A High Energy Density Lithium/Dichloroisocyanuric Acid Battery System

D. L. Williams,* J. J. Byrne, and J. S. Driscoll

Monsanto Company, New Enterprise Division, Boston Laboratory, Everett, Massachusetts

ABSTRACT

The N-chloro compound, dichloroisocyanuric acid (DCA), has been discharged *vs.* lithium in organic nonaqueous electrolytes. The Li/2M $LiClO_4$ (methyl formate)/DCA system has an open-circuit voltage of 4.0v. The solubility of DCA in 2M $LiClO_4$ (methyl formate) is 13 w/o (weight per cent) or 0.65M. Chronopotentiometry at platinum electrodes indicates an irreversible electrode reaction ($\alpha n_a = 0.074$). However there are no separate voltage plateaus at platinum or carbon. Coulometric and battery discharge data are complex, probably because of precipitates formed during the reduction of DCA in the presence of lithium salts in methyl formate. At constant 3.2v discharges, average current densities are 5.8 and 3.4 ma/cm^2 at 4 and 8 hr, respectively. Excluding grid and container weights 200 whr/lb is achieved in 8 hr. High energy densities (180 whr/lb) are obtained under constant load at 3-10 hr discharge rates. When the cell is activated immediately prior to discharge, self-discharge and anode passivation are relatively minor problems.

Nonaqueous, organic electrolyte batteries can potentially achieve energy densities of 200 whr/lb. Most research in this area has been done using lithium anodes and inorganic cathodes composed of metal salts, such as halides and oxides of silver, nickel, and copper. Problems with these systems are associated with low cathode discharge rates, short activated shelf life, or both.

The system described here uses an organic cathode material, dichloroisocyanuric acid (DCA), which is highly soluble in the electrolyte. The system has been designed primarily for Dry Tape battery (1, 2) use. In this device, a thin-layer battery system is activated as it enters between the current collector heads. Since the collectors are unipotential surfaces, discharge of a tape section is at constant voltage. In this paper, the discharge of the Li/DCA couple is described under both constant voltage and constant load conditions. The constant voltage condition simulates Dry Tape discharge, while constant load is applicable to conventional reserve-activated batteries.

The structure of DCA is shown below.

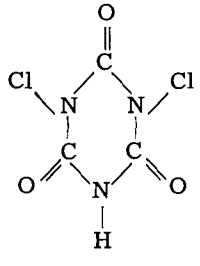

Dichloroisocyanuric acid (DCA)

DCA is a positive N-chloro compound. The two chlorine atoms are formally in the +1 oxidation state. Based on a four-electron transfer, the coulombic capacity of this compound is 32.5 amp-min/g, which is similar to that of cupric fluoride (33.0 amp-min/g). The open-circuit voltage of DCA *vs.* lithium is 4.0v, which is approximately 0.4v higher than that of a lithium/cupric fluoride cell.

Experimental

Materials.—Cells were discharged in an argon atmosphere. Materials were transferred in a glove box when possible. Materials were obtained and purified as follows:

Methyl formate—Matheson Coleman & Bell Spectroquality—Purified by contact with Linde 4A molecular sieve, followed by distillation;

Lithium perchlorate—G. Frederick Smith Company—Dried under vacuum (<1 Torr) for 72 hr at 130°C;

Lithium ribbon—Foote Mineral Company—Thickness 0.38 mm, used as received:

Dichloroisocyanuric acid (DCA)—Monsanto Company, ACL-70®—Ground with mortar and pestle, and dried under vacuum (<0.5 Torr) over P_2O_5, for 24 hr;

Carbon black—Shawinigan Chemicals Ltd., Shawinigan acetylene black, 50% compressed—Dried under vacuum (<1 Torr) at 130°C for 24 hr;

Carbon fibers—H. I. Thompson Company—Cut in Waring blender and dried under vacuum (<1 Torr) at 130°C for 24 hr;

Polypropylene nonwoven separator—Pellon Corporation—Thickness 0.076 mm, used as received.

Cathode preparation.—The cathode plate was prepared by blending dry powders of dichloroisocyanuric acid (83%), carbon black (16%), and carbon fibers (1%), and pressing them at 300 psi (0.21 kgf/mm^2). The loading was approximately 100 mg/cm^2 of total material, which corresponded to 2.5 amp-min/cm^2 of active material. This gave a cathode plate, or tape, which was 1 mm thick.

Cell discharge.—Cathode contact was made by pressure against a platinum collector. Contact to a lithium tab was made with an alligator clip. Cell weights and energy densities were calculated on the weights of the anode, cathode, electrolyte, and separator.

Discharge at constant voltage employed a Harrison Laboratory 6200B power supply to maintain the desired cell voltage across a 1-ohm resistor, which was then connected across the test cell. The circuit is shown schematically in Fig. 1. All other circuitry was standard. Average voltage and ampere-minute values were obtained by planimeter integration of recorder outputs.

Results and Discussion

Development of the system.—In the initial stage of this program, lithium was discharged in half-cell experiments using a Luggin capillary and a high resistance normal calomel electrode (NCE). About 30 electrolyte-solvent systems were screened for use with a lithium anode (3). Observations of gassing and electrolyte-anode changes, as well as steady-state voltages at several currents, and oscilloscope traces of polarization were determined. Methyl formate was found to

* Electrochemical Society Active Member.

Key words: battery, lithium, dichloroisocyanuric acid, chloramines, chlorine compounds, methyl formate.

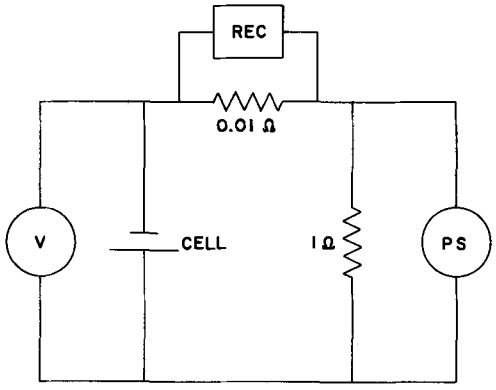

Fig. 1. Schematic of constant voltage discharge circuit

be the best solvent for the support of high current densities, and $LiClO_4$ was the best of the solutes tested. At 100 ma/cm², anodic polarization of lithium anodes in 1M solutions of $LiClO_4$ in methyl formate (MF) was 0.8v. The analysis of polarization relaxation showed that 0.2v could be attributed to resistance polarization.

During the second stage of this investigation, several cathode materials were mixed with carbon and discharged *vs.* lithium in 1M $LiClO_4$ (MF). On the basis of these results, DCA was chosen for further study. A study of the effect of $LiClO_4$ molarity on the discharge characteristics of this cathode showed a decided advantage for a 2M concentration. At higher molarities the viscosity and density of the electrolyte increase, and the conductivity decreases as shown in Fig. 2.

The solubility of DCA in 2M $LiClO_4$ (MF) is 0.65M, or 13 w/o. This value was determined by iodine-thiosulfate titrations of saturated solutions. The solubility varies only slightly with $LiClO_4$ concentration. The dissolved DCA however, changes the 2M $LiClO_4$ (MF) solution conductivity from 2.4×10^{-2} to 1.7×10^{-2} ohm^{-1} cm^{-1}, and changes the kinematic viscosity from 1.0 centistokes to 1.5 centistokes.

DCA voltammetry.—Chronopotentiometric data are shown in Table I for DCA and for trichloroisocyanuric acid (TCA) in 2M $LiClO_4$(MF). Values for $i\tau^{1/2}/C$ are constant for each compound and are 2/3 as large for the dichloro- as for the trichlorocompound. Since battery efficiencies of over 50% are realized for DCA, based on a 4-electron transfer, the 4-electron transfer is assumed for the chronopotentiogram of DCA. Similarly for TCA we assume a 6-electron transfer. Using the Sand equation, the calculated diffusion coefficient is 1.4×10^{-6} cm²/sec for each compound. Analysis of the DCA chronopotentiometric potential-time curve (platinum electrode) showed the reduction to be irreversible. Figure 3 shows a plot of E *vs.* log $(\tau^{1/2} - t^{1/2})/\tau^{1/2}$ from which a value of $\alpha n_a = 0.074$ can be calculated (4). There is no evidence of separate voltage plateaus either in these experiments or with a carbon-epoxy electrode (5).

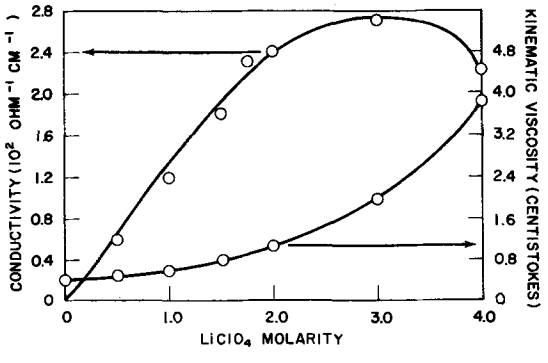

Fig. 2. Conductivity and viscosity of $LiClO_4$ (MF) solutions

Table I. Chronopotentiometric data of DCA and TCA in 2M $LiClO_4$ (MF)

Compound	Concentration C, moles/liter	Current density i, ma/cm²	Transition time τ, sec	$\frac{i\tau^{1/2}}{C}$
DCA	0.025	2.0	28	415
DCA	0.025	3.0	12	415
DCA	0.025	5.0	4	400
DCA	0.050	5.0	15	395
DCA	0.050	7.0	6	345
DCA	0.050	10.0	4	400
TCA	0.022	5.0	7	610
TCA	0.022	3.0	14	605

$$\frac{n_{DCA}}{n_{TCA}} = \frac{i\tau^{1/2}/C_{DCA}}{i\tau^{1/2}/C_{TCA}} \simeq \frac{400}{600}$$

$$D = \left(\frac{2i\tau^{1/2}}{n\pi^{1/2}FC}\right)^2 = 1.4 \times 10^{-6}\ \text{cm}^2/\text{sec}$$

assuming $n_{DCA} = 4$, $n_{TCA} = 6$

Coulometric experiments, using a smooth platinum electrode, yielded a precipitate on the electrode surface. Infrared spectra indicated the product to be similar to cyanuric acid. LiCl also precipitates on the electrode since the solubility of LiCl in the electrolyte is only 0.12M. Figure 4 shows a coulometric voltage-time plot obtained at constant current, 0.010 ma/cm². There is an initial increase in voltage followed by voltage oscillations and continued reduction at a lower potential. The voltage oscillations are believed to be caused by coverage of the surface by a precipitate and subsequent breakdown of this layer. Finally, a more stable, porous, precipitate layer is developed, and the voltage adjusts to compensate for the reduced diffusion rate and decreased active area at the electrode. The initial voltage increase may be explained by the decreased overpotential required to grow formed crystals relative to that required for the nucleation of crystals.

Cell discharge characteristics.—The lithium-DCA cell component weights are shown in Table II. The cathode plate is prepared with 83% dichloroisocyanuric acid and 17% carbon. A void structure of 60-70% is obtained by using the high structure Shawinigan acetylene black and carbon fibers.

The constant voltage discharge characteristics of this cell are also shown in Table II. A static discharge time of 4 hr simulates a residence time of 4 hr on the

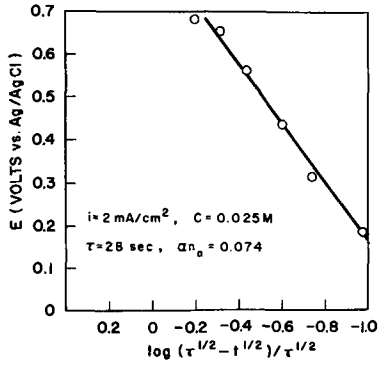

Fig. 3. Analysis of DCA chronopotentiometric data

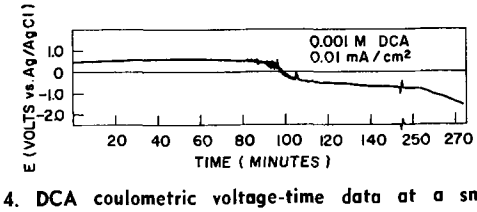

Fig. 4. DCA coulometric voltage-time data at a smooth Pt electrode.

Table II. Constant voltage discharge test of the Li/2M $LiClO_4$ (methyl formate)/DCA system

Cell weights	mg/cm²
Anode, 0.38 mm lithium ribbon	15.5
Separator, 0.08 mm polypropylene	2.6
Electrolyte, 0.073 ml/cm² (d = 1.15 g/ml)	83.5
Cathode	
DCA	77.8
Shawinigan acetylene black	14.5
Carbon fibers	1.0
	194.9

Electrical characteristics at 3.2v

Discharge time, hr	Avg. current density, ma/cm²	Energy density, whr/lb	Cathode efficiency, %
4	5.8	173	57
8	3.4	200	69
18	1.6	216	71

collector plate in a dynamic Dry Tape test. At 3.2v, this simulated tape throughput gives an average current density of 5.8 ma/cm², 57% cathode efficiency, and 173 whr/lb. This energy density is based on the weight of the anode, cathode, separator and electrolyte. With increased discharge time the average current decreases, and the efficiency and energy density increase. With a simulated 18-hr residence time, 216 whr/lb is obtained.

The current and energy density profiles for the constant voltage discharge of the system are shown in Fig. 5. At constant voltage, the greatest drain occurs when the cathode is fresh, and the electrochemical reaction competes effectively with self-discharge reactions. The current minimum and plateau, observed in Fig. 5, are not indicative of electrode reaction complications, since the chronopotentiometric data were regular. The cause may be due to precipitation effects, since minima and plateaus have been observed in coulometric experiments at smooth electrodes where precipitates were formed.

Cathode efficiencies averaged 60-70% in these tests. Most of the remaining capacity is left undischarged on the tape, as determined by iodine-thiosulfate titrations. After an 18-hr discharge test, 67% had reacted electrochemically, 25% remained unreacted and 8% had decomposed.

The system described above was also discharged under constant load conditions. Data are shown in Fig. 6 for a 3-hr rate (20-ohm) discharge. A voltage minimum and plateau are discernible, and the voltage drops sharply beyond 2.5v. The initial closed circuit voltage is 3.6v at this drain rate, which is 0.4v below the open-circuit value. The average voltage is 3.1v to a 2.0v cut-off.

A series of discharges was run through various resistances. The energy density data are shown in Fig. 7. The energy density of the system rose sharply with

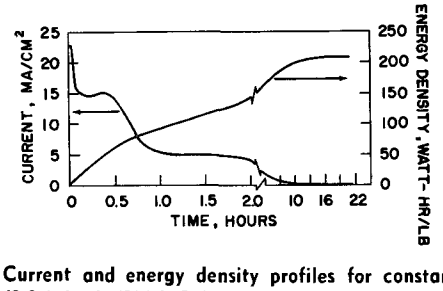

Fig. 5. Current and energy density profiles for constant voltage discharge (3.2v) for Li/2M $LiClO_4$ (MF)/DCA.

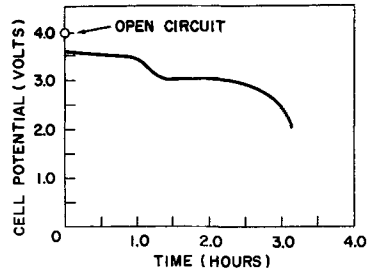

Fig. 6. Discharge of the Li/DCA cell at the 3-hr rate (20 ohms)

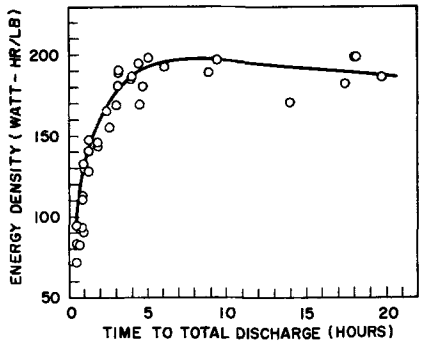

Fig. 7. Energy density of Li/DCA cells as a function of drain rate at constant load (2.0v cut-off).

time to the 3-hr rate and then levelled off. At low discharge rates, methyl formate evaporation was a problem because of the test cell design, and discharges of longer than 20 hr were not attempted. Flash currents of 200 ma/cm² were obtainable at short circuit. As in the constant voltage tests, the efficiencies were about 60%, and most of the remaining capacity was left in the cathode, undischarged.

Conclusion

The lithium-DCA couple is a high energy density battery system that can be discharged effectively at the 3-10 hr rates to give energy densities of 180 whr/lb. Work is in progress to increase the coulombic efficiency and current density of this cell.

Acknowledgment

This work was supported by the NASA Lewis Research Center, Cleveland, Ohio, under Contracts NAS3-7624 and NAS3-9431. The authors thank William Nagle, contract monitor, and M. L. Bhaskara Rao for helpful discussion of this work.

Manuscript submitted May 20, 1968; revised manuscript received *ca.* Sept. 12, 1968. This paper was presented at the Chicago Meeting, Oct. 15-19, 1967, as Paper 15.

Any discussion of this paper will appear in a Discussion Section to be published in the December 1969 JOURNAL.

REFERENCES

1. B. A. Gruber, *Proc. 18th Annual Power Sources Conference*, 94 (1964).
2. B. A. Gruber and J. J. Byrne, *New Scientist*, **35**, 74 (1967).
3. J. S. Driscoll, D. L. Williams, A. S. Borsanyi, and J. J. Byrne, "Research and Development of the Dry Tape Battery Concept," Contract No. NAS3-7624, Final Report, 1967.
4. P. Delahay, "New Instrumental Methods in Electrochemistry," pp. 184-187, Interscience Publishers, New York (1954).
5. H. S. Swofford and R. L. Carman, *Anal. Chem.*, **38**, 966 (1966).

Chromium Coatings Prepared by Chemical Vapor Deposition

Gene F. Wakefield

Chemical Materials Research and Development Laboratory, Texas Instruments Incorporated, Dallas, Texas

ABSTRACT

The formation by chemical vapor deposition (CVD) of chromium metal as coatings on various substrates was studied using the reaction

$$CrCl_2 + H_2 \rightarrow Cr + 2HCl$$

Process parameters of temperature, gas flow rate, and chromium chloride concentration influenced the deposition rate. The chromium metal deposited had properties similar to high-purity "iodide" chromium. Surface appearance and grain structure differed from materials such as titanium, deposited in earlier studies. This is suggested to result from difference in the controlling mechanism of the reduction reaction and evidence for this mechanism was observed.

The commercial use of Chemical Vapor Deposition (CVD) processes for preparation and forming of metallurgical materials is increasing. Several practical aspects are encouraging this investigation into the nature and application of CVD process methods. One aspect is the capability of producing a wide variety of shaped materials, such as boron or silicon carbide (1) filaments, since the deposit usually conforms to the contour of the substrate. Another is production of materials of controlled purity, such as semiconductor grade silicon (2) or tungsten metal (3). Another is the ability to form materials having unusual or unique properties such as anisotropic pyrolytic graphite (4).

The CVD preparation of bulk chromium metal has commonly been carried out by the transfer reaction utilizing chromous-chromic iodide equilibrium or simply thermal decomposition on a heated filament (5). A mass of coarse, loosely bound crystals usually results. This material is commercially available with a stated purity of 99.99%.

Preparation of unalloyed chromium coatings has been carried out (6) by the thermal dissociation of organochromium compounds such as dicumene chromium, $Cr[C_6H_5CH(CH_3)_2]$. Because of their low boiling points, use of such compounds is a convenient procedure for obtaining chromium in a vapor state, and the compounds can be decomposed at moderate temperatures. Care must be exercised over the reaction conditions to avoid the introduction of carbon from the organic radical decomposition.

The procedure designated as "chromizing" (7) is used for preparation of chromium-containing coatings. Chromizing differs from the present subject in that it is limited to diffused coatings, which consist of an alloy containing a major concentration of the substrate material. The coating mechanism often involves displacement in addition to reduction reactions. Because of its vapor pressure, chromium can be evaporated and condensed on a substrate material. This procedure can produce high-purity metal, but is usually restricted to thin coatings.

The applications of chromium as a bulk material or as a coating on another material are usually for corrosion resistance, appearance, or high-temperature strength. The vapor process is a preferred preparation method to obtain a high-purity metal and thus a relatively ductile material. This study was conducted to investigate the deposition process for the formation of high-purity chromium metal, primarily as coatings on various metal substrates, although the method is also applicable to bulk metal preparation.

Equipment

Equipment for CVD processes consists basically of a controlled supply of reaction gases delivered into a heated reaction area where the gases impinge on the deposition site. The reaction which occurs produces the desired material as a solid product, and the remainder of the products are given off as gases.

The equipment used in this study contained all equipment for measurement and control of the parameters in the process in a single control unit. Temperature controllers for the system were Honeywell Versatronik temperature controllers (accuracy ±5°C) on the chromium reservoir and argon purifying furnaces and a Honeywell Pyro-Volt proportional controller (accuracy ±2°C) for reactor temperature. Gas flows were measured with Brooks Sho-Rate flow meters having a stated accuracy of 5%, and the meters were calibrated with a Precision Scientific Company wet test meter having a stated accuracy of 0.5%. The results of the calibrations showed a deviation of less than 3% from the smoothed curve values.

A schematic diagram of the reactor used is shown in Fig. 1. Two gas streams of controlled flow rate and composition entered the top of the reactor. The hydrogen chloride-argon stream flowed through the heated bed of chromium metal where reaction (A) produced $CrCl_2$. The hydrogen stream flowed around the chloride generation chamber and mixed with the exiting $CrCl_2$-argon stream in the nozzle above the specimen. The diameter of the reactant nozzle (0.62 in.) and the nozzle to substrate distance (1.5 in.) were adjusted to give a uniform deposition over a 1 in. diameter circle. Thus, uniform mixing of reactants over at least this area was indicated. The specimen rested on a support above the center of the heater. Temperature of the heater was controlled by a thermocouple-actuated controller on a saturable core reactor. Calibration of the control was done with an optical pyrom-

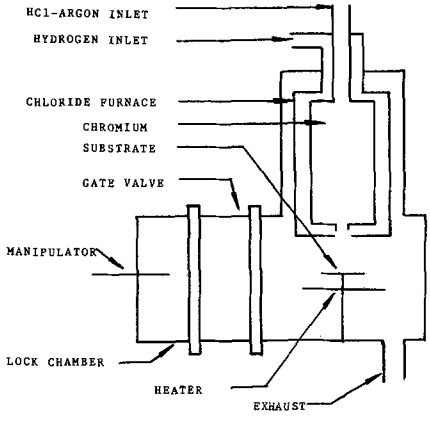

Fig. 1. Schematic diagram of CVD reactor

Table I. Data for chromium depositions

Point	Rate mg/cm² observed	Rate, calculated Eq. [1]	$k \times 10^{-5}$ l / Mole-sec	Rate, calculated Eq. [2]	$H_2^{0.85} \times [CrCl_2]^{0.92} \times 10^{6}$*
−1, 1, −1	0.41	0.48	4.63	0.42	0.88
−1, 1, 1	1.25	1.25	4.78	1.23	2.61
−1, −1, 1	0.72	0.82	4.98	0.68	1.44
−1, −1, −1	0.21	0.04	4.30	0.18	0.49
1, −1, −1	0.34	0.30	6.93	0.34	0.49
1, 1, 1	1.72	1.51	6.58	1.77	2.61
1, 1, −1	0.62	0.74	6.95	0.60	0.88
1, −1, 1	0.96	1.06	6.67	0.97	1.44
0, 0, 0	0.77	0.77	5.67	0.77	1.36

Variable Level	−1	0	1
X_1 sample temperature, °C	1200	1275	1350
X_2 $CrCl_3$ concentration, %	0.15	0.225	0.30
X_3 flow rate, l/min	8.0 l Argon 2.0 l Hydrogen	8.0 l Argon 8.0 l Hydrogen	8.0 l Argon 14.0 l Hydrogen
X_4 deposition rate, mg/cm²/min			

* Concentrations in moles/liter at 900°C.

eter using a sample containing a black body hole. The gate valve and lock chamber permitted the insertion and removal of specimens without the introduction of impurity gases into the system. Exclusion of impurities was a major aid in obtaining consistent experimental results and permitting more rapid operation.

Gases in the reactant stream were hydrogen, purified by passage through a palladium diffusion purifier; argon, purified by passage over a bed of heated titanium chips; and chromium chloride generated by the reaction of high-purity hydrogen chloride gas and chromium metal. The substrate material used for most of the chromium depositions was a niobium alloy, B-66[1] (89% Nb, 5% Mo, 5% V, 1% Zr), although deposition on other materials has produced essentially the same results.

The reaction

$$2HCl(g) + Cr(s) \xrightarrow{\text{argon}} CrCl_2(g) + H_2(g) \quad (A)$$

occurred in the chloride generating chamber at a temperature of 900°C. The reversal of this

$$H_2(g) + CrCl_2(g) \rightarrow Cr(s) + 2HCl(g) \quad (B)$$

occurred at the substrate surface in the presence of excess hydrogen and at higher temperatures.

Experimental Plan

A statistical plan of the experimental variables of reactor temperature, chromium chloride concentration, and flow rate[2] of gases was carried out to determine the influence of these upon the rate of metal deposition. The basic design (8) of the series was a two-level, three-variable cube with fourfold replication at the center of the cube. Such a plan was selected because it can be analyzed by Analysis of Variance, and Multiple Regression and Correlation Analysis to identify the first order and the interaction effects of the variables. The mathematical description from this standard analysis is strictly empirical since it is based on assumed linearity of the model.

Listing of the experiments and the resulting deposition rates is given in Table I. The concentrations are given in terms of molar per cent. The flows were measured at 25°C although the values given are calculated for the gases heated to 900°C assuming ideal gas laws, as this is more representative of the actual deposition conditions.

[1] Westinghouse Astronuclear Laboratory, Pittsburgh, Pennsylvania.

[2] Note that the flow rate change was accomplished by variation of the hydrogen flow.

Results and Discussion

The resulting deposition rate data are plotted *vs.* the three independent variables in Fig. 2a, 2b, and 2c. The curves exhibit self-consistency and indicate that each of the three variables contributes positively to the deposition rate. The mathematical analysis of the results, based on a linear model for the system, is given in Table II and is in agreement with this conclusion. This analysis yields the deposition rate equation

$$\text{Rate } X_4 = 1.74 \times 10^{-3} X_1 + 2.94 X_2 + 0.128 X_3 - 3.127 \quad [1]$$

Statistical analysis of the deposition rate data indicates that the variables are significant at the 95% confidence level. On the basis of the T values of Table II, the major influence exerted on the deposition rate results was the flow rate of gases, with a lesser influence exerted by the chromium chloride concentration, while the reaction temperature has the least effect. Process studies indicate that for these experimental conditions the deposition is controlled by several, rather than a single, identifiable factor.

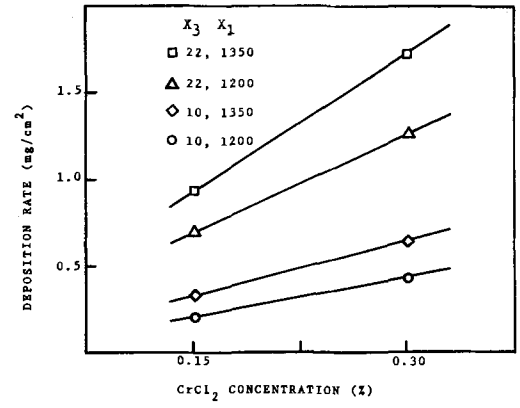

Fig. 2a. Deposition rate of chromium from statistical plan

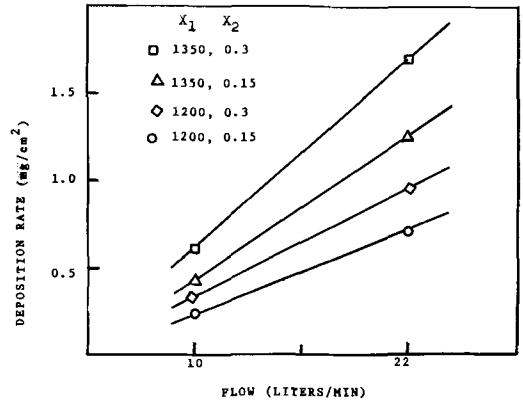

Fig. 2b. Deposition rate of chromium from statistical plan

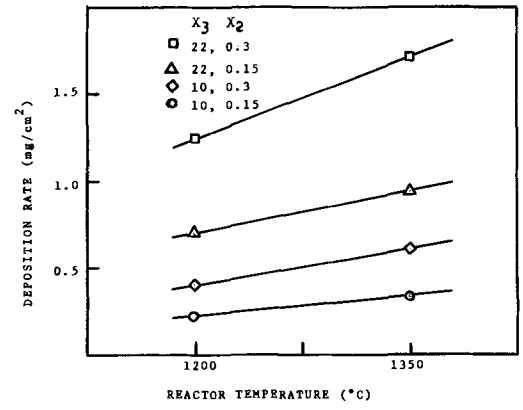

Fig. 2c. Deposition rate of chromium from statistical plan

Table II. Multiple regression and correlation analysis of chromium depositions

Variable	Regression coefficient	Observed T value	T for 95% level
X_1	1.741×10^{-3}	1.99	2.36
X_2	2.941	3.36	2.36
X_3	1.277×10^{-1}	5.84	2.36

Intercept: −3.127
Standard error of estimate: 0.185
Multiple correlation coefficient: 0.9359

A second mathematical analysis of the data was made, based on a classical kinetic model. This analysis used only concentration of reactants without regard to flow rate. The dependence of deposition rate on the concentrations of the reactants was derived as an equation of the form

$$R = k[H_2]^{0.85}\,[CrCl_2]^{0.92} \qquad [2]^3$$

The values of k and the calculated rates using this equation are given in columns 4 and 5 of Table I, and illustrated in Fig. 3. The average deviation from the mean of the values is less than 8% of the value, which is near the limits within which the experimental variables could be fixed.

The exponents on the concentrations of the rate Eq. [II] indicate approximate first order in both reactants. First order dependence on the chromium chloride concentration is reasonable in relation to the availability of chromium chloride for reaction. For these experiments, the gas phase concentration of hydrogen varied from 60 to 500 times that of the $CrCl_2$. At such excess concentrations, an apparent first order dependence with hydrogen was not expected and could more likely also have been affected by variation in flow rate since the experimental parameters were varied in a fashion which did not entirely separate the flow rate and hydrogen concentration effects.

A Factorial Analysis of Variance indicated no interaction between the variables significant at the 95% confidence level. An Arrhenius plot of the deposition rate is shown in Figure 4. The data divide into four separate lines, and the lines of the higher flow rate (A and B) have a slope of 10 kcal/mole. The separation of the curves substantiates the independence of the variables. The slope of the lower flow rate lines (C and D) is 14 kcal/mole. The average slope of these curves is 12 kcal. The thermodynamic value of ΔH for this reduction can be calculated from the data (9) for ΔH: $\Delta H = -14{,}710 - 2.38T + 1.91 \times 10^{-3}\,T^2$. For the midrange of temperatures studied, $\Delta H_{calc} = 13$ kcal/mole. This value is in reasonable agreement with the values observed in this study.

From the temperature dependence of k, a value can be calculated for the effective energy of activation for the over-all reduction reaction. The values of k are shown on the Arrhenius plot of Fig. 4 and indicate an activation energy of 12 kcal/mole from the slope. This value is in reasonable agreement with the values of ΔH from the rate data and the thermodynamic calculation.

An apparent efficiency of the reaction can be obtained from the ratio of the amount of chromium retained on the sample to that passed over the sample. This ratio varied from 0.05 to 0.07 for the lower hydrogen concentration, and 0.07 to 0.10 at the higher hydrogen concentration. This efficiency is lower than would occur at equilibrium conditions, as shown in Table III, because the sample interrupted only a portion of the gas stream.

A photomicrograph of a cross section of a chromium deposit is shown in Fig. 5a displaying the absence of

[3] Average deviation on coefficients: $[H_2] = 0.85 \pm 0.03$, $[CrCl_2] = 0.92 \pm 0.07$

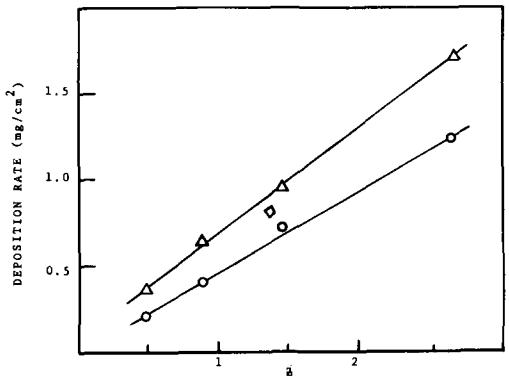

Fig. 3. Deposition rate of chromium vs. concentrations, $Z = [H_2]^{0.85} \times [CrCl_2]^{0.92} \times 10^6$; △ 1350°C; ○ 1200°C; □ 1275°C.

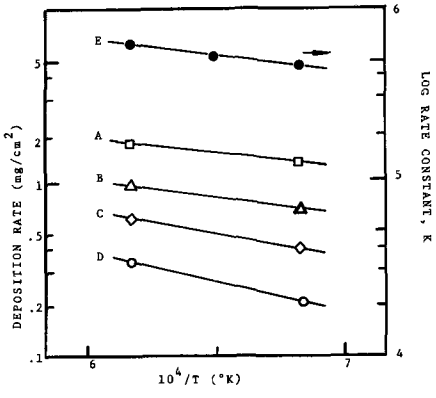

Fig. 4. Arrhenius plot of chromium deposition data

Line	Flow	$CrCl_2$ conc.
A	22	0.3
B	22	0.15
C	10	0.3
D	10	0.15
E	Rate constant, K	

a reaction between the coating and the niobium substrate. The columnar grain structure of the deposit is commonly observed with CVD materials. The uneven top surface shows many crystal facets and shapes. A photograph of this surface is shown in Fig. 6, together with a deposit of titanium prepared in a similar fashion; a considerable difference in appearance is noted. Other coating characteristics noted during some of the experimentation are shown in Fig. 5b, where the appearance of voids in the coating is related to the rate of formation of the deposit.

The morphology of the surfaces of materials obtained by vapor deposition can be sometimes correlated (10) on the basis of the supersaturation ratio (S) defined as the ratio of the observed metal vapor pressure (Pa) to the equilibrium vapor pressure (Po), *i.e.*,

$$S = \frac{Pa}{Po}$$

Table III. Equilibrium values for hydrogen reduction of chromium chloride

T, °C	Reactant pressure $CrCl_2$	Reactant pressure H_2	Unreacted $CrCl_2$	Per cent $CrCl_2$ reduced
1200	0.0015	0.2	0.00012	92.0
1200	0.0015	0.64	0.00004	97.5
1200	0.0030	0.2	0.00042	86.0
1200	0.0030	0.64	0.00017	94.5
1275	0.00225	0.5	0.00015	95.5
1350	0.0015	0.2	0.00017	88.7
1350	0.0015	0.64	0.00006	96.0
1350	0.0030	0.2	0.00057	81.0
1350	0.0030	0.64	0.00023	92.4

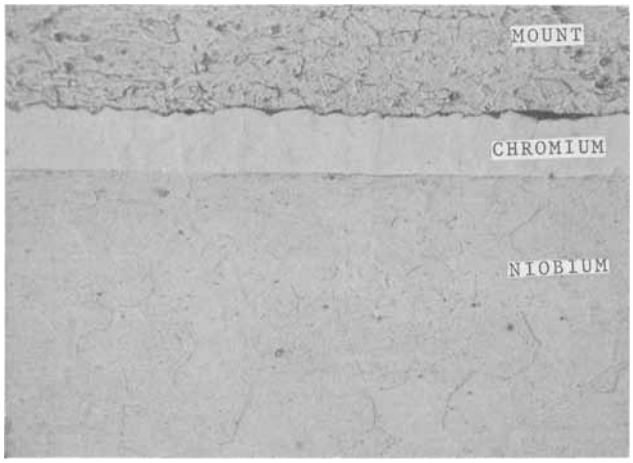

Fig. 5a. Chromium deposit cross section; deposition rate 0.6 μ/min. Magnification 350X.

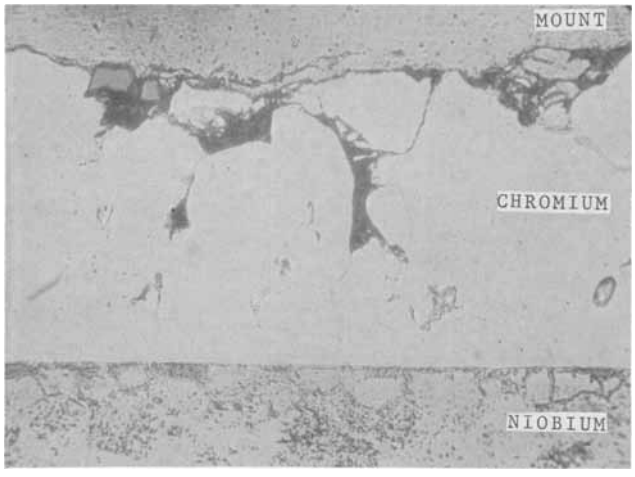

Fig. 5b. Chromium deposit cross section; deposition rate 5 μ/min Magnification 385X.

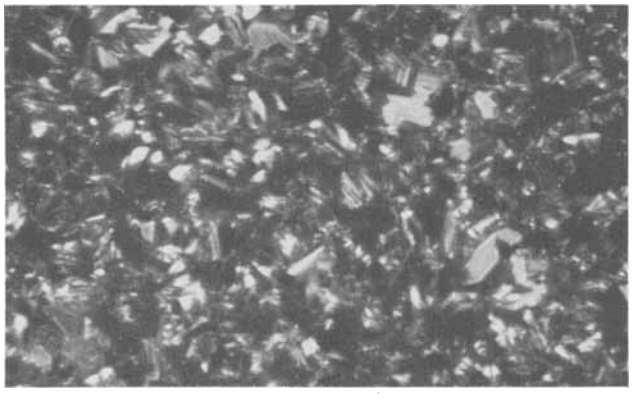

Fig. 6a. Surface of as-deposited chromium (250X)

In general, high values of S result in discontinuous deposits such as powders, dendrites, etc., while low values of S result in a more regular deposit. For the specific data discussed here, the value of S (see Table IV) changes from 110 to less than one; for the latter case, the equilibrium vaporization flux is greater than the net deposition rate. This calculated vaporization flux would be 0.15 mg/cm^2/min at 1200°C and 2.65 mg/cm^2/min at 1350°C.

The difference in surface appearance of the chromium and titanium deposits was interpreted as resulting from different deposition mechanisms. The titanium deposited in an "epigranular" fashion and thus had a smooth surface. The supersaturation ratio for this deposit was approximately 10^3.

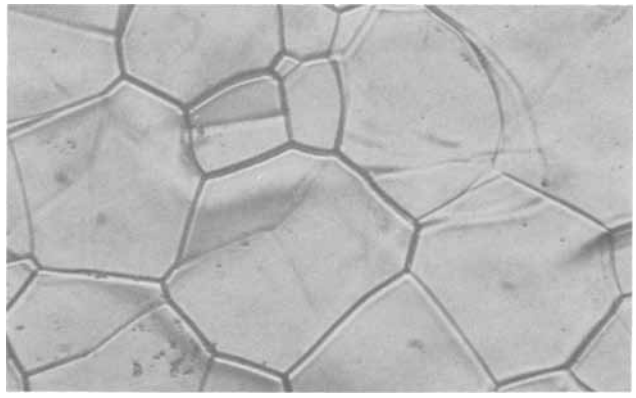

Fig. 6b. Surface of as-deposited titanium (150X)

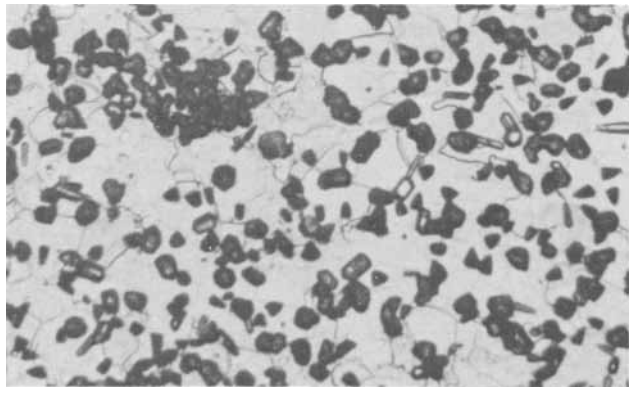

Fig. 7. Initial growth of chromium on niobium (400X)

Chromium apparently has a tendency to form agglomerates when deposited at these supersaturation values either due to preferential adsorption of the reactants or to surface diffusion of the adsorbed species after deposition. This is demonstrated by the photograph in Fig. 7 of the surface of a sample where the deposition was terminated and examined at an early stage during the deposition. The chromium deposit had formed as isolated nodules. At a slightly later stage in the deposition, coalescing of the nodules to form larger islands, and then finally a continuous coating, was observed. The voids observed in a cross section of a coating which had been deposited rapidly could easily result from mismatch as the islands coalesced.

The metals obtained were relatively soft, Rockwell B75, and ductile, as would be expected to result from a vapor deposition process, and could undergo a 4T bent test without fracture.

Conclusions

The formation of high-purity coatings of chromium metal by the CVD process using hydrogen reduction of chromous chloride was investigated. The reaction mechanism was controlled by several variables rather than a single variable. For the range of variables investigated, the rate of metal deposition onto a substrate can be described by the equation

$$\text{Rate mg/cm}^2\text{/min} = k[H_2]^{0.85}[CrCl_2]^{0.92}$$

Table IV. Chromium deposition supersaturation ratio data

T °K	P_o − log atm	P_s − log atm	log S
1300	8.336	6.29	2.05
1400	7.222	6.10	1.12
1500	6.260	5.92	0.36
1600	5.421	5.62	0 20
1700	4.686	5.30	−0.62

where $k = 4.67 \times 10^5$ at 1200°C and 6.78×10^5 at 1350°C. The activation energy calculated from the temperature dependence of k is 12 kcal/mole. An approximate first order dependence on the concentrations of both reactants is indicated even though the gas phase concentration of hydrogen varied from 60 to 500 times the stoichiometric requirements.

Acknowledgments

The valuable assistance of Charles A. Cockrum and other personnel at Texas Instruments is gratefully acknowledged. This information is partially the result of a program to "Investigate and Evaluate Chemical Vapor Deposition for Application of High Temperature Oxidation Resistant Coatings to Refractory Metals," Contract AF33(615)3046, sponsored by Chemical Processing Branch of the Manufacturing Technology Division, Air Force Materials Laboratory.

Manuscript submitted April 24, 1967; revised manuscript received Aug. 30, 1968. This paper was presented at the Philadelphia Meeting, Oct. 9-14, 1966, as Paper 223.

Any discussion of this paper will appear in a Discussion Section to be published in the December 1969 JOURNAL.

REFERENCES

1. R. L. Hough, "Continuous Silicon Carbide Filaments," paper presented at American Chemical Society Meeting, Phoenix, Ariz., Jan. 19-21, 1966.
2. E. A. V. Ebsworth, "Volatile Silicon Compounds," The MacMillan Co., New York (1963).
3. J. H. Oxley, E. A. Beidler, J. M. Blocher, Sr., C. S. Lyons, R. S. Park, and J. H. Pearson, "Fluoride Tungsten," paper presented at 5th Plansee Seminar, Reutte/Tyrol, Austria, June 22-26, 1964.
4. R. O. Grisdale, A. C. Pfister, and W. A. Van Roosbroeck, *Bell System Tech. J.*, **271**, 30 (1951).
5. D. R. Mosher, U.S. Dept. Comm. Report PB 63628 (1943).
6. J. H. Oxley, M. F. Browing, N. D. Veigel, and J. M. Blocher, Jr., *Ind. Eng. Chem. Prod. Research and Development*, **1**, 102 (1962).
7. T. P. Hoar and E. A. G. Croom, *J. Iron Steel Inst. (London)*, **169**, 101 (1951).
8. S. Ehrenfeld, and S. Littauer, "Introduction to Statistical Method," McGraw-Hill Publishing Co., New York (1965).
9. H. A. Doerner, U.S. Bur. Mines Tech. Paper 577 (1937).
10. R. D. Gretz, "Structure of Deposits" in "Vapor Deposition," C. F. Powell *et al.*, Editor, John Wiley & Sons, Inc., New York (1966).

An Experimental Investigation of a High-Voltage Electron-Bombardment Ion Thruster

David C. Byers

Lewis Research Center, National Aeronautics and Space Administration, Cleveland, Ohio

ABSTRACT

The performance of a mercury electron-bombardment thruster at large values of net accelerating potential is described. A 20-cm diameter thruster was tested at values of ion beam current and net accelerating potential up to 0.165 amp and 70 kv, respectively. A maximum beam power of about 10 kw was obtained. The maximum supportable electric field strength between accelerator grids was approximately constant at 2×10^6 v/m for spacings between 0.5 and 3.0 cm. The ion chamber performance was qualitatively similar to that at low accelerating voltage. The energy dissipated per beam ion in the ion-chamber discharge was related to the percentage of Child's law ion current extracted over a wide range of accelerator spacings and potentials. The maximum percentages of Child's law current transmitted were about 60 and 80% for thrusters with 20 and 7.5-cm diameter accelerator grids, respectively, and were essentially independent of grid spacing and thickness. Ion focusing characteristics, at ion beam current densities of about 10 amp/m^2, indicated that the ratio of center-to-center grid spacing to grid thickness should be between about 2.5 and 4 to avoid direct ion impingement.

The power efficiency was measured and found to be consistent with data taken with low voltage thrusters operated at similar conditions. A power efficiency of 0.8 was obtained at a net accelerating potential of 18 kv and rose to 0.88 at a net accelerating potential of 36 kv. Over-all thruster efficiencies of about 0.80 and 0.82 were obtained at net accelerating potentials of 28 and 36 kv, respectively.

The operation of an electron-bombardment ion thruster at high values of net acceleration potential is described. The electron-bombardment thruster is an ion source conceived by H. R. Kaufman (1) of the NASA Lewis Research Center. This source consists basically of a discharge chamber, where ions are produced by electron bombardment, and a grid system which electrostatically accelerates ions produced in the discharge chamber.

The present interest in the electron-bombardment ion source is its attractiveness as a space thrust system (2). The present paper emphasizes parameters germane to this application. This ion source is, however, capable of operation over a wide range of electrical and physical parameters and with a variety of atomic species. Electron bombardment thrusters have operated at net ion accelerating potentials from 400v (3) to the 70 kv operation reported herein. Source diameters have ranged from 5 cm (4) to 1.5m (5). The propellants most utilized to date with this source have been mercury and cesium. Large atomic masses are of interest for thruster application due to the increase of thrust per beam ion with ion mass. This source has, however, been operated with a variety of gases (6) and molecular types (7). In addition, the electron-bombardment thruster has demonstrated extremely long term, stable operation (8).

The operation of electron-bombardment thrusters at high values of net acceleration potential has promise of increasing the over-all thruster efficiency (1). Higher specific impulses (and therefore higher accelerating voltage) also become more necessary as

mission difficulty increases and propulsion system specific mass decreases (9). This investigation was carried out to determine the operating characteristics of mercury electron-bombardment thrusters at net ion accelerating potentials between 10,000 and 70,000v. Previous thruster data had been limited to a maximum potential of approximately 10,000v (10).

The discharge chamber efficiency and the current carrying characteristics of the high voltage grid system were investigated and compared with data obtained at low values of net accelerating potential (11). Ion impingement currents were measured and compared with an existing analysis (12) extrapolated to high voltage. Over-all thruster efficiencies are discussed both as a function of propellant utilization efficiency and net accelerating potential and in addition are compared with low voltage data.

Apparatus and Procedure

Thruster

The electron-bombardment ion thruster utilized in this program is shown in Fig. 1. The principle of operation of the thruster has been described in many references [*e.g.*, ref. (10)]. In brief, a mercury vaporizer was heated with steam slightly above atmospheric pressure to provide close thermal control of the vaporizer. Interchangeable vaporizer orifices were utilized to change propellant flow rates. The propellant flowed into the ionization chamber through an annular slot distributor. A small screen was placed between the vaporizer and the distributor to prevent plasma leakage to the vaporizer (13).

Electrons are emitted from the cathode and reach an energy nearly equal to the potential difference between the anode and the cathode. These electrons, which are constrained by an axial magnetic field, ionize some of the mercury. The mercury ions diffuse to the accelerator grid region and are accelerated into the exhaust beam.

For all tests, a 20-cm diameter anode was used. The cathode was tantalum ribbon 0.05 mm thick, 40 mm long, and about 5 mm wide.

Accelerator grid system.—A typical accelerator configuration is shown in sketch a.

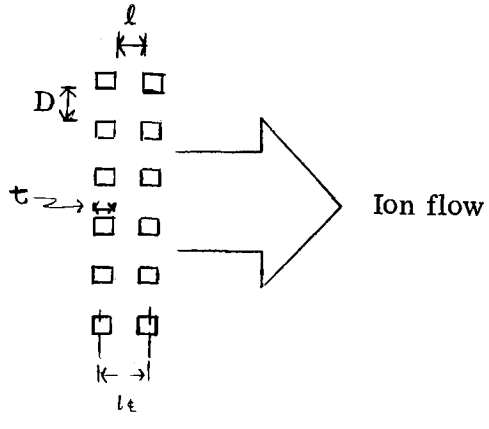

Sketch a

The value of the ratio of center-to-center grid spacing to hole diameter, l_t/D, was varied between 0.5 to 3.0 by insertion of shims between the downstream insulators and the screen grid extensions (Fig. 1). The screen and accelerator grids were of equal thickness unless otherwise stated. All the data presented in the figures of this report were taken with accelerator grids with hole diameters of 2.2 cm because, as will be later explained, the use of larger holes, 5 cm, led to undesirable thruster performance.

Insulators.—The high voltage thruster was initially designed with spherical insulators scaled from insulators used successfully up to about 10 kv. The 5-cm diameter aluminum oxide spheres were capable of supporting 22 kv before severe flashover occurred. Insulators utilizing shielded negative terminals were also fabricated and tested. These tests are presented in the section Results and Discussion. The final design, shown in Fig. 2, was capable of withstanding potentials up to 250 kv in vacuum.

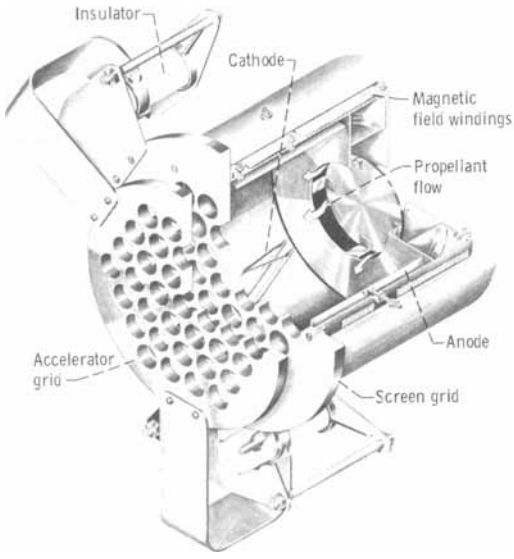

Fig. 1. 20 cm Kaufmann thruster

Facility

The facility was one of the 5-ft diameter, 16-ft long vacuum tanks at the NASA Lewis Research Center. The tank has three 32-in. oil diffusion pumps feeding into a common ejector pump followed by a mechanical pump. Cryogenic pumping (liq. N_2) was used in conjunction with the diffusion pumps so that thruster operation was possible in the 10^{-6} Torr pressure range. A more complete description of this facility is included in ref. (14).

Measurements

All electrical measurements in this program were made with standard meters with an accuracy of about 3% at full scale deflection. The propellant utilization efficiency could not be fixed to much better than 5%. This accuracy was estimated from measured variation in neutral propellant flow rate from several tests where the same orifice size was utilized.

Results and Discussion

The results of the high voltage breakdown characteristics over insulators and between accelerator grids are described first. The ion chamber performance is considered next. The effects of accelerator parameters on the maximum attainable ion current are then presented. Finally, a discussion of over-all thruster efficiencies at high voltage is presented.

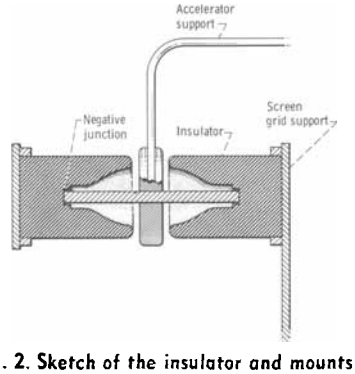

Fig. 2. Sketch of the insulator and mounts

High Voltage Breakdown Studies

The maximum value of the ion current or thrust per unit area of a Child's law current limited system is directly proportional to the square of the electric field supported by the accelerator grid system (15). The value of the maximum supportable field strength in vacuum has, in general, been found to decrease with increasing spacing (16). The voltage breakdown characteristics of accelerator grids at spacings of interest in this program (roughly 0.5-5 cm) were therefore studied.

In addition, initial tests indicated that spherical insulators were unacceptable for use at the intended voltage levels. A test program was carried out to find a suitable insulator design.

All the breakdown tests described below were carried out at pressures less than 1 x 10^{-5} Torr. Breakdowns should then be independent of pressure (17).

Insulator studies.—Spherical insulators (such as utilized in low voltage thrusters), 5 cm in diameter, were found to break down at 22 kv. A program was carried out to improve the insulator design to meet the voltage requirements of the study. The guideline for this program was the data of ref. (18) and (19) which indicated that the primary cause of insulator flashover was electron emission initiating at the negative metal-dielectric junction.

The final insulator design (Fig. 2) was found to eliminate insulator flashover breakdown up to voltages of 250 kv, at which point the insulator failed due to puncture through the dielectric. This design increased the flashover voltage for two reasons. First, the electric fields which can liberate electrons are reduced near the negative junction, as suggested by Ref. (18). Second, the discharge at the negative junction was constrained to the hollowed out section of the insulator.

Plate breakdown studies.—Breakdown tests between simulated accelerator grids were carried out in a bell jar facility. The effects of spacing and surface conditioning on the maximum supportable electric field strength were investigated at voltages up to 285,000v. The grids were attached to independent holders which were connected to high voltage feedthroughs at opposite ends of the bell jar. This mounting technique eliminated the need of spacing insulators and allowed comparison of grid-to-grid breakdown separate from insulator flashover.

Stainless steel plates 0.31 cm thick and 25 cm in diameter were fabricated. Plain plates and plate sets with up to 37 holes (all holes 2.54-cm diameter) were utilized. The edges of one side of each of the plates were left unfinished while the edges of the opposite side were machined to approximately 0.06 cm radius.

The results of these tests are presented in Fig. 3, where the maximum supportable field strength is plotted against the face-to-face spacing between the plates. Above the maximum field strength the breakdowns would become nearly continuous. In addition, this field strength was the highest that could be supported without breakdowns for times greater than about 5 min after prolonged conditioning, *i.e.*, repeated breakdowns. A breakdown was defined as a discharge between the plates greater than 1 ma (which tripped the power supplies).

Figure 3 shows that the maximum supportable electric field does decrease with increasing spacing as expected. The fields are, however, considerably greater than the maximum supportable fields for low voltage thruster operation, which are generally from 2 to 3 x 10^6 v/m (12). Figure 3 also shows that the maximum field is somewhat dependent on the number of holes. In general, the voltage breakdown level decreased with the number of holes drilled in the plates. Although not shown, the critical electric field was larger when rounded edges rather than

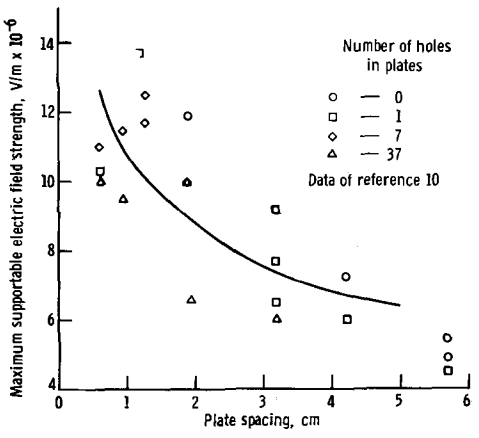

Fig. 3. Effect of spacing on the maximum supportable electric field strength between stainless steel plates. Plate diameter, 25 cm; hole size, 2.2 cm.

square edges faced each other. This difference in critical electric field was, however, always less than 20%. It is seen that the data agree relatively well with the data of ref. (20), which were taken with unpolished stainless steel plates.

It was found that the characteristics of the breakdowns which occurred at spacings less than 1 cm spacing differed substantially from those of breakdowns at spacings greater than 1 cm. At the smaller spacings the breakdowns were localized, data were quite repeatable, and the current between the plates approached zero at the maximum voltage difference, after conditioning for a few minutes. At larger spacings, however, breakdowns were not localized; the leakage current did not decrease significantly with time near the maximum field strength. In addition, the data at large spacings were never repeatable to much closer than about 20%.

Thruster breakdown tests.—Data were taken throughout the thruster program of the maximum supportable field during thruster operation (utilizing the improved insulator design previously described). The results are shown in Fig. 4. Comparing these data with Fig. 3 it is seen that the levels of field strength are approximately a factor of 3 or 4 lower than those obtained in the bell jar tests. The data do not, however, show significant degradation from field strengths obtained previously with thrusters operating at lower voltages. The reason for the low maximum supportable field strength between grids of operating thrusters, as compared with breakdown between plates of the same physical geometry in vacuum, is not certain. During operation, however, the grids of a thruster suffer ion impingement, and become heated to about 700°K (12). These factors would probably tend to reduce the maximum supportable field strength.

Ion Chamber Performance

For flight applications, the energy required to form a beam ion is of importance. This energy, eV/ion,

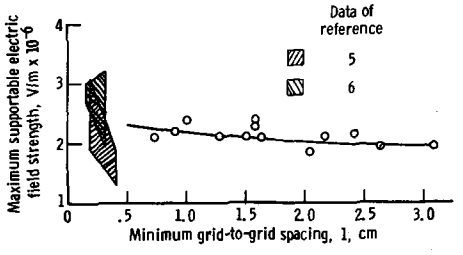

Fig. 4. Maximum supportable electric field strength between the accelerator grids of the operating electron bombardment thruster as a function of the grid spacing; *t*, 1.18 cm; *D*, 2.2 cm; 37-hole grid.

is defined as

$$\text{eV/ion} = \frac{\Delta V_I (J_I - J_B)}{J_B} \qquad [1]$$

All symbols are defined in the symbol list.

The ion chamber was tested over a large range of thruster operating conditions. In general, the qualitative trends were the same as those obtained with low voltage thrusters utilizing tantalum cathodes. Figure 5 shows the eV/ion as a function of the propellant utilization efficiency, net accelerating potential, ion-chamber discharge potential, and magnetic field strength. As is generally true (10) the eV/ion increased with propellant utilization efficiency, decreased with net accelerating potential, and exhibited a minimum at some value of both ion chamber potential difference and magnetic field strength. These data are not optimum for a 20-cm thruster. Use of a discharge chamber configuration employing a hollow cathode (21) or different propellant introduction modes (22) would probably lower the chamber losses.

Discharge stability.—During the investigation it was found that some limits had to be placed on various thruster parameters in order to maintain stable thruster operation. The instability of the discharge would manifest itself both by breakdowns from the thruster anode potential to ground and by quenching of the ion-chamber discharge. Such instabilities are similar to those experienced during operation with short anodes (7, 10). The factors most strongly affecting the discharge stability were the propellant utilization efficiency and the accelerator grid hole size. The grid spacing and thickness did not significantly affect stability over the range of values tested.

The discharge chamber was unstable with the 2.2 and 5.0-cm diameter grid holes at propellant utilization efficiencies greater than about 0.90 and 0.30, respectively. Data presented herein at propellant utilization efficiencies greater than these values (with the specified hole sizes) were taken during repeated breakdowns and/or discharge quenching.

Operation with the large hole grids was characterized by very severe breakdowns which would often destroy the cathode. When wire mesh was placed over the screen grid holes (sketch b), breakdowns

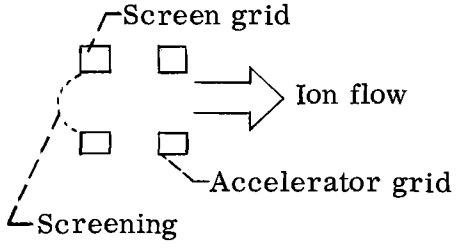

Sketch b

from the anode to ground were eliminated. Use of such screens proved unsatisfactory, however, because the mesh would quickly burn through. In addition, the eV/ion was 2 to 3 times that obtained without mesh screening.

The above statements indicate that the accelerator field can interact with the ion chamber plasma. The grid hole size strongly affected the maximum propellant utilization efficiency that could be attained. The data suggest that discharge quenching, at high utilization efficiencies, may be inherent with the grid geometries required at high voltage.

Accelerator spacing and net accelerating voltage.—Throughout the test it was found that the eV/ion was strongly dependent on the accelerator geometrical and electrical parameters within the region of stable discharge operation. Accelerator grids with hole diameters of 2.2 cm and 7 or 37 holes were utilized for the tests discussed below. The ratios of center-

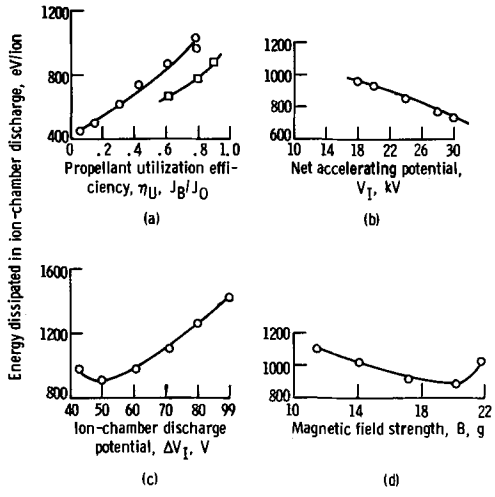

Fig. 5. Ion chamber performance as a function of several thruster parameters. ΔV, 50v; V_I, 20 kv; J_O, 0.165 amp; η_U, 0.79; B, 17.4g; R, 0.8; l_ℓ/D, 1.29; D, 2.2 cm; t, 18 cm; 37-hole grid, unless otherwise noted.

to-center spacing and grid thickness to the hole diameter were varied between 0.8 to 2.5 and 0.34 to 0.86, respectively.

Figure 6 shows the energy loss per beam ion as a function of the center-to-center grid spacing. The center-to-center spacing was chosen because it allows reasonable agreement with Child's law currents (11) and with predicted values of charge-exchange ion impingement currents (12). It is seen from Fig. 6 that the eV/ion tends to increase with both grid spacing and thickness at fixed values of accelerating voltage and propellant utilization efficiency (the hole size was constant for the data of Fig. 6).

To present data concisely over a wide variety of operating conditions, the eV/ion was plotted as a function of the ratio of beam current to the Child's law current predicted by use of the center-to-center grid spacing (11). This ratio is hereafter referred to as percentage of Child's law, and for reference is given by Eq. [2]

$$\left(\frac{J_B}{J_{CH}}\right) = 2.59 \times 10^{10} \frac{J_B l_\ell^{\,2}}{A_A \Delta V_T^{3/2}} \qquad [2]$$

Figure 7 shows this variation and is typical of all data taken in that the energy lost per beam ion always rose monotonically with the percentage of Child's law.

Comparison of Fig. 5(a) and 7 show that the eV/ion is less sensitive to the propellant utilization

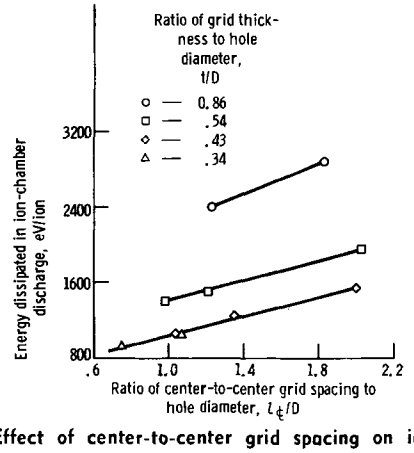

Fig. 6. Effect of center-to-center grid spacing on ion chamber performance. ΔV_I, 50v; V_I, 16 kv; J_O, 0.165 amp; η_U, 0.12; B, 17.4g; R, 0.8; D, 2.2 cm; 7-hole grid.

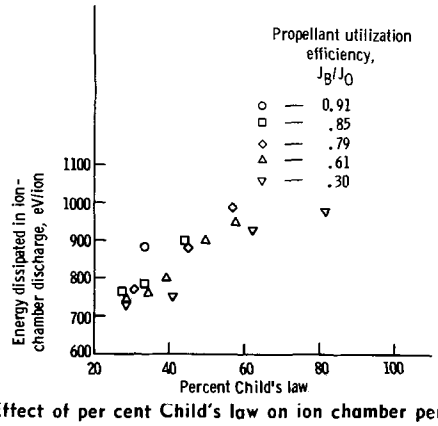

Fig. 7. Effect of per cent Child's law on ion chamber performance. ΔV_I, 50v; J_O, 0.165 amp; *B*, 17.4g; *R*, 0.8; l_t/D, 1.29 cm; *D*, 2.2 cm; *t/D*, 0.54; 37-hole grid.

efficiency when the percentage of Child's law current, rather than the net accelerating potential, is held constant. This fact is more clearly demonstrated by Fig. 8 which presents, at one grid spacing, the variation of eV/ion with propellant utilization efficiency at three values of percentage of Child's law ion current.

For the data of Fig. 8, at a fixed percentage of Child's law, an increase of propellant utilization efficiency from 0.3 to 0.9 corresponded to increases of ion beam current and net accelerating potential by factors of about 3 and 2, respectively. At a fixed propellant utilization efficiency, the net accelerating potential decreased (Eq. [1]) by a factor of about 1.4 as the percentage of Child's law current increased from 30 to 50%.

Figure 9 shows that to a good approximation the eV/ion was not a strong function of grid spacing if the accelerating voltage was adjusted to provide a constant percentage of Child's law ion current. The data of Fig. 6 (fixed net accelerating potential, 7 hole grid) indicate that the eV/ion nearly doubled as the spacing ratio increased from 0.8 to 2.0. The increase

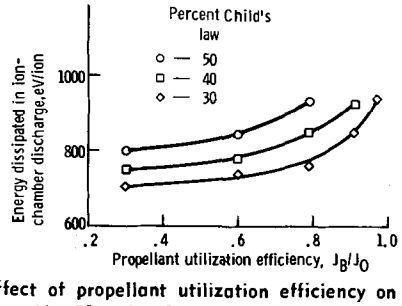

Fig. 8. Effect of propellant utilization efficiency on ion-chamber performance. ΔV_I, 50v; J_O, 0.165 amp; *B*, 17.4g; l_t/D, 1.29; *D*, 2.2 cm; *t/D*, 0.535; 37-hole grid.

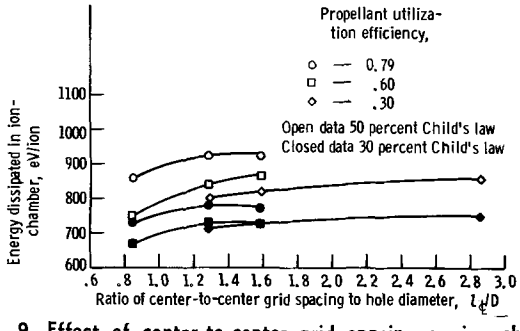

Fig. 9. Effect of center-to-center grid spacing on ion chamber performance at several values of per cent Child's law and propellant utilization efficiency. ΔV_I, 50v; J_O, 0.165; *B*, 17.4g; *R*, 0.8; *D*, 2.2 cm; *t/D*, 0.54; 37-hole grid.

in eV/ion for the same spacing ratio variation at fixed percentage of Child's law current (Fig. 9) was about 15%.

The basic energy requirement of producing a beam ion is, of course, most strongly a function of propellant type and the geometrical and electrical parameters of the ionization chamber (23). Within this framework, however, the accelerator parameters can play an important role in determining the eV/ion.

The ion extraction efficiency could be a function of either the ion sheath withdrawal area or long range extraction phenomena such as axial electric field gradients in the discharge chamber. Figures 7 and 8 of ref. (24) indicate that small changes in the percentage of Child's law can result in large variation in ion sheath withdrawal area. Reference (24) indicates, for example, that the sheath area increased by about 50% when the ion current was varied to decrease the per cent Child's law from approximately 27 to 17%. On the other hand, increased extraction efficiency is almost certain to change the plasma parameters, at least near the accelerator grids. Variation of the electron temperature, for example, could affect the ion drift velocity toward the accelerator grids (23).

A consequence of the above discussion is that the eV/ion does not decrease indefinitely with increasing net accelerating potential. For a fixed grid spacing the energy expended per beam ion will decrease with increasing acceleration voltage up to the voltage limit determined by grid-to-grid breakdown. In order to increase further the acceleration potential it is necessary to increase the grid spacing. An increase in spacing has the effect (Eq. [2]) of increasing the percentage of Child's law current represented by a given ion beam current density and net accelerating potential, and as previously seen, the eV/ion will increase. This implies a serious limitation in the attainable discharge power losses or beam current densities with simple two grid accelerators at large spacings.

Beam Current Density Measurements

The maximum beam current density of an ion source is of interest, particularly for thruster applications due to the direct influence of maximum beam current density on the maximum attainable thrust per unit area. Calculation of the grid aperture effect (11) indicated that no decrease in the maximum transmitted percentage of Child's law ion current would occur due to operation at high voltage (large spacings).

Grid spacing.—Figure 10 shows the variation of the maximum percentage of Child's law current as a function of the ratio of accelerator grid spacing to hole diameter. Data for both the 37 and 7 hole grids (sketch c) are included in Fig. 10. The maximum beam current was determined by the "knee" method of ref. (11) and can contain considerable error due to the difficulty of locating the knee exactly. Briefly, the "knee" method is the determination of the total voltage between the grids at which the impingement current begins to rise rapidly when the thruster is

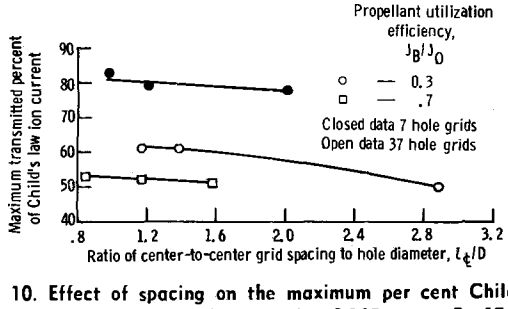

Fig. 10. Effect of spacing on the maximum per cent Child's law ion current transmitted. ΔV_I, 50v; J_O, 0.165 amp; *B*, 17.4g; *R*, 0.8; *D*, 2.2 cm; *t/D*, 0.54.

operated at a constant beam current. For a fixed spacing the Child's law ion current can be calculated for the "knee" voltage and the data of Fig. 10 is the ratio of the actual ion current at the "knee" to the calculated Child's law value.

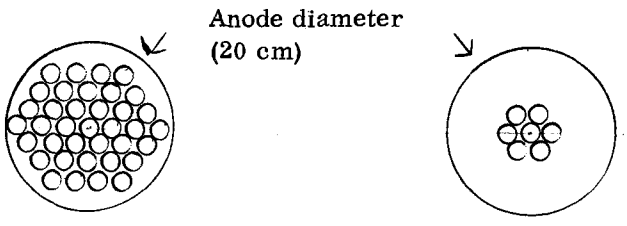

It is seen from Fig. 10 that the value of the maximum percentage of Child's law current does not vary significantly with grid spacing for a fixed number of holes. The general levels of maximum percentage of Child's law ion currents were higher for the 7 hole than the 37 hole system. The defining diameters, within which all holes were contained, were about 7.5 and 20 cm, respectively, for the 7 and 37 hole configurations. It was found the closing the central 7 holes on the 37 hole system increased the maximum transmitted percentage of Child's law ion current for the remaining 30 holes but the maximum current from the thruster was reduced.

It is likely that there was a larger variation in the discharge ion density across the 37 hole system than the 7 hole system. The radial ion number density gradient is probably most strongly affected by the basic geometry of the discharge chamber which had a constant anode diameter for both grid configurations. The presence of a large ion density gradient thus might lead to defocusing of the central holes before the outer holes become defocused as the total thruster current approaches the Child's law current limit.

Focusing characteristics.—Tests were performed with 7-hole accelerator grids in order to evaluate the focusing characteristics over a large range of spacings and grid thicknesses. Figure 11 shows the ratio of ion impingement to ion beam current as a function of grid spacing at three values of percentage of Child's law ion current. The data were taken at fixed values of ion beam current, ratio of net to total accelerating potential, and propellant utilization efficiency.

It is seen from Fig. 11 that the variation of the impingement current with spacing is a function of both the percentage of Child's law ion current and the ratio of grid thickness to hole diameter. In general, at 30% of Child's law the impingement current decreased slightly with increasing grid thickness and was rather insensitive to the grid spacing. At 80% of Child's law ion current the impingement current is, however, a rather sensitive function of the grid geometry. The ion beam appeared to defocus at both large and small spacing for the thinner grids (data were not taken with the thickest grids at a large enough spacing for defocusing to occur). As the grid thickness increased, both the maximum and minimum spacing at which defocusing initiated increased.

The data of Fig. 11 indicate that if thruster operation at a large value of percentage of Child's law is desired, care is necessary in selection of the grid geometry in order to operate at low values of impingement current. If the thruster is to be operated at a low percentage of Child's law, the impingement will be substantially constant over a wide range of grid geometries. The lack of dependence of the impingement current upon the grid configuration at low values of per cent Child's law is probably due to the fact that in this region the ion beam becomes strongly focused into the center of the accelerator holes [see Fig. 9 and 10 of ref. (24)]. As the value of the percentage of Child's law increased, the ion beam spreads, due to sheath readjustment, and the ion focusing becomes more strongly dependent on the specific grid geometry.

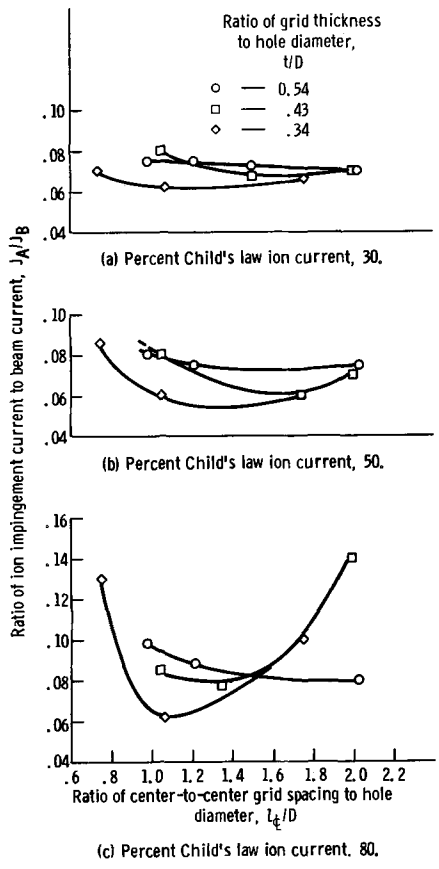

Fig. 11. Effect of grid spacing on the ratio of ion impingement current to beam current, 7-hole system; J_O, 0.165 amp; η_U, 0.12; R, 0.8.

Charge-exchange ion impingement.—In the region of good ion focusing, the value of impingement current due to charge-exchange has been calculated in ref (12). The value of the charge-exchange currents in the present investigation will differ from those of ref. (12) due to the large differences in net accelerating potential and spacings utilized. For fixed values of neutral mass flow rate, propellant utilization efficiency and open area, the values of the charge-exchange current will be considerably larger than at low voltage operation. The cross section for charge exchange does decrease somewhat with increasing voltage. Large uncertainties exist in the literature, however, regarding the exact variation, *e.g.*, ref. (25-27). For purposes of later calculation the charge-exchange cross section will be assumed to be constant at 5×10^{-15} cm^2 for the net accelerating potentials (15,000-70,000v) used in this investigation.

Figure 12 shows the variation of the ratio of impingement to beam current as a function of grid spacing. These data were taken with the 37-hole grid system with a grid thickness to hole diameter ratio of 0.54. This grid thickness ratio was selected as it allowed operation over a wide range of percentage of Child's law ion currents and accelerator grid spacings (Fig. 11). Also shown are the calculated values of the impingement to beam current ratio obtained by use of equation (B16) of ref. (12). This equation is given below with the charge-exchange cross section assumed to be 5×10^{-15} cm^2 rather than 6×10^{-15} cm^2 as in ref. (11).

$$\frac{J_A}{J_B} = 2.63\,(1-\eta_U)J_O\left[1.5\frac{l_t}{A_A}+\sqrt{\frac{\beta V_I^{3/2}A_I f(R)}{A_O^2\eta_U J_O}}\right] \quad [3]$$

It is seen from Fig. 12 that, in general, the values of ion impingement were within about a factor of 2 of those predicted from the calculated charge-exchange impingement current of ref. (12). This agreement, ap-

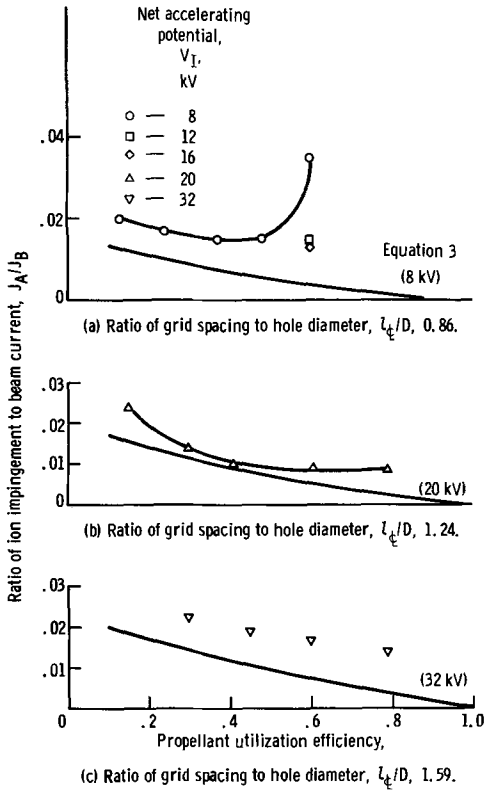

Fig. 12. Effect of propellant utilization efficiency on the ion impingement current. ΔV_I, 50v; J_O, 0.165 amp; *B*, 17.4g; *R*, 0.8; *D*, 2.2 cm; *t/D*, 0.54; 37-hole grid.

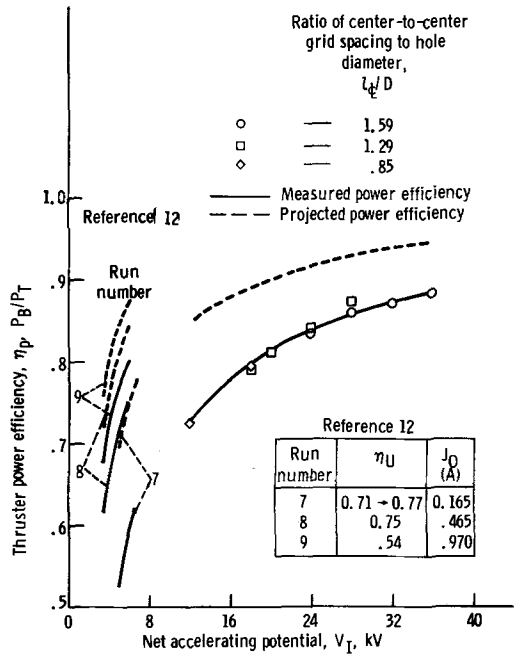

Fig. 13. Effect of net accelerating potential on thruster power efficiency ΔV_I, 50v; J_O, 0.165 amp; *B*, 17.4g; *D*, 2.2 cm; 37-hole grid; *t/D*, 0.54; *R*, 0.8; η_U, 0.8 except where otherwise noted.

proximately the same as that obtained at low voltage (12), held as long as care was taken to operate in the aforementioned region of good focusing. It is thus likely that the impingement in the good focusing region was due primarily to charge-exchange ions. The data of Fig. 11 (7-hole grid) also agreed with Eq. [3]. The higher values of impingement arose primarily because the low utilization efficiencies and reduced open area at which the 7-hole grids were operated.

Power Efficiency

One of the primary advantages of high-voltage operation is the increase to be expected in the power efficiency, or ratio of beam power to total expended power. As was previously shown (Fig. 9), the value of the energy loss per beam ion does not vary substantially over a large range of spacings so that the power efficiency can be expected to reflect directly the increasing ion beam energy.

Figure 13 shows the power efficiency as a function of the net accelerating potential for three values of accelerator spacing. Power losses in the cathode, magnet, accelerator, and ion chamber were included in these data. The power efficiency is a steadily increasing function of net accelerating potential for a fixed value of propellant utilization efficiency. Unfortunately power supply limitations did not allow data to be taken in excess of approximately 70 ma of ion beam current with net accelerating voltages in excess of 50 kv. It was found that the combination of large neutral propellant flow rates and ion beam power would result in vacuum system pressure increases which would lead to anode to ground breakdown. The upper limits were neutral flow rates of about 0.2 equivalent ampere and beam power levels of approximately 7000w at net accelerating potentials in excess of 20 kv.

The data of Fig. 13 indicate that the value of the power efficiency was greater than 0.80 at net accelerating potentials larger than 20 kv. Reduction of the eV/ion would not appreciably affect these data. Because of the small ion beam currents (imposed by Child's law considerations) these losses were always less than 150w. The use of permanent magnets and hollow cathodes (21) would reduce the power losses by about 300w or more. The cathode power of the tantalum cathodes was typically about 12% of the total thruster power; that of a hollow cathode is about 2%. The increase in power efficiency that would result from a 300w saving is shown by the projected power efficiency on Fig. 13.

Also shown on Fig. 13 are data taken at low voltage with a 20-cm-diameter thruster (12). Magnet and cathode losses of 150 and 200w, respectively, were used to determine these power efficiencies. The data selected from ref. (12) were those closest to 0.80 propellant utilization efficiency and which were available over some range of net accelerating potential. The power efficiency, at a fixed net accelerating potential, is not strongly affected by variation of the propellant utilization efficiency between about 0.60 and 0.80. A comparison between the low and high voltage power efficiencies can, therefore, be made.

The extrapolated power efficiencies at high voltage best match the data of ref. (12) when the value of the neutral flow rates were approximately equal. In general, the value of the power efficiency increased with the neutral flow rate at a fixed propellant utilization and net accelerating potential. This occurred because of fixed losses that did not vary significantly with ion beam current. The high and low voltage data, with the assumed savings of 300w, show that thruster power efficiencies in excess of 0.85 and 0.90 should be obtained at net accelerating potentials greater than about 10 and 20 kv, respectively.

Over-all Thruster Efficiency

The over-all thruster efficiency as a function of the net accelerating potential is shown in Fig. 14(a). For reference the same data is plotted as a function of specific impulse in Fig. 14(b). The projected power efficiencies from Fig. 14 were utilized in calculation of over-all efficiency. It is seen that the over-all efficiency should be greater than 0.80 for net accelerating potentials greater than 16 kv at propellant utilization efficiencies of 0.90 or larger. To achieve this over-all efficiency at lower propellant utilizations would require higher net accelerating potentials.

Data are not presented at values of propellant utilization efficiency greater than 0.91 since this was the largest value at which the thruster operated

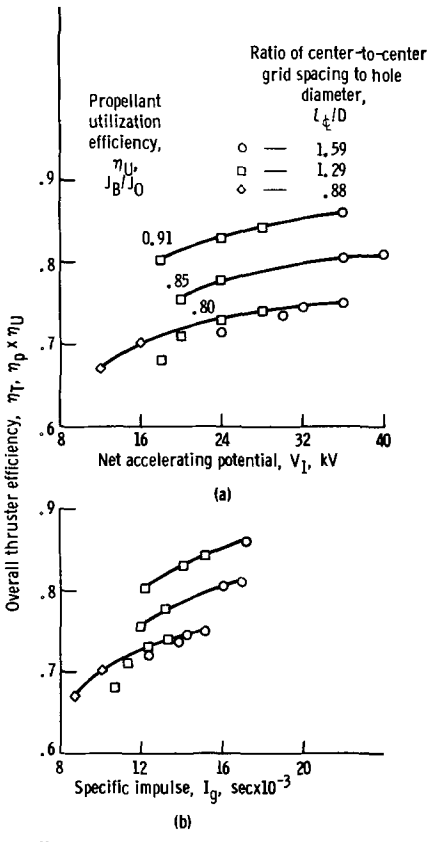

Fig. 14. Over-all thruster efficiency as a function of net accelerating potential and specific impulse. ΔV_I, 50v; J_O, 0.165 amp; B, 17.4g; D, 2.2 cm; t/D, 0.54; R, 0.8.

stably. From previous consideration it would appear that the maximum stable propellant utilization efficiency could probably be increased by decreasing the grid hole size. Because of the spacings required for high voltage (Fig. 4), however, and the fact that there exists a maximum ratio of center-to-center spacing to hole diameter [ref. (11) and Fig. 11] for good ion focusing the hole diameters could not be significantly reduced.

Concluding Remarks

It was found that the maximum supportable electric field strength between accelerator grids of operating thrusters was about 2×10^6 v/m over a large range of spacings. This field strength refers to grid-to-grid breakdowns after 2 to 20 hr conditioning.

The qualitative variations in eV/ion were found to be quite similar to that at low voltage. In addition, the eV/ion was nearly independent of the net accelerating potential and center-to-center grid spacing if the propellant utilization efficiency and per cent of Child's law current were held constant.

It was found that the ratio of center-to-center grid spacing to grid thickness should be between 2.5 and 4 to provide good ion focusing. The value of the grid thickness alone did not strongly affect the ion focusing, however, unless the beam current was in excess of approximately 50% of Child's law value.

The maximum values of ion beam current density were about 80 and 55% of the Child's law value for 7 and 37 hole grid systems, respectively. The maximum current densities were nearly independent of spacing. The accelerator impingement current, at beam current densities less than the maximum, were essentially those predicted from charge exchange interactions.

The thruster power efficiency can be expected to be in excess of 0.85 at all net accelerating potentials greater than 20,000v. The over-all thruster efficiency (the product of the power and utilization efficiencies) was limited to 0.86 in the present study because of discharge chamber stability problems and was substantially less for most conditions investigated. High current densities at high voltage probably require more complex accelerator grid systems to avoid stability problems and excessive ion chamber losses.

SYMBOL LIST

A_A	open area of accelerator on screen grid, m^2
A_I	flow area of ions, m^2
A_O	nominal thruster area, m^2
B	magnetic field strength, w/m^2
D	accelerator plate hole diameter, m
$f(R)$	$1/R^{3/2} + 3/R - 4$
I_{sp}	specific impulse, sec
J	current, amp
J_O	current equivalent neutral flow rate, amp
j	current density, amp/m^2
l	grid-to-grid spacing, cm
l_c	center-to-center grid spacing, cm
m	mass, kg
q	charge of an electron, C
R	ratio of net-to-total accelerating potential, $V_I/V_{I+} + \lvert V_A \rvert$
t	accelerator grid thickness, cm
V	potential, v
ΔV	potential difference, v
β	$4\epsilon_o/9\sqrt{2q/m} = 3.86 \times 10^{-9}$ mks units for Hg_g^{+1} ions
ϵ_o	permittivity of free space, 8.85×10^{-12} $C^2/(N)(m^2)$
η	efficiency

Subscripts

A	accelerator
B	beam
CH	Child's law
I	ion chamber
n	neutral
p	power
T	total
U	utilization

Manuscript submitted May 15, 1968; revised manuscript received Sept. 19, 1968. This paper was presented at the Boston Meeting, May 5-9, 1968, as Paper 170D.

Any discussion of this paper will appear in a Discussion Section to be published in the December 1969 JOURNAL.

REFERENCES

1. H. R. Kaufman and P. D. Reader, "Progress in Astronautics and Rocketry," Vol. 5, pp. 3-20, Electrostatic Propulsion, D. B. Langmuir, E. Stuhlinger, and J. M. Sellen, Jr., Editors, Academic Press Inc., New York (1961).
2. D. J. Kerrisk and H. R. Kaufman, "Electric Propulsion for Primary Spacecraft Propulsion," Paper 6-424 presented at AIAA New York Meeting (1967).
3. B. A. Banks, Paper presented at Third International Conference on Electron and Ion Beam Science and Technology, Boston, May 6-9, 1968.
4. W. R. Kerslake, J. F. Wasserbauer, and P. M. Margosian, *AIAA Journal*, 5, 683 (1967).
5. S. Nakanishi, and E. V. Pawlik, AIAA Paper No. 67-725 (1965).
6. P. D. Reader, "First International Conference on Electron and Ion Beam Science and Technology," Robert Bakish, Editor, pp. 925-935, John Wiley & Sons, Inc., New York (1965).
7. D. C. Byers, W. R. Kerslake, and J. S. Grobman, NASA TN D-2401 (1964).
8. P. D. Reader and E. V. Pawlik, NASA TN D-4055.
9. E. Stuhlinger, "Ion Propulsion for Space Flight," pp. 150-151, McGraw-Hill Book Co., New York (1964).
10. P. D. Reader, NASA TN D-1163 (1962).
11. W. R. Kerslake, NASA TN D-1168 (1962).
12. W. R. Kerslake, NASA TN D-1657 (1963).
13. S. Nakanishi, NASA TN D-3535 (1966).
14. T. A. Keller, "Transactions of the Seventh National Symposium on Vacuum Technology," pp. 161-167, Pergamon Press, London (1960).
15. H. R. Kaufman, NASA TN D-261 (1960).
16. D. Alpert, D. A. Lee, and H. E. Tomasche, "Proceedings of the International Symposium on In-

sulation of High Voltages in Vacuum," pp. 1-12, MIT Press, Cambridge (1964).
17. K. W. Arnold, R. B. Britton, S. C. Zanon, and A. S. Denholm, Proc. of Sixth Int. Conf. on Ionization Phenomena in Gases, Paris, 1963.
18. M. J. Kofoid, *AIEE Trans.*, Part III, **79**, 991 (1960).
19. M. J. Kofoid, *ibid.*, **79**, 999 (1960).
20. C. Germain and F. Rohrback, in Proc. of Sixth Int. Conf. on Ionization Phenomena in Gases, Paris 1963.
21. R. T. Bechtel, G. A. Csiky, and D. C. Byers, AIAA Paper 68-88 (1968).
22. P. D. Reader, NASA TN D-2586 (1965).
23. H. R. Kaufman, NASA TN D-3041 (1965).
24. E. V. Pawlik, P. M. Margosian, and J. F. Staggs, NASA TN D-2804 (1965).
25. A. von Engel, "Ionized Gases," p. 112, Clarendon Press, Oxford (1955).
26. R. M. Kushnir, B. M. Palyukh, and L. A. Sena, *Bull. Acad. Sci. USSR*, **23**, 995 (1959).
27. I. Popescu Iovitsu and N. Ionescu-Pallas *Soviet Phys.-Tech. Phys.*, **4**, 781 (1960).

Electrolytic Degradation and Electrode Structure

William A. Nystrom*

Stackpole Carbon Company, St. Marys, Pennsylvania

ABSTRACT

The anode degradation of electrographitic materials was investigated in concentrated oxyacid electrolytes and in saturated brine solutions. Both light microscopy and electron microscopy were used to follow the progressive attack of the graphite surface. The rate of wear in the concentrated oxyacid electrolytes could be correlated with the relative tendency to form graphite intercalation compounds, and a number of interesting possibilities are suggested for the use of such a process. In brine solutions, it was observed that the binder materials were attacked more rapidly than were the graphitized coke particles, and the pattern of attack within the coke particles was observed to follow the original coke structure.

Graphitic materials are found in many commercial applications. Certainly one of the most important of these is the use of graphite electrodes in electrolysis cells. When used as a cathode, and barring the formation of compounds, graphite can be expected to last indefinitely. However, in chlorate and in chlor-alkali cells, graphite is used either solely or else periodically as an anode material where it is subjected to strongly oxidizing conditions. Since it is only due to the high irreversibility of the oxygen evolution process in brine solutions that chlorine can be generated, it is inevitable that some water is discharged to yield molecular oxygen and carbon dioxide at the anode. It is the formation of this latter product along with the chemical oxidation of graphite by chlorate which results in graphite electrode wear.

In this study, the anodic degradation of carbonaceous electrode materials was investigated in both brine solutions and in concentrated oxyacids. Although the behavior of electrode materials in concentrated oxyacids has been previously reported by Thiele (1), it was felt that another look at this phenomenon might yield useful information as to possible relationships between anode wear and both macro and microstructures. Also, the effect on anode wear of various mixtures of the oxyacids has not been previously reported. The experiments in brine solutions were carried out to either verify or disprove certain widely held generalizations as to the effect of microstructure on anode wear. These were (*i*) anodes consisting of a large proportion of coarse filler particles wear more slowly than do anodes which have a fine filler particle size and (*ii*) regions consisting of binder material wear faster than do the adjacent filler particles.

Experimental Procedure

Degradation in concentrated oxyacid electrolytes.—A schematic illustration of the electrolysis cell for the anodic degradation studies in concentrated oxyacids is shown in Fig. 1. This cell consisted of a 1500-cc Pyrex vat into which was fitted a cylindrical, type 302 stainless steel cathode. For the most part, cylindrical anodes measuring approximately 2 in. high by 0.5 in. in diameter were used in this study. They were positioned as indicated in the center of the cell. The effect of various oxyacids and mixtures of oxyacids on electrode wear was studied by using a special high-purity grade of extruded electrographitic rod having an ash content of less than 0.001%. As will become apparent, the results obtained for this material are to be regarded only as generalizations; changes in the specific nature of the electrode material will give rise to different rates of attack although the general features common to a given type of material are expected to remain the same.

The concentrated oxyacids investigated in this study included sulfuric acid, nitric acid, phosphoric acid, and mixtures of phosphoric and nitric acids. All of these acids were of reagent-grade quality. Test anodes were corroded at constant total current, and the electrolysis time was monitored by a stop watch. At the end of selected intervals of electrolysis time, the current was switched off, and the diameters of the test anodes were measured by a micrometer. In selected cases, photographs of the degraded samples were also taken for a record of the nature of the anodic attack. The test anodes were then placed back into the electrolysis cell and electrolyzed for the next interval of time, etc., until the point of complete destruction of the anode was achieved. The specific values of the selected interval times varied with the nature of the electrolyte and were chosen so as to obtain a reasonable number of data points for plotting the electrode diameter as a function of time.

Degradation in brine solutions.—The experimental setup for the electrolysis runs in the saturated sodium

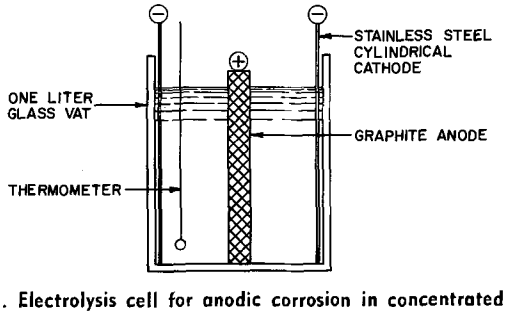

Fig. 1. Electrolysis cell for anodic corrosion in concentrated oxyacid electrolytes.

* Electrochemicaal Society Active Member.
Key words: graphite, electrode, wear, structure, electrolysis.

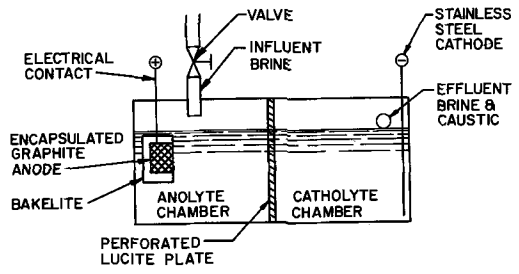

Fig. 2. Electrolysis cell for anodic corrosion in saturated brine solution.

chloride electrolyte is shown in Fig. 2. The cell consisted of a 1-l Lucite box which was subdivided by means of a perforated Lucite plate into two equal 500-cc compartments. The anode compartment, or anolyte chamber, was continuously fed fresh, saturated brine solution at the rate of 7 cc/min, thus creating a positive pressure head to prevent intermixing of the caustic produced in the catholyte chamber with the anolyte chamber brine. A vent was placed in the side of the catholyte chamber to allow the continuous removal of caustic and brine during the electrolysis run.

The graphite samples used for these experiments consisted of 0.5-in. diameter extruded rods of electrographitic materials which were encapsulated in Buehler No. 1385AB transoptic mounting powder. The surface exposed to the electrolysis consisted of the 0.5-in. diameter cross section of the extruded rod which was polished using conventional metallographic procedures to a Linde B finish (0.05μ) before commencing electrolysis. Electrical connection to the encapsulated samples was made by drilling and tapping a metal screw into intimate contact with the graphite, as is shown in Fig. 2. Stop-off lacquer was used to insulate the surface of the screw from the electrolyte.

The results found for two basic types of electrographitic electrode materials are reported herein. They consisted, respectively, of a pitch-coke, pitch-binder material and a petroleum-coke, pitch-binder material. The latter material also contained a conventional linseed oil impregnation treatment whereas the former material was tested in the untreated condition. Both of these materials are composed of relatively coarse particles of filler particles although of necessity some fines are also present. Their microstructures are representative of typical anode materials.

Reagent-grade sodium chloride and high-purity demineralized water were used to prepare the saturated brine solutions. The acidity of the influent brine was adjusted to pH 4 using reagent-grade hydrochloric acid or caustic soda as necessary. A type 302 stainless steel cathode was used in all of these experiments.

Prior to electrolysis but subsequent to polishing, a fiducial mark was scribed onto the surface of the graphite samples in order to facilitate the location of selected areas which were photographed in the as-polished condition. Each sample was then electrolyzed at 158 ma/cm^2 in the brine solution for the sequence of times of 1, 2, 4, 8, 16, and 32 hr, at the end of each specific time of which it was removed from the solution, carefully dried, and the previously selected areas were located and photographed. The samples were then placed back in the cell and electrolysis continued for the next interval of time until the desired 32 hr of electrolysis on a given sample had been realized (this gave a nominal sample wear of about 1 mil). In this manner, a sequence of photographs were prepared which illustrated the nature of the electrode wear in relation to its microstructure as a function of time. As before, deposition time was monitored by means of a stop watch. The photographs of the surface microstructure of the degraded anodes were taken at a magnification of 250X (reduced to 235X for publication) as this was adequate to discern the pattern of sample attack. All work of this nature was performed on a Bausch and Lomb metallograph.

After the photomicrographs of the 32 hr of anode electrolysis had been taken, the samples were submitted to electron microscopy in order to determine the fine-scale features of the anode wear. Two-stage replicas of the samples were prepared by replicating the degraded surfaces with Bioden RFA acetyle cellulose. Preshadowed carbon replicas of the plastic originals were then prepared using chromium as the preshadow. The resulting composites were immersed in acetone and the plastic dissolved away to give the two-stage carbon replicas. The examination of these replicas was performed on a JEM 30 electron microscope manufactured by the Japan Electron Optics Laboratory Company, Ltd.

As it was desirable to know the true magnification of the electron micrographs as well as to distinguish between hills and holes on the replicated surfaces, 0.365μ diameter latex balls were placed on the plastic first-stage replicas prior to chromium preshadowing. In the final image of the surface, those formations which show shadowing on sides opposite to the shadowed sides of the latex balls correspond to raised projections on the graphite surface. Those which show shadowing on the same side as the latex balls correspond to depressions or cracks in the corroded sample surface.

Results and Discussion

Degradation on oxyacid electrolytes.—The composition and operating conditions of the oxyacid electrolytes used in this study are given in Table I along with the value of the time interval selected for the measurements of electrode diameter as a function of electrolysis time. Table II lists the experimental data obtained from these runs, part of which was used to prepare Fig. 3, which presents the data in a graphical fashion for the phosphoric and nitric acid combinations. Also shown in Fig. 3 are the results for elec-

Table I. Composition and operating conditions of the oxyacid electrolytes

Electrolyte*	Anodic current, amp	Time interval, min
H_3PO_4	10	120
2 Pt H_3PO_4 1 Pt HNO_3	10	30
2 Pt H_3PO_4 1 Pt HNO_3	5	60
1 Pt H_3PO_4 1 Pt HNO_3	10	15
HNO_3	10	5
H_2SO_4	10	5

* The specific gravities of these acids are: H_2SO_4, 1.84 g/cc; HNO_3, 1.42 g/cc; H_3PO_4, 1.71 g/cc.

Table II. Experimental data for oxyacid degradation

Electrolyte	Current, A	Time, min	Avg diameter, mil
H_3PO_4	10	0	561
		120	464
		240	225
		290	50
2 Pt H_3PO_4 1 Pt HNO_3	10	0	561
		30	503
		60	415
		90	304
2 Pt H_3PO_4 1 Pt HNO_3	5	0	561
		60	492
		120	410
		180	305
		240	120
1 Pt H_3PO_4 1 Pt HNO_3	10	0	560
		15	490
		30	398
		45	288
		60	136
HNO_3	10	0	561
		5	500
		10	414
		15	307
		20	204
H_2SO_4	10	0	561
		15	296

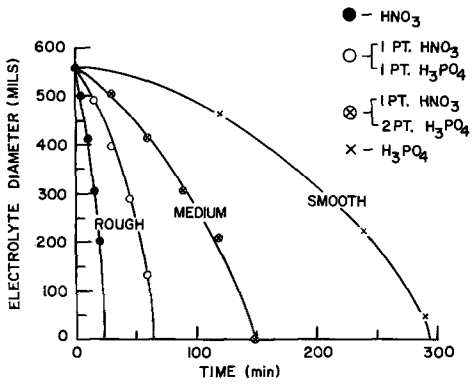

Fig. 3. Anodic degradation in HNO_3-H_3PO_4 electrolytes

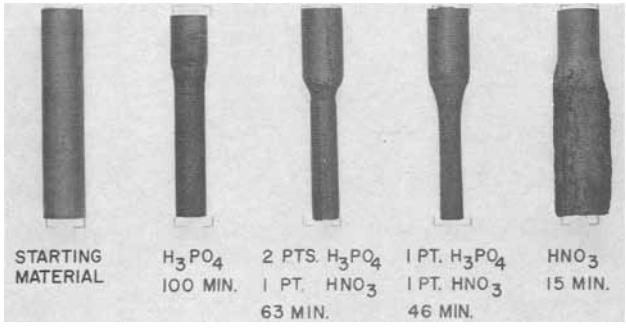

Fig. 4. Anodic corrosion of electrographitic material in concentrated oxyacids. Anode current, 10 amp; electrolyte temperature, 25°C.

trolysis in nitric acid and in phosphoric acid alone. It is quite obvious from these data that the higher the ratio of nitric acid to phosphoric acid in the electrolyte, the faster is the degradation rate of our purified graphite electrodes. Also, the higher the nitric acid content of the electrolyte, the rougher the degraded electrode surface becomes. Figure 4 shows this aspect of the electrode degradation quite nicely as those samples which were degraded in electrolytes having appreciable percentages of phosphoric acid present smooth surfaces whereas the sample corroded in concentrated nitric acid is covered with a voluminous degradation product. In the latter case, if the degradation product is washed off the electrode, a core of relatively undisturbed material is found; but the point is that this operation is not required for corrosion in phosphoric acid containing electrolytes. Also, the smoothest corroded surface is found in the case of degradation in pure phosphoric acid; with the addition of higher percentages of nitric acid, there is a progressive deterioration in electrode smoothness along with the increasingly faster degradation rates. Electrolytes containing up to about one part of nitric acid to two parts of phosphoric acid give a relatively smooth degraded surface. At intermediate nitric acid contents (one part nitric acid to one part phosphoric acid), a roughening of the corroded surface is noticeable, and at high concentrations of nitric acid of from two parts of nitric acid to one part of phosphoric acid on to pure nitric acid, very rough surfaces are formed along with the voluminous corrosion products previously mentioned. The quality of surface finish obtained as a function of phosphoric acid content is also shown schematically on Fig. 3.

The theoretical explanation for the observed differences in the anodic degradation behavior of pure nitric acid and of pure phosphoric acid on graphite has been given previously by Thiele. He states, "Graphite does not swell in alkalies and in acids of the phosphoric acid group, in that these bodies do not penetrate into its structure and oxidation only occurs at the surface with the formation of humic acid

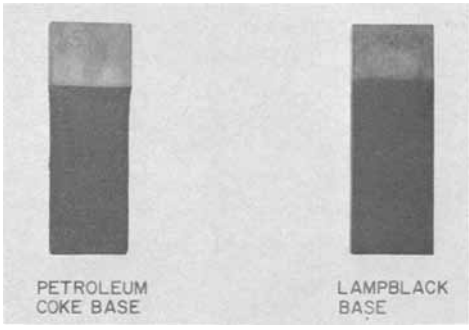

Fig. 5. Anodic corrosion of gas-baked carbons in 35% nitric acid solution. Anode C.D., 144 asf; electrolyte temperature, 25°C; time, 1 hr.

and carbon dioxide. Acids of the sulfuric acid group (including nitric acid) on the other hand, penetrate into the interior of the graphite crystal. The graphite swells, and the carbon atoms become accessible to oxidation." The explanation of the differences in degradation behavior therefore lies with the formation of graphite intercalation compounds in the case of strongly oxidizing acids such as perchloric, sulfuric, and nitric acids; weakly oxidizing acids such as phosphoric acid give only an exterior surface attack of the graphite. In this connection, it is interesting to note Fig. 5 which compares the degradation of two gas-baked carbons in nitric acid under the conditions given in Table III. One immediately notes the much more pronounced attack of the petroleum-coke base sample as compared to the lampblack-base sample. Hence, those materials which possess structures which are capable of being graphitized show a much more pronounced rate of degradation in nitric acid than do the black-base materials which can be only partially graphitized. Obviously, it is the tendency to form intercalation compounds in the case of the coke-base structure which is creating the difference here even though the usual voluminous degradation products are not present. This result suggests the use of anodic degradation in nitric acid or nitric acid-phosphoric acid combinations as a method of evaluating the potential degree of graphitizability of carbonaceous material. For example, those gas-baked materials which show the greatest degree of degradation after electrolysis for a selected period of time may be the ones which will yield the most graphitic structures upon graphitization.

In addition, the results obtained for the degradation of graphitic materials in phosphoric acid and nitric acid mixtures also suggests two more uses for this technique. The first of these is as a destructive test for electrode quality with respect to macrostructural defects such as internal cracking and lamination. Figure 6 illustrates this possibility by showing the results obtained for three different electrolysis-electrode material combinations. Sample No. 1 was a fine-grained, extruded electrographitic material which was corroded in phosphoric acid to about 75% destruction. One notes the presence of wormlike holes on the corroded surface which indicate the presence of internal cracks and gaps in this material. Sample No. 2 is the same material except corroded in concentrated nitric acid for a short period. In this instance, the presence of lamellar layers is easily noticed in the voluminous corrosion products. Indeed, on sectioning and polishing a sample of the as-received material, it was found to consist of a distinctly cored structure which was created by the extrusion process. Sample No. 3 consisted of a relatively coarse-grained,

Table III. Anodic degradation of gas-baked carbons

Electrolyte	1:1 HNO_3
Current density	144 asf
Electrolysis time	60 min
Electrolyte temperature	25°C

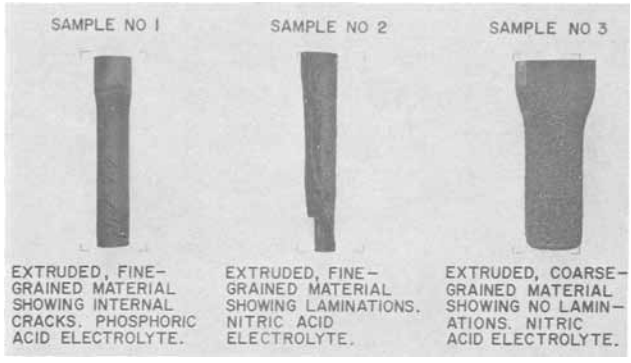

Fig. 6. Comparison of anodically corroded electrographitic materials.

extruded electrographitic material which did not contain either a cored structure or internal microcracks. On removal of the voluminous surface sludge formed in this case, one sees only a severely corroded surface indicating to some extent the size of the filler particles.

Another possibility for this technique lies in the potential use of these electrolytes as electrochemical machining and polishing media for carbon and graphite materials. The data of Table II and Fig. 3 indicate that one can vary the rate of wear and quality of surface finish produced by the oxyacids by suitable manipulations in electrolyte composition. In fact, these data are susceptible to the following theoretical analyses:

If we assume that the rate of wear (or decrease in volume) is a linear function of the total coulombs of electricity passed through the system, we have

$$-\Delta V = KI\,\Delta t \qquad [1]$$

where K is a constant dependent on both the electrolyte and the electrode material, I is the current, V is the electrode volume, and t is the electrolysis time. For a cylindrical anode, Eq. [1] becomes

$$-\Delta\left(\frac{\pi D^2}{4}h\right) = KI\Delta t \qquad [2]$$

where D is the electrode diameter and h is the depth of immersion of the electrode in the electrolyte. Since the depth of immersion can be treated as a constant during a given electrolysis run, integration of Eq. [2] and solving for the electrode diameter as a function of time gives

$$D_t = \left(D_o^2 - \frac{4KIt}{\pi h}\right)^{1/2} \qquad [3]$$

where D_t is the electrode diameter at time, t and D_o is the initial electrode diameter at time zero. Equation [3] indicates that we should have a parabolic decrease of the electrode diameter as a function of time until at time $t_{D_t=0}$ the electrode should be completely consumed, where $t_{D_t=0}$ is defined by

$$t_{D_t=0} = \frac{\pi h D_o}{4KI} \qquad [4]$$

Figure 3 shows that the electrode wear does indeed follow a parabolic curve for cylindrical anodes in these solutions, and Table IV lists the values of the experimental constant K and the time of corrosion for zero electrode thickness calculated from Eq. [4] and compared to the actual value obtained by the extrapolation of the data of Fig. 3 to zero electrode thickness. Also given in Table IV are the calculated K values for two electrolysis runs conducted in the same electrolyte and on the same type of electrode material but for the two different values of the total current of 5 and 10 amp. The reasonably good agreement of the K values for these two runs show that our initial assumption that the rate of electrode wear is a linear function of the total coulombs passed through the system is valid. If there were not so, K would be a function of the current density, which it is not. Hence, by first determining the value of the experimental constant K for a given combination of electrolyte and electrode material by a simple degradation test using a cylindrical anode, one can then choose those operating conditions such as current and time to produce the desired electrochemical machining for any given nominal surface area on this material. In fact, one might choose to use a combination of two separate electrolysis treatments in order to first achieve rapid electrochemical machining of the graphite part (*e.g.*, by using one part nitric acid to one part phosphoric acid) followed by a period of electrolysis in phosphoric acid alone to produce polishing of the electrochemically machined surface. The one requirement remaining to be met (as with all electrochemical machining techniques) is that one be able to achieve a uniform current distribution over those areas where machining is desired. In many cases, this can be attained by the use of thieving, stop-off procedures, and conforming counter electrodes.

Table IV. Experimental and calculated degradation parameters

Electrolyte	Current, A	Avg K, in.^{3}/amp hr	$t_{D_t=0}$/min	
			Calc	Exp
H_3PO_4	10	0.0094	314	296
2 Pt H_3PO_4 1 Pt HNO_3	10	0.021	141	149
2 Pt H_3PO_4 1 Pt HNO_3	5	0.023	257	265
1 Pt H_3PO_4 1 Pt HNO_3	10	0.047	63	64
HNO_3	10	0.130	23	23

Although the specific use of sulfuric acid has not been previously mentioned save for references to its effects by Theile, it should be obvious from the data of Table II that sulfuric acid could be substituted for nitric acid to produce the same effects described above. In fact, sulfuric acid containing electrolytes may well give a better surface finish than that found for the comparable nitric acid-phosphoric acid mixtures owing to its more syrupy nature [see, for example, the general theory of electropolishing as given by Tegert (2)]. Also, no use was made of perchloric acid additions to replace the nitric acid owing to the explosive hazards which present themselves when one uses this acid in the presence of organic materials.

Degradation in brine solutions.—The composition and operating conditions of the brine electrolyte are given in Table V. Photomicrographs of the anodic wear produced under these conditions of a typical oil impregnated, pitch bonded, petroleum-coke base electrographitic material are shown in Fig. 7 to 13. Figure 7 is a photograph of the sample in the as-polished condition prior to electrolysis. A number of relatively large coke particles as well as a considerable number of dark black pores of varying sizes are present in this area of the sample. Also, a number of light gray, structureless areas are present in this photomicrograph which indicates pores which have been successfully impregnated with the conventional linseed oil treatment. With increasing electrolysis time of this material in the pH 4 brine solution, a progressive deterioration of the sample occurs with the most rapid attack being noted at the boundaries of the graphitized coke particles. In fact, after 32 hr of electrolysis, the original coke particles are seen to be standing in relief over the sample surface as is shown by Fig. 13. These results obviously suggest that

Table V. Brine solution composition and operating conditions

NaCl	Saturated solution
pH	4.0
Anode CD	158 ma/cm^2
Temperature	25°C
Agitation	None

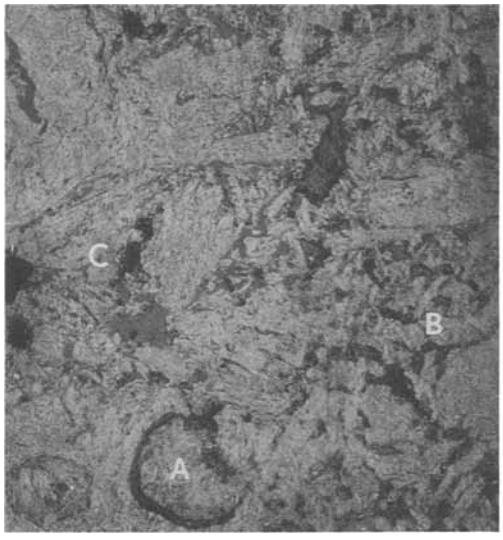

Fig. 7. As-polished, pitch-boned, petroleum-coke base electrographite. Magnification 235X.

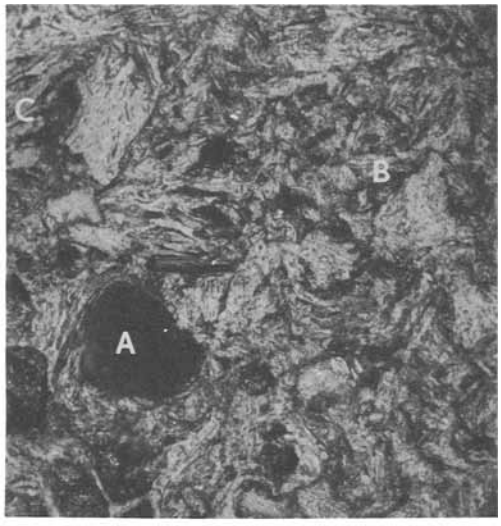

Fig. 10. Four hours of electrolysis on the pitch-bonded, petroleum-coke base electrographite. Magnification 235X.

Fig. 8. One hour of electrolysis on the pitch-bonded, petroleum-coke base electrographite. Magnification 235X.

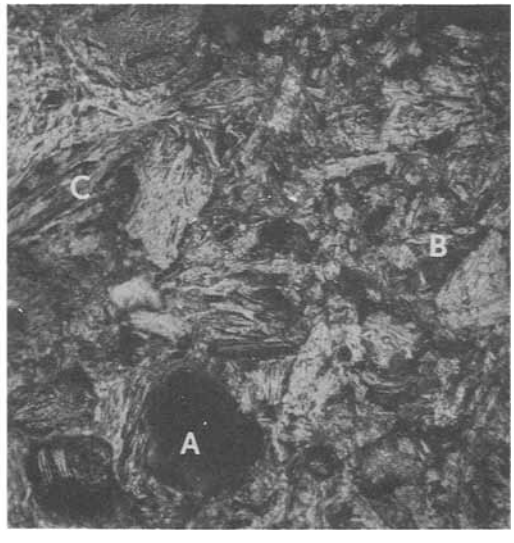

Fig. 11. Eight hours of electrolysis on the pitch-bonded, petroleum-coke base electrographite. Magnification 235X.

Fig. 9. Two hours of electrolysis on the pitch-bonded, petroleum-coke base electrographite. Magnification 235X.

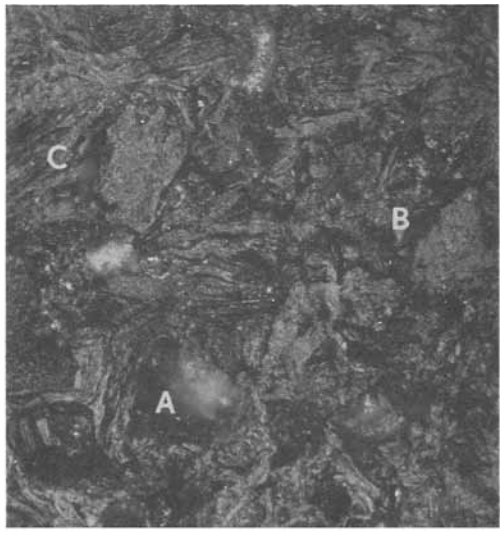

Fig. 12. Sixteen hours of electrolysis on the pitch-bonded, petroleum-coke base electrographite. Magnification 235X.

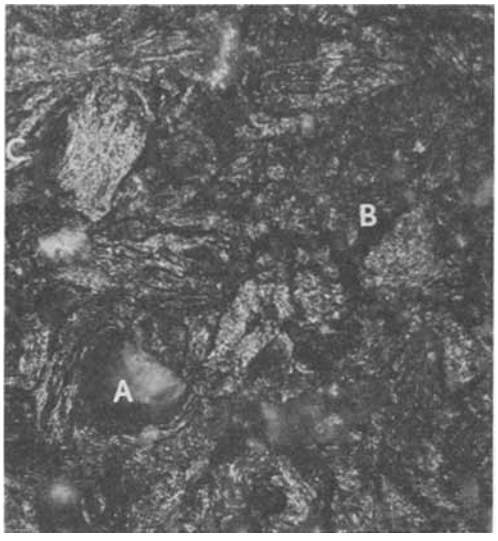

Fig. 13. Thirty-two hours of electrolysis on the pitch-bonded, petroleum-coke base electrographite. Magnification 235X.

it is indeed the binder material which constitutes the weak link in conventional electrode materials. Furthermore, comparison of area A of Fig. 7 with the same area of Fig. 4 reveals that a rather large filler particle has become detached from the electrode between 2 and 4 hr of electrolysis. This obviously points out that, if the filler particles are poorly bonded together, rapid detachment of them from the electrode surface will occur with attendant rapid electrode wear. Also, area B of Fig. 7 is seen to consist of a relatively large number of fine particles of filler particles bonded together. Since finer particles have a larger surface area per unit weight than do coarse particles, they require more binder material on a weight per cent basis to glue them together in the electrode. Hence, this area contains a high proportion of graphitized pitch binder to petroleum-coke filler particles on a unit of surface area basis, and it should therefore have a higher wear rate than the surrounding electrode areas in light of the foregoing observations. That this is indeed the case is borne out by Fig. 13, which shows area B after 32 hr of electrolysis. Obviously, more electrode wear has occurred in this fine-grained area than has occurred over the relatively coarse-grained areas as is shown by the presence in area B of many deeply corroded fissures. This fact probably explains why, as a rule, relatively fine-grained electrodes give poorer performance as evidenced by higher wear rates than do those electrodes prepared from coarser filler particles distribution. It is also interesting to note that the graphitized coke particles are attacked in such a way as to reveal the original lamellar coke structure. This is either due to the presence of microcracks within the coke particle, or more likely, the resistance to electrochemical oxidation of the coke varies in a lamellar fashion with its structure.

For the longer times of electrolysis such as 16 and 32 hr, Fig. 12 and 13 indicate that some pore enlargement has already occurred (compare, for example, area C on these photomicrographs with area C on Fig. 7). This enlargement appears to be due to the wear of binder materials which allows the surrounding filler particles to drop out of the electrode. This results in a progressive enlargening of the pores and permits internal electrolysis and chemical wear of the anode to occur. Of course, the function of conventional oil impregnations of diaphragm cell anodes is to minimize just such internal attack, but the efficacy of the treatment will obviously depend on how many and how well filled are the pores.

As it was observed above that areas of the electrode which represented binder material or probable high binder material concentrations were wearing at a faster rate than the surrounding filler material, it was decided to anodically degrade a pitch-bonded, pitch-coke base electrographitic material having the same approximate particle size distribution as the petroleum-coke based samples. The photomicrographs of this study are shown as Fig. 14 through 20, where Fig. 14 shows the as-polished surface of this material. Although this material is obviously wearing away

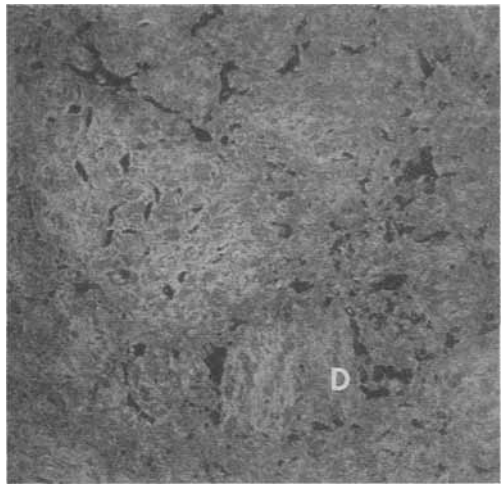

Fig. 14. As-polished, pitch-bonded, pitch-coke base electrographite. Magnification 235X.

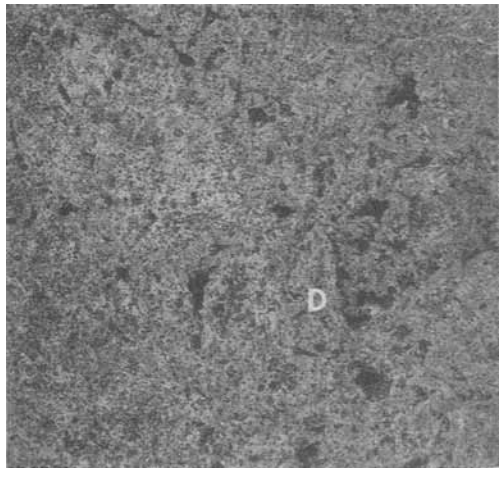

Fig. 15. One hour of electrolysis on the pitch-bonded, pitch-coke base electrographite. Magnification 235X.

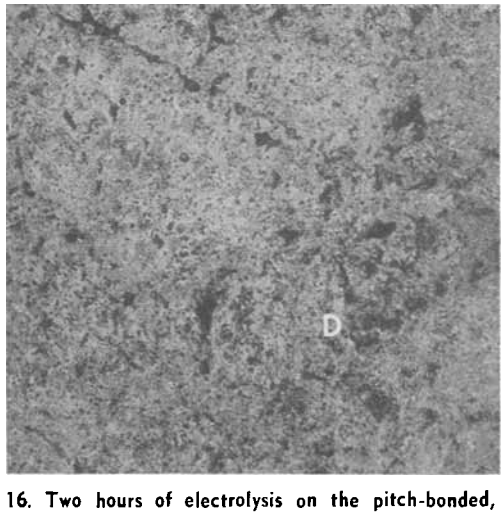

Fig. 16. Two hours of electrolysis on the pitch-bonded, pitch-coke electrographite. Magnification 235X.

Fig. 17. Four hours of electrolysis on the pitch-bonded, pitch-coke base electrographite. Magnification 235X.

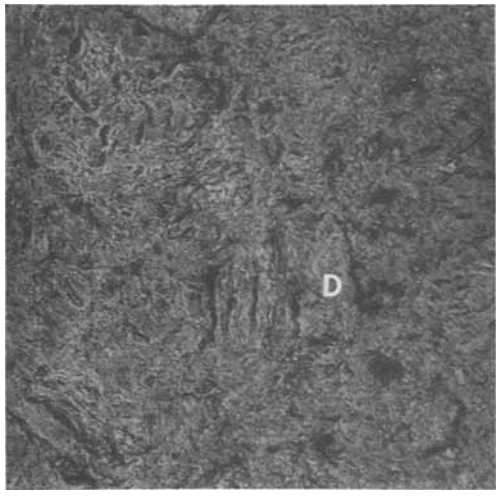

Fig. 18. Eight hours of electrolysis on the pitch-bonded, pitch-coke base electrographite. Magnification 235X.

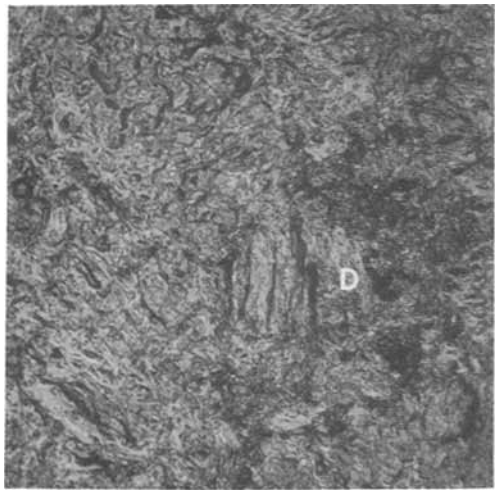

Fig. 19. Sixteen hours of electrolysis on the pitch-bonded, pitch-coke base electrographite. Magnification 235X.

progressively with time, as all carbon and graphite materials will do under these conditions, its degraded surface presents a rather nondescript appearance consisting of a wavy pattern of corroded channels uniformly distributed over the sample surface. Save for a few local areas such as area D where there was obviously a poor bond developed between adjacent agglomerates of particles, the sharp delineation of

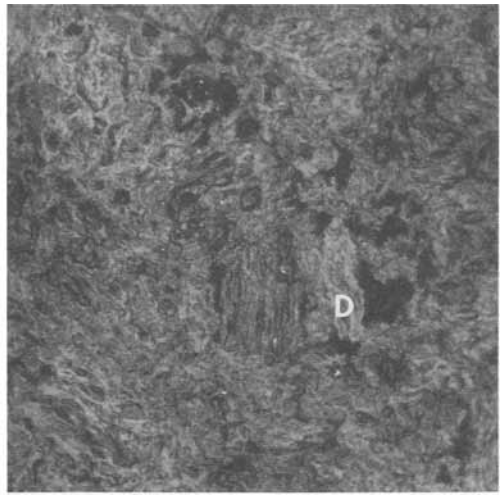

Fig. 20. Thirty-two hours of electrolysis on the pitch-bonded, pitch-coke electrographite. Magnification 235X.

the filler particles as observed for the petroleum-coke whose sample is absent here. Rather, a relatively uniform over-all pattern of wear is observed. This observation agrees well with the previously mentioned fact that the pitch-binder areas wear faster than the petroleum-coke areas inasmuch as in this material all areas should represent graphitized pitch-coke and should therefore be wearing uniformly. Such is indeed the case. Unfortunately, the over-all wear rate of this material is substantially greater than that observed for the pitch-bonded petroleum-coke base material previously examined. This was to be expected, however, as all components of this electrode are now wearing at the much higher rate of graphitized pitch coke rather than at the lower wear rate of graphitized petroleum-coke.

The nature of the really fine-scale attack of the graphitized coke particles is shown in Fig. 21, which is an electron micrograph of the anode surface of the petroleum-coke base sample after 32 hr of electrolysis. It is seen that the fine-scale pattern of wear consists of the formation of small "islands" of material surrounded by corroded channels. Such a pattern of attack is reminiscent of intergranular attack in fine-grained metals. As the size of the observed "islands" of graphitic material is of the same order of magnitude as the expected graphitic crystallite size (*e.g.*, 0.1μ), it may well be that something of a similar nature is occurring here, with the less organized material between the graphite crystallites being more susceptible

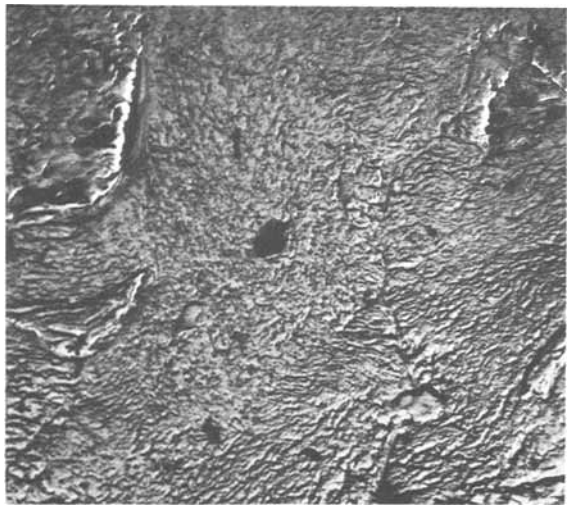

Fig. 21. Electron micrograph of the pitch-bonded, petroleum-coke base sample after 32 hr of electrolysis showing the intersection of a number of particles and the nature of the fine-scale wear of the electrode. Magnification ca. 4200X.

to electrolytic oxidation. This suggests a possible fruitful area for further research efforts in the future.

In view of the fact that air oxidation studies have shown that the pitch-binder areas of pitch-bonded samples are oxidized away more readily than the filler particles, the use of static air oxidation tests to evaluate potential electrode material ingredients as to their resistance to oxidation might be a possibility. Unfortunately, in this respect however, the supply of available electrode materials is limited from both a cost and a material standpoint and is of questionable reproducibility from shipment to shipment. Therefore, further improvement in anode quality will probably depend to a large extent on how well the existing technology can continue to use the known processes of fabrication and the available materials to make a more sound and defect-free anode with respect to such macrofactors as internal cracking, separations and laminations, and the uniformity of and the quality of various impregnation treatments.

Summary and Conclusions

The anodic degradation of graphitic materials was investigated in both concentrated oxyacid electrolytes and in brine solutions. From the oxyacid studies it was seen that:

(*A*) The relative resistance to anodic degradation in a given oxyacid is governed by the presence or absence of a graphite or graphitizable structure in conjunction with the relative tendency of the oxyacid to form a graphite intercalation compound. A possible use of this technique would therefore be to correlate the degree of graphitizability of a material with its rate of degradation in an intercalation compound forming concentrated oxyacid solution. Materials having a high degree of graphitization may degrade more rapidly than those whose degree of graphitizability is lower.

(*B*) The possibility of using mixtures of oxyacids to machine and polish carbon and graphite materials electrochemically is a good one. In particular it was seen that if an empirical constant, which relates electrode wear to current density and which contains both electrolyte and electrode material factors, is first evaluated by a simply cylindrical anode degradation test, it ought to be possible to choose those solutions which will give the desired machining rate and surface finish on a working part of any desired shape. This is, of course, subject to the provision that conforming cathodes or the judicious use of stop-off lacquer is used to bring about a uniform, nominal current density over the corroding surface.

From the studies in brine solutions it was seen that:

(*A*) The areas between the graphitized coke particles, which presumably represent graphitized pitch-binder materials, wear slightly faster than the surrounding material. As a result, any poorly bonded particles are quickly detached from the electrode and represent economic loss to the users of graphite electrodes.

(*B*) The graphitized coke particles are attacked in such a way as to reveal the original lamellar coke structure. This may be caused by either microcracking or by lamellar variations in the resistance to electrochemical oxidation of the coke particle.

(*C*) For the longer times of electrolysis, some pore enlargement was noted in unimpregnated materials or around those pores which were not adequately impregnated to start with. This enlargement appears to be due to wear of the binder materials which allows particles to drop out of the electrode. With time, this results in a progressive enlargening of the pores and permits internal electrolysis of the anode to occur.

(*D*) A fine-scale attack within the graphitized coke particles was also observed by electron microscopy. It consisted of the formation of small islands of material surrounded by corroded channels. Such a pattern of attack is reminiscent of intergranular attack in fine-grained metals. Indeed, the size of the observed islands of resistant material is of the same order of magnitude as the expected graphite crystallite size which suggests that something of a similar nature is occurring here.

Acknowledgment

The author wishes to express his appreciation to the Stackpole Carbon Company for allowing him to publish this paper. Further thanks are also due Mr. Thomas Valentine for metallography, Miss Linda Thorwart for electron microscopy, and Miss Mary Lou Bankovic for typing.

Manuscript submitted July 22, 1968; revised manuscript received *ca.* Aug. 19, 1968. This paper was presented at the Boston Meeting, May 5-9, 1968, as Paper 266.

Any discussion of this paper will appear in a Discussion Section to be published in the June 1969 JOURNAL.

REFERENCES

1. H. Thiele, *Trans. Faraday Soc.*, 1033 (1938).
2. W. J. Tegart, "The Electrolytic and Chemical Polishing of Metals," Pergamon Press, New York (1959).

pH Changes at Anion Selective Membranes under Realistic Flow Conditions

T. R. E. Kressman

The Permutit Company Ltd., London, England

and F. L. Tye

The Ever Ready Company (Great Britain) Ltd., London, England

ABSTRACT

The flow conditions and solution concentrations used in the investigation were similar to those present in practical electrodialysis cells. The concentration of hydroxyl ions which appeared on the receiving side of the polarizing anion selective membrane was measured as a function of current density. The important finding was the large effect traces of dissolved organic matter in the feed water had on the onset and concentration of alkali produced in the receiving stream. For unpoisoned membranes an i_o/c value of 4000 amp cm equiv^{-1} was obtained. This is an order of magnitude greater than reported in previous studies.

Multicompartment electrodialysis depends on the principle that the transference number of the counterion in an ion-selective membrane is greater than the transference number of the same ion in the surrounding solution (1). Thus for the layer of solution adjacent to the membrane on the donating side (2) there is for each ion an inequality in electrical migration and counterions are removed through the membrane at a greater rate than they are replaced from the bulk solution. Continuity of counterion migration is maintained by convective and diffusive transport from the bulk solution. As the membrane surface is approached the contribution due to convective transport decreases.

It is customary to simplify the real situation (3, 4) by postulating a layer of thickness δ (cm) adjacent to the membrane in which convective transport normal to the membrane is zero. By assuming a smooth flat membrane surface and a homogeneous current distribution it is then possible to describe the steady state for a single electrolyte by the following equation.

$$\frac{i(\bar{t}-t)}{\mathbf{F}} = \frac{D(c-c')}{\delta} \qquad [1]$$

where i is the current density (amp cm^{-2}), $\bar{t}$ and t are the counterion transference numbers in the membrane and solution, respectively, **F** is the faraday, D the diffusion coefficient of the electrolyte in the external solution (cm^2 sec^{-1}), and c and c′ are the concentrations of electrolyte in solution in the bulk and at the membrane interface, respectively, (g equiv cm^{-3}). c′ is less than c. (The situation on the receiving side is described by transposing c and c′, and c′ is greater than c).

The maximum inequality in electrical migration that can be balanced by diffusive transport is obtained when the solution concentration at the membrane interface is zero ($c' = 0$). From Eq. [1] the critical current density i_c at this condition is

$$i_c = \frac{DC\mathbf{F}}{(\bar{t}-t)\delta} \qquad [2]$$

At current densities higher than i_c additional current carriers are necessary. These are hydroxyl ions through anion-selective membranes and hydrogen ions through cation-selective membranes (5, 6). While this appears true for anion-selective membranes (7, 8) the amount of hydrogen ion transport through cation-selective membranes above the critical current density is much less than expected, and additional transport mechanisms have had to be invoked (7-11). This behavior with cation-selective membranes is not fully understood, but need not concern us further as the situation at the anion-selective membrane has proved to be of much greater importance in practical electrodialysis. A refinement is that the transport of hydroxyl ions through anion-selective membranes should commence not when the conditions are such that the interfacial concentration has fallen to zero but at a current density slightly lower than the critical value of Eq. [2] when the interfacial concentration is sufficiently small for the natural hydroxyl ion concentration of the donating solution to be competitive as an alternative migratory species (5, 6, 12).

In the vicinity of and above the critical current density the effects described give rise in practical electrodialysis units to (*i*) increased ohmic resistance due to layers of reduced concentration on the donating sides of membranes, (*ii*) increased counter concentration potentials across the membranes, (*iii*) reduced coulombic separation efficiencies, and (*iv*) transport of hydroxyl ions through the anion-selective membranes to make the receiving stream alkaline (12). Of these effects (*iv*) has the most serious repercussions (12, 13) as it results in the precipitation of hydroxides and carbonates of the alkaline earth metals which are present in most natural waters.

It is mandatory that electrodialysis units be operated below the critical current density. This is an important limitation since economically, current densities higher than the accepted critical values are desirable (13-16). Although suitable programming of electrodialysis operation (17) can reduce the economic effect of this limitation, the onset of hydroxyl ion transport through anion-selective membranes at the critical current density is probably the most serious restriction to electrodialysis at the present time (18).

All the effects (*i*)-(*iv*) above have been used to study polarization phenomena. Cooke (7, 8) and Cooke and van der Walt (19) have demonstrated the advantages of the concentration potential method whereby actual interfacial concentrations are deduced. The method is most useful at current densities less than the critical value. Unfortunately the theoretical basis is less convincing in the vicinity of the critical current density when the potential due to different interfacial electrolyte concentrations may be complicated by pH values which also differ on the two sides of the membrane. Voltage-current or voltage-time plots to indicate an increased ohmic resistance and an in-

Key words: Anion-selective membranes, concentration polarization, desalination, electrodialysis, limiting current density, multicompartment cells, organic poisoning.

creased counter concentration potential under critical conditions (9, 20-24) have the merit of simplicity. A small yet damaging transport of hydroxyl ions at current densities less than the main critical value could, however, be undetected by the voltage method. Cooke and van der Walt have mentioned this possibility (19), and in practical units such conditions could also arise from nonuniform flow distribution, inhomogeneous membranes (25), and nonuniform current distribution. Cooke (26) has improved the sensitivity of the method, without entirely removing the objections, by the use of overpotential which is obtained by subtracting an extrapolated estimate of the voltage of a hypothetical unpolarized condition from the voltage of the real polarized condition. The expected decrease in coulombic efficiency has been observed above the critical current density (5, 6, 27, 28) but is not sufficiently sensitive to be useful. The measurement of *p*H changes, (5, 6, 11, 21) particularly of alkalinity on the receiving side of the membrane utilizes the most serious effect of polarization and is, therefore, the most direct method. Cooke has criticized the *p*H method (7), but his arguments apply only to cation-selective membranes with their low hydrogen ion transport above the critical current density. The measurement of alkalinity on the receiving side of the membrane has been preferred in this work.

While systems stirred mechanically (11, 19) and by natural convection (5, 7, 8, 11, 21, 23, 26) have provided valuable insight into the polarization phenomena, the uncertainties in extrapolating to practical systems are too great for these results to be of real value to the designer. Flowing systems must be used (6, 9, 19, 20, 22, 24, 28) under hydrodynamic conditions which approximate as closely as possible to those present in practical units (24). Data from flowing systems of small exposed membrane area, *e.g.*, 0.64 cm^2 (19), where the entry and exit conditions to the compartment may have a disproportionate influence on the hydrodynamic conditions within the compartment, must be regarded with caution. Block (25) has demonstrated the heterogeneity of many commercial membranes, and Solt (29) and Cooke (26) have reported particular examples. It is, therefore, important that the scale of scrutiny should be appropriate. From the design viewpoint this is a further argument against the use of very small areas of membrane. For flowing systems it is also desirable to provide information on flow distribution so that one can ascertain that the noted effects are not seriously complicated by stagnant regions within the compartment. The value of F-diagrams (30, 31) in this respect does not appear to have been appreciated.

The present work formed part of a design study, and everything possible was done to ensure that conditions were similar to those that would be present in the actual stack. Compartment dimensions, compartment filling, linear flow rate, and exit and entry arrangements were identical. It was not practical in the laboratory to carry out very prolonged runs, and we compromised by following the *p*H of the receiving solution for 3 hr. Our important findings are consequent on the continuation of runs for this period. No information is given on the duration of runs in previous studies (6, 19, 20, 22, 24). Theoretically (Eq. [2]) and experimentally (11, 17) the critical current density is directly related to the donating-side concentration. Thus the polarization limitation is first apparent at the most dilute donating concentration in the unit, *i.e.*, the effluent concentration of the dialysate stream. This study was therefore carried out with a donating concentration equivalent to the planned concentration of the dialysate effluent.

Experimental

The membrane and flow arrangement is shown in Fig. 1. The anion-selective membrane whose polarization was under examination was at position 3. The

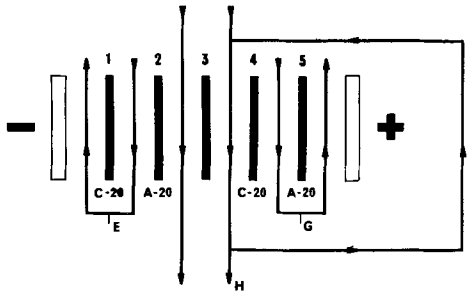

Fig. 1. Membrane and flow arrangement

donating and receiving solutions for this membrane flowed through compartments 2-3 and 3-4, respectively.

Membranes.—Two membranes were used in position 3, Permaplex A-20 (The Permutit Company Ltd.) and T.N.O. C-60 (Nederlandse Centrale Organisatie voor toegepast—Natuurwetenschappelijk Onderzoek). Permaplex A-20 and C-20 membranes were used in positions 1, 2, 4, and 5.

Permaplex A-20 is of the heterogeneous type and consists of a finely divided conventional anion exchange resin imbedded in an inert polyethylene binder with an inert reinforcing fabric of fine open mesh pressed against each face (32). The basic membrane has been described (5), and the influence of the reinforcing fabric is similar to that already noted for the cation-selective type (33).

The homogeneous membrane T.N.O. (34, 35) A-60 is based on a polyethylene film in which styrene and a few per cent of divinyl benzene have been polymerized. Quarternary ammonium groups are introduced on the aromatic nuclei by established procedures. In regard to the homogeneity, the comments of Block (25) and Cooke (26) are noteworthy.

Cell design.—Each compartment was bounded by two membranes (or a membrane and an electrode) and a Klingerit gasket 0.127 cm thick. The plan of the gasket for compartment 2-3 is shown in Fig. 2. The central square area is 27 x 27 cm. Rectangular holes A registered with similar holes in other components of the stack to form the supply conduits to the compartment. Similarly holes B formed part of the withdrawal conduits.

Flow between conduits and the compartment was via inserts C (36). The inserts were 0.127 cm thick, to correspond with gasket thickness, and were made from rigid epoxy resin. A series of small circular tunnels, 0.051 cm diameter, on the thickness center-line and spaced with centers 0.127 cm apart formed the connecting passages. Experience has shown that these inserts prevent intercompartmental solution leakage which is a serious problem in other stack designs (37).

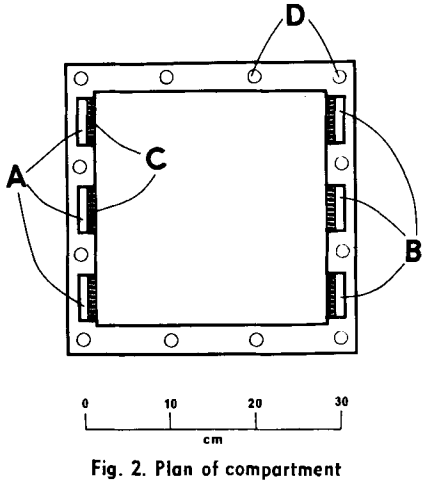

Fig. 2. Plan of compartment

The solution thus entered substantially all along one edge of the compartment and left by exits substantially all along the opposite edge (38). Such an arrangement encouraged uniform liquid distribution. Good distribution was further aided by a close fitting filling of a corrugated perforated sheet of polyvinyl chloride (39, 40) which was orientated so that flow resistance was greater in the forward than in the sideways direction (40), *i.e.*, with the corrugations normal to the direction of flow. This orientation promotes turbulent flow (24), thus reducing δ and increasing the critical current density (Eq. [2]). The polyvinyl chloride sheet was 0.025 cm thick and perforated with holes of diameter 0.23 cm to give an open area of 44.5%. The amplitude and wave length of the corrugations was 0.064 cm and 0.43 cm, respectively. A slightly higher pressure was maintained in the compartments on either side of compartment 2-3 so that the membranes conformed to the corrugated filling thereby ensuring a uniform 0.127 cm thickness throughout compartment 2-3.

The gasket for compartment 3-4 was similar except that solution now flowed between the other two edges, *i.e.*, at 90° to the flow in compartment 2-3. The filling was also turned through 90° to maintain the corrugations normal to the direction of flow. The remaining compartments were similar. Each end assembly consisted of an impregnated carbon electrode in a rigid polyvinyl chloride mounting, and a steel backing plate. The whole was held together by suitably insulated nuts and 1.27 cm diameter threaded rods, which passed through holes D.

To establish hydrodynamic suitability of the compartment design, additional experiments were made to obtain an F-diagram (30) and a log (pressure loss)-log (flow rate) plot (24).

Operating conditions.—The feed to compartment 2-3 was 0.01N NaCl. This compartment was bounded by two anion-selective membranes to avoid bulk concentration changes which complicate the interpretation of polarization data (6). The feed to compartments 1-2, 3-4, and 4-5 was 0.2*N* NaCl.

The flow rate in compartment 2-3 was 1500 cm^3 min^{-1} (7.3 cm sec^{-1}). The flow rate in compartment 3-4 was 1000 cm^3 min^{-1} and the feed-and-bleed rate 100 cm^3 min^{-1}.

The transport of hydroxyl ions to compartment 3-4 was measured by monitoring *p*H at position H. The *p*H was also monitored at positions E and G to ensure that the effects noted at H were not complicated by the *p*H changes which occurred in the electrode compartments. A series of current densities was used and at each the run duration was 3 hr. In this time 270 liters of solution passed through compartment 2-3. Unless stated otherwise hydroxyl ion transference numbers were calculated from measurements made at the finish of the 3-hr runs.

Room temperature was used for all runs. There are claims that critical current density is not very dependent on temperature (11, 41).

Power supply was single phase, 50 cycles sec^{-1} with full wave rectification unless otherwise noted.

Some experiments were also carried out in a smaller cell (exposed area 10 x 10 cm). General design principles, gasket thickness, and linear flow rates were identical with those used in the larger cell. There was no significant difference between the results obtained with the two cells.

Concentration of organic matter.—During the program it became necessary to assess the amount of organic matter in the solutions fed to the electrodialysis cell. The standard procedure of measuring the oxygen absorbed by the solutions from acid permanganate under precisely specified conditions was adopted. We used 4 hr at 27°C (42) which is one of several conditions that are standard practice. The results depend on the oxidation conditions chosen and the various procedures are, therefore, not directly comparable. The concentration of organic matter is obtained in terms of oxygen absorbed (O.A.) from permanganate and is expressed throughout this work as ppm O.A. Unpublished work at the Permutit Laboratories has shown that an approximate weight concentration for the organic matter present in these studies may be calculated by mutliplying ppm O.A. by three.

The chemical method is time consuming, and it was frequently more convenient to use an optical method (43) in which the optical density of a solution is compared with that of triply distilled water at a wavelength of 3000Å. Silica cells 10 cm in length were necessary for the required sensitivity. For the organic matter present in these studies, optical absorbency is related to chemically determined concentrations by the following equation

$$\frac{30 \times \text{optical density}}{\text{optical path length (cm)}} = \text{ppm O.A.}$$

Results and Discussion

Hydrodynamic considerations.—Consider liquid A flowing through a vessel and suppose at some instant a property of the liquid, *e.g.*, color, concentration, etc., is changed so that from this instant a second liquid, B, enters the vessel. A plot from this instant of the fraction of the new liquid B in the effluent against the ratio, effluent volume/vessel volume, is an F-diagram (30). Holdback, which may be determined from the F-diagram, is the fraction of liquid A that is in the vessel after a volume of liquid B equal to the volume of the vessel has entered the vessel (30). If perfect piston flow exists in the vessel, holdback is zero. If flow is confined to a narrow channel with a large proportion of the liquid in the vessel stagnant, then holdback approaches unity. Holdback for our compartment design was 0.05. With Newtonian fluids perfect piston flow is not possible due to the viscous drag of the walls of the vessel and in our case also of the compartment filling. A value of 0.05 for the holdback indicates very good flow distribution and a close approach to perfect piston flow.

The change in the log (pressure loss) *vs.* log (flow rate) plot from unit slope to a higher value occurred at a linear flow rate of 2.2 cm sec^{-1}. (Linear flow rates are not corrected for compartment filling.) This is in general agreement with Wilson's reported slope change at 4.4 cm sec^{-1} with a similar filling and identical filling orientation (24). His compartment was thinner so the higher figure is to be expected. In compartment 3-4 the flow rate was 7.3 cm sec^{-1}, which is above the point of slope change, and we conclude that the flow in our work was of turbulent type. Seko (44) has deduced from the value of the slope that flow is of turbulent type in Asahi's design of compartment in the same region of linear flow rates. [Although Seko (44) cites 1.51 for the slope, the plot given has a value of only 1.26.]

Polarization experiments.—Permaplex A-20 was studied first. Initial results were puzzling in that the amount of alkali found in the receiving stream under apparently identical conditions was quite irreproducible. Further, although a steady state should be attained fairly quickly the *p*H of the receiving stream in polarizing runs, *i.e.*, those in which there was hydroxyl ion transference, drifted upward and had not reached a steady value after 3 hr or even, when runs were extended, after 6 hr.

Our first constructive results were obtained from a cyclic series of runs in which current density was increased and then decreased in successive steps. Hydroxyl ion transport, shown in Fig. 3, exhibited hysteresis. The hydroxyl ion transference number when current density was decreasing was much higher than had previously been obtained when current density was increased.

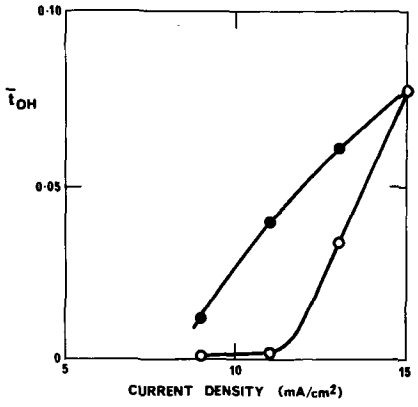

Fig. 3. Hydroxyl ion transference number vs. current density, Permaplex A-20. ○ after increase in current density, ● after decrease in current density.

These results might be explained by an accumulation of hydroxyl ions within the membrane. Thus during the run at 15 ma cm^{-2} hydroxyl ions accumulated, and the subsequent gradual release of these from the membrane when current density was decreased caused the hydroxyl ion transference number to be higher than the values obtained on the increasing part of the cycle. To check this suggestion the effect of prior conversion of the membrane to the hydroxyl form by immersion in alkali was investigated. Figure 4 shows that hydroxyl ions initially present were cleared from the membrane in 90 min at 4 ma cm^{-2} and in 60 min at 7 ma cm^{-2}. Thus at the higher current densities used in the cyclic series, 9-15 ma cm^{-2}, one would expect any hydroxyl ion content present at the start of a run to be cleared from the system after about 40 min. Certainly no effect on measurements taken after 3 hr would be expected. Further evidence against this suggestion was obtained by suddenly dropping the current density to 5 ma cm^2 during a run on the decreasing part of the cycle whereupon the hydroxyl ion transference number fell to zero.

For the work described so far demineralized water was used to prepare the sodium chloride solutions. The anion-exchange resin in the unit was weakly basic and of a type which removed very little of the organic matter in the supply water (Metropolitan Water Board, London). During the investigation the organic content of the M.W.B. supply water varied between 0.7 and 1.5 ppm O.A., and most of this passed into the electrodialysis cell. The affinity of the organic matter in supply waters for strongly basic anion-exchange resins and the accompanying fouling problems are well known (45, 46). The functional groups in Permaplex A-20 and in most anion-selective membranes are strongly basic. Accumulation of organic matter by the membrane would thus be expected and might result in a gradually increasing polarization tendency. Hysteresis could be explained in these terms.

For the next stage of the work the sodium chloride solutions were prepared with M.W.B. water that had been demineralized by mixed bed ion exchange with a strongly basic anion-exchange resin. The solutions were further treated by passage through trap columns (4 in. diameter x 18 in.) of De-Acidite FF (The Permutit Company Ltd.) in the chloride form immediately before entering the electrodialysis cell. By this means the organic matter in the solutions fed to the cell was reduced more than tenfold to 0.06 ppm O.A. With these conditions the upward drift of pH with time was rectified except in the sensitive region between pH 6 and 8 (Fig. 5). pH was constant for at least the final hour. Figure 6 shows that hysteresis had also disappeared. This demonstrates that our earlier difficulties were the result of organic matter in the influent solution accumulating on the anion-selective membrane. The only previous workers to report a reversibility or hysteresis examination are Cowan and Brown (20) and they noted irreversibility. Since they used a flowing system and treated municipal water to prepare their solutions it is possible that organic matter may have been the responsible factor in this case also.

Figure 6 clearly shows there is no sharp onset of hydroxyl ion transport with either of the membranes examined but a gradually accelerating increase in transference number. Similarly Cooke and van der Walt (19) found no sharp change in interfacial concentration at a particular current density in flowing systems although this was observed under naturally convective conditions (7, 8). The compartment filling presumably causes local variations in linear flow rate, film thickness δ and current density which could blur the effects of criticality. However Cooke and van der Walt (19) have indicated there was no sharp change in interfacial concentration even in the absence of compartment filling. Poor flow distribution on a macroscopic scale could account for the interfacial concentration results (19), but is unlikely in the present

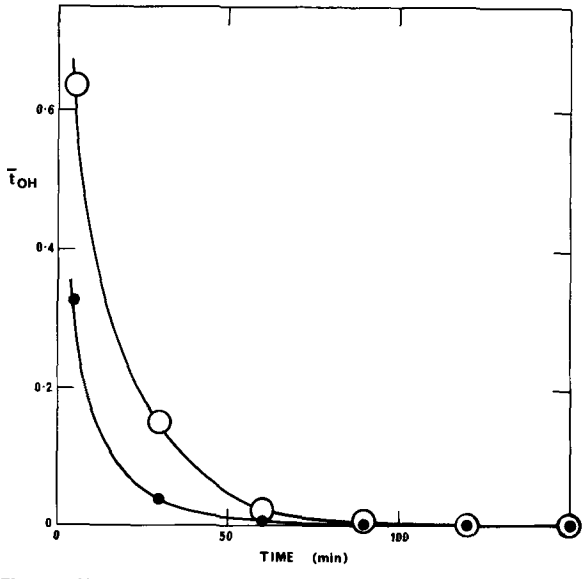

Fig. 4. Hydroxyl ion transference number vs. time, Permaplex A-20 initially in hydroxyl form. ○ current density 4 ma/cm^2; ● current density 7 ma/cm^2.

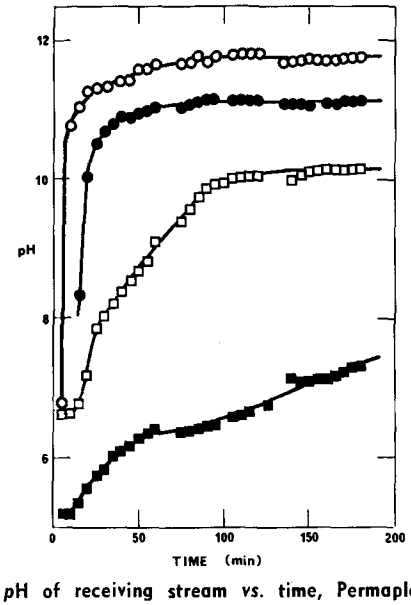

Fig. 5. pH of receiving stream vs. time, Permaplex A-20, organic matter 0.06 ppm O.A. ○ current density 12 ma/cm^2; ● current density 10 ma/cm^2; □ current density 8 ma/cm^2; ■ current density 5 ma/cm^2.

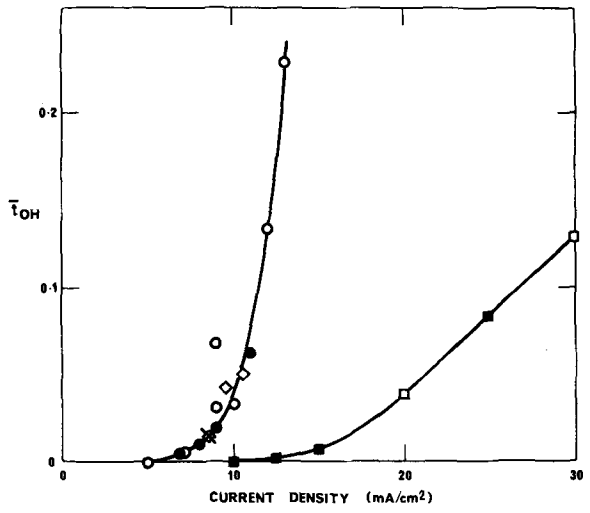

Fig. 6. Hydroxyl ion transference number vs. current density, organic matter 0.06 ppm O.A. ○ Permaplex A-20, after increase in current density; ● Permaplex A-20, after decrease in current density; × Permaplex A-20, three-phase supply; ◇ Permaplex A-20, battery supply; □ T.N.O. A-60, after increase in current density; ■ T.N.O. A-60, after decrease in current density.

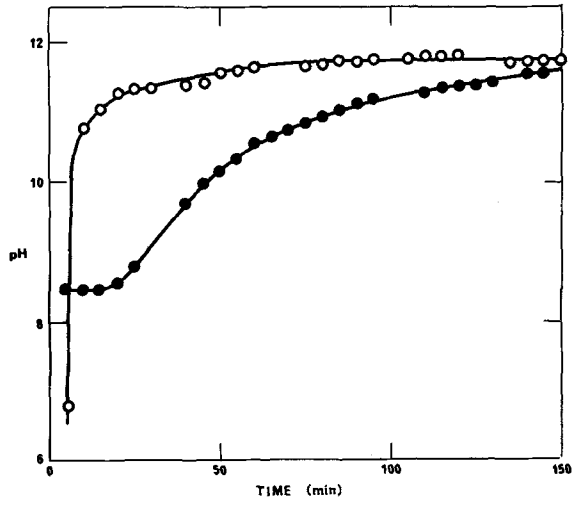

Fig. 7. pH of receiving stream vs. time, Permaplex A-20, organic matter 0.06 ppm O.A. ○ used membrane, 12 ma/cm²; ● new membrane, 45 ma/cm².

work in view of the holdback of only 0.05. Cooke (26) favors an explanation in terms of a variation in δ on the membrane surface. A much smaller variation in δ would be expected in a naturally convective system (26), and hence the criticality observed in this case (7, 8) is explained. Absence of sharp changes could also be explained by nonuniform current distribution due to membrane heterogeneity on a macroscopic (25, 26, 29) or microscopic scale. The latter could result from partial poisoning of the membrane. The absence of sharp changes in flowing systems emphasizes the dangers of using methods dependent on such effects. The rapidity of change is unimportant in the pH method, and in principle the amount of acid required to maintain any desired pH in the receiving stream is directly calculable from data such as is shown in Fig. 6.

Mention has been made in the literature of effects due to periodic changes in current (47, 48). It seemed desirable to ascertain whether the periodicity of current that results from full wave rectification of single phase a.c. was affecting our data. A few experiments were therefore carried out with full wave rectification of three phase a.c., where the amplitude of the ripple is much less, and with a battery source. Figure 6 indicates that there was no significant difference in the hydroxyl ion transference number with the three types of power supply.

Although the T.N.O. A-60 membrane used for the data in Fig. 6 was new, the Permaplex A-20 membrane had previously been in contact for three runs with solutions which had not been subjected to precautions to reduce organic matter. Further runs were therefore made with a series of new Permaplex A-20 membranes using solutions in which the organic matter had been reduced to 0.06 ppm O.A. The surprising result was that under these conditions the critical region was much higher at 35-40 ma/cm². Furthermore the phenomenon of an upward pH drift reappeared and steady values were not obtained within the period of the runs. The difference between the two conditions is illustrated in Fig. 7. For the first 150 min of operation, at least, hydroxyl ion transport through a new membrane at 45 ma/cm² was less than that through the used membrane at 12 ma/cm². A steady pH was reached with the used membrane after 80 min, but such was not achieved after 150 min with the new membrane.

The following points have now emerged. The critical current density region of new unpoisoned Permaplex A-20 membrane under our specified flow conditions is much higher than might be suspected from the literature. The critical region is, however, very sensitive to the condition of the membrane in that even an influent with as little organic matter as 0.06 ppm O.A. caused steady deterioration during the short time of a run. Further a few hours running with an influent containing 0.7-1.5 ppm O.A. which is by no means an excessive level, *i.e.*, the condition of the used membrane, reduces the critical current density approximately fourfold. The apparently steady, reproducible and reversible conditions obtaining for the data on Permaplex A-20 in Fig. 6 must have occurred because the amount of organic matter accumulated by the membrane during the runs was small relative to the amount already on the membrane at the start of this series.

Further work served to confirm the above interpretation. Runs were carried out in which current density was varied so as to maintain a constant concentration of alkali in the receiving stream. A new membrane was used for each run. Figure 8 shows that a much faster reduction of current density was necessary when the organic matter in the influent solution was 0.7-1.5 ppm O.A. than when it was 0.06 ppm O.A. However, even with an influent containing only 0.06 ppm O.A. of organic matter a fairly rapid reduction in current density was necessary. Obviously it was de-

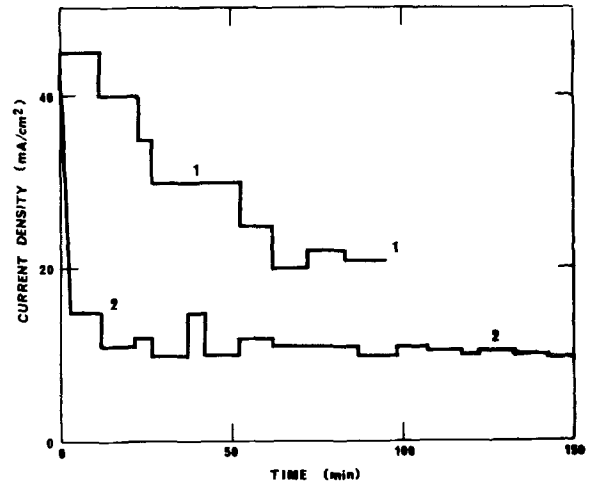

Fig. 8. Current density vs. time, receiving stream alkalinity 0.0027*N*, new Permaplex A-20. 1, organic matter 0.06 ppm O.A.; 2, organic matter 0.7-1.5 ppm O.A.

sirable to show that no reduction in current density was required when organic matter was completely absent from the influent solutions. In spite of considerable effort we were unable to produce solutions of this purity on the scale required. By the use of activated carbon (Chlorosorb, British Carbo Norit Union) columns (4 in. diameter x 18 in.) after the DeAcidite FF trap columns the influent organic matter was halved to 0.03 ppm O.A. (49), but pH drift indicating membrane poisoning still occurred with this solution.

In another series the effect of deliberately poisoning a Permaplex A-20 membrane for various times was studied. Poisoning was carried out at 5 ma cm^{-2} by passage of a 0.01*N* solution containing 0.85 ppm O.A. Reasonably reproducible results were obtained only if the poisoning was followed by a 6-hr conditioning run carried out at 5 ma cm^{-2} with the 0.06 ppm O.A. influent solutions, before proceeding to the standard pH runs. Even then the results after the longest poisoning of 16 hr were very scattered. For this work the normal compartment filling was omitted, and the membrane was supported by rigid plastic strips (2 mm wide) spaced parallel to the direction of flow and with centers 1.0 cm apart. The results shown in Fig. 9 clearly demonstrate the extreme sensitivity of Permaplex A-20 to poisoning by organic matter. After six or more hours poisoning it appears from Fig. 9 that there is substantial hydroxyl ion transport at any current density. This behavior is similar to that shown by bipolar membranes (50) and could result from acidic groups of the organic matter that are free, *i.e.*, in excess of those participating in bonds with the membrane, causing the surface to become cation selective. Cooke (26) has made similar comments.

The T.N.O. A-60 membrane was unaffected by 20-hr poisoning runs. While this cannot be extrapolated to long-term performance it does represent a remarkable difference from the sensitivity of Permaplex A-20. Other differences which may be related to the same prime cause are the ready attainment of steady-state conditions with new T.N.O. A-60 membranes and a lower critical current density region. The structure of the two membranes is of course quite different. Cooke and van der Walt (15) have provided evidence that with Permaplex A-20 the diffusion layer is not entirely irradicable by stirring as it is with a homogeneous A.M.F. membrane. This may be due to the Permaplex A-20 being of the heterogeneous type (19) or to its fabric reinforcement (32). A few runs with a new homogeneous A.M.F. membrane showed that this also was different to the T.N.O. A-60 membrane. The A.M.F. membrane showed a critical current density region as high as 45-50 ma cm^{-2} and the same upward drift of pH with influent solution containing 0.06 ppm O.A., indicating sensitivity to organic poisoning. We, therefore, think that the lower critical current density region and the short term insensitivity to poisoning of T.N.O. A-60 are not due to its homogeneous structure,

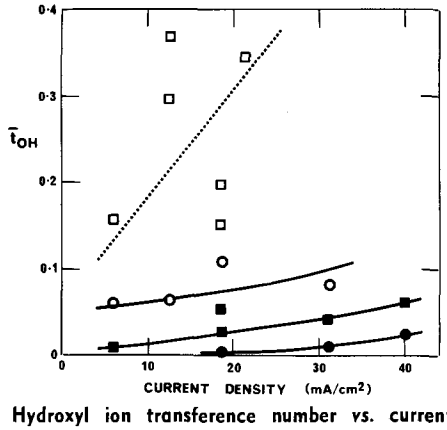

Fig. 9. Hydroxyl ion transference number *vs.* current density, Permaplex A-20. ● after poisoning for 0 hr; ■ after poisoning for 2 hr; ○ after poisoning for 6 hr; □ after poisoning for 16 hr.

but rather that it was partially poisoned at the outset of the work. Obviously this is only supposition, and the nature of the poison is unknown although it may be remarked that the membrane was stored with a T.N.O. C-60 membrane from which a little polystyrene sulfonate may have been leached. Cooke (26) has shown that polystyrene sulfonate poisons anion-selective membranes. Although the present paper has dealt only with poisons introduced with the water it is clear there must be absolutely no tendency for the cation-selective membrane to shed soluble polymeric anions which would poison anion-selective membranes. Wegelin (51) noted that homogeneous membranes were less resistant than heterogeneous membranes to the effects of poisoning by a polluted water from the Rhine.

General comment on organic poisoning.—Information on the deleterious effects on strongly basic anion-exchange resins of organic matter, tenaciously absorbed from water, accumulated during the 1950's (45, 46, 52-54). Similar problems would be expected with anion-selective membranes which in the main have similar structure and functional groups. One might anticipate even greater difficulties as there is no frequent regeneration procedure and the additional force of electrical potential is present to drive the organic matter into the membrane. It is thus surprising that prior to about 1962 there is hardly a mention of undesirable effects due to organic matter. Analyses of waters to be treated do not contain figures for organic matter. Resistance to organic fouling is not a specified membrane requirement. Even in major works there is no discussion related to organic matter in water sources. Since 1962 there has been a gradual awakening (12, 13, 18, 37, 44, 55, 56) although comments are mostly limited to unsupported statements. Even in 1963 Wilson (24), studying polarization to explain the failure of the Free State Geduld plant to meet design predictions, did not appear to give any consideration to organic poisoning of the membranes. Few authors (26, 29, 51) have provided positive information on organic poisoning.

Although the precise nature of organic matter in water varies with location and season, much is known in general terms (57). It is sufficient for the present purpose to note only that these materials, collectively termed humic and fulvic acids, have acidic groups of pK value about 4 (46, 58) and a range of molecular weights which includes a fraction capable of penetrating, albeit slowly, the interior of ion-exchange materials (26, 45, 46). There is no sparsity of acid groups in the molecules. Unpublished work at the Permutit laboratories indicates equivalent weights of around 100. Van der Waals' forces between the organic acids and the organic framework of the ion-exchanger (46) probably contributes to the tenacious binding, and in this respect the performance of the new inorganic membranes (59, 60) would be interesting.

Organic acids adsorbed on an ion-selective membrane can effect the critical current density region in three ways. First, as already mentioned, they can provide a surface of acid groups which is cation selective and results in a membrane of bipolar character (50). Second, the adsorption of a species of zero or low mobility on the most accessible membrane sites must result in the counterions having to reach less accessible sites before being subjected to the selective influence of the membrane. This is equivalent to an increase in δ in Eq. [2]. Finally the heterogeneous distribution of low mobility species in the membrane will divert current to paths where such species are relatively few, thus causing nonuniform current distribution on a microscopic scale.

The results obtained with new Permaplex A-20 membranes and indicated with homogeneous A.M.F. membranes show that, with properly designed compartments and suitable hydrodynamic conditions, i_c/c

values of about 4000 amp cm equiv^{-1} may be achieved. This value corresponds to a value of δ of 0.0008 cm which seems reasonable. Previous workers have reported much lower critical i_c/c values. For example at our linear flow rate, Cowan's formula for filled compartments (41) yields a figure of 340 amp cm equiv^{-1}, and Mandersloot and Hicks (61) obtained about 400 amp cm equiv^{-1}. One is tempted to suspect the influence of organic poisoning. Seko (44) on the other hand found no critical polarization up to 1000 amp cm equiv^{-1} which was the highest value he studied. A critical value of 4000 amp cm equiv^{-1} leaves ample scope for the choice of an economically optimum current density. We conclude, therefore, that the main limitation to electrodialysis is not polarization *per se* but poisoning of the anion-selective membrane which reduces the critical current density region to an economically unattractive level.

Conclusion

The measurement of pH changes at the anion-selective membrane is advocated for determination of critical current density regions.

Organic acids in the feed water, even in very small concentrations, drastically reduce critical current density.

For unpoisoned membranes the critical i_c/c values are much higher than has previously been appreciated and leave scope for an economic choice of current density.

The main limitation on electrodialysis is not polarization *per se* but poisoning of the anion-selective membranes.

Acknowledgments

The authors thank, S. K. Ahsanuddin for his persistent and careful experimental work, the Directors of The Permutit Company Ltd. for permission to publish, and one of them (FLT) thanks the Directors of The Ever Ready Company (Great Britain) Ltd., for permission to present the paper at the Boston Meeting of The Electrochemical Society.

Manuscript submitted May 31, 1968; revised manuscript received *ca.* Sept. 10, 1968. This paper was presented at the Boston Meeting, May 5-9, 1968, as Paper 236.

Any discussion of this paper will appear in a Discussion Section to be published in the December 1969 JOURNAL.

REFERENCES

1. K. H. Meyer and W. Straus, *Helv. Chim. Acta*, **23**, 795 (1940).
2. T. R. E. Kressman and F. L. Tye, *Trans. Faraday Soc.*, **55**, 1441 (1959).
3. L. L. Bircumshaw and A. C. Riddiford, *Quart. Rev.*, **6**, 157 (1952).
4. V. G. Levich, "Physicochemical Hydrodynamics," Prentice Hall Inc., Englewood Cliff, N. J. (1962).
5. T. R. E. Kressman and F. L. Tye, *Discussions Faraday Soc.*, **21**, 185 (1956).
6. N. W. Rosenberg and C. E. Tirrell, *Ind. Eng. Chem.*, **49**, 780 (1957).
7. B. A. Cooke, *Electrochim. Acta.*, **3**, 307 (1961).
8. B. A. Cooke, *ibid.*, **4**, 179 (1961).
9. A. M. Peers, *Discussions Faraday Soc.*, **21**, 124 (1956).
10. V. J. Frillette, *J. Phys. Chem.*, **61**, 168 (1957).
11. T. Uchino, S. Nakaoka, H. Hani, and T. Yawataya, *J. Electrochem. Soc. Japan* (Overseas Ed.,), **26**, E129 (1958).
12. L. H. Shaffer and M. S. Mintz in "Principles of Desalination," p. 232, K. S. Spiegler, Editor, Academic Press, London (1966).
13. W. K. W. Chen in "Encyclopedia of Chemical Technology," Kirk-Othmer, 2nd ed., Vol. 7, p. 846, John Wiley & Sons Inc., London (1965).
14. T. A. Kirkham, *Chem. Eng.*, **63**, 185 (1956).
15. D. A. Cowan, Advances in Chemistry, Series No. 27, 224 (1960).
16. R. E. Lacey, E. W. Lang, and E. L. Huffman, Advances in Chemistry, Series No. 38, 168 (1963).
17. F. L. Tye, *Trans. Instn. Chem. Engrs.*, **41**, 72 (1963).
18. W. M. T. Boby and G. S. Solt, *Dechema Monographien*, **47**, 569 (1962).
19. B. A. Cooke and S. J. van der Walt, *Electrochim. Acta*, **5**, 216 (1961).
20. D. A. Cowan and J. H. Brown, *Ind. Eng. Chem.*, **51**, 1445 (1959).
21. M. Block and J. A. Kitchener, *This Journal*, **113**, 947 (1966).
22. "Demineralisation of Electrodialysis," J. R. Wilson, Editor, p. 15, Butterworths, London (1960).
23. K. S. Spiegler, Advances in Chemistry, Series No. 38, 179 (1963).
24. J. R. Wilson, *Trans. Inst. Chem. Engrs.*, **41**, 3 (1963).
25. M. Block, *Chem. and Ind.*, 2099 (1967).
26. B. A. Cooke, First International Symposium on Water Desalination, U.S. Dept. of the Interior, **2**, 219 (1965).
27. A. G. Koblyanskii and A. O. Ulitin, *Russ. J. Appl. Chem.*, **34**, 2553 (1961).
28. S. M. Partridge and A. M. Peers, *J. Appl. Chem.*, **8**, 49 (1958).
29. G. S. Solt, First International Symposium on Water Desalination, U.S. Dept. of the Interior, **2**, 13 (1965).
30. P. V. Danckwerts, *Chem. Eng. Sci.*, **2**, 1 (1953).
31. D. J. Lewis and F. L. Tye, *J. Appl. Chem.*, **9**, 279 (1959).
32. F. L. Tye, British Pat. 823,077.
33. J. W. Jarvis and F. L. Tye, *J. Chem. Soc.*, **1961** 4483.
34. J. F. A. Hazenberg and B. P. Knol, South African Pat. 1754/58.
35. J. F. A. Hazenberg, *Dechema Monographien*, **47**, 487 (1962).
36. J. B. Davis, British Pat. 887,732.
37. O. B. Volckman, Advances in Chemistry, Series No. 38, 133, (1963).
38. T. R. E. Kressman, F. L. Tye, and G. S. Solt, British Pat. 845,186.
39. C. van Hoek, U.S. Pat. 2,735,812.
40. Ref. (22), p. 240.
41. D. A. Cowan, *Dechema Monographien*, **47**, 559 (1962).
42. "The Examination of Waters and Water Supplies," (Thresh, Beale and Suckling), revised by E.W. Taylor, 7th ed., p. 222, J. and A. Churchill, London (1958).
43. A. L. Wilson, *J. Appl. Chem.*, **9**, 501 (1959).
44. M. Seko, *Dechema Monographien*, **47**, 575 (1962).
45. A. L. Wilson, *J. Appl. Chem.*, **9**, 352 (1959).
46. N. W. Frisch and R. Kunin, *J. Am. Water Works Assoc.*, **52**, 875 (1960).
47. G. W. Jernstedt, *Metal Finish, (N. Y.)*, **45**, 68 (1947).
48. C. Forgacs and R. Matz, *Dechema Monographien*, **47**, 601 (1962).
49. F. L. Tye, British Pat. 914,511.
50. V. J. Frilette, *J. Phys. Chem.*, **60**, 435 (1956).
51. E. Wegelin, Proc. Symposium "The Less Common Means of Separation," The Institution of Chemical Engineers, p. 43 (1963).
52. P. F. J. Bogers, *Water (Holland)*, **38**, 299 (1954).
53. R. V. Skold and J. F. Wilkes, *Ind. Eng. Chem.*, **47**, 90 (1955).
54. N. W. Frisch and R. Kunin, *ibid.*, **49**, 1365 (1957).
55. W. G. B. Mandersloot, First International Symposium on Water Desalination, U.S. Dept. of the Interior, **2**, 461 (1965).
56. J. W. Minken, Int. Atomic En. Tech. Rept. No. 51, AEC Accession No. 31/94 (1966).
57. R. F. Packham, *J. Soc. Water Treatment Examination*, **13**, 316 (1964).
58. T. R. E. Kressman, *ibid.*, **13**, 332 (1964).
59. J. I. Bregman and R. S. Braman, *J. Coll. Sci.*, **20**, 913 (1965).
60. K. S. Rajan, D. B. Boies, A. J. Casolo, and J. I. Bregman, *Desalination*, **1**, 231 (1966).
61. W. G. B. Mandersloot and R. E. Hicks, I and EC Process Design and Development, **4**, 304 (1965).

The Standard Potential of Glucose Oxidase

F. R. Duke,[1]* R. N. Kust,[2] and L. A. King[3]

Departments of Chemistry, Texas A&M University, College Station, Texas, and Purdue University, Lafayette, Indiana

ABSTRACT

Glucose oxidase was titrated with Cr(II) and with Ti(III) over a pH range from 5.0 to 6.0, and a temperature range of 25° to 40°C. The two inorganic reagents were used, rather than just one, to ensure that there was no specific interaction between the enzyme and the reagent. Simultaneously, it was shown that the stoichiometry of the enzyme-inorganic reductant reaction was identical to that of the enzyme-glucose reaction and that the reduction products were identical in each case. Thus, it is shown that the potentials found are truly those which apply in the enzymatic oxidation of glucose. Glucose could not be used as reductant in the potentiometric studies because neither the enzyme nor the glucose reacts at the electrode. The values of E_o' (median reduction potential at pH 7) are —0.061v at 40°C, —0.028v at 30°C, and —0.008v at 25°C.

Glucose oxidase (EC 1. 1.3.4) from Aspergillus niger catalyzes the reaction: β-D-glucose + $O_2 \xrightarrow{E}$ gluconolactone + H_2O_2. The enzyme contains, as prosthetic groups, two molecules of flavin adenine dinucleotide (FAD) per mole of protein (1). Past potentiometric studies of the enzyme result in rather gross disagreement (2, 3), which needs to be resolved. Furthermore, it is of fundamental importance to determine the degree of cooperation between the flavin molecules. For example, if the two FAD moieties are closely associated in the reduction, a four-electron step might be expected for complete reduction; on the other hand, if the flavins occupy remote and nearly identical positions in the enzyme molecule, a single two-electron step might be expected. If they occupy remote but differing functions in the protein, two two-electron steps might occur. Finally, semiquinoid intermediates could show up in coupled or uncoupled one-electron reductions.

A group of flavins including FAD have been subjected to careful potentiometric study (4); in addition, the flavin-containing "old yellow" enzyme was the subject of a study by Vestling (5). Lowe and Clark found that at high acidities there was appreciable formation of semiquinoid material when FAD was reduced. Studies by Beinert and Sands (6) and by Mason *et al.* (7) indicate no semiquinoid intermediates are formed in the mechanics of glucose oxidase action. Gibson *et al.* (8) reached the same conclusion in an extensive mechanistic study.

The glucose-gluconolactone system and the enzyme system do not react at electrodes. To surmount this difficulty, Vestling used a potential mediator which equilibrated with old yellow enzyme and also with the electrode. In the present study, the inorganic reductants, Cr(II) and Ti(III), were the reductants chosen because they indicate readily and reversibly at platinum electrodes, and, although they were indicating at considerable potential difference from their standard potentials, the high impedance detector used still allowed for reversible measurements. It remained to show that the reaction with the inorganic reductants produced the identical reduction product of the enzyme with the same stoichiometry as did glucose.

Experimental

The glucose oxidase was obtained from Nutritional Biochemicals Corporation, pure grade. The buffers used were cp sodium acetate-acetic acid mxitures and cp cacodylic acid and its sodium salt.

The titanium (III) and chromium (II) solutions were prepared by reduction of Ti(IV) and Cr(III) using a Jones reductor in a chloride solution; electrolytic reduction of Ti(IV) was also employed to avoid the presence of Zn^{++} in the solutions. No difference was found between the solutions containing Zn^{++} and those not containing it. The glucose was reagent grade.

Potentiometry.—A cell consisting of a 25 ml glass vessel with a sealed-in platinum electrode, a microcalomel electrode, and a small opening covered with a serum cap, was placed in a small black box. Deaerated enzyme solution, 1 mg/ml, was added by means of a Roger Gilmont Teflon syringe. The electrode vessel was continuously purged with argon which had been passed over tantalum chips heated to 800°C to remove oxygen. The reducing agent in solution was added through the serum cap using a Vernier type Roger Gilmont Teflon syringe calibrated to the nearest microliter.

The potential between the electrodes was measured on an L & N K3 potentiometer; a Kiethley 603 electrometer was used in place of a galvanometer as a null instrument. After each addition, the potential change with time was registered on a Rustrak recorder attached to the electrometer. When a reading had come to a steady state (about 5-10 min), the potentiometer was adjusted to null the electrometer, and the potential was read from the potentiometer.

Stoichiometry.—The desired amount of enzyme was weighed and transferred to a centrifuge tube equipped with a rubber serum cap. The tube was thoroughly flushed with argon, then filled to the desired amount with buffer solution. After the enzyme dissolved, the solution was centrifuged, and a known volume (about 11 ml) of the clear liquid was transferred to an argon-flushed Beckman 40 mm pathlength spectrophotometer cell. The cell had a glass top sealed on with Apiezon W wax. The top had two holes in it which were closed with serum caps. All transfers of solutions were done with hypodermic syringes and considerable care was exercised to exclude oxygen. The solutions contained typically 2 mg enzyme per ml.

The absorption of light at 450 mμ was followed by a Beckman Model DB spectrophotometer for some of the experiments. In these cases, oxidized enzyme was used on both sample and reference sides of the instrument. Glucose was added, using a Roger Gilmont 0.2 ml micrometer syringe, to the reference side, resulting in an apparent decrease in transmittance as seen by the instrument. A Beckman Model DU spectrophotometer was used for the remaining experiments, with ordinary demineralized water as a reference. These experiments were conducted conventionally with the glucose added to the sample cell. A small Teflon covered stirring bar was inside the cell to mix the reagents after each addition.

* Electrochemical Society Active Member.
[1] Present address: Department of Chemistry, University of Iowa, Iowa City, Iowa.
[2] Present address: Department of Chemistry, University of Utah, Salt Lake City, Utah.
[3] Present address: Department of Chemistry, Air Force Academy, Colorado.

Kinetic experiments.—All solutions were prepared in vigorously deoxygenated water or 0.05M acetate buffer solutions, pH 5.5. The enzyme concentration was about 2 mg/ml, and in distilled water solution, the resulting pH was about 4.5. All solutions were kept in volumetric flasks stoppered with rubber serum caps. At no time in their use were the solutions exposed to air. Methylene blue concentration was 10^{-3} M.

The enzyme was reduced stoichiometrically with each reductant. In turn, the methylene blue was added with the micrometer syringe and the rate of appearance of the 450 mμ band was measured with the Beckman DB.

Results and Discussion

Stoichiometry.—The molar absorbency index for glucose oxidase has been determined to be 28.2 x 10^3 cm^{-1} (7). Using this value, the stoichiometry of the glucose-enzyme reaction ranged between 1.9 and 2.1 β-glucose molecules oxidized per mole of enzyme. A plot of moles of β-glucose *vs.* moles of enzyme reacted yielded a straight line, showing that the stoichiometry is constant throughout the titration. The stoichiometry of the reaction with Cr(II) and Ti(III) was found, by potentiometry, to correspond to the addition of two hydrogen atoms to each flavin. As it turns out, the potential of the flavin in the enzyme is sufficiently far removed from that of FAD that the break in the potential measured only the enzyme, even though there might be some free FAD present.

To show that the reduction products of the enzyme were indifferent to the nature of the reducing agent, the rate of reoxidation of the stoichiometrically reduced enzyme was studied using methylene blue as oxidant, and using the inorganic reagents and glucose as reductants. The kinetic results were not analyzed in detail, but plots of rate of appearance of the 450 mμ peak of the enzyme *vs.* time under carefully controlled conditions with respect to concentrations and starting time yielded plots which were coincident irrespective of the nature of the reducing agent. Thus, it was concluded that the inorganic reagents yielded a reduced enzyme identical to that formed using glucose.

Potentiometry.—Reproducible potentials were not obtained even in diffuse fluorescent light. After some time of futile experimentation, it was found that placing the cell in a black light-proof box yielded reproducible results. The photoexcitation of flavins has been noted previously, and the added energy is reflected in the potential observed (9).

Only one break in the titration curves was found. A typical titration curve is shown in Fig. 1. This break corresponded to a two-electron reduction of the enzyme. The precision was such that there could have been a small percentage of semiquinoid material present. In general, however, the flavins in the enzyme acted like independent identical molecules. This does not mean that a cooperative or coupled effect may not be involved as the enzyme reacts with glucose. It does suggest, however, that the two FAD molecules occupy remote and identical, as far as the potentiometric titration is concerned, sites in the protein.

The E_o (median potential at pH 7) for the enzyme is calculated from the data using the Nernst expression

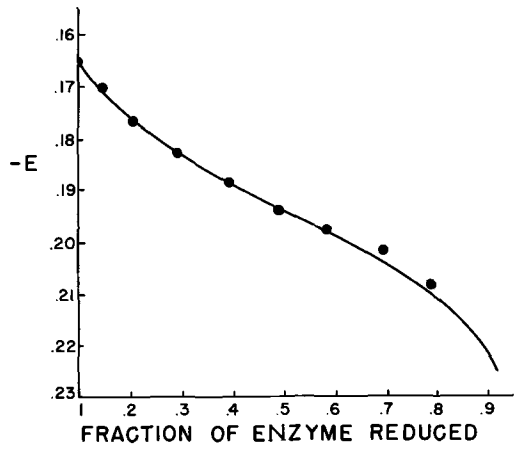

Fig. 1. Titration curve of glucose oxidase using $CrCl_2$ as titrant at 25°C. This curve is typical of all titrations resulting in the values in Table I.

and shown in Table I. The enzyme is a considerably more energetic oxidant than is FAD (E_o' = — 0.219v).

The results of Yamano *et al.* (2) who found E_o' = + 0.08v, may be in error because they simultaneously measured the potential and the absorbance at 450 mμ. It is known that light may affect the potential observed (9). The high reduction potential found is probably a reflection of photoexcitation.

On the other hand, Walter (3) kept light from the sample being titrated; he used leucosafranin which had been reduced by dithionite as titrant and methylene blue was the potential mediator. It is possible that one of the dyes or some of the reduction products of dithionite preferentially combine with the oxidized form of the enzyme as found by Swoboda and Massey (10), to lower the potential to the value of —0.144 v for E_o'. An alternate explanation is that titanium and chromium complexes of the reduced enzyme are formed which raise the standard reduction potential in the work here presented. However, it would be highly coincidental for these two metal ions to combine with the reduced form of the enzyme to the same extent. At any rate, our values fall close to half way between those previously reported.

Acknowledgments

This work was supported in part by a grant from the Robert A. Welch Foundation and in part by a grant from the U.S. Public Health Service (AM 07986).

Manuscript submitted July 3, 1968; revised manuscript received *ca.* Aug. 27, 1968.

Any discussion of this paper will appear in a Discussion Section to be published in the December 1969 JOURNAL.

REFERENCES

1. D. Keilin and E. F. Hartree, *Biochem. J.*, **42**, 221 (1948).
2. T. Yamano, Y. Miyake, and K. Aki, *Tokashima J. Exptl. Med.*, **7**, 169 (1960).
3. M. J. Walter, *Biochem. Biophys. Acta*, **128**, 504 (1966).

Table I. Reduction potentials of glucose oxidase

Red. agent	Ox. agent	pH	Buffer	Temp, °C	E°_{pH} (SCE)	$E_{1/2}$ (SCE)*	E°_{pH} (NHE)	E_o' (pH7)
Cr^{+2}	gluc. ox.	5.5	cacodylic A.	40	−0.2050	0.2366	+0.0316	−0.061
Cr^{+2}	gluc. ox.	5.5	cacodylic A.	30	−0.1760	0.2415	0.0655	−0.026
Cr^{+2}	gluc. ox.	5.5	cacodylic A.	32.5	−0.1810	0.2402	0.0592	−0.032
Cr^{+2}	gluc. ox.	6.0	cacodylic A.	25	−0.1940	0.2444	0.0504	−0.0086
Ti^{+3}	gluc. ox.	5.0	acetate	30	−0.1482	0.2415	0.0933	−0.029
Ti^{+3}	gluc. ox.	5.0	acetate	30	−0.1476	0.2415	0.0939	−0.028
Ti^{+3}	gluc. ox.	5.2	acetate	30	−0.1603	0.2415	0.0812	−0.028
Ti^{+3}	gluc. ox.	5.6	acetate	30	−0.1810	0.2415	0.0605	−0.026

* R. G. Bates, "Electrometric pH Determination, Theory and Practice." p. 201, John Wiley & Sons, Inc., New York (1954).

4. H. J. Lowe and W. M. Clark, *J. Biol. Chem.*, **221**, 983 (1956).
5. C. S. Vestling, *Acta Chemica Scand.*, **9**, 1600 (1955).
6. H. Beinert and R. H. Sands in "Free Radicals in Biological Systems," p. 17, Academic Press, Inc., New York (1961).
7. H. S. Mason, T. Nakamura, I. Yamazaki, E. Spencer, and D. Nebert, Abstracts of the Fifth International Congress of Biochemistry, Moscow, 1961, p. 466.
8. Q. H. Gibson, B. E. P. Swoboda, and V. Massey, *J. Biol. Chem.*, **239**, 3927 (1964).
9. G. Strauss and W. J. Nickerson, *J. Am. Chem. Soc.*, **83**, 3187 (1961).
10. B. E. P. Swoboda and V. Massey, *J. Biol. Chem.*, **241**, 3409 (1966).

Thallium-Thallous Halide Reference Electrodes in Propylene Carbonate

Friedrich G. K. Baucke and Charles W. Tobias*

Inorganic Materials Research Division, Lawrence Radiation Laboratory, and Department of Chemical Engineering, University of California, Berkeley, California

ABSTRACT

The performance of thallium amalgam-thallous halide electrodes with thallium concentrations from 1 to 20 a/o (atomic per cent) has been investigated in propylene carbonate (PC). Measurements of bias potentials, polarization measurements, and comparison of emf's of amalgam concentration cells without transference with data on cells in aqueous solutions show reversibility and good stability of the electrodes. The solubilities of thallous chloride, bromide, and iodide were found in the order of 1 to 5 x 10^{-6} moles/1000 ml. The pure thallium-thallous chloride electrode was also found to be suitable for reference purposes in propylene carbonate.

In recent years propylene carbonate, PC (mp: —48°C, bp: 242°C, dielectric constant: 64.5 at 25°C) has attracted much interest as an ionizing solvent for application in high energy density batteries. For measurements of thermodynamic properties of electrolytes and for studies of electrode processes in this solvent a reversible reference electrode of the second kind is required, which, for practical reasons, should involve a halide as sparingly soluble salt since this allows the experimental establishment of concentration cells without transference. Halides of sufficiently low solubilities in PC include mercurous, silver, and thallous halides.

At first sight the calomel and the mercury-mercurous bromide electrodes promise to be suitable systems. Mercurous chloride and bromide, however, disproportionate instantaneously when they are added to solutions of the corresponding alkali halides in propylene carbonate. Disproportionation also takes place in absence of indifferent halides; only the reaction rate is very low. Slow disproportionation of mercurous chloride has been reported to occur in contact with solutions of the corresponding halides in acetonitrile (1) and in dimethyl sulfoxide (2). Rapid spontaneous reaction, however, has not been reported thus far.

The low intrinsic solubility of silver chloride in propylene carbonate (2 x 10^{-5} mol/1000 ml) (3) suggests the application of the silver-silver chloride electrode in this solvent. However, excess chloride ions increase the solubility to such an extent that it becomes approximately equal to the excess chloride concentration (3-5). We have, therefore, not investigated further the application of this electrode in propylene carbonate.

The thallium amalgam-thallous chloride electrode is a reliable reference electrode in aqueous solutions, especially for measurements above 80°C, and is commercially available with 40 w/o (weight per cent) thallium as "Thalamid-Elektrode" (6). Recently it has been shown by Smyrl and Tobias (2) and by Cogley and Butler (7) that it is also reversible and well suited as a reference electrode in dimethylsulfoxide solutions. Furthermore, the solubilities of thallous chloride, bromide, and iodide determined by means of emission spectroscopy are in the order of 5 x 10^{-6} (TlCl), 1 x 10^{-6} (TlBr), and 2 x 10^{-6} (TlI) moles/1000 ml solvent and hence an order of magnitude below that of silver chloride. These values yield solubility products in the order of 10^{-12} to 10^{-11} (moles/1000 ml) (8), if complete dissociation and no complex formation of the salts at these low concentrations is assumed. Quantitative tests on the effect of excess halides on the solubility of thallous halides have not been performed in the frame of this study. Unlike in the case of silver chloride, however, no effect could be discerned by visual observation.

Therefore it seemed promising to examine the behavior of thallium amalgam electrodes in connection with thallous halides in propylene carbonate. Lithium chloride (10^{-3}M), lithium bromide (0.1M), and potassium iodide (0.1M) were chosen as indifferent electrolytes because of their relatively high solubility in PC; the thallium concentration of the amalgams ranged from 1 to 20 a/o (atomic per cent). The experiments also included measurements on oxide free thallium metal electrodes covered with an electrolytically formed layer of thallous chloride.

Experimental

Propylene carbonate (Jefferson Chemical Company, Houston, Texas) was distilled at 0.5 mm Hg by means of a commercially available column[1] packed with stainless steel helices.[2] The reflux ratio was 50 to 60, the head temperature 65°C. The first 10% and the last 20% of the solvent were discarded.

Because of the high tendency of the solvent to dissolve stopcock greases the receiver system of the column was designed with glass drip tips and needle valve stopcocks[3] equipped with Teflon "O"-rings.

Gas chromatographic analysis[4] of the product showed the presence of two impurities at very low concentration, one of which could be identified as water. The

* Electrochemical Society Active Member.

[1] Semi-CAL Series 3650, Podbielniak, Franklin Park, Illinois.
[2] Helipak, Podbielniak.
[3] Delmar Scientific Laboratories, Inc., Maywood, Illinois.
[4] Conditions of these runs were: Ucon HB 2000 (polar) on graphite in glass columns, at 152°C, carrier gas: Helium; 5 μl samples. Propylene carbonate did not decompose in this column.

concentration of water as determined by the Fischer method was below 5 ppm.

Thallous chloride (reagent grade, Fisher Scientific Company, New York) and thallous bromide and iodide (prepared by precipitation from aqueous solutions of thallous nitrate with the corresponding alkali halides) were dried *in vacuo* with phosphorus pentoxide. In contact with PC they are slightly sensitive to light; the effect increases with increasing molecular weight of the halides. Solutions and galvanic cells were, therefore, kept in dark as far as possible.

Thallium wire used for preparation of amalgams and thallium electrodes was 99.999% pure (United Mineral and Chemical Corporation, New York). The surface was freed from oxide by washing with oxygen-free water under argon atmosphere. The silvery white metal dissolved readily in mercury. The thallium concentrations of the amalgams were determined by the acidimetric titration method given by Richards and Daniels (9).

Electrolyte solutions, amalgams, and cells were prepared in dry argon atmosphere inside a glove box, which could be evacuated to below 1μ Hg. The argon passed a U-tube with dried magnesium perchlorate for removal of water and a U-tube with BTS catalyst[5] for removal of oxygen. The water content was 1 ppm by volume.[6]

The Pyrex cells used for equilibrium emf and polarization measurements consisted of six compartments, five of which were equidistant from a center compartment (Fig. 1). This arrangement permitted the combination of any two of six reference electrodes for test purposes.

Electrode cups containing about 5 ml of the amalgam exposed 0.5 and 1 cm^2 of the metal surface to the electrolyte. The amalgams were covered with a thin adherent layer of thallous halide. Since it was found that propylene carbonate tends to creep between glass and amalgams, a tightly fitting Teflon "O"-ring was attached to the glass stem of the platinum contact below the mercury surface preventing contact between electrolyte and platinum.

The cells were tightly sealed, and 1 atm of argon was maintained over the solution throughout the measurements. The temperature was kept at 30° ± 0.02°C.[7]

Thallium-thallous chloride electrodes were prepared from thallium wire. Thallous chloride well adhering to the metal surface was formed by anodization inside the sealed cells with current densities of 0.2 ma/cm^2 for a period of 30 min, yielding an amount of 0.85 mg TlCl/cm^2 and an average layer thickness of 1.2 x 10^{-3} mm. Dissolution of this layer was prevented by presaturating the electrolyte solutions with thallous chloride.

Electrode potentials and overvoltages were measured with a potentiometric electrometer.[8] Constant current was supplied by a constant current power supply[9] and measured with a multirange electrometer.[10] Each of the six electrodes of each cell studied was subjected to positive and negative galvanostatic polarization (from 10^{-8} to 10^{-6} amp/cm^2), as counter and reference electrodes served any two of the other amalgam- or thallium-thallous chloride electrodes.

Results

Bias potentials.—Thallium amalgam (1-20 a/o)-thallous halide and thallium-thallous chloride electrodes were set up in propylene carbonate solutions of the corresponding alkali halides. Measurements of bias potentials and electromotive forces were conducted at 30°C for at least six months.

[5] BASF, Ludwigshafen, Germany.
[6] "Moisture Monitor," Consolidated Electrodynamics Corp., Pasadena, California.
[7] This temperature was chosen for the purpose of direct comparison of the data in PC with those given by Richards and Daniels for 30°C (9).
[8] Keithley potentiometric electrometer, Model 630.
[9] Electronics Measurements, Inc., Model 613.
[10] Keithley multirange electrometer, Model 601.

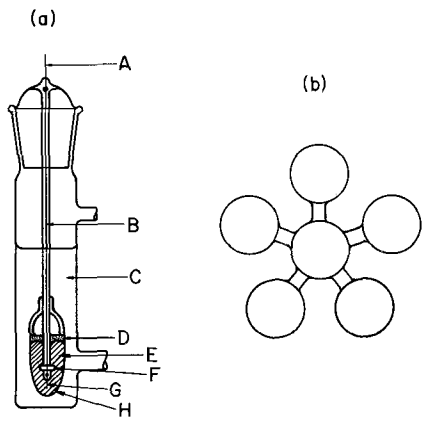

Fig. 1. (a) Single electrode compartment: A, 1 mm ϕ platinum wire; B, tungsten in uranium-glass seal; C, electrolyte; D, sparingly soluble salt (TlCl); E, amalgam; F, Teflon O-ring; G, platinum tip; H, glass cup. Fig. 1 (b). Combination of six electrode compartments.

Bias potentials of "good" amalgam electrodes never exceeded 0.05 mv, and it could be foretold from the appearance of the surface when, in few cases, they had higher values (up to 3 mv). Good electrodes had a certain appearance: Their surface was completely covered with a thin layer of very fine crystals of thallous halide. The velvet layer was produced by shaking the amalgam before it was immersed into the solution; the salt spread readily over its surface and was not removed on wetting with propylene carbonate solution. Salt in excess over the adherent quantity was usually ejected out of the electrode cups by this procedure; its presence was found to be unnecessary for a good performance of the electrodes. Only a few amalgam electrodes could either not completely be covered with thallous halide or lost the coherence of the adherent film on wetting with propylene carbonate. They showed patches of shiny amalgam, and their bias potentials were up to 3 mv and not quite constant.

Solid thallium wires employed as metal phases for thallium-thallous chloride electrodes were immersed in the PC solutions saturated with thallous chloride. Acting as electrodes of the first kind they exhibited bias potentials of less than 0.2 mv and constant emf's with amalgam-thallous chloride electrodes showing identical states of metal and surfaces. Directly after anodization and formation of the thallous chloride layer the potentials were usually off by several hundred millivolts; they changed, however, rapidly returning to their preceding value: Bias potentials were below 1 mv after 2 hr and below 0.2 mv after 6 hr. The erroneous potentials directly after anodization seem to be caused by nonuniform concentrations of electrolytes in the freshly formed layer of thallous chloride.

Polarization measurements.—In order to characterize their actual performance and reversibility, the electrodes were subjected to positive and negative polarization with current densities from 10^{-8} to 10^{-6} amp/cm^2.

The overvoltages of amalgam-thallous halide electrodes were in every case proportional to the current flowing; no hysteresis could be observed (Fig. 2). Overvoltages of electrodes with 9 a/o thallium were corrected for the iR-drop obtained from resistance measurements at 10,000 Hz between corresponding electrodes and the electrode in the center compartment. The corrected overvoltages allow the calculation of i_o^*, the effective exchange current density

$$i_o^* = \frac{RT}{n\mathbf{F}} \left(\frac{\partial i}{\partial \eta} \right)_{\eta \to 0}$$

Its magnitude is determined by the slowest reaction at

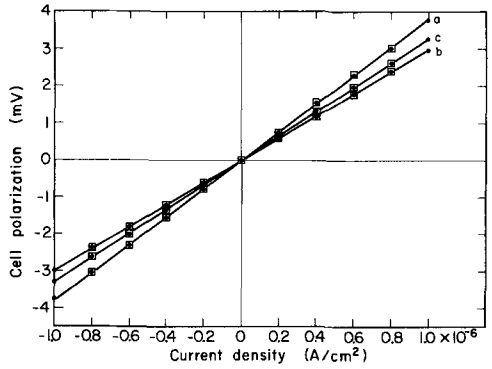

Fig. 2. Typical behavior of thallium amalgam electrodes under current. Cell polarization refers to potential measured between two identical electrodes. Ohmic drop included. ● ascending current density; □ descending current density. a, Tl(1.15% by weight), Hg/Tl I(s), KI(0.1 m); b, Tl(7.56% by weight), Hg/Tl I(s), KI(0.1 m); c, Tl(17.87% by weight), Hg/TlBr(s), LiBr(0.1 m).

the electrode surface. For the electrode

$$9\ \text{a/o Tl(Hg)/TlCl(sat'd), LiCl}(10^{-3})\text{M}$$

i_o* is in the order of 2 to 5 x 10^{-5} amp/cm².

Concentration cells.—Richards and Daniels investigated thermodynamic properties of thallium and its amalgam from 0.33 w/o to saturation (over 40 w/o) in concentration cells without transference and used aqueous 2% thallous sulfate as electrolyte (9). As long as only the reversible electrode reaction determines the potential of the electrodes, the electromotive forces of these cells should be independent of the electrolyte, its concentration, the solvent, and whether the electrodes are of the first or second kind. The emf's should only depend on the ratio of the thallium activities of the amalgam.

Accordingly, electromotive forces between thallium amalgam electrodes of the second kind with different thallium concentrations (1-20 a/o) and with thallous chloride, bromide, and iodide as sparingly soluble salts and also thallium-thallous chloride electrodes were measured in concentration cells without transference in solutions of corresponding alkali halides at 30°C. The values were compared with those for aqueous solutions at the same temperature given by Richards and Daniels. For more correct interpolation the literature data were treated by a method used by Lewis and Randall (10). As illustrated in Table I, agreement of these interpolated values with our measurements was in every case better than 0.1 mv.

Discussion

The results reported indicate that thallium amalgam electrodes in connection with thallous chloride, bromide, and iodide as sparingly soluble salts as well as thallium-thallous chloride electrodes with electrolytically formed thallous chloride layer are suitable as constant, reproducible, and reversible reference electrodes of the second kind in propylene carbonate solutions. The three amalgam electrodes provide a wide and useful range of applicability, especially for thermodynamic measurements in cells without transference, since they allow the selection of the most soluble and most suited halide of a given cation to be studied. The concentration of thallium in the amalgam may be chosen within broad limits (9), however, concentrations below 1% by weight are not recommended. It is to be emphasized that oxygen has strictly to be excluded from the system, since solid thallium and its amalgam undergo oxidation very rapidly.

When the amalgam electrode is used as a reference electrode in connection with a solution containing other than halide ions, and therefore a liquid junction is involved, the choice of the thallium halide is optional. Since alkali bromides are more soluble than chlorides, and because the thallous bromide is less sensitive to light than is the iodide, the use of the bromide electrode may be preferable, with LiBr as the supporting halide.

Solid thallium-thallous chloride electrodes are somewhat less reproducible than the amalgam electrode and require a longer time after their preparation for equilibration. However, these electrodes may have advantages for "practical" reference purposes. For example, it may be convenient to be able to insert a thin wire into a galvanic cell under study, a requirement that is rather difficult to meet by amalgam electrodes.

Table I. Comparison of the emf's of thallium amalgam concentration cells in propylene carbonate with values reported for aqueous solutions at 30°C by Richards and Daniels (9)

[Values in right-hand column were obtained by interpolating (10) from the plot: $\left|\frac{-E}{0.06015}\log X_{Tl}\right|$ *vs.* X_{Tl}.]

Solute in propylene carbonate	Tl-conc'n in amalgam w/o	Tl-conc'n in amalgam mole fraction	Experimental emf, mv cell A	Experimental emf, mv cell B	EMF in aqueous Tl_2SO_4 according to Richards & Daniels (9)
TlCl (sat'd)	0.862	0.0085	55.95	56.00	56.0
LiCl (10^{-3}m)	4.750	0.0467	27.15	27.20	27.1
	9.104	0.0895	41.28	41.26	41.3
	22.20	0.219	29.21	29.23	29.2
	pure Tl/TlCl	1.00			
TlBr (sat'd)	1.032	0.0102	58.98	59.00	59.1
LiBr (0.13m)	5.823	0.0574	50.01	49.98	49.9
	17.84	0.176	16.36	16.38	16.4
	25.42	0.251			
TlI (sat'd)	1.152	0.0113	59.90	59.85	59.8
KI (0.1m)	6.441	0.0633	44.35	44.40	44.3
	17.30	0.170	14.45	14.47	14.5
	23.61	0.233			

Acknowledgments

The authors are indebted to Dr. A. Newton and Dr. G. Shalimoff, Lawrence Radiation Laboratory, Berkeley, for their contribution to gas chromatographic and spectroscopic analyses and to Professor H. Gerischer, Munich, Germany, for helpful discussions.

The work was carried out under the auspices of the United States Atomic Energy Commission.

Manuscript submitted Dec. 11, 1967; revised manuscript received Aug. 9, 1968.

Any discussion of this paper will appear in a Discussion Section to be published in the June 1969 JOURNAL.

REFERENCES

1. K. Cruse, E. P. Goertz, and H. Petermöller, *Z. Elektrochem.*, **55**, 405 (1951).
2. W. H. Smyrl and C. W. Tobias, *This Journal* **113**, 754 (1966).
3. J. N. Butler, Solubility and Complex Formation Equilibria of Silver Chloride in Propylene Carbonate, TLI #210, Tyco Laboratories, Inc., Waltham, Mass.
4. J. N. Butler, *Anal. Chem.*, **39**, 1799 (1967).
5. J. N. Butler, D. R. Cogley, and W. Zurosky, *This Journal*, **115**, 445 (1968).
6. Schott u. Gen., Mainz, Germany.
7. D. R. Cogley and J. N. Butler, *This Journal*, **113**, 1074 (1966).
8. R. Jasinski, Tyco Laboratories, Inc., Waltham, Mass., Bibliography on the Uses of Propylene

Carbonate in High Energy Density Batteries, private communication, 1967. Y. C. Wu and H. L. Friedmann, *J. Phys. Chem.*, **70**, 501 (1966).
9. T. W. Richards and F. Daniels, *J. Am. Chem. Soc.*, **41**, 1732 (1919).
10. G. N. Lewis and M. Randall, "Thermodynamics," McGraw-Hill Book Co., New York, Toronto, London, revised ed. by K. S. Pitzer and L. Brewer (1961). G. N. Lewis and M. Randall, *J. Am. Chem. Soc.*, **43**, 233 (1921).

The Electrochemical Oxidation of Adsorbed Hydrogen and Carbon Monoxide on Noble Metals and Their Alloys

R. J. Roethlein*[1] and H. J. R. Maget*

R & D Laboratory, Direct Energy Conversion, General Electric Company, West Lynn, Massachusetts

ABSTRACT

The mechanism of electrochemical oxidation of H_2-CO mixtures was investigated on noble metals (Pt, Rh, Ru) and their alloys (Pt-Rh, Pt-Ru), by a voltage pulse technique. The relative coverage of adsorbed hydrogen in the presence of CO was found to be approximately 5% for all of the Pt-Rh alloys investigated and the total surface coverage dependent on the alloy surface area. For Pt-Ru alloys the degree of hydrogen coverage in the presence of CO was found to be a function of the Ru content of the alloy.

Considerable interest has been raised in the past few years concerning the electrochemical oxidation of reformate gas mixtures containing varying amounts of H_2, CO, CH_4, and CO_2. Conventional electrocatalysts, such as platinum black, commonly employed as anodes for the oxidation of hydrogen have displayed severe polarization losses under current drain when H_2 is substituted with reformate gases at temperatures ranging from ambient to 90°C. Investigations of the various components in reformate gases have shown that CO_2 and CH_4 do not affect directly electrode polarization during the oxidation of hydrogen, but act merely as diluents in the fuel mixture. CO has been shown to be strongly adsorbed on many electrode materials and does not oxidize until an appreciably high overvoltage (~0.4v) is reached. Studies (1-7) conducted on both smooth and platinized platinum have shown that CO replaces most of the adsorbed hydrogen and is preferentially adsorbed on the electrode surface; these authors have also shown that CO adsorption occurs in at least two isomeric forms. Earlier investigations of CO adsorption on supported platinum substrates (8) employing infrared techniques have labelled these isomers as linear (one site adsorption) and bridge (two site adsorption).

Several binary noble metal alloys permit the oxidation of hydrogen containing CO as part of the fuel gas mixture (9,10); these catalysts have shown an exceptional tolerance for carbon monoxide in reformate fuels and are far more resistant to poisoning than platinum. These authors conclude that the improved performance of these catalysts appears to result from the greater availability of sites for hydrogen adsorption rather than through promotion of the oxidation of carbon monoxide. It was the purpose of this work to determine the quantity of hydrogen and carbon monoxide adsorbed on some of these catalyst materials and thereby gain some understanding of the over-all oxidation process. Rapid voltage scanning techniques were employed so that investigation of the adsorption effects of hydrogen and carbon monoxide on smooth alloy and metal surfaces could be determined. These techniques also kept the rate of CO adsorption from solution at a minimum.

* Electrochemical Society Active Member.
[1] Present address: R & D Laboratories, Sprague Electric Company, North Adams, Massachusetts.

Experimental

Study electrodes were composed of 30 mil diameter polished metal wires obtained from Engelhard Industries and sealed in soft glass tubes having coefficients of expansion similar to those of the wires. The metals consisted of pure platinum, rhodium, ruthenium, and binary platinum alloys of the latter noble metals; see Table I for exact composition. The geometric area for each sample depended on the length of wire extending from the glass capillary tip, but ranged between 0.15 and 0.35 cm^2. The experiments were carried out in a standard three-compartment Pyrex glass test cell, each section separated from the other by fritted glass disks. All potentials refer to a hydrogen saturated platinum-black electrode in 3*N* H_2SO_4 which was prepared from doubly distilled water and reagent grade chemicals. All tests were carried out at either 25° or 80°C + 1° in a P.M. Tamson constant temperature oil bath, and the gases used in these experiments were research grade quality.

A triangular wave voltage ramp was obtained by means of a Servomex waveform generator used in conjunction with a Wenking 61R fast-rise potentiostat in applying potential ramps on the test electrode. Current variations were measured across a 10 ohm standard resistor and recorded on a 551 Dual Beam Tektronix Oscilloscope using a type-D plug-in. Simultaneously, the voltage change across the test electrode could be monitored on the other oscilloscope beam via a type-L plug-unit. Traces were then photographed with a C-12 Polaroid Oscilloscope camera.

The instrumentation and procedure followed for electrode precleaning prior to the adsorption of the oxidizable species was similar to that employed by Gilman (1-3). The electrolyte was thoroughly saturated with CO and the test electrode brought to an oxygen evolution potential of 1.8v for 30 sec to remove oxidizable impurities from the electrode. The electrode potential was then lowered to 1.3v and molecular oxygen was swept from solution after which the electrolyte was allowed to become quiescent for an additional 60 sec at this potential. The electrode potential was then lowered to the desired adsorption potential for various durations or adsorption times. A linear anodic potential ramp was then imposed on the electrode during which adsorbed CO was oxidized and the electrode surface was covered with adsorbed oxygen.

Table I. Charge due to CO and H_{ads} oxidation on noble metals and alloys 80°C

Alloy wt. %	Q_H	Q_H^{CO}	Q_H^{CO}/Q_H	Q_{CO}	$Q_{CO}/Q_H - Q_H^{CO}$
Pt	0.272	0.014	0.052	0.560	2.17
95 Pt- 5 Rh	0.249	0.012	0.048	0.485	2.04
90 Pt-10 Rh	0.241	0.009	0.037	0.420	1.81
80 Pt-20 Rh	0.459	0.027	0.059	0.940	2.15
70 Pt-30 Rh	0.577	0.021	0.036	1.10	1.98
60 Pt-40 Rh	1.11	0.056	0.050	2.31	2.20
50 Pt-50 Rh	1.26	0.065	0.052	2.65	2.21
5 Pt-95 Rh	0.647	0.029	0.045	1.63	2.61
100 Rh	0.731	0.034	0.047	1.58	2.26
95 Pt- 5 Ru	0.494	0.041	0.083	0.868	1.92
90 Pt-10 Ru	0.910	0.161	0.177	1.46	1.95
85 Pt-15 Ru	0.766	0.137	0.179	1.14	1.81
60 Pt-40 Ru	0.306	0.060	0.195	0.410	1.67
100 Ru	0.595	0.179	0.300		

Q_H = total charge for H_{ads} oxidation.
Q_H^{CO} = total charge for H_{ads} oxidation in CO-saturated solution.
Q_{CO} = total charge for CO oxidation.
All Q-values expressed in millicoulombs/cm² geometric area.

The same procedure was followed after thoroughly purging the solution with N_2 and the traces obtained from both runs were superimposed on the same photographic plate so that the charge due to surface oxidation could be eliminated and to permit a more accurate determination of the charge due to CO oxidation. Measurements of the quantity of hydrogen adsorbed on the same electrode surface were also made. All potentials were previously adjusted via a Fluke potentiometer and potential sweep speeds the order of 100 v/sec were used in order to minimize the measurement of currents due to diffusional processes.

Results

The smooth wire electrodes were examined by a voltage pulse technique in order to determine the charge due to the oxidation of hydrogen and carbon monoxide adsorbed on the electrode surface. Following the electrode precleaning procedure described in the experimental section, the electrode potential was held at an adsorption potential until hydrogen or carbon monoxide adsorption on the electrode surface was complete. In the case of H_{ads} full surface coverage was realized in less than 50 msec.

Figure 1 shows typical traces obtained on a Pt-Ru electrode in a nitrogen and carbon monoxide saturated system. The shaded areas being the regions of interest: Q_{CO} = CO oxidation, Q_H = hydrogen oxidation, and Q_H^{CO} = hydrogen oxidation in the presence of CO. Q represents the charge due to the oxidation of the adsorbate in millicoulombs per square centimeter of geometric area. The charge due to hydrogen oxidation in the presence of CO, Q_H^{CO}, decreased rapidly with increasing adsorption times and reached a steady value after approximately 10 sec; however, adsorption times

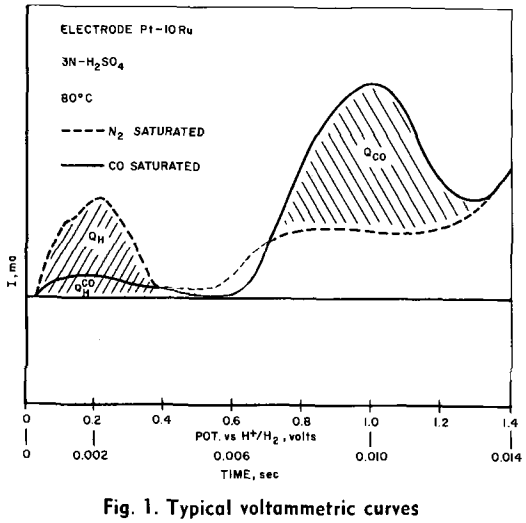

Fig. 1. Typical voltammetric curves

the order of 60 sec were employed since it has been reported (1) that the final CO molecules may adsorb slowly. The quantity of adsorbed hydrogen oxidized was attributed to the charge measured between the start of the sweep up to 0.4v where hydrogen coverage is zero and double layer charging begins (11).

Hydrogen saturation coverages were measured from a starting potential of +0.030v in order to minimize effects due to hydrogen evolution. A correction for the capacity contribution to the charge in the presence and absence of CO was applied to the values obtained by integration of the area under the curves between +0.030 and 0.400v. Since the double layer capacity is almost constant in this potential range (12) a value of 40 μfd/real cm² (13), in the absence of an organic adsorbate, and 8 μfd/real cm² (14) in the presence of CO was employed in making the corrections. The surface roughness of each electrode was also taken into consideration in applying the corrections. The double-layer contribution to the charge due to CO oxidation is negligible since they tend to cancel one another (3, 15) in the presence and absence of CO.

Measurements of hydrogen coverage were made using the current and time coordinates that provided the largest amount of display. These values were also checked by the method of hydrogen codeposition (1), where the electrode after a precleaning cycle was held at an adsorption potential of +0.400v and a cathodic sweep applied to hydrogen evolution potentials. Analysis of the charge due to hydrogen deposition in the presence and absence of CO was in good agreement with the values obtained by the application of anodic sweeps.

With sweep speeds ranging from 50 to 200 v/sec, the amount of charge due to the oxidation of adsorbed hydrogen and carbon monoxide maintained a constant value after repeated measurements employing the fore-mentioned potential sequence on Pt and all of the Pt-Rh alloys tested below 50 w/o rhodium. Both rhodium and the Pt-95 Rh alloy did show a small increase in charge within the first few potential cycles, possibly indicating an increase in surface area. However, after several cycles reproducible values were obtained. On pure ruthenium it was found that for anodic potentials greater than 1.4v an oxide formed on the electrode surface which could only be removed by mechanical polishing. Consequently, electrode precleaning on the material was carried out at an applied potential of 1.0v, and all measurements of hydrogen adsorption were made by anodic potential ramps that did not exceed 1.0v. Charge measurement on the Pt-Ru alloys tested, employing the original potential sequence, did not show any significant variation during repeated measurements or oxide build-up on the surface.

Electrode surface reproducibility was measured as a function of sweep rate and adsorption time for the

amount of charge required to oxidize hydrogen from an electrode surface held at an adsorption potential of 0.030v. For a wide range of sweep speeds (5-2000 v/sec) the charge corresponding to the oxidation of hydrogen has an average deviation of less than 2%. Measurements of charge variation as a function of adsorption time has shown that under the worst condition (violent gas bubbling through the electrolyte) the number of sites lost to impurity adsorption has been low. With gas bubbling, adsorption times of the order of 60 sec produce a 5% loss in charge; after 180 sec 18% of the sites were covered with impurities.

The degree of hydrogen coverage on platinum and rhodium was measured as a function of potential at 25°C; for platinum, hydrogen adsorption is present up to 0.300v, in contrast to rhodium which is relatively free of adsorbed hydrogen at potentials greater than 0.200v. No significant change in the range of hydrogen coverage was noted on these metals when the electrolyte temperature was raised to 80°C. Measurements of hydrogen coverage on pure ruthenium as a function of potential were difficult, except at low adsorption potentials $\leq$ 0.05v, due to the rather ill defined double layer region obtained during an anodic or cathodic voltage sweep. High electrode capacity has been attributed to the adsorption of oxygen at potentials in the region of the double layer (16).

The charge due to the oxidation of CO as a function of adsorption potential was also investigated on several materials. Figure 2 shows that for platinum at 80°C the total charge is constant up to an adsorption potential of 0.700v. At some potential between 0.700 and 0.800v CO is no longer adsorbed on the electrode surface. This is in contrast to values obtained at 25°C on platinum where the charge due to CO adsorption was constant up to 0.900v. This may suggest that adsorbed oxygen forms on platinum at slightly lower potentials as the temperature is increased. To insure removal of any oxide formed at higher potentials during the pretreatment procedure an additional step was added to the potential sequence. Prior to the adsorption step the electrode was cathodized for 1 sec at 0.100v and then brought to the appropriate adsorption potential for 60 sec duration.

A similar investigation was carried out on two platinum alloys; 50% Rh-Pt and 15% Ru-Pt. For these materials the charge due to CO oxidation was a steady value up to adsorption potentials of 0.600v. At 0.700v the charge due to CO oxidation was too small on both materials, see also Fig. 2. The behavior of rhodium toward CO oxidation was similar to that of the alloys, Fig. 3; the charge remained constant up to an adsorption potential of 0.600v on a prereduced surface. Higher oxides, however, were not fully removed until significantly lower adsorption potentials were achieved. At 0.400v some residual oxide still remained on the surface preventing a saturation coverage with carbon monoxide.

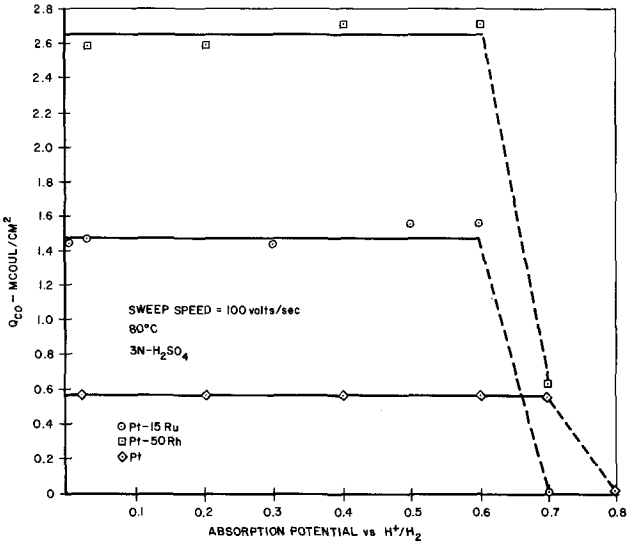

Fig. 2. Charge due to CO oxidation as a function of potential

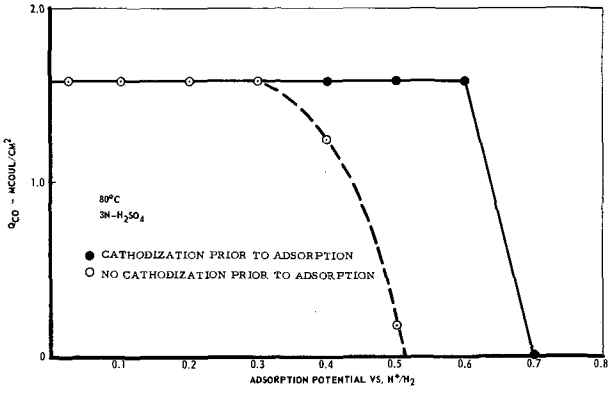

Fig. 3. Charge due to CO oxidation on rhodium as a function of potential.

The charge due to the oxidation of hydrogen and carbon monoxide measured for saturation coverages at 80°C on pure metals and several Pt-Rh and Pt-Ru binary alloys is summarized in Table I. The analysis of the data obtained on the various metals and alloys is based on two assumptions: that the values obtained for Q_H represent adsorbed hydrogen coverages approaching saturation and that the adsorption of CO molecules takes place mainly on those sites previously covered with adsorbed hydrogen. The results indicate that for Pt-Rh alloys the quantity of hydrogen adsorbed on a smooth electrode surface in a CO-saturated condition is directly related to the amount of hydrogen it can adsorb in the absence of carbon monoxide. Although values for the charge due to adsorbed hydrogen vary with each electrode because of its roughness factor the ratio of hydrogen coverage in the presence of CO to that obtained in its absence remains fairly consistent for this whole series of alloys; values of Q_H^{CO}/Q_H vary slightly from 3.5 to 6.0%.

Ruthenium and the binary alloys of this series do not however follow the previously described relationship. For these materials the quantity Q_H^{CO}/Q_H, seems to reach a plateau and does not vary significantly. Pure ruthenium, however, exhibits a higher percentage of hydrogen coverage which may possibly be a maximum for this series.

If the assumption is maintained that CO molecules adsorb on the same sites previously occupied by adsorbed hydrogen, then charge comparison for these two species indicates that approximately a two to one ratio exists for platinum, rhodium, and most of the alloys. Providing a two-electron transfer is necessary for the complete oxidation of carbon monoxide, then these values may be a good indication that the main form of CO bonding to these materials at 80°C is of the linear type.

Discussion

From the studies conducted on pure metals and alloy wire electrodes some observations can be made regarding the role these catalysts play in oxidizing impure hydrogen. For alloys of the Pt-Rh series, adsorption data indicate that the amount of charge due to hydrogen coverage in a CO saturated solution, Q_H^{CO}, is a function of electrode surface area. For pure platinum, rhodium, and their alloys, the relative hydrogen coverage in the presence of CO compared to hydrogen coverage without CO present on the same surface is approximately 5% and independent of alloy composition. This would indicate that the same proportion of sites are available for hydrogen adsorption in the presence of CO on Pt and on the Pt-Rh alloys.

Since the oxidation of CO occurs on all of these alloys at potentials far removed from the region of

hydrogen oxidation, catalytic activity for the electrochemical oxidation of H_2 would then be confined to those residual sites not covered with adsorbed CO. It would seem then that catalytic activity of these alloys is not due to a larger portion of sites available for hydrogen adsorption but to some other factor which will enhance activity for specific alloy compositions, such as a higher total surface area.

The adsorption data obtained on the Pt-Ru alloys indicate that for these materials the degree of hydrogen coverage in the presence of CO is dependent on the Ru content of the alloy. The relative degree of hydrogen surface coverage (Q_H^{CO}/Q_H) in a CO saturated solution increased rapidly up to approximately 10 w/o ruthenium; at this point approximately 20% of the electrode surface is covered with residual hydrogen. The value remained fairly constant on the remaining higher weight per cent ruthenium alloys tested. Thus specific alloy composition of the Pt-Ru series shows a greater tendency to adsorb hydrogen in the presence of reformate fuels. The results obtained on pure ruthenium agree with this observation since values for the relative hydrogen coverage are higher for the pure material than for any of the alloys.

Manuscript submitted Sept. 15, 1967; revised manuscript *ca.* Aug. 13, 1968.

Any discussion of this paper will appear in a Discussion Section to be published in the December 1969 JOURNAL.

REFERENCES

1. S. Gilman, *J. Phys. Chem.*, **67**, 78 (1963).
2. S. Gilman, *ibid.*, **66**, 2657 (1962).
3. S. Gilman, *ibid.*, **67**, 1898 (1963).
4. S. B. Brummer and J. I. Ford, *ibid.*, **69**, 1355 (1965).
5. A. B. Fasman, G. L. Padyokoua, and D. V. Sokolskii, *Dokl. Akad. Nauk. SSR*, **150**, 856 (1963).
6. S. Schuldiner and T. B. Warner, *Electrochim. Acta*, **11**, 307, (1966).
7. R. A. Munson, *J. Electroanalyt. Chem.*, **5**, 292 (1963).
8. R. D. Eischens and W. Pliskin, "Advances in Catalysis," Vol. X, p. 18, Academic Press Inc., New York (1958).
9. L. W. Niedrach, D. W. McKee, J. Paynter, and I. F. Danzig, *Electrochem. Technol.*, **5**, 318 (1967).
10. L. W. Niedrach, D. W. McKee, J. Paynter, and I. F. Danzig, *ibid.*, **5**, 419 (1967).
11. F. G. Will and C. A. Knorr, *Z. Elektrochem.*, **64**, 258 (1960).
12. A. Slygin, A. Frumkin, and W. Medvedovsky, *Acta Physicochim., URSS*, **4**, 911 (1936).
13. S. Schuldiner and R. M. Roe, *This Journal*, **110**, 332 (1963).
14. T. B. Warner and S. Schuldiner, *ibid.*, **111**, 992 (1964).
15. S. B. Brummer, *J. Phys. Chem.*, **71**, 2838 (1967).
16. G. P. Khomchenko, A. F. Lunev, and K. N. Bogdanouskaya, *Electrokimiya*, **1**, 1352 (1965).

Electrochemical Methods for the Measurement of High-Temperature Diffusion in Metals

D. O. Raleigh and H. R. Crowe

Science Center, North American Rockwell Corporation, Thousand Oaks, California

ABSTRACT

Previous determinations of the diffusion coefficient of silver in single-crystal Ag-Au alloys at 394° by the measurement of diffusion-limited currents in solid electrolyte cells Ag|AgBr|Au have been extended to cover the complete alloy composition range and to determine the effects of electrode surface preparation, direction of diffusion, compositional cycling, and use of a bulk Ag-Au alloy as the starting electrode. In addition, the experimental and theoretical principles are discussed more thoroughly. In selected systems, the method permits the accurate measurement of D values as low as 10^{-16} cm^2/sec, at a time scale of about 1 hr per data point, over the range of miscibility of diffusant and solute metals, with a single cell. In the present study, D values from duplicate runs in the range 10^{-14} cm^2/sec agreed to ~3%. The method permitted, for the first time, direct comparison of D values corresponding to inward and outward diffusion in a substitutional solid system. Out-diffusion D values were systematically higher, a result attributed to vacancy injection. Extension of the present and related methods to fused salt electrolytes and other solid electrode materials is discussed.

In a previous publication (1), preliminary results were reported on a high-temperature electrochemical method for the rapid and sensitive measurement of low-level diffusion in selected metal systems. In applying the method to the diffusion of silver in silver-gold alloys at 400°C, it was found possible to measure D values of order 10^{-14} cm^2/sec at five points in the alloy composition range 10-60 a/o Ag in a one-day experiment with one metal sample. By contrast, conventional metallurgical techniques involving radiotracers and sectioning generally cannot be extended below $D \sim 10^{-11}$ cm^2/sec and require several weeks of annealing as well as precise sectioning techniques. In the application reported, the method involved the measurement of diffusion-limited currents in the solid electrolyte cell Ag|AgBr|Au. In the present work, we report more extensive studies on the Ag-Au system, examining the theoretical and experimental principles more thoroughly and discuss the applicability of this and related methods to other metallic and electronically conducting systems.

Key words: silver diffusion in gold, electrochemical diffusion method, solid electrolytic cell.

The cell Ag|AgBr|Au is one of a class of solid electrolyte cells, (Me or X)|MeX|M', termed polarization cells, which contain one electrode that is electrochemically reversible to the electrolyte and one which is chemically inert toward it. If an external voltage is applied to such cells, there is a wide range of the voltage over which there can be no steady-state ionic current. For instance, if the Ag side of the cell Ag|AgBr|Au is made negative, a steady-state electrolytic current could only occur through electrodissociation of the AgBr or oxidation of the Au. If the cell

voltage is kept below the values required for these reactions, no steady-state faradaic process is available to permit current flow. Under these conditions, the Au electrode is current-blocking and, in essence, functions like a capacitor. Wagner (2) has pointed out that in such cells the applied voltage V uniquely fixes the chemical activities of the electrolyte components at the inert electrode surface. In the present cell, for instance, the activity of metallic silver at the gold surface is given by $a_{Ag} = \exp(-V\mathbf{F}/RT)$. The activity in this case is manifested as a partial monolayer of electrodeposited silver (3, 4) which, on application of the voltage, is achieved on the time scale of the electrode double-layer charging. If the charging process is carried out at a cell temperature where the diffusivity of silver in gold is negligible, the ionic cell current drops to zero on its completion.

Suppose, however, that the temperature has a value at which the silver diffusivity is appreciable. In this event, silver at the surface will migrate into the gold, but the cell will act to maintain the surface concentration by electrodepositing more silver. The result will be an ionic cell current that is precisely equivalent to the flux of diffusing silver into the electrode at the fixed surface concentration. In consequence of the value of the Faraday constant, one can measure directly and continuously a material transport of $\sim 10^{-11}$ moles/sec as a 1 μa current.

Because of the action of the cell to maintain a fixed surface concentration of the diffusant, it becomes possible by the use of voltage-step techniques to determine D values over a wide composition range. If, in the above case, the applied voltage is maintained at the value V, the diffusion current will persist until the rate of the diffusion process becomes negligible. At this point, the Au electrode has the characteristics of an Au-Ag alloy of silver activity a_{Ag}. If the applied voltage is now changed to a value V', corresponding to a new surface activity a_{Ag}', the situation corresponds to a well-known solution of the diffusion equation. If C_0 and C_1 are the silver concentrations corresponding to a_{Ag} and A_{Ag}', the diffusion flux will be given by

$$J = -D\frac{dC}{dx}\bigg|_{x=0} = -D(C_1 - C_0) \times \left[\frac{d}{dx}\operatorname{erfc}\frac{x}{2\sqrt{Dt}}\right]_{x=0} = (C_1 - C_0)\left(\frac{D}{\pi t}\right)^{1/2} \quad [1]$$

and the corresponding diffusion current by the well-known Cottrell equation

$$i = \mathbf{F}A(C_1 - C_0)(D/\pi t)^{1/2} \quad [2]$$

where A is the electrode area. Thus, if concentrations C_1 and C_0 corresponding to activities a_{Ag}' and a_{Ag} are known (as is the case for the Ag-Au system), a plot of i *vs.* $t^{-1/2}$ should yield a straight line whose slope may be used to derive D. Repeated cell voltage changes would then permit measurement of D in sequential steps across the alloy composition range. Moreover, because of the capability to apply voltage steps that either increase or decrease the surface diffusant concentration, it becomes possible to study not only the conventional "in-diffusion," but extractive or "out-diffusion" as well.

Several factors deserve consideration. First, one should distinguish between the gold electrode potential, relative to the silver potential, and the actual voltage applied to the cell. Where the former directly fixes a_{Ag}, the latter may also contain contributions from polarization at the Ag electrode and iR drop in the electrolyte. If these were appreciable, the result would be an uncertainty and a time variation in the value of a_{Ag}. In fact, one or both of these are invariably important in the early stages of applying a voltage step, and determine the "sharpness" of the step with respect to time scale for the surface activity change. When a voltage step is applied to a cell of this type, the step voltage initially appears across the electrolyte as iR drop and, on the time scale of the RC time constant of the cell, is transferred to the current-blocking electrode. Accordingly, the Cottrell equation becomes applicable at times large compared with the electrode charging time. In our own cells, the charging time is in the millisecond range, permitting diffusion current analysis for times at least as short as 1 sec. Residual portions of the double layer charging persist out to $\sim$ 5 sec but, since the charging is essentially complete at much shorter times, this will only have the effect of adding a transient increment to the diffusion current.

If the electrolyte resistance is large, the iR drop associated with residual double layer charging and even early portions of the diffusion current may be appreciable. This was not the case in our cells, where currents for $t > 1$ sec were in the microampere range and the electrolyte resistance was several ohms, but may well be the case in other systems. In such instances, potentiostatic arrangements with resistance compensation may be employed (5). Likewise, counter electrode polarization may be removed as a factor by the use of a potentiostat with a reference electrode, though, as previously reported (1), this was found unnecessary in our system.

A further consideration is the general presence of a low-level electronic current in such cells. While conduction in our own electrolyte was predominantly ionic, there is in many such cell systems a small steady-state electronic current at any finite applied voltage. This current exists as a consequence of a stoichiometry gradient in the electrolyte and is constant at any particular voltage (2, 6). In a cell Me|MeX|M' with n-type electronic conduction, the current is given by

$$i_e = (\sigma_e{}^o RTA/L\mathbf{F})[1 - \exp(-V\mathbf{F}/RT)] \quad [3]$$

where $\sigma_e{}^o$ is the specific electronic conductivity of MeX at equilibrium with metallic Me, and L and A are the thickness and area of a cylindrical electrolyte pellet. For cells with p-type or mixed electronic conduction, analogous expressions apply. The important point, however, is that, since the electronic current is constant at a given potential, it appears merely as a nonzero intercept in a plot of i *vs.* $t^{-1/2}$. Thus, it is not necessary to know the magnitude or type of conduction in advance. This current, however, together with the electrode charging, defines a lower limit for the size of diffusion currents that may be measured. As mentioned previously (1), it is required that the diffusion current be large enough to be seen against the steady-state electronic current once the double-layer charging process is complete. This depends on the values of D, ΔC, $\sigma_e{}^o$, and the electrode charging kinetics, but can be examined empirically in a given cell system by seeing whether the current in response to a particular voltage step contains a well-defined region of $t^{-1/2}$ variation.

Finally, in examining successive D values across a composition range by applying sequential voltage steps, it is necessary to know how long to wait between successive steps. Ideally, to conform exactly to the boundary conditions for the Cottrell equation, one should wait until the diffusant becomes uniformly distributed throughout the electrode at the concentration corresponding to the previous step. In practice, however, this is often not possible. In our own system, we study D values $\sim 10^{-14}$ cm^2/sec. For a 0.1 cm thick electrode, this would require a characteristic wait time of $x^2/D = (0.1)^2/(10^{-14}) = 10^{12}$ sec! However, several regressions from such a prohibitive wait time are possible. For instance, if one waits merely until the diffusion current becomes negligibly small on the current-measuring apparatus, the electrode will behave to all intents and purposes as though the diffusant were uni-

formly distributed. Even this approximation, however, leads to inconveniently long waits between steps, because of slowness of $t^{-1/2}$ current decay. If currents were recorded up to a minimal time t_1 and we required the current to drop to 1% of its value at t_1 before applying the next step, this would require a wait time $\tau = 10^4\ t_1$. Experimentally, it has been found that much shorter waits may be tolerated, but it is of interest to inquire theoretically why this should be so.

The relevant diffusion problem is one in which we start with a substrate with uniform initial diffusant distribution C_0 and change the surface concentration successively to fixed values C_1, C_2, etc. at equal time intervals τ, the electrode geometry being appropriate to semi-infinite linear diffusion. In our actual system, the uniform initial concentration is achieved either exactly by use of an alloy electrode whose bulk composition is the same as the surface composition fixed by the starting voltage V_0, or is achieved to satisfactory approximation by a sufficiently long initial wait at V_0. An exact analytic solution to the multistep diffusion problem is possible, but only for the case where D is composition-independent. While D indeed varies with composition in our system, it is instructive to present the composition-independent solution and inquire as to what may be a reasonable approximate form for a nonconstant D.

The solution for a constant D may be derived analytically by a treatment described by Carslaw and Jaeger (7), but a simpler approach that supplies the same answer and gives more insight into the physical situation is to make use of the superposition principle (8). In this, one may arbitrarily subdivide a diffusion process into a number of conveniently treated constituent contributions, solve the diffusion problem separately for each, and then sum the solutions. Consider in the present case that we label as Ag_{01} each silver atom deposited on the electrode surface during voltage step $V_0 \rightarrow V_1$ and similarly label each silver atom that is deposited to replace an Ag_{01} atom when it diffuses into the electrode. Likewise we label as Ag_{12} each Ag atom that is deposited during step $V_1 \rightarrow V_2$ or that replaces an Ag_{12} atom on the surface, and so on for further steps. Then the effect of voltage V_1 is to maintain a fixed surface concentration of Ag_{01} atoms, the effect of V_2 is to maintain simultaneously fixed concentrations of Ag_{01} and Ag_{12}, and so on. The net result is that for each newly introduced species of Ag atom, the boundary condition for the Cottrell equation is obeyed for all time, irrespective of previous and subsequent steps. Accordingly, the total current after n steps is given by a sum of Cottrell terms for each constituent Ag species

$$\begin{aligned} i = {} & \mathbf{F}A(C_n - C_{(n-1)})\,(D/\pi)^{1/2}t^{-1/2} \\ & + \mathbf{F}A(C_{(n-1)} - C_{(n-2)})\,(D/\pi)^{1/2}(t+\tau)^{-1/2} + \cdots \\ & \mathbf{F}A(C_2 - C_1)\,(D/\pi)^{1/2}[t + (n-2)\tau]^{-1/2} \\ & + \mathbf{F}A(C_1 - C_0)\,(D/\pi)^{1/2}[t + (n-1)\tau]^{-1/2} \quad [4] \end{aligned}$$

where t is the time after application of the nth step. Note that for $t << \tau$, only the first term on the right shows time variation. (For $t \leq 0.1\tau$ and equal-sized concentration jumps, the error in neglecting t in the other terms is $\leq 1\%$.) Thus, for the nth step, the slope of a plot of i *vs.* $t^{-1/2}$ for data in this time range is unaffected by prior steps, as we have found experimentally. Since the terms for prior steps are effectively constant, the effect on the i *vs.* $t^{-1/2}$ plot is merely to shift its intercept.

This analysis for the case of a constant D suggests that, for a nonconstant D that varies smoothly and gradually with composition, a reasonable approximate expression for the diffusion current should be similar in form to Eq. [4]. We assert, in fact, that we may conceptually separate the contributions from the various steps so that for times $t << \tau$ following the latest step, only the current associated with this step will be varying as rapidly as $t^{-1/2}$, the others varying with time in some manner similar to $(t + n\tau)^{-1/2}$. Thus, a Cottrell expression involving the D for the latest step should still give the slope of the i *vs.* $t^{-1/2}$ plot.

It is useful to consider what we mean by the D for a given step when D is, in fact, composition-dependent. The D values we measure determine the chemical, as opposed to the tracer, diffusion coefficient. That is, we are measuring the D associated with the diffusion of Ag into a substrate at diffusant concentration $C_{(n-1)}$ from a surface concentration C_n. This is inevitable in any study of chemical diffusion. We follow the practice in the literature (9) of assigning the effective D value we obtain to the median composition $\frac{1}{2}(C_{(n-1)} + C_n)$, designating it by $D_{(n-1)n}$.

Given the experimental fact that the D value is not appreciably influenced by the application of prior steps, we need not actually acquire an approximate form of Eq. [4] to evaluate D when it varies with composition. It is instructive, however, to do so, both to see what increments to the current intercepts we might expect, and to explore the general physical picture. Consider that a second step has just been applied and $i(t)$ for $t << \tau$ is being studied. Since the diffusion associated with the prior step has been taking place for the relatively long time $t + \tau$, the characteristic penetration depth associated with it will be large compared with that for the second step. Accordingly, the bulk of the substrate region involved in this diffusion will be in the same composition range as when the step was first applied, there being only a small compositional perturbation near the surface from the subsequent step. Likewise, in a multistep diffusion process, each past previous step would be associated with a greater penetration depth. While the differences between these depths would not be as great as between any of them and the step just applied, it is also true that the contributions of past steps to the total current should be much diminished as new steps are applied. Thus, it may be a reasonable approximation to assume that each contributing diffusion proceeds with the D value originally associated with it, so that Eq. [4] is modified to

$$\begin{aligned} i = {} & \mathbf{F}A(C_n - C_{(n-1)})\,(D_{(n-1)n}/\pi)^{1/2}t^{-1/2} \\ & + \mathbf{F}A(C_{(n-1)} - C_{(n-2)})\,(D_{(n-2)(n-1)}/\pi)^{1/2}(t+\tau)^{-1/2} \cdots \\ & + \mathbf{F}A(C_2 - C_1)\,(D_{12}/\pi)^{1/2}[t + (n-2)\tau]^{-1/2} \\ & + \mathbf{F}A(C_1 - C_0)\,(D_{01}/\pi)^{1/2}[t + (n-1)\tau]^{-1/2} \quad [5] \end{aligned}$$

The usefulness of this expression is that, since the coefficient of each term $(t + j\tau)^{-1/2}$ is the slope of the i *vs.* $t^{-1/2}$ curve obtained from that step, we may evaluate the equation from existing data to see what the intercept shifts should be.

Experimental

As described previously (1), a working cell consisted of a single-crystal AgBr pellet springloaded between a square of Ag foil and the appropriate gold electrode. For the latter, gold single crystals and 50:50 a/o Ag-Au alloy single crystals were employed in different runs. The electrodes were shaped from larger crystals and provided with a smooth, planar surface by spark cutting, followed by mechanical polishing and electropolishing. Because of the short diffusion length involved ($\sqrt{Dt} \approx 10^{-6}$ cm), it was critically important to have the smoothest possible electrode surface with minimal surface damage. In the early runs with pure Au electrodes, the electropolishing was carried out in fused 1:1 NaCl-KCl at 750° at a constant current of $\sim$ 150 ma/cm^2. In the later runs, including all the alloy runs, an aqueous electropolish was employed, using an H_2SO_4-containing saturated thiourea solution (10). In all cases, a specular surface was obtained. Electron micrographs showed no significant roughness down to 500Å. Laue diffraction patterns showed slight to moderate surface damage, unavoidable in a soft metal such

as gold. In general, the aqueous polish gave more consistent results and less surface damage.

In the runs with a pure Au electrode, the assembled cell was outgassed and heated under vacuum to just below the AgBr melting point with an applied voltage corresponding to a 10 a/o alloy composition at 400°. Interface contact was achieved by flash-melting the electrolyte in the neighborhood of the electrodes or, in one run, by prolonged annealing under pressure just below the melting point. No difference in results was noted. In the gold alloy runs, essentially the same procedure was followed, except that at each temperature, a potential corresponding to the 50:50 composition at that temperature was maintained. Following the interface contacting, the cell was cooled to the operating temperature, placed under an argon flow, and allowed to equilibrate for about an hour. All runs were made at approximately 394°. Minor temperature variations from run to run and within a run were accounted for in the D value calculations by employing a diffusion enthalpy factor from the data of Slifkin *et al.* (11) as will be discussed later.

As reported previously (1), the cell voltage and voltage steps were applied via a straightforward battery-voltage divider setup in which a mercury relay provided noise-free stepping between two preadjusted d-c bias levels. The cell current was recorded by the previously described low-impedance amplifier-recorder arrangement.

Following cell equilibration at the operating temperature (394°), voltage steps were applied at 75-min intervals and the cell current recorded in each case. The voltages employed were generally chosen to correspond to 10 a/o composition intervals in the completely miscible Au-Ag solid solution system. In runs with eight cells in all, the alloy composition range 10-90 a/o Ag was covered for both pure Au and 50:50 Ag:Au alloy as the initial electrode material, and for the two electrode surface preparation techniques described. Cell currents in the range 0-10 μa were read with a sensitivity of 0.01 μa. Cell voltages corresponding to the various compositions ranged 10-231 mv and were set to the nearest millivolt with a resolution of 0.1 mv. At the end of a run, the cells were removed from the furnace assembly and the gold electrode area determined by photographing and weighing the photograph cutout. In all cases, the electrolyte was found to be bonded tenaciously to both electrodes. Electrodes to be used in subsequent runs were repolished mechanically and electrolytically.

For the cell voltages corresponding to the various compositions, the most careful relevant studies were those of Wachter (12) and of Kubaschewski and Huchler (13). Wachter measured the emfs of solid-electrolyte concentration cells Ag|AgCl|Ag-Au for seven different alloy compositions over the approximate range 200°-400° and derived emf-composition plots at 200° and 400°. Kubaschewski and Huchler used similar cells, but with silver-ion-containing Thuringia glass as a solid electrolyte. Eleven alloy compositions were studied in the range 300°-600°. Because of the small temperature coefficient of emf ($\lesssim$0.1% per °C), data at 400° could be employed for our cell systems. Smooth emf-composition curves at 400° were drawn separately from the Wachter and Kubaschewski-Huchler data and a best median curve drawn between them. The average discrepancy of the median curve from either of the parent curves was 3½%.

Results

In all cases, plots of i *vs.* $t^{-1/2}$ were linear over a wide time range. This was the case for both forward (in-diffusion) and reverse (out-diffusion) steps. Figure 1 shows a typical plot for a forward step, showing the time range 6-4500 sec, the latter time being wait time τ (75 min). At times below 10 sec, currents showed a general upturn from linearity attributable

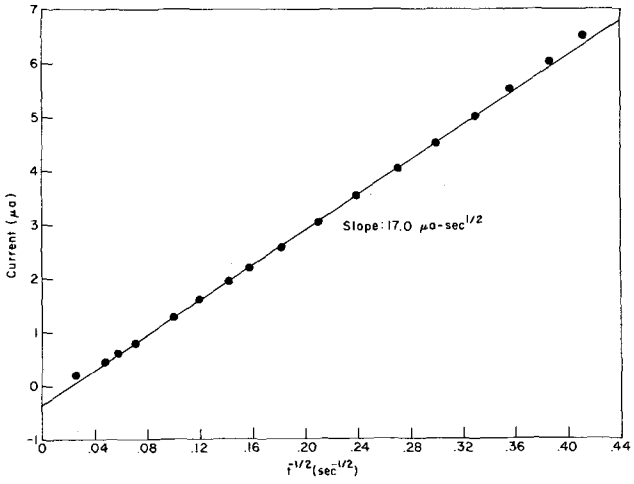

Fig. 1. Current-time data, run 2, 20 → 30 a/o Ag compositional step.

to residual double layer charging. At times in excess of several hundred seconds, there were often small drifts from linear variation, 0.1-0.3 μa at most. Since these were larger than expected from the nonlinearity in $t^{-1/2}$ in Eq. [5] and did not show a consistent direction, they probably represent small furnace temperature drifts. In general, the time range 10-100 sec was used for the slope determinations.

The current intercept in Fig. 1, of opposite sign from the forward diffusion current, represents the sum of the electronic cell current and the time-independent terms in Eq. [5], as previously discussed. All current intercepts were compared with predictions based on Eq. [3] and [5], using the prestep cell current in the equilibrated cell and the current intercept from the first step to predict electronic currents at other cell voltages, and using the slopes of the i *vs.* $t^{-1/2}$ curves to evaluate the terms in Eq. [5]. The match with predictions ranged fair to excellent, the discrepancy averaging 15%. In each case, the qualitative variation predicted for the series of steps in question was observed. The scatter is believed to reflect the sensitivity of the steady-state electronic cell current to temperature fluctuations and low-level impurities.

Several duplicate runs were used to measure the reproducibility of the D values determined. In three early runs, pure Au electrodes, polished by the fused salt technique, were used for 10 a/o forward steps in the composition span 10-60 a/o Ag. In the first two runs, the same Au electrode was simply repolished and used in a new cell. In the third run, a new Au electrode crystal was employed. D values for each composition deviated from their mean by an average of 3%. In addition, duplicate runs were carried out with two 50:50 Ag-Au alloy electrodes, using the aqueous electropolish technique, for 10 a/o forward and reverse steps in the composition span 50-90 a/o Ag. Forward-step D values agreed to an average of 3% and reverse-step values to 10%. As will be discussed later, the latter result is a consequence of the inherently more irreproducible nature of the extractive diffusion process.

The main source of the 3% factor for forward steps is believed to be temperature uncertainty in the runs. Because of the predominant interest in the electrochemical aspects of these runs, insufficient attention was admittedly paid to temperature control. In consequence, the cell temperature was only defined to about ½°. Since Slifkin's data indicates a temperature dependence of D in the Ag-Au system of 5% per °C at our temperature, an approximate 2½% figure can be applied to errors in temperature definition.

In run 8, a pure Au starting electrode was employed, using the aqueous electropolish technique. A series of eight 10 a/o forward steps covered the composition

range 10-90 a/o Ag. This was followed by four 10 a/o reverse steps, the entire run requiring two days. Because of the wide composition range covered, and the more reliable, damage-free surface produced by the aqueous electropolish, the results of this run will be used as a standard of comparison with other runs and with data in the literature.

The most recent and careful study of diffusion in the Ag-Au system has been carried out by Slifkin *et al.* (11) with radiotracer techniques, using nine alloy compositions and temperatures 635°-1010°C. Measurements at lower temperatures were not possible because of the prohibitively low D values. The results, however, were presented in the form of empirical expressions for the various compositions, which could be used to predict values at lower temperatures. Radiotracer diffusion coefficients D^* at 394° were calculated from these expressions and interpolated values taken at our compositions. These were converted to chemical diffusion coefficients by the use of the Darken equation

$$D = D^* [1 + (d \ln \gamma_{Ag})/(d \ln N_{Ag})] \quad [6]$$

a procedure which has previously been found reliable in the Ag-Au system (14). Here, γ_{Ag} and N_{Ag} are the activity coefficient and mole fraction of Ag in the alloy. Since $d \ln \gamma_{Ag} = d \ln a_{Ag}$ and the emf in the Wachter and Kubaschewski-Huchler concentration cells is given by $-F\mathcal{E} = RT \ln a_{Ag}$, the Darken equation reduces to

$$D = D^* \left[1 - \frac{FN_{Ag}}{RT} \frac{d\mathcal{E}}{dN_{Ag}} \right] \quad [7]$$

where $d\mathcal{E}/dN_{Ag}$ can be evaluated directly from the emf-composition curve. Values for the bracketed term ranging from 2.56 to 3.18 were obtained.

Figure 2 shows the run 8 diffusion coefficient data for forward steps and compares it with values calculated from Slifkin's data. All our D value-composition curves showed the same smooth compositional variation with a minimum close to 50%. The slightly different compositional behavior reported previously (1) was found to be the result of less carefully chosen voltage values from the Wachter and Kubaschewski emf-composition data. In Fig. 2, D values in the range 10-50 a/o Ag agree with those calculated from Slifkin's data to an average of 25%, which is reasonable, considering the extrapolation represented and the use of the Darken equation. The calculated values, however, do not show a minimum and hence deviate progressively at more silver-rich compositions. Slifkin's data, however, included a D value-composition plot for Ag at 875° that showed the same type of minimum as ours in the neighborhood of 50 a/o Ag. The appearance of this minimum at 875° and not at 394° is related to the empirical expressions employed. In these expressions, of the usual form $D^* = D^*_0 \exp(-Q/RT)$, a minimum occurs at 875° because of increases in both D^*_0 and Q with increasing silver content. At 394°, the exponential term dominates and no minimum is predicted. Since only small changes in D^*_0 and Q are required to create the minimum at 394°, it is felt that its absence is an artifact of extrapolating the empirical expressions to this temperature. The narrow range of Q values reported (40.2 to 44.5 kcal/mole) and the reasonable agreement with a fair portion of our data allow the use of an average Q value in this range to correct our D values for run-to-run temperature variations of several degrees, as was done.

Figure 3 shows the effect of surface preparation technique on the D value results. The curve for runs 2, 3, and 4 represents an average of the closely agreeing D values from these runs. In these runs, a fused salt electropolish was used, while the aqueous polish was used in run 8. The former curve is seen to be higher by a factor 1.4 to 1.6. As we have noted, aqueous polishing gave more consistently specular surfaces and less surface damage. One effect of aqueous polishing may have been a lower microscopic surface roughness. In this respect, surface roughness is a factor in diffusion measurements if the scale of the roughness is large compared with the characteristic diffusant penetration distance. In this event, in our own experiments, the effect would be to increase the electrode area A in the Cottrell equation. The somewhat greater surface damage from the fused salt polish, however, may also play a role. The reasonable partial agreement between the run 8 values and the extrapolations from Slifkin's data would indicate that the roughness factor in run 8 was not severe. It should be pointed out that these effects of surface preparation are not unique to the electrochemical method, but would be common to any method that measured D values from characteristic diffusant penetration distances this small (30-100Å). In the measurement of larger D values, such effects become correspondingly smaller.

In several runs, the effect of previous compositional cycling was studied. In run 3, for instance, 10 → 60 a/o Ag steps of 10 a/o size were applied to a pure Au electrode, followed by a step 60 → 50 and a repeat 50 → 60 a/o step. A 7% higher D value was obtained for the repeat step. Following this, the cell was stepped to 90 a/o in three further steps, reverse-stepped to 10 a/o in one large step, and the first 10 → 20 a/o step repeated. A 10% larger D value was obtained. In

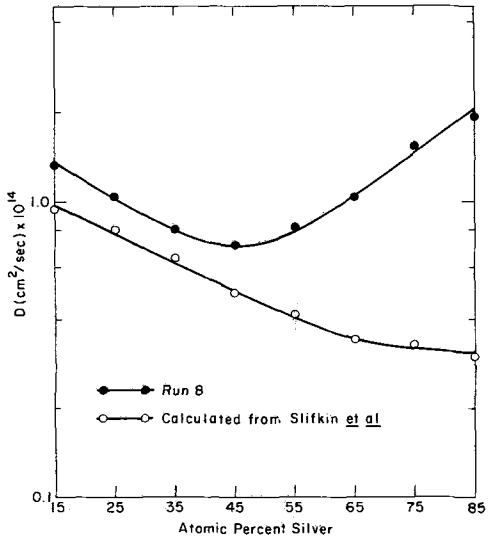

Fig. 2. Calculated and measured (run 8) chemical diffusion coefficient of Ag into Ag-Au alloys at 394°.

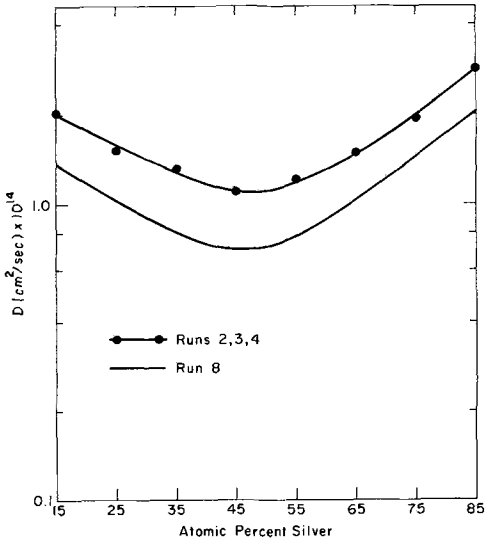

Fig. 3. Comparative in-diffusion D values from runs 2, 3, 4 (fused salt electropolish) and run 8 (aqueous electropolish).

run 4, the same initial sequence 10 → 60 → 50 → 60 a/o was followed, yielding an 8% higher D value for the repeat 50 → 60 step. The cell was then stepped back to 10 a/o in 10 a/o steps and the entire 10 → 60 step sequence repeated. The respective D value increases in these five steps were 15%, 17%, 52%, 70%, and 97%. It was concluded that extensive cycling over the composition range results in significantly increased D values, the increase increasing with the extent of cycling. As will be discussed, the development of surface roughness is felt to be responsible.

The above effect made it a possibility that the D value for any given step in a step sequence may be influenced by the application of prior steps, even for a simple, unidirectional sequence. To check this possibility, it was desirable to do experiments on a bulk Ag-Au alloy of known composition, with steps starting at this composition. For this purpose, 50:50 alloy electrodes were employed in runs 6, 7, and 9. In run 6, the composition was stepped 50 → 10 →50 in eight consecutive 10 a/o steps while, in duplicate runs 7 and 9, the same was done for the range 50 → 90 → 50. A composite D value-composition curve for the forward steps in these three runs is shown in Fig. 4, together with the run 8 (pure Au) curve for comparison. All the electrodes were prepared by the aqueous polishing technique. The good match of the 50-90 points in runs 7 and 9 with the run 8 values shows that no significant "memory" effects are involved in a simple forward step sequence across the composition range. In run 6, however, where the 10 → 50 forward steps were preceded by a reverse step sequence, the D values are about 14% higher. This would indicate that a reverse step sequence introduces such a "memory" into a subsequent forward step sequence.

The electrochemical method permitted, for the first time, a direct comparison between D values corresponding to in-diffusion and out-diffusion in a solid-state system. Wagner and co-workers (15, 16) have examined the process of out- or extractive diffusion from solid-solution alloys in connection with liquid-metal leaching and selective anodic dissolution, but quantitative measurements were not made. In general, no distinction has been made between in-diffusion and out-diffusion in terms of D values. Indeed, the macroscopic equations developed from Fick's laws are symmetric in this regard, permitting no such distinction. Nonetheless, since the electrochemical method permitted such measurements, it was of interest to make them.

In all the measurements, the reverse-step D values showed the same general compositional variation as the forward-step values, but were invariably higher. This was true even when comparing the first reverse step on a 50:50 alloy (50 → 40) with the corresponding forward step (40 → 50) on a pure Au electrode, where cycling effects could not be involved. Likewise, an isolated reverse step in a sequence of forward steps (*e.g.*, 10 → 20 → 30 → 40 → 50 → 60 → 50 → 60) gave a higher D than the corresponding forward step on each side of it. Moreover, as previously noted, more scatter in duplicate runs was observed for reverse steps. Figure 5 shows the combined forward and reverse D values for 50:50 alloy runs 6, 7, and 9.

Forward-reverse D value ratios were available from some 30 steps in various runs. When plotted as a function of composition on a common graph, however, they showed too much scatter to ascertain even a well-defined compositional trend. Scatter between duplicate runs was as great as between runs under different conditions. Accordingly, a smoothing procedure was adopted. In each run, such as in Fig. 5, where a range of forward and reverse D values was obtained, a best smooth curve was drawn through each set of points and the factor relating the two curves determined at each composition. The smoothed data from the various runs clustered together in the range 10-50 a/o Ag, but showed considerable scatter at more silver-rich compositions. In the 10-50 range, the average values of the D_{rvs}/D_{fwd} ratio at 15, 25, 35, and 45 a/o Ag were 1.34, 1.32_5, 1.31_5, and 1.33_5, suggesting a composition-independent ratio of 1.33 ± 1% in this range. At more Ag-rich compositions, there were indications of a general increase, but the scatter of the data was too great to ascertain this.

Finally, in several runs, the effect of step size was examined. In four instances, 10 a/o compositional steps were split into two constituent 5 a/o steps. No significant difference in D values was obtained. In addition, however, in several runs with pure Au electrodes, terminating at high Ag concentrations, a final reverse step was applied to restore the initial pre-step 10 a/o Ag composition. In these cases, considerably enhanced D values were obtained. For the 60 → 10 step in run 2, we obtained $D = 3.4 \times 10^{-14}$ cm²/sec, compared with an average of 1.30×10^{-14} cm²/sec for forward steps in the 10-60 range and an expected average reverse-step D of 1.73×10^{-14} cm²/sec from the use of the 1.33 factor for D_{rvs}/D_{fwd}. For a 90 → 10 step in run 3, a D value of $10.9_5 \times 10^{-14}$ cm²/sec was obtained, clearly in excess of the average D value expected from smaller steps in the run. In such cases, it is apparent that the sudden gross compositional change at the electrode surface results in a drastic alteration in the nature of the surface, making comparison with smaller-sized steps questionable. Finally, it should be

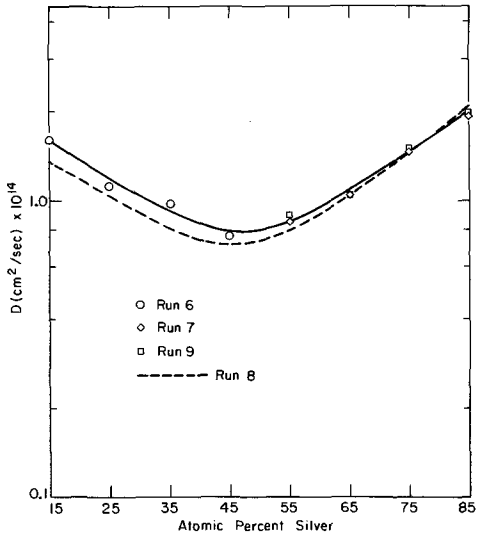

Fig. 4. Comparative in-diffusion D values from runs 6, 7, 9 (Ag-Au alloy electrode) and run 8 (Au electrode).

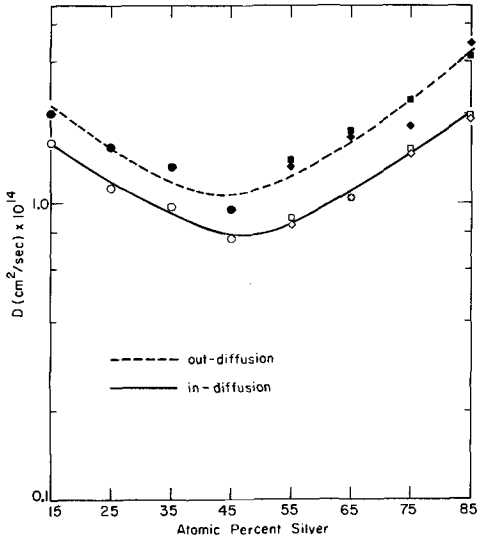

Fig. 5. Comparative in-diffusion and out-diffusion D values for runs 6, 7, and 9. Point designations as in Fig. 4.

pointed out that in all reverse steps, where one is dealing with an anodic removal of Ag into the electrolyte, co-anodization of Au may be ruled out on both thermodynamic and experimental grounds, independent voltammetric experiments in our laboratory having shown that a potential of ~0.6v is required for Au oxidation.

Discussion

In discussing the results, one needs some sort of microphysical picture to describe diffusion processes occurring on and in the neighborhood of the electrode surface. Specifically, explanations must be offered for the observed enhancement of out-diffusion and for the apparent generation of surface roughness in this process. In what follows, we offer what we feel to be a plausible model on the basis of present understanding in this area.

Metallic silver and gold have the same crystal structure (fcc), almost equal lattice parameters, and form a continuous series of substitutional solid solution alloys. Accordingly, diffusion occurs by a vacancy mechanism. In the process of in-diffusion, the Au concentration will be increasing from the surface of the electrode to the interior. Hence, in accordance with Fick's first law, there must be, through any fixed plane parallel to and several atom layers below the surface, an Au flux toward the surface as well as the Ag flux away from it. Therefore, to maintain the fixed Ag:Au ratio in a thus-defined "surface region," more Ag must be plated onto the surface than is diffusing through this plane. Thus, the electrode is growing towards the electrolyte from such a fixed plane. We consider the surface growth in terms of the usual kink-step-terrace picture (16, 17). Previous work in our laboratory (3, 4) has shown that, when a voltage step appropriate for in-diffusion occurs, there is a rapid and uniform enhancement of the Ag concentration in the first atom layer. This, plus considerations of entropy, kink-step populations, and simple kinetics insures that Ag atoms will be deposited mainly on terrace sites, where they may possibly be considered "ad-atoms" (17). To maintain compositional homogeneity, Ag atom diffusion toward step and kink sites must be accompanied by Au atom diffusion, ultimately from the electrode interior. It is suggested that free exchange occurs between Ag atoms on terrace sites and underlying Au atoms, and that the resulting mixture of Ag and Au atoms on terrace sites, in the ratio fixed by the electrode potential, migrates to step and kink growth sites. Thus, plated Ag atoms may be incorporated into the electrode either by migration to such sites or by exchange with Au at terrace sites. In either event, subsequent in-diffusion occurs by the arrival of vacancies from within the electrode. A relatively orderly surface growth pattern is expected, not unlike that for low-current electroplating. An equilibrium concentration of vacancies is assumed to exist throughout the electrode and to be built in on the growing surface at step and kink sites.

In the process of out-diffusion, the same arguments as above require that a reverse voltage step result in a very large concentration of vacancies at terrace sites, produced by electrolytic stripping. In a 50 → 40 a/o Ag step, for instance, one-third of the surface Ag atoms present would be stripped off in several milliseconds. By contrast, one may estimate from Shewmon (18) that the equilibrium vacancy mole fraction in Au at ~400° should be about 3×10^{-8}. Since the diffusion rate by a vacancy mechanism is proportional to the local vacancy concentration, it is apparent that if all or even an appreciable fraction of the electrolytically created vacancies migrated into the electrode interior, there should be an enormous enhancement from the in-diffusion rate in the 30-100Å effective diffusion distances we are studying. The relatively modest enhancement we observe suggests that most of them coalesce on the surface, but that, from strictly random atom movements, enough are "injected" into the interior to cause the observed effect. What we expect, then, is a local supersaturation of the vacancy concentration. Since the exact degree of supersaturation might well be a matter of the precise electrode surface or interface condition, the observed scatter for reverse-step D values is reasonable.

Vacancies thus produced that are not injected into the interior could migrate to step and kink sites, but it seems more likely, from their large concentration, that most of them would coalesce to form local patches. Since the "floors" of such patches are also subject to Ag stripping and vacancy coalescence during the continued out-diffusion process, one has a mechanism for the generation of surface roughness. Harrison and Wagner (15) have asserted, from a macroscopic argument, that a plane alloy surface is unstable during the selective leaching of a component by liquid metal extraction or electrolysis, and that a rugged interface develops. The surface roughness thus introduced would account for the enhanced forward-step D values obtained after a series of reverse steps, both in the runs where cycling effects were encountered, and in the 50:50 alloy runs for the 10 → 50 steps.

In the case of large (60 → 10 and 90 → 10) reverse steps, we are of course dealing with electrolytic dissolution of the major portion of the electrode surface. In such a situation, one actually expects the effective collapse of the entire electrode surface. The observed enhancement of the diffusion rate would then not be surprising in view of the greater likelihood of excess vacancy incorporation.

Applications

In this section, we would like to discuss some of the general applications and limitations of electrochemical methods in studying diffusion in metals and other solid electronically conducting systems at elevated temperatures. Some of the limitations were mentioned in the previous communication. For instance, it is necessary in cells Me|MeX|M′ to employ an electrolyte MeX that does not react chemically with substrate electrode M′. In metal-electrode systems, this requires a metal M′ that is reasonably more noble than Me, and remains a basic limitation. M′, however, might well be a chemically saturated electronically conducting material, such as a compound semiconductor. In this case, one requires the absence of chemical addition and replacement reactions with the electrolyte. It may be possible, in fact, to study thin-layer diffusive doping in systems such as, for instance, Ag or Cu in CdS. A precaution in such systems would be to insure that the diffusion current does not result in excessive iR drop in the semiconductor, or to compensate for such effects, either instrumentally or in the data analysis. A distinct possibility that follows from the ability to conduct out-diffusion as well as in-diffusion would be the creation of junctions, such as by following a long in-diffusion period with a short-lived out-diffusion. Selective doping of particular surface areas might be accomplished by suitable shaping of the solid electrolyte, either in pellet or evaporated-film configuration, or by conventional masking.

While the above-described methods were developed for solid electrolytes, one may in principle conduct similar studies with fused salt electrolytes. In our own laboratory, we have observed suitable polarization characteristics in the cell Ag|AgBr(l)|Pt. While steady-state cell currents were higher than for AgBr(s) cells, they showed the expected voltage dependence for electronic currents and can be handled by the use of current-compensating potentiostatic power supplies. A variation would be the use of the diffusant compound in question, MeX, as a dilute solute in an inert fused-salt solvent such as an alkali halide mix. There remains, however, a range of un-

explored solid electrolytes (halides of Cu, Pb, Cd, Tl, alkali and alkaline earth metals) as well.

We have noted that a diffusion current, to be observable in cells of this type, must be large enough to be seen against the steady-state cell current for a reasonable time after the electrode interface is charged. While current compensation can be used to remove a portion of the steady-state cell current, residual currents and noise define a lower limit. The Cottrell equation (Eq. [2]) shows the factors involved in the size of the diffusion current. Electronic and noise effects increase linearly with cell area A, so A is not a parameter of interest. The quantity $\Delta CD^{1/2}$ is the controlling one. Since the maximum value of ΔC in the system is the diffusant solubility C_s, there is an inverse relation between the lowest detectable value of D and C_s. In our own system (complete solubility), D values $\sim 10^{-14}$ cm^2/sec were measured readily; less accurate values several orders of magnitude lower could have been measured with one or several large steps. Using this as a criterion for the lower-limit size of $C_sD^{1/2}$, a dopant-level C_s of 2 x 10^{18} carriers/cm^2 with a D value of 10^{-9} cm^2/sec could be studied, provided similar influences of the interface charging time and steady-state cell current prevailed.

An important consideration in our own work was the activity-composition relation in the Ag-Au system, in that the surface diffusant concentration could not be fixed electrochemically without these data. In alloy systems with wide solid solution ranges, such data would be required, either from pre-existing work or from a separate series of concentration-cell experiments with a number of alloys of suitable composition. In systems with C_s small enough to obey Henry's law, a knowledge of this solubility would suffice. These considerations, however, apply to systems with relatively small D values.

In systems where the D value is large enough for $\sqrt{Dt}$ to be comparable with the thickness of a thin-film electrode in a reasonable time t, a number of methods are available for determining D and C_s in the same experiment. In the coulometric titration method of Wagner (19), for instance, the cell voltage can be stepped from one value to another, the cell permitted to equilibrate completely, and the total charge transfer used to determine the material dissolved corresponding to the known change in activity level in an electrode of known volume. In another method, Rickert (20) has shown in the case of oxygen diffusion in silver, that D and C_s may be separated by studying semi-infinite linear diffusion and inward diffusion from the surface of a cylinder in separate cells, since the differing forms of the diffusion equations for the two cases allow such separation when $\sqrt{Dt}$ is comparable with the radius of the cylinder. Rapp (21) has measured both D and C_s, in studying oxygen diffusion in copper, by analysis of the current-time function where an electrode is being saturated with oxygen by joined cells on either side.

In systems with relatively high D values, some intriguing experiments should be possible by using separate cells on a common electrode to "transmit" and "receive" the diffusant. A possible arrangement of this type would be Me|MeX|M'|MeX|Me. If both cells are initially set to define a low, common value of a_{Me} in a slab or foil electrode of metal M', and the voltage on one is stepped to an appreciable a_{Me}, metal Me will be transmitted into M' from this cell and, when it arrives at the other side, will be anodically stripped by the second cell, giving rise to an observable stripping current. Eventually, the same current is seen in both cells, corresponding to the steady-state flux of diffusant down a known, linear activity gradient. The steady-state flux and the time required to reach it provide determinations of D and C_s. The method is analogous to the well-known "lag time" method for studying gas permeation in solid membranes (22). A plot of the integrated diffusion current in the second cell as a function of time would give a linear "steady-state" portion which may be back-extrapolated to the time axis to give lag time $\tau = x^2/6D$, where x is the electrode thickness. A sequence of alternating a_{Me} increases on the two sides would in principle permit determination of D and C_s values over the full range of diffusant activities. In a variation of this approach, it might be possible to study surface diffusion on a metallic specimen by means of Me|MeX> "probe" cells (Me wires coated with MeX), serving as diffusant sources and sinks at various points on the surface.

Finally, mention should be made of possible galvanostatic methods for studying diffusion electrochemically. In an alloy cell Me|MeX|M'-Me, for instance, we may apply a constant current sweep that anodically strips Me from the alloy and monitor the potential-time variation. In this, the sweep ultimately depletes the alloy surface of diffusant, resulting in a potential surge; the "transition time" for this is given by the Sand equation (23). An alternative galvanostatic method was employed by Rapp in the above-mentioned copper-oxygen study (21), where D was measured from the slope of a current-time function plot. Such methods do not offer any advantages over potentiostatic ones in separating D and C_s, are subject to interference from double layer charging and electronic cell currents, and give a mean value of D when compositional variation is involved, but may supply useful and rapidly obtained complementary data in suitable circumstances.

Acknowledgments

The authors are extremely grateful to Professor Lawrence M. Slifkin for the gift of a 50:50 Ag:Au alloy single crystal and to Mr. James Savage of our laboratory for growing several gold single crystals. Helpful discussions and suggestions from Professor Carl Wagner and Dr. A. Sosin are gratefully acknowledged. The authors are grateful to Professor Carl Wagner for pointing out that the diffusion treatment in the present case should include a correction to account for the movement of the electrode boundary during diffusion. Because of its complexity, this correction will be discussed in a future communication.

Manuscript submitted June 17, 1968; revised manuscript received *ca.* Aug. 21, 1968.

Any discussion of this paper will appear in a Discussion Section to be published in the June 1969 JOURNAL.

REFERENCES

1. D. O. Raleigh, *This Journal*, **114**, 493 (1967).
2. C. Wagner, *Proc. Int. Comm. Electrochem. Thermo. Kinetics (CITCE)*, **7**, 361 (1957); *Z. Elektrochem.*, **60**, 4 (1956).
3. D. O. Raleigh, *J. Phys. Chem.*, **70**, 689 (1966).
4. D. O. Raleigh, *ibid.*, **71**, 1785 (1967).
5. G. Lauer and R. A. Osteryoung, *Anal. Chem.*, **38**, 1106 (1966).
6. D. O. Raleigh, "Progress in Solid State Chemistry," Vol. 3, Ch. 3, pp. 104-7, H. Reiss, Editor, Pergamon Press, Oxford (1967).
7. H. S. Carslaw and J. C. Jaeger, "Conduction of Heat in Solids," pp. 62-64, Oxford University Press, London (1957).
8. See, for instance, J. Crank, "The Mathematics of Diffusion," pp. 11-12, Oxford University Press, London (1957).
9. P. G. Shewmon, "Diffusion in Solids," pp. 14-15, McGraw-Hill Book Co., New York (1963).
10. P. A. Jacquet, *Met. Rev.*, **1**, 157 (1956).
11. W. C. Mallard, A. B. Gardner, R. F. Bass, and L. M. Slifkin, *Phys. Rev.*, **129**, 617 (1963).
12. A. Wachter, *J. Am. Chem. Soc.*, **54**, 4609 (1932).
13. O. Kubaschewski and O. Huchler, *Z. Elektrochem.*, **52**, 170 (1948).
14. See, for instance, ref. (9), pp. 125-7.
15. J. D. Harrison and C. Wagner, *Acta Met.*, **7**, 722 (1959).

16. H. W. Pickering and C. Wagner, *This Journal*, **114**, 698 (1967).
17. B. E. Conway and J. O'M Bockris, *Electrochim. Acta*, **3**, 340 (1961).
18. Ref. (9), p. 57.
19. C. Wagner, *J. Chem. Phys.*, **21**, 1819 (1953).
20. H. Rickert and R. Steiner, *Z. Physik. Chem. N.F.*, **49**, 127 (1966).
21. R. A. Rapp, Vienna Symposium, IAEA, Sept. 1967.
22. R. M. Barrer, "Diffusion in and through Solids," p. 217, Cambridge University Press (1951).
23. See, for instance, P. Delahay, "New Instrumental Methods in Electrochemistry," p. 182, Interscience Publishers, New York (1954).

Void Fraction and Current Density Distributions in a Water Electrolysis Cell

J. E. Funk
University of Kentucky, Lexington, Kentucky

and J. F. Thorpe
University of Cincinnati, Cincinnati, Ohio

ABSTRACT

An analytical basis defining the steady-state conditions occurring in an electrolysis cell is stated. Several assumptions are made which permit a theoretical determination of the void fraction and current density distributions. The effect of void fraction and inlet velocity on cell performance is shown. Experimental data for the void fraction and slip ratio occurring in an electrolysis cell are presented. It is found that the slip ratio is near unity. This result is of importance in defining the cell void fraction distributions and is prerequisite to an analysis of pressure drop in electrolysis cells.

There has been a renewed interest recently in the water electrolysis process. This is due to the potential of this process for life support systems in both space and deep-sea applications (1, 2). The water electrolysis process is also being considered on a large scale in connection with industrial complexes which can desalt water, produce power and other products such as hydrogen, oxygen, ammonia, ammonium nitrate, and nitric acid (3, 4). The energy source for such a complex could be a very large nuclear reactor which would be coupled to a large electrolyzer system (5).

In the design of water electrolyzers there is a need for basic engineering information concerning electrode materials, electrolytes, electrolyzer control, and the two-phase hydrodynamics and heat transfer. The current density distribution and the pressure drop, in particular, are two areas of research in which there is little published data. Concurrent with these problems is that of predicting the void fraction (or slip ratio) in an electrolysis cell. The present paper presents the results of the first of two research programs (6) designed to fill this need. The first program is an experimental and analytical investigation of void fraction (or slip ratio) in an electrolysis cell. This program is prerequisite to the second research program which involves an experimental investigation of pressure drop in an electrolysis cell. Both programs require an analytical model for experimental data reduction. The first part of this paper presents the analytical basis while the later section presents the void fraction and slip ratio data. The pressure drop data and correlations will be presented in a separate paper since this work is still in progress.

The electrolysis process is complicated because of the simultaneous occurrence of coupled, nonlinear transport of mass, momentum, and energy in the presence of electrochemical reactions in the electrolyte and on the electrodes. The precise definition of these processes requires the statement and simultaneous solution of a set of coupled, nonlinear, partial differential equations. In view of the magnitude of the task of solving this set of equations, one dimensional (or hydraulic) equations will be used to define the flow in an electrolysis cell configuration such as is sketched in Fig. 1. The approach is essentially that which has been outlined by Brodkey (7) and used extensively in the field of two-phase flow (7-9). In this problem, however, there is the additional complication of interchannel cross flow through the porous membrane.

The first significant work on such a problem was by Tobias (10) who discussed previous work and then presented an analytical solution for the void fraction subject to the assumptions: (*a*) zero cell inlet velocity, (*b*) no membrane in the cell, (c) gas velocity independent of void fraction, and (*d*) constant electrode polarization.

Aside from Tobias' work there seem to be no significant publications directly applied to the water electrolyzer cell. There are, however, several papers on electrochemical machining (ECM) in which an allied problem is discussed (11-14). The purpose of this paper is to present a more general analytical basis for the flow in an electrolyzer cell and to provide some preliminary experimental data which may be useful in electrolyzer engineering.

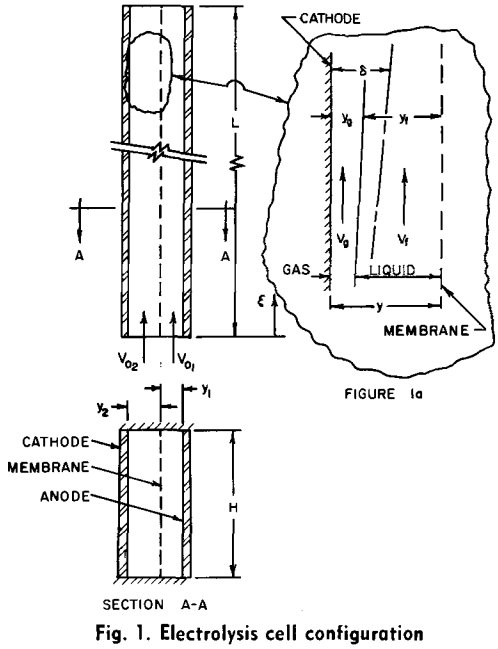

Fig. 1. Electrolysis cell configuration

Analytical Basis

Consider the electrolysis cell configuration sketched in Fig. 1. The electrolyte flow is from the bottom toward the top in a cell of width H and length L. The cell consists of two parallel channels separated by a membrane. Flow in the hydrogen side consists of a mixture of hydrogen gas and electrolyte in a thin rectangular channel (H by y_2) formed between the membrane and cathode. Flow in the oxygen side consists of a mixture of oxygen gas and electrolyte in a rectangular channel (H by y_1) formed between the membrane and anode. The membrane is assumed to be porous to OH^- ions and possibly to liquid electrolyte. Subscript 1 denotes the flow properties on the oxygen side while subscript 2 denotes properties on the hydrogen side. Various species within a given channel are identified by the subscripts g for gas, f for electrolyte, and i for hydroxyl ion. Since only an alkaline electrolyte is considered, the hydrogen ion is neglected.

The transverse current density (current flux) ϕ in the cell is a function of axial position ξ. If the cell is vertical then ξ is identical with the coordinate z. The current flux generates hydrogen gas on the cathode at the local mass flux rate $\dot{m}_{2g}$. The hydrogen gas flows upward with average velocity V_{2g} in some equivalent area proportional to the dimension y_{2g}. The gas bubbles, or voids, are contained within an electrolyte layer near the cathode surface which is called the hydrogen bubble layer of thickness δ_2.

The liquid electrolyte flow on the hydrogen side occurs with average velocity V_{2f} in an equivalent area proportional to y_{2f} where

$$y_2 = y_{2g} + y_{2f} \qquad [1]$$

A similar flow configuration exists on the oxygen side where oxygen gas is liberated on the anode at the local mass flux rate $\dot{m}_{1g}$ and then flows upward with average velocity V_{1g} in an equivalent area proportional to y_{1g}. The oxygen bubble layer thickness is δ_1 and the electrolyte flow on the oxygen side has velocity V_{1f} in an area proportional to y_{1f} where

$$y_1 = y_{1g} + y_{1f} \qquad [2]$$

A hydroxyl ion flux occurs through the membrane which has the net effect of transporting H_2O from the cathode side to the anode side of the cell. In addition to the ion flux, the membrane may be porous to the liquid electrolyte. These fluxes through the membrane are denoted by $\dot{m}_i$ and $\dot{m}_f$, respectively.

The definitions and derivations which follow will apply to either hydrogen or oxygen sides of the cell so that, in the interest of simplifying the notation, the numerical subscript will be omitted.

The gas quality x, sometimes called the flowing quality, is defined by the equations

$$x = \frac{w_g}{w}\,;\ (1-x) = \frac{w_f}{w} \qquad [3]$$

where

$$w_g = \rho_g A_g V_g = \text{mass flow rate of gas} \qquad [4]$$

$$w_f = \rho_f A_f V_f = \text{mass flow rate of liquid} \qquad [5]$$

$$w = w_g + w_f = \text{total mass flow rate} \qquad [6]$$

and ρ_f = liquid density, ρ_g = gas density, $A_f = Hy_f$ = area occupied by liquid, $A_g = Hy_g$ = area occupied by gas, V_f = average liquid velocity, and V_g = average gas velocity.

The gas volume fraction α, sometimes called the void fraction, and the liquid holdup $(1-\alpha)$ are defined by

$$\alpha = \frac{A_g}{A}\,;\ (1-\alpha) = \frac{A_f}{A} \qquad [7]$$

where

$$A = A_g + A_f = Hy \qquad [8]$$

If Eq. [3] to [7] are combined, the following equation is obtained

$$\left(\frac{1-\alpha}{\alpha}\right) = \sigma\left(\frac{1-x}{x}\right)\left(\frac{\rho_g}{\rho_f}\right) \qquad [9]$$

where σ is the slip ratio (also called the phase velocity ratio) defined by

$$\sigma = \frac{V_g}{V_f} \qquad [10]$$

In general, the slip ratio σ depends on pressure p, void fraction α, mass flow rate w, channel area A, density ratio ρ_g/ρ_f, and channel orientation (15-17). That is, in general

$$\sigma = \sigma(p,\alpha,w,A,\rho_g/\rho_f) \qquad [11]$$

One of the major efforts of two-phase flow research is to determine the function σ.

Most of the engineering quantities of interest in an electrolysis cell, such as ohmic resistance of electrolyte or pressure drop, are functions of the void fraction α; the void fraction depends, in turn, on the slip ratio σ which is generally unknown. There are several models which express the void fraction-slip ratio relationship (15-17). The simplest model is called the fog-flow or homogeneous model in which σ is taken to be unity.

Continuity equations.—Assuming the flow in the cell to be steady, application of the law of conservation of mass to the gas and liquid electrolyte phases of Fig. 1a yields the following equations

$$\frac{d}{d\xi}(\rho_g y_g V_g) = \dot{m}_g \qquad [12]$$

$$\frac{d}{d\xi}(\rho_f y_f V_f) = -\dot{m}_g + (\pm)\dot{m}_i + (\pm)\dot{m}_f \qquad [13]$$

where the mass flux rate $\dot{m}_g$ is given by

$$\dot{m}_g = \lambda_g \phi \qquad [14]$$

and

$$\lambda_g = \frac{M_g}{\epsilon_g} \qquad [15]$$

The atomic weight of the gas is M_g while its valence on electrolytic decomposition is ϵ_g. The proportionality constant λ_g is the electrochemical equivalent.

The mass flux $\dot{m}_f$ is nonzero only if the membrane is porous to liquid electrolyte; if the membrane does have this porosity, then both the magnitude and sign of the term $\dot{m}_f$ depend on the pressure distributions along the two sides of the membrane.

The hydroxyl ion flux $\dot{m}_i$ can be related to the flux $\dot{m}_g$ from the equation of the electrochemical reaction occurring in the channel. On the cathode side, for example, the equation is

$$\textit{cathode:} \qquad 2H_2O + 2e^- \rightarrow 2\,OH^- + H_2 \qquad [16]$$

For every gram of hydrogen generated on the cathode side, there are 17g of hydroxyl ions passing through the membrane; this ion flow is provided by the liquid electrolyte phase. Thus on the cathode side, the minus (—) sign is selected for $\dot{m}_i$ and

$$\textit{cathode:} \qquad \dot{m}_i = -17\dot{m}_g \qquad [17]$$

On the anode side, the electrochemical reaction is

$$\textit{anode:} \qquad 2\,OH^- \rightarrow \frac{1}{2}O_2 + H_2O + 2e^- \qquad [18]$$

Thus for every gram of oxygen generated, there are 2.125g of hydroxyl ions flowing through the membrane into the oxygen channel. In this instance, the plus (+) sign is selected for $\dot{m}_i$ and

$$\textit{anode:} \qquad \dot{m}_i = 2.125\dot{m}_g \qquad [19]$$

Using the definitions made previously, the continuity equations can be rewritten in the forms

$$\frac{d}{d\xi}(\rho_g \alpha \sigma y V_f) = \lambda_g \phi \quad [20]$$

$$\frac{d}{d\xi}[\rho_f(1-\alpha)yV_f] = (\gamma - 1)\lambda_g\phi + (\pm)m_f \quad [21]$$

where

$$\left\{ \gamma = \begin{matrix} -17 \text{ cathode side} \\ +2.125 \text{ anode side} \end{matrix} \right\} \quad [22]$$

Equation of motion.—Application of the law of motion to the two-phase mixture flowing in the channel between membrane and electrode gives the equation

$$\alpha\rho_g \frac{d}{d\xi}\left(\frac{\sigma^2 V_f^2}{2}\right) + (1-\alpha)\rho_f \frac{d}{d\xi}\left(\frac{V_f^2}{2}\right) + \frac{dp}{d\xi} + \frac{2\tau}{y} + [\alpha\rho_g + (1-\alpha)\rho_f]g\frac{dz}{d\xi} + \frac{\sigma\lambda_g\phi V_f}{y} = 0 \quad [23]$$

In deriving this equation, the following assumptions have been made

(*a*) The production of gas has been assumed to occur at the electrode surface from liquid electrolyte which is at rest on the electrode surface. This gas must be accelerated to the gas velocity V_g by the gas phase pressure gradient. This effect is represented by the momentum flux term which is the last term of Eq. [23].

(*b*) The transverse pressure gradient has been assumed negligible so that the same axial pressure gradient occurs in each phase.

Energy equation.—The energy transport of the gas phase will be assumed negligible due to the low thermal conductivity and heat capacity of the gas compared to the electrolyte. Application, then, of the first law of thermodynamics to the liquid electrolyte gives the equation

$$\rho_f V_f \frac{dT}{d\xi} = \frac{R\phi^2}{C_f(1-\alpha)y} + \frac{\mu\Phi}{C_f} \quad [24]$$

where R is the electrical resistance of the electrolyte-bubble mixture, C_f is the liquid specific heat, and μ is the viscosity. The first term on the right side is the electrical dissipation while the second term is the viscous dissipation.

Electrical equations.—Consistent with the one-dimensional transport equations of continuity, momentum, and energy, stated above, is a one-dimensional transport equation of charge within the electrode gap. However, such an equation will involve ion mobilities, electrochemical reactions, and other complicated processes and will not be presented here. Rather, the electrical phenomena will be represented by a simple form of Ohm's law.

Let the sum of the electrode polarization and decomposition potentials be denoted by ΔE while the applied voltage is E. Then the voltage E' available for overcoming Ohmic resistance of the two-phase electrolyte is given by

$$E' = E - \Delta E \quad [25]$$

and

$$E' = \phi R_c \quad [26]$$

where R_c is the Ohmic resistance of the cell. This resistance consists of a membrane resistance R_m in series with resistances R_1 and R_2 of the electrolyte-bubble mixtures in the oxygen and hydrogen channels of the cell. That is

$$R_c = R_1 + R_m + R_2 \quad [27]$$

The resistances R_1 and R_2 are functions of the properties of pure liquid electrolyte, the void fraction α, and the temperature T.

The cross section of a channel occupied by gas at position ξ is proportional to y_g. This void is distributed within some bubble layer of thickness δ. The void fraction α' based on bubble layer thickness (that is, the void fraction within the bubble layer) is defined by

$$\alpha' = \frac{y_g}{\delta} \quad [28]$$

The resistance within the bubble layer is some function of α' rather than α.

The total transverse resistance, per unit cross sectional area perpendicular to y, is

$$R = r_{tp}\delta + r_f(y - \delta) \quad [29]$$

where r_{tp} is the two-phase resistivity in the bubble layer and r_f is the liquid electrolyte resistivity. The quantity r_f is, in general, temperature dependent. That is

$$r_f = r_f(T) \quad [30]$$

The two-phase resistivity, in the bubble layer, is a function of α' assumed to be of the form

$$r_{tp} = r_f f(\alpha') \quad [31]$$

The function f is determined from some void fraction-resistivity model which assumes a homogeneous distribution of bubbles within an electrolyte matrix. The simplest such relation would be

$$f(\alpha') = \frac{1}{1-\alpha'} \quad [32]$$

Tobias (10) proposed that

$$f(\alpha') = \frac{1}{(1-\alpha')^{1.5}} \quad [33]$$

while Mashovet's (18) equation is

$$f(\alpha') = \frac{1}{1 - 1.78\alpha' + \alpha'^2} \quad [34]$$

Mashovet's equation is empirical and valid for spherical inclusions forming void fractions up to 74%.

It can be noted that

$$\alpha' = \frac{y}{\delta}\alpha \quad [35]$$

so that Eq. [29] can be written as

$$R = r_f\left[(y - \delta) + \delta f\left(\frac{y}{\delta}\alpha\right)\right] \quad [36]$$

The electrode polarization overvoltages are assumed to obey Tafel (19) equations of the form

$$\Delta E_p = a + b \ln \phi \quad [37]$$

where a, b are constants depending on electrode material, electrolyte, temperature, and pressure. Denoting the decomposition potential by ΔE_d, then

$$\Delta E = \Delta E_{p1} + \Delta E_{p2} + \Delta E_d \quad [38]$$

Equations [25], [26], [27], [36], [37], [38] can be combined to give an implicit relation between the applied voltage E, current density ϕ, void fractions α_1, α_2, bubble layers δ_1, δ_2, and temperatures T_1, T_2. That is

$$\phi = \phi(E, \phi, \alpha_1, \alpha_2, \delta_1, \delta_2, T_1, T_2) \quad [39]$$

Recapitulation.—The equations above represent a one-dimensional approximation of the processes occurring within the electrolysis cell. As they stand, they involve more unknowns than there are equations so that additional relations are required. Additional equations will be the equations of state of oxygen and hydrogen gases, empirical relations for the shear stresses, and either empirical or theoretical expressions for the slip ratios. Although this is a complicated system it does represent a sound description of the electrolysis cell hydrodynamics and could be programmed for computer solution if desired.

One of the objectives of the present paper is to present a parametric study of void fraction and current density distributions as functions of certain input variables. Consistent with this limited objective are certain simplifying assumptions which can be listed as follows:

(*A*) Both gas and liquid flows are assumed to be incompressible and isothermal. This assumption permits a great analytical simplification of the problem in that it decouples the continuity and resistivity equations from the momentum and energy equations.

(*B*) The bubble layers are assumed to extend completely across the channels. This assumption is justified from experimental visual observations which show the bubble layer to fill the channel except in a short entrance region.

(C) The membrane is assumed to be permeable only to the hydroxyl ion flux and not to liquid electrolyte.

With the above assumptions, the system of equations reduces to a set in which there are only three more unknowns than equations; these unknowns are the applied voltage E and the slip ratios σ_1, σ_2. If E, σ_1, σ_2 are regarded as parameters, then the system of equations can be solved simultaneously for the α and ϕ distributions; this suggests a parametric study of the effect of slip ratios σ_1, σ_2 and cell voltage E on void fraction and current density distributions. Since integration of the equations will bring the cell inlet velocity into the problem as a boundary condition, the inlet velocity will also be a parameter.

Void fraction and current density distributions.— Equations [20], [21], can now be written in the forms

$$\frac{d}{d\xi}(\alpha\sigma y V_f) = \frac{\lambda_g}{\rho_g}\phi \qquad [40]$$

$$\frac{d}{d\xi}[(1-\alpha)yV_f] = (\gamma-1)\frac{\lambda_g}{\rho_f}\phi \qquad [41]$$

Assuming the electrolysis cell is vertical ($\xi = z$) and integrating these equations from inlet ($z = 0$) to some point z, it can be shown that

$$\frac{\alpha}{1-\alpha} = \frac{\frac{\rho_f}{\sigma\rho_g}I}{(\gamma-1)I + \Gamma_0} \qquad [42]$$

where

$$\Gamma_0 = \left(\frac{y}{L}\right)\left(\frac{\rho_0 V_0}{\phi_0 \lambda_g}\right) \qquad [43]$$

$$I = \int_0^{z^0} \phi^0 dz^0 \qquad [44]$$

$$\phi^0 = \frac{\phi}{\phi_0} \qquad [45]$$

$$z^0 = \frac{z}{L} \qquad [46]$$

Equation [42] can be applied to either the oxygen or hydrogen sides by affixing subscripts 1 or 2, respectively, to the quantities α, σ, γ, Γ_0, ρ_g. The subscript 0 denotes inlet conditions where $\alpha = 0$. The superscript 0 denotes dimensionless quantities.

The electrical requirement can now be expressed by the equation

$$E - [(a_1 + a_2) + (b_1 + b_2)\ln\phi + \Delta E_d] = \phi\{R_m + r_f[y_1 f(\alpha_1) + y_2 f(\alpha_2)]\} \qquad [47]$$

Equation [47] along with two equations of the type [42] are a set of three equations in three unknowns α_1, α_2, ϕ and four parameters E, σ_1, σ_2, V_0. These equations have been programmed for numerical solution on a digital computer and solved for a specific cell design as defined in Table I. The computations were carried out using Mashovet's equation [34] for f along with the assumption that the slip ratios σ_1, σ_2 on the two sides of the cell are the same.

Table I. Cell design and conditions

Geometry	Properties	Parameters
y_1 = 1/16 in. y_2 = 1/8 in. H = 2 in. L = 48 in.	p = 300 psi T = 160°F 6M KOH ΔE_d = 1.2v r_f = 0.31 ohm-in. R_m = 0.58 ohm-in.^{2}	σ = 1.1, 10 V_0 = 0.05, 0.25 ft/sec E = 3, 5.3, 8.9v

Polarization overvoltages

ϕ, amp/ft^2	ΔE_{p1}, v	ΔE_{p2}, v
0	0	0
400	0.38	0.17
800	0.43	0.21
1200	0.46	0.24
1600	0.48	0.25

The results are displayed in Fig. 2, 3, and 4. Figure 2 shows dimensionless current density distributions as functions of cell voltage and slip ratio. The effect of slip ratio is more pronounced at higher cell voltages and the reason lies in the effect of slip ratio on void fraction. As the slip ratio increases the void fraction decreases causing a decrease in the ohmic resistance

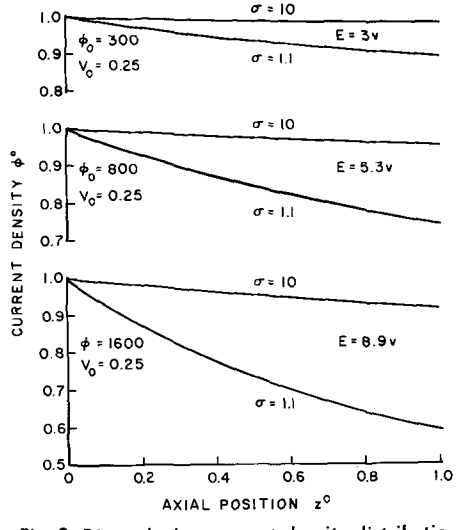

Fig. 2. Dimensionless current density distribution

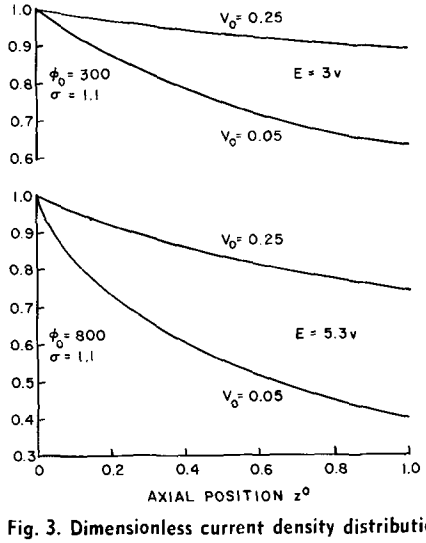

Fig. 3. Dimensionless current density distribution

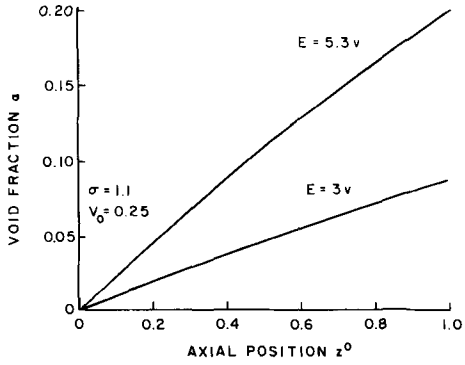

Fig. 4. Axial void fraction distribution

of the electrolyte. At high cell voltages the void fraction will be high and more sensitive to the slip ratio.

Figure 3 shows the effect of the inlet velocity and cell voltage on current density distributions for a slip ratio of 1.1. It is seen that cell inlet velocity is very important and becomes most important for higher cell voltages. This effect is due to the fact that at higher electrolyte velocities the cell void fraction is lower.

Figure 4 shows the void fraction distributions along the cell for two different cell voltages and a slip ratio of 1.1. The void fraction distributions were found to be practically identical in the two sides of the cell so that only single curves are shown in Fig. 4. This result occurs because the inlet velocities were assumed equal in both hydrogen and oxygen channels and is discussed in more detail below.

Approximate relations.—In a forced convection electrolysis cell, the liquid throughput mass flow rate will ordinarily be much larger than the mass rate of conversion of liquid to gas. In other words the term Γ_0 of Eq. [42] is much larger than the term $(\gamma - 1)I$. Under such circumstances, Eq. [42] simplifies to

$$\alpha = \frac{1}{1 + \frac{\rho_g}{\rho_f}\sigma\frac{\Gamma_0}{I}} \qquad [48]$$

Suppose, in designing a cell, the channel dimensions, y_1, y_2 of the oxygen and hydrogen sides are to be chosen so that the void fractions α_1, α_2 are the same in the two flow channels. Equation [48] then will show that

$$\frac{y_1}{y_2} = \left(\frac{\lambda_{g1}}{\lambda_{g2}}\right)\left(\frac{\rho_{g2}}{\rho_{g1}}\right) \qquad [49]$$

where it has been assumed that the cell inlet velocities and slip ratios are identical. Now

$$\frac{\lambda_{g1}}{\lambda_{g2}} = 8\,; \quad \frac{\rho_{g2}}{\rho_{g1}} \cong \frac{1}{16}$$

Therefore

$$\frac{y_1}{y_2} = \frac{1}{2}$$

This result is expected because there are 2 moles of hydrogen gas formed for each mole of oxygen gas; this result serves as a check on the analytical formulation. It should be emphasized, however, that simply setting $y_1 = 1/2\ y_2$ will not assure equal void fractions in the two channels because the inlet velocities V_{20}, V_{10} will not necessarily be equal. The values V_{20}, V_{10} depend strongly on the pressure distributions in the two parallel channels.

By combining the expression [48] with an approximation for the pressure drop across the cell it could be shown that the pumping power of an electrolyzer is related to void fraction through an equation independent of electrical resistance. Use of these relations would make possible an optimization study of total cell power requirements with respect to the cell parameters.

The results shown in Fig. 2, 3, and 4 indicate the importance of the slip ratio to the axial current density distribution. This parameter also plays an important role in the axial pressure distribution. For these reasons the experimental apparatus described below was constructed. One of the main objectives of this apparatus was the experimental determination of the slip ratio for both hydrogen and oxygen gases.

Experimental

Apparatus.—The flow loop used to perform the electrolysis experiments is shown schematically in Fig. 5. The loop comprises a pump, filter, rotameters and valving, the electrolyzer cell, and separators for the hydrogen and oxygen gases. The cell has an entrance length of 20 in. to allow the flow to become established before entering the electrolyzer section. As shown in Fig. 6, the cell is made up of two rectangular channels separated by a semipermeable membrane. The membrane is polystyrene coated Nylon held between two thin slotted pieces of Plexiglas. Polystyrene coated Nylon is used as the membrane because it combines low channel cross flow with acceptable electrical resistance.

The electrodes are segmented axially, and the current flow to each of the six sections is controlled. Pressure taps are placed axially along the cell at the inlet to each of the electrode sections and at the channel outlet on both anode and cathode sides. The axial pressure distribution is measured and recorded for each experiment. The void fraction is measured by means of a gamma ray attenuation system utilizing a Cesium 137 source of 0.62 Mev gamma rays. This system is shown schematically in Fig. 7.

A typical experiment is run by first setting the electrolyte flow on both the hydrogen and oxygen sides of the cell. The same voltage is then applied to

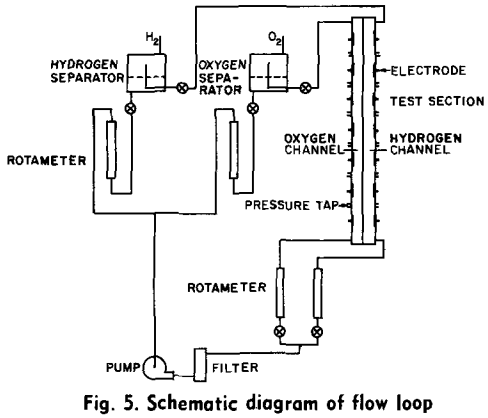

Fig. 5. Schematic diagram of flow loop

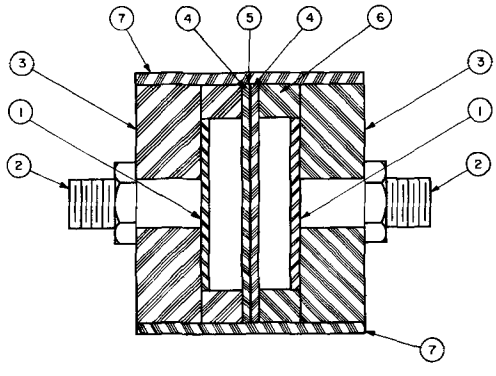

Fig. 6. Electrolysis cell cross section: 1, electrodes; 2, electrode terminals; 3, Plexiglas back up plates; 4, slotted Plexiglas membrane support; 5, semipermeable membrane; 6, channel spacers; 7, Plexiglas straps.

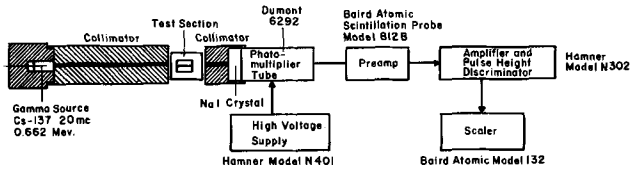

Fig. 7. Void fraction detection system

each of the six electrode sections. The total current flow is recorded and is used to calculate the total mass flow of gas at the channel outlet. The total vapor flowrate is calculated by assuming that the hydrogen and oxygen gases are saturated with water vapor. The outlet void fraction is determined from the gamma ray attenuation. The total 3-min count was measured three times and averaged. The void fraction is calculated directly from the increased (over-all liquid) count when the gases are present.

Results.—The experimental results are shown in Fig. 8 through 12. Figures 8 and 9 show the data plotted so that Eq. [9] can be used directly to determine the slip ratio, σ. The limits of experimental error are also shown and indicate that the experimental accuracy becomes very poor at low void fractions. These results indicate that the slip ratio is very near unity in both channels and possibly slightly higher (about 1.1) in the hydrogen channel. This result is consistent with calculations made assuming that there is no interaction among the flowing bubbles and that the bubbles are small. Visual observation shows that the flow is bubbly; there are a large number of finely dispersed bubbles. Photographs taken in a static cell using the same electrodes and electrolyte show that the bubble diameter is between 0.002 and 0.007 in. The bubbles are large enough so that the surface tension effect on pressure is negligible and small enough so that their terminal rise velocity is very small.

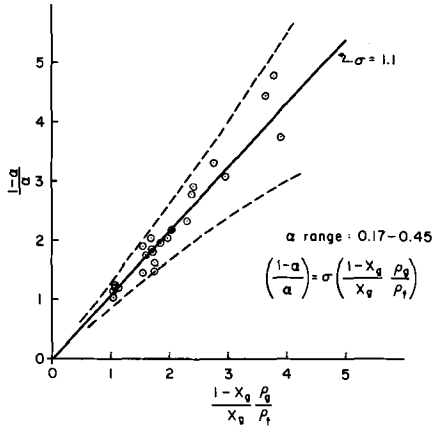

Fig. 8. Experimental void fraction, hydrogen channel, design 8. Cross section, 1 x 0.181 in.; six segmented electrodes, 1 x 5¾ in.; electrolyte, 1N KOH; temperature, 80°-100°F; pressure, 1 atm; inlet velocity, 0.3-0.8 ft/sec; current density, 180-400 amp/ft^2; - - - limits of experimental error.

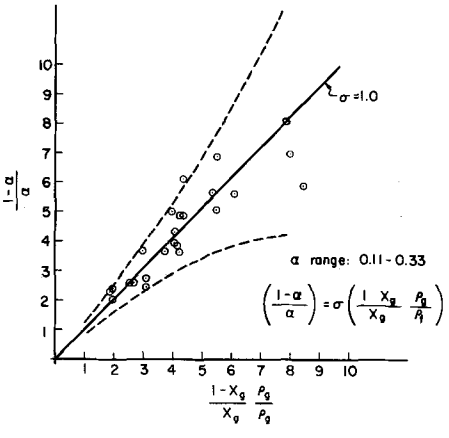

Fig. 9. Experimental void fraction, oxygen channel, design 8. The description is the same as Fig. 8.

Figures 10 and 11 show outlet void fraction as a function of quality. This is a common way of presenting two phase flow experimental data and the $\sigma = 1$ curve is calculated directly from Eq. [9]. Bankoff's model is discussed in ref. (16) in which it is shown that

$$\sigma = \frac{1-\alpha}{K-\alpha} \qquad [50]$$

where K is a parameter which is determined from the transverse distribution of velocity and voids in the channel. A value of $K = 0.89$ provides agreement between Bankoff's theory (16) and the Martinelli-Nelson correlation (20) and is shown in Fig. 10 and 11 for this reason.

Figure 12 shows outlet void fraction *vs.* the channel outlet gas volume fraction for both hydrogen and oxygen. The definition of β is

$$\beta = \frac{\sigma\alpha}{\sigma\alpha + (1-\alpha)} \qquad [51]$$

which, when combined with [50] yields

$$\alpha = K\beta \qquad [52]$$

For a slip ratio of unity the simple result that $\alpha = \beta$ is obtained. Both $\sigma = 1$ and $K = 0.89$ are shown on Fig. 12.

Discussions and Conclusions

The major conclusions drawn from the earlier part of the investigation have been stated earlier in conjunction with Fig. 2, 3, and 4. It was shown, quantitatively, that the slip ratio and inlet velocity are important electrolysis cell design variables.

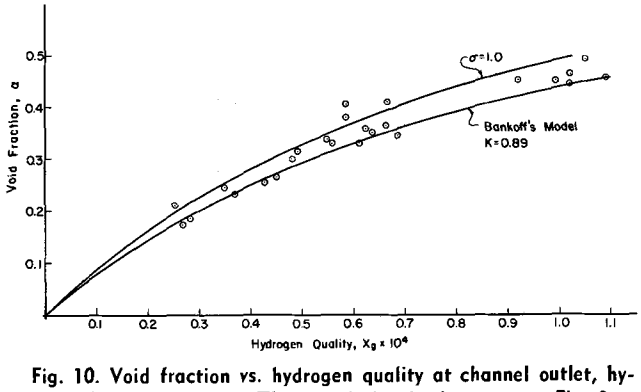

Fig. 10. Void fraction vs. hydrogen quality at channel outlet, hydrogen channel, design 8. The description is the same as Fig. 8.

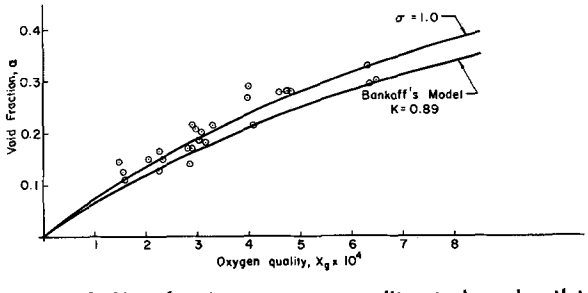

Fig. 11. Void fraction vs. oxygen quality at channel outlet, oxygen channel, design 8. The description is the same as Fig. 8.

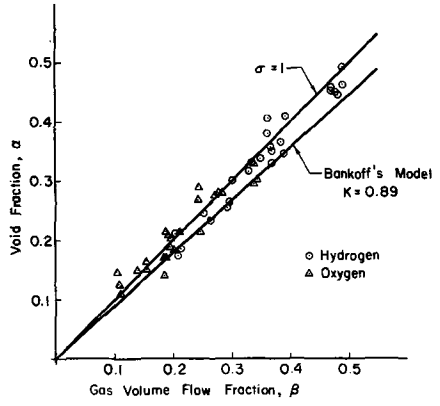

Fig. 12. Void fraction vs. gas volume flow fraction, design 8. The description is the same as Fig. 8.

The experimental results indicate that the slip ratio is, for practical purposes, equal to unity. This experimental result has been obtained from void fraction measurements and means that the void fraction can be determined directly from Eq. [42] by setting $\sigma = 1$. In an experimental apparatus, the current density distribution is measured so the void fraction is then given explicitly by Eq. [42] with $\sigma = 1$.

The current density distribution is not known, *a priori*, in designing a cell, and in this situation the void fraction and current density distribution must be determined simultaneously by using Eq. [42] (with $\sigma = 1$) along with the other equations described earlier.

Since the pressure drop calculations required in reducing experimental pressure drop data are directly dependent on the slip ratio, use of the above data can be made in formulating pressure drop correlations. Such experimental data is presently being obtained and pressure drop correlations are being developed. When this work is completed it will be presented in a separate paper.

A critical test of any analytical model for predicting the performance of an electrolysis cell is a comparison of measured current density and void fraction distributions with those predicted analytically. Such a direct comparison was not possible from the work described in this paper due to the uncertain electrical properties of the membrane which was designed primarily to permit accurate and reliable void fraction measurement and pressure drop data. Future work is planned to overcome this limitation of the existing apparatus.

Acknowledgment

This research was sponsored by the National Science Foundation under Grant NSF-GK-775.

NOMENCLATURE (Consistent Units)

$a,b,$	constants in the equation describing polarization over voltage (Eq. [37])
A	channel flow area
C_f	specific heat of the electrolyte
E	voltage applied to the cell
E'	voltage drop in the two phase electrolyte
ΔE_d	water decomposition potential
ΔE_p	electrode polarization overvoltage
ΔE	sum of ΔE_d and ΔE_p
g	gravitation constant
H	channel width
I	integral of the nondimensional current density defined by Eq. [44]
L	electrolyzer cell length
$\dot{m}$	local mass flux
M	atomic weight
p	pressure
r_f	liquid electrolyte resistivity
r_{tp}	resistivity of the two-phase bubble layer
R	total cell transverse resistance
R_c	ohmic resistance of the cell
R_m	membrane resistance
T	temperature
V	fluid velocity
w	mass flow rate
x	gas quality or gas mass fraction
y	channel thickness
z	vertical coordinate

Greek Letters

$\alpha,$	void fraction based on channel thickness
α'	void fraction based on bubble layer thickness
β	gas volume flow fraction
γ	defined by equation 22
Γ_0	non-dimensional parameter defined by equation 43
δ	bubble layer thickness
ϵ_η	valence upon electrolytic decomposition
λ_η	constant defined by equation 15
μ	viscosity
ξ	axial position coordinate
ρ	density
σ	slip ratio or phase velocity ratio
τ	wall shear stress
ϕ	current density
Φ	viscous dissipation function

Subscripts

0	channel inlet conditions
1	anode side
2	cathode side
g	gas
f	liquid
i	hydroxyl ion

Superscripts

0	nondimensional quantity

Manuscript submitted June 10, 1968; revised manuscript received *ca.* Sept. 1, 1968. This paper was presented at the Boston Meeting, May 5-9, 1968, as Paper 182.

Any discussion of this paper will appear in a Discussion Section to be published in the December 1969 JOURNAL.

REFERENCES

1. F. P. Rudek and N. Belasco, Report AMRL-TDR-63-32, Wright-Patterson AFB Ohio (1963).
2. J. F. Hall, Autogram D329, General Electric Co., Missile and Space Division, Philadelphia, Pa., (1963).
3. M. Steinberg, "Production of Industrial Chemicals by Chemonuclear Processes," paper presented at Nov. 1964 Am. Nucl. Soc. Meeting, San Francisco (1964).
4. G. Seaborg, *Forbes*, Dec. 15, 1967.
5. R. L. Costa and P. G. Grimes, "Electrolysis as a Source of Hydrogen and Oxygen," paper presented at the A.I.Ch.E. Symposium on the Import of Low Cost Nuclear Power, Houston, Feb. 19-23, 1967.
6. J. F. Thorpe and J. E. Funk, "Electrolysis Cell Research I," Eng. Exp. Station Report, University of Kentucky, Lexington, Ky. (1968).
7. R. S. Brodkey, "The Phenomena of Fluid Motions," Addison-Wesley Publishing Co., Reading, Mass. (1967).
8. J. F. Thorpe, "Fluid Flow," Chap. 5 of ASHRAE Handbook of Fundamentals, New York (1967).
9. L. S. Tong, "Boiling Heat Transfer and Two-Phase Flow," John Wiley & Sons, Inc., New York (1965).
10. C. W. Tobias, *This Journal*, **106**, 833 (1959).
11. K. Kawafune *et al.*, *Ann. CIRP*, **15**, 65/1 (1967).
12. H. Opitz *et al.*, *ibid.*, **15**, 263 (1967).
13. S. Maeda *et al.*, *Jap. Soc. Prec. Eng.*, **2**, 126 (1967).
14. J. Hopenfeld and R. R. Cole, *Trans. ASME, J. Eng. for Indust.*, **88**, 455 (1966).
15. S. Levy, *Trans. ASME, J. Heat Trans.*, **82**, 113 (1960).
16. S. G. Bankoff, *ibid.*, **82**, 265 (1960).
17. M. M. El-Wakil, "Nuclear Power Engineering," McGraw-Hill Book Co., New York (1962).
18. V. P. Mashovets, *J. Appl. Chem. USSR*, **24**, 391 (1951).
19. R. A. Foust, Jr., "Survey of Electrochemical Technology Applicable to Water Electrolysis," Allison Div. GM Corp., Report EDR 3687, V. 2, (1964).
20. R. C. Martinelli and D. B. Nelson, *Trans. ASME*, **70**, 695 (1948).

Field Dependence of the Tafel Slopes for Formation of Anodic Oxide Films

S. G. Christov and S. Ikonopisov

Department of Physical Chemistry, Higher Chemico-Technological Institute, Sofia (Darvenitza), Bulgaria

ABSTRACT

An explanation of the field dependence of Tafel slopes for formation of anodic oxide films is proposed on the basis of an earlier general consideration of charge transfer over potential barriers. An expression for the activation energy as a function of the field strength is derived which contains a quadratic term arising from the shifting of both the barrier top and the equilibrium position of the ion under the influence of the electric field. The treatment includes the usual parabolic approximation of a continuous potential-energy function in the regions of its maximum and minimum. A comparison with the experimental data for anodic oxidation of Ta, Nb, and Al shows this approximation to be quite satisfactory. The theoretical expression permits the determination of the actual barrier parameters at a given field strength $\mathcal{E}_0$ near the experimental field range, as well as an extrapolation to zero field strength. This theory is applicable equally well to any possible mechanism of the current flow in the anodic formation of oxide layers.

The growth of homogeneous oxide layers during anodization of film-forming metals such as Al, Ta, Nb, Zr, etc., in a suitable electrolyte is interpreted by passage of ions across the oxide, surmounting some potential energy barrier in their way. Measurable rates of growth require considerable electric fields (more than 10^6 v/cm)[1] so that the ionic transitions can be considered to occur only in the direction of the field.

On the basis of elementary kinetic considerations, one obtains the well-known equation for ionic current density

$$j_i = A \exp [-W(\mathcal{E})/kT] \qquad [1]$$

with the activation energy being a linear function on the field strength $\mathcal{E}$

$$W(\mathcal{E}) = W_0 - aq\mathcal{E} \qquad [1a]$$

where W_0 is the activation energy in the absence of an external field ($\mathcal{E} = 0$), a the activation distance, and q the charge on the moving ion. The pre-exponential factor A has a different meaning depending on the assumptions for the kind and location of the potential barrier. In this respect, the various theories could be classified on the basis of the following three assumptions:

(*a*). *Internal control.*—According to Verwey's model (1), the limiting factor is the rate at which ions move from one interstitial position to another. It was proposed later (2-4) that the high field produces Frenkel defects (pairs of interstitial cations and cation vacancies) by drawing out metal ions in interstitial positions. Recently, a new theory for the internal control was developed by Dignam (5) on the basis of a dielectric mosaic model of the anodic oxide film.

(*b*). *Interface control.*—Mott and Cabrera (6, 7) considered as rate determining the first barrier which metal ions have to surmount to enter the oxide. This was shown to be the case with anodization of sputtered tantalum films (8). Jukova and Odynec (9) assumed that the electrochemical reactions at the oxide/electrolyte interface play a certain role in the growth of nonporous anodic films as well.

(*c*). *Internal-interface control.*—That is an extension of the mentioned models for including effects of space charge due to ions in transit, so that barriers at the metal/oxide interface and within the oxide both play a part in controlling the ionic current flow (10-13).

Equation [1] with expression [1*a*] for $W(\mathcal{E})$ has been experimentally confirmed many times. However, some measurements have shown that, for anodization of tantalum, the reciprocal Tafel slope

$$\partial \ln j_i/\partial\mathcal{E} = -\partial W/\partial\mathcal{E}$$

is field dependent, which is inconsistent with expression [1*a*]. It was proved by Young (14, 15) that this dependence could best be described if the activation energy is represented by an expression of the form

$$W(\mathcal{E}) = B - \alpha\mathcal{E} + \beta\mathcal{E}^2 \qquad [2]$$

where B, α, and β are positive constants. Later this expression was found to be in excellent accord with the data for the growth of anodic oxide films on aluminum (16) and niobium (17, 18) as well.

Various theoretical interpretations of Eq. [2] have been proposed by Young (19), Dignam (5, 20) and Ibl (21). All of them, however, are based on special assumptions concerning the shape of the barrier or the oxide film properties. There exists, however, another possibility to explain the appearance of the quadratic term in Eq. [2], which ensues from more general properties of the potential barriers. This approach has already been applied by Christov in the cases of electrode kinetics (22 a,b,c), electron emission (23), and chemical kinetics (24). A deduction is given below, leading directly to expression [2] which is the usual form of determining the ionic conduction of oxide layers by means of Eq. [1].

Derivation of the Expression for Activation Energy

Figure 1 shows the potential energy $V(x)$ of an ion as a function of distance x in the direction of the electric field.[2] The curve $V_0(x)$ represents the potential barrier which the ion has to overcome in passing from one equilibrium position ($x = 0$) to another ($x = L$) in the absence of an external field, and curve $V(x)$, the barrier in the presence of a linear electric field with strength $\mathcal{E}$. Hence

$$V(x) = V_0(x) - q\mathcal{E}x \qquad [3]$$

where q is the charge of the ion. By the action of the field, the barrier is lowered by the magnitude ΔW, expressed approximately by

[1] The total current is $j = j_i + j_e$, with j_i the ionic and j_e the electronic current; j_e is negligibly small at high fields, but at $\mathcal{E} < 10^6$ v/cm exceeds j_i many times and makes it indeterminable.

[2] We consider the more general case of a barrier which is asymmetrical in the absence of an external field, which will be the case with control by the entrance barrier. The same results are obtained in the case of a symmetric barrier, too.

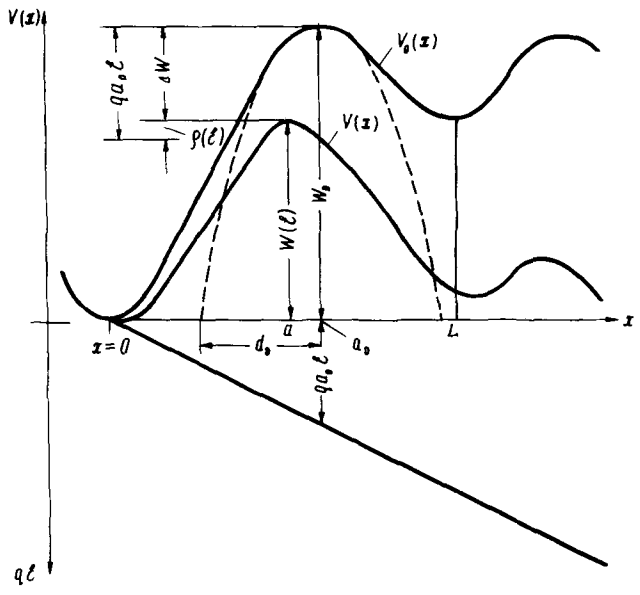

Fig. 1. Potential energy of the mobile ion vs. distance. The shifting of the barrier top is illustrated: $V_0(x)$, in the absence of external field; $V(x)$, when an external electric field is applied.

$$\Delta W = W_0 - W(\mathcal{E}) \approx a_0 q\mathcal{E} \qquad [4]$$

Here, a_0 determines the position of the barrier top when $\mathcal{E} = 0$, *i.e.*, the maximum of the function $V_0(x)$. From that follows the conventional expression [1*a*] for the ion transfer activation energy $W(\mathcal{E})$. Such a deduction ignores the shifting of the potential energy maximum from $x = a_0$ to $x = a$. Accounting for this, the lowering of the barrier is accurately given by (see Fig. 1) (22c)

$$\Delta W = W_0 - W(\mathcal{E}) = a_0 q\mathcal{E} - \rho(\mathcal{E}) \qquad [5]$$

where the quantity $\rho(\mathcal{E})$ increases with $\mathcal{E}$ and could be neglected only if the field strength is sufficiently low.

On principle, an exact expression for the activation energy $W(\mathcal{E})$, including the term $\rho(\mathcal{E})$, could be derived by the analytical method for determining of the maximum of potential energy $V(x)$, if the form of the function $V_0(x)$ in Eq. [3] is known. Explicit expressions for $W(\mathcal{E})$ are easily obtained for simple models of potential barriers,[3] but they have only limited applicability for some special cases.

A rather general solution of the problem may be obtained without any hypotheses about the entire barrier shape, by means of a simple method, proposed earlier by Christov (22c). This method is based on the usual parabolic approximation of the function $V_0(x)$ in the region of its maximum (transition state), which may be written in the form (22 b, c)

$$V_0(x) = W_0\left[1 - \frac{(x-a_0)^2}{d_0^2}\right] \qquad [6]$$

where d_0 is the half-width of a parabolic barrier of height W_0 (Fig. 1). If the region of validity of this approximation is sufficiently wide, the height of the barrier $V(x)$ at not very high fields may be easily found by calculating the maximum of the function

$$V(x) = W_0\left[1 - \frac{(x-a_0)^2}{d_0^2}\right] - q\mathcal{E}x \qquad [7]$$

[3] Such are, for instance, the parabolic barrier (22b) and the Schottky image force barrier (23), on which the potential of the electric field is superimposed. With more complicated functions (such as the Eckart potential in combination with an electric potential (22a), the condition of the maximum $dV/dx = 0$ leads to transcendental equations; that is why only approximate solutions are possible in this case (22a).

which is obtained from Eq. [3] and [6]. Thus, from the condition $dV/dx = 0$, we obtain the position of the maximum

$$a = a_0 - \frac{d_0^2}{2W_0} q\mathcal{E} \qquad [8]$$

and the barrier height

$$W(\mathcal{E}) = W_0 - a_0 q\mathcal{E} + \frac{\gamma_0^2 a_0^2}{4W_0} q^2\mathcal{E}^2 \qquad [9]$$

where $\gamma_0 = d_0/a_0$.

A comparison of Eq. [5] with Eq. [9] gives the correctional term for $W(\mathcal{E})$

$$\rho(\mathcal{E}) = \frac{\gamma_0^2 a_0^2 q^2}{4W_0}\mathcal{E}^2 = \frac{q^2}{2L_a}\mathcal{E}^2 \qquad [10]$$

where

$$L_a = -\left(\frac{d^2V}{dx^2}\right)_{x=a} = \frac{2W_0}{d_0^2} = \frac{2W_0}{\gamma_0^2 a_0^2} \qquad [11]$$

is the curvature of the barrier [7] at the top ($x = a$), which is a constant, *i.e.*, is independent on the top displacement ($L_a = L_{a_0}$).

Expression [9] coincides with the empirical relation [2] provided that

$$B = W_0, \quad \alpha = a_0 q, \quad \text{and} \quad \beta = \frac{\gamma_0^2 a_0^2 q^2}{4W_0} \qquad [12]$$

The dependence [9] would clearly be exact enough on condition that the curvature at the top of the real barrier $V(x)$ remains constant when the field changes, so that it could be represented by expression [11] for the curvature of the parabolic barrier [7]. Then, according to Eq. [11] and [12]

$$\beta = \frac{q^2}{2L_a} = \frac{q^2}{2L_{a_0}}$$

will really be a constant. The smaller the curvature L_{a_0}, *i.e.*, the flatter the barrier in absence of an external field, the wider the field region, within which the foregoing condition will be valid. According to Eq. [11], L_a decreases with the increase of the quantity $\gamma_0 = d_0/a_0$ which is a criterion for the deviation of the barrier from a parabolic shape (for the latter $\gamma_0 = 1$). The possible cases are $\gamma_0 < 1$ ($d_0 < a_0$) and $\gamma_0 > 1$ ($d_0 > a_0$); *i.e.*, the real barrier may be wider or narrower than the corresponding parabolic barrier, having the same curvature at the top.

At sufficiently high fields, one should expect the parabolic approximation [7], appropriate to low fields, to be invalid, since a considerable change of the field will surely cause a noticeable change in the curvature of the barrier top ($L_a \neq L_{a_0}$). It is possible, however, to approximate the upper part of the barrier with a parabolic function of type [7] in each not very wide region of fields between $\mathcal{E}_0$ and $\mathcal{E}_0 + \Delta\mathcal{E}$, if the quantities W_0, a_0, and d_0 (or $\gamma_0 = d_0/a_0$) are referred to a certain value of the field $\mathcal{E} = \mathcal{E}_0$ (instead of $\mathcal{E} = 0$) and if $\mathcal{E}$ is replaced by $\mathcal{E} - \mathcal{E}_0$. In this way, we obtain again expression [2]

$$W(\mathcal{E}) = B - \alpha\mathcal{E} + \beta\mathcal{E}^2 \qquad [13]$$

where

$$\begin{cases} B = W_0^* + a_0^* q\,\mathcal{E}_0 + \dfrac{\gamma_0^{*2} a_0^{*2} q^2}{4W_0^*}\mathcal{E}_0^2 \\ \alpha = a_0^* q + \dfrac{\gamma_0^{*2} a_0^{*2} q^2}{2W_0^*}\mathcal{E}_0 \\ \beta = \dfrac{\gamma_0^{*2} a_0^{*2} q^2}{4W_0^*} \end{cases} \qquad [13a]$$

The system of three equations [13*a*] permits computation of the three unknown parameters W_0^*, a_0^*, and γ_0^* of the barrier at a certain value of the field strength $\mathcal{E}_0$ on the basis of the experimental data for the constants B, α, β in the given field region (from $\mathcal{E} = \mathcal{E}_0$ to $\mathcal{E} = \mathcal{E}_0 + \Delta\mathcal{E}$).

If the more simple expression [9], *i.e.*, relation [12] is used instead of equation [13] with coefficients [13*a*], one might calculate from the experimental data for B, α, and β the quantities W_o, a_o, and γ_o which will then represent the apparent barrier parameters in the absence of a field ($\mathcal{E} = 0$). It is quite improbable, indeed, for the dependence [2], which is established in a fairly narrow field range at very high fields (between 10^6 and 10^7 v/cm), to hold true with the same values of the coefficients B, α, and β right up to $\mathcal{E} = 0$. Therefore, the quantities W_o, a_o, and γ_o, computed by means of Eq. [12], should represent a very far-reaching extrapolation, having no direct physical significance as far as these quantities cannot be identified with the true barrier parameters in absence of an electric field.

In the above consideration, only the shifting of the barrier top is taken into account. A more general treatment should include also the displacement of the initial equilibrium position of the ion under the influence of the external field from $x = 0$ to $x = x_o$, which cannot be neglected if the potential well is wide. Such a situation is represented in Fig. 2. Then the lowering of the barrier is given by

$$\Delta W = W_o - W(\mathcal{E}) = a_o q\mathcal{E} - [\rho(\mathcal{E}) - \rho'(\mathcal{E})] \quad [14]$$

The quantity $\rho'(\mathcal{E})$ could be found using again (22c) the familiar parabolic approximation of the potential energy about the equilibrium position, *i.e.*

$$V_o(x) = \frac{f_o x^2}{2} \quad [15]$$

in the absence of external field ($\mathcal{E} = 0$) and

$$V(x) = V_o(x) - q\mathcal{E}x = \frac{f_o x^2}{2} - q\mathcal{E}x \quad [16]$$

if not a very high electric field is applied. The quasi-elastic force constant f_o is related to the frequency of the harmonic ion vibration

$$\nu_o = \frac{1}{2\pi}\sqrt{\frac{f_o}{m}} \quad [17]$$

where m is the mass of the ion. From Eq. [16], we find for the equilibrium position

$$x_o = \frac{q\mathcal{E}}{f_o} \quad [18]$$

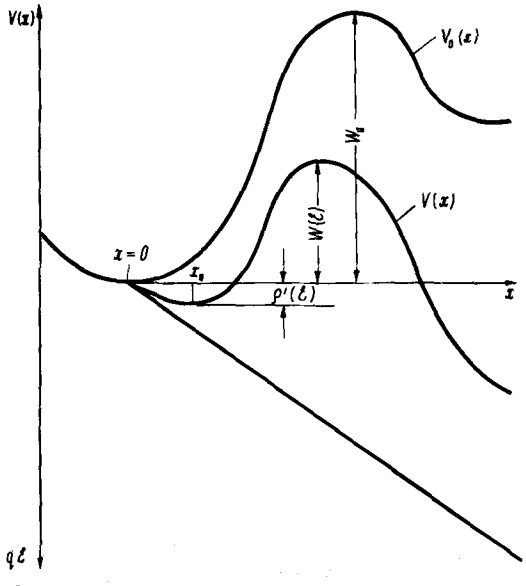

Fig. 2. Potential energy vs. distance for illustrating the shifting of the equilibrium position of the ion in addition to the barrier top displacement: $V_o(x)$ in the absence, and $V(x)$ in the presence, of external electric field.

and for the potential energy minimum

$$V(x_o) = \rho'(\mathcal{E}) = -\frac{q^2\mathcal{E}^2}{2f_o} \quad [19]$$

Equations [10], [14], and [19] lead to the expression

$$W(\mathcal{E}) = V(a) - V(x_o) = W_o - a_o q\mathcal{E} + \left(\frac{\gamma_o^2 a_o^2 q^2}{4W_o} + \frac{q^2}{2f_o}\right)\mathcal{E}^2 \quad [20]$$

which is identical with the empirical relation [2] if we set

$$B = W_o, \quad \alpha = a_o q,$$

$$\beta = q^2\left(\frac{\gamma_o^2 a_o^2}{4W_o} + \frac{1}{2f_o}\right) = \frac{q^2}{2}\left(\frac{1}{L_a} - \frac{1}{L_o}\right) \quad [21]$$

Here the curvature L_a at the barrier top is given by Eq. [11] and the curvature L_o at the equilibrium position is determined from Eq. [16] and [17] by

$$L_o = -\left(\frac{d^2V}{dx^2}\right)_{x=x_o} = -f_o = -m(2\pi\nu_o)^2$$

When $|L_o| >> |L_a|$ Eq. [21] turns into relations [12]. If the barrier parameters W_o, a_o, γ_o, and f_o are related to a given value of the field strength $\mathcal{E} \neq 0$, we obtain in a similar manner again Eq. [2] with

$$\begin{cases} B = W_o^* + a_o^* q\mathcal{E}_o + \left(\dfrac{\gamma_o^{*2} a_o^{*2} q^2}{4W_o^*} + \dfrac{q^2}{2f_o^*}\right)\mathcal{E}_o^2 \\ \alpha = a_o^* q + \left(\dfrac{\gamma_o^{*2} a_o^{*2} q^2}{2W_o^*} + \dfrac{q^2}{f_o^*}\right)\mathcal{E}_o \\ \beta = \dfrac{\gamma_o^{*2} a_o^{*2} q^2}{4W_o^*} + \dfrac{q^2}{2f_o^*} \end{cases} \quad [22]$$

These expressions include relations [13*a*] as limiting cases for large values of the force constant f_o^* (*i.e.*, for $|L_o^*| >> |L_a^*|$), for which the terms containing f_o^* become negligible.

Comparison with Experimental Data[4]

Effect of barrier top shifting.—We will first assume that the potential well in the initial position of the ion is not very wide (Fig. 1). Then using Eq. [13*a*] and available experimental data for B, α, and β, one can compute the quantities W_o^*, a_o^*, and γ_o^* at a given value of the field strength $\mathcal{E}_o$. As such, we take $\mathcal{E}_o = 10^6$ v/cm, which is closed by the usual experimental field range. The extrapolated barrier parameters at $\mathcal{E} = 0$ may also be calculated by means of Eq. [12*a*].

Tantalum.—The relation [2] was established by Young (14, 15) who investigated the anodizing of Ta at temperatures between 0° and 95°C and fields between 4.5 x 10^6 and 7.5 x 10^6 v/cm. Taking for the ion charge a value $q = 5e$, the experimental data yield $B = 2.185$ ev; $\alpha = 3.497 \times 10^{-7}e$ cm; $\beta = 1.675 \times 10^{-14}e$ cm²/v. The barrier parameters calculated by Eq. [13*a*] with $\mathcal{E}_o = 10^6$ v/cm are as follows

$$W_o^* = 1.852 \text{ ev}; \quad a_o^* = 6.325 \times 10^{-8} \text{ cm}; \quad \gamma_o^* = 1.114$$

The apparent values at $\mathcal{E} = 0$, computed by Eq. [12] are

$$W_o = 2.185 \text{ ev}; \quad a_o = 6.995 \times 10^{-8} \text{ cm}; \quad \gamma_o = 1.094$$

Niobium.—The kinetics of anodization of Nb in 0.2*N* H_2SO_4 was investigated by Young and Zobel (17) in the field range from $\mathcal{E} = 3 \times 10^6$ to $\mathcal{E} = 4.5 \times 10^6$ v/cm and at temperatures 25° and 75°C. The values B =

[4] This comparison does not concern the case of two-barrier control.

Table I. Kinetic parameters for anodizing of niobium in different electrolytes

		H_2SO_4	HCl	HNO_3	H_3PO_4
Experimental data	I_o, A cm^{-2}	5.72×10^{-7}	3.57×10^{-7}	8.0×10^{-10}	7.5×10^{-13}
	α', 10^{-6} cmV^{-1}	1.63	1.23	4.78	7.40
	β', 10^{-14} cm^{2}V^{-2}	9.74	5.20	37.7	54.0
Values of the constants in Eq. [2] with $A = 10^{7.44}$ A/cm^2	α, $10^{-7}e$ cm	0.4118	0.311	1.201	1.870
	β, $10^{-14}e$ cm^{2}V^{-1}	0.246	0.1314	0.9525	1.364
	B, ev	0.796	0.808	0.962	1.146
Apparent barrier parameters by Eq. [12] ($\mathcal{E} = 0$)	a_o, 10^{-8} cm	0.824	0.621	2.415	3.740
	W_o, ev	0.796	0.808	0.962	1.146
	γ_o	2.148	2.097	1.585	1.337
Barrier parameters by Eq. [13a] $\mathcal{E}_o = 10^6$ v/cm^{-1}	a_o^*, 10^{-8} cm	0.725	0.569	2.034	3.194
	W_o^*, ev	0.757	0.778	0.932	0.973
	γ_o^*	2.380	2.248	1.853	1.442

2.167 ev; $\alpha = 1.074 \times 10^{-7}e$ cm; $\beta = 8.36 \times 10^{-15}e$ cm^2/v were found. For $\mathcal{E}_o = 10^6$ v/cm, these data lead to

$$W_o^* = 2.068 \text{ ev}; \quad a_o^* = 1.814 \times 10^{-8} \text{ cm}; \quad \gamma_o^* = 2.90$$

and at $\mathcal{E} = 0$

$$W_o = 2.167 \text{ ev}; \quad a_o = 2.148 \times 10^{-8} \text{ cm}; \quad \gamma_o = 2.506$$

The growth of anodic oxide films on this metal was found by Shatalov and Bondareva (18) to be very sensitive to the nature of the anodizing electrolyte. As such normal aqueous solutions of H_2SO_4, HCl, HNO_3, or H_3PO_4 have been used. A law of the form

$$j_i = I_o \exp(\alpha'\mathcal{E} - \beta'\mathcal{E}^2) \qquad [23]$$

proved to fit the data very well. Depending on the electrolyte, however, quite different values for the constants I_o, α', and β' were obtained (*see* Table I). Unfortunately, these measurements have been made at 20°C only. The needed constants $B = (\ln A - \ln I_o)kT$; $\alpha = \alpha'kT$; $\beta = \beta'kT$ could be obtained from Eq. [23], if a value for A is assumed. For the purpose, a value $\lg A = 7.44$ was adopted, which is the mean value from available data ($A = 10^{7.24}$ and $10^{7.64}$ A cm^{-2}) for this constant (13, 17). (If any of these values for A were assumed instead of the mean value, the value for B would differ no more than ±2%.) The estimated values for the quantities in question are given in Table I. One can clearly see the strong dependence of the barrier parameters on the nature of the anodizing electrolyte.

Aluminum.—Unfortunately, the numerous investigations of the dependence $j_i(\mathcal{E},T)$ were carried out in conditions which do not provide the opportunity to determine the field dependence of the Tafel slope. The only data (16) available for this purpose were obtained at a single temperature ($T = 298.2$°K); therefore, only the term $A \exp(-B/kT) = 10^{-29}$ amp/cm^2 is known. If a value $A = 10^8$ amp/cm^2 is taken by analogy with the values of this constant for Ta and Nb [as the quoted authors have also done (16, 20)], we can find the values

$$A = 2.19 \text{ ev}; \quad \alpha = 2.38 \times 10^{-7}e \text{ cm}; \quad \beta = 7.4 \times 10^{-15}e \text{ cm}^2/\text{v}$$

Hence, the barrier parameters at $\mathcal{E}_o = 10^6$ v/cm will be

$$W_o^* = 1.96 \text{ ev}; \quad a_o^* = 7.44 \times 10^{-8} \text{ cm}; \quad \gamma_o^* = 1.16$$

and at $\mathcal{E} = 0$

$$W_o = 2.19 \text{ ev}; \quad a_o = 6.793 \times 10^{-8} \text{ cm}; \quad \gamma_o = 1.249$$

Effect of displacement of ion equilibrium position.—Assuming that the potential well of the ion is wide (Fig. 2), so that the curvatures L_o and L_a at the equilibrium position ($x = x_o$) and at the barrier top ($x = a_o$) are of the same order ($L_o \sim L_a$), we have to use Eq. [21] or [22]. However, the experimental data for the constants B, α, and β in the empirical relation [2] are not sufficient for computing all the barrier parameters W_o, a_o, γ_o, and f_o. Taking into account; Eq. [17], we can calculate the force constant f_o if the frequency of ion vibration ν_o is known [it may not be the same at very low and very high fields ($\mathcal{E} > 10^6$ v/cm)].

According to the models of Verwey (internal control) and Mott-Cabrera (interface control), ν_o is the vibrational frequency of the ions in the oxide or in the metal, respectively. This is known (25) to vary from 5×10^{12} s^{-1} to 10^{13} s^{-1} [Young (26) also assumed for ZrO_2, a value of $\nu_o = 10^{13}$ s^{-1} as reasonable]. With these limiting values for ν_o, the values for f_o and for the term $q^2/2L_o$ in the expression [21] are given in Table II. The quotient $(q^2/2L_o)/\beta$, which indicates the effect of displacement of potential well minimum, is also given. The term $q^2/2L_o$ appears to have small effect on the constant β from expression [21]. Hence, the real value of γ_o would not be much different than that, calculated by means of Eq. [12] in which the term $q^2/2L_o$ is disregarded.

Table II. Estimation of the effect of displacement of potential well minimum

	f_0 10^5 dynes/cm	$q^2/2L_0$ 10^{-17}e cm²/v	$100\,(q^2/2L_0)/\beta$ %
Ta	11.8-2.95	1.7-6.78	0.1-0.4
Nb	6.07-1.52	3.3-13.2	0.4-1.6
Al	1.76-0.44	4.1-16.4	0.55-2.2

The values are calculated for: $\nu_0 = 10^{13}$ and $\nu_0 = 5 \times 10^{12}$ s^{-1}.

In the mosaic model of Dignam (5), the importance of this term cannot be estimated. However, it is clear that depending on the accepted model the term $q^2/2L_0$, related to the potential well, may be less or more or as important as the term $q^2/2L_a$ related to the barrier peak.

Discussion

The first attempt to explain the empirical equation [2] was made by Young (19) on the basis of a postulated variation of the activation energy with the condenser pressure. Dignam (20) pointed out that the effect of condenser pressure is probably too small to account for the observed phenomena. In any case, there are no experimental data for the magnitude of this effect with the oxides in question.

Dignam (20) derived an expression of the form [2] in principle in the same way as earlier done by Christov (22) *i.e.*, by determining the maximum and the minimum of the potential energy. Dignam described the potential curve in absence of external field with special functions, namely a clipped parabolic, a cosine, and a Morse function, and found that the third function gave best agreement with the experimental data. The Morse function, however, has no maximum, so that the linear potential of the electric field has to be superimposed to give a maximum of the resulting potential energy. This picture obviously does not agree with the periodic variation of the ion potential in the oxide and therefore is not acceptable from physical standpoint, as already was remarked by Young and Zobel (17). That is why the agreement found by Dignam between the theoretical expression derived by using the Morse potential and the experimental data cannot be regarded as a real justification for the assumption of this potential.[5]

Recently, Ibl (21) showed that relation [2] could be derived on the basis of the transition-state theory if the polarization of the dielectric is taken into account. This possibility presupposed an internal control for the growth of the oxide layer and is consistent with Dignam's mosaic model only (21).

In contrast to the above explanations, it is shown in the present paper that the field dependence of Tafel slopes in anodic oxidation has to be expected without any special assumptions if only we determine more accurately the change of the barrier height, caused by the electric field. The appearance of the quadratic term in expression [2] for the activation energy is a result of shifting the position of the barrier top, as well as the equilibrium position with the field. This can be taken into account quantitatively, using the method proposed by Christov (22b, c), which includes the usual parabolic approximation of a continuous potential energy function in the regions of its maximum and minimum. In supposing that only the displacement of the barrier peak is important, we can compute the barrier parameters from the experimental data in a unique way. Thus, one concludes that for Ta and Al the parabolic approximation is valid in a wide barrier region because the quantity γ_0 (or γ_0^*), which accounts for the deviation from the parabolic shape, proved to be very close to unity. The larger value for γ_0 at some conditions of anodizing of niobium is an indication for a rather flat barrier, which also seems not to be improbable. Assuming that the shifting of the potential energy minimum is sufficiently significant, we obtain more or less smaller values for γ_0; however, this seems not to be really the case from the viewpoint of both the theories of the internal and the interface control.

Equations [13*a*] and [22] permit the determination of the actual barrier parameters at a given field strength $\mathcal{E}_0$ near the experimental field range instead of the very doubtful extrapolation up to $\mathcal{E} = 0$ by means of Eq. [12].

The theoretical interpretation of the field dependence of Tafel slopes, proposed earlier (22a, b, c), is based on general properties of the potential barriers, including changing of their shape under the influence of a variable factor. Therefore, the results obtained in this work present an immediate application of this theory to the case of anodic formation of oxide films, which is valid independently of any special assumption on the nature and the location of the potential barrier, *i.e.*, about the concrete mechanism of ion current flow.

The theoretical expression [9] for the activation energy agrees well with the experiment as far as it predicts the order of the observed deviations from Eq. [1] with [1*a*] (Tafel-Frenkel relation) in anodic oxidation of film-forming metals. The quadratic term in Eq. [9] becomes, indeed, appreciable in the investigated high-field range (10^6-10^7 v/cm) if the values of barrier parameters corresponding to the experimental data at a given field strength are introduced. This conclusion is valid in a larger extent if the more general expression [20] is considered.

An inspection of Table I clearly shows that the barrier parameters for anodic oxidation of Nb vary strongly with the change of the electrolyte. It is not the aim of the present paper to discuss this dependence which is an indication for a change of the oxide structure. On the basis of the theory presented here, it is possible, however, to determine the variations of both the dimensions and the shape of the barrier with the change of the physical properties of the homogeneous oxide films, depending on the conditions of anodization.

It must be stressed that, from the standpoint of the theory developed previously (22), relation [2] is only an approximate expression, which is valid for a not very large variation of the field. In wider field ranges, one should expect the appearance of higher order terms (22c) as seems to be the case of the electrolytic deposition of silver (27). However, such deviations from relationship [2] are not observed in the restricted ranges of the field in which the anodic formation of oxide films has been investigated at present.

Manuscript submitted June 24, 1968; revised manuscript received Sept. 30, 1968.

Any discussion of this paper will appear in a Discussion Section to be published in the December 1969 JOURNAL.

[5] It is very doubtful that the potential energy of the ion near its equilibrium position may be expressed by Morse function, which is appropriated to diatomic molecules. Using the (non-periodic) clipped parabolic curve, Dignam (20) assumes a fixed barrier peak, so that the quadratic term in expression [2], arising entirely from the shifting of the potential minimum, proved to be very small.

REFERENCES

1. E. J. W. Verwey, *Physica*, **2**, 1059 (1935).
2. C. P. Bean, J. C. Fisher, and D. A. Vermilyea, *Phys. Rev.*, **101**, 551 (1956).
3. J. F. Dewald, *Phys. Chem. Solids*, **2**, 55 (1957).
4. D. A. Vermilyea, *This Journal*, **104**, 427 (1957).
5. M. J. Dignam, *ibid.*, **112**, 722 and 729 (1965).
6. N. F. Mott, *Trans. Faraday Soc.*, **43**, 429 (1947).
7. N. Cabrera and N. F. Mott, *Repts. Progr. Phys.*, **12**, 163 (1948-1949).
8. D. Mills, L. Young, and F. G. R. Zobel, *J. Appl. Phys.*, **37**, 1821 (1966).
9. I. S. Jukova and L. L. Odynec, "Fizika poluprovodnikov i metallov," AN SSSR, p. 5 (1964).
10. H. E. Haring, *This Journal*, **99**, 30 (1952).
11. J. F. Dewald, *Acta Met.*, **2**, 340 (1954).
12. J. F. Dewald, *This Journal*, **102**, 1 (1955).

13. L. Young, *Trans. Faraday Soc.*, **52**, 502 (1956).
14. L. Young, *Proc. Roy. Soc. (London)*, **A 258**, 496 (1960).
15. L. Young, *ibid.*, **A 263**, 395 (1961).
16. M. J. Dignam, D. Goad, and M. Sole, *Can. J. Chem.*, **43**, 800 (1965).
17. L. Young and F. G. R. Zobel, *This Journal*, **113**, 277 (1966).
18. A. Ya. Shatalov, and T. P. Bondareva, *Zh. Fiz. Khim.*, **38**, 868 (1963).
19. L. Young, *This Journal*, **110**, 589 (1963).
20. M. J. Dignam, *Can. J. Chem.*, **42**, 1155 (1964).
21. N. Ibl, *Electrochim. Acta*, **12**, 1043 (1967).
22a. S. G. Christov, *Z. Electrochem.*, **62**, 567 (1958); *see* p. 578.
22b. S. G. Christov, *ibid.*, **64**, 840 (1960); *see* p. 841.
22c. S. G. Christov, *Z. Electrochem.*, **67**, 117 (1963).
23. S. G. Christov, *Phys. Stat. Sol.*, **6**, 55 (1964); *see* p. 62.
24. S. G. Christov, *J. Res. Inst. Catalysis Hokkaido Univ.*, In press.
25. C. Kittel, "Introduction to Solid State Physics," part 5, (Translated in Russian) Moscow (1963).
26. L. Young, *Trans. Faraday Soc.*, **55**, 632 (1959).
27. A. R. Despić and J. O'M. Bockris, *J. Chem. Phys.*, **32**, 389 (1960).

Eu^{2+} Activated Aluminosilicate Phosphors

A. Wachtel*

Westinghouse Electric Corporation, Bloomfield, New Jersey

ABSTRACT

Within the system $xSiO_2$ $(1 - x)Al_2O_3:Eu^{2+}$, there exist two maxima of luminescence intensity: "phosphor I" a $x = 0.9$-0.95 consisting of mullite + amorphous SiO_2 and "phosphor II" at $x = 0.15$-0.175 consisting of mullite + θAl_2O_3. Excitation, emission, and ESR spectra of both phosphors are the same. It is concluded that in each case, Eu^{2+} is located at the interface between mullite and the second phase.

Recent investigations by a number of authors (1-11) have shown that Eu^{2+} is an efficient activator in a variety of phosphor matrices. In the present study, an attempt is made to characterize the luminescent phases which occur in the system $xSiO_2$ - $(1\text{-}x)Al_2O_3:Eu^{2+}$ reported by Jaffe (12).

Experimental

Solid-state reaction between SiO_2 and Al_2O_3, even from hydrated raw materials, is known to be very slow (13) and normally confined to the immediate vicinity of contact between the two reactants. The usual method to overcome this difficulty is by use of gel coprecipitates for which various techniques are reported by authors investigating aluminosilicates (14-19). A simple technique suitable for the present study consisted of adding excess alcoholic NH_4OH to a solution of $Al(NO_3)_3$ + $Eu(NO_3)_3$ + $Si(OC_2H_5)_4$ in about 70% alcohol. Hydrolysis of the $Si(OC_2H_5)_4$ then proceeds in the interstices of the mixed $Al,Eu(OH)_3$ gel and produces a quasihomogeneous raw material which requires very little thermal diffusion for subsequent compound formation. The gels were then water-washed, dried at up to 950°C, and fired in air followed by grinding and refiring in a reducing atmosphere. The air firing was at 1250°C, except where it was intentionally varied, while the temperature of the second firing was maintained at 1100°C.

Fluorescence intensity was measured under 254 nm excitation, using a Spectra Brightness Spot Meter at the "blue" ($\bar{z}$) setting whose sensitivity nearly coincides with the spectral energy distribution of the phosphors.

Emission and IR absorption spectra were obtained on commercial instruments. Excitation and absolute reflectance spectra were measured on an instrument designed by Thornton (20), the latter by the method of Middleton and Sanders (21).

Results

Figure 1 shows the fluorescence intensity as a function of composition. The fact that at this temperature pure mullite was obtained at $0.6Al_2O_3 \cdot 0.4SiO_2$, as well as the presence of only those unreacted components which are in excess over this ratio, may be taken as evidence that equilibrated reaction products were obtained. It should be noted that well-defined single phases (θAl_2O_3, $3Al_2O_3 \cdot 2SiO_2$, amorphous SiO_2) are non- or poorly luminescent, while there are two strongly luminescent compositions, arbitrarily designated as phosphors I and II, each consisting of two phases, one of which is mullite. In these phosphors, the strongest x-ray diffraction line of mullite (210) is seen to be about one-tenth of the height in the pure compound; moreover in the weaker phosphor (II), there is a sixfold decrease in line height which occurs as one goes from $x = 0.2$ to $x = 0.175$. Since over this interval the mullite concentration differs by only 12.5%, the increase in luminescence is primarily associated with decreased particle size, *i.e.*, increased surface area of the mullite.

Figure 2 shows emission spectra of phosphor I as a function of Eu concentration, and Fig. 3 shows the absorption (1- absolute reflectance) and the excitability of the sample with 3 x 10^{-3}Eu/0.925 $SiO_2 \cdot 0.075Al_2O_3$.[1] The fluorescence of this phosphor is very

[1] All concentrations are expressed in gram atoms. Reproducibility of excitation spectra of phosphors prepared with minor variations was good as pertains to general features, but they frequently differed in relative peak heights. An additional peak at 205 nm was also noted on occasion.

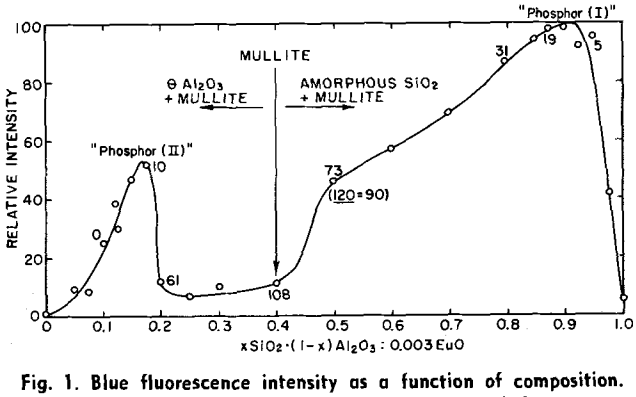

Fig. 1. Blue fluorescence intensity as a function of composition. Numbers in figure denote the relative height of the 210 x-ray reflection of mullite.

* Electrochemical Society Active Member.

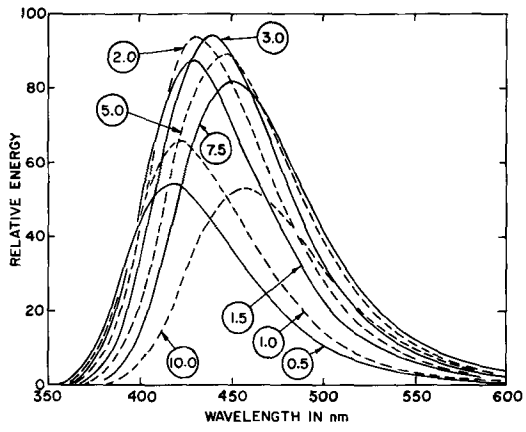

Fig. 2. Special energy distribution of $0.925SiO_2$ $0.075Al_2O_3$: $10^{-3}xEu^{2+}$. Values of x are shown in figure.

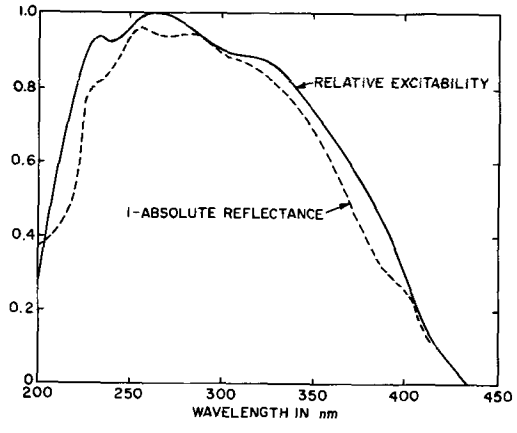

Fig. 3. Excitability and absorption plotted as 1-absolute reflectance of $0.925SiO_2 \cdot 0.075Al_2O_3 : 3x10^{-3}Eu^{2+}$.

intense, and under 254 nm excitation values of quantum efficiency approaching unity have been measured. The pronounced shift of emission to longer wavelength which occurs with increasing Eu can be explained by the region of overlap with the excitation spectrum where self-absorption and re-emission at longer wavelength occurs. Accordingly, this has also been observed to occur (to a lesser extent) with increasing particle size, *i.e.*, decreased scattering of the powder layer. The optimum Eu concentration of phosphor II lies in the neighborhood of $1.5 \times 10^{-3}Eu/0.175SiO_2 \cdot 0.825Al_2O_3$. Its spectral distributions are essentially the same as those of phosphor I with equal Eu concentration. As already seen in Fig. 1, the fluorescence of phosphor II is considerably weaker; moreover in contrast to phosphor I, it is unstable in that the activator begins to oxidize at only slightly elevated temperatures, *e.g.*, 100°C. The weak luminescence of $3Al_2O_3 \cdot 2SiO_2 + Eu^{2+}$ is broader (half-width = 118 nm) and peaks at 460 nm. Its excitability is essentially the same as that of the two phosphors, although only two peaks located at 268 and 304 nm were detected.

Trivalent Eu, unless stabilized in a suitable matrix, is readily reducible under present experimental conditions, and Eu^{2+} may therefore be assumed to exist, at least as a separate compound with θAl_2O_3, $3Al_2O_3 \cdot 2SiO_2$, or amorphous SiO_2. Among IR absorption bands characteristic for these substances, a fairly strong band was also noted at 1390 cm^{-1} which, however, is present only in the two phosphor compositions and in $3Al_2O_3 \cdot 2SiO_2 + Eu^{2+}$, but absent in $\theta Al_2O_3 + Eu^{2+}$, amorphous $SiO_2 + Eu^{2+}$, and a sample of phosphor I, prepared without Eu.

Figure 4 shows ESR spectra of phosphors I and II at 4.2K and 9447 megacycles, plotted as the derivative of absorption. The sample weights were arbitrary, but

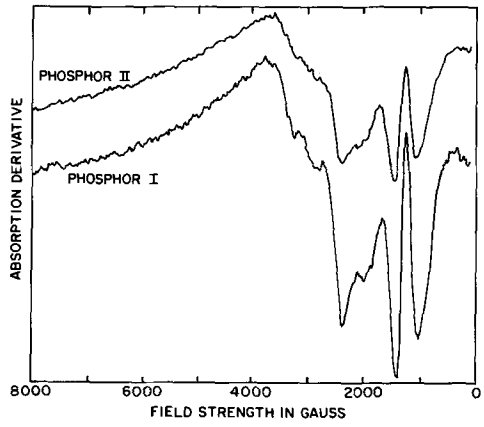

Fig. 4. Electron spin resonance at 4.2K of Eu^{2+} in phosphors I and II, plotted as the derivative of 9447 mc absorption as a function of magnetic field strength.

by correcting to the same amount of Eu in the cavity, the spin density of phosphor II is found lower by a ratio of 1.44. [2] Otherwise, the spectra are identical and therefore indicate that the environment of Eu^{2+} is the same in both phosphors.

The present materials appear to be characterized by dispersions of $3Al_2O_3 \cdot 2SiO_2 + Eu^{2+}$ in another matrix. In the case of phosphor I, this consists of amorphous SiO_2 whose relatively structureless appearance makes it possible to show the presence of the mullite directly. This is seen in Fig. 5a where one notes particles of 100Å most easily discernible near the periphery. When the prefiring of the phosphor was carried out at 1500°C, the SiO_2 was converted to α-cristobalite which is readily noted in Fig. 5b; moreover, the small particles are now absent which means that the mullite has also undergone extensive particle growth. For both reasons, it is evident that the area of contact between the two phases must have diminished. Prefiring at 1600°C causes fusion to an opalescent glass which, after grinding and refiring at 1100°C, was found to contain considerably less α-cristobalite. Figure 5c shows that the over-all structure of this phosphor consists of an amorphous matrix containing evenly dispersed particles, again of about 100Å in size. Moreover, x-ray powder diffraction analysis of this specimen indicates the presence of the same amount of mullite as a separate phase, *i.e.*, it has not dissolved irreversibly in the silica. The small particles, therefore, consist at least in part of mullite which is in contact with amorphous silica.

Figure 6 shows the dependence of fluorescence intensity of prefiring temperature. X-ray powder diffraction analyses taken on one of the series (gel precipitates, NH_3-refired) show the relative height of the 101 reflection of α-cristobalite, and the samples prepared at 1250°, 1500°, and 1600°C are the ones shown in the previous three figures. At least qualitatively, there is a correlation between fluorescence and the crystallinity of the SiO_2 in contact with $3Al_2O_3 \cdot 2SiO_2$, and therefore by inference, the area of the interface. By way of illustration, Fig. 6 also shows that refiring in H_2 is preferable to NH_3, and that a raw material of the same over-all composition but consisting of a mechanical mixture (prepared by wet slurry) of $Al(OH)_3$, $SiO_2 \cdot xH_2O$, and $Eu(NO_3)_3 \cdot 6H_2O$ is not sufficiently reactive to provide the needed dispersion until it is fused.

Discussion

The present system is probably unique in the sense of requiring not one but two host matrices to evoke luminescence. This admittedly unorthodox conclusion follows from direct experimental evidence (Fig. 1)

[2] The phosphors contained 2×10^{-3} Eu/mole. Assuming complete incorporation in phosphor I, this ratio indicates 1.39×10^{-3} Eu/mole in phosphor II which is in good agreement with the optimum activator concentration in this composition.

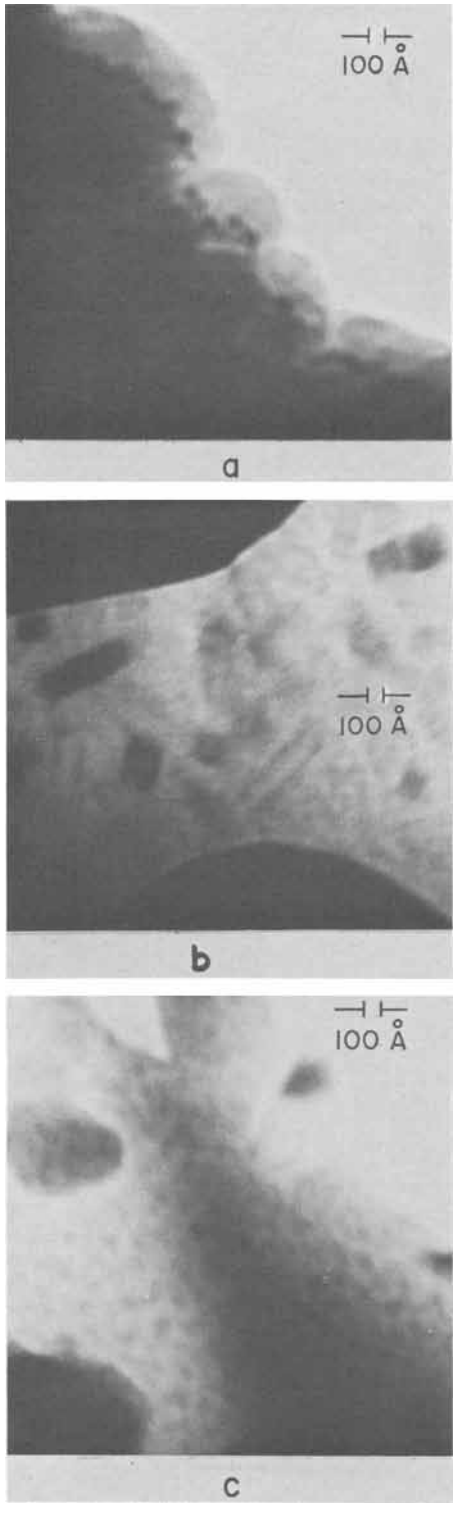

Fig. 5. Transmission electronphotomicrographs of thin edges of $0.925SiO_2 \cdot 0.075Al_2O_3$:3 x $10^{-3}Eu^{2+}$, prefired at: a, 1250°C; b, 1500°C; c, 1600°C.

and is supported by other data which may be summarized as follows.

1. The ionic size of Eu^{2+} (1.09Å) is too large to allow incorporation into Al_2O_3(Al^{3+} = 0.51Å) or $3Al_2O_3 \cdot 2SiO_2$(Si^{4+} = 0.41Å). The disordered lattice of amorphous SiO_2 is known to accommodate large ions; however, no luminescence was noted in this compound until Al is introduced. Then, luminescence rises very steeply and, therefore, one might wish to ascribe this effect to charge compensation such as $2Al^{3+} + Eu^{2+} = 2Si^{4+}$. Maximum luminescence obtains, however, at a Al/Eu ratio near 50/1 where a separate phase (mullite) is already detectable. Moreover, the need for charge compensation is questionable especially in the disordered SiO_2 network, where vacancy formation has little meaning and a configuration such as $2Eu^{2+} = 1Si^{4+}$ seems equally plausible.

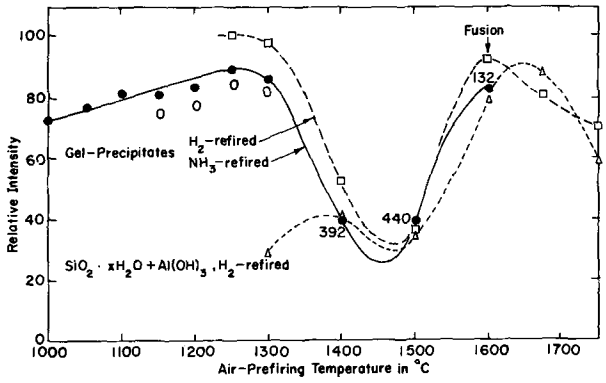

Fig. 6. Blue fluorescence intensity of $0.925SiO_2 \cdot 0.075Al_2O_3$:3 x $10^{-3}Eu^{2+}$ as a function of prefiring temperature. Different techniques of preparation are shown in figure.

2. Luminescence does not require the presence of free SiO_2, since the same excitation and emission spectra are obtained in both phosphors. Although Eu^{2+} is unstable in phosphor II (apparently no effective means of charge compensation is operative) the identical spectra suggest the presence of the same activator center in both phosphors. This further supported by the same ESR absorption of Eu^{2+}. The IR absorption band observed only in compositions containing both $3Al_2O_3 \cdot 2SiO_2$ and Eu^{2+} further supports this conclusion. The fact that this absorption occurs also in the absence of excess SiO_2 or Al_2O_3 indicates that the environment of Eu^{2+} is uniquely determined by its association with $3Al_2O_3 \cdot 2SiO_2$, while only the radiative emission probability of this center is influenced by the presence of the second phase.

3. The dependence of luminescence on the particle size of the mullite phase in phosphor (II) (steep slope between $x = 0.175$ and 0.2 in Fig. 1) and on the crystallinity of SiO_2 (Fig. 5 and 6) suggests that it depends on the area of the interface and consequently, that it originates therein. Owing to the presence of SiO_4 and AlO_4 tetrahedra, as well as AlO_6 octahedra in the structure of aluminosilicates, the interface with neighboring similar units in SiO_2 or Al_2O_3 is likely to involve sharing of oxygen bonds and is therefore not merely mechanical.

The model proposed for the present system may be thought of as Eu^{2+} ions dispersed in the interface between mullite and the second phase and whereby the concentration of activator centers obviously increases with decreasing particle size of the mullite. Alternately, the "association" of Eu^{2+} with mullite may consist of one of the luminescent compounds, *e.g.*, $EuAl_2Si_2O_8$ reported by Jaffe (12, 22). The latter would then be similar to the system $Zn_3(VO_4)_2$ - ZnO recently described by Bernikov and Zelikin (23), *i.e.*, the dispersion of a phosphor in an excess of one of its constituent oxides. It is attractive from the standpoint that at least in the absence of excess SiO_2 or Al_2O_3, Eu^{2+} must form a separate phase, and that the luminescence presently observed in $3Al_2O_3 \cdot 2SiO_2 + Eu^{2+}$ is at least at slightly longer wavelength[3] and can be weak because of its low (activator) concentration. This model would, however, require that only one such compound, *e.g.*, $EuAl_2Si_2O_8$, can exist regardless of over-all stoichiometry which is contrary to Jaffe's results, and that in the present environment, its spectral energy distribution is altered. Finally, the luminescence intensity of a discrete Eu^{2+} compound should not be so strongly influenced by dispersion in the mullite-silica or mullite-alumina interface. Instead, it

[3] The emission of $EuAl_2Si_2O_8$ peaks at 510 nm (22).

should depend on its concentration which would be maximized at Al/Si ratios other than those presently found to yield maximum luminescence (Fig. 1). In view of these considerations, the former model involving discrete Eu^{2+} activator sites appears to be more plausible.

Acknowledgment

The author is indebted to Miss I. Walinski for phosphor preparation and measurements, and also wishes to thank G. Wagner, R. Fitzmaurice, C. K. Lui Wei, and W. A. Thornton for valuable help and discussions.

Manuscript submitted Aug. 8, 1968; revised manuscript received *ca.* Sept. 18, 1968. This paper was presented as a Late News Paper at the Boston Meeting, May 5-9, 1968.

Any discussion of the paper will appear in a Discussion Section to be published in the December 1969 JOURNAL.

REFERENCES

1. J. G. Jenkins and A. H. McKeag, *This Journal*, **97**, 415 (1950).
2. P. M. Jaffe and E. Banks, *ibid.*, **102**, 518 (1955).
3. A. Wachtel, *ibid.*, **107**, 199 (1960).
4. W. L. Wanmaker and J. W. ter Vrugt, *Philips Research Repts.*, **22**, 355 (1967).
5. P. M. Jaffe, U.S. Pat. 3,359,210, Dec. 19, 1967.
6. W. A. McAllister, *This Journal*, **115**, 535 (1968).
7. M. V. Hoffman, *ibid.*, **115**, 560 (1968).
8. T. L. Barry, Paper presented at the Boston Meeting, May 5-9, 1968, as Paper 55.
9. G. Blasse, W. L. Wanmaker, and J. W. ter Vrugt, *ibid.*, Paper 56.
10. C. F. Chenot, *ibid.*, Paper 57.
11. C. C. Lagos, *ibid.*, Paper 58.
12. P. M. Jaffe, *ibid.*, Recent News Paper and U.S. Pat. 3,359,211 Dec. 19, 1967.
13. J. Trömel *et al.*, *Ber. deut. Keram. Ges.*, **34**, 397 (1957).
14. J. Ossaka, *Nature*, **191**, 1000 (1961).
15. S. Otani and A. Kojima, *Kogyo Kagaku Zasshi*, **67**, 239 (1964).
16. S. Otani *et al.*, *ibid.*, 1509 (1964).
17. A. Leonard, S. Suzuki, J. Fripiat, and C. De Kempe, *J. Phys. Chem.*, **68**, 2608 (1964).
18. J. Fripiat, A. Leonard, and J. B. Uytterhoven, *ibid.*, **69**, 3274 (1965).
19. S. Aramaki and R. Roy, *Am. Mineralogist*, **48**, 1322 (1963).
20. W. A. Thornton, Electrochem. Soc. Enlarged Abstracts, **14**, No. 1, 26 (1965).
21. W. E. K. Middleton and C. L. Sanders, *J. Opt. Soc. Am.*, **41**, 419 (1951).
22. P. M. Jaffe, U.S. Pat. 3,359,210, Dec. 19, 1967.
23. S. L. Berdnikov and Ya. M. Zelinkin, *Optics and Spectroscopy*, **19**, 339 (1965).

Effects of Impurities on the Luminescence Processes in YVO_4: Eu

Tsuyoshi Kano and Yoshiro Otomo

Central Research Laboratory of Hitachi Ltd., Kokubunji, Tokyo, Japan

ABSTRACT

Effects of impurities on the photoluminescence, cathodoluminescence, and thermoluminescence of YVO_4:Eu are investigated. Such impurities as Zr, Th, Mo, or W that would give charge defects in the crystal lattice lead to strong quenching of cathodoluminescence, weak or no quenching of photoluminescence at room temperature, and remarkable change of the glow curve. Energy transfer from lattice to Eu by way of excited Eu-O state that is sensitive to trapping by charge defects in the lattice is proposed from the specific quenching of photoluminescence below glow-peak temperature in the Mo- or W-doped phosphor.

Efficient host sensitization in YVO_4:Eu was first indicated by Van Uitert *et al.* who observed the remarkable deviations from a linear dependence of the emission intensity on the Eu^{3+} content in the regions of low concentration by 254 nm or 366 nm uv excitations (1). Since YVO_4:Eu was developed for use in color picture tubes by Levine and Palilla (2), excitation and energy transfer processes in various orthovanadate phosphors have been reported and discussed by many authors (3-13), but more experimental bases are required to make clear the mechanism of these processes. In this paper, the effects of charge defects introduced by impurities on the luminescence intensity and the thermoluminescence properties with 254 nm uv, 365 nm uv, or 10 kv cr (cathode-ray) excitation were investigated to explain the excitation and energy transfer processes in YVO_4:Eu.

Experimental

The powder samples were prepared by firing the precipitates obtained from a mixture of component solutions at 1250°C for 2 hr with sodium pyrovanadate flux. The Eu content was 5 m/o (mole per cent). Various impurities in the form of oxides or oxyacids were intimately mixed with the precipitates before firing. The contents of impurities in this paper refer to the amounts of impurities added before firing. The firing of vanadate precipitates serves as a suitable method of preparing samples for the purpose of this paper, because it can constantly provide bright phosphors for laboratory scale experiments. Nb and Ta in the final products were analyzed by x-ray fluorescence method with IKF-3 x-ray spectrometer made by Rigaku Denki Company, Ltd. A high-pressure mercury lamp (100w) was used for long wave uv (mainly 365 nm) exciting light source and a low-pressure mercury lamp (10w) with a quartz tube was used for short wave uv (mainly 254 nm) exciting light source. For the cathodoluminescence measurement, the phosphors were settled on a metal panel in thin layers (0.06 g/cm^2) and irradiated with 10 kv electrons at 1 μa/cm^2. Luminescence spectra were obtained using Hitachi recording spectrophotometer EPS-2R which gives spectral energy distribution curves automatically corrected for the characteristics of the system. Excitation spectra were obtained with Hitachi spectrofluorometer MPF-2, using 40w hydrogen lamp as a light source and sodium salicylate as a reference phosphor showing constant quantum yields in the wavelength region studied. The thermoluminescence measurements were carried out by a conventional technique, using an EMI 6256S photomultiplier as a detector.

Results

The effects of such added impurities as Ce, Pr, Nd, U, Th, Mo, W, Nb, or Ta on the luminescence intensities of YVO_4:Eu with 365 nm uv, 254 nm uv, or cr excitation are shown in Fig. 1. As shown, these impurity effects can be classified into three types: (*A*) the strong quenching which is independent of the way of excitation, (*B*) the strong quenching of cathodoluminescence, weak quenching of photoluminescence by short-wave uv excitation and no remarkable effect observed on photoluminescence by long wave uv excitation, and (*C*) minor effects observed. Type A, B, and C are typically observed by the doping of rare earth impurities, group IV or VI elements and group V elements, respectively. By Ce- or U-doping, the quenching effects on the cathodoluminescence and the photoluminescence by 365 nm uv excitation were found to be of the same degree, but minor quenching effects were observed on the photoluminescence by 254 nm uv excitation. This difference is explained in the following way. Ce- or U-doping causes coloration of samples which gives rise to absorption of luminescence. When the phosphors are excited deeply from the surface by 365 nm uv or cr, the absorption of luminescence by those impurities is expected to be stronger than that when the phosphors are excited at the surface by 254 nm uv which is shorter than the absorption edge (about 320 nm). The dopings of other impurities shown in Fig. 1, on the other hand, do not result in the remarkable coloration of samples. Thus, the effects of Ce- or U-doping can be interpreted to belong to type A essentially. Type A quenching is ascribed to the interaction between electronic energy levels of impurity ions and excited electronic energy levels of Eu that are commonly involved in the luminescence process with uv excitation and in the process with cr excitation. This type of interaction is expected to be observed between many rare earth ions which transfer energy with each other by resonance. To estimate the quenching effect by this mechanism, an important parameter is a critical transfer distance Ro, which is defined as the distance of a donor-acceptor pair at which the probability of energy transfer from the donor to acceptor becomes equal to the probability of the internal transition of the donor (14). For the quenching of Eu^{3+} luminescence by Nd^{3+}, Ro was estimated to be 12.8Å from the analysis of the decrease of emission intensity of Eu^{3+} by Nd^{3+} (14). By using this value, it is estimated that Eu^{3+} luminescence decreases by half by 0.9 a/o Nd^{3+} in YVO_4:Eu. This is in qualitative agreement with the result shown in Fig. 1. Type B quenching, on the other hand, is ascribed to the action of charge defects in the highly excited lattice, since it is characteristic of those ions that give surplus charges replacing constituent ions. Other luminescence properties of Mo or W-doped phosphors which are characterized by type B quenching will be described in the following and the detailed discussion of type B quenching will be given in the next chapter.

Minor effects of type C may be due to the lack of energy levels interacting strongly with Eu^{3+} and also due to the lack of charge defects formed by incorporation of the impurities. The anxiety that the minor effects of type C might be due to small amounts of these impurities actually incorporated in the final products could be eliminated by analyzing the content of Nb or Ta in the final products by x-ray fluorescence spectroscopy which confirmed the nearly quantitative incorporation of these elements.

The thermoluminescence of YVO_4:Eu has already been reported (12, 15). The remarkable changes of the glow curve as a result of Mo- or W-doping were found after uv irradiation at 77°K as are shown in Fig. 2. The doping of Mo or W gives rise to a new glow peak at the expense of the native glow peak by 254 nm uv excitation. By 365 nm uv excitation, however, no thermal glow was observed in the Mo-doped phosphor and only a little glow was observed in the W-doped phosphor. These thermoluminescence properties of Mo- or W-doped phosphors provide contrasts to those of undoped phosphor which exhibits nearly identical glow curve by 365 nm uv excitation with that by 254 nm uv excitation. By cr excitation of the Mo-doped YVO_4:Eu, a similar glow curve with that by 254 nm uv excitation was obtained. By keeping the irradiated Mo-doped YVO_4:Eu at 77°K for 30 min in the dark, 20% decrease of the resultant light sum was observed. As for the case of the doping of group IV elements, strong or complete quenching of the native glow-peak was observed by Th- or Zr-doping. No remarkable new peak, however, appears in this case. The difference between the effects of group IV elements and group VI elements may be related to the difference of substituted sites, V site by Mo or W and Y site by Zr or Th being expected to be substituted, respectively.

The glow curves of YVO_4 not activated with Eu are shown in Fig. 3. Several glow peaks were found in the sample which had been fired without flux. A simpler glow curve was obtained with the sample fired

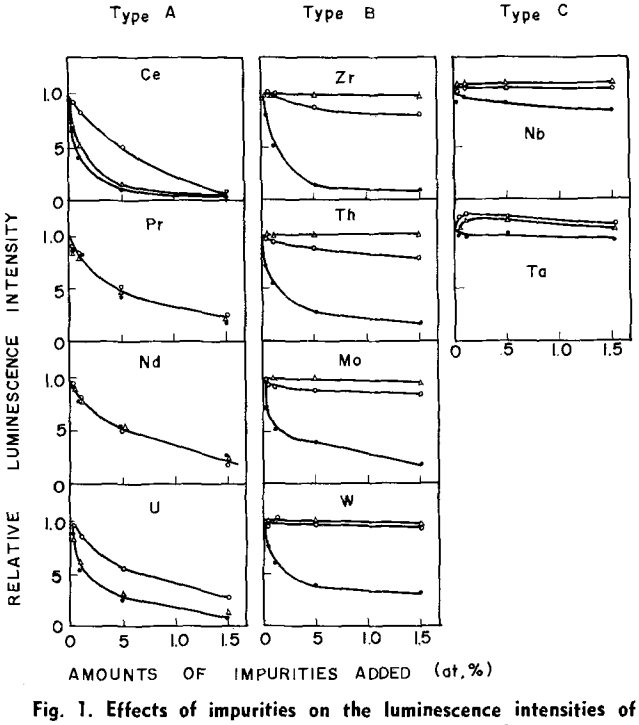

Fig. 1. Effects of impurities on the luminescence intensities of YVO_4:Eu excited with 365 nm uv (△), 254 nm uv (○), or cathode rays (●) at room temperature.

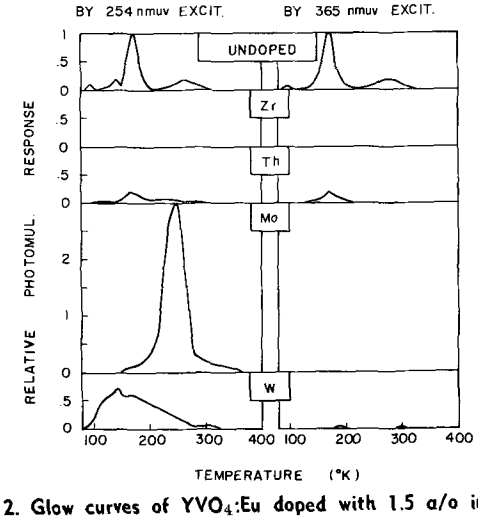

Fig. 2. Glow curves of YVO_4:Eu doped with 1.5 a/o impurities. Heating rate, 25°K/min.

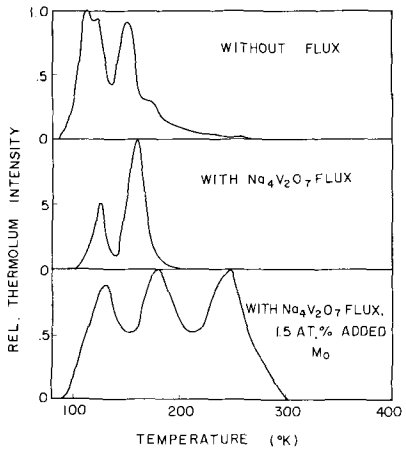

Fig. 3. Glow curves of YVO_4; heating rate, 25°K/min; after 254 nm uv excitation at 77°K.

with flux, where only two peaks were distinguished. The glow peaks that disappeared as a result of using flux may be due to some crystal defects that are removed by using flux. The major glow peak at 160°K lies very near to the reported value, 164°K (12) and corresponds to the major glow peak of undoped YVO_4:Eu. By Mo-doping, a new glow peak around 240°K appears in the glow curve of YVO_4 or YVO_4:Eu. From these glow curve measurements, it is obvious that the trapping levels of YVO_4:Eu lie not in the excited state of Eu but in the host lattice and charge defects introduced by impurity dopings strongly affect the native trapping level or provide new levels.

In Fig. 4, the spectra of photoluminescence and thermoluminescence are compared by observing the dependences of the transmitted light intensity on the cut-off wavelength of filters. The thermoluminescence spectrum of Mo-doped YVO_4:Eu appears to be similar with that of photoluminescence of YVO_4:Eu.

Cathodoluminescence spectrum of YVO_4:Eu and that of Mo-doped YVO_4:Eu are compared in Fig. 5, where no difference of spectral energy distribution was observed. Excitation spectrum of YVO_4:Eu and that of Mo-doped YVO_4:Eu are shown in Fig. 6. Mo-doping decreases the luminescence intensity only under short wavelength region, as is consistent with the results shown in Fig. 1.

Temperature dependences of the luminescence intensity of Mo-doped YVO_4:Eu by cr, 254 nm uv, or 365 nm uv excitation are compared with those of undoped YVO_4:Eu in Fig. 7. By 254 nm uv excitation, stepwise temperature-dependent quenching of luminescence is induced by Mo-doping at low temperatures. Increasing

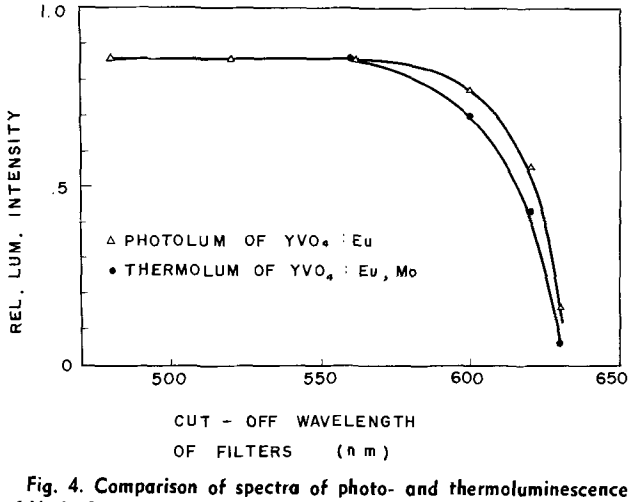

Fig. 4. Comparison of spectra of photo- and thermoluminescence of YVO_4:Eu.

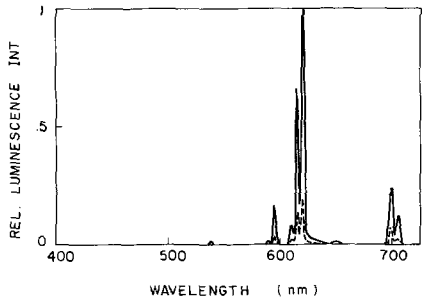

Fig. 5. Cathodoluminescence spectra of YVO_4:Eu (solid line) and 1.5 a/o Mo added YVO_4:Eu (broken line) at room temperature.

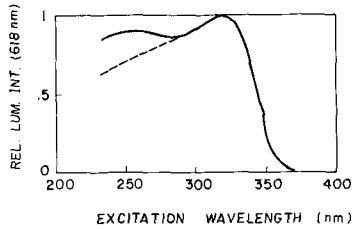

Fig. 6. Excitation spectra of YVO_4:Eu (solid line) and 1.5 a/o Mo added YVO_4:Eu (broken line) at room temperature.

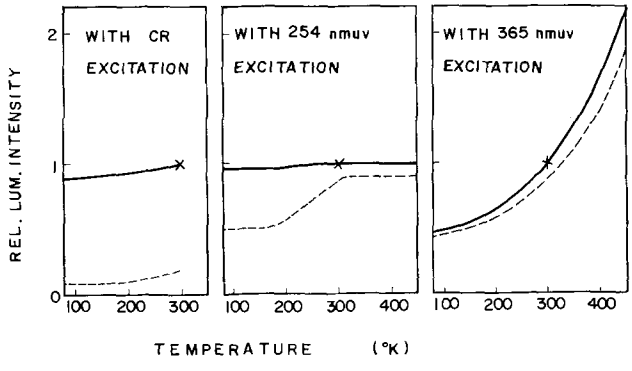

Fig. 7. Temperature dependences of luminescence intensities of YVO_4:Eu - - - - doped with 1.5 a/o Mo; ——— undoped.

quenching effects with the decrease of temperature are also observed with cr excitation, while marked effects of Mo-doping are not found from 77° to 450°K with 365 nm uv excitation. The luminescence spectra do not depend much on temperature except that a feeble host luminescence, which is cut by a filter, appears at low temperatures. In Mo- or W-doped YVO_4:Eu with 254 nm uv excitation, correlations between the temperature dependences of photoluminescence intensities and the glow curves are shown in Fig. 8. As shown in the figure, quenching by Mo- or W-doping occurs below the temperature around which thermoluminescence appears. The decrease in luminescence intensity at low temperature is not due to simple energy storing, be-

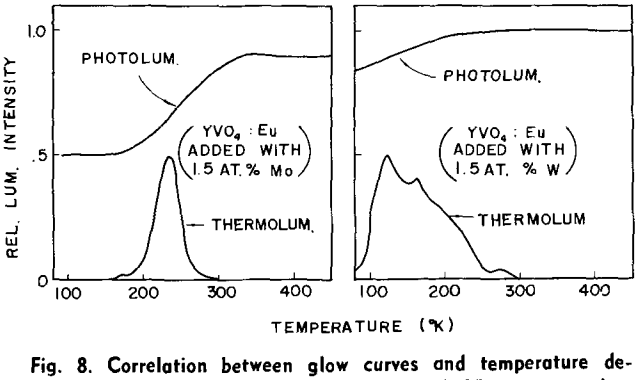

Fig. 8. Correlation between glow curves and temperature dependences of photoluminescence intensities with 254 nm uv excitation.

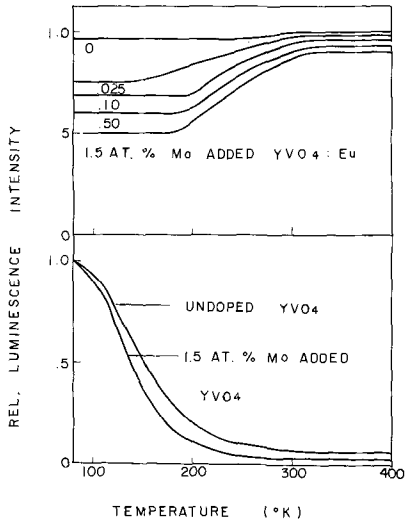

Fig. 9. Effects of Mo doping on the temperature dependence of luminescence intensities with 254 nm uv excitation. In the case of the host luminescence of YVO_4, normalized intensities are shown.

cause the resultant thermoluminescence intensity is orders of magnitude weaker than the luminescence intensity under excitation. In the case of Mo-doped YVO_4:Eu, steady intensity of photoluminescence was instantly obtained from the beginning of excitation at 77°K where the number of filled traps giving rise to thermoluminescence was increasing. This result indicates that the quenching induced by Mo-doping below glow-peak temperature is not due to the filled traps which will give rise to thermoluminescence at elevated temperatures. Figure 9 shows the temperature dependences of luminescence intensities of YVO_4:Eu doped with various amounts of Mo and the effect of Mo-doping on the temperature dependence of the host luminescence of YVO_4. In the case of host luminescence, specific quenching due to Mo-doping at low temperatures does not occur in contrast with the case of the luminescence of Eu in YVO_4:Eu. An explanation for the specific quenching effect of Mo-doping at low temperatures is given below.

Discussion

It has been indicated by Van Uitert *et al.* that the excitation of YVO_4:Eu by 254 nm uv or 366 nm uv proceeds through the host process because the relative brightness per Eu content increases with the decrease of Eu concentration (1). The identical excitation spectra of related vanadate phosphors around 320 nm reported by Palilla *et al.* show that the exciting energy is absorbed by VO_4^{3-} ions and is transferred to activators (4), but the broad absorption or excitation band in the shorter wave uv region has been the subject of discussions (7, 9). Recently Mooney and Toma indicated a continuous overlap of π-bonding orbitals of vanadate ions and f orbitals of the rare earth ion to explain the efficient photoluminescence of YVO_4:Eu (13).

The specific quenching of Eu luminescence below the glow peak temperature in Mo-doped YVO_4:Eu provides another experimental basis for the discussion on the nature of interaction between the host lattice and Eu. Various possible quenching mechanisms are discussed in the following. There are several possible stages from absorption of exciting light to emission of luminescence on which Mo-centers can play a part. The quenching due to ineffective additional absorption by impurity ions has been indicated in the luminescence quenching of $CaWO_4$ or $MgWO_4$ by Fe, Cr, Cu, or Mn by Kröger (16). Following this mechanism, quenching effects are stronger with long wave uv excitation than with short wave uv excitation in the neighborhood of absorption edge. The quenching due to Mo-doping, however, is rarely observed by 365 nm uv excitation and appreciable by 254 nm uv excitation in contradiction of the prediction of the above mechanism. Absorption of the red luminescence by doped Mo-center may be negligible, because it does not affect the white body color of the phosphor. It is evident from the minor effect of Mo-doping with 365 nm uv excitation that the emitting state of Eu, $^5D_0$, does not suffer quenching interaction from the doped Mo center. Therefore, the doped Mo center is supposed to act in the intermediate luminescence process. By the way, P substituted for V in YVO_4:Eu reduces luminescence of Eu but enhances host luminescence in YVO_4 (10). These effects result from the cutting of the energy transferring chain by PO_4^{3-} group substituted for VO_4^{3-} group. If this mechanism is dominant in Mo-doped YVO_4:Eu, native feeble host luminescence observed at 77°K should be enhanced at the expense of the luminescence from Eu. Such enhancement of host luminescence by Mo-doping could not be observed. In the case of Y_2W_{1-x} Mo_x O_6: Eu, it has been reported that doped Mo plays a role of sink in the course of exciton migration with subsequent energy dissipation (17). It seems hard to explain by this mechanism the temperature-dependent quenching due to Mo doping in YVO_4:Eu, because the host luminescence in YVO_4 does not suffer this specific quenching. It is to be noted in this discussion that the exciton migration in the lattice of YVO_4:Eu is supposed to be comparatively rapid even at 77°K, because only a feeble host luminescence could be observed in YVO_4:Eu at 77°K. This feeble host luminescence in the case of YVO_4:Eu provides an interesting contrast to the remarkable host luminescence in Ca WO_4:Sm at low temperatures (18). The phonon-assisted energy transfer from lattice to an activator suggested in the case of YVO_4:Sm by Ropp (9) may have few connections with the quenching by doped impurities, because the phonons in the host lattice may not be so sensitive to doped impurities. It is most likely that highly excited states of Eu-O state which is closely coupled with the lattice suffer quenching interaction from doped Mo center at low temperatures. The broad excitation spectra of various Eu-activated mixed oxides in the region from 220 to 310 nm have been assigned as charge transfer bands by Blasse (19). It is quite possible that the charge transfer state play a part in the energy transfer process from lattice to an activator. This possibility has already been referred to in the case of $CaWO_4$:Sm (18). As a higher energy state to which Eu^{3+} is excited by receiving energy from the vanadate lattice with short wave uv excitation, the charge transfer state is preferred to excited states of Eu^{3+} perturbed by crystal field, because the sensitivity to charge defects in the lattice is expected to be higher in the former than the latter. The continuous overlap of π-bonding orbitals of the VO_4^{3-} group and f orbitals of Eu^{3+} proposed by Mooney and Toma to explain the efficient energy transfer (13) might contribute to the trapping by doped Mo center below glow peak temperature. The quenching is explained by assuming that the charge transfer state of Eu is sensitive to the charge trapping action of doped Mo center at low temperatures and as a result, its energy is transferred to the doped Mo center and dissipated nonradiatively there or stored. The trap depth of the doped Mo center was roughly estimated from the initial rise of thermoluminescence to be distributed from 0.48 to 0.65 ev. The condition indicated by Bräunlich (20) should be checked before the establishment of the value.

Finally, it is to be indicated that the comparison between glow curve and temperature dependence of luminescence of insulating phosphors, preferably doped with impurities giving surplus charges, will provide useful information concerning intermediate processes from excitation to luminescence.

Acknowledgments

The authors are indebted to Dr. M. Emoto of this laboratory for the continuous support and encouragement throughout this work, to Dr. H. Yamamoto of this laboratory for useful discussions, to Miss Y. Iijima for the assistance in experiments, and to Mr. M. Hayashi for the analyses of samples.

Manuscript submitted June 26, 1968; revised manuscript received Sept. 4, 1968. This paper was presented at the Boston Meeting, May 5-9, 1968, as Paper 38.

Any discussion of this paper will appear in a Discussion Section to be published in the December 1969 JOURNAL.

REFERENCES

1. L. G. Van Uitert, R. C. Linares, R. R. Soden, and A. A. Ballman, *J. Chem. Phys.*, **36**, 702 (1962).
2. A. K. Levine and F. C. Palilla, *Appl. Phys. Letters*, 5, 118 (1964).
3. L. H. Brixner and E. Abramson, *This Journal*, **112**, 70 (1965).
4. F. C. Palilla, A. K. Levine, and Maija Rinkevics, *ibid.*, **112**, 776 (1965).
5. Jean Loriers, Jean-Pierre Denis, and Jean-Pierre Briffaut, *C. R. Acad. Sc. Paris*, **262**, 496 (1966).
6. J. R. O'Connor, *Appl. Phys. Letters*, **9**, 407 (1966).
7. R. K. Datta, *Trans. Met. Soc. AIME*, **239**, 355 (1967).
8. J. R. O'Connor, *ibid.*, **239**, 362 (1967).
9. R. C. Ropp, *J. Opt. Soc. Amer.*, **57**, 1240 (1967).
10. M. A. Aia, *This Journal*, **114**, 367 (1967).
11. S. Z. Toma, F. F. Mikus, and J. E. Mathers, *ibid.*, **114**, 953 (1967).
12. S. G. Polick and H. N. Hersh, Electrochem. Soc. Dallas Meeting Extended Abstracts, I-3 **16**, 4, Abstract 69 (1967).
13. R. W. Mooney and S. Z. Toma, *J. Chem. Phys.*, **46**, 4544 (1967).
14. E. Nakazawa and S. Shionoya, *ibid.*, **47**, 3211 (1967).
15. T. Kano and Y. Otomo, *Chem. Soc. Japan*, Annual Meeting, **1**, 572 (1967).
16. F. A. Kröger, "Some Aspects of the Luminescence of Solids," Elsevier Publishing Company Inc., New York (1948).
17. G. Blasse and A. Bril, *J. Chem. Phys.*, **45**, 2350 (1966).
18. Th. P. J. Botden, *Philips Research Repts.*, **6**, 425 (1951).
19. G. Blasse, *J. Chem. Phys.*, **45**, 2356 (1966).
20. P. Bräunlich, *J. Appl. Phys.*, **38**, 2516 (1967).

Spectroscopic Identification of Europium-Oxygen Complexes in Calcium Fluoride

R. L. Amster and C. S. Wiggins

The Bayside Laboratory, Research Center,
General Telephone & Electronics Laboratories Incorporated, Bayside, New York

ABSTRACT

The emission and excitation spectra for $CaF_2:Eu^{3+}$ have been analyzed. The spectra have been attributed to four main Eu^{3+} species. Three of these species are composed of $Eu^{3+} - O^{2-}$ complexes which arise as a result of the charge compensation of Eu^{3+} substituting in a Ca^{2+} site. The complexes have been associated with both $(Eu - O)^+$ and $(Eu_2 - O_2)^{2+}$ groups with the relative concentration of the complexes depending on the total Eu^{3+} concentration. Broad and intense uv excitation spectra have been identified as $Eu^{3+} - O^{2-}$ charge transfer bands. The high intensity of $^5D_0 - {}^7F_0$ transitions attests to the linear asymmetry of the complexes at the Eu^{3+} site.

Replacement of Ca^{2+} in CaF_2 by trivalent europium requires compensation of the excess positive charge (1, 2). This may be effected by the inclusion of an interstitial fluoride ion or by the isomorphous substitution of an O^{2-} ion for a F^- ion adjacent to the cation site. The latter mode of compensation predominates when $CaF_2:Eu^{3+}$ is prepared in an oxidizing atmosphere (1).

The presence of an oxide ion in the immediate vicinity of Eu^{3+} gives rise to charge transfer bands in the absorption and fluorescence excitation spectra of several Eu^{3+} activated materials (3). For example, Blasse and Bril (4) have observed broad uv bands in the fluorescence excitation spectra of $NaGdO_2:Eu^{3+}$ which they attribute to charge transfer from O^{2-} to Eu^{3+}. Their observations are in agreement with Jørgensen's (5) interpretation of the uv absorption spectra of Eu^{3+} in solution. Similarly, Kingsley and Prener (6) have reported observing an intense charge transfer band when CdS is introduced into $CdF_2:Eu^{3+}$; the absorption peaking at 283 nm is associated with the $Eu^{3+} - S^{2-}$ complex. It was the intention of this investigation to examine the charge transfer bands in the spectra of $CaF_2:Eu^{3+}$ (prepared in air) in an attempt to identify the $Eu^{3+} - O^{2-}$ complexes formed through the mechanism of charge compensation. The identification was assisted by studying the effects of linear asymmetry at the europium site as a result of compensation by O^{2-} ions. Blasse and co-workers (7) have studied several Eu^{3+}-activated phosphors in which there exists linear asymmetry at the Eu^{3+} site. They observed that the generally forbidden $^5D_0$-$^7F_0$ transition in Eu^{3+} gives rise to unusually high fluorescence intensity in the compounds examined. The intense $^5D_0$-$^7F_0$ fluorescence is explained by inclusion of a linear term in the crystal field expansion (8).

Since the $^5D_0$-$^7F_0$ transition cannot be split by a crystal field, the appearance of more than one $^5D_0$-$^7F_0$ emission line for $CaF_2:Eu^{3+}$ can be interpreted as proof of the existence of more than one symmetry site for Eu^{3+} ions charge compensated by oxide ions. Eu^{3+} ions in CaF_2 can be expected to yield emission and fluorescence excitation spectra which depend on local europium site symmetry. In the present study, several Eu^{3+} species with different site symmetries are identified by isolating groups of emission and excitation lines which undergo equivalent intensity changes with variations in europium concentrations.

Experimental Procedure

Preparation of $CaF_2:Eu^{3+}$.—Calcium fluoride activated with Eu^{3+} was prepared by a high-temperature, 1050°C, reaction between CaF_2 (Fisher Reagent grade) and anhydrous EuF_3 (Trona Division, American Potash Company). The reaction was carried out in open alu-

mina crucibles in a muffle furnace which had openings to permit free flow of air through the furnace.

Emission spectroscopy.—Emission spectra were recorded in terms of energy *vs.* wavelength with a radiometer which includes a 3/4M Spex grating monochromator and an ITT 4013 photomultiplier [S-20 response, sapphire window]. Correction for instrumental sensitivity was obtained by comparison with a standard lamp and applied automatically.

Excitation spectroscopy.—A double monochromator, consisting of two ¼-meter Jarrell-Ash monochromators linked and driven together was used to select the excitation wavelength from the output of a 900-watt xenon-arc source. Correction for the lamp output spectrum as well as the transmission of the double monochromator was applied automatically.

Experimental Results

When CaF_2:Eu^{3+} is excited by 3130Å radiation, fluorescence emission is observed between 5000 and 7100Å. The four most intense emission lines are located at 6308, 6162, 5809, and 5731Å (Fig. 1). As the Eu^{3+} concentration is increased from 0.002 to 0.02 gram atom mole CaF_2, these lines remain nearly constant in intensity giving no indication of Eu^{3+} concentration quenching. However, emission lines at 5763, 6100, and 6262Å show some increase in intensity with rising Eu^{3+} concentration (Fig. 2). The first set of Eu^{3+} emission lines is attributed to a specie I while the second set is associated with specie IV to be discussed below. Excitation spectra for emission lines attributed to specie I are identical and contain lines at 5731, 5281, 4622, and 4594Å (Fig. 3). In addition, two broad uv excitation bands are observed at 3000 and 3150Å and are accompanied by a series of lines in the 3500-4200Å region (Fig. 4). The broad uv bands are attributed to charge transfer absorptions in Eu^{3+} — O^{2-} groups; lines in the 3500-4200Å region are associated with f-f transitions of europium in these groups. The intense sharp line at 5731Å which is observed in emission and excitation is identified with the $^5D_0$-$^7F_0$ transition in Eu^{3+} which occupies a linearly asymmetric site in specie I.

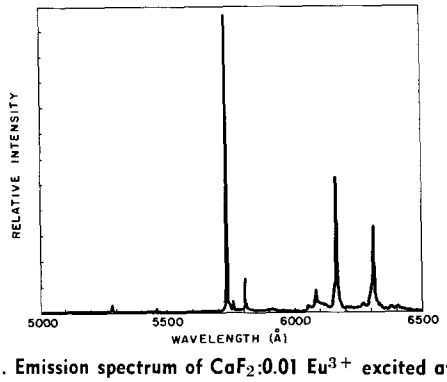

Fig. 1(a). Emission spectrum of CaF_2:0.01 Eu^{3+} excited at 3130Å

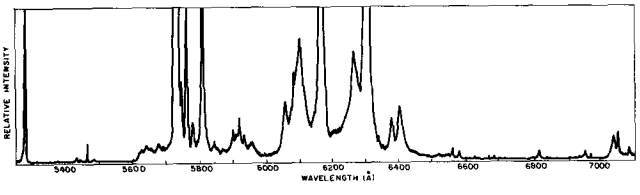

Fig. 1(b). Emission spectrum of CaF_2:0.01 Eu^{3+} excited at 3130Å; high gain.

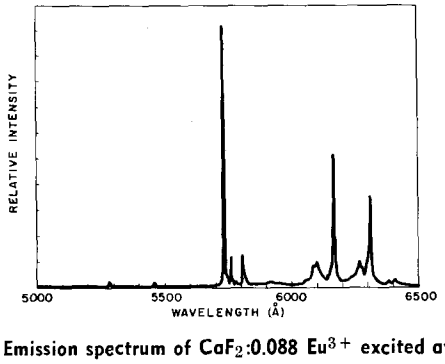

Fig. 2. Emission spectrum of CaF_2:0.088 Eu^{3+} excited at 3130Å

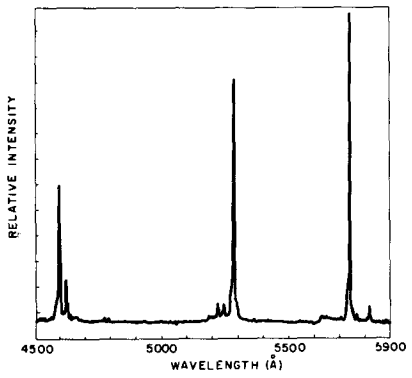

Fig. 3. Visible excitation spectrum of CaF_2:0.02 Eu^{3+} for specie I emission at 6308Å.

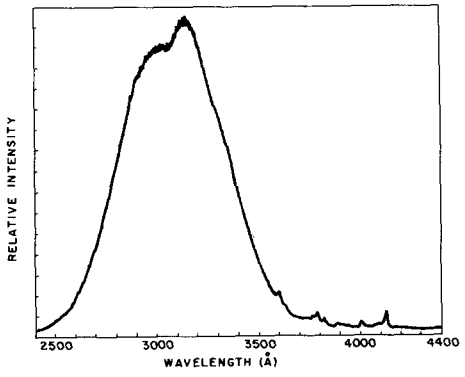

Fig. 4. Ultraviolet excitation spectrum of CaF_2:0.01 Eu^{3+} for specie I emission at 5732Å.

Spectral lines and bands associated with specie I are listed in Table I. The wavelengths listed are nearly identical with those observed by Feofilov and Stepanov (1, 9) for "Type-I" CaF_2:Eu^{3+}; it is clear that specie I reported herein and type I discussed by Feofilov are the same entity and can be identified as a Eu^{3+} — O^{2-} complex with nonlinear symmetry. The spectral transitions were assigned by comparing the spacings of emission and excitation lines in different spectral regions. The lack of equal spacing between spectral lines within any set of $^5D_0$-^7F_J emissions indicated that the lines were not of vibronic nature. These lines were, therefore, identified with pure electronic transitions with the aid of results obtained for $LaCl_3$:Eu^{3+} by DeShazer and Dieke (10). The sharp fluorescence line at 6308Å may be assigned to a $^5D_0$-$^7F_2$ transition. This would indicate an unusually large separation of the $^7F_2$ terminal level involved in this transition from those $^7F_2$ terminal levels associated with the $^5D_0$-$^7F_2$ emission lines at 6054 and 6162Å. The line at 6308Å, therefore, may instead be associated with a $^5D_0$-$^7F_3$ transition. Present evidence, however, does not allow for a definite assignment to the 6308Å emission line. It is clearly not attributable to a transition from a $^5D_1$ state since it is strongly excited by selective absorption into the $^5D_0$ level.

The relative intensities of the specie I charge-transfer bands vary with concentration. The lower wavelength band becomes relatively less intense at higher Eu^{3+} concentration and is just observable when [Eu^{3+}] = 0.088 g-atom/mole CaF_2. Exciting a given CaF_2:Eu^{3+}

Table I. Emission and excitation spectra of specie I

Emission, Å	Excitation, Å	Transition
7088 }		
7055 }		$^5D_1$-$^7F_6$ or $^5D_0$-$^7F_4$
7043 }		
6960		$^5D_0$-$^7F_4$
6933		$^5D_0$-$^7F_4$
6823		$^5D_0$-$^7F_4$
6583		$^5D_1$-$^7F_5$
6564		$^5D_1$-$^7F_5$
6553		$^5D_1$-$^7F_5$
6526		$^5D_1$-$^7F_5$
6406		$^5D_0$-$^7F_3$
6382		$^5D_0$-$^7F_3$
6308		$^5D_0$-$^7F_2$ or $^5D_0$-$^7F_3$
6162		$^5D_0$-$^7F_2$
6054		$^5D_0$-$^7F_2$
5957		
5934		$^5D_0$-$^7F_1$
5920		$^5D_0$-$^7F_1$
5870		$^5D_1$-$^7F_3$
5843		$^5D_1$-$^7F_3$
5809	5808	$^5D_1$-$^7F_3$
5781		$^5D_1$-$^7F_3$
5778		$^5D_1$-$^7F_3$
5746		$^5D_1$-$^7F_3$
5735	5732	$^5D_0$-$^7F_0$
5684		
5678		
5656		
5642		$^5D_1$-$^7F_2$
5627		
5488		$^5D_1$-$^7F_1$
5447		$^5D_1$-$^7F_1$
5436		$^5D_1$-$^7F_1$
5284	5281	$^5D_1$-$^7F_0$
	4622	$^5D_2$-$^7F_0$
	4594	$^5D_2$-$^7F_0$
	3500-4200	Unassigned f-f transitions
	3150 }	$Eu^{3+}-O^{2-}$ charge transfer
	3000 }	bands

sample at the maximum of each of the broad uv bands leads to no differences in emission spectra. Apparently, specie I is composed of two separate $Eu^{3+} - O^{2-}$ entities with identical emission spectra but with charge transfer transitions of different energies. In a later section of this paper, spectra of specie I will be compared with those of other species to be discussed. Identification of the various types of Eu^{3+} groups present will then be made and the intensity dependence of the charge transfer bands upon Eu^{3+} concentration will be discussed.

Excitation of CaF_2:0.002 Eu^{3+} by 2537Å radiation leads to emission between 4500 and 7000Å (Fig. 5a). As the Eu^{3+} concentration is increased from 0.002 g-atom Eu^{3+}/mole CaF_2 to 0.02 g-atom Eu^{3+}/mole CaF_2, a large group of emission lines decreases in intensity and disappears upon further increase in europium concentration to 0.088 g-atom/mole CaF_2 (Fig. 5b and 5c). This group of lines is associated with specie II. (Specie II emission in the 4500-6000Å region is more readily observed in a high-gain recording of the emission spectrum of CaF_2:0.002 Eu^{3+}; Fig. 6.) The most intense emission line for this specie is observed at 6162Å. This line, which is accompanied by a less intense line at 6172Å, coincides with the most intense line of specie I. The excitation spectrum for the 6162Å emission contains, in addition to the excitation spectrum for specie I, lines at 5379 and 4669Å and a band peaking at 2600Å (Fig. 7 and 8). The specie I excitation spectrum can be distinguished from that of specie II because the latter does not appear in excitation spectra of specie I for emission lines other than 6162Å. The group of lines associated with specie II is listed in Table II. The emission spectrum of this specie II agrees closely with that of "type II" reported by Feofilov and Stepanov (1, 9) for CaF_2:Eu^{3+} prepared in the absence of oxygen and the presence of graphite. Specie II is, therefore, associated with Eu^{3+} ions which are not charge compensated by oxide ions. Since Eu^{3+} ions of specie II do not form $Eu^{3+} - O^{2-}$ charge transfer complexes, the broad uv excitation band at 2600Å may then be ascribed to "host" absorption. Since CaF_2 is transparent to 2600Å radiation, the presence of occluded hydroxyl and oxygen anions in air fired CaF_2 probably accounts for the broad uv absorption band (11). For trivalent europium a maximum of three $^5D_0$-$^7F_1$ transitions is allowed.

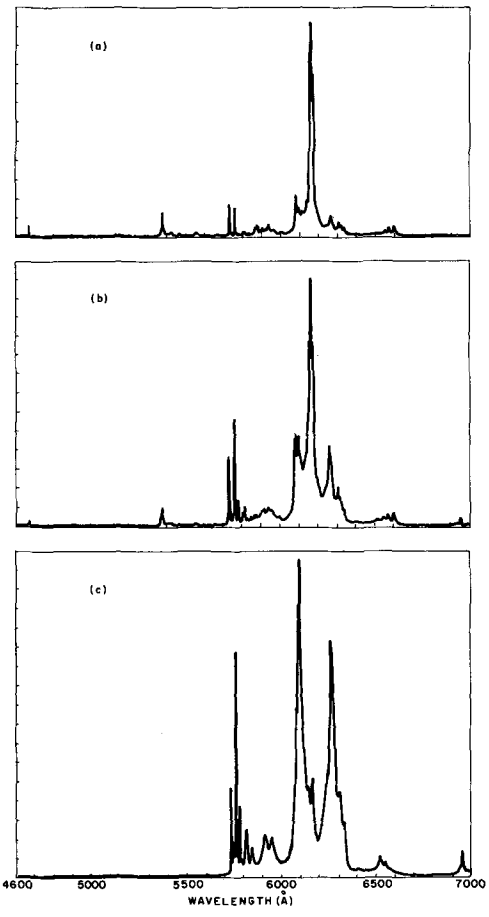

Fig. 5. Emission spectrum of (a) CaF_2:0.002 Eu^{3+}; (b) CaF_2: 0.02 Eu^{3+}; (c) CaF_2:0.088 Eu^{3+} excited at 2537Å.

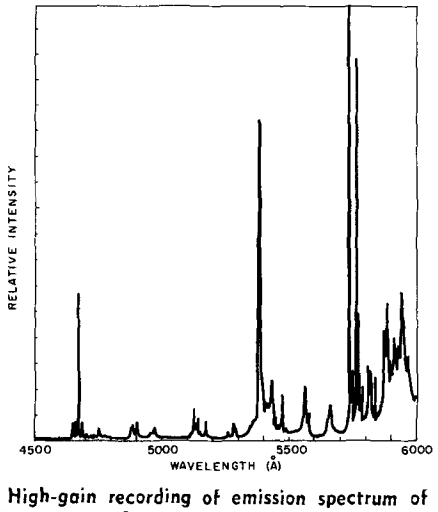

Fig. 6. High-gain recording of emission spectrum of CaF_2:0.002 Eu^{3+} excited at 2537Å; emission covers 4500-6000Å range.

Observation of more than three such lines in the emission spectrum of specie II indicates that this specie is a collection of Eu^{3+} ions occupying dissimilar symmetry sites. These Eu^{3+} ions are most probably charge compensated by nearby interstitial fluoride ions or experience nonlocalized compensation giving rise to cubically symmetric Eu^{3+} sites.

As has been observed from spectra shown in Fig. 5a, excitation of CaF_2:0.002 Eu^{3+} by 2537Å radiation yields line emission at 6262, 6082, and 5763Å in addition to emission associated with species I and II. (Specie I can be excited by 2537Å since the low-wavelength tails of specie I charge transfer bands extend below 2500Å.) As the Eu^{3+} concentration is increased to 0.02 g-atom Eu^{3+}/mole CaF_2, lines at 6262, 6100, 6082, and 5763Å

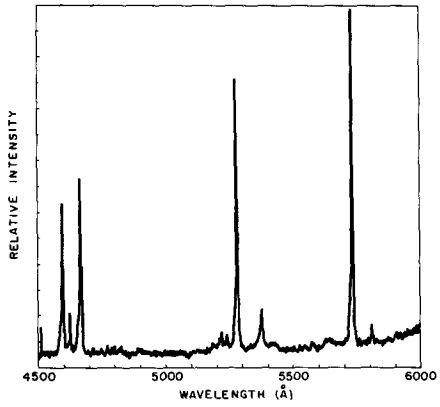

Fig. 7. Visible excitation spectrum of CaF_2:0.002 Eu^{3+} for emission at 6162Å emission.

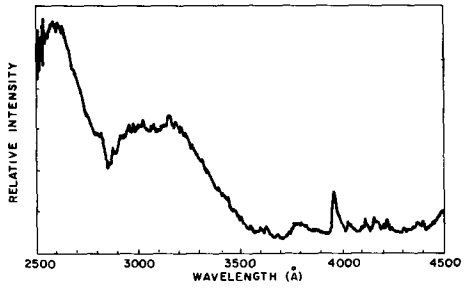

Fig. 8. Ultraviolet excitation spectrum of CaF_2:0.002 Eu^{3+} for emission at 6162Å.

become prominent, while those lines attributable to specie II diminish in intensity (compare Fig. 5a and 5b). A further increase in Eu^{3+} concentration to 0.088 g-atom Eu^{3+}/mole CaF_2 leads to an increase in the intensity of lines at 6100 and 6262Å relative to that at 6082Å; this concentration increase also leads to increased emission at 5781, 5915, and 5951Å and to a group of lines near 6530Å (Fig. 5c). Increasing the Eu^{3+} concentration leads to the appearance of emission from two additional species: a specie III emitting primarily at 6262, 6082, and 5763Å and a specie IV emitting at 6262, 6100, and 5763Å. (Lines and bands associated with species III and IV are listed in Tables III and IV.) The latter specie is observed primarily at high Eu^{3+} concentrations. Excitation of CaF_2:0.02 Eu^{3+} by 5763Å radiation leads to the emission of two lines of nearly equal intensity at 6082 and 6262Å (Fig. 9a),

Table II. Emission and excitation spectra of specie II

Emission, Å	Excitation, Å	Transition
6600		$^5D_1$-$^7F_3$
6571		$^5D_1$-$^7F_3$
6554		$^5D_1$-$^7F_3$
6172		$^5D_0$-$^7F_2$
6162		$^5D_0$-$^7F_2$
6000		$^5D_0$-$^7F_1$
5962		$^5D_0$-$^7F_1$
5942		$^5D_0$-$^7F_1$
5930		$^5D_0$-$^7F_1$
5918		$^5D_0$-$^7F_1$
5908		$^5D_0$-$^7F_1$
5882		$^5D_1$-$^7F_3$
5881		$^5D_1$-$^7F_3$
5865		$^5D_1$-$^7F_3$
5838		$^5D_1$-$^7F_3$
5660		$^5D_1$-$^7F_2$
5560		$^5D_1$-$^7F_2$
5468		$^5D_1$-$^7F_1$
5425		$^5D_1$-$^7F_1$
5380	5379	$^5D_1$-$^7F_1$
5284		$^5D_1$-$^7F_0$
5170		$^5D_2$-$^7F_3$
5142		$^5D_2$-$^7F_3$
5124		$^5D_2$-$^7F_3$
4976		$^5D_2$-$^7F_2$
4962		$^5D_2$-$^7F_2$
4882		$^5D_2$-$^7F_2$
4670	4669	$^5D_2$-$^7F_0$
	2600	Host excitation

Table III. Emission and excitation spectra of specie III

Emission, Å	Excitation	Transition
6938		$^5D_0$-$^7F_4$
6856		$^5D_0$-$^7F_4$
6338		$^5D_0$-$^7F_3$
6322		$^5D_0$-$^7F_3$
6262		$^5D_0$-$^7F_2$
6245		$^5D_1$-$^7F_4$
6082		$^5D_0$-$^7F_2$
5946		$^5D_0$-$^7F_1$
5911		$^5D_0$-$^7F_1$
5763		$^5D_0$-$^7F_0$
5281	5281	$^5D_1$-$^7F_0$
4638	4638	$^5D_2$-$^7F_0$
4616	4618	$^5D_0$-$^7F_0$
	3500-4200	Unassigned f-f transitions
	2750	$Eu^{3+}-O^{2-}$ charge transfer band

Table IV. Emission and excitation spectra of specie IV

Emission, Å	Excitation	Transition
6978		$^5D_0$-$^7F_4$
6950		$^5D_0$-$^7F_4$
6550		$^5D_1$-$^7F_3$
6530		$^5D_1$-$^7F_3$
6320		$^5D_0$-$^7F_3$
6262		$^5D_0$-$^7F_2$
6140		$^5D_1$-$^7F_4$
6100		$^5D_0$-$^7F_2$
5951		$^5D_0$-$^7F_1$
5915		$^5D_0$-$^7F_1$
5844		$^5D_1$-$^7F_3$
5814		$^5D_1$-$^7F_3$
5794		$^5D_1$-$^7F_3$
5781		$^5D_1$-$^7F_3$
5776		$^5D_1$-$^7F_3$
5761	5761	$^5D_0$-$^7F_0$
5747		$^5D_1$-$^7F_3$
	5285	$^5D_1$-$^7F_0$
	4638	$^5D_2$-$^7F_0$
	4618	$^5D_2$-$^7F_0$
	3500-4500	Unassigned f-f transitions
	2750	$Eu^{3+}-O^{2-}$ charge transfer band

while excitation of the CaF_2:0.088 Eu^{3+} by 5763Å gives rise to emission lines at 6100 and 6262Å (Fig. 9b). This supports the conclusion that specie III and IV have the 5763Å and 6262Å emissions in common but differ in the wavelength position of the emission near 6100Å. The relative intensities of spectral lines corresponding to emission from the $^5D_2$, $^5D_1$, and $^5D_0$ levels of a given Eu^{3+} specie are not a function of Eu^{3+} concentration. There is no evidence for concentration quenching of $^5D_2$ or $^5D_1$ accompanied by an enhancement of emission from the $^5D_0$ level. Appearance of specie III and specie IV emission and simultaneous disappearance of emission from specie II on increasing the concentration of Eu^{3+} is readily ascribed to a change in absolute concentrations of the individual species. The changes in emission intensities may not be attributed to a concentration dependent variation of fluorescent lifetimes of the ^5D_J levels.

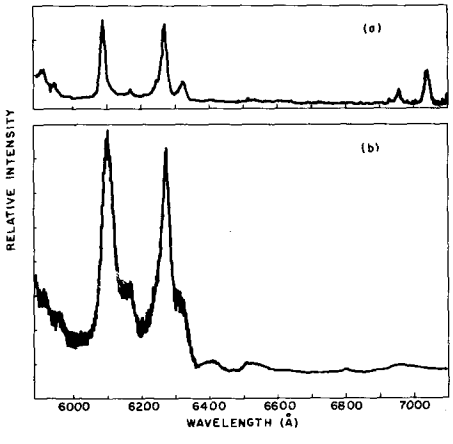

Fig. 9. Emission spectrum of (a) CaF_2:0.02 Eu^{3+} and (b) CaF_2: 0.088 Eu^{3+} excited at 5763Å.

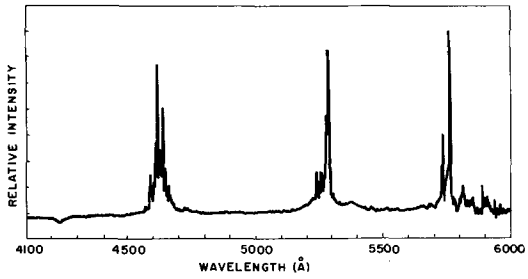

Fig. 10. Visible excitation spectrum of CaF_2:0.02 Eu^{3+} for emission at 6262Å.

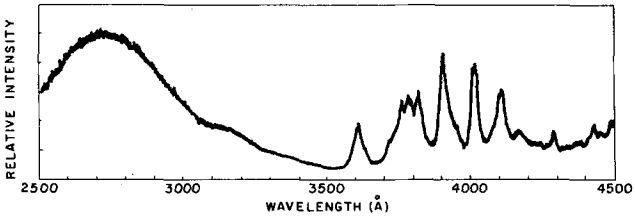

Fig. 11. Ultraviolet excitation spectrum of CaF_2:0.02 Eu^{3+} for emission at 6262Å.

Excitation spectra for the primary specie III and IV emissions (6262, 6100, 6082, and 5763Å) are identical; as an example, the excitation spectra for 6262Å emission in CaF_2: 0.02 Eu^{3+} are shown in Fig. 10 and 11. The resemblance between excitation and emission spectra for species III and IV indicates that the site symmetry for Eu^{3+} ions involved in these $Eu^{3+} - O^{2-}$ complexes are similar. A comparison of the four europium species mentioned now follows.

Discussion

Kreitman and Barnett (12) have calculated the concentration dependent probabilities for finding a given impurity ion in various clusters in a face-centered cubic lattice. In CaF_2, for example, for concentrations of impurity up to 0.05 g-atom/mole CaF_2, the impurity ions are predominantly isolated from each other (singles) or form nearest and next-nearest neighbor pairs. Above a concentration of 0.05 g-atom/mole CaF_2, the probability for finding singles and pairs becomes less than that for finding triads and higher order clusters.

In the present investigation the impurity concentration of Eu^{3+} in CaF_2 ranged from 0.002 to 0.02 g-atom/mole CaF_2 and from 0.042 to 0.088 g-atom/mole CaF_2. For low europium concentrations (0.002-0.02 g-atom range) most Eu^{3+} ions are single or paired. For single (isolated) Eu^{3+} ions, the charge compensation by oxide ion can be achieved by an O^{2-} ion replacing F^- in a site adjacent to Eu^{3+}. The Eu^{3+} ion would, thus, possess C_{3v} site symmetry (Fig. 12a). A nearest neighbor pair of Eu^{3+} ions can be compensated by a pair of oxide ions (occupying F^- ion sites), forming a bridge between the europium ions (Fig. 12b). The Eu^{3+} ions in such a bridged pair possess C_{2v} site symmetry. For next-nearest neighbor pairs, one may assume that the individual Eu^{3+} ions are too far separated to interact appreciably. Therefore, when O^{2-} compensated, such a Eu^{3+} ion pair may be considered to form two slightly interacting $(Eu - O)^+$ complexes. Thus, the Eu^{3+} ion in each complex may be treated as possessing somewhat perturbed C_{3v} symmetry with emission excitation spectra similar to nonperturbed $(Eu - O)^+$ complexes.

X-ray crystallographic evidence exists for the formation of both $(LnO)^+$ and $(Ln_2O_2)^{2+}$ complexes in rare earth oxides and oxy-salts (13). In addition, Forrester and McLaughlin (14) have interpreted ESR measurements of Tm_2O_3-activated CaF_2 in terms of Tm^{3+}-Tm^{3+} nearest neighbor cation pairs bridged by two charge compensating oxide ions. Such evidence

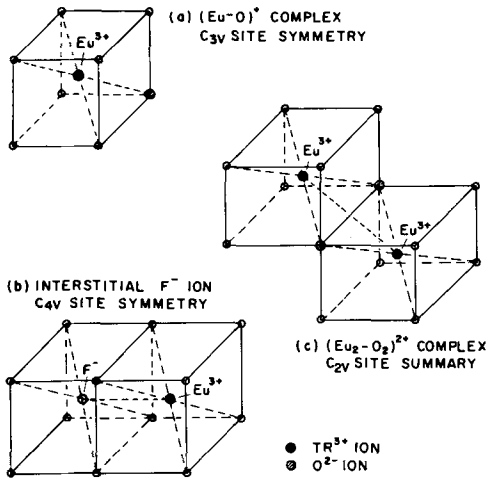

Fig. 12. Modes of charge compensation for Eu^{3+} in CaF_2

supports the contention that Eu^{3+} when O^{2-} compensated exists as $(Eu - O)^+$ and $(Eu_2 - O_2)^{2+}$ entities.

In the higher Eu^{3+} concentration range, more europium ions are clustered in triads and high-order groups than exist as singles or pairs. However, assuming again that next-nearest neighbor interaction of Eu^{3+} ions can be ignored, most triads can be looked upon as associations of singles or pairs and singles. The emission and excitation spectra of Eu^{3+} ions in these triads will probably be similar to the spectra of singles and pairs with any differences ascribed to weak interactions with nearby $Eu^{3+} - O^{2-}$ complexes.

Barnes and Hincott (15) have shown that the wavelength of the charge transfer band of $Eu^{3+} - O^{2-}$ complexes increases with an increase in the number of ligands coordinated to the Eu^{3+} ion. Thus, the charge transfer band associated with 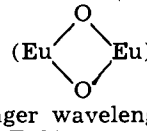 complexes is expected to lie at longer wavelengths than that associated with an isolated Eu^{3+} ion coordinated to a single oxide ion.

For specie I Eu^{3+} in CaF_2 (Table I), the charge transfer bands associated with this specie are at the longest wavelength observed for such bands, suggesting that the entity discussed is a 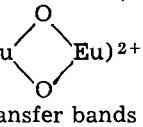 complex. The appearance of two charge transfer bands for specie I excitation has earlier been attributed to the presence of two separate entities. One of these may be identified as an isolated $(Eu_2 - O_2)^{2+}$ complex. The second may be a $(Eu_2 - O_2)^{2+}$ complex which forms part of a triad or high cluster and is far enough removed from other Eu^{3+} ions in the cluster to exhibit a $(Eu_2 - O_2)^{2+}$-type spectrum. Since europium-oxygen charge transfer bands shift to longer wavelength with increased coordination of O^{2-} to Eu^{3+}, the longer wavelength transfer band in specie I can be ascribed to the $(Eu_2 - O_2)^{2+}$ group weakly coordinated to a nearby $Eu^{3+} - O^{2-}$ grouping. It may be recalled that the probability for isolated $(Eu_2 - O_2)^{2+}$ pair formation decreases with increased Eu^{3+} concentration while the probability for triad formation increases. Therefore, the increase in the relative intensity of the long wavelength charge transfer band with Eu^{3+} concentration can be attributed to the increased presence of pairs that are parts of higher-order clusters.

For both specie III and IV, the charge transfer excitation band is observed at 2750Å which is appreciably lower in wavelength than the charge transfer band of specie I. This indicates that the Eu^{3+} ions in the species III and IV are coordinated to fewer O^{2-} ligands than are Eu^{3+} ions of specie I. Specie III,

which is prevalent at lower concentrations, is, therefore, associated with an isolated $(Eu - O)^+$ complex. Specie IV, which is observed at higher Eu^{3+} concentrations is associated with a $(Eu - O)^+$ complex which is next-nearest neighbor to another $(Eu - O)^+$ or $(Eu_2 - O_2)^{2+}$ group, *i.e.*, it is part of a next-nearest neighbor pair or part of a triad.

Finally, as previously noted, failure to observe a $Eu^{3+} - O^{2-}$ charge transfer band for specie II indicates that the Eu^{3+} ions involved are far removed from oxide ions. The number of $^5D_0$-$^7F_1$ emissions observed for specie II is greater than the maximum allowed assuming complete removal of $^7F_1$ degeneracy. Thus, specie II is the collection of all Eu^{3+} ions in both noncompensated and F^- ion compensated sites. Europium compensated by an oxide ion not localized at the Eu^{3+} site would also be included in specie II. Specie II Eu^{3+} ions compensated by an interstitial F^- ion would possess C_{4v} symmetry which, according to group theoretical calculations, would allow for a $^5D_0$-$^7F_0$ transition. Judd (8), however, in his discussion of hypersensitive rare earth ion transitions states that the linear asymmetry at a rare earth ion required for observation of such transitions must involve symmetry distortion caused by nearest neighbor ions. Since F^- ions compensating Eu^{3+} in CaF_2 are not nearest neighbor to Eu^{3+}, one may conclude that they are ineffective in distorting the local Eu^{3+} symmetry sufficiently to allow observation of a $^5D_0$-$^7F_0$ transition.

Acknowledgments

The authors gratefully acknowledge helpful discussions with F. Palilla, G. Gashurov, and O. Sovers.

Manuscript submitted July 22, 1968; revised manuscript received Sept. 16, 1968.

Any discussion of this paper will appear in a Discussion Section to be published in the December 1969 JOURNAL.

REFERENCES

1. I. V. Stepanov and P. P. Feofilov, *Sov. Phys. Doklady*, **1**, 350 (1956).
2. J. Makovsky, *Phys. Rev. Letters*, **15**, 953 (1965).
3. G. Blasse, *J. Chem. Phys.*, **45**, 2356 (1966).
5. C. K. Jørgensen, *Molecular Phys.*, **5**, 271 (1962).
6. J. D. Kingsley and J. S. Prener, *Phys. Rev.*, **126**, 458 (1962).
7. W. C. Nieuwpoort and G. Blasse, *Solid State Comm.*, **4**, 227 (1966).
8. B. R. Judd, *J. Chem. Phys.*, **44**, 839 (1966).
9. P. P. Feofilov, *Doklady Akad. Nauk. S.S.S.R.*, **99**, 731 (1954).
10. L. G. DeShazer and G. H. Dieke, *J. Chem. Phys.*, **38**, 2190 (1963).
11. J. Rolfe, F. R. Lipsett, and W. J. King, *Phys. Rev.*, **123**, 447 (1961).
12. M. M. Kreitman and D. L. Barnett, *J. Chem. Phys.*, **43**, 364 (1965).
13. P. Cara, *Compte rend., Ser. C.* **262**, 992 (1966).
14. P. A. Forrester and S. D. McLaughlin, *Phys. Rev.*, **138A**, 1682 (1965).
15. J. C. Barnes and H. Pincott, *J. Chem. Soc.*, **1966** 842.

Strain Compensation in Silicon by Diffused Impurities

T. H. Yeh* and M. L. Joshi

IBM Components Division, East Fishkill Facility, Hopewell Junction, New York

ABSTRACT

A method to avoid dislocation generation in boron or phosphorus-diffused layers is presented. This method, called strain compensation, considerably reduces dislocation generation in the diffused layers. This strain compensation is brought about because impurities such as tin and boron, or tin and phosphorus, have been diffused simultaneously into the silicon, with tin counteracting the stresses produced by the solute lattice contraction of the boron or the phosphorus. Transmission electron micrographs are provided as evidence of this phenomenon.

Diffusion of high concentration of impurity in silicon is known to introduce stresses in the lattice and cause the generation of dislocations in the diffused region. Such dislocations, particularly those due to phosphorus and boron, have been the subject of detailed study in the past (1-11). The amount of maximum stress being induced in the silicon lattice by the homogeneously distributed impurity is understood to be dependent on both the size of the impurity atom relative to the size of the lattice site it occupies in the silicon matrix and on the maximum solubility of the impurity in the silicon at the diffusion temperature. On the basis of Pauling's tetrahedral covalent radii, both phosphorus and boron radii are smaller than that of silicon (12). Also, the maximum solid-solubility of these two elements in silicon (13) is relatively high. Therefore, the amount of maximum stress introduced by them can easily exceed the elastic limit of silicon (14). Heavy homogeneous doping of phosphorus and boron in Si is, however, not expected to introduce dislocations. An impurity gradient with the concentration in the surface exceeding a critical limit is necessary for the generation of misfit dislocations. There are two well-known basic theories on diffusion induced misfit dislocations, one by Prussin (3) and the other one by Queisser (4). Modifications of these theories also exist (5-11) but have no substantial advantage over them. Prussin's theory shows that the total number of dislocations generated via diffusion is directly proportional to the surface concentration, C_o. This concentration has to be in excess of the critical concentration, C_g, for which the surface stress exceeds the elastic limit of silicon. Queisser, on the other hand, considers the total integrated doping Q as a criterion for dislocation generation. In order to avoid dislocation generation in these diffused layers, one generally has to diffuse these impurities (B and P) into the silicon in such a way that the total number of solute atoms per unit surface area of the diffused layer, Q, is below a certain critical value (4). This can be achieved by either diffusing these impurities at concentrations well below their solid solubility limits, *i.e.*, in the case of where the surface concentration of the boron- or phosphorus-diffused layer is below 3×10^{19} cm^{-3} or 5×10^{20} cm^{-3}, respectively, with a relatively large diffusion length (4, 8); or alternatively, by diffusing these impurities to the limit of solid solubility, but with a small diffusion length (15). This is so be-

* Electrochemical Society Active Member.

cause Q[1] is proportional to the product of Co and $(Dt)^{1/2}$, where Co is the surface concentration of the diffused impurity in silicon and $(Dt)^{1/2}$ is the diffusion length.

In this article, a method to avoid dislocation generation in boron or phosphorus-diffused layers is presented. This method—strain compensation—considerably reduces dislocation generation in either boron- or phosphorus-diffused layers, even though these surface concentrations exceed the limits mentioned above.

Experimental procedure.—Silicon wafers of <111> orientation were cut from Czochralski-grown boron or phosphorus-doped single crystals. The net impurity concentration of these crystals was on the order of 10^{16} cm^{-3}. Wafers were lapped and chemically polished to remove surface damage. (The dislocation etch-pit count on one of the wafers was taken and was found to be less than 500/cm^2.) The silicon wafers were annealed at 1000°C for about an hour in an open tube through which dry nitrogen flowed. This treatment was used only as a precaution to eliminate any remnant strains in the surfaces of the wafer. One of the wafers was again tested for etch-pit count and was found to show no increment in dislocation content, thereby indicating that the chemical polishing did actually remove almost all of the surface strains. Diffusions were carried out in the evacuated capsules (16) (<10^{-6} mm Hg) at 1200°C for 60, 120, and 180 min. For the single diffusion of phosphorus, boron, or tin, certain amounts of crushed powders obtained from the doped silicon crystal of that particular impurity with known concentrations were included in the capsule as the source of diffusion. For the simultaneous diffusion of tin and boron, or tin and phosphorus, equal amounts of crushed powders obtained from these two doped silicon crystals (such as tin-doped and boron-doped, or tin-doped and phosphorus-doped) of known concentrations were included in the capsule as the sources of diffusions. For the phosphorus-, boron-, or tin-doped silicon source, concentrations of 1.7 x 10^{21} cm^{-3}, 1.7 x 10^{20} cm^{-3}, and 8 x 10^{19} cm^{-3}, respectively, were employed.

Chemical staining was used on a bevelled sample to determine its diffusion depth, and a four-point probe was used to measure its sheet resistivity. The surface concentration of the boron or phosphorus-diffused sample was then determined according to Irvin (17). Radiotracer technique was used to determine the tin's profile in a tin-and-boron- or in a tin-and-phosphorus-diffused wafer.[2]

Transmission electron microscopy examination was used to study the dislocations induced in the phosphorus- or boron-diffused layers; it was also used to study or confirm the absence of dislocations in the phosphorus-tin-, or boron-tin-diffused layers. X-ray diffraction technique was used to study the changes of lattice parameter of silicon due to boron, phosphorus, or tin impurities. Details of these two techniques have been described elsewhere (8, 18).

Results and Discussion

Table I summarizes the diffusion data. In the case of single diffusion, the wafers in the capsule achieve the same concentration as the source powders at the surface after equilibrium conditions are established at the diffusion temperature. However, in the case of simultaneous diffusion, it was found that the surface concentration of those phosphorus- or boron-diffused wafers are almost one-half the values of those singularly diffused P or B wafers. They are 8.0 x 10^{20} cm^{-3} and 6.5 ~ 7.5 x 10^{19} cm^{-3}, respectively, instead of 1.7 x 10^{21} cm^{-3} and 1.7 x 10^{20} cm^{-3}. This result can be explained by the flux continuity in the mass transport phenomenon. When the tin-doped and the boron-doped silicon source powders are simultaneously included in the capsule, the tin-doped source actually acts as a sink for the boron-doped source, and *vice versa*. (These sample wafers, although they act as a sink for both of the sources, actually constitute a negligible fraction of surface area when compared to the surface area of the silicon powders.)

If one assumes that (*i*) that the vacuum space offered very little resistance to mass transport, (*ii*) the rate of evaporation of impurity is much higher than the rate of diffusion of that impurity in the solid, and (*iii*) the diffusivity of that impurity in the source and in the sink are the same and are constant, then the impurity profiles in the source and in the sink can

Table I. Diffusion data

Temp, °C	Time, min	Boron X_j, μ	Boron C_o, cm^{-3}	Boron and Sn* X_j, μ	Boron and Sn* C_o, cm^{-3}
1200	180	7.9	1.7 x 10^{21}	6.8	6.5 x 10^{19}
1200	60	4.4	1.7 x 10^{21}	3.9	7.5 x 10^{19}
		Phosphorus		**Phosphorus and Sn***	
Temp, °C	Time, min	X_j, μ	C_o, cm^{-3}	X_j, μ	C_o, cm^{-3}
1200	180	10.5	1.6 x 10^{21}	9.0	8.0 x 10^{20}
1200	120	8.6	1.7 x 10^{21}	7.4	8.0 x 10^{20}
1200	60	5.9	1.7 x 10^{21}	5.5	8.0 x 10^{20}

X_j = Junction depths; C_o = surface concentration of the diffused impurity in silicon.
* Those C_o and X_j are for boron or phosphorus only. Tin's X_j and C_o in the presence of boron or phosphorus are shown in Fig. 1a and 1b.

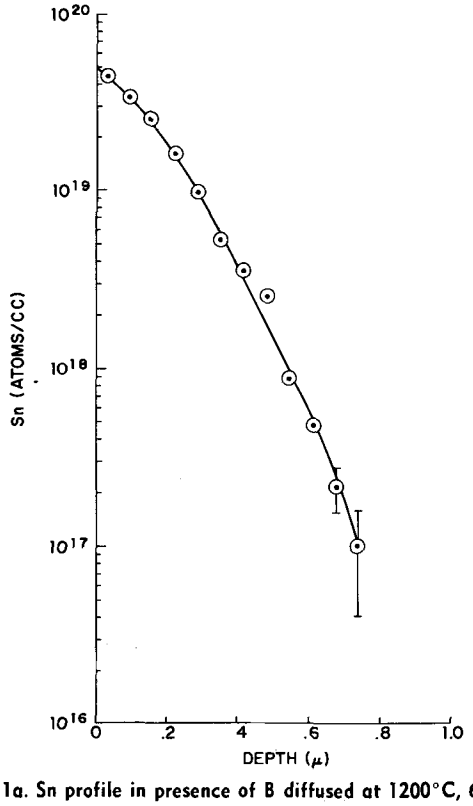

Fig. 1a. Sn profile in presence of B diffused at 1200°C, 60 min

[1] For diffusion from a constant source, the quantity of impurity having entered the wafer at time, t, is given by

$$Q = \int_0^t j(x,t)\,dt = (C_o/\sqrt{\pi})\ 2\sqrt{Dt};\ \text{where } j(x,t)\Big|_{x=0} = -D\frac{\partial c}{\partial x}\Big|_{x=0} = \frac{D\,C_o}{\sqrt{\pi Dt}}\exp\left(-\frac{x^2}{4Dt}\right)\Big|_{x=0} = C_o\sqrt{\frac{D}{\pi t}}$$

[2] The detailed analysis of the Sn^{113} is described in a separate paper entitled "Diffusion of Tin in Silicon" by T. H. Yeh, S. M. Hu, and R. H. Kastl, published in Journal of Applied Physics, August, 1968.

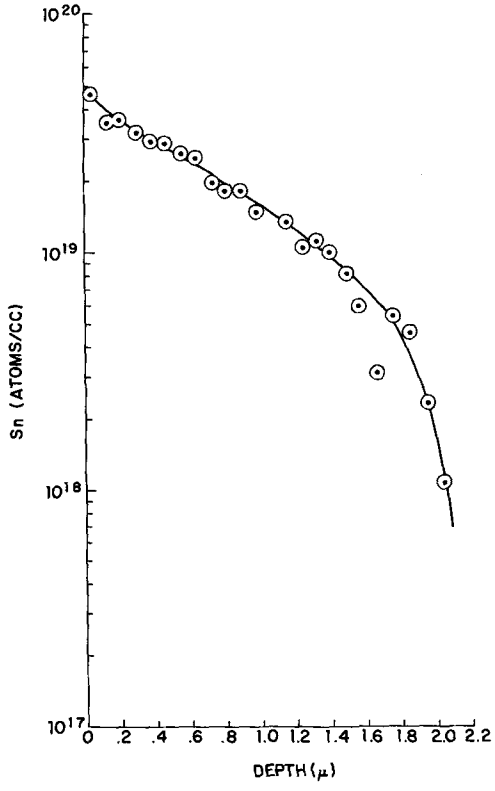

Fig. 1b. Sn profile in presence of P diffused at 1200°C, 120 min

be expressed, respectively, by the following equations

$$C_I(x,t) = C_{I_i}\left[1 - \frac{A_{II}}{A_I + A_{II}}\operatorname{erfc}\left(\frac{x}{2\sqrt{Dt}}\right)\right] \quad [1]$$

and

$$C_{II}(x,t) = C_{I_i}\frac{A_I}{A_I + A_{II}}\operatorname{erfc}\left(\frac{x}{2\sqrt{Dt}}\right) \quad [2]$$

which must satisfy the following initial and the boundary conditions

$$C_I(x,0) = C_{I_i} \text{ for all } x \quad [3]$$

$$C_{II}(x,0) = 0 \text{ for all } x \quad [4]$$

$$C_I(x,t) = C_{I_i} \text{ as } x \to \infty \text{ for all } t \quad [5]$$

$$C_{II}(x,t) = 0 \text{ as } x \to \infty \text{ for all } t \quad [6]$$

and

$$-A_I D\left.\frac{\partial C_I}{\partial x}\right|_{x=0} = -A_{II} D\left.\frac{\partial C_{II}}{\partial x}\right|_{x=0} \quad [7]$$

where subscripts I and II denote the source and the source and the sink, respectively, C_{I_i} is the initial concentration of the source, and the A's are the surface areas. From Eq. [2] it is seen that the surface concen-

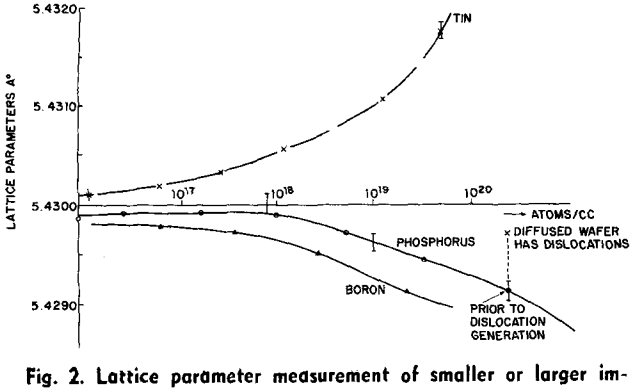

Fig. 2. Lattice parameter measurement of smaller or larger impurity atoms in silicon.

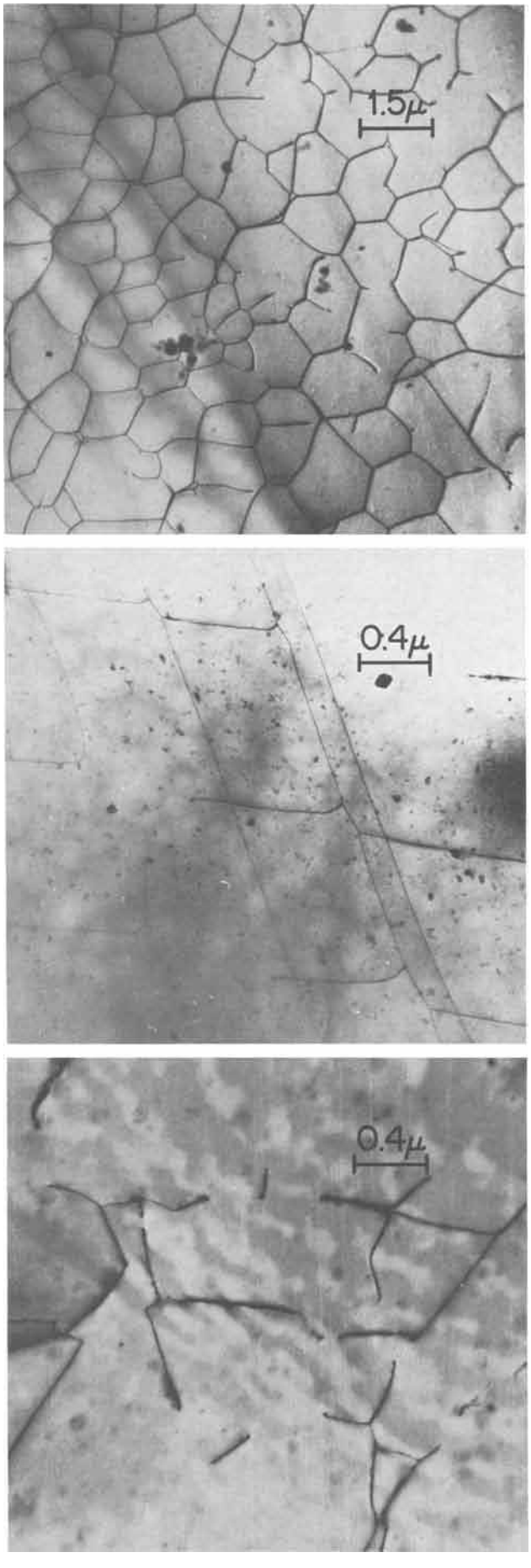

Fig. 3. Dislocations generated by (a) (top) P, (b) (center) B, (c) (bottom) Sn alone in the diffused layers having surface concentrations of 1.7 x 10^{21}, 1.7 x 10^{20}, and 8 x 10^{19} cm^{-3}, respectively.

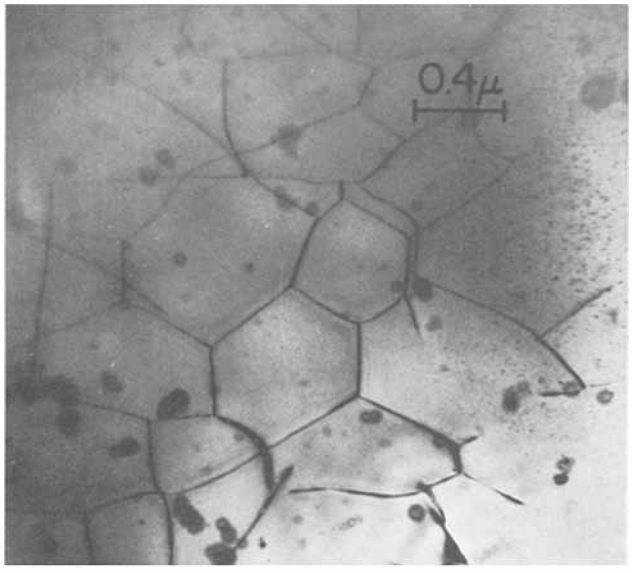

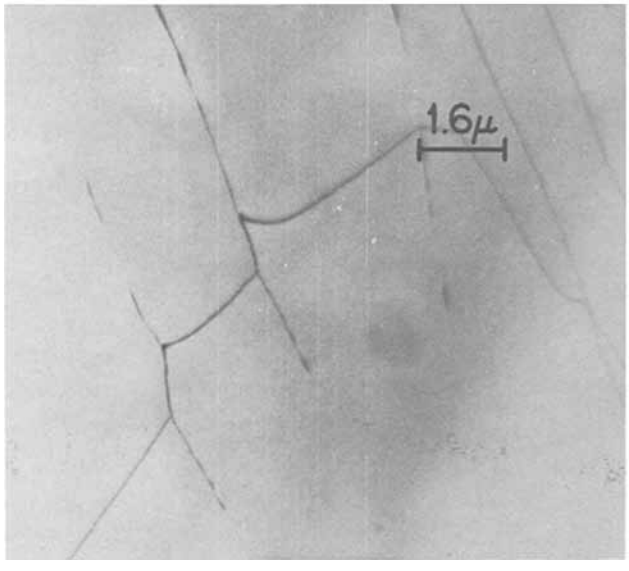

Fig. 4. Dislocations generated by (a) (top) P and (b) (bottom) B alone in the diffused layers having surface concentrations of 8.0 x 10^{20} and 6.5 ~ 7.5 x 10^{19} cm^{-3}, respectively.

tration of the wafer is given by

$$C_0 = C_{II}(0,t) = C_{I_i}\frac{A_I}{A_I + A_{II}} \qquad [8]$$

Since both powdered sources are of the same particle size and have equal amounts in the capsule, they therefore have the same surface area. Consequently, the surface concentration of the wafer, according to Eq. [8], should be one-half of the value of the initial concentration of the source.

Because tin is a neutral impurity in silicon, a radiotracer technique was used to determine its profile. Figures 1a and 1b are the tin's profile in a tin-boron- or in a tin-phosphorus-diffused wafer. The surface concentration of tin in both of these samples (~5 x 10^{19} cm^{-3}) is only about one-half of the value of tin diffused alone into silicon (8 x 10^{19} cm^{-3}), as it should be according to Eq. [8]. This, in turn, further substantiates the surface concentration values of boron or phosphorus, determined by sheet resistivity and junction depth measurements, in the presence of tin, as given in Table I.

Examination by x-ray diffraction of bulk-doped silicon with impurities having larger (Sn) or smaller (P and B) atom sizes than that of the silicon showed distinct measurement differences in the lattice parameters (Fig. 2). The important result of this x-ray examination is that the impurity having the larger atomic size also had the larger lattice parameter, *i.e.*, lattice expansion of silicon, whereas those impurities having the smaller atomic size also had the smaller lattice parameter, *i.e.*, lattice contraction of silicon. Also, their respective lattice differences increase with increasing impurity concentrations. However, bulk-doped crystals with the highest possible concentration of either P, B, or Sn did not produce dislocations. This is understandable since only impurity gradients cause dislocations. Dislocations are produced only in the diffused wafers when either one of these impurities exceeds a certain concentration level at the surface. For P, B, and Sn, this critical level is 5 x 10^{20} cm^{-3}, 3 x 10^{19} cm^{-3}, (ref. 7, 8) and 10^{19} cm^{-3}, respectively. The cross point in Fig. 2 indicates such a lattice parameter measurement in the surface layer of the phos-

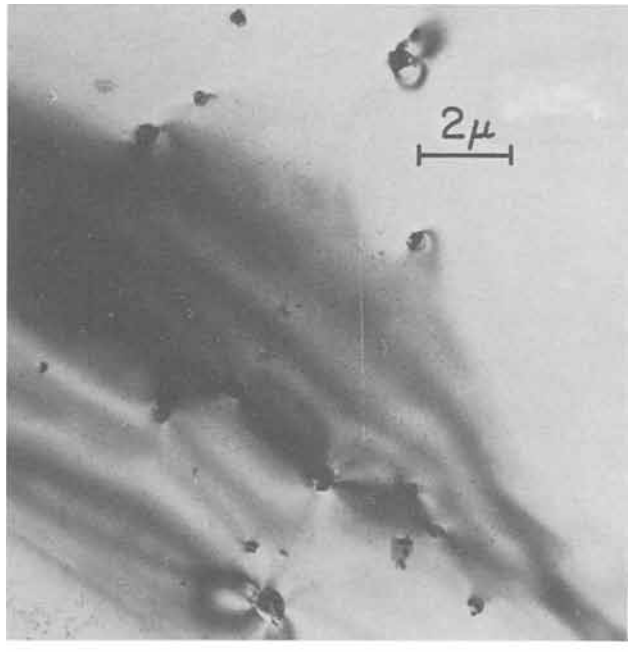

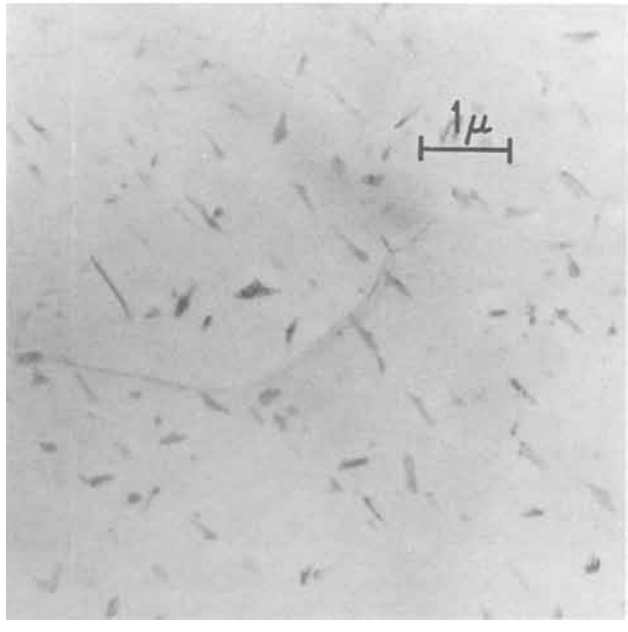

Fig. 5. No dislocations in (a) (top) P+Sn simultaneously diffused layer having surface concentrations of 8.0 x 10^{20} cm^{-3} for phosphorus and of 5.0 x 10^{19} cm^{-3} for tin; (b) (bottom) B+Sn simultaneously diffused layer having surface concentrations of 7.5 x 10^{19} cm^{-3} for boron and of 5.0 x 10^{19} cm^{-3} for tin.

phorus-diffused wafer. It shows a return of the lattice parameter in the diffused surface to a value corresponding to the lattice parameter of silicon with lower concentrations of phosphorus as dopant (18), strong evidence that the strained lattice tends to relax when the dislocations are produced.

Figure 3 shows an electron micrograph of the dislocations produced by the P, B, and Sn alone in the diffused layers having surface concentrations of 1.7 x 10^{21} cm^{-3}, 1.7 x 10^{20} cm^{-3}, and 8 x 10^{19} cm^{-3}, respectively; the dislocation densities for those samples are in the order of 10^9, 10^8, 10^7 cm^{-2}, respectively. If the surface concentrations of phosphorus or boron diffused wafers have reduced to 8.0 x 10^{20} cm^{-3} and 6.5 ~ 7.5 x 10^{19} cm^{-3} (from 1.7 x 10^{21} cm^{-3} and 1.7 x 10^{20} cm^{-3}), respectively, the dislocation densities for those samples are also reduced to about 10^8 and 5 x 10^6 cm^{-2} (from 10^9 and 10^8 cm^{-2}), respectively, as evidenced in Fig. 4a and 4b, by the electron micrographs.

However, when those simultaneously diffused P-Sn or B-Sn wafers were examined by transmission electron microscopy (even though they have the same surface concentrations as those singly diffused wafers, namely, 8 x 10^{20} cm^{-3} and 6.5 ~ 7.5 x 10^{19} cm^{-3}) they clearly show the lack of dislocations. Figures 5a and 5b are the electron micrographs of those simultaneously diffused wafers. From this result one can conclude that the stresses ordinarily caused by the phosphorus or boron atoms in silicon have been compensated by the stress caused by the tin atoms to the extent that no relief of the stresses in the lattice is necessary.

Furthermore, preliminary results indicate that Ge can also be used for strain compensation in silicon with boron or phosphorus, *i.e.*, simultaneously diffused P-Ge or B-Ge in silicon produces no dislocations in the diffused layers.

Conclusion

A method to avoid dislocation generation in boron- or phosphorus-diffused layers is presented. This method, strain compensation, considerably reduces dislocation generation in either boron- or phosphorus-diffused layers, even though their surface concentrations are exceeded by the critical values (4, 8). The strain compensation is brought about through simultaneous introduction into silicon of impurities such as tin and boron, or tin and phosphorus. Since the TCR (tetrahedral covalent radius) of tin is larger than that of Si, whereas the TCR of boron and phosphorus is smaller than that of Si, it is felt that the silicon lattice, which would be expanded by tin atoms, counteracts the contraction ordinarily due to phosphorus or boron is either eliminated or considerably reduced below the elastic limit.

Acknowledgments

The authors wish to thank Dr. S. M. Hu for his critical comment on the manuscript, and Dr. R. H. Kastl for obtaining the profiles of Sn^{113} through the radiotracer technique.

Manuscript submitted May 2, 1968; revised manuscript received Aug. 28, 1968.

Any discussion of this paper will appear in a Discussion Section to be published in the December 1969 JOURNAL.

REFERENCES

1. Y. Sato and H. Arata, *J. Appl. Phys. Japan*, **3**, 511 (1964).
2. J. E. Lawrence, *This Journal*, **113**, 819 (1966).
3. S. Prussin, *J. Appl. Phys.*, **32**, 1876 (1961).
4. H. J. Queisser, *ibid.*, **32**, 1776 (1961).
5. J. Washburn, G. Thomas, and H. J. Queisser, *ibid.*, **35**, 1909 (1964).
6. G. H. Schwuttke and H. J. Queisser, *ibid.*, **33**, 1540 (1962).
7. D. P. Miller, J. E. Moore, and C. R. Moore, *ibid.*, **33**, 2648 (1962).
8. M. L. Joshi and F. Wilhelm, *This Journal*, **112**, 185 (1965).
9. R. C. McDonald, G. G. Ehlenberger, and T. R. Huffman, *Solid State Elec.*, **9**, 807 (1966).
10. W. Czaja, *J. Appl. Phys.*, **37**, 3441 (1966).
11. E. Levine, J. Washburn, and G. Thomas, *ibid.*, **38**, 81 (1967).
12. L. Pauling, "The Nature of the Chemical Bond," 3rd ed., p. 256, Cornell University Press, Ithaca, N. Y. (1960).
13. F. A. Trumbore, *Bell System Tech. J.*, **39**, 205 (1960).
14. G. L. Pearson, W. T. Read, Jr., and W. L. Feldmann, *Acta Met.*, **5**, 181 (1957).
15. T. H. Yeh, W. D. Rosenberg, and G. H. Schwuttke, Recent News Paper presented at the Society Chicago Meeting, Oct. 15-17, 1957.
16. W. J. Armstrong and M. C. Duffy, *Electrochem. Technol.*, **4**, 475 (1966).
17. J. C. Irvin, *Bell Sys. Tech. J.*, **41**, 387 (1962).
18. M. L. Joshi, C. H. Ma, and J. Makris, *J. Appl. Phys.*, **38**, 725 (1967).

The Preparation and Properties of Amorphous Silicon

R. C. Chittick, J. H. Alexander, and H. F. Sterling

Standard Telecommunication Laboratories Limited, Harlow, Essex, England

ABSTRACT

A radio-frequency glow discharge is used to deposit films of amorphous silicon from silane gas on to substrates at 25°-650°C. These films have resistivities at 21°C of up to 10^{14} ohm-cm and have large temperature coefficients of resistivity. A photoconductive effect is observed which reaches a maximum for films deposited at 300°C, and a sample is compared with a CdS cell. The effects of heat-treatment, ageing, and doping on the properties of amorphous silicon are reported. The variation of properties with deposition temperature is related to the structural changes with temperature that have been observed for this material.

Various processes are available for the deposition of silicon. The element may be transported by vacuum evaporation, for example, or be deposited from the vapor phase by the chemical reduction of a suitable compound. When the substrate is heated, crystalline deposits are obtained, and under certain conditions single crystal or epitaxial growth takes place. Silicon in the crystalline form is well characterized, and its electrical behavior is understood.

The vapor depositions of silicon onto unheated substrates are microcrystalline or "amorphous" in form and exhibit electrical properties which significantly depart from those of the crystalline state. Since the microcrystallinity or degree of amorphousness is un-

defined and very process dependent, the same consistency of standard electrical properties in comparison with single crystal silicon is not obtained.

Silane gas is a useful and important source material for the preparation of high-purity elemental silicon in crystalline form. By pyrolysis at 1000°C it liberates silicon and can be used for the bulk preparation of semiconductor grade material. In order to suppress gas phase decomposition of silane, the pyrolysis is usually carried out at reduced pressure.

If silane gas at low pressure is subjected to a high-frequency electrodeless glow discharge, the deposition of amorphous or vitreous silicon takes place (1). Although higher electron temperatures exist in the gas it is molecularly near room temperature, so that deposition on to virtually cold substrates results in very short range ordering in the structure which is not necessarily of tetrahedral form. In appearance the material resembles the crystalline form but breaks with a conchoidal fracture. Electrically it has a room temperature resistivity of up to 10^{14} ohm-cm with a large temperature coefficient. Specimens deposited under certain conditions exhibit marked photoconductive effects.

The object of this paper is to report details of the apparatus and method used and to give results of some electrical measurements which have been made.

Experimental Technique

The apparatus used is comparatively simple (Fig. 1). A silica tube 3 cm diameter and 40 cm long acts as the reaction chamber and is fed with pure silane gas through a flow meter and needle valve. (The silane used in these experiments was obtained from Matheson and was nominally 50 ohm-cm p-type as crystalline silicon.)

The gas pressure is reduced by means of a vacuum pump, fitted with a throttle valve, so that the dynamic pressure can be set in the range 0.1-1 Torr and measured on a McLeod gauge. A radio-frequency coil surrounds this reaction tube and stimulation is provided by a 500w oscillator operating at 1 MHz. Deposition of amorphous silicon takes place on the walls of the reaction tube and in the glow discharge area generally. Substrates placed in this area are coated at a rate of a few microns per hour. Provision is also made for substrates to be heated during deposition or subsequently, so that structural changes, associated with ordering and the onset of crystallization and their electrical effects, can be studied. Since the heating of a susceptor and the provision of a glow initiating field are derived from the same oscillatory source, modifications have been made to the tuned circuit so that these effects can be varied independently.

During the first stages of deposition the film is yellow changing to red by transmitted light and shows interference colors by reflection. As growth proceeds toward 1μ thickness, the film becomes opaque and black when deposited on polished surfaces and looks matt gray on rough surfaces. Experimental work has shown that deposition rates may be speeded up considerably, but the effect of these increased rates on the properties of the material has not yet been assessed.

Special care was taken with apparatus design and with the experimental techniques to ensure that oxygen and other atmospheric gases were excluded from the reaction chamber during deposition. A leak rate of less than 1 Torr per liter volume over 24 hr is always maintained.

Samples for measurement have been prepared mainly on glass substrates (Corning glass 7059 7/16x 1/2 in.) with two evaporated aluminum electrodes in either coplanar or parallel planar form. Temperature measurement was carried out optically using an infrared pyrometer (Thermodot TD6B). Electrical measurements were made with a Keithley electrometer (610B) and film thicknesses with a Talystep.

Electrical Resistivity

Measurements carried out on coplanar samples gave the following results. A number of samples were grown at 21°C with thicknesses from 0.2 to 4 μm and an electrode spacing of 1 mm. The resistivity was inversely proportional to the thickness, that is, normal conduction in a uniform material (Fig. 2). Assuming $I = A \exp(-\phi/kT)$, with A a constant independent of temperature, a discrete activation energy (ϕ) of 0.8-0.83 ev was obtained for these samples. It was found also that the resistance was directly proportional to the electrode separation. A typical resistivity value for amorphous silicon deposited at room temperature by this technique is 1.5 x 10^{10} ohm-cm at a field of 100 v/cm.

On parallel-planar samples (Al-Si-Al sandwich), measurements indicate a higher value for the electrical resistivity of the material. For example, at a field of 100 v/cm a value of 2.5 x 10^{14} ohm-cm was obtained. Similar high resistivity values have been obtained for evaporated silicon films (2).

Variation of Resistivity with Deposition Temperature

The effect of deposition temperature on the resistivity of amorphous silicon is plotted in Fig. 3, curve a. Measurements were carried out at 21°C, and from the curve it will be seen that the resistivity decreases with increasing deposition temperature, the effect being most marked between 250° and 500°C. At temperatures above 500°C, the resistivity stabilizes near 4 x 10^4 ohm-cm. No depositions were carried out above 650°C on glass.

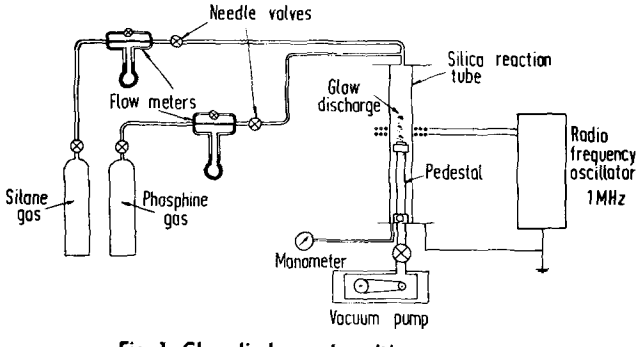

Fig. 1. Glow discharge deposition apparatus

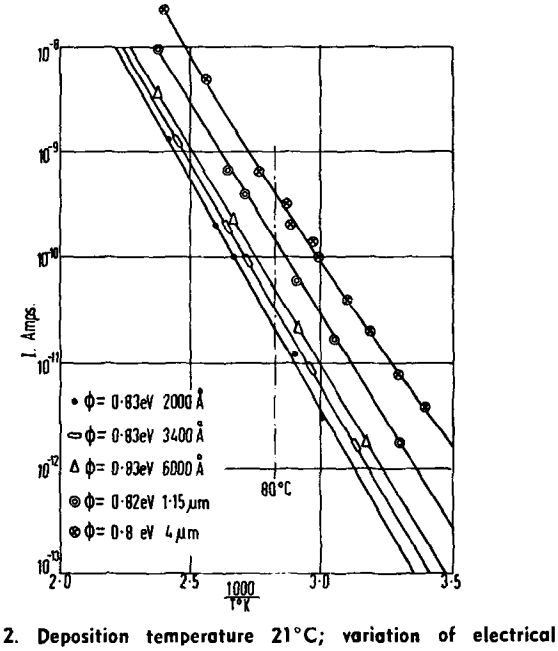

Fig. 2. Deposition temperature 21°C; variation of electrical conduction with temperature for various thicknesses.

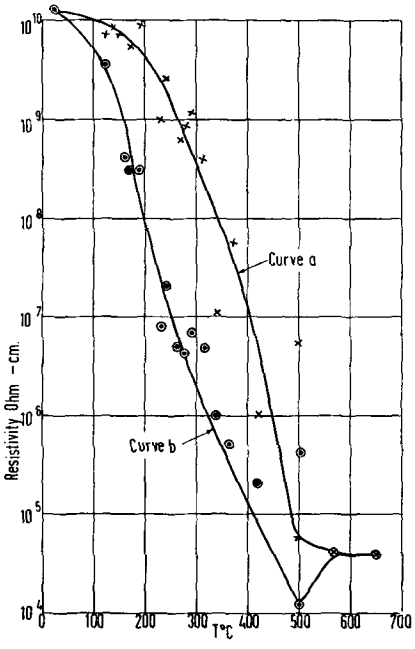

Fig. 3. Resistivity measured as a function of deposition temperature at 21°C. Curve a, dark; curve b, light (20 ft candles).

Variation of Activation Energy with Deposition Temperature

It is interesting to note that well-defined activation energies have been observed over fairly large temperature ranges. A sample deposited at 21°C has an activation energy of 0.8-0.85 ev over the range 0°-150°C. For 160°C deposited samples the activation energy is 0.65-0.7 ev for the temperature range 21°-80°C and for 80° to 150°C is 0.8-0.85 ev. The changeover appears to increase with increasing deposition temperature until ϕ = 0.65-0.7 ev over the whole range 21°-150°C for deposition temperatures of 270°-300°C. Further increases in deposition temperature give lower activation energies. At the low resistivity plateau (4 x 10^4 ohm-cm, Fig. 4) the activation energy = 0.21 ev. It can be seen from the curves that the resistivity changes from 1.5 x 10^{10} ohm-cm at 21°C to 1 x 10^6 at 140°C for material deposited at room temperature.

Optical Properties

A photoconductive effect has been observed in samples of amorphous silicon and shows a dependence on deposition temperature (Fig. 3, curve b). The effect is absent in room temperature depositions, but reaches a maximum for near 300°C depositions and decreases with further temperature increase. A decrease in resistivity of about 3 orders of magnitude is obtained from dark to normal laboratory illumination (100 ft candles). Under these conditions the frequency response of cells made from this material appears to be superior to those made from cadmium sulfide. A commercial cadmium sulfide cell was compared with a glow-discharge deposited silicon cell. Both were exposed to chopped light from a tungsten lamp and their responses, adjusted to have the same value at 5 Hz, were displayed on an oscilloscope. At a frequency of 2000 Hz the silicon cell output dropped by 50% compared with a fall in output of 93% for the particular CdS cell used. This comparison is shown in Fig. 5. The dependency of the photocurrent on light intensity is sublinear $I = (Int)^n$ where, in this case $0.5 \leq n \leq 0.85$. In these measurements a tungsten filament light source was used in conjunction with neutral density filters.

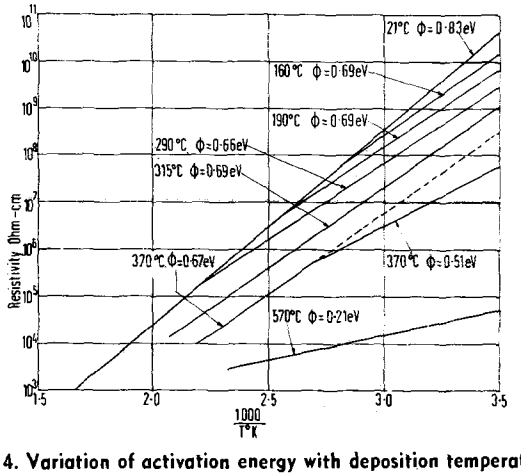

Fig. 4. Variation of activation energy with deposition temperature

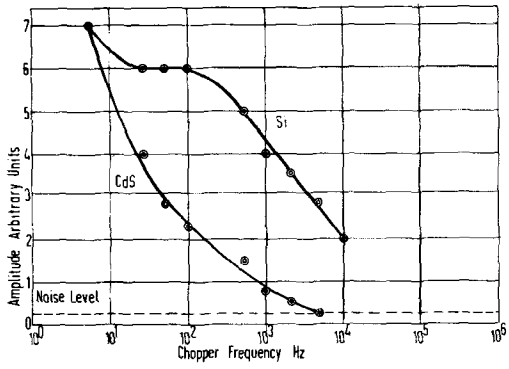

Fig. 5. Relative time responses of photoconductivity in amorphous silicon and cadmium sulfide.

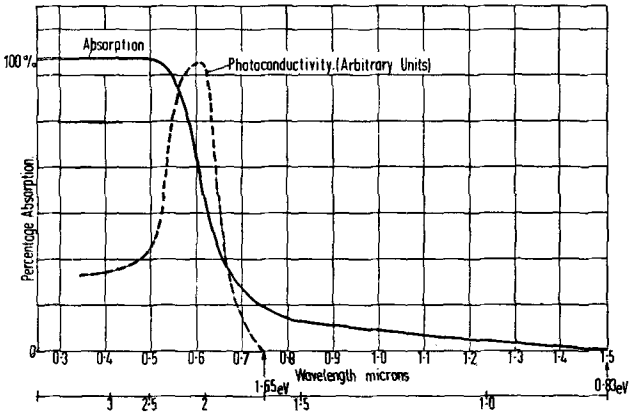

Fig. 6. Optical absorption and photoconductivity for amorphous silicon deposited at 300°. Film thickness, 5000A; interference fringes on the absorption spectrum which occur from 0.7μ to higher wavelengths have been neglected.

A smeared absorption edge between 1.5 μm and 0.5 μm (Fig. 6) is obtained for amorphous silicon films. This is consistent with the concept of localized states at the band edges. The onset of the photoconductivity, however, is at 0.75 μm and reaches a maximum at about 0.6 μm. Carriers are, therefore, not being produced by photon energies below 1.65 ev. Possibly transitions in the energy range 0.8-1.65 ev occur only to the localized states at the band edges.

If this is the case, a voltage dependence of the threshold energy would be expected at high fields since there is a possibility of Poole-Frenkel emission or tunneling from the localized states.

This has yet to be investigated as only low field measurements have been made. Further experimental work is being carried out on absorption and spectral response of this material.

Heat-treatment

Heat-treating films to temperatures above those of deposition changes their electrical properties. For example, when heated, room temperature films become

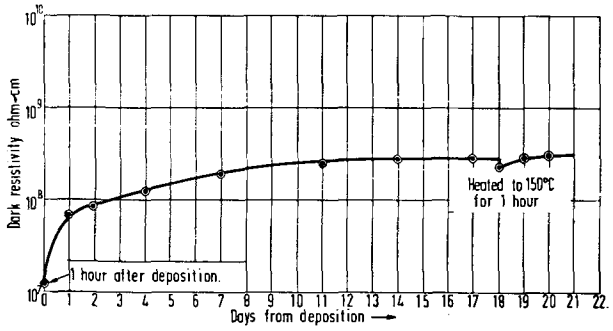

Fig. 7. Ageing in air of amorphous silicon grown at 300°C

photoconducting and, at the same time there is a drop in dark resistivity. A sample grown at room temperature and heated to 400°C for 2 hr has properties which approach those of a sample grown at this temperature.

Samples grown at temperatures between 21° and 150°C show no change in activation energy with heat treatment at 150°C under an applied field of 100 v/cm.

Ageing

Films of amorphous silicon grown under certain conditions exhibit ageing effects in resistivity as has been reported by other workers for germanium (3). The effect of ageing in air on glow discharge deposited material appears to be dependent on deposition temperature. Films grown from 21° to 200°C show no significant ageing effect either short term (1 hr) or long term (6 months). At deposition temperatures of 500°C and above, ageing effects are not noticeable. However in the intermediate range of temperatures 200°-500°C an ageing effect is apparent and has a broad maximum around 300°C.

Figure 7 shows the ageing curve for a sample grown at 300°C. The first point corresponds to the dark resistivity measured 1 hr after deposition. As can be seen, the ageing rate is greatest just after deposition and falls off in time until the resistivity approaches stability between 2 and 3 weeks after deposition. A slight decrease in resistivity occurs when the material is heat treated for 1 hr at 150°C. These effects of ageing and their interrelation with heat-treatment need further study.

Parallel Planar Structures

The current-voltage characteristics for these structures reveal an ohmic region at low field intensities of less than 10^4 v/cm. Under fields greater than this until breakdown occurs at 10^5 v/cm there is a relationship $I = A \exp \alpha V^{1/2}$ (see Fig. 8) where α is inversely proportional to the absolute temperature and the square root of film thickness. Hence we have the expression of the form $I \propto \exp. (\epsilon\beta E^{1/2}/kT)$ with β the Schottky or Poole-Frenkel coefficient, which suggests Schottky or Poole-Frenkel emission. However there is no quantitative agreement between theory and practical results.

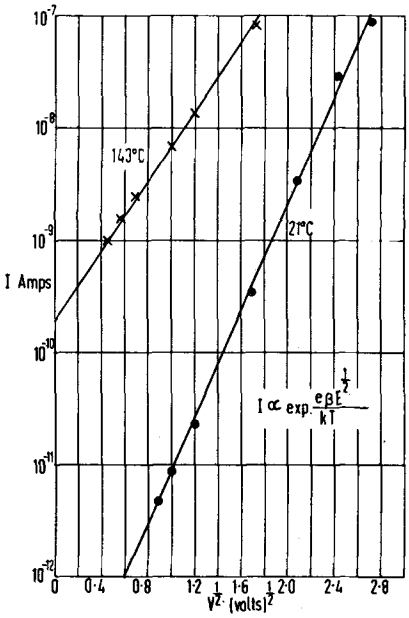

Fig. 8. Current/voltage characteristics for Al-Si-Al sandwich structure at 21° and 143°C.

Effects of Doping

The electrical effects of the addition of significant impurities in crystalline silicon are well known and understood. Experiments were carried out to assess the effect of adding phosphorus to amorphous silicon during the deposition. Phosphine was chosen for this purpose, diluted with hydrogen, and added to the silane prior to its decomposition. Quantities of 40-200 ppm of phosphine in silane did not give the dramatic changes in resistivity which would normally be associated with these doping levels in single crystal silicon. The resistivity was reduced by a factor of 20 to 100 on samples deposited at room temperature depending on the doping level. However these samples were unstable, but stabilized after heat treatment at 150°C in air. Results were as follows:

ppm phosphine in silane	Activation energy, ev	Resistivity 21°C ohm-cm
40	0.83	10^{10}
100	0.77	4×10^9
200	0.75	2×10^9

Films deposited above 200°C still show relatively high resistivities at the doping levels previously mentioned. However, instability made accurate measurements difficult, so only approximate figures are possible. An undoped sample deposited at 280°C has a typical resistivity near 6×10^8 ohm-cm. A sample deposited from silane doped with 200 ppm of phosphine at this temperature gives a resistivity value of the order of 10^6 ohm-cm.

The photoconductive effect is reduced as doping increases. Experiments were also carried out at extremely high doping levels, *i.e.*, 0.4 and 4.0% of phosphine in silane. Room temperature deposition at these levels showed resistivities of 1×10^6 to 1×10^4 ohm-cm.

Although some discrete activation energies were found they tended to vary with time. Room temperature samples were more stable than others grown at higher temperatures. Figure 9 refers to these measurements.

In order to assess the amount of phosphorus incorporated in amorphous silicon for a given gas percentage the material was investigated by electron-probe analysis. A gas mixture containing 50% phosphine in silane showed an actual phosphorus in silicon content of near 30%. A second mixture containing 5% phosphine in silane gave a figure of approximately 1% phosphorus in silicon.

Discussion

Many of the properties of amorphous silicon are dependent on the temperature of deposition, for example, there is a gradual drop of resistivity with temperature and an increase in photoconductivity up to a maximum. This suggests that structural differences exist when material is deposited at different temperatures, and it seems apparent that some transition of structure occurs as evidenced by the photoeffects. In other words, these changes are not seen as a straight transition from amorphous to diamond structure with temperature, but indicate that some intermediate structure is involved.

It has been shown by Coleman and Thomas (4) for amorphous silicon and by Grigorovici and Manaila (5) for amorphous germanium, that the structure contains fivefold planar rings of atoms as well as the more normal sixfold puckered rings of the crystalline material.

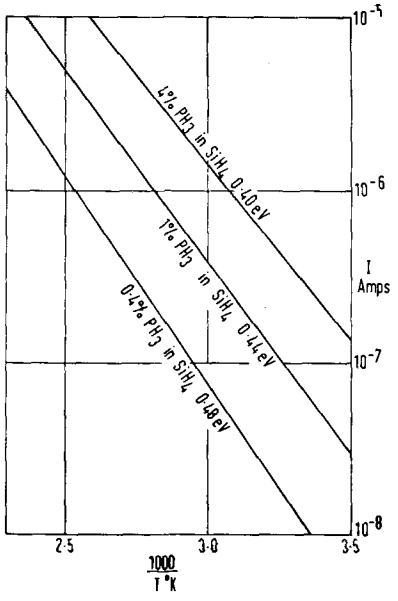

Fig. 9. Inverse temperature-current characteristics for phosphorous doped amorphous silicon; deposition temperature 21°C.

This fivefold structure is stable up to temperatures in excess of 500°C. Films grown at up to 500°C have been shown to be amorphous when deposited on cleaved single crystal magnesium oxide, however, the specimens used for electrical evaluation were deposited on glass which contain a mixture of potential impurities, some of which are known to have an effect on the crystallization rate of these amorphous films.

Acknowledgment

The authors wish to thank their colleagues at STL for helpful discussions and with the measurements. Thanks are also due to Mrs. S. Y. Hughes for work concerned with sample preparation and to the management of STL for permission to publish this work.

Manuscript submitted July 11, 1968; revised manuscript received Sept. 10, 1968. This paper was presented at the Boston Meeting, May 5-9, 1968, as Paper 74.

Any discussion of this paper will appear in a Discussion Section to be published in the December 1969 JOURNAL.

REFERENCES

1. H. F. Sterling and R. C. G. Swann, *Solid State Electronics*, **8**, 653 (1965).
2. E. I. Adirovich and Yu M Yuabov, *Soviet Physics —Doklady*, **9**, 296 (1964).
3. P. A. Walley and A. K. Jonscher, *Thin Solid Films*, **1**, 367 (1967/68).
4. M. V. Coleman and D. J. D. Thomas, *Phys. Stat. Sol.*, **24**, K111 (1967).
5. R. Grigorovici and R. Manaila, *Thin Solid Films*, **1**, 343 (1967/68).

Growth Rate and Surface Morphology Studies in the $GeCl_4$-H_2 System

V. J. Silvestri*

International Business Machines Corporation, Thomas J. Watson Research Center, Yorktown Heights, New York

ABSTRACT

Growth rate studies of the $GeCl_4$-H_2 reaction are reported for an epitaxial system. The experimentally observed deposition rates are described in terms of a "quasi-equilibrium" model in which only a limited portion of the gas achieves equilibrium composition. Smooth surfaces are obtained under conditions where epitaxial growth appears to be mass transport controlled. For any given Ge concentration, the observed dependence of growth rate on temperature and substrate orientation indicates that a surface limitation controls growth at lower growth temperatures. When this condition prevails, structured deposits result. Structureless surfaces are favored by operating at high temperatures and low Ge concentrations.

Since the initial work by Theurer *et al.* (1), the reduction of $GeCl_4$ with hydrogen for epitaxial deposition of germanium has been used extensively (1-11). Cave and Czorny (2) and Goorissen and Bruijning (10) have described the epitaxial process as it applies to the preparation of semiconductor devices. Hornberger (3) studied the low-temperature growth aspects of the reduction system. Miller and Grieco (11) studied the etch reactions involving Ge-HCl and Ge-$GeCl_4$. These authors (4-9) investigated growth conditions and surface morphology for different crystallographic orientations, and Grossman (12) has described a kinetic theory for the origin of auto-doping for the epitaxial process.

With increasing complexity of device structures, requirements on epitaxial smoothness and doping control have become more critical, and further understanding of the factors affecting surface character and doping appeared warranted. The present study was undertaken partially to meet these needs.

Experimental results obtained for the analogous $SiCl_4$-H_2 reaction indicate that the silicon deposition systems in use are mass transport limited (13). Reisman and Berkenblit (14) have defined two distinct types of mass transport limitations which are considered below. In the first, the over-all reaction or deposition rate depends simply on the rate of introduction of gaseous reactants into the reaction chamber. In such a case, complete mixing occurs, chemical equilibrium is essentially achieved, and we have an "input-limited" system. The second type of mass transport limitation, called "lateral gas flow limited," results when the chemical deposition reaction is so rapid compared to the rate of transport of reactants through the gas phase by all processes (*i.e.*, diffusion, convection, turbulent flow, *etc.*) that large gradients of reactants and products exist throughout the chamber. In this latter case,

* Electrochemical Society Active Member.

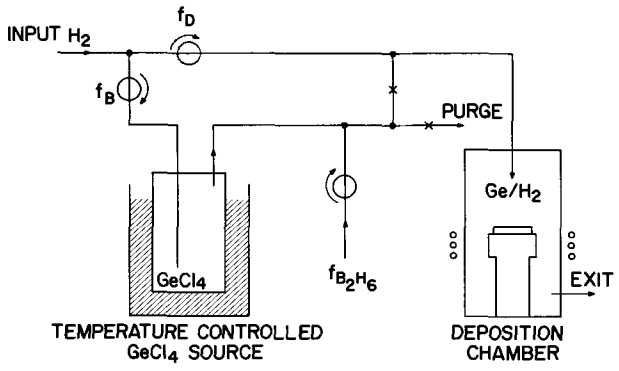

Fig. 1. Pertinent features of the $GeCl_4$-H_2 system

typical of many epitaxial growth systems, portions of the input gas flow by the heated substrates unreacted, and the portion which is unreacted is very dependent on system geometry and flow conditions. The "quasi-equilibrium" model as proposed by Sedgwick (15) for the $SiCl_4$ reduction treats in a simple way systems which are subject to this second mass transport or a "lateral gas flow limited" case. Using Lever's (16) thermodynamic data, Sedgwick was able to explain the main features of reported Si growth data by assuming that a varying but limited portion of the input gas reacted, depending on the exact conditions employed.

An initial goal of this work was the investigation of growth phenomena, in order to determine experimentally growth limitations in the analogous Ge system. Subsequent studies were aimed at relating these growth studies to the surface morphology of the films.

Experimental

The essential features of the experimental system employed in the investigation are shown schematically in Fig. 1. The temperature of the high-purity $GeCl_4$ source could be varied from —40° to 25°C. In addition, the system contained a hydrogen dilution line which bypassed the $GeCl_4$ bubbler. It was therefore possible to vary the Ge/H_2 ratio[1] flowing into the reaction chamber by either changing the vapor pressure at the $GeCl_4$ source, while keeping the total flow constant, or by adding pure hydrogen through the dilution line (f_D) at a fixed $GeCl_4$ source temperature. This latter method maintains a constant germanium flux through the deposition chamber at varying gas velocity. Linear gas stream velocity changes could also be made at a constant Ge concentration by adjusting both the $GeCl_4$ vapor pressure and the hydrogen flow.[2] By using these experimental approaches, one can examine the effects of flux, concentration, and linear gas stream velocity on the course of the $GeCl_4$-H_2 reaction.

Chemical analysis of the germanium content of effluent gas provided assurance that for the flow rates (f_B) employed through the $GeCl_4$ source, saturation of the vapor was achieved for all experimental conditions to be described.

All substrates had been polished to mirror smoothness with sodium hypochlorite as described by Reisman and Rohr (18). Standard cleaning procedure prior to deposition consisted of a 2-min etch in a 3:1 solution of H_2O; NaOCl (5%). After rinsing in distilled water, the substrates were dried in a high-pressure nitrogen stream. They were then heated in the reactor at $T >$ 700°C for 15 min in order to complete the cleaning operations.

Depositions took place on Ge substrates placed perpendicular to the gas stream. A 1-in.-diameter germanium pedestal acted as the susceptor in the rf heated system, and comprised 25% of the internal cross-sectional area of the reaction tube. Deposition of germanium occurred only on the heated substrate and pedestal sides, since the reactor walls were water cooled to prevent any reduction of the halide. Substrate temperature was measured using an optical pyrometer, and was controlled by means of a thermocouple embedded in a well in close proximity to the Ge wafer. The depositions were carried out for the most part on <110> oriented substrates. In order to determine if growth rate was orientation dependent, <111>, <211>, <100> oriented surfaces were employed for a few specific experiments. Thickness measurements were obtained on the epitaxial layers using infrared interference (17) or angle lapping techniques. For doping experiments, diborane mixed in high-purity hydrogen was used. Carrier concentrations were determined from Hall effect, differential junction capacitance, and 4-point probe techniques.

Total deposition experiments were conducted in order to compare theoretical[3] with experimental deposition rates. In such cases, the material weighed included the Ge deposited on the substrate and the heated area of the germanium pedestal.

Results

Growth rate data.—Growth rate was found to be independent of deposition time for all experimental conditions employed. Growth rate was evaluated as a function of substrate temperature, Ge/H_2 ratio variation, and linear gas stream velocity. In Fig. 2, the Ge/H_2 ratio or Ge input flux variations were achieved by changing the vapor pressure at the $GeCl_4$ source while keeping the total flow or linear gas stream velocity constant. The data shown in Fig. 2 indicate a strong growth rate dependence with temperature in the lower temperature range (region *A*) at each Ge/H_2 input ratio. At higher temperatures (region *B*), there is little or no growth rate dependence with temperature.

In Fig. 3, growth rate is shown as a function of Ge/H_2 ratio at two substrate temperatures, 700° and 780°C. It is to be noted that the growth rate at 700°C shows a maximum as the Ge/H_2 ratio is increased, while flow rate is held constant (at the same value as that used to take the data shown in Fig. 2).

An alternative way of changing the Ge/H_2 ratio which at the same time maintains a constant Ge flux

[3] Appendix.

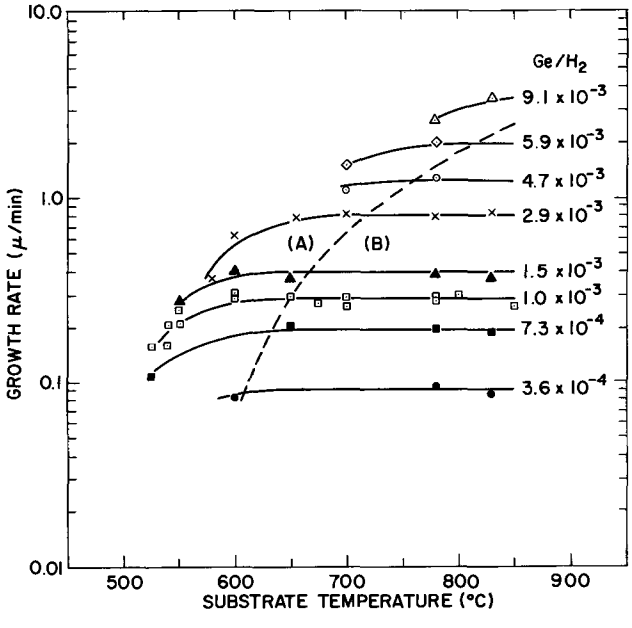

Fig. 2. Growth rate as a function of varying substrate temperature for different Ge/H_2 inputs at a constant linear gas stream velocity of 175 cm/min. The dashed curve is taken from Fig. 9.

[1] The Ge/H_2 ratio is defined as the ratio of moles of $GeCl_4$/min, divided by the moles of H_2/min flowing into the reaction chamber.

[2] The linear gas stream velocity is referred to the total flow in cc/min at room temperature divided by the entire cross-sectional area of the reaction tube. It should be noted that this is a reference point only and, since the pedestal perturbs flow, the average linear gas stream velocity is higher along the sides of the pedestal than on the top.

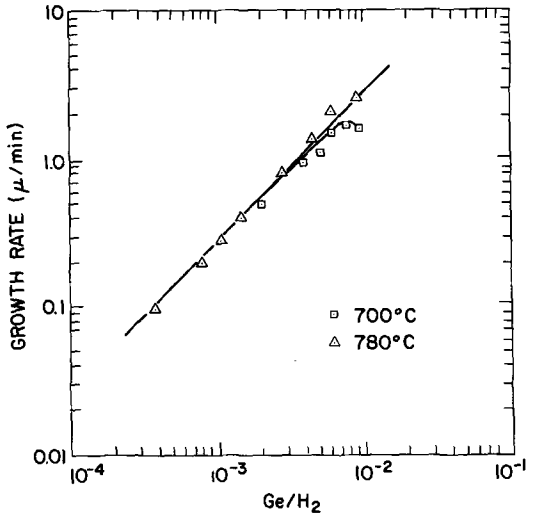

Fig. 3. Growth rate as a function of $GeCl_4$ input for a constant linear gas stream velocity of 175 cm/min.

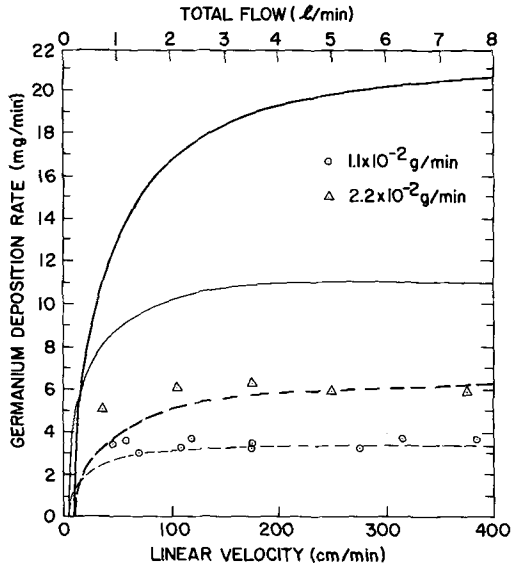

Fig. 4. Germanium deposition rate as a function of linear gas stream velocity at constant germanium tetrachloride flux values. Temperature, 780°C. ——— theoretical; – – – theoretical ÷ 3.3.

involves dilution of the $GeCl_4$ source effluent at a constant source temperature and bubbler flow. This method leads to the data points shown in Fig. 4 where each point is representative of a different linear gas stream velocity and Ge vapor phase concentration. Data are shown for two different germanium input rates. The germanium deposition rates shown as experimental points in Fig. 4 were calculated from growth rates measured on the substrate and the assumption of a uniform growth over the entire heated region of the susceptor.[4] The solid and dashed curves in Fig. 4-7 represent theoretical rates computed in two ways to be discussed in the following section. Experimental data shown in Fig. 5 and 6 are based on the weighed amount of Ge deposited on the substrate plus susceptor. Figure 5 data were obtained under conditions similar to Fig. 2 and 3 in which Ge concentration was varied at a constant linear gas stream velocity. Figure 6 gives total Ge deposition rate in mg/cm²/min under conditions of constant Ge/H_2 ratio and varying linear gas stream velocity. The constant Ge concentration was achieved by readjusting the vapor pressure at the $GeCl_4$ source

[4] In Fig. 6, both the growth rate on the substrate and the total amount of Ge deposited were assessed. Using the growth rate data on the substrate and assuming an equal and uniform thickness over the heated susceptor, the total amount of Ge deposited could be calculated on the basis of area ratio and agreed in every case to within better than 20% with the value as measured by net weight gain.

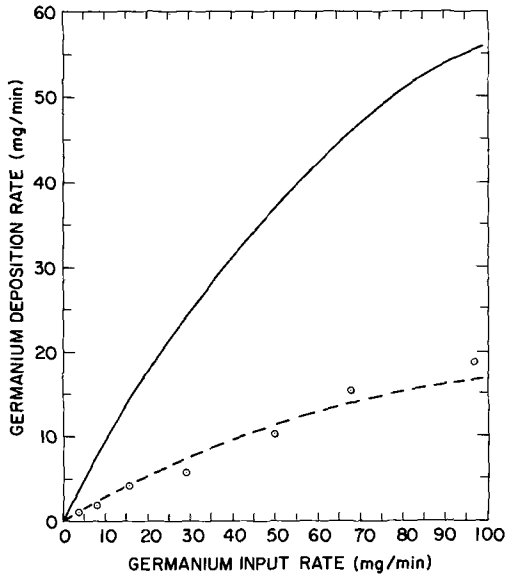

Fig. 5. Germanium deposition rate for varying germanium input rates at a linear gas stream velocity of 175 cm/min. Temperature, 780°C. ——— theoretical; – – – theoretical ÷ 3.3.

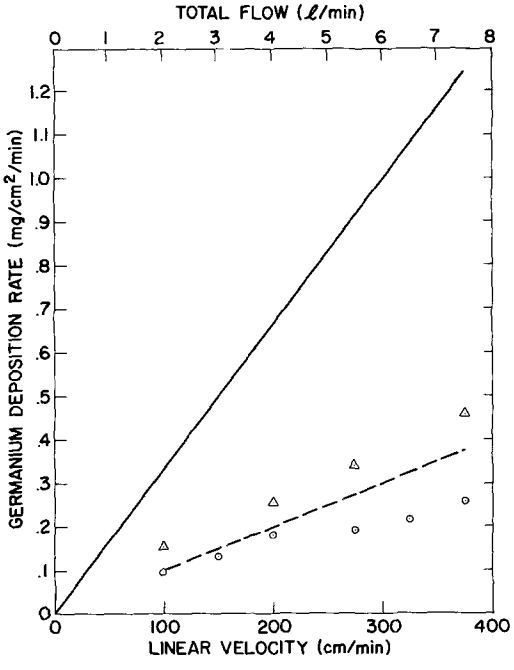

Fig. 6. Germanium deposition rate as a function of varying linear gas stream velocity at a constant Ge concentration. $Ge/H_2 = 1.1 \times 10^{-3}$. ——— theoretical; – – – theoretical ÷ 3.3; △, deposition rate on the substrate with an SiO_2 masked susceptor; ⊙, deposition rate on the substrate and the Ge susceptor.

for each linear gas stream velocity change. The data shown as circles and triangles differ in the following way. The circles represent deposition rates which are based on the total Ge deposited on both the substrate and the susceptor having a total heated area of approximately 18.5 cm². For the data points given as triangles, the Ge susceptor was masked with an SiO_2 film (upon which Ge will not nucleate). The deposition rates shown for this latter case are therefore calculated from the total amount of Ge deposited solely on substrates having areas of approximately 4.4 cm². The data in Fig. 4, 5, and 6 have been acquired since they are pertinent to the discussion of the effects of mass transport limitations on surface morphology to follow.

In order to compare the experimental deposition rates with the theoretical rates as a function of temperature, we have plotted in Fig. 7 deposition rate for

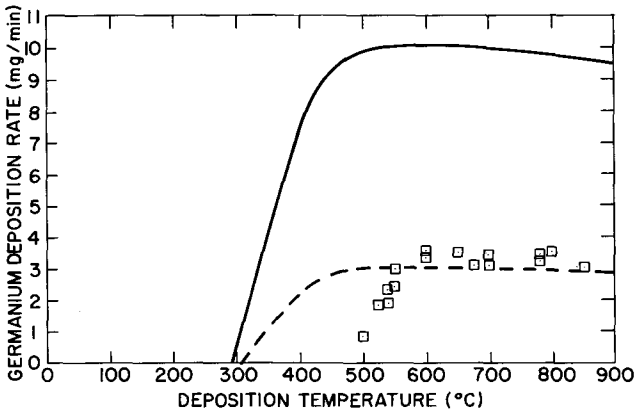

Fig. 7. Comparison of theoretical deposition rates with deposition temperature variation. $Ge/H_2 = 1.0 \times 10^{-3}$. ——— theoretical curve; – – – theoretical curve ÷ 3.3; ⊡, experimental data.

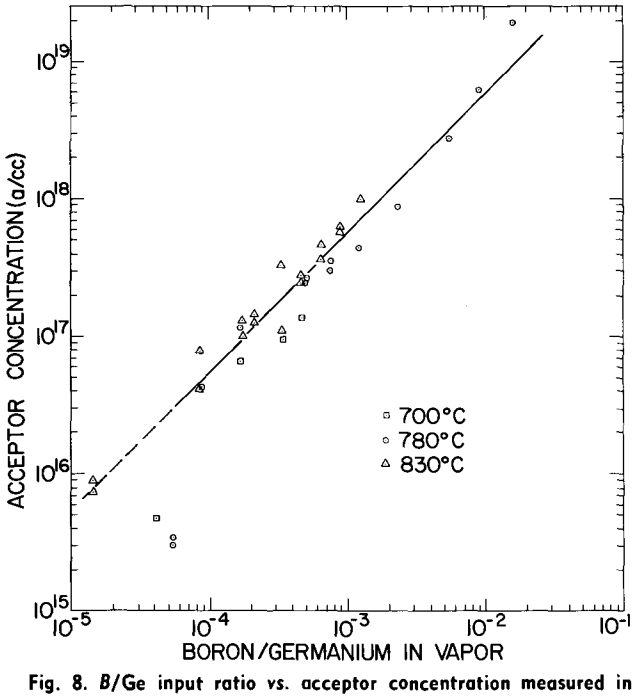

Fig. 8. B/Ge input ratio vs. acceptor concentration measured in the deposited layers for three substrate temperatures for a constant total flow of 3.5 liters/min.

a specific Ge/H_2 input value. The germanium deposition rates shown were evaluated from the growth rate data given in Fig. 2 by assuming a uniform growth rate over the entire pedestal. In Fig. 8, the input B/Ge ratios are plotted *vs.* the acceptor concentration measured electrically in the epitaxial layer.

Surface morphology.—Upon microscopic examination of surfaces grown under the conditions described for Fig. 2, it became obvious that the surface morphology of the epitaxial deposits was related to the temperature-concentration conditions used for growth of the films. To analyze this observation more thoroughly, the substrate temperature was varied at a constant Ge/H_2 ratio and *vice versa*. It was found that: (*a*) increases in substrate temperature over certain intervals for a given Ge/H_2 ratio will yield progressively smoother surfaces; (*b*) increasing the Ge/H_2 ratio for a constant substrate temperature will produce more structured surfaces; (c) changes in surface morphology were observed irrespective of substrate orientation. Epitaxial layers investigated included <211>, <111>, <110>, and <100> oriented surfaces. Figure 9 summarizes the above-described observations. The microscopic evaluations of surface morphology placed the samples in one of two categories having either smooth or structured

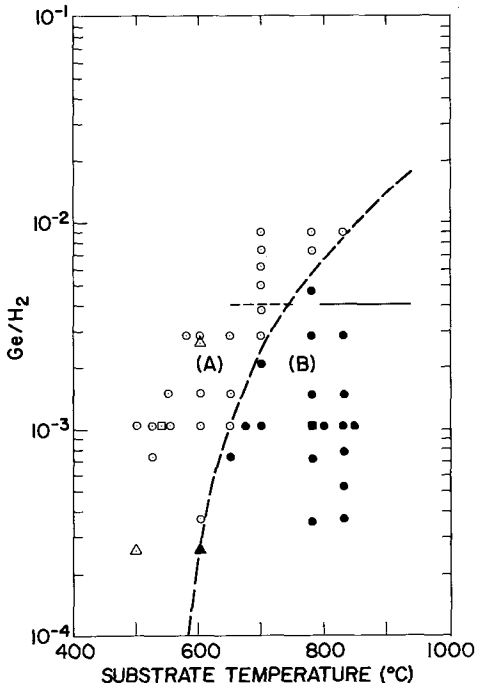

Fig. 9. Morphology diagram for the $GeCl_4$-H_2 system. The solid points indicate smooth surfaces; open points, structured surfaces. The dashed curve demarks conditions for obtaining smooth and structured surfaces. Triangles are data from Ref. (3). The horizontal dashed and solid lines at 4×10^{-3} show, respectively, the temperature intervals at which authors in Ref. (7) and (8) observed structured and smooth surfaces. The squares indicate conditions at which <111>, <110>, <211>, and <100> orientations were employed.

films. Deposits were considered "structured" which exhibited growth figures characteristic of the particular substrate orientation employed. Smooth surfaces exhibited essentially a mirror finish and were free of growth figures. The morphology diagram, Fig. 9, describes the surface morphology of the epitaxial layers obtained for various substrate temperature-Ge/H_2 input conditions employed. The solid points (region *B*) define the temperature-Ge/H_2 combinations where smooth surfaces were obtained. Open symbols designate conditions (region *A*) where structured surfaces result. The square symbols in Fig. 9 represent data for the four different substrate orientations mentioned above. For the conditions represented by the solid square in region *B*, no growth rate variation with substrate orientation was observed. In region *A* for the experimental condition represented by the open square, the following growth rate variations with substrate orientation were observed: <211>, 0.11 μ/min; <111>, 0.15 μ/min; <110>, 0.17 μ/min; <100>, 0.20 μ/min. The data shown as triangles are data derived from previously published reports in which similar morphological observations were made (3). The solid horizontal line at a Ge/H_2 value of 4.0×10^{-3} gives the temperature interval for which Sheftal *et al.* (7, 8) obtained smooth surfaces. The horizontal dashed line indicates the temperature span for which the same authors report structured surfaces.

Discussion

In Fig. 2, region *B*, both the observed independence of growth rate with temperature at a particular Ge/H_2 ratio and increase in growth rate with germanium input in Fig. 3 indicate that region *B* of Fig. 2 represents mass transport limited growth. In addition, it has been observed that for the experimental conditions in region *B*, Fig. 2, growth morphologies on the various orientations are similar (Fig. 9) and that there is no growth rate dependence found with these variations of surface orientation. In contrast, in region *A* of Fig. 2, growth

rate varies with both temperature and surface orientation.

The comparison of the theoretical deposition rates based on the total amount of Ge deposited with linear gas stream velocity, concentration, and temperature in Fig. 4-7 further supports these conclusions.

The theoretical deposition rates shown in Fig. 4-7 as solid curves are based on thermodynamic calculations. The computer calculations for the Ge-H-Cl system included the gas species $GeCl_4$, $GeCl_2$, $GeHCl_3$, HCl, and H_2, and were made in the manner reported by Lever (16) for the analogous Si-H-Cl system. For the case of a mass transport limited system which is "input limited," one would expect the theoretical deposition rate based on a thermodynamic calculation of chemical equilibrium to be identical to the observed deposition rate. In Fig. 4-7, we note that, although the shapes of the theoretical curves resemble the experimental data, the experimental rates are much lower than theory predicts. In Fig. 5 where data are given for a single linear gas stream velocity, it was found that the experimental data could best be approximated by dividing the theoretical rates by a constant factor, 3.3. This proportionality between the theoretical and experimental rates is explainable if we consider the second possible kind of mass transport limitation discussed earlier, namely, where "lateral gas flow" is rate limiting and the deposition rate is very dependent on system geometry.

In the Si-H-Cl system, Sedgwick proposed in accordance with this second mass transport case that the deposition rate D in g/min in many epitaxial systems may be represented to first order by

$$D = J \cdot \alpha\beta \qquad [1]$$

where J is the flux of Ge in g/min into the reaction tube and α the theoretical efficiency factor based on equilibrium calculations. The actual fraction of incoming gas which equilibrates with the heated Ge surface and consequently attains this theoretical efficiency is designated as β. The remaining fraction of gas $(1 - \beta)$, in this model, streams by unreacted. The magnitude of this remaining fraction is highly geometry dependent, and could comprise either a large or small portion of the total gas input.

Applying Eq. [1] with $\beta = 0.3$ to the theoretically calculated curves (solid lines), we obtain the dashed lines in Fig. 4-7. We note that, while the data of these figures are in much closer agreement to the theoretical predictions, some discrepancy exists. The assumption of a constant β factor for the system is not expected to be valid in a system with varying linear gas stream velocity, particularly under conditions of very low velocities where equilibration is more complete and at very high linear gas stream velocities when residency times of molecules in the vicinity of the susceptor become short. In Fig. 4, the higher deposition rates at the lower velocities, where there is a longer gas residence time and in general better gas mixing, actually indicate an increase in the value of β. Consistent with this, the experimental data in Fig. 6 at the higher linear gas stream velocity show an apparent decrease in β. The experimental data shown in Fig. 6 are of two types. The points represented by circles were obtained from the total Ge deposited on both the substrate and the pedestal, whereas the points shown as triangles are from the Ge deposited solely on the substrate. The intent of obtaining the experimental data involving the SiO_2 coated pedestal (triangles) was (*a*) to evaluate the effect of gas velocity on deposition rate for a Ge surface perpendicular to the gas stream (Ge wafer only) separately from the case in which heated Ge surfaces are both perpendicular and parallel (wafer plus pedestal sides) to the gas stream (circles), and (*b*) to observe the effect on β of reducing the total heated Ge surface area. The ratio, substrate plus pedestal to substrate area for the two sets of data in Fig. 6, is 4.2 and a β of 0.1 was found for the reduced area experiments (triangles) at a velocity of 100 cm/min. Assuming uniform growth, the expected β at this same velocity, for the larger area data (circles), would be 0.42; experimentally it is found to be 0.3.

This difference in β for the two sets of data in Fig. 6 is expected if we attribute the variation to gas depletion effects. These are effects which one would normally consider to be operative in a mass transport limited system. The earlier cited results, namely for the data in Fig. 6 (circles), indicated that growth rate could be considered essentially uniform to within 20% and would imply that reasonably good mixing of the gas occurs at heated surfaces. In view of these results, one would therefore expect the growth rate to increase with a reduced available surface area due to a reduced gas depletion effect.

The general features of both sets of data in Fig. 6, which include the dependence of growth rate on surface area, clearly indicate mass transport limited behavior.

The foregoing experimental growth data support, therefore, the conclusion of a specific type of mass transport limited system, *i.e.*, "lateral gas flow limited" in the higher temperature intervals, where only approximately 1/3 of the gas flowing through the reaction tube is capable of diffusing to and reacting with the heated Ge surface.[5]

The hypothesis that mass transport control of growth is more readily achieved at higher temperatures is further supported by the results of doping experiments. It was found that the boron concentration in the epitaxial Ge layers deposited at 700°, 780°, and 830°C increased linearly with gas phase B_2H_6 content and independently of temperature. The input B/Ge ratios shown could be obtained experimentally by either varying the diborane or the germanium input to the system. The linear nature of the results are in agreement with the work reported by Goorissen (10), and are expected for a mass transport controlled system. The data show a distribution ratio C_s/C_v of 0.0125 between the solid and vapor, where C_s = B/Ge ratio in the solid and C_v = B/Ge ratio in the vapor.

In Fig. 7, the theoretical curves fail to explain the temperature dependency of deposition rate in the low-temperature region. In Fig. 2 (region *A*), we note that temperature-dependent regions on the plot cover a wide range of substrate temperatures and input concentrations. Experimental evidence suggests that in these temperature-dependent intervals the growth rate is no longer dominated by mass transport, but instead is inhibited by a surface limitation. This is consistent with the model proposed by Reisman and Berkenblit (14). In the present study, structured surfaces were consistently observed for surface limited experimental conditions and the growth rate has been found to vary with substrate orientation. These observations are in agreement with orientation studies which have been reported by Givargizov *et al.* (8, 7) for similar growth conditions. The surface morphology changes described previously would further suggest that a different growth limiting mechanism is involved.

It will be noted that the conditions for smooth surfaces in Fig. 9 (region *B*) are for high substrate temperatures and low Ge/H_2 ratios. The intimate relationship of the morphology data illustrated in Fig. 9 to the growth rate data in Fig. 2 has been demonstrated by superimposing the "dashed curve" of Fig. 9, which demarks conditions for obtaining smooth and structured surfaces, on the growth rate data in Fig. 2. It can be seen that the dashed curves in Fig. 2 and 9 divide the data into a region *B* where mass transport limited growth conditions prevail and smooth surfaces

[5] Independent experimental observations which also support these conclusions have been made by Papazian (25). Using a reaction chamber of smaller diameter, such that a greater portion of the inside cross-sectional area was blocked by the heated pedestal surface, Papazian observed a β of 0.56 for comparable growth conditions.

are obtained, and a surface rate limited region *A* where structured surfaces are obtained.

In summary, the above studies have shown: (*a*) that deposition rates observed for the system studied can be explained using a "quasi-equilibrium" model; (*b*) the temperature and substrate orientation independence of growth rate, for a specific Ge/H_2 input value at higher temperatures, indicate a mass transport controlled system. Smooth surfaces are obtained under such conditions; and (c), at lower temperatures, dependence of growth rate on both temperature and substrate orientation indicates that surface limitations predominate. This latter case is coincident with structured surfaces.

APPENDIX

The theoretical calculations made use of the following equations along with the appropriate vant Hoff expressions relating the equilibrium constant, *K*, with temperature.

$$Ge(s) + 4HCl(g) = GeCl_4(g) + 2H_2(g) \quad [A\text{-}1]$$

$$[1a] \quad \log K_1 = \frac{6730}{T} - 8.02$$

$$Ge(s) + 2HCl(g) = GeCl_2(s) + H_2(g) \quad [A\text{-}2]$$

$$[2a] \quad \log K_2 = \frac{-465}{T} + 1.12$$

$$Ge(s) + 3HCl(g) = GeHCl_3(g) + H_2(g) \quad [A\text{-}3]$$

$$[3a] \quad \log K_3 = \frac{7580}{T} - 7.45$$

Equation [1*a*] is based on room-temperature enthalpy and entropy data for Ge(s), H_2(g), HCl(g) (19) and $GeCl_4$ (20) corrected for temperature using the tables of Kelley (21). The linear relationship for $\log K_1$ is the best fit of data corrected for a number of temperatures in the temperature interval 400°-1100°K. Sedgwick's (22) equilibrium data, Eq. [4*a*], for the reaction

$$GeCl_4(g) + Ge(s) = 2GeCl_2(g) \quad [A\text{-}4]$$

$$[4a] \quad \log K_4 = \frac{-7660}{T} + 10.25$$

were used along with Eq. [1*a*] to obtain Eq. [2*a*]. The reported K_4 data for reaction [A-4], was extrapolated to include the entire range of the calculations.

Thermodynamic data for $GeHCl_3$ are not known, and the room-temperature enthalpy and entropy were estimated by linear interpolation for the series GeH_4, GeH_3Cl, GeH_2Cl_2, $GeHCl_3$, and $GeCl_4$. This procedure is based on the assumption that bond energies are additive in generating the above series. Approximations of this type have been demonstrated in the analogous carbon series and were used in estimating heats for the Si series (16). Using this method, $\Delta H°_{298}$ was estimated at 90 ± 10 kcal from the room-temperature enthalpy of $GeCl_4$ and an estimated enthalpy of from 0 to −12 kcal for GeH_4. The approximation of the GeH_4 enthalpy was obtained using the approach of Roth and Schwartz (23) in which estimations of enthalpies are made by plotting heats of formation against an atomic number. An interpolated room-temperature entropy of 75.6 eu was used since the linear assumption was found to hold well for the above series for calculated values for GeH_4, $GeHCl_3$, and $GeCl_4$ as reported by Kelley (24). Equation [3*a*] was written assuming that $\Delta H°_{298}$ and $\Delta S°_{298}$ for reaction [A-3] is constant for the temperatures of the calculations.

Because of the large uncertainty in the thermodynamic constants for $GeHCl_3$, the enthalpy of formation was varied between −100 and −85 kcal. The enthalpy value changes for $GeHCl_3$ had no effect on the values of predicted deposition rates at higher temperatures; however, below 500°C, the use of a heat of formation value of −100 kcal caused significant reduction in predicted deposition rate. Equation [3*a*] was written using a −100 kcal value for $GeHCl_3$(g). The theoretical calculations were made adopting the approach described by Lever (16).

The thermodynamic efficiency, α, was defined as reported earlier by Sedgwick (15) for the analogous Si-H-Cl system

$$\alpha = \frac{\eta_{input} - \eta_{equi}}{\eta_{input}}$$

where, in general, η is the ratio of the total density of Ge atoms in the gas phase divided by the total density of Cl atoms in the gas phase summed over all species. η_{input} refers to the input gas consisting of $GeCl_4$ and H_2 and is, therefore, 0.25. η_{equi} refers to the gas phase Ge/Cl ratio at equilibrium. This efficiency value was employed in Eq. [1] to obtain the theoretical curves shown.

The thermodynamic calculations show that, above 600°C for Ge/H_2 ratios $< 3 \times 10^{-3}$, the efficiency is above 0.8 and that the reaction of $GeCl_4$ with hydrogen yields predominantly Ge and HCl as reaction products.

Acknowledgments

The author wishes to acknowledge gratefully, in particular, T. O. Sedgwick and R. F. Lever for their sustained interest, stimulating discussions, and critical evaluations throughout the course of this work. In addition, the author wishes to thank R. Gereth, A. Reisman, R. A. Laff, and Mrs. S. A. Papazian for their helpful suggestions. Thanks also to A. G. Blachman and M. E. Cowher for electrical data, and W. P. Hornberger who designed the original experimental system.

Manuscript submitted July 29, 1968; revised manuscript received Sept. 5, 1968. This manuscript was presented in part at the Dallas Meeting, May 7-12, 1967, as paper 104, and at the Chicago Meeting, Oct. 15-19, 1967, as paper 163.

Any discussion of this paper will appear in a Discussion Section to be published in the December 1969 JOURNAL.

REFERENCES

1. H. C. Theurer, J. J. Keimaek, H. H. Loar, and H. Christensen, *Proc. IRE*, **48**, 1964 (1960).
2. E. F. Cave and B. R. Czorny, *RCA Rev.*, **24**, 523 (1963).
3. W. P. Hornberger, AFCRL Contract # AF19(628)-2468, Sci. Reports # 1, 2, 3, and 4, July 1963, Dec. 1963, June 1964, and July 1965.
4. E. I. Givargizov, *Soviet Phys.-Solid State*, **5**, 840 (1963).
5. E. I. Givargizov and N. N. Sheftal, *Soviet Phys. "Doklady,"* **8**, 441 (1963).
6. E. I. Givargizov, *Fiz. Tverd. Tela*, **6**, 1804 (1964).
7. N. N. Sheftal and E. I. Givargizov, *Soviet Phys.-Cryst.*, **9**, 576 (1965).
8. E. I. Givargizov and N. N. Sheftal, "Crystal Growth," Proc. 1966, Boston, H. Steffen Peiser, Editor.
9. N. N. Sheftal, E. I. Givargizov, B. V. Spitsyn, and A. M. Kevorkov, "Growth of Crystals," Vol. 4, p. 15, Consultants Bureau, New York (1966).
10. J. Goorissen and H. G. Bruijning, *Philips Tech. Rev.*, **26**, 194 (1965).
11. K. J. Miller and M. J. Grieco, *This Journal*, **111**, 1099 (1964).
12. J. J. Grossman, *ibid.*, **110**, 1065 (1963).
13. E. G. Bylander, *ibid.*, **109**, 1171 (1962).
14. A. Reisman and M. Berkenblit, *ibid.*, **113**, 146 (1966).
15. T. O. Sedgwick, *ibid.*, **111**, 1381 (1964).
16. R. F. Lever, *IBM J. Res. Develop.*, **8**, 460 (1964).
17. W. G. Spitzer and M. Tanenbaum, *J. Appl. Phys.*, **32**, 744 (1961).
18. A. Reisman and R. L. Rohr, *This Journal*, **111**, 1425 (1964).
19. O. Kubaschewski and E. Evans, "Metallurgical Thermochemistry," Pergamon Press, New York (1968).

20. D. F. Evans and R. E. Richards, *J. Chem. Soc.*, **1952**, 1292.
21. K. K. Kelley, Bureau of Mines Bull. 584, U. S. Govt. Printing Office, Washington, D. C. (1961).
22. T. O. Sedgwick, *ibid.*, **112**, 496 (1965).
23. W. A. Roth and O. Schwartz, *Z. Physik. Chem.*, **134**, 456 (1928).
24. K. K. Kelley and E. G. King, Bureau of Mines Bull. 592, U. S. Govt. Printing Office, Washington, D. C. (1961).
25. S. A. Papazian, Private communication.

Application of Multilayer Potential Distribution to Spreading Resistance Correction Factors

P. A. Schumann, Jr.,* and E. E. Gardner*

IBM Corporation, Components Division, East Fishkill Facility, Hopewell Junction, New York

ABSTRACT

The potential distribution of a flat circular area contact on a multilayered structure of infinite radial extent is presented. The solution is applied to the three-point spreading resistance probe and appropriate correction factors are obtained. This solution is compared with existing solutions, and it is shown that there is disagreement with the published values for the insulating back surface case but agreement with the conducting back surface. The results were checked with an electrolytic tank and good agreement was obtained.

All of the four-point potentiometric and spreading resistance probes require a knowledge of the potential distribution due to a point or finite area contact. Many authors (1-10) formulated solutions to the point contact problem with infinite and finite geometries, but with only one layer of material on a perfectly insulating or conducting substrate. Other authors (11-13) have discussed the finite area contact in similar geometries. Very early work (14-17) has been published for point contacts on multilayered structures but very few calculations were carried out. A numerical analysis (18) was made of a finite area contact on a multilayered structure. This paper outlines a technique of solving for the potential distribution due to a finite area contact on a multilayered geometry which is infinite in extent in the radial coordinate direction. This solution is then applied to the spreading resistance probe (19-23) to derive correction factors. Part of the model was used previously to derive correction factors for the delta probe (24).

The geometry considered is shown in Fig. 1. A flat circular probe makes a contact of radius, a, with the top surface of the semiconductor. Cylindrical coordinates are used as shown. The sample is infinite in extent in the r direction. There are three regions of different resistivity. Region 1 has a resistivity ρ_1 and a thickness h_1. Region 2 has a resistivity ρ_2 and a thickness d. Region 3 has a resistivity ρ_3 and is infinitely thick.

Several assumptions made which limit the accuracy and usefulness of the technique are:

1. The area contact is uniform. When a point is brought in contact with a sample, both the point and sample deform. Since neither are perfectly smooth or clean, the area of contact between the two is not uniform. The contact is usually made up of a collection of small contact areas. It is assumed here that the collection of small contact areas can be treated together as a single contact of effective radius, a.

2. The metal-semiconductor contact is ohmic. A small area metal-semiconductor contact is not ohmic in general. But experience has shown that in most cases, if low current levels are used, the resistance of the contact is not a function of current direction or magnitude.

3. There are no resistive layers between the contact and semiconductor. In silicon, particularly, it is obvious that there is always present an oxide of silicon on the surface. This is tied in with the first assumptions and it is further assumed that the pressure of the point is sufficient to break through the oxide.

4. Low current levels are used. It is necessary to use low current levels because of heating effects, high field effects, and junction effects.

5. All layers are of the same conductivity type. This is merely a restriction on the applicability of the solutions. For cases where a junction is present, it can be assumed that the junction insulates and an infinite resistivity can be used.

6. The resistivity is homogeneous throughout each layer. In actual practice, the resistivity change at an interface is never abrupt. This is a mathematical approximation to reality.

7. Laplace's equation is valid. It is not strictly true that Laplace's equation can be used to solve this type of problem. Charge accumulation or depletion occurs at the boundary between semiconductor regions of different resistivity depending on the bias conditions. We assume that this is a second order effect in many types of problems employing low current levels. Exact solutions taking into account charge accumulation or depletion at the inter-

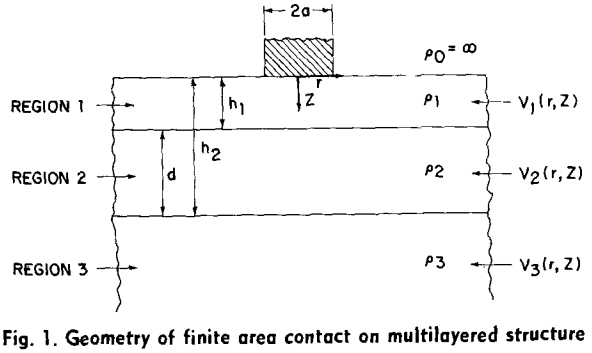

Fig. 1. Geometry of finite area contact on multilayered structure

* Electrochemical Society Active Member.

face between layers would require solution of Poisson's equation. Poisson's equation is nonlinear for this type of problem and solutions have been obtained for only a few one dimensional cases (25-27). Solutions for two dimensions are unknown to the authors.

8. The current distribution at the contact-semiconductor interface can be determined by the electrostatic analog of a flat disk in a semi-infinite medium. In order to carry over Laplace's equation from electrostatics to a current flow problem, a current analog model must be developed. By assuming a surface current distribution both under the contact and elsewhere on the surface it is possible to eliminate mixed boundary conditions in the solution of Laplace's equation.

Only the last two assumptions bear at all on the mathematics of the problem. We are in a sense completely wrong in using Laplace's equation, but the complete problem is not easily solved. Also, we believe that the effects due to the charge accumulation will be small, and, furthermore, comparisons between the spreading resistance probe using these solutions and other techniques are favorable.

It is important to produce the current analog of the electrostatic problem and provide a boundary condition under the contact. In certain cases (12) it is possible to avoid this second problem by solving two simultaneous integral equations. It did not look feasible to attempt this in the case considered. In all cases where checks have been possible, these solutions converge to the solutions presented by other authors for special cases.

The first six assumptions limit the applicability of the mathematics to reality. They are necessary conditions for the solutions as presented and seem reasonable in light of experience. The first four are of very minor importance to the four-point probe techniques, but become important to the spreading resistance measurements.

The mathematical solutions are valid for the problem as described under these assumptions, but no general statement can be made about how well the mathematical model matches the physical situation. Rather, each individual limit taken on the solution must be considered and evaluated.

To proceed with the solution of the problem, the sample is divided into three regions as shown in Fig. 1. Cylindrical coordinates are used, and it is noted that there will be symmetry in the θ direction. Potential V_1 (r,z) is the solution for region 1, V_2 (r,z) for region 2, and V_3 (r,z) for region 3. The solutions take the form

$$V_n(r,z) = \frac{I\rho_1}{2\pi a}\left\{\int_0^\infty \frac{e^{-\lambda z}\sin(\lambda a)J_0(\lambda r)\,d\lambda}{\lambda} + \int_0^\infty \frac{\theta_n(\lambda)e^{-\lambda z}\sin(\lambda a)J_0(\lambda r)\,d\lambda}{\lambda} + \int_0^\infty \frac{\psi_n(\lambda)e^{\lambda z}\sin(\lambda a)J_0(\lambda r)\,d\lambda}{\lambda}\right\} \quad n = 1,2,3 \quad [1]$$

The boundary conditions for this type of problem are relatively standard with the exception of the current distribution under the contact. These boundary conditions are:

Surface

$$\frac{\partial V_1(r,z)}{\partial z} = 0 \quad \text{when } r > a \text{ and } z = 0 \quad [2]$$

$$\frac{\partial V_1(r,z)}{\partial z} = \frac{-I\rho_1}{2\pi a(a^2-r^2)^{1/2}} \quad \text{for } r \leq a \text{ and } z = 0 \quad [3]$$

These first two conditions relate to the field at the surface. Equation [2] states that there is no current flow out of the surface away from the contact. Equation [3] is developed from considerations of the current flow under a flat circular contact on an infinite geometry.

Region 1

$$\lim_{r\to\infty} V_1(r,z) = 0 \quad [4]$$

First Interface

$$\frac{1}{\rho_1}\frac{\partial V_1(r,z)}{\partial z} = \frac{1}{\rho_2}\frac{\partial V_2(r,z)}{\partial z} \quad \text{for } z = h_1 \quad [5]$$

$$V_1(r,z) = V_2(r,z) \quad [6]$$

The equations at the interfaces state that the current density must be the same across the boundary and that the potential is continuous.

Region 2

$$\lim_{r\to\infty} V_2(r,z) = 0 \quad [7]$$

Second interface

$$\frac{1}{\rho_2}\frac{\partial V_2(r,z)}{\partial z} = \frac{1}{\rho_3}\frac{\partial V_3(r,z)}{\partial z} \quad [8]$$

for $z = h_2$

$$V_2(r,z) = V_3(r,z) \quad [9]$$

Region 3

$$\lim_{r\to\infty} V_3(r,z) = 0 \quad [10]$$

$$\lim_{z\to\infty} V_3(r,z) = 0 \quad [11]$$

These conditions are then imposed on the solutions given in Eq. [1] to specify $\theta_n(\lambda)$ and $\psi_n(\lambda)$. This results in a series of linear equations which can be solved with determinants. In general, if N is the number of layers of finite thickness, a $2N$ by $2N$ determinant must be solved. The solution to the equations for two layers are

$$\theta_1(\lambda) = \frac{k_1e^{-2\lambda h_1} + k_2e^{-2\lambda h_2}}{1 - k_1e^{-2\lambda h_1} - k_2e^{-2\lambda h_2} + k_1k_2e^{-2\lambda d}} = \psi_1(\lambda) \quad [12]$$

$$\theta_2(\lambda) = \frac{k_1 + k_1e^{-2\lambda h_1} + k_2e^{-2\lambda h_2} - k_1k_2e^{-2\lambda d}}{1 - k_1e^{-2\lambda h_1} - k_2e^{-2\lambda h_2} + k_1k_2e^{-2\lambda d}} \quad [13]$$

$$\psi_2(\lambda) = \frac{(1 + k_1)k_2e^{-2\lambda h_2}}{1 - k_1e^{-2\lambda h_1} - k_2e^{-2\lambda h_2} + k_1k_2e^{-2\lambda d}} \quad [14]$$

$$\theta_3(\lambda) = \frac{k_1 + k_2 + k_1k_2 + k_1e^{-2\lambda h_1} + k_2e^{-2\lambda h_2} - k_1k_2e^{-2\lambda d}}{1 - k_1e^{-2\lambda h_1} - k_2e^{-2\lambda h_2} + k_1k_2e^{-2\lambda d}} \quad [15]$$

and

$$\psi_3(\lambda) = 0 \quad [16]$$

where

$$k_1 = \frac{\rho_2 - \rho_1}{\rho_2 + \rho_1} \quad [17]$$

and

$$k_2 = \frac{\rho_3 - \rho_2}{\rho_3 + \rho_2} \quad [18]$$

For most probe problems, only the potential at the surface is important, and since $\theta_1(\lambda) = \psi_1(\lambda)$

$$V_1(r,0) = \frac{I\rho_1}{2\pi a}\int_0^\infty \frac{[1 + 2\theta_1(\lambda)]\sin(\lambda a)J_0(\lambda r)}{\lambda}\,d\lambda \quad [19]$$

This specifies the potential at any point on the surface. But, for a spreading resistance measurement, the potential drop due to current flow through the contact area is needed. Since the contact probe will average out any gradients in potential that exist

$$V_S = \frac{\int_0^a\int_0^{2\pi} V_1(r,0)\ \mathrm{r}\,\mathrm{d}r\,\mathrm{d}\theta}{\int_0^a\int_0^{2\pi} \mathrm{r}\,\mathrm{d}r\,\mathrm{d}\theta} \quad [20]$$

which is the spreading resistance voltage or self potential of the contact. Substituting Eq. [19] for $V_1(r,z)$ and noting there is no dependence on θ

$$V_S = \frac{I\rho_1}{\pi a^2}\int_0^\infty \frac{[1 + 2\theta_1(\lambda)]\sin(\lambda a)J_1(\lambda a)}{\lambda^2}\,d\lambda \quad [21]$$

It is almost always more convenient to work with a dimensionless system. This can be obtained in this case by letting $t = \lambda a$. In dimensionless form, the solutions for the surface take the form

$$V_1(R,0) = \frac{I\rho_1}{2\pi a}$$

$$\int_0^\infty \left[\frac{1 + k_1e^{-2H_1t} + k_2e^{-2H_2t} + k_1k_2e^{-2Dt}}{1 - k_1e^{-2H_1t} - k_2e^{-2H_2t} + k_1k_2e^{-2Dt}}\right] \frac{\sin t\, J_0(Rt)}{t}\,dt \quad [22]$$

and

$$V_S = \frac{I\rho_1}{\pi a}$$

$$\int_0^\infty \left[\frac{1 + k_1e^{-2H_1t} + k_2e^{-2H_2t} + k_1k_2e^{-2Dt}}{1 - k_1e^{-2H_1t} - k_2e^{-2H_2t} + k_1k_2e^{-2Dt}}\right] \frac{\sin t\, J_1(t)}{t^2}\,dt \quad [23]$$

where

$$D = \frac{d}{a} = \frac{h_2 - h_1}{a} = H_2 - H_1,\ R = \frac{r}{a},\ \text{and}\ Z = \frac{z}{a} \quad [24]$$

These functions can be integrated as a convergent series for $\theta_1(t/a)$ can be found. The series can be integrated term by term and values for V_1 $(R,0)$ and V_S can be found from the new series. However, in practice it was found to be much quicker to integrate the functions numerically using Simpson's rule rather than sum the series.

The three-point spreading resistance probe as commonly used in our laboratory (22) is shown in Fig. 2. Current is passed between the inner probe and one of the outer probes. The voltage is measured between the inner probe and the other outer probe. By superposition, the measured voltage will be given by

$$\Delta V_2 = V_S - 2V_1(s,0) + V_1(2s,0) \quad [25]$$

Superposition is valid in this situation since the probe spacing is large compared to the radius of contact.

Using the values given in Eq. [22] and [23]

$$\Delta V_2 = \frac{I\rho_1}{4a}$$

$$\left\{\frac{4}{\pi}\int_0^\infty \left[\frac{1 + k_1e^{-2H_1t} + k_2e^{-2H_2t} + k_1k_2e^{-2Dt}}{1 - k_1e^{-2H_1t} - k_2e^{-2H_2t} + k_1k_2e^{-2Dt}}\right] \sin t\left[\frac{J_1(t)}{t^2} - \frac{J_0(St/2)}{t} + \frac{J_0(St)}{2t}\right] dt\right\} \quad [26]$$

where

$$S = 2s/a$$

Or,

$$\Delta V_2 = \frac{I\rho_1}{4a} I_2 \quad [27]$$

Since $I\rho_1/4a$ is the normal spreading resistance obtained from a flat circular contact on an infinitely thick sample, I_2 is the appropriate correction factor. Numerically calculated values of I_2 are shown in Fig. 3 and 4 for two different probe spacings.

In these figures, note that the correction factor approaches one for large values of H_1. The case where $k_1 = 1$ is the insulating back surface condition and

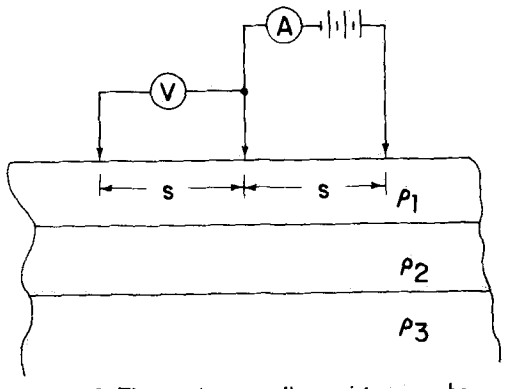

Fig. 2. Three-point spreading resistance probe

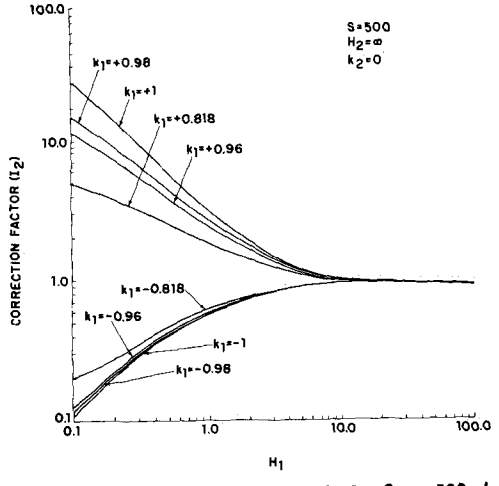

Fig. 3. Values of the correction factor I_2 for $S = 500$, $k_2 = 0$, and $H_2 = \infty$ plotted for various values of k_1 between ± 1 as a function of H_1.

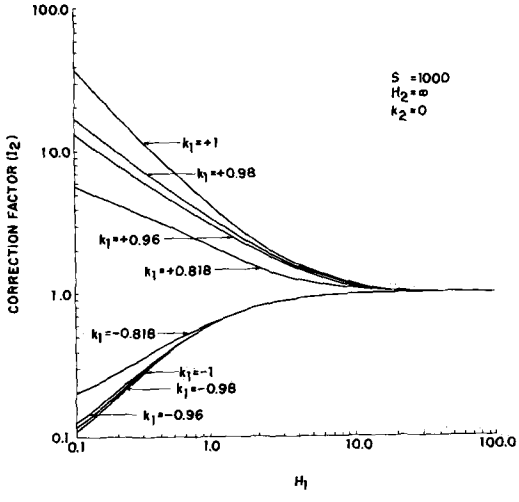

Fig. 4. Values of the correction factor I_2 for $S = 1000$, $k_2 = 0$, and $H_2 = \infty$ plotted for various values of k_1 between ± 1 as a function of H_2.

was solved by Dickey (13) using an image system. These values differ from Dickey's by about 25% at $H_1 = 0.1$ and 10% at $H_1 = 1.0$. Agreement is good at large H_1. This is due to the inaccuracy of his image system which renders it only applicable for large H_1. For the case where $k_1 = -1$, conducting back surface, good agreement is obtained between these solutions and results published by Foxhall and Lewis (12). As would be expected, this solution also goes to the cylinder resistance for small H_1.

The function I_2 was also calculated for $k_2 = \pm 1$, and the dependence on D studied. There is very little dependence on this parameter in most cases. The same

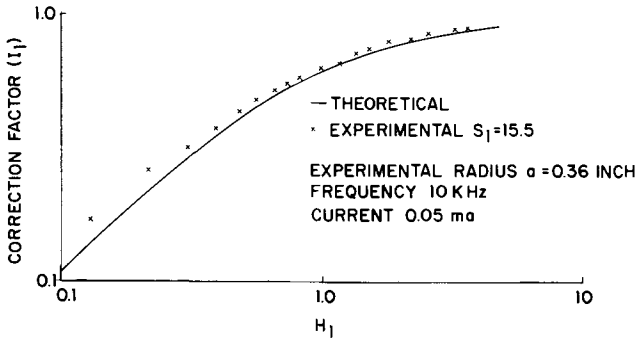

Fig. 5. Comparison of experimentally obtained correction factor from an electrolytic tank with theoretical values for $a = 0.36$ in., $S = 15.5$, $I = 0.05$ ma, and $f = 10$ kHz.

is true of the probe spacing as noted by comparing Fig. 3 and 4.

A useful method of checking these results is the electrolytic tank. A tank was constructed which could hold a 0.01M KCl aqueous solution with a nominal resistivity of 700 ohm-cm. For the conducting back surface case, $k_1 = -1$, the results are shown in Fig. 5. An a-c power supply was used and operated at a frequency of 10 kHz at a current of 0.05 ma. Good agreement is obtained between the experimentally and theoretically determined correction factors. The experimental value was obtained by measuring the resistivity of the solution with a four-point probe. Then knowing the resistivity and depth of the solution, an experimental correction factor can be obtained. The slight divergence at small H_1 is probably due either to measurement errors in the depth of the solution or to the fact that the conducting back surface was neither perfectly conducting nor infinitely thick.

Solutions to this type of problem have been obtained for more complicated geometries and an extrapolation to N layers has been obtained where N is the number of layers of different resistivity and finite thickness. With a many layered solution, approximations can be made to graded profiles through the use of step functions. Such a case is shown in Fig. 6. Here various approximations up to $N = 4$ are made to an exponential resistivity profile that decreases from a value of 0.5 ohm-cm at the surface to 0.0050 ohm-cm at the interface in a distance of $H_1 = 2.0$. The resultant correction factor was calculated for each case and is shown in Fig. 7 as a function of the number of layers

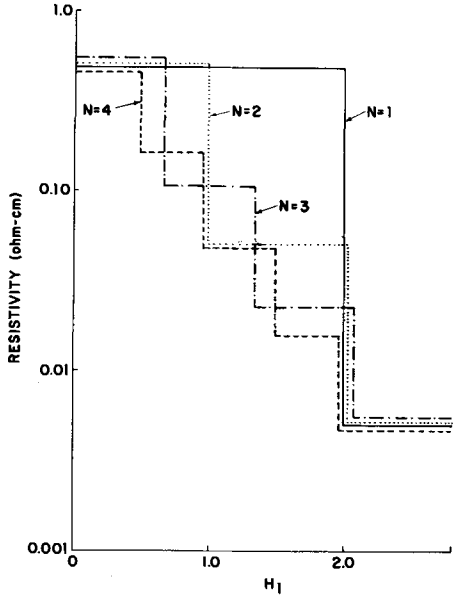

Fig. 6. Step function approximation to an exponential profile. The value of resistivity at the surface is 0.5 ohm-cm and at the interface is 0.005 ohm-cm.

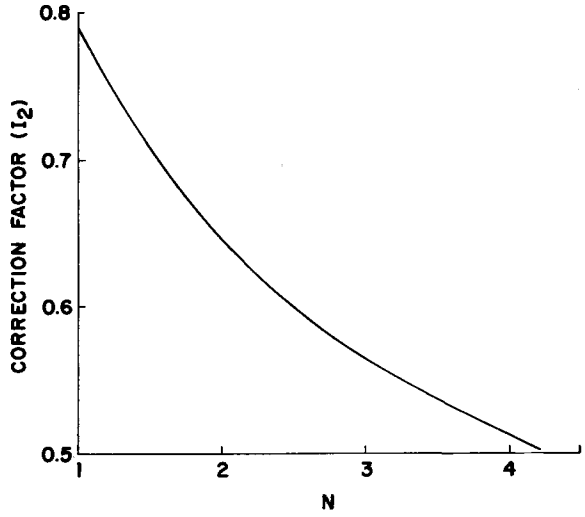

Fig. 7. Correction factor for approximated decreasing experimental resistivity profile plotted as a function of the number of layers used for approximation.

or steps. It is apparent that there is a strong dependence on the profile and that care must be taken in interpreting resistivity profiles obtained with a spreading resistance probe. This is certainly an area for further investigation.

An outline of the solution to the potential distribution due to a finite area contact on a multilayered structure has been given. It was applied only to a particular version of the three-point spreading resistance probe. The same solutions are applicable to all the four-point potentiometric probes, inline, square, over-under, and delta, and to all the spreading resistance probes, two-point, another three-point, and one-point. In all cases where other valid solutions have been found, this solution will converge to the published values if appropriate limits are taken. In addition, it provides a much wider range of application and can be extended to finite horizontal geometries through images and to N layers.

The application of the mathematics to the physical situation leaves some question. Perhaps the largest unanswered question is whether Laplace's equation is a valid representation of the physics when semiconductors are used. Also, there is much yet to be done with graded profiles rather than the step changes required by this analysis. However, in the use of the mathematics to problems such as the spreading resistance, good experimental agreement has been found between this and other techniques (21, 22). It would seem then that the mathematics is a fairly good approximation to reality in most cases. Great care must be used though in indiscriminate use of the integrals as each limit and assumption must be analyzed for that specific problem.

Acknowledgment

The authors would like to acknowledge the contributions of E. F. Gorey in much of the experimental work. They also would like to recognize the efforts of W. H. Stocklin, C. Sakkas, and H. Young for the programming of the IBM 7090 computer for the numerical solutions presented.

Manuscript submitted June 6, 1968; revised manuscript received Aug. 26, 1968. This paper was presented in part at the Philadelphia Meeting. Oct. 10-14, 1967, as Paper 165.

Any discussion of this paper will appear in a Discussion Section to be published in the December 1969 JOURNAL.

REFERENCES

1. L. B. Valdes, *Proc. IRE*, **42**, 420 (1954).
2. A. Uhlir, *Bell Syst. Tech. J.*, **34**, 105 (1955).
3. F. M. Smits, *ibid.*, **37**, 711 (1958).

4. L. J. Swartzendruber, N.B.S. Report 8066 (1963).
5. P. A. Schumann and L. S. Sheiner, *Rev. Sci. Instr.*, **35**, 959 (1964).
6. F. Keywell and G. Dorosheski, *ibid.*, **31**, 833 (1960.
7. M. A. Logan, *Bell Syst. Tech. J.*, **40**, 885 (1961).
8. D. E. Vaughan, *Brit. J. Appl. Phys.*, **12**, 414 (1961).
9. L. J. Swartzendruber, N.B.S. Technical Note 199 (1964).
10. L. J. Swartzendruber, N.B.S. Technical Note 241 (1964).
11. A. Gray, G. B. Mathews, and J. M. MacRobert, "A Treatise on Bessel Functions," MacMillan and Co., London (1952).
12. G. F. Foxhall and J. A. Lewis, *Bell System Tech. J.*, **43**, 1609 (1964).
13. D. H. Dickey, Paper presented at the Pittsburgh Meeting of the Society, April 15-18, 1963, Paper 57.
14. J. N. Hummel, *Z. Geophysik*, **5**, 89 (1929).
15. J. N. Hummel, *ibid.*, **5**, 288 (1929).
16. S. Stefanesco and C. N. Schlumberger, *J. Phys.*, **1**, 132 (1930).
17. W. R. Smythe, "Static and Dynamic Electricity," McGraw-Hill Book Co., New York (1950).
18. P. A. Schumann and J. F. Hallenback, *This Journal*, **110**, 538 (1963).
19. R. G. Mazur and D. H. Dickey, *ibid.*, **113**, 255 (1966).
20. E. E. Gardner, Paper presented at the Buffalo Meeting of the Society, Aug. 11-14, 1965, Paper 101.
21. E. E. Gardner, Paper presented at Symposium on Manufacturing In-Process Control and Measuring Techniques for Semiconductors in Phoenix, March 9-11, 1966.
22. E. E. Gardner, P. A. Schumann, and E. F. Gorey, Paper presented at the Philadelphia Meeting of the Society, Oct. 10-14, 1966, Paper 139.
23. E. E. Gardner, J. F. Hallenback, and P. A. Schumann, *Solid-State Electronics*, **6**, 311 (1963).
24. P. A. Schumann, and E. E. Gardner, *Trans. AIME*, **233**, 602 (1965).
25. S. P. Morgan and F. M. Smits, *Bell System Tech. J.*, **39**, 1573 (1960).
26. Y. F. Chang, *Solid State Electronics*, **10**, 281 (1967).
27. H. K. Gummel and D. L. Scharfetter, *J. Appl. Phys.*, **38**, 2148 (1967).

Polymorphism in Silver Telluride at High Pressures and Temperatures

Mario D. Banus* and Mary C. Finn

Lincoln Laboratory,[1] Massachusetts Institute of Technology, Lexington, Massachusetts

ABSTRACT

The phase diagram of Ag_2Te at pressures to 40 kbar and temperatures to 300°C has been determined by resistivity, DTA, and x-ray diffraction measurements. Two high-pressure phases were found. Ag_2Te II, which has a resistivity ~4 times that of the atmospheric pressure monoclinic phase Ag_2Te I, is stable between 22 and 25 kbar. Ag_2Te III appears above 25 kbar. Its resistivity is about half that for Ag_2Te I. X-ray diffraction patterns for both high-pressure phases can be indexed on tetragonal cells with different lattice parameters.

The structures of Ag_2Se and Ag_2Te are orthorhombic and monoclinic, respectively, at room temperature. The electrical properties of both chalcogenides could best be studied by measurements on single crystals. However, it is not possible to grow single crystals of the room-temperature phases from the melt because each has a transformation to a face-centered-cubic phase at 133° and 148°C, respectively. When melt-grown single crystals are cooled through this transformation, they become highly polycrystalline. Since the molar volume increases on entering the high-temperature phase, the application of pressure raises the transition temperature from the low-temperature phase. If the phase boundary intersected the liquidus at a higher pressure, single crystals of the desired phase might be grown from the melt under pressure. [The polymorphism of stoichiometric Ag_2Te at atmospheric pressure is complicated by a second transformation to a body-centered-cubic phase occurring at 802°C, near its melting point (1, 2).]

A pressure-temperature phase study of Ag_2Se (3) was carried out by measuring the change of resistivity with temperature and pressure to 48 kbar. This showed that the rate of increase of the transition temperature between the orthorhombic and face-centered-cubic phase decreased with increasing pressure, so that this phase boundary was not expected to meet the liquidus. Resistivity measurements and x-ray diffraction studies, which were made to over 50 kbar at room temperature, showed no change from the low-temperature orthorhombic phase.

Preliminary experiments by the same methods on Ag_2Te showed a somewhat steeper initial slope for the boundary between the monoclinic and face-centered-cubic phases, and also gave evidence for additional phases at high pressure. This paper reports a more detailed investigation of the pressure-temperature phase diagram of Ag_2Te by electrical resistivity, differential thermal analysis, and x-ray diffraction measurements.

Experimental

All experiments were performed on samples cut from an n-type ingot, grown from the melt by the horizontal Bridgman technique. The composition of the ingot is very close to stoichiometric, since the carrier concentration is only 1 x $10^{17}/cm^3$. [It is necessary to specify the composition because the transition temperature between the Ag_2Te phases at atmospheric pressure depends strongly on sample stoichiometry. Thus, it was reported (1, 2) that the temperature of the monoclinic to face-centered cubic transition decreases from 145° ± 3°C on the Ag-rich side to 105°C on the Te-rich side of the stoichiometric compound.] Electrical resistivity (four-lead) and differential thermal analysis measurements under hydrostatic pressures to 18 kbar and temperatures to about 400°C were made in a 1-in.-diameter by 4-in.-high piston-cylinder device using isopentane or a mixture of isoamyl alcohol and n-pentane as the pressure-transmitting fluid. A carefully insulated resistance-wound furnace surrounded the sample inside the pressure chamber. The maximum temperature was limited by the thermal decomposition of the liquids. Resistivity measurements under hydrostatic conditions to 28 kbar and temperatures to about 100°C were made in a liquid cell (4) containing the same liquids. This cell was heated by circulating hot oil through the jacket around the cylinder restraining rings. Temperatures in both devices

* Electrochemical Society Active Member.
[1] Operated with support from the U.S. Air Force.

were measured with Cr-Al thermocouples in thermal contact with but electrically isolated from the specimens. No corrections were made for the effect of pressure on the emf of the thermocouples.

The structures of the phases have been studied by obtaining x-ray diffraction powder patterns for samples squeezed between diamond Bridgman anvils of the type first described by Piermarini and Wier (5). Since the anvil configuration results in substantial pressure gradients across the sample, more than one phase may be present. Even with a finely collimated x-ray beam, portions of more than one phase may be intercepted by the beam, especially if one of the phases has a very narrow pressure range. Where the unknown structures have symmetries other than cubic or close-packed hexagonal, however, patterns which are unambiguously single phase are essential for correct indexing. The problem was solved by using the Bassett modification of the diamond anvil squeezer (6) which permits visual observation of the phases with a metallographic microscope. Since the Ag_2Te is not transparent, reflected light, either normal or polarized, was used. Figure 1 is a photomicrograph taken through the anvil diamond showing the three phases of Ag_2Te. The desired phase could be positioned in the area of the x-ray beam by changing the loading on the piston diamond while observing the growth, disappearance, or movement of the phases. It was necessary to wait for about 24 hr after a pressure change to allow phase change or motion to go to completion. Sample flow or kinetics of the phase transformations may have caused the slow change in phase locations. Photomicrographs made before and after the 200-300 hr exposures for the x-ray diffraction patterns showed that no further changes took place during the exposures.

Results and Discussion

Phase diagram.—In our first experiments, the resistivity was measured as a function of temperature at various fixed pressures between atmospheric and 16 kbar. The phase change to face-centered-cubic Ag_2Te with increasing temperature was readily observed by the sharp increase in resistivity, fourfold at 1 atm, accompanying this transformation (Fig. 2). The transition temperature was found to increase smoothly from 148° ± 1°C at atmospheric pressure to 193° ± 3°C at 6 kbar. This increase was expected because the molar volume is greater for the face-centered-cubic phase than for the monoclinic phase. At about 8 kbar, however, there was an abrupt increase in the slope of the transition temperature *vs.* pressure curve (*see* Fig. 4, below). In order to check this unexpected result, the transition temperatures were then determined by means of differential thermal analysis measurements. The results of these measurements are in good agreement with the resistivity data. The shape of the temperature-pressure curve suggested the presence of a triple point at about 8 kbar, resulting from the intersection with the boundary of a high-pressure phase.

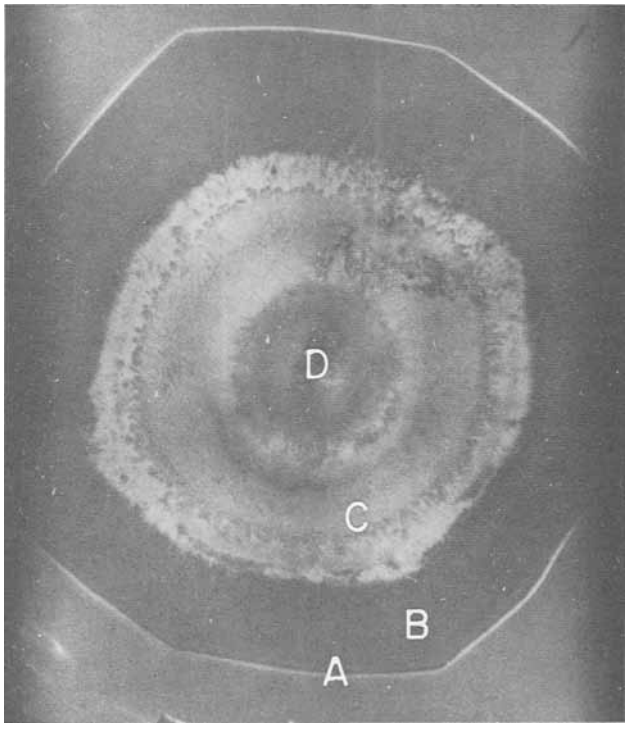

Fig. 1. Photomicrograph of Ag_2Te pressed between diamond Bridgman anvil faces and viewed by reflected light: *A*—outline of 0.5-mm-diameter piston-diamond face; *B*—Ag_2Te I; *C*—Ag_2Te II; *D*—Ag_2Te III.

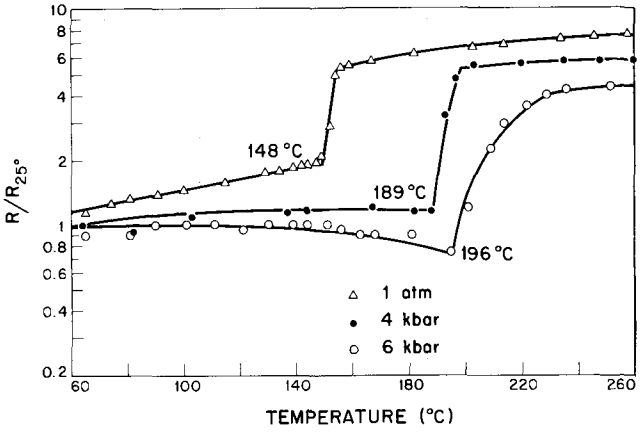

Fig. 2. Relative resistivity of Ag_2Te vs. temperature at constant pressure. Temperatures for monoclinic to fcc transition indicated.

Resistivity *vs.* pressure measurements were then made at room temperature to confirm the existence of a high-pressure phase. These measurements show an abrupt increase in resistivity by a factor of 4 at 22.0 ± 0.5 kbar, followed by an abrupt decrease by a factor of 7 at 25.0 ± 0.5 kbar. The resistivity-pressure curves (Fig. 3) are very similar in shape to the curves for cesium (7) used to establish the phase boundaries of cesium III, which has a pressure stability range of only 1.5 kbar at room temperature. These curves therefore indicate that transformations occur first to a phase (Ag_2Te II) of higher resistivity than the monoclinic phase (Ag_2Te I) and then to a phase (Ag_2Te III) with the lowest resistivity.[2] With increasing temperature, the magnitude and sharpness of the resistivity changes decrease so that accurate phase boundary data cannot be obtained by resistivity *vs.* pressure measurements above ~75°C. However, at 8 and 10 kbar, resistivity *vs.* temperature curves showed changes in slope which are characteristic of phase changes, although it is more difficult to determine the precise temperature of the transition.

The pressure-temperature diagram based on these data is shown in Fig. 4. The slope of the boundary between Ag_2Te II and Ag_2Te III suggests that it is this boundary which gives the triple point at 8 kbar and 200°C. Thermodynamic considerations require a second triple point including Ag_2Te I. However, the data are not sufficient to show whether this point is between Ag_2Te I, II, and III at about 10 kbar and 175°C or between Ag_2Te I, II and the face-centered cubic phase very close to the triple point shown. In the latter case, the I-II and II-III boundaries do not intersect. The phase diagram shows that it is not possible to grow

[2] We have adopted Roman numerals to designate these phases because this is the customary usage in the literature on high-pressure research. It should be noted that Frueh has used Roman numerals to identify the three phases of Ag_2Te which are stable at atmospheric pressure, but this procedure has not been followed by other investigators of Ag_2Te, and it is contrary to the usual practice of designating atmospheric pressure phases by lower-case Greek letters.

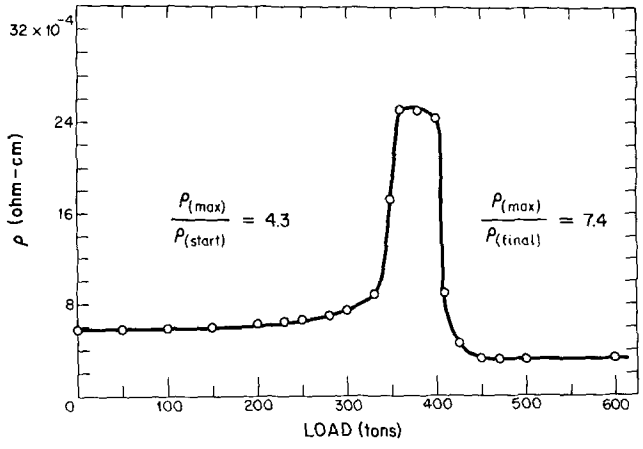

Fig. 3. Resistivity (four-lead) vs. increasing load for Ag_2Te in hydrostatic system at 25°C; 330 tons corresponds to 22 kbar and 410 tons corresponds to 25 kbar.

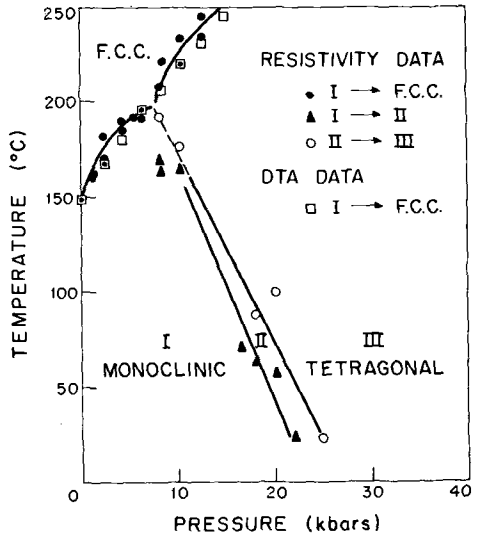

Fig. 4. Pressure-temperature phase diagram of Ag_2Te from resistivity and DTA data.

crystals of the room temperature Ag_2Te I phase from the melt at high pressure.

Resistivity measurements (four-lead) were also made at room temperature to ~90 kbar in a quasihydrostatic system using AgCl as the pressure medium. The abrupt resistivity changes at 22.5 and 25 kbar were duplicated. Above 26 kbar, the resistivity increases slowly by about 15% to a maximum between 44 and 48 kbar, then gradually decreases by ~20% to 90 kbar. These small gradual changes probably do not result from further structural changes but rather from the effect of pressure on the conduction mechanism, complicated by decreases in sample dimensions due to compression.

Structure of high-pressure phases.—The diffraction patterns of both high-pressure phases have been indexed on tetragonal cells. A summary of the d-spacings and indexing is given in Table I. Table II lists the lattice parameters and densities of Ag_2Te I, II, and III. The diffraction pattern at atmospheric pressure agrees with the pattern for monoclinic structure reported by Frueh (8). There is an increase in density of 12% between Ag_2Te I at 1 atm and Ag_2Te II at 24 kbar, part of which is due to the compressibility of the monoclinic structure. The 5% density increase between Ag_2Te II at 24 kbar and Ag_2Te III at ~40 kbar is probably due mostly to the change in molar volume at the transition rather than to compressibility.

Table I. Indexing of x-ray patterns for high-pressure Ag_2Te-II and Ag_2Te-III

hkl	Ag_2Te-II d-spacing (Å)	Intensity	hkl	Ag_2Te-III d-spacing (Å)	Intensity
002	3.06	0.5	310, 221	2.78	0.5
300	2.95	9	301, 112	2.67	1
310	2.82	10	311	2.53	10
311	2.57	4	202	2.46	1
202	2.51	<0.5	400	2.17	8
321	2.31	1	410, 302	2.11	8
400	2.25	1	411	1.99	<0.5
302, 410	2.15	<0.5	322	1.90	0.5
330	2.10	<0.5	213	1.80	<0.5
411, 003	2.04	8	402	1.76	<0.5
113	1.94	5	511	1.65	<0.5
402	1.80	0.5	521	1.56	0.5
510	1.75	<0.5	440	1.53	0.5
511	1.70	0.5	413	1.46	<0.5
313	1.65	<0.5	423	1.40	0.5
521	1.60	<0.5	324	1.29	0.5
530	1.53	1	424, 115	1.20	0.5
610	1.47	2	524	1.10	<0.5
620	1.41	1			
541	1.36	1			
513	1.31	2			
700	1.28	1			
711, 640	1.24	<0.5			
721	1.20	<0.5			
722	1.14	<0.5			
810	1.11	<0.5			

Table II. Phases of Ag_2Te

I Monoclinic (1 atm)	II Tetragonal (24 kbar)	III Tetragonal (40 kbar)
a = 8.13Å	a = 8.92Å	a = 8.68Å
b = 4.48		
c = 8.09	c = 6.09	c = 6.09
β = 112°55′	c/a = 0.68	c/a = 0.70
M = 4	M = 8	M = 8
ρ = 8.40 g/cc	ρ = 9.41 g/cc	ρ = 9.91 g/cc

The space groups for the high-pressure phases have not been determined. Although the two phases have the same c-parameter and similar a-parameters, they probably have different space groups, since the intensity distribution is quite different for the two diffraction patterns. For example, compare the 310, 311, 400, and the 410, 302 doublet reflections. The electrical and optical properties emphasize the sharp difference between these two phases. The structure of Ag_2Te III appears to be isotypic with that of high pressure Ag_2S (9), the space group of which has not been determined either. The ratio of the unit cell volumes between Ag_2Te III and the high pressure Ag_2S (1.31) is similar to the ratio of the atomic volumes for tellurium and sulfur (1.32). Thus, in its high-pressure behavior, Ag_2Te appears to be similar to Ag_2S rather than to Ag_2Se, which has no high-pressure phases to more than 45 kbar (3).

Acknowledgments

The authors are pleased to acknowledge the assistance of Messrs. T. E. Stack and R. Westberg in carrying out the high-pressure measurements, and thank Mrs. M. J. Button for reading the x-ray diffraction patterns. We thank, also, Dr. A. J. Strauss for providing us with the ingot of Ag_2Te.

Manuscript submitted July 19, 1968; revised manuscript received Sept. 19, 1968. This manuscript was presented at the Boston Meeting, May 5-9, 1968, as Paper 73.

Any discussion of this paper will appear in a Discussion Section to be published in the December 1969 JOURNAL.

REFERENCES

1. A. J. Frueh, Jr., *Am. Mineralogist*, **46**, 659 (1961).
2. F. C. Kracek, C. J. Ksanda, and L. J. Cabri, *ibid.*, **51**, 14 (1966).
3. M. D. Banus, *Science*, **147**, 732 (1965).

4. A. Jayaraman, A. R. Hutson, J. H. McFee, A. S. Coriell, and R. G. Maines, *Rev. Sci. Instr.*, **38**, 44 (1967).
5. G. J. Piermarini and C. R. Wier, *J. Res. Nat. Bur. Stds.*, **66A**, 325 (1962).
6. W. A. Bassett, T. Takahashi, and P. W. Stook, *Rev. Sci. Instr.*, **38**, 37 (1967).
7. A. Jayaraman, R. C. Newton, and J. M. McDonough, *Phys. Rev.*, **159**, 527 (1967).
8. A. J. Frueh, Jr., *Z. Krist.*, **112**, 44 (1959).
9. L. H. Adams and B. L. Davis, *Am. J. Sci.*, **263**, 363 (1965).

Electron Beam Exposure of Silicones

Yasuo Yatsui, Toshitake Nakata, and Kazuo Umehara

Research and Development Center, Sanyo Electric Company, Ltd., Hirakata, Osaka, Japan

ABSTRACT

An investigation has been carried out on silicone etch-resists which can be exposed by electron beam irradiation. Thin silicone films with a thickness of about 5000 and 10,000Å were irradiated by scanning electron beam accelerated at 10 and 25 kv, over defined area. The thicknesses of silicone films after development were measured for each different irradiation charge density; thus the exposure characteristics of a few kinds of silicones were obtained. With the most sensitive silicone, methylvinylpolysiloxane, it was possible to form developed pattern with irradiation charge density 8.8 x 10^{-7} coulombs/cm^2 at 10 kv. The chemical resistances of the electron beam irradiated silicone films to the chemical reagents which were thought to be the constituents of common etchants were also investigated. It has been shown that flood-beam irradiation onto the developed silicone films was effective to increase chemical resistance and adhesive force to the substrate. Such silicone resists are practically useful to almost all etchants other than sulfuric acid.

It has been well known that electron beam irradiation causes cross-linking of polymers (1). In several alterations of the chemical and physical natures of the cross-linked polymers, the change of polymer solubility to organic solvents can be utilized for the formation of submicron sized etch-resist patterns by sectional electron beam irradiation over the polymer films.

Etch-resists that have been used for the above mentioned purposes were in almost all cases photosensitive resins which can be cross-linked essentially by uv light irradiation; these resins are also successsfully cross-linked by electron beam irradiation (2). If other materials having high sensitivities not to uv light but to the electron beam, and having good resistance to acids and alkalis were obtained, these materials would be better for electron beam sensitive etch-resists.

As the silicones are among the more chemically stable classes of compounds, cross-linking of a few kinds of silicones by electron beam irradiation was tried for the formation of the etch-resists. Although some experiments have been done to form silicone films by electron beam irradiation, their processes were fairly slow since silicones were supplied onto the surface of substrate from vapor phase along with electron bombardment (3-11). In other experiments the precoated organosilicon compound, triphenylsilanol, was polymerized by electron beam, but its sensitivity was also low (12-13). Recently it was proposed to use electron beam irradiated silicones as diffusion barriers (14).

To put silicones to practical use as etch-resist, the following conditions should be met: (*i*) the possibility of making thin and uniform silicone films with a thickness less than 1μ; (*ii*) high cross-linking sensitivity by electron beam irradiation; (*iii*) good chemical resistances of the cross-linked silicones. As a result of investigations concerning the radiation chemistry of polymers, it has been shown that the polymerization degree and the organic groups contained in polymers play important roles in cross-linking by irradiation (15), and so several silicones having different polymerization degree and organic groups were employed.

Experimental Procedure

The electron beam apparatus used in the experiments was Japan Electron Optics Laboratory's JSM type scanning electron microscope. Although this apparatus can form a fine electron beam with diameter less than 0.1μ, the electron beam was focused to 1-2μ diameter, so as to obtain uniform exposure over the area of raster scan which was nearly square.

Exposing charge density is given by

$$Q\,(\text{coulombs/cm}^2) = i \times t/s$$

where i is the electron beam current in amperes, t is the scanning time in seconds, and s is the scanning area in square centimeters. To vary the exposing charge density, ranging from 10^{-8} to 10^{-4} coulombs/cm^2, the scanning time and scanning area were varied with the beam current held constant.

Exposure conditions by the electron beam were as follows: beam current, 10^{-10} amp; accelerating voltage, 10 and 25 kv; scanning area, 4 x 10^{-4} — 10^{-2} cm^2; scanning time, 1.1-1279 sec; scanning lines, 125, 250, and 500 lines/frame.

The silicones used in the experiments and their properties are listed in Table I.

Silicones were dissolved into isoamylacetate which was found to be the most suitable solvent for the silicones; solutions were spun onto mirror-polished silicon slices, after which the solvent was volatilized thoroughly at room temperature. If the dilution rate was appropriate, uniform films with arbitrary thicknesses from 500 to 20000Å were easily obtained by this method. In the following experiments 5000 or 10000Å films were employed. After the drying was completed samples were inserted into the scanning electron microscope and subjected to the electron beam irradiation. Irradiated samples were then soaked in isoamylacetate for 2 min for the purpose of development. The residual film thickness after development will depend on the quantity of the irradiation charge. Development longer than 2 min made no observable change in residual film thicknesses determined by the exposure conditions. For the expression of the exposure characteristics of silicones for electron beam irradiation, the relations between the irradiation charge density and film thickness remaining after development were adopted. Resist removal during development was uniform over the entire exposed surface, whether the irradiation charge densities are high or low. Because the thicknesses of the exposed film areas were too small to measure by an interferometer, interference color was

Key words: electron beam exposure, etch-resist, silicone.

Table I. Silicones used in the experiments

Silicones	Organic groups	Remarks
SH 200 (10^5 c.s.)[1]	Methyl	Oil, polymerization degree 1400[3]
SH 200 (2.5×10^6 c.s.)[1]	Methyl	Oil, polymerization degree 2600[3]
TSE 200[2]	Methyl	Gum, polymerization degree 15000-20000
SH 410[1]	Methyl, vinyl	Gum, vinyl; more than 1 m/o ?[4]
SH 430[1]	Methyl, vinyl	Gum, vinyl; less than 1 m/o ?[4]
SH 440[1]	Methyl, phenyl	Gum, phenyl; about 10 m/o ?[4]

[1] Toray Silicone Company, Japan.
[2] Tokyo Shibaura Electric Company, Japan.
[3] Calculated from viscosity.
[4] Precise data are not available.

adopted as the measure of thickness. Precise relations between interference colors and silicone film thicknesses on silicon substrates were obtained previously with relatively large area silicone films whose thickness could be measured by an interferometer. The same conditions were applied in all interference color observations.

Resistances of electron beam irradiated silicones to the common chemical agents were also examined. In these experiments, silicone films about 5000Å thick were employed. Since it had been shown in the preliminary experiment that flood-beam irradiation with high charge density after development increased chemical resistance and the adhesive force of silicones, charge densities irradiated prior to the chemical test were 10^{-5} and 10^{-4} coulombs/cm^2. Flood-beam irradiation corresponds to the postbake process of photosensitive resins. The irradiated silicone films were then immersed in chemical reagents for 15 min at room temperature, and diminution of film thickness was measured by interference color observation. Some errors in measurement would occur, for refraction constant may be altered by absorption of chemical reagent, and interference color may change independently with thickness. However these errors would be negligible.

Experimental Results

Exposure characteristics of silicones listed in Table I with thicknesses about 5000 and 10000Å for the electron beam accelerated at 10 and 25 kv are shown in Fig. 1-a, b as the relations between the charge density and the percentages of residual film thicknesses after the development relative to the thickness before development. The charge density which results in 90% residual film thickness is designated as efficient charge density, and for convenience these quantities may be used as the comparison of the sensitivities of silicones. Efficient charge densities of the silicones with thickness about 5000Å for the electron beam accelerated at 10 kv are listed in Table II.

Although the electron beam current was 10^{-10} amp in those cases, irradiation by an electron beam carrying 10^{-12} amp was also tried, but the exposure characteristics were identical with that obtained by the electron beam carrying 10^{-10} amp within the limits of experimental error. So we may conclude that there exists no reciprocity failure in the range of these electron beam currents.

The chemical resistances of silicones irradiated by the electron beam accelerated at 10 kv are listed in

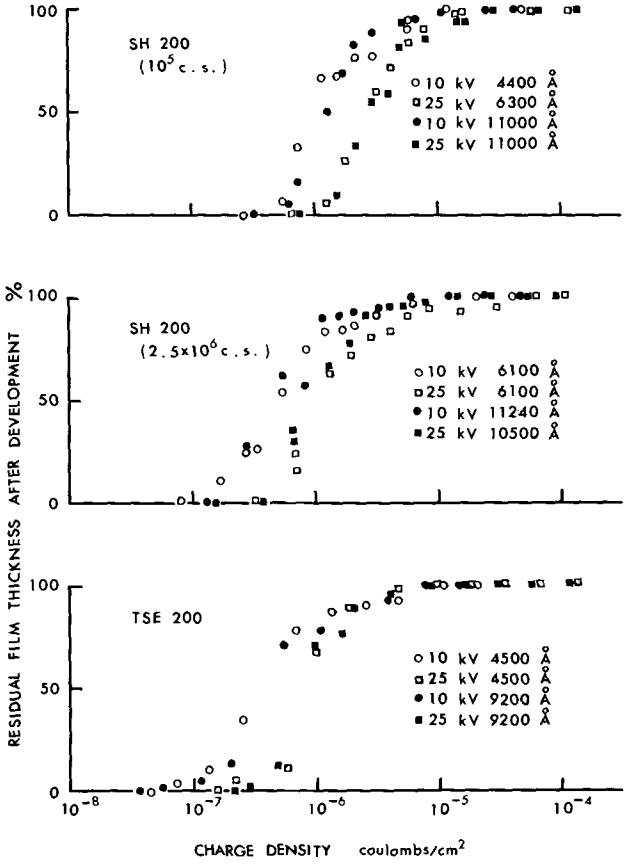

Fig. 1a. Exposure characteristics of silicones, SH 200 (10^5 c.s.), SH 200 (2.5×10^6 c.s.), and TSE 200.

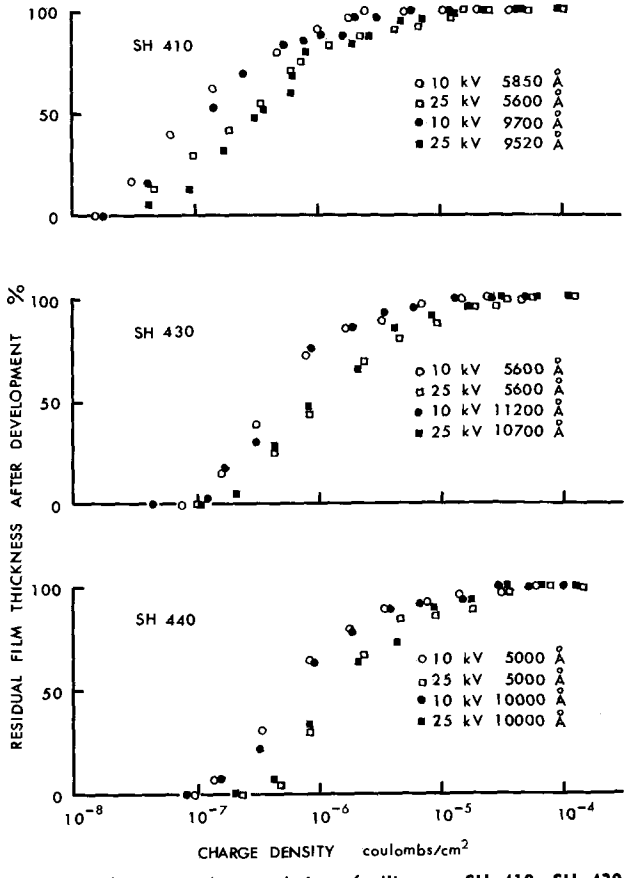

Fig. 1b. Exposure characteristics of silicones, SH 410, SH 430, and SH 440.

Table II. Efficient charge density for silicones

Silicones	Efficient charge density, coulombs/cm²
SH 200 (10^5 c.s.)	3.9×10^{-6}
SH 200 (2.5×10^6 c.s.)	2.9×10^{-6}
TSE 200	2.2×10^{-6}
SH 410	8.8×10^{-7}
SH 430	2.8×10^{-6}
SH 440	5.0×10^{-6}

Table III. In this table residual film thicknesses after immersion in chemical reagents for 15 min at room temperature are expressed in percentages relative to the film thickness before immersion (5000Å). The left-hand figures in each column are the results for films irradiated with 10^{-5} coulombs/cm² charge densities, and the right-hand figures for those with 10^{-4} coulombs/cm² charge densities. For the comparison, methylvinylpolysiloxane and dimethylpolysiloxane were also immersed in boiling trichloroethylene, but no dissolution or peeling were seen in these cases.

Although the silicone films were dissolved slowly in hydrofluoric acid (49%), they were dissolved very little in buffered etchant, and SiO_2 of which thickness was 3000Å was successfully etched without damage of resist films (Fig. 2).

To know the resolution of silicone resist, line exposure of SH 200 (10^5 c.s.) of which thickness was about 3000Å was carried out using 0.1μ electron beam, and developed pattern about 0.4μ was obtained as shown in Fig. 3. It was difficult to obtain a finer exposure line because of the spreading of exposure area by scattering of electrons in the resist and substrate.

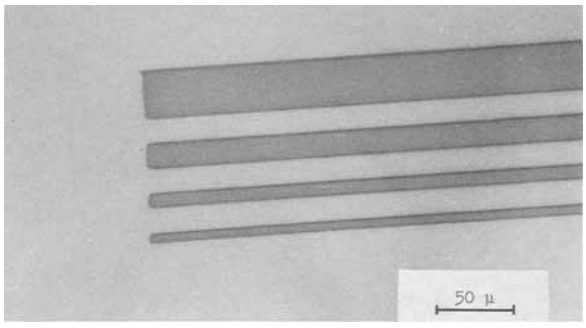

Fig. 2. Etching test of 3000Å SiO_2 by buffered etchant, using SH 200 (10^5 c.s.) resist, after stripping off the resist.

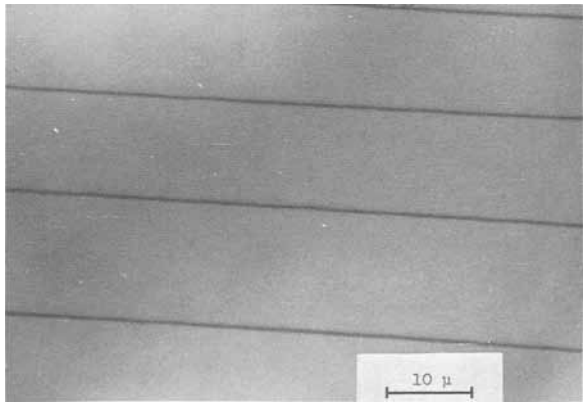

Fig. 3. Fine line pattern of SH 200 (10^5 c.s.), exposed by 0.1μ beam at 25 kv, after development. Line width is about 0.4μ.

Discussion and Conclusions

It can be seen that the silicones show decreasing sensitivity in the order of those having vinyl groups, methyl groups, and phenyl groups. Especially, methylvinylpolysiloxane thought to contain more than 1 m/o (mole per cent) vinyl groups shows a few times higher sensitivity than the conventional photoresists for electron beam exposure (16). The high sensitivity of methylvinylpolysiloxane to the electron beam is reasonable and to some extent anticipated. The relatively low sensitivity of methylphenylpolysiloxane may be explained by the radiation protective effect of phenyl groups for the cross-linking, which is well known in the study of radiation chemistry (17). According to this phenomenon, the energy transferred from the bombarding electron to the molecule, will be further transferred to the phenyl groups, and the bombarding energy is diminished without causing any chemical reaction. When more sensitive silicone is required, one containing phenyl groups must be avoided.

Comparison between silicones that have the same methyl groups but different polymerization degrees shows that one having higher polymerization degrees has higher sensitivity. However in the matter of contrast, silicones having higher polymerization degrees show poorer contrast than those having lower polymerization degrees.

Silicones were more sensitive to the electron beams accelerated at 10 kv than to those accelerated at 25 kv because the energy transfer to the resist per unit length increases as the energy of the incident electrons decreases. However no dependences on the film thickness were seen within the limits of experimental error.

The chemical resistance of silicones exposed to the electron beam is poor to sulfuric acid, and in this case films were dissolved completely in 1 min, so the silicone resist cannot be used in etchant containing sulfuric acid. Also some damage to the resist was seen with hydrofluoric acid and in a sodium hydroxide solution. However higher irradiation charge density provided by flood-beam irradiation improved the resistance to those reagents. For instance, in the case immersing TSE 200 in hydrofluoric acid for 15 min, films subjected to 10^{-4} coulombs/cm² irradiation showed only 33% decrease in thickness, while those subjected to 10^{-5} coulombs/

Table III. Residual film thicknesses expressed in percentage relative to those before immersion in chemical reagents
Left-hand figures in each column are the result for 10^{-5} coulombs/cm² irradiation
and right-hand figures are for 10^{-4} coulombs/cm² irradiation.

Chemical reagents	SH 200 10^5 c.s.	SH 200 2.5×10^6 c.s.	TSE 200	SH 410	SH 430	SH 440
Trichloroethylene	100%/100%	100/100	100/100	100/100	100/100	100/100
Methylalcohol	100/100	100/100	100/100	100/100	100/100	100/100
Sodium hydroxide (10%)	100/100[1]	100/100	0/0[3]	100/100	90/89	92/94[1]
Chromic acid (saturated)	100/100	100/100	100/100	100/100	100/100	100/100
Phosphoric acid (85%)	100/100	100/100	100/100	100/100	100/100	100/100
Hydrochloric acid (35%)	100/100	90/100	87/92	95/100	100/100	94/100
Hydrofluoric acid (49%)	54/82	59/79	33/67	78/77	86/85	43/85
Sulfuric acid (95%)	0/0[2]	0/0[2]	0/0[2]	0/0[2]	0/0[2]	0/0[2]
Nitric acid (65%)	100/100	100/100	87/92	100/100	100/100	100/100
Aqua regia	100/100	100/100	87/92	100/100	93/96	98/100

[1] Shrinking and partial peeling of the films were seen.
[2] Dissolved in 1 min.
[3] Films were lost by peeling.

cm^2 showed 67% decrease. Such silicone films come to have perfect resistance to the buffered hydrofluoric acid that is ordinarily used to etch SiO_2. Resistances to the other acids were excellent, and these facts demonstrate that the silicone films subjected to flood-beam after development are useful as an etch-resist for the etchants composed of the acids or alkalis listed in Table III except for sulfuric acid. The difficulty involved in stripping of the resists after etching may be anticipated as the result of excellent resistances to the organic solvents. To remove exposed resist films, swabbing with cotton after boiling in trichloroethylene for 20 min is required. Soaking in sulfuric acid at room temperature is also effective, if it is permissible.

It is expected that the oxygen atoms contained in silicones make strong metal-oxygen bonds at the interface of resist and substrate. In fact, adhesion of irradiated silicone films to a silicon substrate was excellent.

In conclusion, silicones can be good material for electron sensitive resist in place of the conventional photosensitive resists because of the high sensitivity to the electron beam, strong resistance to most chemical etchants, and good adhesion to the substrate.

Acknowledgment

The authors wish to express their thanks to H. Fukuda for his assistance in operating the scanning electron microscope, and to Dr. T. Hayashida for his encouragement during this work.

Manuscript submitted May 20, 1968; revised manuscript received Sept. 12, 1968.

Any discussion of this paper will appear in a Discussion Section to be published in the December 1969 JOURNAL.

REFERENCES

1. R. M. Black and E. H. Reynolds, *Proc. IEE*, **112**, 1226 (1965).
2. R. F. M. Thornley and T. Sun, *This Journal*, **112**, 1151 (1965).
3. R. W. Christy, *J. Appl. Phys.*, **31**, 1680 (1960).
4. L. Mayer, *ibid.*, **34**, 2088 (1963).
5. H. T. Mann, *ibid.*, **35**, 2173 (1964).
6. R. W. Christy, *ibid.*, **35**, 2179 (1964).
7. H. Holland and L. Laurenson, *Vacuum*, **14**, 325 (1964).
8. J. M. Hlavin, and R. A. Fotland, 1st Intern. Conf. on Electron and Ion Beam Sci. and Tech., 231 (1965).
9. G. W. Hill, *Microelectronics and Reliability*, **4**, 109 (1965).
10. D. S. Allam, C. T. H. Stoddart, and P. R. Stuart, *ibid.*, **5**, 19 (1966).
11. T. H. P. Chang and W. C. Nixon, *J. Sci. Instrum.*, **44**, 231 (1967).
12. K. R. Shoulder, P B Report, 171027.
13. T. P .Woodman, *Brit. J. Appl. Phys.*, **16**, 359 (1965).
14. E. D. Roberts, Presented at 3rd Intern. Conf. on Electron and Ion Beam Sci. and Tech.
15. A. Charlesby, *Proc. Roy. Soc.*, **A222**, 60 (1954).
16. K. Kanaya, K. Tanaka, and T. Yuasa, Proc. 6th Intern. Congr. Electron Microscopy, Kyoto (1966).
17. M. Koike, and A. Danno, *J. Phys. Soc. Japan*, **15**, 1501 (1960).

Carbon in Epitaxial Silicon

P. Rai-Choudhury,* A. J. Noreika, and M. L. Theodore

Westinghouse Research Laboratories, Pittsburgh, Pennsylvania

ABSTRACT

Epitaxial Si layers have been doped with carbon from a silicon tetrachloride-methane system, and the carbon content has been chemically analyzed. The levels of carbon content range from 9.7×10^{17} atoms C/cm^3 (undoped) through 2.6×10^{19} atoms C/cm^3 (moderate doping), to a saturation content which induces complete conversion to SiC. Influence of the carbon content on the crystalline perfection of the Si layers is found to be negligible up to concentrations of 10^{18} atoms C/cm^3; at concentrations near 10^{19} atoms C/cm^3 many polycrystalline inclusions are formed. Spreading resistance measurements which reveal doping profiles show significant increases in resistance only in layers which can show some change of phase. Direct evidence is presented demonstrating that the retention of carbon in the deposited layers is both by diffusion induced substitution and by chemical reaction. The retention of excess carbon interstitially is inferred.

Epitaxial Si layers, grown in the presence of carbon contaminants, are often observed to contain crystallographic defects. Some of these defects, *e.g.*, tripyramids, are presumed to arise from the formation of SiC platelets at the substrate surface (1,2). No data are available, however, which directly relate the carbon impurity concentrations to the type or number of defects which are formed.

Studies of carbon in bulk Si are more quantitative. Bulk Si, regardless of the method of preparation, has been reported to retain at least 3×10^{18} atoms C/cm^3 (3). This impurity level represents the substitutional saturation limit of carbon in Si at the melting point (3,4); hence, retention of this concentration at lower temperatures denotes a supersaturation of carbon in Si.

The present study seeks the following: (*i*) to confirm the quantitative measurements for concentrations of carbon in bulk Si; (*ii*) to extend these measurements to carbon in epitaxial Si deposits; (*iii*) to alter controllably carbon concentrations in epitaxial Si; and (*iv*) to correlate the relative numbers of observable defects with known carbon impurity concentrations.

* Electrochemical Society Active Member.

Experimental

Epitaxial layers of Si were grown in a conventional horizontal reaction chamber by the hydrogen reduction of $SiCl_4$ as well as by the pyrolysis of silane. Chemically polished Si(111) wafers were used as substrates. Heating of the substrates was done via the rf heating of a SiC coated graphite susceptor on which the substrates lay. Predeposit etching of the substrates with water vapor (5) was done *in situ*. Group V doping of the layers where desired was accomplished by injecting phosphine into the main gas stream. The source carbon supplied to the growing Si layers arrived via

the gas flow as a methane (CH_4)-hydrogen mixture. The partial pressure of silicon tetrachloride was held constant at 8 x 10^{-3} atm; all relative $(C/Si)_g$ ratios were produced by altering only the methane partial pressure.

The carbon contents of both the epitaxial deposits and the substrates (bulk) were analyzed chemically. The method of analysis (see Appendix) imposed a lower limit on the weight of the Si sample, *viz.*, 0.3g at which 20 ppma could be detected unambiguously. Two epitaxial layers from a single experiment with substrates removed provided the necessary 0.3g of Si.

The sirtl etch technique (6) and optical microscopy were used to note surface defects. Precipitates and/or inclusions were detected by transmission electron microscopy (TEM) of thin regions near the surface and identified where possible by transmission electron diffraction. The layers were subjected to both TEM and Lang topographical x-ray analyses to obtain a measure of crystalline perfection. Spreading resistance measurements gave resistance profiles (7) of the layers together with any resistance inhomogeneities which may have been carbon induced.

Results

The experimental data are presented relative to increasing levels of carbon (gas phase) doping. Carbon concentrations of the various silicon samples are presented in Table I and compared there to bulk data. The thicknesses of all deposits were nominally 200μ (grown at $\simeq$ 1 μ/min), the initial 70μ of which were deposited with no carbon doping. To provide a standard resistivity, all deposits were phosphorus doped to a level which would provide n-type, 30 ohm-cm Si.

$(C/Si)_g$ = 0.—With no intentional carbon doping, the carbon content of the epitaxial Si layers formed by the hydrogen reduction of $SiCl_4$ was 2.3 x 10^{18} atoms C/cm^3. This concentration was approximately half that observed in bulk specimens, the latter value comparing favorably with data published by Schink (3). Layers prepared by the pyrolysis of silane showed a still smaller carbon concentration, as noted in Table I.

The crystalline perfection of these layers was typically good. TEM studies and x-ray topographic examinations showed no precipitatelike inclusions or stacking faults. The observed dislocation densities were of the order of 10^2/cm^3.

$(C/Si)_g$ = 1/80; $(C/Si)_g$ = 1/34.—Specimens grown in both the $(C/Si)_g$ = 1/80 and $(C/Si)_g$ = 1/34 concentrations were physically very similar. Dislocation densities and resistivities of both differed negligibly from those of the deposits described in section 3.1. Unlike the latter (undoped) deposits, however, small, roughly circular inclusions occasionally appeared. The small size ($\sim$0.1 mm) and the sparse numbers ($< 1/cm^2$) made identification impossible. No attempt was made to characterize further these particular inclusions. The carbon content of deposits with $(C/Si)_g$ = 1/34 was 3 x 10^{18} atoms C/cm^3 concentration measurements were not made on the $(C/Si)_g$ = 1/80 specimens.

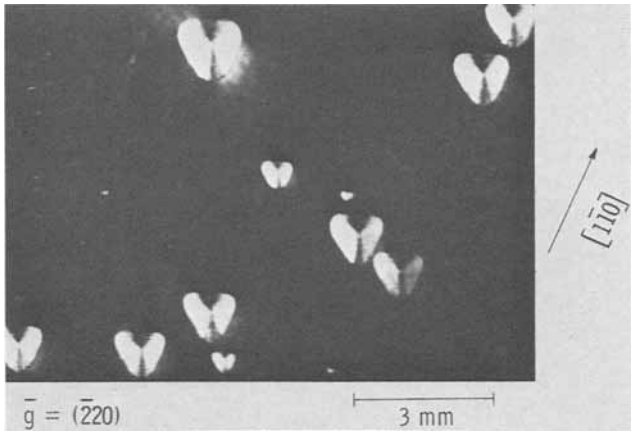

Fig. 1. X-ray topograph of an epitaxial Si layer doped with moderately high level of carbon. Triangular features correspond to polycrystalline inclusions.

$(C/Si)_g$ = 3/10.—At $(C/Si)_g$ = 3/10 the carbon concentration was found to be 2.6 x 10^{19} atoms C/cm^3. Visual observation of the deposited surfaces showed the epitaxial layer to be interspersed with large equilateral triangular shapes. Analyses of electron diffraction patterns of thinned surface regions of these areas identified them as mixed polycrystalline regions of Si and graphite. It is possible, however, that regions more removed from the surface may have had sufficient time to form SiC during the extended growth period. Normal edge dimensions of the triangular shapes ranged from 0.3 to 1.5 mm, the larger ones being more numerous. Figure 1, a Lang x-ray topograph, shows the general two-dimensional shape of these regions and indicates an intense strain at their junction with the epitaxial deposit. The figure also shows, in marked contrast, the relative absence of additional strain-induced effects in the epitaxial component of the deposit, the dislocation density nominally being the same as in undoped layers. To determine the three-dimensional shape, the deposits were sectioned. When viewed in cross section, the polycrystalline regions again appeared triangular, the vertex angles being extremely obtuse, *viz.*, $\sim$ 170° - 175° and the maximum thickness being $\sim$ 140μ.

To gain some measure of the carbon content of the polycrystalline regions, the deposits were annealed in hydrogen for 6 hr at 1050°C. In the thinned regions of the triangular areas, after the anneal there was complete conversion of the Si to SiC (both α and β-forms, $\beta > \alpha$), *i.e.*, the carbon to Si ratio was at least unity. In the epitaxial region of the deposit, the anneal had precipitated the small agglomerates shown in the micrograph, Fig. 2. This region had been, prior to anneal, devoid of any contrast producing objects. The agglomerates failed to give an electron diffraction pattern, but the originally high concentration of carbon suggests they are carbon precipitation out of solid solu-

Table I. Carbon content of silicon

Sample No.	Method of silicon preparation	Approximate dislocation density, No./cm^2	Carbon concentration in silicon, atoms C/cm^3	Macroscopic effects of carbon on surface
1	Bulk, float zone	10^5	5.1 x 10^{18}	None
2	Bulk, Czochralski	0	5.9 x 10^{18}	None
3	Epitaxial silicon from $SiCl_4$, undoped	10^2	2.3 x 10^{18}	None
4	Epitaxial silicon carbon doped $(C/Si)_g$ = 1/34	10^2	3.0 x 10^{18}	Polycrystalline areas
5	Epitaxial silicon from $SiCl_4$, carbon doped, $(C/Si)_g$ = 3/10	10^2	2.6 x 10^{19}	Triangular polycrystalline areas
6	Epitaxial silicon from SiH_4, undoped	—	9.3 x 10^{17}	None

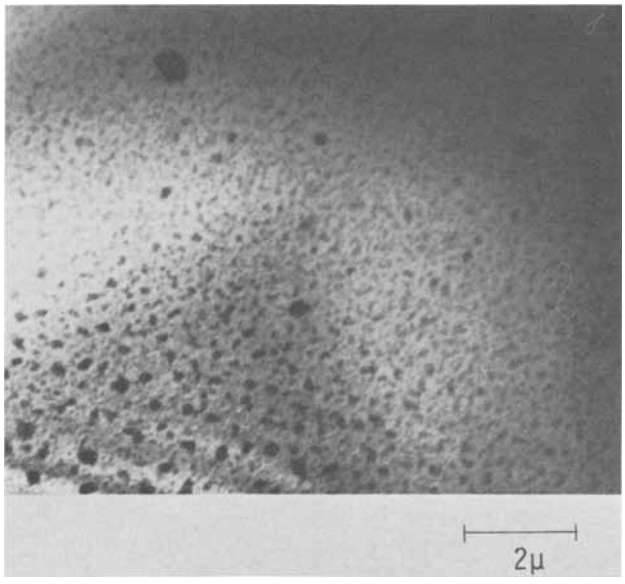

Fig. 2. Transmission electron micrograph of an annealed, carbon-doped, epitaxial deposit. Annealing temperature, 1050°C; depositing temperature, 1225°C.

tion. Resistivity measurements corresponded closely to those of undoped (carbon) deposits.

$(C/Si)_g = 1/2$.—Layers produced at this level of carbon doping mainly consisted of polycrystalline regions of Si and graphite; the epitaxial component of the deposit represented about 30% of the surface area. The polycrystalline regions possessed no simple geometric shapes. Average resistivities continued to be of the order of 30 ohm-cm.

$(C/Si)_g = 1$.—At $(C/Si)_g = 1$, the deposit was completely polycrystalline. Electron diffraction showed the presence of both Si and SiC. Spreading resistance measurements showed a marked increase in resistance at the onset of carbon injection. The resistivity up to the time of carbon doping was 30 ohm-cm; the equivalent spreading resistance is 3.5×10^4 ohms; after doping the spreading resistance rose to 10^6 ohms.

$(C/Si)_g = 5/1$.—The deposited layers at this doping level were completely composed of polycrystalline SiC, the average crystal size being 2000Å. Both α and β forms were detected, the latter form predominating. Spreading resistance measurements gave values greater than 10^7 ohms.

Discussion

The experimental results described above noted that carbon, chemically introduced during the epitaxial growth of Si, either (*i*) reacted to form SiC, or (*ii*) initiated the formation of mixed polycrystalline areas of Si and graphite, or (*iii*) might be incorporated in yet another way, *e.g.*, interstitially. Growths of both the SiC layers and of the unreacted polycrystalline areas were likely to have had similar beginnings, *viz.*, at pyrocarbon nuclei. The reduction of methane to carbon for methane concentrations equivalent to $(C/Si)_g > 1/8$ at 1200°C was based on thermodynamic calculations, *i.e.*, the input partial pressures of methane are equal to or greater than the equilibrium value. At 1200°C, SiC formation from $SiCl_4$, CH_4, and H_2 involves the reaction (8)

$$Si(s) + C(s) \rightarrow SiC(s)$$

and was observed in the present study for $(C/Si)_g > 1/2$. Its inhibition in the range, $1/8 < (C/Si)_g < 1/2$, however, was unexpected. Initial speculation linked the effect to the reaction kinetics and suggested a minimum carbon concentration below which SiC was not formed.

The generation of both reacted and unreacted polycrystalline regions from carbon nuclei was partly confirmed through measurements of the thicknesses of these deposits. Depths of the large triangular regions produced where $(C/Si)_g = 3/10$ corresponded to growth initiated during the deposition of the first few doped monolayers. Similar findings were noted for all ratios of greater magnitude; the few inclusions observed in layers where $(C/Si)_g$ had been 1/80 or 1/34 showed no such correspondence. The predicted pyrocarbon formation for $(C/Si)_g \geq 1/8$ thus coincided with the onset of polycrystalline layer formation. The presence of the small triangular regions (Fig. 1) demonstrated that some nucleation may occur at later stages of growth. Polycrystalline growth in lightly doped layers was regarded as a rare event.

An intriguing feature of the polycrystalline regions produced where $(C/Si)_g = 3/10$ was the pyramidal shape which they adopted. The three faces of the pyramid, inclined to the surface of the deposit, showed no simple crystallographic relationship with the surface plane. The bounding edges of the face parallel to the substrate surface, however, aligned themselves along the three <110> directions common to the adjacent epitaxial (111) surface. A possible explanation considered is the packing of newly arrived Si and C atoms. Close packing of atoms on the original Si(111) surface occurs along equivalent <110> directions. Surface steps of atomic dimensions generally lie along these directions. Si atoms engaged in forming an epitaxial layer favor such steps as nucleation sites, hence align themselves along them (and the <110>'s). If a foreign element, *e.g.*, carbon, was interposed during the Si buildup and was able to assimilate the others of its species, a region, out of register with the epitaxial Si, would be formed. The subsequent build-up of such a region is that of an expanding island bounded by Si atoms, the latter favoring <110> alignment. It was only fortuitous that the triangular shape of the island was maintained for the $(C/Si)_g$ ratio of 3/10, the necessary condition being some critical balance between the island's expansion rate (the ability of the island to inhibit epitaxial growth) and the rate of Si arrival. A more rapid Si arrival might contain the island within a given surface area, then begin to overlap and give it a roughly circular shape. A slower Si arrival rate would allow the island to spill over. Since the ratio between the Si arrival rate and island formation rate were functions of the respective partial pressures of Si and of the carbon impurities, the results of the present experiments contained examples from both sides of the critical condition. To a first approximation the results seemed consistent.

In the bulk Si, the carbon concentration occasionally exceeds the predicted solubility limit. In epitaxially deposited Si, a controlled carbon excess can be introduced which may be several orders of magnitude greater than the solubility limit. Presumably there is physical trapping of carbon during the rapid growth of an epitaxial deposit if deposition occurs in a carbon-bearing atmosphere (a number of metals are known to trap inert gases) (9, 10). Equilibrium processes dissolve carbon into the Si lattice up to the solubility limit. Any excess trapped carbon is then, for practical purposes, retained interstitially if it fails to (*i*) form SiC, or (*ii*) diffuse and segregate with other carbon atoms. Since neither SiC nor carbon precipitates were observed in deposits which nevertheless contained excess carbon, interstitial accommodation of carbon is inferred.

Conclusions

The carbon content of bulk silicon substrates as measured by the method described here agrees well with those reported by Schink. Epitaxial silicon layers are found to have concentrations of carbon in excess of the substitutional solid solubility limit. These concentrations are determined by the epitaxial growth conditions, *viz.*, partial pressure of methane, and a continuous range of carbon concentration between

pure Si and SiC seems attainable. The crystalline perfection of the epitaxial layer is not affected by the presence of carbon in concentrations up to 10^{18} atoms/cm^3. At levels of carbon concentration near 10^{19} atoms/cm^3 many polycrystalline inclusions are formed with only a small increase in the dislocation density. The presence of a mixture of graphite and Si is observed by transmission electron diffraction from the polycrystalline regions. These regions are converted into SiC by appropriate postdeposit annealing schedules. In the presence of excess methane, thin partially oriented layers of both α and β-SiC are grown. Annealing of epitaxial regions results in the formation of numerous microprecipitates, attributed partly to the precipitation of excess carbon from solid solution. In undoped deposits, an order of magnitude excess of carbon, together with the absence of observable precipitates of carbon or SiC, implies the presence of interstitial carbon. Electrical properties such as resistivity are not affected by increasing concentrations of carbon until the onset of SiC formation.

Acknowledgment

The authors wish to thank Dr. W. J. Takei, Mr. R. J. Pfeil, Mr. W. J. Cifone, and Mr. J. H. Rieger for assistance with the experimental work. The constructive comments of Dr. J. E. Johnson were greatly appreciated.

Manuscript submitted May 15, 1968; revised manuscript received *ca.* Sept. 5, 1968. This paper was presented at the Boston Meeting, May 5-9, 1968, as Paper 79.

Any discussion of this paper will appear in a Discussion Section to be published in the December 1969 JOURNAL.

REFERENCES

1. G. R. Booker, *Phil. Mag.*, **11**, 1007 (1965).
2. M. Inoue, *This Journal*, **112**, 189 (1965).
3. N. Schink, *Solid-State Electr.*, **8**, 767 (1965).
4. W. R. Runyan, "Silicon Semiconductor Technology," p. 253 McGraw-Hill Book Co., New York (1965).
5. T. L. Chu, G. A. Gruber, and R. Stickler, *This Journal*, **113**, 156 (1966).
6. E. Sirtl and A. Adler, *Z. Metallk.*, **52**, 529 (1961).
7. R. G. Mazur and D. H. Dickey, *This Journal*, **113**, 255 (1966).
8. M. L. Pearce and R. W. Marek, *J. Am. Ceram. Soc.*, **51**, 84 (1968).
9. A. D. LeClaire and A. H. Rowe, A.E.R.E. Report M/R 1417 (1957).
10. K. B. Blodgett and T. A. Vanderslice, *J. Appl. Phys.*, **31**, 1017 (1960).

APPENDIX

Determination of Carbon in Silicon

A new technique is used for carbon analysis in Si. Carbon content is determined by measuring concentrations of CO_2 with a Leco (Laboratory Equipment Corporation) low carbon analyzer. Initially, a Si specimen is burned together with several combustion accelerators in oxygen in an induction furnace. The Si combusts at temperatures greater than 1670°C, all the carbon being oxidized. A catalyst furnace converts residual CO into CO_2. The gas is dried by passing it through anhydrous magnesium perchlorate, then swept into a collection trap. After a predetermined collection interval, the trap is isolated, then heated. The heated CO_2 is swept out of the trap by a stream of helium into a thermal conductivity cell. The output of the cell, amplified and integrated, gives a measure of the carbon content.

The accelerators which are used include lead chromate and iron chip. These are preburned in a ceramic crucible to minimize their inherent content. When the Si sample is to be burned, excess iron chip, of the order of 1.5-2.0g per 0.3g of Si, is added to the preburned accelerators. The excess iron chip yields 12-16 μg of carbon on burning. By assuming conservatively that a 3 μg increase, over the amount introduced by the excess iron chip, can be detected accurately by the apparatus, and by restricting the weight of Si to at least 0.3g, a reasonable lower detection limit of carbon in Si is 20 ppma. The method is reproducible within 10%.

A comparison of results obtained by chemical analysis with those from infrared data (measuring only substitutional carbon) on a Si specimen containing carbon showed the following: carbon (chem) ~ 47 ppma; carbon (I.R.) ~ 13 ppma measured by the Dow Corning Corporation, Hemlock, Michigan; carbon (I.R.) ~ 17 ppma measured in this laboratory at liquid nitrogen temperature using the calibration curve of Newman and Willis.[1]

[1] R. C. Newman and J. B. Willis, *J. Phys. Chem. Solids*, **26**, 373, 1965.

Technical Notes

RF Sputter Etching—A Universal Etch

P. D. Davidse

IBM Components Division, East Fishkill Facility, Hopewell Junction, New York

Photosensitive resists are widely used to define patterns that are to be etched in thin films. The definition obtained depends on the quality and adhesion of the resist film, the nature of the material to be etched, and the etchant used. With materials that are difficult to etch, strong chemicals are needed, which often results in a degradation of the resist adhesion, leading to a high degree of undercutting. In some cases, the adhesion of the resist to the surface can be improved considerably by surface treatments or by applying a so-called conversion coating (1), thus reducing the degree of undercutting. However, because chemical etching proceeds in all directions, there will always be some undercutting. An oversimplified comparison of etching profiles is given in Fig. 1.

D-C sputtering has been used for etching of metals to bring out their grain structure (2). For this, the sample to be etched is made the cathode of a conventional d-c glow discharge. With this method, it is also possible to etch insulators by depositing on the insulator a metal stripe or grid pattern (or by placing a metal grid on the insulator) to which the cathode voltage is applied (2). The spacing between the metal lines has to be small, since neutralization of the accumulated positive charge on the exposed insulator surface takes place by secondary emission from the metal lands. This method is limited also because nonuniform etching of the insulator material takes place due to a focusing effect and because metal sputtered from the metal line patterns can be deposited on the exposed

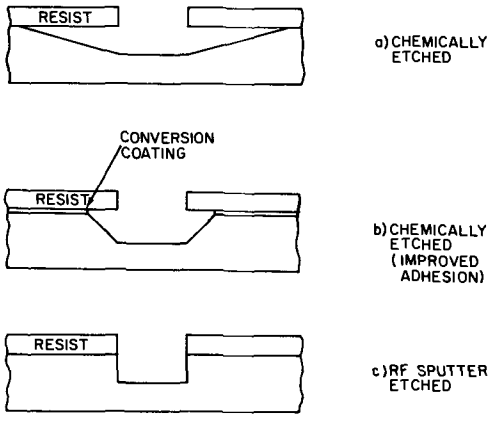

Fig. 1. Etching profiles (simplified)

insulator surface (3). Therefore, this method has been used mainly for the study of the structure of insulators. Similar studies have been made using an ion beam, with which alumina and fused silica were etched (4).

D-C sputtering can be used successfully to etch metal line patterns by using a thicker metal film as a mask. This method's drawbacks are the possibility of arcing between isolated lands and the possibility of dielectric breakdown of insulator films when they are present in the structure to be etched (5). Another disadvantage of the d-c sputtering method is that an extra film deposition and chemical etching step is needed to produce the desired metal mask pattern. These limitations do not exist with the method which is the subject of this publication. With RF sputter etching it is, in principle, possible to etch patterns or holes in any metal, semiconductor, or insulator using standard photoresist materials as masks.

Apparatus

Figure 2 shows a system used for RF sputter etching. The samples are placed on a circular electrode that is mounted on the base plate of a bell-jar vacuum system. This electrode is similar to the electrode used for the deposition of insulator films by RF sputtering (6). After the system has been evacuated, argon is bled in to obtain a pressure of from 2 to 15 x 10^{-3} Torr. A glow discharge is then started by applying RF power to the electrode. The RF power supply is capacitively coupled to the electrode to allow the build-up of a negative d-c bias on the front of the electrode, hereafter referred to as the "cathode." The self-biasing effect is caused by the difference in electron and ion mobility and is necessary to affect sputtering.

The power supply was a crystal-controlled 1 kw amateur radio transmitter with a frequency of 13.56 MHz. The progress of the sputter etching can be followed by observing the removal on a monitor sample or by determining the etch rate or etch time in a trial run.

Although a grounded counter electrode or "anode" parallel to the RF electrode can be used, operation is simplified by its omission, which only slightly lowers the removal rate. Without the "anode," the samples can be more readily observed during the experiment, and the system is easier to load and unload. The basic character of a glow discharge system is not changed because of the presence of many grounded metal parts in the system, *e.g.*, the baseplate and the cathode shield. Because the metal cathode itself is also sputtered, the bell jar will be coated very quickly with a metal film, thus making observation of the samples difficult. This problem can be greatly reduced by placing the samples on a fused quartz plate that rests on the cathode. However, as will be discussed later, it is desirable to keep the samples reasonably cool, which can be more readily achieved when the samples are placed directly on the water-cooled metal electrode. In this case, a fused quartz plate with cut-outs for the samples can be placed on the cathode.

The cathode, which has a diameter of 8¾ in., can hold nineteen 1¼ in. silicon wafers. These wafers are placed in a hexagonal configuration, *i.e.*, one wafer in the center surrounded by two concentric hexagons of six and twelve wafers each. The wafer-to-wafer variation in removal rate was generally less than 2%.

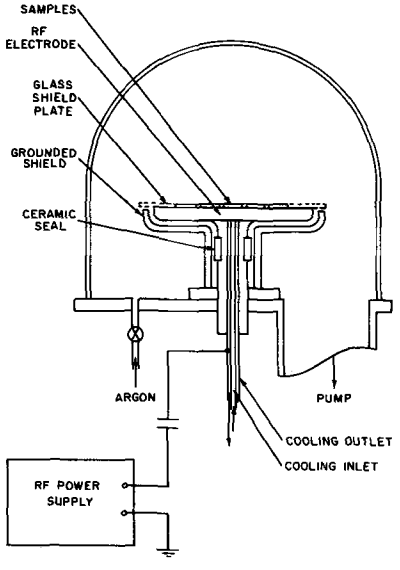

Fig. 2. RF sputter etching system

Experimental

With this etching technique, land patterns or holes have been etched in thin films of the following materials: aluminum, tantalum, Cr-SiO, nichrome, silicon nitride, and RF sputtered and thermally grown silicon dioxide. Film thickness ranged between 500 and 20,000Å.

RF sputter etching has been found to be especially useful for the etching of Cr-SiO films to make thin film resistors. Figure 3 illustrates the procedure to make such resistors. A 1000-2000Å-thick Cr-SiO film is evaporated (7) onto the substrate, followed by the deposition of the contact metallurgy. Next, a photoresist film is applied, the required contact land pattern is developed, and the exposed metal film is etched away (Fig. 3a). Subsequently, a second layer of photoresist is applied, and the resistor pattern is developed (Fig. 3b). At this point, exposed resistive material would normally be etched away chemically. However, chemical etching is difficult with Cr-SiO films, especially when the SiO concentration is high. Very strong chemicals have to be used, which often results in ill-defined edges and attack of the contact metallurgy. These problems do not exist when the exposed cermet is removed by subjecting the sample to RF sputtering (Fig. 3c), after which the photoresist is removed (Fig. 3d).

Figures 4 and 5 illustrate the good definition that can be obtained with this method. The substrates used were 1¼ in. silicon wafers precoated with a 1.5μ-thick film of RF sputtered silicon dioxide. The pattern

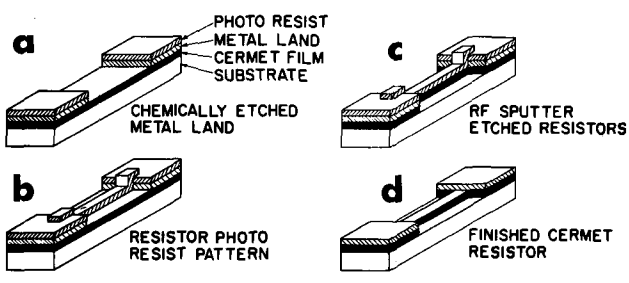

Fig. 3. Sputter-etching of thin-film resistors

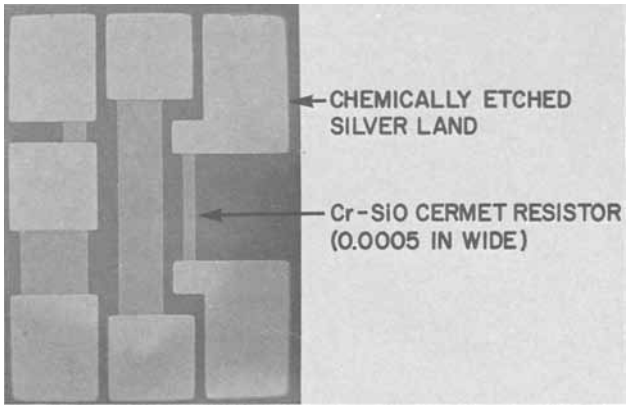

Fig. 4. RF sputter etched Cr-SiO cermet resistors (substrate: silicon wafer precoated with 1.5μ of RF sputtered SiO_2).

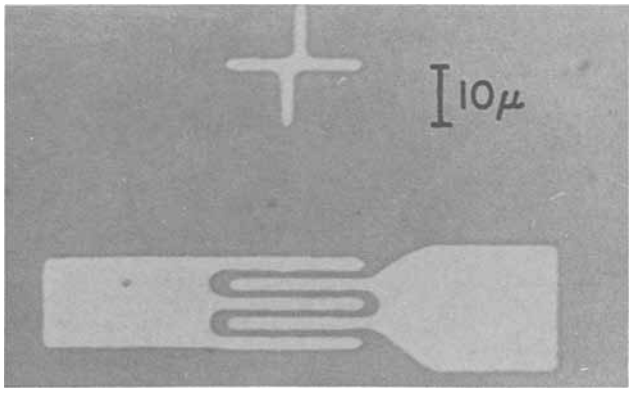

Fig. 5. Fine-line test pattern

shown in Fig. 4 was a unit cell of which there were more than 1200 on each wafer; Fig. 5 shows a fine-line test pattern.

The resist used was KTFR (Kodak Thin Film Resist). Since in RF sputter etching the resist material is also sputtered, it is necessary that the resist film be thick enough to last through the sputter etching. Figure 6 shows the removal rates for various materials as a function of RF power. The KTFR removal rate at a given power level was found to be comparable to the rate for the materials that were etched. As indicated in Fig. 6, this rate is considerably higher for what were believed to be incompletely cured resin films. Later experiments showed that the relatively high removal rate in this case was more likely associated with the presence of relatively high concentrations of reactive gases, such as oxygen and hydrogen, in the sputtering atmosphere. Deliberate addition of these gases was found to give a very high photoresist removal rate with a simultaneous lower removal rate for inorganic materials, thus making this a means for photoresist removal. It has also been found that the photoresist removal rate is strongly dependent on the sample temperature during sputter etching, as expected. The removal rate for a photoresist pattern was generally found to be lower than the rate for a continuous resist film. Similar observations were made when positive resists were used. Removal of the resist after sputtering was found to be somewhat more difficult than usual; however, standard stripping techniques could still be used, *i.e.*, stripping in a J-100 solution followed by rinsing with or without the use of a cotton swab.

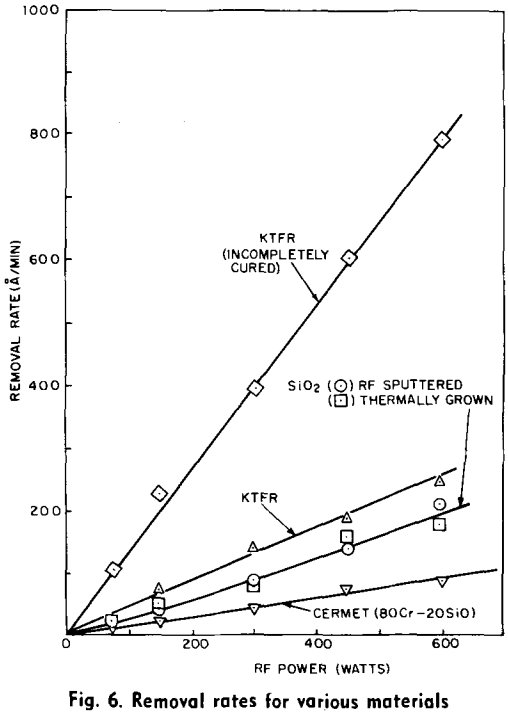

Fig. 6. Removal rates for various materials

In all the experiments, the wafers were mounted on the water-cooled cathode using a high-vacuum grease to provide good thermal contact. Without good contact, extensive degradation of the resist takes place at high power levels. Occasionally, even with good thermal contact, spots have been observed in the resist film after sputtering. However, after removal of the resist, no evidence of spots could be seen on the underlying films.

When the photoresist is incompletely developed, some resist material is left behind at the edges. These "feathered" edges and any debris that is left on the material to be etched are cleaned up during the sputtering operation.

Figure 7 illustrates the sharpness of a step sputter etched in silicon, indicating that absence of undercutting can be achieved. It should also be noted that the polishing marks on the original surface have been smoothed out where material has been removed.

Discussion

The two main advantages of RF sputter etching are, obviously, its universality and the absence of undercutting. The former feature allows the evaluation of new materials for device applications without having to search for suitable etchants first. Once device feasibility has been demonstrated, efforts can be made to find satisfactory chemical etchants. A disadvantage of

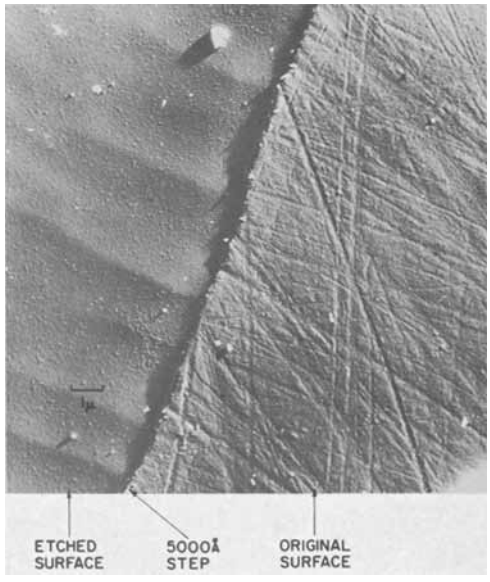

Fig. 7. RF sputter etched step in silicon showing absence of undercutting.

this universality is that the etching continues after the material of interest has been removed. Therefore, careful monitoring of the etching process is necessary. The absence of undercutting is an especially desirable feature where dimensional control is necessary, *e.g.*, precision thin film resistors.

Because the photoresist material is also removed by RF sputter etching, the technique is of practical interest mainly for films that are relatively thin, *i.e.*, several microns or less.

Conclusions

RF sputter etching is a practical technique that can be used in semiconductor and thin film studies. It allows the etching of virtually any material using standard photoresist materials and techniques to define the areas that are to be etched. This characteristic and the absence of undercutting are the attractive features of the technique.

Acknowledgments

The author is greatly indebted to L. R. Koster for his significant contributions in the first phase of this work. He would like to thank Miss M. H. Whitehill for her assistance with the photoresist work and J. J. Van Steenburgh for his assistance with some of the sputtering experiments. He is grateful to C. S. Standley and D. P. Cameron for Fig. 7.

Manuscript submitted Feb. 17, 1967; revised manuscript received June 21, 1968. This paper was presented at the Thirteenth National Vacuum Symposium, San Francisco, Oct. 26-28, 1966.

Any discussion of this paper will appear in a Discussion Section to be published in the December 1969 JOURNAL.

REFERENCES

1. Kodak Industrial Data Book No. P-7, p. 17, Eastman Kodak Co., Rochester, N. Y. (1962).
2. G. V. Spivak, I. N. Prilezhaeva, and O. I. Savochkina, *Doklady Akad. Nauk SSSR*, **88,** 511 (1953).
3. G. V. Spivak *et al.*, *ibid.*, **114,** 1001 (1957).
4. R. A. Dugdale and S. D. Ford, *Trans. Brit. Cer. Soc.*, **65,** 165 (1966).
5. M. P. Lepselter, *Bell System Tech. J.*, **45,** 247 (1966).
6. P. D. Davidse and L. I. Maissel, *J. Appl. Phys.*, **37,** 574 (1966).
7. M. Beckerman and R. E. Thun, *Trans. 8th Symp. Am. Vac. Soc.*, p. 905 (1961).

Transmission Electron Microscopy of As-Grown PbSe Single Crystals

H. Abrams* and R. N. Tauber

Department of Metallurgy and Materials Science and the Materials Research Center, Lehigh University, Bethlehem, Pennsylvania

The preparation of thin foils of the compound semiconductor PbSe for transmission electron microscopy has not been reported previously. This note describes the preparation technique and some observations made on as grown thin foils of PbSe.

Single crystals were grown by the Bridgman-Stockbarger technique in an evacuated capsule, containing a molten charge of nominally stoichiometric PbSe. The growth conditions were 6°C/cm temperature gradient through the reported melting point of 1065°C (1) and a lowering rate of 2 mm/hr. These conditions resulted in single crystal PbSe having a dislocation density measured by standard etch pit methods (2) of approximately 6 x 10^6 cm^{-2}. Slices cut with a {100} orientation were thinned for electron microscopy using the following procedure.

Thin foils which may have had surface contamination were prepared using the material removal etch reported by Coates *et al.* (3). After polishing the specimen on both sides with 600 grit silicon carbide to a thickness of about 300μ it was immersed in a solution consisting of 5 volumes of 45% aqueous KOH, 5 volumes of ethylene glycol, and 1 volume of 30% H_2O_2. The solution was maintained at room temperature and agitated with a magnetic stirrer. A relatively uniform bright surface was obtained within a few minutes, and it took from 3 to 6 hr to thin down to a thickness of about 1μ. The polishing rate decreased with time due to depletion of the H_2O_2. However, the solution could be reactivated by the addition of H_2O_2, thereby increasing the polishing rate. When the solution loses its polishing ability it turns a pale yellow color. A highly polished surface and removal of yellow-brown surface stains was achieved by immersing the sample in a 1:1 acetic acid-water solution for a few seconds and then rinsing in deionized water. The 1μ thick sample was then mounted on a Teflon block using apiezon wax and polished for an additional 8 hr. The sample became progressively smaller and thinner until a suitable foil was obtained. The sample was floated off the Teflon holder in reagent grade trichloroethylene, rinsed in deionized water, and mounted on a copper grid for observation in a Hitachi 11B electron microscope, operated at 100 kv.

Figure 1 is a diffraction pattern of a {100} orientation for an as grown PbSe specimen. The most prominent extra diffraction spots (points A and B) correspond to a d spacing of 2.83Å. This value is in error less than 3%, since the PbSe pattern was used as an internal standard. This d spacing corresponds closely to the (111) d spacing (2.855Å) of Pb. Also it could possibly arise from a (200) reflection of Pb_2O_3

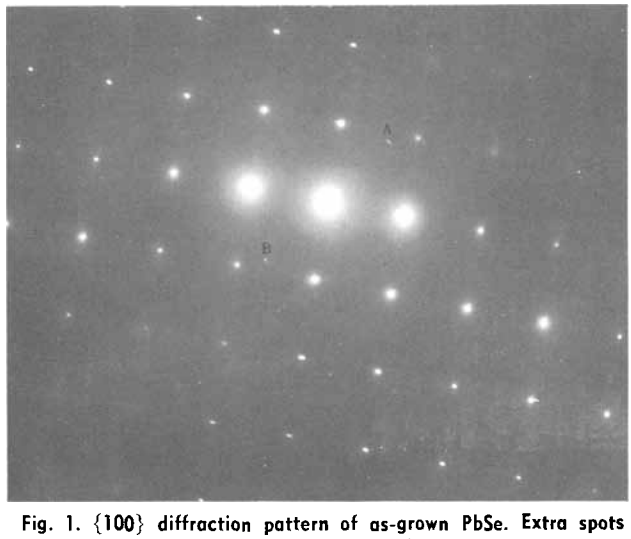

Fig. 1. {100} diffraction pattern of as-grown PbSe. Extra spots at points A and B may be due to precipitated Pb.

* Electrochemical Society Active Member.

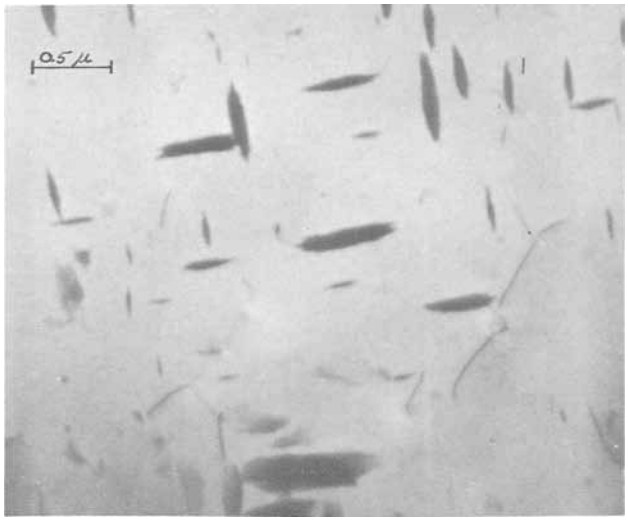

Fig. 2. Transmission electron micrograph of as-grown PbSe. Particles on the order of 0.6 x 0.15 μ, oriented in a <100> direction are observed.

(2.75Å) or a (210) reflection of $PbSeO_3$ (2.735Å), either of which may have deposited on the surface during the thinning procedure. Additional weak spots can be attributed to both Pb and $PbSeO_3$.

An electron micrograph of a region of the as grown PbSe foil is shown in Fig. 2. The micrograph shows about 10 v/o of ellipsoidally shaped particles on the order of 0.6 x 0.15μ, oriented in a <100> direction. It is difficult to determine the exact shape of these particles since they may be inclined to the plane of the foil. The Widmanstatten pattern formed by these particles indicates that they grew by a diffusion limited precipitation process. Relating these particles to the extra diffraction spots reveal they may be due to Pb. Precipitation of Pb can occur in PbSe (4), due to the retrograde nature of the Pb solidus boundary (5). However, in accordance with the PbSe phase diagram near stoichiometry (5, 6) the amount of precipitate should be several orders of magnitude less than that observed here. In order to account for the large volume fraction of second phase observed, either the retrograde solubility is much larger than has been previously reported or the specimen grew nonstoichiometrically. The latter is more plausible since some of the more volatile Se component may have been lost during the growing procedure.

The presence of a two-phase structure has important implications for use of this semiconductor in electronic applications. Further experiments are in progress to ascertain what growth conditions lead to the observed two-phase structure.

Acknowledgment

This work was supported by the National Science Foundation under Grant No. GK-1607.

Manuscript submitted July 25, 1968; revised manuscript received Sept. 8, 1968.

Any discussion of this paper will appear in a Discussion Section to be published in the December 1968 JOURNAL.

REFERENCES

1. A. E. Goldberg and G. R. Mitchell, *J. Chem. Phys.*, **22,** 220 (1954).
2. M. Norr, *This Journal*, **109,** 1113 (1962).
3. D. G. Coates, W. D. Lawson, and A. C. Prior, *ibid.*, **108,** 1038 (1961).
4. H. Abrams, Ph.D. Dissertation, Lehigh University 1968 (University Microfilms, Ann Arbor, Mich.).
5. R. F. Brebrick and E. Gubner, *J. Chem. Phys.*, **36,** 170 (1961).
6. K. Izaki and N. Ohashi, *J. Phys. Soc. Jap.*, Supp. II, **18,** 143 (1963).

Preparation of $Cd_xHg_{1-x}Te$ Crystals by the Vertical-Zone Melting Method

E. Z. Dziuba

Institute of Physics, Polish Academy of Sciences, Warsaw, Poland

The solid solution system $Cd_xHg_{1-x}Te$ has become in recent years an object of intensive scientific research (1) in view of its interesting electrical and optical properties and related theoretical considerations as well as the theory of its energy band structure. A wide range of the variation of the electrical and optical properties makes this material also interesting from a practical point of view (2).

Material obtained by the methods described in the publications (1) does not satisfy the basic requirements of homogeneity of the crystals. Crystals obtained by the Bridgman method have high gradients of composition due to strong segregation into individual components during the solidification process (3). Difficulties in preparing a homogeneous and single-crystalline solid solution $Cd_xHg_{1-x}Te$ are connected with the strong tendency toward segregation and the high mercury vapor pressure.

It is known that the Bridgman method makes it possible to obtain single-crystalline homogeneous material, provided that the segregation can be prevented. Low vapor pressure of the components is not essential in this method, as it is in the horizontal-zone melting method which can also be used for preparing materials which have a tendency toward segregation. It is also possible to use the horizontal-zone melting method for other materials for which the equilibrium condition between vapor, liquid, and solid phases is known (4).

The method of preparing homogeneous single-crystalline $Cd_xHg_{1-x}Te$ alloys described in this work combines benefits of both the Bridgman and horizontal-zone melting methods. This method, although it is very similar to the method used for purification and crystallization of CdTe (5), embodies more complicated phenomena but simpler operating conditions. Both methods consist of pulling the material through a hot zone in a vertically arranged quartz tube. The difference lies in the presence of an empty space in a part of the tube[1] in the method presented in this paper, whereas in the method given in paper (5) the tube is full of charge.

The preparation of homogeneous $Cd_xHg_{1-x}Te$ crystals, the discussion of the operating conditions, and the description of the experimental arrangement are presented in this paper. The $Cd_xHg_{1-x}Te$ solid solutions were prepared from high-purity HgTe and CdTe obtained previously (7, 8). The appropriate quantity of HgTe and CdTe is placed into the quartz container

[1] The method given in paper (9) also contains an empty space in the tube. As the part containing the empty space is kept at room temperature, mercury vapor transport occurs to this part. This method therefore cannot be used with $Cd_xHg_{1-x}Te$.

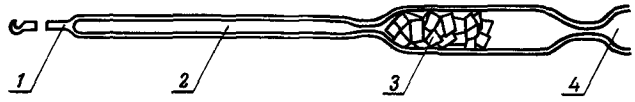

Fig. 1. The quartz arrangement for tightly filling the tube: 1—holder, 2—tube, 3—container, 4—vacuum.

connected to a quartz tube as shown in Fig. 1. After evacuation, both container and tube are sealed off from the vacuum apparatus and put into a horizontal heater having a temperature of about 650°C. The heater temperature is raised to the melting point of the $Cd_xHg_{1-x}Te$ composition in about 24 hr. This process is necessary in order to avoid the danger of explosion due to high mercury vapor pressure which occurs when the liquid phase, rich in mercury component, is present (6).

After the solid CdTe is completely dissolved into the liquid system, the heater, together with the quartz arrangement, is turned to a vertical position to charge the tube. The tube with liquid $Cd_xHg_{1-x}Te$ is removed from the heater for quick solidification and cut off from the container. As an empty space of about 1 cm^3 is present in the tube in the region of the tube-container junction, no other additional operations for cutting off the tube from the container are necessary.

The quartz tube, tightly filled with the macroscopically homogeneous polycrystalline $Cd_xHg_{1-x}Te$, is placed vertically in a furnace having its hot zone wider than the length of the empty part of the tube (Fig. 2). Starting with the tube partly empty, it is lowered through the hot zone.

After the pass of the tube, there are three parts to the ingot: the first part in which the composition of the crystal changes from x' to x_0, the second part (the longest) in which there is a constant composition of $x = x_0$, and the third part in which the composition changes from x_0 to $x = 0$.

Fused at T_0°K in the upper part of the hot-zone, 2 (Fig. 2), the melt flows down and forms the liquid phase, 4. The crystal, 5, grows from this melt.

In the first part, due to segregation (Fig. 3) the crystal with the composition x' grows from the melt

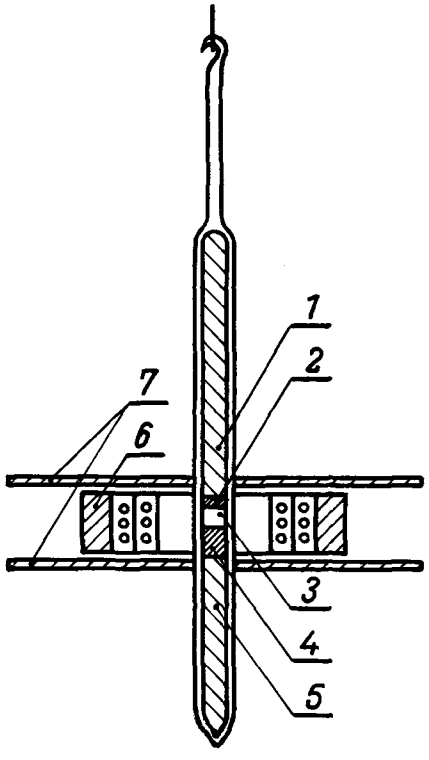

Fig. 2. The principle of arrangement for preparation of single crystals of $Cd_xHg_{1-x}Te$: 1 and 5—solid, 2 and 4—liquid, 3—vapor, 7—ceramic shells, 6—heater.

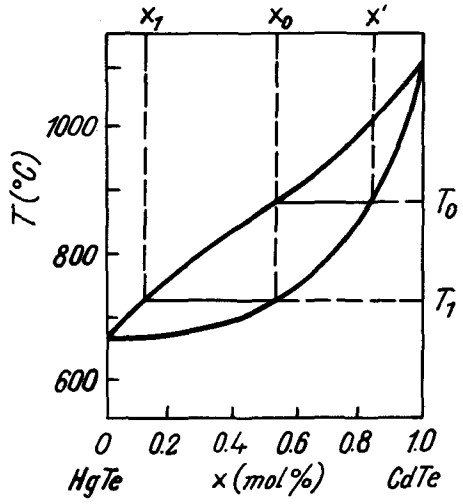

Fig. 3. The solidus-liquidus diagram for $Cd_xHg_{1-x}Te$ (3): x_0, composition in dynamic steady state; x' and $x = 0$, the composition at the start and at the end of the process; x_1, composition of the melt in dynamic steady state; T_0, melting point, and T_1, solidification point in dynamic steady state.

with the composition x_0. This causes the change of the composition of the liquid phase, 4, from x_0 to x_1.

In the second part, in dynamic equilibrium, the composition of the crystal in the lower part of the tube, 5, must be equal to the composition of the material in its upper part, 1, because the melt with the composition x_0 flows down and compensates for the decrease of the value of the components, due to the crystallization process. In this equilibrium condition, the composition of the liquid phase in the lower part of the tube, 4, changes from x_0 at the surface to x_1 at the bottom of the liquid volume.

In the third part, at the end of the crystallization process when the hot zone has reached the upper end of the tube, the liquid phase there is not compensated and, due to segregation, the crystal grows with various compositions from x_0 to $x = 0$.

In the equilibrium condition, in the second part of the ingot, the gradient of the composition of the liquid phase, 4, has constant slopes if all parameters, such as speed of the tube, the temperature of the hot zone, and the transport of the material from the upper, 2, to the lower, 3, part of the tube, are constant. The speed of the tube and temperature of the hot zone are easy to control, but the transport of the material from the upper to lower part of the tube is difficult to control. If the material flows down in the form of large drops, local changes in the composition of the liquid phase, 4, are produced. If, however, the temperature of the vapor phases, 3, are sufficiently high, the transport of the material from the upper to lower part of the tube occurs by small drops or by evaporation. To preserve these phenomena, it is necessary to maintain the high temperature of the hot zone and large gradient of temperature in the upper and lower parts of the hot zone.

The apparatus which was used to obtain the $Cd_xHg_{1-x}Te$ crystals is shown in Fig. 2. The tube, about 12 cm long and having a 7-mm inner diameter and a 10-mm outer diameter, is lowered at a constant rate, 5 mm/hr. The hot zone, about 2 cm long, is produced by resistance heater and two ceramic shells. To maintain the hot-zone temperature constant, the current supplying the heater is controlled. The magnitude of the current was established by direct observation of the melting process when the tube was starting to move. This observation of the melting process is possibly due to the empty part of the tube and required no other additional experiments.

Direct observation of the reflection from the ingot surface in visible light established that the prepared material consisted of several large single crystals. The

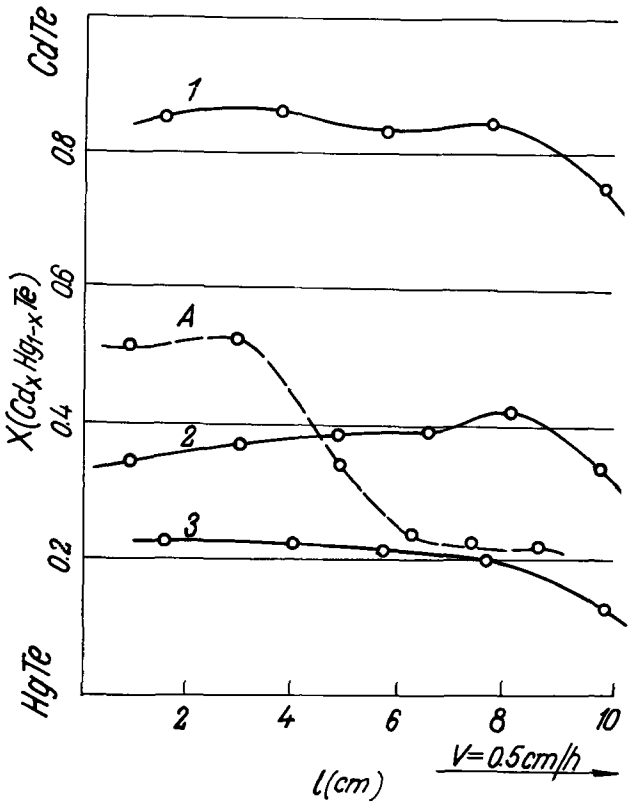

Fig. 4. Distribution of the $Cd_xHg_{1-x}Te$ alloy composition along the ingot.

ingot was cut into samples of about 20 mm length. The average composition of each sample was determined by estimating its density as described in Ref. (8). This method is very simple; and, due to linear variation of the density from $\rho = 8.1$ g/cm³ for HgTe to $\rho = 5.9$ g/cm³ for CdTe, the precision of the measurements is sufficiently high to allow the determination of the composition of the $Cd_xHg_{1-x}Te$ system to within less than 1% (8).

The average composition of the typical samples as a function of their position in the ingot is shown in Fig. 4. It is evident from Fig. 4 that the segregation is not observed over a large portion of the ingots. The change in the composition due to segregation appears only in the third part of the ingot where the liquid phase in the lower part of the tube was not compensated by the material flowing from the top downward. To determine the influence of the fluctuation of the hot-zone temperature on the composition of alloy, the temperature of the hot zone was lowered while pulling the tube. The result is shown in Fig. 4, curve *A*. It can be seen that a large change in the composition occurs in the region grown while the temperature was lowered. It is therefore possible that the fluctuations in the composition along the ingots, as seen from curves 1, 2, and 3 in Fig. 4, are mainly due to the instability of the hot-zone temperature.

Acknowledgments

I wish to express my gratitude to Professor L. Sosnowski for his research guidance and interest and to Drs. J. Baranowski, E. Cruceanu, R. R. Galązka, A. Jendrzejczak, A. Mycielski, and N. Niculescu for their assistance and discussions in the course of this work.

Manuscript submitted March 3, 1968; revised manuscript received Sept. 6, 1968.

Any discussion of this paper will appear in a Discussion Section to be published in the December 1969 JOURNAL.

REFERENCES

1. C. Verié and E. Decamps, *Phys. Stat. Sol.*, **9**, 797 (1965); C. Verié, *ibid.*, **17**, 889 (1966). R. R. Galazka and L. Sosnowski, *ibid.*, **20**, 113 (1967), and other work to which references have been given in the publications mentioned above.
2. P. W. Krusu, M. D. Blue, J. H. Garfunkel, and W. D. Saur, *Infrared Phys.*, **2**, 53 (1962). C. Verié and R. Grabner, *Compt. Rend.*, **261**, 3349 (1965). J. Melugailis and A. J. Strauss, *Appl. Phys. Letters*, **8**, 179 (1966).
3. B. Ray and M. P. Spencer, *Phys. Stat. Sol.*, **22**, 371 (1967).
4. E. Cruceanu and N. Nistor, *This Journal*, **113**, 955 (1966).
5. M. R. Lorenz and R. E. Halstead, *ibid.*, **110**, 343 (1963).
6. R. F. Brebrick and A. J. Strauss, *ibid.*, **26**, 989 (1968).
7. Z. Dziuba, *Acta Phys. Polon.*, **26**, 897 (1964).
8. R. R. Galazka, *ibid.*, **24**, 791 (1963).
9. F. K. Heuman, *This Journal*, **109**, 345 (1962).

Three-Point Probe Heating Effects in Silicon

P. A. Schumann, Jr.,* J. F. Hallenback, Jr., M. R. Poponiak, and C. P. Schneider

IBM Components Division, East Fishkill Laboratory, Hopewell Junction, New York

The three-point probe (1-9) is a useful tool for the evaluation of the resistivity of semiconducting epitaxial layers deposited on substrates of the same conductivity type. Its main advantage is that it is relatively easy to set up and operate. It also is one of the few "nondestructive" techniques to measure layer resistivity. It has the disadvantage of being imprecise and having a short life.

The short life of the probe is due to the extreme thermal conditions that exist under the probe at breakdown, conditions so severe that the silicon can even be melted. This short life increases the imprecision, of which a major part is due to wear of the probe and resultant drift. The older d-c and a-c methods (1-4) were most severe on the probe. However, newer techniques involving pulse (6) or rapid shut-off (8) systems have improved this situation.

* Electrochemical Society Active Member.

The data presented in this paper were taken with a modified Dumas probe reported on earlier (4), operating at a load of 35 g/point. The points are steel with a radius of curvature of 0.001 in. A description of the measurement electronics is presented in a recent publication (8).

The forming of point contact diodes is a well-known phenomenon (10). Its relation to the three-point probe has not been discussed in the literature. Figure 1 shows the change in the shape of an I-V curve for a three-point probe taken with half-wave rectified 60 Hz power supply. When the current is first applied, the curve looks as shown in Fig. 1a. Then, as the current is increased (1b and 1c), the curve balloons out, increasing the breakdown voltage and decreasing the current necessary to achieve breakdown. This effect can contribute to imprecision if the measurement procedure is not precisely duplicated. Once an appropriate forming

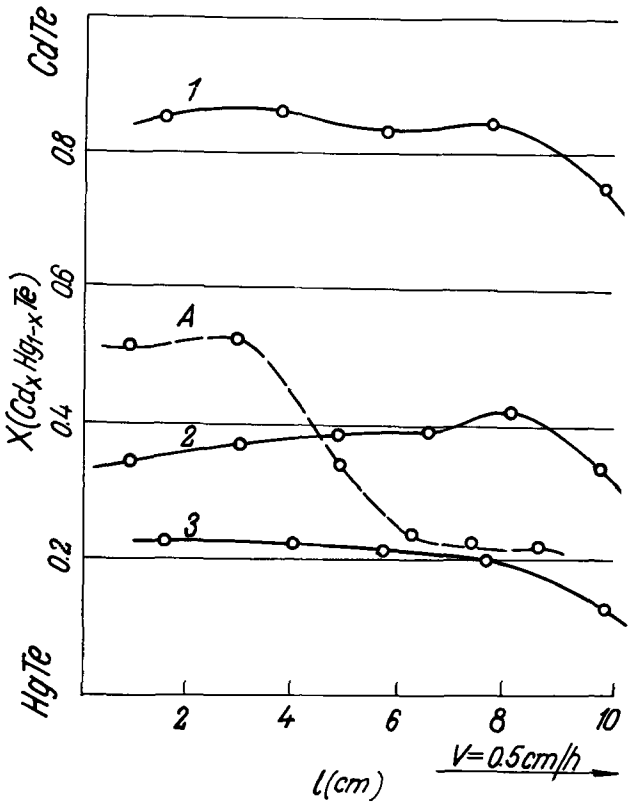

Fig. 4. Distribution of the $Cd_xHg_{1-x}Te$ alloy composition along the ingot.

ingot was cut into samples of about 20 mm length. The average composition of each sample was determined by estimating its density as described in Ref. (8). This method is very simple; and, due to linear variation of the density from $\rho = 8.1$ g/cm³ for HgTe to $\rho = 5.9$ g/cm³ for CdTe, the precision of the measurements is sufficiently high to allow the determination of the composition of the $Cd_xHg_{1-x}Te$ system to within less than 1% (8).

The average composition of the typical samples as a function of their position in the ingot is shown in Fig. 4. It is evident from Fig. 4 that the segregation is not observed over a large portion of the ingots. The change in the composition due to segregation appears only in the third part of the ingot where the liquid phase in the lower part of the tube was not compensated by the material flowing from the top downward. To determine the influence of the fluctuation of the hot-zone temperature on the composition of alloy, the temperature of the hot zone was lowered while pulling the tube. The result is shown in Fig. 4, curve *A*. It can be seen that a large change in the composition occurs in the region grown while the temperature was lowered. It is therefore possible that the fluctuations in the composition along the ingots, as seen from curves 1, 2, and 3 in Fig. 4, are mainly due to the instability of the hot-zone temperature.

Acknowledgments

I wish to express my gratitude to Professor L. Sosnowski for his research guidance and interest and to Drs. J. Baranowski, E. Cruceanu, R. R. Galązka, A. Jendrzejczak, A. Mycielski, and N. Niculescu for their assistance and discussions in the course of this work.

Manuscript submitted March 3, 1968; revised manuscript received Sept. 6, 1968.

Any discussion of this paper will appear in a Discussion Section to be published in the December 1969 JOURNAL.

REFERENCES

1. C. Verié and E. Decamps, *Phys. Stat. Sol.*, **9**, 797 (1965); C. Verié, *ibid.*, **17**, 889 (1966). R. R. Galazka and L. Sosnowski, *ibid.*, **20**, 113 (1967), and other work to which references have been given in the publications mentioned above.
2. P. W. Krusu, M. D. Blue, J. H. Garfunkel, and W. D. Saur, *Infrared Phys.*, **2**, 53 (1962). C. Verié and R. Grabner, *Compt. Rend.*, **261**, 3349 (1965). J. Melugailis and A. J. Strauss, *Appl. Phys. Letters*, **8**, 179 (1966).
3. B. Ray and M. P. Spencer, *Phys. Stat. Sol.*, **22**, 371 (1967).
4. E. Cruceanu and N. Nistor, *This Journal*, **113**, 955 (1966).
5. M. R. Lorenz and R. E. Halstead, *ibid.*, **110**, 343 (1963).
6. R. F. Brebrick and A. J. Strauss, *ibid.*, **26**, 989 (1968).
7. Z. Dziuba, *Acta Phys. Polon.*, **26**, 897 (1964).
8. R. R. Galazka, *ibid.*, **24**, 791 (1963).
9. F. K. Heuman, *This Journal*, **109**, 345 (1962).

Three-Point Probe Heating Effects in Silicon

P. A. Schumann, Jr.,* J. F. Hallenback, Jr., M. R. Poponiak, and C. P. Schneider

IBM Components Division, East Fishkill Laboratory, Hopewell Junction, New York

The three-point probe (1-9) is a useful tool for the evaluation of the resistivity of semiconducting epitaxial layers deposited on substrates of the same conductivity type. Its main advantage is that it is relatively easy to set up and operate. It also is one of the few "nondestructive" techniques to measure layer resistivity. It has the disadvantage of being imprecise and having a short life.

The short life of the probe is due to the extreme thermal conditions that exist under the probe at breakdown, conditions so severe that the silicon can even be melted. This short life increases the imprecision, of which a major part is due to wear of the probe and resultant drift. The older d-c and a-c methods (1-4) were most severe on the probe. However, newer techniques involving pulse (6) or rapid shut-off (8) systems have improved this situation.

* Electrochemical Society Active Member.

The data presented in this paper were taken with a modified Dumas probe reported on earlier (4), operating at a load of 35 g/point. The points are steel with a radius of curvature of 0.001 in. A description of the measurement electronics is presented in a recent publication (8).

The forming of point contact diodes is a well-known phenomenon (10). Its relation to the three-point probe has not been discussed in the literature. Figure 1 shows the change in the shape of an I-V curve for a three-point probe taken with half-wave rectified 60 Hz power supply. When the current is first applied, the curve looks as shown in Fig. 1a. Then, as the current is increased (1b and 1c), the curve balloons out, increasing the breakdown voltage and decreasing the current necessary to achieve breakdown. This effect can contribute to imprecision if the measurement procedure is not precisely duplicated. Once an appropriate forming

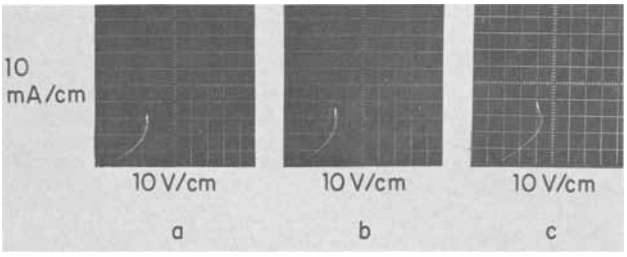

Fig. 1. AC I-V characteristics

action has taken place, the curve may be retraced with no change in the characteristics. If too much current is applied, however, the breakdown will drop to a lower value, and retracing will not bring the voltage up to its original value.

For most of the point radii and loads used (1-7), the silicon under the point is plastically deformed. If an electrical breakdown is achieved and the surface of the silicon is examined, however, a very different effect is observed, depending on the electrical conditions under which the measurement is made. Figure 2 is a micrograph showing the area under all three points after a breakdown has been measured with a d-c system (4). The damage under the voltage probe is purely mechanical, but that under the forward and reverse biased probes is a combination of mechanical and thermal. The diameter of the center damaged area is about 25.0 μm and that of the large ring is about 115.0 μm. The center damaged area has the appearance

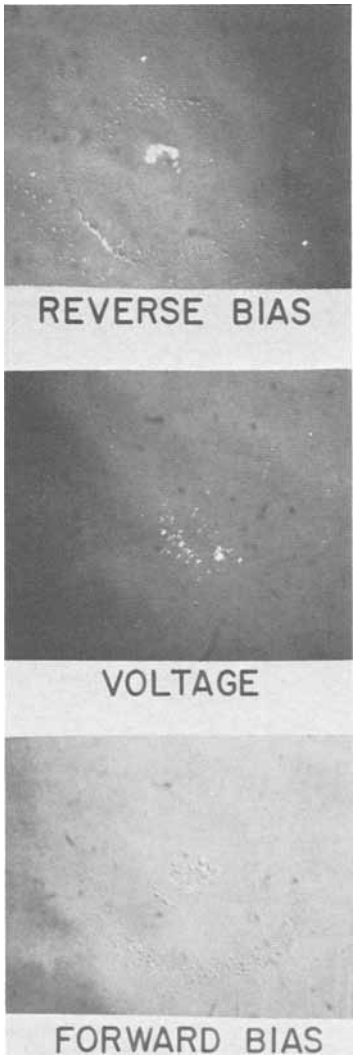

Fig. 2. Damaged area under all three probes after breakdown. Magnification *ca.* 200X.

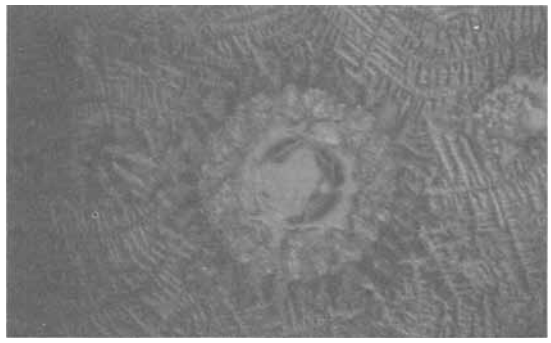

Fig. 3. Melted area under reverse biased probe with d-c breakdown system. Magnification 560X.

of having been melted. There seems to be very little difference between the forward and reverse biased points.

Photographs taken of the damaged area on silicon surface under the reverse biased point can be used to indicate heating effects. Figure 3 shows the melted region under the reverse biased probe for a d-c system, which is the worst offender. This is an extreme case, showing recrystallization of the silicon in a dendrite structure. The diameter of the center hole is 74 μm and that of the larger circle is 46 μm. Figures 4 through 6 show the effect on silicon measured using a d-c ramp with rapid shut-off (8), contrasted with a repetitive-pulse technique with pulse widths of 100 and 1 μs. Figures 7 and 8 show the effect for a single-pulse system, with the same pulse widths as above.

It is easy to see that a reduction in the pulse width or duty cycle reduces the damage to the silicon. Although there is some difference between the single-pulse and repetitive-pulse system, the difference is not great. Also it is clear from the damaged area under the rapid shut-off system that the time spent at breakdown is important. In this case the shut-off occurs in

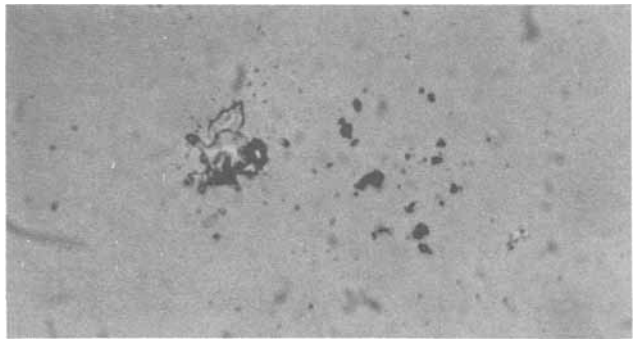

Fig. 4. Damaged area under reverse biased probe on d-c breakdown system with electronic shut off. Magnification *ca.* 225X.

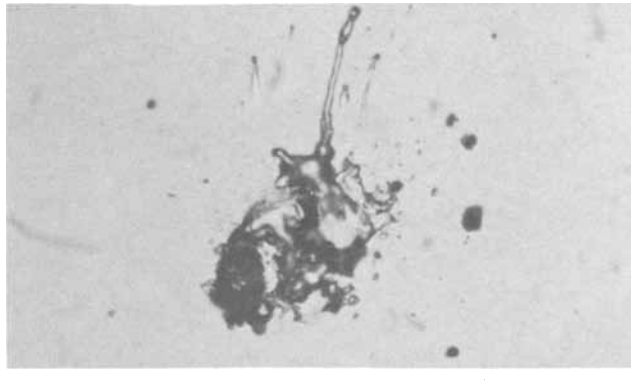

Fig. 5. Damaged area under reverse biased probe by a pulsed three-point probe with a repetition rate of 100 pulses/sec and a pulse width of 100 μsec. Magnification *ca.* 225X.

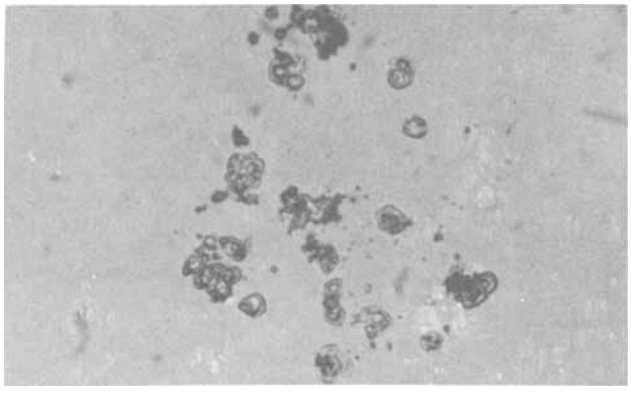

Fig. 6. Damaged area under reverse biased point for repetition rate of 100 pulses/sec with a pulse width of 1 μsec. Magnification ca. 225X.

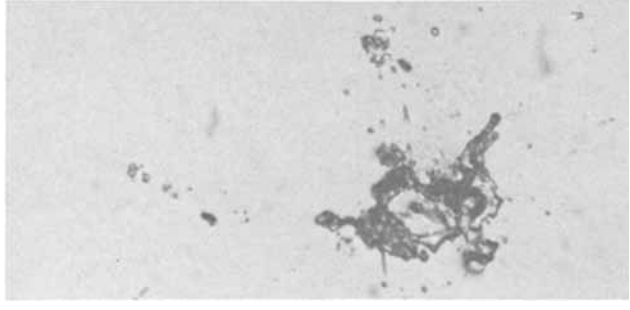

Fig. 7. Damaged area under reverse biased point for single-pulse system with a pulse width of 100 μsec. Magnification ca. 225X.

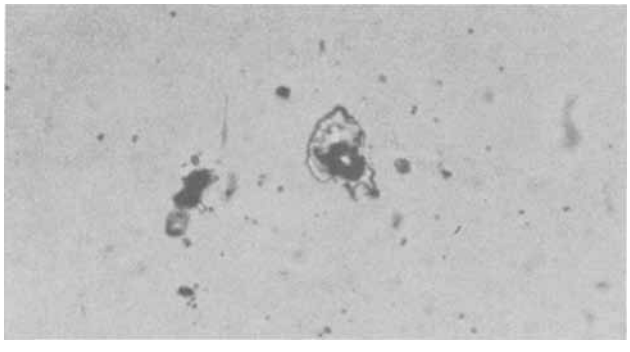

Fig. 8. Damaged area under reverse-biased probe for single-pulse system with a pulse width of 1 μsec. Magnification ca. 225X.

about 1 μ sec after breakdown is reached. The damage for this system is equivalent to that of a pulse system with a pulse width of 1 μsec.

Several breakdown voltage levels are obtained in a typical sample, as shown in Fig. 9. Here the breakdown voltage as a function of time is plotted for a single-pulse system. The structure of the trace is not completely understood, but the second level is probably similar to thermal breakdown and the third level due to melting of the sample. Similar results, although on a larger time scale, were reported by Agatsuma (11) for point contact diodes.

A further complication to the pulse technique is demonstrated in Fig. 10. A repetitive-pulse technique was used with a pulse rate of 15 Hz. A sampling scope was used to read the peak voltage. The oscillator had a peak output of 200v, with a 50 ohm termination. These data were taken on an n/n^+ silicon epitaxial layer with a resistivity of about 0.1 ohm-cm. Note that the readings approach the d-c value but have no apparent upper limit. This type of dependence on pulse width or duty cycle is certainly different than would be expected of a pn junction. These results confirm the trend Allen, Clevenger, and Gupta (6) observed, using their pulse technique.

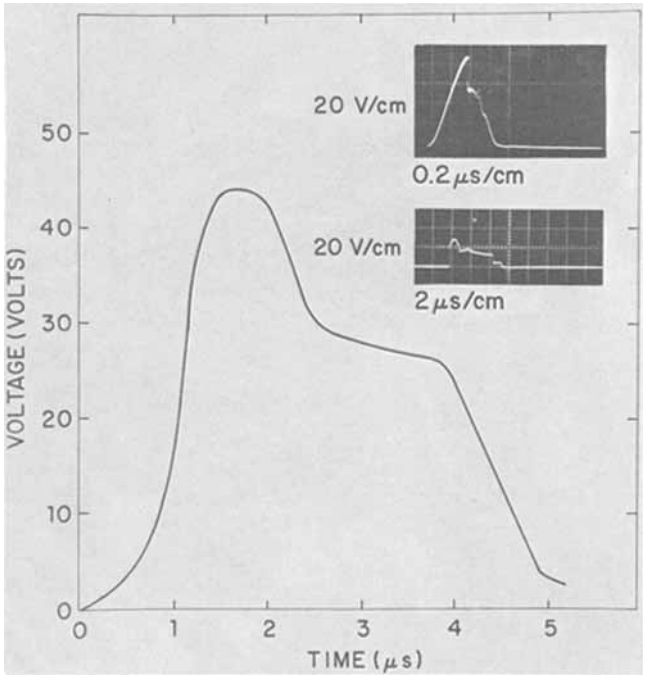

Fig. 9. Pulsed voltage-time characteristics

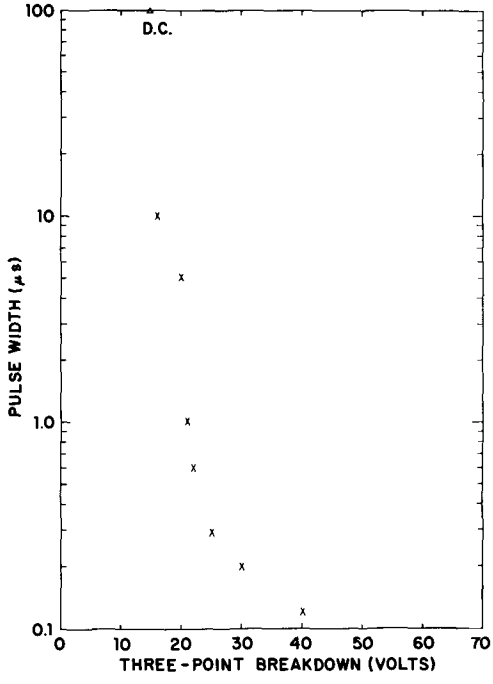

Fig. 10. Effect of pulse width on three-point probe voltage breakdown.

In addition, for a pn junction, the breakdown voltage should increase for an increase in ambient temperature. This is not the case for the three-point probe as shown in Fig. 11. The breakdown voltage is nearly a linearly decreasing function of temperature. The coefficient of temperature variation for this 0.2 ohm-cm n-type sample is 0.0795 v/°C.

Several conclusions can be drawn from these data.

1. It is apparent that the electronics used for the measurement of three-point probe breakdown voltage must be shut off within 1 μsec after breakdown has been reached in order to avoid excessive damage to the silicon and point material. This can be accomplished with either a d-c ramp or pulse technique.

2. Many of the heating phenomena suggest that the three-point probe is not measuring a true avalanche

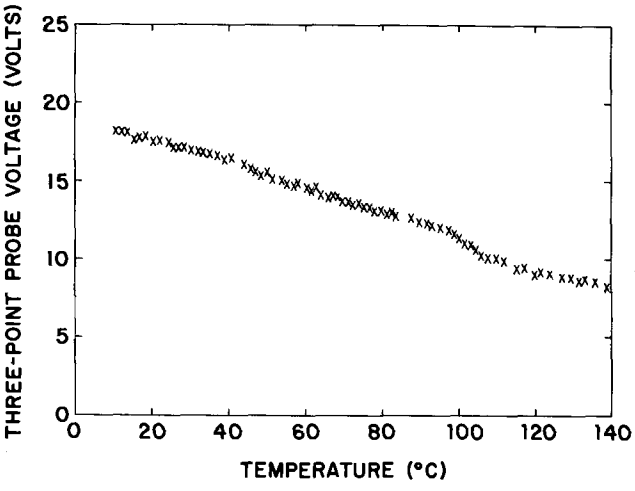

Fig. 11. Three-point probe breakdown voltage as a function of temperature for an n-type silicon sample.

breakdown in its common use but a thermal breakdown effect.

3. The effects of forming and duty cycle are important in determining the breakdown voltage and must be considered in the calibration of a system.

4. The temperature rise under the point is very severe and can lead to an apparent melting of the silicon under the point. The power at breakdown is about 1w, and for the areas of contact normally encountered for these types of probes a power density as much as 10^7 w/cm^2 is possible. This is certainly a high enough power density to melt silicon if it is held at this level for a long enough time.

Acknowledgment

The authors would like to acknowledge the assistance of Miss Lucy A. Pietrogallo for some of the experimental data and of Mr. A. Dupnock for some of the photographs.

Manuscript submitted Feb. 19, 1968; revised manuscript received Sept. 6, 1968.

Any discussion of this paper will appear in a Discussion Section to be published in the December 1969 JOURNAL.

REFERENCES

1. E. E. Gardner, J. F. Hallenback, Jr., and P. A. Schumann, Jr., *Solid-State Electron.*, **6**, 311 (1963).
2. J. Brownson, *This Journal*, **111**, 919 (1964).
3. P. J. H. Dobbs and F. S. Kovacs, *Semicond. Prod.*, **7**, 28 (1964).
4. E. E. Gardner and P. A. Schumann, Jr., *Solid State Electron.*, **8**, 165 (1965).
5. M. H. Norwood, *This Journal*, **112**, 875 (1965).
6. C. C. Allen, L. H. Clevenger, and D. C. Gupta, *ibid.*, **113**, 508 (1966).
7. H. Frank, *Phys. Status Solidi*, **19**, 401 (1966).
8. P. A. Schumann, Jr., J. F. Hallenback, Jr., M. R. Poponiak, and C. Schneider, To be published in *Semicond. Prod.*
9. P. A. Schumann, Jr., and A. Dupnock, *Electrochem. Technol.*, **6**, 218 (1968).
10. L. P. Hunter, "Handbook of Semiconductor Electronics," McGraw-Hill Book Co., New York (1962).
11. T. Agatsuma, *Proc. IEEE*, **54**, 1207 (1966).

Brief Communications

A Deep Donor Level in n-type Silicon Carbide

M. J. Moore

Associated Semiconductor Manufacturers Ltd., Stockport, Cheshire, England

The results of recent investigations (1, 2) on the electro- and photoluminescence of silicon carbide p-n junctions have pointed to the possible presence of a low lying donor state between 0.4 and 0.6 ev below the bottom of the conduction band. The purpose of this note is to present strong evidence for the existence of a group of deep energy states from the measurement of the electrical properties of silicon carbide.

Measurements of Hall coefficient have been made from room temperature to about 1000°C on three n-type single crystals of commercial grade silicon carbide. Details of the experimental arrangements have been outlined in a previous paper (3). The electron concentration n, obtained from the Hall coefficient R, by means of the familiar expression

$$n = 3\pi/8Re$$

is shown as a function of reciprocal temperature in Fig. 1.

From room temperature to about 400°C the variation of carrier concentration is what one would expect with the excitation and eventual exhaustion of electrons from partially compensated nitrogen impurity levels at an energy which, for commercial grade crystals, is generally between 0 and 0.1 ev, depending on the concentration of ionized nitrogen centers. However, beyond 400° and up to 1000°C there is rather unusual behavior of the electron concentration with a rapid rate of increase with increasing temperature. In some semiconductors this behavior is not uncommon and is attributed to the excitation of elec-

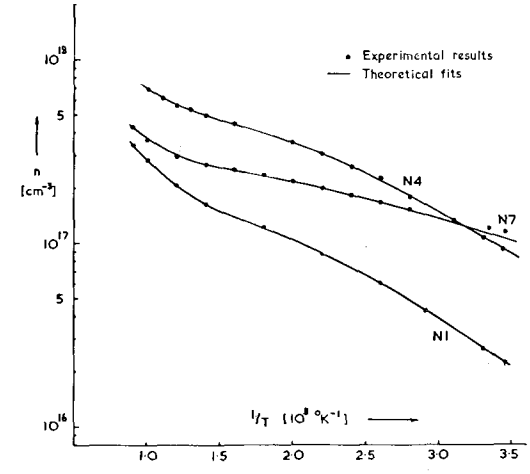

Fig. 1. Reciprocal temperature variation of carrier concentration for three n-type silicon carbide crystals.

trons across the band gap. Hexagonal silicon carbide however, has a band gap of approximately 3 ev and the intrinsic carrier concentration at 1000°K would be of the order of 10^{10} cm^{-3} which is clearly several orders of magnitude less than the concentrations involved at this temperature.

The presence of a second group of donor levels would explain the qualitative features of the experimental data in Fig. 1. A quantitative examination of these results, taking into account the proposed deep levels would begin with the expression for the carrier concentration derived from the condition for electrical neutrality within the crystal, *viz.*

$$n = N_d - N_a - N_d f_d + N_1(1 - f_1) \qquad [1]$$

where the Fermi factors f_d, f_1 are given by

$$f_d = \left(1 + \frac{g_d N_c}{n} \exp -\epsilon_d/kT\right)^{-1}$$

$$f_1 = \left(1 + \frac{g_1 N_c}{n} \exp -\epsilon_1/kT\right)^{-1}$$

with

$$N_c = 2\left[\frac{2\pi m^* kT}{h^2}\right]^{3/2}$$

The concentrations of shallow donor, deep donor, and compensating acceptor centers are, respectively N_d, N_1, and N_a and the corresponding donor activation energies are ϵ_d and ϵ_1. The factors g_d, g_1 depend on the type of binding between an electron and the corresponding ionized donor center. If the binding is unpaired with respect to the electron spin then these factors would be equal to ½ whereas for paired binding they would be equal to 2. For a nitrogen donor we would expect $g_d = ½$.

Because of the nature of the Fermi factors f_d and f_1, the analyses may be carried out in two parts. First, with the effective mass of the electron $m^* = 0.7$ m and $g_d = ½$, N_1 is put equal to zero and N_d, N_a, and ϵ_d are adjusted to give the best fit to the experimental data from room temperature to the temperature at which the point of inflexion is apparent. Following this, g_1 is put equal to ½, and values of N_1 and ϵ_1 are found which explain the dependence of carrier concentration over the remaining range of temperature. The values obtained by this procedure are given in Table I and the theoretical fits are shown in Fig. 1.

Table I. Values obtained

Specimen	N_d	N_a $cm^{-3} \times 10^{15}$	N_1	ϵ_d ev	ϵ_1
N1	2.0	1.78	0.41	0.09	0.50
N4	1.64	1.04	0.85	0.09	0.50
N7	3.40	3.07	0.48	0.04	0.54

The departure of theoretical curves from the experimental results at high temperatures with values of ϵ_1 different from those in Table I gives an indication of the error in ϵ_1. This is such that ϵ_1 is not likely to be greater by a factor of 14% or less by a factor of 7% than the tabulated values. It will also be appreciated that as ϵ_1 is contained with temperature T under the exponential in Eq. [1] then the value of ϵ_1 required for the best fit is quite insensitive to variations in the choice of the other variables. For example, on repeating the second part of the analyses with $g_1 = 2$ it is found that the "best fit" values of ϵ_1 are only 5% greater than those given above.

Manuscript received Oct. 17, 1968.

Any discussion of this paper will appear in a Discussion Section to be published in the December 1969 JOURNAL.

REFERENCES

1. A. Addamianio, R. M. Potter, V. Ozarow, *This Journal*, **110**, 517 (1963).
2. G. F. Kholuyanov, *Sov. Phys. (Solid State)*, **7**, 2620 (1966).
3. E. W. J. Mitchell and M. J. Moore, Int. Conf. on Semiconductors, Paris, p. 235 (1964).

Depositing Silicon Nitride Layers at Low Temperature Using a Photochemical Reaction

M. G. Collet

Philips Research Laboratories, N. V. Philips' Gloeilampenfabrieken, Eindhoven-Netherlands

In the past two years much has been written on the use of silicon nitride in semiconductor technology (1, 2). The subject is of interest because it has appeared that silicon nitride layers can be very dense. This makes them very effective as diffusion masks and less susceptible to ion drift than silicon dioxide layers.

The work of Elgin and Taylor (3) and Emeléus and Stewart (4) on the photosensitized decomposition of hydrazine (N_2H_4) and silane (SiH_4) made us investigate whether it is possible to use a photosensitized reaction between these components to deposit a nitride layer at temperatures as low as room temperature.

We used a closed quartz walled system filled with a mixture of approximately equal quantities of silane and hydrazine with a total pressure of about 5 Torr. Mercury vapor with a partial pressure of 10^{-3} Torr was added to the mixture.

When irradiated with 2537Å uv light the mercury atoms are excited to the $^3P_1$ state. On collision with silane or hydrazine molecules the mercury atoms release the absorbed energy, thereby decomposing the silane or hydrazine. By way of a reaction sequence not yet investigated, the decomposition products form a deposit on the substrate, which may consist for example of silicon or germanium.

In Fig. 1 a comparison is made between the infrared absorption spectra of silicon nitride layers grown at 200°C with uv light and at 900°C with the pyrolytic process ($SiH_4 + NH_3$).

The spectrum for the low temperature process shows an absorption band at 4.7μ, which has also been found for sputtered nitride (5) and has been attributed to Si ≡ N or Si-H bonds. Apart from this band there is no difference with the spectrum for pyrolytic nitride. On this evidence and because the refractive index $n = 2$ we assume the layers to be silicon nitride.

At deposition temperatures lower than 150°C the infrared absorption spectrum showed an Si-O absorption band as well. This is probably caused by contamination of the hydrazine with hydrazine hydrate or water. Ultra dry hydrazine should permit deposition of silicon nitride at room temperature.

Table I compares the properties of pyrolytic nitride and the low-temperature variety. The values given are

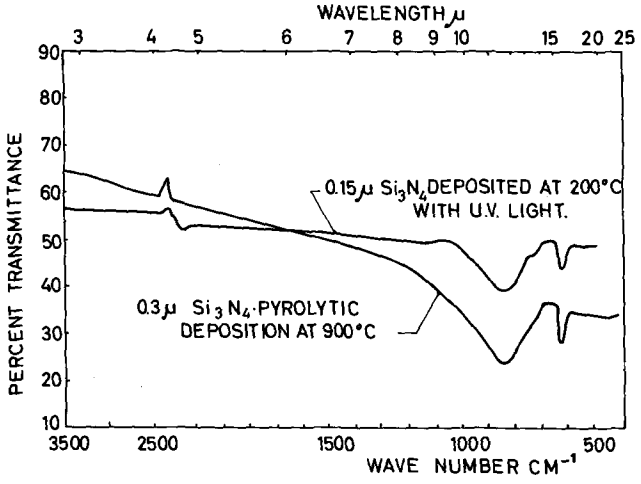

Fig. 1. Infrared absorption spectra of pyrolytic and low-temperature nitride.

only approximate because both processes cover a range of possible values depending on growth conditions.

However, the lower deposition temperature clearly results in less dense layers and with the density all other properties change as well. Thus it is possible to vary the properties of the layers by varying the deposition temperature or by applying various heat-treatments.

At 200°C the photosensitized deposition of silicon nitride on oxidized silicon wafers induces no change in surface states or oxide charge densities. Deposition at a temperature of 450°C influences the oxide-silicon interface in the same way as the well-known hydrogen or wet nitrogen anneal (6).

Table I. Si_3N_4 layers grown at 200°C with uv light and at 900°C from $SiH_4 + NH_3$

	T, °C	Dielectric strength, v cm^{-1}	Dielectric constant, ϵ_r	Etch rate ($NH_4F \cdot HF$) μ min^{-1}
$SiH_4 + NH_3$	900	10^7	6.0	0.001
$SiH_4 + N_2H_4$	200	10^6	5.5	0.1

The most attractive possibilities of the photosensitized process lie in the covering of ready-made devices with a nitride layer impenetrable to air, moisture, Na ions, and other ambient impurities. Some preliminary experiments on this application have given promising results.

Manuscript received Sept. 30, 1968.

Any discussion of this paper will appear in a Discussion Section to be published in the December 1969 JOURNAL.

REFERENCES

1. S. M. Hu, *This Journal*, **113**, 693 (1966).
2. T. L. Chu, C. H. Lee, and G. A. Gruber, *ibid.*, **114**, 717 (1967).
3. J. P. Elgin and H. S. Taylor, *J. Am. Chem. Soc.*, **51**, 2059 (1929).
4. H. J. Emeléus and J. Stewart, *Trans. Faraday Soc.*, **32**, 1577 (1936).
5. A. R. Janus and G. A. Shirn; *J. Vac. Science Techn.*, **4**, 37 (1967).
6. E. Kooi, *Philips Research Repts.*, **20**, 578 (1965).

High Current Density Chlorate Cell Using Platinized Anodes

J. R. Newberry,*[1] W. C. Gardiner,** A. J. Holmes,[2] and R. F. Fogle[3]

Olin Mathieson Chemical Corporation, New Haven, Connecticut

ABSTRACT

Sodium chlorate was produced in a monopolar cell having platinized titanium anodes and steel cathodes. A high current density was used in order to minimize cell costs. A 144-amp cell was built and tested in a continuous experiment for 31 days. The energy requirements were 6300 kwhr d.c./ton $NaClO_3$. The replacement platinum which may not have been optimized was shown as 5.3 g/ton $NaClO_3$. The cell operated at 1 amp/in.^{2}, and 110°C. The cell feed contained approximately 190g NaCl and 330g $NaClO_3$ per liter. Cell effluent contained 110g NaCl and 580g $NaClO_3$ per liter. The average cell voltage was 3.7. The pH was 6.7. This process is the subject of U.S. Patent 3,043,757. A cell with variable electrode spacings and height was used to indicate that ⅛ in. spacing would be preferred with electrodes 3 ft high in the commercial cell design.

Sodium chlorate is prepared commercially by electrolyzing sodium chloride in an undivided cell to form hypochlorite, which in turn reacts chemically to form chlorate in the cell and/or associated vessels.

The process has been described by Forester (1) and Knibbs and Palfreeman (2). Commercial cells with graphite anodes having become standard practice, the corrosion of graphite has dictated operation generally below 50°C. Current densities below 0.5 amp/in.^{2}, and heat exchange devices to provide cooling, are customary.

About the time that the possibilities for electrolyzing brine with platinized titanium electrodes were indicated (3), Olin had made some interesting observations in chlorate cell studies. The cell voltage with platinized electrodes was lower than expected and, as a result, considerably higher current densities were possible when customary cell voltages were applied. Considering the expected stability of platinum, it was reasonable to explore operation at higher temperature. Increased temperature appeared practical and offered additional advantages involving increased solubility of chlorate. As more chlorate was soluble at higher temperature, the possibility of forming product crystals simply by cooling the cell effluent was apparent. Since cell effluents, relatively concentrated in chlorate, were feasible, it was possible to operate with more sodium chloride in the electrolyte. This increased concentration of NaCl served to reduce both cell voltage and the formation of by-product perchlorate. This process was developed in a series of laboratory cells and when a reasonable approach to economics, competitive with those for conventional cells, was indicated a commercial cell and flow system were designed.

Experimental and Results

After exploratory experiments indicated a high current density might be used to justify the cost of platinized anodes, a 9-amp cell was designed using a 4-liter glass vessel placed on a hot plate with a magnetic stirrer. The vessel was closed with a 1-in.-thick Lucite cover carrying pH electrodes, leads for a level controller, anode and cathode leads, a thermometer, and connections for adding dilute hydrochloric acid and for removing cell gas and water vapor. A condenser separated water vapor from cell gas. The liquid level controller maintained 2.5 liters of electrolyte in the cell by actuating a valve to return condensate to make up for evaporation. A pH controller fed 1% hydrochloric acid to the cell to maintain the electrolyte at pH 7.

The electrodes suspended from the cover by 1/16-in.-diameter metal wires were each 3 in. square and 1/16 in. thick. They were completely submerged in the electrolyte. The anode was platinum-plated titanium and the cathode was either mild steel or platinized titanium. Spacers formed by making saw cuts in small Teflon strips were slipped over the bottom of the electrodes to maintain the distance at ⅛ in.

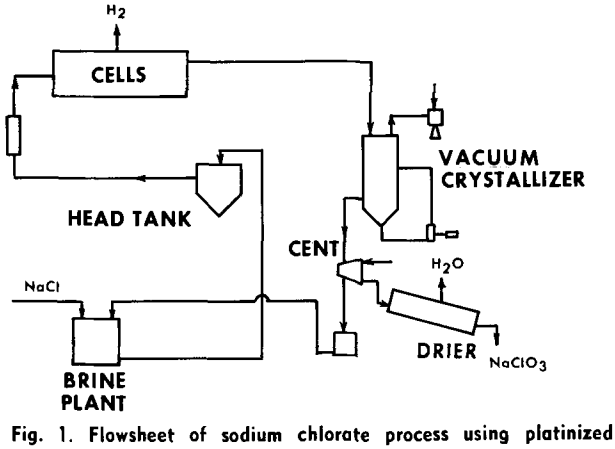

Fig. 1. Flowsheet of sodium chlorate process using platinized titanium anodes.

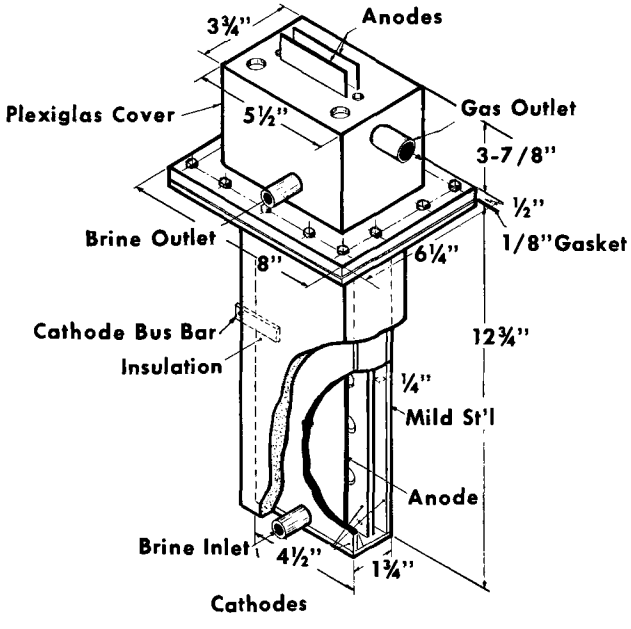

Fig. 2. Diagram of 144-amp monopolar cell.

* Electrochemical Society Active Member.
** Electrochemical Society Active Member Representative of a Patron Member Company.
[1] Present address: 120 Laurel Terrace, Cheshire, Connecticut.
[2] Present address: 22 Terrace Court, Ballston Lake, New York.
[3] Present address: 1317 W. Princeton, Ontario, California.

Table I. Typical data: 9-amp cell operated at 111°C

Hours	NaCl-gpl	$NaClO_3$-gpl	pH	Volts	% C.E. $NaClO_3$	% C.E. Gas	Kwhr d.c./ton Chem.	Kwhr d.c./ton Gas	Lb HCl/ ton
2532	96	757	7.3	3.90	93.5	—	5770	—	35
2556	92	750	7.0	3.92	98.5	94	5450	5770	54
2580	89	735	6.85	3.97	78.5	88	6850	6240	5
2604	91	710	6.6	3.98	60	92	7500	6030	12
2629	109	689	6.95	4.00	100	93	5500	5940	15
2701	97	795	6.65	4.40	95	96	6000	5800	28
Avg.	96	739	6.9	4.03	87.6	93	6178	5956	25

Table II. Perchlorate formation as chloride is depleted

Hours	NaCl-gpl	$NaClO_3$-gpl	$NaClO_4$-gpl	pH	Volts
1673	93.7	752	1.39	6.6	3.58
1697	77.7	785	3.27	6.9	3.67
1720	60.5	791	4.22	6.85	3.72
1747	34.5	821	4.55	7.0	3.77
1771	9.0	860	5.42	7.0	3.84
1795	7.9	882	8.13	6.9	3.88
1820	3.3	886	21.1	6.5	3.99
1881	2.2	901	37.6	6.5	3.90
1866	2.3	913	47.8	6.7	3.98
1892	1.6	908	61.5	6.7	3.97

Table III. Comparison of platinized titanium and steel cathodes

Period hr	Cathode Pt or Fe	NaCl-gpl	pH	Temp °C	Volts
3516	Pt	91	6.5	109	3.76
3843	Fe	92	6.9	112	3.47
3540	Pt	96	6.4	111	3.61
3795	Fe	96	6.8	112	3.36
3819	Fe	96	6.9	110	3.44
3564	Pt	106	6.7	110	3.64
3771	Fe	106	7.0	112	3.31

The cell was charged with a solution containing approximately 750 gpl $NaClO_3$, 100 gpl NaCl, and 2 gpl $Na_2Cr_2O_7$. It was stirred and heated to the boiling point which varied from 105° to 110°C.

Every 24 hr, the electrolyte was analyzed and a portion was removed which contained an amount of chlorate equivalent to the daily production. Solid NaCl was added to the cell at this time to replace the salt that had been consumed. Gas samples were taken daily and analyzed in an Orsat apparatus for Cl_2 and O_2. Current efficiency was calculated from the chlorate analysis and gas analysis. Periodically, current, voltage, temperature, pH, condensate volume, and acid consumption were measured.

Table IV. Platinized titanium anodes in "144-amp cell"

Plated area 132 in.^{2}, average thickness = 0.00017 in., current used 132 amp

Ampere-hours	Wt loss, g	g Pt/ton $NaClO_3$
50,618	0.2615	8.6
28,699	0.115	6.9
63,711	0.713	19.4*
97,330	0.299	5.3

* Cell ran dry.

Typical data are presented in Table I. The two methods of measuring current efficiency show wide variations. Estimates of the chlorate produced suffer from analytical errors of very concentrated solutions and from any operating upsets that may have occurred during the period. The gas analyses indicate current efficiencies only at the time of sampling.

Perchlorate formation.—The effect of allowing NaCl to be depleted is shown in Table II. Normal practice is to maintain approximately 100 gpl NaCl to minimize formation of perchlorate.

Cathode material.—A platinized titanium cathode was used for much of the test but, in the period 3400-3700 hr, two cathodes lost their platinum. After the second failure, a steel cathode was used and a lower voltage resulted as shown in Table III. The difference seems to be 0.2-0.3v.

Proposed sodium chlorate process.—During the operation of the 9-amp cell with platinized titanium anodes, a processing scheme for recovery of solid chlorate was developed (4). The electrolysis of NaCl to $NaClO_3$ was carried out at temperatures of about 105°-123°C, the boiling range of the electrolyte. Water

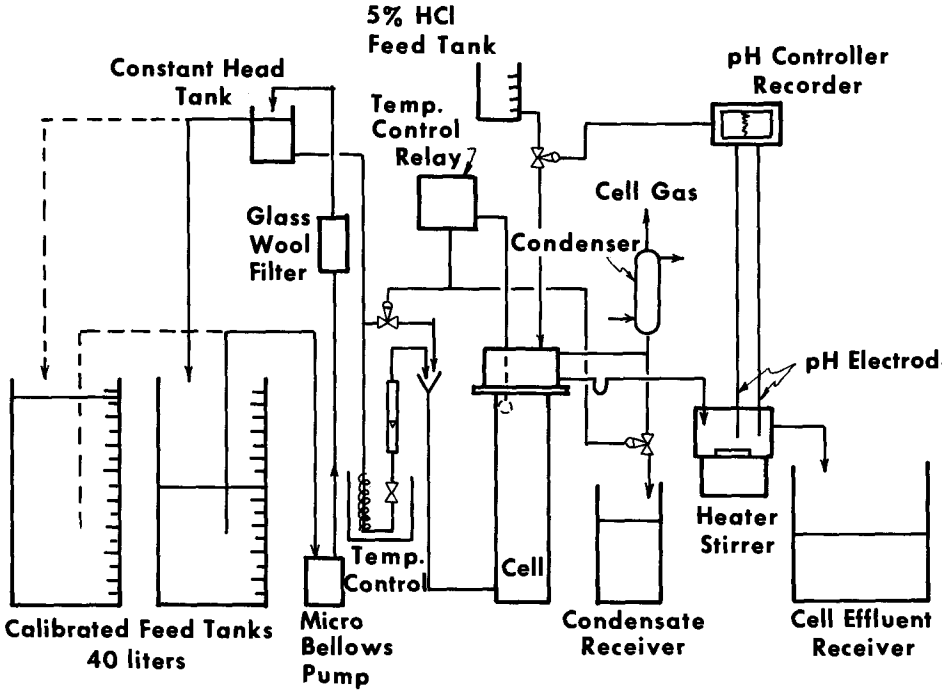

Fig. 3. Process flowsheet for 144-amp cell.

Table V. Data on "144-amp cell" operated continuously for 31 days at 132 amp

Amp-hr since start	Cell feed, gpl NaCl	Cell feed, gpl $NaClO_3$	Cell effluent, gpl NaCl	Cell effluent, gpl $NaClO_3$	Avg volts	Current efficiency, %	Kwhr/ton $NaClO_3$ (b)	Lb HCl/ton $NaClO_3$ (d)	Cell temp °C	Cell pH
155175(a)	194	334	80	473	4.56	76	6480	98	106	7.1
168057	193	352	104	577	3.69	81	6240	74	110	6.9
180402	191	328	114	604	3.72	80	6400	38	109	6.5
193120	192	330	96	580	3.70	79	6400	41	108	6.5
206354	191	318	139	628	3.67	81	6260	19	109	6.8
217642(c)	—	—	—	—	—	—	—	—	—	6.8
220746	192	330	119	637	3.70	86	5920	41	108	6.8
230962	192	330	105	572	3.72	81	6320	44	108	6.8
233504	189	326	113	671	3.71	82	6360	27	108	6.8
236699	189	326	118	603	3.68	78	6540	23	108	6.8
240359	189	326	187	326	3.67	80	6360	31	108	6.8
Avg.	191	332	112	580	3.67	81	6300	48	108	6.7

(a) Four days of continuous operation preceding sampling. Start at 143,029 amp-hr.
(b) Energy consumption based on $NaClO_3$ weighed.
(c) Cell inlet plugged with solids. Solids removed without interrupting current. Platinum loss 0.299g in 97,330 amp-hr.
(d) 100% basis; used as hydrochloric acid.

was evaporated with cell gas and removed from the cell. The effluent liquor from the cell was cooled; in a plant, this would be done preferably by flashing off further water from the liquor in a crystallizer. Sodium chlorate crystallized out and was separated, washed, and dried. The wash water and filtrate were recycled. Sodium chloride was added as purified brine to the recycle liquor. A flowsheet of this process is shown in Fig. 1.

A larger monopolar cell was built to test the platinized titanium anode further in conjunction with the proposed chlorate process.

144-Ampere monopolar cell.—A second chlorate cell was designed with 144 in.^{2} of anode surface to be operated at 144 amp. It is illustrated in Fig. 2. During an initial run, the platinum plating failed and the anodes were replated with 132 in.^{2} of coated surface. Thereafter, the cell was operated at 132 amp.

The cell was in two parts: a steel cell body with a top flange and a flanged Plexiglas dome. The steel cell body has a perforated steel partition providing a cathode between two anodes. Two platinized titanium anodes are suspended through slots in the dome and are spaced ¼ in. from the cell body and central partition. The anode surfaces were platinized over an area 3 in. x 12 in. (3 in. x 11 in. the second time). Sel Rex Corporation's Platinex L.S.III proprietary plating solution was used. The anodes were weighed before and after plating.

The cell was operated under the conditions of current density, electrolyte concentration, and temperature as proposed for commercial operation. Current was adjusted manually, but an integrating ampere-hour meter was depended on for current efficiency calculations. The cell feed selected was 195 gpl NaCl, 330 gpl $NaClO_3$, and 2 gpl Na_2Cr_2O7. The expected cell effluent was 95 gpl NaCl and 750 gpl $NaClO_3$. The cell effluent was cooled to room temperature and solid $NaClO_3$ crystallized and filtered off. The filtrate was returned to the feed tank along with solid salt and water.

The system was perfected to operate overnight and week ends with the arrangement shown in Fig. 3. Each

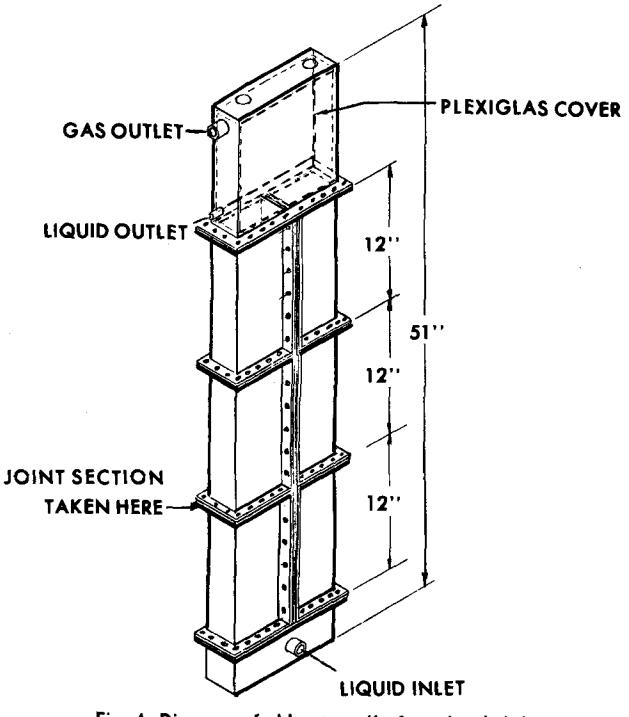

Fig. 4. Diagram of chlorate cell of varying height.

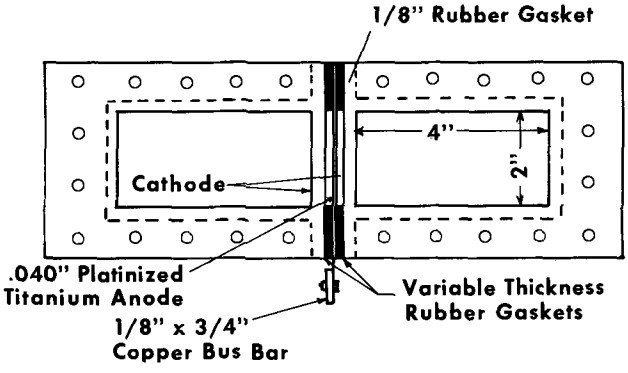

Fig. 5. Cross section of experimental chlorate cell.

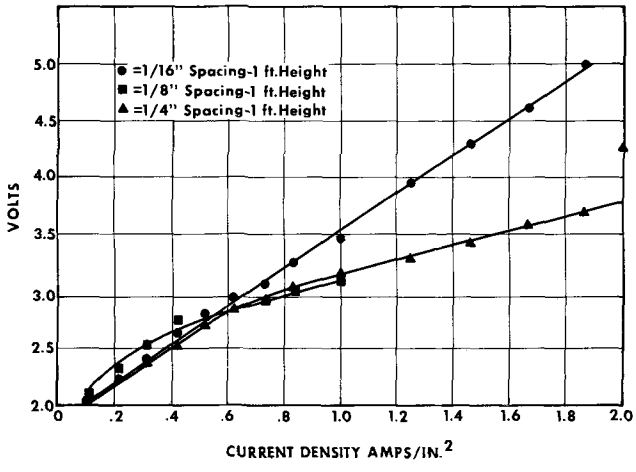

Fig. 6. Effect of anode-cathode spacing on cell voltage.

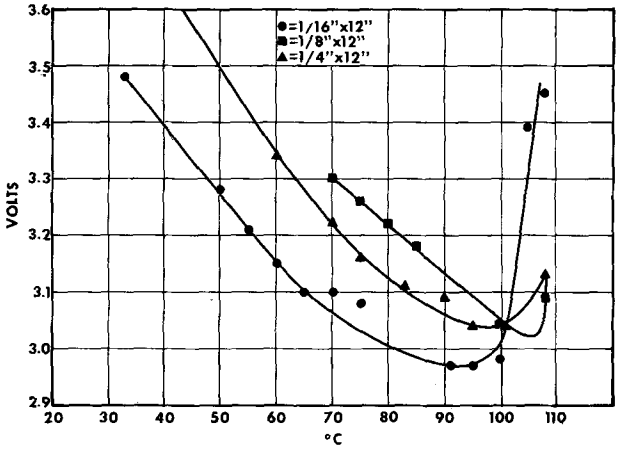

Fig. 7. Effect of temperature on cell voltage.

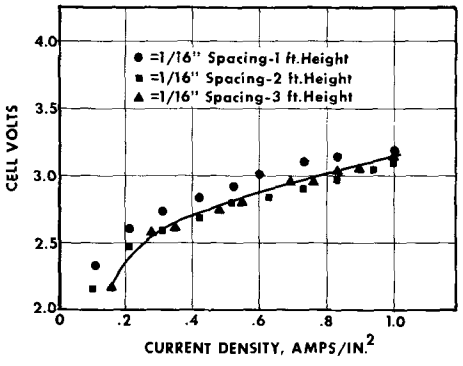

Fig. 8. Effect of electrode height on cell voltage.

feed tank and the cell effluent receiver had 4 days' capacity. The liquor in the cell effluent receiver was weighed and sampled, then cooled and filtered. One feed tank could be prepared while the other was in operation. It was found necessary to pass the cell feed liquor through a glass coil and needle valve immersed in a thermostat to maintain constant flow. The cell temperature was maintained by automatically returning the required amount of condensate to the cell. The *p*H was controlled by passing the cell effluent through a *p*H cell with glass and calomel electrodes. A controller-recorder actuated a valve feeding dilute hydrochloric acid to the cell. It was found that the *p*H electrodes also worked satisfactorily in the cell.

Platinum life.—The anodes were weighed four times to determine platinum loss. The data are given in Table IV. The cell feed failed during one test and resulted in a high platinum loss. If this measurement is excluded, the other three averaged 6.95 g/ton $NaClO_3$.

Operating data for 31 days of continuous operation are given in Table V. There was a short stoppage of cell feed, but the current was not interrupted. The current efficiency based on $NaClO_3$ averaged 81% and energy consumption averaged 6300 kwhr/ton $NaClO_3$.

Electrode height and spacing study.—A companion experiment to the 144-amp process study was made to evaluate the effect of electrode spacing and cell temperature.

A flanged cell was constructed to contain a single pair of vertical electrodes. The cell was arranged so that adjustment in gasket thickness could be employed to provide various interelectrode distances. Additionally, the cell was built in three sections (Fig. 4 and 5), 1 ft high, to study height and spacing with electrodes 1, 2, and 3 ft high. Data taken with this setup are shown graphically in Fig. 6, 7, 8.

Discussion

The data reported in Tables IV and V were collected in a 31-day operation. The data in Table V indicate current efficiencies and energy requirements in kwhr d.c./ton $NaClO_3$ based on the $NaClO_3$ weighed.

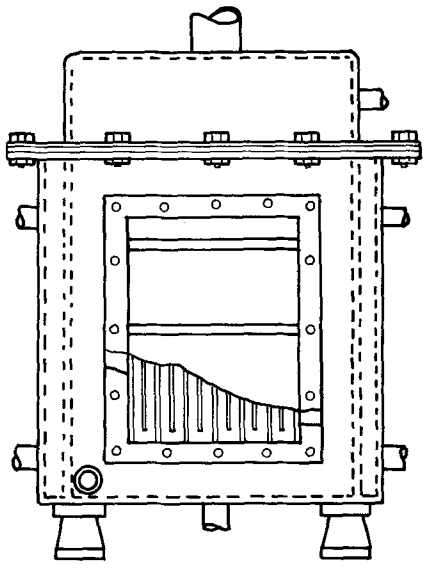

Fig. 9. Diagram of monopolar chlorate cell.

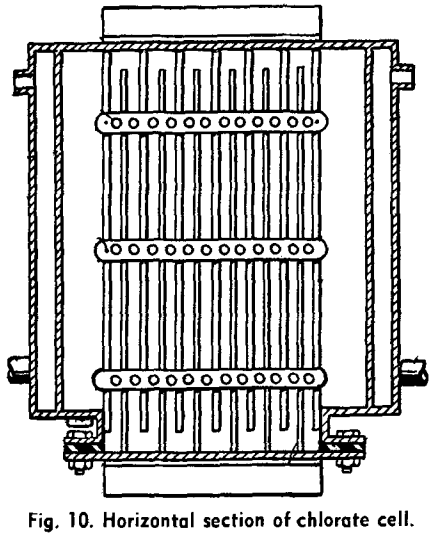

Fig. 10. Horizontal section of chlorate cell.

Experimental work was halted before the platinum loss was fully explored. The operation had become better controlled during the experiment, permitting the hope that platinum losses might be reduced further with increasing skill in operation.

Comparisons of energy requirements reported for various cells and the expectation of improving the operation reported in Table V prompted the design of a commercial cell (5) to operate at 30,000 amp. Study of Fig. 8 indicated that an electrode 3 ft high was workable. An electrode gap of ⅛ in. was chosen from Fig. 6 and 7. A cell was designed as shown in Fig. 9 and 10. As can be seen, the rectilinear cell contained vertical steel cathodes. The sheet anodes were platinized titanium fixed to a titanium header. Twenty anodes, 2 x 2.5 ft, were planned for the 30,000-amp cell. The header and anode assembly slides into the side of the cell and is bolted in position. Teflon spacers are inserted in the cathodes to prevent short-circuiting.

The cell cover is a Fiberglas reinforced polyester dome. Bus connections are made from one cell body to the succeeding anode header by removable bus sections.

Summary

Experiments in bench-scale apparatus established the feasibility of a chlorate cell having platinized titanium anodes and steel cathodes. A 144-amp cell

demonstrated operation for 1 month at 1 amp/in.^{2}. The cell temperature was approximately 110°C. An energy consumption of 6300 kwhr d.c./ton $NaClO_3$ was shown. A commercial cell of 30,000-amp capacity was designed. The process flow visualizes crystallizing by cooling effluent cell liquor. No internal cooling is required for the cell.

Manuscript submitted April 30, 1968; revised manuscript received Sept. 21, 1968. This manuscript was presented at the Chlorates and Perchlorates Symposium at the Boston Meeting, May 5-9, 1968, as Paper 260.

Any discussion of this paper will appear in a Discussion Section to be published in the December 1969 JOURNAL.

REFERENCES

1. F. Forester, *Trans. Am. Electrochem. Soc.*, **46**, 23 (1924).
2. N. V. S. Knibbs and H. Palfreeman, *Trans. Faraday Soc.*, **16**, 402 (1921).
3. J. B. Cotton, *Platinum Metals Rev.*, **2**, 45 (Apr. 1958).
4. A. J. Holmes, U. S. Pat. 3,043,757 (1962).
5. A. J. Holmes and W. C. Gardiner, U. S. Pat. 3,055,821 (1962).

Electrochemical Oxidation of Multicomponent Hydrocarbon Fuels

I. Studies with n-Octane Based Fuels Containing Aromatic, Olefinic, and Naphthenic Components

Eugene Luksha[1] and Eugene Y. Weissman*[,2]

General Electric Company, Direct Energy Conversion Operation, West Lynn, Massachusetts

ABSTRACT

The classes of compounds found in liquid hydrocarbon fuels were studied to determine their effect on the electrochemical performance of direct oxidation anodes. Experiments were conducted on porous platinum black, Teflon electrodes in 95 weight per cent phosphoric acid at temperatures between 150° and 200°C. It was found that the performance of anodes operating on binary mixtures of n-octane and small amounts of hydrocarbon additives depends on the nature of the additive. For aromatic additives, an increase in molecular weight or complexity of the aromatic molecule will result in an increase in anode overvoltage. For olefin additives, there is a distinct relationship between the type of olefins and performance. The anode overvoltage decreases as the number of allylic hydrogen atoms increases. The cyclic olefin (six-membered ring) is aromatic in character due to an apparent dehydrogenation mechanism preceding the oxidation step. Iso-paraffins, in any proportion, do not affect anode performance of normal paraffins having the same number of carbon atoms. Sizable performance gains can be made by increasing cell operating temperatures. If a cell could be operated at 250°C, materials permitting, as much as a ten-fold increase in cell performance could be obtained, based on a linear extrapolation of existing data.

Because of economic necessity, commercial fuels will be used in practical fuel cell devices. While indirect utilizations, such as by steam-reforming, are realizable today, it is the direct electrochemical oxidation process which requires considerably more understanding and improvement. It forms the subject of this paper.

Commercially available fuels generally consist of complex mixtures of hydrocarbons, primarily straight and branched aliphatics, olefins, naphthenes, and aromatics. The aliphatic compounds, both straight and branched-chained, are relatively reactive in fuel cells, while the unsaturated and cyclic compounds are considerably more difficult to oxidize (1) and have been designated as "unreactive." These types of compounds are believed to adsorb on an electrode surface more strongly than aliphatic compounds, forming an inert ad-layer (2). For this reason, it is necessary to know the tolerance of an operating fuel cell anode to these "unreactive" compounds.

Experimental

The model fuel taken into consideration was split into its principal components: paraffins, olefins, naphthenes, and aromatics, as is shown in Fig. 1. The proportions of these components vary widely with the type and origin of the fuel. Normal octane was chosen as the base fuel and various quantities of single unreactive components were added to it. These additives were chosen on the basis that they are all found in relatively high concentrations in various types of hydrocarbon fuels (3-5) and have boiling points lower than 175°C, the practical upper temperature limit of the electrodes used in this work. As a result, compounds containing more than 1 ring, as, for example, indanes, indenes, tetralins, and naphthalenes, were not considered since they all have boiling points in excess of 175°C. Since hydrocarbons with condensed rings were eliminated, only alkylbenzenes, 1-ring naphthenes, in addition to the olefins and paraffins were studied.

The compounds shown in Fig. 1 were added to n-octane in varying concentrations. Polarization curves were taken using the binary solution as a fuel. These polarization curves were measures of the decrease in cell performance caused by the addition of the "unreactive" components.

The experimental equipment has been described elsewhere (6). The following conditions apply to the present work:

1. The electrodes used were 7.6 x 7.6 cm (46 cm^2 active geometric area) platinum-Teflon-screen composites of a type previously described (7). The platinum loading was 35 mg/cm^2 and the composition: 85 weight per cent (w/o) Pt-15 w/o TFE. The current-collecting screen was generally gold-plated expanded tantalum (5 Ta 10 4/0), and sometimes wire-woven platinum (45 mesh).

* Electrochemical Society Active Member.
[1] Present address: Gould-National Batteries, Incorporated, Research Division, Minneapolis, Minnesota 55414.
[2] Present address: Globe-Union, Incorporated, Corporate Applied Research Center, Milwaukee, Wisconsin 53201.

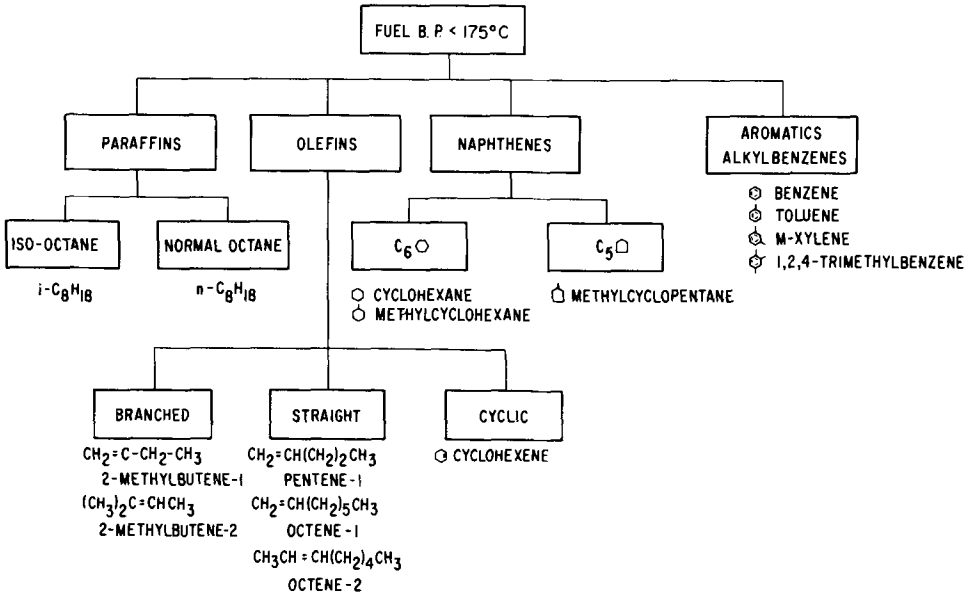

Fig. 1. Principal components of the model fuel.

2. The reference electrodes were hydrogen electrodes in the same electrolyte.

3. The electrolyte was 95 w/o phosphoric acid and, as mentioned above, the maximum practical operating temperature compatible with this electrode structure was found to be 175°C.

4. The counterelectrodes (cathodes) consisted of platinum-Teflon-platinum screen (woven, 45 mesh) composites with the same composition and loading as the anodes.

5. The experimental procedure for obtaining the polarization data was identical for each fuel studied. When the cell reached the desired temperature, the fuel was introduced at a flow rate of 20 μl/min [3] and the O.C.V. was allowed to stabilize for approximately ½ hr. The fuel flow rate was determined by observing the pressure drop across a calibrated capillary.

6. Prior to the start of each run, the anode potential was raised to approximately 1v for 30 sec in order to activate the electrode. The current was then shut off and the potential was allowed to stabilize. This point was recorded as the O.C.V.

7. A Kordesch-Marko bridge was used to control the current through the cell. To determine the initial portion of the polarization curve, small increases in the current were made in the range of 0-1 amp (0-22 ma/cm²). At each current setting, the anode potential was allowed to stabilize, before being recorded. Above 1 amp, the current changes were made in steps of ½ amp until the anode potential reached approximately 0.6v Above this potential, current increases were made in smaller steps as the limiting current was approached. The limiting current was taken as that current at which the anode potential would no longer stabilize. Following each run, the fuel was purged from the anode with nitrogen for 10 min. With the nitrogen purge on, the anode potential was brought up to about 1v to remove traces of fuel from the electrode surface.

Results and Discussion

Binary mixtures.—Aromatic additives.—Anode performance losses for n-octane with up to 5 mole per cent (m/o) additions of benzene, toluene, m-xylene, and 1, 2, 4 trimethylbenzene are summarized in Fig. 2.

There appears to be an effect on anode performance, in terms of molecular weight and degree of complexity of the additive, with the heavier, more complex additives, causing higher anode overvoltages.

The effects are generally small since the concentrations of the additives are small. It is expected that differences may become more pronounced as the concentrations of the additives increase.

In spite of some scatter in the experimental data, certain trends have been observed for the change in anode performance as a function of the additive complexity. Thus, the anode performance penalty for an n-octane fuel containing 3 m/o of various aromatics is shown to increase with an increase in the number of methyl groups in the aromatic molecule. Similar results were obtained with 1 m/o aromatic solutions (Fig. 3).

Naphthene additives.—The naphthenes that were evaluated can be divided into two classes: the six-

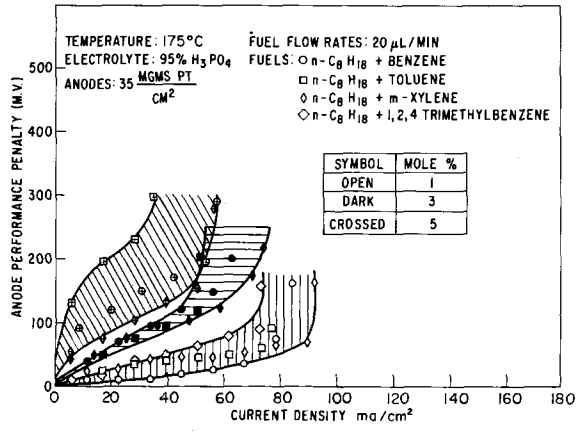

Fig. 2. Anode performance penalty for aromatics at 175°C.

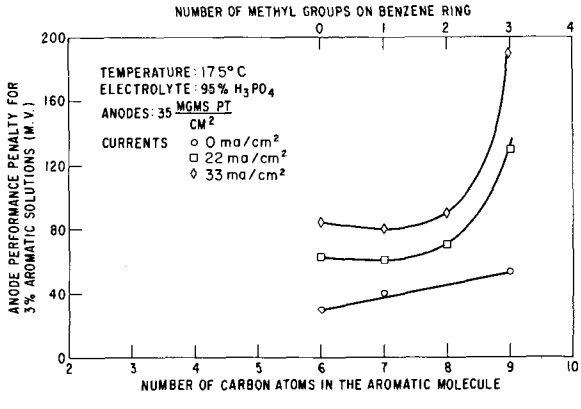

Fig. 3. Anode performance penalty vs. number of carbon atoms on the aromatic additive.

[3] This corresponds to 10 times the theoretical requirement of octane at 30 ma/cm².

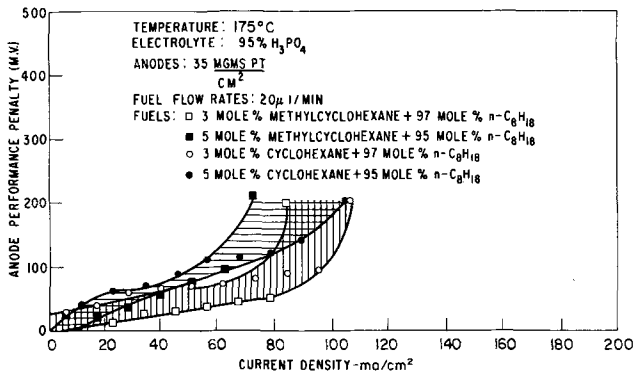

Fig. 4. Anode performance penalty for cyclohexyl naphthenes at 175°C.

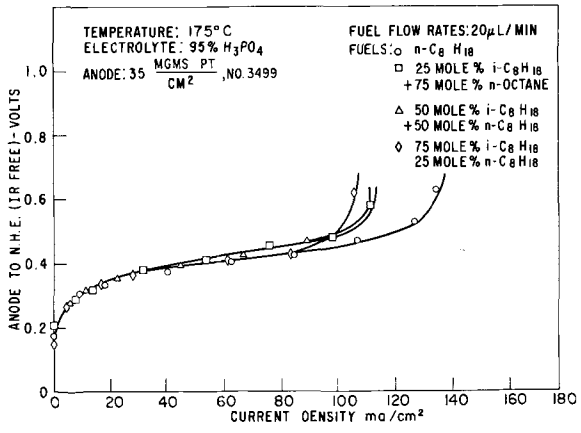

Fig. 5. Anode polarization for n-octane and i-octane mixtures at 175°C.

membered ring types which, under anode operating conditions, may be dehydrogenated to aromatics, and the five-membered ring types which appear to behave like paraffins.

The anode performance losses for n-octane based fuels containing varying amounts of cyclohexane and methylcyclohexane are shown in Fig. 4.

It appears that cyclohexane is more harmful to anode performance than methylcyclohexane, possibly because the presence of the electrophilic methyl group in the latter species would make dehydrogenation to an aromatic structure more difficult, and it is the aromatic structure that would cause the higher anode overvoltages.

In the study of the napthenes, probably the most significant result found was the high tolerance of a fuel cell anode to rather high concentrations of cyclopentyl naphthenes. No performance penalty was observed for these compounds for concentrations of up to 15 m/o and current densities up to 100 ma/cm².

Olefin additives.—The anode performance loss for various n-octane-olefin fuel mixtures is summarized in Table I. There appears to be a relationship between the type of olefin (straight-chained, branched, cyclic) and performance. The straight-chained olefins are apparently the most difficult to oxidize. The chain length of the linear olefin is of little importance to anode performance, except at high current densities, as is evident when one compares octene-1 with pentene-1. Here, at least, the detrimental effect of higher molecular weights is not apparent. The position of the double bond in the olefin molecule also plays a role in determining the anode performance penalty. As the double bond is moved toward the center of the molecule, the anode performance penalty is slightly reduced. This result can be seen by comparing octene-1 with octene-2 in Table I.

The branched olefins do not appear to cause any significant performance penalty when present in concentrations up to 5 m/o.

All these facts may be related to the number of allylic hydrogen atoms that the olefins contain (column 2, Table I). On a qualitative basis, given a series of hydrocarbons containing a single double bond, the olefin containing the largest number of allylic hydrogen atoms will be least harmful to anode performance. This appears to be the case here. An explanation of the phenomenon awaits further clarification.

The cyclic olefins, cyclohexane derivatives, form a separate class of compounds and exhibit higher anode overvoltages than the other types of olefins. These compounds are probably dehydrogenated under anodic conditions (*see* also, negative values of anode performance loss for cyclohexene in Table I) to aromatics, and as a result behave more like aromatics than like olefins. One point that should be emphasized is that an unsaturated six-membered ring is extremely detrimental to anode performance no matter what may be the degree of unsaturation.

Mixtures of normal and branched paraffins.—Polarization curves for cells operating on fuels consisting of mixtures of normal and iso-octanes, with 25-75 m/o iso-octane, show no change in performance as compared to pure n-octane (see Fig. 5). This indicates that branched and straight-chained paraffins having the same number of carbon atoms are very similar in reactivity. This is a useful result since it increases the flexibility of a choice of multicomponent fuels for specific performance requirements.

Multicomponent mixtures.—The above results were for mixtures of n-octane with single "unreactive"

Table I. Anode performance loss for addition of olefins at 175°F

Fuel composition, mole %	No. allylic hydrogen atoms	Electrode No.	Surface area, m^2/g	Anode performance loss,* mv						
				0 ma/cm²	22 ma/cm²	33 ma/cm²	55 ma/cm²	77 ma/cm²	99 ma/cm²	i_L ma/cm²
99% n-octane + 1% octene-1	2	1051**	—	9	0	0	0	0	30	90
97% n-octane + 3% octene-1	2	1051**	—	20	20	25	55	120	—	72
95% n-octane + 5% octene-1	2	1051**	—	50	45	75	150	—	—	53
99% n-octane + 1% octene-2	5	1059**	—	5	0	0	0	0	0	107
97% n-octane + 3% octene-2	5	1059**	—	25	15	20	20	25	20	97
95% n-octane + 5% octene-2	5	1059**	—	35	30	35	48	120	—	74
99% n-octane + 1% 2-methylbutene-2	9	3543	11.01	0	0	0	0	0	—	89
97% n-octane + 3% 2-methylbutene-2	9	3543	11.01	5	0	0	0	0	—	86
95% n-octane + 5% 2-methylbutene-2	9	3543	11.01	5	0	0	0	5	—	84
99% n-octane + 1% 2-methylbutene-1	5	3497	9.42	20	0	0	0	0	0	121
97% n-octane + 3% 2-methylbutene-1	5	3497	9.42	30	0	0	0	0	0	114
95% n-octane + 5% 2-methylbutene-1	5	3497	9.42	40	0	0	0	0	10	107
99% n-octane + 1% pentene-1		3544	10.22	10	0	0	7	20	34	110
97% n-octane + 3% pentene-1		3544	10.22	20	35	50	52	55	73	98
95% n-octane + 5% pentene-1		3544	10.22	20	35	50	52	55	98	96
99% n-octane + 1% cyclohexene		3515	—	−5	40	47	50	40	—	89
97% n-octane + 3% cyclohexene		3515	—	−10	75	80	98	115	—	75
95% n-octane + 5% cyclohexene		3515	—	−50	135	127	—	—	—	50

* Defined as the increase in anode potential over that measured for pure octane at the same conditions.
** Electrodes supported on Pt screen.

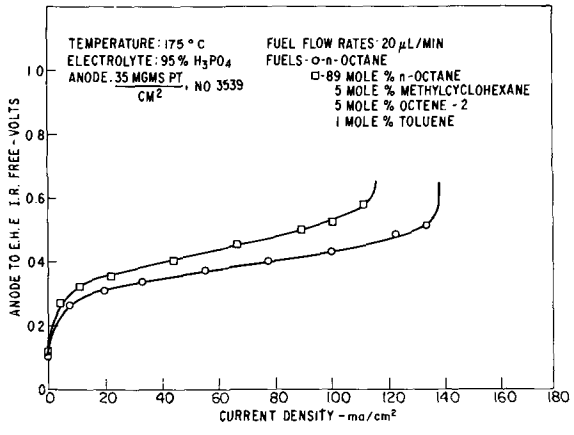

Fig. 6. Anode polarization curves for a fuel mixture consisting of 89 mole % n-octane, 5 mole % methylcyclohexane, 5 mole % octene-2, and 1 mole % toluene at 175°C.

components. Experiments were conducted in which several "unreactive" components were added to n-octane. The polarization curve of an anode operating on a fuel consisting of 89 m/o n-octane, 5 m/o methylcyclohexane, 5 m/o octene-2, and 1 m/o toluene is shown in Fig. 6. The concentrations of each of the additives were determined from binary mix data, so that the anode performance penalty for each of these components is roughly 50 mv at 30 ma/cm^2.

The outstanding feature of these results is that the cumulative effect of the "unreactives" does not appear to be additive. In fact, the performance loss is similar to that obtained for the corresponding binary mixtures, meaning that at these concentration levels each ingredient is not independent of the others present in the mixture.

This seems to suggest that, should a multicomponent mixture be chosen with any combination of ingredients, the performance penalty will be the one roughly corresponding to the "worst offender" in the mixture, as exhibited in a binary mixture with octane.

The main question, then, becomes one of establishing the influence of the other possible performance-determining parameters, such as the fuel flow rate.

Anode performance at other temperatures.—In an effort to determine the magnitude of a performance gain that may be obtained by increasing the operating temperature, several cells containing typical "unreactive" compounds were run at 150°, 175°, and 200°C. The data at 150° and 200°C are given elsewhere (8), while the data obtained at 175°C are given in this paper.

The log of the current at anode potentials of 0.4v for various fuels at 150°, 175°, and 200°C was plotted against $1/T$. From the Arrhenius-type relationship shown in Fig. 7, an approximate activation energy of 13 kcal/gmole is obtained; this is indicative of a strong temperature dependence. Although the data do not form a true straight line, probably because a variety of fuels were used, the trend toward significantly increased anode performance is evident. A linear extrapolation to a cell operating temperature of 250°C, for example, indicates the possibility of obtaining about a tenfold increase in performance, assuming, of course, that compatible electrode structures are available.

Conclusions

The performance of a platinum-activated anode oxidizing binary mixtures of n-octane and various small amounts (generally 1-5 m/o) of hydrocarbon additives in hot concentrated acid electrolytes (95% H_3PO_4 at 175°C) depends on the nature of the additive. Thus:

1. For aromatic additives, an increase in molecular weight or degree of complexity of the aromatic molecule (*e.g.*, number of methyl groups) will determine a corresponding increase in anode overvoltage.

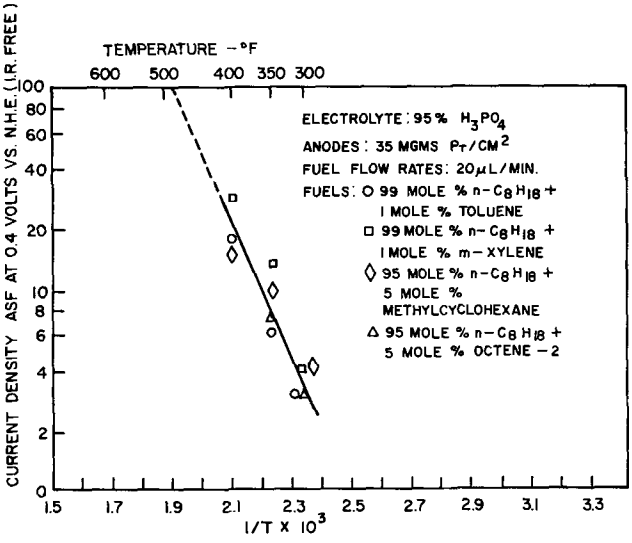

Fig. 7. Current at an anode potential of 0.4v *vs.* $1/T$.

2. For naphthene additives, the opposite appears to be true (when comparing methyl cyclohexane to cyclohexane). These findings are, however, in need of further experimental evidence.

3. For olefin additives, there is a distinct relationship between the type of olefin (straight-chained, branched, or cyclic) and performance; on an over-all basis, the number of allylic hydrogens in the noncyclic additive molecule appears to set a characteristic trend, with the anode overvoltage decreasing as the number of allylic hydrogens increases.

The cyclic olefin is quite aromatic in character due to an apparent dehydrogenation mechanism preceding the oxidation step. Specifically, six-membered cyclic olefins are very harmful to the performance of the anode both on a relative basis (compared to the other types of olefins) and on an absolute basis.

4. Iso-paraffins (in any proportion) do not affect the performance of normal paraffins having the same number of carbon atoms.

The detrimental effects of various additives, as obtained from performance data of binary mixtures (with octane), are not cumulative. Therefore, a multicomponent mixture will not necessarily contribute more to the rise of the anode overvoltage than the single "worst offender" in the mixture.

Sizable performance gains can be made by increasing cell operating temperatures. For example, if compatible materials and electrode structures were available so that a cell could be operated at 250°C, as much as a tenfold increase in cell performance would be possible, based on a linear extrapolation of the existing data.

Acknowledgments

This work is a part of the program under contract DA 44-009-AMC-479(T) with the U.S. Army Mobility Equipment Research and Development Center, Fort Belvoir, Virginia, to develop a technology which facilitates the design and fabrication of practical military fuel cell power plants for operation on ambient air and hydrocarbon fuels.

The authors are grateful for the able assistance of Mr. Lucien Brassard who performed much of the experimental work, and Mr. J. Foley for the manufacturing of most of the electrodes and preparation of the catalytic mixes used in the present study.

Manuscript submitted Jan. 29, 1968; revised manuscript received Aug. 30, 1968. This paper was presented at the ACS Meeting, Miami, April 9-14, 1967, Symposium on Electrochemical Processes, as paper 93.

Any discussion of this paper will appear in a Discussion Section to be published in the December 1969 JOURNAL.

REFERENCES
1. W. T. Grubb and C. J. Michalske, *Proc. Ann. Power Sources Conf.*, **18**, 17 (1964).
2. S. Gilman Tech. Summary Report No. 7, "Hydrocarbon-Air Fuel Cells," U.S.A. Engineers R & D Labs. (now: U.S. Army Mobility Equipment R & D Center), Ft. Belvoir, Va., Jan. 1965-June 1965, No. AD-474379L, pp. 2-76.
3. "Chemistry of Petroleum Hydrocarbons," Reinhold, New York (1954).
4. "Hydrocarbon Analysis," ASTM STP 389 (1965).
5. Y. M. Paushkin, "The Chemical Composition and Properties of Fuels for Jet Propulsion," Pergamon Press, New York (1962).
6. H. J. R. Maget and P. J. Chludzinski, in "Hydrocarbon Fuel Cell Technology," B. S. Baker, Editor, p. 429 ff., Academic Press, New York (1965).
7. L. W. Niedrach and H. R. Alford, *This Journal*, **112**, 117 (1965).
8. E. Luksha and E. Y. Weissman, Tech. Summary Report No. 9, "Hydrocarbon-Air Fuel Cells," U.S.A. Engineers R & D Labs. (now: U.S. Army Mobility Equipment R & D Center), Ft. Belvoir, Va., Jan. 1965-June 1965, No. AD-640521, pp. 3-11.

Electrochemical Oxidation of Multicomponent Hydrocarbon Fuels

II. Long-Term Performance Studies with n-Octane Based Fuels Containing Aromatic, Olefinic, and Naphthenic Components

James F. Lennon, Eugene Luksha,[1] and Eugene Y. Weissman*,[2]

General Electric Company, Direct Energy Conversion Operation, West Lynn, Massachusetts

ABSTRACT

The long-term anode performance with hydrocarbon fuels may be different from what can be predicted from short-term polarization data. This is due to such time-dependent factors as accumulation of inert adlayers on the electrode surface and the progressive structural deterioration of the electrode. A study of the time-dependent aspects of hydrocarbon anode performance was made. The experiments were conducted on practical platinum/Teflon electrodes in 95 weight per cent phosphoric acid at 175°C. Characteristics of extended time *vs.* performance were described for n-octane and n-octane containing various single and multiple additives. It was found that the influence of various hydrocarbon additives on short-term performance of an octane anode cannot necessarily be applied toward prediction of long-term performance. Several additives do not appear to affect performance on a cumulative detrimental basis. However, when a certain total additive limit has been exceeded, the decrease in anode performance can be severe, over extended periods of operation. The cycling characteristics associated with the process of direct electrochemical oxidation of hydrocarbons have been described in terms of several distinct modes of performance fluctuation prior to the establishment of steady-state conditions.

For the most part, studies of the various aspects of direct hydrocarbon oxidation are based on short-term measurements. It is recognized that long-term anode performance with hydrocarbon fuels may be different from what can be predicted from short-term polarization data. This is due to such time-dependent factors as the accumulation of inert ad-layers on the electrode surface. Another important contribution to such performance changes is a progressive structural deterioration of the electrode. A study of the long-term effects that various "unreactive" additives (*e.g.*, aromatics, olefins, naphthenes) may have on the performance of fuel cells operating on n-octane was made in order to determine whether there may be cumulative inhibition of the active sites on the anode as a function of time by these additives.

Other long-term effects of various additives in multicomponent, octane-based fuels, are changes in the characteristics of performance cycling, which is present when hydrocarbons are oxidized directly with phosphoric acid electrolytes.

It is the purpose of this study to provide information and shed some light on these time-dependent aspects of anode performance.

Experimental

The life testing installation has been described earlier (1). The electrodes (both anode and cathode) were of the same types described elsewhere (2) (35 mg Pt/cm^2, 85% Pt-15% TFE, gold-coated Ta screen for anodes, Pt screen for cathodes).

The following experimental procedure was used: After establishing the desired gas flow rates (in general: 20 μl fuel/min; corresponding to 10 times the stoichiometric requirement of octane at 1 amp and 10 times the stoichiometric requirement of oxygen supplied in the air stream to the cathode[3]) and isothermal conditions (175°C), the open-circuit potential was recorded. Thereafter, an initial polarization curve was taken.

After these initial data were obtained, the cell current was maintained in general at 1.5 amp (33 ma/cm^2), by means of Electro-Products, Model EFB, d-c power supply units. The *IR*-included anode *vs.* H_2/H^+ potential and cell current were continuously recorded with Varian two-channel strip chart recorders. *IR*-free potential data were also obtained, by means of a Kordesh-Marko bridge. These data were logged, together with cell potentials and resistances.

The circulating electrolyte concentration was maintained at 95-98% H_3PO_4 by means of controlled-rate addition of water to the electrolyte sump.

At the end of each test (usually caused by excessive electrolyte leakage through the anode), a final polarization curve was taken. The cell was then disassembled and the anode was cleaned. If desired, its surface area was measured by the B.E.T. method.

Whenever time permitted, initial surface area measurements on anodes prior to assembly were also made. The method itself, as applied to whole electrodes, has been described by Weissman (3).

* Electrochemical Society Active Member.
[1] Present address: Gould-National Batteries, Incorporated, Research Division, Minneapolis, Minnesota 55414.
[2] Present address: Globe-Union, Incorporated, Corporate Applied Research Center, Milwaukee, Wisconsin 53201.

[3] These are not the minimum required flow rates; they were selected so as to eliminate any possibility of concentration polarization biases on the life test results but not optimized (in terms of minimum values) since this was outside the scope of the experiment.

Whenever necessary, the polarization curve data points were determined after suitably preactivating the anodes at anode potentials greater than 0.90v *vs.* H_2/H^+, and subsequently waiting for the output to stabilize at what would have been the average anode potential under cycling conditions for a fixed current density. This wait period was usually of the order of 3-4 min. In this way, cycling disturbances were avoided, without affecting the values to be measured.

Interpretation of the Test Data

Characteristics of extended performance vs. time data.—As mentioned above, direct hydrocarbon oxidation in phosphoric acid is characterized by spontaneous performance cycling. One of the objectives of the present work was quantitatively to define differences in the behavior of octane and various octane-based binary and multicomponent fuel mixtures, in terms of the frequency and/or the amplitude of anode potential fluctuations at constant current. The interpretation of such differences can be refined by noting that in each case the time required for the onset of cycling can be divided into four distinctly different periods:

I. The induction period—a short interval of time, normally 1-2 hr, during which there is a large increase in anode potential, from its open-circuit value.

II. The ripple period—follows the induction period and is of short duration; up to 2 hr. During this time interval, the anode potential starts fluctuating at high frequencies (*e.g.*, several times a minute) and low amplitudes (*e.g.*, 10-20 mv).

III. The onset-of-cycling period—sometimes indistinguishable from the actual cycling mode of operation (IV, below). When it occurs, it lasts a few hours, or less, and is characterized by performance cycling at frequencies that are sometimes higher and sometimes lower than during the actual cycling operation that follows; the corresponding amplitudes are always smaller (*e.g.*, 20-80% of actual cycling amplitudes).

IV. The cycling period—characterizes the onset of steady-state anode operation. Here, the performance fluctuations have been established to their full extent, according to the experimental conditions and the species being oxidized.

The anode potential will change from its minimum to its maximum value according to a set pattern. This pattern can be used to define differences in the behavior of various fuels of interest in terms of frequency and amplitude of performance cycling (*see* Results and Discussion).

As time goes on, various modes of degradation occur (*e.g.*, progressive catalyst inhibition by a relatively nonreactive ad-layer, or structural degradation of the anode). These may be responsible for observable changes in the characteristics of performance cycling. It sometimes appears that these changes are auto-compensatory in nature; thus, a certain increase in frequency appears to be associated with a decrease in amplitude and *vice versa*.

Processing and significance of the experimental data.—The high-loading unsupported platinum anodes used in the present work, while sufficiently active catalytically to yield meaningful results, at least on a comparative basis, present the drawback of structural variance with time. This variance is sufficiently severe to make it necessary not to consider the "last-stage" data for comparison purposes since they are often influenced by high rates of electrolyte leakage through the anode.

Two methods of data interpretation were used:

1. Use of available polarization curve data to define various performance points (*e.g.*, anode potential at given current densities) at various chronological stages; say, at the beginning and at the end of a run. These are, essentially, extent-of-degradation data.

2. Averaging of cycling data, from recorder traces, and graphical representation of the resulting changes of performance with time. These are the typical life test curves, supplying information on the total life for a set of predetermined conditions, as well as the individual durations of the various periods of operation (induction, ripple, *etc.*).

Results and Discussion

n-Octane oxidation.—Six anodes were tested with pure n-octane in order to establish a graphical frame of reference for the results obtained with various fuel mixtures. The changes in anode potential with time occupy a band whose boundaries represent the range of anode performance for the electrodes tested (Fig. 2 and 3). The abrupt break in the curve after the initial several hours is an indication of the onset of steady-state operation (cycling).

Figure 1 summarizes the cycling characteristics observed with n-octane. The time to start cycling (periods I + II + III) and the frequency of cycling once it has started are plotted against current density. It is seen that the time to start cycling and the cycling frequency are related to operating current density. No significant trends for the amplitude values could be obtained. Period III of cycling was often indistinguishable from period IV, and period II (ripple) was sometimes negligibly small.

Normal octane with single additives.—The life test data for n-octane containing a single additive indicate

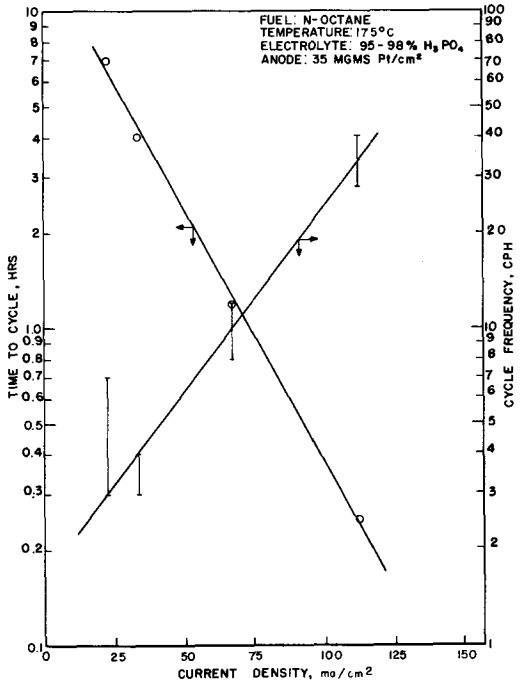

Fig. 1. Anode cycling characteristics as a function of current density.

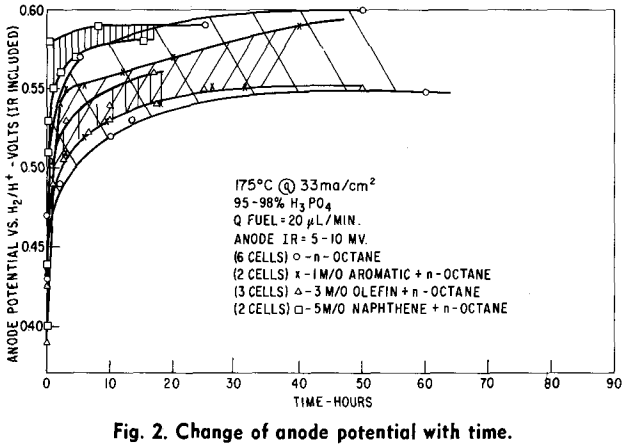

Fig. 2. Change of anode potential with time.

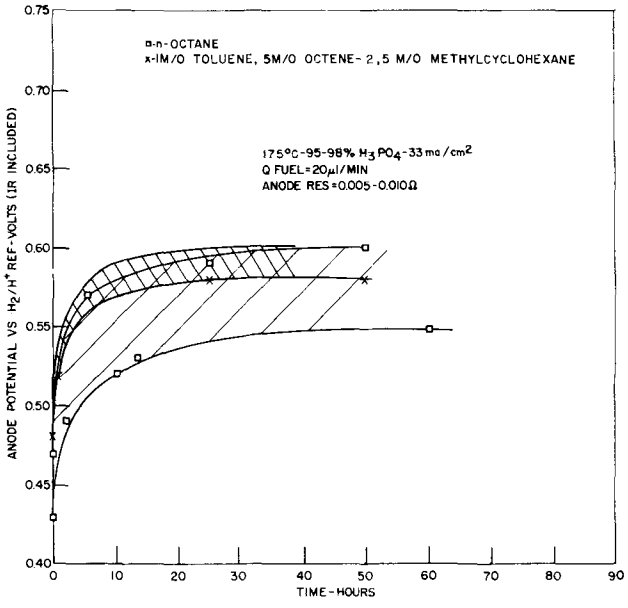

Fig. 3. Change of anode potential with time.

that there were no significant performance differences in the cycling period for the octane + 1% aromatic and octane + 3% olefin data as compared to pure octane. These similarities can be seen clearly in Fig. 2 where the performance-time curves for the fuels containing olefins and aromatics fall within the n-octane band. It can also be seen that anodes operating on octane + 5% naphthene fuels polarize more extensively during a relatively short initial time interval. Even after this brief interval, the performance-time curve is situated within the upper portion of the n-octane band while the latter has most of its data clustered in its lower portion.

The only significant differences in the cycling characteristics of octane plus single additives as compared to pure octane oxidation are the increased cycle frequencies, roughly 3 times higher, for the binary fuels.

Normal octane with several additives.—It has been shown in short-term tests (4) that there are no cumulative effects for multiple additions of "unreactives" up to a total of 11 mole per cent (m/o) additives. It was shown, in fact, that the performance penalty roughly corresponded to the "worst offender."

Figure 3 represents performance-time data for four cells operated on mixtures of 50/50 normal and iso-octane[4] containing 11 m/o additives (1% aromatic, 5% naphthene, 5% olefin). For the purposes of comparison, the experimental n-octane band is superimposed over this curve. A sharp increase in anode potential is first exhibited, up to a value of about 0.575v where the potential finally stabilizes. The multicomponent fuel data fit roughly within the upper portion of the n-octane band. The approximately 40 mv penalty over the performance of pure n-octane, based on the 5% naphthenes being the "worst offender" under these conditions, is substantiated by these graphical representations. This is due to the fact that most of the n-octane results fall within the lower portion of the performance-time band while the multicomponent data are clustered close to the upper limit.

Life test data obtained where increasing amounts of the "unreactive" components were added to n-octane are shown diagrammatically in Fig. 4 and 5. It is evident that sizable performance penalties are paid for concentration levels greater than 11% even to the extent of a 180 mv[5] deviation from n-octane performance, representing approximately 50% of the cell output *IR* included. This performance drop occurs within the first 25 hr of operation, where effects of anode deterioration are minimal. Figure 6 is a graphic representation of the decrease in current density, at a given polarization, with increasing concentrations of the "unreactive" components in n-octane. It should be noted that the current densities are normalized in terms of real B.E.T. surface areas measured on the pure electrodes. The spread of the data increases at higher concentrations of "unreactives."

An analysis of the cycling characteristics of these multicomponent fuels for operation at 33 ma/cm^2 indicated that the frequency and amplitude of cycling did not appear to exhibit any of the trends reported for n-octane and n-octane with single additive mixtures. In fact, there were no appreciable changes of the frequency of cycling with time.

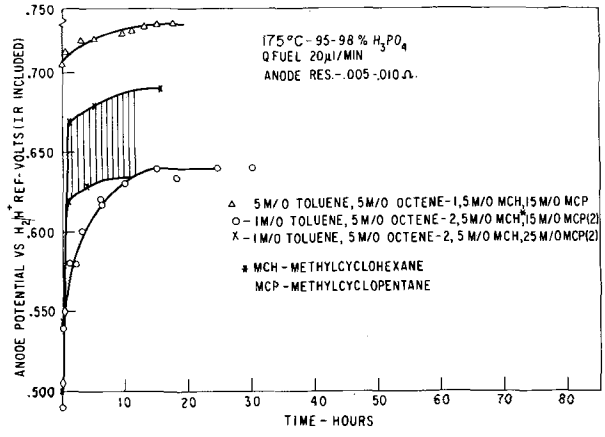

Fig. 4. Change of anode potential with time.

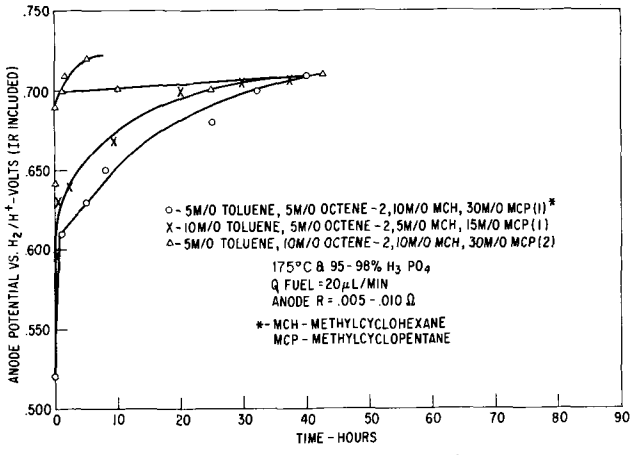

Fig. 5. Change of anode potential with time.

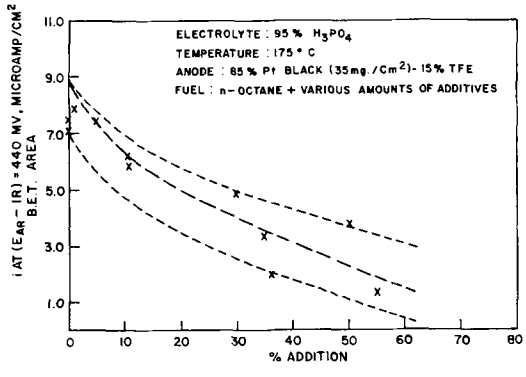

Fig. 6. True current densities as a function of the total amount of additives.

[4] It has been previously shown (4) that there are no performance differences between anodes operating on n-octane and on n-octane + i-octane mixtures.

[5] Note that the detrimental effect of octene-1, as compared to octene-2, is particularly obvious with high amounts of additives (30 m/o).

Conclusions

1. The differences between anode overvoltages for the oxidation of pure octane and of octane with various hydrocarbon additives appear only to be significant in the context of short-term operation, in most cases up to 25 hr.

2. For longer runs, characteristic of real fuel cell operation, differences in anode performance are reduced to practically insignificant levels; this holds true as long as the cumulative amount of additives does not exceed a certain limit. At least for the conditions imposed in the present work, *i.e.* a platinum loading of 35 mg/cm^2, 95% phosphoric acid at 175°C, and excess flow rates of reactants, this limit was found to be 11 m/o.

Acknowledgments

This work is part of the program under contract DA 44-009-AMC-479(T) with the U.S. Army Mobility Equipment Research and Development Center, Fort Belvoir, Virginia, to develop a technology which facilitates the design and fabrication of practical military fuel cell power plants for operation on ambient air and hydrocarbon fuels.

The authors are grateful for the able assistance of Mr. G. Serena who performed much of the experimental work, and Mr. J. Foley for the manufacturing of most of the electrodes and preparations of the catalytic mixes used in the present study.

Manuscript received Jan. 29, 1968. This paper was presented at the ACS Meeting, Miami, April 9-14, 1967, Symposium on Electrochemical Processes, as paper 94.

Any discussion of this paper will appear in a Discussion Section to be published in the December 1969 JOURNAL.

REFERENCES

1. P. J. Chludzinski and J. F. Lennon, Technical Summary Report No. 5, "Hydrocarbon-Air Fuel Cells," U.S.A. Engineers R & D Labs. (now: U.S. Army Mobility Equipment R & D Center), Ft. Belvoir, Va., Jan. 1964-June 1964, No. AD-612766, pp. 4-216.
2. L. W. Niedrach and H. R. Alford, *This Journal*, **112**, 117 (1965).
3. E. Y. Weissman, *ibid.*, **114**, 658 (1967).
4. E. Luksha and E. Y. Weissman, *ibid.*, **116**, 118 (1969).

PbO_2 in the Lead-Acid Cell

I. Formation from Three Typical Oxides

Jeanne Burbank*
Naval Research Laboratory, Washington, D. C.

and Everett J. Ritchie*
Eagle-Picher Industries, Incorporated, Joplin, Missouri

ABSTRACT

Three representative lead oxides for storage battery fabrication were mixed with water and H_2SO_4 to paste consistency. Each of these was hand pasted into antimonial and pure lead circular grids of standard SLI thickness. The plates were cured according to common practice for each oxide. The small circular plates were anodized in an electrolytic cell mounted directly on an x-ray machine, and the diffraction patterns recorded at intervals throughout 72 hr of formation in 1.0585 sp gr H_2SO_4. Beta PbO_2 was identified as the reaction product. At the end of formation, nominally 150% of theoretical requirement, the morphology of the PbO_2 was examined by electron microscopy. The crystals varied from small prismatic individuals to complex spherulitic formations.

Positive plate materials of the lead-acid cell have received intensive study in recent years because of massive failure of nonantimonial submarine cells in which the positive active material suffered catastrophic softening early in life. It was shown that similar cells, pasted with identical materials but having antimonial lead grids, gave longer service life. The difference in performance was attributed to the difference in electron morphology of the PbO_2 crystals, which in the case of the antimonial cells remained characteristically prismatic and dendritic, while those in a softening paste were nondescript spheroids, readily detached from the plate upon gassing on overcharge. These results have led to a systematic examination of the electron morphology of PbO_2 crystals in the lead-acid cell. It has been indicated that the electron morphology is related to the materials originally present in the paste (1-6). As a continuation of the study, the present investigation of positive plate oxides was undertaken.

Materials and Methods

Three representative commercial oxides for storage battery fabrication were used in this study, designated respectively *A*, *C*, and *H*, Table I. These are characterized in Tables II and III which show the particle size ranges and spectrographic analyses.

Pastes of each oxide, water, and sulfuric acid were mixed in a laboratory dough-type mixer in three pound batches, Table IV. Each of the pastes was hand pasted into special grids and cured and dried according to standard practice for each type of oxide. Plates containing pastes of oxides *A* and *H* were racked, and placed in a steam-filled oven to set the paste, followed by drying at about 105°C. Plates containing paste *C* were flashed, rolled, stacked, and cured for 24 hr in an

Table I. Description of oxides *A*, *C*, and *H*

Oxide	Description	Specific surface (m^2/g)	Median particle radius (μ)*
A	A milled, nonleady litharge having a mixed composition of orthorhombic and tetragonal PbO	0.18	3.9
C	A leady litharge containing 25% free lead produced by ball milling	0.97	1.8
H	A furnace oxide containing 25% Pb_3O_4	0.28	2.15

* Equivalent spherical radius.

* Electrochemical Society Active Member.

Table II. Particle size distribution of oxides A, C, and H

Size range* (μ)	Oxide A (w/o)	Oxide C (w/o)	Oxide H (w/o)
0.0-0.015	0.03	0.9	0.02
0.015-0.03	0.05	1.2	0.06
0.03-0.06	0.14	2.2	0.22
0.06-0.125	0.38	4.2	0.7
0.125-0.25	1.0	6.5	1.8
0.25-0.5	2.0	10.0	4.7
0.5-1.0	5.4	12.0	11.5
1.0-2.0	13.0	15.0	28.0
2.0-4.0	39.0	15.0	34.0
4-8	20.0	14.0	16.3
8-16	14.5	12.5	2.57
16-32	4.1	5.8	0.13
32-64	0.4	0.7	—
Plastic <0.5	3.6	25	7.5
Granular >0.5	96.4	75	92.5

* Equivalent spherical radius.

Table III. Spectrographic analysis of oxides A, C, and H

Element or compound	Oxide A (w/o)	Oxide C (w/o)	Oxide H (w/o)
Ag	0.0005	0.00039	0.00039
Al_2O_3	0.00018	0.00005	0.00065
$BaSO_4$	<0.00020	<0.00020	0.00022
Bi	0.0026	0.017	0.020
CaO	0.00074	0.00020	0.0068
Cu	0.00034	0.00027	0.00048
Fe	0.00023	0.00009	0.0017
MgO	0.00053	0.00005	0.00084
Mn	Not detected	Not detected	0.00002
SiO_2	0.0020	0.00058	0.0074

Table IV. Pasting data

Oxide	A	C	H
Initial water (cc/lb)*	50	50	53
1400 sp gr H_2SO_4	40	40	39
Final water (cc/lb)*	None	None	5
Paste density (g/in.^{3})*	65	65	66
Pasting properties	Fair	Good	Good

* These units of metric-English systems are in common use in storage battery technology.

Table V. Spectrographic analyses of grid metals

Element	Pure lead (w/o)	Antimonial lead (w/o)
Sb	Not detected	7.0
Sn	Not detected	0.3
As	Not detected	0.062
Bi	0.018	0.016
Cu	0.00015	0.0064
Fe	0.0017	0.00078
Mn	0.00002	0.00002
Mg	0.00014	0.00028
Si	0.00075	0.00044
Mo*	Not detected	Not detected
Cd	Not detected	Not detected
Ag	0.0014	0.0015
Ni	0.00005	0.00005
Ca	0.0004	0.0002

* Data given for elements from Mo to Ca are of lower precision.

insulated box, followed by 40 hr in a closed oven at 40.9°C. Conventional square grids for use as counter-electrodes were pasted and cured at the same time, with the same materials.

The special and conventional square grids fabricated for this study were cast from pure lead and nominal 7% lead-antimony alloy. Spectrographic analyses of the grid metals are given in Table V. The special grids were small circles, 47 mm diameter, designed to fit the electrolytic cell mounted directly on an x-ray goniometer, permitting registration of diffraction patterns during anodic treatment (7).

Table VI. Anodization treatments

Oxide	Grid metal	Average plate thickness (mm)	Dry active material weight (g)	Amp-hr (theory)	Amp-hr (actual)	%
A	Pb-Sb	1.8288	7.6	1.79	1.165	65.08
		1.8288	6.3	1.49	2.252	151.15
		1.7018	6.4	1.51	2.304	128.72
	Pb	2.1082	8.2	1.94	3.024	155.9
C	Pb-Sb	2.1336	7.5	1.75	2.63	150.2
	Pb	2.1336	8.6	2.03	3.053	150.25
H	Pb-Sb	1.7018	7.0	1.65	2.52	152.7
	Pb	1.9304	8.7	2.05	3.024	147.51

Radiographs of each of the circular plates were made prior to any electrochemical treatment with a Faxitron 804 table-top radiographic system. The small disk plates were mounted in turn in the electrolytic cell, backed by a circle of pure lead to effect electrical contact, and rotated at 60 rpm throughout the anodization of about 72 hr or less in certain instances, Table VI. A preliminary soak of 20-30 min was given in the electrolyte, 1.0585 sp gr H_2SO_4. Anodic oxidation took place from one side only in the x-ray cell assembly, and the current density was approximately 4 ma/cm^2 on the submerged half of the electrode. Using Cu $K\alpha$ radiation, x-ray diffraction patterns were registered from the cured plate surfaces, and from samples of the paste removed from the grids, ground to pass No. 120 sieve, and mounted in the conventional manner for diffractometric registration. Following the soaking period, and at intervals throughout the anodic oxidation, diffraction patterns of the surfaces of the plates were recorded also. Positive plate polarization was followed continuously by means of a standard Hg, Hg_2SO_4 reference electrode.

Upon completion of anodization, usually about 150% of theoretical requirement on a weight basis, the plates were blotted and dried in air at room temperature. The active material was removed from the grids for electron microscope examination by carbon replication and further x-ray diffraction study by the same methods used in the earlier studies (1-6). All electrochemical experiments were performed at room temperature which varied from 20.0° to 25.2°C.

Results, Discussion, and Conclusions

The radiographic examination of the cured plates showed that, from a practical standpoint, the grids were fairly well filled with paste, and were free of large voids or skips. There were, however, hidden cracks in some pellets, and some areas of the grid bars were not in good intimate contact with the paste. A difference was observed between the radiographic density exhibited by the paste of oxide C and that of the other two oxides. It is seen in Fig. 1 that the paste containing oxide C is markedly more uniformly dense than that of oxide A, which was adopted as a standard for comparison of all plates. While it is true that the plates containing oxide C averaged thicker than the others, Table VI, there were variations among all specimens that eliminate thickness as the sole cause of this difference in radiographic density. Also, it may be observed from the figure that the plate of oxide A is distinctly more grossly porous than the paste resulting from oxide C. This was true of all specimens of pastes A and H when similarly compared with all those containing oxide C. Further, cross-pellet cracking was most prominent in oxide C as a general characteristic, as was poor contact with the grid bars.

Of particular significance is the difference in the relative amounts of small particles in the three oxides, Table II. It is generally accepted that even nonplastic materials such as silica will exhibit plastic behavior if particle size is sufficiently reduced, and even more pronouncedly if the particle shape is also favorable (8). Particles exhibiting plastic behavior are usually 1μ or less in diameter, and the percentage of particles in each oxide falling within this range has been indi-

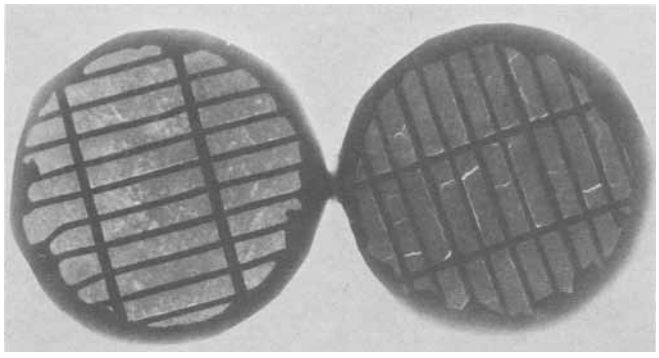

Fig. 1. Representative macroradiographs of unoxidized, cured plates containing pastes from oxide *A (left)* and *C (right)*. The dense packing of oxide C is shown by its greater opacity to x-rays, giving a darker image than that of paste *A*. The distribution of macroporosity in paste *A* is shown by the fairly uniform mottling. Thin white lines are cracks, visible along some grid bars in paste *A*, but larger and more extensive in paste *C* where shrinkage resulted in cross-pellet cracking as well as parting from the grid bars. Similar radiographs from plates containing paste *H* resembled the one shown for paste *A*.

cated as "plastic" and the larger fractions as "granular" in Table II. The handling and curing properties of pastes fabricated from the oxides depend to a large extent on the relative amounts of plastic and granular material present. For example, on the basis of the above radiographic examinations, it is seen that paste *C* suffers greater shrinkage during curing than either paste *A* or *H*. Neglecting the fact that the curing reaction of oxide *C* must include the step of oxidation of the free metallic lead particles present in this type of oxide, and considering only the distribution of particle sizes in the original oxides, Table II, it is to be expected that the oxide containing the lowest percentage of "granular" size particles would undergo the most pronounced shrinkage. The pasting properties, Table IV, of each of the oxides also may be related to the relative amounts of granular and plastic size particles. Oxide *A* contained only 3.6% of plastic material, and gave a paste described as "fair" in pasting quality. Oxides *C* and *H* had 25 and 7.5% plastic material, respectively, and both had "good" pasting properties. This suggests that 3.6% plastic material is too low to impart satisfactory workability to the mix, 7.5% is sufficient, while 25% is excessive, leading to undesirable shrinkage cracking. Investigation of the rheological properties of these and other representative oxides combined with radiographic study of pasting and curing would be of interest. As a result, optimum workability could be realized, and pellet cracking and arcing along grid bars could be minimized and possibly eliminated.

All identifications of solid crystalline materials given in this report were made by x-ray diffraction analyses. Reference diffraction patterns are listed in Table VII giving the card numbers in the standard file (9).

X-ray diffraction patterns from bulk specimens of the cured pastes showed the major component to be tribasic lead sulfate in all three. The surfaces of plates made with oxides *A* and *H* were primarily basic lead carbonate, hydrocerussite, and the surfaces of plates made with oxide *C* were largely tribasic lead sulfate. Residual PbO and, in the case of oxide *H*, Pb_3O_4 were also detected.

When plates containing oxides *A* and *H* came into contact with the dilute H_2SO_4 solution, the gassing of CO_2 was visible, and during the preliminary soaking period all traces of the superficial layers of basic lead carbonate were rapidly eliminated. Crystalline $PbSO_4$ formed on the surface of all three types of plate during the soaking period. At this same time, Pb_3O_4 in paste *H* was converted to PbO_2 and $PbSO_4$ and resulted in a marked purplish coloration in this kind of plate.

Table VII. The x-ray diffraction patterns

Compound	ASTM (9) card number	Remarks
$PbSO_4$	5-0577	Excellent match is obtained for this material; on occasion, the weak line at 5.38 is missing and, with lesser amounts of $PbSO_4$ present, only the strong lines are detected.
β PbO_2	8-185	Excellent match is obtained for this material with the exception of the line at 2.21 which did not appear in the electrochemical products of this study. There was some indication of preferred orientation in some of the electrodeposits, although not to a strong degree.
PbO (tetragonal)	5-0561	Excellent match is obtained for this material. On occasion, preferred orientation causes divergence from the standard intensities.
PbO	5-0570	Excellent match is obtained for this material.
Pb_3O_4	8-19	Excellent match is obtained for this material.
$Pb_3(CO_3)_2(OH)_2$	13-131	This reference card gives the best match for this material when observed as a reaction product on a surface; it arises from an oriented deposit with the basal planes lying in the surface. Because of the strong tendency for this material to form oriented deposits, the lattice parameters given on this card are in error. *See* also card 14-8 and Ref. (10) and (11).
$3PbO \cdot PbSO_4 \cdot H_2O$	6-0282	This reference card gives a fairly good match for identification of this material although weak lines are often missing and relative intensities may vary.
	6-0287	This reference card also gives a fairly good match for this material; however, the preparation contained some $4PbO \cdot PbSO_4$ and lines from this compound must be subtracted from the pattern. Bode and Voss (12) have given a pattern for this compound that compares favorably with the two given above. Comments: Identification of this material by x-ray diffraction in a mixture such as the battery paste is made on the basis of strong lines which fortunately are unique for this material.

The plates were individually anodically oxidized and details of the anodizations are given in Table VI. The positive plate polarization during oxidation followed the expected pattern previously reported by Ikari, Yoshizawa, and Okada (13); one example is

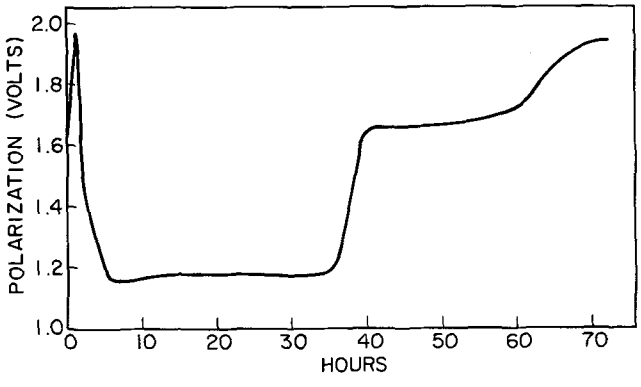

Fig. 2. Plate polarization during anodic oxidation. The polarization is given relative to the standard Hg, Hg_2SO_4 reference electrode, and is a typical example. Theoretically, if the process were 100% efficient, oxidation would have been complete at 48 hr at the constant current of approximately 4 ma/cm^2. The initial rise in polarization is attributed to an initial increase in resistance caused by continued deposition of $PbSO_4$ in the plate. This is followed by a lowering of resistance as the grid metal becomes covered with conducting PbO_2. When sufficient PbO_2 has been formed in the paste mass, between 36 and 40 hr in this case, the potential rises owing to the high oxygen overpotential on PbO_2, and ultimately climbs to the high terminal value when oxygen evolution becomes the major reaction during the final 10 hr of oxidation.

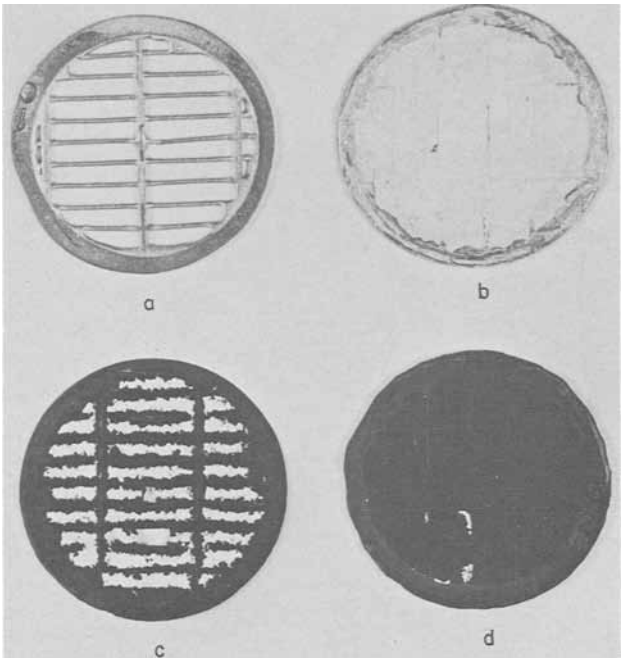

Fig. 3. Small circular plates at various stages of the study: (*a*) Small grid prior to pasting. (*b*) Small plate after pasting and curing. (*c*) Small plate after partial anodization. Black β PbO_2 first appeared adjacent to the grid bars and gradually extended into the central pellet areas as anodization continued. The white areas were $PbSO_4$. In plates containing oxide *A*, a considerable residue of the white layer remained at the outer central surfaces of the pellets after passage of a total of 150% of the theoretical charge requirement. (*d*) Final appearance of small plates containing pastes *C* and *H*. The pastes appeared essentially totally oxidized to β PbO_2. Plates containing oxide *C* were very dark, nearly black, and plates containing oxide *H* were lighter in color. The pockets of white material in the lower left quadrant are residual $PbSO_4$ that were not oxidized possibly because they were not in good electrical contact with the remainder of the pellets. It seems likely that these encrustations would be associated with cracks between the grid metal and paste visible in the radiographs of Fig. 1.

shown in Fig. 2. The actual values of the polarization will, of course, vary with the rate or current density, concentration of the electrolyte, and various *IR* losses in the system such as plate thickness, compactness of the $PbSO_4$ coating on the outer surface of the plates, *etc.*

As the anodic oxidation progressed, dark brown to black β PbO_2 developed near the grid bars, and spread gradually toward the pellet centers. Paste *A* became converted to PbO_2 at the edges and interior of the pellets, but retained a surface coating of $PbSO_4$ at the pellet centers. Pastes *C* and *H* appeared essentially completely oxidized, paste *C* giving a very dark blackish plate while paste *H* was lighter in color. Figure 3 shows the general appearance of the plates at various stages of the work.

After formation, electron microscopy showed a range of morphologies with the individual crystallites varying from about 0.5 to less than 0.1μ. Some prismatic crystals with branching suggestive of multiple twinning were present in paste *A*, and appeared less frequently in the other two pastes. Agglomerates, up to several microns in size, of prismatic crystallites were present in all pastes. Paste *H* gave rise to the largest individual crystallites about 0.5μ diameter. Oxide *C* resulted in many remarkably uniform 0.1μ crystallites arranged in spiraling layers terminated by one central individual crystallite, and forming spheroidal agglomerates, Fig. 4-7. Although not clearly apparent in all of the electron micrographs, it is believed that the aggregates are compound spikes of dendritic growth covered with sessile crystallites of

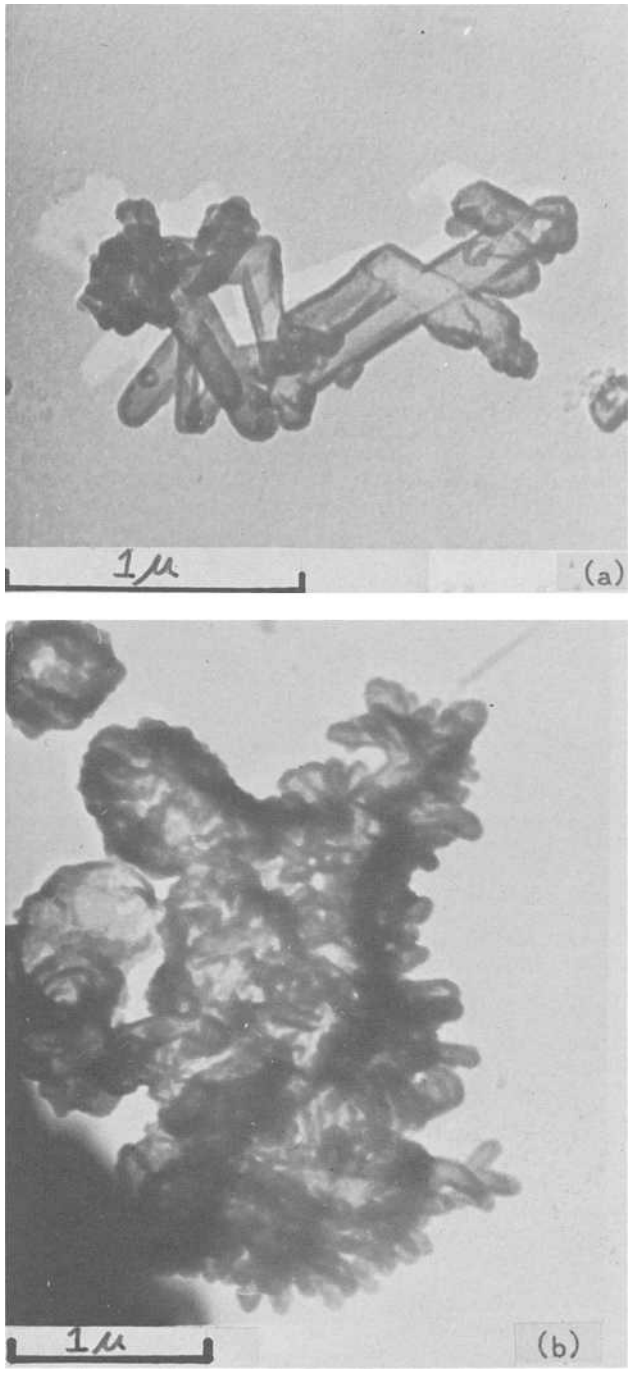

Fig. 4. Prismatic crystals of PbO_2: (*a*) This group of crystals is representative of the type referred to as prismatic individuals with branching suggestive of multiple twinning. They were found more frequently in paste *A* than in *C* and *H*. This is believed to be an early stage in the growth of more extensive clusters of similar prismatic crystals shown in (*b*). (*b*) Christmas tree dendrites of PbO_2 possibly composed of true whiskers. This may be a more advanced stage of growth of clusters of crystals such as shown in (*a*). Markers equal 1μ.

varied size and morphology. It is possible that the agglomerates may arise from the coarse particles present in the original oxides.

Differences in PbO_2 morphology from the three different oxides were recognizable, and the photographs have been selected to illustrate these differences. Paste *A* appeared to give rise to true spherulites, paste *C* produced spheroidal agglomerates of small crystals from which emerged dendritic spikes of somewhat larger crystals, and paste *H* produced irregular-shaped clusters of even larger crystals. Because the largest individual crystals appeared in the paste that

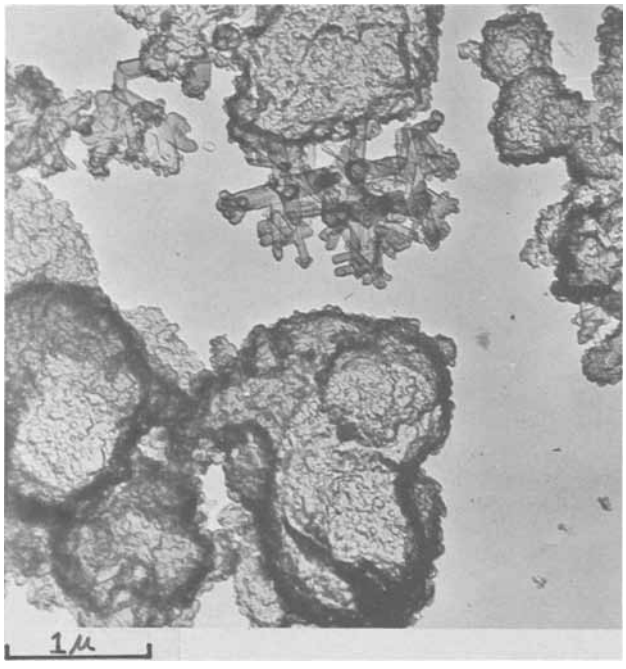

Fig. 5. Spherulites and prismatic crystals which were characteristic of PbO_2 grown from paste A. It is possible that the spherulites originated from dendrites such as shown here and in Fig. 4 through development of overgrowths of sessile crystallites on the originally smooth surfaces of the whiskerlike crystals. Marker equals 1μ.

originally contained Pb_3O_4, it seems likely that the PbO_2 particles resulting from chemical reaction with H_2SO_4 acted as growth-promoting nuclei. Despite these differences, it would not be possible to identify any single isolated crystal form as coming from a specific paste, because of the range of individual and agglomerate shapes and sizes in each sample. This is not surprising in view of the fact that all three pastes were primarily composed of the same material after curing, namely tribasic lead sulfate. The morphologies observed in this study are essentially identical with those developed by anodic oxidation of the pure phases examined earlier (5, 6).

It did not appear to make a major significant difference in morphology if the three oxides used in this study were anodized on pure lead or antimonial lead

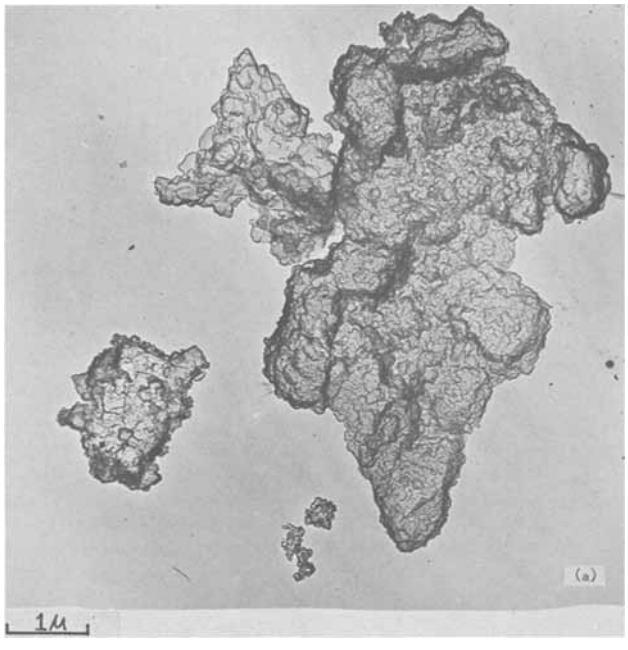

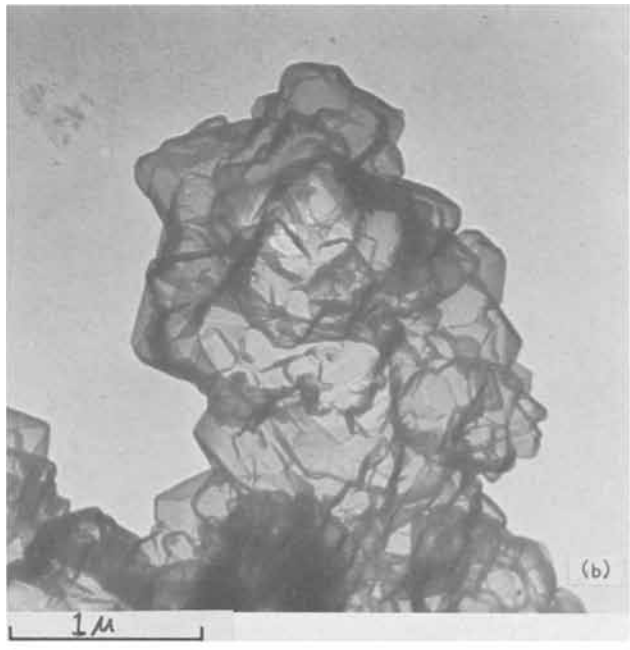

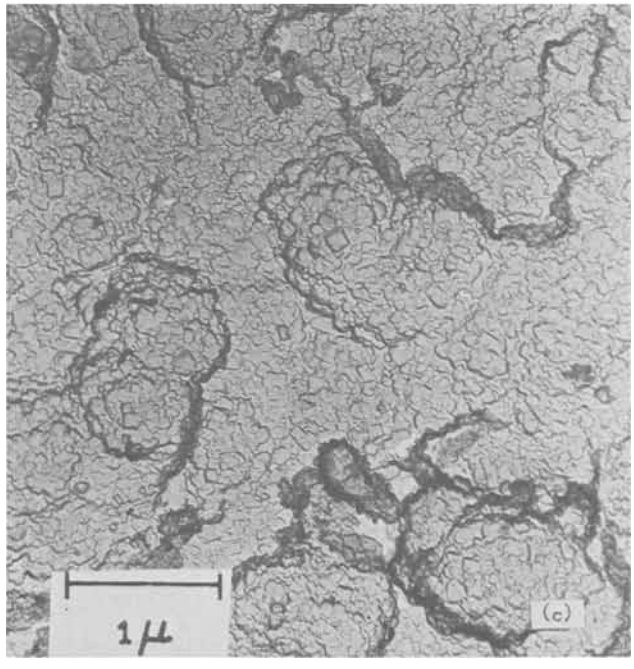

Fig. 6. Spheroidal and dendritic growths fairly typical of PbO_2 from paste C: (a) The similarity in general outline of the emergent dendritic spike to the main body of this nodular mass of crystals is strongly suggestive that the smaller crystals have grown on, and filled in a similar underlying dendritic growth of the larger crystals. This is also suggested by the appearance of the smaller mass at the left which shows a spherulite of larger crystals partially coated with outgrowths of the smaller crystals. (b) Detail of a dendritic spike. (c) Spiraling layers of small prismatic crystals make up the spherical nodules. The uniformity in size of these crystallites indicates that they represent one stage in the PbO_2 growth mechanisms, possibly the final stage. Markers equal 1μ.

grids. This is in contrast to previous observations; however, in the earlier study (4), formation was performed by commercial manufacture, probably under considerably different conditions of current density, temperature, and relative volume of electrolyte to plate area, details not revealed by the manufacturer. Furthermore, the oxides used in this study were of different manufacture, and it may be considered very significant that these gave rise to well-developed prismatic crystallites when formed on pure lead as well

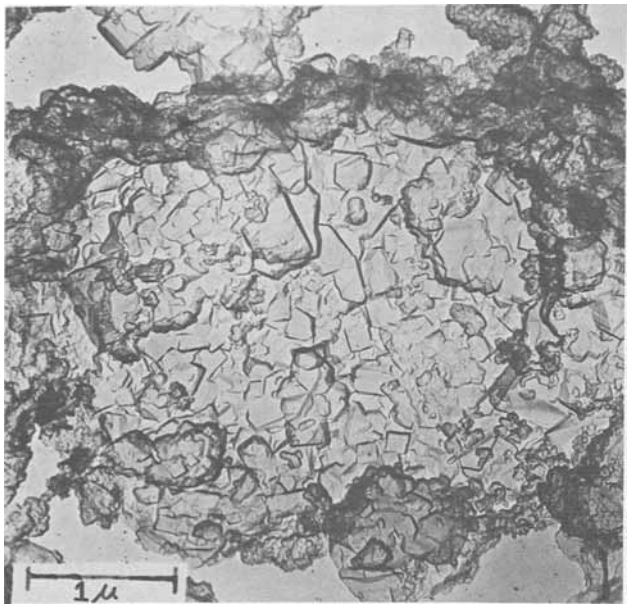

Fig. 7. Clusters of large prismatic crystals like this were characteristic of PbO_2 grown in paste *H*. The clusters took the form of irregular aggregates some approaching ovoids and others, like this one, were rhomboidal in outline. The decoration at the edges with much smaller crystallites was also fairly typical, and again suggests that the small crystals grow on the surfaces of the larger ones, and may represent a final growth stage in the anodic oxidation. Marker equals 1 μ.

as on antimonial lead. Further investigation of the float characteristics of these oxides will be of interest to determine whether the prismatic morphology and attendant paste strength is retained on both antimonial and nonantimonial grids.

The largest crystallites of PbO_2 developed in paste *H* containing Pb_3O_4, suggesting that this oxide may be of particular interest for further investigation. The relatively large agglomerates of these bigger crystals may form a submicroscopic network of considerable strength that may enhance the durability of a plate fabricated from this oxide.

Acknowledgment

The work of one of us (EJR) was performed under a research contract with the International Lead Zinc Research Organization.

Manuscript received June 28, 1968.

Any discussion of this paper will appear in a Discussion Section to be published in the December 1969 JOURNAL.

REFERENCES

1. J. Burbank and C. P. Wales, Naval Research Lab. Report 5773, "The Lead Calcium Battery Part 3—Submarine Cells," May 29, 1962.
2. J. Burbank, "Batteries," D. H. Collins, Editor, p. 43, Pergamon Press, New York (1963).
3. J. Burbank, *This Journal*, **111**, 765 (1964).
4. J. Burbank, *ibid.*, **111**, 1112 (1964).
5. J. Burbank, *ibid.*, **113**, 10 (1966).
6. J. Burbank, "Power Sources 1966," D. H. Collins, Editor, p. 147, Pergamon Press, New York (1967).
7. J. Burbank and C. P. Wales, *This Journal*, **111**, 1002 (1964).
8. W. A. Weyl and W. C. Ormsby, Chap. 7 in "Rheology," Vol. 3, F. R. Eirich, Editor, p. 249, Academic Press, New York (1960).
9. "Powder Diffraction File," Am. Soc. Test. Mater., Philadelphia.
10. J. M. Cowley, *Acta Cryst.*, **9**, 391 (1956).
11. G. Todd and E. Parry, *Nature*, **202**, 386 (1964).
12. H. Bode and E. Voss, *Electrochim. Acta*, **1**, 318 (1959).
13. S. Ikari, S. Yoshizawa, and S. Okada, *J. Electrochem. Soc. Japan (Overseas Ed.)*, **27**, E 186 (1959).

An Electrochemical Method of Preventing Embrittlement in High-Strength Steel Types 1062 and 4037 During Hydrochloric Acid Pickling

A. W. Lui* and R. R. Rogers*

Mines Branch, Department of Energy, Mines and Resources, Ottawa, Ontario, Canada

ABSTRACT

It is shown that a high-strength steel of Type 1062 or 4037, either covered with nonmetallic scale or with the scale removed by blasting with an aqueous slurry of No. 220 aluminum oxide, can be pickled in hydrochloric acid without (*a*) the occurrence of embrittlement, (*b*) the loss of an appreciable amount of metal, or (c) an important change in appearance, when it is maintained within a range of potentials which is specific for each combination of steel and nonmetallic material on the surface of the steel. Any nonmetallic material remaining on the steel after the pickling can be removed by ultrasonic vibration in water. After such treatment, the steel remains unembrittled during plating with cadmium in a stable cyanide bath.

Frequently Type 1010 low-carbon steel, having the specification shown in Table I, is electroplated with other metals to protect it from corrosion, to improve its appearance, *etc.* Prior to plating, the steel ordinarily is degreased and then pickled in hydrochloric or sulfuric acid to remove oxides and other undesirable materials. During the pickling process, metal is dissolved at small anodic areas of the steel, and hydrogen gas is evolved at small cathodic areas.

The situation is different in the case of "high-strength" steels such as Types 1062 and 4037, typical analyses of which are shown in Table I. Such steels absorb part of the hydrogen produced during acid pickling, with the result that they may become severely embrittled. In present-day practice, these steels are baked at a comparatively high temperature after plat-

* Electrochemical Society Active Member.

Table I. Analyses of steel Types 1010, 1062, and 4037 (%)

Constituent	Specification for low-carbon steel (Type 1010)	Analyses of "high-strength" steels used in the present research (%) Steel Type 1062	Steel Type 4037
Carbon	0.08-0.13	0.64	0.40
Manganese	0.30-0.60	1.03	0.76
Silicon	—	—	0.31
Molybdenum	—	—	0.26
Phosphorus	0.04 max.	<0.02	<0.02
Sulfur	0.05 max.	<0.02	<0.02

ing, to eliminate this hydrogen embrittlement. This procedure has certain disadvantages.

Bednar, Dingley, and Rogers (1) already have described a method of pickling high-strength steel of Types 1062 and 4037 without significant embrittlement as indicated by the bend test. This method involves (*a*) removal of oxides, *etc.*, by hydrochloric acid with the use of ultrasonics, (*b*) treatment in copper sulfate solution, (*c*) treatment in a solution of nitric and acetic acids, and (*d*) water rinsing using ultrasonics. Following this procedure, the steels may be plated with a good, very adherent coating of cadmium in a stable cyanide bath [described in an earlier paper (2)] without embrittlement. Equally good results may be obtained when the steels are plated with zinc or copper using stable cyanide baths (3, 4). A new procedure for plating these high-strength steels with silver in a stable bath, without embrittlement, is described in a paper soon to be published.

More recently, this laboratory has become interested in the possibility of pickling high-strength steel without embrittlement by making it anodic in a cell in which the electrolyte is hydrochloric or sulfuric acid. It was assumed that the hydrogen produced would be evolved on the cathode of the cell, *i.e.* at some distance from the high-strength steel. It was believed that such a procedure could be more useful than the one described above (1) under certain circumstances.

The Steels as Received

The high-strength steel pins of Types 1062 and 4037 used in these experiments (chemical analyses in Table I) were 0.4 cm in diameter. Those of Type 1062 were 8.3 cm long and had been austempered in the bainitic range giving a Rockwell C hardness of 52-56. When received, they were covered with a uniform thin blue oxide scale. Those of Type 4037 were 6.7 cm long and had been quenched and tempered giving a Rockwell C hardness of 51-55. When received they were covered with a thin, very porous film of copper together with smutty black material. No attempt was made to pickle more complicated objects made of these steels by the new electrochemical method which has been described here.

Experimental Equipment

The equipment used in these experiments was standard with the following exceptions:

(*a*) Lorco Liquamatte wet-blasting equipment Model 22 using an air-line pressure of 80 psi.

(*b*) Sonogen ultrasonic generator LG-150 (25 kc, 150w) equipped with an LT-60 transducerized tank. (All ultrasonic treatments were performed in distilled water.)

(*c*) Electrical equipment which has been described elsewhere (5).

This included:

1. A glass test cell containing hydrochloric acid as the electrolyte. A high-strength steel pin was used as one electrode, and two platinum sheets connected in parallel as the other electrode.
2. A potentiostat which could be used to maintain the potential of the immersed steel pin at any desired value.
3. A standard saturated calomel electrode which was used in determining either (*a*) the uncontrolled potential of the steel pin, or (*b*) the controlled potential of the steel pin when connected with the platinum electrode.

(*d*) A Hounsfield notched bar bending jig attached to a tensometer machine. During bend testing, the unnotched pin was supported at two points 3 cm apart. Pressure applied to a 0.32-cm-diameter mandrel forced the pin into the gap between these two points until it broke or until a bend of 90° had been produced without breaking. This bending through 90° required 7 min. If the pin remained unbroken, it was arbitrarily assumed to be free of significant embrittlement.

Experimental Procedures and Results

Preventing blasted pins from embrittlement.—During this part of the research, each steel pin was prepared, prior to its use in an experiment, by degreasing in trichlorethylene vapor, blasting with an aqueous slurry of No. 220 aluminum oxide to remove the oxides and other undesirable material from the surface, thorough rinsing with distilled water, and drying.

In the first experiment, a blasted pin of steel Type 1062, free from significant embrittlement, was connected to a standard calomel electrode (SCE) and both were placed in the test cell which contained 250 ml of 0.1*N* hydrochloric acid at room temperature (about 23°C). After 5 min, the potential of the pin *vs.* the calomel electrode was recorded. The pin then was removed from the acid, rinsed with distilled water, and dried in air. Finally, it was bent in the Hounsfield testing machine to determine whether or not it would break due to embrittlement. Four other similar experiments were performed and then the percentage of this set of five pins which had broken during the test was calculated. Five similar experiments were performed with the pins immersed in the acid for only 3 min. The information obtained in this way is given in Table II.

Five additional experiments were performed in each of which a pin of Type 1062 steel was connected with a platinum electrode and the two were immersed in 250 ml of 0.1*N* hydrochloric acid. In each case, the potential of the pin was maintained for 5 min at —1.0v *vs.* SCE by means of the potentiostat. This was followed by rinsing, drying, and testing in the Hounsfield machine as before. The experiments then were repeated using 3 min instead of 5 min.

The procedure described in the last paragraph was repeated using potentials of —0.9, —0.8 . . . 0.3 and 0.4v *vs.* SCE.

The information obtained in the above experiments is summarized in Table II. Similar information, obtained with pins of steel Type 4037, is presented in Table III.

In the case of the pins of steel Type 1062, it is seen that:

1. The potentials of the pins which had been pickled in the acid without any externally applied potential were between —0.56 and —0.54v *vs.* SCE, and 60% of those pins were broken when bend tested regardless of whether they had been 5 or 3 min in the acid.

Table II. Embrittling effect of 0.1*N* hydrochloric acid on blasted pins of steel Type 1062, at different applied potentials and treatment times

Externally applied potential *vs.* SCE (volt)	Pins broken (%) 5-Min treatment	3-Min treatment	Current density at pin surface (amp/sq ft)
−1.0 to −0.9	100	100	−24
−0.8 to −0.7	100	90	−7
−0.6	80	80	−2
(−0.56 to −0.54)*	60	60	—
−0.5 to −0.1	0	0	10 to 20
0.1 to 0.4	0	0	27 to 40

* No external potential applied.

NOTE: The steel pins were anode in the tests in which the externally applied potential was −0.5 or higher.

Table III. Embrittling effect of 0.1N hydrochloric acid on blasted pins of steel Type 4037, at different applied potentials and treatment times

Externally applied potential *vs.* SCE (volt)	Pins broken (%) 5-Min treatment	3-Min treatment	Current density at pin surface (amp/sq ft)
−1.0 to −0.7	100	100	−80 to −4
−0.6	100	80	−2
−0.5	80	80	−1
(−0.50 to −0.47)*	60	40	—
−0.4 to −0.1	0	0	2 to 14
0.1 to 0.5	0	0	24 to 31

* No external potential applied.
NOTE: The steel pins were anode in the tests in which the externally applied potential was −0.4 or higher.

2. All of the pins which had had an externally applied potential of −1.0 or −0.9v *vs.* SCE for 5 or 3 min were broken in the bend test.
3. At least 80% of the pins which had had an externally applied potential of −0.8, −0.7, or −0.6v *vs.* SCE were broken in the test, regardless of the length of pickling treatment.
4. None of the pins which had had an externally applied potential between −0.5 and 0.4v *vs.* SCE were broken in the test, regardless of the length of the pickling treatment.

The results obtained with the Type 4037 pins showed some similarity to those obtained with the Type 1062 pins. Here, none of the pins which had had an externally applied potential between −0.4 and 0.5 were broken, regardless of the length of the pickling.

After pins of both steels had been pickled in 0.2*N* hydrochloric acid (instead of 0.1*N*) for 5 min at an externally applied potential between −0.4 and −0.1v, none of them were broken in the bend test; *i.e.*, no significant embrittlement had occurred. No experiments were performed in which the hydrochloric acid content was below 0.1*N* or above 0.2*N*.

Since acid pickling solutions become less acid and their iron contents increase during use, experiments similar to the above were performed with pickling solutions which were 0.05*N* in hydrochloric acid and 0.05M in ferric or ferrous chloride. It was found that none of the pins were broken after 5 min pickling in these solutions when the externally applied potentials were as follows:

Steel Type 1062

Ferric chloride solution : −0.3 to −0.1v
Ferrous chloride solution : −0.4 to −0.2v

Steel Type 4037

Ferric chloride solution : −0.3 to −0.1v
Ferrous chloride solution : −0.4 to −0.3v

These data show that, even after one half of the hydrochloric acid in a 0.1*N* solution has been changed to ferric or ferrous chloride, there was a range of applied potentials at which no significant embrittlement occurred in pins of Types 1062 and 4037.

The pickling of high-strength steel pins in hydrochloric acid without embrittlement would be of comparatively little importance if a large amount of metal were to be dissolved during the operation, or if even a thin nonmetallic coating were to remain on the surface. Accordingly, the rate of solution of each metal during the pickling, and the appearance of each metal after the pickling, were investigated. As shown in Table IV, the rates of metal loss during 10-min pickling treatments of Type 1062 pins in 0.1*N* hydrochloric acid at applied potentials between −0.5 and −0.1v varied between 0.36×10^{-4} and 3.58×10^{-4} g/cm²/min. The rates for Type 4037 pins at applied potentials between −0.4 and −0.3v varied between 0.33×10^{-4} and 1.75×10^{-4} g/cm²/min. All of these rates are too low to be of importance. The appearance of these metals changed very little during these pickling treatments, as determined by inspection at a magnification of 60X.

Table IV. Rates of metal loss from blasted steel pins during immersion for 10 min in 0.1N hydrochloric acid with various anodic potentials applied

Applied potential *vs.* SCE (volt)	Rate of metal loss (g/cm²/min) Steel Type 1062	Steel Type 4037
−0.5	0.36×10^{-4}	
−0.4	0.94	0.33×10^{-4}
−0.3	1.69	1.75
−0.2	2.64	
−0.1	3.58	

It is important to note that (as shown in Table II), as the applied potential was increased from about −0.5 to about 0.4v, the current density at the steel surface was increased greatly. Although the pins continued to be in the unembrittled condition, the rate of solution of the metal in the acid increased a great deal and the metal surface became considerably rougher. Somewhat similar observations were recorded in Table III.

All of the experiments already referred to were repeated using sulfuric acid instead of hydrochloric acid. Since the results obtained in these experiments were of less practical interest than those obtained with hydrochloric acid, they have not been included in this paper.

Preventing unblasted pins from embrittlement.—In this part of the research, each steel pin was prepared for experiment by merely degreasing in trichloroethylene vapor. No attempt was made to remove or change the nature of the other nonmetallic material originally present on the pins.

It was found that, after pins of steel Type 1062, prepared as described in the previous paragraph, had been pickled for 15 min in 0.1*N* hydrochloric acid at an applied potential between −0.1 and +0.5v, they were free from embrittlement. When the applied potential was between +0.3 and +0.5v and the final surface had been water rinsed and treated ultrasonically, the surface was clean and comparatively smooth (*see* Table V). As shown in the same table, almost the same results were obtained with steel Type 4037.

Electroplating cadmium on steel Types 1062 and 4037 after anodic pickling in hydrochloric acid.—Geyer, Lawless, and Cohen (6) have stated, "Electroplating processes are recognized as the most common source of detrimental hydrogen embrittlement, and cadmium-electroplating processes are considered to be among the most serious offenders." However, in the present research it was found that high-strength steel pins of Types 1062 and 4037 could be plated with adherent cadmium in a stable bath (2) without embrittlement, providing that their surfaces had been given a preliminary preparation consisting of electrolytic treatment in hydrochloric acid, water rinsing, and ultrasonic treatment as described in this paper.

Summary

Degreased high-strength steel of Type 1062 or 4037, covered with oxide or other foreign material produced during previous metallurgical treatment, can be pickled with hydrochloric acid at about 23°C without embrittlement, if it is maintained within a certain range of electrical potentials while the pickling is in progress.

Table V. Effect of applied potential on the embrittlement of unblasted steel and the nature of the surface after water rinsing and ultrasonic treatment (15 min in 0.1N hydrochloric acid)

Type of steel	Potential applied to steel *vs.* SCE	No embrittlement produced	Surface clean and smooth after water rinsing and ultrasonic treatment
1062	−0.1 to +0.2	Yes	No
	+0.3 to +0.5	Yes	Yes
4037	−0.1 to +0.1	Yes	No
	+0.2 to +0.5	Yes	Yes

Any foreign material remaining on the metal surface can be removed by ultrasonic treatment in distilled water. The exact range of electrical potentials giving satisfactory results during the pickling depends on the composition of the metal being treated, the nature of the nonmetallic material on the surface of the metal prior to the pickling, and the length of the treatment time. The metal is dissolved at an insignificant rate and the nature of its surface is practically unaffected during the electrolytic treatment if the proper electrical potential is used.

The following alternate procedure may be used in the case of these steels. After degreasing, the steel is blasted with an aqueous slurry of No. 220 aluminum oxide to remove the undesirable nonmetallic material from the surface, thoroughly rinsed with distilled water, and dried. It then is pickled in hydrochloric acid while being maintained within a certain range of electrical potentials, and the foreign material still adhering after this treatment is removed thoroughly by ultrasonic treatment in distilled water and rinsing.

Steel Type 1062 or 4037 prepared by one of the procedures just described may be electroplated with adherent cadmium in a stable cyanide bath without becoming embrittled.

Since steels of the same type vary somewhat from batch to batch, the most suitable operating conditions for pickling each new batch of steel should be determined before regular production is commenced.

The electrodes used in these experiments were of high-strength steel and platinum. Obviously, in an industrial operation the platinum would be replaced by a cheaper material.

Sulfuric acid was found to be less satisfactory than hydrochloric acid as a pickling agent for the high-strength steels investigated.

Manuscript submitted Sept. 7, 1967; revised manuscript received Sept. 5, 1968.

Any discussion of this paper will appear in a Discussion Section to be published in the December 1969 JOURNAL.

REFERENCES

1. J. Bednar, W. Dingley, and R. R. Rogers, *Electrochem. Tech.*, **4**, 497 (1966).
2. W. Dingley and J. Bednar, *Tech. Proc. Am. Electroplaters' Soc.*, **51**, 66 (1964).
3. W. Dingley and J. Bednar, *ibid.*, **50**, 71 (1963).
4. W. Dingley, J. Bednar, and R. R. Rogers, *Plating*, **53**, 602 (1966).
5. J. D. Sudbury, O. L. Riggs, Jr., and D. A. Shock, *Corrosion*, **16**, 47t (1960).
6. M. M. Geyer, G. W. Lawless, and B. Cohen, "Hydrogen Embrittlement in Metal Finishing," H. J. Read, Editor, p. 109, Reinhold Publishing Corp., New York (1961).

Hydride Sources for Diffusion of Dopants into Silicon-on-Sapphire Films

D. J. Dumin

RCA Laboratories, Radio Corporation of America, Princeton, New Jersey

ABSTRACT

Mixtures of B_2H_6, PH_3, AsH_3 diluted in H_2 have been used as a source for diffusion into thin silicon-on-sapphire films after the films had been grown. Films 1-2 μm thick of initial resistivity greater than 100 ohm-cm have been reproducibly doped from 0.01 to 1 ohm-cm, both P- and N-type. Films have been doped to resistivities higher than 10 ohm-cm, but not reproducibly. This process has been used to produce either thin heavily doped layers on the surface of the thin film or, after a drive-in step, a uniformly doped film. The doping process was studied as a function of dopant gas flow rate and temperature.

Numerous sources of P- and N-type impurities have been used to dope bulk silicon and silicon epitaxial layers (1). In general, the doping of epitaxial layers of silicon has been performed during growth of the layer (2), allowing for the control of either uniformly doped layers or the production of doping profiles that would be extremely difficult to obtain after growth using diffusion only (3). The solid-solid diffusion process has been found to be both convenient and reproducible, but after diffusion the silicon surface is covered with a doped oxide layer (4).

In general, the techniques used to dope silicon films grown heteroepitaxially on sapphire and spinel have paralleled the techniques used to dope homoepitaxial silicon (5). The use of the gaseous hydrides added to the gas stream during growth of silicon on quartz and beryllium oxide have been reported (6). Fabrication of diodes, transistors, and integrated circuits in silicon-on-sapphire films have used processing steps similar to those used in processing bulk silicon devices (7).

The use of gaseous hydrides in both oxidizing and reducing atmospheres as sources of P- and N-type impurities for the selective doping of silicon has been reported (8). These reports have indicated that the use of an oxidizing atmosphere to provide a doped oxide as the source of impurity tended to produce wafers more uniformly and reproducibly doped than the use of a reducing atmosphere of H_2 or an inert atmosphere of He. Using a hydride in an oxidizing atmosphere results in essentially a solid-solid diffusion process.

During the fabrication of silicon-on-sapphire circuits, it has often been necessary to modify transistor or diode characteristics after the devices had been fabricated. A relatively simple system that we investigated was the use of the gaseous hydrides B_2H_6, AsH_3, and PH_3 in H_2 mixtures as diffusion sources. The silicon surfaces after diffusion were not covered by an oxide layer and uniform doping of layers 0.2-1.0 μm could be obtained in relatively short periods of time. This paper describes the results of experiments performed on the doping of thin silicon films.

Experimental

Wafer preparation.—The wafers used in these experiments were (100) silicon grown on $(1\bar{1}02)$ flame fusion sapphire at temperatures between 1050° and 1100°C using previously described techniques (9).

No dopant was intentionally added to the films during growth, but the films were usually P-type, doped with varying amounts of Al from the Al_2O_3 substrate (10). Previous experiments of growing thin silicon films on 10 ohm-cm P- and N-type bulk silicon wafers indicated that impurities in the SiH_4 source produced silicon doped N-type with carrier concentrations of about $10^{14}/cm^3$. After the Al had been removed from the films by segregation in a thermal oxide (11), the films of silicon on sapphire were N-type with resistivities above 10 ohm-cm and Hall mobilities over 400 $cm^2/vsec$. The films were 1-2 μm thick as determined by using *IR* interference techniques (12).

The diffusion step was carried out by first heating the wafer to the desired hydride deposition temperature in hydrogen. The wafer was held at deposition temperature for 1 min after which the dopant was added to the hydrogen flow. The deposition time in all cases was 5 min. The system was flushed for 1 min in H_2 after deposition from the hydride, and then the temperature was lowered to room temperature. The system used to grow and dope the films has been previously described (9).

At this stage in the processing, the wafers contained both a doped layer on the surface and, because the processing took place in H_2, a somewhat variable amount of aluminum originating from the H_2 reduction of the Al_2O_3 substrate. The aluminum could be removed by segregation in a thermal oxide (11) which also caused redistribution of the desired impurities. Since, in general, P-type impurities tend to segregate in a thermal oxide and N-type impurities do not (13), the redistribution step also caused some reduction in the amount of boron in the films. The presence of aluminum in the films and its removal after the diffusion step complicate the analysis of the data and these complications are discussed below. In the cases where the diffusion was performed at temperatures below 1050°C and only a limited amount of aluminum was introduced into the films, the impurities could be redistributed by heating the wafer in He at 1200°C for 30 min.

P-type doping: boron.—The boron diffusions were carried out using B_2H_6-H_2 mixtures varying in composition from 10^{-6} to 10^{-2} mole per cent (m/o). At B_2H_6 concentrations greater than 10^{-2} m/o, elemental boron was deposited on the wafer surface. At hydride concentrations less than 10^{-3} m/o, the boron apparently diffused into the silicon as fast as it was produced, and a P+ layer of silicon was formed on the surface of the silicon, rather than an elemental boron layer.

Two profiles of resistivity *vs.* silicon thickness are shown in Fig. 1 for two boron layers deposited on a 1 μm-thick silicon film. The boron concentration in the gas stream was $7.5 \cdot 10^{-4}$ m/o at two deposition temperatures of 1050° and 1150°C. The resistivity was measured using a four-point probe using the total film thickness to determine the thickness correction factor (14). The silicon was removed by anodic oxidation involving maximum temperatures of 60°C (15). The aluminum autodoping had been removed from these films, and both films were N-type with resistivities greater than 100 ohm-cm prior to boron doping. In the film doped at 1050°C, a layer of P-type silicon was observed on the surface of the wafer with the N-type silicon remaining below the diffused layer to the silicon-sapphire interface. The depth of diffusion of 0.1 μm is in good agreement with a complementary error function type of diffusion using published values of diffusion constant for boron (16). The wafer diffused at 1150°C was P-type throughout. This was probably due not only to the greater depth of diffusion of the boron at 1150°C but also to the enhanced aluminum autodoping.

A series of plots in Fig. 2 show the variation in carrier concentration in the films due to changes in the

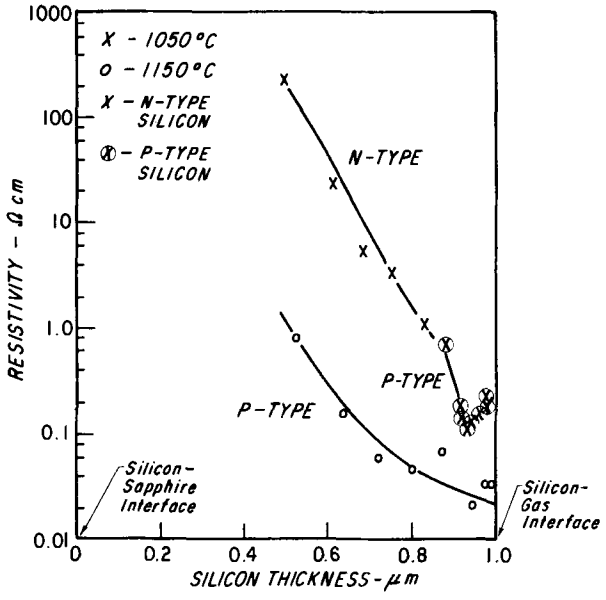

Fig. 1. Doping profiles using B_2H_6 to dope 1-μm-thick, high-resistivity N-type silicon-on-sapphire films. B_2H_6 concentration in H_2 was 2×10^{-5} m/o.

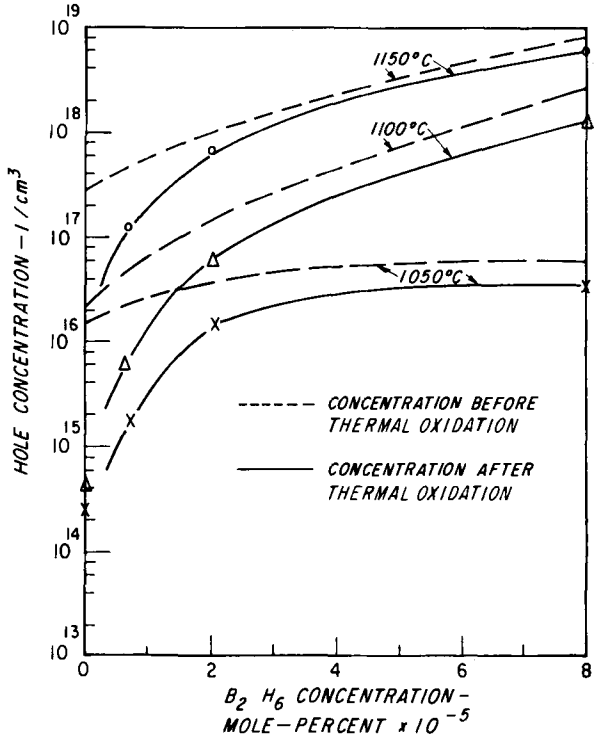

Fig. 2. Carrier concentration in 1-μm silicon-on-sapphire films as a function of gas concentration and temperature. Dashed lines—data taken before aluminum removal by thermal oxidation; solid lines—data taken after aluminum removal by thermal oxidation.

B_2H_6 gas concentration and deposition temperature. These wafers were doped using the cycle: 1 min H_2; 5 min B_2H_6-H_2; 1 min H_2 described above. Hall data were taken both before and after the boron had been redistributed by diffusion in a dry O_2 ambient at 1200°C for 1 hr.

The carrier concentration was determined by using $N = 1/\rho e\mu$ where ρ is the resistivity and μ is the Hall mobility. The ratio of drift to Hall mobility was assumed to be unity. Before oxidation, the wafers contained both the heavily boron doped layer on the silicon surface and any aluminum autodoping that was present. After the oxidation, the boron was redistributed throughout the film and the aluminum was

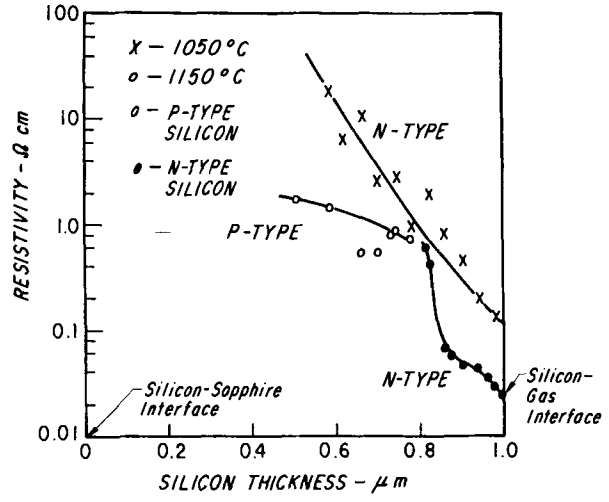

Fig. 3. Doping profiles using PH_3 to dope 1-μm, high-resistivity N-type silicon-on-sapphire films. PH_3 concentration in H_2 was $7.5 \cdot 10^{-5}$ m/o.

removed by segregation in the oxide (11). Some of the boron no doubt also segregated in the thermal oxide (13). Thus, within the error of neglecting the amount of boron that might have segregated in the oxide, the data presented in Fig. 3 represent the amount of boron introduced into the silicon during the deposition step. The hole concentration measured in 2-μm-thick films was about ½ of that shown in Fig. 2 when the 2-μm-thick films were subjected to the same diffusion cycle.

The reproducibility of the boron doping system was tested by attempting to dope several wafers to the same resistivity on successive days. The results of one of these experiments are shown in Table I. The wafers were doped at 1000° and 1100°C for 5 min in $2 \cdot 10^{-5}$ m/o B_2H_6 in H_2. Before thermal oxidation, one set of wafers had resistivities of about 0.14 ± 0.02 ohm-cm. After aluminum removal through the thermal oxidation at 1200°C, the resistivity had risen to 0.23 ± 0.04 ohm-cm. This represents reproducibility to about 30-40%. Wafers doped to resistivities about 1 ohm-cm showed a somewhat larger spread in resistivities with typical values ranging between 1 and 2 ohm-cm after aluminum removal. The resistivity varied over a wafer surface about as much as it varied from wafer to wafer.

Data taken on arsenic doped films are included in Table I and are discussed below.

N-type impurities: phosphorus and arsenic.—Wafers of high-resistivity silicon on sapphire were doped with phosphorus and arsenic *via* the decomposition of PH_3-H_2 and AsH_3-H_2 mixtures, respectively. Two profiles of phosphorus diffusions performed at 1050° and 1150°C are shown in Fig. 3. The PH_3 concentration in H_2 was $7.5 \cdot 10^{-5}$ m/o using the 1-5-1 min cycle described above. These data were taken by measuring the sheet resistance of the films on a four-point probe after successive anodic oxidations. The aluminum introduced into the films was not removed. This accounts for the P-N junction observed in the film doped at 1150°C. At 1150°C, the diffusion length for aluminum is about 0.85 μm and for phosphorus is about 0.5 μm. These numbers predict that a P-N junction should be observed between 0.15 and 0.5 μm below the silicon surface, in reasonable agreement with the observed junction depth of 0.2 μm. The wafer doped at 1050°C was N-type throughout. The resistivity continually rose as the thickness was reduced indicating the effect of the decrease in phosphorus concentration. No layer of P-type silicon was observed at the silicon-sapphire interface in the 1050°C doped film due to the aluminum autodoping. This would be expected from data taken previously on thin silicon-on-sapphire films in this temperature range (10).

Attempts to measure the diffusion profile accompanying arsenic diffusion were unsuccessful for diffusion times of 5 min and temperatures below 1150°C. This reflects the lower diffusion constant of arsenic in silicon. That arsenic was indeed present in the films is however, shown when the carrier concentration data is discussed.

Plots of carrier concentration in the films as a function of hydride gas concentration and deposition temperature are shown in Fig. 4 for both phosphorus and arsenic doped silicon. The data shown in Fig. 4 were taken after a 1-hr oxidation in dry O_2 at 1200°C. Before oxidation, many of the films were P-type with varying resistivity due to the aluminum autodoping. As in the case of the boron doped wafers, increasing either the hydride concentration or the diffusion temperature increased the doping density. The carrier concentration of films doped with arsenic was almost one order of magnitude less than the concentration in the phosphorus doped films, reflecting the fact that the diffusion constant of arsenic in silicon is almost two orders of magnitude lower than the diffusion constant of phosphorus at 1150°C (17).

At diffusion temperatures of 1050°C or below, the diffusion of arsenic into the silicon was sufficiently slow to lead to nonreproducibility in the films doped using the 1-5-1 min diffusion cycle. The reproducibility of the arsenic doping system at an 1150°C deposition temperature is shown in Table I where, under nearly identical conditions, the resistivity of doped silicon layers varied around 0.5 ± 0.1 ohm-cm after aluminum removal. Before aluminum removal, the films were P-type with resistivity about 0.3 ohm-cm. The reproducibility of the phosphorus diffusions was similar to that cited for the boron under similar doping conditions. As in the case of the boron doped films, increasing the initial film thickness decreased the

Table I. Test of doping reproducibility

Resistivity as doped (ohm-cm)	Resistivity after thermal oxidation (ohm-cm)	
0.13	0.20	1100°C B_2H_6 deposition
0.14	0.20	
0.16	0.27	
1.5	2.0	1000°C B_2H_6 deposition
0.75	1.0	
1.0	1.5	
P-type	0.59	1150°C AsH_3 deposition
P-type	0.44	
P-type	0.42	

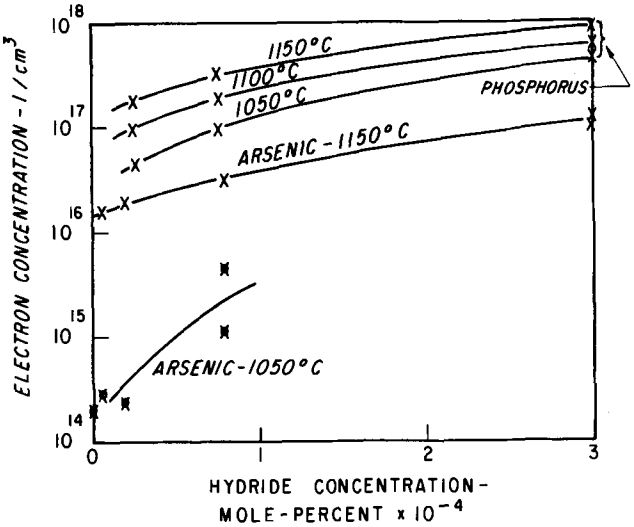

Fig. 4. Carrier concentration of N-type films as a function of hydride concentration and temperature. Many of these films were P-type prior to aluminum removal. Data presented were taken after aluminum removal.

carrier concentration in the films, but the product of carrier concentration and film thickness was approximately constant.

Discussion and Conclusions

The process of using a gas to maintain a constant surface concentration of impurity as a doping source should lead to a diffusion profile which follows the complementary error function (18). The diffusion profiles measured in Fig. 1 and 3 show that a diffusion front was obtained at about the depth of diffusion expected, but the data were not sufficiently accurate to be used as a measure of the diffusion profile. In Fig. 3, a hint of a complementary error function profile might be assigned to the 1150°C diffusion, but any concrete conclusions would be highly speculative. The shallowness of the diffusions precluded accurate measurements of the profile.

The total amount of impurity diffused into the silicon was calculated from the data shown in Fig. 2 and 4 and compared with the amount that would be expected under a complementary error function type of diffusion. For the N-type impurities, phosphorus and arsenic, no segregation of the impurity in a thermal oxide should be observed (13); thus, analyzing the concentration data after impurity redistribution by the 1200°C oxidation step should be valid. In the case of phosphorus in silicon, diffusion is a faster mechanism than thermal oxidation and the ratio $K/\sqrt{D} \approx 0.17$, where K is the parabolic rate constant for oxidation and D is the diffusion constant. This implies that the impurity would diffuse faster than the oxidation front would advance. For arsenic, $K/\sqrt{D} \approx 1.0$ and thus it would be possible for the oxidation front to overtake a portion of the diffusion impurity. This, of course, neglects segregation of the impurity in the oxide or in the silicon. The measured values of carrier concentration accompanying the phosphorus diffusion fit reasonably well the values expected for a complementary error function diffusion. The total carrier concentration varied as the square root of the diffusion constant as would be predicted (18). The carrier concentrations accompanying the arsenic diffusion were lower than predicted and this may have been due to the oxidation front overtaking some of the impurity. The carrier concentrations considered in the case of arsenic diffusion were well below the values needed for degeneracy and thus it has been assumed that the carrier concentration is an accurate measure of the impurity concentration.

The hole concentration measured in the case of the boron diffusions did not fit the error function complement type of diffusion. It appeared as if less boron was being included in the films than was expected. Again, it has been assumed that the hole concentration is an accurate measure of the boron concentration. Since boron segregates in a thermal oxide, the lowering of the hole concentrations measured could be attributed to inclusion of boron in the oxide. Since the boron diffusions were found to be reproducible, the fact that the carrier concentration data did not fit the complementary error function type of diffusion meant that the data shown in Fig. 2 had to be taken at various temperatures before it was possible to use the boron doping system accurately.

One of the purposes of these experiments was to provide a system for the alteration of diode and transister properties after device fabrication. In Fig. 5, the alteration of the characteristics of through-diffused silicon-on-sapphire diodes (19) is shown. Initially, the diodes had reverse breakdown voltages of 220v and forward series resistance of $2 \cdot 10^5$ ohms. The silicon was 10 ohm-cm, N-type, 1.3μ thick. The wafer was broken into several parts. Boron and phosphorus were diffused into the different pieces to produce silicon doped to different levels according to the data presented in Table I and Fig. 2 and 4. After deposition of the thin boron layer and subsequent drive-in, the

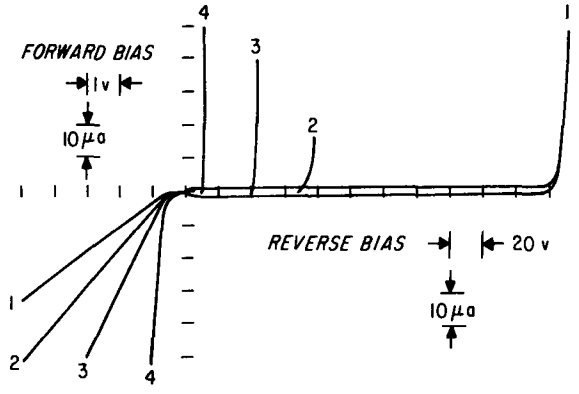

Fig. 5. Alteration of forward and reverse diode characteristics after boron diffusion: 1—Initial characteristics. 2—Portion diffused in $7 \cdot 10^{-6}$ m/o B_2H_6 in H_2 at 1000°C for 5 min. Drive-in was 1200°C dry O_2 for 30 min. 3—Portion diffused in $7 \cdot 10^{-6}$ m/o B_2H_6 in H_2 at 1050°C for 5 min. Drive-in was 1200°C dry O_2 for 30 min. 4—Portion diffused in $8 \cdot 10^{-5}$ m/o B_2H_6 in H_2 at 1150°C for 5 min. Drive-in was 1200°C dry O_2 for 30 min.

diode resistivity had been lowered on one piece of the wafer to 5 ohm-cm, on another portion to 2.5 ohm-cm, and on a third portion to 0.5 ohm-cm with the breakdown voltage being lowered to 70, 40, and 10v, respectively. The phosphorus doped portions of the wafer showed similar changes in diode resistances and breakdown voltages. The gas phase doping of the films did not change the position of the junction, which was determined by microscopically examining the diode under large reverse bias and noting the position of the light emission (20). The breakdown voltages observed in these diodes always correlated well with the breakdown expected on bulk silicon of similar resistivity (21).

Attempts were made to raise the reverse breakdown voltage of diodes made in P-type silicon by partially compensating the material with phosphorus. This has not been reproducibly accomplished.

The surfaces of bulk silicon wafers were doped using the doping schemes described above. Diodes have been manufactured either by uniformly doping the wafer and etching mesas or by diffusion through holes in an oxide mask. P^+N diodes have been produced at deposition temperatures as low as 800°C and N^+P diodes at temperatures above 900°C. The minority carrier lifetime in the starting N-type silicon was of the order of 5-10 μsec and after P^+N diode fabrication was between 1-5 μsec (22). Diffused resistors have also been produced in bulk silicon with values of resistance varying between 10-4000 ohms/sq.

The use of the hydride in hydrogen sources has thus been utilized to dope both thin silicon-on-sapphire films on bulk silicon wafers. The doping of the thin films proved to be reproducible. A sufficient amount of data needed to determine reproducibility on the bulk silicon wafer was not taken; however, the production of diodes with only a small amount of degradation of minority carrier lifetime indicated that the use of the hydride-hydrogen diffusion system may have applications in doping of bulk silicon. At present, the use of the hydride-hydrogen diffusion system appears to be no more reproducible than existing doped oxide systems as sources for diffusion, but the fact that the doped silicon surface is not covered by an oxide after diffusion tends to simplify some device fabrication steps. Helium was used as the carrier gas when it was desirable to avoid oxidation of the silicon surface during the drive-in step.

Acknowledgments

The assistance of R. F. Adams and R. O. Wance during the performance of these experiments is gratefully acknowledged.

Manuscript submitted April 19, 1968; revised manuscript received Aug. 23, 1968.

Any discussion of this paper will appear in a Discussion Section to be published in the December 1969 JOURNAL.

REFERENCES

1. "Integrated Silicon Device Technology, Vol. IV—Diffusion," Research Triangle Institute, Durham, N.C. (1964), and references contained in bibliography.
2. S. R. Bhola and A. Mayer, *RCA Rev.*, **24**, 511 (1963).
3. S. Nakanuma, *IEEE Trans.*, **ED-13**, 578 (1966).
4. F. M. Smits, *Proc. IRE*, **46**, 1049 (1958); J. Scott and J. Olmstead *RCA Rev.*, **26**, 357 (1965).
5. P. H. Robinson and C. W. Mueller, *Trans. Met. Soc. AIME*, **236**, 268 (1966).
6. B. A. Joyce, R. J. Bennett, R. W. Bicknell, and P. J. Etter, *ibid.*, **233**, 556 (1965); H. M. Manasevit, D. H. Forbes, and I. B. Cadoff, *ibid.*, **236**, 275 (1966).
7. C. W. Mueller and P. H. Robinson, *Proc. IEEE*, **52**, 1487 (1964); F. P. Heiman, *IEEE Trans.*, **ED-13**, 855 (1966); A. Miller, *Electronics*, **40**, 171 (1967); R. Zuleeg and P. Knoll, *Electron Letters*, **3**, 137 (1967).
8. M. C. Duffy, D. W. Foy, and W. J. Armstrong, *Electrochem. Technol.*, **5**, 29 (1967); M. S. R. Heynes, *ibid.*, **5**, 25 (1967); M. S. R. Heynes, and P. G. G. van Loon, Paper 92, ECS Meeting, Dallas, May 7-12, 1967; W. G. Dautzenberg, Y. W. Hsueh, and B. R. Wilkins, Paper 91, ECS Meeting, Dallas, May 7-12, 1967.
9. D. J. Dumin, *J. Appl. Phys.*, **38**, 1909 (1967); D. J. Dumin and P. H. Robinson, *ibid.*, **39**, 2759 (1968).
10. D. J. Dumin and P. H. Robinson, *This Journal*, **113**, 469 (1966); P. B. Hart, P. J. Etter, B. W. Jervis, and J. M. Flanders, *Brit. J. Appl. Phys.*, **18**, 1389 (1967).
11. H. Edagawa and Y. Morita, *J. Phys. Soc. Japan*, **18**, 460 (1963); A. S. Grove, O. Leistiko, Jr., and C. T. Sah, *J. Appl. Phys.*, **35**, 2695 (1964); C. S. Fuller and F. H. Doleiden, *J. Appl. Phys.*, **29**, 1264 (1958).
12. D. J. Dumin, *Rev. Sci. Instr.*, **38**, 1107 (1967).
13. A. S. Grove, O. Leistiko, Jr., and C. T. Sah, *J. Appl. Phys.*, **35**, 2695 (1964).
14. L. B. Valdes, *Proc. IRE*, **42**, 420 (1954).
15. A. G. Revesz, *This Journal*, **114**, 629 (1967).
16. A. D. Kurtz and R. Yee, *J. Appl. Phys.*, **31**, 303 (1960).
17. C. S. Fuller and J. A. Ditzenberger, *ibid.*, **25**, 1439 (1954); C. S. Fuller and J. A. Ditzenberger, *ibid.*, **37**, 544 (1956).
18. P. G. Shewmon, "Diffusion in Solids," McGraw-Hill Book Co., New York (1963).
19. D. J. Dumin and R. S. Silver, *Solid State Electron.*, **11**, 353 (1968).
20. A. G. Chynoweth and R. G. McKay, *Phys. Rev.*, **102**, 369 (1956).
21. S. M. Sze and G. Gibbons, *Appl. Phys. Letters*, **8**, 111 (1966).
22. R. S. Silver, RCA Labs., Private communication.

Preparation and Properties of Boron Carbide Continuous Filaments

J. B. Higgins, A. Gatti, and J. J. Gebhardt

Space Sciences Laboratory, General Electric Company, Missile and Space Division, Space Technology Center, Philadelphia, Pennsylvania

ABSTRACT

Boron carbide filaments are promising reinforcements for use in both resin and metal composites because of their potentially high strength, high elastic modulus, and low density. This paper discusses the preparation and properties of such filaments from the viewpoint of their ultimate usefulness in such applications. Continuous boron carbide filaments were vapor deposited on tungsten substrates having a boron precoat from mixtures of boron trichloride, methane, and hydrogen at 1 atm and temperatures between 1100° and 1200°C. Deposition rates were considerably less than for boron alone; a close relationship was seen between the stoichiometry of the feed gas, filament composition, and mechanical properties. In extended runs, average strengths of 390,000 psi were achieved, with individual values as high as 474,000 psi (1-in. gauge). Elastic modulus values up to 62 x 10^6 psi were also characteristic of the product. In prototype epoxy resin composites of less than optimum uniformity and homogeneity, bend strengths up to 244,000 psi and moduli up to 54 x 10^6 psi were measured at 85 v/o filaments, indicating that efficient transfer of stress to the filaments occurred.

The vapor deposition of refractory high-melting materials on static filamentary substrates was first undertaken on a broad scale by Moers and Agte in 1931 (1). Only within the past few years, however, has this technique been sufficiently well developed to permit preparation of continuous coated filaments on a scale approaching that of pilot-plant production. While both elemental boron and silicon carbide (2, 3) have been prepared in quantity, boron carbide in this form has not been studied in detail, although its bulk mechanical properties mark it as a promising candidate for use in filament reinforced composites.

In order to obtain boron carbide by vapor deposition from easily obtained gaseous species, it is most convenient to reduce a halide and pyrolyze a hydrocarbon simultaneously. Boron can be obtained at reasonable rates by the reduction of boron trichloride with hydrogen at temperatures above about 1000°C (4), while the thermal decomposition of methane can also be brought about, although at lower rates in the same temperature region (5). This temperature requirement necessitates the use of an electrically conductive refractory filament for a substrate, since it must retain sufficient strength at deposition temperatures to be drawn through a continuous deposition reactor. The number of such materials is limited to those in the refractory metal group and since, of these, tungsten is most easily available in quantity, it is the most logical choice. However, because it is very dense (18.9 g/cm^2) and will thus raise the total density of the final filament considerably, only the thinnest available substrate can be used. Thus, the basic outlines of the deposition scheme can be summarized as follows: deposition temperature, above 1050°C; pressure, 1 atm;

reactants, boron trichloride, methane, and hydrogen; substrate, tungsten filament, 0.5-1.0 mil.

Experimental Procedure

Preliminary experiments were carried out using a static filament or hot-wire reactor in which the deposition surface consisted of resistance-heated, vertically suspended tungsten filaments 0.5 and 1 mil thick, spring loaded to compensate for expansion on heating. Data from these experiments were used to obtain preliminary correlations between reaction conditions and the stoichiometry and mechanical and chemical properties of the deposits. These conditions were used as a starting point in the process study for preparing continuous filaments.

In order to prepare continuous lengths of filament, a series of connected 1-in. ID horizontal tubular compartments was arranged to permit the substrate to pass along the common axis while reactant gases were passed at right angles to the filament. The use of connected compartments or stages was required in order to obtain a uniform temperature profile along the filament as it became thicker with the deposit. Gas director plates were also inserted in the compartments parallel to the filament to constrict the gas stream as it passed across the filament and thereby achieve a higher mass flow rate to the deposition surface. Electrical contact to the filament as well as sealing against the atmosphere was achieved by the use of mercury wells located in the dividers between each stage and at each end of the reactor. Prior to entry into the reactor, the filament substrate was heated in an atmosphere of hydrogen to remove impurities and residual lubricant. The filament was unwound from its original shipping reel and through the reactor to the take-up spool by means of a small variable speed motor. Tension was adjusted by means of a simple friction brake on the de-reeling spool. Gas flows and temperatures were independently variable for each deposition stage. Early in the experimental program, it was found advantageous to deposit a precoating of boron on the substrate after cleaning, both for stabilizing the substrate temperature and for increasing the surface area of the substrate during carbide deposition. The bulk of the filament thus consisted of boron with a relatively thin shell of boron carbide on the outside. Figure 1 is a sketch of the deposition apparatus which was evolved during the program and which comprised the final deposition system in which the majority of filament preparation runs was made.

As was stated earlier, conditions used for preparation of continuous lengths of filament were based on those which gave the best deposits in the static hot-wire experiments. Temperatures in the two boron precoat stages of the reactor (*see* Fig. 1) were varied at two levels (1050°-1100°C and 1100°-1195°C). In the boron carbide deposition section of the reactor, temperatures were also varied at two levels, about 790°-1030°C and 1010°-1150°C, along the length of the heated-boron-coated filament. The initial or hydrogen cleaning stage was kept at about 900°C throughout.

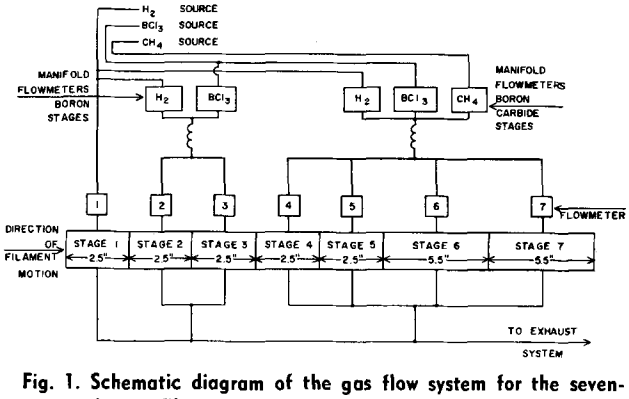

Fig. 1. Schematic diagram of the gas flow system for the seven-stage continuous filament reactor system.

Boron-to-carbon mole ratios in the feed gas were varied from 1.1 to 11.5 in hydrogen, while total gas feed rate to the boron carbide stages was kept between about 1375 and 1630 cc/min. Filament speed was adjusted to produce filaments thicker than 2.5 mils where possible and was usually around 18 in./min. These conditions and associated test data are summarized in Table I.

Typical specimens from each run were tested for tensile strength (1-in. gauge length) and elastic modulus (15-in. gauge length) on a standard Instron Testing Machine at a crosshead speed of 0.020 in./min. Selected specimens were also examined by optical and electron microscopy as well as by x-ray diffraction, while microstructure was studied on smooth unpolished fracture cross sections. To evaluate preliminary composite behavior, epoxy-coated filaments were hand laid by standard techniques developed for making small experimental boron-epoxy (Epon 815) beam composites. These were flexure tested in three-point loading, both before and after a water-boiling treatment, using a span of approximately 0.7 in.

Results

Deposition rate.—Of primary importance in the development of a practical process for manufacturing continuous filament by vapor deposition is the rate at which material is deposited on the substrate. In the deposition of boron carbide filament, the rate, which may be dominated by diffusion processes or by the rate of chemical reaction at the surface, was determined by measuring the filament diameter before and after deposition, and using a geometric averaging procedure to compensate for the increase in substrate surface area during the deposition. In both the static hot-wire and the continuous filament apparatus, the deposition rate for boron carbide was diffusion limited judging from the activation energy derived from Arrhenius plots of deposition rate *vs.* reciprocal temperature (Fig. 2). In the case of the continuous filament reactor, the higher energy of activation is believed to be due to the preliminary coating of boron deposited prior to deposition of boron carbide and which was included in the diameter measurement. This step is known to have been essentially surface reaction controlled from rates measured in the boron deposition stages alone. A pronounced reduction in deposition rate was observed when even small quantities of methane were added to the boron trichloride-hydrogen mixture used to obtain only boron deposits, suggesting the possibility of an interference in the boron deposition mechanism by methane or some of its decomposition products. However, although a num-

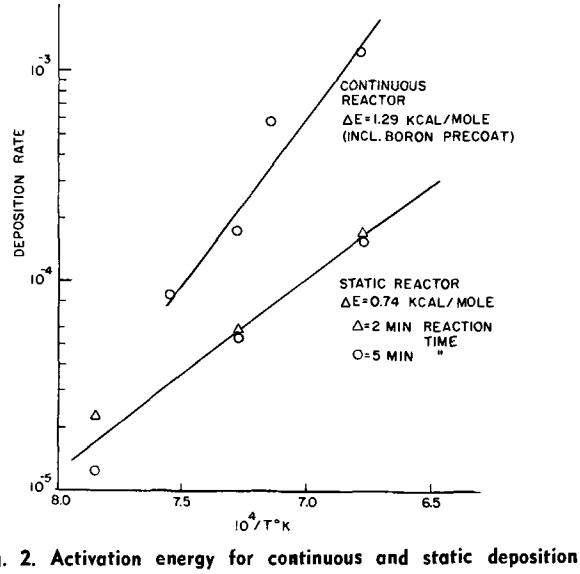

Fig. 2. Activation energy for continuous and static deposition of boron carbide.

Table I. Deposition parameters and properties of continuous B_4C filaments*

Run No.	Stage 1 Filament speed in./min	Stage 1 H_2 cc/min	Gas flows cc/min Stages 2 & 3 H_2	Stages 2 & 3 Mol fraction BCl_3	Stages 2 & 3 Total flow cc/min	Stages 4-7 H_2	Stages 4-7 CH_4	Stages 4-7 Mol fraction BCl_3	Stages 4-7 Total flow cc/min	Temperature readings, °C Stage No. 1	2	3	4	5	6	7	Filament diam mils	Physical properties Tensile strength psi × 10^{-3} Low	Average	High	No. of tests	Modulus psi × 10^{-6}
34	9.5	115	0.622	0.378	370	0.501	0.040	0.459	1507	900	1100	1120	1105	1090	1070	1050	2.75		326	410	16	62
35	9.5	115	0.622	0.378	370	0.501	0.040	0.459	1507	900	1035	1140	1100	1000	1055	1050	3.07	262	270	340	19	57
36	19.5	115	0.622	0.378	370	0.463	0.113	0.424	1632	900	1070	1070	1050	1070	1095	1070	2.10	216	153	197	5	60
37	19.5	115	0.622	0.378	370	0.463	0.113	0.424	1632	900	1060	1055	1010	1030	1055	1160	2.15	108	279	337	6	59
38	19.5	115	0.622	0.378	370	0.463	0.113	0.424	1632	900	1060 *L*	1055	1010	1030 *H*	1165	1150	2.35	252	279	236	6	55
39	19.5	115	0.622	0.378	370	0.463	0.113	0.424	1632	900	1055	1080	1085	1130	1170	1135	2.62	86	187	254	6	55
40	19.5	115	0.622	0.378	370	0.463	0.113	0.424	1632	900	1195	1195	1020	1075	1120	1090	3.15	179	217	313	5	55
41	19.5	115	0.622	0.378	370	0.463	0.113	0.424	1632	900	1185 *H*	1195	960	1050 *L*	965	980	3.0	164	232	392	6	57
42	19.5	115	0.622	0.378	370	0.463	0.113	0.424	1632	900	1170	1170	800	1005	945	940	2.70	162	315	291	6	60
43	19.5	115	0.622	0.378	370	0.463	0.113	0.424	1632	900	1080	1075	790	990	930	910	1.93	197	239	349	6	61
44	19.5	115	0.622	0.378	370	0.463	0.113	0.424	1632	900	1060 *L*	1050	790	1070 *L*	960	985	1.96	243	312	302	5	58
45	13.5	115	0.648	0.352	455	0.519	0.068	0.413	1407	900	1060	1050	790	1070	960	985	3.27	222	256	231	5	58
46	18.0	115	0.648	0.352	455	0.526	0.054	0.420	1387	900	1060	1050	790	1070	960	985	2.75	103	154	266	6	60
47	18.0	115	0.648	0.352	455	0.531	0.047	0.422	1377	900	1060	1050	790	1070	960	985	2.62	194	245	432	10	59
48	18.0	115	0.648	0.352	455	0.531	0.047	0.422	1377	900	1060	1050	790	1070	960	985	2.62	280	364	344	13	58
49	18.0	115	0.648	0.352	455	0.531	0.047	0.422	1377	900	1060	1050	790	1070	960	985	2.62	268	309	364	6	61
50	18.0	115	0.648	0.352	455	0.531	0.047	0.422	1377	900	1060	1050	790	1070	960	985	2.62	320	350	364	6	60
51	18.0	115	0.648	0.352	455	0.531	0.047	0.422	1377	900	1060	1050	790	1070	960	985	2.5	244	342	385	6	60
52	18.0	115	0.648	0.352	455	0.531	0.047	0.422	1377	900	1060	1050	790	1070	960	985	—	—	—	—	—	—
																	2.65	281	390	474	6	62

* Data illustrating the effect of temperature on deposition rate (filament thickness) are enclosed in boxes, where *H* denotes a high temperature range and *L* a low one.

Table II. Bend test results for B_4C filament reinforced epoxy microbeams

Average beam dimensions (mils)	Strength KSI	Volume fraction filaments	Strength KSI	Volume fraction filaments
1*D* 24.7 high × 44.1 wide Span 0.748 in.	237	0.85	211	0.65
	244	0.84	192	0.69
	230	0.77	188	0.65
	231	0.73	181	0.63
	232	0.64	180	0.65
1*W* 25.9 high × 55.7 wide Span 0.717 in.	128	0.51	134	0.49
	168	0.55	113	0.46
	136	0.53	137	0.69
	146	0.52	142	0.53
3*D* 23.8 high × 45.2 wide Span 0.763 in.	178	0.62	189	0.61
	160	0.66	210	0.62
	188	0.62	184	0.58
	200	0.64	182	0.59
	197	0.62	178	0.58
3*W* 26.4 high × 38.0 wide Span 0.699 in.	64	—	145	0.60
	93	—	143	0.60
	172	0.56	148	0.59
	154	0.64	137	0.59
	142	0.62	132	0.57

D = Tested as received.
W = Tested after 2-hr soak in boiling water.

ber of mechanisms can be hypothesized which involve, for example, an interaction of hydrocarbon fragments with dichloroborine ($BHCl_2$), a suspected intermediate in the deposition of boron, or a surface adsorption or desorption selectivity for more stable fragments, they cannot easily be tested for validity from the data obtained in the preparative type of experiment.

The experimental variable having the greatest effect on deposition rate, as estimated from filament diameter, was temperature. Variations in the boron-carbon ratios in the feed gas, or in total feed rate, did not produce noticeable differences in filament diameter, nor did changes in the hydrogen content of the feed gas mixture. Certain data in Table I are set off in groups with the identifying code "*H*" and "*L*" representing high and low temperature levels on the average for boron deposition stages and carbide deposition stages. All other experimental factors remained constant throughout this series of runs. Examination of these data shows that high temperature in the second and third (boron deposition) stages, only 5 in. long, and low temperature in the remaining (carbide deposition) stages, 16 in. long (Runs 41, 42 *vs.* Runs 36-39), produced thicker filament than the reverse situation. This is not unexpected since the deposition rate of boron under conditions similar to those prevailing in the second and third stages was controlled by the rate of reduction, while carbide deposition was apparently diffusion limited.

Filament Properties.—Physical properties and morphology. The continuous boron carbide coated boron filaments were between 1.8 and 3.5 mils thick and were dense, hard, and black, exhibiting a somewhat grainy dull surface rather than a shiny smooth appearance (Fig. 3). The formation of isolated islands or patches or a different appearance was occasionally observed (Fig. 4) and appeared to be associated with a perturbation in deposition conditions. Also observed from time to time were isolated nodules believed to be due to the adherence of soot or other solid particles to the substrate. In cross section (Fig. 5), the filaments consisted of a number of concentric rings which resulted from interruption of the deposition process when the filament left one stage, and passed through the mercury contact into the next stage. However, the number of rings was also increased by fluctuations in deposition temperature, which indicates that deposition rate variations due to temperature and perhaps chemical changes can lead to the formation of inhomogeneous deposits. The occurrence of longitudinal cracks or splits (Fig. 6) was also noted in some cases both during and after deposition. These are believed to be due to the relief of asymmetric residual stresses, al-

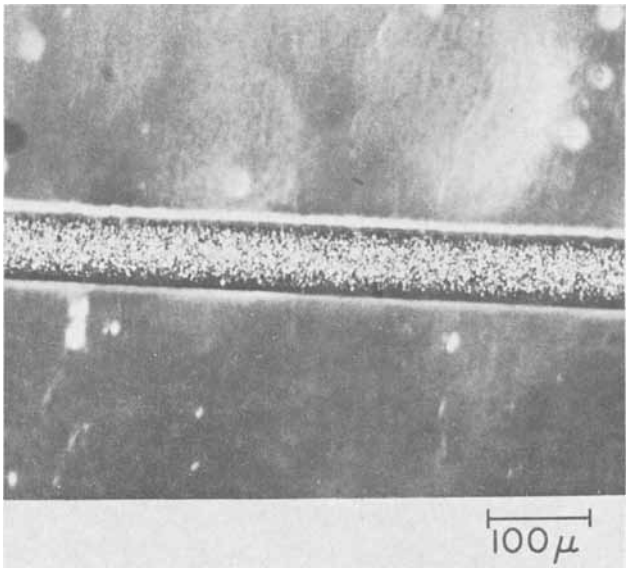

Fig. 3. Surface of boron carbide filament

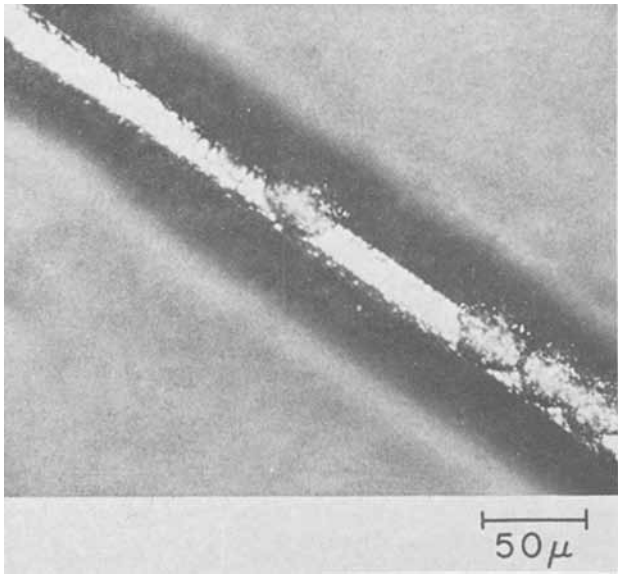

Fig. 4. Isolated regions of nonhomogeneous deposit

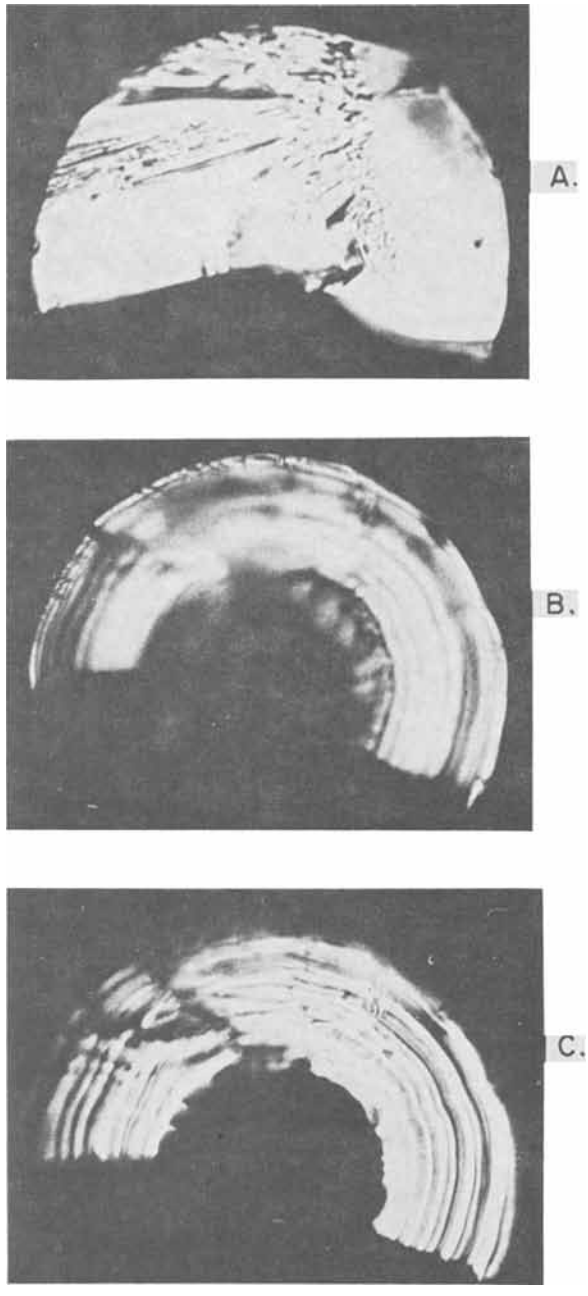

Fig. 5. Cross section of boron carbide filament showing radial structure: (A) before etching; (B) after etching (outer skin in focus); (C) after etching (core and interior in focus). (1210X)

though the probable origins of such stresses (volume expansion of the core due to formation of tungsten borides, differences in thermal expansion coefficients) do not lead in themselves to asymmetry. It can be speculated that the asymmetry was due to the manner in which the gas was fed across the filament, and that temperature gradients and variations in rate as a result of this led to the development of unequal stresses on either side of the filament. Such longitudinal cracks rarely resulted in filament breakage, however, although they tended to cause curvature.

The filament surfaces at higher magnification showed the familiar "corncob" appearance associated with deposition on a tungsten substrate [Fig. 7(*A*)], when the coating was thin (0.1 mil). Thicker coatings obscured the nodule surface as shown in Fig. 7(*B*). On a finer scale, there are significant differences between the filament shown in Fig. 7(*A*) and those made without methane (boron). Figure 8 is an electron photomicrograph of a boron filament, while Fig. 9 is a similar picture of a boron carbide filament. The latter contains isolated nodules which may be boron carbide nuclei. If these inhibit the formation of boron nuclei and in addition grow more slowly because of the more complex chemistry of the boron carbide system, the lower rate of boron carbide deposition may be explained.

Structure, stoichiometry, and mechanical properties. The major differences revealed by x-ray diffraction studies of boron carbide coated boron filaments and elemental boron filaments, both deposited on tungsten substrates at similar temperatures, consisted of (*a*) an alteration of the relative intensities of the lines due to the borided core phases, WB_4 and W_2B_5, denoting a change in phase concentration ratios, and (*b*) the presence of at least one additional diffraction line, indicative of another phase.

The diffraction halos obtained from the boron-carbon filaments were characteristic of a noncrystalline or vitreous structure. Although the diffraction positions (2θ) of the halos appeared to be similar to those produced by vitreous boron, their precise centroid positions could not be determined because of the high degree of overlap with many of the remaining sharp diffraction lines associated with the core phases. Beyond these observations, no direct statement can be

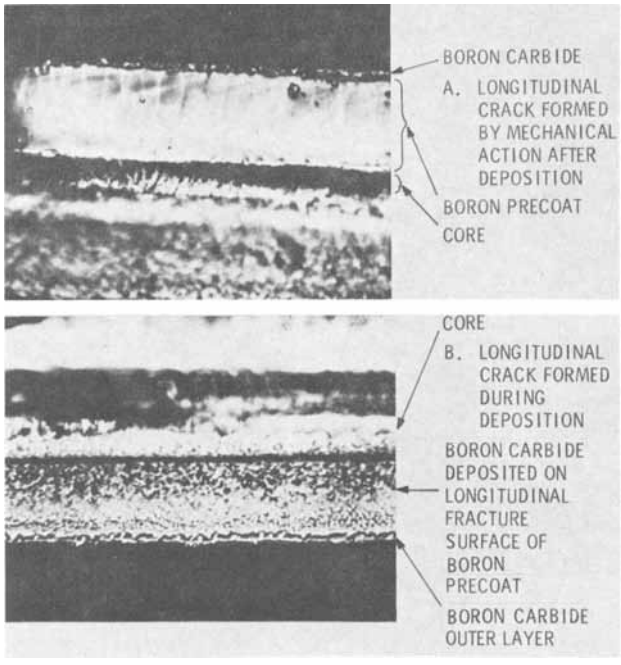

Fig. 6. Detail of longitudinal cracks formed before and after deposition in boron carbide filament (685X).

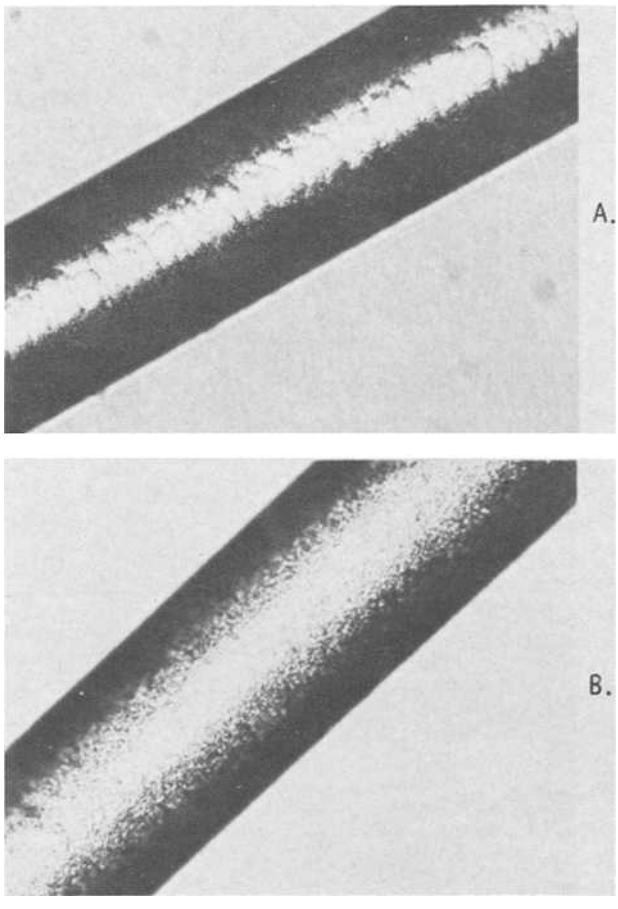

Fig. 7. (*A*) Thin boron carbide coating (0.1 mil) on boron filament; (*B*) thick boron carbide coating (0.4 mil) on boron filament. (200X)

made from the x-ray data concerning the exact crystallographic structure of the boron-carbon deposits nor about the basic structural unit which comprises it.

Electron microprobe studies did, however, establish that carbon was present in the inner deposit, having most probably diffused in from the outer layer during deposition. Hot 50% hydrogen peroxide attacked this inner layer but not the outer boron carbide layer. Although one may conclude that the as-deposited boron-carbon material is certainly more stable chemically than the inner layer into which carbon had probably diffused, there was no direct way to arrive at specific structures or stoichiometries for these two phases, nor even to establish that the outer layer was boron carbide.

Deposits consisting of only the boron-carbon material with no boron precoated were prepared in the static reactor. These were tested for mechanical properties as well as analyzed chemically for boron and carbon. The correlations which were made are presented in Fig. 10 and 11. Figure 10 shows elastic modulus and tensile strength values as functions of weight per cent (w/o) carbon in the deposit, while Fig. 11 relates feed gas composition to the composition of the deposit. A maximum in both tensile strength and modulus was observed at 27.5 w/o carbon or nearly 25 atomic per cent (a/o). This corresponds to a ratio of three boron atoms to each carbon atom, or a boron deficient deposit from the standpoint of the theoretical boron-carbon ratio of 4 to 1. A mixture of about 2.7 moles of boron carbide (B_4C) per mole of carbon would correspond to the composition observed at the maximum. A composition of 28 a/o carbon was observed by Glaser, Moskowitz, and Post (6) to be the maximum carbon content which can be contained in the so-called boron carbide lattice by filling the holes between boron icosahedra. This was deduced from measurements of density, electrical resistivity, and 2θ values of the (10.4) and (20.1) x-ray reflections as functions of carbon content which showed sudden slope changes or maxima at about 28 a/o. Above this carbon content, free graphite was observed to be present. It would, therefore, appear that the filament material corresponding to the maxima in both tensile

Fig. 8. Electron micrograph of a vitreous boron filament

Fig. 9. Electron micrograph of a boron carbide filament

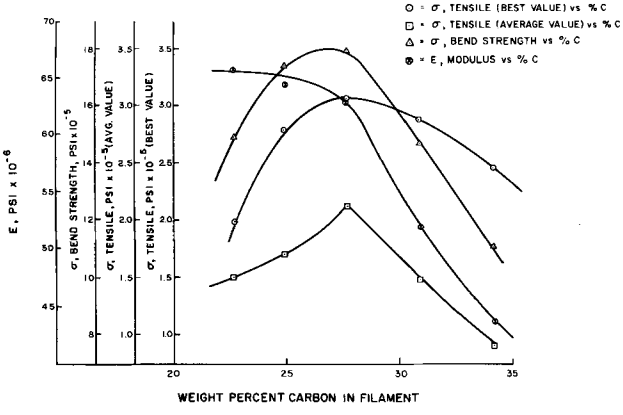

Fig. 10. Strength and modulus data *vs.* carbon content for B_4C filaments.

strength and modulus consisted of boron carbide saturated or nearly saturated with carbon. In view of the heterogeneous character of the filaments submitted for analysis, due to variations in gas composition and temperature along the filament as deposition progressed, a value of 25 a/o may be regarded as being substantially in agreement with the finding of Glaser *et al.* However, no certain evidence could be obtained as to the existence of a carbon phase on the high carbon side of the maximum and further speculation about the phase composition is not warranted.

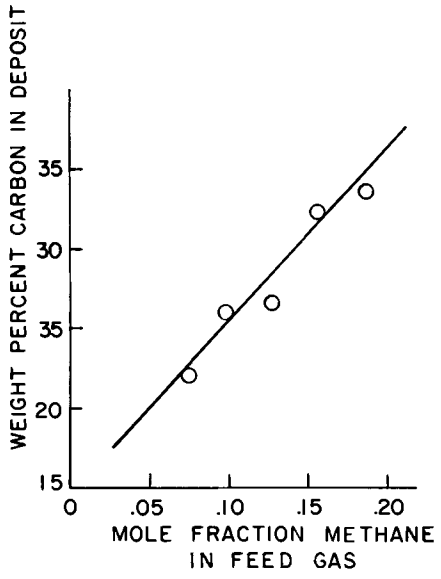

Fig. 11. Weight per cent carbon in deposit *vs.* mole per cent methane in feed gas.

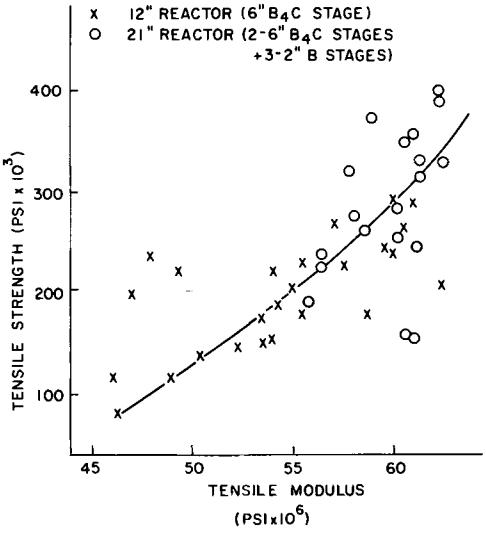

Fig. 12. Relation between tensile strength (psi x 10^3) and modulus (psi x 10^6).

Mechanical test data were obtained for all of the continuous preparative runs which produced filament consisting of a layer of the boron carbide deposited over the boron precoat. Filament diameters varied between 1.8 and 3.6 mils, depending on the deposition conditions. The outer boron carbide layer usually comprised between 4 and 20% of the total filament volume, again depending on the conditions.

Average tensile strengths varied between 150,000 and 390,000 psi with a maximum single value of 474,000 psi. Modulus values lay between 55 and 62 x 10^6 psi and include the contribution of the lower modulus boron precoat layer. Statically prepared filament, with no boron precoat, gave a modulus value maximum of 70 x 10^6 psi. In the continuous filament, although considerable scatter was noted, high tensile and high modulus values appeared to be associated (Fig. 12) as they were in the case of the static filaments (Fig. 10). This lends some support to the contention that the maximum values discussed above in relation to stoichiometry may indeed be structure-related rather than due to deposition conditions.

Composite studies.—In order to obtain preliminary performance data concerning the boron carbide filaments in connection with composite reinforcement, experimental beams were prepared using an epoxy

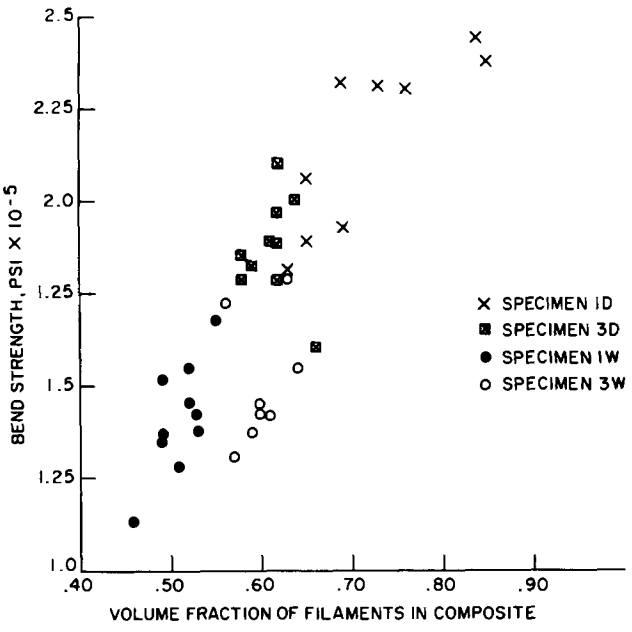

Fig. 13. Bend strength *vs.* volume fraction for B_4C filaments, epoxy microbeam composites.

resin system (Epon 815) cured with methyl nadic anhydride and DMP-30. Incomplete wetting of the fibers was eliminated by refluxing the filaments in methanol prior to formation of the beam. After curing for 2 hr at 95°C and 16 hr at 127°C, the beams measured approximately 23 mils by 40-50 mils in cross section and were tested in three-point bending using a span of about 0.7-0.75 in. Results are shown in Table II for several different volume per cent filament contents. Figure 13 shows these results graphically in terms of bend strength *vs.* volume per cent (v/o) filaments in the composite, before (series 1*D* and 3*D*) as well as after (series 1W and 3W) exposure to boiling water for 2 hr. In both cases, strength was proportional to filament concentration but, while specimen series 1*D* appeared not to have been damaged by the water treatment, specimen series 3*D* had lower strengths at comparable volume fractions. Transfer of the load stress from the resin matrix to the reinforcing filament was efficient, assuming the rule of mixture to be valid for bend test results. A bending modulus of 54 million psi was calculated for a reinforced beam containing 85 v/o filaments having a modulus of 62 million.

Summary

Continuous filaments of boron carbide were prepared on a boron coated tungsten substrate by simultaneous reduction of boron trichloride with hydrogen and decomposition of methane at temperatures between 1050° and 1195°C. Filament thickness varied between 1.8 and 3.6 mils, depending on deposition conditions and filament draw speed.

Deposition rates yielded an activation energy suggestive of a diffusion-controlled mechanism for the over-all rate of the combined reactions, although boron deposition alone was observed to have been surface reaction rate controlled using the same reactor and conditions. An interference effect of methane either in nucleation or in gaseous intermediate interactions may have been responsible.

The boron-carbon deposits were vitreous and noncrystalline, yielding only broad diffuse halos in x-ray diffraction studies. They appeared to consist of a solution or mixture of vitreous carbon in vitreous boron carbide, deduced from chemical behavior and analysis. The boron carbide layer comprised between 4 and 20% of the total filament volume, depending on deposition conditions. Diffusion of carbon into the precoat layer occurred during deposition.

A maximum in the tensile strength and elastic modulus of filaments containing no boron precoat occurred at 27.5 w/o carbon, a composition equivalent to a mole ratio of 2.7 boron carbide to carbon or 7.4 w/o carbon in boron carbide.

Average tensile strengths of the continuous boron carbide filaments with a boron precoat lay between 150,000 and 390,000 psi with a single high value of 474,000 psi. Modulus varied between 55 and 62 million psi. Boron carbide filaments with no boron precoat had modulus values up to 70 million psi.

Flexure test results for epoxy resin beams reinforced with continuous boron carbide filaments both before and after boiling in water indicated that the filaments were well bonded and possibly more resistant to hydrolytic attack than boron filaments. Flexure strengths were proportional to the volume per cent of filaments in the composites.

Acknowledgments

The authors express their thanks to Dr. E. Feingold, Mr. J. M. Berry, and Mr. T. A. Harris, Jr., for assistance during the deposition studies and in characterizing filament structure and behavior. This work was sponsored by the Non-Metallic Materials Division of the Air Force Materials Laboratory, Wright-Patterson AFB, Ohio, under Contract AF33(615)-1644, and the authors wish to extend their appreciation for permission to publish these results.

Manuscript submitted Jan. 18, 1968; revised manuscript received Sept. 13, 1968. This manuscript was presented at the Dallas Meeting, May 7-12, 1967, as Paper 210.

Any discussion of this paper will appear in a Discussion Section to be published in the December 1969 JOURNAL.

REFERENCES

1. C. Agte and K. Moers, *Z. Anorg. Allgem. Chem.*, **198**, 233 (1931); K. Moers, *ibid.*, **198**, 243 (1931).
2. A. H. Lasday and C. P. Talley, *SAMPE*, **10**, D1 (1960); R. B. Reeves and J. J. Gebhardt, *ibid.*, **10**, D13 (1960).
3. F. Galasso, M. Basche, and D. Kuehl, *Appl. Phys. Letters*, **9**, (1) 37 (1966).
4. D. R. Stern and L. Lynds, *This Journal*, **105**, 676 (1958).
5. R. J. Diefendorf, *J. Chim. Phys.*, **59**, 815 (1960).
6. F. W. Glaser, D. Moskowitz, and B. Post, *J. Appl. Phys.*, **24**, (6), 731 (1953).

A Comparison Between the Properties of Anodic Oxide Films on Aluminum Obtained in Different Alkali Nitrate Melts at Various Temperatures[1]

Luigi Campanella
Italian National Researches Council, Institute of Analytical Chemistry, University, Rome, Italy

and Arminio Conte
C.S.N. Casaccia, Industrial Chemistry Laboratory (CNEN), Rome, Italy

ABSTRACT

Crystalline form, hardness, kinetic parameters, coating ratio, and resistance to corrosion of the films produced in lithium-containing melts are reported and compared with results obtained in (Na,K)NO_3 fused mixtures at higher temperatures.

The nature and properties of oxide films obtained on the surface of aluminum samples by anodization in fused mixtures of $NaNO_3$-KNO_3 at 300°C have been previously investigated (1, 2). These films were found to be very hard and compact, with a nonporous partially crystalline structure; their corrosion resistance to acid and alkali solutions was found to be higher than the oxides prepared by anodization in aqueous H_2SO_4 solutions; some of their physical properties (specific gravity, flexibility, resistance to high temperatures, adherence, color and appearance, reflectivity, dielectric constant) were also determined and related to the experimental conditions of preparation. The production of oxide films on aluminum surfaces by anodization in the fused eutectic $LiNO_3$-KNO_3, at 160°C, has also been described (3).

In the present communication, the properties of the films produced at lower temperatures in lithium-containing melts are reported and compared with results obtained in (Na,K)NO_3 fused mixtures at higher temperatures.

Experimental

The preparation and purification of the solvent ($NaNO_3$-KNO_3, 59.3% by weight KNO_3 and $LiNO_3$-KNO_3, 59.4% by weight KNO_3) were reported elsewhere (4).

The Ag/Ag^+ reference electrodes were prepared as previously described (4). The test electrodes were cylindrical rods (1 cm) of Al Raffinal AP-O-H 80 (99.99% purity); the samples to be anodized were prepared from the above-mentioned aluminum sheets and their dimensions were 5 x 5 x 0.2 cm. Before immersion in the melt, the specimens were degreased with toluene, chemically polished for 30 min in NaOH solutions (5% by weight), rinsed in distilled water, and air dried. After exposure to the fused nitrates, the samples were cooled in air. The auxiliary electrode was contained in a Pyrex tube with a medium porosity glass frit disk sealed at the bottom end. The Pyrex cell assembly was of the type previously described (4). All the experiments were performed with the cell open to air, at 160° or 300°C according to the melt used. An AMEL 561 Corrograph was used for the electrochemical measurements.

For the determination of the oxide amount, the original oxide was removed without attacking the metal, by immersion in 35 ml/liter 85% H_3PO_4 + 20 g/liter CrO_3 solution, operating at 100°C (Edwards mixture).

The films were stripped from the metal substrate by Treadwell and Obrist's modified method (13).

Results and Discussion

By x-ray analysis, no substantial difference was found between films obtained at 160°C in (Li,K)NO_3, and, at 300°C in (Na,K)NO_3, α, η, γ Al_2O_3 (1), with a prevalence of α and γ, were revealed. The hardness—measured by Brinnell's suitably modified method—of oxide films prepared by anodization at 160°C in (Li,K)NO_3 was found to be approximately 30% lower than that obtained in (Na,K)NO_3 melts at 300°C.

In Fig. 1, potential *vs.* time curves of aluminum electrodes are reported. They were recorded by a recorder electrometer without drawing any current. It can be seen that, without preanodization (curve *a*), the potential, after 10 hr, is not yet stabilized and does not increase to a more positive value, unlike what is observed in (Na,K)NO_3 melts (1). After anodization at +5v for 30 min (curve *b*) and 1 hr (curve *c*), and at +24v for 5 min (curve *d*), the potential decreases slowly to the value observed at open circuit. Only after preanodization at +24v for 5 hr, the potential seems to have attained a constant more positive value.

The equation

$$i = 2\,a\,n\,\nu\,e^{-(W+qaE)/KT} = A\,e^{BE}$$

where i = ionic current, a = activation distance, n = number of mobile ions per unit volume, ν = interstitial ion frequency of vibration in simple harmonic motion, W = potential energy barrier that must be jumped by the ions in order to reach the next site, q = charge on the ion, E = electrical field, K = Boltzmann's constant, and T = absolute temperature, is the key expression for the growth kinetics, if the high-field ionic conductivity approximation ($qaE >> KT$) is applied to the theory of growth mechanism of anodic oxide films.

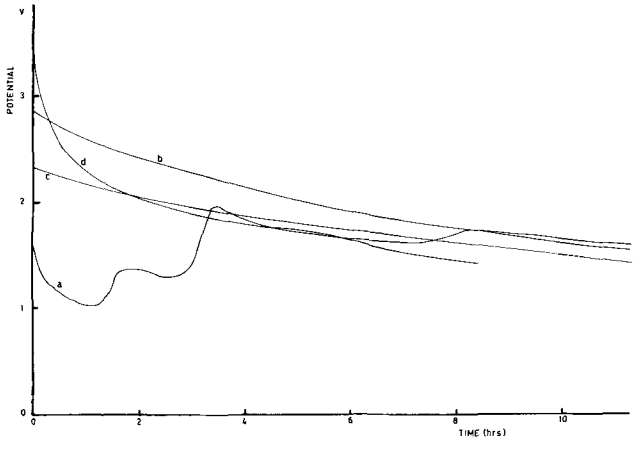

Fig. 1. Potential *vs.* time curves of aluminum electrodes: (a) without preanodization; (b) after anodization at +5v, 30 min; (c) after anodization at +5v, 1 hr; (d) after anodization at +24v, 5 min.

[1] Work carried out with the aid of the Italian C.N.R.

Table I. Corrosion of Al electrodes anodized under the following conditions. (*a*) (Li,K)NO_3, 160°C, +24v; (*b*) (Na,K)NO_3, 300°C, +5v [see Ref. (1)]; (*c*) aqueous H_2SO_4 solution [see Ref. (5)]; (*d*) same as (*a*), electrolysis performed without separated cathodic compartment, Fe as cathode material; (*e*) same as (*d*), 18-8 SS as cathode material

Corroding solution	Time of contact with the corroding solution (hr)	Weight loss (mg/cm²) (*a*)	(*b*)	(*c*)	(*d*)	(*e*)
NaOH 1*N*	1	2.57	1.47	3.68	2.74	3.56
NCl 1*N*	72	0.51	10.46	1.73		0.96
H_2SO_4 1*N*	24	0.11	0.12	0.42		
HNO_3 1*N*	24	0.16	0.23	0.74		
Na_2CO_3 1M	24	0.71	0.18	0.84		

The logarithmic form of the above equation is

$$\log i = \log A + B\,E$$

Values of E, determined by oxide thickness measurements (performed by DERMITRON apparatus manufactured by Unit Process Assemblies Inc., New York, and operating by virtue of eddy currents induced in metallic surfaces) were used for the determination of a and B, that resulted in 1.8Å and 1.5 10^{-6} cm v^{-1}, respectively, for oxides prepared in (Li,K)NO_3. The higher values of a determined in a previous study (2) —7.6Å—, concerning the anodization in (Na,K)NO_3, can be explained if the different values of temperature are considered.

The coating ratio (ratio of coating weight to metal loss) values determined for different anodization times and applied voltages were always found to be 1.8 (theoretical value). The film thickness was remarkably lower as compared to values obtained by anodization in (Na,K)NO_3 melts, ranging from approximately 1μ (1v, 30 min) to 3.9μ (24v, 2 hr).

In Table I, the results of corrosion tests of aluminum samples anodized at +24v, 160°C, in (Li,K)NO_3 melts are reported and compared with those referring to aluminum oxides prepared in H_2SO_4 aqueous solutions (15% w/v) (5) and in (Na,K)NO_3 fused mixtures at 300°C. It can be seen that the corrosion resistance to NaOH and Na_2CO_3 solutions of samples anodized in (Li,K)NO_3 at 160°C is markedly lower than for samples prepared in (Na,K)NO_3 at 300°C, but still high when compared with films obtained in H_2SO_4 solutions. The corrosion resistance to H_2SO_4 and HNO_3 solutions is slightly improved for oxides prepared in (Li,K)NO_3 relative to those obtained in (Na,K)NO_3. The markedly low corrosion in 1*N* HCl may be ascribed to the competition between Cl^- and H_2O, as occurring for oxides prepared in aqueous solutions. Presence of H_2O in our oxides could be postulated if the nature of $LiNO_3$ is considered and is really confirmed by the results of the weight loss (found = 0.1 mg/cm²) determinations of anodized aluminum samples when oven dried at 240°C. The water absorption appears also to be influenced by the presence of lithium in the anodization bath; while no weight change is observed for Al samples previously anodized in (Na,K)NO_3 when contacted with H_2O at 100°C for 30 min (sealing conditions), 0.1 mg/cm² weight gain is observed for samples anodized in (Li,K)NO_3; this is probably due to the higher porosity of the latter films because of the acidity of the electrolyte.

An important point to be investigated also for the purpose of practical application is the influence on the oxide properties of the products of the cathodic reduction of the solvent and of the cathode materials undergoing dissolution. It was shown by calculations (6, 7) and experimentally (8) that the first reduction process of nitrate melts is

$$NO_3^- + 2\,e \rightarrow NO_2^- + O^{2-}$$

Other processes involve oxide ion formation and evolution of various gaseous products. In basic melts, aluminum oxides undergo dissolution (1); therefore, in (Na,K)NO_3, it is worthwhile to operate with separated anodic and cathodic compartments. We have seen that this is unnecessary with (Li,K)NO_3 melts, owing to the more acidic character of Li^+ ions and consequent association with oxide ions (9, 10).

As regards the presence in the melts of species produced by reaction of cathode materials with the reduction products of the solvent (11, 12), no differences were observed in coating ratio values using Pt, Fe, 18-8 stainless steel as cathodes. On the contrary, the corrosion resistance to basic and acid aqueous solutions is lowered, as can be seen from columns (*d*) and (*e*) in Table I, when the oxide films are obtained using Fe and 18-8 SS as cathodes.

Manuscript submitted July 25, 1968; revised manuscript received Sept. 11, 1968.

Any discussion of this paper will appear in a Discussion Section to be published in the December 1969 JOURNAL.

REFERENCES

1. A. Conte and L. Campanella, *Electrochim. Metall.*, **3**, 183 (1968).
2. L. Campanella and A. Conte, In print.
3. L. Campanella, Patent for Italian National Researches Council, Rome, Italy, In print.
4. A. Conte, *Electrochim. Acta*, **11**, 1579 (1966).
5. L. Campanella, *Rass. Chim.*, **3**, 85 (1965).
6. A. Conte and M. D. Ingram, *Electrochim. Acta*, In print.
7. H. E. Bartlett and K. E. Johnson, *Can. J. Chem.*, **44**, 2119 (1966).
8. H. S. Swofford and H. A. Laitinen, *This Journal*, **110**, 814 (1963).
9. M. Francini and S. Martini, EUR (Euratom reports), 2496 e.
10. R. Kohlmuller, *Ann. Chim.*, **4**, 1183 (1959).
11. H. E. Bartlett and K. E. Johnson, *This Journal*, **114**, 64 (1967).
12. A. Conte and S. Casadio, *Ric. Sci.*, **36**, 443 (1966).
13. B. Turi and L. Campanella, *Ric. Sci.*, **34**, 201 (1964).

On the Mechanism of Anodic Chlorate Oxidation

O. de Nora, P. Gallone,* C. Traini, and G. Meneghini

Oronzio de Nora, Impianti Elettrochimici, Milan, Italy

ABSTRACT

Anodic polarization curves were determined on smooth Pt, Pt-coated Ti, PbO_2-coated graphite, and PbO_2-coated Ti. Operating conditions were typical for industrial perchlorate production, *i.e.* 1.6 moles/liter $NaClO_4$, while $NaClO_3$ concentration was ranging between 0.47 and 4.7 moles/liter, at 50°C, *p*H 6-7. For solutions containing $NaClO_4$ only, the anodic current potential diagram is rectilinear, irrespective of any presence of NaF or $Na_2Cr_2O_7$. If $NaClO_3$ also is present, the diagram shows a strong inflection. For each set of conditions, current efficiency and anode potential were determined *vs.* current density. This allowed two separate curves for ClO_3^- conversion rate and O_2 evolution rate, respectively, to be plotted *vs.* anode potential. Tafel linearity for ClO_3^- conversion is thus obtained on Pt and on PbO_2 under all conditions, with a slope ranging between 0.1 and 0.12. This fact supports the view that ClO_3^- is oxidized through a path involving primary discharge of ClO_3^- with formation of ClO_3 radicals and that charge transfer is in most cases the rate-determining step.

The over-all reaction of anodic chlorate oxidation is

$$ClO_3^- + H_2O = ClO_4^- + 2H^+ + 2e^- \quad E^o = 1.19v \quad [1]$$

The potential-*p*H equilibrium diagram (Fig. 1) runs parallel to that of water oxidation reaction

$$2H_2O = O_2 + 4H^+ + 4e^- \quad E^o = 1.228v \quad [2]$$

Accordingly, the *p*H value affects the thermodynamic equilibrium of both reactions in the same direction and by the same amounts. In other words, it is impossible, on purely thermodynamic arguments and for any established electrode potential, to favor anodic production of perchlorate rather than oxygen evolution, or *vice versa,* simply by changing the *p*H value.

As to the kinetic behavior of oxygen evolution according to reaction [2] on an unreactive electrode such as platinum, a wealth of experimental evidence indicates that oxygen overvoltage is *p*H independent (1). Accordingly, the concern expressed by former authors (2, 9) without any produced evidence about the adverse effect that alkalinity might have on chlorate conversion efficiency, due to the competing reaction involving OH^- discharge, seems unfounded and only based on a prejudice widespread in the past that the charge transfer between the electrode and the electrolyte can involve only ions and not the undissociated water molecule itself or any other uncharged species.

On the other hand, the kinetic independence of the oxygen evolution reaction from *p*H does not necessarily imply a similar behavior of reaction [1]. However, this has also been experimentally evidenced on smooth platinum (3). For lead dioxide anodes, the results are somehow conflicting. This may possibly be explained by the fact that lead dioxide cannot be considered as a perfectly unreactive material, so that different preparative methods, as well as previous performance conditions, may lead to somewhat different results. At any rate, it is to be pointed out that whereas Schumacher (4) finds that current efficiency is not affected by *p*H, according to Narasimham (5) it shows an increase under more alkaline conditions, contrary to what former authors (2, 9) would have expected, in principle, to occur. The equilibrium potentials of reactions [1] and [2] differ by less than 40 mv; therefore, only if the concomitance of all operating conditions that may affect the two kinetics, such as current density, temperature, anode potential, adsorbed discharge inhibitors and catalysts, is such as to bring about a definite increase of the overvoltage proper to reaction [2] over that of reaction [1] will chlorate conversion occur at a satisfactory current efficiency.

* Electrochemical Society Active Member.

As for other oxidation reactions (6), there are two possible pathways along which chlorate conversion may proceed as a preliminary assumption, so that only through experimental verification may conclusions, if any, be drawn about the path that is actually followed by the electrode process. One of these, which we shall call the primary reaction mechanism, would involve a direct electron withdrawal from the chlorate ion, as a first step, followed by a homogeneous reaction of the free radical with water. According to the other possible pathway, which we shall call the secondary reaction mechanism, the water molecule would be involved in the charge transfer step, with the production of surface oxides (or adsorbed oxygen-containing species, *e.g.* OH or O); such entities would then perform as oxidants of the chlorate ion diffusing toward the substrate or being coadsorbed at the electrode surface.

Table I displays in chronological order the several reaction mechanisms that have been proposed so far. A critical review of the several theories has been made by Schumacher (4*a*). It may be observed here that neither the first proposed mechanism (7) nor most of those suggested later (2, 5, 9) are based on any strong experimental evidence, but mainly on speculations, some of which, as noted above, are affected by preconceptions such as the possible role played by a supposed OH^- discharge. Sugino and Aoyagi (8) were, to

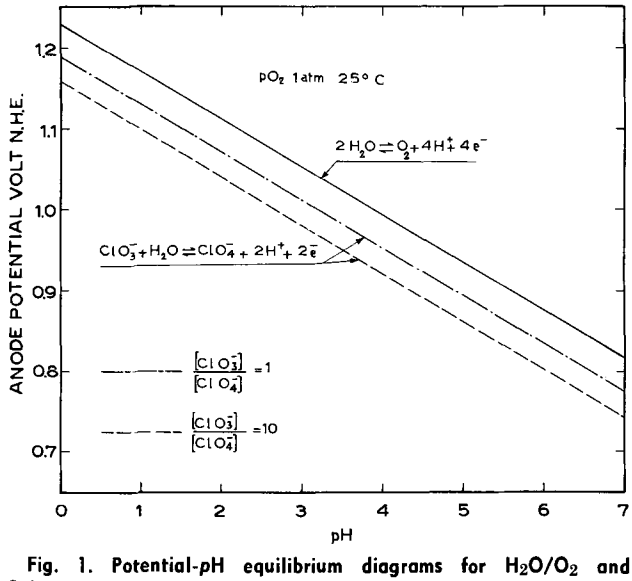

Fig. 1. Potential-pH equilibrium diagrams for H_2O/O_2 and ClO_3/ClO_4^-.

Table I. Proposed mechanisms for anodic chlorate oxidation

Over-all reaction: $ClO_3^- + H_2O \rightarrow ClO_4^- + 2H^+ + 2e^-$

A.	Primary discharge of ClO_3^-		
(I)	Oechsli (7)		
	$2ClO_3^- + H_2O \rightarrow ClO_4^- + ClO_2^- + 2H^+ + O + 2e^-$		(a)
	$ClO_2^- + O \rightarrow ClO_3^-$		(b)
(II)	Knibbs (2)		
	$2ClO_3^- \rightarrow 2O_2ClO + 2e^-$		(a)
	$O_2ClO + OClO_2 \rightarrow O_2Cl—O—O—Cl_2$		(b)
	$O_2Cl—O—O—ClO_3 + H_2O \rightarrow ClO_4^- + ClO_3^- + 2H^+$		(c)
(III)	Sugino and Aoyagi (8)		
	$2ClO_3^- \rightarrow 2ClO_3 + 2e^-$		(a)
	$2ClO_3 + H_2O \rightarrow ClO_3^- + ClO_4^- + 2H^+$		(b)
	$ClO_3^- \rightarrow ClO_3 + e^-$		(c)
	$OH^- \rightarrow OH + e^-$		(d)
	$ClO_3 + OH \rightarrow ClO_4^- + H^+$		(e)
(IV)	Narasimham, Sundararajan, and Udupa (5)		
	$ClO_3^- \rightarrow ClO_3 + e^-$		(a)
	$ClO_3 + H_2O \rightarrow ClO_4^- + 2H^+ + e^-$		(b)
B.	Secondary reaction of ClO_3^- with discharged oxygen		
	Bennett and Mack (9)		
	Grotheer and Cook (10)		
(V)	$H_2O \rightarrow O + 2H^+ + 2e^-$		(a)
	$ClO_3^- + O \rightarrow ClO_4^-$		(b)

our knowledge, the first to investigate the correlation between anode potential and current density. By their method, which was essentially potentiokinetic, they were able to observe two stages of potential in 1.4M $NaClO_3$ at 17°C. Since the first stage, occurring between 1.7 and 1.9v, corresponds (mostly) to oxygen evolution and the second stage, higher than 2.3v, corresponds (mostly) to chlorate oxidation, said authors interpret their results by assuming that chlorate oxidation proceeds through a primary discharge step. However, as will become apparent in further discussion, the two potential stages referred to above do not supply by themselves any evidence in favor of the primary discharge mechanism, as advocated by said authors.

Strangely enough, Grotheer and Cook (10) have been the only investigators that, prior to the present study and as late as 1967, seem to have based their considerations on the most classical and elucidating of all experimental methods, which consists in carrying out intensiostatic current-potential measurements and representing them on a Tafel diagram. By plotting the results thus obtained with two different solutions, which respectively contained sodium chlorate alone and sodium perchlorate alone, they found that both plottings fall on an identical, practically straight, line. The natural conclusion of said authors is that the same anodic process occurs in both cases. This is true because, within the low current density range they have investigated (up to 10 ma/cm^2), the only process that practically does occur is oxygen discharge in either solution, since chlorate conversion efficiency is practically nil at such low current densities. Accordingly such determinations do not seem to supply sufficient experimental evidence in favor of a secondary reaction mechanism between ClO_3^- and adsorbed oxygen as proposed by said authors. Actually, some of the experimental findings disclosed and discussed in the following seem to bring more support to the primary reaction assumption.

Experimental Procedure and Results

The laboratory cell is represented in Fig. 2. The glass container had a capacity of approximately 1 liter and was kept at the desired temperature by a water jacket connected with a thermostat. A top cover provided sufficient tightness to avoid appreciable evaporation losses, which would impair the accuracy of gas volume measurements.

The anodic O_2 gas was collected by a bell hanging over the anode and partially submerged to a depth of approximately 5 cm; from the bell, the gas was drawn into a measuring burette. Current efficiency (C.E.) of O_2 production was determined by comparison with the gas evolved from a standard coulombic cell with Pt electrodes and containing 5% NaOH, connected in

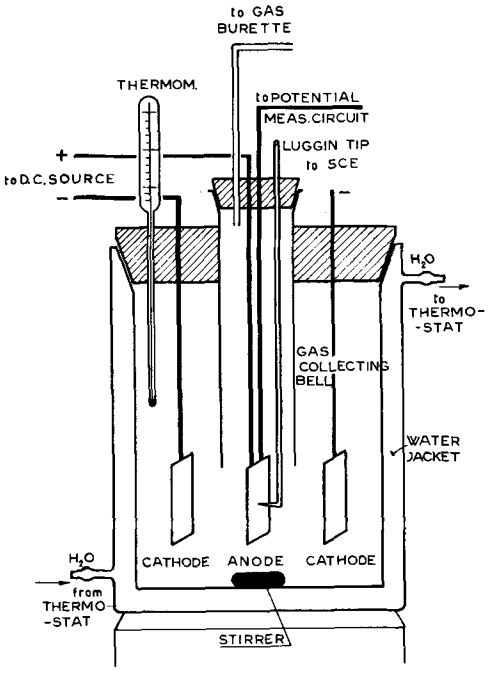

Fig. 2. Experimental cell

series with the laboratory cell. The solution was kept under agitation only during anode potential measurements but not during current efficiency evaluation runs, in order not to facilitate O_2 gas losses. Blank tests were performed with a solution containing $NaClO_4$ only, so that O_2 C.E. had to be 100% and showed that the determination may be affected with a maximum error of ± 1% unit of C.E. The minimum amount of gas collected in any further run was 30 cm^3; each run was repeated at least twice under the same conditions and the average gas volume reading determined. Chlorate conversion efficiency was calculated by subtracting O_2 conversion efficiency from 100.

The several anodic samples were made of 1-x 5-cm rectangular strips suspended in the solution. Both surfaces were made to operate by placing the anode between two counterelectrodes 2 cm apart from the anode. The counterelectrodes used were of nickel, iron, stainless steel, and platinized titanium. With all of these materials, the current efficiency of hydrogen evolution was found to be 100% within the limits of measuring accuracy (±1%). The anodic materials investigated were smooth Pt, platinized titanium, and PbO_2 deposited either on graphite or on titanium (14), the thickness of the deposit being about 5 mm on graphite and 2 mm on titanium. The PbO_2 coating was polished after electrodeposition with fine emery paper of the quality used for metallographic samples. The Pt coating on Ti was of a quality giving very low overvoltage under Cl_2 discharge in NaCl electrolysis. Further tests with this material were discontinued after verifying that chlorate conversion efficiency was very low (less than 10%) also at the highest $NaClO_3$ concentration investigated (4.7 moles/liter). The PbO_2 deposits on graphite and on Ti were found in preliminary tests to have a practically equivalent anodic performance. Accordingly, PbO_2-coated titanium was used throughout the subsequent tests as described in the following. The anode potential was measured by means of a saturated calomel electrode connected with the negative terminal of the electronic voltmeter. The positive terminal of the voltmeter was in direct metallic connection with the anodic structure at a point practically unaffected by ohmic drops. The readings were converted to the NHE scale by conventionally adding 0.25v, whereby any liquid junction effects have been neglected.

The investigation was carried out with particular regard to intermediate conditions that are met with

in industrial $NaClO_4$ production. Accordingly, the temperature was 50°C and the pH value was kept between 6 and 7. $NaClO_4$ concentration was maintained at 1.6 moles/liter (195 g/liter) throughout the tests, after ascertaining that its influence on the kinetics is very small, if any. As to $NaClO_3$ concentration, its effect on the kinetics was investigated between 0.47 and 4.7 moles/liter.

In order to obtain good reproducibility, anode prepolarization was found to be indispensable. This was carried out before every run at 100 ma/cm² on Pt and at 200 ma/cm² on PbO_2. The anode was kept at said C.D. for 30 min, after which the run was started at the lowest C.D. value as shown on the Tafel diagram. Each C.D. value was kept for the time required to collect at least 30 cm³ O_2 for current efficiency determination, whereafter the corresponding anode potential was measured.

Such procedure, besides allowing good reproducibility, brings about as a further consequence a marked decrease of the pronounced hysteresis that would otherwise be observed in the descending branch of the polarization diagram for smooth Pt, when $NaClO_3$ is present in the solution.

Figure 3 represents the Tafel diagrams obtained on Pt and PbO_2 in 1.6 moles/liter $NaClO_4$ with and without NaF or $Na_2Cr_2O_7$ additions. Under all conditions, Tafel linearity is obtained through the C.D. range investigated (0.02-1 amp/cm²). Whereas the presence of 2 g/liter NaF markedly increases O_2 overpotential and the slope on both Pt and PbO_2, the addition of 3 g/liter $Na_2Cr_2O_7$ affects the overpotential substantially only on Pt, and to a definitely minor extent on PbO_2.

Figures 4 and 5 show Tafel diagrams on Pt and PbO_2, respectively, for solutions containing 1.6 moles/liter $NaClO_4$ and $NaClO_3$ in different amounts from 0.47 to 4.7 moles/liter. A comparison with Fig. 3 shows the strong polarization effect of $NaClO_3$ at all concentrations. This effect becomes independent of $NaClO_3$ concentration when the latter approaches 1 mole/liter. However, it is less marked on PbO_2 than on Pt; furthermore, at higher $NaClO_3$ concentrations, the steep potential transition observed on Pt straightens out on PbO_2, so that the polarization curve acquires Tafel linearity, although with a steep slope (0.17).

Figure 6, referring to Pt, shows the strong dependence of chlorate conversion efficiency on current density at all $NaClO_3$ concentrations. Figure 7 represents such dependence for PbO_2. Current efficiency appears to be definitely lower on PbO_2 than on Pt only at relatively low C.D.'s and $NaClO_3$ concentration. The difference, even though still appreciable at 1 amp/cm² and 4.7 moles/liter $NaClO_3$, shows a tendency to level off above these values.

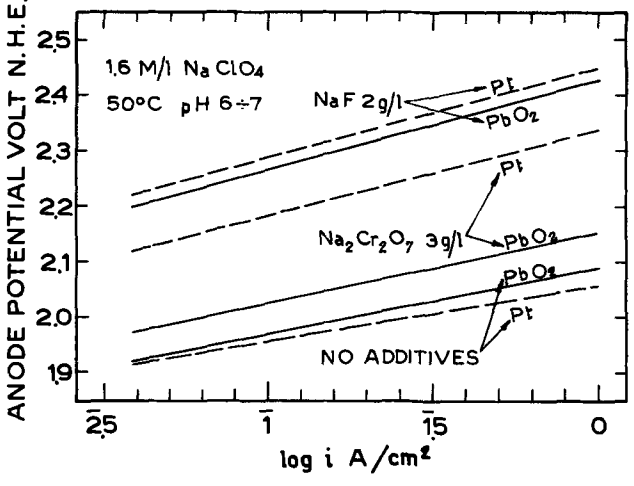

Fig. 3. Polarization curves on Pt and PbO_2 in 1.6 moles/liter $NaClO_4$ at 50°C, pH 6 ÷ 7, with and without NaF or $Na_2Cr_2O_7$.

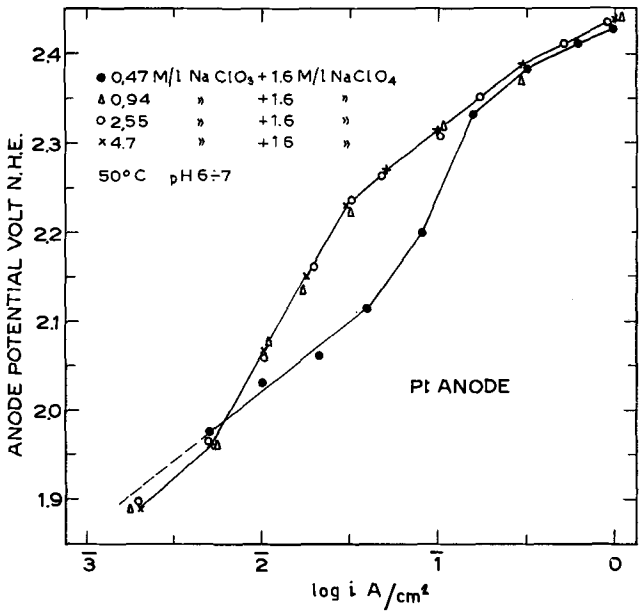

Fig. 4. Polarization curves on smooth Pt at different $NaClO_3$ concentrations.

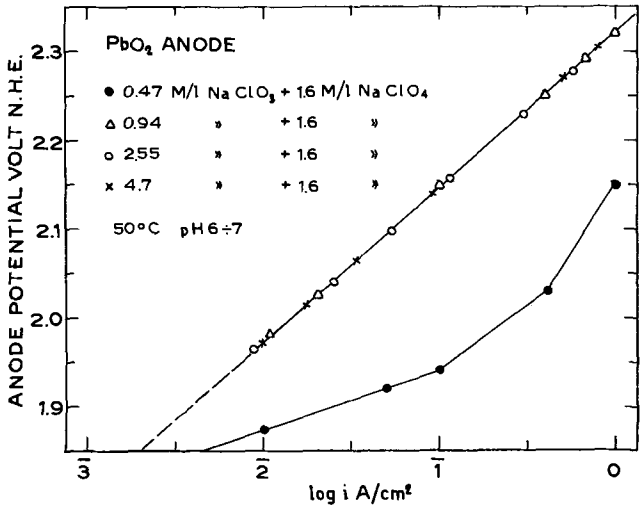

Fig. 5. Polarization curves on PbO_2 at different $NaClO_3$ concentrations.

The effect of NaF or $Na_2Cr_2O_7$ addition on anode polarization and conversion efficiency in a solution containing 0.94 mole/liter $NaClO_3$ and 1.6 moles/liter $NaClO_4$, can be evaluated from Fig. 8 for Pt and Fig. 9 for PbO_2. The presence of 2 g/liter NaF markedly raises polarization on PbO_2 and to a lesser extent on Pt, so that the two corresponding curves become quite close to each other. For both materials, the C.E. is improved throughout the C.D. range, the extent of such improvement being definitely more substantial on PbO_2.

Figure 8 also shows that, by the addition of 3 g/liter $Na_2Cr_2O_7$, polarization and C.E. are decreased on smooth Pt for C.D. lower than 0.1 amp/cm²; at higher C.D., the polarization is slightly increased and this is accompanied by a slight decline in C. E. at equal anode potentials. As regards PbO_2, it can be seen from Fig. 9 that $Na_2Cr_2O_7$ addition lowers the polarization curve throughout the C.D. range, with an associated sharp decline in C.E.

Discussion

The above results, with particular regard to Fig. 3, 4, and 5, show that anodic polarization on Pt and on PbO_2 is strongly influenced by the presence of ClO_3^-

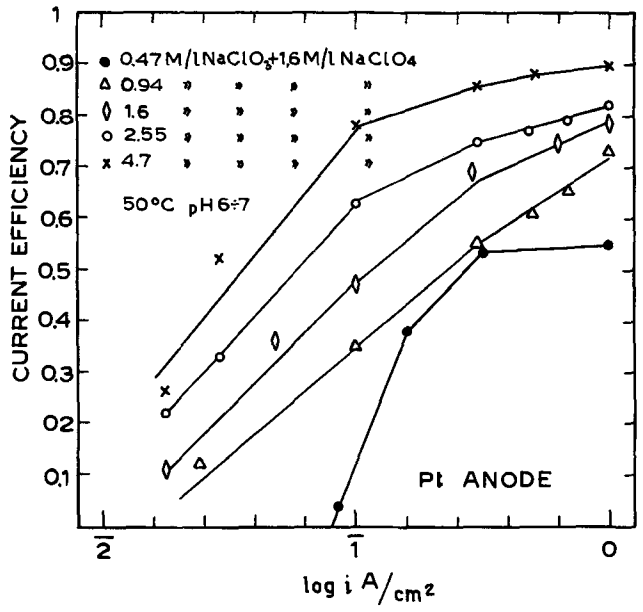

Fig. 6. ClO_3^- conversion efficiency vs. current density on smooth Pt at different $NaClO_3$ concentrations.

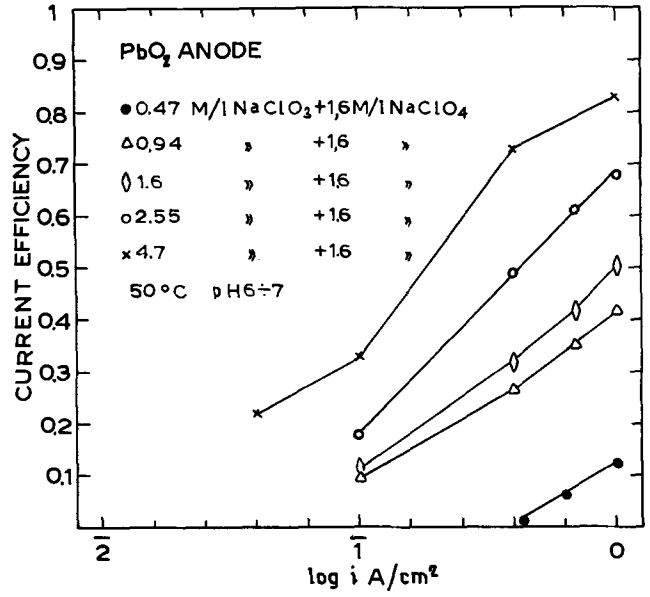

Fig. 7. ClO_3^- conversion efficiency vs. current density on PbO_2 at different $NaClO_3$ concentrations.

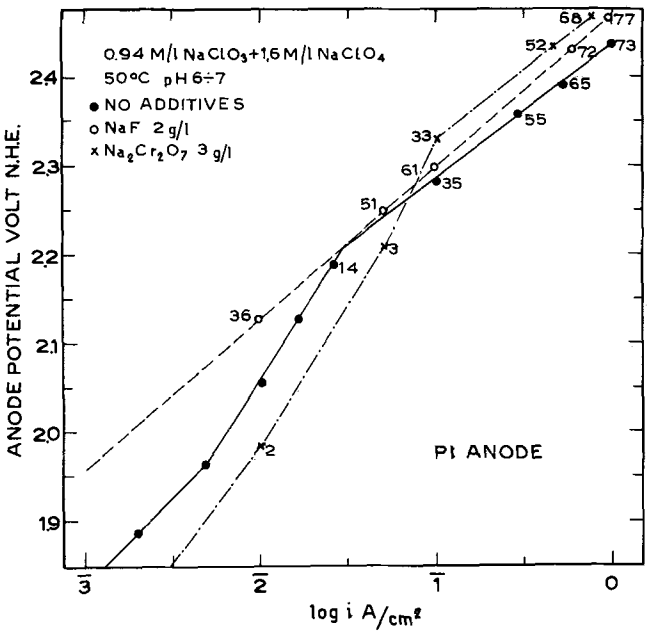

Fig. 8. Effect of NaF and $Na_2Cr_2O_7$ on anodic polarization and current efficiency on smooth Pt (per cent C. E. values marked along each plotting).

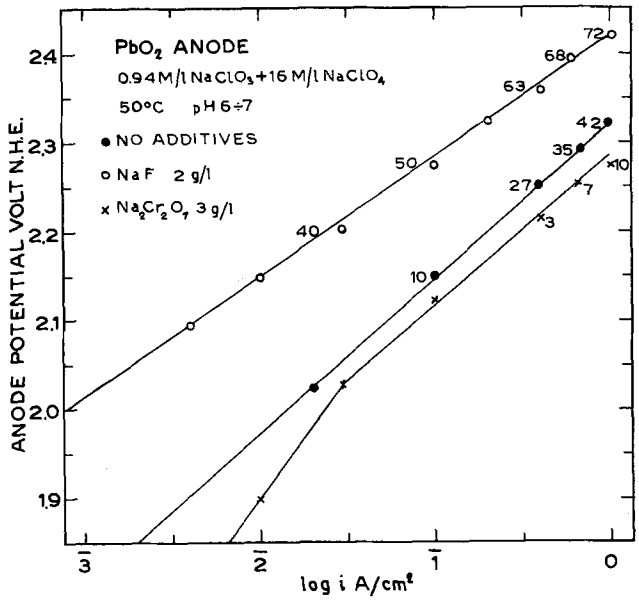

Fig. 9. Effect of NaF and $Na_2Cr_2O_7$ on anodic polarization and current efficiency on PbO_2 (per cent C. E. values marked along each plotting).

ions, on account of their progressive adsorption at the interface as electrostatic attraction increases with potential. Consequently, the water molecules adsorbed at the interface are gradually displaced by ClO_3^- ions, which thus hinder the primary discharge of water and oxygen evolution. This is evidenced, in particular, by the strong inflection generally observed on Pt at all $NaClO_3$ concentrations and also on PbO_2 in the lower concentration range, the somewhat different behavior of the two anode materials being attributable to their different specificity in adsorbing ClO_3^- ions. With regard to the shape of the inflection shown by the curves of Fig. 4, it may be noted that it begins at some potential lower than 1.9v and terminates above 2.3v, which corresponds quite closely to the two stages observed by Sugino and Aoyagi in their potentiokinetic investigation (8). However, this does not provide by itself any evidence in favor of the mechanism of primary ClO_3^- discharge; indeed, besides water displacement from the double layer as postulated above, the further possibility may in principle be visualized that the active sites of high oxygen adsorption energy are progressively blocked by the adsorbed ClO_3^- ions, with a consequent modification of the oxide film and a rise in oxygen discharge overpotential. This could allow the adsorbed ClO_3^- ions to react with oxygen in the modified oxide film, so that ClO_3^- oxidation would occur as a secondary reaction with the chemisorbed oxygen atoms resulting from the primary discharge of water. Such assumption would be in line with the anodic interaction that has been investigated by others (11, 12) between chemisorbed oxygen and ClO_4^- ions in perchloric acid solutions. Evidence of this interaction, which also gives rise to a strong inflection in the polarization curve, has been obtained with experiments conducted in ^{18}O-labeled $HClO_4$ in nonlabeled water (11). In our present case, however, a similar assumption involving interaction between the anion and chemisorbed oxygen seems to be contradicted, in favor of the primary discharge mechanism, by some other experimental evidence discussed here.

Since only the two over-all reactions [1] and [2], *i.e.* ClO_3^- oxidation and O_2 evolution, take place at the anode with complementary current efficiencies, it is possible from the experimental results described above to work out both reaction rates as a function of anode potential and represent them in terms of two partial currents i_1, i_2, respectively, so that $i_1 + i_2 = i$. Such representation, as given in Fig. 10 through 13 for different operating conditions, shows the remarkable fact that the rate of reaction [1] is invariably characterized by Tafel linearity, its slope being generally between 0.11 and 0.12. This provides strong support to the assumption that chlorate oxidation may take place following a pathway that starts with primary discharge of ClO_3^- and proceeds independently of anodic water oxidation throughout the investigated C.D. range. Moreover, since a slope of about 0.12 is typical of an electrode process in which the charge transfer reaction is rate determining, conclusion may be drawn that formation of the ClO_3^- radical is the most likely rate-controlling step in the over-all process leading to ClO_4^- production.

As can be seen in Fig. 10, an increase in $NaClO_3$ concentration c enhances the ClO_3^- conversion rate at a definite constant potential; this is expressed by the positive value of the partial differential coefficient $\delta \log i_1/\delta \log c$, which in the lower potential range is about 0.5, with a tendency to diminish in the higher range. On the other hand, O_2 evolution is strongly inhibited by the adsorbed ClO_3^- ions and depends on the amount of $NaClO_3$ also in the concentration range throughout which the relevant polarization curve remains unaffected (Fig. 4).

Figure 11 illustrates the anodic performance of PbO_2, which is essentially similar to that formerly described for Pt. It is, however, to be noted that the partial differential coefficient $\delta \log i_1/\delta \log c$ is now only about 0.4 in the lower potential range, while O_2 evolution is

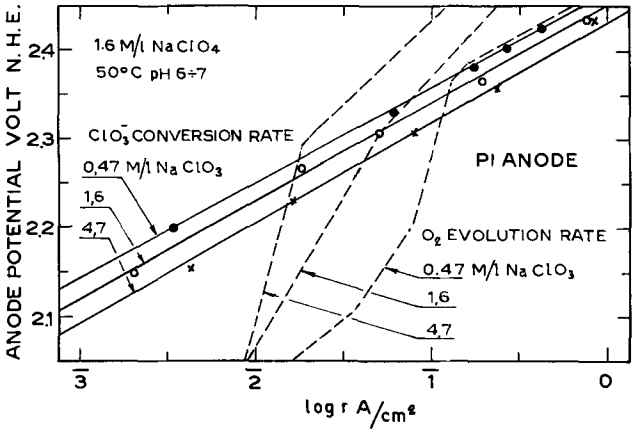

Fig. 10. ClO_3^- conversion and O_2 evolution rates on smooth Pt expressed in amp/cm² vs. anode potential at different $NaClO_3$ concentrations.

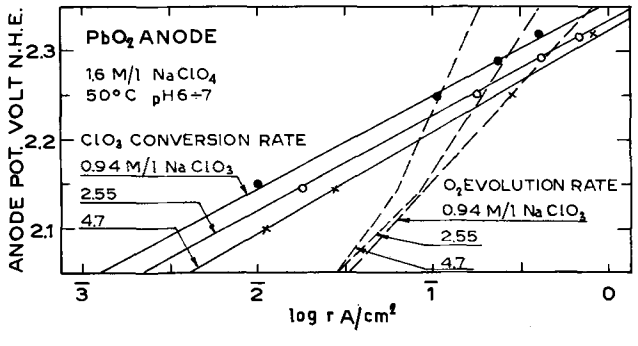

Fig. 11. ClO_3^- conversion and O_2 evolution rates on PbO_2 expressed in amp/cm² vs. anode potential at different $NaClO_3$ concentrations.

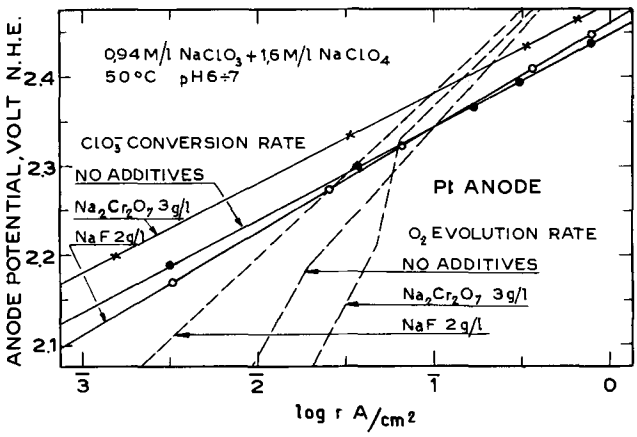

Fig. 12. Effect of NaF and $Na_2Cr_2O_7$ on ClO_3^- and O_2 evolution rates on smooth Pt expressed in amp/cm² vs. anode potential.

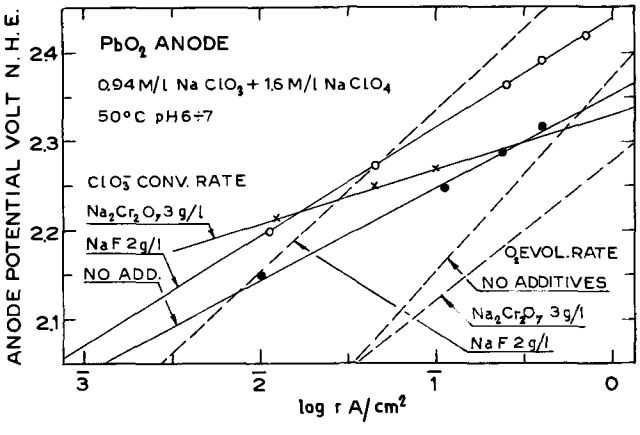

Fig. 13. Effect of NaF and $Na_2Cr_2O_7$ on ClO_3^- and O_2 evolution rates on PbO_2 expressed in amp/cm² vs. anode potential.

inhibited by the presence of $NaClO_3$ to a substantially lesser extent than on Pt.

The influence of additives on the two reaction rates is evidenced by Fig. 12 for Pt and by Fig. 13 for PbO_2. In the case of smooth Pt, the presence of 2 g/liter NaF not only exerts a strong inhibiting action on O_2 evolution, but also slightly improves ClO_3^- conversion in the lower potential range. On the contrary, the addition of 3 g/liter $Na_2Cr_2O_7$ inhibits ClO_3^- conversion on Pt, while catalyzing O_2 evolution. Moreover, while NaF tends to increase the slope of the Tafel line related to ClO_3^- conversion, $Na_2Cr_2O_7$ tends to decrease it. Accordingly, the effects of the two additives are opposite in all respects.

With PbO_2 anodes (Fig. 13), the presence of 2 g/liter NaF inhibits both reaction rates, but O_2 evolution is affected to a much greater extent than ClO_3^- conversion; this explains the improvement in faradic efficiency obtained by NaF addition, which also increases the ClO_3^- conversion slope from the original value of 0.1 to the value of 0.12. As to the effect of $Na_2Cr_2O_7$ on PbO_2 anodes, it is distinguished by the peculiar characteristic that, besides inhibiting ClO_3^- conversion in the C.D. range up to 0.3 amp/cm² and enhancing O_2 evolution rate by a factor that increases with C.D., it markedly lowers the slope of both plottings so that the slope of ClO_3^- conversion is depressed from 0.1 without additives to 0.05 after adding 3 g/liter $Na_2Cr_2O_7$. It ensues that, while persistence of Tafel linearity still provides support to the assumption of the primary discharge mechanism also in this case, the fact that the slope is definitely smaller than 0.1 indicates that the charge transfer would no longer be the rate-determining step and that this is now to be identified with a subsequent step, such as desorption of ClO_3 radicals or a further electrochemical reaction be-

tween radicals and ions. The interaction between a lead anode and chromic acid was originally investigated by Elbs and Nübling (13). They have thus demonstrated that anodic treatment of lead in a chromic acid solution may result in anodic passivation with the build-up of a layer of lead chromate and/or lead dioxide, or else it may cause anode dissolution, depending on chromic acid concentration. Therefore, we wished to carry out some tests to ascertain whether the lead dioxide coating is modified by the presence of CrO_4^{2-} or $Cr_2O_7^{2-}$ ions under the conditions prevailing in our present research. We have accordingly submitted the PbO_2 anode to polarization at 0.3 amp/cm² in 0.1 and 1% chromic acid solution. Electrolysis was conducted for several hours and the tests were repeated in 1.6 moles/liter $NaClO_4$ + 1.6 moles/liter $NaClO_3$ with different $Na_2Cr_2O_7$ additions up to 5 g/liter.

After none of such runs was any anode weight loss measurable. However, after each run the aspect of the anode surface had changed and some pale yellowish hues were visible, which presented interferential characteristics. Such aspect is different from the black metallic luster of a freshly prepared and polished PbO_2 coating, as well as from the gray and dull appearance of anode samples after operating in solutions containing no chromate. It must therefore be concluded that the superficial structure of the PbO_2 substrate is somehow modified by interaction with $Cr_2O_7^{2-}$ ions, with probable build-up of a chemisorbed layer.

Conclusion

The rectilinear character of ClO_3^- conversion rate, when plotted in a current potential diagram, under all investigated conditions, leaves little doubt that ClO_3^- oxidation should be considered as the consequence of a primary discharge reaction involving ClO_3^- ions. It would indeed be difficult to reconcile the constancy of the reaction mechanism throughout the C.D. range with the drastic modification of the chemisorbed oxygen layer that is shown to occur at the same time by the strong inflection of the oxygen evolution curve.

Since the slope of the Tafel line is generally between 0.1 and 0.12, the rate-determining step of over-all reaction [1] should be identified with the charge transfer reaction

$$ClO_3^- \rightarrow ClO_3 + e^-$$

This is in accordance with either one of mechanisms (II) and (IV) in Table I. As to mechanisms (I) and (III), they seem less likely to occur for a number of reasons. First of all, they both involve adsorbed H_2O molecules in a charge transfer reaction;[1] on the other hand, since water is gradually driven out and replaced by ClO_3^- ions in the adsorbed layer, it is difficult to visualize how the reaction rate can thus proceed with Tafel linearity. Moreover, mechanism (I) involves the production and recombination of an unlikely intermediate product such as ClO_2^- according to step (*a*) and, in addition, the production and subsequent reaction rate of chemisorbed oxygen according to step (*b*) should also be affected by the gradual modification of the chemisorbed layer, as observed above; this, again, would be difficult to reconcile with Tafel linearity.

The only slope departure from values between 0.1 and 0.12 has been observed on PbO_2 in the presence of $Na_2Cr_2O_7$. On the assumption of mechanism (II), this would be attributable to a slowing down of the desorption step (*b*). However, the assumption of mechanism (IV) provides an interpretation that is possibly even more in line with the present findings. In fact, the results represented in Fig. 13 indicate that the presence of $Cr_2O_7^{2-}$ ions in the adsorbed layer has the effect of enhancing O_2 evolution by counteracting the tendency of electrosorbed ClO_3^- ions to drive out the H_2O molecules. By supposing, then, that the electrochemical step (*b*), involving adsorbed water, becomes rate determining, a theoretical calculation according to the method used by Bockris (1) would give a slope value of about 0.04, which is quite close to the value of 0.05 as determined in the present investigation.

[1] Step (*d*) in mechanism (III) should obviously be modified as follows: $H_2O \rightarrow H^+ + OH + e^-$.

Manuscript submitted May 9, 1968; revised manuscript received Sept. 18, 1968. This manuscript was presented at the Boston Meeting, May 5-9, 1968, as Paper 270.

Any discussion of this paper will appear in a Discussion Section to be published in the December 1969 JOURNAL.

REFERENCES

1. J. O'M. Bockris, "Modern Aspects of Electrochemistry," pp. 226-229, Academic Press, London (1954).
2. N. V. S. Knibbs and H. Palfreeman, *Trans. Faraday Soc.*, **16**, 402 (1920).
3. A. Legendre, *Chem. Ing. Tech.*, **34**, 379 (1962).
4. J. C. Schumacher, D. R. Stern, and P. R. Graham, *This Journal*, **105**, 151 (1958).
4a. J. C. Schumacher, "Perchlorates," pp. 6 and 79, Reinhold Publishing Corp., New York (1960).
5. K. C. Narasimham, S. Sundararajan, and H. V. K. Udupa, *This Journal*, **108**, 798 (1961).
6. B. E. Conway, N. Marincic, D. Gilroy, and E. Rudd, "Electrode Processes, Transactions of the 1966 Symposium," E. Yeager, H. Hoffman, and E. Eisenmann, Editors, p. 128, The Electrochemical Society, Inc., New York (1967).
7. W. Oechsli, *Z. Elektrochem.*, **9**, 807 (1903).
8. K. Sugino and S. Aoyagi, *This Journal*, **103**, 166 (1956).
9. C. W. Bennett and E. L. Mack, *Trans. Am. Electrochem. Soc.*, **29**, 323 (1916).
10. M. P. Grotheer and E. H. Cook, *This Journal*, **6**, 221 (1968).
11. A. N. Frumkin, "CITCE Proceedings Ninth Meeting (1957)," p. 396, Butterworths Scientific Publications, London, (1959).
12. P. Delahay, "Double Layer and Electrode Kinetics," pp. 269-273, Interscience Publishers, New York (1965).
13. K. Elbs and R. Nübling, *Z. Elektrochem.*, **9**, 776 (1903).
14. J. C. Grigger, "The Encyclopedia of Electrochemistry," C. A. Hampel Editor, pp. 762-764, Reinhold Publishing Corp., New York (1964).

Catalytic Enhancement of Carbon Monoxide and Reformer Gas Oxidation in Fuel Cells By Sodium Tungsten Bronzes

L. W. Niedrach* and H. I. Zeliger[1]

General Electric Research and Development Center, Schenectady, New York

It has been previously shown that the electro-oxidation of carbon monoxide and reformer gas at platinum black fuel cell anodes can be appreciably enhanced by the incorporation of tungsten oxides into the electrodes (1). The purpose of the present note is to discuss a similar promotional effect that has since been observed with sodium tungsten bronzes.

The tungsten bronzes, which were discovered by Wöhler (2) were so named because of their metallic properties, *e.g.* luster and electrical conductivity. Actually they are neither alloys nor metallic compounds, but, rather, mixed oxides having the general formula M_xWO_3. M is generally an alkali or alkaline earth metal, but other metals can be substituted. The values of x can vary from 0 to 1.0. In the case of the sodium bronzes, compounds covering essentially the full range of x values are known. Other systems are restricted to narrower ranges. While the compounds have been looked upon as containing mixed valences of +5 and +6 tungsten, the physical properties are best interpreted on the basis of an interstitial distribution of the substituent metal and free electrons in a tungsten trioxide matrix (3). The properties of tungsten bronzes have been reviewed in detail elsewhere (4-6).

Experimental

Three approaches were adopted for the preparation of the high area materials desired for use in fuel cell electrodes. All employed high temperatures and, because of the dissociative equilibria involved, were somewhat empirical with regard to the adjustment of the x value.

Fusion of tungsten, tungsten trioxide, and sodium tungstate.—An intimate mixture of the starting materials was heated in a porcelain crucible until a homogeneous melt was obtained (7). After cooling to room temperature, excess Na_2WO_4 and WO_3 were removed by boiling in dilute NaOH. The product bronze was collected over a filter, washed, and dried. One advantage of this method is that one may quickly obtain bronzes with high x values (0.8-1.0) that are otherwise difficult to prepare. A disadvantage is that the bronze powders are attacked slowly by NaOH to liberate hydrogen and form soluble sodium tungstate. The product can be ball milled to obtain a high surface area material (4-6 m^2/g).

Reaction of higher bronzes with WO_3.—One can obtain bronzes with low x values by heating an intimate mixture of a bronze having a high x value with WO_3 either in a vacuum or under an inert atmosphere *e.g.*, argon), at temperatures ranging from 500° to 850°C for durations of from 2 to 66 hr. The reaction occurs *via* a dissociation of the higher bronze to give free sodium which reacts with the WO_3. This reaction is described by Straumanis (7).

Reaction of WO_3 with NaI.—Tungsten trioxide reacts with sodium iodide to form a bronze with the liberation of iodine (7). This reaction can be carried out at 600°-650°C either in a vacuum or under an inert atmosphere (argon). This method is useful for obtaining bronzes of intermediate x values.

The properties of the sodium tungsten bronzes prepared are summarized in Table I. All were examined by x-ray diffraction. Values of x were obtained from the lattice parameters using the data of Straumanis (7).

Teflon-bonded electrodes were prepared with several of the bronzes (surface area 4-6 m^2/g) in admixture with platinum black (surface area, 20 m^2/g) using procedures that have previously been described

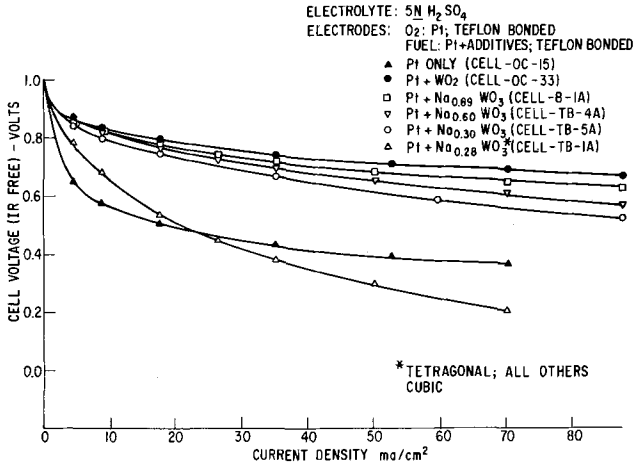

Fig. 1. Effect of several tungsten bronzes on the performance of CO-O_2 fuel cells at 25°C.

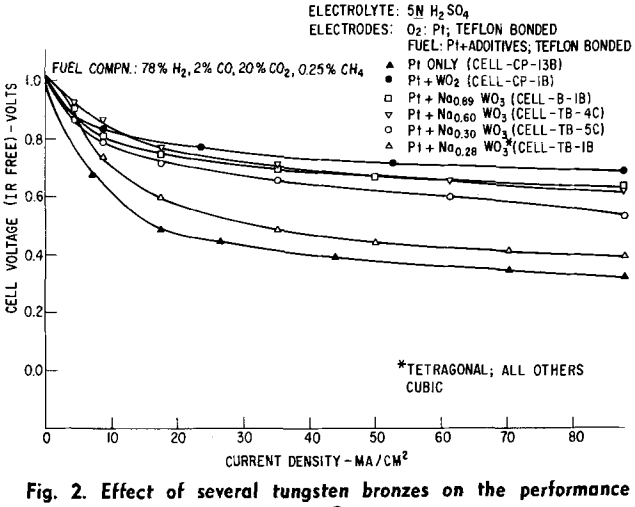

Fig. 2. Effect of several tungsten bronzes on the performance of reformer gas-O_2 fuel cells at 25°C.

* Electrochemical Society Active Member.

[1] Present address: Scientific Consultants, 81 Rockledge Road, Hartsdale, New York 10530.

Table I. Properties of sodium tungsten bronzes

Nominal x	Actual x	Procedure	Color	Lattice
1.0	1.0	Method 1—fused in air	Yellow-brown	Cubic
0.9	0.89	Method 1—fused in air	Yellow-brown	Cubic
0.8	0.76	Method 1—fused in vacuum; 850°C, 4.5 hr	Red-brown	Cubic
0.7	0.68	Method 2*—in vacuum; 500°C, 66 hr	Red-violet	Cubic
0.7	0.66	Method 3—in argon; 650°C, 5 hr	Red-violet	Cubic
0.6	0.60	Method 3—in argon; 600°C, 2 hr	Dark-violet	Cubic
0.5	0.48	Method 2*—in vacuum; 500°C, 66 hr	Blue	Cubic
0.5	0.53	Method 2*—in argon; 800°C, 1 hr	Blue	Cubic
0.5	0.53	Method 3—in vacuum; 600°C, 8 hr	Blue	Cubic
0.4	0.43	Method 2*—in vacuum; 500°C, 66 hr	Blue	Cubic
0.3	0.30	Method 2*—in vacuum; 500°C, 24 hr	Blue	Cubic
0.3	0.28	Method 1—fused in air	Dark blue	Tetragonal

* $Na_{0.89}WO_3$ (4 m^2/g) used as starting material.

(8). All the electrodes contained 34 mg Pt/cm^2, 6.8 mg bronze/cm^2, and Teflon binder (DuPont's T-30 Teflon) amounting to 10% of the combined weight of platinum and bronze. A film of 1.6 mg Teflon/cm^2 was used on the gas side of all electrodes.

The electrodes were evaluated in fuel cells at 25°C on both carbon monoxide and a synthetic reformer gas (78% H_2, 2% CO, 20% CO_2, and 0.25% CH_4) fuel. In all cases, the counterelectrode (operated on pure oxygen) was a Teflon-bonded platinum black electrode containing 34 mg Pt/cm^2 and prepared in the same manner as the other electrodes. Both electrodes had a working area of 11.4 cm^2. The electrolyte was 5*N* H_2SO_4. All measurements were made with a Kordesch-Marko bridge (9).

Results and Discussion

Performance data for cells with the bronze-containing electrodes are shown in Fig. 1 and 2 in the form of *IR*-free current-voltage curves obtained with carbon monoxide and synthetic reformer gas fuels, respectively. Included in the figures for reference purposes are similar curves obtained with a fuel electrode containing platinum only, as well as with an electrode containing WO_2 as an additive. This oxide of tungsten had previously been found to be the best among those examined (1).

These data show that the cubic bronze additives result in a considerable improvement over straight platinum, while the tetragonal bronze provides little or no improvement. The data also show that, as the value of x in the cubic bronzes (M_xWO_3) increases, the promotional effect also increases. This parallels the results previously obtained with the tungsten oxides, the lower oxides showing greater catalytic promotion than the higher oxides (1). As is evident, the promotional effect of the bronze with $x = 0.89$ for both carbon monoxide and synthetic reformer gas is only slightly less than the best tungsten oxide (WO_2).

Summary and Conclusions

Relatively high surface area sodium tungsten bronzes (4-6 m^2/g) have been prepared. These materials serve as promoters for the catalytic oxidation of carbon monoxide and reformer gas in fuel cells much the same as the tungsten oxides. The effectiveness of the bronze promoters increases with increasing sodium content.

Acknowledgment

This is a part of the program under contracts DA-44-009-AMC-479(T) and DA-44-009-ENG-4909, ARPA Order No. 247, with the U.S. Army Mobility Equipment Research & Development Center, Ft. Belvoir, Virginia, to develop a technology which will facilitate the design and fabrication of practical military fuel cell power plants for operation on ambient air and hydrocarbon fuels.

Manuscript submitted April 2, 1968; revised manuscript received Sept. 9, 1968.

Any discussion of this paper will appear in a Discussion Section to be published in the December 1969 JOURNAL.

REFERENCES

1. L. W. Niedrach and I. B. Weinstock, *Electrochem. Technol.*, **3**, 270 (1965).
2. F. Wöhler, *Ann. Chem. Phys.* [2], **29**, 43 (1823).
3. P. M. Stubbin and D. P. Mellor, *Proc. Roy. Soc. N.S. Wales*, **82**, 225 (1948).
4. M. J. Sienko, *Advan. Chem. Ser.*, **39**, 224 (1963).
5. H. R. Shanks, P. H. Sidles, and G. C. Danielson, *ibid.*, p. 237.
6. A. S. Ribnick, B. Post, and E. Banks, *ibid.*, p. 246.
7. M. E. Straumanis, *J. Am. Chem. Soc.*, **71**, 679 (1949).
8. L. W. Niedrach and H. R. Alford, *This Journal*, **112**, 117 (1965).
9. K. Kordesch and A. Marko, *ibid.*, **107**, 480 (1960).

A Dual Reference Electrode System for Molten Carbonate Cells with Immobilized Electrolyte

E. S. Argano*, [1] and J. Levitan*

Institute of Gas Technology, Chicago, Illinois

The growing interest in the electrochemistry of molten and solid electrolytes brought up the problem of reliable reference electrodes in those high-temperature media.

The corrosivity of molten electrolytes at high temperatures is one of the main problems in the design of reference electrodes and half-cell systems. Reference electrodes reversible to cations such as Na (1-3), Al (4), Pb (5), and Ag (6), and to anions such as the chlorine electrode in chloride melts (7, 8) and the oxygen electrode in borates (9) are being used.

In the case of molten carbonate systems, several types of reference electrodes have been used. The Danner-Rey Ag/Ag^+ electrode (10) has been frequently used in such media and, according to Janz and Conte (11), it has a useful life of about 30 days. Gas

* Electrochemical Society Active Member.
[1] Present address: Istituto di Ricerche Breda, viale Sarca 336, I 20126 Milan, Italy.

reference electrodes are the most reliable in molten carbonate systems because junction potentials are avoided. The Pt/O_2-CO_2 electrode has been investigated by Janz *et al.* (12, 13) and Stepanov *et al.* (14-16) and was found to be thermodynamically reversible and stable with time. This type of gas electrode, using Pt or Au, was used by Schenke and Broers (17) and Borucka (18) for studies in carbonate melts.

When dealing with carbonate fuel cell systems, Moss and Gibbens (19) used a "potential probe" consisting of a Ag wire placed within the immobilized electrolyte, and Trachtenberg (20) used an "idle" electrode consisting of a porous Ag electrode situated in the cathode compartment. The "reference wire" electrode used by Broers and Schenke (21) eliminated the effect of spurious currents by using a carbonate film "bridge" as the liquid junction, but the third electrode was supplied with a mixture of CO_2 and air of unknown composition.

For evaluating properties of individual anodes and cathodes in molten carbonate fuel cells with immobilized electrolytes, the use of proper gas reference electrodes provides reliable and accurate information.

This article reports an improved design for a gas reference electrode for conducting electrochemical studies in molten carbonate cells with an immobilized electrolyte. Two reference electrodes are provided in the same cell assembly.

The present design is shown in Fig. 1.

A pure gold wire (99.999% purity, 0.020 in. in diameter) is enclosed in an alumina tube (*C*) (6 mm in diameter). The lower end of the gold wire is immersed in a closely packed powder of immobilized electrolyte (*D*). An inner alumina tube (OD = 2 mm) situated a few centimeters above the electrolyte level is used to introduce the reference gas mixture. The gas mixture consisting of CO_2 and O_2 (P_{CO_2} = 2/3 atm, P_{O_2} = 1/3 atm) has the most noble potential (14, 15) for this system and was taken as an arbitrary zero point.

The tubes (*C*) of the reference electrodes are located in two symmetrical cylindrical cavities (*G*) containing paste electrolyte.

The electrolyte junction between the reference tubes and the cell electrolyte is obtained through two 0.5-mm-diameter holes: *E* in tube *C* and *J* in ring *H*. The two inner junctions (*J*) were symmetrically located with respect to the electrolyte disk (*I*).

The half-cell housing consists of an outer alumina ring (*H*) (ID = 25 mm) sealed to the bottom alumina tube (*N*) with an alumina-phosphate mixture heated at 1000°C. The electrolyte disk (*I*) (diameter = 25 mm) seated on the bottom tube (*N*) and a similar tube pressed on the top of the electrolyte provide the sealing between the anodic and cathodic compartments of the cell.

The advantage of the present design over the previous three electrode assemblies (19-21) of immobilized electrolyte cells is the ability to maintain a definite and independent atmosphere in the reference chamber. When operated, the reference electrodes and the cell were maintained at 700°C.

An immobilized electrolyte composed of a mixture of inert ceramic and a carbonate ternary mixture (8% Li_2CO_3, 52% Na_2CO_3, and 40% K_2CO_3 melting at 650°C) was used with the present design. The a-c (1000 cps) resistance at 700°C of the reference electrodes *vs.* one of the cell electrodes was found to increase with time from 1 to 2 k-ohm after 30 days of operation. This is probably due to the depletion of carbonates in the pockets (*G*) because of carbonate creeping and decomposition. It can be avoided if tube *C* is sealed to ring *H* but, in this case, the reference tubes are not interchangeable during the operation of the cell. Experiments were conducted for evaluating the long-term stability of the reference electrode. The potential difference at 700°C between the two reference electrodes constructed from the same material and fed by the same gas mixture was ±0.5 mv at the beginning of the test, increased to ±1.5 mv after 10 days of operation, and then did not change during the subsequent 2 months.

A typical polarization curve of a molten carbonate cell with the described reference electrodes (an Au cathode and a porous Ni anode) is shown in Fig. 2.

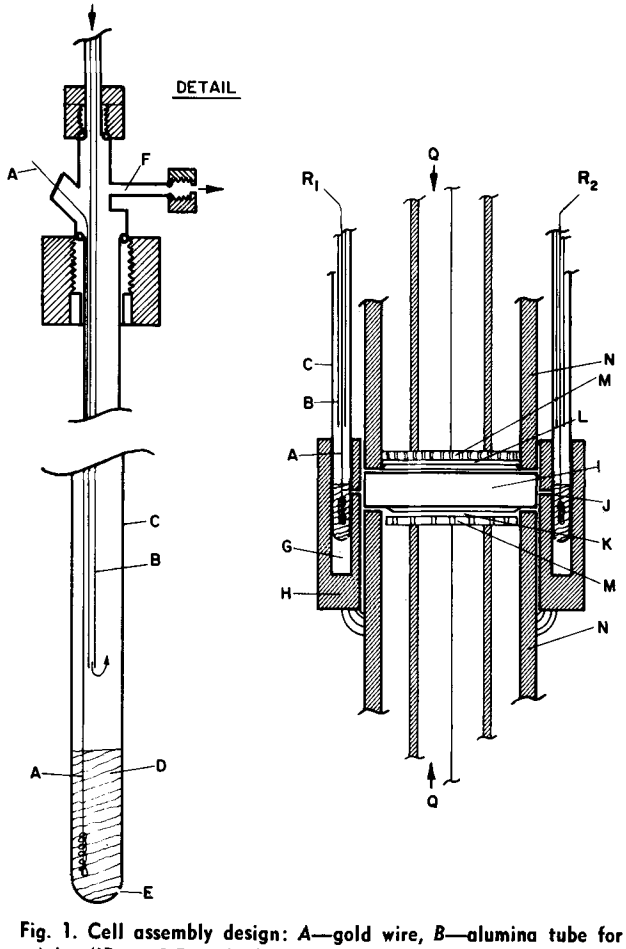

Fig. 1. Cell assembly design: *A*—gold wire, *B*—alumina tube for gas inlet (ID = 1.5 mm), *C*—alumina tube of reference electrode, *D*—paste electrolyte of reference electrode, *E*—hole in tube *C* (diameter 0.5 mm), *F*—gas outlet tube of reference electrode, *G*—paste electrolyte pocket (diameter 6 mm), *H*—alumina ring for reference electrodes, *I*—paste electrolyte disk of cell, *J*—hole for junction with cell electrolyte (diameter 0.5 mm), *K*—cell cathode, *L*—cell anode, *M*—current collector, *N*—alumina tubes of cell assembly, *Q*—gas inlets to cell electrodes.

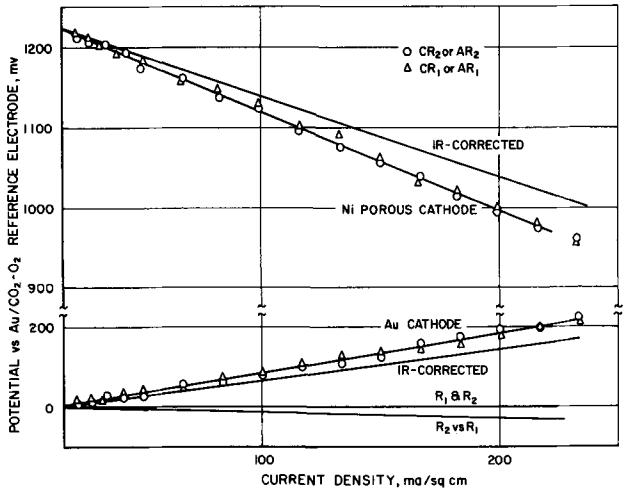

Fig. 2—Typical polarization curve of a molten carbonate cell with an Au cathode and a porous Ni anode.

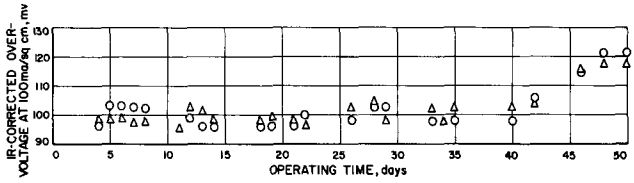

Fig. 3—*IR*-corrected polarization plotted against time of operation.

When the anodic and cathodic polarizations of the cell were measured *vs.* both reference electrodes, the electrode polarization was obtained with ±2 mv accuracy. However, at increased current density, the potential difference between the two reference electrodes increased (15 mv at 200 ma/cm^2). This is presumably due to the nonsymmetrical potential distribution within the electrolyte disk in the vicinity of the inner junctions (*J*) connecting the electrolyte disk (*I*) with the electrolyte pockets where the reference electrodes are located. The single-electrode ohmic components were measured *vs.* both reference electrodes using a standard interruption technique. An *IR*-corrected polarization plotted against time of operation is shown in Fig. 3. The polarization of the porous Ni anode (corrected for *IR* drop) was recorded against both reference electrodes at a current density of 100 ma/cm^2. A mean anodic polarization of 100 ±2.5 mv was measured. The main source of error in this measurement is involved in reading the oscillograms. A failure of the anode was detected after 40 days of operation of that experimental cell.

In conclusion, this design has several advantages:

(*A*) Single-electrode polarization data can be obtained with a known accuracy.

(*B*) The reference electrodes are interchangeable and can be substituted during the operation of the cell without disturbing the cell operation.

(*C*) Long-time stability of the reference electrodes was achieved using immobilized electrolyte in the reference tube and intermediate tubes as well as in the intermediate pocket.

(*D*) The described design can be applied to other electrochemical systems with immobilized and solid electrolytes.

Acknowledgment

This work is sponsored by Pratt & Whitney Aircraft Division of United Aircraft Corporation as part of the TARGET Fuel Cell Program. This support is gratefully acknowledged.

Manuscript received June 24, 1968.

Any discussion of this paper will appear in a Discussion Section to be published in the December 1969 JOURNAL.

REFERENCES

1. K. Hauffe, *Z. Elektrochem.*, **46,** 348 (1940).
2. K. Hauffe and A. L. Vierk, *ibid.*, **53,** 151 (1949).
3. A. A. Kolotii, *Zh. Prikl. Khim.*, **38,** 2706 (1965).
4. R. G. Verdieck and L. F. Yntema, *J. Phys. Chem.*, **48,** 268 (1944).
5. B. P. Artamonov, *Tr. Gos. Inst. Prikl. Khim.*, **33,** 39 (1940).
6. S. N. Flengas and E. Rideal, *Proc. Roy. Soc. (London)*, **A223,** 443 (1956).
7. A. Wachter and J. H. Hildebrand, *J. Am. Chem. Soc.*, **52,** 4655 (1930).
8. S. Senderoff and R. J. Labrie, *This Journal*, **102,** 77 (1955).
9. Y. K. Delimarskii and G. D. Nazarenko, *Ukr. Khim. Zh.*, **27,** 458 (1961).
10. G. Danner and M. Rey, *Electrochim. Acta*, **4,** 274 (1961).
11. G. J. Janz and A. Conte, *ibid.*, **9,** 1269 (1964).
12. G. J. Janz, F. Colom, and F. Saegusa, *This Journal*, **107,** 581 (1960).
13. G. J. Janz and F. Saegusa, *Electrochim. Acta*, **7,** 393 (1962).
14. G. K. Stepanov and A. M. Trunov, *Dokl. Akad. Nauk SSSR*, **142,** 866 (1962).
15. A. M. Trunov and G. K. Stepanov, *Tr. Inst. Elektrokhim., Ural'sk Filial Akad. Nauk SSSR*, **2,** 97 (1961).
16. I. N. Ozerianaiya *et al.*, *ibid.*, **7,** 91 (1965).
17. M. Schenke and G. H. J. Broers, Reprint No. 25, 5th Intern. Power Source Symp., Brighton, England, Sept. 20-22, 1966.
18. A. Borucka, Paper presented at Fuel Cell Symp., 154th Natl. Meeting Am. Chem. Soc. Div. Fuel Chem., Chicago, Sept. 11-15, 1967; abstracted in *Preprints*, **11,** No. 3, 186.
19. R. L. Moss and H. R. Gibbens, *Cobalt*, **28,** 115 (1965).
20. I. Trachtenberg, *This Journal*, **111,** 110 (1964).
21. G. H. J. Broers and M. Schenke, "Hydrocarbon Fuel Cell Technology," B. S. Baker, Editor, p. 225, Academic Press, New York (1965).

Luminescence of YVO_4:In

S. Faria* and Carl W. Fritsch, Jr.

Sylvania Electric Products Incorporated, Chemical and Metallurgical Division, Towanda, Pennsylvania

Yttrium vanadate, YVO_4, has been activated by most of the trivalent rare-earth (RE) elements (1). The first investigators to activate YVO_4 with another trivalent element, Bi^{3+}, which is not a rare earth, were Toma *et al.* (2) and Datta (3). Their activation with Bi^{3+} resulted in broad-band emission with a maximum at about 550 nm. Although unactivated YVO_4 (1) is in itself a broad-band emitter with a maximum around 435 nm, incorporation of Eu^{3+} (or other RE elements) quenches the matrix emission band and produces characteristic RE line emission.

In this paper, we report that indium, another activator which is not a rare earth, was successfully incorporated in YVO_4 matrix, giving rise to broad-band emission. The emission peak for YVO_4:In is between the matrix emission and Bi emission, *i.e.*, around 470 nm. Some preliminary results on the photoluminescence and cathodoluminescence characteristics of YVO_4:In are presented here.

* Electrochemical Society Active Member.

Phosphor Preparation and Measurements

Procedures similar to those described in the literature for the preparation of YVO_4:Eu (1-3) were followed except for the use of 99.99% In_2O_3 (obtained from Indium Corp. of America). The excitation and emission spectra were measured from phosphor plaques using a Perkin-Elmer spectrofluorimeter and a Hitachi-Perkin-Elmer MPF-2A, respectively. Cathodoluminescence and fluorescent lamp data were also obtained using the conventional techniques.

Effect of In *in* YVO_4

Increasing the In concentration in YVO_4 shifts the emission to longer wave lengths. Figure 1 represents the normalized emission spectra depicting the effect of 0.25 and 5.0 mole per cent (m/o) In substitution

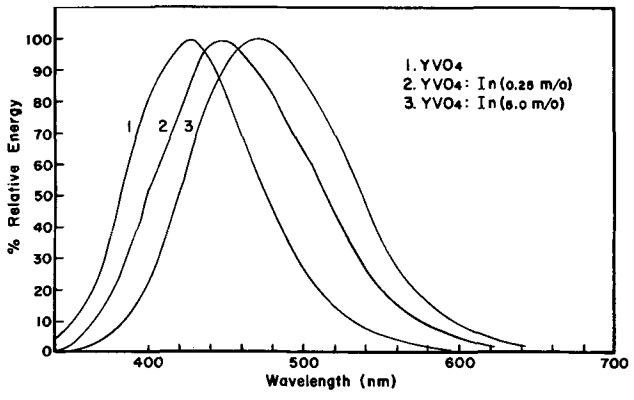

Fig. 1. Emission spectra of: 1—YVO_4, 2—YVO_4:In (0.25 m/o), 3—YVO_4:In (5.0 m/o).

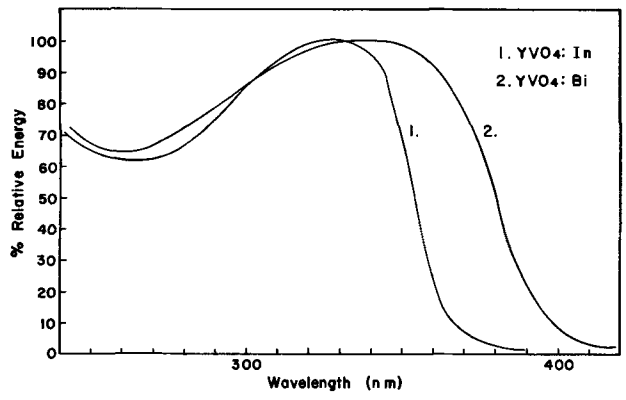

Fig. 2. Excitation spectra of: 1—YVO_4:In (5 m/o) compared to 2—YVO_4:Bi (4 m/o).

for Y^{3+} in YVO_4. Note that 0.25 m/o In shifts the peak of unactivated YVO_4 about 300Å, while 5.0 m/o In shifts it close to 450Å. Per cent plaque brightness with three different ultraviolet mercury excitations at various In concentrations are presented in Table I.

Optimum In concentration for 2537 and 3250Å excitation is about 2 m/o. With 3650Å excitation, however, the maximum was found to be around 7 m/o In.

The blue emission of YVO_4:In was compared to $Sr_2P_2O_7$:Sn and $Ca_5F(PO_4)_3$:Sb, two well-known blue-emitting fluorescent lamp phosphors. Table II shows the lamp brightness results in lumens (mainly 2537Å excitation).

Excitation Spectra of In *vs.* Bi

The normalized excitation spectrum for YVO_4:In was compared to that of Bi and shown in Fig. 2. Note that the excitation peak for In is 330 nm, while for Bi it is around 345 nm. The indium excitation band is much narrower than that of Bi. The excitation spectrum of unactivated YVO_4 is the same as that of YVO_4:In.

In Fig. 3 are plotted the emission spectra of YVO_4, YVO_4:In, and YVO_4:Bi. The separation between the In and Bi peaks is about 100 nm.

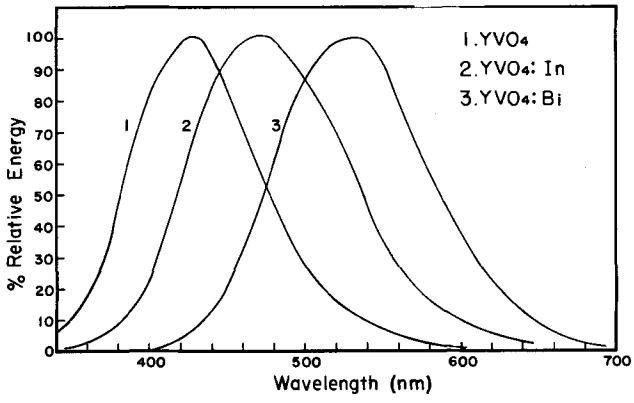

Fig. 3. Comparison of emission spectra of YVO_4, YVO_4:In, and YVO_4:Bi.

Table I. Per cent plaque brightness of YVO_4:$In_{(x)}$ as a function of exciting wave lengths

(x) m/o In	2537Å	3250Å	3650Å
0	48	60	37
0.25	66	81	50
0.50	90	89	60
1.00	97	95	71
2.00	100	100	85
3.00	99	100	88
5.00	95	96	95
7.00	91	93	100
10.00	76	90	91

Table II. Lamp brightness comparison (40T12)

	0 Hr lumens	100 Hr lumens
$Sr_2P_2O_7$:Sn (Type 243)**	1506	1382
$Ca_5F(PO_4)_3$:Sb (Type 244)**	2241	2148
YVO_4:In (2 m/o)	1344	1180

** Sylvania Type No.

Table III. Cathode-ray brightness

m/o In	Brightness (ft-L)
0.25	3.8
2.00	5.5
5.00	5.2

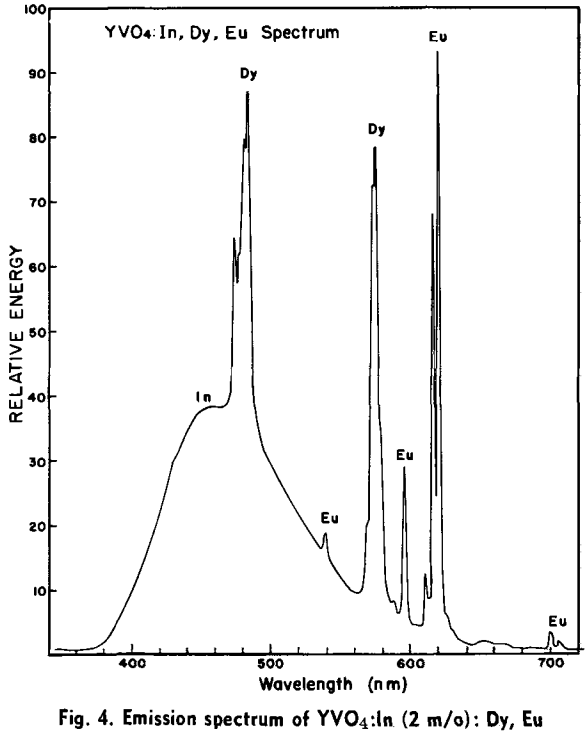

Fig. 4. Emission spectrum of YVO_4:In (2 m/o): Dy, Eu

Cathodoluminescence Properties

Under cathode-ray bombardment, YVO_4:In also showed blue luminescence. Table III shows the brightness results in foot-lamberts (ft-L) for three In concentrations. (About 4.4 mg/cm² of phosphor were settled on 1.5 x 1.5-in. glass slides and bombarded with 12 kv, 6 μa cathode rays.)

The brightness of the 2.0 m/o In sample represents about 60% of the brightness of the normal blue cathode-ray phosphor, ZnS:Ag.

Effect of Eu and Dy

When small amounts of Eu and/or Dy (500 ppm, respectively) were added together with In, we obtained the emission spectrum shown in Fig. 4. Note that the Eu and Dy emission lines are superimposed over the YVO_4:In emission band. Over 1 m/o of Eu or Dy additions tend to quench the YVO_4:In band. On the other hand, high In (1-2 m/o) additions to YVO_4:Eu (5 m/o) do not seem to affect the Eu lines or the Dy lines.

Summary

Indium has been found to activate the YVO_4 matrix, yielding a phosphor with a broad-band emission. The position of the emission peak is dependent on the In concentration. Increasing the In content shifts the emission peak toward longer wave lengths. Optimum ultraviolet-excited and cathodoluminescence brightness appears at about 2 m/o In.

A possible mechanism of energy transfer in YVO_4:Bi has been discussed by Toma (2) and Datta (3). They have assumed that energy absorbed by the matrix is transferred by a radiationless process to the activator center. We suspect that a similar mechanism applies to In-activated YVO_4.

Manuscript submitted June 28, 1968; revised manuscript received Aug. 14, 1968. This paper was presented at the Boston Meeting, May 5-9, 1968, as a Late News Item.

Any discussion of this paper will appear in a Discussion Section to be published in the December 1969 JOURNAL.

REFERENCES

1. F. C. Palilla, A. K. Levine, and M. Rinkevics, *This Journal*, **112**, 776 (1965).
2. S. Z. Toma, F. F. Mikus, and J. E. Mathers, *ibid.*, **114**, 953 (1967).
3. R. K. Datta, *ibid.*, **114**, 1057 (1967).

The Luminescence of YVO_4:Dy, YVO_4:Dy,Eu, and YVO_4:Dy,Tb

S. Faria* and D. T. Palumbo

Sylvania Electric Products Incorporated, Chemical and Metallurgical Division, Towanda, Pennsylvania

Rare-earth (RE) vanadate crystals prepared by Brixner and Abramson (1) showed, besides their main host emission, additional luminescent multiplets ascribed to other RE impurities. Similar multiplets were observed by Palilla and co-workers (2) in their extensive luminescence investigation of RE activated YVO_4. Among the RE impurities usually detected were Er, Sm, Tm, Dy, and Eu. The characteristic line emission of these RE and their position in the visible spectrum are easily identified in the vanadate matrix by spectrophotometric measurements.

Dy multiplets in particular are quite evident, even when using yttrium salts of high purity. Concentrations of Dy as low as 1-2 ppm give distinctive lines superimposed over the broad spectrum of YVO_4. The location of the Dy multiplets is centered at about 475 and 575 nm.

Because of its intense emission at low concentrations, we investigated Dy as a primary activator in YVO_4. We also studied the effect other RE's, particularly Eu and Tb, have on the luminescence characteristics of YVO_4:Dy, particularly in fluorescent lamps.

Experimental

YVO_4, YVO_4:Dy, YVO_4:Dy:Eu, *etc.*, were prepared by dry blending high-purity oxides (99.99%) of yttrium, dysprosium, europium, and terbium with excess ammonium metavanadate and firing at 1750°F for 2 hr in open quartz crucibles. After cooling, the phosphors were washed in 10% caustic solution to remove the excess vanadium pentoxide.

Emission spectra were measured with a Hitachi-Perkin-Elmer spectrophotometer, Model MPF-2A. Fluorescence brightness was obtained from both low- and high-pressure (2537 and 3650Å) mercury vapor lamps. The per cent red output from the high-pressure mercury vapor lamps was measured using a Corning red filter #2418 (CS2-62).

Experimental Results

Response of YVO_4:Dy.—Besides being an excellent host for RE activators, YVO_4 is a self-activated phosphor. Its broad band emission spectrum with maximum at about 440 nm has been previously reported (2). Low levels of Dy, as well as other RE's, quench the matrix band and emit their own characteristic lines. We found that the Dy concentration for optimum luminescence ranged between 0.2-0.4 m/o (mole per cent) as shown in Fig. 1. There is a considerable decrease in the emission intensity with Dy content above 1 m/o.

The main Dy transitions are the $^4F_{9/2} \rightarrow {}^6H_{15/2}$ (475 nm) and the $^4F_{9/2} \rightarrow {}^6H_{13/2}$ (575 nm). Other weak transitions are reported at longer wave lengths (3). An unresolved but typical Dy emission spectrum is shown in Fig. 4.

Effect of Eu on YVO_4:Dy.—While maintaining the Dy at 0.3 m/o, Eu was added at various concentrations. No detrimental effect is observed in the Dy intensities until Eu content supersedes the Dy content. The ratio of Eu (619 nm) lines to Dy (575 nm) increases linearly up to about 1500 ppm Eu. Figure 2 shows that a ratio of Eu/Dy emission of 1 is obtained when Eu is approximately 3000 ppm. Amounts of Eu around this concentration improve the color rendition

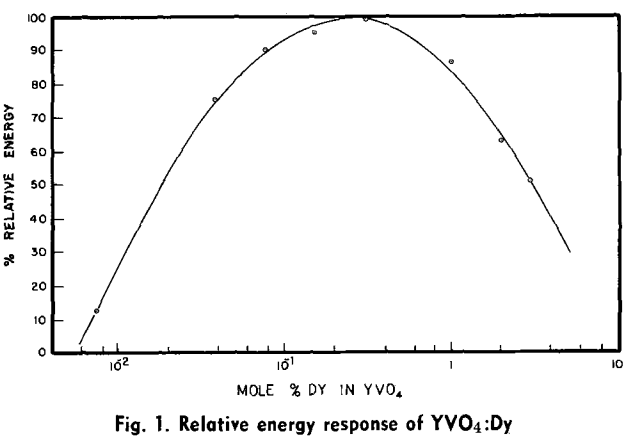

Fig. 1. Relative energy response of YVO_4:Dy

* Electrochemical Society Active Member.

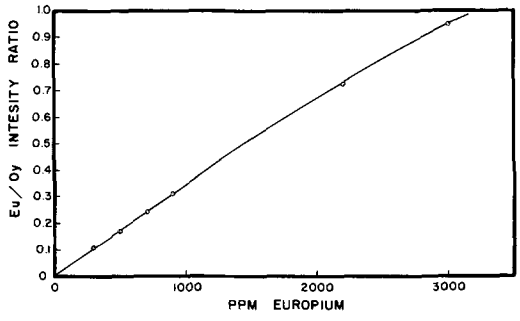

Fig. 2. Ratio of Eu (619 nm) emission to Dy (574 nm) emission

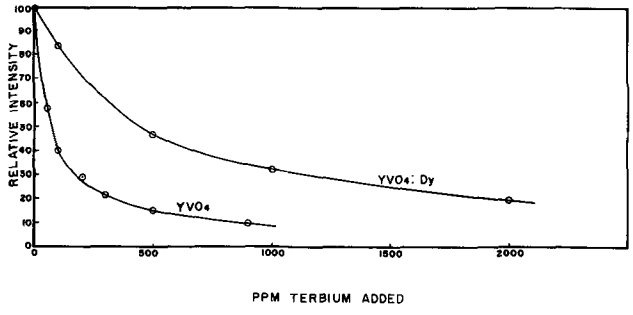

Fig. 3. Effect of Tb on YVO_4 and YVO_4:Dy emission

of the phosphor in high-pressure mercury vapor lamps.

Response of YVO_4:Dy *to* Tb.—Unlike Eu, Tb strongly quenches the Dy emission. At 100 ppm Tb, the YVO_4:Dy emission intensity is reduced to 85% and, at 500 ppm Tb, less than 50% of the original intensity remains as shown in Fig. 3. The strong quenching effect of Tb was even more pronounced in pure YVO_4, 100 ppm Tb reducing the broad band emission intensity of YVO_4 to about 40%.

Fluorescent lamp results.—Figure 4 compares the two broad emission bands of $Ca_5F(PO_4)_3$:Sb (0.06), Mn (0.07), the well-known cool white fluorescent lamp phosphor, with that of the emission of YVO_4:Dy (0.3 m/o). Table I shows the low-pressure mercury vapor lamp data for YVO_4:Dy at various Dy concentrations. An initial brightness of about 76 lpw was obtained with what we consider an optimum Dy concentration; however, there is considerable drop in light output after 100 hr of lamp operation.

YVO_4:Dy was also evaluated in high-pressure mercury vapor (HPMV) lamps. The lumens per watt

Table I. Lumens per watt of YVO_4:Dy in low-pressure lamps

m/o Dy	0 Hr	100 Hr
0.10	62.4	51.3
0.28	75.0	67.2
0.30	75.8	63.5
2.8	30.0	29.0

Table II. Lumens per watt of YVO_4:Dy *vs.* YVO_4:Eu in HPMV lamps

	175w			400w		
	0 Hr	100 Hr	% Red (100 Hr)	0 Hr	100 Hr	% Red (100 Hr)
YVO_4:Dy (0.3 m/o)	57.5	53.3	1.31	63.0	58.1	2.53
YVO_4:Eu (5.0 m/o)	54.0	51.4	14.50	60.8	55.8	15.6

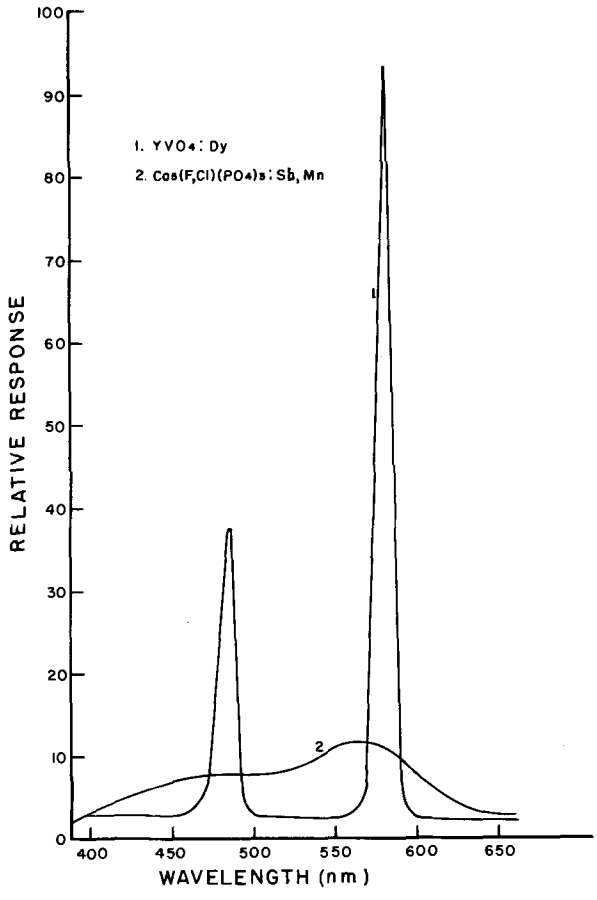

Fig. 4. Comparison of YVO_4:Dy emission with $Ca_5F(PO_4)_3$:Sb, Mn

were compared to that of YVO_4:Eu as shown in Table II. Because of the lack of red emission, this phosphor is not used directly in HPMV lamps. With the addition of Eu, the red rendition of the phosphor is improved. When appreciable amounts of Eu (1 m/o) are added, the red emission intensity increases considerably.

Summary

We have described the effects of Eu and Tb on the luminescence characteristics of YVO_4:Dy. While Eu in moderate amounts (Eu = Dy) does not quench the Dy emission, Tb in very small amounts (Tb << Dy) rapidly quenches the Dy emission.

Lamp data were presented showing that YVO_4:Dy may be used in both low- and high-pressure mercury vapor lamps with interesting results.

Manuscript submitted July 19, 1968; revised manuscript received Sept. 11, 1968. This manuscript was presented at the Boston Meeting, May 5-9, 1968, as Paper 37.

Any discussion of this paper will appear in a Discussion Section to be published in the December 1969 JOURNAL.

REFERENCES

1. L. H. Brixner and E. Abramson, *This Journal*, **112**, 70 (1965).
2. F. C. Palilla, A. K. Levine, and M. Rinkevics, *ibid.*, **112**, 776 (1965).
3. G. H. Dieke and H. M. Crosswhite, *Appl. Opt.*, **2**, 675 (1963).

A New Radio-Frequency Inductive Plasma Sputtering Process for Surface Coating

P. Beucherie, M. Block, and J. G. Wurm*

EURATOM, Ispra Establishment of the C.C.R., Chemistry Department, High Temperature Chemistry Section, Ispra, Italy

High-quality thin film coatings are increasingly required in various fields such as the chemical space, nuclear, and electronic industries. The basic cathode sputtering process and the high vacuum evaporation method have both been used extensively for most coating purposes (1). For high-quality coatings, cathode sputtering was preferred, but this method is handicapped by its very low sputtering speed. So, in the last few years, the tendency was to increase the sputtering efficiency with the addition of different auxiliary devices.

In the literature are described several low-energy sputtering devices with two or three auxiliary electrodes and thermionic cathodes (2-4). Furthermore, the addition of a strong magnetic field increased the ion concentration and therefore the sputtering yield. The development of the R-F sputtering, as reviewed by Davidse (5), paved the way to the deposition of thin insulator films. The deposition of Ta metal and Ta_2O_5 by superimposed R-F and d-c sputtering was described by Vratny (6). The increase in sputtering efficiency, obtained from all these improvements, was penalized by more complicated and costly sputtering equipment. It was the purpose of our investigation to find a more compact and simplified device with an acceptable sputtering efficiency for industrial coating applications. It was also thought that the device should be suitable for coating tubes inside. Therefore, the basic cathode concept has been discarded, and the ionized plasma was confined inside an inductive R-F coil made of the material itself to be sputtered. The ions which are created under the impulses of the R-F electromagnetic field bombard the material of the coil and sputter its surface atoms into the surrounding space. Also, a substrate interposed on the trajectories of the sputtered "microparticles" will be coated with a very uniform and dense layer.

Description of the Process

The general schema of the equipment is illustrated by Fig. 1 and 2. The inductor coil, 7, made of the material to be sputtered is placed inside a vacuum enclosure consisting of a metallic base, 4, and a glass bell, 10. Through the base, 4, are inserted: the insulated R-F connections, 6, for the inductor coil and the argon admission line made of a capillary tube, 8, directed toward the axis of the inductor coil. The amount of gas to be admitted is regulated by a precision needle valve, 9. The samples, 5, to be coated are fixed around the inductor coil; however, the preferential position will be in the axis of this latter. The R-F current is supplied to the inductor coil by a R-F generator, 1, S.T.E.L. with an adjustable frequency from 5 to 12 MHz. Between the generator, 1, and the inductor, 7, is switched in a R-F transformer, 3, with a variable capacity, 2. The pumping group consists of a diffusion pump, 12, Leybojet 3000 liters/sec followed by a Roots pump, 14, of 250 m^3/hr and a preliminary pump, 15, of 60 m^3/hr.

Operating Method

The samples to be coated are carefully cleaned in an organic solvent bath; also, an electrolytic attack might be useful in some cases. Then the samples are fixed in their sputtering position. According to their geometrical configuration, a rotation of the samples would be necessary, particularly for the outside coating of tubes. A vacuum of 10^{-5} to 10^{-6} Torr is maintained for some time, until the residual and adsorbed gases are eliminated. Through the needle valve, an argon leak stream about 0.2 Torr liters/sec is introduced into the coil axis by the refractory capillary which is about 5 cm long with a 0.4-mm hole. As soon as the R-F current is switched on, a blue-colored plasma is formed inside the inductor coil (Fig. 3), and the argon line pressure, measured between the needle valve and the capillary, increases from 50 to about 250 Torr. Due to the bombardment by the gas ions, the inductor reaches a temperature of about 600°-1000°C according to the nature of the metal, the geometry of the coil, and the injected R-F power. Example: for a niobium inductor composed of seven turns (wire diameter 3 mm) with a coil diameter of 25 mm, the total consumed power is about 3 kva and the coil temperature around 900°C. The temperature of the sample to be coated depends mainly on its distance from the inductor. A metal sheet fixed at a 10-15 cm distance from

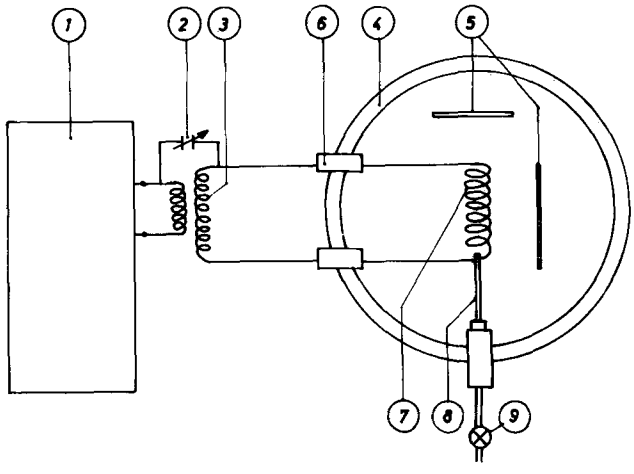

Fig. 1. Schematic diagram of the HF inductive sputtering apparatus: 1—HF generator, 2—variable capacity, 3—HF transformer, 4—vacuum enclosure, 5—sample, 6—HF connections, 7—inductor coil, 8—capillary gas inlet, 9—needle valve.

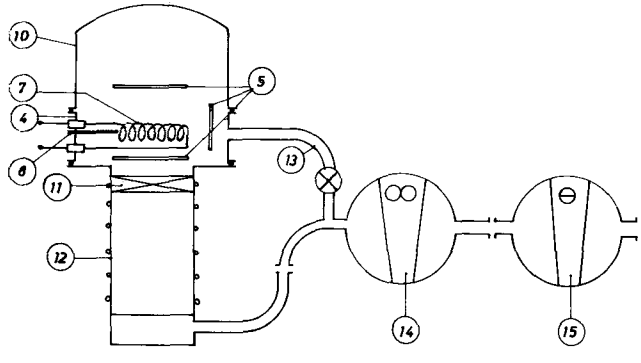

Fig. 2. General view of the bell jar and assembly of the pumping system: 4—vacuum enclosure, 5—sample, 7—inductor coil, 8—capillary gas inlet, 10—bell jar, 11—valve baffle, 12—diffusion pump, 13—bypass, 14—Roots pump, 15—preliminary pump.

* Electrochemical Society Active Member.

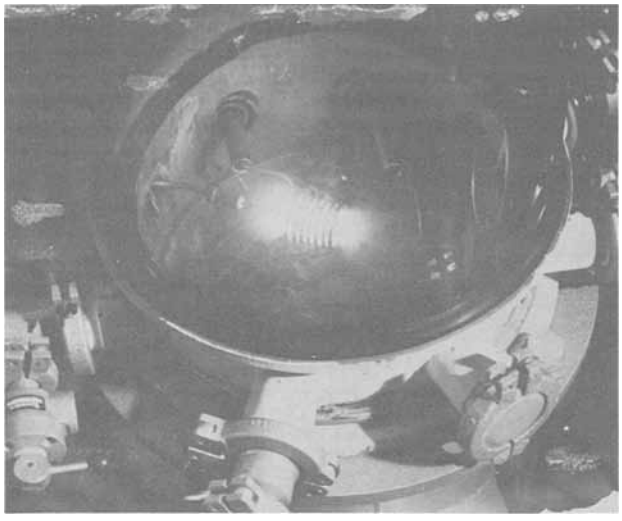

Fig. 3. View of the plasma inside inductor coil

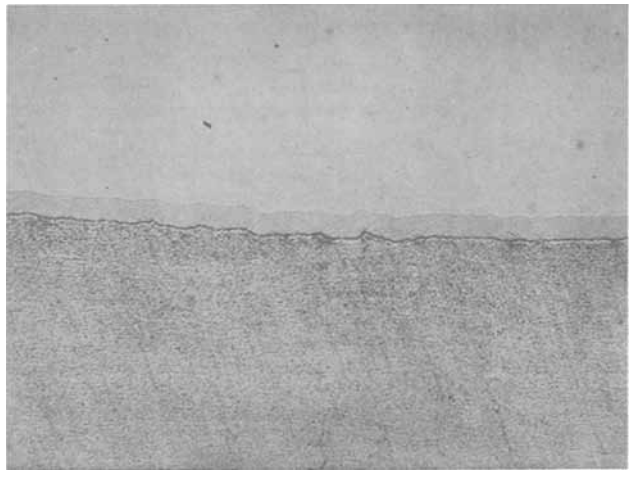

Fig. 4. Photomicrograph of stainless steel sample coated with 15μ of niobium.

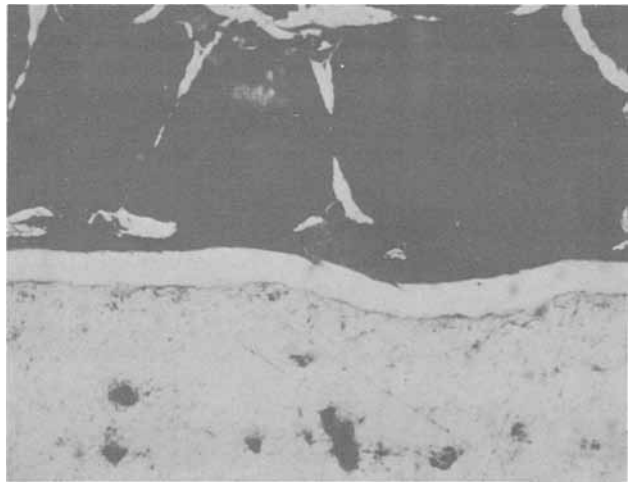

Fig. 5. Photomicrograph of niobium sample coated with 14μ of molybdenum.

the coil can reach a temperature of 60°-100°C. For special coating purposes, a cooling or a heating device for the sample has been set up. The capacity of the pumping group must be calculated in order to maintain inside the enclosure a dynamic vacuum of about 10^{-3} to 10^{-4} Torr despite the permanent argon stream flow through the capillary. As a matter of fact, the pressure inside the vacuum enclosure is less than uniform. In the center of the inductor coil where the plasma takes place, a maximum concentration of the gaseous ions is reached, and the pressure may be estimated to about 10^{-1} to 10^{-2} Torr. Outside the inductor coil a pressure gradient will be established going from 10^{-1} Torr to about 10^{-3} to 10^{-4} Torr at the place where the sample to be coated is fixed. The sputtering rate, which can be defined as the ratio of the sputtered atoms to the number of incident ions, depends on the nature of the metal and the energy of the gaseous ions bombarding it. The coating speed depends on that sputtering rate and, moreover, on the geometry of the system. Coating thicknesses from 0.1 to 0.5 μ/min can easily be obtained. In some special cases, as for instance the inside coating of tubes, a much higher deposition speed can be reached.

Furthermore, the coating speed may be increased by connecting several inductors together, either in series or in parallel. For all refractory metals having a high melting point, the inductor coil is usually composed of a wire. For metals with a melting point lower than 1100°C, it is more advisable to use a water-or air-cooled tube. With inductors made of cooled tubes, it is possible to inject more power and therefore also to increase the sputtering rate. For the sputtering of metals a neutral gas (essentially argon) is preferred, but it is also possible to make use of the reactive gases such as nitrogen or oxygen. In this case, called "reactive sputtering," the sample will be coated with the corresponding nitride or oxide.

Because of the high energy concentration in a restricted volume, delimited by the inductor coil, the microparticles ejected from the latter hit the sample with an appreciable kinetic energy. Consequently, the deposited films are strongly adherent, very dense, and regular in thickness. As there are only two R-F connections to the inductor coil, the effective space in the enclosure is very large and the metallization of samples with various shapes is easy.

Also, this method, well suited for metallizing tubes inside, is of particular interest to the chemical, nuclear, and electronic industries. We have deposited films of various thicknesses up to 20μ of metals such as Nb, W, Ta, Zr, Ti, Fe, Co, Ni, Cu, Al, Pt, Ir, Au, and also alloys of Ni-Cr and stainless steel on all kinds of substrates such as other metals, alloys, ceramics, glass, graphite, plastics, and even paper. As an example: a niobium layer of 8-10μ has been deposited inside of a Zircaloy tube of 50 mm diameter. The film adherence was not altered after a thermal cycling of 250 hr at 500°C (*see* Fig. 4 and 5).

For industrial coating purposes, this new coating process can be compared favorably with cathode sputtering and vacuum evaporation; it is essentially characterized by its great sputtering rate, the excellent quality of the deposits which are obtained, and its extreme operating simplicity.

Manuscript submitted April 11, 1968; revised manuscript received Aug. 8, 1968.

Any discussion of this paper will appear in a Discussion Section to be published in the December 1969 JOURNAL.

REFERENCES

1. L. Holland, "Vacuum Deposition of Thin Films," Chapman and Hall Ltd. (1960).
2. Earl H. Blevis, Private communication, R. D. Mathis Co., 1345 Gaylord St., Long Beach Calif. 90813, Feb. 1965.
3. W. H. Huss, S.C.P. and Solid State Tech., Dec. 1966, p. 50.
4. J. W. Nickerson and R. Moreson, *La Vide,* No. 120, **20,** 437 (1965).
5. P. D. Davidse, S.C.P. and Solid State Tech., Dec. 1966, p. 30.
6. F. Vratny, *This Journal,* **114,** 505 (1967).

The Corrosion of Zinc in KOH Solutions

T. P. Dirkse* and R. Timmer

Calvin College, Grand Rapids, Michigan

ABSTRACT

The corrosion rate of zinc in KOH solutions has been measured under a variety of conditions. Amalgamation and the presence of zincate ions lower this rate of corrosion. The effect of increasing KOH concentration on the rate of corrosion is different for nonamalgamated zinc than for amalgamated zinc. The temperature effect is also different for the two types of zinc electrodes.

One of the problems associated with the use of zinc electrodes in alkaline solutions is the reaction of zinc with the electrolyte to produce hydrogen. This reaction has two disadvantages. It uses up the zinc, *i.e.*, it is a self-discharge reaction. Also, the evolution and buildup of hydrogen are undesirable if an alkaline cell containing zinc electrodes is to operate in the sealed condition.

The reaction can be described as a corrosion reaction. Over the years there has been considerable interest in the corrosion of zinc but hardly any work has been published on the corrosion of zinc in alkaline solution.

Snyder and Lander (1) studied the evolution of hydrogen from commercial zinc electrodes containing 2% polyvinylalcohol and encased in a cellulosic separator material. They found that the amount of hydrogen evolved in a given time decreased as the electrolyte changed from 30 to 45% KOH. It decreased with increasing HgO content up to 4%, and it also decreased with decreasing temperature. Furthermore, the presence of zincate in the electrolyte increased the amount of hydrogen evolved.

Ruetschi (2) also studied the corrosion rate of amalgamated zinc in alkaline solutions. His experimental arrangement avoided the use of separators and additives. He used a specified weight of powdered material, but no surface area values were given. Consequently, the rate of corrosion per unit surface cannot be determined from his data. The corrosion of amalgamated zinc was found to increase with increasing temperature. It increased with increasing KOH concentrations, contrary to the results of Snyder and Lander (1). Furthermore, the presence of zincate ions decreased the rate of corrosion except in KOH solutions less than 2*N*. Here the zincate ion appeared to have a catalytic effect.

The main discrepancies between the work of Rüetschi and that of Snyder and Lander are (*i*) the effect of zincate ion and (*ii*) the effect of increasing KOH concentration on the corrosion rate of amalgamated zinc. Some of this difference may be due to the way in which the data were obtained. Snyder and Lander used as the corrosion rate the steady state achieved after about 30 days. Rüetschi started taking measurements less than 24 hr after the zinc and KOH were brought in contact with each other. Thus, in the work of Snyder and Lander, the electrolyte composition at the time measurements were taken was likely somewhat different from that at the time the corrosion began. Furthermore, in the work of Snyder and Lander the corrosion rate was likely also affected by the polyvinyl alcohol and the separator material.

The present work on the corrosion of zinc in alkaline solutions was undertaken for two reasons: (*i*) because so little work has been reported on this matter; and (*ii*) to establish basic information on the effect of KOH concentration, amalgamation, zincate ion, and temperature on this process. These values are needed so that one can determine, with such information as a background, the effect of additives and impurities on the corrosion rate of zinc in a battery system.

Experimental

The apparatus consisted of a sealed glass tube about 2.5 x 20 cm to which a calibrated pipette was attached, Fig. 1. The entire assembly, except for the outlet of the pipette, was immersed in a liquid constant temperature bath. Two pieces of zinc (99.999%) wire, 12.7 x 0.15 cm, were placed in the electrolyte. Thus the surface area exposed to the electrolyte was 12 cm^2.

As hydrogen was evolved, electrolyte was forced into the pipette. Consequently, the rise in the electrolyte level in the pipette was a measure of the rate at which hydrogen was evolved. In each run a blank (containing no zinc wire) was included to correct for minor fluctuations due to changes in barometric pressure. Corrections were also made for vapor pressure, etc., and the results were then expressed as micromoles of hydrogen evolved per square centimeter of electrode area. Measurements were begun within an hour after the apparatus was assembled.

Amalgamation was done by dipping the zinc wire in a $HgCl_2$ solution (50 g/liter) for 30 sec. No work was done to determine the effect of varying degrees of amalgamation.

Results

A typical set of data is shown on Fig. 2. The slope of these lines served as a measure of the rate of corrosion, *i.e.*, rate of hydrogen evolution. This rate was

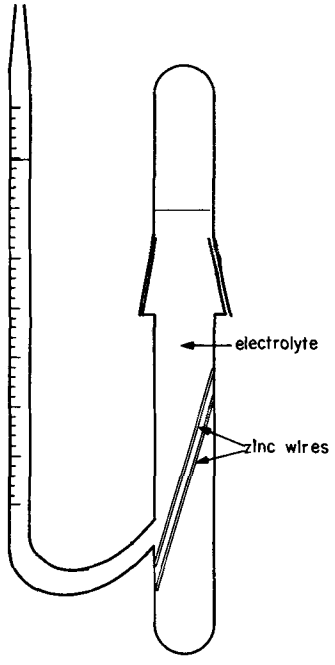

Fig. 1. Experimental arrangement

* Electrochemical Society Active Member.

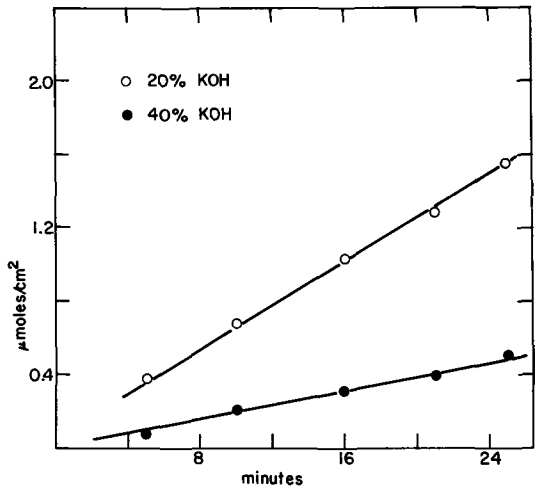

Fig. 2. Rate of hydrogen evolution from nonamalgamated zinc at 25°C.

measured in 20, 30, 35, 40, and 45% KOH and in these same solutions saturated with zinc oxide. Both amalgamated and nonamalgamated zinc electrodes were used and every run was made at two temperatures, 25° and 44°C.

The variation of the rate of corrosion with these differing conditions can be seen on Fig. 3-8. Figure 3 shows the effect of temperature in plain KOH solutions while Fig. 4 shows the effect for solutions saturated with ZnO. On this and other figures, lines are drawn through most of the data points. However, on such lines minor fluctuations are not necessarily significant. Some duplicate runs were made and, especially at the lower rates, the uncertainty may approach ±20%.

In the plain KOH solutions, Fig. 3, temperature seems to have little effect, but, surprisingly, the small difference that there is indicates a lower corrosion rate at the higher temperature. In the zincate solutions, the temperature effect also is small, but here the higher corrosion rate generally occurs at the higher temperature. In any event, the difference in corrosion rates at 25° and 44°C is small.

Figure 3 also illustrates the effect of KOH concentration. Increasing KOH concentrations bring about a reduced corrosion rate as was found by Snyder and Lander (1). When the solutions are saturated with zincate, this regularity does not exist, but rather the

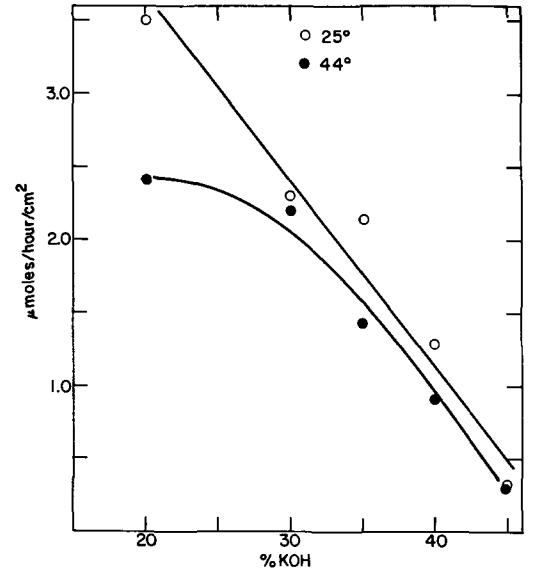

Fig. 3. Rate of hydrogen evolution from nonamalgamated zinc as a function of KOH concentration and temperature.

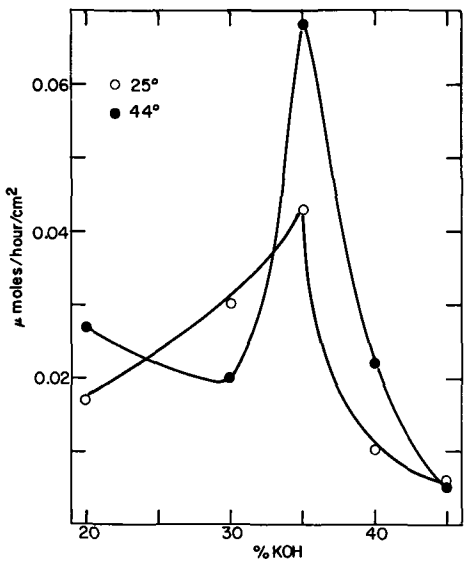

Fig. 4. Effect of dissolved ZnO on the rate of hydrogen evolution from nonamalgamated zinc. All solutions are saturated with ZnO.

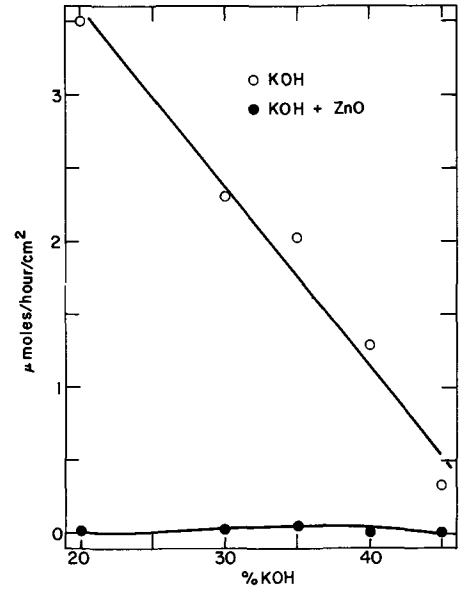

Fig. 5. Rate of hydrogen evolution from nonamalgamated zinc at 25°C.

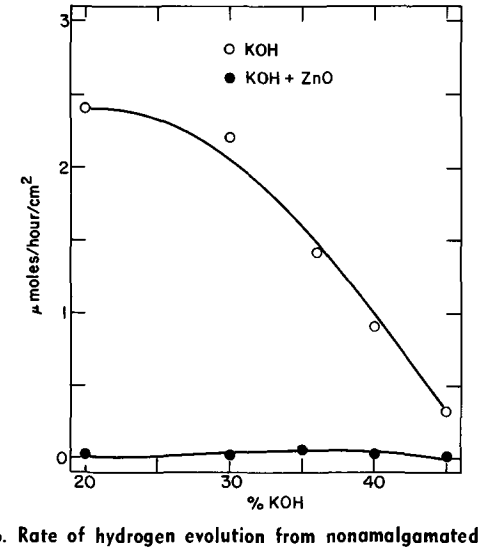

Fig. 6. Rate of hydrogen evolution from nonamalgamated zinc at 44°C.

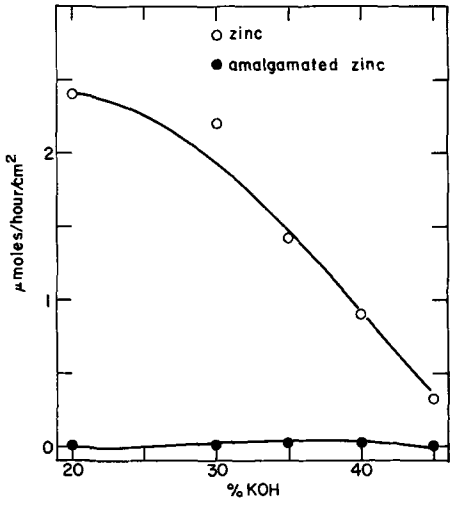

Fig. 7. Rate of hydrogen evolution at 44°C

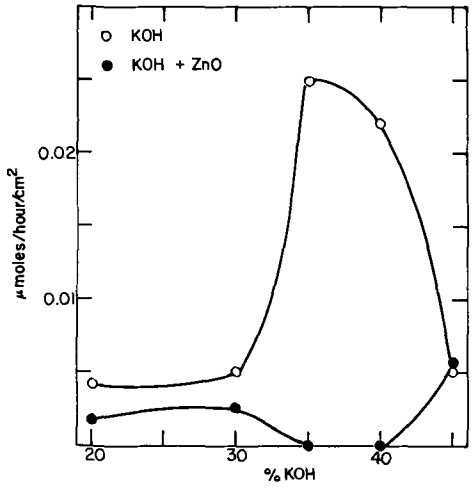

Fig. 8. Rate of hydrogen evolution from amalgamated zinc at 44°C.

corrosion rate increases up to about 35% KOH and then decreases, Fig. 4. Note that the ordinate scale on Fig. 4 is considerably smaller than that on Fig. 3.

The effect of zincate ion can be seen by comparing Fig. 3 and 4, but it is shown more directly on Fig. 5. The solutions designated as KOH + ZnO were all saturated with ZnO so that the zincate concentration increases markedly in going from 20 to 45% KOH. Figure 6 shows the effect of zincate ion at 44°C.

Amalgamation of the zinc electrode also brings about a marked reduction in the corrosion rate, Fig. 7. The amount of amalgamation was not varied so that the effect of increasing quantities of mercury on the corrosion rate cannot be determined from our data.

It is interesting to note that saturating a KOH solution with ZnO has about the same effect in reducing the rate of corrosion as does amalgamation, compare, *e.g.*, Fig. 6 and 7. When both factors are present there is a slight decrease over either one alone, Fig. 8. The effect of temperature and KOH concentration on the corrosion of amalgamated zinc is shown on Fig. 9.

Discussion

No other reported work was found for the corrosion rate of nonamalgamated zinc in KOH solutions except for a few data reported by Snyder and Lander (1). They found, as we have, that the corrosion rate decreased with increasing KOH concentration. Results such as those shown on Fig. 2 and 3 are the basic data against which other factors or conditions can be compared.

A possible mechanism involves the following processes:

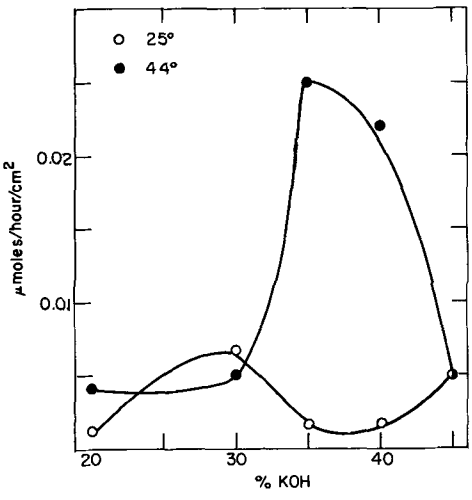

Fig. 9. Rate of hydrogen evolution from amalgamated zinc in KOH solutions.

$$2H_2O + 2e \rightarrow H_2 + 2\,OH^- \qquad E^\circ = -0.828v \quad [1]$$

$$Zn + 2\,OH^- \rightarrow Zn(OH)_2 + 2e \qquad E^\circ = 1.245v \quad [2]$$

$$Zn + 2\,OH^- \rightarrow ZnO + H_2O + 2e \qquad E^\circ = 1.248v \quad [3]$$

Reactions [2] and [3] may each involve several steps as in the anodic treatment of zinc.

Combining [1] and [2], the over-all reaction is

$$Zn + 2H_2O \rightarrow H_2 + Zn(OH)_2 \qquad E^\circ = 0.417v \quad [4]$$

Combining [1] and [3] gives

$$Zn + H_2O \rightarrow ZnO + H_2 \qquad E^\circ = 0.420v \quad [5]$$

For both over-all reactions the driving force, energetically, is favorable and practically the same. The reason the reaction is as slow as it is arises from the overvoltage for the hydrogen evolution, reaction [1]. The initial rate of reaction [4] is

$$\text{rate} = K_4\,(a_{H_2O})^2 \quad [6]$$

while that for reaction [5] is

$$\text{rate} = k_5 \cdot a_{H_2O} \quad [7]$$

A plot of log rate *vs.* log a_{H_2O} should then give a slope of 2 for reaction [4] and a slope of 1 for reaction [5] if these reactions are rate controlling. Making such a plot of the data in ref. (3) gives a slope of 1.6. A similar plot of our data for plain zinc in KOH solutions at 25° gives a slope somewhat larger than 1.5, Fig. 10. This may mean that both reactions [4] and [5] take place. These reactions do agree with the effect of KOH concentration on the rate of corrosion. As KOH concentration increases, the activity of the water decreases, resulting in a lower rate for reaction [1]. This then may be the controlling process.

Amalgamation reduces the corrosion rate of zinc. Our results for amalgamated zinc do agree with other reported work so far as comparisons can be made. The behavior of amalgamated zinc is definitely different from that of nonamalgamated zinc. The corrosion of amalgamated zinc appears to reach a maximum in 30-35% KOH while the rate for nonamalgamated zinc decreases with increasing KOH concentration. Further, the corrosion rate of nonamalgamated zinc decreases in going from 25° to 44° while that of amalgamated zinc increases.

Amalgamating the electrode raises the hydrogen overvoltage considerably and slows down reaction [1] which again limits the over-all corrosion reaction. The value of this overvoltage varies with temperature and KOH concentration (4), and this may partly affect the change of corrosion rate with these conditions. The overvoltage has a minimum value at about 9M KOH.

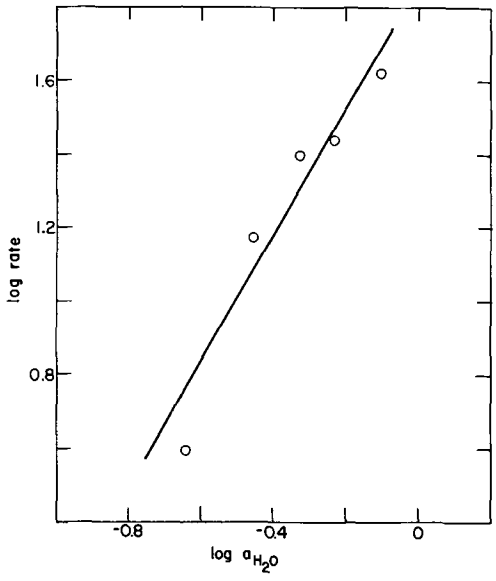

Fig. 10. Log rate vs. log a_{H_2O} plot for hydrogen evolution from zinc in KOH solutions at 25°C.

The corrosion rate appears to have a maximum value at this concentration, Fig. 9.

The presence of zincate ions also reduces the rate of hydrogen evolution. This was observed by Rüetschi (2) but not by Snyder and Lander (1).

When ZnO is dissolved in KOH solutions, reaction [8], the activity of the water is lowered

$$ZnO + H_2O + 2\,OH^- \rightarrow Zn(OH)_4^= \qquad [8]$$

and this should decrease the rate of reaction [1]. However, the rate decrease that was observed, *e.g.*, in 20% KOH, was far greater than could be accounted for by this process alone. Consequently, some other or additional influence of zincate ion must be present.

A more likely explanation is that suggested by Rüetschi (2), *i.e.*, the corrosion rate also depends on the rate of dissolution of interfacial ZnO or $Zn(OH)_2$. In KOH solutions saturated with ZnO, the oxide or hydroxide produced by the corrosion reaction cannot readily dissolve in the electrolyte. Consequently, it remains on the surface of the zinc and protects the zinc underneath from further reaction. The extent to which the zinc is protected depends on the porosity of the corrosion product. This same phenomenon could account for the lack of complete reproducibility in our results. Our solutions were not shaken during the course of a given determination. For the corrosion product to continue to dissolve, it was then necessary for that which had dissolved to be transported away from the zinc surface either by diffusion or convection. Our results then were modified somewhat by the randomness of this material transport.

In conclusion, reactions [1] to [3] serve as a satisfactory mechanism for the initial corrosion of zinc in KOH solutions. With pure zinc the process is controlled by reaction [1]. With amalgamated zinc, reaction [1] is the limiting process because of the higher hydrogen overvoltage. When zincate ion is present other processes, such as dissolution of the corrosion product, may become rate controlling.

Still unaccounted for is the fact that the corrosion rate for nonamalgamated zinc is slightly lower at 44° than at 25°C. This cannot be attributed to decreasing activity of water or to increasing hydrogen overvoltage as the temperature is raised. Further, one would expect the rate of dissolution of ZnO or $Zn(OH)_2$ to be greater at the higher temperature. This leaves as a possible explanation the suggestion that the corrosion product at 44° is more dense than at 25°C. This more dense product affords a more complete covering of the zinc at the higher temperature and lowers the corrosion rate. It has been pointed out (5) that below 35°-40°C a $Zn(OH)_2$ is a stable form while above this temperature ZnO is the stable phase. Gilbert (6) found that the corrosion of zinc is distilled water at 85° produced only ZnO, while at room temperature the product was ZnO + various types of $Zn(OH)_2$. Furthermore, $Zn(OH)_2$ is more soluble than ZnO. Thus it is a possibility that the corrosion of nonamalgamated zinc in alkaline solutions at 25° produces a less dense, and more soluble, product than that which is produced at 44°. Consequently, a more protective covering is formed at the higher temperature giving rise to a lower rate of corrosion.

Acknowledgment

This work was carried out under a Contract with the United States Air Force Aero Propulsion Laboratories.

Manuscript submitted July 12, 1968; revised manuscript received Nov. 4, 1968.

Any discussion of this paper will appear in a Discussion Section to be published in the December 1969 JOURNAL.

REFERENCES

1. R. N. Snyder and J. J. Lander, *Electrochem. Technol.*, **3**, 161 (1965).
2. P. Rüetschi, *This Journal*, **114**, 301 (1967).
3. Chih-Ping Chang, Cheng-Chung Li, and Shian-Te Shieh, *Hua Hsueh Hsueh Pao*, **29**, 236 (1963).
4. Z. A. Iofa, L. Vikomlev, and V. S. Bagotskii, *Zhur. Fiz. Khim.*, **35**, 1571 (1961).
5. G. F. Hüttig and H. Möldner, *Z. anorg. u. allgem. chem.*, **211**, 368 (1933).
6. P. T. Gilbert, *This Journal*, **99**, 16 (1952).

Controlled Current Deposition of Zinc from Alkaline Solution

S. Arouete,*[1] K. F. Blurton,*[2] and H. G. Oswin*[2]

Leesona Moos Laboratories, Great Neck, New York

ABSTRACT

Electrodeposition of zinc onto foil electrodes from alkaline zincate solutions with direct current results in dendritic or black, porous mossy deposits. Smoother deposits are obtained with a pulsed current source or periodic reversal of current. The nature of the deposit with pulsed charging depends on the current density, the amount of charge passing through the electrolytic cell, the on time, and off time. The optimum values of these parameters are dependent on the cell geometry and the differences between the apparatus used in the present study and a cell containing a secondary zinc electrode are discussed.

Secondary silver/zinc batteries are severely limited in applications where a high energy/weight ratio is desirable because of their limited cycle life at high depths of discharge. In contrast to the insoluble oxidation product formed at other negative electrodes, the oxidation product of the zinc electrode is highly soluble in strong alkali, forming $Zn(OH)_4^{2-}$ as the principal product. This species has the ability to form highly stable supersaturated alkaline solutions (1). In a silver/zinc battery, the concentration of zincate after discharge is estimated at one molar, and where there is restricted diffusion the electrolyte may supersaturate to two or three times this concentration (1). During the subsequent charging cycle, the zincate discharges at the zinc electrode in a nonadherent dendritic or mossy form. This results in a loss of capacity of the secondary zinc electrode.

From the viewpoint of battery technology the three most important morphologies associated with zinc deposition from alkaline solution on foil electrodes are smooth, mossy, and dendritic deposits (2, 3). Smooth deposits are formed at low overpotential with vigorous stirring of the electrolyte. The other two deposits are noncompact. The mossy deposit is black and porous and is formed at low overpotentials, while the dendritic deposits are formed at high overpotentials. The transition from moss to dendrites corresponds to the onset of mass transport control and is characterized by a critical current density which is temperature dependent (2). Thus the overpotential is controlling only to the extent that it determines whether the deposition is mass-transport controlled. Since mass transport plays such an important role in producing dendrites it appeared profitable to follow a previous suggestion and work with interrupted current sources (2), where the concentration gradient is allowed to collapse and reform during metal deposition.

Much of the work to date on improving the capacity of Ag/Zn batteries has been aimed at improving the electrode separators. This has given some success (4) but the cycle life and depth of discharge are still limited by nonadherency of the zinc deposit and dendrite formation. In order to lengthen the cycle life of the Zn electrode, it is necessary to form on the surface an even, adherent, porous deposit during charge. The sole object of the present study has been to investigate the parameters which control the deposit adherency and dendrite formation when charging a zinc electrode with an interrupted current source. Constant current deposition was chosen first because growth of zinc dendrites is controlled by the rate of transport of zincate ions to the electrode surface and second because controlled current charging is a preferred mode of battery charging.

Experimental Procedure

The electrolyte composition was aqueous 43% KOH solution made 1.13M in Zn(II). Reagent grade chemicals were used without further purification. A 130 ml rectangular cell was used which permitted the working electrode to be mounted vertically and parallel to the counter electrode. Sheet zinc was used as the working electrode. Its area was usually 22 cm^2 but this could be varied by coating with epoxy adhesive. In most of the experiments the counter electrode was either gold or platinum foil, but there was no difference in the results when the counter electrode was nickel foil. The temperature was regulated at 30°C in all of the experiments.

A constant current source was developed which provided direct current or pulses of varying on and off times. Current regulation was $\pm 0.25\%$ over the range of 10^{-3} to 1.2 amp, and the pulse rise and fall time was approximately 4 μsec. The quoted values of the current density are those for the on time and are based on the geometric area of the electrode. For the investigation of the periodic reversal of current a constant current source was connected to a time switch.

The deposits were characterized by viewing under a 50X magnification microscope, by preparing cross-sectional photomicrographs of 1000X magnification of the center of the electrode and by measurement of deposit adherency. The adherency of the deposit was determined by essentially the same procedure as Romanov (5). After deposition the electrode was removed from the solution, washed, dried, and weighed. The visible moss was then readily removed by brushing with a tissue. An adherent, compact deposit always remained which could not be removed by the most vigorous brushing. The technique was not precise but it did give an estimate of the amount of nonadherent deposit.

Results

Since the deposit morphology is different above a critical current density from that below it, experiments have been performed at constant current in the two regions. In the present work the value of the critical current density was 21 ma/cm^2.

Charging with a pulsed current source at currents less than the critical current density.—In this series of experiments the deposit was initially compact and adherent, but after a certain time moss usually appeared. Regardless of the extra charge passed thereafter the maximum weight of zinc deposited adherently after the appearance of moss corresponded to only about 6 coulombs/cm^2. This additional weight of zinc cor-

* Electrochemical Society Active Member.
[1] Present address: Yardney Electric Corporation, New York, New York.
[2] Present address: Energetics Science Inc., 4461 Bronx Blvd., New York, New York.

Table I. Adherency of zinc deposit formed at low current densities. Total charge passed in each experiment 18 coulombs/cm²

Current density, ma/cm²	Charge passed before appearance of mossy deposit, coulombs/cm²	Quantity of adherent deposit, coulombs/cm²	Quantity of nonadherent deposit, coulombs/cm²	Mode of charging
4	2.4	3.6	14.4	Direct current
4	3.1	4.0	14.0	Pulsed current 25 msec on, 25 msec off
4	4	5.3	12.7	Pulsed current 2.5 msec on, 2.5 msec off
10	4	6.1	11.9	Direct current
10	9	14.0	4.0	Pulsed current 2.5 sec on, 2.5 sec off
10	15.0	16.5	1.5	Pulsed current 30 msec on, 30 msec off
10	No moss formed	18.0	0	Pulsed current 30 msec on, 45 msec off
10	No moss formed	18.0	0	Periodic reversal of current 12 sec cathodic 8.4 sec anodic

responds to the period during which both compact and mossy deposits form simultaneously. Hence the quantity of adherent deposit is related to the time of appearance of moss. The longer the appearance of moss is delayed the larger the fraction of adherent deposit. Thus in Table I, if charging was continued beyond 18 coulombs/cm² very little extra zinc would have been deposited adherently in the cases where moss had already appeared.

The deposit adherency obtained by pulse charging at current densities less than the critical current density is dependent on the value of the charging current, the ratio of the on to off time and the numerical values of the on and off times (Table I). As expected, the more adherent deposits were produced with the longer off times. In fact, moss was not formed on the electrode when charging at 10 ma/cm² with the on time 30 msec and the off time 45 msec, respectively, until 38 coulombs/cm² of charge had been passed. Presumably moss formation could be eliminated entirely by pulse charging with short pulse lengths and small values of the on to off time ratio, but under those conditions the deposition or charging time would be lengthy.

It has been observed previously (6) that the potential-time variation gives an indication of the formation of dendrites. Similarly the presence of moss is shown by the potential-time curve in the activation control region (Fig. 1). The shape of this curve varied slightly in different experiments, possibly due to impurities in the electrolyte (7), but once moss is formed there is a small, but significant, decrease in the overpotential during the on time. This decrease in overpotential is presumably due to the decrease in the true current density resulting from the increase in electrode surface area. The equilibrium potential of the mossy deposit was 7-10 mv more cathodic than that of a zinc foil

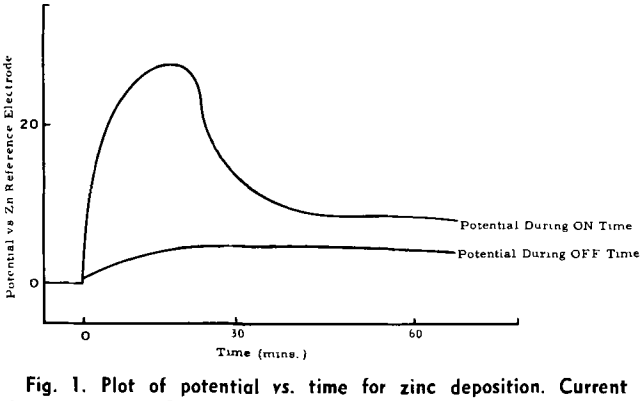

Fig. 1. Plot of potential vs. time for zinc deposition. Current density 10 ma/cm², on time 1 sec, off time 1 sec.

(Fig. 1) in agreement with the work of Bek and Kudryavtsev (8, 9).

Charging with pulsed current source at currents greater than the critical current density.—Preliminary experiments with pulsed current charging at current densities greater than the critical current density indicated that adherent deposits were formed with on and off times of the order of 10 msec, but that dendritic deposits were formed with on and off times of the order of seconds. Subsequent work showed that four factors control the nature of the deposit using a pulsed current source, constant electrolyte composition, and constant temperature. They are current density, the quantity of charge passed, the on time, and the off time. This was confirmed by choosing a set of charging conditions and varying each in turn. For comparison, Fig. 2 shows the deposit obtained with direct current at 40 ma/cm². The current efficiency for deposition in the experiments represented by Fig. 3 to 7 was never less than 85%, whereas the corresponding value in those experiments where dendrites were formed was always very low due to the large amount of hydrogen evolution.

The effect of the pulsed current density is shown in Fig. 3 and 4. The deposit at 40 ma/cm² (Fig. 3) is smoother than that at 80 ma/cm² (Fig. 4). The more even deposits are obtained with the lower current densities, providing these remain above the critical current density. However, due to surface roughening during electrodeposition the true current density may decrease below the critical value causing the formation of nonadherent mossy deposits. The surface roughness increases slightly as the quantity of charge increases (Fig. 5 and 6) and when 200 coulombs/cm² of charge was passed, a small amount of moss formed at the bottom of the electrode. The effect of off time is shown

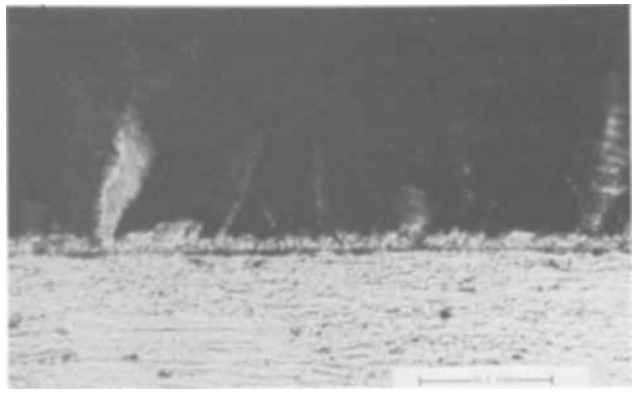

Fig. 2. Photomicrograph of zinc deposit produced by direct current charging. Current density 40 ma/cm², quantity of charge passed 25.8 coulombs/cm².

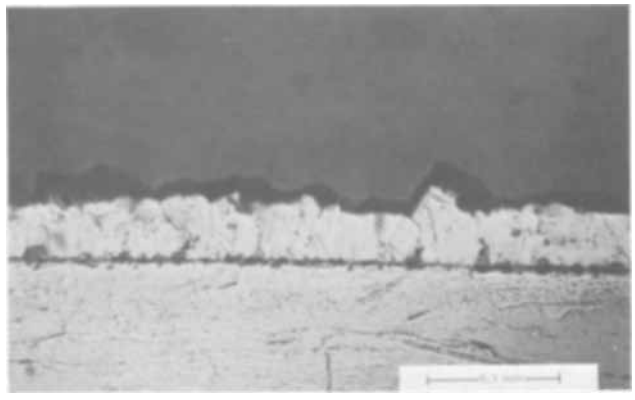

Fig. 3. Photomicrograph of zinc deposit produced by pulsed current charging. Current density 40 ma/cm², time on 10 msec, time off 10 msec, quantity of charge passed 60 coulombs/cm², current efficiency for deposition 85%.

Fig. 4. Photomicrograph of zinc deposit produced by pulsed current charging. Current density 80 ma/cm^2, time on 10 msec, time off 10 msec, quantity of charge passed 60 coulombs/cm^2, current efficiency for deposition 85%.

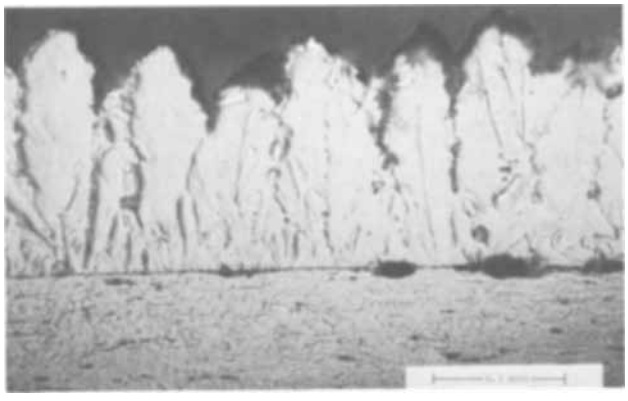

Fig. 5. Photomicrograph of zinc deposit produced by pulsed current charging. Current density 40 ma/cm^2, time on 10 msec, time off 8 msec, quantity of charge passed 200 coulombs/cm^2, current efficiency for deposition 95%.

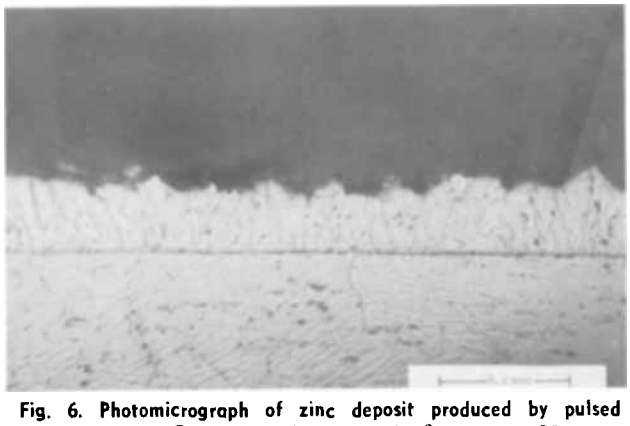

Fig. 6. Photomicrograph of zinc deposit produced by pulsed current charging. Current density 40 ma/cm^2, time on 10 msec, time off 8 msec, quantity of charge passed 60 coulombs/cm^2, current efficiency for deposition 90%.

in Fig. 3, 6, and 7. For a constant on time, the deposit is less dendritic the longer the off time. It is important to note that the ratio of on to off time is not by itself decisive. Thus with a constant current density a more dendritic deposit was obtained with the on and off times both 10 sec than with values of 10 msec. In all cases viewing the deposit cross-sections with polarized light showed that the direction of crystallization of the deposit is independent of the substrate.

At current densities above the critical current density the potential-time curves were similar to those obtained with pulsing under activation control (Fig. 1) but now the overvoltage was approximately 50 mv showing the formation of adherent deposits.

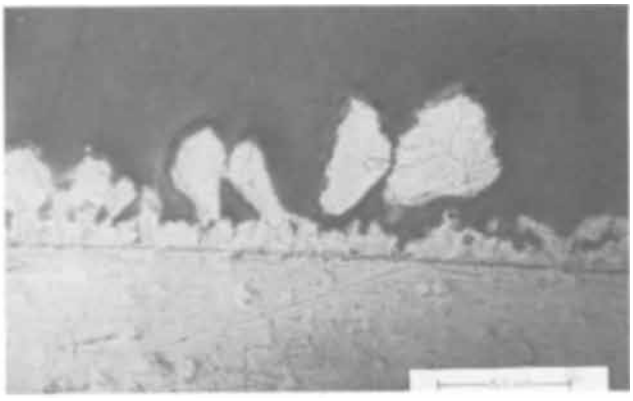

Fig. 7. Photomicrograph of zinc deposit produced by pulsed current charging. Current density 40 ma/cm^2, time on 10 msec, time off 4 msec, quantity of charge passed 60 coulombs/cm^2, current efficiency for deposition 86%.

The dependency of the nature of the deposit on current density, on time, and off time indicates that extremely smooth deposits can be obtained with the current density slightly greater than the critical value for moss deposition, with a short on time (10 msec or less), and an on/off time ratio as small as possible.

Charging with periodic reversal of current.—Deposition with periodic reversal of current was performed with two ratios of the cathodic and anodic period; one of 3.3/2.55 sec, respectively, and the other of 12/8.4 sec, respectively. At a constant current density the deposit was similar with the two charging modes.

Only small quantities of charge were passed when charging at current densities less than the critical current density (*i.e.*, no greater than 30 coulombs/cm^2) and no moss was formed on the electrode (Table I). At higher current densities (greater than the critical current density) larger quantities of charge were passed. Again no moss was formed but the deposit was rough although there was little dendritic growth. With this technique it was found possible to obtain a relatively even deposit with the passage of 900 coulombs/cm^2 of charge at a current density of 100 ma/cm^2. The potential-time curves were similar to the previous cases (Fig. 1) only in this case giving a cathodic overpotential of 100 mv and the current efficiency for electrodeposition was again in the range of 85-95%.

Discussion

Dendritic deposits are formed when the rate of the electrode reaction is controlled by the mass transport of the electroactive species to the electrode surface, *i.e.*, when the surface concentration of the electroactive species is less than the bulk concentration. The beneficial effect of pulsed current charging at current densities greater than the critical current density is probably due to the modification of the ionic concentration gradient during the off period. The transport of ions to the electrode surface during the off period occurs by convection and by diffusion. In the present study the contribution of convective mass transport far outweighed that of diffusive flow due to the relatively large volume of electrolyte.

Convective flow will be limited in a practical cell due to the restricted motion of the electrolyte by the separator. During battery charging, convection may arise from chance vibrations or from changes occurring at the electrode/electrolyte interface, *e.g.*, due to the difference in density between zincate saturated and zincate free KOH solution, due to hydrogen evolution or due to the volume change during the reduction of zinc oxide to zinc. Differentiation between these stirring modes is important for the effect of the former within the battery matrix is probably negligible, whereas stirring at the electrode surface will be more significant.

The less dendritic deposit obtained with pulse charging at 80 ma/cm² and on and off times 10 msec (Fig. 4) than with direct current charging at half the charge rate (Fig. 2) is due to the elimination of the electrostatic force between the electrode and electroreducible anion during the off period. Thus ionic transport by electrical migration is expected in the electrolytes used in the present study during the current on period because the ratio of the concentration of supporting electrolyte to the concentration of zincate ions is very much less than 50, the value considered to be necessary to suppress migratory currents (10). This decreases the rate of mass transport during charge since the transport of an anion to the cathode is involved. Hence during the on period the mass transport of zincate ion to the electrode is hindered and the interfacial concentration of zincate ion is less than it would be when there is no potential applied to the electrode, *i.e.*, during the off period.

Studies on the electrodeposition of copper (11, 12) indicated that the beneficial effect of periodic reversal of current is the delay in the onset of concentration polarization. It is probable that this is also the explanation for the prevention of the formation of zinc dendrites although we have performed insufficient experiments to confirm this hypothesis in detail.

In agreement with the conclusion of Bek and Kudryavtsev (8, 9) we believe that the elimination of the mossy zinc deposit by selected modes of pulse charging and by periodic reversal of current is due to the dissolution of the active mossy deposit during the open circuit or anodic period. This theory is supported by the observations that the equilibrium potential of the mossy zinc deposit is 5-10 mv more cathodic than that of the zinc foil (8) (Fig. 1) and that small quantities of gas are evolved during the current off period. This indicates that the current efficiency for zinc deposition should be less than 100%. However the experimental values of the current efficiency were always high (95-100%) and it was not possible to determine whether this slight departure of the current efficiency from the theoretical value is confirmation of the above theory or merely a measure of the experimental precision.

The numerical values of the current density and on and off times are not directly applicable to a cell consisting of a secondary zinc electrode for in that case, the large surface area of the porous zinc electrode and the restricted transport of the zincate ions must be considered. However this study does indicate the order of magnitude of the parameters, which it is necessary to control, in order to increase the cycle life of a secondary zinc electrode by improving zinc deposit adherency.

Manuscript submitted June 24, 1968; revised manuscript received Oct. 14, 1968. This paper was presented at the Chicago Meeting, Oct. 15-19, 1968 as Paper 34.

Any discussion of this paper will appear in a Discussion Section to be published in the December 1969 JOURNAL.

REFERENCES

1. T. P. Dirkse, *This Journal*, **102**, 497 (1955).
2. J. E. Oxley, C. W. Fleischmann, and H. G. Oswin, Proceedings of the 20th Annual Power Sources Conference, May 1966.
3. J. E. Oxley, G. K. Johnson, and H. G. Oswin, Paper presented to the Electrochemical Society Meeting, October 1965.
4. H. K. Farmery and W. A. Smith, "Batteries," p. 179, D. H. Collins, Editor, Pergamon Press, Inc., New York (1963).
5. V. V. Romanov, *Zhur. Priklad. Khim.*, **34**, 2692 (1961).
6. J. E. Oxley and C. W. Fleischmann, Quarterly Report No. 1 to NASA, Contract NAS 5-9591, September 1965.
7. R. W. Powers, Progress Report No. 1 to ILZRO, Project No. ZE120, October 1966.
8. R. Yu. Bek and N. T. Kudryavtsev, *Zhur. Priklad. Khim.*, **34**, 2013 (1961).
9. R. Yu. Bek and N. T. Kudryavtsev, *ibid.*, **34**, 2020 (1961).
10. I. M. Kolthoff and J. J. Lingane, "Polarography," Vol. 1, 2nd Edition, Interscience Publishers, Inc., New York (1952).
11. A. Hickling and H. P. Rothbaum, *Trans. Inst. Metal Finishing*, **34**, 53 (1957).
12. A. Hickling and H. P. Rothbaum, *ibid.*, **34**, 199 (1957).

Current Distribution on a Plane Electrode below the Limiting Current

W. R. Parrish and John Newman

Inorganic Materials Research Division, Lawrence Radiation Laboratory, and Department of Chemical Engineering, University of California, Berkeley, California

ABSTRACT

The current distribution on a short, plane electrode in the wall of a flow channel is calculated at various fractions of the limiting current. Near the limiting current, the current density exceeds the local limiting value near the downstream end of the electrode.

An important geometry in electrochemical industries involves channel flow between two plane, parallel electrodes as shown in Fig. 1. A complicated procedure for treating this problem is outlined in ref. (1). This is based on the concept (2) that concentration variations are restricted to thin diffusion layers near the electrodes, which allows separate treatment of the diffusion layer and the potential distribution outside the diffusion layer. This concept has been applied to the rotating disk electrode (3, 4). However, it is difficult to treat the channel problem, and the present paper is restricted to the consideration of one electrode. If the distance between the electrodes is much greater than the length of the electrodes, each electrode behaves independently. This assumption greatly simplifies the determination of the current and concentration distributions on the electrodes.

The following assumptions will also be made:

1. The electrode is embedded in an infinite, plane, insulating wall.
2. Fully developed, laminar flow prevails, and the velocity can be approximated by a linear profile near the wall, within the diffusion layer.

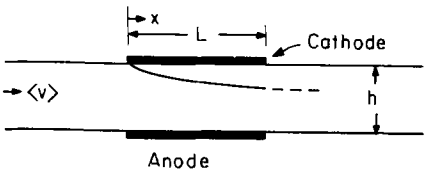

Fig. 1. Plane electrodes in the walls of a flow channel

3. Dilute-solution theory with constant physical properties is applicable.

4. The transport equations used here apply to either the deposition of an ion of a single salt or the reaction of an ion in an excess of supporting electrolyte. The effect of ionic migration for intermediate cases is not considered.

Mathematical Formulation of the Problem

The mode of approach is described in ref. (1-3). The potential in the electrolytic solution outside the diffusion layer satisfies Laplace's equation in two-dimensional form

$$\frac{\partial^2\Phi}{\partial x^2} + \frac{\partial^2\Phi}{\partial y^2} = 0 \qquad [1]$$

where Φ is the potential measured by a reference electrode of the same type as the working electrode. The appropriate boundary conditions are

$$\partial\Phi/\partial y = 0 \text{ at } y = 0 \text{ for } x < 0 \text{ and } x > L \qquad [2]$$

$$\partial\Phi/\partial y = -i/\kappa_\infty \text{ at } y = 0 \text{ for } 0 < x < L \qquad [3]$$

Equation [2] applies to the insulating surface bounding the electrode, and Eq. [3] relates the normal potential gradient to the electrode current density, where κ_∞ is the conductivity of the solution outside the diffusion layer.

Wagner (5) gives the solution of Eq. [1] subject to conditions 2 and 3

$$\Phi = \Phi^* - \frac{1}{2\pi\kappa_\infty}\int_o^L i(x') \ln\left[(x-x')^2 + y^2\right] dx' \qquad [4]$$

where Φ^* is an integration constant reflecting the arbitrary zero of potential. The potential Φ_o near the electrode surface is then

$$\Phi_o = \Phi^* - \frac{1}{2\pi\kappa_\infty}\int_o^L i(x') \ln (x-x')^2 dx' \qquad [5]$$

This should be regarded as the potential of the solution outside the diffusion layer extrapolated to the electrode surface as if the actual current distribution prevails but there is no concentration variation near the electrode.

Another integral equation can be developed for the diffusion layer (1). The limiting current distribution for such a plane electrode is[1]

$$i(x) = -\frac{n\mathbf{F}Dc_\infty}{(1-t)\Gamma(4/3)}\left(\frac{b}{9Dx}\right)^{1/3} \qquad [6]$$

where b, a constant, is the slope of the velocity profile at the wall ($b = \partial v_x/\partial y$ at $y = 0$). We assume here that the concentration variation is confined to a thin region near the electrode surface. Thus the velocity profile within this diffusion layer is linear in y. This approximation is valid when $L < 0.02 \langle v\rangle h^2/D$. Equation [6] applies when the concentration of the reactant is zero at the electrode surface. Application of Duhamel's theorem (9) to Eq. [6] gives a relationship between the current density distribution and the surface concentration, for currents below the limiting current.

[1] This equation is correct for the limiting cases considered here. For a binary electrolyte, D is the diffusion coefficient of the salt. With excess supporting electrolyte, t is zero and D is the diffusion coefficient of the reactant ion or molecule. The indiscriminate use of this equation to describe the effect of migration in intermediate cases is subject to criticism (1, 10, 11).

$$i(x) = -\frac{n\mathbf{F}D}{(1-t)\Gamma(4/3)}\left(\frac{b}{9D}\right)^{1/3}\int_o^x \frac{dc_o(x')}{dx'}\frac{dx'}{(x-x')^{1/3}} \qquad [7]$$

In many cases the electrode kinetics allow the current density and the surface overpotential η_s to be related by an exponential expression

$$i(x) = i_o\left(\frac{c_o}{c_\infty}\right)^\gamma \left[\exp\left\{\frac{\alpha Z\mathbf{F}}{RT}\eta_s\right\} - \exp\left\{-\frac{\beta Z\mathbf{F}}{RT}\eta_s\right\}\right] \qquad [8]$$

where α and β are characteristic parameters of the electrode reaction, and i_o is the exchange current density at the bulk concentration. The exchange current density at the electrode is taken to be proportional to the surface concentration, c_o, raised to the power γ. The surface overpotential is related to the electrode potential V by

$$\eta_s = V - \Phi_o - \eta_c \qquad [9]$$

where η_c is the concentration overpotential and is taken to be (2)

$$\eta_c = -(RT/Z\mathbf{F})\left[\ln (c_\infty/c_o) - t\,(1 - c_o/c_\infty)\right] \qquad [10]$$

where

$$Z = -z_+z_-/(z_+ - z_-) \text{ for a single salt}$$

$$Z = -n \text{ with supporting electrolyte} \qquad [11]$$

If there is an excess of supporting electrolyte, the transference number t will be zero.

Instead of the integral Eq. [7], it might have been possible to treat the diffusion layer with some sort of power series in x, similar to the method used for the rotating disk (3). However, even with the disk, a power series introduces numerical difficulties which can be avoided with an integral equation (4). This is demonstrated in Fig. 2, recalculated for the rotating disk with an integral equation similar to Eq. [7]. Comparison with Fig. 7 of ref. (3) shows that the curves are nearly the same with one important exception. The current density can rise above the limiting current near the edge of the disk and then go through a maximum as the limited supply of reactant becomes decisive. However, it cannot rise again near the edge of the disk as shown in the earlier work. Thus, from a practical point of view, the integral equation is superior to a power series and will be used in the present work.

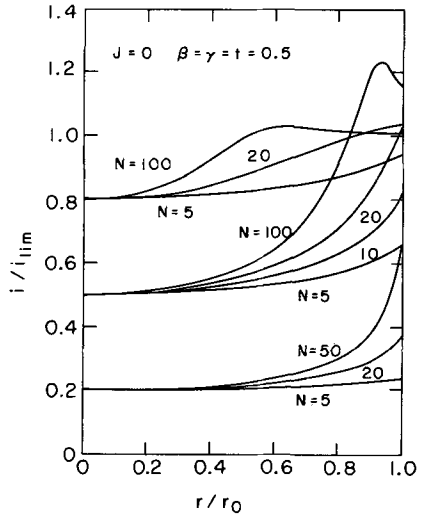

Fig. 2. Current distribution on a rotating disk for Tafel kinetics ($i_o << i_{avg}$). The parameters N and J are the dimensionless limiting and exchange current densities, respectively, as defined in ref. (3).

Numerical Calculations

To determine the current and concentration distributions along the electrode, Eq. [5] and [7] must be solved along with Eq. [8], [9], and [10]. The integral in Eq. [5] was evaluated by Simpson's method. The singularity at $x' = x$ was removed by adding and subtracting $i(x)$ as suggested by Kantorovich and Krylov (6). For a given distribution of total overpotential $\eta_c + \eta_s$, the integral Eq. [7] was solved in conjunction with Eq. [8] and [10] by the method of Acrivos and Chambré (7). It might be noted that Eq. [7] is a special form of a more general equation which can be applied to other flow geometries, for example, the rotating disk electrode.

The number of intervals required to obtain accurate results varied between 50 and 140, depending on the uniformity of the current distribution. The answers were checked by increasing the number of intervals and were considered to be satisfactory if they did not vary by more than 1% with an increase of 20 intervals.

The following iteration procedure was used:

1. The current density was specified at $x = 0$. Since $c_o = c_\infty$ at $x = 0$, this also specifies the total overpotential at $x = 0$. As a first guess, this total overpotential was assumed to apply over the entire electrode.
2. For a given distribution of total overpotential, the current density and surface concentration were determined from Eq. [7], [8], and [10].
3. From the current distribution, new values of the total overpotential were calculated from Eq. [5] and [9]. If the new and old values of the total overpotential differed by more than 0.01%, these values were averaged (usually with unequal weights on the two values) and put back into step 2.

This procedure appears to work well over almost the entire range between the secondary and limiting current distributions. Convergence was always achieved in less than 35 iterations for the cases considered.

Results

The number of parameters required to describe a given situation can be minimized by defining three dimensionless quantities:

$$J = \frac{ZFL}{RT\kappa_\infty} i_o \qquad [12]$$

$$N = -\frac{nZF^2Dc_\infty}{(1-t)RT\kappa_\infty}\left(\frac{L^2b}{D}\right)^{1/3} \qquad [13]$$

$$\delta = \frac{ZFL}{RT\kappa_\infty}|i_{avg}| \qquad [14]$$

These are analogous to those defined for the rotating disk problem (3). J, N, and δ can be regarded as dimensionless exchange, average limiting, and average current densities. The limiting current corresponds to $\delta = 0.807N$. The total number of parameters required to define the problem will now be seven, J, N, and δ, the transference number, t, and α, β, and γ characteristic of the electrode reaction.

The two extreme cases are the primary and limiting current distributions, shown in Fig. 3. The primary current occurs when the electrode is reversible and there are no concentration effects ($N = \infty$ and $J = \infty$). Wagner (5) gives the primary current distribution as

$$i/i_{avg} = (1/\pi)\,[x/L - (x/L)^2]^{-1/2} \qquad [15]$$

When the current is limited solely by the rate of mass transfer through the diffusion layer, the limiting current distribution, obtained from Eq. [6], is

$$i/i_{avg} = (2/3)\,(x/L)^{-1/3} \qquad [16]$$

The secondary current will result when there is a surface overpotential but no mass transfer effects.

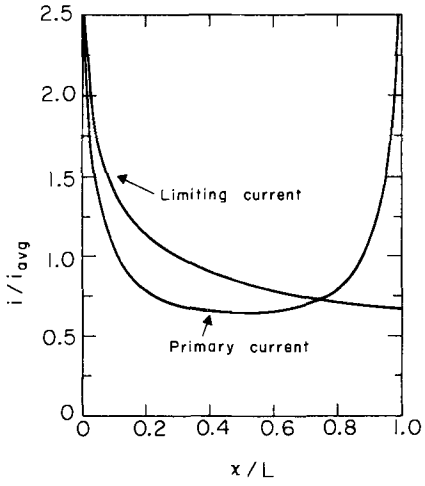

Fig. 3. Primary and limiting current distributions on a plane electrode.

For sufficiently small currents ($\delta << J$), the polarization law 8 can be linearized to

$$i = (\alpha + \beta)\,(ZF/RT)\,i_o\eta_s \qquad [17]$$

Wagner (5) calculated secondary current distributions as a function of the coefficient in Eq. [17]. A linear approximation can also be made if the current distribution is fairly uniform, say $\delta < 0.5$, even if J is small.

If, on the other hand, the average current is much greater than the exchange current ($\delta >> J$), Tafel polarization will apply

$$\eta_s = -(RT/ZF\beta)\,[\ln|i| - \ln i_o] \qquad [18]$$

(For anodic currents, the term in α would be retained.) Gnusin, Poddubnyi, Rudenko, and Fomin (8) determined the secondary current distribution as a function of the average current.

Before considering the case where mass transfer effects are important, we compared our calculated secondary distributions with those in these two papers. Comparison for the rotating disk (3) served as a check on the mass transfer calculations.

Because mass transfer effects occur at higher current densities, we used a Tafel polarization law in subsequent work considering concentration variations. Figure 4 shows the current distribution for $N = 100$

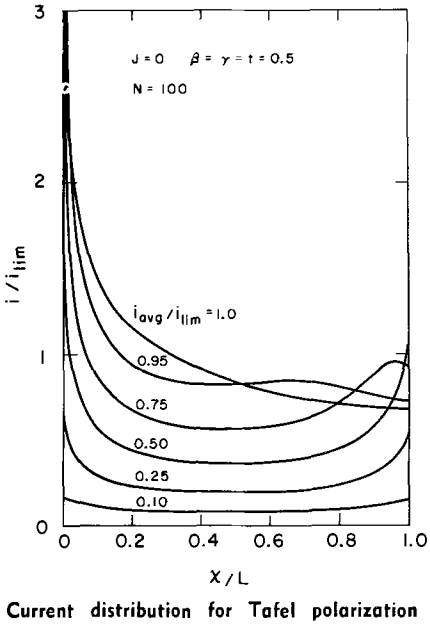

Fig. 4. Current distribution for Tafel polarization at various fractions of the average limiting current.

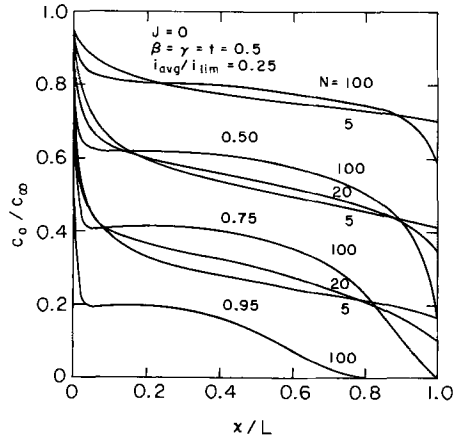

Fig. 5. Surface concentration distribution for Tafel polarization near the limiting current.

and average current densities at various fractions of the average limiting current. At low currents, the distribution is close to the secondary distribution, and mass transfer becomes important only at higher currents. At greater than about 75% of the limiting current, the current cannot continue to increase near the end of the electrode because of mass transfer limitations.

Concentration profiles are shown in Fig. 5 for various values of N. For the case of $N = 100$ at 75 and 95% of the limiting current, there is a slight increase of reactant concentration near the front of the electrode ($x/L \approx 0.1$), resulting from the rapid drop in current density near the front of the electrode. The concentration then has a chance to increase a little before the current density begins to increase.

In Fig. 6 the ratio of the maximum to minimum current density has been plotted against the fraction of the limiting current, giving an indication of the uniformity of the current distribution. At a given fraction of the limiting current, the current distribution becomes less uniform with increasing N. In all cases the effect of mass transfer resistance is to make the current distribution more uniform near the back end of the electrode.

Conclusions

Current distributions on a plane electrode in the wall of a flow channel are calculated while taking into account concentration variations near the electrode, electrode kinetics, and the ohmic potential drop in the bulk of the solution. The procedure is similar to that for a rotating disk, leading to the conclusion that the diffusion layer can be treated by a general method for hydrodynamic situations where the velocity derivative at the electrode surface is known. Thus, for geometric arrangements where the diffusion layer can be treated and where it is also possible to treat the potential distribution outside the diffusion layer, current density calculations can be carried out in the manner illustrated for the plane and the disk.

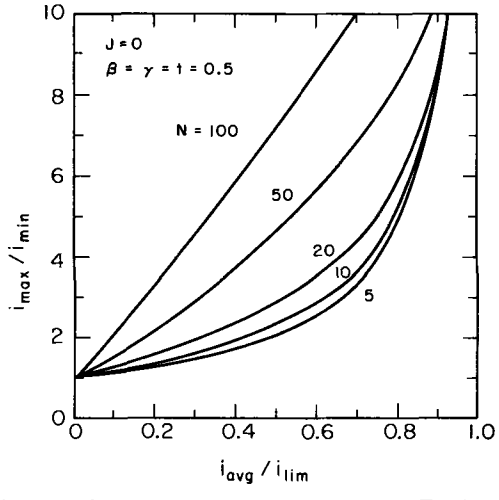

Fig. 6. Ratio of maximum to minimum current for Tafel polarization vs. the fraction of the average limiting current.

Acknowledgment

This work was supported by the United States Atomic Energy Commission.

Manuscript submitted April 19, 1968; revised manuscript received Sept. 17, 1968.

Any discussion of this paper will appear in a Discussion Section to be published in the December 1969 JOURNAL.

Nomenclature

b	$= 6 \langle v \rangle / h$, velocity derivative at the wall of the channel, sec^{-1}
c_o	concentration at electrode surface, $mole/cm^3$
c_x	bulk concentration of reactant, $mole/cm^3$
D	diffusion coefficient of reactant or of binary electrolyte, cm^2/sec
$\mathbf{F}$	Faraday's constant, 96,487 coul/equiv
h	height of channel, cm
i	normal current density at electrode surface, amp/cm^2
i_o	exchange current density, amp/cm^2
i_{avg}	average current density, amp/cm^2
i_{lim}	average limiting current density, amp/cm^2
J	dimensionless exchange current density (see Eq. [12])
L	length of electrode, cm
n	number of electrons produced when one reactant ion or molecule reacts
N	dimensionless limiting current (see Eq. [13])
R	universal gas constant, joule/mole-deg
t	transference number of reactant
T	absolute temperature, °K
$\langle v \rangle$	average velocity, cm/sec
V	potential of electrode, volt
x	distance along electrode, cm
y	normal distance from electrode, cm
z_i	charge number of species i
Z	see Eq. [11]
α, β, γ	parameters in kinetic expression (see Eq. [8])
$\Gamma(4/3)$	$= 0.89298$, the gamma function of 4/3
δ	dimensionless average current density (see Eq. [14])
η_c	concentration overpotential, volt
η_s	surface overpotential, volt
κ_x	conductivity of bulk solution, $ohm^{-1}\text{-}cm^{-1}$
Φ	potential in bulk solution, volt
Φ_o	potential in bulk solution extrapolated to electrode surface, volt

REFERENCES

1. John Newman, *Ind. Eng. Chem.*, **60**, 12 (1968).
2. John Newman, *Intern. J. Heat Mass Transfer*, **10**, 983 (1967).
3. John Newman, *This Journal*, **113**, 1235 (1966).
4. John Newman, *ibid.*, **114**, 239 (1967).
5. Carl Wagner, *ibid.*, **98**, 116 (1951).
6. L. V. Kantorovich and V. I. Krylov, "Approximate Methods of Higher Analysis," p. 101, translated by Curtis D. Benster, Interscience Publishers, Inc., New York (1959).
7. Andreas Acrivos and P. L. Chambré, *Ind. Eng. Chem.*, **49**, 1025 (1957).
8. N. P. Gnusin, N. P. Poddubnyi, E. N. Rudenko, and A. G. Fomin, *Elektrokhim.*, **1**, 452 (1965).
9. H. S. Carslaw and J. C. Jaeger, "Conduction of Heat in Solids," p. 30, Oxford University Press, Inc., New York (1959).
10. John Newman, *Advances in Electrochemistry and Electrochemical Engineering*, **5**, 87 (1967).
11. John Newman, *Ind. & Eng. Chem. Fundamentals*, **5**, 525 (1966).

Mechanism of Inhibiting Stress Corrosion Cracking of 18-8 Stainless Steel in $MgCl_2$ by Acetates and Nitrates

H. H. Uhlig* and E. W. Cook, Jr.

Department of Metallurgy and Materials Science,
Massachusetts Institute of Technology, Cambridge, Massachusetts

ABSTRACT

Modest additions of sodium acetate, nitrate, iodide, or benzoate to $MgCl_2$ test solution boiling at 130°C are found to increase resistance to or inhibit stress corrosion cracking of 18-8 stainless steel. The critical applied potential in $MgCl_2$ solution (—0.145v) above which, but not below, cracking occurs is shifted in the noble direction by extraneous salt additions. When the shift exceeds the corrosion potential for 18-8 in the same solution, cracking is apparently inhibited. On the other hand, salt additions, *e.g.*, $FeCl_3$, which shift the corrosion potential in the noble direction may induce or accelerate stress corrosion cracking.

The critical potential is interpreted as that value above which but not below Cl^- ions adsorb on imperfection sites of plastically deforming metal in amount adequate to cause failure (stress sorption cracking). The present data do not support an electrochemical mechanism of stress corrosion cracking based on anodic dissolution of metal ions at the tip of a crack, nor the mechanism dependent on continuous cracking of a surface oxide film.

The phenomenon of failure of ductile metals by cracking when stressed in tension and exposed to specific anions is still not well understood. Several theories have been proposed since the time stress corrosion cracking (scc) was first observed, the most important of which are: (*i*) electrochemical, based on dissolution of metal ions at the base of a notch or crack acting as anode in contact with metal elsewhere acting as cathode; (*ii*) progressive cracking of a brittle surface oxide film; (*iii*) reduction of surface energy or weakening of metal bonds by adsorption of specific anions at the root of a notch or crack. There is supporting evidence for each theory, but no general consensus as yet that any one of them can adequately account for the general phenomena of scc (1).

The mechanism by which extraneous salts, when added to damaging solutions, act as inhibitors of scc, and in some instances as accelerators, challenges each of the currently discussed theories and provides the basis for the present paper. The work reported at present began with our observation that a few per cent of a salt, *e.g.*, sodium acetate or sodium iodide, added to the usual boiling concentrated $MgCl_2$ test solution for 18-8 stainless steel effectively inhibited scc. This fact excited curiosity as to how such additions could in principle affect any supposed electrochemical process occurring within the growing crack, particularly when the added salt had no readily discernible major effect on cathodic or anodic polarization behavior, and certainly had little effect on the conductivity of an already good conducting solution [$\kappa = 0.27$ ohm^{-1} cm^{-1} at 146°C (2)]. The cracking of an oxide film, if one construes the passive film to be an oxide, did not seem to be involved in view of the fact that polarization measurements of stainless steels in $MgCl_2$ solution indicated absence of passivity (2, 3). Visible patches of surface oxide, if any, that may form during tests in $MgCl_2$ are equally evident on specimens which do not crack as well as on those which do. And the effect of applied potential to either initiate or to prevent cracking is found whether or not an inhibiting anion is present.

The inhibiting effect of various salts, including NaCl (4), Na_2CO_3 (5, 6), Na_2HPO_4 (6), and others, on the stress corrosion cracking of mild steel in boiling nitrate solutions has been reported previously by several investigators. Nitrates have been reported to act as inhibitors for scc of mild steel in hot NaOH solutions (7). Such additions were used over many years as a practical measure to avoid damage of locomotive boilers containing alkaline boiler waters. Additions of sulfates, fluorides, or nitrates to halide salt test solutions were reported to inhibit scc of a titanium alloy (8% Al, 1% Mo, 1% V) stressed at room temperature (8). Edeleanu (9) reported that 1% $NaNO_3$ added to boiling 20% NaCl solution had an accelerating effect on scc of 18-8 stainless steel. However, the function of nitrates to protect against rather than to stimulate scc of austenitic stainless steels in boiling $MgCl_2$ was reported by Rideout and Mittleberg (10) and more recently by Couper (11). We confirmed the inhibiting effect of nitrates in $MgCl_2$ test solution and showed that several other salts are similarly effective.

Experimental

Specimens 1-3/4 x 3/16 x 0.04 in. (4.5 x 0.5 x 0.1 cm) were sheared from commercial type 304 stainless steel sheet, originally 1/16th in. thick as received and subsequently cold rolled to 0.04 in. (36% reduction of thickness). Longest dimension was in the rolling direction. Some specimens were tested as such; others called "annealed" were heated in argon at 1050°C and water quenched. All specimens were abraded to No. 0 emery paper, degreased in benzene, pickled initially in 25 v/o (volume per cent) H_2SO_4, 25 v/o HCl at 90°C if a tenacious oxide covered the surface, and pickled finally in any event in 15 v/o HNO_3, 5 v/o HF at 90°C for 5 min. Specimens were immediately bent beyond the elastic limit into the shape of a C using a special vise, then transferred to the test apparatus by means of a metal holder adjusting the final span to 1-7/16th in. (3.7 cm), carefully avoiding springback. A compressed spring was used to maintain essentially constant flow stress of the porcelain insulated specimen during the test, and an electric clock recorded time to failure. For polarization measurements, or when a controlled potential was applied throughout the test, usually a type 304 stainless steel wire, 0.025-in. diameter, was spot welded to one end of the specimen. The wire was encased in sections of capillary glass tubing in order to reduce impressed current reaching the wire. Other details of the test apparatus, constructed largely of commercial zirconium, have been described previously (12, 13).

For polarization or controlled potential measurements, the Heathkit or Wenking potentiostats were used. The glass cell for such measurements holding

* Electrochemical Society Active Member.

about 200 ml of test solution was designed with two side arms opposite one another, holding auxiliary electrodes of platinized titanium, and a center arm into which a saturated calomel electrode at room temperature was placed. Glass frit disks separated $MgCl_2$ solution of the arms from the boiling solution in the test cell. Measurements of potential made beforehand showed that IR drop in the $MgCl_2$ solution at the prevailing applied current in the region of the critical potential was so low (approximately 10 $\mu a/cm^2$) that the position of the calomel electrode with respect to the stainless steel specimen made no appreciable difference and hence no correction of potential was needed. Because of accumulating electrode reaction products, polarization runs were usually not extended beyond 50 hr.

The test solution containing 33g anhydrous $MgCl_2$ per 100 ml saturated solution boiled at 130°C, a temperature which was maintained during the test. This solution, which is less concentrated than the usual $MgCl_2$ test solution boiling at 154°C, was chosen in order to allow greater solubility of salts added as inhibitors. Because of variable cracking times characteristic of different batches of $MgCl_2$, originating in large part from variable pH, the reagent salt used for all the tests was a mixture of several 25-pound shipments. Per cent salt additions were calculated on the weight of the $MgCl_2$ solution. When the added salt in the stipulated amount was found to alter the *p*H of the $MgCl_2$ solution saturated at room temperature (measured with a glass electrode), the pH was adjusted to the original value (5.2) by adding NaOH or HCl. The boiling point, which was found to be changed by about 1°C or less by the salt additions, was always adjusted to 130°C by adding a small amount of water.

Results

Almost any salt added to the $MgCl_2$ test solution, if sufficiently soluble, was found to act as an inhibitor of scc, with some salts being more effective than others. The requirement of a salt suited to the present study, other than solubility, included lack of obvious reaction with $MgCl_2$ or with the test specimen. Inhibition was observed in similar degree whether cold rolled or annealed stainless steel was used.

The effects of $NaNO_3$, NaI, and sodium benzoate additions on time to failure of annealed 18-8 stainless steel are shown in Fig. 1, 2, and 3. The effect of sodium acetate on failure times of cold rolled or annealed stainless steel is shown in Fig. 4. A small amount of added sodium benzoate was found to be an effective inhibitor, but maximum inhibition was limited by the small solubility of the salt in the boiling $MgCl_2$ solution, hence time to failure was essentially constant above 0.05%. In Fig. 1, 2, and 4, each point is usually the average time to failure of 2 to 3 specimens. In Fig. 3, each point represents one specimen. A few additional runs in which EDTA was added up to 1.5% showed some degree of inhibition, but the general dissolution rate of the specimen was so high that failure times were not considered reliable.

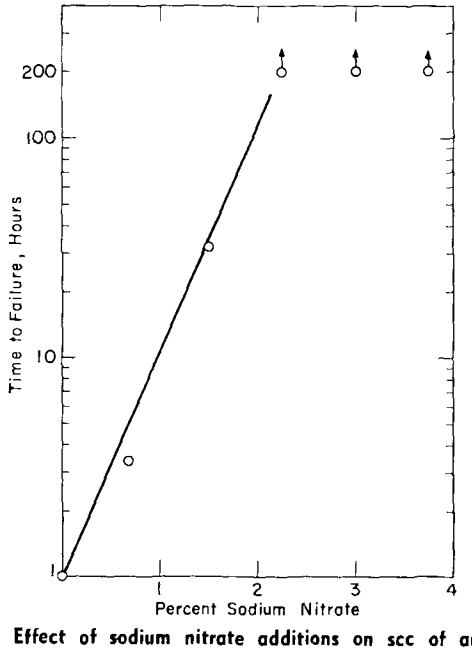

Fig. 1. Effect of sodium nitrate additions on scc of annealed 18-8 stainless steel in $MgCl_2$ boiling at 130°C.

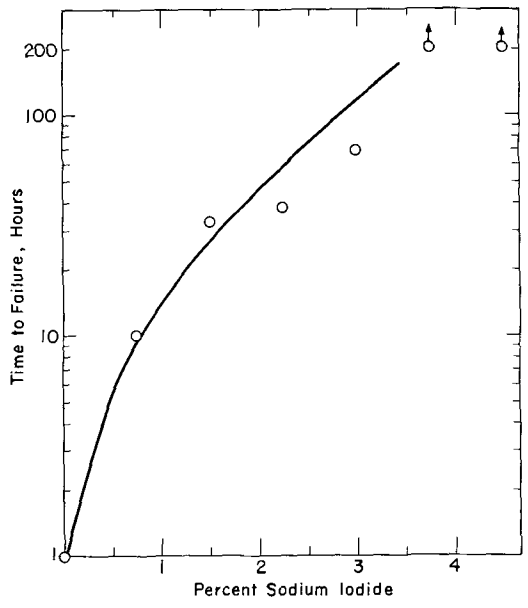

Fig. 2. Effect of sodium iodide additions on scc of annealed 18-8 stainless steel in $MgCl_2$ boiling at 130°C.

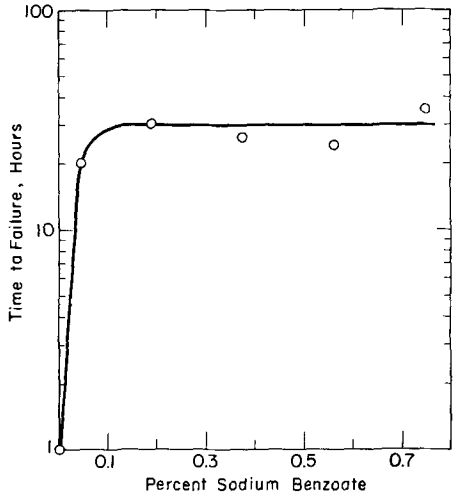

Fig. 3. Effect of sodium benzoate additions on scc of annealed 18-8 stainless steel in $MgCl_2$ boiling at 130°C. (Solution is saturated above 0.05%.)

Consecutive runs using the same test solution demonstrated that the inhibiting salts do not function by gradually reacting with and depleting the test solution. The cracking time, for example, of a second specimen placed in a test solution used for a previous test containing either 1% sodium acetate, or 2% sodium nitrate, or 3% sodium iodide was the same as the first specimen within the usual experimental scatter (14).

Tests under controlled applied potential were carried out in $MgCl_2$ solution both with or without additions of sodium acetate or sodium nitrate at two concentrations (Fig. 5, 6, 7). The lower concentration in each case did not inhibit against cracking in the absence of an applied potential, whereas the higher con-

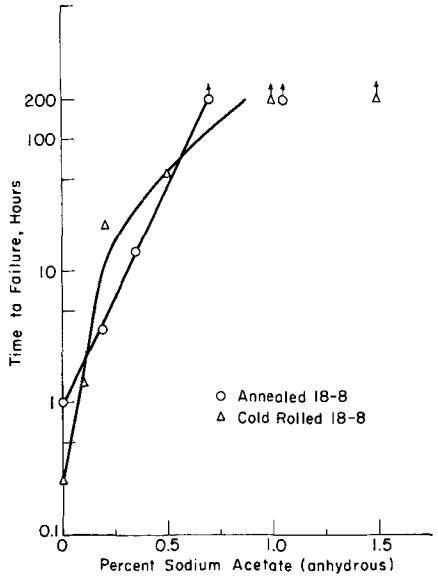

Fig. 4. Effect of sodium acetate additions on scc of cold-rolled and annealed 18-8 stainless steel in $MgCl_2$ boiling at 130°C.

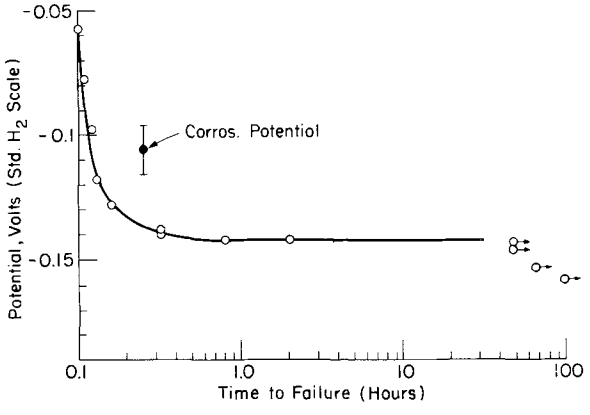

Fig. 5. Effect of applied potential on time to failure of cold-rolled 18-8 stainless steel in $MgCl_2$ boiling at 130°C.

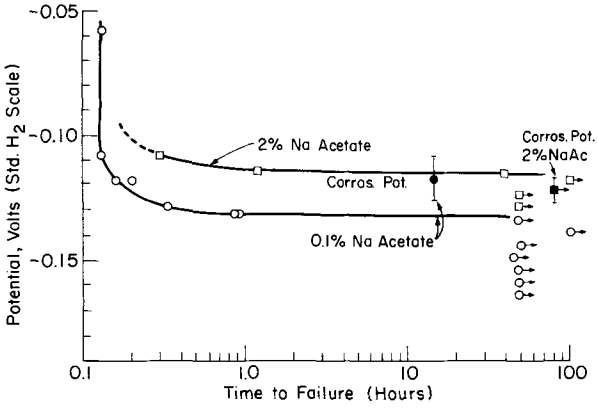

Fig. 6. Effect of applied potential on time to failure of cold-rolled 18-8 stainless steel in $MgCl_2$ solution with sodium acetate additions boiling at 130°C. (2% sodium acetate addition is inhibiting.)

centration prolonged resistance to failure for at least 50 hr. A definite critical potential was established for each test solution above which cracking occurred in times that decreased with increase of potential (noble direction) and below which cracking did not occur within the maximum test period. The critical potential was sharply defined, usually to within a few millivolts. The value presently obtained for cold rolled 18-8 in $MgCl_2$ boiling at 130°C is —0.145 ± 0.0015v (std. H_2 scale). This value was checked subsequently by H. Lee of this Laboratory. Values reported previously by other investigators fall within the same approximate range, although they are not strictly comparable because of differing test conditions. Barnartt and van Rooyen (2) reported —0.16v for annealed 18-8 in $MgCl_2$ boiling at 146°C. Brennert (15) reported about —0.16v for annealed or cold worked 18-8 in 40% $CaCl_2$ at 100°C; —0.14v for cold worked 18-8 in 24% $CaCl_2$ at 100°C, and —0.18v in 60% $CaCl_2$ at 100°C. Smialowski and Rychik (3) reported a value of about —0.15v for annealed 18-8 type 302 stainless steel in $MgCl_2$ boiling at 125°C.

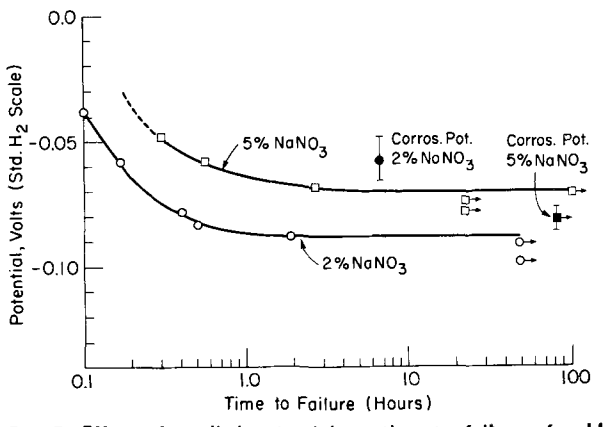

Fig. 7. Effect of applied potential on time to failure of cold-rolled 18-8 stainless steel in $MgCl_2$ solution with sodium nitrate additions boiling at 130°C. (5% $NaNO_3$ addition is inhibiting.)

Data presented in Fig. 6 and 7 show that both nitrates and acetates shift the critical potential in the noble direction. A summary of critical and corrosion potentials is given in Table I.

Discussion

Of considerable importance were observations that the corrosion potential as recorded after several hours was typically more noble than the critical potential for those solutions in which cracking was produced in absence of polarization, but that the reverse situation applied, namely the corrosion potential was more active than the critical potential in solutions in which cracking was not produced. However, in the latter solutions, cracking could nevertheless be induced by anodically polarizing the specimens to any value above the critical potential. The added salts, in other words, become effective inhibitors through their ability to shift the critical potential to a value more noble than the corrosion potential. The added salts may have the supplementary effect of shifting the corrosion potential in either the active direction (as for sodium acetate) or in the noble direction (as for $NaNO_3$). But if cracking is to be avoided in the absence of polarization, the corrosion potential must apparently lie at a value that is consistently active to the critical potential. Whether cracking occurs or not beyond the present maximum test period presumably depends on whether the corrosion potential eventually drifts to a value more noble than the critical value. It also follows that any oxidizing salt which shifts the corrosion potential to more noble values should in general accelerate scc. This is

Table I. Critical and steady-state corrosion potentials (std. H_2 scale) of cold-rolled 18-8 stainless steel in $MgCl_2$ boiling at 130°C

	Critical potential	Corrosion potential
$MgCl_2$	−0.145v	−0.11v
+ 0.1% Sodium acetate	−0.132	−0.12
+ 2% Sodium acetate	−0.116	−0.12
+ 2% $NaNO_3$	−0.090	−0.06
+ 5% $NaNO_3$	−0.070	−0.08

found to be the case, as for example with $FeCl_3$ additions to the $MgCl_2$ test solution as reported by Edeleanu (9).

In carrying out the described tests, it was observed that reproducibility of failure times was much improved under conditions of controlled potential compared to conditions of simple immersion. This observation sets aside previous arguments that tests on stress corrosion cracking lack characteristic reproducibility because of minute irregularities in the specimen surface acting as notches or stress raisers, or because of unknown residual surface stresses varying from specimen to specimen. Variations of either surface or stress are apparently less important in carefully prepared specimens than are variations in the corrosion potential. The latter usually drifts with time in the noble direction probably because of surface alloy composition changes or because of changes in activity of dissolved metal ions, or because of slowly adsorbing Cl^- ions.

The dependence of scc on the relation of the corrosion potential to the critical potential has significant implications with regard to the electrochemical mechanism of cracking based on supposed anodic dissolution of alloy at the tip of an advancing crack, in contact with cathodic areas along the walls of the crack or at the outer surface of the specimen. Were this mechanism to apply, cathodic protection against scc could be expected only if the specimen were polarized to a potential equal to or more active than the open-circuit anode potential representing conditions at the tip of the crack. The critical potential is obviously not such an open-circuit anode potential because the corrosion potential in presence of acetates or nitrates of sufficient concentration to inhibit scc is more active than the critical potential. This order of potentials is impossible for any conceivable operating galvanic cell. Hence the critical potential must have another interpretation.

The cathode reaction, on the other hand, fits the electrochemical model. In view of the fact that cracking occurs in boiling $MgCl_2$ solution in absence of O_2 (12), the cathode reaction must involve hydrogen evolution. The *p*H of $MgCl_2$ boiling at 130°C is 1.17 as presently measured with a platinized platinum electrode over which purified hydrogen was bubbled. Hence the cathode open-circuit potential for 18-8 stainless steel in the $MgCl_2$ test solution is $(-2.3\ RT/F)$ *p*H or —0.094v. For the corresponding galvanic cell, the corrosion potential must always be more active than this value, which in general is observed for $MgCl_2$ and for $MgCl_2$ with sodium acetate additions. For $NaNO_3$ additions, the cathode reaction is expected to involve NO_3^- reduction; hence the corrosion potential in this case is understandably more noble than —0.094v (Table I).

Since the critical potential is not the open-circuit anode potential, it is suggested that it must correspond instead to the potential at which adsorption of Cl^- occurs at metal surface imperfections at the tip of the advancing crack. Only at potentials more noble than the critical value are Cl^- ions adequately adsorbed; at values more active than the critical potential Cl^- ions are desorbed. When the prevailing potential favors Cl^- adsorption, it is supposed that the weakening of metallic bonds or the corresponding reduction of surface energy allows a crack to grow (stress sorption cracking) (16); otherwise in absence of Cl^- adsorption, cracks do not either initiate or grow. When extraneous anions are present which do not of themselves cause cracking when adsorbed on the metal surface, competition between the ions for available sites requires that the potential be made more noble in order to achieve the required Cl^- concentration within the double layer essential for adsorption and cracking. Hence, whenever the competing anion shifts the critical potential to a value more noble than the corrosion potential, adequate adsorption of Cl^- is not possible and the anion acts as an inhibitor.

A parallel situation is found in the critical potential necessary to initiate pitting corrosion in the stainless steels and several other passive metals exposed to chloride solutions. Cathodic protection against pitting consists of polarizing the stainless steel to any value below its critical potential for pitting; it is not necessary to polarize to the open-circuit anode potential which is considerably more active. Additions of extraneous anions, *e.g.*, $SO_4^=$, NO_3^-, ClO_4^-, or OH^- consistently shift the critical potential in the noble direction, presumably by competitively adsorbing with Cl^- for sites on the alloy surface (17). If the shifted critical potential exceeds the corrosion potential or the open-circuit cathode potential, the added salt acts as an effective inhibitor. Here stress is not necessary and adsorption can occur at random on the alloy surface. Rosenfeld and Maximtschuk (18) using radioactive Cl^- showed that Cl^- adsorbs on metallic chromium to an increasing extent the more noble the applied potential (increased anodic polarization). Extraneous anions, *e.g.*, $SO_4^=$ or OH^-, in sufficient concentration prevented adsorption of Cl^- even on anodically polarized chromium. Similar conditions probably apply, although at different potentials, to adsorption of Cl^- on a stainless steel surface either at room temperature leading to pitting or at 130°C leading to stress corrosion cracking.

One distinguishing feature of conditions affecting pitting compared to those affecting scc is that stainless steels are passive in aerated chloride solutions in which pitting may occur, but they show no evidence of passivity when exposed to the $MgCl_2$ test solution. Previously reported potentiostatic anodic polarization curves for 18-8 stainless steel in $MgCl_2$ test solution boiling at 146°C (2) or at 125°C (3) show absence of a passive current density. The 18-8 alloy is also not passive in $MgCl_2$ boiling at 130°C to which sodium acetate is added as shown by polarization curves of Fig. 8. A passive current density is not observed even at relatively noble potentials.

The present measurements, therefore, do not support either an electrochemical mechanism of stress corrosion cracking depending on anodic dissolution of metal ions at the tip of a growing crack or the mechanism depending on continuous cracking of an oxide or passive film. Instead they support a mechanism based on potential-dependent adsorption of Cl^- ions presumably on imperfection sites generated at the surface of the plastically yielding metal. It is predicted that critical potentials for scc of other metals, *e.g.*, carbon steels and Ti alloys, will also be found to lack identity with open-circuit anode potentials and that the critical potentials will be similarly shifted in the noble direction by extraneous anions which act as inhibitors.

Acknowledgment

This research was supported by the United States

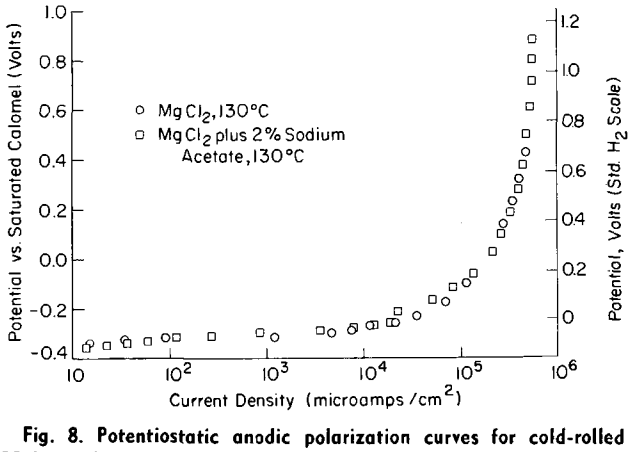

Fig. 8. Potentiostatic anodic polarization curves for cold-rolled 18-8 stainless steel in $MgCl_2$ solution and in $MgCl_2$ + 2% sodium acetate solution boiling at 130°C.

Army Research Office—Durham to whom the authors express their appreciation.

Manuscript received May 1, 1968. This paper was presented at the Montreal Meeting, Oct. 6-11, 1968, as Paper 423.

Any discussion of this paper will appear in a Discussion Section to be published in the December 1969 JOURNAL.

REFERENCES

1. Conference on Fundamental Aspects of Stress Corrosion Cracking, Ohio State University, September 1967, To be published.
2. S. Barnartt and D. van Rooyen, *This Journal*, **108**, 222 (1961).
3. M. Smialowski and M. Rychik, *Corrosion*, **23**, 218 (1967).
4. M. Smialowksi in "Proceedings of the First International Congress on Metallic Corrosion," p. 296, Butterworths, London (1962).
5. J. Jones, *Trans. Faraday Soc.*, **17**, 102 (1921).
6. R. Parkins and R. Usher, ref. (4), p. 289.
7. W. Schroeder and A. Berk, "Intercrystalline Cracking of Boiler Steel and its Prevention," U.S. Bur. Mines Bull. 443, Washington, D.C. (1941).
8. T. Beck and M. Blackburn, Preprint AIAA-ASME Conf., Palm Springs, Calif., March 1967.
9. C. Edeleanu, *J. Iron Steel Inst.*, **173**, 140 (1953).
10. S. Rideout and R. Mittleberg, U.S. A.E.C. Report CONF-778-3 (1964).
11. A. Couper, "Minimizing Stress Corrosion Cracking of Austenitic Stainless Steels" presented at Annual Conference, NACE, Cleveland, Ohio, March 18-22 (1968).
12. H. Uhlig and J. Lincoln, *This Journal*, **105**, 325 (1958).
13. H. Uhlig and J. Sava, *Trans. ASM*, **56**, 361 (1963).
14. V. S. Agarwala and H. H. Uhlig, Unpublished results.
15. S. Brennert, *Jernkont. Ann.*, **144**, 560 (1960).
16. H. H. Uhlig in "Physical Metallurgy of Stress Corrosion Fracture," T. Rhodin, Editor, p. 9, Interscience Publishers, New York, 1959.
17. H. Leckie and H. Uhlig, *This Journal*, **113**, 1262 (1966).
18. I. Rosenfeld and W. Maximtschuk, *Z. Physik. Chem.*, **215**, 25 (1960).

An Electrochemical Mass Transport-Kinetic Model for Stress Corrosion Cracking of Titanium

T. R. Beck*

Boeing Scientific Research Laboratories, Seattle, Washington

and E. A. Grens, II*

Department of Chemical Engineering, University of California, Berkeley, California

ABSTRACT

The purpose of this work has been to develop a quantitative model for the electrochemical kinetic and mass transport processes in a propagating stress corrosion crack and to use the model to gain insight into manner in which these processes influence propagation. Analysis of the problem led to a system of simultaneous differential equations which with their appropriate boundary conditions were solved by computer implemented numerical methods. Comparison of computed behavior with experimental stress corrosion cracking data for a titanium alloy has guided the development of the model and the specification of critical stress corrosion cracking experiments. Such comparisons indicate that there is a halide ion current to the crack tip with some hydrogen ion discharge in the region downstream from the tip. A significant fraction of the current entering a crack appears to be involved in formation of soluble titanium ions in parallel with oxide formation on the walls.

Stress corrosion cracking (SCC) of Titanium: 8%Al-1%Mo-1%V (Ti: 8-1-1) alloy under potentiostatic conditions in halide salt solutions has previously been described (1). The main features observed were that chloride, bromide, and iodide ions appeared to be the unique SCC agents in aqueous solutions and that SCC velocity and anodic current entering the crack were approximately linearly related to applied potential.

Kinetic data for oxidation of newly generated Ti: 8-1-1 surfaces and hydrogen ion reduction thereon have also been presented (2) and order of magnitude values of the exchange current densities for these reactions determined. Some qualitative ideas about the electrochemical mechanisms in a propagating crack based on the kinetic data were also described (2). However, the influence of mass transport phenomena within the propagating crack in establishing the relationship between potential and propagation velocity has not been seriously examined. The only prior analysis found of potential drop in a stress corrosion crack was that of Hines (3). His analysis is not applicable to titanium and in many other situations, because his assumption regarding uniform wall reactions and absence of any transport restrictions aside from those on current are not consistent with the kinetic data (2).

In the present work an attempt has been made to study more rigorous models for a propagating crack, which account for transport of species involved in reactions at the tip and along the crack walls as well as for the kinetics of the wall reactions. Experimental work continued concurrently with development of the model has provided data for comparison with the model and has guided its development. Some of this experimental work has been reported elsewhere (4), and the salient points are summarized herein.

The model has been derived to be consistent with the experimental findings on crack propagation behavior summarized in Table I and the basic principles of mass transport in electrolytes. The reason for the selectivity to Cl^-, Br^-, and I^-, ions appears to be outside of the scope of the present work, but the model as now formulated appears to be at least in qualitative

* Electrochemical Society Active Member.

Table I. Experimental stress corrosion cracking data for Ti:8-1-1 alloy to which the model must comply (1, 4)

1. SCC occurs only in the presence of Cl^-, Br^-, and I^- ions in aqueous solution.
2. SCC velocity is approximately linearly related to potential over a range of about 2v with zero-velocity intercept at −900 mv (SCE) for duplex annealed Ti:8-1-1.
3. Anodic current flowing into a propagating crack is approximately linearly related to potential with zero-current intercept at about −800 mv.
4. Under potentiostatic conditions SCC velocity is relatively independent of particular alkali or alkaline earth cations present or pH of the bulk solution.
5. Velocity varies with bulk concentration of halide to about the ¼ power becoming asymptotic to a limiting velocity at zero bulk concentration.
6. Activation energy for velocity is about 3.5 kcal/mole.
7. On open-circuiting the current to a propagating crack the initial open-circuit potential is only slightly below the initially applied potential in a range of applied potentials up to +200 mv. At more anodic applied potentials the value of the initial open-circuit potential approaches +200 mv asymptotically. A slow potential transient on open circuit occurs over a period of 10^{-2} to 100 sec with a final approach to about −800 mv.

agreement with the other observations, although its quantitative predictions are dependent on parameter values not all of which can be independently determined. It does not, and cannot, represent nor explain phenomena in the region of atomic dimensions at the very tip of a crack where actual fracture of the metal structure takes place. The effects of mechanical and metallurgical factors (2) are also not considered. These can influence the present results through their effect on the crack opening angle and the electrochemical kinetics parameters.

As will be seen, the model is not in complete quantitative agreement with all of the experimental data, but the source of certain deviations can be inferred. Later modifications to the model may serve to reduce these discrepancies. Nevertheless the model has provided valuable insight into the operation of mass transport phenomena which exert considerable influences on the course of SCC. It has guided our conception of many aspects of the SCC process and has often served to define critical SCC experiments. Further, it is believed that progress in understanding the electrochemistry of stress corrosion cracking can only be achieved by such continuous interplay of theory and experiment.

Model Formulation

The SCC model described here is based on consideration of a straight sided crack in a specimen of sufficient thickness that effects in the transverse direction are not appreciable. As shown in Fig. 1, this crack is subdivided into three basic regions: the "tip zone" ($\delta^t \leq y \leq \delta^p$) where the cleavage process takes place; the inner region or "monolayer zone" ($\delta^p \leq y \leq \delta$) where a first monolayer of oxide is formed on the metal surface; and the outer region or "multilayer zone" ($\delta \leq y \leq l$) where the oxide layer increases in thickness. Based on model studies of several possible reaction mechanisms, some of which are mentioned briefly later, assumptions have been made for the reactions occurring in these three zones which yield model behavior corresponding to experimental SCC measurements.

In the tip zone the reaction

$$Ti + mX^- \rightarrow TiX_m + me^- \qquad \text{Reaction (I)}$$

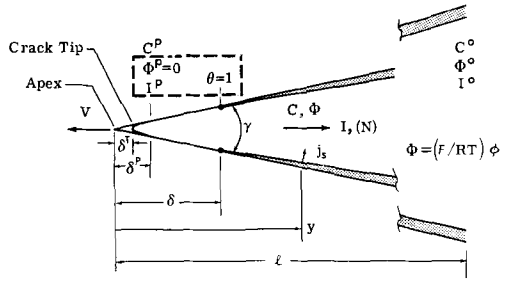

Fig. 1. Mass-transport-kinetic model for SCC

is assumed to take place and is presumably the reaction responsible for SCC. This assumption is based on calculations (described later) indicating the need for a net current of halide ions corresponding to about a monolayer in the tip zone. It is not known whether the halide ion tip current is due to electrochemical reaction or to charging of the electrical double layer, but either can be expressed by reaction (I).

Oxidation of titanium

$$Ti + 2H_2O \rightarrow TiO_2 + 4H^+ + 4e^- \qquad \text{Reaction (II)}$$

is assumed to occur on the walls in both the monolayer and multilayer zones. In the first of these it is assumed to be governed by Tafel-type kinetics (2) and to be accompanied by the displacement of halide ion from the titanium halide or adsorbed halide ion layer formed in the tip zone. This displacement mechanism is required to explain the observed nonlinear relationship of velocity to halide concentration (Table I, Item 5). In the multilayer zone, reaction (II) is governed by high field conduction (2) and thus has considerably different kinetic behavior than in the monolayer zone.

Hydrogen ion reduction

$$H^+ + e^- \rightarrow H \text{ (dissolved in metal)} \qquad \text{Reaction (III)}$$

is also assumed to occur in the monolayer zone where the potential at δ^p appears to be close to the mixed potential in acid solution for reactions (II) and (III). The amount of hydrogen ion reduced is small (on the order of a monolayer), and the hydrogen formed is assumed to go into the metal. Hydrogen ion reduction has been omitted in the multilayer zone because at a potential anodic to the mixed potential the current density would become small relative to reaction (II).

The mass transport and kinetic effects for this model have been analyzed subject to several fundamental assumptions discussed below.

Quasi-steady-state crack propagation.—It is assumed that the time constant for changes in the electrochemical variables is small compared to the period of crack propagation so that the system is essentially at steady state in respect to velocity and to concentration and potential gradients. The velocity, V, is assumed to be either uniform or the stepwise jumps small enough compared to the dimensions affecting mass transport that the velocity can be considered uniform. The mechanism of crack initiation is not considered.

Uniform small-angle crack.—The crack angle observed visually on the sides of SCC specimens and on optical photomicrographs of sectioned cracks to within 10^{-4} cm from the crack tip is on the order of 1-4°. Electron fractography indicates transcrystalline cleavage-type failure of the alpha titanium phase, indicating a curvature of atomic dimensions at the crack tip at a distance δ^t from the apex. There is thus a region of unknown crack angle from the atomic dimensions of the tip to 10^{-4} cm from the geometric apex of the crack, but the simplest assumption regarding shape is that the angle, γ, is uniform from the crack tip to the full length of the crack. Some branching of cracks has been observed on photomicrographs, but the effect will not be considered here.

Electrolyte completely fills crack.—It is assumed that capillary forces are sufficient to fill the crack with electrolyte completely at least to the tip zone.

Continuum treatment is applicable.—The lower boundary for the model is the position, δ^p, where the electrical double layers on the two walls intersect. Continuum mass transport flux equations and electrochemical kinetics data obtained from plane electrodes are assumed applicable at distances larger than δ^p from the apex. The continuum model of mass transport is not entirely applicable at distances close to

δ^p from the apex because of interference by the field of the diffuse part of the double layer. Unfortunately, as will be seen in the solutions, many of the electrochemically significant events in the crack occur not far from δ^p. The breakdown of the continuum conditions is one of the more serious criticisms that can be levied a posteriori against the model.

A one-dimensional representation is applicable.—The width of the small-angle crack is assumed to be small enough that there are negligible concentration and potential gradients normal to the axis of the crack. Actually, because there is no slip at the walls and the relative velocity of electrolyte to walls is on the order of 10^{-3} to 10^{-1} cm/sec, a near-parabolic velocity gradient would be expected. The transverse concentration gradient therefore must be assumed to be leveled by diffusion.

Halide ion is the SCC agent at the crack tip.—As stated earlier, the requirement of a limiting halide ion mass transport rate evolved from the preliminary calculations and was therefore added as a fundamental to the model. This requirement, moreover appeared consistent with the experimental SCC results in Table I. Further justification for elimination of other species is given here.

The other species which might be considered as the SCC agents in aqueous solutions are H_2O, OH^-, H^+, or alkali metal cation. The metal cation can be eliminated because SCC occurs with near equal velocity in the halogen acid solutions. Further, the potential gradient in the crack is in the wrong direction for either H^+ or metal cation to be the primary reactant at the tip. The hydroxyl ion can be eliminated because it is a SCC inhibitor if it is present in high concentration in respect to halide ions (1).

Water is eliminated as the primary SCC agent at the crack tip for several reasons. The reaction consuming H_2O would be the formation of a titanium oxide and hydrogen ions. As will be shown later, ohmic drop with H^+ ion the sole charge carrier cannot account for the large differences between the applied potential and the reversible potential for formation of TiO_2 in acid solutions (—1100 mv vs. SCE).[1] Therefore, this potential difference would have to be explained as activation overpotential. However, this is inconsistent with the linear relationship of velocity to potential and the low activation energy. An exponential velocity-potential relationship and at least an order of magnitude greater activation energy for velocity would be observed.

Tip is at the mixed potential.—It has been found that exchange current densities for reactions (II) and (III) are relatively large on newly generated metal surface so that the short circuit current density is on the order of 1 amp/cm² (2). It was therefore initially assumed that the potential at δ^p was the mixed potential for reactions (II) and (III) (about —800 mv) in the acid solution resulting from reaction (II) on the walls. In later calculations mixed potentials more negative than the —800 mv resulting from reactions (I) and (III) were examined.

Under these basic assumptions the SCC model can be represented mathematically by consideration of the mass transport and kinetic relationships involved.

Kinetic relationships.—The kinetic relationships express local reaction rate (or current) per unit wall area for the reactions enumerated. They consider the dependence of these rates on the potential and species concentrations existing in the electrolyte at the point in question.

In the multilayer zone ($\delta \leq y \leq l$) the formation of oxide through the oxide film is governed by the high-field equation taken in a form modified from Vetter (5).

$$j_s = j_o \exp\left\{\frac{B(\Phi - \Phi_e - \Phi_f - X}{\frac{A}{V}\int_{\delta^p}^{y} j_s\, dy}\right\} \quad [1]$$

This relates the local transfer current density, j_s, to exchange current density, j_o and the potential gradient in the oxide film. The exponential term B is the high-field-conduction constant nondimensionalized in respect to potential, the quantity in parenthesis is the nondimensionalized potential drop across the oxide film, and the denominator is the film thickness. The individual terms are defined under Nomenclature, and values of the parameters used are given in Table II.

In Eq. [1], X represents a surface overpotential defined by the kinetic expression

$$j_s = i_o\, 2 \sinh\left\{\frac{n'}{2} X\right\} \quad [2]$$

This expression was used because the current density spanned both the linear and Tafel overpotential regions, and its use avoided discontinuities in the calculations. The transfer coefficient has been assumed to be one-half. The value of exchange current density, i_o, was assumed to be the same as that for bare metal, i_m, in absence of experimental data for this parameter.

In the monolayer zone ($\delta^p \leq y \leq \delta$), where the surface coverage with oxide is θ, the kinetic equation for reaction (II) has the form (2)

$$j_s = i_m\,(1-\theta)\,2 \sinh\left\{\frac{n}{2}(\Phi - \Phi_e)\right\} + j_o\,\theta \exp\left\{\frac{B(\Phi - \Phi_e - \Phi_f - X)}{t_o}\right\} \quad [3]$$

The first term on the right is the Tafel expression for formation of oxide on bare metal. Mathematically, full coverage of oxide could never be achieved with only this term because this current goes to zero as the oxide coverage, θ, approaches unity. Therefore, it was assumed that formation of oxide on oxide, governed by the high-field equation, has commenced before the first monolayer is complete. The second layer was assumed to shift to the surface and help complete the first monolayer. This procedure gave a smooth transition at $\theta = 1$ from the Tafel to high-field conduction kinetics. The transfer coefficient in the Tafel term was assumed to be one-half in absence of more precise data. Order of magnitude values of the exchange current densities have been obtained experimentally (2).

The oxide coverage, θ, can be related to reaction occurring in the monolayer zone by

$$\theta = \frac{1}{Q_o V}\int_{\delta^p}^{y} j_s\, dy \quad [4]$$

Table II. Values of parameters used in mass transport kinetic model

D_+	$= 1 \times 10^{-5}$ cm²/sec
D_-	$= 1 \times 10^{-5}$ cm²/sec
D_{II}	$= 6 \times 10^{-5}$ cm²/sec
z_+	$= +1$
z_-	$= -1$
z_{II}	$= +1$
γ	= 0.05 radians (3°)
i_{II}	$= 2 \times 10^{-7}$ amp/cm²*
i_m	$= 2 \times 10^{-2}$ amp/cm²*
i_o	$= 2 \times 10^{-2}$ amp/cm²
j_o	$= 10^{-12}$ to 10^{-6} amp/cm²
m	$= 2$
n	$= -1$
n'	$= 1$
B	$= (6 \times 10^{-6}$ cm/v)/(F/RT)
A	$= 4.85 \times 10^{-5}$ cm³/coulomb
ϕ_e	$= -1040$ mv*
ϕ_{II}	$= -180$ mv*
Q_o	$= 425 \times 10^{-9}$ coulomb/cm²
Q_r	$= 425 \times 10^{-9}$ coulomb/cm²
δ^p	$= 10^{-6}$ cm
l	$= 10^{-4}$ cm
C_-°	$= 6 \times 10^{-4}$ mole/cm³ (0.6M)
V	$= 1 \times 10^{-2}$ cm/sec

[1] Potentials in this paper are on the SCE scale.

* Based on data obtained in 12M HCl (2).

where Q_o is the charge density of a monolayer of oxide.[2]

In the monolayer zone hydrogen ion reduction was considered simultaneously with oxide formation on bare metal (2,4). At open circuit, it appears that hydrogen ion reduction occurs over the whole crack length, resulting in the mixed potential of —800 mv (2). A Tafel expression with a transfer coefficient of one-half was assumed.

$$j_H = i_H \frac{C_H}{C_{H^\circ}} (1 - \theta) \exp \{\tfrac{1}{2}(\Phi - \Phi_H)\} \quad [5]$$

The exchange current density, i_H, was estimated from kinetic studies on new Ti:8-1-1 surface (2). Hydrogen ion reduction in the multilayer oxide region was not considered for the calculations, as there the potential is more anodic to the mixed potential.

The net generation of hydrogen ions is thus defined by

$$j = j_s - j_H \quad [6]$$

Mass transport relationships.—The treatment of mass transport in this model is based upon the one-dimensional assumption discussed above and the use of a coordinate system moving with the propagating crack. Under these conditions there are no convective transport terms, and the fluxes of the significant species along the axis of the crack are (using the Nernst-Einstein approximation for mobilities)

$$N_+ = -D_+ \frac{dC_+}{dy} - z_+ D_+ C_+ \frac{d\Phi}{dy} = 0 \quad [7]$$

$$N_- = -D_- \frac{dC_-}{dy} - z_- D_- C_- \frac{d\Phi}{dy} \quad [8]$$

$$N_H = -D_H \frac{dC_H}{dy} - z_H D_H C_H \frac{d\Phi}{dy} \quad [9]$$

The flux of the alkali cation is zero because it does not participate in reactions (I) to (III).

The current density at any point in the crack can be related to these fluxes

$$i = \mathbf{F} \sum z_i N_i \quad [10]$$

and electroneutrality is assumed to hold at all points

$$\sum z_i C_i = 0 \quad [11]$$

By application of conservation requirements for halide and hydrogen ions in the crack of linearly increasing section

$$\nabla \cdot N_- = \frac{dN_-}{dy} + \frac{N_-}{y} = \begin{cases} \dfrac{2m}{4\mathbf{F}\gamma y} j_s & @ \ \delta^p \leq y \leq \delta \\ 0 & @ \ \delta \leq y \leq l \end{cases} \quad [12]$$

$$\nabla \cdot N_H = \frac{dN_H}{dy} + \frac{N_H}{y} = \frac{2}{\mathbf{F}\gamma y} (j_s - j_H) \quad [13]$$

where the right-hand side terms represent the sources arising in the reactions at the crack walls. No such equation is necessary for the cation as Eq. [7] integrates directly to (with $C_+ = C_+^\circ$ at $\Phi = \Phi^\circ$)

$$C_+ = C_+^\circ \exp \{-z_+ (\Phi - \Phi^\circ)\} \quad [14]$$

If Eq. [7] through [9] are summed after being multiplied by their appropriate charge numbers the diffusion terms can be eliminated by use of [11] to give an equation for potential.

$$\frac{d\Phi}{dy} = -\frac{N_H/D_H + z_- N_-/D_-}{z_-^2 C_- + z_+^2 C_+ + C_H} \quad [15]$$

The side conditions for these equations which correspond to a case of specified propagation velocity (and thus halide flux to tip), tip potential, and external solution concentrations are

At

$$y = \delta^p \ ; \ N_- = N_-^p, N_H = 0, \Phi = \Phi^p$$

$$y = \delta \ ; \ N_- = 0 \ [3]$$

$$y = l \ ; \ C_- = C_-^\circ, C_+ = C_+^\circ, C_H = 0 \quad [16]$$

The model is then represented by the equation system comprising the differential Eq. [12], [13], [14], [8], and [9] together with the kinetic expressions [1], [3], and [5] and the side conditions [16]. Although manipulation can reduce this directly to three second order ordinary differential equations in C_+, C_H, and Φ, the nonlinear nature of these equations precludes analytic solution. In this work a numerical solution of the equation system was developed.

Numerical Procedure

The ordinary differential equations describing the SCC model can be put in the form of five simultaneous first order equations in N_-, N_H, C_-, C_H, and Φ by substitution of Eq. [15] into [8] and [9] and insertion of the kinetic expressions [1], [3], and [5] into [12] and [13].[4] Unfortunately this equation system has boundary conditions on N_-, N_H, and Φ at $y = \delta^p$ and on C_- and C_H at $y = l$ preventing direct solution as an initial value problem.

The method used here was, after suitable nondimensionalizations had been introduced, to assume the values for C_- and C_+ at $y = \delta^p$ (actually of C_- at $y = \delta^p$ and Φ at $y = l$ which is equivalent through [11] and [14]) and solve as an initial value problem, the assumed values being corrected until convergence on the required conditions at $y = l$ was satisfied. The initial value problem was solved at each iteration of this procedure by a Runge-Kutta-Gill integration (8). The selection of successive initial value assumptions followed a Newton-Raphson second order iteration procedure in two variables with the required partial derivative being approximated by first order finite difference representations for steps of 1% (reduced during iteration to 10^{-3}%) in the iteration variables.

This calculational procedure was implemented by a FORTRAN IV program and an IBM 7094 digital computer. The computation became time consuming (convergence of assumed initial values difficult) when conditions approaching a limiting propagation velocity (very high potential drop in the crack) were approached and concentrations C_- and C_H at the tip became very small, but otherwise was quite efficiently converging in about 2 to 4 Newton-Raphson iterations.

The calculation described here allowed evaluation of model performance under any desired set of system parameters and operating conditions.

Results

All calculations were conducted for values of system parameters believed representative of the Ti:8-1-1 halide solution system and for operating conditions corresponding to those for which experiments had been conducted. Values of the parameters used are given in Table II. In the special cases where other values are used it is so stated. The only parameter listed that came from the stress corrosion cracking experiments is the angle, γ. The diffusivities are approximate values. The exchange current densities are order of magnitude values estimated from electrochemical kinetics experiments (2). The value of B in the high-field conduction equation came from Johansen *et al.* (6). The value of A was calculated from the density of bulk rutile. The reversible potentials for oxidation and hydrogen ion reduction were from Latimer (7), converted to the SCE scale. The charge

[2] The charge density of an adsorbed oxide ion layer is assumed for first layer.

[3] This condition results from the fact that there is no net consumption of halide ion in the propagation process.

[4] Equation [15] constitutes the fifth equation, along with Eq. [8], [9], [12], and [13] as modified.

density of a monolayer of oxide is based on one oxide ion per titanium atom in the basal plane.

In the course of the development of the model described above, calculations were also made for several alternative sets of assumed reactions. Two such cases of historical interest in the development will be described; they can be considered as simplifications of the final model as presented. At the time that the model formulation was begun all of the data in Table I were not available. Items 5, 6, and 7 in Table I, for example, resulted from testing the consequences of the models. It was also not recognized initially that the mixed potential for reactions (II) and (III) in acid solution (and the zero-current intercept; item 3) is —800 mv and the tip potential was initially assumed to be —900 mv from the zero-velocity intercept (Table I, item 2).

The failure of these simplified or alternative models for any reasonable parameter values to yield calculated behavior even roughly corresponding to experimental observations led to the model presented in this work and indicated certain important features of the propagation mechanism.

Case I, with no tip current or H^+ reduction.—The first calculations were made before the kinetic data for hydrogen ion reduction on bare metal were available and i_H was in effect assumed zero. The potential of the tip was assumed to be —900 mv based on the zero-velocity intercept. The tip current, being unknown, was assumed to be zero, its importance not yet being recognized. With no tip current, reaction (I) was not considered, and therefore no halide displacement was involved. In test of this model a typical velocity of 10^{-2} cm/sec was chosen for the initial calculation. The experimental values of current and potential for this velocity are, respectively, about 200 μa/cm and —500 mv (1).

Results of the initial calculation are given in Table III. Lower and upper bound levels of j_o of 10^{-12} and 10^{-6} amp/cm^2 (2) were used. It is seen that a 10^6 fold variation of j_o gave only a fourfold change in the current and about twofold change in the potential drop. The reason for this behavior is that for higher values of j_o the resistive oxide layer is built up faster thus limiting the current. Also for faster oxide layer formation, greater rates of generation of hydrogen ion and higher conductivities for the electrolyte will be encountered, and therefore a relatively smaller potential change will result. Calculated currents approach the same order of magnitude as obtained by experiment, but the potential drop is low by more than an order of magnitude. This low potential drop arises in the fact that the hydrogen ion carries most of the current in the model and hydrogen ion concentration increases toward the tip.

Case II, with tip current and H^+ reduction but no halide displacement.—After examination of case I, it became apparent that a lower conductivity must be obtained in the crack in order to obtain potentials compatible with experimental values. A reasonable way to obtain a lower conductivity was to have a mass transport limiting current density of halide ion in the monolayer zone near δ^p such that the ionic concentration at δ^p would become small. Results of

Table III. Comparison of results of calculations to experimental SCC data for V = 10^{-2}cm/sec

	SCC Experiments (1)	Calculations			
			Case I	Case II	Case III
j_o, amp/cm^2	—	10^{-12}	10^{-6}	10^{-8}	10^{-8}
I^p, μa/cm	—	0	0	7.2	8.7
I°, μa/cm	200	30	120	27	8.8
ϕ^p, mv(SCE)	−800	−900	−900	−900	−1145
ϕ°, mv(SCE)	−500	−888	−875	−777	−990
$\Delta\phi$, mv	300	12	25	123	155
C^p_-/C°_-	—	1.6	2.6	10^{-3}	2×10^{-3}

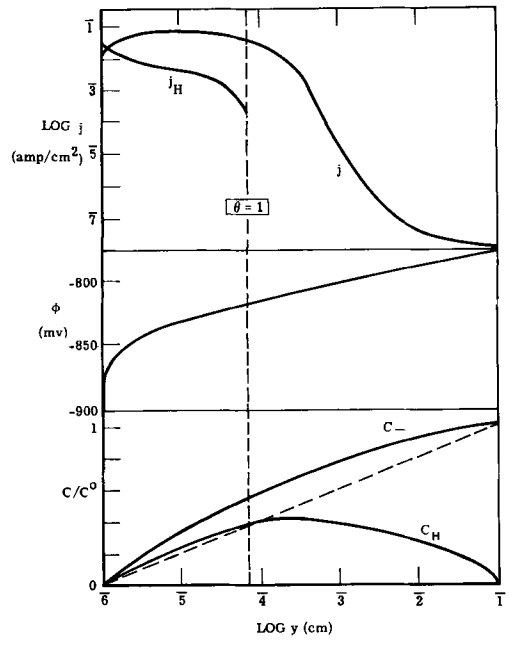

Fig. 2. Calculated current density, potential, and concentration as a function of position in a propagating stress corrosion crack according to model of case II.

the calculation with limiting mass transport are shown in Table III and plots of flux, potential, and concentration *vs.* position in the crack are shown in Fig. 2. It was found that a tip current of 7.2 μa/cm was close to the value of the limiting current, as it gave a concentration of halide ion at δ^p a factor of 10^{-3} times that of the bulk solution. The potential drop now approached the right order of magnitude and could be increased further by approaching the limiting mass transport rate more closely, thus giving a lower concentration at δ^p. The current, I°, was still low (using a value of j_o giving an approximate fit to the experimental kinetic data [2]), but this was considered to be due to the low potential as yet achieved.

It turned out that the limiting tip current corresponds to the order of magnitude for one monolayer of adsorbed halide ions or of titanium dihalide, the thermodynamically stable form at the tip potential (7). The tip current can be defined as $I^p = 2qQ_xV$, which for $I^p = 7.2$ μa/cm, $Q_x = 425$ μcoulomb/cm^2 (for dihalide), and $V = 10^{-2}$ cm/sec, gives $q = 0.85$ of a monolayer. The values of the parameters used in the model are not sufficiently precise that the model cannot distinguish between a monolayer of adsorbed halide ions or a monolayer of titanium dihalide, but it is significant that the order of magnitude of a monolayer is indicated. If the dihalide is formed, it is necessary, however, that it remain adsorbed until it enters the monolayer zone because it is known to be soluble and fully ionized; dissolution would give Ti^{++} as a current carrier, resulting in an increase rather than a decrease in halide ion concentration toward the tip.

The mass transport limiting case was then tested by further SCC experiments in which the bulk concentration of halides was varied. In concentrated solutions (1-10M) the observed velocity (4) was found to correspond to the value calculated for a limiting mass transport rate of halide ions from the bulk solution to the tip zone forming a monolayer therein but with no wall reactions in the region $\delta^p \leq y \leq l$. This calculation is represented by the dashed line in the concentration plot in Fig. 2. Examination of the model shows that this is a limiting case for high concentration electrolytes, thus providing a degree of verification.

On the other hand, the model predicts an approximately linear relation of velocity to concentration,

whereas approximately a 1/4 power relationship was observed, becoming asymptotic to a finite lower limit velocity in distilled water (Table I, item 5). The implication is that unless water molecules are also a stress corrosion agent, halide must be conserved in the crack by displacement or by hydrolysis in order to have SCC in distilled water.[5] Halide displacement tested in a much simplified mass transport model (4) gave results semiquantitatively in agreement with the velocity *vs.* concentration data. The model was therefore modified to include halide displacement.

Case III, with tip current, H^+ reduction, and halide displacement.—In the final form of the model as presented it was assumed that the equivalent of a monolayer of adsorbed halide ion was formed in the tip zone and that this was displaced by oxide on the basis of equal surface coverage. The exchange current densities for oxidation of freshly generated bare metal surface and hydrogen ion reduction thereon (2) were also assumed applicable to the surface covered with adsorbed halogen.

Initial calculations including halide displacement indicated propagation velocities much higher than those observed would be required in order to obtain a limiting mass transport rate and an appreciable potential drop. The reason for this, of course, was that the halide ion was regenerated and built up a higher concentration in the monolayer zone. The simplest change to reduce this discrepancy was to start at a more negative potential at δ^p such that a greater amount of hydrogen ion discharge occurred in the monolayer zone near δ^p, thus lowering the concentration of H^+, and X^- by the electroneutrality condition. This required no change in formulation of the model. It was consistent with the expectation of some oxidation of titanium to Ti^{++} which is the thermodynamically stable oxidized form at negative potentials (7, 9) (E° = −1870 mv), although the amount of Ti^{++} formed would have to be relatively small so as to be neglected in the transport equations. Trial values of tip potential were used until a limiting mass transport rate was achieved at δ^p consistent with velocity and monolayer halide coverage in the tip zone.

Results of calculations for case III are given in Table III and Fig. 3. By starting at the more negative potential the rate of oxidation of titanium was decreased in respect to hydrogen ion reduction. (Further, $j_s = 0$ at potentials more negative than ϕ_e.) This resulted in a lower hydrogen ion concentration in the crack and a larger potential drop. But the potential drop was not large enough to overcome the effect of starting at the more negative potential, and a longer time was required to complete the first monolayer and less total oxide was formed. The total current was therefore also too low as compared to experimental SCC data in Table III. Although there is some hydrogen ion discharge in the monolayer zone the net resulting charge density cannot be greater than $Q_x + Q_o$ in the present formulation. If $Q_x + Q_o$ were exceeded, there would be a net flux of hydrogen ions toward the tip giving a potential gradient in the wrong direction. (It may also be noted that j_H increases initially with distance in Fig. 3 due to increase in hydrogen ion concentration whereas j_H decreased initially in Fig. 2 because the concentration term had not been added to Eq. [5] at the time the calculation was made.)

Although in principle it is possible to achieve as large a potential drop as desired by going to a sufficiently low concentration at δ^p, one very serious problem remains. Examination of the model formulation and results shows that most of the potential drop occurs in the monolayer zone with a very large potential gradient at δ^p. For a concentration at δ^p that is a factor of 10^{-3} times that of the bulk solution (0.6M) the potential gradient at δ^p is over 10^6 v/cm. This is a level at which dielectric breakdown could occur and is higher by at least an order of magnitude than can be supported in continuum electrolyte. Such factors have limited voltage drop calculated by the model to less than about 200 mv while, experimentally, velocity was observed to be linear with potential over a range of nearly 2v. Thus it is apparent that an additional source of a large potential drop must exist.

[5] It is proposed that chloride at a parts-per-million level remaining in the metal from the reduction process is the source in the distilled water experiments. Experiments are underway to test this hypothesis.

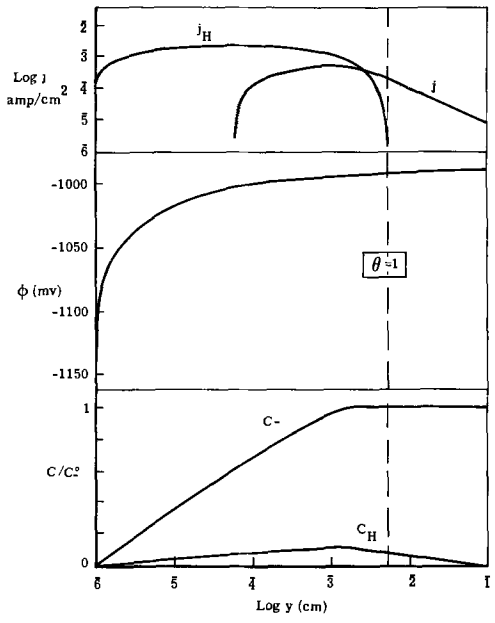

Fig. 3. Calculated current density, potential, and concentration as a function of position in a propagating stress corrosion crack according to model of case III.

It should also be pointed out that where there was some latitude of choice in the exact value of the parameters, values (Table II) were chosen that would tend to maximize the potential drop. For example, $\delta^p = 10^{-6}$ cm which gives a crack width at that point of 5Å is probably about an order of magnitude too small. No experimental value was available for i_o so it was assumed to be equal to i_m, whereas it would be expected to be considerably smaller than i_m. The value of $j_o = 10^{-8}$ used in case II and III is four orders of magnitude larger than the experimental value for titanium (6). The Flade potential was also assumed zero whereas a value of about ½v would be reasonable in comparison to other metals (5). That the model was incapable of producing a potential drop comparable to experiment in spite of this bias shows either that there is a large potential drop in the tip zone or that additional species existing in the electrolyte in the crack must be taken into account. Experiments with a Luggin capillary probe and calculations show that the large potential drop does not occur at the mouth of the crack. As described under limitations, the production of soluble titanium ions in the crack is suspected as the reason for the high potential drop in the SCC experiments.

Comparison of Model Behavior to Experimental Results

We will try to show here to what extent the calculated results for the model developed in this work agree with the experimental data in Table I and thus satisfy our original requirement. In some areas the agreement is quantitative and others qualitative, as an extensive investigation of the effects of all parameters has not yet been made. Some answers are outside of the scope of the present formulation and further experimental work and modeling are required. However, in this comparison, explanations for some observed characteristics of SCC can be obtained.

Only Cl^-, Br^-, *and* I^- *produce SCC in aqueous solution.*—The explanation of this observation is outside of the scope of any transport kinetic model such as the present formulation. Two possibilities are suggested: Perhaps other anions are absorbed in the oxide on the walls of the crack and never reach the tip zone; or they may not have the required surface transport properties to reach the tip within the tip zone.

Linear relation of velocity to potential.—The velocity is apparently limited by mass transport of halide ions in the monolayer zone close to δ^p giving a potential drop which is linear with tip current. The zero-velocity intercept is more cathodic than the mixed potential for reactions (II) and (III) because a cathodic current is required to decrease the halide concentration in the crack to a low enough level to stop propagation.

Linear relation of current to potential.—It can be shown that current flowing into the crack under potentiostatic conditions is linearly related to rate of creation of new surface or to velocity (2). Because velocity is linearly related to potential, current is therefore linearly related to potential. The zero-current intercept is at the mixed potential for reactions (II) and (III) on the crack walls at the acid condition developed in the crack.

Independence of velocity with cation.—The velocity is limited by halide ion transport in the monolayer zone and, with the formation (and reduction) of hydrogen ion that occurs, this phenomena is little affected by the decreased amount of other cations present. (Certain heavy metal chlorides such as cupric chloride, however, give inhibition at open circuit, because they establish a potential in the anodic protection zone for chloride.)

Nonlinear relation of velocity to concentration of halide ions.—This behavior is related to displacement of halide ion by oxide in the monolayer zone, which leads to local circulation of halide ions and a strongly nonlinear relation of halide concentration in the tip region, and thus to bulk concentration of halide.

Activation energy for velocity of approximately 3.5 kcal.—The activation energy for diffusion of species in aqueous solutions is also about 3.5 kcal (10). If the velocity were limited by a chemical or electrochemical reaction, a considerably higher activation energy would be expected. An activation energy of 3.5 kcal for velocity, although not proof of a limiting mass transport, is strong supporting evidence.

Open-circuit transient potential.—The initial open-circuit plateau potential up to an applied potential of +200 mv is only slightly below the applied potential because only the outer IR drop in the crack, which is small according to the model, disappears rapidly. The inner IR drop near δ^p would continue if the velocity remains initially unchanged (at time less than 10^{-2} sec from open circuit) and the tip current for reaction (I) is supplied by local circulation in conjunction with reaction (III), hydrogen ion reduction. There is however, also a need for reduction of other species such as higher valence titanium ions to continue the oxidation on the walls. Further kinetics experiments and model modification need to be done on this aspect.

The time of the potential transient, however, is consistent with the mass transport model. The time constant for a diffusional process is given approximately by $\tau = L^2/D$. The length associated with a diffusivity of 10^{-5} cm^2/sec and transient time of 10^{-2} to 100 sec is 3×10^{-4} to 3×10^{-2} cm consistent with position of peak concentration and value of l in the model. The final potential reached on open circuit is the mixed potential of —800 mv.

Limitations of Model and Calculations

While the mass transport kinetic model is qualitatively, and in some respects quantitatively, in agreement with the experimental stress corrosion cracking data, no real proof of its validity can be claimed. Some of its limitations and areas where it has indicated that further investigation is required are described here.

Mechanisms in tip zone not considered.—As mentioned earlier no continuum model such as this can be applied to the tip zone where distances approach the order of magnitude of atomic spacing. Complete understanding of stress corrosion cracking will require that atomic scale mechanisms at the tip be described. At best the model shows that halide ions disappear into the tip zone but gives no indication of whether electrochemical reaction or only adsorption occur. It also cannot consider the effect of the nature of the metal lattice which is manifested in this region. The transport mechanism within the tip zone itself also remains to be elucidated.

Geometry of crack imprecisely known near tip.—The crack angle, γ, is an important parameter in the model. Although it has been measured for the outer part of a crack to within about 10^{-4} cm from the tip the precise shape in the monolayer zone is not known. This turns out to be an important zone in respect to concentration and potential gradients in the model. The tip radius may be considerably larger than atomic as indicated by Elliott (11), but calculations have indicated that the angle and value of δ^p do not have a large influence on the magnitude of the potential drop near δ^p.

Continuum model breaks down near δ^p *where large changes in potential occur.*—Figures 2 and 3 show that the potential gradient is steepest and most of the potential drop occurs in a zone near δ^p where the applicability of the continuum treatment is doubtful. Originally it was hoped that the model could account for the entire apparent potential drop observed in the experiments; however, these studies have not supported that expectation. A change in the model to include generation and transport of soluble titanium ions as described below may change this situation to some extent, but it is a possibility that at least a part of the potential drop must be assigned to phenomena outside of the continuum region.

Limited accuracy of kinetic data used.—It should be counted as a strength of the model that it forced recognition of the important parameters and a need to evaluate them by independent experiments. Thereby new data were obtained on electrochemical kinetics on newly generated titanium surfaces. It has become evident however, that more data and more precise data are required, including:

(*a*) kinetics of hydrogen ion reduction on bare metal;
(*b*) kinetics of formation of first layer of oxide;
(*c*) kinetics of formation of soluble titanium ions;
(*d*) kinetics of a, b, c on adsorbed halide film;
(*e*) kinetics of formation of oxide on oxide surface;
(*f*) Flade potential (assumed zero in calculations).

Formation and transport of soluble titanium ions not included.—No consideration of possible formation and transport of soluble titanium ions has been included in this model, largely because no kinetic data for formation of Ti^{++} or Ti^{+++} on newly generated titanium surfaces have been available. It has, however, become increasingly clear from the interplay of theoretical model development and experiments that soluble titanium species must be formed. This is implied by need for a potential at δ^p more negative than the mixed potential for reactions (II) and (III) in case III. Also initial open-circuit plateau slightly below the applied potential up to +200 mv (Table I, item 7) suggests a reversible titanium ion couple capable of providing a current to continue crack propagation. Potential-*p*H diagrams (9) for titanium also show that in acid solution the soluble ions are

more thermodynamically stable than the oxide. The oxide apparently owes its existence at all in acid solution to favorable kinetics (*i.e.*, rate of formation much greater than rate of dissolution). Formation of soluble species in parallel with oxide has been reported under certain conditions for iron (12) and for zinc (13). When necessary data are obtained for titanium this mechanism can be included in further model developments.

Conclusions

In this work a quantitative electrochemical mass transport kinetic model has been formulated for stress corrosion cracking of titanium alloy, which has given some new insights into mechanisms in a propagating crack. In particular the model studies have indicated:

1. That the propagation of the crack requires a flux of halide ions to the tip zone. The limiting mass transport rate of these halide ions corresponds to the order of magnitude of one monolayer of halide ions or titanium halide.
2. That a mechanism such as displacement or hydrolysis exists to release of the bound halide from the walls within the crack in order for the model to be consistent with observed velocity *vs.* concentration data.
3. That reduction of hydrogen ions in the crack in the region outside of the tip zone occurs at the negative potential of this zone but the amount must be small to be consistent with the direction of the potential gradient.
4. That the model as now formulated cannot account for the large difference between the applied potential in SCC experiments and the reversible potential for oxidation of newly generated titanium surface. This potential difference either exists outside the region of the model within the tip zone or it must be accounted for in a revised model formulation. Several experimental results point to formation of soluble titanium species in parallel with formation of oxide on new titanium surface which if included in the model may produce the required potential drop.

In addition, as an important general contribution, the model has forced quantitative thinking about the electrochemistry in a crack. This has required obtaining new kinetic data for freshly generated titanium surfaces and suggested key stress corrosion cracking experiments.

Acknowledgment

This work was partially supported by NASA/Headquarters Contract NAS 7-489.

Manuscript submitted June 7, 1968; revised manuscript received *ca.* Oct. 2, 1968. This paper was presented at the Dallas Meeting, May 7-12, 1967, as Paper 147.

Any discussion of this paper will appear in a Discussion Section to be published in the December 1969 JOURNAL.

NOMENCLATURE

A	$M/z\mathbf{F}\rho = 4.85 \times 10^{-5}$ cm³/coulomb for rutile
B	constant in high field equation (nondimensionalized in respect to potential)
C	concentration, mole/cm³
D	diffusivity, cm²/sec
$\mathbf{F}$	Faraday, 96,500 coulomb/equiv or 23,060 cal/v equiv
I	current along axis of crack in unit width specimen, amp/cm
i	current density in cross section of crack, amp/cm²
i_o	exchange current density with suitable subscript, amp/cm²
j	current density, amp/cm²
l	crack length to position where current enters from sides, cm
M	molecular weight, g/mole
m	coefficient in reaction (I)
N	flux, mole/cm² sec
n	number of electrons in rate-determining step
Q	charge density of surface species, coulomb/cm² Q_o for oxide, Q_x for halide
q	number of monolayers
R	gas constant, 1.987 cal/deg mole
T	temperature, °K
t	thickness, cm
t_o	thickness of first monolayer of oxide, cm
V	crack propagation velocity, cm/sec
X	activation overpotential, nondimensionalized
y	distance from apex of crack, cm
z	equiv/mole
γ	crack angle, radians
δ	distance from crack apex to position where monolayer of oxide is complete, cm
δ^p	distance from crack apex to position where electrical double layers intersect, cm
δ^t	distance from apex to crack tip, cm
θ	oxide coverage, dimensionless
ρ	density, g/cm³
τ	time, sec
ϕ	potential, volts or mv
Φ	$(\mathbf{F}/RT)\phi$, dimensionless potential ($\mathbf{F}/RT$ = 38.9 v^{-1} at 25°C)

Subscripts

$+$	cation
$-$	halide ion
e	equilirium potential
f	Flade potential
H	hydrogen ion
m	metal (exchange current density for oxide on metal)
o	oxide (exchange current density for oxide on oxide)
s	surface
x	halide

Superscripts

o	bulk
p	position in crack where double layers intersect
t	crack tip

REFERENCES

1. T. R. Beck, *This Journal*, **114**, 551 (1967).
2. T. R. Beck, *ibid.*, **115**, 890 (1968).
3. J. G. Hines, *Corrosion Sci.*, **1**, 21 (1961).
4. T. R. Beck, Presented at Stress Corrosion Conference, Ohio State University, Sept. 1967, and unpublished work.
5. K. S. Vetter, "Electrochemical Kinetics," (translation) Academic Press, New York (1967).
6. H. A. Johanson, G. B. Adams, and P. Van Ryssselberghe, *This Journal*, **104**, 339 (1957).
7. W. Latimer, "Oxidation Potentials," 2nd ed., Prentice-Hall, Englewood Cliffs, N.J. (1952).
8. S. Gill, *Proc. Camb. Phil. Soc.*, **47**, 96 (1951).
9. M. Pourbaix, "Atlas of Electrochemical Equilibria," Pergamon Press, New York (1966).
10. S. Glasstone, K. J. Laidler, and H. Eyring, "The Theory of Rate Processes," McGraw-Hill Book Co., New York (1941).
11. H. A. Elliott, *Proc. Phys. Soc.*, **59**, 208 (1947).
12. M. Nagayama and M. Cohen, *This Journal*, **109**, 781 (1962).
13. H. Kaesche, *Electrochim. Acta*, **9**, 383 (1964).

Internal Stress of Electroless Metal Films on Single Crystal Silicon

H. E. Austen

Process R&D Department, The National Cash Register Company, Dayton, Ohio

and R. D. Fisher

Materials Research Department, Ferroxcube Corporation, Saugerties, New York

ABSTRACT

The internal stress of electroless nickel and cobalt films on silicon single crystals was measured as a function of thickness and experimental conditions. The internal stress was measured using an interference technique to determine the bending produced by films in the thickness range of 500-5,000Å. The stress was found to be tensile and isotropic for both metals. The stress in electroless nickel films is greater than in similar cobalt films. The stress decreases with thickness which is in contrast to vacuum evaporated nickel and cobalt films which exhibit a stress independent of thickness.

The electroless deposition of nickel, cobalt, and their alloys was reported by Brenner in 1946 (1). Since then, considerable literature on the electroless deposition process has been published, and the physical properties of the deposits have been studied. Graham and coworkers have recently published the results of an extensive investigation of the structure and mechanical properties of electroless nickel (2), and there is increased interest in electroless cobalt, which may be prepared with magnetic characteristics applicable to digital recording media (3).

A property of electroless deposits which has not been extensively studied is the internal stress characteristics. Knowledge of the stress is of theoretical interest due to the relatively small crystalline size and to the inherent phosphorus content of the deposit. Practical interest lies in preparation conditions which may minimize internal stress to promote adhesion and prevent cracking or buckling of the coatings on certain substrates.

In this investigation, the internal stress of electroless nickel and cobalt films were measured as a function of film thickness and experimental conditions.

Experimental

Electroless cobalt and nickel films were deposited on the (111) crystal face of optically polished, single crystal, silicon wafers. The method of determining the internal stress in this investigation was developed by Hoffman and Finegan (4, 5) based on the theory of bending of thin plates (6). The contours of the silicon wafers were determined with, and without, the deposit. From these contours the bending due to the film was determined, and, from this bending and the thickness of the film, the internal stress was calculated.

Electroless deposition conditions.—The silicon substrates were prepared by cleaning ultrasonically in an organic solvent, immersing in hot concentrated nitric acid, rinsing in distilled water, immersing in 30% hydrofluoric acid, rinsing in distilled water, immersing in 20% hydrofluoric acid containing 0.2 g/l $PdCl_2$, and placing in the electroless solution. Two solution concentrations were used to deposit each metal, as follows:

(a) Concentrated Solutions	g/l
$CoCl_2 \cdot 6H_2O$ or $NiCl_2 \cdot 6H_2O$	30
NH_4Cl	50
$(NH_4)_2C_6H_5O_7 \cdot H_2O$ (diammonium citrate)	65
$NaH_2PO_2 \cdot H_2O$	15
NaOH	to *p*H 8.2
Temperature: 84° ± 1°C	

(b) Dilute Solutions	g/l
$CoCl_2 \cdot 6H_2O$ or $NiCl_2 \cdot 6H_2O$	7.5
NH_4Cl	12.5
$H_3C_6H_5O_7$ (citric acid)	19.8
$NaH_2PO_2 \cdot H_2O$	7.0
NH_4OH	to *p*H 8.2
Temperature: 84° ± 1°C	

The time of deposition was varied to obtain deposits ranging in thickness from 500 to 5,000Å out of the four solutions.

Thickness measurement.—The thickness of the electroless films was generally determined by assuming bulk density to be equal to the pure metal, *i.e.*, 8.9 g/cm^3 for both nickel and cobalt, and weighing the deposit on a microbalance. The measurements were checked in thin films by using the Tolansky method (7) and agreed within about 10%.

Stress measurement.—The measurement was made by determining the bending produced in the silicon wafer by the deposit on the face of the wafer. The contour of the face was determined from the interference pattern of sodium light reflected between the face and an optical flat on which the wafer lay. The pattern was photographed, using reference marks, prior to deposition. After deposition, the deposit was stripped from the back of the wafer and the interference pattern again photographed. From these photographs the contours in a line between the reference marks were plotted. Subtraction of the two curves then gave a curve of the bending produced by the deposit. In this investigation, silicon wafers 0.008 in. thick by ¾-⅞ in. diameter were used to give the desired degree of bending. Stress measurements were generally made on five deposits, and the average results were plotted as a function of thickness.

Stress calculation.—The thickness of the deposited film was generally calculated from the weight of deposit and the bulk density of the metal as previously discussed. The thickness of the silicon wafer was measured with a micrometer. Young's modulus and Poisson's ratio were calculated for the (111) plane from the elastic constants.

The curve of bending is normalized by plotting the difference between it and a straight line drawn from one end to the other. The curve is assumed to be a parabola of the form $y = k\,x^2$. At four equally spaced points on the "y" axis, the average x distance to the curve is determined. The values of y *vs.* the square of the average distance $\overline{X}^2$ is plotted, and the straight line fitting these points has a slope whose value is k.

The stress is calculated as

$$\text{Stress} = \frac{E\,h^2\,k}{3\,t\,(1-\mu)}$$

where E is Young's modulus = 1.748×10^{12} dynes/cm^2 calculated from elastic constants, μ is Poisson's ratio = 0.266 calculated from elastic constants, h is thickness of substrate, cm, k is slope of y *vs.* $\overline{X}^2$ plot, cm^{-1}, and t is thickness of deposited film, cm.

Experimental Results

Electroless nickel.—The internal stress of the electroless nickel deposits, parallel to the surface, was found to be tensile and isotropic over the range of 500-5000Å whether deposited from the dilute or concentrated solutions. The tension per unit length, *i.e.*, normalized bending force, *vs.* thickness is shown in Fig. 1.

The tension per unit length from both the dilute and concentrated solutions increases rapidly between 500 and 2000Å, but increases more rapidly for films prepared from the concentrated solution. From 2000-5000Å, the tension per unit length from the dilute solution increases very little, while from the concentrated solution there is a continuous increase.

The internal stress, derived by dividing tension per unit length by thickness, approaches a maximum at about 1000Å from the dilute solution and at about 1400Å from the concentrated solution (Fig. 2). The stress from the dilute solution reached a maximum not much lower than the maximum from the concentrated solution (3.2 *vs.* 3.75 dynes/cm^2 x 10^9). At greater thicknesses the stress appears to decrease to some constant value which is higher for the concentrated solution. However, at 5000Å the deposit from the concentrated solution has a tension per unit length twice that from the dilute solution.

Electroless cobalt.—The internal stress of the cobalt deposits, parallel to the surface, was also found to be isotropic and tensile over a thickness range of 500-3000Å from the dilute or concentrated solutions. The tension per unit length, *i.e.*, normalized bending force *vs.* thickness, is shown in Fig. 3.

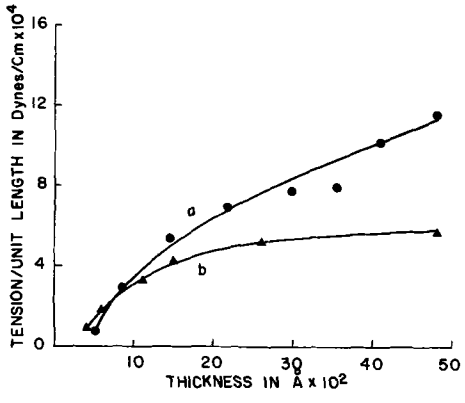

Fig. 1. Tension per unit length *vs.* thickness for electroless nickel: (a) deposits from concentrated solution; (b) from dilute solution.

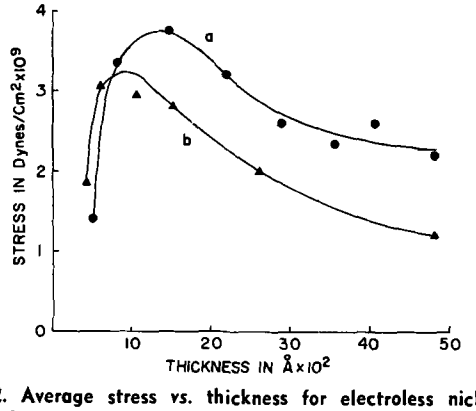

Fig. 2. Average stress *vs.* thickness for electroless nickel: (a) deposits from concentrated solution; (b) from dilute solution.

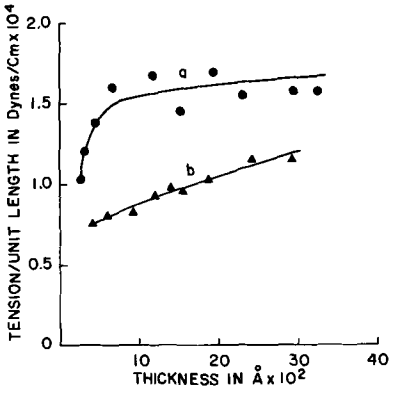

Fig. 3. Tension per unit length *vs.* thickness for electroless cobalt: (a) deposits from concentrated solution; (b) from dilute solution.

The tension increases linearly from 500 to 3000Å when cobalt films are prepared from the dilute solution. However, in the case of concentrated solutions, the tension increases rapidly from 500Å to approximately 1000Å and then remains relatively constant with increasing thickness over the range measured. The tension per unit length is larger for films deposited from concentrated solutions than for films deposited from dilute solutions, regardless of the thickness.

However, the internal stress calculated from the tension per unit length decreases rapidly from a thickness of 500 to 2000Å, and from 2000 to 3000Å is relatively constant (Fig. 4). The stress exhibited by films from the dilute and concentrated solutions is nearly identical at a thickness of 3000Å. However, in thin films, *e.g.*, at 500Å, the stress is much larger in films deposited from the concentrated solution.

Discussion

The method utilized to measure the internal stress detects the presence of anisotropic stresses by producing an asymmetric interference pattern. Previous techniques for measuring the internal stress assumed that the stress was isotropic. Our results show that electroless cobalt and nickel films exhibit an isotropic stress and that the average stress is a function of thickness. These results are in contrast to vacuum evaporated cobalt and nickel films which exhibit a stress independent of thickness (8, 9).

The curves of tension per unit length *vs.* thickness, and stress *vs.* thickness, for nickel, indicate that the initial stress is compressive but rapidly becomes tensile so that the average stress is zero at about 300-400Å. The deposits from concentrated solutions show a rapidly increasing tension per unit length, initially, but then show a smaller, nearly constant rate of change at

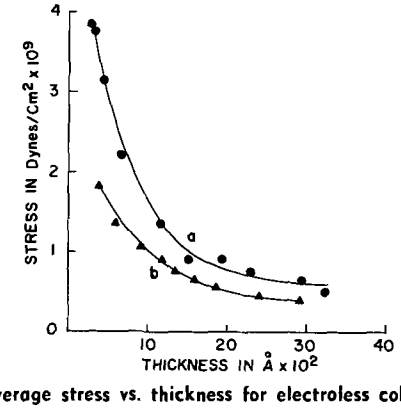

Fig. 4. Average stress *vs.* thickness for electroless cobalt: (a) deposits from concentrated solution; (b) from dilute solution.

thicknesses greater than about 2000Å. The deposits from dilute solutions also show an initially rapid increasing tension per unit length, but the rate of change decreases and becomes nearly constant at a considerably lower tension value, but at about the same thickness.

When the data are plotted as stress *vs.* thickness the stress shows a rapid increase, to a maximum and a gradual leveling off to a nearly constant value of 5000Å or more. Again, it appears that the initial stress was probably compressive. Also, the concentrated solution produces a higher maximum and levels off at a higher thickness value.

The curves for cobalt also indicate a rapidly increasing initial stress, but the data do not indicate that the initial deposit is compressive from either the concentrated or dilute solutions. The deposits from the concentrated solutions reach a higher tension per unit length than those from dilute solutions, and then level off to nearly constant tension at about 1000Å. However, the deposits from dilute solutions show nearly a constant rate of change of tension per unit length with thickness and the rate of increase is greater than for the concentrated solution. Extrapolation of the curves indicates the stresses would be equal at approximately 10,000Å.

In both cases there appears to be a change in the mechanism producing stress at thicknesses between 500 and 1000Å. It is interesting to note that electron transmission micrographs of chemical deposits on "Formvar" have shown that the deposits first become continuous at thicknesses of about 500Å; the observed change in stress mechanism may be associated with such a structural change.

The stress in nickel is much higher than in cobalt at similar thicknesses. Below about 1000Å, there appears to be considerable difference between the two metals. For example, the tensile stress of cobalt below 1000Å is decreasing rapidly with increasing thickness while the tensile stress of nickel is increasing rapidly. While the data for nickel indicate the initial deposit may be compressive, that for cobalt indicates extremely high tensile stress in the initial deposit. It should be noted that there is a possibility that the stress mechanism operates much more rapidly with change in thickness of cobalt and the maxima might be present at thicknesses below that at which measurements were made.

The experimental data on stress in chemically deposited films and on the structure of these films are not sufficient to allow a theoretical explanation as to the origin and mechanism of the stress. However, an explanation for the difference in stress observed for cobalt and nickel might be that the codeposited phosphorus is insoluble in cobalt (10) but in the case of nickel may form a supersaturated solid solution of phosphorus dissolved in crystalline nickel (2). As a consequence, the phosphorus in cobalt films should occur at crystallite boundaries as elemental phosphorus or as a cobalt phosphide which might reduce the generation of internal stress associated with any interaction or crystallite boundary relaxation. In the case of nickel this would not occur due to formation of a solid solution. This mechanism would agree with that proposed by Hoffman (11).

Summary of Results

Electroless cobalt and nickel films exhibit an isotropic tensile stress at thicknesses greater than 500Å whether deposited from relatively dilute solutions or from concentrated solutions. However, deposits from concentrated solutions exhibit higher stress values.

The stress in nickel deposits is greater than in cobalt deposits at equivalent thicknesses by a factor of about four.

A maximum tensile stress in electroless nickel films occurs at a thickness of approximately 1000Å while no maximum in stress was observed for cobalt films over the thickness range investigated.

Manuscript submitted June 25, 1968; revised manuscript received Oct. 2, 1968.

Any discussion of this paper will appear in a Discussion Section to be published in the December 1969 JOURNAL.

REFERENCES

1. A. Brenner and G. E. Riddell, *J. Research Natl. Bur. Standards*, **3**, 31 (1946).
2. A. H. Graham, R. W. Lindsay, and J. J. Read, *This Journal*, **112**, 401 (1965).
3. R. D. Fisher and W. H. Chilton, *ibid.*, **104**, 485 (1962).
4. J. D. Finegan and R. W. Hoffman, *J. Appl. Phys.*, **30**, 597 (1959).
5. J. D. Finegan and R. W. Hoffman, AEC Tech. Rept. 15, Case Institute of Technology, Cleveland, Ohio, 1961.
6. S. P. Timoshenko, "Theory of Plates and Shells," McGraw-Hill Book Co., New York (1940).
7. S. Tolansky, "Surface Microtopography," Interscience Publishers, Inc., New York (1960).
8. R. W. Hoffman and E. C. Crittenden, Jr., *Phys. Rev.*, **78**, 349 (1950).
9. E. Klokholm and S. Berry, *This Journal*, **115**, 823 (1968).
10. Cobalt Monograph, Centre D'Information Du Cobalt, Brussels, Belgium 185 (1960).
11. J. D. Finegan and R. W. Hoffman, AEC Tech. Rept. 18, Case Institute of Technology, Cleveland, Ohio, 1961.

Effect of Electroless Nickel Substrate on Coercive Force and Microstructure of Certain Co-P Films

V. Morton and R. D. Fisher

Ferroxcube Corporation, Saugerties, New York

ABSTRACT

The influence of electroless nickel as a substrate on the coercive force and microstructure of certain electroless cobalt films was examined. Cobalt films on electroless nickel substrates exhibit (*i*) deposits which may contain a lesser proportion of amorphous or fine grained cobalt, (*ii*) a more pronounced [10$\bar{1}$0] preferred orientation perpendicular to the plane of the deposit relative to similar deposits on a Mylar-adhesive substrate, and (*iii*) higher coercive force values relative to similar deposits on a Mylar-adhesive substrate. The data suggests that the increase in coercive force may be due to a decrease in the amorphous characteristics of cobalt films prepared on electroless nickel in comparison to such films on Mylar.

Chemically deposited cobalt films may exhibit coercive force values from a few oersteds to over one thousand oersteds depending on the experimental conditions (1, 2). In general, investigators have utilized pretreated Mylar (3-5) (polyethylene terephthalate), Mylar with an adhesive (6), glass (7), brass (8), or Be-Cu (1) as a substrate or base material. The influence of the substrate or base material on the coercive force and microstructure of electroless cobalt films has not been extensively studied under given experimental conditions. Consequently, a preliminary study was made as to the influence of the substrate on the coercive force and microstructure of electroless cobalt films. The experimental conditions were fixed and the magnetic properties of electroless cobalt films on nonconductive and conductive substrates were evaluated. The substrates were Mylar-adhesive and Mylar-adhesive coated with electroless nickel. The cobalt film thickness was varied on each substrate from approximately 1000 to 10,000Å and the coercive force and microstructure as a function of thickness were evaluated on each substrate.

Experimental Conditions

Cobalt deposition.—Electroless cobalt films were prepared from the following solution:

$CoCl_2 \cdot 6H_2O$	(cobalt chloride)	0.0315M (Co^{++})
$NaH_2PO_2 \cdot H_2O$	(sodium hypophosphite)	0.03M (H_2PO_2)
NH_4Cl	(ammonium chloride)	0.234M
$H_3C_6H_5O_7 \cdot H_2O$	(citric acid)	0.0934M

*p*H: 8.2 with NaOH
Temperature: 80°C

Nickel deposition.—Electroless nickel was deposited on the Mylar-adhesive substrate from the following solution:

$NiCl_2 \cdot 6H_2O$	(nickel chloride)	0.0315M
NH_4Cl	(ammonium chloride)	0.2338M
$H_3C_6H_5O_7 \cdot H_2O$	(citric acid)	0.0945M
$NaH_2PO_2 \cdot H_2O$	(sodium hypophosphite)	0.0664M

*p*H: 8.2
Temperature: 80°C
Time: 60 sec

Substrates.—Mylar substrates were precleaned and dip coated with an adhesive and cured (3). The Mylar-adhesive substrates were then overcoated in certain instances with electroless nickel from the preceding solution. The Mylar-adhesive surface was sensitized with stannous chloride and activated in the usual manner (3).

Magnetic measurements.—M-H loop measurements were made with an instrument similar to that of Howling (6). A maximum field of 1000 oersteds was applied to measure the M-H loop.

Thickness measurements.—The thickness was generally determined by the weight-density relationship assuming a bulk density for Co-P of 8.6. In general, this method agreed with interference and x-ray techniques which were used to check the thickness estimation from time to time.

X-ray diffraction.—A Norelco x-ray diffractometer was used to determine the crystallographic orientations in the plane of deposit. The specimens were examined in normal reflection geometry using the flat specimen holder. Filtered cobalt Kα radiation was used. A silicon powder standard was used to adjust the instrumental conditions so that they were constant for each specimen examined. The integrated intensities and the proportion of the sum of the integrated intensities attributable to each observed x-ray reflection were determined. The integrated intensities were obtained by integrating the area under each diffraction profile observed.

Experimental Results and Discussion

Magnetic properties.—The coercive force of electroless cobalt as a function of thickness on the Mylar-adhesive and electroless nickel substrates is shown in Fig. 1. The coercive force of cobalt films on both substrates is greatly dependent on the film thickness.

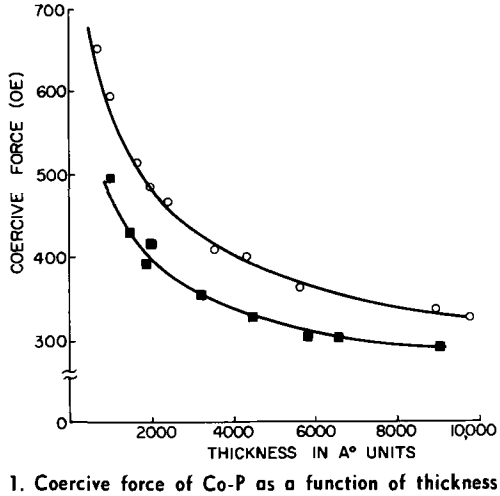

Fig. 1. Coercive force of Co-P as a function of thickness on adhesive coated Mylar, ■, and on electroless Ni-adhesive-Mylar, ●.

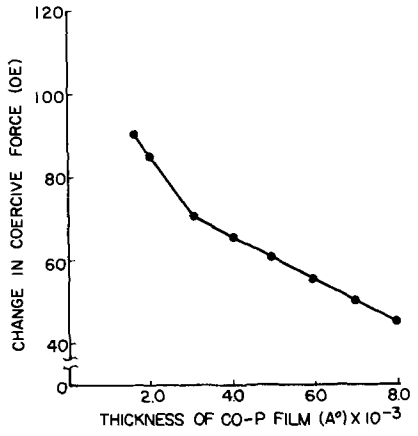

Fig. 2. Change in coercive force of Co-P as a function of thickness due to overcoating the adhesive-Mylar substrate with electroless nickel.

On the Mylar-adhesive substrate, the coercive force decreases from 495 oe at 1000Å to 295 oe at 9000Å. However, on Mylar-adhesive coated with electroless nickel, the coercive force decreases from 660 oe at 600Å to 350 oe at 9000Å. It is apparent that electroless nickel surfaces promote a higher coercive force cobalt deposit than on the Mylar-adhesive base. The increase in coercive force of similar Co-P deposits as a function of thickness due to electroless nickel on Mylar-adhesive substrate is shown in Fig. 2.

Structure

To examine the influence of the electroless nickel substrate on the structure of the Co-P film, deposits prepared on Mylar-adhesive and on the Mylar-adhesive-electroless nickel substrate were examined by x-ray diffraction. The results are shown in Tables I and II.

In the Co-P films on the Mylar-adhesive substrate, only two diffraction peaks were detected; namely, the $(10\bar{1}0)$ and the $(10\bar{1}1)$. Deposits showed a $[10\bar{1}0]$ preferred orientation perpendicular to the plane of deposit but random in the plane. The one-half amplitude peak width of the $(10\bar{1}0)$ reflection remained nearly constant with increasing thickness indicating that the particle size was essentially constant or that any tendency toward peak narrowing due to particle size increase was offset by a tendency to peak broadening caused by micro stress and resultant lattice strain or by lattice imperfections with the net effect being a

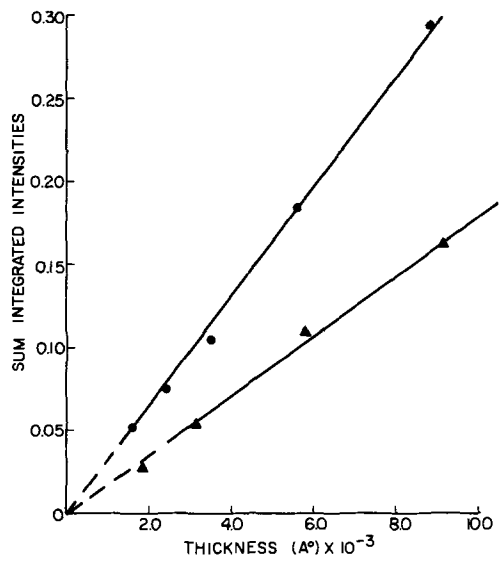

Fig. 3. The sum of the integrated x-ray intensities for all reflections of Co-P as a function of thickness on adhesive-Mylar substrate, ▲, and on electroless nickel-adhesive-Mylar substrate, ●.

constant peak width. However, Co-P films prepared on the nickel substrates exhibited three diffraction peaks, the $(10\bar{1}0)$, $(10\bar{1}1)$, and (0002). The deposits initially exhibit a [0002] preferred orientation perpendicular to the plane of the deposit. As thickness increases, the [0002] orientation decreases and the $[10\bar{1}0]$ orientation becomes predominant. That the diffraction planes indicated were lying preferentially in the plane of deposit but random in that plane was verified by the use of a modified Schulz (9) device. The half amplitude peak width was measured for both the $(10\bar{1}0)$ and (0002) peaks. The $(10\bar{1}0)$ peak width decreases significantly with increasing thickness whereas the (0002) peak width remains nearly constant. Because of the possibility of nonuniform lattice strain or anisotropic lattice defects, definite interpretation of the peak width measurements cannot be made. However, if these factors are assumed to be essentially constant, the data suggests that the particles oriented with $(10\bar{1}0)$ planes in the plane of deposit increases in size with increasing thickness.

A plot of the sum of the integrated intensities of Co-P films as a function of thickness on electroless Ni Mylar-adhesive and Mylar adhesive is shown in Fig. 3.

Table I. X-ray diffraction results for Co-P deposits on an adhesive-Mylar substrate

Thickness, Å	Peak breadth* $10\bar{1}0$	Peak breadth* 0002	∫ Intensity $10\bar{1}0$	∫ Intensity 0002	∫ Intensity $10\bar{1}1$	∫ Intensity $11\bar{2}0$	Σ (∫ Int.)	∫ Int.$_{(hkil)}$/Σ (∫ Int.) × 100 $10\bar{1}0$	0002	$10\bar{1}1$	$11\bar{2}0$
1400†	—	—	—	—	—	—	—	—	—	—	—
1800	0.40°	—	0.0089	—	0.0202	—	0.0291	30.6	—	69.4	—
3150	0.43°	—	0.0316	—	0.0267	—	0.0583	54.2	—	45.8	—
5800	0.40°	—	0.0836	—	0.0274	—	0.1110	75.3	—	24.6	—
9150	0.41°	—	0.1370	—	0.0265	—	0.1635	83.8	—	16.2	—

* Peak breadth in degrees 2θ.
† Diffraction peaks could not be accurately measured.

Table II. X-ray diffraction results for Co-P deposits on a Ni-P substrate

Thickness, Å	Peak breadth* $10\bar{1}0$	Peak breadth* 0002	∫ Intensity $10\bar{1}0$	∫ Intensity 0002	∫ Intensity $10\bar{1}1$	∫ Intensity $11\bar{2}0$	Σ (∫ Int.)	∫ Int.$_{(hkil)}$/Σ (∫ Int.) × 100 $10\bar{1}0$	0002	$10\bar{1}1$	$11\bar{2}0$
1600	0.53°	0.43°	0.0104	0.0252	0.0170	—	0.0526	19.8	47.9	32.3	—
2400	0.49°	0.42°	0.0244	0.0276	0.0237	—	0.0757	32.3	36.5	31.2	—
3500	0.46°	0.41°	0.0493	0.0285	0.0273	—	0.1051	46.9	27.1	26.0	—
5600	0.43°	0.45°	0.1303	0.0303	0.0257	—	0.1863	69.9	16.3	13.8	—
8850	0.39°	0.47°	0.2404	0.0213	0.0316	—	0.2933	82.0	7.3	10.7	—

* Peak breadth in degrees 2θ.

The sum of the integrated intensities, in both cases, is linear with thickness. However, a greater intensity sum is observed for Co-P films on electroless nickel, the difference increasing with thickness. Since all observed x-ray reflections are random in the plane of deposit and the deposits are magnetically isotropic in the deposition plane, the linearity of the intensity sums with thickness would seem to indicate that most of the particles which have a size sufficient for coherent diffraction have one of the orientations observed and as one orientation increases (or decreases) there is a corresponding decrease (increase) in other orientations so that the total reflected x-ray intensity is essentially constant per unit volume in each experimental case. This data would be consistent with an assumption that there may be more amorphous cobalt (very fine grained material below the resolution of the x-ray wavelength used) on the Mylar-adhesive substrate than in the case of an electroless nickel substrate. However, to establish the relative content of amorphous material in the films would require more highly refined x-ray measurements.

Based on a semiparticulate model for the coercive force of cobalt films, it would be expected that a decrease in coercive force would occur in deposits which contained a large number of amorphous or fine particles. This would agree with the experimental observation that cobalt films on Mylar exhibit lower coercive force values than those on electroless nickel substrates.

Conclusion

The influence of an electroless nickel substrate on the microstructure of electroless cobalt is to produce a more pronounced [10$\bar{1}$0] preferred orientation perpendicular to the plane of the deposit.

Cobalt films prepared on electroless nickel Mylar base materials exhibit higher coercive force than similar deposits on Mylar. If a smaller proportion of amorphous (fine grained) cobalt were present in the former, one may reasonably assume that the coercive force would be increased.

Acknowledgment

The authors would like to thank The National Cash Register Company for permission to publish this work which the authors performed at this company. Also, we would like to thank W. H. Chilton and P. E. Henry for sample preparation and x-ray data collection.

Manuscript submitted June 25, 1968; first revised manuscript received *ca.* Sept. 12, 1968, second revised manuscript received Oct. 2, 1968.

Any discussion of this paper will appear in a Discussion Section to be published in the December 1969 JOURNAL.

REFERENCES

1. Lloyd D. Ransom and Victor Zentner, *This Journal*, **111**, 1423 (1964).
2. J. S. Judge, J. R. Morrison, D. E. Speliotis, and G. Bate, *ibid.*, **112**, 681 (1965).
3. J. S. Judge, J. R. Morrison, and D. E. Speliotis, *ibid.*, **113**, 547 (1966).
4. M. G. Miksic, R. Travieso, A. Arcus, and R. H. Wright, *ibid.*, **113**, 360 (1966).
5. Y. Moradzadeh, *ibid.*, **112**, 891 (1965).
6. R. D. Fisher and W. H. Chilton, *ibid.*, **109**, 485 (1962).
7. D. E. Speliotis, J. S. Judge, and J. R. Morrison, *J. Appl. Physics*, **37**, 1158 (1966).
8. R. D. Fisher, "IEEE Transactions on Magnetics," Vol. Mag-2, No. 4, 681 (1966).
9. L. G. Schulz, *J. Appl. Phys.*, **20**, 1030 (1949).

Electrochemistry and Photopotentials of Phenazine in Methanol Solutions

David N. Bailey,[1] David M. Hercules, and David K. Roe*[2]

Department of Chemistry and Laboratory for Nuclear Science, Massachusetts Institute of Technology, Cambridge, Massachusetts

ABSTRACT

Linear-potential-scan voltammetry and coulometry have been used to study the electrochemistry of phenazine in methanol solutions. Parallel work (reported elsewhere) was done on the photochemistry of this compound and the combined results led to elucidation of the species involved in the development of photopotentials which occurred upon illumination of phenazine solutions. Acid-base processes dominated the electrochemistry; in acid solution the reactant at a cathode was the diprotonated phenazine, yielding a stable semiquinone radical which was further reduced in a separate step to dihydrophenazine. Oxidation of the products proceeded readily. In buffered solutions of the neutral range, the reactant was monoprotonated phenazine and the over-all rate was strongly influenced by the protonation step; a single reduction wave of two electrons occurred and reoxidation yielded phenazine. Photopotentials in acid solution were due to diprotonated phenazine and photochemically produced semiquinone radical of the same species. In neutral buffered solutions the photochemical product was dihydrophenazine and the photopotential was due to this species and monoprotonated phenazine.

Interest in the redox behavior of phenazine-based compounds stems from their use as dyestuffs as well as from recognition of the biological importance of some phenazine derivatives. Prior to any recorded voltametric measurements of phenazine, it was established that a stable, one-electron reduction product (semiquinone) was formed during potentiometric titrations using suitable solvents. A review of this subject was prepared by Michaelis (1). Following this, Müller (2, 3) showed that the same information about formal potentials and semiquinone intermediates of a number of compounds could be obtained from polarograms. He found (4, 5), however, that some dyes, including several phenazine derivatives, gave an anoma-

* Electrochemical Society Active Member.
[1] Present address: Department of Chemistry, Gustavus Adolphus College, St. Peter, Minnesota 56082.
[2] Present address: Oregon Graduate Center, Portland, Oregon 97225.

lous wave which preceded the normal or expected reduction wave. Phenazine was included in the survey (5) of compounds but the only information given was that the prewave preceded the main reduction wave by a maximum of 75 mv at a pH of 4.06. Apparently the prewave was not found at a lower pH where the semiquinone was stable. Most of the compounds giving prewaves did so at concentrations of 10^{-5} to 10^{-4} *M*. At higher concentrations the prewave did not increase in magnitude. It is generally accepted now that these anomalous prewaves were due to adsorption of the product of the reduction, as described by Brdicka (6, 7). Somewhat later, Kaye and Stonehill (8) reported the polarographic behavior of phenazine, pyridine, and quinoline. They used 10% ethanol-water solutions with HCl or buffers covering the pH range from 1 to 13 and also 1*M* H_2SO_4. These pH values were measured for nonalcoholic buffers. At pH values below 2, two distinct reduction processes were found; the first wave had an $E_{1/2}$ of +0.09v *vs.* S.C.E. at pH = 0, shifting to −0.02v at pH = 1.93, and the second wave was independent of acidity over this range at −0.18v. Between pH = 3.95 and 13.0, only one wave was found with $E_{1/2}$ values ranging between −0.20 and −0.76v. The interpretation of these polarographic observations is the same as that given by Michaelis (1): when the medium's pH was below pK_a of the protonated semiquinone radical, the latter was a stable intermediate. They calculated pK_a = 3.8 for the radical and 3.2 for phenazinium ion. It was noted that phenazine had no bacteriostatic properties, while several other compounds which gave stable semiquinones at pH of *ca.* 7 were antibacterial. In the series of polarograms given by Kaye and Stonehill there is no clear indication of a prewave at concentrations of 2 to 4 x 10^{-4}*M*. Müller (5) found fully developed prewaves of many compounds, including phenazine, at the same or lower concentration.

Laitinen and Mosier (9) used double layer capacity measurements to survey the adsorption of a number of compounds on the DME. For phenazine, they reported that at −0.8v *vs.* S.C.E. surface adsorption was 50% complete at a solution concentration of 7.6 x 10^{-5}*M*. The solution was 0.1*M* in $NaClO_4$ and neutral (unbuffered). Thus it appears that the adsorbed species was the reduction product of phenazine (dihydrophenazine) since the half wave potential was considerably positive of −0.8v. Müller's study (5) of the concentration dependence of the prewave of phenazine and derivatives is in general agreement with the capacity measurements. He also tried adding ethanol in some cases, the effect of which was to decrease slightly the prewave of α-oxyphenazine. How phenazine's behavior was changed by ethanol was not stated.

Finally, it may be noted that polarographic half-wave potentials for phenazine and 59 of its derivatives have been measured (10).

The occurrence of photopotentials on irradiation of solutions of certain organic compounds has been known for many years (11). Historically, the Becquerel effect, as it is frequently named, was observed as a change in emf measured between two inert metal electrodes immersed in a solution when only one of the electrodes was irradiated by visible or ultraviolet light. Unpoised electrodes would be expected to be subject to relatively large potential changes from impurities, so the majority of such measurements are of qualitative value only. Surash and Hercules (12) found that when proper attention was given to purity of the system, reproducible photopotentials were obtained from a variety of compounds in nonaqueous solutions. Phenazine in ethanol produced a photopotential of −345 mv *vs.* a silver wire coated with silver chloride. Kuwana (13) has recently reviewed the subject of photopotentials and the related photochemistry.

On the basis of the detailed photochemistry of phenazine now available (14), an understanding of the photopotentials produced by products of the photoreduction process is possible. This paper presents the relevant information on the electrochemistry of the system and from this we can deduce what is the potential-determining couple in irradiated phenazine solutions.

Experimental

Details of the preparation of solutions and choice of chemicals have been described (14). Methanol was used as solvent in all cases, except as noted.

All current-potential curves were obtained with a potentiostat based on the details given by Enke and Baxter (15). Depending on the potential scan rate, the curves were recorded either on a Houston Instruments HR-100 X-Y plotter or a Tektronix Type 536 oscilloscope equipped with suitable preamplifiers and Model C-12 camera. Potential scan signals were derived from an internal circuit (15) or from a Wavetek Function Generator.

Polarographic measurements were made with a Heath EUW-19-6 dropping mercury electrode assembly. Maximum possible uncompensated resistance in a 0.1*M* HAc, 0.1*M* NaAc, and 0.1*M* NaCl methanol solution was measured to be 350 ohms near the end of drop life. This resistance was the value measured between counter and indicator electrodes using an Industrial Instruments RC conductivity bridge at 1 kHz. Electrodes were arranged at approximately the three corners of an equilateral triangle so that relatively little solution resistance was compensated. Consequently, concentrations were adjusted so that the maximum iR drop due to uncompensated resistance was less than 2 mv for all curves subject to quantitative interpretation.

Most measurements involving cyclic potential scans were made with a platinum electrode (0.096 cm^2) in an all-glass cell. The counter electrode was a spiral platinum wire enclosed in a porous glass sleeve (Corning 7930 glass). The reference electrode was silver-silver chloride in a 0.125*M* NaCl solution of methanol; isolation from the cell solution was provided by a porous glass plug. Uncompensated resistance was 100 ohms using the same solution referred to in the polarographic case.

Coulometric reduction was done with the same cell with a 1 cm^2 platinum electrode. Potentiostatic control was from a Jaissle Model 300 R potentiostat. Coulombs were measured with a hydrogen-nitrogen coulometer (16). The determination of the number of electrons per molecule, or n-values, was made from a plot of evolved gas volume against peak current at a microelectrode measured by a linear voltage scan. Coulometric electrolysis was stopped during these measurements.

Prepurified nitrogen was used to remove dissolved oxygen.

Hydrogen ion activities were measured in a relative manner with a conventional pH meter and standard electrodes which were normally stored in water. Calibration was routinely performed with aqueous buffers before a measurement; however, the meter reading was occasionally calibrated against a suitable methanol buffer (17-19). Thus, all readings were converted to the pH* scale which is relative to a standard solution of hydrogen ions in methanol. This procedure produced consistent results provided pH* $> \sim 3$. Below this point, the measurements lacked linearity and credibility. Consequently, we resorted to calculation of pH* for all HCl solutions. Activities of HCl in methanol are available (20) and De Ligny *et al.* (18) have calculated chloride ion activities up to 0.1 molal. Since some of our solutions were 0.2*M*, it was necessary to extrapolate the curve, but the probable error from this is <0.1 of a pH* unit. Calculated and measured values of pH* matched with discrepancies of <0.1 unit.

Results and Discussion

Most of the measurements of direct pertinence to the following discussion were made within two pH* ranges: 1 to 2.6 (hydrochloric acid) and 8 to 10 (acetic acid-acetate buffer). Phenazine, denoted by P, exists in the monoprotonated form, PH^+, in acid solution; above pH* of about 6 only the uncharged molecule is found. This information on protonation is based on the results of HCl titrations of phenazine in methanol (containing *ca.* 0.1*M* NaCl). The midpoint pH* of the titration was 4.4, which we take as the logarithm of the reciprocal of the equilibrium constant, pK_{a1}, for the process $PH^+ = P + H^+$ under these conditions. This is a very reasonable value for pK_{a1} in view of the value 3.2 reported (8) for 10% ethanol solutions. Cationic acids typically undergo only small changes in pK_a upon change from aqueous to alcoholic media. Neutral red, a phenazine derivative, was reported (21) to have pK_a values of 7.4 and 8.2 in water and methanol.

Evidence for the occurrence of the reaction $PH_2^{2+} = PH^+ + H^+$ was based on the observation that the yellow color of phenazinium ion was half-changed to an orange color in 65% (10*M*) H_2SO_4 in water. The Hammett acidity function, H_0, has a value (22) of −5 at this concentration of H_2SO_4, but this value cannot apply to a cationic base without major corrections. The factors to be considered are the term log (f_{++}/f_+), where the *f*'s are activity coefficients of the acid and base, association of ions and also the change in dielectric constant to a methanol medium. We estimate pK_{a2} to be more positive than −5, but the order of magnitude is a hazardous guess. A lower limit of pK_{a2} will be discussed later from kinetic measurements.

Cyclic voltammograms of phenazine at low values of pH* are shown in Fig. 1 and 2. Changes of peak potentials with pH*, as identified on the voltammograms, are given by the respective lines of Fig. 3. Up to pH* = 2.6, which was the lowest HCl concentration (0.0041*M*) used, the two reductions and their respective anodic counterparts did not quite meet the criteria (23) of diffusion control at scan rates of about 33 mv/sec or greater: that is, separations of peak potentials ($E_{p4} - E_{p1}$ and $E_{p3} - E_{p2}$) were 62 to 65 mv instead of 57 mv. However, this small deviation,

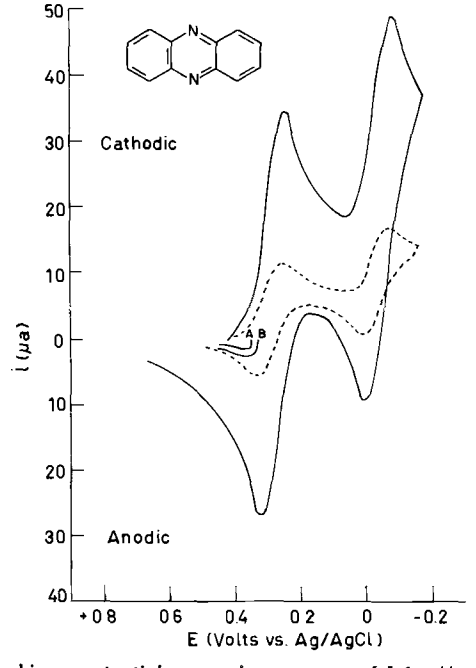

Fig. 1. Linear-potential-scan voltammogram of 1.6 *mM* phenazine in methanol containing 0.1M HCl and 0.1M NaCl. Scan rates are 33 (solid line) and 3.3 (dashed line) mv/sec. Curves A and B are anodic scans initiated from photopotentials.

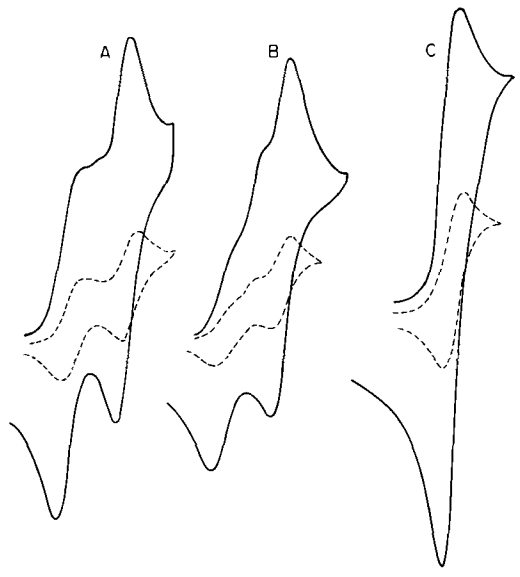

Fig. 2. Linear-potential-scan voltammogram of phenazine in methanol: (a) 0.16 *mM*, pH* = 2.6; (b) 1.6 *mM*, pH* = 2.6; (c) 0.16 *mM*, pH* = 4.9. Solutions (a) and (b) contained 0.0041M HCl and 0.1M NaCl; solution (c) contained 0.067M chloroacetic acid and 0.1M NaCl. Scan rates are 33 (solid line) and 3.3 (dashed line) mv/sec.

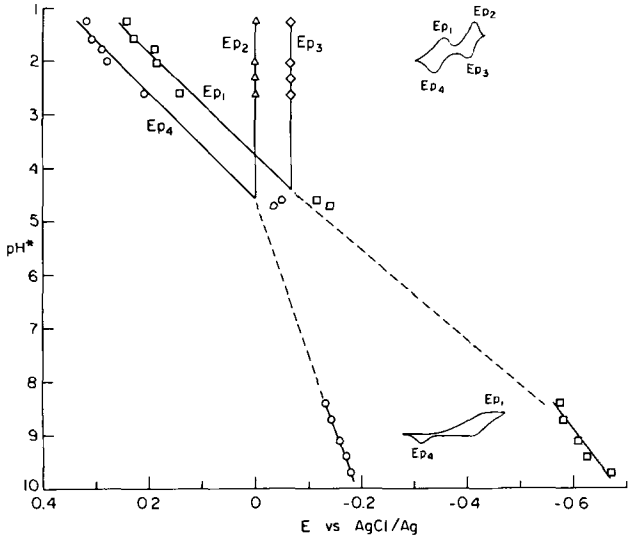

Fig. 3. Peak potentials as a function of pH*. Peaks are identified on inset curves.

corresponding to a heterogeneous rate constant of about 0.01 cm/sec according to the calculations of Nicholson (24) is not very essential at this point. Coulometry at a constant potential of 0.05v with pH* = 1.2 resulted in a value for the number of electrons in the first cathodic peak of $n = 1$. The product of the electrolysis was a stable, green solution which gave an ESR spectrum identical to that reported (25) for the protonated semiquinone radical. Comparison of the relative height of the four peaks leads to the conclusion that each is a one-electron step.

On the basis of the results of pH* dependence and coulometry, the electrode reaction at E_{p1} and E_{p4} involved the sequence

$$PH^+ + H^+ \rightleftarrows PH_2^{2+} \quad [1a]$$

$$PH_2^{2+} + e^- \rightleftarrows PH_2^+ \quad [1b]$$

and at E_{p2} and E_{p3} the reaction was

$$PH_2^{\cdot +} + e^- \rightleftarrows PH_2 \quad [2]$$

The directions of the reactions are to the left for E_{p1} and E_{p2} and to the right for E_{p3} and E_{p4}.

There were, however, two aspects of the first reaction which were subject to analysis by linear sweep methods but not apparent to previous polarographic measurements. Conditions were possible under which the rate of protonation of PH^+, reaction [1a], caused a decrease of the first cathodic current peak and when this protonation rate was made slow enough, a new peak appeared which was apparently the direct reduction of PH^+. Two examples are shown in Fig. 2a and b; note that there is no change in the appearance of the remaining peaks. From an analysis of this behavior of the first cathodic peak, we have set a lower limit on the value of pK_{a2} of phenazine. Table I summarizes the current peaks at three scan rates and for three solutions. These data were processed by the method of analysis given by Nicholson and Shain (23), who found that for the case of a first order chemical reaction preceding a reversible charge transfer the following empirical equation applied

$$\frac{i_k}{i_d} = \frac{1}{1.02 + 0.471\sqrt{a}/K\sqrt{l}} \qquad [3]$$

Here, i_k is the observed, kinetically-influenced current and i_d is the diffusion-controlled current which would be found in the absence of a chemical step; a is $\nu nF/RT$, in which ν is the potential scan rate; K is the equilibrium constant for the preceding chemical reaction, which is equal to $[H^+]/K_{a2}$ for this case; and l equals $(k_f + k_b)$ for a first order chemical reaction, or $([H^+]k_f + k_b)$ for reaction [1a]. We have taken i_d at 3.3 mv/sec to be diffusion controlled since essentially the same value was observed for all values of pH* up to 2.3. At 0.1*M* HCl, $i_d/\nu^{1/2}$ was constant for $\nu < 10$ mv/sec, giving $D = 2.2 \times 10^{-5}$ cm²/sec. For higher scan rates, i_d was calculated from this value; the ratios of i_k/i_d are given in the table and the resulting values of $k\sqrt{l}$. Now if the maximum possible value of k_f is taken to be 10^{10} liters/mole sec, then the upper limit of K_{a2} is found to have an average value of 107 ± 20. More realistically, pK_{a2} appears to be —2, subject also to the accuracy of the estimate of k_f. Since the two reactants in Eq. [1a] have the same charge, a rather low value for k_f was taken. [For purposes of comparison, see the tabulations of Eigen and De Maeyer (26) and of Strehlow (27)].

In solutions in which the ratio of HCl to phenazine was 10 or less, by increasing the phenazine concentration, the additional current peak mentioned previously appeared between the two cathodic peaks at the lowest scan rates, as shown in Fig. 2b. Similar curves were also obtained with buffers prepared with trichloroacetic acid. However, it was found that the effect was greater at a given scan rate with dilute HCl solutions than with high capacity buffers of higher pH*. This additional peak increased with increasing scan rate at the expense of the first cathodic peak; no other changes in the voltammogram were noted. A reasonable interpretation would be that the direct reduction of PH^+ occurred when reaction [1a] became sufficiently slow. In dilute HCl solutions, the decrease in rate was exaggerated because the activity of H^+ was not held as uniform in the diffusion layers as when buffers were present in high concentrations. Thus, pseudo-first-order conditions were not maintained.

With increasing pH* above 2.6, the peak ascribed to direct reduction of PH^+ became dominant and merged with E_{p2} by pH* = 5.0, shown in Fig. 2c. The anodic counterpart, E_{p4}, also shifted negative in potential until it merged into the tail of the wave at E_{p3}. Since pK_a (8) for dissociation of $PH_2^{\cdot+}$ was at least about 0.6 units larger than pK_{a1} of PH^+, E_{p4} persisted to slightly higher pH* values than did E_{p1}. For the curve shown in Fig. 2c, the peak heights corresponded to a two-electron process by comparison with the other curves. Also, the separation of peak potentials was 65 mv at low scan rates in well-buffered solutions.

Further increases in pH* have the significant effect shown in Fig. 4. The cathodic process has shifted negative by nearly 0.5v for a pH* change of 4. Increasing scan rates caused the cathodic curve to flatten and $i_p/\nu^{1/2}$ decreased markedly, as is illustrated by the normalized curves of Fig. 5. Further diagnostic characteristics of the cathodic wave were a negative potential shift with increasing scan rate of both half-peak potential and peak potential (—18 and —40 mv per 10-fold increase in ν, respectively, for rates up to 5 v/sec) and a change of about —70 mv per unit pH* increase, as shown in Fig. 2. Coulometry at —0.7v revealed that two electrons were involved in the overall reduction. As the cathodic current decreased during bulk electrolysis, the anodic wave increased cor-

Table I. Kinetic data for the reaction $PH^+ + H^+ \rightleftarrows PH_2^{2+}$

pH*	ν mv/sec	$\sqrt{a}$	$i_d\mu A^{(a)}$	i_k/i_d	$K\sqrt{l}$
2.02	3.3	0.36	1.20	1	
	33	1.14	3.80	0.92	8.9
	330	3.60	12.0	0.80	7.4
2.31	3.3	0.36	1.20	1	
	33	1.14	3.80	0.88	4.5
	330	3.60	12.0	0.71	4.3
2.61	3.3	0.36	1.20	1	
	33	1.14	3.80	0.83	3.0
	330	3.60	12.0	0.58	2.4

(a) Phenazine concentration was 0.16 *mM*; methanol solution contained HCl and 0.1*M* NaCl. Diffusion currents are calculated from experimental values at 3.3 mv/sec and pH* = 1.2.

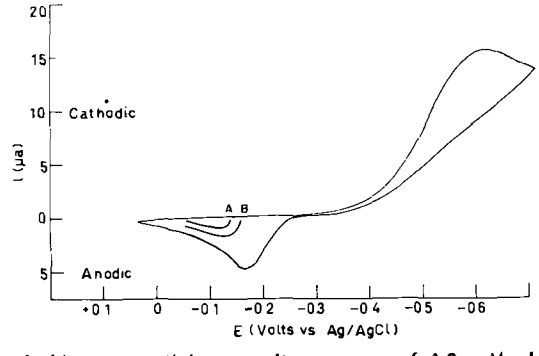

Fig. 4. Linear-potential-scan voltammogram of 1.2 *mM* phenazine in methanol solution of 0.1*M* acetic acid, 0.1*M* sodium acetate, and 0.1*M* sodium chloride; pH* = 9.4; scan rate 33 mv/sec. Curves A and B are anodic scans initiated from photopotentials.

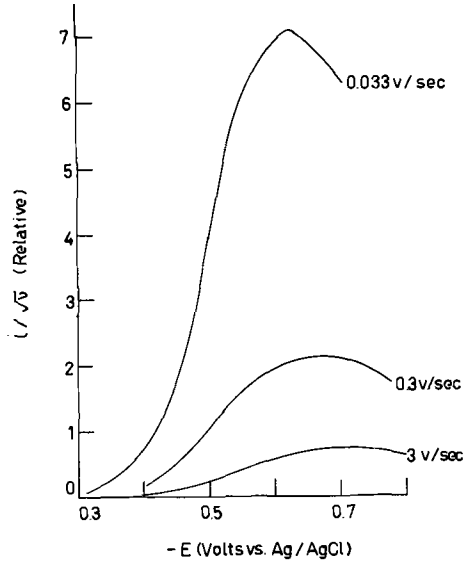

Fig. 5. Normalized voltammograms of phenazine at various scan rates; acetate buffer of pH* = 9.4.

respondingly and no additional current peaks were found.

Several polarographic observations were also made with acetate buffers. Reduction at a DME was a single wave; the rising part of the wave had an average slope of 45 mv when plotted as E *vs.* log $(i_d - i)/i$ for a drop time of about 6 sec. At $pH^* = 8.4$, the diffusion current *vs.* square root of height of mercury column was reasonably linear for drop times greater than 4 sec; below this value the plot curved toward a zero-order dependence on mercury column height.

A diffusion coefficient of the neutral phenazine species was calculated from the polarographic limiting current at $pH^* = 8.4$. Using the Ilković equation and $n = 2$, a value of $D = 3.0 \times 10^{-5}$ cm^2/sec was calculated. This is in fair agreement with the value of 2.2×10^{-5} cm^2/sec calculated from the peak current from a linear scan of 3.3 mv/sec at $pH^* = 5.0$ where the single wave most closely has the characteristic diffusion-controlled shape. Extrapolated to zero scan rate, the value increased to 2.8×10^{-5} cm^2/sec. None of these calculations included a spherical term in the diffusion equation. Also, in anticipation of a one-electron initial step of the over-all process, the term $n^{3/2}$ of the Randles-Sevcik equation was replaced by $(n_1 + n_2)n_1^{1/2}$ in which the subscripts indicate the sequence of electron addition. Nicholson and Shain (28) have shown that this modification is necessary when a single current wave consists of two charge transfers coupled by a chemical reaction; evidence for this assignment of steps is given below. To a certain extent, the diffusion coefficient values given here may appear to be larger than generally reported for similar compounds. However, the difference in viscosity of methanol and water is sufficient to account for the increase. Kaye and Stonehill (8) did not give a diffusion coefficient from their measurements, but assuming they employed the same capillary characteristics for phenazine as for the other compounds investigated, we calculate $D = 8 \times 10^{-6}$ cm^2/sec for phenazine in 1:10 ethanol-water; viscosity of this solvent is 1.32 while that of methanol is 0.55 at 25°C.

Consideration of the above information on the reduction of phenazine over the investigated pH^* range leads to the following four equations as a reaction sequence for solutions giving single cathodic and anodic waves

$$P + H^+ \rightleftarrows PH^+ \qquad [4a]$$

$$PH^+ + e^- \rightleftarrows PH\cdot \qquad [4b]$$

$$PH\cdot + H^+ \rightleftarrows PH_2\cdot^+ \qquad [5a]$$

$$PH_2\cdot^+ + e^- \rightleftarrows PH_2 \qquad [5b]$$

The combination of [4a] and [4b] is based on the marked decrease in $i_p/\nu^{1/2}$ with increasing scan rate (23). If [4b] is not a reversible step, the effect is essentially the same; there appears to be no reason to assume [4b] to be irreversible in view of the results shown for pH^* of 1 to 5. None of the model kinetic systems which have been analyzed shows this characteristic, except a catalytic cycle. We exclude this possibility from having a major role, although it has been found as hydrogen evolution during reduction of many nitrogenous compounds (29), because the diffusion coefficient is constant for a wide range of conditions and the change of the shape of the voltammogram with increasing scan rate of a catalytic reaction (23) is toward that of a peaked, normal diffusion-controlled wave. Figure 5 shows that the opposite was found, in qualitative agreement with the calculated curves (23) for the case of a chemical step preceding charge transfer. There is one important respect in which our measurements deviate from the results of the calculations of Nicholson and Shain (23) for a preceding reaction: with increasing scan rate, the half-peak potential should shift anodic if the sequence is indeed [4a] followed by [4b]; a cathodic shift was found. The explanation can be found in the effect of reaction [5a]. A following chemical reaction shifts E_p (and the half-peak potential) in the cathodic direction (23) with increasing scan rate, becoming constant with increasing scan rate when a/k_f $[H^+]$ exceeds a value of about 10. Here $k_f[H^+]$ applies to reaction [5a], which is considered to be irreversible because of [5b]. The reduction potential of $PH_2\cdot^+$ is positive of the region where [4b] commences, as is evident from the anodic wave of Fig. 4 and further is typical of protonated hydrocarbons, as was shown by Hoijtink *et al.* (30). Thus, at slow scan rates, the effect of [5a] dominates and a cathodic shift amounting to a maximum of −30 mv per 10-fold increase in ν is expected. However, the effect of [4a] at low scan rates also causes a small cathodic shift in E_p (while $E_{p/2}$ moves anodic), as is shown in the calculated current functions (23). It is not known how these criteria, calculated for independent cases, will behave when combined. Certainly the qualitative aspects are correct. As further proof, we found that the half-peak potential became independent of scan rate in the vicinity of 10 to 70 v/sec, in spite of a large ohmic drop in the cell under these conditions. It is interesting to note that no new waves due to intermediates were found at these scan rates.

Calculation of rate constants for reaction [4a] would not be expected to be realistic if the reduction actually occurs as written. Characteristics of peak currents are unique to the boundary conditions assumed for a system and they lose their significance when additional steps occur. We found that the quantity $K\sqrt{l}$ was not constant when Eq. [3] was used; for example, k_f ranged from 10^{12} to 10^{13} liters/mole sec and k_b ranged from 10^8 to 10^9 sec^{-1}. Indications are that k_f of [4a] is a diffusion-controlled constant. The absence of an anodic wave due to the proposed intermediate PH· would require (23) that $a/k_f[H^+]$ for [5a] be less than 0.1. At $\nu \cong 100$ v/sec and $[H^+] = 10^{-8}$ M, this condition gives $k_f \cong 4 \times 10^{12}$ liters/mole sec for [5a].

In the high pH^* range, the anodic wave shifted negative in potential by 31 mv/pH^* unit. Distortion of this curve occurred because of the time lag between reversal of direction of the linear potential scan and the start of the anodic process. There is no doubt that the oxidation is the reverse of the over-all reduction sequence since no cathodic peak was found adjacent to this wave upon a second reversal of direction of potential scan. Also the area of the anodic wave approached the area of the cathodic wave with increasing scan rate.

Since previous investigations (5, 9) indicated that dihydrophenazine was adsorbed on mercury electrodes, it is important to assess the magnitude of this effect under the conditions of our experiments. Due to the many complications causing deviations from simple diffusion control of voltammogram curves, adsorption effects were difficult to locate except at pH^* of about 5. Here the peak anodic wave exceeded the peak cathodic wave by 5% at $\nu = 33$ mv/sec; according to measurements of the curve of Fig. 2c. At low scan rates the difference was too small to measure and at high scan rates (333 mv/sec) the cathodic wave became influenced by the prior chemical step, Eq. [4a]. Wopschall and Shain (31) recently treated the cases of reactant and product adsorption and from their results, one would conclude that the experimental evidence showed that dihydrophenazine was weakly adsorbed from methanol solution.

Photopotentials were measured with 2 mM solutions of phenazine at $pH^* = 1.4$ and also at $pH^* = 9.4$. Cyclic scans were recorded with a platinum electrode and the solution was illuminated at a distance of 15 cm from an AH-6 mercury vapor lamp. In acid solution, the initial potential was 0.45v and unsteady. After a few seconds of illumination the potential moved in a negative direction, first rapidly then more

slowly until a potential of 0.330v was attained after about several minutes. At this point the solution was a definite yellow-green color due to the formation of photoreduced products. Additional curves were measured during illumination; there were no major changes in the curves from those shown in Fig. 1. The potential of E_{p1} shifted about 10 mv negative and the current decreased slightly with time. The other current peaks increased about 5%, an effect most probably due to the thermal convections from the light source. Anodic potential scans started from the photopotential showed a small wave; examples have been added to Fig. 1, lines A and B. These waves increased with time. Using the electrochemical results, the interpretation of these observations is rather direct. The product of photoreduction (14) in acid was the protonated semiquinone radical, $PH_2^{\cdot+}$ and therefore, the potential-determining couple was $PH_2^{2+}/PH_2^{\cdot+}$ (Eq. [1b]), as was clearly shown by the measured potential and current-potential curves. The observed decrease of current of E_{p1} is quite as expected from the gradual conversion of PH^+ to $PH_2^{\cdot+}$, as is the increase in the anodic current wave starting from the photopotential.

The situation with the acetate buffer corresponds more closely to the conditions employed by Surash and Hercules (12) than does the above. Here, the initial potential was about zero volt and also unsteady. After about 10 min of illumination a potential of —0.2v was reached. Again, no marked changes in the voltammogram were noted, except a gradual increase with time of the anodic wave as measured from the photopotential, as shown by curves A and B of Fig. 4. Absence of new current peaks during illumination showed that the photoreduction intermediates were short lived as was established from photochemical studies and the product was PH_2 (14). Thus the potential-determining couple was PH^+/PH_2 since the intermediate oxidation state was not thermodynamically stable. Kuwana (13) expressed the view that photopotentials are due to the fully reduced species and not radical intermediates. This view certainly applies to phenazine in acetate buffer solution. Also, the very slow decay of photopotentials (12) after cessation of illumination is suggestive of diffusional and convective mixing of solution between the exposed and light-baffled parts of the cell.

Finally, it may be noted that the time-rate of change of photopotentials and the anodic waves clearly reflected the large difference in quantum efficiencies (14) of the photoreduction of phenazine in HCl and acetate buffer solutions. In the first solution, the quantum efficiency was 0.094 moles/einstein while in the latter it was 0.011 moles/einstein.

Acknowledgments

This work was supported in part through funds provided by the U.S. Atomic Energy Commission under Contract AT(30-1)-905. D. N. Bailey held National Science Foundation (1963-1966) and National Institutes of Health (1966-1968) fellowships which are acknowledged with appreciation. The authors are thankful to Kenneth B. Legg for help with the photopotential measurements and to Donald W. Shive for critical discussions.

Manuscript submitted July 5, 1968; revised manuscript received *ca.* Oct. 28, 1968. This paper was presented at the Boston Meeting, May 5-9, 1968 as Paper 201.

Any discussion of this paper will appear in a Discussion Section to be published in the December 1969 JOURNAL.

REFERENCES

1. L. Michaelis, *Chem. Rev.*, **16**, 243 (1935).
2. O. H. Müller and J. P. Baumberger, *Trans. Electrochem. Soc.*, **71**, 181 (1937).
3. O. H. Müller, *Ann. New York Acad. Sci.*, **40**, 91 (1940).
4. O. H. Müller, *J. Biol. Chem.*, **145**, 425 (1942).
5. O. H. Müller, *Trans. Electrochem. Soc.*, **87**, 441 (1945).
6. R. Brdicka, *Z. Electrochem.*, **48**, 278 (1942).
7. R. Brdicka, *Collection Czechoslov. Chem. Communs.*, **12**, 522 (1947).
8. R. C. Kaye and H. I. Stonehill, *J. Chem. Soc.*, **1952**, 3240.
9. H. A. Laitinen and B. Mosier, *J. Am. Chem. Soc.*, **80**, 2363 (1958).
10. Yu. S. Rosum, S. B. Sebryanyi, E. F. Karaban, V. P. Chernetskii, and M.I. Drankina, *J. General Chem. U.S.S.R.*, **34**, 2622 (1964).
11. E. Bequerel, *Compt. rend.*, **9**, 144, 561(1839).
12. J. J. Surash and D. M. Hercules, *J. Phys. Chem.*, **66**, 1602 (1962).
13. T. Kuwana, "Photoelectrochemistry and Electroluminescence" in "Electroanalytical Chemistry," Vol. 1, A. J. Bard, Editor, Marcel Dekker, Inc., New York (1966).
14. D. N. Bailey, D. M. Hercules, and D. K. Roe, Submitted to *J. Amer. Chem. Soc.*, 1968.
15. C. G. Enke and R. A. Baxter, *J. Chem. Educ.*, **41**, 202 (1964).
16. J. A. Page and J. J. Lingane, *Anal. Chim. Acta*, **16**, 175 (1957).
17. R. G. Bates, "Determination of pH—Theory and Practice," p. 226, John Wiley & Sons, New York (1964).
18. C. L. De Ligny, P. F. M. Luykx, M. Rehbach, and A. A. Wieneke, *Rec. Trav. Chim.*, **79**, 669 (1960).
19. *Ibid.*, p. 713.
20. B. E. Conway, "Electrochemical Data," pp. 94, 97, Elsevier, New York (1952).
21. L. S. Guss and I. M. Kolthoff, *J. Amer. Chem. Soc.*, **62**, 249 (1940).
22. M. J. Jorgenson and D. R. Hartter, *ibid.*, **85**, 878 (1963).
23. R. S. Nicholson and I. Shain, *Anal. Chem.*, **36**, 706 (1964).
24. R. S. Nicholson, *ibid.*, **37**, 1351 (1965).
25. (a) K. H. Hausser, A. Häbich, and V. Franzen, *Z. Naturforsch.*, **16a**, 836 (1961); (b) Y. Matsunaga and C. A. McDowell, *Proc. Chem. Soc.*, **1960**, 175; (c) D. W. Schiesser and P. Zvirblis, *J. Chem. Phys.*, **36**, 2237 (1962); (d) L. D. Tuck and D. W. Schiesser, *J. Phys. Chem.*, **66**, 937 (1962).
26. M. Eigen and L. De Maeyer, "Technique of Organic Chemistry," Vol. VIII, Part II, Chap. XVII, Friess, Lewis and Weissberger, Editors, Interscience, New York (1963).
27. H. Strehlow, *ibid.*, chapt. XV.
28. R. S. Nicholson and I. Shain, *Anal. Chem.*, **37**, 178 (1965).
29. (a) J. Koutecky, *Collection Czechoslov. Chem. Communs.*, **18**, 311 (1953); (b) M.v. Stackelberg and H. Fassbender, *Z. Electrochem.*, **62**, 834 (1958); (c) M. v. Stackelberg, W. Hans, and W. Jensch, *ibid.*, p. 839.
30. G. J. Hoijtink, J. van Shooten, E. de Boer, and W. Y. Aalbersberg, *Rec. Trav. Chim.*, **73**, 355 (1954).
31. R. H. Wopschall and I. Shain, *Anal. Chem.*, **39**, 1514 (1967).

Energy Considerations in Electron Beam Welding

P. G. Klemens[1]

Westinghouse Research Laboratories, Pittsburgh, Pennsylvania

ABSTRACT

An expression is obtained for the depth of penetration of an electron beam in terms of the thermal conductivity of the solid and other parameters of the material. In the case of a moving beam, the penetration decreases with speed; an expression for the decrease of penetration is obtained in terms of the thermal diffusivity. An electron beam technique is described which may be a useful method for measuring thermal diffusivities.

Although electron beams have been used successfully as a tool in cutting and welding materials, and although a large body of empirical information is now available on how this tool can be used to good advantage, our knowledge of the actual processes induced by the electron beam in the target material is incomplete. Ideally we would like to know the details of the atomic processes which govern the penetration of the electron beam (1); however, there is also a prior need to understand the penetration process on a macroscopic level. The present paper considers the energy balance and energy loss mechanisms on a macroscopic basis and shows how these energy considerations govern to a large extent the penetration of the electron beam, although there are some assumptions which have to be made, the validity of which can only be examined on a microscopic basis. It is shown that, provided the beam is sufficiently narrow and its energy content high enough, the penetration in the stationary case is mainly governed by thermal conduction. If the beam is not narrow, a second energy loss mechanism becomes important, the flow of vapor out of the hole made by the beam. In the case of a moving beam, the penetration is reduced by the extra energy requirement of melting the material ahead of the cut, and an expression is found for the decrease of penetration depth as function of the forward velocity of the beam. Finally it is pointed out that since this loss of penetration depth depends on the thermal diffusivity, an electron beam technique may be a convenient way of measuring thermal diffusivity in circumstances when measurements of temperature gradients of temperature variations inside a solid are difficult.

The present treatment depends mainly on energy flow considerations; it applies not only to electron beams, but to any other method which delivers a high flux of energy in a beam of narrow cross section. It may, in particular, apply under appropriate circumstances to laser welding.

Stationary Beam

Consider a narrow electron beam impinging on a surface. Let the voltage be V, the current J, so that the energy flow is $W = VJ$. Suppose in the steady state the beam has cut a deep hole, of depth D, and diameter l, and let $D >> l$. Let T_m be the melting point of the material, and let the vapor inside the hole be of temperature T_v. Presumably there is a sheath of molten material between the vapor core and the surrounding solid; unfortunately, very little is known about what occurs precisely within the hole. But note that by the above definition l is the diameter of the "key hole" formed by the beam and not the width of the molten metal which, by the usual definition, gives the weld width.

The electrons penetrate the hole in an unknown and extremely complicated manner, although some x-ray photographs give information about the spatial distribution of the absorption (2). We shall assume (*a*) that x-rays remove only a negligible fraction of the total power, and (*b*) no matter how the energy loss of the electrons by interaction with the vapor and the walls of the hole is distributed spatially, this energy is rapidly transported within the hole, so that the wall is of uniform temperature.

The energy which is delivered by the beam is dissipated by various mechanisms: by heat conduction into the solid, by energy transported away by vapor, and by radiant energy.

If the hole is deep and narrow, conduction becomes most important. The temperature gradient at the solid-liquid interface is of order T_m/l, so that the heat carried away by conduction is of order $\kappa(T_m/l)\pi lD$, where κ is the thermal conductivity. The heat flow is thus roughly independent of the hole diameter, but proportional to the hole depth D. Therefore, as long as the other energy loss mechanisms are relatively small, the conduction depends on the depth of the hole, which is therefore proportional to beam power; this result is insensitive to the hole diameter, which must be determined by other considerations.

In greater detail, the heat conduction for a length D through a cylinder of inside diameter l and inside temperature T_m, and outside diameter L and temperature T_o is given by (3)

$$W_1 = 2\pi D\kappa \frac{T_m - T_o}{\ln(L/l)} \qquad [1]$$

There is thus a weak dependence on l. We must now choose the radius $L/2$ outside which the material is at the ambient temperature T_o. We find that strictly speaking the process is not stationary and L increases with time. However, as long as the cylinder is not infinitely long but of finite length D, we expect the conduction to be enhanced by the addition of an extra dimension as soon as L becomes comparable to D; at that point a stationary state is more closely approached. We therefore identify $L/2$ with D, noting that any error will only enter into [1] logarithmically, so that

$$W_1 = 2\pi D\kappa \frac{T_m - T_o}{\ln(2D/l)} \qquad [2]$$

In many typical cases, $\ln(2D/l)$ ranges from 3 to 5.

Equating W_1 to the total power of the beam, W, one obtains for the depth of the hole

$$D = \frac{W \ln(2D/l)}{2\pi\kappa(T_m - T_o)} \qquad [3a]$$

$$\simeq \frac{4W}{2\pi\kappa(T_m - T_o)} \qquad [3b]$$

In a typical case of a 15-kw beam and in a metal for which thermal conductivity $\kappa = 1$ watt-cm-deg^{-1}, and $T_m = 1500°C$, one would expect a penetration of the order of 6 cm. If the diameter of the hole is 0.2 cm, this makes $\ln(2D/l) = 4.2$, consistent with our approximation.

Some typical values of D for various materials deduced from [3a] are shown in Table I.

[1] Present address: Department of Physics, The University of Connecticut, Storrs, Connecticut 06268.

Table I. Beam penetration for 15 kw beam, $l = 0.2$ cm:optimum values

Material	T_m, °C	K, watt-cm-deg^{-1}	D, cm
Copper (pure)	1080	4.5	1.5
Copper alloy (20μ ohm-cm)	1080(?)	0.8(?)	10
Iron	1540	0.7	9
Stainless steel	1600(?)	0.14	50*
Tungsten	3380	1.0	2.0
Rocks, various	2000(?)	0.02(?)	400**

* The thermal conductivity of stainless steel is a room temperature value; it may be considerably higher near T_m, resulting in a substantial reduction of D. The value may thus turn out to be closer to that for the copper alloy.

** We have neglected the "dilution" of the beam by electron scattering which causes variations in the temperature of the vapor with depth, and would invalidate the present argument in extreme cases. We have also disregarded the factor of time, which is again of great importance in such extreme cases.

One must recognize that these values are optimum values deduced on the assumption that other heat loss mechanisms are inoperative. Furthermore, it has been assumed that the hole is long and thin and of uniform temperature, and that the solid material which had to be removed to form the hole has been removed without inhibiting the entrance of the beam. In the case of the 400-cm hole calculated for rock, this is certainly a questionable assumption. Limitations due to electron scattering are discussed in an associated paper by Schubert and Schumacher (4).

Let us now consider competing heat loss mechanisms. The material inside the hole is partly in the form of liquid, partly in the form of vapor. The latter probably occupies the major fraction of the volume. The vapor emits electromagnetic radiation and also streams out of the hole, carrying away energy. The black body radiation out of a hole of area l^2 is

$$W_r = 6 \times 10^{-12}\, T_v^4 l^2 \text{ w} \qquad [4]$$

and even if $T_v \simeq 3000$°K, this is clearly negligible.

The energy loss by vapor flow is more important. Let us assume the vapor to emerge with the velocity of sound v, at a temperature T_v. Let d_o be the density of the solid, C its heat capacity per unit volume, and let d be the density of the vapor. The heat capacity per unit volume of the vapor is thus

$$\frac{d}{2d_o} C \qquad [5]$$

the factor 2 being included because the vapor atoms have only translational, not vibrational, energy. The energy flow due to the vapor is thus

$$W_{II} = l^2\, v\, C\, T_v \frac{d}{2d_o} \qquad [6]$$

Invoking the perfect gas law, and assuming that the vapor issues at or near atmospheric pressure

$$\frac{d}{d_o} \simeq 3 \times 10^{-4} \frac{T_v}{300} \simeq 10^{-6}\, T_v \qquad [7]$$

so that

$$W_{II} = \frac{1}{2} \times 10^{-6}\, C\, v\, l^2\, T_v^2 \qquad [8]$$

In a typical case, when $C \simeq 3.5$ joule/cm^3/deg, $T_v = 3000$°K, and $v = 5 \times 10^4$ cm/sec

$$W_{II} \simeq 8 \times 10^5\, l^2 \text{ w} \qquad [9]$$

For beam energies of the order of 10 kw, this loss becomes important when l exceeds say 0.1 cm. In the case of vacuum welding the pressure in the hole is only about ¼ atm (1), and W_{II} is correspondingly decreased.

We now recognize two possible cases: when $W_{II} < W$ and when $W_{II} > W_I$. In the former case the energy balance is

$$W_I = W - W_{II} \qquad [10]$$

where W_I is determined by conduction and proportional to the depth of penetration. The vapor loss W_{II} is proportional to l^2 or the cross-sectional area of the hole. It is thus advantageous to keep l^2 as small as possible.

The factors which control l^2 are obscure, but the minimum requirement is a narrow beam, for l cannot be less than the beam diameter. Another requirement is that the beam does not wander, and that it is not broadened by atmospheric scattering. Alternatively it is desirable to have a large beam power. Inasmuch as it is difficult to concentrate a large beam power into a small area, the condition

$$W > W_{II}$$

is equivalent to a requirement on the beam power density, namely

$$\frac{W}{l^2} > 5 \times 10^{-7}\, C\, v\, T_v^2 \qquad [11]$$

which is the harder to fulfill, the greater the vaporization temperature of the material.

In the typical case quoted above, the critical beam power density below which substantial penetration is certainly impossible is 80 kw/cm^2. In actual practice the beam power density should exceed this value by a substantial factor.

If $W < W_{II}$, we have different conditions altogether. The beam does not drill a deep hole, but eats its way into the material gradually, leaving a relatively wide depression. No vapor cloud forms in that depression, but material is removed until D is comparable to l. Further penetration is governed by the speed with which material can evaporate from a liquid surface of area l^2 kept at some temperature intermediate between the melting temperature T_m and the vaporization temperature T_v. The temperature reached in the steady state depends on the power density W/l^2. Furthermore, since a large amount of liquid is present, the progress of the erosion will depend on how that liquid will flow and possibly refreeze; this in turn depends on the direction of gravity and on surface tension effects.

Moving Beam

It is generally observed that the depth of penetration is less for a moving beam than for a stationary beam, and that this depth decreases as the forward speed of the beam is increased. This is readily understood as a consequence of the additional energy requirement of moving the beam. Since heat is left behind in the wake of the moving beam, less heat needs to be conducted away, so that the penetration decreases.

As the beam is moved forward, material has to be melted at the front of the beam, and material resolidifies at the back. The heat required to do so consists in part of heat required to raise the temperature of the material to T_m, and in part of the latent heat of melting. The latent heat of melting is given up and, as we may assume, completely regained at the back face where the liquid metal resolidifies. The moving hole leaves behind a wake of heat. Originally this heat was concentrated in a small region immediately behind the hole, at a temperature T_m. The fact that it subsequently spreads out does not affect the amount of heat involved. The additional heat required to move the hole is therefore

$$W_{III} = D\, l\, V\, C\, T_m \qquad [12]$$

where D is the depth of the hole, l its diameter, V the forward speed of the moving beam, C the heat capacity per unit volume, and T_m the melting temperature.

The energy balance is now

$$W = A_1 D + A_2 + A_3 D V \quad [13]$$

where $A_1 D$ is W_I of Eq. [2], A_2 is W_{II} of Eq. [6], and $A_3 DV$ is W_{III} of Eq. [12]. The depth of penetration is now given by

$$D = \frac{W - A_2}{A_1 + A_3 V} \quad [14]$$

and in the stationary case

$$D_o = (W - A_2)/A_1 \quad [15]$$

which is given by Eq. [10] and [3] as

$$D_o = \frac{2W - l^2 V\, C\, T_v\, d/d_o}{\pi\, \kappa\, T_m} \ln\left(\frac{2D_o}{l}\right) \quad [16]$$

Strictly speaking, A_1 is not quite constant because it contains the factor $\ln(2D/l)$, but we may approximate this by $\ln(2D_o/l)$, since it varies only relatively weakly.

While [14] and [15] give the magnitude of D and the manner in which it decreases with speed V, it is also of interest to consider the speed V_c for which the penetration is halved. From [14] we obtain

$$V_c = \frac{A_1}{A_3} = \frac{2\pi\,\kappa}{C\, l \ln(2D/l)} \quad [17]$$

In most cases when $\ln(2D/l) = \ln(D_o/l) \simeq 3$

$$V_c = \frac{2\pi\kappa}{3Cl} \quad [18]$$

In the case of a typical metal for which $\kappa/C \simeq 1$ cm^2/sec, taking $l = 0.2$ cm, one finds

$$V_c = 10 \text{ cm/sec} = 240 \text{ in./min.}$$

In stainless steel for which $\kappa/C = 0.04$ cm^2/sec

$$V_c = 0.4 \text{ cm/sec} = 10 \text{ in./min.}$$

In the case of a poor thermal conductor such as concrete, where $\kappa/C = 0.005$ cm^2/sec,

$$V_c = 0.05 \text{ cm/sec} = 1.3 \text{ in./min.}$$

Experimental data on concrete (5) indicate that half the penetration is lost at a forward speed of about 2.5 in./min. The order of magnitude of the agreement is satisfactory; the discrepancy may be due to a number of factors, in particular the crudeness of our theory, but also the variability in the thermal diffusivity of concrete.

Determination of Thermal Diffusivity

The fact that the penetration of the electron beam decreases with forward speed in a manner which depends on the thermal diffusivity of the solid material makes it possible to measure the thermal diffusivity by means of an electron beam. One would have to measure the penetration at two or more forward speeds and determine V_c from the relation

$$D = D_o\,[1 + V/V_c]^{-1} \quad [19]$$

If one also measures the diameter of the cut, l, one can calculate the thermal diffusivity κ/C from [18], or better still, from [17].

The interesting point is that this method of determining κ/C does not depend on the detailed assumptions which we have made. All which is really required is that thermal conduction is the only heat loss mechanism which depends on D, and that the other mechanisms (vapor flow, *etc.*) are independent of D. Then an energy balance equation of the form [13] holds, and V_c is independent of A_2.

If the thermal diffusivity depends on temperature, this method will yield the diffusivity in the vicinity of the melting temperature T_m. Since thermal diffusivity measurements at elevated temperatures are notoriously difficult to carry out, and subject to large and incompletely understood errors, the electron beam method may well be competitive with other methods. Basically, this method is equivalent to a transient method involving a line source of heat, but it avoids the use of thermocouples embedded in the solid.

It would be interesting to attempt quantitative measurements of thermal diffusivity on materials of known properties.

Some Further Problems

Although the present considerations do give an over-all description of the beam penetration which seems to agree with what has been observed, at least in some cases, there are a number of questions which have yet to be answered.

The most important question is to determine the factors which govern the "key-hole" diameter l, an important parameter in our considerations. Clearly the beam diameter sets a lower limit to l, but there could be mechanisms which tend to make l wider than the beam diameter.

A second question is whether the hole is really of uniform diameter and whether the temperature within it is uniform. This has been assumed in our considerations, and although the heat conducted away is not very sensitive to variations in diameter along the length of the hole, there is a need to investigate the mechanism of hole formation in greater detail.

Perhaps the greatest need is to find out what happens when the hole is relatively wide and thermal conduction is only a minor mechanism of heat transport. In that case the present considerations are inapplicable (except possibly that the variation of depth with forward speed is still given correctly). It is unlikely that a simple answer exists in this case but further investigations are clearly needed.

Manuscript received Jan. 24, 1968. This paper was presented at the Boston Meeting, May 5-9, 1968, as Paper 144.

Any discussion of this paper will appear in a Discussion Section to be published in the December 1969 JOURNAL.

REFERENCES

1. H. Schwarz, Mechanism of High-Power-Density Electron-Beam Penetration in Metal, in "Electron and Ion Beam Science and Technology," R. Bakish, Editor, p. 158. John Wiley & Sons, Inc., New York (1965).
2. B. W. Schumacher, Some Observations on High-Power Electron Beams Under Water, in "Electron and Ion Beam Science and Technology," 3rd International Conf., R. Bakish, Editor, p. 236, John Wiley & Sons, Inc., New York (1968).
3. M. Jakob, in "Heat Transfer," p. 132, John Wiley & Sons, New York (1949).
4. D. C. Schubert and B. W. Schumacher, Effect of Electron Scattering in the Metal Vapor on the Energy Dissipation in the Cavity Present During Electron Beam Welding, in "Electron and Ion Beam Science and Technology," 3rd International Conf., R. Bakish, Editor, p. 269, John Wiley & Sons, Inc., New York (1968).
5. B. W. Schumacher, Electron Beam Cutting of Rocks and Concrete, *op. cit.*, p. 447.

An Investigation of the Differences Between NaCl and $NaClO_3$ as Electrolytes in Electrochemical Machining

James P. Hoare,* Mitchell A. LaBoda,*
Michael L. McMillan,† and Augustine J. Wallace, Jr.

Electrochemistry Department, Research Laboratories, General Motors Corporation, Warren, Michigan

ABSTRACT

Constant potential polarization curves were obtained on steel rotating disk anodes in concentrated NaCl and $NaClO_3$ electrolytes, and steady-state polarization curves were obtained on stationary soft iron anodes in NaCl, $NaClO_3$, $NaNO_3$, and $Na_2Cr_2O_7$ solutions. The results show that the metal removal reaction is activation controlled and that $NaClO_3$ electrolytes are reduced to NaCl with extended periods of electrochemical machining. Tests conducted in a flow system showed that up to 50 g/l of NaCl could be tolerated in a concentrated $NaClO_3$ electrolyte (350 g/l) before the excellent machining properties of the electrolyte become impaired. Wild cutting electrolytes (NaCl) do not form protective films on ferrous metals, whereas noncutting electrolytes ($Na_2Cr_2O_7$) form too highly protecting films of γ-Fe_2O_3. The good dimensional control is obtained with electrolytes ($NaClO_3$) which behave in an intermediate way and possess a sharp transition from the passive to the transpassive state.

For a number of years, electrochemical machining (ECM) has been known as a highly effective metal removal method for machining hardened metals at high metal removal rates without producing process-induced stresses and wearing of the machining tool. Until recently, development of ECM as an industrial process has been slow because of the lack of dimensional control when NaCl, $NaNO_3$, or acids were used as the electrolyte. Most developmental efforts (1) have been aimed at improvements in the use of NaCl electrolytes without the required success necessary for industrial usage.

Operating with the concept that satisfactory dimensional control necessitated the uncovering of a new electrolyte, LaBoda and co-workers (2), after an intensive screening effort, reported that $NaClO_3$ electrolyte possesses excellent ECM properties. Metal removal rates were obtained as high as 0.001 in./sec for a hardened Carpenter Ni-Cr steel having a Rockwell hardness of 60C and the finish of the machined surface measured from 1 to 5 μin.

To understand the nature of the processes taking place in the ECM operation, an intense, comprehensive investigation of ECM systems is being carried out at the General Motors Research Laboratories. This report describes the results of some of these studies.

Experimental

Because the experimental conditions for actual ECM (high flow rates, high currents, small distance between anode and cathode, among others) are very complex, the only hope for obtaining meaningful data on such a system is to design experiments in which a minimum number of uncontrolled parameters exist.

Rotating disk studies.—Since the ECM processes take place under conditions of high flow rates of electrolyte, a study of the corrosion process using the controlled hydrodynamic conditions of the rotating disk (3) was carried out.

The rotating disk was made by potting a rod (0.3 cm in diameter) of 5160 steel hardened to Rockwell 60C in epoxy and grinding the face of this assembly to expose a circular area of the steel to the electrolyte. Rotational speeds between 160 and 7550 rpm were employed. A saturated calomel electrode (SCE) served as a reference electrode and a copper cylinder (0.318 cm in diameter) was the counter electrode.

After the anode and cathode were ground, polished and anodically cleaned, the electrodes were mounted in the glass cell shown in Fig. 1 and the anode and cathode were spaced to the desired distance by Lucite spacers. Anodic polarization curves were taken potentiostatically in NaCl (250 g/l) and $NaClO_3$ (350 g/l) electrolytes. Vacuum fusion, electron probe, and electron diffraction techniques were used to study the steel surfaces electrochemically machined in both NaCl and $NaClO_3$ electrolytes.

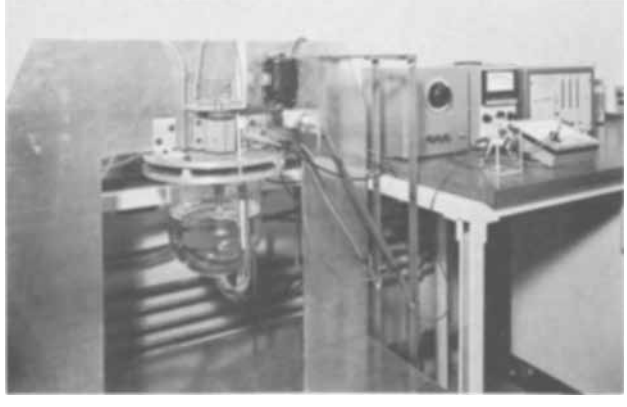

Fig. 1a. Rotating disk electrode system

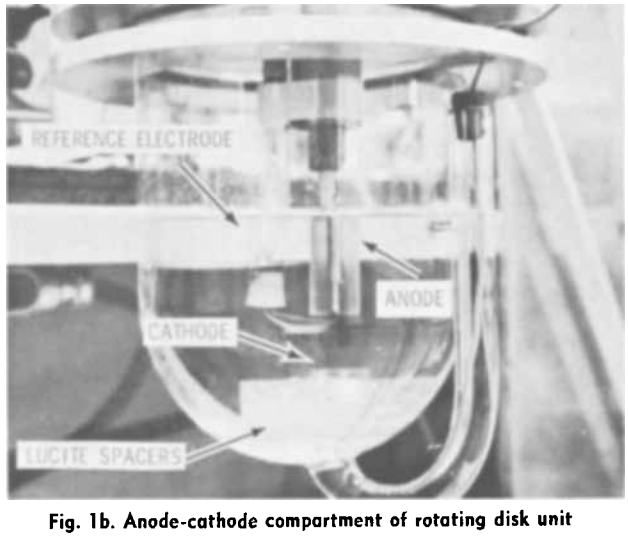

Fig. 1b. Anode-cathode compartment of rotating disk unit

* Electrochemical Society Active Member.
† Electrochemical Society Student Member.

With the controlled hydrodynamic conditions obtained with the rotating disk technique, an analysis of the system for Cl^- and ClO_3^- ion for a given amount of iron machined was carried out to help answer questions about what happens during ECM over extended periods of time. In this case the rotating disk was composed of a 5160 steel rod insulated from the electrolyte with stopoff tape and held in a neoprene stopper. As the rod was progressively machined away, the experiment was halted and the rod was repositioned in the stopper to expose an additional amount of the rod.

Exactly 3.50 liters of $NaClO_3$ solution (600 g/l) were placed in the cell and the rod was machined at about 35 amp/cm^2 (from a 115v, 15-amp power supply) at 7000 rpm. The amount of charge passed was determined with an electronic coulometer. Samples of the electrolyte were taken at various times by halting the experiment long enough to allow the sludge to settle. At the end of the experiment, the remaining electrolyte was filtered and both the filtrate and sludge were analyzed to obtain an over-all material balance. The Cl^- ion was analyzed by titration with $AgNO_3$ (4) and ClO_3^- ion was reduced with excess $FeSO_4$ and back-titrated with $Na_2Cr_2O_7$. In addition, the sludge was also analyzed for Fe using the Zimmermann-Reinhardt method (6), and for H_2O by weight loss after drying in an oven. The entire cell was thermostated to room temperature by immersion in a large water bath.

Test panel studies.—Since the analytical results indicated that the ClO_3^- ion was degraded to Cl^- ion with time, it seemed desirable to study the effect of the presence of Cl^- ion in the $NaClO_3$ electrolyte on the ECM properties. For this study, a flow system (Fig. 2) was used consisting of a centrifugal pump, a solution reservoir, and a cell fixture (Fig. 3). The cell was a circular cavity (2.5 cm in diameter and 1.15 cm deep) in one side of an epoxy block (5 x 5 x 7 cm) into which extended a copper tube which served as the cathode. The anodes were test panels (2.5 x 7.5 x 0.062 cm) of 1008 steel which were held in place over the face of the cell with a neoprene gasket and Lucite end plate so that the initial gap space between the test panel and the copper tube cathode was 0.0507 cm. After the test panels were cleaned, dried, weighed, and anodically activated, they were electrochemically machined for 1 min at 62 amp/cm^2 at 25°C with an electrolyte flow rate of 4.5 l/min. At the end of each run, the panels were rinsed in water, dried, and reweighed. Each test was run in triplicate.

A topographic microscope (7) was used to examine the profile of the panel surface after ECM. As noted in Fig. 4, the high current density (hcd) region on the panels is an annular ring opposite the annulus of the copper pipe cathode. In $NaClO_3$ solutions virtually all of the metal removal took place in the hcd region.

As NaCl was added to the $NaClO_3$ electrolyte, the anode surface was examined in the low current density (lcd) region for any attack of the surface outside of the hcd region. In one group of experiments, the $NaClO_3$ concentration was held constant at 350 g/l while the NaCl concentration was increased from 0.5 through 15, 30, 45, 60, and 100 to 150 g/l. In a second set of experiments, the ionic strength was kept constant by lowering the $NaClO_3$ concentration by the required amount as the NaCl concentration was increased.

Steady-state polarization studies.—Because the rotating disk studies indicated that the corrosion process at the anode surface was activation controlled, potentiostatic polarization studies were carried out on the more convenient stationary bead electrodes with better control of the parameters affecting the electrochemical properties of the system. From an observation of the curves obtained earlier (2), it was decided that a more careful determination of the polarization curves was required to help in the understanding of the passivating nature of these electrolytes. Since it was observed in the actual ECM operation, for a given set of experimental conditions, that $NaClO_3$ gave excellent dimensional control, $NaNO_3$ gave relatively good control, NaCl gave serious wild cutting, and Na_3PO_4, Na_2CO_3, and $Na_2Cr_2O_7$ gave no cutting at all, these steady-state polarization studies were undertaken to shed light on the ECM behavior of these electrolytes.

To remove any complicating influence of nonferrous components in the anode metal, anodes were fashioned in the form of small beads (~0.13 cm in diameter) melted at the end of soft iron wires plated with soft iron. The iron bead was held in the reducing part of a burning H_2 jet for a few minutes to reduce surface oxides. Tight-fitting Teflon spaghetti was slipped over the wire and pressed against the base

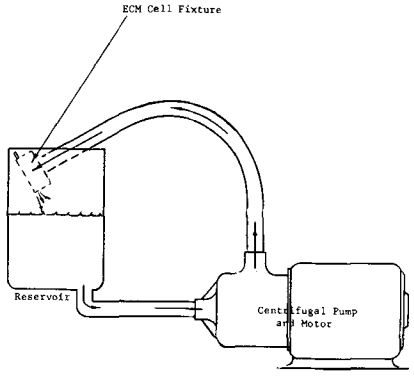

Fig. 2. Schematic illustration of assembled ECM apparatus

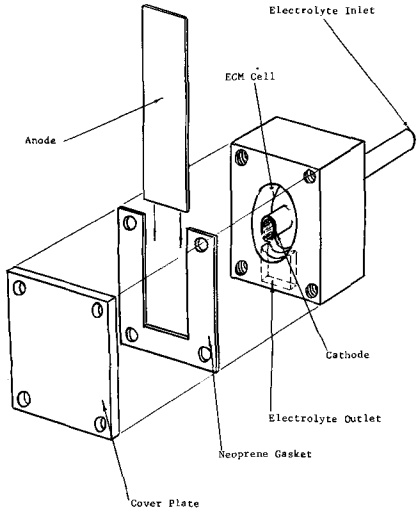

Fig. 3. ECM cell fixture

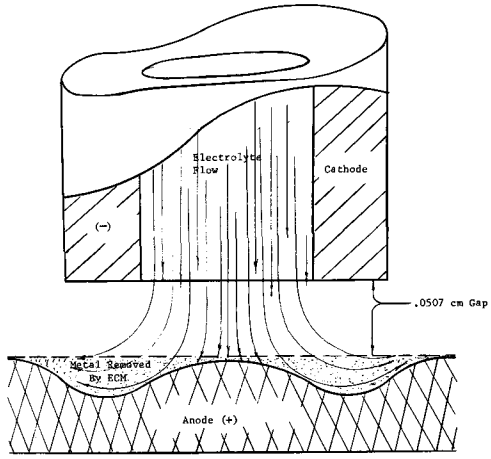

Fig. 4. Profile hcd area in relation to the cathode tube

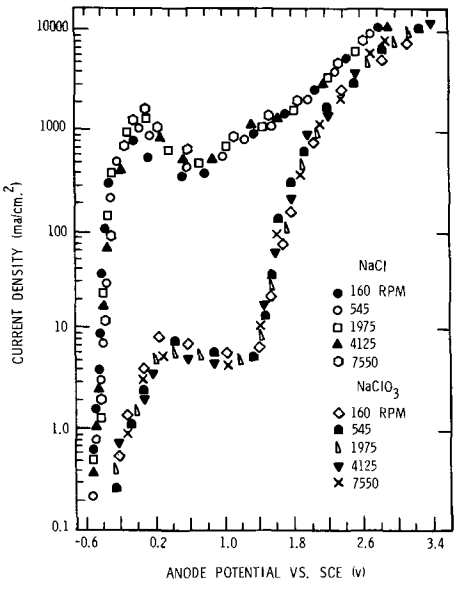

Fig. 5. Current density vs. anode potential for 250 g/l NaCl and 350 g/l $NaClO_3$ with disk rotational speed as parameter. Anode-cathode spacing = 4.83 cm.

of the bead. Then the bead was imbedded in molten polyethylene so that only a hemisphere of the bead was exposed (8). After mounting three beads in a clean Teflon dual cell (9), they were soaked in triply distilled water for about 24 hr with numerous changes of water to leach out impurities in the system.

The test solutions (made from reagent grade chemicals) were as follows: $NaClO_3$, 350 g/l; $NaNO_3$, 350 g/l; NaCl, 275 g/l; $Na_2Cr_2O_7$, 100 g/l. In a second clean Teflon cell which held about 12 cc of solution, the given electrolyte was preelectrolyzed between removable Pt electrodes for 16 hr. By withdrawing the Pt preelectrolysis electrodes, the circuit was broken and any H_2O_2 formed was removed by saturating the solution with hydrogen gas. A large Pt gauze was used as the counter electrode and a SCE as the reference electrode. After the solution was saturated with nitrogen, the iron test electrodes were removed from the first cell and sealed in the test compartment of the second cell.

The polarization curve was obtained by determining the steady-state current on a Keithley electrometer, Model 600A, and recorded on a Honeywell strip recorder for the stepwise increases and decreases in the potential controlled by a Wenking 61R potentiostat. Although the steady-state value was reached within a few minutes in most cases, periods of time up to 25 min were required in some regions. The solution was stirred by bubbling either purified N_2 or O_2 through the test compartment at a rate of at least 300 cc/min to minimize mass transfer effects, and the temperature was 25° ±1°C.

Table I. Results of extended electrochemical machining in $NaClO_3$

Sample No.	Weight of rod machined (g)	Coulombs passed	Grams/liter C_{NaClO_3}	Grams/liter C_{NaCl}
1	0.562	2299	595.99	0.478
2	3.089	12331	595.70	0.617
3	5.738	22781	595.21	0.875
4	10.882	43681	594.17	1.426
5	21.280	85481	592.09	2.573
6	42.164	169290	588.34	4.600
7	82.838	332519	582.67	7.656
8	169.698	688028	569.10	14.958

Results

Rotating disk studies.—A plot of the potential of the steel anode as a function of the log of the apparent current density for various speeds of rotation of the disk in both NaCl and $NaClO_3$ solutions is given in Fig. 5. It is seen that over the range of rotational speeds studied virtually no effect of the rate of rotation was observed on the polarization curves.

Table I contains the results of the analysis for Cl^- ion and ClO_3^- ion for extended periods of ECM in $NaClO_3$ solutions. It is seen that the amount of Cl^- ion builds up in solution while the ClO_3^- ion concentration decreases during the ECM process. There is a linear relationship between the grams of metal removed and the buildup of NaCl in solution as well as between the moles of iron machined and the moles of $NaClO_3$ reduced. The average value of the moles of iron machined to the moles of $NaClO_3$ reduced is 3.95.

The possibility that the reduction of ClO_3^- ion to Cl^- ion takes place at the cathode is the subject of current investigations and is not considered further in this report.

Both vacuum fusion and electron probe analyses indicated a high percentage of oxygen on the surface of disks machined in $NaClO_3$ but none on the surface of those machined in NaCl. Reflection electron diffraction studies confirmed these findings by detecting a film of γ-Fe_2O_3 on specimens machined in $NaClO_3$ but not on those machined in NaCl.

Test panel studies.—The results of these studies are given in Table II and Fig. 6. With NaCl concentrations below 50 g/l in either group A or B tests, the weight of metal removed did not sensibly change compared to the results from the pure $NaClO_3$ control solution. Above 50 g/l of NaCl, the weight of the metal removed increased with each addition of NaCl to the electrolyte but was independent of the amount of $NaClO_3$ in solution. Also associated with the increased metal removal due to the increased NaCl concentration is the

Table II. Results after ECM in $NaClO_3$, NaCl, or mixed $NaClO_3$-NaCl electrolytes

Solution	$NaClO_3$ (g/liter)	NaCl (g/liter)	Cell voltage	Metal removal (g)	Diameter hcd* ECM (mm)	Appearance of lcd* Etching	Appearance of lcd* Staining
Control	350	—	8.5	0.1057	12.5	None	None
Control	—	230	5	0.2300	15	All over	None
Mixed A	350	0.5	8	0.1099	12.5	None	None
Mixed A	350	15	8	0.1235	13	Ring groove	None
Mixed A	350	30	7.5	0.1168	12.5	Ring groove	None
Mixed A	350	45	7.25	0.1109	12.5	Ring groove	None
Mixed A	350	60	7	0.1404	13	Ring groove	Slight
Mixed A	350	100	6.75	0.2117	12	Ring groove	Black-rust
Mixed A	350	150	6.25	0.2155	10.5	Ring groove	Black-rust
Mixed B	350	0.5	8.75	0.1057	12.5	None	None
Mixed B	325	13.75	8.25	0.1053	11.8	Ring groove	None
Mixed B	300	27.5	8.25	0.1037	12.3	Ring groove	None
Mixed B	275	41.25	8	0.1006	11.8	Ring groove	None
Mixed B	250	55	7.25	0.1624	10.6	Ring groove	None
Mixed B	225	68.75	7.5	0.1432	11.5	Ring groove	Black-rust
Mixed B	175	96	7.5	0.1479	9.6	Ring groove	Black-rust
Mixed B	80	148	6.25	0.2324	11.5	Ring groove	Black-rust

* Hcd—High current density.
Lcd—low current density.

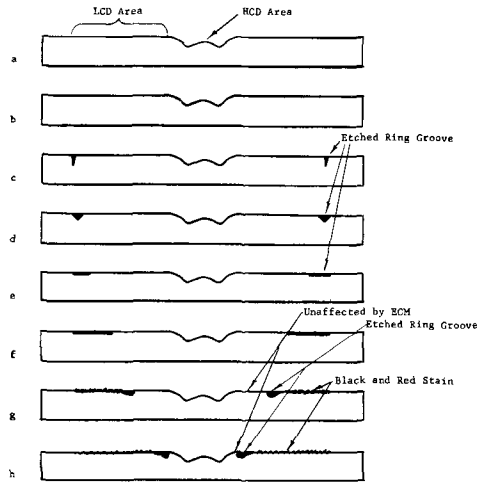

Fig. 6. Profile of hcd and lcd areas after electrochemical machining in a 350 g/l $NaClO_3$ solution with: (a) 0 g/l NaCl, (b) 0.5 g/l NaCl, (c) 15 g/l NaCl, (d) 30 g/l NaCl, (e) 45 g/l NaCl, (f) 60 g/l NaCl, (g) 100 g/l NaCl, and (h) 150 g/l NaCl.

increasingly larger surface area attacked during the ECM process.

Steady-state polarization studies.—A summary of the typical results obtained on soft iron in the various electrolytes is displayed in Fig. 7. Open symbols represent the data for increasing potentials and filled symbols for decreasing potentials. Repeated cycles of polarization gave virtually the same results. All curves shown were obtained in O_2-saturated solutions except one in N_2-saturated $NaClO_3$ solution (x's in Fig. 7). The N_2 and O_2 curves were similar, but the currents in general were lower in the case of N_2-stirring.

A vertical dashed line is drawn arbitrarily at 10 ma/cm² to correspond to the region in which the ECM process takes place. It must be kept in mind that the potentials recorded in Fig. 7 are referred to a reference electrode and are not the total cell potentials commonly reported in the ECM literature. How the potentials in Fig. 7 are related to the reported ECM cell potentials is not important to this discussion since the relative shapes of the polarization curves are the matters of interest.

Discussion

From the rotating disk studies, it is seen that the metal removal process under these conditions is activation controlled rather than limited by a mass transfer step.

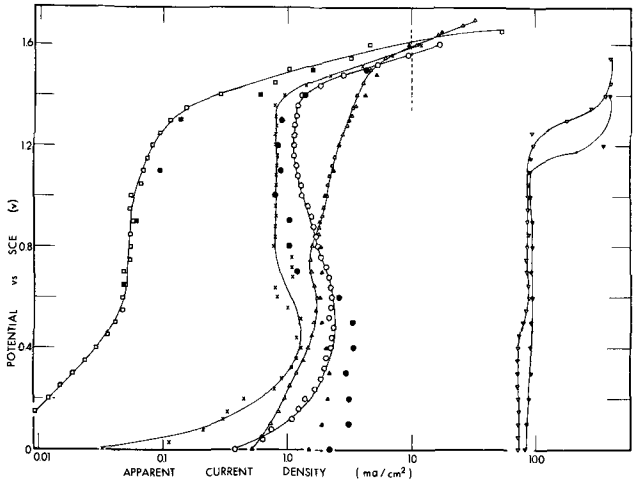

Fig. 7. Steady-state potentiostatic polarization curves of soft iron in concentrated solutions of the following electrolytes: ○, ● — $NaClO_3$; △, ▲ — $NaNO_3$; ▽, ▼ — NaCl; □, ■ — $Na_2Cr_2O_7$. Open symbols indicate data for increasing potentials; filled, for decreasing potentials. All of these solutions were saturated with O_2. A curve in N_2-saturated $NaClO_3$ solution is shown by the x's.

The data of Table I show that $NaClO_3$ is reduced to NaCl with extended periods of ECM operation and the test panel studies confirm that the presence of NaCl in $NaClO_3$ electrolytes produces unacceptable wild cutting above a certain limiting concentration (50 g/l). Since a film of γ-Fe_2O_3 is detected on the surfaces of test samples machined in $NaClO_3$ but not in NaCl electrolytes, it appears, at first sight, that the presence of an oxygen-containing anion (or good oxidizing agent) is required for the electrolyte to have acceptable ECM properties. However, this cannot be the complete story, because electrolytes based on chromates, phosphates, or carbonates produce no cutting under the conditions where $NaClO_3$ gives excellent cutting. Results of the steady-state polarization studies provide data from which a possible explanation for these findings may be made in the light of accepted theories of passivation (10).

Consider first the curve for $NaClO_3$ (circles in Fig. 7). At the lowest potentials, the system is active, and Fe goes into solution as Fe^{++} ions which can then be oxidized by dissolved oxygen to Fe^{+++} ions (11). As the potential becomes more noble, the current increases until a critical current is reached, after which the surface becomes passivated by the formation of a film of γ-Fe_2O_3 and the current falls to smaller values. At still more anodic potentials, the film breaks down, the system becomes transpassive, and the current (rate of reaction) increases rapidly. It is assumed that ECM cutting takes place in this transpassive region.

As a typical example of electrochemical machining (2), currents of the order of 300-1200 amp/in.² were passed between the work sample (anode) and the tool (cathode) at cell potentials between 12 and 15v. With such enormous currents, the iR drop across the anode-cathode gap may assume large values. As machining takes place, the gap between the anode and the exposed face of the tool increased with a resultant increase in iR drop. Consequently, the potential of the surface of the worked piece falls to less noble values where cutting does not occur. Since the difference between cutting and not cutting takes place over a very short gap length, the machined surface is a faithful reproduction of the tool giving the high precision recorded by LaBoda and McMillan (2).

In the case of the $NaNO_3$, which is known to cut with little wild cutting, the polarization curve (triangles in Fig. 7) is similar to the $NaClO_3$ curve except that the transition from passivity to transpassivity is not as sharp. As a result, cutting can take place over a wider gap distance, and the precision with $NaNO_3$ is not as good as with $NaClO_3$. In the transpassive region, the $NaNO_3$ curve lies at more noble potentials than does $NaClO_3$. For a given potential, the rate of cutting (current density) is less for $NaNO_3$ than for $NaClO_3$, in agreement with the observation that $NaNO_3$ cuts slower than $NaClO_3$.

The steady-state polarization curve for NaCl (inverted triangles in Fig. 7) lies in a current density range nearly two orders of magnitude higher than that for $NaNO_3$ and $NaClO_3$. Since cutting can occur even at the lowest potentials given in Fig. 7, the gap space over which cutting is permitted in this case is very large. As reported (2), the undesirable wild cutting obtained with this electrolyte produces a complete lack of dimensional control.

After the polarization curves were obtained, the cell was opened and the electrolyte examined. With $NaNO_3$ and $NaClO_3$, the beads were black or had areas of red rust on them. Rust in the solution was not soluble, so that if the solution was filtered, the filtrate was colorless. With NaCl, the beads were light gray, and the solution was clear but yellow colored. In the NaCl electrolyte, a soluble iron salt is formed instead of a protective film of γ-Fe_2O_3 in the cases of $NaNO_3$ and $NaClO_3$; and this situation keeps iron in a highly active state even in regions of high potential. To have good

Table III. Rest potentials on soft Fe in O_2-saturated, concentrated salt solutions

Salt	Concentration (g/l)	Potential vs. SCE (mv)	Remarks
NaCl	275	−590	Wild cutting
$NaNO_3$	350	−480	Good cutting
$NaClO_3$	350	−350	Excellent cutting
$Na_2Cr_2O_7$	100	−140	No cutting

dimensional control, the electrolyte must passivate the iron surface at potentials below cutting, and the polarization curve must exhibit a sharp transition from the passive to the transpassive region.

To obtain a suitable ECM electrolyte, these data predict that an oxygen-containing anion is a necessary prerequisite to produce the passivating film required for dimensional control. The chromates appear to be likely candidates since a protective film of γ-Fe_2O_3 is formed on Fe in these electrolytes (*e.g.*, 12, 13). However, a solution of $Na_2Cr_2O_7$ did not produce any cutting in the potential range where $NaClO_3$ cuts.

Examination of the steady-state polarization curve obtained in $Na_2Cr_2O_7$ (squares in Fig. 7) shows that the Fe is so well protected that the curve is shifted to current densities about two orders of magnitude lower than those in $NaClO_3$. Although a sharp transition from the passive to the transpassive region exists, the transpassive region for $Na_2Cr_2O_7$ still lies at higher potentials than that for $NaClO_3$. In practice, it is found that cutting with poor surface finishes due to sparking can be obtained with $Na_2Cr_2O_7$ at much higher potentials (above 30v).

Other passivating electrolytes, such as Na_2CO_3 and Na_3PO_4, do not give any cutting. It is likely that their polarization curves are similar to the $Na_2Cr_2O_7$ curve because these electrolytes produce highly protective films of γ-Fe_2O_3 (14, 15).

There is an interesting correlation between the rest potential in O_2-saturated solutions and the ECM properties as shown in Table III. The potentials are the average of three independent determinations. As the potential becomes more noble, one progresses from wild cutting through good dimensional control to no cutting. This correlation, of course, is related to the passivating nature of the electrolyte since the test potentials are mixed potentials (16, 17).

By comparing the polarization curves for Fe anodes in O_2- and N_2-saturated $NaClO_3$ solution, it is seen that the presence of O_2 increases the current density.

Apparently, $NaClO_3$ electrolytes occupy a privileged position. Their polarization curves not only have the sharp transition from the passive to the transpassive region of the highly passivating electrolytes but also have transpassive regions lying at the least noble potentials.

Manuscript submitted Aug. 20, 1968; revised manuscript received Oct. 24, 1968.

Any discussion of this paper will appear in a Discussion Section to be published in the December 1969 JOURNAL.

REFERENCES

1. C. R. Allison, Creative Manufacturing Seminar, ASTME (1963-1964); G. K. Vandenburgh, *ibid.*, (1964-1965); R. R. Rupender, *ibid.*, (1966); J. Hopenfeld and R. R. Cole, *ibid.*, (1966).
2. M. A. LaBoda and M. L. McMillan, *Electrochem. Technol.*, **5**, 340, 346 (1967).
3. A. C. Riddiford, in "Advances in Electrochemistry and Electrochemical Engineering," C. Tobias, Editor, Vol. 4, p. 47, Interscience Publishers Inc., (1966).
4. H. H. Willard, N. H. Furman, and E. K. Bacon, "A Short Course in Quantitative Analysis," p. 135, D. Van Nostrand & Co., New York (1957).
5. Hooker Chemical Co., Bulletin No. 99A, Niagara Falls, New York (1961).
6. A. A. Blair, "The Chemical Analysis of Iron," p. 248, Lippincott (1918).
7. R. L. Saur, *Rev. Sci. Instruments*, **29**, 1023 (1958).
8. J. P. Hoare, *GM Eng. J.*, **9**, No. 1, 14 (1961).
9. J. P. Hoare, *This Journal*, **109**, 858 (1962).
10. Symposium on Passivity, *Z. Elektrochem.*, **59**, 591 (1955).
11. W. Feithneckt and G. Keller, *Z. Anorg. Chem.*, **262**, 61 (1950).
12. T. P. Hoar and U. R. Evans, *J. Chem. Soc.*, **134**, 2476 (1932).
13. M. Cohen and A. F. Beck, *Z. Elektrochem.*, **62**, 696 (1958).
14. M. J. Pryor and M. Cohen, *This Journal*, **100**, 203 (1953).
15. H. H. Uhlig, D. N. Triadis, and M. Stern, *ibid.*, **102**, 59 (1955).
16. C. Wagner and W. Traud, *Z. Elektrochem.*, **44**, 391 (1938).
17. J. P. Hoare, in "Advances in Electrochemistry and Electrochemical Engineering," P. Delahay, Editor, Vol. 6, p. 226, Interscience Publishers Inc., (1967).

Electrolytic Production of Perchlorate by Lead Dioxide Anodes

Takashi Osuga and Shojiro Fujii

Sanwa Chemical Co. Ltd., 1-8, Kanda Nishikicho, Chiyoda-ku, Tokyo, Japan

and Kiichiro Sugino* and Taro Sekine

Department of Applied Electrochemistry, Tokyo Institute of Technology, Ookayama, Meguro-ku, Tokyo, Japan

ABSTRACT

An outline is given of an electrolytic process for the production of sodium perchlorate using a pure lead dioxide anode. In this process, a saturated solution of sodium chlorate is electrolyzed batchwise at an anodic current density of 25 amp/dm² at 50°C; current efficiency, about 70% with more than 99% conversion of chlorate to perchlorate; cell voltage, 4.5-5.0v. The process has been operated successfully for more than two years without renewal of the anodes. In relation to the above, the results of basic research on anode potential and current efficiency for perchlorate formation from chlorate are also given.

Although we had perfected a new electrolytic process of producing perchlorate using lead dioxide as the anode about two decades ago in both the laboratory and on a semicommercial scale (1), production using the new process was not carried out in Japan until 1965, when Sanwa began to produce perchloric acid with this process. The principal reason for the delay was the small demand for perchlorate in Japan after the war. When the Pacific Engineering Company of the United States started to produce perchlorate using a lead dioxide anode, we decided to put our

* Electrochemical Society Active Member.

process in practical use. Because of the small demand for perchlorate, we constructed a small-sized perchlorate plant to produce perchloric acid as the final product. This report mainly describes the outline of the process operated in Sanwa Chemical's plant.

Basic Research on Anode Potential and Current Efficiency for Perchlorate Production from Chlorate

In 1953 one of the authors (K. Sugino) and Dr. S. Aoyagi presented a paper entitled "Mechanism of the Electrolytic Formation of Perchlorate" at the New York Meeting of the Society in which the current *vs.* potential curves for the anodic process of chlorate at platinum were shown. The results were subsequently published (2). The curves were obtained by a kind of polarographical technique at a platinum microanode. In a moderately concentrated solution of chlorate two stages of potential were definitely observed on the curves. In the first or lower stage, the potential was between 1.5-1.7v and in the second or higher stage, it was more positive than 2.1v (*vs.* SCE).

As a result of controlled potential electrolysis, it was clarified that the first stage was the potential of oxygen evolution and the second stage was the potential at which the formation of perchlorate occurred.

From the detailed experiments on the above phenomena, it was proved that the first step of this process is the direct discharge of ClO_3^- at a higher potential than that of oxygen evolution.

Recently, from a practical point of view, the current *vs.* potential curves for perchlorate formation were again measured at the platinum and at the lead dioxide anodes by one of the authors (T. Sekine) and his collaborators by using controlled potential electrolyzer (3). They are shown in Fig. 1 and 2.

At the platinum anode curves similar to those of Sugino and Aoyagi were obtained and two potential stages were clearly observed. On the other hand, at the lead dioxide anode, the curves did not indicate such stages. They showed a steep increase of current at around 1.8-1.9v (*vs.* SCE) and were observed as a simple exponential relationship. However, as shown in Fig. 3, when the chlorate solution of *p*H 11.4-12.0 was used, curves having two potential stages were obtained and the lower stage was found to be the potential of oxygen evolution. Accordingly the potential at which the current began to flow in Fig. 2

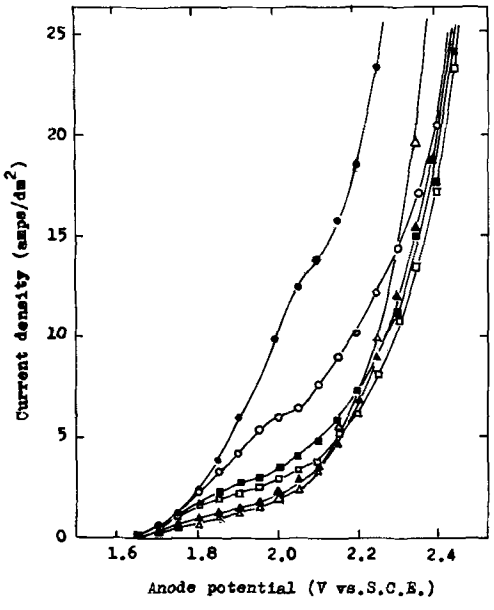

Fig. 1. Current *vs.* potential curves at platinum anode in various concentrations of chlorate solution. ●, $NaClO_3$, 1 mole/l; ○, $NaClO_3$, 2 mole/l; ■, $NaClO_3$, 3 mole/l; □, $NaClO_3$, 4 mole/l; ▲, $NaClO_3$, 5 mole/l; △, $NaClO_3$, 6.4 mole/l (saturated solution).

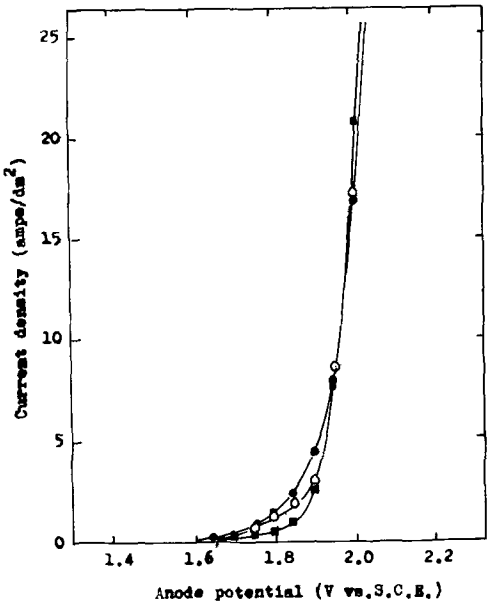

Fig. 2. Current *vs.* potential curves at lead dioxide anode in various concentrations of chlorate solution. ●, $NaClO_3$, 1 mole/l; ○, $NaClO_3$, 3 mole/l; ■, $NaClO_3$, 6.4 mole/l (saturated solution).

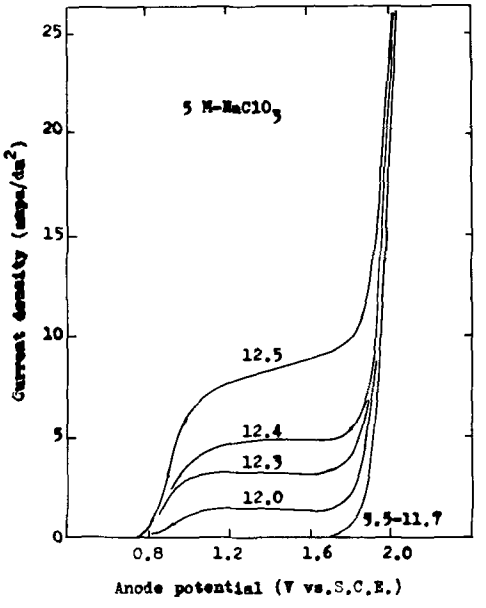

Fig. 3. Current *vs.* potential curves at lead dioxide anode in chlorate solution of different *p*H.

indicated the potential of perchlorate formation at the lead dioxide anode.

The mechanism of perchlorate formation at the lead dioxide anode may be somewhat different from that at the platinum anode. It is presumed to be due to the simultaneous discharge of ClO_3^- and OH^-, followed by the combination of the radicals formed. This was proposed as a possible route by Sugino and Aoyagi in the paper described above.

It was found that the potential at which the current corresponding to perchlorate formation began to flow was about 0.25v lower than that at the platinum anode in the same concentration. In addition, the increase of anode potential with increasing current density was very small up to high current density such as 30 amp/dm^2, but at the platinum anode, the potential increased steadily with increasing current density as shown in Fig. 1. This is an interesting characteristic of the lead dioxide anode and it is the main reason for the smaller cell voltage than that at the platinum cell, especially at high current density.

Table I. Bench scale experiment*

Anode	Lead dioxide
Cathode	18-8 stainless steel
Electrolyte	Saturated solution of $NaClO_3$ containing 2 g/l of NaF
Current	600 amp
Current density, anodic	20 amp/dm²
Temperature	50°C
Conversion	99.5%
Current efficiency	72%

* Data from ref. (1).

It was thought for a long time that the current efficiency for perchlorate formation from chlorate at the lead dioxide anode was not so high when the electrolysis was continued until almost all the chlorate was converted to perchlorate, although a high value could be expected as an instantaneous current efficiency. Therefore, about 2 g/l of sodium fluoride were added to the cell liquor to maintain the over-all current efficiency above 70%. Thus, one of the authors (K. Sugino) and his collaborators reported about 80% current efficiency in a laboratory cell and 72% current efficiency in a 600 amp cell when more than 99% of chlorate was converted to perchlorate (4) as shown in Table I. These results were later confirmed by Schumacher *et al.* (5).

Recently one of the authors (T. Sekine) carried out a detailed study on the current efficiency for perchlorate formation at the lead dioxide anode. From the results, it seems that a high current efficiency could be obtained at the lead dioxide anode without any additive such as sodium fluoride. A few examples are shown below:

Results of controlled potential electrolysis.—Electrolyses at the lead dioxide anode were carried out in various concentrations of chlorate solution (1-6M $NaClO_3$) at a certain potential in the range of 1.85-2.10v (*vs.* SCE). The examples with 6M solution are condensed in Table II. In the table about 90% (87-89%) of current efficiency was marked at the potential of 1.90-2.10v (*vs.* SCE), without addition of sodium fluoride in the electrolyte in the initial stage of electrolysis.

Combining the above results with those obtained at the platinum anode, the influence of anode potential on the current efficiency in 5M solution, for instance, is shown in Fig. 4. From the curve, it is also clear that the potential corresponding to the formation of perchlorate at the lead dioxide anode is about 0.25v more negative than that at the platinum.

Results of almost complete conversion of chlorate to perchlorate by constant current electrolysis (6).—The current efficiencies for perchlorate formation are shown in Table III when more than 80% of the chlorate is converted to perchlorate. A decline in current efficiency was observed in the final stage of electrolysis as shown in the table. The results indicate that with lead dioxide a current efficiency of 65-70% was obtained even when about 99% of chlorate was converted to perchlorate.

However, it should be pointed out that commercial chlorate contains a very small amount of bichromate as a contaminant. As shown in Table III, in the case of the lead dioxide anode, it was found that this contaminant showed a strong negative effect on the current efficiency. It was also found that the addition of sodium fluoride partly compensates the negative effect of bichromate thus contributing to maintain a high current efficiency. Accordingly we are still using this additive.

In regard to the effects of temperature on current efficiency, a remarkable difference was found between platinum and lead dioxide. In the case of platinum, it has been reported that the current efficiency increases with lower temperature. On the other hand it was found that in the case of lead dioxide the current efficiency increased with higher temperature as shown in Fig. 5. This may be a phenomenon suitable from a practical point of view. However, we had operated at 50°C considering another mechanical factor.

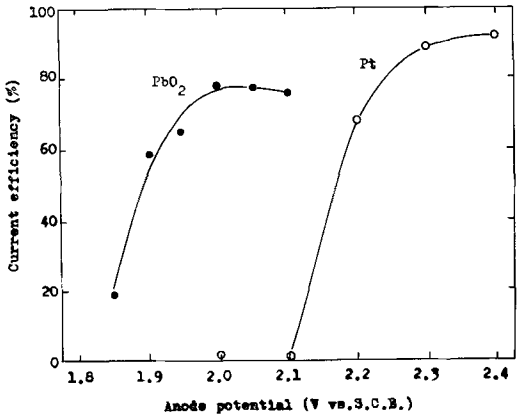

Fig. 4. Relation between anode potential and current efficiency with both lead dioxide and platinum anode in 5M $NaClO_3$. ●, Lead dioxide, ○, platinum.

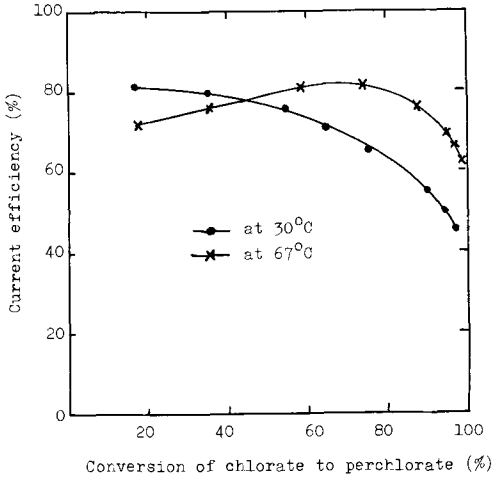

Fig. 5. Influence of temperature on current efficiency

Table II. Example of controlled potential electrolysis*

Anode potential (v *vs.* SCE)	Concentration of electrolyte $NaClO_3$ (mole/l)	Current density (average) (amp/dm²)	Amount of current (amp · hr)	$NaClO_4$ (mmole/l)	Current efficiency (%)
1.90	6.39	2.40	1.59	25.7	86.7
1.95	6.39	14.1	2.90	48.5	89.6
2.00	6.39	14.5	2.46	41.2	89.0
2.05	6.39	28.5	2.74	44.5	87.0
2.10	6.23	35.9	2.09	34.8	89.0

* Anode: PbO_2, cathode: Pt, temperature: 25°C.

Table III. Example of electrolysis in process of complete conversion*

Concentration of electrolyte $NaClO_3$ (mole/l)	Current density (amp/dm²)	Temperature (°C)	Conversion (%)	Current efficiency (%)
5.67	20	50	80.5	80.5
			94.1	76.2
			96.8	73.5
			98.8	69.2
5.98†	42	50	97.9	51.3

* Anode: PbO_2, cathode: stainless steel.
† Electrolyte contains 0.03 g/l of Na_2CrO_4.

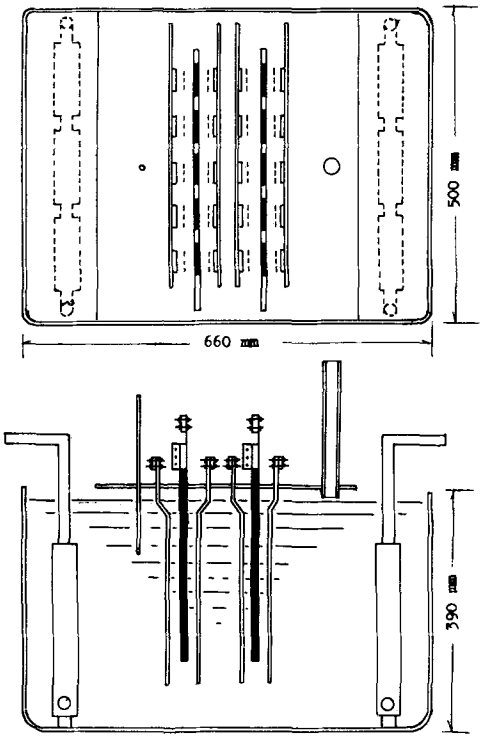

Fig. 6. Cell design

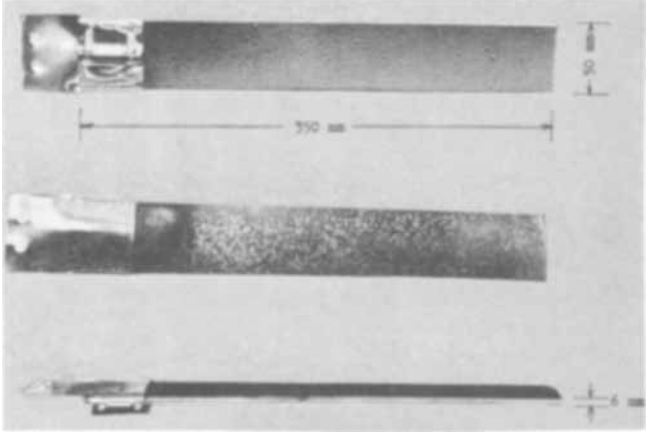

Fig. 7. Lead dioxide anode

Cell Design

The Sanwa perchlorate cell now used is almost the same as that being used in the production of bromate (7). Figure 6 is a diagram of the Sanwa perchlorate cell showing construction and dimensional features.

The cell body is constructed of a sheet iron rectangular tank 660 mm long x 500 mm wide x 390 mm high. The inside surface of the body are all lined with hard polyvinylchloride sheet. A plate of the same hard polyvinylchloride is placed on top of the cell and supports 10 anodes and 20 cathodes. These are arranged in 6 rows running the length of the cover. Down the middle are two rows of 5 anodes and on either side of the rows is a row of 5 cathodes.

The lead dioxide anodes,[1] which are shown in Fig. 7, are 50 mm wide, 6-7 mm thick, and 350 mm long and extend about 65 mm above the cover. The stainless steel cathodes (18-8) are 35 mm wide, 3 mm thick, and 300 mm long. The distance from an anode to the nearest cathode is about 10 mm. Six stainless steel cooling boxes are placed in both ends of the cell and act somewhat as a cathode.

[1] The method used in making the lead dioxide anode was reported in the previous paper (7).

Hydrogen discharged at the cathodes caused sufficient circulation of the cell liquor. It was vented through the roof from each cell.

Although the present cell is operated in a 500 amp capacity, it is possible to bring it up to a 1000 amp cell by doubling the electrode assembly in the container.

A 5000 amp cell can be constructed by combining five unit cells lengthwise. Cells of larger capacities, some 10,000 amp, can also be constructed with lead dioxide anodes of the same size.

The Process

Each cell was filled with 85 liters of a solution of sodium chlorate nearly saturated. Its concentration was 736 g/l $NaClO_3$. To increase the current efficiency, 2 g/l of sodium fluoride was added to the cell liquor. The cells were operated batchwise and each portion of cell liquor was electrolyzed to a final chlorate content of 5-6 g/l before being discharged.

Cell temperature was kept as constant as possible ranging from 47° to 52°C. A current of 500 amp was carried by each cell.

The anodic and cathodic current densities were 25 amp/dm^2 and 35 amp/dm^2, respectively. Current efficiency averaged 70% or a little less based on the analysis of unconverted chlorate. The potential drop across each cell ranged from 4.5 to 5.0v (average 4.7v). Accordingly, energy consumption is estimated to be 3 kw-hr (d.c.) or a little more for each kilogram of sodium perchlorate.

The operation characteristics are listed in Table IV.

The process has been operated successfully for more than two years without renewal of the anodes. It indicated that the loss, if any, may be very small. However, an experiment was made to determine the loss of the anode by using a practical cell. The results are shown in Table V. Conditions of electrolysis are the same as in Table IV.

The data showed that practically no loss resulted after the anode had been used for about three months. A few anodes sustained a very small loss which averaged 8.1 mg/1000 amp-hr.

After electrolysis, the cell liquor was treated with a small amount of calcium chloride to remove fluoride. The resulting solution was then evaporated to a desired concentration. By cooling the concentrated solution at 20°C, about 75-80% sodium per-

Table IV. Operation characteristics

Capacity	85 l/cell
Cell feed	$NaClO_3$ 736 g/l
	NaF 2 g/l
Cell effluent	$NaClO_3$ 5-6 g/l
	$NaClO_4$ 892 g/l
	NaF 2 g/l
Current, amperage	500
Current density, anodic	25 amp/dm^2
cathodic	35 amp/dm^2
Temperature	47°-52°C
Cell voltage	4.5-5.0v (average 4.7v)
Current efficiency (average)	70%
Power consumption	3 kw-hr (d.c.)/kg $NaClO_4$

Table V. Weight loss of lead dioxide anode

Anode No.	Duration of electrolysis: 81 days Weight of anode Before test (g)	After test (g)	Loss (g)
1	1133	1133	0
2	1098	1096	2
3	1118	1116	2
4	990	990	0
5	957	957	0
6	899	899	0
7	885	884	1
8	960	959	1
9	849	847	2
10	958	958	0
Total	9847	9839	8

Average
0.081% by weight for 982.1 kamp-hr
8.1 mg/kamp-hr

chlorate crystallized out as monohydrate. The mother liquor was subsequently returned to the evaporator. In Sanwa Chemical Company, 60% perchloric acid is being produced by treating sodium perchlorate thus obtained with hydrochloric acid.

Manuscript submitted Aug. 5, 1968; revised manuscript received Sept. 30, 1968. This paper was presented at the Boston Meeting, May 5-9, 1968, as Paper 272.

Any discussion of this paper will appear in a Discussion Section to be published in the December 1969 JOURNAL.

REFERENCES

1. K. Sugino, *Bull. Chem. Soc. Japan*, **23**, 115 (1950).
2. K. Sugino and S. Aoyagi, *This Journal*, **103**, 166 (1956).
3. S. Obara, I. Ohara, and T. Sekine, *J. Electrochem. Soc. Japan*, (Denkikagaku), **36**, 291 (1968).
4. K. Sugino and M. Yamashita, *ibid.*, **15**, 61 (1947); see also ref. (1).
5. J. C. Schumacher, D. R. Stern, and P. R. Graham, *This Journal*, **105**, 151 (1958).
6. C. W. Nam and T. Sekine, Unpublished results.
7. T. Osuga and K. Sugino, *This Journal*, **104**, 448 (1957).

Solid Electrolyte Coulometry; Silver Sulfide Bromide Electrolyte

John H. Kennedy and Fred Chen*

Department of Chemistry, University of California, Santa Barbara, California

ABSTRACT

The properties of a coulometer utilizing a highly conductive solid electrolyte have been investigated. The system consists of silver sulfide bromide as electrolyte, between a silver and a gold electrode. A new faster method of preparation for silver sulfide bromide was developd, and the conductivity was re-examined with measurements extending to −60°C. Coulombs of charge are recorded by plating silver on the gold electrode and then recovered by stripping the silver from the gold electrolytically. Under carefully controlled conditions more than 99% of the silver plated on the gold could be stripped off. However, long charging periods gave low results, while idle periods between charging and stripping gave high results.

In a recent paper, the properties of a new type of coulometer using a solid electrolyte were described (1). Silver halides have been found to be of interest as solid electrolytes because of their high conductivity. This conductivity could be increased by the addition of divalent impurities, *i.e.*, $S^=$ (2). More important, however, silver halides react with silver chalcogenides (3, 4), or with alkali halides (5, 6), to produce compounds with ionic conductivities $> 10^3$ higher than the conductivities of silver halides. The aim of this research is to study the properties of a coulometer using a solid electrolyte of high conductivity, specifically using silver sulfide bromide (Ag_3SBr). Although less conductive, Ag_3SBr was chosen over Ag_3SI because of the higher decomposition potential of bromide *vs.* iodide.

Experimental

Preparation.—Ag_3SBr has been prepared by mixing AgBr and Ag_2S (7) and this method (I) was used initially.

(I). Stoichiometric amounts of AgBr (Matheson, Coleman and Bell) and of Ag_2S (A. McKay Inc.) were mixed together and heated at 280°C for several weeks. X-ray powder diffraction patterns showed the absence of Ag_2S, after the mixture was heated for seven weeks.

The long heating time required and often inhomogeneous product led us to studying other possible methods including the following one based on coprecipitation.

(II). 100 ml solution of 1F Na_2S and 1F NaBr (or KBr) were mixed by pouring together into an empty beaker. The mixture was stirred for several minutes, after which 100 ml of 3F $AgNO_3$ was added. The precipitate formed was digested near the boiling point and then allowed to stand for 12 hr. After filtration, it was dried at 200°C for two days. X-ray powder diffraction patterns showed no Ag_2S present. Preparations normally contained some excess AgBr to prevent any presence of Ag_2S which is an electronic conductor.

Key words: coulometer; coulometry; electrolyte, solid; silver sulfide bromide; electrolytic integrator.

* Electrochemical Society Student Member.

For our electrochemical studies, the Ag_3SBr used was prepared by the new procedure (II), because the preparation time was considerably shorter.

Ag_3SBr was found to be stable to air and could be kept at room temperature. Like many silver compounds, it was unstable to light, with the formation of metallic silver. Metallic silver was also formed when Ag_3SBr was heated for long periods at > 200°C.

X-ray diffraction patterns.—For x-ray powder studies a Phillips Electronics X-ray diffraction unit No. 12045 was used with CuKα rays (1.54178Å) at 40 kv.

Values of crystal spacings found for Ag_3SBr were in good agreement with the values reported by Reuter and Hardel (8). The crystal structure of Ag_3SBr is a body center cube with silver atoms on the faces of the crystal. Ag_3SBr has an anti-perovskite structure with the bromine atoms in the corners of the cube and the sulfur atom in the center. The distance between the nearest silver atoms was 4.8073Å and the distance between the nearest bromine atoms was 6.7984Å.

Using Pauling's ionic radii values for Ag^+, Br^-, and $S^=$, the relative volume occupied by the atoms in the cube was 0.262. The large amount of void volume allows for the easy migration of silver ions.

Pellet preparation.—Pellets were prepared with a Perkin-Elmer evacuable die (186-0025), 0.5 in. diameter. As an example, 0.25g powdered silver was pressed at 6000 psi, followed by 0.5g silver sulfide bromide pressed at 6000 psi, and finally 0.5g powdered gold pressed at 6000 psi. The whole pellet was then put under vacuum for 5 min after which it was pressed at 60,000 psi and held under this condition for 1 min. The pressed silver and gold powders served as electrodes for the pellet, and the boundary lines between electrolyte and electrode have been found to be extremely sharp (1). The electrode area of the pellets was 1.27 cm^2.

The pressed material had a density of 6.22 g/cm^3 which is 95% of the theoretical density based on unit cell dimensions (6.52 g/cm^3).

For polarization and cyclic voltammetry studies, pellets with a silver reference electrode were used.

This reference electrode was prepared by cutting the silver electrode into two parts. One silver electrode was operated in the usual manner while the smaller section was used as a reference electrode. The electrode area of the gold electrode remained 1.27 cm^2 for these pellets, but the working silver electrode was approximately 1 cm^2.

Electrochemical measurements.—A Beckman Electroscan 30 was used for cyclic voltammetry and recorded charge-strip cycles at constant current. A Harrison 6112A DC power supply was used for residual current measurements. For long charge-strip cycles at constant current, a Bissett-Berman E-cell digital coulometer was used. A General Radio Inc. 1650A impedance bridge was used for resistance measurements. For studies at temperatures other than ambient, an Associated Testing Lab (SW-5101) Environmental Chamber was used.

Results and Discussion

Resistivity.—Resistance of Ag_3SBr pellets of various thickness were measured using 1000 cycles a-c signal. The resistance of the pellets was found to be proportional to the thickness of the pellets (Fig. 1). The intercept at zero thickness shows little, if any, contact resistance. The resistivity calculated from the slope was 80 ohm-cm at 25°C. This value is an order of magnitude smaller than the value reported by Reuter and Hardel (9). This difference may be attributed to the extremely low contact resistance of compressed powder electrodes.

Addition of AgBr to Ag_3SBr increased the resistance of the pellets proportionally to the amount of AgBr added, up to 20% per mole excess AgBr (Fig. 2). To avoid the possible presence of excess Ag_2S, which is an electronic conductor, most of the preparations contained some excess AgBr in the Ag_3SBr.

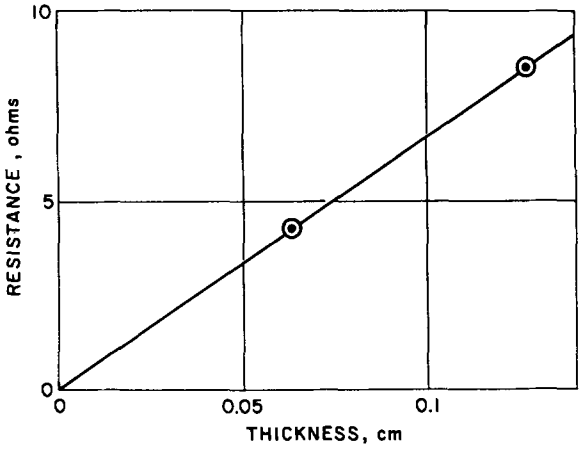

Fig. 1. Resistance of Ag_3SBr pellets

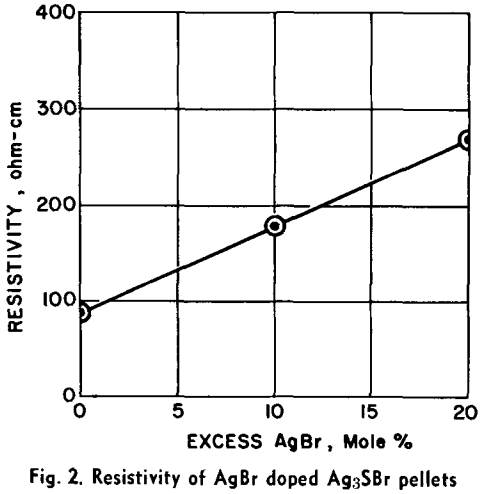

Fig. 2. Resistivity of AgBr doped Ag_3SBr pellets

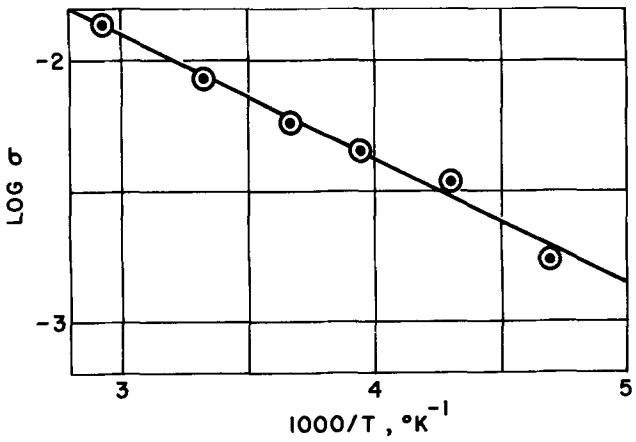

Fig. 3. Temperature dependence for Ag_3SBr conductivity

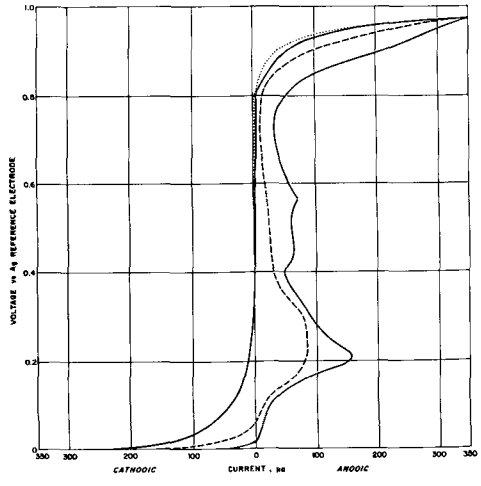

Fig. 4. Cyclic voltammetry of Ag_3SBr. Scan rate = 2 mv/sec; solid line — first sweep, anodic direction first; dashed line — second anodic sweep; dotted line — second cathodic sweep.

Grain boundary conduction, so important to AgBr (1), was not a factor for Ag_3SBr since annealing pellets at 150°C for seven days decreased the conductivity by only 10%.

The conductivity of Ag_3SBr as a function of temperature is shown in Fig. 3. The activation energy was found to be 4.3 kcal/mole. This activation energy is compared with other highly conductive solid electrolytes in Table I.

Cyclic voltammetry.—Cyclic voltammetry was used to examine the electrode reactions which took place on the gold electrode. The potential of the gold electrode was measured *vs.* the silver reference electrode. In general, one anodic peak was observed before the final cut-off, although small peaks between 0.4 and 0.6v were often observed on the first sweep only (Fig. 4). The main anodic peak was observed on the first and succeeding cycles and was about —0.2v *vs.* the silver reference electrode. This peak can be attributed to the following reaction

$$S^{=} \rightarrow S + 2e^{-} \qquad E^{\circ} = +0.203\text{v } vs. \text{ Ag ref.}$$

The final cut-off voltage is probably due to the following reaction

Table I. Activation energy for solid electrolytes

Compound	Activation energy, kcal/mole	Temp. range, K°	(Ref.)
Ag_3SBr	5.5	285-673	(9)
Ag_3SBr	4.3	213-343	Present paper
Ag_3SI	4.0	285-500	(7)
Ag_3SI	3.3	273-373	(4)
Ag_4I_5	2.3	323-523	(11)

$Br^- + Au \rightarrow AuBr + e^-$ $E^\circ = +0.834$v *vs.* Ag ref.

although two other reactions may proceed depending on reversibility and operating current density

$Br^- \rightarrow \frac{1}{2}Br_2 + e^-$ $E^\circ = +0.994$v *vs.* Ag ref.

$3Br^- + Au \rightarrow AuBr_3 + 3e^-$ $E^\circ = +0.910$v *vs.* Ag ref.

The peak positions (corrected for iR drop) were affected by scan rate indicative of irreversibility, and the cathodic reaction was not even observed in the reverse direction although it may have been masked by the reduction of Ag^+ at zero volts. The fact that sulfide can be oxidized at < 0.5v, but the reverse reaction does not proceed forms the basis for a positive error mechanism. It is also important to note that the peak is larger on the first sweep and recovers after a long waiting period.

Charge-strip curves.—The voltage drop during stripping of silver from the gold electrode should remain equal to iR until the gold surface becomes depleted of silver (1), at which time the voltage should rise until it reaches the Ag/Ag_3SBr, AuBr/Au potential plus iR. Figure 5 shows stripping curves for charges of 10 and 36 μa for 1000 sec. The gold surface had been oxidized to 0.5v *vs.* silver before plating. In both cases, the 0.5v end-point voltage was reached at 1000 $\pm$ 1 sec. A three electrode system showed that the end voltage was predominantly a potential developed at the gold electrode as it began to oxidize (Fig. 6).

During the charge cycle, the system is a silver-silver couple and the only voltage drop should be iR. However the voltage drop was higher because of polarization effects, and using a three electrode system, it was found to be predominantly on the silver electrode (Fig. 7). After long charging periods this polarization became significant and increased to the decomposition voltage of the electrolyte. Using a current interruptor circuit almost no change in resistance was found during the charge cycle.

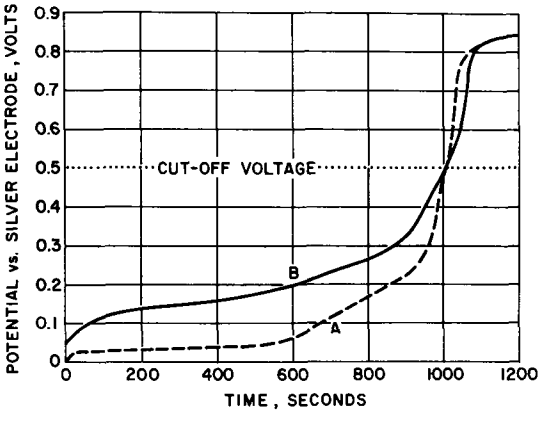

Fig. 5. Stripping curve for Ag_3SBr. (A) Charge: 1000 sec at 10 μa; stripping current: 10 μa; (B) charge: 1000 sec at 36 μa; stripping current: 36 μa.

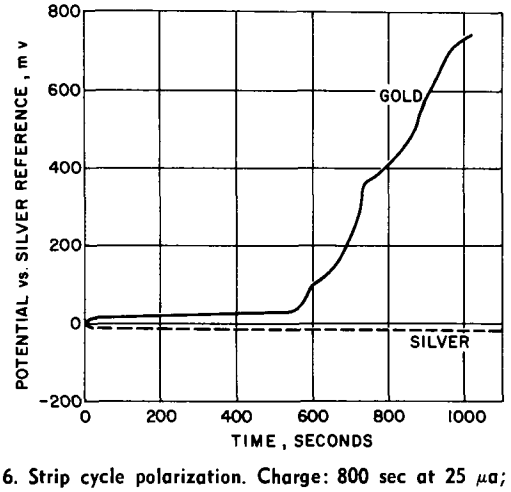

Fig. 6. Strip cycle polarization. Charge: 800 sec at 25 μa; stripping current: 25 μa.

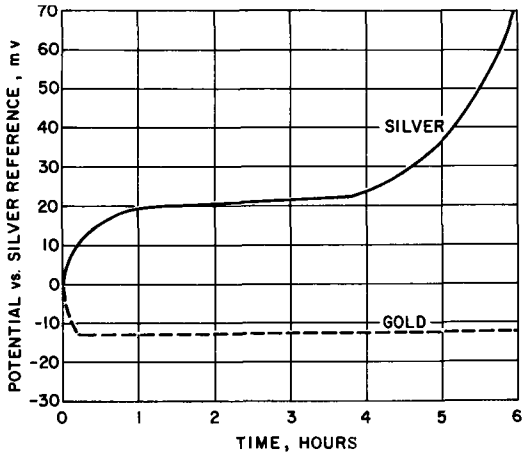

Fig. 7. Charge cycle polarization. Charge: 21,600 sec at 25 μa

Polarization.—The observed polarization (η) on the silver electrode during the charge cycle could be represented by Tafel's equation

$$\eta = a + b \log I$$

For charge, the values of a and b were 63 and 10.0 mv, respectively, and the exchange current density was 5×10^{-7} μa/cm^2.

This value for exchange current is much lower than the Ag/Ag^+ couple in an aqueous electrolyte and may be the result of electrode/electrolyte effects giving rise to much smaller effective areas. A similar situation was observed by Takahashi and Yamamoto (4) who decreased silver electrode polarization by using a silver amalgam electrode.

An increase in polarization on the silver electrode during charge took place after a certain time, and this can also be attributed to a decrease in active area.

Controlled potential electrolysis.—Electrolysis at controlled potential (50-600 mv for 24-72 hr) was carried out to determine the final residual current for the pellets, and the results are shown in Table II. Assuming that no ionic contribution remains after this time the residual current can be used to calculate the upper limit of electronic conductivity contribution. Using the equation of Wagner (10), the electronic conductivity must be less than 0.002% of the total conductivity. Current which flows at cut-off voltage will

Table II. Residual current and leakage current results

Sample	Time o.c., hr	i_R Final residual current, nano-amp	Charge lost, μcoul	i_L Leakage current, nano-amp
Pure Ag_3SBr	1	100	428.7	119.0
	25	100	4,091.8	45.4
	100	100	15,399.0	42.7
Pure Ag_3SBr	1	200	1,118.0	310.6
	50	300	8,924.2	49.5
	100	200	17,670.6	49.0
Ag_3SBr with 20% AgBr	1	80	350.6	97.3
	25	60	2,594.0	28.0
	100	60	6,548.4	18.2
Ag_3SBr with metallic silver	1	3,300	6,307.8	1,752.0
	25	3,000	13,221.6	146.0

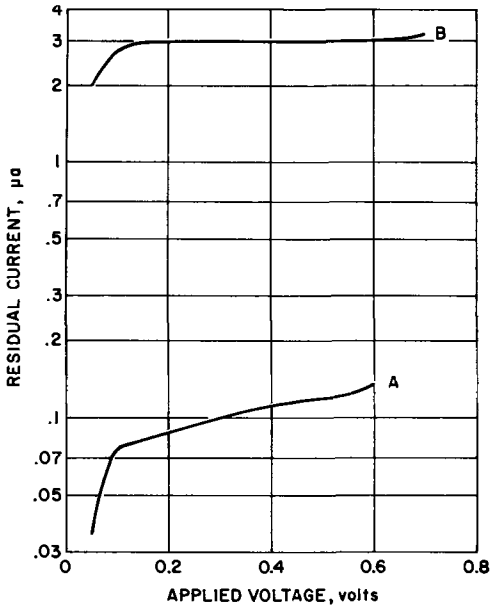

Fig. 8. Residual current. Controlled potential electrolysis. (A) Ag_3SBr; (B) Ag_3SBr containing metallic Ag from decomposition.

also determine the lower limit at which the coulometer can be used.

The residual current of Ag_3SBr pellets, containing metallic silver, (curve B, Fig. 8) was ten times higher than the residual current of pure Ag_3SBr pellets (curve A, Fig. 8). Reuter and Hardel (9) have reported the electronic conductivity of Ag_3SBr as a function of temperature. An extrapolation of their results, shows that at room temperature, the electronic conductivity would be 7.95×10^{-6} (ohm-cm)$^{-1}$. Using this value for electronic conductivity in Wagner's equation

$$i_o = (RT/LF)\ \sigma_o$$

the electronic current would be 3.23 μamp. This value is in good agreement with the residual current we have found for Ag_3SBr containing metallic silver but not for pure Ag_3SBr.

Because the observed residual current may still contain other contributions (note that a strictly flat plateau was not observed) the value of 2.6×10^{-7} (ohm-cm)$^{-1}$ for σ_o is only approximate, but probably represents the maximum electronic contribution.

Leakage current.—After a pellet was driven to a high voltage (0.5-0.6v, the open circuit voltage would decay with time. A number of μcoulombs had to be passed in order to return the pellet to the original voltage. The charge lost can be considered in terms of a leakage current (i_L)

$$i_L = Q/T_{o.c.}$$

where Q is the total charge lost and $T_{o.c.}$ is the open circuit time.

If no electronic shorting existed, the open circuit voltage would not decay and no charge would be lost ($Q = 0$, $i_L = 0$). On the other hand, if all the residual current observed above (i_R) were electronic then i_L would equal i_R. As can be seen from Table II, i_L for Ag_3SBr is initially equal to (or even greater than the final i_R), but decreases to a value about half of i_R. Unfortunately, during this time, the open circuit voltage is decaying, and when it decreases below the plateau value for i_R one would expect the leakage current to decrease. This is what was observed for Ag_3SBr containing metallic silver. Within the first hour at open circuit the voltage dropped to <50 mv and i_L decreased very rapidly (Table II).

Table II shows the results for a number of pellets. Since i_L is significantly lower than the residual current (i_R), i_R must still contain some ionic contributions. Based on the i_L values, the electronic conductivity must be less than 1.2×10^{-7} (ohm-cm)$^{-1}$ or 0.001% of the total conductivity for Ag_3SBr.

Table III. Timing accuracy for Ag_3SBr coulometers

Current μa	Charge time, sec 50 Avg. error	50 Std. dev.	100 Avg. error	100 Std. dev.	250 Avg. error	250 Std. dev.
10	+4.6%	2.3%	+5.8%	1.6%	+3.2%	0.26%
36	−0.2	1.5	−0.1	0.8	−0.6	0.38
100	−1.8	1.3	−0.7	0.6	−0.6	0.30
360	−0.8	0.3	−0.7	0.2	−1.2	0.17

Note: Results represent average of eight determinations.

Timing accuracy.—Timing accuracy for the silver sulfide bromide coulometers was checked for currents of 10-360 μa and for periods of 50-250 sec. The charge ranged from little more than a monolayer (approximately 300 μcoulombs) to about 300 atomic layers on the average. In the current range 36-360 μa, the average error was about —1% in almost all cases, Table III. This error was due to silver remaining on the gold electrode and could be recovered at controlled potential at very low currents.

Results of continued cycling are shown in Fig. 9. Usually the first few cycles gave a relatively large error, due to conditioning effects at the gold electrode surface. In general, less charge was recovered on the first cycles than plated, and could result from either (*i*) reduction of a species during charge that is not re-oxidized during strip, or (*ii*) formation of silver during charge which is not stripped. The latter process, *i.e.*, formation of "inactive" silver, might include migration of silver into the gold via grain boundaries. For fresh pellets possibly containing gold oxide or gold sulfide surfaces, the first mechanism appears more likely.

In general, ten cycles were run and the average of the last eight determinations was used for Table III. This value was usually quite close to the asymptotic value, *e.g.*, in Fig. 9 the average of the last eight cycles was 248.3 sec (—0.68% error) while the asymptotic value was 249.2 sec (—0.32% error). The asymptotic value was not reported in Table III since in several instances the value could not be determined in ten cycles because of random fluctuations.

Charge hold.—The time at open circuit between charging and stripping has been called charge hold (1). Silver sulfide bromide pellets gave positive errors as charge hold time increased. The results are shown in Fig. 10. Two processes are postulated for read-out errors. The first process is the formation of inactive silver (1) on the gold electrode leading to small negative errors (Table III). The second process is the oxi-

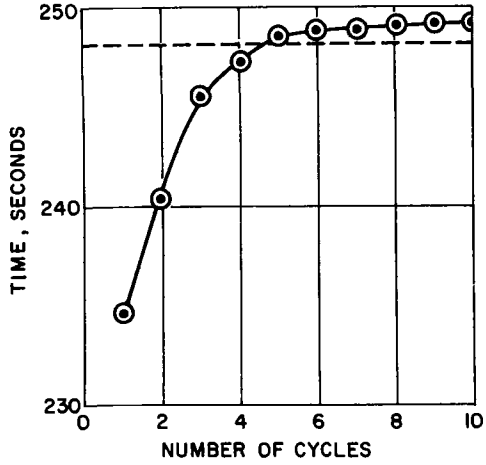

Fig. 9. Timing accuracy results. Charge: 250 sec at 100 μa; stripping current: 100 μa.

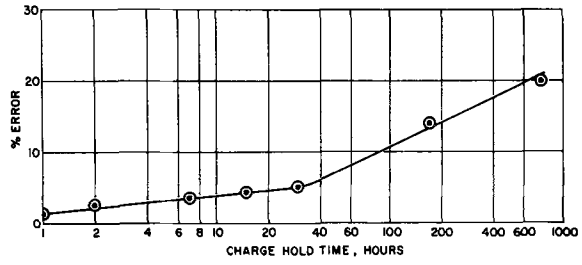

Fig. 10. Charge hold results. Charge: 1000 sec at 50 μa; stripping current: 50 μa.

dation of sulfides on the gold electrode at 0.2-0.4v which leads to a positive error. With a charge hold period, the second process dominates and the net effect is a positive error. The positive error appears because the arbitrarily chosen cut-off voltage (0.5v) was above the potential at which sulfide ion at the gold electrode is oxidized. Thus, additional charge is required before the gold surfaces reach 0.5v. As mentioned earlier, the reaction is not reversible so that positive errors can also be observed on succeeding cycles. Thus, irreversible (*e.g.*, kinetically slow compared to the operating current) processes can give rise to both negative errors for fresh pellets (conditioning) and positive errors after a charge hold period.

Charge capacity.—A practical consideration is the amount of silver which can be transferred to the gold and subsequently stripped without losing accuracy or shorting from silver growth. Table III shows that negative errors of —1.2% were observed with charges of 90,000 μcoulombs, (25 μa-hr). It also shows that negative errors increased as the amount of charge transferred to the gold increased. For large charges (>10 μa-hr) and no charge hold, larger negative errors were observed (Fig. 11). However, most of the high charge studies were carried out with no conditioning (set B on Fig. 11), and the errors were considerably smaller with conditioning (set A on Fig. 11).

One pellet was given a charge of 417.6 μa-hr and a —13% error was observed on stripping. Another possible mechanism for negative errors during stripping of such large charges is that the silver plate may be thick enough to allow under-cutting. That is, silver would be oxidized close to the gold during stripping leaving silver metal in the electrolyte region not connected electrically to the gold electrode. In support of this mechanism, charge lost for these pellets could not be recovered by controlled potential electrolysis.

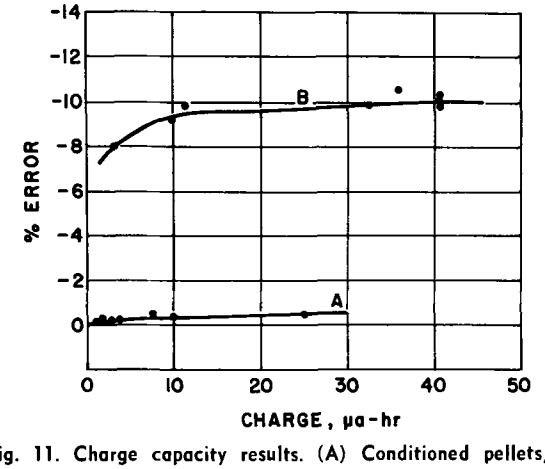

Fig. 11. Charge capacity results. (A) Conditioned pellets; (B) non-conditioned pellets.

Conclusion

Both AgBr (1) and Ag_3SBr have been found to be useful as solid electrolytes for coulometers. Ag_3SBr, because of its much higher conductivity can be used at currents up to 1 ma/cm² (compared to 0.1 ma/cm² for AgBr) and larger amounts of charge could be transferred without shorting by silver dendrites. Also, Ag_3SBr exhibited no room temperature annealing effects, and the resistance was more stable with time. On the other hand, Ag_3SBr showed a significant positive error due to build up of sulfide on the gold electrode when stored for longer than 100 hr while AgBr coulometer showed a negative error.

For highest accuracy, silver coulometers containing silver sulfide bromide as a solid electrolyte must be operated under controlled conditions. These conditions include current densities of 28-280 μa/cm², preconditioning of the gold electrode to the cut-off voltage, charge capacities of 1,400 to 70,000 μcoul/cm², and immediate read-out. Under these conditions coulometer read-out error will be less than 1%.

Acknowledgment

The authors thank Dr. L. Webber for helpful discussions and Bissett-Berman Co. for providing specialized test equipment. One of the authors (F. C.) is indebted to the Latin American Scholarship Program of American Universities; the University of California, Santa Barbara, and the Instituto para la Formacion y Aprovechamiento de Recursos Humanos for financial support.

Manuscript submitted July 22, 1968; revised manuscript received Sept. 30, 1968.

Any discussion of this paper will appear in a Discussion Section to be published in the December 1969 JOURNAL.

REFERENCES

1. J. Kennedy, F. Chen, and A. Clifton, *This Journal*, **115**, 918 (1968).
2. J. Teltow, *Z. Phyz. Chem.*, **1950**, 213 (1950).
3. V. Reuter and K. Hardel, *Naturwissenschafter*, **48**, 161 (1961).
4. T. Takahashi and O. Yamamoto, *Electrochim. Acta*, **11**, 779 (1966).
5. J. Bradley and P. Greene, *Trans Faraday Soc.*, **62**, 2069 (1966).
6. B. B. Owens and G. R. Argue, *Science*, **157**, 308 (1967).
7. V. Reuter and K. Hardel, *Z. anorg. allg. Chem.*, **340**, 158 (1965).
8. V. Reuter and K. Hardel, *ibid.*, **340**, 168 (1965).
9. V. Reuter and K. Hardel, *Ber. Bunsegesellchaft.*, **70**, 82 (1966).
10. C. Wagner, *Z. Elektrochem.*, **60**, 4 (1956).
11. J. Bradley and P. Greene, *Trans. Faraday Soc.*, **63**, 424 (1967).

Linear Sweep Studies of the Oxygen Electrode in Nonaqueous Media

Kinetics Studies on Smooth Platinum Electrodes

Jorge E. A. Toni*[1]

Corporate Applied Research Group, Globe-Union Incorporated, Milwaukee, Wisconsin

ABSTRACT

The electrochemical reduction of oxygen was studied in phenyltrimethylammonium hexafluorophosphate-nitrosodimethylamine solutions. The kinetic effects of different levels of water concentration were also investigated. The electrode studies indicated that the oxygen reduction in nonaqueous media is a complex mechanism. The postulated electrode process in the systems studied includes first, a series of surface processes on the electrode (adsorption, interaction between oxygen and platinum, reduction of the film formed) and second, two partially mass transport dependent steps with chemical kinetics complication (ECE mechanism).

The reduction of oxygen in aqueous media is a classical problem in electrochemistry; nevertheless, new ideas about the electrode process mechanisms are continuously being postulated. However, the study of the mechanism of oxygen reduction in nonaqueous media and particularly in aprotic systems can be considered a relatively recent problem, and perhaps it will receive in the future as much attention by the electrochemists as the study in aqueous solutions.

In an absolutely aprotic solvent, if the reduction of oxygen occurs, it has to be fundamentally different than in water. This condition is difficult to achieve experimentally because moisture (a proton source) is one of the most difficult impurities to eliminate from nonaqueous solvents and water concentrations in the order of 5×10^{-4}M (10 ppm), only one order of magnitude lower than the oxygen concentration, are often present in the best purified solvents.

However, the possibility of eliminating or at least decreasing to a minimum, the effect of protons (without increasing hydroxyl concentration) is a fascinating approach and creates new horizons for the study of the oxygen reduction. Moreover, the study of the oxygen reduction in aprotic media is of interest from the point of view of energy conversion because it permits the study of very high energy couples with alkali metals as anodes (1).

The initial studies of the reduction of oxygen in nonaqueous media were done by Kolthoff and collaborators (2-4). Lately, and in part during the progress of the present research, several other papers have appeared (5-12), and in some cases quantitative data was shown (8, 9, 12). In general, there is agreement that the reduction of oxygen in aprotic media occurs in two principal steps, quasi-reversible and irreversible, respectively. Maricle and Hodgson (5) were the first to postulate that the first step is a one electron reduction of oxygen to superoxide. For the second step the data are not so clear because of difficulties in studying this reduction process. Generally, it is not very reproducible and occurs at such negative potentials that the curve practically is superimposed on the depolarization limiting of the electrodes. However, Sawyer *et al.* postulated first (8) that the reduction corresponds to the reduction of O_2^- to $O_2^=$, and later (12) that OH^- is one of the products. Johnson *et al.* (7) have studied the effect of cations on the E_p of this reduction. Several attempts were made to characterize the superoxide formation. They included chemical (5) and esr (5, 9) experiments. The present discussion summarizes our study on the reduction of oxygen, in a new aprotic solvent, N-Nitrosodimethylamine (NDA) (13). The research was done with smooth platinum electrodes. The technique most frequently used during the present research was linear sweep voltammetry in the direct or cyclic fashion. The diagnostic criteria developed by Nicholson and Shain (14) were a powerful tool for the interpretation of the results. Our conclusions about the mechanism are in some ways different than previous investigations. We have recognized that small (<20 ppm) traces of protons (water) were impossible to remove completely and were always present. We assign an important role to them in the mechanism. The effect on increasing water concentration was also studied and did help in the interpretation of the over-all mechanism.

Key words: oxygen reduction, nonaqueous media, nitrosodimethylamine.

* Electrochemical Society Active Member.

[1] Present address: USAECOM, Attn: AMSEL-KL-P, Fort Monmouth, New Jersey 07703.

Experimental

The NDA was obtained from Eastman Kodak Company. The two main impurities which generally may accompany the solvent are water and peroxides. The peroxides were eliminated by treatment with Al_2O_3 or Li and the removal of water required a pretreatment and distillation. The solvent was dried for at least twenty-four hours with P_2O_5 or molecular sieves, type 4A; after filtering off the drying agent, the NDA was vacuum distilled from molecular sieves, type 4A, which had been dried previously at 200°C. The distillation was performed at a pressure of 2 mm of mercury and only the fraction which distilled in the range 26°-28°C was collected. If all the previous steps have been performed properly, the only impurity observable by vapor phase chromatography (VPC) is water and its concentration as determined by VPC, is usually reduced to about 20-30 ppm. The gas chromatograph used was an F & M 810 with a thermal conductivity detector as the sensing device. The chromatograph was programmed in the following way: Two 1½ foot copper columns packed with Carbowax (10%) 20 M on Fluoropak 80M were used. Bridge current was 150 ma. Injection post temperature was 160°C. Detector temperature was 180°C. The program temperature scale was 100°C-150°C. Upscale temperature rate of scan was 30°/min. Downscale temperature rate of scan (fixed) was 40°/min. The post injection interval was 0 min, and the upper limit interval was 6 min. The flow rate of helium carrier gas was 40 ml/min. The sample size was 20 μl.

Phenyltrimethylammonium-hexafluorophosphate (ϕMe_3NPF_6) which was used as supporting electrolyte was obtained from K&K Laboratory and dried at 95°C under vacuum for at least 8 hr. Prepurified nitrogen and oxygen were from Airco Company. They were passed through concentrated sulfuric acid and

P_2O_5 or Drierite. The solutions were saturated with oxygen by bubbling the gas through the solution. The concentration of oxygen in the solutions was obtained by applying the volumetric titration method suggested by Coetzee and Kolthoff (2) with slight modifications. The final titration of the excess of Fe(II), which has not reacted with the oxygen present, was performed by a ceric (sulfate) continuous potentiometric titration in order to eliminate the interaction between Ce(IV) and NDA. The concentration of oxygen in a O_2 saturated solution of 0.5m ϕMe_3NPF_6-NDA was 5×10^{-3}M.

The test electrode was a conventional platinum disk electrode which was polished to a 1μ surface finish. Its geometrical area was 7.8 mm^2. The reference electrode was a Ag/AgCl (0.1M KCl), with a salt bridge of 1m $LiClO_4$-NDA which had a potential of —25 mv *vs* SCE (1). A Luggin capillary was used to decrease the uncompensated resistance. Its value, determinated using the conventional study of ratio E_{in}/E_{out} *vs.* frequency was 33 ohms. Simple calculations can show that the IR drop effect is in the experimental error. The counter electrode was a pyrolytic graphite rod. Extreme precautions were taken to eliminate contamination of moisture with the solutions. Vapor phase chromatography of solutions prior to and after electrochemical studies did not show any appreciable increase in water concentration.

The potentiostatic equipment used for this research consisted of combinations of operational amplifier circuits such as originally suggested by DeFord (15) and modified by Shain (16) and co-workers.

Results and Discussion

Figure 1a shows a typical cyclic scan of oxygen in ϕMe_3NPF_6-NDA, and it also shows the base line of residual current which is obtained when the solution is purged free of oxygen by the use of nitrogen. It can be seen that the cyclic voltammogram consists of at least four sections. The scan starts at OV *vs.* the Ag/AgCl electrode and proceeds in a cathodic direction. With oxygen present a prepeak or hump-shaped wave is obtained at approximately —0.4v *vs.* Ag/AgCl. Before this wave has been completed, a well-developed reduction peak occurs at —1.0v *vs.* Ag/AgCl. (In future discussions we will speak of this reduction peak as peak I.) Well beyond peak I a second reduction peak (called in later discussion peak II) is observed just prior to the decomposition potential of the electrolyte at the platinum electrode surface. At this point the scan was reversed and proceeds in the anodic direction. The first observable feature is that there is no anodic peak close to peak II and that an anodic peak occurs at —0.8v *vs.* Ag/AgCl. This anodic peak is related to the first cathodic peak, peak I (Fig. 1b). Figure 1b is typical for the first step in performance of oxygen electrochemically on smooth platinum in the electrolyte system described above. We will label the anodic peak, IA. Since the difference in peak potential between peaks I and IA (Fig. 1b) is approximately 200 mv we cannot consider the reaction to be reversible (14). The criteria for reversibility are such that the peak separation for the cathodic and anodic peaks should be equal to 58 mv/n which is much smaller than the 200 mv observed above. On the other hand, cathodic peak II does not show any signs of reversibility since no anodic peak corresponds to it.

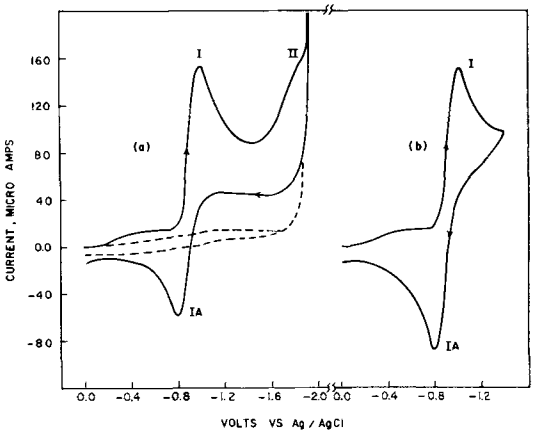

Fig. 1. Typical cyclic voltammogram of oxygen in 0.5m ϕMe_3NPF_6-NDA; concentration 5×10^{-3}M (saturated); scan rate, 100 mv/sec. Two minute hold at 0.0v with agitation; 30 sec rest period prior to scanning; - - - - residual current. (a) complete cyclic voltammogram. (b) cyclic voltammogram of the first step.

The over-all mechanism, as will be shown in the progress of the discussion, is a complex one which includes several steps. They involve a series of surface processes on the electrode and two partially mass transport dependent cathodic steps.

Surface Process

Accumulation of Oxygen on the Surface

In previous work with lithium perchlorate and NDA (1) we had observed that the first cathodic peak current for the reduction of oxygen in that media was dependent on the length of time we held the potential at 0.0v *vs.* Ag/AgCl. This was presumed to be due to a slow adsorption of oxygen on the surface of the platinum electrode. In substantially the same manner we have made studies in the phenyltrimethylammonium hexafluorophosphate-NDA system. It was observed that if we held the potential at 0.0v for longer periods of time, peak I increased in height to a maximum value. Plotting the peak current *vs.* the length of the holding time at 0.0v the peak current reached a maximum value and leveled off as the holding time increased. An auxiliary experiment to demonstrate this effect was also performed in which the solution was stirred and the only change in the form of the curve obtained was that the steady-state value at the maximum peak current was achieved more rapidly. This indicates diffusion control adsorption occurring on the electrode surface since a maximum value would be reached at maximum or saturation coverage. It is therefore suggested that this portion of the mechanism is simply described by the equation:

$$O_2 \text{ solution} \rightleftharpoons O_2 \text{ surface}$$

Interaction between the oxygen and the platinum electrode.—As noted earlier in this paper there appears to be an electroactive species which gives a prepeak or hump before the major oxygen reduction step in cathodic peak I. It is possible that some form of platinum oxide or mixture of platinum oxides are formed on the platinum surface. This is not a new concept since many others have proposed that this occurs with the oxygen electrode in aqueous media. However, we refer to Kolthoff and Tanaka (17) which relates the potential for the reduction of the platinum oxides to the *p*H of the solution and have found that at very high *p*H the reduction of the oxide occurs at a potential region near that of the present hump.

In addition, we have found that the prepeak is observed only after prolonged potentiostatic holds. In the experiments described in the previous section using increasing potentiostatics holds at 0.0v, the prepeak starts to rise after 30 sec of holding. To establish that oxygen was necessary at the surface before this prepeak would be obtained, we ran the following series of experiments all by linear voltammetry. (Fig. 2). One experiment shows the formation of the prepeak when the solution is saturated with oxygen both during the hold and during the scan. The second experiment shows the effect of exposing the electrode to oxygen only during the hold period then purging the solution with nitrogen for 15 min and rescanning. The result of this experiment is that the prepeak shows, but no following oxygen reduction wave (peak I) appears. The third experiment was

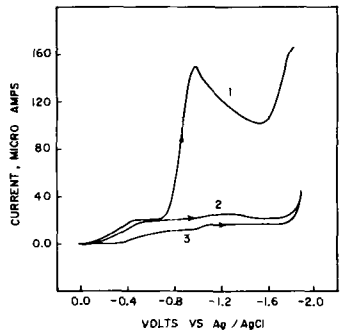

Fig. 2. Relation of the prepeak with the presence of oxygen. Scan rate 100 mv/sec. Curve 1, oxygen saturated solution; 2, oxygen purging only during hold, scan after 15 min purging with N_2; 3, residual current after 15 min hold at 0.0v with N_2 purge.

carried out in the same manner as the first two with the exception that the solution was purged with nitrogen for 15 min, and then the voltammetric scan was carried out. This curve shows neither the prepeak nor the oxygen reduction wave. Thus, it is our conclusion that oxygen is necessary to form the species on the surface which gives the prepeak in a voltammogram. The mechanistic step could be written as follows

$$O_{2ads.} + Pt \rightarrow Pt_xO_y \text{ surface}$$

Other interpretation, suggested by one of the reviewers, is that the prepeak reduction wave "may actually be some other oxidation product such as a free radical formed by the interaction of oxygen with organic impurity or solvent decomposition product."

Reduction of Oxygen

As was explained before (Fig. 1), the electrochemical reduction of oxygen on smooth platinum in ϕMe_3NPF_6-NDA, appears to occur in two steps. They both apparently are irreversible, but since the first cathodic wave peak I has an anodic counterpart, peak IA at potentials close to the cathodic peak, we would, therefore, classify the reaction as quasireversible. The peak potentials are affected by the increase of the scan rate showing a negative shift for the reduction processes and positive shifts for the anodic one. This behavior is also a typical qualitative diagnostic test for cases which do not include a reversible system.

We also knew that the reduction of oxygen is in part mass transport controlled and the reduction current can be considered an additive function of the reduction of oxygen adsorbed and oxygen transported by diffusion from the bulk of the solution. These conclusions were drawn from experiments with stirred solutions. If the solution is stirred during the scan, the reduction current increased greatly. With stirring the anodic peak, IA, decreases, showing that the product of the first reduction is not accumulated on the electrode surface.

To summarize the information we have at this point of the discussion and before passing to more detailed studies, it is believed that after the accumulation and interaction of oxygen with the electrode, the oxygen reduction appears to occur in two steps; one quasireversible, the other completely irreversible. These processes are in part transport controlled. We will pass now to the study of the first step of the reaction.

First step in presence of minimal amounts of water. —The first step of the reaction (that is, peaks I and IA, Fig. 1b) looked promising for a detailed study. It shows both the cathodic and the anodic processes, and peak I is separated well enough in potential from reduction wave, peak II, to give us a chance to study peaks I and IA without interference from the second wave. On the other hand, the second reduction is so close to the depolarization limits of the platinum electrode that it is very difficult to get valid information about peak II.

The main study includes the effect of scan rate on the peak current. The diagnostic techniques of Shain *et al.* (14, 18-21) were studied extensively. Their diagnostic interpretations of appropriate voltammetric experiments can give an enormous amount of information about the mechanism of the reaction. We have run experiments covering a range of practically five orders of magnitude in scan rate (V), from 10 mv/sec to 680 x 10^3 mv/sec. The experiments here were cyclic voltammograms which included only the first step. The scans were run from 0.0v *vs.* Ag/AgCl to an appropriate potential after the peak generally no more negative than 200 mv past the first cathodic peak potential, E_pI. All the experiments had a potentiostatic hold at 0.0v for 2 min with agitation and oxygen passing through the solution for the first minute. Then just prior to scanning the stirring was stopped, the oxygen passed over the surface of the solution, and the solution was allowed to become quiescent for 30 sec. Figure 3 is representative of all the voltammetric studies obtained by this method. It includes experiments run at different times over a period of 6 months. The figure includes the plots of current functions $I_{pI}/V^{1/2}$ *vs.* V. (I_p = peak current, V = scan rate.) The representation of $I_p/V^{1/2}$ is used to normalize the results at different scan rates and relate them with a true reversible case from which the curve has to be a straight line parallel to the abscissa because $I_p = kV^{1/2}$ for a reversible electrochemical reaction. This study includes series without water added. The analysis of Fig. 3 leads to the conclusion that we might interpret the data as diagnosing an ECE mechanism (18) (electron transfer, chemical reaction, electron transfer) exemplified in a general way by

$$A \underset{E_1^o}{\overset{n_1e}{\rightleftharpoons}} B \overset{k}{\rightarrow} C \underset{E_2^o}{\overset{n_2e}{\rightleftharpoons}} D$$

where E^o = formal potential.

For an ECE mechanism $I_p/V^{1/2}$ is larger at low scan rates than at fast scan rates. A similar behavior is only found for reactions with a cyclic (catalytic) reaction (14). However, for these catalytic cases the increase of $I_p/V^{1/2}$ at low scan rate is much greater than was observed in our experiments. Our case only shows a ratio of 2 to 1 between the values obtained at 10 mv/sec and the values over 5.5 x 10^4 mv/sec. This ratio fits perfectly for an ECE mechanism where $n_1/n_2 = 1$ and $E_1^o = E_2^o$ or $\Delta E^o = 0$ (18). These conclusions mean that after the electrochemical reduction of A to B a chemical process takes place which transforms B into C. Then C is electrochemically reduced to D at the same or very close to the same potential at which A is reduced to B. That is why at low scan rates the peak current consists of contributions of both electron transfer reactions. In the slow scan case there is enough time for the chemical interaction of B to C but very fast sweeps do not allow sufficient time for this chemical reaction.

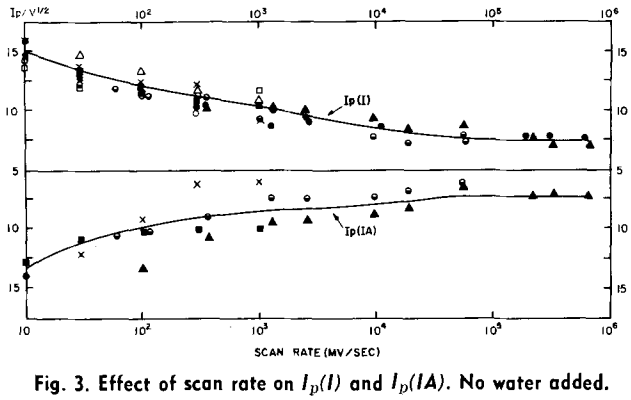

Fig. 3. Effect of scan rate on $I_p(I)$ and $I_p(IA)$. No water added.

Thus, the current observed is only due to the first electron transfer. However, it is well to note that our case must have the same number of electrons transferred in the first case $A \rightleftharpoons B$, n_1 as in the second electron transfer, $C \rightleftharpoons D$, n_2.

An ECE mechanism can have four different cases relative to the reversibility or irreversibility of the individual charge transfers (18) (*R-R*, *R-I*, *I-R*, *I-I*, where *R* = reversible and *I* = irreversible). To characterize the case with $\Delta E = 0$, the effect of scan rate on the anodic peak is important. Only in the case where both electron transfers are reversible will an anodic peak be obtained at all the scan rates over the entire scan rate range. Figure 3 shows that we have that case. Consequently, we can say now that our first step includes two reversible, or at least very close to reversible, equal electron transfers in the ECE mechanism. Our assumption that the first step could be considered quasireversible is thus confirmed.

We consider interesting to include at this point of the discussion a similar type of series of experiments but with 0.25% by volume of H_2O before postulating the mechanism for the first step. Figure 4 shows the results of those experiments. It is notorious a larger spreading of the experimental points and the traced line is only tentative. The concentration of water present is lower than that required for other complicating effects which will be discussed in the next section of this paper. In this case, the peak I current function at low scan rate was always larger and the ratio was slightly over 2. However, the currents at fast scan rates were practically the same as those without water added.

Taking into consideration the data discussed above and the system under study, we think that it is very possible that an ECE case can be postulated. Perhaps a combination of an ECE mechanism and disproportionation reaction occur. The steps may well be related to traces of protons present in the system.

$$A + n_1 e \rightleftharpoons B \xrightarrow{k} C + n_2 e \rightleftharpoons D$$
$$\uparrow \qquad\qquad\qquad\qquad \uparrow$$
$$\underset{k^1}{\longleftarrow}$$

This case has not been studied theoretically yet. It should give larger current functions at low scan rates (because of regeneration of *A*) than a simple ECE mechanism. The latter type of behavior is the type of results which have been observed (especially in the case of addition of low concentration of water) in our experiments.

Summarizing the data available for the first step of the electrochemical reduction of O_2 on platinum we postulate that when no protons are available a one-electron reaction may occur. When protons are available as impurities or at low levels, a ECE mechanism is possible. A disproportionation of O_2^- or HO_2 should be considered in the postulation.

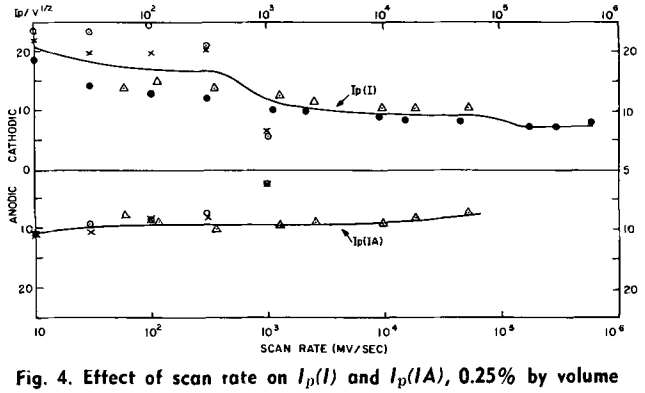

Fig. 4. Effect of scan rate on $I_p(I)$ and $I_p(IA)$, 0.25% by volume of water.

No protons available

$$O_2 + e \overset{E^o}{\rightleftharpoons} O_2^-$$

disproportionation

$$2\,O_2^- \rightarrow O_2 + O_2^=$$

protons available (traces, low concentration)

$$O_2 + e \overset{E_1^o}{\rightleftharpoons} O_2^- + H^+ \xrightarrow{k} HO_2 + e \overset{E_2^o}{\rightleftharpoons} HO_2^-$$

disproportionation

$$2\,O_2H \rightarrow O_2 + O_2H_2$$

Effect of increasing level of water concentration on the mechanisms.—This study of the effect of moisture has given results which permitted us to obtain more information about the second reduction step, peak II, and in this way a better understanding of the over-all oxygen reduction process. We have run several series of experiments with increasing concentrations of water studying simultaneously only the first step, (peaks I and IA) and also the complete reaction (peaks I, IA, and II). Experiments were run at 100 mv/sec and we started with solutions of 0.5m ϕMe_3NPF_6-NDA, which contained low concentrations of H_2O (30-60 ppm) (Fig. 1) and then added appropriate amounts of H_2O (dispensed from a micro syringe) to obtain increases in water concentration. In many cases the unit increase in water concentration was of the order of 0.02%, as was required for the experiments performed. In all other respects the conditions utilized in the experiments with water were the same as in those run without water. With the data thus obtained it has been possible to study the effect of H_2O concentration on both the peak current and peak potential of each of the major voltammetric peaks. The presence of water has affected all the peaks by increasing the current peak heights and has also affected the peak potentials. Figure 5 shows these effects and the curves in the figure should be compared to the curves in Fig. 1 where the amount of water was minimal.

The results are representative of experiments at five different concentration levels of H_2O: 0.006%, 0.20%, 0.40%, 0.80%, and 1.60% by volume, which give a picture of the drastic changes which occur with increasing levels of water concentration. Figures 6, 7, and 8 are the plots of I_p and E_p of the peaks as a function of concentration of water, and cover the

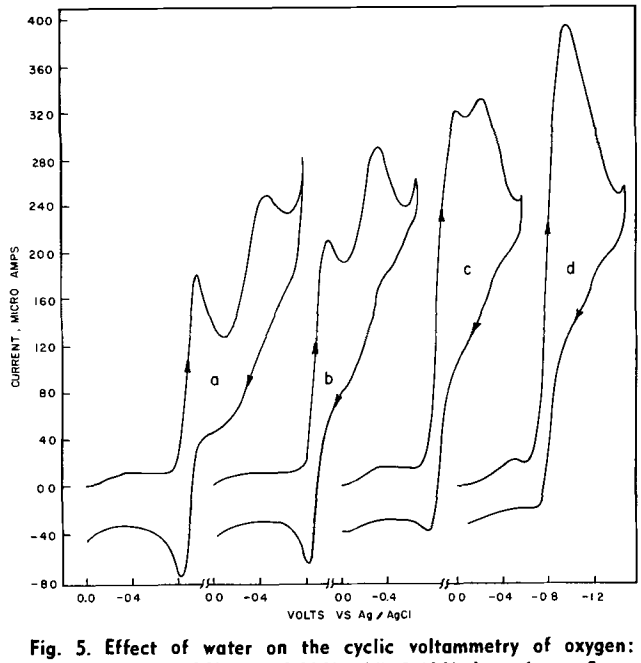

Fig. 5. Effect of water on the cyclic voltammetry of oxygen: (a) 0.20%; (b) 0.40%; (c) 0.80%; (d) 1.60% by volume. Same conditions of Fig. 1.

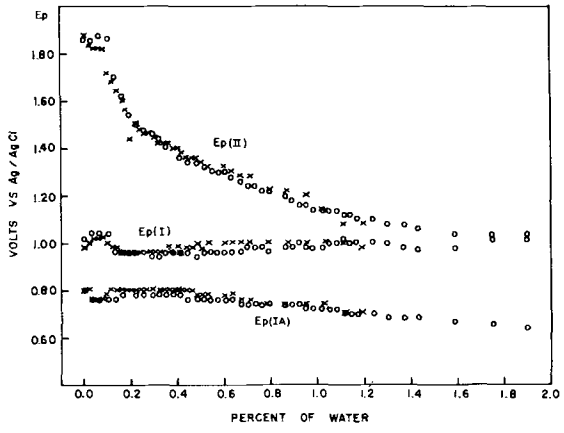

Fig. 6. Effect of increasing concentration of water on peak potentials.

whole range of water concentration levels studied. In Fig. 5 it is noticeable that the prepeak also was affected by the increase in water content of the electrolyte, but this effect has not been fully evaluated.

The effect of water (Fig. 6) on E_pI and E_pIA is not significant but is very pronounced on the second reduction peak, peak II. With increasing water concentration the peak II potential shifts to positive values and finally merges into peak I. It is interesting to note that the peak potential shift follows the following logarithmic equation

$$E_{pII} = -2.15 + 0.06 \log (H_2O) \qquad [1]$$

The value 0.06 would indicate that there is one electron per molecule of water if the reaction is reversible, but as this second step is completely irreversible (Fig. 1), we should include the transfer coefficient α in the equation, which for a value of 0.5 would give two electrons involved in the reaction.

Figure 7 which is the study of I_pI, shows how the peak I current increases until it reaches a steady value. As the figure shows, the increase in current is not continuous and there is an inflection at approximately 0.3-0.4% of H_2O. The current reached at this small plateau is virtually one-half of the maximum current obtained at water concentration levels over 1.2%. This observation can be interpreted as a change in mechanism and perhaps as a change in the number of electrons transferred. We will go back to this observation later during the discussion of the over-all reaction.

Figures 8a and 8b are the same type of study but for I_pII and I_pIA. These experiments possessed larger errors attributable to the difficulty in selecting a realistic base line from which to measure the peak currents. For peak II, it was decided to use the criterion (14) which says that the base line should follow the current-time curve for a potentiostatic hold immediately after the first peak. To obtain the base lines it was necessary to run the experiments at all the concentrations of water studied. For the anodic peak we chose to fix the base line from the base line obtained in the experiments without added water. This criterion possesses larger errors and gave values at high concentrations of water which apparently cannot be realistic from the shape of the peak (Fig. 5d), but it gave some idea about the progressive decrease of the anodic peak until it leveled off or disappeared. The reduction peak II, Fig. 8a, gradually decreases and merges into peak I. It is interesting that the maximum amount of current observed for peak II is of the same order and at the same range of water concentration as the peak current values at the inflection plateau observed for the peak I (Fig. 7). The rise in current of peak II at the beginning of the water additions has to be interpreted carefully because peak II is very close to the potential of the electrolyte decomposition wave at these water concentrations. At this point we prefer to leave the discussion of the results with increasing water concentration to the next section where the over-all mechanistic process is discussed.

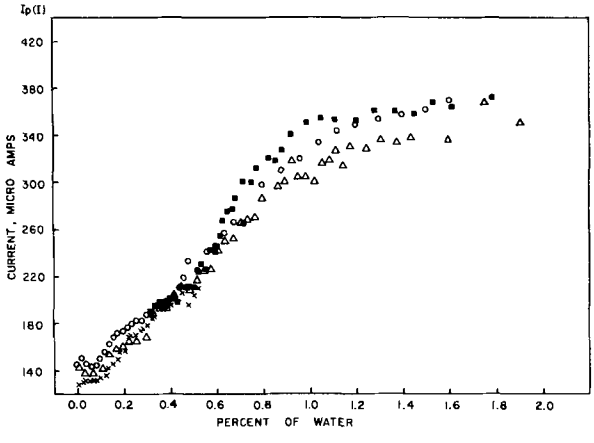

Fig. 7. Effect of increasing concentration of water on I_p (I)

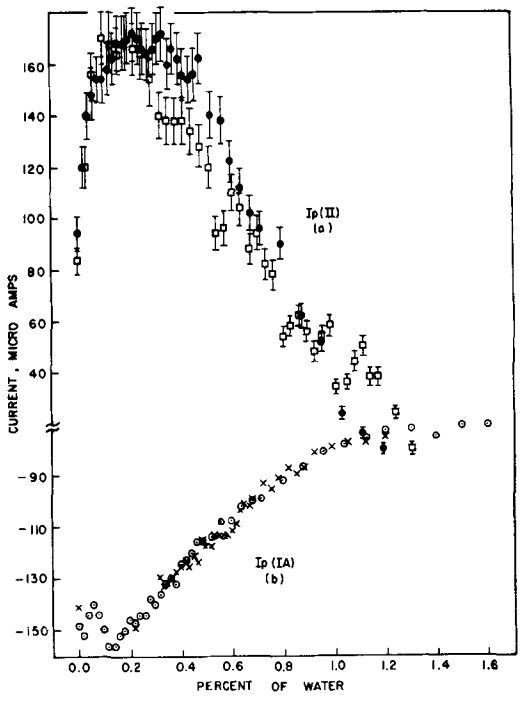

Fig. 8. Effect of increasing concentration of water on (a) $I_p(II)$ and (b) $I_p(IA)$.

Postulation of the complete mechanism.—The experiments described in the last section suggest several conclusions. These conclusions, combined with those obtained in the section of this paper covering step I, permit one to arrive at a hypothetical over-all mechanism for the oxygen reduction. It is believed that the second peak can be the reduction of peroxide to hydroxide, and the strong effect of the presence of water is perhaps an indication of the necessity of proton availability for this latter reduction step.

$$HO_2^- + 2e + H^+ \rightarrow 2\,OH^- \qquad E_3^\circ = f\,(H^+)$$

or following Eq. [1]

$$HO_2^- + 2e + H_2O \rightarrow 3\,OH^-$$

Perhaps in a system completely aprotic this reduction would not occur or is related to the cations which are present (7, 11). The increase in concentration of H_2O has to change the reduction in a way to approximate the reaction in aqueous media. The inflection observed in Fig. 7, the ratio of current between

this point and the maximum amount of current, and the same levels of current at the inflection point for peak I and peak II can suggest that (*a*) at that concentration of H_2O there is the same number of electrons transferred for both reductions (very possibly two), and (*b*) that the inflection for the increase of peak I is obtained when the reaction

$$O_2 + 2H^+ + 2e \rightarrow H_2O_2$$

is predominant.

At a water concentration (0.3-0.4%) the above mechanism would hold. At the other extreme where no protons are available the scheme below would hold.

$$O_2 + e^- \rightleftharpoons O_2^-$$

However, with water or proton concentrations intermediate between aproticity and 0.3 to 0.4% water the reaction could change from a one electron reaction to a two-electron reaction. This can result in a complex intermediate mechanism such as we suggested in the section on step I of the oxygen reduction.

Finally we want to note that at concentration levels over 1.2% H_2O, peak I arrives at a steady value, peak II merges with peak I, and the anodic peak IA disappears or decreases to a minimum. Thus, at 1.2% or higher concentrations of water it can be said that $E_1^\circ = E_2^\circ = E_3^\circ$ since all of the three reactions, having these formal potentials, have now been enclosed and included in peak I. Also, at or above this water concentration (1.2%) the cathodic reduction reaction conforms closely to a four electron reaction of the type postulated below.

$$O_2 + 2H^+ + 4e \rightarrow 2\,OH^-$$

The summary of the electrode process can be now postulated in the following way

$$O_2 \rightleftharpoons O_2 \text{ surface}$$

$$O_2 \text{ surface} + Pt \rightarrow O_xPt_y$$

$$O_2 \rightleftharpoons O_2^- \xrightarrow[k]{e^-,\ (H^+)} HO_2 \rightleftharpoons HO_2^-,\ (H_2O_2) \xrightarrow{2e^-,\ (H^+)} 2\,OH^-$$

(with k^1 on the reverse step; $2e, (H^+)$ over the whole sequence; (H^+) under the first step)

We have postulated our reaction considering the proton as the active specie from the addition of H_2O. We realize that this postulation of the reactions is tentative, because we do not have information about the dissociation of water in NDA and we expect that the mechanism can be expressed using water in place of protons as the active specie.

We also recognize that the postulation has to be confirmed by the determination of the number of electrons involved in the different steps (which from initial experiments looks difficult) or at least by identification of the different species postulated. The lack of time prevented further work covering these two areas.

Acknowledgment

The author gratefully acknowledges the technical assistance of R. L. Zwaagstra and the valuable discussions with Professor Irving Shain and W. E. Elliott. This research was supported by United States Army Mobility Equipment Research and Development Center, Fort Belvoir, Virginia, Contract No. DA-44-009-AMC 1552(T).

Manuscript submitted Aug. 9, 1968; revised manuscript received Oct. 28, 1968. This paper was presented at the Chicago Meeting, Oct. 15-20, 1967, as Paper 7.

Any discussion of this paper will appear in a Discussion Section to be published in the December 1969 JOURNAL.

REFERENCES

1. J. E. Toni *et al.*, USAERDL, Contract No. DA-44-009-AMC-1552(T), Final Report, July 1967.
2. J. F. Coetzee and I. M. Kolthoff, *J. Am. Chem. Soc.*, **79**, 6110 (1957).
3. I. M. Kolthoff and T. B. Reddy, *This Journal*, **108**, 980 (1961).
4. L. A. Knecht and I. M. Kolthoff, *Inorg. Chem.*, **1**, 195 (1962).
5. D. L. Maricle and W. G. Hodgson, *Anal. Chem.*, **37**, 1562 (1965).
6. M. E. Peover and B. S. White, *Chem. Comm.*, **10**, 183 (1965).
7. E. L. Johnson, K. H. Pool, and R. E. Hamm, *Anal. Chem.* **38**, 183 (1966).
8. D. T. Sawyer and J. L. Roberts, *J. Electroanal. Chem.*, **12**, 90 (1966).
9. M. E. Peover and B. S. White, *Electrochem. Acta*, **11**, 1061 (1966).
10. M. E. Peover and J. S. Powell, *J. Polarogr. Soc.*, **12**, 106 (1966).
11. E. L. Johnson, K. H. Pool, and R. E. Hamm, *Anal. Chem.*, **39**, 888, (1967).
12. A. D. Goolsby and D. T. Sawyer, *ibid.*, **40**, 83 (1968).
13. W. E. Elliott *et al.*, NASA CR-54187, First Quarterly Report, July-September, 1964.
14. R. S. Nicholson and I. Shain, *Anal. Chem.*, **36**, 706, (1964).
15. D. D. DeFord, Division of *Anal. Chem.* 133rd Meeting ACS, San Francisco, April 1958.
16. W. L. Underkofter and I. Shain, *Anal. Chem.*, **35**, 1778 (1963).
17. I. Kolthoff and N. Tamaka, *ibid.*, **26**, 632 (1954).
18. R. S. Nicholson and I. Shain, *ibid.*, **37**, 178 (1965).
19. D. Polcyn and I. Shain, *ibid.*, **38**, 376 (1966).
20. D. Polcyn and I. Shain, *ibid.*, **38**, 370 (1966).
21. R. Wopschall and I. Shain, *ibid.*, **39**, 1527 (1967).

Technical Notes

Methods for Studying the Solution Chemistry Within Stress Corrosion Cracks

B. F. Brown, C. T. Fujii, and E. P. Dahlberg

Naval Research Laboratory, Washington, D.C.

A major obstacle to a better understanding of the fundamentals of stress corrosion cracking (SCC) has been the almost total lack of information about the nature of the corrodent within a growing stress corrosion crack, particularly near the advancing edge. While it is generally conceded that the local chemistry within the stress corrosion crack differs considerably from that of the bulk solution, the demonstration of this difference has been deterred by inaccessibility and the problems of obtaining representative samples of solution. The present communication describes methods by which the stress corrosion process is interrupted in such fashion as to permit opening the crack without undue mixing of the corrodent within it, and to enable one to analyze the small amount of corrodent present without undue chemical changes in the interval between termination of the SCC test and the completion of the analysis.

The specimens used were for the most part rectangular and about 3 mm thick, with a saw cut at the middle of the long dimension. A metal wedge was pressed into the saw cut using a vise, thus stressing the root of the saw cut in tension. The specimen was then placed in either distilled water or 3½% NaCl solution (*p*H 6.5), with the wedge either paraffin coated or kept above the waterline to prevent galvanic effects. Some of the aluminum alloy specimens were long bars slotted at one end (parallel to the rolling plane) and stressed by opening the slot elastically with a set screw.

After the stress corrosion crack had propagated a suitable distance (a centimeter or so), the specimen was removed from the solution and immersed in liquid nitrogen to freeze the corrodent in the crack in place and also to minimize any side reactions which might alter the composition of the corrodent until the analytical operation could be effected. The specimen was subsequently removed from the liquid nitrogen and broken apart in a vise or with pliers to expose the frozen solution on the SCC surfaces for analysis immediately on thawing. Some of the early experiments were conducted in a glove box filled with dry nitrogen (1), but it was found that in general they can be conducted satisfactorily in the open air.

The inherent difficulties of microanalysis on the microvolume of solution available at the crack tip, the rugged fracture surface, and the obvious requirement of rapid analysis to prevent solution changes suggested a simple *in situ* approach to the problems of determining the solution chemistry of interest, *i.e.*, the acidity and the soluble metallic constituents. (A listing of the acid and ion indicators used for this purpose is given in Tables I and II.) The test method involved the use of indicator-impregnated filter paper or indicator-coated silica gel (60-80 mesh) prepared by saturating the paper or gel with dilute aqueous solutions of indicator, and drying completely. The congo-red and alkacid papers were obtained commercially; the others were all prepared as described above. The silica gel particles were sprinkled on the chilled fracture surface and provided a point-to-point indicator as the specimen warmed up and the corrodent melted. The strips of filter paper were simply pressed firmly on the moist fracture surface, and the color changes over the moist replica of the crack impressed on the paper were observed. In the normal procedure one-half the specimen was used for *p*H determination and the other half for the qualitative test for the ion species of interest. Several specimens of each alloy type were analyzed in this manner to encompass the range of indicators prepared and to bracket the *p*H within as narrow a range as possible.

The results of these test methods on two commercial alloys, 7075 Al alloy and Ti-8%Al-1%Mo-1%V, and a vacuum-melted carbon-deoxidized 0.45%C steel are summarized in Table III. The color changes observed after sprinkling silica gel coated with bromocresol green indicator on the fracture surface of 7075 Al and 8-1-1 Ti alloy specimens suggested local variation in the acidity. The individual silica gel particles ranged in color from the yellow of *p*H 3.8 or lower, through a medium green, to the less acid blue of *p*H 5.4 or higher. Generally, the region of highest acidity was at the advancing edge of the crack with a gradual decrease in acidity in the direction of the initial root

Table I. Acid indicators: ranges and associated color changes

Acid indicator	*p*H range	Color change†
1, Bromocresol green*	5.4-3.8	B-Y
2, Bromophenol blue	4.6-3.0	B-Y
3, Congo red*	5.0-3.0	R-B
4, Thymol blue	2.8-1.2	Y-R
5, Alkacid paper	5.5-3.5	G-Y-O

† B, blue; Y, yellow; R, red; G, green; O, orange.
* Those marked with asterisk used both in paper and on silica gel. All others in paper only.

Table II. Ion indicators: uses and color changes

Ion indicator	Test	Color change for positive test
1, Potassium ferrocyanide	Fe^{+3}	Pale yellow to blue
2, Sodium thiocyanate	Fe^{+3}	Colorless to red
3, Potassium ferricyanide*	Fe^{+2}	Yellow to blue
4, Aluminon reagent	Al^{+3}	Orange to red
5, Alizarin Red S*	Al^{+3}	Yellow to red

* Those marked with asterisk used both in paper and on silica gel. All others in paper only.

Table III. Test results for acidity and metallic ions in solution within the stress-corrosion crack

Alloy	Maximum *p*H detected at crack front	Soluble ions* Al^{+3}	Fe^{+3}	Fe^{+2}
7075 Al	3.5	+	N.T.	N.T.
0.45C Steel	3.8	N.T.	–	+
8-1-1 Ti	1.7	+	N.T.	N.T.

* + present; – absent; N.T. no test.

of the crack. However, within the regions of high or low acidity, local variations of acidity were discernible, *i.e.*, yellow and green silica gel particles were observed at the acid end and yellow, green, and blue particles at the less acid end of the fracture surface.

The pH paper tests permitted more accurate estimates of the acidity. The 7075 Al alloy and 0.45 C steel specimens indicated pH values of 3.5 and 3.8, respectively, near the advancing crack tip. In both cases the pH may actually have been slightly lower, but it was not sufficiently low to yield a positive congo-red test (pH 3.0). The 8-1-1 Ti specimen produced a decidedly positive congo-red test (pH 3.0 or lower), and further testing with thymol blue indicator showed an acidity as low as pH 1.7 at the crack tip.

In all three alloys, the relatively acid condition of the corrodent within the advancing crack suggests that the corrosion products are soluble. For the 7075 Al alloy and the 8-1-1 Ti alloy, positive tests for aluminum ions (Al^{+3}) were obtained with both aluminon and alizarin indicators in the region of highest acidity near the extreme edge of the advancing crack.[1] The 0.45 C steel specimens gave positive tests for the presence of ferrous ion (Fe^{+2}) but showed the absence of ferric ion (Fe^{+3}) in two independent tests, the ferricyanide and thiocyanate papers. Again the blotted imprint of the ferrous ion "blue" from one-half the specimen matched that of the region of highest acidity from the complementary half of the specimen. The results thus indicate that the corrodent is adequately immobilized by freezing, a requirement for the successful application of the test methods. Tests on unchilled, broken SCC specimens indicate that the freezing of the solution does not alter the solution chemistry, *i.e.*, similar indications of acidity were obtained. Thus, it can be concluded confidently that the test results are valid and represent the state of the solution at the termination of the SCC test.

The concurrence of higher acidity with the presence of the metallic ions in the region of the crack root suggests that the acidity is the result of hydrolysis of the metallic constituent released by anodic dissolution. The extreme edge of the advancing crack is generally thought to be anodic to the rest of the specimen and thus is consumed in the corrodent by the electrochemical reaction $M \rightarrow M^{+z} + ze^-$, where M is the metal in question and z the electronic charge involved. Subsequent hydrolysis represented by the general equation.

$$M^{+z} + xH_2O \rightleftarrows M(OH)_x^{(z-x)} + xH^+$$

would produce the increase in acidity observed in all the specimens used in this investigation. Such a mechanism has been offered for reactions within pits protected by an oxide film in the corrosion of Al and Fe in alkaline medium (2). It is likely that the present findings may also be applicable to other alloys which are susceptible to SCC and which contain metals the ions of which are hydrolysis prone. These results would suggest the possibility of SCC control by methods which would inhibit the hydrolysis or neutralize the acidity.

A knowledge of the acidity and the solution chemistry, obtainable by the methods described, would generally be useful in interpreting SCC and specifically be helpful in evaluating the applicability of SCC models such as the film-formation and oxide-rupture model.

[1] The presence of acidity and Al^{+++} ions within stress-corrosion cracks in Ti-Al alloys was predicted by M. Pourbaix in a seminar at NRL in 1967.

Acknowledgments

Much of the experimental work reported herein was conducted by Mr. R. L. Newbegin. This work was supported by the Advanced Research Projects Agency of the Department of Defense as part of the coupling program on stress-corrosion cracking established by ARPA Order 878.

One of the authors (B.F.B.) would like to acknowledge the stimulating value, in planning the present work, of lecture series by Dr. Evans and Dr. Hoar delivered at Cambridge University while he was a postdoctoral guest in Dr. Hoar's laboratory.

Manuscript submitted Aug. 22, 1968; revised manuscript received *ca.*, Nov. 15, 1968.

Any discussion of this paper will appear in a Discussion Section to be published in the December 1969 JOURNAL.

REFERENCES

1. E. P. Dahlberg, C. T. Fujii, and B. F. Brown, Report of NRL Progress, August 1968, pp. 28-29.
2. H. Kaesche, "Die Korrosion der Metalle," pp. 268 and 279, Springer-Verlag, New York (1966).
3. P. T. Gilbert and S. E. Hadden, *J. Inst. Metals*, **77**, 237 (1950).

The Anodic Voltammetry and Electrolytic Oxidation of Corypalline

G. F. Kirkbright,[1] J. T. Stock,* R. D. Pugliese,[2] and J. M. Bobbitt

Department of Chemistry, University of Connecticut, Storrs, Connecticut

Recent papers on the general (1) and electrolytic (2) oxidation of phenols suggested to us the possible application of electrolytic oxidation to the synthesis of isoquinoline alkaloids. A preliminary communication from this laboratory (3) has outlined the successful electrolytic and photochemical oxidation of one of the simpler isoquinoline alkaloids, corypalline (I). More recently, two studies of the ferricyanide oxidation of corypalline have appeared (4). Qualitatively, the results are similar to those now presented.

This paper describes studies leading to the optimization of conditions for the electrolytic oxidation of corypalline to the "carbon-carbon dimer" N, N'-dimethyl-6, 6'-dimethoxy-7, 7'-dihydroxy-1, 1', 2,2', 3,3', 4,4'-octahydro-8,8'-biisoquinoline (II). The method developed is simple, quite rapid, and relatively efficient. These studies strongly indicate the feasibility of the application of electrochemical oxidation to the synthesis of complex natural products (1, 5). It is especially noteworthy that an aliphatic tertiary nitrogen does not interfere significantly with the reaction.

Experimental

Voltammograms at a platinum wire microelectrode that was rotated at 600 rpm were recorded by an

* Electrochemical Society Active Member.

[1] Present address: Department of Chemistry, Imperial College of Science & Technology, London S. W. 7, England.

[2] Present address: Texaco Research Laboratories, Beacon, New York.

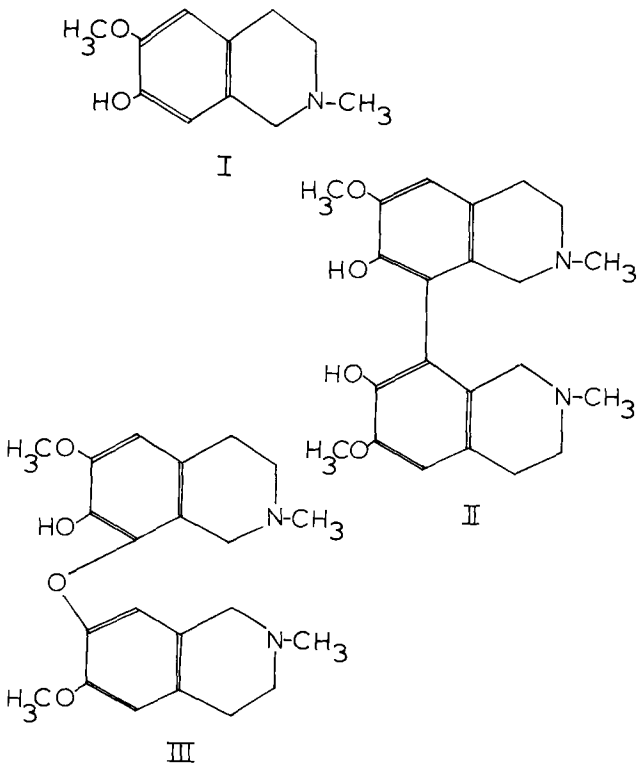

L&N type E electrochemograph. Preparative electrolyses were carried out with a Wenking potentiostat. The cathode compartment was formed by epoxy cementing a medium-porosity glass filter crucible to the inner wall of the 150-ml beaker used as an electrolysis cell. The semicyclindrical platinum gauze anode had a half-circumference of 82 mm and was 52 mm high. A 50 mm x 80 mm rectangle of platinum foil rolled into a loose spiral was used as a cathode. The anolyte was agitated by a magnetic stirrer bar and by a stream of nitrogen.

Corypalline (6) was prepared (7) from isovanillin by a modification of a general synthesis of 1,2,3,4-tetrahydroisoquinolines (8).

Preparative electrolyses were monitored by thin-layer chromatography (TLC) on microscope slides coated with Merck silica gel GF. Ammonia: methanol (3:100 v/v) was used as developing solvent and the spots were visualized with iodine vapor or Dragendorf's reagent. R_f values were corypalline, 0.65; compound (II), 0.4. A yellow product that awaits identification remained at the origin.

Two grams of corypalline suspended in 100 ml of 0.1M $Na_2B_4O_7$ were placed in the cell, and the cathode compartment was filled simultaneously to the same level with 0.1M $Na_2B_4O_7$. The suspension was stirred rapidly, and nitrogen was slowly bubbled near the anode, which was maintained at a potential of +0.35v. The electrolysis was terminated when all solid had dissolved and the current had fallen by 25% from the essentially constant reading obtained in the presence of solid.

After removal from the cell, the anolyte was allowed to stand for several hours (preferably overnight) to allow precipitation of the first crop of compound (II). This was filtered off and dried. The filtrate was transferred to a 500 ml separating funnel and 20 ml of ammonia (sp gr 0.90) were added. The solution was extracted with four 100 ml portions of chloroform and the extracts were combined, dried over anhydrous $MgSO_4$ and taken to dryness under reduced pressure in a rotary evaporator. The residue was dissolved in 25 ml of chloroform, and the volume was reduced to 15 ml by gentle warming. After cooling in ice water, the recovered corypalline was filtered off. A second crop of compound (II) was obtained from the filtrate by evaporation to dryness, dissolution in 50 ml of ethanol, evaporation to a volume of 10 ml, cooling in ice-water, and filtering. The combined crops were recrystallized from ethanol, to yield (II), mp 235°-236°C, undepressed by the addition of a known specimen of compound 6 (3).

Results and Discussion

Preliminary investigations (9) have shown that, although compound (II) is the major oxidation product of corypalline, a 2-5% yield of an oxygen-linked dimer (III) can also be obtained. No attempts to isolate this minor product were made in the present work.

All potentials are with respect to the saturated calomel electrode.

Voltammetry.—The starting potentials of the single anodic waves given by compounds (I) and (II) were almost identical and, in acid and strongly alkaline media, the drawn-out wave merged into the decomposition wave of the medium. Definition was better in 0.1M $NaHCO_3$ (pH 8.4) or 0.1M $Na_2B_4O_7$ (pH 9.0), and the current approached limiting conditions over the approximate potential range +0.6 to +0.8v (Fig. 1, curve 2). No conditions were found that would permit the oxidation of corypalline without attack on the compound (II) formed by this oxidation. The marked current decay with time observed in $NaHCO_3$ was not significant in $Na_2B_4O_7$, in which a linear current-corypalline concentration relationship could be obtained at any potential in the approximate range +0.2 to +0.5v.

Controlled potential electrolysis.—Preliminary electrolyses of corypalline in CH_3COOH-CH_3COONa (pH 4.6), $NaHCO_3$, $Na_2B_4O_7$, and Na_2CO_3 showed $Na_2B_4O_7$ to be the most promising medium. Conditions finally chosen involved the electrolysis of a suspension of corypalline in 0.1M $Na_2B_4O_7$ at a potential of +0.35v. Partial destruction of compound (II) is then minimized, because the oxidation current of a saturated solution of corypalline is much larger than the current given by a saturated solution of compound (II) Fig. 1, curves 1 and 3). The current remained approximately constant while solid corypalline was present and began to diminish soon after the anolyte had become homogeneous. Experiments with unsaturated corypalline solutions showed that the logarithm of the current decreased linearly with time until the amount of electricity reached approximately 80% of that theoretically required for the oxidation of corypalline to compound (II). Deviation from linearity and fall-off in slope then occurred as shown in Fig. 2, reflecting the increasing competitive oxidation of compound (II). TLC near the deviation point showed the

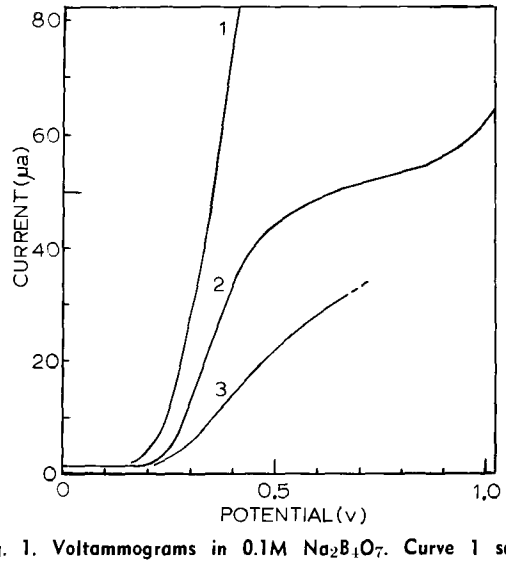

Fig. 1. Voltammograms in 0.1M $Na_2B_4O_7$. Curve 1 saturated with corypalline; curve 2, 0.001M in corypalline; curve 3, saturated with compound II.

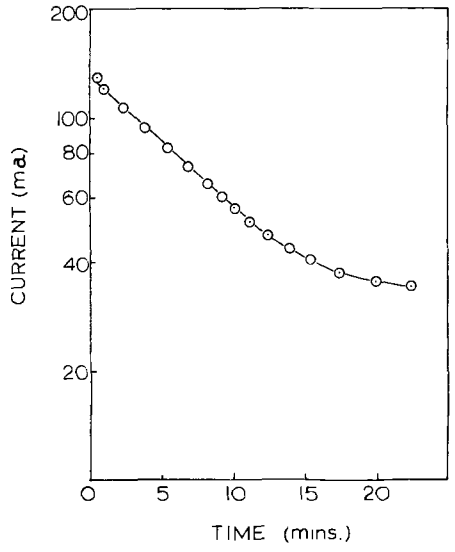

Fig. 2. Current-time relationship for 0.0075M corypalline in 0.1M $Na_2B_4O_7$.

presence of considerable amounts of corypalline and of compound (II). The concentrations of both compounds fell on further electrolysis and buildup of the concentration of a deep yellow further oxidation product proceeded rapidly.

Seven preparative runs with from 0.4 to 3.0g of corypalline gave yields of 44-60% (average 55%), based on recovered corypalline. The current efficiency for the preparation of compound (II) probably exceeds 60%. Differing percentage yields are almost certainly due to variations in the techniques used for isolation and purification of the product.

These studies are being extended to derivatives of corypalline and to other phenolic derivatives of isoquinoline.

Acknowledgments

Preliminary voltammetric observations and some pilot controlled-potential oxidations were made by A. Marchand, K. H. Weisgraber, and Dr. A. Vinod (née Varma). This work was supported in part by grant GP-7601 from the National Science Foundation.

Manuscript submitted Sept. 27, 1968; revised manuscript received Nov. 3, 1968.

Any discussion of this paper will appear in a Discussion Section to be published in the December 1969 JOURNAL.

REFERENCES

1. A. I. Scott, *Quart. Rev.*, **19**, 1 (1965).
2. F. J. Vermillion, Jr., and I. A. Pearl, *This Journal*, **111**, 1392 (1964).
3. J. M. Bobbitt, J. T. Stock, A. Marchand, and K. H. Weisgraber, *Chem. & Ind.* (London) 2127 (1966).
4. M. Tomita, K. Fujitani, Y. Masaki, and K.-H. Lee, *Chem. Pharm. Bull.*, **16**, 251 (1968); B. Umezawa, O. Hoshino, H. Hara, and J. Sakakibara, *ibid.*, **16**, 381 (1968).
5. W. I. Taylor and A. R. Battersby, Editors, "Oxidative Coupling of Phenols," Marcel Dekker, New York (1967).
6. R. H. F. Manske, *Can. J. Res.*, **B15**, 159 (1937).
7. J. M. Bobbitt, D. N. Roy, A. Marchand, and C. W. Allen, *J. Org. Chem.*, **32**, 2225 (1967).
8. J. M. Bobbitt, J. M. Kiely, K. L. Khanna, and R. Ebermann, *ibid.*, **30**, 2247 (1965).
9. A. S. Steinfeld, Ph.D. Thesis, University of Connecticut (1968).

Brief Communication

Potential-Wetting Effects of Platinum Electrodes

L. Nanis* and G. F. Rowell

School of Chemical Engineering, University of Pennsylvania, Philadelphia, Pennsylvania

Oxygen on the platinum electrode has been the subject of much attention. Summaries of previous work may be found in recent reviews by Gilman (1) and Hoare (2). The precise nature of the oxygen on the electrode is an issue which is apparently unresolved as yet. The wetting behavior of surfaces is known to be strongly dependent on traces of surface compounds. A critical change in wetting of a platinum anode in 1*N* H_2SO_4 (room temperature) was noted in studies of the oxidation of dissolved hydrogen (3). The apparatus used incidentally permitted rapid (2-3 sec) drainage of a layer of acid 2.4 mm thick from a vertical smooth platinum electrode, 9 x 9 cm, and also permitted observation of the electrode surface. It was noticed that the drainage behavior was influenced by the potential of the electrode. The nature of the draining electrolyte film was correlated with electrode potential by commencement of drainage when the electrode potential was near the hold plateau of 0.74 $\pm$0.02v during transient decay (open circuit) from above 1v.

For drainage beginning above 0.76v (with respect to a reversible hydrogen electrode in the H_2 saturated 1*N* H_2SO_4), total wetting occurred initially. For drainage initiated when the electrode was below 0.70v, the surface was not truly wetted but isolated beads of electrolyte remained. Correspondingly, the total drainage was noticeably more rapid from the poorly wetted surface. In the range between 0.70 and 0.76v, the drainage behavior included mixed features, *i.e.*, initial partial wetting. The wetting behavior noticed here should be added to consideration of the nature of the adsorbed oxygen layer on platinum.

Acknowledgment

The support of NASA (Grant NSG-316) is gratefully acknowledged.

Manuscript submitted Oct. 21, 1968.

Any discussion of this paper will appear in a Discussion Section to be published in the December 1969 JOURNAL.

REFERENCES

1. S. Gilman, "The Anodic Film on Platinum Electrodes," in Electroanalytical Chemistry, vol. 2, pp. 132-189, M. Dekker, Inc., New York (1965).
2. J. P. Hoare, "The Oxygen Electrode on Noble Metals" in Advanced Electrochemistry and Electrochemical Engineering, Vol. 6, pp. 202-255, Interscience Publishers, New York.
3. G. F. Rowell, "Platinum Oxide Electrode," M. S. Thesis, Chemical Engineering, University of Pennsylvania, 1967.

* Electrochemical Society Active Member.

High-Temperature Oxidation of Co-10 w/o Cr Alloys

I. Microstructure of Oxide Scales

P. K. Kofstad[1] and A. Z. Hed

Metal Science Group, Battelle Memorial Institute, Columbus Laboratories, Columbus, Ohio

ABSTRACT

Oxidation of Co-10 w/o Cr alloy results in an outer CoO layer, an inner CoO layer with inclusions of Cr_2O_3 and $CoCr_2O_4$, and an internal oxidation zone. Both oxide layers contain appreciable porosity and the morphology of the inclusions is a function of temperature. The microstructure of scales formed during oxidation is presented. It is assumed that the rate-controlling step is the solid state diffusion of Co-ions in the CoO phase, while gaseous oxygen is rapidly transported across pores. The pores short-circuit the solid state diffusion process and enhance oxidation, while Cr_2O_3 and Co-Cr spinel inclusions inhibit the oxidation.

Cobalt-chromium alloys serve as a basis material for production of a family of Co-base superalloys for high-temperature applications. To increase the service lifetime and use temperatures of these alloys, an understanding of their chemical stability and, particularly, their oxidation resistance is of paramount importance.

The development of oxidation-resistant alloys has to a large extent been empirical and therefore has failed to provide a detailed understanding of mechanisms of alloy oxidation. The work reported here is a part of a general study on the different mechanisms governing the oxidation behavior of Co-Cr alloys. This paper describes some microstructural and morphological aspects of the scales formed during oxidation of Co-10 w/o (weight per cent) Cr alloys and their influence on the scaling rate.

Oxidation of Co-Cr alloys has been studied by Preece and Lucas (1) in the range 0-40 w/o Cr and by Phalnikar, Evans, and Baldwin (2) in the range 0-48 w/o Cr. Davin, Coutsouradis, and Habraken (3) studied the oxidation behavior of pure cobalt and of Co-Cr alloys containing 10 and 35% Cr.

The study by Phalnikar *et al.*, was the most extensive of these. According to these authors, the main feature of the oxidation behavior of Co-Cr alloys above 900°C is that the oxidation of this system increases with increasing amounts of chromium up to about 10 w/o Cr. Beyond this level, the oxidation rate decreases with increasing chromium content up to 20-30 w/o Cr, after which the oxidation rate again increases up to unalloyed chromium. Their metallographic studies revealed that small additions of chromium cause formation of duplex scales: the outer layer consists mainly of CoO, while the inner layer consists of CoO, Cr_2O_3, and the spinel $CoCr_2O_4$. They found that Cr_2O_3 and the spinel do not form continuous layers but are dispersed in the CoO matrix of the inner layer. They concluded that the rate-controlling process in the oxidation of low-chromium-content Co-Cr alloys is solid-state diffusion of cobalt in CoO. They attributed the continuous increase in the oxidation rate up to 10% Cr to the doping effect of the scale, according to the semiconductor valence approach of alloy oxidation (Wagner theory). However, no detailed analysis was given.

It must be emphasized that, for the Wagner theory to hold, the concentration of the dopant (chromium in this case) must be higher than the native-defect concentration at the ambient oxygen pressure. No data for the solubility of chromium in CoO were reported, either in their work or elsewhere. If we take the solubility of chromium in NiO as a measure of that of chromium in CoO (see below), the use of the semiconductor valence approach in explaining the oxidation of Co-Cr alloy with more than a few per cent chromium does not appear justified.

Meyer and Rapp (4) found that no more than 1% Cr will dissolve in NiO, yet the oxidation rate of Ni-Cr alloys increases continuously up to 5% Cr (5). If the Wagner theory were to be used, a saturation of the NiO scale with Cr would have occurred at 1% Cr, and the oxidation rate should not increase above that chromium percentage. Similar behavior should be expected for the oxidation of Co-Cr alloys. No explanation of the increased rate has as yet been given.

Phalnikar *et al.*, attributed the decrease of the oxidation rate at high chromium concentration to a "blocking" effect by either Cr_2O_3 or spinel. The relative abilities of Cr_2O_3 and spinel to impart oxidation resistance were not evaluated.

This paper reports on the microstructures of scales formed on Co-10 w/o Cr alloy and suggests how these can account for the increased oxidation rate at high temperatures. Thermogravimetric data on this alloy will be given in a following paper (9).

Experimental Procedure

An alloy with the nominal composition Co-10 w/o Cr was prepared in a vacuum furnace and cast into tapered zirconite sand molds. Subsequent analysis showed the actual composition to be 9.62 w/o Cr. After grit blasting, the ingots were heat treated at 1175°C for 2 hr, and then forged. The ingots were cold rolled down to plates of 0.070-in. thickness. After rolling, the plates were reblasted, cut to specimens 1 x 0.75 in., then subsequently ground on emery paper and diamond polished. This procedure removed some 2-4 mils.

Specimens were oxidized in the temperature range 800°-1300°C at oxygen pressures from 0.2 to 760 Torr. A Crusilite furnace was used, with a Mullite tube as a reaction chamber held by a Barber-Coleman controller within 3°C. Weight gains were continuously recorded with a Cahn R-H electrobalance and an AZAR Leeds and Northrup recorder. The balance was used with a full range of 2g, a recording range of 20 mg, and a sensitivity of 0.1 mg. The system could be evacuated to 10^{-5} Torr by a 450-liter CVC diffusion pump and an Edwards mechanical pump. The pressures were measured by CVC-ionization and thermocouple gauges. The polished specimen, washed in water and trichloroethylene, was attached to an annealed Pt-10 Rh wire and dropped into the hot zone by a magnetic device while the system was under high vacuum. Oxygen was then introduced by a Granville-Phillips metering valve to the desired pressure. Below 10 Torr O_2, oxygen was continuously pumped through the apparatus during the run. After oxidation proceeded to the desired extent, the samples were raised into the cool part of the furnace, oxygen was introduced into the reaction chamber, and the specimens were taken out and quenched in molten lead-bismuth

[1] Present address: Central Institute for Industrial Research, Blindern, Oslo, Norway.

alloy, which in turn was rapidly cooled. This was done to prevent spallation of the scale. Some samples were than chosen for metallographic study, x-ray analysis, and electron-probe microanalysis. A Picker x-ray machine was used to determine the different compounds in the scale. A Kenny electron-microprobe analyzer was used for the probe analysis. Since the oxides at room temperature are poor electrical conductors, a layer of carbon 250Å thick was deposited on the specimens. The limit of detection is 0.1%, while the actual resolution is ± 0.5%.

Microstructure of Oxide Scales

The oxidation of the Co-10 w/o Cr specimens results in two-layered scales. The outer layer consists of columnar grains of CoO and the inner of CoO, Cr_2O_3, and the spinel $CoCr_2O_4$. A small area of chromium internal oxidation is present to varying degrees under all oxidation conditions. Various features of the oxide scales are illustrated in Fig. 2 through 15.

Electron-probe microanalyses were performed on a few samples. A typical result is shown in Fig. 1. The outer scale contained less than 0.1 Cr, which is the limit of detection of the apparatus. In the inner layer, no regular gradient of chromium was found, instead, an irregular distribution of high chromium and high cobalt content was found. As described below, the spinel appears as a dispersion in the CoO matrix, and an accurate determination of its composition is not possible by electron-probe microanalysis. We will therefore refer to it as $CoCr_2O_4$, although it must be borne in mind that the actual composition may vary from $Co_{1.3}Cr_{1.8}O_4$ to $CoCr_2O_4$ (11).

Detailed metallographic studies of specimens oxidized under different conditions were performed. Different etching agents were tried to reveal the different constituents of the scale. The following etching agent was found to be most effective: 80 parts lactic acid, 10 parts HNO_3, 10 parts H_2O_2, and 5 parts HCl. This agent completely etched out the Cr_2O_3 and attacked the CoO, to some extent. The spinel is slightly more resistant to the etchant than is the CoO. We were able to determine the distribution of the three constituents in the scale by comparing the metallographic cross section before and after etching.

The only other phase found in the outer layer consists of small Co_3O_4 precipitates within the grains and at the grain boundaries. This confirms the electron-microprobe results, that no measurable Cr_2O_3 is present in this part of the scale.

The deviation from stoichiometry of CoO increases with temperature and partial pressure of oxygen and, at 1200°C and 1 atm O_2, reaches 1.5% excess oxygen (6). When CoO is cooled, the excess oxygen precipitates in the form of Co_3O_4. The concentration of these precipitates should, therefore, increase with increasing temperature and oxygen partial pressure. This effect was not easily observed, however, since the degree of precipitation depends critically on the quenching procedure, which was not accurately reproducible from sample to sample. Nevertheless, a small effect of temperature can be seen in the scales of specimens oxidized at 1000° and 1200°C (Fig. 3 and 4, respectively). Assuming a uniform quenching of the sample, a gradient of these precipitates should be present in the outer scale according to the decreasing oxygen activity. Such an effect is, however, probably masked by the temperature gradients in the samples during cooling and by extensive precipitation at the grain boundaries, which causes a depletion of Co_3O_4 in the grains near these boundaries. In addition, the gradient of excess oxygen in the outer layer may be small compared with that in the inner layer. It may be noted that the appearance of the outer scale is similar to scale formed during oxidation of unalloyed cobalt (7,8).

The interface between the inner and outer layers shows the geometry of the original alloy surfaces (Fig. 2, 3, and 4.). We therefore concluded that this interface in fact represents the original alloy surface. To further substantiate this, a notched specimen was oxidized. The notch dimensions were accurately measured and compared with dimensions of the inner-outer layer boundary at the notch after oxidation. Very good agreement was found.

The microstructure of the inner layer depends largely on the temperature of the oxidation. At low temperatures one can see a general striation with dark and bright layers (Fig. 2 and 3), while at high temperatures the appearance of the inner layer is more uniform. The details of this behavior are described below.

Spinel Morphology

The spinel morphology in the scale depends largely on temperature and to a lesser degree on the oxygen partial pressure of the oxidizing atmosphere. Various

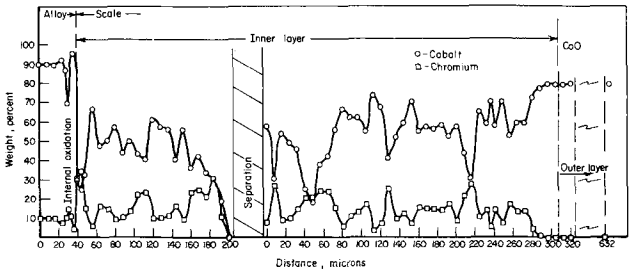

Fig. 1. Profile of cobalt and chromium content in a scale produced on a Co-10 w/o Cr alloy oxidized at 1100°C in air for 17 hr. Note: A slight depletion of chromium followed by an increase is observed at the alloy-oxide interface in the internal-oxidation region. The sum of cobalt and chromium is not constant due to porosity. The outer layer contains only cobalt.

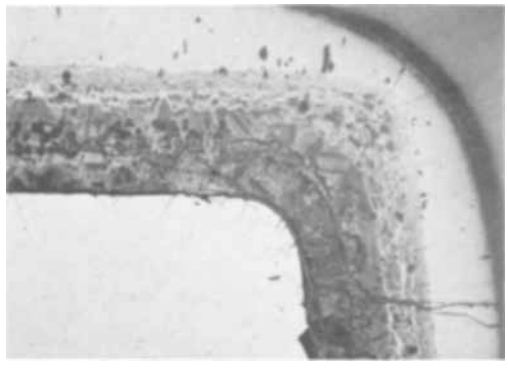

Fig. 2. Corner of a Co-10 w/o Cr specimen oxidized at 900°C in air for 193 hr. Note the decrease in the density of spinel decoration at original alloy grain boundaries from the inner-outer layer interface toward the alloy. Magnification of Fig. 2-4 is *ca.* 50X.

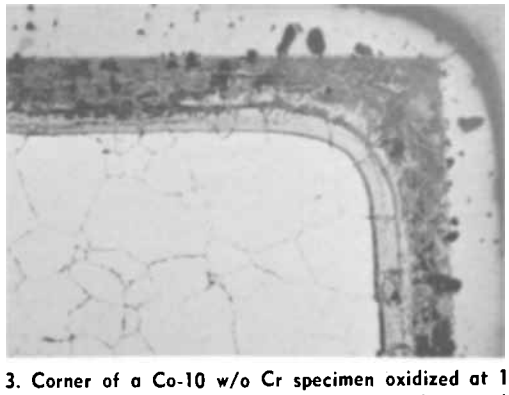

Fig. 3. Corner of a Co-10 w/o Cr specimen oxidized at 1000°C in air for 11 hr. Note the pyramidal pores in outer layer and irregularly shaped pores in the inner layer. Spinel decorations are larger than at 900°C.

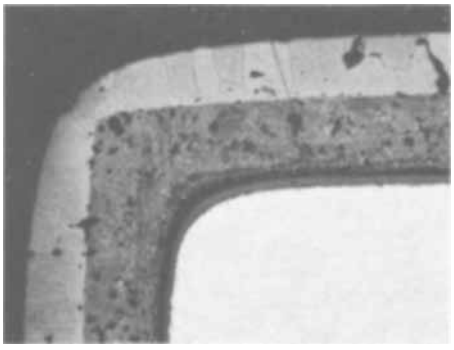

Fig. 4. Corner of a Co-10 w/o Cr specimen oxidized at 1200°C in 100 Torr O_2 for 3 hr. Note: No spinel decoration of the original grain boundaries is present, and irregularly shaped pores are quite evenly distributed.

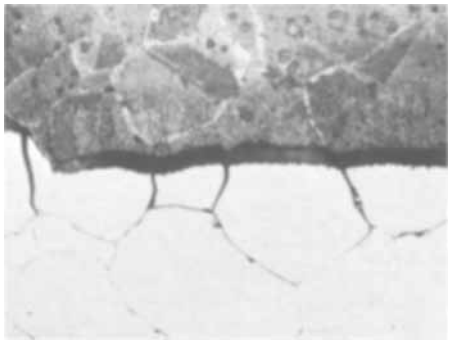

Fig. 5. Alloy-scale interface of specimens of Fig. 2. Note the internal oxidation of alloy grain boundaries and their continuation in the scale as spinel decoration, along with fine dispersion of spinel within the "grains." Magnification of Fig. 5-10 is *ca.* 250X.

features of the spinel growth are illustrated in Fig. 5 through 10.

Figure 5 shows the metal-oxide interface of a sample oxidized at 900°C in air. The grain boundaries in the alloy are etched out, and one can see their continuation in the scale outlined by lighter colored spinel. The etching out of the grain boundaries in the alloy is due to preferential internal oxidation of chromium to Cr_2O_3 at the grain boundaries. Also, fine internal oxidation along the metal-oxide interface occurs, and correspondingly, a fine dispersion of spinel in the CoO inner scale is present. A similar behavior is illustrated in Fig. 6, which shows a specimen oxidized at 900°C and 10 Torr oxygen. Due to the lower partial pressure of oxygen, the internal oxidation is slightly more severe along the metal-oxide interface than along the grain boundaries.

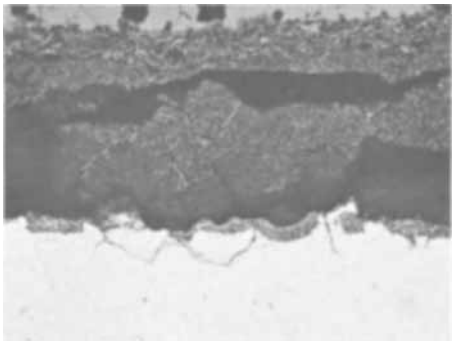

Fig. 6. Alloy-scale interface of a Co-10 w/o Cr specimen oxidized at 900°C in 10 Torr O_2 for 70 hr. Note the more intense internal oxidation at the interface than in air (Fig. 5), and "grain-boundary" decoration by spinel.

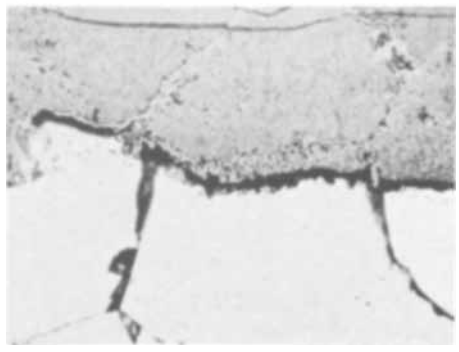

Fig. 7. Alloy-scale interface of a Co-10 w/o Cr specimen oxidized in air at 1000°C for 140 hr. Note the large grains due to annealing during oxidation; spinel decoration is lighter and spinel dispersion coarser than in Fig. 5.

Figure 7 shows the metal-oxide interface of a sample oxidized at 1000°C in air. The grains in the alloy are larger (due to annealing at temperature during oxidation) than in the sample oxidized at 900°C. Furthermore, in the oxide, the spinel decoration along the original grain boundaries in the alloy is less marked and the individual spinel particles are larger in size than those obtained at 900°C.

In Fig. 8 the metal-oxide interface of the specimen oxidized at 1100°C and 100 Torr O_2 is shown. The decoration of the spinel along the original grain boundaries of the alloy has disappeared completely, and the spinel particles are much larger. Figures 9 and 10 show the metal-oxide interface of specimens oxidized at 1200°C in 100 and 10 Torr O_2, respectively. At 100 Torr the spinel has formed relatively large platelets dispersed in a CoO matrix, while at 10 Torr less CoO matrix is left. (The dark background is epoxy that filled a network of pores near the metal-oxide inter-

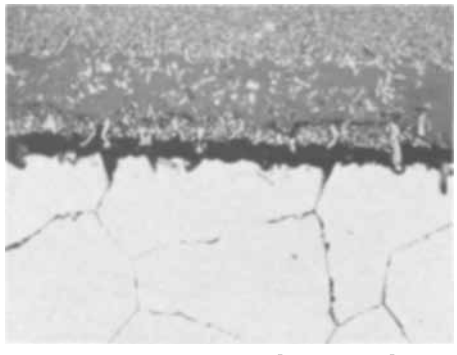

Fig. 8. Alloy-scale interface of a Co-10 w/o Cr specimen oxidized at 1100°C in 100 Torr O_2 for 20 hr. Note: No spinel decorations are present in the scale.

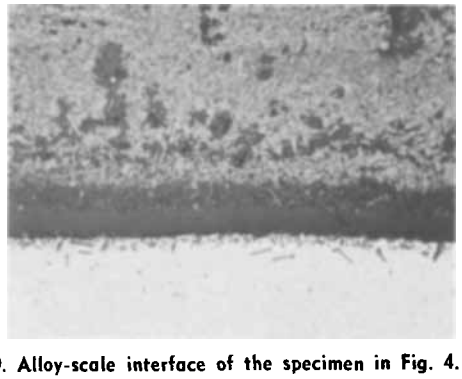

Fig. 9. Alloy-scale interface of the specimen in Fig. 4. Note the line of pores and very coarse spinel. (Spinelization occurs probably partly within the internal oxidation region.)

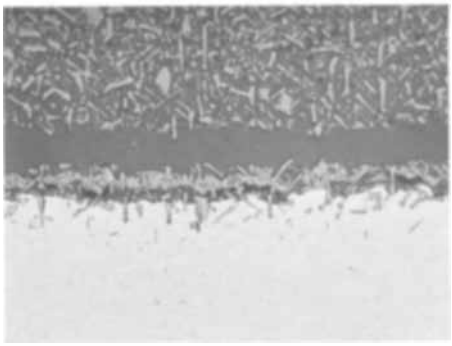

Fig. 10. Alloy-scale interface of a Co-10 w/o Cr specimen oxidized at 1200°C in 10 Torr O_2 for 1.5 hr.

face. The actual pores in this case could be smaller than seen in the photograph.)

From these observations we conclude that the size of the spinel particles and their location in the scale depend largely on temperature. At low temperatures the spinel is finely dispersed and is formed along the original grain boundaries of the alloy. With higher temperatures, the spinel particles grow in size and become more uniformly distributed in the oxide, and the decoration along the original grain boundaries in the alloy disappears.

The distribution of the spinel may also be affected by the history of the oxidizing sample. An example is given in Fig. 11, which shows the scale of a sample oxidized at 900°C in air. The spinel decoration of the original alloy grain boundaries near the outer part of the inner layer shows small "grain" size (which is probably not the oxide grain size), but the size increases as the metal-oxide interface is approached. This feature is due to the fact that the sample was cold rolled and that the grain size before oxidation was relatively small. During oxidation, the alloy is simultaneously annealed, and the grain size in the alloy increases correspondingly. When the temperature is raised, this behavior changes accordingly. In Fig. 3, which shows a sample oxidized at 1000°C, only a very narrow range of small "grains" next to the interface between the inner and outer layers is observed. At and above 1100°C (Fig. 12 and 14) the spinel outlines of the original grain boundaries in the alloy have disappeared.

Porosity in the Scale

Different kinds of pores are observed in the scales. In the outer layer triangular pores are found, the tops of which always point toward the outer oxide surface. This is illustrated in Fig. 13. This kind of pore occurs in almost all of the outer layers (Fig. 2, 3, 11, and 12). To further identify the geometry of these pores, a cross section of the outer layer at a small angle with the outer surface was prepared (see Fig. 14). As

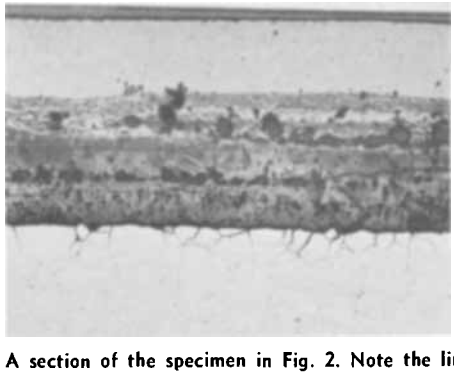

Fig. 11. A section of the specimen in Fig. 2. Note the line of irregularly shaped pores and the behavior of spinel decoration. Magnification ca. 50X.

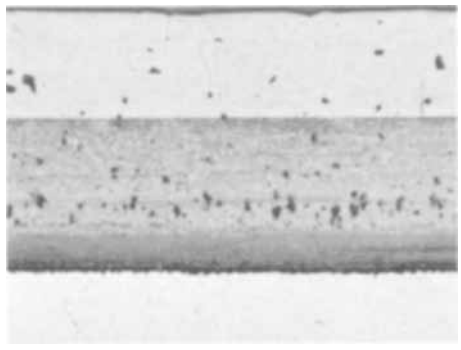

Fig. 12. Section of the specimen in Fig. 8. Note spinel dispersion and slight striation in the inner layer. Magnification ca. 50X.

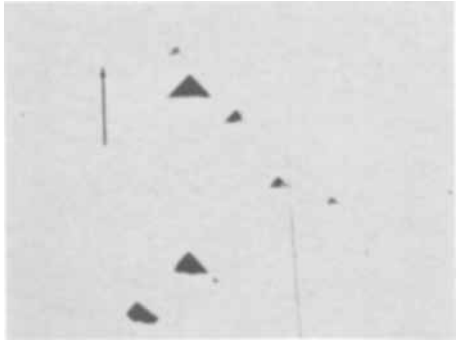

Fig. 13. Perpendicular cross section of the outer layer of a Co-10 w/o Cr specimen oxidized at 1100°C in air for 119 hr. Note the triangular form of the pores in this layer. The arrow is pointing toward the oxide gas interface. Magnification ca. 125X.

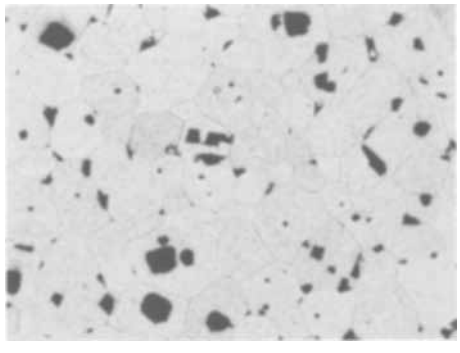

Fig. 14. Tapered cross section of the outer layer of a Co-10 w/o Cr specimen oxidized at 1200°C in 100 Torr O_2 for 35 hr, showing the rectangular shape of the pores parallel to the alloy surface. Magnification ca. 100X.

viewed in this direction, the pores tend to be rectangular. We therefore conclude that these pores tend to be rectangularly shaped pyramids whose tops are pointing toward the outer oxide surface.

The inner layer contains only irregularly shaped pores (Fig. 2, 3, 11, and 12), which may be divided into three groups: (*i*) large pores that sometimes coalesce to form a line of pores, (*ii*) very small pores or micropores distributed evenly throughout the matrix, and (*iii*) pores associated with the chromium oxide in the scale.

The amount of porosity was estimated from the dimensions of the scale and the weight gain of the specimen. In such an estimate one must consider differences in porosities of the inner and outer layers. Assuming that the outer layer is fully dense, the inner layer would be 39% porous. Assuming that the pores are equally distributed throughout both layers, the average porosity would be 27%. The actual values lie

between these limits, and it is estimated that the mean values amount to 33-35% porosity in the inner layer and 3-6% porosity in the outer layer.

In a consideration of the porosity, it is also of interest to estimate the volume change upon converting the alloy to the oxide. Comparisons were made of the thickness of the consumed part of the alloy and the thickness of the inner oxide layer. As an example, in one case the thickness of the consumed alloy was 0.53 mm, while the thickness of the inner layer was 0.93 mm, which amounts to an increase of 75%. As discussed above, the interface between the inner and outer oxide layers reflects the position of the original surface of the alloy. This means that this interface is continuously displaced outward, relative to the center of the specimen during oxidation.

The expanding inner layer puts the outer layer under tension. This tension is probably partially accommodated for by the growth process of the outer layer (involving outward migration of cobalt ions) and partially by plastic deformation and creep. It is proposed that the pyramid-like pores in the outer layer result from mechanical shear and deformation.

The porosity in the inner layer is to a large extent due to the outward migration of cobalt ions to form the outer layer (see Discussion, below). It is not improbable that volume change associated with the oxide formation also causes stresses that in turn may be alleviated by local loss of adherence to the alloy substrate. This may yield porosity in the form of bands observed in some metallographic cross sections.

Discussion

High-temperature oxidation of Co-10 w/o Cr results in the formation of a two-layered oxide scale and a small internal oxidation zone. The over-all oxidation is approximately parabolic (9). In this context only a brief qualitative discussion will be made, while a more detailed treatment of the reaction mechanism is presented elsewhere (9).

The outer layer of the scale consists of CoO and the inner layer consists of CoO with dispersed $CoCr_2O_4$ and Cr_2O_3, while the inner oxidation zone involves formation of Cr_2O_3 in the alloy. The scale, particularly the inner layer, contains appreciable porosity. The demarcation between the outer and inner layers represents the original surface of the alloy.

The parabolic oxidation indicates that the reaction is controlled by solid-state diffusion. However, since the scale is two-layered and consists of several oxide phases, the transport through the scale becomes complex.

When considering the solid-state diffusion processes in the scale, the relative rates of diffusion of cobalt, chromium, and oxygen in CoO, Cr_2O_3, and $CoCr_2O_4$ are of primary importance. Available self-diffusion data show that Co diffusion in CoO (10) is more than three orders of magnitude faster than diffusion of Co or Cr in $CoCr_2O_4$ (11,12) and two orders faster than that of Cr in Cr_2O_3 (13). Oxygen diffusion in CoO (14), Cr_2O_3 (15), and , probably, in $CoCr_2O_4$ is slower than that of the cations. In a discussion of the transport processes in the scale growth, solid-state oxygen diffusion can therefore be neglected, and diffusion of the cations through $CoCr_2O_4$ is negligible compared with that of Co in CoO. As in oxidation of unalloyed cobalt (10,15,16), the solid-state Co diffusion in the CoO phase is probably the predominant process in the oxidation, and the presence of the dispersed $CoCr_2O_4$ particles in the inner layer serves to reduce the effective solid-state diffusion area.

If one neglects the surface oxide formed prior to the start of the actual oxidation run, the initial oxidation at atmospheric or subatmospheric pressures probably involves the simultaneous formation of Cr_2O_3 and CoO. After a continuous film is built up, the oxidation becomes diffusion controlled. The microprobe data (Fig. 1) show that the solubility and /or diffusion of Cr in CoO is low; the continued oxidation thus involves Co diffusion outward through the CoO phase by a vacancy mechanism, and reaction with oxygen takes place at the outer surface. In this manner the CoO phase grows on top of the original alloy surface. Simultaneously, oxygen dissolves in the alloy phase and internally oxidizes the chromium to Cr_2O_3. The Cr_2O_3 is formed as discrete particles in the metal in a zone at the scale-metal interface. At the lower temperatures (*e.g.*, 900° and 1000°C), a marked internal oxidation takes place at grain boundaries in the metal, but this preferential internal oxidation at grain boundaries disappears at higher temperatures. With increasing temperature, the Cr_2O_3 particle size increases. The internal oxidation of chromium depletes the alloy phase in chromium, and the metal at the scale-metal interface probably consists of essentially pure Co. The Cr_2O_3 particles are immobile with respect to cobalt; they serve as internal markers, and the first Cr_2O_3 particles (which subsequently react with CoO to form $CoCr_2O_4$) delineate the original alloy surface.

Considerable porosity is formed as a result of the reaction mechanism. After the outer layer of CoO is formed, with the absence of solid-state oxygen diffusion in CoO, oxygen for the internal oxidation can be obtained only through a decomposition of CoO at the metal-scale interface. While the oxygen is consumed in the internal oxidation, the correspondingly formed cobalt ion diffuses outward through the CoO layer. For each oxygen atom that is consumed through internal oxidation, one CoO molecule is simultaneously removed from the CoO layer at the metal-scale interface. This may result in cavity formation at the inner boundary of the CoO layer. This cavity formation is counteracted by a volume increase of the metal due to the internal oxidation and possibly by plastic deformation of the outer CoO layer.

If physical contact remains between the CoO layer and the metal, the Co metal between internal Cr_2O_3 particles will diffuse outward through the CoO scale. However, the Co supply between the Cr_2O_3 particles is limited. Due to slow diffusion through Cr_2O_3, these particles block the supply of cobalt from underlying areas, and the Cr_2O_3 particles probably serve as sites or areas for cobalt vacancy condensation. As a result, cavities or porosity accumulate at the surface of the Cr_2O_3, particularly the surface facing the outer layer.

This porosity correspondingly reduces the available area for solid-state diffusion of cobalt, but it probably does not limit the oxidation, as discussed in the literature (17). The cobalt oxide on the cavity facing the outer surface decomposes; the cobalt diffuses outward, while the oxygen gas is probably rapidly transferred across the cavity to the inner surface, where it in turn reacts with cobalt. In this manner, CoO is formed beneath the original alloy surface. The Cr_2O_3 particles partially become surrounded by pores and partially by CoO. The Cr_2O_3 and CoO gradually react to form the spinel $CoCr_2O_4$. In all the oxide scales examined in this study, spinel rather than Cr_2O_3 is present, while Cr_2O_3 is observed only next to the metal phase. The inner layer of the oxide scale is formed by the combination of the internal oxidation and the transport of gaseous oxygen across the cavities in the inner layer. The outer layer is formed through outward diffusion of cobalt in the areas where the outer layer is in solid contact with the CoO matrix of the inner layer.

It is difficult to estimate accurately the amount of porosity that is formed in the scale. Part of the porosity stems from the vacancy condensation described above. Some of the porosity is also directly related to the alloy composition. Thus, the flux of cobalt ions that react with oxygen at the outer surface is larger than the cobalt flux reacting with oxygen at the scale-metal interface. Since we have 9.6 w/o or 11.7 a/o (atomic per cent) Cr in the alloy, about 17 a/o of the oxygen at this interface is consumed by chromium to form Cr_2O_3. This means that 17% more cobalt ions react with oxygen at the CoO-gas interface than at the scale-metal interface, leaving a corresponding amount of

porosity in the scale. Other factors affecting the porosity are sintering and plastic deformation, both of which will tend to reduce porosity.

In an over-all consideration of the oxidation rate, the blocking of the transport of cobalt within the scale by the spinel phase and the rapid, short-circuiting transport of oxygen across the cavities must be considered. This will be treated in a separate paper (9).

Acknowledgment

This work was supported by NASA under Research Grant NGR-36-002-070.

Manuscript submitted Sept. 3, 1968; revised manuscript received Oct. 28, 1968. This paper was presented at the Montreal Meeting, Oct. 6-11, 1968, as Paper 413.

Any discussion of this paper will appear in a Discussion Section to be published in the December 1969 JOURNAL.

REFERENCES

1. A. Preece and G. Lucas, *J. Inst. Metals*, **81**, 219 (1952-1953).
2. C. A. Phalnikar, E. G. Evans, and W. M. Baldwin, Jr., *This Journal*, **103**, 429 (1956).
3. A. Davin, D. Coutsouradis, and L. Habraken, *Cobalt*, **35**, 69 (1967).
4. Meyer and R. A. Rapp, Ph.D. Dissertation, Ohio State University (1968).
5. C. Wagner and K. E. Zimens, *Acta Chem. Scand.*, **1**, 547 (1947).
6. B. Fisher and D. S. Tannhauser, *J. Chem. Phys.*, **44**, 1663 (1966).
7. J. Paidassi, M. G. Vallée, and P. Pepin, *Mem. Scient. Rev. Met.*, **62**, 789 (1965).
8. J. Krüger, A. Melin, and H. Winterhager, *Cobalt*, **33**, 176 (1966).
9. P. Kofstad and A. Z. Hed, *This Journal*, **116**, 229 (1969).
10. R. E. Carter and F. D. Richardson, *Trans. AIME*, **200**, 1244 (1954); **203**, 335 (1955).
11. A. Morkel and H. Schmalzried, *Z. Phys. Chem. Neue Folge.*, **32**, 76 (1962).
12. R. Sun, *J. Chem. Phys.*, **28**, 290 (1958).
13. W. C. Hagel and A. U. Seybolt, *This Journal*, **108**, 1146 (1961).
14. B. A. Thompson, Ph.D. Dissertation, Rensselaer Polytechnic Institute, 1962, University Microfilms, Ann Arbor, Michigan, 1963.
15. S. Mrowee, T. Walee, and T. Werber, *Bull. Acad. Polon. Sci.*, **14**, 179 (1966).
16. J. A. Snide, J. R. Myers, and R. K. Saxer, *Cobalt*, **36**, 157 (1967).
17. Examples are given in: P. Kofstad, "High Temperature Oxidation of Metals," p. 272, John Wiley & Sons, New York (1966).

High Temperature Oxidation of Co-10 w/o Cr Alloys

II. Oxidation Kinetics

P. K. Kofstad[1] and A. Z. Hed

Metal Science Group, Battelle Memorial Institute, Columbus Laboratories, Columbus, Ohio

ABSTRACT

Thermogravimetric studies of the oxidation kinetics of Co-10 w/o Cr have been carried out in the temperature range 800°-1300°C at oxygen pressures from 0.05 to 760 Torr. The over-all oxidation is parabolic, and the oxygen pressure dependence of the rate constant can be expressed by $k_p \propto p_{O_2}^{1/n}$, where n varies from 3 at 900° to 2.5 at 1300°C. The oxidation is faster than that of pure cobalt. The oxide scale is double-layered and consists of an outer CoO layer and an inner layer of $CoCr_2O_4$ and Cr_2O_3 particles embedded in a CoO matrix. The inner layer also contains 30-35 v/o (volume per cent) porosity. It is concluded that the oxidation is controlled by Co-vacancy diffusion in the CoO-phase. The spinel inclusions inhibit the oxidation by decreasing the effective diffusion area in the scale. The pores partially short-circuit the solid-state diffusion through the scale due to oxygen transport across the pores; the porosity then serves to increase the oxidation. Semiconductor valence effects due to dissolution of chromium in the CoO phase are concluded to be of minor importance as regards the relative oxidation behavior of pure cobalt and Co-10 w/o Cr alloy.

In the previous paper (1) (hereafter referred to as I) the microstructure of scales formed in oxidation of Co-10 w/o (weight per cent) Cr are described. In this paper the results of thermogravimetric oxidation rate studies in the temperature range 800°-1300°C at oxygen pressures ranging from 0.05 to 760 Torr are reported and discussed.

The oxide phases formed in high-temperature oxidation of Co-10 w/o Cr comprise CoO, Cr_2O_3, and $CoCr_2O_4$ (1). In the following is given a brief survey of reported data on the diffusion in these oxides and of oxidation of cobalt.

Literature Survey

Diffusion in CoO, Cr_2O_3, *and* $CoCr_2O_4$.—CoO is a metal-deficient oxide in which metal vacancy defects predominate. From studies of nonstoichiometry and electrical conductivity of CoO as a function of temperature and partial pressure of oxygen, Fisher and Tannhauser (2) have concluded that the cobalt vacancies may be neutral or singly or doubly charged, depending on the temperature and partial pressure of oxygen. Doubly charged vacancies predominate in a region next to the Co-CoO phase boundary, singly charged vacancies are dominant at higher oxygen pressures, and neutral vacancies are important in a region next to the CoO-Co_3O_4 phase boundary. Accordingly the electrical conductivity at near-atmospheric pressures is proportional to $p_{O_2}^{1/4}$ and the self-diffusion of cobalt in CoO (950°-1350°C and 1-10^{-3} atm O_2) is proportional to $p_{O_2}^{1/3}$ at 1 atm O_2 and to about $p_{O_2}^{1/4}$ at 10^{-3} atm O_2 (2-4). At an oxygen pressure of 5 x 10^{-3} atm, i.e., when the vacancy concentration and diffusion coefficient is proportional to $p_{O_2}^{1/4}$, the Co-tracer diffusion coefficient is given by $D_{Co}^{T} = 1.7 \times 10^{-3} \exp(-38{,}000/RT)$. The observed activation energy of 38 kcal/mole partially represents the activation energy of diffusion of the vacancies

[1] Present address: Central Institute for Industrial Research, Blindern, Oslo, Norway.

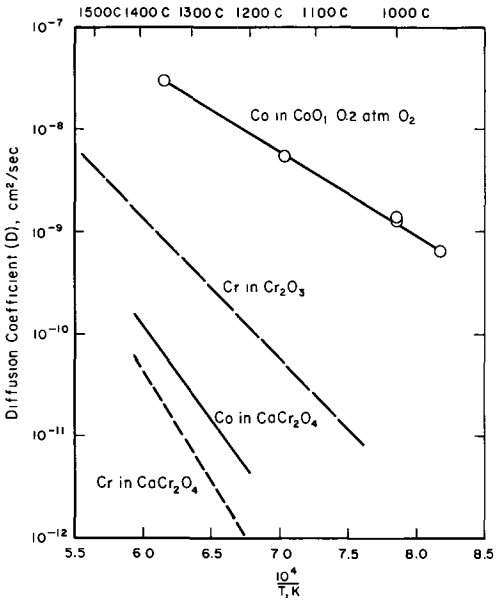

Fig. 1. Comparative plots of cation diffusion in CoO, Cr_2O_3, and $CoCr_2O_4$.

(~30-32 kcal/mole) and partially the heat of formation of the singly charged vacancies (4). The temperature dependence of $D_{Co}{}^T$ at 0.2 atm O_2 is shown in Fig. 1. The oxygen diffusion coefficient in CoO has been found to be three orders of magnitude lower than that of cobalt at high temperature (5, 6).

The defect structure and diffusion mechanism in Cr_2O_3 have not been unequivocally determined (7-14). However, Cr ions are the faster moving ionic species in Cr_2O_3, and the diffusion coefficient of Cr is approximately three orders of magnitude faster than that of oxygen at high temperatures (9, 14). Cr-diffusion is sensitive to pretreatment of the oxide specimens (hot-pressing *vs.* sintering) and probably to impurity content (9). Hagel and Seybolt (9) found that the self-diffusion coefficient of chromium is independent of oxygen pressure. They suggest that the best value for the tracer self-diffusion coefficient is given by $D_{Cr}{}^T = 0.167 \exp(-61{,}100/RT)$ (Fig. 1).

$CoCr_2O_4$ is a normal spinel. It may be nonstoichiometric with its composition ranging from $CoCr_2O_4$ to $Co_{1.3}Cr_{1.8}O_4$ at 1200°-1400°C (15). Although the exact diffusion mechanism is not known, the diffusion coefficients of the cations in the $CoCr_2O_4$ phase are appreciably slower than in Cr_2O_3 (15, 16). This is illustrated in the comparative plot in Fig. 1. As regards potential protective properties in compact oxide scales, the spinel phase is expected to be by far the best oxide.

Oxidation of cobalt.—The oxidation of high-purity cobalt above 950°C results in the formation of a compact scale of CoO (4, 9, 17-20). The oxidation follows a parabolic rate equation

$$\frac{dx}{dt} = \frac{k_p}{x} \qquad [1]$$

where x is the scale thickness, t is time, and k_p the parabolic rate constant. For dense scales x is related to the total weight gain, Δm, through $x = (\Delta m)/YdA$, where Y is the average weight fraction of oxygen in the oxide, d is the oxide density, and A is the surface area.

Through the Wagner theory k_p can be expressed in terms of the diffusion coefficient of cobalt in CoO. Experimental and calculated values of k_p are in good agreement (4). k_p is approximately proportional to $p_{O_2}{}^{1/3}$ at 1-10^{-2} atm. Below 950°C formation of Co_3O_4 takes place at high oxygen pressures. When CoO-

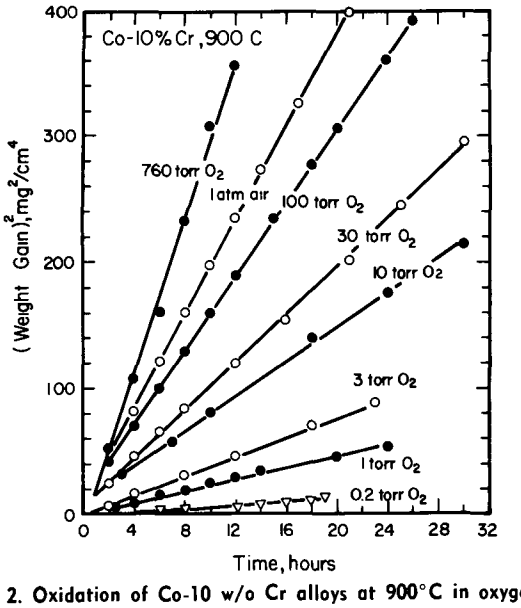

Fig. 2. Oxidation of Co-10 w/o Cr alloys at 900°C in oxygen at pressures from 0.2 to 760 Torr oxygen. Parabolic plot.

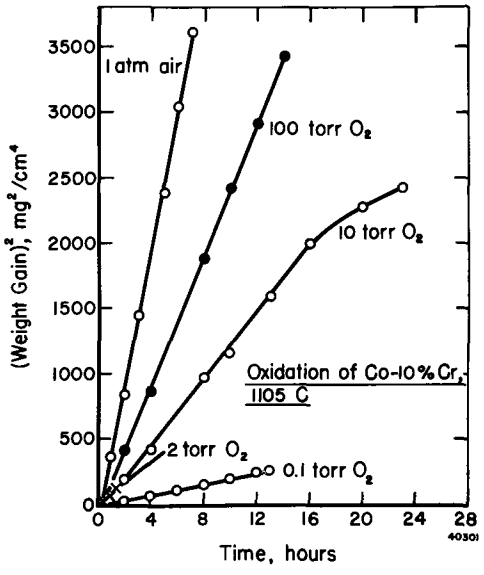

Fig. 3. Oxidation of Co-10 w/o Cr alloys at 1105°C in oxygen at pressures from 0.1 to 100 Torr oxygen. Parabolic plot.

Co_3O_4 scales are formed, k_p becomes independent of the ambient partial pressure of oxygen (4).

Experimental Results

The experimental procedure has been described in I. The results of the thermogravimetric studies are presented in Fig. 2-8. Figures 2, 3, and 4 show parabolic plots of the oxidation of Co-10 w/o Cr at different oxygen partial pressures from 0.1 to 760 Torr at temperatures of 900°, 1105°, and 1200°C, respectively. In all cases the oxidation is well described by a parabolic rate equation. Under some conditions (*e.g.*, at 100 Torr O_2, at 1200°C), one observes breaks or periodic changes within the over-all parabolic oxidation.

The oxidation exhibits a marked oxygen-pressure dependence. This is illustrated in Fig. 5, in which the parabolic rate constant is plotted as function of p_{O_2}. The pressure dependence can be expressed by $k_p \propto p_{O_2}{}^{1/n}$,[2] where n gradually changes from approximately 3 at 900°C to 2.5 at 1300°C. This pressure dependence is similar to that for oxidation of unalloyed cobalt with CoO scales, although for cobalt oxidation the values of n tend to be slightly higher.

In the temperature range 900°-1300°C, the Co-10 w/o Cr alloy oxidizes faster than unalloyed cobalt.

[2] k_p in Fig. 5 is related to k_p in Eq. [1] by the factor $(yd)^{-2}$.

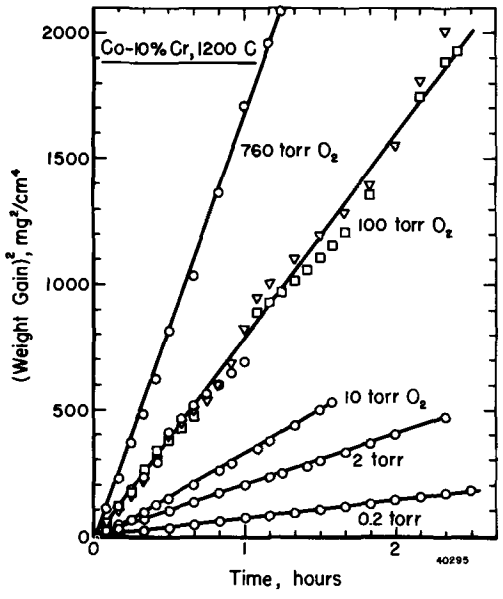

Fig. 4. Oxidation of Co-10 w/o Cr alloys at 1200°C in oxygen at pressures from 0.2 to 760 Torr oxygen. Parabolic plot.

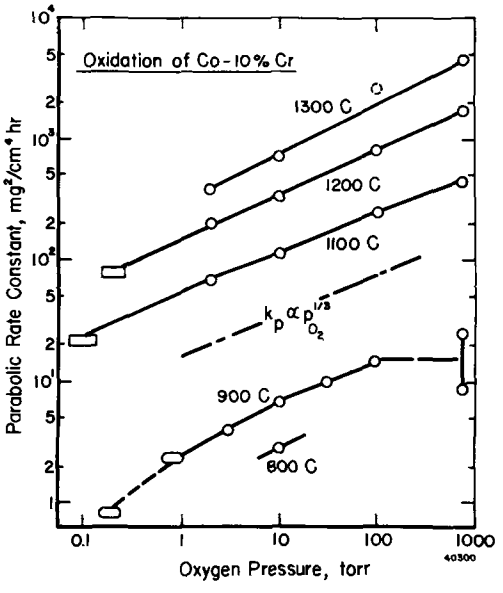

Fig. 5. Parabolic rate constants for oxidation of Co-10 w/o Cr alloys as a function of oxygen pressure at temperatures ranging from 800° to 1300°C.

This is illustrated in Fig. 6, which shows a comparative Arrhenius plot of the parabolic rate constant for oxidation of the Co-10 w/o Cr alloy and of unalloyed cobalt at 100 Torr oxygen. The activation energy for oxidation of the alloy is greater (~46 kcal/mole) than that for oxidation of unalloyed cobalt (35 kcal/mole), and thus the alloy oxidizes progressively faster with increasing temperature as compared with unalloyed cobalt.

At oxygen pressures below 0.1 Torr the oxidation tends to deviate from parabolic behavior during the initial oxidation. This is illustrated in Fig. 7, which shows a linear plot of the oxidation of the Co-10 w/o Cr alloy at 0.05 Torr O_2 at 900°, 1000°, 1100°, and 1200°C, respectively. At the three lower temperatures the oxidation tends to be linear.

After longer periods of oxidation the initial linear oxidation gradually transforms to parabolic oxidation. This is shown in the combined linear and parabolic plot of extended oxidation at 900°C and 0.05 Torr O_2 in Fig. 8.

Discussion

Although the oxidation kinetics of unalloyed cobalt and the Co-10 w/o Cr alloy are similar, they differ in

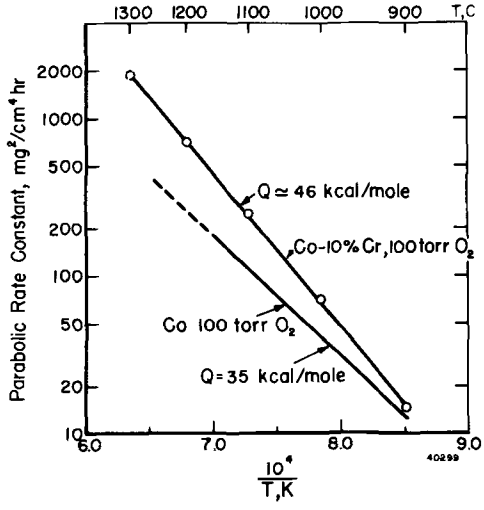

Fig. 6. Arrhenius plot of the parabolic rate constant for oxidation of Co-10 w/o Cr and of unalloyed cobalt at 100 Torr oxygen.

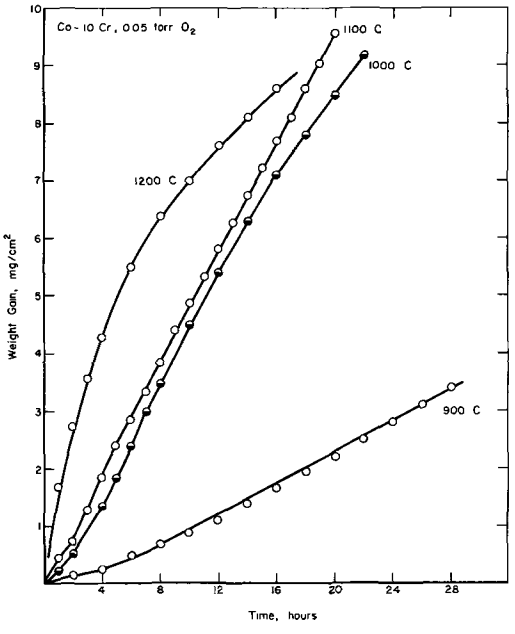

Fig. 7. Oxidation of Co-10 w/o Cr alloys in 0.05 Torr oxygen in the range 900° to 1200°C. Linear plot.

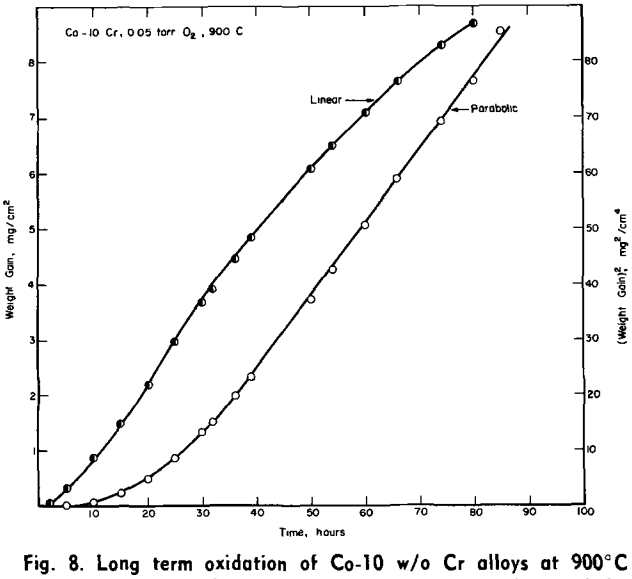

Fig. 8. Long term oxidation of Co-10 w/o Cr alloys at 900°C in 0.05 Torr oxygen. The scale on the right refers to the parabolic plot (circles), the scale on the left refers to the linear plot (half filled circles).

some respects: (*i*) above 900°C the alloy oxidizes faster than does cobalt, (*ii*) the activation energy for the alloy is higher than for cobalt (~46 *vs.* 35 kcal/mole), and (*iii*) the results suggest a slightly higher oxygen pressure dependence of k_p for the alloy than for cobalt.

It is concluded that a cation diffusion in the CoO phase is rate-determining in oxidation of both cobalt and the alloy (1). From this over-all consideration it may be speculated whether the differences in oxidation are completely or partially due to the effect of dissolved trivalent chromium in the CoO phase and the corresponding changes in defect concentrations and diffusion characteristics. If this effect is to be important, the solubility of chromium must be higher than the native cobalt vacancy concentration in pure CoO. The nonstoichiometry amounts to about 1% at 1200°C and 1 atm O_2.

There are no definite data available on the chromium solubility in CoO. However, the microprobe studies on scales of oxidized Co-10 w/o Cr specimens suggest a solubility less than 0.1 w/o Cr. Even if the solubility is higher than this by a factor of ten, it is difficult to explain the results at higher temperatures in terms of the semiconductor valence approach. Such considerations also completely fail to explain a gradual increase of the oxidation rate with increasing chromium concentration from pure cobalt to Co-10 w/o Cr as observed by Phalnikar *et al* (21). We conclude that semiconductor valence effects are of no or of minor importance in explaining the differences in oxidation behavior between pure cobalt and the Co-10 w/o Cr alloy. As noted in I, the same considerations also apply to dilute Ni-Cr alloys. We propose in the following that the differences are due to the differences in composition, microstructure, and porosity of the oxide scales.

The oxide scales on the alloy are double-layered; the outer layer consists of CoO and the inner layer of a CoO matrix with inclusions of $CoCr_2O_4$ (and of Cr_2O_3 near the metal-scale interface) (1). The inner layer, in addition, contains 30-35% porosity. Due to the low diffusion rates in $CoCr_2O_4$ and Cr_2O_3 compared to that of Co in CoO (Fig. 1), the inclusions serve as diffusion barriers and decrease the total cross-sectional area available for transport of the reactants through the scale. The pores, on the other hand, may increase the oxidation, as gaseous oxygen can be transported across the pores, and the gas transport serves to partially short-circuit the solid-state diffusion in the scale (22). When the gas transport is rapid, the oxidation may still be solid-state diffusion-controlled and parabolic, as is found in this work. The blocking of the spinel and the gas transport across the pores are proposed to be the main reasons for the difference in oxidation behavior between cobalt and dilute Co-Cr alloys.

When expressing these effects in terms of a mathematical model, one should as regards the blocking of the spinel consider the morphology, particle size, and distribution of the spinel in the scale. As described in I these factors are a function of temperature, pretreatment of the specimens, and, to some extent, the partial pressure of oxygen. An accurate and detailed description appears to be extremely complicated, and we will at this stage only propose an approximate and general model. The blocking effect of the spinel will depend on the average cross-sectional area of the spinel relative to the total area, and this will in turn depend on the total volume and the particle size of the spinel.

The volume of the spinel relative to that of the entire scale in the temperature range studied is probably only a weak function of temperature. The justification for this statement is that the microprobe studies revealed no marked chromium gradient in the scale and no extensively chromium depleted regions in the alloy at the alloy-scale interface. After the double-layered scale is formed, cobalt and chromium are, as a first approximation, consumed at the same relative rates. Cr_2O_3 is observed as an internal oxide and is present in the scale close to the alloy-scale interface. In the oxide the Cr_2O_3 rapidly reacts with CoO to form the spinel. In the following it will be assumed that the relative amount of Cr_2O_3 and $CoCr_2O_4$ in the total scale is a constant and is independent of temperature.

The size of the spinel particles increases with temperature (1). Their size will partially be governed by the size of the internally formed Cr_2O_3 particles and partially by the subsequent reaction of these with CoO. It is not unreasonable to assume that the processes governing the growth of the spinel particles are thermally activated or diffusion-controlled and that the size is an increasing exponential function of temperature.

Only one plane parallel to the alloy surface needs to be considered for the blocking effect of the spinel; obviously that plane is the one in which the cross-sectional area of the spinel is the largest in the scale. Since all the spinel particles in this plane had a similar history of growth, their size distribution will be relatively narrow. It is not unreasonable, therefore, to describe this dispersion by a sum of equal particles with a single size parameter r. One may then postulate

$$r = r_0 \exp(-Q/RT) \qquad [2]$$

where Q is the activation energy associated with the increase of r with temperature. Q cannot yet be evaluated, since the processes involved in the growth of Cr_2O_3 and spinel are not established.

The total volume of the spinel is proportional to r^3, while the surface area and the blocking cross-section, S, are proportional to r^2. When the total volume is constant with temperature, S can be expressed in terms of r

$$S = \frac{B}{r} = S_0 \exp(Q/RT) \qquad [3]$$

B is a constant which includes the volume of the spinel and a geometrical factor. As a first approximation it is assumed that the shape of the spinel particles do not change with temperature, and S_0 is therefore constant. The available cross-section for diffusion of cobalt through the scale is decreased by the amount S. When this effect is included in the expression for growth of CoO on pure cobalt (Eq. [1]), one obtains

$$\frac{dx}{dt} = k_p \frac{\left[1 - \frac{S_0}{A}\exp\left(\frac{Q}{RT}\right)\right]}{x} = \frac{k_p'}{x} \qquad [4]$$

where the blocking effect is expressed per unit area to retain the units. The effect of the spinel relative to that of cobalt according to Eq. [4] is illustrated schematically in Fig. 9. It should be noted that Eq. [4] does not predcit a straight-line relationship in an Arrhenius plot of the parabolic rate constant k_p', but within experimental errors and reproducibility this deviation may in many cases be difficult to determine. Since many pairs of S_0 and Q can yield the observed behavior, it is impossible at this stage to speculate on the actual values of S_0 and Q.

Although the pores serve as a barrier to the solid state diffusion, it is concluded, as discussed above and in I, that the pores enhance oxidation through rapid gaseous transport of oxygen across the pores. This gaseous transport may be considered to partially short-circuit the solid state diffusion in the scale. In terms of Eq. [4], this means that the total diffusion length x is shortened by the total pore length in a line perpendicular to the surface. If one assumes as a first approximation that the pore volume relative to the scale volume is a weak function of temperature, the reduction in the solid state diffusion length can

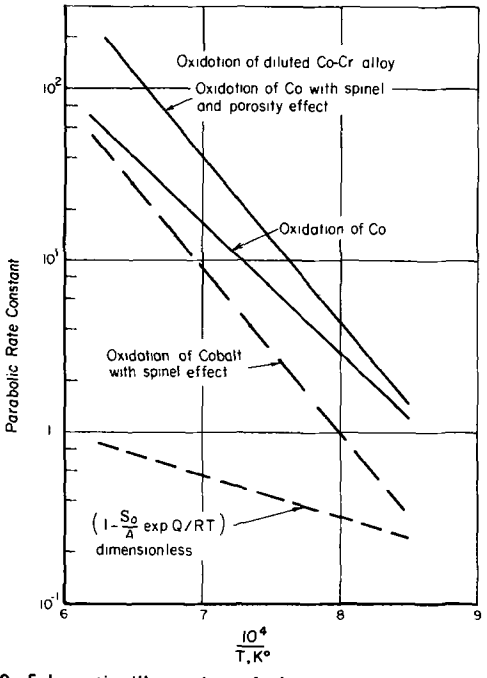

Fig. 9. Schematic illustration of the effects of spinel blocking and gaseous oxygen transport across pores on the oxidation behavior.

be expressed by $x\ (1-\gamma)$. γ is then approximately constant with temperature and depends on pore geometry and is proportional to the cube root of the fraction of the pore volume. With such a correction Eq. [4] takes the form

$$\frac{dx}{dt} = k_p \frac{\left[1-\frac{S_o}{A}\exp\left(\frac{Q}{RT}\right)\right]}{x(1-\gamma)} = \frac{k_p''}{x} \qquad [5]$$

The effect of the gaseous transport is to increase the oxidation rate as illustrated schematically in Fig. 9 ($\gamma = 0.77 = 1.1\ \sqrt[3]{0.32}$). Furthermore, the combined effects of spinel blocking and gaseous transport across scales may explain the oxidation behavior of Co-10 w/o Cr relative to that of cobalt.

At this stage Eq. [5] only represents an approximate phenomenological description of the oxidation of dilute Co-Cr alloys. It is as yet difficult to verify the details of the model through independently measured parameters, but it is believed that the main concepts provide a correct description of the over-all oxidation behavior. Some effects which have been observed experimentally were not accounted for in Eq. [5]. These include the preferential decoration by spinel at the original alloy grain boundaries in the oxide scales (1) at low temperature and low pressures. This effect cannot be dealt with mathematically; however, it is not inconsistent with the kinetic results and the role ascribed to the spinel. We observed in I that the spinel decoration is enhanced at low pressures; this will result in more effective blocking of Co diffusion and therefore lower k_p. This feature can explain the larger n (in $k_p = C\ p_{O_2}^{1/n}$) observed for the oxidation of the alloy.

The origin of this preferential decoration is due to the decreased outward migration of cobalt with decreasing pressure and a corresponding tendency for a preferential oxidation of chromium and a relatively larger amount of the spinel in the scale. For the same reason internal oxidation becomes more pronounced with decreasing oxygen pressure. At very reduced partial pressures of oxygen, *e.g.*, by oxidation in H_2/H_2O atmospheres, selective oxidation of Cr is to be expected as, for instance, observed in Ni-Cr alloys.

The fluctuations around the parabolic behavior, very marked at 1200°C and 100 Torr O_2 (Fig. 4), are probably a side effect. It is not unreasonable to ascribe this to the alleviation of stresses that cause local loss of adherence, producing marked lines of porosity in the scale.

In one of the three runs, the number of marked striations in the scale was found to be equal to the number of cycles in the weight gain. We do not understand, however, why this behavior was so marked at the special conditions, 1200°C and 100 Torr O_2. (Three different runs exhibited the same cyclic behavior, while for other temperatures and pressures this cycling is not so pronounced.

The oxidation of Co-Cr alloys with more than 10 w/o Cr decreases with increasing Cr-content. This is concluded to be due to the fact that an increasingly larger part of diffusion cross-section consists of the spinel, and a minimum in the oxidation rate for Co-Cr alloys are reached when essentially the whole scale consists of the spinel. These features will be discussed elsewhere in connection with the oxidation behavior of Co-25 w/o Cr (23).

With decreasing oxygen pressures it is a general phenomenon in oxidation of metals that phase boundary reactions at the scale surface become increasingly important during initial oxidation, and at very reduced pressures the reaction becomes diffusion controlled only after a relatively thick scale has been built up. This behavior is observed in this study during oxidation at 0.05 Torr (Fig. 7 and 8).

Conclusions

We conclude in this work that the mechanism governing the oxidation of Co-10 w/o Cr at high temperatures is solid-state diffusion of Co cations in the inner layer of a CoO network via a vacancy mechanism. This diffusion is influenced by two factors: (*i*) the porosity of the inner layer, which enhances oxidation, and (*ii*) spinel inclusions, which inhibit oxidation. The first effect is almost temperature independent, while the second effect decreases with increasing temperatures, due to the growth of the spinel particles. The oxygen-pressure dependence of the parabolic rate constants results mainly from the defect structure known in CoO; however, due to enhanced preferential-internal-oxidation grain boundaries at low pressures, the values of n in $k_p = C\ p_{O_2}^{1/n}$ are slightly smaller than those for pure CoO. Semiconductor valence effects due to dissolution of chromium in the CoO phase are believed to have minor or no influence on the oxidation rate of Co-10 w/o Cr alloys. At very low pressures, phase boundary reactions are of great importance for relatively long initial periods.

Acknowledgment

This work was partially supported by NASA under NGR 36-002-070. The authors wish to thank Mr. R. O. Dodds who carried out a large part of the experimental work.

Manuscript submitted Sept. 3, 1968; revised manuscript received Oct. 28, 1968. This paper was presented at the Montreal Meeting, Oct. 6-11, 1968, as Paper 413.

Any discussion of this paper will appear in a Discussion Section to be published in the December 1969 JOURNAL.

REFERENCES

1. P. K. Kofstad and A. Z. Hed, *This Journal*, **116**, 224 (1969).
2. B. Fisher and D. S. Tannhauser, *J. Chem. Phys.*, **44**, 1663 (1966).
3. R. E. Carter and F. D. Richardson, *Trans. AIME*, **200**, 1244 (1959); **203**, 336 (1956).
4. P. Kofstad, "High Temperature Oxidation of Metals," John Wiley & Sons, New York (1966).
5. B. A. Thompson, Ph.D. Dissertation, Rensselaer, Polytechnic Institute, 1962, University Microfilms, Ann Arbor, Michigan, 1963.
6. J. B. Holt, *Proc. Brit. Ceram. Soc.*, **9**, 157 (1967).
7. K. Hauffe and J. Block, *Z. Phys. Chem.*, **198**, 232 (1951).

8. W. A. Fischer and G. Lorenz, *Arch. Eisenhüttenw.*, **28**, 497 (1957).
9. W. C. Hagel and A. U. Seybolt, *This Journal*, **108**, 1146 (1961).
10. J. A. Crawford and R. W. Vest, *J. Appl. Phys.*, **35**, 2413 (1964).
11. W. A. Fischer and G. Lorenz, *Z. Phys. Chem. Neue Folge*, **18**, 308 (1958).
12. R. Lindner and A. Åkerström, *ibid.*, **6**, 162 (1956).
13. L. C. Walters and R. E. Grace, *J. Appl. Phys.*, **8**, 2331 (1965).
14. W. C. Hagel, *J. Am. Ceram. Soc.*, **48**, 70 (1965).
15. A. Morkel and H. Schmalzried, *Z. Phys. Chem. Neue Folge*, **32**, 76 (1962).
16. R. Sun, *J. Chem. Phys.*, **28**, 290 (1958).
17. J. A. Snide, J. R. Myers, and R. K. Saxer, *Cobalt*, **36**, 157 (1967).
18. J. Paidassi, M. G. Vallée, and P. Pepin, *Mem. Sci. Rev. Met.*, **62**, 789 (1965).
19. D. W. Bridges, J. P. Baur, and W. M. Fassell, Jr., *This Journal*, **110**, 614 (1963).
20. J. Krüger, A. Melin, and H. Winterhager, *Cobalt*, **33**, 176 (1966).
21. C. A. Phalnikar, E. W. Evans, and W. M. Baldwin, Jr., *This Journal*, **103**, 429 (1956).
22. A. Brückman, *Corrosion Science*, **7**, 51 (1967).
23. P. K. Kofstad and A. Z. Hed, *This Journal*, **116**, 224 (1969).

Preparation, Optical and Dielectric Properties of Vapor-Deposited Niobium Oxide Thin Films

M. T. Duffy, C. C. Wang,* A. Waxman, and K. H. Zaininger

RCA Laboratories, Radio Corporation of America, Princeton, New Jersey

ABSTRACT

Thin dielectric films of niobium oxide have been deposited on silicon and quartz substrates by pyrolysis of the niobium alcoholate $Nb(OC_2H_5)_5$ at 450°C in an oxidizing ambient. Optical measurements have been made on these films in the spectral range 0.2-2.6 μm. Information on dispersion, fundamental absorption edge, and absorption coefficient (as related to photon energy) has been obtained. An electrical evaluation of the films has been made, including dielectric properties and MOS behavior.

The recent advances in the technology of microelectronics have led to extensive research on the physical, chemical, and electrical characteristics of MOS structures (1). Studies (2) on the SiO_2-Si system have shown the important role of the insulator-semiconductor interface in determining device behavior. The stringent requirements imposed on thin film dielectrics, including surface passivation, diffusion masking, radiation resistance, and varied applications, have stimulated interest in noncrystalline dielectric materials other than SiO_2 (1).

It is the purpose of this paper to report the preparation, structural, optical, and dielectric properties of niobium oxide thin films, MOS (metal-oxide-silicon) structures using this oxide have been fabricated and evaluated. The results of the MOS characteristics are reported.

Experimental

Thin film deposition.—Thin dielectric films of niobium oxide have been deposited on silicon, germanium, and quartz substrates by the pyrolysis of the niobium-alcoholate, $Nb-(OC_2H_5)_5$, in an oxidizing ambient. The alcoholate vapors were transported to the rf-heated substrates by helium carrier gas. Deposition conditions were optimized by varying the alcoholate vapor pressure, the deposition temperature, and total flow rate of gases. The following deposition parameter values gave uniform coherent films:

Substrate temperature:	450°C
Niobium-alcoholate source temperature:	115°C
Helium carrier flow rate:	325 cc/min
Other gases: helium flow rate:	2500 cc/min
oxygen flow rate:	820 cc/min

Faster flow rates than indicated here favored heavy deposition at the center of the substrate, while slower flow rates favored deposition at the periphery of the substrate.

The deposition apparatus is illustrated in Fig. 1. The reaction chamber is made of quartz and has a length of 20 cm and an internal diameter of 35 mm. A graphite susceptor having a pyrolytic graphite coating was used for heating the substrates. It was cylindrical in shape, 1¼ in. diameter and ¾ in. long. The apparatus was arranged in the vertical position and the vapor path between generator and deposition chamber was kept as short as possible. Air or water was circulated through the outer jacket of the depo-

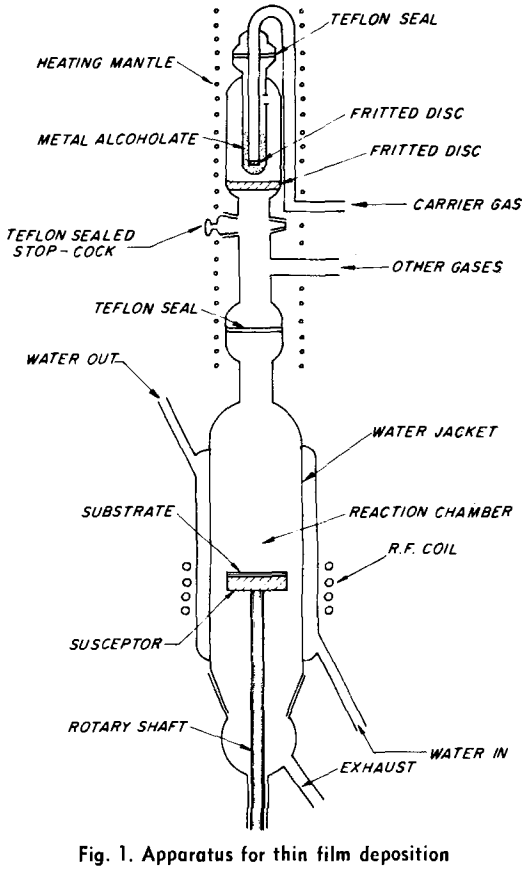

Fig. 1. Apparatus for thin film deposition

* Electrochemical Society Active Member.

sition chamber to cool the inner tube. The susceptor was rotated at 10 rpm during film formation in order to facilitate uniform deposition. Silicon substrates had residual SiO_2 films of about 30Å prior to deposition. This oxide thickness was measured by ellipsometry after the cleaning procedure.

Optical measurements.—Transmission measurements were made on films deposited on quartz substrates in the spectral range 0.2-2.6 μm using a Cary Model 14 spectrometer with a similar quartz substrate in the reference beam. Ellipsometric measurements were made to determine film thickness and refractive index at the mercury wavelength 5461Å in the case of films thinner than 2000Å. Film thickness in excess of 2000Å was determined from the conditions for maxima and minima in the transmittance curves using the refractive index values obtained by ellipsometry. The conditions are (3):

$$T = T_{max} \quad \text{for} \quad n_1 d = (2m + 2)\,\lambda/4$$

$$T = T_{min} \quad \text{for} \quad n_1 d = (2m + 1)\,\lambda/4$$

when $n_2 \gtrless n_1 \lesseqgtr n_0$; where T is the transmittance, n_0, n_1, and n_2 the refractive indices of air, film, and substrate, respectively. The factor m is an integer, d the film thickness, and λ the corresponding wavelength of light.

From the above results, information on optical dispersion, absorption coefficient, fundamental absorption edge, and interband transition has been obtained.

Dispersion data were obtained from the conditions for maxima and minima in transmittance and the calculated thickness of the films. The absorption coefficient has been obtained from transmittance and dispersion curves using the relationship (4)

$$T = I/I_0 = \frac{(1-R)^2}{e^{\alpha d} - R^2 e^{-\alpha d}} \qquad [1]$$

which includes effects of multiple internal reflection but excludes interference effects which cause variation of transmittance with wavelength; T is the transmittance, α the absorption coefficient, R the reflectivity, d the film thickness, and I/I_0 the ratio of transmitted and incident intensities.

MIS measurements.—A variety of methods is available to determine electrical properties of the MIS system such as density, capture cross section and response time of interface states, surface recombination velocity, and surface mobility. We have restricted ourselves to the MIS capacitance (C-V) (5-7) and MIS conductance (G-V) (8) techniques. These are by far the most frequently employed methods due to the simplicity of fabricating test structures, the ease of making (automatic) measurements, and the extent of information that can be obtained.

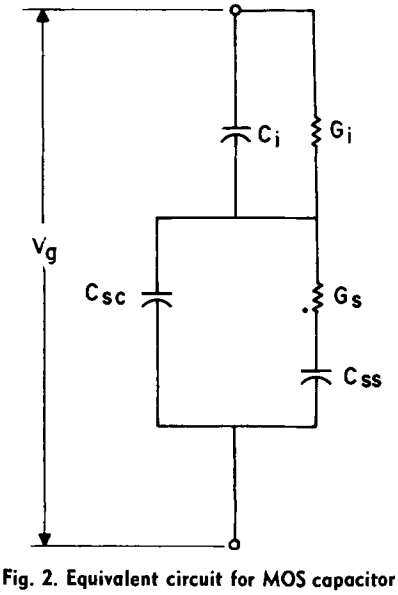

Fig. 2. Equivalent circuit for MOS capacitor

Equivalent circuit of MIS capacitor.—In order to be able to interpret the results of such measurement, a useful equivalent circuit has to be available. The impedance of an MIS capacitor has been derived by several authors (9, 10). However, their equivalent circuits are as complicated as the mathematical models they used and are of little practical use. The circuits have to be simplified considerably if they are to be useful in interpreting experimental results. A generally accepted simplified equivalent circuit that accounts for oxide loss and interface states has been derived and is shown in Fig. 2. C_i and G_i represent the capacitance and conductance of the insulator, C_{sc} is the capacitance of the semiconductor space charge region, and G_s and C_{ss} are the conductance and capacitance, respectively, associated with interface states, all per unit area. For n-type material C_{sc} is given by (11, 12)

$$C_{sc} = \frac{\epsilon_s}{\lambda_n} \frac{\left(1 - e^{+q\psi_s/kT} + \frac{P_B}{N_D} e^{-q\psi_s/kT}\right)}{\left(e^{q\psi_s/kT} - \frac{q\psi_s}{kT} - 1 + \frac{P_B}{N_D} e^{-q\psi_s/kT}\right)^{1/2}} \qquad [2]$$

where ψ_s is the semiconductor surface potential, ϵ_s the semiconductor dielectric constant, k is the Boltzmann constant, T is the temperature, q is the electronic charge, P_B the bulk density of holes, and N_D is the donor concentration. The Debye-length λ_n is defined by (12)

$$\lambda_n^2 = \frac{2(kT/q)\epsilon_s}{N_D q} \qquad [3]$$

The calculation of the a-c conductance for interface states for any type of distribution of states has been derived (13) and yields the following expression:

$$G_s = \frac{\omega^2 q^2}{kT} \int_{E_i}^{E_F} \frac{\tau(E_t) N_{ss}(E_t)\, f(E_t)\,[1 - f(E_t)]}{1 + \omega^2 \tau^2(E_t)}\, dE_t \qquad [4]$$

where ω is the radian frequency of measurement, $N_{ss}(E_t)$ is the density of states/cm²-ev, f is the Fermi function. The expression $\tau(E_t)$ is given by

$$\tau(E_t) = \frac{f(E_t)}{\sigma(E_t) <V_n> n_s} \qquad [5]$$

where $\sigma(E_t)$ is the capture cross section of the states at energy E_t, $<V_n>$ is the thermal velocity, and n_s is the density of electrons at the interface.

The high-frequency MIS capacitance method.—It is quite clear that the performance of the equivalent circuit discussed above is a function of frequency, and that measurements made at an arbitrary frequency could lead to erroneous conclusions. If the measuring frequency is sufficiently high so that surface states cannot follow the applied signal, then the surface state capacitance becomes zero (12), and the MIS capacitance reduces to its high-frequency form, *i.e.*, the series combination of C_i and C_{sc}. When this condition is satisfied, then the MIS capacitance is unambiguously related to the semiconductor surface potential. However, there is a difference between an experimentally determined high-frequency C-V characteristic and one computed for an identical structure without surface states, and that is the voltage due to the total charge in surface states. By finding the difference between the measured voltage for a given capacitance (and thereby ψ_s) and its "ideal" value, ΔV, one can determine the total charge that can be trapped in surface states during the measurement period and the surface state density as a function of ψ_s (or energy). The effective density of surface states, as reflected to the insulator-semiconductor interface, N_{ss},

is then given for any particular value of capacitance (and thereby ψ_s) as

$$N_{ss} = \frac{C_i \Delta V}{1.6 \times 10^{-19}} = \frac{(\epsilon_i \Delta V)}{(1.6 \times 10^{-19} t_i)} \quad [6]$$

where ϵ_i and t_i are the insulator dielectric constant and thickness, respectively. If the experimental curve lies toward more negative voltage than the ideal one, the charge in surface states is positive; if it lies toward more positive voltage, the charge is negative. A typical example of a comparison between experimental and ideal curves is shown in Fig. 3.

For the use of the MIS capacitance technique in the study of surface properties various assumptions and approximations have been made in the past which are not always justified. However, it has been shown (7) that MIS capacitance measurements can yield interesting and meaningful results if the proper experimental conditions are established and care is taken in the interpretation of the experimental results. Thus, we use the C-V technique cognizant of its limitations (7).

The actual measurement of the samples is carried out at a frequency of 1 MHz using an automatic C-V plotter. This system has been described previously (14).

The MIS conductance technique.—An alternate technique which is useful in making quantitative determinations of interface states in MIS structures is the measurement of the dependence of the a-c conductance on measurement frequency and applied bias. As indicated in the equivalent circuit in Fig. 2, interface states contribute an a-c loss due to the inability of charge in the states to follow an applied a-c signal. The lag occurs because of the finite time it takes carriers to move in and out of interface states. The conductance due to this effect is given in Eq. [4]. This equation has the following general features:

1. At any given test frequency, the maximum contribution that a state makes to the conductance occurs when the semiconductor Fermi level is at the energy of the state.
2. At a given surface potential, the expression G_s/ω, that is the ratio of the conductance to the radian frequency, peaks at a radian frequency given by $\omega\tau = 1.98$ and $G_s/\omega = 0.4\ qN_{ss}\ A$ (A is the area).
3. The time constant of the state is inversely proportional to the surface density of electrons at a given surface potential.

The measured a-c conductance can be used in conjunction with the equivalent circuit in Fig. 2 to obtain the dependence of G_s on frequency, at a given voltage. An analysis of the equivalent circuit in Fig. 2 yields the following expression for G_s.

$$G_s = G_m \left(1 + \frac{C_{sc}}{C_i}\right)^2 - G_i \left(\frac{C_{sc}}{C_i}\right)^2 \quad [7]$$

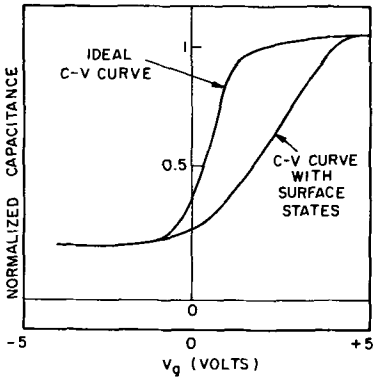

Fig. 3. Comparison between ideal and experimental C-V curves for an n-type MOS capacitor.

where G_m is the measured a-c conductance at a given voltage, and G_i, C_{sc}, and C_i are also determined for this applied voltage.

Since $G_s/\omega = 0.4\ qN_{ss}\ A$ at $\omega\tau = 1.98$, the surface state density can be determined as a function of surface potential and, hence, energy.

The samples are measured using an automatic C-V and G-V plotter which makes use of a phase-sensitive detector. Data can be taken from 10 Hz to 100 kHz. This system has been described elsewhere (15).

Dielectric constant measurement.—The determination of the dielectric constant of an insulating film is normally carried out by determining the capacitance of a parallel plate capacitor made from this material, coupled with a measurement of the capacitor area and insulator thickness. When one of the plates is a semiconductor instead of a metal, the measurement is only then meaningful if it can be assured, by the application of the proper bias, that the semiconductor surface is in heavy accumulation (or inversion).

Our measurements were carried out using the automatic measurement arrangements mentioned above as well as a Boonton Electronics and a GR-1608 Impedance Bridge while maintaining the above conditions. The measurements on adherent contacts of known area were all three-terminal capacitance measurements which yield the direct capacitance between the two plates, excluding all stray capacitances that may exist to other parts of the structure. The thickness of the insulating film was determined by the use of an ellipsometer.

Results and Discussion

Niobium oxide films with thicknesses ranging from 500 to 3000Å have been obtained. The deposition rate was usually ~70-80 Å/min using the flow rates previously mentioned. The films were inert to most acids but could be etched in dilute HF, giving an etch rate of 60 Å/min in 1:4/HF:H_2O.

Structure of films.—The surface structure of the films was examined using the scanning electron microscope. The films have extremely smooth surfaces as shown in the electron micrographs (Fig. 4). No film deterioration was observed as a result of the electron beam. Low glancing angle electron diffraction patterns [Fig. 5(a)] indicated that the films were amorphous. Films, which were annealed in He at 850°C, still showed an amorphous structure as revealed by the electron diffraction pattern [Fig. 5(b)]. However, a film which was removed from the susceptor after heating to >1200°C in inert gas gave an x-ray powder

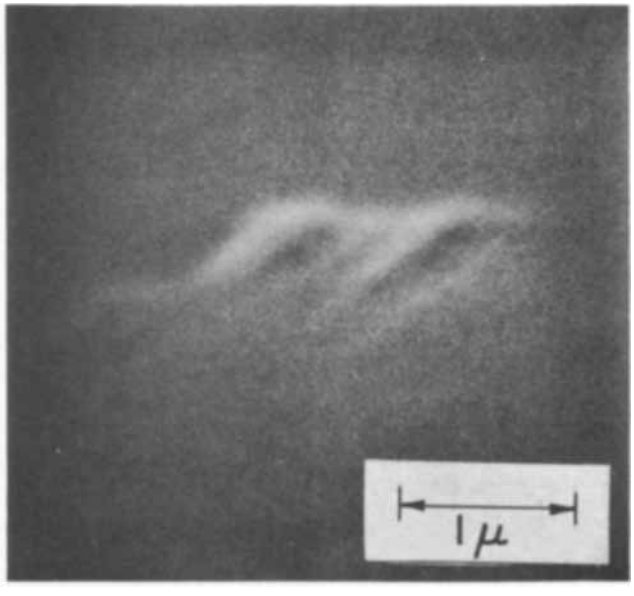

Fig. 4. Scanning electron micrograph of thin film Nb_2O_5

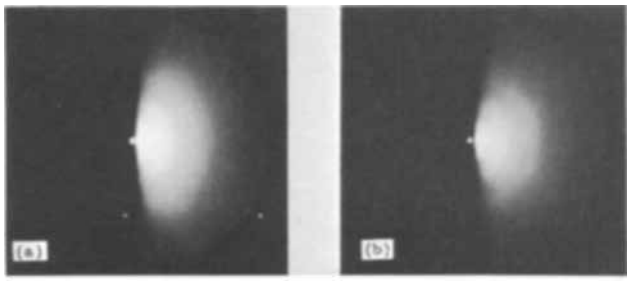

Fig. 5. Electron diffraction patterns of thin film Nb_2O_5: *(a)* before annealing, *(b)* after annealing.

pattern which could be identified as single-phase Nb_2O_5. No other phase was detected. This suggests that the initial material was Nb_2O_5, though the exact formula is not known. The crystallization behavior contrasts with the case of anodic niobium oxide, which has been reported to "recrystallize" at 500°-600°C.

Optical properties.—The dispersion data of the Nb_2O_5 films are plotted in Fig. 6. The data were fitted by the Hartmann equation (16):

$$n(\lambda) = a + b/(\lambda - \lambda_0)^{1.2} \quad [8]$$

where n is the refractive index and a, b, and λ_0 are constants. The experimental points are best fitted by:

$$n_{Nb_2O_5} = 2.0 + 1.1/(\lambda/10^3\,\text{Å} - 1.9)^{1.2} \quad [9]$$

These values are about 15% lower than reported by Young (16) for anodic films and 5% lower than reported by Burgiel *et al.* (17) for sputtered films. These differences may be attributed to differences in preparation.

Optical transmission of an Nb_2O_5 film is illustrated in Fig. 7 showing absorption and interference effects.

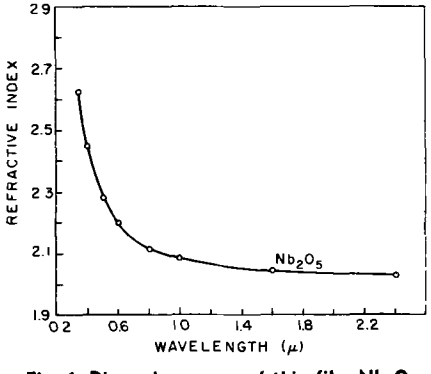

Fig. 6. Dispersion curves of thin film Nb_2O_5

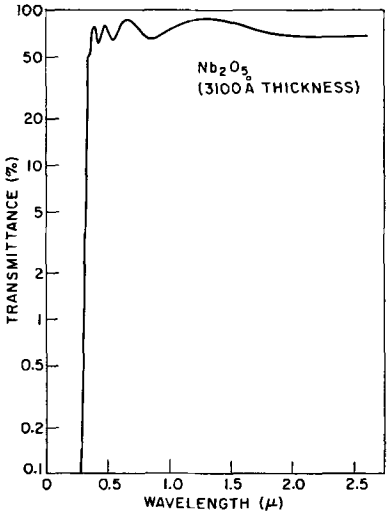

Fig. 7. Optical transmission of thin film Nb_2O_5

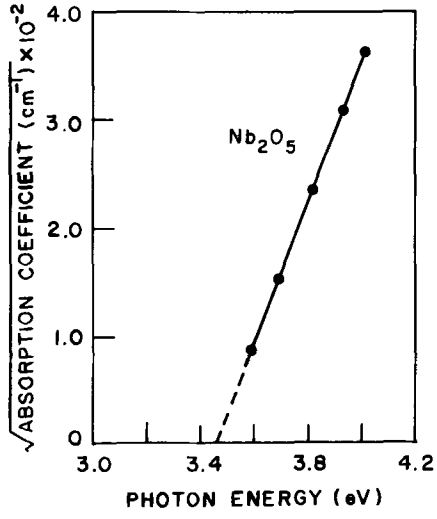

Fig. 8. Square root of absorption coefficient *vs.* photon energy for thin film Nb_2O_5.

Figure 8 is a plot of the square root of the absorption coefficient *vs.* photon energy. The linear nature of this plot suggests that excitation across the bandgap is by indirect transition, even though the magnitude of the absorption coefficient falls within the range expected for direct transition (18). The high value of this coefficient indicates that the absorption is intrinsic rather than by impurities. The intercept in Fig. 8 gives the value of the fundamental absorption edge as 3.48 ev, which is in fair agreement with values reported for oxides prepared by other methods (19-21). However, this value may be influenced by the donor concentration of the oxide as indicated by the work of Vratny and Micale (23). This value, as may be expected, is lower than the values obtained from photoconductivity experiments on anodic oxide films.

MOS behavior of Nb_2O_5*-silicon contacts.—High-frequency capacitance measurements.*—We have fabricated a large number of MOS contacts using Nb_2O_5 as a gate insulator directly on (111) silicon. A 1 MHz C-V curve, obtained with an Hg-probe on a 900Å film, is shown in Fig. 9. From this curve, it can be seen that interface state density and oxide charge can be kept to values which readily allow modulation of the silicon surface potential. We will have more to say about interface state density after we discuss a-c conductance measurements.

Generally, we have found that the positive oxide charge for Nb_2O_5 can be kept below 5 x 10^{11}/cm^2 so that flatband voltages for a 1000Å oxide on 10 ohm-cm, p-type silicon are less than 1v. This number includes oxide charge as well as work function difference due to gate contacts.

The Nb_2O_5-silicon interface generally exhibits a room-temperature hysteresis of the slow trapping

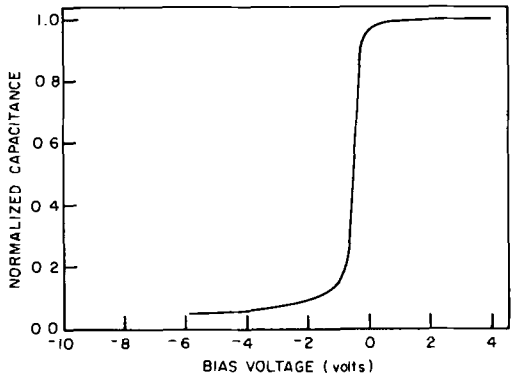

Fig. 9. Normalized C-V curve for an n-type MOS capacitor with 900Å Nb_2O_5 as gate insulator.

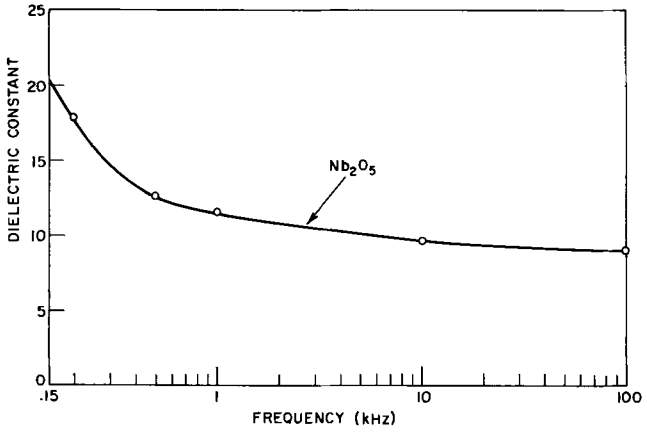

Fig. 10. Variation of oxide dielectric constant with frequency for thin film Nb_2O_5.

type. That is, for increasing negative gate voltage, the flat band voltage shifts to more negative values. Generally, this type of hysteresis is strongly dependent on deposition conditions, but can be reduced by annealing.

Bias-temperature tests at 200°C in an inert ambient show that these films are not an effective barrier against ionic motion. Positive charge is observed to move toward the silicon interface under the influence of positive gate voltage.

The dielectric strength as determined from MOS contacts is about 5 x 10^6 v/cm. The electrode area was 0.11 mm^2.

Frequency dependence of dielectric constant.—During our MOS impedance measurements, we have observed that the dielectric constant of Nb_2O_5 is frequency dependent. A plot of oxide dielectric constant dependence on frequency is shown in Fig. 10. As is seen from this plot, significant changes in dielectric constant can occur over a wide range of frequencies (100 Hz-100 kHz). However, variations in this frequency dependence have been observed as a function of deposition conditions. The value of the dielectric constant of ~11 ± 2 at 1 kHz is unusually low compared to a value of ~40 reported for amorphous anodic oxide films (16). At the present time, no explanation exists for this difference.

A-C conductance in MOS contacts.—A-C conductance measurements as a function of voltage have been made on Nb_2O_5-silicon MOS contacts over a range of frequencies from 100 Hz to 150 kHz. In Fig. 11, the G-V data at two frequencies, 100 and 10 kHz, are shown. The sample consisted of a 1000Å Nb_2O_5 film on 10 ohm-cm p-type silicon. As discussed earlier in this paper, the peak in the conductance is due to the presence of interface states. The peak occurs at the voltage determined by Eq. [7]. The shift of the peak toward positive voltage with decreasing frequency is indicative of a distribution of interface states in energy rather than a single level of states at a discrete energy.

Using Eq. [4] and [7], we have analyzed the G-V data for a number of samples, both p- and n-type. The density of states is found to increase toward both band edges, with a minimum in density occurring near midgap. Typical densities at flat-bands for n- and p-type samples are 1.5-2.0 x 10^{11} states/cm^2-ev. The time constant at flat bands is 3.2 μs and the capture cross section for the interface states is 2.5 x 10^{-17} cm^2. The capture cross section is found to be relatively independent of energy.

In analyzing the G-V data to determine interface states, it is important to note that the variation in frequency of ϵ_i, and hence the oxide capacitance, increases the difficulties in calculating the surface conductance due to interface states. Referring to Eq. [7], the measured a-c conductance is made up of two terms: one due to oxide loss, and the other due to interface states. The oxide loss term must be eliminated to obtain G_s. Equation [7] represents the formula which is used to do this. However, due to frequency dependence of C_i, the term $G_i\ (C_{sc}/C_i)^2$ will not be the same at a given voltage for each frequency. Hence, to determine the interface state density accurately, the dependence of ϵ_i (hence, C_i) on frequency must be determined.

It is also interesting to note the dependence of a-c conductance on voltage beyond accumulation. In Fig. 12, the voltage dependence for two frequencies is shown. It can be seen that the voltage dependence changes as a function of frequency. For example, in the region of —12 to —20v on a 1000Å Nb_2O_5 film on 10 ohm-cm silicon, the a-c conductance changes from being relatively independent at 10 kHz to linear dependence at 100 kHz.

We propose a tentative model to explain this effect. Since the Nb_2O_5 has a relatively narow band gap (3.48 ev) compared to SiO_2, the silicon valence band lies considerably closer to the Nb_2O_5 valence band. Hence, hole injection into the insulator is possible. Under these conditions, the current in the insulator will be space charge limited. In the case where shallower trapping can occur in the insulator, it is well known that d-c current is given by (22)

$$J = \frac{9}{8}\epsilon_i\,\mu_h\theta\,\frac{V^2}{L^3} \qquad [11]$$

where ϵ_i is the insulator dielectric constant, μ_h the hole mobility, θ a factor which describes the relative occupation of the trap and the valence band, and L the insulator thickness.

The a-c conductance will then be proportional to V, and the constant of proportionality related to θ. It is not difficult to show that θ is frequency dependent, with the frequency dependence determined by the

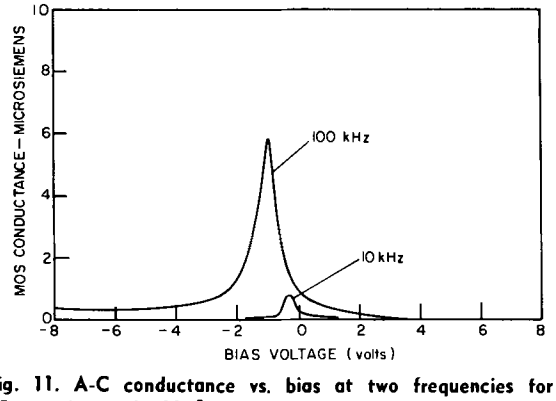

Fig. 11. A-C conductance vs. bias at two frequencies for an MOS capacitor with 1000Å Nb_2O_5 film.

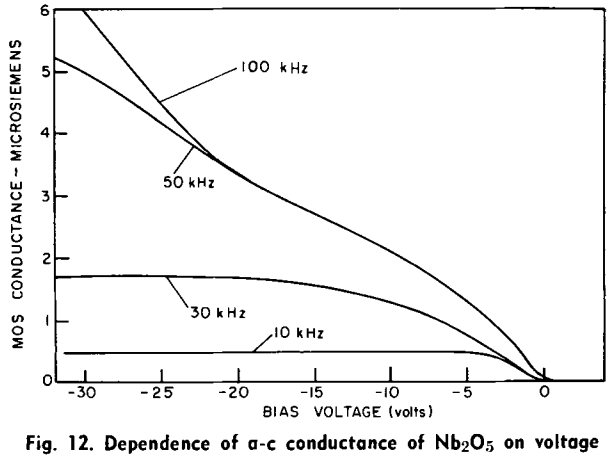

Fig. 12. Dependence of a-c conductance of Nb_2O_5 on voltage at several frequencies.

trap capture cross section and trap location. θ will increase from a low value ($<<1$), to a maximum of one at frequencies above $\frac{1}{2}\pi\,\tau_t$, where $\tau_t = (n_t\sigma_p <v>)^{-1}$ n_t is the density of filled hole traps, σ_p the capture cross section, and $<v>$ the thermal velocity. The exact frequency dependence will be determined by the trap distribution.

In Fig. 12, we see this type of behavior. For 10 kHz the dependence on voltage is very slight, while for 100 kHz the linear dependence is quite apparent. Further work is being done in this area to extend it to the point where information can be determined about trap properties in the insulator.

Acknowledgments

We wish to thank C. Arasim, R. Lenskold, G. Mark, and R. Soltis for assistance in the experimental work, and R. Paff, W. Roth, and B. Seabury for x-ray, electron diffraction, and scanning microscope measurements.

Manuscript submitted July 5, 1968; revised manuscript received Sept. 19, 1968. This paper was presented at the Boston Meeting, May 5-9, 1968, as Paper 17.

Any discussion of this paper will appear in a Discussion Section to be published in the December 1969 JOURNAL.

REFERENCES

1. E. S. Schlegel, *IEEE Trans. Elect. Dev.*, **ED-14**, 728 (1967).
2. A. G. Revesz and K. H. Zaininger, *RCA Rev.*, **29**, 22 (1968).
3. O. S. Heavens, "Optical Properties of Thin Solid Films," Dover Publications, Inc., New York (1965).
4. H. Y. Fan, "Reports on Progress in Physics," Vol. XIX, Physical Society of London (1956).
5. L. M. Terman, *Solid State Electron.*, **5**, 285 (1962).
6. K. Lehovec, A. Slobodskoy, and J. L. Sprague, *Phys. Stat. Sol.*, **3**, 447 (1963).
7. K. H. Zaininger and G. Warfield, *IEEE Trans.*, **ED-12**, 179 (1965).
8. E. H. Nicollian and A. Goetzberger, *Bell System Tech. J.*, **46**, 1055 (1967).
9. F. Berz, *J. Phys. Chem. Solids*, **23**, 1795 (1962).
10. K. Lehovec and A. Slobodskoy, *Solid State Electron.*, **7**, 59 (1964).
11. R. Lindner, *Bell System Tech. J.*, **41**, May 1962, 803-831.
12. K. H. Zaininger, "Semiconductor Surface Physics" in "Field Effect Transistors," J. T. Wallmark and H. Johnson, Editors, Prentice Hall, Inc., Englewood Cliffs, N.J. (1966).
13. K. Lehovec, *Appl. Phys. Letters*, **8**, 48 (1966).
14. K. H. Zaininger, *RCA Rev.*, **27**, 341 (1966).
15. J. Shewchun and A. Waxman, *Rev. Sci. Instr.*, **37**, 1195 (1966).
16. L. Young, "Anodic Oxide Films," Academic Press, New York (1961).
17. J. C. Burgiel *et al.*, *This Journal*, **115**, 729 (1968).
18. R. H. Bube, "Photoconductivity of Solids," John Wiley & Sons, Inc., New York (1960).
19. L. Apker and E. A. Taft, *Phys. Rev.*, **88**, 58 (1952).
20. R. E. Salomon, G. E. Adams, and W. M. Graven, *This Journal*, **110**, 1163 (1963).
21. D. C. Conlon and W. P. Doyle, *J. Chem. Phys.*, **35**, 752 (1961).
22. A. Rose "Concepts in Photoconductivity and Allied Problems," Interscience Publishers, New York (1963).
23. F. Vratny and F. Micale, *Trans. Faraday Soc.*, **59**, 2739 (1963).

Theory of Dielectric Breakdown in Solids

J. J. O'Dwyer

Physics Department, Southern Illinois University, Carbondale, Illinois

ABSTRACT

A short review is given of current trends in research on the theory of dielectric breakdown in solids; in particular the theory of thermal breakdown is discussed for the case in which the dielectric conductivity is explicitly field dependent. A new possibility for avalanche breakdown is also examined. The field in the dielectric is considered to be nonuniform because of the space charges created by collision ionization, and the enhanced field adjacent to the cathode causes field emission which is many orders of magnitude greater than would be expected from a mean field calculation.

The theory of dielectric breakdown of solids has been divided by custom into three areas (1-3), *viz.*, thermal, intrinsic, and avalanche. Most recent work has been along the lines of developing the theory of thermal breakdown by explicit inclusion of the field strength dependence of the conductivity (4, 5), or of presenting an avalanche theory which takes account of the nonuniformity which will arise in the field strength due to the charges which are the products of collision ionization (6). Theories of intrinsic breakdown would then be seen as yielding a critical field strength of order of magnitude of the field strength at which collision ionization within the material becomes significant, rather than a critical field for direct comparison with the experimental breakdown field.

A brief introduction will first be given to the ideas underlying the various theories of breakdown which have been current for some time; recent developments will then be discussed in more detail.

All theories of thermal breakdown can be derived from the basic equation

$$C_v \frac{dT}{dt} - \text{grad}\,(K\,\text{div}\,T) = \sigma F^2 \qquad [1]$$

where C_v is the specific heat per unit volume, dT/dt is the time derivative of the temperature T, K is the thermal conductivity, F the field strength, and σ the electrical conductivity. Since σ is almost always a strongly varying function of temperature, the solution of [1] is complicated even for the simplest geometry of boundary conditions. The most usual approaches have been to solve [1] for the simple limiting cases: (*A*) Steady state solution in which the time derivative term is set equal to zero. (*B*) Short time solution in which the thermal conduction term is ignored. An alternative approach would be to give a numerical solution to the complete equation for the simple case of plane parallel geometry.

The conclusions of standard thermal breakdown theory have been well tested experimentally; generally speaking they are valid at high temperatures where the ratio of electrical to thermal conductivity is large.

Theories of intrinsic breakdown regarded the breakdown strength as an intrinsic property of the material; the calculation of the critical field strength then corresponded to the failure of some specified process to achieve a stable situation with the conducting electrons. Different physical processes by which an electron can lose the energy it gains from the electric field then specify the various theories of intrinsic breakdown strength. All such theories predict a specific temperature dependence of the breakdown strength but assume that it is thickness independent. This led to much experimental work on the temperature dependence of the breakdown strength, with occasional measurements showing a slight thickness effect.

The simplest theory of avalanche breakdown is based on order of magnitude arguments, which lead to the conclusion that forty generations of collision ionization products will form a critical avalanche (7). If d is the dielectric thickness and $\alpha(F)$ the field dependent mean ionization rate per unit path length, then the critical field strength will be given by

$$\alpha(F_c)\,d = 40 \qquad [2]$$

If we assume that the field dependence of the collision ionization function is given by

$$\alpha(F) = \alpha_0 \exp(-H/F) \qquad [3]$$

where α_0 is a constant ionization rate and H is a field strength characteristic of the material, the thickness dependence of the critical field strength is then given by

$$H/F_c = \ln(\alpha_0 d/40) \qquad [4]$$

This result predicts a monotonic decrease of breakdown strength with increasing thickness of about the magnitude observed over not too great a range of thickness.

The work described in this introduction has been extensively reviewed and discussed in the general references (1-3).

Thermal Breakdown of Thin Films

Recently the breakdown of thin films has been interpreted as thermal; the measured temperature and field strength dependence of the prebreakdown conduction has been used in the equation

$$JFd = \Gamma(T - T_0) \qquad [5]$$

where J is the current density, Γ is the thermal conductance per unit area, T_0 the ambient temperature, T the temperature of the dielectric (which is assumed to be constant throughout the film), F the mean field strength, and d the dielectric thickness. This equation has been fully discussed by Whitehead (7) for the case in which σ is not an explicit function of F, but depends on it implicitly through its temperature dependence.

Various forms for the temperature and field strength dependence of J have been given. Klein and Gafni (4) working on silicon oxide films 3000-50,000Å thick use

$$J = \sigma_0 F \exp\{a(T - T_0) + bF\} \qquad [6]$$

in which both σ_0, a, and b are functions of T_0. They also note a Schottky like expression also fits well to their results, but prefer [6] because of consequent algebraic simplicity. For the same substance in films 1000-10,000Å thick Hartman *et al.* (8) give

$$J = C_1 d \exp\{-(\phi - \alpha_1 F^{1/2})/kT + \alpha_2 F^{1/2}\} \times [1 - \exp\{-F(\alpha_2 + \phi/kT)^2\}] \qquad [7]$$

where C_1 is a constant, d is the dielectric thickness, and α_1, α_2, and ϕ are constants of the material. This is an interesting expression since it contains an explicit dependence on the dielectric thickness, and also a factor which gives an ohmic current for low field strengths. Because of this ohmic dependence [7] leads to $J \propto dF = V$ at low field strengths (V is the voltage); for high field strengths [7] becomes approximately

$$J = C_1 d \exp\{-(\phi - \alpha_1 F^{1/2})/kT + \alpha_2 F^{1/2}\} \qquad [8]$$

so that current density is directly proportional to dielectric thickness for a given mean field strength, but not for a given voltage. Results of this general nature had already been found for silicon oxide in the thickness range 1-4μ by Hirose and Wada (10). Sze (5) working on silicon nitride films found that for high field strengths

$$J = C_2 F \exp\{-(\phi - \alpha_3 F^{1/2})/kT\} \qquad [9]$$

where C_2, ϕ, and α_3 are constants. He also explicitly stated that no thickness dependence was found over the range 500-2900Å.

A wide diversity of choice is, therefore, available for the functional form of the current in Eq. [5], and since the expressions are all empirical it is difficult to find reasons for preferring one to another. We shall use [8], and in making this choice there are three distinct points of difference from other possibilities: (*i*) The explicit field strength dependence is given by an exponential factor in $F^{1/2}$ rather than in F. (*ii*) An explicit thickness dependence is included. (*iii*) The exponential factor in $F^{1/2}$ gives the total explicit field strength dependence of the current; it does not, as in [9], give the field strength dependence of the conductivity. That these two cases may be very difficult to distinguish experimentally has been shown by Hanscomb *et al.* (9) in work on sodium chloride.

Substituting [8] in [5]

$$C_1 F d^2 \exp\{-(\phi - \alpha_1 F^{1/2})/kT + \alpha_2 F^{1/2}\} = \Gamma(T - T_0) \qquad [10]$$

Following Whitehead (7) the critical field strength is found by differentiating both sides of [10] with respect to T and then using [10] to simplify the result. One readily finds

$$kT_c^2/(\phi - \alpha_1 F_c^{1/2}) = T_c - T_0 \qquad [11]$$

which with the use of [10] and the assumption $T_c \simeq T_0$ gives

$$F_c^{1/2} = (\phi - kT_0 \ln C)/(\alpha_1 + kT_0\alpha_2) \qquad [12]$$

where

$$C = C_1 d^2 F_c(\phi - \alpha_1 F_c^{1/2})/\Gamma k T_0^2 \qquad [13]$$

The result is written in this way since ln C is a slowly varying function of F_c and T_0. If $\alpha_1/\alpha_2 >> kT_0$ then

$$F_c^{1/2} = (\phi - kT_0 \ln C)/\alpha_1 \qquad [14]$$

which was derived by Sze (5) using the current form [9]. Equation [14] predicts that $F_c^{1/2}$ decreases linearly with increasing temperature; this has been verified by Sze (5) for the case of silicon nitride. Equation [12] predicts a similar but more rapid decrease of $F_c^{1/2}$ with increasing temperature.

Although the logarithm of the dimensionless quantity [13] varies slowly with any of the variables contained in it, there is a possibility of several orders of magnitude change in dielectric thickness which would lead to a change of one order of magnitude in the logarithm. The square root of the breakdown field strength should vary linearly with the logarithm of dielectric thickness.

Avalanche Breakdown

There have been two principal lines of development to the 40 generations theory of avalanche breakdown described above.

In the first due to Forlani and Minnaja (10) the assumption of uniform field strength between the electrodes is retained, but the electron emission from the cathode is explicity introduced. Although their theory is complicated, the thickness dependence of the critical field strength can be found from an order of magni-

tude argument. The current injected into conduction levels from the cathode will be given by the Fowler-Nordheim expression

$$J_{\text{Inj}} = J_0 \exp\left\{-\frac{4(2m)^{1/2}\phi^{3/2}}{3\hbar e F}\right\} \quad [15]$$

where J_0 is the pre-exponential quantity and ϕ the effective work function. If the lattice vibrations in the dielectric are ineffective in slowing down the electrons in the strong field, then the collision ionization rate per unit length will be given approximately by

$$\alpha = e F/E_g \quad [16]$$

where E_g is the energy required for a collision ionization. Then

$$J(d) = J_{\text{Inj}} \exp(e F d/E_g)$$

$$= J_0 \exp\left\{-\frac{4(2m)^{1/2}\phi^{3/2}}{3\hbar e F} + \frac{e F d}{E_g}\right\} \quad [17]$$

Zero exponent in [17] corresponds approximately to the onset of irreversible changes in the dielectric, and if one takes the breakdown criterion as being that value of F for which the exponent in [17] becomes positive,[1] then the critical field strength is given by

$$F_c^2 = \frac{4(2m)^{1/2}\phi^{3/2}E_g}{3\hbar e^2 d}$$

Inserting values of the appropriate order of magnitude one finds

$$F_c \simeq 3 \times 10^4/d^{1/2}\ V \cdot \text{cm}^{-1} \quad [18]$$

with d measured in cm. Burdenstein and Hayes (11) have verified this result for silicon oxide in the thickness range 10^3-10^4Å. However, the thermal critical field strength of [12] (also alternative avalanche theories to be described below) exhibits a variation of a factor 3 in the breakdown strength for a thickness variation of one decade; measurements over at least several decades of thickness would be required to verify the $d^{-1/2}$ dependence.

The other main line of development of avalanche breakdown theory has resulted from the realization that the space charges caused by the build up of the avalanche should result in a nonuniform field strength distribution. If one drops the assumption of a uniform field, then a natural basic theoretical assumption is constancy of current. A space charge controlled theory of avalanche breakdown was proposed by O'Dwyer (6) assuming that electron current was continuous, and that the collision ionization function was of the form [3]. In this theory it was also assumed that the relatively unmobile holes arranged themselves in such a way that Poisson's equation is satisfied and continuity of electron current is preserved but without contributing to the current themselves. This leads to a relation for the mean critical field strength $\overline{F_c}$ which requires computation, but can be written approximately as

$$H/\overline{F_c} = 8 \cdot 5 \ln(\alpha_0 d) - 2 \quad [19]$$

This theory suffers from a similar defect to the 40 generations theory in that it contains contradictory assumptions; the holes must move to satisfy Poisson's equation, and yet it is assumed that they make no contribution to the current.

A theory of current flow due to collision ionization has been given by O'Dwyer (12). Anode and cathode are assumed to be blocking; both continuity of current and field distribution in accordance with Poisson's equation are strict requirements of the theory. The ionization rate per unit volume per unit time is assumed to be of the form (c.f. Eq. [3])

[1] A weak point in this assumption is that $J_0 \sim 10^7$ amp·cm^{-2}.

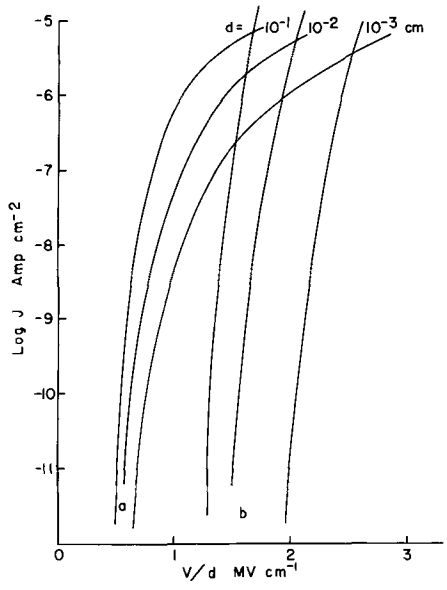

Fig. 1. Double ejection current and cold emission current for various values of the dielectric thickness: (a) double ejection current, (b) cold emission current.

$$I = (\alpha_n n^+ \alpha_p p) \exp(-H/F) \quad [20]$$

where α_n and α_p are constants and n and p are the electron and hole densities. In order to make the equations tractable it is also assumed that

$$\alpha_n/\alpha_p = \mu_n/\mu_p$$

where μ_n and μ_p are the effective electron and hole mobilities.

The computation of the current voltage characteristics is somewhat lengthy, but is given in a dimensionless form in ref. (12). Making the following assumptions about the constants of the dielectric:

$$H = 5 \times 10^6\ \text{V} \cdot \text{cm}^{-1}$$

$$\alpha_n = 2.5 \times 10^7\ \text{sec}^{-1}$$

$$\mu_n = 10^{-3}\ \text{cm}^2\ \text{volt}^{-1}\ \text{sec}^{-1}\ ^2$$

$$\mu_p/\mu_n = 5 \times 10^{-7}$$

one obtains the set of current-voltage characteristics shown in Fig. 1. On the same diagram are plotted the Fowler-Nordheim emission curves for an electrode with 1.50 ev net work function, and subject to a field equal to that caused by the space charge distribution of the double ejection current. The intersection point of these curves corresponds to a mean field strength for which injection from the electrodes can no longer be ignored; the injection would be a most steeply rising function of applied voltage, very much steeper than a Fowler-Nordheim law, and some ten orders of magnitude larger than the injection current as calculated from the mean field strength. If this point of intersection is regarded as the mean critical field strength determining breakdown, then this critical field strength is thickness dependent. The form of this thickness dependence is shown in Fig. 2. Also included on the same diagram for the sake of comparison are thickness dependences for thermal breakdown and the avalanche theories expressed by Eq. [18] and [19], using the same data as above.

Discussion

Since all dielectric breakdown must be in a sense thermal, it is difficult or even impossible to make an ultimate distinction between thermal breakdown and any other type of instability. This is clearly demonstrated by recent work in which the explicit (and strong) field dependence of the conductivity is in-

[2] Collision ionization would not be feasible with such a low value of true mobility. The figure quoted is for effective mobility which may be many orders of magnitude lower than the true mobility.

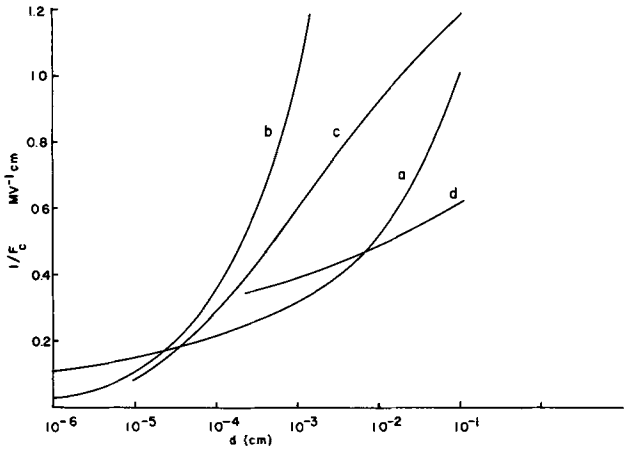

Fig. 2. Thickness dependence of the critical field strength according to various theories: (a) thermal with Schottky field dependence, (b) cathode emission with collision multiplication, (c) cathode emission with collision multiplication and nonuniform field, (d) cathode emission arising from nonuniform field caused by double ejection.

cluded in thermal breakdown theory. However, in the region of so called electrical breakdown the dependence of the conduction current on the electric field still remains; the problem is one of extreme sensitivity. Budenstein and Hayes (11) claim that the conductivity of the breakdown path increases by ten orders of magnitude within 100 n · sec., while Klein (3) mentions current densities of order 10^6-10^{10} amp · cm^{-2} in the discharge path. It is clear that adequate theoretical description of these phenomena faces severe difficulty. Avalanche theories have attempted to give an approximate explanation of the sharp rise in current. As discussed above the basic assumptions of the theory have been either constancy of field strength or constancy of current. The first assumption is self-contradictory in the presence of collision ionization, the second can be made consistent, but the truth is probably somewhere in between. For thin films and consequently few generations of collision ionizations the uniform field assumption should be a reasonable one, provided that the current injected from the cathode is not too great. Distortion of the field depends on the density of charge, and even a single collision ionization between cathode and anode will make this large if the current level is high. On the other hand, it is unlikely that field distortion can ever be ignored in thicker films in which relatively many generations of collision ionization will occur; the constant current assumption will, therefore, be a better starting point, although probably not an adequate one. Recent experimental work by Cooper and Elliott on KBr (14) has supported the assumption of field enhancement in front of the cathode. Measurements of breakdown strength over many decades of thickness will probably not give unambiguous support to one theory or another, since it is likely that the breakdown mechanism will change as the thickness changes.

Measurements of the field strength dependence of the current over many decades of thickness could be more rewarding and may help with the vexing question of identifying the mechanism of the conductivity. Certainly in this situation d-c conductivity measurements must be explained in terms of continuous current, and a change from conditions in which space charge is important to those in which it is not should be clearly manifest.

Manuscript submitted May 15, 1968; revised manuscript received Oct. 31, 1968. This paper was presented at the Boston Meeting, May 5-9, 1968, as Paper 5.

Any discussion of this paper will appear in a Discussion Section to be published in the December 1969 JOURNAL.

REFERENCES

1. R. Stratton, *Prog. in Dielectrics*, **3**, (1961) 235.
2. J. J. O'Dwyer, "The Theory of Dielectric Breakdown of Solids," (1964).
3. N. Klein, "Advances in Electrons and Electron Physics" (1968) In press.
4. N. Klein and H. Gafni, *IEEE Trans. on Electron Devices*, **ED-13**, 281 (1966).
5. S. M. Sze, *J. Appl. Phys.*, **7**, 2951, (1967).
6. J. J. O'Dwyer, *J. Phys. Chem. Solids*, **28**, 1137 (1967).
7. F. Seitz, *Phys. Rev.*, **76**, 1376 (1949).
8. S. Whitehead, "Dielectric Breakdown of Solids" (1951).
9. T. E. Hartman, J. C. Blair, and R. Bauer, *J. Appl. Phys.*, **37**, 2468 (1966).
10. J. R. Hanscomb, K. C. Kao, J. H. Calderwood, J. J. O'Dwyer, and P. R. Emtage, *Proc. Phys. Soc.*, **88**, 425 (1966).
11. F. Forlani and N. Minnaja, *Phys. Stat. Solidi*, **4**, 311 (1964).
12. P. P. Budenstein and P. J. Hayes, *J. Appl. Phys.*, **38**, 2837 (1967).
13. J. J. O'Dwyer, *ibid.*, **39**, 4360 (1968).
14. R. Cooper and C. T. Elliott, *ibid.*, **17**, 481 (1966).

Reactively Sputtered Oxide Films

M. L. Lieberman*[1] and R. C. Medrud

Research and Development Laboratories, Corning Glass Works, Corning, New York

ABSTRACT

Oxide films of eleven metals have been prepared by reactive sputtering. The use of refrigerated substrates resulted in amorphous films in eight of the metal-oxide systems. Crystallization of the amorphous films gave rise to metastable, high-temperature polymorphs of WO_3, Ta_2O_5, and Bi_2O_3, and an unidentified tellurium oxide phase. High-oxidation-state compounds of silver, antimony, and lead were prepared. Optical properties of some films were examined. Films with a high refractive index and low optical absorption were prepared by crystallization of the highly absorbing, amorphous, bismuth oxide films.

Sinclair and Peters (1) have previously shown that it is possible to prepare amorphous metal-oxide films on uncooled substrates by reactive sputtering. They found, however, that lead oxide films prepared in this manner were crystalline and suggested that refrigerated substrates might give rise to amorphous deposits.

For the present investigation, an apparatus has been constructed which has provisions for substrate refrigeration and multicathodic reactive sputtering. Consequently, it is possible to increase the number of

* Electrochemical Society Active Member.
[1] Present address: Sandia Laboratories, Albuquerque, New Mexico 87115.

amorphous single- and mixed-metal-oxide films prepared by reactive sputtering. Secrist and Mackenzie (2) have found that amorphous films, of some systems at least, prepared by a variety of methods can properly be called glasses. If the amorphous, reactively sputtered films are indeed glasses, they should be structurally similar to supercooled liquids. This suggests that the controlled crystallization of such films may give rise to metastable high-temperature phases. Since many oxides have never been prepared as amorphous bulk materials, the crystallization of the amorphous films may produce metastable phases which cannot be prepared by other methods.

The results presented in this paper are limited to single-metal-oxide films.

Experimental

Reactive sputtering.—An apparatus has been constructed which provides for the simultaneous rotation and refrigeration of substrates during reactive sputtering. Substrates are cooled with liquid nitrogen to increase the possibility of obtaining amorphous films. With the present cathode geometry, rotation of the substrates gives rise to films which are more uniform in thickness than could otherwise be obtained. Rotation also serves to aid in the dissipation of heat from the substrate surfaces, since the substrates are only in the plasma region for a small part of each revolution. In addition, rotation permits the preparation of mixed-metal-oxide films by means of the simultaneous reactive sputtering of several independent cathodes. Selection of the various sputtering parameters can be used to obtain some degree of composition control in the mixed-metal-oxide films.

The basic sputtering unit, shown schematically in Fig. 1, is a modified Edwards Evaporation Plant with a 19 in. diameter stainless steel bell jar. The salient feature of the system is a liquid-nitrogen-cooled stainless steel Dewar which was fabricated to specifications by Hofman Laboratories, Inc. The baseplate of the Dewar is a 17 in. diameter, 0.625 in. thick copper plate. The Dewar neck has an outer diameter of 1.5 in. and an inner diameter of 1.0 in. In the region of the rotary seal, the Dewar walls are welded to a stainless steel pipe of the same dimensions.

Substrates (ground and polished Corning Code 7900 glass), typically 1 x 3 x 0.050 in., are supported by screws which go about halfway through the Dewar baseplate. The Dewar is filled with liquid nitrogen to a height of approximately 3 in. above the baseplate before sputtering is initiated. This height is automatically maintained by means of a Hofman P/N 3718 liquid nitrogen level controller (not shown) connected to 200-liter liquid nitrogen supply Dewar.

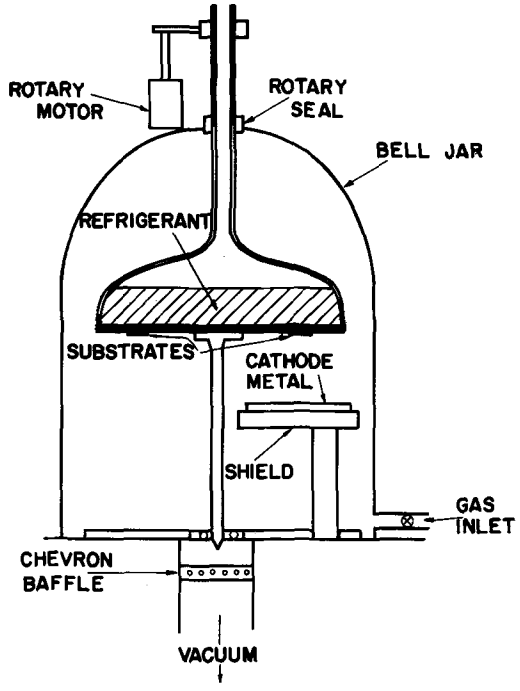

Fig. 1. Reactive sputtering apparatus

A rotary motor, located outside of the vacuum system, turns the Dewar via a V-belt arrangement. The rate of rotation, typically 120 rpm, is regulated by a speed controller. A stainless steel post is screwed to the bottom of the Dewar baseplate; this post fits into a bearing attached to the baseplate of the vacuum system. Since two bearings are also located in the rotary seal area, the Dewar is positioned to within small tolerances. Consequently, the torque applied to the Dewar during its rotation causes only a slight wobble, approximately ± 0.06 in. vertical displacement at the outer edge of the Dewar baseplate.

The rotary seal is a differentially pumped section contained between Viton O-rings which are lubricated with Apiezon H or T grease. The weight of the Dewar is supported by one of the two bearings located in the seal area. With the Dewar rotating prior to refrigeration, a vacuum in the 10^{-6} to 10^{-7} Torr range is typically obtained.

Sector-shaped metal plates with 60° angle and 6.75 in. radius are used as cathodes in the sputtering. Water cooling is provided through the cathode supports. When multicathodic sputtering is performed, the cathodes are positioned adjacent to each other. Separate power supplies are available for three cathodes. Table I lists the manufacturer's reported purity for each of the metals. Except for tellurium, silicon, and cadmium, all metals were purchased in plate form. The tellurium was purchased in lump form and vacuum melted in a graphite mold to obtain a plate. During removal from the mold, the plate broke into several pieces. Since tellurium sputters much faster than aluminum, the cathode support was covered with aluminum foil and the tellurium pieces were fitted together over the foil. An analysis of a tellurium oxide film based on spark-source mass spectrometry indicated about 0.2 w/o (weight per cent) Al. Silicon powder (—325 mesh) was granulated with ~5% sugar, hydrostatically pressed at 15,000 psi, fired in oxygen at 400°C, and then fired in argon from 400° to 1350°C. The resulting plate made a suitable silicon cathode. Purity of the plate was not determined, since residual impurities from the sugar would form volatile compounds during reactive sputtering, most of which would be removed by the pumping system. A cadmium cathode was cast from material of unknown purity.

Reactive sputtering was performed in a nominally 1:1 argon-oxygen gas mixture obtained from the Matheson Co., Inc. Cathode potentials applied to most metals were in the range 1200-2400v, but potentials applied to nickel, silicon, tungsten, and tantalum were in the range 3000-4800v. Total gas pressure was generally in the range 10-30 x 10^{-3} Torr. The cathode-substrate spacing was about 1.4 in., except for the

Table I. Cathode metals

Cathode metal	Supplier	Reported purity, %
W	a	99.95 minimum
Bi	b	99.999
Pb	b	99.99
Sn	b	99.99
Te*	b	99.99
Sb	b	99.999
Ag	c	99.99
Ta	b	99.9
Cd		
Si†	b	99.99
Ni	b	99

(a) Sylvania Electric Products, Inc.
(b) United Mineral and Chemical Corp.
(c) Gallard-Schlesinger Chemical Mfg. Corp.
* Obtained in lump form.
† Obtained as —325 mesh powder.

tellurium cathode in which case it was 1.8 in. Substrates were cleaned with 2-5% HF, distilled water, and Fisher Certified ACS methanol. Filmed substrates were removed from the vacuum system on the day following the reactive sputtering.

X-ray and optical measurements.—All films were examined by x-ray diffraction at room temperature on a General Electric XRD-5 diffractometer equipped with a Hamner detection system and a pulse height analyzer. Cu Kα radiation with a Ni filter was used. Scanning rates of 2.0 and 0.2 deg/min were employed. All phase identifications were made from x-ray diffraction data and, unless otherwise mentioned, the source was the ASTM Powder Diffraction Data File.

Specular reflectance measurements were made in the visible and near infrared by means of Perkin-Elmer Model 350 and Beckman Model DK-2R spectrophotometers. Refractive index n was determined as a function of wavelength from the relation

$$nt = m\lambda/4 \quad [1]$$

where t is the film thickness, λ is any wavelength at which a reflectance extreme occurs, and m is an integer which describes the order of interference. The value of t was determined with a CEJ Multimi 3000D multiple-beam interferometer, values of λ were determined from the reflectance measurements, and values of m could be readily assigned at low orders of interference. Reflectance measurements made with the Perkin-Elmer Model 350 spectrophotometer were corrected for nonnormal incidence, although the 20° incidence resulted in a correction of n of only 1% for a lead oxide film. Reflectance maxima corresponding to optical thicknesses less than $5\lambda/4$ were not used, because of the dispersion errors encountered at low orders of interference (3, 4).

The extinction coefficient k ($\bar{n} = n\text{-}ik$) was determined as a function of wavelength by the method described by Ennos (4). The evaluation of k at any wavelength is primarily determined by the difference in reflectance values measured from filmed and unfilmed areas of an aluminum-backed substrate. This method is particularly suitable for the determination of low k values. For these determinations, all spectrophotometric measurements were made with the Beckman Model DK-2R spectrophotometer.

Results

Film crystallinity.—The as-deposited films were examined by means of x-ray diffraction. Only oxide films of cadmium, nickel, and silver were crystalline. The common cubic forms of CdO and NiO were observed. Both compounds showed a strong (111) preferred orientation. The silver oxide films were black as deposited and became light brown when heated at 100°C. The black films contained AgO, Ag_2O, and a small amount of Ag. The color change on heating was caused by the conversion of AgO to the more stable Ag_2O. These films were prepared under conditions similar to those used by Rollins and Weichman (5). The phases observed confirm their interpretation of resistance measurements being associated with the presence of a higher oxide of silver (Ag_2O_{1+x}, $0 \leq x < 1$).

Crystallization of amorphous films.—Filmed substrates were cut into two or three pieces which were subjected to various thermal treatments in a small furnace. The time of thermal treatment had no apparent effect on whether or not crystallization would occur, but sometimes had an effect on the particular phases obtained when crystallization did occur. Results of various thermal treatments are summarized in Table II. The tabulated thermal treatments are the lowest temperature treatments for which crystallinity was detected by x-ray diffraction. Near the crystallization temperatures, the thermal treatments were generally conducted at intervals of 50°C, although few treatments were carried out below 250°C. The silicon oxide films were not heated above 500°C, at which temperature they were still amorphous.

Table II. Phase identification

Oxide of	Thermal treatment for crystallization Temp, °C	Time, hr	ASTM x-ray card or other reference	Phases
Cd			5-0640	CdO
Ni			4-0835	NiO
Ag			Ref. (24), 12-793, 4-0783	AgO + Ag_2O + Ag
Sn	250	1	5-0467	SnO_2
Bi	250	1	16-654	δ-Bi_2O_3
	250	>1	Ref. (15)	β-Bi_2O_3
Pb	250	1	Ref. (7)	$Pb_{12}O_{19}$
W	350	1	6-0707, 5-0363	$H_{0.5}WO_3$, WO_3 (orthorhombic)
Te	400	3	11-693	TeO_2 + unknown phase
Sb	550	72	11-690, 11-694	Sb_2O_5, Sb_2O_4
Ta	650	3	Ref. (8, 9)	δ-Ta_2O_5
Si	500	3		Amorphous

Crystallization of the oxide films of tin, antimony, and lead produced phases which exist in bulk form at room temperature and pressure. Films of tin oxide crystallized as the rutile analog of SnO_2, as reported by Sinclair and co-workers (6). The antimony oxide films showed either Sb_2O_4 or mixtures of Sb_2O_4 and Sb_2O_5. One of the first lead oxide films, prepared prior to provisions for substrate rotation, crystallized as a mixture of β-PbO_2 and $Pb_{12}O_{19}$. All other lead oxide films crystallized as $Pb_{12}O_{19}$ alone. The diffraction data for $Pb_{12}O_{19}$ obtained in this investigation are in agreement with those given by White and Roy (7), with the exception of the d value for the first and strongest reflection. They reported $d = 3.268$Å which is not consistent with their indexing. The value should be 3.158Å which also agrees with the data obtained in this work. An error of 1° in the scattering angle would account for this difference.

Oxide films of tantalum, tungsten, and bismuth crystallized as metastable, high-temperature phases. The diffraction data for the tantalum oxide films are in good agreement with those reported by Terao (8) and by Sarjeant and Roy (9) for δ-Ta_2O_5. Two different phases occurred in the tungsten oxide films. The first was found in one of the initial tungsten oxide films prepared, and the x-ray diffraction data for it closely resemble the data for $H_{0.5}WO_3$ reported by Glemser and Naumann (10). The formation of a hydrogen-containing compound is not surprising, since Sosniak (11) and Stern and Caswell (12) have shown that hydrogen is a major gaseous impurity in sputtering systems. All other tungsten oxide films resembled the orthorhombic WO_3 structure which, in bulk form, has a stability range from 330° to 720°C (13). To the authors' knowledge, this phase has not been previously obtained at room temperature. The only published diffraction data for this phase are lattice constants as a function of temperature (13, 14). From such data, it is apparent that the diffraction pattern of the orthorhombic form closely resembles that of the room-temperature monoclinic form, except that the former polymorph has no unique $hk\bar{l}$ reflections. A comparison of the authors' diffraction data with the ASTM data for the monoclinic form is given in Table III.

The polymorphic transformations which occur in the bismuth oxide system have been discussed by Gattow and Schütze (15) and Levin and Roth (16). A flow diagram presented by the former authors (15) is shown in Fig. 2. Although the β-modification is metastable, it has been obtained at room temperature by quenching the melt (9, 15, 16). The existence of δ-Bi_2O_3 has been shown by high-temperature x-ray diffraction techniques (15, 16), but an attempt to obtain this polymorph at room temperature by quenching was unsuccessful (16).

Table III. X-ray diffraction data for tungsten and tellurium oxides

Tungsten oxide films		WO_3 (monoclinic) ASTM 5-0363			Tellurium Oxide films		TeO_2 ASTM 11-693		
d	I	hkl	d	I	d	I	hkl	d	I
3.829	82	001	3.835	100	4.31	2			
		020	3.762	95	4.08	2	101	4.068	13
3.658	100	200	3.642	100	3.90	3			
		011	3.408	5	3.42	6	110	3.404	35
3.35	4	120	3.339	50	3.25	18			
		11$\bar{1}$	3.106	50	3.12	2	111	3.107	13
3.077	18	111	3.073	50	3.045	75			
		021	2.681	75	2.986	100	102	2.988	100
		20$\bar{1}$	2.659	60	2.596	2			
		201			2.540	<1	112	2.536	1
2.626	40		2.615	90					
		220			2.450	1			
		22$\bar{1}$	2.170	50	2.419	1			
2.150	14	221	2.147	60			200	2.407	20
		31$\bar{1}$	1.989	35	2.396	1			
1.975	4	311	1.964	30	2.353	<1			
1.912	4	002	1.916	50			201	2.296	3
		040	1.877	50	2.151	1	210	2.151	3
		140			2.111	2			
1.824	10		1.818	75					
		400			2.070	1	211	2.071	5
		112	1.805	40			113		
					2.036	<1		2.033	1
1.794	8	112	1.791	50			202		
		202			1.937	5			
			1.705	60					
		022			1.910	16	004	1.904	11
		202			1.877	13	212	1.873	55
1.690	5		1.686	55					
		041			1.794	2			
		14$\bar{1}$	1.645	25			203	1.746	3
		141			1.711	6			
1.640	11	401	1.636	65			220	1.701	13
							114		
		420			1.662	14		1.661	20
		42$\bar{1}$	1.513	45			221		
1.504	4	421	1.498	35			213	1.641	5
					1.635	9			
					1.597	9			
							301	1.569	3
					1.521	4	310	1.521	9

Crystallization of the amorphous bismuth oxide films (Table II) occurs readily at 250°C. The Bi_2O_3 polymorph which originally forms is the cubic δ-modification. Whereas Levin and Roth (16) reported a lattice constant of 5.66Å for this polymorph at 750°C, the present authors have obtained a value of 5.53Å at 25°C. If it is assumed that the thermal expansion of δ-Bi_2O_3 is linear over the temperature range 25°-750°C, and Levin and Roth (16) have shown that this is a good assumption for all Bi_2O_3 polymorphs, the calculated coefficient of linear thermal expansion is 24 x 10^{-6}/°C. This value is identical with that reported by Levin and Roth (16) for the temperature range 625°-800°C.

The δ-Bi_2O_3 polymorph undergoes a transformation to the β-modification, accompanied by a color change

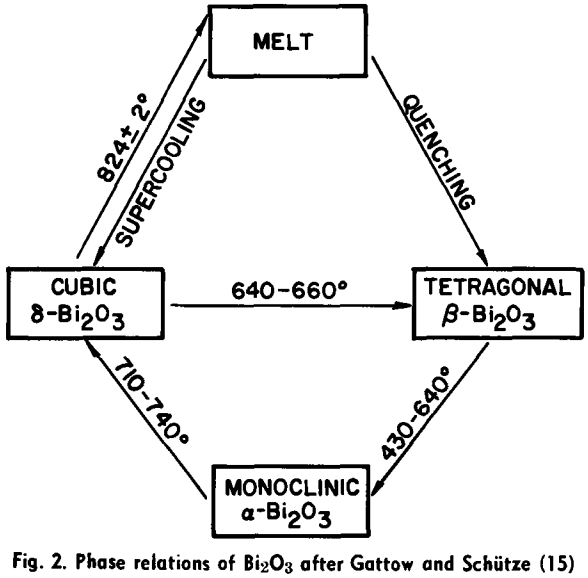

Fig. 2. Phase relations of Bi_2O_3 after Gattow and Schütze (15)

from brown to yellow, if the thermal treatment is extended beyond about 1 hr. Although both modifications are metastable at room temperature, the transformation is in the direction of increasing stability. No further phase transformations occurred when a film was heated at 295°C for 71 hr. Presumably, higher temperatures would result in conversion of the β-modification to the stable α-modification.

Whereas amorphous tellurium oxide films are transparent and nearly colorless, the thermally crystallized films are opaque and white. These features, and the appearance of "splatter" marks, distinguish crystallized tellurium oxide films from other crystallized films. The observations suggest the evolution of gas from the films. Amorphous α-TeO_3 is reported (17) to decompose to Te_2O_5 and then to the stable TeO_2 at 400°C, the temperature at which the films crystallized. Consequently, the presence of large amounts of the higher oxides in the amorphous films is indicated. This was qualitatively verified by observing the effervescent reaction which occurred when amorphous tellurium oxide films were immersed in a 30% NaOH solution. Bulk Te_2O_5, and presumably TeO_3, react in this manner (17), whereas TeO_2 does not yield an effervescent reaction. Such observations only indicate the presence of the higher oxides; the presence of TeO_2 is not excluded. Therefore, the films are designated $TeO_{2+x}(0 < x \leq 1)$.

X-ray diffraction analyses show that crystallization of the amorphous TeO_{2+x} films commences with the formation of an unidentified phase. This phase transforms to tetragonal TeO_2 when heated for a longer period of time or at a higher temperature. It was not possible to obtain a good diffraction pattern of the unidentified phase alone. A comparison of the ASTM data for tetragonal TeO_2 and the data obtained from a representative film containing both phases is given in Table III. High-temperature x-ray diffractometry has shown that bulk TeO_2 undergoes no polymorphic transformations when heated to its melting point in air. The data for the unidentified phase do not suggest formation of the orthorhombic or high-pressure TeO_2 polymorphs (18). The unidentified phase may represent a higher oxide of tellurium, but the diffraction data are not in sufficient agreement with those reported (19) for TeO_3 phases prepared by hydrothermal methods to give definite identification.

Optical properties.—Optical properties of some amorphous films are shown in Fig. 3 and 4. Individual films are identified by numbers which refer to the sputtering run and by letters which refer to the various substrates used in any given run. The order of increasing refractive index is the same as the order of increasing extinction coefficient. The uncertainty in the refractive index of any film is within ± 4% and is primarily due to the uncertainty in the film thickness. For the oxide films of tungsten, tellurium, and tin, $k \leq 0.002$ at $\lambda \geq 450$ mμ. The experimental uncertainty in k is estimated to be within ± 0.003 for the lowest k values.

Few tin oxide films were obtained which were thick enough for optical measurements, because the tin cathode melted unless sputtered at a very low deposition rate. Amorphous bismuth oxide and lead oxide films are brown in transmission, whereas the other amorphous films are nearly colorless. The crystalline oxide films of cadmium, nickel, and silver are all colored; CdO is yellow, and the others are black.

Reactively sputtered bismuth oxide films have long been used as high-refractive-index dielectric films. The main problem associated with such films is the presence of optical absorption. Clapham (20) has examined the effect of gas composition used in sputtering on optical absorption. He found that the absorption is minimized when the ratio of argon to oxygen flow rates is about 100:1. In his work, optical properties were determined for films deposited on glass substrates, while electron diffraction patterns were ob-

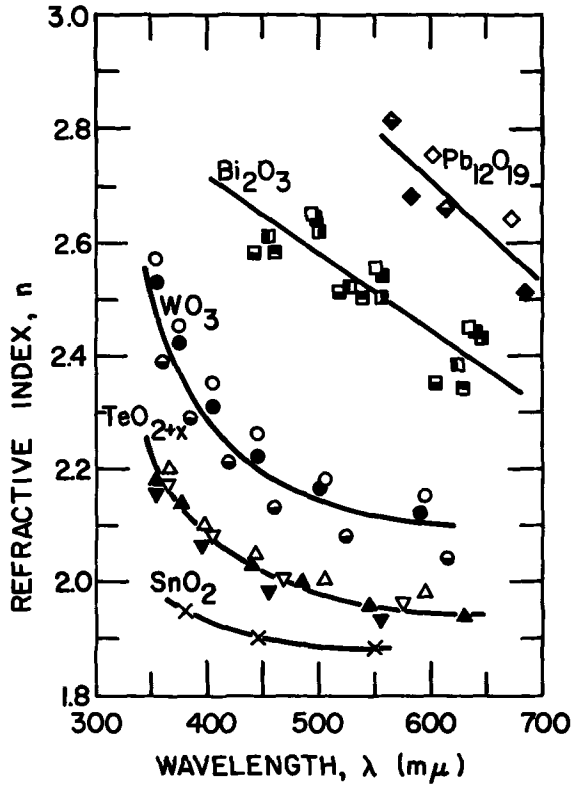

Fig. 3. Refractive index of amorphous films as a function of wavelength. Identification and thickness of films: $Pb_{12}O_{19}$—◇, 69F, 3840Å; ◈, 9H, 4060Å; ◆, 8A, 2730Å; Bi_2O_3—■, 20A, 3290Å; □, 20B, 3240Å; ◧, 20D, 3320Å; ⬓, 5A, 2580Å; ⬒, 66B, 2690Å; ◧, 66D, 2620Å; WO_3—○, 79B, 3450Å; ◒, 80A, 3780Å; ●, 74G, 3490Å; TeO_{2+x}—△, 68E, 3760Å; ▽, 67A, 2930Å; ▼, 67D, 2880Å; ▲, 24D, 4870Å; SnO_2—X, 19D, 2930Å.

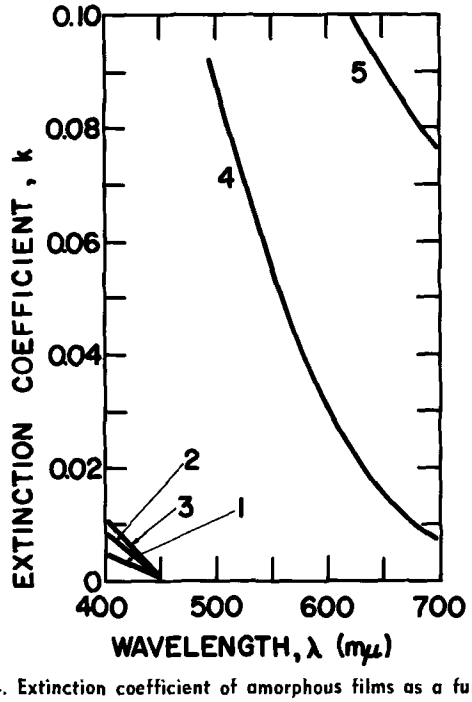

Fig. 4. Extinction coefficient of amorphous films as a function of wavelength. Identification of films: 1—SnO_2; 2—TeO_{2+x}; 3—WO_3; 4—Bi_2O_3; 5—$Pb_{12}O_{19}$.

tained for films deposited on carbon supports. The films were identified as α-Bi_2O_3.

In the present investigation, both optical and structural properties were determined for films deposited on glass substrates. The refractive index data obtained for the amorphous bismuth oxide films are in excellent agreement (well within experimental error) with those obtained by Clapham (20). The value of the extinction coefficient of the amorphous films at 550 mμ is 0.056, which is in reasonable agreement with the value of 0.07 reported by Clapham for a film prepared with a large excess of oxygen in the gas mixture. Transformation of the amorphous bismuth oxide to the β-modification, however, results in a large decrease in optical absorption without any detectable change in the refractive index. Extinction coefficient values of β-Bi_2O_3 films were determined in the usual manner and are compared with Clapham's (20) minimum-absorption values in Fig. 5. Values presented for the amorphous films are those shown in Fig. 4. The values obtained for β-Bi_2O_3 films are lower than Clapham's minimum-absorption values. These results show that optical absorption in bismuth oxide films is highly dependent on structure. Films of low absorption and high refractive index can be prepared via the crystallization of amorphous- or δ-Bi_2O_3 films of high absorption which have been prepared by reactive sputtering in an excess-oxygen gas mixture. Consequently, gas composition need not be a carefully controlled sputtering parameter.

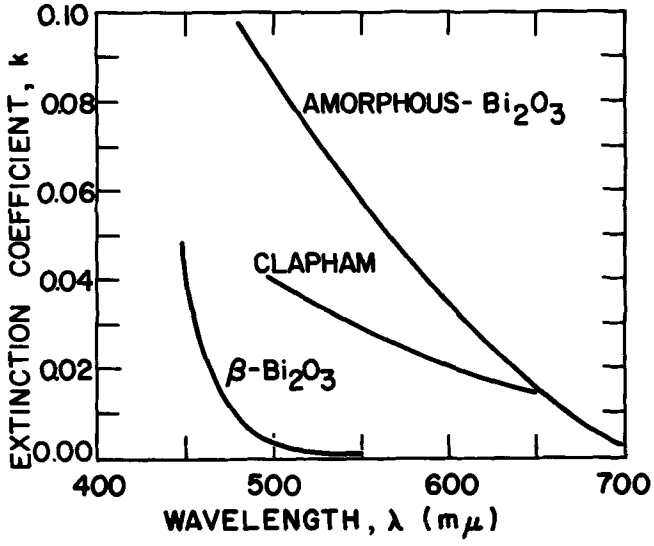

Fig. 5. Comparison of extinction coefficients of Bi_2O_3 films obtained in this investigation with those obtained by Clapham (20).

Discussion

The amorphous metal oxides prepared in this work, with the exception of SiO_2, have not been reported to form bulk glasses. Amorphous films of SiO_2 and SnO_2 have been prepared by reactive sputtering by Sinclair and Peters (1). Those of Ta_2O_5 have been prepared by reactive sputtering by Gerstenberg and Calbick (21). The other amorphous films have apparently not been reported. Only crystalline lead oxide films have been prepared by reactive sputtering by Lappe (22) and Sinclair and Peters (1). Substrate refrigeration was used in this work to maximize the number of amorphous materials prepared. That it had this effect was shown by the preparation of amorphous Bi_2O_3 with substrate refrigeration and crystalline δ-Bi_2O_3 without it.

Sarjeant and Roy (9) have examined the phases of metal oxides obtained from splat cooling and other rapid-quenching techniques. They were unable to prepare amorphous Bi_2O_3, Ta_2O_5, SnO_2, or WO_3 (except in the presence of some crystalline WO_3). In the present investigation, all of these metal oxides were prepared as amorphous films. Consequently, the deposition of reactively sputtered films on refrigerated substrates represents a more effective method of quenching than the techniques employed by Sarjeant and Roy (9).

The crystallization of the amorphous films often produces metastable high-temperature phases which

suggests that such films can be regarded as supercooled liquids. In particular, the formation of δ-Bi_2O_3 on crystallization of the amorphous Bi_2O_3 is good evidence that these films are structurally comparable to supercooled melts (see Fig. 2). If glass is defined as an amorphous, rigid, supercooled melt, such films can be considered to be glasses. Sinclair (23) has expressed the opinion that glass films be defined as those having an amorphous structure and a sufficiently high viscosity so that the structure is rigid. According to this definition, the amorphous films prepared in the present investigation must be regarded as glass films.

Crystallization of the amorphous WO_3 films usually gave rise to the orthorhombic modification rather than the higher-temperature tetragonal modification obtained by Sarjeant and Roy (9). The amorphous films, if supercooled liquids, would have been expected to crystallize initially as the tetragonal modification, and then transform to the orthorhombic modification. The possibility exists that this may have occurred, but the tetragonal to orthorhombic transformation occurred too quickly to be observed.

From the phases observed, it is apparent that the metal atoms of films reactively sputtered in an excess-oxygen atmosphere are frequently in high oxidation states. This is not meant to imply that the highest oxidation states are always obtained. Rather, it indicates that the lower oxidation states, which may be more common in some of the metal oxides prepared by other techniques, are not necessarily to be expected from the highly energetic sputtering process.

Acnowledgments

The authors wish to thank Dr. Peter R. Segatto for supplying some of the sputtering equipment, reading the manuscript, and giving helpful advice throughout the work. Spectrophotometric measurements provided by Mr. Herbert Hoover are particularly appreciated. Finally, the authors gratefully acknowledge the technical assistance of Mr. Oliver W. Kendall and Miss Brenda Boller in the film preparations and x-ray diffraction analyses, respectively.

Manuscript submitted July 11, 1968; revised manuscript received *ca.* Oct. 1, 1968. This paper was presented in part at the Dallas Meeting, May 7-12, 1967, as Paper 20.

Any discussion of this paper will appear in a Discussion Section to be published in the December 1969 JOURNAL.

REFERENCES

1. W. R. Sinclair and F. G. Peters, *J. Am. Ceram. Soc.*, **46**, 20 (1963).
2. D. R. Secrist and J. D. Mackenzie, *ibid.*, **48**, 487 (1965).
3. G. Koppelmann and K. Krebs, *Z. Physik*, **145**, 486 (1956).
4. A. E. Ennos, *J. Opt. Soc. Am.*, **52**, 261 (1962).
5. T. L. Rollins and F. L. Weichman, *Phys. Stat. Sol.*, **15**, 233 (1966).
6. W. R. Sinclair, F. G. Peters, D. W. Stillinger, and S. E. Koonce, *This Journal*, **112**, 1096 (1965).
7. W. B. White and R. Roy, *J. Am. Ceram. Soc.*, **47**, 242 (1964).
8. N. Terao, *Japan. J. Appl. Phys.*, **6**, 21 (1967).
9. P. T. Sarjeant and R. Roy, *J. Am. Ceram. Soc.*, **50**, 500 (1967).
10. O. Glemser and C. Naumann, *Z. anorg. u. allgem. Chem.*, **265**, 288 (1951).
11. J. Sosniak, *J. Vac. Sci. Technol.*, **4**, 87 (1967).
12. E. Stern and H. L. Caswell, *ibid.*, **4**, 128 (1967).
13. J. A. Perri, E. Banks, and B. Post, *J. Appl. Phys.*, **28**, 1272 (1957).
14. C. Rosen, E. Banks, and B. Post, *Acta Cryst.*, **9**, 475 (1956).
15. G. Gattow and D. Schütze, *Z. anorg. u. allgem. Chem.*, **328**, 44 (1964).
16. E. M. Levin and R. S. Roth, *J. Res. Nat. Bur. Std.*, **68A**, 189 (1964).
17. W. A. Dutton and W. C. Cooper, *Chem. Rev.*, **66**, 657 (1966).
18. S. S. Kabalkina, L. F. Vereshchagin, and A. A. Kotilevets, *Sov. Phys.-JETP*, **24**, 251 (1967).
19. M. Maurin and J. Moret, *C. R. Acad. Sci., Paris, Ser. C*, **226** (1), 22 (1968).
20. P. B. Clapham, *Brit. J. Appl. Phys.*, **18**, 363 (1967).
21. G. Gerstenberg and C. J. Calbick, *J. Appl. Phys.*, **35**, 402 (1964).
22. F. Lappe, *J. Phys. Chem. Solids*, **23**, 1563 (1962).
23. W. R. Sinclair, *Glass Industry*, **49**, 22 (1968).
24. V. Scatturin, P. L. Bellon, and A. J. Salkind, *This Journal*, **108**, 819 (1961).

Optimization of Electroluminescent Efficiencies for Vapor-Grown $GaAs_{1-x}P_x$ Diodes

C. J. Nuese, J. J. Tietjen, J. J. Gannon, and H. F. Gossenberger

RCA Laboratories, Princeton, New Jersey

ABSTRACT

A series of $GaAs_{1-x}P_x$ diodes have been prepared by a vapor-phase growth technique to investigate the effects of current-spreading, absorption, impurity concentrations, and alloy composition on room-temperature electroluminescent efficiencies. It is shown that for maximum efficiencies, a diode structure should be prepared with a p^+ surface layer to enhance current spreading, and a $GaAs_{1-x}P_x$ "window" containing about 10% more GaP than the p-n junction region to reduce absorption losses. It is also shown that the most efficient radiative recombination originates on the p-side of the junction; low acceptor concentrations and high donor concentrations which are required for strong electron injection into the p-side of the junction are thus found to result in highest electroluminescent efficiencies. Slow compositional grading between the GaAs substrate and the $GaAs_{1-x}P_x$ p-n junction also resulted in increased efficiencies. A drop-off in efficiency near the direct-indirect transition for values of x increasing from 0.38 was found to be severe, however, a corresponding increase in the spectral sensitivity of the eye was found to provide a broad maximum in diode brightness at emission wavelengths near 6800Å ($x \approx 0.38$). Planar uncoated diodes have provided brightness values in excess of 300 ft-L at 10 amp/cm^2 with external efficiencies of 2×10^{-4} at 6400Å. Plastic encapsulants can be readily used as domes to increase external efficiencies by a factor of 3, or as directional lenses to provide beam-widths as narrow as 7°.

Several semiconductor compounds have been considered for d-c room-temperature visible-light-emitting diodes, the most promising to date being GaP, $GaAs_{1-x}P_x$, and $Al_{1-x}Ga_xAs$. In GaP, high external efficiencies ($\approx$ 2%) have been measured (1), although much of the radiation is in the infrared. Recent results for solution-grown $Al_{1-x}Ga_xAs$ have also been very encouraging (2) (0.4% for shaped, coated diodes emitting at 6500Å). The work reported here is concerned with determining the potential of the system $GaAs_{1-x}P_x$ for the fabrication of electroluminescent diodes. Such devices have application as small indicating lamps, for alpha-numeric displays, and in various optical systems requiring a particular emission wavelength (*e.g.*, to match a detector or photosensitive device).

In order to optimize $GaAs_{1-x}P_x$ electroluminescent efficiencies, it is desirable to separate the relevant parameters and to determine the importance of each. For this purpose, a vapor-phase growth technique is particularly well-suited. With it, one can individually control such parameters as alloy composition, junction depth, impurity concentration, and compensation, etc.; this is not the case for diffused diodes where many of these parameters are strongly interrelated. In addition, the ease of successively depositing different type layers of $GaAs_{1-x}P_x$ is found to be important for the fabrication of diodes with reduced absorption losses and uniform light emission.

The vapor-phase growth of $GaAs_{1-x}P_x$ p-n junctions has previously been employed for the fabrication of injection lasers capable of pulsed room-temperature (3) or c-w operation at 77°K (4). In addition, vapor-phase growth has been used to clarify the effects of absorption, temperature, and impurity concentrations on the quantum efficiency of GaAs noncoherent diodes (5). For this research, similar growth techniques have been used to prepare $GaAs_{1-x}P_x$ junction structures specifically designed for visible-light-emitting sources operating in the spontaneous mode.

Experimental Procedure

The $GaAs_{1-x}P_x$ used in this study was deposited epitaxially on <100>-oriented n-type GaAs substrates by an open-tube vapor-phase growth technique which has been described previously (6). Briefly, arsine and phosphine are used as the source of arsenic and phosphorus, while HCl gas is used as a transport agent for the gallium. Donor and acceptor doping is accomplished by using hydrogen-selenide gas and Zn vapor, respectively.

The electroluminescent diodes were prepared in an n-p-p^+ structure, as shown in Fig. 1, by grading the phosphorus concentration, x, from zero at the GaAs substrate to about 0.4-0.6 just below the p-n junction. Following junction formation, a further increase in phosphorus concentration was employed to provide a high-energy-gap "window" for the junction radiation. A p^+ layer was used in the outermost portion of the window in order to spread the current laterally from beneath small surface contacts so that the radiative recombination would occur uniformly over the p-n junction. It should be noted that the structure of Fig. 1, consisting of various impurity concentrations and alloy compositions, is prepared in one continuous growth operation and, unlike diffused and (usually) solution-regrown diodes, does not require an additional high temperature process to form or anneal the p-n junction.

Diode fabrication procedures were similar to those used for vapor-grown GaAs electroluminescent diodes (5). An array of small Ag-Mn ohmic contacts (7) was evaporated to the as-grown p-type epitaxial surface, and a continuous Au-Sn contact was evaporated to a lapped surface of the n-type GaAs substrate. Individual chips, 1 mm^2, were cleaved from the wafer, mounted on

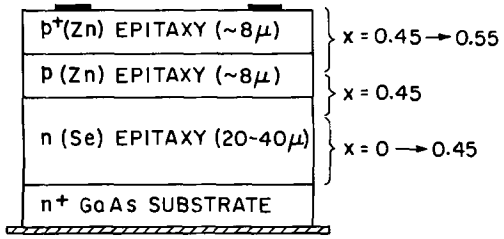

Fig. 1. Vapor-grown $GaAs_{1-x}P_x$ electroluminescent diode structure. Light emission passes through the p and p^+ layers and is emitted from the uppermost p^+ surface.

a transistor header, and contacted with Au leads on an ultrasonic bonder.

The external quantum efficiency was measured with a calibrated, large-area silicon solar cell (Hoffman 2A) placed in close proximity to the uppermost p-type light-emitting surface of the diode. Emission from the four cleaved edges of the diode was not measured by this technique, and therefore, the reported efficiency values are estimated to be low by about 10%. Spectral measurements were taken on a Spex 1700 grating monochromator with an S-1 photomultiplier and associated amplifying and recording electronics. All electrical and optical measurements were taken with applied current densities and/or duty cycles small enough to avoid adverse heating effects.

Donor and acceptor impurity concentrations were approximated by comparison with epitaxial Hall samples prepared under similar growth conditions. $GaAs_{1-x}P_x$ alloy compositions were occasionally determined by x-ray diffractometry, but were usually approximated from the junction emission energy and the known relationship (6) between energy gap and alloy composition.

Results and Discussion

Current spreading and absorption.—To evaluate the performance of the diode structure of Fig. 1, we first examine the importance of the p^+ layer in spreading the current from beneath the dot contacts (Fig. 2). The microphotograph of Fig. (2a) shows an extreme example of current localization beneath the contacts, which is found to occur for diodes without (or with too thin) a p^+ layer. A typical junction acceptor concentration of 3×10^{18} holes/cm^3 ($\rho \approx 10^{-2}$ ohm-cm) is too low to provide adequate lateral conduction between the contacts. Such localization is undesirable because a large fraction of the emission is blocked by the metalization and reflected back into the (absorbing) semiconductor. For Fig. (2b), an 8μ thick p^+ layer of Zn-doped $GaAs_{1-x}P_x$ with $p \approx 3 \times 10^{19}$ cm^{-3} ($\rho \approx 10^{-3}$ ohm-cm) was vapor-grown above a similar p-n junction. Here, the light emission is relatively uniform over the 4 mm^2 junction area, even though less than 6% of the p^+ surface is metalized. A doping concentration of about 3×10^{19} cm^{-3} was found empirically to best enhance the current spreading. This n-p-p^+ structure was then used in all subsequent experiments.

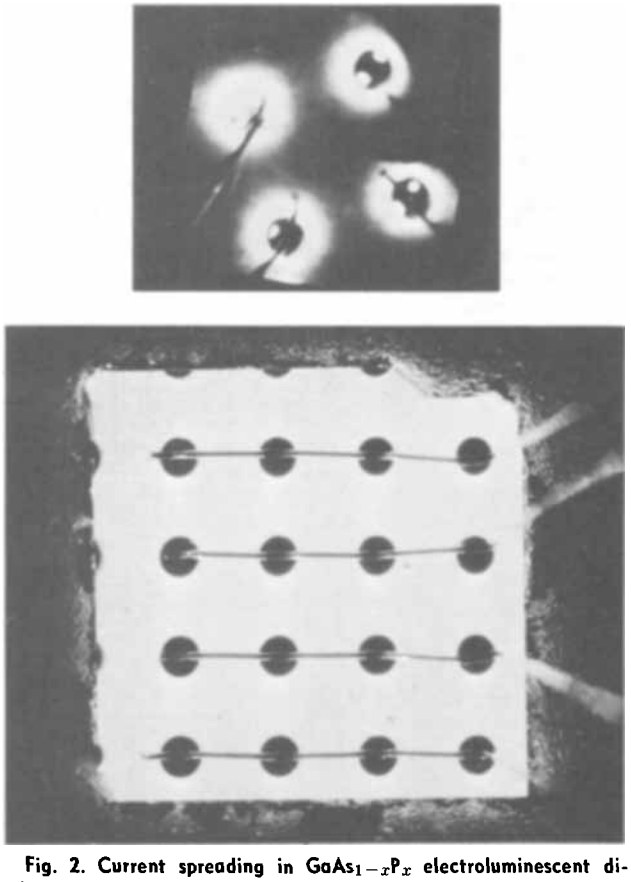

Fig. 2. Current spreading in $GaAs_{1-x}P_x$ electroluminescent diodes. All of the illumination for these microphotographs was provided by the band-gap diode emission. $T = 300°K$. For both photos, ohmic contacts are 0.005 in. diameter dots located on 0.020 in. centers. (a, top) Extreme current localization beneath ohmic contacts, which is caused by absence of p^+ layer. (b, bottom) Uniform light emission enhanced by presence of 8μ thick p^+ surface layer doped to 3×10^{19} cm^{-3}.

It is well known that room-temperature absorption losses significantly limit the external efficiencies of near-band-gap-emitting electroluminescent diodes (5, 8-10). One technique for reducing this absorption is with a higher-energy-gap window adjacent to the p-n junction (11), so that the lower energy junction emission travels to the semiconductor surface with little attenuation. We have previously reported the use of $GaAs_{1-x}P_x$ windows with vapor-grown GaAs electroluminescent diodes (5), and have also found such windows effective for reducing the absorption losses of the $GaAs_{1-x}P_x$ diodes described here.

A series of 6 $GaAs_{1-x}P_x$ wafers were prepared as described above, each with a window of different alloy composition above the p-n junction, but as alike as possible in alloy composition ($x \approx 0.41$) at the junction and in impurity concentrations ($n = 2 \times 10^{18}$, $p = 3 \times 10^{18}$, $p^+ = 3 \times 10^{19}$ cm^{-3}). For these wafers, the p and p^+ layers were each about 8μ thick, and the compositional grading to provide the window was initiated about 2μ beyond the p-n junction, so as not to alter the junction recombination process. The external quantum efficiency of diodes prepared from these wafers is plotted in Fig. 3 as a function of the difference in phosphorus composition, Δx, between the surface and the junction.

The improvement in external efficiency (by a factor of about 3) for windows with $\Delta x = 0.1$ is attributed to reduced absorption losses. The effectiveness of the window for the structure used here is always limited by high free-carrier absorption in the p^+ layer, even at photon energies significantly less than bandgap. Calculations with p-type GaAs (for which room-temperature absorption data are available) indicate that one should expect a reduction in absorption on the order of 3 for a structure similar to that in Fig. 1.

The decrease in relative external efficiency for $\Delta x > 0.1$ is mainly due to inadequate current spreading which is observed for contacts applied to phosphorus-rich $GaAs_{1-x}P_x$. At increased phosphorus concentrations, the surface conductivity of the p^+ layer decreases due to lower hole mobilities, as well as to a reduction in the solubility of Zn in $GaAs_{1-x}P_x$ at the

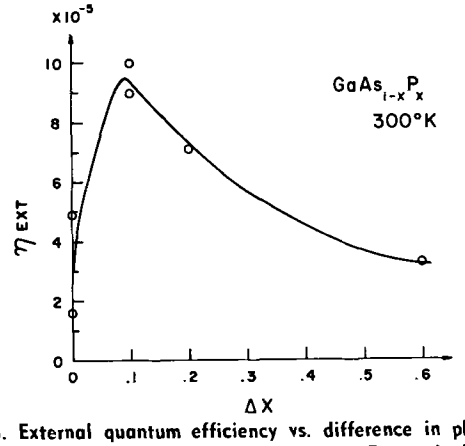

Fig. 3. External quantum efficiency vs. difference in phosphorus composition, Δx, between surface and junction. External efficiencies have been corrected slightly to normalize variations in emission wavelength.

growth temperature (775°C) (14). It is also possible that excessive strain due to lattice mismatch or to differences in thermal expansion coefficients (15) can reduce the junction efficiency whenever the alloy composition in the window is graded too rapidly. The effect of grading on junction efficiencies is again mentioned below.

Impurity concentrations.—After optimizing the p^+ layer to obtain light uniformity and the phosphorus-rich window to reduce absorption, a series of 11 wafers was prepared to determine the effects of impurity concentrations on junction efficiency. For one group of 5 wafers, the doner (Se) concentration was maintained at 2×10^{18} cm^{-3}, and the acceptor (Zn) concentration was intentionally varied from wafer to wafer between 1×10^{18} and 3×10^{19} cm^{-3}. For the second group of 6 wafers, the Zn concentration was held at 3×10^{18} cm^{-3}, while the Se concentration was varied between 6×10^{16} and 5×10^{18} cm^{-3}. For all of the wafers, the p^+ layer was maintained at 3×10^{19} cm^{-3} to ensure good current spreading.

The results of room temperature efficiency measurements for diodes fabricated from these wafers are shown in Fig. 4 and 5. Also included are similar results for GaAs vapor-grown diodes from a previous publication (5). Immediately apparent is the lower efficiencies (by a factor of about 25) for the $GaAs_{1-x}P_x$ diodes as compared to those of GaAs. A reduction in $GaAs_{1-x}P_x$ efficiencies for alloy compositions near the direct-indirect transition has been observed previously (22, 23), and is evaluated further below. However, also interesting in Fig. 4 is the relatively gradual drop-off in efficiency for $GaAs_{1-x}P_x$ diodes that occurs with increasing acceptor concentrations at a value as low as 3×10^{18} cm^{-3}. This effect is probably due to two factors. First, for high acceptor concentrations ($p \approx 10^{19}$ cm^{-3}), the absorption coefficient remains large for photon energies less than bandgap (13), due to large free-carrier absorption. Thus, a high-energy-gap window would then be much less effective in reducing absorption and would result in a reduction in external efficiencies (but not internal efficiencies) at high acceptor concentrations.

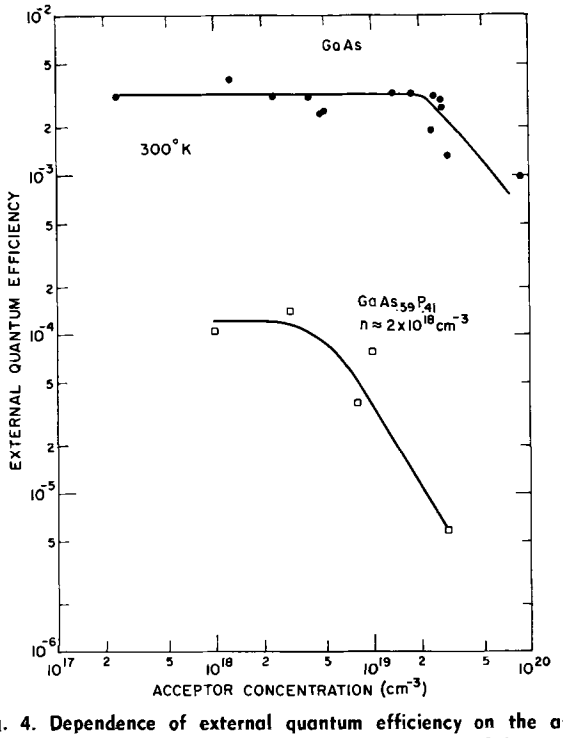

Fig. 4. Dependence of external quantum efficiency on the acceptor concentration on the p-side of the junction. $x \approx 0.41$, $n = 2 \times 10^{18}$ cm^{-3}, $p^+ = 3 \times 10^{19}$ cm^{-3}, T = 300°K. Efficiencies were corrected slightly for small variations in emission wavelength. GaAs data are from previous publication (5).

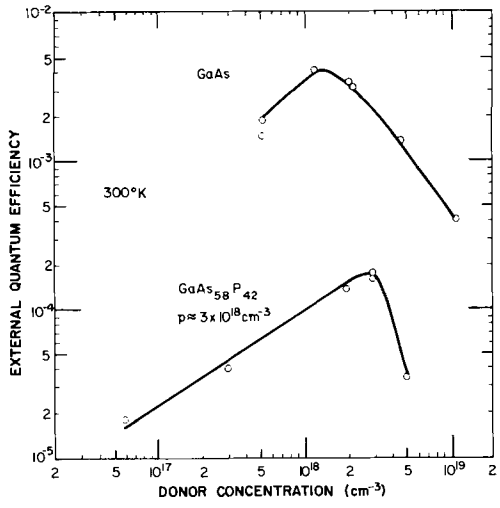

Fig. 5. Dependence of external quantum efficiency on the donor concentration on the n-side of the junction. $x \approx 0.41$, $p = 3 \times 10^{18}$ cm^{-3}, $p^+ = 3 \times 10^{19}$ cm^{-3}, T = 300°K. Efficiencies were corrected slightly for small variations in emission wavelength. GaAs data are from previous publication (5).

Second, the electron injection efficiency into the radiatively efficient p-region, which is given by (16)

$$\gamma_{n\to p} = \frac{1}{1 + \sqrt{\frac{p\mu_p}{n\mu_n}}} \qquad [1]$$

decreases by at least a factor of 3 for an increase in acceptor concentration from 1×10^{18} cm^{-3} to 5×10^{19} cm^{-3}. In general, the electron injection efficiency, $\gamma_{n\to p}$, in $GaAs_{1-x}P_x$ junctions with alloy compositions near the direct-indirect transition ($x = 0.44$) would be expected to decrease (as compared to GaAs junctions) due to the large drop-off in electron mobility, μ_n, from its GaAs value (17, 18). The reduction in μ_n (and μ_n/μ_p) would require a smaller acceptor concentration and/or a larger donor concentration to maintain the electron injection efficiency for $GaAs_{1-x}P_x$ junctions equal to that for GaAs diodes. The fact that the efficiency peaks do occur at lower acceptor concentrations (Fig. 4) and higher donor concentrations (Fig. 5) for $GaAs_{1-x}P_x$ than for GaAs is consistent with this injection process.

In Fig. 5, the initial increase in efficiency with increasing donor concentration is again partly due to increasing electron injection into the p-region, according to Eq. [1]. Over the range of doping studied here, $\gamma_{n\to p}$ would increase by about a factor of 3, somewhat less than the observed efficiency increase in Fig. 5. The peak in efficiency occurs at about $n = 3 \times 10^{18}$ cm^{-3}, higher than that for GaAs, as mentioned previously. The very sharp fall-off in efficiency for $n = 4\text{-}5 \times 10^{18}$ cm^{-3} is not clearly understood, but may be related to metallurgical imperfections (*e.g.*, Se-precipitation) which occur at such high donor concentrations (19).

The electron injection model suggested by Fig. 4 and 5 is based on the assumption of efficient recombination occurring primarily on the p-side of the junction, an assumption which is supported by photoluminescence measurements on bulk n- and p-type epitaxial wafers. Room temperature photoluminescence of p-type wafers consists of a strong near-band-gap peak; however, for n-type wafers such peaks are very weak by comparison.

The fact that the radiation originates primarily from the p-side of the junction is also independently confirmed by examination of the spectral half-widths for these diodes. The half-width, $\Delta\lambda$, plotted in Fig. 6 as a function of the donor or acceptor concentration, remains relatively constant at about 160Å over the entire range of donor concentrations, but increases significantly with increasing acceptor concentration. Such an

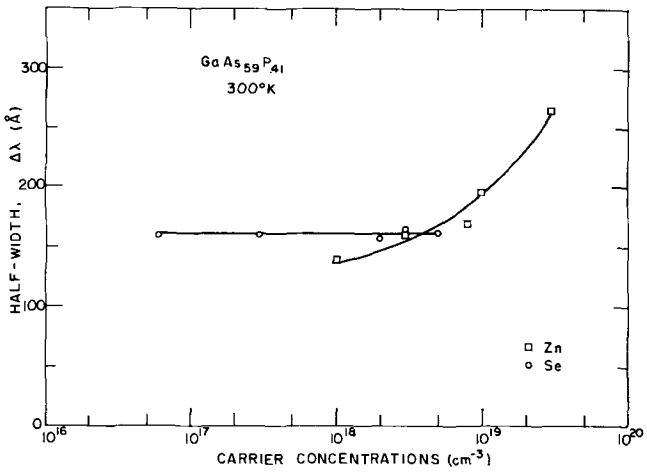

Fig. 6. Spectral half-width, $\Delta\lambda$, vs. donor and acceptor concentrations for $GaAs_{0.59}P_{0.41}$. T = 300°K.

increase is well known to result from impurity band tailing, which demonstrates, in this case, that the acceptor impurity, and therefore the p-side of the junction, is the effective origin of efficient recombination. This is also the case for $GaAs_{1-x}P_x$ diffused p-n junctions (20, 21).

The possibility of the spectral half-widths of Fig. 6 being distorted by a preferential absorption of the high-energy emission edge does exist; however, an expected increase in absorption at high acceptor concentrations would cause a decrease in spectral half-widths, contrary to Fig. 6.

Alloy composition.—For $GaAs_{1-x}P_x$ diodes having compositions near the direct-indirect transition ($x \approx 0.44$), a drop-off in efficiency with increasing phosphorus concentration has been previously noted (22, 23). In Fig. 7, the extent of this effect is clearly depicted, showing a decrease in efficiency by almost 3 orders of magnitude between 6800Å ($x \approx 0.38$) and 6000Å ($x \approx 0.60$). Such behavior is caused by the transfer of electrons from the direct [000] conduction band minimum to the six indirect <100> minima (23),

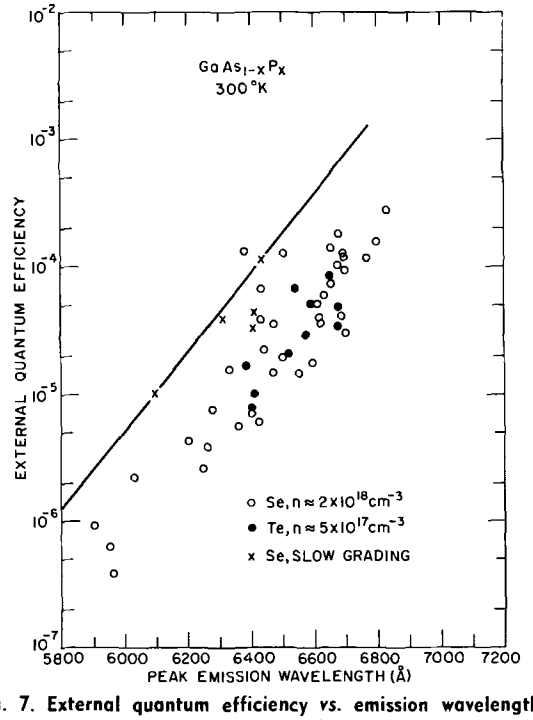

Fig. 7. External quantum efficiency vs. emission wavelength for $GaAs_{1-x}P_x$ junction diodes. T = 300°K. All diodes are planar and uncoated. o Se, n = 2 x 10^{18} cm^{-3}, graded at 2 %/μ; x Se, n = 2 x 10^{18} cm^{-3}, graded at 1 %/μ; o Te, n = 5 x 10^{17} cm^{-3}.

or to "shallow" donor states associated with the indirect minima (24). At 6800Å, planar uncoated diodes yield average efficiencies of 3-4 x 10^{-4}, with best efficiencies anticipated to be at least as high as 1 x 10^{-3} (by extrapolating the best efficiency results at shorter wavelengths, where many more wafers were prepared).

Several of the diodes with highest efficiencies in Fig. 7 were obtained by grading the alloy composition more slowly between the GaAs substrate and the $GaAs_{1-x}P_x$ p-n junction. Whereas typically the phosphorus concentration, x, was graded at a rate of about 2%/μ, most of the highest efficiency diodes were prepared from a few wafers which were graded at a rate of 1%/μ. With the slower grading, not only were efficiencies higher, but a faint dark grid-network (25) (faintly observable in Fig. 2b), which had always been present in the more rapidly graded samples, was not detected. The lower efficiencies and the grid-like array of dark "lines" are believed to be due to strain-induced dislocation arrays caused by rapid grading.

Also note in Fig. 7 that comparable efficiencies have been obtained for $GaAs_{1-x}P_x$ diodes employing either Se or Te as the donor impurity. However, to date, Te donor concentrations in $GaAs_{1-x}P_x$ have been limited by growth conditions to about 5 x 10^{17} cm^{-3}, whereas the Se donor concentrations in Fig. 7 are typically 2 x 10^{18} cm^{-3}. Thus, if the dependence of efficiency on Te concentration is similar to that for Se (Fig. 5), and if Te can be incorporated into the lattice at concentrations comparable to those of Se, then Te should provide still higher efficiencies than those shown in Fig. 7.

Perhaps of greater interest than the external quantum efficiency of visible-light-emitting diodes is their brightness, which takes into consideration the spectral sensitivity of the human eye. The Luminosity Factor (26), F, plotted in Fig. 8, accounts for the eyes' dependence on spectral wavelength, peaking at a value of 1.0 for its maximum response at 5550Å green light, and decreasing rapidly toward zero for near-infrared radiation.

The brightness, B, of a planar electroluminescent diode is proportional to the power radiated per unit area of source, and to the Luminosity Factor of the human eye. For a monochromatic-source approximation, the brightness can be expressed as

$$B \text{ (in ft-L)} = \frac{7.8 \times 10^5 F \eta_{ext} I}{\lambda A} \qquad [2]$$

In Eq. [2], η_{ext} is the external quantum efficiency, λ is the peak emission wavelength in microns, I is the applied diode current in amperes, and A is the observed light-emitting area. The relative brightness of $GaAs_{1-x}P_x$ diodes, also plotted in Fig. 8, is determined primarily by the strong wavelength dependence of F and of η_{ext}, and is seen to peak at emission wavelengths of 6700-6800Å. The dependence of brightness on alloy composition (or wavelength) is much less severe than the efficiency dependence, varying by less than a factor of 3 between 6200 and 7100Å. Highest brightness values at room temperature for these diodes are about 300 ft-L for applied current densities of 10 amp/cm^2. However, these results have been obtained with diodes emitting at 6400-6600Å, which corresponds to those compositions for which the largest number of wafers have been grown. By concentrating on the 6700-6800Å range, only slightly higher brightness values than the 300 ft-L can be expected.

Diode encapsulants.—Thus far we have treated the optimization of material parameters for electroluminescent efficiencies of planar $GaAs_{1-x}P_x$ diodes. However, a simple planar structure is relatively inefficient for diodes of $GaAs_{1-x}P_x$ (and of most other III-V compounds), because of large internal reflections at the semiconductor-air interface. The critical angle,

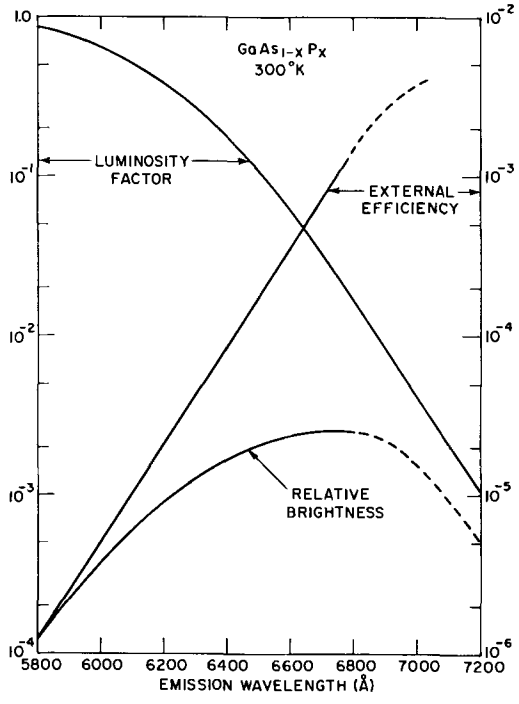

Fig. 8. Luminosity factor, external quantum efficiency, and brightness as a function of $GaAs_{1-x}P_x$ emission wavelength. T = 300°K.

Φc, for total internal reflection (*i.e.*, the largest angle which incident radiation can subtend and still be diffracted from the crystal), is defined by the equation (27)

$$\sin \Phi c = n_o/n_1 \qquad [3]$$

where n_1 and n_o are the refractive indices for the semiconductor and for the surrounding medium, respectively. For a $GaAs_{1-x}P_x$-air interface, the large mismatch in refractive index ($\approx$ 3.6 for $GaAs_{1-x}P_x$, 1.0 for air) defines a critical angle of only 16°, so that a large fraction (about 98%) of the randomly oriented junction radiation is totally reflected back into the semiconductor (28), and efficiently absorbed.

A convenient technique for reducing these reflection losses is by "capping" the planar diode with a transparent material which more closely matches the large refractive index of $GaAs_{1-x}P_x$. Plastic caps (including urethanes, epoxies, lucites, etc.) have been successfully employed for this purpose; however, two requirements are imposed on such caps. The first is, obviously, a high refractive index to increase Φc for radiation at the semiconductor-plastic interface, while the second is appropriate shaping to transmit most of the radiation from the semiconductor into the air without large reflection losses at the plastic-air interface. Theoretically, no efficiency improvement is obtained for a perfectly planar coating, regardless of its refractive index.[1] Actually, improvements of $\approx$ 40% occur for such coatings because of optical inhomogeneities and small deviations from planarity.

One shape which is particularly convenient for improving efficiencies is that of a hemispherical dome, shown in the insert of Fig. 9. For such a shape, the efficiency improvement can be calculated from (28)

$$\frac{\eta_{dome}}{\eta_{air}} = \frac{1 - \cos(\Phi c)_{dome}}{1 - \cos(\Phi c)_{air}} \qquad [4]$$

and is plotted in Fig. 9 as a function of the index of refraction for the coating material.

[1] When a planar plastic coating is deposited on the planar diode, the critical angle of the semiconductor → plastic interface is increased from Φc to Φc'. All of the junction radiation with Φc < Φ < Φc' is diffracted into the plastic, but is incident on the plastic → air interface at an angle greater than its critical angle, and is totally reflected within the plastic. Very thin anti-reflective coatings which utilize interference effects are not considered here.

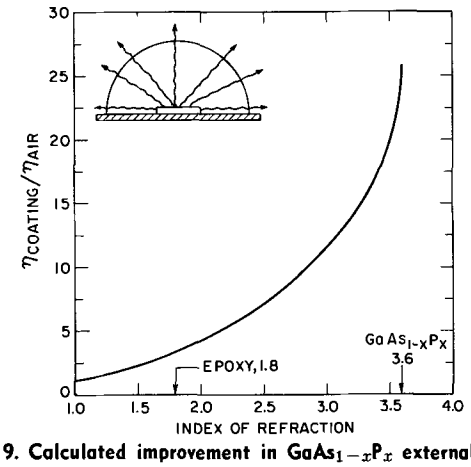

Fig. 9. Calculated improvement in $GaAs_{1-x}P_x$ external quantum efficiencies provided by hemispherical dome with arbitrary index of refraction. Absorption losses are neglected.

It is readily apparent that large improvements can be attained for high-index-of-refraction materials (as much as a factor of 26 for a perfectly matched, non-absorbing, transparent material). However, plastics, etc. which are commercially available to date, have refractive indices no larger than about 1.8, so that caps of these materials can only be expected to improve efficiencies by a factor of about 3. Experimentally, plastic caps have been used which do improve efficiencies by a factor of about 3 (from approximately 0.03 to 0.1%) for $GaAs_{1-x}P_x$ with emission wavelengths near 6500Å. At 6800Å, external efficiencies of at least 0.3% should thus be attainable with such caps. We should add that these efficiency improvements do not lead to similar gains in diode brightness, because the lens-like action of the hemisphere magnifies the observed diode area, thus increasing A in Eq. [2].

Besides improving the external efficiency of a planar electroluminescent diode, a plastic cap also can be used as a spherical lens for applications requiring a source with beam-like directionality. By molding (*e.g.*, in Teflon) a plastic lens to the shape shown in Fig. 10, a diode may be readily located at the primary focal length of the lens so that nearly all of the junction radiation is focused into a narrow beam. Figure 10 shows the experimental far-field radiation patterns for three initially identical $GaAs_{1-x}P_x$ diodes which were capped with plastic lenses of different shapes. The focal length, l, of the lens is calculated from the equation (29)

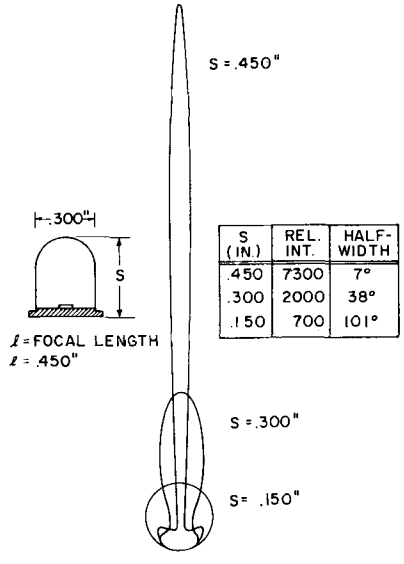

Fig. 10. Far field radiation patterns for $GaAs_{1-x}P_x$ diodes capped with a plastic lens.

$$\frac{n}{l} = \frac{n-1}{r} \qquad [5]$$

where n is the refractive index of the plastic, having a spherical surface of radius r. For the diodes in Fig. 10, $n = 1.5$ and $r = 0.15$ in., yielding $l = 0.450$ in. Particularly significant in Fig. 10 is the very narrow (7° half-width) beam obtained for the diode mounted at the focal length of the lens. Compared with the hemispherically shaped diode ($s = 0.150$ in.), an order of magnitude increase is also noted in its peak intensity. A room temperature electroluminescent source which can be operated on d.c. and provide a narrow beam of efficient visible light could compete with laser diodes in many applications, especially since laser diodes operate only under pulse conditions and at low duty cycles at room temperature.

Conclusions

Room temperature electroluminescent efficiencies of $GaAs_{1-x}P_x$ visible-light-emitting diodes are significantly lower than those of GaAs diodes. It is well known that this is primarily due to electron transfer from the efficient [000] conduction band minimum to the relatively inefficient <100> minima (or to states associated with them). However, in addition to this effect, the present study has revealed that several other parameters must be considered to achieve maximum efficiencies in $GaAs_{1-x}P_x$ diodes. For the diodes studied here, maximum efficiencies were obtained by employing:

(*i*) Strong electron injection into the radiatively efficient p-side of the junction. This is accomplished by using relatively low acceptor concentrations and high donor concentrations ($n \approx p \approx 3 \times 10^{18}$ cm^{-3}) adjoining the p-n junction.

(*ii*) Adequate current spreading at the diode surface to prevent current localization beneath the metallic contacts. This is effected by incorporating a p^+ layer at the surface of the diode.

(*iii*) Slow compositional grading between the GaAs substrate and the p-n junction, resulting in reduced strain and increased efficiencies.

(*iv*) Semi-transparent windows of phosphorus-rich $GaAs_{1-x}P_x$ to reduce absorption. Here, the exact composition of the window is important, with maximum effectiveness being realized with alloys containing about 10% more phosphorus than the junction region. Also, the use of transparent domes of high-index-of-refraction materials can improve both the external quantum efficiency and the directionality of the emitted radiation.

In addition, to achieve maximum brightness in this alloy series, it is necessary to prepare diodes which emit at about 6800Å. At this wavelength, an optimum compromise is obtained between the diode efficiency and the spectral sensitivity of the human eye.

Finally, using a vapor-phase growth method such as that employed in this study, the complex structures dictated by the above considerations can be readily fabricated.

Acknowledgments

The authors would like to thank H. P. Maruska and R. Bednars for preparing some of the wafers used here, and C. W. Benyon for ultrasonically bonding the diodes. We furthermore gratefully acknowledge the helpful discussions and suggestions of L. R. Weisberg. The research reported in this paper was sponsored in part by the Air Force Cambridge Research Laboratories, Office of Aerospace Research, under Contract F19628-68-C-0190.

Manuscript submitted Aug. 26, 1968; revised manuscript received *ca.* Oct. 16, 1968. This paper was presented at the Boston Meeting, May 5-9, 1968, as Paper 103.

Any discussion of this paper will appear in a Discussion Section to be published in the December 1969 JOURNAL.

REFERENCES

1. R. A. Logan, H. G. White, and F. A. Trumbore, *Appl. Phys. Letters*, **10**, 206 (1967).
2. H. Rupprecht, J. M. Woodall, and G. D. Pettit, IEEE Semiconductor Laser Conference, Las Vegas, Nevada, November 1967.
3. J. J. Tietjen, J. I. Pankove, I. J. Hegyi, and H. Nelson, *Trans. AIME*, **239**, 385 (1967).
4. H. Nelson, RCA Laboratories, Private communication.
5. C. J. Nuese, J. J. Tietjen, J. J. Gannon, and H. F. Gossenberger, *AIME Transactions Metallurgical Soc.*, **242**, 400 (1968).
6. J. J. Tietjen and J. A. Amick, *This Journal*, **113**, 724 (1966).
7. C. J. Nuese and J. J. Gannon, *ibid.*, **115**, 327 (1968).
8. D. E. Hill, *Bull. Am. Phys. Soc.*, **10**, 97 (1965).
9. W. N. Carr, *IEEE Trans. Electron. Devices*, **ED-12**, 53 (1965).
10. T. Gonda, M. F. Lamorte, P. Nyul, and H. Junker, *IEEE Trans. Quantum Electron.*, **QE-2**, 74 (1966).
11. S. V. Galginaitis, *J. Appl. Physics*, **36**, 460 (1965).
12. W. J. Turner and W. E. Reese, *J. Appl. Phys.*, **35**, 350 (1964).
13. D. E. Hill, *Phys. Rev.*, **133**, A866 (1964).
14. L. L. Chang and G. L. Pearson, *J. Phys. Chem. Solids*, **25**, 23 (1964).
15. E. D. Pierron, D. L. Parker, and J. B. McNeeley, *J. Appl. Phys.*, **38**, 4669 (1967).
16. T. Nakano, K. Fujikawa, and T. Oku, *Japan J. Appl. Phys.*, **6**, 665 (1967).
17. J. J. Tietjen and L. R. Weisberg, *Appl. Phys. Letters*, **7**, 261 (1965).
18. C. M. Wolfe, C. J. Nuese, and N. Holonyak, Jr., *J. Appl. Phys.*, **36**, 3790 (1965).
19. M. S. Abrahams, C. J. Buiocchi, and J. J. Tietjen, *ibid.*, **38**, 760 (1967).
20. C. M. Wolfe, M. D. Sirkis, C. J. Nuese, N. Holonyak, Jr., O. L. Gaddy, O. T. Purl, and W. E. Kunz, *ibid.*, **36**, 2087 (1965).
21. C. J. Nuese, G. E. Stillman, M. D. Sirkis, and N. Holonyak, Jr., *Solid-State Electronics*, **9**, 735 (1966).
22. M. Pilkuhn and H. Rupprecht, *J. Appl. Phys.*, **36**, 684 (1965).
23. H. P. Maruska and J. I. Pankove, *Solid-State Electronics*, **10**, 917 (1967).
24. N. Holonyak, Jr., C. J. Nuese, M. D. Sirkis, and G. E. Stillman, *Appl. Phys. Letters*, **8**, 83 (1966).
25. C. J. Nuese and J. J. Tietjen, To be published.
26. W. T. Walsh, "Photometry," Appendix IV, Dover Publications, Inc., New York (1965).
27. F. A. Jenkins and H. E. White, "Fundamentals of Optics," p. 15, McGraw-Hill Book Co. Inc., New York (1957).

Mechanical Loss and Conduction Mechanism in Iron-Phosphate Glass

R. A. Miller and Kent W. Hansen[1]

Research and Development Laboratories, Corning Glass Works, Corning, New York

ABSTRACT

Mechanical loss measurements were made on an iron-phosphate glass (55% FeO_x-45% P_2O_5 on a mole basis). The activation energy (0.59 ev) determined from the mechanical-loss data compared favorably with those (0.55-0.57 ev) obtained from dielectric-loss and d-c conductivity data on a similar glass. The correlation of these results is consistent with a "hopping" model for electrical conduction in iron-phosphate glasses.

Electrical conduction in semiconducting oxide glasses has been shown to result primarily from electrical charge transfer by electrons and/or holes (1). Two mechanisms have been proposed to explain the conduction. One of these is conduction by band states (2), the other by trapped states (3).

Thermoelectric power measurements made on 55 m/o (mole per cent) FeO_x-45 m/o P_2O_5 semiconducting glasses have been shown to be essentially independent of temperature (4). This would tend to imply that the carrier concentration is insensitive to temperature and, thus, that the conduction cannot be explained on the basis of band states. However, one of the consequences of narrow-band conduction, *i.e.*, conduction in bands of width kT or less, is a thermoelectric power essentially independent of temperature (5). This temperature independence can also be explained on the basis of trapped states by a "hopping" process wherein, for the glass mentioned above, the charge carriers migrate between Fe^{+3} and Fe^{+2} ions. A feature of this hopping process is that the charge carriers are not free to move throughout the glass, but are trapped at cation sites due to the polarization induced by the carriers themselves. In such a process the conduction mobility is a thermally activated process, while the carrier concentration is independent of temperature (6).

A hopping process should show both a mechanical and a dielectric loss with the same activation energy. Furthermore, that activation energy should be equal to the d-c-conduction activation energy. Dielectric loss and electrical conductivity data do exist for semiconducting oxide glasses, but to our knowledge the mechanical loss in a semiconducting oxide glass has never been investigated.

Here mechanical loss will be characterized by internal friction expressed as the logarithmic decrement. Internal friction is a measure of the capacity of a vibrating body to convert some of its mechanical energy of vibration into heat. In a perfectly elastic solid a periodic stress gives rise to a periodic strain in phase with the stress and there is no mechanical energy loss. Real materials are not perfectly elastic, however, and the strain lags behind the applied stress. This results in a loss of elastic energy analogous to the case of dielectric loss. A convenient measure of the mechanical energy loss is the logarithmic decrement which is just π times the phase angle by which the strain lags the stress. Internal friction in glass usually arises from the movement of some of the constituents of the glass, but any process which is capable of causing the strain to lag the applied stress will give rise to internal friction.

Mechanical loss measurements have been made on a glass containing 55 m/o FeO_x-45 m/o P_2O_5, and the results correlated with dielectric loss and electrical conductivity data.

Key words: semiconducting glass, iron-phosphate glass, mechanical loss, modulus relaxation, dielectric loss, d-c conductivity, electron hopping.

[1] Present address: Semiconductor Products Division, Motorola Incorporated, Phoenix, Arizona.

Experimental

The apparatus used to determine the internal friction and Young's modulus for the samples investigated in this work is essentially that described by Marx (7). Briefly, it is a composite oscillator employing two 18.5° x-cut quartz bars; one to drive the system, and one to monitor the amplitude of the strain. Samples were cemented to this driver-gauge combination to form the complete three-component composite oscillator.

The samples themselves were in the form of polished bars of square cross section, ⅛ in. on a side. This is the same cross-sectional size as the quartz and eliminates any question of loss arising from area mismatching at the specimen-quartz interface. The lengths of the samples were determined by the consideration that some multiple of the fundamental resonant length (a half wavelength of the longitudinal stress, strain, or displacement) leaves about a 6-in. dummy section between a half-wavelength sample positioned at the center of the furnace and the driver-gauge combination maintained at or near room temperature outside the furnace. The sample lengths were cut and ground so that frequency mismatching of the samples to the driver and gauge was always less than 0.1% at room temperature.

The samples were heated in a differentially wound vertical tube furnace. To minimize thermal gradients, a silver core was inserted in the furnace, and to minimize convection currents, the top was sealed off completely and the bottom opening made as small as possible. In the center region of the furnace, the maximum temperature variation along the specimens was less than 2°C from room temperature to 500°C. Temperatures were determined by means of a 5-mil chromel-alumel thermocouple placed adjacent to the samples in the furnace.

The composite resonator was driven by a Hewlett-Packard 200T precision oscillator that had been modified to permit fine adjustments of frequency (to within 1 Hz) and to permit operation to 200 kHz. Frequencies were determined by a Hewlett-Packard 5245L electronic counter. The driver and gauge voltages were determined with high-impedance, Hewlett-Packard 400D vacuum tube voltmeters.

The mechanical-energy loss expressed as the logarithmic decrement δ may be defined as the ratio of the energy loss ΔE per cycle in the material to twice the total vibrational energy E stored in the material per cycle

$$\delta = \frac{\Delta E}{2E} \qquad [1]$$

Marx has shown that for a system such as described here, the decrement for the total system (quartz plus sample) is proportional to the ratio of the voltage

applied across the driver V_d to that measured across the gauge V_g

$$\delta = K\frac{V_d}{V_g} \qquad [2]$$

where K is a constant which may be determined initially by measuring the half width of the resonance peak (7). To determine the decrement of a half-wavelength sample, each set of measurements requires two specimens, one a half-wavelength shorter than the other. The decrement δ_s of a half-wavelength sample can be found from the total decrement δ_1 determined with longer sample and δ_2 with the shorter sample by the relation

$$\delta_s = (m_1\,\delta_1 - m_2\,\delta_2)/m_s \qquad [3]$$

where m_1 is the mass of the longer sample plus the mass of the quartz, and m_2 is the mass of the shorter sample plus the mass of the quartz. The quantity m_s is the mass of the extra half wavelength of sample or the difference between m_1 and m_2 if the samples are uniform. Similarly, the resonant frequency f_s of the half-wavelength sample can be found from

$$f_s = (m_1 f_1 - m_2 f_2)/m_s \qquad [4]$$

where the subscripts have the same meanings as before.

The temperature of the furnace was increased at the rate of one degree per minute, and simultaneous readings of the driver voltage, gauge voltage, resonant frequency, and temperature were taken every 5 min. Sets of measurements were made at both 50 kHz and 150 kHz. Strain amplitudes of the order of 10^{-7} were employed at both frequencies. The decrements calculated for each temperature from Eq. [3] are shown as a function of temperature in Fig. 1. The resonant frequency values calculated for each temperature from Eq. [4] were converted to relative Young's moduli Y_T/Y_0 by the relation

$$Y_T/Y_0 = (f_T^2/f_0^2)/(1 + \alpha\Delta T) \qquad [5]$$

and are shown as a function of temperature in Fig. 2. Here Y_T and Y_0 are the high-temperature and room-temperature Young's moduli, respectively; f_T and f_0 are the high-temperature and room-temperature resonant frequencies, α is the linear coefficient of thermal expansion, and ΔT is the temperature difference. For convenience, all values have been plotted at only 20° intervals.

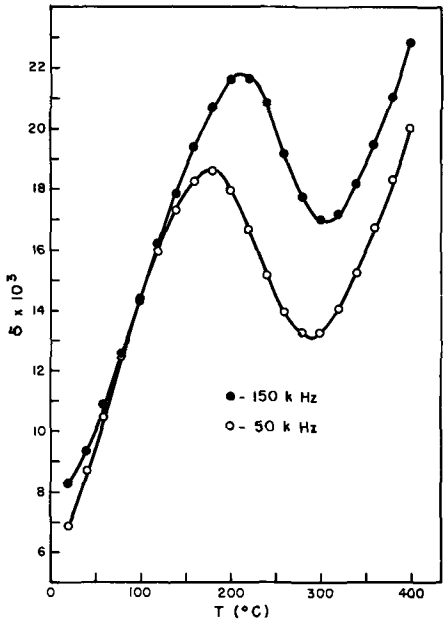

Fig. 1. Logarithmic decrement calculated from 50 kHz and 150 kHz data as a function of temperature for an alkali-free 55 m/o FeO_x-45 m/o P_2O_5 glass with an Fe^{+3}/Fe_{Total} ratio of 0.813.

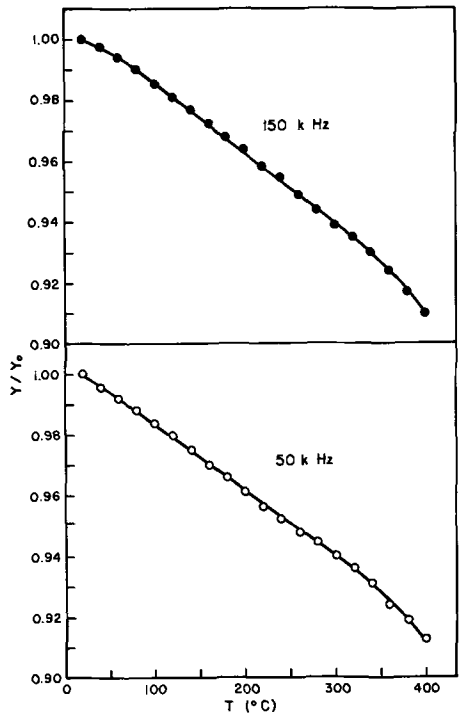

Fig. 2. Fractional change in Young's modulus calculated from 50 kHz and 150 kHz data as a function of temperature for an alkali-free 55 m/o FeO_x-45 m/o P_2O_5 glass with an Fe^{+3}/Fe_{Total} ratio of 0.813.

All measurements were made at atmospheric pressure. Experiments have shown that losses arising from air damping are of the order of 10^{-4}, or an order of magnitude smaller than found in this work, and are in fact on the order of the uncertainty in the measurements. From measurement considerations and reproducibility experiments we feel that the uncertainty in the loss values is of the order of 10% and the uncertainty in the modulus values is of the order of 2%.

Direct-current resistivity and dielectric measurements were made on samples 2 in. in diameter x 2 mm thick. Three-terminal gold electrodes were applied in accordance with ASTM specifications. The resistance was measured with a Beckman Ultrohmeter at a potential of 20v. A detailed description of the conductivity and dielectric loss measurements is given in ref. (8).

Results and Discussion

The material used in this investigation was a 55 m/o FeO_x-45 m/o P_2O_5 semiconducting glass. Chemical analysis gave an $Fe^{+3}/Fe^{+2} + Fe^{+3}$ ratio of 0.813 and a total alkali oxide content of less than 0.05 w/o (weight per cent). The samples were n-type as determined by thermoelectric power measurements. Other pertinent basic data for this glass are a room-temperature Young's modulus of 7.16 x 10^{11} dynes/cm^2 and a linear thermal expansion coefficient of 8.0 x 10^{-6}/°C.

Each of the mechanical-loss curves shown in Fig. 1 is typical of internal friction in glass. First, there is a background loss which increases rapidly at higher temperature and arises from the relaxation of the glass network itself. No attempt has been made to subtract this background loss from the data. Superimposed on this background is a broad loss peak arising from some other relaxation process taking place within the structure. The loss peak at 150 kHz is shifted to a higher temperature than that occurring at 50 kHz, implying that this is a thermally activated relaxation process. Each peak appears to be of the

Debye form

$$\delta = \Delta \frac{\omega\tau}{1 + \omega^2\tau^2} \qquad [6]$$

where Δ is the relaxation strength, ω is 2π times the vibrational frequency, and τ is the relaxation time and is of the form $\tau_0 e^{H/kT}$, where k is Boltzmann's constant, T is the absolute temperature, and H is the activation energy for the relaxation process. The breadths of the peaks indicate that they cannot be explained on the basis of a single relaxation time, and in general one might expect a distribution of relaxation times for a relaxation process occurring in a random network such as glass. Anderson and Bommel have shown that the effects of such a distribution not only broaden the loss peaks beyond that expected from a single relaxation time, but they also thermally broaden them, skew them, and increase the maximum absorption as the frequency is increased (9). All these effects are present here, although it should be noted that the higher loss at 150 kHz can also be due in part to the fact that the background loss itself is larger at the higher temperature.

For a broad distribution such as this, the most probable activation energy in the distribution $\overline{H}$ can be found from the relation

$$\ln \frac{f_2}{f_1} = \frac{\overline{H}}{k}\left(\frac{1}{T_1} - \frac{1}{T_2}\right) \qquad [7]$$

where f_2 and f_1 are the resonant frequencies of the two samples at T_2 and T_1, which are the absolute temperatures of the internal-friction peak maxima. The activation energy $\overline{H}$ calculated from Fig. 1 is 0.59 ev, where $T_1 = 177°C$ and $T_2 = 212°C$, corresponding to frequencies of 50 kHz and 150 kHz, respectively. Because the loss peaks are quite broad, the inability to locate the position of the peak maxima to better than $\pm 2°C$ results in an uncertainty of about 12% in this activation energy.

There is good reason for believing that the relaxation strength Δ of Eq. [6] is itself proportional to $(kT)^{-1}$, and one should use the temperature of the maxima from a $\delta \cdot T$ *vs.* $1/T$ plot to find activation energies. This has in fact been done, and the activation energy found is 0.04 ev less than that given above. Since this result is encompassed in the uncertainty of the previous value, and since there is no reason to believe that the background damping should follow such a relation, we prefer not to show this procedure.

The occurrence of internal friction is usually accompanied by a fractional decrease in the modulus of the same order of magnitude as the internal friction. Figure 2 would appear to show only an ordinary decrease in the modulus with temperature. However, closer examination of the 150 kHz values, where the loss peak and, thus, dispersive effects appear at higher temperatures, shows that the initial slope of the curve differs from that seen throughout most of the temperature range investigated. Thus, the modulus *vs.* temperature curve would appear to approach the temperature range considered here with a smaller slope. This is not so evident from the 50 kHz values, but here the dispersive effects due to the relaxation peak would come into play about 35°C lower in temperature, so that the smaller-slope region due to the ordinary decrease in modulus with temperature lies entirely to the left of this curve. At temperatures above 340°C, where one might again expect to see a modulus unaffected by the stress-induced relaxation, the modulus fall-off with temperature due to the gradual softening of the glass is large enough to mask any other effects. In other words, at these frequencies, we are probably able to see only the dispersive region of the modulus in the temperature range over which the measurements were made.

The absence of any significant concentration of alkali in the glass eliminates the possibility that a loss of the magnitude found here is due to the stress-induced movement of alkali ions. Neither can the loss be realistically attributed to the stress-induced diffusion of Fe^{+2} or Fe^{+3} ions or of singly bonded oxygen ions. If these were responsible for this loss, one would expect to find an activation energy more nearly like the 1.3 ev found for the former (10) or the 2-3 ev found for the latter (11) in silicate glasses. Dielectric loss and resistivity measurements yielded similar results. Experiments carried out on a glass of identical composition but with a slightly different $Fe^{+3}/(Fe^{+2} + Fe^{+3})$ ratio of 0.793 [glass 1, ref. (8)] showed a dielectric loss peak with an activation energy between 0.55 and 0.57 ev, and a d-c-conduction activation energy of 0.57 ev. It thus appears that a relaxation associated with the motion of the charge carriers (here localized electrons) is responsible for the observed mechanical loss. The relaxing unit in this case acts as both an elastic and an electric dipole. This behavior is entirely consistent with the model proposed by Heikes and Johnston (6).

The uncertainties associated with the activation energies for both the dielectric and mechanical loss prevent a meaningful comparison of the pre-exponential τ_0 in the expression for the relaxation time. The agreement is, however, order of magnitude ($\sim 10^{-13}$ sec).

Although an activation energy for the mechanical loss was determined on the basis of only two frequencies, it is significant that the activation energy agreed with that found from dielectric-loss and d-c-conductivity data. Equality of activation energies can, of course, be coincidental. The equality of these particular activation energies, however, is certainly as one would expect in a hopping process and would seem to lend strong support to a hopping mechanism for electrical conduction.

Conclusions

1. A mechanical loss and modulus relaxation attributable to the stress-induced movement of electrons in a semiconducting glass has been detected.
2. The similarity of the values of the activation energy calculated from the mechanical loss, dielectric loss, and d-c conductivity suggests that the same mechanism is operative in the two loss processes and quite probably in the d-c conductivity.
3. The ability to detect a mechanical loss associated with the motion of the charge carriers gives further weight to a hopping process of conduction in a semiconducting glass.

Acknowledgment

It is a pleasure to acknowledge Mr. D. M. Jenkins and Mr. F. W. Voorhees for their experimental assistance and Mrs. J. R. Ketcham for typing the final manuscript.

Manuscript submitted June 13, 1968; revised manuscript received Nov. 4, 1968.

Any discussion of this paper will appear in a Discussion Section to be published in the December 1969 JOURNAL.

REFERENCES

1. J. D. Mackenzie, "Modern Aspects of the Vitreous State," Vol. III, p. 126, J. D. Mackenzie, Editor, Butterworth, Inc., Washington (1964).
2. P. L. Bayton, H. Rawson, and J. E. Stanworth, *This Journal*, **104**, 237 (1957).
3. M. Munakata, *Solid-State Electronics*, **3**, 159 (1960).
4. K. W. Hansen, *This Journal*, **112**, 994 (1965).
5. R. R. Heikes, "Transition Metal Compounds," p. 2, E. R. Schatz, Editor, Gordon and Breach Science Publishers (1964).
6. R. R. Heikes and W. D. Johnston, *J. Chem. Phys.*, **26**, 582 (1957).

7. J. Marx, *Rev. Sci. Instr.*, **22**, 503 (1951).
8. K. W. Hansen and M. T. Splann, *This Journal*, **113**, 895 (1966).
9. O. L. Anderson and H. E. Bommel, *J. Am. Ceram. Soc.*, **38**, 125 (1955).
10. M. P. Borom, *Dissertation Abstr.*, **26**, 7192 (1966).
11. I. Mohyuddin and R. W. Douglas, *Phys. and Chem. Glasses*, **1**, 7 (1960).

Flame Emission Analysis for Sodium in Silicon Oxide Films and on Silicon Surfaces

J. E. Barry, H. M. Donega, and T. E. Burgess

Sprague Electric Company, North Adams, Massachusetts

ABSTRACT

A flame emission spectrophotometric method has been developed for the determination of ultramicro amounts of sodium present in thin silicon oxide films and on cleaned silicon surfaces. Ultrapure 5% hydrofluoric acid is used as the solvent and the sodium measured directly in the solution by flame emission analysis. This method, which has a sodium detection limit of 0.2 ppb, is used in place of the more contamination-prone neutron activation analysis to determine sodium distribution profiles in thin silicon oxide films as well as to measure the sodium contamination level of cleaned silicon surfaces. Sodium contamination on the surface of a single silicon wafer, having a surface area of approximately 16 cm^2, can be detected down to 8×10^{11} Na atoms/cm^2.

The presence of trace impurities in silicon oxide films grown on silicon surfaces has recently been the subject of many investigations. Field-effect measurements made on metal-oxide-semiconductor structures have indicated that the number of surface charges per cm^2 at the silicon-silicon oxide interface are directly related to the presence of certain impurities (1). Further studies have confirmed the fact that the presence of alkali metal impurities, especially sodium, both in the silicon oxide film and at the silicon-silicon oxide interface contribute significantly to the instability of the metal-oxide-semiconductor structure (2-4).

Previous studies of the distribution of sodium in silicon oxide films grown under a variety of conditions have been made by neutron activation analysis (5-7). The flame emission method not only offers the high sensitivity necessary for this application, but at the same time essentially eliminates the obvious inherent shortcomings of activation analysis.

The flame emission method has also been successfully applied to the determination of the sodium contamination level of cleaned silicon surfaces for which neutron activation analysis is most seriously limited.

Experimental

Flame photometry.—Flame photometric analysis consists essentially of the emission of characteristic radiation by a metallic element as the result of atomization of a solution of the element into a flame of sufficient thermal energy to excite the metal atom. The intensity of the emitted radiation is directly proportional to the number of atoms excited by the flame and therefore to the concentration of the element in solution. The light emitted is resolved by a monochromator into specific wavelengths, and the radiation intensity in the selected spectral region measured using a suitable detector system. The instrument is calibrated with standard solutions of the element of interest in order to establish a relationship between the measured emission intensity of a known characteristic spectral line and the concentration of the element in solution. Similar intensity measurements are made on the sample solutions and converted to concentrations by comparison to the calibration curve.

The spectral emission line used for the determination of sodium is the unresolved doublet at 589.0/0.6 mμ. This is the most sensitive of all lines employed in flame photometry (8). Its use results in an extremely sensitive method for sodium and calibration curves which are linear even at extremely low concentrations.

Equipment.—For this work a Beckman Model DU spectrophotometer was used equipped with the following Beckman accessories: (*i*) 9200 flame attachment, (*ii*) a-c power supply, (*iii*) 4020 atomizer-burner assembly, (*iv*) W128719 oxygen burner sheath, (*v*) 4310 multiplier phototube (1P28), (*vi*) 100 megohm phototube resistor.

The purpose of the oxygen burner sheath was to shield the flame from the ambient air and air-borne dust. Use of the sheath reduced any turbulence, improved the stability of the flame, and as a result increased the detection limit by approximately a factor of two.

Only polyethylene ware was used throughout this study for all sample handling and storage of solutions to eliminate possible contamination by leaching of sodium from glass. Polyethylene cups were used as sample containers in the spectrophotometer and standard solutions were stored in polyethylene bottles. All of the equipment was cleaned immediately prior to use by rinsing first in distilled water and finally distilled-deionized water.

Preparation of standards.—Two calibration curves covering the ranges 0-100 ppb Na and 0-10 ppb Na in 5% HF were prepared from standards made by diluting a water solution containing 1000 ppm Na (as sodium chloride). The final hydrofluoric acid concentration was adjusted to 5% in all standard solutions to coincide with the use of 5% HF to etch the silicon surfaces.

Figure 1 shows the sodium calibration curve covering the range 0-10 ppb Na in 5% HF. The instrument was adjusted for 0% transmission with the dark current control using a 5% HF blank. The 100% transmission was set using the sensitivity controls and a 10 ppb sodium standard in the same 5% HF. This procedure was repeated each time a measurement was made. Based on the data obtained in preparing this curve, the optimum precision of the method was determined to be ± 0.2 ppb Na and the limit of detection 0.2 ppb Na corresponding to 2.6×10^{13} atoms of sodium.

Method of analysis.—The scope of this study included not only the measurement of the sodium contamination level of cleaned silicon surfaces but also the determination of the distribution of sodium in

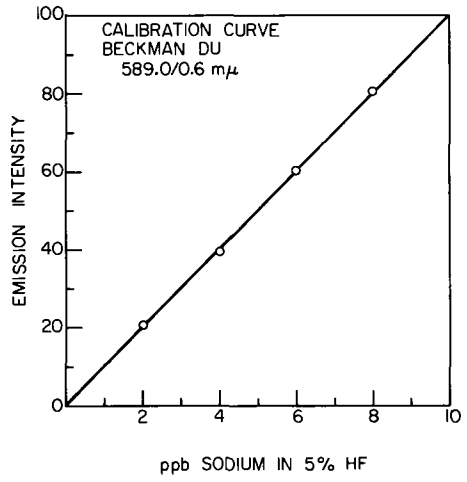

Fig. 1. Calibration curve for Beckman DU flame spectrophotometer at 589.0/0.6 mμ.

silicon oxide films grown on silicon wafers. Generally, the silicon wafers were treated to a dissolution step designed to remove the sodium and isolate it in a measured volume of 5% HF. The sodium content of the hydrofluoric acid was then determined by flame emission analysis. From this data the sodium concentration of the oxide film or the sodium contamination level of the silicon surface was calculated. The 5% HF solution which dissolves silicon oxide films at a fairly uniform rate of 300 Å/min was prepared by volumetric dilution of an ultrapure reagent grade (minimum 40%) hydrofluoric acid manufactured by E. Merck Inc., Darmstadt, Germany, and distributed by Brinkmann Instruments Inc. Silicon wafers were cleaned before analysis by exposure to a 10% HCl-90% H_2 atmosphere at 1250°C for 30 min. This treatment removed 15μ of silicon from the surface. The sodium remaining on these surfaces or distributed in 6000Å oxide films thermally grown in a dry oxygen atmosphere on similarly prepared surfaces was measured.

To determine the level of sodium contamination on cleaned silicon surfaces, each wafer was placed in a clean polyethylene beaker and 5 ml of 5% HF added. After a 2-min exposure time, the hydrofluoric acid was transferred to a photometer cup and the sodium measured directly by flame emission analysis. The same process was repeated with additional hydrofluoric acid for either a maximum of four rinses or until the sodium content was reduced to a value equivalent to the detection limit. The total sodium determined was then related to the individual wafers on a surface area basis. The surface area of each wafer was approximately 16 cm^2.

A similar procedure was used to determine the distribution of sodium in thermally grown silicon oxide films on silicon surfaces. In this case, the individual wafers were placed in clean polyethylene beakers and 5 ml of 5% HF added. After a predetermined period of time, the hydrofluoric acid was transferred to a polyethylene photometer cup and the sodium measured directly by flame emission analysis. Immediately after transfer of the acid, the wafer and the beaker were rinsed several times with distilled-deionized water, the washings discarded, and an additional volume of hydrofluoric acid added. This process was repeated until the oxide film was completely removed in several increments. The sodium determined was then related to the thickness of the oxide removed on a concentration basis.

Results and Discussion

The results of a study of the distribution of sodium in thermally grown silicon oxide films are given in Table I. Eighteen silicon wafers were used having an oxide thickness of 6000Å and a surface area of 16 cm^2.

Table I. Distribution of sodium in thermally grown silicon oxide films

Silicon oxide removed (Å)	Sodium atoms: Group A (Avg. 4 wafers)	Sodium atoms: Group B (Avg. 14 wafers)
50	3.4×10^{14}	4.5×10^{14}
1200	7.5×10^{13}	
1200	3.0×10^{13}	
1200	5.6×10^{13}	
1200	5.6×10^{13}	
900	1.3×10^{14}	
250	2.8×10^{14}	3.9×10^{14}
5700	3.5×10^{14}	4.4×10^{14}

For the study, the wafers were divided into two groups. Group A represents the average data from four individual wafers in which the oxide was removed in several small increments. Group B represents the average data from 14 wafers in which the initial 50Å of oxide at the surface and the final 250Å at the silicon-silicon oxide interface were removed in identical fashion to group A. However, the intermediate 5700Å was removed in a single step rather than in several small increments.

The data show excellent agreement between the two studies. For the initial 50Å of oxide at the surface an average of 3.4 x 10^{14} atoms of sodium in group A and 4.5 x 10^{14} in group B are found. For the intermediate 5700Å of oxide, the total number of sodium atoms in group A, 3.5 x 10^{14}, compares favorably with a corresponding value of 4.4 x 10^{14} atoms for group B. In the final 250Å of oxide, which essentially represents the level of sodium contamination at the silicon-silicon oxide interface, group A has an average of 2.8 x 10^{14} atoms of sodium and group B, 3.9 x 10^{14} atoms.

The results of this study show, first, that the average sodium profile for group A is generally in good agreement with the average distribution of sodium determined for group B. Second and most important, the average sodium content determined for the intermediate 5700Å of oxide in group A, which is based on five separate acid cuts and includes five individual flame measurements, agrees well with the comparable data determined for group B, which involves only a single acid cut and a single flame measurement. This excellent agreement eliminates contamination during the analysis as a source of error since group A involved five times as much handling as group B.

Figure 2 is a comparative study of the distribution of sodium in thermally grown oxide films made by both neutron activation analysis and flame emission analysis. The lower curve represents the average data taken from four individual profile studies made by flame emission analysis of silicon wafers having an oxide thickness of 6000Å. The upper curve, represented by a

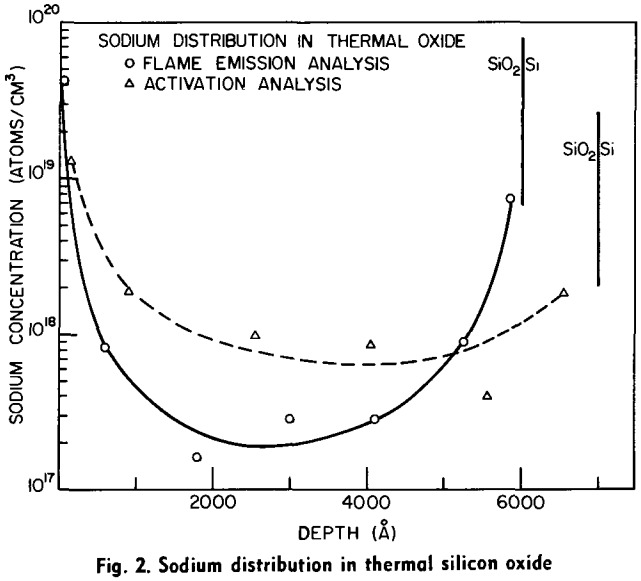

Fig. 2. Sodium distribution in thermal silicon oxide

Table II. Sodium on the surface of HCl vapor-etched silicon wafers

Lot No.	Wafer No.	Sodium atoms/cm²
1	1	$<8.2 \times 10^{11}$
	2	$<8.2 \times 10^{11}$
	3	1.4×10^{13}
	4	$<8.2 \times 10^{11}$
	5	$<8.2 \times 10^{11}$
2	1	$<8.2 \times 10^{11}$
	2	$>9.1 \times 10^{13}$
	3	$>1.6 \times 10^{14}$
	4	$>3.3 \times 10^{14}$
	5	$<8.2 \times 10^{11}$
3	1	4.2×10^{13}
	2	7.7×10^{12}
	3	4.3×10^{12}
	4	1.1×10^{13}
	5	5.4×10^{12}

broken line, is a plot of the average data from two individual profile studies made by neutron activation analysis of silicon wafers having an oxide thickness of 7000Å. Except for a slight difference in thickness, the oxide films were prepared in an identical manner by thermal oxidation in a dry oxygen atmosphere, in the same furnace but not at the same time. The shapes of the two sodium distribution curves are the same and the only difference between the two curves is the slightly higher concentration of sodium both at the surface and the silicon-silicon oxide interface in the 6000Å films analyzed by the flame emission method.

In general, the sodium profile obtained by flame emission is in relatively good agreement with that obtained by neutron activation analysis. The slight difference between the two profiles is no more than would be observed if both studies had been made by activation analysis alone.

Besides the study of the distribution of sodium in thermally grown oxide films, flame emission analysis has one other significant application; this is in the measurement of the level of sodium contamination on silicon surfaces prior to oxide formation. This is of importance since it is related to the level of sodium contamination found in the oxide grown on such a surface.

Table II shows the results of a study to determine the level of surface contamination on silicon wafers after HCl vapor-etch cleaning. The surface sodium remaining after cleaning was removed by dissolution in a measured volume of 5% HF and quantitatively measured by flame emission analysis. The data was obtained from three lots of silicon wafers cleaned at different times. The results are reported as atoms of sodium per square centimeter based on a total surface area of 16 cm².

The data show considerable lot-to-lot variation in the level of surface sodium contamination as well as some piece-to-piece variation within the same lot. Lot No. 2, for example, had contamination levels ranging from below the analytical detection limit, 8.2×10^{11} sodium atoms/cm², to greater than 3.3×10^{14} sodium atoms/cm².

No direct comparison between these results and results obtained by other methods of analysis such as spark source mass spectroscopy is available; however, the values measured compare favorably with the 8×10^{14} silanol (Si-OH) groups per square centimeter found on fully hydrated silicon dioxide surfaces (9). This suggests that at least a portion of the protons of these silanol groups on the natural oxide which would form on the HCl-etched surface in air would be replaced by sodium in the presence of this contaminant to give Si-O-Na. This oxide and the sodium contaminant is easily removed by 5% HF (10).

Summary

Flame emission spectrophotometry has been successfully applied to both the study of the distribution of sodium in thermally grown silicon oxide films and to the measurement of the level of sodium contamination on silicon surfaces.

The limit of detection for the method is 0.2 ppb Na, corresponding to 2.6×10^{13} atoms of sodium. When applied to a silicon surface having an area of 16 cm², the detection limit is 8×10^{11} atoms/cm².

The sensitivity and detection limit of flame emission spectrophotometry is approximately equivalent to that obtained by neutron activation analysis and comparable results have been obtained by both methods in determining the distribution of sodium in silicon oxide films.

Manuscript submitted July 24, 1968; revised manuscript received Oct. 14, 1968. This paper was presented at the Boston Meeting, May 5-9, 1968, as Paper 306 RNP.

Any discussion of this paper will appear in a Discussion Section to be published in the December 1969 JOURNAL.

REFERENCES

1. E. R. Snow, A. S. Grove, B. E. Deal, and C. T. Sah, *J. Appl. Phys.*, **36**, 1664 (1965).
2. E. Yon, W. H. Ko, and A. B. Kuper, *IEEE Trans.* **ED-13**, 276 (1966).
3. J. R. Matthews, W. A. Griffin, and K. H. Olson, *This Journal*, **112**, 899 (1965).
4. E. Kooi, *Philips Research Repts.*, **21**, 477 (1966).
5. D. R. Fewer and W. L. Gill, Texas Instruments, Inc., Technical Report No. RADC-TR-66-345 (1966).
6. T. M. Buck, F. G. Allen, J. V. Dalton, and J. D. Struthers, *This Journal*, **114**, 862 (1967).
7. J. F. Osborne, G. B. Larrabee, and V. Harrap, *Anal. Chem.*, **35**, 1144 (1967).
8. J. A. Dean, "Flame Photometry," McGraw-Hill Book Co., New York (1960).
9. R. K. Iler, "The Colloid Chemistry of Silica and Silicates," Cornell University Press, Ithaca, New York (1955).
10. G. B. Larrabee, K. G. Heinen, and S. A. Harrell, *This Journal*, **114**, 867 (1967).

Metallic Inclusions and Cellular Substructure in $Pb_{1-x}Sn_xTe$ Single Crystals

J. F. Butler and T. C. Harman

Lincoln Laboratory,[1] Massachusetts Institute of Technology, Lexington, Massachusetts

ABSTRACT

Electrolytic etching has revealed metallic inclusions and a cellular substructure in a number of $Pb_{1-x}Sn_xTe$ single crystals. The existence of metallic inclusions and cellular substructure in the interior of some Bridgman-grown crystals is explained by the mechanism of constitutional supercooling. Metallic surface inclusions, which are possibly due in part to reaction with the quartz growth vessel, were observed on as-grown surfaces of Bridgman- and vapor-grown crystals. Growth conditions have been found which result in $Pb_{1-x}Sn_xTe$ crystals free of bulk metallic inclusions and cellular substructure.

There has recently been considerable interest in fabricating infrared devices of $Pb_{1-x}Sn_xTe$ because its bandgap can be reduced, probably to zero width, by adjusting the Pb:Sn ratio (1). This offers the promise of intense radiation sources and intrinsic photodetectors covering the wavelength region between about 5μ and the far infrared. So far, injection laser action (2) has been observed to 28.1μ and photovoltaic detection (3) has been demonstrated to 30μ in $Pb_{1-x}Sn_xTe$ diodes. Metallic inclusions and cellular substructure are highly undesirable in these semiconductor devices, causing, for example, sinks for nonradiative recombination of electrons and holes, leakage paths across p-n junctions, and nonplanarity in diffused p-n junctions. Such metallic inclusions and cellular substructure have been observed in some single crystals of $Pb_{1-x}Sn_xTe$. This paper describes the method used to identify these macroscopic defects and presents growth conditions that can be used to avoid them. It is shown that the occurrence of metallic inclusions and cellular substructure in various $Pb_{1-x}Sn_xTe$ crystals grown from different liquidus compositions is consistent with a model of constitutional supercooling at the growth interface between liquid and solid.

Experimental Procedure and Results

Single crystals of $Pb_{1-x}Sn_xTe$ were grown by the Bridgman technique and by closed tube vapor transport. These methods have been described in detail elsewhere (2, 4). For Bridgman growth a mixture of the elements is sealed in a carbonized evacuated fused silica ampoule and reacted at a temperature 50°C above the liquidus. The ampoule is then lowered out of the high temperature region of the vertical furnace at a rate of 1 cm/day. The temperature gradient in the furnace is approximately 10°C/cm. Bridgman-grown single crystals are commonly 15 cm long and 2.5 cm in diameter. Vapor growth is carried out in a special fused silica ampoule using a vapor source consisting of a two-phased alloy of composition $(metal)_{0.51}(Te)_{0.49}$. The evacuated, sealed ampoule is placed in the furnace at approximately 825°C in a small temperature gradient of about 0.25°C/cm. Nearly stoichiometric crystals with linear dimensions up to several millimeters are formed on the walls. Before opening the growth ampoules the vapor grown crystals are usually annealed for lengthy periods at temperatures between 400° and 600°C.

The presence of metallic inclusions and cellular substructure is revealed by microscopic examination of samples electrolytically etched in a solution of 20g KOH, 45 ml H_2O, 35 ml glycerol, and 20 ml ethanol. This is a well-known polishing etch for PbTe (5). The samples are biased anodically and are thoroughly rinsed in distilled water after etching. The stirred solution is used at room temperature. At a current density of 0.5 a/cm^2 the $Pb_{1-x}Sn_xTe$ crystal is polish-etched at a rate of approximately 30 μ/min. Metallic inclusions, if present, acquire an orange film but otherwise remain intact. They remain as protuberances on the deeply etched semiconductor surface. At a current density of approximately 0.05 a/cm^2, the solution is suitable for obtaining dislocation density measurements or, in the present case, showing cellular substructure.

Figure 1 shows the surface of a sample cut from the last-to-freeze end of $Pb_{1-x}Sn_xTe$ crystal A-2 which was grown from a liquid with excess metal and etched at a current density of 0.5 a/cm^2. The weighed out proportions corresponded to the composition $(Pb_{0.70}Sn_{0.30})_{0.5063}Te_{0.4937}$. For the 400g ingot, it was estimated that at the growth temperature about 7 mg of Te was present in the vapor space above the liquid. Thus, the weighed out composition and actual liquidus composition are very nearly identical. The first-to-freeze solidus composition of A-2 was determined to be approximately $(Pb_{0.80}Sn_{0.20})_{<0.50}Te_{>0.50}$ from electron microprobe and Hall coefficient measurements (4). This photomicrograph, which shows an unusually large number

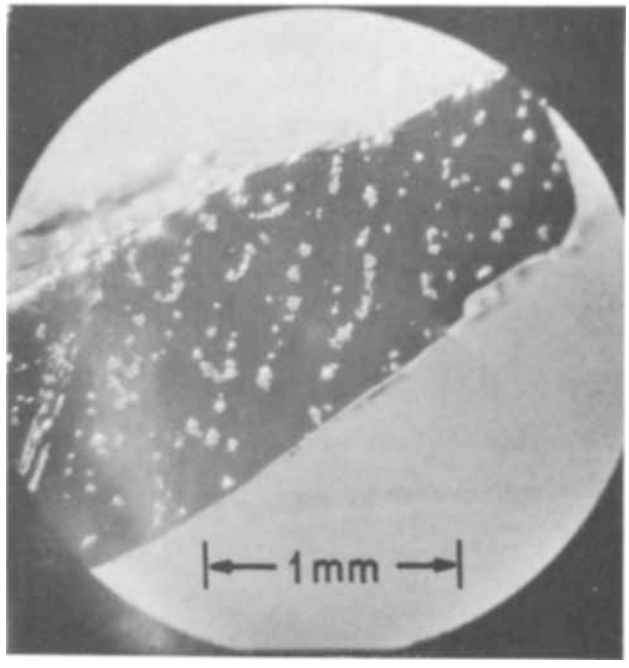

Fig. 1. Etched sample from last-to-freeze end of $Pb_{1-x}Sn_xTe$ crystal A-2 containing a large number of metallic inclusions. Unannealed.

[1] Operated with support from the U.S. Air Force.

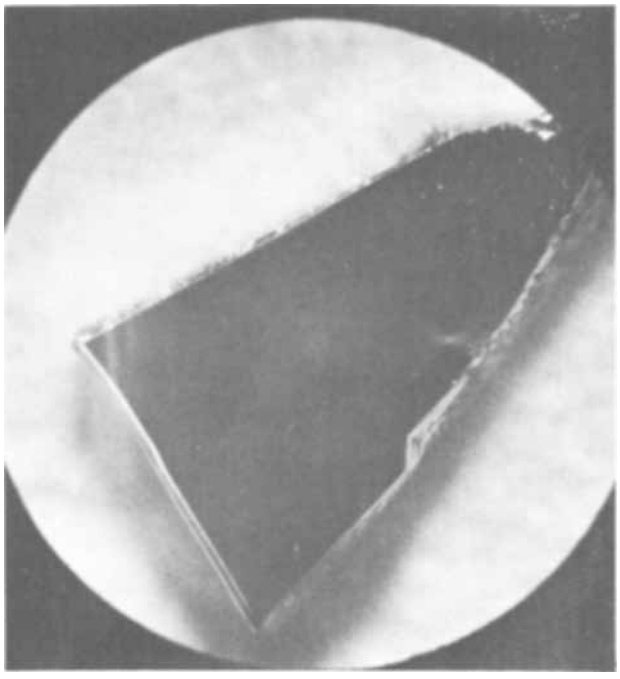

Fig. 2. Etched unannealed sample of $Pb_{1-x}Sn_xTe$ crystal A-4 in which no bulk metallic inclusions are observable; magnification is same as in Fig. 1.

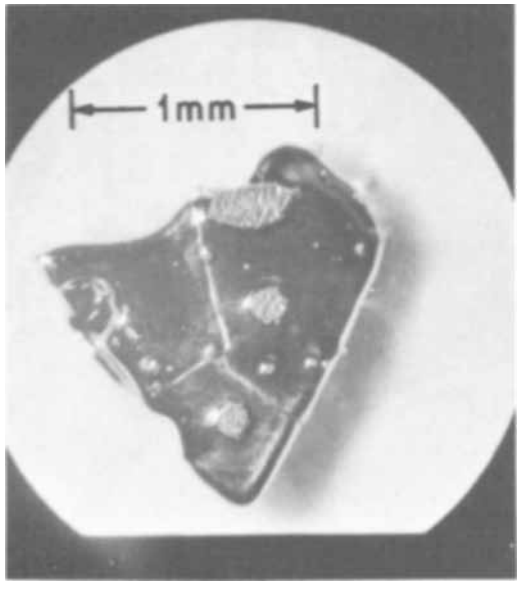

Fig. 3. Etched crystal from last-to-freeze end of $Pb_{1-x}Sn_xTe$ crystal A-2 after 850°C anneal for seven days.

of light spots, presents an extreme example of the presence of bulk metallic inclusions in Bridgman grown crystals. The inclusions observed range in size from a few microns to over 0.1 mm in diameter. The 100% metallic composition (Pb-Sn alloy) of the inclusions was determined by chemical and electron microprobe analyses.[1] Figure 2 shows for comparison purposes a sample of crystal A-4, which was grown from a Te-rich melt of composition $(Pb_{0.70}Sn_{0.30})_{0.49}Te_{0.51}$ and etched in the same manner. No metallic inclusions were observed in this crystal.

A section of the sample cut from the last to freeze end of A-2 is shown in Fig. 3 after isothermally annealing for seven days at 850°C in the presence of a metal-rich powder of composition $(Pb_{0.8}Sn_{0.2})_{0.5125}Te_{0.4875}$. The inclusions have apparently migrated and coalesced, forming larger metal

[1] Electron microprobe analysis was carried out by M. C. Finn.

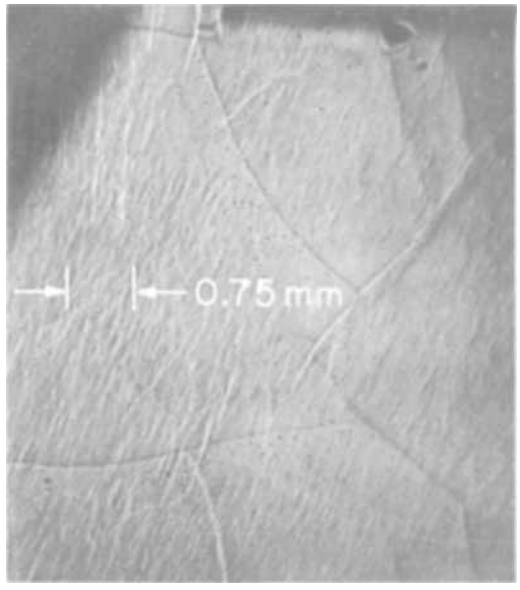

Fig. 4. Slowly etched sample from the first end to freeze of Bridgman grown $Pb_{1-x}Sn_xTe$ crystal A-2 containing cellular substructure. Unannealed.

regions with a smaller number density. A photomicrograph of the surface of a specimen obtained near the first end to freeze of a crystal A-2 is shown in Fig. 4. This sample was etched at the slower rate to show the cellular substructure. At the fast rate, only a few metallic inclusions were observed in a 1 cm^2 area. The pronounced mosaic pattern evident in Fig. 4 was found throughout the crystal and is believed to be due to preferential etching at the cell boundaries.

Table I indicates the presence or absence of metallic inclusions and cellular substructure in several crystals of $Pb_{0.8}Sn_{0.2}Te$. Bulk metallic inclusions, when present, varied in number from essentially zero at the first end to freeze to a maximum at the opposite end of each crystal. The density of bulk inclusions in the as-grown solid decreased as the composition of the melt became richer in Te. Surface metallic inclusions, which had physicochemical characteristics identical to the bulk metallic inclusions, were observed rather uniformly distributed over the exterior surfaces of the crystals. A second $M_{0.49}Te_{0.51}$ crystal was grown which was free of both bulk and surface metallic inclusions. The inner surface of the silica growth ampoule for this crystal had been carbonized by the reduction of acetone, whereas the former crystal was grown in an ampoule carbonized by the reduction of natural gas.

A number of the vapor grown crystals were etched by the technique previously described. No evidence for the presence of either metallic inclusions or cellular substructure was found in the bulk of these

Table I. Presence or absence of metallic inclusions and cellular substructure in crystals of $Pb_{0.8}Sn_{0.2}Te$

	Liquid composition	Bulk inclusions	Surface inclusions	Low-angle grain boundaries
Bridgman technique	$M_{0.506}Te_{0.494}$	Present	Present	Present
	$M_{0.500}Te_{0.500}$	Present	Present	Present
	$M_{0.496}Te_{0.504}$	Present	Present	Present
	$M_{0.493}Te_{0.507}$	Present	Present	Present
	$M_{0.49}Te_{0.51}$	Absent	Present*	Absent
	$M_{0.49}Te_{0.51}$	Absent	Absent*	Absent
	Source composition			
Vapor-growth technique	$M_{0.51}Te_{0.49}$	Absent	Present	Absent

* See text.

crystals. However, metallic inclusions in the surface layers of crystals vapor grown from metal-rich sources were observed in all crystals. In the case of crystals vapor grown from a Te-rich source, no metal inclusions were evident in the surface layers directly exposed to the vapor. However, even in this latter case, metallic inclusions were seen on surfaces in contact with the inner walls of the quartz growth capsule. This result indicates that surface inclusions may be due at least in part to a chemical reaction of $Pb_{1-x}Sn_xTe$ with the surface of the silica growth tube.

Discussion

We believe the bulk metallic inclusions and cellular substructure are due to constitutional supercooling during growth. The mechanism of constitutional supercooling has been previously used to explain cellular growth and other defects in various crystals (6). In the present case, segregation of excess metal (relative to the composition at the maximum melting temperature) at the liquid-solid interface of the growing crystal is postulated to be the basic cause of the observed macroscopic imperfections. Figures 5 and 6 illustrate the relationships between the phase diagrams of $Pb_{1-x}Sn_xTe$ and the pertinent parameters which are usually employed in standard discussions of constitutional supercooling phenomena (6). Figure 5 shows an idealized equilibrium phase diagram for $Pb_{1-x}Sn_xTe$ near the stoichiometric composition. It is well established that the position of the maximum melting point is on the Te-rich side of the binary phase diagram in both the Pb-Te (7) and Sn-Te (8) systems. Furthermore, the data presented in ref. (4) give strong evidence that the maximum melting point is on the Te-rich side for the pseudobinary alloys, $Pb_{1-x}Sn_xTe$. As evident from data given in ref. (4), for $x = 0.2$ the maximum melting temperature is approximately 890°C, and the intersection of the solidus line with the stoichiometric line occurs at about 525°C. Figure 6a shows schematically the variation of the metal-Te ratio across the interface between the melt and solid of a growing crystal. The buildup of the metal-Te ratio in the liquid at the interface depends on the growth rate and would be absent for an infinitesimally slow rate. Pertinent compositions are shown at the liquidus and solidus temperatures in Fig. 5. It is evident that the equilibrium freezing temperature in the liquid will vary with position as a result of varying the metal-Te ratio. The variation of freezing temperature is shown schematically in Fig. 6b. Also shown are two possible actual temperature gradients. For the less steep line there is a region of instability where the liquid is locally supercooled. Rapid quenching will occur in this region causing spurious nucleation and leading to cellular substructure. In addition, the rapidly quenched solid material should

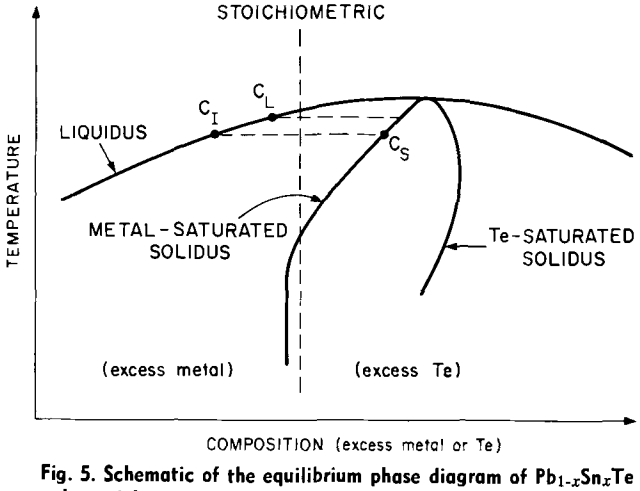

Fig. 5. Schematic of the equilibrium phase diagram of $Pb_{1-x}Sn_xTe$ near the stoichiometric composition.

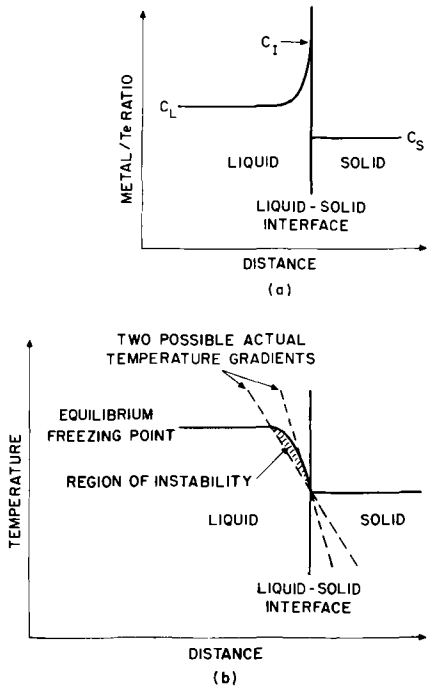

Fig. 6(a) Schematic of Metal-Te ratio near the freezing interface of a growing crystal of $Pb_{1-x}Sn_xTe$. C_L, C_I, and C_S are the Metal-Te ratios in the liquid at the interface and in the solid, respectively. (b) Schematic of equilibrium freezing temperature variation near freezing interface along with two possible gradients of the actual temperature and a region of instability.

contain metal-rich liquid as a second phase at the higher temperatures and two solid phases at lower temperatures, *i.e.*, $Pb_{1-x}Sn_xTe$ and metal.

This qualitative explanation for the occurrence of macroscopic defects suggests some practical methods of avoiding them. As may be seen from Fig. 5, C_I, C_L, and C_S will be identical at the maximum melting point composition; hence, growth from a liquid of this composition should eliminate constitutional supercooling. Crystal growth from a melt composition richer in Te than the maximum melting point composition should also yield crystals free of metallic inclusions. We believe the $M_{0.49}Te_{0.51}$ crystals mentioned previously were grown from a melt near or on the excess Te side of the maximum melting point composition. These crystals were free of bulk metallic inclusions and cellular substructure. According to Fig. 6b, constitutional supercooling can also be prevented by imposing a steep enough temperature gradient or by reducing the slope of the freezing temperature curve by decreasing the growth rate.

Acknowledgments

We wish to thank Dr. J. O. Dimmock for helpful discussions and M. S. Woodworth, A. E. Paladino, and J. H. Boghos for technical assistance.

Manuscript submitted June 17, 1968; revised manuscript received Oct. 1, 1968. This paper was presented at the Boston Meeting, May 5-9, 1968, as Paper 72.

Any discussion of this paper will appear in a Discussion Section to be published in the December 1969 JOURNAL.

REFERENCES

1. J. O. Dimmock, I. Melngailis, and A. J. Strauss, *Phys. Rev. Letters*, **16**, 1193 (1966).
2. J. F. Butler and T. C. Harman, *Appl. Phys. Letters*, **12**, 347 (1968).
3. A. R. Calawa, I. Melngailis, and T. C. Harman, IEEE Solid State Device Research Conference, Boulder, Colorado, June 17-19, 1968.
4. A. R. Calawa, T. C. Harman, M. Finn, and P. Youtz, *Trans. AIME*, **242**, 374 (1968).
5. M. K. Norr, *This Journal*, **109**, 433 (1962).

6. See, for example, M. Tanenbaum in "Semiconductors," p. 91, N. B. Hannay, Editor, Reinhold Publishing Corp., New York (1959); and W. Bardsley, J. S. Boulton, and D. T. J. Hurle, *Solid-State Electronics*, **5**, 395 (1962).
7. R. F. Brebrick and R. S. Allgaier, *J. Chem. Phys.*, **32**, 1826 (1960).
8. R. F. Brebrick, *J. Phys. Chem. Solids*, **24**, 27 (1963).

The Solution of Aluminum Phosphide in Aluminum

Sylvan Z. Beer*[1]

Westinghouse Research Laboratories, Pittsburgh, Pennsylvania

ABSTRACT

The solubility of aluminum phosphide in molten aluminum was measured over the temperature range of 900°-1200°C. This was done by equilibrating molten aluminum with solid aluminum phosphide, pouring off and quenching the aluminum, and analyzing the quenched metal. The heat of solution is calculated to be 18.1 kcal. From the measured solubility, approximate dissociation pressures at different temperatures were calculated.

The physical properties of AlP are the least known of the family of III-V intermetallic compounds possessing the zinc blende structure. This is largely due to the difficulties encountered in preparing and handling single crystals. Of the various applicable methods for growing single crystals of AlP, growth from solution in aluminum stands out because it presents the possibility of accurate control of impurity levels. To grow single crystals from molten aluminum under optimum conditions, requires a detailed knowledge of the solubility of AlP in aluminum as a function of temperature. Such data could also provide a means for roughly estimating some thermodynamic properties of AlP, which are at present almost totally lacking. For these reasons the solubility of AlP in molten aluminum was measured and is presented in this publication.

Experimental

The solubility was measured by holding the molten aluminum in contact with aluminum phosphide in an equilibration crucible until equilibration and then inverting the furnace to cause the molten aluminum to fall into a cold catch crucible, thus quenching-in any dissolved phosphorus.

The aluminum phosphide was prepared by the method described previously (1). Briefly, aluminum (Alcoa, 99.999%) was etched in a 96% phosphoric acid-4% nitric acid mixture and air dried. It was then placed in an alumina boat (Morganite) in one end of a closed-end mullite tube which had a borosilicate glass extension at the open end. Red phosphorus (United Mineral, 99.999%) was placed about midway along the length of the mullite tube. The tube was pumped at less than 10^{-6} Torr for 24 hr and sealed off. It was then placed in a horizontal two-zone furnace with the hot end kept at 1450°C while the glass end, to which the phosphorus distills, was kept at about 450°C. The tube was withdrawn from the furnace at a rate of about 6 mm/day keeping the phosphorus end at constant temperature. The larger crystals of AlP which grew this way were extracted (2) and used for these experiments.

For the solubility measurements, the aluminum phosphide was placed in a high purity alumina crucible (Morganite), previously baked out at 900°C for at least 24 hr. In this was also placed a 2g piece of aluminum (Alcoa, 99.999%) which had been etched with a mixture of 96% phosphoric acid-4% nitric acid and air dried. The crucible was then placed vertically in a quartz vessel with the catch-crucible (a long closed-end alumina tube) placed in inverted position against the equilibration crucible. The two were held tightly together by means of a spring compressed in the cold end of the quartz tube. The lower end of the tube was inserted into the furnace. The upper end of the catch crucible was kept at room temperature by means of muffin fans. The quartz tube was sealed at the top with a wax-sealed ground joint. It was then evacuated and heated slowly to the equilibrating temperature. The temperature was held constant to ±1°C for 20-24 hr to attain equilibration. After equilibration, the vessel was inverted and molten aluminum was dropped into the catch crucible and quenched. On solidification, the aluminum was removed, etched with the phosphoric-nitric mixture and analyzed for phosphorus by the colorimetric phosphovanadomolybdate method (3).

Analytic procedure.—About one gram of the metal was dissolved in a dilute aqua regia solution. Because the method was found to be sensitive to acidity, the solution was then heated almost to dryness, rediluted, and transferred to a 100 ml volumetric flask. To this was added 5.0 ml of 70% perchloric acid, 10 ml of 0.75M sodium sulfate solution, and 10.00 ml of a vanadium stock solution prepared in the following manner. To a mixture of 400 ml of water and 25 ml of 8*N* perchloric acid, 1.17g of ammonium metavanadate was added. The mixture was then diluted to 500 ml with water.

The unknown mixture in the 100 ml flask was stirred and to it was added 20.00 ml of a molybdenum stock solution. The latter was prepared by dissolving 35g of ammonium molybdate tetrahydrate in one liter of water. The unknown mixture was then diluted to the 100 ml mark. The absorbance was determined one hour later with a Cary spectrophotometer at 390μ against a similar solution containing no phosphorus. This was converted to concentration through the use of a calibration curve prepared as above using potassium dehydrogen phosphate as the phosphorus source. The over-all precision of the method was found to be within 3%. It was found to be insensitive to aluminum in the range encountered here.

Discussion of Results

The results of the measurements are shown in Fig. 1. It can be seen that the solubility as a function of the inverse absolute temperature falls on a straight line. The line was extrapolated to low temperatures for reasons to be discussed later. The slope of the line is equivalent to a ΔH solution of 18.1 kcal.

It is most convenient to analyze these results according to the method of Wagner (4), as further developed by Schottky and Bever (5), Hall (6), Vieland

* Electrochemical Society Active Member.
[1] Present address: Special Metals Corporation, New Hartford, New York.

6. See, for example, M. Tanenbaum in "Semiconductors," p. 91, N. B. Hannay, Editor, Reinhold Publishing Corp., New York (1959); and W. Bardsley, J. S. Boulton, and D. T. J. Hurle, *Solid-State Electronics*, **5**, 395 (1962).
7. R. F. Brebrick and R. S. Allgaier, *J. Chem. Phys.*, **32**, 1826 (1960).
8. R. F. Brebrick, *J. Phys. Chem. Solids*, **24**, 27 (1963).

The Solution of Aluminum Phosphide in Aluminum

Sylvan Z. Beer*[1]

Westinghouse Research Laboratories, Pittsburgh, Pennsylvania

ABSTRACT

The solubility of aluminum phosphide in molten aluminum was measured over the temperature range of 900°-1200°C. This was done by equilibrating molten aluminum with solid aluminum phosphide, pouring off and quenching the aluminum, and analyzing the quenched metal. The heat of solution is calculated to be 18.1 kcal. From the measured solubility, approximate dissociation pressures at different temperatures were calculated.

The physical properties of AlP are the least known of the family of III-V intermetallic compounds possessing the zinc blende structure. This is largely due to the difficulties encountered in preparing and handling single crystals. Of the various applicable methods for growing single crystals of AlP, growth from solution in aluminum stands out because it presents the possibility of accurate control of impurity levels. To grow single crystals from molten aluminum under optimum conditions, requires a detailed knowledge of the solubility of AlP in aluminum as a function of temperature. Such data could also provide a means for roughly estimating some thermodynamic properties of AlP, which are at present almost totally lacking. For these reasons the solubility of AlP in molten aluminum was measured and is presented in this publication.

Experimental

The solubility was measured by holding the molten aluminum in contact with aluminum phosphide in an equilibration crucible until equilibration and then inverting the furnace to cause the molten aluminum to fall into a cold catch crucible, thus quenching-in any dissolved phosphorus.

The aluminum phosphide was prepared by the method described previously (1). Briefly, aluminum (Alcoa, 99.999%) was etched in a 96% phosphoric acid-4% nitric acid mixture and air dried. It was then placed in an alumina boat (Morganite) in one end of a closed-end mullite tube which had a borosilicate glass extension at the open end. Red phosphorus (United Mineral, 99.999%) was placed about midway along the length of the mullite tube. The tube was pumped at less than 10^{-6} Torr for 24 hr and sealed off. It was then placed in a horizontal two-zone furnace with the hot end kept at 1450°C while the glass end, to which the phosphorus distills, was kept at about 450°C. The tube was withdrawn from the furnace at a rate of about 6 mm/day keeping the phosphorus end at constant temperature. The larger crystals of AlP which grew this way were extracted (2) and used for these experiments.

For the solubility measurements, the aluminum phosphide was placed in a high purity alumina crucible (Morganite), previously baked out at 900°C for at least 24 hr. In this was also placed a 2g piece of aluminum (Alcoa, 99.999%) which had been etched with a mixture of 96% phosphoric acid-4% nitric acid and air dried. The crucible was then placed vertically in a quartz vessel with the catch-crucible (a long closed-end alumina tube) placed in inverted position against the equilibration crucible. The two were held tightly together by means of a spring compressed in the cold end of the quartz tube. The lower end of the tube was inserted into the furnace. The upper end of the catch crucible was kept at room temperature by means of muffin fans. The quartz tube was sealed at the top with a wax-sealed ground joint. It was then evacuated and heated slowly to the equilibrating temperature. The temperature was held constant to ±1°C for 20-24 hr to attain equilibration. After equilibration, the vessel was inverted and molten aluminum was dropped into the catch crucible and quenched. On solidification, the aluminum was removed, etched with the phosphoric-nitric mixture and analyzed for phosphorus by the colorimetric phosphovanadomolybdate method (3).

Analytic procedure.—About one gram of the metal was dissolved in a dilute aqua regia solution. Because the method was found to be sensitive to acidity, the solution was then heated almost to dryness, rediluted, and transferred to a 100 ml volumetric flask. To this was added 5.0 ml of 70% perchloric acid, 10 ml of 0.75M sodium sulfate solution, and 10.00 ml of a vanadium stock solution prepared in the following manner. To a mixture of 400 ml of water and 25 ml of 8*N* perchloric acid, 1.17g of ammonium metavanadate was added. The mixture was then diluted to 500 ml with water.

The unknown mixture in the 100 ml flask was stirred and to it was added 20.00 ml of a molybdenum stock solution. The latter was prepared by dissolving 35g of ammonium molybdate tetrahydrate in one liter of water. The unknown mixture was then diluted to the 100 ml mark. The absorbance was determined one hour later with a Cary spectrophotometer at 390μ against a similar solution containing no phosphorus. This was converted to concentration through the use of a calibration curve prepared as above using potassium dehydrogen phosphate as the phosphorus source. The over-all precision of the method was found to be within 3%. It was found to be insensitive to aluminum in the range encountered here.

Discussion of Results

The results of the measurements are shown in Fig. 1. It can be seen that the solubility as a function of the inverse absolute temperature falls on a straight line. The line was extrapolated to low temperatures for reasons to be discussed later. The slope of the line is equivalent to a ΔH solution of 18.1 kcal.

It is most convenient to analyze these results according to the method of Wagner (4), as further developed by Schottky and Bever (5), Hall (6), Vieland

* Electrochemical Society Active Member.
[1] Present address: Special Metals Corporation, New Hartford, New York.

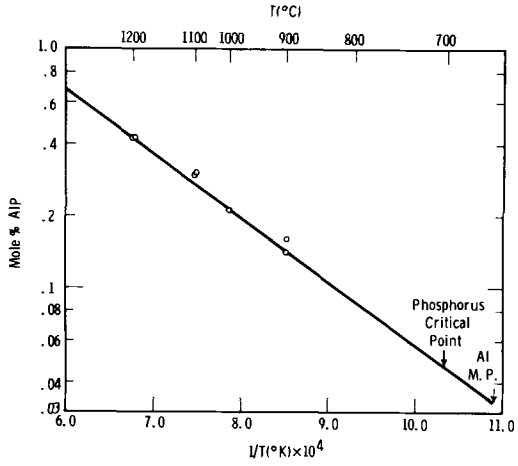

Fig. 1. Solubility of aluminum phosphide as a function of reciprocal absolute temperature. The data line is extrapolated to lower temperatures to indicate the relationship to the phosphorus critical temperature and the aluminum melting point.

(7), and others. Based on the quasi chemical approach and on the assumption that the solution is regular and that the excess free energy is given by $F^E = -wX(1-X)$, where w is the interaction parameter and X is the mole fraction of the solute, an equation determining the solubility was derived. It is given in the form

$$-\ln[4X(1-X)] = \frac{\Delta S^f}{R}\left[\frac{T_m}{T} - 1\right] - \frac{w}{4RT}(1-2X)^2 \quad [1]$$

where ΔS^f is the entropy of fusion and T_m is the melting point of the compound. The value of w is the only quantity which cannot be readily estimated. It has been shown for other III-V compounds to be a function of temperature (8). The evaluation of w as a function of temperature can be accomplished using Eq. [1] over the range of measured solubility. To do this requires the evaluation of both T_m and ΔS^f.

In order to obtain an estimated melting temperature, the melting temperatures of the other III-V's were plotted as a function of the atomic number. In Fig. 2 this was done utilizing the gram atomic number in accordance with the method of Lichter (9). The gram atomic number is simply the average atomic number of each III-V compound. Plotting the relationship in

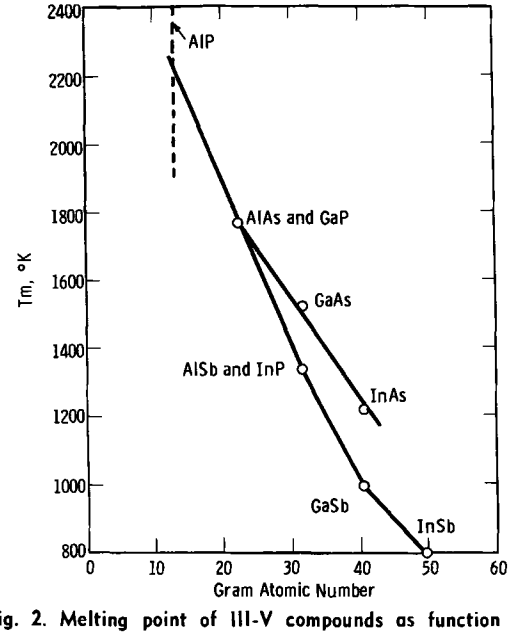

Fig. 2. Melting point of III-V compounds as function of gram atomic number.

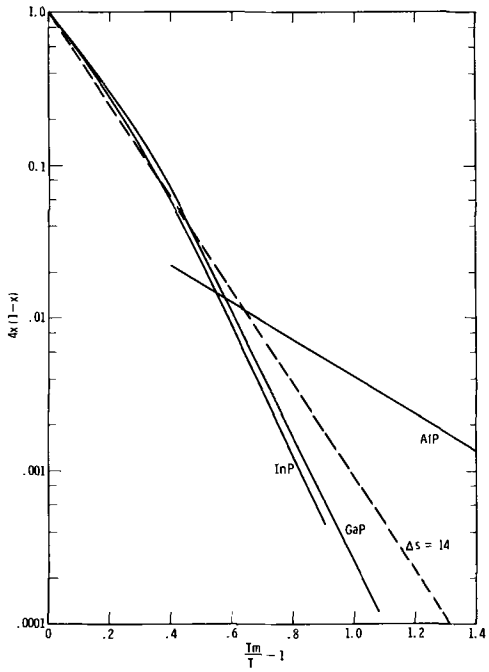

Fig. 3. Plot of ln $4X(1-X)$ as a function of $T_m/T-1$ for III-V phosphides. The $\Delta S = 14$ line is the average of many compounds plotted by Hall (6).

this way has the particular advantage in that all the compounds can be placed on the same graph conveniently, From this plot it can be seen that fairly reasonable straight lines can be drawn for the arsenides, the gallium compounds, and to some extent the antimonides. On this basis the AlP melting point can be estimated to be 2200°K.

The value of ΔS^f can be calculated directly from a plot of $\ln[4X(1-X)]$ against $T_m/T-1$. At low temperature, where the solubility is also low, a straight line relationship can be expected as a first order approximation. This plot is shown in Fig. 3. The relationship is seen to be fairly linear with a slope determined to be 5.9 eu. This is rather small compared with the other III-V phosphides and the other III-V compounds which average around 14 eu. Estimating the entropy of melting according to the method used by Thermond (8) for GaP and GaAs yields a value of about 16 eu. The experimental value is however close to that of the elements Ge and Si. The small value found experimentally may perhaps be attributed to the highly ionic nature of aluminum phosphide and its low solubility and low degree of dissociation in the metallic aluminum.

Utilizing the calculated values of ΔS^f and T_m in Eq. [1], the temperature dependence of w can be approximately determined. The relationship plotted in Fig. 4 is given by

$$w = 2.131 - 1.167T \quad [2]$$

As in the case of other III-V compounds (8), the value of w is found to follow closely a linear function of temperature.

Basic to the regular solution-quasi chemical approach the partial free energy of the V-species of compound is given as

$$\bar{F}^E = RT \ln \gamma_V = w(1-X)^2 \quad [3]$$

Rewriting this in terms of pressure, the vapor pressure of phosphorus in equilibrium with aluminum phosphide can be calculated from the relationship

$$p^{1/2}{}_v = p^{1/2}{}_{ov}\, X\, e^{(1-X)^2 w/RT} \quad [4]$$

where p_v is the equilibrium pressure of the P_2 species of phosphorus and p_{ov} is the pressure of pure phosphorus at temperature T. The equation cannot be used

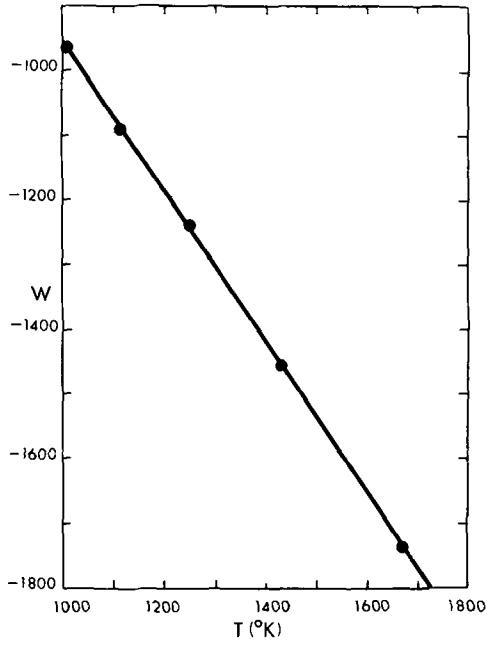

Fig. 4. Interaction parameter w as a function of absolute temperature.

directly because as can be seen from Fig. 1, the measurements are well above the critical temperature of phosphorus, 695°C (10). However, by utilizing the solubility data of GaP in Ga and by rewriting the equation in the form

$$\frac{p^{1/2}_{AlP}}{p^{1/2}_{GaP}} = \frac{X_{AlP}}{X_{GaP}} \frac{e^{(1-X)^2 w/RT}}{e^{(1-X)^2 w/RT}} \qquad [5]$$

the useful temperature range of the equation can be extended. Solution of this equation requires both the solubilities of the GaP in Ga and the solubility of AlP in Al over the same temperature range as well as the value of w for each compound over the same range. An equation for w for GaP has been given by Thurmond (8). Thus, the pressure ratios in Eq. [5] over the range of 800° to 1200°C is found to be 1.9 x 10^{-6} to 8 x 10^{-7}. From the known pressure-temperature relationship of GaP (11), the pressure of phosphorus in equilibrium with aluminum phosphide is found to lie in the range of 5 x 10^{-10} to 3 x 10^{-6} Torr over the same temperature range.

Because of the exponential dependence of the calculated pressure on the solubility of phosphides in the molten metals, the errors in the calculated pressures can be rather considerable. The values so obtained must, therefore, be regarded as first approximations.

Acknowledgment

I wish to thank Mr. R. Jox for his assistance in some of this work.

This work was supported in part by the Bureau of Ships Contract Nos.-94326.

Manuscript submitted May 8, 1968; revised manuscript received Nov. 7, 1968. This paper was presented at the Chicago Meeting, Oct. 15-19, 1967, as Paper 184.

Any discussion of this paper will appear in a Discussion Section to be published in the December 1969 JOURNAL.

REFERENCES

1. S. Z. Beer, *Trans, A.I.M.E.*, **242**, 424 (1968).
2. S. Z. Beer, *This Journal*, **114**, 634 (1967).
3. I. M. Kolthoff and P. J. Elving, "Treatise on Analytical Chemistry," Part II, Vol. 5, Interscience Publishers, New York (1961).
4. C. Wagner, *Acta Metallurgica*, **6**, 309 (1958).
5. W. F. Schottky and M. B. Bever, *ibid.*, **6**, 320 (1958).
6. R. N. Hall, *This Journal*, **110**, 385 (1963).
7. L. J. Vieland, *Acta Metallurgica*, **11**, 137 (1963).
8. C. D. Thurmond, *J. Phys Chem. Solids*, **26**, 785 (1965).
9. B. D. Lichter, University of Washington, Private communication.
10. T. D. Farr, Tennessee Valley Authority, Chemical Engineering Report No. 8, U.S. Govt. Printing Office, Washington 25, D.C.
11. W. D. Johnston, *This Journal*, **110**, 117 (1963).

The Determination of Phase Boundaries and Thermodynamic Functions in the Iron-Oxygen System by EMF Measurements

H. F. Rizzo,[1] R. S. Gordon, and I. B. Cutler

Division of Materials Science and Engineering, University of Utah, Salt Lake City, Utah

ABSTRACT

Coulometric titration in a high-temperature cell employing a stabilized zirconia electrolyte was used successfully in the determination of phase boundaries and related thermodynamic data in the iron-oxygen system. The standard free energy of formation of oxygen-deficient wüstite was determined between 540° and 1200°C. Values agree to within 500 cal of the most critically reviewed data. The free energy of reaction for the formation of magnetite from wüstite and oxygen was determined between 900° and 1200°C. The composition of the iron-rich boundary of wüstite was found to decrease very slightly in oxygen content with increasing temperature. For all practical purposes, however, the composition of the boundary can be considered constant at $FeO_{1.05}$. The compositions of oxygen-rich wüstite agreed fairly well with existing data. Evidence was presented, however, for the existence of additional phases in the region of the Fe-O diagram between the presently reported oxygen-rich wüstite and magnetite. The temperature for the Fe, Fe_xO, Fe_3O_4 three-phase equilibrium was found experimentally to be 610° ± 10°C. Extrapolation of low temperature ($T < 900$°C) Fe_zO-Fe_3O_4 equilibrium data resulted in lower transformation temperatures.

The use of emf measurements on galvanic cells, utilizing solid electrolytes such as stabilized zirconia, yttria, and thoria has led to the production of valuable thermodynamic data in numerous oxide systems. The standard molal free energies of formation of oxides such as FeO (1, 2), Fe_3O_4 (1), CoO (1, 2), Cu_2O (3), NiO (1, 2), and MoO_2 (4) have been determined at elevated temperatures in numerous studies.

The high-temperature galvanic cell is especially suited for studying the thermodynamic properties of defect oxide phases. By employing the technique of coulometric titration, which involves varying the composition of the oxide phase electrochemically, it is possible, in principle, to measure the activity of oxygen as a continuous function of composition over the entire phase field of a nonstoichiometric phase (5-9). Thus information such as thermodynamic activities, phase boundaries, and the existence of defect phases is readily obtained by this method.

It is the purpose of this paper to explore the feasibility of employing a solid electrolyte galvanic cell in conjunction with the technique of coulometric titration in the determination of phase boundaries in an oxide system. The iron-oxygen system was selected since there is considerable information on the phase boundaries in the literature, principally that of Darken and Gurry (10).

Experimental

Two kinds of experimental cells were employed: (*i*) closed-end tube cell, and (*ii*) three electrode cell. The electrolyte in the former cell is a closed-end, 10 in. long, 13/16 in. diameter calica-stabilized zirconia tube (0.85 ZrO_2 + 0.15 CaO). The basic arrangement of this cell is shown schematically in Fig. 1. The open end of the zirconia tube, which was exposed to air, was the oxygen reference potential used as the cathode. The outside of this tube was exposed to a purified argon (10-25 cm³/min) or helium atmosphere.[2] The FeO sample electrode was held in place by an alumina disk supported by a molybdenum wire. A 1-mil thick platinum electrode separated the FeO sample from the alumina. A Pt, Pt-13Rh 10-mil thermocouple was attached to the bottom of this platinum electrode. The platinum wire was also used to measure the cell voltage and as the lead wire for the titrating current. A ½-in. platinum electrode was placed around the outside of the zirconia cell within ¼ in. from the bottom of the cell. This electrode was used to monitor the oxygen pressure within the inert cell atmosphere using the air electrode (cathode) as the oxygen reference potential. The platinum electrode used in the cathode (the open end exposed to air) also had a 10 mil Pt, Pt-13Rh thermocouple attached and was used in the same manner as described for the anode. A spring-loaded mullite tube ensured good contact between the platinum electrode and the air cathode.

Three compositions were studied in the closed-end tube cell

$$\text{Pt, Fe-Fe}_x\text{O} \;\Big|\; \begin{matrix}0.85\ ZrO_2\\ +\\ 0.15\ CaO\end{matrix} \;\Big|\; \text{air } (P_{O_2} = 0.18 \text{ atm}), \text{Pt} \qquad \text{(I)}$$

$$\text{Pt,Fe}_2\text{O}^3\text{-Fe}_3\text{O}_4 \;\Big|\; \begin{matrix}0.85\ ZrO_2\\ +\\ 0.15\ CaO\end{matrix} \;\Big|\; \text{air } (P_{O_2} = 0.18 \text{ atm}), \text{Pt} \qquad \text{(II)}$$

$$\text{Pt,FeO}_y{}^4 \;\Big|\; \begin{matrix}0.85\ ZrO_2\\ +\\ 0.15\ CaO\end{matrix} \;\Big|\; \text{air } (P_{O_2} = 0.18 \text{ atm}), \text{Pt} \qquad \text{(III)}$$

$$\frac{1}{x} < y < \frac{1}{z}$$

The cell potentials are given by Eq. [1] and [2] in which $\bar{F}'_{O_2}$ and $\bar{F}''_{O_2}$

$$E = [(\bar{F}''_{O_2} - F^\circ_{O_2}) - (\bar{F}'_{O_2} - F^\circ_{O_2})]/4\mathbf{F} \qquad [1]$$

$$= \frac{RT}{4\mathbf{F}} \ln \frac{P''_{O_2}}{P'_{O_2}} \qquad [2]$$

are the partial molal free energies of oxygen at the anode and cathode, respectively, $F^\circ_{O_2}$ is the standard molal free energy of (ideal gas at one atmosphere pressure) oxygen, P'_{O_2} and P''_{O_2} are the partial pres-

[1] Present address: Air Force Weapons Laboratory, Kirtland Air Force Base, New Mexico.

[2] The gas was purified by passing it in succession over anhydrous magnesium perchlorate, ascarite, heated copper or titanium-zirconium turnings, and ascarite.

[3] Evidence will be presented that indicates the presence of more than one wüstite-type defect phase between $FeO_{1.05}$ and $FeO_{1.33}$. Therefore, reference to the Fe_zO-Fe_2O_4 two-phase region corresponds to the most oxygen-rich wüstite-type phase in equilibrium with Fe_3O_4 or an over-all composition slightly less oxygen-rich than $FeO_{1.33}$ (*i.e.* Fe_3O_4).

[4] FeO_y is used to denote the composition within the single phase region because the O/Fe ratio ($=y$) is used to describe the composition.

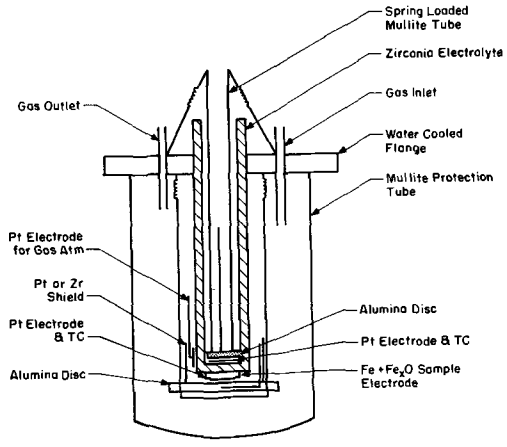

Fig. 1. Schematic of galvanic cell with zirconia electrolyte closed-end tube.

sures in atmospheres of diatomic oxygen at the anode and cathode, respectively, and **F** is the Faraday constant.

In these experiments the oxygen pressure at the cathode (P''_{O_2}) was always a constant (P_{O_2} [air] ≈ 0.18 atm), the partial pressure of oxygen in the atmosphere at Salt Lake City, Utah. Thus, from a measured emf, the oxygen pressure (P'_{O_2}) was calculated for the two phase mixtures, Fe-Fe$_x$O (I) and Fe$_z$O-Fe$_3$O$_4$ (II). In addition, the oxygen pressure was obtained for any arbitrary composition (y) in the wüstite phase (FeO$_y$) by coulometric titration in cell III. Isothermal titration experiments were conducted at temperatures between 800° and 1200°C in both directions across the wüstite phase. In addition to the titration experiments, heating and cooling experiments were performed with cells I and II. From these experiments, the oxygen activity was determined as a function of temperature (500°-1200°C) in the two-phase equilibrium mixtures Fe-Fe$_x$O and Fe$_z$O-Fe$_3$O$_4$.

The three-electrode cell consists of three electrodes in a cylindrical zirconia electrolyte (1 in. diameter, 0.75 in. high) as can be seen in Fig. 2. In the coulometric titration studies, one of the bottom Fe-Fe$_x$O electrodes was used to titrate oxygen in or out of the top electrode, while the other bottom electrode was used to record the open-circuit emf.

A mullite tube was fitted inside the top wüstite electrode so that incoming gas would flow from the cathode to the anode and thus lower the possible reduction of wüstite *via* the gas phase from the anode which is at a lower oxygen partial pressure. The entire asembly was spring loaded to insure good electrical contacts. The top sample electrode and one Fe-Fe$_x$O reference electrode were instrumented with Pt, Pt-13Rh thermocouples.

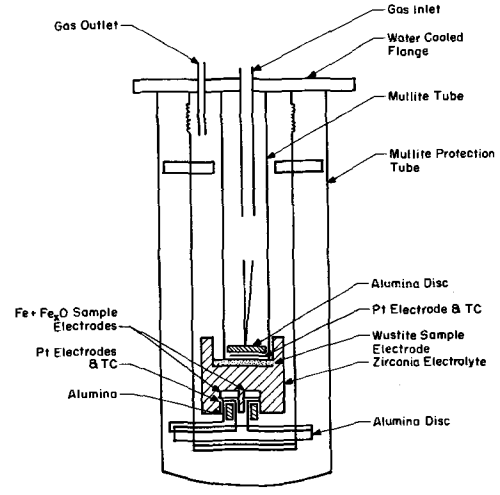

Fig. 2. Schematic of galvanic cell with three-sample electrode cylindrical shaped zirconia electrolyte.

Two compositions were studied with the three-electrode cell.

$$\text{Pt, Fe-Fe}_x\text{O} \left| \begin{matrix} 0.85\text{ZrO}_2 \\ + \\ 0.15\text{CaO} \end{matrix} \right| \text{Fe}_z\text{O-Fe}_3\text{O}_4\text{, Pt} \qquad \text{(IV)}$$

$$\text{Pt, Fe-Fe}_x\text{O} \left| \begin{matrix} 0.85\text{ZrO}_2 \\ + \\ 0.15\text{CaO} \end{matrix} \right| \begin{matrix} \text{FeO}_y\text{, Pt} \\ (y \text{ variable}) \end{matrix} \qquad \text{(V)}$$

Isothermal titration experiments were conducted in both directions with cell V across the entire wüstite phase. Heating and cooling studies were conducted on cell IV. From the emf measured as function of temperature, the activity of oxygen (P_{O_2}) in the Fe$_z$O-Fe$_3$O$_4$ system was evaluated between 700° and 1200°C. In order to calculate the pressure of oxygen at the cathode (Fe$_z$O-Fe$_3$O$_4$), the pressure at the anode must be known. The oxygen potentials for the Fe-Fe$_x$O equilibrium are reasonably well known (10, 11-16). These potentials were also measured with the closed-end tube cell (I) described previously. Since this paper will concern itself primarily with the determination of the phase boundaries in the Fe-O system, the description of the experimental details connected with coulometric titration within single phase wüstite, FeO$_y$, are given elsewhere (5, 17).

The electrolytes used in this study, with the exception of one of the closed-end tubes which was made by Zircoa Corporation, were fabricated in this laboratory. The zirconia was —325 mesh Wah Chang "S" Reactor Grade which is 99.9% pure and hafnia free. Reagent grade CaCO$_3$ (Baker's 1288) was the principal source of CaO. The complete description of the fabrication of the electrolyte can be found elsewhere (17). Each electrolyte was subjected to a vacuum test (1-2 x 10^{-3} mm Hg) to insure that it was impervious. It is noted here that the real test for an impervious electrolyte was the absence of any sample oxidation (emf drift with time) during an experiment.

The closed-end tube electrode samples used in this study varied from pure iron (less than 25 ppm impurities) to samples containing 85.5% iron and 14.5% oxygen by weight. The pure iron sample electrode was prepared at Battelle Memorial Institute by zone melting in a hydrogen atmosphere. Compositions containing 85.5 and 82 w/o (weight per cent) iron were prepared by dry mixing reagent grade Fe$_2$O$_3$ (99.0% minimum) with iron powder (GAF HP carbonyl 99.6-99.9%). Samples were dry pressed in ½ in. steel dies and heated in a tungsten vacuum furnace between 950°-1000°C for 19 hr at a pressure of 2 x 10^{-5} mm Hg. A sample containing 77 w/o iron was prepared by oxidation of iron wire (99.96%) in a H$_2$O/H$_2$ atmosphere at 900°C. This powdered sample was used in the three-electrode cell for the variable wüstite electrode. The other Fe-Fe$_x$O reference electrodes were powdered samples containing 85% iron. The sample weights and thicknesses varied between 0.0922 and 0.3385g and 0.023 and 0.10 cm, respectively.

Platinum electrodes were perhaps not the best choice to use with wüstite because of the solubility of iron in platinum. The predominant effect would be loss of iron in the wüstite electrode. Darken and Gurry (10) determined that there was zero solubility of platinum in any wüstite or magnetite composition. The solubility of iron in platinum at 1300°C is about 13%, based on the measurements of Taylor and Muan (18) for a partial pressure of oxygen corresponding to the Fe$_z$O-Fe$_3$O$_4$ equilibria. Therefore, in the lower temperature range (1057°-1200°C) of this study, it is very doubtful that the solubility of iron in a 1-mil thick platinum electrode will affect the results.

Results

In this paper only results connected with the phase boundaries are reported. The presentation and analysis of the titration data in single phase wüstite can be found elsewhere (5, 17).

Fe-Fe_xO *equilibria.*—The reaction for cell (I) is

$$x\,Fe + \tfrac{1}{2}\,O_2\,(0.18\,atm) = Fe_xO;\ \Delta F_3 \qquad [3]$$

When reaction [4] is added to reaction [3]

$$\tfrac{1}{2}\,O_2\,(1\,atm) = \tfrac{1}{2}\,O_2\,(0.18\,atm);\ \Delta F_4 \qquad [4]$$

the desired reaction [5], *i.e.*, the formation of Fe_xO from the elements in their standard states, is obtained.

$$x\,Fe + \tfrac{1}{2}\,O_2\,(1\,atm) = Fe_xO;\ \Delta F_5 \qquad [5]$$

Using Eq. [5a] the standard free energy of formation of Fe_xO (ΔF_5) was

$$\Delta F_5 = \Delta F_3 + \Delta F_4 = -n\mathbf{F}E_I + RT \ln (0.18)^{1/2} \qquad [5a]$$

evaluated from temperature profiles of cell I for the two-phase mixture (Fe, Fe_xO) between 540° and 1200°C. A linear least squares analysis of 156 data points obtained from six separate experiments resulted in Eq. [6].

$$E_I\ (mv) = 1354.0\ (\pm 1.0) - 0.36488\ (\pm 0.00109)\ T\ (°K) \qquad [6]$$

The actual data are tabulated elsewhere (17). In Fig. 3 a portion of these data is presented in addition to those for the Fe_zO-Fe_3O_4 region (cell II). The results substantiated that the fit was linear between 540° and 1200°C. Substitution of Eq. [6] into [5a] gave Eq. [7] for the standard free energy of formation of Fe_xO in calories

$$\Delta F_5 = -62{,}452 \pm 46 + 15.127\ (\pm 0.05)\ T\ (°K) \qquad [7]$$

The partial pressure of oxygen in equilibrium with the phases Fe and Fe_xO as a function of temperature is given by Eq. [8]. The standard enthalpy and entropy for reaction [5] were evaluated from the temperature dependence,

$$\log P_{O2} = \frac{-27{,}295 \pm 20}{T} + 6.6115 \pm 0.0218 \qquad [8]$$

of ΔF_5 and are $-62{,}452 \pm 46$ cal/mole and -15.127 ± 0.05 cal/mole deg, respectively.

These results agree well with the data of other workers (10, 12-16, 19) and should be more accurate since the use of air as a reference electrode eliminates one of the principal sources of error, namely, the thermodynamic properties of gaseous phases or other two-phase coexistence mixtures which are used to establish the partial pressure of oxygen at the reference electrode. The results of this study for the standard free energy of formation of iron-rich wüstite are compared with previous data in Table I. Any errors due to thermal emf's caused by possible temperature gradients across the electrolyte would be minimized, since the primary temperature-measuring thermocouple was attached to the Pt electrode in contact with the Fe-Fe_xO sample electrode. The use of air as an electrode does result in a higher cell potential across the electrolyte which could result in greater electronic conduction. However, there was no evidence of this behavior since the data were reproduced from heating and cooling profiles and also from a number of experiments in which different zirconia tubes were employed. The reported transference number data on the zirconia-base electrolytes (20, 21) indicate that there are practically no measurable electronic or other charge-carrying species other than oxygen ions in the oxygen partial pressure range covered in this study.

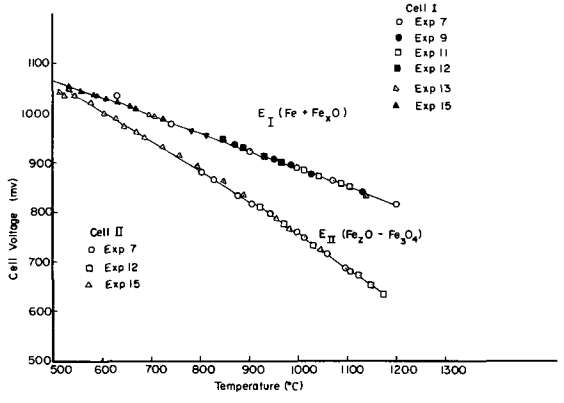

Fig. 3. Cell potentials for Fe-Fe_xO, Fe_zO-Fe_3O_4 equilibria closed-end tube.

Table I. Comparison of the standard free energy of formation of $Fe_{0.95}O$ obtained from this and previous studies

Investigators	Temperature $-\Delta F_f$ ($Fe_{0.95}O$) in calories 1000°K	1500°K
This study	47,325	39,752
Chipman (13)	47,600	39,800
Kleman (12), Vallet and Raccah (16)	47,230	39,743
Humphrey, King, and Kelley (14)	47,850	40,000
Wicks and Block (15)	47,350	39,050
Ackerman and Sandford (19)	47,761	39,850

Fe_zO-Fe_3O_4 *equilibria.*—The reaction for cell (II) is

$$\frac{3}{4z-3}\,Fe_zO + \tfrac{1}{2}\,O_2\,(0.18\,atm) = \frac{z}{4z-3}\,Fe_3O_4;\ \Delta F_9 \qquad [9]$$

Combining Eq. [4] and [9] results in Eq. [10].

$$\frac{3}{4z-3}\,Fe_zO + \tfrac{1}{2}\,O_2\,(1\,atm) = \frac{z}{4z-3}\,Fe_3O_4;\ \Delta F_{10}$$

$$\Delta F_{10} = -n\mathbf{F}E_{II} + RT \ln (0.18)^{1/2} \qquad [10]$$

The reaction for cell (IV) is:

$$x\,Fe + \frac{z}{4z-3}\,Fe_3O_4 = Fe_xO + \frac{3}{4z-3}\,Fe_zO;\ \Delta F_{11} \qquad [11]$$

Using established data for the Fe-Fe_xO equilibria (ΔF_5), the free energy of reaction [10] is given by Eq. [12].

$$\Delta F_{10} = -\Delta F_{11} + \Delta F_5 = n\mathbf{F}E_{IV} + \Delta F_5 \qquad [12]$$

Voltage-temperature profiles for cells (II) and (IV) are plotted in Fig. 3 and 4. The emf values for cell IV (Fig. 4) were obtained after titration into the Fe_3O_4 single-phase region at 1000° and 1100°C after which the sample was reduced to a composition slightly more oxygen deficient than magnetite. The reduction of the sample was apparently achieved through the gas phase by the lower oxygen potential of the two other Fe-Fe_xO sample electrodes. The cell voltage was recorded continuously and, after a steady-state constant voltage was achieved, emf-temperature profiles were made. Cell voltages were reproduced both on cooling and on heating to within ± 1 mv above 950°C. Another measure of the accuracy and reproducibility is to compare the emf difference between cell (I) and (II) with that of cell (IV). The agreement between 800° and 1100°C was within ± 2 mv.

An analysis of the emf-temperature curves in Fig. 3 and 4 indicates that the partial molal enthalpy of oxygen for the Fe_zO-Fe_3O_4 equilibria is not constant over the temperature range 700°-1200°C. A linear least squares fit was performed over several temperature ranges and the results are presented in Table II. A linear least squares analysis of all the data above

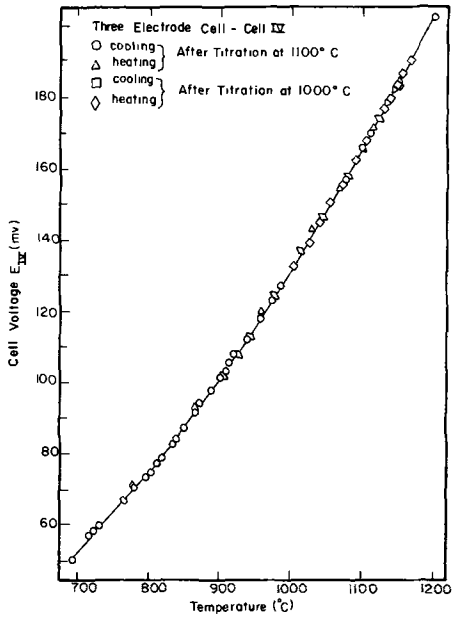

Fig. 4. Cell potentials for cell (IV) at different temperatures

900°C for the free energy of reaction between Fe_xO and Fe_3O_4 in Eq. [10] is given by Eq. [13].

$$\Delta F_{10}(\text{cal}) = -75{,}985 \pm 194 + 30.550 \pm 0.15\,T(°K) \quad [13]$$

The partial pressure of oxygen between 900° and 1200°C for the reaction is given by Eq. [14] and corresponds to the most oxygen-rich wüstite phase (Fe_xO) in equilibrium with Fe_3O_4. Excellent agreement exists between

$$\log P_{O_2} = \frac{-33{,}210 \pm 85}{T} + 13.354 \pm 0.064 \quad [14]$$

Eq. [14] and Darken and Gurry's data at 1100° (10). However, above 1200°C the partial pressure of oxygen is less than that reported by Darken and Gurry. The partial molal enthalpy and entropy of oxygen for the Fe_xO-Fe_3O_4 equilibrium are −75,985 ± 194 cal/mole and −30.550 ± 0.15 cal/mole deg, respectively. It is emphasized again that the data for the Fe_xO-Fe_3O_4 equilibria correspond to compositions containing an

Table II. Linear least squares fit of partial pressure of oxygen in equilibrium with Fe_xO + Fe_3O_4 and cell voltage E_{II}

Cell	Exp. No.	Temp range, °C	$-\log P_{O_2} = A + B\,(1/T) \times 10^4$ A	B	$-\Delta H_O^*$ Cal/mole
IV	1	925-1200	−13.6012 ± 0.053	3.3531 ± 0.00706	76,719 ± 160
IV	1	700-925	−11.624 ± 0.098	3.1170 ± 0.0106	71,317 ± 240
IV	1	700-1200	−12.512 ± 0.223	3.2130 ± 0.0267	73,513 ± 610
II	15	900-1075	−13.467 ± 0.111	3.3326 ± 0.0140	76,250 ± 320
II	15	1075-1200	−15.898 ± 0.258	3.665 ± 0.0364	83,855 ± 830
II	15	900-1200	−14.102 ± 0.133	3.412 ± 0.0176	78,068 ± 400
II	12	950-1200	−13.533 ± 0.068	3.348 ± 0.009	76,602 ± 205
II	12	900-950	−12.2795 ± 0.173	3.19515 ± 0.0207	73,105 ± 470
II	12	900-1200	−13.420 ± 0.056	3.332 ± 0.0074	76,235 ± 170
			$E_{II(mv)} = A + BT$ (°K) A (mv)	B (mv/°K)	$-\Delta H_O^{**}$
II	7	951-1109	1651.2 ± 12.5	−0.70186 ± 0.0119	76,160 ± 575
II	7	804-951	1534.4 ± 7.0	−0.60626 ± 0.0079	70,773 ± 320
II	7	804-1109	1596.0 ± 6.2	−0.65998 ± 0.0065	73,614 ± 285
II	15	851-1048	1647.7 ± 4.6	−0.70005 ± 0.0049	75,998 ± 210
II	15	497-743	1485.6 ± 7.7	−0.55569 ± 0.0123	68,552 ± 355
II	15	746-851	1526.7 ± 17.9	−0.59256 ± 0.0226	70,417 ± 825
II	15	497-1048	1522.0 ± 3.6	−0.35633 ± 0.00264	70,201 ± 165

* $\Delta H_O = \frac{-2.303 \times 1.987}{2} B \times 10^4$ ** $\Delta H_O = -A(\text{mv}) \times 46.124$

Table III. Comparison of the Fe_xO-Fe_3O_4 equilibrium oxygen pressures obtained in this and previous studies

Investigator	Equation	Fe, Fe_xO, Fe_3O_4 transformation temperature, °C
This study (900°-1200°C) O/Fe ~ 1.33	$\log P_{O_2} = -33{,}210/T + 13.354$	604
Kleman (12) Vallet and Raccah (16) (900°-1250°C)	$\log P_{O_2} = -33{,}400/T + 13.510$	611
Darken and Gurry (10) (1100°-1400°C)	$\log P_{O_2} = -35{,}200/T + 14.75$	697

over-all oxygen to iron ratio between 1.25 and 1.31. Equation [14], giving the equilibrium oxygen pressure for the equilibrium between magnetite and the most oxygen-rich phase of wüstite, is compared with the equations of other workers in Table III. Included also in the table are the Fe, Fe_xO, Fe_3O_4 transformation temperatures obtained by equating the oxygen pressure for the Fe_xO-Fe_3O_4 equilibrium with that for the Fe-Fe_xO equilibrium (Eq. [8]).

Iron-rich boundary of wüstite.—The composition of wüstite in equilibrium with iron as a function of temperature is well established. The phase boundaries for wüstite determined by Darken and Gurry (10) are widely accepted by most investigators. A compilation of these data along with more recent data on the Fe-O system is presented in Table IV. The data for the Fe-rich boundary support the selection of $FeO_{1.05}$ as the composition.

The change in composition with temperature of the boundary was studied by determining the temperature coefficient of oxygen pressure at constant composition for a series of compositions close to the boundary. The three-electrode cell was employed. The cell voltages (E_V) for compositions between $FeO_{1.0536}$, $FeO_{1.058}$, and $FeO_{1.067}$ as a function of temperature are shown in Fig. 5.

It is noted that the temperature coefficients of cell voltage at constant composition decreased from 0.06 mv/°C ($FeO_{1.067}$) to 0.02 mv/°C ($FeO_{1.053}$), which if extrapolated to $FeO_{1.05}$ would be 0.003 to 0.01 mv/°C. If the composition of Fe_xO in equilibrium with Fe_xO + Fe was $FeO_{1.05}$ at 800°C and invariant, the temper-

Table IV. Compilation of phase boundary data for Fe-O system

Source of data	Temp, °C	Composition (O/Fe) of two-phase regions: Fe_xO-Fe	Fe_xO-Fe_3O_4
Barbi (22)	700	1.055	1.091
	800	1.052	1.102
	850		1.107
	900	1.049	1.113
	950		1.117
	1000	1.046	1.122
Meussner (11)	700	1.058	1.103
	850	1.049	1.122
	1000	1.048	1.139
Ackerman and Sandford (19)	750	1.056	1.113
	799	1.052	1.120
	909	1.054	1.132
	1004	1.052	1.137
Gerdanian and Dode (23)	800	1.051	1.115
Darken and Gurry (10)	800	1.049	1.113
	900	1.049	1.129
	950		1.135
	1000	1.049	1.141
	1100	1.048	1.154
	1150		1.160
	1200	1.049	1.164
	1300	1.050	1.180
	1400	1.053	1.197
Swaroop and Wagner (24)	950	1.051	
	1000	1.050	
	1050	1.049	
	1100	1.049	
	1150	1.049	
	1200	1.050	
	1250	1.050	
This study	800		1.087
	894		1.110
	1000		1.135-1.147
	1100		1.145-1.155

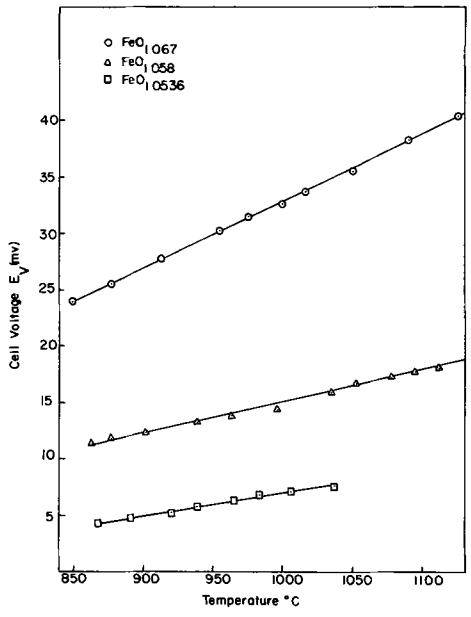

Fig. 5. EMF vs. temperature for compositions $FeO_{1.0536}$, $FeO_{1.058}$, and $FeO_{1.067}$ in cell (V).

ature coefficient for $FeO_{1.05}$ in this cell would be zero. Therefore, assuming that the extrapolated coefficient of 0.01 mv/°C is real and that the composition $FeO_{1.05}$ is not invariant, the true composition of wüstite in equilibrium with iron at temperatures greater than 800°C would be more iron rich. From a knowledge of the ratio of cell voltage per coulomb which was determined from the titration experiments, the change in composition over a 300° temperature rise was calculated to be + 0.00077 using a slope of 0.01 mv/°C. This decrease in O/Fe ratio corresponds to $FeO_{1.04923}$. Thus the assumption that $FeO_{1.05}$ is constant over the temperature range between 1057° and 1200°C has been well substantiated.

Oxygen-rich boundary of wüstite.—The oxygen-rich boundary of wüstite was determined by the technique of coulometric titration. The boundary is readily identified by a plateau in either a P_{O_2} or emf *vs.* composition (O/Fe) plot. In Fig. 6 a plot of P_{O_2} *vs.* O/Fe is given which is representative of the titration experiments in both cell configurations. This particular experiment was conducted at 1139°C in the three-electrode

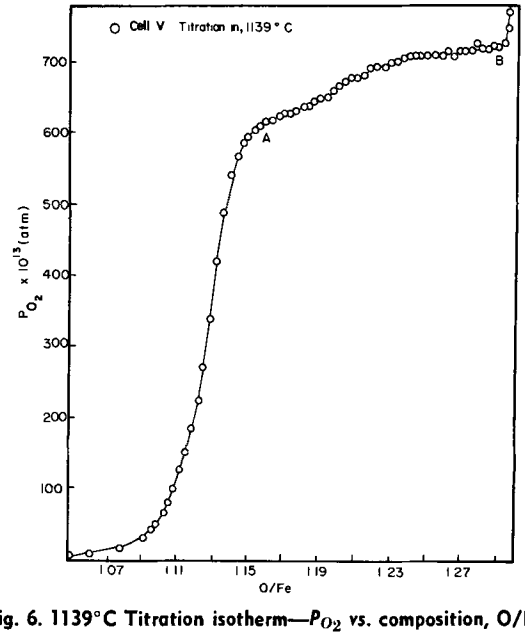

Fig. 6. 1139°C Titration isotherm—P_{O_2} vs. composition, O/Fe

cell. It is noteworthy that the oxygen pressure (activity) is a continuous function of composition until an O/Fe ratio of about 1.15 (composition A on Fig. 6) is reached. This composition corresponds to the oxygen-rich wüstite boundary presently reported on the phase equilibrium diagram (refer to Table IV). The oxygen pressure at composition B (O/Fe ~ 1.29) corresponds to the Fe_zO-Fe_3O_4 equilibrium value measured in this study (5, 17) and by other investigators (10, 12, 16). The rapid increase in oxygen potential at a composition (O/Fe) of 1.29, which is less than the magnetite composition (1.33) is due probably to the presence of a polarizing layer of magnetite at the electrode.

The fact that the oxygen potential at composition A is lower than that at B indicates tentatively that the composition of wüstite at A is not in equilibrium with magnetite. Between compositions A and B a series of single- and two-phase regions was observed. These were detected by a series of composition ranges with variable and constant oxygen activity, *i.e.*, variable and constant cell emf. If the composition range between A and B was a single two-phase region, as is now believed, the equilibrium oxygen activity (cell emf) should not vary with the composition as observed in this study but be constant until the magnetite composition is reached.

It is important to emphasize that the composition where the first two-phase region (A on Fig. 6) was observed corresponds to the presently accepted oxygen-rich boundary of wüstite. These compositions are listed at different temperatures in Table IV. It is also noted that the difference in oxygen pressure between points A and B corresponds to differences in cell voltage of ≈ 5-10 mv. These small differences in partial pressure (~ 1 x 10^{-11} atm) would be difficult to determine in normal gas equilibration techniques. For example, ratios of P_{CO_2}/P_{CO} (~8) in this oxygen pressure region are difficult to control precisely. A plot of the log P_{O_2} *vs.* 1/T for the oxygen pressure corresponding to the first two-phase region (composition A) observed in the titration studies at different temperatures led to Eq. [15].

$$\log P_{O_2} = \frac{-33{,}633 \pm 230}{T} + 13.567 \pm 0.176 \qquad [15]$$

This equation is very close to that reported earlier (Eq. [14]) for the true Fe_zO-Fe_3O_4 (*i.e.*, O/Fe at 1.33) potential and compares well with reported data (10, 12, 16). The small difference between Eq. [14] and [15] easily illustrates how the difference in oxygen potential between compositions corresponding to A and B in Fig. 6 could be overlooked in the less precise gas equilibration studies.

In order to justify further the results of this study in connection with the oxygen-rich boundary of wüstite, it is informative to review briefly the results of previous workers in establishing the oxygen-rich boundary of wüstite.

The phase boundaries corresponding to the Fe_zO + Fe_3O_4 equilibrium are not well established, and considerable difficulty was experienced by many investigators working in this region of the Fe-O system (10-12, 19, 25, 26). It is believed by the authors that this difficulty stems from the fact that there is a series of two-phase regions existing between the commonly accepted oxygen-rich wüstite boundary and Fe_3O_4. One of the principal reasons frequently given for failure to determine this boundary sharply is that nucleation of magnetite is the slow or rate-determining step. This explanation is difficult to understand when one considers the following:

1. At temperatures such as 1100°-1200°C diffusion of iron is fairly rapid (27, 28).
2. The crystal structures of FeO_y and Fe_3O_4 are basically the same, at least with respect to the anion packing.

3. Lattice parameter measurements indicate that the Fe_3O_4 structure can be derived by continuous removal of iron cations from the wüstite structure (29).

4. Oxygen potential measurements by Barbi (30) made during the reduction of Fe_2O_3 to Fe + Fe_xO did not indicate any evidence of a phase boundary between Fe_3O_4 and FeO_y.

5. A good epitaxial relation exists between FeO_y and Fe_3O_4, with a coherent boundary between the two phases (31, 32).

6. The rate of decomposition of FeO_y to Fe_3O_4 is very fast and a low activation energy process (33).

7. The single crystal structure is not destroyed by repeated reduction and oxidation of Fe_3O_4 to FeO (32).

8. Experimental evidence (neutron and high-temperature x-ray diffraction) has been found for clusters of defects present in wüstite which basically have the structure of magnetite (34, 35). Libowitz (36) has derived a relationship between oxygen pressure and composition based on the model proposed by Roth, wherein the principal defect in wüstite is assumed to be a Fe^{3+} interstitial associated with two iron vacancies. This model predicted correctly the P_{O_2} *vs.* composition (O/Fe) dependence in single-phase wüstite between 1057° and 1200°C (5).

In summary, ample evidence exists that magnetite-type clusters of defects are always present in wüstite, especially oxygen-rich wüstite. These defects may be responsible for the number of two-phase regions observed in this study. The presence of these defects should not only provide sites for nucleation but should also enhance its rate as well. Considering the difficulties encountered by other investigators in determining the Fe_zO-Fe_3O_4 equilibrium boundary, it is very difficult to rationalize that the principal cause is the slow nucleation of magnetite. In summary, one might expect from these facts to find a continuous solid solution between $FeO_{1.05}$ and $FeO_{1.33}$ (Fe_3O_4).

A summary of the two-phase regions observed in the P_{O_2} composition isotherms (5, 17), which were obtained from the coulometric titration experiments, is presented in Table V. In this table the oxygen-rich compositions to which titration was extended in addition to the compositions where two-phase regions were observed are listed. Compositions listed without a range for the two-phase region correspond to the composition at which there was a definite break in the oxygen activity-composition curve. The partial pressure of oxygen corresponding to the most oxygen-rich composition titrated is also listed.[5] A plot of the Fe-O phase diagram with selected reference data showing the oxygen-rich boundary of wüstite is presented in Fig. 7. The compositions where two-phase regions were noted are included in this figure.

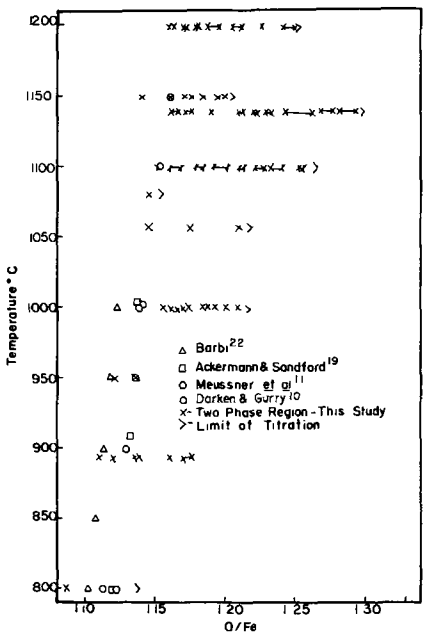

Fig. 7. Two-phase regions observed between oxygen-rich wustite and magnetite.

The results of the coulometric titration studies indicate the presence of as many as eight different two-phase regions between oxygen-rich wüstite and magnetite at temperatures between 1100° and 1200°C. The principal proof was the constant oxygen potential, *i.e.*, cell emf, observed over a finite composition range. These phases were found to exist over a narrow pressure range corresponding to a total cell voltage change from 5 to 10 mv with differences of 0.3 mv between some two-phase regions. The emf-temperature coefficient for cells III and V in the oxygen pressure range between FeO_y and Fe_3O_4 is 0.67 and 0.36 mv/°C, respectively. Thus, the duplication of isotherms would require very accurate temperature measuring and control equipment. Since this equipment was not available, the experimental technique employed was to use a constant voltage supply and then correct the cell emf to a particular temperature. Temperature measurements were made frequently between cycles to ensure a constant temperature. Fluctuations were normally within ± 1°C. Although differences (~ 0.3 mv) between successive two-phase regions were diffi-

[5] This study was not initially intended to determine phase boundaries in the iron-oxygen system so that many of the titration experiments used to establish the isotherms were stopped once a partial pressure of oxygen determined from the cell emf corresponded to the reported value for the Fe_zO-Fe_3O_4 two-phase equilibrium.

Table V. Compilation of two-phase regions observed in wüstite regions determined from coulometric titrations

	Temperature in °C for isotherms							
	894°	950°	1000°	1057°	1100°	1139°	1150°	1200°
O/Fe	1.110	1.12	1.135-1.142	1.145	1.15	1.161-1.165	1.140	1.158-1.161
$-\log P_{O_2}$	15.301	13.942	12.754	11.796	10.92	10.211	10.096	9.260
O/Fe	1.119-1.121		1.155-1.162	1.175	1.16-1.166	1.171-1.178	1.160	1.169-1.171
$-\log P_{O_2}$	15.275		12.733	11.68	10.906	11.202	10.046	9.236
O/Fe	1.135-1.138		1.165-1.170	1.121	1.177-1.183	1.190	1.170	1.177-1.180
$-\log P_{O_2}$	15.229		12.725	11.60	10.898	11.187	10.031	9.222
O/Fe	1.16		1.171-1.184		1.191-1.202	1.209-1.212	1.175	1.186-1.195
$-\log P_{O_2}$	15.187		12.723		10.872	11.168	10.022	9.215
O/Fe	1.170-1.175		1.187-1.193		1.210-1.213	1.219-1.222	1.182	1.204-1.211
$-\log P_{O_2}$	15.148		12.721		10.865	10.158	10.000	9.187
O/Fe			1.20-1.21		1.221-1.228	1.229-1.232	1.195	1.226
$-\log P_{O_2}$			12.717		10.853	10.154	9.982	9.171
O/Fe					1.232-1.241	1.242-1.261	1.198-1.200	1.241-1.25
$-\log P_{O_2}$					10.846	10.148	9.974	9.156
O/Fe					1.253-1.256	1.267-1.277		
$-\log P_{O_2}$					10.832	10.144		
O/Fe						1.280-1.293		
$-\log P_{O_2}$						10.139		
Maximum composition for titration	1.176	1.135	1.122	1.222	1.266	1.30	1.205	1.250
$-\log P_{O_2}$	14.932	13.88	12.40	11.592	10.721	11.097	9.966	9.159

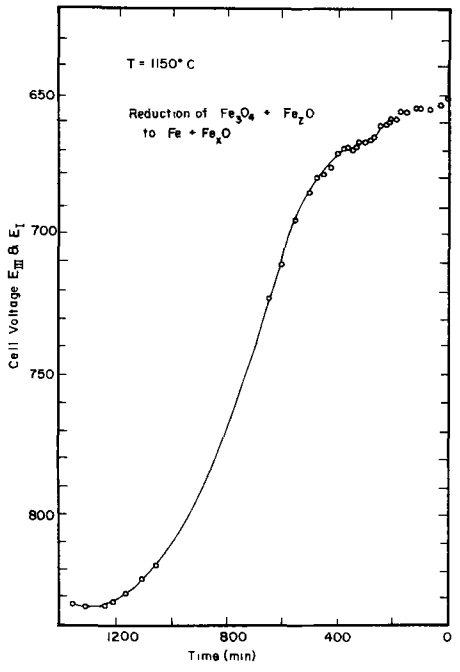

Fig. 8. Reduction of Fe_zO + Fe_3O_4 at 1150°C

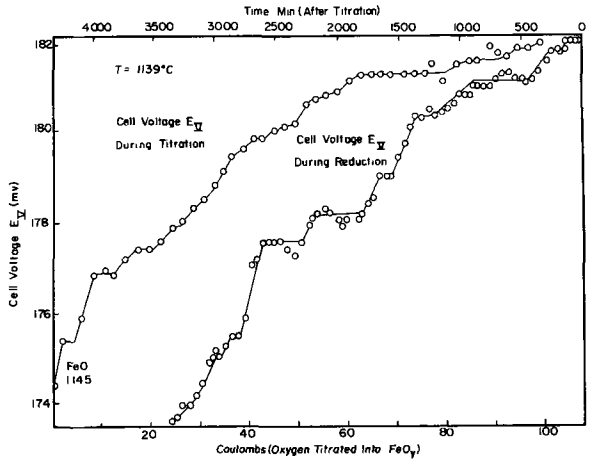

Fig. 9. Cell voltage E_V at 1139°C during reduction and titration

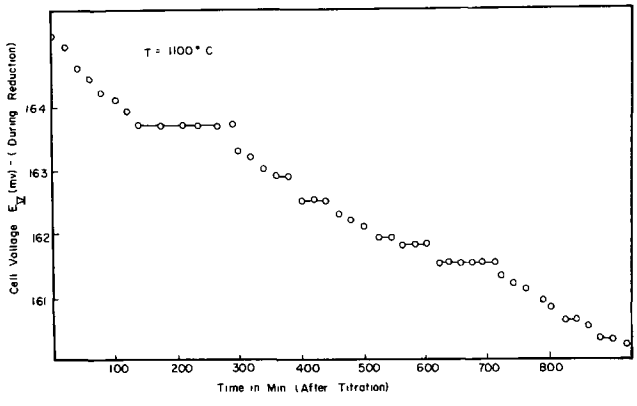

Fig. 10. Reduction of Fe_zO + Fe_3O_4 at 1100°C, E_V vs. time

cult to reproduce, the gradual increase in cell emf (5-10 mv) between compositions represented by points A and B on Fig. 6 was easily reproduced and was well within experimental error.

The initial evidence for additional two-phase regions was obtained by observing the cell emf as a function of time under reducing conditions. In Fig. 8 the cell emf as a function of time for a closed-end tube cell operating at 1150° is plotted. Titrations were carried out at 1057° and 1075°C; then the temperature was increased to 1150°C, and the change of emf with time was recorded. The reducing potential was either a zirconium getter or molybdenum wire used in the cell assembly. In cell (V) it was most likely the Fe-Fe_xO electrodes. Similar reduction data were obtained in both cells at other temperatures.

Tare and Schmalzried (37) used the reverse of this technique to determine the oxidation rate constant for the phase-boundary reaction in the oxidation of iron to wüstite. For the phase-boundary reaction to be controlling, no concentration gradients can exist in the sample so that equilibrium is established throughout. The rate-controlling mechanism is the transfer of oxygen from the surface of the sample to the gas phase. This transfer would be expected to be a low activation energy process and perhaps might explain why the general shape of the reduction curves in this study (17) remains the same for different temperatures (1090°-1200°C). The important conclusion to draw from these reduction studies is the presence of several constant emf regions in reducing Fe_3O_4 to wüstite. These constant emf regions indicate the presence of two coexisting phases which are being reduced providing the reduction is phase boundary controlled. Linear reduction rates have been observed in wüstite by a number of workers (37-41).

An example of a titration experiment at 1139°C into magnetite followed by a reduction on the same sample can be seen in Fig. 9. The titration portion corresponds to the last 60 cycles (60 out of the total of 87 hr of titration) in which the titration current varied from 1.50 to 1.25 ma with titration and emf measuring times of 26.5 and 35.5 min, respectively. With the rapid rise of cell emf at $FeO_{1.316}$ the titrations were stopped, and the resultant cell emf as a function of time during reduction is plotted on this same figure. There is a good correlation between these curves for the two-phase regions. The wavy portions in the reduction curves are most likely due to the temperature variations. A similar plot for reduction after titration to composition $FeO_{1.186}$ at 1100°C is shown in Fig. 10. It is noteworthy that a constant emf was recorded in some cases up to 200 min. A summary of additional reduction and titration results for two-phase regions is given in Table VI.

Similar reduction experiments were conducted in which oxygen rich magnetite was reduced into the Fe_zO-Fe_3O_4 coexistence region. The data from these experiments conducted in both cell configurations are shown in Fig. 11. The reduction reaction for the closed-end tube (exp. 12) started within 1 mv of the Fe_3O_4-Fe_2O_3 two-phase region. It is clear that in this composition range ($1.33 < O/F < 1.5$) the absence of any emf-time plateaus indicates that only single phase Fe_3O_4 is being reduced. However, in the FeO_y-Fe_3O_4 composition range (*i.e.*, $1.15 < O/F < 1.33$) numerous plateaus were observed.

In summary, it has been demonstrated that a number of two-phase regions exist between oxygen-rich wüstite and magnetite. They can be reproduced within experimental accuracies of measuring the temperature and cell emf's between different cells. The actual delineation of the phase regions will require greater precision and accuracies in controlling the temperature in addition to better control of the partial pressure of oxygen existing in the cell atmosphere.

Transformation temperature for decomposition of wüstite to magnetite.—The temperature corresponding to the decomposition of wüstite into magnetite has been reported to be between 565° and 620°C (16, 19, 42). This temperature can be uniquely determined by the triple point where iron, magnetite, and a particular composition of wüstite are in equilibrium. At this temperature the phase boundaries merge and the oxygen pressure is unique. Thus, extrapolations of Eq. [8] and [14], which relate the partial pressure of

Table VI. Summary of two-phase regions observed between $FeO_{1.05}$-$FeO_{1.333}$ by coulometric titration and reduction experiments

Reduction time min in two-phase region	E_T, mv
T = 1000°C	
Exp 1, cell (V)	
initial composition	$FeO_{1.325}$
35	135.8
40	134.6
30	134.2
500	133.9
Exp 7, cell (III)	
initial composition	$FeO_{1.162}$
60	134.8
25	131.9
100	130.7
50	128.7
60	126.5
Exp 7, cell (III)	
composition range	
from titration	E_T, mv
1.156	133.5
1.153	
1.147	132.0
1.144	
1.141	
1.138	130.7
1.134	129.8
T = 1100°C	
Exp 1, Cell (V)	
initial composition	$FeO_{1.221}$
80	165.2
50	164.2
300	163.5
150	162.8
250	161.0
150	160.5
50	160.0
50	159.2
150	158.6
50	157.4
150	156.8
Exp 1, cell (V)	
initial composition	$FeO_{1.150}$
150	163.7
20	162.9
40	162.5
100	161.5
20	160.6
20	160.2
Exp 1, Cell (V)	
initial composition	$FeO_{1.175}$
20	162.5
10	161.5
20	160.5
15	159.5
Exp 7, cell (III)	
initial composition	$FeO_{1.149}$
40	163.5
40	161.0
25	159.0
30	158.0
Exp 7, cell (III)	
initial composition	$FeO_{1.24}$
300	169.0
300	163.5
Exp 7, cell (III)	
initial composition	$FeO_{1.31}$
25	165.1
210	162.1
Composition range	
from titration	E_T
Exp. 12, cell (III)	
1.188	
1.173	164.5
1.170	
1.168	165.2
1.159	
1.156	162.8
1.156	
1.147	162.3
Exp. 12, cell (III)	
1.172	
1.165	166.3
1.162	
1.160	165.4
1.158	
1.154	164.3
1.148	
1.144	162.7
T = 1200°C	
Exp. 12, cell (III)	
50	194.6
25	189.6

E_T for experiments 7 and 12 (closed-end tube cell) was determined from the relationship, $E_T = E_I$ (Eq. [6]) $- E_{III}$.

oxygen in equilibrium with Fe-Fe_xO and Fe_xO-Fe_3O_4 to the temperature where the pressure of oxygen is the same and unique, should define the transformation temperature. The extrapolation of Eq. [8] for the Fe + Fe_xO equilibrium is valid in this temperature range. However, Eq. [14] describing the Fe_xO + Fe_3O_4 equilibrium should not be extrapolated below 900°C (per previous discussion in the section Fe_xO-Fe_3O_4 equilibria). The transformation temperatures obtained from a linear extrapolation of the equation for log P_{O_2} of the Fe_xO-Fe_3O_4 equilibrium are presented in Table VII. The transformation temperatures listed were determined as a function of the temperature range from which the equation describing the Fe_xO-Fe_3O_4 equilibrium was derived. The resultant temperatures (417°-547°C) obtained from extrapolation of low-temperature data appear unrealistic and are hard to explain. This same behavior was also noted by Vallet and Raccah (16). The transformation temperature of 614° ± 7°C derived from the extrapolation of high-temperature data (900°-1200°C) indicates good agreement with the results of Vallet and Raccah.

Table VII. Transformation temperature of wüstite into magnetite from Fe-Fe_xO and Fe_xO-Fe_3O_4 oxygen partial pressures

Temp. range °C*	Cell	Exp. No.	Transformation temp. °C Fe, Fe_xO, and Fe_3O_4 in equilibrium
497-743	II	15	417
746-851	II	15	490
804-951	II	7	477
700-925	IV	1	508
900-950	II	12	547
850-1075	II	15	605
951-1109	II	7	608
925-1200	IV	1	619
950-1200	II	12	620
1075-1200	II	15	733
Intersection of Eq. [8] and [14]			604
Intersection of Eq. [8] and [15]			638

* The temperature range in which the equation, $-\log P_{O_2} = A + B\,(1/T) \times 10^4$, for the Fe_xO + Fe_3O_4 equilibrium was derived and used with the Fe-Fe_xO equilibrium (Eq. [8]) to calculate the triple point.

The transformation temperature was measured experimentally by the use of cell (V) with the composition $FeO_{1.08}$ as the cathode. The cooling and heating profiles (1050°-450°C, 19 hr each) are shown in Fig. 12, as the X-Y plot of a Pt, Pt-13Rh thermocouple emf vs. E_V (mv) for the cell reaction. When the cell emf is zero, both electrodes have the same oxygen potential corresponding to the Fe-Fe_3O_4 equilibrium. The temperatures obtained were 620° and 599°C for cooling and heating, respectively. The 620°C obtained upon cooling was extrapolated to a point where the slope, $dE_V/dE_{Pt,\ Pt\text{-}13Rh} = 0$.

Conclusion

The usefulness of a solid electrolyte galvanic cell in determining phase boundaries and thermodynamic functions in the iron-oxygen system has been demonstrated. Tentative evidence for the existence of more than one defect phase between wüstite and magnetite has been presented from coulometric titration experiments.

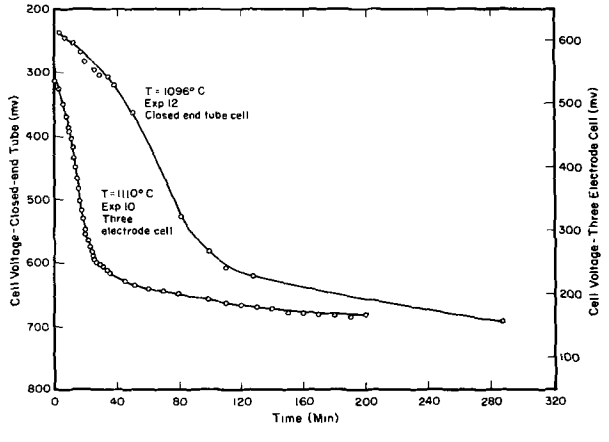

Fig. 11. Reduction of Fe_3O_4 at 1096° and 1110°C

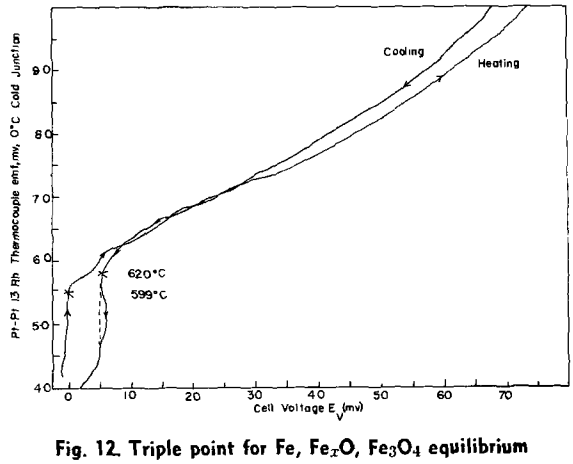

Fig. 12. Triple point for Fe, Fe_xO, Fe_3O_4 equilibrium

Acknowledgment

The writers are indebted to the Research Committee of the University of Utah for providing funds for the research. The principal author is grateful to Brigadier General Raymond A. Gilbert and the Air Force for affording the opportunity to continue studies in the Ph.D. program.

Manuscript submitted March 4, 1968; revised manuscript received *ca.* Sept. 23, 1968. This paper is based on part of a thesis submitted by one of the authors (H.F.R.) in partial fulfillment of the requirements for the Ph.D. Degree at the University of Utah, June 1968.

Any discussion of this paper will appear in a Discussion Section to be published in the December 1969 JOURNAL.

REFERENCES

1. Kalevi Kiukkola and Carl Wagner, *This Journal*, **104**, 308 (1957).
2. Kalevi Kiukkola and Carl Wagner, *ibid.*, **104**, 379 (1957).
3. F. E. Rizzo, L. R. Bidwell, and D. F. Frank, *Trans. AIME*, **229**, 593 (1967).
4. R. A. Rapp, *ibid.*, **227**, 371 (1963).
5. H. F. Rizzo, R. S. Gordon, and I. B. Cutler, Proc. National Bureau of Standards Symposium on Mass Transport in Oxides, October 1967, NBS special publication 296, pp. 129-142 (August 1968).
6. Kalevi Kiukkola, *Acta Chem. Scand.*, **16**, 327 (1962).
7. R. F. Ksenofontova, I. A. Vasil'era, and Ya. I. Gerasinov, *Proc. Acad. Sci. USSR., Chem Sect.*, **143**, 314 (1962) (in English).
8. T. L. Markin and R. J. Bones, *At. Energy Res. Estab. (Gr. Brit.)* report No. 4040 (April 1962).
9. C. B. Alcock, S. Zadon, and B. C. H. Steele, *Proc. British Ceram. Soc.*, **8**, 231 (June 1967).
10. L. S. Darken and R. W. Gurry, *J. Am. Chem. Soc.*, **67**, 1398 (1945).
11. R. A. Meussner, L. E. Richards, and C. T. Fujii, *Report of NRL Progress*, p. 26, Naval Research Lab., Washington, D. C.
12. M. Kleman, *Mem. Science Review Metall.*, **62**, 457 (1965).
13. J. Chipman, *Pure Appl. Chem.*, **5**, 669 (1962).
14. G. L. Humphrey, E. G. King, and K. K. Kelley, U. S. Bur. Mines Rep. Invest., No. 4870 (1952).
15. C. E. Wicks and F. E. Block, Bull, 65, U. S. Bur. of Mines, p. 57 (1963).
16. Pierrie Vallet and Paul Raccah, *Mem. Scien. Rev. Metall.*, **62**, 1 (1965).
17. H. F. Rizzo, "Thermodynamics of the Fe-O System by Coulometric Titration in High Temperature Galvanic Cells," unpublished Ph.D. Thesis, University of Utah (1968).
18. R. W. Taylor and A. Muan, *Trans. AIME*, **224**, 550 (1962).
19. R. J. Ackerman and R. W. Sandford, Jr., "A Thermodynamic Study of Wüstite Phase," *U. S. At. Energy Comm. ANL-7250*, Sept. 1966.
20. Hermann Schmalzried, *Elektrochem.*, **66**, 572 (1962).
21. B. C. H. Steele and C. B. Alcock, *Trans AIME*, **223**, 1359 (1965).
22. G. B. Barbi, *J. Phys. Chem.*, **68**, 2912 (1964).
23. P. Gerdanian and M. Dodé, *Compt. rend.*, **258**, 892 (1964).
24. B. Swaroop and J. B. Wagner, Jr., *Trans AIME*, **239**, 1215 (1967).
25. E. R. Jette and Frank Foote, *ibid.*, **105**, 276 (1933).
26. P. K. Foster and A. J. E Welch, *Trans. Faraday Soc.*, **52**, 1626 (1956).
27. P. F. J. Landler and K. L. Komarek, *Trans AIME*, **236**, 138 (1966).
28. L. Himmel, R. F. Mehl, and C. E. Birchenall, *ibid.*, **197**, 827 (1953).
29. H. J. Goldschmidt, *J. Iron Steel Inst.* (London), **146**, 157 (1942).
30. G. B. Barbi, *Trans. Faraday Soc.*, **62**, 1589 (1966).
31. R. F. Mehl and E. L. McCandless, *Trans AIME*, **125**, 531 (1937).
32. N. Buinov, A. Komar, M. Zhuravleva, and G. I. Chufarov, *J. Tech. Phys.* (USSR), **9**, 1649 (1939).
33. L. Himmel, "Kinetics of High Temperature Processes," p. 135, W. D. Kingery, Editor, John Wiley & Sons, Inc., New York (1959).
34. W. L. Roth, *Acta Cryst.*, **13**, 140 (1960).
35. F. Koch, Private communication.
36. G. G. Libowitz, Proc. National Bureau of Standards Symposium on Mass Transport in Oxides, October 1967, NBS special publication 296, pp. 109-118. (August 1968).
37. J. B. Tare and H. Schmalzried, *Trans AIME*, **236**, 444 (1966).
38. K. Hautte, "Oxidation of Metals," translated by Karl Vorres, Plenum Press, New York, p. 253 (1965).
39. J. M. Quets, M. E. Wadsworth, and J. R. Lewis, *Trans AIME*, **218**, 545 (1960).
40. J. M. Quets, M. E. Wadsworth, and J. R. Lewis, *ibid.*, **221**, 1186 (1961).
41. F. Pettit, R. Yinger, and J. B. Wagner, Jr., *Acta Met.*, **8**, 617 (1960).
42. F. H. Emmett and J. F. Shultz, *J. Am. Chem. Soc.*, **55**, 1376 (1933).

Technical Notes

Luminescence of Some Bismuth-Activated Oxides

S. Z. Toma* and D. T. Palumbo

Sylvania Electric Products, Inc., Chemical and Metallurgical Division, Towanda, Pennsylvania

Y_2O_3 has the so called C-type structure with two yttrium sites characterized by C_2 and S_6 symmetry. The cations are 6-coordinated in both sites. Bismuth luminescence in this and several other matrices has been studied (1-3). Broad absorption and emission bands are usually observed with energies quite dependent on the particular environment of Bi^{3+} ion. The present work concerns further study of bismuth luminescence in Y_2O_3 and the isomorphous oxides of scandium and gadolinium.

* Electrochemical Society Active Member.

Experimental

Samples of Y_2O_3:Bi were prepared from luminescent grade yttrium oxide (~99.99%). Appropriate amounts of bismuth and yttrium oxalates were acetone blended and dried. The mix was ignited to the oxide for 1 hr at 700°C and refired for 3 hr at 1100°C. A sample of

$(Y_{0.99}E_{0.01})_2O_3$ was prepared by firing coprecipitated oxalates at 1200°C for 3 hr.

All spectra were obtained at room temperature with a Hitachi-Perkin-Elmer MPF-2A spectrophotofluorimeter. This instrument, although uncorrected, provided better separation of the excitation and emission bands due to its grating optics. Minimum excitation and emission slit widths possible were used, consistent with the sample brightness. The excitation monochromator bandpass was 10Å in most measurements, while that for the emission monochromator was 10-20Å. An HTV-R213 photomultiplier was used.

Results and Discussion

Figures 1 and 2 show the emission spectra of Y_2O_3:Bi (0.5 a/o) for a number of different excitation wavelengths. The excitation spectra for the two emissions

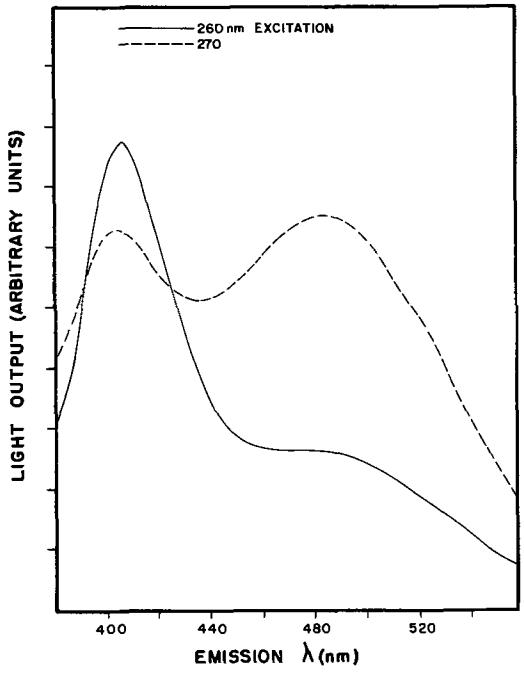

Fig. 1. Emission spectra of Y_2O_3:Bi with short uv wavelength excitations.

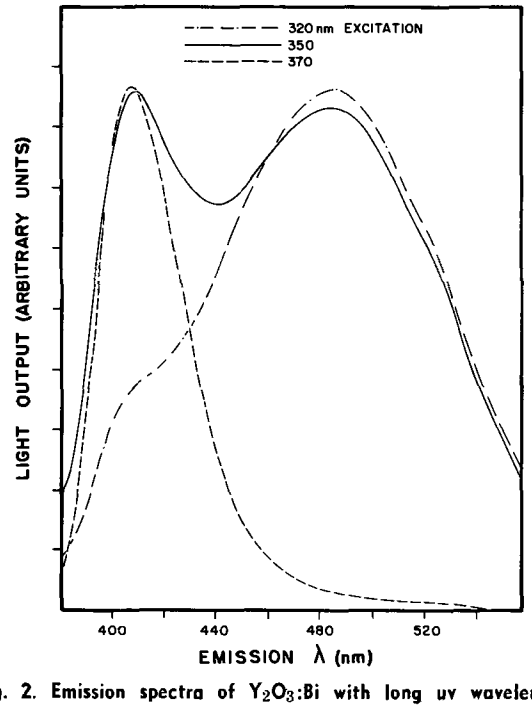

Fig. 2. Emission spectra of Y_2O_3:Bi with long uv wavelengths excitations.

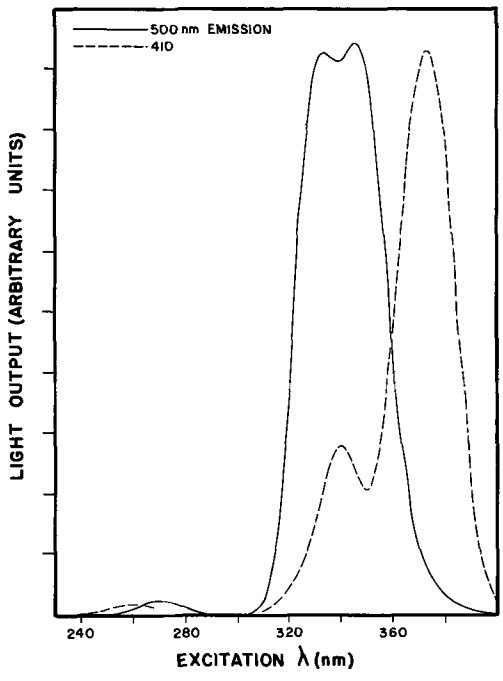

Fig. 3. Excitation spectra of Y_2O_3:Bi for the two emissions

are shown in Fig. 3. A sample formulated with 1 a/o bismuth *i.e.*, $(Y_{0.99}Bi_{0.01})_2O_3$, gave similar results. Comparison of the band maxima in the spectra of Sc_2O_3, Y_2O_3 and Gd_2O_3 activated with bismuth appears in Table I.

Incorporation of an activator ion with $6s^2$ electrons in a matrix allows a number of new electronic states, *e.g.*, $s^2 \rightarrow sp$ transitions, activator-matrix states, and "dimer" states resulting from the proximity and interaction of activator ions. "Dimer" absorption in thallium-activated alkali halides is the subject of recent works (4, 5). Activator-matrix states, those not characteristic of the free ion levels, have been considered in bismuth activated YVO_4, $YNbO_4$, Y_2WO_6 (3), and Y_2O_3 (2). The free ion $s^2 \rightarrow sp$ transitions give rise to four excited states, which for L — S coupling, are $^3P_0$, $^3P_1$, $^3P_2$, and $^1P_1$. With j — j coupling the levels are $(j_1, j_2)_J = (1/2, 1/2)_0$, $(1/2, 1/2)_1$, $(3/2, 1/2)_2$, $(3/2, 1/2)_1$. Selection rules imply the transitions to J = 1 levels to be strongest, and symmetry considerations predict complete splitting of all degenerate levels in C_2 symmetry. Within the limits of instrumental resolution (10Å) we were not able to detect any structure in the observed bands.

The electronic transitions responsible for the observed excitation and emission bands are difficult to ascertain from the present work. However, since two emissions are observed with bismuth addition, each having characteristic excitation bands, two distinct emitting centers may be present and be associated with the two sites in these oxides. Evidence for Eu^{3+} absorption (6) and emission (7) from both sites of Y_2O_3 has been reported. The two sites of Eu^{3+} can give differing, broad excitation bands and this is shown in Fig. 4 where the band for the 582.3 emission (7) extends to

Table I. Comparison of the band maxima in the spectra of Sc_2O_3, Y_2O_3, and Gd_2O_3 activated with bismuth

	Sc_2O_3	Y_2O_3	Gd_2O_3
Emission (nm)	403	407	418
Excitation bands	372	373	379
	336	340	345
	258	258	270
Emission	479	483	480
Excitation bands	348	346	347
	328	333	337
	272	270	270

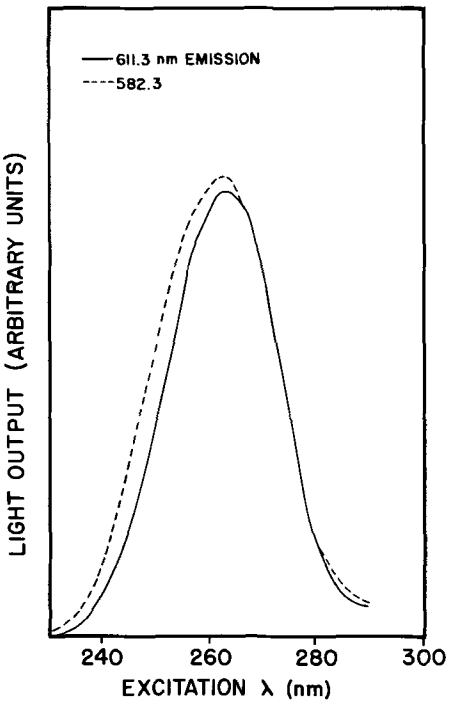

Fig. 4. Broad excitation bands for the 611.3 and 582.3 nm line emissions in Y_2O_3:Eu.

shorter wavelength than that for the 611.3 nm line. Analogously, the excitation and emission spectra of Y_2O_3:Bi may be understood by assuming that bismuth occupies both sites in Y_2O_3, each having characteristic excitation and emission.

The possible effect of long or short distance interaction between two bismuth centers would complicate the assignment of the observed excitation bands. For example, since the green emission overlaps the excitation band of the blue emission, the latter's excitation bands may have some contribution from the green band excitations. Such interactions can occur to some extent due to this overlap (8) and bismuth concentrations and spectral measurement conditions were selected to minimize such effects.

Although narrow band emissions due to trivalent rare earths are well studied in Y_2O_3, much less has been reported about activators with broad absorptions and emissions in this matrix. These are of some interest in studies of the general questions of two sites and activator-matrix states in Y_2O_3. We have observed that pure Y_2O_3 and Y_2O_3:Tl(2a/o), prepared in air, have broad emissions under x-ray and 254 nm excitations, respectively (9). The emission color is yellow for Y_2O_3:Tl and uv-blue for the pure matrix.

Manuscript submitted June 28, 1968; revised manuscript received *ca.* Nov. 10, 1968. This paper was presented at the Boston Meeting, May 5-9, 1968, as Paper 32.

Any discussion of this paper will appear in a Discussion Section to be published in the December 1969 JOURNAL.

REFERENCES

1. W. A. Runciman, *Proc. Phys. Soc.*, **A68**, 647 (1955).
2. R. K. Datta, *This Journal*, **114**, 1137 (1967).
3. G. Blasse and A. Bril, *J. Chem. Phys.*, **48**, 217 (1968).
4. M. P. Fontana and W. J. Van Sciver, *Phys. Rev.*, **168**, 960 (1968).
5. G. K. Herb, M. P. Fontana, and W. J. Van Sciver, *ibid.*, **168**, 1000 (1968).
6. N. C. Chang and J. B. Gruber, J. *Chem. Phys.*, **41**, 3227 (1964).
7. H. Forest and G. Ban, *This Journal*, **115**, 64C (1968).
8. D. L. Dexter, *J. Chem. Phys.*, **21**, 836 (1953).
9. D. T. Palumbo and S. Z. Toma, To be published.

Epitaxially Grown Guard Rings for GaAs Diodes

C. M. Wolfe* and W. T. Lindley*

Lincoln Laboratory,[1] Massachusetts Institute of Technology Lexington, Massachusetts

In this paper we present a technique for fabricating guard rings for GaAs p-n junction and Schottky barrier avalanche diodes. To obtain uniform avalanche diodes it is necessary to prevent breakdown at the edges of the diodes. Although this can be done by etching mesas, GaAs diodes fabricated in this manner often show surface leakage, deterioration with time, or even complete failure at the surface. Even when the diodes are hermetically sealed in an inert atmosphere, or the surfaces are coated with pyrolytic silicon dioxide or silicon nitride, these problems are not completely eliminated. Edge breakdown has been prevented in silicon devices by using diffused guard ring structures (1). To avoid the problems involved in diffusing guard rings in GaAs, we have developed a method for growing guard rings in an epitaxial reactor which is compatible with current GaAs epitaxial technology.

These epitaxially grown guard rings have been used for both p-n junction and Schottky barrier diodes (2) on <100> orientated GaAs. The two diode configurations are shown in Fig. 1. For the Schottky barrier diode the Au or other high work function metal must extend out over the n^- regions. In this guard ring structure edge breakdown is suppressed by utilizing two diodes in parallel: an annular outer diode of lightly doped material (guard ring) and an inner diode of heavier doped material (diode). Since the same voltage is applied across both diodes, the heavier doped inner diode breaks down first in reverse bias. The space charge region of the annular guard ring isolates the junction interface of the inner diode. Due to the smaller area of the annular guard ring, it does not contribute significantly to the reverse leakage current.

The mesas for these diodes are etched and the guard rings are grown in an epitaxial reactor utilizing the $AsCl_3$-Ga-H_2 flow system (3) by a technique previously described (4). With this system the mesa etching can be carried out in a high-purity gaseous ambient, and relatively uncompensated GaAs guard rings with doping levels in the 10^{14}-10^{15} cm^{-3} range can be grown. Higher resistivity, more heavily compensated n-type material can be obtained by introducing trace amounts of O_2 into the reactor during growth.

The process used for making the guard rings around p-n junctions is illustrated in Fig. 2. Figure 2(a) shows the initial p^+-n-n^+ layer structure with an etch mask consisting of an array of SiO_2 disks on the p^+ region and a layer of SiO_2 on the n^+ region. The layer structure is produced by growing an epitaxial n-type layer (10^{15}-10^{17} cm^{-3}) on an n^+ substrate ($\sim 10^{18}$ cm^{-3}) and then either diffusing Zn into the n layer or growing a Zn-doped ($\sim 10^{19}$ cm^{-3}) epitaxial layer on the n re-

* Electrochemical Society Active Member.

[1] Operated with support from the U.S. Air Force.

Key words: gallium arsenide, epitaxy, semiconductor devices.

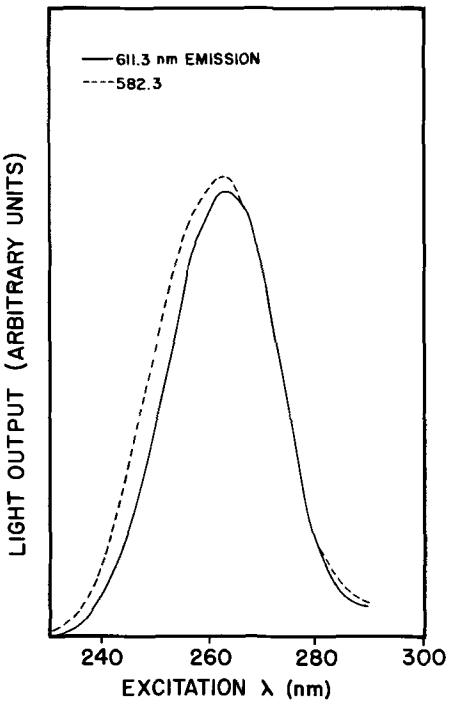

Fig. 4. Broad excitation bands for the 611.3 and 582.3 nm line emissions in Y_2O_3:Eu.

shorter wavelength than that for the 611.3 nm line. Analogously, the excitation and emission spectra of Y_2O_3:Bi may be understood by assuming that bismuth occupies both sites in Y_2O_3, each having characteristic excitation and emission.

The possible effect of long or short distance interaction between two bismuth centers would complicate the assignment of the observed excitation bands. For example, since the green emission overlaps the excitation band of the blue emission, the latter's excitation bands may have some contribution from the green band excitations. Such interactions can occur to some extent due to this overlap (8) and bismuth concentrations and spectral measurement conditions were selected to minimize such effects.

Although narrow band emissions due to trivalent rare earths are well studied in Y_2O_3, much less has been reported about activators with broad absorptions and emissions in this matrix. These are of some interest in studies of the general questions of two sites and activator-matrix states in Y_2O_3. We have observed that pure Y_2O_3 and Y_2O_3:Tl(2a/o), prepared in air, have broad emissions under x-ray and 254 nm excitations, respectively (9). The emission color is yellow for Y_2O_3:Tl and uv-blue for the pure matrix.

Manuscript submitted June 28, 1968; revised manuscript received *ca.* Nov. 10, 1968. This paper was presented at the Boston Meeting, May 5-9, 1968, as Paper 32.

Any discussion of this paper will appear in a Discussion Section to be published in the December 1969 JOURNAL.

REFERENCES

1. W. A. Runciman, *Proc. Phys. Soc.*, **A68**, 647 (1955).
2. R. K. Datta, *This Journal*, **114**, 1137 (1967).
3. G. Blasse and A. Bril, *J. Chem. Phys.*, **48**, 217 (1968).
4. M. P. Fontana and W. J. Van Sciver, *Phys. Rev.*, **168**, 960 (1968).
5. G. K. Herb, M. P. Fontana, and W. J. Van Sciver, *ibid.*, **168**, 1000 (1968).
6. N. C. Chang and J. B. Gruber, J. *Chem. Phys.*, **41**, 3227 (1964).
7. H. Forest and G. Ban, *This Journal*, **115**, 64C (1968).
8. D. L. Dexter, *J. Chem. Phys.*, **21**, 836 (1953).
9. D. T. Palumbo and S. Z. Toma, To be published.

Epitaxially Grown Guard Rings for GaAs Diodes

C. M. Wolfe* and W. T. Lindley*

Lincoln Laboratory,[1] Massachusetts Institute of Technology Lexington, Massachusetts

In this paper we present a technique for fabricating guard rings for GaAs p-n junction and Schottky barrier avalanche diodes. To obtain uniform avalanche diodes it is necessary to prevent breakdown at the edges of the diodes. Although this can be done by etching mesas, GaAs diodes fabricated in this manner often show surface leakage, deterioration with time, or even complete failure at the surface. Even when the diodes are hermetically sealed in an inert atmosphere, or the surfaces are coated with pyrolytic silicon dioxide or silicon nitride, these problems are not completely eliminated. Edge breakdown has been prevented in silicon devices by using diffused guard ring structures (1). To avoid the problems involved in diffusing guard rings in GaAs, we have developed a method for growing guard rings in an epitaxial reactor which is compatible with current GaAs epitaxial technology.

These epitaxially grown guard rings have been used for both p-n junction and Schottky barrier diodes (2) on <100> orientated GaAs. The two diode configurations are shown in Fig. 1. For the Schottky barrier diode the Au or other high work function metal must extend out over the n^- regions. In this guard ring structure edge breakdown is suppressed by utilizing two diodes in parallel: an annular outer diode of lightly doped material (guard ring) and an inner diode of heavier doped material (diode). Since the same voltage is applied across both diodes, the heavier doped inner diode breaks down first in reverse bias. The space charge region of the annular guard ring isolates the junction interface of the inner diode. Due to the smaller area of the annular guard ring, it does not contribute significantly to the reverse leakage current.

The mesas for these diodes are etched and the guard rings are grown in an epitaxial reactor utilizing the $AsCl_3$-Ga-H_2 flow system (3) by a technique previously described (4). With this system the mesa etching can be carried out in a high-purity gaseous ambient, and relatively uncompensated GaAs guard rings with doping levels in the 10^{14}-10^{15} cm^{-3} range can be grown. Higher resistivity, more heavily compensated n-type material can be obtained by introducing trace amounts of O_2 into the reactor during growth.

The process used for making the guard rings around p-n junctions is illustrated in Fig. 2. Figure 2(a) shows the initial p^+-n-n^+ layer structure with an etch mask consisting of an array of SiO_2 disks on the p^+ region and a layer of SiO_2 on the n^+ region. The layer structure is produced by growing an epitaxial n-type layer (10^{15}-10^{17} cm^{-3}) on an n^+ substrate ($\sim 10^{18}$ cm^{-3}) and then either diffusing Zn into the n layer or growing a Zn-doped ($\sim 10^{19}$ cm^{-3}) epitaxial layer on the n re-

* Electrochemical Society Active Member.

[1] Operated with support from the U.S. Air Force.

Key words: gallium arsenide, epitaxy, semiconductor devices.

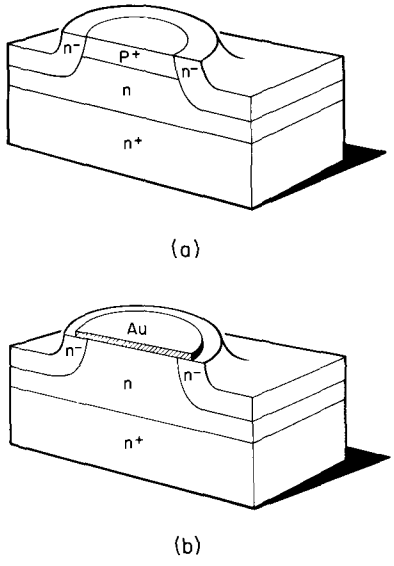

Fig. 1. Guard ring structures for (a) a p-n junction diode and (b) a Schottky barrier diode. For the Schottky barrier diode the Au must extend out over the n^- regions.

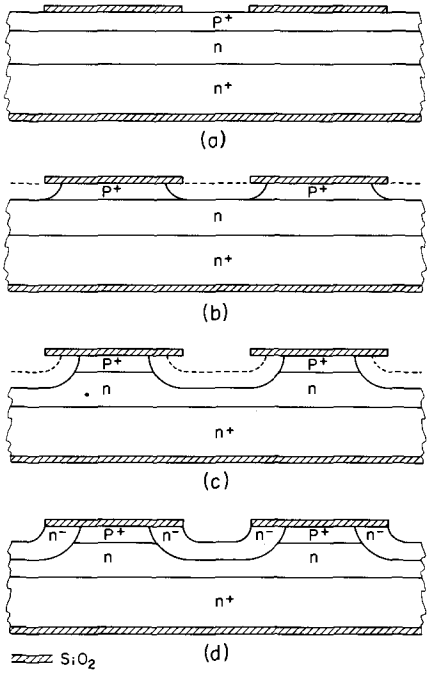

Fig. 2. Guard ring fabrication process for p-n junction diodes: (a) initial p^+-n-n^+ layer structure with an etch mask of SiO_2 disks on the p^+ region and a layer of SiO_2 on the n^+ region; (b) removal of the excess p^+ layer before insertion in the furnace to avoid contamination of the epitaxial reactor; (c) high-temperature furnace etching step to ensure clean mesa surfaces; (d) growth of the lightly doped guard rings over the etched mesas.

gion. The SiO_2 is then deposited on both sides of the epitaxial structure by the pyrolytic decomposition of SiH_4 in the presence of O_2 at 300°C. Islands of SiO_2 are defined by standard photolithographic techniques. To prevent severe undercutting during the subsequent high-temperature furnace etching, there must be good adherence between the SiO_2 and the p^+ layer. This can be attained by ensuring a clean and oxide-free GaAs surface before SiO_2 deposition. Circles of SiO_2 as small as 2 mils in diameter on <100> orientated material have been cycled from room temperature to 900°C to room temperature with no loss of adherence. The n^+ side of the wafer must be coated with SiO_2 to reduce autodoping of the initial growth. When the n^+ side of the wafer is not coated with SiO_2, the resulting diodes

Table I. Etching conditions for {100} seeds

H_2 flow through $AsCl_3$	100 ml/min
H_2 dilution flow	150 ml/min
Gallium temperature	850°C
Etching temperature	800° ± 2°C
Growth temperature	750°C
Furnace thermal time constant	~200 min
or avg. cooling rate (800°-750°C)	5°C/min

exhibit premature reverse breakdown which is characteristic of a heavily doped region at the n-n^- interface.

Before inserting the layer structure into the epitaxial reactor, the excess p^+ layer is removed [Fig. 2(b)]. A solution of $5H_2SO_4$-$1H_2O_2$-$1H_2O$, allowed to cool for about 5 min before use, can be used to controllably remove p^+ layers several microns thick. This step in the process is necessary to avoid reactor contamination from the heavily doped p^+ layer. When the excess p^+ layer is removed by high-temperature furnace etching, it is difficult to obtain lightly doped n-type material for the guard rings in the growth step. For the Schottky barrier diode configuration this pre-etch is not necessary.

To ensure a clean n-n^- interface the exposed mesas of the layer structure are re-etched in the high-purity atmosphere of the epitaxial reactor [Fig. 2(c)]. This step is performed by inserting the layer structure in a flat temperature region of the furnace at a temperature somewhat higher than the temperature that is used for growth. After thermal equilibration, the H_2 through the $AsCl_3$ is turned on and the furnace is allowed to cool to the growth temperature. Etching occurs during the cooling of the furnace. The conditions we have used to obtain etch depths from 1 to 5μ are listed in Table I. Larger amounts can be removed by initiating the etch cycle at higher temperatures. Etch conditions, however, will vary from one system to the next due in part to differences in furnace cooling rates. We have found that at an etching temperature of 800°C, compared to higher temperature etching, the etch depth is very temperature dependent. Thus, good temperature control is required to reproducibly remove small amounts of material. This furnace etching process undercuts the SiO_2 at about the same rate that it etches into the sample. Caution must also be taken to avoid etching through to the n^+ layer. When this occurs, the resulting diodes exhibit premature breakdown due to autodoping of the n-n^- interface.

In the next step [Fig. 2(d)] the n^- guard ring is grown over the etched mesas. The growth of lightly doped n^- material in this system has previously been discussed in some detail (3-5). Growth must be obtained by a surface catalyzed reaction to prevent nucleation of the GaAs on the SiO_2. Unlike the small area {100} growth through holes in an oxide (6), where it is difficult to terminate growth before the oxide is overgrown, this essentially large area {100} growth is sufficiently slow to make growth termination noncritical. The requirements on the doping level of the n^- guard ring are also not critical. We have found that it is only necessary that the doping level of the n^- guard ring be about a factor of five below that of the doping level of the n region of the diode. The approximate doping level of the guard ring is determined from Hall measurements on layers simultaneously grown on high-resistivity substrates.

Schottky barrier diodes with the structure which was shown in Fig. 1(b) have been fabricated by electroplating a semi-transparent gold film (~100Å) onto the active diode area and over part of the epitaxially grown guard ring. By looking at the visible light emission (7) from these diodes when they are biased into reverse breakdown, the uniformity of the avalanche breakdown can be observed. For diodes fabricated on this same material with no guard ring, the breakdown light emission is entirely at the perimeter. Figure 3 shows the light emission from one diode of an array of 3.5-mil diameter diodes which have epitaxial guard

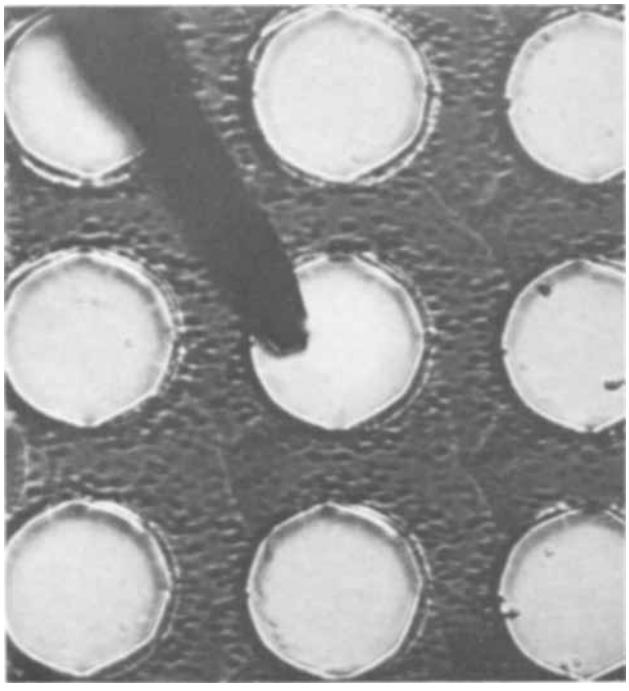

Fig. 3. An array of 3.5 mil diameter semitransparent Au-GaAs Schottky barrier diodes with epitaxial guard rings. Reverse bias visible light emission pattern is shown for the center diode.

rings. The breakdown voltage of these diodes is higher than those without a guard ring and the breakdown is entirely in the center active region. The slight nonuniformity in the light emission is due to material inhomogeneity. These diodes have also been used as avalanche photodetectors and show a gain in excess of 100 when biased near their reverse breakdown.

We believe that this epitaxial process for the formation of GaAs guard rings provides a useful and efficient technique for eliminating surface problems and suppressing edge breakdown in GaAs p-n junction and Schottky barrier avalanche diodes.

Acknowledgment

The authors would like to thank L. Krohn, Jr., G. A. Lincoln, Jr., and R. T. Cerretani for their excellent assistance in this work.

Manuscript received Sept. 4, 1968.

Any discussion of this paper will appear in a Discussion Section to be published in the December 1969 JOURNAL.

REFERENCES

1. R. L. Batdorf, A. G. Chynoweth, G. C. Dacey, and P. W. Foy, *J. Appl. Phys.*, **31**, 1153 (1960); A. Goetzberger, B. McDonald, R. H. Haitz, and R. M. Scarlett, *ibid.*, **34**, 1591 (1963).
2. W. T. Lindley, R. J. Phelan, Jr., and C. M. Wolfe, IEEE Solid-State Device Research Conference, Boulder, June 17-19, 1968.
3. J. R. Knight, D. Effer, and P. R. Evans, *Solid-State Electronics*, **8**, 178 (1965); D. Effer, *This Journal*, **112**, 1020 (1965).
4. C. M. Wolfe, A. G. Foyt, and W. T. Lindley, *Electrochem. Technol.*, **6**, 208 (1968).
5. E. W. Mehal and G. R. Cronin, *ibid.*, **4**, 540 (1966); D. E. Bolger, J. Franks, J. Gordon, and J. Whitaker, *Proc. Intern. Symp. Gallium Arsenide, Reading, 1966* (Institute of Physics and The Physical Society, London), p. 16 (1967); M. Maruyama, S. Kikuchi, and F. Hasegawa, Paper presented at the Boston Meeting, May 5-9, 1968, as Paper 62.
6. D. W. Shaw, *This Journal*, **113**, 904 (1966).
7. A. E. Michel, M. I. Nathan, and J. C. Marinace, *J. Appl. Phys.*, **35**, 3543 (1964).

Properties of Ion-Implanted GaAs Diodes

P. E. Roughan and K. E. Manchester

Research and Development Center, Sprague Electric Company, North Adams, Massachusetts

GaAs p-n junction diodes have been produced by the implantation of 80 kev singly charged zinc ions into n-type GaAs substrates of carrier concentration 2.4 x 10^{16} cm^{-3}. The implantation was carried out at room temperature, into wafers cut parallel to the <110> direction. The apparatus employed has been previously described by Manchester *et al.* (1).

After implantation, the wafers were covered with an evaporated layer of SiO_x and annealed at 650°C in argon for various periods of time. The protective oxide layer was then removed, the wafer diced into squares approximately 20-25 mils on a side, and the dice bonded to standard headers. Measurements were then carried out on the forward and reverse current-voltage characteristics, the capacitance-voltage relationship, and the light emission properties of the diodes.

The annealing behavior of implanted GaAs does not, at present, appear to be as consistent as that for silicon. In the latter case, relatively mild anneal cycles (*e.g.*, a minimum of 600°C for 10 min in the case of phosphorus implants) are sufficient to produce diodes with excellent characteristics. However, for GaAs, we have found that, in some cases, brief anneals (30 min to 3 hr) are sufficient to produce diode properties, while, in other cases extended annealing periods, of the order of 10 hr and longer, appear to be necessary before diode properties are obtained. This behavior appears to be related to ion dose; for example, all of the samples implanted with 10^{16} ions cm^{-2} required only brief annealing periods, while most, but not all, of the samples implanted with 10^{15} ions cm^{-2} required long anneals. Furthermore, extended annealing (up to 15 hr) of high dose samples produced no significant changes in diode properties, while those low dose samples which required long anneals displayed quite different diode properties.

Figure 1 shows curve tracer displays of the I-V characteristics for two typical diodes, one of each type. Part (a) of this figure shows the characteristics for a diode obtained by the implantation of 10^{16} Zn^+ ions cm^{-2}, followed by an anneal for 3 hr at 650°C. A good thermally diffused diode produced in background material of similar carrier concentration would show the same characteristic. Part (b) of this figure illustrates the diode characteristic obtained for a sample implanted with 10^{15} Zn^+ ions cm^{-2}, then annealed for 18 hr at 650°C. The most significant difference here is the extremely large value of reverse breakdown voltage, ~115v. The forward characteristic also indicates a higher series resistance. Schroeder and Dieselman (2) have presented I-V data on Zn-implanted GaAs diodes which exhibit rather large reverse currents and soft breakdown characteristics. A maximum anneal temperature of 250°C, however, was employed by these authors, which is probably insufficient to remove the radiation damage.

Figure 2 illustrates the capacitance-voltage relationships, again for two typical diodes. Linear dependencies are obtained for C^{-2} and V for diode C8-11,

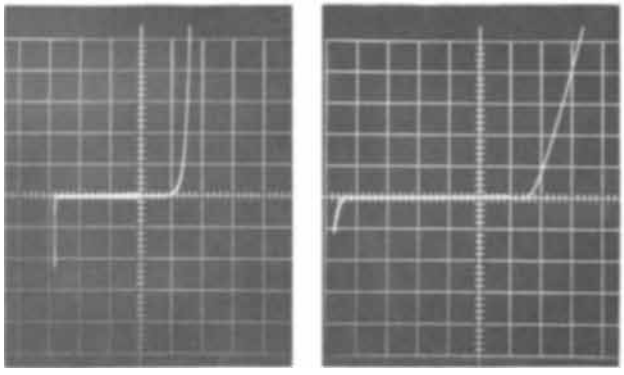

Fig. 1. Curve tracer displays of I-V characteristics of Zn-implanted diodes: a (left) dose 10^{16} ions cm^{-2}, anneal 3 hr, 650°C, in Ar (scales: vertical, 0.01 ma/div.; horizontal, 10 v/div. reverse, 0.5 v/div. forward); b (right) dose 10^{15} ions cm^{-2}, anneal 18 hr, 650°C, in Ar (scales: vertical, 0.05 ma/div.; horizontal, 20 v/div. reverse, 1 v/div. forward. Origin has been shifted one division to the right.)

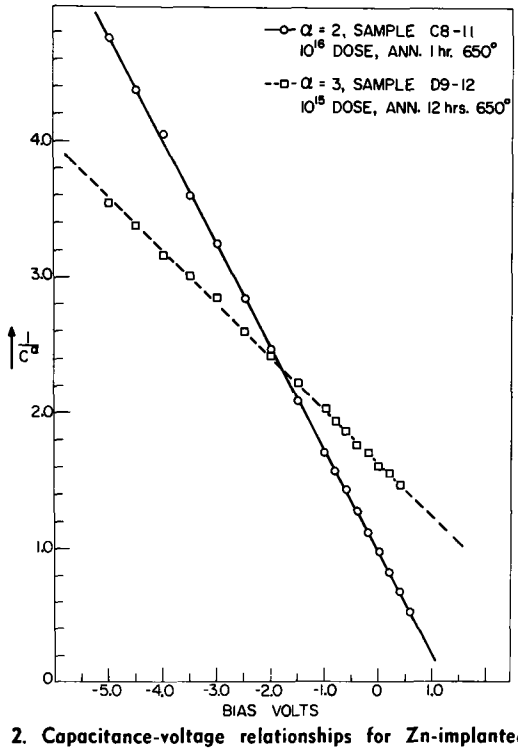

Fig. 2. Capacitance-voltage relationships for Zn-implanted diodes.

which had been annealed for 1 hr at 650°C, and between C^{-3} and V, for diode D9-12, an 18-hr anneal. Thus, the high dose units, for which only a brief anneal is required, exhibit the characteristics of a typical abrupt junction, while the low dose units, annealed for longer periods, show graded junction behavior. In fact, if one calculates an impurity grading coefficient from the slope of the C^{-3} *vs.* V plot, the rather low value of a $\simeq 10^{20}$ cm^{-4} is obtained, as opposed to the typical value of a $\geqslant 10^{22}$ cm^{-4} for normal graded junctions.

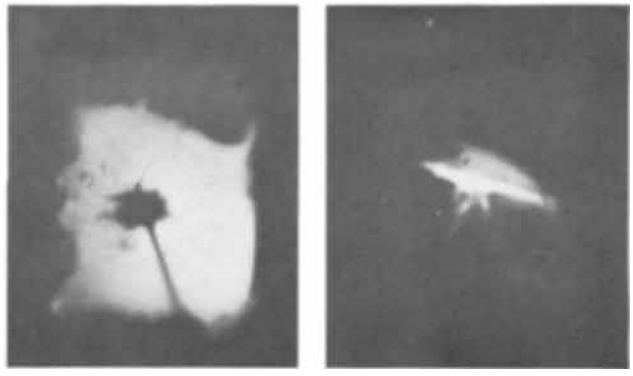

Fig. 3. Infrared emission for an implanted GaAs diode: a (left) top view of diode; b (right) side view of diode.

Both types of diodes emit light when biased in the forward direction. As might be expected, however, power outputs and efficiencies are considerably higher in the case of the abrupt junction types. Figure 3 shows the light emission characteristics of an implanted GaAs diode, as observed on the screen of an image converter. The best emitters have shown power outputs of 0.7-0.8 mw at external efficiencies of ~0.5% at room temperature. Spectral measurements indicate that the peak of the emission occurs at $\lambda = 0.92$ μm.

Summary

GaAs diodes have been fabricated by room-temperature implantation of 80 kev Zn^+ ions. Preliminary data indicate that, by suitably altering implantation conditions, two types of diodes can be obtained, *i.e*, abrupt junction units, formed using a high-dose implant and brief annealing periods, or graded-junction units formed with a low dose implant after extended annealing. The former display I-V and light emission characteristics comparable to good thermally diffused diodes. The latter exhibit high forward resistances and large reverse breakdown voltages; they are perhaps more appropriately described as p-i-n structures, produced by smoothing out the implanted profile (assumed to be Gaussian) by thermal diffusion during the long annealing periods.

Manuscript submitted Feb. 20, 1968; revised manuscript received Oct. 23, 1968. This paper was presented at the Chicago Meeting, Oct. 15-19, 1967, as Paper 172.

Any discussion of this paper will appear in a Discussion Section to be published in the December 1969 JOURNAL.

REFERENCES

1. K. E. Manchester, C. B. Sibley, and G. Alton, *Nucl. Instr. and Methods*, **38**, 165 (1965).
2. J. B. Schroeder and H. D. Dieselman, *Proc. IEEE*, **55**, 125 (1967).

Brief Communications

Measurement of Anodic Oxide Film Thickness by Electroreflectance Interferometry

B. J. Holden and F. G. Ullman*

Electrical Materials Laboratory, Department of Electrical Engineering, University of Nebraska, Lincoln, Nebraska

In this Communication, we describe a new spectrophotometric method for the measurement of the thickness of oxide films on tantalum and niobium[1] with which the wavelengths of reflectance maxima and minima can be measured with a precision of better than 0.1%.

In a study of room temperature electroreflectance from tantalum oxide films on tantalum by the electrolyte method (1), oscillatory spectra, extending from just inside the oxide absorption edge (about 4.4 ev) to photon energies less than the edge by more than a factor of two, were observed (2). It was apparent that the measured response was proportional to the slope of the reflectance spectrum since the wavelengths of the zero crossings corresponded closely to the reflectance maxima and minima. However, the mechanism responsible for the observed electric field-induced modulation was not immediately obvious. Calculations of the Franz-Keldysh effect, using Aspnes' theory (3), showed it to be too small at photon energies much less than the absorption edge to account for the observed modulation which ranged from about 0.01 to 1.0%. However, at the field strengths used in these experiments, about 10^6 v/cm, an electrostrictive compression of the oxide of the order of 0.001% can be expected for an assumed linear compressibility of the oxide of about 10^{-12} cm^2/dyne. The calculated changes in reflectance for thickness changes of this order are in good semiquantitative agreement with the observed changes. (We are indebted to B. O. Seraphin for suggesting electrostriction to be the mechanism responsible for our observations.)

The change in reflectance resulting from such small thickness changes is directly proportional to the slope of the reflectance spectrum if dispersion in the optical constants of the film and substrate is small. Using phase-sensitive detection, we found that the wavelengths of the zero crossings could be determined with a reproducibility of better than 0.1%. These results suggested that film thicknesses could be measured by this new technique, which we have termed "electroreflectance interferometry," with a precision approaching that obtainable by multiple beam interferometry (4) or shearing interference microscopy (5). However, our method has the additional advantage of being nondestructive, *i.e.*, no steps, scratches, or metallic overlays are required. Further, since the effect can frequently be observed in a region of low film absorption, the calculation of film thickness, in this case, is straightforward.

Taking into account the phase shift on reflection at the film-substrate interface, and neglecting film absorption ($k_1 = 0$), the film thickness, s, for normal incidence, is

$$s = (m\lambda/4n_1)\{1-(1/m\pi)[\tan^{-1}(2n_1k_2/(n_2^2-n_1^2+k_2^2))]\} \quad [1]$$

where λ = wavelength of zero crossing, n_1 = real part of refractive index of film, n_2 = real part of refractive index of substrate, k_2 = imaginary part of refractive index of substrate, and m is an integer, odd for minima and even for maxima, if the refractive index of the film is less than that of the substrate. The appropriate values of the interference order, m, are obtained by first estimating the film thickness, without the phase correction, from the photon energy increment between adjacent maxima or minima. An incorrect choice of m is then readily detected since this will result in a monotonic variation in calculated thickness with increasing m instead of a random variation about an average value.

A block diagram of our instrumentation is shown in Fig. 1 and typical spectra obtained from samples of tantalum oxide on tantalum and niobium oxide on niobium are shown in Fig. 2. The samples were anodized in 2% boric acid solution buffered to a pH of 6-7 with NH_4OH.[2] The measurement conditions are given in the figure caption. The calculated tantalum oxide thicknesses, their mean, the mean deviation, and the sources of constants used in the calculation are shown in Table I. For niobium oxide, consistent results are obtained only for obviously incorrect, or nonintegral, values of the interference order, m. Apparently, the refractive indices of our films differ significantly from the published values (6) used for these calculations.

Because of the electrolyte, this method is limited to wavelengths longer than the vacuum ultraviolet which, at best, imposes a short wavelength cutoff of about 1800Å. Consequently, this technique is limited to films sufficiently thick for at least the first reflectance minimum to be at greater than 1800Å. For such thin films there would be only one observable zero crossing; consequently, it is more accurate to use the wavelength of the electroreflectance maximum to calculate the film thickness in this case. This is accomplished by calculating numerically the wavelength

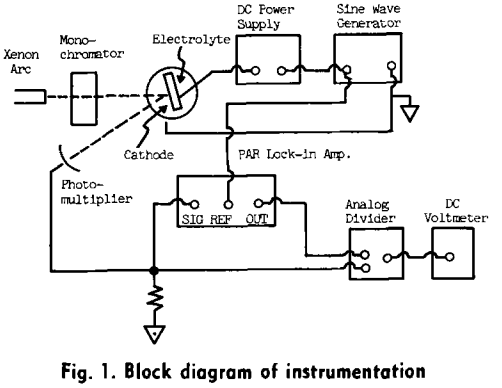

Fig. 1. Block diagram of instrumentation

* Electrochemical Society Active Member.
Key words: tantalum oxide, niobium oxide, anodic film, thickness measurement.

[1] Other materials have not yet been tried.

[2] One sample of niobium was anodized in 0.2*N* H_2SO_4 with no change in results.

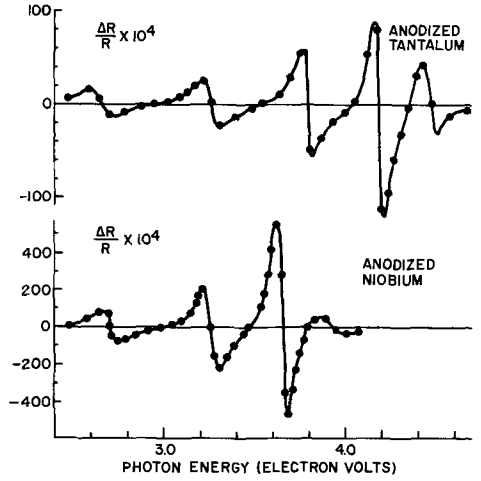

Fig. 2. Electroreflectance spectra of anodized tantalum and niobium. Upper curve, one mil tantalum foil anodized to 200v. Measurement made in boric acid electrolyte (1.0M KCl solutions were also used with no change in results) with 160v d-c bias and 35 Hz, 50v peak-to-peak sine wave modulation. Lower curve, one mil niobium foil anodized to 118v. Measurement made in boric acid (0.2*N* H_2SO_4 was also used) with 35v d-c bias and 35 Hz, 70v peak-to-peak sine wave modulation.

of the maximum in the ratio of the derivative of the reflectance with respect to thickness to the reflectance, $(dR/ds)/R$, as a function of thickness in the appropriate spectral range for comparison with the experimental result. We have been able to measure electroreflectance maxima for tantalum oxide films estimated to be as thin as about 70Å as shown in Fig. 3. The vertical bars in the figure indicate the width of the noise in these measurements. The measurement conditions are given in the caption. Photomultiplier shot-noise and the inherently lower precision in locating a maximum, rather than a zero crossing, limit the precision in this case to values as poor as 10%. Calculation of film thicknesses from these and similar data await the determination of the refractive index for this spectral region.

The results in Table I indicate a precision for thickness determination of about 0.6% (0.3% is more typical of other measurements) whereas the reproducibility in the determination of the zero crossing wavelengths was better than 0.1%. Since the applied field varied from zero to its maximum value in these measurements, the measured change in reflectance is not directly proportional to just the first derivative of reflectance with respect to film thickness but may depend on higher derivatives as well. To determine if

Table I. Calculation of film thickness from experimental electroreflectance zeros for 200v tantalum oxide film

Experimental zero crossing, Å	Order, m	$\frac{m\lambda}{4n_1}$, Å	Metal absorption correction, Å	Thickness, Å
3788	9	3680	97	3583
3492	10	3673	87	3586
3275	11	3697	82	3615
3065	12	3616	78	3538
2968	13	3690	76	3614
2846	14	3629	74	3555
2775	15	3645	73	3572

Average: 3580 Å
Average Deviation: ±21 Å

Note: The two longest wavelength zeros in Fig. 2 were excluded because of the excessively small signal-to-noise ratio in this spectral region.
The values of the optical constants used in this calculation were:
$n_1 = 2.14 + 0.292\ (\lambda/10^3\text{Å} - 2.305)^{-1.2}$ (ref. 7)
$n_2 = 3.5$, $k_2 = 2.4$ } (Ref. 10)

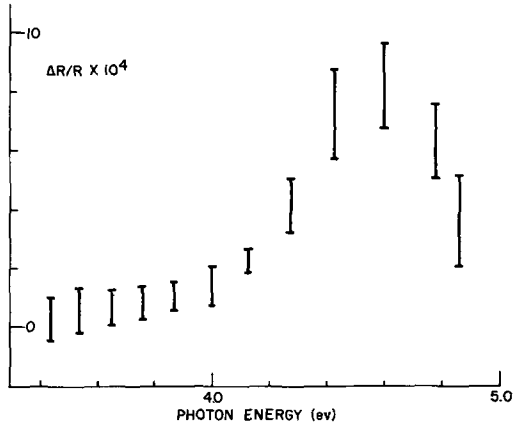

Fig. 3. Electroreflectance spectrum of 1 mil tantalum foil anodized to 3v. Measurement made in boric acid with 1.5v d-c bias and 35 Hz, 3.0v peak-to-peak sine wave molulation.

neglect of these higher order derivatives in the thickness calculations was contributing to the apparent experimental error, we calculated the magnitude of the second derivative term. The effect of including the second derivative on the calculated thickness was less than 0.05%, and therefore only the first derivative term is significant. The most likely explanation for the observed error is the choice of the optical constants used in the thickness calculations. The optical constants of tantalum and niobium oxide are not known at all wavelengths of interest and particularly, at wavelengths shorter than 3000Å. In any case, reported values vary by as much as 10% (7-9) and seem to depend on methods and conditions of preparation. The optical constants of tantalum and niobium are also not known except at a few wavelengths (10, 11). However, these appear only in the phase correction term which is nearly constant and therefore, the error resulting from assuming these to be the same for all wavelengths is significant but less serious.

We are carrying out ellipsometer measurements on anodic and reactively sputtered films on various substrates. With the optical constants obtained from these results, we hope to achieve the ultimate precision of better than 0.1% that is expected with this technique.

Acknowledgment

The authors would like to thank the Fansteel Metallurgical Corporation for donating samples of tantalum and niobium foil.

Manuscript received Sept. 30, 1968.

Any discussion of this paper will appear in a Discussion Section to be published in the December 1969 JOURNAL.

REFERENCES

1. M. Cardona, K. L. Shaklee, and F. H. Pollak, *Phys. Rev.*, **154**, 696 (1967).
2. F. G. Ullman and B. J. Holden, *Bull. Am. Phys. Soc.*, **12**, 1132 (1967).
3. D. E. Aspnes, *Phys. Rev.*, **153**, 972 (1967).
4. O. S. Heavens, "Optical Properties of Thin Solid Films," Chap. 5, Dover Publications, Inc., New York (1965).
5. J. Dyson, *Physica*, **24**, 532 (1958).
6. L. Young, *Canad. J. Chem.*, **38**, 1141 (1960).
7. L. Young, *Proc. Roy. Soc.*, **A244**, 41 (1958).
8. J. C. Burgiel, Y. S. Chen, F. Vratny, and G. Smolinsky, Electrochemical Society Symposium, "Optical Properties of Dielectric Films," May, 1968.
9. M. T. Duffy, K. H. Zaininger, and C. C. Wang, *ibid.*
10. S. Kumagai and L. Young, *This Journal*, **111**, 1411 (1964).
11. L. Young and F. G. R. Zobel, *ibid.*, **113**, 277 (1966).

YPO_4:Ce Phosphor Sensitized by Thorium Ions

Kenzo Awazu and Katsutoshi Muto

The Central Research Laboratories, Mitsubishi Electric Corporation, Amagasaki, Japan

The efficient uv emitting phosphor, $BaSi_2O_5$:Pb is well known and commercially used (1, 2). Recently Ropp has described YPO_4:Ce as the uv phosphor which has two emission peaks near 3500Å (3, 4). The photoluminescent material had an integrated output of only 36% of the commercial $BaSi_2O_5$:Pb phosphor when excited by 2537Å.

In the present communication, we report on the YPO_4:Ce phosphor sensitized by Th ions. The sensitized phosphor is 150% more efficient than $BaSi_2O_5$:Pb phosphor when excited by the low pressure mercury discharge lamp. The result may be explained by energy transfer from Th to Ce ions.

The phosphor was prepared by precipitating solution of yttrium with a dilute solution of phosphoric acid. Mixture of the ions was made, including soluble salts of the activator Ce ions and the sensitizer Th ions, before precipitation. The material as produced was then fired to form the phosphor composed of the desired solid solution of phosphates. Firing was accomplished in air or in a slightly reducing atmosphere at 1200°C.

Measurements of fluorescent spectra were made employing a Beckman model DU spectrometer with 1P28 photomultiplier. The spectra were not corrected for the sensitivity of the tube.

The emission spectra of $BaSi_2O_5$:Pb and YPO_4:Ce phosphors are given in Fig. 1. As a photoluminescent material, YPO_4:Ce sensitized by Th ions, the most efficient phosphor, had an integrated output of 150% of the commercial $BaSi_2O_5$:Pb phosphor when excited by a low-pressure mercury discharge lamp and measured under identical condition as shown in Fig. 1. YPO_4:Ce and one which contained a trace of Nd^{3+} ions and other rare earth ions had an integrated output of only 60 and 20%, respectively. It is clear that Nd^{3+} ions and other impurities reduce the emission intensity of YPO_4:Ce phosphor, whereas Th ion sensitizes the phosphor.

The excitation spectra of YPO_4:Ce phosphor and the Th-sensitized phosphor are given in Fig. 2. The peak of the new excitation band in the Th-sensitized

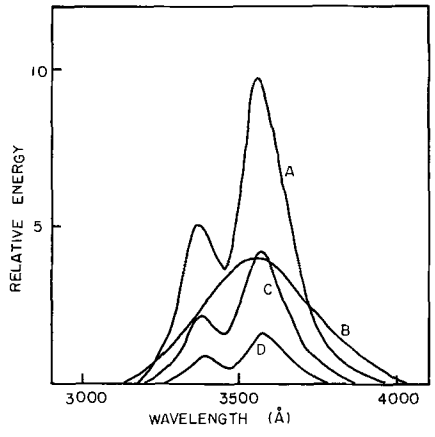

Fig. 1. Radiometric comparison of uv emitting phosphors: A, YPO_4:6.3 a/o Ce 0.1 a/o Th; B, Ba Si_2O_5:Pb; C, YPO_4:6.3 a/o Ce; D, YPO_4:Ce which contained a trace of Nd^{3+} impurity.

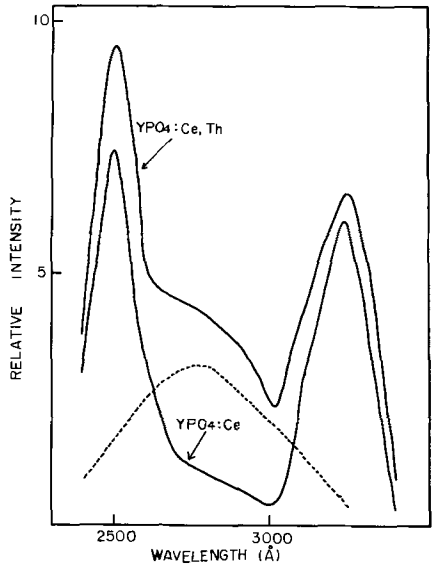

Fig. 2. Excitation spectra of YPO_4:Ce and Th sensitized phosphors.

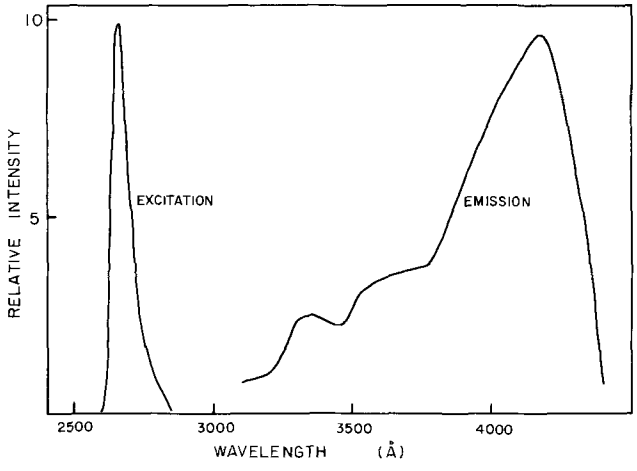

Fig. 3. Emission and excitation spectra of YPO_4:Th

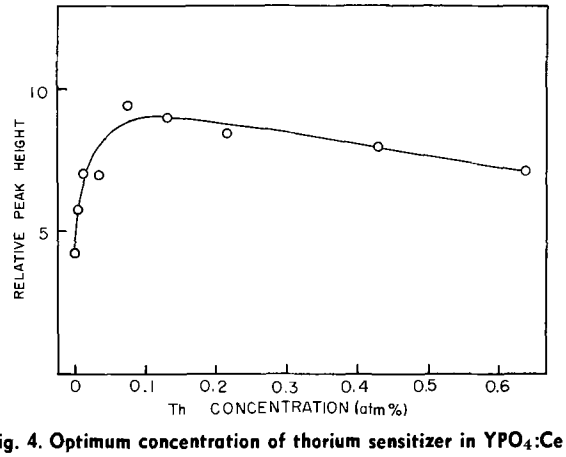

Fig. 4. Optimum concentration of thorium sensitizer in YPO_4:Ce

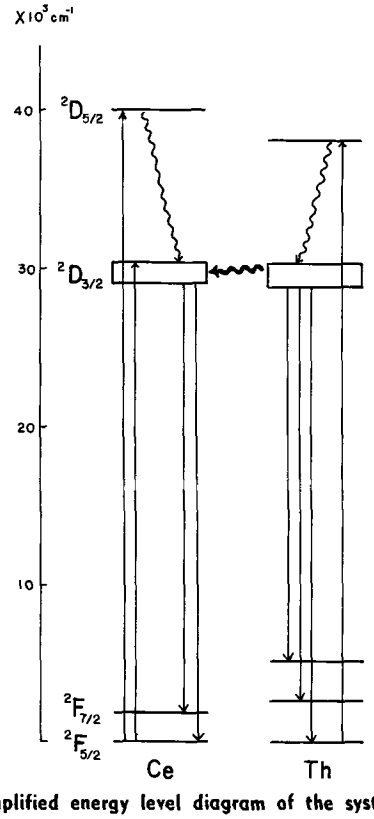

Fig. 5. Simplified energy level diagram of the system YPO_4:Ce, Th.

phosphor is near 2750Å, whereas in YPO_4:Th phosphor, the excitation peak is near 2650Å as shown in Fig. 3. Thus one is led to the conclusion that the new excitation band is probably due to the excitation of thorium ions in YPO_4:Ce, which are disturbed by Ce ions.

As shown in Fig. 4 for photoluminescence, the optimum sensitizer concentration for the YPO_4:6.3 a/o Ce composition is about 0.1 a/o.

The trivalent ion, Ce^{3+}, has an electronic structure containing one 4f electron. The allowed multiplet terms for $4f^1$ configuration are $^2F_{7/2}$ and $^2F_{5/2}$. The energy separation of these two levels is about 1800 cm^{-1}, from which one may obtain the spin-orbit coupling coefficient for a 4f electron in cerium; ξ 4f (Ce) = 514 cm^{-1}, in fair agreement with other estimates (5). The 5d levels $^2D_{3/2}$ at 40,000 cm^{-1} and $^2D_{5/2}$ at 30,860 cm^{-1} are 9140 cm^{-1} apart, from which ξ 5d (Ce) = 3656 cm^{-1}. The value is different from the other estimate (5).

The simplified energy diagram of the system Ce, Th:YPO_4 is shown in Fig. 5. It is considered that the excitation energy is transferred from the fluorescent level of Th ion to the $^2D_{3/2}$ level of Ce ion.

Manuscript received Oct. 28, 1968.

Any discussion of this paper will appear in a Discussion Section to be published in the December 1969 JOURNAL.

REFERENCES

1. R. H. Clapp and R. J. Ginther, *J. Opt. Soc. Am.*, **37**, 355 (1947).
2. J. W. Gilliland and M. S. Hall, *Electrochem. Technol.*, **4**, 378 (1966).
3. R. C. Ropp, *This Journal*, **115**, 531 (1968).
4. R. C. Ropp, *ibid.*, **115**, 841 (1968).
5. R. Lang, *Can. J. Research*, **A13**, 1 (1935); **A14**, 127 (1936).

Quantum Efficiency Spectra of Photoluminescent Materials

W. A. Thornton*

Advanced Development Department, Lamp Division, Westinghouse Electric Corporation, Bloomfield, New Jersey

ABSTRACT

A method for synthesizing accurate quantum efficiency spectra of luminescent materials, over a range of exciting wave length and temperature, is described. By (*a*) using pure monochromatic exciting radiation, (*b*) correcting for changes, with temperature and exciting wave length, of the spectral energy distribution, (c) correcting for inconstancies in response of the standard excitation material, and (*d*) using measured absolute diffuse reflectance data for a standard material, the method removes the rather drastic assumptions usually made in such optical measurements to reduce the labor involved but which often introduce large errors. New data on the quantum efficiency spectra of some important phosphors are presented, together with new data on the dependence of spectral energy distribution, excitation spectrum, and diffuse reflectance on exciting wave length and temperature; subordinate data on chromaticity and luminosity are included.

One of the important intrinsic characteristics of a phosphor is its quantum efficiency; the determination of quantum efficiency spectra (1) as exciting wave length or temperature varies involves the measurement of emission, excitation, and reflectance spectra, any one of which is a demanding task if accuracy is necessary. There are three major requirements for the accurate determination of the variation of quantum efficiency with exciting wave length and temperature: (*a*) The emission spectrum must be measured against that of a source of known spectral energy distribution, and the variation of this emission spectrum with exciting wave length and temperature must be determined. If variation of emission spectrum is neglected, errors of as much as 50% in the resulting quantum efficiency values can occur. (*b*) The excitation spectrum must be measured against that of a phosphor of known excitability, since it is usually highly inconvenient and often impossible to measure the incident exciting intensity directly. The assumption, for example, that the excitability of sodium salicylate is independent of wave length may result in a 20% error (2). In the excitation measurements, the emission of the phosphor must either be measured by means of a photon detector which is independent of wave length, or must be sampled at a chosen wave length and corrected to total photon output by the emission spectrum data of (*a*). Only the second alternative seems to be practical. (c) The reflectance spectrum must be measured against that of a reference sample of known absolute reflectance (3). Neglect of phosphor reflectance altogether can, of course, result in errors of a factor of ten in the quantum efficiency values, while assumptions concerning the reflectance of some standard sample can, at least in the 200-300 nm region, be in error by tens of per cent. Because there is so much labor involved in the correct determination of a spectrum of quantum efficiency, the usual procedure is to neglect many of the above factors with the result that such spectra are so rough as to give only a general idea of the behavior of a phosphor with change of exciting wave length or temperature. The usual excitation spectrum or temperature dependence curve is also a rough approximation for the above reasons. Useful as these approximations may be in the absence of more accurate data, there is the danger of being seriously misled. The objective of this paper is to provide a method of obtaining emission, excitation, reflectance, and quantum efficiency spectra, as exciting wave length and temperature vary, by avoiding the usual assumptions and approximations which introduce sizable errors in the results, and to provide examples of the spectra obtained. These examples constitute, in addition, much new data on the luminescent materials described.

The luminescent materials for which data are included are listed in Table I with approximate raw molar composition and preparation conditions.

Key words: phosphor, luminescence, quantum efficiency, spectrum, excitation, temperature, reflectance, chromaticity, luminosity.

*Electrochemical Society Active Member.

Procedure

Spectral energy distributions.—Equipment.—Adequate precision in the spectral energy distribution (SED) is obtainable if well-known procedures are used with care. Here, two Bausch and Lomb 500-mm 33-86-45-01 grating monochromators were used. High-pressure or medium-pressure (4) mercury lamps, quartz-iodine (5) incandescent lamps, or 1000-w water-cooled Hanovia 771B-32 hydrogen lamps (6) were used; in some cases synthetic quartz (7) lenses were used to fill the entrance aperture of the first monochromator with source radiation. The first monochromator had a 600 groove/mm grating blazed for 150 nm in order to favor transmission around 200 nm wave length. The rejection factor (ratio of transmission in pass band to transmission outside the pass band) of this monochromator was more than 10^4; some trace of mercury line emission other than the excitation wave length nevertheless leaks through and is identified, used as an accurate check on the wave length scale, and then removed from the data to be analyzed. For comparison, a 2-mm thick Corning 9863 filter shows a measured rejection ratio of 22, and a typical metal-dielectric interference filter shows a measured ratio of about 40 in the ultraviolet (254 nm) and about 500 in the visible.

The intermonochromator optics (Fig. 1) provided about a 0.3 magnification on the phosphor sample of the slit image; this results in two favorable effects, intensification of the exciting radiation on the sample (photons/sec-cm^2) and increase of the collecting solid angle of reflected or emitted radiation from the sample into the second monochromator. It will be seen that for optimum throughput the input and output optical arrangement must be symmetrical; *i.e.*, the magnification must be the same, and as great as optical registry problems will allow. Focus and alignment are done arbitrarily at 254 nm; aberrations at other wave lengths are not harmful because calibration is always done by accurate substitution of the appropriate reference sample at the normal sample position.

The total useful range of wave length is 190-850 nm, the short wave length cut-off due to air absorp-

Table I. Luminescent materials

Calcium halophosphate: Sb,Mn	CaO	P_2O_5	Mn	Sb	F	Cl	Cd	Air, 3 hr, 1200°C covered.
Bluish white	4.7	1.5	0.05	0.10	1.0	0.5	0.05	
Cool white	4.7	1.5	0.08	0.10	1.0	0.5	0.05	
White	4.7	1.5	0.12	0.10	1.0	0.5	0.05	
Warm white	4.7	1.5	0.17	0.10	1.0	0.5	0.05	
Zinc silicate: Pb,As,Mn	ZnO	SiO_2	Mn	Pb	As			Air, 3 hr, 1300°C, covered.
	8.6	5.0	0.5	0.008	0.0005			
Calcium silicate: Pb,Mn	$CaCO_3$	SiO_2	Mn	Pb	CaF_2			Air, 4 hr, 1200°C, covered.
	5.3	6.3	0.17	0.02	0.05			
Magnesium fluorogermanate: Mn	MgO	MgF_2	GeO_2	Mn				Air, 40 hr, 1100°C, uncovered.
	2.9	0.4	0.8	0.004				
Strontium magnesium phosphate: Sn	SrO	P_2O_5	MgO	Sn				Forming gas, 3 hr, 1200°C, covered.
	2.66	1.0	0.3	0.03				

Magnesium tungstate (NBS Sample #1027)
Sodium salicylate

tion and the long wave length cut-off due to reduction in photomultiplier sensitivity. The accessible range of temperature of the phosphor sample is approximately −170° to +300°C, although the upper limit is uncertain, and sample temperature is maintained by helium at 1 atm. The sample can is shown in Fig. 2. The synthetic quartz window between the monochromator space and the sample space is necessary to confine the helium atmosphere to the latter,

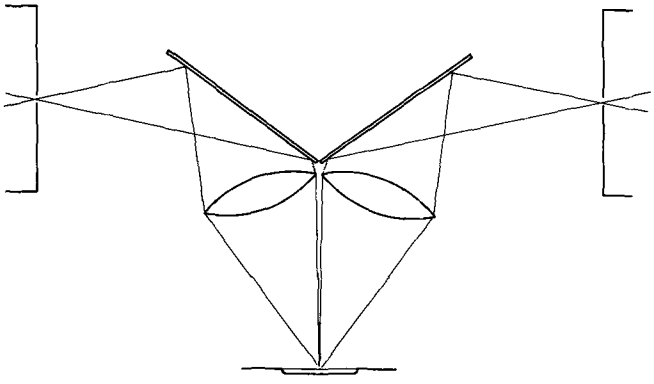

Fig. 1. Optics between the two monochromators showing symmetrical arrangement for incoming and outgoing radiation at the sample position.

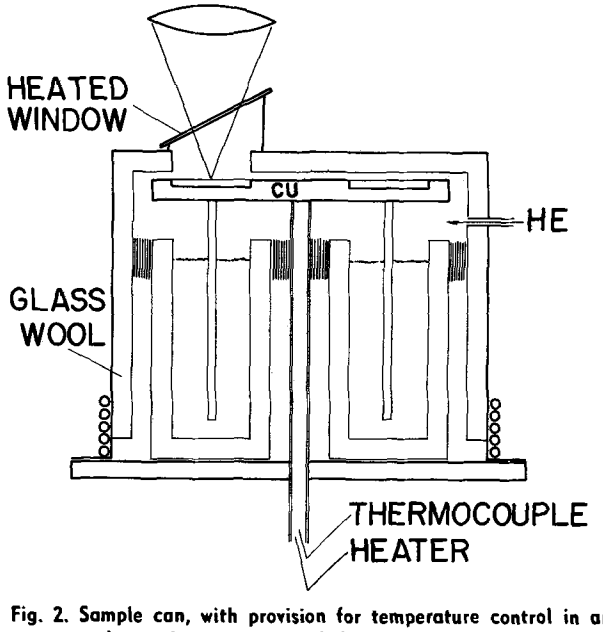

Fig. 2. Sample can, with provision for temperature control in an inert atmosphere, showing sample holder at focus of lens, liquid nitrogen Dewar, copper cooling vanes.

is slightly heated to prevent frosting when the sample is held at low temperature, and is mounted at an angle to avoid reflections from input into output monochromators. The second monochromator is identical to the first except that its grating is blazed for 300 nm radiation. Typical slit width was 2 mm, equivalent to resolution (line width at half maximum) of 6-7 nm. Detector was a 2-in. diameter end-on EMI 9558 photomultiplier (8), of which the sensitivity [amperes output per watt of input radiation per ampere of dark current (9)] is extremely high.

In the work covered by this paper the intention was to use phosphor powder layers so thick that transmission of both exciting and emitted radiation is negligible. The phosphor samples were made by filling bright aluminum dishes, 2 mm deep by 1¼ in. diameter. The transmission of strongly absorbed radiation is certainly nearly zero and for radiation which is only moderately or weakly absorbed the reflectance of the aluminum is about the same as an infinitely thick phosphor layer (≈90%), so the net result must be quite representative of a powder layer which is infinitely thick. With a little practice the top surface of the phosphor in the filled dish can be made visually flawless. The smooth phosphor surface is made by a gentle wiping action with a glass plate, using only light pressure. This method does produce some orientation of the phosphor crystals which can be detected as anisotropy in emission and reflection, as the azimuthal angle is varied and the angle of elevation fixed. The variations, however, are fortunately of the order of 1%. All phosphors and reference materials were sieved through 200 mesh, which did not cause a particle size separation but removed agglomerates.

Calibration.—Accurate calibration of the monochromator-photomultiplier combination requires a radiant source of known emission spectrum which should have the size, shape, and diffuseness of the phosphor samples to be measured subsequently, in order that identical geometry may be used and optical apertures filled in exactly the same way. This ideal situation was achieved as follows. A smoked and bleached MgO sample which had been calibrated accurately for absolute diffuse reflectance (by the partial sphere method mentioned later) was placed in the sample position; the size and shape of this reference sample is the same as that of typical phosphor samples. Radiation from a National Bureau of Standards calibrated quartz iodine incandescent lamp QL-33 (operated at the standard 6.50-amp condition) shone directly onto this reference MgO sample. NBS states that no atmospheric absorption takes place between 250-1100 nm, that 100 hr of operation causes less than 1% variation in output, and that absolute errors in calibration of the incandescent lamp output are less than 8% near 250 nm and less than 3% in the visible and infrared; this does not imply that one

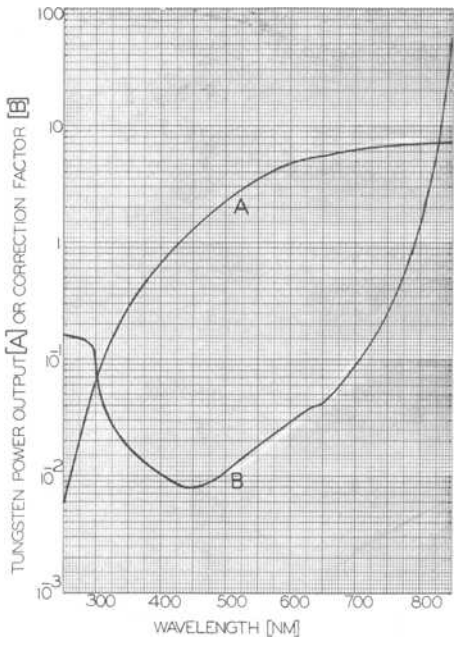

Fig. 3. Power output (A) of standard tungsten lamp per unit area per unit wave length, at a given distance, and correction factor (B) of analyzing monochromator obtained with the standard lamp.

visible region is in error with respect to another by as much as 3%.

The NBS values for the emission of this incandescent lamp (microwatts per square centimeter per nanometer at 43 cm distance) are given in Fig. 3, curve *A*. These values were corrected by the measured absolute reflectance of the MgO sample even though this reflectance varied only between 95 and 97%. The product of these factors was taken to be the radiation intensity entering the optics of the monochromator. The output of the monochromator, scanned through the range 250-850 nm, was used to calculate the final correction curve:

$$\frac{\text{NBS intensity (Reflectance of MgO)}}{\text{(Monochromator Signal)}}$$

shown in Fig. 3, curve *B*, and it is seen that the correction factor becomes as large as 10^4 in the near infrared region, into which the emission of some phosphors extends. The magnitude of this correction factor, even with the excellent S-20 photosurface, together with the requirement of good accuracy in correction over this range, makes the use of a correcting device unallowable, in the writer's opinion. The use of a computer for this step is, on the other hand, satisfactory, particularly since other spectra and integrated quantities in addition to the usual spectral energy distribution are computed at the same time.

Data analysis.—For each combination of exciting wave length and temperature, a recorder trace is used as the baseline, obtained from an inert material of similar reflectance to that of the phosphor sample in the sample position. The oxide or carbonate of magnesium is suitable. This baseline is normally quite flat and gives the signal level due to stray light, photomultiplier noise, and bias settings of the amplifier and recorder. However, it is absolutely indispensable to determine this baseline and to use it as the reference for the desired emission spectrum, rather than to assume that the "zero" level is independent of wave length, since under some conditions there are at least traces of visible components from the source leaking through the first monochromator, as well as second-order effects and peculiarities of grating reflectance. These nonuniformities in the baseline are usually small but often not negligible. From this raw spectrum, data are taken every 10 nm if the spectrum contains only the usual broad emission bands; otherwise the wave length interval is chosen narrow enough to sample adequately whatever structure is in the spectrum. For example, if the SED of zinc silicate:Mn is analyzed both at 2-nm and at 8-nm intervals, computed values of integrated quantities such as chromaticity, total watts, total lumens, *etc.*, vary by ½ to 2 parts per thousand. The computer program makes use of the quadrature formula known as Simpson's Rule (10).

These data are punched into a computer program in which are stored the tristimulus values for spectrum colors (11) and the correction data described in the preceding section. The total computation may be summarized as follows:

Spectral distributions (relative and normalized)
  Energy
  Photons
  Lumens
Total energy E
Total photons Q
Tristimulus values X, Y, Z
Trichromatic coefficients x, y, u, v
Color temperature, mean wave length, luminosity factor (Y/E)

For each phosphor, 30 or more spectral energy distributions were determined, by correction against the NBS standard lamp; five temperatures (—160°C, —60°C, room temperature RT = 25°C, 100°C, 200°C) and six or more pure exciting wave lengths were used. All of the measured spectra are used in determination of other data to be presented. Examples of SED variation with temperature or exciting wave length are given in Fig. 4-11 for "cool white" calcium halophosphate:Sb,Mn, strontium magnesium phosphate:Sn, magnesium fluorogermanate:Mn, and magnesium tungstate; each of these SED's is normalized to constant peak height. Some integrated quantities calculated from the SED which are independent of phosphor efficiency are, for example, chromaticity and luminosity factor. In Fig. 12 and 13 of trichromatic coefficient data, the dashed lines are contours of equal exciting wave length and the solid lines of equal temperature; the arrows indicate dominant wave length (11) in nanometers. Figure 12 shows the peculiar behavior of the chromaticity of the calcium halophosphate phosphors due to different dependence on exciting wave length of the blue antimony band and the yellow manganese band. Figure 13 shows the large chromaticity variation of strontium magnesium phosphate:tin due to the strong dependence of the ratio of violet to orange band output on both temperature and exciting wave length. Figures 14-16 are contour plots,

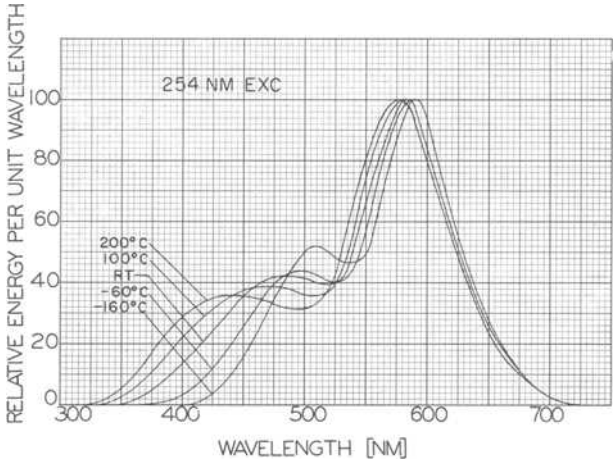

Fig. 4. Spectral energy distributions of cool white calcium halophosphate phosphor excited at 254 nm and at various temperatures.

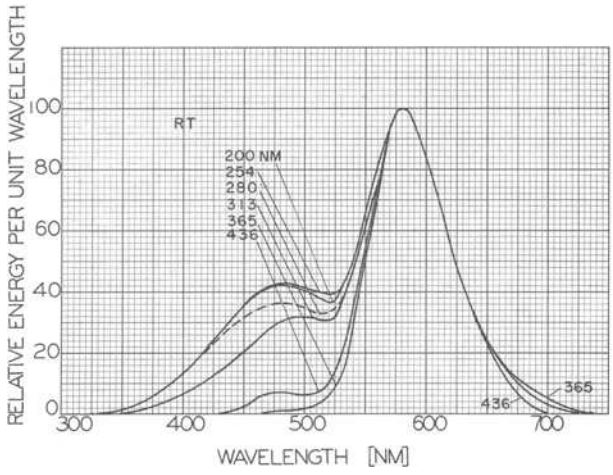

Fig. 5. Spectral energy distributions of cool white calcium halophosphate phosphor excited at various wave lengths and at room temperature.

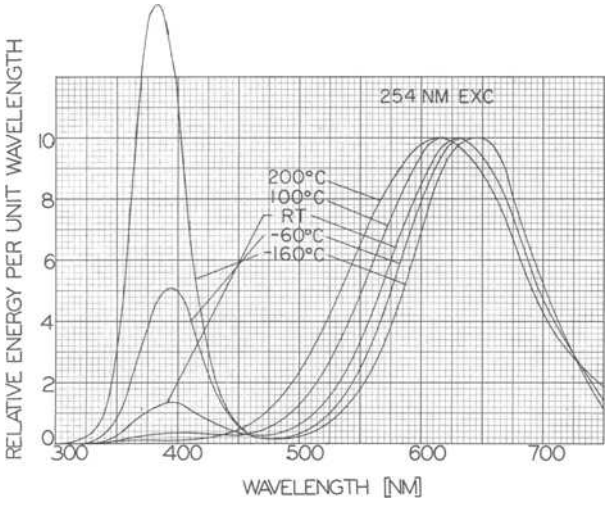

Fig. 6. Spectral energy distributions of strontium magnesium phosphate:Sn phosphor excited at 254 nm and at various temperatures.

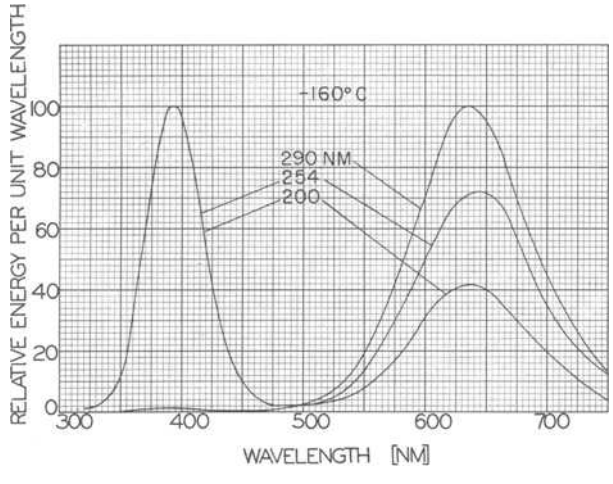

Fig. 7. Spectral energy distributions of strontium magnesium phosphate:Sn phosphor excited at various wave lengths and at −160°C.

of luminosity factor Y/E for three phosphors, over the range of excitation wave length in which the material is appreciably excited. These figures demonstrate the importance of such changes in the SED, in that, unless one uses a detector with equal response to photons of all wave lengths, corrections which are both large and accurate must be made for these changes.

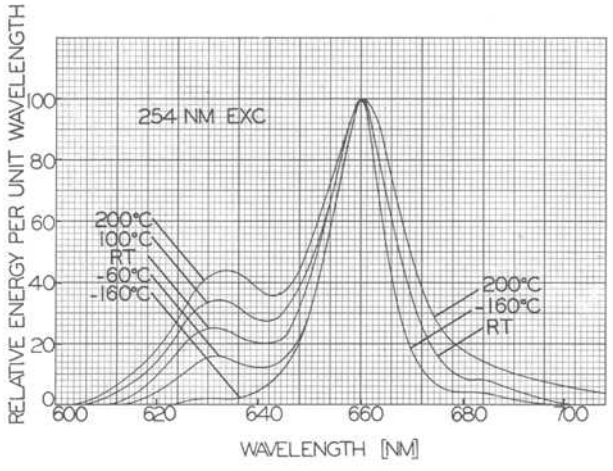

Fig. 8. Spectral energy distributions of magnesium fluorogermanate:Mn phosphor excited at 254 nm and at various temperatures.

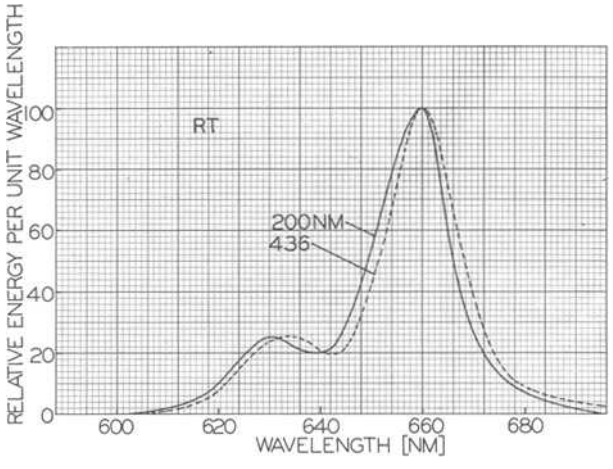

Fig. 9. Spectral energy distributions of magnesium fluorogermanate:Mn phosphor excited at various wave lengths and at room temperature.

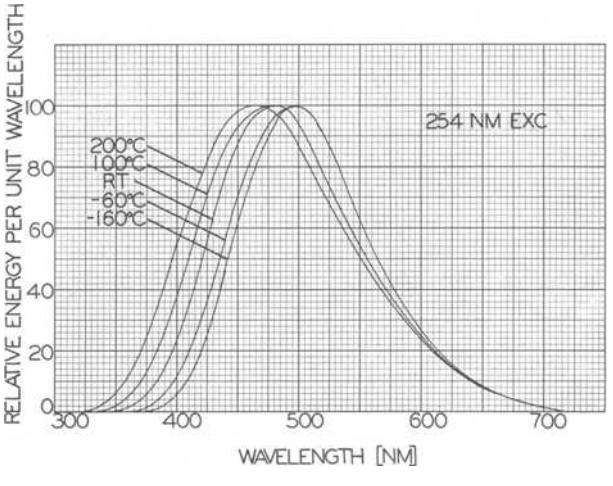

Fig. 10. Spectral energy distributions of magnesium tungstate (NBS No. 1027) phosphor excited at 254 nm and at various temperatures.

It is convenient to define the quantity Q_w as the number of emitted photons within a certain wave length "window" as defined by Fig. 17, in which the total area under the curve is total photons Q. Thus the ratio Q/Q_w is characteristic of the SED of a phosphor at a given combination of exciting wave length and temperature (λ,T) and is used later in the calculation of the quantum efficiency spectra. The window may be specified anywhere on the SED but is usually taken

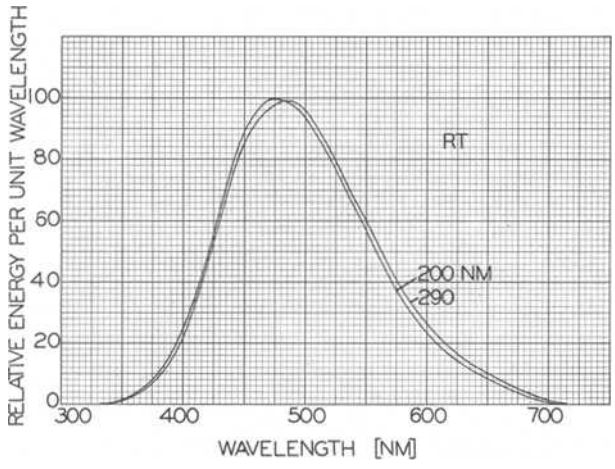

Fig. 11. Spectral energy distributions of magnesium tungstate (NBS No. 1027) phosphor excited at various wave lengths and at room temperature.

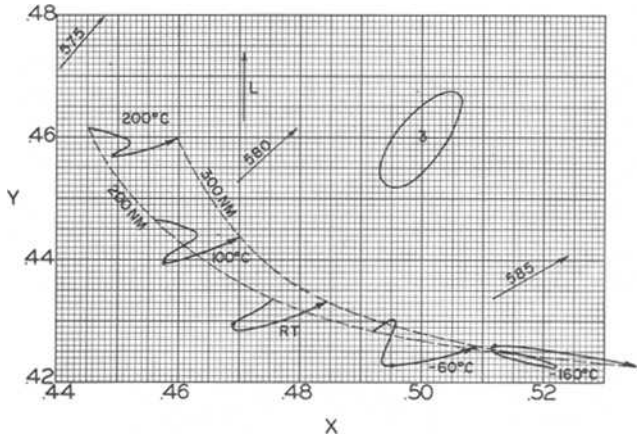

Fig. 12. Chromaticity of warm white calcium halophosphate phosphor at various exciting wave lengths and temperatures plotted on the 1931 CIE diagram. Dashed lines: equal exciting wave length. Solid lines: equal temperature; dot: 254 nm excitation. Numbered arrows: dominant wave length with respect to Illuminant C. Arrow "L": direction of maximum luminosity increase. Ellipse: MacAdam three-step oval.

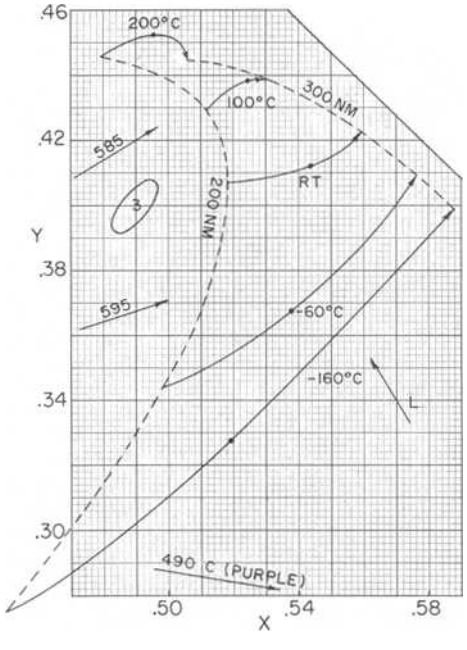

Fig. 13. Chromaticity of strontium magnesium phosphate:Sn phosphor. Similar to Fig. 12.

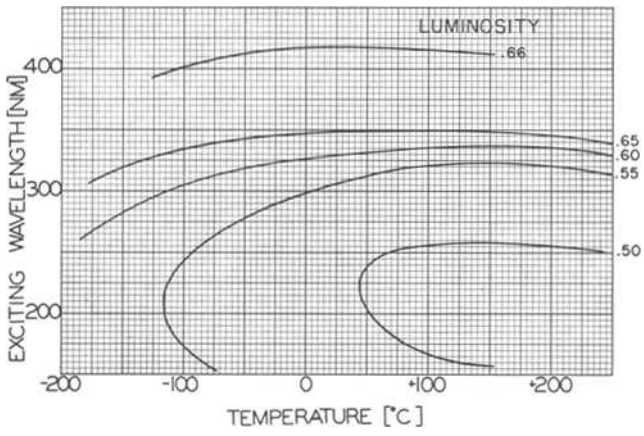

Fig. 14. Luminosity factor Y/E (see text) of cool white calcium halophosphate phosphor as a function of exciting wave length and temperature.

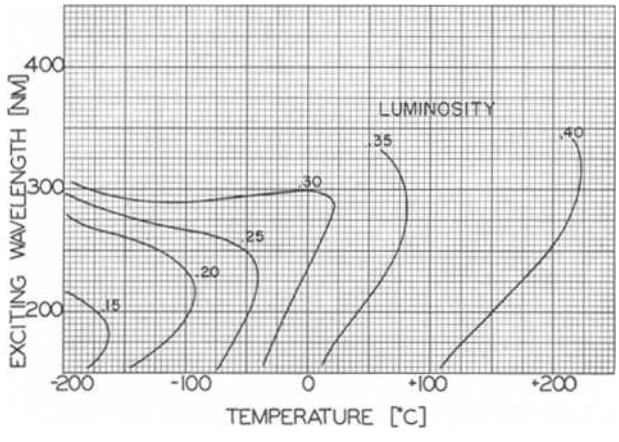

Fig. 15. Luminosity factor Y/E (see text) of strontium magnesium phosphate:Sn as a function of exciting wave length and temperature.

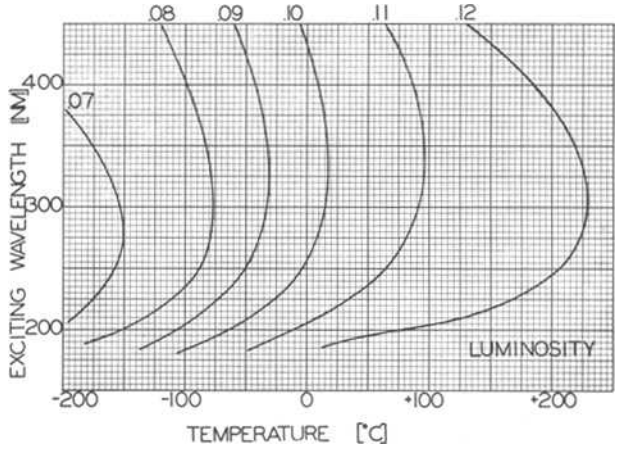

Fig. 16. Luminosity factor Y/E (see text) of magnesium fluorogermanate:Mn as a function of exciting wave length and temperature.

near one or another emission peak, for maximum signal as will be seen, and then retained as a constant of the phosphor; for example the chosen window wave lengths of the halophosphate phosphors are 480 or 580 nm and that of zinc silicate:Mn is 528 nm. Plots of Q/Q_w as this ratio depends on exciting wave length and temperature appear in Fig. 18 for a bluish white calcium halophosphate phosphor for window wave length of 580 nm, for strontium magnesium phosphate:tin at 600 nm (Fig. 19), and for zinc silicate:Mn (Fig. 20) at a window wave length of 528 nm. In each case the window width is 8 nm at half maximum.

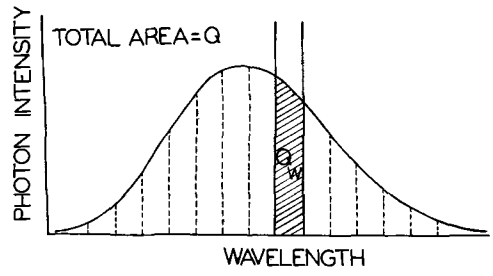

Fig. 17. Definition of the quantity Q_W, the number of photons detected in an interval at "window wave length" W chosen near the peak of a major emission band.

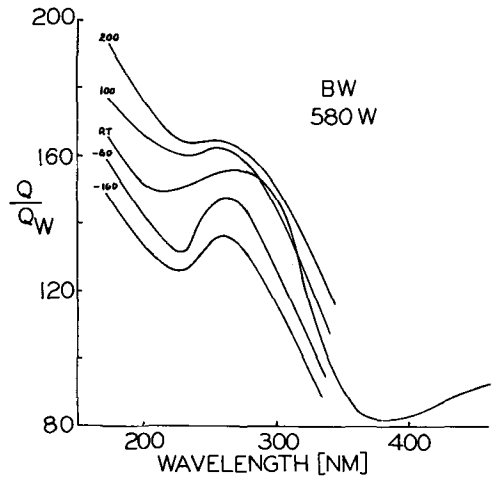

Fig. 18. The variation of Q/Q_W with wave length and temperature for bluish white calcium halophosphate phosphor when the chosen "window wave length" is 580 nm and window width is 8 nm at half maximum. When 480 nm is chosen for this phosphor (near the peak of the blue band) the Q/Q_W curves which result bear a rather inverse relationship to those pictured here. The dependence shown is of course due to the varying excitability of the blue and yellow emission bands, and to shifts in position of these bands.

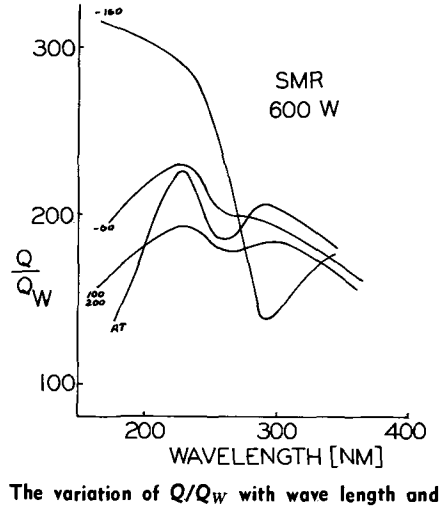

Fig. 19. The variation of Q/Q_W with wave length and temperature for strontium magnesium phosphate:tin. The large variation at —160°C is due to the appearance of the strong violet emission band at low temperature and short-wave excitation.

Excitation spectra.—Equipment.—The equipment described in the preceding section is used also for obtaining excitation spectra. Since phosphors of known excitability were used in the normal sample position as excitation standards, it is necessary neither to determine the transmission of the first monochromator as a function of wave length nor to know the output of the various source lamps *vs.* wave length. The 1000-w hydrogen lamp or the quartz-iodine incandescent lamp

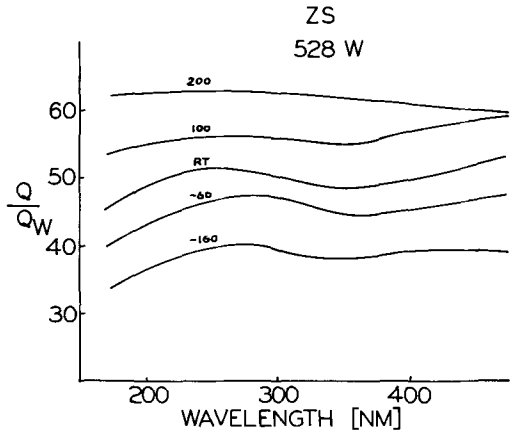

Fig. 20. The variation of Q/Q_W with wave length and temperature for zinc silicate:Mn. The predominant variation with temperature is due to broadening of the single emission band with increasing temperature (the window width, or monochromator resolution which is a function of slit width, remaining constant at 8 nm width at half maximum.

was used in the source position and the first monochromator was scanned over the appropriate wave length range with either the standard or unknown phosphor in sample position. The second monochromator was set at the chosen, constant window wave length W characteristic of each phosphor in turn. The standard phosphor was always measured at room temperature (and remeasured at short intervals) and removed before the unknown phosphor(s) were exposed to other temperatures; it was assumed and verified that the source lamp output and standard phosphor behavior changed very little between calibrations.

Calibration.—A standard phosphor is used so that the visible light emitted by this standard can be simply related to the intensity of ultraviolet radiation incident upon the phosphor. The ideal standard would be a phosphor which emitted some constant number of visible photons for every 100 u.v. photons incident, independent of the wave length of the incident radiation, and of the temperature of the phosphor. No phosphor is known, at present, to have such a "flat" response even over a limited wave length region, although a number of phosphors approach this condition closely enough to be very useful. For accurate work, it is best simply to measure the characteristics of the phosphor which is to be used as the standard, and to correct for the deviations from constant output. Sodium salicylate has been used as the primary standard in the present work, and much use has been made of the University of Rochester data (2, 12) on this material. Kristianpoller and Knapp (2) measured the visible quantum output per ultraviolet quantum incident from 175 to 350 nm; this curve is used in the present work as a correction curve from which to obtain the incident ultraviolet intensity with good accuracy. These authors showed that the quantum efficiency is about 20% higher at liquid nitrogen temperature and that its dependence on wave length at low temperature is very similar to that at room temperature.

Before using the above data for correcting the response of sodium salicylate, it is necessary to make sure that there is no appreciable change in emission spectrum as incident wave length varies from 175 to 350 nm. (If such a change in spectrum occurs, it would mean that the University of Rochester data quoted above would be valid only for their particular phototube; another phototube with a different wave length sensitivity would yield a different correction curve.) Fortunately, it turns out that at room temperature the emission spectrum of sodium salicylate is quite independent of excitation wave length (Fig. 21). At 200°C, however, there is an appreciable shift toward the green. In the present work, this standard phosphor is used only at room temperature where the University

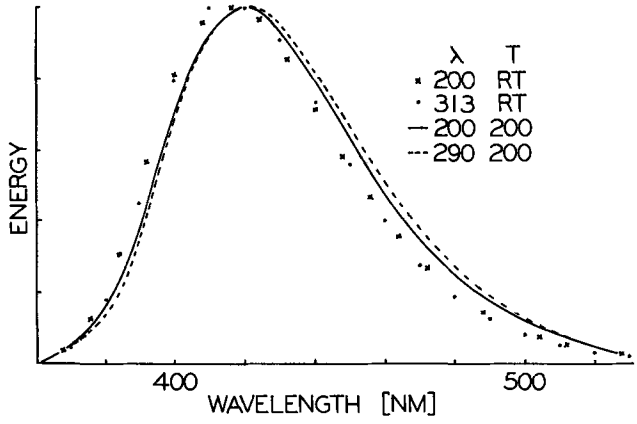

Fig. 21. Spectral energy distributions of sodium salicylate excitation standard, at various exciting wave lengths and temperatures.

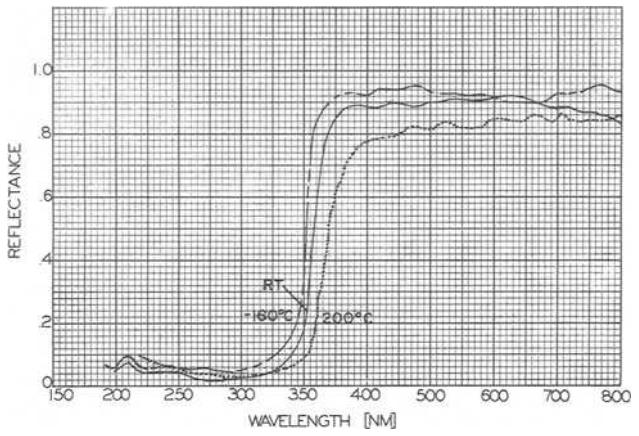

Fig. 22. Absolute diffuse reflectance of sodium salicylate excitation standard, at various exciting wave lengths and temperatures.

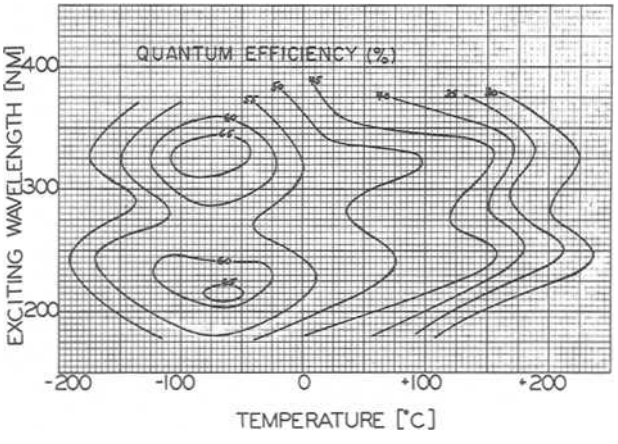

Fig. 23. Quantum efficiency of sodium salicylate excitation standard, at various exciting wave lengths and temperatures.

of Rochester data should be completely applicable. Sodium salicylate emits with good quantum efficiency (12-14) (≈50%, *see* remarks below), is easily deposited (15) on glass slides or directly on the phototube, and is stable in air or vacuum. Allison, Burns, and Tuzzolino (16) find that quantum efficiency values for lots of sodium salicylate from four different suppliers differ by no more than 3% at 254 nm; the implication is that the dependence of quantum efficiency on wave length will be about the same also for samples of different origin. The fluorescent yield of sodium salicylate is stable for long periods of time in dry air or clean vacuum and under 254 nm radiation (17).

There is disagreement concerning the absolute quantum efficiency of sodium salicylate, no doubt due to errors in interpretation of data. In 1964 papers were published which gave the quantum efficiency at room temperature and an exciting wave length of 254 nm as 0.99 (16), 0.50 (13), and 0.25 (18). Nygaard (13) measured the quantum efficiency as a function of layer thickness and obtained a maximum efficiency of 0.50 ± 0.05 at 1-2 mg/cm², defined as visible photons emitted per ultraviolet photon *incident*. Sodium salicylate reflects roughly 5% of the 254 nm radiation, so Nygaard's value defined as quanta emitted per quantum absorbed would be about 0.53. Studer (14) has measured the absolute quantum efficiency under the same conditions and obtained a value of 0.60 + 0.05. Kristianpoller (12) arrives at a value of 0.64. The writer, by comparison to the absolute quantum efficiency of $MgWO_4$ (NBS No. 1027; *see* section on Synthesis of quantum efficiency spectra—Quantum efficiency standard) and to standard calcium halophosphate phosphors,[1] repeatedly obtains a value of about 0.5 for sodium salicylate. It seems that the extreme values quoted above are incorrect, and in any case such a range of values emphasizes the pitfalls in a measurement of absolute quantum efficiency.

As a matter of possible interest, the reflectance and quantum efficiency spectra of sodium salicylate are given in Fig. 22 and 23; procedures for obtaining these are described later.

In some cases the incident ultraviolet intensity may be needed at wave lengths longer than the 350 nm limit to which sodium salicylate may be used. Another organic compound, dihydroxynaphthalazine (DHN), has been measured by the University of Rochester group (19) to have almost constant quantum efficiency between 200 and 470 nm. We have used corrected values for DHN as the excitation standard between 350 and 470 nm, usually in the form of a thick powder layer; it is also easily evaporated and has similar properties in layers equal to or greater in thickness than about 2μ.

Finally, we have used the smoked and bleached MgO reference sample in the sample position, and the calibration of the second monochromator, to determine the intensity of exciting radiation, particularly in the visible, from the quartz iodine lamp.

Data analysis.—When a phosphor exhibits more than one emission band in its spectral energy distribution, the response or excitability of one band (that is, the intensity of emission within the band) generally depends on exciting wave length and temperature in a different manner than that of another band. For example, it is well known that the yellow emission band in halophosphates activated by manganese and antimony is much more strongly excited by near-ultraviolet wave lengths, say 365 nm, than is the blue band in the same phosphor even when the bands are equally excited at shorter wave lengths. Actually, if one chooses two wave lengths present in the same emission band of a given phosphor, emission at one wavelength will in general exhibit a different dependence on exciting wave length and temperature than emission at the other wave length. These two phenomena are of course related to the shifts with exciting wave length and temperature in spectral energy distribution, chromaticity, and luminosity already mentioned. It is sometimes of practical interest to determine the excitability of one emission band relative to another. The method adopted here is to assign a "window wave length" denoted by W to each emission band of interest; W is approximately the wave length of the peak of the emission band at $\lambda = 254$ nm and room temperature. In obtaining the excitation data the detector could "see" only the emission at window wave length W as exciting wave length and temperature were varied. The excitation data are corrected to equal numbers of incident exciting photons and are normalized to unity at 254 nm.

[1] Which, from fluorescent lamp performance, must have a quantum efficiency in the neighborhood of 0.80-0.85.

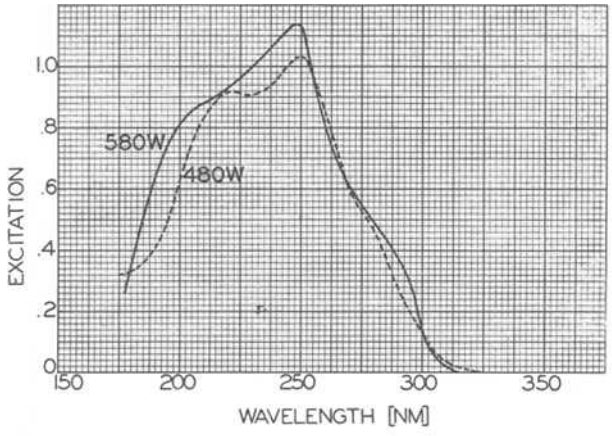

Fig. 24. Excitability of the blue antimony band (480W) and the yellow manganese band (580W) in bluish white calcium halophosphate phosphor at room temperature. Normalized at 254 nm.

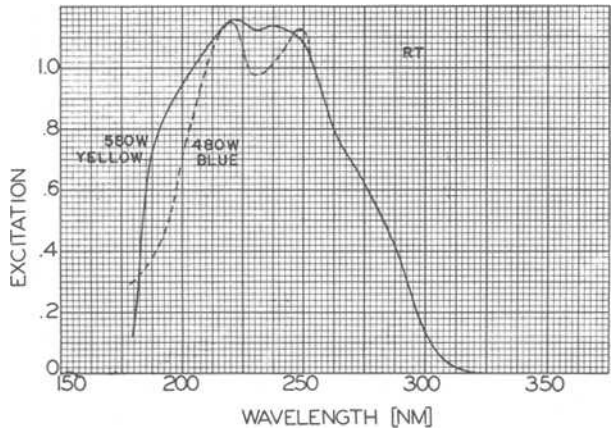

Fig. 25. Excitability of the blue antimony band (480W) and the yellow manganese band (580W) in warm white calcium halophosphate phosphor at room temperature. Normalized at 254 nm.

Figures 24 and 25 show, for example, the excitability of the blue antimony band (480W) and the yellow manganese band (580W) at room temperature in a "bluish white" and a "warm white" calcium halophosphate, and indicate the increased relative excitability at 220 nm of both blue and yellow bands in the latter phosphor with the higher manganese activator content; Fig. 26 shows excitabilities of the former phosphor at more extreme temperatures. Figure 27 demonstrates the different violet and orange band excitability at room temperature in strontium magnesium phosphate:

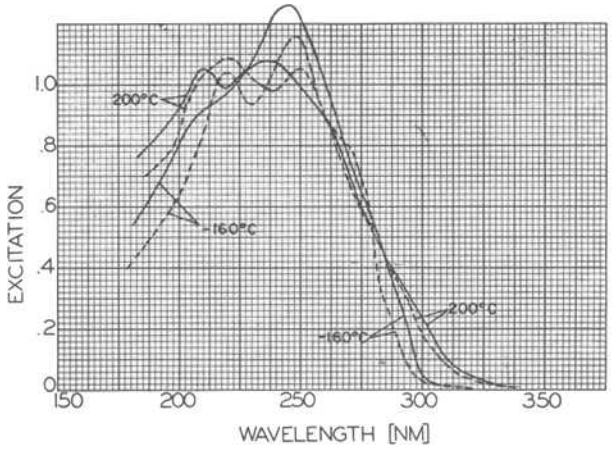

Fig. 26. Excitability of the blue band (dashed curves) and yellow band (solid curves) of the phosphor of Fig. 24 at more extreme temperatures.

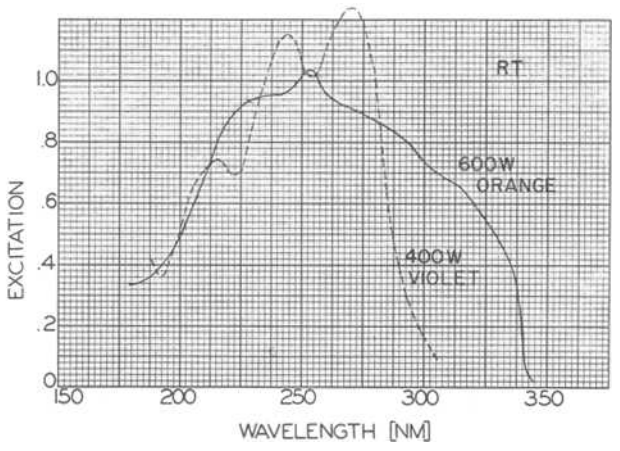

Fig. 27. Excitability of the violet band (400W) and the orange band (600W) in strontium magnesium phosphate:Sn phosphor at room temperature.

tin; Fig. 28 does similarly for calcium silicate:Mn,Pb. In these figures, the ordinate is proportional to Q_w/Q_{INC} where Q_{INC} is the number of photons of wave length λ incident upon the phosphor sample.

Reflectance spectra.—Equipment.—The equipment described in the section on Spectral energy distributions—equipment is used also for obtaining reflectance spectra. A material of known reflectance was used as standard, in the normal sample position. Either the hydrogen lamp or the tungsten lamp was used as source. The wave length drives of the two monochromators were connected and the two scanned together over the appropriate wave length range with either the standard reflecting sample or the unknown phosphor in sample position. The standard reflecting sample was always measured and maintained at room temperature as in the case of the excitation standard.

Calibration.—The reflectance of a layer of phosphor for various wave lengths of incident radiation must be measured absolutely; that is, the actual ratio of total radiation reflected to total radiation incident, ordinarily given in per cent, must be determined. A smoked layer of MgO, which appears to be the best standard known, is quite stable in the visible region of the spectrum, but at wave lengths shorter than 300 nm varies in reflectance depending on the time, wave length, and intensity of radiation to which it is exposed (3). The solution seems to be to form such a layer, bleach it thoroughly with short-wave ultraviolet radiation, measure its reflectance on an absolute basis throughout the spectrum of interest, and immediately compare it to that of a secondary standard of which fresh samples can easily and repro-

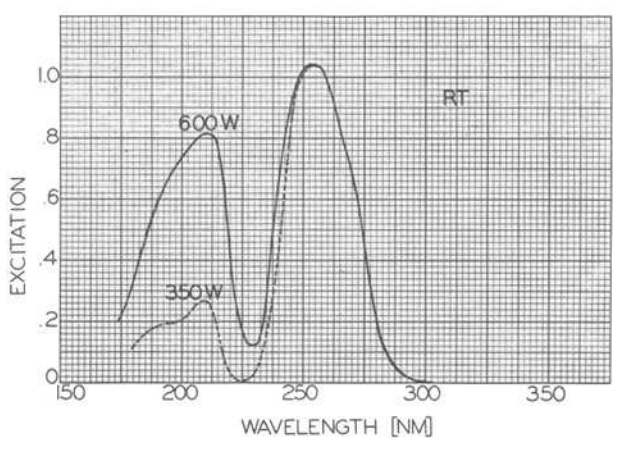

Fig. 28. Excitability of the ultraviolet band (350W) and the orange band (600W) in calcium silicate:Mn,Pb phosphor at room temperature.

ducibly be made. This procedure has been carried out as follows.

The "partial sphere" method (3) is a convenient and very accurate determination of the diffuse reflectance of a layer of material, provided the reflectance of that material at wave lengths of interest is greater than 0.5, and preferably greater than 0.8. On the other hand, the entire inside surface of a sphere must be uniformly covered with an opaque coating of the material of which the reflectance is desired, so it is a technique suitable for calibrating a standard diffuse reflector, but too time consuming and difficult to use for routine determination of reflectance. A section (cap) of about 0.1 of the area is cut out of the sphere but coated in the same way as the remainder of the sphere. The measurement consists of introducing a beam of radiation of the required wave length into a small port in the sphere and measuring the radiation escaping from the same or another port under two conditions: (*a*) with the cap in position, completing the sphere, and (*b*) with the cap removed, and radiation also escaping through the cap area. The ratio of intensities at the exit port with and without the cap in position, together with the dimensions of the sphere, cap, and ports, determines the absolute diffuse reflectance of the sphere coating.

Sections were cut from 500-ml spherical Pyrex boiling flasks, the edges ground, and matched sets of the parts were obtained. A single slot about 8 by 32 mm was cut in the hemisphere at the focus of the slit image from the first monochromator; the same slot served as exit port into the symmetrical optics of the second monochromator. Light-sensitive paper on the sphere surface was used to find the image position. It is necessary that the incoming radiation not strike the cap area. A reversible motor and screw moved the cap in and out of position; in the "out" position only a flat black surface was visible through the cap area from the interior of the sphere. The Pyrex sphere parts were carefully cleaned and aluminized inside, a precaution which almost completely corrects, apparently, for the fact that usable thicknesses of materials are not completely opaque; the highly reflecting aluminum throws transmitted radiation back into the material layer in much the same way as would added thickness of the material to be measured. A number of aluminum disks were mounted flush on the inside surface of the hemisphere, to be removed finally and used as the standard samples. All glass parts were smoked by burning magnesium ribbon (Mallinckrodt, 0.125 x 0.006 in.) in air; the parts were assembled in hemispheres and rotated about an axis roughly 45° to the horizontal, 2 or 3 in. above the burning Mg ribbon, until the MgO coating on the inside of the sphere parts was about 0.5 mm in thickness. The sphere and cap were then mounted in position in the sample can of the double monochromator (Fig. 29).

In the present equipment, the inside sphere diameter with the coating in place was 97.2 mm and the cap diameter was 52.0 mm. The equation (3) relating the ratio of the signal N_0 with the cap off to the signal with the cap on reduces to

$$\frac{N_0}{N} = \frac{1 - R\ (1.0089)}{1 - R\ (1.088)}$$

where R is the absolute diffuse reflectance of the coating. The "sensitivity" of the method, *i.e.* ratio of per cent change in N_0/N to per cent change in R, varies from 10 at $R = 0.95$ to 1.0 at $R = 0.78$ to 0.15 at $R = 0.5$. It is for this reason that the method becomes inaccurate for materials of low reflectance. A calculation showed that the sphere and cap dimensions used resulted in approximately optimum sensitivity. Reflectance measurements were made between 200 and 700 nm, followed by bleaching of the coating by a bare quartz LPMV lamp for different intervals, and remeasurement of reflectance. The results are shown in Fig. 30. Reflectance in the visible was reproducible

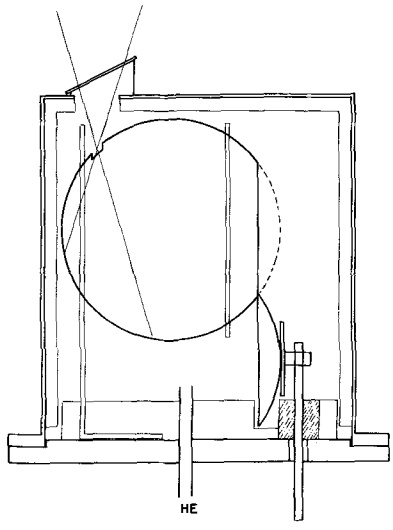

Fig. 29. Assembled attachment for measuring by the "partial sphere" method the absolute reflectance of the inner sphere wall coating; *cf.* Fig. 2.

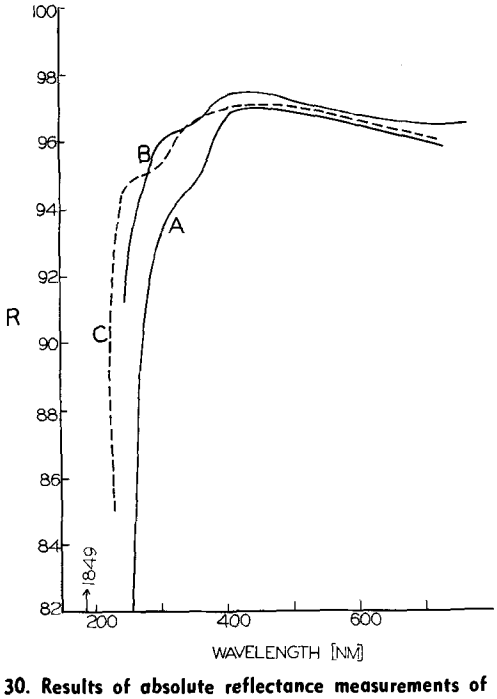

Fig. 30. Results of absolute reflectance measurements of smoked MgO on aluminum. (*A*) As deposited. (*B*) After 115-hr bleach under unfiltered quartz LPMV lamp. (*C*) After 250-hr bleach under same conditions.

to about 0.004. Bleaching increased the reflectance at 254 nm, for example, from 0.82 to 0.95. It appears that reflectance remains relatively low in the region of 200 nm.

The detachable samples were removed from the inside of the sphere wall and immediately used to calibrate the reflectance of samples of fired MgO and of magnesium carbonate block, which were then used as secondary standards. The $MgCO_3$ block (20) was found to have the same reflectance values within 1% as those reported by Taylor (21) in 1931.

Data analysis.—The proportion of radiation reflected from a thick layer of phosphor in per cent of incident radiation is plotted against exciting wave length and temperature. The ordinate in the figures to follow is $r_P R_S / r_S$ where r_P is the signal due to the reflected radiation from the unknown phosphor P, R_S is the absolute reflectance of the standard reflecting sample, and r_S is the signal from this standard sample, all measured at a given wave length λ. Figure 31 for zinc

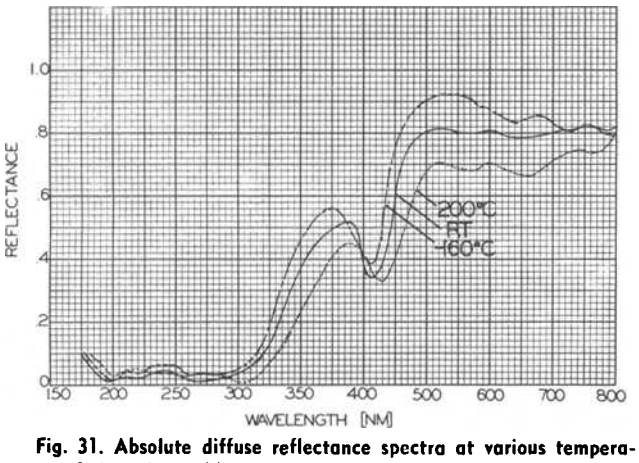

Fig. 31. Absolute diffuse reflectance spectra at various temperatures of zinc silicate:Mn.

silicate:Mn and Fig. 32 for magnesium fluorogermanate:Mn are representative of the results, and Fig. 33 for cool white halophosphate is an example of a contour plot of similar data.

Synthesis of quantum efficiency spectra.—Quantum efficiency standard.—We have not yet in this laboratory attempted measurement of absolute quantum efficiency. The alternative is to choose a value of absolute quantum efficiency from the literature, for a particular phosphor under particular conditions, upon which some reliance can be placed. It is a fortunate circumstance that the National Bureau of Standards has accumulated a number of phosphors in sufficient quantity that they are available for distribution in small lots. Many groups concerning themselves with phosphor comparison now have sets of these standard phosphors in their possession, and thus have common standards to which reference may be made. Bril (22) has made what appear to be careful measurements of the absolute quantum efficiencies of a number of the NBS standard phosphors. Such measurements must specify exciting wave length and temperature, however. To obtain adequate intensity, Bril used a HPMV lamp and filter combination which, rather than constituting a monochromatic source, rendered his spectrum of exciting wave lengths peculiar to his equipment. If a given phosphor shows appreciable difference in excitability by the wave lengths incident upon it, the resulting quantum efficiency value will be ill defined. However, magnesium tungstate (NBS 1027) is about equally well excited by 254 nm and by all the wave lengths present in Bril's measurement (245-280 nm) and for this reason Bril's value of 0.84 ought to be quite reliable and is assumed for reference purposes in this paper.

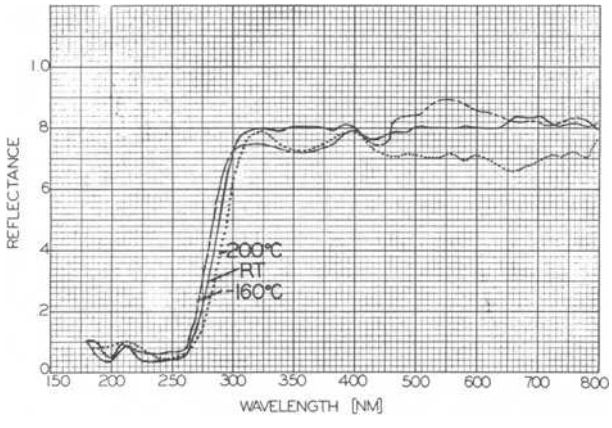

Fig. 32. Absolute diffuse reflectance spectra at various temperatures of magnesium fluorogermanate:Mn.

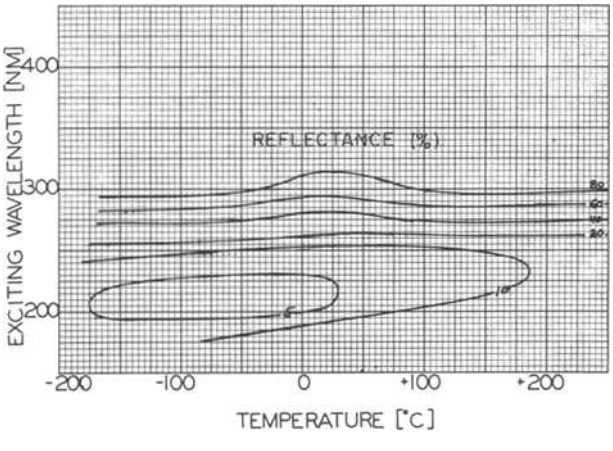

Fig. 33. Contour plot of absolute diffuse reflectance at various wave lengths and temperatures of cool white calcium halophosphate phosphor.

Calculation procedure.—We define quantum efficiency as the total number Q of quanta emitted by the phosphor divided by the total number of (exciting) quanta absorbed by the phosphor Q_{ABS}. We recognize that the number of photons absorbed by the phosphor Q_{ABS} is equal to the number incident Q_{INC} multiplied by the fraction absorbed, which is $(1 - R)$ if R is the fraction reflected and the phosphor layer is thick enough that no transmission occurs. Therefore,

$$QE = \frac{Q}{Q_{\text{INC}}(1-R)} = \frac{Q/Q_W}{(1-R)} \cdot \frac{Q_W}{Q_{\text{INC}}} = \frac{Q/Q_W}{(1-R)} \cdot X \qquad [1]$$

The quantum efficiency of a phosphor thus depends on three measurable quantities: (*a*) the factor Q/Q_W which is a measure of the emission spectrum, and which will change when the spectrum changes; (*b*) the factor Q_W/Q_{INC} which is a measure of the excitability of the phosphor and for which we use the symbol X; (*c*) the diffuse reflectance R. The great difficulty lies in the determination of the excitability Q_W/Q_{INC} since the actual total number of photons, either incident upon the sample or emitted at the window wave length, is extremely difficult to measure. The problem is dealt with as follows. Returning to Eq. [1], and discarding Q_W temporarily, we can write for two phosphors

$$\frac{QE_1}{QE_2} = \frac{Q_1}{Q_2} \frac{Q_{INC_2}(1-R_2)}{Q_{INC_1}(1-R_1)} \qquad [2]$$

For phosphor 2 we use magnesium tungstate (NBS 1027) and Bril's quantum efficiency value of 0.84 for 254 nm excitation at room temperature. We measure Q_1 and Q_2 at the same incident intensity, 254 nm wave length, and room temperature. Then for unknown phosphor P

$$QE_{P,254,T_R} = 0.84 \left(\frac{Q_P}{Q_{1027}} \right)_{254,T_R} \left(\frac{1 - R_{1027,254,T_R}}{1 - R_{P,254,T_R}} \right) \qquad [3]$$

and this is the method used for comparing quantum efficiencies of two phosphors at a given excitation wave length and temperature. The procedure is to measure the emission spectra of the two phosphors under identical conditions (same intensity and wave length λ of incident radiation, same monochromator slit widths, same photomultiplier gain), convert to the photon spectrum, and integrate by computer; this determines Q_P/Q_{1027}. Absolute diffuse reflectances R_P and R_{1027} are also determined, and then the unknown quantum efficiency calculated.

In comparing quantum efficiencies of phosphors at different exciting wave lengths (λ) and/or temperatures (T), one cannot in general hold the incident

intensity constant, or at least it is inconvenient to do so. It is also inconvenient to measure the total quantum output $Q_{P,\lambda,T}$ of the unknown and reference phosphors at each combination of wave length and temperature, primarily because the emission spectrum of the unknown and the standard must be measured under identical conditions, and the total quanta computed. The next logical step is, therefore, to remove these restrictions. First we rewrite Eq. [3] to read

$$QE_{P,254,T_R} = 0.84\left[\frac{(Q/Q_W)'_P}{(Q/Q_W)''_{1027}}\left(\frac{Q_{W_P}}{Q_{W_{1027}}}\right)'''\right]_{254,T_R}\left(\frac{1-R_{1027,254,T_R}}{1-R_{P,254,T_R}}\right) \quad [4]$$

If we assume that emission spectra are independent of intensity, then the three factors in the square brackets may be measured at arbitrary intensities of incident radiation, as indicated by the primes. Second, the ratio of quantum efficiency of unknown phosphor P at arbitrary wave length λ and temperature T to that under the standard conditions is, from Eq. [1],

$$\frac{QE_{P,\lambda,T}}{QE_{P,254,T_R}} = \frac{(Q/Q_W)_{P,\lambda,T}}{(Q/Q_W)_{P,254,T_R}}\,\frac{1-R_{P,254,T_R}}{1-R_{P,\lambda,T}}\,\frac{X_{P,\lambda,T}}{X_{P,254,T_R}} \quad [5]$$

By definition,

$$\frac{X_{P,\lambda,T}}{X_{P,254,T_R}} = \frac{\left(\frac{Q_W}{Q_{INC}}\right)_{P,\lambda,T}}{\left(\frac{Q_W}{Q_{INC}}\right)_{P,254,T_R}} = \left[\frac{\left(\frac{Q_W}{Q_{INC}}\right)_\lambda}{\left(\frac{Q_W}{Q_{INC}}\right)_{254}}\right]_{P,T} \times \left[\frac{\left(\frac{Q_W}{Q_{INC}}\right)_T}{\left(\frac{Q_W}{Q_{INC}}\right)_{T_R}}\right]_{P,254} \quad [6]$$

Since only phosphor P is involved, for which window wave length W is assigned, the raw signal S_W is proportional to Q_W; S_W is the detector output with the second monochromator set at window wavelength W. The last factor in [6], if incident intensity Q_{INC} is held constant, is essentially a normalized temperature dependence factor.

Substituting [6] in [5] and multiplying by [4] results in the final expression

$$QE_{P,\lambda,T} = 0.84\,\frac{\left(\frac{Q}{Q_W}\right)'_{P,\lambda,T}}{\left(\frac{Q}{Q_W}\right)''_{1027,254,T_R}}\left(\frac{Q_{W_P}}{Q_{W_{1027}}}\right)'''_{254,T_R}\left(\frac{1-R_{1027,254,T_R}}{1-R_{P,\lambda,T}}\right)\left[\frac{\left(\frac{S_W}{Q_{INC}}\right)_\lambda}{\left(\frac{S_W}{Q_{INC}}\right)_{254}}\right]_{P,T}\left(\frac{S_{W_T}}{S_{W_{T_R}}}\right)_{P,254} \quad [7]$$

$$a\,\frac{b}{c} \qquad d \qquad \frac{e}{f} \qquad \frac{g}{h} \qquad j \quad [7a]$$

This expression for quantum efficiency makes the experimental work reduce to a series of independent measurements which can be carried out for the most part at arbitrary lamp intensity, arbitrary signal amplification, and in an order which suits the convenience of the experimenter rather than is dictated by the requirement of equivalent conditions.

Factors (a), (c), and (e) in Eq. [7a] are constants of the standard magnesium tungstate phosphor. Factor (d) is the ratio of "photons out the window" for the unknown and standard phosphors, determined once at 254 nm and room temperature by measuring the window signals S_W and correcting them to photons by the same correction factors used by the computer in calculating a photon spectrum. Factors (b), (f), and (g) are the only three factors which vary with λ and T, and correspond of course to the emission, reflectance, and excitability of the unknown phosphor at λ and T. To determine factor (b), a series of emission spectra is measured, ordinarily at the five temperatures −160°, −60°, +25° (T_R), +100°, and +200°C, and at six or seven exciting wave lengths including 200, 230, 254, 280, 313, 365, 405, 436, and 546 nm or others depending on the results of the excitation measurements; Q and Q_W are read off from the computer results and Q/Q_W plotted and smoothed as λ and T vary, as in Fig. 18-20. From this family of curves $(Q/Q_W)_{P,\lambda,T}$ is read off for every 10 nm at each of the five temperatures. Factor (f) is, in the computer program, actually

$$1 - \frac{r_P R_S}{r_S}$$

Q_{INC} in factors (g) and (h) is the raw signal S_W, derived from sodium salicylate, which is multiplied by a correction factor (2) at each wave length. Factor (g/h) is the excitability X of Eq. [1] normalized to that at 254 nm. Factor (j) is the ratio of window output of phosphor P at temperature T to that at room temperature T_R, excited at 254 nm.

The computer program corresponding to Eq. [7] is

$$QE = PT\,\frac{[(Q/Q_W)_{P,\lambda,T}]}{\left(1-\left[\frac{r_P}{r_S}\right]R_S\right)_{P,\lambda,T}}\,\frac{[S_{W_\lambda}]}{ISH} \quad [8]$$

where

$$P = 0.84\,\frac{(Q_{W_P}/Q_{W_{1027}})_{254,T_R}}{(Q/Q_W)_{1027,254,T_R}}\,(1 - R_{1027,254,T_R})$$

a constant which relates the output of phosphor P to that of the standard,

$$T = \left(\frac{S_{W_T}}{S_{W_{T_R}}}\right)_{P,254}$$

a constant for a given temperature,

$$IS = Q_{INC_\lambda}$$

and consists of a deck I of stored data of $S_{W\lambda,T_R}$ for sodium salicylate and a deck S of stored data from Ref. (2) which correct data I to actual incident intensity. Deck I is related to source output and is checked periodically and changed if necessary.

$$H = \left(\frac{S_W}{Q_{INC}}\right)_{P,254,T}$$

and is a normalizing factor comparing all excitabilities to that at 254 nm. The three bracketed quantities in Eq. [8] are fed to the computer at 10-nm intervals over the entire wave length range. Constants P, T, H are fed in on the title card. R_S, I, and S are stored in permanent card decks, I being changed only when the source is changed. The computer readout provides, for every 10-nm wave length interval, the computed value of quantum efficiency, the absolute reflectance, and the normalized excitability.

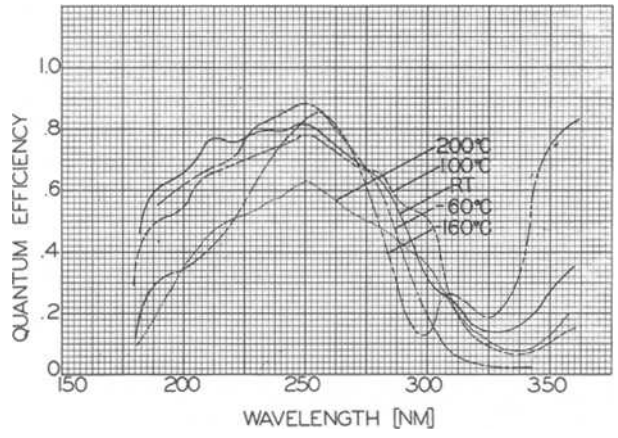

Fig. 34. Quantum efficiency spectra at various temperatures of zinc silicate:Mn.

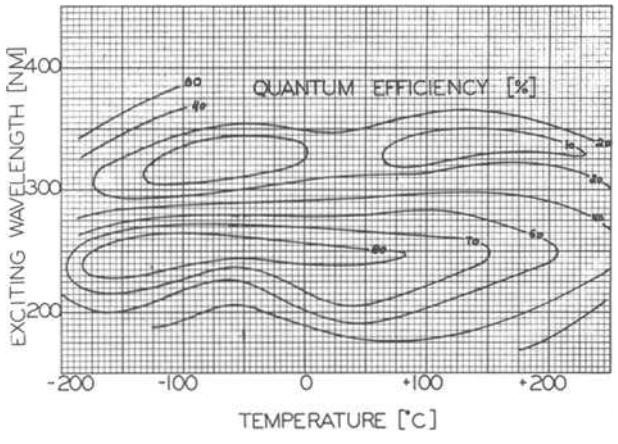

Fig. 35. Contour plot of the data of Fig. 34

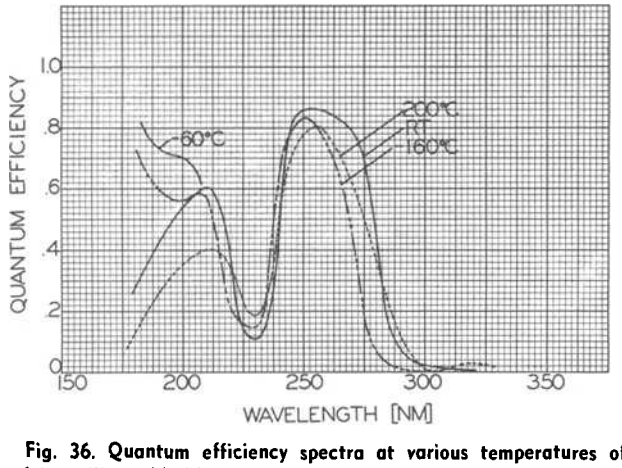

Fig. 36. Quantum efficiency spectra at various temperatures of calcium silicate:Mn,Pb.

Resulting QE spectra.—Figure 34 is an example of the final computed quantum efficiency spectra, for zinc silicate:Mn. Although the *QE* at 350 nm increases strongly near liquid nitrogen temperature, the output of this phosphor will remain low because reflectance (Fig. 31) remains high; obviously this is a case where such complete measurement is necessary in order to understand the phosphor behavior; Fig. 35 shows the same data presented as a contour plot. Figure 36 shows the *QE* spectra of calcium silicate:Mn, Pb and their similarity to the excitation curves of Fig. 28. Figure 37 shows a contour plot which is rather typical of calcium halophosphate:Sb,Mn.

Lumen output.—This calculated quantity represents the relative number of lumens one should expect

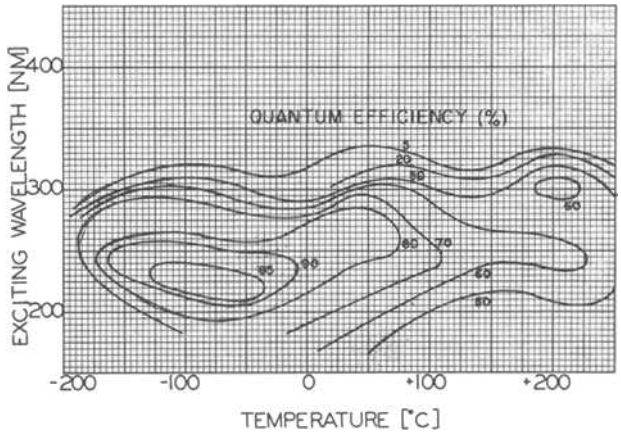

Fig. 37. Contour plot of quantum efficiency as a function of exciting wave length and temperature of white 3500K calcium halophosphate phosphor.

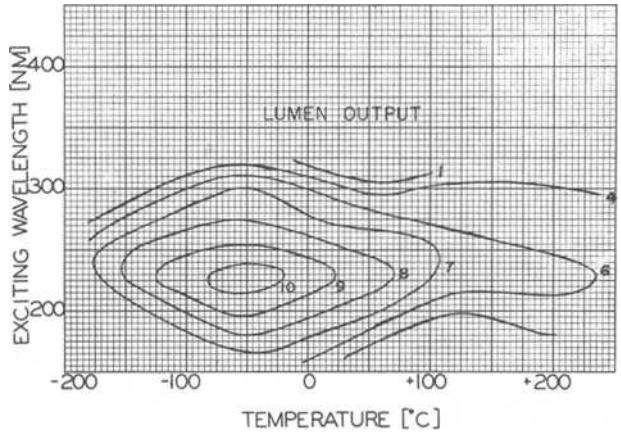

Fig. 38. Lumen output (lumens emitted per exciting photon absorbed) contours *vs.* exciting wave length and temperature, of warm white calcium halophosphate phosphor.

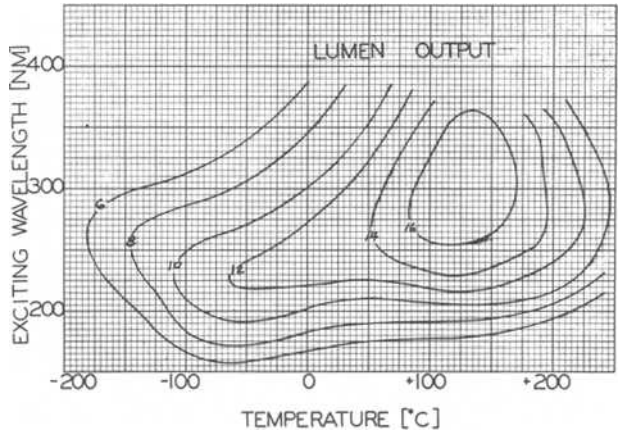

Fig. 39. Lumen output (lumens emitted per exciting photon absorbed) contours *vs.* exciting wave length and temperature, of magnesium fluorogermanate:Mn.

from a lamp made with the given phosphor at optimum coating weight, excited by a discharge generating a certain constant number of (ultraviolet) photons at a single wave length λ, and operating at bulb wall temperature T. "Lumen output" is defined here as (Y/Q) QE, where Y/Q is the ratio of lumens emitted to total photons emitted by the phosphor at λ, T and is derived from the relative quantities Y and Q calculated by the computer for each spectral energy distribution. "Lumen output" is thus simply lumens emitted divided by photons absorbed and is plotted as

equal-lumen-output contours against exciting wave length and temperature. Figure 38 represents warm white halophosphate and Fig. 39 magnesium fluorogermanate: Mn.

Acknowledgments

It is a pleasure to acknowledge the helpful contributions of many associates. Many thanks are due G. R. Hagen for the computer programs and assistance with their use, D. A. Larson for some useful source lamps, J. W. McNall and H. F. Ivey for helpful comment, and especially E. J. Ham, R. J. Mahalik, and W. R. Wheatley for much good assistance.

Manuscript submitted July 23, 1968; revised manuscript received Nov. 7, 1968. This paper was presented at the San Francisco Meeting, May 9-13, 1965, as Paper 38.

Any discussion of this paper will appear in a Discussion Section to be published in the December 1969 JOURNAL.

REFERENCES

1. *See*, for example, A. Bril and W. van Meurs-Hoekstra, *Philips Res. Repts.*, **19**, 296 (1964), and other work by the Philips group.
2. N. Kristianpoller and R. A. Knapp, *Appl. Opt.*, **3**, 915 (1964).
3. *See*, for example, W. E. K. Middleton and C. L. Sanders, *J. Opt. Soc. Am.*, **41**, 419 (1951).
4. For example, Model 420-U2, George W. Gates and Co., Franklin Square, L.I., N.Y.
5. R. Stair, W. E. Schneider, and J. K. Jackson, *Appl. Opt.*, **2**, 1151 (1963).
6. Engelhard Hanovia, Inc., Hanovia Lamp Division, Newark, N. J.
7. For example, "suprasil" by Engelhard Industries, Amersil Quartz Division, Hillside, N. J. (transmission greater than 50% at 160 nm).
8. Whittaker Corp., Gencom Division, Plainview, L. I., N. Y.
9. A useful figure of merit brought to the writer's attention by W. Lehmann.
10. "The Mathematics of Physics and Chemistry," Margenau and Murphy, p. 460, Van Nostrand (1943).
11. "Handbook of Colorimetry," M.I.T., The Technology Press (1936).
12. N. Kristianpoller, *J. Opt. Soc. Am.*, **54**, 1285 (1964).
13. K. J. Nygaard, *Brit. J. Appl. Phys.*, **15**, 597 (1964).
14. F. J. Studer, Opt. Soc. Amer. Spring Meeting 1965, Abstract FB15.
15. R. A. Knapp, *Appl. Opt.*, **2**, 1334 (1963).
16. R. Allison, J. Burns, and A. J. Tuzzolino, *J. Opt. Soc. Am.*, **54**, 747 (1964).
17. R. Allison, J. Burns, and A. J. Tuzzolino, *ibid.*, **54**, 1381 (1964).
18. F. Inokuchi, *ibid.*, **54**, 842 (1964).
19. N. Kristianpoller and D. Dutton, *Appl. Opt.*, **3**, 287 (1964).
20. Distributed by C. L. Huisking and Co., Inc., New York.
21. A. H. Taylor, *J. Opt. Soc. Am.*, **21**, 776 (1931).
22. A. Bril, in "Luminescence of Organic and Inorganic Materials," Kallmann and Spruch, Editors, p. 479, Wiley, New York (1962).

Particle Size and Morphology of Zinc Sulfide

II. Thermal Recrystallization Effects

R. A. Brown*

Radio Corporation of America, Electronic Components and Devices, Lancaster, Pennsylvania

ABSTRACT

The action of heat on ZnS:0.015% Ag, 2% sodium chloride flux results in rapid intra-aggregate coalescence, followed by the subsequent growth of the primary zinc sulfide particles. At temperatures between 700° and 1100°C, the rate of growth of the particles during the initial, fast recrystallization follows the empirical equation $D^{4/5} = kt$, where D is the average particle diameter at a firing time t. An Arrhenius activation energy of 13 ± 2 kcal was obtained for this stage of the growth process. An inverse relationship exists between the initial zinc sulfide aggregate size and the particle size of the resultant phosphor. This suggests that the agglomerate structure does not collapse completely during the period of coalescence.

Luminescent zinc sulfide phosphors are usually prepared by firing zinc sulfide precipitate with a suitable activator and flux at moderately high temperatures. Although the mechanism of flux action in initiating thermal recrystallization is not always clearly understood, it is well known that the presence of a flux has a marked influence, not only on luminescent emission (1, 2), but also on crystal structure (3) and particle size (4). Common fluxes employed in zinc sulfide type phosphors include the halogen salts of ammonium, the alkali metals, and the alkaline earth elements.

Leverenz (5) has shown that during firing particle volumes may change by a factor of 10^8. The data of Bube (6) indicate that, in the presence of a flux, a limiting particle size of about 6μ is attained, irrespective of the temperature employed, whereas in the absence of a flux, and at temperatures of 900°-1350°C, the particles continue to grow. Smith (7), following earlier work by Gugel (8), has studied the chemical nature of the flux and has suggested that, since the alkali or alkaline earth halides are liquid at normal firing temperatures, solid solution may occur with the zinc sulfide. Contrast this with the work of Houben (9) who studied the ZnS-NaCl system and found no zinc sulfide in the fused sodium chloride phase. The activator may also be responsible for changes in morphology or crystal structure. For example, Gashurov and Banks (10) have demonstrated that the wurtzite-sphalerite transition in the ZnS:Cu system is initiated by a separate phase of cuprous sulfide.

Recently, Bodi (11) and Bodi and Tufts (12) have attempted to give a more detailed description of the changes in particle size and morphology which occur during the thermal recrystallization of zinc sulfide containing a sodium chloride flux. Bodi (11) found that particle sizes obtained from air sedimentation rates were much larger than those given by gas adsorption measurements. From this he concluded that during the early stages of heating zinc sulfide has a highly porous structure. Electron microscopic studies carried out by Bodi and Tufts (12) supported this observation. On the basis of these results, the latter workers showed that rapid coalescence of intra-aggregate grains occurs within the first few minutes of firing.

* Electrochemical Society Active Member.

A previous paper (13) examined the influence of various preparative conditions on the particle size and habit of zinc sulfide obtained by precipitation methods. Of the parameters studied, pH had a marked effect on particle size. In addition, the size varied inversely with the rate of precipitation. Preparation of the zinc sulfide in strongly acid solution resulted in the formation of aggregates, of the order of 1 to 5μ, which were irregular, globular masses. If the precipitation was carried out in the presence of certain additives, such as ammonium acetate or ammonium formate, irregularly shaped platelets resulted. In all cases, zinc sulfide obtained from strongly acid, neutral, or alkaline solution was precipitated in the sphalerite form, although occasionally a small amount (<2%) of wurtzite was also detected.

The object of the present work was to investigate thermal recrystallization effects in zinc sulfide precipitate. With this object in mind, attempts have been made to: (*a*) obtain a phenomenological description of the changes in morphology and particle size which occur during heating; (*b*) determine what relationship, if any, exists between the initial zinc sulfide particle size and that of the final phosphor; (c) obtain quantitative data on the rate of growth of the particles during the initial stages of recrystallization. Most of this work was carried out with ZnS:0.015% Ag, 2% sodium chloride flux, and 1% sulfur as the starting material. Note that these are weight per cent values.

Experimental

A detailed account of the precipitation of zinc sulfide by the addition of gaseous hydrogen sulfide to an aqueous solution of zinc sulfate has been given elsewhere (13). In order to obtain reproducible results in the firing series, phosphor samples were prepared by a dry-blending process, following the usual procedures. By way of example, a typical experiment involving the firing of zinc sulfide at 700°C is described below.

Test samples of 3.5g of ZnS:0.015% Ag, 2% sodium chloride, containing 1% sulfur, were fired in air at 700°C using 10 cm^3 covered "Vitreosil" crucibles. During the heating, samples were removed at regular intervals of time from periods of 1 min up to 4 hr. Subsequently, specimens were examined by electron microscopy and Coulter counter methods, for the determination of the size and shape of the particles, and by x-ray powder and electron diffraction procedures, to ascertain the crystal structure.

Firings were carried out at temperatures in the range 700°-1100°C. In addition, different "types" of precipitate (for example, zinc sulfide obtained at various rates of precipitation and in the presence of conventional buffering agents) were used as the starting material. For comparison, 3.5g specimens of pure zinc sulfide containing no flux or activator as additives were fired for various lengths of time at 700° and 800°C. It should be pointed out that the thermal effects depend on factors such as the sample size, configuration of the firing vessel, and rate of cooling. Consequently, the results obtained should be regarded as relative.

Results and Discussion

A typical firing sequence at 700°C for a ZnS:0.015% Ag phosphor containing 2% sodium chloride as flux and 1% sulfur is illustrated in Fig. 1. The original precipitate was prepared from 1M zinc sulfate solution at 25°C, using a hydrogen sulfide flow of 0.82 liter/min. Initially, the precipitate is in the form of highly aggregated, globular masses approximately 2μ in size, as shown in Fig. 1 (*a*). After firing for 2.5 min [Fig. 1(*b*)], there is a roughening in the surface texture and some coalescence of adjacent grains has taken place. At 4.5 min [*see* Fig. 1(*c*)], rapid intra-aggregate coalescence occurs, resulting in the formation of many, small particles having a size of the order of 0.2μ. Following this coalescence, the large particles grow at the expense of smaller ones by normal growth processes (14, 15). This is demonstrated in Fig. 1(*d*) to 1 (*h*) which show the gradual assimilation of the zinc sulfide particles during the 4-hr firing period. After 4 hr, the final size attained is approximately 4μ; the particle has lost all traces of the globular form, and instead shows evidence of crystal facets. These results agree with the observation of Bodi and Tufts (12).

A summary of the particle size measurements obtained for the firing series, together with the crystal structure as determined by x-ray powder diffraction methods, is given in Table I. Note that the particle sizes obtained by the Coulter counter procedure differ widely from those given by electron microscopic examination. This confirms the findings of Bodi (11). Apparently, the size given by the Coulter counter represents that of the zinc sulfide aggregates, whereas electron microscopic observation provides the size and shape of the primary zinc sulfide particles which compose the agglomerates. During the early stages of heating, the aggregate size does not change appreciably. In contrast to this, the primary zinc sulfide particles grow very rapidly within an agglomerate.

The data of Table I also show that during the recrystallization an appreciable amount of wurtzite may be formed. Higher firing temperatures made this even more evident. For example, after heating for 10 min the amount of wurtzite present was 14% at 700°C and 27% at 900°C. During the remainder of the 4-hr heating cycle, the quantity of hexagonal phase present gradually diminishes at each of these temperatures.

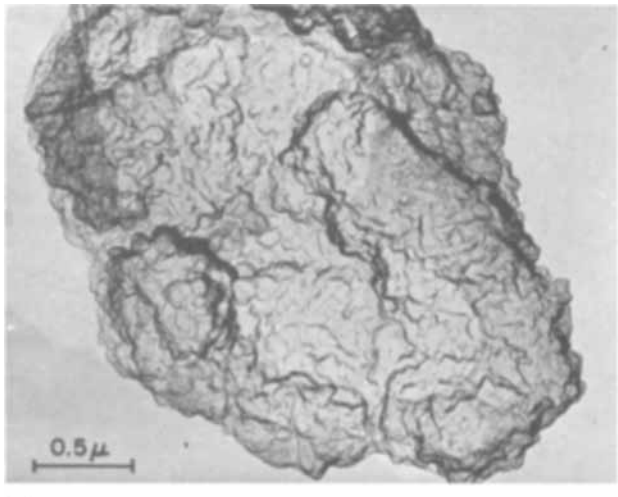

(a)

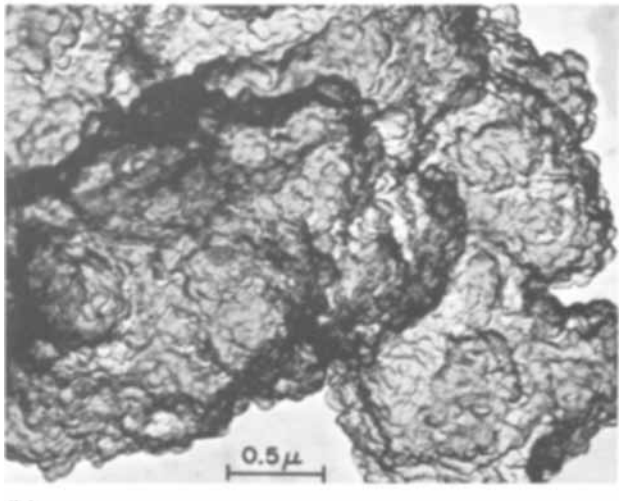

(b)

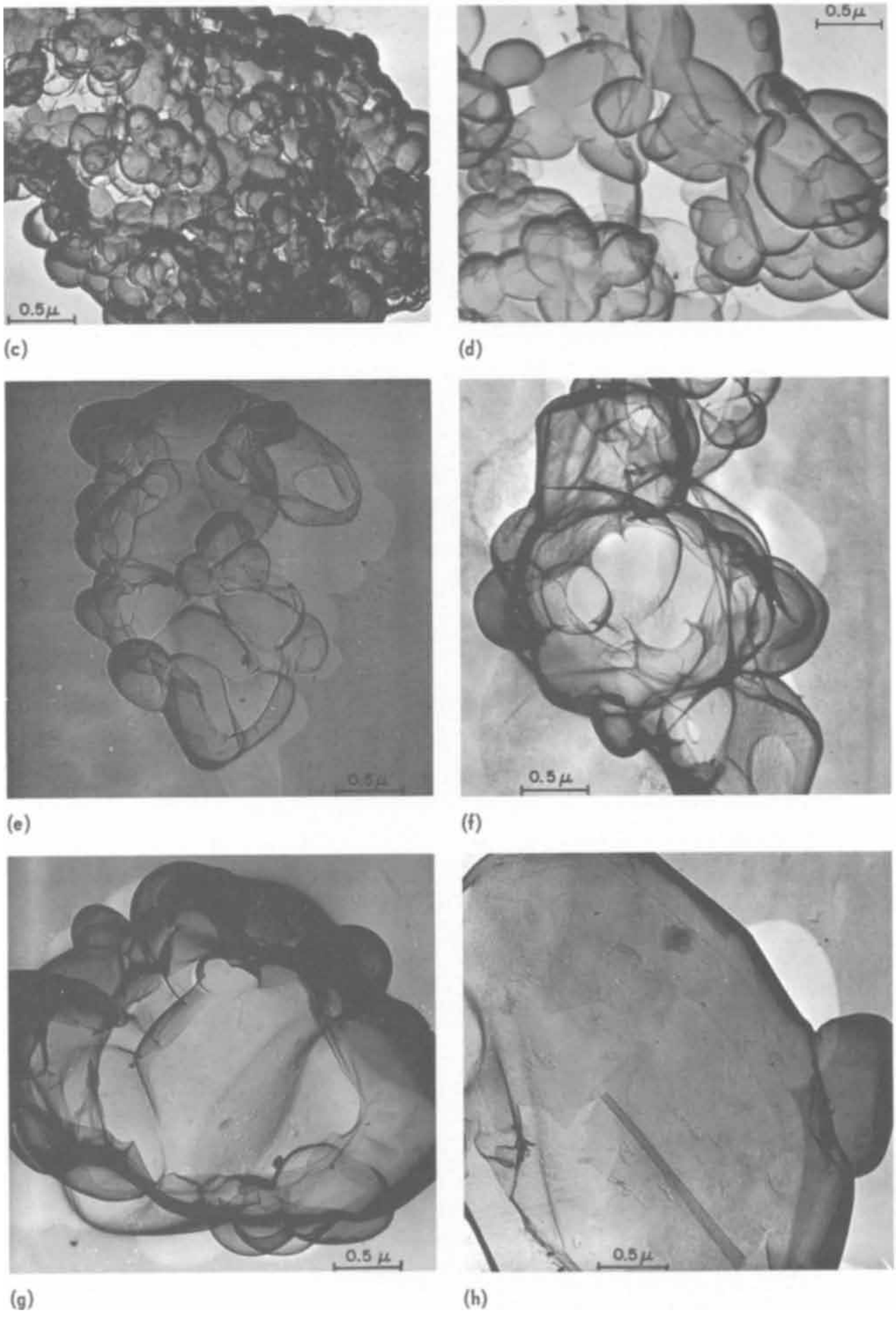

Fig. 1. Firing sequence at 700°C for ZnS:0.015% Ag, 2% NaCl flux: *(a)* 0 min, *(b)* 2.5 min, *(c)* 4.5 min, *(d)* 10 min, *(e)* 0.5 hr, *(f)* 1 hr, *(g)* 2 hr, *(h)* 4 hr. Initial ZnS precipitated from $ZnSO_4$ with H_2S.

Table I. Influence of temperature on the particle size and crystal structure of ZnS:0.015% Ag, 2% NaCl

Duration of firing (min)	Particle size (μ) Coulter counter 700°C	900°C	1100°C	Electron microscopy 700°C	900°C	1100°C	Wurtzite in cubic host (%) 700°C	900°C	1100°C
1	3.2	3.1	3.1				4	5	16
2	3.2	3.0	3.0		0.17	0.45	4.5	15	36
3	3.1	3.0	3.0	0.07	0.27	0.8	5	24	55
4	3.1	2.9	3.0				8	25	75
5	3.1	2.9	3.3	0.17	0.65	1.4	13	27	78
10	2.9	3.1	5.0	0.32	1.6	3.3	14	27	86
15	2.7	3.1	7.7	0.6			8	24	100
30	2.6	4.7	8.5	1			6	22	100
60	2.5	5.9	10.0	2			4	20	100
120	3.0	6.5	11.0	3			2	10	100
180	3.3	6.8	13.6				2	7	100
240	3.3	7.0	14.0				1.4	6	100

NOTE: The Coulter counter values represent the median point by number of particles.

Brown (13) has shown that the initial zinc sulfide precipitate is poorly crystalline and essentially cubic, although it may contain a small amount of wurtzite. Apparently, during the period of coalescence that occurs in the first few minutes of firing, the hexagonal form grows more rapidly than the cubic. However, since sphalerite is the more stable form at temperatures below the transition point of 1020°C (16), the initial rapid crystallization is followed by a slower rearrangement during which the wurtzite present is gradually converted to sphalerite.

Since it was desirable to obtain a more quantitative understanding of the thermal recrystallization processes, an attempt was made to determine whether the rate of increase in particle size at a given temperature would obey the same type of relationship as that observed during grain growth in ceramic systems. For many systems, grain growth is observed to follow the empirical equation (17, 18)

$$D^n = kt$$

where

D = average diameter of the grains
n = a constant
k = the rate constant
t = time

On the basis of this equation, a plot of log D *vs.* log t should be a straight line with a slope of $1/n$. Nicholson (19) has shown that an activation energy for the growth process can be obtained directly from a plot of —log t against 1/T, where T = temperature (°K), for an arbitrarily selected constant D.

Figure 2 shows the relationship between log D and $1/t$ at temperatures of 700°, 900°, and 1100°C. Since the particle sizes were estimated from an electron microscopic examination, the values should, perhaps, be regarded as relative rather than absolute. For comparison, the particle growth observed in the same system by Bodi (11) at 1200°C, determined from surface area measurements, is also given. These results confirm that a linear dependence does, in fact, exist. Since the measured slope of these lines is 5/4, the relationship between average particles size D at a firing time t may be expressed by the empirical equation $D^{4/5} = kt$. A plot to determine the Arrhenius activation energy for the growth processes was derived from the data of Fig. 2, with the use of an arbitrarily chosen constant D of 1μ. From this plot, given as Fig. 3, the activation energy for the thermal recrystallization of zinc sulfide, 2% sodium chloride flux during the initial stage of firing was calculated to be 13 ± 2 kcal. Secco (20) and MacKinnon *et al.* (21) have studied the self-diffusion of ions in polycrystalline zinc sulfide. Although the movement of the zinc ions was found to be the rate-determining step, the results obtained were not straightforward to interpret. An apparent activation energy of 30.5 kcal was derived for a mechanism involving the interstitial diffusion of zinc; for a bulk diffusion model, a value of 61.5 kcal was obtained. A detailed discussion of the activation energy in terms of rate processes and mechanisms is not within the scope of this paper. However, the value of 13 kcal obtained for the recrystallization processes is considerably lower than that of 30.5 kcal calculated for interstitial diffusion, or 61.5 kcal given for self-diffusion of the rate-controlling (zinc) ion. This result could be interpreted in terms of a boundary diffusion model, as suggested by the work of Nicholson (19).

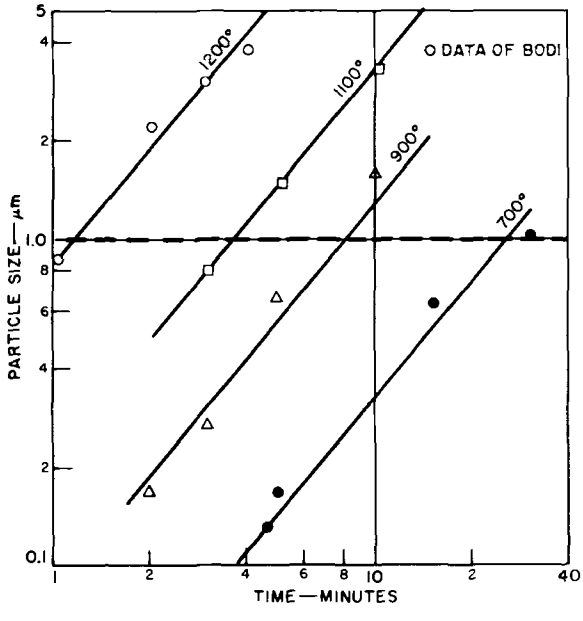

Fig. 2. Rate of particle growth in ZnS:0.015% Ag, 2% NaCl flux

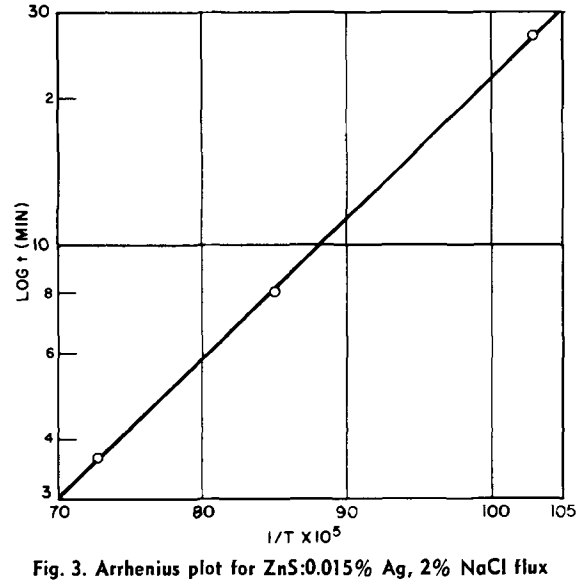

Fig. 3. Arrhenius plot for ZnS:0.015% Ag, 2% NaCl flux

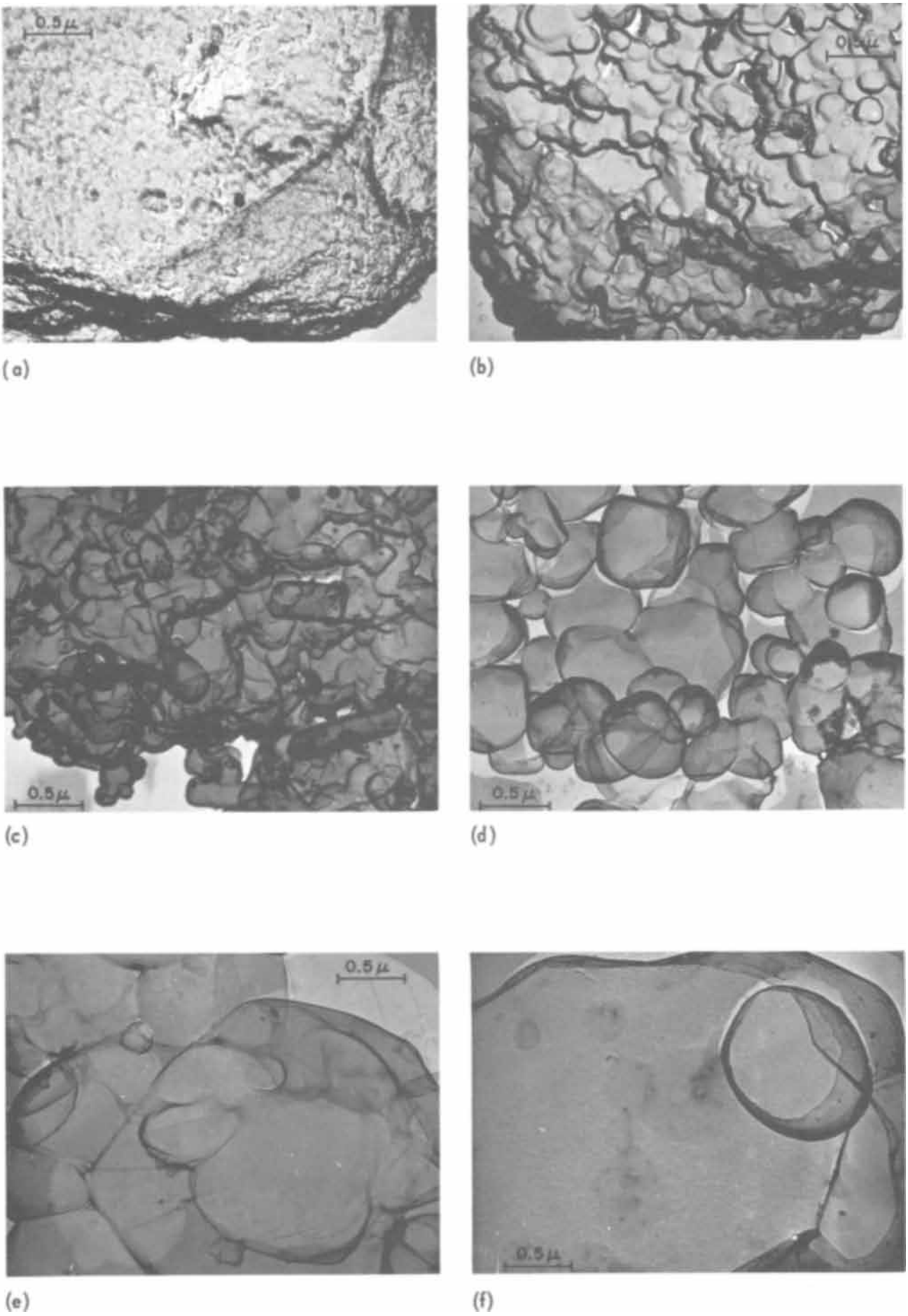

Fig. 4. Firing sequence at 700°C for ZnS:0.015% Ag, 2% NaCl flux: *(a)* 1 min, *(b)* 5 min, *(c)* 10 min, *(d)* 15 min, *(e)* 3 hr, *(f)* 4 hr. Initial ZnS precipitated from $ZnSO_4$-ammonium formate with H_2S.

Figure 4 illustrates a firing sequence at 700°C for a different zinc sulfide powder. In this case, the starting material was precipitated with hydrogen sulfide from a zinc sulfate solution containing an ammonium formate buffer. As such, it would consist of smaller particles with a tendency to aggregate as platelets. In general, the recrystallization follows the same pattern as that noted above, namely intragrain coalescence followed by the growth of the fundamental zinc sulfide particles. The composition of the phosphor is again ZnS:0.015% Ag, 2% sodium chloride flux with 1% sulfur. An interesting type of behavior is demonstrated in Fig. 4(c). A new crystalline phase is observed to form from an apparently amorphous precipitate. Electron diffraction analyses of the two areas showed that they were both hexagonal zinc sulfide, in spite of the fact that the unheated precipitate was essentially cubic. This confirms the observation made above, that during the rapid thermal recrystallization comparatively large amounts of wurtzite may result.

All of the zinc sulfide precipitates examined so far, irrespective of the initial size or morphology of the particles, have follwed this same pattern of recrystallization. Note that this applies only to zinc sulfide containing sodium chloride as a flux. In the absence of additives, pure zinc sulfide showed no noticeable changes, either in particle size and morphology, or in crystal structure, even when heated at temperatures up to 800°C for periods of 2-4 hr.

Another aspect of this work was the determination of any relationship that might exist between the aggregate size of the initial zinc sulfide precipitate and the particle size of the resultant phosphor. Previous work (13) (summarized above) has shown that the size of the zinc sulfide aggregates can be controlled most readily by varying the rate of precipitation. Consequently, zinc sulfide obtained at different precipitating rates was used as the starting material in the preparation of ZnS:0.015% Ag phosphors. A summary of the results obtained is presented as Fig. 5, which shows an inverse relationship between aggregate size of the precipitate and phosphor particle size. Thus, the relatively small zinc sulfide aggregates, such as would be obtained by rapid precipitation, show considerable particle growth on heating [Fig. 5(*b*)]. On the other hand, the larger aggregates prepared at a slow rate of precipitation do not grow to the same extent [Fig. 5(*a*)]. It is well known that fine particles are more "reactive" than coarse ones, owing to their higher surface energy. The behavior of the zinc sulfide precipitates is in accord with this general observation. This finding, together with Coulter counter measurements reported above, suggests that the aggregate structure does not collapse completely during the thermal recrystallization. Apparently, following the intragrain coalescence, the submicron particles are still held together within the framework of the original zinc sulfide agglomerate.

In summary, this work has confirmed that the thermal recrystallization of zinc sulfide, in the presence of a sodium chloride flux, proceeds by coalescence within an aggregate followed by fusion of the primary zinc sulfide particles. During heating, very pronounced changes occur in particle size, morphology, and crystal structure within a period of a few minutes. Contrast this with the fact that, during the preparation of zinc sulfide luminophors, firing times up to several hours in duration are frequently employed. During the early stage of recrystallization, the rate of particle growth can be expressed by an equation similar to that used in describing grain growth in metals or ceramic systems, namely $D^{4/5} = kt$, where the symbols have the meanings given above. In addition, it was shown that there is an inverse dependence between initial aggregate size and the particle size of the resultant phosphor. Consequently, these studies have led to a clearer understanding of the relationship between the physical properties of zinc sulfide precipitate and those of the phosphor, and have shown some of the factors which are important in controlling the particle size of zinc sulfide phosphors.

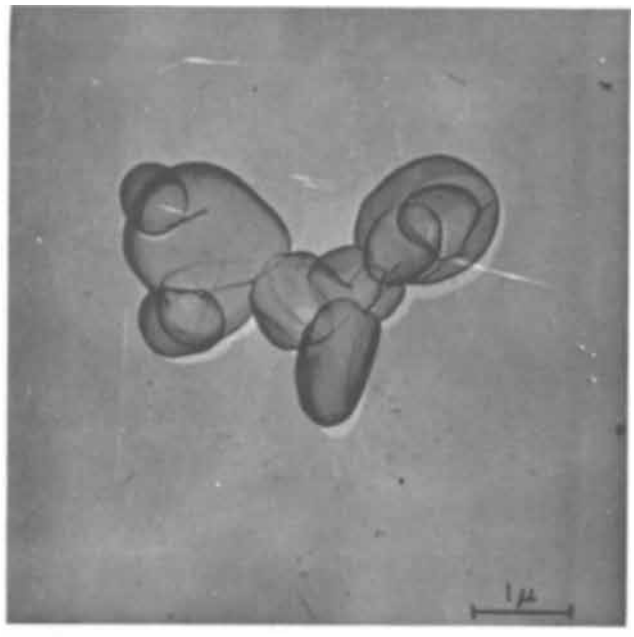

(a)

(b)

Fig. 5. Influence of initial aggregate size (S) on ZnS:0.015% Ag, 2% NaCl flux: (*a*) S = 3-4μ, (*b*) S = 0.5μ. Firing conditions —800°C for 1 hr.

Acknowledgments

The author expresses his gratitude to Dr. L. Woontner for providing the electron photomicrographs used, and for valuable discussions. Thanks are due to E. W. Bomgardner for assistance with the preparatory work. For helpful discussions and suggestions, especial thanks are due to Dr. A. L. Smith.

Manuscript submitted Oct. 3, 1968; revised manuscript received Nov. 13, 1968.

Any discussion of this paper will appear in a Discussion Section to be published in the December 1969 JOURNAL.

REFERENCES

1. S. Rothschild, *Trans. Faraday Soc.*, **42**, 635 (1946).
2. F. A. Kroeger and J. E. Hellingman, *This Journal*, **93**, 156 (1948).
3. B. Bartels, Ph.D. Thesis, University of Leipzig (1933).
4. A. Schleede and H. Gantzckow, *Z. Phys. Chem.*, **106**, 37 (1923).
5. H. W. Leverenz, *Science*, **109**, 187 (1949).
6. R. H. Bube, *J. Chem. Phys.*, **20**, 715 (1952).
7. A. L. Smith, *This Journal*, **96**, 75 (1949).
8. V. M. Gugel, *Bull. Acad. Sci. U.R.S.S., Ser. Phys.*, **9**, 539 (1945).
9. J. Houben, *Mettalurgie*, **9**, 592 (1912).
10. G. Gashurov and E. Banks, *This Journal*, **114**, 1143 (1967).
11. L. J. Bodi, *Proc. Int. Conf. Luminescence, Budapest, 1966*. Preprints, Vol. II, pp. 139-143.
12. L. J. Bodi and C. F. Tufts, *Science*, **143**, 872 (1966).
13. R. A. Brown, *Electrochem. Technol.*, **6**, 246 (1968).
14. W. D. Kingery, "Introduction to Ceramics," pp. 354-369, John Wiley & Sons Inc., New York (1960).
15. H. E. Buckley, "Crystal Growth," pp. 23-35, John Wiley & Sons Inc., New York (1951).
16. E. T. Allen and J. L. Crenshaw, *Z. Anorg. Chem.*, **79**, 130 (1913).
17. R. L. Coble, *J. Appl. Phys.*, **32**, 793 (1961).
18. Y. Ida, *J. Am. Ceram. Soc.*, **41**, 397 (1958).
19. G. C. Nicholson, *ibid.*, **48**, 214 (1965).
20. E. A. Secco, *Can. J. Chem.*, **42**, 1396 (1964).
21. A. J. MacKinnon, R. R. Martin, and E. A. Secco, *ibid.*, **42**, 2334 (1964).

Diffusion Pipes in Silicon NPN Structures

F. Barson,* M. S. Hess,* and M. M. Roy

Components Division, International Business Machines Corporation, East Fishkill Laboratory, Hopewell Junction, New York

ABSTRACT

Diffusion pipes in silicon NPN structures were investigated both by electrical measurements and by microsectioning. It was found that certain crystalline defects, specifically stacking faults and edge dislocations, can act as sites for the formation of such pipes. The presence of gold doping at these lattice defects greatly increases the incidence of pipes, apparently by offering a path of enhanced diffusivity for phosphorus from the emitter.

"Pipes" in NPN transistor structures may be defined as localized n-type regions extending through the p-type base. They appear electrically as a low resistance path, or near short circuit, between the emitter and collector and can be a significant cause of yield loss in device fabrication. Although these defects have been known for years, little has been reported in the literature as to their cause and cure. Goetzberger and Stephens (1) showed that localized diffusion pipes could result from small bits of impurities, specifically phosphorus, on the wafer surface. Enhanced diffusion along dislocations has also been reported (2, 3), although not actually correlated to pipes in device structures.

The scarcity of references on pipes is perhaps partly due to the fact that their incidence has been minimized by dust control in the diffusion areas, and also by the availability of silicon crystals with relatively few imperfections. However, with the advent of complex integrated circuit fabrication, the perfection of the silicon may be degraded by the increased number of high-temperature epitaxial and diffusion cycles required (4). Also, in most cases, a greater total area of the silicon wafer contains active device structures, which increases the probability of a defect occurring in an area which is susceptible to damage by such defects. Hence, the possibility arises once again that yield loss due to pipes can be quite severe.

In the present work, the effects of various process steps and of certain crystalline defects have been investigated as to their influence on the incidence of diffusion pipes. It has been found that stacking faults and edge dislocations can act as sites for pipes, and that the probability of the occurrence of pipes is greatly increased when the wafers are doped with gold.

Electrical Measurements

During development of a specific integrated circuit, a situation did arise in which yields suffered severely from an incidence of pipes. Electrical tests indicated emitter-to-collector shorts, even though the base widths were not abnormally narrow, and it was sometimes possible to demonstrate the presence of diffusion pipes by microsectioning. The process at that time employed epitaxial silicon wafers, a capsule boron base diffusion process (5), and an open-tube, gaseous source phosphorus emitter diffusion similar to that described by McDonald *et al.* (6). The wafers were gold-doped for lifetime control, and the total emitter area (the area susceptible to pipes) was about 60 sq mils per chip.

Variations in several of the process parameters were made in an attempt to discover a particular operation or operations which caused the large incidence of pipes. The results are shown in Table I. In the "standard" gold process, gold from a metallic film deposited on the back of each wafer was diffused during an 1150°C reoxidation following the boron base diffusion.

Experiment 1 in the table consisted of varying the surface concentration (C_0) of the emitter diffusion. The highest concentration was obtained with a two-zone P_2O_5 diffusion, and the lower ones were done with the usual gaseous source. The phosphorus surface concentrations listed in the table were computed

Table I. Effect of process parameters on junction yield

Experiment No.	Parameter	Variable	No. of wafers	Yield (%) Range	Yield (%) Avg
1	Emitter diffusion (std Au process)	$C_0 = 1.5 \times 10^{20}$ cm^{-3}	6	0-2	0.6
		$C_0 = 6 \times 10^{20}$ cm^{-3}	7	0-1	0
		$C_0 = 3 \times 10^{21}$ cm^{-3}	7	0-4	0.5
2	Boron source powder (std Au process)	"*A*"	7	0-30	7.0
		"*B*"	6	0-30	10.0
		"C"	5	0	0
3	Au *vs.* no Au	Abraded/Au	4	0-2	1
		Etch/Au	4	0-16	4
		Abraded/no Au	5	28-57	42
		No Au	5	5-56	35
4	Au diffusion	970°C Au/post-emitter depn.	5	0	0
		970°C Au/post-emitter reoxn.	5	25-42	35

* Electrochemical Society Active Member.

from the measured junction depths and sheet resistivities by use of Irvin's curves (7). No improvement in yield resulted from changing either the surface concentration or the impurity source. Experiment 2 compared the results of using three separately prepared boron-doped silicon powders as the impurity source for the sealed-capsule base diffusions. The small differences in yield shown in the table probably are not significant, particularly since source "*A*" was used in the previous experiment.

The third experiment involved the gold diffusion process, and wafers with and without gold were compared. An additional variation included chemical etching *vs.* abrasion as a cleaning technique before evaporating gold on the back of the wafers. Here it can be seen that a dramatic increase in yield (*i.e.*, a decrease in pipes) was obtained by omitting gold from the process. The method of surface preparation before gold deposition had little, if any, effect.

Although it improved the junction yield significantly, the omission of gold was not acceptable in this particular process, since lifetime control was necessary. Hence, experiment 4 in Table I was performed to learn whether gold added later in the process might be less harmful. Indeed, it can be seen that, if the gold is added after the final reoxidation (but not before), the yield approximates that of wafers without gold. It should be noted that the gold diffusions in both parts of experiment 4 were done at 970°C. Hence, it is the point in the process, rather than the temperature, at which gold is introduced which is significant in affecting the incidence of pipes. Although the addition of gold as a final process step seems to be an effective cure for pipes, it is a practical one only if the gold diffusion cycle is compatible with the previous diffusions. In Table I, for example, gold was necessarily added at a lower temperature in experiment 4 than in the "standard" gold process. In general, the impurity profiles (base width, *etc.*), as well as the amount of gold doping required, must be considered for any specific design before such a process can be applied.

Microsectioning Studies

In order to study any influence of crystalline defects on the formation of pipes, and also to attempt to get a more quantitative measure of pipe densities, microsectioning techniques were employed. Figure 1 illustrates the use of a conventional bevel section. To examine a large area of the base region, where pipes are visible, a low-angle bevel of about 1° was used. The diffusions were done over a large area, or even over the entire wafer, and were adjusted to produce abnormally wide bases. By such techniques, and by making several microsections across each wafer, a total base area of perhaps a tenth of a square centimeter could be scanned for pipes and counts of pipe densities could be made semiquantitatively. A copper staining technique, which plates out copper on n-type regions, was used to make the pipes and the junctions visible. Incidentally, it is noted that in a bevel section (Fig. 1) a pipe is observed as a small n-type spot in the p-type base region.

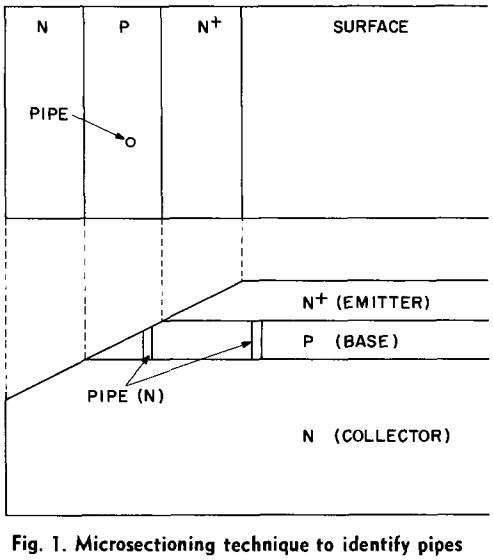

Fig. 1. Microsectioning technique to identify pipes

Table II. Pipe densities for various substrates and gold diffusions

	Nonepitaxial	Epitaxial, low stacking fault count	Epitaxial, high stacking fault count
A. No gold	3×10^3/cm²	0.4×10^3/cm³	7×10^3/cm³
B. Au at 970°C after final reoxidation	0.8×10^3	0.8×10^3	9×10^3
C. Au at 1150°C during postboron reoxidation	8×10^3	5×10^4	$>10^5$

Crystalline Defects as Sites for Pipes

To make a correlation between pipes and crystalline defects, it is advantageous to use wafers with very high defect densities. For example, it was possible to grow epitaxial silicon films with very high stacking fault counts by repeated oxidation and heat cycling of the substrate prior to epitaxial growth. Although this is not a completely reproducible effect, some wafers with over 10^5 stacking faults per square centimeter were obtained for this work.

In addition to wafers with very high stacking fault densities, epitaxial wafers with much greater perfection, and also nonepitaxial wafers, were diffused and microsectioned to investigate pipe densities. Three variations were made with regard to gold doping in this experiment, based on results of the electrical measurements previously made: (*a*) no gold at all was used; (*b*) gold was added at 970°C, following final reoxidation, to minimize pipe formation; and (c) gold was added at 1150°C, before the emitter diffusion, to enhance pipe formation.

Table II lists the resulting pipe densities as determined by microsectioning. It can be seen that these results completely verify the electrical measurements. Gold added after final reoxidation is essentially equivalent to the omission of gold entirely, so far as pipes are concerned. The addition of gold earlier in the process increases the incidence of pipes by approximately an order of magnitude.

Of equal interest is the observation that the epitaxial material with very high stacking fault densities contained many more pipes than did the more perfect material. Good quality epitaxial material appeared equivalent to nonepitaxial material with respect to pipe formation. In the case of highly faulted epitaxial material with gold added prior to emitter diffusion, the density of pipes was found to be on the same order as the stacking fault density, *i.e.* over 10^5/cm². Figure 2 is a photomicrograph of a bevel section illustrating

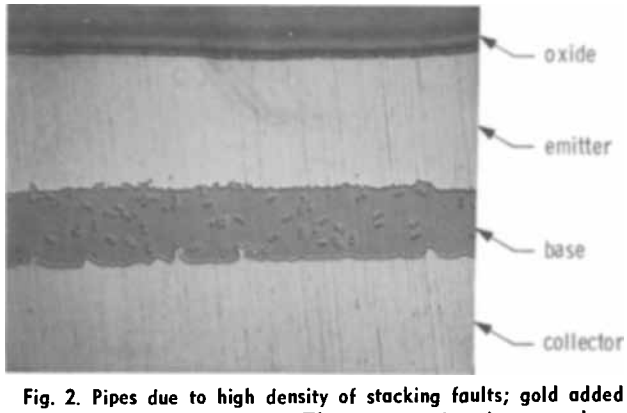

Fig. 2. Pipes due to high density of stacking faults; gold added during boron reoxidation cycle. The apparent junction raggedness is principally due to scratches introduced in lapping. This is aggravated by the low angle of the bevel in microsectioning.

this extremely high incidence of pipes. Since the wafer was (111)-oriented, the appearance of pipes in pairs showing a three-fold symmetry is particularly significant. The appearance of the pipes, plus the statistical correlation with stacking faults, suggests strongly that there may be a one-to-one correspondence of the pipe pairs and stacking faults.

To test this hypothesis, similar structures were produced in which the phosphorus was diffused through an oxide mask having an irregular shape. The corners of this masking pattern could then be used as fiducial marks to locate specific stacking faults prior to microsectioning, as well as the pipes themselves after beveling and staining. Figure 3 illustrates that an almost one-to-one correlation does in fact exist. The location of the base region from Fig. 3(*b*) is indicated on the original wafer surface in Fig. 3(*a*). A comparison of the figures shows the correspondence between the stacking faults, as indicated by the triangular figures on the surface, and the pipes, which appear as small n-type spots in the base region of the microsection. A few exceptions are at the stacking faults lettered *A,B,C* in the figure, which do not have any corresponding pipes. The converse has also been observed in other such studies, *i.e.*, a few pipes which correspond to no visible stacking faults. Thus, in spite of the good correlation, stacking faults alone are neither a completely necessary nor a completely sufficient condition for the formation of pipes.

A significant observation in Fig. 3(*b*) is that pipes occur only under the phosphorus-diffused, or "emitter," region and not in the remainder of the base region. This leads to the conclusion that the pipes are a result of enhanced phosphorus diffusion along the crystalline defects, rather than simply some sort of impurity precipitation at these sites. It may also be noted that the depth to which this diffusion extends is appreciable. In the microsections shown, the emitter depth is slightly over 1μ and the base width is also almost 1μ. In spite of this excessively wide base, some pipes can be seen extending at least this far beyond the emitter diffusion front. It is also interesting that, in nearly all cases, there are pipes at two, rather than at all three, corners of the triangular traces of the stacking faults. Actually, of course, the faulted area is in the shape of an inverted tetrahedron with its apex at the substrate-epitaxy interface. Possibly one face of this tetrahedron is a multiple fault, which would result in a more complex defect along two edges of the tetrahedron than the stair-rod dislocations ordinarily anticipated.

Since in many cases the edges of stacking faults act as sites for pipe formation, it might be expected that edge dislocations extending through the base region would act the same. It is more difficult to demonstrate a one-to-one correspondence here, since it is not easy to locate either pipes or dislocations nondestructively with high precision. By analogy to the results above with stacking faults, however, one might hope to use

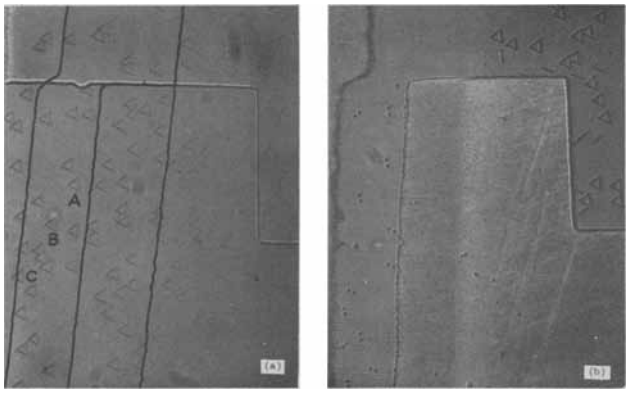

Fig. 3. Correlation of stacking faults and pipes: *(a)* top view showing stacking faults, *(b)* microsection showing pipes.

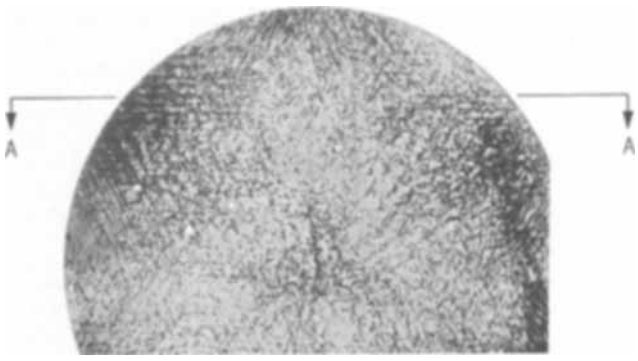

Fig. 4. Topograph of highly dislocated wafer. Microsection location is indicated at *A-A*.

gold-doped wafers with high dislocation counts in order to produce enough pipes that at least a statistical correlation could be found.

Silicon wafers from a crystal grown by the floating-zone technique, and containing a very high dislocation density, were used for this work. The dislocation array in one such wafer is shown in Fig. 4, which is an x-ray transmission topograph made by use of the scanning oscillator technique (8). The wafer is once more (111)-oriented, so that the rows of dislocations run in <110> directions. This wafer was diffused, with gold included, and microsectioned to search for pipes.

In preparing the wafer for microsectioning, it was cleaved, *i.e.* broken precisely along a <110> direction, parallel to the rows of dislocations. The approximate location of the microsection is shown in Fig. 4, with "*A-A*" indicating the cleaved edge. Figure 5 is a photomicrograph of the stained section itself. The arrangement of diffusion pipes in straight rows, following the dislocation array, is quite striking. This plus the fact that the pipe density was highest near the wafer edge, where dislocations were also most dense, is taken as an indication that edge dislocations can indeed act as sites for pipe formation.

Although it is perhaps an obvious point, it should be recalled that these dislocations were grown in the crystal and extend generally from top to bottom of the wafer. Dislocations parallel to the surface, such as might result from high concentration impurity diffusions (9), would not normally extend through the base region and would not be expected to cause pipes.

Summary and Conclusions

It has been demonstrated, both by electrical measurements and by microsectioning techniques, that stacking faults and dislocations can act as sites for diffusion pipes in double-diffused silicon npn structures. The presence of such defects alone is not sufficient to cause pipes; however, the addition of gold doping to the crystal greatly increases the probability of pipe formation at such sites. Since pipes so formed occur only under the emitter, or phosphorus-diffused region, it is concluded that an enhanced diffusion effect is involved rather than simply a precipitation of impurities about the crystalline defects. It seems most likely, however, that a clustering of gold about the

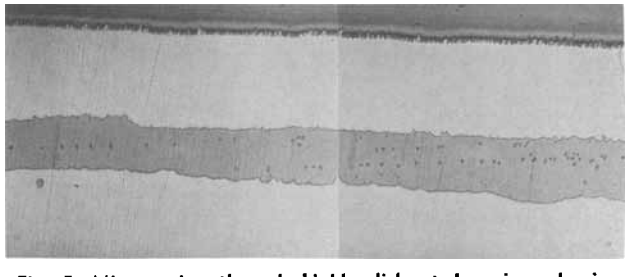

Fig. 5. Microsection through highly dislocated region, showing pipes along <110> direction.

dislocations or stacking faults produces this path of easy diffusion.

Although it has not been demonstrated experimentally, it is tempting to speculate that other fast-diffusing impurities might act in a manner similar to gold in causing these diffusion pipes. Copper, for example, which is known to segregate at crystalline defects (10-12), would seem to be a likely suspect. Thus, the experimental observation that heavily faulted material exhibits an increased incidence of pipes, even without the deliberate addition of gold, may be due to the inadvertent presence of a similar impurity through contamination.

When the use of gold is necessary for lifetime control, its effect in causing pipes can be minimized by adding it at the end of the process, following emitter reoxidation. However, this assumes that the heat cycle for gold diffusion is compatible with the completed device structures. Otherwise, some compromise may be required in the gold diffusion temperature and, hence, in the amount of gold doping used.

Acknowledgments

The authors are indebted to Dr. G. H. Schwuttke for the x-ray topographs used in the work on dislocations, and to Mr. T. Nagasaki for his patient and skillful microsectioning work.

Manuscript submitted July 2, 1968; revised manuscript received Oct. 16, 1968. This manuscript was presented at the Boston Meeting, May 5-9, 1968, as Paper 95.

Any discussion of this paper will appear in a Discussion Section to be published in the December 1969 JOURNAL.

REFERENCES

1. A. Goetzberger and C. Stephens, *This Journal*, **109**, 604 (1962).
2. H. J. Queisser, K. Hubner, and W. Shockley, *Phys. Rev.*, **123**, 1245 (1960).
3. P. V. Pavlov, V. A. Panteleev, and A. V. Maiorov, *Soviet Phys.-Solid State*, **6**, 305 (1964).
4. E. D. Jungbluth and P. Wang, *J. Appl. Phys.*, **36**, 1967 (1965).
5. W. J. Armstrong and M. C. Duffy, *Electrochem. Technol.*, **4**, 475 (1966).
6. R. A. McDonald, G. G. Ehlenberger, and T. R. Huffman, *Solid-State Electron.*, **9**, 807 (1966).
7. J. C. Irvin, *Bell System Tech. J.*, **41**, 387 (1962).
8. G. H. Schwuttke, *J. Appl. Phys.*, **36**, 2712 (1965).
9. S. Prussin, *ibid.*, **32**, 1876 (1961).
10. W. C. Dash, *ibid.*, **27**, 1193 (1956).
11. G. H. Schwuttke, *This Journal*, **108**, 163 (1961).
12. J. E. Lawrence *ibid.*, **112**, 796 (1965).

Electrochemically Controlled Ion Exchange

I. Mechanism

S. Evans,* M. A. Accomazzo,* and J. E. Accomazzo

Rocketdyne, A Division of North American Rockwell Corporation, Canoga Park, California

ABSTRACT

The results of coulometric and mass balance analyses have been used to elucidate the mechanism of this demineralization process. Essentially, undissociated fixed groups (*e.g.*, weak acid or weak base) that are ionized as a result of the electrochemical reactions partake in an ion exchange process. The properties of weak acid and weak base ion exchange resins are incorporated into the electrodes. The simultaneous removal of anions and cations is undertaken in neutral solution. Regeneration of the electrodes is accomplished by polarity reversal.

The exchange of cations at chemically oxidized carbon electrodes that were coupled to Ag-AgCl electrodes has been previously discussed (1,2). Essentially weak acid groups that were present on the surface of the treated carbons were ionized as a result of electrochemical reactions, and took part in an ion exchange process.

The objective of this effort was to investigate the feasibility of electrochemically controlling ion exchange at electrodes that contained commercial weak acid and weak base, ion exchange resins, respectively.

Experimental

The mixtures used for electrode preparation were made by the addition of graphite, Norit, and ion exchange resin to a xylene solution of Kraton binder (Shell Chemical Co.). The cation-responsive mixture consisted of: 20% Kraton, 30% acid-treated Norit (1), 15% graphite, and 35% Amberlite CG-50 (weak acid, ion exchange resin). The anion-responsive mixture consisted of: 20% Kraton, 15% untreated Norit, 15% graphite, and 50% Amberlite CG-4B (weak base, ion exchange resin). Mixtures were painted onto one face of a graphite backing with an artist's paintbrush; the area covered by the mixture was 1.5 cm^2. Generally, five layers were applied; each layer was allowed to dry (about 1 hr) before subsequent painting.

The cell (Fig. 1) was a small glass vial in which the three electrodes were fixed in the positions shown.

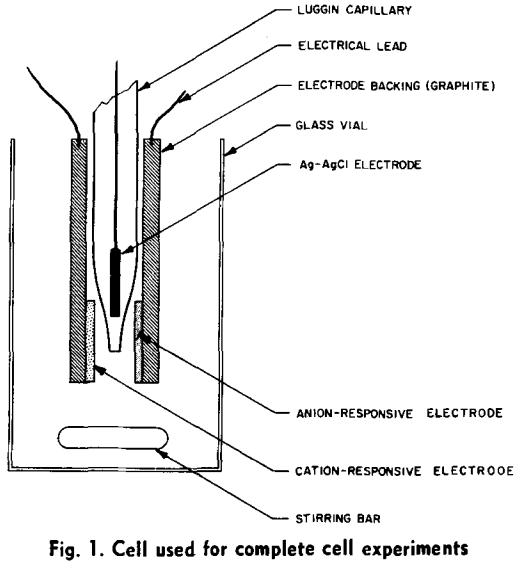

Fig. 1. Cell used for complete cell experiments

Key words: electrochemically controlled ion exchange, cation-responsive electrodes, anion-responsive electrodes, anion exchange studies, cation exchange studies.

* Electrochemical Society Active Member.

Table I. Complete cell studies
(Series D, Cell 10)

Run number	Coulombs	Cycle[a]	Efficiency, per cent Na+	Efficiency, per cent Cl-	pH	Na+ Equiv. × 10^4[b] Ads	Na+ Equiv. × 10^4[b] Des	Cl- Equiv. × 10^4[c] Ads	Cl- Equiv. × 10^4[c] Des
1[d]	3.6	D	106	108	7.5	0.40		0.40	
2	3.6	D	97	110	7.6	0.36		0.41	
3	3.6	D	83	119		0.31		0.44	
4	3.6	D	112	85		0.42		0.32	
5	3.6	R	94	100	6.8		0.35		0.37
6	3.6	R	87	73			0.32		0.27
7	3.6	R	91	83			0.32		0.31
8	3.6	R	88	52	8.2		0.33		0.19
9[e]	6.4	D	71	82		0.47		0.54	
10[e]	7.2	D	92	93	6.3	0.69		0.69	
11[e]	7.2	R	74	59	7.0		0.55		0.44

[a] D = demineralization, R = regeneration.
[b] Equivalents of Na+ adsorbed or desorbed on entire cation-responsive electrode.
[c] Equivalents of Cl- adsorbed or desorbed on entire anion-responsive electrode.
[d] Current: 1.0 ma; test solution analysis = 476 ppm Na+; 734 ppm Cl-; 1210 ppm NaCl.
[e] Current: 2.0 ma.

The potential at each of the ion-responsive electrodes was detected through a Luggin capillary which contained a silver wire coated with silver chloride. This Ag-AgCl electrode was in contact with the electrolyte (*e.g.*, 1200 ppm NaCl). The electronic instrumentation has been described previously (3).

All of the test solutions were analyzed for sodium with a Beckman DU Spectrophotometer with flame attachment, and were titrated potentiometrically for chloride ion. The solution *pH* was determined with a digital *pH* meter (E. H. Sargent and Co.).

Results and Discussion

Several hundred electrodes were prepared and evaluated. The tabulated results of representative experiments with one pair of electrodes are shown in Table I. Each run involved pipetting 10 cc of 1200 ppm NaCl solution into the vial which contained the electrodes (Fig. 1). After passage of a constant current through the cell, the solution was analyzed for sodium and chloride ions, and the *pH* was determined. The efficiency for each run was determined from the ratio of the measured change in sodium or chloride ion concentration to the change calculated by Faraday's law.

When current was passed such that the polarity of the cation-responsive electrode was negative, sodium and chloride ions were efficiently removed from the solution with little change in *pH* (demineralization cycles, Table I). Sodium and chloride ions were efficiently released to the solution during regeneration. Regeneration was accomplished by reversing the polarity.

Cation-responsive electrode potentials (Fig. 2) recorded during demineralization and regeneration showed some dependence on the sequence of cycles. Regeneration followed by demineralization (Fig. 2, Run 5) occurred at lower potentials than consecutive regeneration cycles (Run 6). Demineralization undertaken after regeneration occurred at lower potentials than consecutive demineralization cycles. This has been discussed previously (1, 2). Similar cyclical dependence was observed at the anion-responsive electrode.

The cell potential (total potential) recorded during demineralization and regeneration is shown in Fig. 3. The cyclical behavior of the individual electrodes is reflected in these curves. Most of the total cell potentials for demineralization and regeneration at 1.0 ma were less than 1.0v (Fig. 3). Increasing the current to 2.0 ma did not result in doubling the potential.

The processes occurring in complete cells are shown in Table II. During demineralization, the electrochemical reactions involve the generation of OH^- and H^+ at the cation- and anion-responsive electrodes, respectively. Demineralization (removal of NaCl) occurs to the extent that the generated OH^- and H^+ are utilized in the ionization of acidic and basic groups, respectively. The reactions occurring at the cation-responsive electrode have been elucidated (1,2) with the results of coulometric experiments wherein the cation-responsive electrode was coupled to an Ag-AgCl electrode (half-cell studies).

The rate of exchange of weak acid groups (or weak base) is dependent on the *pH* within the resin; the *pH* determines the ratio of ionized to un-ionized groups. In the electrochemical process, it is the localized *pH* generated at the electrode interface that

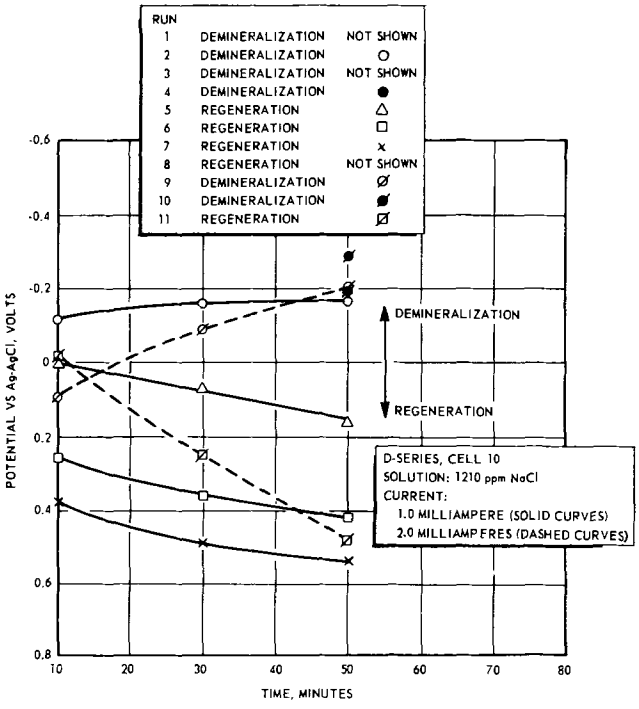

Fig. 2. Complete cell studies: cation-responsive electrode potentials recorded during demineralization and regeneration.

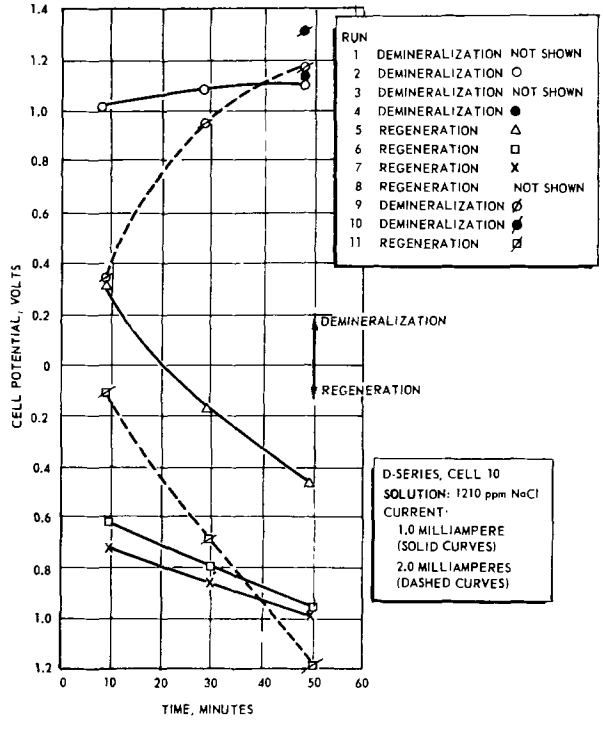

Fig. 3. Complete cell studies: total cell potentials recorded during demineralization and regeneration.

Table II. Representation of complete cell experiments

Cation-responsive-electrode (Cathode)	Demineralization	Anion-responsive electrode (Anode)
$H_2O + e^- \rightarrow H_{ADS} + OH^-$	Electrochemical	$H_2O - 2e^- \rightarrow O_{ADS} + 2H^+$ or $2H_2O - 4e^- \rightarrow O_2 + 4H^+$
$RCOOH + OH^- \rightarrow RCOO^- + H_2O$	Ionization	$RNH_3OH + H^+ \rightarrow RNH_3^+ + H_2O$
$RCOO^- + Na^+ \rightarrow RCOONa$	Exchange	$RNH_3^+ + Cl^- \rightarrow RNH_3Cl$
	Regeneration	
Cation-responsive-electrode (Anode)		Anion-responsive electrode (Cathode)
$H_{ADS} - e^- \rightarrow H^+$	Electrochemical	$H_2O + e^- \rightarrow H_{ADS} + OH^-$
$RCOONa + H^+ \rightarrow RCOOH + Na^+$	Exchange	$RNH_3Cl + OH^- \rightarrow RNH_3OH + Cl^-$

dictates the ratio of ionized and un-ionized groups. The ion exchange groups are in close proximity to this interface.

The polarity is reversed to achieve regeneration (Table II). The hydrogen which was adsorbed on the cation-responsive electrode during demineralization is oxidized during regeneration, resulting in the formation of a localized high concentration of hydrogen ions; the low pH results in regeneration of the spent form (1). Additionally, water is oxidized; the resulting low pH is favorable to regeneration. At the anion-responsive electrode, the OH^- formed results in a localized high pH that is favorable to regeneration. In accordance with the mechanism presented, there is no change in pH during efficient demineralization or regeneration.

The ion exchange capacities of electrodes have been evaluated chemically (2). During consecutive demineralization experiments, it has been possible electrochemically to achieve about 90% of the chemically determined value. The capacity of the electrodes evaluated was of the order of 2.0×10^{-4} equiv. of NaCl.

The electrochemical process is undertaken in neutral solution; negligible exchange was found to take place chemically at these electrodes in neutral solution. The anion- and cation-responsive electrodes are regenerated simultaneously; chemical regeneration must be undertaken with each electrode individually.

Acknowledgment

This work was supported by the Office of Saline Water, U. S. Department of the Interior, under Contract 14-01-0001-334.

Manuscript submitted July 1, 1968; revised manuscript received Oct. 11, 1968. This paper was presented at the Boston Meeting, May 5-9, 1968, as Paper 229.

Any discussion of this paper will appear in a Discussion Section to be published in the December 1969 JOURNAL.

REFERENCES

1. S. Evans and W. S. Hamilton, *This Journal*, **113**, 1314 (1966).
2. S. Evans, W. S. Hamilton, and J. E. Lewis, *Electrochem. Technol.*, **6**, 153 (1968).
3. S. Evans, *This Journal*, **113**, 165 (1966).

Electrochemically Controlled Ion Exchange

II. Transport Processes

M. A. Accomazzo* and S. Evans*

Rocketdyne, A Division of North American Rockwell Corporation, Canoga Park, California

ABSTRACT

At present, the highest current density that has resulted in the efficient removal of ions is approximately 1.5 ma/cm^2. Chemical ion exchange rates were determined at ion exchange sheets prepared in a manner similar to electrode fabrication. It was concluded that transport through the binder limited the rate of exchange. A simple model was used to predict the critical current density for the process.

The mechanism and feasibility of the electrochemically controlled ion exchange process has been previously discussed (1-3). Essentially, undissociated fixed groups (*e.g.*, weak acid or weak base) that are ionized as a result of the electrochemical reactions partake in an ion exchange process. The properties of weak-acid and weak-base ion exchange resins are incorporated into the electrodes. The anion-responsive electrode (ARE) consists of a weak base ion exchange resin, carbons, and a binder. The cation-responsive electrode (CRE) contains a weak acid ion exchange resin, carbons, and a binder.

During demineralization (ARE is made positive), acid is generated electrochemically at the ARE.

$$H_2O - 2e^- = 2H^+ + O_{ADS} \qquad [1]$$

Key words: electrochemically controlled ion exchange, cation-responsive electrodes, anion-responsive electrodes, anion exchange studies, cation exchange studies, ion exchange kinetics.

* Electrochemical Society Active Member.

The resulting low pH, localized in the vicinity of the weak-base ion exchange resin favors exchange.

$$\frac{RNH_3OH}{resin} + HCl = \frac{RNH_3Cl}{resin} + H_2O \qquad [2]$$

The electrochemical generation of base at the CRE

$$H_2O + e^- = OH^- + H_{ADS} \qquad [3]$$

results in a localized high pH which favors ion exchange at the weak-acid ion exchange resin.

$$\frac{RCOOH}{resin} + NaOH = \frac{RCOONa}{resin} + H_2O \qquad [4]$$

Polarity reversal results in regeneration of the anion and cation resin to the free base and acid form, respectively.

At present, the highest current density that has resulted in the efficient removal of ions is approximately 1.5 ma/cm^2. A current density of 15 ma/cm^2 has been passed between the electrodes, but the resulting current efficiency for ion removal was low. Under these conditions, the acid and base produced at the electrodes was being released to the solution; interaction between acid and base and the ion exchange resins was thus obviated. Hence, at present, it appears that the current density for this process is being limited by the ion exchange kinetics of the electrodes.

Ion Exchange Kinetics

Although theories of ion exchange kinetics are still being developed, a recent paper by Helfferich (4) is helpful in describing the ion exchange kinetics that could be expected at the electrodes.

During demineralization, the ion exchange reactions at the electrodes are given by Eq. [2] and [4]. It has been long known that ion exchange kinetics is controlled by diffusion. Two types of diffusion control are considered; namely, film diffusion and particle diffusion.

Film Diffusion

Film diffusion, which occurs in the solution, is the mechanism by which ions are transported to the ion exchange surface. In the preceding reactions, NaOH and HCl must diffuse to the weak-acid and weak-base resin surfaces, respectively. Film diffusion control is well understood. If an ion exchanger of surface area A is placed in a solution of volume V with an initial concentration C_o, the concentration of the solution, C, as a function of time is given as

$$C = C_o\, e^{-ADt/V\delta} \qquad [5]$$

Particle Diffusion

Particle diffusion is the mechanism by which ions are transported in the resin phase. Particle diffusion in strong-acid and strong-base ion exchangers is very rapid (4). Consequently, at low concentrations the ion exchange process at strong ion exchangers would be under film diffusion control. Weak-acid and weak-base ion exchange kinetics, however, can be many orders of magnitude lower (than strong). This results from the fact that most of the fixed ionogenic groups are undissociated. The concentration of mobile ions is therefore low; this results in slowing the diffusion process greatly. If the solution in contact with the resin can cause ionization (*e.g.*, Eq. [4], weak-acid resin in contact with NaOH), the limiting kinetics are controlled by the particle diffusion of the co-ion, namely OH^-. This is quite an unusual situation in ion exchange kinetics; the rate of ion exchange would be dependent on the solution concentration of the co-ion. Analytical expressions have been developed for the rate of reaction of weak-acid and weak-base ion exchangers (4). For a slab of thickness x_o placed in an infinite volume of solution at concentration C_A^o, the fractional attainment of equilibrium is given by

$$F = \left(\frac{2\,\overline{D}_A\,\overline{C}_A^o\,t}{x_o^2\,\overline{C}} \right)^{1/2} \qquad [6]$$

For a limited volume of solution, V, the surface concentration would decrease with time. This would result in slowing the diffusion rate. Under these conditions, the fractional attainment of equilibrium can be represented by

$$F = \frac{x}{x_o} \qquad [7]$$

where x is related to time by the following expression

$$t = \frac{V^2}{\overline{D}_A\,\overline{C}\,A^2} \left[\overline{C}_A^o \ln \frac{\overline{C}_A^o}{\overline{C}_A^o - A\overline{C}x/V} - \frac{A\overline{C}x}{V} \right] \qquad [8]$$

The expression for time, t, obtained when the logarithm is expanded is

$$t = \frac{\overline{C}x^2}{\overline{C}_A^o\,\overline{D}_A} [1/2 + 1/3\,yx + 1/4\,(yx)^2 + 1/5(yx)^3 + \ldots] \qquad [9]$$

where

$$y = \frac{A}{V}\frac{\overline{C}}{\overline{C}_A^o} \qquad [10]$$

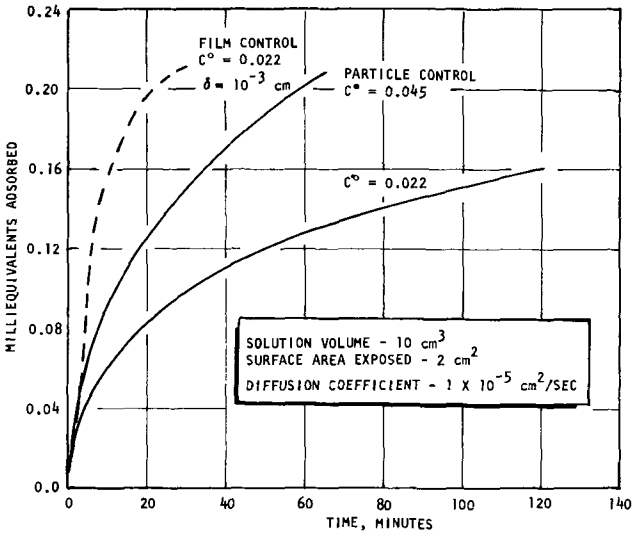

Fig. 1. Theoretical rate of ion exchange assuming particle or film diffusion control.

Figure 1 is a plot of Eq. [9] for two different initial concentrations. The concentrations chosen (C^o) were those described. The capacity value ($\overline{C}$), represents an experimentally determined capacity for the coupons. The best possible diffusion coefficient was assumed. Also shown is the rate of ion uptake for coupons under film diffusion control with adequate agitation.

Experimental

Chemical ion exchange rates were determined at ion exchange sheets prepared in a manner similar to electrode fabrication (3). Ion exchange resin in fine powder form was mixed with a binder (46% Kraton 101, 46% Nujol, 8% Piccotex) that was initially dissolved in xylene. The solution was then poured onto glass and the xylene was allowed to evaporate. The remaining sheet (approximately 1 mm thick) was peeled from the glass and cut into 1 cm squares. The resulting coupons were spent and regenerated before being used in kinetic studies.

Ion uptake as a function of ion exchange resin, solution concentrations, and time was determined by placing the coupon in 10 cc of solution for a given length of time. Depending on the resin used, the solution was analyzed for change in sodium or chloride ion concentration, using a Beckman DU Spectrophotometer with flame attachment or by potentiometric titration, respectively.

Results and Discussion

Weak-base ion exchange.—Coupons containing a weak-base resin in the hydroxide form (Amberlite CG-4B) were studied in 10 cc of HCl test solution (two concentrations). The results presented in Fig. 2 clearly indicate particle diffusion control. In fact, the data closely follow the curves predicted from the theoretical model (Fig. 1).

Similar tests were conducted with the weak-base resin in the chloride form and a test solution of Na_2SO_4 (two concentrations). According to theory, the rate of ion uptake should be under film diffusion control. However, the data in Fig. 2 clearly show particle diffusion control.

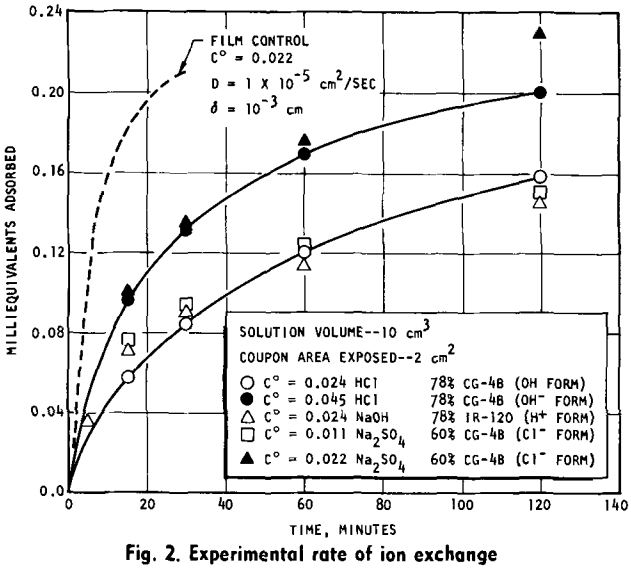

Fig. 2. Experimental rate of ion exchange

Strong-acid ion exchange.—Coupons containing a strong-acid resin in the hydrogen form (Amberlite IR-120) were studied in 10 cc of NaOH test solution. At the concentration used (0.024*N*), the coupons' kinetics should be under film diffusion control. However, again the data shown in Fig. 2 indicate particle diffusion control.

Critical current density.—The results of the chemical rate studies clearly indicate that ion exchange kinetics at sheets prepared in a manner similar to electrode fabrication is severely limited. Apparently, the method of preparation causes the ion exchange particles to be separated or coated by the binder system. Hence, it is the diffusion through the binder which controls the rate of ion uptake. Since the ionic concentration between the particles is low, the diffusion process is slow.

Now consider an electrode (CRE) placed in an NaCl solution (Fig. 3). Inside the electrode, OH^- ions are being produced electrochemically at carbon sites according to Eq. [3]. For 100% demineralization efficiency, based on Faraday's Law, the OH^- ion must be involved in ion exchange by Eq. [4]. This means that current must be carried across the electrode-solution interface solely by the transport of Na^+ and Cl^- ions; if OH^- does aid in current transport across the interface, good efficiencies cannot be obtained. Hence, it is the transport of NaCl inside the electrode that limits the rate of the process because it is at a low concentration (~0.02*N*). However, that portion of the electrode that has been converted to the Na^+ form contains a high concentration (~2*N*) of mobile sodium ions. If the ion exchange resin beads were in contact with each other, this would provide a path for rapid transport of sodium ions. However, the chemical rate studies previously described clearly indicated that the ion exchange particles were separated.

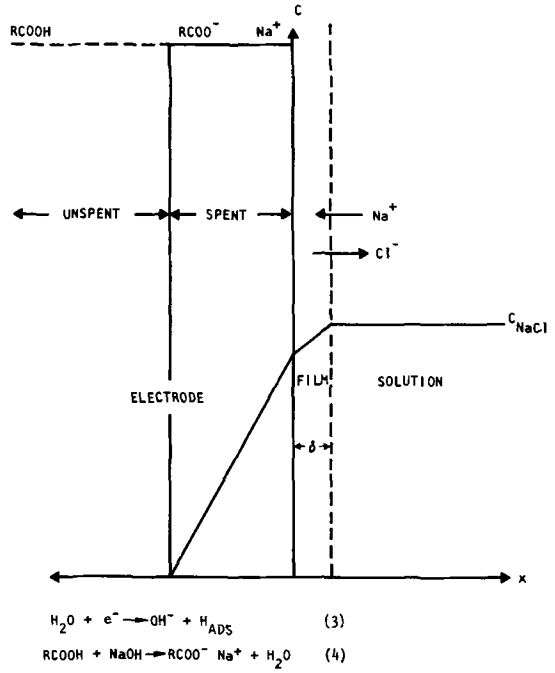

Fig. 3. Concentration profile at cation-responsive electrode

With the above considerations in mind and realizing that the application of a homogeneous model for an electrode is a poor assumption and only a first approach, one can write the usual critical current density expression

$$(I/A)_{crit} = \frac{\mathbf{F}D\bar{C}_s}{x(1-t^*)} \qquad [11]$$

The above equation shows that the critical current density is directly proportional to the surface concentration of the transported ion and inversely proportional to the depth of penetration. For a reasonable depth of 0.25 mm, a transport number of 0.5, a diffusion coefficient of 1 x 10^{-5} cm^2/sec, and a surface concentration of 0.02*N*, one obtains a critical current density of 1.5 ma/cm^2. This is in agreement with previous experimental results (1-3). However, if one could utilize the mobile ions in the ion exchange resin which are at a concentration of approximately 2*N*, one would calculate a critical current density of 150 ma/cm^2. Of course, solution transport would now limit the current density.

Research is now focused on methods of electrode fabrication which will allow rapid transport in the resin phase to occur.

SYMBOLS

F	fractional uptake by resin
x_o	slab thickness, cm
t	time, seconds
$\bar{C}_A^o$	concentration of co-ion at ion exchanger surface, equiv./liter
$\bar{C}$	concentration of fixed ionogenic groups, equiv./liter (capacity), 4.5
$\bar{D}_A$	diffusion coefficient of co-ion in ion exchanger, cm^2/sec
δ	effective film thickness, cm
C	solution concentration, equiv./liter
C_o	initial solution concentration, equiv./liter
V	solution volume, cm^3
D	diffusion coefficient, cm^2/sec
A	surface area exposed to solution, cm^2
x	thickness of slab converted from molecular form to ionic form, cm
t^*	transport number
I	current, milliamperes
$\mathbf{F}$	Faraday's constant
$\bar{C}_S$	concentration at ion exchange surface, equiv./liter

Acknowledgment

This work was supported by the Office of Saline Water, U. S. Department of the Interior, under Contract 14-01-001-1316.

The authors are grateful to Mrs. J. E. Accomazzo and Mr. K. A. Lossett for their assistance in this study.

Manuscript submitted July 1, 1968; revised manuscript received Oct. 11, 1968. This paper was presented at the Boston Meeting, May 5-9, 1968, as Paper 238.

Any discussion of this paper will appear in a Discussion Section to be published in the December 1969 JOURNAL.

REFERENCES

1. S. Evans and W. S. Hamilton, *This Journal*, **113**, 1314 (1966).
2. S. Evans, W. S. Hamilton, and J. E. Lewis, *Electrochem. Technol.*, **6**, 153 (1968).
3. S. Evans, M. A. Accomazzo, and J. E. Accomazzo, *This Journal*, **116**, 307 (1969).
4. F. Helfferich, *J. Phys. Chem.*, **69**, 1178 (1965).

Technical Notes

Stability of the Solid State Cell $Ag/Ag_3SI/I_2$

Boone Owens,*,[2] G. R. Argue,*,[1] I. J. Groce,[2] and L. D. Hermo[2]

Atomics International, A Division of North American Rockwell Corporation, Canoga Park, California

In the past, there has been a fluctuating interest in solid state batteries (1). The interest waned primarily because of lack of any high-conductivity solid electrolyte. A material that was frequently utilized as a solid electrolyte was AgI; the highest specific conductivity reported for compressed powdered AgI was nominally 10^{-4} (ohm-cm)$^{-1}$ at 25°C (2, 3). The compound Ag_3SI was reported to have an ionic conductivity of 10^{-2} (ohm-cm)$^{-1}$ at 25°C (4). Because of the high ionic conductivity of this material, it appeared attractive as a solid state electrolyte, and Takahashi and Yamamoto (5-8) have extensively investigated cells of the type $Ag/Ag_3SI/I_2$.

The present investigation was carried out to determine the feasibility of developing a solid state battery, utilizing the electrolyte Ag_3SI, that could be operated at elevated temperatures. However, the system was found to exhibit a considerable amount of instability at the elevated temperatures. This note reports the degradation of the electrolyte by the cathode according to the reaction

$$I_2(g) + Ag_3SI(s) \rightarrow 3\,AgI(s) + S(s) \qquad [1]$$

Reaction [1] has not been reported in the papers on the $Ag/Ag_3SI/I_2$ solid-electrolyte cell.

Experimental

Reagent-grade or 98% pure materials were used in these experiments. The Ag_3SI was prepared by the combination of AgI and Ag_2S, following Takahashi's procedure (7).

Cells of the type $Ag/Ag_3SI/X$, where X represents the electroactive cathode material, were fabricated in the configuration reported by Takahashi and Yamamoto (7). In addition to I_2 cathodes, a number of other materials, including $CuBr_2$, V_2O_5, S, NiO_2, and MnO_2, were also investigated.

The reactivity of Ag_3SI with I_2 gas was determined by measuring the change in weight of powdered samples of Ag_3SI after these solid samples had been exposed to controlled atmospheres of Ar, equilibrated with I_2 at pressures of 0.18 Torr (65°C) or 8.2 Torr (70°C). The iodine pressures were maintained at the indicated values by having present in the reaction vessel excess solid I_2 at T = 70°C or a mixture of RbI and RbI_3 at T = 65°C. Vapor pressures of I_2 were calculated from literature data (9, 10). A sample of Ag_2S was also run for comparative purposes.

Results and Discussion

Table I shows initial open-circuit voltages observed for the cathode systems investigated. Cell voltages were obtained as a function of temperature for the resultant electrochemical couples. All of the solid state cells underwent an irreversible loss in voltage at elevated temperatures (100°-400°). This property of the cells suggested that the chemical components were not compatible and therefore the stability of the electrolyte to I_2 was investigated.

The results of the weight gain experiments are given in Table II. It was assumed that the weight changes were due to the addition of I_2 to the samples and that no volatile products were formed. All of the samples gained weight, and in an amount consistent with 1 mole of I_2 per mole of solid reactant. The data are in agreement with Eq. [1] for Ag_3SI and with the reaction

$$I_2(g) + Ag_2S(s) \rightarrow 2AgI(s) + S(s) \qquad [2]$$

for the Ag_2S. The powder patterns of the products confirmed that AgI and S were formed and no significant difference (other than relative intensities) was detected in the x-ray patterns of the products of the two reactions.

No thermodynamic data have been reported in the literature for Ag_3SI and, consequently, the free energy change for reaction [1] is not known. However, reaction [2] has a standard free energy change of −22 kcal at 25°C (for solid components). Therefore, unless the reaction

$$AgI + Ag_2S \rightarrow Ag_3SI \qquad [3]$$

has a free energy change more negative than −22 kcal, reaction [1] would be expected to be thermodynamically favored.

The results show that reaction [1] readily occurs. In view of this instability of Ag_3SI in the presence of I_2 vapor, it is necessary to re-evaluate the usefulness of this material as a solid state battery electrolyte, and to reconsider the results of Takahashi's investigations. In the cells that Takahashi fabricated, the iodine was present in the cathode as crystalline I_2 rather than any complex with reduced activity, and the observed cell emf was 675 mv at 20°C, slightly below the calculated $Ag-I_2$ potential of 687 mv. In addition, it was reported that the emf was unchanged by storage of

Table I. Cathodes for the $Ag/Ag_3SI/X$ solid state cells

Cathode (X)	Measured voltages at 25°C[a]
	v
V_2O_5 + C + Ag_3SI	0.46
$CuBr_2$ + C + Ag_3SI	0.73
I_2 + C + Ag_3SI	0.68
S + Na_2S + MoS_2 + Ag_3SI	0.22

[a] All voltages decreased to at least 0.2v after exposure to elevated temperatures.

Table II. Reaction of I_2 with Ag_2S and Ag_3SI

Reaction time (hr)	Weight gain (moles of I_2 per mole of sample)		
	Ag_3SI at 65°C I_2 pressure = 0.18 Torr	Ag_3SI at 70°C I_2 pressure = 8.2 Torr	Ag_2S at 70°C I_2 pressure = 8.2 Torr
0	0	0	0
14	—	0.50	0.78
20	—	0.72	0.87
107	—	0.93	0.95
432	0.94	—	—

* Electrochemical Society Active Member.
[1] Present address: General Telephone and Electronics Laboratories, Inc., Bayside, New York.
[2] Present address: Gould Ionics Inc., Canoga Park, California.
Key words: battery, decomposition, electrolyte, iodide, iodine, silver, solid, sulfide, sulfur, thermodynamic.

the cells for over 1 yr. This would infer that elemental I_2 is in stable contact with the Ag_3SI electrolyte layer.

Based on the results of the present investigation, it seems unlikely that a cell $Ag/Ag_3SI/I_2$ would be stable unless some means of preventing the I_2-Ag_3SI reaction were in effect. Upon fabrication of the indicated cell, degradation of the Ag_3SI at the electrolyte-cathode interface should occur according to reaction [1]. The product of this degradation is predominately AgI which can function as a Ag^+ conducting solid electrolyte. However, the internal resistance of such a cell should increase as the electrolyte-cathode reaction occurs. If the products of the electrolyte-cathode reaction form in a sufficiently dense layer, impermeable to I_2, then the resulting cell

$$Ag/Ag_3SI/AgI, S/I_2,C$$

could function in the manner observed by Takahashi. The cell is now essentially a

$$Ag/AgI/I_2$$

cell with the electrolyte phase now consisting of a bilayer of Ag_3SI and AgI-S.

An alternate method in which the bilayer electrolyte could be fabricated *in situ* would be to discharge the cell immediately upon its fabrication. The cell reaction product AgI would then form at the electrolyte-cathode interface, without the concurrent formation of the S.

It therefore appears that, although the compound Ag_3SI has a high ionic conductivity, its application to solid electrolyte cells involving the combination

$$Ag + \tfrac{1}{2} I_2 \rightarrow AgI$$

is quite limited. In this type of cell, the effective electrolyte must be AgI rather than Ag_3SI. Lower emf cells such as

$$Ag/Ag_3SI/S$$

would be thermodynamically stable. However, they would have the disadvantages of low emf, low power density, and possibly kinetic restrictions in the current densities that could be attained.

Acknowledgments

The authors wish to thank Drs. James E. Oxley, Leo E. Topol, and Samuel Yosim for helpful discussions during the course of this investigation.

Manuscript received Aug. 7, 1968. This paper was presented in part at the 153rd ACS Meeting, April 1967.

Any discussion of this paper will appear in a Discussion Section to be published in the December 1969 JOURNAL.

REFERENCES

1. J. N. Mrgudich, "Solid Electrolyte Batteries" in "The Encyclopedia of Electrochemistry," Ed. by C. A. Hampel, p. 84, Reinhold Publishing Corp., New York (1964).
2. J. N. Mrgudich, *This Journal*, **107**, 475 (1960).
3. J. N. Mrgudich, P. J. Bramhall, and J. J. Finnegan, "IEEE Transactions on Aerospace and Electronic Systems," Vol. AES-1, No. 3, p. 290 (1965).
4. B. Reuter and K. Hardel, *Naturwissenschaften*, **48**, 161 (1961).
5. T. Takahashi and O. Yamamoto, *Denki Kagaku*, **32**, 610 (1964).
6. T. Takahashi and O. Yamamoto, *ibid.*, **33**, 346 (1965).
7. T. Takahashi and O. Yamamoto, *Electrochim. Acta*, **11**, 779 (1966).
8. T. Takahashi and O. Yamamoto, *ibid.*, **11**, 911 (1966).
9. L. E. Topol, *Inorg. Chem.*, **7**, 451 (1968).
10. H. T. Gerry and L. J. Gillespie, *Phys. Rev.*, **40**, 269 (1932).

Improved Methods for Deposition of Thin-Film Zn_2SiO_4:Mn Phosphors

George M. di Giacomo

Westinghouse Defense and Space Center, Aerospace Division, Baltimore, Maryland

In this paper, two methods are described for the deposition of Zn_2SiO_4:Mn in a polycrystalline thin-film form: (*a*) vapor phase reaction; (*b*) vacuum evaporation. Vapor phase reaction is a chemical process in which the reactant is transported as a compound to the sample surface. The resultant product is then obtained by thermal decomposition and hydrogen reduction by maintaining the sample surface at a higher temperature than the source of reactant vapors (1).

In the vapor reaction process, the halides of the constituent materials were used to form zinc orthosilicate by the following reaction:

$$SiCl_4 + 2\,ZnCl_2 + 4\,CO_2 + 4\,H_2 = Zn_2SiO_4 + 8\,HCl + 4\,CO$$

Manganese was added in the form of $MnCl_2$ as a dopant.

A metered flow of 50 cc/min CO_2 and 40 cc/min H_2 was bubbled through a room-temperature bath of $SiCl_4$. The evaporation rate of $SiCl_4$ was controlled by diverting some of this gas flow around the liquid. The small part of the gas bubbled through the $SiCl_4$ bath carried 1-2 ml of liquid into the reaction.

Mixing with the solid constituents and the deposition took place in a two-zone reaction furnace lined with a quartz tube. The solid constituents, 3g $ZnCl_2$ and 0.1g $MnCl_2$, were placed in a crucible in the first zone, the mixing zone. These solids were vaporized by heating this zone at 550°-600°C. An orifice at the end of this zone caused turbulence in the flow and resulted in mixing of constituents before they entered the reaction zone.

In the reaction zone, the substrates were held on a large flat quartz plate to insure even heat distribution. This section was heated to 1100°-1200°C. By-product gases were exhausted.

The substrates used were quartz, sapphire, and silicon wafers with an oxide thickness of 1μ.

The second method of depositing $ZnSiO_4$:Mn phosphor material in a thin-film form involves the vacuum evaporation technique developed by Feldman (2). This is a two-step process. First, a commercial Zn_2SiO_4:Mn phosphor is evaporated onto a substrate. During the evaporation, the phosphor decomposes into its more stable molecular components and condenses on the substrate as a film composed of a mixture of these materials. The second step then involves the recombination of these components into the crystalline phosphor on the substrate by firing the layer in air. The problem encountered using this method was that it was difficult to cover a given substrate with an even film. It seemed to be a matter of chance whether a smooth, even film condensed as various cleaning techniques and substrate conditions were used. In order to increase the

affinity between the evaporated material and the substrate, a seeding technique was developed. The substrate was first coated with a film of ZnO of about 200-300Å thickness. The method used to deposit the ZnO was first to "nucleate" the substrate with a few seconds' exposure to evaporating Ag. Over this, metallic zinc was evaporated to a thickness of about 200-300Å. The seeding with silver promotes a smooth, even film of Zn. The Zn-coated substrate was then removed from the vacuum and placed in an air or O_2 atmosphere furnace at 200°C in order to oxidize the Zn film completely. After the process, the conventional evaporation and baking process described by Feldman (2) was used to develop the zinc orthosilicate film.

Films resulting from both these techniques luminesced green under 2537Å u.v. and glow discharge bombardment excitation. When compared to powder Zn_2SiO_4:Mn excited by the same technique, the best films were from ¼ to ½ as bright as the powder. The thicknesses of the layers were from 0.2 to 0.5μ. Thicker films could have been deposited. The quality of the film varied from foggy to clear. The best clear films were highly transparent (est 75%) but not as bright as some of the foggy films.

The advantage of using the vapor deposition technique was that the film could be deposited on different substrate shapes such as a cylinder of curved surface. This technique could also be used where a vacuum chamber is not available. The advantage of the vacuum evaporation techniques was that a smooth, even film of this difficult-to-deposit material was condensed with much greater regularity.

Manuscript submitted Oct. 5, 1966; revised manuscript received Oct. 18, 1968.

Any discussion of this paper will appear in a Discussion Section to be published in the December 1969 JOURNAL.

REFERENCES

1. C. F. Powell, I. E. Campbell, and B. W. Gonser, "Vapor Plating," John Wiley & Sons, Inc., New York (1955).
2. C. Feldman and M. O'Hara, *J. Opt. Soc. Am.*, **47**, 300 (1957).

Dependence of the Composition of the Anodic Layer on the Oxidation Potential of Lead in Sulfuric Acid

D. Pavlov, C. N. Poulieff, E. Klaja, and N. Iordanov

Institute of Physical Chemistry, Bulgarian Academy of Sciences, Sofia, Bulgaria

ABSTRACT

Potentiostatic oxidations of lead in 1*N* H_2SO_4 were performed in the potential range between −900 and +1400 mv (with respect to the mercury/mercury sulfate electrode). The anodic layer was subjected to x-ray diffraction and chemical analysis. According to the phases present three potential ranges are discerned. From −956 to about −300 mv only $PbSO_4$ is present. From −300 to +900 mv large amounts of $PbSO_4$ and PbO-tet are formed, as well as small amounts of $PbO \cdot PbSO_4$, $3PbO \cdot PbSO_4 \cdot H_2O$, $5PbO \cdot 2H_2O$ or PbO orthorhombic and α-PbO_2. Above +900 mv the divalent lead compound content decreases, while that of α-PbO_2 rapidly increases. Above +1200 mv β-PbO_2 is formed.

Many of the processes taking place during anodic oxidation of lead in sulfuric acid can be elucidated by identifying the compounds which constitute the anodic layer.

X-ray and electron diffraction methods (1-4) as well as electrochemical techniques (5-9) have been used for the identification of the phases occurring in the anodic layer. In the potential range between the equilibrium potentials of the $Pb/PbSO_4$ and $PbSO_4/PbO_2$ electrodes diffraction lines of tetragonal PbO were found by Lander (1) and Burbank (2). Lander explained the formation of this compound in terms of solid-state reactions between lead and lead dioxide. Later, Rüetschi and Cahan (3) found lines of α-PbO_2 in the anodic layer. The coincidence of diagnostic diffraction lines of alpha lead dioxide with those of tetragonal lead oxide caused some workers to deny the formation of tetragonal lead oxide (3, 7).

If diffraction methods alone are used the identification of the individual phases is ambiguous owing to the overlapping of numerous diagnostic reflections, brought about by close similarities in the crystal structures of the various lead oxides and hydroxides.

In two previous papers (8, 9) one of us studied the behavior of the $Pb/PbSO_4$ electrode in H_2SO_4 upon anodic polarization. It was established that it behaves first as a lead sulfate electrode, then, over a large interval, as a lead oxide one, and, lastly, at very high polarizations, as a lead dioxide electrode. However, the potentiometric identification of the compounds formed (8, 9) is also somewhat uncertain because of the very close values of the equilibrium potentials of lead oxides, hydroxides, and basic sulfates. Furthermore, not every compound present in the anodic layer is potential determining at open circuit.

These difficulties in the identification of the phases of the anodic layer inherent in the diffraction and electrochemical methods led to differences in the model of the structure of the anodic layer (4, 6).

The purpose of the present paper is to study the changes in the phase composition of the anodic layer at different oxidation potentials of the lead electrode in H_2SO_4. In the present investigation the x-ray analysis and electrochemical techniques were supplemented by appropriate chemical determinations which make it possible to eliminate the ambiguities resulting from the limitations of these techniques.

Results and Discussion

Electrochemical measurements.—High-purity 99.9999% lead electrodes with dimensions 16 x 11 x 1 mm were subjected to oxidation in electrolytically purified, analytical-grade 1*N* H_2SO_4. The oxidation was performed by means of an electronic potentiostat in the cell described in previous works (8, 9). The mercury/mercury sulfate electrode was used as reference. All potentials are given with respect to this electrode. Between −900 and +900 mv the oxidation was carried out during 72 hr, while above +900 mv the oxidation time was only 24 hr. After each oxidation run the quantity of electricity was determined graphically from the i/t curves. Figure 1 gives the calculated quantities of electricity at the various potentials. The steep rise of the curve above +1300 mv must be ascribed to oxygen evolution reaction proceeding parallel to the oxidation of the metal.

The potential change of the electrode was recorded during several minutes after the interruption of the polarization in order to study the electrochemical behavior of the anodic deposit. The results of these measurements are shown in Fig. 2. The equilibrium potentials of the tetragonal lead oxide (PbO-tet) and normal lead sulfate electrodes in 1*N* H_2SO_4 are also shown in the figure. Three regions of behavior can be discerned on the potential/time curves: lead sulfate, lead oxide, and lead dioxide (8, 9).

X-ray diffraction studies.—After performing the electrochemical measurements the electrodes were washed, dried, and introduced in the sample holder of the Müller-Mikro 111 diffractometer. The diffraction patterns were recorded with filtered copper radiation and the following goniometer settings: goniometer speed $2°2\theta$/min, and slits 1°/1°/0.1 mm. The intensity of the strongest line of each pattern was taken as 100. The diffractometer traces were measured down to $d = 1.60$Å.

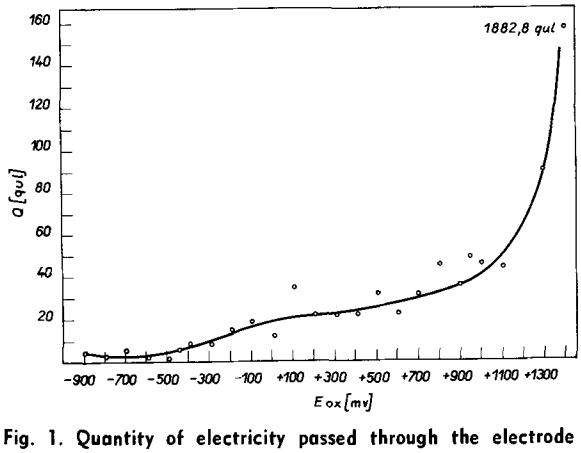

Fig. 1. Quantity of electricity passed through the electrode at different oxidation potentials.

Key words: x-ray diffraction, lead oxide, lead sulfate, anodic oxidation of lead.

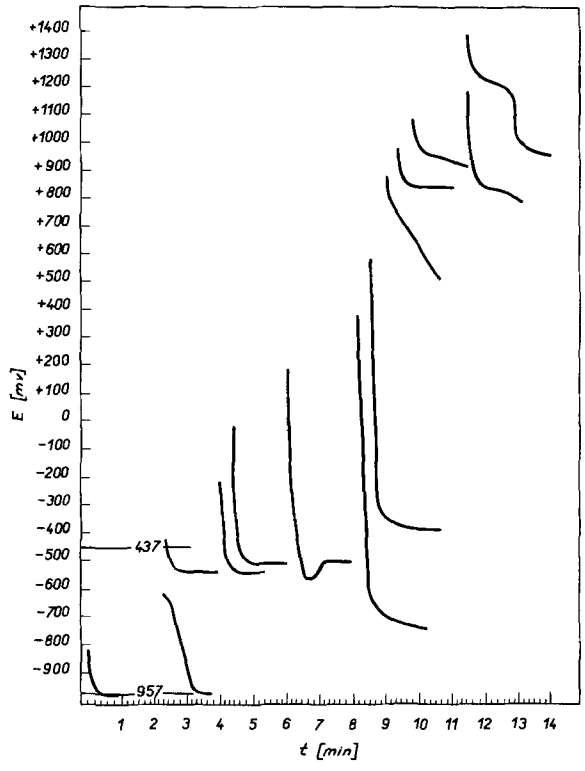

Fig. 2. Change of the electrode potentials with time on open circuit: E = —437 mv, PbO-tet/Pb; E = —957 mv, $PbSO_4$/Pb.

The following method was adopted in order to insure an unambiguous assignment of each diffraction line. For each diffraction line the dependence of the relative intensity (I) of each reflection was plotted against the oxidation potential (E); that is, it was referred to a non-x-ray parameter. Thus each diffraction line was assigned to a particular compound both on the basis of its interplanar spacing and of the shape of its I/E curve. The diffraction lines were then separated into groups having an identical or closely resembling shape of the I/E curves over the whole potential range. This was done under the assumption that normally the relationships between the intensities of the diffraction lines of the various compounds are preserved in mixtures. Therefore, the resemblance in the curve I/E should indicate that they belong to the same compound. Differences in the I/E curve of a given reflection can be due either to texture effects or to coincidences with reflections belonging to other compounds. The appearance of new lines in the x-ray diffraction patterns or a drastic change in the I/E curve are brought about by the formation of additional phases in the anodic deposit at some oxidation potentials.

The diffraction patterns of the electrodes contained all lines belonging to $PbSO_4$ and to lead from 4.24 to 1.60Å (16). The I/E curve for $PbSO_4$ is illustrated in Fig. 3 by the diffraction line with d = 3.00Å.

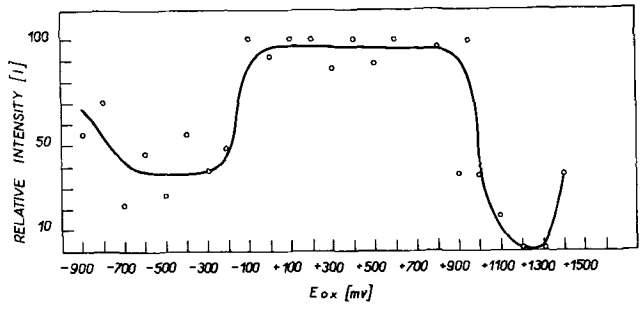

Fig. 3. Intensity of the d = 3.00Å reflection of $PbSO_4$ at different oxidation potentials.

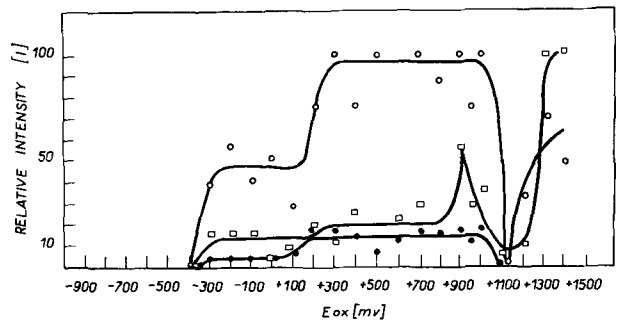

Fig. 4. Intensity of the diffraction lines, □ d = 3.12Å, ○ d = 2.80Å, ● d = 1.67Å, at different oxidation potentials.

In the diffraction patterns of electrodes anodized at potentials more positive than —300 mv additional strong lines were recorded with interplanar spacings 3.49, 3.12, 2.80, 2.12, 1.85, and 1.67Å. The relative intensity changes of the 3.12, 2.80, and 1.67Å lines are given in Fig. 4, while the potentials at which the remaining lines occur are given in Table I. The line with d = 3.12Å is notably broadened. It coincides with the strongest reflections in the x-ray patterns of α-PbO_2 (10) and of tetragonal PbO (11). On the other hand, both PbO-tet and β-PbO_2 show reflections with d = 2.80Å, the relative intensity being 62 for the former and 100 for the latter. The coincidences between these diffraction lines have been the cause of the discussion which has originated during the last years concerning the formation of PbO-tet. This problem can be unambiguously solved only by applying additional non-x-ray identification techniques. Alpha- and β-PbO_2 are both strong oxidizing agents, while PbO-tet possesses no oxidizing properties. We made use of this difference in behavior of the above compounds in order to assign the diffraction lines with d = 3.12 and 2.80Å. After recording the x-ray pattern the anodic deposit was removed from the surface of the electrode. The powder thus obtained and the electrode were placed in an iodine determination flask and the amount of lead dioxide was determined iodometrically, using the method described by Diehl and Toph (12). These determinations were duplicated on a sec-

Table I.

d = 3.49 β-PbO_2 (9)		d = 2.13 PbO-tet (10)		d = 1.85 α- and β-PbO_2 (9)	
E_{mv}	I	E_{mv}	I	E_{mv}	I
+1200	19	−300	2	+500	3
+1300	45	−100	4	+1200	11
+1400	52	0	3	+1300	46
		+100	3	+1400	39
		+200	6		
		+300	3		
		+400	5		
		+500	4		
		+600	3		
		+950	4		
		+1000	2		

Table II.

d = 3.25 $3PbO \cdot PbSO_4 \cdot H_2O$ I = 100 (14)		d = 3.06 $5PbO \cdot 2H_2O$ PbO-orth.	I = 70 (15) I = 100 (11)	d = 2.95 $PbO \cdot PbSO_4$ I = 100 (16)	
E_{mv}	I	E_{mv}	I	E_{mv}	I
−200	6	0	4	−400	1
−100	3	+100	6 (B)	−300	6
+100	6	+300	10	−200	7
+200	8	+500	5	−100	10
+300	7	+700	9	0	5
+400	3	+800	6	+100	5
+600	6			+200	6
+700	7			+300	5
				+600	2
				+700	5

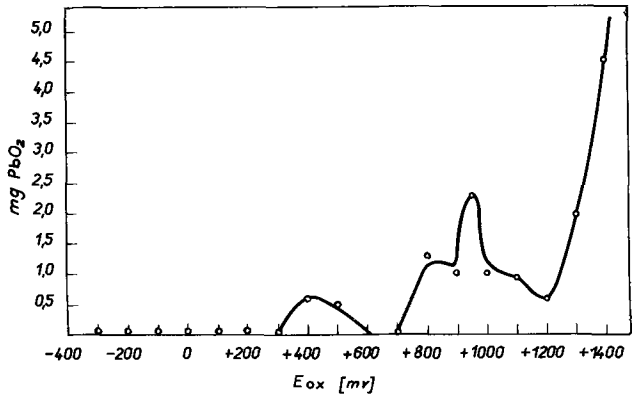

Fig. 5. Amount of lead dioxide in the anodic layer at different oxidation potentials.

ond series of electrodes by photometric determinations of lead dioxide with o-tolidine (13). The results of both series of measurements were in agreement. Figure 5 shows the iodometrically determined amount of PbO_2 contained in the anodic layer of the electrodes oxidized between —200 and +1400 mv. The anodic layer does not contain lead dioxide up to the oxidation potential +400 mv, nor between +600 and +700 mv. However, the 3.12 and 2.80Å reflections already occur at —300 mv. The relative intensity of the latter is nearly equal to that of $PbSO_4$ between +300 and +1000 mv. It can be assumed therefore that these diffraction lines indicate the presence of tetragonal PbO in the anodic layer.

The 3.12 reflection at potentials up to +800 mv is due to PbO-tet. Only at +400 and +500 mv does the reflection of alpha dioxide coincide with that of the tetragonal oxide. In the standard x-ray diffraction pattern of tetragonal oxide this reflection is strongest (relative intensity 100), while in the PbO-tet it appears as a very weak line. In the standard x-ray diffraction pattern the 2.80 reflection has a relative intensity of 62. In the diffraction pattern of anodically obtained PbO-tet in sulfuric acid its intensity is considerably enhanced. This change in the intensities of these lines may be ascribed to preferred orientation. In order to test this assumption a series of oxidations was performed between —200 and +900 mv on wire electrodes, x-ray diffraction photographs of which were subsequently taken in a conventional 57.3-mm Debye-Scherrer camera. The diffraction ring corresponding to the 110 reflection of PbO-tet (d = 2.80Å) exhibited marked orientation texture effects. This indicates that the tetragonal lead oxide crystals are preferentially oriented with the texture axis [110] oriented along the axis of the wire. In the x-ray diffraction pattern the remaining lines of PbO-tet in the interval considered are the following: d = 2.51 (I = 11); 2.12 (1); 1.99 (8); 1.87 (37); and 1.67 (24). The lines with d = 2.51 and 1.99Å were not recorded in our diffraction pattern. The 1.87 reflection coincides with a normal lead sulfate line. Reflections with d = 2.12 and 1.67Å are observed in the potential range between —300 and +1000 mv. Up to potential +1000 mv the 1.67Å reflection shows the same shape of the I/E curve as the 2.80Å reflection, indicating formation of PbO-tet.

Figure 2 shows that following anodization between —400 and +800 mv, on interrupting the polarization, the electrode potential at open circuit is arrested in the interval between —450 and —750 mv. According to the x-ray data, PbO-tet is formed in the same potential range. Consequently, the potential arrest observed under open-circuit conditions should be ascribed to the presence of lead oxide in the anodic layer.

A comparison between Fig. 4 and 5 indicates that the increase in relative intensity of the 3.12 reflection above +900 mv is due to the alpha dioxide formed during anodization. The strong intensities at potentials above +1300 mv (Fig. 4) show that the major part of the anodic layer above this potential is constituted by alpha lead dioxide. From the diffraction lines of the standard x-ray pattern of alpha lead dioxide which do not overlap with lead sulfate reflections only those with d = 2.73 and 1.64Å are absent. In some oxidation runs minor amounts of α-PbO_2 occur in electrodes anodized at —100, 0, and +200 mv. This shows that between —200 and +900 mv the formation of α-PbO_2 is determined by fortuitous factors.

The diagnostic diffraction lines of β-PbO_2 are those with interplanar spacings 3.49, 2.80, and 1.85Å. The remaining reflections coincide with those of lead and lead sulfate. The 3.49 reflection occurs at potentials more positive than +1200 mv (Table I). The increase in relative intensity of the 2.80Å reflection (Fig. 4) for electrodes anodized at potentials above +1200 mv is also brought about by the presence of β-PbO_2. The 1.85 line is due both to beta and to alpha dioxide.

Apart from these reflections the diffractometer traces of electrodes anodized at potentials more positive than —400 mv contained some very weak lines. These are given in Table II together with the oxidation potentials at which they appear. The reflection with d = 3.25Å coincides with the strongest line of $3PbO \cdot PbSO_4 \cdot H_2O$ (14). The reflection with d = 3.06Å coincides with the strongest line of orthorhombic PbO (10) and with the 3.05Å reflection of $5PbO \cdot 2H_2O$ (relative intensity I = 70) (15). It is thus impossible to differentiate these two compounds only by means of the x-ray diffraction pattern. The reflection with d = 2.95Å coincides with the strongest line of $PbO \cdot PbSO_4$ (15), Pb_2O_3 (I = 90) (17). However, the remaining strong lines of Pb_2O_3, 3.03 (I = 70), 2.85 (40), 2.31(80), and 1.78(50), do not occur in the diffraction patterns of the electrodes, thus clearly indicating that this compound is not formed in the anodic deposit. Consequently the observed reflection with d = 2.95Å should be assigned to $PbO \cdot PbSO_4$.

On the basis of the x-ray data and of the electrochemical behavior of the electrode the potential range investigated can be divided into three regions according to the composition of the anodic layer:

(A) Lead sulfate region: from —956 to —300 mv. The deposit is built up by $PbSO_4$ crystals.

(B) Lead oxide region: from —300 to about +900 mv. Apart from lead sulfate the deposit contains substantial amounts of tetragonal lead oxide. Minor amounts of $PbO \cdot PbSO_4$, $3PbO \cdot PbSO_4 \cdot H_2O$, and $5PbO \cdot 2H_2O$ or PbO-orthorhombic are also formed. At some potentials small amounts of orthorhombic α-PbO_2 also occurs. In previous electrochemical investigations (8, 9) it was established that the lead oxide region begins between —450 and —500 mv. The x-ray data yield a more positive value for the beginning of the second region. This difference is probably due to the lower sensitivity of the x-ray diffraction technique.

(C) Lead dioxide region. It lies at potentials more positive than +900 mv. However, the composition depends strongly on the oxidation potential and changes with the oxidation time. The major component of the anodic layer in this region is α-PbO_2. Beta-PbO_2 begins to form at potentials more positive than +1200 mv.

The present experimental results show that both tetragonal PbO and α-PbO_2 are formed in 1N H_2SO_4 although it is known that these compounds originate in alkaline media. Obviously the mechanism of the alkalinization of the lead electrode during anodic oxidation must be elucidated in order to explain this contradiction.

Such a mechanism for the alkalinization of the solution in the near-electrode potential was suggested in previous work (8). This mechanism is based on the hindered diffusion of SO_4^{2-} in the intercrystalline spaces of $PbSO_4$.

The composition of the anodic layer depends not only on the oxidation potential but on the quantity of

electricity passed at each potential as well. Any attempt to elucidate the mechanism of the processes which take place in the anodic oxidation of lead should take into account these two parameters.

Acknowledgments

Thanks are due to I. Tomov and Z. Iordanova, of the same institute, for x-ray diffraction measurements.

Manuscript received Oct. 14, 1968.

Any discussion of this paper will appear in a Discussion Section to be published in the December 1969 JOURNAL.

REFERENCES

1. J. J. Lander, *This Journal*, **98**, 213 (1951); **103**, 1 (1956).
2. J. Burbank, *ibid.*, **103**, 87 (1956).
3. P. Rüetschi and B. D. Cahan, *ibid.*, **104**, 406 (1957).
4. J. Burbank, *ibid.*, **106**, 369 (1959).
5. E. B. Krivolapova and B. N. Kabanov, *Trudy Soveshch. po Elektrokhim., Moscow*, p. 539 (1953).
6. P. Rüetschi and R. T. Angstadt, *This Journal*, **111**, 1323 (1964).
7. E. Sato and T. Shiina, *J. Electrochem. Soc. Japan*, **32**, 148 (1964).
8. D. Pavlov, *Ber. Bunsengesell.*, **71**, 398 (1967).
9. D. Pavlov, *Electrochim. Acta*, **13**, 2051 (1968).
10. N. E. Bagshaw, R. L. Clarke, and B. Halliwell, *J. Appl. Chem.*, **16**, 180 (1966).
11. ASTM, X-Ray Powder Data File, 5-0561, 5-0570.
12. N. H. Furman, "Standard Methods of Chemical Analysis," 6th Edition, 62 Vol. 1, p. 578, D. Van Nostrand Co. (1962).
13. G. Kraft, "Handbuch der analytischen Chemie, Band IV, Ge, Pb," p. 201, Springer-Verlag, Berlin (1966).
14. H. Bode and E. Voss, *Electrochim. Acta*, **1**, 318 (1959).
15. G. Todd and E. Parry, *Nature*, **202**, 386 (1964).
16. J. D. Esdaile, Ph.D. Thesis, University of Adelaide (1963).
17. W. B. White and R. Roy, *J. Am. Ceram. Soc.*, **47**, 242 (1964).

The Influence of Ternary Alloying Additions on the Galvanic Behavior of Aluminum-Tin Alloys

D. S. Keir, M. J. Pryor,* and P. R. Sperry

Metals Research Laboratories, Olin Mathieson Chemical Corporation, New Haven, Connecticut

ABSTRACT

The effect of a series of ternary alloying additions on the galvanic behavior of Al-Sn base alloys has been investigated. A group of soluble ternary elements including Bi, Zr, Mg, and Ag expands the aluminum lattice, stabilizes the Al-Sn solid solution and either maintains or enhances the high galvanic currents observed in an aluminum alloy-steel couple in sodium chloride solution. A group of soluble ternary elements including Si, Zn, Cu, and Mn contracts the aluminum lattice, rejects tin from solid solution, and markedly decreases the galvanic current. A group of comparatively insoluble ternary alloying additions including Co, Ni, Fe, and As has little effect on galvanic current but reduces the anodic efficiency of the Al-Sn base alloy anodes.

A previous study (1) of the galvanic corrosion characteristics of aluminum alloyed with group IV metals showed that alloying aluminum with as little as 0.1% tin resulted in a major change in corrosion and galvanic corrosion characteristics in chloride solutions. For instance, the corrosion potential in 0.1*N* NaCl was debased from around —0.5 to —1.2 volts[1] while the current in a galvanic couple with an equal area of mild steel was enhanced by a factor of around fifty times. Other group IV alloying additions including germanium, silicon, titanium, and zirconium did not result in a similar major change in corrosion characteristics.

The dramatic effect of tin as an alloying addition was attributed to its ability to enter the surface oxide film as Sn^{4+} ions thereby creating additional cation vacancies. It was shown experimentally that the a-c resistivity of the surface oxide film on the aluminum-tin alloy in sodium chloride solution was almost two orders of magnitude lower than that of similar films on pure aluminum; this effect was attributed to lowered ionic resistance.

The galvanic behavior of dilute aluminum-tin alloys was not particularly reproducible unless the alloy castings were subjected to a thermal treatment designed to insure maximum retained solid solubility of tin in aluminum. This involved soaking the alloys at around 620°C followed by quenching in still water. This treatment was effective because of the existence of a small but significant solubility loop in the aluminum tin equilibrium diagram at this temperature where a maximum of around 0.1% tin may be dissolved (2, 3). When the maximum amount of tin was retained in metastable solid solution by this homogenizing treatment, the corrosion potential and a-c resistivity of the surface oxide film were debased to the maximum degree, and galvanic current output was maximized. A lower temperature thermal treatment at 400°C resulted in precipitation of most of the tin retained by homogenizing. Such precipitation treated (heterogenized) aluminum-tin alloys showed much more noble corrosion potentials, significantly higher film resistivity, and greatly reduced galvanic corrosion currents. These results demonstrated that tin in the alloy could not pass effectively into the surface oxide unless it was retained in solid solution.

In view of the foregoing, it was felt important to determine the effects of ternary alloying additions on the galvanic behavior of aluminum-tin alloys. Such effects might well be related to the influence of the ternary alloying addition on the solid solubility of tin in aluminum. No information appears to exist on this point in the literature partly because of the difficulty of studying changes in small solid solubilities by conventional metallurgical methods. However, in the aluminum-tin system the measurement of galvanic current provides an accurate means of locating the phase boundary (1). The particular ternary alloying additions investigated included iron, magnesium, bismuth,

* Electrochemical Society Active Member.
[1] All potentials in this paper are expressed on the standard hydrogen scale.

zirconium, zinc, manganese, copper, silver, nickel, arsenic, and cobalt. Iron and silicon were also investigated both singly and in combination because these are common impurities in aluminum.

Experimental and Results

Material preparation.—Alloys were prepared from superpurity (99.992%+) aluminum, high-purity tin, and high-purity elemental ternary alloying additions. Ternary alloys containing magnesium, bismuth, zirconium, zinc, manganese, copper, silver, iron, nickel, arsenic, and cobalt were prepared using a constant tin content of 0.2 w/o (per cent by weight). The ternary alloying additions were added in amounts varying from 0.012% to approximately 1.0% depending on their solubility in aluminum. The alloys were prepared as small chill castings measuring 1.25 x 1.4 x 10 cm using the technique described previously (1). The chemical compositions are given in Table I. Similar castings of selected binary alloys were also prepared, Table II.

Aluminum-tin-iron-silicon alloys were likewise prepared from 99.992% pure aluminum with high-purity iron, silicon, and tin as alloying additions. The nominal tin content of these alloys was 0.14 w/o. A variety of iron and silicon contents of up to about 0.3 w/o was investigated, Table III. The castings were prepared by the direct chill method. The ingots measured 7.5 x 15 x 100 cm. The pouring temperature of the melt was 720° ± 5°C, with an initial drop rate of 7.5 cm/min during the start-up, being succeeded by a final constant drop rate of 11 cm/min. The molten metal head was held constant in the mold at a value of 6 cm. Gaseous chlorine at a flow rate of 2500 cc/min was passed through each melt from 8 to 13 min before casting to insure a low hydrogen level in the ingots. Each ingot was cut into 7.5 cm long sections for use in the galvanic corrosion studies.

Thermal treatment of castings.—All castings were homogenized to insure uniform distribution of tin and of the other alloying additions. A homogenizing temperature of 620° ± 3°C was employed. Most alloys were held for 16 hr and were then quenched in still water. The alloys containing zinc, magnesium, and arsenic were homogenized for a reduced time of 6 hr in order to minimize loss of volatile ternary alloying additions.

Experimental method.—Specimens were machined from the castings in the form of square rods having dimensions of 0.5 x 0.5 x 8.0 cm. In the galvanic experiments only 5 cm of the rod (10 cm^2) were immersed in the electrolyte. The machined specimens were degreased in benzene, etched in 1*N* NaOH for 5 min, washed, dried in acetone, and exposed to dry air over phosphorus pentoxide for 24 hr and weighed.

Mild steel cathodes had an area of 10 cm^2. Their chemical composition and method of preparation was described earlier (1).

Galvanic couples of 10 cm^2 of the appropriate aluminum alloy coupled to 10 cm^2 of mild steel in 0.1*N* NaCl at 25° ± 0.05°C were investigated using the cell and experimental method described earlier by two of the authors (4). Galvanic currents and cell potentials were recorded continuously for 48 hr, the standard duration of all galvanic experiments in this paper. After each experiment had been terminated the aluminum anode was freed from corrosion product by treatment in 2% chromic-5% phosphoric acid at 85°C, after which it was rinsed, dried, and reweighed. The steel cathode was cleaned in 1:1 HCl inhibited with 3% of rhodine 41, rinsed, dried, and reweighed. All steel cathodes were effectively protected against corrosion.

Results.—The results of the galvanic experiments on homogenized Al-Sn alloys containing a variety of ternary alloying additions are shown in Table I. The experimental data include the numbers of coulombs flowing in 48 hr, the closed-circuit cell potentials, and the anodic efficiencies.

From Table I, only bismuth caused a major increase (more than 50%) in the galvanic corrosion current. A group of alloying additions comprising Mg, Ag, Zr, Co, and Fe, had little effect on the galvanic current and cell potential, although the iron addition caused a large drop in anodic efficiency. The remaining alloying additions caused a reduction in galvanic current together with an ennobling in cell potential with the major effects stemming from the addition of Cu, Zn, or Mn. The closed-circuit cell potentials for these three elements are in the range obtained from homogenized binary Al-Sn alloys with tin contents in the range of 0.04-0.06% (1).

Table II shows the number of coulombs flowing in galvanic couples with pure aluminum and selected binary alloys including tin. With the exception of tin, all other elements (Bi, Zr, As, and Si) reduced galvanic output in binary alloys.

Iron and silicon are major impurities found in commercial grades of aluminum and, hence, were investigated in more detail. Table III lists the galvanic data obtained from a range of homogenized Al-Sn alloys with varying amounts of iron and silicon.

The data from Table III are plotted in Fig. 1 and 2 as the individual effects of iron and silicon, at approximately constant silicon and iron levels, respectively. It may be seen that increasing iron results in a modest decrease in galvanic current together with decreasing efficiency as $FeAl_3$ accumulates in the alloy. Figure 3 shows that the cell potential change is relatively insensitive to the presence of iron up to 0.2%. Alloying with silicon (Fig. 2) results in a major decrease in galvanic current accompanied by a drastic displacement in cell potential in the noble direction

Table I. Effects of minor alloying additions on galvanic characteristics Al-0.2% Sn alloy anode coupled to steel in 0.1*N* NaCl solution

Alloy composition	Coulombs in 48 hr	Cell potential-volts (*vs.* H_2)	Anodic efficiency, %
Al-0.2% Sn	850, 930	−1.08	40
Al-0.2% Sn-0.16% Bi	1210, 1580	−1.16	52
Al-0.2% Sn-1.10% Mg	790, 1010	−1.09	54
Al-0.18% Sn-0.094% Zr	790, 810	−1.09	50
Al-0.19% Sn-0.013% Ag	970, 1040	−1.09	48
Al-0.17% Sn-0.021% Co	630, 900	−1.07	52
Al-0.19% Sn-0.076% Fe	800, 840	−1.15	32
Al-0.20% Sn-0.012% As	690, 690	−1.11	41
Al-0.19% Sn-0.096% Ni	310, 370	−0.96	55
Al-0.20% Sn-1.05% Zn	35	−0.74	67
Al-0.18% Sn-0.10% Cu	30	−0.64	59
Al-0.20% Sn-0.84% Mn	25	−0.55	52

Table II. Galvanic output of some high-purity binary alloys coupled to steel in 0.1*N* NaCl solution

Alloy	Coulombs in 48 hr
Al + 0.12% Sn	810, 831, 881
Al + 0.075% Bi	15, 17
Al + 0.17% Zr (1)	4, 6
Al + 0.083% As	6, 6
Al + 0.20% Si (1)	9, 44
99.997% pure Al (1)	20, 21

Table III. Effects of iron and silicon content on galvanic characteristics of Al-0.14% Sn alloy anodes coupled to steel in 0.1*N* NaCl solution

Alloy composition (w/o) Sn	Fe	Si	Coulombs in 48 hr	Anodic efficiency, %
0.13	0.003	0.002	810, 831, 881	61, 66, 62
0.14	0.04	0.05	402, 440, 550	61, 64, 56
0.13	0.04	0.29	32, 36, 41	67, 64, 68
0.14	0.066	0.13	135, 164, 148	62, 64, 64
0.14	0.15	0.14	30, 45, 64	57, 56, 62
0.14	0.19	0.065	406, 494, 511	38, 40, 40
0.13	0.20	0.30	37, 40, 41	63, 63, 60
0.14	0.27	0.14	130, 138, 124	37, 36, 34
0.13	0.33	0.065	268, 279, 300	35, 34, 34
0.14	0.34	0.31	36, 34, 79	60, 63, 58

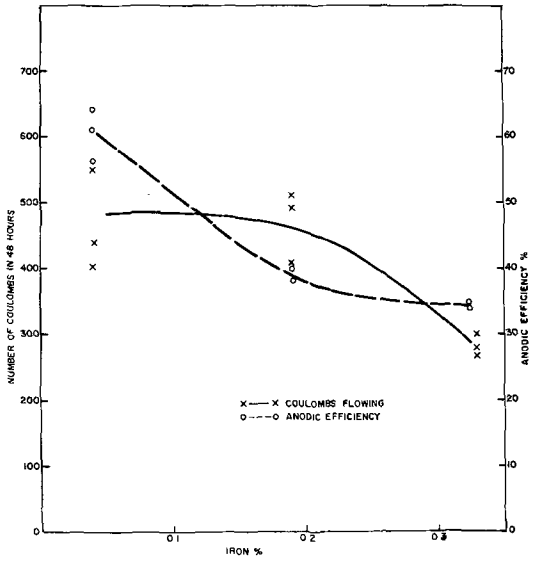

Fig. 1. Relation between iron content (silicon content 0.05-0.065%), coulombs flowing in 48 hr, and anodic efficiency in galvanic couples of Al-0.14% Sn base alloys and mild steel in 0.1*N* NaCl at 25°C.

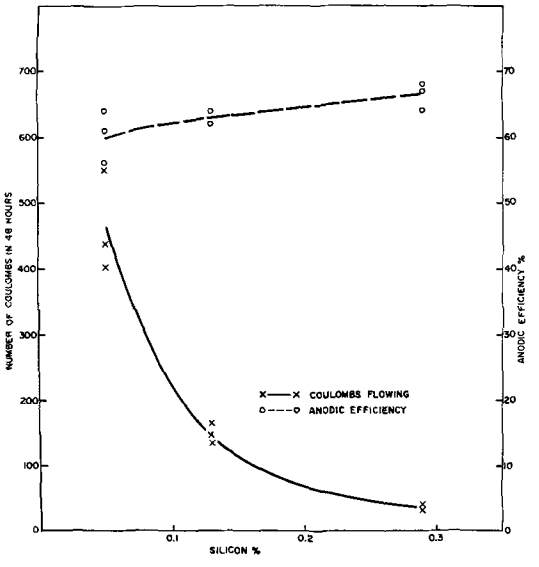

Fig. 2. Relation between silicon content (iron content 0.04-0.066%), coulombs flowing in 48 hr, and anodic efficiency in galvanic couples of Al-0.14% Sn base alloys and mild steel in 0.1*N* NaCl at 25°C.

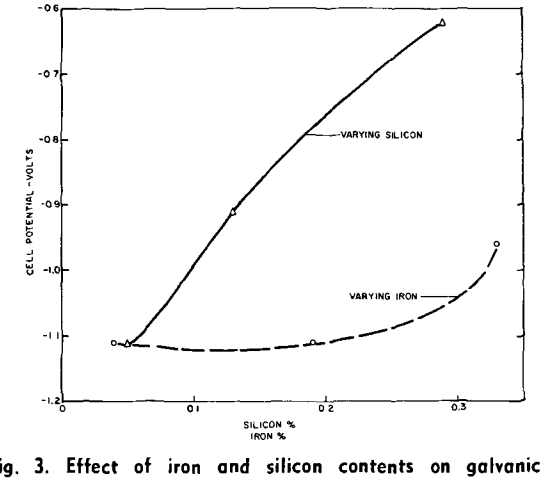

Fig. 3. Effect of iron and silicon contents on galvanic cell potential.

(Fig. 3). Anodic efficiency increases slightly with increasing silicon content.

Discussion

It was previously found that tin in aluminum can enter the surface aluminum oxide film only if it is initially dissolved in the aluminum solid solution. A ternary alloying or impurity element could conceivably modify the effect of tin on the galvanic properties in one of two ways:

(*i*) it could also enter the oxide and further change its defect structure, or

(*ii*) it could affect the solid solubility of tin in aluminum so that it influences the effectiveness of tin in an indirect manner.

If (*i*) was true, it would be expected that an element such as bismuth, which enhances the effect of tin would increase the galvanic current in a binary alloy. Table II shows that this is not so. Furthermore, it is well known that binary zinc additions to aluminum shift the potential in the active direction and yet this element annihilates the effect of tin (Table I). Clearly ternary alloying effects in Al-Sn base alloys cannot be related to the influence of the ternary alloying additions themselves on the surface oxide films.

Since (*i*) above is not a valid explanation of the results in Tables I and III, the tin solubility considerations outlined in (*ii*) can be examined. In an earlier paper (1) it was demonstrated that only the tin retained in solid solution in the alloy could enter the surface oxide film and modify its conductivity. Tin retained in an aluminum solid solution is recognized as being a strong expander of the FCC lattice with the expansion being reported as +0.0045 Å/w/o of tin in solution (2). This is a surprisingly large effect which is comparable with the effect of magnesium in also expanding the aluminum lattice (+0.0052 Å/w/o).

Since tin expands the aluminum lattice, it would appear that it should be compatible with other solid solution elements which are also lattice expanders. By contrast, lattice contractors could well result in the rejection of tin from solid solution which would reduce the galvanic corrosion current and ennoble the potential of the alloy. Insoluble elements should have no effect on the solubility of tin, but if present as electronically conducting second phase particles should reduce anodic efficiency.

The available data required to support or reject these contentions is summarized in Table IV (5-7). This

Table IV. Solubility and lattice changes due to alloying aluminum

Element	Solubility in w/o at 600°C*	Change in Al lattice, Å/w/o*	Goldschmidt atomic radius A**	
Sn	0.10	+0.0045	1.58	
Bi	0.2 at 657°C	—	1.82	Expanders
Mg	3.6	+0.0052	1.60	
Zr	0.15	—	1.60-1.61	
Ag	17.6	+0.00002	1.44	
Al	—	—	1.43	
Co	0.02 at 657°C	—	1.25-1.26	Limited Solubility
Fe	0.025	—	1.26-1.28	
As	—	—	1.25	
Ni	0.028	—	1.25	
Zn	14.6	−0.0003	1.37	Contractors
Cu	2.97	−0.0022	1.28	
Mn	1.03	−0.0033	1.12-1.37	
Si	1.00	−0.0017	1.17	

* Data for solubility at 600°C and change in lattice from ref. (5); other solubility data from ref. (6).
** Data from ref. (7).

table contains solubility limits at 600°C for the various ternary elements[2] together with what quantitative information is available relative to their effect in expanding or contracting the aluminum lattice (5). Complete information is not available on this point for all the ternary elements; in such cases, the Goldschmidt atomic radius has been used (7). This number normalizes the atomic radius for a coordination number of 12 which is applicable to aluminum. Where lattice expansion or contraction data is also available, the agreement between the values quoted and the Goldschmidt atomic radius is good.

The elements in Table IV are organized into three groups, as follows:

1. Elements which are soluble at the quantity added and which expand the aluminum lattice. These include Bi, Mg, Zr, and Ag.
2. Elements which are soluble at the quantity added and which contract the aluminum lattice. These include Zn, Cu, Mn, and Si.
3. Elements which are insoluble at the quantity added.

If the groupings in Table IV are compared with the electrochemical results in Tables I and III, an excellent correlation is found to exist. The lattice expanders Bi, Zr, Mg, and Ag do not degrade the electrochemical properties normal to binary Al-0.2% Sn alloys. Indeed the very large bismuth atom results in a major enhancement of galvanic current and a further debasement in cell potential. Silver slightly enhances the galvanic current, whereas magnesium and zirconium have essentially no effect on the electrochemical behavior. These results can be interpreted as meaning that the presence of ternary lattice expanders either permits the binary solid solubility of tin to be maintained at around 0.11% or else, in the case of bismuth, to be enhanced.

The lattice contractors, Zn, Cu, Mn, and Si, all have the opposite effect on galvanic characteristics. They reduce to a major degree the galvanic corrosion current and ennoble the cell potential. The effect is greatest for manganese, which, at the quantity added, results from Table IV in the largest total lattice contraction. Clearly as the ternary element contracts the aluminum lattice tin is rejected from solid solution and the logical (1) reduction in galvanic corrosion current results. Comparison with earlier work on binary aluminum-tin alloys suggests that in the ternary Al-Sn-Mn system less than 0.05% tin is retained in solid solution.

The insoluble elements, Co, Fe, As, and Ni, generally have a small effect on galvanic current. Up to their small solubility limits they are all lattice contractors (Table IV) so should slightly reduce galvanic current. This effect is in fact found in Table I with the greatest current decrease being found with nickel which also has the largest solid solubility. As these elements are added over and above their solubility limits, they form intermetallic compounds. Since these are usually good electronic conductors, they can act as good local cathodes and so can promote local action on the alloy anodes. Accordingly, the effect over and above the solid solubility limit is principally to reduce anodic efficiency without further affecting galvanic current. This effect is elucidated in Tables I and III and also in Fig. 1 for iron.

The combined effect of silicon (a lattice contractor) and iron (an insoluble element) is of greatest interest because these are common impurities in aluminum. The individual effects of these elements are shown in Fig. 1 and 2. Their combined effect is shown in Table III which shows that the galvanic current is controlled by the silicon content and the anodic efficiency by the iron content.

This work provides further support of the contention that only the tin retained in solid solution can enter the surface oxide film and modify its conductivity and through this means, the electrochemical behavior of the alloy. Accordingly, the effects of ternary alloy additions follow closely the effects of these elements on the solid solubility of tin in aluminum.

[2] Information on arsenic is not available, but its solubility should be very low.

Acknowledgment

The authors wish to thank the Aluminum Division of the Olin Mathieson Chemical Corporation for their support of this work and for their permission to publish the results.

Manuscript received Sept. 16, 1968.

Any discussion of this paper will appear in a Discussion Section to be published in the December 1969 JOURNAL.

REFERENCES

1. D. S. Keir, M. J. Pryor, and P. R. Sperry, *This Journal*, **114**, 777 (1967).
2. A. H. Sully, H. K. Hardy, and T. J. Heal, *J. Inst. Metals*, **76**, 269 (1950).
3. H. K. Hardy, *ibid.*, **80**, 431 (1951-2).
4. M. J. Pryor and D. S. Keir, *This Journal*, **105**, 629 (1958).
5. "Aluminum," K. R. Van Horn, Editor, Vol. I, pp. 362, 399, ASM, Metals Park, Ohio (1967).
6. H. W. L. Phillips, Annotated Equilibrium Diagrams of Some Aluminum Alloy Systems, Inst. of Metals Monograph and Report Series No. 25, London (1959).
7. C. J. Smithells, "Metals Reference Book," Vol. I, pp. 140, 141, 4th ed., Plenum Press, New York (1967).

Anodic Polarization of Titanium and Titanium Alloys in Hydrochloric Acid

Milton Levy* and Gilbert N. Sklover

Army Materials and Mechanics Research Center, Watertown, Massachusetts

ABSTRACT

Commercially pure titanium and the alloys studied exhibited active to passive transitions in HCl. Increasing the acid concentration increased the critical current density for passivity and the dissolution current density in the passive range and shifted the critical potential for passivity in the noble direction. Increasing the temperature served only to increase the critical current density for passivity and the dissolution current density in the passive range. Activation energies for the anodic polarization process were the right order of magnitude for a reaction controlled by reactivity at the metal surface. For the α-β alloy 6Al-6V-2Sn the critical current density for passivity increased as the ratio of amounts of beta to alpha phase decreased with increasing strength level. The dissolution is accelerated probably, by the galvanic effects and the unfavorable area ratio. Ti 75A, a commercially pure metal, had a smaller critical current density for passivity value than did the alloys, which was expected. Secondary current density increases were observed for all the alloys at potentials above +1.0v. For the 13V-11Cr-3Al alloy such behavior was attributed to transpassivity. For the other alloys the phenomena was attributed to pitting or localized corrosion. The commercially pure metal remained passive in this potential range. The addition of Fe^{3+} and Cu^{2+} (0.03M) to the HCl facilitated passivation of the metal and its alloys. Pitting of several of the alloys occurred in HCl but not in H_2SO_4.

The anodic behavior in acid media of pure titanium and titanium alloyed with selected amounts of noble elements has been reported by several investigators (1-7). Relatively few data on the anodic behavior of commercial titanium alloys are available (8-10).

In previous work (8) the anodic behavior of α-β titanium alloy 6Al-6V-2Sn was studied in sulfuric acid as a function of temperature, acid concentration, selected ion additions to the electrolyte, yield strength level, and microstructure of the alloy. For comparison, commercially pure α titanium and a β alloy containing 13V-11Cr-3Al were also studied. The present investigation extends this study to hydrochloric acid media, additional commercially available titanium alloys, and considers the directionality of the metal specimen.

Experimental Procedure

The metal and alloys studied were commercially pure α Ti75A in the annealed condition, α-β titanium 6Al-6V-2Sn heat-treated to strength levels of 140, 160, and 180 ksi, β titanium 13V-11Cr-3Al in the as-received mill anneal condition, α-β titanium 8Al-1Mo-1V in both the single and duplex annealed condition, and annealed α-β titanium 6Al-4V alloy.

The potential sweep method of potentiostatic polarization (sometimes called potentiodynamic polarization) was used. The electrode potential was continuously changed at a constant rate of 5000 mv/hr (83.3 mv/min) and current simultaneously recorded. A Wenking potentiostat in conjunction with a motor potentiometer for automatic programming of the operating potential and an x-y recorder were employed to automatically record current *vs.* voltage. The automatic potential sweep technique (as opposed to potential step) yields the most reproducible results because of the high resolution offered by continuous recording. The critical potentials for passivity determined by the potential step method agree within ±10 mv of those obtained from the potential sweep technique at the same traverse rate. The critical current densities for passivity are greater when the potential sweep technique is used. The polarization cell and general procedure have been described previously (8).

Polarization measurements were made in 5, 12, and 20% hydrogen saturated hydrochloric acid electrolytes at temperatures of 35, 50 and 65°C ±1°C. Reproducibility was within experimental error (<3%).

For the directionality studies cylindrical specimens of 1 cm^2 surface area were machined both parallel (longitudinal) and perpendicular (transverse) to the working direction. Because of the many similarities in behavior, a number of the polarization curves obtained are not presented.

Results and Discussion

Polarization of Ti-6Al-6V-2Sn

Effect of concentration of electrolyte.—Figure 1 shows the anodic behavior of Ti-6Al-6V-2Sn (180 ksi strength level) at 65°C in 5, 12 and 20% HCl. Increasing the acid concentration increases the critical current density for passivity or maximum dissolution current density and the critical potential for passivity is shifted in the noble direction. The dissolution current density in the passive range was highest in 20% HCl. The higher the value of the corrosion current in the passive state, the less stable the passive state. Similar behavior was observed at other strength levels and temperatures except at the lowest temperature (35°C) where the curves were characterized by the

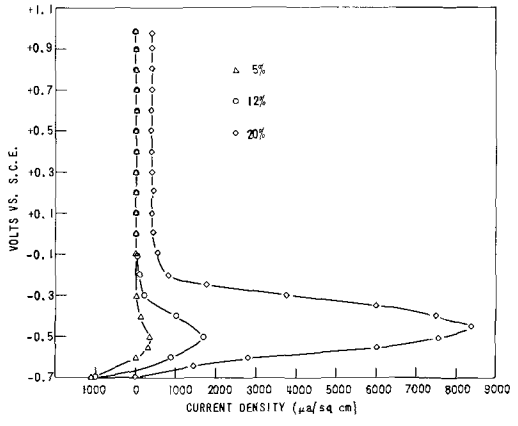

Fig. 1. Effect of concentration of HCl on polarization of Ti-6Al-6V-2Sn (180 ksi) at 65°C.

* Electrochemical Society Active Member.

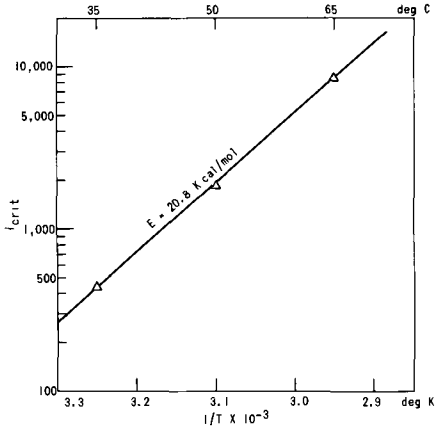

Fig. 2. Arrhenius plot for Ti-6Al-6V-2Sn (180 ksi) in 20% HCl

extremely small currents required to passivate the alloy and the negligible extent of their active regions.

Effect of temperature.—The critical current density for passivity for the alloy (140, 160, 180 ksi strength levels) in 5, 12, and 20% HCl increases considerably as temperature is increased from 35° to 60°C. The critical potential for passivity is unaffected. Figure 2 shows log critical current density for passivity plotted against the reciprocal of absolute temperature. The result is a linear dependency which can be expressed by the Arrhenius equation and an activation energy of 21 kcal/mol calculated. This activation energy is the right order of magnitude for a reaction controlled by chemical reactivity at the surface rather than a diffusion controlled reaction.

Effect of strength level.—Anodic polarization curves for Ti-6Al-6V-2Sn at strength levels of 140, 160 and 180 ksi in 20% HCl at 65°C are shown in Fig. 3. The critical current density for passivity increases with increasing strength level. The dissolution current density in the passive range also increased at the higher strength levels. The critical passive potential shifts in the more noble direction at the 180 ksi strength level. X-ray diffraction analysis showed that the β phase content decreases from 36 to 23 to 17% with a corresponding increase in α phase as the strength level increases from 140 to 160 to 180 ksi. It is probable that the alloying additions in the alloy produce a significant potential difference between the α and β phases which causes the relatively high dissolution currents. The dissolution current increases as the ratio of amounts of β to α phases decreases with increasing strength level. Dissolution may be accelerated both by the galvanic effects and the unfavorable area ratio.

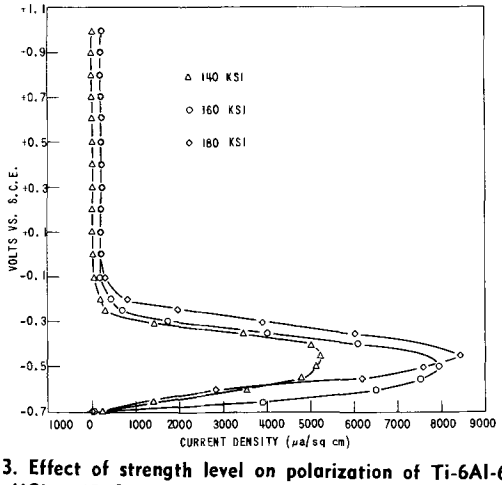

Fig. 3. Effect of strength level on polarization of Ti-6Al-6V-2Sn in 20% HCl at 65°C.

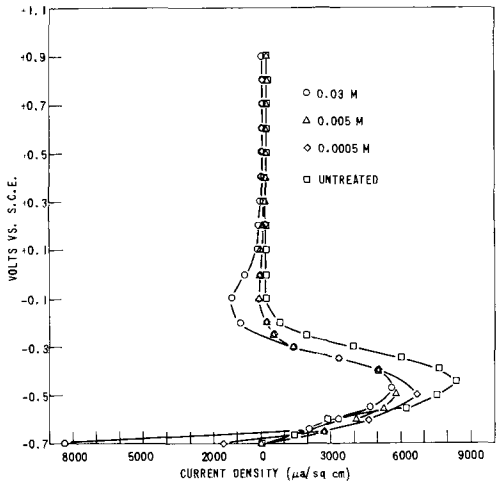

Fig. 4. Effect of $FeCl_3$ concentration on polarization of Ti-6Al-6V-2Sn (180 ksi) in 20% HCl at 65°C.

Effect of Fe *and* Cu *additions.*—Fe^{3+} and Cu^{2+} were added to the HCl electrolyte in the form of $FeCl_3$ and $CuSO_4$. Figure 4 shows the effect of the Fe addition on the polarization behavior of Ti-6Al-6V-2Sn (180 ksi) in 20% HCl at 65°C. The critical current density for passivity decreases with increasing Fe concentrations. At all concentrations of Fe there is some inhibition of the anodic reaction. At the maximum Fe concentration (0.03M) the polarization current density becomes negative and recrosses the zero current to a positive value at some point in the passive range. According to Mueller (11) this behavior indicates that passivity is stable and a stable passive potential exists. The lower value for the corrosion current density in the passive range at the 0.03M Fe concentration also indicates a more stable passive state. The electrochemical process associated with the cathodic currents is probably hydrogen ion reduction, particularly because the cathodic current occurred at a potential more active than the hydrogen electrode value of the electrolyte. Similar cathode currents have been reported for other metals by Greene *et al.* (12) and Myers *et al.* (13) who suggested they were related to the chemical reduction of hydrogen ions. The effect of cupric ions on the polarization behavior of the alloy in 20% HCl at 65°C is shown in Fig. 5. The Cu^{2+} ion reduces the critical current density for passivity. The reduction increases with increasing Cu^{2+} concentration. At 0.03M concentration the maximum dissolution current is approximately one-third that of the untreated solution. The Cu^{2+} ion achieves greater inhibition than the Fe^{3+} ion. Cobb and Uhlig (4) and Levy (8) reported that ferric and cupric ions are effective inhibitors for the corrosion of titanium and several titanium alloys in other acid media.

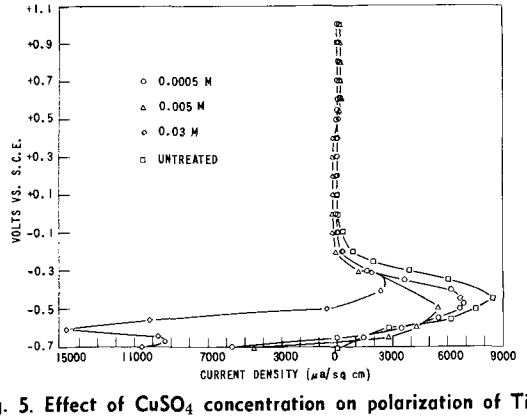

Fig. 5. Effect of $CuSO_4$ concentration on polarization of Ti-6Al-6V-2Sn (180 ksi) in 20% HCl at 65°C.

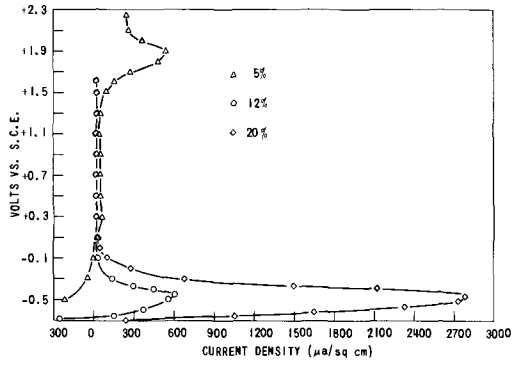

Fig. 6. Effect of HCl concentration on polarization of commercially pure Ti 75A at 65°C.

Polarization of Commercially Pure Ti 75A

Effect of concentration of HCl.—Figure 6 shows anodic polarization curves for Ti 75A in 5, 12, and 20% HCl at 65°C. The maximum dissolution current density increases with increasing HCl concentration. The critical potential for passivity is essentially the same in both 12 and 20% solutions. At the lowest HCl concentration, the curve is characterized by the negligible extent of the active region and a very small current is required to passivate the metal. At a potential of +1.5v different behavior is observed in 5% HCl solution. A secondary active-passive transition is observed. Although Levy (8) reported transpassive behavior for Ti 13V-11Cr-3Al in H_2SO_4, transpassivity has not been reported for commercially pure titanium. Why it should occur only in 5% HCl is not understood. Perhaps it does not represent true transpassive behavior but rather is an artifact.

Effect of temperature.—Figure 7 shows the effect of temperature on the polarization of the metal in 20% HCl. Paralleling the effect of concentration, the critical current density for passivity increases with increasing temperature. The rate of increase corresponds to an activation energy of about 20 kcal/mol. At 35°C, even at the 20% acid concentration, a relatively small current is required to passivate the metal. The dissolution current density in the passive range is of very low order of magnitude at all temperatures. Of course, the lower the value of the corrosion current in the passive state, the more stable the passive state.

Effect of Fe^{3+} *additions.*—Figure 8 shows the effect of $FeCl_3$ additions on the polarization behavior of Ti 75A in 20% HCl at 65°C. $FeCl_3$ in concentrations of 0.005 and 0.0005M accelerates anodic dissolution, 0.03M $FeCl_3$ reduces the maximum dissolution current density slightly. At this concentration cathodic current densities are observed in the passive range which indicates a more stable passive potential exists.

Polarization of Ti 8Al-1Mo-1V

Concentration of HCl.—Figure 9 shows anodic polarization curves for the alloy as a function of HCl

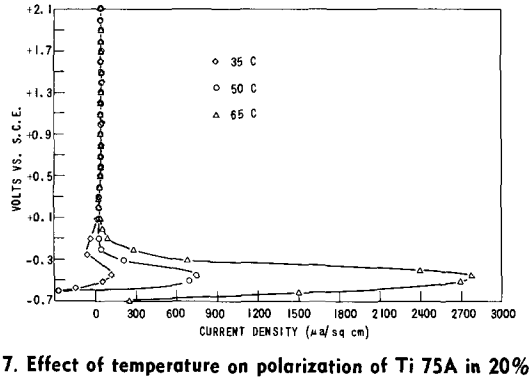

Fig. 7. Effect of temperature on polarization of Ti 75A in 20% HCl

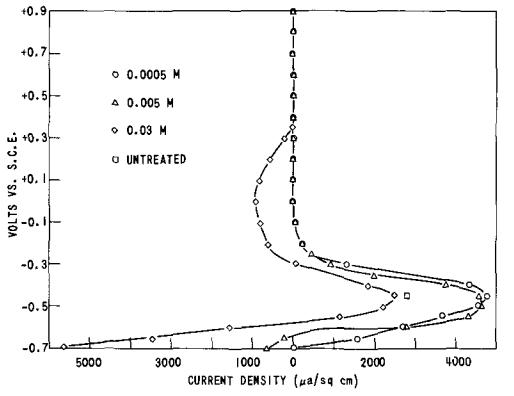

Fig. 8. Effect of $FeCl_3$ concentration on polarization of Ti 75A in 20% HCl at 65°C.

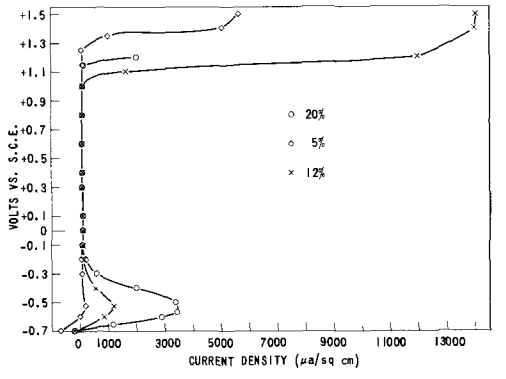

Fig. 9. Effect of concentration of HCl on polarization of Ti-8Al-1Mo-1V (duplex annealed) at 65°C.

concentration at 65°C. The maximum dissolution current density increases with increasing concentration. The critical potential for passivity remains essentially the same. Note the negligible extent of the active region in 5% HCl even at 65°C. At potentials between +1.0 to +1.25v, depending on the concentration, a secondary anodic reaction occurred. Such behavior is usually attributed to transpassivity. However, pitting occurred at these potentials indicating that the reaction was not one involving general dissolution or transpassivity.

Effect of temperature.—Figure 10 shows anodic polarization curves for the alloy in 20% HCl as a function of temperature. The critical current density for passivity increases with increasing temperature at a rate corresponding to an activation energy of about 20 kcal/mol. At 65°C the passive state is less stable since the value for the dissolution current density in the passive state is greater. There is no significant change in the critical potential for passivity. Pitting occurred at all temperatures at potentials above +1.1v where

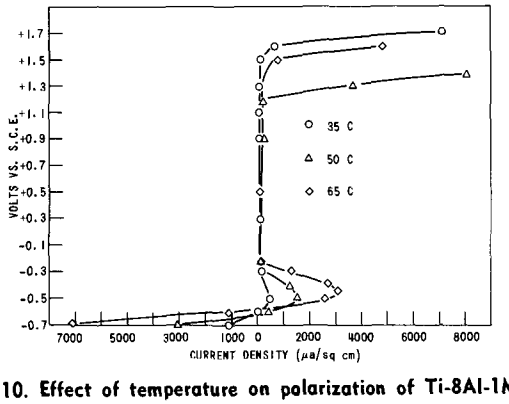

Fig. 10. Effect of temperature on polarization of Ti-8Al-1Mo-1V (single anneal) in 20% HCl.

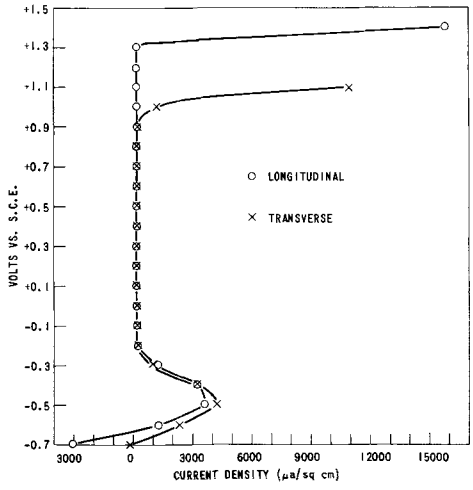

Fig. 11. Effect of directionality on polarization of Ti-8Al-1Mo-1V (duplex anneal) in 20% HCl at 65°C.

the current density increased appreciably. The potential at which pitting occurred varied with temperature.

Effect of directionality.—The anodic behavior of the alloy in both longitudinal and transverse directions in 20% HCl and 65°C is shown in Fig. 11. The maximum dissolution current density for the specimen fabricated in the transverse direction (machined normal to the working direction) was greater than that fabricated in the longitudinal direction (parallel to the working direction). Pitting occurred in both transverse and longitudinal specimens but at a more noble potential in the longitudinal specimen (+1.3v *vs.* +0.9v).

Effect of heat-treatment.—The effect of heat-treatment on the polarization of Ti 8Al-1Mo-1V in 20% HCl at 65°C is shown in Fig. 12. The critical current density for passivity and the critical potential for passivity are essentially the same for the alloy in the single and the duplex annealed condition. Localized corrosion (pitting) of the single and duplex annealed alloy occurred at potentials of +1.0 and +1.3v, respectively.

Polarization of Ti 13V-11Cr-3Al

Effect of concentration of electrolyte.—Figure 13 shows the polarization behavior of the alloy in 5, 12, and 20% HCl solutions at 65°C. The critical current density for passivity increases with the increasing HCl concentration, and the critical potential for passivity shifts in the more noble direction. Although not shown in Fig. 13, above +1.0v a secondary reaction was ob-

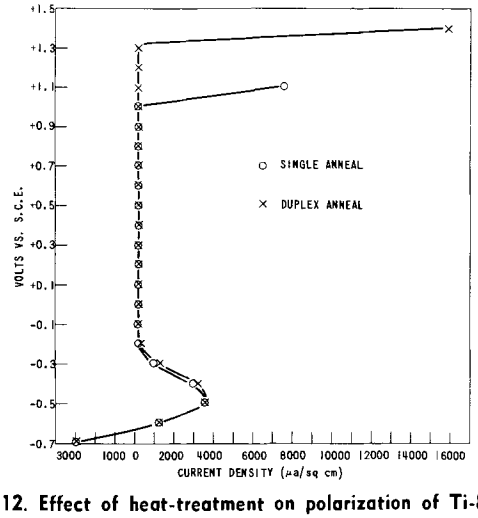

Fig. 12. Effect of heat-treatment on polarization of Ti-8Al-1Mo-1V in 20% HCl at 65°C.

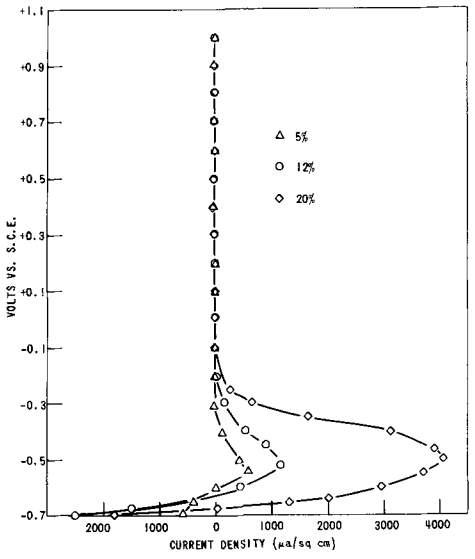

Fig. 13. Effect of HCl concentration on polarization of Ti-13V-11Cr-3Al at 65°C.

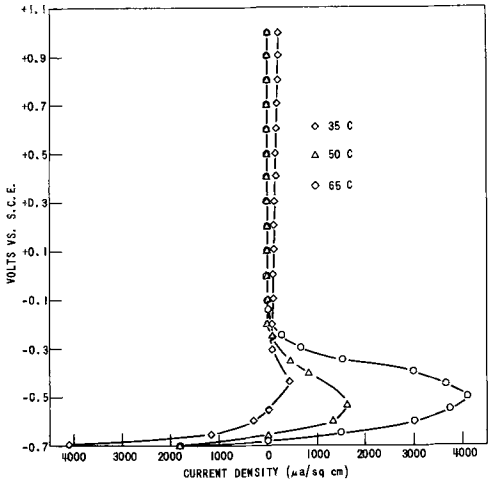

Fig. 14. Effect of temperature on polarization of Ti-13V-11Cr-3Al in 20% HCl.

served at all HCl concentrations and was characterized as transpassive behavior due to the 11% chromium content of the alloy.

Effect of temperature.—Figure 14 shows that the critical current density for passivity increases with increasing temperature. The activation energy for the polarization process (about 20 kcal/mol) is the right order of magnitude for a reaction controlled by chemical reactivity at the surface The alloy exhibited transpassive behavior at all temperatures at potentials above + 1.0v (not shown).

Effect of Cu^{2+}.—Figure 15 shows the effect of $CuSO_4$ on the polarization of Ti-13V-11Cr-3Al in 20% HCl at 65°C. Corrosion is accelerated by the addition of $CuSO_4$ in concentrations of 0.005 and 0.0005M. The anodic reaction is markedly stifled in 0.03M solution. Note the cathodic currents in the passive range which indicate that the passivity is stable.

Polarization of Ti-6Al-4V

Effect of temperature.—The temperature dependence of the anodic polarization process is shown in Fig. 16. The critical current densities for passivity and the dissolution current densities in the passive range increase with increasing temperature. Again the activation energy is the right order of the magnitude for a chemical controlled reaction rather than diffusion controlled. Paralleling the effect of temperature, in-

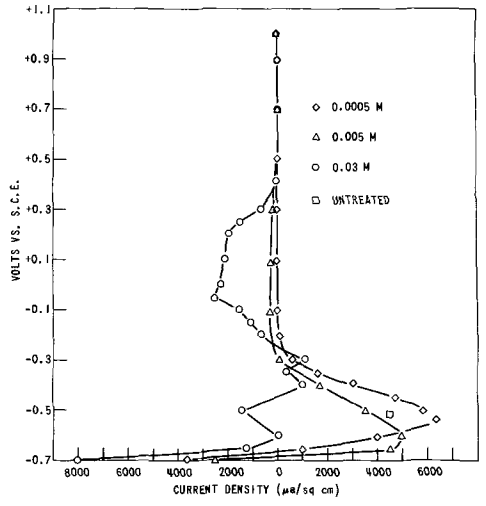

Fig. 15. Effect of $CuSO_4$ concentration on polarization of Ti-13V-11Cr-3Al at 65°C.

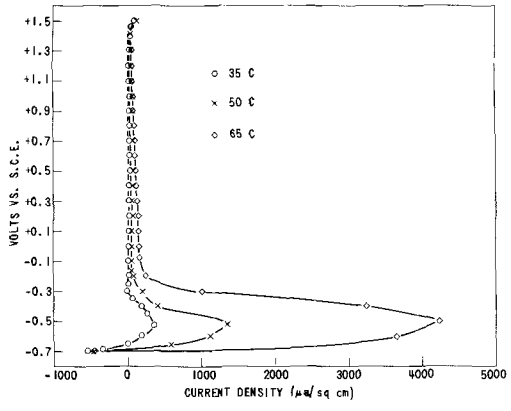

Fig. 16. Effect of temperature on polarization of Ti-6Al-4V in 20% HCl.

creasing the HCl concentration increased the critical current for passivity.

Comparison of Polarization Behavior of Titanium and Alloys

The anodic behavior of commercially pure titanium and several alloys in 20% HCl at 65°C are compared in Fig. 17. Based on maximum dissolution current, α-β Ti-6Al-6V-2Sn shows the least corrosion resistance followed by β Ti-13V-11Cr-3Al, α-β Ti-6Al-4V, α-β 8Al-1Mo-1V (10%β), and α Ti75A, in order of increasing corrosion resistance. Since the anodic polarization process was shown to be controlled by reactions occurring at the surface, metal composition and structure should achieve their greatest effect. Composition gradients in a metal create galvanic cells causing accelerated attack of anodic areas. A pure metal or homogeneous single phase alloy, therefore, is usually more corrosion resistant than an impure or multiphase alloy which appears to be the case here. The critical potential for passivity is essentially the same for the metal and the alloys which means that the alloying does not significantly alter the critical potential for passivity. The dissolution current densities in the passive range were of very low order of magnitude for all alloys indicating stable passivity. The commercially pure Ti 75A remains passive throughout the potential range (from —0.2 to +2.3v). All the alloys exhibit secondary reactions above potentials of +1.0v. The secondary reaction for the Ti-13V-11Cr-3Al alloy (+1.1v) is attributed to transpassivity. In this region of potential, chromium becomes oxidized to its hexavalent soluble state. The secondary current increase associated with the remaining alloys Ti-6Al-6V-2Sn,

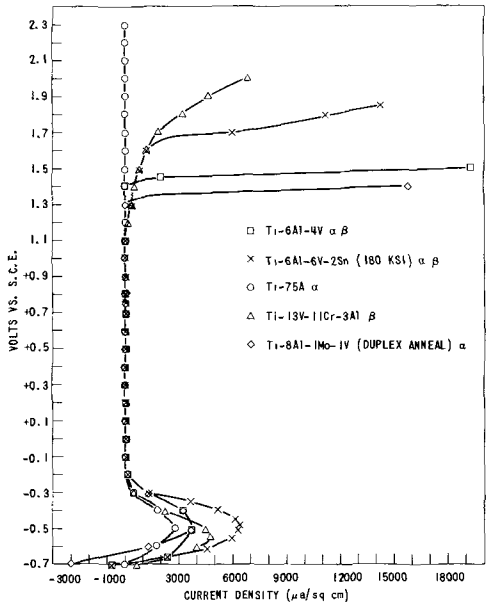

Fig. 17. Comparison of polarization behavior of titanium and alloys in 20% HCl at 65°C.

Ti-6Al-4V, Ti-8Al-1Mo-1V is attributed to localized corrosion or pitting. It should be noted here that the pitting observed in HCl solutions was not observed in H_2SO_4 solutions.

Summary

Commercially pure titanium and the alloys studied exhibited active to passive transitions in HCl. Increasing the acid concentration increased the critical current density for passivity and the dissolution current density in the passive range and shifted the critical potential for passivity in the noble direction. Increasing the temperature served only to increase the critical current density for passivity. Activation energies for anodic dissolution in the active region were the right order of magnitude for a reaction controlled by reactivity at the metal surface. For the α-β alloy 6Al-6V-2Sn the critical current for passivity increased as the ratio of amounts of beta to alpha phase decreased with increasing strength level. The dissolution is accelerated probably, by the galvanic effects and the unfavorable area ratio. Ti 75A, a commercially pure metal had a smaller critical current for passivity value than did the alloys, which was expected. Secondary current density increases were observed for all the alloys at potentials above +1.0v. For the 13V-11Cr-3Al alloy such behavior was attributed to transpassivity. For the other alloys the phenomena was attributed to pitting or localized corrosion. The commercially pure metal remained passive in this potential range. The addition of Fe^{3+} and Cu^{2+} (0.03M) to the HCl facilitated passivation of the metal and its alloys. Pitting of several of the alloys occurred in HCl but not in H_2SO_4.

Manuscript submitted July 15, 1968; revised manuscript received Oct. 21, 1968. This paper was presented at the Chicago Meeting, Oct. 15-19, 1967, as Paper 55.

Any discussion of this paper will appear in a Discussion Section to be published in the December 1969 JOURNAL.

REFERENCES

1. M. Stern and H. Wissenberg, *This Journal*, **106**, 755 (1959).
2. M. Stern and H. Wissenberg, *ibid.*, **106**, 759 (1959).
3. D. Schlain and J. S. Smatko, *ibid.*, **98**, 417 (1952).
4. J. R. Cobb and H. H. Uhlig, *ibid.*, **98**, 13 (1952).
5. N. D. Tomashov, R. M. Altovsky, and G. P. Chernova, *ibid.*, **108**, 113 (1961).
6. M. E. Straumanis and P. C. Chen, *ibid.*, **97**, 234 (1951).
7. A. Takamura, *Corrosion*, **23**, 306 (1967).

8. M. Levy, *ibid.*, **23**, 236 (1967).
9. J. M. Peters and J. R. Meyers, *ibid.*, **23**, 326 (1967).
10. J. C. Griess, Jr., *ibid.*, **24**, 96 (1968).
11. W. A. Mueller, *Can. J. Chem.*, **38**, 576 (1960).
12. N. D. Greene, C. R. Bish, and M. Stern, *This Journal*, **108**, 836 (1961).
13. J. R. Myers, F. H. Beck, and M. G. Fontana, *Corrosion*, **21** 277 (1965).

Two-Dimensional Nucleation in Electrocrystallization

R. D. Armstrong and J. A. Harrison

Department of Physical Chemistry, University of Newcastle upon Tyne, Newcastle upon Tyne, England

ABSTRACT

The transient and steady-state responses of electrodes under conditions where two-dimensional nucleation is rate determining are considered.

The suggestion that the formation of two-dimensional nuclei was rate determining in electrocrystallization was first made by Erdey-Gruz and Volmer (1). This view was subsequently not accorded much attention since (*i*) no experimental evidence could be obtained to support it, and (*ii*) it was thought by analogy with crystal growth from the vapor phase that the presence of large numbers of screw dislocations in real surfaces would control the kinetics of electrocrystallization. More recently it has been demonstrated that two-dimensional nucleation can be experimentally observed in situations where the number of dislocations is drastically reduced, *e.g.*, the deposition of Ag on to Ag single crystals (2), the formation of anodic films on Hg and Hg amalgams (3-9), the deposition of Ni on to Hg (10), and the formation of a monomolecular layer of pyridine, also on Hg (11).

It is the purpose of this communication to formulate the transient and steady-state responses of unbounded electrodes[1] under conditions where two-dimensional nucleation occurs, and to consider the significance of the results.

Potentiostatic Conditions

For the formation of a single layer of a phase on an unbounded electrode surface, the *i-t* transient under potentiostatic conditions (where the rate constants V and A are time independent) has been shown to be (3, 12)

$$i = q_{mon}\,\pi V^2 A t^2 \exp\left(-\frac{\pi t^3 V^2 A}{3}\right) \qquad [1]$$

for a nucleation rate (A) constant in time, or

$$i = q_{mon}\,2\,\pi V^2 N_0 t \exp\,(-\pi t^2 V^2 N_0) \qquad [2]$$

for a fixed number of nuclei (N_0) formed at $t = 0$. The symbols are defined near the end of the paper. [1] and [2] thus give the transient and steady-state responses for the special case of the formation of a single layer. Experimentally this situation often arises in the formation of anodic phases on mercury electrodes, but in general the process will not stop after the formation of the first layer. A derivation of the *i-t* transient for the formation of successive layers under conditions of progressive nucleation has been attempted by computer simulation (3). A much simpler approach in which the dependence of the transient on the rate constants for successive layers can be seen more clearly is as follows.

A patch of the n^{th} layer (dS_n) formed at time u, will generate a current due to the succeeding layer at a time t given by

$$di_{n+1} = q_{mon}\,3\beta_{n+1}(t-u)^2 \exp\,[-\beta_{n+1}(t-u)^3]\,dS_n$$

so that the total current due to the formation of the $(n+1)$ layer is

$$i_{n+1} = q_{mon}\int_0^t 3\beta_{n+1}(t-u)^2 \exp\,[-\beta_{n+1}(t-u)^3]\,\frac{dS_n}{du}\,du$$

$$= \int_0^t 3\beta_{n+1}(t-u)^2 \exp\,[-\beta_{n+1}(t-u)^3]\,i_n\,du \qquad [3]$$

Since i_1 is known [1] the current contributions from successive layers can be evaluated by numerical integration using a calculating machine. For the case where $\beta_1 = \beta_2 = \ldots \beta_n$ (which is the case expected for metal deposition) the resulting *i-t* transient with the component layer currents are shown in Fig. 1. It is apparent that in the steady state the current is constant and is the same magnitude as the maximum current due to the first layer, *i.e.*

$$i(t \to \infty) \approx q_{mon}(\pi V^2 A)^{1/3}\,(2)^{2/3} \exp(-2/3) \qquad [4]$$

(obtained by differentiating [1]).

Thus evidence for two-dimensional nucleation can only be obtained at short times, by observation of the rising section and subsequent damped oscillation of the current. The *i-t* transient for three dimensional nucleation when overlap effects are included (6) (Fig. 2) differs significantly from that for two-dimensional nucleation only in that damped oscillations are not observed before the steady state is reached. It should be stressed however that the model used for the evaluation of the *i-t* transient for three-dimensional nucleation is somewhat unrealistic, differing essentially from that for two-dimensional nucleation only in that it does not recognize the finite size of atoms. It is for this reason that oscillations due to the formation of individual atom layers are not predicted. We should generally expect to observe three-dimensional nucleation in deposition on to heterogeneous substrates where the spreading of a monomolecular layer over the surface may be inhibited so that the outward growth becomes comparable with the lateral growth.

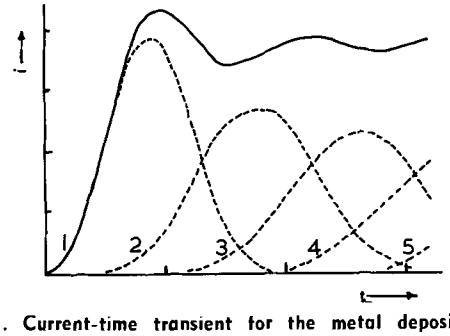

Fig. 1. Current-time transient for the metal deposition case, together with currents for individual layers.

[1] These are taken to be electrodes where edge effects are negligible.

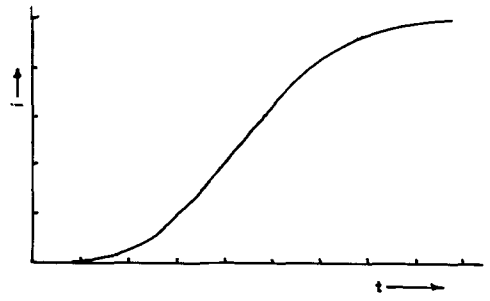

Fig. 2. Current-time transient for three-dimensional nucleation, taking into account overlap.

The present results extend the computer simulations (3) which were not taken to sufficiently long times to show the damping of the current oscillations, and which also showed an artifact in that the curves depended separately on V and A which is not substantiated by the present analysis.

The steady state i-E relationship is given by [4]. The prediction of the i-E curve demands a knowledge of the potential dependence of V and A. The dependence on potential[2] would be expected to be the same as that of a normal electrochemical rate constant, *i.e.*

$$V = V_{\eta=o}\left[\exp\left(\frac{\alpha z\mathbf{F}\eta}{RT}\right) - \exp\left(\frac{-(1-\alpha)z\mathbf{F}\eta}{RT}\right)\right] \quad [5]$$

provided that average potentials (7) are of significance in determining the rate.

The potential dependence of A is of the form (1, 2, 12)

$$A = \text{const.}\exp\left(-\frac{\text{const}}{\eta}\right) \quad [6]$$

Neither [5] nor [6] can be regarded as proved although [6] has been in some measure substantiated (2). [In the earlier work (3-5) on the formation of anodic films on mercury and mercury amalgams the potential dependence of V and A for individual layers is obscured by ohmic overpotential effects.]

Galvanostatic Conditions

For the formation of a single layer from N_o instantaneously nucleated centers under galvanostatic conditions $V(t)$ is given by

$$S_{ex} = N_o\pi\left(\int_0^t V(t)\,dt\right)^2 \quad [7]$$

where

$$S_{ex} = -\ln\left(1 - \frac{it}{q_{mon}}\right) \quad [8]$$

[7] and [8] use the relationships given by Avrami (13).

Solving [7] gives

$$V(t) = \frac{1}{2(\pi N_o)^{1/2}}\frac{i}{(q_{mon}-it)}\left[\ln\left(\frac{q_{mon}}{q_{mon}-it}\right)\right]^{-1/2} \quad [9]$$

The form of V as a function of t is given in Fig. 3. This has a minimum at a time

$$t = \frac{q_{mon}(e^{1/2}-1)}{ie^{1/2}} \quad [10]$$

If an exponential dependence of V on η is assumed the corresponding η-t relationship can be derived.

For the growth of successive layers with a time dependent rate of nucleation the transient condition cannot be solved. However the steady-state i-E relationship for the metal deposition case is again given by [4]. For a crude approximation to the nonsteady-state condition we can assume that as one layer is

[2] It is important that η is referred to the appropriate monolayer reversible potential (7).

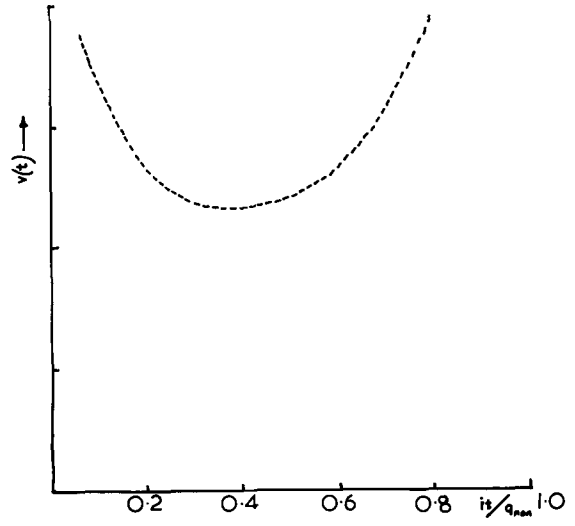

Fig. 3. Dependence of the rate of advance of an edge (V) on time for instantaneous nucleation under galvanostatic conditions.

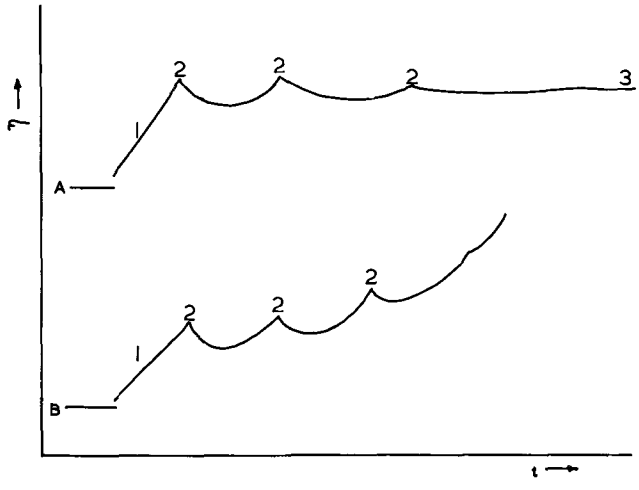

Fig. 4. Schematic η-t transients: A, metal deposition case; B, anodic film case. 1, double layer charging; 2, period of high nucleation rate; 3, steady state.

completed the potential rises to a high value for a short time to produce effectively N_n nuclei instantaneously. The η-t relationships are shown in Fig. 4, and such transient conditions have been observed for the electrodeposition of Ag on to Ag[2] (although on a bounded electrode, where the steady state given by [4] is not expected) and for the formation of calomel on Hg (14, 15).

Diffusion Effects

A situation which is very likely to arise in metal deposition is that a transport process either on the surface or in the solution procedes incorporation into the nucleus. A completely rigorous solution of the problem is difficult. However the problem can be simplified by calculating two limiting cases: (*i*) the diffusion zones are confined to individual nuclei; and (*ii*) the diffusion zones have overlapped so that only a concentration gradient at right angles to the surface exists.

Case (i).—The calculation of the current-time characteristic for the formation of a single layer can be achieved by relaxing the condition that V is time independent. The rate of advance of the radius is assumed to be controlled by hemicylindrical diffusion symmetrically about an axis at right angles to the 2D nucleus. The exact solution for the simple growth of one nucleus has been given by Frank (16).

$$R(t) = S\sqrt{Dt} \quad [11]$$

S is a constant which depends on $\frac{(C^* - C^o)M}{\rho}$ and can be obtained from equations or calibration curves given in the paper.

Application of the Avrami theorem (13) gives analogues of [1], [2]

$$i = q_{mon}\pi S^2 D \exp(-\pi S^2 D N_o t) \quad [12]$$

$$i = q_{mon}\pi S^2 D A t \exp\left(\frac{-\pi S^2 D A t^2}{2}\right) \quad [13]$$

The forms of [12] and [13] are shown in Fig. 5 and 6. It is to be noted that the form of Fig. 6 is the same as that of Eq. [2] and experimentally indistinguishable from it.

Case (*ii*).—This limiting situation is likely to arise when a large number of nuclei are formed initially and the individual diffusion zones soon disappear. When the growth is controlled by linear diffusion, with Nernst equilibrium only at the growing patches the current-time curve can be calculated as for the adsorption of organic molecules (17, 18). The expression assuming a linear isotherm is (19)

$$i = \frac{zFA'C^*D^{1/2}}{\pi^{1/2}t^{1/2}} - \left\{\left(\frac{zFA'^2C^{*2}D}{m}\right)\left(\exp - \frac{z\mathbf{F}\eta}{RT}\right)\right.$$
$$\left.\exp\left[\frac{C^{*2}DA'^2t}{m^2}\left(\exp - \frac{2z\mathbf{F}\eta}{RT}\right)\right]\right.$$
$$\left.\operatorname{erfc}\left[\frac{C^*D^{1/2}A't^{1/2}}{m}\left(\exp - \frac{z\mathbf{F}\eta}{RT}\right)\right]\right\} \quad [14]$$

which is to be compared with the well-known situation

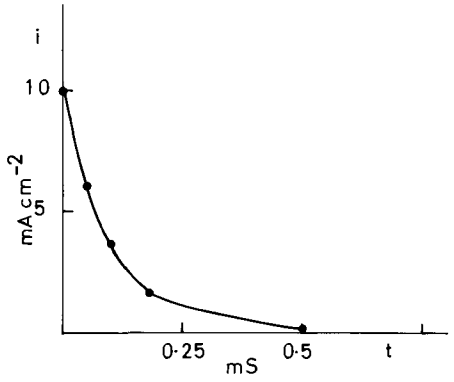

Fig. 5. Current-time transient for instantaneous two-dimensional nucleation with diffusion control.
$\pi S^2 D q_{mon}$ = 10 ma cm^{-2}
q_{mon} = 1.0 mcoul cm^{-2}
N_o = 10^6

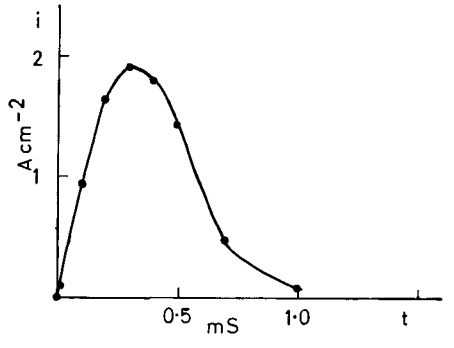

Fig. 6. Current-time transient for progressive two-dimensional nucleation with diffusion control.
$q_{mon}\pi S^2 DA$ = 10^7 ma cm^{-2} sec^{-1}
A = 10^6 sec^{-1}
q_{mon} = 1.0 mcoul cm^{-2}

when the whole of the surface appears to be active to cations approaching the surface

$$i = zFAC^*\left[1 - \exp\left(-\frac{z\mathbf{F}\eta}{RT}\right)\right]\frac{D^{1/2}}{\pi^{1/2}t^{1/2}} \quad [15]$$

Conclusions

Since the steady-state response for metal deposition under conditions where the formation of two-dimensional nuclei is rate determining has no remarkable features, evidence for 2D nucleation must be obtained from transient experiments. An exact time dependent analysis is only possible under potentiostatic conditions because two potential dependent parameters are involved.

Due to the presence of (*i*) a large number of bounded areas and (*ii*) large numbers of dislocations (possibly screw dislocations) which act as growth sites, in real metallic surfaces it may not be possible to observe the predicted i-t or η-t oscillations even if 2D nucleation occurs. However there are certain other indications that 2D nucleation and growth control the rate of metal deposition, *e.g.*, the successful prediction of change of orientation with potential based upon the equilibrium orientation of a 2D nucleus (20).

Manuscript received Oct. 22, 1968.

Any discussion of this paper will appear in a Discussion Section to be published in the December 1969 JOURNAL.

SYMBOLS

A nucleation rate (cm^{-2} sec^{-1})
A' area of the electrode (cm^2)
C^* concentration in the bulk of the solution (mole cm^{-3})
C^o concentration at the surface (mole cm^{-3})
D diffusion coefficient (cm^2 sec^{-1})
i current density (amp cm^{-2})
i_n current density due to the n^{th} layer
m number of moles in a monolayer of area A'
M molecular weight
N_o number of nuclei formed instantaneously (cm^{-2})
l height of edge (cm)
$q_{mon} = \frac{z\mathbf{F}l\rho}{M}$ charge involved in the formation of a monolayer (coulombs cm^{-2})
R Radius of center (cm)
S_n fraction of area covered by n^{th} layer
S_{ex} fraction of area with no account taken of overlap
V rate of advance of an edge (cm sec^{-1})
t, u } time (sec)
$\beta_n = \frac{\pi V_n^2 A_n}{3}$
η crystallization or nucleation overpotential (volts)
ρ density (g ml^{-1})

REFERENCES

1. T. Erdey-Gruz and M. Volmer, *Z. physik. Chem.*, **157**, 165 (1931).
2. E. Budeoski, W. Bostanoff, T. Vitanoff, Z. Stoinoff, A. Kotzewa, and R. Kaischew, *Phys. Stat. Sol.*, **13**, 577 (1966); *Electrochim. Acta*, (1966).
3. A. Bewick, M. Fleischmann, and H.R. Thirsk, *Trans. Faraday Soc.*, **58**, 2200 (1962).
4. M. Fleischmann, K. S. Rajagopalan, and H. R. Thirsk, *ibid.*, **59**, 741 (1963).
5. M. Fleischmann, J. Pattison, and H. R. Thirsk, *ibid.*, **61**, 1256 (1965).
6. R. D. Armstrong, M. Fleischmann, and H. R. Thirsk, *J. Electroanal. Chem.*, **11**, 208 (1966).
7. R. D. Armstrong and M. Fleischmann, *Z. physik. Chem.*, (1967).
8. R. D. Armstrong, M. Fleischmann, and J. W. Oldfield, *J. Electroanal. Chem.*, **14**, 235 (1967).
9. R. D. Armstrong, D. F. Porter, and H. R. Thirsk, *J. Phys. Chem.*, **72**, 2300 (1968).
10. M. Fleischmann, J. A. Harrison, and H. R. Thirsk, *Trans. Faraday Soc.*, **61**, 2742 (1965).
11. R. D. Armstrong, *J. Electroanal. Chem.*, **20**, 168 (1969).
12. M. Fleischmann and H. R. Thirsk in "Advances in Electrochemistry and Electrochemical Engineer-

ing," Vol. 3, p. 123, P. Delahay, Editor, John Wiley & Sons, Inc., New York (1963).
13. M. Avrami, *J. Chem. Phys.*, **9**, 177 (1941).
14. D. C. Cornish, S. N. Das, D. J. G. Ives, and R. W. Pittman, *J. Chem. Soc.*, A, 111 (1966).
15. B. Behr, *J. Electroanal. Chem.*, **19**, 373 (1968).
16. F. C. Frank, *Proc. Roy. Soc.*, **A201**, 586 (1950).
17. P. Delahay and I. Trachtenberg, *J. Am. Chem. Soc.*, **79**, 2355 (1957).
18. W. H. Reinmuth, *J. Phys. Chem.*, **65** 473 (1961).
19. D. J. Astley, J. A. Harrison, and H. R. Thirsk, *J. Electroanal. Chem.*, **19**, 325 (1968).
20. N. A. Pangarov and V. Velinov, *Electrochim. Acta*, **11**, 1753 (1966).

A New Cell for Electrochemical Studies at Elevated Temperatures: Design and Properties of a Cell Involving a Combination of Thorium Oxide-Yttrium Oxide and Zirconium Oxide-Calcium Oxide Electrolytes[1]

Ju. D. Tretyakov[2]

Moscow State University, Moscow, U.S.S.R.

and Arnulf Muan

Department of Geochemistry and Mineralogy, The Pennsylvania State University, University Park, Pennsylvania

ABSTRACT

A "double-cell" involving a combination of ZrO_2-CaO and ThO_2-Y_2O_3 solid electrolytes has been developed for emf measurements at elevated temperatures. The cell utilizes the desirable properties of the ZrO_2-CaO electrolyte at relatively high oxygen pressures and the desirable properties of the ThO_2-Y_2O_3 electrolyte at very low oxygen pressures to make it operative over a considerably wider range of oxygen pressures than has been possible with previously described cells.

Galvanic cells involving solid electrolytes with oxygen-ion conductivity are being used widely in investigations of thermodynamic and kinetic properties of materials at elevated temperatures (1, 2). Such cells also have potential applications as fuel cells (3).

The most commonly used electrolyte is a solid solution of zirconia and lime [85 m/o (mole per cent) ZrO_2, 15 m/o CaO], which at moderately high temperatures (*e.g.*, 700°-1400°C) is a practically pure ionic conductor over a wide range of oxygen pressures (P_{O_2}). This electrolyte performs well even at oxygen pressures above 1 atm. For instance, a preliminary investigation (4) has shown that appreciable hole conductivity at 1000°C appears only if $P_{O_2} > 100$ atm. However, the 85% ZrO_2 15% CaO electrolyte is not suitable at very low oxygen pressures because of the appearance of electronic conductivity according to the reaction

$$O_O \rightarrow \tfrac{1}{2} O_2\,(g) + V_O^{\cdot\cdot} + 2e' \qquad [1]$$

where O_O is an oxygen atom in a regular oxygen site, $V_O^{\cdot\cdot}$ is a doubly ionized oxygen vacancy, and e' is an excess electron. Applying the method of coulometric titration, Tretyakov (5) found that the average value of the ionic transference number, $\bar{t}_i$,[3] was $\geqq 0.99$ (and hence the average value of the electronic transference number, $\bar{t}_e$, $\leqq 0.01$) if

$$\log_{10} P_{O_2} \geqq -\frac{60.5 \cdot 10^3}{T} + 23.5 \qquad [2]$$

Thoria-yttria solid solutions (with 5-10 m/o Y_2O_3) (7, 8) have been found to be a more satisfactory electrolyte than ZrO_2-CaO at very low oxygen pressures. However, the ThO_2-Y_2O_3 electrolyte has the serious disadvantage of developing a significant hole conductivity at moderate oxygen pressures. This hole conductivity has been shown (9) to be strongly temperature dependent.

The present work has two main objectives: (*a*) to design a galvanic cell which combines the desirable properties of the ThO_2-Y_2O_3 electrolyte at very low oxygen pressures and the desirable properties of the ZrO_2-CaO electrolyte at relatively high oxygen pressures; (*b*) to determine the conditions of appearance of electronic conductivity in the ThO_2-Y_2O_3 electrolyte of this cell as a function of temperature.

Description of the Cell

The design of the cell is shown schematically in Fig. 1. The feature of main interest is the two concentric, impervious tubes, an outer 85 m/o ZrO_2 15 m/o CaO tube[4] and an inner 92 m/o ThO_2 8 m/o Y_2O_3 tube,[4] each closed in one end. The two tubes separate the electrode to be investigated, located inside the inner tube, from the reference electrode, located outside the outer tube, allowing only transport of oxygen ions through the double electrolyte. In the space between the two electrolyte tubes there is a partially oxidized Co strip which acts as a buffer, keeping the

[1] Contribution No. 67-80 from College of Earth and Mineral Sciences, The Pennsylvania State University, University Park, Pa.

[2] At the time of this work, Dr. Tretyakov was a visiting scientist at the Pennsylvania State Unversity under the 1967-1968 U.S.S.R.-U.S.A. exchange scholar program.

[3] According to Wagner (6)

$$\bar{t}_i = \frac{\int_{\mu_O'}^{\mu_O''} t_i \, d\mu_O}{\mu_O'' - \mu_O'}, \qquad [3]$$

where t_i is the true value of the ionic transference number, and μ_O' and μ_O'' are the oxygen chemical potentials on the two sides of the solid electrolyte.

[4] The tubes were manufactured by the Zirconium Corporation of America. The dimensions and impurity levels of the tubes (in wt. %) are approximately as follows: ZrO_2-CaO tube (12″ long, ½″ O.D., ⅜″ I.D.): Aluminum, 0.09%; Iron, 0.07%; Magnesium, 0.15%; Titanium, 0.07%; Silicon, 0.29%. ThO_2-Y_2O_3 tube (12″ long, ⅜″ O.D., 9/32″ I.D.): Aluminum, 0.02%; Boron, 0.002%; Calcium, 0.001%; Cobalt, 0.003%; Copper, 0.002%; Iron, 0.03%; Magnesium, 0.005%; Molybdenum, 0.001%; Nickel, 0.001%; Potassium, 0.001%; Silicon, 0.06%; Sodium, 0.003%.

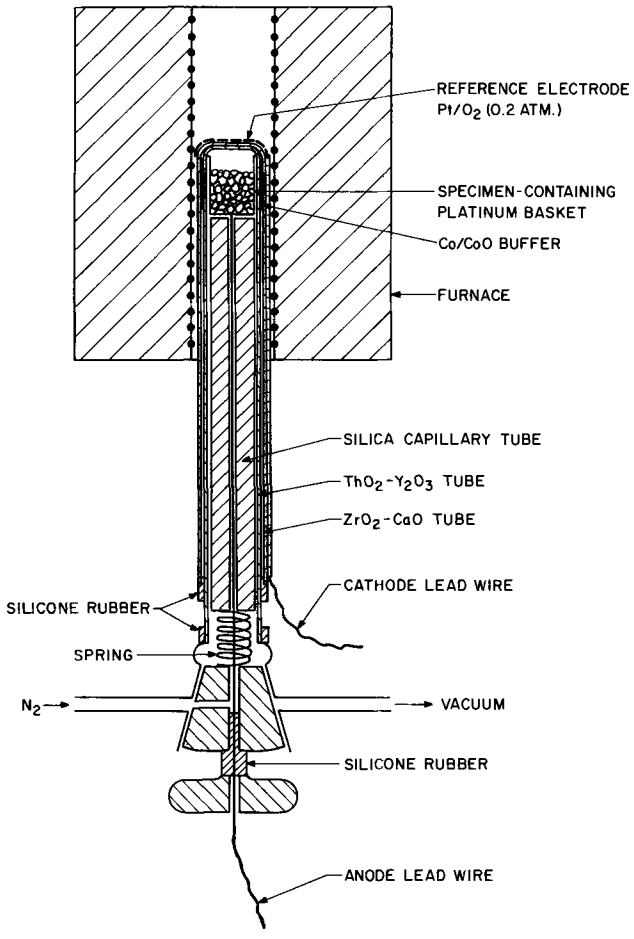

Fig. 1. Schematic diagram showing main features of new cell combining ThO_2-Y_2O_3 and ZrO_2-CaO electrolytes for electrochemical studies at elevated temperatures (compare text).

oxygen pressure in this space equal to that of the Co/CoO equilibrium at a given temperature. The rest of the space between the tubes is filled with nitrogen gas, and the two tubes are attached to each other with a gas-tight silicone rubber seal which is indifferent to the gaseous phase up to 200°C. The same sealing technique is used to attach the ThO_2-Y_2O_3 tube to the ground-glass joint at the lower end of the apparatus.

The material to be investigated is contained in a small platinum basket (~7 mm OD, ~15 mm long) near the closed end of the ThO_2-Y_2O_3 tube. A silica-glass capillary tube occupies the major part of the remaining volume inside the ThO_2-Y_2O_3 tube. The remaining, free volume inside the ThO_2-Y_2O_3 tube is small and accurately known [the method of precise determination of free volume of such a chamber has been described elsewhere (10)]. The tip of the inner surface of the ThO_2-Y_2O_3 tube, as well as the outer surface of the tip of the ZrO_2-CaO tube, is coated with a porous platinum film. Good contact is ensured between the specimen-containing platinum basket and the ThO_2-Y_2O_3 electrolyte by means of a spring at the lower end of the apparatus. This spring exerts pressure on the silica-glass capillary tube inside the ThO_2-Y_2O_3 tube. A platinum wire attached to the specimen-containing basket goes through the silica-glass capillary tube, through the male part of the ground-glass joint (silicone rubber sealing), and to a very sensitive potentiometer. The reference electrode consists of platinum gauze in contact with air (P_{O_2} = 0.21 atm) and wired firmly to the platinum film at the outer surface of the tip of the ZrO_2-CaO tube. A platinum lead wire is attached to the platinum gauze. The wire as well as the Pt-Pt 10% Rh thermocouple wires used to measure temperature are insulated from the electrolyte by alumina capillary tubes. The cell is heated by a Kanthal-wound microfurnace (15 mm ID, 150 mm long) with low heat capacity. The EMF of the cell is measured with a Guildline 9160-1 potentiometer assembly, which includes a narrow galvanometer combined with a photocell amplifier.

Experimental Procedures Used in Testing the Performance of the Cell

The platinum basket with the material to be investigated is introduced into the ThO_2-Y_2O_3 tube. The latter is evacuated, heated to 50°-60°C, and filled with nitrogen at pressure slightly in excess of 1 atm. The ThO_2-Y_2O_3 tube is then closed by turning the glass graded seal, and the cell is heated to the maximum temperature of the experiment (in the present case usually 1100°C). In order to maintain the electrolyte tubes impervious as long as possible, it is important to change the temperature of the cell slowly—in no experiments did the rate of heating or cooling exceed 300°C/hr.

The emf's of the following cells were measured in order to check the performance of the apparatus under various experimental conditions:

$$\text{air } (P_{O_2} = 0.21 \text{ atm}) \,|\, \text{Pt} \,|\, ThO_2(Y_2O_3) \,|\, ZrO_2(CaO) \,|\, \text{Pt} \,|\, \text{air } (P_{O_2} = 0.21 \text{ atm}) \quad (A)$$

$$O_2(P_{O_2} = 1 \text{ atm}) \,|\, \text{Pt} \,|\, ThO_2(Y_2O_3) \,|\, ZrO_2(CaO) \,|\, \text{Pt} \,|\, \text{air } (P_{O_2} = 0.21 \text{ atm}) \quad (B)$$

$$\text{Fe,Fe}_{1-x}\text{O} \,|\, \text{Pt} \,|\, ThO_2(Y_2O_3) \,|\, ZrO_2(CaO) \,|\, \text{Pt} \,|\, \text{air } (P_{O_2} = 0.21 \text{ atm}) \quad (C)$$

$$\text{Mn,MnO} \,|\, \text{Pt} \,|\, ThO_2(Y_2O_3) \,|\, ZrO_2(CaO) \,|\, \text{Pt} \,|\, \text{air } (P_{O_2} = 0.21 \text{ atm}) \quad (D)$$

The electrode $Fe,Fe_{1-x}O$ was prepared by sintering a pelletized mixture of high-purity metal and Fe_2O_3 (molar ratio 4:1) in an evacuated and sealed silica tube at 1000°C for 24 hr. The electrode Mn,MnO was prepared by sintering a pressed mixture of Mn metal and Mn_3O_4 (molar ratio 5:1) in an alumina container in a nitrogen atmosphere at 1100°C for 24 hr. Measurements of the emf's of the cells were made over the temperature range 700°-1100°C.

Results of these measurements for the four cells are shown in Fig. 2. The results presented are typical of the more extensive sets of data which were obtained; for sake of clarity the number shown has been reduced. Cell (*A*) produces the emf of zero ±0.5 mv over the entire temperature range, showing that there is practically no emf developed in our apparatus in addition to that created by the different oxygen potentials on the two sides of the double solid electrolyte according to the equation

$$E = \frac{1}{2\mathbf{F}} \int_{\mu_o'}^{\mu_o''} t_i \, d\mu_o \qquad [4]$$

where **F** is Faraday's number, t_i is the transference number of oxygen ions, and μ_o' and μ_o'' are the oxygen potentials on the inner surface of the ThO_2-Y_2O_3 electrolyte and on the outer surface of the ZrO_2-CaO electrolyte, respectively. The emf of cell (*B*) is in good agreement (deviations $\leqq$ 0.7 mv) with the value calculated from Eq. [4], assuming $t_i = 1$, *i.e.* $E = 1/2\mathbf{F}\ (\mu_o'' - \mu_o') = RT/4\mathbf{F} \ln P_{O_2}''/P_{O_2}'$. This is remarkable, in view of the fact that a ThO_2-Y_2O_3 solid electrolyte, when used alone, has considerable hole conductivity under similar conditions. For instance, Wimmer, Bidwell, and Tallan (9) have shown that in the cell

$$O_2(P_{O_2} = 0.08 \text{ atm}) \,|\, \text{Pt} \,|\, ThO_2(Y_2O_3) \,|\, \text{Pt} \,|\, O_2(P_{O_2} = 1 \text{ atm})$$

the average ionic transference number is as low as ~0.7, independently of temperature in the range of 900°-1500°C.

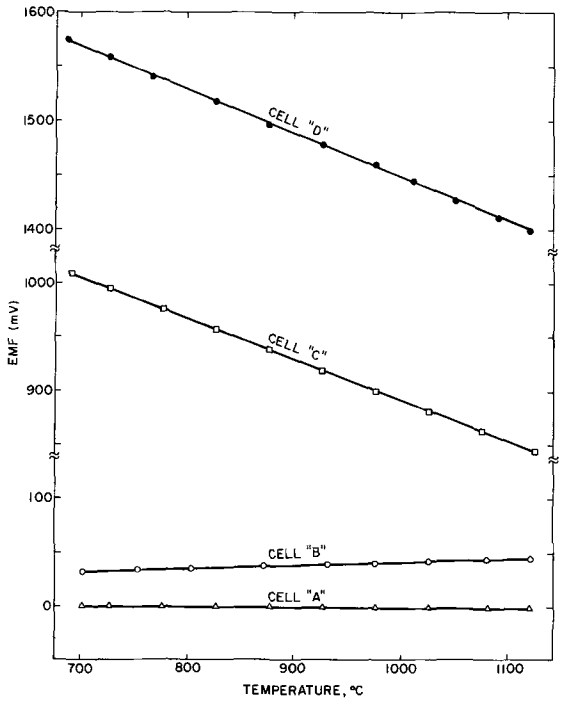

Fig. 2. Experimentally determined emf values as a function of temperature for cells "A," "B," "C," and "D" as described in the text.

In the double solid electrolyte shown in Fig. 1, practically pure ionic conductivity is maintained also at low oxygen pressures. Thus, the Gibbs free energies ΔG^o for the reaction Me + 1/2 O_2 = MeO (M = Fe,Mn) calculated from the emf's of cells (*C*) and (*D*) are in good agreement with the data of Chipman (11) and of Coughlin (12).

Determination of Conditions for Occurrence of Electronic Conductivity in the ThO_2-Y_2O_3 Electrolyte of the Present Cell

Theoretical background.—The occurrence of electronic conductivity at low oxygen pressures, and its pressure dependence according to

$$[e'] = K' P_{O_2}^{-1/4} \qquad [5]$$

are to be expected on the basis of reaction [1] (*see* p. 331). The corresponding mass-action expression is

$$P_{O_2}^{1/2}[V_o^{\cdot\cdot}][e']^2 = K \qquad [6]$$

For the ThO_2-Y_2O_3 electrolyte, $[V_o^{\cdot\cdot}] = \frac{1}{2}[Y'_{Th}] = Y_2O_{3_{total}}$ = constant. The ionic transference number may be written

$$t_i = \frac{\sigma_i}{\sigma_i + \sigma_e} = \frac{1}{1 + K''[e']} \qquad [7]$$

assuming that electronic conduction σ_e is proportional to $[e']$. Inserting Eq. [5] into Eq. [7], one obtains

$$t_i = \frac{1}{1 + (P_{O_2}^*/P_{O_2})^{1/4}} \qquad [8]$$

where $P_{O_2}^* = (K' \cdot K'')^4$. It is seen from Eq. [8] that $P_{O_2}^*$ is the oxygen pressure which corresponds to $t_i = 0.5$. Inserting Eq. [8] into Eq. [4] and taking into account that $\mu_o = \mu_o^o + RT \ln P_{O_2}^{1/2}$, one obtains (3) the following expression

$$E = \frac{RT}{F} \ln \frac{(P_{O_2}^*)^{1/4} + (P_{O_2''})^{1/4}}{(P_{O_2}^*)^{1/4} + (P_{O_2'})^{1/4}} \qquad [9]$$

If $P_{O_2'} << P_{O_2}^* << P_{O_2''}$, Eq. [9] yields the expression

$$P_{O_2}^* = P_{O_2''} \exp\left(-\frac{4E_sF}{RT}\right) \qquad [10]$$

where E_s is the potential of a galvanic cell in which the equilibrium oxygen pressure on one side of the solid electrolyte is determined by the self-dissociation of the electrolyte ($P_{O_2}^* >> P_{O_2'}$), leading to the occurrence of electronic conductivity.

Experimental.—The method of coulometric titration was used in the present investigation to measure E_s over a wide temperature range. In cell (*A*) (*see* p. 332) oxygen was removed from the inner compartment of the ThO_2-Y_2O_3 tube by the application of a suitable external voltage. The titration current varied between 0.2 and 2 ma, and every charge consisted of 0.5-1 coulomb. After every charge, the external circuit was disconnected, and the emf was measured. High and very unstable emf values, resulting from polarization of the electrolyte, were followed by stable emf values corresponding to equilibrium states of the system. One of the curves showing emf as a function of charge at 900°C is presented in Fig. 3. It is seen that the emf increases during the initial stage of the coulometric titration and then reaches a practically constant value. Results of the determination of the free volume of the inside of the cell show that the titration curves of Fig. 3 are consistent with a complete removal of the oxygen which was originally present in this compartment of the cell. If the solid electrolyte is stable under similar conditions and is impervious to oxygen, the curve emf = $f(q)$ would go toward infinity. Stability of the maximum emf value proves gas-tightness of the solid electrolyte tube. The stable, fixed plateau-value of the emf results from proper dissociation of the ThO_2-Y_2O_3 electrolyte, *i.e.* emf = E_s in Eq. [10]. The results of the determination of E_s as a function of temperature, as shown in Fig. 4, can be expressed by the following equation:

$$E_s(V) = 2.87 - 7 \cdot 10^{-4} T (\pm 0.02, 1000°\text{-}1400°K)$$

From this equation and Eq. [10] it follows that for the ThO_2-Y_2O_3 electrolyte

$$\log_{10} P_{O_2}^* = -\frac{56.25 \cdot 10^3}{T} + 13.36 \ (1000°\text{-}1400°K) \qquad [11]$$

Assuming that the range of applicability of the ThO_2-Y_2O_3 electrolyte is limited by the oxygen-pressure range in which the average value of the ionic transference number t_i is $\geqq 0.99$, and taking into account the analysis of Vetcher (14), one obtains

$$\log_{10} P_{O_2}^{**} = -\frac{56.25 \cdot 10^3}{T} + 17.36 \ (1000°\text{-}1400°K) \qquad [12]$$

where $P_{O_2}^{**}$ is the minimum value of the oxygen pres-

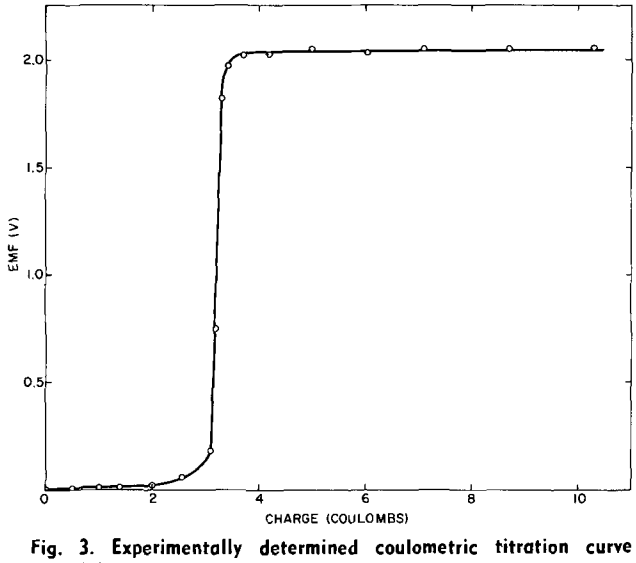

Fig. 3. Experimentally determined coulometric titration curve for cell "A" (compare text).

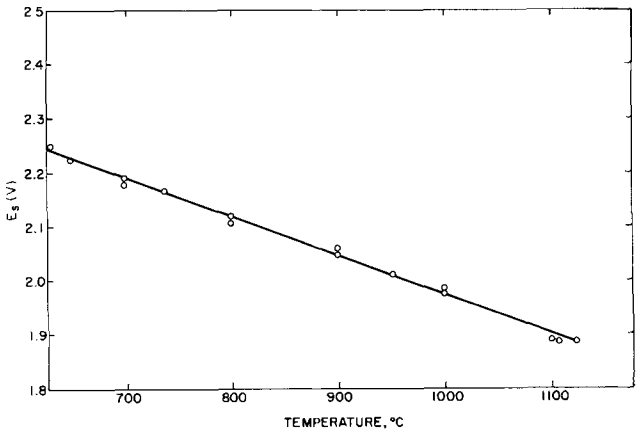

Fig. 4. Experimentally determined values of E_s as a function of temperature for ThO_2-Y_2O_3 electrolyte of the present cell (compare text).

sure for which electron transport in the solid electrolyte causes an error in the determination of the thermodynamic emf not exceeding 1% (the usual limit of accuracy in such measurements).

General Considerations and Conclusions

In applying the ThO_2-Y_2O_3 solid solution as electrolyte in galvanic cells, one must take into account that direct contact between the electrolyte and the electrode to be investigated may result in considerable decrease of the emf because of polarization effects (15), surface contamination, oxidation of the electrode, or reaction between the electrolyte and the adjacent solid phases. Hence, it would be more correct to consider Eq. [11] as the condition of applicability of the ThO_2-Y_2O_3 solid electrolyte only if there is no direct contact between the electrolyte and the solid phases of the electrodes, *i.e.* if equilibrium between electrolyte and solid phases is established through the gas phase only.

Acknowledgment

The authors wish to thank A. G. King of the Zirconium Corporation of America for his cooperation in making ThO_2-Y_2O_3 tubes available on short notice.

Manuscript submitted July 25, 1968; revised manuscript received Dec. 6, 1968.

Any discussion of this paper will appear in a Discussion Section to be published in the December 1969 JOURNAL.

REFERENCES

1. H. Schmalzried, "Thermodynamics," Vol. 1, p. 93, IAEA, Vienna (1966).
2. "Proceedings, Electromotive force measurements in High-Temperature Systems," Institute for Mining and Metallurgy, London (1968).
3. J. Weissbart and R. Ruka, *This Journal*, **109**, 723 (1962).
4. B. Steele and C. B. Alcock, Personal communication.
5. Ju. D. Tretyakov, *Vesn. Mosk. Univ., Ser. II, Khim.* (In press).
6. C. Wagner, *Z. Physik. Chem.*, **B21**, 25 (1933).
7. B. C. H. Steele and C. B. Alcock, *Trans. Met. Soc. AIME*, **233**, 1359 (1965).
8. T. L. Markin and M. H. Rand, "Thermodynamics," p. 145, Vol. 1, IAEA, Vienna (1966).
9. J. M. Wimmer, L. R. Bidwell, and N. M. Tallan, *J. Am. Ceram. Soc.*, **50**, 198 (1967).
10. Ju. D. Tretyakov, *Neorg. Materials (USSR)*, **2**, 501 (1966).
11. J. Chipman, *J. Pure Appl. Chem.*, **5**, 361 (1962).
12. J. P. Coughlin, *U.S. Bur. Mines Bull.*, 542 (1954).
13. H. Schmalzried, *Z. Elektrochem.*, **66**, 572 (1962).
14. A. A. Vetcher, *Russ. J. Phys. Chem.*, **41**, 685 (1967).
15. A. R. Kaul, M. S. Dissertation, University of Moscow (1967).

Studies of Electrooxidation of Dextrose in Neutral Media

M. L. B. Rao[1] and Roger F. Drake*

Monsanto Research Corporation, Boston Laboratory, Everett, Massachusetts

ABSTRACT

Electrooxidation of dextrose on platinized platinum electrodes has been studied in phosphate buffer at *p*H 7.4. Rest potentials are interpreted as mixed potentials. Galvanostatic curves have been observed to exhibit oscillatory voltage behavior. In the range of potentials investigated gluconic acid is observed as the reaction product and is found to inhibit oxidation of dextrose due to adsorption on the electrode surface. From the measurements of the adsorption characteristics of the acid, the oscillatory voltage behavior of the galvanostatic curves have been ascribed to kinetic effects of formation of the product and the potential dependence of its adsorption.

Anode-cathode couples based on redox components of the blood are under investigation in a program to study the feasibility of an implantable fuel cell for an artificial heart (1). The possibility of utilizing the dextrose in blood as fuel for this purpose is contemplated. Therefore, tests are carried out at the blood *p*H of 7.4.

Literature on the electrochemistry of dextrose is limited. Polarographic reduction of the carbohydrate was treated by Delahay and Strassner (2). Bockris, Piersma, and Gileadi (3) reported electrooxidation of dextrose in aqueous alkali at high temperature. Mention is made of dextrose oxidation in acid media by Bagotsky and Vasilyev (4). In contrast to previous investigations, this paper is devoted exclusively to a detailed analysis of the electrooxidation of dextrose in neutral media.

* Electrochemical Society Active Member.
[1] Present address: P. R. Mallory, Inc., Laboratory for Physical Science, North West Industrial Park, Burlington, Mass.

Experimental

Electrodes.—The working electrode is a 3 cm^2 platinized platinum sheet spot welded to a platinum wire, which is embedded in a glass tube. Before platinizing, the electrode surface is cleaned in concentrated nitric acid and flamed. It is then platinized at 10-20 ma/cm^2 for 10-20 min in a H_2PtCl_6 platinizing solution.

The counter electrode is a platinized platinum gauze of apparent area 10 cm^2.

A standard calomel electrode (SCE), immersed in the electrolyte through a Luggin capillary situated at the working electrode, serves as the reference for the measurement of potential.

Electrolyte and cell.—Reagent grade chemicals and distilled water are used to prepare the solutions. The electrolyte is a 1M phosphate buffer (19.85g K_2HPO_4, 22g $Na_2HPO_4 \cdot 12H_4O$, and 29g NaCl per liter) of pH 7.4. Known amounts of dextrose or gluconic acid or both are added to the electrolyte as required. Measurements are carried out at room temperature employing freshly deaerated solutions. An H-type cell with a fine sintered glass frit separating the two compartments is used in the experiments.

Measuring procedure and equipment.—The rest potential of the working electrode is first determined in the deaerated dextrose solution. The electrode is then set at the value of the rest potential by means of a potentiostat. At predetermined time intervals, the potentiostat circuit is switched off and a constant anodic current is passed by means of a galvanostatic circuit and a mercury wetted relay switch. On application of the galvanostatic current, the working electrode assumes more positive values. When the electrode potential exhibits a point of inflection in the range of 0 to +0.25v (*vs.* SCE), the galvanostatic current is switched off, and the electrode is returned to the control of the potentiostat. Between measurements, the electrolyte is stirred by bubbling nitrogen for 40 sec. When the gas is turned off, an additional 60 sec is allowed to obtain minimum turbulence. The galvanostatic pulse is again applied, and the sequence of operation is repeated for further measurements. In the absence of the potentiostatic circuit, it is observed that the decay of the electrode potential subsequent to anodization to the initially observed rest potential is slow and is not reproducible, possibly due to formation of platinum oxides or sorption of the reaction product. By utilizing the potentiostatic circuit, either the reduction of platinum oxide or the desorption of the product is accomplished, and thus reproducible surface conditions are established.

A 610A Keithley Electrometer, Wenking Potentiostat, Tektronix Oscilloscope Model 545 with Type-L Plug-in unit, a strip chart recorder, 6200-B Harrison D.C. power supply, and a mercury relay (Potter & Brumfield JM1-121-11) are used in the experiment. The circuitry is conventional.

Product analysis.—In order to determine the product, anodization is carried out at constant current employing small volumes of 0.5M dextrose solution and a large area working electrode. The potential of the electrolysis is restricted to $<+0.2$v (*vs.* SCE). The spent solution is analyzed for products by thin layer chromatography.

Results

Open-circuit behavior of dextrose half-cell.—On bright platinum electrodes immersed in a 0.01-0.5M dextrose solution in the deaerated electrolyte, the rest potential is in the range of -0.1 ± 0.05v. Platinized platinum electrodes, however, attain rest potentials of -0.65 ± 0.05v. Experiments reveal that the rest potential of the electrode is sensitive to the previous history of the electrode and impurities in the solution. This behavior is illustrated from data in Table I.

Dextrose oxidation.—Typical galvanostatic curves observed during the anodization of platinized platinum electrodes in 0.5M dextrose solution in the saline phosphate buffer are illustrated in Fig. 1. Curves 1 through 5 are for apparent current densities 4.26, 3.26, 2.6, 1.86, 1.3, and 0.66 ma/cm². The roughness factor of the electrode as determined by electrochemical hydrogen coverage is in the range of 80-150.

The total coulombic charge required to reach the point of inflection A in Fig. 1 varies with current density and is quantitatively represented in Fig. 2, curve 1. Voltage oscillations are observed in the current density region 2.6-1.3 ma/cm². At current densities of 0.66 ma/cm², voltage oscillations are not observed except just prior to occurrence of the point of inflection (*cf.* Fig. 1, curve 5).

Table I. Open-circuit potential established on platinized-platinum electrode in 0.5M dextrose solution in phosphate buffer (pH = 7.4)

Experimental condition	Observed open-circuit potential (volts *vs.* calomel)
Just after immersion of the electrode in the solution	−0.56
Solution deaerated with N_2 for 20 min	−0.65 ± 0.05
Subsequent to subjecting to cathodic pulse at 1 ma for 2 min	−0.66
Subsequent to subjecting to anodic pulse at 10 ma for 1 min	+0.15v
3 min after the anodic pulse	−0.55
20 min after the anodic pulse	−0.65 ± 0.05
On stirring the solution by introducing air	−0.1
Unstirred solution saturated with air	−0.56
Electrode potential subsequent to potentiostating at −0.66v (potentiostat requires ± <0.01 ma to maintain the potential)	−0.66

In order to understand the dextrose oxidation behavior, further experiments were carried out in the electrolyte solution containing 0.01, 0.05, 0.10M of the active material. The nature of the galvanostatic curves obtained in these experiments was similar to those represented in Fig. 1. However, at lower concentrations of dextrose, no oscillatory behavior was observed.

Considering the time (t or τ) required to attain the transition point A as the termination of oxidation of dextrose, the data are analyzed for constancy in it and $i\tau^{1/2}/c$, as in the measurement of coulometric adsorption coverage and in chronopotentiometry, respectively. The results indicate that neither it nor $i\tau^{1/2}$ is constant.

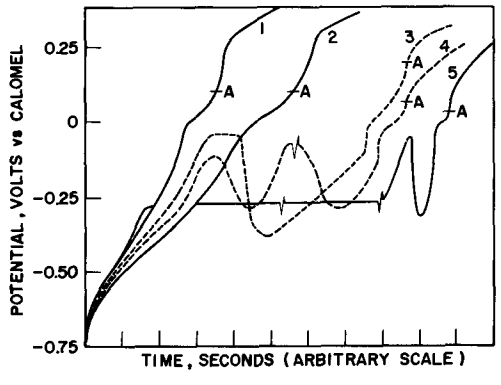

Fig. 1. Nature of dextrose curves. Curves 1 to 5 are for current densities 4.26, 3.26, 2.6, 1.86, 1.3, and 0.66 ma/cm², respectively. Electrolyte: 0.5M dextrose in phosphate buffer (pH = 7.4); electrode: (Roughness factor 150).

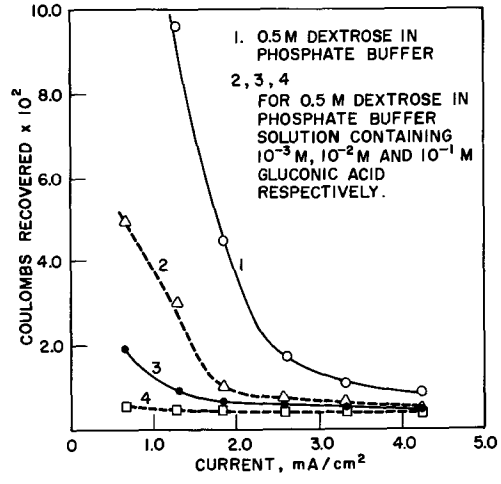

Fig. 2. Effect of gluconic acid on oxidation of dextrose. Curve 1, 0.5M dextrose in phosphate buffer. Curves 2, 3, and 4 are for 0.5M dextrose in phosphate buffer solution with 10^{-4}M, 10^{-2}M, and 10^{-1}M gluconic acid, respectively.

Under experimental conditions gluconic acid is observed as the product of dextrose electrooxidation. Stirring as well as increasing the temperature of the solution favors the requirement of higher charge coulombs to attain the transition point A in the galvanostatic curves.

Evaluation of the effect of the products of oxidation of dextrose on the behavior observed in Fig. 1 is made by obtaining polarization curves in 0.5M dextrose solution containing 0.001, 0.010, and 0.100M gluconic acid. The nature of the curves obtained in these experiments is similar to the ones in Fig. 1, except that the current density at which voltage oscillations occurred decreases with an increase in the concentration of gluconic acid. The charge coulombs required to reach the point of inflection A in Fig. 1 decreases at all current densities with increasing gluconic acid concentration in the dextrose solution. The results are represented in Fig. 2, curves 2, 3, and 4.

The platinized platinum electrodes used in the above experiments assume open-circuit voltages of +0.05 ± 0.05v in deaerated gluconic acid solution (10^{-4} to 10^{-1}M) in the saline buffer electrolyte. Anodic charging curves on the platinized platinum electrodes are taken in the electrolyte with and without gluconic acid in order to examine whether there is evidence for the oxidation of gluconic acid. These experiments are carried out from the open circuit voltage as well as from —0.65v (*vs.* SCE). The latter potential is chosen since it is the open-circuit voltage of dextrose solution. It is observed that in either case, the nature or coulombic charge required to reach the point of inflection on the anodic curve was not significantly different in the two solutions. This suggested gluconic acid does not undergo further oxidation in the voltage range of investigation.

In order to understand the mechanism of inhibition of dextrose oxidation induced by gluconic acid (*cf.* Fig. 2, curves 2-5), the adsorption characteristics of the acid were studied. The method of investigation consisted of taking cathodic charging curves of platinized platinum electrodes immersed in the saline buffer of the electrolyte at various levels of gluconic acid content. Taking the charging curves from different initial potentials, Q_H, the hydrogen coverage was determined as a function of potential. In this procedure, the difference in Q_H observed in the two solutions at any given potential would reflect the number of hydrogen adsorption sites which are occupied by gluconic acid. This procedure and method of computation of θ, the fraction of total surface covered by gluconic acid, is similar to that employed by Breiter and Gilman (5) for obtaining the potential dependence of adsorption of methanol in acid electrolyte. For example, the hydrogen coverage of an electrode was 83.3 mc/cm² at —0.2v. This value was observed to have changed to 73.3, 61.7, and 51.3 mc/cm² in the presence of 0.0001, 0.01, and 0.5M gluconic acid concentration, respectively. Based on the results the θ_{GA} values of 0.12, 0.26, and 0.38, respectively, were calculated. Similar computation of observed data yielded the variation of θ_{GA} with potential at different concentrations of gluconic acid and this is shown in Fig. 3. θ_{GA} for gluconic acid is potential dependent, and the maximum adsorption occurs in the region of —0.35 to —0.2v (*vs.* SCE).

Discussion

The open-circuit potentials in Table I, exhibited by oxide-free platinized platinum electrodes immersed in dextrose-containing saline phosphate buffer solution, may be considered as mixed potentials of the following reactions

$$O_2 + 4H^+ + 4 \rightarrow 2H_2O$$
$$E^o_{pH7.4} = +0.55v \text{ } vs. \text{ calomel} \quad [1]$$
$$R\text{-}CHO + H_2O \rightarrow R\text{-}COOH + 2H^+ + 2e$$
$$E^o_{Dextrose,\ pH7.4} = -0.625v \text{ } vs. \text{ calomel (6)} \quad [2]$$
$$2H^+ + 2e \rightarrow H_2 \quad E^o_{pH7.4} = 0.68v \text{ } vs. \text{ calomel (7)} \quad [3]$$

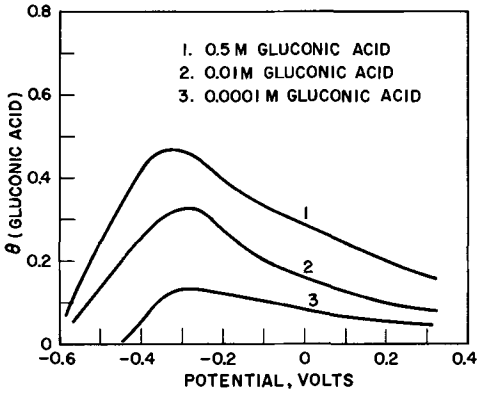

Fig. 3. Variation of surface coverage of gluconic acid with electrode potential.

where R- represents the $CH_2OH(CHOH)_4$ group of the dextrose molecule.

Considering the facts that (*i*) the open-circuit potentials are sensitive to the presence of oxygen; (*ii*) gluconic acid has been identified as reaction product; and (*iii*) the open-circuit potentials are close to the reversible hydrogen electrode potentials; it is suggested that the rest potentials are mixed potentials of reactions represented in Eq. [1], [2], and [3]. In thoroughly deaerated solutions, the effect of reaction in Eq. [1] is negligible because of very low partial pressure of oxygen.

The electrooxidation products of dextrose in the electrolyte obviously depend on the polarization voltage of the electrode. In the voltage range of investigation, *i.e.*, from —0.65 to +0.2v (*vs.* SCE) gluconic acid is found as a reaction product. It is also noted that gluconic acid does not seem to undergo further oxidation in this voltage region, and has a tendency to adsorb on the electrode (Fig. 3). In the presence of gluconic acid, dextrose oxidation was noticed to be inhibited (cf. Fig. 2, curves 2 to 4). These facts suggest that production of gluconic acid and its tendency to adsorb on the electrode results in a decrease in active surface area for dextrose oxidation and, hence, the inhibition of the oxidation reaction. The low material efficiency observed for the reaction is thus explained.

The oxidation curves of dextrose are complicated as shown from the oscillatory voltage behavior represented in Fig. 1 and also from the analysis of the results which revealed lack of constancy in the computed values of it or $i\tau^{1/2}/c$. The complexities seem to arise due to kinetic effects of potential-dependent adsorption-desorption phenomena associated with the product, gluconic acid. The behavior may be explained phenomenologically.

Curves 1 through 5 in Fig. 1, observed for the dextrose oxidation reaction, may be grouped into three categories: (*i*) high current density region wherein no oscillatory voltage behavior is observed [*cf.* curves 1 and 2]; (*ii*) intermediate current density region for which oscillatory voltage behavior is observed as in curves 3 and 4; and (*iii*) the low current density region for which the oscillatory behavior is observed only prior to the attainment of the point of inflection A. As indicated, gluconic acid is the oxidation product. Since gluconic acid has been found to inhibit the oxidation of dextrose (Fig. 2, curves 2, 3, and 4), and since the extent of inhibition depends on the concentration of gluconic acid, it is of interest to consider the effect of pseudoequilibrium of adsorption of the electrogenerated acid in the system. The quantity of gluconic acid present under kinetic conditions in the diffusion layer and on the electrode depends upon the rate of production of the acid, *i.e.*, current density, and the rate of desorption and diffusion of the acid into the bulk of the solution. The experiments carried out under stirred electrolyte condition favor the pas-

sage of higher charge coulombs until attainment of the inflection point in comparison to unstirred solution. Based on this information it is inferred that both desorption and diffusion processes contribute to the removal of gluconic acid from the vicinity of the electrode, the latter being rate limiting. In the high current density region, presumably, the rate of production of the acid exceeds the rate of diffusion of the product into the bulk of solution, and hence a large concentration of the acid predominates at the electrode. The presence of a large concentration of gluconic acid at the electrode decreases the active area of the electrode, due to the pseudoequilibrium for the adsorption of the acid. Thus, the transition point A may be said to be reached soon because of a large decrease in active surface area. The potential dependence of adsorption is probably of secondary importance on curves 1 and 2 in Fig. 1 as they are inferred to be operating under the influence of a high concentration of adsorbable species. Because of the changes in active surface area of the electrode during the measurement, neither it or $it^{1/2}/c$ would be constant.

At medium current densities, the rate of production of gluconic acid and the rate of diffusion of the species away from the electrode are hypothesized to be approximately equal. This results in a steady concentration of gluconic acid in the diffusion layer. Under these conditions, for the pseudoequilibrium of adsorption of the acid, the potential dependence as observed in Fig. 3 becomes important. Thus, during anodization, when the electrode crosses the potential of maximum adsorption of the acid, desorption of the adsorbed species is favored. At this point, the effective surface area for dextrose oxidation increases, resulting in a decrease in the reaction overpotential, and the reversal of potential occurs. As the reaction proceeds, once again the accumulation of gluconic acid occurs; adsorption takes place, resulting in a decrease in surface area for dextrose oxidation. The latter process increases the reaction overpotential. Repetition of the aforementioned sequence results in oscillatory voltage behavior. The voltages at the turning point of the oscillatory voltage behavior observed for Fig. 1, curves 3 and 4, correspond reasonably well with the potential dependence of adsorption observed in Fig. 3, and thus the mechanism is substantiated.

In the low current density region, the rate of production of gluconic acid is presumed to be less than the rate of diffusion of the acid into the bulk of the solution, and hence a low concentration of the acid exists in the vicinity of the electrode. Under this condition the decrease in surface area due to adsorbed gluconic acid is small and the reaction proceeds uninhibited.

Termination of the dextrose oxidation at medium and low current density regions possibly occurs because of slow accumulation and adsorption of impurities. The impurities may be oxidation products of gluconic acid, and may have been generated from the very low partial currents effective for such reactions. This suggested that the oxidation products of gluconic acid would also effect the inhibition of dextrose oxidation. The effect of temperature to favor higher charge coulombs during electrooxidation of dextrose may be understood in terms of increased rate of removal of gluconic acid from the vicinity of the electrode, due to an increase in the value of diffusion coefficient of the species.

In earlier studies on small amplitude voltage oscillations, the behavior was observed for the oxidation of formaldehyde in sulfuric acid by Koch (6). The author has proposed the accumulation and desorption of a polymer product as the cause for the oscillatory behavior. Based on the results of this paper, the mechanism of the formation of a polymer product is an unlikely cause for the oscillatory voltage behavior observed in the case of dextrose oxidation.

It is recognized that the carbohydrate under investigation exists in two optical isomers. In the dextrose reduction reaction on mercury it is shown that only the open chain aldehyde form of the material is the electroactive species. Because of the inhibiting effect of the product of oxidation observed in the present experiments, it is not clear whether the activity of dextrose for oxidation at platinum depends on the structural and configurational parameters. Further insight into the problem has to come subsequent to the development of electrocatalysts capable of oxidizing the carbohydrate without the complication of adsorption of the product.

Acknowledgment

The authors wish to thank Dr. David L. Williams for helpful discussions, Mr. A. R. Doig, Jr., for providing the thin layer chromatographic analysis, and Mr. P. W. Orthmann and Mr. W. P. Brissette for technical assistance. This work was sponsored by the National Heart Institute, United States Department of Health, Education, and Welfare, contract PH43-66-976.

Manuscript submitted Aug. 9, 1968; revised manuscript received Nov. 20, 1968. This paper was presented at the Boston Meeting, May 5-9, 1968, as Paper 184.

Any discussion of this paper will appear in a Discussion Section to be published in the December 1969 JOURNAL.

REFERENCES

1. National Heart Institute Contract PH43-66-976 with Monsanto Research Corp., Boston Lab., Everett, Mass.
2. P. Delahay and J. B. Strassner, *J. Am. Chem. Soc.*, **74**, 893 (1952).
3. J. O'M. Bockris, B. J. Piersma, and E. Giliadi, *Electrochim. Acta*, **9**, 1329 (1964).
4. V. S. Bagotzky and Yu. B. Vasilyev, *ibid.*, **9**, 869 (1964).
5. M. W. Breiter and S. Gilman, *This Journal*, **109**, 622 (1962).
6. D. F. A. Koch, Proc. 1st Australian Conference on Electrochemistry, 1963, J. A. Friend, F. Gutmann and J. W. Hayes, Editors, p. 657, Pergamon Press, (1965).
7. C. W. Mansfield, "Oxidation Reduction Potentials of Organic Systems," Williams & Wilkins Co., Baltimore (1960).

Electroosmosis in Ion-Exchange Membranes

N. Lakshminarayanaiah

Department of Pharmacology, University of Pennsylvania School of Medicine, Philadelphia, Pennsylvania

ABSTRACT

Application of an electric field to the system, electrolyte solution ⇌ membrane ⇌ electrolyte solution, gives rise to unidirectional flow of solvent phenomenologically called electroosmosis. The volume of this transference depends primarily on membrane water content and the concentration of the electrolyte solution bounding the membrane on either side. For the passage of 1**F** of electricity, the quantity of electroosmotic flow in dilute solutions is shown by some investigators to be dependent on current density, while others claim it to be independent of current density. Recent measurements indicate that membranes with low water contents (less than about 14%) produce water flows independent of current density, while those with higher water contents show current dependence. However, at external concentration greater than 0.1*N*, the current dependence of water flow disappears and the flow decreases with increase in external concentration. These results and others are discussed in terms of existing theories of electroosmosis in charged membranes.

Application of an electric field to the system, electrolyte solution ⇌ membrane ⇌ electrolyte solution, causes not only transference of ions but also flow of liquid through the membrane. The number of moles of ions and of water transported for the passage of 1**F** of electricity are called ion transference number ($\bar{t}_i$) and water transference number ($\bar{t}_w$), respectively (overbar refers to membrane phase). The total water transport composed of two components—water of ion hydration and water transported electroconvectively—is designated purely phenomenologically by the well-known term electroosmosis. The flow of water usually takes place in the direction in which the counterions move and as a result the counterions move faster than coions, since they experience less resistance to movement than coions.

Electroosmosis is observed with all types of membranes. It is due to the presence of charged groups arising either by adsorption of one or more ionic species from solution onto the walls of the pores or by fixation to the membrane matrix by an appropriate chemical process. Presence of these fixed groups in an aqueous electrolyte medium leads to the type of ionic distribution associated with the electrical double layer.

All electrokinetic phenomena have been attributed to interactions between flow of electricity and flow of liquid in the double layer (1). A slipping plane between the fixed charges and the diffuse part of the double layer of opposite total charge density is usually envisaged and the electrical potential in this plane is identified with the zeta (ζ) potential. The classical theory of electroosmosis centers round the parameter ζ which cannot be measured directly. Without using this concept of ζ potential, Schmid and Schwarz (2-8) have dealt with the different electrokinetic phenomena in detail considering the membrane as a system composed of fine pore capillaries in which solution of fixed charges and their counterions existed. Disregarding this membrane structure, electrokinetic phenomena have been treated by the methods of thermodynamics of irreversible processes by Staverman (9) and Kedem and Katchalsky (10). Spiegler (11), on the other hand, using a pore model, has given a very illuminating treatment "in generality falling between Schmid's and Staverman's."

Some of our new results and those already existing in the literature are reviewed in the light of the equations developed by Schmid, Spiegler, and others (12, 13).

Key words: double layer, electroconvection, electroosmotic permeability, friction coefficient, ion transport number, membrane conductance, membrane fixed charge density, membrane porosity, surface charge density, water transport number, zeta potential.

Experimental

A number of investigators have measured water transport through various ion-selective membranes using different ions and a variety of techniques and cell designs (12-48). Basically two methods, one based on weight changes (12, 16, 34, 35, 44) and the other based on volume changes (13, 16-22, 24-30, 33, 36-39, 41-43, 45-48) have been used to measure total transport of water through ion-exchange membranes. Weight method is accurate with flexible membranes which are likely to move back and forth during electrolysis. It has the other advantage that volume changes due to salt transport, electrode reactions, and small temperature fluctuations need not be considered seriously. It calls for meticulous care in transferring solutions and washing the apparatus. In contrast, experiments by the volume method are easy to perform, provided temperature fluctuations are well controlled by a thermostat held constant to ± 0.01°. Its chief advantage is the innumerable number of experimental runs that may be carried out by simply reversing the direction of current flow in each succeeding run. The membrane movement may be controlled by the techniques described elsewhere (18, 39). All our new results given in this paper and those results referred to herein are obtained by the volume method (13, 18, 25, 27, 36, 39, 42, 46).

Results and Discussion

The work relating to electroosmosis in permselective membranes has been recently reviewed by Lakshminarayanaiah (49). Since then a few more papers dealing with different aspects of electroosmotic water flow have appeared (38-48). These and some of our new results are examined to emphasize the effects of different membrane parameters on $\bar{t}_w$.

Effects of various factors on $\bar{t}_w$.—Two major factors which act directly to control the amount of electroosmosis (*i.e.*, $\bar{t}_w$) in membranes are the water content of the membrane and the concentration of the external electrolyte solution. Normally $\bar{t}_w$ is found to decrease with decrease in the water content and to increase with the decrease in the electrolyte concentration. The data of Lakshminarayanaiah (42) realized for phenolsulfonate (PSA) membranes and given in Table I illustrate these effects. It should be noted that $\bar{t}_w$ values are determined by both the electrolyte concentration and the water content. To isolate the influence of one on $\bar{t}_w$ from the influence of the other is difficult. Recently, we have measured $\bar{t}_w$ keeping the external electrolyte concentration constant at 0.01*N*

Table I. $\bar{t}_w$ values for phenolsulfonate (PSA) membrane as functions of external NaCl concentration and water present in the membrane (42)

External electrolyte normality	Water content g H_2O/g wet membrane	Current density ma/cm²	$\bar{t}_w$
0.10	0.622	0.5-10.1	37.2
0.50	0.606	0.5-10.1	18.2
1.00	0.602	0.5-10.1	11.0
2.00	0.568	0.5-10.1	6.1
3.00	0.558	0.5-10.1	3.9
5.20	0.540	0.5-10.1	2.1

Table II. $\bar{t}_w$ values for AMF C-104 membrane with 0.01*N* solution

Current density ma/cm²	Li^+	Na^+	K^+	Rb^+	Cs^+
0.32	10.0	5.8	4.5	4.0	4.3
1.58	9.5	6.3	3.7	3.6	4.1
3.15	10.1	6.2	4.0	3.7	4.3
15.75	10.0	6.4	3.4	4.1	4.4
Water content: g H_2O/g wet membrane	0.132	0.121	0.118	0.115	0.112

but varying the nature of the cation. These new results obtained for AMF C-104 membranes and shown in Table II indicate that, besides showing the effect of the nature of the cation on $\bar{t}_w$, $\bar{t}_w$ does decrease with decrease in the membrane water content. The independent demonstration of the effect of the other factor, *i.e.* at constant water content increase of electrolyte concentration will decrease $\bar{t}_w$, is quite difficult, as electrolyte invasion of the membrane following increase in external concentration will always affect the membrane water content.

There are a few other factors which also affect $\bar{t}_w$ rather indirectly by affecting the water content of the membrane. They are, the temperature, the degree of crosslinking of the membrane, the fixed charge density of the membrane, and the current density employed in the measurement of $\bar{t}_w$.

Recently George and Courant (43) examined the effect of temperature and found $\bar{t}_w$ to decrease slightly with increase in temperature in the range 10°-40°C. Usually increase of temperature decreased the membrane water content and so the observed $\bar{t}_w$ variation with temperature was in accordance with the change in the water content of the membrane.

The effect of crosslinking on $\bar{t}_w$ depends on the way crosslinking affects again the membrane water content. The data of Lakshminarayanaiah (13) obtained for differently crosslinked polymethacrylic acid (PMA) membranes in contact with 0.01*N* NaOH solution are shown in Fig. 1. At any given current density, $\bar{t}_w$ value is greater the lower the crosslinking, because the membrane with the lower degree of crosslinking has higher water content.

The effect of fixed charge density on $\bar{t}_w$ is quite complex. No systematic study of this effect exists in the literature. Its effects may, however, be inferred from studies made on a number of membrane systems. In Table III are given the values of $\bar{t}_w$ derived by Lakshminarayanaiah and co-workers (27, 36, 39) for three membrane systems. In the case of PMA membrane whose water content is greater than PSA membrane, the $\bar{t}_w$ value is less than that of the PSA membrane. This follows from the fact that the water associated with an equivalent of counterion in PMA membrane is less than that of the PSA membrane. But the same is not seen in the case of untreated collodion membrane which in spite of an internal molality of 10.4 is still cation selective giving a water flow of 7.4 moles in the direction of the cation flow. These facts by themselves are acceptable but taken together

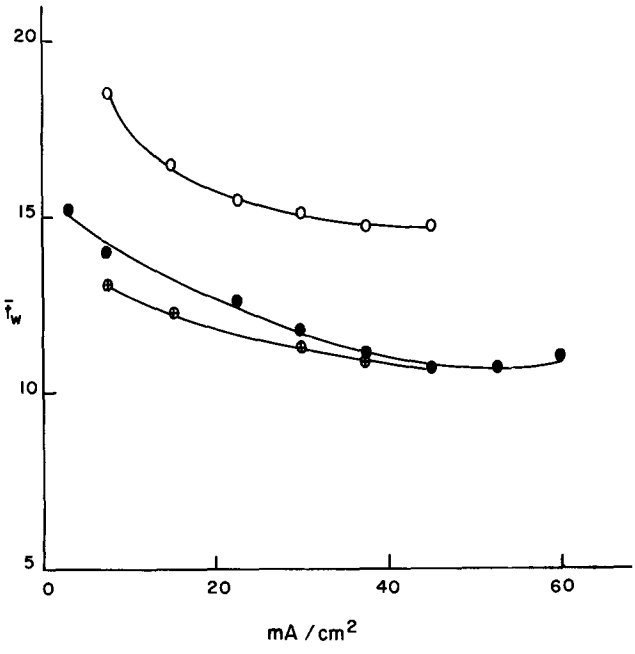

Fig. 1. $\bar{t}_w$ plotted as a function of current density for PMA membranes differently crosslinked with 5% (○), 10% (●) and 15% (⊕) ethylene glycol dimethacrylate. Data taken from Ref. (13).

belie belief in generalizations about membrane behavior.

Studies of the dependence of $\bar{t}_w$ on current density using dilute solutions (0.01*N*), in whose environment there is little invasion of the membrane by the coion, are not definitive. Mackay and Meares (24) in 1959 reported complete independence of $\bar{t}_w$ on current strength employing NaCl solutions in the concentration range 0.01-1.0*N*. Carr *et al.* (29) obtained the same current independence of $\bar{t}_w$ with 0.02*N* KCl solution. Similar results have been obtained by others (30, 34) using higher concentrations and moderate current densities. At very high current densities, however, $\bar{t}_w$ decreased (30) and this decrease was attributed to membrane polarization. In contrast, Lakshminarayanaiah (13, 18, 42, 46, 49, 50) for the first time in 1956 using 0.01*N* solutions showed (Fig. 1 and Table IV) that $\bar{t}_w$ depended on current density displaying two main characteristics: (*a*) at low current densities $\bar{t}_w$ rose to a high value, and (*b*) at high currents it attained a limiting value. Subrahmanyan and Lakshminarayanaiah (25, 26, 42) showed later that these relationships changed as the concentration of external electrolyte was increased to 0.1*N* and above when $\bar{t}_w$ became independent of current density (see Table I). The results for Na^+ ion (0.01*N*) obtained by Lakshminarayanaiah (13, 18, 46) for three different mem-

Table III. Membrane characteristics

Electrolyte solution 0.1*N*	Membrane type	Water content g H_2O/g wet membrane	$\bar{m}_1$	$\bar{m}_2$	$\bar{X}$	$\bar{t}_1$	$\bar{t}_w$	Reference
KOH	PMA	0.68	3.16	0.07	3.09	0.92	7.8	(27)
NaCl	PSA	0.62	1.40	0.03	1.37	0.90	37.3	(36)
KCl	Collodion	0.31	10.4	9.4	1.0	0.60	7.4	(39)

PMA = 10% crosslinked polymethacrylic acid.
PSA = crosslinked phenolsulfonic acid.
Collodion = untreated collodion cast on a glass plate.
$\bar{m}_1$ = mole/1000g membrane water (counterion).
$\bar{m}_2$ = mole/1000g membrane water (coion).
$\bar{X}$ = mole/1000g membrane water (membrane fixed charge groups).
$\bar{t}_1$ = transference number of counterion.
$\bar{t}_w$ = transference number of water.

Table IV. $\bar{t}_w$ as a function of current density for membranes in 0.01N NaCl solution

Current density ma/cm²	Crosslinked (10%) PMA (13, 18)	Crosslinked PSA (46)	Polyethylene-polystyrene sulfonic acid AMF C-103 (46)
0.32	—	62.1	9.6
1.58	—	39.3	7.0
3.00	15.3	—	—
3.15	—	32.9	7.0
7.50	14.0	—	—
15.75	—	24.7	6.9
22.50	12.6	—	—
30.00	11.8	—	—

Table V. $\bar{t}_w$ values for AMF C-103 membrane in 0.01N solution (46)

Current density ma/cm²	Rb^+	Cs^+
0.32	4.9	4.8
1.58	4.9	4.9
3.15	4.5	4.9
15.75	4.6	5.0

branes at different current densities are given in Table IV. These results are further confirmed by the work of George and Courant (43) who used leached membranes (Nepton CR-61) in 0.01N NaCl solution. The water content of PMA, PSA, and AMF C-103 membranes were 0.68, 0.59, and 0.18g H_2O/g wet membrane, respectively. Lakshminarayanaiah and Subrahmanyan (46) used AMF C-103 membrane in 0.01N RbCl or CsCl solution and obtained values for $\bar{t}_w$ shown in Table V. It is seen that $\bar{t}_w$ is completely independent of current density. The water contents of the membrane in Rb^+ and Cs^+ forms were 14 and 13%, respectively (46). This pointed to the fact that water content of the membrane controlled current dependence of $\bar{t}_w$; that is, at water contents greater than 14% $\bar{t}_w$ depended on current density, whereas at lower values it did not depend on current density. To check this further, we measured $\bar{t}_w$ with AMF C-104 membrane which has a low water content in 0.01N solutions. The results of Table II confirm the independence of $\bar{t}_w$ on current density where the water content of membrane in different ionic forms is less than 14%.

Evaluation of Schmid's theory of electroosmosis.— All of the results obtained by different investigators under a variety of conditions cannot be explained by any one of the existing theories of electroosmosis. Let us consider the theory of electroconvection in fine capillary membrane systems proposed by Schmid and Schwarz (4, 6). They related the ratio of convection current Δi (*i.e.*, $\Delta i = i - i'$ where i is current flowing through the membrane in presence of an applied field and i' is current flowing in absence of solvent flow) to total current to the fixed ion concentration and radius r of the membrane pores. Thus

$$(i - i')/i = \Delta i/i = (\mathbf{F}^2\bar{X}^2r^2)/(8\bar{\eta}\bar{k}_i) \quad [1]$$

where $\mathbf{F}$ is faraday, $\bar{X}$ is fixed charge density of the membrane expressed in moles/liter, $\bar{\eta}$ is viscosity of pore liquid, and $\bar{k}_i$ is specific conductance of pore liquid. Despic and Hills (17, 51) have cast this into the form

$$\bar{\lambda} - \bar{\lambda}' = (10^3\mathbf{F}^2\bar{X}r^2)/(8\bar{\eta}) \quad [2]$$

($\bar{\lambda}$ is equivalent conductance measured electrically and $\bar{\lambda}'$ is equivalent conductance derived from self-diffusion coefficient) and found it inapplicable to PMA rods (17).

To make a critical check of Eq. [2], we measured the equivalent conductance ($\bar{\lambda}$) and self-diffusion coefficient $\bar{D}$ of ^{22}Na using PSA and AMF membranes in the usual way (52). These results are given in Table VI. From $\bar{D}$ values, $\bar{\lambda}'$ values were derived using the Nernst-Einstein relation

$$\bar{D} = (RT)/(z\mathbf{F}^2)\bar{\lambda}' = 2.66 \times 10^{-2}\bar{\lambda}' \quad [3]$$

$$\text{for } z = 1$$

Using the bulk viscosity value for water in Eq. [2], values for r, the radius of membrane pores, were calculated. These calculated values are compared in Table VI with the values derived by water flux measurements described by Lakshminarayanaiah (53). The agreement in the case of tight membranes (AMF C-103 and C-104) is good, whereas with PSA membrane the agreement is bad. From these results, it is thus concluded that Schmid's theory of electroconvection is applicable to tight membranes of low water content.

Another equation of Schmid's theory which involves $\bar{t}_w$ may be used to make a further check on the validity of the pore model chosen by Schmid who in developing the theory of electroosmosis has used the equations derived by Bjerrum and Manegold (54) and Manegold and Solf (55). He showed that electroosmotic permeability D_i per ampere is given by

$$D_i = \frac{\mathbf{F}\bar{X}D_h d}{\bar{k}} \quad [4]$$

where D_h is permeability defined as the volume of solution transferred in unit time through unit membrane area under unit pressure difference, d is membrane thickness, and $\bar{k}$ is specific conductance of the membrane.

Some of the data derived again for the three membranes (PSA and AMF C-103 and C-104) by Lakshminarayanaiah (18, 46, 53) are used here to check Eq. [4]. Values of $\bar{t}_w$ calculated according to Eq. [4] and those obtained by direct measurement are shown in the last two columns of Table VII. The agreement between the calculated and measured values is poor in the case of PSA membranes and very good in the case of AMF membranes. This check also goes to show that the Schmid theory is applicable to tight

Table VI. Electrical conductance and self-diffusion coefficient (^{22}Na) of membranes in Na form. Test of Eq. [2]

Membrane	Specific conductance $\bar{k} \times 10^3$ (ohm^{-1} cm^{-1})	Fixed charge capacity $\bar{X}$ (mole/liter)	Equivalent conductance $\bar{\lambda}$ (equiv.$^{-1}$ ohm^{-1} cm^2)	Self-diffusion coefficient $\bar{D}$ (cm^2 sec^{-1})	$\bar{\lambda}'$ Eq. [3]	$\bar{\lambda} - \bar{\lambda}'$	$\bar{r}$ (A) Eq. [2]	Water*** flux
PSA*	15.3	1.00	15.30	2.65×10^{-6}	9.97	5.33	61.5	37.7
AMF C-103**	1.8	0.92	1.95	5.74×10^{-8}	0.22	1.73	11.7	10.0
AMF C-104**	1.4	1.10	1.27	7.33×10^{-8}	0.28	0.99	8.0	7.9

* Values taken from Ref. (18).
** New results.
*** The r values from water flux measurements for PSA and AMF C-103 membranes are taken from Ref. (53). The r value for C-104 is a new result.

Table VII. Values for different membrane parameters

Membrane	$\bar{X}$ (equiv./cm³) × 10³	d (cm)	$\bar{k}$ (ohm⁻¹ cm⁻¹) × 10³	$\left(\frac{D_h}{\text{cm}^3}\right)$ / dyne sec × 10¹³	$\left(\frac{D_i}{\text{cm}^3}\right)$ / coulomb × 10³ (Eq. [3])	$\left(\frac{\bar{t}_w}{D_i \times F}\right)$ / 18 (calc)	$\bar{t}_w$ (exp)
Na-PSA*	1.0	0.029	15.3	141	16.4	88	62
Na-AMF C-103**	0.92	0.013	1.8	2.08	1.33	7.1	6.9
Na-AMF C-104**	1.1	0.015	1.4	0.92	1.05	5.6	6.2

* Values taken from Ref. (18, 53).

** New results except $\bar{t}_w$ and D_h values for AMF C-103 membrane which are taken from Ref. (46, 53).

membranes whose water contents are about 14% or less. The capillary model therefore seems to be quite realistic for evaluating both electroconvection and total water transport.

Evaluation of surface charge density of membrane pore liquid.—In order to explain the current dependence of $\bar{t}_w$, Lakshminarayanaiah (13, 49) assumed a capillary model for the membrane and derived the relation

$$\bar{t}_w = (r\mathbf{F})/(36\sigma) \qquad [5]$$

where σ is the surface charge density per square centimeter of the pore liquid. For any i^{th} pore in the membrane, a value of r_i/σ_i can be assigned. If the membrane was "heteroporous," it was postulated that at low currents liquid in pores of larger radii and lower surface charge became mobilized and gave a larger value for $\bar{t}_w$. In most cases, it is possible, unless the membrane is very homogeneous, $\sigma_i \neq \sigma$ and $r_i \neq r$ where σ and r are the average values for all the n pores in the membrane. These averages, which can be written as $\sigma = \sum_i \sigma_i/n$ and $r = \sum_i r_i/n$ $(i = 1,2 \ldots n)$, become effective at high currents and gave limiting values for $\bar{t}_w$.

The average values of r given in Table VI for PSA and AMF membranes and the values of $\bar{t}_w$ given in Tables II and IV may be used in Eq. [5] to derive values for σ. Some of these values are shown in Table VIII in which are included some values derived by Frumkin (56) by directly measuring the current flowing (*i.e.*, the charge) from a dropping mercury electrode to a pool of mercury containing the electrolyte solution. The agreement is surprisingly good and, if this is genuine, it seems to give credence to the reality of the capillary model chosen for the membrane. This is the first time water transport values have been used to derive values for the surface charge density of the pore liquid in a membrane.

Effect of friction between membrane parameters on $\bar{t}_w$.—In contrast to the capillary model approach, Winger *et al.* (12) made a phenomenological approach and wrote the following relationship for an ideal system in which there were no interactions between the different membrane components.

$$\bar{t}_w = (\bar{t}_1\bar{n}_1/z_1) - (\bar{t}_2\bar{n}_2/z_2) \qquad [6]$$

where $\bar{n}_1$ and $\bar{n}_2$ are the numbers of moles of water associated with cation and anion, respectively. When valencies $z_1 = z_2 = 1$, Eq. [6] becomes

$$\bar{t}_w = \bar{t}_1\bar{m}_w - \bar{n}_2 \qquad [7]$$

Table VIII. Surface charge in different systems

System	(μcoulomb/cm²)
PSA + 0.01*N* NaCl : Eq. [5]	40.5
AMF C-103 + 0.01*N* NaCl : Eq. [5]	38.3
AMF C-104 + 0.01*N* NaCl : Eq. [5]	34.1
1*N* NaCl saturated with Hg_2Cl_2 (Frumkin)	47
1*N* H_2SO_4 saturated with Hg_2Cl_2 (Frumkin)	39

where $\bar{m}_w = \bar{n}_1 + \bar{n}_2$. According to Eq. [7], Winger *et al.* (12) found a linear relationship between $\bar{t}_w$ and $\bar{t}_1$. On the contrary, Kressman *et al.* (35) and Lakshminarayanaiah and Brennen (39) found no such linear behavior although the latter found a linear relationship between $\bar{t}_w$ and $\bar{m}_w$ for untreated collodion membrane. The straight line relationships between $\bar{t}_w$ and $\bar{t}_1$, and $\bar{t}_w$ and $\bar{m}_w$ never gave, on extrapolation according to Eq. [7], agreeing values for $\bar{n}_2$ for any given anion. Further, the data of Lakshminarayanaiah (39, 42) showed that it was impossible to interrelate different membrane parameters by simple relationships. The observation that ions and water moved through the membrane with the same linear velocities noted by Kressman *et al.* (35) has not been observed by other workers. However, Eq. [7] predicts that this would take place only when $\bar{t}_1 = 1$ and $\bar{n}_2 = 0$ (*i.e.*, complete absence of coions). These conditions reduce Eq. [7] to

$$\bar{t}_w = \bar{m}_w \qquad [8]$$

This equation has been deduced by Lakshminarayanaiah and Subrahmanyan (46) assuming a capillary model for the membrane in the form

$$\bar{t}_w = 55.56/\bar{m}_1 \qquad [9]$$

where $\bar{m}_1$ is the molality of the counterion in the membrane.

Although the data of Table IV are obtained under these conditions, the values of $\bar{t}_w$ in the case of PSA membrane are higher than $\bar{m}_w$ ($\bar{m}_w \approx 40$) at 0.32 ma/cm² and at higher currents lower than $\bar{m}_w$. In the case of the other two membranes, the values of $\bar{t}_w$ are lower than $\bar{m}_w$ ($\bar{m}_w$ for PMA membrane $\approx$ 17.6 and for AMF C-103 $\approx$ 11). This deviation of $\bar{t}_w$ from values predicted by Eq. [8] is due to omissions of interactions between different components—membrane matrix, counterion, and water—of the membrane system. Spiegler (11) has considered these interactions in detail and has shown that the ratio of the fluxes of free water (J_3) and mobile counterion (J_1) is given by

$$J_3/J_1 = \bar{C}_3/[\bar{C}_1 + \bar{C}_3(\bar{X}_{34}/\bar{X}_{13})] \qquad [10]$$

where $\bar{C}_1$ and $\bar{C}_3$ are the concentrations of counterion and water in the membrane and $\bar{X}_{34}$ and $\bar{X}_{13}$ are the friction coefficients between water-membrane matrix and counterion-water, respectively. Equation [10] shows that only when $\bar{X}_{34}/\bar{X}_{13} = 0$ both ions and water move with the same linear velocity. For the condition $J_1 = 1$ (*i.e.*, $\bar{C}_2 = 0$ and $J_3 = \bar{t}_w$) Eq. [10] takes the form in which it has been derived by Dorst *et al.* (57)

$$viz., \quad 1/\bar{t}_w = (\bar{C}_1/\bar{C}_3) + (\bar{X}_{34}/\bar{X}_{13}) \qquad [11]$$

The relevant data from the work of Tombalakian *et al.* (30) have been used by Dorst and Staverman (58) to derive values for the ratio $(\bar{X}_{34}/\bar{X}_{13})_{HCl}/(\bar{X}_{34}/\bar{X}_{13})_{NaCl}$,

Table IX. Water transport numbers and frictional coefficients

Membrane	NaCl $1/\bar{t}_w$	NaCl $\bar{C}_1/\bar{C}_3$	NaCl $\bar{X}_{34}/\bar{X}_{13}$	KCl $1/\bar{t}_w$	KCl $\bar{C}_1/\bar{C}_3$	KCl $\bar{X}_{34}/\bar{X}_{13}$	$(\bar{X}_{13})_{NaCl}/(\bar{X}_{13})_{KCl}$
1 — 2*	0.0625	0.0322	0.0303	0.0699	0.0332	0.0367	1.21
1 — 6B*	0.1820	0.0643	0.1177	0.2080	0.0681	0.1399	1.19
1 — 8*	0.2220	0.0800	0.1420	0.2380	0.0865	0.1515	1.07
1 — 10*	0.2500	0.0909	0.1591	0.2780	0.1000	0.1780	1.12
10% PMA‡	0.0925	0.0495	0.0430	0.1062	0.0538	0.0524	1.22
PSA‡	0.0400	0.0214	0.0186	0.0500	0.0159	0.0341	1.83
AMF C-103††	0.1430	0.0583	0.0847	0.2260	0.0633	0.1627	1.92
AMF C-104**	0.1590	0.0762	0.0828	0.2560	0.0760	0.1800	2.17

Membrane	RbCl $1/\bar{t}_w$	RbCl $\bar{C}_1/\bar{C}_3$	RbCl $\bar{X}_{34}/\bar{X}_{13}$	CsCl $1/\bar{t}_w$	CsCl $\bar{C}_1/\bar{C}_3$	CsCl $\bar{X}_{34}/\bar{X}_{13}$	$(\bar{X}_{13})_{RbCl}/(\bar{X}_{13})_{CsCl}$
PSA††	0.0512	0.0173	0.0339	0.0510	0.0174	0.0336	0.99
AMF C-103††	0.2130	0.0675	0.1455	0.2040	0.0608	0.1432	0.98
AMF C-104**	0.2570	0.0706	0.1864	0.2330	0.0723	0.1607	0.86

Membrane	$(\bar{X}_{13})_{NaCl}/(\bar{X}_{13})_{RbCl}$	$(\bar{X}_{13})_{KCl}/(\bar{X}_{13})_{RbCl}$
PSA	1.82	0.99
AMF C-103	1.72	0.89
AMF C-104	2.25	1.03

* Taken from Ref. (30).
‡ Taken from Ref. (18).
†† Taken from Ref. (46).
** New data.

i.e. $(\bar{X}_{13})_{NaCl}/(\bar{X}_{13})_{HCl}$. They found this ratio to be approximately constant and to lie between 5 and 6 for a number of membranes. The results of similar calculations made for a variety of membranes and for different alkali metal ions but containing the same anion (except in the case of 10% PMA which contained OH^- ion) are shown in Table IX. For different combinations of cations, the ratio $(\bar{X}_{13})_{M_1^+}/(\bar{X}_{13})_{M_2^+}$ lies between 1 and 2. In view of this constancy Eq. [11] can be written for two electrolytes M_1 and M_2 as

$$[(1/\bar{t}_w) - (\bar{C}_1/\bar{C}_3)]_{M_1} = \text{Constant}\,[(1/\bar{t}_w) - (\bar{C}_1/\bar{C}_3)]_{M_2} \quad [12]$$

and from this, as pointed out by Dorst and Staverman (58), $\bar{t}_w$ for M_2 may be inferred, provided all the required data for M_1 and the values of $\bar{C}_1$ and $\bar{C}_3$ for M_2 are known. Since $\bar{C}_2 = 0$ for the membrane phase, the nature of the anion should have little effect on the ratio $(\bar{X}_{13})_{M_1^+}/(\bar{X}_{13})_{M_2^+}$.

Conclusions

1. Effects of various factors have shown that $\bar{t}_w$ is primarily controlled by the membrane water content and the concentration of the electrolyte solution surrounding it. $\bar{t}_w$ values decrease with decrease in water content and increase in electrolyte concentration.

2. $\bar{t}_w$ is independent of current density at external concentrations greater than 0.1*N*. In dilute solution (0.01*N*) it depends on current density if the water content of the membrane is greater than about 14%. This dependence disappears if the water content is less than about 14%.

3. The Schmid theory of electroconvection and electroosmosis has been tested and found to be inapplicable to membranes of high water content and applicable to membranes of low water content.

4. For the first time the surface charge density of moving pore liquid has been estimated from $\bar{t}_w$ data and found to be about 35 μcoulombs/cm^2.

5. That ions and water move through the membrane with the same linear velocity has been found to be an exception rather than the rule.

6. The value for the ratio of the friction coefficients $(\bar{X}_{13})_{M_1}/(\bar{X}_{13})_{M_2}$ has been found to lie between 1 and 2 for all the alkali metal ions in dilute solution contrary to the value of about 5.5 found by Dorst and Staverman for $(\bar{X}_{13})_{NaCl}/(\bar{X}_{13})_{HCl}$.

Acknowledgments

Some of the original experimental work described in this paper was supported by a grant from the Office of Saline Water, U. S. Department of the Interior.

Manuscript submitted May 17, 1968; revised manuscript received Oct. 25, 1968. This paper was presented at the Boston Meeting, May 5-9, 1968, as Paper 240.

Any discussion of this paper will appear in a Discussion Section to be published in the December 1969 JOURNAL.

NOMENCLATURE

Subscripts 1, 2, 3, and 4 refer to counterions, coions, water, and membrane, respectively. Often, subscript w is used instead of 3 for water. Terms with bars on top refer to the membrane phase.

$\bar{C}$	Concentration (mole cm^{-3})
d	Thickness of membrane (cm)
$\bar{D}$	Self-diffusion coefficient (cm^2 sec^{-1})
D_h	Hydraulic permeability (cm^3 dyne^{-1} sec^{-1})
D_i	Electroosmotic permeability (cm^3 amp^{-1} sec^{-1})
Δ	Difference
$\bar{\eta}$	Viscosity of pore liquid (g cm^{-1} sec^{-1})
$\mathbf{F}$	Faraday's constant (coulomb equiv.$^{-1}$)
i	Current flowing through the membrane (amp)
i'	Current flowing through the membrane in absence of solvent flow (amp)
J	Flux (mole cm^{-2} sec^{-1})
$\bar{k}$	Specific conductance of membrane (ohm^{-1} cm^{-1})
$\bar{k}_i$	Specific conductance of pore liquid (ohm^{-1} cm^{-1})
$\bar{\lambda}$	Equivalent conductance measured (ohm^{-1} cm^2 equiv.$^{-1}$)
$\bar{\lambda}'$	Equivalent conductance derived (ohm^{-1} cm^2 equiv.$^{-1}$)
$\bar{m}$	Molality (mole/1000g H_2O)
$\bar{m}_w$	Moles of water associated with 1 equiv. counterion
n	Number of pores in the membrane per unit area
$\bar{n}$	Number of moles of water associated with an ion
N	Normality (equiv./liter)
R	Gas constant (erg deg^{-1} mole^{-1})
r	Radius of membrane pore (cm)
σ	Surface charge density (coulomb cm^{-2})
T	Absolute temperature
$\bar{t}_i$	Ion transference number (i = 1, 2)
$\bar{t}_w$	Water transference number (moles/**F**)
$\bar{X}$	Fixed charge density (mole cm^{-3})
$\bar{X}_{ij}$	Friction coefficient between components i and j (dyne sec cm^{-1} mole^{-1})
z	Valency
ζ	Zeta potential (v)

REFERENCES

1. J. Th. G. Overbeek, in "Colloid Science," Vol. 1, p. 197, H. R. Kruyt, Editor, Elsevier Publishing Co., New York (1952).
2. G. Schmid, *Z. Electrochem.*, **54**, 424 (1950).
3. G. Schmid, *ibid.*, **55**, 229 (1951).
4. G. Schmid and H. Schwarz, *ibid.*, **55**, 295 (1951).
5. G. Schmid and H. Schwarz, *ibid.*, **55**, 684 (1951).
6. G. Schmid and H. Schwarz, *ibid.*, **56**, 35 (1952).
7. G. Schmid, *ibid.*, **56**, 181 (1952).
8. G. Schmid, *J. Chim. Phys.*, **55**, 163 (1958).
9. A. J. Staverman, *Trans. Faraday Soc.*, **48**, 176 (1952).
10. O. Kedem and A. Katchalsky, *ibid.*, **59**, 1918, 1931, 1941 (1963).
11. K. S. Spiegler, *ibid.*, **54**, 1408 (1958).
12. A. G. Winger, R. Ferguson, and R. Kunin, *J. Phys. Chem.*, **60**, 556 (1956).
13. N. Lakshminarayanaiah, *Proc. Indian Acad. Sci.*, **A55**, 200 (1962).
14. K. S. Spiegler, *This Journal*, **100**, 312C (1953).
15. W. R. Walters, D. W. Weiser, and L. J. Marek, *Ind. Eng. Chem.*, **47**, 61 (1955).
16. Y. Oda and T. Yawataya, *Bull. Chem. Soc., Japan*, **28**, 263 (1955); **29**, 673 (1956); **30**, 213 (1957)

17. A. Despic and G. J. Hills, *Disc. Faraday Soc.*, **21**, 150 (1956).
18. N. Lakshminarayanaiah, Thesis, London University (1956).
19. J. W. Lorimer, E. I. Boterenbrood, and J. J. Hermans, *Disc. Faraday Soc.*, **21**, 141 (1956).
20. R. J. Stewart and W. F. Graydon, *J. Phys. Chem.*, **61**, 164 (1957).
21. N. W. Rosenberg, J. H. B. George, and W. D. Potter, *This Journal*, **104**, 111 (1957).
22. J. G. McKelvey, Jr., K. S. Spiegler, and M. R. J. Wyllie, *ibid.*, **104**, 387 (1957).
23. G. Schulz, *Z. Anorg. Allgem. Chem.*, **301**, 97 (1959).
24. D. Mackay and P. Meares, *Trans. Faraday Soc.*, **55**, 1221 (1959).
25. V. Subrahmanyan and N. Lakshminarayanaiah, *Current Sci.*, **29**, 307 (1960); *Bull. Chem. Soc., Japan*, **34**, 587 (1961).
26. V. Subrahmanyan, Thesis, Madras University (1961).
27. G. J. Hills, P. W. M. Jacobs and N. Lakshminarayanaiah, *Proc. Roy. Soc., (London)*, **A262**, 257 (1961).
28. D. K. Hale and D. J. McCauley, *Trans. Faraday Soc.*, **57**, 135 (1961).
29. C. W. Carr, R. McClintock, and K. Sollner, *This Journal*, **109**, 251 (1962).
30. A. S. Tombalakian, H. J. Barton, and W. F. Graydon, *J. Phys. Chem.*, **66**, 1006 (1962).
31. F. Runge, F. Wolf, and R. Backman, *Dechema Monograph*, **47**, 465 (1962).
32. W. Dorst, P. L. Polak, R. Caramazza, and A. J. Staverman, *Gazz. Chim. Ital.*, **92** 1241 (1962).
33. M. Block and K. S. Spiegler, *This Journal*, **110**, 577 (1963).
34. T. R. E. Kressman, P. A. Stanbridge, and F. L. Tye, *Trans. Faraday Soc.*, **59**, 2129 (1963).
35. T. R. E. Kressman, P. A. Stanbridge, F. L. Tye, and A. G. Wilson, *ibid.*, **59**, 2133 (1963).
36. N. Lakshminarayanaiah and V. Subrahmanyan, *J. Polymer Sci.*, **A2**, 4191 (1964).
37. N. Krishnaswamy and V. K. Indusekhar, *Indian J. Technol.*, **2**, 169 (1964); **3**, 358 (1965).
38. N. Lakshminarayanaiah, *J. Phys. Chem.*, **70**, 1588 (1966).
39. N. Lakshminarayanaiah and K. R. Brennen, *Electrochim. Acta*, **11**, 949 (1966).
40. G. B. Willis and E. N. Lightfoot, *Ind. Eng. Chem. Fundamentals*, **5**, 114 (1966).
41. A. S. Tombalakian and W. F. Graydon, *J. Phys. Chem.*, **70**, 3711 (1966).
42. N. Lakshminarayanaiah, *Desalination*, **3**, 97 (1967).
43. J. H. B. George and R. A. Courant, *J. Phys. Chem.*, **71**, 246 (1967).
44. R. Arnold and D. A. Swift, *Austr. J. Chem.*, **20**, 2575 (1967).
45. T. S. Brun and P. Vaula, *Ber. Bunsenges. Physik. Chem.*, **71**, 824 (1967).
46. N. Lakshminarayanaiah and V. Subrahmanyan, *J. Phys. Chem.*, **72**, 1253 (1968).
47. Y. Kobatake, M. Yuasa, and H. Fujita, *ibid.*, **72**, 1752 (1968).
48. E. M. Scattergood and E. N. Lightfoot, *Trans. Faraday Soc.*, **64**, 1135 (1968).
49. N. Lakshminarayanaiah, *Chem. Rev.*, **65**, 525 (1965).
50. N. Lakshminarayanaiah, *Current Sci.*, **28**, 321 (1959).
51. A. Despic and G. J. Hills, *Trans. Faraday Soc.*, **51**, 1260 (1955).
52. F. Helfferich, "Ion Exchange," p. 334 and p. 315, McGraw-Hill Book Co. Inc., New York (1962).
53. N. Lakshminarayanaiah, *Biophys. J.*, **7**, 511 (1967).
54. N. Bjerrum and E. Manegold, *Kolloid-Z.*, **43**, 5 (1927).
55. E. Manegold and K. Solf, *ibid.*, **55**, 273 (1931).
56. A. Frumkin, *Z. Physik. Chem.*, **103**, 55 (1923). A table of values for σ exists in Ref. (1), p. 150, also taken from A. Frumkin, *Erg. Exakt. Naturw.*, **7**, 235 (1928).
57. W. Dorst, A. J. Staverman, and R. Caramazza, *Rec. Trav. Chim.*, **83**, 1329 (1964).
58. W. Dorst and A. J. Staverman, *ibid.*, **86**, 61 (1967).

Technical Note

Limitations of the Determination of the True Surface Area of Spongy Metals with the Help of A-C Polarization Measurements

Carl Wagner*

Max-Planck-Institut für physikalische Chemie, Göttingen, Germany

Pickering (1) has recently used a-c impedance measurements in order to determine the change in true surface area of Cu-Au samples subject to anodic dissolution of Cu with a sponge of Au-rich alloy surrounding the core of the sample. Impedance measurements were conducted in 1M H_2SO_4 with a negligible a-c component of the faradaic current. In this context the question has been raised under which conditions the ohmic resistance of the electrolyte in the sponge of Au-rich alloy affects the impedance measurements. The following elements of a model of the sponge may be considered (*i*) channels of uniform width and finite length whose axes are normal to the surface of the sample, (*ii*) wedgelike grooves, and (*iii*) conical pits.

The a-c impedance of each of these elements has been calculated by de Levie (2, 3). His equations can be used directly with suitable modifications for the special conditions considered in this paper.

The following general symbols are used

$j = (-1)^{1/2}$
κ double layer capacity per unit true surface area,
ρ resistivity of the electrolyte,
ω angular frequency of the alternating current.

(*i*) For the impedance Z_1 of a single channel of radius r and depth $L >> r$ de Levie (4) has derived an expression involving the ohmic resistance of the electrolyte in the pore per unit length ($=\rho/\pi r^2$) and the impedance of the double layer capacity in a pore of unit length ($=\frac{1}{2}\pi r j\omega\kappa$)

$$Z_1 = \left[\frac{\rho}{\pi r^2 \cdot 2\pi r j\omega\kappa}\right]^{1/2} \cdot \coth\left[\left(\frac{\rho}{\pi r^2} \cdot 2\pi r j\omega\kappa\right)^{1/2} L\right] \quad [1]$$

For the following calculation, it is expedient to introduce the real parameter

* Electrochemical Society Active Member.

$$u_1 = (2\omega\kappa\rho r^{-1})^{1/2} L \quad [2]$$

and to rewrite Eq. [1] as

$$Z_1 = \frac{j^{1/2}u_1 \cdot \coth (j^{1/2}u_1)}{2\pi r L j\omega\kappa} \quad [3]$$

Using a series expansion (5) for $j_1^{1/2}u_1 \cdot \coth j^{1/2}u_1$ one obtains

$$Z_1 = \frac{1}{2\pi r L j\omega\kappa}\left[1 + \frac{1}{3}(j^{1/2}u_1)^2 - \frac{1}{45}(j^{1/2}u_1)^4 + \frac{2}{945}(j^{1/2}u_1)^6 - \frac{1}{4775}(j^{1/2}u_1)^8 + \dots\right]$$

$$= \frac{1 + \frac{1}{45}u_1^4 - \frac{1}{4775}u_1^8 \dots}{2\pi r L j\omega\kappa} + \frac{\frac{1}{3}u_1^2 - \frac{2}{945}u_1^6 + \dots}{2\pi r L\omega\kappa} \quad [4]$$

The surface area of the wall of the channel is $2\pi rL$. The contribution of the bottom of the channel is disregarded since $L >> r$. Thus the admittance of the double layer capacity C_1 is

$$2\pi r L j\omega\kappa = j\omega C_1 \quad [5]$$

In view of Eq. [5], one may rewrite Eq. [4] as

$$Z_1 \cong \frac{1 + \frac{1}{45}u_1^4 - \frac{1}{4775}u_1^8 - \dots}{j\omega C_1} + \frac{\frac{1}{3}u_1^2 - \frac{2}{945}u_1^6 + \dots}{\omega C_1} \quad [6]$$

(*ii*) The impedance Z_2 of a groove of width $2b$ and depth L per unit length has been calculated by de Levie (3) as

$$Z_2 = \frac{\rho}{\tan\beta}\frac{I_0(\lambda)}{\lambda I_1(\lambda)} \quad [7]$$

In Eq. [7] $\beta = \sin^{-1}(b/L)$ is half the angle between the walls at the bottom of the groove, I_0 and I_1 are the modified Bessel functions of zero and first order, respectively, and the variable λ is defined as

$$\lambda = 2(\rho L/\zeta \sin\beta)^{1/2} \quad [8]$$

where $\zeta = (j\omega\kappa)^{-1}$ is the double layer impedance per unit true surface area. In a metal sponge as present in Pickering's experiments, L is much greater than b and accordingly $\beta << 1$. Hence

$$\sin\beta \cong \tan\beta \cong b/L \quad [9]$$

Thus Eq. [8] may be rewritten as

$$\lambda = 2j^{1/2}u_2 \quad [10]$$

where the dimensionless real parameter u_2 is defined as

$$u_2 = (\omega\kappa\rho b^{-1})^{1/2} L \quad [11]$$

The modified Bessel function of order ν is represented by the series expansion (6)

$$I_\nu(\lambda) = (\tfrac{1}{2}\lambda)^\nu \sum_{k=0}^{k=\infty} \frac{(\tfrac{1}{2}\lambda)^{2k}}{k!(\nu + k)!} \quad [12]$$

Further, one has the auxiliary formula

$$\frac{1}{1+\epsilon} = 1 - \epsilon + \epsilon^2 - \epsilon^3 + \dots \quad \text{if } \epsilon < 1 \quad [13]$$

Substituting Eq. [9], [10] and [12] in Eq. [7] and using Eq. [13], one obtains

$$Z_2 = \frac{1 + \frac{1}{12}u_2^4 + \dots}{2j\omega\kappa L} + \frac{\frac{1}{2}u_2^2 + \dots}{2\omega\kappa L} \quad [14]$$

The surface area of the walls of a narrow groove ($\beta << 1$) per unit length is $2L$. Thus the admittance of the double layer per unit length of the groove is

$$2bj\omega\kappa = j\omega C_2 \quad [15]$$

where C_2 is the double layer capacity per unit length of the groove. Thus Eq. [14] may be rewritten as

$$Z_2 = \frac{1 + \frac{1}{12}u_2^4 + \dots}{j\omega C_2} + \frac{\frac{1}{2}u_2^2 + \dots}{\omega C_2} \quad [16]$$

(*iii*) The impedance Z_3 of a conical pit with the radius r at its opening and the depth L has also been calculated by de Levie (3)

$$Z_3 = \frac{2\rho}{\pi r \tan\beta}\frac{I_1(\lambda')}{\lambda' I_2(\lambda')} \quad [17]$$

where $\sin\beta = r/L$ and

$$\lambda' = 2(2\rho L/\zeta \sin\beta) = 2j^{1/2}u_3 \quad [18]$$

and the dimensionless real parameter u_3 is given by

$$u_3 = (2\omega\kappa\rho r^{-1})^{1/2} L \quad [19]$$

Substituting Eq. [12], [18], and [19] in Eq. [17] with $\tan\beta \cong r/L$ if $r << L$ and using Eq. [13], one obtains

$$Z_3 = \frac{1 + \frac{1}{72}u_3^4 + \dots}{j\pi r L\omega\kappa} + \frac{\frac{1}{6}u_3^2 + \dots}{\pi r L\omega\kappa} \quad [20]$$

The surface area of the wall in a conical pit ($r << L$) is πrL. Thus the admittance of the double layer of the pit is

$$\pi r L j\omega\kappa = j\omega C_3 \quad [21]$$

where $C_3 = \pi rL\kappa$ is the double layer capacity of the pit. Thus Eq. [20] may be rewritten as

$$Z_3 \cong \frac{1 + \frac{1}{72}u_3^4 + \dots}{j\omega C_3} + \frac{\frac{1}{6}u_3^2 + \dots}{\omega C_3} \quad [22]$$

The solutions in Eq. [6], [16], and [22] are very similar. Thus they may be discussed jointly. If u_1, u_2, or u_3 is much less than unity, the value of Z_n for $n = 1, 2, 3$ is given by $(j\omega C_n)^{-1}$ as the limiting value for negligible ohmic resistance. The total impedance of a sample is given by the reciprocal of the sum of the individual admittances $j\omega C_n$. Thus, if the contribution of the metal surface between channels, grooves, or pits is disregarded, the total impedance Z of a sample involving a large number of channels, grooves or pits may be written as

$$Z \cong \frac{1 + \beta_n u_n^4}{j\omega C} + \frac{\alpha_n u_n^2}{\omega C} \quad \text{if } u_n << 1 \quad [23]$$

where C is the total double layer capacity, the parameters u_n for $n = 1, 2, 3$ are given by Eq. [2], [11], and [19], and the coefficients α_n and β_n for the three models are

$$\alpha_1 = \frac{1}{3}; \quad \alpha_2 = \frac{1}{2}; \quad \alpha_3 = \frac{1}{6} \quad [24]$$

$$\beta_1 = \frac{1}{45}; \quad \beta_2 = \frac{1}{12}; \quad \beta_3 = \frac{1}{72} \quad [25]$$

It is noteworthy that according to Eq. [23] even for $u_n = 1$ the change in the imaginary term is relatively small. The predominating effect is due to the second real term in Eq. [23]. Therefore, if u_n is not much less than unity, the bridge used by Pickering can be balanced only if during dissolution of Cu from a Cu-Au sample with increasing depth L corresponding to an increasing value of u_n in the model one adjusts not only capacitor C_5 but also resistor R_2 shown in Fig. 2 of Pickering's paper (1). Numerical estimates show that in most runs reported by Pickering values of u_n for each model were sufficiently small so that use of the limiting relation

$$Z = (j\omega C)^{-1} \quad [26]$$

is appropriate. This is in accord with Pickering's (1) observation that values of C calculated from Eq. [26] for measurements of Z with different frequencies do not differ to a large extent.

The ratio of the real part to the amount of the imaginary part of the impedance calculated in Eq. [23] is in essence proportional to u_n^2, *i.e.*, according Eq. [2] [11], and [19], proportional to the resistivity ρ of the solution, the square of the depth L, and the angular frequency ω, and inversely proportional to the width of the channel, groove, or pit expressed either by r or b. Thus the effect of a finite ohmic resistance of the electrolyte in the sponge is quite low if the depth L is small. In most of Pickering's experiments, L was less than 10^{-4} cm. Care, however, must be exercised if L is greater. Eventually, it is recommendable to use a low rather than a high a-c frequency if one intends an evaluation of measurements with the help of Eq. [26].

Since no model represents adequately the odd geometry of a metal sponge, Eq. [23] cannot be used for a quantitative evaluation of experimental data obtained for a metal sponge. Equation [23], however, can be used in order to estimate the limits for the applicability of a-c impedance measurements and their evaluation with the help of Eq. [26] for an approximate determination of the true surface area. In this context it is important to notice that an estimate based on Eq. [23] gives in essence the same result for all three models.

Acknowledgment

The author is grateful to Dr. H. W. Pickering for critical comments.

Manuscript submitted Aug. 19, 1968.

Any discussion of this paper will appear in a Discussion Section to be published in the December 1969 JOURNAL.

REFERENCES

1. H. W. Pickering, *This Journal*, **115**, 690 (1968).
2. R. de Levie, Advances in Electrochemistry and Electrochemical Engineering, **6**, 355 (1967).
3. R. de Levie, *Electrochim. Acta*, **10**, 113 (1965).
4. Ref. 2, Eq. (96) and (98).
5. Handbook of Mathematical Functions, M. Ambramowitz and I. A. Stegun, Editors p. 85, Eq. 4.5.67, Dover Publications, New York (1965).
6. Handbook of Mathematical Functions, p. 375, Eq. 9. 6. 10.

Crystal Growth and Properties of Mica-Like Potassium Niobates

K. Nassau, J. W. Shiever, and J. L. Bernstein

Bell Telephone Laboratories, Incorporated, Murray Hill, New Jersey

ABSTRACT

Large single crystals of KNb_3O_8 and $K_4Nb_6O_{17}$ can be grown by Czochralski pulling from the melt. In the case of KNb_3O_8 a small amount of excess K_2O is used to avoid incongruent crystallization. Both materials show pronounced cleavage very similar to that of mica. The electrical properties of KNb_3O_8 are also very similar to those of mica, making this material a possible mica substitute as well as being an interesting new dielectric material in its own right. KNb_3O_8 is orthorhombic $Pmmm$, with $a = 8.91 \pm 0.01$Å, $b = 10.66 \pm 0.01$Å, $c = 3.77 \pm 0.01$Å, not the previously reported perovskite structure. Other characteristics determined include optical, mechanical, and chemical properties. When exposed to atmospheres between about 25 and 85% relative humidity, $K_4Nb_6O_{17}$ becomes a trihydrate, with higher hydration above about 85% relative humidity. Optical, electrical, and structural properties of all three forms of $K_4Nb_6O_{17}$ are described.

A total of nine compounds between Nb_2O_5 and K_2O have been discussed in recent studies. Reisman and Holtzberg (1) reported K_3NbO_4, $KNbO_3$, $K_4Nb_6O_{17}$, KNb_3O_8, and "$K_6Nb_{44}O_{113}$" in their equilibrium phase diagram based on differential thermal analysis. Guerchais (2) added to these $K_4Nb_2O_7$ and $K_2Nb_8O_{21}$ from his formation reaction powder x-ray diffraction study and found two other phases instead of "$K_6Nb_{44}O_{113}$." Whiston and Smith (3) in their single crystal x-ray diffraction study added the unit cell dimensions of $K_{12}Nb_{14}O_{41}$, "$K_4Nb_6O_{17}$," KNb_3O_8, "$K_2Nb_8O_{21}$," and $K_6Nb_{44}O_{113}$ to the well known perovskite structure of $KNbO_3$. Several of these identifications must, however, be questioned.

Since KNb_3O_8 is stated to melt incongruently (1), the platy crystals obtained by Whiston and Smith from a melt of the composition are expected to be the adjacent compound $K_6Nb_{44}O_{113}$ (1) or $K_2Nb_8O_{21}$ (2). It is indeed possible to index the $K_2Nb_8O_{21}$ pattern of Guerchais (2) with the Whiston and Smith KNb_3O_8 cell parameters thus confirming the probable identity of these two compounds. The cell parameters given by Whiston and Smith for acicular $K_4Nb_6O_{17}$ do not apply to any of the three platy forms of that composition described below, but do fit the diffraction lines of Guerchais' "third compound" in the $K_2Nb_8O_{21}$-$K_6Nb_{44}O_{113}$ region. There are other inconsistencies which are however not relevant to the present study. Except for $KNbO_3$, none of the crystals obtained in these studies was analyzed or characterized other than by x-ray diffraction and sometimes brief statements of crystal morphology, nor could the powder x-ray diffraction patterns be indexed.

Reisman and Holtzberg (1) state that crystals of $K_4Nb_6O_{17}$ and KNb_3O_8 are birefringent, the former being similar in appearance to mica, the latter occurring as rectangular plates. The growth of $K_4Nb_6O_{17}$ crystals by slow solidification of the melt has also been reported by Kestigian *et al.* (4), who gave extensive analysis details and some electrical measurements. They observed moisture absorption, but it appears that all measurements and analyses were performed on freshly dried material and accordingly the hydrates described below were not observed.

Among the factors which produce confusion in this system may be mentioned incongruent melting, extreme metastability (5) with excessive annealing times needed to obtain the final equilibrium compounds, as well as extensive hydrate formation, again probably including some metastability. The growth and detailed study of single crystals provides one way of avoiding many of these difficulties. We have grown crystals of KNb_3O_8 and $K_4Nb_6O_{17}$, and have characterized these, as well as the hydrates of $K_4Nb_6O_{17}$, by chemical analysis, x-ray diffraction, optical, and electrical measurements.

Crystal Growth of KNb_3O_8 *and* $K_4Nb_6O_{17}$

Niobium oxide (Kawecki Chemical Company, optical grade, highest impurity Ta < 100 ppm) and potassium carbonate (Fisher Scientific Company, reagent grade, highest impurity Na < 200 ppm) were ground together in stoichiometric amounts and fired overnight and reground three times at 500°, 700°, and 800°C. This material was melted in a platinum crucible heated by a 450 kHz radio frequency generator. In the case of KNb_3O_8 a small amount of excess K_2CO_3 was added at this point to avoid the incongruent melting point. The addition of 1 w/o (weight per cent) K_2CO_3, corresponding to approximately 2 m/o (mole per cent) excess potassium was found to be suitable. The temperature was controlled with a platinum sheathed platinum/platinum 10% rhodium thermocouple immersed in the melt. Growth was performed by the Czochralski pulling technique as previously described (6). The uncorrected optical pyrometer temperature of the melt during growth was about 1275°C for KNb_3O_8 and 1220°C for $K_4Nb_6O_{17}$, as usually, somewhat higher than the melting temperatures.

Crystals could readily be nucleated at the end of a platinum wire. Growth rates of ½-1 in./hr gave crystals of satisfactory size and quality. These crystals were oriented and cut into seed crystals which were used for further pulling experiments. Growth in a direction perpendicular to the cleavage was difficult due to the easy separation along the cleavage in both materials.

The orientation of crystals could be rapidly determined by the observation of a cleavage fragment between crossed polarizers. Figure 1 shows the observed biaxial interference figures, and their relation to the crystallographic axes of both materials. Growth along a, c, and intermediate directions yield crystals with

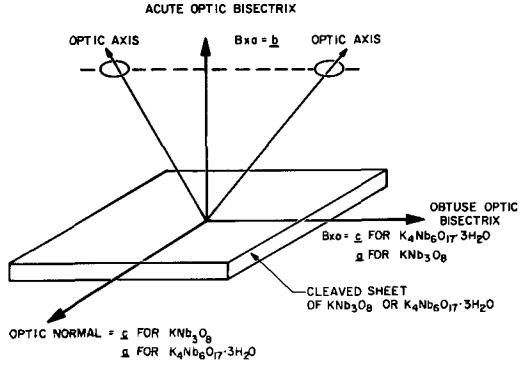

Fig. 1. Relationship of optical and crystallographic axes in KNb_3O_8 and $K_4Nb_6O_{17}\cdot 3H_2O$.

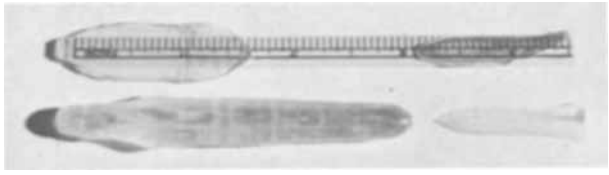

Fig. 2. Crystals and cleaved sheets of KNb_3O_8 (left) and $K_4Nb_6O_{17}\cdot 3H_2O$ (right).

oval cross-sections, the cleavage plane always lying in the widest part. Growth approximately half-way between a and b also proceeded readily. As-grown and cleaved c-axis grown crystals are shown in Fig. 2. The growth of crystals up to 4 in. in length and 7/8 in. diameter from a crucible 1½ in. diameter and 1½ in. deep indicates that this process should present no difficulties if performed on a larger scale. There was a pronounced tendency of crystals to twin with parallel growth at relatively small angles close to the cleavage plane, but this could be avoided by the choice of undeformed seeds and by maintaining a steady growth temperature.

Satisfactory crystal growth of KNb_3O_8 was also obtained in a single Bridgman-type experiment, by lowering a 3½ in. long tapered crucible at a rate of 1 in./day through a furnace having a 20°/in. temperature gradient. Even without refinements, crystals up to ⅜ in. in size were obtained.

Measurement Techniques

Powder x-ray diffraction patterns were obtained in a Phillips 114.6 mm Debye-Scherrer Camera with V filtered CrKα radiation. Single crystals were examined by means of a precession camera using Zr filtered MoKα radiation.

Differential thermal analysis was performed in a Dupont 900 machine in platinum cups in flowing air at a heating rate of 20°/min. Densities were determined by flotation in a thallium formate-malonate-water mixture at 60°C, and pycnometrically in alcohol at room temperature, with estimated accuracies ±0.2 and ±0.05 to 0.1, respectively.

Refractive indexes were determined by measuring the real and apparent thickness of parallel cleavage sheets under the microscope in white light. Optical transmission curves (unpolarized) were determined on a Cary Model 14 double beam spectrophotometer and a Perkin-Elmer Model 421 double beam grating spectrophotometer. Electrical measurements were performed on a General Radio Type 1620A capacitance measurement assembly. Electrodes were applied with silver conducting paste.

Table II. Indexed powder x-ray diffraction pattern of KNb_3O_8 (using a = 8.91Å, b = 10.66Å, c = 3.77Å)

h, k, l	d calc, Å	d obs, Å	I obs
010	10.66	10.58	vs
110	6.84	6.83	s
020	5.33	5.31	w
120	5.47	4.56	w
210	4.11	4.12	w
001	3.77	3.75	s
220	3.42	3.42	vs
111	3.30	3.35	w
130	3.30	3.28	vs
021	3.08	3.14	s
121	2.91	2.87	m
201	2.88		
310	2.86	2.83	vw
211	2.78	2.78	vw
230	2.78	2.70	w
040	2.66	2.65	s

Water absorption studies were performed by storing about 0.5g samples in small Teflon cups over constant humidity reagents in 500 ml screw-capped jars. The specimens were weighed every day until constant weight was reached, usually after two days. At least two samples were run at each humidity.

Properties of KNb_3O_8

Crystal data.—The unit cell dimensions obtained on a single crystal of KNb_3O_8 are shown in Table I, together with the calculated and observed densities. The Laue symmetry and systematic absences indicated the possible space groups *Pmmm*, *Pmm*2, or P222. The absence of response in a laser-induced single crystal harmonic generation experiment (7) demonstrated the probable presence of a center of symmetry, thus indicating the space group to be *Pmmm*. The previously reported perovskite structure (3) does not appear to refer to the KNb_3O_8 compound as discussed in the first part of this paper. The powder x-ray diffraction pattern is shown in Table II, with indexing based on the single crystal unit cell parameters. The observed d spacings are generally similar to those of Guerchais (2), except that we do not observe his very strong line at 8.44Å (for which there would be no index) but instead observe the 110 reflection to occur at 6.83Å.

The similarity of mechanical behavior, also shown in Table I, with that of mica suggests a similar structure. Mica type materials, using muscovite $KAl_2(AlSi_3O_{10})(OH)_2$ as representative, contain (8) triple layer sheets composed of alumina octahedra (sharing edges) with alumino silicate tetrahedra sheets (sharing corners) on each side. These triple layers are held together by K^+ ions. A somewhat similar

Table I. Some properties of KNb_3O_8, $K_4Nb_6O_{17}$, and $K_4Nb_6O_{17}$ hydrates

Compound	KNb_3O_8	$K_4Nb_6O_{17}\cdot xH_2O$		
		$x = 0$	$x = 3$	$x \approx 4½$
Structural data				
System	Orthorhombic	Orthorhombic	Orthorhombic	Orthorhombic
Space group	*Pmmm*		$P22_12_1$ (or $P22_12$)	$P22_12_1$ (or $P22_12$)
Unit cell dimensions, Å	a = 8.91 ± 0.01 b = 10.66 ± 0.02 c = 3.77 ± 0.01	a = 7.58 ± 0.20 b = 32.3 ± 0.8 c = 6.40 ± 0.20	a = 7.85 ± 0.01 b = 37.67 ± 0.10 c = 6.46 ± 0.01	a = 7.82 ± 0.01 b = 41.09 ± 0.10 c = 6.42 ± 0.01
Unit cell volume, Å³	V = 358	V = 1567	V = 1910	V = 2063
Proposed molecules per unit cell	n = 2	n = 4	n = 4	n = 4
Calculated density, g/cc	$d_{x\text{-ray}}$ = 4.14		$d_{x\text{-ray}}$ = 3.43	$d_{x\text{-ray}}$ = 3.18
Measured density, g/cc	d_{obs} = 4.15 ± 0.05		d_{obs} = 3.37 ± 0.1 3.5 ± 0.2	
Mechanical data				
Hardness, Mohs	2½	2½	2½	<1
Cleavability	Pronounced	Pronounced	Pronounced	Pronounced
Flexibility of cleaved sheet	Flexible along a and c	Slightly brittle along a*, very brittle along c*	Brittle along a and c	Slightly brittle along c*, flexible along a*
Optical data				
Interference figure	Negative biaxial	Biaxial	Negative biaxial	Biaxial
Refractive indexes	$n\alpha$ = 1.92 $n\beta$ = 2.10 $n\gamma$ = 2.20		$n\alpha$ = 2.22 $n\beta$ = 2.36 $n\gamma$ = 2.43	
Transparency region, μ	0.36 to 5		0.36 to 2½ 3½ to 5½	

* Oriented by the interference figure assuming the relationship of Fig. 1 applies as for $K_4Nb_6O_{17}\cdot 3H_2O$.

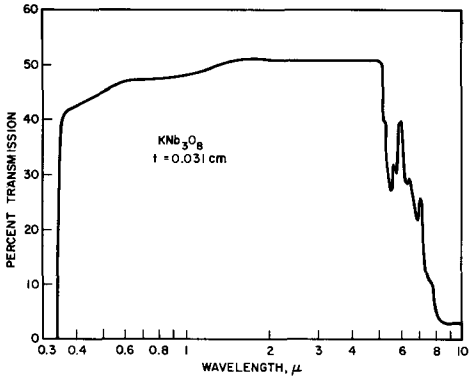

Fig. 3. Optical transmission curve of KNb_3O_8

structure with similar mechanical properties (9), is observed for potassium tetrafluo-aluminate, $KAlF_4$, where sheets of aluminum octahedra, sharing corners, are again held together by K^+ ions. An analogous structure consisting of single or multiple sheets of niobium-oxygen octahedra, held together with K^+ ions is accordingly suggested for KNb_3O_8. Detailed structural work is however expected to be difficult due to the easy deformation of the material due both to the cleavage as well as the flexibility.

Mechanical and optical properties.—The mechanical and optical data are also included in Table I. The relationship of the optical to the crystallographic directions is shown in Fig. 1.

The most notable characteristic of KNb_3O_8 is the highly developed cleavage. In this it greatly resembles mica, except that KNb_3O_8 is appreciably more flexible than mica. Delamination occurs on bending, with separations down to one micron. The crystal is colorless and highly transparent with essentially no absorption in the 0.5-5μ region as shown in Fig. 3 and with the remarkably high refractive indices shown in Table I.

Chemical properties.—Chemical analysis using x-ray spectrochemical analysis on an HF-HNO_3 solution shows the crystals to have the composition KNb_3O_8 as shown in Table III. Differential thermal analysis indicates no phase changes occur below a melting point of 1205° ± 10°C, compared to the reported value of 1234° (to <1213)°C (1).

KNb_3O_8 does not show any detectable reaction with water, in contrast to the closely related $K_4Nb_6O_{17}$. It dissolves in hot HF, but is not attacked by other acids or alkalies either cold or hot. A number of impurities at the 1 to 2 m/o level were added to the melt and the distribution coefficients (ratio of concentration of impurity in crystal to concentration of that impurity in the melt) determined. Most of these contained two ions at one time. Distribution coefficients and colors are shown in Table IV. More than one color is listed when the material is strongly dichroic or trichroic. In the cases of chromium (yellow-green) the impurity was predominately physically trapped, possibly due to too rapid growth, the clear crystal remaining colorless; distribution coefficients were not determined in this case.

Table III. Analyses in weight per cent

	K	Nb	O + H (by difference)
KNb_3O_8, Sample S122			
Observed	8.8	62.5	28.7
Calculated for KNb_3O_8	8.77	62.52	28.71
$K_4Nb_6O_{17} \cdot 3H_2O$, Sample S129			
Observed	54.2	15.0	30.8
Calculated for $K_4Nb_6O_{17} \cdot 3H_2O$	53.6	15.04	31.35

Table IV. Distribution coefficient (k) and colors of various impurity combinations in KNb_3O_8

Sample	Color	Impurities	k
159, 161	Yellow, brown	Ta	1.2
		V	0.5
163	Colorless	Rb	0.9
		Na	0.5
168	Colorless	Ba	0.5
		Ti	0.5
169	Yellow, green	Cr	—
173	Yellow, brown, purple	W	0.8
		Mo	0.9

Electrical properties.—The dielectric constant (D) and loss tangent (tan δ) were determined as a function of frequency at room temperature as shown in Fig. 4 and 5, and the dielectric constant as a function of temperature at 10^4 Hz as shown in Fig. 6.

The room temperature dielectric constant of 9.5 and loss tangent of less the 0.0005 at 10^6 Hz may be compared with the equivalent values of 6.5-9.0 and 0.0003 for highest quality natural muscovite mica (10). Further electrical measurements will be reported by J. F. Puluka, who has observed a dielectric breakdown strength of greater than 3 kv/mil as compared to 3 to 6 kv/mil for mica (11). KNb_3O_8 appears to be highly resistant to radiation damage; exposure to 20 Mrads of 1 meV electrons produced only approximately twice the change in loss tangent produced in mica (11).

In view of the importance of natural mica and the relative lack of success in growing synthetic mica as a substitute (12) despite extensive work at the Bureau of Mines and elsewhere (10), there is still a need for a comparable dielectric material which can be grown in large crystals in a controlled manner. KNb_3O_8 shows considerable promise in this respect.

Properties of $K_4Nb_6O_{17}$

Crystals of $K_4Nb_6O_{17}$ become completely brittle and develop many small cleavage cracks after a number of days at ambient conditions. This is caused by re-

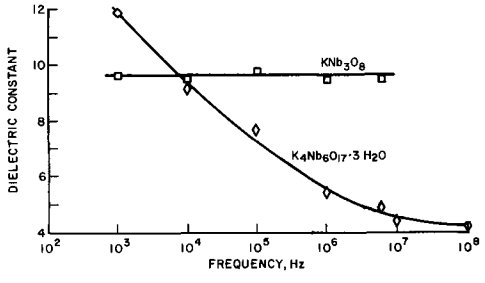

Fig. 4. Dielectric constant variation with frequency of KNb_3O_8 and $K_4Nb_6O_{17} \cdot 3H_2O$.

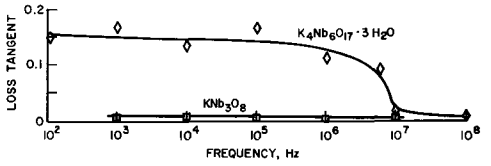

Fig. 5. Loss tangent variation with frequency of KNb_3O_8 and $K_4Nb_6O_{17} \cdot 3H_2O$.

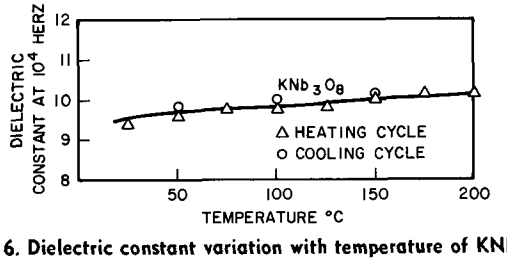

Fig. 6. Dielectric constant variation with temperature of KNb_3O_8

action with moisture as described in the next section. All of the water is driven off by heating to 150°-200°C. Because of this reaction only a limited number of properties were determined. The dielectric constant and the loss tangent show small peaks at 148°C, as shown in the curves of Fig. 7 and 8. They do not, however, show up on the differential thermal analysis curve of Fig. 9, which also indicates a melting point of 1155°C; the value given by Reisman and Holtzberg is 1163°C. The only measurement reported by Kestigian, who grew thin plates by the slow solidification of a nonstoichiometric melt, was a dielectric constant of 10.7 at 10^3 Hz which was reported not to change appreciably over the range —50° to 400°C, not really inconsistent with the data of Fig. 7.

Lattice parameters of $K_4Nb_6O_{17}$ were obtained from selected area electron diffraction during examination in a Siemens electron microscope operating at 111 kv. The data is given in Table I and was used to index the powder x-ray diffraction pattern given in Table V. The powdered and well-dried crystal sample was sealed into a capillary tube with wax.

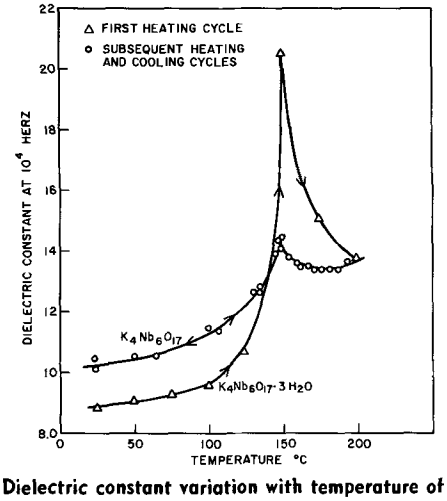

Fig. 7. Dielectric constant variation with temperature of $K_4Nb_6O_{17}$ and $K_4Nb_6O_{17}\cdot 3H_2O$.

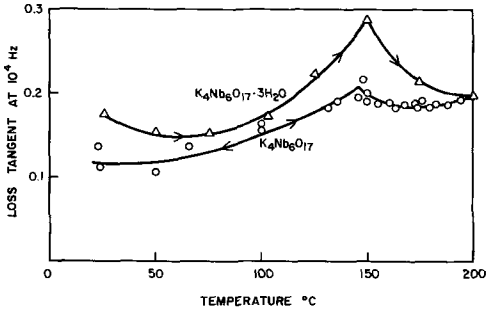

Fig. 8. Loss tangent variation with temperature of $K_4Nb_6O_{17}$ and $K_4Nb_6O_{17}\cdot 3H_2O$.

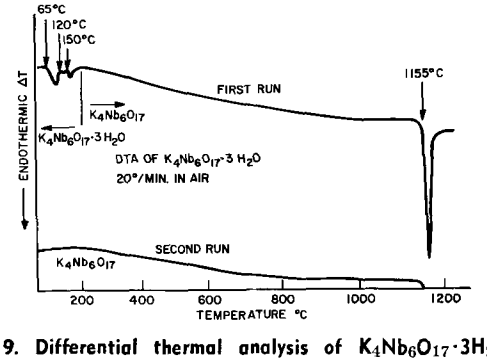

Fig. 9. Differential thermal analysis of $K_4Nb_6O_{17}\cdot 3H_2O$ and $K_4Nb_6O_{17}$.

Table V. Indexed powder x-ray diffraction pattern of $K_4Nb_6O_{17}$ (using $a = 7.58$Å, $b = 32.3$Å, $c = 6.40$Å)

hkl	d_{calc}, Å	d_{obs}, Å	I_{obs}
040	8.08	8.08	s
140	5.53	5.58	vw
041	5.02	5.06	w
200	3.79	3.79	w
210	3.76		
230	3.57	3.52	w
180	3.56		
211, 190	3.24		
0, 10, 0	3.23	3.23	m
002, 221	3.20	3.17	w
012	3.18		
260	3.10	3.08	vw
032	3.07		
270	2.929	2.924	s
132	2.843	2.846	m
*		2.712	w
		2.521	w
		2.350	vw
		2.206	s
		2.115	vw
		2.081	w
		1.952	m

* No unique indexing for lines at lower spacings.

This pattern does not agree with any of Guerchais' patterns (2), nor can it be indexed using the $K_4Nb_6O_{17}$ parameters of Whiston and Smith (3). It had been suggested that the structure is complex and of monoclinic symmetry (4); we find it to be orthorhombic.

Occurrence of $K_4Nb_6O_{17}$ Hydrates

In view of the changes occurring in $K_4Nb_6O_{17}$ on exposure to the atmosphere, the reaction with both CO_2 and H_2O was investigated. No reaction with CO_2 was observed, but absorption of water occurred readily. This had been noted by Kestigian *et al.* (4), who did not however observe the formation of hydrates.

Experiments on the water absorption of sintered powders did not yield reproducible results, presumably due to the presence of metastable intermediates (5). The use of powdered single crystal material completely avoided these problems and gave the data of Table VI. By transferring samples to higher and lower humidities, the water absorption was found to be reversible; all the water could also be removed again by storage in a desiccator over Drierite. Reproducibility was poor only in the 98% humidity atmosphere, where water condensation occurs very readily.

As shown in Fig. 10, the stable compound between about 25 and 85% relative humidity is $K_4Nb_6O_{17}\cdot 3H_2O$, which is therefore the composition normally encountered in the laboratory. Above about 85% humidity the fully hydrated compound is probably $K_4Nb_6O_{17}\cdot 4\frac{1}{2}H_2O$, although more water may be involved.

The differential thermal analysis curve of $K_4Nb_6O_{17}\cdot 3H_2O$ is shown in Fig. 9. The occurrence of the water loss in three steps is not significant, since the shape of the pattern changes with the heating rate. At all heating rates there is no water remaining above

Table VI. Variation of composition of $K_4Nb_6O_{17}\cdot XH_2O$ with humidity

Chemical*	Relative humidity, %	PH_2O, mm Hg	x
Drierite	~0	~0	0.0
$ZnCl_2\cdot \frac{1}{2}H_2O$	10	2.4	0.15
$LiCl\cdot H_2O$	15	3.6	0.0
$CaCl_2, 6H_2O$	32	7.6	3.2
$K_2CO_3\cdot 2H_2O$	43	10.0	3.1
$NaBr\cdot 2H_2O$	58	13.8	3.1
H_2SO_4:H_2O*	80	19	2.9
$Na_2CO_3\cdot 10H_2O$	87	20.7	4.4
$CuSO_4\cdot 5H_2O$	98	23.3	4.8, 5.1, 5.3

* Substance in equilibrium with its saturated solution in a confined space to give the humidity shown, except for Drierite (no water) and the sulfuric acid-water mixture which had a density of 1.20.

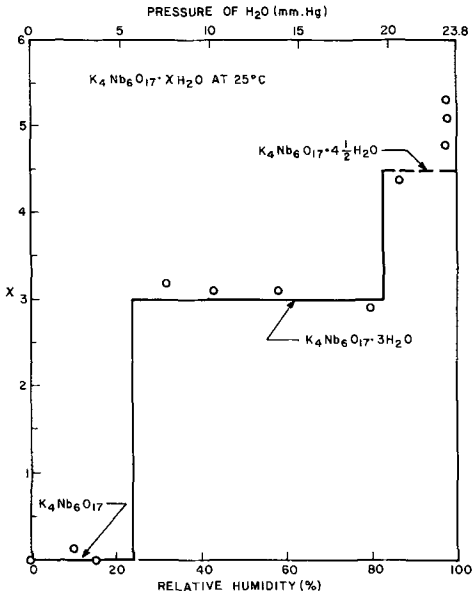

Fig. 10. Humidity-composition diagram for $K_4Nb_6O_{17}\cdot XH_2O$

150°C, and subsequent heating cycles retrace the lower curve of Fig. 9, now pertaining to anhydrous $K_4Nb_6O_{17}$.

Properties of $K_4Nb_6O_{17}$ Hydrates

The composition $K_4Nb_6O_{17} \cdot 3H_2O$ is the stable form below 65°C and between about 25 and 85% humidity. The crystals produced from $K_4Nb_6O_{17}$ by atmospheric water absorption are colorless, clear in thin layers, but with a silver sheen due to internal delamination, perhaps at grain boundaries at low angles to the cleavage plane in thicker sections. They cleave readily but show great brittleness, resembling the brittle micas. The addition of chromium to the melt produced yellow crystals; microscopic examination however showed that the color was due to trapped melt, the crystal remaining in fact colorless.

The optical transmission curve is shown in Fig. 11. The strong absorption near 3μ is consistent with either OH-bonded water or water of crystallization. The intensity of this absorption corresponds only to about 0.1 moles H_2O/mole $K_4Nb_6O_{17}$, because a freshly grown sample of $K_4Nb_6O_{17}$ with a short exposure to the atmosphere had been used. The optical constants listed in Table I were somewhat variable, presumably dependent on the humidity. The dielectric constant and loss tangent variation with temperature and frequency is shown in Fig. 4, 5, 7, and 8. The strong dispersion at 10^7 Hz in Fig. 5 presumably originates in the water content.

The single crystal parameters of $K_4Nb_6O_{17}\cdot 3H_2O$ are given in Table I. The Laue symmetry and systematic absences indicate the most probable space group to be $P22_12_1$. Due to the low quality of the diffraction patterns arising from the bent crystals, the space group $P22_12$ cannot be completely eliminated.

The b parameter was found to be slightly variable, again presumably dependent on the humidity, and

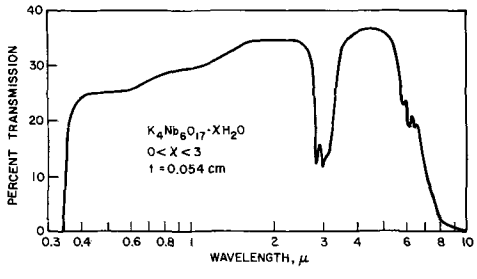

Fig. 11. Optical transmission curve of $N_4Nb_6O_{17}\cdot XH_2O$

Table VII. Indexed powder x-ray diffraction pattern of $K_4Nb_6O_{17}\cdot 3H_2O$ (using $a = 7.85$Å, $b = 37.9$Å, $c = 6.46$Å)

hkl	d_{calc}, Å	d_{obs}, Å	I_{obs}
020	18.95	19.0	m
040	9.48	9.50	vs
060	6.32	6.32	s
151	4.17	4.16	vw
071	4.15		
231	3.24	3.24	w
002	3.23		
012, 191	3.22		
0, 12, 1	2.837	2.832	s
1, 11, 1	2.834		
*	*	2.354	w
		2.215	w
		2.097	w
		1.995	w
		1.894	m
		1.714	m
		1.581	m

* No unique indexing for lines at lower spacings.

Table VIII. Indexed powder x-ray diffraction pattern of $K_4Nb_6O_{17}\cdot 4\frac{1}{2}H_2O$ (using $a = 7.82$Å, $b = 41.09$Å, $c = 6.42$Å)

hkl	d_{calc}, Å	d_{obs}, Å	I_{obs}
020	20.54	20.53	m
040	10.27	10.30	vs
060	6.85	6.89	s
0, 10, 2; 340; 2, 14, 1	2.53	2.53	vw
0, 16, 1; 370; 331	2.38	2.38	vw
0, 18, 0; 272	2.28	2.28	w
1, 16, 1; 361		2.27	w
0, 20, 0; 123; 0, 19, 1	2.05	2.05	m
Six possibilities	—	1.82	w

the value of 37.9Å was used in the indexed powder x-ray diffraction pattern of Table VII. This, as well as the pattern of $K_4Nb_6O_{17}\cdot 4\frac{1}{2}H_2O$ in Table VIII, is based on traces taken on a General Electric XRD 3 diffractometer with Ni filtered CuKα radiation at a rotation rate of 0.2°/min. The sample consisted of a slurry of powdered $K_4Nb_6O_{17}$ crystal in water on a microscope slide covered with tape. As the water evaporated, the pattern changed slowly from that given in Table VIII ($K_4Nb_6O_{17}\cdot 4\frac{1}{2}H_2O$) to that in Table VII ($K_4Nb_6O_{17}\cdot 3H_2O$).

In the presence of water $K_4Nb_6O_{17}\cdot 4\frac{1}{2}H_2O$ spontaneously separates into thin laminations. A single crystal of $K_4Nb_6O_{17}$ surrounded by a thin walled glass tube partially filled with water gave the fully hydrated compound, presumably $K_4Nb_6O_{17}\cdot 4\frac{1}{2}H_2O$. The single crystal parameters are given in Table I. As in the case of $K_4Nb_6O_{17}$ the probable orthorhombic space group is $P22_12_1$ or $P22_12$. Neither of the two hydrate diffraction patterns or unit cell dimensions were the same as any of those listed by Guerchais (2) or by Whiston and Smith (3).

The change in unit cell volume in going from $K_4Nb_6O_{17}$ to the hydrates is 28.6Å^3/H_2O for $K_4Nb_6O_{17}\cdot 3H_2O$ and 27.6Å^3/H_2O for $K_4Nb_6O_{17}\cdot 4\frac{1}{2}H_2O$. These values are in the range observed in inorganic hydrates (*e.g.*, 24.7 for $KAl(SO_4)_2\cdot 12H_2O$, and 30.0 for $Ca_2Al(OH_2)Br\cdot 2H_2O$) and confirm the hydrate formula for $K_4Nb_6O_{17}\cdot 4\frac{1}{2}H_2O$.

Only the b spacing changed appreciably with the variation in water content of the $K_4Nb_6O_{17}$ hydrates. Mica and related materials consist of layers of single or multiple sheets of linked octahedra and/or tetrahedra with alkali ions between the sheets. A similar structure composed of sheets of linked NbO_6 octahedra, with K^+ ions between the sheets, appears likely for the $K_4Nb_6O_{17}$ compounds. On this basis the water molecules would probably occur as a hydration sphere about the potassium ions.

Acknowledgments

The authors wish to thank E. W. Anderson for assistance with some of the electrical measurements, Mrs. A. S. Cooper and D. J. Nitti for the powder

photographs, T. T. Perry for the refractive index determinations, D. L. Wood for the optical transmission data, R. D. Heidenreich for the electron diffraction results, J. F. Puluka for permission to use some of his unpublished electrical data, and S. C. Abrahams for helpful discussions.

Manuscript submitted July 25, 1968; revised manuscript received *ca.* Nov. 10, 1968. This paper was presented at the Montreal Meeting, Oct. 6-11, 1968, as Paper 453.

Any discussion of this paper will appear in a Discussion Section to be published in the December 1969 JOURNAL.

REFERENCES

1. A. Reisman and F. Holtzberg, *J. Am. Chem. Soc.*, **77**, 2115 (1955).
2. J. E. Guerchais, *Bull. Soc. Chim. Fr.*, p. 103 (1962).
3. C. D. Whiston and A. J. Smith, *Acta Cryst.*, **19**, 169 (1965).
4. M. Kestigian, F. D. Leipziger, J. R. Carter, and F. G. Garabedian, *J. Am. Ceram. Soc.*, **49**, 517 (1966).
5. A. Reisman, F. Holtzberg, and M. Berkenblit, *J. Am. Chem. Soc.*, **81**, 1292 (1959).
6. K. Nassau and A. M. Broyer, *J. Am. Ceram. Soc.*, **45**, 474 (1962).
7. S. K. Kurtz and T. T. Perry, *J. Appl. Phys.*, **39**, 3798 (1968).
8. L. Bragg and G. F. Claringbull, "Crystal Structures of Minerals," p. 253 ff., Cornell University Press, Ithaca, New York (1965).
9. H. M. Gladney, *J. Appl. Phys.*, **38**, 4980 (1967).
10. H. R. Shell, "Micas, Natural and Synthetic," in Kirk-Othmer Encyclopedia of Chemical Technology, 2nd Edition, Vol. 13, pp. 398-424, Interscience Publishers, New York (1967).
11. J. F. Puluka, To be published.
12. B. Petkof in "Mineral Facts and Problems", Bureau of Mines, Bulletin 630, U.S. Government Printing Office, Washington, D.C., 1965.

Solid State Properties of Some Valve Metal Oxides

Ashok K. Vijh*

Research and Development Laboratories, Sprague Electric Company, North Adams, Massachusetts

ABSTRACT

Lattice energies and heats of atomization have been calculated for HfO_2, ZrO_2, Al_2O_3, Nb_2O_5, and Ta_2O_5 from thermochemical (see text, however) data by the use of the appropriate Born-Haber cycles. An attempt has been made to explore the relation of these quantities to certain fundamental properties, *e.g.*, melting points, boiling points, heats of formation, dielectric constants, forbidden gaps, *etc.*, which are a measure of the general physical and chemical nature of substances. Average bond energy values as well as MO bond dissociation energies for these oxides have also been calculated and discussed. Possible relation of these and related matters to heats of hydration and solution, and, heat capacities and thence temperature coefficients of band gaps have been briefly indicated.

On anodization in suitable electrolytes, Ta, Nb, Al, Zr, and Hf form thick (*ca.* > 1000Å) oxide films (1) which are of considerable interest as dielectric materials in electrolytic capacitors. It is of some importance, therefore, to attempt to obtain quantities which, in general, are diagnostic of a variety of mechanical, thermal, chemical, and electrical properties of these substances. In case of ionic compounds, such a quantity is lattice energy whereas the corresponding parameter for covalent compounds is the heat of atomization (2). Like many other materials of technological interest, these oxides are partially ionic and partially covalent (1). Here, an attempt has been made to calculate both the lattice energies and heats of atomization and compare each with various fundamental properties of these oxides, *e.g.*, heats of formation, melting points, and dielectric constants, etc.

Lattice Energies and Heats of Atomization

The lattice energies have been calculated from thermochemical data[1] by use of the appropriate Born-Haber cycle (3). The values obtained as well as the thermochemical data used in these calculations, together with the source references for these data, have been shown in Table I. The only previous value available in the literature is for Al_2O_3 (3). Our value for lattice energy per mole (at 25°C) for Al_2O_3 in Table I (3651.5 kcal) compares favorably with the older value (3663 kcal/mole), also obtained by Born-Haber cycle, quoted by Waddington (3). The heats of atomization have also been obtained from the thermochemical data listed in Table I, by means of the shorter Born-Haber cycle.

In Table II, lattice energies per equivalent as well as heats of atomization per equivalent for these oxides have been compared with the corresponding dielectric constants, melting points, boiling points, and heats of formation per equivalent. In order to explore the significance of these data in more detail and to permit discussion of these properties individually, each one of these properties has been plotted separately against the corresponding lattice energies per equivalent and heats of atomization per equivalent in the various graphs shown here. It may be concluded from Table II and from Fig. 1-4, that, in general, with increasing heat of atomization per equivalent, melting point (Fig. 1), heat of formation per equivalent (Fig. 2), boiling point (Fig. 3), all increase and dielectric constant decreases (Fig. 4). Again, lattice energy, in general, may be concluded to be related to these quantities in a way opposite to that of heat of atomization.

It may be noted that the comparisons are not entirely satisfactory, *e.g.*, shaded points in Fig. 1, 3, and 4 do not really follow a relation either with the heats of atomization or lattice energies. All these points, it may be mentioned, represent Al_2O_3. This is probably not entirely unexpected, since the heat of sublimation for aluminum, which makes a substantial contribution to heat of atomization of aluminum oxide and some contribution to the lattice energy of Al_2O_3 is, in the present context, unusually low. The reason being that, aluminum, unlike Ta, Nb, Zr, and Hf, is not a transition metal. For improved estimates one must invoke

* Electrochemical Society Active Member.

[1] Values of the heat of formation of O^{2-} from O cannot be obtained by thermochemical measurements, since O^{2-} ion is unstable. An estimate of this quantity is usually made by first calculating the theoretical lattice energy of an oxide by a Madelung type computation (assuming 100% ionicity) and then applying the Born-Haber cycle. One of the referees is thanked for pointing this out to us.

Table I.*

Oxide	$-\Delta H°_{form.}$ (kcal · mole^{-1}, 25°C)	Successive ionization potentials of the respective metals, kcal					$A_{O^{-2}}$,† kcal · mole^{-1}	$\Delta H_{diss}O_2$, kcal/g atom	$(\Delta H_{Sub})_{metal}$‡ kcal/g atom	U, 25°C kcal · mole^{-1}
		1	2	3	4	5				
HfO_2	271.5 (5)	160 (6)	344 (6)	485 (7)	715 (7)		156 (8)	59.5 (9)	163.2 (9)	2569.7
ZrO_2	258.2 (5)	158 (6)	302.8 (6)	530 (6)	791.8 (6)		156 (8)	59.5 (9)	142 (9)	2613.8
Al_2O_3	399 (5)	138 (6)	434.1 (6)	655.9 (6)			156 (8)	59.5 (9)	75 (9)	3651.5
Ta_2O_5	499.9 (5)	182 (6)	374 (6)	507.5 (7)	761 (7)	1037 (7)	156 (8)	59.5 (9)	185 (9)	7670.4
Nb_2O_5	463.2 (5)	158.7 (6)	330.3 (6)	579.8 (6)	883 (6)	1152 (6)	156 (8)	59.5 (9)	185 (9)	8018.3

* The numbers in the parentheses indicate the reference from which a particular value has been obtained.
† $A_{O^{-2}}$ is the energy required to form O^{-2} from O atom.
‡ The values of $[\Delta H_{Sub.}]_{metal}$ have been taken as the same as the heats of formation of gaseous atoms of the respective metal from its standard state, *i.e.*, crystalline form of element. In general, $[\Delta H_{Sub.}]_{metal} = [\Delta H_{fusion}]_{metal} + [\Delta H_{Vap.}]_{metal}$ and hence the values used are valid since metals usually evaporate to monoatomic gases [see ref. (4), pp. 82, 86].

Table II.*

Oxide	Lattice energy, kcal/equiv. 25°C	Heat of atomization, kcal/equiv.	Heat of formation, kcal/equiv.	Dielectric constant	M. Pt., °K	B. Pt., °K
HfO_2	642.4	138.42	−67.9	20-22 (1)	3063 (10)	~5700 (12)
ZrO_2	653.4	129.8	−64.5	22-25 (1)	2950 (10)	4600 (11)
Al_2O_3	608.6	121.25	−66.5	8-10.5 (1)	2300 (10)	3280 (11)
Ta_2O_5	767.4	116.64	−50.0	27.6 (1)	2150 (10)	
Nb_2O_5	801.8	113.07	−46.3	41.4 (1)	1733 (10)	3227 (13)

* The numbers in parentheses indicate the reference from which a particular value has been obtained.

a "correction factor" to take into account the lack of unfilled d orbitals and thence low cohesive energies of aluminum. This, of course, is not very straightforward.

In case of Fig. 3, no data seem to exist for the boiling point of Ta_2O_5.

Significance of Various Graphs (Fig. 1-4)

Since melting points increase systematically with heats of atomization and not lattice energies (Fig. 1), it may be concluded that the solid-state cohesion of these oxides is determined predominantly by covalent aspects of their bonding (2; *cf.* 1). Identical qualitative conclusions would also follow from Fig. 2-4 (2). No quantitative estimates, however, can be made regarding partial ionicity and covalence in these oxides. This is because the various procedures for estimating the nature of bonding in solids often yield widely different results (4). Further, since the Born-Haber lattice energies are not true thermochemical values for the case of oxides, it is not valid to compare them with the theoretical lattice energies for the purposes of obtaining per cent ionicity. It has been recently pointed out to us that Pauling's criteria for per cent ionic character (*cf.* 1) are not applicable to solids (4a).

It may also be stated, by analogy with some previous work (2), that the magnitude of various other properties diagnostic of the general stability of these oxides would be largely determined by the covalent aspects of their bonding. Some of these properties are: heats of fusion and evaporation, dielectric strengths, activation energies for the creation of dislocations and other physical "faults," and band gaps.

Band Gaps and Their Temperature Dependence

It may be noted that no attempt has been made in the foregoing discussion to relate heats of atomization or lattice energies of these oxides, to the corresponding values, ΔE, of the forbidden gaps. Since relation to the heats of formation per equivalent has already been examined (Fig. 2), it follows that the relation to the energy of the forbidden gap, ΔE, would exhibit the same trend. This is because, recently, it has been shown that, for a great variety of semiconducting compounds, especially ones with high ΔE values and specifically for Al_2O_3, Ta_2O_5, Ga_2O_3, In_2O_3, TiO_2 (and,

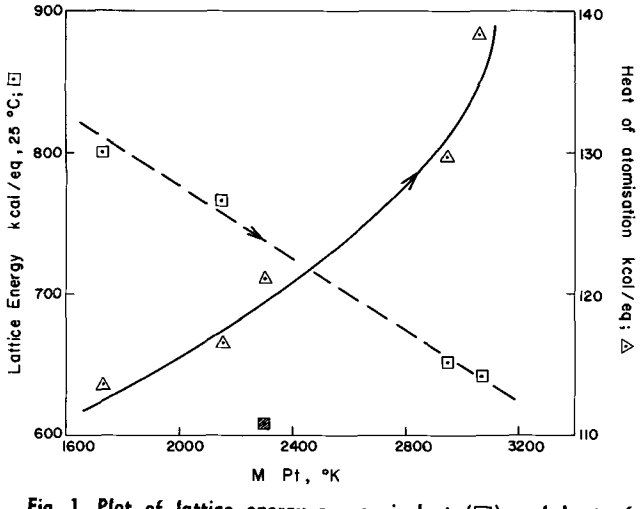

Fig. 1. Plot of lattice energy per equivalent (⊡) and heat of atomization per equivalent (△) against melting points.

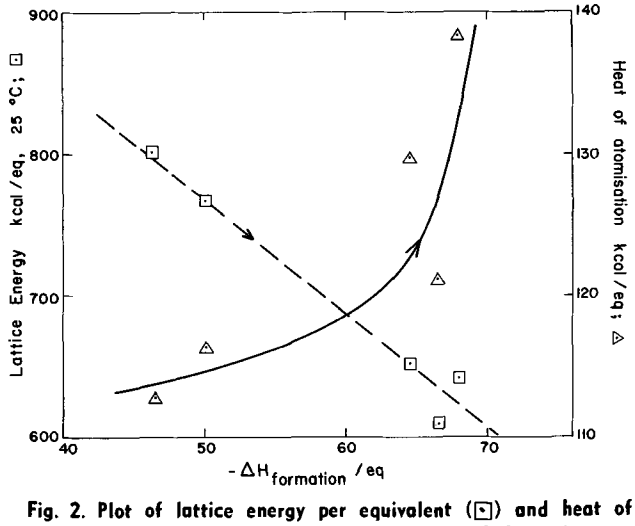

Fig. 2. Plot of lattice energy per equivalent (⊡) and heat of atomization per equivalent (△) against heats of formation per equivalent.

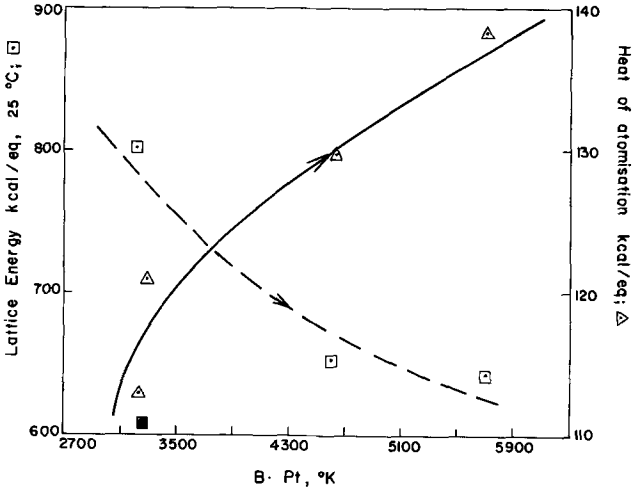

Fig. 3. Plot of lattice energy per equivalent (⊡) and heat of atomization per equivalent (△) against boiling points.

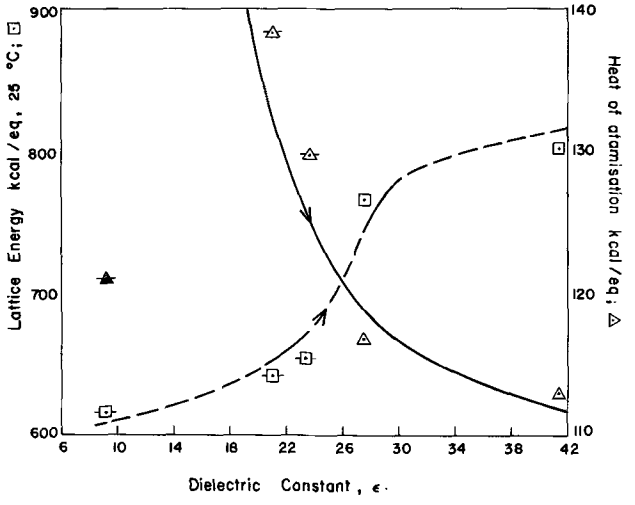

Fig. 4. Plot of lattice energy per equivalent (⊡) and heat of atomization per equivalent (△) against dielectric constants for various oxides.

presumably, other polyvalent oxides), $\Delta E \simeq 2$ x heat of formation per equivalent (14).

The values of heat capacity at constant pressure, C_p, available in the literature (15) are for Nb_2O_5, Ta_2O_5, and Al_2O_3 only. For these three substances, C_p has a value 3.13 ± 0.1 cal/deg equiv. (15). Since C_p is directly related to $\partial(\Delta E)/\partial T$, the temperature coefficient of the band gap, it follows that the change in the band gap with changing temperature for these three substances is approximately the same (16).

It has been tacitly assumed in the foregoing discussion that concepts valid for crystalline substances can also be applied to amorphous oxides as indeed would be obtained on anodization. This is essentially valid, though approximately so, since the short range structure and crystalline order is still maintained intact in amorphous substances and even in melts; *e.g.*, band theory of solids can be applied to these states (*i.e.*, amorphous and molten) exactly the same way as to the crystalline substances, except that the bands tend to be diffuse and thence the consequent approximations (17).

Relation of Lattice Energies to Heats of Hydration and Solution

The lattice energies of compounds are also related to their heats of hydration and heats of solution (18). In fact, Lattice energy = Heat of hydration — Heat of solution.

Heats of solution are usually a small fraction (*ca.* 5%) of heats of hydration, and, experimental values are unknown for the present oxides. It may be concluded, therefore, that the lattice energies reported in Table I are also an approximate measure of the heats of hydration of the corresponding oxides. This is confirmed by a direct theoretical estimation of standard free energies of hydration for oxides and their comparison with the lattice energies calculated in Table I. These estimations have been carried out as follows (19).

The molal free energy changes associated with the conversion of the lattice into individual ions in the ideal gas state at one atmosphere pressure may be represented by $\Delta\mathring{G}_L$, which is related to the lattice energy U (see, Table I) by the equation (19)

$$\Delta\mathring{G}_L = -U - 7.4\,(a + c) \qquad [1]$$

where a is the number of anions and c that of cations in one molecule of the given oxide, *e.g.*, Al_2O_3.

The standard free energies of hydration for a cation and anion may be estimated semi-empirically by the equations (19)

$$(\Delta\mathring{G}_h)_{Cat} = -164\,Z^2 + /(r+ + 0.75) \qquad [2]$$

and

$$(\Delta\mathring{G}_h)_{An} = -164\,Z^2-/(r- + 0.35) \qquad [3]$$

Where $Z+$ and $Z-$ are the respective cationic and anionic charges and $r+$ and $r-$ are the crystallographic radii of the cation and anion, respectively; the factors 0.75 and 0.35 are in Angstroms and are the empirical corrections that must be made to the crystallographic radii to make the latter agree with the radii as determined by the Born equation, which are presumably equivalent to the gas phase ionic radii (undefinable and unknown). The $\Delta\mathring{G}_L$, $(\Delta\mathring{G}_h)_{Cat}$, $(\Delta\mathring{G}_h)_{An}$ and $(\Delta\mathring{G}_h)_{oxide}$, determined, per mole, by this procedure for every one of the five oxides have been shown in Table III.

It may be emphasized that no corrections for per cent ionic character are necessary in the lattice energies used here since if the oxides were entirely covalent, one would replace the lattice energy by heat of dissociation into ions (*e.g.*, for HCl) and not corresponding heats of atomization (18).

Bond Energies and Bond Dissociation Energies

If the spin correlation stabilization energies, which are usually small, are ignored (20), the heats of atomization (Table II) per equivalent would be identical

Table III.

Oxide	$\Delta G°_L$*	$(\Delta G°_h)_{cat}$†	$(\Delta G°_h)_{An}$†, ‡	$(\Delta G°_h)_{oxide}$*
HfO_2	2598	1701	393	2487
ZrO_2	2642	1690	393	2476
Al_2O_3	3688	1170	393	3519
Ta_2O_5	7722	2866	393	7697
Nb_2O_5	8070	2752	393	7469

* Values are kcal mole^{-1}.

† Values are kcal g-ion^{-1}.

‡ For the hypothetical ion O^{-2}; hypothetical because the ultimate anion formed for, *e.g.*, Al_2O_3 would depend on the pH of the solution, *e.g.*, AlO_2^- in certain alkaline solutions.

Notes:

All values in this table are approximate since no rigorous procedures are available for calculating $\Delta G°_h$ of individual ions; approximations become particularly serious for the polyvalent ions as in the present case [see ref. (18) and (19)].

Data on ionic radii have been obtained from ref. (5), p. F-89.

Values of $(\Delta G°_h)_{cat}$ are much more reliable than $(\Delta G°_h)_{An}$, since empirical corrections to Born's radii have been shown to give much more accurate results in case of cations than in case of anions (19).

Table IV.

Oxide	Heat of atomization, kcal/equiv. of oxide	MO bond energy, kcal · mole^{-1} of the bond	MO bond dissociation energies, kcal · mole^{-1} 25°C		
			1	2	3
HfO_2	138.4	148	184	—	—
ZrO_2	129.8	142	173	182	151
Al_2O_3	121.2	132	158	116	120
Ta_2O_5	116.6	123	167	215	195
Nb_2O_5	113	122	115	181	93

Notes:
MO bond dissociation energies under 1 have been calculated by us from Pauling's equation

$$D_{MO} = \tfrac{1}{2}\,(D_{MM} + D_{OO}) + 23.06\,(X_M - X_O)^2,$$

in kcal · mole^{-1} of MO (21); Pauling calls it bond energy. However, since he assumes an isolated diatomic molecule in his procedure, MO in this case, these bond energies are bond dissociation energies and in case of a diatomic molecule are equal to bond energies.

MO bond dissociation energies under 2 above have been obtained from ref. (22) and have been determined by a variety of experimental and theoretical procedures. See ref. (22) for the assessment of accuracies of these values.

MO bond dissociation energies under 3 were obtained from ref. (23) and were determined by different procedures of widely differing accuracies.

The quantity of interest in the present discussions is MO bond energy, an average value obtained by Howald's method and represents the average strength of MO bond as it occurs in the oxide of interest; MO bond dissociation energies refer to isolated MO bonds and are not relevant to the arguments developed here. They have been presented here, however, for the purposes of comparison and for emphasizing the distinction between bond energies and bond dissociation energies.

to the average bond energies (not bond dissociation energies for particular bonds). An attempt has also been made here to calculate the MO (metal-oxide) bond energies for these oxides, by taking into account spin correlation stabilization energies (20). The values obtained have been compared with the values of heats of atomization in Table IV. This procedure for the calculation of bond energies involves reference to Howald's (20) "valence state atoms" [see Table III in ref. (20)] and an assumption that, $\alpha = Q$, since Q values are not available. This assumption amounts to ignoring the contribution of coordinate valence to the bonding. It may be noted in Table IV that the bond energies are consistently slightly higher than the corresponding values for heats of atomization per equivalent.

It is clear from Table IV, however, that replacing heats of atomization by bond energies in various plots (Fig. 1-4) would not change the nature of arguments presented here.

In Table IV, values of (last) bond dissociation energies estimated by us by Pauling's method (21) and experimental values of other workers have also been shown for the sake of comparisons with bond energies. The relative significance of various quantities in Table IV has been explained in the notes to that Table.

Acknowledgments

The author would like to thank Dr. R. S. Alwitt and Dr. D. M. Smyth for some general discussion on matters related to the content of this paper. Thanks are also due to Professor R. A. Howald of Montana State University for a personal communication on the procedures for calculation of bond energies. A recent personal communication from Dr. M. Tosi of Argonne National Laboratory [ref. (4a)] and the helpful comments of the referees are gratefully acknowledged.

Manuscript submitted Sept. 9, 1968; revised manuscript received Nov. 18, 1968.

Any discussion of this paper will appear in a Discussion Section to be published in the December 1969 JOURNAL.

REFERENCES

1. G. C. Wood and C. Pearson, *Corrosion Science*, **7**, 119 (1967); L. Young, "Anodic Oxide Films, Academic Press, New York (1961).
2. A. A. Vorob'ev in "Chemical Bonds in Semiconductors and Solids," p. 177, N. N. Sirota, Editor, Consultants Bureau, New York (1967), *idem, Russ. Chem. Rev.*, **36** (6), 440 (English Trans.) (1967), Consultants Bureau, New York.
3. T. C. Waddington in "Advances in Inorganic and Radiochemistry," Vol. 1, p. 158, H. J. Emleleus and A. G. Sharpe, Editors, Academic Press, New York (1959).
4. J. L. Birman, *Phys. Rev.*, **109**, 810 (1958).
4a. M. Tosi, Personal communication.
5. "Handbook of Chemistry and Physics," 45 Edition, p. D-38, The Chemical Rubber Co. (1964-65).
6. K. B. Harvey and G. B. Porter, "Physical Inorganic Chemistry," p. 80, Addison-Wesley Publishing Co., Inc. (1963).
7. R. Parsons, "Electrochemical Constants," p. 2, Butterworths (1959).
8. Ref. (4), p. 102.
9. Ref. (5), p. F-94.
10. Ref. (5), pp. D-35 to D-37.
11. I. E. Campbell, "High Temperature Technology," p. 31, John Wiley & Sons, Inc. (1956).
12. Ref. (5), p. B-147 and the following pages.
13. Ref. (5), p. D-36.
14. A. K. Vijh, *J. Phys. and Chem. Solids*, accepted for publication.
15. R. Rossini *et al.*, "Selected Thermodynamic Properties," Natl. Bureau Standards Circular 500, U.S. Govt. Printing Office, Washington, D. C. (1952).
16. N. N. Sirota, in "Chemical Bonds in Semiconducductors and Solids," p. 7, N.N. Sirota, Editor, Consultants Bureau, New York (1967).
17. D. R. Lamb, "Electrical Conduction Mechanisms in Thin Insulating Films," p. 9, Methuen and Co., Ltd., London (1967).
18. B. E. Conway and J. O'M. Bockris in "Modern Aspects of Electrochemistry," Vol. I, J. O'M. Bockris and B. E. Conway, Editors, Butterworths, London (1954).
19. D. A. Johnson, *J. Chem. Ed.*, **45**, 236 (1968).
20. R. A. Howald, *ibid.*, **45**, 163 (1968); also private communication to A. K. Vijh.
21. L. Pauling, "The Nature of Chemical Bond," p. 79 and Appendix XII, Cornell University Press (1960).
22. V. I. Vendeneyere *et al.*, "Bond Energies, Ionization Potentials and Electron Affinities," p. 29, St. Martin's Press, New York (1966).
23. "Handbook of Chemistry and Physics," 47th Ed., F-89, The Chemical Rubber Co. (1966-67).

The Electrical Conductivity and the Crystal Structure of Silver Iodide

Takehiko Takahashi,* Katsumi Kuwabara, and Osamu Yamamoto

Department of Applied Chemistry, Faculty of Engineering, Nagoya University, Nagoya, Japan

ABSTRACT

The electrical conductivity of silver iodide pressure moulded into pellets at 2.0 tons/cm^2 was measured and the crystal structure of γ-AgI was investigated by means of x-ray diffraction. The conductivity of γ-AgI decreases gradually as the heating and cooling operations are repeated. The decrease is attributed to the phase transition of γ- to β-phase. In the case of β-AgI the conductivity is not changed by the heating procedure. The activation energies of conduction for γ- and β-AgI at near room temperature are about 7.0 and 9.5 kcal/mole respectively. The crystal structure of the compressed γ-AgI differs from the ideal zinc blende structure. The modified structure has been suggested to be the average one which has silver ions distributed randomly over the ideal position of the ideal zinc blende structure and the four positions surrounding the ideal position.

Studies on high ionic conductive solids have been carried out in our laboratory for several years and some compounds have been found to have high ionic conductivity (1-6). These compounds, such as Ag_3SI (1) and $Ag_4HgSe_2I_2$ (3), were synthesized using silver iodide as a main material. Silver iodide is, therefore, of interest as a mother compound of the high ionic conductivity solid electrolytes.

A number of reports (7-13) have shown polymorphism in silver iodide. At atmospheric pressure, three forms of silver iodide are said to exist: face-centered cubic, hexagonal, and body-centered cubic forms. The third, α-phase, is famous for typical "average structure."

The electrical conductivity of α-phase is the order of 10^0 ohm^{-1}cm^{-1}, which is 10^4 or 10^6 times larger than that of the γ- or β-phase. It is known that the charge carrier in the α-phase is the silver ion.

Silver iodide is usually precipitated by the reaction between silver nitrate solution and potassium iodide solution at room temperature. It is, however, impossible to prepare a single crystal stable at normal pressure, and silver iodide is generally a mixture of γ- and β-phase (14). Accordingly, the electrical conductivities reported were mean values.

The purposes of the present study were to measure the electrical conductivity of γ- and β-phase silver iodide separately, to survey the conductivity change with time, and to make clear the correlation between the electrical conductivity and the crystal structure of silver iodide.

Experimental

Preparation of the starting materials.—Silver iodide is precipitated by the following reaction in the low cubic form under the condition that silver is in excess of the stoichiometric proportion (15)

$$AgNO_3 + KI \rightarrow AgI \downarrow + KNO_3$$

By the addition of KI (aq) into excess $AgNO_3$(aq) with constant stirring, γ-AgI containing a small amount of β-AgI was obtained. In order to get as pure γ-phase as possible, the dried precipitate was gently ground in a mortar.

Electrical conductivity and x-ray diffraction measurements were performed with a pellet type specimen. The γ-AgI pellets, 13 mm in diameter and about 2 mm thick, were formed by a hand press. It is known that the β-phase tends to precipitate if iodide ion is in excess (15). However, in this study, β-AgI was prepared by heating the compressed γ-AgI for a long time at 200°C.

* Electrochemical Society Active Member.

Conductivity measurement.—Apparatus for conductivity measurements is shown in Fig. 1. To measure the conductivity change with time and temperature, the apparatus was placed in an electrical oven, the temperature of which was changed from room temperature to 160°C. An impedance bridge at 1 kHz was used to measure the electrical conductivity.

X-ray diffraction.—A copper anode tube was operated at 15 ma and 35 kv. The goniometer scan speed was selected to 1°/min in the qualitative analysis.

A sample holder made in our laboratory was used to follow the change in structure at higher temperatures.

In the structure analysis, the goniometer scan speed was reduced to ¼°/min. The observed intensities discussed later are the mean values of the diffraction lines obtained from twelve samples.

Results and Discussion

Stability of γ-AgI.—The structure of silver iodide changes with temperature and pressure (16-22).

As a first step, the dependency of the conductivity on pressure was examined. The pellet type samples made at 0.5 to 6.0 tons/cm^2 were used to measure the electrical conductivity σ. The results are shown in Fig. 2. Up to about 2.5 tons/cm^2, σ increases; between 2.5 and 4.0 tons/cm^2, σ is nearly constant; and in the range above 4.0 tons/cm^2, the curve has a descending plateau. These three parts of the curve should be compared with the phase relationship of AgI drawn by Davis and Adams (23) which reveals agreement with the phases found by them at room temperature. The low pressure part in Fig. 2 corresponds to the II' phase (low fcc) in their diagram, the middle part to the IV

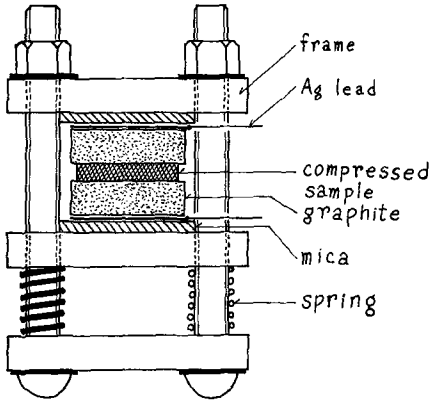

Fig. 1. Apparatus for conductivity measurement

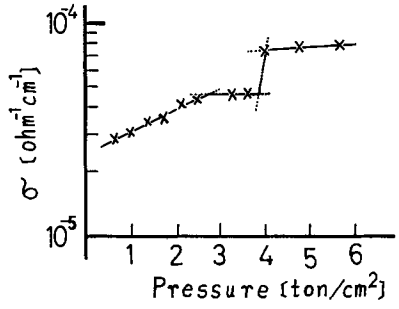

Fig. 2 Conductivity of γ-AgI compressed at various pressures at room temperature.

phase (ortho), and the higher pressure part to the III phase (fcc).

It has been reported that γ-AgI is metastable and β-AgI transforms to γ-AgI when being ground in a mortar or strongly pressed. In the second part of this report, therefore, the change of the conductivity with time was followed at room temperature. σ remains essentially constant and there is no change in the x-ray pattern with time.

From these facts it is suggested that the γ-AgI pellet is stable at room temperature.

Conductivity.—γ-AgI.—As mentioned above, γ-AgI has been found to have a high stability at room temperature, but it is affected by heating. Initial experiments showed that when the specimen was annealed for 10 hr at 60°C, σ was observed to be lower than the initial value by about one order of magnitude. After being annealed for several hours at 100°C, σ decreased considerably.

Thus, the conductivities were measured at several temperatures in the range between room temperature and 100°C. The temperature of the specimen was kept constant for one or two hours in conductivity measurement.

The results are shown in Fig. 3. Curve A was obtained with the initial heating operation. Curve B shows the result for the cooling operation after the initial heating. Curves C, D, and E correspond to the results for successive heating operations. These curves are fairly linear and the conductivity tended to decrease as the operations were repeated. The activation energy of conduction is obtained from these slopes to be about 7.0 kcal/mol.

The repetition of heating and cooling in the range of room temperature to 160°C makes the slope larger and the linearity poorer. Curve F in Fig. 3 shows the result in the case where the heating operation was done after the heating procedure represented by Curve E had been performed. The σ values are found to decrease by about one order in the cooling operation next to the heating. Finally, σ values are fixed to the positions shown by the open circles.

β-AgI.—It is ordinarily very difficult to prepare pure β-AgI. Even if the pellet type specimen is heated over 10 hr at 200°C, it is not possible to completely prevent γ-AgI forming. The sample so treated may be regarded as pure β-AgI so far as the conductivity measurement is concerned. In practice, the conductivity change of β-AgI with time is not observed and the presence of a trace of γ-AgI has been neglected in this experiment.

Two kinds of electrodes, graphite and silver plates, were used to check the effect of electrode materials, but no effect was detected.

Figure 4 shows the conductivity curve of β-AgI. There exists a slight displacement between the curves for temperature descending and ascending. This may be due to supercooling of the α-phase. This hysteresis was observed in every measurement extended to 160°C. The activation energy is calculated from the slope of the linear portion of the curve near room temperature and is found to be about 9.5 kcal/mole, which is larger than that of γ-AgI.

Conductivity and phase transition.—The electrical conductivities of a number of solid electrolytes are known to be changed by phase transition. For example, the electrical conductivity of Ag_2HgI_4 (24, 25) is about 10^{-7} ohm^{-1} cm^{-1} at room temperature, the phase of which is demonstrated as β-Ag_2HgI_4. When it transforms to α-Ag_2HgI_4 at 50°C which has an "average" structure (26), the conductivity becomes about 10^{-3} ohm^{-1} cm^{-1}.

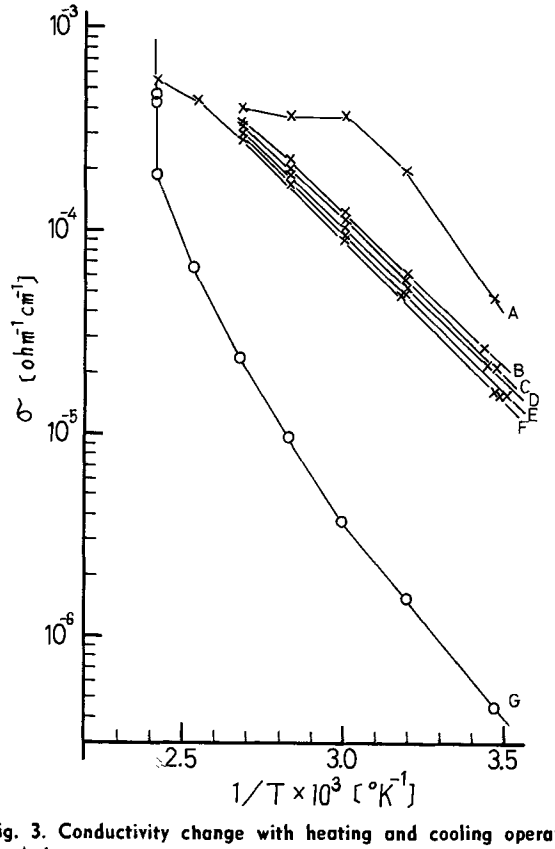

Fig. 3. Conductivity change with heating and cooling operation for γ-AgI.

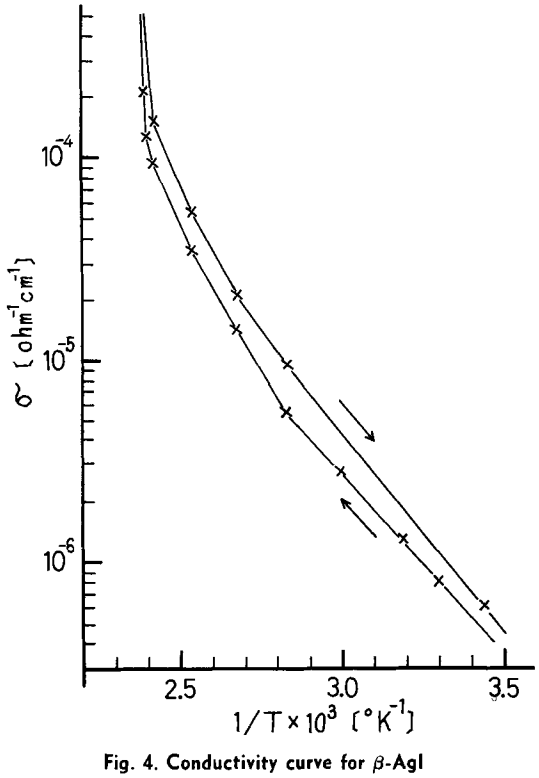

Fig. 4. Conductivity curve for β-AgI

The polymorphism or phase transition of AgI has been investigated by many authors. Mrgudich (27) studied pellet type AgI. In his study on solid electrolyte batteries, he measured the conductivity of compressed AgI powder pellets. According to his results, the presence of a deformed hexagonal phase was an important factor in determining the conductivity, and the face-centered cubic phase, i.e., γ-phase, gave some resultant decrease in conductivity.

On the other hand, different phenomena were observed in the present investigation. X-ray diffraction patterns were taken in order to find the reason why the conductivity change was observed when the heating and cooling operations were repeated with pellet type γ-AgI. The results are shown in Fig. 5. The profile (a) is that of the sample immediately after the conductivity was measured at room temperature. The three peaks are fairly broad. The pattern (b) was taken at 120°C. In addition to the three peaks in (a), a few small peaks which belong to β-AgI are seen. They grow moderately as the heating operation is repeated. At 170°C which is above the transition temperature 147°C, four peaks are obtained as are seen in (c). This pattern is typical for the body-centered cubic lattice. After being annealed for 1 hr at 170°C, the sample was cooled to room temperature, and the x-ray diffraction pattern was taken again. The more complex peaks shown in (d) are those of β-AgI which have been identified by the help of ASTM card. The ratios of their intensities differ slightly from the data indicated in ASTM data. This difference suggests that the lattice distortion is induced by heating of the pellet.

To compare the diagram of the pellet with that of the powder sample, x-ray diffraction profiles were taken at room temperature, 100°, and 170°C. The results with powders shown in Fig. 6 agreed approximately with those of the pellet. The (d) in Fig. 6 differs from (d) in Fig. 5. The agreement of the intensity ratios in Fig. 6 with ASTM data is better than that in Fig. 5.

From these results it is confirmed that the face-centered phase transforms to the hexagonal phase in the course of repetition of heating and cooling. This consideration coincides with Burley's study (13).

Thus, the change of conductivity in γ-AgI can be attributed to the phase transition. The decrease in

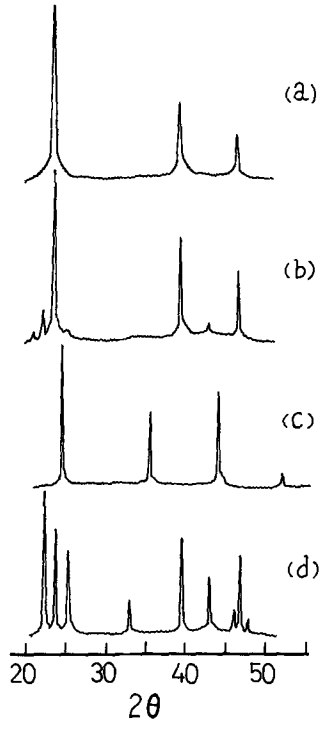

Fig. 5. X-ray diffraction of compressed γ-AgI at various temperatures.

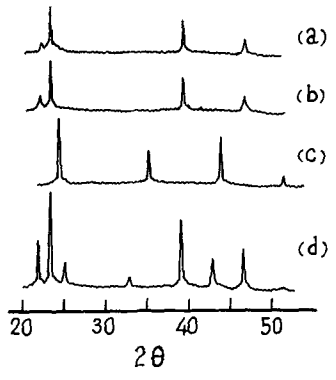

Fig. 6. X-ray diffraction of γ-AgI powder at various temperatures

conductivity of the γ-phase is not due to the presence of the face-centered cubic phase, but to the transition of the γ- to β-phase.

Structure of compressed γ-AgI.—The crystal structure of γ-AgI was analyzed by Wilsey (28) in 1921 and confirmed by Davey (29) in 1922. According to their powder x-ray diffraction studies, γ-AgI has a face-centered cubic lattice of zinc blende type. On the other hand, a hexagonal structure of wurtzite type was reported as a result of the optical studies with relation to iodyrite by Aminoff (30) in 1922. In addition, the fact that the silver atoms in β-AgI are distributed at random among four positions situated tetrahedrally around the ideal position in the wurtzite structure was found on the basis of oscillation studies by Helmholz (31) in 1935.

As can be seen in the previous sections, pellet type γ-AgI gives a hundred times larger conductivity than that of β-AgI at room temperature, and its activation energy of conduction is comparatively low. Moreover, a little breadth in x-ray diffraction peaks is observed and separation of the peaks corresponding to $CuK\alpha_1$ and $K\alpha_2$ is insufficient. These data suggest that compressed γ-AgI may have some structural peculiarity.

In fact, our observed intensities did not agree with the expected. Thus, a modified structure model may be introduced like (b) in Fig. 7, which differs from that of ideal zinc blende (a). The intensities of the diffraction lines were calculated by the following formula in order to compare with the experimental data

$$I = A \cdot \frac{1 + \cos^2 2\theta}{\sin^2\theta \cos\theta} \cdot P \cdot |F|^2 \qquad [1]$$

where I is the relative intensity, A the absorption factor, the second term the Lorentz-polarization factor containing the Bragg angle θ, P the multiplicity of lattice plane, F the structure factor. The last term F is expressed by the following relation

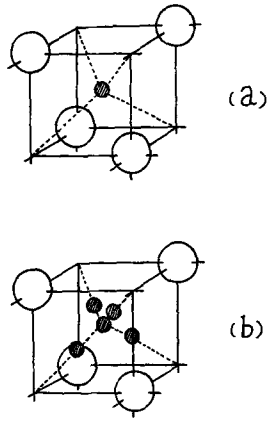

Fig. 7. Crystal structure of γ-AgI showing 1/8 of unit cell, (a) ideal zinc-blende structure, (b) proposed average structure.

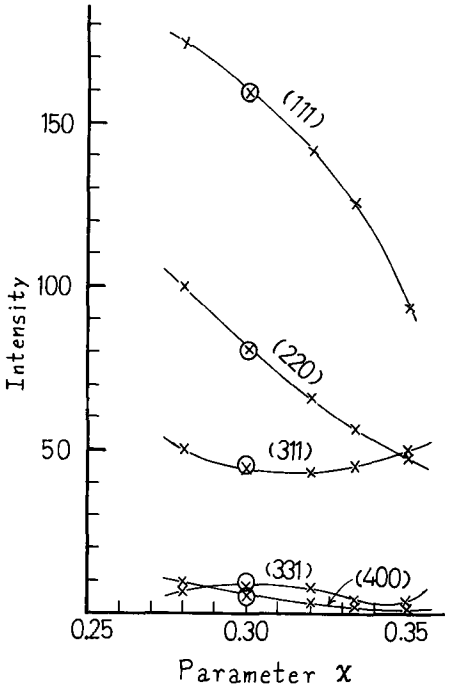

Fig. 8. Calculated intensity as a function of the parameter x 16 (e) of F $\bar{4}$3m.

$$F = F(hkl) = \sum_i f_i \exp 2\pi i\,(hx_i + ky_i + lz_i) \quad [2]$$

$$= A(hkl) + iB(hkl) \quad [3]$$

$$A(hkl) = \sum_i f_i \cos 2\pi\,(hx_i + ky_i + lz_i) \quad [4]$$

$$B(hkl) = \sum_i f_i \sin 2\pi\,(hx_i + ky_i + lz_i) \quad [5]$$

$$f_i = f_{io} \exp\,(-\bar{B} \sin^2\theta/\lambda^2) \quad [6]$$

where h, k, l are the Miller's indices, f_i the modified atomic scattering factor of the i-th atom related to the atomic scattering factor f_{io} and the Debye factor $\bar{B}$ by Eq. [6], x_i, y_i, z_i the parameters of the i-th atom.

The ideal lattice of γ-AgI is that of the zinc-blende type and the space group is F $\bar{4}$3 m (32). A parameter in 16(e) is 0.25 in ideal zinc blende but it may be changed in the compressed γ-AgI.

In this calculation, the Debye factor plays an important role in an attempt to conform to the experimental intensities. Therefore both x in 16(e) and $\bar{B}$ were roughly examined and then the range of x was limited to 0.28-0.35, and $\bar{B}$ was kept constant at 5.0. This $\bar{B}$ is somewhat larger than that of the ordinary compound at room temperature, but reasonable for the "average structure" like α-AgI (33).

Figure 8 shows the intensities as a function of x. The open circles are the observed intensities. The agreement of the calculated intensities with the observed ones is the best when $x = 0.30$.

In addition, the reliability index R was computed with the aid of next equation

$$R = \frac{\Sigma||F_{obs}| - |F_{calc}||}{\Sigma|F_{obs}|} \quad [7]$$

where F_{obs} and F_{calc} are the observed and calculated structure factors respectively. The obtained R is 0.115 which suggests that the above calculation of the intensity is highly reliable.

From these results, a new average structure is confirmed in which silver atoms are randomly distributed over four possible sites placed tetrahedrally around the ideal site in zinc blende, similarly over the ideal position. The distance between the ideal and the tetrahedral sites is 0.60Å, which is greater than the amplitude of the simple oscillation of a silver atom.

The low activation energy in conduction, the large ionic conductivity at room temperature, and the insufficiency of the separation between $K\alpha_1$ and $K\alpha_2$ in x-ray diffraction may be obviously interpreted by the disordered or averaged structure in compressed γ-AgI.

Manuscript submitted Sept. 30, 1968; revised manuscript received Nov. 19, 1968.

Any discussion of this paper will appear in a Discussion Section to be published in the December 1969 JOURNAL.

REFERENCES

1. T. Takahashi and O. Yamamoto, *Denki Kagaku,* **32,** 610 (1964).
2. T. Takahashi, O. Yamamoto, K. Tsukade, and A. Baba, *ibid.,* **35,** 32 (1967).
3. T. Takahashi, O. Yamamoto, and K. Kuwabara, *ibid.,* **35,** 264 (1967).
4. O. Yamamoto and T. Takahashi, *ibid.,* **35,** 651 (1967).
5. T. Takahashi, K. Kuwabara, and O. Yamamoto, *ibid.,* **35,** 682 (1967).
6. T. Takahashi, K. Kuwabara and O. Yamamoto, *ibid.,* **36,** 530 (1968).
7. L. W. Strock, *Z. physik. Chem.,* **B25,** 441 (1934).
8. L. W. Strock, *ibid.,* **B31,** 132 (1936).
9. L. W. Strock and V. A. Brophy, *Am. Mineralogist,* **40,** 94 (1955).
10. M. L. Huggins, Transition in Silver Halides in "Phase Transformation in Solids," Chap. 8. Smoluchowski *et al.,* Editors, John Wiley & Sons, New York (1951).
11. J. W. Mansen, *J. Phys. Chem.,* **60,** 806 (1956).
12. A. J. Majumdar and R. Roy, *ibid.,* **63,** 1858 (1959).
13. G. Burley, *Am. Mineralogist,* **48,** 1266 (1963).
14. R. Bloch and H. Moeller, *Z. physik. Chem.,* **A152,** 245 (1931).
15. N. H. Kolkmeijer and J. W. A. van Hengel, *Z Krist.,* **88,** 317 (1934).
16. A. Van Valkenburg, *J. Research, Nat. Bur. Standards,* **68A** 97 (1964).
17. H. C. Duecker and E. R. Lipincott, *Science,* **146,** 1295 (1964).
18. W. A. Bassett and T. Takahashi, *Am. Mineralogist,* **50,** 1576 (1965).
19. A. Neuhaus and E. Hinze, *Ber. Bunsenges. Physik. Chem.,* **70,** 1073 (1966).
20. R. N. Schock and S. Katz, *J. Phys. Chem. Solids,* **28,** 1985 (1967).
21. M. J. Moore and J. S. Kasper, *J. Chem. Phys.,* **48,** 2446 (1968).
22. R. N. Schock and S. Katz, *ibid.,* **48,** 2094 (1968).
23. B. L. Davis and L. H. Adams, *Science,* **146,** 519 (1964).
24. J. A. A. Ketelaar, *Z. physik. Chem.,* **B26,** 327 (1934).
25. J. A. A. Ketelaar, *Z. Krist.,* **87,** 436 (1934).
26. I. Nitta, "X-ray Crystallography I.," p. 457, Maruzen, Tokyo (1959).
27. J. N. Mrgudich, *This Journal,* **107,** 475 (1960).
28. R. B. Wilsey, *Phil. Mag.,* **42,** 262 (1921).
29. W. P. Davey, *Phys. Rev.,* **19,** 248 (1922).
30. G. Aminoff, *Z. Krist.,* **57,** 180 (1922).
31. L. Helmholz, *J. Chem. Phys.* **3,** 740 (1935).
32. International Tables for X-ray Crystallography, Vol. I, Kynoch Press, Birmingham (1952).
33. S. Hoshino, *J. Phys. Soc. Japan,* **12,** 315 (1957).

Thermal Cycling and Surface Reconstruction in Aluminum Thin Films

C. J. Santoro

Motorola Semiconductor Products Division, Phoenix, Arizona

ABSTRACT

The appearance of "annealing hillocks" on heat treated aluminum films has been previously reported. Thin films of Al, deposited on passivated wafers, were annealed for various lengths of time in the temperature range 200°-500°C. The effects of grain size, alloying and surface passivation on hillock formation, were studied. It is the purpose of this report to summarize the effect of thermal cycling on similar films and to show in more detail the size and appearance of the hillocks. Aluminum was deposited on oxidized silicon substrates in a vacuum of about 10^{-8} Torr. Grain sizes at the deposition temperature were on the order of $<1\mu$, 1μ, and 5μ. Manual cycling was carried out between a hot stage in N_2 and a room temperature heat sink. Control samples were annealed (uncycled) for equivalent times-at-temperature. Photomicrographs of the surface at its various stages of reconstruction were taken and scanning electron micrographs provided a more detailed view of individual hillocks and their surroundings. At the higher temperatures (425°C) thermal cycling increases the number of hillocks by factors of 2 or 3, with the typical hillock density estimated to be approximately $10^6/cm^2$. Cycling also increases the size of the protrusions, and hillocks as high as 3.5μ have been observed growing out of a 0.7μ film. Experiments employing glass passivation confirm earlier results that surface reconstruction can be eliminated.

Aluminum thin films have found wide application in the semiconductor industry. As interconnections on a semiconductor device or integrated circuit the aluminum, usually in contact with a thin layer of SiO_2 on a Si wafer, may be subject to forces tending to change its structure. This is especially true if thermal excursions are encountered. If an aluminum film on an oxidized silicon substrate is heated sufficiently above its deposition temperature abnormal localized growths, "annealing hillocks," appear (1, 2). This effect has also been reported for lead, tin, and indium films (3) on substrates of lower thermal expansivity. Paddock and Black (1) have reported increases in hillock density with increasing time, temperature, and impurity content for aluminum films on silicon held at elevated temperatures. Similar features exist for the other metal films.

d'Heurle *et al.* (2) do not attempt an explanation of the growth phenomena for their aluminum on silicon films; Paddock and Black (1) attribute this growth to increased grain boundary diffusion. Caswell *et al.* (3) feel that the presence of cross slip in their film provides evidence for plastic deformation but find it difficult to explain the presence of sufficiently large strains even though the films are on low expansion coefficient substrates.

It is the purpose of this report to summarize some experiments studying the effect of thermal cycling on this surface reconstruction phenomena and to comment further on the mechanisms responsible for the size, density, and external morphology of the hillocks.

Experimental

The aluminum films used in this investigation were vacuum deposited at less than 10^{-8} Torr using 99.999% pure aluminum wire on a braided tungsten filament. The filaments were outgassed with a high temperature anneal before each evaporation. The substrates, p-type silicon with 1μ of thermally grown oxide on a polished surface, were thoroughly cleaned and dried before deposition. A dehydration and final surface cleaning were accomplished by heating the wafers to several hundred degrees centigrade while under vacuum. Both cleaning and deposition temperatures were achieved with a tungsten wound radiation heater and monitored with a Pt-Pt 10% Rh thermocouple, mounted on a "dummy" wafer. Three deposition temperatures were used to produce 7000Å thick films of various grain sizes; room temperature (28°C), 200°C, and 400°C. The average grain sizes of the films deposited at these temperatures were in the range less than 1μ, 1μ, and 5μ, respectively.

Thermal cycling was performed manually between a hot stage in a tube furnace and a massive aluminum block held at room temperature. Temperature control was ±2°C and a N_2 atmosphere was used. A 15 min cycle time was selected. Control samples were run for the same time-at-temperature as the cycled ones.

Observation of the surface reconstruction was accomplished in three ways. During anneal (*i.e.*, after each cycle) surfaces were examined by standard optical microscopy (up to 2000X). This enabled estimates of hillock density at various stages of development to be made. Three stage replication and shadowing permitted the use of an electron microscope (10,000X to 20,000X) for viewing individual hillocks. Employment of a scanning electron microscope (up to 20,000X) with its large depth-of-field allowed examination of individual hillocks from a variety of incident directions and yielded much information about the details of hillock morphology.

Results

The effect of thermal cycling on surface reconstruction is rather dramatic. Figures 1 and 2 illustrate this for 7000Å aluminum films deposited at 200°C having a grain size of about 1μ. Both films were annealed in a dry N_2 atmosphere at 430°C and hillock growth was apparent in either case. The uncycled film (Fig. 1) has had a continuous 2½ hr anneal and the "uncycled hillock density" (ρ_u) is about $5 \times 10^5/cm^2$. This includes hillocks of base diameter about 1μ or larger whose typical height is close to 1.5μ.

Figure 2 shows an identically prepared film which has undergone ten 15 min cycles at 430°C (equivalent time-at-temperature as the film of Fig. 1). The "cycled hillock density" (ρ_c) is $1.5 \times 10^6/cm^2$ while the average height has increased to almost 3μ.

Similar experiments (*i.e.*, 430°C anneal) have been carried out for films deposited at room temperature and also at 400°C. The corresponding hillock densities are given for all these films in Table I and sample data is plotted in Fig. 3. A nearly logarithmic dependence on deposition temperature is indicated. For

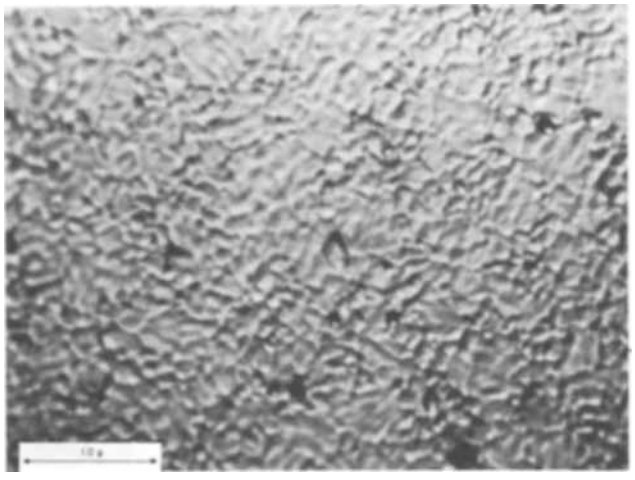

Fig. 1. Optical micrograph of 7000Å Al film annealed 2½ hr at 430°C, 4360X.

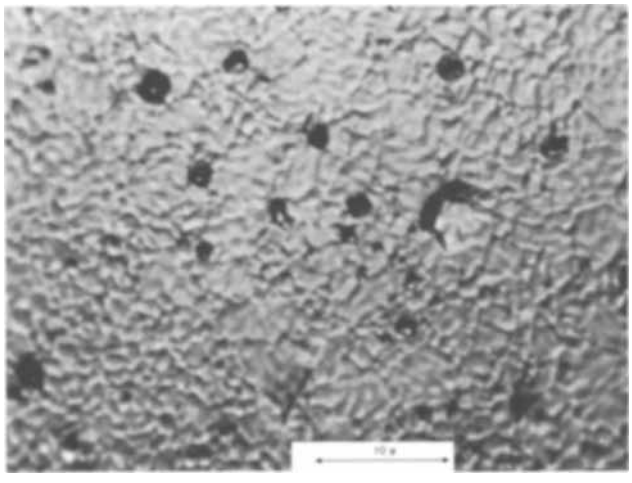

Fig. 2. Optical micrograph of 7000Å Al film annealed in ten, 15 min cycles at 430°C, 4360X.

the room temperature films densities are high and the sizes were generally just greater than 1μ. For the films deposited at 400°C densities are considerably lower. In all cases the estimates of hillock number are rough since the relatively low number (especially in the larger grained specimens) prevents obtaining good counting statistics.

Both large and small grain films were annealed at temperatures below that of deposition. In the case of large grains (5μ) no hillock formation was observed at anneal temperatures of 175°C, and 237°C for either cycled or uncycled samples. For the smaller grained (1μ) films deposited at 200°C some hillocks were observed for an anneal at 179°C. Here the densities are $\rho_c \approx 5.2 \times 10^5/cm^2$ and $\rho_u \approx 2.8 \times 10^5/cm^2$. These data are included in Table I.

Several films were passivated by depositing films of SiO_2 at 150°C with thickness 1000Å to 1μ. As was reported for constant temperature anneals (1), thermal cycling produced no hillocks in the passivated state.

Table I. Hillock densities for films deposited at room temperature and 400°C

T_e, °C	T_a, °C	ρ cycled	ρ uncycled	ρ_c/ρ_u
R.T.	430	$8.7 \times 10^7/cm^2$	$4.0 \times 10^7/cm^2$	2.2
200	430	$1.5 \times 10^6/cm^2$	$5.0 \times 10^5/cm^2$	3.0
400	430	$3.4 \times 10^4/cm^2$	$6.0 \times 10^3/cm^2$	5.7
R.T.	223	$6.0 \times 10^6/cm^2$	$3.2 \times 10^0/cm^2$	1.9
200	179	$5.2 \times 10^5/cm^2$	$2.8 \times 10^6/cm^2$	1.8
400	237	0	0	—
	175			

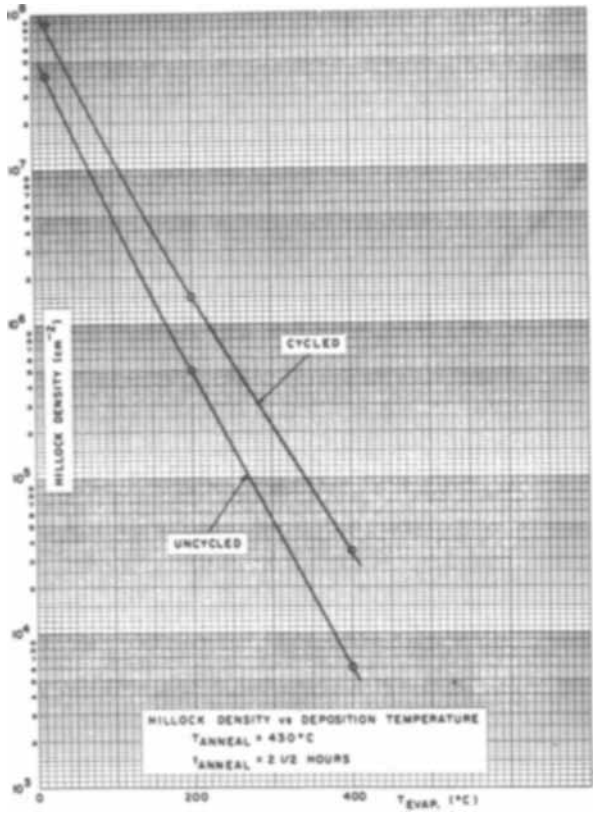

Fig. 3. Dependence of hillock density on deposition temperature for films annealed at 430°C.

The shape of the hillocks is determined by the granular structure of the film. The hillocks may be divided into three general classes based on the grains from which they originate. Figure 4 shows the three grain patterns present in these films. Growth from a configuration similar to 4a can result in an "edge" hillock such as shown in Fig. 5. Configurations 4b and 4c yield hillocks such as the flat-topped one shown in Fig. 6 and the spire-like one shown in Fig. 7. Edges corresponding to the surrounding boundaries are apparent in both of the latter types.

Discussion

The primary reason for hillock development is the disparity in linear expansion coefficient between the silicon substrate ($\alpha_{Si} = 3.3$ ppm/°C) and the deposited Al film ($\alpha_{Al} = 23.6$ ppm/°C). The film is in "size equilibrium" with the substrate at the temperature of evaporation (T_e) whereas at the anneal temperature (T_a) a strain, ϵ, is introduced on the film given by

$$\epsilon = \frac{L_{Al}(T_a) - L_{Si}(T_a)}{L(T_e)}$$

where $L(T_e)$ is the size (diameter) of the substrate and film at deposition and $L_{Al}(T_a)$ and $L_{Si}(T_a)$ are the sizes of each if they are allowed to expand freely from T_e to T_a. To a first approximation, then, this

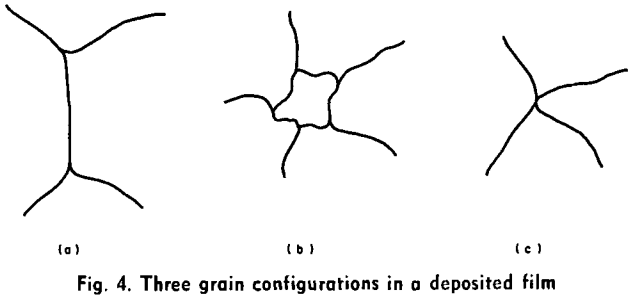

Fig. 4. Three grain configurations in a deposited film

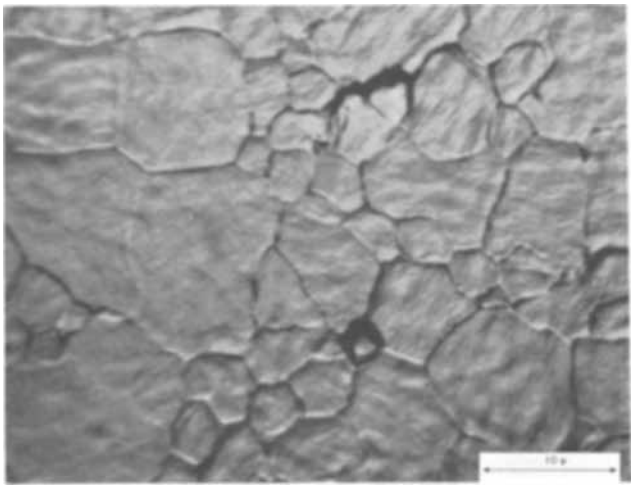

Fig. 5. "Edge hillock" in 7000Å film, 4360X

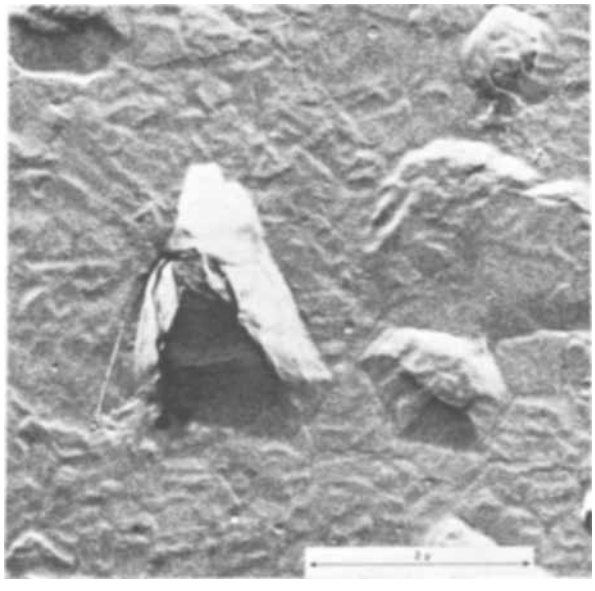

Fig. 6. Electron micrograph of a shadowed replica of a flat-topped hillock, 36,000X.

Fig. 7. Scanning electron micrograph of 3μ high hillock in 7000Å film, 27,900X.

strain can be expressed

$$\epsilon = [\bar{\alpha}_{Al} - \bar{\alpha}_{Si}]\ (T_a - T_e)$$

where the $\bar{\alpha}$'s are some appropriate average values (in a linear approximation α is a constant) of the coefficients of thermal expansion of the layers. In the cases where $T_a > T_e$ the Al film is placed under a compressional ($\epsilon > 0$) stress proportional to ϵ and hence to $[\bar{\alpha}_{Al} - \bar{\alpha}_{Si}]$ and $\Delta T = T_a - T_e$. Using the aforementioned coefficients of expansion, a $\Delta T = 250°C$, and an elastic modulus of 9×10^6 psi for aluminum, we have obtained a rough estimate of this stress to be about 40,000 psi. Paddock (1) has calculated a value of 60,000 psi for similar conditions. A more elaborate calculation (6) employing the appropriate stress function (7) for axially coupled cylinders yields a value on the order of 25,000 psi with a slight radial dependence. It is to relieve this compressional stress that mass transport forming the hillocks occurs at the elevated temperature. In an uncycled anneal the hillock growth continues until equilibrium at the higher temperature is achieved. When a specimen undergoes thermal cycling, however, there is a reversal of the stress patterns during the cooling cycle. Since hillock formation relieves some of the compressional stresses present on heating, and since the aluminum atoms are mobile at temperatures above the recrystallization point (150°C) one expects some relief of the tension stresses, present during cooling, while the film is above the recrystallization temperature, and the aluminum atoms are still mobile. Because one does not expect a reversibility to exist in the mass motion causing hillock formation, this relief is probably accomplished by gross thinning of the film or by grooving or separation at grain boundaries. The film then approaches the higher temperature equilibrium, except in a thinner, "hillocked" state. The reapplication of heat, in a subsequent heating cycle, once again causes compressional forces to rise, and new hillocks as well as the growth of older ones are promoted. Hence one anticipates the increase in both hillock size and number when films are thermally cycled.

It is noteworthy that this relief-upon-cooling may also explain the growth of hillocks in the cases where $T_a < T_e$. In one such case where $T_e = 200°C$, and $T_a = 179°C$ a sparse but nevertheless significant hillock population was seen (Fig. 8). Since cooling in a vacuum after evaporation is generally slow there may have been sufficient time for reordering and hence the establishment of a film which appears to have been deposited at an "effective T_e," lower than the anneal temperature. This reordering is certainly present in all the films deposited at higher temperatures and hence any quantitative evaluation of stresses which would certainly involve a knowledge of T_e requires an assumption about this effective value.

In one model for hillock formation, grain boundary diffusion is postulated as the controlling mass transport mechanism. It is assumed that films containing a high grain boundary density relieve the compressional forces by diffusion down these boundaries to nucleat-

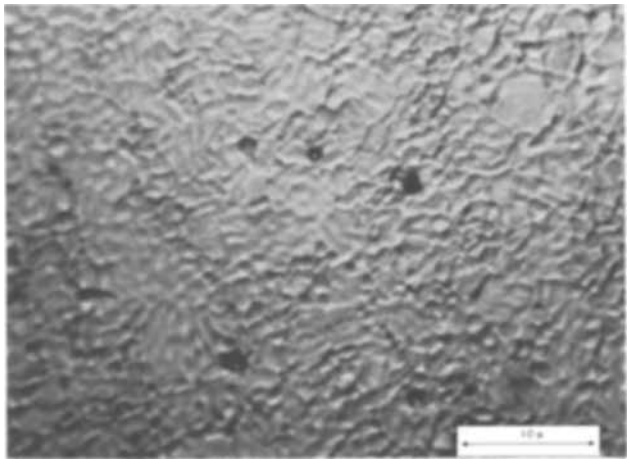

Fig. 8. Hillocks formed in an anneal below the deposition temperature, 4360X.

ing sites when the hillocks form. The evidence of higher hillock density on the "cold-deposited" small grain films, and films doped with silicon is pointed to in support of this mechanism.

It is presently felt that the formation and growth of hillocks is a creep (4) phenomenon. Although primarily diffusion controlled, this is a lattice rather than a boundary process in which the surface is plastically deformed due to atomic motion in the bulk of the film. Dorn (5) has shown that creep occurs in bulk aluminum at temperatures above 400°C for stresses as low as 3000 psi. The calculations above estimate the stress levels in these films to be greater than 25,000 psi. Hence it is not unreasonable to consider reconstruction of the film as being due to creep under the influence of this rather high compressive stress. No experiments have been performed during this investigation to try to determine which mechanism of creep is operating during the reconstruction process.

It is interesting to postulate the effect of many thermal cycles on the aluminum. Hillock growth is highly anisotropic, this random thickening of the film takes place as mass is locally "piled-up" during the heating cycle. The hillock formation is not reversible, however, and hence some "thin-spots" are likely to occur after many cycles. The stress levels in these less thick regions may be considerably higher than the remaining films—high enough, perhaps to cause separation along a grain boundary. This is expected to occur during cooling at temperatures below 150°C where the mobility of Al atoms is restricted and tension forces of sufficient magnitude to pull grains apart, may exist.

Summary

In summary, then, the presence of high compressive stresses and elevated temperatures, coupled with the observation of creep in bulk aluminum, lends evidence to the creep mechanism of hillock formation.

The effect of thermal cycling is seen to increase the over-all hillock density since a renewed compressive stress accompanies each heating cycle. This is due to the fact that some relief of the tensile stress, present during cooling, must occur above the recrystallization temperature. This relief is not simply the reverse of the hillock formation but is most probably a bulk reordering of the film accompanied by some grain boundary separation. The repeated cycling of the film, then, produces hillocks as well as enlarging those already formed. In the extreme case of many cycles, grain boundary separation leading to "opens" may be expected to occur.

Acknowledgments

The author is indebted to Mr. J. R. Black for his stimulating guidance throughout the work and to Mr. R. Mattox and Miss H. Kelley for experimental assistance. Indebtedness is expressed to the Reliability Section of the Jet Propulsion Laboratory for some of the scanning micrographs used in this work.

Manuscript submitted Oct. 8, 1968; revised manuscript received Nov. 20, 1968.

Any discussion of this paper will appear in a Discussion Section to be published in the December 1969 JOURNAL.

REFERENCES

1. A. Paddock and J. R. Black, "Hillock Formation on Aluminum Thin Films," presented at the Boston Meeting, May 5-9, 1968, as Paper 98.
2. F. d'Heurle, L. Berenbaum, and R. Rosenberg, *Trans. AIME*, **242**, 502 (1968).
3. H. L. Caswell, J. R. Priest, and Y. Bodo, *J. Appl. Phys.*, **34**, 3261 (1963).
4. C. E. Dieter, Jr., "Mechanical Metallurgy," p. 335, McGraw-Hill Book Co., New York (1961).
5. J. E. Dorn, "Creep and Recovery," p. 255, A.S.M. Menlo Park, Ohio, (1957).
6. M. Rodgers, Motorola S.P.D., Private communication.
7. S. Timoshenko and J. N. Goodier, "Theory of Elasticity," p. 384, McGraw-Hill Book Co., New York.

Electrically Conducting Photoluminescent ZnSe Films

Alvin M. Goodman

RCA Laboratories, Princeton, New Jersey

ABSTRACT

Electrically conducting photoluminescent ZnSe films have been prepared by evaporation onto suitably cleaned, heated sapphire ($1\bar{1}02$ orientation) substrates. The presence of electrical conductivity is shown to be correlated with (*a*) the degree to which the (111) planes of the films are parallel to the substrate surface, and (*b*) preferred orientation of these planes about the normal to the substrate. Crude electroluminescent comb cells utilizing these films have been fabricated.

The purpose of this paper is to describe a technique for producing electrically conducting photoluminescent (PL) ZnSe films of micron thickness. This type of film should be useful for the fabrication of electroluminescent (EL) devices (1, 2). With one possible exception,[1] it has not been feasible in the past to produce such films although much effort has been expended toward this objective (4-6). The method used here is basically that developed by Fonger (4-6) to produce photoluminescent insulating ZnSe films; it was found, however, that by proper selection and preparation of the substrate material, electrically conducting films could be produced.

[1] The one possible exception to this is in the work reported by Dobbs (3) in which the films were heavily doped with Cu to a concentration of from 500 to 5000 ppm. It seems probable that in that work the conductivity was due to metallic Cu which had precipitated along grain boundaries.

Film Preparation

A series of ZnSe films were produced using an evaporation technique developed by Fonger (4-6). Since that work has been described in great detail, only the essentials will be described here.

A cross-section view of the multiple arm evaporation chamber used in this work is shown in Fig. 1. The evaporation chamber and the associated heaters and heat shields are mounted inside the bell jar of a Kinney evaporation system equipped with a 4 in. diffusion pump and a liquid nitrogen trap. The system ordinarily pumped down to pressure in the range $10^{-6} = 10^{-5}$ Torr. The evaporation chamber is constructed of quartz and has five arms extending from its bottom. Three of the arms are short, closed at the lower end, and inclined (at an angle of 13° with respect to the vertical) to point toward the center of the substrate.

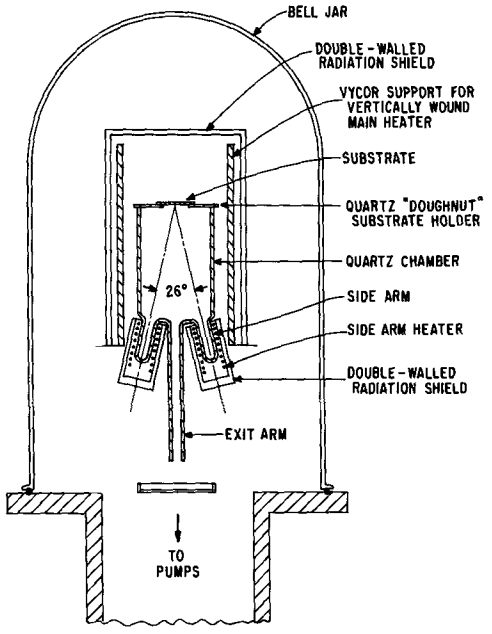

Fig. 1. Cross-section schematic view of the multiple-arm evaporation chamber.

They are intended for use with high-evaporation-temperature materials and were used in the present work. The other two arms are long and vertical. One of these (not shown in Fig. 1) is closed at the lower end and is intended for use in evaporating material at a relatively low temperature; it was not used in this work. The remaining arm emanating from the center of the chamber bottom is open and serves to evacuate the chamber to the bell jar and the pumps.

Each of the evaporating arms has its own tungsten coil heater and radiation shield. There is also a heating coil and radiation shield which surrounds the main chamber. The power to each of the heaters is individually controlled and metered. A thermocouple between the main heater and the chamber was used to monitor the chamber temperature and thus the substrate temperature. Various substrates and substrate preparation procedures were used and these are discussed in detail in the following section. The substrate holder was a quartz plate with a beveled hole in the center through which the evaporants reached the substrates.

The usual procedure for the deposition of a film was the following:

1. The chamber and substrate holder were thoroughly cleaned in aqua regia and rinsed in distilled water. The weight of the substrate was measured.

2. A measured amount of ZnSe powder was placed in one of the short inclined arms of the chamber and a similar amount of NaCl was placed in another. The amount was in each case typically ~ 100 mg. The ZnSe powder[2] was prefired in a reducing atmosphere (H_2 or forming gas) at ~ 1000°C to remove volatile impurities and to increase the crystallite size. The larger crystallite size is desirable to decrease "rocket flights" of the particles due to self-propulsion as they volatilize nonuniformly. The use of the coevaporant NaCl was shown by Fonger to result in much greater reproducibility of PL in ZnSe films (6). The probable effect of the use of NaCl as a coevaporant is the introduction of Cl as a coactivator for the red-orange "self-activated" luminescence of ZnSe.

3. Loosely packed plugs of quartz wool were inserted over the ZnSe and NaCl to prevent spattering during evaporation.

4. The chamber was placed in the vacuum system and the substrate holder and the substrate were positioned as shown in Fig. 1. The arm heaters and the chamber radiation shield were placed as shown in Fig. 1.

5. After putting the bell jar in place, the system was pumped down and baked by applying power to all heaters. The power to the main heater was adjusted to obtain the desired chamber temperature. The power to the arm-heaters was adjusted to keep the arms hot (hopefully near the chamber temperature) but much below the temperature at which rapid evaporation occurs.

6. When the chamber temperature stabilized, the power to the arms containing the NaCl and the ZnSe was increased and the evaporation was started. Typical evaporation times were ~ 15 min. After this, the power to all heaters was turned off and the system was allowed to cool. The film was then removed from the vacuum system and the weight gain of the substrate was determined. Typically the deposit weights were of the order of 1 mg.

[2] "Luminescent grade" ZnSe powder obtained from the General Electric Company.

Table I. Photoluminescence, conductivity, and electroluminescence in ZnSe evaporated films

Substrate material	Substrate preparation	Substrate temperature, °C	PL	Conducting	EL
Quartz	Unknown	400	No	No	No
Quartz	[a]	670	Yes	No	No
Quartz	[b]	670	Yes	No	No
$(1\bar{1}02)$ Sapphire	[a]	670	Yes	No	No
$(1\bar{1}02)$ Sapphire	[b]	670	Yes	Yes	Yes
SiO_2 on Si	[a]	670	Yes	No	No
SiO_2 on Si	[b]	670	Yes	No	No
Si_xN_y on Si	[a]	670	Yes	No	No
Al_2O_3	[b]	670	Yes	Weakly in spots	Doubtful
Pt on $(1\bar{1}02)$ sapphire	[b]	670	No	No	No

[a] Cleaned in 1:1 mixture of H_2O_2 (30% solution) and H_2SO_4 (~96% solution) followed by a thorough rinse in distilled water. [b] Washed in Calgonite, thoroughly rinsed in distilled water, boiled in trichlorethylene, and air dried.

Film Properties

The films were tested for photoluminescence by illuminating them with near-uv light (3660Å) and visually observing the resulting visible (red-orange) luminescence. The photoluminescent efficiency was not measured; however, the visually observed brightness (of the films which exhibited luminescence) appeared to be approximately equal to that of films grown by Fonger (6) at similar substrate temperatures. The quantum efficiency of those films was of the order of 3%.

The films were tested for conductivity by measuring the resistance between two In-Ga electrodes painted on the films or between Pt electrodes which had been evaporated onto one of the sapphire substrates before deposition of the ZnSe film.

A variety of substrates, substrate preparation procedures, and temperatures were used; the most significant results are summarized in Table I. The only combination that resulted in an electrically conducting, photoluminescent film was that of (*i*) a $1\bar{1}02$ oriented sapphire substrate prepared by washing in Calgonite,[3] rinsing thoroughly in distilled water and boiling in trichlorethylene, and (*ii*) use of a high substrate temperature during film deposition. The observed conductivity between "painted-on" In-Ga electrodes was non-ohmic and light was observed emanating from the periphery of the negative electrode. Between two Pt contacts which had been evaporated onto one sapphire substrate before deposition of the ZnSe, the conductivity was ohmic and no luminescence was observed. The current-voltage plots for these cases are shown in Fig. 2.

[3] Calgonite is a laboratory cleaning agent for glassware obtained from Fisher Scientific Company. It contains soap, carbonates, silicates, and a water conditioner, i.e., glassy sodium phosphate.

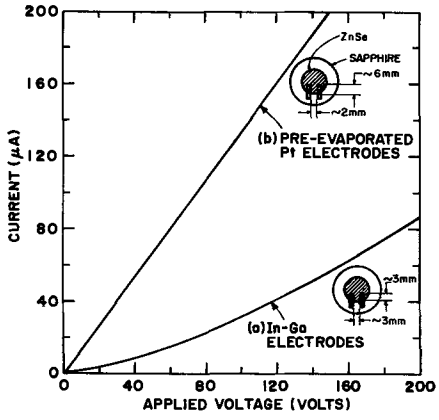

Fig. 2. Current-voltage characteristics of a ZnSe film between identical electrodes: (a) In-Ga "painted-on," (b) previously evaporated Pt.

An order of magnitude estimate of the resistivity of the conducting films is about 300 ohm-cm. Detailed studies of the electrical characteristics of the films were not carried out.

A crude electroluminescent comb cell using a conducting, photoluminescent ZnSe layer is described in the Appendix.

In an effort to determine why only the films grown on sapphire which had previously been cleaned using procedure b of Table I were conducting and the others were not, the films were examined using high magnification light microscopy, x-ray methods (Laue and diffractometry), and electron diffraction. The results are discussed below.

In Fig. 3 are shown 4 micrographs of ZnSe films for different growth conditions. In (a) the substrate was quartz at 400°C. There is no granularity apparent; the film is smooth though slightly cloudy.

In (b), the substrate was also quartz but at 670°C. The granularity here is apparent; the maximum grain dimension is about 2μ with the average probably somewhat smaller than 1μ. In (c) the substrate was sapphire at 670°C. The maximum grain size may be slightly larger than for (b) but the difference is certainly not striking. In (d) the substrate was an evaporated layer of Pt on sapphire. The grain size is not significantly different from either (b) or (c). In other cases (not shown) with different substrates and substrate preparation procedures but using the same substrate temperature (670°C) during deposition, the film grain size was not noticeably different from (b), (c), or (d). To summarize, the grain size was larger when deposition of the ZnSe occurred on higher temperature substrates but was relatively independent of the substrate material and cleaning procedure.

The x-ray results on the same samples showed that all were either predominately or entirely cubic ZnSe but that there were significant differences in crystallinity and orientation (7). These results are summarized in Table II.

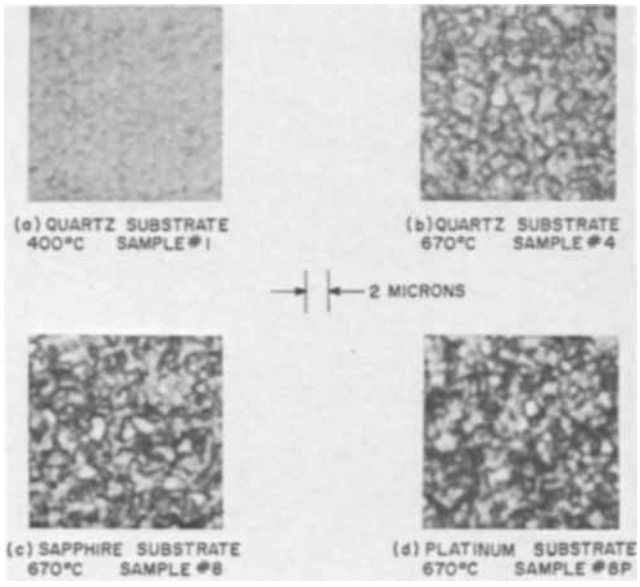

Fig. 3. Photomicrographs of ZnSe films for 4 different growth conditions: (a) quartz substrate 400°C, sample No. 1, (b) quartz substrate 670°C, sample No. 4, (c) sapphire substrate 670°C, sample No. 8, (d) evaporated platinum layer (on sapphire) at 670°C, sample No. 8P.

The back-reflection Laue pattern showed the presence of polycrystalline rings for all samples. In each case, the rings were continuous, indicating no detectable azimuthal ordering in planes not parallel to the surface. The rings were sharp and resolved ($K\alpha_1$-$K\alpha_2$) except for sample No. 1; this was interpreted as being due to a smaller particle size in sample No. 1. Sample No. 8 produced sharp continuous rings but fewer of them indicating a higher degree of preferred orientation; *i.e.*, more planes were parallel to the surface (111) and fewer planes were oriented at an angle to the surface.

Diffractometry indicated that all of the samples were single phase ZnSe (cubic) and had preferred orientation in the (111) direction relative to the substrate. There was, however, a difference in degree. Sample No. 8 was most highly oriented and showed only (111) reflections and higher orders. Samples No. 4 and No. 16 were less highly oriented in the (111) direction than No. 8. Sample No. 1 gave the poorest crystalline pattern and was only slightly oriented in the (111) direction. Sample No. 8P was the most randomly oriented ZnSe of the lot.

"Omega scans" (rocking curves) were obtained for each of the samples by keeping the detector stationary on the 111 reflection and scanning through the θ angle. The width at half maximum intensity was measured for each sample and is given in Table II. The important observation here is that the smallest half-width (3.1°) was obtained for sample No. 8 and that

Table II. Results of x-ray and electron diffraction analyses of ZnSe evaporated films

Sample	Substrate	Temp, °C	X-ray results	Peak half-width in omega-scan	Electron diffraction results
1	Quartz	400	Gave poorest crystalline pattern (relative to other samples) and was only slightly oriented in (111) direction. Had smallest crystallite size	>10°	Polycrystalline rings with little if any orientation in reflections other than (111). The (111) reflection shows some orientation. Some hexagonal phase ZnSe can also be identified
4	Quartz	670	Somewhat higher degree of crystallinity than No. 1 and slightly more highly oriented in (111) direction than No. 1	5°	Similar to sample No. 1 except that no hex phase is present
8	Sapphire (cleaning procedure b of Table 1)	670	Most highly oriented in (111) direction and only the (111) peak and its higher orders were observed on the trace	3.1°	Sample gives pattern of rings showing preferred orientation about the normal to the surface for all rings with the (111) most highly oriented. All rings are cubic ZnSe
8P	Pt on sapphire	670	Most randomly oriented ZnSe of the lot	—	—
16	Sapphire (cleaning procedure a of Table I)	670	Results very similar to those for sample No. 4	4°	Similar to sample No. 1

Fig. 4. Electron diffraction patterns of ZnSe for different growth conditions.

this is still much greater than the value which might be expected for a good single crystal ($\sim 0.1°$).

Four of the samples were also examined by reflection electron diffraction using 100 kev electrons at near grazing incidence (8). The diffraction patterns are shown in Fig. 4 and a summary of the interpretation is given in Table II. The significant point here is that the (111) planes are highly oriented about the normal to the film surface for sample No. 8 and that they are not for the other samples.

Discussion

The results of the last section show clearly that electrical conductivity of the film is correlated with a high degree of crystalline grain orientation. This result tends to support the following speculation of Fischer on the reason for lack of conductivity in polycrystalline ZnSe films (9). Fischer suggests that depleted Schottky barriers form between grains of a polycrystalline ZnSe layer thus causing it to be insulating. It follows then that a high degree of crystalline orientation of the grains should give rise to less disorder and thus fewer electronic interface states along the grain boundaries. This is illustrated in Fig. 5 where in (a) the high density of electronic interface states gives rise to larger depletion regions and a higher barrier than in (b) where the interface state density is low. While the foregoing reasoning is not "a proof," it does constitute a strong plausibility argument.

In order to determine how the procedure for cleaning the substrates affected the crystallinity of the deposited films, two sapphire substrates were examined by scanning electron microscopy (10). One of these had been prepared using cleaning procedure "a"—"cleaned" in 1:1 mixture of H_2O_2 (30% solution) and H_2SO_4 ($\sim$ 96% solution) followed by a thorough rinse in distilled water. The other was prepared using cleaning procedure "b"—washed in Calgonite, thoroughly rinsed in distilled water, boiled in trichlorethylene, and air dried. The substrate prepared using cleaning procedure "a" showed considerably more contamination remaining on the surface than the other substrate although both were relatively clean. Two more or less typical areas are shown in Fig. 6.

The work described thus far has (hopefully) answered one question about the nature of conductivity (or lack of it) in ZnSe films. It leads, however, to many more questions. It is appropriate to set the stage for possible future work by explicitly asking some of these questions:

1. What are the electronic properties of these films? carrier density? carrier mobility?
2. What would be the effect of using other crystalline substrates? For example, spinel, GaAs, Ge, etc.
3. What would be the effect of doping on the electrical conductivity and luminescence of these films?
4. Are these films useful for device purposes?

To give a definitive answer to any of these questions is beyond the scope of the present work. However, a first and admittedly very crude step toward an answer to the last question is described in the Appendix.

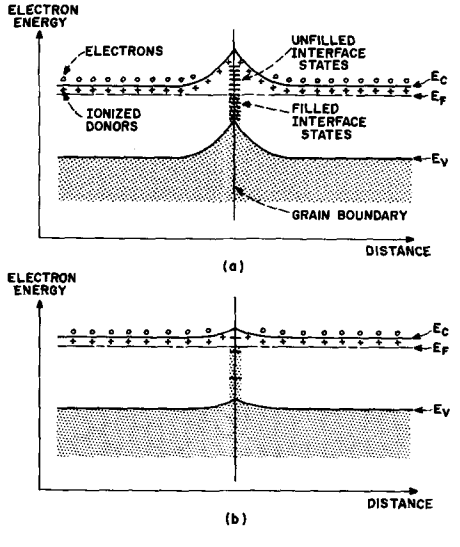

Fig. 5. Models of the energy-band-diagram at a grain boundary: (a) high electronic interface-state density, (b) low electronic interstate density.

Conclusion

Electrically conducting photoluminescent ZnSe films have been prepared by vacuum evaporation onto suitably cleaned, heated sapphire ($1\bar{1}02$ orientation) substrates.

The presence of electrical conductivity has been shown to be correlated with (*a*) the degree to which the (111) planes of the film are parallel to the substrate surface, and (*b*) preferred orientation of these planes about the normal to the substrate.

The results are in agreement with and tend to confirm a model suggested by Fischer for explaining the lack of conductivity in other ZnSe films.

Acknowledgment

The author owes a debt of gratitude to a number of people for their help during the course of this work. Among these are W. H. Fonger who gave much val-

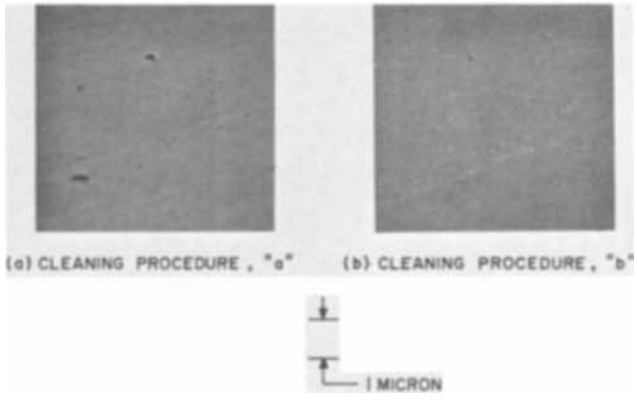

Fig. 6. Scanning electron micrographs of sapphire substrates cleaned in two ways. See Table I and text.

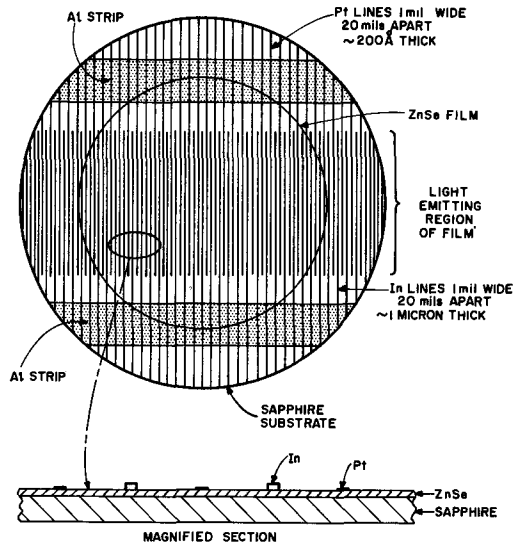

Fig. 7. Electroluminescent comb cell structure

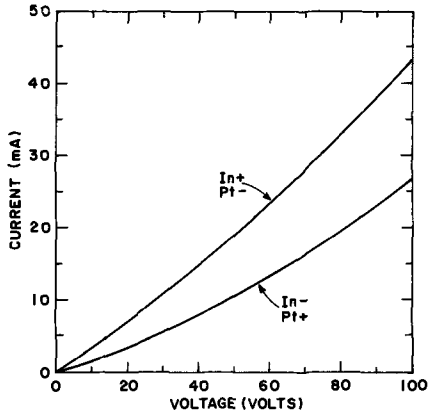

Fig. 8. Current-voltage characteristic of a ZnSe film electroluminescent cell.

uable advice as well as the use of his vacuum system, J. Breece who rendered capable assistance in the preparation of the films, M. D. Coutts, R. J. Paff, W. C. Roth, and R. T. Smith for their help in the film and substrate analyses, and A. G. Fischer for useful discussions and advice.

Manuscript submitted Oct. 23, 1968.

Any discussion of this paper will appear in a Discussion Section to be published in the December 1969 JOURNAL.

APPENDIX

An Electroluminescent Comb Cell

A crude electroluminescent cell using the comb structure illustrated in Fig. 7 was fabricated on each of two conducting luminescent ZnSe layers by evaporation of metal electrodes through appropriate masks. The current voltage characteristics of the two devices were similar though not identical; one of these is shown in Fig. 8. The observed light when viewed through the microscope appeared to come principally from the edges of the negative electrode regardless of whether it was Pt or In. The mechanism was probably that of impact ionization described by Fischer (2). When the Pt lines were positive, however, some light did appear to come from their edges and was probably due to hole injection. At a power input of 5w the light from the cell was visible in dim room light. No further work has been done to improve the performance of these devices or to analyze the radiative mechanisms involved.

REFERENCES

1. A. G. Fischer, *Physics Letters*, **12**, 313 (1964).
2. A. G. Fischer, Electroluminescence in II-VI Compounds in "Luminescence of Inorganic Compounds," Paul Goldberg, Editor, Academic Press, New York (1966).
3. J. D. Dobbs, Low Field DC Excited Electroluminescence in Evaporated ZnSe Films in "Proceedings of the Symposium on Radiative Recombination," Dunod, Paris (1965).
4. A. G. Fischer, W. H. Fonger, and A. S. Mason, Investigation of Carrier Injection Electroluminescence," Semiannual Scientific Report No. 2, Contract No. AF19(604)8018, August 15, 1962.
5. A. G. Fischer, W. H. Fonger, and A. S. Mason, "Investigation of Carrier Injection Electroluminescence," Semiannual Scientific Report No. 3, Contract No. AF19(604)8018, February 15, 1963.
6. A. G. Fischer, W. H. Fonger, and A. S. Mason, "Investigation of Carrier Injection Electroluminescence," Semiannual Scientific Report No. 4, Contract No. AF19(604)8018, August 15, 1963.
7. Carried out by R. J. Paff and R. T. Smith.
8. Carried out by W. C. Roth.
9. A. G. Fischer, Internal Report (unpublished).
10. Carried out by M. D. Coutts.

Photoexcitation and Luminescence in Redox Processes on Gallium Phosphide Electrodes

K. H. Beckmann and R. Memming

Philips Zentrallaboratorium, Hamburg, Germany

ABSTRACT

The mechanism of the charge transfer between energy states of electrons in GaP electrodes and redox systems was studied. Measurements of the photoexcitation of electrons in GaP have shown that not only the conduction and valence band but also surface states are involved in the charge transfer at the interface. Electroluminescence is observed if minority carriers are injected into the electrode. The corresponding recombination process is compared with that of the photoluminescence. Quenching effects are discussed.

In a recent paper (1) we reported on some electrochemical properties of GaP-electrodes. In connection with those studies we already discussed the reduction mechanism of certain oxidizing agents. Some results indicated that not only the conduction and the valence band but also surface states are involved in charge transfer reactions. This assumption is based mainly on investigations of redox reactions in which minority carriers are consumed. In this case the reaction rate may be controlled by light excitation. In the present paper the corresponding excitation mechanism is reported.

In connection with those studies, measurements of the luminescence produced by light or current injection give valuable information about the charge transfer mechanism on GaP surfaces. As mentioned in a previous paper we observed electroluminescence in GaP after addition of an oxidizing agent (1). Similar effects were observed with ZnS electrodes in electrolytes containing oleum (2). In this paper the corresponding recombination mechanisms are reported.

Experimental

All experiments were performed with single crystals of GaP oriented in the <111> direction. Whereas the n-type material was doped with tellurium, the p-type crystals contained zinc and oxygen. In both cases the density of free carriers was about $10^{17}/cm^3$. Before each measurement the electrodes were etched in HCl.

The current-potential curves were measured using a Wenking potentiostat. In the electroluminescence experiments the electrolyte was streaming along the surface in order to increase the supply of oxidizing agent near the surface. In this case the electrode potential was modulated by square wave pulses (28 Hz) leading to current peaks up to 100 ma/cm². The photoluminescence was excited by chopped radiation (12.5 Hz) from a mercury arc or a tungsten lamp. Schott glass filters BG 18 and a copper sulfate solution in the incident and RG 5 in the emitted beam were used. The spectral distribution was measured using a Leiss monochromator and a photomultiplier or a PbS-cell. The corresponding signal was amplified (lock-in amplifier) and displayed on a recorder.

Results and Discussion

Photoexcitation mechanism.—The charge transfer between a semiconductor electrode and an electrolyte may occur via the conduction or the valence band of the semiconductor. From current-voltage curves it can generally be concluded which band is involved in the corresponding charge transfer. Typical curves of the interfacial current *vs.* electrode potential for n- and p-type GaP-electrodes are plotted in Fig. 1 and 2. In the anodic region the current increases exponentially at a p-type electrode whereas a saturation current was observed with an n-type electrode. This means that only the valence band is involved in the corresponding process (anodic dissolution). The mechanism of the anodic dissolution itself will not be discussed here; it was recently published elsewhere (1).

When polarizing the GaP-electrode cathodically hydrogen evolution occurs. Since the cathodic current does not increase at cathodic potentials for a p-type electrode obviously only conduction electrons are involved in this process. The number of electrons available for the evolution of hydrogen and consequently the interfacial current may be increased by illuminating the electrode (see Fig. 2).

If $K_3[Fe(CN)_6]$ is added as an oxidizing agent to a solution of 3*N* NaOH a cathodic current was observed also with p-type material without illumination (Fig. 2). From this result it may be concluded that the reduction of $[Fe(CN)_6]^{3-}$ in alkaline solutions proceeds mainly via the valence band.[1] As shown in Fig. 2, however, not only the valence band is involved since the reduction current is slightly increased by illumination of the electrode. As we reported recently (1) in acid solution the dark current is much lower and the light effect stronger than in alkaline solutions, *i.e.*, in this case only few electrons from the valence band are consumed.

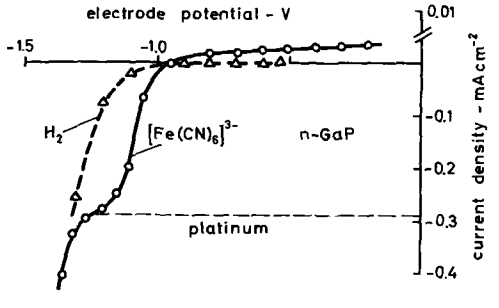

Fig. 1. Interfacial current *vs.* electrode potential for an n-type GaP-electrode in 3*N* NaOH before and after addition of 10^{-2}M $K_3[Fe(CN)_6]$ (electrode potential measured against saturated calomel electrode).

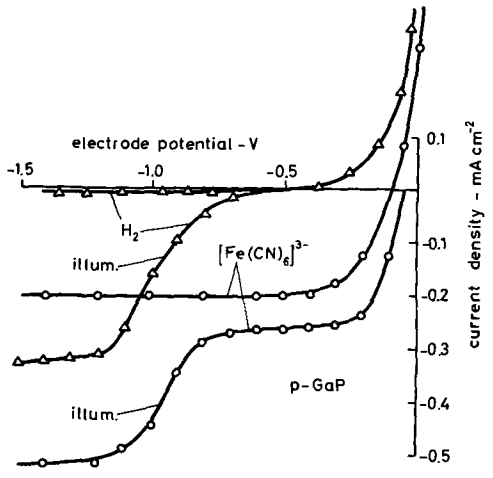

Fig. 2. Interfacial current *vs.* electrode potential for a p-type GaP-electrode in 3*N* NaOH before and after addition of 10^{-2}M K_3 $Fe(CN)_6$.

In order to study this reduction process more accurately the following experiment was performed. A p-type GaP electrode was illuminated by monochromatic light. The change of the cathodic current normalized to unit intensity of the incident radiation was then measured at weak cathodic polarization as a function of the wavelength of the incident light. As shown in Fig. 3 the photocurrent in 1*N* H_2SO_4 due to hydrogen evolution starts to rise near 2.0 ev and reaches a maximum at about 2.75 ev (curve a). Figure 4 shows the absorption spectrum of GaP as it was measured by Subashiev and Abagyan (3). Comparing the increase of the photocurrent with the absorption spectrum it is quite obvious that electrons by a band-band transition are consumed for the discharging of hydrogen ions. With $K_3[Fe(CN)_6]$ present in the solution we observed an additional broad peak in the excitation spectrum at an energy of about 1.6 ev (curve b in Fig. 3). This is a very weak current peak, since its maximum value differs from the main peak at 2.75 ev by about four orders of magnitude.

Similar experiments have been performed with other oxidizing agents, such as persulfate and ceric ions. In these cases we also observed a small current peak in the same energy range around 1.6 ev as it is demonstrated for $K_2S_2O_8$ in Fig. 3 (curve c). The experimental results differ only in so far as the maximum value of the current at 1.6 ev depends on the type of oxidizing agent used for these measurements.

Since the current peak at 1.6 ev appears at an energy smaller than the band gap of GaP (2.25 ev) it has to be concluded that surface states are involved in the charge transfer for the reduction of certain oxidizing agents. As shown in Fig. 5 surface states may be filled by optical excitation with electrons from the valence band. In this figure the energetic positions of the conduction and valence band, of surface states and of the electronic states of the oxidizing agent are indicated. The model for the latter states has been developed by Gerischer (4). According to it these states

[1] It should be mentioned that the large shift of the rest potential occurring for n- and p-type electrodes in opposite directions after addition of the oxidizing agent is due to the formation of electron-hole pairs. The mechanism of this effect was described previously (1).

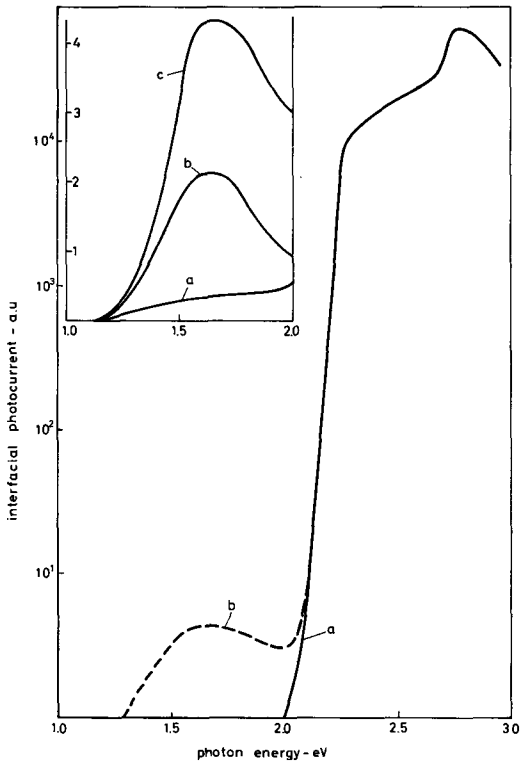

Fig. 3. Interfacial photocurrent as a function of the photon energy of the incident light. The low energy range plotted in an enlarged scale in Fig. 3a. Curve a; 1*N* H_2SO_4; curve b; 1*N* H_2SO_4 + 10^{-1}M $K_3[Fe(CN)_6]$; curve c; 1*N* H_2SO_4 + 10^{-1}M $(NH_4)_2S_2O_8$. (Photocurrent normalized to unit intensity of incident light).

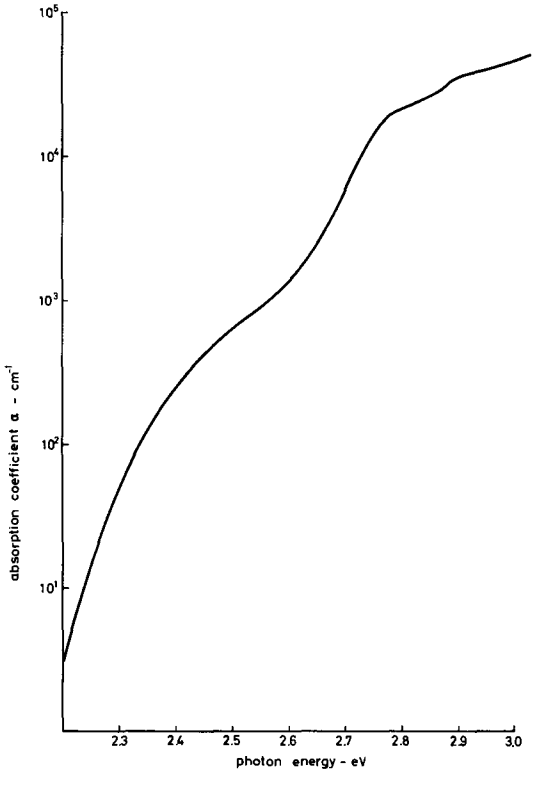

Fig. 4. Absorption spectrum of GaP from ref. (3)

within the electrolyte show an appreciable broadening so that overlapping with states of different energetic positions in the solid electrode is possible. Charge transfer between the solid and those states within the electrolyte occurs horizontally, *i.e.*, at constant energy. Thus transitions of electrons from surface

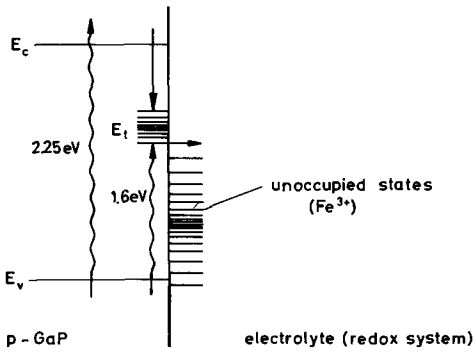

Fig. 5. Schematic energy diagram of p-GaP and redox system (photoexcitation model).

states into the electrolyte lead to the increase in the reduction current. An excitation of an electron from a surface state into the conduction band can be ruled out since in that case the hydrogen evolution should also be excited through photons of 1.6 ev, which is not the case (see Fig. 3 curve a).

As mentioned above in the case of $[Fe(CN)_6]^{3-}$ ions a charge transfer also occurs (see Fig. 2) via the valence band. Consequently the unoccupied states (Fe^{3+}) of this system overlap with the energy levels of the valence band and of the surface state as indicated in Fig. 5, *i.e.*, in alkaline solutions more with valence band and in acid solutions more with the surface states. According to Fig. 3 the reduction current is also increased by exciting electrons directly from the valence into the conduction band. From this fact it can be concluded that electrons are also transferred directly from the conduction band into the unoccupied state of the redox system. Since the band gap of GaP is quite large it seems to be rather unlikely that the unoccupied states of the redox system also overlap with the energy levels of the conduction band. We therefore prefer to assume that electrons excited into the conduction band are trapped by the surface states and then transferred to the Fe^{3+} states. The quantum efficiency for the latter possibility is much larger than for the transition from the valence band into the surface state because of the large absorption cross section for a band-band transition.

Electroluminescence.—As mentioned above the reduction of $[Fe(CN)_6]^{3-}$ ions proceeds partly via the valence band of GaP, *i.e.*, holes are injected. For similar studies with germanium and silicon electrodes the injection current was quantitatively determined using the "thin slice" method (5), *i.e.*, the number of holes was detected by a pn-junction alloyed on the reverse side of the electrode. Since the diffusion length of minority carriers in GaP is only about 1μ (see below), it was impossible to apply this method. Another possibility to detect minority carriers injected from the electrolyte into the crystal is given by luminescence measurements.

GaP is a semiconductor with relatively good luminescence properties. The electroluminescence produced by passing a current through a forward biased pn-junction of GaP was studied by several authors (6). In order to produce electroluminescence by injecting holes during the reduction process we had to take an n-type GaP-electrode. The electroluminescence spectrum obtained with $K_3[Fe(CN)_6]$ as an oxidizing agent is plotted in Fig. 6. Since no electroluminescence was observed without ferricyanide ions it is proved that the electroluminescence is indeed produced by the charge transfer during the reduction process. The same spectral distribution was obtained with a variety of other oxidizing agents such as ceric ions, hydrogen peroxide, and persulfate.

In the spectral distribution of the electroluminescence two peaks are visible, at 1.2 and 1.55 ev. Ac-

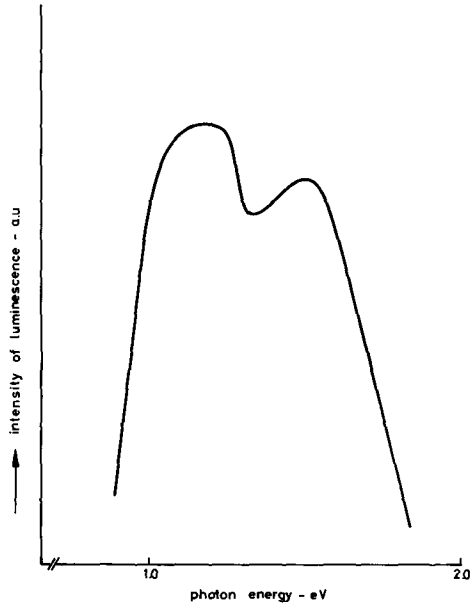

Fig. 6. Electroluminescence spectrum of n-GaP in 1*N* H_2SO_4 + 1M $K_3[Fe(CN)_6]$.

cording to the literature only one luminescence peak was found with pn-junctions. In this case the peak appeared in the range of 1.4-1.9 ev depending mainly on the spatial separation of the Zn and O which participate in this recombination (7). This could lead to the assumption that at least one of our peaks (1.55 ev) would fit into this range and could be explained by the same recombination mechanism as it was found for pn-junctions. This assumption, however, may be ruled out by two arguments: (*A*) According to investigations with pn-junctions (8) the luminescence is due to a corresponding transition between an oxygen and a zinc level within the p-type material. Since we studied the luminescence in n-type electrodes we could not observe the same type of luminescence. (*B*) In the case that still small traces of zinc and oxygen in our n-type material were responsible for the 1.55 ev peak one should expect at the same wavelength a peak in the luminescence spectrum produced by photoexcitation. We performed corresponding measurements with n-type electrodes immersed into an electrolyte free from ferricyanide or any other oxidizing agent. As demonstrated in Fig. 7 only one peak at 1.2 ev appears in the photoluminescence spectrum. At 1.55 ev practically no luminescence was observed.

Comparing the spectrum in Fig. 6 and 7 it is quite evident that the photoluminescence coincides in the spectral distribution very well with low energy peak (1.2 ev) of the electroluminescence. Consequently the luminescence at 1.2 ev may be attributed to one and the same recombination transition within the bulk of n-type GaP independent from the excitation mechanism. The levels within the forbidden zone involved in this transition mechanism are not known. For demonstration only we marked in Fig. 8 the corresponding recombination as a transition between a level within the band gap and the valence band. Whether this is the case or a transition occurs between the conduction band and a certain level or between two levels within the forbidden zone is open for discussion. In order to interpret the appearance of the second peak in the electroluminescence spectrum we have to consider the boundary conditions for the excitation process of the photo- and electroluminescence. In both cases minority carriers are injected. Since the photoluminescence is very weak in n-type GaP we had to use light for the excitation covering a greater spectral range between $\approx$2 ev and higher energies. For all energies of the exciting light below 2.75 ev the penetration depth is large compared with the diffusion length (1μ) of the minority carriers. In the case of the excitation of the electroluminescence, however, holes are injected directly at the surface. Consequently, the probability for a recombination near the surface is much higher. From this consideration it may be concluded that the second peak (1.55 ev) is due to a radiative transition via surface states. This assumption is supported by the fact that a current peak in the excitation spectrum of the photocurrent (see Fig. 3) was observed at practically the same energy (1.6 ev). Since we related this current peak with the optical excitation of an electron from the valence band into a surface state (see Fig. 5) we have to postulate that the electroluminescence is due to a transition from the same surface state into the valence band (Fig. 8).

As mentioned above the luminescence is very weak. The quantum efficiency amounts to about 10^{-6}. Since p-type GaP has much better luminescence properties it seems to be much more favorable to study injection luminescence with p-type instead of n-type electrodes. In the case of p-type electrode we had only to take a redox system with which it is possible to inject electrons. Principally such an experiment could be performed using a strong reducing agent (4). We tested a variety of corresponding redox systems, but we did not find any reducing agent with which it was possible to inject electrons into the conduction band. Probably the position of the conduction band in the absolute energy scale is so high so that it does not overlap with the occupied energy states of a corresponding reducing agent.

Quenching effects.—In the preceding chapters we described the mechanisms of the excitation and the radiative transition via surface states. Now we want

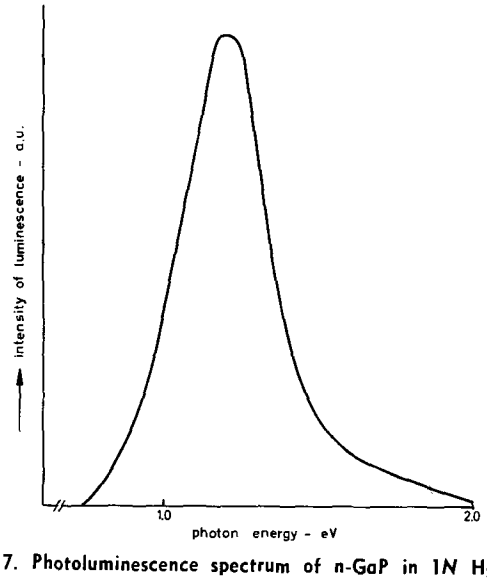

Fig. 7. Photoluminescence spectrum of n-GaP in 1*N* H_2SO_4 at rest potential.

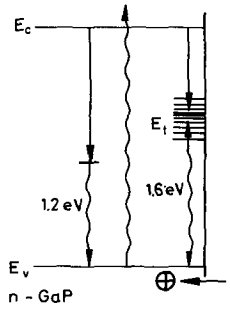

Fig. 8. Schematic energy diagram of n-GaP (electroluminescence model).

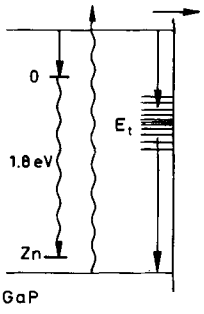

Fig. 9. Schematic energy diagram of p-GaP (quenching of photoluminescence).

to discuss the influence of interfacial properties on the bulk photoluminescence.

As mentioned before the quantum efficiency for photoluminescence in appropriately doped p-type GaP is much larger than in n-type material. According to the literature the red luminescence at 1.8 ev is due to a transition between an oxygen donor and a zinc acceptor term as demonstrated in Fig. 9. In the case that minority carriers recombine via surface states or are consumed for a surface reaction one should expect that the quantum yield of the bulk luminescence depends on the penetration depth of the exciting light.

We performed corresponding measurements with a p-type electrode keeping the electrode potential constant at the rest potential. The result is plotted in Fig. 10 (circles). Values for the penetration depth were taken from the absorption curve in Fig. 4. In order to get some quantitative information from the curve presented in Fig. 10 we derived a simple relationship between luminescence intensity and surface parameters as follows. The recombination rate is given by

$$U = \frac{\delta n\,(x)}{\tau} \qquad [1]$$

$\delta n\ (x)$ is the density of charge carriers excited at a certain distance x from the surface and $1/\tau$ is the rate constant for the luminescent transition. The intensity I of the light emitted from the whole specimen is obtained by integrating Eq. (1)

$$I = \frac{\alpha}{\tau}\int_0^\infty \delta n\,(x)\,dx \qquad [2]$$

(α is a factor which includes the quantum efficiency of the corresponding transition).

The relationship between the generation and recombination process is given by the continuity equation:

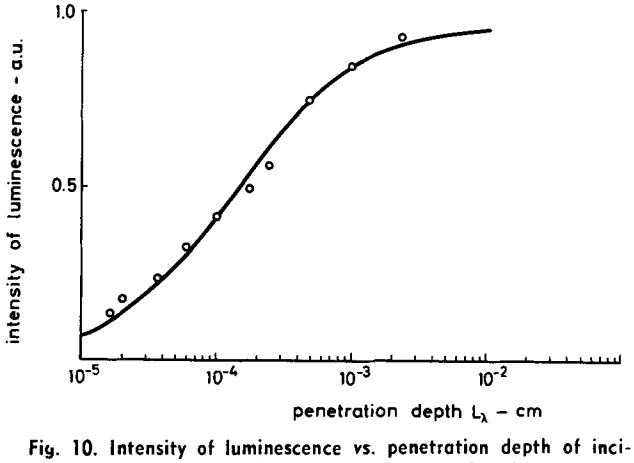

Fig. 10. Intensity of luminescence vs. penetration depth of incident light for p-GaP in 1N H_2SO_4 (values for L_λ obtained from Fig. 4).

$$D\frac{\partial^2 \delta n}{\partial x^2} - \frac{\delta n}{\tau} + g(x) = 0 \qquad [3]$$

$g(x)$ is the generation rate and is related to the number of incident photons P by

$$g\ (x) = \frac{P}{L_\lambda} e^{-x/L_\lambda} \qquad [4]$$

(L_λ = penetration depth of incident light and D = diffusion constant).

The surface parameters may be introduced via the boundary conditions. We assume that minority carriers recombine via surface states or are consumed for a charge transfer into the electrolyte, s and k are the corresponding rate constants. Under stationary conditions the transition rate at the surface equals the diffusion current toward the surface

$$(s + k)\ \delta n = D\frac{\partial\, \delta n}{\partial x}\Big/_{x=0} \qquad [5]$$

Solving the continuity Eq. [3] one obtains using Eq. [1]-[5]

$$I = \frac{I_0}{L_n + L_\lambda}\left(L_\lambda + \frac{D}{s + k + D/L_n}\right) \qquad [6]$$

(L_n = diffusion length of minority carriers). This equation is already normalized in so far as I_0 is the intensity of the photoluminescence if no quenching at the surface occurs. Moreover it should be mentioned that Eq. [6] is valid only in this simple form for the case that the penetration depth is smaller than the sample thickness. As soon as the penetration depth is of the order of the sample thickness we actually observed a decrease of the luminescence intensity (not plotted in Fig. 10).

According to Eq. [6] the diffusion length may be determined easily provided that $s + k >> D/L_n$. Then

$$L_n = L_\lambda \quad \text{for} \quad I = \frac{I_0}{2}$$

The theoretical function of I *vs.* L_λ calculated for large values of s and k ($L_\lambda >> D/s + k$) is also plotted in Fig. 10 (solid line). The best fit was obtained with $L_n = 1.5\mu$. According to this result it has to be concluded that $s + k > 10^5$.

Since according to the Shockley-Read model the surface recombination velocity s depends on the position of the Fermi level at the surface (9, 10) it should be possible to vary the luminescence intensity by changing the band bending, *i.e.*, the electrode potential. This effect, however, turned out to be very small. In order to measure those small variations of the luminescence intensity we increased the sensitivity of our experimental arrangement by modulating the electric field at the surface. This differential method has the advantage that scattered exciting light is not detected. The differential potential dependence of the luminescence ($d\,I/d\,U_E$) ("differential luminescence") as measured by superimposing a 50 mv a-c signal on the external d-c voltage is plotted in Fig. 11a. For comparison the interfacial d-c photocurrent (hydrogen evolution) measured in the same potential range is shown in Fig. 11b. Since the maximum of the differential luminescence coincides with the inflection point of the interfacial photocurrent curve obviously the charge transfer of minority carriers across the interface is responsible for the potential dependence of this luminescence. An influence of the surface recombination velocity s on the differential luminescence may be ruled out because then, according to the bell shaped potential dependence of s[10], two peaks of different signs should have appeared.

This experiment does show the quenching of the red luminescence by charge transfer across the interface. The quenching efficiency is very low and the lumi-

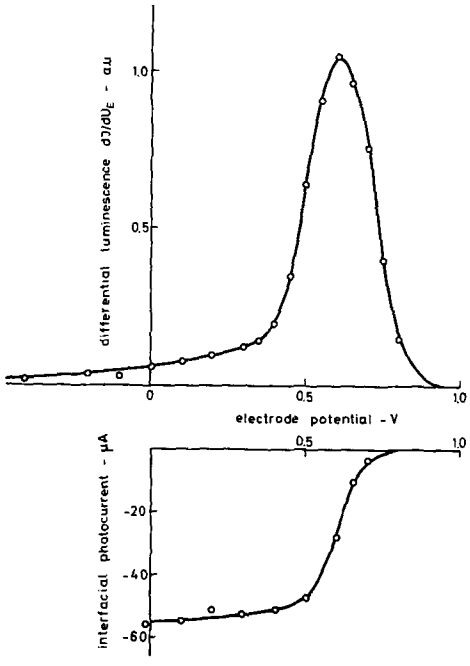

Fig. 11. Differential luminescence (a, top) and photocurrent (b, bottom) as a function of the electrode potential for p-GaP in 1*N* H_2SO_4.

nescence is varied by only few per cent of its total intensity in the corresponding potential range. Since we observed, on the other hand, a strong dependence of the luminescence intensity on the penetration depth of the incident light (Fig. 10) we have to conclude that surface recombination is chiefly responsible for the quenching. This is in agreement with results obtained by Gershenzon and Mikulyak (11) who performed similar measurements with dry surfaces. Why the surface recombination is not changed by varying the electrode potential remains a problem. Since at low depth of penetration the intensity of the luminescence is considerably reduced compared to its value obtained by exciting with radiation of greater penetration depth, the only possible explanation is given by the assumption that not only one discrete but a whole spectrum of energy levels of the surface states on GaP exists. This assumption is supported by the fact that also in the photocurrent spectrum (Fig. 3) the current peak due to the excitation of electrons from the valence band into surface states is very broad. Moreover, other measurements have shown that the quantum yield for the cathodic photocurrent determined at low penetration depths is very low (10^{-2}). This result also indicates that surface recombination is the dominant factor in the luminescence quenching.

The charge transfer by which the luminescence is partly quenched is a cathodic process (cathodic photocurrent in Fig. 11b), *i.e.*, electrons are consumed for discharging hydrogen ions. From the thermodynamic point of view hydrogen evolution is expected to occur only below −0.27v and not at such a high anodic potential as +0.8v. On the other hand, electrons and holes are not in thermodynamic equilibrium under illumination because the number of electrons excited by light is by several orders of magnitude larger than that in the dark ($n_o \approx 10^{-16}$ for $p_o = 10^{17}$). Moreover, according to capacity measurements flat band position is obtained with p-type GaP at +0.1v in 1*N* H_2SO_4, *i.e.*, below +1.0v the energy bands are bent downward at the surface. In the corresponding electric field within the space charge region the electron-hole pairs created by light are separated: electrons move toward the surface and holes in the opposite direction which leads to a reduction of the electric field (surface photovoltaic effect). On the other hand we kept the electrode potential and consequently the potential drop within the space charge region constant. In this case the electrons excited by light are forced to pass the interface. This leads to a cathodic reaction process, *i.e.*, the hydrogen evolution.

In the derivation of Eq. [6] we introduced the charge transfer as a diffusion determined term. This is not correct, of course, if the photovoltaic effect is responsible for the charge transfer. This fact, however, has no influence on the qualitative description of the quenching by charge transfer.

Acknowledgment

The authors are indebted to Ir. R. Ch. Peters from the Philips Research Laboratories in Eindhoven for supplying single crystals of GaP. Thanks are also due to Ing. J. Haberkamp and Ing. G. Kürsten for performing the measurements.

Manuscript submitted Sept 23, 1968. This paper was presented at the Boston Meeting, May 5-9, 1968, as Paper 65.

Any discussion of this paper will appear in a Discussion Section to be published in the December 1969 JOURNAL.

REFERENCES

1. R. Memming and G. Schwandt, *Electrochim. Acta*, **13**, 1299 (1968).
2. L. J. van Ruyven and F. E. Williams, *Phys. Rev. Letters*, **16**, 889 (1966).
3. W. K. Subashiev and S. A. Abagyan, in Physics of Semiconductors, Proc. 7th Intern. Conference, Paris 1964, p. 225.
4. H. Gerischer, *Z. Phys. Chem. N. F.*, **26**, 223 (1930).
5. R. Memming and G. Schwandt, *Surface Sci.*, **4**, 109 (1966).
6. *See e.g.*, M. Gershenzon, in "Luminescence of Inorganic Solids," p. 603, by P. Goldberg, Editor, Academic Press, New York (1966).
7. P. J. Dean, C. H. Henry, and C. J. Frosch, *Phys. Rev.*, **168**, 812 (1968).
8. J. Starkiewicz and J. W. Allen, *Phys. Chem. Solids*, **23**, 881 (1962).
9. W. Shockley and W. T. Read, *Phys. Rev.*, **87**, 835 (1952).
10. D. T. Stevenson and R. J. Keyes, *Physica*, **20**, 1041 (1954).
11. M. Gershenzon and R. M. Mikulyak, *Appl. Phys. Letters*, **8**, 245 (1966).

Growth of Zinc-Doped Gallium Phosphide by the Water Vapor Transport Method

Lars C. Luther

Bell Telephone Laboratories, Incorporated, Murray Hill, New Jersey

ABSTRACT

Large Zn-doped GaP crystals have been grown epitaxially on GaAs and GaP substrates. The presence of oxygen as an uncontrolled and perhaps major impurity is inferred from photoluminescence data. Carrier concentrations and total Zn concentrations were obtained from electrical measurements and analytical techniques. The variation of the room-temperature hole concentration with the Zn partial pressure of the growth ambient is in qualitative agreement with a calculated curve using an estimated value of the intrinsic carrier concentration at the growth temperature.

Frosch (1) has described a water vapor transport method for epitaxial deposition of GaP. The purpose of this paper is to describe the application of this technique to the preparation of large-area Zn-doped GaP crystals and to present data on the Zn incorporation.

Experimental

A schematic diagram of the apparatus is given in Fig. 1. Wet hydrogen is passed over a GaP source heated to 1100°C. The source reacts with the water producing phosphorus, Ga_2O, and hydrogen. As these gases are carried over a GaAs or GaP seed crystal placed in a temperature gradient of 6°-10°C/cm and centered at 1075°C, the decomposition reaction is reversed and GaP is deposited on the seed as well as the walls of the furnace tube. The Zn vapor is introduced into the growth ambient by passing dry hydrogen over a heated source of Zn and mixing the gas into the wet hydrogen at 900°C upstream from the GaP source. At this temperature no zinc oxide will precipitate out. The flow rate of the hydrogen carrier gas ranged from 130 to 450 cm^3/min but generally was held at 300 cm^3/min. A constant water vapor pressure of around 3 Torr was used in the majority of the runs; however, pressures as high as 10 Torr and as low as 0.3 Torr were tried. The source temperature was varied between 1100° and 1150°, while that of the seed ranged from 1020° to 1100°C. The average growth rate was 15 μ/hr. A wide range of Zn partial pressures (0.09-34 Torr) was used, the limitation on the high-pressure side being the voluminous Zn deposits which rapidly blocked the gas flow before significant epitaxial growth was achieved.

Gallium was obtained from Alcoa or Alusuisse and had a purity of 99.9999%. United Minerals and Chemical Company was the supplier of 99.998% pure Zn. The GaAs substrates obtained from the Monsanto Chemical Company in the form of <111> oriented slices were cut from undoped, boat-grown ingots. The carrier concentration was 10^{15} cm^{-3} and the dislocation count 10^5 cm^{-2}. The arsenic (B) faces of the slices were polished with bromine in alcohol on rotating Pellon cloth. The GaP seeds were made from epitaxial layers grown on GaAs substrates in the same manner as the Zn-doped material described below. Immediately before a run the GaAs substrate was etched in a mixture of 3 parts conc sulfuric acid and 1 part each of "Superoxol" (30% H_2O_2) and water. GaP seeds were etched in *aqua regia* or a methanol solution of chlorine. Polycrystalline source GaP was prepared by a method developed by Frosch (2), in which gaseous phosphorus was passed over gallium in a quartz boat placed in a temperature gradient of 1000°-1130°C.

Epitaxial growth of gallium phosphide on gallium arsenide under the conditions employed was reproducible only when a phosphorus pressure higher than the decomposition pressure of GaP was maintained over the GaAs seed during the heat-up period (10

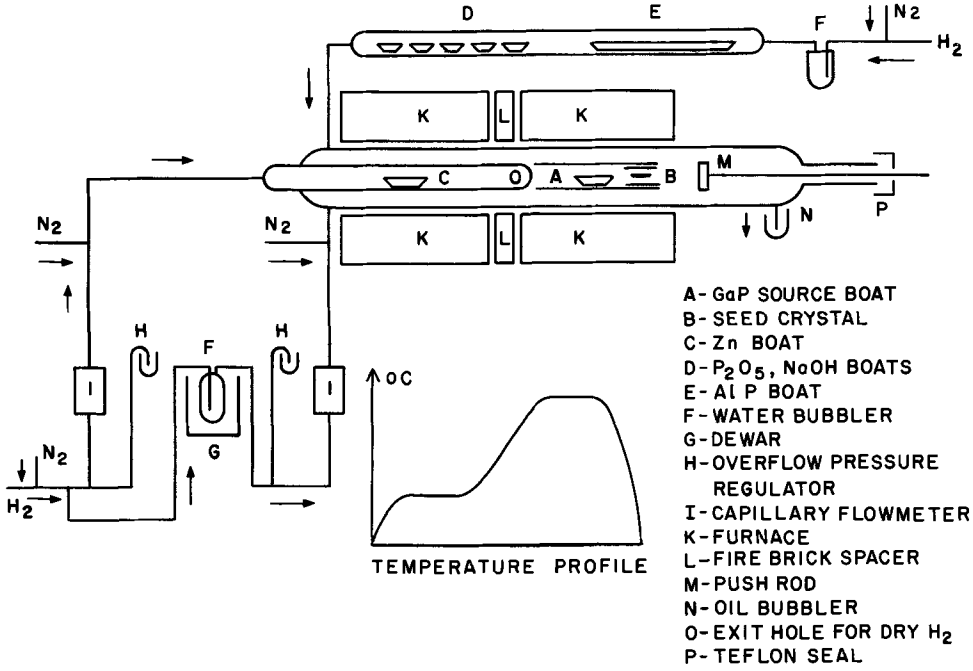

Fig. 1. Schematic diagram of apparatus. Arrows indicate gas flow.

min). The bulky (20-30g) source heats up more slowly than the seed. At the same time the decomposition pressure of GaAs is nearly ten times greater than that of GaP. Thus, after loading, the seed will soon start to decompose forming gallium on its surface. If the phosphorus pressure is too low, this gallium will not be converted to GaP but will aggregate in small spheres which later may act as centers for unoriented growth when the source comes to temperature and the phosphorus pressure increases. The phosphine used to produce the protective phosphorus pressure was generated by passing wet hydrogen over aluminum phosphide in the same kind of apparatus as used in the synthesis of GaP.

The resistivities of the crystal plates obtained in this study were measured using the Van der Pauw method. Ohmic contacts were made by applying d-c pulses to gallium-wetted gold or tungsten wires resting directly on the etched surface. Etchants recommended by Abrahams and Buiocchi (3) and Richards and Crocker (4), shown by Saul (5) to reveal dislocations, were used on some of the crystals to obtain an estimate of the dislocation density on the (111) phosphorus face, or growth face. The homogeneity of the material was tested by successive lappings followed by resistivity measurements and etch pit counts. Finally, the photoluminescence of the crystal was measured. At liquid nitrogen temperature an u.v. lamp was used to excite red fluorescence which was analyzed and measured with a photomultiplier tube (RCA 7326).

Results and Discussion

Size and quality of crystals.—The GaAs substrates used had a semicircular shape with a diameter of 30 mm. The thickness of the GaP layer was not uniform but decreased going from the center to the long edges, *i.e.*, the edges parallel to the furnace tube. A crystal grown during 60 hr would typically have a maximum thickness of 1 mm. Sometimes a central flat, about 1 cm broad, had developed with irregular terraces leading down towards the edges. A picture of one such crystal is reproduced in Ref. (6).

The etch pit counts for vapor-transported GaP grown directly on the GaAs seeds were found to be of order 10^5 cm^{-2} although a low count of order 10^4 cm^{-2} was sometimes observed. No reduction in this density was achieved by using GaP substrates. Photomicrographs of some typical, etched surfaces are found in Fig. 2(A,B,C). Etch grooves due to stacking faults were observed in a very few crystals.

Table I lists the results of the homogeneity tests. Since the crystals were lapped on the growth face, the properties of the first grown layers were measured last.

Electrical properties.—The Hall mobilities measured for four crystals at room temperature are plotted in Fig. 3 against the Zn partial pressure of the growth ambient. Using interpolated mobility values from this plot, resistivities obtained on a large number of crystals were converted to carrier concentrations. In Fig. 4, the dependence of the carrier concentration on the Zn partial pressure is displayed. At high Zn partial pressures the hole concentration varies as the square root of the Zn pressure. This is the expected behavior for an extrinsic semiconductor for which the fractional ionization of the acceptors is constant. Evidence for such a constant 50% ionization efficiency at room temperature has been given in Ref. (6).

The square root dependence has also been observed by Trumbore (7) over a limited range of concentrations in solution growth of Zn-doped GaP. From Trumbore's data one may calculate the Zn partial pressure over a gallium solution of GaP and Zn from which a crystal with a given Zn concentration can be grown. Thus a crystal containing 1×10^{18} cm^{-3} Zn can be grown at 1040°C from a gallium solution with a Zn concentration of 4×10^{-2} atom per cent. Adopting an activity coefficient of 0.5 for the Zn and a vapor pressure of 2500 Torr one can calculate a partial zinc pressure of 0.5 Torr for this gallium solution. For comparison the water vapor transport system described here required a partial Zn pressure of 0.6 Torr to yield a crystal containing 1×10^{18} cm^{-3} Zn.

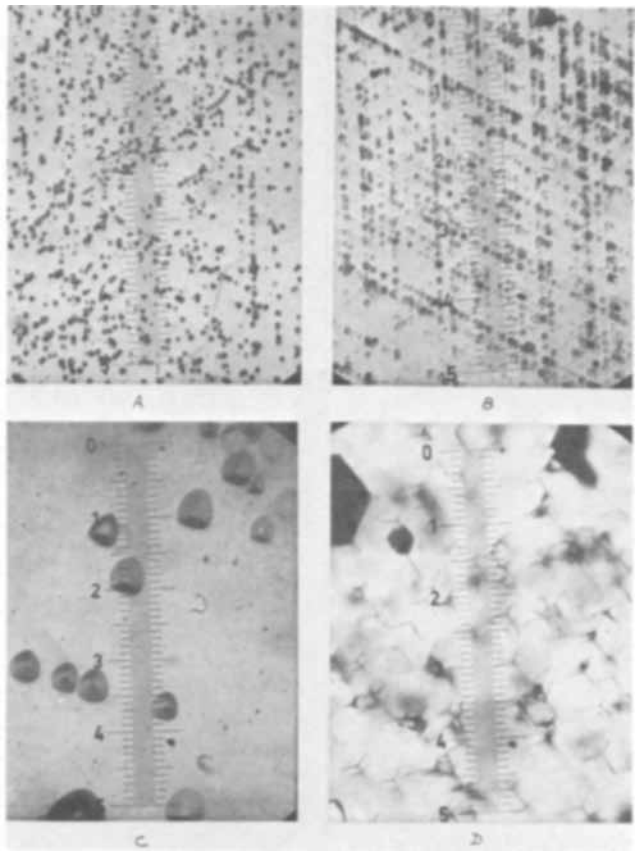

Fig. 2. Etch pits and imperfections on (111) phosphorus faces of vapor-grown GaP crystals. Etch pit density 3×10^5 cm^{-2} (A) and 4×10^5 cm^{-2} (B), one numbered scale unit = 0.15 mm. (C) Etch pits at higher magnification, one numbered scale unit = 0.024 mm. (D) Bulk imperfections, one numbered scale unit = 0.087 mm.

A set of four crystals were selected for surface barrier capacitance measurements and wet chemical analysis. In the latter the zinc was coprecipitated with copper and the precipitate analyzed by x-ray spectroscopy (8). The results are shown in Table II and are plotted in Fig. 4. Due to the fractional ionization of the Zn the total Zn concentration is higher than the hole concentration.

Additional information about impurity concentrations was obtained from spark source mass spectrometry analysis of one sample. The results are summarized in Table III. We note that the concentration of silicon was less than 5×10^{15} cm^{-3}, in agreement with an expected value extrapolated from the data given by Frosch, Thurmond, White, and May (9). Secondly we observe that the concentration of other donors as

Table I

Thickness (mm)	Resistivity (ohm-cm)	Etch pit count (cm^{-2})
Sample No. I		
0.49	0.085	5×10^5
0.42	0.086	6×10^5
0.30	0.083	5×10^5
0.20	0.095	4×10^5
0.12	0.107	5×10^5
Sample No. II		
0.37	0.056	2×10^5
0.28	0.056	2×10^5
0.20	0.056	3×10^5
0.14	0.061	3×10^5
0.05	—	8×10^5

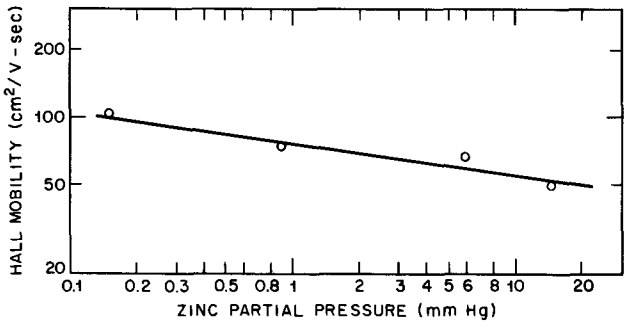

Fig. 3. Room-temperature mobility of Zn-doped, vapor-grown GaP plotted against Zn partial pressure of growth ambient.

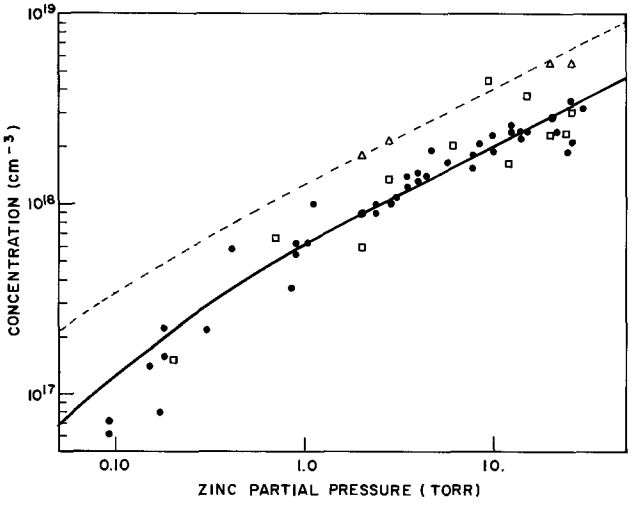

Fig. 4. Carrier and total Zn concentrations as functions of zinc pressure: •, room-temperature carrier concentration from resistivity and Hall data; □, carrier concentration from capacitance measurements (averaged); △, total Zn concentration from wet chemical analysis; ——, calculated room-temperature carrier concentration; - - -, calculated total Zn concentration.

measured by mass spectrometry is small compared to the Zn concentration. This leads us to the conclusion that no significant amount of compensation has occurred. The hole concentration obtained from the resistivities and the interpolated mobilities indicate that the Zn is only about 50% ionized at room temperature. A similar room-temperature ionization efficiency has been measured in Zn-doped, halogen-transported GaP (6).

As shown in Fig. 4 we observe a distinct fall-off in the hole concentration at the lowest Zn partial pressures. This effect may be due to a donor, *e.g.* oxygen, which eludes mass spectrometric analysis or to a transition to intrinsic material at the growth temperature, 1075°C. Recent band gap measurements by M. B. Panish and H. C. Casey (10) indicate that the band gap decreases nonlinearly with temperature and that previous extrapolations to high temperatures have resulted in overestimates of the band gap. Based on the new band gap measurements the intrinsic carrier concentration has been estimated to be 2.6×10^{17} cm^{-3} at 1100°C. Using a value of 3×10^{17} together with the observed room-temperature ionization efficiency of 50% the curves in Fig. 4 were calculated. As can be seen the room-temperature hole concentrations follow this curve quite well. However, the scatter in the data is too large to claim more than qualitative agreement.

If the interpretation of the fall-off in the Zn concentration is correct and the intrinsic carrier concentration is as high as several $\times 10^{17}$ cm^{-3}, the silicon incorporation data of Frosch *et al.* (9) will have to be given a new interpretation. Instead of operating entirely in the extrinsic range as claimed, the authors probably grew silicon-doped crystals in the intrinsic range only. The agreement between the carrier concentration data and the predictions of their model must be considered inconclusive, because of the amphoteric character of the silicon impurity which was ignored in the model. For solution-grown GaAs it has been demonstrated by Rosztoczy (11) that the conductivity type depends on the growth rate and therefore is the result of nonequilibrium growth conditions.

Photoluminescence.—The photoluminescence spectrum of the Zn, oxygen-doped GaP crystals always exhibited two broad bands at 1.84 and 1.96 ev, measured at 77°K. Dean, Frosch, and Henry (2) have shown that 1.96 ev bands are due to Si-Si and Si-S pair recombination. The 1.84 ev band has been shown to consist of two almost overlapping spectra (12). One is due to an exciton bound to a Zn-O complex, while the other arises from pair recombination between a Zn-O complex donor and a Zn acceptor. Thus the presence of oxygen in the crystals was clearly indicated. Due to the large scatter in the photoluminescence data, no correlation of the intensity of the 1.84 ev band with any controllable experimental variables could be established.

Table III. Impurities in sample C from spark source mass spectrometry

Element	atoms/cm³
Carbon	9×10^{16}
Nitrogen	2×10^{16}
Silicon	$<5 \times 10^{15}$
Zinc	3×10^{18}
Arsenic	3×10^{19}
All others	$<3 \times 10^{15}$

Acknowledgments

I am grateful to H. G. White for $N_A - N_D$ measurements and to Miss S. Vincent for the chemical analyses. D. Malm carried out the mass spectrometric analysis. H. C. Montgomery kindly assisted me with the Hall measurements. To C. J. Frosch and F. A. Trumbore and C. D. Thurmond, I owe thanks for helpful discussions.

Manuscript submitted Sept. 12, 1968; revised manuscript received Nov. 18, 1968.

Any discussion of this paper will appear in a Discussion Section to be published in the December 1969 JOURNAL.

REFERENCES

1. C. J. Frosch, *This Journal*, **111**, 180 (1964).
2. P. J. Dean, C. J. Frosch, and C. H. Henry, *J. Appl. Phys.*, **39**, 5631 (1968).

Table II. Total Zn and carrier concentrations

Sample	Zn partial pressure (Torr)	Total Zn* concentration (cm⁻³)	N_A-N_D (cm⁻³)	Room-temp. carrier concentration (From resistivity data) (cm⁻³)
A	2.0	1.8×10^{18}	$5.4\text{-}6.5 \times 10^{17}$	1×10^{18}
B	2.9	2.2×10^{18}	$1.1\text{-}1.6 \times 10^{19}$	1×10^{18}
C	20	5.5×10^{18}	$1.5\text{-}3.2 \times 10^{18}$	3×10^{18}
D	26	5.5×10^{18}	$1.9\text{-}4.2 \times 10^{18}$	3×10^{18}

* Wet chemical analysis.

3. M. S. Abrahams and C. J. Buiocchi, *J. Appl. Phys.*, **36**, 2855 (1965).
4. J. L. Richards and A. J. Crocker, *ibid.*, **31**, 611 (1960).
5. R. H. Saul, *This Journal* **115**, 1184 (1968).
6. L. C. Luther and D. D. Roccasecca, *ibid.*, **115**, 850 (1968).
7. F. A. Trumbore, H. G. White, M. Kowalchik, R. A. Logan, and C. L. Luke, *ibid.*, **112**, 782 (1965).
8. C. L. Luke, *Anal. Chim. Acta.*, **41**, 237 (1968).
9. C. J. Frosch, C. D. Thurmond, H. G. White, and J. A. May, *Trans. Met. Soc. AIME*, **239**, 365 (1967).
10. H. C. Casey, Unpublished.
11. F. E. Rosztoczy, *This Journal*, **115**, 244C (1968).
12. C. H. Henry, P. J. Dean, and J. D. Cuthbert, *Phys. Rev.*, **166**, 754 (1968).

Electrical Properties of Silicone Films on Silicon

M. Conti and F. Tegagni

Research and Development Laboratories of S.G.S. SpA., Agrate Brianza, (Milano), Italy

ABSTRACT

The electrical properties of silicone resin films on silicon have been investigated by means of MIS structures. The silicones considered are commercially available methyl phenyl compounds successfully employed in passivating high voltage silicon devices. As contrasted to thermally grown silicon dioxide, well cured silicones feature rather low values of Q_{SS} in the range of few 10^{10} cm^{-2}. However, the surface recombination velocity is appreciably higher, in the range 10-10^2 cm/sec. There is a room temperature trapping instability similar to the one encountered in silicon nitrides. The critical field for the onset of trapping is in the range 0.5-1 x 10^6 v/cm which is significantly lower than that for silicon nitride. The conduction current through the films is a rapidly increasing function of the applied voltage. This behavior is similar to that of silicon nitride although the currents are higher for the same electric fields.

For several years silicone resins and rubbers have been used in passivating silicon devices. Actually, in spite of the many efforts made to establish a suitable planar technology, the best way to obtain high voltage diodes and transistors seems to be silicone passivation. Many publications have been devoted to the chemistry and application of silicones in the electrical industry (1-3). More specifically Kern (4) reported some effects of resin composition on the production of donor or acceptor states at the silicon-silicone interface. The experience gained in developing high voltage devices (up to 1500v) convinced us that some silicone resins should have very good properties such as fixed space charge Q_{ss}, a low density of fast states D_{st}, and low bulk conduction. We also found that the reverse current of relatively large diodes in which the surface contribution was dominant was of the same order of magnitude as in the best passivated planar devices. As a consequence, the contribution of surface recombination had to be essentially the same.

For lack of published data a systematic study of the interface properties of silicone films on silicon was undertaken. Measurements were performed on MSS (Metal Silicone Silicon) capacitors and silicone insulated gate diodes. The capacitors allow the measurement of fixed surface charge density Q_{ss} through CV plots and flatband voltage displacement (5).

Silicone films feature a room temperature trapping instability as encountered in silicon nitride (6); however, the critical field is rather small, in the range of 0.5-1 x 10^6 v/cm. Conduction current through the silicone film was measured through guard ring MSS capacitors. Recombination velocity was examined through the gate diode technique first reported by Grove and Fitzgerald (7).

Final interface properties and, of course, device performance are heavily determined by cure schedule; long cure times result in the best electrical performances.

Experimental

The silicones investigated are commercially available resins especially designed for electrical industry applications. The investigation has been restricted to three types made by different manufacturers, which in the following will be referred to as A, B, and C silicones. They are basically methyl phenyl compounds diluted in xylene or toluene. Type A silicone is a high purity resin which is claimed to be made in glass equipment under carefully controlled laboratory conditions. The high purity is ensured by spectrographic analysis specifications which guard against metal contamination. This compound does not contain any catalyst.

Types B and C are general purpose resins, designated to improve the surface resistivity of insulating materials in electrical circuitry. Type B contains a catalyst, type C does not.

The samples studied were prepared on 10-20 ohm-cm n-type silicon wafers which were first lapped, 30μ etched, polished, and finally 10μ etched to remove most of the mechanically damaged surface.

The wafers were then covered with silicone diluted in toluene to get a sufficiently low viscosity fluid. The wafers were spun up to 4000 rpm on standard resist spinners and then cured. Curing schedule was 2 hr at 65°C, 2 hr at 150°C, and finally from 60 to 200 hr at 220°C. The silicone film thickness was measured by stripping away the silicone in certain areas of the wafer and recording the total height variation between the bare surface and the silicone-coated silicon surface by means of a Talysurf 4 surface inspection test set. The thickness of silicone A samples was typically 1μ $\pm$ 5% and was found to be in agreement with capacity measurements in accumulation situation (see paragraph on fixed surface charge).

In MSS capacitors the central electrode is surrounded by a guard ring electrode which is useful in avoiding surface leakage effects during conduction current measurements. Aluminum thickness was normally 7000Å. In gated diode experiments, silicon dioxide passivated diodes were first obtained by standard planar technology. After having measured the surface recombination velocity, the aluminum and oxide were etched off and the wafers covered by silicones and then cured with the same schedule as with MSS capacitors. To obtain proper gates and contacts, 7000Å aluminum was evaporated and masked.

Most of the measurements refer to silicone A since the reproducibility and the electrical performance of this compound are quite good, whereas B and C materials give high values of Q_{ss} and D_{st}. With type A resin the manufacturer recommends a minimum curing time of 4 hr at 250°C. However, a strong change in characteristics is detectable even after 60 hr. From 100 to 200 hr can be considered as a curing time sufficient to get the complete stabilization of the resin. Figure 1 shows a typical MSS CV plot after 60 hr at 220°C. The transition from accumulation to depletion is quite smooth and is due to a high density of surface states. Figure 2 refers to the same sample after 140 hr (curve a) and 200 hr (curve b) at 220°C. As can be seen, the transition is steeper and the flat-band-voltage is highly reduced. The CV plot depends also on the operating frequency. When the frequency decreases, the flat-band-voltage shifts toward negative gate voltages and at very low frequencies the CV plot features the well-known minimum capacity (7 Hz). Samples cured for 200 hr are significantly similar to those cured for 140 hr, although the longest cures result in a smaller flat-band-voltage spread between 100 kHz and 23 Hz. The density of fast states D_{st} has been computed using the method first reported by Terman (8) and subsequently improved by Berglund (9). At the middle of the energy gap, the state density is rather low, in the range of 10^{10} cm^{-2} ev^{-1}, as can be computed by the low frequency CV plot (80 Hz plot of Fig. 2b).

As the energy is increased toward the conduction band, the state density increases and reaches up to 10^{12} cm^{-2} ev^{-1} in the energy range 0.15-0.30 ev below the conduction band. This can be computed accounting for the flat-band-voltage reduction at 100 kHz and 1 MHz. At such frequencies even the states in the above-mentioned energy interval are not sufficiently fast to follow the surface potential variations (10).

Both silicones B and C feature large and negative flat-band-voltages (see Fig. 3), even when the curing time is increased to 200 hr at 220°C. Furthermore, the transition to the depletion mode is quite smooth.

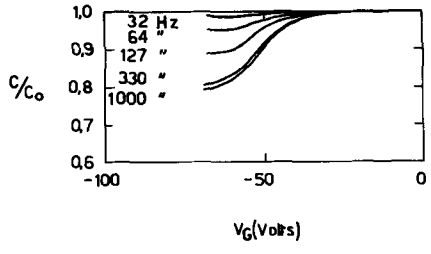

Fig. 1. Type A silicone. CV plots after a 60 hr cure at 220°C

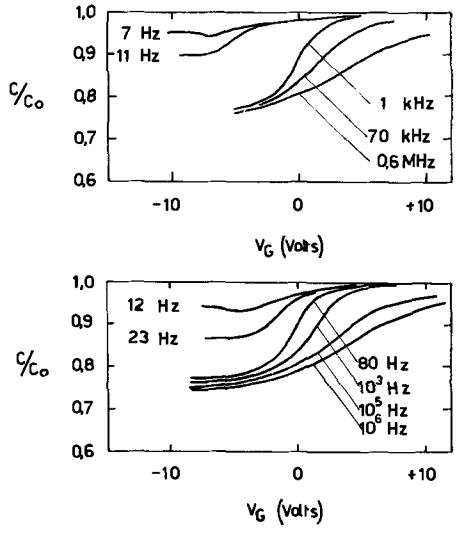

Fig. 2. Type A silicone. CV plots after a 140 hr cure at 220°C (curve a, top) and a 200 hr cure at 220°C (curve b, bottom), silicone thickness 1 μ.

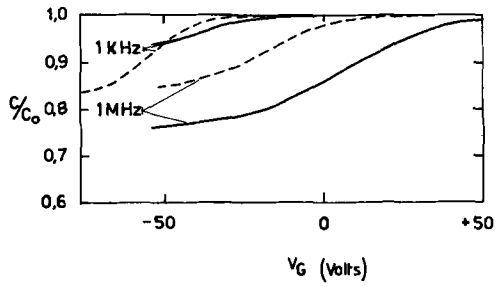

Fig. 3. Typical CV plots of type C (solid lines) and type B silicones (dotted lines).

Trapping effects.—When the electric field is raised above a critical value, the MSS capacitor features a permanent shift in CV characteristics. This instability was previously reported for silicon nitride and is currently ascribed to the trapping of carriers in the dielectric. The critical field strongly depends on the curing schedule. Figure 4 refers to the plot of flat-band-voltage *vs.* bias voltage for a type A-MSS capacitor after 60 hr (dotted line) and after 140 hr (solid line) at 220°C. The additional 80 hr curing time raised the critical field from 5 x 10^5 to 7 x 10^5 v/cm. The sample was given a further 220°C 60 hr curing but no noticeable increase in the trapping field was detected. When bias voltage is changed, a certain time interval is required before the new equilibrium condition is reached. There is a marked difference in the time interval between positive and negative bias of the metal electrode. When the electrode is made positive, the relaxation is controlled by a fast time constant in the range of a few seconds, followed by a much longer one in the range of minutes. When the gate is made negative, there is no fast time constant; the relaxation is controlled by a very long time constant in the range of half an hour. The critical field is strongly dependent on whether measurements are performed in absolute dark or not. Performances so far reported are "dark" performances and a noticeable reduction in the critical field (1-2 x 10^5 v/cm) is obtained when even a small light flux strikes the sample. A light-induced reduction of the trapping field is detectable at wavelengths up to 1.2μ.

Fixed surface charge density Q_{ss}.—As explained in ref. (5), p. 280, the fixed surface charge density Q_{ss} can be computed by the expression

$$Q_{ss}\frac{X_o}{\epsilon_S\epsilon_0} = -V_{FB} + \phi_M - \phi_S$$

where X_o is the silicone thickness, $\epsilon_S = 2.7$ is the silicone dielectric constant, V_{FB} is the low frequency flat-band voltage, ϕ_M and ϕ_S are the metal-silicone and the silicon-silicone barrier heights. The factor

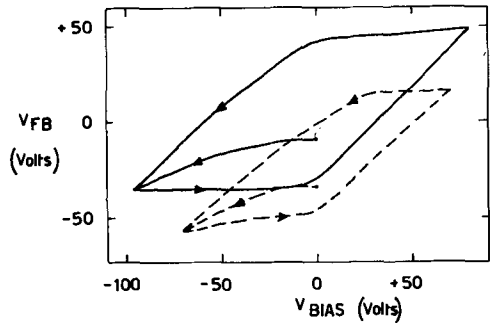

Fig. 4. Dependence of flat-band-voltage on curing conditions of the MSS type A silicone capacitor, with a symmetrical bias stress. Curing time and temperature 60 hr at 220°C (dotted lines) and 140 hr at 220°C (solid lines).

Table I. Fixed surface charge values

Silicone	Cure Time, hr	Cure Temperature, °C	Q_{ss}, cm^{-2}
A	60	220	4-7 × 10^{11}
	140	220	<1 × 10^{11}
	200	220	<3 × 10^{10}
B	Up to 200	220	~10^{12}
C	200	220	~4-10 × 10^{11}

$\epsilon_s\epsilon_0/X_0$ can be quickly obtained from the CV plots when the silicon surface is strongly accumulated (metal electrode heavily positive). In the absence of experimental data for $\phi_M - \phi_S$, the silicon dioxide values have been employed with aluminum against 10 ohm-cm n-type silicon: $\phi_M - \phi_S \simeq -0.4$v (11).

Fixed surface charge values are summarized in Table I.

Surface recombination velocity.—Measurements of the surface recombination velocity were performed by the well established technique of measuring the reverse current of gated diodes as a function of gate voltage. Silicon dioxide passivated diodes were first obtained and measured. The surface recombination velocity S_0 results were typically $S_0 = 10$ cm s^{-1} and Fig. 6 shows a typical plot of reverse current *vs.* gate voltage (dotted line). The aluminum and oxide were etched off, the wafers covered by silicones, and then cured. A typical plot of reverse current *vs.* gate voltage for type A silicone is shown in Fig. 5. As can be seen, the reverse current features the well-known bump when the surface under the gate is depleted. Notice that the gate voltage corresponds to the beginning of depletion in the very low frequency CV plot. The surface recombination velocity as obtained from many measurements resulted in

$$S_0 = 10 - 20 \text{ cm s}^{-1}$$

which is a value not much higher than the best performances measured in annealed oxides (12).

Conduction current.—Guard ring MSS capacitors were employed to measure the conduction current through silicone films. Typical plots at 25°C are reported in Fig. 6.

The conduction performance may be compared with that of silicon nitride which also features a strong dependence on electric field. As reported in ref. (13),

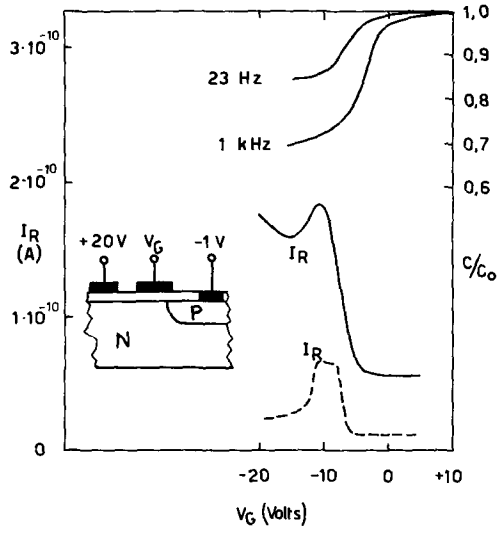

Fig. 5. Reverse current of a silicone insulated gate diode (solid line) as a function of gate voltage V_G. The top curves are CV plots of the gate. Silicon resistivity is 6 ohm-cm and silicone thickness is 1μ (type A). The dotted line plot is the reverse current of the same gated diode when insulated with 0.3μ of thermal silicon dioxide.

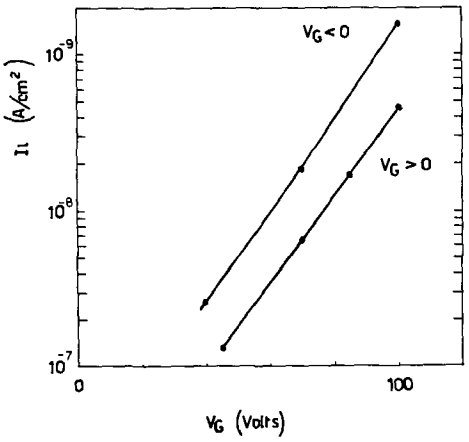

Fig. 6. Current *vs.* applied voltage in 1μ thick type A silicone. Curing time is 140 hr at 220°C.

nitrides are much better as insulators since twice the electric field is required for the same current density. The silicone dielectric strength is strongly dependent on temperature and varies from sample to sample. While at room temperature an electric field up to 10^6 v/cm can be successfully supported, at 90°C few samples survive the electric stresses in excess of 5 x 10^5 v/cm. In measuring conduction currents, the same succession of time constants is found as reported in the section on Trapping effects. This depends obviously on the fact that both conduction current and electric field at the silicone-silicon interface are controlled by the trapping of carriers in the silicone.

Discussion and Conclusions

The silicone-silicon interface properties can be interpreted in terms of the well-established theory currently employed with silicon dioxide (14). Major differences are (*i*) frequency dependent flat-band-voltage, and (*ii*) permanent shift in flat-band-voltage when the critical field is exceeded.

Frequency dependent effects were shown to be due both to fast state density at the silicon dielectric interface (10) and to tunnelling of carriers through the dielectric into dielectric traps (so-called slow states) (15). Although tunnelling effects cannot be entirely excluded, both frequency dependent CV plots and surface recombination measurements can be explained in terms of a proper fast state distribution.

In fact, a low state density at the middle of the energy gap is consistent with a low value of recombination velocity S_0. On the other hand, at zero gate voltage the gated diode reverse current is many times higher than in oxide insulated diodes. This can be explained by the relatively large fast state density far from the middle of the energy gap which has been shown to account for the shift of flat-band-voltage at high frequencies.

Trapping effects in silicones begin at electric fields smaller than in other useful dielectrics. For instance, silicon nitride features critical fields in the range of 2-4 x 10^6 v/cm. From the high voltage device point of view, the room temperature trapping instability is insignificant since the silicone critical field is two or three times higher than the breakdown field of high voltage silicon devices. Actually, in several hundred volt devices, both diodes and transistors, the breakdown field hardly exceeds 2-4 x 10^5 v/cm as opposed to a critical trapping field of 7-10 x 10^5 v/cm. However, as the temperature is raised, the dielectric strength of the silicone film drastically decreases. This is probably the main reason why silicone passivated devices require a significant relaxation in electrical specification as the operating temperature exceeds the 100°-125°C level.

Acknowledgment

The authors wish to thank D. J. Fitzgerald for the many helpful discussions throughout this investigation.

Manuscript submitted Sept. 3, 1968; revised manuscript received Nov. 8, 1968.

Any discussion of this paper will appear in a Discussion Section to be published in the December 1969 JOURNAL.

REFERENCES

1. C. Eaborn, "Organosilicon Compounds," Butterworths Scientific Publishers, London (1960).
2. S. Fordham, "Silicones," C. Newnes Ltd., London (1960).
3. R. N. Heals and F. M. Lewis, "Silicones," Reinhold Publishing Co., New York (1959).
4. Edward L. Kern, "The Electronic Effect of Junction Coating Resins on Active Semiconductor Surfaces," 153rd Meeting of the Am. Chem. Soc., April 10-14, 1967, Miami, Florida.
5. A. S. Grove, "Physics and Technology of Semiconductor Devices," John Wiley & Sons, Inc., New York (1967).
6. T. L. Chu, J. R. Szedon, and S. H. Lee, *Solid State Electron.*, **10**, 897 (1967).
7. A. S. Grove and D. J. Fitzgerald, *ibid.*, **9**, 783 (1966).
8. L. M. Terman, *ibid.*, **5**, 285 (1962).
9. C. N. Berglund, *Trans. IEEE on El. Dev. EDI3*, **10**, 701 (1966).
10. K. Lehovec and A. Slobodskoy, *Solid State Electron.*, **7**, 59 (1964).
11. B. E. Deal, E. H. Snow, and C. A. Mead, *J. Phys. Chem. Solids*, **27**, 1873 (1966).
12. D. J. Fitzgerald and A. S. Grove, *Surface Science*, **9**, 317 (1968).
13. S. M. Sze, *J. Appl. Phys.*, **38**, 2951 (1967).
14. See for instance, E. H. Nicollion and A. Goetzberger, "The Si-SiO_2 Interface—Electrical Properties as determined by the MIS Conductance Technique," *Bell System Tech. J.*, **46**, 1055 (1967).
15. F. P. Heiman and G. Warfield, *IEEE Trans. El. Dev. EDI3*, 167 (1965).

Etching Characteristics of Silicon Carbide in Hydrogen

J. M. Harris,* H. C. Gatos,* and A. F. Witt*

Department of Metallurgy and Center for Materials Science and Engineering, Massachusetts Institute of Technology, Cambridge, Massachusetts

ABSTRACT

It was found that the etching rate of alpha (hexagonal) silicon carbide in hydrogen at high temperatures (above 1550°C) varies with the susceptor material on which the inductively heated silicon carbide rests. Molybdenum exhibits the most pronounced effect increasing the etching rate by about one order of magnitude over that on all other susceptors (W, Nb, Ta, C) employed. Finite etching rates were also observed on α-silicon carbide exposed to inert gas atmospheres at elevated temperatures and were attributed to hydrogen residually present in the susceptors. It was concluded that catalytic action of the susceptor material is involved in the etching process.

It is well known that in the case of silicon, vapor etching prior to vapor growth greatly improves the perfection of the deposited layer (1). However, depending on experimental conditions, vapor etching may compete with the growth process. For example, experiments with silicon carbide in a hydrogen atmosphere have shown that no effective epitaxial growth could be obtained above 1750°C because of the prevailing high etch rates (2-4).

The present experiments were undertaken in connection with our studies on the epitaxial growth of silicon carbide. During these studies it became apparent that the etching rate of α-SiC (hexagonal) in hydrogen is substantially affected by the susceptor material used for induction heating. Temperatures below 1550°C were not considered since the etching rates are very small.

Experimental Procedure

The etching experiments were carried out on α-SiC platelets (0.15 cm^2) of (0001) orientation in a 1.5 in. ID, horizontal, water-cooled, quartz reaction tube. Three different susceptor materials, Ta, C, and SiC-coated carbon were used for inductive heating of the system. Figure 1 (a, b, c) shows schematically the arrangement of the sample and the susceptors. Secondary susceptor strips of Mo, Nb, and W (about 5 cm^2 and 0.5 mm thick) were placed on the primary susceptors as indicated in Fig. 1b.

Etching rates (in microns per hour) were determined from the sample weight changes and of the (0001) area face. Area measurements were made with a planimeter on low magnification (16X) photographs of the samples. The etching rates represent the change in the over-all thickness of the sample. Prior to use the susceptors were etched in a 5:1, conc HF: conc HNO_3 solution; the α-SiC platelets were etched in KOH and cleaned in acetone and then distilled water.

Before introducing the hydrogen the reaction tube was purged with argon or helium while the system was brought up to the desired temperature. The tube was also purged with the inert gas after the termination of the etching experiment to prevent hydrogen embrittlement of the metallic susceptors. The indicated temperatures are uncorrected optical pyrometer readings of the susceptor. All gases employed were >99.999% pure. The experimental results were reproducible to within ± 15%.

Results

Etching in hydrogen.—The results of etching experiments with α-SiC on the various susceptors in a

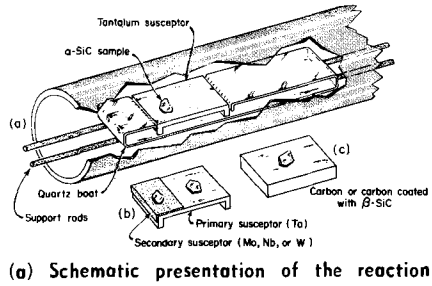

Fig. 1. (a) Schematic presentation of the reaction tube, (b) secondary susceptor, (c) susceptor.

* Electrochemical Society Active Member.

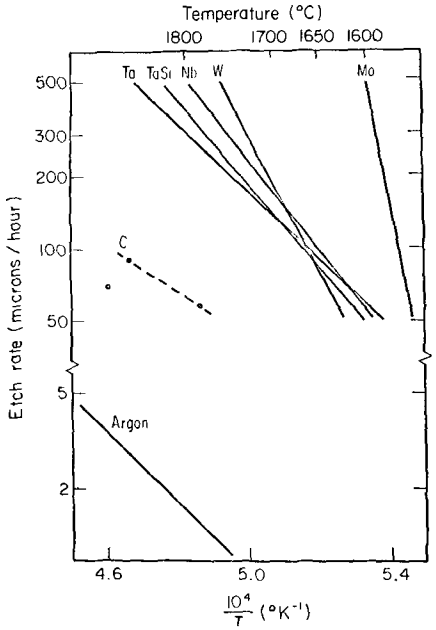

Fig. 2. Effect of susceptor materials on the etching rate of α-SiC in hydrogen. The data obtained with the carbon susceptor are somewhat uncertain because of carbon transfer to the SiC (see text). The published results for SiC decomposition in argon under static conditions are also shown. For clarity the numerous experimental points are omitted. They exhibited a standard deviation less than 5%.

hydrogen atmosphere are presented in Fig. 2. For convenience published results for the etching of α-SiC on tantalum silicide (2,3) and for the α-SiC decomposition in argon (5) are also included. All experiments were performed with a hydrogen flow rate of 2 l/min (measured under atmospheric pressure at room temperature). Those on TaSi had been performed with a flow rate of 2.5 l/min and those in argon had been carried out under static conditions.

The results obtained in the etching experiments on carbon susceptors (Fig. 2) are of limited accuracy due to carbon deposits which could be observed on the SiC surface in contact with the susceptor after etching at high temperatures (>1800°C). Such deposits are apparently the result of carbon transfer from the susceptor to the sample.

Figure 2 shows that the etching rates of α-SiC inductively heated on Ta, TaSi, Nb, and W susceptors in hydrogen are similar. While the apparent activation energies for the etching process on these susceptors (as determined from the slopes of Fig. 2) are not substantially different from that on the carbon susceptor, the corresponding etching rates are considerably higher. In the case of Mo susceptors it is seen that markedly greater etching rates and a stronger temperature dependence prevail.

When carbon susceptors coated with TiC or with Ti-Ta alloy were employed the weight of the α-SiC samples did not change at temperatures up to 1750°C and for etching times up to 20 min. However, a net weight increase was observed after 30 min at 1700°C when a carbon susceptor coated with β-SiC (cubic) was employed. This weight increase was apparently the result of mass transfer of SiC from the susceptor to the sample as a result of the prevailing thermal gradients. Figure 3 shows a typical example of polycrystalline β-SiC deposit on an α-SiC substrate by thermal transport in argon.

The etching rates of the (0001) and (000$\bar{1}$) basal surfaces of α-SiC were studied by masking one of the two with a nonreactive carbon deposit. It was found that the silicon (0001) surface exhibits somewhat higher etching rates than the carbon (000$\bar{1}$) surface. At 1725°C this difference in etching rates was found to be approximately 15%. The etching rates of the basal planes did not significantly change whether or not the surface under investigation was facing the susceptor during etching.

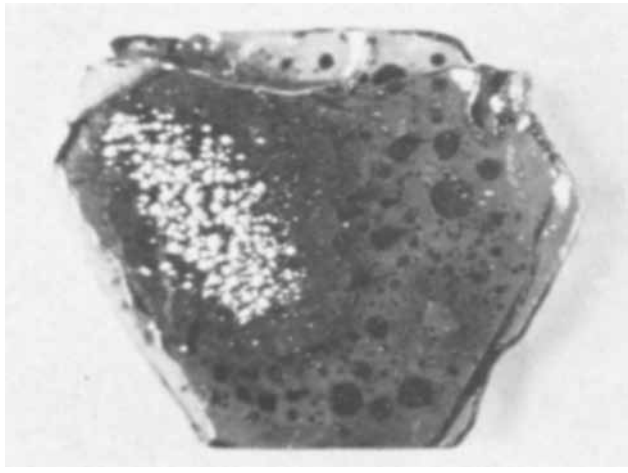

Fig. 3. α-SiC sample after 6 min exposure to argon at 1850°C on a tantalum susceptor. The β-SiC deposit appearing as bright spots is the result of mass transfer from other α-SiC samples simultaneously exposed to the etching conditions. Magnification approx. 6X.

The basal planes were identified by their etching characteristics (6). In hydrogen the carbon surface exhibited well defined dislocation etch pits whereas the silicon surface showed irregular attack and occasional hexagonal pits (see Fig. 4).

Etching in inert gas atmospheres.—Etching experiments were carried out in argon and helium on Ta and Mo susceptors. The results of these experiments are summarized in Fig. 5. It is seen that α-SiC undergoes significant etching when exposed to argon or helium. The etching rate on Mo is considerably higher and exhibits stronger temperature dependence than on Ta susceptors. It is of interest to note that above 1700°C

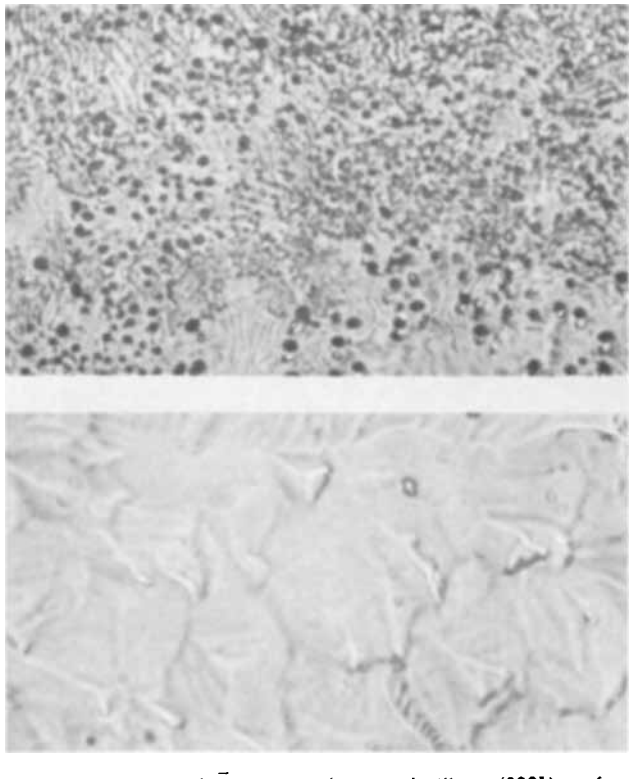

Fig. 4. Carbon (000$\bar{1}$) surface (top) and silicon (0001) surface (bottom) of α-SiC after 20 min exposure to hydrogen at 1650°C on a tantalum susceptor (see text) (100X).

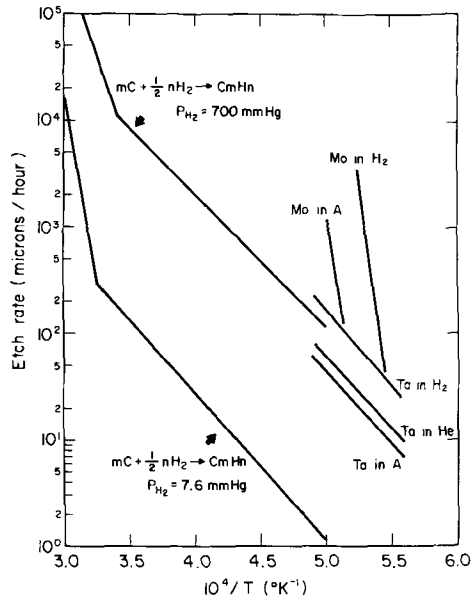

Fig. 5. Etching behavior of α-SiC in argon and helium on tantalum and molybdenum susceptors. The interaction of graphite and hydrogen at high temperatures (7) is also shown (see text).

the etching rate on Mo in an argon atmosphere is higher than on Ta susceptors in hydrogen.

In several experiments it was observed that SiC was deposited in the form of α-SiC from samples at higher temperatures to samples at lower temperatures when several α-SiC samples were exposed simultaneously to argon on Ta susceptors (Fig. 3). Such temperature differences were caused by varying thermal contact of the samples with the susceptor.

Transport experiments in hydrogen.—Etching experiments on Mo susceptors revealed that about 85% of the weight loss of the α-SiC samples could be accounted for by a corresponding weight increase of the Mo susceptor. A chemical analysis of the susceptor after an etching experiment showed that the molar ratio Si/C was now greater than one.

The distribution of the transferred material on the susceptor was investigated by placing SiC samples on Ta susceptors at a fixed distance (3 mm) from the leading and trailing edge of secondary Mo susceptors respectively and exposing them at 1600°C to a hydrogen atmosphere. Figure 6 shows the data of the silicon

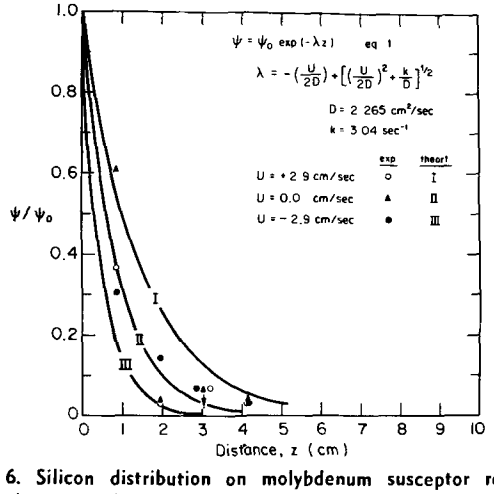

Fig. 6. Silicon distribution on molybdenum susceptor resulting from etching of α-SiC in hydrogen at 1650°C. The normalized concentrations were obtained by extrapolating the data of the chemical analysis to zero distance from the source. Curves I, II, and III represent the concentration profiles based on Eq. [1] (see text).

analyses plotted in normalized concentration *vs.* distance from the source.

If it is assumed that the component distribution in the vapor phase is determined by diffusion from the source in the presence of convection and chemical reaction then the steady state solution of the diffusion equation is (8)

$$\psi = \psi_0 \exp(-\lambda z) \qquad [1]$$

where ψ is the concentration of the component in the vapor phase; $\lambda = (U/2D) + [(U/2D)^2 + (k/D)]^{1/2}$, where D is the diffusion coefficient, U is the gas flow rate, k is an over-all first order rate constant, and z is the distance from the source. When Eq. [1] was applied to the measured distribution of silicon in Mo, the best agreement with the experimental data was obtained for $D_{Si/H_2} = 2.3$ (cm²/sec) and $k = 3.0$ (sec^{-1}). This value for the diffusion constant of silicon in hydrogen at 1600°C appears to be reasonable[1] and is taken as an indication that this mechanism of silicon vapor transfer is plausible under the given conditions.

The results of the above analysis are presented as solid lines in Fig. 6 for the various hydrogen flow rates investigated. No analysis for the carbon data was attempted since the carbon concentrations on the susceptor material were too low to permit an accurate analysis of its distribution.

It was also observed that higher effective etching rates on Ta susceptors occurred when a piece of Mo was placed on the primary susceptor near (but not in contact with) the α-SiC sample. This effect was found to decrease exponentially with distance of separation and became negligible when the distance of the Mo piece was in excess of 15 mm from the sample. At flow rates of 2 l/min such an increase in etching rate was observed on samples placed up or down-stream relative to the Mo piece.

These transport experiments constitute evidence of chemical interaction between the SiC sample and the susceptor. Evidence of chemical interaction was also present whenever etching occurred. At the lower temperatures the susceptor changed color underneath the sample. At higher temperatures the outline of the SiC sample was clearly imprinted on the susceptor by the interaction.

Discussion

It was found that the etching rates of α-SiC in hydrogen, argon, or helium are strongly dependent on the susceptor material on which the samples were inductively heated. It was also found that there was no visible interaction between SiC and the susceptor material unless etching of SiC took place. Apparently during the etching process carbon is removed from SiC as hydrocarbons and the silicon, which forms no stable gaseous compound at these temperatures, reaches the susceptor via surface diffusion or the vapor phase. The experimental results can be accounted for by assuming that a key step in the etching process is the formation of atomic hydrogen which interacts with the SiC to form stable volatile hydrocarbons. On this basis the etching rates should reflect the catalytic effectiveness of the susceptor in forming atomic hydrogen. Consistent with this requirement is the fact that the etching rate of Mo susceptors is much greater than on W susceptors, since it is well known that Mo is more effective than tungsten in converting molecular into atomic hydrogen (10). It should also be noted that the solubility of H_2 is greater in Mo than in W (11). Since the processes considered were not under equilibrium conditions no attempt was made to treat them thermodynamically.

It is not clear at present as to whether the atomic H reacts directly with SiC or with carbon resulting from the decomposition of SiC. It is of interest to note, however, that the reaction rate between graphite and hydrogen (below 2400°C) is directly proportional to the partial pressure of atomic hydrogen (7), and that

[1] A value of $D_{Si/H_2} = 3.2$ cm²/sec for 1100°K was calculated (9) using Chapman-Enskog parameters.

the apparent activation energy for the low temperature hydrogen-carbon reaction is very close to that observed for the etching process on Ta (Fig. 5).

Regarding the observed etching in inert atmospheres, it is believed that it is due in part to residual hydrogen being released from the susceptor upon heating. The materials employed as susceptors are known for dissolving hydrogen which they release slowly at high temperatures (12).

Acknowledgment

The authors wish to acknowledge the Advanced Research Projects Agency under contract SD-90 for sponsoring this research. One of us (J.M.H.) wishes to acknowledge IBM for an IBM Resident Study Fellowship.

Manuscript submitted June 17, 1968; revised manuscript received Nov. 12, 1968. This paper was presented at the Boston Meeting, May 5-9, 1968, as Paper 68.

Any discussion of this paper will appear in a Discussion Section to be published in the December 1969 JOURNAL.

REFERENCES

1. G. A. Lange and T. Stavish, *RCA Rev.*, **24**, 488 (1963); K. E. Bean and P. S. Gleim, *This Journal*, **110**, 265C (1963).
2. T. L. Chu and R. B. Campbell, *This Journal*, **112**, 8, 955 (1965).
3. R. B. Campbell and T. L. Chu, *ibid.*, **113**, 8, 825 (1966).
4. H. C. Chang, Final Report Contract AF 19 (604)-8499, AFCRL-63-61, December 1962.
5. R. N. Ghoshtagore, *Solid State Electronics*, **9**, 178 (1966).
6. K. Brack, *J. Appl. Phys.*, **36**, 3560 (1965).
7. J. T. Clarke and B. R. Fox, *J. Chem. Phys.*, **46**, 827 (1967).
8. R. W. Walker, *ibid.*, **34**, 2196 (1961).
9. J. A. Conwicke, M.I.T. Private communications.
10. G. E. Moore and F. C. Unterwald, *J. Chem. Phys.*, In Press.
11. G. E. Moore and F. C. Unterwald, *ibid.*, **40**, 2626, 2639 (1964).
12. G. E. Moore, Private communication.

The Effect of Substrate Orientation on the Incorporation of Zinc and Selenium in Vapor-Grown Gallium Phosphide

R. C. Taylor*

International Business Machines Corporation, Research Division, Yorktown Heights, New York

ABSTRACT

Vapor-grown GaP doped with radioactive Zn^{65} and Se^{75} has been prepared by a halogen transport method. The dopant concentration in the crystals ranged from the mid 10^{15} to mid 10^{19} atoms/cm^3. By means of radiotracer and electrical measurements, it was found that the degree of incorporation of the dopant into the growing crystal is dependent on the substrate orientation. Zinc was incorporated into (111)A face growths more readily than into (111)B face growths by a factor of from 12- to 25-fold, depending on zinc concentration in the vapor. Selenium was incorporated into (111)B face growths more readily than into (111)A face growths by a factor of from 4- to 35-fold. Growths on (100) or (110) substrates accepted zinc or selenium dopants to about the same extent as the preferentially doped polar [(111)A or (111)B] face. It was found that selenium had a limit of solubility in an electrically active form of about 4×10^{18} cm^{-3}. The solubility limit for zinc was not reached at 10^{19} cm^{-3}. Studies were also made of undoped and selenium doped growths on higher index orientations. A model is presented to account for the observed orientation effect based on the properties of the (111) double layer.

In earlier publications (1, 2), we reported the effect of substrate orientation on the electrical, optical, and paramagnetic resonance properties of vapor-grown GaP, both undoped and doped with sulfur or selenium. The orientations studied were the polar (111)A (Group III atom) and (111)B (Group V atom) surfaces. It was found that donor impurities were apparently incorporated far more readily into growths on (111)B substrates. Nominally undoped GaP deposited onto (111)B substrates of either GaAs or GaP was n-type and had a resistivity of about 1 ohm-cm, a carrier concentration in the low 10^{16} cm^{-3} range due to a residual sulfur impurity, and a mobility of 170-190 cm^2/v-sec at room temperature. Undoped samples grown on (111)A substrates were high-resistivity (10^3-10^4 ohm-cm) p-type due to a deep acceptor impurity. Growth in sulfur or selenium dopant fluxes sufficient to increase the carrier concentration of (111)B face growths to the low 10^{17} cm^{-3} range increased the resistivity of the still p-type (111)A face growths by two orders of magnitude due to compensation. Similar orientation dependence has also been reported for vapor-grown GaAs (3, 4) and for GaP deposited on GaAs (5).

In the present investigation, in order to gain a more quantitative picture of the magnitude of the effect of substrate orientation on impurity incorporation, radiotracer techniques were employed in conjunction with electrical measurements to determine the true dopant concentrations. Radioactive Se^{75} and Zn^{65} were selected as the dopants so that both donor and acceptor incorporation could be studied. Studies were also extended to the (100) and (110) basic planes with radioactive Zn and Se doping and to higher index planes with no doping and with nonradioactive Se doping.

Experimental

The vapor-grown GaP crystals were prepared by a phosphorous trichloride transport method (1, 6). The apparatus and growth conditions used were the same

* Electrochemical Society Active Member.

as those of Ref. (1). The gallium source temperature was 900°C, the substrate temperature 800°C, and the total hydrogen flow rate was 100 cc/min, of which 50 cc/min passed through the PCl_3 bubbler at −30°C to give a PCl_3 flux of 1.2×10^{-3} moles/hr. In order to employ radioactive species, the H_2Se tank normally used in doping was replaced by hydrogen, and pellets of the radioactive elements were placed in the doping line at the appropriate temperature to attain the desired vapor pressure. When radioactive Zn and Se were in use, 20% of the hydrogen diluent gas was passed over the radioactive material. Depending on the dopant temperature, this resulted in a dopant flux of between 10^{-10} and 10^{-5} moles/hr.

Gallium arsenide substrates were cut from Czochralski pulled crystals. When nominal (111)A and (111)B growths were made, the GaAs substrates were actually oriented 2° off the basic planes. The substrates were mechanically and chemically polished with an H_2SO_4-H_2O_2 etch before introduction into the system. In most cases of (111) growth, A and B oriented substrates were mounted side by side on a vertical holder so that growth occurred on both in the same run.

Average growth rates were 14 μ/hr on (111)A faces, 8 μ/hr on (111)B faces, and 10 μ/hr on (100) and (110) faces. Film thicknesses were approximately 250μ.

After removal of substrates and edge growth, the same section of each GaP growth was used for both radiotracer and electrical measurements. Radiotracer measurements were done by gamma scintillation counting and the Van der Pauw method was used for the electrical measurements. In order to check for doping uniformity through the thickness of the samples, the growths were lapped and remeasured several times. No significant gradients were found.

Results

Zn^{65} and Se^{75} doping of growths on (111)A and (111)B planes.—The results of doping (111)A and (111)B face GaP growths with Zn^{65} and Se^{75} are shown in Tables I and II. The only variable in the growth conditions was the dopant vapor pressure which increases from the top of the tables to the bottom. Each pair of (111)A and (111)B samples was grown in the same run to insure identical conditions. With the exception of 589 and 590, all samples were grown on GaAs substrates. It is clear from both the radiotracer and electrical data that (111)A face growths incorporate Zn far more readily than do (111)B face growths, while the heaviest Se doping is found in samples grown on (111)B faces.

Zinc-doped crystals grown on (111)A faces show a uniform increase in carrier concentration and Zn^{65} concentration as the Zn vapor pressure increases, with a corresponding decrease in resistivity and mobility. Liquid nitrogen electrical data show a carrier freezeout of two orders of magnitude at the low zinc concentrations and no freezeout at the higher concentrations, indicating impurity band conduction at about 10^{18} cm^{-3} (7). The superiority of GaP substrates which was demonstrated in Ref. (1) for n-type samples is shown here for p-type samples by the fact that sample 589 had a liquid nitrogen mobility of 1873 cm^2/v-sec, far higher than any obtained when using GaAs substrates. This is probably due to superior crystal structure of samples grown on GaP substrates.

The properties of Zn-doped crystals grown on (111)B faces show that a very small amount of Zn is taken up on this face, insufficient in fact to compensate the residual background donor impurity in the first five samples. This impurity has been shown by photoluminescence to be sulfur, both by identification of the sulfur exciton line in undoped samples and the zinc-sulfur pair band in Zn-doped samples (1). The amount of sulfur impurity varies with purity of the PCl_3 and in this series of samples is $1\text{-}2 \times 10^{17}$ cm^{-3}, which is the concentration of Zn^{65} required to convert the crystals to p-type.

Selenium-doped crystals grown on (111)A faces show electrical behavior similar to that of the Zn-doped (111)B face growths. As in the Zn case, the lowest doping levels were not sufficient to compensate the carriers of the opposite type that were already present. These growths were high-resistivity p-type, as were undoped samples, until about 10^{16} Se^{75} atoms/cm^3 had been added. [We had previously found about 10^{16} cm^{-3} deep acceptors in (111)A face growths and tentatively identified them as Ga vacancies (2).]

In the more heavily doped (111)B face growths, the Se^{75} concentration and room-temperature carrier con-

Table I. Results of Zn^{65} doping

Sample No.	Substrate orient.	Zn^{65} conc (cm^{-3})	$\frac{Zn_{(111A)}}{Zn_{(111B)}}$	Cond. type	ρ (ohm-cm) RT	n(p) (cm^{-3}) RT	μ (cm^2/v-sec) RT
589	(111)A GaP	1.3×10^{17}	39.4	p	0.48	1.0×10^{17}	128
590	(111)B GaP	3.3×10^{15}		n	—	—	—
573	(111)A	3.9×10^{17}	24.3	p	0.23	3.0×10^{17}	90
574	(111)B	1.6×10^{16}		n	0.41	1.1×10^{17}	135
577	(111)A	4.8×10^{17}	19.3	p	0.22	3.9×10^{17}	75
578	(111)B	2.5×10^{16}		n	0.42	1.1×10^{17}	129
569	(111)A	1.5×10^{18}	18.5	p	0.097	1.1×10^{18}	57
570	(111)B	8.1×10^{16}		n	0.56	1.2×10^{17}	94
571	(111)A	3.0×10^{18}	17.6	p	0.054	2.2×10^{18}	52
572	(111)B	1.7×10^{17}		n	0.91	6.9×10^{16}	100
579	(111)A	6.3×10^{18}	13.7	p	0.036	5.4×10^{18}	32
580	(111)B	4.6×10^{17}		p	0.49	1.7×10^{17}	76
583	(111)A	1.4×10^{19}	11.7	p	0.022	1.2×10^{19}	25
584	(111)B	1.2×10^{18}		p	0.13	7.3×10^{17}	68

Table II. Results of Se^{75} doping

Sample No.	Substrate orient.	Se^{75} conc (cm^{-3})	$\frac{Se_{(111B)}}{Se_{(111A)}}$	Cond. type	ρ (ohm-cm) RT	n(p) (cm^{-3}) RT	μ (cm^2/v-sec) RT
547	(111)A	3.2×10^{15}	4.4	p	—	—	—
548	(111)B	1.4×10^{16}		n	—	—	—
555	(111)A	5.9×10^{15}	16.8	p	2×10^6	—	—
556	(111)B	9.9×10^{16}		n	0.54	9.8×10^{16}	117
565	(111)A	3.1×10^{16}	31.8	n	11.0	1.0×10^{16}	57
566	(111)B	9.9×10^{17}		n	0.075	8.4×10^{17}	99
557	(111)A	5.2×10^{16}	34.7	n	4.0	2.0×10^{16}	78
558	(111)B	1.8×10^{18}		n	0.057	1.2×10^{18}	90
561	(111)A	8.1×10^{16}	37.2	n	1.1	4.3×10^{16}	129
562	(111)B	3.0×10^{18}		n	0.061	2.0×10^{18}	51
563	(111)A	1.2×10^{17}	58.2	n	1.2	4.0×10^{16}	129
564	(111)B	7.0×10^{18}		n	0.051	1.7×10^{18}	71
550	(111)A	3.0×10^{18}	—	n	0.058	1.2×10^{18}	87
551	(111)B	$\sim 5 \times 10^{19}$		n	—	—	—

centration increase with Se vapor pressure to about 2×10^{18} cm^{-3}. Above this point, Se^{75} concentration continues to rise while the carrier concentration levels off. (A temperature run on one sample showed that $N_d - N_a$ became independent of temperature at 4×10^{18} at about 400°C. This sample had a room-temperature carrier concentration of 2.1×10^{18} and a Se^{75} concentration of 1.3×10^{19} cm^{-3}.) The solubility limit of Se in an electrically active form has been reported by Trumbore (8). Above 4×10^{18} cm^{-3}, Se probably enters the GaP lattice in the form of Se precipitates or neutral complexes such as $V_{Ga}Se_3$ as has been proposed for Se in GaAs (9, 10). It should be remembered that undoped (111)B face growths contain 10^{16}-10^{17} carriers cm^{-3} due to a sulfur impurity so the electrical carrier concentration figures are a sum of the ionized sulfur plus selenium.

The magnitude of the effect of substrate orientation [(111)A and (111)B] on the incorporation of Zn and Se in GaP growths as determined from the radiotracer data is shown in Fig. 1. The ratio of Zn^{65} in GaP grown on a (111)A face to that on a (111)B face is plotted against the Zn^{65} in the (111)A face growths, and the ratio of Se^{75} in (111)B face growths to that in (111)A face growths is plotted against the Se^{75} in the (111)B face growths. It can be seen that, with Zn doping, the orientation effect ratio [Zn on (111)A to Zn on (111)B] increases with decreasing Zn concentration from 12 at 1.4×10^{19} cm^{-3} to 24 at 3.9×10^{17} cm^{-3}. The fact that the highest ratio, 39, does not fall on the line through the other data might be due to the use of GaP substrates for that pair. The concentration dependence of the orientation effect for Se doping is greater than in the Zn case and is in the reverse direction. The ratio increases with increasing Se concentration from 4 at 1.4×10^{16} cm^{-3} to 37 at 3.0×10^{18} cm^{-3}. Points above this concentration are possibly unreliable due to formation of Se precipitates or gallium selenide.

In Fig. 2 and 3, we have plotted the effect of dopant flux on Zn incorporation in GaP grown on (111)A substrates and on Se incorporation in GaP grown on (111)B substrates. The Zn^{65} line in Fig. 2 and the Se^{75} line in Fig. 3 were obtained from samples for which the dopant pellets were weighed before and after the run to determine the number of moles transported and then the resulting Zn^{65} and Se^{75} concentrations were measured in the GaP growths. The carrier concentration lines show the room-temperature carrier concentrations corresponding to the radiotracer concentrations from Tables I and II. In the cases of both Zn^{65} and Se^{75} doping, there is an approximately linear dependence of dopant in the GaP growth on dopant concentration in the vapor. The carrier concentration line in Fig. 3 clearly shows the electrically active solubility limit of Se in the GaP. The corresponding line in Fig. 2 shows that no precipitation or separation of Zn in an inactive form is evident up to a concentration of 10^{19} cm^{-3}.

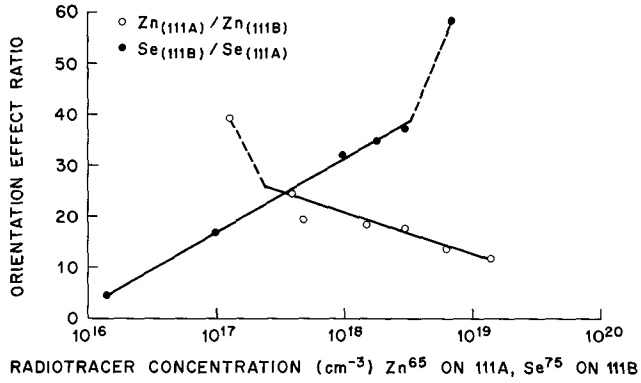

Fig. 1. Concentration dependence of the orientation effect for Zn and Se doping of (111)A and (111)B face GaP growths.

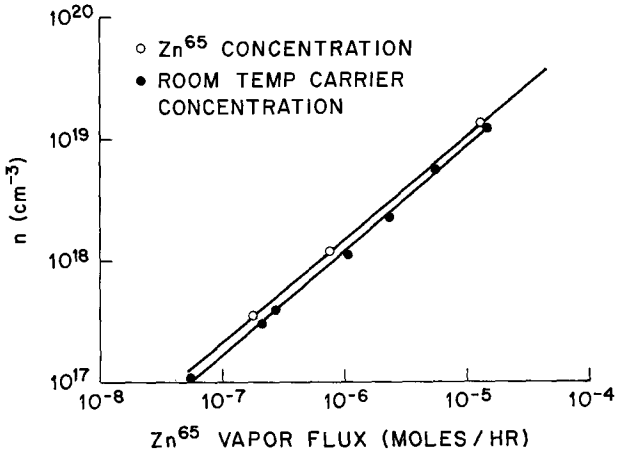

Fig. 2. The effect of zinc vapor flux on Zn^{65} concentration and room-temperature carrier concentration in GaP grown on (111)A substrates.

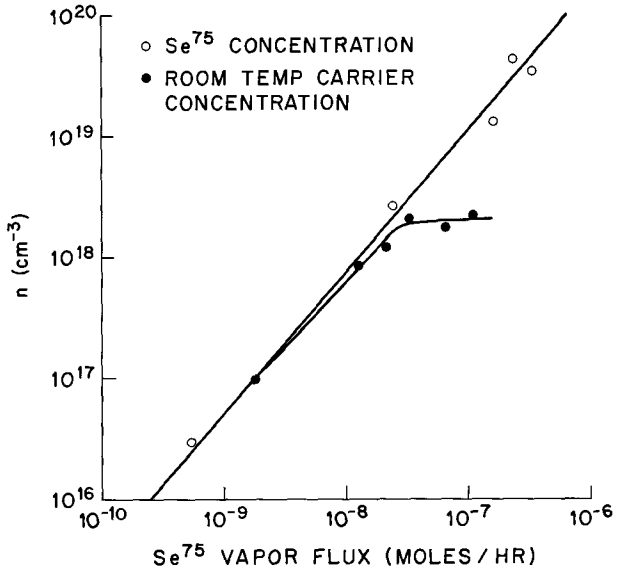

Fig. 3. The effect of selenium vapor flux on Se^{75} concentration and room temperature carrier concentration in GaP grown on (111)B substrates.

Although no runs were actually made in which both Zn and Se were present in the vapor at the same time, an idea of the results may be had by combining the data for Zn and Se doping and assuming no vapor phase interaction between the dopants. The data for Zn and Se doping of both (111)A and (111)B face growths is plotted against dopant flux in Fig. 4. The interesting thing to note is that, in the dopant flux region where the data overlap, the lines for Se doping of a (111)A face growth and Zn doping of a (111)A face growth coincide, and both have the same slope. Thus, while Se prefers (111)B face growths and Zn prefers (111)A face growths, the (111)A face has no preference as to which one it incorporates and is more inert toward both than the (111)B face is to Se. The large effect is that the (111)B face prefers Se to Zn by a factor of 1000. Therefore, when both Se and Zn are present in the vapor in equal concentrations, a (111)A face growth should be compensated and a (111)B face growth should be strongly n-type. These observations might be a fortuitous combination of the orientation effect and dopant distribution coefficients and apply only to the case of Zn and Se under the conditions of these experiments.

There was an interesting effect of Se doping on the growth rates of (111)A and (111)B face growths and on the surface morphology of (111)B face growths.

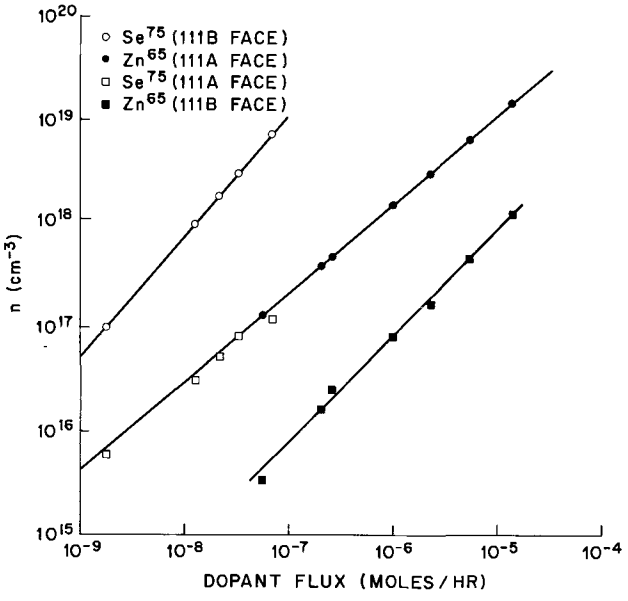

Fig. 4. The effect of dopant flux on Zn^{65} and Se^{75} concentration in GaP crystals grown on (111)A and (111)B substrates.

Zinc doping had no effect on either. When the Se concentration on (111)B face growths reaches the mid 10^{19} cm^{-3} range, the growth rate abruptly changes from the normal 8 μ/hr to about 2 μ/hr. When the concentration on (111)A face growths reaches the mid 10^{18} cm^{-3} range, the rate changes from 14 μ/hr to about 20 μ/hr. This occurs both when the two faces are growing together in the same run or when the two faces are introduced into the system separately. The change on the (111)B face could be due to the formation of selenium precipitates causing strain and impeding normal growth, but there is no apparent reason for the increase in the (111)A growth rate. Such a decrease in growth rate was reported by Hara and Akasaki (11) in sulfur-doped, vapor-grown GaP. However the decrease cannot be due to depletion of GaCl vapor by formation of Ga chalcogenides as they postulated, or the (111)A face growth rate would also decrease. The drop in rate must be associated with changes at the crystal surface. Changes in growth rate and morphology of epitaxial GaAs with doping level have also been reported (12).

The effect of Se concentration on (111)B growth surface morphology is shown in Fig. 5. The greatest change in the surface morphology occurs in the low 10^{18} cm^{-3} range where there is relatively little change in the orientation effect ratio [Se on (111)B to Se on (111)A]. The morphology change is probably associated with the appearance of Se precipitates, and does not occur on (111)A face growths. X-ray studies showed all of these growths to be single crystal.

Zn^{65} and Se^{75} doping of growths on (100) and (110) planes.—Zn^{65} and Se^{75} doped GaP growths were also made on the other two basic orientations, (100) and (110). The results of the radiotracer measurements on Zn-doped samples are given in Table III. The dopant flux for these samples, as determined from the weight loss of the Zn pellet, was 3.6×10^{-7} moles/hr. The values in the table for (111)A and (111)B orientations are those that would be expected from Fig. 1 and 2 for this dopant flux. The Se^{75} radiotracer and electrical results are given in Table IV. The (111)A and (111)B data are for two samples from Table II grown at the same Se pressure. It can be seen that for both Zn and Se doping, the GaP grown on (100) and (110) faces incorporates the dopant to about the same degree as does the GaP grown on the preferentially doped polar face. Zinc is taken up in (100) and (110) growths almost as well as in (111)A growths and the Se uptake in (100) and (110) growths is close

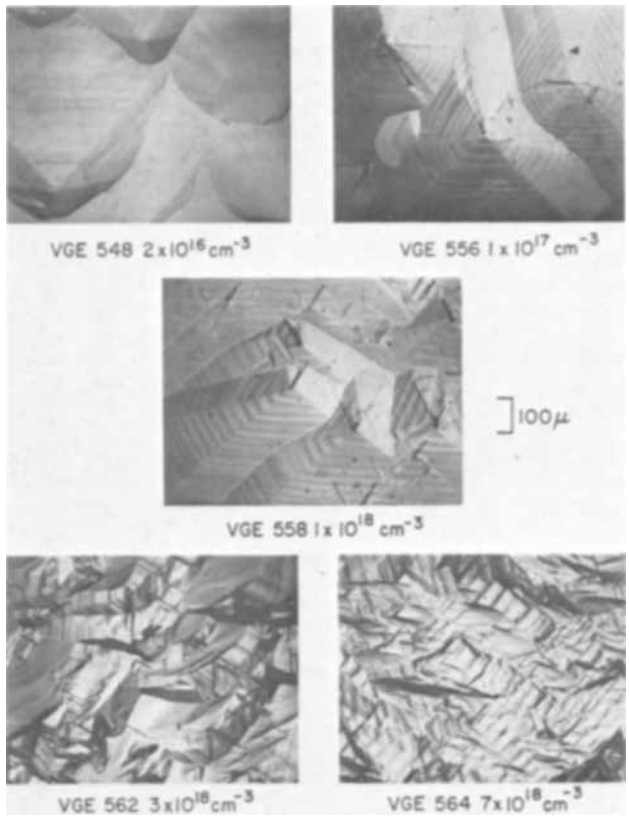

Fig. 5. The effect of selenium concentration on the surface morphology of GaP crystals grown on (111)B substrates.

to that in (111)B growths. The electrical data, while giving the correct relative order of dopant incorporation on the basic planes, do not show the true magnitude of the orientation effect due to varying degrees of compensation. A nominally undoped (110) growth is n-type with a resistivity of 50-100 ohm-cm, a carrier concentration in the low 10^{16} cm^{-3} range, and low mobility. Undoped (100) growths are n-type with a resistivity of 10^3 to 10^4 ohm-cm.

Growth on higher index planes.—In order to see if misorientation from the basic (111) plane had any effect on the anisotropy of impurity incorporation, several higher index planes were studied. The planes were misorientations from the (111) plane in the direction of both the (100) plane [(h11) planes] and the (110) plane [(hh1) planes]. For example, the misorientation in the (100) direction was 5°, 10°, 19.3° [(211) plane], and 29.4° [(311) plane]. Also included was the (310) plane which is a (h10) plane. The complete list of orientations studied is shown in the stereographic triangle of Fig. 6. With the exception of the (100) and (110) planes, both the "A" and "B" faces of each orientation were investigated by slicing the wafers in half, reversing one half, and growing on both halves in the same run. The A and B faces of all the (h11) and (hh1) orientations were distinguishable with a standard $NaOH-H_2O_2$ etch.

In all cases, with the exception of the (100), (110), and (310) planes, there was a pronounced orientation effect on electrical properties of the deposited GaP. All undoped samples grown on "B" faces were n-type with

Table III. Zn^{65} doping of basic planes

Sample No.	Substrate orient.	Zn^{65} (cm^{-3})	$\frac{Zn^{65}_{(111A)}}{Zn^{65}_{(basic)}}$
609	(110)	2.8×10^{17}	2.2
610	(100)	2.6×10^{17}	2.4
—	(111)A	6.2×10^{17}	1.0
—	(111)B	2.8×10^{16}	22.2

Table IV. Se^{75} doping of basic planes

Sample No.	Substrate orient.	Se^{75} conc (cm^{-3})	$\frac{Se_{(111B)}}{Se_{(basic)}}$	Cond. type	ρ (ohm-cm) RT	n (cm^{-3}) RT	μ (cm^2/v-sec) RT
557	(111)A	5.2×10^{18}	34.7	n	4.0	2.0×10^{16}	78
558	(111)B	1.8×10^{18}	1.0	n	0.057	1.2×10^{18}	90
559	(100)	5.3×10^{17}	3.4	n	0.52	9.9×10^{16}	121
560	(110)	1.6×10^{18}	1.1	n	0.33	4.0×10^{17}	47

resistivities between 0.1 and 10 ohm-cm and carrier concentrations of 2×10^{16} to 4×10^{17} cm^{-3} (depending on the purity of the PCl_3 used). "A" face growths were either p-type or semi-insulating with resistivities of 10^5 ohm-cm and higher. Carrier concentrations, where measurable, were 10^{12} cm^{-3} or less. Similar findings were made by Groves (5) on growths on (211) planes. Properties of undoped growths on (100) and (110) planes were mentioned in the previous section. Growths on both sides of the (310) wafer were n-type with resistivity of about 50 ohm-cm and a carrier concentration in the low 10^{16} cm^{-3} range. Growths were also made on the above orientations using hydrogen selenide doping. No radioactive species were present for a quantitative determination, but electrical measurements showed the persistence of the orientation effect. It is clear therefore that the orientation effect exists on all (h11) and (hh1) planes, and does not exist on (h10) planes. In the absence of radiotracer data, it is difficult to know if there is any diminution of the effect as misorientation from the (111) plane increases.

Surface morphology of growths was significantly affected by misorientation from the (111) plane, and in each (h11) and (hh1) higher index orientation there was a substantial difference between the "A" and "B" morphologies. There was no difference in morphology between growths on the two sides of the (310) plane. Misorientation from the (111) plane had little effect on the growth rates of undoped growths on the "A" and "B" faces.

Discussion

Some of the more striking features about Zn and Se doping of vapor-grown GaP that are brought out by the radiotracer and electrical data are: the linear dependence of dopant concentration in the crystal on dopant flux in the vapor; the opposite direction of the concentration dependence of the orientation effect in the case of Zn and Se; the persistence of the orientation effect on all (h11) and (hh1) planes and the absence of the effect on (h10) planes; the similarity in behavior between the (100) and (110) planes and the preferentially doped polar plane for both Zn and Se doping.

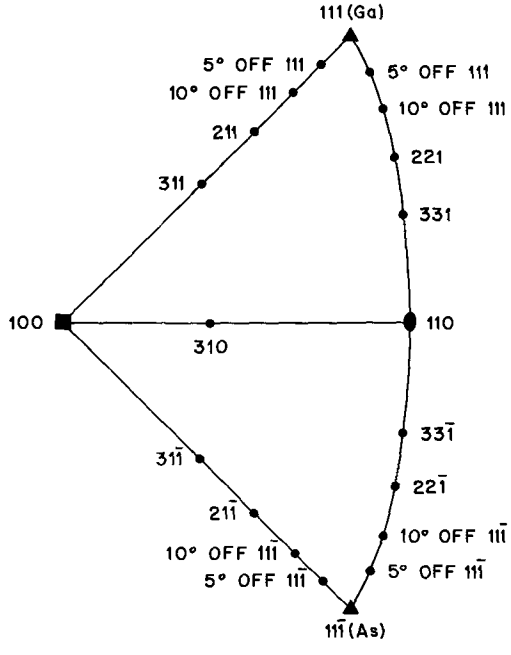

Fig. 6. Stereographic triangle showing the higher index and basic orientations studied in section on *Growth on higher index planes.*

The approximately linear dependence of dopant concentration in the crystal on dopant flux is surprising in that the 800°C growth temperature is well within the extrinsic region for Zn- and Se-doped GaP. According to the model presented by Kroger (13) for equilibrium doping of an extrinsic semiconductor, there should be a square root dependence of ionized acceptor or donor concentration on the vapor concentration of the dopant, and at 800°C all of the zinc and selenium are ionized. A linear dependence should occur only in the intrinsic semiconducting region. Trumbore (8) did find a square root dependence for Zn-doped solution-grown GaP, but a linear dependence for Se-doped material at carrier concentrations where extrinsic behavior was expected. A linear dependence was observed by Luther (14) for Zn-doped, vapor-grown GaP and a linear dependence has been found for Cd-doped, vapor-grown GaP (14, 15). Zinc and Se doping of GaP during vapor growth therefore appears to be a non-equilibrium process.

The direction of the concentration dependence of the Se-doping orientation effect suggests that the effect will disappear when the (111)B growth Se concentration falls to the low 10^{15} cm^{-3} range. It is possible that at such low concentrations the doping becomes an equilibrium process, the deposition being limited only by the input rate of the selenium and independent of the substrate surface. As the selenium pressure increases, the incorporation into the crystal becomes a kinetically controlled process and more and more orientation dependent. Other investigators reporting orientation effects have dealt with concentrations in the range of 10^{17} carriers cm^{-3} and above for donors on (111)B faces (3, 5). There is no obvious explanation for the opposite direction of the concentration dependence of the orientation effect for Zn doping. It is possible that surface nucleation sites become saturated at the higher concentrations so that incorporation on (111)A surfaces is lessened. The effect might also be related to the fact that the diffusion coefficient of Zn is far greater than that of Se in GaP, and that the diffusion coefficient increases with Zn concentration (16). This might allow for redistribution of the Zn in the heavily doped (111)A growths in such a way as to lessen the orientation effect. The approach to equilibrium which might be occurring in Se doping would not be observable with the Zn since higher dopant concentrations are present.

The persistence of the polarity orientation effect through all of the (h11) and (hh1) higher index planes may possibly be explained on the basis of Sangster's model (17). According to this model, all high-index nonbasic orientations are stepped structures consisting of "treads" and "risers" of the basic planes. The (h11) planes are stepped structures consisting of (100) treads and (111) risers and the (hh1) planes are composed of (111) treads and (110) risers. All of these planes can be resolved into stacks of (111) double layers. Thus, aside from the fact that the planes are stepped, they have essentially (111) characteristics and would be

expected to show the polar nature of the basic (111) plane. When h becomes greater than 5 on (h11) planes, the axes become indistinguishable from (100) so that the polarity effect should cease. This has been confirmed in the case of GaAs growth rates by Shaw (18). The (h10) planes *e.g.*, (310) and (210), which are combinations of (100) and (110) planes, are composed of (100) treads and (110) risers and should therefore show no polarity effects.

The behavior of GaP growths on (100) and (110) faces suggests that there is a similar mechanism involved in Zn incorporation on (111)A, (100), and (110) planes and in Se incorporation on (111)B, (100), and (110) planes. The similarity can again be found in Sangster's model of the nucleation and growth process on the basic planes. A Zn atom being incorporated into GaP on a Ga site on a (111)A, (100), or (110) plane will attach itself to two surface P atoms with no increase in dangling surface bonds and no nucleation barrier. In contrast, on a (111)B surface the Zn atom will attach itself to only one surface P atom. It will be loosely held and in the presence of low Zn pressure in the vapor stream might tend to re-evaporate. The analogous situation exists with Se doping. Selenium going onto a P site in GaP will bond to two surface Ga atoms on (111)B, (100), and (110) surfaces, but to only one on a (111)A surface.

Acknowledgments

The author wishes to thank W. J. Haag, R. Robinson, and S. Baliozian for their technical assistance, Dr. S. E. Blum for supplying substrate material, Dr. J. F. Woods for the electrical data, and J. E. Lewis for the radiotracer data.

Manuscript submitted Oct. 17, 1968; revised manuscript received Nov. 25, 1968.

Any discussion of this paper will appear in a Discussion Section to be published in the December 1969 JOURNAL.

REFERENCES

1. R. C. Taylor, J. F. Woods, and M. R. Lorenz, *J. Appl. Phys.*, **39**, 5404 (1968).
2. R. C. Taylor and R. S. Title, *Appl. Phys. Letters*, **11**, 355 (1967).
3. F. V. Williams, *This Journal*, **111**, 886 (1964).
4. R. R. Moest, *ibid.*, **113**, 141 (1966).
5. W. O. Groves, "Crystal Growth," Proceedings of the International Conference on Crystal Growth, H. S. Peiser, Editor, p. 669, Pergamon Press, Oxford, England (1967).
6. W. G. Oldham, *J. Appl. Phys.*, **36**, 2887 (1965).
7. M. M. Cohen and F. D. Bedard, *ibid.*, **39**, 75 (1968).
8. F. A. Trumbore, H. G. White, M. Kowalchik, R. A. Logan, and C. L. Luke, *This Journal*, **112**, 782 (1965).
9. L. J. Vieland and I. Kudman, *J. Phys. Chem. Solids*, **24**, 437 (1963).
10. G. Schottky, *ibid.*, **27**, 1721 (1966).
11. T. Hara and I. Akasaki, *J. Appl. Phys.*, **39**, 285 (1968).
12. Kh. A. Magomedov, Yu. N. Yarmukhamedov, and N. N. Sheftal, *Soviet Phys. Cryst.*, **11**, 578 (1966).
13. F. A. Kroger, "Chemistry of Imperfect Crystals," North Holland Publishing Co., Amsterdam (1964).
14. L. C. Luther and D. D. Roccasecca, *This Journal*, **115**, 850 (1968).
15. Zh. I Alferov, V. I. Korolkov, M. K. Trukan, and S. P. Chaschin, *Soviet Phys. Solid State*, **7**, 1915 (1966).
16. L. L. Chang and G. L. Pearson, *J. Appl. Phys.*, **35**, 374 (1964).
17. R. C. Sangster, "Compound Semiconductors," Vol. 1, p. 241, Reinhold Publishing Corp., New York (1962).
18. D. W. Shaw, *This Journal*, **115**, 405 (1968).

Technical Notes

Sparking Voltages Observed on Anodization of Some Valve Metals

R. S. Alwitt* and A. K. Vijh*

Research & Development Laboratories, Sprague Electric Company, North Adams, Massachusetts

Wood and Pearson (1) recently presented some experimental results for breakdown voltages of anodic oxide films on valve metals. Breakdown voltage was defined as the voltage at which visible sparking was observed to start or, in the absence of sparking, the steady voltage that was achieved at constant current. We have repeated some of their measurements and extended the work to another electrolyte system. Our results are in general agreement with those of Wood and Pearson except for the case of aluminum. This difference is critical since it weakens a correlation presented by those authors and suggests some other correlations which are presented here.

Wood and Pearson attempted to associate the tendency for breakdown with the type of bonding in the oxide. It is essential to explore such connections between electrical and other properties in order to arrive at a unified theory of the properties of anodic oxides. An important point in their analysis is that a higher melting point corresponds to a greater degree of ionic bonding. However, for at least some of these oxides the dependence of melting point on cohesive forces (2) indicates the opposite, a higher melting point corresponds to a greater degree of covalent bonding. This point will be pursued in the Discussion Section.

Experimental

Foil and wire specimens of aluminum, niobium, tantalum, and zirconium, of the highest purity available, were chemically polished and then anodized at room temperature in either 3% aqueous ammonium tartrate or 39% w/w ammonium pentaborate in ethylene glycol. The anodization current density was 0.5 ma/cm^2 in all cases except for zirconium in ammonium tartrate where 5 ma/cm^2 was used because of the low current efficiency for oxide formation.

* Electrochemical Society Active Member.

Table I. Comparison of sparking voltages in two electrolytes

Metal	Purity, %	Type	Sparking voltage: Glycol borate	Sparking voltage: 3% NH_4 tartrate: Our results	Sparking voltage: 3% NH_4 tartrate: Wood & Pearson	Dielectric constant	$-\Delta H_f$/eq, kcal/eq
Al	99.97	Foil	442		245	8-10	65.3
	99.99	Wire	—	350 (210)	—		
Zr	99.88 + 0.1 Hf	Foil	325 (200)	315 (100)	300	22-25	64.6
Ta	99.9+ (electronic grade)	1 mil Foil	250	275 (205)	195-200	28	50.0
		0.5 mil Foil	—	205			
Nb	(electronic grade)	Foil	215	190	165-190	41	46.3
		Wire	—	170	—		

Notes: 1. Sparking voltage defined as voltage at which sparking began over entire sample surface, accompanied by rapid voltage fluctuations.
2. Voltages in parentheses indicate approximate points where large decrease in dV/dt occurred usually accompanied by gas evolution.

Results

Our observations of anodization and subsequent breakdown were similar to those reported by Wood and Pearson. The notable exception was that we saw sparking with all metals, including aluminum. For aluminum in ammonium tartrate this was achieved by taking great care to eliminate sources of contamination in both the electrolyte and the atmosphere above the solution. Otherwise, no sparking was observed and voltages close to those reported by Wood and Pearson were obtained, with corrosion on the specimen stem at the solution/air interface.

The breakdown voltages we observed are listed in Table I along with values taken from Table III of Wood and Pearson (1). The ranking of metals in both electrolytes was the same, but differed from the results of Wood and Pearson in that the breakdown voltage for aluminum was higher than that for zirconium. For the cases of tantalum and niobium, use of metal obtained from different sources did not affect the ranking.

Discussion

The fact that we observed the same ranking of breakdown voltage in two electrolytes of very different composition makes more tenable the suggestion advanced by Wood and Pearson (1) that sparking breakdown reflects some basic property of the oxides. Certainly this same ranking would not be realized in all electrolytes, probably because of chemical interactions between solute species and oxide. Aluminum is particularly susceptible to such complications. A glycol borate electrolyte was chosen for this study since this system was known to produce an amorphous oxide on aluminum at 100% current efficiency with little incorporation of species from the electrolyte (3). It is believed that under the conditions of these experiments the tartrate electrolyte behaves very much like the glycol borate.

Because of the higher sparking voltage obtained with aluminum, our results offer no correlation with oxide melting point. We do find an inverse correlation between sparking voltage and oxide dielectric constant (1) (Table I), and direct correlation with both a-c resistivity of the oxide (4) and heat of formation per equivalent (5) (Table I).

Since the sparking voltage is a poorly defined property of a complex phenomenon it is difficult to assign a physical significance to these correlations. It has been shown for many compounds, including valve metal oxides, that $-\Delta H_f$/eq. is approximately equal to half the value of the forbidden band gap (5). This suggests a correlation between sparking voltage and band gap which would reflect the often cited (but as yet unproven) electronic nature of the breakdown.

Although a correlation between sparking voltage and melting point is no longer found to exist, the attempt of Wood and Pearson (1) to connect a higher melting point with increased ionic bonding merits further discussion. It has been demonstrated recently (2) that the melting points of these oxides increase systematically with increasing heats of atomization per equivalent (*i.e.*, approximate values of average metal-oxygen bond energies) and not with lattice energies per equivalent. This is illustrated in Fig. 1. Bond energies emphasize the covalent aspects of cohesion whereas lattice energies represent the ionic aspects (2). This indicates that the melting point is largely determined by the covalent part of the bonding. It has been concluded elsewhere (2) that various properties diagnostic of electrical and thermal stability of these oxides are largely influenced by bond energy and not by lattice energy. The dielectric breakdown is probably related to the thermal and electrical stability of these materials.

It is important to emphasize that the ionic component of solid-state cohesion is denoted accurately only by lattice energies. Secondary quantities like melting points and (calculated) per cent ionic character are only crude measures of ionic cohesion in solids and are valid only for extremely ionic compounds, such as fluorides of the alkali and alkaline earth metals.

If per cent ionic character of solids is to be calculated, the criteria of Wells are to be preferred to those of Pauling, since it has been recently pointed out that Pauling's criteria for determining ionicity yield gross overestimates of ionic character when applied to solids (6). Wells' procedure predicts predominantly covalent character for these oxides as indicated by the calculations of Wood and Pearson.

Some recent experiments, modelled after those of Waring and Benjamini on silicon (7), deserve brief mention here since they may stimulate further consideration of the sparking process on valve metals.

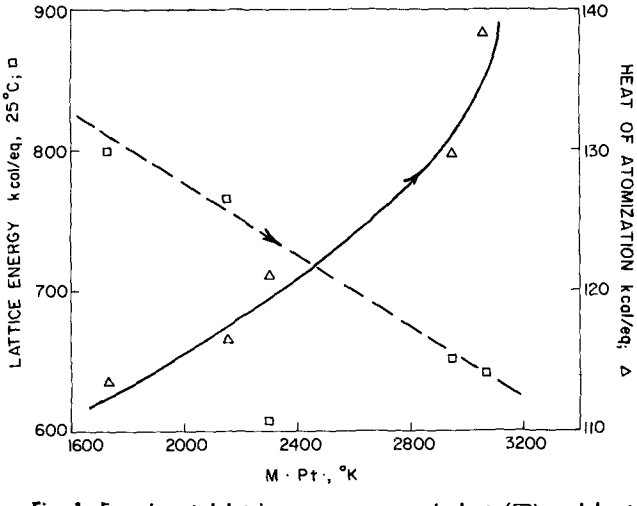

Fig. 1. Experimental lattice energy per equivalent (□) and heat of atomization per equivalent (△) vs. melting point for ZrO_2, HfO_2, Al_2O_3, Ta_2O_5, and Nb_2O_5; for details, see ref. (2).

Waring and Benjamini observed sparking during the anodization of silicon in a solution of KNO_3 in ethylene glycol. To help determine the region in which the sparks were generated they bubbled neon against the silicon wafer. When these bubbles passed near a spark they gave a brilliant red-orange flash characteristic of a neon discharge. From this they concluded that the sparks were associated with a strong field that extended into the solution.

In our experiments on Al, Ta, and Zr anodes in the glycol borate electrolyte the same characteristic neon flashes were observed. On each of these metals, as well as on Si (7), copious gas evolution accompanied sparking. This suggests that sparking may be the electrical discharge through gas generated at the anode surface. When neon becomes mixed with this gas it imparts its characteristic color to the discharge.

However, when the experiment was conducted in the aqueous tartrate electrolyte no red flashes were seen on Nb, Ta, or Zr anodes even though considerable sparking was evident. It was thought significant that in this aqueous solution oxygen is probably the gas generated at the anode, whereas it has been found in our laboratory that the gas generated at Al anodes in the glycol borate electrolyte is a mixture of CO, H_2, and CH_4 (8). Mixtures of neon with each of these three gases were bubbled against Ta anodes in the aqueous tartrate electrolyte, but in no case could a neon discharge be produced.

Thus, when glycol is the electrolyte solvent an effect due to sparking can be detected on the solution side of the oxide/solution interface. In an aqueous electrolyte the same test provides no information. We cannot yet offer an explanation for this.

Acknowledgments

One of the authors (A. K. V.) would like to thank Dr. M. Tosi of Argonne National Laboratory for a personal communication which clarified some of the matters discussed in this paper.

Manuscript received Oct. 28, 1968.

Any discussion of this paper will appear in a Discussion Section to be published in the December 1969 JOURNAL.

REFERENCES

1. G. C. Wood and C. Pearson, *Corr. Sci.*, **7**, 119 (1967).
2. A. K. Vijh, *This Journal*, **116**, 353 (1969).
3. W. J. Bernard and J. W. Cook, *ibid.*, **106**, 643 (1959).
4. G. C. Wood and C. Pearson, *Nature*, **208**, 547 (1965).
5. A. K. Vijh, *J. Phys. Chem. Solids*, To be published.
6. M. Tosi, Personal communication to A. K. Vijh; see also, M. Tosi, "Cohesion of Ionic Solids in Born Model," in "Solid State Physics," Vol. 16, F. Seitz and D. Turnbull, Editors, Academic Press, New York (1964).
7. W. Waring and E. A. Benjamini, *This Journal*, **111**, 1256 (1964).
8. R. W. Santway, Private communication.

Point Defect Concentrations as an Aid in Calculating Thermodynamic Activities

C. G. Carson, III, W. R. Bitler, and G. Simkovich

Metallurgy Section, Department of Materials Science, The Pennsylvania State University, University Park, Pennsylvania

Since the definition of thermodynamic activity and activity coefficient by Lewis (1), the determination of these quantities has been the concern of many investigators. A large number of experimental methods for determining these quantities have evolved through the years (2). Techniques for subsequent evaluation of activities within multicomponent systems by integration of the Gibbs-Duhem equation also have been advanced considerably during this time (3-6).

During an investigation on the effect of nonhydrostatic stress on the activity of interstitials in solid solution, it was necessary to obtain thermodynamic data on the lithium-tin system. This note deals with a method for deriving such data, which, while based on the familiar concepts of the defect solid state (7), to the writers' knowledge has not been utilized as a means of determining thermodynamic activities. The main purpose of this note is to draw attention to the method outlined as a possible means of obtaining thermodynamic activities in a few selected systems which might prove difficult to measure by other more standard methods (2).

In the following the most important assumption that is made is that the activity coefficients of the charged point defect species remain constant over the range of interest. Such an assumption, often made in defect chemistry studies (8), implies that the defect concentrations fall within the range where Henry's law holds, *i.e.*, the dilute solution range.

Consider first the dissolution of a donor atom, *e.g.*, lithium, into pure elemental semiconductor silicon

$$D_{(g)} = D^+ + n \qquad [1]$$

where D^+ indicates a donor positively charged with respect to the undisturbed lattice and n denotes a quasi-free electron. If the concentrations of these defects are less than the degeneracy limit and the donor is completely ionized, one may apply the mass action principle to Eq. [1] to obtain

$$K_1 = \frac{N_{D^+}{}^{0} N_n{}^{0}}{P_{D(g)}{}^{0}} \qquad [2]$$

where N indicates the concentration of the species, and the superscript zero indicates the selected standard state for the species considered.

We assume that the silicon is doped only with the donor, D, and that the intrinsic concentrations of defects are small in comparison to the donor concentrations. Under these assumptions, electrical neutrality requires

$$N_{D^+}{}^{0} = N_n{}^{0} \qquad [3]$$

so that Eq. [2] may be written

$$K_1 = \frac{(N_{D^+}{}^{0})^2}{P_{D(g)}{}^{0}} = \frac{(N_n{}^{0})^2}{P_{D(g)}{}^{0}} \qquad [4]$$

If we now consider the dissolution into silicon of a donor from a binary or multicomponent alloy, whose components other than the donor are insoluble in silicon, and follow the procedure leading to Eq. [4], we obtain

$$K_1 = \frac{N_{D^+} N_n}{P_{\underline{D}(g)}} = \frac{(N_{D^+})^2}{P_{\underline{D}(g)}} = \frac{(N_n)^2}{P_{\underline{D}(g)}} \qquad [5]$$

where the underscored D indicates the donor in an external solution. Utilizing the definition of the activ-

ity of the i-th species, a_i, as

$$a_i = \frac{P_i}{P_i^\circ} \qquad [6]$$

and equating Eq. [4] and [5] yields, on rearranging

$$a_D = \frac{P_{D(g)}}{P_{D(g)}^\circ} = \left(\frac{N_{D^+}}{N_{D^+}^\circ}\right)^2 = \left(\frac{N_n}{N_n^\circ}\right)^2 \qquad [7]$$

Thus, if the assumptions made in arriving at Eq. [7] are correct, one may obtain the activities of the donor from measurement of the concentration of dissolved donor or the concentration of quasi-free electrons.

To obtain electron concentrations, one may, as one possibility, utilize electrical conductivity (κ) measurements. Since donor doped silicon crystals conduct mainly by the movement of electrons one has

$$\kappa = N_n \mu_n e \qquad [8]$$

where μ_n is the mobility of the electrons and e is the electronic charge. Substitution of Eq. [8] into Eq. [7] gives

$$a_D = \left(\frac{\kappa/\mu_n}{\kappa^\circ/\mu_n^\circ}\right)^2 \qquad [9]$$

Thus, measurement of the electrical conductivity and knowledge of the mobilities, which, it is noted, do change extensively over small concentration ranges (9), permits one to calculate the activity of the donor.

Should the concentration of intrinsic defects and the presence of other doping agents be significant in comparison to that of the donor, then these must also be taken into account.

Let us assume that such is the case and that the doping agent, other than the donor, is an acceptor, A.

The intrinsic equilibrium constant, K_{int}, relating concentrations of defects in silicon may be expressed as (8)

$$K_{int} = N_n N_p \qquad [10]$$

where p indicates a positive hole.

Charge neutrality, in the case where both acceptors and intrinsic defect concentrations are comparable to the donor, is given as

$$N_n + N_{A^-} = N_p + N_{D^+} \qquad [11]$$

where A^- indicates the acceptor, A, substituting for silicon and bearing an effective negative charge in comparison to the undisturbed lattice.

Use of Eq. [10] and [11] permits one to obtain the concentration of electrons as

$$N_n = \frac{N_{D^+} - N_{A^-} + [(N_{A^-} - N_{D^+})^2 + 4K_{int}]^{1/2}}{2} \qquad [12]$$

Once again, utilizing Eq. [2], [5], and [6], one may obtain

$$a_D = \frac{P_{D(g)}}{P_{D(g)}^\circ} = \frac{N_{D^+} N_n}{N_{D^+}^\circ N_n^\circ} \qquad [13]$$

Knowledge of K_{int} and the various defect concentrations permits one to calculate the activities of the donor through use of Eq. [12] and [13].

For example, consider the case of silicon in contact with a Li-Sn alloy melt. The equilibrium concentration of lithium ions in silicon in contact with pure lithium metal has been determined by Reiss *et al.* (10). The solubility of lithium in boron doped silicon in equilibrium with a lithium-tin alloy has been measured by Reiss and Fuller (11). From these data the activities of Li in the external phase, Li-Sn, is calculated utilizing Eq. [13] based on pure lithium as the selected standard state. Table I lists their pertinent data and the calculated activities for $T = 339°C$ with $K_{int} = (5.96 \times 10^{15})^2$ and for $T = 404°C$ with $K_{int} = (2.06 \times 10^{16})^2$.

Activity coefficients for the lithium in the Li-Sn system have also been calculated and are listed in Table I. Extreme negative deviation from Raoultian behavior is noted.

The lithium activities calculated show remarkable constancy considering the wide range of concentrations studied and indeed indicate that the assumptions made in arriving at Eq. [12] and [13] are valid.

It should be noted that at zero acceptor concentrations Eq. [12] reduces to

$$N_n = \frac{N_{D^+} + [N_{D^+}^2 + 4K_{int}]^{1/2}}{2} \qquad [14]$$

so that intrinsic concentrations may be neglected only when

$$N_{D^+}^2 > 4K_{int} \qquad [15]$$

Since information such as mobilities and concentrations of intrinsic defects is well known for the elemental semiconductors silicon and germanium the use of these substances in the method outlined requires the least amount of experimental effort. However, the application of this method to an ionic semiconductor or an ionic compound is also feasible.

Finally, it should be noted that although we have considered electrical conductivities as a means of measuring defect concentrations, any method giving these concentrations may be utilized.

In summary, we have outlined a method for obtaining activities of a component common to two condensed phases. The method utilizes the measurement of point defect concentrations in one of these phases and is based upon dilute solution theory. The method is restrictive but may, on occasion, prove useful in systems where concentrations and mobilities of point defects are well known.

Acknowledgment

Support of this research by the Army Research Office—Durham under Project No.: 200 145 011 332D,

Table I. Calculated lithium activities and activity coefficients in the Li-Sn system

T°C	Alloy comp, w/o Li	$N^\circ_{Li^+}$	N_{Li^+}	N_{B^-}	N_n (Eq.[12])	a_{Li^+} (Eq. [13])	$\gamma_{Li \text{ in } Sn}$
339	0.18	6.0×10^{17} cm^{-3}	2.82×10^{15} cm^{-3}	0.82×10^{15} cm^{-3}	7.05×10^{15} cm^{-3}	0.55×10^{-4}	0.19×10^{-2}
			4.0	6.0	5.05	0.56	0.19
			9.6	22.4	2.35	0.63	0.21
			15.3	39.3	1.40	0.60	0.20
			74.0	195.0	0.30	0.62	0.21
			234.0	693.0	0.10	0.65	0.22
	0.61	6.0×10^{17}	7.10×10^{15}	0.795×10^{15}	9.89×10^{15}	1.95×10^{-4}	0.21×10^{-2}
			8.86	6.10	7.49	1.84	0.19
			17.7	22.5	4.00	1.97	0.21
			26.0	36.5	2.70	1.95	0.21
			135.0	198.0	0.55	2.06	0.22
			432.0	700.0	0.15	1.80	0.19
404	0.18	1.10×10^{18}	7.11×10^{15}	0.820×10^{15}	23.99×10^{15}	1.41×10^{-4}	0.47×10^{-2}
			8.10	6.0	21.67	1.45	0.49
			12.3	22.4	16.16	1.64	0.55
			16.0	39.3	12.01	1.59	0.53
			63.0	195.0	3.15	1.64	0.55
			177.0	693.0	0.80	1.17	0.39

Contract No.: DA-31-124-ARO-D-432 is gratefully acknowledged.

Manuscript received Sept. 27, 1968.

Any discussion of this paper will appear in a Discussion Section to be published in the December 1969 JOURNAL.

REFERENCES

1. G. N. Lewis, *Proc. Am. Acad.*, **43**, 259 (1907); *Z. physik. Chem.*, **61**, 129 (1907).
2. C. Wagner, "Thermodynamics of Alloys," pp. 88-95, Addison-Wesley Publishing Co., Reading, Mass. (1962).
3. L. S. Darken, *J. Am. Chem. Soc.*, **72**, 2909 (1950).
4. C. Wagner, *op cit.*, pp. 19-22.
5. R. Schuhmann, Jr., *Acta Met.*, **3**, 219 (1955).
6. N. A. Gokcen, *J. Phys. Chem.*, **64**, 401 (1960).
7. C. Wagner, *ibid.*, **57**, 738 (1953).
8. F. A. Kröger, "The Chemistry of Imperfect Crystals," John Wiley & Sons, New York (1964).
9. W. W. Tyler and H. H. Woodbury, *Phys. Rev.*, **102**, 647 (1956).
10. H. Reiss, C. S. Fuller, and A. J. Pietruszkiewicz, *J. Chem. Phys.*, **25**, 650 (1956).
11. H. Reiss and C. S. Fuller, *J. Metals*, **8**, 276 (1956).

Studies on Chlorate Cell Process

III. Depolarization of Cathodic Hydrogen Evolution in the Bipolar Chlorate Cell Process

M. M. Jaksić,* B. Z. Nikolić, D. M. Karanović, and C. R. Milovanović

Electrochemistry Department, Institute of Chemistry, Technology, and Metallurgy, Beograd, Yugoslavia

ABSTRACT

The cathode process of hydrogen evolution in chlorate cells, including possible depolarization, has not been studied to date. High hydrogen polarization at graphite electrodes delayed the industrial application of bipolar cells for more than 80 years. A new method of depolarization has been developed which consists of depositing on the cathode side of a graphite electrode metallic chromium and/or an addition of small amounts of molybdate. The finely divided cathode molybdenum deposit decreases the cathode polarization for the hydrogen evolution reaction (h.e.r.). The Tafel lines obtained on metallized graphite exhibit nearly the same slopes as the ones for the parent metals, but are shifted to more positive values. This represents a further extension of the methods for depolarized hydrogen cathode evolution with metallized graphite (8, 9).

Bipolar chlorate cells have found recent acceptance in industry because of their high permissible current densities, low potential drops in the electrodes, simple design, and high capacity (1, 2). The bipolar construction of the cell allows copper bus bars and their connections to graphite electrodes to be almost completely eliminated (except for the first and the last electrode connection). Thus, contact resistances are practically avoided. However, the higher the current density, the higher is the electrode polarization, especially at graphite electrodes. The aim of the present paper is to show that depolarization of h.e.r. on graphite can be achieved with a corresponding cell voltage reduction, to match that of iron cathodes, at least.

Some Aspects of the Depolarized Hydrogen Cathode Evolution together with Suppressed Hypochlorite Reduction

There are two possible cathode reactions that could take place inside chlorate cells:

(*a*) Hydrogen evolution (main reaction)
$2H_2O + 2e \rightarrow H_2 + 2OH^-$
(*b*) Reduction of hypochlorite (side reaction)
$ClO^- + H_2O + 2e \rightarrow Cl^- + 2OH^-$

The cathode current losses due to hypochlorite reduction are governed by diffusion of its ions toward the electrode surface and could be suppressed by concentration polarization at a high enough current density (3).

Müller (4) introduced dichromate addition to the electrolyte in the industrial chlorate cell process to suppress cathode hypochlorite reduction and to achieve a suitable *p*H buffering effect as well as iron corrosion inhibition. The chromate action was theoretically explained by the formation of a thin cathode surface layer, probably consisting of chromium oxides, which decreases the effective surface area and hence provides hypochlorite ion concentration polarization and thus prevents its cathodic reduction.

Nagai and Takei (5) reported practically complete suppression of cathodic reduction of hypochlorite ions at chromium-plated 18Cr-8Ni stainless steel. The electrolyte was without added chromate ions, which supported the theory established by Müller (4). However, unplated 18Cr-8Ni stainless steel by itself did not suppress hypochlorite cathode reduction (5).

It is well known that in electrolysis, even from acid solutions, the cathode diffusion layer is alkaline in respect to the bulk solution because of the h.e.r. and metal electrodeposition often is accompanied by hydroxide formation.

Vander Poorten (6) recently examined the reduction of chromic acid in the presence of chloride ions and pointed out by potentiostatic current/potential curves, some sudden transitions before hydrogen evolution, indicating the formation of a resistant layer on the electrode, which was considered as a "cathodic passivation" layer.

Wagner (7) showed theoretically that there exists a critical potential difference across the cathode diffusion boundary layer of the order of, or greater than, $kT/|z_i| \cdot e = 0.025/|z_i|$, (where k is the Boltzmann constant, T temperature in °K, z_i hypochlorite ion valence, or that of another reducible anion, and e the electronic charge), providing the adverse potential gradient for negatively charged hypochlorite ions so that their reduction is effectively suppressed. As long as the current density or potential difference is relatively low, chromate reduction takes place, but it will practically cease after a sufficient cathode layer of chromium oxide is formed. After that all anions, chromate as well as hypochlorite, will be repulsed by an adverse potential gradient. In this manner an effective diaphragm is formed without causing an excessive *IR*-drop or electrode polarization. The theoretical considerations of Wagner (7) are in accordance with results of Maroni *et al.* (10) and Kolthoff and Shams el Din (11).

Maroni *et al.* (10) showed the cathode reduction of hypochlorite to be governed by diffusion in sodium chloride solutions and the electrode potential to be changed to more positive value with sudden chromate addition, which then in a short time decreases to the previous one.

Kolthoff and Shams el Din (11) pointed out the appearance of a strongly adhering monomolecular film consisting of chromium oxide and hydroxide mixture, insoluble and resistant in strong acid solutions.

Effective depolarization of the h.e.r. can be obtained with a number of metals, as shown by Zholudev and Stender (13). However, precious metals are excluded for the present application because of high price and limited availability.

In previous papers, the authors (8, 9) have pointed out that thin cathode deposits of active metal forms of molybdenum or cobalt change the polarization characteristics of graphite for the h.e.r. The Tafel lines obtained on metallized graphite exhibit nearly the same slopes as the ones on molybdenum or cobalt metal, but are shifted to more positive values of potential.

Two methods of depolarization for the h.e.r. in bipolar chlorate cells with graphite electrodes have been

* Electrochemical Society Active Member.

developed. The first one results from an electrolytic chromium deposition over the whole surface of the cathode side of the graphite electrode in sufficient thickness that polarization characteristics similar to those of the deposited metal itself are obtained.

The second one, much simpler, more effective, and more economical, is based on the previously developed method of depolarization of the h.e.r. in mercury cell decomposers (8). This consists of depositing active molybdenum from molybdate in a negligible amount over the graphite cathode surface.

Molybdenum has a double effect: it decreases the polarization for the h.e.r., and it increases the potential gradient in the chromium oxide diaphragm. The latter effect results from the fact that all the current of the h.e.r. is now predominantly concentrated in fewer pores, *i.e.* only those at the bottom of which there are sites of an extremely small amount of molybdenum. The increased potential gradient effectively suppresses further reduction of chromate, molybdate, or hypochlorite in accordance with Wagner's theory (7).

Vanadium could be expected to have a similar effect.

The combination of the two methods seems also to be useful and effective.

Experimental

The effect of the depolarized h.e.r. has been studied by comparing the polarization curves on graphite, iron, 18Cr-8Ni stainless steel, chromium, molybdenum, cobalt, and on molybdenized, chromized, cobaltized, and vanadized surfaces of graphite. Two electrolytes for chlorate production were investigated: 310 gpl sodium chloride at *p*H 6.2 and 8.0, with chromate content of 4.8 gpl. Available chlorine concentrations during investigations were at steady state in respect to *p*H, load, and current density of prepolarization (14), and hence were equal in all measurements.

Cathodic polarization was carried out in an apparatus illustrated in Fig. 1. The intention was to achieve conditions as close as possible to those in industrial electrolytic chlorate production. Special precautions, such as pre-electrolytic purification treatment, were not undertaken since, in the range of current densities (1-300 ma/cm^2) of practical importance, the influence of impurities in reagent-grade sodium chloride solution can be neglected. The apparatus used was of glass-Teflon construction in order to avoid any organic material as impurity. The temperature was kept constant at 40°C ± 0.2°C by means of a water thermostat.

Cathode potentials were measured *vs.* SCE by means of VTVM (*p*H-mv meter type PHM 22R, Radiometer, Copenhagen). The tip of the Luggin capillary was about 0.03-0.05 cm diameter and touched the cathode. The pseudo-ohmic polarization at higher current densities was determined galvanostatically and subtracted from the measured values of potential.

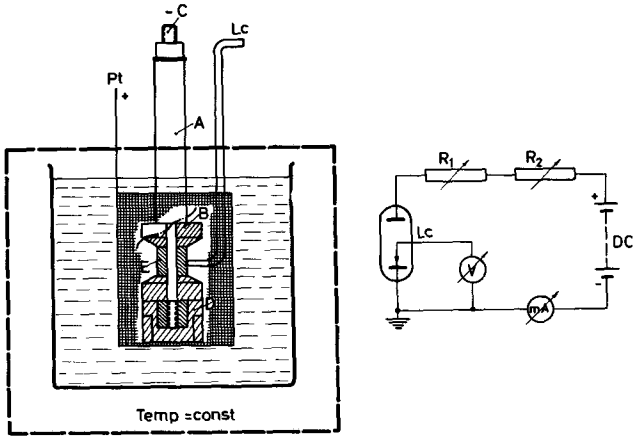

Fig. 1. Apparatus for measurement of hydrogen overpotential on various cathodes: Pt(+), Winkler platinum counterelectrode (anode); E, cathode of various materials; Lc, Luggin capillary; C, cathode connecting screw (nickel); D, Teflon fastener device with nickel nut; A and B, Teflon connections; mA, multirange milliammeter; V, vacuum-tube voltmeter; R_1 and R_2, variable resistors; DC, d-c supply.

Polarization curves were taken in the usual way using platinum counterelectrode and a saturated calomel reference electrode connected *via* a bridge to the Luggin capillary.

The approximate value of the emf of the galvanic cell

$$Pt(Pt)\ H_2/H_3O^+,\ 300\ gpl\ NaCl,\ H_2O//SCE$$

was calculated for *p*H 8.00 and 40°C, and overvoltages were obtained by subtracting this value (740 mv) from measured potentials.

Cathodic polarization of metallic chromium, cobalt, and molybdenum was carried out in the same apparatus as presented in the previous paper (8) since the metal electrodes were in the form of sheet.

The cathodes with exposed apparent surface areas of approximately 1.0 cm^2 (12 mm diameter) for sheet electrodes and 3.0 cm^2 for cylindrical electrodes were prepared as follows.

The molybdenum electrode was made of pure molybdenum sheet received from Climax Molybdenum Company, New York, type TZM [*cf.* (8)]. The electrode was mechanically polished and, after the usual cleaning with detergents, it was cathodically prepolarized in the investigated solution for 2 hr at a current of 100 ma.

The cobalt electrode was formed of electrolytically prepared pure cobalt sheet obtained from International Nickel Limited, London [*cf.* (9)] and prepolarized in the investigated solution, as was the molybdenum electrode.

The chromium electrode was formed of pure chromium sheet also obtained from International Nickel Limited, London, Batch GSKY, prepared electrolytically in the following purity: C, 0.01%; Al, 0.005%; Ni, 0.01/0.02%; Mn, 0.01%; Sn, 0.01/0.02%; Zn, 0.01%; B, 0.001%; Pb, 0.005%; Mo, 0.01%; Mg, 0.001%; Ti, 0.01%; S, 0.002%; Si, 0.01%; P, 0.005%. The electrode was mechanically polished and after proper cleaning with detergents it was cathodically prepolarized, as was the molybdenum one.

The mild steel [*cf.* (8)] and 18Cr-8Ni stainless steel electrodes were formed of technical materials, prepared and prepolarized as above.

Chlorate cell quality graphite blocks of SIGRI Elektrographit, Meitingen, type EKS special grade for chlorate cells, were carefully abraded with No. 600 grit emery cloth and then prepolarized as above.

Molybdenized graphite was obtained by submerging the prepared graphite electrodes in saturated sodium molybdate solution for 1 day, followed by immediate cathode prepolarization in the investigated solution as described for metallic molybdenum.

Cobaltized graphite was prepared by the procedure described in the previous paper (9).

Chromatized graphite was prepared as follows. Graphite blocks of SIGRI, type EKS, were carefully abraded and pretreated as described by Vaasos *et al.* (15), and then a chromium deposit was obtained from tetrachromate baths by the modified Bornhauser method (16). This consists of plating from a bath of chromic oxide (CrO_3) 300 gpl, NaOH 59-60 gpl, H_2SO_4 0.6-0.75 gpl, and ethanol (96%) 1 ml/liter, at a temperature of 16°-22°C and a current density of 150 amp/dm^2. The anode was insoluble Pb90-Sb10 alloy. Prepolarization was carried out as for all other electrodes.

Vanadized graphite was obtained by submerging the prepared graphite electrode in a saturated solution of sodium vanadate for 1 day, followed by immediate cathodic prepolarization in the investigated solution as for the other electrodes.

Polarization curves were also taken for electrodes made of the same graphite and impregnated with lin-

seed oil according to a recently described method (17).

All values presented in this paper refer to the electrolyte with 4.8 gpl of sodium chromate and at pH 8.0. At the pH value of 6.2, the Tafel lines were shifted to more negative values by about 30 mv. The reproducibility of potentials was better in the presence of chromate ions, though the values were practically the same.

Results and Discussion

The Tafel lines obtained for various electrodes are given in Fig. 2, 3, and 4. Reproducibility of the Tafel lines in ascending and descending direction of measurements repeated several times was better than ±10 mv.

The Tafel lines were fitted to the function

$$\eta = a - b \log i = b \log \frac{i_o}{i}$$

by the least-squares method for evaluating the slopes and intercepts (Table I).

Results show that the polarization characteristics of graphite have been changed considerably by depositing very small quantities of metal on its surface. The Tafel lines of metallized graphite for the h.e.r. are shifted to more positive values of potential, even compared to those for the metals themselves, while exhibiting nearly the same slopes.

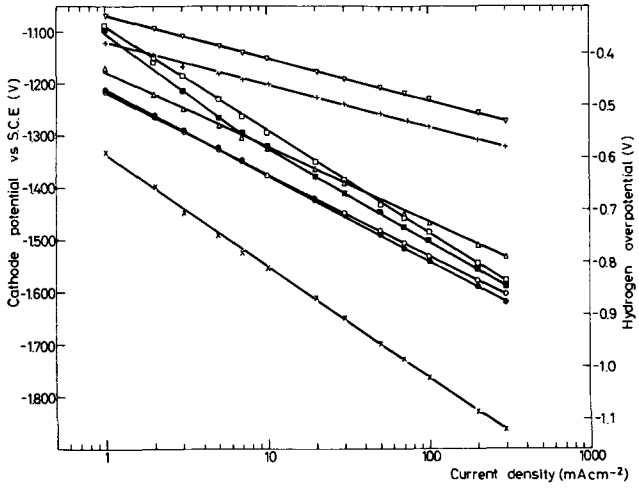

Fig. 2. Tafel plot of experimental results for various cathodes at 40°C: ×, graphite; ●, 18Cr-8Ni stainless steel; ○, chromatized graphite; ■, mild steel; □, vanadized graphite; △, molybdenized graphite-C; +, cobalt; ▽, cobaltized graphite.

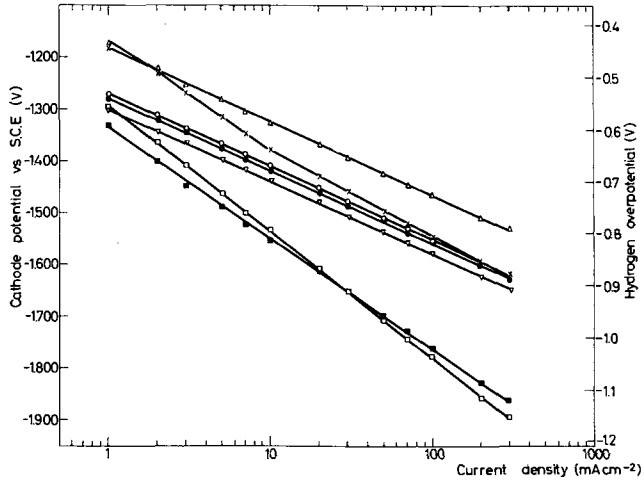

Fig. 3. Tafel plot of experimental results for various cathodes at 40°C: □, graphite; ■, graphite impregnated with linseed oil; ▽, graphite impregnated with linseed oil and molybdenized; ●, molybdenum; ○, molybdenized graphite-A; ×, molybdenized graphite-B; △, molybdenized graphite-C.

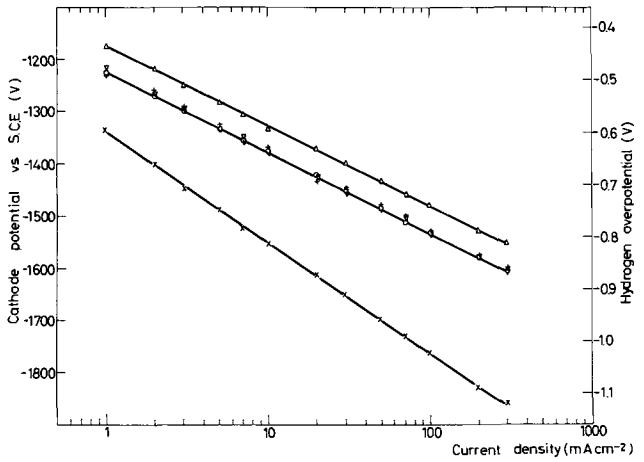

Fig. 4. Tafel plot of experimental results for various cathodes at 40°C: ×, graphite; ▽, 18Cr-8Ni stainless steel; +, chromatized graphite; ○, chromium; △, chromatized and molybdenized graphite.

The chromium deposit of 40-60μ thickness over the graphite surface shifts the Tafel line to values as positive as for 18Cr-8Ni stainless steel or metallic chromium (Fig. 4). To provide additional protection, the strongly adhering deposit of chromium in the chlorate cell process is covered further with chromium oxides obtained by chromate reduction. After anodic graphite is used up during the chlorate cell production, the chromium could be recovered by conventional processing and used once again for deposition on new graphite surfaces. Hence, thin deposits of chromium could substitute for large weights of steel cell body and cathode plates of monopolar cells. The addition of dichromate to the electrolyte is eliminated as are many copper lead-ins and bus bars. Thus, all voltage drops at contacts and through metal are reduced.

As in the previous paper (8), a small addition of molybdate to graphite or the solution completely changes the polarization characteristics of the electrode. Tafel lines for molybdenized graphite are shifted to more positive values and, especially at higher current densities, they are even more positive than for iron. Subsequent addition of molybdate to the investigated chloride solution, *i.e.* over 0.5 gpl, does not fur-

Table I. Tafel constants[a] for the h.e.r. on various cathodes at 40°C

	Cathode material	$-a$, mv	b, mv	β	$-\log i_o$
1.	Graphite	606	207	0.300	2.928
2.	Mild steel	377	194	0.320	1.942
3.	18Cr-8Ni stainless steel	470	163	0.380	2.879
4.	Chromium	487	156	0.399	3.124
5.	Molybdenum	539	141	0.442	3.831
6.	Cobalt	385	79	0.787	4.878
7.	Chromized graphite	479	155	0.401	3.098
8.	Cobaltized graphite	331	80	0.775	4.127
9.	Molybdenized graphite—A[b]	527	143	0.436	3.701
10.	Molybdenized graphite—B[c]	448	181	0.344	2.480
11.	Molybdenized graphite[d]	439	144	0.432	3.054
12.	Chromized and molybdenized graphite	434	152	0.407	2.907
13.	Vanadatized graphite	354	196	0.318	1.810
14.	Graphite impregnated with linseed oil	552	245	0.254	2.255
15.	Graphite impregnated with linseed oil and molybdenized	560	140	0.442	3.991

[a] $\eta = a - b \log i = b \log i_o/i$, where η is the overpotential in mv, i is the current density (ma/cm²), i_o is the exchange current density (ma/cm²), $b = RT/\beta F$.

[b] Graphite impregnated in saturated sodium molybdate solution and prepolarized in presence of chromate ions.

[c] Graphite electrode impregnated in saturated molybdate solution and prepolarized in presence of chromate ions, but without molybdate ions in sodium chloride electrolyte.

[d] Graphite electrode impregnated in saturated sodium molybdate solution and prepolarized in sodium chloride solution with molybdate ions and without chromate ions.

ther change Tafel lines, which is in accordance with Wagner's theory (7), as well as with the previous paper of the present authors (8). Polarization characteristics of graphite impregnated with linseed oil are also improved by the addition of molybdate to the investigated solution (Fig. 3). The molybdenum deposit is stable as long as it is cathodically protected, but it is renewed in a short time by the next cathodic polarization of the electrode after the electrode has been without load.

The fact that molybdenized graphite exhibits the same slope of the Tafel lines as for the metal itself suggests that there is some metallic form of coating. The observed highly catalytically active black dots probably represent molybdenum oxide reduced to the metal by adsorbed hydrogen atoms. Further cathodic evolution of hydrogen keeps molybdenum in reduced form during the process. Our investigation has shown that the coating is not catalytically active for hydrogen oxidation in fuel cells, as pointed out by Feuillade (18) for molybdenum oxides deposited on carbon. The coating oxidizes if it is not cathodically protected and loses its activity. It needs repeated cathodic polarization to regain its previous activity and Tafel line slope.

An interesting behavior of molybdenized graphite has been observed: the Tafel line was shifted to more positive values of potential if molybdate was added prior or together with chromate (Fig. 3). However, the electrode impregnated in molybdate solution and prepolarized with chromate present in, but molybdate absent from, the sodium chloride solution exhibits an intermediary transition behavior between the two considered cases (Fig. 3).

A chromatized graphite electrode, impregnated in saturated molybdate solution and polarized in the presence of molybdate ions in a chloride solution, exhibits the same behavior as the molybdenized graphite just considered (Fig. 4). Its polarization characteristics are independent of molybdate concentration over 0.5 gpl in solution.

Voltage-current characteristics of a suitably scaled-up bipolar cell (21) for the usual chlorate process conditions as well as for molybdate addition to the electrolyte are presented in Fig. 5, comparing the depolarizing effects achieved under industrial processing conditions.

Addition of molybdate to the investigated electrolyte in the case of metal electrodes (Co, Mo, Fe) does not change their polarization characteristics. However, it has been pointed out that the Tafel line shifts to more positive values of potential for the stainless steel electrode in the presence of molybdate ions in the solution. The appearance of molybdenum black over its exposed surface was also observed. This fact could be of importance for monopolar cells also.

The addition of vanadate was also tried, and its presence exhibits an appreciable depolarization too (Fig. 2).

An investigation was also made of the influence of cobalt coating on the graphite surface, obtained by the described method (9). The effect (Fig. 2) was stronger than with molybdenized graphite as was previously observed in caustic soda solution. However, due to the well-known catalytic effect of cobalt ions (12) on decomposition of hypochlorite, an effective cathode protection of the deposited cobalt should be provided all during the process.

Effect of molybdate on chlorate and hypochlorite stability.—Molybdates, and mainly Mo^{5+} ions, have been used as promoters for the catalytic activity of some other ions such as osmium for chlorate reduction in strong acid solution (19, 20). The catalytic action of molybdate for hydrogen peroxide decomposition is also well known. Therefore, an investigation was made of the effect of molybdate in the chlorate cell process, as well as on hypochlorite and chlorate decomposition.

Sodium molybdate in the amount of 1 gpl, was added separately to hypochlorite and chlorate solutions at pH

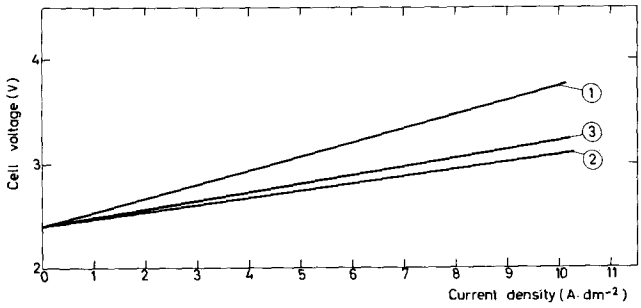

Fig. 5. Voltage-current characteristics of a scaled-up bipolar chlorate cell and the effect of depolarization in industrial process conditions: 1, usual cell conditions (unimpregnated graphite, TUP, Dubrovnik, Yugoslavia); 2, molybdenized graphite as cathode (chromate absent); 3, molybdenized graphite as cathode (dichromate content 4.0 gpl).

8.0 and their concentrations were followed as a function of time at 40°C. During more than 20 hr of investigation, no significant decomposition was observed.

In an apparatus for continuous chlorate production described recently by the authors (21), the influence of 1.0 gpl molybdate on chlorate cell current efficiency was investigated. No significant change in current efficiency was observed for the same pH and under otherwise similar conditions (flow, current density, temperature, concentration) of the process. Apparently the promoting effect of Mo^{5+} ions is possible only under strongly acidic conditions and in the presence of strong reducing or catalyzing agents, which are excluded in the usual industrial electrolytic chlorate process. The Mo^{5+} ions in the chlorate cells exist only inside the strongly alkaline cathode diffusion layer and for a short time, because they are further reduced to metallic molybdenum or an oxide of lower valence at least. Therefore, one could conclude that the small addition of molybdate has no significant influence on current efficiency in the chlorate cell process. The anodic effect is the same as for chromate ions themselves (22).

Miscellaneous observations.—The present methods thus improve the polarization characteristics for the h.e.r. at the graphite electrode by 200-300 mv with the molybdenized surface, more than 500 mv with the cobaltized, and about 150 mv with chromatized graphite.

In conclusion, current flow normal to the exposed graphite side surface for the electrochemical process in bipolar cells provides minimized paths through electrodes and hence enables application of higher current densities with reduced cell voltage. At the same time, small additions of molybdate provide a depolarizing effect for the h.e.r., similar to iron, which allows high current densities for bipolar chlorate cells (Fig. 2).

Therefore, an impregnation of graphite with molybdate is suggested, as well as the addition of 0.1-0.2 gpl to the electrolyte, as a suitable method for continuous cathode depolarization in a bipolar chlorate cell process.

In the previous paper, the authors (21) have pointed out the strong buffering effect of hypochlorous acid-hypochlorite ions just in the pH region providing the maximum conversion rate to chlorate. Thus, an application of the described depolarization methods provides the possibility for reducing dichromate addition, which is important for the chlorate crystallization process.

The methods of depolarization for the h.e.r. described here seem to be very advantageously applicable to all electrolytic processes having graphite or other porous cathodes, such as is the case for water and hydrochloric acid electrolysis, and should lead to lower cell voltages.

Acknowledgments

This work was supported and carried out by the Institute of Chemistry, Technology, and Metallurgy of Beograd, Yugoslavia, and Faculty of Chemical Technology of Split, University of Zagreb, Split, Yugoslavia.

The authors are deeply indebted to Professor Dr. A. R. Despić of Beograd for his personal interest in this work and his contributions to the direct preparation of the paper.

The authors wish also to express their gratitude to all members of the Electrochemistry Department of the Institute for their suggestions and stimulating discussions in connection with the present paper.

Manuscript submitted July 11, 1968; revised manuscript received *ca.* Dec. 5, 1968. This paper was presented in part at the Chlorates and Perchlorates Symposium at the Boston Meeting, May 5-9, 1968, as paper 259.

Any discussion of this paper will appear in a Discussion Section to be published in the December 1969 JOURNAL.

REFERENCES

1. D. G. Elliott, *Tappi*, **51**, 88A (1968).
2. *Can. Chem. Process.*, **50**, 85 (1966).
3. L. Hammar and G. Wranglén, *Electrochim. Acta*, **9**, 1 (1964).
4. E. Müller, *Z. Elektrochem.*, **5**, 469 (1899); **7**, 398 (1900); **8**, 909 (1902); **32**, 399 (1926).
5. T. Nagai and T. Takei, *J. Electrochem. Soc. Japan*, **25**, 373 (1957).
6. H. Vander Poorten, *Electrochim. Acta*, **10**, 809 (1965).
7. C. Wagner, *This Journal*, **101**, 181 (1954).
8. M. M. Jaksic and I. M. Csonka, *Electrochem. Technol.*, **4**, 49 (1966), and M. M. Jaksic, *Kem., Ind. Zagreb*, **12**, 45 (1963).
9. M. M. Jaksić, D. R. Jovanović, and I. M. Csonka, "Depolarization of Sodium Amalgan Decomposition with Cobaltized Graphite in the Mercury Cell Process," Paper presented at Istanbul CITCE-Colloquium on Corrosion and Electrochemical Thermodynamics, Istanbul, Sept. 12-16, 1967, submitted to *Electrochim. Acta.*
10. J-C. Maroni, E. Authier-Cabibel, and B. Tremillon, *Bull. Soc. Chim. France*, **1959**, 127.
11. I. M. Kolthoff and A. M. Shams el Din, *J. Phys. Chem.*, **60**, 1564 (1956).
12. M. W. Lister, *Can. J. Chem.*, **34**, 479 (1956).
13. M. D. Zholudev and V. V. Stender, *Zh. Prikl. Khim.*, **31**, 719 (1958).
14. D. Landolt, Ph.D. thesis, Eidgenössischen Technischen Hochschule, Zürich, Prom. Nr. 3673 (1965); N. Ibl and D. Landolt, *This Journal*, **115**, 713 (1968).
15. B. H. Vassos, F. J. Berlandi, T. E. Neal, and H. B. Mark, *J. Anal. Chem.*, **37**, 1655 (1965).
16. E. Bertorelle, "Trattato di galvanotecnica," p. 536, Ulrico Hoepli, Milano (1960).
17. M. M. Jaksić and I. M. Csonka, *Electrochem. Technol.*, **5**, 473 (1967).
18. G. Feuillade, "EPE," Vol. 2, No. 2, p. 1 (1966).
19. I. M. Kolthoff and I. Hodara, *J. Electroanal. Chem.*, **5**, 2, 165 (1963).
20. A. J. Boyle, V. V. Hughey, and C. C. Casto, *Ind. Eng. Chem., Anal. Ed.*, **16**, 370 (1944).
21. M. M. Jaksić, I. M. Csonka, B. Z. Nikolić, and A. R. Despić, Paper 257 presented at Electrochem. Soc. Meeting, Boston, May 5-9, 1968.
22. T. S. Filippov, V. I. Eberil, R. A. Agapova, and G. N. Razygraeva, *Zh. Prikl. Khim.*, **40**, 2488 (1967).

Process for Coating Tin-Free Steel with Layers of Metallic Chromium and Chromium Oxide

Nobuo Fukuda, Shigeru Yonezaki, Hajime Nitto, Minoru Kamada, Hidejiro Asano, and Kazukiyo Terayama

Yawata Iron & Steel Company, Limited, Chiyoda-ku, Tokyo, Japan

ABSTRACT

Tin-free coated steels are attracting attention as new container materials. As a result of studies that have been conducted since 1957 on tin-free steel, a double-layered chromium-chromium oxide tin-free coated steel (T.F.S.) has been developed. The properties of T.F.S. are excellent because each layer compensates for the others' deficiencies; namely, pin holes in the chromium are sealed by the chromium oxide and thermal cracking of the oxide layer is minimized by the underlying chromium metal layer. T.F.S. can be produced by a one-step cathodic treatment, using dilute chromic acid solution containing sulfate ion. The thicknesses of each layer may be controlled independently by treating conditions. The manufacturing equipment for this process is similar to that used in the electrotinning process. However, plating bath and tank lining materials must be carefully selected.

A rise in the price of tin due to the shortages and the instability of production, as well as inroads being made by aluminum and plastics producers into the market for container materials, has compelled can manufacturers and steel makers to take greater interest in the development of low-cost steel base container materials, such as tin-free steel (T.F.S.).

Against this background, competition for T.F.S. development is being waged throughout the world, and T.F.S. should soon enter an age of practical application. In anticipation of such a trend, development of T.F.S. was initiated in 1957.

After studying the feasibility of such processes as electrolytic phosphating, nonelectrolytic and electrolytic chromating, nickel and chromium plating, it was concluded that the double-layered T.F.S. consisting of an upper layer of chromium oxide and an underlayer of metallic chromium was most effective.

The chief merit of the double-layered T.F.S. is that the pinholes in the metallic chromium layer are sealed by the chromium oxide layer. Thermal cracking of the chromium oxide layer is minimized by the metallic chromium layer.

If the coating layers are too thin, the corrosion resistance is poor and, if too thick, the lacquer adhesion is poor. After determining the optimum film thickness (*see* Table I) for the most favorable combination of corrosion resistance and lacquer adhesion, commercial production was started on double-layer T.F.S. in 1967 on a unique high-speed production line (maximum 1200 fpm).

The purpose of this report is to describe briefly the production process for T.F.S.

Table I. Quality specification

Item	Coating weight (mg/dm² surface)
Metallic chromium	0.7 ~ 1.5
Chromium oxide	0.3 ~ 0.6

Table II. Comparison of coating film composition with conventional chromium plating and T.F.S. process at same plating conditions (Bath temp: 50°C)

Name of treatment	Concentration of plating solution	Plating condition: Current density, amp/dm²	Plating condition: Plating time, sec	Coating weight: Metallic Cr, mg/dm²	Coating weight: Cr oxide, mg/dm²
Conventional chromium plating	CrO_3:250 g/liter $SO_4^=$:2.5 g/liter	40	3	2.5	0.03
Plating solution for T.F.S. process	CrO_3:45 g/liter $SO_4^=$:0.45 g/liter	40	3	2.6	0.6

Process for Double-Layered T.F.S.

The mechanism of double-layered film deposition.—In conventional chromium plating, a solution containing about 250 g/liter of CrO_3 (chromium trioxide) and about 2.5 g/liter of sulfate ion is used. However, in order to obtain a double-layered T.F.S., in a single step, a solution containing less than 50 g/liter of CrO_3 and a small amount of sulfate ion is used.

Utilizing a solution for a double-layered T.F.S., samples were prepared and compared with samples of the ordinary chromium-plated steel. In both instances, the same current density, plating time, and bath temperature were used. As shown in Table II, the thickness of the chromium on the T.F.S. samples was about the same as that on the samples from the conventional chromium-plating solution, whereas the chromium oxide layer on T.F.S. was several hundred times thicker. Further, the thickness of the chromium oxide film gradually decreased if the samples were immersed in the solution before being dried as shown in Fig. 1.

From the results of these two experiments, it has been concluded that the chromium oxide film is the undissolved residue of intermediate products of reduction produced during chromium plating.

The key problem is how to develop this intermediate product into a double-layered T.F.S. in a single electrolysis step.

Outline of the process.—The new T.F.S. is produced by a process similar to electrotinning as shown in Fig. 2.

The steel base strip is prepared for plating in the same manner as for tinplate. The steel strip is first

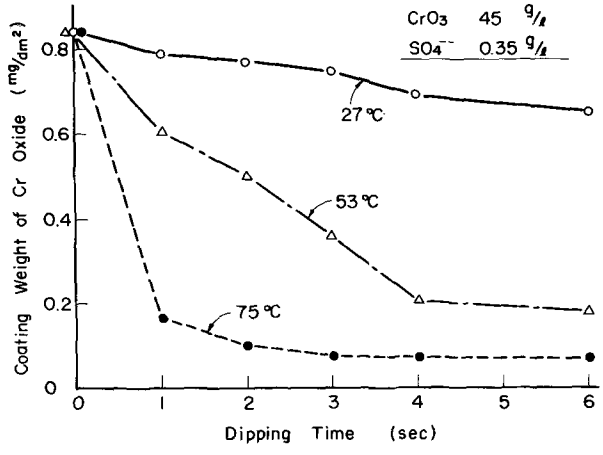

Fig. 1. Influence of dipping time in treating solution on chromium oxide coating weight.

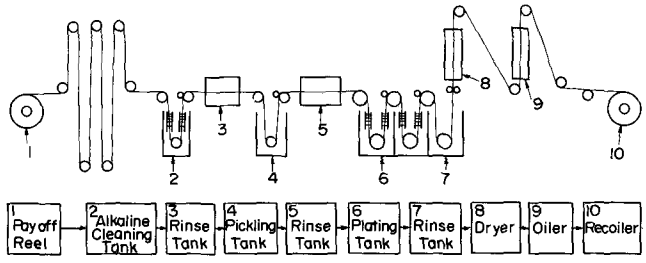

Fig. 2. T.F.S. plating line layout

washed by the alkaline cleaning method to remove completely all stains and oil on the surface. For double-reduced strip, cleaning must be particularly thorough. To obtain optimum surface properties, electrolytic alkaline cleaning is recommended. After rinsing with water, the strip is pickled with sulfuric acid at room temperature. Then the strip is treated cathodically in a plating bath to form a double-layered film on its surface. After removing the strip from the plating solution, it is rinsed in warm water, dried in hot air, and oiled.

Plating solution.—The plating is conducted in solutions having the compositions given in Table III. The fact that this solution is considerably less concentrated than that used for conventional chromium plating, as noted earlier, explains why it is possible to obtain a double-layered film in one-step electrolysis. Other advantages also accrue from use of a weaker solution.

It is cheaper, in the first place, and, even when used in a high-speed line, the drag-out (depletion) of chromic acid is less than that of conventional plating solution, so there is no need to recover CrO_3.

Second, it is less corrosive, having about one fifth of the chromic acid concentration used in conventional plating solutions. Hence, roll and lining materials present less problems.

Third, it is less of a health hazard to plant workers because CrO_3 fumes generated during electrolysis are proportionately weaker than those produced in conventional chromium plating.

Current efficiency for the deposition of metallic chromium and the line speed total current curve.—Unlike the electrotinning or galvanizing processes, the current efficiency of chromium plating varies with the current density and the bath temperature. This process exhibits similar characteristics. Hence, coating weight cannot be kept constant simply and linearly by adjusting current density to line speed if the line speed changes.

Since in chromium plating a drop in current density causes a corresponding drop in current efficiency, it may be necessary to actually increase current density to compensate for a drop in current efficiency when the line slows down. For this reason, the line speed-total current curve does not pass through the zero-point.

The line speed *vs.* total current curve for the new T.F.S. line, depositing 1 mg/dm² of metallic chromium is shown in Fig. 3.

Coating weight control of chromium oxide.—As already indicated, the oxide layer of the film, being an intermediate residue of the plating process, dissolves when reimmersed in the plating solution without electrolytic action. When plating in a vertical tank, it was found that the oxide film dissolved on parts of the strip not facing the anode, (*e.g.*, parts A, B, C, and D in Fig. 4). Thus, in multitank continuous plating, the oxide film is produced and dissolved alternately.

Table III. Plating solution of T.F.S. process

Concentration	CrO_3	<50 g/liter
	$SO_4^=$	<0.5 g/liter
Temperature of plating solution		50° ~ 60°C

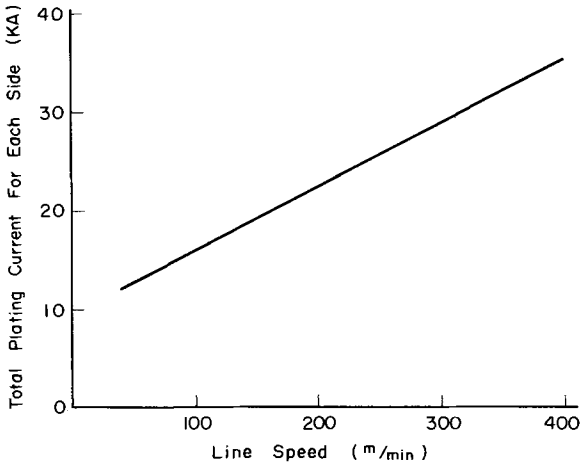

Fig. 3. Total current-line speed curve for 1.0 mg/dm² metallic chromium in actual line (width: 800 mm).

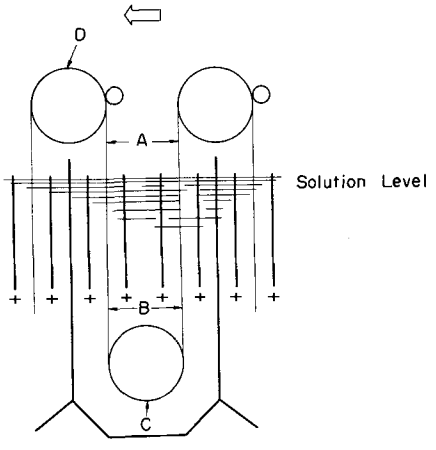

Fig. 4. Cross-sectional view of vertical plating tank

This behavior becomes even more severe at higher bath temperatures.

If electrodeposition and dissolution of chromium oxide occur alternately, the effect of each pass on the deposition of chromium oxide should become greater toward the rear pass. The contribution ratio of each pass to the deposition of chromium oxide was measured in the actual line. It was found that most of the chromium oxide deposits in the last tank as had been anticipated. This shows that, by controlling the current in the last tank, it is possible to control the amount of chromium oxide deposition independently of the amount of metallic chromium deposition. Actually, in this process the amount of chromium oxide deposition is controlled by the current in the last tank and the bath temperature.

Plating Equipment

Since a clean strip surface is also necessary for T.F.S., equipment for pretreatment is essentially the same as for electrotinning:

The pretreating section has an alkaline dunk tank, alkaline scrubber, electrolytic alkaline cleaning tank, pickling tank, and scrubber tank. Tank lining and roll material are also the same as used in electrotinning.

A predip tank, plating tanks, and rinse tanks are used in the plating section, the number of plating tanks depending on how much metallic chromium is to be required, on current capacity, and on line speed.

Vertical plating tanks are best since it has been found that in horizontal plating gas generated during electrolysis produces surface defects on the underside of the strip.

Lead-tin alloy is used for the anode. The space between the anode and strips is 25-40 mm.

The conductor roll is made of copper with a chromium-plated surface similar to that employed in electrotinning. The roll and tank lining material should be selected carefully because chromic acid solution is oxidizing; ordinary rubber, for instance, is corroded by chromic acid and the life of the lining becomes short; moreover, it reacts with chromic acid and increases the Cr^{+++} and sulfate ion in the plating solution. As shown in Fig. 5, increased Cr^{+++} reduces conductivity of the plating solution; sulfate ion increase changes the plating solution and makes operation difficult.

After testing various roll and lining materials, a special resin resistant to chromic acid corrosion was developed as shown in Fig. 6. This material is as easily fabricated into rolls or linings as ordinary rubber, whereas polypropylene and PVC are hard to make and tend to crack with aging.

This new resin has been used with very satisfactory results for hold-down rolls, sink rolls, and linings of plating tanks.

To prevent surface defects caused by plating solution remaining on the strip, a hot water rinse is used. Rinse water is supplied continuously to reduce chromic acid and sulfate ion concentrations, but losses from drag-out are so slight that no attempt is made to recover the chromic acid.

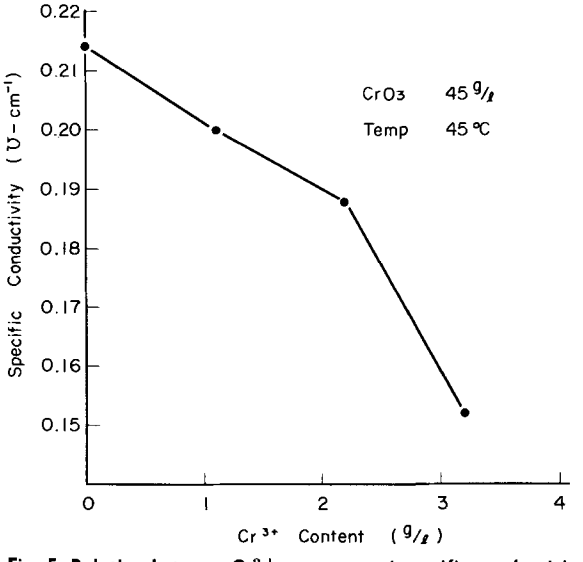

Fig. 5. Relation between Cr^{3+} content and specific conductivity

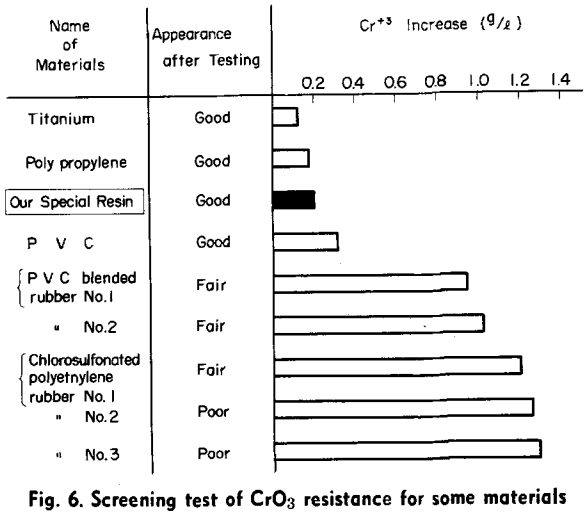

Fig. 6. Screening test of CrO_3 resistance for some materials

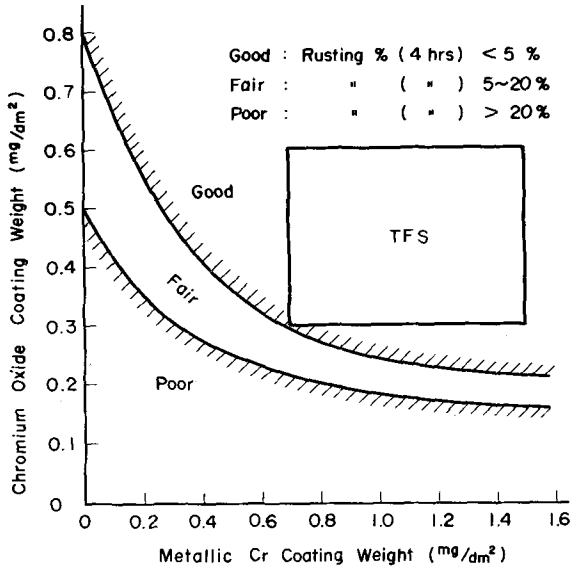

Fig. 7. Relation between salt spray test and coating weight

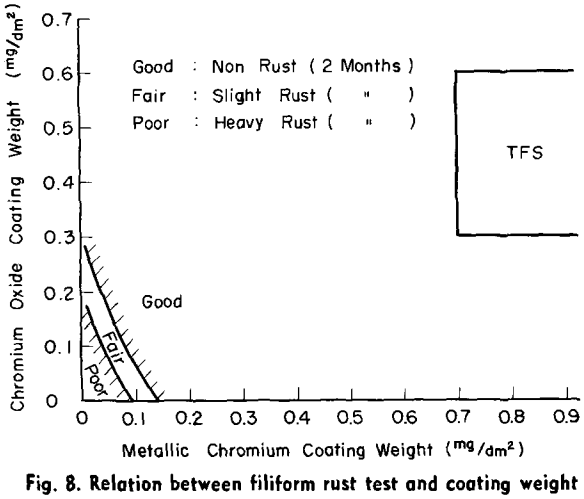

Fig. 8. Relation between filiform rust test and coating weight

The strip is dried by blowing hot air of 150°C on it before it goes through the electrostatic oiler.

Installation of a fume exhauster system is recommended to expel fumes generated during electrolysis.

Quality

The T.F.S. described herein is used for containers of carbonated beverages, beer, and various foodstuffs, also for bottle caps, battery cases, motor oil cans, pails, liquid detergent cans, and PVC laminated sheets.

To find the optimum coating weights of chromium oxide and metallic chromium required to produce adequate levels of corrosion resistance and lacquer adhesion for such a wide range of uses, the following tests were carried out.

Tests for Quality of Coating

Corrosion resistance of an unlacquered sheet.—First, as a general corrosion test, the corrosion resistance of an unlacquered sheet was evaluated by the salt spray method and the relation between the coating weights of each layer of the film and corrosion resistance was examined. As shown in Fig. 7, the coating specification of the T.F.S. was found to be satisfactory.

Filiform rust test.—Filiform rusting after lacquering is very undesirable because it greatly reduces the market value of a canned product.

The relation between each layer of the film and the filiform rusting is shown in Fig. 8. As this figure shows, the double layer of the T.F.S. prevents filiform rusting.

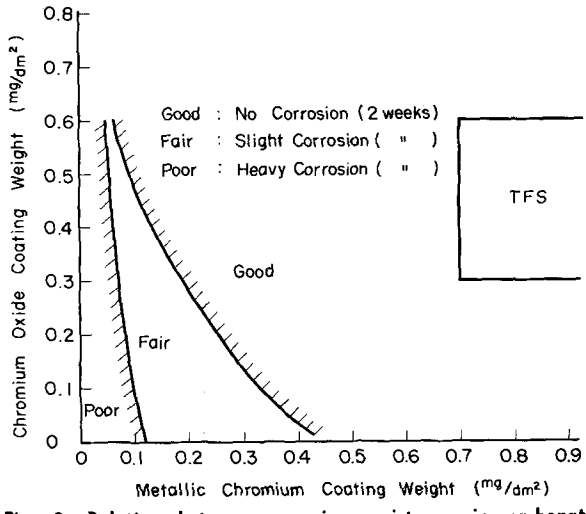

Fig. 9. Relation between corrosion resistance in carbonated beverage and coating weight.

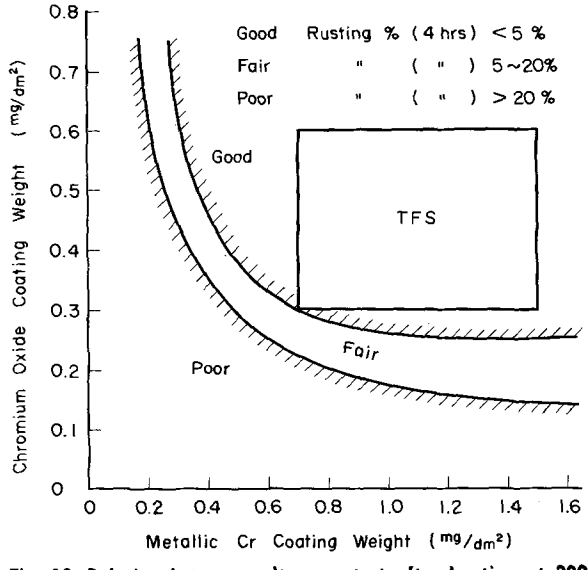

Fig. 10. Relation between salt spray test after heating at 200°C × 10 min and coating weight.

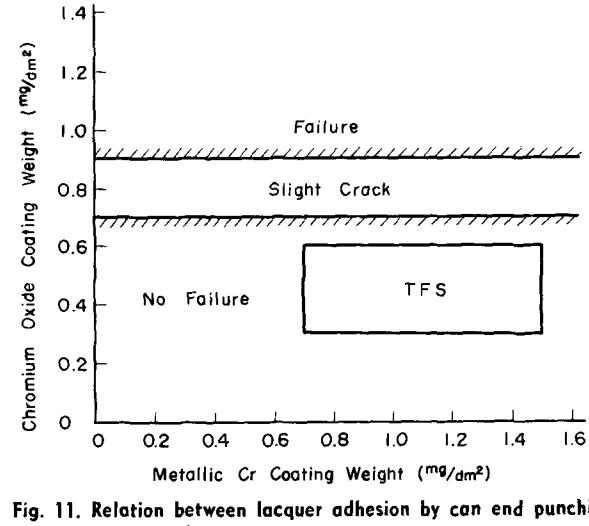

Fig. 11. Relation between lacquer adhesion by can end punching test and coating weight.

Corrosion resistance in carbonated beverage (lacquered sample).—The results of a corrosion test in carbonated beverage are shown in Fig. 9.

As this figure shows, the double layer of the T.F.S. coating insures excellent corrosion resistance in carbonated beverages.

Corrosion resistance after heating.—T.F.S. can be used for the inner surface of an unlacquered can. In this instance, one side of the sheet will be heated prior to fabrication and packing. Accordingly, the corrosion resistance of T.F.S. was examined after heating for 10 min at 200°C by the salt spray test. The results were satisfactory as shown in Fig. 10.

Lacquer adhesion.—The relation between the coating weight and lacquer adhesion of T.F.S. was examined by means of the can and punching test. The results are shown in Fig. 11. As this figure shows, lacquer adhesion deteriorates as the coating weight of oxide chromium exceeds 0.7 mg/dm², keeping in mind that the coating weight of metallic chromium is not related to lacquer adhesion. Also in this test, the specifications of the T.F.S. proved to be satisfactory.

Conclusions

1. The specifications for our T.F.S. are: metallic chromium, 0.7-1.5 mg/dm²; chromium oxide, 0.3-0.6 mg/dm².

If T.F.S. has the above coating weights, it exhibits satisfactory results for such tests as the salt spray test (4 hr), filiform rust test, corrosion test in carbonated beverage, salt spray test after heating, and the lacquer adhesion test by can end punching.

2. A manufacturing process was developed that produces tin-free steel in a one-step electrolytic treatment. Equipment used in this process is also described.

Manuscript submitted Sept. 25, 1967; revised manuscript received *ca.* Oct. 1968. This paper was presented at the Protective Coatings Symposium at the Chicago Meeting, Oct. 15-19, 1967, as Paper 208.

Any discussion of this paper will appear in a Discussion Section to be published in the December 1969 JOURNAL.

Plating Stresses from Electroless Nickel Deposition on Beryllium

R. M. Shemenski, J. G. Beach,* and R. E. Maringer

Battelle Memorial Institute, Columbus Laboratories, Columbus, Ohio

ABSTRACT

Commercial electroless nickel coatings on beryllium are shown to produce residual stresses of appreciable magnitude at the coating-substrate interface. A 0.005-in. layer of electroless nickel deposited on one side of a 0.010-in. beryllium strip induced residual compressive stresses in the beryllium substrate as high as 33,000 psi as calculated from the curvature of the plated composite. Evidence is presented to indicate that at least a substantial part of this residual stress is the result of a solid-state reaction and accompanying volume change in the coating during normal stress-relief annealing of the composite near 200°C. This is believed to be an ordering reaction associated with formation of the Ni_3P precipitate phase. The effect of temperature change on the level of induced stress in a nickel-beryllium composite due to a difference in coefficients of thermal expansion was investigated. The net difference in coefficients of thermal expansion increased in the temperature range 25°-50°C to a maximum value of $(\alpha_{Ni} - \alpha_{Be})_T = 1.9 \times 10^{-6}$ to 2.6×10^{-6} $\left(\frac{\text{in./in.}}{\text{°C}}\right)$, and then decreased approximately linearly up to 200°C at a rate of $\sim 6 \times 10^{-9} \left(\frac{\text{in./in.}}{\text{°C}}\right) / \text{°C}$.

Electroless nickel plating is a general term applied to processes based on the controlled, autocatalytic reduction of nickel cations by means of hypophosphite anions on certain catalytic surfaces in the presence of water (1-4). Brenner *et al.* listed the advantages of electroless nickel deposition as (*a*) deposition of uniform thickness in recesses as well as exposed areas, (*b*) no excessive build-up on projections or edges, and (*c*) elimination of the need for electroplating power sources and equipment (1-4). Coatings obtained by the electroless nickel process are typically α-nickel containing 8-10% by weight of phosphorus and minor amounts of other residual elements (5). The structure of electroless nickel deposits has been subject to considerable altercation. Differences in structure, composition, and properties of electroless nickel deposits are attainable, depending on the type of electroless nickel bath and operating parameters for deposition of a specific electroless nickel alloy. Brenner described electroless nickel as "fine-grained coherent deposits with a laminated structure sometimes imposed upon a columnar structure" (1). On the other hand, Gutzeit *et al.* (2, 5) reported that "electroless nickel coatings have the structure of an amorphous solid substance with liquid-like disorder of the atoms," this amorphous character being dependent of the nature of the substrate for deposits up to 0.010 in. in thickness. Goldenstein *et al.* (6) and Ziehlke *et al.* (7) also found catalytic nickel deposits to be amorphous by using x-ray and electron-diffraction techniques. They found that the amorphous structure reverted exothermically to a crystalline phase mixture of Ni + Ni_3P at low temperatures. Graham *et al.* (8, 9), Dixmier and Doi (10), and Randin *et al.* (11) all reported that electroless nickel had a very fine grain size of the order of 10^{-6} cm, and that the as-plated deposit was a supersaturated solid solution of phosphorus in nickel [$Ni_{(P)}$] as a metastable intermediate state between that of a mixture of Ni + P and the equilibrium system of $Ni_{(P)}$ + Ni_3P.

Dixmier and Doi found that this structure was a heavily faulted fcc-hcp structure, with the phosphorus atoms located interstitially in the hcp layers (10). Albert *et al.* showed that the structure was essentially a strained fcc-nickel lattice (12). Apart from these

* Electrochemical Society Active Member.

Corrosion resistance after heating.—T.F.S. can be used for the inner surface of an unlacquered can. In this instance, one side of the sheet will be heated prior to fabrication and packing. Accordingly, the corrosion resistance of T.F.S. was examined after heating for 10 min at 200°C by the salt spray test. The results were satisfactory as shown in Fig. 10.

Lacquer adhesion.—The relation between the coating weight and lacquer adhesion of T.F.S. was examined by means of the can and punching test. The results are shown in Fig. 11. As this figure shows, lacquer adhesion deteriorates as the coating weight of oxide chromium exceeds 0.7 mg/dm², keeping in mind that the coating weight of metallic chromium is not related to lacquer adhesion. Also in this test, the specifications of the T.F.S. proved to be satisfactory.

Conclusions

1. The specifications for our T.F.S. are: metallic chromium, 0.7-1.5 mg/dm²; chromium oxide, 0.3-0.6 mg/dm².

If T.F.S. has the above coating weights, it exhibits satisfactory results for such tests as the salt spray test (4 hr), filiform rust test, corrosion test in carbonated beverage, salt spray test after heating, and the lacquer adhesion test by can end punching.

2. A manufacturing process was developed that produces tin-free steel in a one-step electrolytic treatment. Equipment used in this process is also described.

Manuscript submitted Sept. 25, 1967; revised manuscript received *ca.* Oct. 1968. This paper was presented at the Protective Coatings Symposium at the Chicago Meeting, Oct. 15-19, 1967, as Paper 208.

Any discussion of this paper will appear in a Discussion Section to be published in the December 1969 JOURNAL.

Plating Stresses from Electroless Nickel Deposition on Beryllium

R. M. Shemenski, J. G. Beach,* and R. E. Maringer

Battelle Memorial Institute, Columbus Laboratories, Columbus, Ohio

ABSTRACT

Commercial electroless nickel coatings on beryllium are shown to produce residual stresses of appreciable magnitude at the coating-substrate interface. A 0.005-in. layer of electroless nickel deposited on one side of a 0.010-in. beryllium strip induced residual compressive stresses in the beryllium substrate as high as 33,000 psi as calculated from the curvature of the plated composite. Evidence is presented to indicate that at least a substantial part of this residual stress is the result of a solid-state reaction and accompanying volume change in the coating during normal stress-relief annealing of the composite near 200°C. This is believed to be an ordering reaction associated with formation of the Ni_3P precipitate phase. The effect of temperature change on the level of induced stress in a nickel-beryllium composite due to a difference in coefficients of thermal expansion was investigated. The net difference in coefficients of thermal expansion increased in the temperature range 25°-50°C to a maximum value of $(\alpha_{Ni} - \alpha_{Be})_T = 1.9 \times 10^{-6}$ to 2.6×10^{-6} $\left(\frac{\text{in./in.}}{\text{°C}}\right)$, and then decreased approximately linearly up to 200°C at a rate of $\sim 6 \times 10^{-9} \left(\frac{\text{in./in.}}{\text{°C}}\right) / \text{°C}$.

Electroless nickel plating is a general term applied to processes based on the controlled, autocatalytic reduction of nickel cations by means of hypophosphite anions on certain catalytic surfaces in the presence of water (1-4). Brenner *et al.* listed the advantages of electroless nickel deposition as (*a*) deposition of uniform thickness in recesses as well as exposed areas, (*b*) no excessive build-up on projections or edges, and (*c*) elimination of the need for electroplating power sources and equipment (1-4). Coatings obtained by the electroless nickel process are typically α-nickel containing 8-10% by weight of phosphorus and minor amounts of other residual elements (5). The structure of electroless nickel deposits has been subject to considerable altercation. Differences in structure, composition, and properties of electroless nickel deposits are attainable, depending on the type of electroless nickel bath and operating parameters for deposition of a specific electroless nickel alloy. Brenner described electroless nickel as "fine-grained coherent deposits with a laminated structure sometimes imposed upon a columnar structure" (1). On the other hand, Gutzeit *et al.* (2, 5) reported that "electroless nickel coatings have the structure of an amorphous solid substance with liquid-like disorder of the atoms," this amorphous character being dependent of the nature of the substrate for deposits up to 0.010 in. in thickness. Goldenstein *et al.* (6) and Ziehlke *et al.* (7) also found catalytic nickel deposits to be amorphous by using x-ray and electron-diffraction techniques. They found that the amorphous structure reverted exothermically to a crystalline phase mixture of Ni + Ni_3P at low temperatures. Graham *et al.* (8, 9), Dixmier and Doi (10), and Randin *et al.* (11) all reported that electroless nickel had a very fine grain size of the order of 10^{-6} cm, and that the as-plated deposit was a supersaturated solid solution of phosphorus in nickel [$Ni_{(P)}$] as a metastable intermediate state between that of a mixture of Ni + P and the equilibrium system of $Ni_{(P)}$ + Ni_3P.

Dixmier and Doi found that this structure was a heavily faulted fcc-hcp structure, with the phosphorus atoms located interstitially in the hcp layers (10). Albert *et al.* showed that the structure was essentially a strained fcc-nickel lattice (12). Apart from these

* Electrochemical Society Active Member.

differing opinions, there is significant agreement that as-plated electroless nickel is a metastable structure characterized by some degree of atomic disorder which tends toward the equilibrium $Ni_{(P)} + Ni_3P$ structure upon heating. X-ray diffraction studies of nickel phosphide (Ni_3P) indicated that it has a body-centered tetragonal structure ($a = 8.91$Å, $c = 4.39$Å). When precipitated in a parent nickel lattice, it shows a preferred orientation with the {111} planes of fcc nickel parallel to the {110} planes of Ni_3P. Furthermore, the average interatomic distance of 2.6Å on the {110} planes of Ni_3P is very close to the interatomic distance of 2.5Å in Ni. The lattice parameter of electroless nickel is 3.52Å (11). The atomic radii of phosphorus and nickel are 1.28 and 1.24Å, respectively, differing by somewhat more than 3%. From changes in lattice parameter with phosphorus content, it is believed that phosphorus content in a stress-relieved nickel deposit is very low, and, therefore, only a little (if any) phosphorus occupies substitutional or interstitial sites in an α-Ni lattice.

Variations in phosphorus content of electroless nickel deposits have a marked influence on the mechanical properties of the coatings. Abrupt changes in tensile properties at approximately 7% by weight phosphorus (49% by volume Ni_3P) were found to indicate a change from a ductile Ni continuous phase at low phosphorus levels to a brittle Ni_3P matrix at high phosphorus contents (9, 13). The response of electroless nickel to heat treatment also is sensitive to phosphorus content, especially at low temperatures. The hardness of deposits with phosphorus content above 9 w/o (weight per cent) remained practically constant for heat treatments of ~5 hr up to 300°C, whereas the hardness of low-phosphorus deposits increased when heat treated at temperatures above 125°C (13). In the high-phosphorus deposits, Graham *et al.* stated that the very low rate of hardening for heat treatments below 200°C seems to be indicative of the presence of an "activation energy barrier," dependent on phosphorus content, that retards the initial stages of transformation of the supersaturated Ni + P solid solution (9). After heat treatment at 200°C, Graham *et al.* reported an increase in hardness at a decreasing rate with increasing phosphorus content up to 9 w/o (9). Goldenstein *et al.* concluded that no transformations occur at 200°C in electroless nickel containing 7-10 w/o phosphorus since their work showed no increase in hardness for 21 hr at that temperature (6). An initial increase in hardness of Ni + 8-10 w/o P from ~500 DPH to ~600 DPH (Rockwell C-50 to 55) within the first few hours followed by no observed change after 617 additional hours at 200°C was found by Lee (14). Ziehlke *et al.* observed no changes in microstructure for samples (7-10 w/o P) heat treated below 400°C (7). Domnikov stated that a slight increase in the microhardness of electroless nickel deposits (phosphorus content not specified) heat treated at 120°-200°C could be explained by an incomplete formation of the Ni_3P phase (15).

This research was part of a larger program to investigate the production of large precision, diffraction-limited mirrors which require a dimensional instability of $<0.033\lambda$ rms or 2.2×10^{-6} cm in the visible region over a moderate temperature range and for long periods of time. The purpose of this particular study was to investigate the effects of commercially processed electroless nickel deposits on dimensional stability of beryllium substrates by comparing the magnitude of residual plating stresses with the micro-yield strength (*i.e.*, the stress to produce a residual plastic strain of 1×10^{-6}) of beryllium. Response of the $Be\text{-}Ni_{(P)}$ system to thermal excursions from ambient temperature to ~200°C (normal stress-relief annealing temperature for electroless nickel) was analyzed to determine the net variation of coefficients of thermal expansion as well as the effect of temperature on microstructural stability. Differences in coefficients of thermal expansion between substrate and coating of the order of 1×10^{-6}/°C are considered pernicious for diffraction-limited mirrors, but could be accommodated in normal applications.

Experimental Procedure

Preparation of beryllium strips.—A beryllium powder, grade S-200 (Brush Beryllium Co., BeO ~ 1.8%) was hot isostatically pressed into a fully dense rectangular block. The faces of this block were milled to an accurate rectangular geometry and rough slabs 0.075 in. thick by 4.75 in. long by 0.625 in. wide were cut off with a water-cooled cut-off wheel. The slabs were assembled into a package and the ends and sides milled by a carbide end mill at 600 rpm (fine hand feed). The final finish on the sides was made according to the standard practice of taking successively finer cuts of 0.010-0.005-0.002-0.002-0.001 in. in depth. Very fine holes approximately 0.025 in. in diameter were made at one end about 0.25 in. from the edge to facilitate handling during plating. The final cuts on the top and bottom surfaces of the strips were made by using an end mill to remove 0.030 in. at 0.005 in./cut from first one side and then the reverse side, ending with cuts of 0.002 in. in one pass in one direction and 0.001 in. on the return pass on both sides to a thickness of 0.030 in. The final strip size as machined was 4.3 x 0.30 x 0.030 in.

These strips were then chemically polished to remove approximately 0.010 in. from all surfaces in a solution composed of:

H_2SO_4 (95-98%)	47 ml
H_3PO_4 (85-87%)	410 ml
H_2O	130 ml
CrO_3	70g
Temperature	160°-170°F
Removal rate	~0.6-0.8 mil/min

The samples were inspected thoroughly and measured accurately, especially to note any curvature or bow-out of the strip. The final strip dimensions were 4.28 x 0.28 x 0.010 in. Twelve identical strips were prepared in this manner and three strips were sent to each of four commercial plating companies using the "KANIGEN"[1] process to be coated with a 0.005-in. layer of electroless nickel on one side; the reverse side was masked in the usual manner employed by each company. The usual outgassing and/or stress-relieving heat treatment (180° ± 20°C for ~5 hr) for electroless nickel was requested for all strips. An additional specimen (No. D-Jan67), prepared in an identical manner and electroless nickel coated by one of the companies 1 yr earlier, was included in this study in order to determine the effect of shelf life on an electroless nickel deposit.

After the plated strips were returned, all dimensions were measured again. The curvature (ρ) of the coated strips was computed from measurements of total strip bow-out made by using a Gaertner Scientific Corporation optical comparator accurate to ±0.00005 in. and was used to calculate the residual plating stresses. Some uncertainty in the level of plating stresses calculated by using a single ρ for the entire composite would be expected due to edge effects and localized irregular curvatures. By measuring ρ over very short distances along representative strips from each group, a random variation in ρ of ±33% maximum was found. Since ρ enters into the calculations in the denominator of one term, a deviation in ρ would not necessarily affect the calculated stresses proportionately. Calculations showed that ±30% seems to be a reasonable estimate of the maximum variation and the nominal accuracy of the plating stresses reported here should be ~±20%. The bow-out of these strips was measured upon heating and cooling by viewing with the Gaertner comparator through an insulated glass window in a laboratory furnace while

[1] Trade-mark registered in the U.S.A. to General American Transportation Corporation.

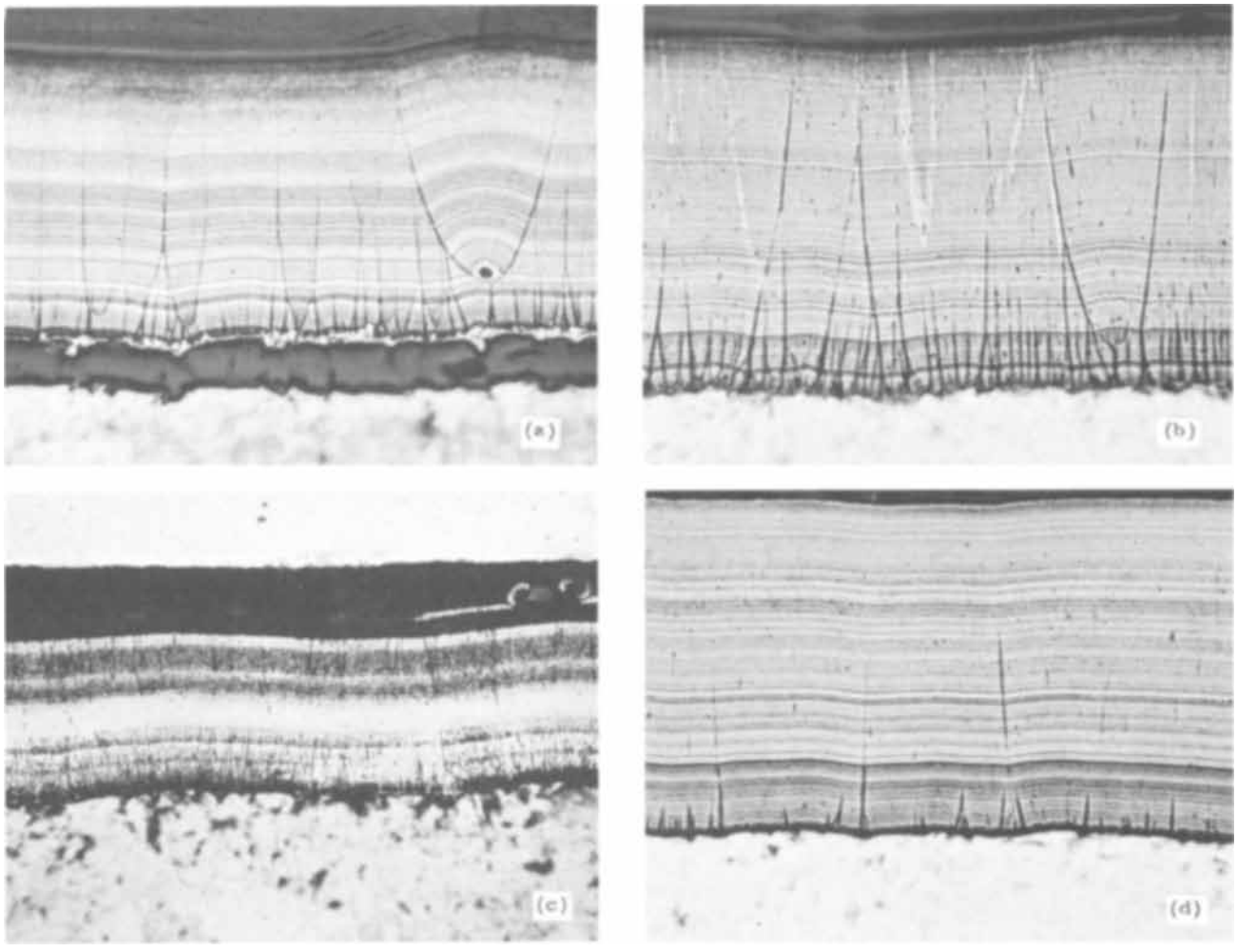

Fig. 1. Electroless nickel plated on beryllium, etched in 50% nitric acid plus 50% acetic acid: (a) specimen A2, 350X; (b) specimen B1, 350X; (c) specimen C1, 350X; (d) specimen D1, 350X.

heating to 200°C in ~3 hr and furnace cooling to room temperature in ~20 hr.

Results

The microstructures of the four commercially prepared electroless nickel deposits are shown in Fig. 1. There were slight differences in microstructure reflecting the different plating conditions used by each commercial plater; however, since the resulting microstructures were similar, any effect of plating conditions should be minimal. The thicknesses of nickel coatings deposited by each plater are summarized in Table I. The residual stresses resulting from plating electroless nickel on thin beryllium strips were calculated based on the model shown in Fig. 2; the derivation used in these calculations is given in the Appendix. The magnitudes of the plating stresses in the Be-$Ni_{(P)}$ composites are summarized in Table II. It is seen that the residual plating stresses (σ_{M2A}) are quite significant when compared with the nominal microyield strength of S-200 grade beryllium (~6000 psi). Temperature for electroless nickel deposition is normally about 90°C. A nickel-coated part is usually given a stress-relief aneal at ~190°C or higher for 1 hr/mil of coating thickness. To evaluate the effect of heat treatment on electroless nickel deposited on beryllium, one specimen from Company A (Specimen A-1) was received in the as-plated condition. This sample was bowed considerably less than the two strips plated and stress relieved by Company A. However, after a heat treatment up to 200°C and furnace cooling, the sample showed a curvature quite comparable with the others received from Company A

Table I. Thickness of electroless nickel deposited on beryllium strips

Company	Specimen identification	End near hole, mils			Center of strip, mils			End opposite hole, mils			Average, mils		
		Be	Ni	Ni + Be	Be	Ni	Ni + Be	Be	Ni	Ni + Be	Be	Ni	Ni + Be
A	A1	9.03	(a)	(a)	9.03	(a)	(a)	9.27	6.4	15.7	9.11	~6	
	A2	10.17	(a)	(a)	9.13	(a)	(a)	10.03			9.77		
	A3	9.57	(a)	(a)	7.67	(a)	(a)	9.93	5.9	15.8	9.06	~6	
B	B1	10.60	5.7	16.3	9.90	6.2	16.1	10.70	5.4	16.1	10.40	5.77	16.17
	B2	10.50	5.7	16.2	9.27	6.7	16.0	10.30	6.1	16.4	10.02	6.17	16.20
	B3	9.80	5.2	15.0	8.03	5.7	13.7	10.13	6.1	16.2	9.37	5.67	14.97
C	C1	8.83	3.40	12.23	8.07	3.56	11.63	8.87	3.36	12.23	8.59	3.44	12.03
	C2	10.03	3.07	13.10	8.93	2.87	11.80	9.87	3.60	13.47	9.61	3.18	12.79
	C3	9.47	3.33	12.80	8.67	4.70	13.37	10.57	3.23	13.80	9.79	3.75	13.32
D	D1	9.90	5.4	15.3	9.60	4.3	13.9	9.50	5.5	15.0	9.47	5.07	14.73
	D2	9.93	4.4	14.3	7.80	5.3	13.1	9.07	5.3	14.4	8.73	5.00	13.93
	D3	9.47	5.0	14.5	8.37	5.2	13.6	9.97	4.7	14.7	9.80	4.97	14.27

(a) Surface too rough to obtain accurate measurements of electroless-nickel-coating thickness.

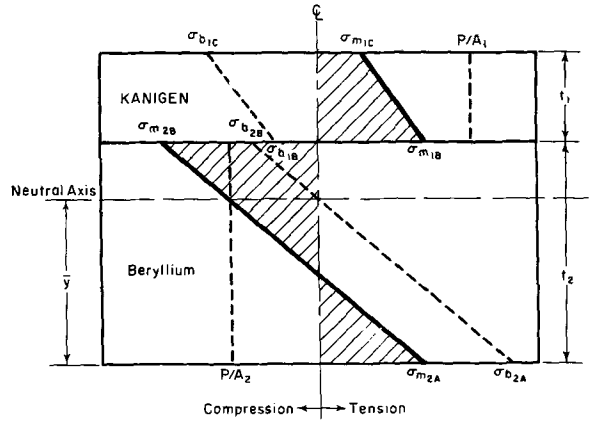

Fig. 2. Schematic representation of typical stress distribution in a cross section of an electroless-nickel-plated beryllium strip.

(see Fig. 3). Another strip (Specimen B-2) initially plated and given a stress-relief anneal by the plater was further heat treated at 240°C for 20 hr. The radius of curvature of this composite decreased from 13.68 to 8.63 in., and the computed maximum fiber stress in the beryllium at the interface ($\sigma_{M_{2B}}$) increased from 19,970 psi (compressive) to 31,670 psi (compressive). The results of the heat treatments are summarized in Table III.

Figure 3 shows the typical response to temperature variations observed for electroless-nickel-coated beryllium strips. The shapes of bow-out *vs.* temperature curves were all quite similar since the rate of change of bow-out with temperature was approximately constant. The only significant difference among all the beryllium strips was the magnitude of initial bow-out; this was reflected by a change in vertical displacement of the curves such as shown in Fig. 3. Strip A-1 (Fig. 3) was tested in the "as-plated" condition; heating to 190°C apparently resulted in a structural change within the $Ni_{(P)}$ layer as indicated by the irreversibility in the heating and cooling curves. Strips A-2 and A-3 were given a stress-relief anneal before testing, and these specimens retraced essentially the same curves upon heating and cooling. These results suggested that a solid-state reaction occurred upon heat treating at ~180°-190°C. This produced a volume change in the electroless-nickel microstructure which was constricted on one side by the beryllium substrate. Hence, an increased curvature of the composite resulted. These tests demonstrated that the $Ni_{(P)}$ deposits are metastable structures and that temperature excursions and/or heat treatments can in fact increase residual stresses which adversely affect dimensional stability. In the absence of structural changes in a coating, a change in curvature with variation in temperature resulted from a temperature dependence of the difference in coefficients of thermal expansion between beryllium and nickel, $\Delta\alpha = (\alpha_{Ni} - \alpha_{Be})_T$. This is seen by the reversibility of the change in bow-out upon heating and cooling observed for the composites. The $\Delta\alpha$ values were calculated by using the radius of curvature of the bowed beryllium-nickel composite as follows (16):

Table III. The effect of heat treatment on electroless nickel plated beryllium

Symbol[a]	Specimen A1 As-plated[b]	Specimen A1 Heat treated[c]	Specimen B2 As-plated plus stress relief anneal[d]	Specimen B2 Heat treated[e]
L, in.	0.0326	0.1108	0.1583	0.2533
ρ, in.	55.97	16.52	13.68	8.63
P, lb	7.32	24.82	34.47	54.37
$\bar{Y}$, mils	6.90	6.90	7.404	7.404
P/A_1, ksi	4.10	13.89	18.76	29.75
P/A_2 ksi	−2.70	−9.15	−11.55	−18.32
σb_{2A}, ksi	5.42	18.37	23.82	37.77
σb_{2B}, ksi	−1.74	−5.90	−8.42	−13.35
σb_{1B}, ksi	−1.19	−4.02	−5.73	−9.09
σb_{1C}, ksi	−4.40	−14.92	−19.27	−30.57
σM_{2A}, ksi	2.72	9.12	12.26	19.44
σM_{2B}, ksi	−4.44	−15.05	−19.97	−31.67
σM_{1B}, ksi	2.91	9.87	13.03	20.66
σM_{1C}, ksi	−0.30	−1.03	−0.51	−0.82

[a] L = deflection, ρ = radius of curvature of bowed strip, P = load, $\bar{Y}$ = neutral axis, σb = bending stress, σM = maximum fiber stress (see Fig. 2 and Appendix).
[b] Electroless nickel plated at 90°C.
[c] Heated to 200°C and furnace cooled.
[d] Stress-relief annealed at 190°C for 5 hr.
[e] Heated to 240°C for 20 hr and furnace cooled.

$$\Delta\alpha = \frac{(t_1 + t_2)\left\{3\left(1 + \frac{t_1}{t_2}\right)^2 + \left(1 + \frac{t_1E_1}{t_2E_2}\right)\left[\frac{t_1^2}{t_2^2} + \frac{1}{t_1E_1/t_2E_2}\right]\right\}}{6\rho\,\Delta T\left(1 + \frac{t_1}{t_2}\right)^2} \qquad [1]$$

Table II. Stress distribution in electroless nickel coated beryllium strips

Symbol[a]	Specimen A 1	Specimen A 2	Specimen A 3	Specimen B 1	Specimen B 2	Specimen B 3	Specimen C 1	Specimen C 2	Specimen C 3	Specimen D Jan. 1967	Specimen D 1	Specimen D 2	Specimen D 3
L	0.0326	0.1348	0.1102	0.1541	0.1583	0.1950	0.0730	0.0689	0.0674	0.0861	0.2753	0.2864	0.2056
b	0.2977	0.2942	0.3043	0.2929	0.2978	0.2966	0.2929	0.2898	0.2880	0.3130	0.2919	0.2913	0.2962
C	3.82	4.11	4.16	4.15	4.15	4.14	4.16	4.14	4.1	3.66	4.10	4.08	4.12
t_1	6	5	6	5.77	6.17	5.67	3.44	3.18	3.75	5.2	5.07	5.00	4.97
t_2	9.11	9.77	9.06	10.40	10.02	9.37	8.59	9.61	9.78	10.5	9.47	8.73	9.80
ρ	55.97	15.73	19.69	14.05	13.68	11.08	29.67	31.13	31.21	19.49	7.77	7.41	10.42
P	7.32	24.81	21.14	33.05	34.47	36.59	8.80	9.49	10.44	24.10	48.21	44.88	37.71
$\bar{Y}$	6.90	6.80	6.87	7.42	7.40	6.88	5.59	5.98	6.30	7.23	6.68	6.29	6.80
P/A_1	4.10	16.87	11.58	19.56	18.76	21.76	8.73	10.30	9.67	14.81	32.57	30.81	25.62
P/A_2	−2.70	−8.63	−7.67	−10.85	−11.55	−13.17	−3.50	−3.41	−3.70	−7.33	−17.44	−17.65	−12.90
σb_{2A}	5.42	19.01	15.36	23.24	23.82	27.32	8.28	8.46	8.88	16.33	37.82	37.37	28.70
σb_{2B}	−1.74	−8.32	−4.89	−9.34	−8.42	−9.88	−4.46	−5.13	−4.93	−7.38	−15.80	−14.47	−12.68
σb_{1B}	−1.19	−5.68	−3.33	−6.37	−5.73	−6.73	−3.04	−4.08	−3.36	−5.03	−10.78	−9.87	−8.64
σb_{1C}	−4.40	−15.21	−12.48	−18.69	−19.27	−22.09	−6.51	−6.56	−6.97	−13.04	−30.35	−30.11	−22.95
σM_{2A}	2.72	10.38	7.69	12.39	12.26	14.15	4.79	5.05	5.17	8.99	20.38	19.73	15.70
σM_{2B}	−4.44	−16.95	−12.56	−20.19	−19.97	−23.04	−7.95	−8.53	−8.63	−14.71	−33.24	−32.12	−26.57
σM_{1B}	2.91	11.19	8.25	13.19	13.03	15.03	5.69	6.22	6.31	9.78	21.79	20.94	16.98
σM_{1C}	−0.30	1.66	−0.90	0.87	−0.51	−0.33	2.22	3.74	2.11	1.77	2.22	0.70	2.67

[a] L = deflection (inch), b = strip width (inch), C = length of bowed strip (inches), t = thickness (mils); ρ = radius of curvature of bowed strip (inches), P = load (ksi), $\bar{Y}$ = neutral axis (mils), A = area (square inches), σb = bending stress (ksi), σM = maximum fiber stress (ksi) (see Fig. 2 and Appendix).

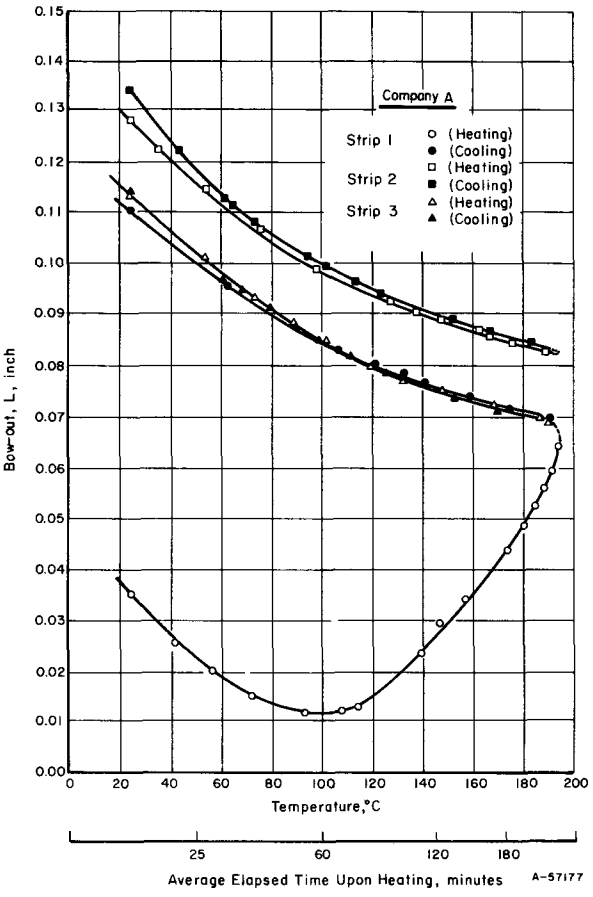

Fig. 3. Response of electroless-nickel-coated beryllium strips from company A to temperature variations.

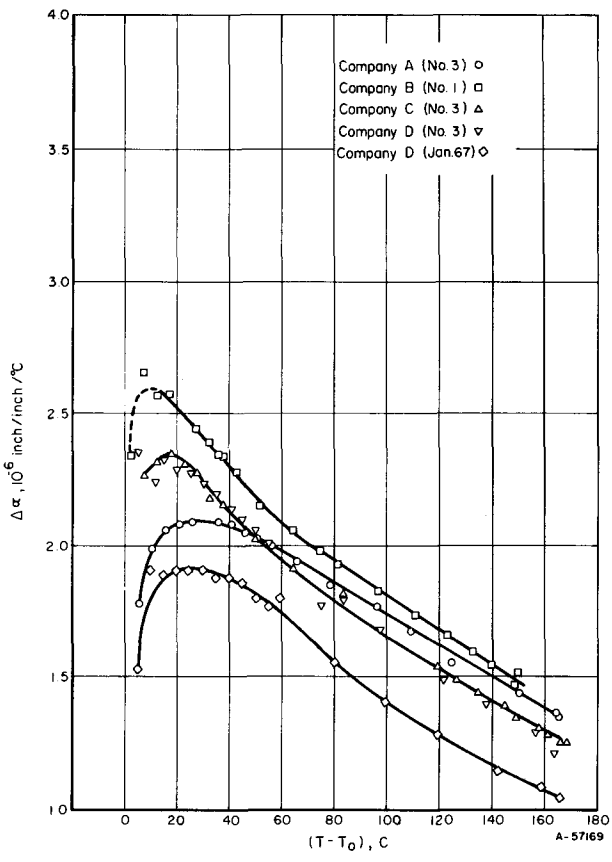

Fig. 4. Variation of the difference in coefficients of thermal expansion between electroless nickel and beryllium with temperature change.

and

$$\rho = \frac{C^2 + 4L^2}{8L} \qquad [2]$$

where ρ is radius of curvature, t is thickness, E is tensile modulus, T is temperature, C is length of bowed-composite, and L is bow-out (*see* Fig. 2). Figure 4 summarizes the variation of $(\alpha_{Ni} - \alpha_{Be})_T$ with change in temperature. The difference in coefficients of thermal expansion initially increased up to a temperature difference of $\Delta T \sim 20°C (T = 25°\text{-}50°C)$, then decreased at an approximately linear rate of

$$\sim 6 \times 10^{-9} \left(\frac{\text{in./in.}}{°C} \right) \Big/ °C$$

up to ~190°C which was the maximum temperature reached in these studies.

Discussion

Since the magnitude of bow-out for the Be-$Ni_{(P)}$ composites was used to calculate residual plating stresses, a thinner substrate allowed greater bending and in fact increased the sensitivity of the stress measurements; however, thin beryllium strips presented some problem in handling during masking, plating, cleaning, etc. Some bending of the strips during handling could have introduced error into the stress calculations. Yet, coated samples from each plating company were very consistent with respect to initial absolute amount of bow-out which suggests that either all strips within each group of three coated specimens were bent the same amount during handling or that the initial bending primarily reflected the specific coating conditions used. This latter explanation is more plausible. Also, the calculations for stress resulting from a difference in coefficients of thermal expansion utilized only the change in bow-out (ΔL) as a function of thermal treatment. Thus, the initial absolute value of bow-out was not a significant factor affecting these calculations and conclusions.

It is recognized that the use of electroless nickel coatings on beryllium will in fact produce deleterious residual stresses within the composite due to such factors as plating stresses, structural instability of the Ni+P lattice, difference in coefficient of thermal expansion, *etc.* Barnes stated that within the present state of technology there exists a necessity for using electroless nickel and that good engineering and process control should mitigate the inherent disadvantages (17). Barnes calculated the stress magnitude for an initially plane, 61-cm-diameter, 5.08-cm-thick, nickel-coated beryllium mirror resulting from a 10°C change in temperature. He reported that the change of stress in the beryllium substrate would be 0.006 ksi (tensile) and, in the nickel layer, 0.70 ksi (compressive). By using bow-out *vs.* temperature data such as shown in Fig. 3, the change in deflection (bow-out) with temperature can be approximated for two ranges of temperature as follows:

$$(T = 0 \text{ to } 100°C) \frac{\Delta L}{\Delta T} \sim 0.38 \text{ mil/°C}$$

$$(T = 100° \text{ to } 200°C) \frac{\Delta L}{\Delta T} \sim 0.2 \text{ mil/°C} \qquad [3]$$

Table IV summarizes the effect of a change in deflection resulting from a given thermal treatment on maximum fiber stresses at a Be-$Ni_{(P)}$ interface. From these data and by using the relationships given in Eq. [3], a change in temperature of 10°C would be expected to change the stress levels in a beryllium substrate and electroless-nickel layer by the following amounts:

Table IV. Effect of change in deflection on maximum fiber stress[a]

Specimen	Condition	Bow-out, L, mils	σ in Be, $\sigma_{M_{2B}}$, ksi	σ in Ni, $\sigma_{M_{1B}}$, ksi	ΔL, mils	$\Delta\sigma_{M_{2B}}$, ksi	$\Delta\sigma_{M_{1B}}$, ksi	$\Delta\sigma_{M_{2B}}$, ksi, ΔL, mil	$\Delta\sigma_{M_{1B}}$, ksi, ΔL, mil
A1	After stress relief	110.8	−15.05	9.87					
A1	As-plated	32.6	−4.44	2.91					
A1					88.2	+10.61	−6.96	+0.123	−0.089
B2	After HT at 240°C (20 hr)	253.3	−31.67	20.66					
B2	After stress relief	158.3	−19.97	13.03					
B2					95.0	+11.70	−7.63	+0.120	−0.092

[a] (−) = compressive stress; (+) = tensile stress.

$$\text{Max } \sigma \text{ in Be}(\sigma_{M_{2B}}): \left(0.38\frac{\text{mil}}{^\circ\text{C}}\right)\left(0.12\frac{\text{ksi}}{\text{mil}}\right)(10^\circ\text{C}) = +0.456 \text{ ksi} \quad [2]$$

$T = 0$-100°C,

$$\text{Max } \sigma \text{ in Ni}(\sigma_{M_{1B}}): \left(0.38\frac{\text{mil}}{^\circ\text{C}}\right)\left(-0.09\frac{\text{ksi}}{\text{mil}}\right)(10^\circ\text{C}) = -0.342 \text{ ksi}$$

$$\text{Max } \sigma \text{ in Be}(\sigma_{M_{2B}}): \left(0.2\frac{\text{mil}}{^\circ\text{C}}\right)\left(0.12\frac{\text{ksi}}{\text{mil}}\right)(10^\circ\text{C}) = +0.24 \text{ ksi}$$

$T = 100$°-200°C,

$$\text{Max } \sigma \text{ in Ni } (\sigma_{M_{1B}}): \left(0.2\frac{\text{mil}}{^\circ\text{C}}\right)\left(-0.09\frac{\text{ksi}}{\text{mil}}\right)(10^\circ\text{C}) = -0.18 \text{ ksi}$$

Whereas the change in compressive stress in an electroless-nickel deposit for a 10°C temperature is in fair agreement with Barnes (17), the residual stress change in a beryllium substrate differs greatly. This difference can be rationalized by considering the derivations used to calculate stress levels. Barnes used a plate model with strain depending only on the temperature change, ignoring any stress relief by bending. A Beam model was used in the present study and stress levels were deflection governed (*see* Appendix) with deformation a function of the relative elastic moduli and thicknesses of a beryllium substrate and the nickel layer. The important difference between these two approaches is that the present study recognized the influence of volume changes of the nickel layer as a determinant of imposed stress. Barnes assumed that since plating is done at 80°-100°C, a stress-free layer is deposited and that subsequent cooling to room temperature produces some stresses in the composite (temperature-governed). This was, indeed, observed here. However, he further assumed that significant stress relief may occur at the 190°C anneal commonly given to electroless-nickel deposits, whereas it was shown that this treatment causes finite volume changes in the Ni+P metastable structure, thereby increasing the magnitude of the residual stresses in the Be-$Ni_{(P)}$ composite.

It is well substantiated in the literature that no precipitation of Ni_3P occurs at temperatures below 200°C. Contraction of a metastable Ni+P lattice detected in this study by a change in curvature upon heating to 200°C is most probably a transformation of the electroless-nickel lattice from a structure of relative disorder to one of higher order. This is likely to be an ordering of nickel and phosphorus atoms in the first stage of forming a Guinier-Preston type of zone. It is evident that more information is needed about the behavior of electroless nickel, not only to define the as-plated structure but also to study the precipitation kinetics and the relative interplay of volume effects and temperature response ($\Delta\alpha$) of an electroless-nickel-coated/metallic substrate composite.

For most applications of electroless nickel, residual stresses of the order found above can be tolerated; however, for diffraction-limited precision optical surfaces, these stresses may produce unacceptable distortions.

Summary

1. Electroless-nickel deposition on beryllium results in a significant level of residual stress within a composite due to both volume effects and temperature response.

2. Upon heating to temperatures below 200°C, a contraction in the metastable Ni+P structure results, presumably from a transformation to a more ordered lattice, probably the first stage in development of G-P zones. This leads to high stresses in the electroless-nickel deposit and its substrate.

3. Temperature-imposed stresses in Be-$Ni_{(P)}$ composites result from a difference in coefficients of thermal expansion. This difference $(\alpha_{Ni} - \alpha_{Be})_T$ increases in the range 25°-50°C and then decreases approximately linearly at a rate of $\sim 6 \times 10^{-9}\left(\frac{\text{in./in.}}{^\circ\text{C}}\right)/^\circ$C.

4. The temperature response of electroless-nickel-plated beryllium was independent of commercial plater and reproducible upon repeated thermal cycling after any volume effects were stabilized.

5. Stresses at the interface of a Be-$Ni_{(P)}$ composite after plating at ~ 90°C and cooling to ambient temperature in the order of 2000-5000 psi can be expected to increase after a stress relief anneal to 10,000-15,000 psi due to volume effects.

Acknowledgment

This research was sponsored by Advanced Research Project Agency under Contract Number DAAH 01-68-C-0018 and Perkin-Elmer Corporation under Subcontract Number 92010-PB.

Manuscript submitted Sept. 30, 1968; revised manuscript received Dec. 6, 1968.

Any discussion of this paper will appear in a Discussion Section to be published in the December 1969 JOURNAL.

REFERENCES

1. A. Brenner, *Metal Finishing*, **52**, 68 (1954).
2. G. Gutzeit, *Plating*, **46**, 1158, 1275, 1377 (1959).
3. A. Brenner and G. E. Riddell, *J. Research NBS*, **37** 1-4 (1946); *Proc. Am. Electroplaters' Soc.*, **33**, 16 (1946).
4. A. Brenner and G. E. Riddell, *J. Research NBS*, **39**, 385-395 (1947); *Proc. Am. Electroplaters' Soc.*, **34**, 156 (1947).
5. G. Gutzeit and E. T. Mapp, *Corrosion Technol.*, **3**, 331 (1956).
6. A. W. Goldenstein, W. Rostoker, F. Schossberger, and G. Gutzeit, *This Journal*, **104**, 104 (1957).
7. K. T. Ziehlke, W. S. Dritt, and C. H. Mahoney, *Metal Progr.*, **77**, 84 (1960).
8. A. H. Graham, R. W. Lindsay, and H. J. Read, *This Journal*, **109**, 1200 (1962).
9. A. H. Graham, R. W. Lindsay, and H. J. Read, *ibid.*, **112**, 401 (1965).
10. J. Dixmier and K. Doi, *Compt. Rend.*, **257**, 2451 (1963).
11. J. P. Randin, P. A. Maire, E. Saurer, and H. E. Hintermann, *This Journal*, **114**, 442 (1967).

12. A. Albert, Z. Kovak, H. R. Lilienthal, T. R. McGuire, and Y. Nakamura, *J. Appl. Phys.*, **38**, 1258 (1967).
13. J. P. Randin and H. E. Hintermann, *Plating*, **54**, 523 (1967).
14. W. G. Lee, *ibid.*, **47**, 288 (1960).
15. L. Domnikov, *Metal Finishing*, **59**, 52 (1961).
16. A. G. H. Dietz, "Engineering Laminates," p. 354, John Wiley & Sons, New York (1949).
17. W. P. Barnes, Jr., *Appl. Optics*, **5**, 701 (1966).

APPENDIX

Calculation of Residual Stresses

Procedures and formulas adapted from (a) S. Timoshenko, "Strength of Materials," pp. 217-219, P. Van Nostrand Co., (b) Albert G. H. Dietz, "Engineering Laminates," p. 354, John Wiley & Sons, New York (1949).

From Dietz: $\delta = \Delta\alpha\Delta T = f(\rho, E_1, E_2, t_1, t_2)$

$$\text{(from Fig. A-1)}\quad P/A = \frac{E\delta L}{L}$$

Assume: coating and strip are the same length (L); then Fig. A-2 is equivalent to Fig. A-1, resulting in the appearance of a net moment as shown in Fig. A-2.

$$M = \frac{EI}{\rho}$$

$$I = \frac{bt^3}{12}$$

$$\frac{PL}{A_1E_1} + \frac{PL}{A_2E_2} = \delta L \qquad [A\text{-}1]$$

$$P\left(\frac{1}{A_1E_1} + \frac{1}{A_2E_2}\right) = \frac{\delta L}{L} \qquad [A\text{-}2]$$

$$P\left(\frac{bt_2E_2 + bt_1E_1}{b^2t_1E_1t_2E_2}\right) = \frac{\delta L}{L} \qquad [A\text{-}3]$$

$$P = \frac{\delta L}{L}\left(\frac{bt_1t_2E_1E_2}{t_1E_1 + t_2E_2}\right) \qquad [A\text{-}4]$$

$$\sigma_{m2} = -\frac{P}{A_2} + \frac{t_2E_2}{2\rho} \qquad [A\text{-}5]$$

$$\sigma_{m1} = +\frac{P}{A_2} - \frac{t_1E_1}{2\rho}$$

Equation [A-5] does not consider the neutral axis; therefore, construct a beam of one material to replace the composite having the same stiffness (AE) and dimensions (b, t_1, t_2) but an irregular cross section (Fig. A-3).

Equivalent stiffness

$$A_1{}^1E_2 = A_1E_1$$

$$E_2b\left(\frac{E_1}{E_2}\right)t_1 = bE_1t_1$$

$$I_y = \frac{bt_2^3}{12} + A_1{}^1d_2{}^2 + \frac{b\left(\frac{E_1}{E_2}\right)t_1^3}{12} + A_1{}^2d_1{}^2 \qquad [A\text{-}6]$$

$$\bar{y}\left(bt_2 + b\frac{E_1}{E_2}t_1\right) = bt_2\frac{t_2}{2} + \left(\frac{E_1}{E_2}\right)bt_1\left(t_2 + \frac{t_1}{2}\right) \qquad [A\text{-}7]$$

$$\bar{y} = \frac{\frac{t_2^2}{2} + \left(\frac{E_1}{E_2}\right)\left[t_1t_2 + \frac{t_1^2}{2}\right]}{t_2 + (E_1/E_2)t_1} \qquad [A\text{-}8]$$

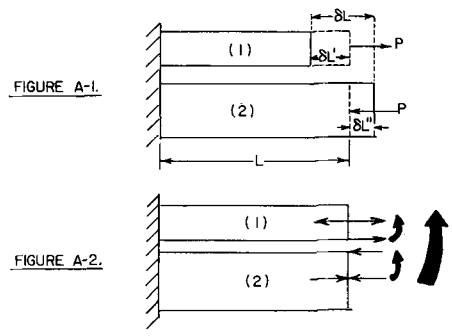

FIGURE A-1.

FIGURE A-2.

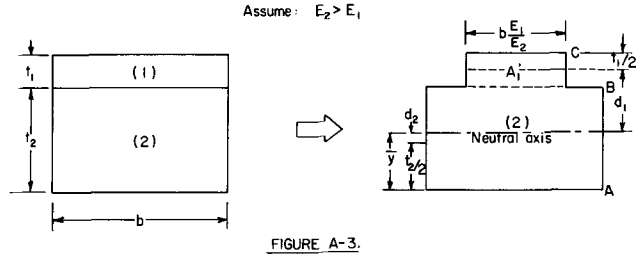

FIGURE A-3.

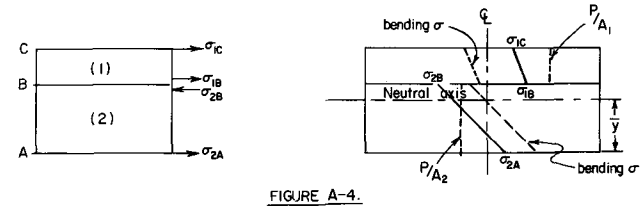

FIGURE A-4.

$$\bar{y} = \frac{\frac{t_2^2}{2} + \left(\frac{E_1}{E_2}\right)\frac{t_1^2}{2} + \left(\frac{E_1}{E_2}\right)t_1t_2}{t_2 + (E_1/E_2)\,t_1} \qquad [A\text{-}9]$$

$$d_2 = \bar{y} - \frac{t_2}{2} = \frac{\left(\frac{E_1}{E_2}\right)t_1^2 + \left(\frac{E_1}{E_2}\right)t_1t_2}{2t_2 + 2t_1(E_1/E_2)} \qquad [A\text{-}10]$$

$$d_1 = \left(t_2 + \frac{t_1}{2}\right) - \bar{y} = \frac{t_2^2 + t_1t_2}{2t_2 + 2t_1\,(E_1/E_2)} \qquad [A\text{-}11]$$

$$I = \frac{bt_2^3}{12} + bt_2\left[\frac{(E_1/E_2)t_1^2 + (E_1/E_2)t_1t_2}{2t_2 + 2t_1\,(E_1E_2)}\right]^2 + \frac{b(E_1/E_2)t_1^3}{12} + (E_1/E_2)\,bt_1\left[\frac{t_2^2 + t_1t_2}{2t_2 + 2t_1\,(E_1/E_2)}\right]^2 \qquad [A\text{-}12]$$

Let:

$$e = \frac{E_1}{E_2}$$

$$I = \frac{b}{4}\left\{\frac{t_2^3 + et_1^3}{3} + \left[\frac{e^2t_1^4t_2 + 2et_1^3t_2^2 + e^2t_1^2t_2^3 + et_1t_2^4 + 2et_1^2t_2^3 + et_1^3t_2^2}{t_2^2 + 2et_1t_2 + e^2t_1^2}\right]\right\} \qquad [A\text{-}13]$$

$$P = \frac{E_2b}{2\rho(t_1 + t_2)}\left\{\frac{t_2^3 + et_1^3}{3} + \left[\frac{et_1t_2(et_1^3 + 2et_1^2t_2 + et_1t_2^2 + t_2^3 + 2t_1t_2^2 + t_1^2t_2)}{t_2^2 + 2et_1t_2 + e^2t_1^2}\right]\right\} \qquad [A\text{-}14]$$

$$P = \frac{E_2b}{2\rho(t_1 + t_2)}\left\{\frac{t_2^3 + (E_1/E_2)t_1^3}{3} + \left[\frac{(E_1/E_2)t_1t_2\{(E_1/E_2)t_1^3 + t_1^2t_2(2(E_1/E_2) + 1) + t_1t_2^2[2 + (E_1/E_2)] + t_2^3\}}{t_2^2 + 2(E_1/E_2)t_1t_2 + (E_1/E_2)^2t_1^2}\right]\right\} \qquad [A\text{-}15]$$

Maximum Fiber Stress: (*see* Fig. A-4)

$E_2 > E_1$

tension = +

compression = −

$$\text{uniform stress} = \frac{P}{A}$$

$$\text{bending stress} = \frac{M\bar{y}}{I}(E_1/E_2) \text{ or } \frac{E\bar{y}}{\rho}$$

$$\sigma_{2A} = -\frac{P}{A_2} + \frac{E_2\bar{y}}{\rho} \quad [A\text{-}16]$$

$$\sigma_{2B} = -\frac{P}{A_2} - \frac{E_2(t_2 - \bar{y})}{\rho} \quad [A\text{-}17]$$

$$\sigma_{1B} = +\frac{P}{A_1} - \frac{E_1(t_2 - \bar{y})}{\rho} \quad [A\text{-}18]$$

$$\sigma_{1C} = +\frac{P}{A_1} - \frac{E_1(t_1 + t_2 - \bar{y})}{\rho} \quad [A\text{-}19]$$

α = coefficient of thermal expansion
T = temperature
ρ = radius of curvature
E = modulus of elasticity
t = thickness
A = area
L = length
M = bending moment
I = moment of inertia
P = load
σ_m = maximum stress
σ_b = bending stress
b = width
$\bar{y}$ = neutral axis
$(E_1)_{Ni(P)} \cong 30 \times 10^6$ psi
$(E_2)_{Be} \cong 44 \times 10^6$ psi

The Infrared Interference Method of Measuring Epitaxial Layer Thickness

P. A. Schumann, Jr.*

International Business Machines Corporation, Components Division, East Fishkill Laboratory, Hopewell Junction, New York

ABSTRACT

The infrared interference method of measuring the layer thickness of silicon layers deposited on heavily doped substrates of the same type is a well-known technique. The correction factors and theoretical models in existence are discussed and their limits of application defined. It is shown that, for most cases, it is not necessary to correct for the profile of impurities in the epitaxial layer due to out-diffusion and autodoping. A new method of calculating the thickness from the interference maxima and minima is presented which includes the phase shift and wave-length dependence of the reflection at the layer-substrate interface. It is shown that, with a spectrophotometer capable of scanning the wave-length range 2.5-50μ, layer thicknesses to 0.8μ can be measured. Comparisons are made between this technique, a stain technique, and the spreading resistance technique for N/N$^+$ and P/P$^+$ silicon with layer thicknesses from 1.5 to 16μ. The precision of the infrared interference technique is quoted and correlation curves between the techniques are presented.

The infrared interference method of measuring the thickness of epitaxial layers deposited on highly doped substrates of the same conductivity type is accepted as a precise and useful technique. It has primarily been used on silicon but some use has been made on germanium. The technique was introduced by Spitzer and Tanenbaum (1) in 1961. Later that same year, Grochowski and Pliskin (2) described improved measurement techniques and compared the infrared interference technique with a stain technique. Albert and Combs (3) discussed the technique, again comparing it with a stain. They developed fringe charts and pointed out that as the reflectivity of the layer-substrate interface was changing with wave length, the positions of the maxima and minima must be determined by the envelope technique. Several of the preceding papers discussed the conditions necessary for interference fringes to be observed. It was pointed out by Schumann, Phillips, and Olshefski (4) that the phase shift on reflection at the layer-substrate interface was a function of wave length and must be accounted for in calculating the thickness. These phase shifts were tabulated (5, 6) and have been used successfully for routine measurement. Two papers (7, 8) were published on the effects of the impurity profile due to out-diffusion and autodoping in the epitaxial layer on the reflection spectra of N/N$^+$ silicon wafers. Abe and Kato (7) describe the reflection in terms of a multilayered step function approximation to a complimentary error function profile. Sato, Ishikawa, and Sagawara (8) developed an effective index of refraction of the layer which accounts for the same type of profile. It is shown in this paper that it is not necessary to account for the impurity profile in the epitaxial layer if errors ranging up to 4% in thickness can be tolerated, provided the wave-length dependence of the phase shift and reflectivity of the layer-substrate interface are incorporated in the calculations.

The precision of the technique is perhaps the best of any of the commonly used semiconductor materials measurements. The multilaboratory three sigma precision of the technique as determined by the ASTM (9) using phase shift corrections and the average of all peaks and valleys obtained for N/N$^+$ silicon layers greater than 5μ is $\pm$ (0.005t + 0.25μ) and for the P/P$^+$ silicon layers is $\pm$ (0.025t + 0.25μ) where t is the thickness of the layer to be measured in microns. For this paper, measurements on three wafers with thicknesses of 2, 4, and 8μ were made with a Perkin-Elmer

* Electrochemical Society Active Member.

621 spectrophotometer over a period of 3 weeks to determine single instrument precision. The reading of the position of a single peak or valley resulted in a standard deviated (pooled) of 0.72%. Thickness obtained from a single peak or valley using the new corrections contained in this report had a standard deviation of 0.82%. In previously published work (2, 3), the technique was compared with various staining procedures but no firm correlation curve was ever established.

The spreading resistance technique (10, 11) of measuring impurity profiles in epitaxial layers is well suited for comparison with the infrared interference technique. The impurity profile thus determined can be compared with the thickness obtained with the infrared interference technique.

Theory

For the reflection from the step function system shown in Fig. 1, neglecting polarization effects which will be small if the angle of incidence is equal to or less than 30°

$$R = \frac{r_1^2 + r_2^2 - 2r_1r_2 \cos(\delta - \phi)}{1 + r_1^2r_2^2 - 2r_1r_2 \cos(\delta - \phi)}$$

where

$$r_1^2 = \left(\frac{n_1 - n_0}{n_1 + n_0}\right)^2, \quad r_2^2 = \frac{(n_2 - n_1)^2 + k_2^2}{(n_2 + n_1)^2 + k_2^2};$$

$$\delta = \frac{4\pi n_1 h}{\lambda}\left(1 - \frac{n_0^2}{n_1^2}\right) \sin^2 \phi_0$$

and

$$\phi = \tan^{-1}\left(\frac{2n_1k_2}{n_1^2 - n_2^2 - k_2^2}\right)$$

where

- n_i is the index of refraction
- k_i is the extinction coefficient
- R is the reflectivity of the layer-substrate system
- r_1^2 is the reflectivity of the air-layer interface
- r_2^2 is the reflectivity of the layer-substrate interface
- θ is the phase shift on reflection at the layer-substrate interface
- ϕ is the angle of incidence
- λ is the wave length in vacuum

The factors n_i and k_i are associated with the real and complex part of the complex index of refraction, $n^* = n - ik$. Polarization effects can be neglected in this case because, at 30° angle of incidence, the error in reflectivity between r_1^2 and an expression including polarization is less than 1% at $\lambda = 50$ μm. Due to the high index of refraction of the epitaxial layer, the angle of incidence at the layer-substrate interface has a maximum of 8° with a 30° angle of incidence at the air-layer interface. The error in r_2^2 is then much less than 1%. Both errors are much less than that at $\lambda = 2$ μm.

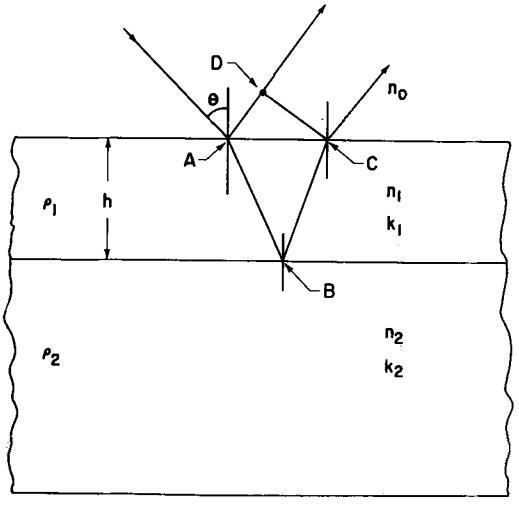

Fig. 1. Basic geometry of infrared interference technique

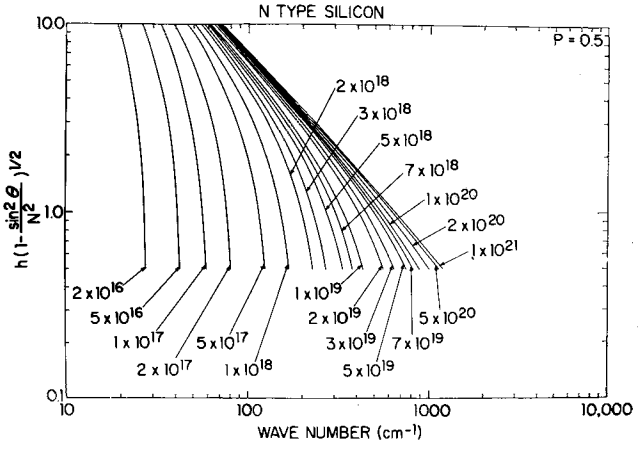

Fig. 2. Sample of thickness charts for N-type silicon. Normalized thickness is plotted as a function of the position of the minima, $P = 1/2$, for various substrate impurity concentrations.

The value of R was numerically calculated and the positions of the maxima and minima determined. This was performed on an IBM 7094 computer using the theory for the optical constants described earlier (4, 12) and produced a series of graphs (13) similar to Fig. 2.[1] The approximate order is usually known, but if not it may be calculated from

$$P_{k+m} = \frac{m\nu_{k+m}}{u_{k+m} - \nu_R} + \frac{1}{2} - \frac{\theta_k u_{k+m} - \theta_{k+m} u_k}{2\pi(\nu_{k+m} - u_k)}$$

where

- P_{k+m} is the order of the $k + m$'th fringe,
- u_i is the wavenumber of the i'th fringe
- θ_i is the phase shift at the layer-substrate interface for u_i

These charts then make it possible to find the thickness of the epitaxial layer without any calculations for the various orders. They include the phase shift corrections, and since they are the position of the actual maxima or minima as observed they preclude the use of the envelope tangent method. The difference between this technique and the phase shift correction scheme will be greatest for very thin layers. Figure 3 shows a calculated reflectivity for an N/N$^+$ structure with a layer thickness of 0.5μ. The position of the maxima is quite different from the tangent point of the envelope curve which is also calculated.

The phase shift corrections apply a correction of about +8% and the charts about +6% to the uncorrected thickness values for thicknesses between 1 and 10μ. For this comparison the phase shift and uncorrected thicknesses were calculated from

$$t_{k+m} = \left(P_{k+m} - \frac{1}{2} + \frac{\theta_{k+m}}{2\pi}\right) \frac{1}{2\nu_{k+m}\,[n_1^2 - \sin^2\phi_0]^{1/2}}$$

[1] Note: A complete set of curves is available from the author on request.

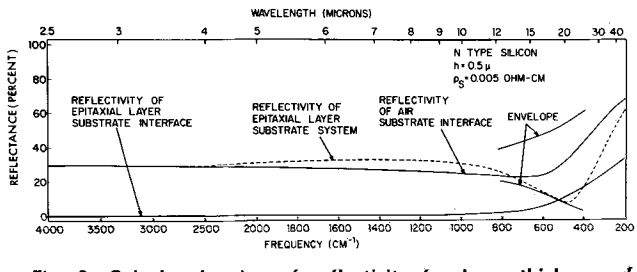

Fig. 3. Calculated value of reflectivity for layer thickness of 0.5μ showing tangent envelope.

Table I. Comparison of infrared interference with various techniques to measure epitaxial thickness showing correlation equations and experimental error of fit of correlation curve

Treatment @1200°C	T1 t_s	T1 t_{IR}	T1 t_{SRP}	T1 t_{SRS}	T1 t_{SRHP}	T2 t_s	T2 t_{IR}	T2 t_{SRP}	T2 t_{SRS}	T2 t_{SRHP}	T3 t_s	T3 t_{IR}	T3 t_{SRP}	T3 t_{SRS}	T3 t_{SRHP}
None	4.75	4.91	5.3	4.9	4.8	6.9	7.30	7.3	7.2	7.1	0.78	1.17	1.32	0.97	0.85
30 min	4.42	4.85	5.3	4.6	4.5	6.5	7.19	7.4	6.7	6.5	0.63	1.21	1.32	0.74	0.65
60 min	—	4.82	5.4	4.2	4.1	—	7.03	7.3	6.3	6.0	—	—	—	—	—
90 min	—	4.72	5.0	4.1	4.1	—	—	—	—	—	—	—	—	—	—
Maximum charge (per cent)	—	3.9	7.4	16.3	14.6	—	3.9	1.3	12.5	15.5	19.3	3.3	0	23.7	23.5

For the uncorrected case θ_{k+m} was assumed to be zero. In all cases, the thickness was obtained for all the maxima and minima observed, and averaged. As many as 12 orders were observed in some cases. The variance of all the thickness values was calculated about the mean and averaged over all the wafers measured. The square root of the average variance is a measure of the consistency of the technique and was 9.2% uncorrected, 5.1% phase shift corrected, and 3.6% chart corrected.

Comparison with Stain and Spreading Resistance

The wafers measured by the infrared interference technique were beveled at a shallow angle and spreading resistance profiles were made. The bevels were later stained with a silver stain (14) whose composition was: 100 ml 48% HF, 2 ml HNO_3, and 1 ml $AgNO_3$ sol.

The silver nitrate solution was composed of 2g $AgNO_3$ in 100 ml H_2O. The stain was developed with illumination and observed under low magnification. As soon as bubbles began to appear, the stain was quenched with water. The thickness thus read is labeled t_S.

The spreading resistance profiles were made by the technique described earlier (11). A sample profile is shown in Fig. 4. Several techniques were used to determine the thickness from the profile. It is clear because it is a profile that there is no definite demarcation of thickness. The slope method used the intersection of the tangent of the downward portion of the profile and the tangent line to the peak value, labeled t_{SRS}. The thickness of maximum impurity concentration is labeled t_{SRP}, and the thickness of half the maximum impurity concentration, t_{SRHP}. These thickness values along with those determined by the infrared interference method are shown in Fig. 4 for that sample. The general relationships between these thickness values and the rms per cent error of the fit of the correlation curves which was obtained by a least squares technique are given in Table I. The best agreement from 1 to 10μ is with the spreading resistance peak technique, as the infrared interference technique indicates a thickness slightly less than the peak concentration.

All wafers studied in this report were grown in a horizontal epitaxial reactor by the hydrogen reduction of $SiCl_4$ at 1210°C with a 2-min postdeposition bake in hydrogen at the deposition temperature.

The half peak technique should be the most accurate indication of the metallurgical interface. The stain technique seems to indicate a position on the profile below the peak. The spreading resistance slope technique and the stain indicate almost the same thickness.

Effect of Altered Profile

Three of the wafers grown by the standard epitaxial process were subjected to various heat treatments in order to alter the impurity profile in the layer. These layers had nominal thickness of 1.77, 4.91, and 7.3μ before heat treatment. The same stain, infrared, and spreading resistance techniques were used to determine thickness. The uncorrected spreading resistance profiles are shown in Fig. 5, 6, and 7. It is apparent from these that the impurity profile was altered significantly by the heat treatments. Table II lists the results obtained by the various thickness methods described. Figure 8 is a plot of the per cent change in thickness from the untreated case as a function of the heat treatment time averaged over all the wafers. The infrared interference technique of measuring the thickness is much less sensitive to changes in the impurity profile than all of the other techniques except the spreading resistance peak method.

The stain technique was not able to resolve those layers which were heat treated more than 30 min. The stain region was too broad and shaded. With the exception of the data point at 60 min, the infrared and spreading resistance values track very well. In all cases, the spreading resistance slope and spreading resistance half-peak values were comparable.

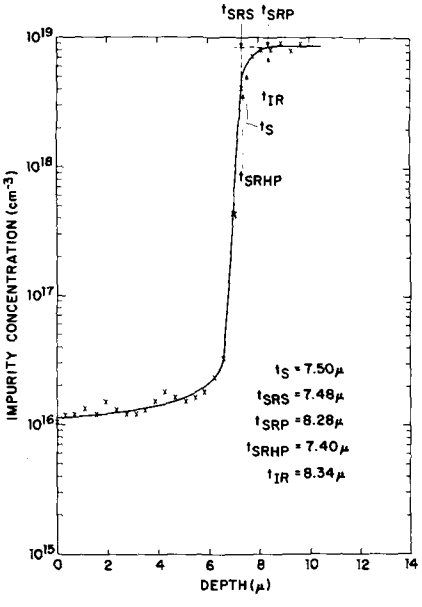

Fig. 4. Sample spreading resistance profile of epitaxial N/N⁺ structure showing position of thickness measurements.

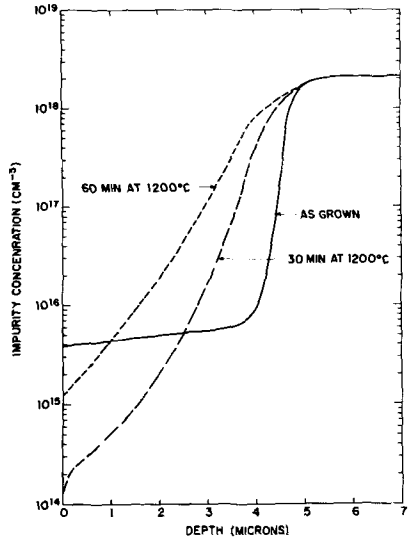

Fig. 5. Effect of heat treatment time at 1200°C on the profile of an N/N⁺ silicon epitaxial layer, T1, as obtained by spreading resistance.

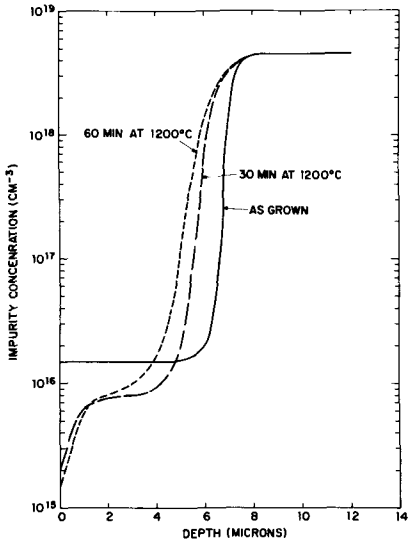

Fig. 6. Effect of heat treatment time at 1200°C on the profile of an N/N+ silicon epitaxial layer, T2, as obtained by spreading resistance.

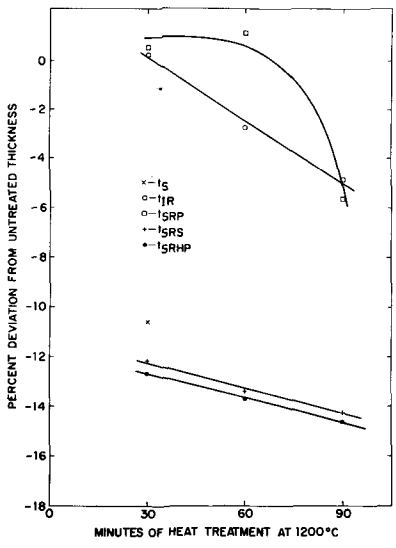

Fig. 8. Per cent deviation from untreated thickness as a function of heat treatment time at 1200°C for the various thickness measurements.

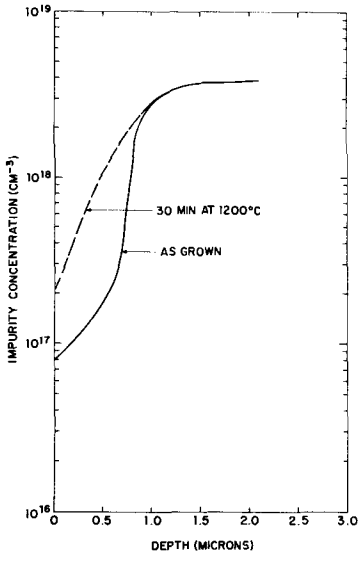

Fig. 7. Effect of heat treatment time at 1200°C on the profile of an N/N+ di silicon epitaxial layer, T3, as obtained by spreading resistance.

Conclusions

Several conclusions can be drawn regarding N/N+ and P/P+ epitaxial silicon from the data presented in this paper:

1. The infrared interference method measured the location in depth of a point on the impurity profile which is close to the maximum impurity concentration. The measured thickness decreases as the profile becomes less abrupt.

Table II. Comparison of various techniques to measure epitaxial layer thickness as a function of heat treatment to alter profiles

Technique	Correlation equation with infrared influence	RMS error of fit, %
Stain	$t_{IR} = 1.054\, t_s + 0.196$	10.1
Spreading resistance slope	$t_{IR} = 1.018\, t_{SRS} + 0.272$	6.6
Spreading resistance peak	$t_{IR} = 0.936\, t_{SRP} + 0.058$	7.5
Spreading resistance half peak	$t_{IR} = 1.022\, t_{SRHP} + 0.327$	7.0

2. The stain method measures a position on the steep portion of the impurity profile which is approximately that given by the spreading resistance slope technique.

3. The infrared interference technique as practiced in this paper is relatively independent of the shape of the impurity profile and thus for the variations in profiles normally encountered it is not necessary to incorporate additional profile corrections. For the drastically altered profiles a maximum change of 4% in thickness was measured.

4. Both the single-instrument and multilaboratory precisions are good for the infrared interference technique as practiced in this paper.

5. The lower limit of measurable thickness is 0.8 μm if a 4% error can be tolerated. Thinner layers can be measured but the effects of the profile become more important.

Acknowledgments

The author would like to acknowledge the experimental assistance of Mr. C. P. Schneider who made the measurements reported. He would also like to thank Mr. C. M. Sakkas for programming the IBM 7094 computer to perform the calculations.

Manuscript submitted April 29, 1968; revised manuscript received ca. Nov. 30, 1968. This paper was presented at the Boston Meeting, May 5-9, 1968, as Paper 82.

Any discussion of this paper will appear in a Discussion Section to be published in the December 1969 JOURNAL.

REFERENCES

1. W. G. Spitzer and M. Tanenbaum, *J. Appl. Phys.*, **32**, 744 (1961).
2. E. G. Grochowski and W. A. Pliskin, Paper presented at Electrochem. Soc. Meeting, Detroit, Oct. 1-5, 1961.
3. M. P. Albert and J. F. Combs, *This Journal*, **109**, 709 (1962).
4. P. A. Schumann, Jr., R. P. Phillips, and P. J. Olshefski, *ibid.*, **113**, 368 (1966).
5. P. A. Schumann, Jr., and R. P. Phillips, IBM Tech. Report, TR 22.182 (1965).
6. P. A. Schumann, Jr., IBM Tech. Report, TR 22.432 (1967).
7. T. Abe and T. Kato, *Japan. J. Appl. Phys.*, **4**, 742 (1965).
8. K. Sato, Y. Ishikawa, and K. Sugawara, *Solid-State Electron.*, **9**, 771 (1966).
9. American Society for Testing and Materials, "Method of Test for Thickness of Epitaxial Layers of Silicon on Substrates of the Same Type by Infrared Reflectance," F80-67T (1967).
10. R. G. Mazur and D. H. Dickey, *This Journal*, **113**, 255 (1966).

11. E. E. Gardner, P. A. Schumann, Jr., and E. F. Gorey, "Measurement Techniques for Thin Films," B. Schwartz and N. Schwartz, Editors, p. 258, Electrochemical Society, New York (1967).
12. P. A. Schumann, Jr., and R. P. Phillips, *Solid-State Electron.*, **10**, 943 (1967).
13. P. A. Schumann, Jr., and C. M. Sakkas, IBM Tech. Report, TR 22.537 (1968).
14. V. Doo, IBM Components Division, Hopewell Junction, Unpublished data.

Preparation and Properties of Epitaxial Gallium Arsenide

M. Maruyama, S. Kikuchi, and O. Mizuno

Central Research Laboratories, Nippon Electric Company, Limited, Kawasaki, Japan

ABSTRACT

High-purity epitaxial layers of n-type gallium arsenide have been grown by vapor deposition, using the reaction of arsenic trichloride with gallium. The purity of the layers was significantly increased when nominal 99.9999+% arsenic trichloride was substituted for nominal 99.999+% material. When the less-pure arsenic trichloride was used, there was a systematic variation in the electrical properties of layers grown in successive runs with the same gallium source. Resistivity and Hall coefficient measurements were made between 300° and 4.2°K. The maximum electron Hall mobilities were 9180, 164,000, and 175,000 cm^2/v-sec at 300°, 77°, and 50°K, respectively. No impurity band conduction was observed even at 4.2°K in pure samples.

Recent work on GaAs (1-4) has indicated that vapor phase epitaxial growth using the reaction (5) of arsenic trichloride with gallium is an excellent method to prepare high-purity and high-mobility gallium arsenide. We have used the method and obtained layers with maximum electron Hall mobility up to 175,000 cm^2/v-sec and room-temperature mobility up to 9180 cm^2/v-sec, carrier concentrations usually being in the range 1 x 10^{14}-4 x 10^{14} cm^{-3}. It is the purpose of this report to describe the preparation and electrical properties of high-purity gallium arsenide epitaxial layers grown from the vapor phase by using the reaction of arsenic trichloride with gallium.

Growth Procedure and Electrical Measurements

Starting materials were gallium (Eagle-Picher Industries 99.99999%), arsenic trichloride (Mining and Chemical Products 99.999% and Mitsubishi Metal Mining Company 99.9999%), and palladium-diffused hydrogen.

The substrates were Cr-doped semi-insulating GaAs (room-temperature resistivity $> 10^8$ ohm-cm) prepared by horizontal boat growth and cut in the (100) plane. The wafers with mirrorlike surfaces were obtained by lapping with Carborundum and mechanical polishing with diamond paste on a rotating pad. They were degreased in boiling trichloroethylene three times and stored in ethyl alcohol. They were lightly etched with the solution of $3H_2SO_4 + H_2O_2 + H_2O$ and finally washed in deionized water before use.

A two-zone furnace was used for this work. The reaction tube, substrate holder, gallium boat, and $AsCl_3$ bubbler were made of high-purity quartz. The dimensions of the reaction tube were about 1m in length and 37 mm ID. Gas supply tubing and valves were made of stainless steel. The quartz parts were cleaned with *aqua regia* and rinsed with deionized water.

The epitaxial process was as follows. Twenty-five grams of gallium were put in the first zone of the reaction tube. The reaction tube was flushed with hydrogen and the furnace was turned on. Both zones were set at 850°C. When the furnace was heated up to the operating temperature, hydrogen was bubbled at a rate of 300 cc/min through the $AsCl_3$ held at 25°C for 1 hr and gallium was completely saturated with arsenic. After the saturation was achieved, the reaction tube was flushed with hydrogen and the furnace was cooled to room temperature. Then the substrate was put in the second zone. The reaction tube was again flushed with hydrogen and the furnace was turned on. The temperatures were held at 850°C for the source gallium and at 730°-750°C for the substrate. The temperature gradient in the vicinity of the substrate was 10°C/cm. The flow rate of the hydrogen gas saturated with $AsCl_3$ at 0°C in the bubbler was about 300 cc/min, corresponding to about 5 x 10^{-5} moles/min of $AsCl_3$. The growth rate was about 15 μ/hr.

The Hall coefficient R_H and resistivity ρ were measured from 300° to 4.2°K on bridge-shaped samples formed by etching. The carrier concentration n was calculated from the relation $n = 1/R_H e$, where R_H is the value measured at 6000 gauss. The electron Hall mobility was calculated from the Hall coefficient measured in low magnetic field (650 gauss).

The donor concentration N_D, acceptor concentration N_A, and donor ionization energy E_D were estimated from R_H *vs.* T curves, using the relation (6)

$$\frac{n(N_A + n)}{(N_D - N_A - n)} = \frac{N_C}{D} \exp\left(-\frac{E_D}{kT}\right)$$

where D is the degeneracy of the donor level, T the absolute temperature, and N_C the effective density of states in the conduction band, given by

$$N_C = 2\left(\frac{2\pi m^* kT}{h^2}\right)^{3/2}$$

where m^* is the density of states effective mass of the electrons. In the present calculation, the values $m^* = 0.0072\ m_e$ (7) and $D = 2$ were used.

Dislocations were revealed on the (111) gallium plane by chemical etching with the solution (8) $3HNO_3 + 4H_2O$. The dislocation density in the layer 5-10μ apart from the epitaxial-substrate interface was less than that in the substrate by a factor of 1-2 as reported previously (9). The dislocation density in the substrate was about 10^3-10^4 cm^{-2}.

Results and Discussion

The epitaxial layers grown in initial experiments exhibited considerable scatter in their electrical properties, with n varying from 10^{13} to 10^{15} cm^{-3} and μ_H at room temperature varying from 1000 to 7000 cm^2/v-sec. This scatter resulted from the presence of leaks in the growth apparatus, and may have been due to contamination by O_2 or H_2O. It was eliminated by using

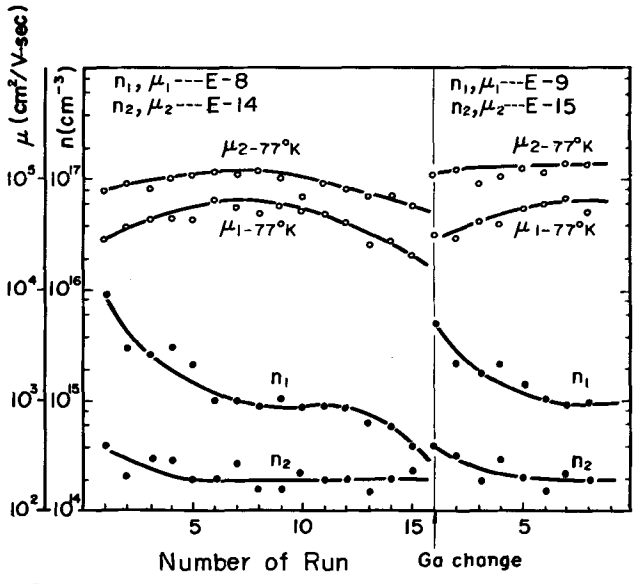

Fig. 1. Variation in the electrical properties of epitaxial layers formed in successive runs of a reaction series. The curves labeled n_1 and μ_1 show the carrier concentrations and the electron Hall mobilities in series E-8 and E-9. The curves labeled n_2 and μ_2 show those quantities in series E-14 and E-15.

apparatus which could be evacuated to pressures of the order of 10^{-4} Torr. All the epitaxial layers described in the rest of this paper were grown with the leak-free apparatus.

Figure 1 shows the electrical properties of the layers grown in successive runs of four reaction series, E-8, E-9, E-14, and E-15. The nominal purity of the $AsCl_3$ used was 99.999+% in series E-8 and E-9, and 99.9999+% in series E-14 and E-15. Each series consisted of about 20 runs with a single gallium source. The source was changed between series E-8 and E-9, and between series E-14 and E-15. The thickness of the growth layers is about 15μ. In Fig. 1, n_1 designates the carrier concentrations at 300°K and $\mu_{1\text{-}77°K}$ designates the electron Hall mobilities at 77°K for the layers prepared in series E-8 and E-9, while n_2 and $\mu_{2\text{-}77°K}$ indicate the corresponding quantities for series E-14 and E-15.

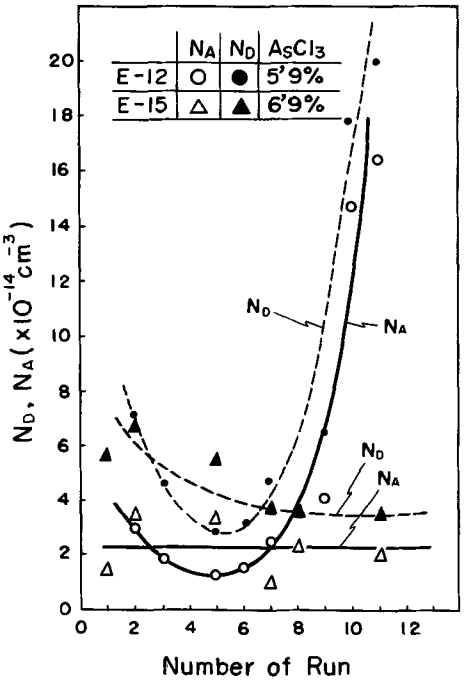

Fig. 2. Variation in the acceptor and donor impurity concentrations obtained in successive runs of two reaction series.

In the first half of series E-8, the electron Hall mobilities at 77°K, $\mu_{1\text{-}77°K}$, increase to a maximum value, while those at 300°K are essentially constant. After the weight of source gallium decreases to about half its original value, n_1 and μ_1 decrease markedly. When the source gallium is replaced by a fresh one (*i.e.*, E-8 → E-9), n_1 and μ_1 recover the original values of the first half of series E-8. In the latter half of series E-8, it was observed that the acceptor concentration N_A increased clearly in successive runs. In some series, the layers were converted from n-type to p-type by con-

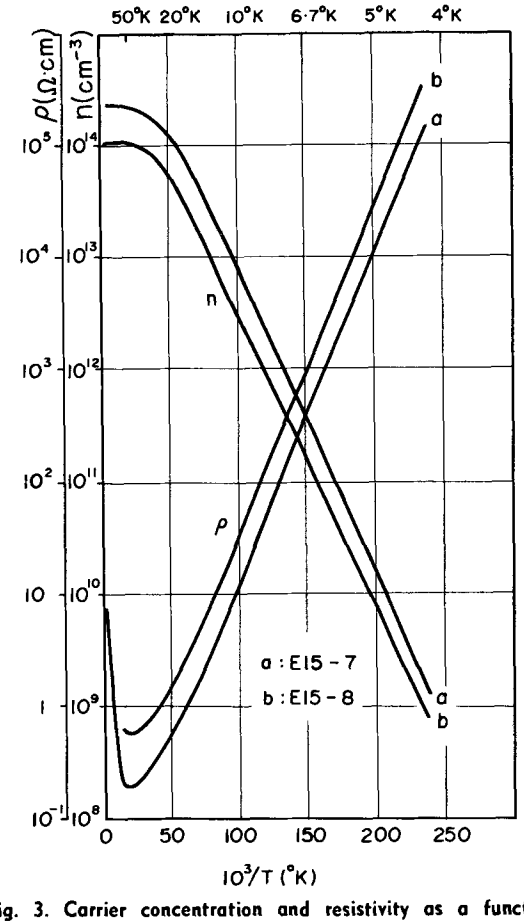

Fig. 3. Carrier concentration and resistivity as a function of temperature in n-type epitaxial GaAs.

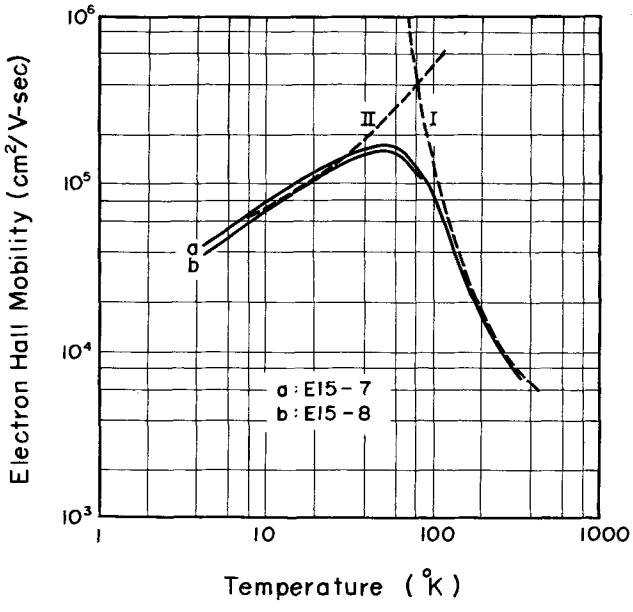

Fig. 4. Mobility as a function of temperature in n-type epitaxial GaAs.

Table I. Properties of high-purity n-type epitaxial GaAs

Sample	$N_D - N_A$ (cm^{-3})	N_D (cm^{-3})	N_A (cm^{-3})	E_D (ev)	μ (cm^2/v-sec) 300°K	77°K	peak (50°K)
15-7	2.6×10^{14}	3.6×10^{14}	1.0×10^{14}	0.0048	8.580	164.000	175.000
15-8	1.2×10^{14}	3.6×10^{14}	2.4×10^{14}	0.0047	9.180	153.000	162.000
15-11	1.6×10^{14}	3.5×10^{14}	1.9×10^{14}	0.0046	8.400	150.000	160.000

tamination with acceptor impurities. When high-purity $AsCl_3$ (99.9999+%) was used, however, no appreciable contamination was observed (*see* the curves for E-14 and E-15). In order to clarify the situation, the calculated values of the acceptor and donor concentrations are plotted in Fig. 2 against the run number for series E-12 and E-15. The same purity $AsCl_3$ was used in series E-12 as in series E-8. It is clearly seen that no appreciable change in N_D and N_A occurred when 99.9999+% $AsCl_3$ was used, in contrast to the case for 99.999+%. From these results, it may be concluded that in the initial runs of a series the source gallium acts as a getter for the acceptor and donor impurities in the $AsCl_3$, but eventually it becomes saturated and is no longer an effective getter. The decrease in N_D and N_A observed in the initial runs of each series must be due to the depletion of impurities from the walls of the reaction tube or from other static parts of the system.

Typical curves for the temperature dependence of ρ, n, and μ_H for high-purity specimens are shown in Fig. 3 and 4. No impurity band conduction is observed even at 4.2°K in pure samples. The most important scattering mechanism between 300° and 100°K seems to be polar optical-mode scattering. Curve I in Fig. 4, computed from the theory (10) for this type of scattering, agrees well with the experimental results. Ionized impurity scattering is dominant below 50°K. Curve II was calculated from the Brooks-Herring theory (11) using the data for sample E15-7. The difference between the theory and experimental results may be due to the difference between zero-field Hall mobility and drift mobility. The highest Hall mobility of 175,000 cm^2/v-sec at 50°K was observed for this sample, in which $N_D = 3.6 \times 10^{14}$ cm^{-3} and $N_A = 1.0 \times 10^{14}$ cm^{-3}. Values of N_D, N_A, E_D, and μ_H obtained for typical samples are given in Table I. For sample E15-7, the mobility at 77°K (164,000 cm^2/v-sec) was decreased to 143,000 cm^2/v-sec when calculated from the high field Hall coefficient.

The dependence of the donor ionization energy on donor concentration is shown in Fig. 5. The value of E_D extrapolated to infinite dilution is approximately 0.005 ev, which is consistent with the previous data (3).

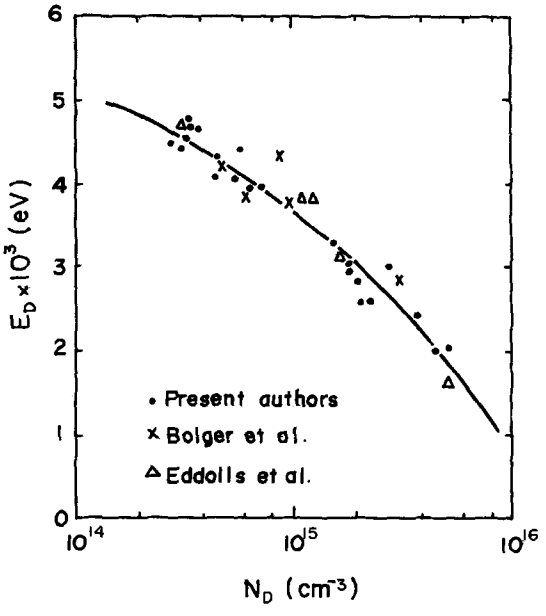

Fig. 5. Dependence of donor ionization energy upon donor concentration.

Acknowledgments

It is a pleasure to thank Drs. Y. Sasaki, S. Asanabe, T. Okada, and Y. Matsukura for useful advice, and Messrs. H. Iwasaki and Y. Kuwano for assistance in the measurements of electrical properties.

Manuscript submitted July 5, 1968; revised manuscript received Nov. 18, 1968. This paper was presented at the Boston Meeting, May 5-9, 1968, as Paper 62.

Any discussion of this paper will appear in a Discussion Section to be published in the December 1969 JOURNAL.

REFERENCES

1. D. Effer, *This Journal*, **112**, 1020 (1965).
2. J. Whitaker and D. E. Bolger, *Solid State Commun.*, **4**, 181 (1966).
3. D. V. Eddolls, J. R. Knight, and B. L. H. Wilson, *Proc. Intern. Symp. Gallium Arsenide, Reading, 1966*, p. 3 (1967).
4. D. E. Bolger, J. Franks, J. Gordon, and J. Whitaker, *ibid.*, p. 16 (1967).
5. J. R. Knight, D. Effer, and P. P. Evans, *Solid State Electron.*, **8**, 178 (1965).
6. G. L. Pearson and J. Bardeen, *Phys. Rev.*, **75**, 865 (1949).
7. T. S. Moss and A. K. Walton, *Proc. Phys. Soc.*, **74**, 131 (1959).
8. H. A. Schell, *Z. Metallk.*, **48**, 158 (1957).
9. F. V. Williams, *Proc. Intern. Symp. Gallium Arsenide, Reading, 1966*, p. 27 (1967).
10. R. L. Petritz and W. W. Scanlon, *Phys. Rev.*, **97**, 1620 (1955).
11. H. Brooks, *Advan. Electron. Electron Phys.*, **7**, 158 (1955).

Algorithms for the Vapor Pressure of Water Over Aqueous Solutions of Salt and Caustic Soda

R. B. MacMullin

R. B. MacMullin Associates, Niagara Falls, New York

ABSTRACT

Incidental to development of a digital computer program for the performance of electrolytic chlor-alkali cells is the necessity of general formulas for calculating the vapor pressure of the aqueous solutions used for the electrolytes. This paper offers algorithms for vapor pressure of pure water, pure NaCl solutions, pure NaOH solutions, and aqueous solutions containing both NaCl and NaOH, within the range of conditions usually encountered in commercial cells of both the mercury and the diaphragm type.

Incidental to development of a digital computer program for the performance of electrolytic chlor-alkali cells is the necessity of a general formula for calculating the vapor pressure of the aqueous solutions used for the electrolytes. The electrolytes usually encountered are:

	Diaphragm cell	Mercury cell
Anolyte	NaCl, >20%, 90°-100°C	NaCl >20%, 50°-90°C
Catholyte	NaOH, 10-14%, 93°-103°C NaCl, 14-20%, 93°-103°C	NaOH, 30-60%, 70°-120°C

The algorithms[1] which follow cover a range of conditions which include the above ranges of interest.

I. Vapor pressure of pure water over the range 10°-150°C.

II. Vapor pressure lowering due to the dissolved NaCl over the range 3M to saturation, and 30°-110°C.

III. Vapor pressure lowering due to the dissolved NaOH: (*a*) over the range 0-12.5M, 20°-110°C, (*b*) over the range 12.5-25M, 20°-110°C.

IV. Combinations of II and III(*a*).

In this paper, temperature is expressed °C; concentration, as Molality (g.f.w./kg H_2O); M for NaCl, N for NaOH; vapor pressure, as Torr (mm Hg).

Vapor Pressure of Pure Water

The steam tables of Keenan and Keyes (1) are based on two formulas taken from the paper by Smith, Keyes, and Gerry (2). The second formula covering the range 10°-150°C is the simpler of the two:

$$\log_{10}\frac{p_c}{p} = \frac{x}{T}\left[\frac{a + bx + cx^3}{1 + dx}\right] \qquad [1]$$

p = vapor pressure in int atm
p_c = critical pressure, 218.167 int atm
T = degrees Kelvin, t°C + 273.16
T_c = critical temperature, 647.27°K
x = $T_c - T$
a = 3.2437814
b = 5.86826×10^{-3}
c = 1.1702379×10^{-8}
d = 2.1878462×10^{-3}

Expressing p as Torr and t as °C, the above formula reduces to the following, which are programmed in sequence:

$$374.11 - t = x \qquad [2]$$

$$\text{antilog}_{10}\left(5.219603 - \frac{x}{t + 273.16}\left[\frac{a + bx + cx^3}{1 + dx}\right]\right) = p_o \qquad [3]$$

This formula reproduces published tables for the vapor pressure of water to within ± 0.02 Torr.

[1] Here used as the art of reducing data involving three or more variables to a single algebraic equation for computer use.

Vapor Pressure Lowering in Pure Salt Solutions

Source of data: International Critical Tables (3), Vol. III, p. 370.

The fractional lowering of vapor pressure due to the solute (in this case NaCl) is expressed

$$R = \frac{(p_o - p)}{p_o M} = \frac{\Delta p}{p_o M} \qquad [4]$$

Since the concentration of NaCl in the table is expressed as w/o (weight per cent), the Molality is

$$M = \frac{\text{w/o NaCl}}{\text{w/o } H_2O} \div 0.0584428$$

Values of 100 R were calculated for each of the data points given in the ICT table quoted above. In Fig. 1, 100 R *vs.* t is plotted for the various concentrations, and R appears to be a linear function of t. In Fig. 2, 100 R *vs.* M. is plotted for the various temperatures, and above 3 M, R appears to be a linear function of M. The lines appear to intersect at the point 100 R = 3.5 at M = 3.0. That is, above 3 M, R may be expressed as follows:

$$R = (M - 3)\ (0.0019772 - 0.00001193\ t) + 0.035 \qquad [5]$$

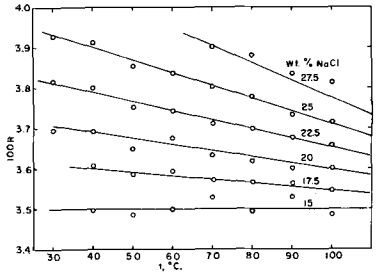

Fig. 1. Vapor pressure lowering, pure aqueous NaCl. Range 15% NaCl to saturation; 40°-110°C.

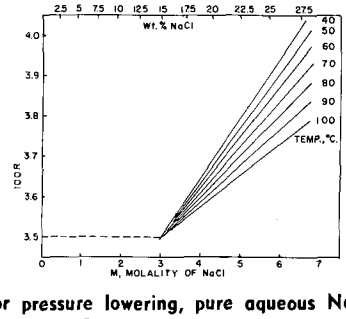

Fig. 2. Vapor pressure lowering, pure aqueous NaCl. Range, 3M to saturation; 40°-110°C.

Since $p = p_o - RMp_o = (1 - RM)p_o$

$$p^+ = [1 - ((M^+ - 3)(1.9772 \times 10^{-3} - 1.193 \times 10^{-5} t^+) + 0.035)\, M^+]\, p_o^+ \quad [6]$$

where the superscripts indicate conditions applicable to the anolyte.

The above formula reproduces most of the data in the ICT tables, at concentrations above 15 w/o NaCl and temperatures from 40° to 110°C, to an accuracy of about ± 0.5 Torr. Several random inconsistencies in the ICT data are apparent.

Below 15 w/o NaCl, it will generally be sufficiently accurate for most purposes, to take $R = 0.035$ at any temperature. For the anolyte problem, the concentration will nearly always be above 15% NaCl, where the sophisticated formula above applies.

Vapor Pressure Lowering in Pure Caustic Soda Solutions

Source of data: International Critical Tables (3), Vol. III, p. 370.

The fractional lowering of vapor pressure due to the solute (in this case NaOH) is expressed

$$R = \frac{\Delta p}{p_o N}$$

Since concentration of NaOH in the ICT table is expressed as C = g NaOH/100g H_2O

$$N = \frac{C}{3.99971} = \text{g.f.w./kg } H_2O$$

100 R has been calculated for all data points given in the ICT table up to $C = 120$ (55% NaOH), at 20°, 40°, 60°, 80°, and 100°C. In Fig. 3, 100 R *vs.* N is plotted for various values of constant t, and one notes that 100 R goes through a maximum at about N = 12.5 Molal.

Case A.—Concentrations < 12.5 Molal (33 w/o of NaOH). In Fig. 4, 100 R *vs.* t is plotted at various values of N. At each value of N, R appears to be a linear function of t. The lines appear to intersect at a common point, 100 $R = 3.17$, $t = 174$°C.

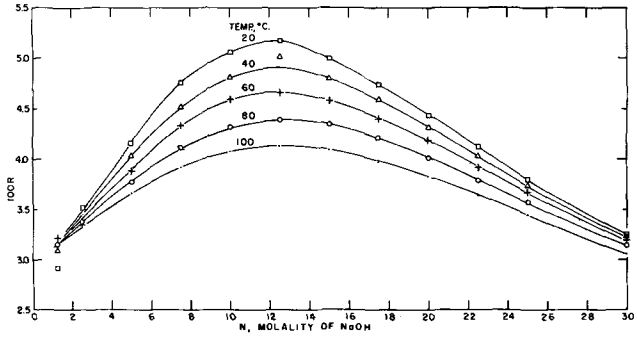

Fig. 3. Vapor pressure lowering, pure aqueous NaOH. Range, 0-30 Molal; 20°-100°C.

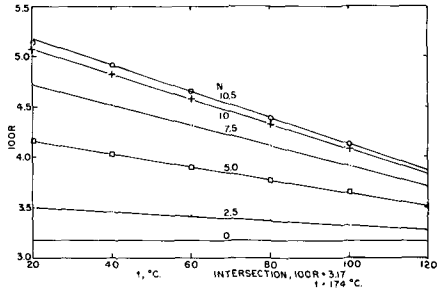

Fig. 4. Vapor pressure lowering, pure aqueous NaOH. Range, 0-12.5 Molal NaOH; 40°-110°C.

Calling the slope of these lines $-dR/dt = m$,

$$R = 0.0317 - m(t - 174)$$

or

$$R = 0.0317 + m(174 - t)$$

The slope of each line was then measured, as per the table which follows:

Molality, N	Slope 100 m $-\Delta$ 100 $R/\Delta t$
0	0
2.5	0.00214
5	0.00636
7.5	0.01000
10	0.01227
12.5	0.01299

In Fig. 5, the negative of the slope, 100 m is plotted against Molality. The curve appears to be close to a quadratic with a maximum at N = 12.5. However, at lower concentration the curve reverses, as shown. A suitable curve fit is obtained by assuming a polynomial of the form

$$m = a + bN + cN^2 + d/N \quad [8]$$

Solving this polynomial for the data given, the following constants are formed

$$a = -8.6715 \times 10^{-5}$$
$$b = 3.368 \times 10^{-5}$$
$$c = -1.354 \times 10^{-6}$$
$$d = 7.88 \times 10^{-5}$$

Hence,

$$R = 0.03170 + (174 - t)(a + bN + cN^2 + d/N) \quad [9]$$

and

$$\Delta p = [(0.03170 + (174 - t)(a + bN + cN^2 + d/N)]N p_o \quad [10]$$

and

$$p = (1 - RN)\, p_o = \{1 + [(t - 174)(a + bN + cN^2 + d/N) - 0.03170]N\} p_o \quad [11]$$

The curves shown in Fig. 3, up to N = 12.5, are actually a plot of Eq. [11]. All the data points fall on these curves, except two, and these are believed to be errors or misprints in the data tabulated in ICT.

Case B.—N >12.5 (33% NaOH) to N = 30 (55% NaOH). Applicable to caustic made in decomposer of a mercury cell.

In Fig. 6, 100 R *vs.* t is plotted at various values of N. At each value of N, within the temperature range of 60°-110°C, R appears to be a linear function of t. The lines appear to intersect at a common point, 100 $R = 2.83$, $t = 198$°C.

Calling the slope of these lines $-dR/dt = m$,

$$R = 0.0283 + m\,(198 - t) \quad [12]$$

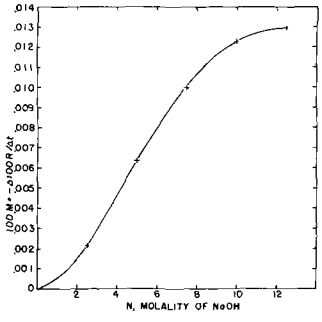

Fig. 5. Temperature coefficient of 100 R for pure NaOH. Range, 0-12.5 Molal NaOH; 40°-110°C.

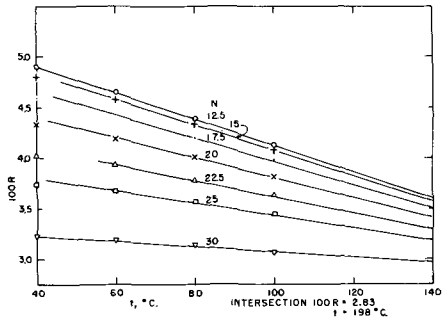

Fig. 6. Vapor pressure lowering, pure aqueous NaOH. Range, 12.5-30 Molal NaOH; 40°-110°C.

The slope of each line was then measured, as per the table which follows

Molality, N	Slope 100 m $-\Delta$ 100 $R/\Delta t$
12.5	0.01319
15	0.01268
17.5	0.01160
20	0.00990
22.5	0.00804
25	0.00616
30	0.00254

In Fig. 7 the negative of the slope 100 m is plotted against Molality. The curve shows a maximum at N = 12.5. As before, a suitable curve fit is obtained by assuming a polynomial of the form

$$m = a' + b'N + c'N^2 + d'/N \quad [13]$$

Solving this polynomial for the data given, the following constants are found

$$a' = 6.2066 \times 10^{-4}$$
$$b' = -2.3155 \times 10^{-5}$$
$$c' = 2.1860 \times 10^{-7}$$
$$d' = -2.920 \times 10^{-3}$$

Hence,

$$R = 0.0283 + (198 - t)(a' + b'N + c'N^2 + d'/N) \quad [14]$$

$$\Delta p = [0.0283 + (198 - t)(a' + b'N + c'N^2 + d'/N)]N\,p_o \quad [15]$$

$$p = (1 - RN)p_o = \{1 + [(t - 198)(a' + b'N + c'N^2 + d'/N) - 0.0283]N\}p_o \quad [16]$$

The curves shown in Fig. 3, from N = 12.5 to N = 30, are actually a plot of Eq. [16]. These curves fit the data from the ICT table very well.

Vapor Pressure Lowering in Diaphragm Cell Liquor

Let Δp_M be the vapor pressure lowering due to the NaCl

Δp_N be the vapor pressure lowering due to the NaOH

$$p^- = p_o^- - \Delta p_M^- - \Delta p_N^- \quad [17]$$

where the minus superscripts refer to the catholyte at t^- °C.

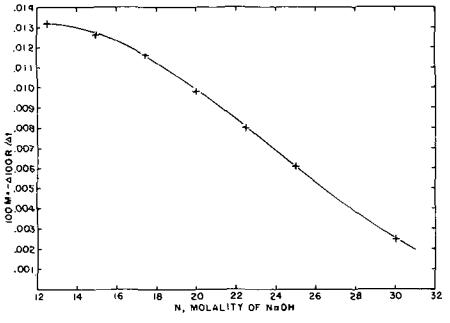

Fig. 7. Temperature coefficient of 100 R for pure NaOH. Range, 12.5-30 Molal NaOH; 40°-110°C.

For the usual cell liquor composition range, M^- will be >3 Molal and N^- <12.5 Molal. The assumption is now made that the Δp_M^- and Δp_N^- are additive, as indicated from Eq. [17].

From II

$$\Delta p_M^- = [(M^- - 3)(0.0019772 - 0.00001193\,t^-) + 0.035]M^-\,p_o \quad [18]$$

From IIIA

$$\Delta p_N^- = [0.03170 + (174 - t^-)(a + bN^- + c(N^-)^2 + d/N^-)]N^-\,p_o \quad [19]$$

$$p^- = \{1 - [(M^- - 3)(0.0019772 - 0.00001193\,t^-) + 0.035]M^- - [(174 - t^-)(a + bN^- + c(N^-)^2 + d/N^-) + 0.0317]N^-\}p_o^- \quad [20]$$

Defining the fractional decomposition of salt in one pass through the diaphragm cell as D, then

$$\frac{N^-}{M^-} = \frac{D}{1 - D} \quad [21]$$

so that, if D is known, there is only one concentration variable, either N^- or M^-.

It is also worth noting that, in a diaphragm cell, the catholyte temperature is always greater than the anolyte temperature. For Hooker cells at rated load, $t^- - t^+$ = approx 3°C.

Example

Figure 8 shows the calculated vapor pressure of diaphragm cell liquor at various concentrations of NaOH and salt decomposition within the range of interest, for a typical temperature of 100°C. Since the solubility of NaCl in NaOH solutions is limited, the saturation line is shown. Only that portion of the plot lying above the saturation line is valid.

Comparison of calculated vapor pressure along the saturation line with experimental data indicates an accuracy within 3%. This is sufficiently good for most engineering purposes. Greater accuracy would require taking into account the interaction between NaCl and NaOH; that is, the slight departure from the assumption that the vapor pressure lowerings of the two solutes are additive.

Programming

For input to a digital computer, the equations can be simplified. The format will depend on the computer used and its program logic. For example, for the Mathatron 8-48 (Mathatronics Division of Barry Wright Corporation, Waltham, Massachusetts),

Eq. [3]

$$c \cdot x \cdot x + b)\,x + a)\,x \div (t + 273.16) \div (1 + d \cdot x) - 5.219603)\,(-1) = \log p_o, \text{antilog} = p_o$$

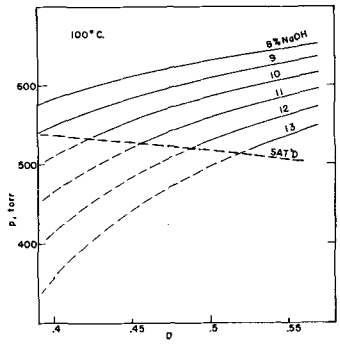

Fig. 8. Vapor pressure of catholyte from a diaphragm cell vs. salt decomposition. Ordinate, Torr. Abscissa, fractional decomposition D. Heavy dashed line shows saturation with NaCl. Valid values of composition and vapor pressure lie above this line.

Eq. [6]

$$1.9772 \cdot 10^{-3} - 1.193 \cdot 10^{-5} \cdot t^{+}) \ (3 - M^{+}) - 0.035) \ M^{+} + 1) \ p_o = p^{+}$$

Eq. [11]

$$cN + b) \ N + a + d \div N) \ (t - 174) - 0.0317) \ N + 1) \ p_o = p$$

Eq. [16]

$$c'N + b') \ N + a' + d' \div N) \ (t - 198) - 0.0283) \ N + 1) \ p_o = p$$

Eq. [20]

$$c \cdot N^{-} + b) \ N^{-} + a + d \div N^{-}) \ (t^{-} - 174) - 0.0317) N^{-} + ((3 - M^{-}) \ (1.9772 \cdot 10^{-3} - 1.193 \cdot 10^{-5} \cdot t^{-}) - 0.035) \ M^{-} + 1) \ p_o = p^{-}$$

Manuscript submitted Oct. 22, 1968; revised manuscript received Dec. 6, 1968. This paper was presented at the Tripartite meeting of the A.I.Ch.E., Montreal, Sept. 25, 1968.

Any discussion of this paper will appear in a Discussion Section to be published in the December 1969 JOURNAL.

REFERENCES

1. Keenan and Keyes, "Thermodynamic Properties of Steam," John Wiley & Sons, New York (1962).
2. L. B. Smith, F. G. Keyes, and H. T. Gerry, *Proc. Am. Acad. Arts and Sci.*, **69**, 137 (1934).
3. International Critical Tables, McGraw Hill Book Co., Vol. III (1928).

Erratum

There was an error in the paper "Accommodation of Lattice Mismatch at Heterojunctions" by R. S. Mroczkowski, A. F. Witt, and H. C. Gatos, **115**, 750 (1968) which was published in the July 1968 issue of the Journal (**115**, 750-752).

In considering the theoretical dislocation density required for the accommodation of an abrupt lattice mismatch in single crystal growth ($\Delta = Sa_o^2/\delta$), inadvertently, the lattice translation in the $a_{(110)}$ direction in the zinc-blende lattice was taken as $a_{(110)} = \sqrt{2}a_o$ instead of $a_{(110)} = \frac{1}{\sqrt{2}} a_o$; the theoretical dislocation density is smaller by a factor of 2 than that indicated in the article. Consequently, a comparison with the experimentally observed dislocation density suggests that part of the lattice mismatch is accommodated by strain. In the light of the present correction, the results seem to confirm the validity of the Van der Merve model.

The authors are grateful to Dr. G. O. Krause, of Texas Instruments, Inc., for bringing this error to their attention.

Cathodic Discharge of Nickel Sulfide in a Propylene Carbonate-$LiClO_4$ Electrolyte

Raymond Jasinski* and Brian Burrows*

Tyco Laboratories, Inc., Waltham, Massachusetts

ABSTRACT

A preliminary evaluation was made of the cathodic discharge of nickel sulfides in $LiClO_4$-propylene carbonate electrolyte. Theoretical energy densities of approximately 400-700 whr/lb are calculated, depending on the choice of the specific nickel sulfide. The nickel sulfides tested had solubilities $<10^{-4}$M in the charged and partially discharged state. High coulombic efficiencies (>50%) were achieved at 1 ma/cm^2. A discharge of 10 ma/cm^2 could be sustained, but at a lower efficiency. The discharge plateau is between 1.8 and 1.4v.

The performances of the most nonaqueous batteries are limited by the positive electrode (1). Positive electrodes with acceptable electrochemical performance have high solubilities and, hence, poor shelf life. Apparently most materials investigated to date, *e.g.*, CuCl, AgCl, CuF_2, must first dissolve in order to discharge (2). However, the metal ions, once in solution, can also reach the negative electrode, generally lithium, and discharge chemically. Problems arising from excessive solubility are particularly insidious in the case of metal chlorides since one of the discharge products, Cl^-, causes further dissolution of the positive plate material (3).

A possible solution of the problems presented by high solubility is to prevent migration of metal ions to the negative electrode with separator membranes. This approach is being studied (4); it presents its own problems in achieving membrane perfection and stability and low ohmic losses. An alternative approach is to employ insoluble plate materials, preferably of good electrical conductivity. This alternative has been the guiding principle behind the work described below.

Transition metal sulfides are particularly insoluble materials in aqueous solutions. In the absence of complex ion formation it was thought likely that these compounds would also be insoluble in aprotic, organic solvents.

The experiments described below on nickel sulfide imply that this material is (*i*) electrochemically active, (*ii*) chemically stable.

The term "nickel sulfide" is actually a generic one. Six stable, crystallographically defined sulfides exist (5): Ni_3S_2, Ni_6S_5, Ni_7S_6, NiS, Ni_3S_4, and NiS_2.

The equivalent weight and energy density of this series of compounds varies as shown in Table I. It was assumed that the reaction products were Li_2S and nickel metal. Li_2S is apparently insoluble in the electrolyte; quantitative data are not available. The higher energy density of the Li/NiS_2 couple reflects the discharge of the $(S\text{-}S)^=$ ion as well as the reduction of divalent nickel.

Clearly the use of materials with high sulfur content provides for high energy densities, approaching that of the Li/CuF_2 couple (740 whr/lb). However, a high energy density is not the only criterion for selecting a positive plate material. A suitable compound must (*a*) be electrochemically active, (*b*) be relatively insoluble, (*c*) not show undesirable side reactions, *e.g.*, electrolyte decomposition and/or formation of soluble intermediates, and (*d*) be compatible with a lightweight electrode structure, *i.e.*, not require large amounts of conducting binder.

Apparatus and Procedure

All electrochemical measurements were carried out in a recirculating argon atmosphere dry box (Vacuum Atmospheres Corporation). The electrolyte was 1M $LiClO_4$ in propylene carbonate (PC). Chronopotentiograms were recorded on an X-Y recorder (Houston Omnigraphic, model HR-98T). To avoid loading of the reference electrode-working electrode cell, a unity-gain voltage follower, constructed from an operational amplifier (Philbrick, type P65AU) was used in the potential measuring circuit. Current was supplied by a constant current power supply (Electronic Measurements, model C633).

Experiments were performed in a three-compartment cell. The working electrode, in the middle compartment, was separated from the counter electrode by a glass frit and from the reference electrode by a Luggin capillary.

In all experiments, the reference electrode was the Li/Li^+ couple (6), formed by immersing a Li rod in PC/$LiClO_4$ (1M) solution. Initially, the counter electrode was a Pt foil. In later experiments, the Pt was replaced by a Li rod to avoid solvent decomposition.

The sulfide electrodes were prepared by mixing the powder with approximately 10% graphite and pressing the mixture between folded, expanded-nickel metal, spot-welded to nickel wire. The sulfides apparently occluded only small amounts of water during pressing in air, since there was only slight evolution of hydrogen in the potential region for water reduction. The coulombic efficiencies were not markedly different when water was rigorously excluded from the system. Electrode thickness was approximately 30 mil.

No attempt was made to optimize material purity or electrode structure in this preliminary survey. The nickel sulfides were prepared as described below and their composition was confirmed by x-ray diffraction.

NiS was formed by reacting 1.5M $NiCl_2 \cdot 6\ H_2O$ with 0.5M $(NH_4)_2S$. The precipitate was washed thoroughly with water, heated at 120°C under N_2, and then transferred to the dry box.

The same procedure was followed for NiS_2 using 0.5M $NiCl_2 \cdot 6\ H_2O$ and 1.5M $(NH_4)_2S$.

Ni_3S_2 was prepared by the reduction of anhydrous $NiSO_4$ by hydrogen at 300°C (7).

Washing of the NiS and NiS_2 precipitates was critical. Discharge of NiS_2 which had not been washed

Table I. Equivalent weight of Li/Ni sulfide couples

Compound	Equivalent weight, g*	Energy density**
Ni_3S_2	67	388
Ni_6S_5	58	450
Ni_7S_6	54	482
NiS	52	500
Ni_3S_4	42	620
NiS_2	38	685

* Including the weight of the required lithium, but not the electrolyte.

** Based on an open-circuit potential of 1.8v (whr/lb).

* Electrochemical Society Active Member.

thoroughly resulted in the formation of a black-brown film in the working electrode compartment. When this cell was removed from the dry box there was a strong odor of H_2S from it. Thoroughly washed NiS_2 does not produce a film or odor.

Qualitative resistivity measurements were made on pressed disks of the nickel sulfides. NiS and NiS_2 were insulators; Ni_3S_2 powder was an electrical conductor. However, the powder, as prepared, contained from 1 to 5% metallic nickel.

Results and Discussion

Discharge behavior.—Half-cell discharge curves of Ni_3S_2, NiS, and NiS_2 are shown in Fig. 1 at 10 ma/cm^2 and in Fig. 2 at 1 ma/cm^2. The theoretical capacity was computed on the basis of complete reduction to metal and sulfide ion. The performance of CuF_2 electrodes, prepared in a similar manner, is also shown in the figures for comparison purposes. It is apparent that the performance of CuF_2 in this configuration is not as good as that of the nickel sulfides. Note, however, the effect of added conductive binder (Fig. 1 *vs.* Fig. 2). Complete utilization of CuF_2 would produce 0.54 amp hr/g CuF_2; complete utilization of Ni_3S_2 would produce 0.46 amp hr/g.

The amounts of graphite binder used for the sulfides are listed in the figures. Since the Ni_3S_2 powder is an electronic conductor, it would be expected that little binder should be needed. Since the conductivities of discharge intermediates, if any, are not known, graphite was added as a precautionary measure.

All discharge curves show an initial section of high potential and short duration which may arise from an impurity, such as sulfur. Figure 1 shows that the discharge curve for a sulfur-carbon electrode falls approximately in the high potential section of the sulfide discharges. Thus, if sulfur is present in the electrode, it probably discharges above 2v (*vs.* Li/Li^+).

The discharge of sulfur at 10 ma/cm^2 is shown in more detail in Fig. 3. After about 1.6% of the material had discharged (2.4v), a yellow-brown substance moved off the electrode into the electrolyte. In view of the electrochemical behavior of sulfur in other

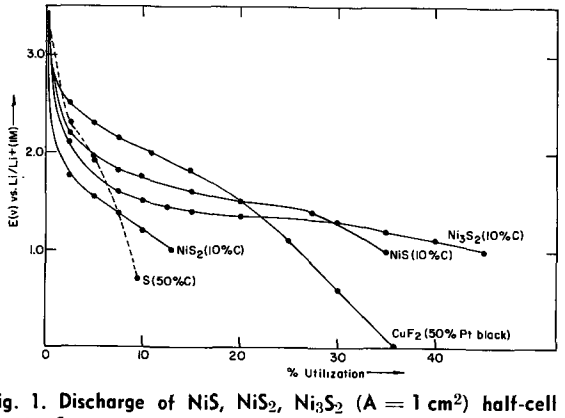

Fig. 1. Discharge of NiS, NiS_2, Ni_3S_2 (A = 1 cm^2) half-cell at 10 ma/cm^2.

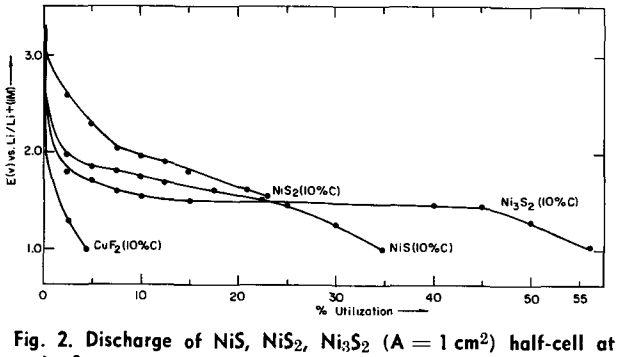

Fig. 2. Discharge of NiS, NiS_2, Ni_3S_2 (A = 1 cm^2) half-cell at 1 ma/cm^2.

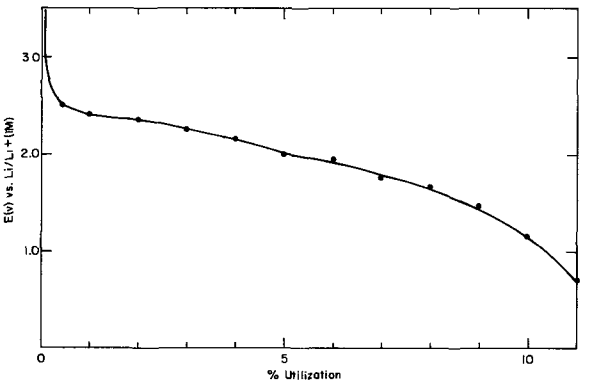

Fig. 3. Discharge of S —50%C (A = 1 cm^2) at 10 ma/cm^2

electrolytes, it is likely that this material is a polysulfide.

In order to explore further the origin of the high potential portion of the nickel sulfide curves, the electrodes were partially discharged and then allowed to return to open circuit for 30 min. If an active impurity were present, it should be eventually consumed and an open-circuit characteristic of the sulfide should be reached. The assumption here is that the presence of partially discharged nickel sulfide will not affect the open-circuit potential of the bulk of the electrode material. The data obtained for Ni_3S_2 and NiS are shown in Fig. 4 where the open-circuit potentials are plotted against the per cent charge delivered at 5 ma/cm^2. The times on open circuit are listed in the figure. A plateau in potential is reached between 1.6 to 1.8v *vs.* Li/Li^+.

The rapid decay in open-circuit potential of the Ni_3S_2 electrode (0-2% discharge) is also consistent with the hypothesis that an impurity is involved. The data for NiS could be interpreted as a larger amount of impurity. Since NiS was precipitated from aqueous solution, some free sulfur is to be expected via the air oxidation of sulfide ion.

Shelf life.—A few qualitative tests were made of nickel sulfide stability in 1M $LiClO_4$/PC electrolyte. Powdered NiS was equilibrated in solution overnight. Supernatent was withdrawn, diluted 1:1 with distilled water, and tested for soluble nickel with dimethylglyoxime (DMG). The test was negative.

A 10^{-4}M $NiCl_2$ solution was used as a control. The addition of DMG to an aqueous solution produced a pink coloration. Diluting the solution 1:1 with $LiClO_4$/PC diminished the intensity considerably. However, some coloration was still visible. The original negative test thus implies that the solubility of NiS in $LiClO_4$/PC is less than 10^{-4}M.

The same test was applied to a partially discharged NiS electrode. The result was also negative, implying that the discharge intermediates, if any, are also insoluble.

A further solubility test consisted of suspending for two days a cleaned lithium rod in solution equilibrated with and containing powdered nickel sulfide. No de-

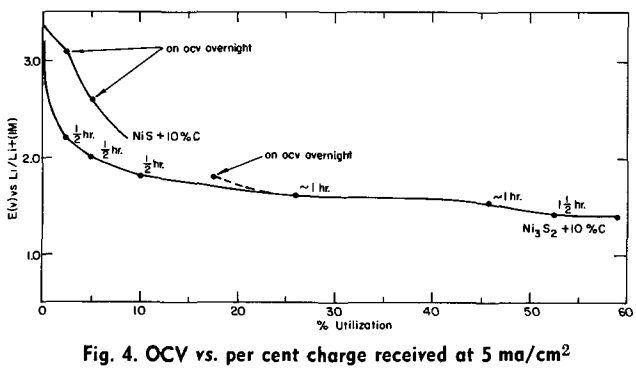

Fig. 4. OCV *vs.* per cent charge received at 5 ma/cm^2

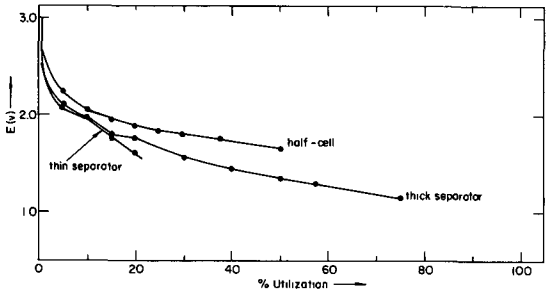

Fig. 5. Discharge of NiS/Li cell at 1 ma/cm^2

posit was noted on the electrode. Finally, a number of electrodes were discharged with interruptions overnight with no adverse effects. A complete cell (see below) was subjected to interrupted discharge, also with no adverse effects. Although further work remains to be done on this subject, it appears that nickel sulfide positives have greater stability than copper halide electrodes. It is important to consider the solubility of the discharge intermediates as well as of the starting plate material, particularly for battery applications which involve large discharge times.

Cell testing.—Because the nickel sulfides discharged well in the half cell, a prototype battery was assembled. The nickel sulfide (NiS) electrode, 2 x 2.5 cm, served as the battery positive electrode. The separator material was glass-fiber filter paper (about 12 mil thick). The plates were held together by small tabs of lithium ribbon, insulated from the positive by the separator, and were immersed in 60 cc of PC/$LiClO_4$ (1M). Comparative discharge curves for the half cell and full cell are shown in Fig. 5. The battery performed well although at a slightly lower potential than the half cell. A thinner separator (¼ thickness) did not seem to improve the discharge of the battery to any extent in this configuration.

Conclusions.—Nickel sulfides can be discharged at high utilization in 1M $LiClO_4$/PC at current densities between 1 and 10 ma/cm^2, *e.g.*, routinely efficiencies greater than 60% are achieved with Ni_3S_2. The discharges of NiS and NiS_2 are more affected by the electrode structure. A single discharge plateau was observed in all the tests conducted. Nickel sulfides have low solubility in the solvent tested ($<10^{-4}$) and, hence, should have a long shelf life. Depending on the specific sulfide chosen, the theoretical energy density may be of the same order as for most metal halides.

Acknowledgment

The authors wish to acknowledge the assistance of Mrs. Susan Kirkland in carrying out the laboratory work as well as the support of the U.S. Navy Air Systems Command under Contract No. N-000-19-68-C-0402.

Manuscript submitted Oct. 14, 1968; revised manuscript received Nov. 22, 1968.

Any discussion of this paper will appear in a Discussion Section to be published in the December 1969 JOURNAL.

REFERENCES

1. K. H. M. Braeuer and J. A. Harvey, Organic Electrolyte High Energy Density Batteries, AD654 818 (May 1967).
2. R. Jasinski, B. Burrows, and P. Malachesky, Final Report, Contract No. N00019-67-C-0680.
3. M. Rao, *This Journal*, **114**, 13 (1967).
4. A. N. Dey, *ibid.*, **115**, 160 (1968).
5. M. Hansen, "Constitution of Binary Alloys," p. 1034, McGraw-Hill Publishing Co., New York (1958).
6. B. Burrows and R. Jasinski, *This Journal*, **115**, 365 (1968).
7. G. Pannetier and J. Abegg, *Bull. Soc. Chim. France*, **1961**, 186.

The Oxidation of Iron-Carbon Alloys at 500°C

W. E. Boggs,* and R. H. Kachik

Applied Research Laboratory, United States Steel Corporation, Monroeville, Pennsylvania

ABSTRACT

When iron is oxidized at 500°C in oxygen at 10 Torr, blisters develop in the scale. This does not occur when the iron is oxidized at 500°C in oxygen at 700 Torr, nor when the iron contains carbon as a cementite precipitate. It appears that the iron oxide scale blisters if cation vacancies can accumulate at the oxide-metal interface. The higher oxygen pressure inhibits scale blistering by promoting more rapid formation of the outer layer of Fe_2O_3, which lowers the rate of vacancy formation and accumulation. The presence of carbon in the substrate inhibits scale blistering by providing additional vacancy sinks, thereby largely preventing the accumulation of vacancies at the oxide-metal interface.

When the iron-carbon alloys are oxidized at 500°C in oxygen at 10 Torr, a decarburized zone appears in the alloy substrate near the oxide-metal interface. This means that, under the experimental conditions, the rate of diffusion of carbon from the alloy substrate exceeds the rate of diffusion of iron into the scale. Decarburization does not occur when the alloy is oxidized at 500°C in oxygen at 700 Torr. This effect of oxygen pressure can be explained if it is assumed that at 10 Torr, carbon oxides are formed at the oxide-metal interface and escape through pores in the scale. At the higher pressure, oxygen enters the pores and is incorporated into the scale, thereby blocking the pores and preventing the escape of carbon oxides.

The results of several investigations of the oxidation of iron-carbon alloys at temperatures above 700°C have appeared in the literature (1-8). Three iron oxide phases, FeO, Fe_3O_4, and Fe_2O_3 are stable in this temperature range, and the reactions between carbon and the oxides are favored thermodynamically. The published information is not directly applicable to the present study, which was conducted at temperatures up to 500°C at which only two oxide phases, Fe_3O_4 and Fe_2O_3, are stable, and at which the reactions between carbon and these oxides are not favored thermodynamically.

* Electrochemical Society Active Member.

Wagner *et al.* (9) have published a general qualitative discussion of the oxidation of metal-carbon alloys. They discussed two general reaction sequences: (*i*) diffusion of carbon to the metal-scale interface, where it reacts with the scale to produce gaseous carbon oxides which may accumulate and cause rupture of the scale, and (*ii*) diffusion of carbon through the scale to react with oxygen at the scale-gas interface. The second sequence would allow decarburization to take place without scale rupture. The possibility of the diffusion of the gases produced in the first sequence through the scale without rupture was not discussed.

Engell (7) oxidized Fe-carbon alloys in air and in CO-CO_2 mixtures over the temperature range 750°-1050°C and found that the specimens oxidized in air decarburized without scale rupture. Chemical analysis of the scale, largely FeO, showed that the solubility of carbon in the scale was so low (0.003%) that transport of carbon (Wagner's second sequence) through the scale was not likely. Therefore, since blistering was not observed, Engell proposed that pores present in the scales on iron-carbon alloys permitted the effusion of the carbon oxides. He further proposed that the pores offered a constant resistance to gas flow at all times such that oxygen could not be transported directly from the gas phase to the metal surface, but rather reacted with CO within the pore to produce CO_2, some of which then reacted with carbon arriving at the base of the pore to produce more CO.

Billings and Smeltzer (8) studied the oxidation of iron-carbon alloys at 800°-950°C in CO-CO_2 atmospheres, conditions under which FeO is the only iron oxide formed. Their conclusions were that, under their experimental conditions, iron oxidation took place in the early stages at random nucleation sites on the surface, and decarburization (and carbon oxidation) took place concurrently at active sites in the areas of exposed iron between the iron oxide nuclei. They argued that a competition occurred between the iron oxidation and the carbon oxidation processes for available adsorbed oxygen. Evidence was presented that as iron oxidation progressed and the surface coverage by FeO became more nearly complete, the decarburization reaction was "stifled" to a large extent. The stifling of direct decarburization by scale growth was accompanied by the onset of partial diffusion control of decarburization as carbon or carbon oxides moved outward through pores between the impinging FeO crystallites. It should be noted that the reduction of FeO by carbon is thermodynamically favored by about 7.7 kcal at 950°C. Thus, it appears likely that CO forms at the Fe-FeO interface and that the carbon, in that form, moves outward through pores in the FeO scale under the experimental conditions of Engell (6, 7) and of Billings and Smeltzer (8).

Although the information cited in the literature is not directly applicable to the present study because of the differences in experimental conditions, the concepts are useful in helping to explain the observed phenomena.

Materials and Experimental Work

An aluminum-deoxidized iron base and five iron-carbon alloys were prepared by vacuum melting. The compositions of these alloys are listed in Table I. The material was hot-rolled to ¼-in. thick plates then trimmed and surface-ground to remove scale and surface defects. The alloys were then cold-rolled into sheet 0.006-0.012 in. thick. The cold-rolled sheet was cut into 2- by 5-cm specimens, which were electropolished in a 15% perchloric-85% glacial acetic acid electrolyte, washed, and vacuum annealed 4 hr at 950°C. After slow cooling (2°C/min) to room temperature in vacuum, the specimens were again electropolished and washed, and then were inserted in the microbalance system. After treatment in hydrogen at a pressure of 10 Torr for 1 hr at 400°C and evacuation for 40 min, the oxidation experiments were begun with adjustment of the specimen temperature and the introduction of oxygen at the required pressure (10).

Table I. Analysis of iron-carbon alloys

Alloy	Composition, %								
	C	Mn	P	S	Si	Cu	Ni	Cr	Al
Iron base	0.003	<0.01	<0.002	0.002	0.008	<0.005	0.022	0.004	0.024
1	0.05	<0.01	<0.002	0.003	0.009	<0.005	0.021	0.004	0.008
2	0.11	<0.01	<0.002	0.002	0.006	<0.005	0.021	0.004	0.008
3	0.22	<0.01	<0.002	0.005	0.006	<0.005	0.004	<0.002	0.14
4	0.50	<0.01	<0.002	0.006	0.006	<0.005	0.004	<0.002	0.14
5	0.99	<0.01	<0.002	0.005	0.008	<0.005	0.004	<0.002	0.14

Results and Discussion

Oxidation of iron at 500°C.—The weight gain *vs.* time curves for the oxidation of the iron base at 500°C and an oxygen partial pressure of 10 Torr are characterized by alternating periods of high and low oxidation rate, Fig. 1. These changes in oxidation rate are associated with scale blistering cycles. It is believed that the blisters in the scale are initiated by vacancy rafts that form under the oxides as vacancies accumulate at the oxide-metal interface. The oxide phase that forms first when iron begins to oxidize under the experimental conditions is Fe_3O_4. This oxide is a cation-deficit p-type semiconductor. The incorporation of oxygen into the Fe_3O_4 lattice produces cation vacancies that move inward through the oxide toward the oxide-metal interface, as iron ions move outward toward the oxide-oxygen interface (10). As iron ions cross over from the metal into the oxide they leave behind at the interface the vacancies which can then, according to Evans (11), accumulate at the oxide-metal interface to form cavities, pass into the metal and react with a vacancy sink such as a dislocation, or pass through the metal (if sheet) and join a cavity in the far side.

The number of vacancy sinks available in a well-annealed metal should be constant at constant temperature. Therefore, the rate of vacancy annihilation at a given temperature should be constant or slowly decrease as the available vacancy sinks are consumed. If the rate of arrival of the vacancies at the oxide-metal interface is higher than the annihilation rate, vacancies will tend to accumulate at the oxide-metal interface and cause the oxide to lose contact with the metal (12). Vermilyea (13) has pointed out that an oxide such as Fe_3O_4, which grows by cation diffusion, will be relatively unstrained, since each new layer is formed at the oxide-gas interface and need only fit the preceding layer. Accordingly, the Fe_3O_4 layer probably is relatively unstrained at the time of separation. However, once contact is lost between the oxide and the metal, iron ions cease to diffuse through the oxide, and the oxide then reacts with ad-

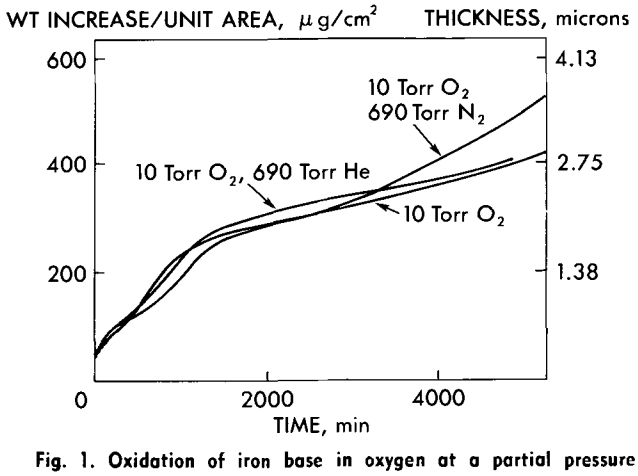

Fig. 1. Oxidation of iron base in oxygen at a partial pressure of 10 Torr.

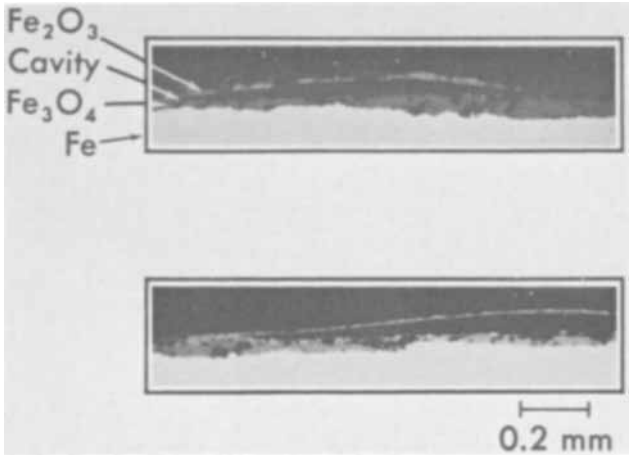

Fig. 2. Oxide blisters formed on iron base at 500°C in oxygen at a partial pressure of 10 Torr. Conditions: top, 500°C, 10 Torr O_2, 690 Torr N_2, 5600 min., bottom, 500°C, 10 Torr O_2, 690 Torr He, 4200 min.

ditional oxygen to become Fe_2O_3. Since Fe_2O_3 grows inward by anion diffusion and has a 2% greater volume than Fe_3O_4 (14), stresses are developed in the oxide, causing it to arch away from the iron substrate in the areas of separation and form the observed blisters, Fig. 2. (On cooling at the termination of an experiment, the difference between the thermal contraction of the oxide and that of the metal causes additional arching of the blister caps.) Eventually, the blister cap cracks and allows oxygen to leak into the cavity, thereby initiating a fresh oxide layer on the exposed metal surface.

The data obtained from the oxidation of the iron base at 500°C and a higher oxygen pressure, 700 Torr, conformed to a smooth, nearly parabolic, curve and there was no evidence of blistering in cross sections of the resulting scale, Fig. 3.

Specimens were oxidized in mixtures of an inert gas such as nitrogen, helium, or argon at a pressure of 690 Torr and oxygen at a pressure of 10 Torr to determine if the observed effect of pressure was the result of squashing of the oxide into the metal at the higher total pressure, 700 Torr. As is shown in Fig. 1 the weight gain curves were similar to those obtained in pure oxygen. Blisters were observed in the scale. Thus, it does not appear that the increase in oxidation rate observed in oxygen at a pressure of 700 Torr can be explained as squashing of the oxide.

The oxide films formed in 1 min and 25 sec at 500°C in oxygen at pressures of 10 and 700 Torr were examined using a polarizing microscope. (The anisotropic phase, Fe_2O_3, is visible under polarized light, whereas the isotropic phase, Fe_3O_4, is dark.) It appeared that the outer, Fe_2O_3 layer, was more complete on the oxide formed at 700 Torr than it was on the oxide formed at 10 Torr. This observation suggests the following mechanism to explain the difference in oxidation behavior observed at the two oxygen pressures. As long as Fe_3O_4 is exposed to gaseous oxygen, cation vacancies are generated at a high rate, diffuse through the scale, and accumulate at the oxide-metal interface, as was discussed in detail above. However, as the surface of the Fe_3O_4 becomes completely covered with a layer of Fe_2O_3, the rate of formation of cation vacancies is drastically reduced and vacancies arriving at the oxide-metal interface can be annihilated at vacancy sinks before they can accumulate. Thus, the oxide formed at 500°C and 700 Torr remains in contact with the metal and thickens more or less continuously under diffusion control.

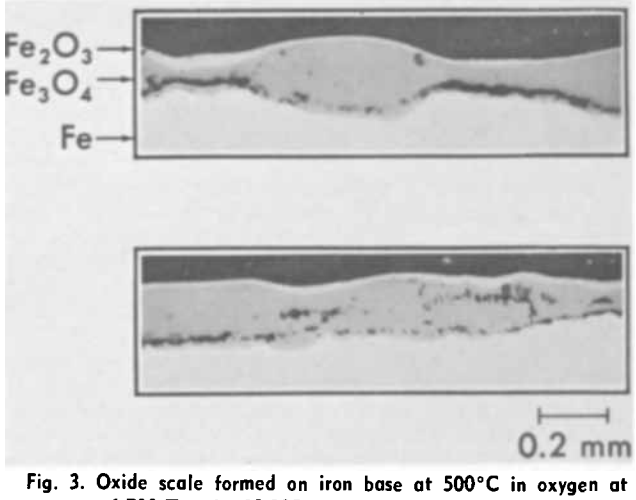

Fig. 3. Oxide scale formed on iron base at 500°C in oxygen at a pressure of 700 Torr for 11,325 min.

Oxidation of iron-carbon alloys at 500°C.—The effect of carbon concentration on the oxidation kinetics at 10 Torr and at 500°C is shown in Fig. 4. The oxidation rate of the iron-carbon alloys was much higher than that of the iron base under these conditions. The effect of carbon concentration on the oxidation kinetics at 700 Torr is shown in Fig. 5. The oxidation rate of the iron-carbon alloys was initially higher than that of the iron base but became lower as the oxidation progressed. The plots of weight gain *vs.* time obtained from the oxidation of the iron-carbon alloys at both oxygen pressures conformed to smooth curves and no evidence of blistering was found in cross sections of the resulting oxide scale, Fig. 6. The data presented in Fig. 4 and 5 show that the over-all scaling rate of the iron-carbon alloys was not increased appreciably at 500°C by increasing the oxygen pressure from 10 to 700 Torr.

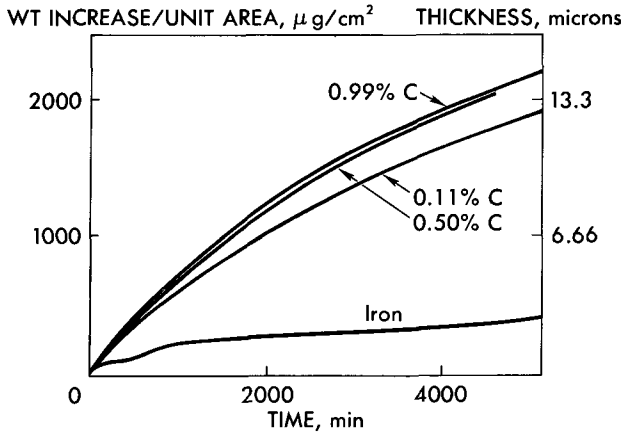

Fig. 4. Effect of carbon concentration on the oxidation of iron-carbon alloys at 500°C in oxygen at 10 Torr.

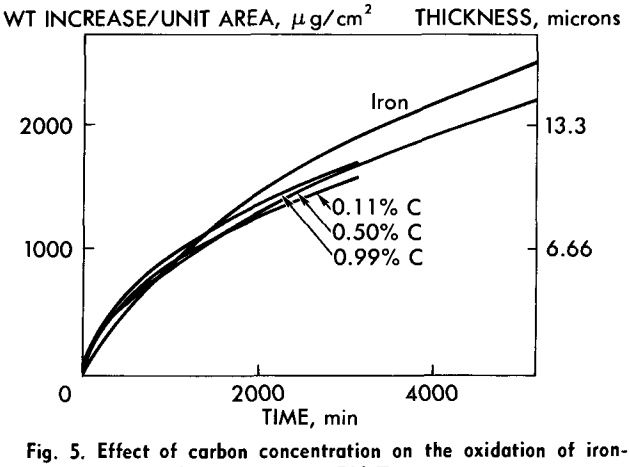

Fig. 5. Effect of carbon concentration on the oxidation of iron-carbon alloys at 500°C in oxygen at 700 Torr.

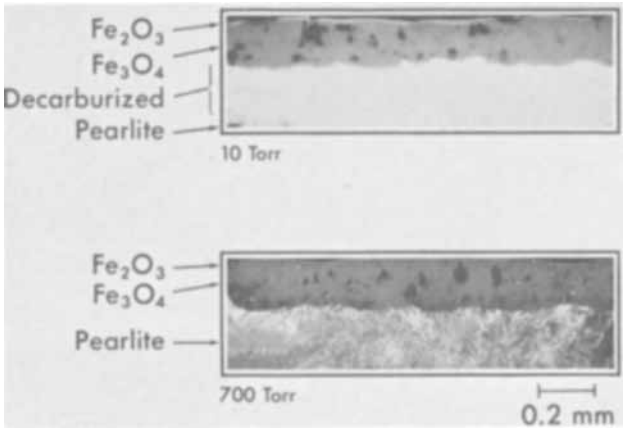

Fig. 6. Effect of oxygen pressure on the decarburization of the iron-0.99% carbon alloy in 5600 min at 500°C.

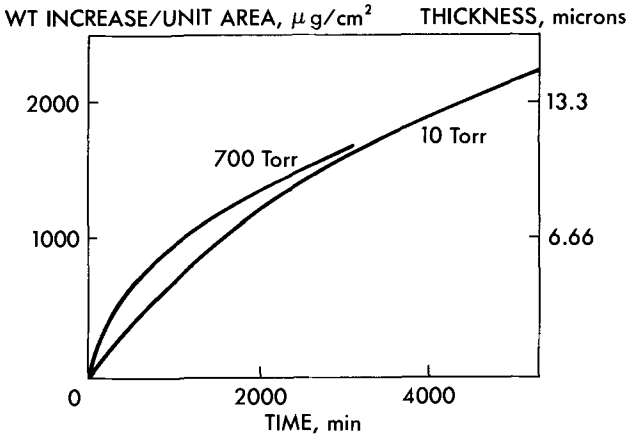

Fig. 7. Effect of oxygen pressure on the oxidation of the iron-0.99% carbon alloy at 500°C.

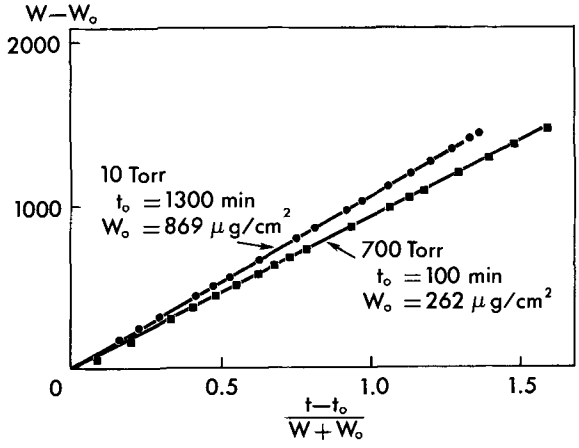

Fig. 8. Parabolic plots of the oxidation of the iron-0.99% carbon alloy at 500°C.

The freedom from scale blistering at 10 Torr exhibited by the iron-carbon alloys, in contrast to the iron base, is believed to be due to a greater number of vacancy sinks (dislocations) generated in the substrate by the precipitation of cementite during specimen preparation and by the subsequent volume decrease associated with decarburization. The vacancy annihilation rate will, therefore, be higher so that there is less tendency for vacancies to accumulate, and the scale will remain in better contact with the metal during the early stages of oxidation than is the case with the oxidation of pure iron. Caplan (12) has shown that cold-worked iron specimens exhibit higher oxidation rates than do well-annealed iron specimens. He has also observed that separations occur between the oxide and the metal with well-annealed material, but not with cold-worked material. He concludes that cold work prevents oxide separation, and thereby increases the oxidation rate, by providing additional sinks for the cation vacancies arriving at the Fe-Fe_3O_4 interface and thus preventing vacancy accumulation. According to Caplan, the cold work is effective, in spite of the annealing that begins as soon as the specimen is heated for oxidation, because extra vacancy sinks are required only at the beginning when the reaction rate is greatest and the vacancy flux a maximum.

The slight increase in initial oxidation rate with increasing carbon concentration can also be explained on this basis. Any slight vacancy accumulation that might occur at the lower carbon concentrations would tend to throttle the flow of iron through the scale to support the oxidation reaction; but at the higher carbon concentrations, enough vacancy sinks are available to annihilate all of the vacancies reaching the oxide-metal interface.

The oxidation of the iron-carbon alloys at an oxygen pressure of 10 Torr is accompanied by decarburization of the substrate. As the oxidation proceeds, a decarburized zone develops in the substrate at the oxide-metal interface and the pearlitic zone retreats toward the center of the specimen, Fig. 6, top. The phenomenon of decarburization below the oxide-metal interface will occur only when the rate of diffusion of carbon in the metal at a given temperature exceeds the rate of diffusion of iron into the scale (15).

In contrast, no decarburized zone appears when the alloy is oxidized at 700 Torr, Fig. 6, bottom. This difference is evident not only in the micrographs of cross sections of specimens oxidized at the two oxygen pressures, but also in the kinetic data, Fig. 7. The weight gain observed in the oxidation of the iron-0.99% carbon alloy at 10 Torr was lower than that observed in the oxidation of the same alloy at 700 Torr by the weight of carbon evolved at the lower oxygen pressure. Parabolic plots of those data are shown in Fig. 8. At 700 Torr the weight-gain data began to exhibit parabolic behavior after about 100 min. In contrast, at 10 Torr the weight gain data began to exhibit parabolic behavior after about 1300 min. The weight gain observed in the oxidation of this alloy at 10 Torr was the net result of the weight gain resulting from the oxidation of iron and weight loss resulting from the simultaneous decarburization.

The effect of oxygen pressure persists even after the experimental conditions have been altered. In a series of experiments with the iron-0.5 carbon alloy, oxidation was begun at 700 Torr and then after 5 min, 100 min, or 1000 min the oxygen pressure was reduced to 10 Torr and the reaction allowed to continue until the total time was 5600 min. Changing the oxygen pressure after 1000 min had little effect on the kinetic data. The specimen oxidized for 1000 min at 700 Torr did not decarburize when the oxygen pressure was reduced; some decarburization occurred in the specimen oxidized for 100 min at 700°C, and normal decarburization was observed in the specimen oxidized for only 5 min at 700 Torr before the pressure reduction, Fig. 9.

Another example of the persistence of the effect of oxygen pressure during scale growth on the subsequent behavior of the oxide is that oxide formed at 10 Torr can be reduced by internal carbon, whereas the oxide formed at 700 Torr cannot be similarly reduced. Specimens of the iron-0.50% carbon alloy were oxidized at 500°C and oxygen pressures of 10 or 700 Torr for 4000 min to produce fairly thick and adherent scales. At the end of this time, the oxygen was removed and the specimens were then allowed to anneal in vacuum for 4400 min at 500°C. A loss in weight was observed for the specimen oxidized at 10 Torr, whereas the weight of the specimen oxidized at 700 Torr remained constant. When the oxide scales produced in

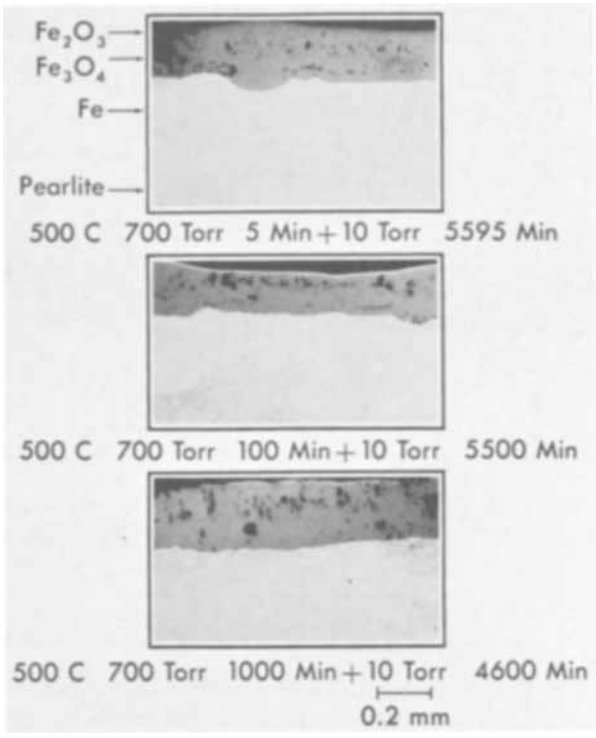

Fig. 9. Sections showing the effect of scale formed on the iron-0.50% carbon alloy at 700 Torr on the subsequent decarburization at 10 Torr.

these two experiments were examined in cross section, it was found that a zone of iron particles, resulting from the reduction of Fe_3O_4 by carbon, had developed near the oxide-metal interface of the specimen oxidized at 10 Torr, Fig. 10. No similar oxide reduction was observed in the specimen oxidized at 700 Torr. The reduction of Fe_3O_4 by carbon is not thermodynamically favored at 500°C. However, it appears that the reduction is permitted by the removal of the gaseous reaction product, CO.

The fact that CO rather than CO_2 was evolved during the vacuum reduction of the oxide was demonstrated by the following experiment: a specimen of the iron-0.11% carbon alloy was oxidized at 350°C in oxygen at 10 Torr for 60 min in the microbalance to form an oxide film containing 64 μg of oxygen. This

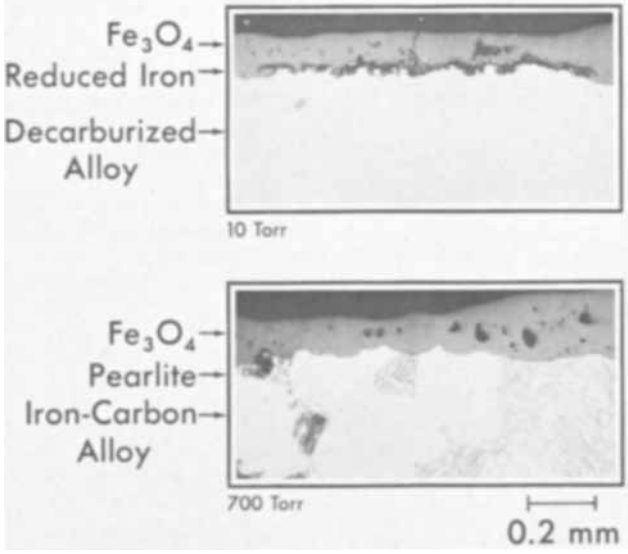

Fig. 10. Scale formed on the iron-0.50% carbon alloy in 4000 min at 10 Torr and 500°C is partially reduced by carbon during a 4400 min vacuum anneal at 500°C. The scale formed at 700 Torr is not similarly reduced during vacuum annealing.

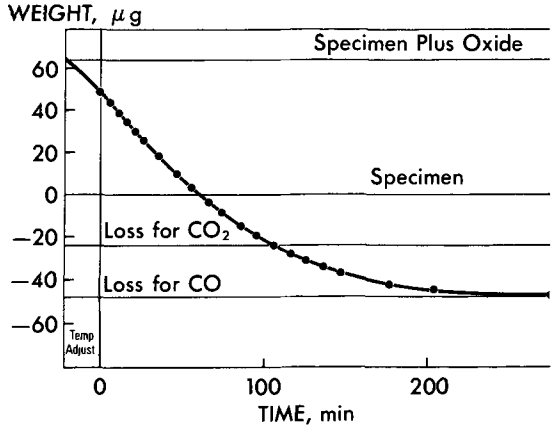

Fig. 11. Vacuum reduction of the oxide formed on the iron-0.11% carbon alloy in 60 min at 350°C in oxygen at 10 Torr.

oxide film was then completely reduced by vacuum annealing at 500°C for 1185 min. The weight losses to be expected from the evolution as CO or CO_2 were calculated from the known weight of the oxide and the amount of carbon required for the reduction. Under the experimental conditions, twice as much carbon would be required to reduce the oxide if CO were the gas evolved than would be required if CO_2 were evolved. As is shown in Fig. 11, the observed weight loss demonstrated that the gaseous reaction product of the vacuum reduction was CO.

A specimen of the iron-0.99% carbon alloy was oxidized at 10 Torr and the gas evolved was trapped in a liquid-nitrogen-cooled finger and determined volumetrically. The iron oxide scale was then completely reduced in hydrogen in order to determine by difference the amount of carbon evolved during the oxidation. The weight of the carbon, trapped as CO_2, amounted to 97.2% of the weight of carbon evolved during the oxidation.

An iron-0.50% carbon alloy specimen was oxidized at 500°C in a gas mixture consisting of helium at a partial pressure of 690 Torr (added first) and oxygen at a partial pressure of 10 Torr. Decarburization of the iron substrate was observed under these conditions in about the same amount as had been observed when the alloy was oxidized in pure oxygen at a pressure of 10 Torr. Thus, the oxygen partial pressure rather than the total gas pressure controls the decarburization process.

In view of the foregoing experimental observations, the most attractive explanation of the pressure dependence of the decarburization involves pores through the oxide that remain open to permit the escape of CO or CO_2 at an external oxygen pressure of 10 Torr but quickly become blocked to prevent decarburization at an oxygen pressure of 700 Torr. In the earliest stages of oxidation, adsorbed oxygen can react with carbon at the alloy surface in the areas between expanding iron oxide nuclei to produce CO. Since, under the experimental conditions, the iron oxide nuclei grow together to form an iron oxide film in a few seconds, the observed amount of decarburization cannot be explained by this direct reaction between carbon and oxygen.

The continuation of decarburization after the formation of an iron oxide film at an oxygen pressure of 10 Torr could be explained by carbon moving through the oxide layer and being emitted into the atmosphere as a gaseous reaction product, CO or CO_2. However, the transport of carbon through the iron oxide film by solid-state diffusion appears unlikely because of the low solubility of carbon in the oxide and because it is difficult to explain the effect of oxygen pressure on the decarburization if the reaction between carbon and oxygen takes place on the outer surface of the oxide. Therefore, it appears that the carbon is oxidized at the oxide-metal interface and that the resulting

gaseous reaction products escape into the atmosphere through pores or faults in the oxide layer.

Thus, it is believed that pores remain in the grain boundaries when iron oxide nuclei grow together. As the oxide thickens at 10 Torr, oxygen entering a pore reacts with CO flowing up from the oxide-metal interface to form CO_2. Some of this CO_2 diffuses back to the base of the pore where it reacts with carbon to produce CO. In this way, a CO-CO_2 atmosphere of low oxidizing potential is maintained within the pore, inhibiting the growth of iron oxide on the pore walls.

However, when the external oxygen pressure is 700 Torr, oxygen enters the pores faster than CO is produced so that the oxidizing potential of the pore atmosphere is much higher. The excess oxygen is incorporated into the iron oxide lattice in the pore walls. Thus, the pores close quickly at the higher oxygen pressure, blocking the escape of gaseous carbon oxides and thereby stopping further decarburization of the alloy substrate.

Except for the direct reaction of oxygen with carbon, none of the possible reactions that could produce gaseous carbon oxides at the oxide-metal interface are favored thermodynamically at 500°C. Thus, the reaction can proceed only if the reaction product can escape from the site of the reaction. When the escape paths are blocked, the reaction stops.

The mechanism for the preferential oxidation of carbon with CO_2 to produce CO at the base of the pore is not clear. Theoretically, under the experimental conditions, the oxidation of iron by CO_2 is slightly favored over the oxidation of carbon by CO_2. Thus, the iron at the base of the pores should be covered with a thin iron oxide layer through which the carbon must pass as it escapes from the iron substrate. The reasons why this thin oxide film does not grow and quickly block the decarburization have not been resolved.

If the proposed mechanism for decarburization of the iron substrate through an oxide scale is valid, it appears that, even at the lower oxygen pressure, the pores should eventually close as the concentration of CO in the pore atmosphere decreases because of the increasing length of the pore and the increasing length of the diffusion paths from the source of the carbon (the Fe_3C phase deep in the iron substrate) to the oxide-metal interface. The kinetic data presented in Fig. 7 for the oxidation of the iron-carbon alloys at oxygen pressures of 10 and 700 Torr tend to support this hypothesis. The rate of oxidation at both pressures is probably quite similar but the decarburization reaction at 10 Torr results in a lower rate of weight increase. After 2000 to 3000 min, the weight-gain rates are similar, which indicates that the decarburization reaction has probably stopped. Furthermore, samples oxidized for extended periods at 10 Torr still have Fe_3C platelets below a decarburized layer despite the fact that decarburization at the early rates should have completely eliminated the carbon. Thus, some mechanism, such as eventual pore closure, evidently exists.

Surface-area measurements by the B.E.T. method using xenon were made on specimens of the iron-0.99% carbon alloy that had been oxidized for 1000 min at 500°C in oxygen at pressures of 10 and 700 Torr, respectively. The oxide formed at 10 Torr had 8 times the surface area of the oxide formed at 700 Torr, presumably because of the surface area of the pores. Unfortunately, the slow evolution of CO from the specimen oxidized at 10 Torr prevented establishment of the adsorption-desorption isotherms with sufficient accuracy for pore-size estimations.

An additional experiment was devised to demonstrate differences in porosity in the scales formed at the two oxygen pressures. Representative specimens of the iron-0.5% carbon alloy were oxidized at 500°C for 3900 min. After this period of time, the temperature was decreased to 350°C and held for 2 hr. The iron diffusion rate outward through the Fe_3O_4 was considerably reduced at the lower tempearture. Consequently, oxygen penetrating through the pores in the oxide was able to convert the oxide in the pore walls to Fe_2O_3 and thereby decorate the pore walls for identification in the metallographic cross sections. The results of these experiments are shown in Fig. 12. Considerable porosity was evident in the scale formed at 10 Torr, but only slight oxygen penetration was observed in the scale formed at 700 Torr.

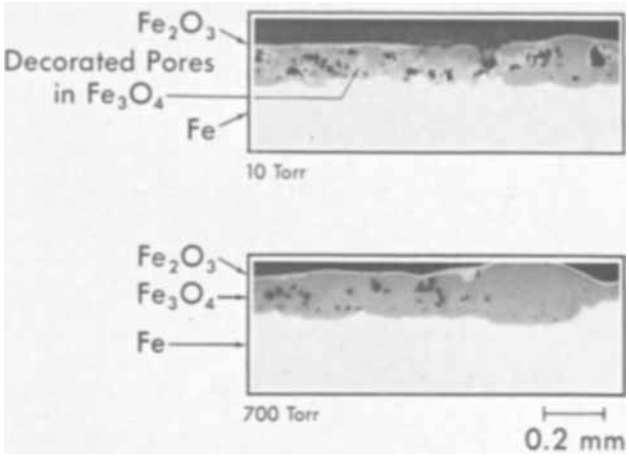

Fig. 12. Effect of oxidizing conditions (oxygen pressure) on the porosity of the scale formed on the iron-0.50% carbon alloy. Specimens first oxidized for 3900 min at 500°C and then 120 min at 350°C.

The distribution of the Fe_2O_3 in these sections suggests that the Fe_3O_4 layer is much less compact than the Fe_2O_3 layer. Most of the pores appear to be concentrated in the lower two-thirds of the Fe_3O_4, and connections between these and the outer layer are relatively rare. Thus, it appears that pore closure occurs near the outer surface of the scale as required for the proposed mechanism for decarburization.

Summary

The oxidation of an iron base and a series of iron-carbon alloys at 500°C in oxygen at pressures of 10 and 700 Torr has been studied in detail. Reasonable explanations have been developed for the various phenomena observed in connection with these oxidation experiments.

Blisters grow in the scale formed on the iron base during oxidation at 10 Torr. It appears that iron-ion vacancies diffuse through the scale and accumulate at the oxide-metal interface at a faster rate than they can be annihilated at vacancy sinks existing in the metal substrate. This causes separation to occur between the oxide and the metal. Subsequent conversion of the Fe_3O_4 to Fe_2O_3 in the scale over the separation introduces strain, which causes the separated area to bow up away from the metal and form the blister. When cracks develop in the blister cap, gaseous oxygen enters the cavity, forming a new oxide layer on the exposed metal, and the process repeats.

Blistering is not observed when the iron base is oxidized at 500°C in oxygen at a pressure of 700 Torr. It appears that the outer phase of the scale, Fe_2O_3, nucleates and grows laterally to form a continuous layer more rapidly at 700 Torr than at 10 Torr. The formation of a continuous layer of Fe_2O_3 reduces the rate of formation of iron-ion vacancies so that those vacancies arriving at the oxide-metal interface can be annihilated at vacancy sinks in the metal and thus do not accumulate at the interface to cause the oxide-metal separations that result in oxide blisters.

The presence of cementite, Fe_3C, in the substrate also tends to prevent the formation of oxide blisters even when these alloys are oxidzed at 500°C in oxygen at a pressure of 10 Torr. It appears that additional vacancy sinks generated by the precipitation of cementite

during specimen preparation and by the volume decrease associated with decarburization increase the vacancy annihilation rate and thus prevent the formation of the oxide-metal separations that occur in the oxidation of iron under similar conditions.

It has also been observed that the iron-carbon alloys decarburize when oxidized at 500°C in oxygen at 10 Torr, but do not decarburize when oxidized at 500°C in oxygen at 700 Torr. This effect of oxygen pressure can be explained if it is assumed that pores develop as the iron and carbon are competitively oxidized, starting with a clean metal surface. Initially, carbon is oxidized and escapes into the atmosphere from sites in the areas between iron oxide nuclei. As the nuclei grow together and the iron oxide thickens, pores or faults are left at the oxide grain boundaries. Carbon from the substrate reacts with CO_2 in the pore atmosphere to form CO. Thus, the pores provide paths for the escape of carbon oxides into the atmosphere. When the external oxygen pressure is 10 Torr, oxygen entering the pores reacts with CO to form CO_2. This mechanism maintains a CO-CO_2 atmosphere of low oxygen activity within the pores, keeping them open.

However, at the higher pressure, 700 Torr, oxygen is able to enter the pores and be incorporated in the iron-oxide lattice. This causes the growth of fresh oxide in the pores, blocking them and preventing the escape of carbon oxides. Since none of the reactions that could oxidize carbon at or near the oxide-metal interface are thermodynamically favored at 500°C, escape of carbon oxides is necesary in order for the reaction equilibrium to be shifted in the direction of carbon oxidation. Thus, once the pores are blocked, carbon oxides cannot escape, and the decarburization reaction stops.

Acknowledgment

The authors gratefully acknowledge the surface area measurements by Dr. Harry Podgurski and Frank N. Davis of the U. S. Steel Fundamental Research Laboratory. The authors also acknowledge the helpful discussions of Dr. Donald Caplan of the Canadian National Research Council and Professor Dr. Hans-J. Engell of the Max-Planck-Institut für Metallforschung.

Manuscript submitted Oct. 8, 1968, revised manuscript received ca. Jan. 16, 1969. This paper was presented at the Montreal Meeting, Oct. 6-11, 1968, as Paper 411.

Any discussion of this paper will appear in a Discussion Section to be published in the December 1969 JOURNAL.

REFERENCES

1. C. Upthegrove and D. W. Murphy, *Trans. Am. Soc. Steel Treat.*, **21**, 73 (1933).
2. A. Portevin, E. Pretet, and H. Jolivet, *Rev. Mét.*, **31**, 101, 186, 219, (1934).
3. C. R. Austin, *Trans. Am. Soc. Metals*, **22**, 31 (1934).
4. C. A. Siebert, *ibid.*, **27**, 752 (1939).
5. D. J. McAdam and G. W. Geil, *J. Research, Nat. Bur. Standards*, **23**, 63 (1939).
6. H.-J. Engell and F.-K. Peters, *Arch. Eisenhüttenw.*, **28**, 567 (1957).
7. K. Bohnenkamp and H.-J. Engell, *ibid.*, **33**, 359 (1962).
8. G. J. Billings, M. S. Thesis: "Oxidation and Decarburization Kinetics of Iron-Carbon Alloys in Carbon Dioxide-Carbon Monoxide Atmospheres." W. W. Smeltzer, Supervisor, McMaster University, Hamilton, Ontario (1966).
9. W. W. Webb, J. T. Norton, and C. Wagner, *This Journal*, **103**, 112, (1956).
10. W. E. Boggs, R. H. Kachik, and G. E. Pellissier, *ibid.*, **112**, 539, (1965).
11. U. R. Evans, "The Corrosion and Oxidation of Metals," p. 836, St. Martin's Press, New York (1960).
12. D. Caplan and M. Cohen, *Corrosion Sci.*, **6**, 321 (1966).
13. D. A. Vermilyea, *Acta Met.*, **5**, 492, (1957).
14. O. Kubaschewski and B. E. Hopkins, "Oxidation of Metals and Alloys," 2nd Ed, p. 10, Academic Press, Inc., New York (1962).
15. N. D. Tomashov, "Theory of Corrosion and Protection of Metals," p. 116, The Macmillan Company, New York (1966).

Polarographic Measurement of the Reaction between o-Chlorobenzalmalononitrile and 2-Diethylaminoethyl Mercaptan (DEAEM)

Pascal A. Tarantino* and Samuel Sass

Research Laboratories, Edgewood Arsenal, Maryland

ABSTRACT

Controlled-potential and first derivative polarography were found to be effective for determining the kinetics of reaction of two electroactive compounds in nonaqueous and partially aqueous media. The mechanism and rate of reaction of o-chlorobenzalmalononitrile with 2-diethylaminoethyl mercaptan were found to be dependent on the relative concentration of the reactants, the solvent medium and temperature. A rapid-scan polarograph with a trielectrode system was used for most of this study.

The purpose of this study was to determine the electrochemical properties (polarography) of o-chlorobenzalmalononitrile (CS) and related compounds in several media and in the presence of a rapidly reacting nucleophile. Since CS is a potent irritant and has been used successfully for riot control, it could be used as a standard of comparison with related compounds. This information could be useful both from the standpoint of analytical methodology and for obtaining a better understanding of structure-activity relationships.

The polarographic reduction of benzalmalononitrile in Prideaux and Ward buffers, pH 4-8.9, with 30% alcohol is reported by Bargain and Delepine (1): in acid media there occurs a single two-electron wave, and in basic media, two waves, each corresponding to one-electron addition. In dimethylformamide (2) benzalmalononitrile gives only one wave with a one-electron addition, indicating the formation of a free

* Electrochemical Society Active Member.

radical. The influence of proton donors (benzoic acid and phenol) in dimethylformamide for this compound (3) has also been reported: with phenol, two reduction waves occur; and when benzoic acid is used, three distinct waves are formed.

Holmes *et al.* reported on the spectral (4) and polarographic analysis (5) of some benzalmalononitriles and related compounds, and on their rates of reaction with potassium cyanide (6), n-butanethiol, and n-butylamine (7), including also a theory for the action of benzalmalononitriles on nerve endings.

Sass *et al.* (8) reported on attempts to utilize aliphatic mercaptan as a reagent for the volumetric analysis of CS and related compounds. This study indicated that more than one thiol adduct could be obtained with CS, depending on the medium and the pH. Under conditions in which a second thiol adduct was obtained, one thiol group was readily removed by titration with iodine.

The work described in the present report represents a study of the polarographic characteristics of CS under conditions that had not been described previously, nor had an aminomercaptan been used heretofore for reaction studies.

Experimental

Reagents.—Preparation of DEAEM.—The free base mercaptan was isolated from the hydrochloride salt, purchased from Evans Chemetics, Inc. The salt was neutralized with a methanol solution of sodium methoxide, decanted from the sodium chloride precipitate, and fractionally distilled in vacuo. The collected DEAEM showed a purity of 99.85%, as indicated by iodine titration.

CS.—A CS sample of 99.5% purity was obtained by recrystallization from an ethanol-water solution, washed with water, and dried *in vacuo*. The white crystalline material melted at 96°C. The purity was determined by volumetric titration (8).

Solvents.—Reagent grade anhydrous methanol and acetone were used with no further purification. The water content for both of these solvents was less than 0.05%. Practical grade acetonitrile was purified by refluxing for 3 hr over phosphorus pentoxide, decanted, distilled, refluxed over potassium carbonate, decanted, and redistilled. The solvent, stored in an amber bottle, contained less than 0.05% water and did not reduce iodine.

Electrolytes.—Lithium nitrate and tetrabutylammonium perchlorate (Bu_4NClO_4) were used as electrolytes. Lithium nitrate, B and A Standard of Purity, was used with no further purification. Tetrabutylammonium perchlorate was prepared from the corresponding bromide salt (9).

Purging gas.—Prepurified nitrogen was used for purging electrolytic solutions before and during the recording of all polarograms and rate studies.

Apparatus.—Polarograph.—A modified version of the ORNL Controlled Potential and Derivative DC Polarograph (10) was used. The new polarograph (ORNL-Q-1988-FES), which is capable of doing rapid regular and first and second derivative d-c polarography,[1] was constructed in our laboratory. It permits a fast scan of the polarograms up to 3 v/min, which was found to be very convenient for reaction-rate study.

Polarographic cell.—A trielectrode cell was all-glass constructed to accommodate a nitrogen gas purger and a three-electrode system. The polarizable electrode was a Smolar type DME with a drop-time (t) of 0.5 sec., a flow rate (m) of 3.85 mg/sec and $m^{2/3}t^{1/6} = 2.18$ $mg^{2/3}/sec^{1/2}$. The reference electrode was an aqueous Ag/AgCl (saturated) system bridged to the test solution by a saturated KCl solution, a 4% KNO_3 agar plug and a sintered glass disk. The counter electrode was a spiral of platinum wire (18 gauge) isolated from the test solution by a 7 mm porous tip Vycor tube filled with the electrolyte used in the cell.

Procedures.—All polarographic work for calibration and rate study was conducted at 25°C by using a water-jacketed cell and a circulating bath with temperature control.

Calibration.—The method of standard addition was used for all calibration at 25°C. The electrolyte (20 ml of 0.1M $LiNO_3$ or Bu_4NClO_4) was placed in the electrolytic cell and purged for 5 min. A given volume of the standard was added, and the purging of the cell solution continued for 1 min longer. The nitrogen purge was diverted to the solution surface, and polarograms were recorded at a scan rate of 1.5 v/min, or as otherwise indicated.

Rate procedures.—The reaction rate between CS and DEAEM was investigated in the solvents listed above. The rates were measured at 25°C under different concentrations of reactants in 20 ml of electrolyte.

A 20-ml volume of electrolyte was placed in the electrolytic cell, purged for 5 min, and the residual current recorded. DEAEM, from a freshly prepared standard, was added to the cell solution to correspond to 1 mM; the system was purged for 1 min, and the purge was diverted to the surface of the solution. After the DEAEM polarogram was recorded, the applied voltage was set on the flat portion of the DEAEM anodic limiting current, and the time-sweep circuit of the recorder was closed to coincide with the addition of CS, and purging was maintained for 30 sec to insure uniform mixing of the solution. The gas purge was diverted to the surface of the solution mixture, and the consumption of the DEAEM was recorded using the preset time-sweep. The monitoring of the rate was continued until the rate curve indicated a 70% consumption of DEAEM.

For cases where both reactants were monitored, derivative polarography was used at a scan rate of 3 v/min. The sequence of preparing the reaction mixture was the same as that described above. The derivative polarograms recorded the DEAEM oxidation peak and the CS reduction peak in about 30 sec. Consecutive derivative polarograms were recorded at time intervals, depending on the speed of the reaction.

Results and Interpretation

Polarography of DEAEM.—The selection of DEAEM as a reactant was based essentially on the desire to more closely approximate thiol associated with amine as in protein (*i.e.*, the cysteine group). Preliminary studies with cysteine indicated that it would be difficult to handle because of instability in any but acidic media. Tests with alkanethiols such as n-pentyl mercaptan showed that, in the absence of added base, the compounds are not polarographically active in the media employed here.

Polarography of DEAEM in various solvents.—DEAEM was calibrated in four different electrolytic media: anhydrous methanol, 50% aqueous methanol, anhydrous acetone containing 0.1M $LiNO_3$, and anhydrous acetonitrile with 0.1M Bu_4NClO_4. Normal and derivative polarography were determined for the calibrations in anhydrous methanol. The other solvents were submitted to only normal polarography.

DEAEM in anhydrous methanol has two waves: one anodic at —0.438v and one cathodic at —0.960v. The first is the oxidation of the thiol, and the second is due to the reduction of the disulfide. The wave and the peak heights are both linear with concentration for the anodic and cathodic diffusion current. The normal and first derivative data for this compound are given in Table I.

The polarograms for DEAEM in 50% aqueous methanol are well defined. The anodic (—0.452v) and the

[1] D. J. Fisher, W. L. Belew and M. T. Kelly, Addition of Rapid Regular, and First and Second Derivative dc Polarography Functions to the ORNL Controlled Potential dc Polarograph, unpublished data.

Table I. Calibration of DEAEM in 0.1M $LiNO_3$ anhydrous methanol

A. Normal polarography

Concentration, mM	Anodic wave $-E_{1/2}$, v	Anodic wave I	Cathodic wave $-E_{1/2}$, v	Cathodic wave I
1.19	0.436	−0.97	0.945	0.046
2.15	0.432	−1.01	0.948	0.046
3.49	0.440	−0.97	0.965	0.046
4.53	0.436	−1.01	0.980	0.046
5.73	0.446	−0.97	0.964	0.092
Average	0.438	−0.99	0.960	0.055

B. Derivative polarography

Concentration, mM	Anodic peak $-E_p$, v	Anodic peak I'	Cathodic peak $-E_p$, v	Cathodic peak I'
1.19	0.470	4.81	0.950	0.32
2.36	0.470	5.26	0.950	0.37
3.49	0.475	5.41	0.960	0.41
4.62	0.470	5.41	0.960	0.41
5.72	0.475	5.41	0.970	0.41
6.79	0.480	5.26	0.975	0.46
Average	0.473	5.26	0.961	0.40

$I = u\,A/C \cdot m^{2/3}t^{1/6}$ and $I' = I$/min.

cathodic (−0.735v) half-wave potentials are constant with increasing concentration; the diffusion current constants are −0.69 and 0.07, respectively. There is very good linearity for both waves with concentration.

The polarographic results for DEAEM in acetone and in acetonitrile are almost identical. The only difference is in the shape of the waves; that in acetonitrile is fairly well defined, and the wave in acetone becomes irregular with increase in concentration. The half-wave potentials are −0.468v and −0.461v for DEAEM in acetone and acetonitrile, respectively. The diffusion current constant is the same for both solvents, about −1.93.

Tautomeric forms of DEAEM.—The anodic diffusion current constant of DEAEM, as indicated by data in Table II, is dependent on the degree of hydrolytic character and on the polarity of the solvent. This current change could be due to several factors such as viscosity and polarity of the solvent, and charge of the electroactive material (11). The pKa for triethylamine and DEAEM in aqueous methanol at 25°C is 9.4 and 7.3, respectively. The lower pKa for DEAEM indicates a less basic amine. These results could indicate the presence of DEAEM in two tautomeric forms:

$$Et_2NCH_2CH_2SH \rightleftharpoons Et_2\overset{\oplus}{\underset{H}{N}}CH_2CH_2S^{\ominus}$$

The formation constant of the charged molecule (or zwitterion) is dependent on the polarity of the medium. The zwitterionic nature for analogous compounds has been shown for 8-mercaptoquinoline and 3 mercaptopyridine (12). In another study (13), the actual percentage of 8-mercaptoquinoline in the zwitterionic form was measured in different solvents (water, 97%; ethanol, 1.3%, acetonitrile, 0.5%; acetone, 0.14%; and ethyl ether, 10^{-5}%). The percentage of DEAEM in the zwitterionic form is probably much greater since it is generally known that aliphatic amines are more basic than the corresponding heterocyclic type.

Table II. Dependence of diffusion current constant of DEAEM on solvent

Solvent medium	I
50% Methanol	−0.64
80% Methanol	−0.87
90% Methanol	−0.96
Anhydrous methanol	−1.15
Anhydrous acetonitrile	−1.88
Anhydrous acetone	−1.92

Table III. Stability of DEAEM in anhydrous methanol

Age of 0.1M standard, hr	Polarographic waves Anodic, μa	Polarographic waves Cathodic, μa	RSH, %
0.1	−12.5	0.5	96
3.0	−12.0	2.0	86
5.0	−11.0	3.6	75
7.0	−10.0	4.9	67
16.0	−8.0	5.5	59
32.0	−0.2	13.3	2

Note: At 0.1 hr the indicated quantity of RSSR, based on its own wave, was of the order of 4%; after 32 hr it was at a level of approximately 98%.

Stability of DEAEM.—Once the DEAEM standard in methanol is placed in a purged electrolyte, consecutive polarograms with time indicate no change in either the anodic or the cathodic wave. However, the stock standard solution, 0.1M DEAEM, changes with time. The data given in Table III indicate that, for this solution, the anodic wave decreases and the cathodic wave increases with time of standing. Although there is no 1:2 correlation between the drop in the anodic wave and the rise of the cathodic wave, it is evident that DEAEM is being converted to its corresponding disulfide (14). According to this time-stability study, the DEAEM standard solution should be used for no more than 5 hr.

Effect of water on the diffusion current of DEAEM.—Four DEAEM standard solutions were prepared, each containing the same concentration (5 mM) in 100%, 90%, 80%, and 50% methanol with 0.1M $LiNO_3$ electrolyte. It was found that the anodic diffusion current decreases with increasing quantities of water present in the electrolyte. The cathodic wave showed some increase. This decrease in height of the anodic wave is probably due to diffusion effects produced by the increasing viscosity or change in dielectric of the methanol-water solution. The data are shown in Table IV.

Polarography of o-chlorobenzalmalononitrile (CS).—CS was the most readily available irritant at the time of this study. Its biological effectiveness had been tested on both animal and man and information made available on some of its chemical reactivity. Under these circumstances, the selection of this compound as a standard of comparison could prove useful for obtaining a better understanding of structure-activity relationships.

Polarography of CS in various solvents.—The calibration of CS was performed in the same media and under the same polarographic conditions as those used for DEAEM.

In anhydrous methanol, CS was calibrated by both normal and derivative polarography. The two cathodic wave heights and derivative peaks of CS are linear with concentration. The half-wave potentials and the maximum derivative peaks are constant for the first wave and peak; but for the second, there is a shift toward a more negative potential with increasing concentration. The average half-wave potentials for the first and the second cathodic waves are −0.896v and −1.635v, and the voltage peaks (Ep) are −0.909v and −1.703v. A summary of this data is shown in Table V.

Table IV. Effect of water concentration on the diffusion current of a 5 mM DEAEM standard

Water, %	DEAEM, μa	RSSR, μa
0	12.5	0.5
10	10.6	0.6
20	9.4	0.7
50	7.2	0.9

Table V. Calibration of CS in 0.1M $LiNO_3$ anhydrous methanol

Concentration, mM	A. Normal polarography: First cathodic wave $-E_{1/2}$, v	First cathodic wave I	Second cathodic wave $-E_{1/2}$, v	Second cathodic wave I
0.99	0.900	2.20	1.605	1.32
1.96	0.895	2.57	1.620	1.32
2.90	0.895	2.52	1.635	1.56
3.85	0.895	2.52	1.645	1.61
4.76	0.895	2.52	1.670	1.64
Average	0.896	2.48	1.635	1.49

Concentration, mM	B. Derivative polarography: First cathodic peak $-E_p$, v	First cathodic peak I'	Second cathodic peak $-E_p$, v	Second cathodic peak I'
0.99	0.925	36.2	1.665	15.1
1.96	0.920	38.0	1.695	12.4
2.90	0.900	37.6	1.700	12.8
3.85	0.900	37.1	1.725	13.3
4.76	0.900	35.3	1.730	13.3
Average	0.909	36.6	1.703	13.8

In 50% methanol a polarogram of CS produces two waves; the first is a wave (—0.79v) having a maximum which can be suppressed with one drop of 1% Titron X-100. With time there occurs a decrease of the CS first wave and a corresponding increase of the second wave (—1.3v). The over-all height of the first and the second wave remains constant. Since this electrolyte contains 50% water, hydrolysis of CS is undoubtedly occurring.

$$ArCH=C(CN)_2 \overset{H_2O}{\rightleftharpoons} ArCHO + CH_2(CN)_2$$

In this experiment an equilibrium was reached at the end of 40 min. A polarogram of o-chlorobenzaldehyde, run under identical conditions, gave a half-wave potential at —1.30v. The fact that the half-wave potential for the known sample of o-chlorobenzaldehyde was identical to the second wave for CS in 50% aqueous methanol was a proof that CS had hydrolyzed.

Polarograms of CS in acetone give only one wave (—0.924v) with a diffusion current constant equal to 4.7. There is an increasing linear deviation at concentration greater than 3 mM.

CS in acetonitrile exhibits two waves, one at —0.941v and the other at —1.766v. The diffusion current constant for the first wave is 4.2 and for the second wave, 0.6. The diffusion current for the first wave has very good linearity with concentration. The second wave is linear up to 2 mM, beyond which it is not reproducible.

Comparison of the polarography of o-chlorobenzaldehyde with that of CS.— o-Chlorobenzaldehyde, which is both an intermediate and a hydrolysis product of CS, was polarographed using the same solvent systems as those described previously. Malononitrile, the other intermediate and also a hydrolysis product, showed no wave in these media. The purpose of these polarograms was to assign a half-wave potential to the aldehyde should it appear during subsequent reaction studies. The polarographic data obtained on o-chlorobenzaldehyde are shown in Table VI. Data cited previously for CS are repeated for comparison.

Polarography of the formation of CS from its intermediates.—In order to confirm the stability of benzalmalononitriles and the dependability of the rate measurement in the electrolyte used for making all standard solutions (0.1M $LiNO_3$ in anhydrous methanol), an experiment was devised employing polarography to follow the formation of CS from its intermediates:

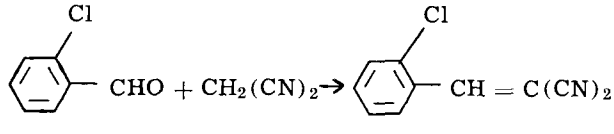

Table VI. Comparison of o-chlorobenzaldehyde with CS in the same electrolytic media

Electrolyte	o-Chlorobenzaldehyde $-E_{1/2}$, v	o-Chlorobenzaldehyde I	CS $-E_{1/2}$, v	CS I
0.1M $LiNO_3$, CH_3OH	1.355	1.15	0.895/1.635	2.48/1.47
0.1M $LiNO_3$, 50% CH_3OH	1.300	1.88	0.790/1.315	1.47/0.23
0.1M $LiNO_3$, $(CH_3)_2CO$	1.405	1.51	0.924/none	4.67/—
0.1M Bu_4NClO_4 CH_3CN	1.605	1.19	0.941/1.766	4.21/0.55

From this information it was intended to prove that the reaction was irreversible and that clear waves could be obtained. The half-wave potentials for the three compounds involved in the above reaction are: CS, —0.896v and —1.635v; malononitrile, inactive; o-chlorobenzaldehyde, —1.355v.

An equimolar mixture of o-chlorobenzaldehyde and malononitrile was polarographed in 0.1M $LiNO_3$, anhydrous methanol. The polarogram, run immediately after mixing, gave only the half-wave potential of the aldehyde. Subsequent polarograms indicated a slow decrease of the aldehyde wave. The solution was left overnight and polarographed again, 24 hr later. By this time the aldehyde wave had completely disappeared and new waves, characteristic of CS, were observed. Calculation, based on diffusion current, indicated a 98% conversion to CS. In a parallel experiment, o-chlorobenzaldehyde and malononitrile were reacted in the same manner. Results from a volumetric titration for CS (8) indicated the same order of conversion to compound.

Electrode processes of DEAEM and CS in methanol. —*DEAEM.*—The aminothiol, when first distilled and polarographed, shows only an anodic wave, that at —0.44v. With aging, the clear, concentrated aminothiol changes to an amber color. Polarograms of the aged aminothiol show, in addition to the anodic wave which is characteristic of the thiol group, a cathodic wave of a much lower current intensity occurs at —0.96v. The magnitude of the cathodic wave is less than 5% of the anodic wave. The second wave is due to a disulfide reduction. The electrode reaction of the aminothiol is not a direct oxidation of mercaptan but, instead, an indirect oxidation of mercury with the formation of mercurous mercaptide (14):

$$Et_2NCH_2CH_2SH + Hg \rightleftharpoons H^+ + Et_2NCH_2CH_2SHg + e$$

Consequently, the anodic current being measured is the oxidation of mercury which is directly related to the mercaptan concentration.

CS.—Normal polarograms of CS give two cathodic waves, the first is well defined and reversible while the second is drawn out and irreversible. The current temperature coefficients for the first and second waves are 2.0 and 2.4% per degree, respectively. The current and the square root of the mercury height gives a linear relationship for both waves. The polarographic wave equation (15) plots of the first CS wave are linear and the n-value averaged to one electron. The reversibility of the first cathodic wave is indicated by the excellent symmetry at its first derivative peak (16) and the linearity of the log-plots mentioned above. Coulometric studies of CS confirmed a one-electron reduction for the first wave; the second wave occurs too close to the background discharge for accurate coulometric determination, but indications are that it is also a one-electron process. Based on these results the following electrode processes are postulated for CS:

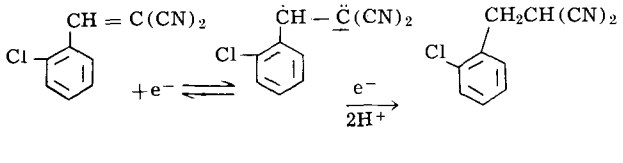

The diffusion current constant (I) of the first CS wave is 2.48 and that for the one-electron process of acetophenone in the same electrolyte is 2.43.

Polarographic reaction rates of CS and DEAEM.—A preliminary investigation of the reaction between CS and DEAEM indicated that when CS is in excess, the decrease in DEAEM content follows a pseudo first-order reaction. When the quantity of DEAEM is equivalent to or is in excess of CS, the reaction is significantly more complex. In the latter case, the CS concentration-time curve shows three slopes: the first, a rapid initial drop which could be indicative of a prior equilibrium, and the other two represent the formation of the mono- and di-adducts of CS-DEAEM. In an attempt to further resolve the formation of two different adducts, the interaction of CS was studied in greater depth.

Reaction rate study of CS with DEAEM.—The derivative polarographic technique was found to be very convenient for monitoring simultaneously the DEAEM (—0.45v) and the CS (—0.92v) derivative peak heights when utilizing a fast scan of 3 v/min (Fig. 1). Both reactant peaks decrease in height, as represented by recordings which occur less than 20 sec apart. A new peak appears at —1.7v and varies as the reaction proceeds; this peak is apparently characteristic of a reaction intermediate and end product, but it could not be quantitated. Plots made of the respective quantity of reactants consumed allowed the determination of reaction rate with respect to each component. These reaction-process curves (Fig. 2, 3, and 4) could be used to determine the nature of the product on an empirical basis at a given time. In the following experiments the rates were measured for four different ratio conditions of the reactants in 20 ml of methanol.

The progress of the reaction at a ratio of CS/DEAEM, 1:1 (20:20 μmoles) is shown in Fig. 2. The initial drop in CS is significantly greater than that of DEAEM. As the reaction proceeds, the curves cross at a point equivalent to a 1:1 reaction (mono-adduct). The continued consumption of DEAEM to approximately 65% of reaction while CS equilibrates at approximately 50% might be explained as the formation of some di-adduct (CS·2RSH).

At a ratio of CS/DEAEM, 2:1 (20:10 μmole) the initial CS drop exceeds that of DEAEM. As the reaction approaches completion, the consumption of reactants becomes equivalent, indicating a 1:1 reaction (CS·RSH, mono-adduct). This experiment is illustrated in Fig. 3.

Experiments in which the excess of DEAEM over CS was run as 2.5:1 (50:20 μmole) and 5:1 (50:10

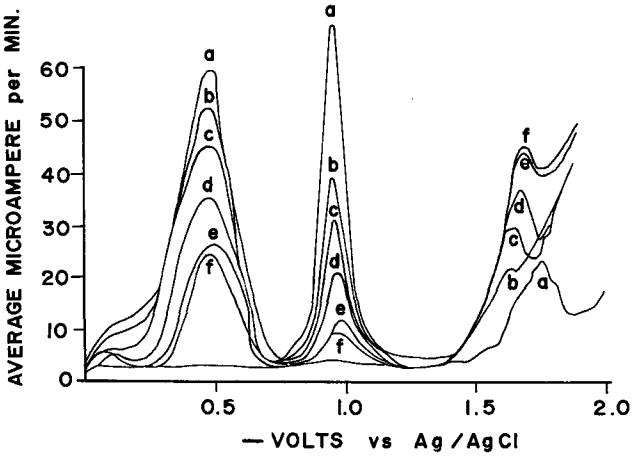

Fig. 1. Derivative reaction rate of 50 μmoles DEAEM with 20 μmoles CS (scan rate 3000 mv/min; Smoler 0.5 sec DME; electrolyte 0.1M $LiNO_3$ methanol; reaction time: a = initial, b = 3.5 min, c = 9.0 min, d = 24 min, e = 73 min, f = 182 min).

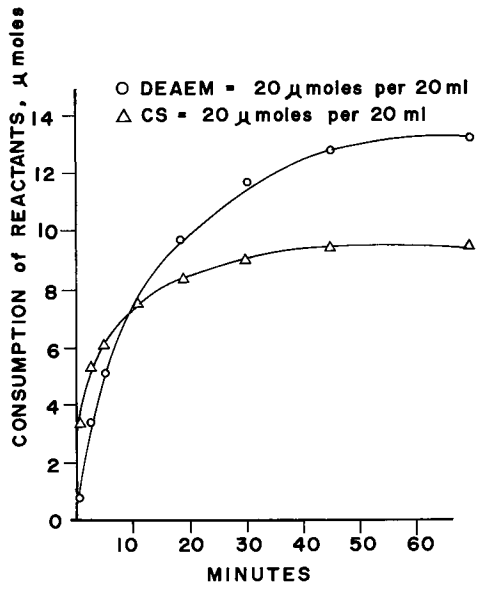

Fig. 2. Consumption of DEAEM and CS during reaction at a molar ratio of 1:1.

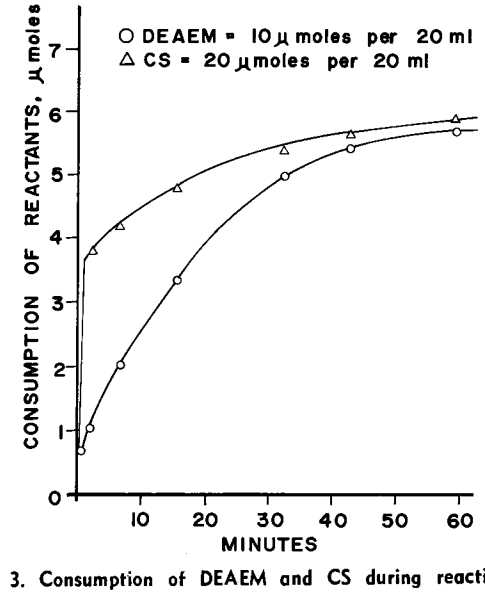

Fig. 3. Consumption of DEAEM and CS during reaction at a molar ratio of 1:2.

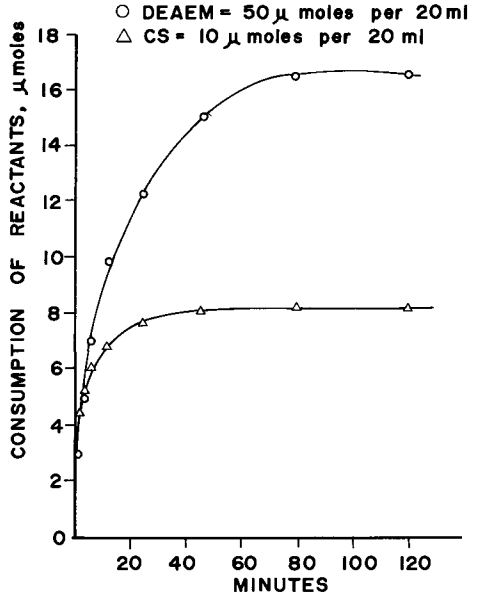

Fig. 4. Consumption of DEAEM and CS during reaction at a molar ratio of 5:1.

μmole) also showed the faster initial drop for CS over that of DEAEM. As the reaction progressed, there was an intersection of the reactant curves that was approximately equivalent to mono-adduct formation. Beyond this point the relative consumption of the components was reversed. At equilibrium or completion of reaction, the ratio of the components consumed was DEAEM/CS, 2:1, indicating the di-adduct (CS·2DEAEM).

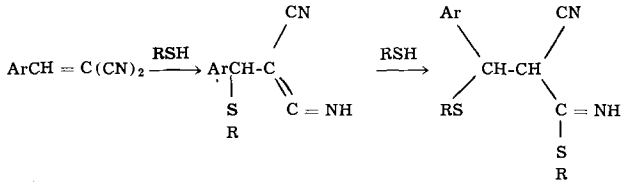

These two experiments, where DEAEM was in excess, also prove that no more than two equivalents of mercaptan are involved in the reaction. The consumption of the reactants for the 5:1 ratio is illustrated in Fig. 4. The structure of the mono-adduct given in the above equation could be explained by the qualitative behavior of the peak at −1.7v; it increases during the formation of the mono-adduct; levels off for some time; and, during the formation of the di-adduct, a slow decrease of this peak takes place.

Table VII summarizes the ratio of reactants (DEAEM/CS) initially mixed and that consumed against time. The tabulated results reflect the same trend as the reaction-progress curves explained above. When CS is in excess, the ratio of reactants represented by the product is one, while at equimolar quantities, the ratio of reactants (DEAEM/CS) is greater than one. The latter result indicates that a mixture of products is being formed. With an excess of DEAEM, the ratio of reactants in the product approaches two, which shows definitely that the di-adduct, $(DEAEM)_2CS$, is the end product.

Reaction rate of CS with DEAEM under varying concentration conditions.—For purposes of reactivity screening, it was found that a ratio of CS to DEAEM of 5:1 could produce the best comparative results, especially when monitored on the basis of mercaptan consumed. Under this condition, only the formation of the mono-adduct is being measured, thus precluding the complexities involved when mixed products are obtained. When CS was maintained in excess from 2:1 and higher, no indication of product other than the mono-adduct was found during a 2-hr rate study.

Millimolarity mixtures of CS and DEAEM in the ratio of 1:1 to 20:1 were polarographed against time at 25°C in 20 ml of anhydrous methanol (0.1M $LiNO_3$). Semilog plots of unreacted mercaptan were made against time on multiple separate determinations for each ratio of reactant. The half-reaction times showed a reproducibility within 3% for the reactants ratio of 3:1 and higher; for ratios of 2:1 and lower, the reproducibility was within 10%. As the ratio of reactants is increased by increasing the concentration of CS, the half-reaction time decreases rapidly at first; when ratios of 5:1 and greater are used, it approaches a constant value.

When the ratio is maintained at 5:1 and the concentration of both reactants is increased, the half-reaction time is decreased. Thus, on the basis of these results, it is imperative that both the ratio and the concentration of the reactants be maintained constant when the reactivity of different analogs and homologs is to be compared. The results showing specific rate constants and half-reaction times *vs.* ratio of reactants and millimolarity are shown in Table VIII.

Reaction rates were determined at 5:1 ratio (CS/DEAEM) in different solvents to determine the effect of solvent on rate. The electrolytes used were 0.1M $LiNO_3$ for 50% methanol, anhydrous methanol, and anhydrous acetone; and 0.1M Bu_4NClO_4 for anhydrous acetonitrile. It was found that the half-reaction times increased in this order: 50% methanol (1 min), anhydrous methanol (6 min), acetonitrile (10 min), and acetone (30 min). The selection of anhydrous methanol as a convenient solvent for screening studies was based on its reasonable half-reaction time, as well as on those criteria discussed previously.

Temperature effect on reaction rate of CS with DEAEM.—The influence of temperature on reaction rates of CS with DEAEM was studied in the range of 15°-40°C. Rates were measured in triplicate for each 5°C increment. The ratio of the reactants was maintained at 5:1 (CS/DEAEM, 5 mM: 1 mM). The DEAEM concentration-time data for these reaction rates were treated as two alternative types of reaction: pseudo first-order and reversible pseudo first-order (Table IX).

(*a*) First order reaction and rate equation: With an excess of CS, DEAEM reacts as designated by DEAEM $\xrightarrow{CS}$ CS·DEAEM. If the initial concentration and the concentration at time, t, of DEAEM are represented by A_o and A, respectively, the integrated rate equation (17) for the reaction is $\ln A = \ln A_o - kt$. A plot of $\ln A/A_o$ *vs.* t should be linear and its slope equal to the first-order rate constant. Experimental results have shown that a plot of the rate data using the above

Table VII. Ratio of reactants (DEAEM/CS) consumed during the course of reaction

	Micromoles of reactants used per 20 ml of electrolyte			
Time, min	10 DEAEM 20 CS	20 DEAEM 20 CS	50 DEAEM 20 CS	50 DEAEM 10 CS
0.5	0.194	0.237	0.312	0.454
2	0.264	0.543	0.421	0.770
5	0.440	0.830	0.916	1.03
10	0.576	1.00	1.09	1.40
15	0.688	1.10	1.35	1.47
20	0.760	1.19	1.52	1.52
25	0.826	1.27	1.57	1.60
30	0.945	1.33	1.57	1.68
40	0.965	1.34	1.62	1.80
50	0.965	1.35	1.73	1.89
60	0.965	1.38	1.76	1.93
70		1.40	1.82	1.97
80			1.81	2.00
100				2.01
120				2.01

Table VIII. Reaction of CS with DEAEM at various ratios of reactants and molarity

CS, mM	DEAEM, mM	CS/DEAEM Ratio	k, min^{-1}	$t_{1/2}$, min
1.0	1.0	1:1	0.0291	23.8
2.0	1.0	2:1	0.0490	14.1
3.0	1.0	3:1	0.0760	9.1
4.0	1.0	4:1	0.0946	7.3
5.0	1.0	5.1	0.1132	6.1
6.0	1.0	6:1	0.1236	5.6
8.0	1.0	8:1	0.1304	5.3
10.0	1.0	10:1	0.1281	5.4
20.0	1.0	20:1	0.1304	5.3
2.5	0.5	5:1	0.0617	11.2
5.0	1.0	5:1	0.1132	6.1
10.0	2.0	5:1	0.1536	4.5
15.0	3.0	5:1	0.1730	4.0
20.0	4.0	5:1	0.2035	3.4

Table IX. Effect of temperature on average specific rate constant and reaction half-time of CS vs. DEAEM (5 mM:1 mM)

	First order		Reversible first-order			
Temperature, °C	$k \times 10^2$, min^{-1}	$t_{1/2}$, min	$k_b \times 10^2$, min^{-1}	$k_f \times 10^2$, min^{-1}	$t_{1/2}$, min	K
15	5.10	13.6	1.82	7.91	8.7	4.40
20	7.92	8.8	1.81	10.6	6.5	5.89
25	11.62	6.0	3.68	16.4	4.2	4.92
30	17.19	4.1	5.02	20.3	3.3	4.00
35	22.17	3.1	7.98	30.7	2.3	3.89
40	25.52	2.7	9.60	33.8	2.1	3.90

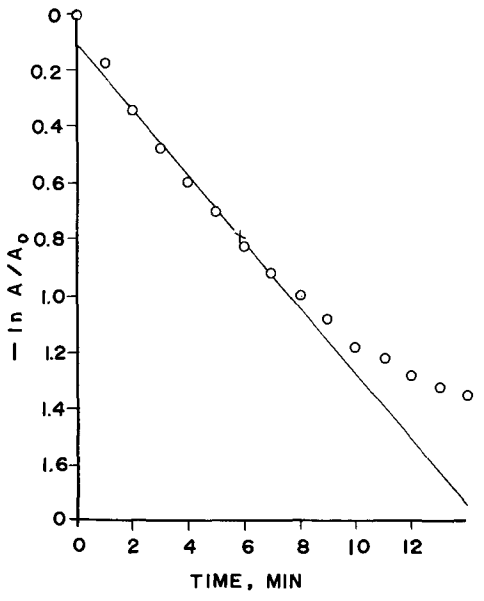

Fig. 5. First order reaction of CS with DEAEM (5:1) at 25°C; $k = 0.1171$ min^{-1} ($t_{1/2} = 5.92$ min).

first-order rate equation gives some deviation at the beginning of the reaction, and a greater deviation close to the end of the reaction (Fig. 5). This observation plus the fact that the isolated mono-adduct, CS·DEAEM, indicated dissociation to the original reactants (when a dilute solution of this product was polarographed with time) lead to the conclusion that the reaction is reversible and the reversible first-order rate equation should be used.

(b) Reversible first-order reaction and rate equation: The reversible reaction of DEAEM with an excess of CS is given by

$$\text{DEAEM} \underset{k_b}{\overset{\text{CS},\ k_f}{\rightleftharpoons}} \text{CS} \cdot \text{DEAEM}$$

The reversible first-order rate equation (18) representing the above reaction is

$$-dA/dt = (k_f + K_b)\,A - k_b A_o \qquad [1]$$

A and A_o were defined above; k_f is the forward rate constant and k_b is the backward (or reverse) rate constant. The integrated form of Eq. [1] is

$$\ln \frac{k_f A_o}{(k_f + k_b)\,A - k_b A_o} = (k_f + k_b)t \qquad [2]$$

The rate constants in Eq. [1] or [2] can be solved readily by the use of an analog computer. If the reaction of CS with DEAEM is permitted to approach equilibrium and A_e is the equilibrium DEAEM concentration, then $dA/dt = 0$ and Eq. [1] becomes

$$(k_f + k_b)\,A_e = k_b A_o \qquad [3]$$

Substitution of Eq. [3] into [2] gives

$$\ln \left(\frac{A_o - A_e}{A - A_e} \right) = (k_f + k_b)t \qquad [4]$$

The slope of this equation is equal to the sum of the forward and reverse rate constants. This slope together with Eq. [3] makes possible the calculation for k_f and k_b. A plot of Eq. [4], using the same concentration-time data which was used for the simple first-order equation, gives excellent linearity for almost the entire reaction with some deviation only after equilibrium of the reaction is reached (Fig. 6).

(c) Arrhenius temperature dependence of rate constants: The reproducibility of the rate constants, for

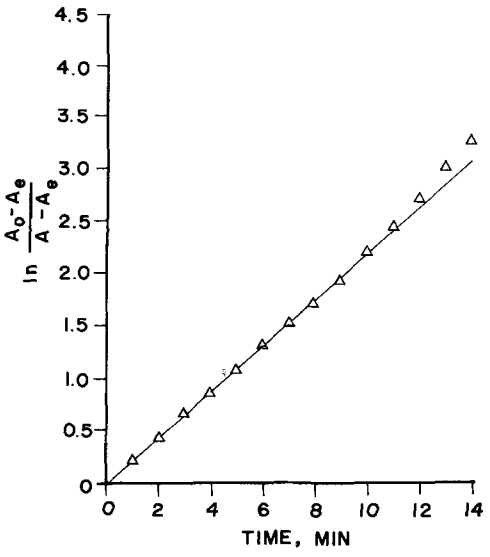

Fig. 6. Reversible first order reaction of CS with DEAEM (5:1) at 25°C, $k_f = 0.1676$ min^{-1} and $k_b = 0.0502$ min^{-1}.

each of the temperature increments, was of the order of 1% for the simple first-order k; for the reversible first-order, the forward rate constant (k_f) was of the order of 7%. The average rate constant for each isotherm (Table IX) was used to calculate $t_{1/2}$'s for the simple and complex (reversible) reaction. For the case of the reversible reaction, the formation constant, K, of the reaction was calculated from the ratio of the forward and reverse reaction constant, k_f/k_b. The average rate constants for the various temperatures given in Table X were used to make two separate Arrhenius plots by using the following equation (19)

$$\ln k = \ln A - \frac{E_a}{RT}$$

The activation energy, E_a, was obtained by equating $-E_a/R$ to the slope of the respective plots (Fig. 7). The value of the universal gas constant, R, is 1.987 cal/mole/degree. The activation energies for the simple and reversible reaction were 13.9 and 11.6 kcal/mole, respectively.

Discussion

The purpose of this investigation was to develop a procedure for a subsequent screening study of the re-

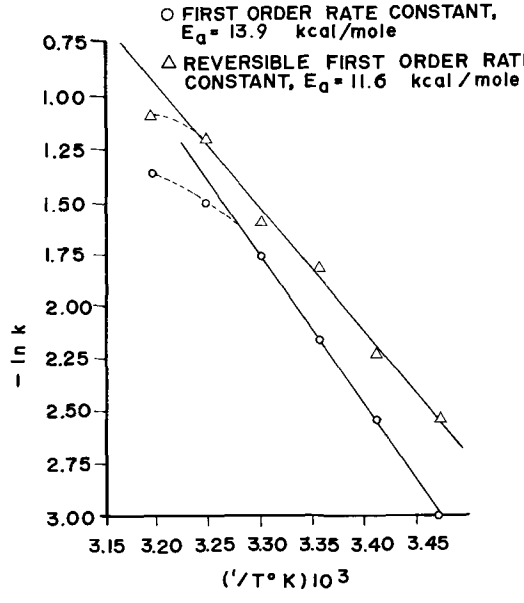

Fig. 7. Arrhenius plot for reaction of CS with DEAEM

activity of benzalmalononitriles and related irritants with a mercaptan. The principal requirements were to select a hydroxylic solvent as close as possible to water and a mercaptan to simulate the protein-thiol present *in vivo*. These requirements were approximated by the use of methanol as the solvent and DEAEM as the mercaptan.

CS and DEAEM were each found to be polarographically active in methanol, acetonitrile, and acetone. Both compounds were found to show linearity for diffusion current *vs.* concentration in the above solvents. The basic reaction being followed was the same regardless of the solvent, with the exception of 50% methanol where hydrolysis was noted. The speed of reaction between CS and DEAEM varies considerably with the polarity of the solvent in the following order: 50% methanol > methanol > acetonitrile > acetone. The magnitude of the zwitterionic form of DEAEM in the above solvents decreases in the same order. The charged aminomercaptan appears to have a major controlling effect on the reaction rate.

The type of reaction occurring was found to depend on the ratio of the starting materials. Thus, in the attempt to elucidate the reaction mechanism between CS and DEAEM, the ratio of initial concentration had to be considered.

CS can add one or two molecules of DEAEM, depending on the relative concentration of the participating reactants. Polarographic rate studies have confirmed the following results:

(*A*) When CS is in excess, the observed rates demonstrate the addition of one molecule of DEAEM based on the thiol consumed.

(*B*) When CS and DEAEM are present in equimolar quantities, rates have shown the establishment of an equilibrium for the mono-thiol addition and a subsequent addition to a site other than the CS α-β double bond.

(*C*) When DEAEM is in excess, the decrease of CS concentration *vs.* time shows three distinctly different slopes (rates). The first one of which could be indicative of the rapid formation of a prior equilibrium; the second, a moderately fast mono-thiol addition; and the third, a comparatively slow, second thiol addition to CS.

Based on the above discussion, a reaction mechanism can be illustrated to explain the mono- and di-addition of DEAEM to CS. The presence of nitrile groups in CS, due to their strong electronegativity effect, makes the α-β double bond in CS highly active and extremely susceptible to nucleophilic attack. The resonance of CS may be represented by the following three structures

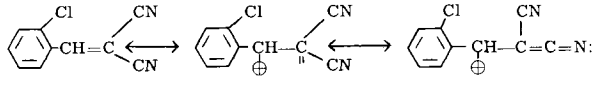

The aminomercaptan, DEAEM, due to its basic nitrogen, exists practically all in its zwitterionic form in polar solvents, and partially in semipolar solvents. In methanol, the following equilibrium exists

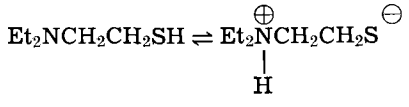

The zwitterion, being a stronger nucleophile, is probably the form of the thiol which takes part in the reaction with CS in methanol as a solvent.

By using the above resonance of CS and the ionic form of DEAEM, the mono- and di-adduct formations can be illustrated as follows

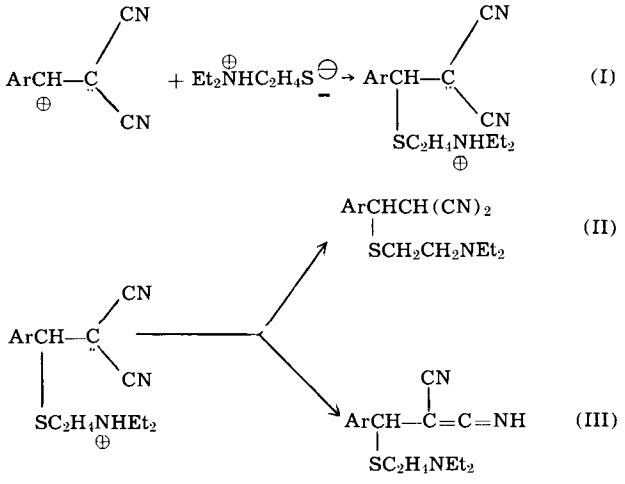

Polarographic indications were that structure (III) occurs in the mono-addition since there is an increase of a new reduction peak at −1.7v. This peak, although not too well defined, can be due only to the reduction of a newly formed conjugated system. The latter system can be initiated only by the free electrons on the alpha carbon in resonance with one of the nitrile groups

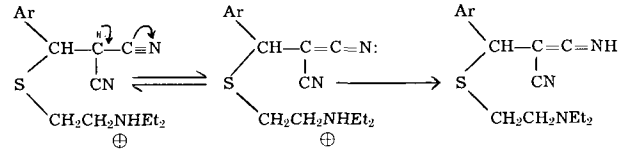

and subsequently stabilized to the imine form by the quaternary nitrogen proton.

The second addition of thiol is possible for structure (III) and not for structure (II). The addition of a second thiol was observed in the rates at equimolar concentration of the reactants, and more definitely as the mercaptan concentration was increased. Under these conditions, at equilibrium the consumption of DEAEM and CS agree with the stoichiometry of CS(DEAEM)$_2$. Thus, the second addition could go through the following steps:

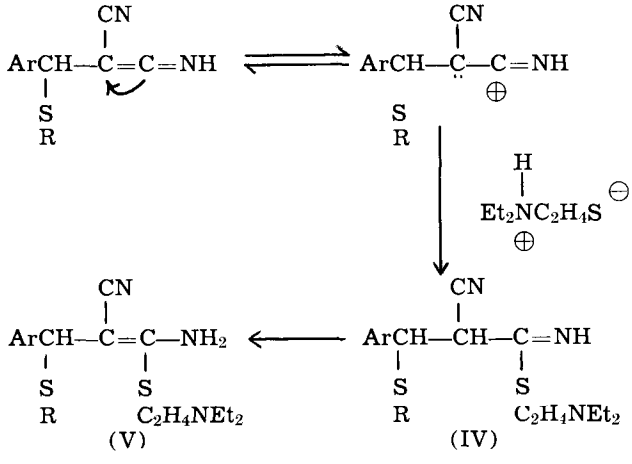

The products (II) or (III) and (V) have been isolated. Their elemental analysis did agree with CS(DEAEM) and CS(DEAEM)$_2$, respectively.

The mono-adduct (III) was a brown oil. The isolated di-adduct was a white solid (mp 82°-84°C) whose IR and NMR spectra conform with structure (V). The imino form represented by structure (IV) is assumed to have existed prior to the end product (V).

The effect of temperature on the reaction rate constants with DEAEM gave excellent linearity between 15°-40°C, which is a good indication of the validity of the reaction rates. The calculated activation energy

was 13.9 kcal/mole for the simple reaction, and 11.9 kcal/mole for the reversible reaction.

Conclusions

A method employing controlled-potential dc polarography was developed for determining the rates of reaction of CS (o-chlorobenzalmalononitrile) and its analogs and homologs with a selected nucleophile, DEAEM (2-diethylaminoethyl mercaptan). Both the irritant and the nucleophile are electrochemically active; and, with derivative polarography, it is possible to measure almost simultaneously the disappearance of the two components during reaction. The developed method employs methanol as the solvent with lithium nitrate as added electrolyte, and a trielectrode system consisting of a rapid dropping-mercury electrode, a Ag/AgCl reference, and a platinum counter electrode.

The products obtained on the reaction of CS and DEAEM were found to be dependent on the concentration of the reactants. Based on rate curves, a 1:1 reactant mixture produces, initially, a monothioether (CS·DEAEM) through addition to the α-β double bond on CS. With CS in excess, the same product is formed. When DEAEM is in excess, a dithioether results, with addition first at the β carbon and then at a nitrile carbon, CS·$(DEAEM)_2$.

At a 5:1 ratio of CS to mercaptan, the half-reaction times in various solvents increased in the following order: aqueous methanol (1 min), methanol (6 min), acetonitrile (10 min), and acetone (30 min).

Manuscript received June 26, 1968. This paper was presented at the Boston Meeting, May 5-9, 1968, as Paper 208.

Any discussion of this paper will appear in a Discussion Section to be published in the December 1969 JOURNAL.

REFERENCES

1. M. Bargain and M. Delepine, *Compt. rend.*, **254**, 130 (1962).
2. *Ibid.*, **255**, 1948 (1962).
3. *Ibid.*, **256**, 1990 (1963).
4. D. J. Currie, C. E. Lough, R. F. Silver, and H. L. Holmes, *Can. J. Chem.*, **45**, 1567 (1967).
5. R. F. Silver and H. L. Holmes, *ibid.*, **44**, 1031 (1966).
6. R. B. Pritchard, C. E. Lough, J. B. Reesor, H. L. Holmes, and D. J. Currie, *ibid.*, **45**, 775 (1967).
7. R. F. Silver, K. A. Kerr, P. D. Frandsen, S. J. Kelley, and H. L. Holmes, *ibid.*, **45**, 1001 (1967).
8. S. Sass, P. M. Davis, I. Master, R. A. Reynolds, E. Roberts, J. Sechrist, and N. Beitsch, Research Labs, Edgewood Arsenal, Internal publication.
9. I. M. Kolthoff and J. F. Coetzee, *J. Am. Chem. Soc.*, **79**, 870 (1957).
10. M. T. Kelley, D. J. Fisher, and H. C. Jones, *Anal. Chem.*, **32**, 1262 (1960).
11. R. B. Purdy, "Electroanalytical Methods in Biochemistry," pp. 96-97, McGraw-Hill Book Co., New York (1965).
12. A. Albert and G. B. Barlin, *J. Chem. Soc.*, p. 2284 (1959).
13. P. D. Anderson and D. M. Hercules, *Anal. Chem.*, **38**, 1703 (1966).
14. I. M. Kolthoff and J. J. Lingane, "Polarography," Vol. 2, pp. 781-82, Interscience Publishers, New York (1952).
15. L. Meitus, "Polarographic Techniques," pp. 217-231, Interscience Publishers, New York (1965).
16. M. T. Kelley, H. C. Jones, and D. J. Fisher, *Anal. Chem.*, **31**, 1475 (1959).
17. A. A. Frost and R. G. Pearson, "Kinetics and Mechanism," p. 13, John Wiley & Sons, Inc., New York, (1961).
18. *Ibid.*, pp. 185-186 (1961).
19. S. Glasstone and D. Lewis, "Elements of Physical Chemistry," pp. 627-628, D. Van Nostrand Co. Inc., New York (1960).

The Combined Adsorption of Cadmium(II) and Thiosulfate on Mercury

Donald J. Barclay and Fred C. Anson*

Gates and Crellin Laboratories of Chemistry, California Institute of Technology, Pasadena, California

ABSTRACT

The combined adsorption of thiosulfate and Cd(II) on mercury, as measured by chronocoulometry, is reported. It is concluded, primarily on the basis of the relationship between the amount of adsorbed thiosulfate and adsorbed Cd(II), that the reaction leading to the thiosulfate induced adsorption of Cd(II) is

$$[S_2O_3^{2-}]_{ads} + CdS_2O_3 \rightleftharpoons [Cd(S_2O_3)_2^{2-}]_{ads}$$

Data is also given on the adsorption of thiosulfate from cadmium-free solutions.

In a previous paper (1) we suggested that the mechanism by which specifically adsorbed and complex-forming anions induce adsorption of white metal cations on mercury involves an interaction between the adsorbed anions and an uncharged metal-anion complex to produce the adsorbed surface species. The inducing anions include iodide (1, 2), bromide (1, 2), chloride (2), and thiocyanate (2, 3, 4). In all previous studies, only the cation adsorption was measured because the concentrations of inducing anions required to produce significant adsorption of cations were too large to permit the application of the convenient chronocoulometric technique (5). For the measurement of the anion adsorption this difficulty is essentially eliminated in solutions of Cd(II) and thiosulfate because substantial Cd(II) adsorption is induced by thiosulfate concentrations in the millimolar range. We therefore studied this system with the chronocoulometric technique in the expectation that simultaneous determination of the adsorption of both cadmium and thiosulfate would enable the composition of the adsorbing species to be identified. The results indicate that, as is true in halide-induced adsorption, the uncharged complex, CdS_2O_3, is the adsorbing species.

The adsorption of thiosulfate on mercury has not previously been studied, but on the basis of a recent classification of anion adsorbability (6) which suggests that soft bases [in Pearson's (7) sense] are strongly adsorbed on positively charged mercury, it seemed reasonable to expect strong specific adsorp-

* Electrochemical Society Active Member.

tion of the thiosulfate anion. The anodic oxidation of mercury in the presence of thiosulfate proceeds according to Eq. [1] (8)

$$Hg + 2\,S_2O_3^{2-} \rightleftarrows Hg(S_2O_3)_2^{2-} + 2\,e \qquad [1]$$

which was the basis of the chronocoulometric determination of the adsorbed thiosulfate. The amount of adsorbed Cd(II) was similarly determined by the procedure previously employed (1).

The adsorption of zinc(II) from thiosulfate solutions and Cd(II) from sulfate solutions was also searched for. In both cases, the adsorption, if any, was less than 0.5 $\mu C/cm^2$.

Experimental

Cadmium adsorption.—The amount of adsorbed Cd(II) was determined by double potential step chronocoulometry with procedures and apparatus that have been previously described (9). The electrode potential was stepped from various initial potentials, E_i to −1000 mv *vs.* S.C.E. where the reduction of Cd(II) is diffusion controlled, and then back to E_i. Adequate time was allowed to elapse following the second potential step to ensure that the thiosulfate adsorption had reached equilibrium before any data points were taken. At the lowest concentrations of thiosulfate employed (1 mM) 5 msec were required. A 20 sec waiting period at E_i after the creation of each new mercury drop electrode was adequate to assure initial adsorption equilibrium.

Thiosulfate adsorption.—Preliminary experiments to determine the amount of adsorbed thiosulfate by double potential step chronocoulometry indicated that the product of the electrode reaction, $Hg(S_2O_3)_2^{2-}$, was also strongly adsorbed, so the correct double layer charging correction could not be obtained in the usual way. The tactic developed in previous chronocoulometric studies with analogous systems (10, 11) was therefore employed to determine the amount of adsorbed thiosulfate: Three single potential step chronocoulometric experiments were performed. First, the electrode was potentiostated at −1000 mv *vs.* S.C.E. where it could reasonably be assumed that no thiosulfate was adsorbed at the low concentrations employed (5 mM or less). The potential was stepped to +150 mv and the resulting charge flow was measured. Least-squares analysis of the charge-time data yielded an intercept equal to the difference in charge on the electrode between −1000 mv and +150 mv, $\Delta Q(-1000 \rightarrow 150)$. The charge on the electrode at +150 mv would be expected to decrease with time until the surface became saturated with adsorbed $Hg(S_2O_3)_2^{2-}$. To overcome this possible source of error no data points at +150 mv were included in the least-squares analysis until enough $Hg_2(S_2O_3)_2^{2-}$ to cover the surface had been generated.

Next, the potential was stepped from −1000 mv to E_i, where thiosulfate was adsorbed, but no electrode reaction proceeds. The resulting step-change in charge gave the difference in the charge on the electrode between −1000 mv and E_i, $\Delta Q(-1000 \rightarrow E_i)$. Finally, the potential was stepped from E_i to +150 and the charge-time data analyzed to give an intercept, I, corresponding to the amount of thiosulfate adsorbed at E_i plus the difference in charge on the electrode between E_i and +150 mv

$$I = F\Gamma_{S_2O_3} + \Delta Q(E_i \rightarrow 150) \qquad [2]$$

From the results of these three experiments the thiosulfate adsorption could be calculated according to Eq. [3]

$$F\Gamma_{S_2O_3} = I - \Delta Q(E_i \rightarrow 150) =$$

$$I - [\Delta Q(-1000 \rightarrow 150) - \Delta Q(-1000 \rightarrow E_i)] \qquad [3]$$

When both thiosulfate and Cd(II) were present the procedure just described could not be used because there is no potential where thiosulfate adsorption can be eliminated before cadmium reduction commences. The appropriate double layer charging corrections in this case were obtained from the double potential step experiments used to measure the cadmium adsorption in which the potential was stepped from E_i to −1000 and back to E_i. These experiments yielded values of $\Delta Q(E_i \rightarrow -1000)_{Cd}$ corresponding to the difference in the charge on the electrode at E_i and −1000 in the presence of adsorbed Cd(II). These values of $\Delta Q(E_i \rightarrow -1000)_{Cd} = -\Delta Q(-1000 \rightarrow E_i)_{Cd}$ were substituted for the last term in Eq. [3] to calculate $F\Gamma_{S_2O_3}$. Reaction [1] proceeds at the diffusion limited rate at +150 mv even in the presence of Cd(II) because the stability of the $Hg(S_2O_3)_2^{2-}$ complex is much greater than the Cd(II)-$S_2O_3^{2-}$ complexes.

The hanging mercury drop electrode was the standard commercially available type (Brinkman Instruments) modified to provide better electrical contact (12).

Reagent grade chemicals [KNO_3, $Na_2S_2O_3$, and $Cd(NO_3)_2$] were used without further purification but thiosulfate solutions were prepared frequently and stored in dark bottles. The ionic strength of all solutions was maintained at unity with potassium nitrate and most experiments were performed at room temperature (25° ± 2°C); the experiments at lower temperatures were performed with the cell immersed in a slurry of ice in a sodium nitrate solution. Solutions were deoxygenated with prepurified nitrogen which was passed through copper turnings at 400°C, a trap maintained at −70°C, and triply distilled water. Triply distilled water was used to prepare all solutions. Potentials are reported in mv *vs.* S.C.E.

Results and Discussion

Adsorption of thiosulfate.—The charge due to adsorbed thiosulfate is plotted as a function of potential in Fig. 1, for 1, 2, 3, and 5 mM concentrations of thiosulfate. Higher concentrations were not used because the uncompensated resistance in the cell seriously degraded the quality of the data above 5 mM. (Typical indications of the presence of errors attributable to uncompensated resistance are intercepts of charge *vs.* $t^{1/2}$ plots that suggest "negative adsorption" or current transients that contain kinks or plateaus instead of a smooth monotonic decay.) The values of $q_{S_2O_3}$ in Fig. 1 could be reproduced within a range of *ca.* ±2 $\mu C/cm^2$.

Inasmuch as this is the first quantitative data on thiosulfate adsorption it is of interest to compare the adsorption of this anion with that of iodide and thiocyanate. In Fig. 2, the charge due to adsorbed

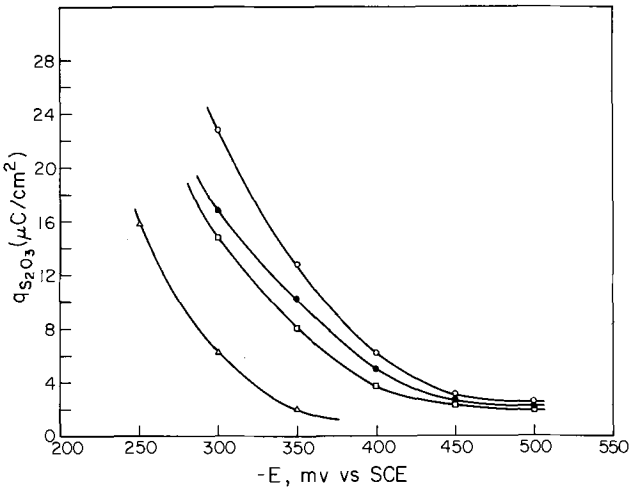

Fig. 1. Dependence of $q_{S_2O_3}$ on E_i. Thiosulfate concentration, mM; Δ, 1.0, □, 2.0; ●, 3.0; ○, 5.0. Each point is the average of several replicate experiments. At more negative potentials than those shown $q_{S_2O_3}$ decreases to values smaller than the experimental reproducibility (~ 0.5 $\mu C/cm^2$).

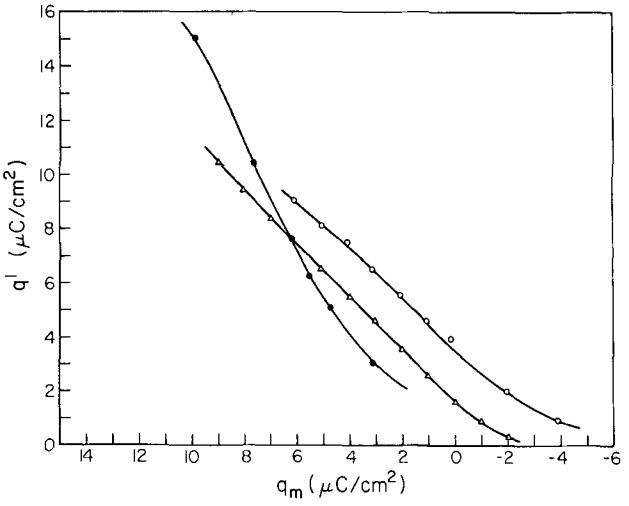

Fig. 2. Comparison of q' (charge due to specifically adsorbed anion) as a function of electrode charge for 4 mM I^- (○), 6 mM NCS^- (△), and 3 mM $S_2O_3^{2-}$ (●). q_m for $S_2O_3^{2-}$ was obtained from chronocoulometric data as described in (1).

anions is plotted *vs.* electrode charge for 4 mM iodide (13), 6 mM thiocyanate (14), and 3 mM thiosulfate. These plots are not strictly comparable because of the concentration differences and because our results were obtained in the presence of 1M potassium nitrate. However, these factors will probably not affect the significant feature of this comparison which is that the adsorption of thiosulfate increases more rapidly with increasing electrode charge than does that of iodide or thiocyanate. The slope $(\partial q_{S_2O_3}/\partial q_m)$, on the linear part of the plot is approximately 2 compared with about 1 for the corresponding iodide and thiocyanate plots. This difference presumably reflects the two-fold greater charge on the adsorbing thiosulfate anion.

The potential at the point of zero charge for a 0.1M solution of sodium thiosulfate (no KNO_3 added) is -540 ± 15 mv as determined by measuring the charge flowing into a d.m.e. (15). This rather negative value suggests that the specific adsorption of the thiosulfate anion is quite strong.

Adsorption of cadmium.—The adsorption of Cd(II) from solutions of varying thiosulfate concentration was determined as a function of potential. The limits on the initial potential, E_i, were set on the anodic side by mercury oxidation and on the cathodic side by the reduction of Cd(II). Figure 3 gives the variation of

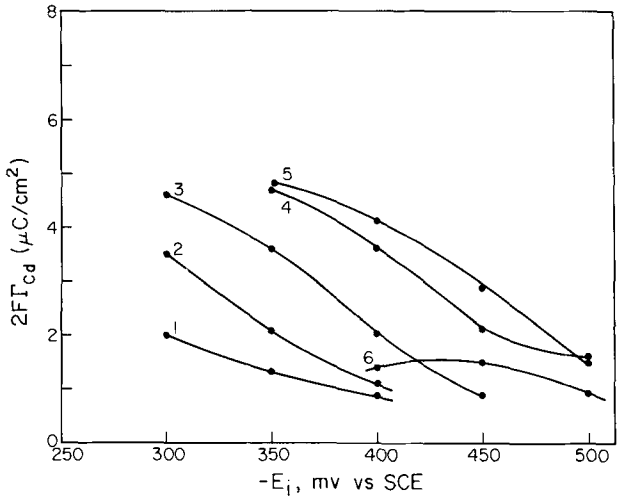

Fig. 3. Potential dependence of Cd(II) adsorption induced by thiosulfate. Cadmium concentration = 0.5 mM. Thiosulfate concentration: 1. 2 mM; 2. 3 mM; 3. 5 mM; 4. 10 mM; 5. 25 mM; 6. 100 mM.

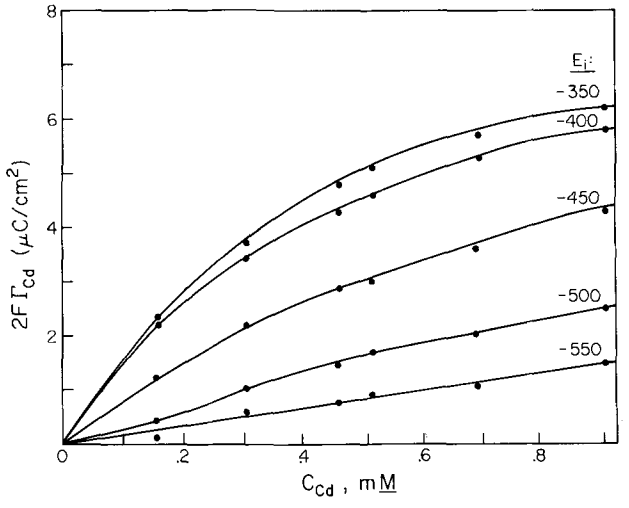

Fig. 4. Dependence of $2F\Gamma_{Cd}$ on Cd(II) concentration in 25 mM $S_2O_3^{2-}$ at various potentials.

$2F\Gamma_{Cd}$ with E_i for concentrations of thiosulfate between 2 and 100 mM and at a Cd(II) concentration of 0.5 mM. Figure 4 is a plot of $2F\Gamma_{Cd}$ *vs.* the Cd(II) concentration in 25 mM thiosulfate where the Cd(II) adsorption was greatest.

Noteworthy points from Fig. 3 are that very low thiosulfate concentrations are adequate to induce the adsorption of Cd(II) and that the maximum adsorption occurs at a thiosulfate concentration of only about 25 mM; with 100 mM thiosulfate the adsorption is quite low, and at higher concentrations it is essentially absent. The strong potential dependence of the adsorption indicates that, as is true with iodide and bromide (1), and thiocyanate (3), specific adsorption of the inducing anion is required for the cation adsorption to occur. Taken together these observations are compatible with the adsorption of a cadmium-thiosulfate complex species by attachment of the complex to a specifically adsorbed thiosulfate anion.

By suitable analysis of double potential step chronocoulometric data (5) any change in the charge on the electrode produced by the adsorption can be determined. For cadmium in thiosulfate solutions the charge changes were very small [*e.g.*, $\Delta Q < 0.3$ $\mu C/cm^2$ when 4.7 $\mu C/cm^2$ of Cd(II) is adsorbed] which suggests that the adsorbing species is not highly charged.

Adsorption of thiosulfate in the presence of Cd(II).—Since both free thiosulfate anions and a cadmium thiosulfate complex appear to be adsorbed from cadmium-thiosulfate solutions, the sum of the two will comprise the values of $\Gamma_{S_2O_3}$ resulting from the chronocoulometric experiments in these solutions (Γ is in moles/cm²)

$$(\Gamma_{S_2O_3})_{total} = \Gamma_{S_2O_3}^{anion} + x\Gamma_{Cd(S_2O_3)_x} \qquad [4]$$

The data in Table I show how $(\Gamma_{S_2O_3})_{total}$ varies as the Cd(II) concentration is increased in 1 mM and 3 mM $Na_2S_2O_3$ solutions. At first, $(\Gamma_{S_2O_3})_{total}$ increases with the Cd(II) concentration, clearly demonstrating that the adsorbing Cd(II) brings additional thiosulfate with it to the electrode surface. However, at the highest Cd(II) concentration (10 mM) $(\Gamma_{S_2O_3})_{total}$ drops well below the value prevailing before any cadmium was added. This behavior results from the fact that with 10 mM Cd(II) a large portion of the total thiosulfate present is converted to the CdS_2O_3 complex leaving a concentration of free thiosulfate which corresponds to a much lower value of $\Gamma_{S_2O_3}^{anion}$. Since this term is the dominant contributor to $(\Gamma_{S_2O_3})_{total}$, the value of the latter decreases accordingly. In short, the decrease in $\Gamma_{S_2O_3}^{anion}$ produced by lowering the free thiosulfate concentration is greater than the increase in $\Gamma_{Cd(S_2O_3)_x}$ resulting from the higher concentration of CdS_2O_3.

Table I. Mixed adsorption of Cd(II) and $S_2O_3^{2-}$

	1 mM $S_2O_3^{2-}$, $E_i = -250$		3 mM $S_2O_3^{2-}$, $E_i = -300$			
T, °C	25	25	0	25	0	25
Cd, mM	moles/cm² × 10^{11}					
	$(\Gamma_{S_2O_3})_{total}$	$\Gamma_{Cd(S_2O_3)_x}$	$(\Gamma_{S_2O_3})_{total}$		$\Gamma_{Cd(S_2O_3)_x}$	
0	7.8	0	11.4	8.0	0	0
0.5	8.0	1.85	13.6	9.5	3.0	1.75
1.0	7.0	1.75	13.7	9.9	3.6	2.3
10.0[a]	3.3	—	10.2	6.6	—	—

[a] $\Delta Q(-1000 \rightarrow E_i)$ could not be evaluated as described in the Experimental Section at this concentration of Cd(II). Instead the difference in $\Gamma_{S_2O_3}$ between E_i and −500 was measured, and by estimating $\Gamma_{S_2O_3}$ at −500 from the calculated concentration of uncomplexed thiosulfate, $\Gamma_{S_2O_3}$ at E_i was evaluated. The error in this procedure will not be large as the adsorption of thiosulfate and Cd(II) at −500 is small.

Data such as those in Table I provide the information needed to deduce the average composition of the cadmium-thiosulfate complex, $Cd(S_2O_3)_x^{2-2x}$ that is adsorbed. When Cd(II) is added to an initially cadmium-free thiosulfate solution the resulting change in $(\Gamma_{S_2O_3})_{total}$ should be given by Eq. [5]

$$\Delta(\Gamma_{S_2O_3})_{total} = \Delta\Gamma_{S_2O_3}^{anion} + x\Gamma_{Cd(S_2O_3)_x} \qquad [5]$$

where Δ signifies the difference between the value obtained after the addition of Cd(II) and the value in the absence of cadmium. $\Delta(\Gamma_{S_2O_3})_{total}$ is obtained directly from the two anodic chronocoulometric experiments based on reaction [1]. $\Gamma_{Cd(S_2O_3)_x}$ is obtained from a cathodic double potential step chronocoulometric experiment in which the Cd(II) is reduced. $\Delta\Gamma_{S_2O_3}^{anion}$ cannot be obtained directly. It was evaluated from the appropriate constant potential adsorption isotherm measured in cadmium-free thiosulfate solutions and the bulk concentration of thiosulfate anion in the cadmium-thiosulfate solutions calculated from the formation constants of the cadmium-thiosulfate complexes (16). This method of evaluating $\Delta\Gamma_{S_2O_3}^{anion}$ assumes that the adsorption isotherm for thiosulfate anion adsorption will remain unchanged in the presence of 3-4 μC/cm² of adsorbed Cd(II). This approximation seems reasonable because almost no change in the charge on the electrode is produced by the adsorption of this amount of Cd(II). The values of x that result from this analysis are given in Table II. The fact that they are close to unity indicates that the predominant adsorbed species is CdS_2O_3 although the experimental uncertainty in the measured adsorptions limits the strength of this conclusion.

Adsorption induced by adsorbed anions.—It has been previously proposed (1) that the mechanism by which specifically adsorbed anions induce the adsorption of white metal cations involves bond formation between adsorbed anions and a metal cation-anion complex. In the particular case of Cd(II) adsorption from iodide solutions the adsorption process was described by a reaction such as

Table II. Average composition of the adsorbed cadmium-thiosulfate complex, $Cd(S_2O_3)_x^{2-2x}$

	$E_i = -300$, $S_2O_3^{2-} = 3$ mM			
Cd(II), mM	0.5		1.0	
T, °C	0	25	0	25
	moles/cm² × 10^{11}			
$\Delta(\Gamma_{S_2O_3})_{total}$, measured	2.2	1.1	2.3	1.5
$\Gamma_{Cd(S_2O_3)_x}$, measured	3.0	1.75	3.6	2.3
$\Delta\Gamma_{S_2O_3}^{anion}$, calculated	−0.7	−0.55	−1.7	−1.3
x, calculated from Eq. [5]	0.97	0.94	1.1	1.2

$\Delta\Gamma_i = \Gamma_i$ with Cd(II) − Γ_i without Cd(II).

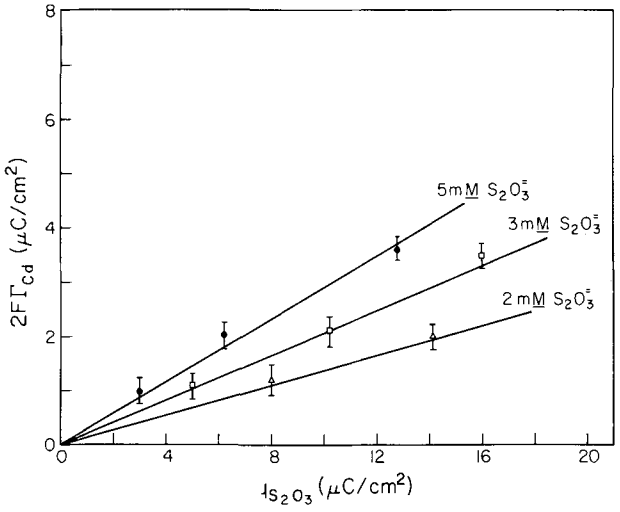

Fig. 5. Correlation between $q_{S_2O_3}$ and $2F\Gamma_{Cd}$ in 2, 3, and 5 mM $S_2O_3^{2-}$. Concentration of Cd(II) was 0.5 mM.

$$(I^-)_{ads} + CdI_2 \rightarrow (I - CdI_2)_{ads} \qquad [6]$$

Evidence to support this proposal included a close correlation between the amount of Cd(II) adsorbed and the quantity of specifically adsorbed anions on the electrode. The same kind of correlation obtains in cadmium-thiosulfate solutions, as is shown in Fig. 5. This figure contains plots of $2F\Gamma_{Cd}$ *vs.* the charge due to adsorbed thiosulfate anions for three different thiosulfate solutions. The plotted values of $q_{S_2O_3}$ are the chronocoulometric values of adsorbed thiosulfate in cadmium-free solutions less a small correction to take account of the decrease in the bulk concentration of free thiosulfate produced by the addition of Cd(II). The linearity of these plots at such low values of $q_{S_2O_3}$ and the fact that all the lines extrapolate to the origin is strong evidence in favor of an adsorption process involving association between adsorbed thiosulfate anions and a Cd(II) complex.

Additional evidence in support of this conclusion comes from experiments testing the effect of temperature on the adsorption. Table III compares the values of $2F\Gamma_{Cd}$ obtained at several thiosulfate concentrations at 25° and 0°C. The uniformly greater Cd(II) adsorption at the lower temperature parallels a greater adsorption of $S_2O_3^{2-}$ at 0°C as measured, at the lower thiosulfate concentration, by anodic chronocoulometry (Table III). The equilibrium constants for the formation of cadmium thiosulfate complexes show temperature dependences too small to account for the increased adsorption on this basis (16). The simplest ex-

Table III. Effect of temperature on the adsorption of cadmium(II) and thiosulfate

A) [Cd(II)] = 0.5 mM

$[S_2O_3^{2-}]$, mM	3		10		25		100	
$-E_i$	T, °C	$2F\Gamma_{Cd}$ (μC/cm²)						
	25	3.5		—		—		—
300	0	6.0		—		—		—
	25	2.1		4.7		4.8		—
350	0	4.7		7.8		7.0		—
	25	1.1		3.6		4.1		1.4
400	0	3.0		6.1		6.7		2.0
	25	0.4		2.1		2.9		1.5
450	0	1.6		3.9		4.3		2.1
	25	0.4		1.1		1.5		0.9
500	0	0.8		1.9		2.9		1.6
	25	—		0.9		0.6		0.5
550	0	—		1.0		1.2		0.7

B) $[S_2O_3^{2-}] = 3$ mM, [Cd(II)] = 0

$-E_i$	T, °C	$q_{S_2O_3}$ (μC/cm²)
	25	16.8
300	0	22.8
	25	10.2
350	0	12.0
	25	5.0
400	0	6.2
	25	2.2
450	0	4.6
	25	2.2
500	0	3.0
	25	1.6
550	0	2.8

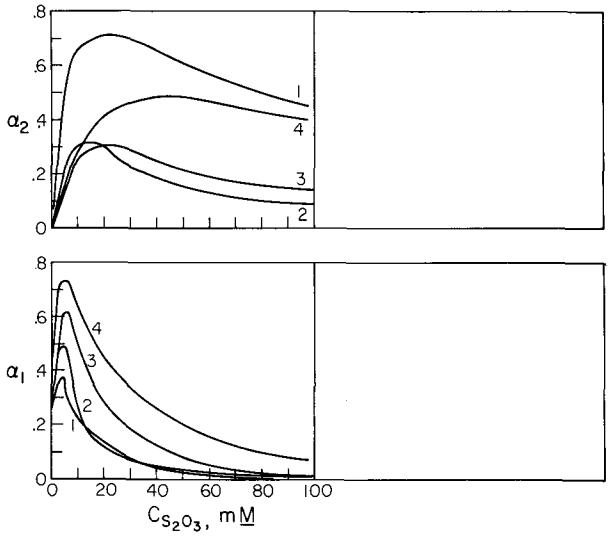

Fig. 6. α_1 and α_2 (the fraction of cadmium present as the mono- and bis-complex) as a function of thiosulfate concentration. There is only fair agreement among the reported values of the cadmium-thiosulfate complex formation constants. Four different sets were employed [1. ref. (17); 2 and 3, ref. (18); 4, ref. (19)] and all lead to the same qualitative deductions about the preponderant species at each thiosulfate concentration.

planation, and the one we prefer, is that the increased adsorption of $S_2O_3^{2-}$ induces increased adsorption of the CdS_2O_3 complex because the adsorption involves bond formation between these two species.

It has been argued previously (1) that reliable information on the composition of adsorbing complexes may be obtained from the dependence of the metal adsorption on the bulk concentration of the complex-forming anion only when the adsorption is evaluated at constant values of adsorbed anion. Unfortunately, the lack of data on thiosulfate adsorption at concentrations above 5 mM prevented the appropriate analysis in this case. However, the fractions of Cd(II) present as the mono- and bis-thiosulfato complexes were computed from some of the reported stability constants and the results are summarized in Fig. 6. The concentration of $Cd(S_2O_3)_2^{2-}$ turns out to be about the same in 5 mM $S_2O_3^{2-}$ as it is in 100 mM $S_2O_3^{2-}$. Since $q_{S_2O_3}$ is much greater at the higher $S_2O_3^{2-}$ concentration, one might expect considerably greater adsorption of Cd(II) at the higher $S_2O_3^{2-}$ concentration if $Cd(S_2O_3)_2^{2-}$ were the adsorbing species. In fact, $2F\Gamma_{Cd(S_2O_3)_x}$ is much greater in 5 mM than in 100 mM thiosulfate even though $q_{S_2O_3}$ is greater at the higher thiosulfate concentration (Fig. 3). This fact is more compatible with the adsorption of the uncharged complex, CdS_2O_3, as was proposed above on other grounds.

Because thiosulfate is an ambidentate anion the site of the proposed bonding between an adsorbed thiosulfate anion and the adsorbing Cd(II)-thiosulfate complex is not obvious. Attachment to one of the oxygen atoms of the adsorbed thiosulfate (which is almost certainly adsorbed via the outer sulfur atom) would appear to be sterically preferable. Nevertheless, a case can be made for the proposition that the same outer sulfur atom which binds the adsorbed thiosulfate ion to the electrode serves as the site of attachment to the electrode surface of the Cd(II) in the adsorbing complex: No adsorption of Zn(II) from thiosulfate media could be detected ($\Gamma < 0.5$ $\mu C/cm^2$) under the same conditions that produced substantial adsorption of Cd(II), *i.e.*, significant adsorption of thiosulfate on the electrode and substantial concentrations of ZnS_2O_3 or $Zn(S_2O_3)_2^{2-}$ in the solution. Since Zn^{2+} is a harder cation than Cd^{2+} (7) it would be expected to have a stronger affinity than Cd^{2+} for the available oxygen atoms in adsorbed thiosulfate anions. The failure of adsorbed thiosulfate to induce any adsorption of Zn(II) thus suggests that attachment through oxygen is not the mechanism by which thiosulfate induces the adsorption of Cd(II).

A related experimental result is the lack of adsorption of Cd(II) from sulfate electrolytes in which $CdSO_4$ is formed and substantial sulfate anion adsorption can be achieved at high positive charges on the electrode. The soft Cd(II) does not avail itself of the opportunity to adsorb via the hard oxygen atoms in the adsorbed sulfate.

The bonding of the Cd(II) in CdS_2O_3 molecules to the sulfur atom of a sulfur-bonded, adsorbed thiosulfate anion poses greater steric difficulties than were encountered in the corresponding iodide-induced adsorption of Cd(II) (1). This difference may account for the lower values of Γ_{Cd} resulting from thiosulfate-induced adsorption even though the Cd(II)-thiosulfate complexes have the higher formation constants.

Acknowledgments

This work was supported by the National Science Foundation. Roger Abel offered immense assistance in the programming and maintenance of the computerized data acquisition and analysis system.

Manuscript submitted Nov. 7, 1968; revised manuscript received *ca.* Dec. 27, 1968.

Any discussion of this paper will appear in a Discussion Section to be published in the December 1969 JOURNAL.

REFERENCES

1. F. C. Anson and D. J. Barclay, *Anal. Chem.*, **40**, 1791 (1968).
2. R. W. Murray and D. J. Gross, *ibid.*, **38**, 392 (1966).
3. F. C. Anson, J. H. Christie, and R. A. Osteryoung, *J. Electroanal. Chem.*, **13**, 343 (1967).
4. G. W. O'Dom and R. W. Murray, *ibid.*, **16**, 327 (1968).
5. J. H. Christie, R. A. Osteryoung, and F. C. Anson, *ibid.*, **13**, 236 (1967).
6. D. J. Barclay, *ibid.*, **19**, 318 (1968).
7. R. G. Pearson, *J. Am. Chem. Soc.*, **85**, 3533 (1963).
8. C. J. Nyman and T. Salazan, *Anal. Chem.*, **33**, 1467 (1961).
9. G. Lauer, R. Abel, and F. C. Anson, *ibid.*, **39**, 765 (1967).
10. F. C. Anson and D. A. Payne, *J. Electroanal. Chem.*, **13**, 35 (1967).
11. B. Case and F. C. Anson, *J. Phys. Chem.*, **71**, 402 (1967).
12. F. C. Anson and B. Epstein, *This Journal*, in press.
13. P. Delahay and D. J. Kelsh, *J. Electroanal. Chem.*, **18**, 194 (1968).
14. R. Parsons and P. C. Symons, *Trans. Faraday Soc.*, **64**, 1077 (1968).
15. G. Lauer and R. A. Osteryoung, *Anal. Chem.* **39**, 1866 (1967).
16. L. G. Sillen and A. E. Martell, "Stability Constants," Special Publication No. 17, The Chemical Society, London, 1964.
17. K. B. Yatsmirskii and L. V. Gus'kova, *Z. neorg. Khim.*, **2**, 2039 (1957).
18. P. K. Migal', N. Kh. Grinberg, and Ya I. Tur'yan, *ibid.*, **4**, 1844 (1959).
19. M. Payszczenska, *Roczniki Chem.*, **33**, 755 (1959).

Theoretical Analysis of Mixed Potentials

David Gray[1] and Allen Cahill

Department of Chemistry, The University of Mississippi, University, Mississippi

ABSTRACT

A mathematical treatment of mixed potential generation is developed from basic electrochemical theories, such that the relationships between rest, mixed, and Nernst potentials are evident. Various approximations of the general mixed potential equations are also developed and discussed.

Single Process Electrode Kinetics

For a simple electrode reaction

$$Ox + ne = R \qquad [1]$$

where Ox is the oxidized species and R is the reduced species. Where the actual charge-transfer valence, z, is equal to the net electrode reaction valence, n, the following may be used

$$i = i^\circ \left[e^{-\alpha \frac{zF}{RT}\eta} - e^{(1-\alpha)\frac{zF}{RT}\eta} \right] \qquad [2]$$

where i is the net current density (often referred to simply as the net current), i° is the exchange current density, α is the transfer coefficient corresponding to the cathodic process, $\mathbf{F}$ is the Faraday, R is the gas constant (different from R used in reaction [1]), T is the temperature in °K, and η is the overvoltage defined as

$$\eta = E - E^{eq} \qquad [3]$$

where E is the applied potential and E^{eq} is the Nernst (equilibrium) potential (1, 2). By the American conventions, i will be positive and η will be negative for a net cathodic process, and i will be negative and η will be positive for a net anodic process.

When diffusion processes are important in reaction [1], Eq. [2] may be rewritten as

$$i = i^\circ \left[\left(1 - \frac{i}{i_c^d}\right) e^{-\alpha \frac{zF}{RT}\eta} - \left(1 - \frac{i}{i_a^d}\right) e^{(1-\alpha)\frac{zF}{RT}\eta} \right] \qquad [4]$$

where i_i^d is the limiting diffusion current density of either the cathodic or the anodic process.

Since the exchange current density, i°, of an electrode reaction is a function of the activities of the reacting species, Delahay and Berzins (3) have introduced the following equation

$$i^\circ = z\mathbf{F}k^\circ a_{ox}^{1-\alpha} a_r^{\alpha} \qquad (n = z) \qquad [5]$$

where k° is the heterogeneous rate constant for electrode reaction [1] and a_i is the activity of the oxidized or reduced species. By defining the standard exchange current density, $i^{\circ\circ}$, as

$$i^{\circ\circ} = z\mathbf{F}k^\circ \qquad \left(\text{or } \frac{z\mathbf{F}k^\circ}{1000}\right) \qquad [6]$$

Spiro (4) has rewritten Eq. [5] as

$$i^\circ = i^{\circ\circ} a_{ox}^{1-\alpha} a_r^{\alpha} \qquad (n = z) \qquad [7]$$

Generally, Eq. [5] and [7] are written with concentrations substituted for activities. This substitution probably causes a large part of the differences in k° and $i^{\circ\circ}$ values as determined by different workers for the same electrode reaction (4).

More complex electrode reactions like

$$pOx + ne = qR \qquad (n \neq z) \qquad [8]$$

where the charge-transfer reaction may occur more than once for the net reaction to occur once have also been considered (1, 5) in evaluating the activity dependence of the exchange current density. For this complex case Eq. [7] may be rewritten as

$$i^\circ = i^{\circ\circ} a_{ox}^{(1-\alpha)\frac{z}{n}p} a_r^{\alpha\frac{z}{n}q} \qquad [9]$$

Equation [9] is often written employing a stoichiometric number, ν, which is the number of times the rate determining step must occur for the net reaction to occur once. The terms, n, z, and ν may be related by

$$\frac{n}{\nu} = z \qquad [10]$$

Mixed Potentials—General

When an electrode is immersed in a solution, there are numerous electrochemical processes which may occur. If one of these processes has a high relative exchange current density to the other possible processes, then it will dominate all processes and the electrode will measure the equilibrium potential of that process, which is calculated by the Nernst equation. When this happens, the electrode is said to be reversible with respect to that particular process. In fact, a practical criterion for reversibility is that the Nernst equation be obeyed. It is important to emphasize that many of the potentials given in standard electrode potential tables are values obtained from thermodynamic data rather than from electromotive force data and caution must be exercised in using them to predict electrode behavior. These values can only be used for electrochemical purposes when the process of interest is kinetically dominating all the other processes which can occur; in other words, when its i° value is considerably higher than the i° values for all the other possible processes.

It is evident that zero net current to an electrode does not necessarily correspond to equilibrium conditions at the electrode when more than one reaction is taking place at the electrode. For the net current to be zero it is only necessary for the sum of the total cathodic currents and the total anodic currents to be zero; that is, the total rate of reductions must equal the total rate of oxidations.

If two or more processes are competitively occurring at the same electrode and at zero net current, a net chemical change or reaction is generally proceeding and the net cathodic and anodic reactions are coupled and they must proceed at the same net rate ($i = i_c + i_a = 0$), and at the same potential, which will be different from the equilibrium potential for any of the processes. This potential is called the mixed potential, and the electrode is called a mixed or polyelectrode. The classic example of mixed potential generation is electrolytic corrosion; that is, when an electrode reacts with the solution in which it is immersed under zero

[1] Present address: Lockheed-Georgia Company, Marietta, Georgia.

net current conditions and at a rest potential which does not appear to be related to the equilibrium potential of the electrode metal or the solution.

The essential idea of mixed potential generation was anticipated by Frumkin (6), Hammett and Lorch (7), and Bronsted and Kane (8) in research on the dissolution rate of sodium amalgam. The classic paper of Wagner and Traud (9) demonstrated that the general behavior of a mixed potential can be explained by the "principle of superpositioning of partial current-voltage curves" of each process involved in the net electrode reaction. Wagner and Traud were aware of the fact (10, 11) that the partial current-voltage curves as well as the mixed potential values must be determined in similar environments. Vetter (12) has pointed out that the mixed potentials, as well as the current-voltage curves, depend greatly on the surface characteristics of the electrode, while the Nernst potentials are independent of the surface properties as shown by Fig. 1. It should also be noted that the partial current-voltage curves are also dependent on the activities of the process components. This is often ignored in graphical determinations of mixed potentials.

The graphical method for determining mixed potentials was initially developed by Wagner and Traud (9). In general, the mixed potential is evaluated by plotting the appropriate partial current-voltage curves as in Fig. 2. The mixed potential, E_m, is the potential at which the net cathodic current for one of the two processes is equal in magnitude to the net anodic current for the other process. In this simple case of two electrode processes, the mixed potential will correspond to two different overvoltages, $\eta_c = E_m - E_2^{eq}$ and $\eta_a = E_m - E_1^{eq}$, where $\eta_c < 0$ and is cathodic and $\eta_a > 0$ and is anodic. The dashed line in Fig. 2 is the over-all current-voltage curve for the mixed electrode. The E_m value will tend toward the E^{eq} value for the process with the highest i° value and it will always be between the equilibrium potentials of the two competing processes. In many cases the cathodic and anodic currents are plotted without regard to sign as in Fig. 3, where the mixed potential is determined by the point of intersection of the partial current-voltage curves. Since mixed potentials are involved in corrosion phenomena, the cathodic current (and also the magnitude of the anodic current) associated with the mixed potential is often referred to as the corrosion current, i_{cor}. The graphical method of evaluating mixed potentials has been expanded for complex systems. Of particular note is the work of Tomashov (13), Hoare (14), and Stern and co-workers (15-17). Hoare (14), and Conway and Bourgault (18) have demonstrated the generation of mixed potentials in systems involving chemisorbed oxygen. Polarographic analysis of mixed potentials has been performed by Kolthoff and Miller (19), and Milicevic (20). Vetter's recent book (12) contains an excellent review of mixed potentials and their importance in interpreting electrolytic corrosion.

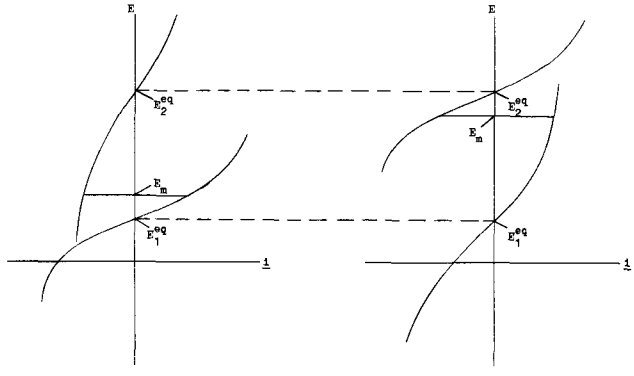

Fig. 1. Dependence of the mixed potential on the relative positions of the partial current-voltage curves.

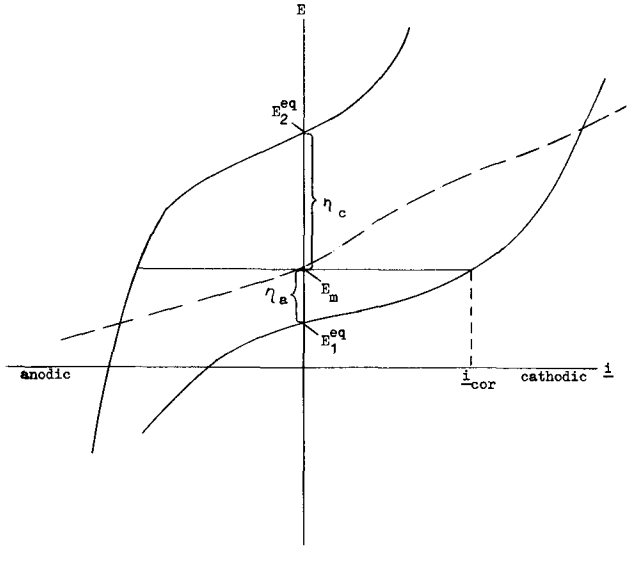

Fig. 2. Graphical determination of a mixed potential generated at a mixed electrode by the coupling of two electrode processes.

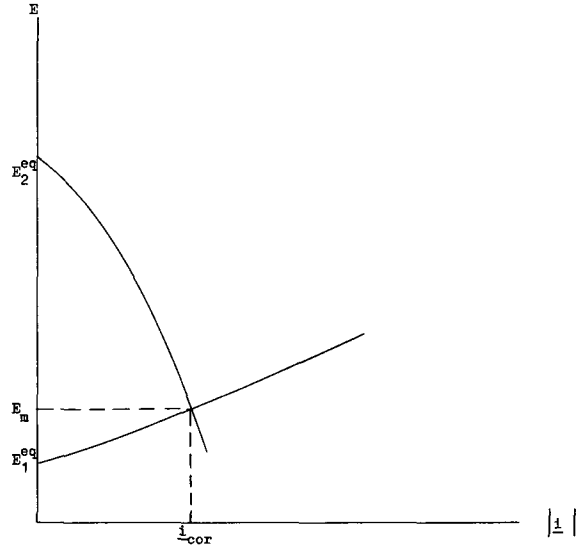

Fig. 3. Graphical determination of a mixed potential generated at a mixed electrode by the coupling of two electrode processes when the cathodic and anodic current densities are taken as absolute values.

Mixed Potentials—Mathematical

If x simultaneous electrode processes

$$\begin{aligned} &Ox_1 + n_1e = R_1 \\ &\vdots \\ &Ox_i + n_ie = R_i \qquad (n_i = z_i) \\ &\vdots \\ &Ox_x + n_xe = R_x \end{aligned} \qquad [11]$$

are occurring at the same electrode and at zero net current to the electrode then one may write for each process

$$\begin{aligned} &\eta_1 = E_m - E_1^{eq} \\ &\vdots \\ &\eta_i = E_m - E_i^{eq} \\ &\vdots \\ &\eta_x = E_m - E_x^{eq} \end{aligned} \qquad [12]$$

where η_i is the overvoltage for the i^{th} process, E_m is the mixed or rest potential of the electrode, and E_i^{eq} is the Nernst potential for the i^{th} process which can be written as

$$E_1^{eq} = E_1^{o} + \frac{RT}{n_1\mathbf{F}} \ln \frac{a_{ox1}}{a_{r1}}$$

$$\vdots$$

$$E_i^{eq} = E_i^{o} + \frac{RT}{n_i\mathbf{F}} \ln \frac{a_{oxi}}{a_{ri}} \qquad (n_i = z_i)$$

$$\vdots$$

$$E_x^{eq} = E_x^{o} + \frac{RT}{n_x\mathbf{F}} \ln \frac{a_{oxx}}{a_{rx}} \qquad [13]$$

where E_i^{o} is the standard electrode potential for the i^{th} electrode process. Each process will be proceeding at a rate which can be expressed by the net current for that process.

$$i_1 = i_1^{o} \left\{ e^{-\alpha_1 \frac{z_1\mathbf{F}}{RT}(E_m - E_1^{eq})} - e^{(1-\alpha_1)\frac{z_1\mathbf{F}}{RT}(E_m - E_1^{eq})} \right\}$$

$$\vdots$$

$$i_i = i_i^{o} \left\{ e^{-\alpha_i \frac{z_i\mathbf{F}}{RT}(E_m - E_i^{eq})} - e^{(1-\alpha_i)\frac{z_i\mathbf{F}}{RT}(E_m - E_i^{eq})} \right\} \qquad [14]$$

$$\vdots$$

$$i_x = i_x^{o} \left\{ e^{-\alpha_x \frac{z_x\mathbf{F}}{RT}(E_m - E_x^{eq})} - e^{(1-\alpha_x)\frac{z_x\mathbf{F}}{RT}(E_m - E_x^{eq})} \right\}$$

The only condition that has been set is that the total net current is zero. Therefore, one may write

$$i_{total} = i_1 + i_2 + \ldots + i_i + \ldots + i_x = \sum_{i=1}^{x} i_i = 0 \qquad [15]$$

It is important to emphasize that it is not necessary to specify which processes are over-all cathodic and which are over-all anodic. If a process is over-all cathodic, then the $(E_m - E_i^{eq})$ terms in Eq. [14] will be negative and the net current for that process, i_i, will be positive, and if a process is over-all anodic, then the $(E_m - E_i^{eq})$ terms will be positive and the net current for that process will be negative.

From Eq. [15] one may write that

$$\sum_{i=1}^{x} i_i = 0 = \sum_{i=1}^{x} i_i^{o} \left\{ e^{-\alpha_i \frac{z_i\mathbf{F}}{RT}(E_m - E_i^{eq})} - e^{(1-\alpha_i)\frac{z_i\mathbf{F}}{RT}(E_m - E_i^{eq})} \right\} \qquad [16]$$

which can be rearranged to

$$\sum_{i=1}^{x} i_i^{o}\, e^{-\alpha_i \frac{z_i\mathbf{F}}{RT}E_m}\, e^{\alpha_i \frac{z_i\mathbf{F}}{RT}E_i^{eq}} = \sum_{i=1}^{x} i_i^{o}\, e^{(1-\alpha_i)\frac{z_i\mathbf{F}}{RT}E_m}\, e^{-(1-\alpha_i)\frac{z_i\mathbf{F}}{RT}E_i^{eq}} \qquad [17]$$

In systems in which the following two conditions exist

$$\alpha_1 = \alpha_2 = \ldots = \alpha_i = \ldots = \alpha_x = \alpha \qquad [18]$$

$$z_1 = z_2 = \ldots = z_i = \ldots = z_x = z \qquad [19]$$

Eq. [17] reduces to

$$e^{-\alpha\frac{z\mathbf{F}}{RT}E_m} \sum_{i=1}^{x} i_i^{o}\, e^{\alpha\frac{z\mathbf{F}}{RT}E_i^{eq}} = e^{(1-\alpha)\frac{z\mathbf{F}}{RT}E_m} \sum_{i=1}^{x} i_i^{o}\, e^{-(1-\alpha)\frac{z\mathbf{F}}{RT}E_i^{eq}} \qquad [20]$$

These two conditions are not very harsh since in most electrode processes z is one and α is one-half. Condition [19] also requires that all the n_i values are equal to z since in this treatment n_i is assumed to be equal to z_i in Eq. [11].

Thus, the mixed potential for x simultaneous processes occurring at the same electrode under conditions [18] and [19] is given by

$$E_m = \frac{RT}{z\mathbf{F}} \ln \frac{\sum_{i=1}^{x} i_i^{o}\, e^{\alpha\frac{z\mathbf{F}}{RT}E_i^{eq}}}{\sum_{i=1}^{x} i_i^{o}\, e^{-(1-\alpha)\frac{z\mathbf{F}}{RT}E_i^{eq}}} \qquad [21]$$

Schneider and Schlegelmilch (21) and Kortüm (22) have derived the following equation for a mixed potential involving two electrode processes occurring at the same electrode with $\alpha = \frac{1}{2}$.

$$E_m = \frac{RT}{z\mathbf{F}} \ln \left\{ \frac{i_1^{o}\, e^{\frac{z\mathbf{F}}{2RT}E_1^{eq}} + i_2^{o}\, e^{\frac{z\mathbf{F}}{2RT}E_2^{eq}}}{i_1^{o}\, e^{-\frac{z\mathbf{F}}{2RT}E_1^{eq}} + i_2^{o}\, e^{-\frac{z\mathbf{F}}{2RT}E_2^{eq}}} \right\} \qquad [22]$$

Obviously Eq. [22] can be obtained from Eq. [21] by setting $x = 2$ and $\alpha = \frac{1}{2}$.

If one electrode process is dominating all the other processes, then the electrode should be reversible to that particular process. From Eq. [21] one can see that if one electrode process is dominant then

$$E_m = E_i^{eq} \qquad [23]$$

where E_i^{eq} is the Nernst potential for the dominant electrode process.

If the complete system of x electrode processes is at equilibrium, then the mixed potential will be given by any of the x Nernst potentials.

Since the Nernst equation is only applicable when both the net current is zero and either one electrode process is kinetically dominating all other possible electrode processes or the system is at equilibrium, Eq. [21] is a more general equation than the Nernst equation. However, it must be remembered that in Eq. [21] both the i_i^{o} value and, of course, the E_i^{eq} value are also dependent on the activities of the electrode process components. Since mixed potential generation implies that a net chemical reaction is proceeding, the values for i_i^{o} and E_i^{eq} will be constantly changing until equilibrium is attained. (If a passive film forms on the electrode then the rate of the coupled electrode processes may become so slow that i_i^{o} and E_i^{eq} will not change noticeably over long periods of time.)

Equation [21] can be written in a more elegant form employing standard exchange current densities and standard electrode potentials by noting that for each electrode process [11] there corresponds the following relationships (refer to Eq. [7])

$$i_1^{o} = i_1^{oo}\, a_{ox1}^{1-\alpha}\, a_{r1}^{\alpha}$$

$$\vdots$$

$$i_i^{o} = i_i^{oo}\, a_{oxi}^{1-\alpha}\, a_{ri}^{\alpha}$$

$$\vdots$$

$$i_x^{o} = i_x^{oo}\, a_{oxx}^{1-\alpha}\, a_{rx}^{\alpha} \qquad [24]$$

Substituting Eq. [13] and [24] into Eq. [21] yields

$$E_m = \frac{RT}{zF} \ln \frac{\sum_{i=1}^{x} i_i^{\circ\circ} a_{oxi} e^{\alpha \frac{zF}{RT} E_i^{\circ}}}{\sum_{i=1}^{x} i_i^{\circ\circ} a_{ri} e^{-(1-\alpha)\frac{zF}{RT} E_i^{\circ}}} \quad [25]$$

Now, if one electrode process is kinetically dominating all the other possible processes, Eq. [25] will give

$$E_m = E_i^{\circ} + \frac{RT}{zF} \ln \frac{a_{oxi}}{a_{ri}} \qquad (z = n) \quad [26]$$

which is the Nernst equation for the dominant electrode process.

Equation [25] is preferred over Eq. [21] since each exponential term in Eq. [25] has to be evaluated only once and Eq. [25] is written in a form which emphasizes the fact that the activity of each species is constantly changing until equilibrium is attained. Equations [21] and [25] also serve to answer questions such as the type raised by Lingane (23) concerning the role of the Pt^{++}/Pt electrode reaction in setting up a hydrogen electrode on platinum. These equations demonstrate that all processes which can occur at an electrode can be taken into consideration when evaluating the rest potential of the electrode. If one process kinetically dominates all the other processes, either because of its high relative $i^{\circ\circ}$ value or because of its high relative activity values, then the rest potential will correspond to the Nernst potential of that process and the electrode can be said to be reversible to that process. If two or more electrode processes are competitively occurring simultaneously at the electrode, then the rest potential will correspond to the mixed potential as determined by either Eq. [21] or Eq. [25].

The overvoltage equations [14] are written for pure charge-transfer rate control. When diffusion processes are significant, Eq. [21] and [25] can be rewritten as (refer to Eq. [4])

$$E_m = \frac{RT}{zF} \ln \frac{\sum_{i=1}^{x} \left(1 - \frac{i_i}{i_{ci}^{d}}\right) i_i^{\circ} e^{\alpha \frac{zF}{RT} E_i^{eq}}}{\sum_{i=1}^{x} \left(1 - \frac{i_i}{i_{ai}^{d}}\right) i_i^{\circ} e^{-(1-\alpha)\frac{zF}{RT} E_i^{eq}}} \quad [27]$$

$$E_m = \frac{RT}{zF} \ln \frac{\sum_{i=1}^{x} \left(1 - \frac{i_i}{i_{ci}^{d}}\right) i_i^{\circ\circ} a_{oxi} e^{\alpha \frac{zF}{RT} E_i^{\circ}}}{\sum_{i=1}^{x} \left(1 - \frac{i_i}{i_{ai}^{d}}\right) i_i^{\circ\circ} a_{ri} e^{-(1-\alpha)\frac{zF}{RT} E_i^{\circ}}} \quad [28]$$

where i_i is the net current for the i^{th} process and i_i^{d} is the limiting cathodic or anodic diffusion current for the i^{th} process. The value for i_i can be calculated as long as a_{oxi} and a_{ri} can be either measured or calculated since the partial current for the i^{th} process is related to the rate of change of the species activities for that process. Of course, these two equations become less reliable as the diffusion processes become stronger.

For more complex electrode reactions, where $z \neq n_i$ and under conditions [18] and [19]

$$\begin{aligned} &p_1 Ox_1 + n_1 e = q_1 R_1 \\ &\cdot \\ &\cdot \\ &p_i Ox_i + n_i e = q_i R_i \qquad (z \neq n_i) \\ &\cdot \\ &\cdot \\ &p_x Ox_x + n_x e = q_x R_x \end{aligned} \quad [29]$$

the exchange current densities for each process can be related by Eq. [9] such that for the i^{th} process

$$i_i^{\circ} = i_i^{\circ\circ} a_{oxj}^{(1-\alpha)\frac{z}{n_i} p_i} a_{rj}^{\alpha \frac{z}{n_i} q_i} \quad [30]$$

Substituting Eq. [30] and the Nernst equation for the i^{th} process (refer to Eq. [13] noting that $n_i \neq z$) into Eq. [21] results in

$$E_m = \frac{RT}{zF} \ln \frac{\sum_{i=1}^{x} i_i^{\circ\circ} a_{oxi}^{\frac{z}{n_i} p_i} e^{\alpha \frac{zF}{RT} E_i^{\circ}}}{\sum_{i=1}^{x} i_i^{\circ\circ} a_{ri}^{\frac{z}{n_i} q_i} e^{-(1-\alpha)\frac{zF}{RT} E_i^{\circ}}} \quad [31]$$

An equation involving both Eq. [21] and Eq. [25] would be very useful when one or more of the x *simultaneous electrode processes occurs* by an unknown mechanism, specifically by an unknown charge-transfer step. In this case, each term in Eq. [25] which involves an unknown mechanism may be replaced by the corresponding term from Eq. [21]. However, reliable data must be available for the exchange current density of the substituted process and, of course, this process must be independent of the other electrode processes. This method would be very useful in systems where complex electrode reactions (*i.e.*, the hydrogen or oxygen electrode reaction) have to be considered.

Approximations of the Mixed Potential Equations

Approximations similar to those made in current-overvoltage studies (1, 12) involving one process may also be made in mixed potential studies involving x simultaneous electrode processes at zero net current.

If the following is true for all the simultaneous processes

$$|E_m - E_i^{eq}| < 0.02 \text{ volt} \qquad \text{(case 1)} \quad [32]$$

and if conditions [18] and [19] are obeyed, provided α is approximately one-half (1), then Eq. [16] may be replaced by

$$E_m = \frac{\sum_{i=1}^{x} i_i^{\circ} E_i^{eq}}{\sum_{i=1}^{x} i_i^{\circ}} \quad [33]$$

by using the approximation $e^x = 1 + x$.

Case 2 corresponds to the familiar Tafel approximation. It is important to note that the statement

$$|E_m - E_i^{eq}| > 0.05 \text{ volt} \qquad \text{(case 2)} \quad [34]$$

must be true for all of the simultaneous electrode processes which are under consideration. The fundamental drawback in this approximation is that before one can write a general mixed potential equation, one must be able to specify which processes are cathodic and which are anodic. For the over-all cathodic processes, the $(E_m - E_i^{eq})$ terms are negative and from Eq. [14] one can write that

$$i_j = i_j^{\circ} e^{-\alpha \frac{zF}{RT} (E_m - E_j^{eq})} \qquad \text{(cathodic)} \quad [35]$$

For the over-all anodic processes, the $(E_m - E_i^{eq})$ terms are positive and from Eq. [14] one can write that

$$i_k = -i_k^{\circ} e^{(1-\alpha)\frac{zF}{RT} (E_m - E_k^{eq})} \qquad \text{(anodic)} \quad [36]$$

Conditions [18] and [19] are followed and since no net current flows the following can be written

$$\sum_{j}^{r} i_j + \sum_{k}^{s} i_k = 0 = \sum_{i}^{x} i_i \qquad [37]$$

where

$$j \neq k \qquad [38]$$

$$r + s = x \qquad [39]$$

From Eq. [37] one obtains

$$\sum_{j}^{r} i_j^\circ \, e^{-\alpha \frac{zF}{RT}(E_m - E_j^{eq})} = \sum_{k}^{s} i_k^\circ \, e^{(1-\alpha)\frac{zF}{RT}(E_m - E_k^{eq})} \qquad [40]$$

Rearranging Eq. [40] yields

$$E_m = \frac{RT}{zF} \ln \frac{\sum_{j}^{r} i_j^\circ \, e^{\alpha \frac{zF}{RT} E_j^{eq}}}{\sum_{k}^{s} i_k^\circ \, e^{-(1-\alpha)\frac{zF}{RT} E_k^{eq}}} \qquad [41]$$

Equation [41] can be rewritten as

$$E_m = \frac{RT}{zF} \ln \frac{\sum_{j}^{r} i_j^{\circ\circ} \, a_{oxj} \, e^{\alpha \frac{zF}{RT} E_j^{\circ}}}{\sum_{k}^{s} i_k^{\circ\circ} \, a_{rk} \, e^{-(1-\alpha)\frac{zF}{RT} E_k^{\circ}}} \qquad [42]$$

If only two simultaneous processes need to be considered under condition [34] and obviously one is over-all cathodic and the other is over-all anodic, the following equation may be written without conditions [18] and [19]

$$E_m = \frac{\alpha_c z_c E_c^{eq} + (1-\alpha_a) z_a E_a^{eq} + \frac{RT}{F} \ln \frac{i_c^\circ}{i_a^\circ}}{\alpha_c z_c + (1-\alpha_a) z_a} \qquad [43]$$

This equation has been given previously by Schneider and Schlegelmilch (21).

Introducing condition [19] into Eq. [43] yields

$$E_m = \frac{\alpha_c E_c^{eq} + (1-\alpha_a) E_a^{eq} + \frac{RT}{zF} \ln \frac{i_c^\circ}{i_a^\circ}}{\alpha_c + (1-\alpha_a)} \qquad [44]$$

Now, introducing condition [18] into Eq. [44] gives

$$E_m = \alpha(E_c^{eq} - E_a^{eq}) + E_a^{eq} + \frac{RT}{zF} \ln \frac{i_c^\circ}{i_a^\circ} \qquad [45]$$

and if α is equal to one-half, Eq. [45] may be written as

$$E_m = \tfrac{1}{2}(E_c^{eq} + E_a^{eq}) + \frac{RT}{zF} \ln \frac{i_c^\circ}{i_a^\circ} \qquad [46]$$

Acknowledgments

The author is indebted to Professor P. Delahay for his instructive comments and to Dr. Andrew Stefani for his interest in publishing this work. This paper is based on part of a dissertation submitted by one of the authors (D.G.) in partial fulfillment of the requirements for a Ph.D. degree.

Manuscript received Dec. 13, 1968.

Any discussion of this paper will appear in a Discussion Section to be published in the December 1969 JOURNAL.

REFERENCES

1. P. Delahay, "Double Layer and Electrode Kinetics," John Wiley & Sons, Inc., New York (1965).
2. B. Conway, "Electrode Processes," Ronald Press Co., New York (1965).
3. P. Delahay and T. Berzins, *J. Am. Chem. Soc.*, **77**, 6448 (1955).
4. M. Spiro, *Electrochim. Acta*, **9**, 1531 (1964).
5. P. Delahay, "Advances in Electrochemistry and Electrochemical Engineering," Vol. 1, P. Delahay, Editor, Interscience Publishers, New York (1961).
6. A. Frumkin, *Z. Physik. Chem.*, **160**, 116 (1932).
7. L. Hammett and A. Lorch, *J. Am. Chem. Soc.*, **54**, 2128 (1932).
8. J. Bronsted and R. Kane, *ibid.*, **53**, 3624 (1931).
9. C. Wagner and W. Traud, *Z. Elektrochem.*, **44**, 391 (1938).
10. P. Delahay, "New Instrumental Methods in Electrochemistry," Interscience Publishers, New York (1954).
11. P. Van Rysselberghe, *J. Phys. Chem.*, **57**, 275 (1953).
12. K. Vetter, "Electrochemical Kinetics," Academic Press, New York (1967).
13. N. Tomashov, *Compt. Rend. Acad. Sci., USSR*, **30**, 621 (1941).
14. J. Hoare, *This Journal*, **109**, 858 (1962); **111**, 988 (1964); **112**, 603, 608, 1129 (1965).
15. M. Stern and A. Geary, *ibid.*, **104**, 56 (1957).
16. M. Stern, *ibid.*, **104**, 559, 645 (1957) **105**, 638 (1958); **106**, 376 (1959).
17. M. Stern and H. Wissenberg, *ibid.*, **106**, 759 (1959).
18. B. Conway and P. Bourgault, *Can. J. Chem.*, **37**, 292 (1959); **38**, 1557 (1960); **40**, 1690 (1962).
19. I. Kolthoff and C. Miller, *J. Am. Chem. Soc.*, **62**, 2171 (1940).
20. B. Milicevic, *Helv. Chim. Acta*, **46**, 671 (1963).
21. H. Schneider and W. Schlegelmilch, *Wiss. Z. Tech. Hochsch. Ilmenau*, **9**, 455 (1963).
22. G. Kortüm, "Treatise on Electrochemistry," Elsevier Publishing Co., New York (1965). See also "Modern Aspects of Electrochemistry," Vol. 1, J. O'M. Bockris, Editor, Plenum Press, New York (1954).
23. J. Lingane, "Electroanalytical Chemistry," Interscience Publishing Co., New York (1958).

Chronopotentiometric Studies in Concentrated Zinc Chloride Solutions

P. Bro* and N. Marincic*

P. R. Mallory & Co. Inc., Laboratory for Physical Science, Burlington, Massachusetts

ABSTRACT

Experimental studies were made of the effect of self-complexation on the cathodic deposition of zinc onto an inert substrate in 0.1-3.0M $ZnCl_2$ solutions with and without a supporting electrolyte. The effect of the self-complexation reactions was accounted for by the use of the apparent transference number of the zinc ion in Sand's equation and a diffusion coefficient of 1.7×10^{-5} cm^2/sec at 25°C. The equations of Morris and Lingane provided a good estimate of the influence of the supporting electrolyte.

The deposition of a metal from a solution of one of its salts in the absence of a supporting electrolyte is accompanied by the depletion of ionic species at the electrode, and the attendant IR drop may be sufficiently large to obscure the potential jumps associated with the onset of other electrode reactions. Chronopotentiometric equations are available (1) for simple reaction systems in fully supporting, partly supporting, and nonsupporting electrolytes, but no treatment has been presented for the partially self-supporting system which results when self-complexation occurs.

Solutions of zinc chloride contain anionic zinc species (2) whose concentration increases when the zinc chloride concentration increases. This is indicated by the transference number of the zinc ion that changes from positive values in dilute zinc chloride solutions to negative values in solutions more concentrated than about two molar (3). The disproportionation of the zinc complexes would be expected to occur sufficiently fast to eliminate any kinetic terms in the chronopotentiometric equations. However, the complexes might be expected to act as a supporting electrolyte, and they might reduce the effective zinc ion concentration at the cathode due to the migration of anionic zinc species.

The purpose of the study was to investigate the self-supporting phenomenon in zinc chloride solutions and to obtain a quantitative description of the self-supporting effect.

Experimental Techniques

Zinc chloride solutions were prepared from analytical grade reagents, and the concentration of the stock solutions was determined with calibrated hydrometers. It is known that zinc chloride solutions undergo hydrolysis with the formation of precipitates (4). When they occurred, they were dissolved by the addition of sufficient $HClO_4$ just to clear the solutions. The supporting effect of the $HClO_4$ is considered in the section on Experimental Results.

A schematic diagram of the cell is shown in Fig. 1. Particular care was exercised in the design of the cell to achieve a uniform current distribution on the cathode. The latter consisted of a circular platinum disk with a diameter of 0.81 cm. It was mounted horizontally at the bottom of a cylindrical cavity with an inner diameter equal to the diameter of the cathode. The cavity was 1.3 cm deep. The zinc counter electrode was located about 3 cm away from the cathode, and it had a diameter of 4 cm. Visual inspection of the zinc deposits on the cathode indicated that a uniform current distribution prevailed under all the conditions of the reported experiments. A reference electrode of zinc was mounted flush with the cavity wall, Fig. 1, and it was located about 0.1 cm away from the cathode.

Conventional circuitry was used for the chronopotentiometric measurements with pulses derived from a 240v stack of lead-acid batteries. An Ebert Electronics, model HD-4, mercury switch gave fast and clean switching at all the currents used. The maximum change in the current during any one pulse was 2.3%, attributable to the changing resistance of the cell during the pulse. The currents were measured with an accuracy of 0.5% with a Greibach model 700 ammeter. A battery derived bias voltage was used in series with the zinc reference electrode to position the pulse suitably on the Tektronix Model 555 CRO screen. The voltage difference between the working electrode and the biased reference electrode was fed to the oscilloscope through a Tektronix Type O preamplifier. IR drops of about 6v and less were encountered, depending on the current densities and solutions used. The traces were recorded photographically, and the time scale of the CRO was calibrated with a Servomex wave form generator, model LF141.

The solutions were deaerated with nitrogen, and a nitrogen blanket was maintained over the solutions. The platinum electrode was restored after every pulse by the anodic dissolution of the zinc to the point of incipient oxygen/chlorine evolution, after which the solution was purged with nitrogen. The restored electrodes were smooth and shiny and they were considered satisfactory for continued use. Anodic currents above about 200 ma/cm^2 resulted in discernible interferences in the subsequent cathodic traces, and, accordingly, this current density was not exceeded during the zinc dissolutions.

The transition times were taken at the point of inflection of the voltage-time curves, and the experiments were restricted to transition times of 5 sec and less to avoid convective disturbances. Because of the

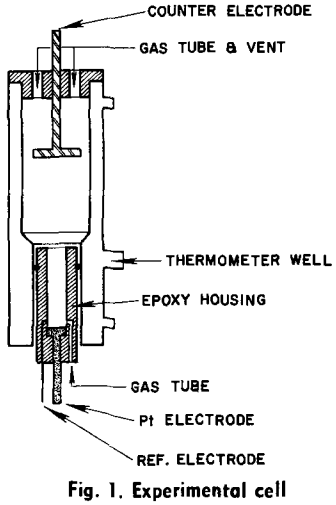

Fig. 1. Experimental cell

* Electrochemical Society Active Member.

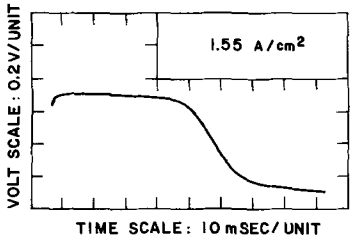

Fig. 2. Chronopotentiogram of 0.6M $ZnCl_2$ in 2.0M $LiClO_4$ at pH 4.9.

high zinc chloride concentrations this necessitated the use of current densities as high as 4.64 amp/cm². The high current densities led to a significant heating of the electrolyte, particularly at the cathode in the absence of a supporting electrolyte, and although the cell was maintained at 25° ± 0.1°C, it is known that higher temperatures occurred during the zinc depositions.

Experimental Results

In the presence of the supporting electrolyte a well-defined voltage step was noted for the transition from zinc deposition to hydrogen evolution on platinum, Fig. 2. In the absence of the supporting electrolyte, however, the depletion of ionic species at the electrode caused a large potential drop that obscured the transition point progressively at the higher current densities for the concentrated $ZnCl_2$ solutions, Fig. 3. An unequivocal transition point could not be defined above 3.0M $ZnCl_2$. A distinguishing feature of the pretransition potential drop that may be seen in Fig. 3 was the change of its time derivative from negative to positive values with an increase in the current density. Although the shape of the transition regions varied noticeably between the runs they did not influence the observed transition times.

The first phase of the experimental work was concerned with the question of the rate-controlling step in the deposition of zinc from the zinc chloride solutions. The known occurrence of anionic zinc species in concentrated zinc chloride solutions (2) suggested the possibility that even if Zn^{+2} could be reduced without kinetic complications at the currents used, the reduction of the chloride complexes might proceed via their dissociation to Zn^{+2}, and the rate of the dissociation reaction might be rate controlling. Delahay (5) showed that a slow reaction step preceding the chronopotentiometric reduction of metal ion complexes should cause $(it^{1/2}/C)$ to decrease with an increase in the current density. No such current dependency was observed in any of the solutions whether a supporting electrolyte was used or not. For example, an $(it^{1/2}/C)$ value of 813 amp $sec^{1/2}$ cm/mole was found for a 2.0M $ZnCl_2$ solution at pH 5.2 with a standard deviation of 3.7% at current densities between 1.17 and 4.64 amp/cm². Since the concentration of the complexes would be expected to depend on the pH of the zinc chloride solutions, the possibility existed that kinetic effects might occur over a limited pH range. $(it^{1/2}/C)$ was found to be independent of the current density in the pH range of interest, pH 3.0 to pH 5.5. Furthermore, $(it^{1/2}/C)$ was independent of the pH in the same pH range. Thus, at pH 4.9 a 0.4M $ZnCl_2$ solution had an $(it^{1/2}/C)$ value of 1006 amp $sec^{1/2}$ cm/mole with a standard deviation of 3.7% over the current density range of 0.19 to 1.94 amp/cm². A 1.0M $ZnCl_2$ solution had an $(it^{1/2}/C)$ value of 1000 amp $sec^{1/2}$ cm/mole with a standard deviation of 8.9% over the pH range of pH 3.0 and pH 5.5.

The absence of a current density effect on the transition time parameter confirmed the absence of convective effects as well. If convection had been present $(it^{1/2}/C)$ should have increased with a decrease in the current density at low current densities. Since convective effects would change $(it^{1/2}/C)$ in the same sense as would kinetic effects, a mutual cancellation of the two effects was precluded. Convective effects were observed for transition times in excess of about 5 sec, but no data are reported for such long transition times.

The preliminary observations indicated that the chronopotentiometric measurements could be made without any kinetic complications, and any effects noted for the influence of the solution parameters on $(it^{1/2}/C)$ should be attributable, therefore, to their influence on the mass transfer process itself.

The transference number of the zinc ion changes from 0.33 in a 0.5M $ZnCl_2$ solution to −0.02 in 2.0M $ZnCl_2$ (3). This indicates that the anionic complexes of the zinc ion become increasingly significant for $ZnCl_2$ concentrations above 0.5M, and if any self-supporting effects were to be present, they would be expected in the more concentrated solutions.

The nature of the $(it^{1/2}/C)$ changes to be expected was ascertained by observing the effect of $LiClO_4$ on the transition time parameter. In a 2.0M solution $(it^{1/2}/C)$ remained constant at 610 amp $sec^{1/2}$ cm/mole with a standard deviation of 8.3% for $ZnCl_2$ concentrations between 0.1 and 3.0M. A decrease in the concentration of the supporting electrolyte from 2.0 to 0.0M $LiClO_4$ led to an increase of $(it^{1/2}/C)$ from 580 to 1070 amp $sec^{1/2}$ cm/mole in a 1.0M $ZnCl_2$ solution, Fig. 4, with a standard deviation of 64.1 amp $sec^{1/2}$ cm/mole about the hand-fitted curve shown in the figure. Therefore, if a self-supporting effect were present, it would cause a decrease of $(it^{1/2}/C)$ with an increase in the $ZnCl_2$ concentration for concentrations greater than about 0.5M $ZnCl_2$ in the absence of $LiClO_4$.

The effect of the $ZnCl_2$ concentration on $(it^{1/2}/C)$ is shown in Fig. 5 for a solution containing no $LiClO_4$ at a constant pH of 4.9. A curve representing the mean value of $(it^{1/2}/C)$ was drawn by trial and error and it gave values of 1120 amp $sec^{1/2}$ cm/mole for the very

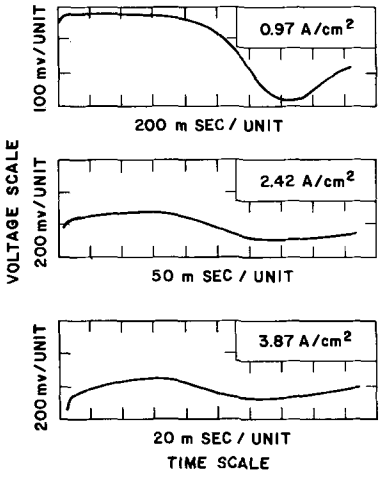

Fig. 3. Chronopotentiograms of 1.0M $ZnCl_2$ at pH 4.9 and various current densities.

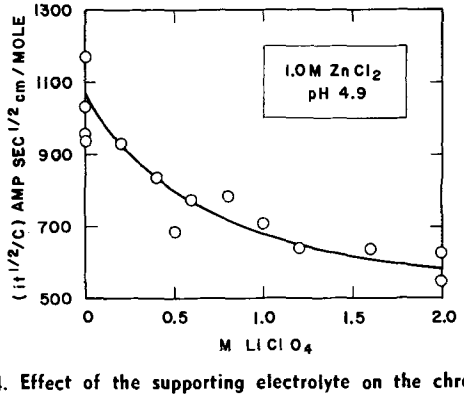

Fig. 4. Effect of the supporting electrolyte on the chronopotentiometric constant.

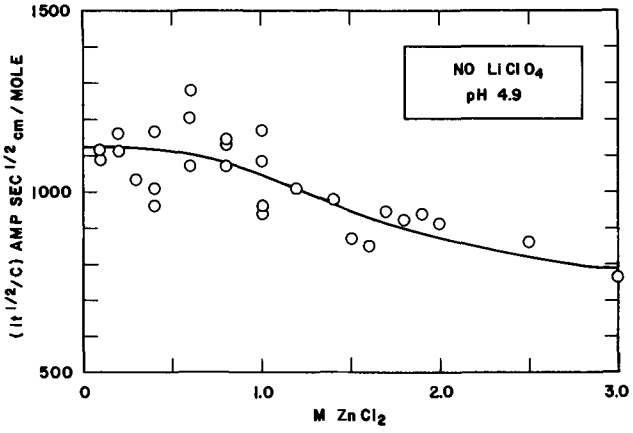

Fig. 5. Self supporting effect in $ZnCl_2$ solutions at pH 4.9

dilute $ZnCl_2$ solutions and 790 amp $sec^{1/2}$ cm/mole for the 3.0M $ZnCl_2$ solution. The standard deviation about the curve shown in Fig. 5 was 80.3 amp $sec^{1/2}$ cm/mole. A considerable scatter was observed for $ZnCl_2$ concentrations of 1.0M and less, and in that region the standard deviation was 93.5 amp $sec^{1/2}$ cm/mole. In the higher concentration range the standard deviation was 48.2 amp $sec^{1/2}$ cm/mole. Within the limitations of these standard deviations the $(it^{1/2}/C)$ values appeared to remain nearly constant for $ZnCl_2$ concentrations below 0.5M, and at higher concentrations it decreased with an increase in the $ZnCl_2$ concentration. Thus, the effect of the complexation reactions was qualitatively equivalent to the use of a supporting electrolyte.

Since $HClO_4$ had been added to maintain a constant pH of 4.9 consideration had to be given to the effect of the $HClO_4$ as a supporting electrolyte. The greatest amount of $HClO_4$ added was 0.73 cm^3 1.0M $HClO_4$ to 200 cm^3 of a 0.1M $ZnCl_2$ solution. It was found (see the following section) that the equations of Morris and Lingane (1) gave a good estimate of the effect of the supporting electrolyte, and, using their equations, it was calculated that the change in $(it^{1/2}/C)$ attributable to the $HClO_4$ would be 4.6% or less.

A series of $ZnCl_2$ solutions were prepared with a minimal amount of $HClO_4$, just sufficient to prevent the precipitation of insoluble hydrolysis products of $ZnCl_2$ and the $(it^{1/2}/C)$ values shown in Fig. 6 were obtained. The same general effect of the $ZnCl_2$ concentration was observed as for the pH 4.9 solutions, except that $(it^{1/2}/C)$ decreased continuously from an extrapolated value of 1300 amp $sec^{1/2}$ cm/mole at a vanishing $ZnCl_2$ concentration. In the higher concentration range, the $(it^{1/2}/C)$ values agreed reasonably well. The minimal $HClO_4$ solution data extrapolated to an $(it^{1/2}/C)$ value of 840 amp $sec^{1/2}$ cm/mole for a 3.0M $ZnCl_2$ solution which may be compared with 790 amp $sec^{1/2}$ cm/mole for the pH 4.9 solution. The data had a standard deviation of 50.8 amp $sec^{1/2}$ cm/mole about the hand-fitted curve shown in Fig. 6.

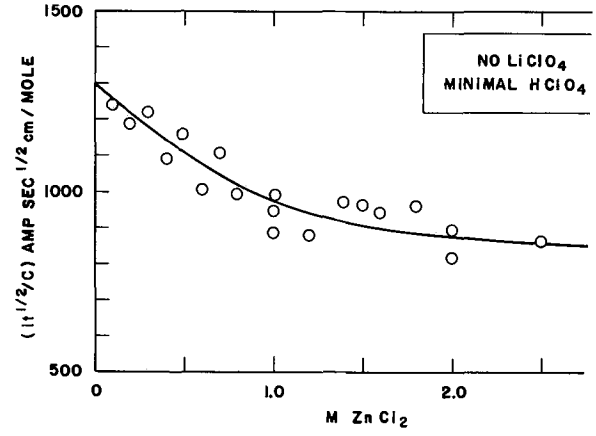

Fig. 6. Self supporting effect in the minimal $HClO_4$ solutions

Several measurements were made with a mercury electrode in the same cell to check for possible surface kinetic and surface roughness effects (the surface area would change during zinc deposition on platinum but not on mercury). An $(it^{1/2}/C)$ value of 593 amp $sec^{1/2}$ cm/mole with a standard deviation of 64 amp $sec^{1/2}$ cm/mole was found for $ZnCl_2$ concentrations below 1.0M $ZnCl_2$ in 2.0M $LiClO_4$ in good agreement with the results for the platinum electrode under the same conditions, *viz.*, 610 amp $sec^{1/2}$ cm/mole. In the absence of a supporting electrolyte the mercury surface changed its shape and size to such an extent on the application of the pulse that well-defined transition times were not obtained.

Discussion

The experimental results established that the deposition of zinc from the zinc chloride solutions was mass transfer controlled, and the chronopotentiometric behavior of the system could be discussed, therefore, in terms of its diffusional and chemical equilibrium characteristics.

Two circumstances impeded an adequate analysis of the diffusion process. The diffusion coefficient used in the chronopotentiometric equations represented an average value obtained by an unknown averaging process, and it was a composite coefficient in the sense that several species contributed to the process which were present in concentration ratios which changed in the gradient region. Furthermore, the diffusion layer became depleted in ionic species and an appreciable ohmic heating of the electrolyte occurred during the diffusion process. Because of these factors the diffusion coefficients calculated from the experimental data are of an heuristic nature.

Case I. Self supporting $ZnCl_2$ *solutions.*—The principal objective of the study was the investigation of the self-supporting effect attributable to the complexation equilibria in the zinc chloride solutions in the absence of an added supporting electrolyte and the search for a quantitative description of the effect. We consider first the experimental $(it^{1/2}/C)$ values extrapolated to a vanishing zinc chloride concentration where ideal solution behavior would be expected and the pertinent Sand equation should apply:

$$(it^{1/2}/C) = \mathbf{F}(\pi D_s)^{1/2}\,(1 - T_+)^{-1}$$

$\mathbf{F}$ = Faraday's constant
T_+ = Transference number of zinc ion
D_s = Diffusion coefficient of zinc chloride

Using the extrapolated, experimental $(it^{1/2}/C)$ values and the reported transference number of the zinc cation of 0.39 (3), the following diffusion coefficients were calculated:

$ZnCl_2$ solution	$(it^{1/2}/C)$ amp $sec^{1/2}$ cm/mole	D_s cm^2/sec
Constant pH 4.9	1120	1.56×10^{-5}
Minimal $HClO_4$	1300	2.15×10^{-5}

These values may be compared with a diffusion coefficient of 1.25×10^{-5} cm^2/sec calculated from the equivalent conductivity of the zinc and chloride ions tabulated by Conway (6). The values agreed well, considering the complexity of the zinc chloride solutions.

The next question concerned the self-supporting effect. The experiments with $LiClO_4$ as a supporting electrolyte had shown that it caused a decrease in $(it^{1/2}/C)$. An analogous effect was observed in the absence of $LiClO_4$ by increasing the zinc chloride concentration in the range where complexation occurred. The transference number of the zinc ion provided a measure of the extent of the complexation reactions, and it was thought that the use of the concentration

dependent transference number in Sand's equation might describe the behavior of the system. In particular, since the diffusion process occurred across an appreciable concentration gradient, the mean transference numbers were used to calculate the diffusion coefficients below from the experimental $(it^{1/2}/C)$ values:

$ZnCl_2$ moles/liter	T_+ mean	pH 4.9 solution $(it^{1/2}/C)$ amp $sec^{1/2}$ cm/mole	pH 4.9 solution D_s cm^2/sec	Minimal $HClO_4$ solution $(it^{1/2}/C)$ amp $sec^{1/2}$ cm/mole	Minimal $HClO_4$ solution D_s cm^2/sec
0.0	0.39	1120	1.56×10^{-6}	1300	2.15×10^{-5}
0.5	0.37	1110	1.65×10^{-6}	1110	1.65×10^{-5}
1.0	0.31	1050	1.80×10^{-5}	970	1.31×10^{-5}
1.5	0.24	950	1.78×10^{-6}	910	1.60×10^{-6}
2.0	0.19	870	1.69×10^{-5}	875	1.70×10^{-5}

The mean value of the diffusion coefficient for each of the two solutions was 1.7×10^{-5} cm^2/sec. In the pH 4.9 solution it remained approximately constant over the entire concentration range whereas it decreased first and then increased as the concentration increased in the minimal $HClO_4$ solution.

The behavior of the experimental D_s values may be contrasted with the expectations for the diffusion coefficient of zinc chloride. The viscosity of zinc chloride solutions increases uniformly by about 30% (7) over the same concentration range, and the activity corrections to the diffusion coefficient calculated from the data in the literature (8) would predict a decrease of D_s between 0 and 1 mole/liter and an increase between 1 and 2 mole/liter. Combining the viscosity and activity corrections, the diffusion coefficient would be expected to decrease about 40% between 0 and 1 mole/liter and increase about 10% between 1 and 2 mole/liter. Qualitatively, this agreed with the behavior observed in the minimal $HClO_4$ solution, but the pH 4.9 solution gave a contrary behavior. The standard deviations of the $(it^{1/2}/C)$ data would give D_s deviations of about 10 and 16% for the minimal $HClO_4$ and the pH 4.9 solutions, respectively, which suggested that the observed D_s patterns might reflect reproducible characteristics of the two solutions. However, in view of the complexity of the diffusion process, we do not attach any fundamental significance to the observed behavior as yet beyond observing that the assumption of a constant diffusion coefficient of 1.7×10^{-5} cm^2/sec provided a reasonably good description of the self supporting effect when the concentration dependent transference number of the zinc ion was used in Sand's equation.

Case II. $ZnCl_2$ *in a supporting electrolyte.*—It was established that the self supporting electrolyte effect in the zinc chloride solutions was analogous to the effect of an added supporting electrolyte, but although the effect could be described formally by the use of the apparent transference number of the zinc ion, it left open the question of how to describe explicitly the effect of a supporting electrolyte. The data obtained in the 2.0M $LiClO_4$ solutions at various $ZnCl_2$ concentrations and in the 1.0M $ZnCl_2$ solutions at various $LiClO_4$ concentrations were used to examine this question.

The 2.0M $LiClO_4$ solutions of zinc chloride may be considered to have been fully supporting at the lower zinc chloride concentrations and the use of Sand's equation for the case of a supporting electrolyte would be justified. The experimental $(it^{1/2}/C)$ value of 610 amp $sec^{1/2}$ cm/mole gave a zinc ion diffusion coefficient of 1.27×10^{-5} cm^2/sec which may be compared with the value of 0.71×10^{-5} cm^2/sec calculated from the equivalent conductivity of the zinc ion at infinite dilution. The agreement appears to be reasonable, but a detailed comparison of the two values will not be pursued. Instead, we focus attention on the changes caused by the supporting electrolyte.

The most complete description available of the effect of a supporting electrolyte is that given by Morris and Lingane (1). The values of $(it^{1/2}/C)$ calculated from their equations [29], [30], and [31] are given below where the equivalent conductivities tabulated by Conway (6) were used.

Molar ratio* $LiClO_4/ZnCl_2$	$(it^{1/2}/C)_{calc}$ amp $sec^{1/2}$ cm/mole	$\left[(it^{1/2}/C)\left(\frac{n_c}{n_0}\right)^{1/2}\right]_{exp}$ amp $sec^{1/2}$ cm/mole	Ratio
0.5	888	950	1.07
1.0	791	817	1.03
1.5	732	748	1.02
2.0	692	729	1.05

* 1.0M $ZnCl_2$.
n_c = viscosity of $LiClO_4$-$ZnCl_2$ solution; n_0 = viscosity of water at the same temperature.

No corrections were introduced for the concentration dependence of the transference number of the zinc ion since the same zinc chloride concentration was used in all the solutions. Since the equations of Morris and Lingane contained no viscosity terms we used experimental viscosity values to adjust the observed $(it^{1/2}/C)$ values to a common basis with the calculated $(it^{1/2}/C)$ values, it being assumed that the product of the diffusion coefficient and the viscosity of a solution would remain constant. A common anion was assumed by Morris and Lingane in the derivation of their equations, and we modified the terms pertaining to the common anion by the use of the mean diffusion coefficient of the chloride and perchlorate ions weighted by their respective formal concentrations. No activity corrections were available, and, therefore, a comparison of the numerical values of $(it^{1/2}/C)$ was not attempted. However, their relative change may be compared as a function of the concentration of the supporting electrolyte.

It may be seen that the equations of Morris and Lingane provided a very good estimate of the effect of the supporting electrolyte on the transition time for the zinc deposition process. The changes in $(it^{1/2}/C)$ were predicted within approximately 5%. Since a meaningful basis existed for the comparison of the changes in $(it^{1/2}/C)$ it was considered that the good agreement resided in the adequacy of the description rather than in fortuity. However, data on other electrolyte systems would be needed to confirm the general applicability of the equations of Morris and Lingane to concentrated solutions of a reducible ion in the presence of a supporting electrolyte.

Conclusions

The complexation reactions in concentrated zinc chloride solutions gave rise to a decrease of $(it^{1/2}/C)$ with an increase in the zinc chloride concentration in the absence of a supporting electrolyte. The changes in the chronopotentiometric constant were analogous to the effect of an added supporting electrolyte, and they were considered to be, tentatively, the result of a self supporting effect attributable to the presence of the complexes in the concentrated solutions.

The self supporting effect could be predicted reasonably well from Sand's equation for the chronopotentiometric constant in the absence of a supporting electrolyte, using a diffusion coefficient of 1.7×10^{-5} cm^2/sec, provided the concentration dependent, apparent transference number of the zinc ion was used to account for the complexation reactions.

The changes in the chronopotentiometric constant attributable to the presence of a supporting electrolyte were predicted quantitatively by the equations of Morris and Lingane.

Manuscript submitted Sept. 11, 1968; revised manuscript received *ca.* Dec. 11, 1968.

Any discussion of this paper will appear in a Discussion Section to be published in the December 1969 JOURNAL.

REFERENCES

1. M. D. Morris and J. J. Lingane, *J. Electroanal. Chem.*, **6**, 300 (1963).

2. L. G. Sillen and B. Liljequist, *Svensk Kemisk Tidsskr.*, **56**, 85 (1944).
3. J. Joussot—Dubien in P. Pascal's, "Nouveau Traite de Chimie Minerale," vol. 5, p. 145, Masson & Co., Paris (1962).
4. *Ibid.*, p. 147.
5. P. Delahay, *Discussions Faraday Soc.*, **17**, 205 (1954).
6. B. E. Conway, "Electrochemical Data," p. 145, Elsevier Publishing Co., New York (1952).
7. J. Joussot—Dubien, *op. cit.*, p. 143.
8. *Ibid.*, p. 142.

Technical Notes

The Anodic Oxidation of CO on Nickel Sulfide in Base

Raymond Jasinski*

Tyco Laboratories, Inc., Waltham, Massachusetts

A number of papers have appeared in recent years on the anodic oxidation of carbon monoxide in basic solutions, *e.g.*, (1-4). Electrochemical oxidation of CO is catalyzed by a variety of metals. However, the rest potentials reported have been significantly more positive than the calculated, thermodynamic value, —0.39v (*vs.* a reversible hydrogen electrode in the same solution), for the reaction

$$CO + 4\,OH^- \rightarrow CO_3^= + 2H_2O + 2e^- \qquad [1]$$

For example, the rest potential for CO on platinum at 23°C has been quoted (2) at +50 mv *vs.* RHE in 1*N* KOH and + 83 mv in 6*N* KOH. In acid the thermodynamic value is —0.105v *vs.* a reversible H_2/H^+ electrode in the same solution.

Recently (2), it has been suggested that the discharge mechanism for CO on platinum, as well as on Raney nickel, takes place according to the following scheme

$$CO + 2\,OH^- \rightarrow CO_3^= + 2H_{ads} \qquad [2]$$

$$2H_{ads} + 2\,OH^- \rightarrow 2H_2O + 2e^- \qquad [3]$$

In effect, the carbon monoxide electrode behaves as a hydrogen electrode operating at low partial pressures of H_2. Alternatively, it has been suggested (4) that CO is first chemically converted to formate ion on Raney nickel, maintaining the same oxidation state, and then to carbonate ion by electrochemical oxidation.

This paper describes the anodic discharge of CO in 6*N* KOH on the compound Ni_3S_2. The equilibrium potentials at 25° and 75°C are negative with respect to the H_2/OH^- electrode in the same solution, although still somewhat more positive than the thermodynamic $CO/CO_3^=$ potential.

Experimental

Ni_3S_2 was prepared from $NiSO_4$ as follows (5): hydrated $NiSO_4$ was dried by programmed heating (<25°C/hr) under a stream of N_2. At 300°C, the temperature and flow of N_2 were kept constant for at least 20 hr to insure thorough drying. When drying was complete, $NiSO_4$ was reduced by H_2 for another day. The principal product was Ni_3S_2, as confirmed by x-ray diffraction measurements. Qualitative measurements on a pressed disk of this material indicate that it is an electronic conductor. However, some metallic nickel was present.

After preparation, the powder was mixed with a Teflon emulsion (~30%) and formed into an electrode in the usual manner (6). The catalyst loadings were variable (see below); no attempt was made to optimize electrode structure for these preliminary experiments.

Electrode testing was carried out in 6*N* KOH in the "floating electrode assembly" (7). Potential measurements were carried out *vs.* a "Dynamic Hydrogen Electrode" (8), calibrated against a commercial platinum electrode under hydrogen in the same solution and at the temperature of operation. Reference electrode stability in the presence and absence of CO was confirmed by periodic checks with a commercial calomel electrode. All potentials are given *vs.* the reversible hydrogen electrode (RHE) in the same solution.

The test electrode (a 1 cm^2 disk) was held at selected potentials with a Wenking potentiostat. Unless otherwise noted, curent readings were taken after steady state had been reached, generally 10-15 min.

A freshly prepared electrode, when first assembled, exhibits a gradually decaying cathodic current below +400 mv, independent of the gas phase (N_2, CO, H_2). After 1-2 hr this current is negligible (<0.01 ma/cm^2). Presumably this current represents the reduction of surface oxide formed during electrode preparation. All data were obtained after this conditioning procedure.

Results

The electrode was first scanned under an atmosphere of N_2. Anodic corrosion current was not observed below +330 mv at 75°C. Hydrogen bubbles are observed to form on the electrode at negative potentials. Under O_2, the electrode is apparently diffusion limited in the same potential range for the cathodic reduction of this gas. Anodic current could not be generated below +330 mv with hydrogen as the fuel; nor could current be generated from methanol, formic acid, or ammonia. However, significant current was sustained when carbon monoxide was present in the gas phase. The actual value of the current was influenced by the catalyst loading and by minor variations in the electrode preparative procedure.

A steady state voltage-current plot for a Ni_3S_2 electrode (20 mg/cm^2) under CO and under H_2 at 75°C is shown in Fig. 1. Figure 2 shows similar data for another Ni_3S_2 electrode (30 mg/cm^2) operated at 25°C. The maximum performance obtained at 75°C has been with an electrode containing 30 mg/cm^2 of catalyst, *i.e.*, 80 ma/cm^2 at +200 mv RHE.

The question arises, of course, whether this electrochemical activity is due to the catalytic oxidation of CO or represents CO-induced corrosion of the electrode material, possibly according to the following sequence

* Electrochemical Society Active Member.

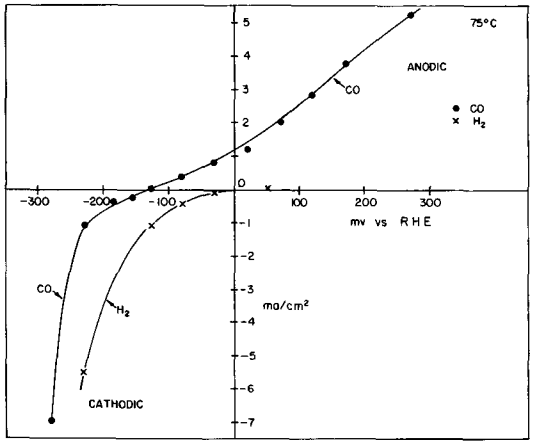

Fig. 1. Steady state voltage current plot for Ni_3S_2 electrode (20 mg/cm^2) under CO and under H_2 at 75°C.

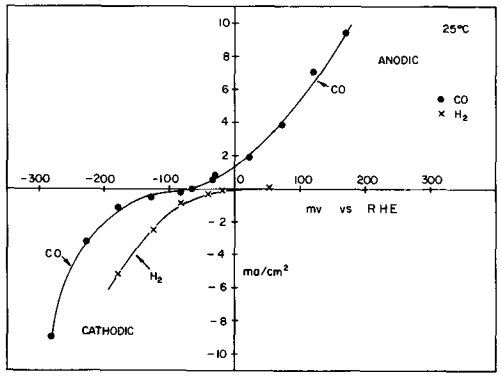

Fig. 2. Steady state voltage current plot for Ni_3S_2 electrode (30 mg/cm^2) under CO and under H_2 at 25°C.

$$Ni_3S_2 + 4CO \rightarrow 3Ni(CO)_4 + 2S^{=} - 4e \quad [4]$$

$$S^{=} + 8\,OH^{-} \rightarrow SO_4^{=} + 4H_2O + 6e^{-} \quad [5]$$

Ignoring Eq. [4], approximately 96 coulombs would result from the oxidation of 30 mg of Ni_3S_2. An experiment was therefore run in which this electrode was held at +100 mv (RHE) and the current followed with time. These data are shown in Fig. 3. There is a gradual improvement in performance (part of the conditioning effect mentioned above) with the current leveling out at ~42 ma/cm^2. The total charge passed was about 430 coulombs, well in excess of that required by Eq. [5]. Furthermore, the electrode was completely intact at the end of the experiment.

Discussion

Ni_3S_2 is stable in 6*N* KOH below +330 mv at 75°C. In this voltage region, Ni_3S_2 will catalyze, at room temperature and at 75°C, the anodic oxidation of carbon monoxide, but not of H_2, NH_3, methanol, or formate ion. This selectivity implies that the mechanism of oxidation does not involve formate ion or gaseous H_2 as intermediates. The reaction product was assumed to be carbonate ion, although this has not yet been confirmed by chemical analysis.

In all experiments with CO as the fuel, equilibrium potentials were more negative than the reversible H_2 electrode in the same solution, as well as the values published for CO on Raney nickel and on platinum (2). At 75°C the equilibrium potential was —180 mv (RHE); at 25°C, —60 mv (RHE).

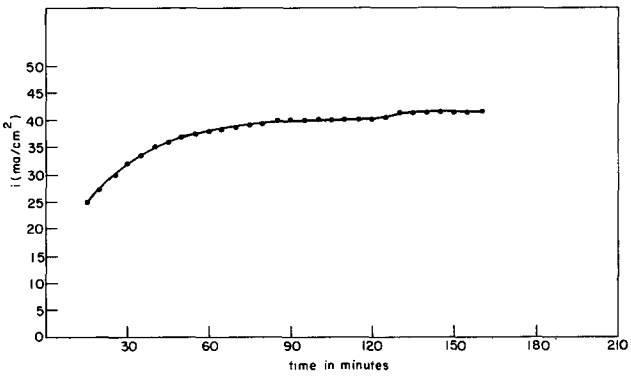

Fig. 3. Current vs. time at +100 mv for CO on Ni_3S_2

Judging from Fig. 1 and 2, the cathodic evolution of H_2 is most likely repressed by the presence of CO; gas bubbles were not observed above —100 mv on the electrode. Because of the negative equilibrium potential and suppression of H_2 evolution, it is unlikely that the anodic oxidation mechanism proceeds through H_{ads} (Eq. [2] and [3]). Detailed mechanistic studies are required to rigorously substantiate this point.

By the use of high catalyst loadings (≧30 mg/cm^2), significant current densities can be obtained, *e.g.*, 80 ma/cm^2 at +200 mv RHE. It is to be expected that optimization of electrode design and the use of higher operating temperatures would further improve performance.

The use of this catalyst in a fuel cell is, of course, obvious. It is suggested, because of the selectivity of Ni_3S_2 to CO in the presence of H_2, that this catalyst could also be used to remove, electrochemically, CO from H_2-CO mixtures. Preliminary experiments indicate that, at a constant potential, the current sustained by this electrode is proportional to the concentration of CO in the gas phase. This also suggests the use of Ni_3S_2 as the basis of a detector for CO in the H_2, N_2, or other "inert" gases.

Preliminary tests were also carried out with an electrolyte one molar in K_2CO_3 and in $KHCO_3$. Performance was poor at 75°C, *e.g.*, 0.1 ma/cm^2 at +180 mv.

Acknowledgments

The author wishes to acknowledge the assistance of Mr. Robert Cattabriga and Miss Susan Carroll, as well as the support of the Air Force Cambridge Research Laboratories, Office of Aerospace Research, under Contract AF 19(628)5549.

Manuscript submitted Oct. 21, 1968; revised manuscript received Nov. 20, 1968.

Any discussion of this paper will appear in a Discussion Section to be published in the December 1969 JOURNAL.

REFERENCES

1. P. Stonehart, "Power Sources," D. Collins, Editor, p. 509, Pergamon Press, New York (1966).
2. K. Hamann, Extended Abstracts, 19th C.I.T.C.E. Meeting, Detroit, Michigan (1968).
3. J. Roberts and D. Sawyer, *Electrochim. Acta*, **10**, 989 (1965).
4. G. Gruneberg, "Brennstoffelemente," W. Vielstich, Verlag Chemie (1965).
5. G. Pannetier, *J. Abegg, Bull. Soc. Chem. France*, **1961**, 186.
6. L. Niedrach and H. Alford, *This Journal*, **113**, 117 (1965).
7. J. Giner and S. Smith, *Electrochem. Technol.*, **5**, 61 (1967).
8. J. Giner, *This Journal*, **111**, 376 (1964).

^{22}Na and ^{14}C Diffusion in a Mixture of Li/Na/KCO_3

R. L. Frederick and E. L. Williams

Fundamental Research, Owens-Illinois Technical Center, Toledo, Ohio

A eutectic ternary mixture of Li_2CO_3, Na_2CO_3, and K_2CO_3 can be formed which will melt around 400°C. As reported by Janz *et al.* (1-3), the eutectic mixture contains Li_2CO_3, Na_2CO_3, and K_2CO_3 in molar ratios of 43.5:31.5:25.0. A similar ratio of 44:30:26 was reported by Rolin *et al.* (4).

A melting temperature of 400°C is 325° to 490°C lower than the melting temperature of the salts in the pure state. Melting temperatures of 500°-600°C make the alkali carbonate mixtures attractive as an electrolyte in high temperature fuel cells. Transport studies in various alkali carbonate melts have been made by Janz *et al.* (2, 5, 6) and by Spedding and Mills (7, 8), but to our knowledge no diffusion measurements have been made in the alkali carbonates below the melting temperature. In the study reported here, the diffusion of Na^+ and $CO_3^=$ ions was measured in a mixture of lithium, sodium, and potassium carbonates near the eutectic mixture by a sectioning technique employing ^{22}Na and ^{14}C tracers. Also, the electric conductivity of this carbonate mixture was measured.

Procedure

Analytical reagent grade chemicals were used to prepare the carbonate mixture which contained Li_2CO_3, Na_2CO_3, and K_2CO_3 in a molar ratio of 41:37:22, respectively. This mixture melts approximately 150°C higher than the true eutectic mixture. The appropriate quantities of raw chemicals for the mixture were melted first at 700° in an alumina crucible and then individual specimens of 1 cm in diameter and approximately 1 cm in thickness were prepared by melting 3-4g of the carbonate mixture in a small zirconia crucible, again at 700°C. Both meltings, as well as the diffusion anneals, were in a CO_2 atmosphere to prevent decomposition of the carbonate. On one surface of each specimen a thin layer of the radioactive isotope was formed by allowing to dry 8-10 drops of an alcohol solution containing the isotope. The ^{14}C isotope was in the form of Na_2CO_3, while the ^{22}Na isotope was in the form of NaCl. The activity of the layer was normally greater than 10,000 counts/min.

For the diffusion to take place, the sample pellets were heat treated in an electric resistance furnace controlled to ±2.0°C of the desired temperature from 18 to 113 hr, depending on the temperature. After the diffusion anneal, the pellets were sectioned and the activity of each section was determined as previously described (9), with the addition that precautions were taken during the sectioning to minimize the absorption of water from the atmosphere. The activity of the sections containing the ^{22}Na isotope was counted by a Nuclear-Chicago single-channel gamma ray spectrometer (Analyzer/Scaler Model 8725 and Scintillation Detector Model DS202V). The activity of the sections containing the ^{14}C isotope was counted by a Nuclear-Chicago liquid scintillation counter (Unilux Model 6850). For the liquid scintillation counting each section was washed off the abrasive paper of the sectioning machine by distilled water into a scintillation counting vial filled with Cab-O-Sil "O."[1] The purpose (10) of the Cab-O-Sil "O" was to keep any precipitates which may form suspended throughout the mixture. To this mixture was added 18 ml of scintillation fluid, which consists of 1-4 dioxane as the solvent and 70 g/liter naphthalene, 4 g/liter of 2,5-diphenyloxazole, 0.1 g/liter of 1,4-bis[2-(5-phenyloxazole)] as solutes. The total volume of the contents of each vial was 23-25 ml.

[1] Cabot Corporation, Boston, Massachusetts.

The electrical conductivity of the carbonate mixture was measured on one of the pellets placed between a silver electrode and a nickel electrode. At temperatures below 275°C, d-c measurements were made with a Tullamore Electrometer (Model VTE-2). At temperatures between 250°-325°C, the resistance was measured by an a-c method with a General Radio Impedance Bridge (Type 1650-A) at 1000 Hz.

Results

In the study reported here, the radioactive isotope diffuses from a thin film into a solid of essentially "infinite" length. Thus, the distribution of the tracer in the solid can be described by the equation

$$A_i = A_0/\sqrt{\pi Dt}\,\exp X_i^2/4Dt \qquad [1]$$

where A_i is the activity concentration of section i at distance X_i from the surface, t is the time of diffusion, A_0 the activity originally at $X_i = 0$, $t = 0$, and D the diffusion coefficient. Thus, plotting A_i *vs.* X_i^2 results in a straight line in which D can be evaluated from the slope.

The results of the tracer diffusion measurements are listed in Table I as the Na^+ and $CO_3^=$ ion diffusion coefficients. It is assumed that the measure of the ^{22}Na and ^{14}C isotope diffusion is in reality a measure of the sodium and carbonate ion diffusion, respectively: that is, there is little or no isotope effect and the ^{14}C is in the $CO_3^=$ ion form. Plots of the diffusion coefficients for each ion *vs.* reciprocal temperature as shown in Fig. 1 reveal a good fit with a straight line and thus is in accordance with the simple Arrhenius equation

$$D = D_0 \exp(-E_a/RT)\ \text{cm}^2/\text{sec} \qquad [2]$$

where D_0 is the frequency factor, E_a is the activation energy, R is the gas constant, and T is the absolute temperature. The values of D_0 and E_a, including the estimated probable error, were evaluated and for the temperature range of 200°-400°C are

For Na^+

$$D_0 = 2.4 \pm 0.4 \times 10^{-3}\ \text{cm}^2/\text{sec} \qquad E_a = 13.0 \pm 0.3\ \text{kcal/mole}$$

For $CO_3^=$

$$D_0 = 1.1 \pm 0.4 \times 10^{-3}\ \text{cm}^2/\text{sec} \qquad E_a = 13.2 \pm 0.3\ \text{kcal/mole}$$

These values were calculated by a least squares treatment of the data.

The values of D_0 and E_a reported here are very similar in magnitude to those reported by Spedding and Mills (7) for Na^+ and $CO_3^=$ diffusion in Li/Na/

Table I. Tracer diffusion in Li/Na/KCO_3 mixture (41:37:22 mole per cent)

Temperature, °C	Diffusion coefficient (cm²/sec) Na^+	Diffusion coefficient (cm²/sec) $CO_3^=$
160	7.0×10^{-9}	—
200	1.9×10^{-9}	7.8×10^{-10}
225	3.0×10^{-9}	—
235	—	2.3×10^{-9}
277	1.5×10^{-8}	—
300	2.5×10^{-8}	1.1×10^{-8}
315	3.7×10^{-8}	—
325	—	1.6×10^{-8}
375	1.4×10^{-7}	3.2×10^{-8}
400	—	5.4×10^{-8}
425	1.7×10^{-7}	—

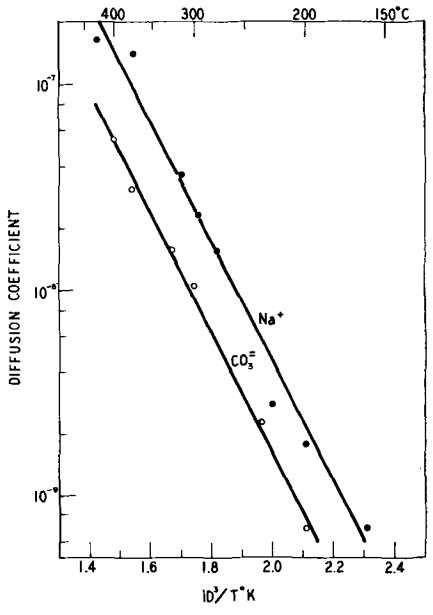

Fig. 1. Diffusion coefficients of both the Na^+ and $CO_3^=$ in the carbonate mixture plotted against reciprocal absolute temperature.

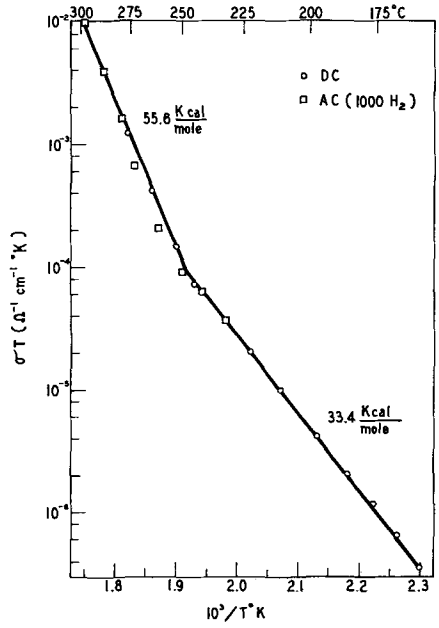

Fig. 2. Electrical conductivity of the carbonate mixture in the temperature range of 150°-300°C plotted as conductivity times temperature vs. reciprocal absolute temperature.

KCO_3 eutectic melt of 43.5:31.5:25.0 mole per cent. Their values for the activation energy are 11.0 and 10.1 kcal/mole for the Na^+ and $CO_3^=$, respectively, and are only slightly lower than those reported here. The largest difference is in the D_0 value for the Na^+. They reported 8.1 x 10^{-3} cm^2/sec for D_0, which is more than three times the value of 2.4 x 10^{-3} cm^2/sec reported here for sodium diffusion in the solid.

The electrical conductivity of the material is shown in Fig. 2. The slope of the best fit straight line to the data corresponds to an activation energy of 33.4 kcal/mole at the lower temperatures and 55.6 kcal/mole at the higher temperatures. The explanation for the change in energies is not known, but it should be noted that both of these energy values are much higher than the activation energies found for the Na^+ and the $CO_3^=$ ions by the tracer measurements.

Acknowledgment

Grateful acknowledgment is made to our colleagues at the Owens-Illinois Technical Center for their helpful comments and discussions.

Manuscript submitted Oct. 28, 1968; revised manuscript received Dec. 16, 1968.

Any discussion of this paper will appear in a Discussion Section to be published in the December 1969 JOURNAL.

REFERENCES

1. G. J. Janz, "Molten Salts Handbook," Academic Press, New York (1967).
2. G. J. Janz and M. R. Lorenz, *J. Chem. Eng. Data*, **6**, 321 (1961).
3. G. J. Janz, E. Neuenschwander, and F. J. Kelly, *Trans. Faraday Soc.*, **59**, 841 (1963).
4. M. Rolin and J. M. Recapet, *Bull. Soc. Chim.*, 2104 (1964).
5. G. J. Janz and M. R. Lorenz, *This Journal*, **108**, 1052 (1961).
6. G. J. Janz and F. Soegusa, *ibid.*, **110**, 452 (1963).
7. P. L. Spedding and R. Mills, *ibid.*, **112**, 594 (1965).
8. P. L. Spedding and R. Mills, *ibid.*, **113**, 599 (1966).
9. E. L. Williams and R. W. Heckman, *Phys. Chem. Glasses*, **5**, 166 (1964).
10. D. G. Ott, C. R. Richmond, T. T. Trugillo, and H. Foreman, *Nucleonics*, **17** (9), 106 (1959).

Brief Communication

Answer to "The Uhlig Defect Model of Oxidation Kinetics" by A. T. Fromhold, Jr.

H. H. Uhlig*

Department of Metallurgy and Materials Science, Massachusetts Institute of Technology, Cambridge, Massachusetts

In the above paper (1), Fromhold criticizes my theory of initial oxidation kinetics first published in 1956 (2) and which was extended to interpret data obtained in my laboratory by MacNairn (2), Pickett and MacNairn (3), and Nwoko (4) on thin-film oxidation behavior of Cu, Ni, and Zn, respectively. Some of the matters discussed by Fromhold repeat his earlier criticisms which were answered in ref. (4) and hence there is no need to repeat the answers here.

By and large, it can be said in summarizing the discussion that Fromhold starts out with different as-

* Electrochemical Society Active Member.

sumptions than mine and reaches different conclusions. The final criterion, of course, of which set of assumptions is better must rest on the accord which is reached with the experimental facts. No theory can hope to survive which is based solely on philosophic speculations and which nowhere along the line makes contact with reality.

Examining some of the details, it should first be made clear that there is usually more than one solution to any differential equation, and the corresponding choice of variables and boundary conditions is arbitrary. The only requirements are that the latter must be self-consistent and that the final solution must have physical significance. I believe that these requirements are adequately met in my solution of the Poisson equation.

Fromhold, using his own particular assumptions, calculates the contribution of the negative space charge layer in zinc oxide to the potential at the metal surface showing that the contribution amounts to only 5.4×10^{-3}v. He concludes that "the space charge for all practical purposes provides an insignificant attenuation of the current." However, using my assumptions instead (2), the analogous calculation for a ZnO film 50Å thick on Zn containing a density n of trapped electrons equal to 0.24×10^{18}/cm^3 is given by $\frac{4\pi ne}{\epsilon}(ly - y^2/2)$ where y is the thickness of oxide, ϵ is the dielectric constant of ZnO (10), e is the charge on the electron (4.8×10^{-10} esu) and l, equal to 1.3×10^{-5} cm, is the theoretically maximum attainable thickness of constant space charge density oxide. The value of l under the above-stated conditions is obtained from the empirical oxidation rate constant k_0 (17/2.3A) equal to $\frac{\epsilon kT}{4\pi ne^2 l}$. The resultant calculated potential is 0.13v which is a substantial contribution satisfactorily accounting for the observed decrease of electron transfer and corresponding slow-down of the oxidation rate after Zn is exposed 140 min to O_2 at 206°C.

The observed change to a higher reaction rate subsequent to the initial reaction rate, giving rise to an observed two-stage logarithmic kinetics, we have ascribed to dissociation of trapped charge at a critical oxide thickness L. Reduced space charge density accounts for a lower retarding potential at the metal surface for electron transfer per unit increase of oxide thickness. The objection is raised that such an abrupt change is "non physical" and out of accord with Boltzmann statistics. But obviously the transition to second-stage kinetics is only abrupt in a relative sense. If more experimental points were obtained in the region of transition, it is expected that the change in growth of oxide would occur over a narrow range of oxide thickness rather than at a single value. Nevertheless, the average value of oxide thickness marking the transition is sufficiently sharp both on examining the experimental data and from the consequences of theory to allow a single oxide thickness to be designated. Further refinements would undoubtedly define a narrow range of oxide thickness instead. This detail has no consequence with regard to the validity of the theory.

In chemical kinetics, when a given reaction results from several concurrent reactions, the standard procedure is to consider that the slowest reaction of the group is the one that limits the over-all reaction. In the thin-film oxidation process, I have considered electron transfer to be the slow process determining the over-all oxidation rate. This does not mean that I have negligently omitted consideration of ion migration, but only that ion migration is a fast process in comparison, and hence it need not be considered in the final rate equation. Carl Wagner, whom Fromhold quotes, showed that for thicker oxide films for which the parabolic equation holds, ion migration is now the slow process and electron transfer and migration in turn can be neglected.

The differentiation between activation energy and free energy is readily resolved. The free energy of oxidation is given by the Gibbs term ΔG for the over-all reaction

$$M + 1/2\, O_2 \rightarrow MO$$

where ΔG is a negative quantity under the usually considered experimental conditions. It involves both ion and electron migration. The activation energy for the above reaction, on the other hand, is given by the term ΔE in the Arrhenius equation where rate = const. $\exp(-\Delta E/RT)$. The value of ΔE can be obtained by plotting the logarithm of the reaction rate constant with the reciprocal absolute temperature T. According to my model of thin film oxidation the expression $d\ ln k_0/d\ 1/T$ becomes equal to $-e(\phi_0 - \chi - v)/k$ where k_0 is the reaction rate constant for first-stage logarithmic kinetics, k is Boltzmann's constant, ϕ_0 is the work function of the metal, χ is the amount by which the oxide alters the work function at the metal-oxide interface, and v is the electron affinity of oxygen adsorbed on the oxide surface. Comparison with the Arrhenius equation makes it quite clear that the energy corresponding to electron transfer from metal to oxide surface as mentioned in my paper is the activation energy and is not the Gibbs free energy term ΔG. The derivation of the expression above was in fact the first which extended to thin film oxidation the empirical relation proposed much earlier by Rideal and Wansbrough-Jones (5) based on observed activation energies for the oxidation of W, Pt, and C.

The discussion of nonconservation of charge is hardly a relevant matter because it is always implied, such as in the similar development of double layer theory in electrolytes, that a simultaneous positive surface charge is formed in the metal as excess negative charge accumulates in the environment. Excess charge, in other words, can and does exist in the oxide as shown by both Volta potential and other type measurements, but the over-all charge including that of the metal must, of course, remain neutral.

The limiting state of affairs at zero oxide thickness is given by negatively charged adsorbed oxygen on the metal surface rather than by a clean metal surface. In other words my described approach to thin film oxidation kinetics includes the limiting case for which volatile oxides are formed (Pt, W, C). Since the negative surface charge now remains constant in time, the linear oxidation equation is obeyed instead of the direct logarithmic, and the expression for the activation energy of oxidation no longer includes the term χ, but is otherwise the same as is given above. This particular assumption in my derivation answers in large part the long discussion by Fromhold on various possible boundary conditions at the oxide-metal interface, as well as detailed matters relating to conservation of charge.

The image charge in the metal is included in my solution of the Poisson equation. The total negative surface charge, on the other hand, made up of oxygen ions adsorbed on the oxide surface is included in my electron affinity term v equal to 3.6 ev. I have assumed that all adsorption sites on the oxide surface are occupied throughout the oxidation process.

As mentioned earlier, the final proof of any oxidation model is its accord with experiment. It may be worthwhile, therefore, to summarize the contributions which are made by the oxidation model which I have proposed.

1. It leads to the derivation of the direct logarithmic equation which represents most thin-film oxidation data for metals in general. It explains why this equation applies only to thin film oxides characterized by a space charge and not to thicker films for which ion migration is controlling. It furthermore explains that thin-film oxidation rates depend on the Curie tempera-

ture, lattice type, and grain orientation because of corresponding changes in work function of the metal.

2. It accounts for observed two-stage logarithmic oxidation behavior of both polycrystalline and single crystal metals and furthermore predicts the thickness at which second-stage logarithmic kinetics begins.

3. It accounts for an observed much lower thin film oxidation rate for zinc compared to Cu and Ni, despite Zn being a chemically more active metal. The difference is ascribed to a calculated higher negative space charge density in ZnO compared to that in Cu_2O or NiO.

4. It provides a theoretical derivation of the Rideal-Jones relation for the activation energy of oxidation dependent on work function of the metal and electron affinity of adsorbed oxygen.

5. It suggests why many metals in the thin film region oxidize in accord with the cubic equation as well as the two-stage logarithmic equation. Only a slight difference in distribution of excess charge in the diffuse space charge layer determines which type equation is followed.

6. It provides for calculating the density of defect sites in metal oxides which for the limited data so far available are in reasonable accord with similar densities calculated independently by others.

Manuscript received Dec. 16, 1968.

Any discussion of this paper will appear in a Discussion Section to be published in the December 1969 JOURNAL.

REFERENCES

1. A. T. Fromhold, Jr., *This Journal*, **115**, 882 (1968).
2. H. H. Uhlig, *Acta Met.*, **4**, 541 (1956).
3. H. Uhlig, J. Pickett, and J. MacNairn, *ibid.*, **7**, 111 (1959).
4. V. Nwoko and H. Uhlig, *This Journal*, **112**, 1181 (1965).
5. E. Rideal and O. Wansbrough-Jones, *Proc. Roy. Soc.*, **123A**, 202 (1929).

Asymmetric Conduction in Thin Film Tantalum/Tantalum Oxide/Metal Structures: Interstitial and Substitutional Impurity Effects and Direct Detection of Flaw Breakdown

Norman N. Axelrod* and Newton Schwartz*

Bell Telephone Laboratories, Incorporated, Murray Hill, New Jersey

ABSTRACT

Asymmetric conduction in a thin film tantalum/tantalum oxide/metal structure depends strongly on the method of preparation of the individual elements as well as the conditions under which the structure is measured. Some of the factors which need to be considered are: (*i*) gas and alloy metal content of the sputtered tantalum film; (*ii*) structural perfection of the tantalum film; (*iii*) nature of the metal counter electrode; and (*iv*) ambient factors such as the presence of moisture during measurement. The principal results from these investigations can be explained on the basis of flaws in the anodic oxide. Evidence exists, however, that some degree of asymmetric conduction exists in nominally flaw-free films.

Many mechanisms have been proposed to explain the rectifying characteristics of anodic oxide films (1). This asymmetric conduction is known to be quite variable and has not been satisfactorily explained in terms of simple solid state band theory.

Two general classes of response can be considered: (2):

(*a*) The homogeneous or uniform response of the entire thin film oxide which depends on the band structure and contact barrier energetics (3-8);

(*b*) The heterogeneous or local response at flaws, (*i.e.*, small areas which differ in electrical properties from the remaining oxide) which may be due to a local variation in the stoichiometry, to a fissure, or to other types of mechanical defects in the oxide (9-11).

Previous studies have indicated that it is possible for both responses to exist. Vermilyea has demonstrated that a transition from type (*a*) to type (*b*) occurs with an increase in anodic oxide film thickness (9). The heterogeneous mechanism, therefore, may be the significant one in the range of film thicknesses used normally for device applications such as capacitors and crossovers. Since flaws may arise in different ways, it is of considerable interest to define the parameters which determine their formation, and to extend the study of nominally flaw-free[1] films to thicknesses greater than those used in Vermilyea's study. A study of these parameters might also result in a definition of the range of metallurgical states of the parent tantalum necessary to obtain reproducible measurements for an investigation of the electronic conduction mechanisms.

The sputtered tantalum-anodic oxide-metal (1b) structure has been shown to have variable asymmetric conduction; the fundamental parameters associated with the asymmetry might be understood if the variability could be controlled. This paper presents some of the factors which determine the asymmetry in this structure; it will be shown that nominally flaw-free films which have nearly symmetric conduction characteristics can be formed in the 2000Å thick range.

Since both homogeneous and heterogeneous responses can exist, each investigator ought to determine the predominant response in the particular samples under investigation. A simple test is reviewed in this study which may allow such a classification.

Sample Preparation

Tantalum films were deposited by sputtering at the rate of about 100 Å/min at argon pressures in the range of 10-20 millitorr of argon. Reactive sputtering techniques (12-15) using small additions of oxygen, nitrogen, methane, or hydrogen in the argon yielded tantalum films with the appropriate amount of the gas going into either interstitial positions or compound formation. Tantalum films alloyed with a variety of different metals were formed by sputtering with wires of the alloying element suspended across the face of a high-purity tantalum cathode (Fig. 1) (16). In all the cases under discussion the structure of the film was the beta-tantalum phase (17) unless specified otherwise. For the studies reported here on the area variation, moisture dependence, and electrolyte contact dependence, the tantalum films were anodized to 100v at 105°C in an ethylene glycol-oxalic acid electrolyte, while for all of the other studies, the anodization was performed at room temperature in a 1% aqueous citric acid solution with a formation voltage of 130v. In both of these anodizations the oxide film thickness was 2300Å. In all of these oxide preparations, the anodization was interrupted at midpoint to allow the back-etching with 0.01% $AlCl_3$ in methanol, although it has been demonstrated that this step does not affect the degree of asymmetric conduction. Metal film counter electrodes, usually gold, were evaporated through masks to form 10-15 capacitors of one size, or else a distribution of sizes (Fig. 2a). Large and small area electrolyte contacts could be isolated on the same anodic film with the use of electroplaters masking tape. The current-voltage characteristics and the non-

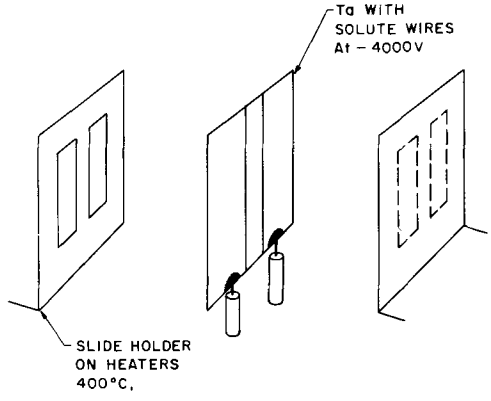

Fig. 1. Tantalum cathode wound with two wires of alloy metal for sputtering onto four glass slides on the two symmetrically placed slide holders.

* Electrochemical Society Active Member.

[1] "Nominally flaw-free" films are those whose breakdown voltages are independent of counter electrode area and are an appreciable fraction of the formation voltage.

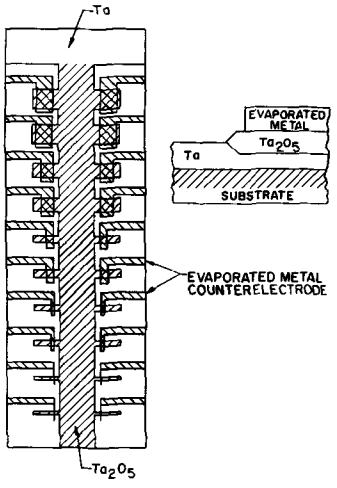

Fig. 2. Structures for the evaluation of printed tantalum oxide capacitors: (a) (left) tantalum anode area variation; (b) (right) schematic capacitor structure.

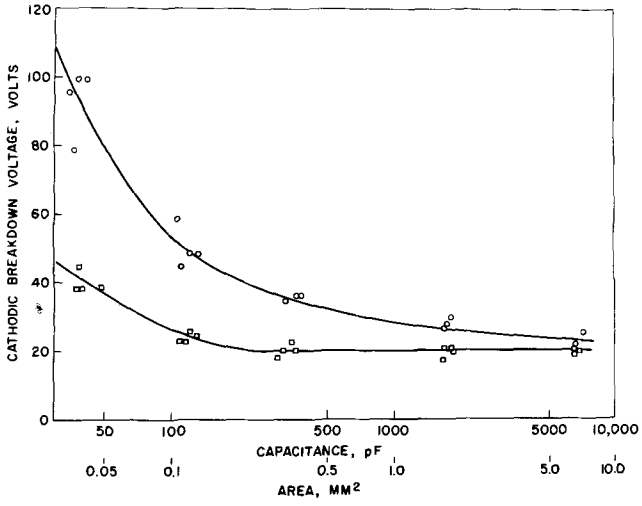

Fig. 3. Cathodic breakdown voltage (Ta^+) as a function of capacitance of printed tantalum oxide capacitors. All oxide formations at 100v at 110°C.

catastrophic breakdown voltages were determined as reported previously (2).

Counter Electrode Area Studies

Vermilyea demonstrated the existence of flaws in anodic oxide films grown on bulk anodes by the use of fine wire contacts and electrodeposition (9, 18). With wire probes, it is possible for the pressure and area of the contact wire on the oxide to vary; in some cases, the wire can puncture the oxide, particularly if the wire had previously conducted current at the site of a local catastrophic breakdown. With evaporated contacts, the pressure problem is avoided, the capacitance of the structure can be measured to assure an appropriate contact and provide information on the area of contact, and there is more flexibility in the kind of experiments that can be done as compared with the use of electrolyte contacts.

A possible ambiguity in the area variation technique illustrated in Fig. 2 is that the perimeter to area ratio increases with decreasing area. If one assumes that flaws are concentrated at the perimeter, and that increasing the perimeter to area ratio increases the probability of making contact to a flaw, the results to be described are incompatible with this assumption.

The results of measurements on the breakdown voltage as a function of the capacitance (*i.e.*, of the calculated area using 26.5 as the dielectric constant and 16.5 Å/v for the anodization constant) for a constant oxide film thickness are shown in Fig. 3 for two different slides prepared under ostensibly identical conditions (2). The reduction in the area of the capacitor sample results in a marked increase in cathodic breakdown voltage. This result is compatible with a model of an oxide film with flaws whose density is on the order of one per 0.05 mm^2 (*i.e.*, with an average separation distance of 0.22 mm). This calculated density assumes one type of flaw which breaks down at a given voltage, but a more realistic treatment would have to include a distribution of flaws breaking down at various voltages.[2]

The difference between the two curves in Fig. 3 may be attributed to two different flaw densities caused by minor changes in the process parameters. In about one third of the samples, the flaw density was so high that no change in cathodic breakdown voltage could be observed in the samples by varying the counter electrode areas.

Large increases in the anodic breakdown voltage when the counter electrode area was decreased from 200×10^{-3} cm^2 to 1×10^{-3} cm^2 have also been reported (20), thus suggesting that flaws can play a role in anodic conduction as well.

[2] See later discussion of direct observation of breakdown at flaws.

The area variation technique utilizing evaporated counter electrodes is a powerful method for detecting flaws if the area of the contact is made small enough. Similar results can be observed with 8*N* sulfuric acid as a contacting electrolyte. For the identical area, where the loosely adherent gold counter electrode was removed with transparent sticky tape, the cathodic and anodic breakdown voltages of the small area samples were significantly larger than those for the large area samples.

Large Area Aqueous Electrolyte Contacts

Studies on anodic oxides have been reported in which aqueous electrolyte contacts were used. To correlate these studies with the present work using metal counter electrodes, the nominal breakdown voltages for both counter electrode types were compared on the same oxide sample. First, the breakdown voltage was determined with a gold counter electrode (see Fig. 4, upper); then the gold counter electrode was removed with aqua regia, the sample reformed at the original anodizing voltage for a short period of time, and then the identical area was contacted with 8*N* sulfuric acid resulting in the lower trace of Fig. 4. This latter sample shows almost complete rectification with a nominal cathodic breakdown voltage of less than 1v, and with anodic breakdown voltages improved over the metal counter electrode sample. Gold counter electrodes were then evaporated over the same area, and results identical to the upper trace in Fig. 4 were ob-

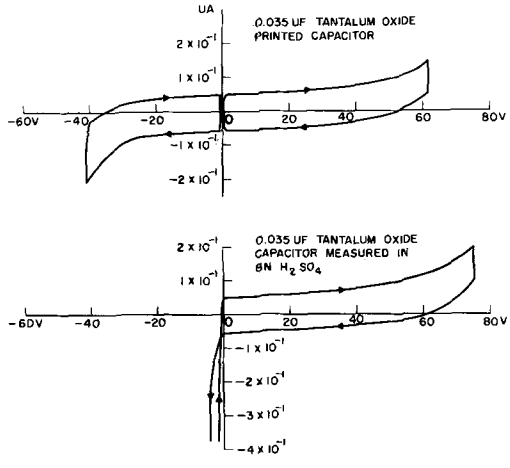

Fig. 4. Comparison of I-V characteristics with gold and aqueous counter electrodes (large area example); positive voltage is for anodic direction (Ta^+).

tained, indicating no irreversible changes occurred in the oxide as a result of these different steps

As indicated in the previous section, however, small area samples showed a similar decrease in cathodic breakdown voltage with an electrolytic contact, but the values of the breakdown voltage were in the 20-30v range. This result indicates that the electrolytic contact results are also area dependent, but with a different sensitivity factor than for the metal counter electrodes. One of the conclusions from this study is that breakdown voltages for gold counter electrodes and for concentrated electrolyte contacts show a similar dependence on the contact area, though the latter contact results in much smaller cathodic breakdown voltages for a given area.

Any model which can be set up to explain these electrolyte results must also take into account concentrations of water less than that associated with an aqueous solution. To investigate this, vacuum baking was employed to remove trace amounts of water from the gold counter electrode samples. Figure 5 shows the breakdown voltage results for both a gold electrode thin film capacitor and a standard tantalum solid electrolytic capacitor. Removal of trace amounts of moisture by heating at 120°C in 10^{-5} Torr vacuum for 3 hr and then cooling in vacuum to room temperature cause a decrease in the anodic breakdown voltage with virtually no change in the cathodic breakdown voltage. These effects are time dependent since applying a voltage of 50v to desiccated samples does not lead to catastrophic breakdown, but a polarization-like phenomenon is observed in which the leakage current decreases with time at constant voltage. An important observation is that the desiccated sample shows almost symmetric breakdown behavior, but with anodic and cathodic breakdown voltages of about one-quarter that anticipated from the 130v anodization voltage. Exposure to room ambient moisture at about 50% relative humidity results in a reversible return of the anodic breakdown voltage to the initial voltage trace. Moreover, the rate of return is proportional to the gold electrode thickness. Small area capacitors comparable to those shown in Fig. 3 with cathodic breakdown voltages in the 100 volts range, do not show this reversible moisture effect, and in fact are quite stable at different moisture levels (see Fig. 6).

The effects of varying degrees of exposure to moisture on the breakdown voltages are pictorially summarized in Fig. 7. The anodic breakdown voltage increases markedly with an increase in the relative humidity, but then has a further smaller increase when an electrolyte contact is used instead of the metal counter electrodes. For the cathodic breakdown voltage, there is essentially no change when the relative humidity is increased, but a decrease results when an electrolyte contact is used.

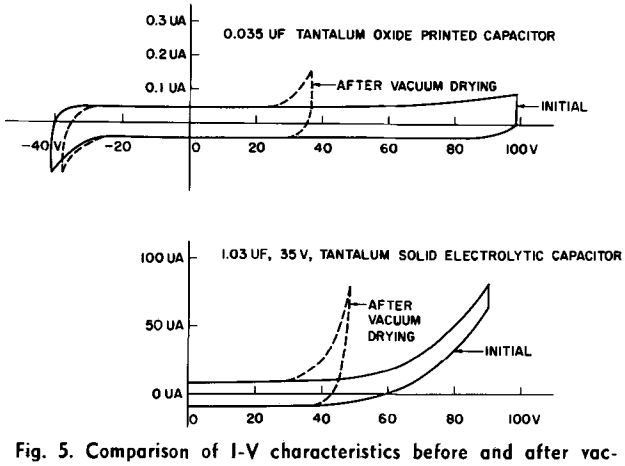

Fig. 5. Comparison of I-V characteristics before and after vacuum baking as determined by the dynamic method; upper-curve, printed tantalum oxide capacitor; lower curve, tantalum solid electrolyte capacitor.

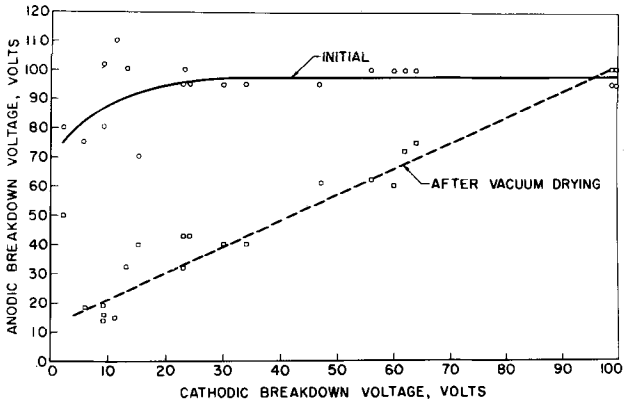

Fig. 6. Correlation of the anodic breakdown voltage of printed tantalum oxide capacitors with the initial cathodic breakdown voltage: solid curve, initial measurement before vacuum drying; dashed curve, after vacuum drying at 120°C. Variation in cathodic breakdown achieved by varying counter electrode area.

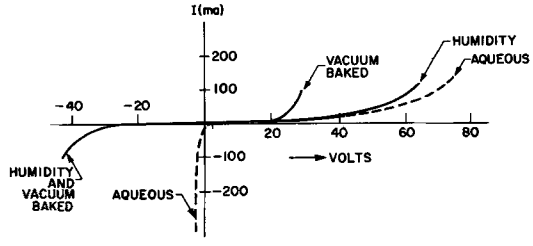

Fig. 7. Comparison of I-V characteristics of capacitor having gold counter electrode before (at 88% relative humidity) and after vacuum baking with capacitor having aqueous electrolyte (8*N* H_2SO_4) contact.

For meaningful models, there should be a well-defined experimental situation to be described. It has been shown above how the contact conditions can affect the results, and we shall discuss below how variations in the fabrication can affect the electrical characteristics. Thus, instead of proposing or reaffirming specific models based on electronic mechanisms or electrochemical processes, a more modest model based on flaws will be used to correlate the above information. It will point up a level of explanation which is currently suitable for a large number of anodic tantalum oxide films, and emphasizes the difficulty in using more sophisticated models when applied to flaws.

It is assumed that flaws are responsible for the cathodic and anodic breakdown voltages. From the data on moisture dependence, three models may be applicable: (*a*) one type of flaw behaves differently with moisture under biases of different signs; (*b*) there are two separate types of flaws; or (*c*) there is essentially one type of flaw with two different parts. For simplicity, we assume that there are two different types of flaws, one of which responds to low moisture content in a certain way in the anodic direction but is not influenced in the cathodic direction, while the other type of flaw is not influenced in the anodic direction and has a response to high levels of moisture (*i.e.*, electrolyte contacts), albeit a different response, in the cathodic direction.

The two major changes with moisture are (*a*) a large change in the cathodic breakdown voltage when going from a sample in high relative humidity to a sample with an electrolyte contact and (*b*) a large change in the anodic direction between a sample being in a dry ambient to being in an ambient with a high relative humidity. The process responsible for (*a*) might be a H^+ or H atom transport, hydrogen embrittlement, or tunneling across a thin section of oxide which becomes important only at high concentrations

of water. Proposed explanations for the latter change, (*b*), have been oxygen bubble formation under anodic bias or the unlikely collapse of the metal film into the flaw to give closer contact with a thinner portion of the oxide. It is difficult to ascribe a conduction reaction under anodic bias in the absence of water with a metal counter electrode.

Since the current flow is so time dependent at low moisture content, it is possible that an electronic mechanism is operative which depends markedly on the absence or presence of water, perhaps affecting some trap levels in the conducting oxide (2).

The influence of water can also be used to explain the marked effects of different metal counter electrodes on the anodic breakdown voltage, with almost no effect produced on the cathodic breakdown voltage (21). In this case, the free energy of formation of the oxide appears to correlate with the ability of the metal counter electrodes to control the moisture level in the anodic film. Electrodes with large negative free energy of formation, such as the Al-Al_2O_3 couple, result in current-voltage characteristics similar to the desiccated sample in the upper trace of Fig. 4, and show little humidity dependence. The large negative free energy of formation for the Al-Al_2O_3 couple may be correlated with its greater adherence which, therefore, provides a high impedance barrier to moisture transpiration.

Electron microscope examination of stripped tantalum oxide films from thin film anodes have revealed a variety of flaws including cracks and recrystallized areas, but these do not appear with the surface density expected from the area variation data.

The rest of this work is concerned with an understanding of the parameters which will eliminate flaw formation as well as direct experimental verification that destructive cathodic breakdown occurs at discrete flaw sites using *in situ* interferometric microscopy. This course has led to more fruitful results than a continued effort to define the flaw-moisture interaction mechanism.

Effect of Composition of Sputtered Tantalum on Breakdown Voltages

The variations in properties of different samples (*e.g.*, see Fig. 3), has impeded the understanding of the mechanisms involved in the conduction process. As discussed above, the moisture and area conditions under which the measurements are made can change the results. Metallurgical parameters in the preparation of sputtered tantalum samples which have been demonstrated to affect the experimental results markedly are the following: (*i*) gaseous impurities (interstitial) (12-15), (*ii*) metallic impurities (substitutional) (16), and (*iii*) sputtering parameters; these determine bcc or β-tantalum formation (22). In what immediately follows only the effects of the interstitial and substitutional impurities are discussed in detail.

One of the principal differences between sputtering vacuum stations is the ambient gas level prior to and during deposition (23). Increasing the content of nitrogen, oxygen, carbon, or hydrogen in the tantalum film in a controlled manner by reactive sputtering has been shown to alter the conduction characteristics severely. This effect can be seen in Fig. 8 for different samples with gold counter electrodes. The maximum relative cathodic breakdown voltage as a function of the reactive gas pressure in Torr has been plotted. The largest changes in the cathodic breakdown voltage for tantalum films reactively sputtered occur at pressures of 5×10^{-5} Torr of oxygen during the sputtering (*i.e.*, 0.25% in Ar or about 12 (atom per cent) in the film). This gives almost symmetric conduction characteristics. However, oxygen pressures less than 10^{-5} Torr have a measurable and reproducibly large effect on the cathodic breakdown voltage. Similar results for other anodic films grown on tantalum sputtered in methane (for the carbon), oxygen, and hydrogen are illustrated in Fig. 8; pressures of these gases of less than 10^{-5} Torr also had large effects on the cathodic breakdown voltages.

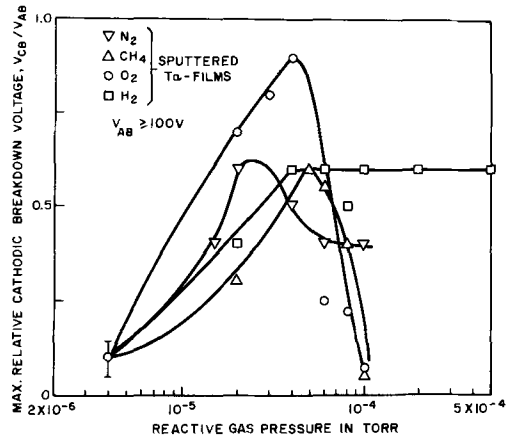

Fig. 8. Maximum relative cathodic breakdown voltage (cathodic breakdown voltage divided by anodic breakdown voltage) vs. reactive gas pressure in Torr for nitrogen, methane, oxygen, and hydrogen (from D. Gerstenberg).

However, the gaseous content of the sputtered tantalum film is but one parameter which determines the properties of the resulting anodic film. An equally important parameter is the metallic impurity content in the tantalum cathode used for the sputtering of the tantalum films (16).

Sputtered alloys of tantalum with molybdenum will be used to illustrate the general effects of alloying on the conduction properties of the thin film tantalum oxide structures, although other metals also have marked effects (16). The preparation of these alloys is illustrated in Fig. 1. The alloying was accomplished by wrapping wires around the cathode as indicated in the figure and then simultaneously sputtering from the wires and the cathode. This yielded uniform films as determined by x-ray fluorescence measurement of the solute element. A tantalum cathode was used whose impurity content was less than 50 ppm per each metallic element in the cathode, with most elements at or below the 10 ppm level. The molybdenum-tantalum alloy films were sputtered in argon under the same conditions which reproducibly gave the lowest cathodic breakdown voltages for tantalum-only controls.

In Fig. 9 the measured anodic and cathodic breakdown voltages are plotted as a function of the atomic per cent of molybdenum as measured in the sputtered films. First, the anodic breakdown voltage is essentially constant up to concentrations on the order of 1-5% of molybdenum in the sputtered film. Second, the cathodic breakdown voltage rises in a semilogarithmic fashion with molybdenum content in the sputtered film. The addition of several hundred parts per million of molybdenum to tantalum cathodes will double the cathodic

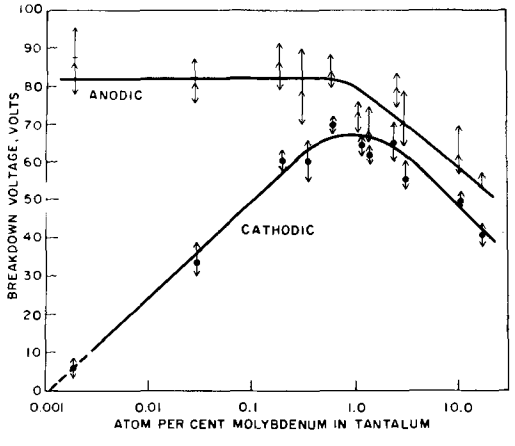

Fig. 9. Cathodic and anodic breakdown voltages vs. the atomic per cent molybdenum in sputtered tantalum films prior to anodization for printed capacitors with gold counter electrodes.

breakdown voltages. Results consistent with this have been obtained using films sputtered from a molybdenum-tantalum alloy cathode. The effect of alloying has been investigated for a wide range of other materials including vanadium, iron, tungsten, cobalt, nickel, copper, gold, and aluminum and, in all cases, over some range of concentration, there has been some increase in the cathodic breakdown voltages.

Thus, changes in the metallic impurities in the cathode and in the ambient residual gas pressures during sputtering can result in changes in the cathodic breakdown of the resulting anodic films; these are, in large measure, responsible for many of the discrepancies seen between thin film samples by different investigators and even between different samples under investigation by the same worker.

The possibility of varying the cathodic breakdown voltage at low concentrations permits further investigation of the flaw problem in a controllable situation. If alloying resulted only in decreasing the density of flaws, then the size of the counter electrode area which has a good chance to be free of flaws should increase with solute concentration. Studies in which counter electrode areas were varied have been made with different concentrations of molybdenum. Measurements consistent with the flaw interpretation, made on separate sets of thin film structures which had been fabricated at different times from different sets of sputtering runs, are shown in Fig. 10.

It is important to note that for small counter electrode areas the breakdown voltages approach constant values; these limiting values are a function of the alloy concentration. Thus, in nominally "flaw-free" films, a homogeneous asymmetric conduction mechanism exists, which can be modified by the addition of alloy agents as molybdenum. This effect may well be associated with band structure modification in the tantalum oxide. The degree of asymmetry in the conduction for these nominally flaw-free films is unusually low; these capacitors appear to have almost symmetric noncatastrophic breakdown voltages.

It should also be noted that the higher concentration alloy films are essentially moisture insensitive; this agrees with the area studies above in which operationally defined flaw-free films are moisture insensitive. There is another interpretation consistent with the area studies on alloy films: instead of, or in addition to, a change in the flaw density there is an alteration of the distribution function over different flaws of the breakdown voltage *vs.* current.

An ion beam probe mass spectrometer has been used to analyze a composite film of (Mo-Ta)-(Mo, Ta)$_2$O$_5$ to verify the presence of Mo in the oxide film. This spectrometer allows analysis of the oxide film in at least 500Å intervals in a 2000Å oxide film. There were positive indications of molybdenum in the anodic oxide films at concentrations compatible with these expected from the grown concentration in the original thin film alloy anode which could also be analyzed.

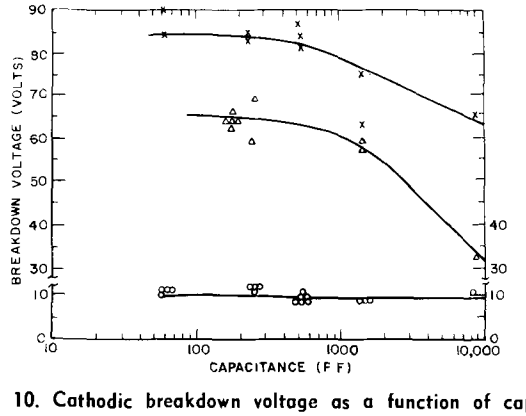

Fig. 10. Cathodic breakdown voltage as a function of capacitance for printed tantalum oxide capacitors formed on sputtered tantalum-molybdenum alloys of different concentrations.

There are some preliminary observations which strongly suggest that the appearance of flaws in the tantalum oxide films are related to minor changes in the surface topography of the sputtered metal film. Additions to the sputtered metal film result in a more uniform metal surface, thereby changing the oxide growth conditions. Tantalum films with a minimum number of microscopic protuberances, or less pronounced protuberances, will result in tantalum oxide films with nearly symmetric I-V characteristics. These conclusions are supported by the *in-situ* microscope observations described in the next section.

Direct Observation of Flaws and Flaw Behavior

Direct observations with a differential interference microscope of flaws, flaws decorated by metallic counter electrodes, growth of the flaws, and irreversible changes at these local inhomogeneities under cathodic voltage provide more direct evidence of the existence and role of the flaws (11).

Tantalum oxide flaws, with and without their surfaces decorated by a thin aluminum counter electrode, are shown in Fig. 11. Decoration by a thick gold counter electrode and the effect of a cathodic voltage are shown in Fig. 12. Here, the irreversible damage at flaws on the application of a cathodic voltage can be seen by comparison of the same field of view before

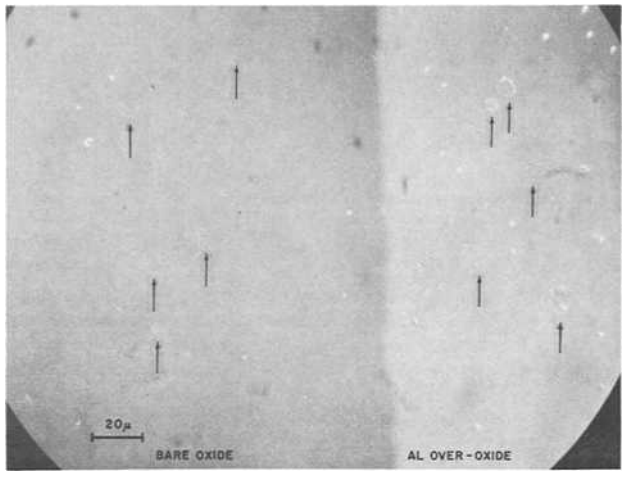

Fig. 11. Nomarski interference microscope (*i.e.*, differential interference microscopy) photograph of tantalum oxide (dark left side of figure) and 400Å aluminum film covering the oxide (light right side of figure). Arrows point to flaws in the oxide and decorated flaws.

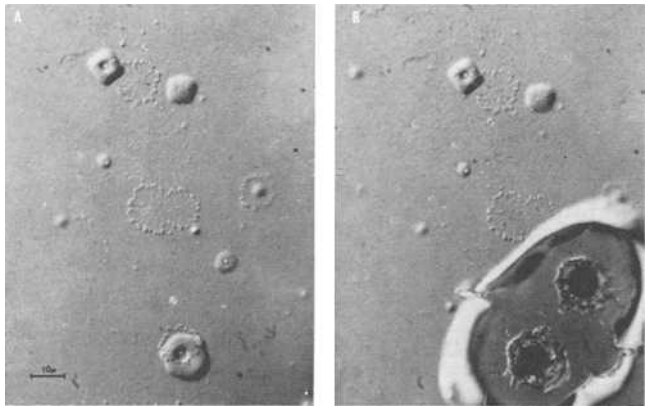

Fig. 12. A (left) Nomarski interference microscope photograph of 2500Å gold counter electrode on tantalum oxide before application of voltage. B (right) Nomarski interference microscope photograph of same field of view as in Fig. 12A after application of cathodic voltage (Ta^-) of 55v.

and after application of voltage; in (A), the flaws are seen before application of voltage, while in (B), the same field of view is shown after application of 55v applied in the cathodic (Ta^-) direction. Similar flaws have been observed, with diameters less than $\frac{1}{2}\mu$ using transmission electron microscopy of carbon replicas. The following observations have also been made using this technique (11):

1. Capacitors have been stressed in the anodic direction to 85v with no optical evidence of irreversible changes; application of 85v in the cathodic direction resulted in irreversible physical changes at the same flaws. This indicates that the flaws are asymmetric in their behavior and supports the hypothesis that the flaws are responsible for the asymmetric conduction.

2. The density of flaws observed under the microscope (*i.e.*, on the order of two per 100μ diameter, or an average area per flaw on the order of 10^{-2} mm^2) as seen in Fig. 11 and 12 is consistent with the order of magnitude of the flaw density obtained from studies of the area dependence of the cathodic breakdown voltage (see Fig. 3). This further supports the hypothesis that the flaws are responsible for the asymmetric conduction.

3. Different flaws in the same field of view have been shown to develop irreversible changes at different rates when the cathodic voltages are applied in steps; these changes stop at different voltages for different flaws in the same field of view. This suggests that the usual method of identifying different conduction mechanisms by the measurement of current-voltage characteristics may only result in the measurement of the distribution function over different flaws of the current-voltage characteristics of the different flaws under one counter electrode.

4. Differential interference microscopic observations of *in situ* growth of flaws indicates that they grow at local imperfections or inclusions in the sputtered tantalum film. Since these films were prepared under clean room conditions, these local imperfections or growths should be less dependent on dirty conditions than such oxide films prepared from sputtered tantalum films deposited under less stringent conditions or from bulk tantalum. Conditions for flaw growth and the flaw density should be different for oxides grown on bulk and thin film tantalum.

5. The current density used for anodization (11, 24), as well as the electrolyte (9), will have an effect on the growth of the flaws.

Summary and Conclusions

The conditions under which the sputtered tantalum films are deposited and the anodic films are grown will strongly affect the conducting properties of the oxide films; the conditions under which the formed films are measured will also determine the results obtained.

Evidence from breakdown measurements as a function of counter electrode area, moisture sensitivity of breakdown voltages, and optical observations indicates that flaws can play a significant role in determining the asymmetric conduction characteristics. It is thought that the presence of metallic and nonmetallic additives in the sputtered film results in a more uniform metal surface which changes the flaw growth during anodization so that the oxide films formed have a less pronounced flaw response.

Previous measurements of the I-V characteristics of tantalum oxide films must be interpreted in the light of results indicating that the flaws may be responsible for the asymmetric conduction and have a distribution of responses on the same film. In order to be meaningful, investigations on conduction mechanisms in tantalum oxide films should demonstrate that the conduction is not flaw dominated; the procedure used here with counter electrodes of different area is a simple method which can be used to establish whether the nominally flaw-free condition has been achieved. This test is only adequate when a counter electrode area of linear dimension of the mean separation between defects is used; in this work, this area is 0.05 mm^2 or less.

Manuscript received Nov. 15, 1968. This paper was presented at the Dallas Meeting, May 7-12, 1967, as Paper 25.

Any discussion of this paper will appear in a Discussion Section to be published in the December 1969 JOURNAL.

REFERENCES

1. A. Guntherschulze and H. Betz, *Ann. Phys.*, **61**, 852 (1931); R. W. Berry and D. S. Sloan, *Proc. IRE*, **47**, 1070 (159); L. Young, "Anodic Oxide Films," Academic Press, New York (1961).
2. N. Schwartz and M. Gresh, *This Journal*, **112**, 295 (1965).
3. Y. Sasaki, *J. Phys. Chem. Solids*, **13**, 177 (1960).
4. H. E. Haring, *This Journal*, **99**, 30 (1952).
5. J. G. Simmons, *Phys. Rev.*, **155**, 657 (1967).
6. J. W. A. Scholte and W. Ch. Van Geel, Philips Research Repts., **8**, 47 (1953).
7. S. Anderson, *J. Appl. Phys.*, **14**, 601 (1943).
8. I. F. M. Walker, *This Journal*, **114**, 55C (1967).
9. D. A. Vermilyea, *J. Appl. Phys.*, **36**, 3663 (1965).
10. M. Kleefstra, *Ann. Radioelect.*, **17**, 223 (1962).
11. N. N. Axelrod, *This Journal*, **114**, 59C (1967).
12. N. Schwartz, M. Gresh, and J. Deaderick, *ibid.*, **109**, 64C (1962).
13. D. A. McLean, N. Schwartz, and E. D. Tidd, *Proc. IEEE*, **52**, 1450 (1964).
14. D. Gerstenberg, *This Journal*, **113**, 542 (1966).
15. D. Gerstenberg and J. Klerer, Proc. Electronic Components Conf., Washington, D. C. (1967).
16. N. N. Axelrod, B. Vromen, H. D. Guberman, D. J. Harrington, and N. Schwartz, *This Journal*, **113**, 51C (1967).
17. M. Read and C. Altman, *Appl. Phys. Letters*, **7**, 5 (1965).
18. D. A. Vermilyea, *J. Appl. Phys.*, **27**, 963 (1956).
19. P. F. Schmidt, F. Huber, and R. F. Schwarz, *J. Phys. Chem. Solids*, **15**, 270 (1960).
20. N. W. Silcox and C. I. Maissel, *This Journal*, **109**, 1151 (1962).
21. N. Schwartz and R. W. Berry, "Thin Film Components" in "Physics of Thin Films," G. Hass, R. E. Thun, Editors, Vol. II, Academic Press, New York (1964).
22. F. Vratny, B. H. Vromen, and A. J. Harendza-Harinxma, *Electrochem. Technol.*, **5**, 283 (1967).
23. J. Sosniak, *J. Vac. Sci. and Tech.*, **4**, 87 (1967).
24. A. Trarusko, N. Ibl, and M. Wiedmer, *This Journal*, **114**, 57C (1967).

Some Evidence for Duplex Film Structuring Within the Anodic Alumina Barrier Layer

G. A. Dorsey, Jr.

Kaiser Aluminum & Chemical Corporation, Department of Metallurgical Research, Spokane, Washington

ABSTRACT

Direct observations of anodic barrier layer oxide, by transmission electron microscopy, provide further evidence for the duplex film structuring suggested earlier, based on infrared data. Anodic films were prepared with a boric acid electrolyte maintained at 60°C and two film layers were observed: the uppermost layer being extremely thin. Only the layer lying next to the metal (primary phase barrier layer) showed a thickness relationship with respect to forming voltage: 14.8 Å/v. The thickness of the uppermost layer (secondary phase barrier layer) was on the order of 200Å and was essentially independent of forming voltage. With the boric acid electrolyte employed at 90°C, a pronounced increase was found in the thickness of the uppermost layer. The thickness of the layer next to the metal surface remained consistent with the ~14 Å/v relationship. Infrared, coating weight, effluent gas detection, and impedance data were also obtained for these coatings and correlated with the data obtained by transmission electron microscopy.

Aluminum, oxidized anodically, may yield coatings that consist of one or more layers. An electrolyte with little tendency to dissolve aluminum oxide, or otherwise interact with the alumina structure, will generally produce only a single nonporous film. Boric acid or near-neutrality ammonium tartrate are examples of this type of electrolyte. Other aqueous electrolytes such as sulfuric, chromic, or phosphoric acids (or organic acids that have the ability to dissolve alumina) will generally yield two anodic oxide layers. The first layer to form is still a nonporous oxide, however further anodic oxidation yields a thicker porous film above this relatively thin layer. Such composite films are referred to as porous layer oxides to distinguish them from coatings that contain only the single nonporous layer. Various models (1-4) for this type of film growth have been proposed and illustrate many of the physical characteristics of these films.

The nonporous oxide is an insulating layer through which current is carried only by ionic diffusion or charge transfer. During the growth of this oxide, the applied voltage must be continually increased in order to maintain a constant rate of formation. If the voltage is increased to some final value (termed the forming voltage) and thereafter maintained constant, the anodization current density will quickly fall to a low value. Indirectly, then, the forming voltage is a measure of the total number of coulombs that were expended toward the formation of this oxide. The thickness of this film is often calculated using an empirical thickness-to-forming voltage relationship of 14 Å/v (5), assuming a negligible or reproducible current flow after forming voltage is attained. Since the voltage drop through this nonporous film constitutes a barrier to further anodic oxidation, this film is commonly referred to as the anodic barrier layer.

Electron microscopy has often been used to study these barrier and porous-layered anodic oxides (1-3, 6-13) via transmission and replication techniques. This has revealed much regarding the pore structure of thick anodic oxides and of the cellular features involved in the growth of both the anodic barrier and porous layers. Barrier layer coatings appear, by electron microscopy, as amorphous pore-free films (12). Only the observation of an ultrastructure at the barrier layer surface (8) suggests the possibility of multilayered effects within this film. Other techniques, however, indicate that there are at least four layered regions of dissimilar electrical resistance (11) within the barrier layer film and, possibly, at least two regions of dissimilar acid solubility (14).

Key words: anodic aluminas, transmission electron microscopy, IR.

Our own work led to a proposal (15-18) based on just such a layering effect since the data suggested a growth mechanism involving a gradual transition from first one barrier layer oxide structure (primary phase) to yield a duplex film structure (primary plus secondary phase of the barrier layer). Deuteration of the anodic barrier layer from aqueous electrolytes implied a hydrogen-bonded trihydrate structure (primary phase barrier layer) whose surface was altered during the course of film formation. This appeared to produce a second barrier layer oxide that was seemingly less dense, with a lower polymer weight, and comprised of μ-hydroxy linkages (secondary phase barrier layer).

While this secondary phase barrier layer is more characteristic of oxides that also contain a porous layer, its structure can also be detected (by IR) in "pure" barrier layer oxide: the latter prepared by conventional methods in boric acid or ammonium tartrate electrolytes. An IR spectrum of the coating surface, via the ATR effect (19), is required to detect this apparently duplex film characteristic since, with these barrier layer films, the secondary phase barrier oxide is present only in the surface region: the bulk of the film being composed of primary phase oxide.

Since these two barrier phases are apparently involved in a growth process through gradual transition, the primary phase may only gradually blend into the secondary phase. There may be no sharp demarkation between them and, unless experimental conditions were sensitive to a subtle differentiation in structuring, such layering effects might not be observable. If such an arrangement actually exists, the duplex barrier layer structure would likely be more apparent, by electron microscopy, with thin films rather than with the thick porous-layered films that are more often studied with this technique.

Oxide solubility is usually low in these barrier layer electrolytes. The oxide is amorphous, by x-ray diffraction, and there is no electrolyte anion incorporation. Accordingly, porous layer oxide is not present in these films: a factor which might otherwise interfere with the detection of the secondary phase barrier layer in cross sections examined by transmission electron microscopy.

Experimental

Anodic aluminas.—Cleaned, etched, and chemically brightened 99.9% Al (alloy 1199) foil coupons were used as the substrate material, and at least four anodized samples were prepared at each of four forming voltages: 20, 50, 100, and 130v. A 2.0M boric acid electrolyte was employed, with stainless steel cathodes, at 60° and 90°C. Anodization was carried out at

25 ma/dm^2 until reaching a preselected forming voltage; afterwards, the current density was allowed to decay to ~3 ma/dm^2 before removing and rinsing the samples. This equilibrium current density (leakage rate) was reached ~ 3 min after attaining forming voltage at 60°C, but *ca.* 15 min were required with the 90°C electrolyte. Two samples were prepared under the latter conditions: a 100v and a 130v coating.

Transmission electron microscopy (TEM).—Thin cross sections of the anodized foils were prepared, using a diamond microknife, with a Reichert OM/U2 ultramicrotome. These were mounted on carbon grids in a Philips EM 100C electron microscope and transmission photomicrographs were obtained at a magnification of 84,000.

The edge of the microknife cut parallel with respect to the anodic oxide, occasionally producing curls in the film. This artifact appears in the photomicrographs as striations that run nearly perpendicular with respect to the metal surface. Also, a layer of carbon, inadvertently deposited on the sample during examination with the electron microscope, sometimes appears as a featureless gray layer at the outer surface of the anodic coating. This film can readily be distinguished from the coating itself, however, by the sharp contrast boundary and by the absence of microknife marks in the carbon layer (further evidence that this is an artifact layer deposited sometime after the anodic film was cross sectioned).

Infrared analysis.—The samples were examined over the 4000-600 cm^{-1} range of the Beckman IR-7, as before (15) using a reflectance attachment set at 45° angle of incidence. These same coating sections, examined by IR, were later cross sectioned for examination with the electron microscope. Thus, we kept a one-to-one correspondence with the data obtained by both techniques.

Far infrared data were not obtained with these samples since earlier work (15) showed that barrier layer oxides absorb, over the range of from 4000 to 35 cm^{-1}, only in the narrow region of 900-to-1000 cm^{-1}.

Effluent gas detection (EGD).—The EGD data were taken in the usual manner, described earlier (20). Since relatively large sample areas were required however, a separate group of samples were prepared at the two lower forming voltages: 20 and 50v. Only the coatings prepared in the 60°C electrolyte were sampled with EGD; the abnormally thick oxide samples (to be discussed later) were not analyzed with the EGD technique.

Impedance measurements.—Impedance measurements were made immediately after anodizing and air drying the same films that were later examined by IR and TEM techniques. The data reported are average values taken from multiple readings with each anodized coupon. A Twin City Testing Corporation Z-Scope (1000 CPS impedance bridge) was employed for these readings, using a 3.5 w/o NaCl media.

Coating weight.—These data were taken in the standard manner (21) using the chromic-phosphoric acid stripping technique. These were the same samples from which sections had been previously removed for impedance, EGD, IR, and TEM measurements. A separate coating weight determination was made with each of the two abnormally thick oxides (prepared in 90°C electrolyte) whereas the remainder, grouped according to forming voltage, were combined for coating weight analysis.

Results and Discussion

Assuming that the rate of oxygen liberation was low or reasonably constant at both electrolyte temperatures, the coatings prepared at 90°C might be expected to be abnormally thick with respect to the forming voltage that was employed. Thicker than would be anticipated from the 14 Å/v relationship, since more coulombs/surface area were expended in their formation.

Based on interpretations of earlier data (15-18), there should be the normal amount (at 14 Å/v) of primary phase oxide in these films. This would be the oxide layer lying next to the metal surface. However the higher electrolyte temperature might be expected to accelerate the postulated transformation rate of primary-to-secondary phase oxide and more than a nominal amount of secondary phase oxide might therefore be found in the barrier layer oxides formed at 90°C (*vs.* 60°C). Note that the secondary phase oxide (if such exists) is still referred to as a form of the barrier layer, even though it is expected that this oxide may be more permeable to the electrolyte (18) and might therefore present only a minor voltage barrier to further oxide growth. Structurally, based on IR data, the secondary phase oxide differs only slightly from the primary phase oxide and appears to form as a gradual transition product of the primary phase. There is no evidence of Al-O-Al linkage in either oxide phase, which is normally associated with a porous layer oxide, nor is there any detectable porosity in these boric-acid-anodized films (this may be seen in the data that follow and in the earlier literature dealing with electron microscopic surface examinations of these same type of films). We will therefore continue to refer to secondary phase oxide as a form of the barrier layer even though the expected characteristics of this oxide do not necessarily constitute a voltage barrier to further anodic oxidation.

Figure 1 shows the coating weight values (micrograms per square centimeter) plotted *vs.* forming voltage for these barrier layer oxides. The two abnormally thick films (abnormal, judging from the anodizing response) show as clearly displaced points above the normal values: at 100 and 130v, respectively. With the exception of these two points, the coating weight data fit a linear relationship with respect to forming voltage. Essentially the same relation may be seen in Fig. 2, which is a plot of total barrier layer IR absorbance *vs.* forming voltage: primary-plus-secondary phase absorbance, since IR cannot accurately distinguish between various admixture compositions.

Again there are two points that are out of line with the remainder. These two points were from the same films that yielded abnormally high coating weight values. Unlike the coating weight determinations which, for weighing accuracy, required a combining of all samples from the same forming voltage, the IR data show individual points for the four separate films that were prepared at each forming voltage. However the

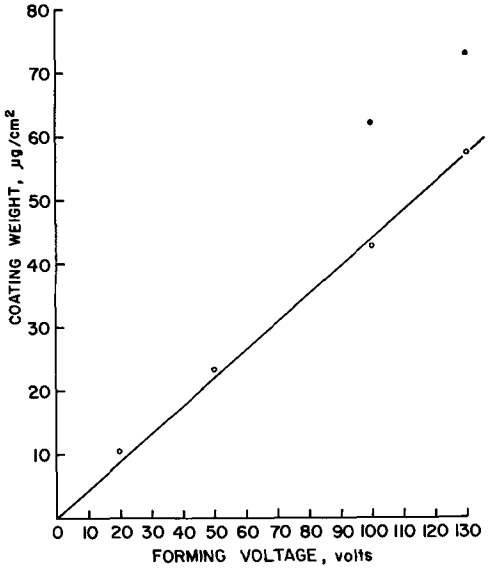

Fig. 1. Coating weight vs. forming voltage. (Solid circles are for abnormally thick films.)

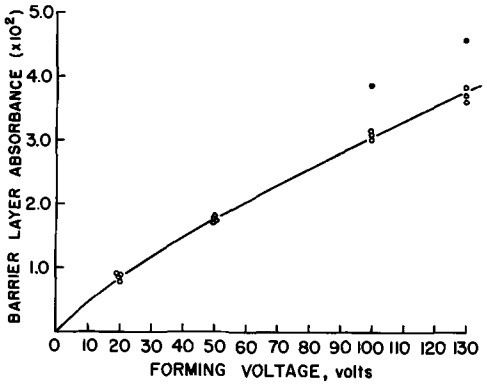

Fig. 2. Infrared absorbance (amount) of barrier layer coatings vs. forming voltage. (Solid circles are for abnormally thick films.)

IR data do not fit a linear relationship with respect to forming voltage; instead, the data seem to give better fit to a curve, as shown in Fig. 2.

Since barrier layer oxides are known to follow a linear thickness-*vs.*-forming voltage relationship (~ 14 Å/v) these IR data present an anomaly. If there are two oxide phases in the barrier layer, but if only one has an appreciable thickness dependence on forming voltage, then this might explain the apparent anomaly in the IR data. However, in order to resolve this question, it would be necessary to determine the various proportions of primary and secondary phases in each of these films.

If such data are to be available at all, then they must come from an examination of the transmission electron microscope data. Earlier reasonings would predict a dark glass-like layer lying next to the metal surface: a low-ordered trihydrate gel, as was suggested (17) in describing the primary phase barrier layer. The thickness of this layer should fit with a nominal 14 Å/v relationship to the forming voltage. Above this layer, there may be a more open structure, less dense and therefore appearing somewhat lighter (more transmittant to the electron beam) in contrast to the lower-lying oxide. This oxide would, as it has been described, be the postulated secondary phase of the barrier layer.

Further, the electron photomicrographs should show an abnormally thick oxide with the two film samples that were prepared at 90°C and gave high values in the coating weight and IR data. The thickness of the primary phase, in these abnormal oxides, should be about the same as that found in all other coatings prepared at the same forming voltage. Only the thickness of the secondary phase (if it can be located in these films) should be different: thicker, perhaps nearly as thick as the primary phase itself.

Figure 3 shows two photomicrographs of coatings prepared with a 20v forming voltage. A carbon deposit is evident on both, but there seemingly are two layers present although the uppermost layer shows only as a thin light band. Figure 4 shows a photomicrograph of a coating formed at 50v. Again there is a lighter uppermost layer, but somewhat thicker than before and better defined. A carbon film still shows but is easily recognized by its light gray shading and by the absence of microknife mark striations that appear in the lower two layers.

Figure 5 shows cross sections of a pair of 100v coatings. Figure 5b is of a coating that appeared to be abnormally thick, seemingly because of an excess of secondary phase barrier layer oxide. The uppermost layer gives the appearance of being composed of a closely packed columnar oxide. It is quite possible, however, that this is an artifact caused by a curling action induced by the cross-cut of the microknife, with this less dense, softer, oxide.

An additional pair of photomicrographs, Fig. 6, exhibit essentially the same features as were seen in Fig. 5. Figure 6b is a cross section of a coating prepared with a 130v forming voltage, but one which yielded abnormally high coating weight and IR absorbance values (total barrier absorbance: primary-plus-secondary layers). The cross section shown in Fig. 6a is also of a 130v coating, but one with a lower coating weight and lower IR barrier layer absorbance.

Quantitative data from these (and their companion) photomicrographs may be seen in Fig. 7, which gives

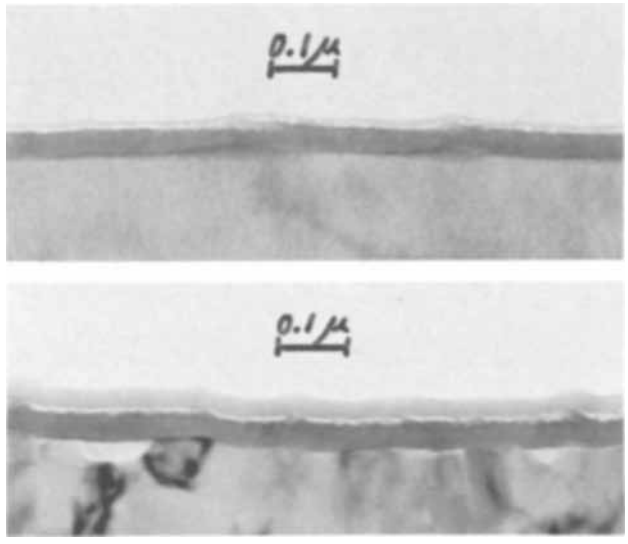

Fig. 3. (a, top, and b, bottom). Cross sections of 20v barrier layer coatings at 84,000 magnification.

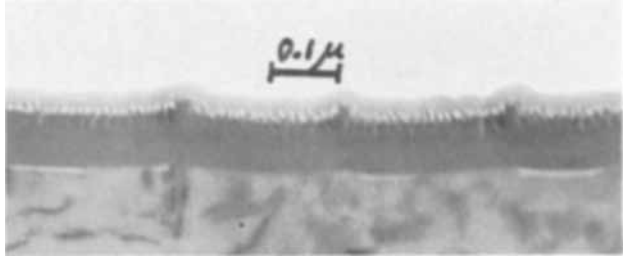

Fig. 4. Cross section of 50v barrier layer coating at 84,000 magnification.

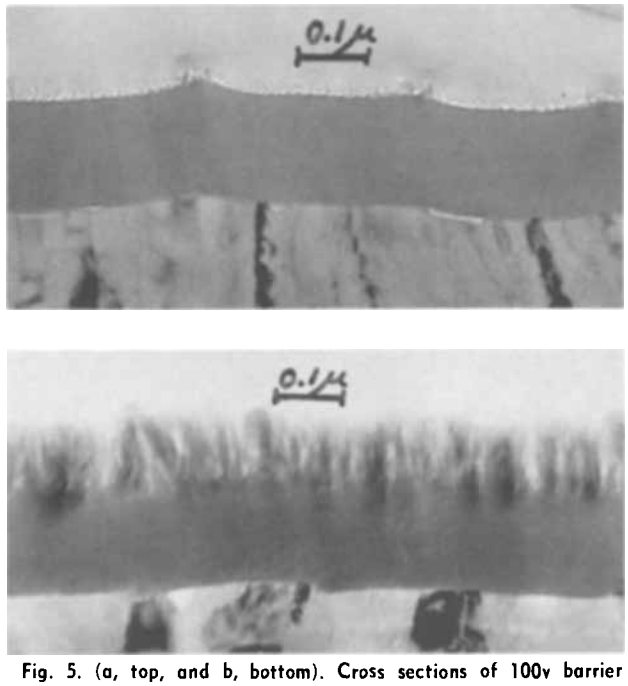

Fig. 5. (a, top, and b, bottom). Cross sections of 100v barrier layer coatings at 84,000 magnification.

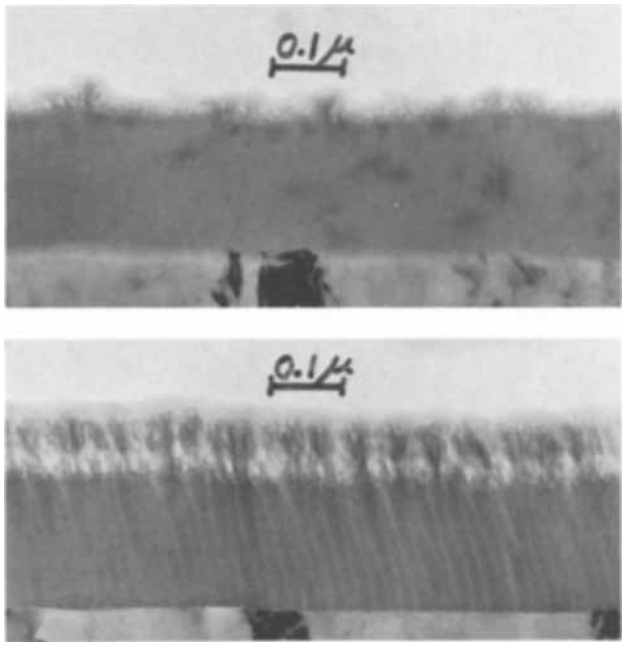

Fig. 6. (a, top, and b, bottom). Cross sections of 130v barrier layer coatings at 84,000 magnification.

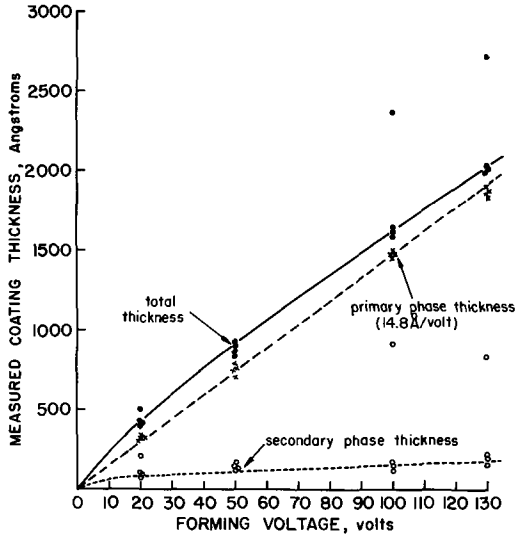

Fig. 7. Measured coating thicknesses (Å) vs. forming voltage

the measured coating thickness data for each group of four coatings that were prepared at the four forming voltages. Three plots are shown, *vs.* forming voltage: total coating thickness, primary phase layer thickness, and secondary phase (uppermost layer) thickness. Even with the abnormally thick coatings (primary-plus-abnormally thick secondary phase barrier layer films) the plot of primary phase barrier layer thickness is linear with respect to forming voltage: 14.8 Å/v. The plot of total coating thickness, *vs.* forming voltage, is displaced upward from this and appears to fit a curve (as do the IR data, Fig. 2) rather than a linear relationship. This is due to the presence of the secondary phase barrier layer, whose thickness seemingly is altered by changes in the anodizing conditions.

There does appear to be a slight thickness increase of this layer as the forming voltage increases: ~ 0.8 Å/v. However the thickness of the secondary phase oxide may be governed more by the temperature and (though minor) by the dissolving action of the electrolyte: both influencing the rate of primary-to-secondary phase transformation. The apparent secondary

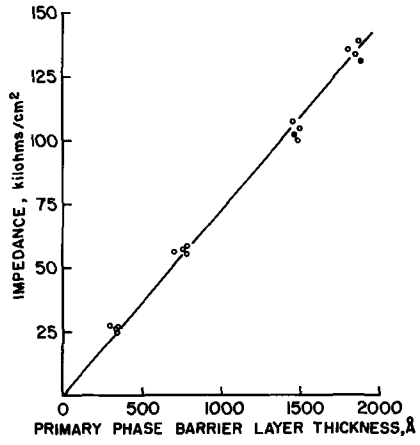

Fig. 8. Impedance values *vs.* primary phase barrier layer thicknesses. (Solid circles are for films with abnormal total thicknesses.)

phase thickness-to-voltage dependence may only be an indirect indication that, at higher forming voltage, the coatings were exposed to the electrolyte for longer time periods.

Figure 8 shows the impedance values that were obtained with these coatings: normal and abnormally thick coatings. As discussed by Hoar and Wood (22), these measured impedance values (at 1000 cps) are due, mainly, only to the capacitance of the barrier layer: not to resistive effects. However there was no measurable difference in impedance between coatings prepared at the same forming voltage regardless of the total coating thickness. This indicates that the impedance of the secondary phase (whatever its actual value) is negligible compared to that of the primary phase barrier layer. It is apparently permeable to the electrolyte and should therefore also have a negligible thickness dependence on forming voltage.

Figure 9 shows EGD data for some of these coatings: those that were normal in thickness, not abnormally thick. The plot is linear with respect to forming voltage and fits with data that were presented and discussed earlier (20). It is interesting to note that, below 300°C, these coatings lost only 1.1 w/o (weight per cent) water *vs.* the 23% water loss experienced by mineralogical trihydrates, when the latter are heated under the same conditions (23). As reported earlier (20) there are indications that the barrier layer oxides lose most of their water of hydration above 400°C, which would indicate a surprisingly tightly bound hydrate network for the primary phase oxide.

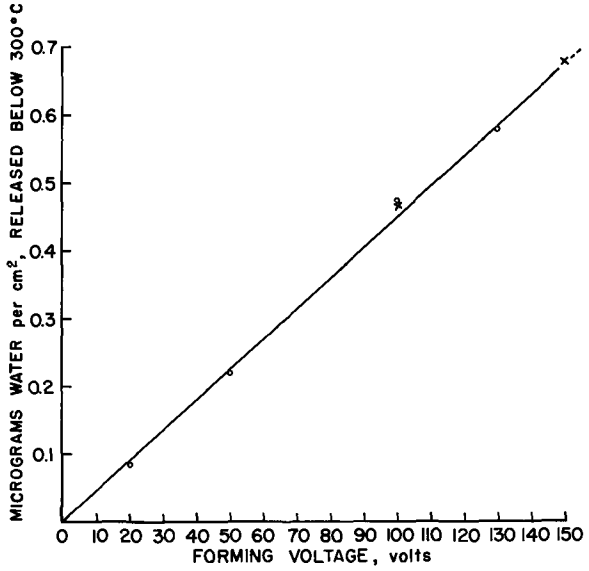

Fig. 9. Effluent gas data (μg H_2O/cm^2) for coatings *vs.* forming voltage. (x points are data points taken from earlier paper (20).)

While there is seemingly reasonable correlation between these various data and discussions, there is one final point that now needs to be developed. With IR data, there is little to distinguish between various admixtures of primary and secondary phase barrier layer oxides. Admixture films prepared in boric acid are especially difficult in this respect since the postulated secondary phase still apparently has a high polymer weight.

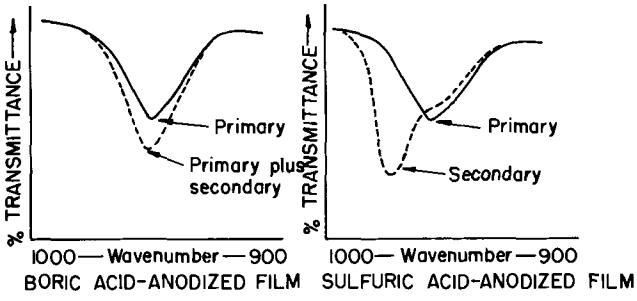

Instead of a band shift with increased quantities of secondary phase, only the band absorbance markedly changes when the barrier film is prepared in boric acid. However, whether the absorbance is due to "pure" primary phase oxide or due to an admixture of primary-plus-secondary phases, the total absorbance of this IR band should correlate with the total thickness of oxide present: thickness as determined independently from the electron photomicrographs.

To make this correlation, it is first necessary to determine the densities and absorbancy indices of the primary and secondary phase barrier layers. This can be done by combining the available data for coatings prepared at a single forming voltage (where the primary phase thicknesses are equal) but where there is a wide variation in secondary phase thickness (itself not a direct function of forming voltage). For coatings prepared at a forming voltage of 100v, the calculated density and absorbancy index values are given in Table I.

Using these single values, with the Beer's law relationship, an "expected IR absorbance" can now be calculated with any of the barrier layer coatings for which electron microscope data are available.

The ratio of primary and secondary phases varied widely among the various barrier layer oxides that were prepared. Still the calculated IR absorbance values, from the electron microscope thickness data, should match with those values found experimentally. This is assuming that there is a one-to-one correlation between the IR identification of primary and secondary phase barrier layer oxides and the duplex layered film effect found by transmission electron microscopy.

Figure 10 shows a plot of calculated-*vs.*-experimental absorbance for each of these barrier layer coatings. This includes coatings with either extreme in secondary phase thickness. The plot is linear and the calculated values fit the experimental data to within 5%. This, and with the preceding discussion,

Table I. Calculated density and absorbancy index values

Oxide type	Density, g/cm³	Absorbancy index, cm²/g
Primary phase barrier layer	2.73	7.34×10^2
Secondary phase barrier layer	2.41	4.13×10^2

Table II. Data obtained with oxide aged in electrolyte

Initial voltage "A," v	Final voltage "B," v	Primary phase thickness, Å At "A"	At "B"	Secondary phase thickness, Å At "A"	At "B"
100	85	1460	1300	210	550

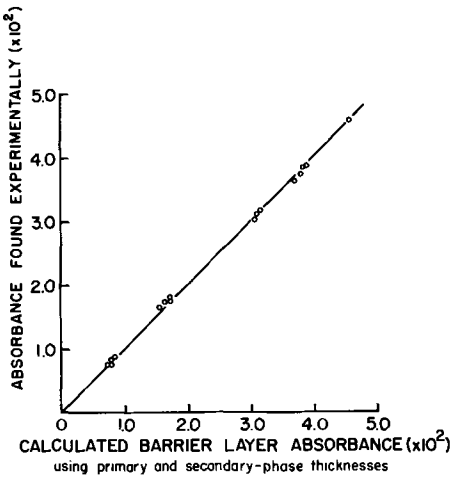

Fig. 10. Calculated IR absorbance data, from coating thickness values, *vs.* experimental absorbance values for each barrier layer coating.

would seemingly indicate that the primary and secondary phases of the barrier layer exist and can be separately identified. The conditions under which these samples were prepared, and the earlier discussion regarding similarities of primary and secondary phase barrier layer IR absorption, argue in favor of regarding the secondary phase as a form of nonporous barrier layer, rather than as a form of porous layer.

One further note regarding the transitions involved with these barrier layer oxides: some cursory data are given in Table II. Primary phase thicknesses were taken by impedance measurements, using the calibration given in Fig. 8, and the secondary phase thickness values were taken from IR data: total absorbance less primary phase absorbance calculated from the impedance estimates of primary phase thickness.

A coupon was taken to the 100v forming voltage, in 2.0M boric acid at 60°C, and then allowed to reach a nominal leakage rate. Afterwards, a section was removed for analysis and the remainder was re-exposed to the boric acid electrolyte for 3 hr at 60°C and 85v.

This type of behavior is essentially the same as the Recovery Effect described by Murphy (24) and Michelson (25). They too discuss a transition effect and, in this respect, their interpretation parallels the preceding discussion.

Acknowledgment

We are indebted to A. T. Melville, D. J. Blew, and Mrs. R. A. Woods, of this laboratory, for their skill and patience in operating the ultramicrotome and obtaining the electron photomicrographs that form the basis of this paper. The author also wishes to thank the Kaiser Aluminum & Chemical Corporation for its support of this work and for its permission to publish these results.

Manuscript submitted Nov. 1, 1968; revised manuscript received Jan 16, 1969.

Any discussion of this paper will appear in a Discussion Section to be published in the December 1969 JOURNAL.

REFERENCES

1. F. Keller, M. S. Hunter, and D. L. Robinson, *This Journal*, **100**, 411 (1953).
2. H. Ginsberg and K. Wefers, *Metall.*, **17**, 202 (1963).
3. H. Akahori, *J. Electronmicroscopy*, **10**, 175 (1961).
4. J. F. Murphy and C. E. Michelson, Proceedings of the Symposium on Anodizing Aluminum, Nottingham University, September 1961. Published by the Aluminum Development Association, London (1962) p. 83 ff.
5. W. Ch. van Geel and B. J. J. Schelen, *Philips Research Rept.*, **12**, 240 (1957).

6. M. Gyenes-Hollo, *Acta Met.*, **8**, 265 (1960).
7. P. E. Doherty and R. S. Davis, *J. Appl. Phys.*, **34**, 619 (1963).
8. J. C. Grosskreutz and G. G. Shaw, *ibid.*, **35**, 2195 (1964).
9. S. Tajima, *Metall.*, **18**, 581 (1964).
10. G. Paolini, M. Masocro, F. Sacchi, and M. Paganelli, *This Journal*, **112**, 32 (1965).
11. A. J. Brock and G. C. Wood, *Electrochim. Acta.*, **12**, 395 (1967).
12. H. A. Francis, *This Journal*, **112**, 1234 (1965).
13. G. C. Wood, J. P. O'Sullivan, and B. Vaszko, *ibid.*, **115**, 618 (1965).
14. D. Altenpohl, *Inst. Radio Engrs. Com. Rec.*, **111**, 35 (1954).
15. G. A. Dorsey, Jr., *This Journal*, **113**, 169 (1966).
16. G. A. Dorsey, Jr., *ibid.*, **113**, 172 (1966).
17. G. A. Dorsey, Jr., *ibid.*, **113**, 284 (1966).
18. G. A. Dorsey, Jr., *ibid.*, **115**, 1053 (1968).
19. J. Fahrenfort, *Spectrochem. Acta*, **7**, 698 (1961).
20. G. A. Dorsey, Jr., *This Journal*, **115**, 1057 (1968).
21. ASTM Test Method B 137.
22. T. P. Hoar and G. C. Wood, *Electrochim. Acta*, **7**, 333 (1962).
23. G. A. Dorsey, Jr., *Anal. Chem.*, **41**, 350 (1969).
24. J. F. Murphy, *Plating*, **54**, 1241 (1967).
25. C. E. Michelson, *This Journal*, **115**, 213 (1968).

Luminescence from Erbium-Activated Group II-VI Compounds Containing Alkali Metal Compensators

S. Larach,* R. E. Shrader, and P. N. Yocom*

RCA Laboratories, Princeton, New Jersey

ABSTRACT

Group II-VI compounds, doped with trivalent erbium, were prepared with alkali-metal compensators. Striking differences are found in the emission spectra, with respect to intensity and spectral character, and the suppression in host-lattice-emission in lithium-compensated materials. The temperature dependence of the $^4S_{3/2} \rightarrow {}^4I_{15/2}$ and $^2H_{11/2} \rightarrow {}^4I_{15/2}$ transitions was studied. Emission appearing with $^4I_{15/2} \rightarrow {}^4G_{11/2}$ excitation was found and was assigned tentatively to the $^2H_{9/2} \rightarrow {}^4I_{13/2}$ transition. A model is proposed for the observed transitions.

Luminescence from rare earths in II-VI compounds has been of interest for many years (1). Such materials have a discrete ion as the principal source of luminescence emission, the f-f transitions yielding narrow emission bands or lines. As part of a general program on the luminescence of rare earths in II-VI compounds, we wish to treat, in this paper, the effect of alkali-metal ions on the luminescence properties of trivalent erbium in zinc sulfide type materials.

Some optical properties of zinc sulfide containing erbium have been reported by Trapeznikova and Shchaenko (2) for materials prepared with fluxes or coactivators as consisting apparently of band and line emission. Rothschild (3) reported that erbium intensified the emission from silver in zinc sulfide, and that phosphors activated with copper and erbium show the expected emission due to copper, and in addition, lines due to erbium at 5300 and 5480Å. However, with erbium alone in zinc sulfide, Rothschild obtained no luminescence. In 1958, luminescence from erbium in zinc sulfide was reported by Trapeznikova (4) as lines superimposed on broad bands, while in 1963, it was reported by Goldsmith *et al.* (5) that electroluminescence from erbium in zinc sulfide could be obtained as the characteristic rare-earth lines, with minimum broad-band emission. Levshin *et al.* (6) reported in 1965 on the cathodoluminescence of zinc sulfide containing rare earths (prepared without coactivator), and found that erbium showed intensive lines at 549, 533.5, and 527.6 mμ. Also in 1965, Kingsley *et al.* (7) reported on short-range energy transfer from noble metals to rare earths, including erbium, in II-VI compounds, and recently Kingsley and Aven (8) published on epr and fluorescence from erbium in zinc selenide containing copper. The general effect of alkali-metal charge compensation on rare earths in II-VI compounds has been reviewed by Larach (9) and is applied to erbium in zinc sulfide in the present paper.

* Electrochemical Society Active Member.

Materials

The ZnS used in the preparation of these materials was luminescent grade, RCA 33-Z-19. To this base material the various doping ions were added as aqueous sulfate solutions. Enough deionized water was then added to make a smooth slurry, and the *p*H was raised to the basic region with NH_4OH. The slurry was then evaporated to dryness. In the cases of the nonalkali-containing samples, manipulations were carried out using polyethylene vessels. Concentrations are in mole per cent.

The firing of the samples was performed under a slow flow of H_2S at 1150°C. The firing was done in a fused silica tube in which the sample was held in a purified fused silica ("spectrasil") boat. Before firing the rare earth-containing samples, the tube and boat were fired with three consecutive, hour-long firings of the undoped ZnS for scavenging purposes. These special firing methods were evolved to achieve reproducibility from sample to sample, as well as to minimize "host-lattice" emission, which, however, could not be eliminated except with alkali-metal additives.

Measurements

Emission spectra were obtained using "host lattice" absorption, *i.e.*, 3280Å at room temperature, and f-f absorptions, as indicated. Due to the temperature dependence of the absorption characteristic, the exciting wavelength was changed with temperature. The exciting wavelength was obtained with a Bausch and Lomb 500 mm grating, in conjunction with a 150w d-c xenon arc lamp. Emission spectra were obtained photoelectronically with a Spex Czerny-Turner grating monochromator, capable of resolving 0.3Å in first order.

Results

Excitation spectra.—That the addition of an alkali-metal affects the basic electronic processes in ZnS is

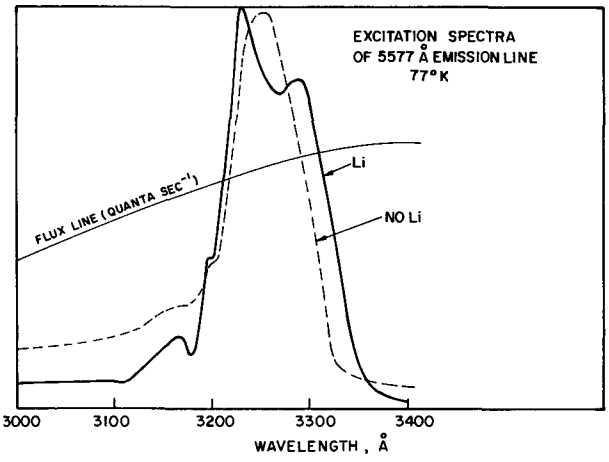

Fig. 1. Excitation spectra of the 5577Å emission from ZnS:Er and ZnS:Er:Li (77°K).

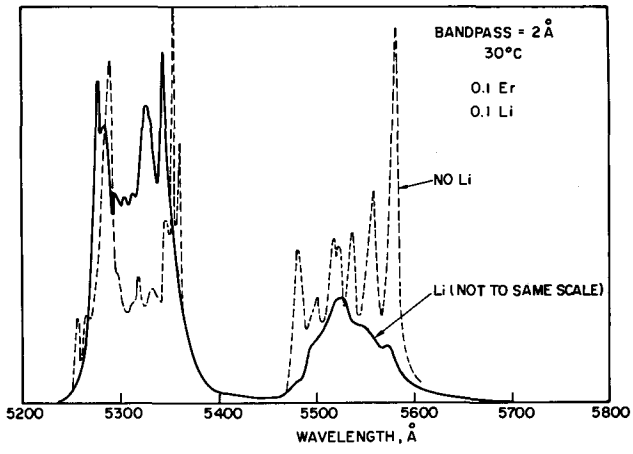

Fig. 3. Emission spectra of manifolds I and II, expanded scale, 30°C, 2Å bandpass. Note that the two spectra are not to the same scale.

shown in Fig. 1. This is a portion of the excitation spectrum of ZnS:Er, with Li and without Li, taken at 77°K. We see that the essentially unstructured excitation spectrum of the non-Li material is changed to a structured spectrum with addition of Li. The structure below 3200Å can be related to host-lattice effects observed in absorption spectra of ZnS materials; however, note the new structure at about 3285Å introduced by Li addition. The flux line (quanta sec^{-1}) is also shown in Fig. 1.

Emission spectra.—The broad-band "lattice-emission," due to vacancies compensated by the rare earth in ZnS (9), is present in ZnS:Er, as shown by curve 1 of Fig. 2. In addition to the broad band peaking at about 4500Å, there are two emission manifolds present, one (I) with a center of gravity at about 5300Å, due to the $^2H_{11/2} \rightarrow {}^4I_{15/2}$ transition, and one (II) manifold centered at about 5500Å, due to the $^4S_{3/2} \rightarrow {}^4I_{15/2}$ transition. Curve 2 is for ZnS:Er:Li, taken with no change in instrumental gain. We see that with Li addition, (*i*) the broad band emission is not detectable, (*ii*) manifold I has increased greatly in intensity, and (*iii*) the smaller increased intensity of manifold II is accompanied by a degradation in the fine structure, and (*iv*) a band at about 4900Å appears, attributable possibly to $^4F_{7/2} \rightarrow {}^4I_{15/2}$ emission. Some of these effects are shown in Fig. 3, where manifolds I and II are shown, with 2Å band-pass. We can clearly see the fine-structure effects of the Li-additive in manifold I, and the degradation of manifold II with Li addition.

The effects of excitation energy are of interest. Thus, as shown in Fig. 4, when 3815Å excitation, which is f-f

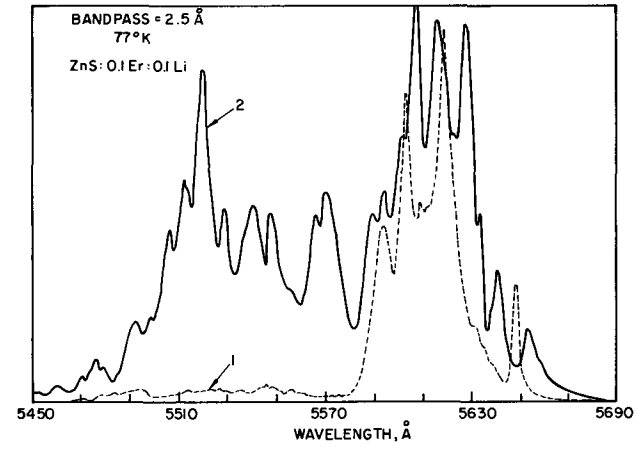

Fig. 4. Emission spectra as a function of exciting wavelength for ZnS:0.1Er:0.1Li; 77°K; curve 1 3815Å excitation, curve 2 3200Å excitation.

in nature, is used, the emission spectrum designated as curve 1 is obtained, at 77°K. When excitation in the host-lattice is used, such as 3200Å, the emission spectrum shown as curve 2 is obtained. It is interesting to compare the results of Fig. 3 and 4. The structured emission from manifold II at room temperature (Fig. 3) terminates close to 5600Å. However, at 77°K, new emission structure appears beyond 5600Å, which is a function of excitation energy (Fig. 4). The materials described in Fig. 5 consist of 0.01 Er and 0.01 Li.

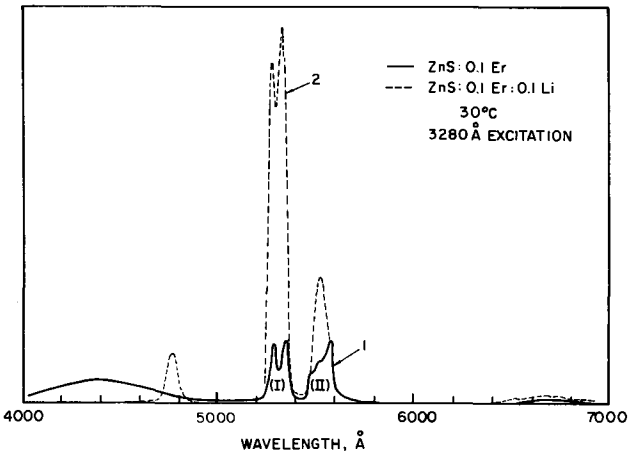

Fig. 2. Spectral distribution curves of photoluminescence from curve 1 ZnS:0.1Er and curve 2 ZnS:0.1Er:0.1Li, under 3280Å excitation (30°C).

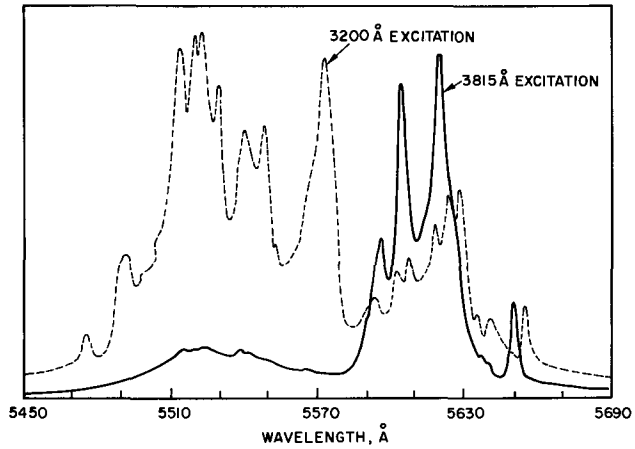

Fig. 5. Emission spectra as a function of exciting wavelength for ZnS:0.01Er:0.01Li; 77°K.

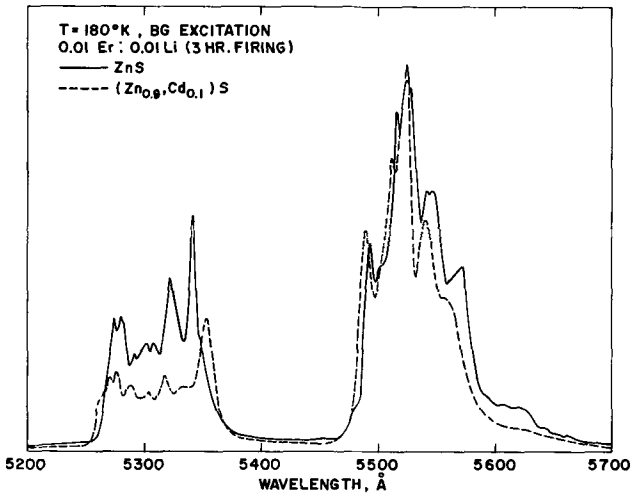

Fig. 6. Emission spectra from ZnS and $(Zn_{0.9}Cd_{0.1})S$, both with Er and Li.

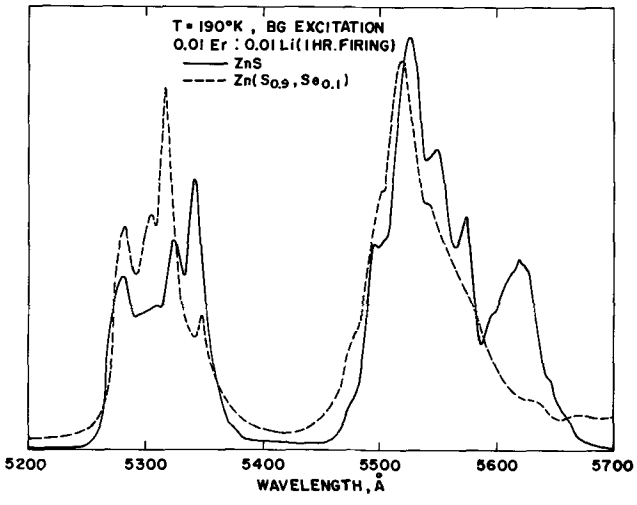

Fig. 7. Emission spectra from ZnS and $Zn(S_{0.9}Se_{0.1})$, both with Er and Li.

Again, we note qualitatively similar effects when 3815Å is used and when 3200Å is used, although quantitative differences are discernible between the two concentrations. The effect of solid solutions of zinc sulfide with cadmium sulfide and with zinc selenide is shown in Fig. 6 and 7. Although the major part of this work was done with lithium as the compensator, similar effects were noted with sodium and with potassium.

Temperature dependence.—The temperature dependence of manifolds I and II is shown in Table I. It is seen that with decreasing temperature, manifold I decreases in intensity. We note that at about 200°K, a new emission (IIA) appears after manifold II, [as we have seen in Fig. 4 at 77°K] which is also shown as a function of temperature. This emission can probably be assigned to $^2H_{9/2} \rightarrow {}^4I_{13/2}$.

Table I. Integrated areas of manifolds I, II, and IIA as a function of temperature

Temp, °K	I	II	IIA	I/[I + II + IIA]	I/[I + II]
333	7.46	1.76		81	81
294	6.40	1.86		77	77
277	4.46	1.76		72	72
256	2.66	1.70		61	61
232	2.55	2.37		53	53
208	2.35	2.80	0.98	39	35
189	1.74	2.91	1.25	29	38
182	1.33	3.10	1.40	23	30
139	0.81	3.23	1.35	15	20

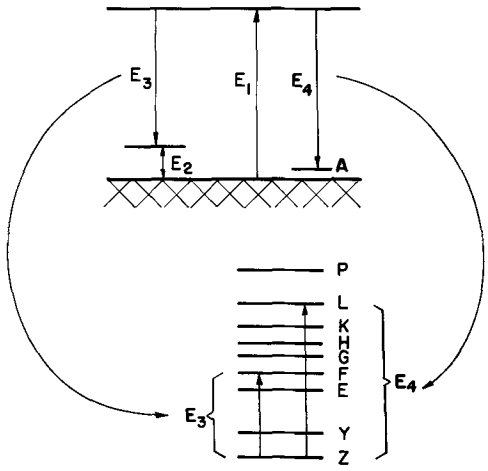

Fig. 8. Proposed model for erbium in zinc sulfide. Arrows upward indicate excitation, arrows downward indicate emission, and the curved arrows indicate energy transfer.

Proposed Model

Bandgap excitation of ZnS:Er results preponderantly in $^2H_{11/2} \rightarrow {}^4I_{15/2}$ and $^4S_{3/2} \rightarrow {}^4I_{15/2}$ emissions. This would indicate that of the roughly 3.7 ev excitation, only about 2.3 ev is available for exciting the erbium ion. This would be the case if the model was that shown in Fig. 8, where $E_2 = 1.4$ ev, and would be the upper limit to the optical acceptor depth, relative to the valence band. Dieleman *et al.* (15) have reported an acceptor depth for alkali metals in cubic zinc sulfide as 1.4 ev. Thus, with bandgap excitation, the energy available for exciting trivalent erbium via an Auger-type transfer would give rise to $^4S_{3/2}$ and $^2H_{11/2} \rightarrow {}^4I_{15/2}$. Level "A" is an acceptor which is available for recombination only at temperatures below 200°K, to excite, via Auger transfer, $^4G_{11/2}$ and/or $^2H_{9/2}$, to yield the manifold IIA emission. However, when 3820°Å photons are used as the exciting source, $^4I_{15/2} \rightarrow {}^4G_{11/2}$ excitation takes place, with $^2H_{9/2} \rightarrow {}^4I_{13/2}$ emission. This emission can also be obtained by exciting into $^2H_{9/2}$ directly from $^4I_{15/2}$ with 4110Å photons.

Site Multiplicity

In the system such as the one under investigation, the problem of site multiplicity and its effects on the luminescence from the rare earth is of great importance. Thus, many of the effects can be interpreted, at least qualitatively, on the basis of erbium in different sites. Another aspect of site multiplicity is indicated in Fig. 4 and 5, where, when Z—K excitation is used, another type of emission spectrum is obtained, as against indirect (bandgap) excitation. ESR-investigations of rare earths in II-VI compounds have been reported recently by Schneider (16) as indicating the existence of a large number of defect centers formed by the rare earth ion associating with, for example, lithium.

Manuscript submitted Nov. 22, 1968; revised manuscript received *ca.* Jan 8, 1969.

Any discussion of this paper will appear in a Discussion Section to be published in the December 1969 JOURNAL.

REFERENCES

1. See for example, H. Tomaschek, *Ann. Phys.*, **75**, 109 (1924).
2. Z. A. Trapeznikova and V. V. Shchaenko, *Sov. Phys. Dokl.*, **1**, 28 (1956).
3. S. Rothschild, *Proc. Intl. Conf. Sol. State Electr. Telecomm*, **4**, Pt. 2, 705 (1958).
4. V. S. Oranovskii and Z. A. Trapeznikova, *Opt. i Spektros.*, **5**, 302 (1958).
5. Goldsmith, Larach, Shrader, and Yocom, *Solid State Comm.*, **1**, 25 (1963).

6. Levshin, Fridman, Chikhacheva, and Shchaenko, *Izv. Akad. Nauk SSSR-Fiz.*, **29**, 500 (1965).
7. Kingsley, Prener, and Aven, *Phys. Rev. Letters*, **14**, 136 (1965).
8. J. D. Kingsley and M. Aven, *Phys. Rev.*, **155**, 235 (1967).
9. S. Larach, *Proc. Int'l. Conf. Lum., Budapest* (1966), 1549 (1968).
10. F. Varsanyi and G. H. Dieke, *J. Chem. Phys.*, **36**, 2951 (1962).
11. S. A. Pollack, *J. Chem. Phys.*, **40**, 2751 (1954).
12. L. G. Van Uitert and L. F. Johnson, *ibid.*, **44**, 3514 (1966).
13. Halperin, Chu, Haber, and Dropkin, "II-VI Semicond. Compounds," p. 68, D. G. Thomas, Editor, Benjamin, New York (1967).
14. S. Larach, R. E. Shrader, and P. N. Yocom, *7th* Rare Earth Resch. Conf., Coronado, Calif. (1968).
15. J. Dieleman, J. W. DeJong, and T. Meijer, *J. Chem. Phys.*, **45**, 3178 (1966).
16. J. Schneider, "II-VI Semicond. Compounds," p. 64, D. G. Thomas, Editor, Benjamin, New York (1967).

Evidence for Eu^{+3} Emission from Two Symmetry Sites in $Y_2O_3:Eu^{+3}$

H. Forest and G. Ban

Zenith Radio Corporation, Chicago, Illinois

ABSTRACT

In $Y_2O_3:Eu^{+3}$ two possible symmetry sites exist for the Eu^{+3} ions, namely S_6 and C_2. The emission spectrum is primarily due to C_2 Eu^{+3} ions but two additional lines are reported corresponding to S_6 Eu^{+3} emissions. The lines were identified by their long lifetime relative to the C_2 emission and represent the Stark splitting of the $^5D_0 \rightarrow {}^7F_1$ transition. This is a pure magnetic dipole transition in S_6 symmetry and consequently has a low oscillator strength. The $^7F_0 \rightarrow {}^5D_1$ absorption transition due to S_6 Eu^{+3} has also been identified. Similar results have been found for the low temperature form of $Gd_2O_3:Eu^{+3}$, which is isostructural with $Y_2O_3:Eu^{+3}$.

Y_2O_3 is a well-known phosphor host material for trivalent activators which are believed to substitutionally occupy Y^{+3} sites (1). The crystal structure of Y_2O_3 is of the rare-earth sequisoxide C-type in which each Y^{+3} ion is surrounded by six oxygens located at the corners of a cube (2). Two of the corners are vacant and can be along a body or face diagonal of the cube which results in two Y^{+3} site symmetries, namely S_6 [1] or C_2, respectively. This is shown in Fig. 1. The unit cell consists of two types of alternating Y^{+3} layers, one composed of only C_2 sites and the other composed of an equal number of S_6 and C_2 sites; the ratio of C_2 to S_6 sites is 3 to 1.

There is some evidence based on paramagnetic studies on $Y_2O_3:Yb^{+3}$ by Mandel and luminescence studies on $Y_2O_3:Bi^{+3}$ by Toma and Palumbo to suggest that in Y_2O_3 activated phosphors, the activator substitutes for both C_2 and S_6 Y^{+3} ions (3). Chang and Gruber in their study of the absorption and luminescence of $Y_2O_3:Eu^{+3}$ have assigned all of their reported emissions to Eu^{+3} ions located at C_2 sites (4). No emissions were found due to S_6 Eu^{+3} ions; however, in the absorption spectrum they report five lines in the region of the $^7F_0 \rightarrow {}^5D_1$ transitions where only three lines are expected based on C_2 symmetry alone. They suggested that the two extra lines are due to Eu^{+3} ions located at S_6 sites, but an assignment was not possible. The present study was initiated in order to establish the two Eu^{+3} symmetry sites in $Y_2O_3:Eu^{+3}$ by searching for the S_6 Eu^{+3} emission.

Symmetry Effects on Eu^{+3} Spectra

The symmetry of the crystal field about the Eu^{+3} ion affects the $4f^6$ absorption and emission spectra in two ways. First, interaction with the crystal field splits the $4f^6$ Eu^{+3} levels, which partly or completely removes the angular momentum degeneracy (Stark effect) and produces a fine structure for each free ion transition. Since the $4f^6$ electrons are substantially shielded from the crystal field by the outer electrons, the Stark splittings are small compared to the spin-orbit coupling. Since the maximum splitting of a level cannot exceed $2J + 1$, the $^5D_0$ level of Eu^{+3} is always a singlet.

The other effect is that the crystal field establishes in part the oscillator strengths of the $4f^6$ transitions. In the case of the free ion all of the $4f^6$ configurations have the same parity so that only magnetic dipole and quadrupole transitions can occur. As is well known, electric dipole transitions are forbidden since this type of transition only connects states of different parity. However, interactions with the crystal field introduce terms into the potential energy part of the Hamiltonian which, depending on the symmetry, can alter the parity of the state. For symmetries which lack a center of inversion these terms are odd and consequently, the parity selection rule breaks down, allowing electric dipole transitions. The selection rules for dipole transitions involving a $J = 0$ emitting or terminal state, which are applicable to the Eu^{+3} $^5D_0$

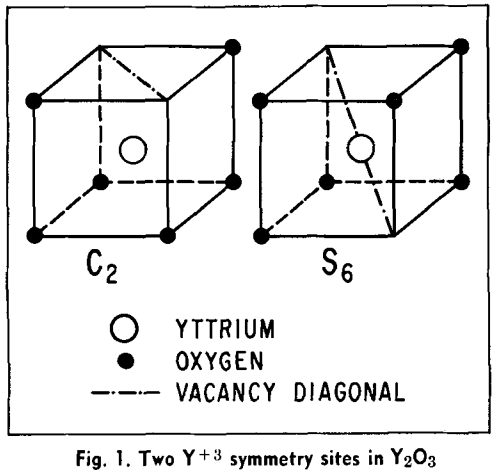

Fig. 1. Two Y^{+3} symmetry sites in Y_2O_3

[1] S_6 is identical to C_{3i}.

state, are: $\Delta J = \pm 1$ for a magnetic dipole transition and $\Delta J = 2, 4, 6$ for an electric dipole transition (5).

In the Eu^{+3} emission spectrum both types of dipole transitions are found: the $^5D_0 \rightarrow {}^7F_1$ is a magnetic dipole transition and the $^5D_0 \rightarrow {}^7F_2$ is an electric dipole transition. Accordingly, when the Eu^{+3} is located at a center of inversion, the $^5D_0 \rightarrow {}^7F_2$ emission should be suppressed and only the $^5D_0 \rightarrow {}^7F_1$ emission should occur. In the above reference, Blasse *et al.* have found this to be true in a series of Eu^{+3} activated phosphors where the inversion symmetry is gradually removed (5). In their phosphors the ratio of the $^5D_0 \rightarrow {}^7F_2$ emission to the $^5D_0 \rightarrow {}^7F_1$ emission was found to increase with asymmetry of the crystal field.

Another factor to consider is the $^5D_0$ lifetime, which will naturally be affected by changes in the probability of the $^5D_0 \rightarrow {}^7F_2$ transition. Since in asymmetric crystal fields electric dipole transitions are more probable than magnetic dipole transitions, an efficient Eu^{+3} emission which consists of the $^5D_0 \rightarrow {}^7F_1$ transition alone will be expected to have a longer radiative lifetime than one dominated by the $^5D_0 \rightarrow {}^7F_2$ transition. Recently, Weber has calculated the $^5D_0 \rightarrow {}^7F_1$ radiative lifetime for C_2 Eu^{+3} ions in Y_2O_3 to be 9.1 msec (6). However, due to the presence of the strong $^5D_0 \rightarrow {}^7F_2$ emission, the observed $^5D_0$ lifetime is actually about 1 msec.

The different nature of the $^5D_0 \rightarrow {}^7F_1$ and $^5D_0 \rightarrow {}^7F_2$ transitions is important in separating the S_6 and C_2 emissions in $Y_2O_3:Eu^{+3}$. Since the C_2 site lacks a center of inversion, its Eu^{+3} emission will be composed of both transitions, which is consistent with Chang and Gruber's assignment (4). On the other hand, the S_6 symmetry site possesses a center of inversion and only the $^5D_0 \rightarrow {}^7F_1$ transition is allowed; consequently, the S_6 $^5D_0$ lifetime is expected to be long compared to the C_2 $^5D_0$ lifetime.

Experimental

The phosphors were prepared by firing stoichiometric mixtures of the oxalates for 2 hr at 600°C followed by 2 hr at 1400°C under an O_2 atmosphere. Most of the measurements were made on powders but some were made on a single crystal of $Y_2O_3:Eu^{+3}$ 5% which was obtained from Lockheed Palo Alto Research Laboratory.

Two Jarrell Ash grating monochromators, a ¼-meter Ebert and a 1-meter Czerny-Turner, were used to obtain the spectral measurements. The Czerny-Turner monochromator, which has a dispersion of 8.2 Å/mm, was used for the emission spectra and lifetime measurements, while both monochromators were used to obtain excitation spectra. In the latter experiments, the Czerny-Turner instrument was used to monochromate the light. In all measurements an RCA 1P21 phototube was used as a detector and the exciting source was either a low pressure Hg discharge lamp (CW or pulse) or a 100w Xe lamp.

Results and Discussion

Emission spectra.—The yellow-red portion of the room temperature emission spectrum of $Y_2O_3:Eu^{+3}$ 6% is shown in Fig. 2. The exciting source was a low pressure Hg lamp which corresponds to excitation in the broad Eu^{+3} absorption band in the short u.v. range. Six lines are found in this region and are listed in Table I. The free ion assignments are based on the position of the emissions predicted by the $4f^6$ Eu^{+3} energy level diagram. The $^5D_0 \rightarrow {}^7F_2$ transition is the dominant emission at 6112.9Å. The emission at 5804.5Å is a narrow singlet and its assignment is clear since the $J = 0$ state is not split by the crystal field. However, there is a question about the number of lines occurring in the region of the $^5D_0 \rightarrow {}^7F_1$ transition. Depending on the site symmetry, this transition can be split into a maximum of only three lines, which corresponds to complete removal of the $^7F_1$ degeneracy. Accordingly, there are one or more extra lines in this

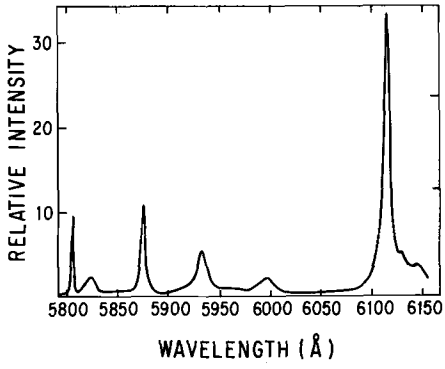

Fig. 2. Yellow-red portion of the emission spectrum of $Y_2O_3:Eu^{+3}$ under 2537Å excitation.

region which can be due to $^5D_1$ emissions or to more than one emitting Eu^{+3} symmetry site. In order to establish the number of additional lines and their origin, the lifetimes of the individual lines were measured using a monochromator to isolate each line.

Table II lists the 1/e lifetimes for the six lines over the concentration range 0.3-10 a/o (atom per cent) Eu^{+3}. The decays were obtained with the pulsed low pressure Hg flash lamp. Some decays were not exponential so that the 1/e lifetimes are to be taken as a convenient reference. It is seen that the five lines marked with asterisks all have roughly the same lifetimes, which indicates that they all originate from the same emitting level. There is little doubt that these are all $^5D_0$ emissions because of unique character of the $^5D_0 \rightarrow {}^7F_0$ singlet. On the other hand, the lifetime of the 5823Å line at low concentrations is too long to belong to this group of lines. Its long lifetime eliminates the possibility of it being a $^5D_1$ emission since the $^5D_1$ level is readily quenched at these concentrations. There are several $^5D_1$ emissions that occur in the 5270Å region and their lifetimes have been measured by us to be about 125-150 μsec. In fact, there is some $^5D_1$ emission overlapping the line at 5873.7Å, which accounts for its slightly shorter lifetime at low Eu^{+3} concentrations. As the Eu^{+3} concentration is increased beyond 1%, the $^5D_1$ emission has been found to decrease relative to the $^5D_0$ emission so that the lifetime of the 5873.7Å line approaches the other four $^5D_0$ values.

The other possibility for the origin of this emission is that the 5823Å line is a $^5D_0 \rightarrow {}^7F_1$ transition which arises from a different Eu^{+3} symmetry site than the other five short-lived $^5D_0$ emissions. We feel that this is the case and the two symmetry sites are S_6 and C_2 mentioned earlier. The emission at 5823Å was not reported by Chang and Gruber, but the five short-lived

Table I. Assignment of $Y_2O_3:Eu^{+3}$ 6% emissions

Wavelength (Å)	Transition
5804.5	$^5D_0 \rightarrow {}^7F_0$
5823.0 5873.7 5934.5 5996.0	$^5D_0 \rightarrow {}^7F_1$
6112.9	$^5D_0 \rightarrow {}^7F_2$

Table II. Lifetimes (msec) of $Y_2O_3:Eu^{+3}$ emissions. The emission wavelengths, in angstroms, refer to the $Y_2O_3:Eu^{+3}$ 6% sample.

C (%)	5804.5*	5823.0	5873.7*	5934.5*	5996*	6112.9*
0.3	1.12	5.5	0.77	1.25	1.06	0.98
1.0	1.07	4.3	0.83	1.0	1.03	1.03
2.0	1.03	2.8	0.98	1.05	1.0	1.05
6.0	1.03	1.2	0.98	1.07	1.02	1.07
10.0	1.00	0.95	0.93	0.92	0.94	0.95

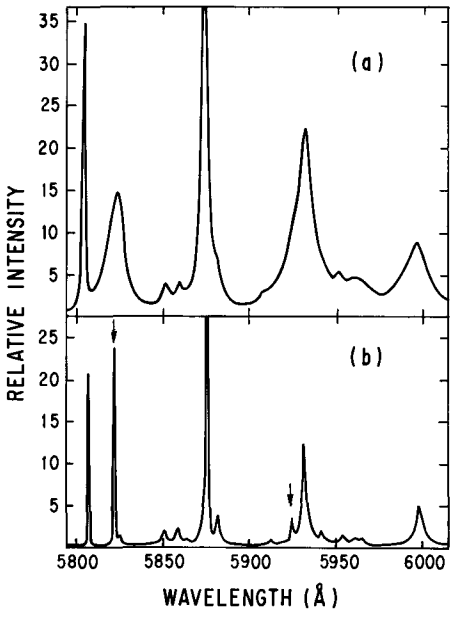

Fig. 3. Emission spectra of Y_2O_3:Eu^{+3} 0.6% under 2537Å excitation: (a) taken at room temperature, (b) taken at 78°K.

ones were and assigned to Eu^{+3} ions situated at C_2 sites. This is reasonable since a strong $^5D_0 \rightarrow {}^7F_2$ transition is possible in C_2 symmetry and the $^5D_0 \rightarrow {}^7F_1$ transition is split into the correct number of Stark components for this symmetry, namely three (4). This suggests that the 5823Å line is an S_6 emission and it will be shown below that this emission possesses all of the characteristics expected for a Eu^{+3} ion situated at an S_6 site.

In the first place, the 5823Å line occurs in the region of the $^5D_0 \rightarrow {}^7F_1$ transition which is the only $^5D_0$ emission allowed in S_6 symmetry. The long lifetime is expected since this transition is a pure magnetic dipole and consequently, has a low oscillator strength. However, the number of Stark components predicted by S_6 is two so that there should be another line in this region which has the same lifetime as the 5823Å line (4). This other Stark component was found but only after the phosphor was cooled to 78°K, where considerable narrowing of the emission spectrum occurs. Figure 3 shows part of the emission spectrum of Y_2O_3:Eu^{+3} 0.6% at room temperature and at 78°K with the two $^5D_0 \rightarrow {}^7F_1$ Stark components indicated by arrows. There is a few angstrom shift in the emission spectrum between room temperature and 78°K. Due to the low Eu^{+3} concentration several weak $^5D_1$ emissions are detected which can easily be indentified by their short lifetime. The lifetime of the two S_6 emissions was found to be identical and equal to 7.7 msec. The lifetime of the C_2 $^5D_0$ emissions at 78°K is about 1.0 msec., which is the same as the room temperature value. The magnitude of the $^5D_0 \rightarrow {}^7F_1$ Stark splitting in each symmetry site is about the same as seen from Table III, which lists the respective lines.

Since the degeneracy of the $^7F_1$ level is not completely removed, one of the S_6 emissions terminates at a doubly degenerate level. This is probably the 5822.3Å line since it is stronger than the 5924.5Å line including an estimated correction for the response of the phototube. We will return to this point.

Gd_2O_3, like all rare-earth oxides, can be made in the cubic C form (8). Therefore, the emission of Gd_2O_3:

Table III. $^5D_0 \rightarrow {}^7F_1$ Emissions, in angstroms, at 78°K

S_6	C_2
5822.3	5875.3
5924.5	5931.5
	5997.9

Eu^{+3} should be similar to Y_2O_3:Eu^{+3} and due to Eu^{+3} ions located at S_6 and C_2 symmetry sites. We have prepared Gd_2O_3:Eu^{+3} and found this to be so.

There is little doubt that the two long-lived emissions found in Y_2O_3:Eu^{+3} and Gd_2O_3:Eu^{+3} are due to S_6 Eu^{+3} ions because of their consistency with crystal field and oscillator strength predictions for the $^5D_0 \rightarrow {}^7F_1$ transition in that symmetry. The splitting of the $^5D_0 \rightarrow {}^7F_1$ transition into two Stark components by S_6 symmetry and its low oscillator strength also supports this assignment.

Excitation spectra.—Some further evidence for the S_6 Eu^{+3} emission in Y_2O_3:Eu^{+3} can be obtained by locating S_6 Eu^{+3} absorptions, which can be used to selectively excite it; two possibilities are the $^7F_0 \rightarrow {}^5D_1$ and $^7F_1 \rightarrow {}^5D_2$ magnetic dipole transitions. Since these two transitions are allowed in C_2 also, their absorption spectra will show lines due to both C_2 and S_6 Eu^{+3} ions. This is in agreement with the five absorption lines reported by Chang and Gruber for the $^7F_0 \rightarrow {}^5D_1$ transition, since this transition is expected to be split into two S_6 and three C_2 Stark components. Assignments of the absorption lines can be established by comparing the S_6 and C_2 Eu^{+3} excitation spectra and determining the preferential emission for each absorption line, since absorptions arising from a particular Eu^{+3} site will be expected to produce the emission of that site. Only the results of the $^7F_0 \rightarrow {}^5D_1$ excitation are reported below. Unfortunately, the absorption spectrum of the $^7F_1 \rightarrow {}^5D_2$ transition, which is composed of many lines, cannot be resolved to the same degree as the $^7F_0 \rightarrow {}^5D_1$ transition. This makes the C_2 and S_6 assignments difficult to establish, but further studies are planned including an analysis of the $^5D_2 \rightarrow {}^7F_1$ emission at low Eu^{+3} concentrations.

Figure 4 shows the absorption spectrum of Y_2O_3:Eu^{+3} 5% in the region of the $^7F_0 \rightarrow {}^5D_1$ absorption transition. This spectrum was taken on a single crystal with a Model 14R Cary absorption spectrophotometer. The five lines agree with those reported by Chang and Gruber. The C_2 and S_6 excitation spectra over the same region are shown in Fig. 5 a and b, respectively. The emission lines at 5823Å and 5873.7Å were used for the excitation spectra since these two lines can be completely isolated by the ¼ meter monochromator. It is seen from Fig. 4 and 5 that every line in the absorption spectrum gives rise to both S_6 and C_2 emission and further there are no lines in the excitation spectra that are not present in the absorption spectrum.

The fact that none of the absorption lines gives one or the other emission exclusively suggests that there may be energy transfer between the S_6 and C_2 Eu^{+3} ions. In some subsequent work, we have found that energy transfer does occur and can proceed in both directions ($C_2 \rightleftarrows S_6$) (9) so that an S_6 or C_2 absorption can produce S_6 and C_2 emission. Due in part to the long lifetime of the S_6 emission, the predominant transfer is $S_6 \rightarrow C_2$. It can be seen in Table II that the S_6 lifetime decreases with increasing Eu^{+3} concentration which is a consequence of the $S_6 \rightarrow C_2$ transfer.

Even though the excitation spectra are complicated by the energy transfer, the assignment of the five ab-

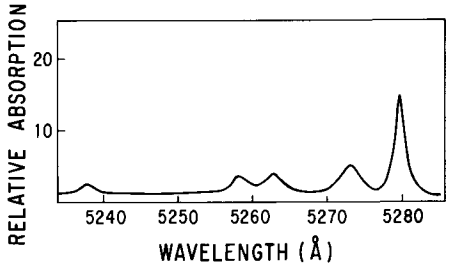

Fig. 4. Absorption spectrum of Y_2O_3:Eu^{+3} 5% corresponding to the $^7F_0 \rightarrow {}^5D_1$ Eu^{+3} transition.

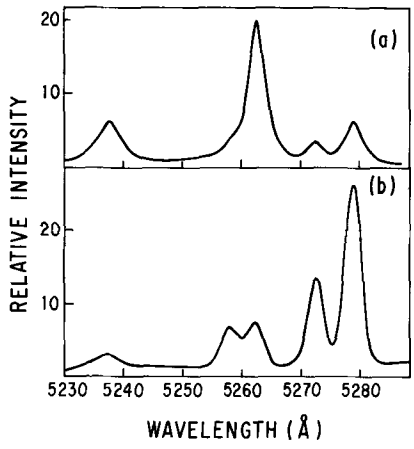

Fig. 5. Excitation spectra of $Y_2O_3:Eu^{+3}$ 5%: (a) emission monochromator set at 5823Å line, (b) emission monochromator set at 5873.7Å line.

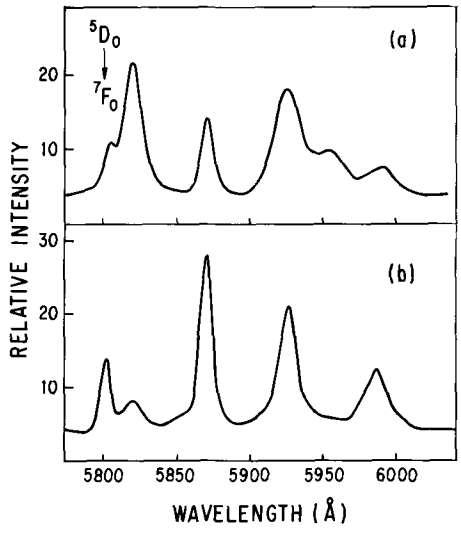

Fig. 6. Part of the emission spectrum of $Y_2O_3:Eu^{+3}$ 5%: (a) Group I excitation, (b) Group II excitation.

sorption lines can still be made. The five lines can be separated into two groups of two and three lines, which are listed in Table IV. The basis for the separation is that the intensity distribution of the lines within each group is constant and only the intensity ratio of Group I to Group II lines varies in each excitation spectrum. In related studies, we have found the latter to depend on Eu^{+3} concentration which is a consequence of the energy transfer dependence. The lines of each group act as a unit and, therefore, are interrelated. It is seen that compared to the lines of Group II, Group I lines are relatively stronger in the S_6 excitation spectrum; this means that this group preferentially excites the S_6 emission. Based on this fact we assign the two lines of Group I to S_6 Eu^{+3} ions and the three lines of Group II to C_2 Eu^{+3} ions. This assignment leads to the correct number of Stark components of the $^7F_0 \rightarrow {}^5D_1$ transition for each symmetry.

If there were no energy transfer, the C_2 and S_6 excitation spectra would only be composed of the Group II and Group I lines, respectively. Since the Group II lines (C_2) are weak in the S_6 excitation spectrum, one can conclude that there is very little $C_2 \rightarrow S_6$ energy transfer.

The above process can be reversed and the emission spectrum can be scanned while exciting at each of the five absorption lines. All five excitations were found to produce one or the other of two emission spectra, where the basic difference was the relative amount of C_2 to S_6 Eu^{+3} emission present. As expected, the two Group I excitations (S_6) yielded the emission spectrum with relatively more S_6 to C_2 Eu^{+3} emission than the three Group II (C_2) excitations. The Group I and Group II emission spectra are shown in Fig. 6a and b, with the respective S_6 and C_2 excitation wavelengths. In Fig. 6a, the S_6 emission at 5823Å is clear but the other one is obscured by the C_2 emission at 5935Å and its presence is detected by a shift toward the shorter wavelengths of the combined emission. By close examination of the two spectra in Fig. 6 the different contributions of the S_6 and C_2 Eu^{+3} emission can be noted and is in accord with the above.

A new feature in Fig. 6a is the presence of a weak emission at about 5959Å. This line is a S_6 Eu^{+3} emission, since it appears with S_6 excitation and also has been found to have a long lifetime. At 78°K this emission resolves into several lines, which indicates that it may be due to vibronic interactions of the S_6 Eu^{+3} $^5D_0 \rightarrow {}^7F_1$ transition.

As is the case with the $^7F_1$ level, the S_6 splitting of the $^5D_1$ level produces a singly and a doubly degenerate Stark level. Based on the relative intensity of the two S_6 absorptions, the more intense low energy absorption at 5262.0Å probably involves the doubly degenerate level. The opposite was found for the $^5D_0 \rightarrow {}^7F_1$ splitting where the high energy emission terminated at the doubly degenerate level. The intensity reversal of the $^5D_0 \rightarrow {}^7F_1$ emission and the $^7F_0 \rightarrow {}^5D_1$ absorption indicates the same type of splitting for the $^7F_1$ and $^5D_1$ levels where the doubly degenerate level is at a lower energy than the singly degenerate level. This is expected since both levels have the same total angular momentum quantum number ($J = 1$) and should, therefore, be split by the crystal field in the same way. A similar situation is found for the $^5D_1$ and $^7F_1$ splitting in $LaCl_3:Eu^{+3}$ (10). The reversal is due to the fact that in absorption the $^7F_0$ level is closer to the doubly degenerate level and in emission the $^5D_0$ level is closer to the singly degenerate level.

Assuming that the degeneracies of the $^7F_1$ and $^5D_1$ levels are properly assigned, the center of gravity of the $^5D_0 \rightarrow {}^7F_1$ and $^7F_0 \rightarrow {}^5D_1$ S_6 transitions can be calculated and compared to the corresponding C_2 transitions. It is found that the center of gravity of both S_6 transitions occurs at higher energies. Although the entire S_6 Eu^{+3} energy level diagram has not been obtained, this implies that the energy separation between the ^5D and ^7F states is greater when the Eu^{+3} is located at the S_6 site. We only mention this as an observation since a discussion of its origin is beyond the scope of this paper.

Table IV. $^7F_0 \rightarrow {}^5D_1$ Excitations in angstroms

Group I	Group II
5262.0	5278.5
5237.5	5272.3
	5257.7

Acknowledgment

The authors wish to thank John Konitzer and Halina Stanczyk for preparing the phosphor samples.

Manuscript submitted Oct. 7, 1968; revised manuscript received Dec. 26, 1968. This manuscript was presented at the Boston Meeting, May 5-9, 1968, as Paper 45.

Any discussion of this paper will appear in a Discussion Section to be published in the December 1969 JOURNAL.

REFERENCES

1. R. A. Buchanan, K. A. Wichersheim, T. L. Weaver, L. E. Sobon, and E. E. Anderson, Sixth Rare Earth Conference 1967, Gatlinburg.
2. R. W. G. Wyckoff, "Crystal Structures," Interscience Publishers, Inc., New York (1965).

3. M. Mandel, *Appl. Phys. Letters*, **2**, 197 (1963); S. Z. Toma and D. T. Palumbo, *This Journal*, **115**, 64C (1968).
4. N. C. Chang and J. B. Gruber, *J. Chem. Phys.*, **41**, 3227 (1964).
5. G. Blasse, A. Bril, and W. C. Nieuwpoort, Int. Conf. on Luminescence 1966, Budapest.
6. M. J. Weber, *Phys. Rev.*, **171**, 283 (1968).
7. N. C. Chang, *J. Appl. Phys.*, **34**, 3500 (1963).
8. A. F. Wells, "Structural Inorganic Chemistry," Third Edition, Oxford University Press, London (1962).
9. H. Forest and G. Ban, To be published.
10. L. G. DeShazer and G. H. Dieke, *J. Chem. Phys.*, **38**, 2190 (1963).

Growth and Characterization of $Ga_xIn_{1-x}Sb$ Solid Solutions Using Temperature-Gradient Zone Melting

Raymond W. Hamaker and William B. White[1]

Materials Research Laboratory, Pennsylvania State University, University Park, Pennsylvania

ABSTRACT

Temperature-gradient zone melting has been utilized to grow a wide range of solid solution compositions of $Ga_xIn_{1-x}Sb$ using indium and lead as zone metals. Single crystal growth was accomplished on {111} InSb seed substrates. Migration velocities as large as 12 x 10^{-7} cm/sec were observed during indium growth experiments, while velocities as large as 7 x 10^{-7} cm/sec were noted during lead growth experiments. All growth runs were performed with the top of the seed substrate at 420°C to provide a reference temperature for the migration experiments. Electron microprobe scans of sections taken along the growth direction have shown gradual increases in the concentration of GaSb in growth layers over the first 2 to 3 mm of solid solution growth. Thereafter, uniform compositional growth is indicated. Photomicrographs of growth surfaces have clearly indicated that growth proceeded by a two-dimensional nucleation mechanism. Etch pit observations taken along the growth direction have indicated noticeable decreases in the dislocation densities of the individual growth layers compared with those in the respective seed substrates.

Since temperature-gradient zone melting (TGZM) was first introduced by Pfann (1, 2) this technique has been utilized to grow both germanium and silicon (3-6) as well as various intermetallic compounds such as GaAs (7), GaP (8-10), SiC (11, 12), InAs (13), and InSb (14). Solid solution growth of $GaAs_yP_{1-y}$ (8-15), $Hg_xZn_{1-x}Te$ (15), and $ZnSe_yTe_{1-y}$ (16) have also been reported recently by various modifications of TGZM. In general, crystals ranging from several millimeters up to several centimeters in length have been grown by this technique.

Growth of solid solutions by any method is difficult and it is important that the resulting crystals be well characterized particularly with respect to compositional zoning. This paper attempts to make a careful examination of the growth of solid solutions by the traveling solvent modification of temperature gradient zone melting using $Ga_xIn_{1-x}Sb$ as a convenient example.

Single crystal layers up to 4 mm in thickness with cross sections of 0.7 x 0.7 cm have been grown using <111> seed orientations of InSb (*i.e.*, both "A" and "B" orientations) at a growth temperature of 420°C. Migration velocity measurements have been made during the growth experiments to determine the effect of changing solid solution composition on crystal growth rate. Chemical etching of growth surfaces has been employed to indicate the type of growth mechanism present. Particular attention was paid to compositional variations and zoning in the resultant growth layers as determined by electron microprobe analysis. Finally, etch pit examinations have been used to determine the relative changes in dislocation density between the individual seed and growth layers.

Experimental

Polycrystalline solid solution charge sections ranging from 3-4 mm in thickness were obtained from ingots (7-10 cm in length) grown at 2-4 mm/hr by a standard vertical Bridgman technique. Indium-rich starting compositions were used to minimize compositional gradients along the growth direction due to segregation during solidification. Single crystal seed sections of InSb were also obtained from Bridgman-grown ingots.

Slow growth rates in the range of 2-4 mm/hr were necessary in the case of solid solution ingots, since faster growth rates usually resulted in a two-phase separation as previously described by Ivanov-Omskii and Kolomiets (17). Such a separation was undesirable for sections that were to be used as charge layers in TGZM experiments, since nonuniform dissolution and unstable zone migration conditions were generally evident from such material. This phase separation was observed through x-ray powder pattern measurements performed on selected thin sections taken normal to the growth direction of an ingot. These measurements indicated either one or two sets of distinct reflection peaks as a function of angular position, which in turn indicated the presence of either one or two solid phases in the crystalline matrix. A Norelco Diffractometer Cu Kα radiation was used.

The uniformity of solid solution sections cut normal to the growth direction of an ingot was determined with an Applied Research Laboratories Electron Microprobe Analyzer. Microprobe beam scans across the individual sections indicated compositional variations in the range of several tenths of a mole per cent (m/o). Scans made along the growth direction indicated compositional variations in the range of 2 m/o over 4 mm of ingot length. The spot size of the scanning electron beam was 10 μm.

Both indium and lead were used as zone solvents in this series of migration experiments. The chemical preparation techniques for both the zone metals and the solids were described previously (14). In order to obtain uniform wetting of the zone metals with the individual solid sections, it was necessary to wet each

[1] Also associated with the Department of Geochemistry and Mineralogy.

layer of solid on a polished silica plate prior to the final assembly of the growth configurations. Subsequent electron microprobe scans have indicated no detectable amounts of silicon in the growth layers of the individual configurations after migration was completed (the limit of detection was about one part in 10^6). Attempts to wet both charge and seed layers together usually resulted in nonuniform wetting. This in turn caused irregular zone migration and unsatisfactory growth conditions.

The rate of zone migration in the individual growth configurations was determined by noting the average velocity of either interface during the first 2 mm of growth with the growth interface initially at 420°C. This was done since no temperature profile could be estimated accurately across either the zone or charge regions during a particular growth experiment because of the unavailability of thermal conductivity data for the two regions. This approximation was reasonable since no significant increases in migration velocity were observed over the limited temperature range for any of the zone configurations. During this series of growth experiments, temperature gradients across the InSb seed substrates ranged from 10° to 12°C/mm, as determined by two-position thermocouple measurements. At the onset of zone migration, the growth interface was not usually visible until ~ 0.2-0.4 mm of growth had occurred. This was due to considerable dissolution of InSb at the top of the seed substrate after the initial mating and wetting of the two specimen layers. Figure 1 shows a pictorial representation of this zone enlargement effect. Indium zones suffered more enlargement than did lead zones. No further changes in zone thickness were noted in any of the migration experiments included in this paper; however, in some experiments where nonuniform wetting had initially taken place, shape irregularities generally increased with zone motion. A telemicroscope assembly having a magnification of x20 and a vernier scale accuracy of 0.005 cm was employed to determine zone movement.

The growth chamber assembly that was used for this series of zone migration experiments has been described in a previous paper (14). Slight evaporation was present during the growth of the solid solutions; however, it was not severe enough to warrant either the use of internal gas pressures within the evacuated chamber or the use of sealed ampoules containing the growth configurations as described by Weinstein and Mlavsky (9).

Results and Discussion

The ten most successful zone migration experiments are listed in Table I. Thick zones were used to minimize interface kinetics effects and this has resulted in an essentially constant zone migration velocity over the entire traverse of the zone. The compositions listed in Table I are those of the polycrystalline feed material. The changing GaSb content of the feed has a pronounced effect on the zone migration velocity and this is shown in Fig. 2. At 10% GaSb concentration, the velocity is nearly halved.

Compositional variations in the growth layers of samples considered in Fig. 2 have been determined by

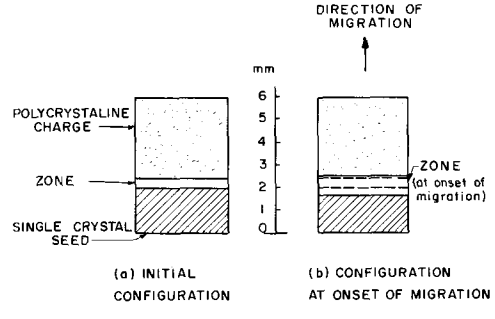

Fig. 1. Pictorial representation of (a) initial zone profile and (b) profile of zone at onset of migration.

Table I. Data for zone migration experiments

Growth run designation	Initial charge composition (X_{GaSb})	Zone thickness (l)	InSb seed orientation
In(1)	0.00	0.90 mm	<111>"A"
In(2)	0.06	0.85	<111>"A"
In(3)	0.27	0.85	<111>"A"
In(4)	0.33	0.90	<111>"B"
In(5)	0.54	0.95	<111>"B"
Pb(1)	0.00	0.90 mm	<111>"A"
Pb(2)	0.13	0.90 mm	<111>"B"
Pb(3)	0.30	0.95 mm	<111>"A"
Pb(4)	0.37	0.85 mm	<111>"B"
Pb(5)	0.47	0.90 mm	<111>"A"

an electron microprobe analysis. Figure 3 indicates the composition of the individual growth layers as a function of distance traversed along the growth direction for indium-rich zones. Figure 4 shows the composition of growth layers as a function of distance traversed along the growth directions for lead-rich zones. All scans were made on sections cut along the growth direction. In all cases, InSb-rich growth layers were evident at the onset of growth. After 2-3 mm of growth, solid solution concentrations became more uniform, indicating that steady-state conditions were approached. Since the indium zones were observed to dissolve more InSb at the onset of a migration run than were the lead zones, it is reasonable to expect that the initial growth layers for indium migration experiments would be more InSb-rich than would be those for lead zone experiments.

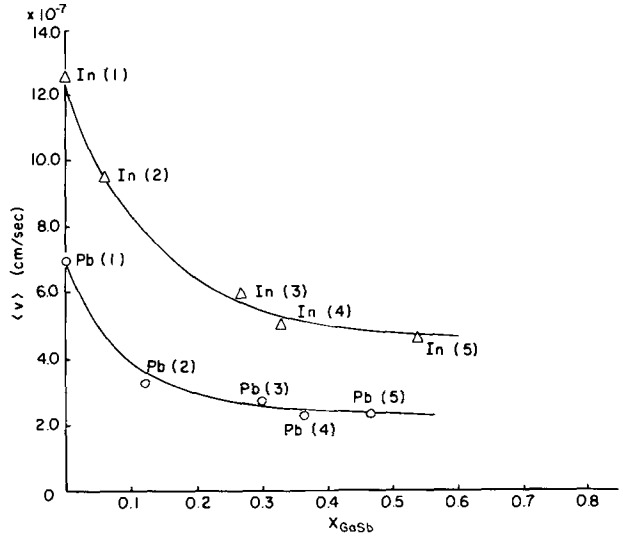

Fig. 2. Migration velocity dependence on solid solution composition in the charge layer for both indium and lead zone configurations.

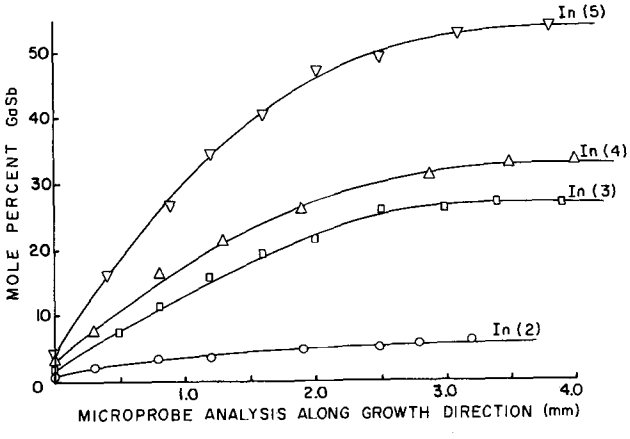

Fig. 3. Solid solution composition along the growth direction for indium zones.

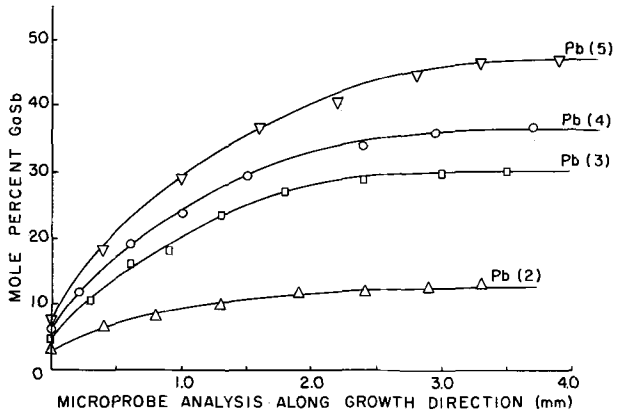

Fig. 4. Solid solution composition along the growth direction for lead zones.

Electron microprobe scans were also made to determine the lead content in the growth layers of solid solution crystals when lead was used as the zone solvent. No detectable amounts of lead were observed in any of the growth regions to a limit of detectability of about one part in 10^5.

Evidence for solid solution crystal growth by the two-dimensional nucleation mechanism has been obtained by etching the regrown region in dilute HCl, after migration of indium zones through the charge sections. Figure 5 shows faceted growth steps observed on an "A" face, while Fig. 6 shows those observed on a "B" face. These step features agree with those for faceted steps observed on pure InSb crystals that were grown under similar growth conditions (14), although the size of the growth steps are somewhat smaller on the solid solution surfaces.

Etch pit observations have been made on polished and chemically etched sections parallel to the growth directions of the individual specimens. Figure 7 shows a photomicrograph of the region bounding the initial growth interface separating the seed and growth regions after migration of an indium zone through a

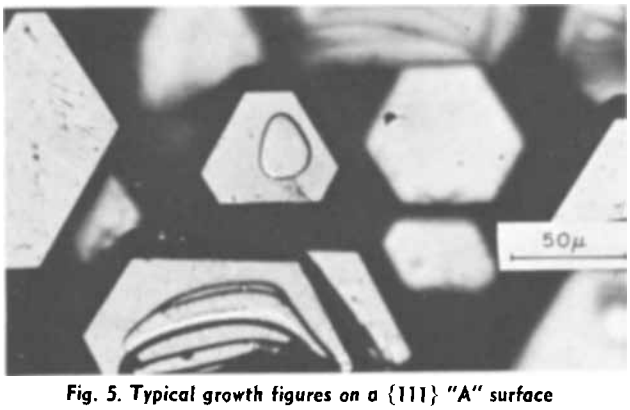

Fig. 5. Typical growth figures on a {111} "A" surface

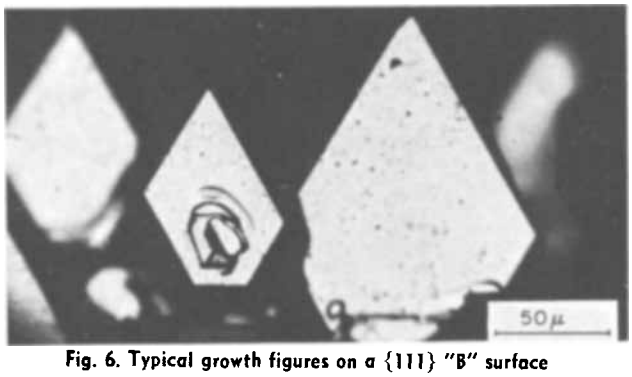

Fig. 6. Typical growth figures on a {111} "B" surface

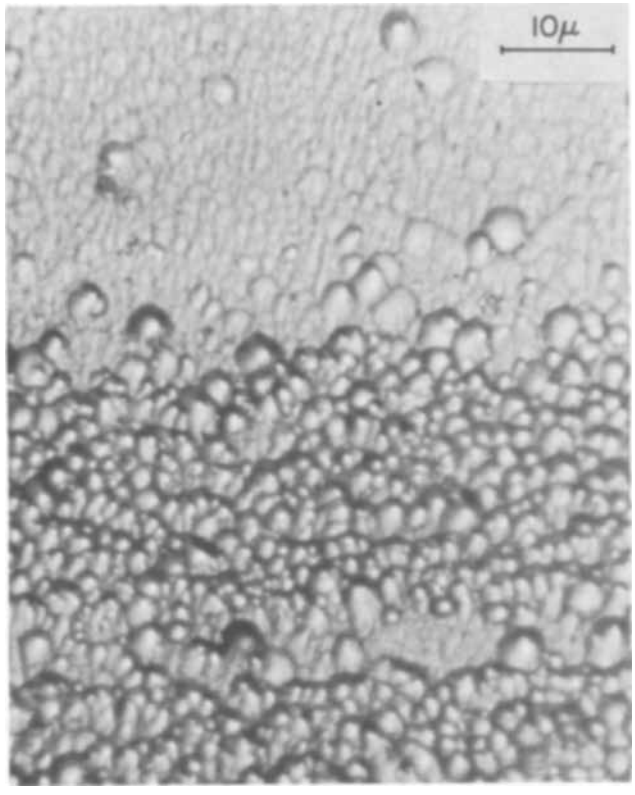

Fig. 7. Etch figures on a surface parallel to the growth direction for a In:InSb $Ga_xIn_{1-x}Sb$ growth experiment.

solid solution charge layer. A noticeable decrease in etch pit density can be observed in the growth region after an initial layer of 20-40 μm of higher etch pit density growth. This initial region of higher etch pit density can be correlated with fine-structure from the electron microprobe scans, which has indicated a rapid change in solid solution composition over the first 25 μm of growth. Such changes in composition have been shown as abrupt in Fig. 3 and Fig. 4, since millimeter scales are used to describe the growth layer composition profiles. Similar etch pit density observations have been noted on growth layers when lead was used as the zone metal as shown in Fig. 8. After the initial region of abrupt compositional change, the etch pit concentrations in the individual growth layers usually decreased by about an order of magnitude. This also agrees with similar observations made on growth layers of pure InSb as shown in Fig. 9. Since a direct correlation of etch pit figures with emergent dislocations is not always present on an etched surface as discussed by Faust (18) and by Sagar and Faust (19) it can only be concluded that the effective dislocation density in a particular growth layer is somewhat less than that in a seed layer for either zone configuration. The most satisfactory etchant used to obtain distinct pit figures on the polished sections was found to be $4H_2O:2HNO_3:1HF$ (by volume). Similar observations of decreased etch pit concentrations in the growth layers of crystals grown by TGZM have been noted by Mlavsky and Weinstein (17), by Weinstein and Mlavsky (9), and by Weinstein *et al.* (20).

The rapid decrease in migration velocity with increasing values of X_{GaSb} for InSb rich solid solutions of (Ga, In)Sb can be reasonably explained by an increased sluggishness of the dissolution interface kinetics for both the indium and lead systems. Evidence of this in both systems has been observed in several migration experiments where the individual grain size in the charge sections was relatively large. In such instances, nonuniform dissolution generally occurred with one grain dissolving more rapidly than an adjacent grain. The growth data from these experiments were sporadic and have not been included in this

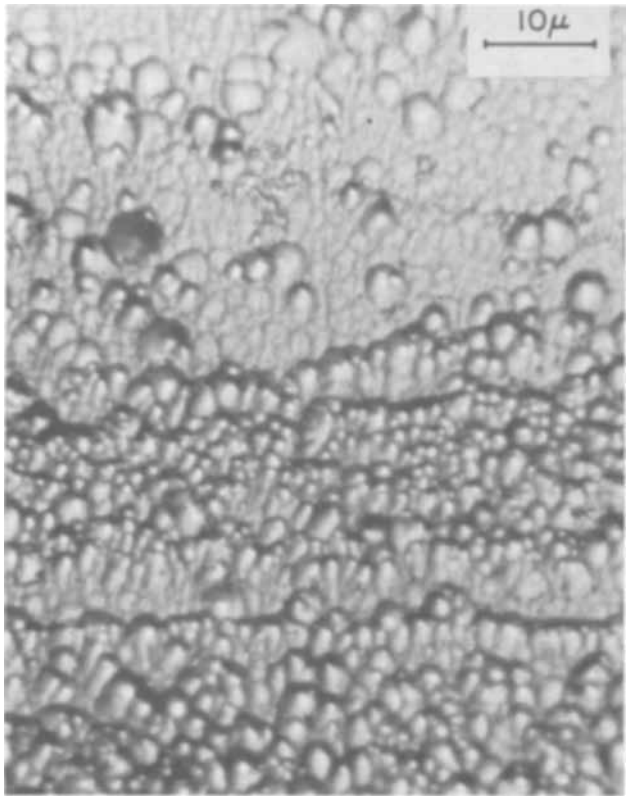

Fig. 8. Etch figures on a surface parallel to the growth direction for a Pb:$Ga_xIn_{1-x}Sb$ growth experiment.

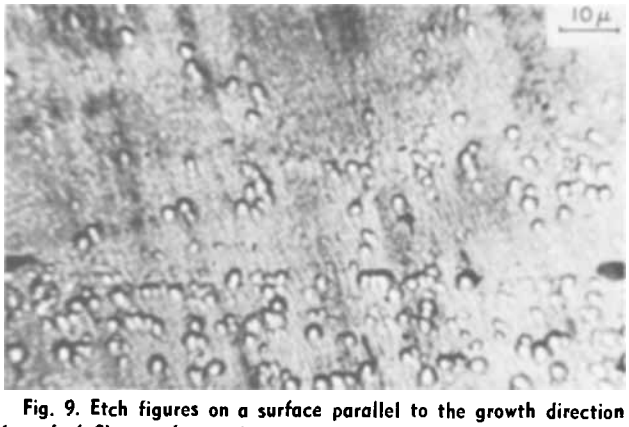

Fig. 9. Etch figures on a surface parallel to the growth direction for a In:InSb growth experiment.

paper. Trumbore *et al.* (21) have observed rapid decreases in the interatomic lattice spacing of InSb rich (Ga, In) Sb solid solutions with small increases in X_{GaSb}. Such decreases in the interatomic spacing could be expected to produce subsequent increases in the interatomic bond energy (*i.e.*, the lattice cohesive energy). An increase in bond energy would, in turn, imply a larger activation energy for the dissolution process as discussed by Jackson and Chalmers (22). Therefore, the rate of zone migration could be expected to decrease in these two systems with increasing X_{GaSb} if dissolution interface kinetics are the rate-controlling factor. Since there was no evidence of migration velocity decreasing during the first few millimeters of growth as successive growth layers were becoming more GaSb-rich, it would appear that atomic interface kinetics at the growth interface of individual growth configuration were rapid enough to allow their over-all effect on zone migration to be negligible.

Another factor that is important in determining the magnitude of the migration velocity in this series of experiments is the liquid diffusion transport term as discussed by Tiller (23) and by Seidensticker (6). Yost (24) has shown that the effective diffusion coefficient for mass transport across an alloy zone is dependent on both the activity of the diffusing substance in the particular solution as well as the viscosity of the liquid. Since no information is available concerning activities or viscosities for either ternary solvent system, no conclusive statement can be made about relative changes in the effective diffusion coefficient of (Ga, In)Sb alloys as a function X_{GaSb}. It is reasonable to conclude, however, that the relative difference in migration velocities between the indium and lead solvent systems could be attributed to differences in viscosity between the two liquids.

A qualitative description of interface conditions during a solid solution: indium:InSb migration experiment can best be explained in terms of the partly hypothetical liquids shown in Fig. 10. After a short transient period in which the solid and liquid compositions at the growth interface equilibrate, the growth interface will be at a temperature of 420°C, while the dissolution interface will be at a temperature of approximately 425°C. At the onset of growth, the liquid compositions at the respective interfaces are indicated by the square and round figures at 420° and 425°C. Equilibrium liquid compositions are considered; however, for sluggish interface kinetics, slight shifts of the square figures on the respective isotherms would be evident to denote nonsaturation conditions at the interfaces. The respective solid compositions are indicated by X_{DI} (dissolution interface) and X_{GI} (growth interface). The respective solid compositions will be denoted as the straight line intercepts on the solid solution binary diagram from the indium end of the Gibbs triangle through the individual points at which the respective liquids lie on the liquidus surface. Actually, these intercepts are tangents to the respective ternary fractionation curves as discussed by Masing (25) and Ricci (26). In the indium-rich region of the ternary diagram, it is reasonable to expect the fractionation curves to be straight lines; Hence a linear extrapolation can be made to indicate

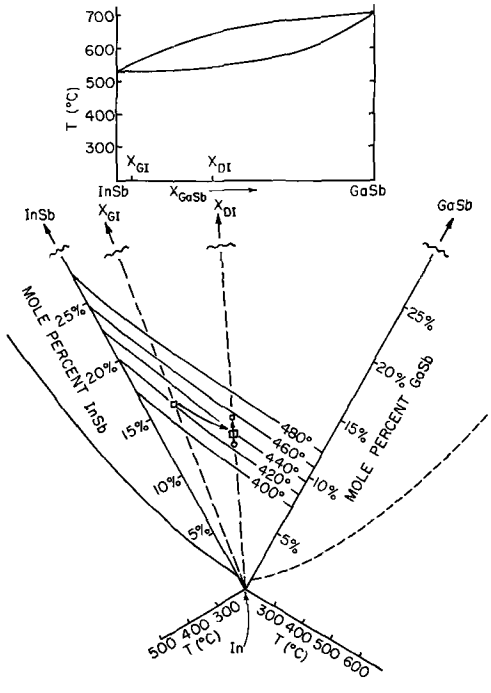

Fig. 10. Portion of a partly hypothetical ternary diagram with bounding binaries for the system In-InSb-GaSb. Since the binary In-GaSb is unknown, the ternary phase boundary connecting the binary eutectics has been omitted. The tie lines connecting the composition of the solid at the growth and dissolution interfaces terminate at different points on the ternary phase boundary and do not necessarily intersect the indium apex.

the general features of solid solution compositions at the respective interfaces during the growth period.

As zone migration progresses, the liquid compositions at the two interfaces change along the paths shown by the arrows. The solid composition at the dissolution interface will remain the same during this period, whereas the solid composition at the growth interface will change gradually until a value of X_{DI} is reached. At this time steady-state conditions have been attained within the zone. The respective interface positions are again indicated by the square and circular figures once both interfaces are in equilibrium (or near equilibrium) with the same composition of solid. Thereafter, both liquid compositions will change along the dotted line from In to X_{DI} with both interfaces being in equilibrium with a solid of composition X_{DI}. A rigorous analysis of this process for similar systems is discussed by Broder and Wolff (8).

Summary

Both indium and lead have provided satisfactory solvent metals for the growth of a wide range of solid solutions of $Ga_xIn_{1-x}Sb$ on InSb substrates. Although it was anticipated that steady-state conditions would occur rapidly within a moving zone, it appears that a region of at least 2-3 mm of growth must occur before steady-state solute conditions exist at the growth interface. This is understandable, since a considerable amount of dissolution initially takes place on an InSb seed prior to zone migration. By utilizing a less soluble seed material it is reasonable to expect that the initial region of nonuniform growth could be decreased considerably.

The growth mechanism operative in this series of TGZM experiments is two-dimensional nucleation. This has been determined by the appearance of faceted growth steps on the {111} surfaces. From the migration velocity dependence on X_{GaSb}, it would appear that dissolution interface kinetics become more sluggish as the GaSb concentration increases. This, in turn, would limit the rate at which solid solution crystals could be grown by this technique.

Noticeable decreases in etch pit density have been observed in the individual growth layers of solid solution crystals compared with those in the respective InSb seed regions, after initial growth regions of 20-40 μm. Since there is usually a high correspondence between the number of observed etch pit figures and emergent dislocations on a crystal surface after polishing and chemical etching, it is reasonable to attribute this observed decrease in etch pit density in the growth region of a solid solution-InSb configuration to a resultant decrease in dislocation density in that region compared with that in the seed region. The initial growth region of higher etch pit density has been attributed to the rapid change in solid solution composition over the first 25 μm of growth as determined by an electron microscope analysis. Such a change in composition could introduce considerable strain, resulting in a high dislocation density at the onset of growth.

Acknowledgments

The authors thank E. W. White, G. R. Zechman, and W. H. Zeigler for obtaining the electron microprobe scan data. The authors also thank J. W. Faust, Jr. for useful discussions concerning the analysis of etch pit observations. R. E. Wilson performed the cutting operations on the crystalline sections used in the TGZM experiments, and W. J. Connor assisted with the initial Bridgman growth work.

This work was supported by the Advanced Research Projects Agency of the U.S. Department of Defense under Contracts SD-132 and DA-49-083.

Manuscript submitted July 22, 1968; revised manuscript received Nov. 27, 1968.

Any discussion of this paper will appear in a Discussion Section to be published in the December 1969 JOURNAL.

REFERENCES

1. W. G. Pfann, J. *Metals*, **7**, 961 (1955).
2. W. G. Pfann, "Zone Melting," 2nd Edition, p. 254, John Wiley and Sons, Inc., New York (1966).
3. J. H. Wernick, *J. Chem. Phys.*, **25**, 47 (1956).
4. J. H. Wernick, *J. Metals*, **9**, 1169 (1957).
5. W. G. Pfann, K. E. Benson, and J. H. Wernick, *J. Electron.*, **2**, 597 (1957).
6. R. G. Seidensticker, *This Journal*, **113**, 152 (1966).
7. A. I. Mlavsky and M. Weinstein, *J. Appl. Phys.*, **34**, 2885 (1963).
8. J. D. Broder and G. A. Wolff, *This Journal*, **110**, 1150 (1963).
9. M. Weinstein and A. I. Mlavsky, *J. Appl. Phys.*, **35**, 1892 (1964).
10. T. S. Plaskett, S. E. Blum, and L. M. Foster, *This Journal*, **114**, 1303 (1967).
11. L. B. Griffiths and A. I. Mlavsky, *ibid.*, **111**, 805 (1964).
12. W. F. Knippenberg and G. Verspui, *Philips Research Repts.*, **21**, 113 (1966).
13. H. P. Kleinknecht, *J. Appl. Phys.*, **37**, 2116 (1966).
14. R. W. Hamaker and W. B. White, *J. Appl. Phys.*, **39**, 1758 (1968).
15. G. A. Wolff, H. E. LaBelle, Jr., and B. N. Das, *Trans. Met. Soc. AIME*, **242**, 436 (1968).
16. J. Steininger and R. E. England, *ibid.*, **242**, 444 (1968).
17. V. I. Ivanov-Omskii and B. T. Kolomiets, *Soviet Physics Solid State*, **1**, 834 (1959).
18. J. W. Faust, Jr., "Compound Semiconductors," Chap. 50, Reinhold Publishing Corp., New York (1962).
19. A. Sagar and J. W. Faust, Jr., *J. Appl. Phys.*, **38**, 2240 (1967).
20. M. Weinstein, H. E. LaBelle, Jr., and A. I. Mlavsky, *J. Appl. Phys.*, **37**, 2913 (1966).
21. F. A. Trumbore, P. E. Freeland, and A. D. Mills, *This Journal*, **109**, 645 (1962).
22. K. A. Jackson and B. Chalmers, *Can J. Phys.*, **34**, 473 (1956).
23. W. A. Tiller, *J. Appl. Phys.*, **34**, 2757 (1963).
24. W. Yost, "Diffusion in Solids, Liquids, Gases," 3d Edition, pp. 156 and 472, Academic Press, New York (1960).
25. G. Masing, "Ternary Systems: Introduction to the Theory of Three Component Systems," p. 60, Reinhold Publishing Corp., New York (1944).
26. J. E. Ricci, "The Phase Rule and Heterogeneous Equilibrium," Chap. 12, D. Van Nostrand Co., Inc., New York (1951).

Illumination and the Photoengraving of Silicon

R. D. Wales*

Lockheed Palo Alto Research Laboratory, Palo Alto, California

ABSTRACT

Equations have been derived for the rate and depth of engraving of near-intrinsic and low-resistivity n-type semiconductor materials. Semiempirical relationships for n-type silicon have been developed from the derived equations. The low-resistivity material, probably due to the defect structure, etched in triangular pits. The high-resistivity material gave very good engravings with a resolution of better than 12μ. The good quality of the pattern and lens is critical in obtaining fine engravings, and the quality and degree of monochromaticity of the illumination affect the resolution and quality of the engraving.

The effects of illumination on semiconductors have been discussed, studied, and theoretical developments presented under conditions in which the semiconductor material itself is not greatly affected (1-7). Few studies have considered the effects of illumination when the semiconductor material is in contact and reacting with an electrolyte solution (2). It is known that illumination aids, or is necessary, for the etching or polishing of n-type semiconductor materials (7-10). The effect of illumination on the "electrode" potential has been examined (2, 3, 6), and several processing techniques and device applications utilize the effects of illumination to obtain desired results (10). Brattain and Bardeen (11) developed a theory for the surface photovoltage of semiconductors which was applied to semiconductor electrodes (6). The theory has been utilized and modified or expanded to fit particular problems. The effects of illumination have been discussed from a theoretical basis and applied to specific problems or effects (1, 2).

The effects of illumination intensity on the chemical engraving (etching) of n-type semiconductors have not been studied, other than to note the requirement for intense illumination. This paper is concerned with the effects of illumination on the rate of solution of an n-type semiconductor in an electrolyte solution, and with the application of the technique to the engraving of silicon.

Theoretical Considerations

Electrochemical studies of the dissolution of silicon have indicated that the electrochemical reaction is activation controlled, at least over a portion of the ranges studied (10). Thus, when the reaction is not at equilibrium, and the rate in one direction is much less than the rate in the other direction, the rate of the electrochemical reaction in terms of the current density, i, is

$$i = z\mathbf{F}C_0 \exp\left(-\frac{n\mathbf{F}E}{RT}\right) \qquad [1]$$

or, as more commonly represented (as the Tafel equation)

$$E = a + b \log i \qquad [2]$$

The symbols in the above equations have the usual meanings, and C_0 is the concentration of the reacting or rate controlling species.

The electrochemical dissolution of n-type silicon has been studied by Turner (10), Flynn (12), Efimov and Erusalimchik (13), and others. They have found that holes are consumed during the anodic dissolution, and that only holes generated in a region much smaller than the diffusion length for holes can take part in the dissolution reaction. Brattain and Garrett (5, 6), Uhlir (14), Gerisher (2), and others have found that illumination affects the anodic electrode potential, or the anodic current, in proportion to the number of holes produced by the illumination. Thus, the rate-controlling specie in the anodic dissolution of n-type silicon are the holes, p, and Eq. [1] can be written as

$$i = k'p \exp\left(-\frac{n\mathbf{F}E}{RT}\right) \qquad [3]$$

where k' is a proportionality constant.

Many of the chemical processes used for etching or engraving semiconductors are electrochemical processes in which the anodic and cathodic reactions occur simultaneously at the surface of the semiconductor. When an n-type semiconductor is engraved in an electrolyte solution in which the rate of reaction or removal of material is controlled by the concentration of holes in the semiconductor, the rate of reaction is represented by Eq. [3]. Since the rate of engraving, dx/dt (where x is the depth of the engraving), is proportional to the rate of removal of material, Eq. [3] can be written as

$$\frac{dx}{dt} = kp \exp\left(-\frac{n\mathbf{F}E}{RT}\right) \qquad [4]$$

The energy absorbed in the surface of the semiconductor by illumination with nonpenetrating radiation results in the generation of hole-electron pairs. If the illumination is fairly intense, and if the probability for thermal release of trapped holes is small, then the traps will be filled and the hole concentration will be affected by the rate of recombination of holes and trapped electrons, cn_tp, or cp^2, and by the hole current into the bulk of the semiconductor. Since no external electrical field has been used, the hole current into the bulk of the semiconductor is the diffusion current and a field-induced (or drift) current. The drift term is negligible in comparison to the diffusion term if the hole concentration during illumination is much less than the electron concentration (1). Thus, the rate of change of hole concentration is

$$\frac{dp(x)}{dt} = q(x) - cp(x)^2 - Dp\frac{\partial^2 p}{\partial x^2} \qquad [5]$$

where q is the rate of generation of hole-electron pairs due to the illumination and c is the recombination probability or rate constant. Furthermore, if it is assumed that the effects of diffusion can be neglected after the semiconductor has been illuminated for a short time, the rate of change of hole concentration in the semiconductor near the electrolyte surface is

$$\frac{dp}{dt} = q - cp^2 \qquad [6]$$

The concentration of holes, p_i produced by the illumination is, by integration of Eq. [6]

* Electrochemical Society Active Member.

$$p_i = \sqrt{\frac{q}{c}} \tanh \sqrt{cq}\, t \qquad [7]$$

If the recombination rate constant is large, steady state is attained rapidly and Eq. [6] (and [7]) reduce to

$$p_i = \sqrt{\frac{q}{c}} \qquad [8]$$

However, if the recombination rate constant is small, steady state is not attained rapidly and Eq. [7] reduces to

$$p_i = qt \qquad [9]$$

During illumination there is a change of potential due to the holes (electrons) produced (photopotential). This photopotential has been given as (2)

$$Vp_1 = \frac{RT}{n\mathbf{F}} \ln \left(1 + \frac{p_i}{p_o}\right) \qquad [10]$$

for n-type materials and, for p-type materials

$$Vp_2 = -\frac{RT}{n\mathbf{F}} \ln \left(1 + \frac{n_i}{n_o}\right) \qquad [11]$$

Assuming that, in a near intrinsic n-type material, the photopotential, Vp, is

$$Vp = Vp_1 + Vp_2 = \frac{RT}{n\mathbf{F}} \ln \frac{1 + \dfrac{p_i}{p_o}}{1 + \dfrac{n_i}{n_o}} \qquad [12]$$

then, since $p_i = n_i$, $p_i >> p_o$, and $p_o + p_i \rightarrow n_o + n_i$, the photovoltage in a near-intrinsic material is small or nearly constant and can be neglected. Thus, the rate of engraving a strongly n-type material is, by combining Eq. [4], [7], and [10], and setting $E = E_o + Vp$

$$\frac{dx}{dt} = \frac{k\sqrt{\dfrac{q}{c}} \tanh \sqrt{cq}\, t}{1 + \dfrac{\sqrt{\dfrac{q}{c}}}{p_o} \tanh \sqrt{cq}\, t} \exp\left(-\frac{n\mathbf{F}E_o}{RT}\right) \qquad [13]$$

If the rate constant for recombination is large, as is generally the case in highly doped materials, Eq. [13] is

$$\frac{dx}{dt} = \frac{k\sqrt{\dfrac{q}{c}} \exp\left(-\dfrac{n\mathbf{F}E_o}{RT}\right)}{1 + \dfrac{\sqrt{\dfrac{q}{c}}}{p_o}} \qquad [14]$$

The rate of engraving of a near-intrinsic n-type material is, by combining Eq. [4] and [7]

$$\frac{dx}{dt} = k\sqrt{\frac{q}{c}} \tanh \sqrt{cq}\, t \exp\left(-\frac{N\mathbf{F}E}{RT}\right) \qquad [15]$$

If the rate constant for recombination is small, as is generally the case in near-intrinsic materials, Eq. [16] may be written as

$$\frac{dx}{dt} = kqt \exp\left(-\frac{n\mathbf{F}E}{RT}\right) \qquad [16]$$

The depth of the engraving is obtained by integration of Eq. [13-16]. The depth of engraving for strongly n-type material is

$$x = \frac{k\sqrt{\dfrac{q}{c}} \exp\left(-\dfrac{n\mathbf{F}E_o}{RT}\right)}{1 + \dfrac{\sqrt{\dfrac{q}{c}}}{p_o}} (t - t_1) \qquad [17]$$

The depth of the engraving for near-intrinsic n-type material is

$$x = \tfrac{1}{2}\, kqt^2 \exp\left(-\frac{n\mathbf{F}E}{RT}\right) - C \qquad [18]$$

where C is an integration constant.

Many simplifying assumptions have been made which may detract from the theoretical significance of the results. The assumptions that the hole current due to diffusion can be neglected, and that the electron concentration need not be considered (other than in terms of the photopotential) in the near-intrinsic material are probably the most questionable assumptions. However, if these assumptions are not made, the solution becomes quite complex. Since the surface is continually moving, if the diffusion term is not neglected the concentration of holes is not only decreasing due to diffusion, but is also increasing due to the holes in the next increment of depth as a function of the concentration and diffusion from the last increment of depth. Thus the simplest assumption is that these effects tend to be equal, and the effect of diffusion neglected. Furthermore, several probable conditions have not been included, such as the possibility of a space-charge region in the semiconductor at the interface, and the approximately equal hole-electron concentrations in the near-intrinsic material. However, it is believed that the major contributors to the engraving rate have been included, and that the engraving process is described by Eq. [13-18].

The rate of generation of hole-electron pairs is a function of the incident light intensity, I, so that q may be represented as

$$k = \alpha I \qquad [19]$$

where α is a constant including the absorption efficiency. The engraving Eq. [14] and [17] for strongly n-type materials can thus be written as

$$\frac{dx}{dt} = \frac{K\sqrt{I} \exp\left(-\dfrac{n\mathbf{F}E_o}{RT}\right)}{1 + \sqrt{I}/I_o} \qquad [20]$$

and

$$x = \frac{k\sqrt{I} \exp\left(-\dfrac{n\mathbf{F}E_o}{RF}\right)}{1 + \sqrt{I}/I_o} (t - t_1) \qquad [21]$$

and the engraving Eq. [16] and [18] for near-intrinsic materials may be written as

$$\frac{dx}{dt} = K'It \exp\left(-\frac{n\mathbf{F}E}{RT}\right) \qquad [22]$$

and

$$x = \tfrac{1}{2}K'It^2 \exp\left(-\frac{n\mathbf{F}E}{RT}\right) - C \qquad [23]$$

where

$$K = k\sqrt{\frac{\alpha}{c}}$$

$$K' = k\alpha$$

$$I_o = p_o\sqrt{\frac{c}{\alpha}}$$

Experimental Technique

The semiconductor materials used in this study were n-type silicon of 190-225 ohm-cm and 0.5-1.5

ohm-cm resistivity oriented on the (100) and (111) planes, respectively. Before use the silicon was immersed in White etch ($1HF/3HNO_3$) for about 1 min to obtain a polished surface. The photoengraving was performed in Dash etch ($1HF/3HNO_3/10HA_3$).

The source of illumination was a General Electric 1000-w theatrical spotlight, and the patterns used were a solar critical focusing chart (Burke and James, Inc., Chicago, Illinois) and a mask with a 21-mm square opening.

The lens system consisted of an 8-in. diameter glass planoconvex lens with a focal length of 14 in. placed about ½ in. after the pattern and about 28 in. from the light source. Further reduction was obtained with either a Wollensak f 4.5 Enlarging Velostigmat 3½ in. focus or a Wollensak-Dumont CRD 75 mm f 1.9 Oscillo-Anastigmat No. C15413 lens.

The light intensity through the lens system to the silicon substrate was measured with a Spectra-Physics 4018 Power Meter. The engraving depth measurements and the pictures of the engraved surface characteristics were made with a Reichert Research Metallograph MeF No. 300/747.

The electrolyte solution was contained in a 2 in. square polystyrene box. The silicon was suspended in the solution in such a manner that the surface to be engraved was 4 mm from the side of the polystyrene box, perpendicular to and in line with the lens system.

The image of the square mask on the silicon averaged about 3.3 mm on a side and was measured to the nearest 0.1 mm on each sample. The precision of the depth measurements was about 5μ at the greater depths increasing to about 2μ at the smaller depths.

Results and Discussion

Illumination intensity and engraving time.—High-resistivity silicon.—The high-resistivity silicon should be near-intrinsic in its responses so that the experimental data should be described by Eq. [23]. Figure 1 indicates graphically the relationship between the engraving depth and the product of the illumination intensity and the square of the engraving time. This data indicates that the integration constant in Eq. [23] is independent of both illumination intensity and engraving time. Thus, the experimental data is described by the semiempirical equation

$$x = 8.05 \times 10^{-10} [It^2 - 2.00 \times 10^5] \qquad [24]$$

for any illumination intensity and/or any engraving time.

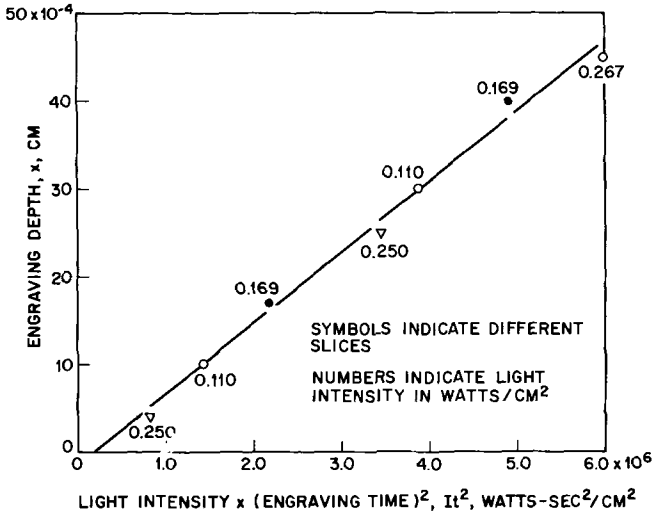

Fig. 1. Illumination intensity, engraving time, and engraving depth relationship for 190 to 225 ohm-cm n-type (100) oriented silicon at room temperature in Dash etch.

This result implies that a certain minimum hole concentration is necessary before engraving commences, the rate of engraving is a function of the concentration of holes (Eq. [16]), and the depth of the engraving is a function of the concentration of holes at the end of the engraving period times the duration of the engraving period. This latter statement implies that the depth of the engraving is independent of the "path" and the same result would be obtained by varying illumination intensity only, varying engraving time only, or varying both illumination intensity and engraving time. Thus Eq. [23] may be written as

$$x = \tfrac{1}{2}K' (It^2 - [It^2]_1) \exp \frac{n\mathbf{F}E}{RT} \qquad [25]$$

Low-resistivity silicon.—The low-resistivity silicon should have a higher concentration of electrons and a low concentration of holes with a high recombination rate constant. Thus, the experimental results obtained with this material should be described by Eq. [20] and [21]. Figure 2 indicates that the engraving depth is a linear function of the engraving time. Rearrangement of Eq. [20] gives

$$\frac{\Delta t}{\Delta x} = \frac{1}{\sqrt{I}K \exp \dfrac{n\mathbf{F}E}{RT}} + \frac{1}{I_0 K \exp \dfrac{n\mathbf{F}E}{RT}} \qquad [26]$$

Figure 3 indicates that the reciprocal of the slopes of the lines in Fig. 2 is a linear function of the reciprocal of the square root of the light intensity. Thus, Eq. [20] is of the correct form for the low resistivity silicon. These results give the semiempirical form of Eq. [21] as

$$x = \frac{5.518 \times 10^{-6} t\sqrt{I}}{1 + 2.649\sqrt{I}} - \frac{5.518 \times 10^{-6} t_1 \sqrt{I}}{1 + 2.649\sqrt{I}} \qquad [27]$$

The value of t_1 can be obtained from the difference between the experimental engraving depth and the depth calculated from the first term on the right side of Eq. [27]. This difference, δ, is described by the relationship

$$\delta = \frac{5.518 \times 10^{-6} t_1 \sqrt{I}}{1 + 2.649\sqrt{I}} \qquad [28]$$

or

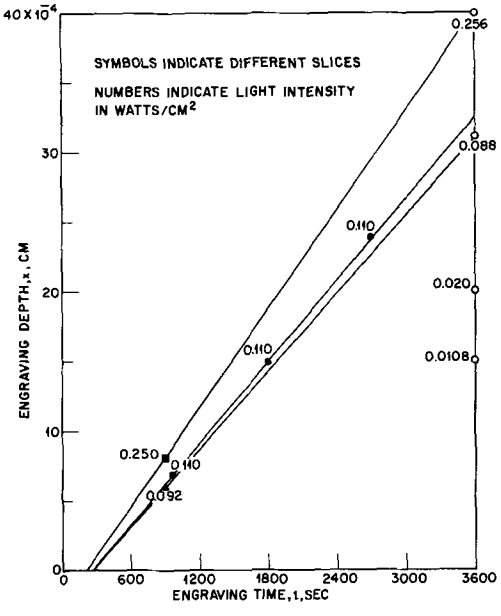

Fig. 2. Engraving time, engraving depth relationship for 0.5 to 1.5 ohm-cm n-type (111) oriented silicon at room temperature in Dash etch.

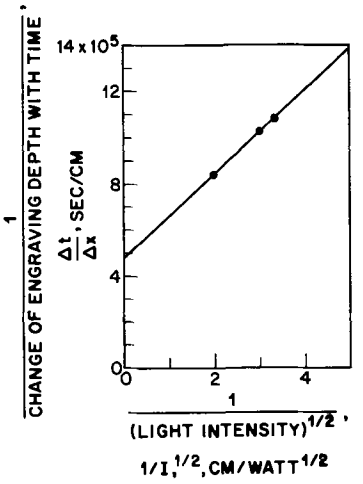

Fig. 3. Rate of engraving (from Fig. 2), illumination intensity relationship.

$$\frac{\delta(1 + 2.649\sqrt{I})}{5.518 \times 10^{-6}} = t_1\sqrt{I} \qquad [29]$$

A plot of the left side of Eq. [29] *vs.* $\sqrt{I}$ is shown in Fig. 4. The slope of the line in this figure gives a value of t_1 or 233 sec. Thus, the semiempirical equation for the low resistivity material is

$$x = \frac{5.518 \times 10^{-6} t\sqrt{I}\left(1 - \dfrac{233}{t}\right)}{1 + 2.649\sqrt{I}} \qquad [30]$$

The values of δ are of such a low magnitude that it is impossible to state conclusively that Eq. [28] is the correct relationship.

Verification of the argument.—Additional experiments utilizing a PEK Industries Model 911 100w mercury arc lamp with a Corning 1-69 infrared filter give results in agreement with the equations presented (Eq. [24] and [30]). The 0.5 to 1.5 ohm-cm material exposed for 1800 sec at 0.982 w/cm^2 was engraved to a depth of 24 x 10^{-4} cm, and when exposed for 8820 sec at 0.016 w/cm^2 was engraved to a depth of 45 x 10^{-4} cm. Calculation of the engraving depth using Eq. [30] gives 23.6 x 10^{-4} cm and 44.9 x 10^{-4} cm, respectively. The 190 to 225 ohm-cm material exposed for 1800 sec at 1.041 w/cm^2 was engraved to a depth of 27 x 10^{-4} cm, and when exposed for the same time at 1.700 w/cm^2 was engraved to a depth of 43 x 10^{-4} cm. Calculation of the engraving depth using Eq. [24] gives 25.6 x 10^{-4} cm and 42.7 x 10^{-4} cm, respectively.

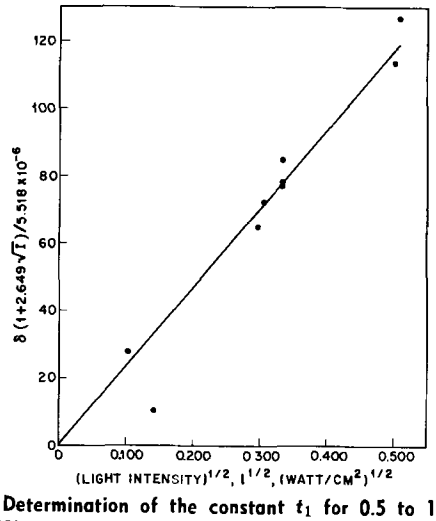

Fig. 4. Determination of the constant t_1 for 0.5 to 1.5 ohm-cm n-type (100) oriented silicon.

Experiments performed with the back of the 195 to 225 ohm-cm material exposed to the solution, with the back masked (with polystyrene film) and with part of the back of the illuminated area exposed to the solution have resulted in (respectively) little or no engraving, engraving as described in this work, and engraving depths equivalent to that in which the total incident illumination is concentrated in only the area for which the back of the sample is insulated from the solution. The 0.5 to 1.5 ohm-cm material was not affected in this manner.

While the effects of masking the back of the 195 to 225 ohm-cm material appear at first glance to be easily explained, such is not the case. Thus, if a space-charge region is developed at the back of the sample, *i.e.*, due to more rapid migration of electrons, it might be postulated that holes would still react at the illuminated surface while electrons react with the solution at the back surface. However, there is (little or) no dissolution of the material. Furthermore, the enhanced dissolution in front of the masked area due to illumination outside this area suggests that migration of holes is not only rapid, but preferentially directed toward the area in front of the mask, where reaction with the solution proceeds. A further complicating factor is that the dissolution reaction (or engraving) proceeds only in the illuminated area when the back is masked. While conclusive results have not been obtained, results suggest that dissolution is enhanced in front of the mask by illumination in unmasked areas in proportion to the illumination on the face opposite the masked surface.

Engraving properties.—The low-resistivity material was not useful for precise engravings. The triangular etch pattern indicated in Fig. 5 has been obtained by other workers (8, 10) and, although they did not indicate orientation, the preliminary treatment used in this work virtually eliminates the possibility that the effect is due to surface faults, although there is a good possibility that it is due to the defect structure (15). Discussions with sales representatives of companies producing material having zero-defect structure have indicated that such pits are not obtained on this material.

The high-resistivity silicon oriented in the (100) plane gives an etched surface as indicated in Fig. 6.

Fig. 5. Pattern obtained on 0.5 to 1.5 ohm-cm, (111) oriented n-type silicon during illumination-induced etching.

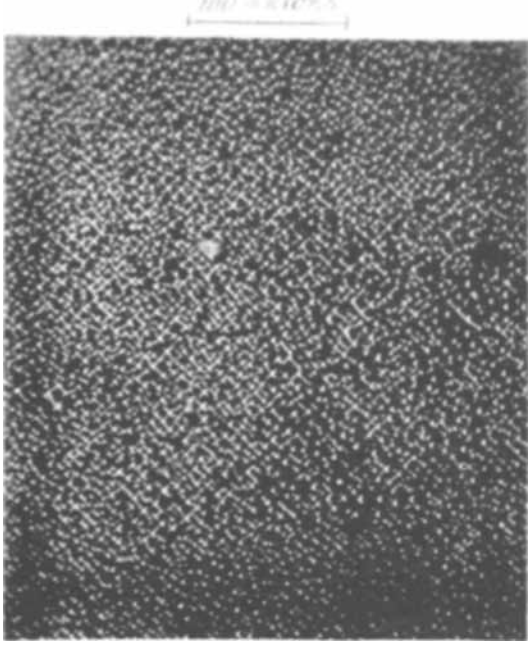

Fig. 6. Pattern obtained on 195 to 225 ohm-cm, (100) oriented, n-type silicon during illumination-induced etching.

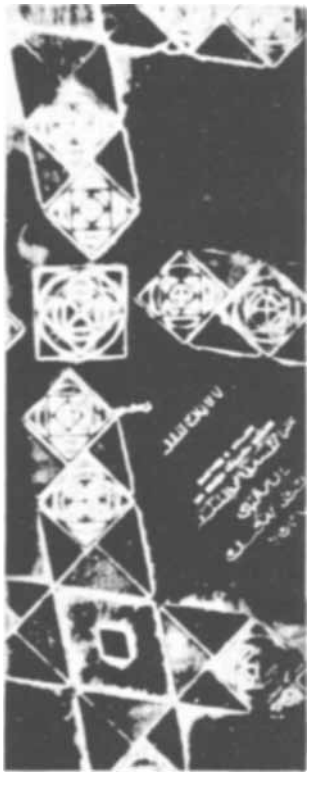

Fig. 7. Engraving obtained on 195 to 225 ohm-cm, (100) oriented, n-type material. The fine lines in the figure are 19-20μ in width on the sample.

This surface is quite good for engravings, the pits being one micron or less in cross-section. Figure 7 is a picture of an engraving in this material using the f 4.5 lens (the better lens). The reduction to the sample is 6.43, the total light intensity was 29 mw and the engraving time was 1 hr. Slightly more than one half the chart is on the sample. The fringe effect is indicated to be about 12μ. That is, there is slight etching indicated up to about 12μ from the light boundary. The only portions of the engraving which are not easily resolved are the portions of the chart consisting of five mil dots spaced five mils apart (black dots on clear area). However, there is a "cross" effect in these areas which is not present in other areas. This effect is probably due to diffraction and can thus be lessened or eliminated by use of a monochromatic light source. The five mil black and clear lines can be easily resolved. There is an over-all etch, but the depth of etch under the center of the black lines is about 4μ compared to about 30μ under the clear lines. On the sample these lines are each about 19-20μ in width. The total depth of the engraving is about 30μ.

The pattern (pictured in Fig. 7) was engraved at a reduction of 10.4 using the mercury arc lamp and infrared filter. The diffraction effect on the 5 mil dots was absent, and the dots were well defined.

Conclusions

The effect of light intensity on the engraving of semiconductors has been indicated. If the recombination rate constant is large, steady-state conditions are attained fairly rapidly and the engraving depth is a linear function of engraving time. If the recombination rate constant is small, the rate of engraving is a function of the instantaneous concentration of holes or the product of illumination intensity and engraving time, and the depth of the engraving is a function of the product of the illumination intensity and the square of the engraving time.

The engraved surface of the (111) material is not satisfactory for fine engravings. The surface consists of steps in a triangular pattern which are probably due to the defect structure of the crystal.

The engraved surface of the (100) material is satisfactory for fine engravings. The surface nonuniformities are 1μ or less. The illumination and lens system used in this study give engravings with a resolution of better than 12μ.

The type of illumination and the lens system become quite critical when fine engravings are desired. Some of the factors, including the more obvious ones, which probably affect the resolution of the engraving and the degree to which it reproduces the original are: (*i*) the pattern: the engraving can be no better than the pattern. (*ii*) The lens system: good lenses must be used to obtain sharp images with good resolution. The depth of field (or focus) of the lenses should be compatible with the depth of the engraving. (*iii*) The light and type of light: the use of monochromatic light of a particular wavelength greatly decreases the possibility of scatter and diffraction through the pattern and lens system, and through the cell wall and engraving solution. (*iv*) The cell window: the window material must not only be inert toward the engraving solution, but must also have good optical properties. (*v*) The diffusion length and other properties of the injected hole-electron pairs, and/or the resistivity of the material: this study indicates that high-resistivity (100) oriented material gives satisfactory results and zero defect structure material may also give satisfactory results. (*vi*) Material crystal form: polycrystalline or monocrystalline material, and the crystal orientation may affect the engraving rate and the type of surface obtained and the defect structure is probably quite important. (*vii*) Technique: the manipulative technique becomes quite critical in obtaining a high degree of resolution. A very stable system and critical means of focus and alignment is necessary.

The back surface of near-intrinsic material should probably be masked if the treatment presented is to be applicable. The study of the effects of masking is beyond the scope of this work, and no attempt has been made to suggest a cause of these effects.

Acknowledgments

This study was supported by the Marshall Space Flight Center, Huntsville, Alabama, Contract NAS 8-20395, and by the Lockheed Independent research program. The author wishes to thank Dr. P. S. Castro

for many valuable discussions and suggestions during the preparation of this paper.

Manuscript submitted Aug. 22, 1968; revised manuscript received Dec. 4, 1968.

Any discussion of this paper will appear in a Discussion Section to be published in the December 1969 JOURNAL.

NOMENCLATURE

a, b	Constants in the Tafel equation
c	Rate constant for recombination
C_o	Concentration of reacting species
C, t_1	Integration constants
Dp	Diffusion coefficient for holes
E	Total potential between bulk of semiconductor and bulk of electrolyte solution
E_o	Total potential E less the photopotential, Vp
$\mathbf{F}$	Faraday
i	Current density
I	Incident illumination intensity
I_o	Equal to $p_o\sqrt{\alpha/c}$
$[It^2]_1$	Equal to C
J	Hole current due to diffusion
k, k'	Constants
K	Equal to $k\sqrt{\alpha/c}$
K'	Equal to $k\alpha$
n	Number of equivalents
n_o	Number of free electrons in the bulk of the semiconductor
n_i	Number of electrons produced during illumination
n_t	Number of bound electrons
p	Number of free holes
p_o	Number of free holes in the bulk of the semiconductor
p_i	Number of holes produced during illumination
q	Rate of generation of hole-electron pairs by incident illumination
R	Gas constant
t	Time
T	Absolute temperature
Vp, Vp_1, Vp_2	Induced photopotential
x	Distance
α	Constant relating illumination intensity and rate of hole-electron pair generation
δ	Representation of second term in Eq. [21]

REFERENCES

1. A. S. Grove, "Physics and Technology of Semiconductor Devices," John Wiley and Sons, Inc., New York (1967).
2. H. Gerischer, *This Journal*, **113**, 1174 (1966).
3. R. S. Muller, *ibid.*, **109** 1195 (1962).
4. M. Balkanski, J. Bardeleben, and A. F. Bogenschutz, *J. chim. phys.*, **57**, 507 (1960).
5. W. H. Brattain and C. G. B. Garrett, *Physica*, **20**, 885 (1954).
6. *Ibid.*, *The Bell System Tech. J.*, **34**, 129 (1955).
7. H. Gerischer, and F. Beck, *Z. physik, Chem. (Frankfurt)*, **23**, 113 (1960).
8. J. H. Braun, *This Journal*, **108**, 588 (1961).
9. D. R. Turner, *ibid.*, **107**, 810 (1960).
10. P. J. Holmes, "The Electrochemistry of Semiconductors," Academic Press, New York (1962).
11. W. H. Brattain, and J. Bardeen, *Bell System Tech. J.*, **32**, 1 (1953).
12. J. B. Flynn, *This Journal*, **105**, 715 (1958).
13. E. A. Efimov and I. G. Erusalimchik, *Doklady Akad. Nauk S.S.S.R.*, **130**, 353 (1960).
14. A. Uhlir, *Bell Syst. Tech. J.*, **35**, 333 (1956).
15. W. Czaja, *J. Appl. Phys.*, **37**, 3441 (1966).

Electrical Properties of Zinc and Cadmium Ion Implanted Layers in Gallium Arsenide

R. G. Hunsperger and O. J. Marsh

Hughes Research Laboratories, Malibu, California

ABSTRACT

Ion implantation has been used to dope high resistivity, single crystal gallium arsenide with cadmium and zinc. Implants were made with 20 kv ions into heated substrates held at 400°C. Electrical characteristics of the implanted layers have been studied as a function of isothermal and isochronal annealing cycles. The surface resistivity, average mobility, and carrier concentration in the layer have been determined by Hall measurements; it has been observed that these electrical properties are dependent on post-implantation annealing and generally tend to improve significantly with annealing at relatively low temperatures for short times. For example, annealing of cadmium implanted samples at temperatures up to 800°C for less than 1 hr was sufficient to increase mobility from a value of 4 cm^2/v sec to approximately 180 cm^2/v sec, and to reduce sheet resistivity from approximately 8 x 10^4 ohm/□ to about 6 x 10^3 ohm/□. Additional annealing for 20 min at 900°C further reduced sheet resistivity to 300 ohm/cm and increased surface carrier concentration to a maximum of 2 x $10^{15}/□^2$. The increased carrier concentration eventually resulted in decreased mobility because of impurity scattering.

Ion implantation has been used to dope gallium arsenide with various elements, producing both n- and p-type layers; proton bombardment has been used to produce electrically isolating semi-insulating layers (1). Initial results have indicated that implantation is a promising method for producing doped regions in gallium arsenide at relatively low temperatures compared with those required for diffusion processes. In addition, ion implanted layers in semiconductors have been found to be more planar than diffused layers (2). Numerous ions have already been implanted in gallium arsenide to produce doped layers, and it is likely that many other ion species also can be used successfully, including some that do not lend themselves well to diffusion techniques. Zinc and tellurium implantations have been reported by Mayer *et al.* (3), and work on zinc implants has also been done by Roughan and Manchester (4). Cadmium implants into

GaAs have been made by Itoh (5), neodymium implants by Gibbons *et al.* (6), and sulfur by Kellet *et al.* (7). This paper describes the electrical characteristics of zinc and cadmium implanted layers in GaAs as a function of implantation parameters and subsequent annealing procedures.

Experimental

Implantations were made into undoped n-type gallium arsenide substrates with room temperature resistivities of 1 to 10 ohm-cm. Substrate wafers 15 mils thick were lapped and subsequently chemically polished to remove surface damage prior to ion implantation. These surfaces were oriented in the <111> direction (± 3°).

All implantations were performed with 20 kv ions. A heated stage was used to maintain the substrate at an elevated temperature (400°C for most samples) during implantation. An arc discharge ion source was used for these implants (8). The pulsed nature of this source makes it very difficult to measure ion current density. The implanted ion densities ranged from 10^{15} to $10^{16}/cm^2$ as determined by Rutherford scattering measurements (9). After implantation the samples were annealed at various temperatures up to 900°C. The annealing was performed in a nitrogen atmosphere, and for temperatures of 600°C or greater the samples were encapsulated in a film of SiO_2 to prevent decomposition of the GaAs and/or outdiffusion of the dopant atoms. The SiO_2 was deposited by decomposition of tetraethyl orthosilicate at 480°C. Below 600°C, extended annealing (24 hr) of the implanted samples showed no observable decomposition of the GaAs even without the protective SiO_2 film.

The electrical characteristics of the implanted layers (sheet resistivity ρ_S, effective surface carrier concentration N_S, and effective mobility μ) were determined using van der Pauw (10) Hall measurement technique. A "cloverleaf" shaped mesa was etched onto the samples to lessen the effect of contact size on the measurements. The junction between the p-type implanted layer and the n-type substrate provided the necessary electrical isolation of the implanted layer during measurement. All Hall measurements were made at room temperature, after the samples were quenched in air from their anneal temperature.

Results and Discussion

Figure 1 shows the change in sheet resistivity as a function of annealing for a sample implanted with approximately $10^{16}/cm^2$ 20 kv zinc ions, with the substrate held at 400°C. The implanted layer was initially p-type (after implantation-before annealing) with a sheet resistivity of approximately 4.5 x 10^4 ohm/□. Annealing at temperatures up to 600° caused the resistivity to decrease. (As one moves to the right on the diagram, each point represents an additional 10 min anneal at the indicated temperature.) Note that

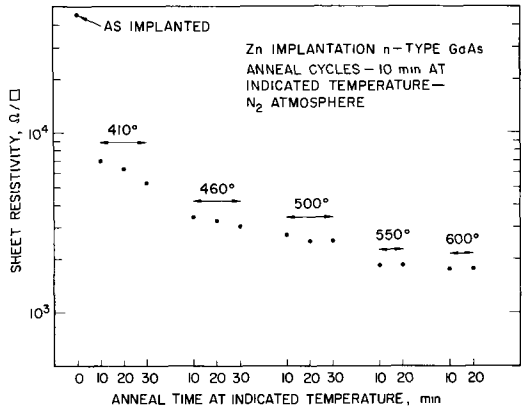

Fig. 1. Variation of sheet resistivity as a result of annealing zinc implanted GaAs.

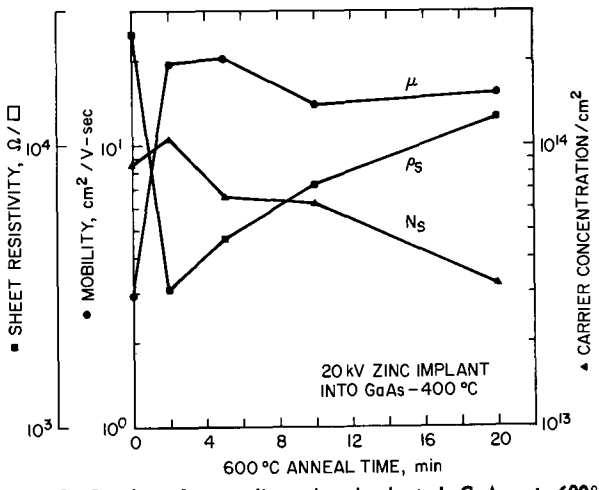

Fig. 2. Results of annealing zinc implanted GaAs at 600°C without surface protection.

most of the decrease in resistivity occurred early in the cycle at temperatures below 450°C. As will be shown later the decrease in resistivity results mainly from improved mobility as crystal damage caused by implantation is annealed away.

It has been found that care must be taken to protect the surface of the sample during anneal at 600°C and above, in order to prevent outdiffusion of the dopant atoms. Outdiffusion of zinc atoms from implanted GaAs has been observed when the surface was not protected during annealing. An example of this effect is shown in Fig. 2, where data are given for a sample annealed at 600°C with no protective covering on the surface. In the first 2 min of the anneal, mobility increased greatly and surface resistivity decreased. After further annealing the sheet resistivity began to increase, while surface carrier concentrations decreased and mobility remained relatively constant. No dissociation of the GaAs was observed when the surface of the sample was viewed under 200X magnification, thus it is felt that the increased sheet resistivity cannot be attributed to dissociation. Instead, it appears to result from outdiffusion of the implanted zinc. The results of an experiment to verify this conclusion are shown in Fig. 3. A sample similar to that of Fig. 2 was annealed at 600°C, but it was covered during the first 10 min by a polished, nonimplanted wafer of GaAs of the same type as the substrate. This cover wafer retarded outdiffusion by reducing the concentration gradient at the surface and thus very little degradation of electrical characteristics was observed. When the cover was removed after 10 min, ρ_S began to increase and N_S began to decrease at rates similar to those observed for the other uncovered sample in Fig. 2. Subsequent

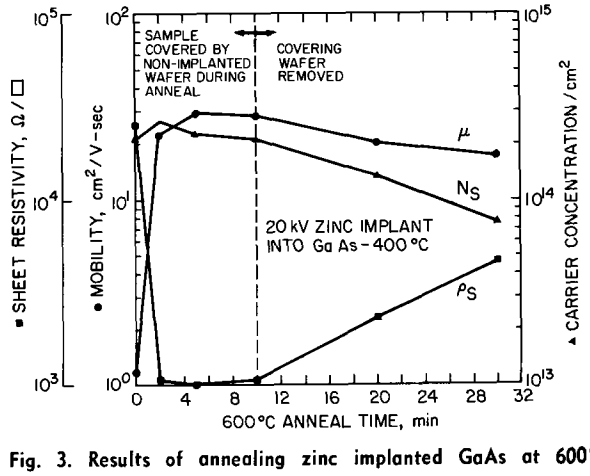

Fig. 3. Results of annealing zinc implanted GaAs at 600°C with surface protection.

to the anneal cycle of Fig. 3 the sample was annealed at 700°C for a total of 30 min without surface protection. This annealing resulted in an increase in ρ_S to 1.04 x 10^4 ohm/□, an increase in μ to 206 cm^2/v-sec, and a decrease in N_S to 2.92 x $10^{12}/cm^2$. Additional evidence of outdiffusion was given by the fact that the cover wafer (although unimplanted n-type material) was found after the anneal to have a p-type layer at the surface which had contacted the implanted layer. A similar effect has been observed for tin implants in GaAs but not for cadmium implants, presumably because tin and zinc diffuse much more rapidly in GaAs than does cadmium. The data of Fig. 2 and 3 emphasize the importance of providing some type of protective covering for ion implanted GaAs during annealing. Such protection can be provided by using a cover wafer or by encapsulating the sample in SiO_2. Both techniques are also effective in preventing the dissociation of GaAs, at least at temperatures up to 900°C.

The use of SiO_2 protective covering allowed the anneal behavior of implanted layers to be studied at elevated temperatures. Figure 4 shows the effect on a typical 20 kv zinc implanted sample of annealing in a series of 10 min anneals from 500° to 900°C. The sample was implanted at 400°C. The sheet resistivity decreased monotonically as a result of increasing mobility, and above 700°C also as a result of increasing carrier concentration. In the temperature range below 700°C the surface carrier concentration first increased and then decreased somewhat with further annealing. The increase is thought to be caused by implanted ions moving to electrically active substitutional positions in the lattice; the decrease is not well understood at present and may be attributed to a number of possible causes. The decrease may result from compensation by defect centers which are released when damage clusters dissociate on annealing. An effect of this type in n-type GaAs has been reported by Fuller, Wolfstern, and Allison (11). The apparent decrease in effective surface carrier concentration may also result merely because the mobility in implanted layers is nonuniform with depth, and the calculation of surface concentration from van der Pauw Hall data is more dependent on the contribution from higher mobility regions. Therefore, even if we assume hypothetically that the concentration profile of electrically active atoms does not change significantly between 500° and 700°C but that the mobility in the more lightly doped regions increases appreciably, the effective mobility in the layer would increase and cause an apparent decrease in the surface concentration N_S. [This effect has been described by Mayer *et al.* (12).]

The relatively large increase in carrier concentration above 700°C results in part from the increased solubility of zinc [7 x $10^{19}/cm^3$ at 700°C to 3 x $10^{20}/cm^3$ at 900°C (13)], in addition to the fact that the doped layer thickens with annealing because of the very rapid diffusion of zinc in GaAs. For an anneal cycle such as that of Fig. 4, calculations based on the work of Shih *et al.* (14) predict a total diffusion depth of as much as 90μ, depending on the initial concentration *vs.* depth profile of the implanted ions. Assuming that there are enough implanted atoms present that the concentration of electrically active (substitutional) zinc per cubic centimeter is constant or increasing with increased solubility, the thickening of the layer because of diffusion would result in a higher measured value for surface concentration per square centimeter.

For a series of isothermal anneals of zinc implanted GaAs, as shown for a typical 20 kv, 400°C implant in Fig. 5, the variation of ρ_S, μ, and N_S with anneal temperature agreed with that observed in the series of 10 min anneals of Fig. 4. In addition, it can be seen from the data of Fig. 5 that much of the change in electrical properties (at temperature up to 700°C) occurred during the first few minutes of each cycle at a new, higher temperature. Mobility increased to a value of about 150 cm^2/v-sec following anneal at 900°C. This behavior is in contrast to that of cadmium implanted samples as shown in Fig. 6 and 7, in that the mobility in the cadmium case peaked after annealing at 800°C and then decreased with further annealing. This difference between the mobility behavior for zinc implants and that for cadmium is believed to result because cadmium diffuses three orders of magnitude more slowly than zinc in GaAs (14, 15). Angle lap and stain techniques on the cadmium implanted samples indicated a junction depth of 0.3μ after the 600°C annealing and showed negligible diffusion after the 900°C anneal (to within the accuracy of measurement of 0.05μ). The junction depth of 0.3μ is considerably greater than the 250Å depth expected from the theoretical Lindhard-Scharff projected range of the ions in amorphous material. It is possible that the larger junction depth is due to channeling and/or enhanced diffusion of the ions during implantation. As more cadmium atoms enter substitutional sites (and become electrically active) as a result of increasing solubility at higher temperature, the doped layer does not thicken as in the case of zinc. Hence the concentration of electrically active cadmium atoms per cubic centimeter increases, and ionized impurity scattering tends to decrease the mobility. A comparison of the observed decrease in mobility with the Brooks-Herring (16, 17) relation for ionized impurity scattering, as-

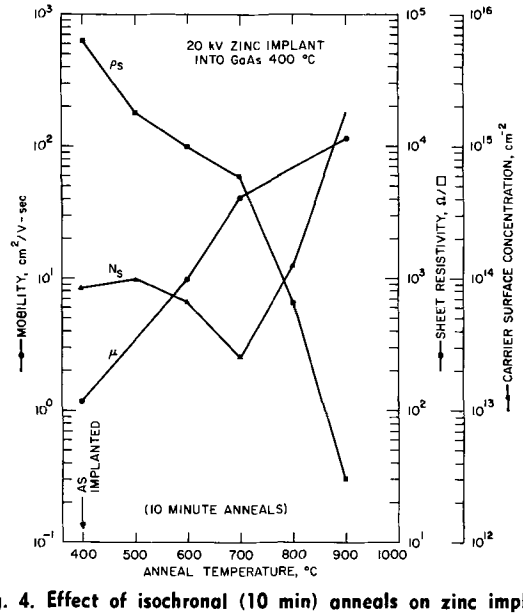

Fig. 4. Effect of isochronal (10 min) anneals on zinc implanted GaAs.

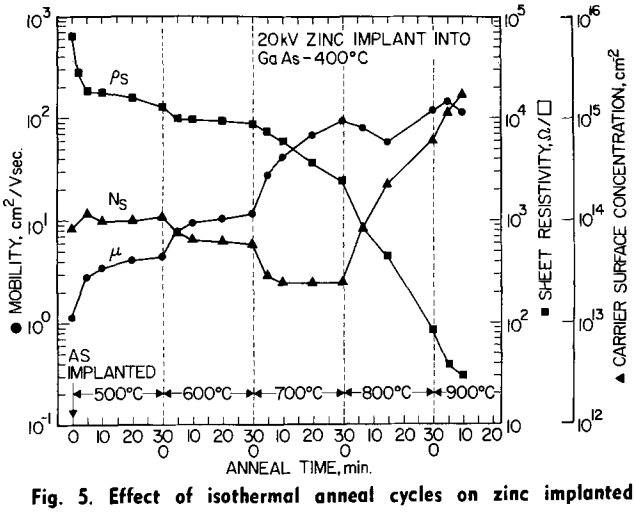

Fig. 5. Effect of isothermal anneal cycles on zinc implanted GaAs.

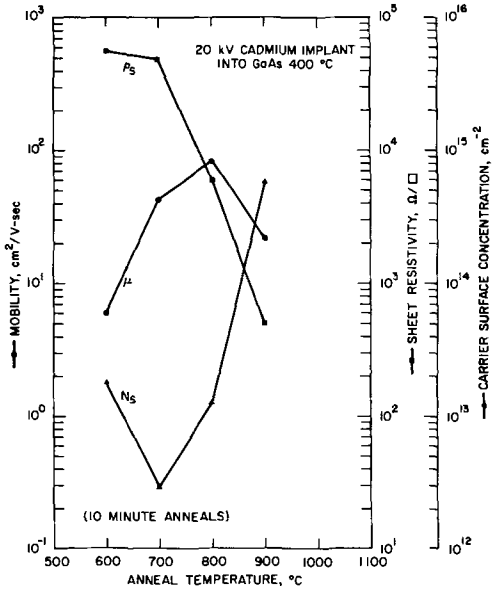

Fig. 6. Effect of isochronal (10 min) anneals on cadmium implanted GaAs.

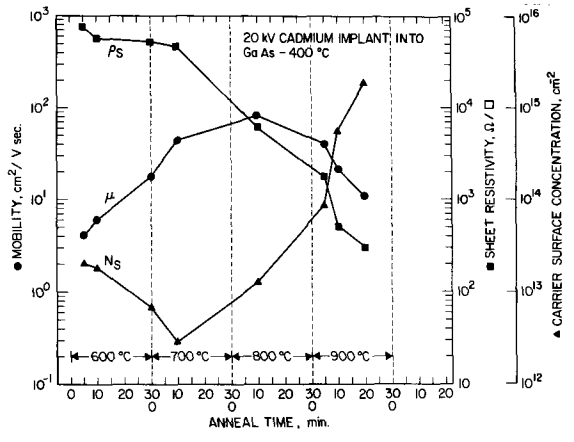

Fig. 7. Effect of isothermal anneal cycles on cadmium implanted GaAs.

suming a lattice mobility of 450 cm²/v-sec (18), shows that the observed mobility decreased somewhat more slowly than would be expected with increasing ion impurity concentration (see Fig. 8). This may result from the competing process of damage annealing, which reduces defect scattering. It can also be seen in Fig. 8 that the mobility remains below the value expected for only ionized impurity scattering until annealing at 900°C for 20 min has been performed. This indicates the presence of lattice damage and resultant defect scattering. Such persistent damage is typical only for the extremely heavy implants (10^{15} to 10^{16} ions/cm²) used in these experiments. The damage produced by smaller doses anneals at temperatures below 600°C (9).

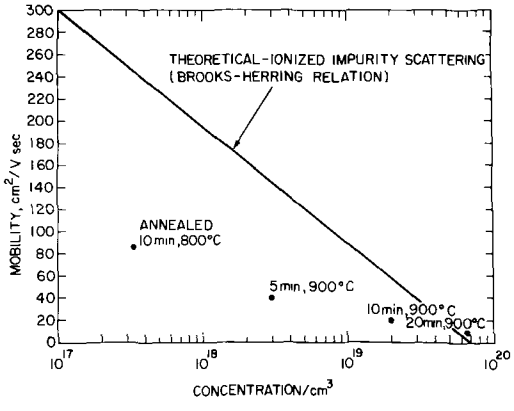

Fig. 8. Variation of mobility with ionized impurity concentration [theoretical curve (16) assumes a hole lattice mobility of 450 cm²/v-sec (18)]. Concentrations were calculated using an implanted layer thickness of 0.3μ obtained from angle section and stain junction depth measurements.

With the exception of mobility, the electrical properties of cadmium implanted samples changed with annealing in a fashion similar to those of zinc implants. The surface carrier concentration increased above 700°C as it did for zinc. For cadmium this increase presumably results almost entirely from the increase in solubility, since negligible diffusion was observed. Another difference between cadmium and zinc implants was that cadmium samples generally had to be annealed to higher temperatures to achieve equivalent values for sheet resistivity and mobility. No measurable p-type layers were obtained in cadmium implanted samples until after anneal at 600°C.

Summary

Ions of both zinc and cadmium can be implanted into GaAs to form p-type layers. The electrical properties of the layers are dependent on post-implantation annealing and generally tend to improve significantly with annealing at relatively low temperatures for short times. The fact that electrical properties continue to change even after considerable annealing is consistent with the results of Rutherford scattering measurements (9), which indicate that for heavily zinc implanted GaAs (dose $\geq 10^{16}$/cm²) considerable damage remains even after annealing at 600°C. For implanted doses $< 10^{16}$/cm² most damage anneals away below 600°C. It also must be remembered that in the case of zinc implants considerable diffusion occurs above 700°C and that this diffusion can affect the electrical properties of the layers. Decomposition of the GaAs and outdiffusion of the implanted atoms during annealing can be limited to an insignificant level by providing a suitable protective covering for the surface of the sample.

Acknowledgments

The authors are grateful to D. Loper and G. Mohr for sample preparation and angle section and stain junction depth measurement.

Manuscript submitted Sept. 9, 1968; revised manuscript received Nov. 25, 1968. This paper was presented in part at the Boston Meeting, May 5-9, 1968, as Paper 133.

Any discussion of this paper will appear in a Discussion Section to be published in the December 1969 JOURNAL.

REFERENCES

1. A. Foyt, W. Lindley, J. Donnelly, and C. Wolfe (Lincoln Laboratory) to be published, *Appl. Phys. Lett.*
2. R. Sherwell, J. Raines, and L. Large, Int. Conf. on Applications of Ion Beams to Semiconductor Technology, Grenoble, May 1967, p. 641.
3. J. Mayer, O. Marsh, R. Mankarious, and R. Bower, *J. Appl. Phys.*, **38**, 1975 (1967).
4. P. Roughan and K. Manchester, To be published, *This Journal.*
5. T. Itoh, To be published.
6. J. Gibbons, J. Moll, and N. Meyer, *Nucl. Instr. Meth.*, **38**, 165 (1965).
7. C. Kellet, W. King, F. Leight, *et al.*, Ion Phys. Corp. AFCRL Cont. Rept. No. 66-367.
8. O. Marsh, J. Mayer, A. Mohr, and R. Ohl, Hughes Res. Labs, NASA Contract (NAS 12-124) Report, "Development of Ion Implantation Techniques for Microelectronics," Oct. 1967.
9. H. Dunlap, R. Hunsperger, and O. Marsh, Hughes Res. Labs, NASA Contract (NAS 12-124) Annual Report, Oct. 1968 (Work currently in progress being performed in collaboration with J. Mayer, T. Picraux and E. Westmoreland at California Institute of Technology, Pasadena.)

10. L. van der Pauw, *Philips Research Repts.*, **13**, 1 (1958).
11. C. Fuller, K. Wolfstirn, and H. Allison, *J. Appl. Phys.*, **38**, 4339 (1967).
12. J. W. Mayer, O. J. Marsh, G. A. Shifrin, and R. Baron, *Can. J. Phys.*, **45**, 4073 (1967).
13. L. Chang and G. Pearson, *J. Phys. Chem. Solids*, **25**, 23 (1964).
14. K. Shih, J. Allen, and G. Pearson, *ibid.*, **29**, 379 (1968).
15. B. Goldstein, "Compound Semiconductors," Vol. 1, p. 347, R. Willardson and H. Goering, Editors, Reinhold, Publishing Co., New York (1962).
16. H. Brooks and C. Herring, *Phys. Rev.*, **83**, 879 (1951).
17. E. Conwell, *ibid.*, **93**, 693 (1954).
18. F. Rosi, D. Meyerhoffer, and R. Jensen, *J. Appl. Phys.*, **31**, 1105 (1959).

The Preparation and Properties of Vapor-Deposited Epitaxial $InAs_{1-x}P_x$ Using Arsine and Phosphine

J. J. Tietjen, H. P. Maruska, and R. B. Clough

RCA Laboratories, Princeton, New Jersey

ABSTRACT

Single crystalline $InAs_{1-x}P_x$ layers have been prepared by a vapor-phase growth technique previously used to prepare very high-quality $GaAs_{1-x}P_x$. These $InAs_{1-x}P_x$ alloys exhibit electron mobilities equivalent to the highest yet reported for this system. Extensive electron mobility data is reported for the alloys at 77°K. At this temperature, a mobility value of 120,000 cm^2/v-sec was measured for InAs, which is slightly higher than previously reported. Vegard's law is obeyed over the entire composition range. Both n- and p-type doping has been achieved during vapor growth to provide a broad range of electrical resistivities and p-n junctions.

$InAs_{1-x}P_x$ alloys have a broad range of band gaps and electron mobilities. Consequently, they have potential advantage for a number of device applications. These include infrared emitting (1) and detecting devices, utilizing their low energy band gaps, and devices operating at high frequencies, which can take advantage of their high mobilities. Although results (2-5) have been reported pertaining to improving the preparation and properties of melt-grown crystals, very little work has involved the vapor-phase growth of these alloys.

Recently, a vapor phase growth method (6) has been described for the growth of $GaAs_{1-x}P_x$ alloys, and the high purity, homogeneity, and crystalline perfection of the crystals prepared by this technique has been demonstrated. With this growth method, Ga is transported as its subchloride via a reaction with HCl gas, and AsH_3 and PH_3 serve as the sources of the group V elements. As a logical extension of this growth technique, a simple substitution of In for the Ga has permitted the preparation of $InAs_{1-x}P_x$ single crystals having very good electrical properties and crystallinity. In addition, both n- and p-type doping has been achieved, and multilayer structures have been prepared.

Experimental

Apparatus and materials.—The apparatus, shown schematically in Fig. 1, is essentially identical to that described previously (6) with the exception that the source Ga is replaced by In. It consists principally of a straight tube through which the pertinent vapors pass. A large bore stopcock separates the growth region from a forechamber which may be purged independently to facilitate insertion and withdrawal of the specimens without contaminating the system. HCl gas, AsH_3, PH_3, and H_2Se (which serves as the n-type dopant source) are all monitored into the apparatus by precision valves and flowmeters. P-type doping is achieved by vaporizing metallic Zn in a heated sidearm and transporting the vapors into the deposition zone with H_2 carrier gas.

With the exception of the use of In,[1] and <100>-oriented InAs single crystalline substrates,[2] the materials employed in this study are as described previously (6). The InAs substrates were mechanically polished to a flat, mirror-smooth finish, and then chemically polished in a solution of 2% by volume of bromine in methanol. Typical substrate dimensions were about 2 cm^2 in area and 0.5 mm thick.

Procedure.—The growth procedure also closely follows that described previously (6). Freshly etched substrates are inserted in the growth chamber and heated in hydrogen at a rate of about 20°C/min. When the substrate temperature reaches 600°C, the AsH_3 flow is started in order to provide an arsenic atmosphere to stabilize the substrate surface. When the final operating temperatures are reached, the HCl flow over the In is started and the epitaxial deposition of InAs occurs. The flow of PH_3 is then initiated and slowly increased to produce a final gas phase mixture of AsH_3 and PH_3 appropriate to the desired alloy composition. The dependence of the alloy composition on the concentration of PH_3 in the AsH_3-PH_3 mixture is presented in Fig. 2. By slowly increasing the PH_3 flow, a region is introduced which is graded in composition from InAs at the substrate to the selected alloy composition. This graded region, which has been as thick as 50μ for phosphorus-rich alloys, is included to minimize strain arising from

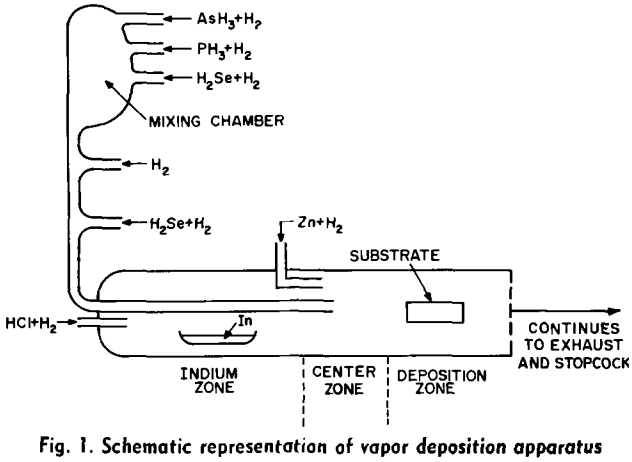

Fig. 1. Schematic representation of vapor deposition apparatus

[1] Purchased from Cominco American, Inc., Spokane, Washington (manufacturer's reported purity is 99.9999%).
[2] Purchased from Monsanto Company, St. Louis, Missouri.

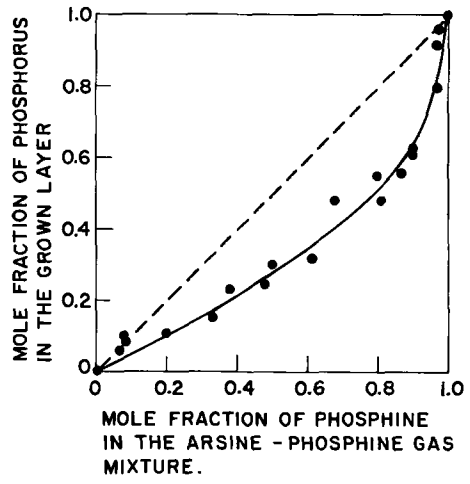

Fig. 2. Dependence of alloy composition on concentration of PH_3 in the AsH_3-PH_3 gas mixture.

differences between the lattice constants of the substrate and the final alloy layer.

The sum of the flow rates of pure AsH_3 and PH_3 are in the range of 20-60 cm³/min. The HCl flow rate is about 5 cm³/min, and between 1 and 2 l/min of hydrogen is used as a carrier. With these flow rates, with a substrate temperature in the range of 675°-725°C, a center zone temperature of 950°-975°C, and an indium zone temperature of between 850° and 950°C, growth rates in the range of ¼ to ½ μ/min are obtained under steady-state conditions. Typical thicknesses for the constant composition region of these deposits have been between 50 and 150μ.

Results and Discussion

Crystallinity and growth morphology.—X-ray analysis by the Debye-Scherrer technique indicates that these layers are single phase, cubic, solid solutions, and show no detectable range of composition. In addition, Laue back-reflection analysis reveals that the layers are epitaxial. The lattice constant is presented as a function of alloy composition in Fig. 3, which demonstrates that Vegard's law of solid solutions is obeyed in this system. This result is in general agreement with those of Folberth (2), and Koster and Ulrich (7). The compositions were determined by chemical analysis (8) with an accuracy of ± 0.5%.

Although no detailed evaluation of the crystalline perfection of these layers was carried out, examination by optical microscopy revealed that macroscopic surface imperfections, such as hillocks, were prevalent only in phosphorus-rich alloys. For alloys containing less than 50% InP, surfaces are obtained which show virtually no gross structure, and to the unaided eye appear to be mirror-smooth.

Electrical properties.—The epitaxial layers were examined by Hall coefficient and resistivity measurements using a technique (6) which permits these measurements to be made on layers as thin as 50μ. Typical electron carrier concentrations for undoped alloys are in the range of 5 x 10^{15} to 1 x 10^{16}/cm³. The electron mobilities are presented as a function of alloy composition in Fig. 4 and 5 for room temperature and 77°K, respectively. The data of other workers (3, 5, 9-11), and the results of a theoretical analysis of Ehrenreich (12) based on polar scattering alone, are included for comparison. In general, the mobility values at room temperature are good. In addition, these data corroborate Ehrenreich's contention that alloy scattering is not dominant in this alloy system, at room temperature. The relatively low mobility values obtained for alloy compositions approaching InP are attributed to strain arising from lattice and thermal-expansion differences between the InAs substrate and the alloy layer. It is anticipated that further compositional grading can alleviate this problem.

The data presented in Fig. 5 are the most extensive data reported for 77°K for this alloy system and compare favorably with the best previously reported mobility values. The mobility value of 120,000 cm²/v-sec for InAs is to be compared to the best previously reported value of 112,000 cm²/v-sec (9). However, the value of 18,000 cm²/v-sec for InP is somewhat lower than the best reported value of 23,400 cm²/v-sec (10).

Doping.—Doping of InAs has been investigated using H_2Se gas as a source of Se for n-type doping, and zinc for p-type doping. Electron concentrations as high as 3 x 10^{19}/cm³ were achieved and in general these crystals exhibit mobilities comparable to the best reported in the literature for untreated samples (11, 13). For example, at carrier concentrations of 1 x 10^{18} and 3 x 10^{19}

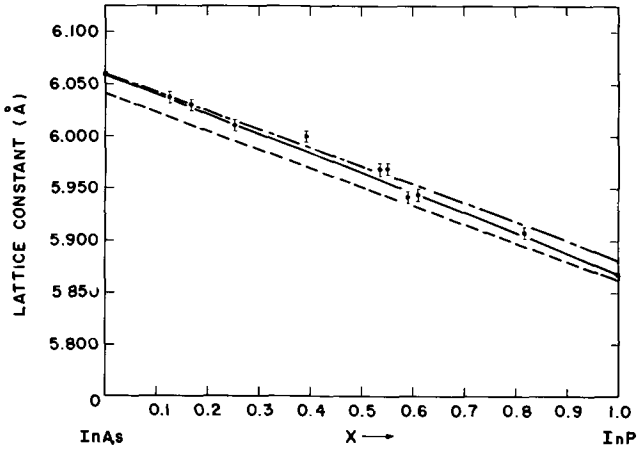

Fig. 3. Dependence of lattice constant on alloy composition in the system $InAs_{1-x}P_x$. The dependence observed by Folberth (2) and Koster and Ulrich (7) is also included: - - - Folberth; — · — Koster and Ulrich; ——— this paper.

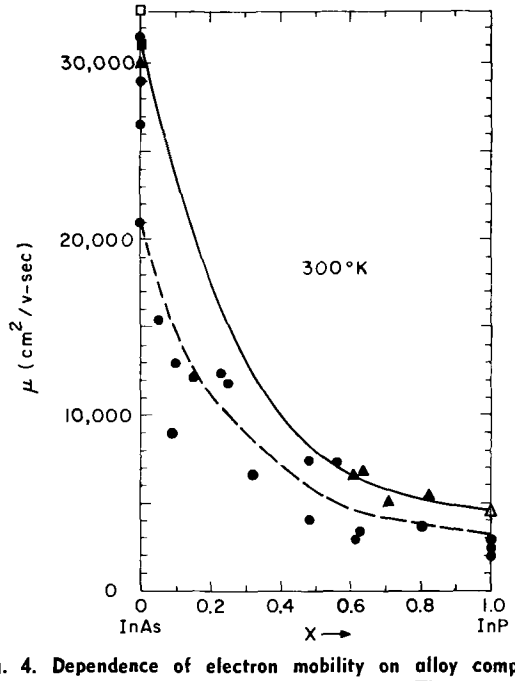

Fig. 4. Dependence of electron mobility on alloy composition in the system $InAs_{1-x}P_x$ at room temperature. The experimental results of other workers and a theoretical analysis of Ehrenreich (12) are also included: - - - Weiss (3); ▲ Winkler, *et al.* (5); ■ Cronin and Borello (9); △ Glicksman and Weiser (10); □ Hilsum and Rose-Innes (11); ——— Ehrenreich; • this paper.

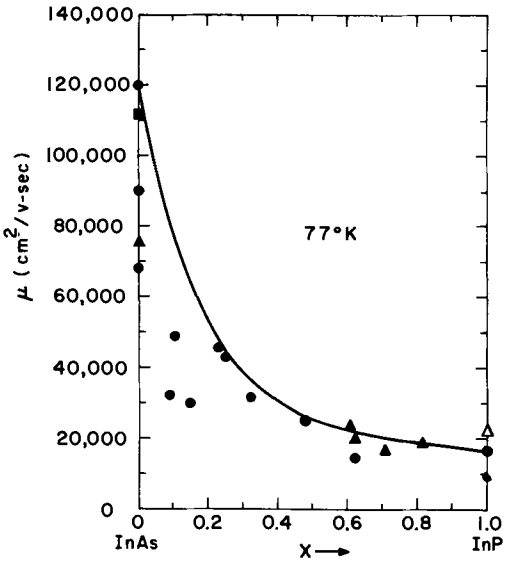

Fig. 5. Dependence of the electron mobility on alloy composition in the system $InAs_{1-x}P_x$ at 77°K. The experimental results of other workers are also included: ▲ Winkler *et al.*; ■ Cronin and Borello; △ Glicksman and Weiser; □ Hilsum and Rose-Innes; ——— this paper.

cm^{-3} the mobility values at room temperatures are 10,000 and 1,500 cm^2/v-sec, respectively. Thus, doping to these high donor concentrations does not degrade the material. With respect to hole concentrations, values in the range of 5 x 10^{17} to 1 x $10^{19}/cm^3$ can be readily obtained, with mobilities of between 150 and 90 cm^2/v-sec for this doping range. These compare with earlier reported values as high as 120 cm^2/v-sec for hole concentrations of about 2 x $10^{19}/cm^3$ (11).

Both n- and p-type doping were also demonstrated for some $InAs_{1-x}P_x$ alloys, and for InP, as characterized by point-contact breakdown and thermal probe measurements. In addition, multilayer structures involving both n- and p-type regions were prepared for selected alloy compositions.

Conclusions

The ability to prepare good-quality $InAs_{1-x}P_x$ alloys by a vapor-growth method previously used for the preparation of $GaAs_{1-x}P_x$ alloys has been demonstrated. Electron mobilities have been obtained for these $InAs_{1-x}P_x$ alloys which are comparable to the best previously reported values for melt-grown material. Both n- and p-type doping can be achieved over a broad resistivity range, and these doped layers can be incorporated in multilayer structures. Vegard's law of solid solutions was found to be obeyed in this alloy system.

Acknowledgments

The authors wish to express their appreciation to D. Richman for valuable suggestions and discussions, and to R. Paff for performing the x-ray analysis. The research reported in this paper was sponsored by the National Aeronautics and Space Administration, Electronics Research Center, under Contract No. NAS 12-538.

Manuscript submitted Sept. 12, 1968; revised manuscript received Dec. 7, 1968.

Any discussion of this paper will appear in a Discussion Section to be published in the December 1969 JOURNAL.

REFERENCES

1. F. B. Alexander *et al., Appl. Phys. Letters,* **4,** 13 (1964).
2. O. G. Folberth, *Z. Naturforsch.,* **10a,** 502 (1955).
3. H. Weiss, *ibid.,* **11a,** 430 (1956).
4. R. Bowers *et al., J. Appl. Phys.,* **30,** 1050 (1959).
5. J. H. Winkler *et al.,* Montreal Meeting, Oct. 6-11, 1968, as Paper 525.
6. J. J. Tietjen and J. A. Amick, *This Journal,* **113,** 724 (1966).
7. W. Koster and W. Ulrich, *Z. Metallk.,* **49,** 365 (1958).
8. B. L. Goydish, To be published.
9. G. R. Cronin and S. R. Borello, *This Journal,* **114,** 1078 (1967).
10. M. Glicksman and K. Weiser, *ibid.,* **105,** 728 (1958).
11. C. Hilsum and A. C. Rose-Innes, "Semiconducting III-V Compounds," p. 132, Pergamon Press Ltd., London (1961).
12. H. Ehrenreich, *J. Phys. Chem. Solids,* **12,** 97 (1959).
13. T. C. Harman *et al., Phys. Rev.,* **104,** 1562 (1956).

Oxygen Doping of Solution-Grown GaP

L. M. Foster and J. Scardefield

IBM Research Division, Yorktown Heights, New York

ABSTRACT

The solubility of oxygen in Zn-doped, solution-grown GaP was determined from the degree of compensation of the Zn by the oxygen electrons. An oxygen content of 7 x 10^{16} cm^{-3} was obtained for crystals grown at 1144°C from Ga-GaP melts that were doped with 0.016 m/o (mole per cent) Ga_2O_3. The solubility of Ga_2O_3 in Ga as a function of temperature was also determined, and a distribution coefficient for oxygen between the solid and liquid of 0.0055 was derived. The implications of these findings for the generation of red luminescence in GaP are discussed.

Visible luminescence of high efficiency can be achieved in GaP that is doped with Zn and oxygen (1-3). Emission is attributed in part to recombination of an electron bound to a neutral Zn-O complex with a hole on a distant Zn acceptor (4), and in part to an exciton bound to a Zn-O nearest neighbor pair (4, 5). At room temperature this emission is centered at about 7000Å. In addition, there is an infrared band that can be resolved at low temperatures into a spectrum characteristic of ordinary pair emission between Zn and O on distant, randomly spaced sites (6). In the last case the oxygen behaves as an isolated, very deep donor at about 0.9 ev below the conduction edge. For the nearest neighbor case, the donor energy is reduced by coulomb interaction to about 0.4 ev.

Zinc is a fairly shallow acceptor in GaP and has been reported at 0.03 ev (7) and, more recently, at about 0.06 ev (8, 9) above the valence band.

Studies of this luminescence in GaP have almost all employed GaP crystals that were obtained by precipitation from dilute Ga-GaP solutions. To a large extent this has been a matter of convenience. How-

ever, it should be noted that attempts to obtain efficient red-emitting GaP from vapor or bulk growth processes have thus far been unsuccessful.

Little was known about the oxygen content of GaP because of the analytical problems attending its detection and measurement. The present investigation is concerned with the determination of oxygen from its electrical behavior in solution-grown GaP crystals that are co-doped with Zn. For this determination it is assumed that oxygen acts as a singly ionized donor and in p-type material compensates one Zn acceptor for each oxygen atom present. The oxygen content of a crystal can be deduced, therefore, from the reduction in hole concentration that is effected by oxygen doping.

The solubility of oxygen in liquid Ga was also determined, and its distribution coefficient between the Ga melt and the solid GaP was obtained.

Experimental

Crystal growth.—GaP stock material was synthesized from Ga and PH_3 in a quartz, open-tube flow system. Unreacted Ga was removed by digestion in hot, aqueous HCl, then the coarsely granular product was freed of surface silica contamination from the glassware by two successive treatments in cold HF solution (25 parts H_2O : 1 part HF).

The degassed charge, consisting of 50g of Ga and 7g of GaP [8 a/o (atomic per cent) P] was encapsulated in quartz. Dopants, as metallic Zn and Ga_2O_3, were added from a side arm in the system prior to sealing it off. A crystal growth experiment consisted of lowering the capsule through a temperature gradient from 1185°C, through the liquidus (1144°C), to 850°C over a period of 16 hr. The precipitated GaP platelets were separated from excess Ga with HCl. Generally, there was no difficulty in selecting one or more single crystal areas from which a ¼ in.-long Hall bar could be cut. The selected platelet was hand-lapped to a uniform thickness and polished on both sides to render it perfectly transparent. This was essential so that the crystal could be examined microscopically for the presence of free Ga. Gallium inclusions had to be avoided since the distribution coefficient for Zn between solid GaP and the melt is very small and the slightest amount of entrapped liquid could contain enough Zn to invalidate its subsequent quantitative determination.

Zinc determination.—It will be seen that the interpretation of the data depends on very accurate knowledge of the acceptor concentration, since the desired information (the degree of compensation that is brought about by oxygen additions) will, in general, be the difference between two considerably larger numbers. Radioactive Zn was employed as the acceptor dopant to provide the necessary precision.

The Zn determinations were made on the actual Hall bars before contacts were applied for transport measurements. The sample activities were compared with those of standards consisting of evaporated aliquots of solutions of the same Zn source. Zinc sources with several different specific activities were used in the investigation to provide suitable sensitivity over the entire composition range. Based on counting statistics alone, the determination was good to ± 2%, except in two cases where it was ±15%. These latter points fell on the smooth curve through the other data, however, so no further mention will be made of them. Radiochemical purity of the isotope was established by gamma ray spectroscopy and half-life determination.

Three confirming experiments were performed where natural Zn was employed as the acceptor dopant, and its concentration was subsequently determined by radioactivation analysis. Since this is a destructive analysis, the Hall measurements were made first, then the contacts were removed by etching prior to neutron activation. In order to achieve high sensitivity in this analysis it was necessary to effect a quite complete chemical separation of the Zn activity from the tremendously greater P^{32} activity. This is accomplished by first taking the sample into solution with hot aqua regia, then separating the Zn, with carrier added, as $ZnHg(SCN)_4$. It was counted in this form and compared with Zn standards that had been irradiated at the same time. The Zn concentrations determined in this manner agreed with those deduced from radioactive Zn doping to within 2%.

Electrical measurements.—Eight-arm Hall specimens were cut ultrasonically from the single crystal platelets. The identical samples were employed for both the electrical measurements and determination of the Zn concentrations. After determination of the Zn content, which is a nondestructive measurement, ohmic contacts were made with Au-Zn alloy dots, and Hall effect measurements were made by conventional d-c techniques. The electrical measurements were checked over a ten-fold range of current values, and at magnetic field strengths from 500 to 10,000 gauss. Hole concentrations were calculated from $p = 1/R_H e$. Only room temperature data were employed.

Results and Discussion

The nominally undoped crystals were n-type, with a room temperature carrier concentration of 2-4 x 10^{16} cm^{-3} and mobility of about 150 $cm^2/v\text{-}sec$, going to 600 at 77°K. A single lot of synthesized GaP was used for all of the low-doped experiments to avoid scatter of the data in this sensitive region due to different amounts of residual background impurities.

The room temperature hole concentration that results from Zn doping of this material in the 10^{16} to 10^{19} cm^{-3} range is shown as the upper curve of Fig. 1. The fact that the hole-to-Zn ratio is anomalous in GaP, being too high for an acceptor energy level of 0.06 ev and actually greater than unity at the extremities of the curve, has been discussed elsewhere (10) and will not be elaborated on here. It will suffice to say that this situation should exist in the Zn-O samples as well and should not affect the interpretation of the hole compensation that is brought about by co-doping with oxygen.

A second series of Zn-doped crystals was made following exactly the same procedure as before, except that Ga_2O_3 was also added to the system. The oxygen addition was constant throughout the series at 0.016 m/o Ga_2O_3, which is approximately the concentration that experience here and elsewhere had shown to

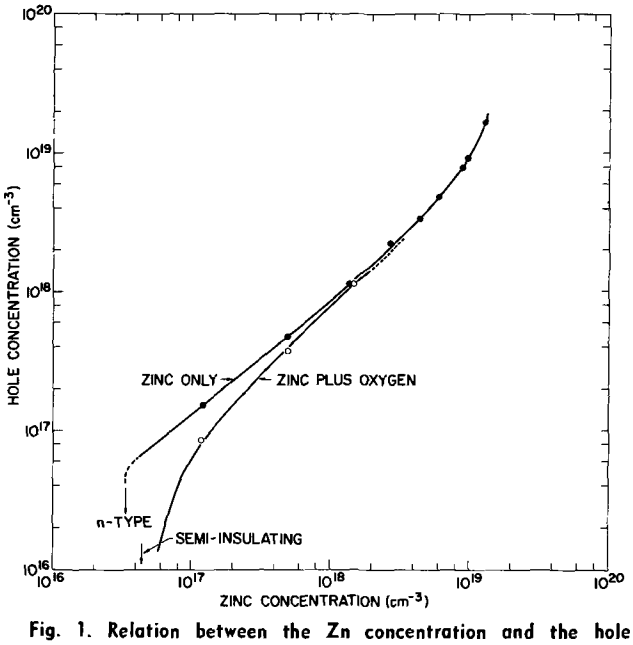

Fig. 1. Relation between the Zn concentration and the hole concentration at 300°K in GaP, with and without oxygen additions.

result in high photoluminescent and electroluminescent efficiencies in the red Zn-O band (2, 11).

The reduced carrier concentration that is brought about by the addition of oxygen is shown as the lower curve in Fig. 1. The reduction, the algebraic difference between the two curves, is essentially constant at 7 x 10^{16} holes cm^{-3} regardless of the Zn concentration up to about 10^{18} cm^{-3}, where this small reduction in carriers becomes lost in the data. At the dilute end, when the hole concentration falls below 7 x 10^{16} cm^{-3}, the compensation of the Zn is complete and the crystal conductivity changes over to very high resistivity n-type, characteristic of a donor deep in the energy gap.

The constant compensation by the added oxygen is not expected behavior; rather, its solubility might be expected to depend on the Zn concentration. Therefore, before the concentration of compensating centers can be identified directly with the oxygen content of the crystal, the situation that obtains when an electrically active solute is added to a crystal of the opposite conductivity type must be examined (13).

When a donor atom dissolves in intrinsic material, the heat of solution includes the energy gain of the electron as it drops to its new equilibrium state at the Fermi level, E^i_f. When the material is doped p-type, the Fermi level lowers to E^p_f and the donor solubility is increased by the Boltzmann factor, exp $(E^i_f - E^p_f)/kT$. However, this is also the factor by which the hole concentration increases when the Fermi level moves from E^i_f to E^p_f. It follows that the donor solubility ratio between p-type and intrinsic material equals the hole ratio, thus

$$\frac{S^p}{S^i} = \frac{\exp(E^i_f/kT)}{\exp(E^p_f/kT)} = \frac{p}{n_i}$$

where E is measured from the valence band, or

$$S^p = S^i \frac{p}{n_i} \qquad [1]$$

where p and n_i are the total and intrinsic holes, respectively. Whether our observation of a constant oxygen content regardless of the Zn concentration is to be expected depends on whether, at the growth temperature, the intrinsic holes predominate over the holes that are contributed by the Zn. We will now consider that aspect.

Determination of n_i.—The intrinsic carrier density at a given temperature can be determined in a number of ways. We will estimate it from the solubility of Zn in GaP as a function of its concentration in the liquid. (These data had been taken while establishing the hole *vs.* Zn relationship for ref. (10); upper curve of Fig. 1 of this paper). It is shown for our crystal growth temperature of 1144°C in Fig. 2. All of the solid does not precipitate at the one liquidus temperature, of course, and the liquidus itself will vary slightly as a function of the Zn concentration in the liquid. This is reflected in the scatter of the data in Fig. 2 as compared to Fig. 1. The Zn concentration in the solid was determined on the small Hall specimen only, but for Fig. 2 this is taken to represent the entire 7g of solid. The error introduced by this approximation is not considered serious for the purpose for which the information is to be used.

Solubility in the solid is determined by the equilibrium (12)

$$Zn(1) + V_{Ga} = Zn^-_{Ga} + p;\ K_1 = \frac{[Zn^-_{Ga}][p]}{[Zn(1)][V_{Ga}]}$$

or

$$Zn^-_{Ga} = \frac{K_1[Zn(1)][V_{Ga}]}{p} \qquad [2]$$

When $p \approx n_i >> Zn^-_{Ga}$

$$Zn^-_{Ga} = \left[\frac{K_1[V_{Ga}]}{n_i}\right][Zn(1)] = K_2[Zn(1)] \qquad [3]$$

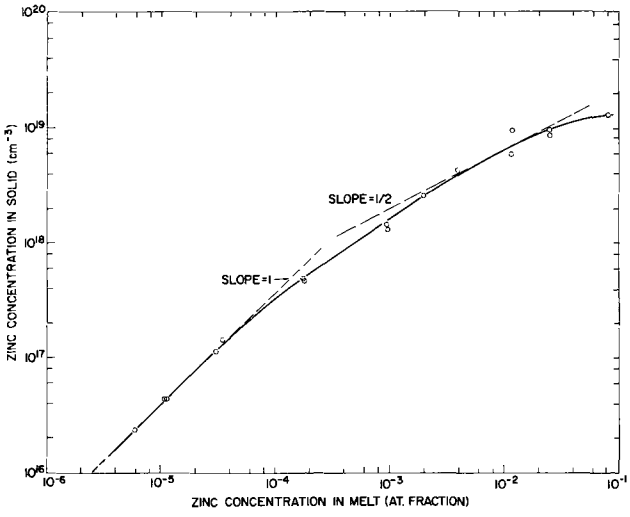

Fig. 2. Zn concentration in solid GaP as a function of its concentration in Ga-GaP melts at 1144°C.

and the Zn dissolved in the solid is directly proportional to its activity in the liquid. This dependence is almost exactly obeyed at low concentrations in Fig. 2.

If the holes are contributed primarily by the zinc, then

$$p \approx Zn^-_{Ga} >> n_i$$

and [2] becomes

$$p = Zn^-_{Ga} = [K_1[V_{Ga}]]^{1/2}[Zn(1)]^{1/2} = K_3[Zn(1)]^{1/2} \qquad [4]$$

and the Zn solubility is proportional to the square root of its concentration in the liquid. A distinct slope of ½ is not seen in Fig. 2 since at the lower side a substantial fraction of holes are still intrinsic, and at the upper side non-ideal behavior of the Zn is becoming evident as the solutions become concentrated. It suffices for our purpose to draw in a ½ slope tangent as seen in Fig. 2.

It remains now to determine the intrinsic hole concentration that, together with the increasing contribution of Zn holes, gives the best fit of the experimental curve between slope 1 and slope ½.

Returning to [2], this cannot be solved explicitly without approximations. However, by invoking the two additional equilibria

$$pn = n^2_i \qquad [5]$$

and the neutrality condition

$$Zn^-_{Ga} + n^- = p \qquad [6]$$

eliminating n and p through simultaneous substitution, and letting $K_4 = K_1[V_{Ga}]$, we obtain

$$Zn^-_{Ga} = \frac{K_4[Zn(1)]}{[n_i^2 + K_4[Zn(1)]]^{1/2}} \qquad [7]$$

By arbitrarily selecting values for n_i to adjust the curve shape, and normalizing to some value of Zn^-_{Ga} (2 x 10^{17} cm^{-3} was chosen) to eliminate the constant, various fits to the experimental curve of Zn^-_{Ga} *vs.* Zn(1) were obtained.

Figure 3 shows the fit for three values of n_i. The solid line is an exact tracing of the experimental curve of Fig. 2. From Fig. 3, n_i is clearly greater than 5 x 10^{17} cm^{-3}. As noted by Trumbore (14), the experimental curve should begin to rise above the theoretical curve when the Zn holes begin to predominate over the intrinsic holes since, rigorously, activities rather than concentrations are required in (4) and the activity coefficient of Zn in Ga is greater than unity in these dilute solutions. We choose 9 x 10^{17} cm^{-3} as the best value for n_i.

Returning now to Fig. 1, it is seen that the constant solubility of oxygen in GaP, irrespective of the

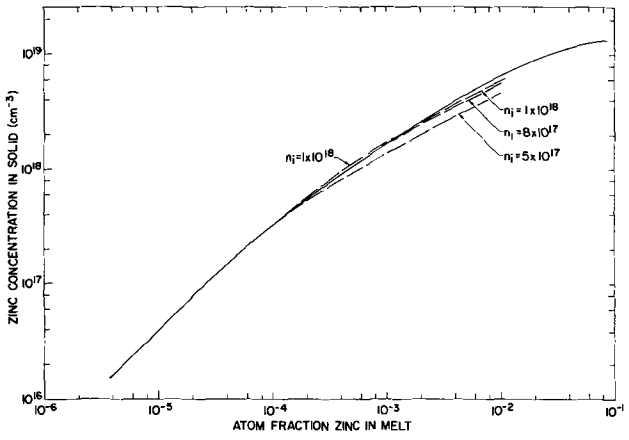

Fig. 3. Comparison of the observed relation between the Zn concentration in the solid vs. liquid at 1144°C with that calculated from various values for the concentration of intrinsic holes.

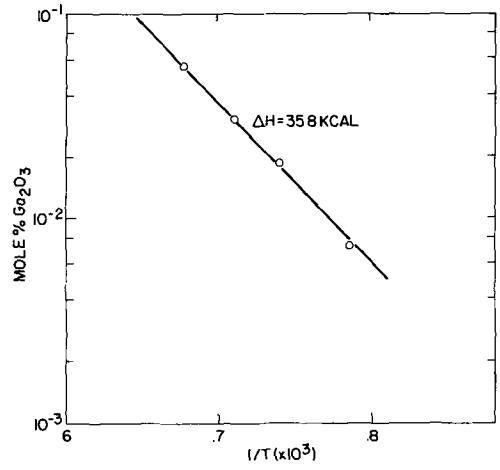

Fig. 4. Solubility of Ga_2O_3 in Ga as a function of temperature

Zn concentration up to almost 10^{18}, is consistent with the large intrinsic hole concentration, according to relation [1]. At Zn concentrations greater than 10^{18} the oxygen solubility would be expected to increase proportional to the increase in Zn. This increase is indicated in Fig. 1 as a dotted line extension of the experimental curve that parallels the "Zn only" curve. The continuation of the curve in this manner is clearly permitted by the data.

Solubility of oxygen in gallium.—In the next section we will determine the distribution coefficient of oxygen between the melt and the solid GaP for the particular conditions employed in this study. Before that can be done, however, the solubility of Ga_2O_3 in Ga must be measured in order to establish the maximum oxygen addition for which such a coefficient would apply.

The solubility was determined by a weight loss method. A solid piece of β-Ga_2O_3 was obtained by flame fusion of Ga_2O_3 powder .The weight of this piece was measured before and after holding it in Ga in a sealed quartz capsule at several temperatures for sufficient times to achieve equilibrium. This ranged from 72 hr at 900°C to 24 hr at 1200°C. Care was taken to ensure that the temperature was uniform over the capsule and did not cycle; otherwise, there could be a continual transport of Ga_2O_3 from the solid piece to the cooler part of the capsule. Before obtaining the weight loss, any Ga that adhered to the piece was removed by boiling in 50% HCl for 3 hr. (In a separate experiment it was established that this treatment did not remove any Ga_2O_3.)

In order to determine the true solubility of oxide in the liquid, it was necessary to correct for that lost in filling the free space of the system. The volatile species is the suboxide, Ga_2O, which is formed in the reaction

$$Ga_2O_3 + 4Ga = 3Ga_2O \qquad [8]$$

for which

$$K = \frac{[p_{Ga_2O}]^3}{[a_{Ga}]^4[a_{Ga_2O_3}]} \approx (p_{Ga_2O})^3 \qquad [9]$$

K had been obtained as a function of T by Cochran and Foster (15). The Ga_2O pressure calculated from [9], together with the known free space in the capsule and the ideal gas relation, $pv = nRT$, permits the calculation of the correction that is to be subtracted from the measured weight loss. The correction ranges from 5.5% at 1200°C to 1% a 1000°C. The final solubility curve is shown in Fig. 4. The consistency of the data is attested to by the straight line plot of log $x_{Ga_2O_3}$ *vs.* $1/T$. From the slope of the line, which is $\Delta H/R$, we obtain an enthalpy of solution of $\Delta H = 35.8$ kcal/mole.

Distribution of oxygen between the melt and solid GaP.—From Fig. 4, the solubility of Ga_2O_3 in Ga at the GaP crystal growth temperature (1144°C) is about 0.034 m/o or approximately twofold greater than the oxygen addition that was employed for the growth of the Zn-O doped crystals. (It is assumed for this purpose that because of their low concentrations the P and Zn do not affect the oxide solubility in the melt.) Therefore, a distribution coefficient, k can be derived for our case which should be applicable to neighboring compositions as well. Again, it is necessary to examine the loss of oxygen to the vapor. In this case, however, since the free space in the system is small (*ca.* 7 ml) and the temperature is moderate, a calculation similar to that in the previous section shows a loss of less than 1%, which can be neglected. From Fig. 1 was obtained an oxygen content of 7 x 10^{16} cm^{-3} for the Zn-O doped GaP crystals. This is an atom fraction of 2.65 x 10^{-6} (considering P and Ga as separate entities). This resulted from an oxygen addition of 0.016 m/o, or 4.8 x 10^{-4} atom fraction, to give a distribution coefficient of 0.0055.

From analysis of the Zn-O exciton and pair band spectra, Henry *et al.* (4) estimated that there were 5 x 10^{16} cm^{-3} Zn-O complexes in GaP crystals that had been grown at 1050°C from a melt that was doped with 0.01 m/o Ga_2O_3. From our distribution coefficient of 0.0055 we too calculate an oxygen content of 5 x 10^{16} cm^{-3} for this case. It is recognized that this perfect agreement must be somewhat fortuitous, considering the approximations that go into the two independent determinations.

Conclusions

The oxygen content of p-type GaP that is grown from Ga-8 a/o P solutions that are doped with 0.016 m/o Ga_2O_3 is 7 x 10^{16} cm^{-3}. This is independent of the acceptor concentration of the crystal up to approximately 10^{18} cm^{-3}. This behavior is consistent with an intrinsic hole concentration at the growth temperature of about 9 x 10^{17} cm^{-3}, which fixes the Fermi level and removes the dependence of the donor solubility on the acceptor content of the sample. Under the experimental conditions of this investigation, the distribution coefficient of oxygen between the solid and liquid is 0.0055. Utilization of this coefficient is limited to Ga_2O_3 additions below 0.034 m/o, which is the solubility of Ga_2O_3 in Ga at the growth temperature of 1144°C.

Some consequences of these findings are noteworthy. Gershenzon *et al.* (11) found that the maximum photoluminescent efficiency in the red Zn-O band was achieved with oxygen additions to the melt of 0.01 m/o Ga_2O_3. From Fig. 4 it is seen that this is essentially the solubility limit of Ga_2O_3 in Ga at their growth temperature of 1050°C. We suggest that the efficiency was limited by the solubility of oxygen in the melt, which in turn limited the solubility in the solid.

There are other observations that confirm this view. Ladany (16) made very large oxygen additions (0.4

m/o Ga_2O_3) to Zn-doped Ga-GaP melts when forming p-n junctions by liquid phase epitaxy onto n-type substrates for the production of EL diodes. Although this is thirty- to forty-fold greater than the oxide addition typically employed in this process (2), the quantum efficiency of the diodes was essentially unchanged. In our laboratory we have observed little difference in the efficiency of red luminescence in GaP whether there was a continuous flow of oxygen through the crystal growth system, whether a small addition of Ga_2O_3 (0.01 m/o) was made, or, as was the case in one instance, a minute accidental admission of air occurred through a crack in the quartz envelope. These observations too can be explained by the very low solubility of Ga_2O_3, which limits the oxygen concentration in the melt to a low value irrespective of the amount of solid oxide phase present.

It appears that because of this low solubility of oxygen in the liquid and its low distribution coefficient between the liquid and solid, the oxygen concentration of 7×10^{16} cm^{-3} that was determined in this work cannot be greatly exceeded. Crystal growth at higher temperatures would increase the oxygen solubility in the liquid according to Fig. 4 and, if the distribution coefficient is insensitive to temperature, this increase would be reflected in a greater oxygen content of the solid. However, practical considerations limit the growth temperature in quartz systems to 1150°-1200°C. From Fig. 1, it is seen that some increase in oxygen solubility should result from increase in Zn doping above the intrinsic range of about 10^{18} cm^{-3}. Whether the increase in Zn-O pairs that could be achieved in this way would result in greater external luminescence efficiencies is doubtful. Concentration quenching can be expected, and the increased free carrier absorption in this doping range begins to darken the crystal.

The very low concentration of the Zn-O luminescent centers in optimally doped GaP suggests that the desired luminescent process might be very vulnerable to degradation by various competing processes. The concentration of impurities such as Si, Ca, Al, Be, and Mg, that form stable oxides, certainly should be maintained well below the oxygen concentration so as not to compete with the Zn. Many other trace impurities that do not form stable oxides could still compete for the electron that is bound to the Zn-O complex and introduce alternative decay paths. The fact that it is difficult to achieve high red luminescence efficiencies reproducibly in GaP probably reflects the difficulty in avoiding very low concentrations of competing centers.

Acknowledgment

The authors wish to thank Mr. J. E. Lewis for performing the radiochemical determinations, Dr. J. F. Woods and co-workers for the electrical measurements, and Mr. R. J. Gambino for supplying the flame-fused Ga_2O_3 for solubility measurements.

Manuscript submitted Nov. 20, 1968; revised manuscript received Dec. 26, 1968.

Any discussion of this paper will appear in a Discussion Section to be published in the December 1969 JOURNAL.

REFERENCES

1. H. G. Grimmeiss and H. Scholz, *Phys. Letters*, **8**, 233 (1964).
2. M. R. Lorenz and M. Pilkuhn, *J. Appl. Phys.*, **37**, 4094 (1966).
3. R. A. Logan, H. G. White, and F. A. Trumbore, *Appl. Phys. Letters*, **10**, 206 (1967).
4. C. H. Henry, P. J. Dean, and J. D. Cuthbert, *Phys. Rev.*, **166**, 754 (1968).
5. T. N. Morgan, B. Welber, and R. N. Bhargava, *ibid.*, **166**, 751 (1968).
6. P. J. Dean, C. H. Henry, and C. J. Frosch, *ibid.*, **168**, 812 (1968).
7. T. Miyauchi, H. Sonomura, and N. Yamamoto, *Jap. J. Appl. Phys.*, **6**, 1409 (1967).
8. J. J. Dean, C. J. Frosch, and C. H. Henry, Private communication.
9. H. C. Casey, Jr., and F. Ermanis, *Bull. Am. Phys. Soc., Series II*, **13**, 376 (1968).
10. L. M. Foster, J. F. Woods, and J. E. Lewis, To be published.
11. M. Gershenzon, F. A. Trumbore, R. M. Mikulyak, and M. Kowalchik, *J. Appl. Phys.*, **37**, 483 (1965).
12. F. A. Kroger, "The Chemistry of Imperfect Crystals," Chap. 16, North-Holland Publishing Co., Amsterdam (1964).
13. F. A. Trumbore, H. C. White, M. Kowalchik, R. A. Logan, and C. L. Luke, *This Journal*, **112**, 782 (1965).
14. R. N. Hall and J. H. Racette, *J. Appl. Phys.*, **35**, 379 (1963).
15. C. N. Cochran and L. M. Foster, *This Journal*, **109**, 144 (1962).
16. I. Ladany, Paper presented at the Montreal Meeting of the Society, Oct. 6-11, 1968, as RNP 610.

Enhanced Gold Solubility Effect in Heavily n-Type Silicon

S. F. Cagnina

Fairchild Semiconductor Research & Development Laboratory, Palo Alto, California

ABSTRACT

Using radiotracer methods, a study has been made of the increased gold solubility in uniformly heavily n-doped silicon. Data for both phosphorus and arsenic showing gold solubility as a function of doping is presented. The gold solubility at 1000°C begins to increase substantially for concentrations of donor impurity in the range 10^{19} cm^{-3}, although a difference in this increase between arsenic doping and phosphorus doping was noted. The data was related quantitatively to an ion pairing model which appeared to best explain the results.

As gold is useful in silicon for controlling minority carrier lifetime, its properties in silicon have been studied extensively (1, 2). An important effect, little studied to date, is the apparent enhanced solubility of gold in n^+ (phosphorus) layers. Wilcox *et al.* (3) found that the presence of a diffused phosphorus layer resulted in higher gold concentration (in excess of the normal solid solubility) in such a layer. Such an effect was not observed for heavily boron-doped layers. In addition, the diffusivity of the gold was found to be retarded significantly by the presence of phosphorus (3). Joshi and Dash (4) studied the distribution of gold in phosphorus diffused silicon and interpreted their results in terms of the Reiss theory (equivalent Shockley-Moll theory) of solubility enhancement. Some authors have attributed this effect to the formation of gold phosphide precipitates as delineated by transmission electron microscopy and x-ray topog-

raphy (5, 6). While precipitation may occur, the present paper is concerned solely with a solubility effect.

The present paper deals with the enhanced solubility of gold in a quantitative manner, contrasting the gold solubility in silicon wafers heavily doped with phosphorus, arsenic, and boron. To avoid precipitation effects and to ensure that a true gold solubility was being measured, only wafers homogeneously doped were used in the experiments. Thus, large dislocation densities generated during the n^+ diffusion (particularly of phosphorus) and any subsequent precipitation of gold were avoided. Special experiments were performed to ascertain that precipitation was not influencing the results.

Theory

Shockley-Moll theory.—For some time now, interactions between impurities in solids have been described in terms of chemical reactions (7). Reiss *et al.* (8) showed how the law of mass action could be applied to explain enhanced solubility of lithium (a donor) in boron-doped silicon. Using thermodynamic arguments, expressions of a general nature were derived relating the donor concentration (*e.g.*, lithium) to the boron concentration. Subsequently, the same theory was reformulated by Shockley and Moll (9) arguing from a somewhat different point of view. In addition to solubility enhancement of lithium, similar effects have been noted for gallium in germanium (10) and for copper in silicon, germanium, and gallium arsenide (11).

To understand how the presence of one charged impurity can affect the solubility of another charged impurity, we shall consider the basic argument present in ref. (9). If an amphoteric impurity (such as gold) is diffused to saturation in silicon containing a p-n junction, then we state that the concentration of neutral impurity should be uniform throughout the silicon since the only "force" acting on the neutral atoms is diffusion. In other words, the concentration of neutral impurity should be independent of the local electropotential or Fermi level. But the impurity atoms in other charge states will be dependent on the Fermi level; in fact, the ratio of the concentration of impurity in any two charge states will be given by the ratio of the Boltzmann factors. Thus the solubility, or total number of atoms in all charge states, will be altered by the presence of other charged impurities if the concentration of these impurities is sufficiently large to affect the Fermi level.

At room temperature, substitutional gold in silicon possesses a donor level $E_D = 0.35$ ev above the valence band edge and an acceptor level $E_A = 0.54$ ev below the conduction band edge (12). The ratio of gold atoms in each charge state is (negative, neutral, and positive, respectively)[1]

$$N_{Au^-} : N_{Auo} : N_{Au^+} = \exp[(E_F - E_A)/kT] : 1 : \exp[(E_D - E_F)/kT] \quad [1]$$

in which E_F is the Fermi level, k is the Boltzmann constant, and T the temperature. In the following analysis we shall assume that the gold solubility is always much less than N_D, the shallow level donor density, and that the shallow level donors are all ionized since at the temperatures considered the Fermi level is not far from midgap.

Using the equation

$$n = N_D + p \quad [2]$$

and the equilibrium relations[2]

$$np = n_i^2 \quad [3]$$

$$n = n_i \exp[E_F - E_i)/kT]$$

it can be shown after a little algebra that

$$N_{Au^-} = [N_{Au^-}]_i \left\{ \frac{N_D + \sqrt{N_D^2 + 4n_i^2}}{2\,n_i} \right\}$$

$$N_{Auo} = [N_{Auo}]_i$$

$$N_{Au^+} = [N_{Au^+}]_i \left\{ \frac{2\,n_i}{N_D + \sqrt{N_D^2 + 4n_i^2}} \right\} \quad [4]$$

in which the bracket $[]_i$ denotes the value of the enclosed quantity in intrinsic silicon. The total gold concentration (*i.e.*, the solubility) is the sum of the above three terms.

$$N_{Au} = N_{Au^-} + N_{Auo} + N_{Au^+} \quad [5]$$

It is clear that solubility enhancement in n-type silicon occurs through the action of the gold acceptor level. Apparently, in the same n-type silicon, a concomitant lowering of the gold concentration in the donor state also occurs. This is a negligible effect since the concentration of gold in the positively charged state is very small to begin with, as solubility enhancement through the action of the gold donor level is heavily doped p-type silicon has not been observed (3). For the gold solubility to be unaffected by a decreasing Fermi level in heavily p-type silicon, then the ratio of positively charged gold to neutral gold should be considerably less than 1, *i.e.*, $\exp[(E_D - E_F)/kT] \ll 1$. Thus, we assume the donor level E_D to be at least 2 kT units below the Fermi level (about 0.2 ev at 1100°C). Neglecting the small contribution of positively charged gold, the gold solubility as a function of doping is then

$$N_{Au} = N_{Au}(N_D = 0) + \left\{ \frac{N_D - 2n_i + \sqrt{N_D^2 + 4n_i^2}}{2n_i} \right\} [N_{Au^-}]_i \quad [6]$$

A prominent feature of the above equation is that the gold solubility begins to increase when $N_D \sim n_i$ [an extrapolated value of n_i is of the order 10^{19} cm^{-3} at 1000°C (14)] the point at which the silicon is no longer intrinsic. Unfortunately, neither the gold energy levels nor n_i are precisely known at temperatures in the range 1000°-1100°C, so that an exact comparison between theory and experiment is not possible. However, in the limit for large values of N_D, the solubility goes as

$$\frac{N_D}{n_i} [N_{Au^-}]_i$$

Therefore, from an experimental plot of N_{Au} *vs.* N_D, we should observe a slope of one on a log-log plot for sufficiently large values of N_D.

Ion pairing.—As the existence of a phosphorus-gold compound (Au_2P_3) is known, one must also consider the possibility of ion pairing between gold and phosphorus and its effect on gold solubility. The most straightforward approach is that of Reiss *et al.* (8) and the techniques used by these authors will be applied to a hypothetical (but not unique) pairing reaction, *i.e.*

$$\{Au\}_{sub,o} + e^- + p^+ \rightleftarrows \{AuP\} \quad [7]$$

in which $Au_{sub,o}$ is a neutral substitutional gold atom, e^- is an electron, P^+ an ionized phosphorus atom, and {AuP} is a neutral gold-phosphorus ion pair. From the law of mass action it follows that

$$\frac{C_p}{(N_{Auo})\,n N_D} = K \quad [8]$$

where C_p is the neutral pair concentration and K is the reaction constant. From Eq. [2], [3], [8] it follows than [see ref. (8)][3]

$$C_p = K(N_{Auo}) \left\{ \frac{N_D^2 + N_D\sqrt{N_D^2 + 4n_i^2}}{2} \right\} \quad [9]$$

[1] Technically, spin degeneracy factors should be included for each level (13). However, omission will not alter the form of the derived expression.

[2] In these expressions, n denotes the electron concentration, p the hole concentration, n_i the intrinsic carrier concentration, and E_i is the intrinsic Fermi level.

[3] Note that in the limit of N_D large compared with n_i, the pair concentration goes as the square of the doping ($C_p \propto N_D^2$). Also this expression assumes $N_{Au} \ll N_D$.

It is important to realize that the occurrence of ion pairing presupposes solubility enhancement through variation of the Fermi level since both are mass action effects. In addition, those phosphorus atoms that pair will no longer contribute an electron to the conduction band and this will therefore affect the Fermi level, particularly the value of N_D to be used in Eq. [6]. Experimentally, it will be shown that solubility enhancement approaches 10^{17} cm^{-3} for dopings in the 10^{19} cm^{-3} -10^{20} cm^{-3} at 1000°C. Since the gold concentration is always much less than the doping concentration, the number of doping atoms removed if pairing does occur will also be much less than the doping concentration and can therefore be neglected. In summation, the total gold solubility in the presence of ion pairing will be the sum of Eq. [6] and Eq. [9].

Experiment

A brief description of the experimental technique employed is as follows: A known amount of nonradioactive gold was tagged with several millicuries of Au^{198} (half life = 2.7 days) in a solution whose volume was 25 ml.[4] From this, 5λ (1λ = 0.001 ml) was pipetted into a test tube which therefore contained a known amount of gold (by volume ratio) as well as a known activity (measured). This therefore served as a calibration standard for the run relating number of gold atoms to counts per minute. Gold was chemplated onto a lapped surface of the silicon wafers to be diffused (usually five, thickness 200μ or less) by injecting the gold chloride solution into a bath of 10:1 hydrofluoric acid (HF) solution in which the wafers lie (3). Plating was allowed to take place for approximately 5 min. The amount of gold plated was approximately two orders of magnitude larger than that needed to satisfy the solid solubility requirements. The wafers were then rinsed with deionized water, blown dry, and diffused.

The solid solubility was measured at a particular temperature by diffusing the wafers to saturation and measuring the bulk gold concentration. To determine the time required for saturation, a series of equally heavily doped n-type wafers were plated with gold as described and each wafer was diffused for varying lengths of time. Heavily doped n-type wafers were used to determine the time to reach saturation since the diffusion rate for gold is progressively lower the higher the doping. This behavior is due to the increased gold substitutional solubility. That the diffusivity should be concentration dependent was first shown in a paper by Frank and Turnbull which discussed the rapid diffusivity of copper in dislocated germanium crystals (15). Like copper in germanium, gold in intrinsic silicon is believed to have a high interstitial diffusivity with low interstitial solubility, and low substitutional diffusivity with high substitutional solubility (16). An expression was derived in ref. (15) which shows that the effective diffusivity should be approximately inversely proportional to the substitutional solubility. The retarded diffusivity of gold in heavily doped n-type silicon was observed during the course of study. For example, a lightly doped wafer was observed to completely saturate with gold in less than a day at 1000°C whereas a heavily doped sample required seven days. As mentioned, a set of heavily doped wafers were plated with gold and diffused varying lengths of time. That time at which the gold concentration no longer changed with added diffusion was taken as the saturation time. Once the saturation time at a particular temperature was determined, wafers of various doping levels were diffused with tracer gold for that length of time and evaluated as previously described.

In order to avoid surface accumulation of gold (17), each wafer was etched to about 60μ after diffusion and treated with hot "Auro Strip," a commercially available cyanide compound which readily dissolves gold. This latter operation is critical, since it was found

[4] Au^{198} obtained from Nuclear Science & Engineering Corporation.

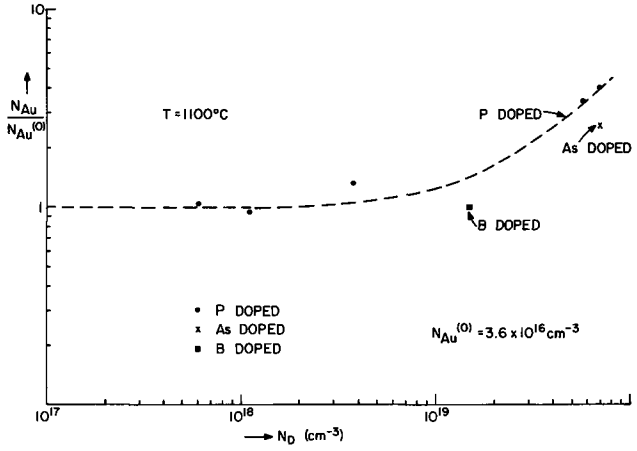

Fig. 1. Gold solubility (normalized with respect to intrinsic solubility) as a function of donor density at 1100°C. The dotted line is intended to represent the locus of experimental points. (Intrinsic solubility at 1100°C, $N_{Au}(o) = 3.6 \times 10^{16} cm^{-3}$.)

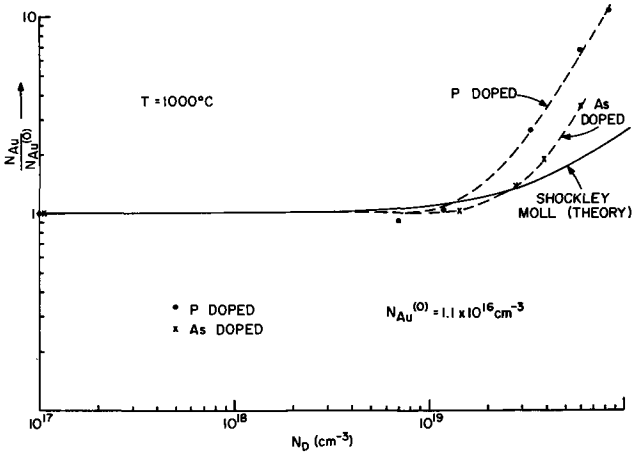

Fig. 2. Gold solubility (normalized with respect to intrinsic solubility) as a function of donor density at 1000°C. The dotted lines are intended to represent the locus of experimental points for the arsenic and phosphorus doped cases. (Intrinsic solubility at 1000°C, $N_{Au}(o) = 1.1 \times 10^{16} cm^{-3}$.)

that a large percentage of the gold contained in the etched silicon plates back onto the wafer. After being rinsed with deionized water and blown dry, the sample was weighed in an anlytical balance to an accuracy of better than 1%. The sample was then dissolved in about 4 ml of HF-HNO_3 mixture and counted repeatedly for times sufficiently long so that the standard deviation was less than 1%. The gamma radiation produced by the Au^{198} was measured using a thallium-activated sodium iodide photodetector assembly in conjunction with an amplifier, single channel analyzer, and scaler. By comparing the count rate of the dissolved wafer with that of the prepared calibration standard, the number of gold atoms in the sample is determined. The weight measurement determines the volume. Thus, the gold concentration is known.

Results and Discussion

The experimental procedure was performed for phosphorus and arsenic (and in one case boron) doped wafers at temperatures of 1000° and 1100°C.[5] Shown in Fig. 1 and 2 are measured gold concentrations at each of these temperatures, normalized with respect to the intrinsic solubility measured as a function of donor density. The donor concentrations were inferred from resistivity measurements using Irving's data (18). Values of intrinsic solubility (*i.e.*, N_D small) found were $(N_{Au})_o = 1.1 \times 10^{16}$ cm^{-3} at 1000°C and

[5] Uniformly antimony doped wafers of sufficiently low resistivity could not be obtained.

$(N_{Au})_o = 3.6 \times 10^{16}$ cm^{-3} at 1100°C, both of which are in excellent agreement with previously reported results (12, 19). Autoradiographs of the gold-doped wafers made by placing an etched sample atop dental x-ray film revealed homogeneity, as best as could be determined, of the gold in the silicon for both the lightly doped and heavily doped samples. Reproducibility of measured gold concentrations from run to run bore out the estimate of about 5% absolute accuracy and better than 2% relative accuracy.

Figure 1, which gives the data for 1100°C diffusions, clearly shows an increased gold concentration (about a factor of 4) for phosphorus doped silicon in the 6 x 10^{19} cm^{-3} concentration range. Unexpectedly, a heavily arsenic doped wafer showed a smaller value of enhanced solubility. A boron doped sample (1.5 x 10^{19} cm^{-3}) gives no indication of the enhanced solubility effect, in agreement with previously reported results (3).

More revealing is the data shown in Fig. 2 which gives the same data for 1000°C. Note that as the temperature is decreased, the silicon becomes more extrinsic for any given value of heavy doping and therefore a larger effect can be expected. Again, heavily arsenic doped wafers showed a consistently smaller value of enhanced solubility than do phosphorus doped samples. Equally interesting is the fact that the slopes of the curve of gold concentration *vs.* donor density is close to a slope of two for both impurities whereas the enhanced substitutional solubility effect predicts a maximum slope of one (see Eq. [6]). At first it was thought that a mobility difference might exist between heavily phosphorus and heavily arsenic doped silicon which might explain the apparent solubility difference.[6] Hall effect measurements made in this laboratory on silicon samples heavily doped with phosphorus and arsenic showed no significant difference in mobility. Mobility difference between phosphorus and arsenic doped silicon has been alleged to exist (20); however, it is too small to explain the difference seen in Fig. 2.

As precipitates of both As and P have been observed in as-grown heavily doped material (21), it is possible that the difference observed could be due to differences in the amount of dopant precipitated. That is, the precipitated As or P could go back into solution at the solubility temperature (and thus be electrically active) whereas the precipitates would be inactive during the resistivity measurement (room temperature).

Since it was recognized that the data used to evaluate the donor concentration from the resistivity (Irvin's data) (18) is a composite made up from various sources, it was decided to re-evaluate Fig. 2 using these original sources. In every case it was found that the shape of the characteristics was approximately the same, the major changes being shifts along the N_D axis.

For comparison purposes, a theoretical curve giving the enhanced substitutional solubility effect (Eq. [6]) is shown in Fig. 2. For this evaluation a value of $n_i = 1.4 \times 10^{19}$ cm^{-3} was used [extrapolated value from data of Morin and Maita (14)]. The parameter $[N_{Au^-}]_i$, the gold concentration in the negatively charged state in intrinsic silicon, was assumed equal to 0.27 $N_{Au}(o)$, where $N_{Au}(o)$ is the gold solubility in intrinsic silicon. Clearly, this curve is inadequate to explain the data. To see if a pairing model might explain these results, the value of gold solubility in excess of the value predicted by Eq. [6] was plotted for phosphorus as a function of doping. In Fig. 3 are shown the resultant points in addition to which is plotted Eq. [9] which gives the predicted pair density. [It was assumed that $KN_{Auo} = (1.2 \times 10^{-39}) N_{Au}(o)$.] As can be seen, good agreement exists between the theoretical curve and the experimental points. In fact, since pairing appears to be the dominant mechanism, no essential assumptions need to be made at which point Shockley-Moll solubility enhancement commences in order to obtain an approximate fit in Fig. 3.

[6] The resistivity is inversely proportional to the mobility.

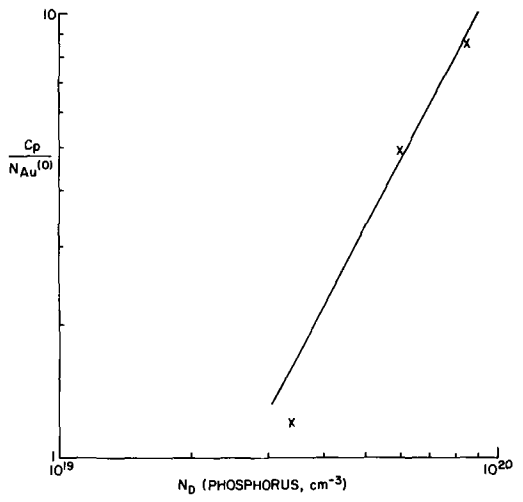

Fig. 3. Pair concentration (normalized with respect to intrinsic solubility) as a function of phosphorus doping. The straight line fit was plotted from Eq. [10] assuming that $KN_{Auo} = (1.2 \times 10^{-39}) N_{Au}(o)$.

As gold and phosphorus are known to form a compound (22) which has also been seen as precipitates in silicon, a pairing model to explain our results is not unreasonable. The author has not been able to find direct evidence of the existence of an arsenic-gold compound but, since arsenic and phosphorus are in the same group in the Periodic Table, their chemical behavior should be similar. Although the data shown for arsenic in Fig. 2 does not cover as wide a range as does that for phosphorus, it too appears to have a slope approximately equal to two. A plot similar to Fig. 3 could also be made for the arsenic case, although it would be less convincing since there are less data.

Joshi and Dash (4), in part, showed a gold profile in a diffused phosphorus region and attempted to correlate the gold concentration at each point with the phosphorus concentration. They pointed to the satisfactory agreement between the gold concentration measured and that predicted by a theoretical Shockley-Moll curve though they still alluded to the formation of gold-phosphorus pairs. Our work corroborates their assertion of gold-phosphorus pairing.

The binding energy for a gold-phosphide pair can be calculated from statistical arguments by considering the product of number of gold atoms in substitutional sites adjacent phosphorus atoms and probability of a "jump" by this gold atom to a pair site. An analysis of this type yields the pair density C_p as

$$C_p = \frac{(N_D)(N_{Au^-})}{N_{Si}} \exp\left[\frac{E_B}{kT}\right] \qquad [10]$$

in which N_{Si} is the density of silicon atoms and E_B is the binding energy. Using the data of Fig. 2 in this expression, we can estimate a binding energy of approximately 1 ev. This number is of the same order as the binding energy of radiation induced pairs in silicon (23).

Effect of dislocations on solubility measurements.— Several special experiments were performed to ascertain any gross precipitation of gold in the bulk silicon after diffusion to saturation. As mentioned previously, autoradiographs of lightly and heavily doped samples indicated uniformity as best as could be determined; however, the resolution of the film used was poor, of the order 10-20 μm. It was thought that if bulk precipitates of gold were influencing the data, then increasing the density of dislocations might increase the measured bulk gold concentration. Accordingly, wafers lightly doped with phosphorus were severely

dislocated by standing the wafers on end and inserting into a 1280°C furnace. The wafers were then fast pulled from the furnace. This procedure was then repeated a number of times (usually 4-6) until the wafers became warped and dislocated as high as 10^7 cm^{-2}. These samples were then annealed in the same furnace, lying flat on a quartz boat. The large dislocation densities produced were thus rendered stable. The same slices were plated with gold and diffused to saturation at 1100°C and pulled quickly from the furnace. Evaluation of the gold concentration proceeded in the fashion given previously. It was found that there was no difference in gold concentration between heavily dislocated and moderately dislocated controls (10^3-10^4 cm^{-3}).

This same experiment was repeated for heavily phosphorus doped wafers ($N_D \sim 5 \times 10^{19}$ cm^{-3}). It was thought that possible formation of auric phosphide precipitates might be influenced by the dislocation count. After diffusion to saturation, wafers were both slow and fast pulled from the furnace. Again, no difference whatever in bulk gold concentration was noted between the dislocated samples and controls.

These experiments do not imply that precipitation does not occur. They do mean that the total amount of gold deep in the bulk, whether precipitated in solid solution or paired with a phosphorus atom at a substitutional site, does not change with dislocation density. Any gold which does precipitate on cooling comes from pair sites or solid solutions; thus the average concentration of gold in the bulk does not change after precipitation.

Segregation of gold in diffused n^+ *regions.*—A dramatic demonstration of the high solubility of gold in diffused n^+ regions was performed as follows: Silicon wafers, which contained diffused silicon diodes on one side, were doped with radiotracer gold from the backside at 900°C using a 2 hr diffusion treatment. Afterward, the slices were back etched (about 15 μm removed) and were then placed in a $POCl_3$ predeposition furnace at a temperature of 1070°C for 15 min. It was found that the phosphorus glass on the backside contained a negligible amount of gold in agreement with an earlier study (24). In all cases unusually large concentrations of gold were found in the 10 μm of backside silicon which contained the n^+ region, whereas the gold concentration in the bulk decreased by two orders of magnitude. The gold-doped wafers without the phosphorus treatment showed a gold concentration (averaged over the central 100 μm of wafer) of approximately 3.8×10^{14} cm^{-3}. Those which received the "gettering" treatment yielded an average gold concentration of approximately 3.5×10^{12} cm^{-3}.

Reverse current *vs.* reverse voltage measurements were made on the diodes fabricated in the gettering samples as well as the gold doped and ungettered ones. For both groups the reverse current varied linearly with reverse voltage on a log-log scale with slope 1/2, corresponding to a p^+n step junction. The current level for the gettered case was approximately two orders of magnitude lower than the ungettered case in agreement with the radiotracer analysis. (The space-charged generation current is directly proportional to the gold concentration.)

Conclusion

The solubility of gold in heavily doped n-type silicon has been measured in such a way as to place a high degree of reliance on the experimental results. Special experiments performed indicated that precipitation of gold was not affecting the data in a deleterious way. A pairing model appears to offer the best explanation for the behavior of gold solubility with doping. Solubility enhancement through action of the Fermi level was found inadequate to explain the data. Probably both of these mechanisms are occurring at the same time, although pairing appears to be the dominant one.

In addition, the enhanced solubility of gold in n^+ regions was effectively demonstrated by using a diffused n^+ region to remove dissolved gold from the silicon bulk.

Acknowledgment

The author wishes to thank K. M. Cooper for his assistance in the experimental portion of this program. In addition, I am grateful to E. H. Snow and W. Oldham for many helpful discussions. Thanks are also due J. Lawrence for his aid with the experiment involving the large dislocation densities and E. Meieran for helping with the radiography.

Manuscript submitted Oct. 18, 1968; revised manuscript received Dec. 29, 1968. This was Recent News Paper 595 which was presented at the Montreal Meeting, Oct. 6-11, 1968.

Any discussion of this paper will appear in a Discussion Section to be published in the December 1969 JOURNAL.

REFERENCES

1. W. M. Bullis, *Solid State Electronics*, **9**, 1943 (1966).
2. S. F. Cagnina and E. H. Snow, *This Journal*, **114**, 1165 (1967).
3. W. R. Wilcox, T. J. LaChapelle, and D. H. Forbes *ibid.* **111**, 1377 (1964).
4. M. L. Joshi and S. Dash, *J. Appl. Phys.*, **37**, 2453 (1965).
5. J. M. Fairfield and G. H. Schwuttke, *ibid.*, **37**, 1536 (1966).
6. E. D. Wolley and R. Stickler, *This Journal*, **114**, 1287 (1967).
7. N. B. Hannay, "Semiconductors," Reinhold Publishing Corp., New York (1959).
8. H. Reiss, C. S. Fuller, and F. J. Morin, *Bell System Tech. J.* **35**, 535 (1956).
9. W. Shockley and J. L. Moll, *Phys. Rev.*, **119**, 1480 (1960).
10. J. O. McCaldin, "Metallurgy of Elemental and Compound Semiconductors," Vol. 12, Interscience Publishers, New York (1960).
11. R. N. Hall and J. H. Racette, *J. Appl. Phys.*, **35**, 379 (1964).
12. C. B. Collins, R. O. Carlson, and C. J. Gallagher, *Phys. Rev.*, **105**, 1168 (1956).
13. J. S. Blakemore, "Semiconductor Statistics," Vol. 3, Pergamon Press, New York (1962).
14. F. J. Morin and P. J. Maita, *Phys. Rev.*, **96**, 28 (1954).
15. F. C. Frank and D. Turnbull, *ibid.*, **104**, 617 (1956).
16. W. R. Wilcox and T. J. LaChapelle, *J. Appl. Phys.*, **35**, 240 (1964).
17. G. J. Sprokel and J. M. Fairfield, *This Journal*, **112**, 200 (1965).
18. J. C. Irvin, *Bell System Tech. J.*, **41**, 387 (1962).
19. F. A. Trumbore, *ibid.*, **39**, 205 (1960).
20. R. A. Logan, J. F. Gilbert, and F. A. Trumbore, *J. Appl. Phys.*, **32**, 131 (1961).
21. G. H. Schwuttke, *ibid.*, **34**, 1662 (1963).
22. H. Haraldsen and W. Blitz, *Z. Elektrochem.*, **37**, 502 (1931).
23. J. W. Corbett, "Electron Radiation Damage in Semiconductors and Metals," Academic Press, New York (1966).
24. J. W. Adamic and J. E. McNamara, Washington Meeting, October 1964, Paper 153.

Oriented Impurity Precipitates in Single Crystals of Sodium Chloride-Barium Chloride

K. N. Swamy Rao and A. S. Parasnis

Department of Physics, Indian Institute of Technology, Kanpur, India

ABSTRACT

Single crystals of sodium chloride pulled from melt containing 1% by weight of barium chloride have been observed to contain a second phase precipitating throughout the interior in the form of thin rods (10-25μ long) and well defined polygonal platelets (10-15μ in size). Two types of rods have been observed, one type oriented along <100> and the other along <110> directions. The platelets are variously in the form of hexagons, octagons, decagons, and rhombi. The hexagonal and octagonal platelets seem to lie on {111} planes. Precipitates disappear on quenching the crystals and reappear on aging the crystals under suitable conditions.

Extraneous phases are known to precipitate in solids when the impurity additive in solid solution begins to exceed the solubility limit as a result of slow cooling. Although a good deal of work has been done on metallic systems of technological importance not much extensive work has been done on nonmetallic solid systems. Alkali halides being transparent to optical wavelengths belong to a convenient class of solids for studying by optical microscopy the processes of precipitation and internal decoration of dislocations. Amelinckx (1) has shown that dislocations in mixed crystals of alkali halides are decorated by particles of a second phase. Suzuki (2) and Toman (3) have studied NaCl-$CdCl_2$ and NaCl-$CaCl_2$ systems by x-ray diffraction techniques and have proposed a model of metastable centers in the form of plate zones due to precipitation. Similarly Lilley and Newkirk (4a, b) have investigated the structural aspects of precipitation in the LiF-MgF_2 system. On the other hand, Dreeben (5) has reported optical microscopic observations on oriented precipitate particles in the CdS-Au system. Precipitates have been observed in KCl crystals by Ewles and Dawson (6), in NaCl crystals by Girard-Nottin and Taurel (7), and in some alkali halide crystals by Bansigir and Schneider (8). In the NaCl-$BaCl_2$ system Harvey (9) has observed decorated dislocations. However, no direct microscopic observation on oriented impurity precipitates in sodium chloride crystals, such as that reported here, seems to have been made.

Experimental Method

The single crystals of sodium chloride used in this investigation were grown in air in the laboratory from melt containing 1% by weight of barium chloride, following a modified Kyropoulos technique (10), the growth rate being 3 mm/hr. The materials used were of B.D.H. Analar grade. As soon as the entire melt had solidified the boule was detached from the chuck holding the seed and was carefully dropped back into the silica crucible in the same furnace. The boule was then cooled at the rate of 1°C/min down to room temperature. Large cubical blocks cleaved from the boule looked turbid. Thin sections of about 0.2 mm thickness were cleaved from the blocks and mounted in Canada balsam for microscopic observations.

Microscopic Observations

On examination under an optical microscope the specimens were found to contain, throughout the interior, precipitates of a second phase. Several different forms were observed (see Fig. 1 to 5).[1] Careful observations made on the geometry of the various precipitate forms enable one to determine the orientations of the precipitates embedded in the NaCl matrix. Most of the precipitates are in the form of either thin rods or hexagonally shaped platelets, but many other forms also are observed (Fig. 1).

Orientation of precipitates in the form of thin rods.— Two types of rods are seen. Those of one type make angles of 45° with the edges of cleavage sections. Figures 2 and 3 show them at lower and higher magnifications, respectively. It is seen that they are oriented along <110> directions. By using the fine focus of the microscope it is possible to see the rods oriented along the other four <110> directions which are inclined to the plane of observation. The second type of rods are parallel to the edges of cleavage sections; this shows that they are oriented along <100> directions. The rods oriented along the third <100> direction normal to the plane of observation would be seen end-on and would appear as "specks." It is, however, possible to follow a "speck" in depth, by using the fine focus, and distinguish it from specks as such. All of the three orientations of <100>-rods are also seen at x in Fig. 2. Clearly they are far less numerous than those of the first type. The length of a <110>-rod is typically in the range of 15-25μ. The lengths of <100>-rods show a wider variation, 5-20μ, but on the whole they are shorter.

Viewed under crossed polarizers, the <110>-rods get extinguished for any orientation of the specimen with the transmission axes of the polarizers, while, for an arbitrary orientation of the specimen, the <100>-rods do not (see Fig. 4a and 4b). This means that either the two types are made of two different materials (one

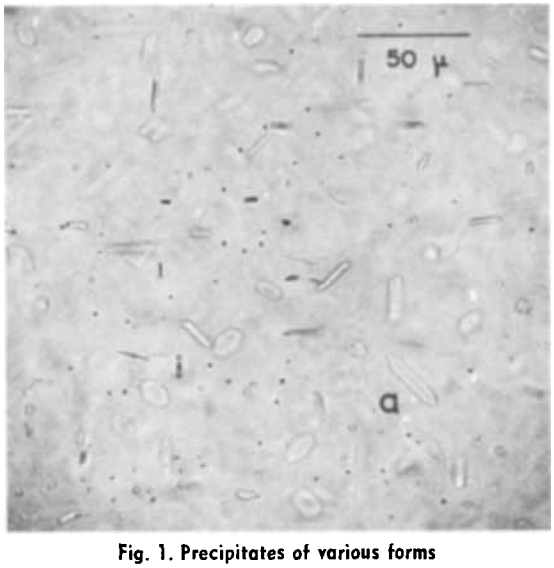

Fig. 1. Precipitates of various forms

[1] The edges of the photomicrographs are parallel to the [100] and [010] directions of the crystals.

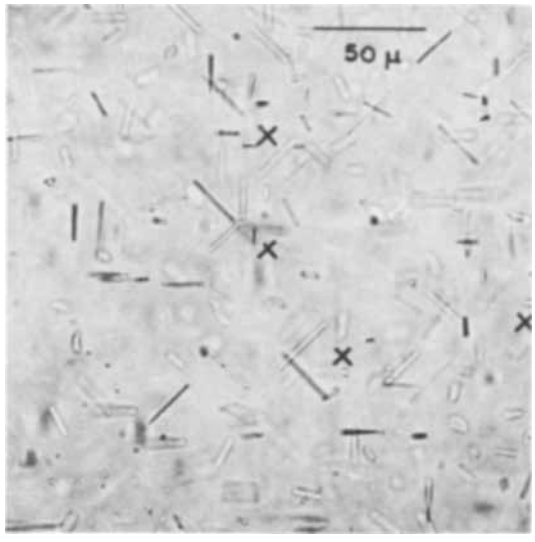

Fig. 2. Precipitates in the form of rods oriented along $<110>$ or $<100>$ directions.

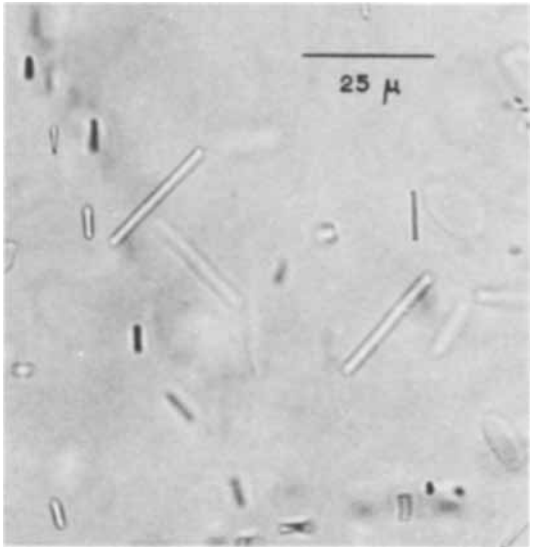

Fig. 3. $<110>$-rods at higher magnification

being noncubic) or they are made of the same material but their optical orientations are different.

Lilley and Newkirk have published (4b) a photomicrograph of precipitate rods which, according to them, do not seem to correspond to any rational low index direction. Both types of rods described in the present work are, however, definitely oriented along simple crystallographic directions in the matrix. Dreyfus (11) also has observed crystallographically oriented rod-like precipitates in the KCl-$SmCl_2$ system.

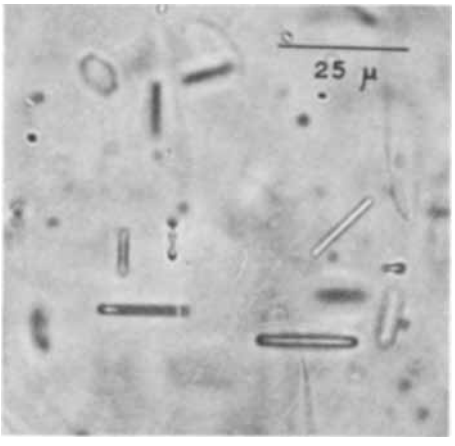

Fig. 4. a. Showing some $<100>$-rods and one $<110>$-rod, viewed by transmitted light.

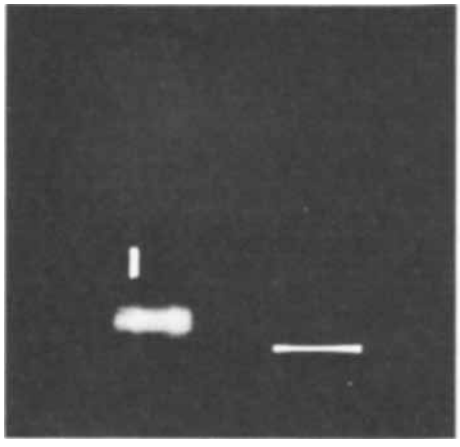

Fig. 4. b. Same area as (a), viewed between crossed polarizers.

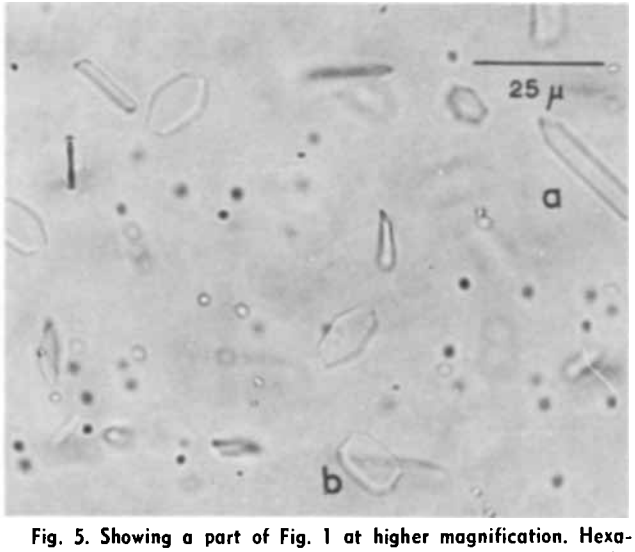

Fig. 5. Showing a part of Fig. 1 at higher magnification. Hexagonal platelets in different orientations and an octagonal platelet are seen.

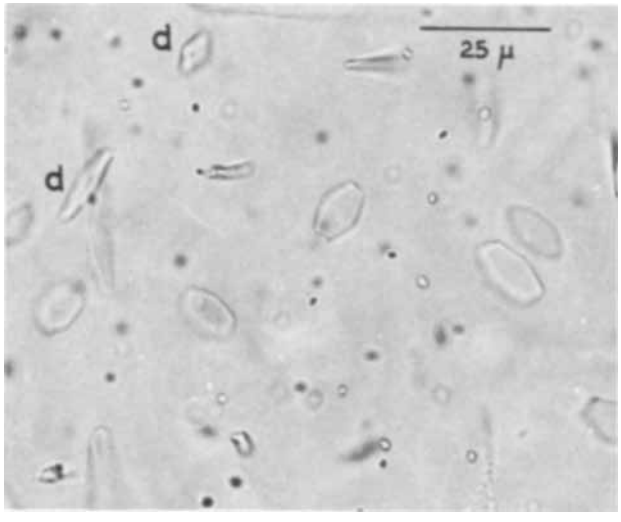

Fig. 6. Several hexagonal platelets and rhombus-shaped platelets

Orientation of precipitates in the form of hexagonal platelets.—Figures 5 to 8 show hexagonal platelets,

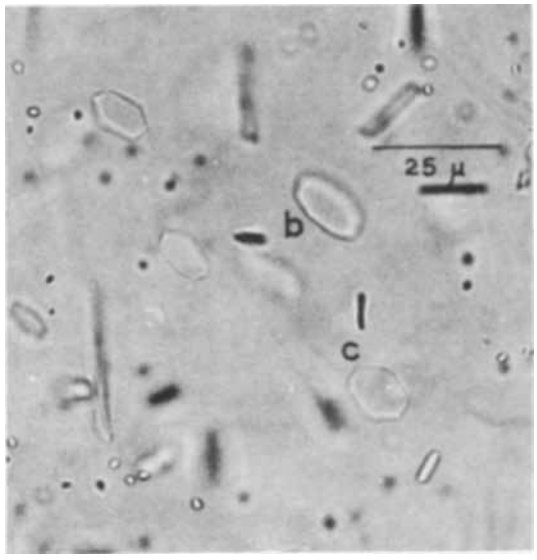

Fig. 7. Platelets in the forms of hexagon, octagon, and decagon seen in relative orientations.

Fig. 8. < 110 >-rods, hexagons, and a decagon

10-15μ in size, as seen on a {001} plane. They are all inclined to the plane of observation, *viz.*, a {001} plane, and although they appear to be irregular they could be regular hexagons in their respective planes. The hexagonal symmetry suggests the possibility that these are {111} planes. Further microscopic observations and x-ray analysis have confirmed that the hexagons in fact lie on {111} planes.

Precipitates of other forms.—(*a*) Figure 5 which is part of Fig. 1 observed at a higher magnification, shows, at "a," an elongated precipitate which appears to be a platelet lying in the plane of observation and oriented along a <110> direction.

(*b*) Figures 5 and 7, at "b," show octagonal platelets. These also are inclined to {001} planes and four different orientations are observed. Thus they, like the hexagonal platelets, seem to lie on {111} planes.

(*c*) Figures 7 and 8 show, at "c," platelets which clearly have ten sides. These decagons too are inclined to {001} planes and preliminary observations indicate that they lie on {111} or near- {111} planes.

(*d*) In Fig. 6 are seen, at "d," platelets which appear to be in the shape of rhombi. They could, however, be rectangular or square platelets and are only seen as rhombi because of their inclination to the plane of observation.

All of these forms are, as can be seen in the photomicrographs, much less numerous than the rods of either kind and the hexagons. In addition to the forms described so far some others also are seen but they are not very prominent.

Nature of Precipitates

The precipitates seen in the present, *viz.*, NaCl-$BaCl_2$, system are all transparent, unlike, for example, those seen by Dreeben (5) in CdS-Au. They are thus some barium compound, not barium metal. It could be barium chloride, hydroxide, or a chloride-hydroxyl complex. Further investigations are in progress to determine the detailed morphology and nature of the precipitates.

All of the precipitates can be dissolved back into the solid by heating the crystal to elevated temperatures below the melting point, and the impurity retained in solution by rapid quenching in air. Such quenched crystals do not show any precipitates when examined under the microscope. Aging the same crystals in air at about 350°C for about 48 hr results in the reappearance of oriented precipitates.

Manuscript received August 19, 1968.

Any discussion of this paper will appear in a Discussion Section to be published in the December 1969 JOURNAL.

REFERENCES

1. S. Amelinckx, "Dislocations and Mechanical Properties of Crystals," p. 50, John Wiley & Sons, Inc., New York (1957).
2. K. Suzuki, *J. Phys. Soc. Japan*, **13**, 179 (1958); *ibid.*, **16**, 67 (1961).
3. K. Toman, *Czech. J. Phys.*, **12**, 542 (1962); *ibid.*, **13**, 296 (1963).
4. E. Lilley and J. B. Newkirk, (a) "Advanced X-ray Analysis," Vol. 7, p. 195, Plenum Press, New York (1964); (b) *J. Mat. Sci.*, **2**, 567 (1967).
5. A. Dreeben, *This Journal*, **112**, 493 (1965).
6. J. Ewles and J. B. Dawson, *Nature*, **186**, 381 (1960).
7. M. Girard-Nottin and L. Taurel, *C. R. Acad. Sci.*, **260**, 4198 (1965).
8. K. G. Bansigir and E. E. Schneider, *J. Appl. Phys.*, **33**, 383 (1962).
9. K. B. Harvey, *Phil. Mag.*, **8**, 435 (1963).
10. K. N. Swamy Rao, Symposium on Solid State Physics, N.P.L., New Delhi, India, 1964 (Unpublished).
11. R. W. Dreyfus, *Appl. Phys. Letters*, **3**, 175 (1963).

Technical Notes

Silicon Dioxide Thermally Grown in a Silicon Nitride Ambient†

Ronald A. Cohen*

MIT Lincoln Laboratory, Lexington, Massachusetts

and R. Wheeler

Sprague Electric Company, Worcester, Massachusetts

Many techniques have been used to reduce the number of surface states and increase the stability of MIS devices. Recently, much of the emphasis has been on the reduction of alkali metal contamination of the silicon dioxide dielectric. Ultraclean processing techniques and material for formation of ultraclean silicon dioxide, replacement of silicon dioxide as the dielectric with silicon nitride as a more effective alkali barrier, and combinations of silicon dioxide with silicon nitride, controlled phosphorus gettering, and most recently, the use of alkali barrier liners (silicon carbide) to replace conventional quartz tube and alumina liner systems have all been tried with varying degrees of success. This note illustrates the use of silicon nitride as an alkali barrier liner analogous to silicon carbide.

Experimental Procedure

MOS structures were fabricated on <100> p-type 10 ohm-cm silicon material by a routine "clean" MOS process (1) with the oxidation being carried out at 1200°C. The normal quartz oxidation tube and high-purity alumina liner were replaced by a single silicon nitride tube.[1] Electron beam probe analysis of the tube material before and after use showed no observable sodium to the limits of the testing technique. The tube was cleaned by etching in a 10/1 solution of distilled deionized water and concentrated HF for 15 min, rinsed for 1 hr in 18 megohm-cm water, dried in a Class 100 ambient overnight, and finally baked in its entire length at 1000°C with oxygen flowing. Capacitance-voltage measurements (2) were used to evaluate the quality of the oxide. In the course of this work it became necessary to shut down and move the apparatus. Later, the furnace was reactivated and resulting experimental wafers were of low quality. The silicon nitride was then recleaned by the above procedure and the resulting wafers were again of high quality.

Results and Discussion

The capacitance-voltage measurements were carried out at room temperature and after a temperature-bias treatment of 300°C under a 1×10^6 v/cm negative field. Shifts in flat band voltage of 0.1-0.7v were obtained corresponding to 1.0 to 8.0×10^{10} q/cm^2. A comparison of this result to those obtained by Schmidt (3) are shown below:

Liner material	$\Delta q/cm^2$
High-purity alumina (3)	3.0×10^{12}
Silicon carbide (3)	4.5×10^{10}
Silicon nitride	$1.0\text{-}8.0 \times 10^{10}$

† This work was sponsored in part by the U.S. Air Force.

* Electrochemical Society Active Member.

[1] Silicon nitride tube was obtained from Haynes Division of Union Carbide, Kalamazoo, Michigan.

It is shown that the high-purity alumina can contaminate the silicon dioxide dielectric and the ordinary quartz tube which cannot be cleaned of alkali metal and must then be scrapped. The silicon nitride tube, if accidentally contaminated, can be cleaned and returned to satisfactory use. There is no data, to our knowledge, that this is possible with the silicon carbide tube.

The advantage of the silicon nitride tube is based on the fact that silicon nitride does oxidize (4) to a small extent. Although the silicon nitride tube itself does not contain or allow alkali metal contamination to pass through it, the interior work area can be contaminated by accident or by poor material control or processing techniques. In addition, silicon nitride also possesses small diffusion coefficients for alkali metals, negligible alkali metal concentration, good thermal conductivity and thermal shock resistance, slow rate of oxidation, availability, and low price.

Conclusions

Alkali barrier liners appear to be greatly superior to conventional quartz tubes and alumina liner systems.

Silicon nitride liners can be recleaned and returned to use if contaminated. Much data are available in the literature on properties of silicon nitride in relation to silicon/silicon dioxide systems. Further experimentation is necessary to determine the relative advantages of silicon nitride and silicon carbide in this application.

Acknowledgments

The authors wish to thank K. Carrol of NASA ERC, Cambridge, Massachusetts, for the electron beam probe analyses. The major portion of this work was performed at NASA's Electronic Research Center, Cambridge, Massachusetts.

Manuscript received Dec. 2, 1968.

Any discussion of this paper will appear in a Discussion Section to be published in the December 1969 JOURNAL.

REFERENCES

1. F. Cocca, R. Cohen, and J. Simonne, *Proc. IEEE*, **55**, 2193 (1967).
2. K. Zaininger, *RCA Rev.*, **27**, 341 (1966).
3. R. Schmidt, Recent Newspaper 308 presented at Boston Meeting of the Society, May 5-9, 1968.
4. N. C. Tombs and F. A. Sewell, Jr., *This Journal*, **115**, 101 (1968).

Variation of Contact Resistance of Metal-GaAs Contacts with Impurity Concentration and Its Device Implication

Kenneth L. Klohn and Lothar Wandinger

Electronic Components Laboratory, U. S. Army Electronics Command, Fort Monmouth, New Jersey

For efficient and reliable operation of microwave semiconductor devices which require high-current densities, it is essential to use the lowest resistance ohmic contacts possible. The generation of excessive ohmic heating (I^2R_s) limits the output which can be achieved by such devices as laser diodes, Gunn oscillators, tunnel diodes, avalanche transit time devices, and high cut-off-frequency varactors. In addition, heat must be dissipated rapidly to prevent any buildup in the bulk material and in the vicinity of the junction. This requires a good thermal path with low resistance from the device to suitable heat sinks. Device cutoff frequency, f_c, is another parameter which is limited by series resistance of which contact resistivity, R_c, is a part. A low f_c, in turn, affects the upper operating frequency and power efficiency. Any degradation in power efficiency generates additional heat which if not removed could result in early device failure and poor reliability.

The formation of an intimate metal-semiconductor contact which exhibits low resistance is dependent on: (*i*) surface preparation, (*ii*) metal deposition conditions, (*iii*) post-deposition alloying, (*iv*) barrier height, (*v*) impurity density of the adjacent semiconductor layer, and (*vi*) uniform wetting between metal and semiconductor. A number of investigators (1-11) have developed various techniques to achieve satisfactory ohmic contacts to GaAs. This note presents techniques and metal-GaAs combinations which produced good ohmic, low resistance contacts at moderate alloying temperatures, and shows how these R_c values vary with substrate impurity density. The metals chosen for this investigation have, for the most part, been used previously on an empirical basis and their quality evaluated by the performance of the completed device. Also, it will be indicated how the results of this investigation reduce the series resistance of laser diodes and consequently improve their potential output power capabilities.

Experimental Procedure

The material used for these experiments was Czochralski and boat-grown GaAs having 10^3-10^5 etch pits/cm^2 and oriented in both the <100> and <111> directions. Wafers were lapped down to 4-6 mils using a 3 μm aluminum oxide grit. Impurity concentrations, determined by the van der Pauw technique (12), varied from 2.8 x 10^{17} to 10^{20} cm^{-3} for Zn-doped material and 1 x 10^{17} to 3 x 10^{18} cm^{-3} for Te-doped material. The wafers were cleaned ultrasonically in trichlorethylene followed by a methyl alcohol rinse. The cleaned wafers were then etched in a warm mixture of $1H_2O:1H_2O_2:3H_2SO_4$ to remove approximately ½-mil and stored under methyl alcohol prior to placing them in the vacuum system or plating solution.

The metals used in this study were Ag, Au-4% Zn, In, and Ni. Ag and Au-4% Zn were applied by evaporation using the metals in wire form with a purity of 99.999%. The metal wire was cleaned in KOH and stored under methyl alcohol prior to evaporation. In each case approximately 6000Å of metal was evaporated on both sides of the substrate at 1-5 x 10^{-6} Torr. Subsequent microalloying was carried out in vacuum by heating the substrate to 300°C for 10 min. The Ag samples received an additional 6000Å of Au on each side which was then heated to 150°C for 5 min. The 2.8 x 10^{17} cm^{-3} samples with Au-4% Zn required an additional sintering operation at 400°C for a few seconds on a strip heater in a forming gas atmosphere.

The nickel contacts were plated with an electroless nickel solution (2), rinsed in H_2O followed by methyl alcohol, and placed in the vacuum system for the alloying step. These samples were also heated to 300°C for 10 min.

The indium contacts on n-type GaAs were applied by electroplating, followed by a rinse in H_2O and methyl alcohol. They were then microalloyed on a strip heater in forming gas at 350°C for 2 min. Following the metalization and microalloying, all samples were diced with a wire saw to 8-10 mil squares.

Resistance measurements were made by using a precision Wheatstone bridge. The resistance due to leads, package, and bulk GaAs was subtracted from the total resistance measured to obtain the contact resistance values. Five to ten dice were measured for each point and averaged. The deviation from the average value was typically —30-+40%. Each point for a given impurity concentration involves a separate metalization and alloying procedure.

Results and Discussion

The value of specific contact resistance *vs.* substrate impurity concentration for Au-4% Zn, Ni, and Ag on p-type GaAs and for In on n-type GaAs is shown in Fig. 1. In order to achieve the values of R_c indicated in the figures, it was necessary to exercise great care to achieve and maintain substrate surfaces free of contamination and minimize any oxides which may have been present. Failure to attain good surface conditions would result in substantially higher contact resistance. The values of substrate impurity concentrations used in these experiments ranged from 2.8 x 10^{17} to 9 x 10^{19} cm^{-3} for p-type GaAs and 1 x 10^{17} to 3 x 10^{18} cm^{-3} for n-type GaAs. They correspond to those normally found when fabricating GaAs laser di-

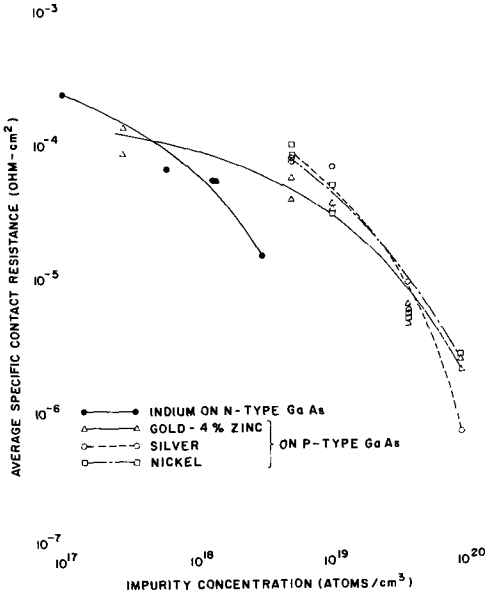

Fig. 1. Average specific contact resistance of gold-4% zinc, silver, and nickel on p-type GaAs and indium on n-type GaAs as a function of GaAs impurity concentration.

odes or emission diodes. Specific contact resistance values measured for p-type GaAs varied from 1.2 x 10^{-4} ohm-cm^2 for Au-4% Zn on 2.8 x 10^{17} cm^{-3} material to 7.3 x 10^{-7} ohm-cm^2 for Ag on 9 x 10^{19} cm^{-3} material and for n-type GaAs with In contacts from 2.5 x 10^{-4} ohm-cm^2 for 1 x 10^{17} cm^{-3} to 1.5 x 10^{-5} ohm-cm^2 for 3 x 10^{18} cm^{-3}.

The curves show only a modest increase of contact resistance with decreasing substrate impurity density of 10^{18} cm^{-3} and lower, but a rapid decrease as substrate doping is increased above 5 x 10^{18} cm^{-3}. In general, the decrease amounted to 1.5 orders of magnitude per order of magnitude increase in doping level. The lowest average R_c value measured was 7.3 x 10^{-7} ohm-cm^2 Ag on 10^{20} cm^{-3} zinc-doped material. It is this behavior which is most important for the design of low series resistance semiconductor devices where heating due to ohmic losses plays an important role, such as in laser diodes.

The desirability of incorporating an n^+ layer adjacent to the metal contact, in order to reduce the series resistance of a device significantly, can be illustrated by calculating the contact resistances and bulk resistance for a typical laser diode such as shown in Fig. 2(a). The n-type material generally used for lasers is 1-3 x 10^{18} cm^{-3}. The p-n junction required for the device is typically generated by the diffusion of Zn at 850°-900°C, yielding a surface concentration of 1-3 x 10^{20} cm^{-3}. Using the dimensions in Fig. 2(a), the experimentally measured contact resistances, and assuming a typical diffusion profile in a 25 μm diffused p-layer with an average density of 4.5 x 10^{19} cm^{-3}, the contact resistance and series resistance for the different layers are calculated and summarized in Table I.

Table I shows that the series resistance R_s for a typical laser structure is of the order of a one tenth of an ohm. In addition, it can be seen that 47% of the total resistance comes from the metal contact to the n-layer. To improve this value a modified structure can be used, as shown in Fig. 2(b). A 3 μm layer can be replaced by an epitaxial n^+-layer doped with Se or Sn with a carrier concentration of 1 x 10^{19} cm^{-3} which represents the highest concentration for any

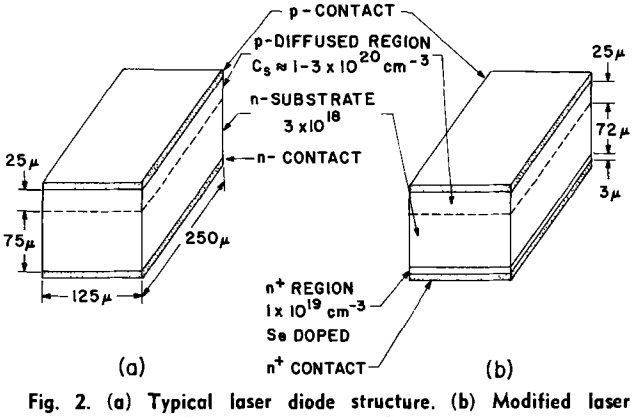

Fig. 2. (a) Typical laser diode structure. (b) Modified laser structure with an n^+ region adjacent to the contact.

Table I. Calculated contact and bulk resistance of typical laser structures based on measured specific contact resistance

Regular structure, Fig. 2(a)			Modified epi-structure, Fig. 2(b)		
Resistance*	(ohms)	Percentage of total resistance	Resistance*	(ohms)	Percentage of total resistance
R_{cp^+}	0.0023	2.3	R_{cp^+}	0.0023	4.1
R_p	0.0223	22.0	R_p	0.0223	39.5
R_n	0.029	28.5	R_n	0.028	49.6
R_{n^+}	—	—	R_{n^+}	0.0006	1.1
R_{cn}	0.048	47.2	R_{cn^+}	0.0032	5.7
R_s	0.1016	100.0	R_s	0.0564	100.0

* R_{cn}, R_{cp^+}, R_{cn^+} = contact resistance to n, p^+, n^+ layers; R_n, R_p, R_{n^+} = bulk resistance of n, p, n^+ layers; R_s = total series resistance.

known n-type dopant for GaAs (13). The p-layer, which is also a big contributor to the R_s, was not changed to illustrate clearly the effect of the impurity concentration of the n-doped semiconductor layer immediately adjacent to the metal layer on the series resistance of a specific device. It can be seen that the R_s of the modified device structure is 44% lower than the one of the original geometry. Significantly, however, the resistance of the n-contact is only 5.7% of the total, a reduction of eight to one. The bulk resistance of the modified structure accounts for 89% of R_s with the n-region being the major contributor. A specific contact resistance of 10^{-6} ohm-cm^2, extrapolated from the In curve at 10^{19} cm^{-3} (Fig. 1) for the n-side and 7.3 x 10^{-7} ohm-cm^2 from the Ag curve at 9 x 10^{19} for the p-side was used in these calculations.

Manuscript submitted Oct. 8, 1968; revised manuscript received Dec. 6, 1968.

Any discussion of this paper will appear in a Discussion Section to be published in the December 1969 JOURNAL.

REFERENCES

1. B. Schwartz and J. C. Sarace, *Solid-State Electronics*, **9**, 859 (1966).
2. W. M. Sharpless, U.S. Patent 2,995,475, Aug. 8, 1961.
3. J. R. Dale and R. G. Turner, *Solid-State Electronics*, **6**, 388 (1963).
4. J. R. Dale and M. J. Josh, *ibid.*, **7**, 177 (1964).
5. W. A. Schmidt, *This Journal*, **113**, 860 (1966).
6. Y. Furukawa and Y. Ishibashi, *Japan J. Appl. Phys.*, **6**, 788 (1967).
7. D. K. Jadus, H. E. Reedy, and D. L. Feucht, *This Journal*, **114**, 408 (1967).
8. K. L. Lawley, J. A. Heilig, and D. L. Klein, *Electrochem. Technol.*, **5**, 374 (1967).
9. Yu. A. Gol'dberg, D. N. Nasledov, and B. V. Tsarenkov, *Instruments and Experimental Techniques*, (6), p. 180, (Nov-Dec. 1966), translation published June 1967, p. 1472.
10. N. Braslau, J. B. Gunn, and J. L. Staples, *Solid-State Electronics*, **10**, 381 (1966).
11. T. B. Ramachandran and R. P. Santosuosso, *ibid.*, **9**, 733 (1966).
12. L. J. van der Pauw, *Philips Tech. Rev.*, **20**, 220, (1959).
13. R. W. Fane and A. J. Goss, *Solid-State Electronics*, **6**, 383 (1963).

Optimum Abrasive Sizes for Minimizing the Polishing Times of Semiconductors

Sumner Mayburg*

Semiconductor Processing Company, Hingham, Massachusetts

The polishing of glass is a combination of fracturing of the surface by the abrasive particle, a flow of material during the time the particle of abrasive produces the scratch, and some chemical action produced by the abrasive polishing slurry (1). Glass polishing technology has been developed with a large number of variables not the least of which is the variability of glass itself. It is not at all surprising that glass polishing is an art which has not been converted to a straight-forward scientifically understood technology.

Much of the art of glass polishing has been carried over to the semiconductor industry. However, for many semiconductor materials, fast chemical polishes have been found which are significantly better than abrasive polishes in producing damage free surfaces. In silicon polishing, where such a chemical polish (2) exists, abrasive polishing is essentially unnecessary. However, in those materials where good chemical polishing has not yet developed, abrasive polishing continues to be an important step in making useful practical structures. In this paper we attempt to treat some practical aspects of abrasive polishing to see what optimization is available.

Abrasive polishing of good single crystals should be simpler to understand than the polishing of glass. The plastic flow temperature and the thermal conductivity of most semiconductor and dielectric single crystals are much higher than glass. Therefore the probability of creating plastic flow during the polishing is greatly reduced. We shall assume that the polishing operation is simply a scratching procedure in which the material being polished is fractured by the hard abrasive particles moving across the surface and that the maximum scratch depth is the diameter of the abrasive particle. This scratch depth is further defined to be the surface roughness.

In a review of the grinding, lapping and polishing of quartz with silicon carbide abrasive, Bond (3) notes that the rate of removal of material is proportional to the size of the abrasive particle used. Soper (4) has observed this same proportionality in the case of garnet abrasive on silicon. The calculations that follow are based on the assumption that the rate of removal is proportional to abrasive size, an assumption which should be verified for each abrasive and material to be polished. In recirculating slurry systems where the abrasive particles are gradually being broken down through use and are being returned to the surface being polished, a simple relationship between rate of removal of material and abrasive particle size is not likely to exist.

Theory

In our discussion we assume that the rate of removal of material is αS where S is the size of the abrasive particles used and α is a constant with respect to S but does depend on the nature of the abrasive and the pressure used during polishing. We assume α is kept constant in a polishing process which consists of using several steps with an abrasive which has been graded into different sizes. Each subsequent step uses a finer grade of abrasive than the prior step, and the final step uses the finest grade of the abrasive available.

Consider the first step; we start with a surface of roughness S_0 and use abrasive particles of size S_1 to remove material. We need to remove a layer of material which is at least an amount S_0. If we do this, the roughness of the surface now becomes determined by S_1 and, assuming that removal of material is produced by a scratching or plowing action, the maximum roughness is S_1. Let t_1 be the time required to remove a layer of material S_0 from the surface then

$$S_0 = \alpha S_1 t_1 \qquad [1]$$

On the second step we want to convert a surface from roughness S_1 to a surface of roughness S_2 with the minimum of polishing time. Thus, we remove a layer of material S_1 but not more.

$$S_1 = \alpha S_2 t_2 \qquad [2]$$

Similarly, we have for the n^{th} step

$$S_{n-1} = \alpha S_n t_n \qquad [3]$$

and for the final step f

$$S_{f-1} = \alpha S_f t_f \qquad [4]$$

From a practical point of view, it is important to minimize the time required to polish the surface. In principle we could polish the roughest surface with the finest abrasive available and have only one step in the polishing operation. However, this may require an impractically long time.

We can minimize the total time of polishing T in the following way: From Eq. [3]

$$T = \sum_{n=1}^{n=f} t_n = \frac{1}{\alpha} \sum_{n=1}^{n=f} \frac{S_{n-1}}{S_n} \qquad [5]$$

In principle, we are free to choose the abrasive size on any step independent of the abrasive sizes on the other steps. In particular, we may choose the abrasive size on the n^{th} step S_n so that T is a minimum.

We have after differentiation

$$\frac{\partial T}{\partial S_n} = \frac{1}{\alpha}\left[-\frac{S_{n-1}}{S_n^2} + \frac{1}{S_{n+1}} \right] = 0$$

since S_n enters in both t_n and t_{n+1}, but nowhere else in Eq. [5]. The condition for minimum T is thus

$$S_n^2 = (S_{n-1})(S_{n+1}) \qquad [6]$$

Also

$$\frac{S_{n-1}}{S_n} = \frac{S_n}{S_{n+1}} \qquad [7]$$

or

$$t_n = t_{n+1} \equiv t \qquad [8]$$

The polishing time on each step should be the same time t for minimum total polishing time T. From Eq. [5] we have

$$T = ft \qquad [9]$$

From Eq. [3], [4], and [8] we may write the products of each step time as

$$\prod_{n=1}^{f} t_n = t_f \cdot t_{f-1} \ldots t_n \ldots t_1 \equiv t^f = \alpha^{-f} S_0/S_f \qquad [10]$$

By combining Eq. [9] and [10] we find for the total time T

$$T = \alpha^{-1} f (S_0/S_f)^{1/f} \qquad [11]$$

* Electrochemical Society Active Member.

as the total time required for the f step polishing operation.

We may minimize the total polishing time T with respect to the number of steps f. From Eq. [11] we find

$$f = \ln (S_0/S_f) \quad [12]$$

With this number of steps

$$T = fe/\alpha \quad [13]$$

with $e = 2.72$.

Discussion

It is especially interesting to note from Eq. [12] that the optimum number of steps is independent of α and depends only on the starting surface roughness S_0 and the finest abrasive available S_f to be used on the final step.

We can estimate f for the case of diamond polishing of a surface produced by a diamond "internal diameter" cutting blade. These blades usually have diamond pieces of size 40μ. The finest diamond abrasive has particle size typically 0.10μ, so that S_f is 0.10μ. We have from Eq. [8]

$$f = \ln 400 = 6 \text{ steps}$$

for minimum polishing time.

If only three polishing stations were available, we would obtain most efficiency by use of Eq. [6] to determine the abrasive sizes to be used on the first and second abrasive polishing station. We have

$$S_1^2 = S_0 S_2$$

$$S_2^2 = S_1 S_f$$

or

$$S_1^2 = S_0 \sqrt{S_1 S_f}$$

Then

$$S_1^3 = S_0^2 S_f$$

or

$$S_1 = (S_0^2 S_f)^{1/3}$$

Similarly, we find

$$S_2 = (S_0 S_f^2)^{1/3}$$

With $S_0 = 40\mu$ and $S_f = 0.1\mu$ as above we have

$$S_1 = 5.5\mu$$

and

$$S_2 = 0.74\mu$$

As another example, consider the abrasive polishing of Si with garnet. We have established (4) a value of α for the garnet abrasive of (1/6) min^{-1}. Suppose we wish to get a final finish of 0.1μ and suppose $S_0 = 40\mu$ is the surface roughness produced by a diamond ID blade slicing. Then the minimum time T given by Eq. [13] is

$$T = 6(2.72)/(1/6) \text{ min}^{-1}$$
$$= 97 \text{ min}$$

where six polishing steps are required. However, if only two polishing steps are available, we find from Eq. [11] that the required time is

$$T = (6 \text{ min}) \ (2) \ (400)^{1/2} = 240 \text{ min}$$

or roughly 2½ times the minimum time.

For a three-step process

$$T = (6 \text{ min}) \ (3) \ (400)^{1/3} = 124 \text{ min}$$

which is only 29% greater than the minimum time. From a practical point of view, a three-step process may be almost as fast as a six-step process when one considers the clean up time required in going from one step of the process to the next step.

Manuscript submitted Oct. 18, 1968; revised manuscript received Dec. 31, 1968. This was Recent News Paper 699 presented at the Montreal Meeting, Oct. 6-11, 1968.

Any discussion of this paper will appear in a Discussion Section to be published in the December 1969 JOURNAL.

REFERENCES

1. L. Holland, "The Properties of Glass Surfaces," Chap. 1, John Wiley & Sons, Inc., New York (1964).
2. J. Regh and G. A. Silvey, *Electrochem. Techol.*, 6, 155 (1968).
3. W. L. Bond, Chap. IX, "Quartz Crystals for Electrical Circuits," R. A. Heising, Editor, D. Van Nostrand Co., Inc., New York (1946).
4. R. B. Soper, Private communications, Semiconductor Processing Co.

Brief Communications

Preparation of Vitreous Materials in the Form of Well-Defined Hollow Cylinders

N. S. Platakis, H. C. Gatos,* and A. F. Witt*

Department of Metallurgy and Materials Science, Massachusetts Institute of Technology, Cambridge, Massachusetts

A method has been developed for the preparation of vitreous materials which essentially overcomes some of the main problems associated with the characterization and study of such materials. These problems are chemical homogeneity (1,2), porosity (or inclusions), and lack of well-defined geometrical shapes.

The system $x\text{As}_2\text{Se}_3 \cdot y\text{Sb}_2\text{Se}_3$ was employed in the present work since in this type of chalcogenide glasses the problem of chemical homogeneity is quite acute. Furthermore due to their very pronounced brittleness, the mechanical preparation of samples with well-defined geometrical shapes is tedious at best.

The salient steps of the new method are as follows: the constituents of the vitreous system are placed, in the desired proportions, in a quartz ampoule (typical dimensions were 1 cm ID and 10 cm long) which is evacuated (to a pressure of approximately 10^{-6} mm Hg) and sealed off. Then the ampoule is fitted to a horizontal shaft of a motor. The shaft-ampoule arrangement can be placed in and out of a horizontal furnace (by moving the motor or by moving the

* Electrochemical Society Active Member.

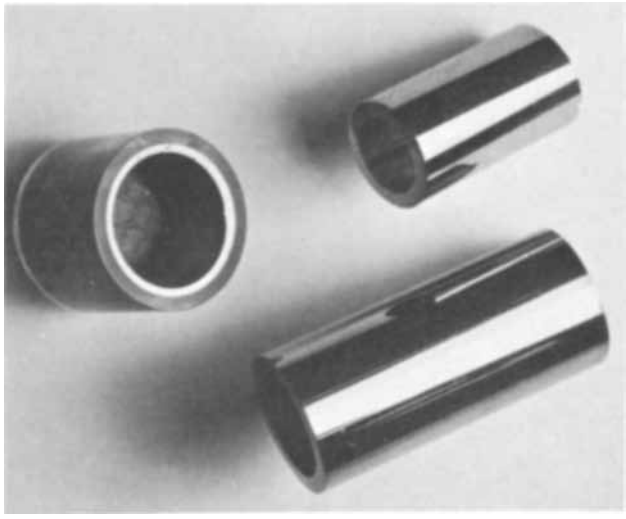

Fig. 1. Hollow cylinder samples of vitreous chalcogenides. The sample on the left is still contained in the quartz tube (after cutting the ampoule). The other two samples have been removed from the quartz tube. Magnification 1X.

furnace) while the ampoule is being rotated in the vicinity of 25 rpm. After the material is molten the ampoule is withdrawn from the furnace and while still under rotation is quenched either in air or other media. (The material can of course be slowly cooled in the furnace if desired.) Subsequently the ampoule containing the vitreous material is cut into the desired lengths (a string saw or ordinary cutting wheels were employed with consistent success). Since the coefficient of thermal expansion of quartz is smaller than that of the chalcogenide glasses, the hollow cylinders of the vitreous material are readily separated from the ampoule by simply immersing the cut pieces into acetone. This obvious requirement that the coefficient of thermal expansion of quartz be smaller than that of the material being prepared (to avoid cracking the cylinder) is essentially met by all materials under consideration (3). Some typical samples of vitreous chalcogenides are shown in Fig. 1.

The hollow cylinders obtained with the present method exhibited no variation in thickness. The thickness could be varied from run to run by controlling the amount of the starting material and the size of the ampoule. It should be pointed out that hollow cylinders are advantageous shapes for quenching since cooling takes place through both their outer and inner surfaces. (In the presence of helium rather than in vacuum quenching can be even more effective.) In fact it was possible to extend the glass formation region of the present system since single phase hollow cylinder samples were obtained with compositions which constantly gave two phase samples by other means of preparation.

No porosity, inclusions, or other macroscopic defects could be detected in the hollow cylinders. This result is not surprising if one considers that solidification proceeds progressively in a layer-type fashion from the outer to the inner part of the cylinders. Because of the rotation, during cooling the melt is in contact with only part of the forming cylinder at any given time. In all instances the hollow cylinder samples exhibited far greater mechanical strength than samples prepared by other methods. Furthermore electron probe analysis along the cylinders and across their thickness revealed no detectable variation in chemical composition.

The hollow cylinder samples lend themselves to electrical measurements (resistivity) which often present serious difficulties. Resistivity measurements were made by immersing the hollow cylinders into silver paste and attaching electrodes in the inner and outer surface (4). The silver paste shorting the inner and outer electrodes was removed by grinding the two ends of the cylinders. For thin-walled cylinders (where the outer area is essentially the same as the inner) the total resistivity R is

$$R = \rho \frac{l}{A}$$

where ρ is the resistivity, l is the length (thickness of cylinder), and A the area of the cylinder. It is apparent that in the present samples the ratio l/A can be made orders of magnitude smaller than in conventional samples and thus facilitate the determination of very large resistance values.

Although the method was primarily applied to the preparation of homogeneous hollow cylinders of vitreous materials it can readily be adopted for a number of polycrystalline materials and even single crystals with the aid of appropriate seeds.

The over-all reproducibility of the method was found to be excellent.

Acknowledgment

This work was supported by the National Aeronautics and Space Administration under grant NGL 22-009-019.

Manuscript received Dec. 20, 1968.

Any discussion of this paper will appear in a Discussion Section to be published in the December 1969 JOURNAL.

REFERENCES

1. R. L. Myuller, V. N. Timofeeva, and Z. U. Borisova, "Solid State Chemistry," Z. U. Borisova, Editor, p. 46; Translated in 1966 by New York Consultants Bureau.
2. A. S. Borshchevskii and D. N. Tret'yakov, *Soviet Physics-Solid State*, **1**, 1360 (1960).
3. B. T. Kolomiets, *Phys. Stat. Sol.*, **7**, 370 (1964).
4. ASTM Designation: D 257-1961.

Homogeneous Impurity Incorporation during Crystal Growth from the Melt

August F. Witt and Harry C. Gatos

Department of Metallurgy and Materials Science, Massachusetts Institute of Technology, Cambridge, Massachusetts

Semiconductor single crystals were grown reproducibly in a Czochralski-type puller with heretofore unattainable dopant homogeneity. No concentration fluctuations of the dopant could be detected by employing the high resolution techniques described elsewhere (1) (linear resolution less than 0.2μ). The effects of thermal asymmetry at the growth interface which are responsible for the commonly observed impurity fluctuations (2) were overcome by dispensing with seed rotation and by virtually eliminating random thermal

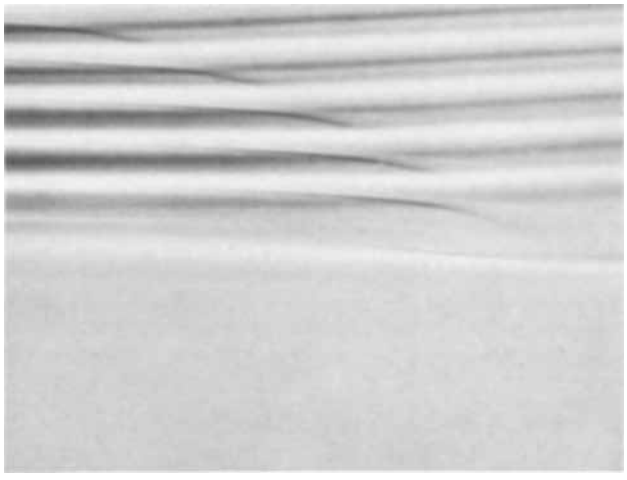

Fig. 1. Impurity distribution in an InSb single crystal as revealed by high resolution etching. The upper part was grown with seed rotation and synchronized crucible rotation in the same direction and exhibits pronounced impurity concentration fluctuations (rotational striations). The "facet" region (upper left part) "off facet" region (upper right part) are clearly delineated. The lower part was grown with crucible rotation alone; it exhibits extremely homogeneous impurity distribution and no rotational striations. Magnification approx. 350X.

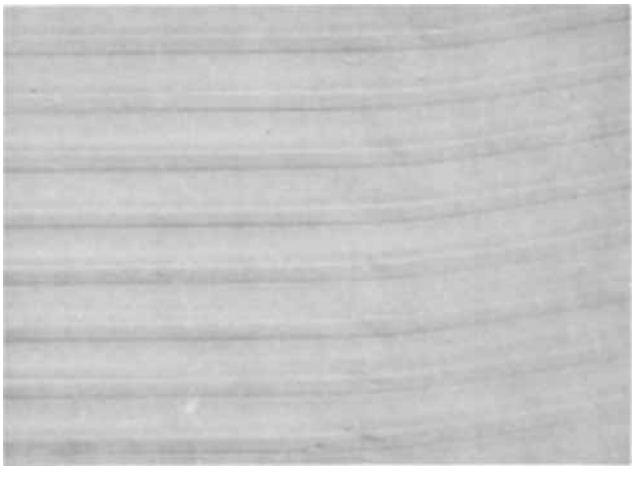

Fig. 2. "Facet" (left-hand side of the figure) to "off facet" (right-hand side) transition regions in InSb pulled under crucible rotation only. The facet region does not exhibit the commonly observed impurity concentration increase; the transition is characterized only by a change of the growth interface from flat to curved. The stripes were introduced by a periodic interruption of crystal pulling so that the growth interface could be clearly delineated. Magnification approx. 360X.

fluctuations in the melt by means of moderate crucible rotation (10-30 rpm).

In previous studies (2,3) it was shown both theoretically and experimentally that thermal asymmetry (whereby the thermal axis does not coincide with the rotational axis) in Czochralski-type pullers leads to fluctuations of the microscopic growth rate which in turn cause the well known impurity striations. Asymmetric heat inputs, which are encountered in nearly all growth systems, establish thermal asymmetry both in the growing crystal and in the melt. Whereas crucible rotation can significantly decrease the effectiveness of thermal asymmetry present in the melt, it does not alter appreciably the thermal configuration in the growing crystal. Thus, when seed rotation is employed, rotational impurity heterogeneities are essentially always present regardless of whether or not crucible rotation is used. Accordingly (and in contrast to the generally held belief), pulling with simultaneous seed rotation and crucible rotation in the opposite

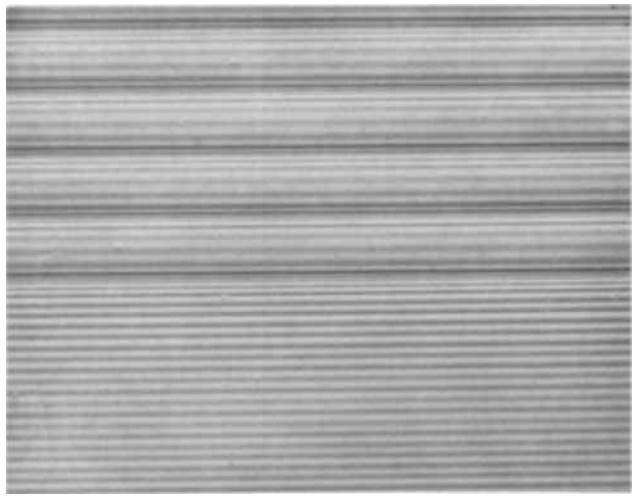

Fig. 3. Growth characteristics of the off facet region of InSb as revealed by vibrational "rate striations." The upper part, grown with seed rotation and synchronized crucible rotation exhibits periodic growth rate changes as seen from the varying spacing of the "rate striations." The lower part, pulled with crucible rotation only, exhibits a constant growth rate (constant spacing of "rate striations") which is a prerequisite for homogeneous impurity incorporation. Magnification approx. 450X.

Fig. 4. Multiple beam interferogram of an etched InSb single crystal. The periodic deflections of the interference fringes in the upper part reflect the impurity concentration fluctuations always present under seed rotation. The homogeneous impurity distribution in the lower part (straight line interference fringes) reflects the growth conditions associated with crucible rotation without seed rotation. Magnification 230X.

direction does not improve the impurity distribution in the resulting crystal. Synchronized crucible and seed rotation in the same direction reduces (but does not eliminate) the commonly observed impurity striations.

By growing without seed rotation, in addition to making any existing thermal asymmetry in the solid ineffective, the growing crystal can readily drift toward the thermal center of the system. This self-positioning process virtually eliminates the effects of thermal asymmetry in the melt and, thus, insures steady-state microscopic growth conditions.

It was further found that in growing with crucible rotation but without seed rotation the facet (on-core) region does not exhibit any noticeable increase in impurity concentration in contradiction to earlier re-

ports (4). The pronounced difference in impurity concentration between the facet and the off-facet regions discussed in these reports was attributed to different growth mechanisms operating in the two regions. In view of the present results a revision of the prevailing views may be necessary.

Experimental results obtained with single crystals of InSb are shown in Fig. 1,2,3, and 4. The crystals were grown in the <111> direction and were studied with techniques discussed elsewhere (1).

Although the bulk of the experiments were performed with InSb, a similar behavior was observed in the case of germanium single crystals. We believe that silicon and other semiconductors should behave likewise. Work is underway to study the electrical characteristics of crystals with the same over-all macroscopic concentration of a given dopant but with different degrees of homogeneity. Preliminary results indicate that the carrier mobilities in InSb are significantly decreased in the presence of impurity fluctuations.

Acknowledgment

This work was supported by the National Science Foundation under contract GK-1653.

Manuscript received Jan. 10, 1969.

Any discussion of this paper will appear in a Discussion Section to be published in the December 1969 JOURNAL.

REFERENCES

1. A. F. Witt, *This Journal*, **114**, 298 (1967).
2. K. Morizane, A. F. Witt, and H. C. Gatos, *ibid.*, **114**, 738 (1967).
3. K. Morizane, A. F. Witt, and H. C. Gatos, *ibid.*, **115**, 747 (1968).
4. K. R. Hulme and J. B. Mullins, *Phil. Mag.*, **4**, 1286 (1959).

Preparation of Rhenium Hexafluoroacetylacetonate

Harvey J. Anderson and Abner Brenner*

National Bureau of Standards, Washington, D. C.

We were interested in preparing the rhenium derivative of hexafluoroacetylacetone (the latter will be designated by F_6AA) for the purpose of using it to produce a deposit of rhenium by chemical vapor deposition. The F_6AA compounds are known to be stable and yet surprisingly volatile for metallic compounds. Van Hemert and co-workers (1) had prepared thin deposits of copper, nickel, and rhodium by passing the F_6AA chelates of these metals mixed with hydrogen through a hot tube.

The metal chelates are usually easily prepared by simple metathesis of the sodium salt of the ligand with the simple metal salt (chloride, nitrate, or acetate) in aqueous or alcoholic media (1-4). A variation consists in adding the ligand directly to a suspension of the metal chloride in carbon tetrachloride (5). Since none of these methods yielded the rhenium chelate, we investigated several other procedures. The only one that was successful is described below.

We prepared the rhenium compound by the destructive distillation of the anhydrous sodium salt of F_6AA with anhydrous rhenium trichloride. Results with the pentachloride were not as satisfactory. The sodium compound was prepared by adding sodium hydride to an excess of F_6AA dissolved in tetrahydrofuran and by evaporating to dryness. In a typical experiment about 7.2g of the sodium salt were intimately mixed in a mortar with 3.0g of $ReCl_3$. The finely ground powder was transferred to a retort through which dry argon was passed during the distillation. The flow of argon aided the removal of the vapors from the hot zone. The delivery tube of the retort was connected to a vessel which was cooled with solid carbon dioxide. The retort was heated slowly in a small pot furnace. At about 125°C the dark vapor of the rhenium compound began to evolve. Heating was continued until the temperature reached about 400°C at which temperature the dark vapors ceased to form.

The rhenium compound in the receiver was collected by dissolving it in petroleum ether. Partial evaporation of the solution followed by cooling with solid carbon dioxide left a crop of dark purple, almost black crystals. These were purified by sublimation. The yield was 34% based on the rhenium trichloride. The following analysis was obtained:

Calculated for $Re(CF_3 \cdot CO \cdot CH \cdot CO \cdot CF_3)_3$		Found
Rhenium	23.1	22.4
Carbon	22.3	22.0
Hydrogen	0.4	0.7

The compound crystallizes in black needles which are soluble in many organic solvents but insoluble in water. The compound is stable in air. The vapor of the compound has a beautiful purple color resembling that of iodine and the organic solutions of the compound have a similar purple color. A few milligrams of the compound placed in a 100 ml flask, which is then transferred to an oven at 100°C, will maintain a purple vapor for about a day. This indicates that the compound is fairly stable to air oxidation. Passage of the vapor mixed with hydrogen through a tube heated to 400°C yielded a rhenium mirror which, however, was rather dark in color. Details of the experiments on chemical vapor deposition of rhenium will be contained in another publication.

Acknowledgment

This work was supported by the Atomic Energy Commission, Division of Research, Chemistry Branch.

Manuscript received Sept. 23, 1969.

Any discussion of this paper will appear in a Discussion Section to be published in the December 1969 JOURNAL.

REFERENCES

1. R. L. v. Hemert, L. B. Spendlove, R. E. Sievers, *This Journal*, **112**, 1123 (1965).
2. R. L. Belford, A. E. Martell, and M. Calvin, *J. Inorg. Nuclear Chem.* **2**, 11 (1956).
3. R. E. Sievers, R. W. Moshier, and M. L. Morris, *Inorganic Chem.*, **1**, 966 (1962).
4. S. J. Lippard, *J. Am. Chem. Soc.*, **88**, 4300 (1966).
5. M. L. Morris, R. W. Moshier, and R. Sievers, *Inorganic Chem.*, **2**, 411 (1963).

Electrocatalysts for Hydrogen/Carbon Monoxide Fuel Cell Anodes

IV. Platinum-Nickel Combinations

D. W. McKee and M. S. Pak

General Electric Research and Development Center, Schenectady, New York

ABSTRACT

The behavior of a series of platinum-base metal binary catalysts as anodes for the oxidation of H_2-CO fuel mixtures has been studied at 85° and 100°C with 85% phosphoric acid electrolyte. Platinum-nickel catalysts show the best tolerance for carbon monoxide and the performance of catalysts with less than 25 w/o (weight per cent) nickel is much superior to that of platinum black. The effect appears to be related to the strength of bonding of chemisorbed carbon monoxide to the alloy surface.

Although platinum black in various forms still remains the most widely used electrocatalyst for fuel cell purposes, for some applications other metals and alloys appears to be superior to platinum alone. For example, in the indirect hydrocarbon system, where the reformer effluent contains small amounts of carbon monoxide, the performance of platinum black anodes is seriously limited by the irreversible chemisorption of carbon monoxide, which causes the anode to polarize rapidly at low current densities. It has recently been found that alloys of platinum-ruthenium (1), platinum-rhodium, and platinum-iridium (2) are much more resistant to poisoning by carbon monoxide than is platinum alone, and improved electrodes for H_2-CO mixed fuels have been developed which utilize these binary catalysts (3).

Synergistic behavior of this type is not confined to alloys of the noble metals, and reports of similar effects are widespread in the catalytic literature. A recent observation by Bond and Webster (4), that addition of small amounts of a transition metal such as nickel, cobalt, or iron increases to a marked extent the hydrogenation activity of platinum catalysts, suggested that such noble metal-base metal combinations might show enhanced activity as electrocatalysts in fuel cell applications. Although corrosive attack of the acid electrolyte on the base metal component was an obvious objection, it was felt that small amounts of base metal incorporated in the platinum lattice might be protected from corrosion in the same way that alloys of copper and gold are known to be resistant to concentrated nitric acid up to 50 a/o (atom per cent) copper (5). The present paper is concerned with the behavior of platinum-base metal catalysts as fuel cell anodes for H_2-CO mixed fuels. Special attention has been devoted to the platinum-nickel combination, which appears to be the most promising of the binary systems investigated.

Experimental

Catalyst preparation and characterization.—A number of platinum-base metal combination catalysts were prepared by a modification of the Adams method previously described (1). This procedure involved fusion of a mixture of chloroplatinic acid and the base metal chloride with an excess of sodium nitrate. After the product was washed to remove soluble salts, the resulting mixed oxides were reduced in suspension with bubbling hydrogen. Before use, the catalysts were dried thoroughly, ground, and sieved through a 400 mesh nylon screen.

The base metal additives was selected so as to fall into one of the following categories:

(i) Platinum-oxide combinations. Metals such as molybdenum, tungsten, chromium, cadmium, and indium would be expected to remain as oxide phases under the conditions of catalyst preparation.

(ii) Alloy combinations. Easily reducible metals such as silver and gold would be expected to form alloy phases with the platinum. Partial alloy formation was also observed in the case of nickel and copper.

(iii) Leachable additives. The reactive metals magnesium, zinc, and tin would be rapidly attacked by the acid electrolyte in the fuel cell, leading to a porous or Raney type platinum structure.

The surface areas of the powdered catalysts were measured in a gas adsorption apparatus by the BET method, using nitrogen as adsorbate at —195°C. The structures of many of the catalysts were examined by means of x-ray diffraction and, for the platinum-nickel series, more detailed studies were made by thermogravimetric analysis. For this purpose, catalyst samples weighing 8-10 mg were contained in a platinum dish suspended from the balance arm of a Cahn Electrobalance coupled with a Fisher Linear Temperature Programmer (Model No. 360). With a stream of 5% hydrogen-nitrogen as reducing gas, initial measurements of weight change at room temperature were followed by measurements of loss in weight of the samples as a function of time, using a constant heating rate of 10°C/min. In this way, information on the reduction characteristics and composition of the catalysts could be obtained.

Evaluation as fuel cell anodes.—As in previous work (3), the catalysts were evaluated in the form of Teflon-bonded anodes in circular cells having 5.06 cm^2 of active electrode area. The catalyst loading was adjusted to about 34 mg/cm^2, and a second electrode containing the same loading of platinum black was used as cathode. The anodes were evaluated with 85% phosphoric acid as electrolyte, with synthetic fuel mixtures containing 2, 5, and 10% carbon monoxide. Oxygen was used as the oxidant, and measurements of anode polarization were made with a Kordesch-Marko bridge, using a separate platinum black electrode as hydrogen reference.

Chemisorption and catalytic activity measurements.—Measurements of the chemisorption of hydrogen and carbon monoxide on the platinum-nickel catalysts and of the gas phase oxidation of carbon monoxide on these materials were carried out in the apparatus described previously (6). This consisted essentially of a calibrated volumetric adsorption apparatus connected *via* a capillary leak to a mass spectrometer (Consolidated Electrodynamics Model 21-610). By this means, the composition of the gas phase in contact with the catalyst could be analyzed at 2-min intervals, and the course of a catalyzed reaction followed as a function of time.

In a typical experiment, a catalyst sample weighing 1.0g was sealed into the apparatus and evacuated to a pressure less than 1×10^{-6} Torr for 16 hr. The catalyst was then reduced at room temperature by treatment with hydrogen/nitrogen mixtures, the hydrogen being admitted slowly into the apparatus by diffusion through a heated palladium thimble. The temperature of the catalyst was then increased slowly to 150°C in contact with hydrogen, and the sample was then evacuated at this temperature for a further period of 16 hr. This procedure was necessary to limit excessive sintering during the reduction process. Adsorption isotherms of hydrogen and carbon monoxide were then determined volumetrically in the usual way. The kinetics of the gas phase oxidation of carbon monoxide were studied by admitting CO-O_2 mixtures to the unreduced catalyst samples and measuring the concentration of carbon dioxide in the gas phase as a function of time. These measurements were generally carried out with the catalyst samples held at 0° and 25°C.

Results and Discussion

Fuel cell performance of platinum/base metal anodes.—A summary of the fuel cell performance of a number of typical platinum/base metal binary catalysts is shown in Table I. The catalysts were tested as anodes for H_2/CO mixtures at 85°C using 85% phosphoric acid as electrolyte. The data are shown as anode *vs.* reference voltages at a number of current densities, the loading of catalyst on the anode being the same in each case. In comparison to platinum black, the lowest polarizations in the presence of carbon monoxide were observed with catalysts containing nickel and copper. Slight to moderate improvement over pure platinum was found with catalysts containing iron, indium, tin, and zinc, although appreciable corrosion of these and other electrodes was observed, as indicated in Table I. The addition of metals such as silver and gold gave rise to a very rapid loss in activity of the catalyst. Alloying with silver and gold is often found to decrease the activity

Table I. Performance of catalysts with H_2/CO mixed fuels

Catalyst No.	85°C Catalyst comp. w/o	85% H_3PO_4 % CO in fuel	34 mg Catalyst/cm² Anode-reference voltage at ma/cm² 20	40	100	200	300
AZ-1	100%Pt	2	0.011	0.025	0.086	0.223	0.328
		5	0.017	0.038	0.184	0.371	0.380
		10	0.032	0.101	0.430	0.505	0.523
NPT-2	Pt-5.4%Ni	2	0.006	0.010	0.022	0.045	0.050
		5	0.005	0.013	0.031	0.071	0.073
		10	0.011	0.017	0.044	0.091	0.090
PCU-1	Pt-5%Cu	2	0.003	0.013	0.034	0.081	0.098
		5	0.013	0.024	0.077	0.172	0.190
		10	0.017	0.035	0.133	0.292	0.329
PCU-4	Pt-10%Cu	2	0.007	0.015	0.051	0.153	0.247
		10	0.018	0.041	0.367	0.557	0.600
PCU-3*	Pt-20%Cu	2	0.397	—	—	—	—
PZN-1*	Pt-7%Zn	2	0.006	0.011	0.031	0.061	0.075
		5	0.008	0.016	0.046	0.098	0.115
		10	0.014	0.028	0.127	0.265	0.265
PZN-15*	Pt-15%Zn	2	0.009	0.017	0.044	0.099	0.172
		5	0.015	0.028	0.089	0.199	0.285
PCR-5*	Pt-5%Cr	2	0.010	0.021	0.093	0.250	0.322
		10	0.025	0.078	0.410	0.570	0.610
PMO-5*	Pt-5%Mo	2	0.029	0.077	0.300	0.475	0.400
PW-5	Pt-5%W	2	0.016	0.039	0.193	0.266	0.188
		5	0.040	0.158	0.425	0.400	0.325
PCO-1*	Pt-5%Co	2	0.000	0.002	0.010	0.035	0.220
		5	0.023	0.054	0.170	0.410	0.830
BPI-1	Pt-10%Bi	2	0.244	0.303	0.395	0.460	0.487
PSN-5	Pt-5%Sn	2	0.018	0.037	0.118	0.175	0.160
		5	0.025	0.057	0.180	0.226	0.178
		10	0.022	0.059	0.308	0.384	0.347
PPB-1	Pt-10%Pb	2	0.052	0.165	0.521	—	—
PCD-1	Pt-10%Cd	2	0.010	0.024	0.083	0.230	—
PIN-5*	Pt-5%In	2	0.009	0.019	0.061	0.137	0.165
		5	0.014	0.028	0.144	0.222	0.257
		10	0.015	0.036	0.160	0.268	0.305
PAU-1	Pt-11%Au	2	0.058	0.193	0.584	0.619	0.619
		5	0.255	0.613	—	—	—
PAG-1	Pt-11%Ag	2	0.191	0.631	0.744	—	—
PMG-5*	Pt-5%Mg	2	0.042	0.241	0.531	0.628	0.660
PSB-5	Pt-5%Sb	2	0.008	0.015	0.035	0.073	0.106
		5	0.015	0.026	0.096	0.214	0.345
		10	0.022	0.046	0.177	0.394	0.454

* Electrode corroded during test.

Table II. Surface areas of platinum-nickel catalysts

Sample No.	Composition w/o	Surface area m²/g
AZ-1	100%Pt	72.9
NPT-14	1.4%Ni	35.2
NPT-3	2.1%Ni	38.4
NPT-13	3.4%Ni	43.9
NPT-2	5.4%Ni	47.6
NPT-1	10.2%Ni	63.1

of the noble metals in gas phase hydrogenation reactions (7). As among all the catalysts tested, only those of platinum-nickel showed good stability, high corrosion resistance and consistently low polarizations in the presence of CO, the properties of this series of catalysts were studied in more detail.

Platinum-nickel catalysts.—Structure. The surface areas of a series of platinum-nickel catalysts, as measured by the BET method, are listed in Table II. A sharp decrease in surface area is indicated on addition of small amounts of nickel to platinum black. The increased tolerance of these catalysts for carbon monoxide does not therefore appear to be a mere surface area effect. On careful reduction of these samples with hydrogen gas at 100°C, the catalysts were found to sinter to a residual surface area of 10-15 m²/g.

Further information on the structure of the Pt-Ni catalysts was obtained by thermogravimetric analysis. Figure 1 shows thermograms obtained with samples of platinum black, Pt-10.2%Ni, and Pt-50%Ni. In all three cases, isothermal treatment with a 5% H_2-N_2 gas mixture resulted in a large weight loss at room temperature. With platinum black, this initial loss could be attributed to reduction of residual platinum oxide to the metal. A further loss in weight on heating to 140°C resulted from desorption of water vapor and no further loss occurred up to temperatures exceeding 300°C. Reduction of Adams platinum black was therefore essentially complete after treatment with diluted hydrogen at room temperature. On the other hand, the thermogram for the Pt-50%Ni sample showed three distinct steps: (*a*) reduction of platinum oxide at room temperature, (*b*) dehydration at 140°C, and (*c*) reduction of nickel oxide at 180°-300°C. The thermogram for the Pt-10.2%Ni sample, however, failed to show a distinct step identifiable as nickel oxide reduction and reduction of this catalyst appeared to be complete at 140°C. This effect was found to be a common feature of catalyst samples containing 10% nickel or less and it seems likely that a true alloy phase is present in these samples. This point is further illustrated in Fig. 2 which shows curves for the total weight loss, the weight loss at room temperature, and the weight loss due to reduction of nickel oxide as functions of the nickel content of the catalysts. Samples containing less than 10% nickel thus showed no evidence of a separate nickel oxide phase.

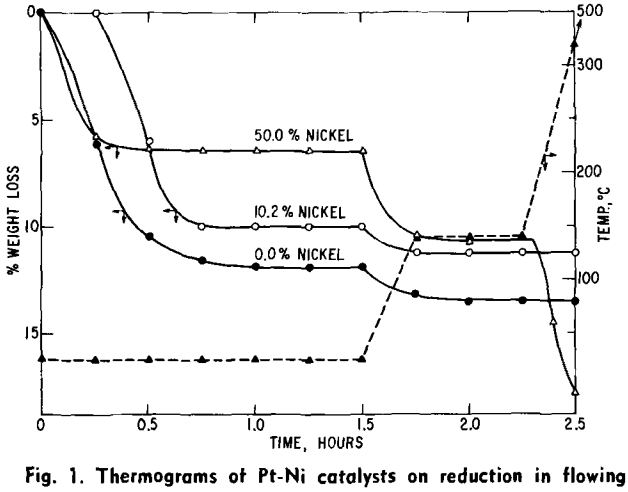

Fig. 1. Thermograms of Pt-Ni catalysts on reduction in flowing 5%H_2/N_2.

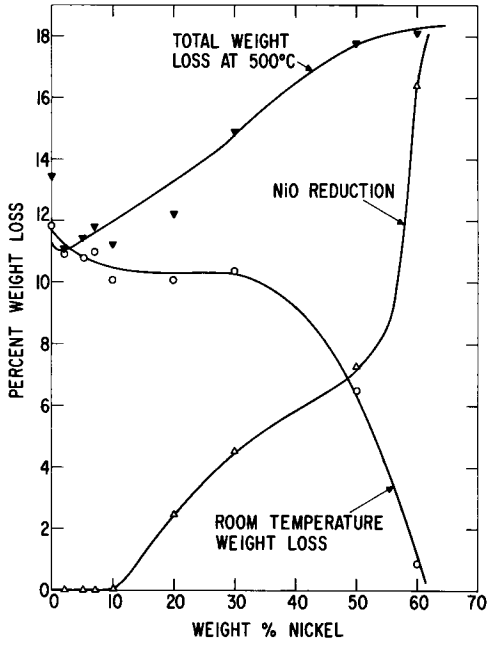

Fig. 2. Weight losses on reduction of Pt-Ni catalysts in 5%H_2/N_2.

Additional evidence for alloy formation was obtained by x-ray diffraction studies. Debye-Scherrer powder patterns obtained with the Pt-Ni catalysts containing 5, 7, and 10% nickel showed clearly the presence of a Pt-Ni alloy phase with lattice spacing $a_0 = 3.86$Å, compared with the spacing of 3.916Å found with platinum black. The existence of this alloy phase may well account for the corrosion resistance and unusual electrochemical activity of this catalyst series.

Fuel cell performance. Typical fuel cell performance data for a Pt-10.2%Ni catalyst are shown in Fig. 3, where anode *vs.* hydrogen reference voltages at 100°C are plotted against current density for H_2-CO fuel mixtures containing 2, 5, 10%CO. Comparable data for a standard platinum black anode under the same conditions are also included in the figure. The improvement resulting from the addition of nickel is very evident. Data obtained at 85°C and 85% H_3PO_4 electrolyte with a 20.3%Ni-Pt anode are shown in Fig. 4 for the three gas mixtures. Also included are comparable data with a 10%CO-H_2 mixture for platinum black and a typical platinum-ruthenium catalyst studied previously (1). It is apparent that the CO tolerance of the Pt-Ni catalyst was definitely superior to the Pt-Ru catalyst.

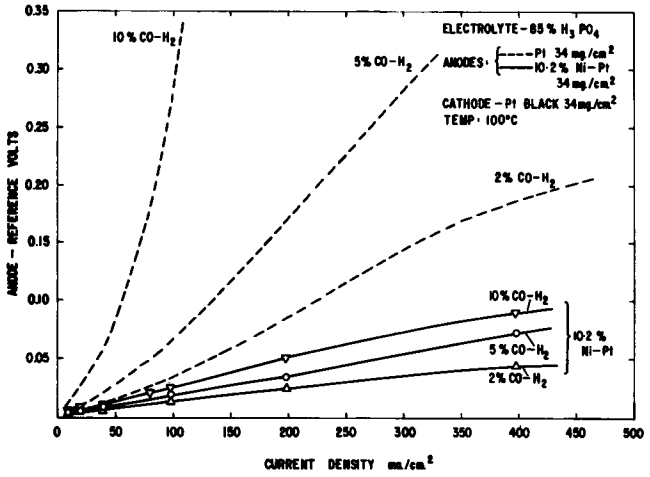

Fig. 3. Performance of 10.2%Ni-Pt and Pt black anodes with H_2-CO mixed fuels, 100°C.

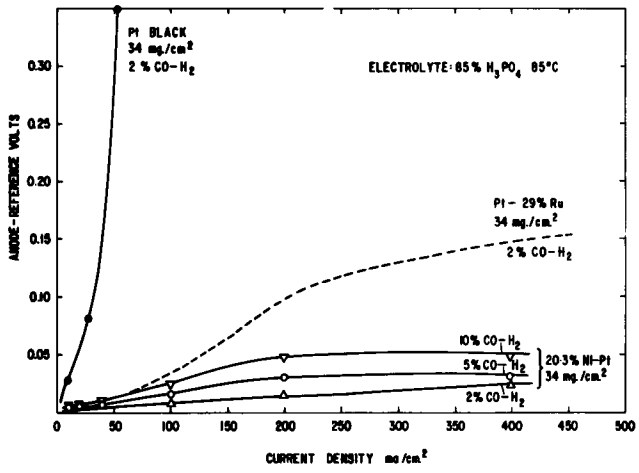

Fig. 4. Performance of 20.3%Ni-Pt anode with H_2-CO mixed fuels, 85°C.

The improved tolerance for carbon monoxide exhibited by these catalysts was also found at lower nickel contents. Figure 5 shows similar data obtained at 85°C with a 5.4%Ni-Pt anode. Even with a 10% CO-H_2 fuel mixture, the polarization of the anode did not exceed 0.1v at 400 ma/cm² C.D. The effect of nickel content on the polarization of the anode is shown in Fig. 6 at a C.D. of 100 ma/cm² for the three gas mixtures. Addition of as little as 2% nickel was apparently sufficient to give rise to a marked improvement in anode performance. Above 30% nickel, corrosion became noticeable and the electrode surface showed a greenish tinge after several hours of operation at 85°C. It is probable that corrosion will become more noticeable at lower nickel contents with increasing temperature. However, below 10% nickel, no trace of corrosion or nickel salts in the effluent electrolyte was observed after tests at 100°C of 3 hr duration. No extended corrosion tests were conducted, and the long-term stability of these catalysts remains uncertain.

In an attempt to provide more detailed information on the nature of the reactions at the anode, analysis of the carbon dioxide content of the effluent gases from a working anode was carried out. Analysis of effluent samples was made with the mass spectrometer after 10-min periods of operation on steady loads at various current densities. Using a Pt-1.4%Ni catalyst as anode and a 5%CO-H_2 fuel mixture, very small amounts of CO_2 were detected in the product gases at current densities below 200 ma/cm². Platinum black electrodes, on the other hand, give rise to large amounts of CO_2 under the same conditions (1). It seems, therefore, that, as with alloys of platinum-ruthenium, platinum-nickel alloy electrodes in the presence of H_2/CO mixed fuels give rise to a higher surface coverage with hydrogen and a higher hydrogen oxidation current than

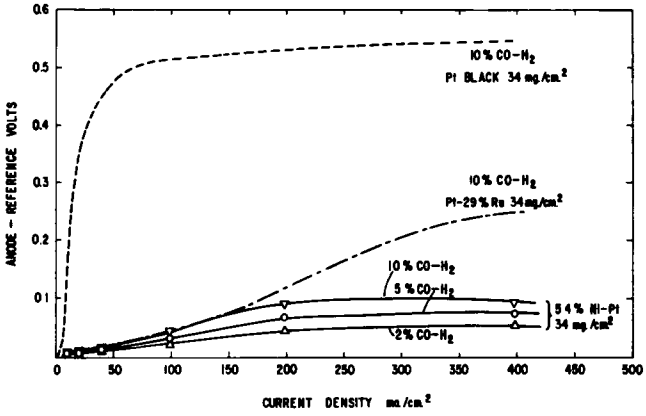

Fig. 5. Performance of 5.4%Ni-Pt anode with H_2-CO mixed fuels, 85°C.

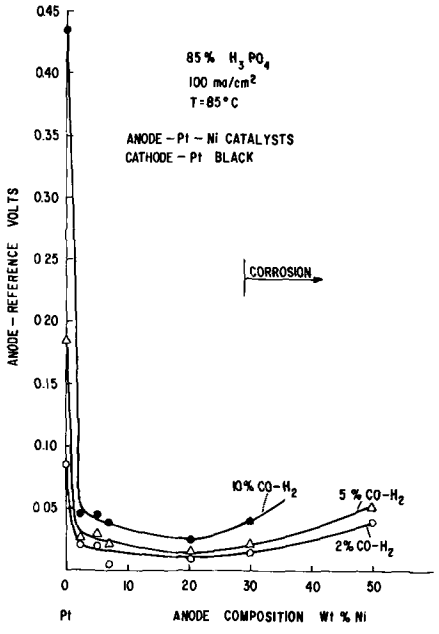

Fig. 6. Effect of nickel content of Pt-Ni anodes with H_2-CO mixed fuels, 85°C.

is the case with pure platinum electrodes, which tend to be rapidly poisoned by the CO in the fuel stream.

Adsorption and catalytic properties.—Previous studies of the co-adsorption and interaction of carbon monoxide and hydrogen from the gas phase on platinum and ruthenium blacks (6) have indicated that CO is much less strongly chemisorbed on ruthenium than on platinum under the same conditions. It seems likely that this fundamental difference in the behavior of the two metals is responsible for the increased CO tolerance exhibited by platinum-ruthenium alloys in fuel cell anodes (1). Similar experiments were therefore carried out with the Pt-Ni catalysts in an attempt to provide a better understanding of the behavior of these materials.

The upper curve in Fig. 7 shows the adsorption isotherm of carbon monoxide at 150°C on a reduced sample of platinum black. The isotherm is of the Langmuir type and adsorption virtually ceases when the metal is covered with a monolayer of adsorbate. At the end of these measurements, the platinum black was evacuated for 16 hr at 150°C and the CO isotherm determined again, as shown in the lower curve of Fig.

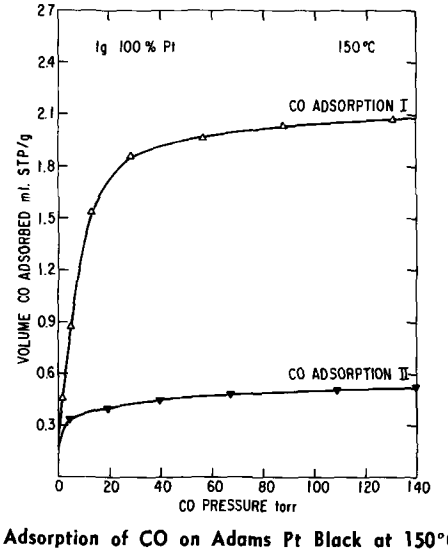

Fig. 7. Adsorption of CO on Adams Pt Black at 150°C: I. adsorption of CO on reduced sample; II. subsequent adsorption of CO after evacuation at 150°C for 16 hr.

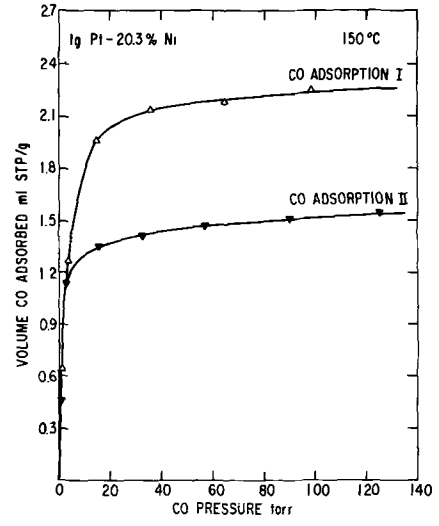

Fig. 8. Adsorption of CO on Pt-20.3%Ni catalyst at 150°C. I. adsorption of CO on reduced sample; II. subsequent adsorption of CO after evacuation at 150°C for 16 hr.

7. If all the chemisorbed CO was desorbed on evacuation, the two isotherms should be coincident. It is apparent, however, that only a small portion (around 25%) of the initially chemisorbed CO could be removed by pumping alone. Similar data for a Pt-20.3% Ni catalyst under the same conditions are shown in Fig. 8. In this case, a much larger fraction (60-70%) of the chemisorbed CO was desorbed by pumping at 150°C for a 16-hr period. The addition of nickel to the platinum thus appears to weaken the bonding of CO to the metal surface.

Fig. 9 illustrates the effect of nickel concentration on the strength of bonding of CO to the catalyst. The solid curve (a) shows the percentage of chemisorbed CO which is desorbable on pumping at 150°C for 16 hr (left-hand ordinate), this quantity reaching a maximum at about 20% nickel. The dashed curve [ordinate (b) on right side] shows the variation in the ratio, volume of CO adsorbed: volume of H_2 adsorbed at 50 Torr and 150°C for the various catalyst samples. A general decrease in this ratio was observed with increasing nickel content of the catalyst. These results suggest that, as in the case of platinum-ruthenium alloys (1), the improved tolerance for CO shown by the alloy catalysts is a result of decreasing CO coverage on the catalyst surface in the presence of hydrogen.

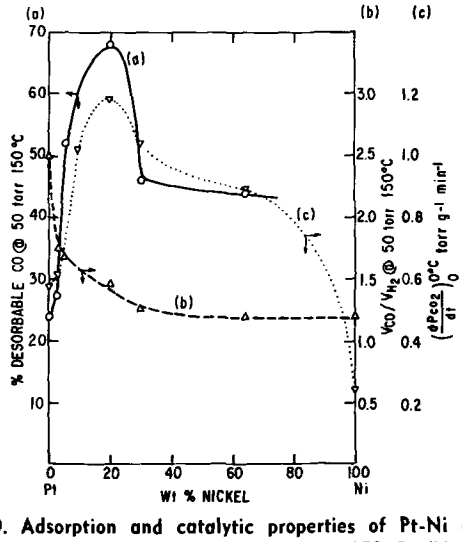

Fig. 9. Adsorption and catalytic properties of Pt-Ni catalysts: (a) per cent desorbable CO at 50 Torr and 150°C; (b) V_{CO}/V_{H_2} at 50 Torr and 150°C; (c) initial rate of formation of CO_2 from 1:1 CO:O_2 mixtures at 0°C, as functions of Ni content.

The Pt-Ni alloy catalysts were also found to be very active for the low-temperature oxidation of carbon monoxide in the gas phase. The formation of CO_2 by the reaction of carbon monoxide and oxygen was found to fit the kinetic expression

$$kT = -P^{o}_{CO} \log (P^{o}_{CO} - P_{CO_2})$$

where P^{o}_{CO} is the initial pressure of carbon monoxide and $P^{o}_{CO_2}$ the pressure of carbon dioxide at time t. A similar expression has been used by Winter (8) to describe the course of the reaction over nickel oxide. The apparent activation energies between 0° and 25°C were in the range 3-5 kcal/mole for all the Pt-Ni catalysts tested. The variation in the initial rate of CO_2 formation at 0°C for an initial ratio of $CO:O_2 = 1.1$ is shown by the dotted curve [ordinate (c) on right side] in Fig. 9. The activity of the Pt-Ni catalysts for this reaction also shows a maximum value at around 20% nickel, in spite of the fact that there is no corresponding maximum in the surface areas of the catalysts.

Although the results of analysis of the fuel cell effluents indicate that electrochemical oxidation of CO plays only a minor role at the Pt-Ni alloy anode, the enhanced activity of these catalysts in the gas phase oxidation of CO may be a reflection of a weaker bonding of carbon monoxide to these alloys than is found with platinum alone.

Conclusions

Of a large number of platinum-base metal combinations tested as anodes in the H_2-CO fuel cell, platinum-nickel catalysts containing 2-20 w/o nickel show an exceptional resistance to poisoning by carbon monoxide. These catalysts are corrosion resistant to phosphoric acid at 100°C and exhibit stable and reproducible performance which equals or exceeds that of the best noble metal alloy catalysts studied previously. The addition of small amounts of nickel to the platinum lattice appears to reduce the heat of adsorption of carbon monoxide on the metal surface resulting in an increase in hydrogen coverage on the electrode during operation of the cell.

Acknowledgments

This work includes parts of the program under contract DAAK-02-67-C-0080 with the U.S. Army Mobility Equipment Research and Development Center, Ft. Belvoir, Virginia, to develop a technology which will facilitate the design and fabrication of practical military fuel cell power plants for operation on ambient air and hydrocarbon fuels.

Manuscript submitted Oct. 17, 1968; revised manuscript received Jan. 23, 1969.

Any discussion of this paper will appear in a Discussion Section to be published in the December 1969 JOURNAL.

REFERENCES

1. L. W. Niedrach, D. W. McKee, J. Paynter, and I. F. Danzig, *Electrochem. Technol.*, **5**, 318 (1967).
2. D. W. McKee, L. W. Niedrach, J. Paynter, and I. F. Danzig, *ibid.*, **5**, 419 (1967).
3. D. W. McKee and A. J. Scarpellino, Jr., *ibid.*, **6**, 101 (1968).
4. G. C. Bond and D. E. Webster, *Chem. Ind. (London)*, **1967**, 878.
5. N. D. Tomashov, "Theory of Corrosion and Protection of Metals," p. 275, MacMillan, New York (1966).
6. D. W. McKee, *J. Catalysis*, **8**, 240 (1967).
7. D. W. McKee, *J. Phys. Chem.*, **70**, 525 (1966); D. A. Cadenhead and N. G. Masse, *ibid.*, **70**, 3558 (1966).
8. E. R. S. Winter, *J. Chem. Soc.*, **1955**, 2726.

The Effect of Electrolyte Flow on the Morphology of Zinc Electrodeposited from Aqueous Alkaline Solution Containing Zincate Ions

R. D. Naybour

Electricity Council Research Centre, Capenhurst, Chester, England

ABSTRACT

The effect of flowing electrolyte on the morphology of zinc electrodeposited from aqueous alkaline solution has been investigated. Aqueous potassium hydroxide solution of 5.8*N* normality containing 19.1 g/dm^3 of dissolved zinc oxide was circulated through a flow tube at flow velocities up to 1.7 m/s, corresponding to Reynold's numbers of up to 13,500. The morphologies of zinc electrodeposits formed on a zinc substrate in the wall of the flow tube were examined over a range of current densities and Reynold's numbers. The results showed that flowing electrolyte under both turbulent flow and laminar flow conditions greatly modified the deposit morphologies. It was possible to construct a morphology, current density, and Reynold's number "phase diagram" to describe the effects of flowing electrolyte on deposit morphology.

The growth of zinc dendrites is a major difficulty in the development of a secondary battery employing zinc as an active material. Consequently, the morphologies of zinc electrodeposited from aqueous alkaline solution containing zincate have been extensively studied in recent years (1-6). It is clear from previous work that dendritic growth occurs during diffusion-limited current conditions, and the rate of growth, rather than the rate of nucleation (2), is the controlling factor. Methods used to control deposit morphologies have included restricting the charging current density to below the limiting current density (1), using current pulses, including both charging and discharging currents (4), and, the use of half-wave, rectified a.c. (5). Each of the above methods have been claimed to prevent the formation of dendrites but, as found in exploratory experiments during the present investigation, they all place limitations on the charging current density without achieving a large increase in the rate at which an acceptable zinc deposit can be formed. Any method of preventing dendritic growth would be successful if the diffusion-depleted

Key words: zinc, morphology, electrodeposition, turbulent, Reynold's number.

layer near the electrode surface was thereby prevented from forming, and it is well known that diffusion-controlled processes in liquids are very dependent on the hydrodynamic conditions. These two conclusions stimulated the present study in which the effect of flowing electrolyte on the morphology of zinc electrodeposits was studied over a range of Reynold's number and current density.

Experimental

The specimen was a single crystal of zinc cut to reveal the basal plane and prepared prior to deposition as previously described (2). The flowing electrolyte apparatus, illustrated diagrammatically in Fig. 1, was designed to obtain Reynold's numbers of up to 10^4 in a tube of length 0.6m and rectangular cross section 0.01 x 0.05m. The specimen was mounted on a holder suitable for examination in the scanning electron microscope. After electropolishing, the specimen was embedded into a hollow plug by means of plasticine. Care was taken to ensure the specimen surface and plasticine were smooth and level with the edges of the plug. The plasticine and specimen surface were covered by a layer of vinyl plastic from an aerosol and, after drying, the plastic was dissolved from the specimen surface. The specimen was then electropolished immediately before placing into the flowing electrolyte apparatus. The removable plug was screwed onto an "O" ring until a previously determined mark indicated the surface of the specimen was level with the inside of the flow tube. After this procedure, the surface of the specimen was about 30μ below the level of the surrounding surface at the start of deposition. During deposition, this difference in surface height decreases until the roughness of the deposit limits the applicability of the Reynold's numbers quoted. The morphologies obtained were not greatly dependent on the charge density and it is concluded that surface modifications to the Reynold's numbers quoted were small. By means of the valves below the flow tube, it was possible to adjust the flow rate in the tube to any value corresponding to Reynold's numbers between 0 and 1.4×10^4. The volume of liquid passing through

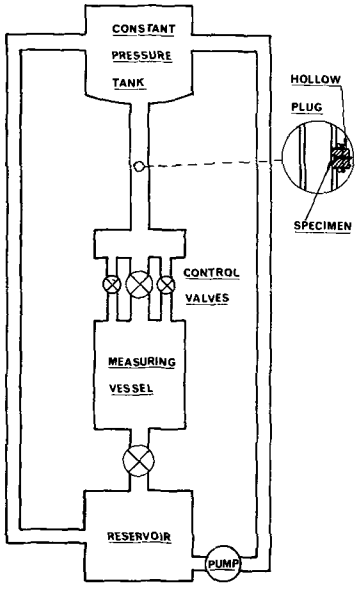

Fig. 1. Schematic diagram of flowing electrolyte apparatus. Inset showing specimen holder.

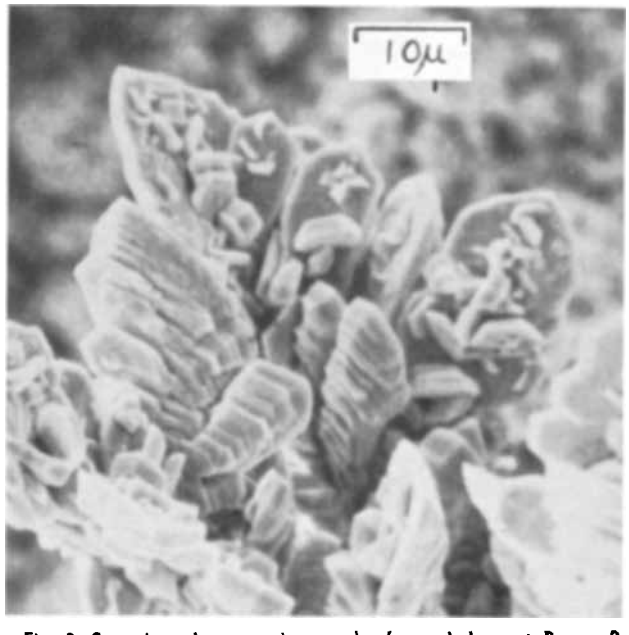

Fig. 3. Scanning electron micrograph of morphology at Re = 0, 12 min at 500 amp/m^2 viewed at 45° (X1500).

Fig. 2. Scanning electron micrograph of morphology at Re = 0, 4 min at 10^3 amp/m^2 viewed at 10° (X1500).

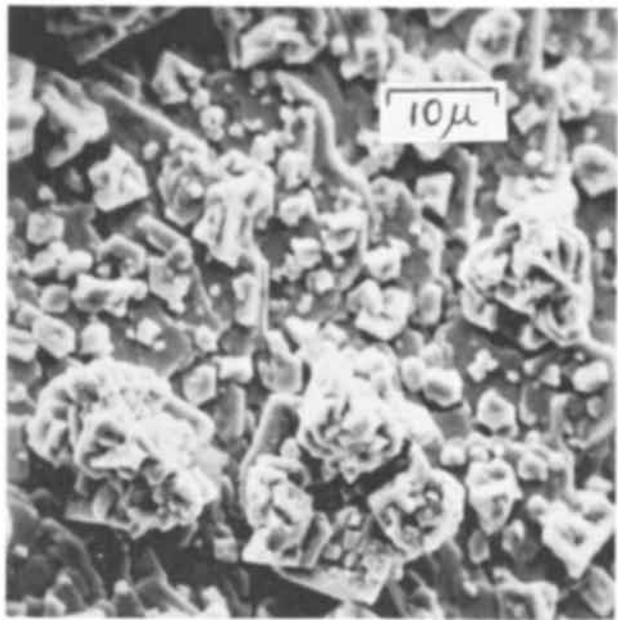

Fig. 4. Scanning electron micrograph of morphology at Re = 0, 8 min at 358 amp/m^2 viewed at 10° (X1500).

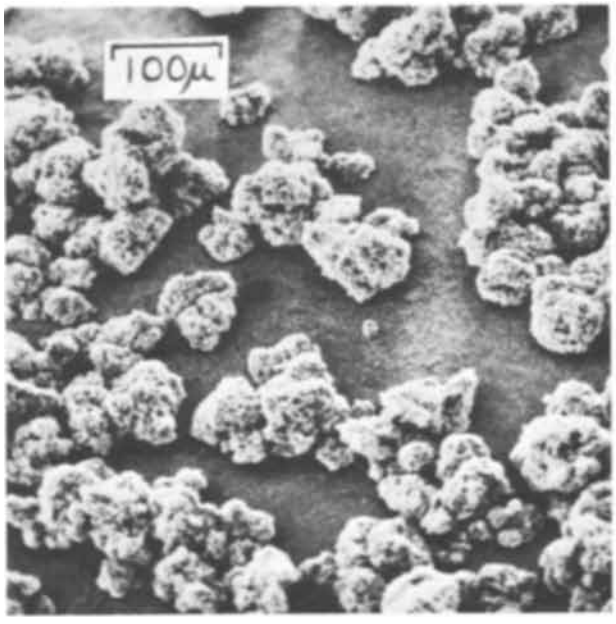

Fig. 5. Scanning electron micrograph of morphology at Re = 0, 20 min at 20 amp/m^2 viewed at 10° (X150).

Fig. 7. Scanning electron micrograph of morphology at Re = 7900, 1 min at 8000 amp/m^2 viewed at 45° (X1500).

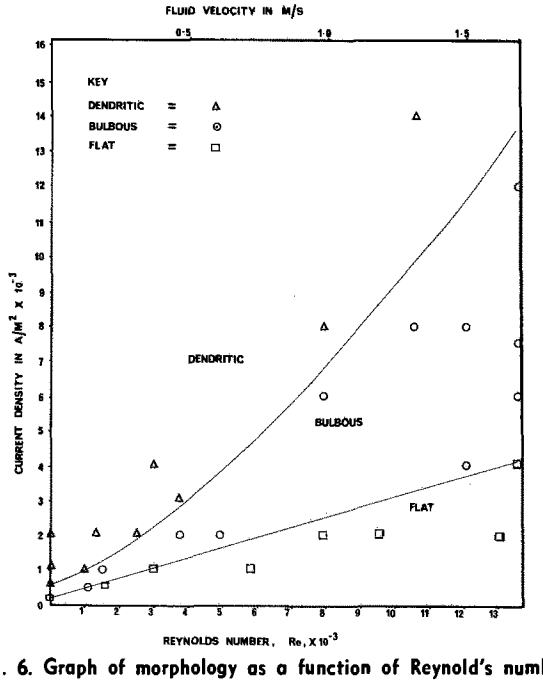

Fig. 6. Graph of morphology as a function of Reynold's number, Re, flow velocity, and current density.

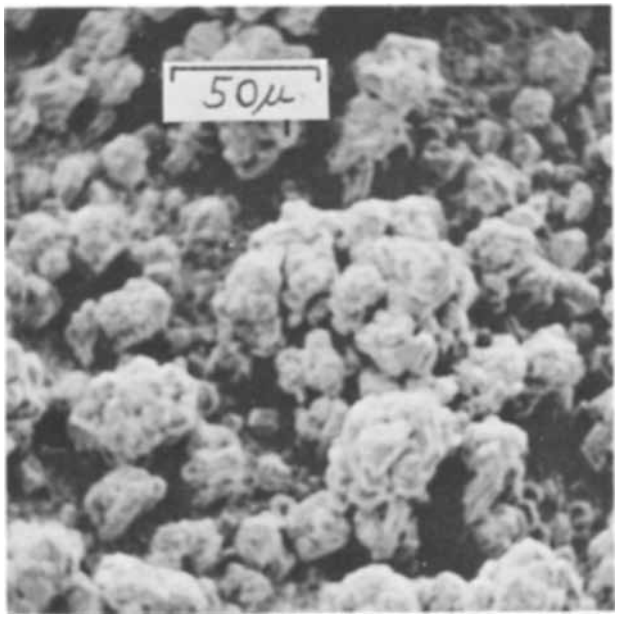

Fig. 8. Scanning electron micrograph of morphology at Re = 7900, 1 min at 6000 amp/m^2 viewed at 45° (X400).

the tube in a given time was measured in the calibrated vessel below the flow tube and the Reynold's number, Re was calculated from Re = aV/ρ where a is the distance between the broader walls of the flow tube, V the average velocity in the flow tube, and ρ the kinematic viscosity. The electrolyte used was made from distilled water and Analar grade potassium hydroxide and zinc oxide. The normality of the solution was 5.8N and the solution contained 19.1 g/dm^3 of dissolved zinc oxide. The density and dynamic viscosity of the electrolyte were measured at 20°C and the value of 1.28 x 10^{-6} m^2/s was calculated for the kinematic viscosity. Experiments were performed at ambient temperature which was in the range 20° ± 2°C so that the error in Re due to temperature variations was ±5%. At high Re, above 8 x 10^3, the high rates of flow were measured to ±8% and the error in Re was therefore around ±10%. Experiments using water and ink as a dye confirmed that the flow was laminar below Re of 1.6 x 10^3 and that turbulence was well developed above Re of 2.5 x 10^3.

Electrodeposition was carried out at constant current using a transistorized potential source, constant to 1 part in 2000, and variable resistances. The anodes were pieces of platinum foil and the zinc single-crystal specimen was the cathode. After deposition, the specimen was removed from the flow tube, washed in distilled water and methanol, and placed in the scanning electron microscope.

Results

Stationary electrolyte.—In stationary electrolyte, the deposit morphologies obtained over the range of current densities were similar to those obtained in our previous work (2). At a current density of 10^3 amp/m^2, the deposit was dendritic as shown in Fig. 2. As the current density was decreased, the dendrites became less needle shaped and more platelike; Fig. 3 is an example of the morphology at 500 amp/m^2.

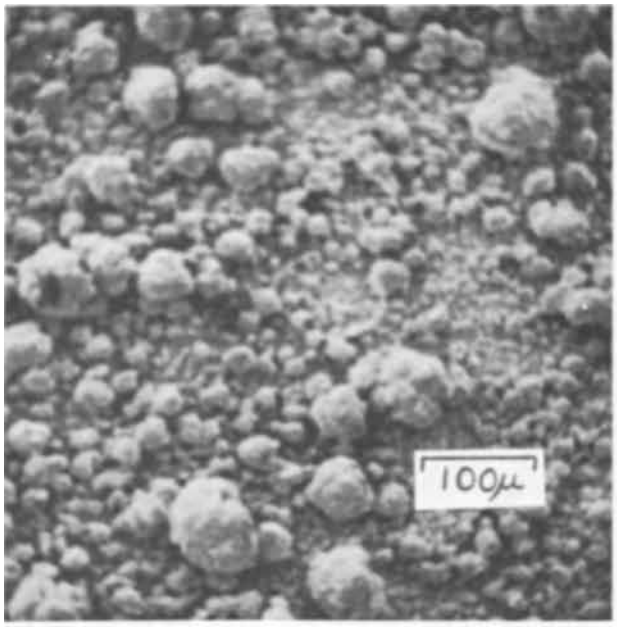

Fig. 9. Scanning electron micrograph of morphology at Re = 7900, 2 min at 3000 amp/m^2 viewed at 10° (X150).

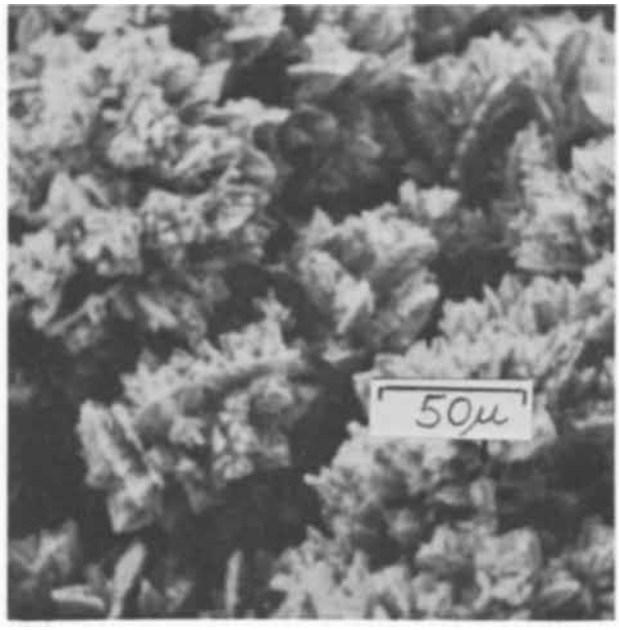

Fig. 11. Scanning electron micrograph of morphology at Re = 13,500, 1 min at 1600 amp/m^2 viewed at 45° (X400).

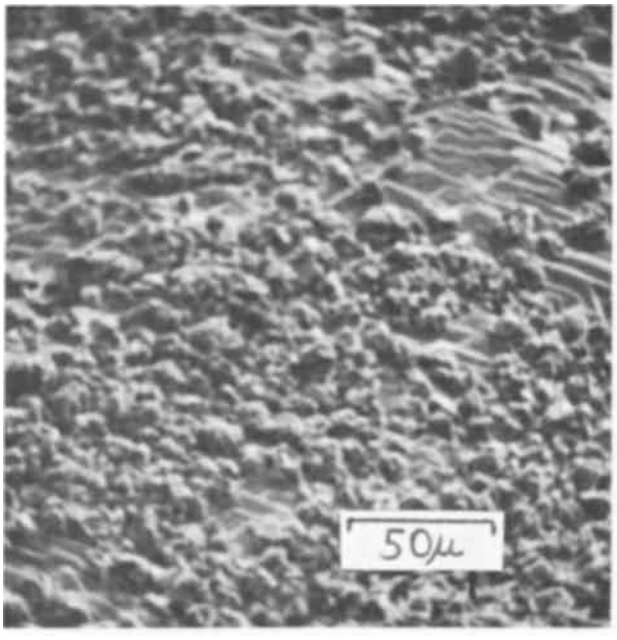

Fig. 10. Scanning electron micrograph of morphology at Re = 7900, 3 min at 2000 amp/m^2 viewed at 45° (X400).

Fig. 12. Scanning electron micrograph of morphology at Re = 13,500, 1 min at 12,000 amp/m^2 viewed at 45° (X400).

Further decrease in current density resulted in a fine granular deposit at 448 amp/m^2 and at 358 amp/m^2 the deposit consisted of a mixture of granular and layerlike deposits as shown in Fig. 4. At 250 amp/m^2, the deposit was essentially granular and layerlike as in Fig. 4 but some bulbous growths were obtained. At 125 amp/m^2, the deposit was in the form of large bulbous growths as shown in Fig. 5.

Flowing electrolyte.—Morphologies produced at current densities up to 16 x 10^3 amp/m^2 and Re up to 14 x 10^3 were examined. Within the above range of current density and Re, three reasonably distinct morphologies were produced. First, at high current densities and low flow rates the deposit was clearly dendritic in form. Increasing the electrolytic movement resulted in a bulbous deposit which was not comparable to any morphology obtained in stationary electrolyte. Finally, at high Re and intermediate current densities the deposit was similar to the flat, granular, deposits obtained at 358 amp/m^2 in stationary electrolyte.

The effect of Re and current density on the type of deposit produced is presented in the form of a "phase" diagram in Fig. 6. The morphologies produced were classified into one of the categories, dendritic, bulbous, or flat. The micrographs in Fig. 7-14 illustrate these three morphologies and the quite sharp transitions among the three types of deposit. Figures 7-10 were obtained at Re = 7.9 x 10^3 and current densities of 8000, 6000, 3000, and 2000 amp/m^2 and show the dendritic deposit at 8000 amp/m^2, the bulbous deposits at 6000 and 3000 amp/m^2, and the flat type at 2000 amp/m^2. The morphologies at Re = 1.35 x 10^4 are shown in Fig. 11-14. The deposit at 16,000 amp/m^2, Fig. 11, was clearly dendritic; that at 12,000 amp/m^2, Fig. 12, was bulbous; and that at 4000 amp/m^2, Fig. 13, was in a transition region between bulbous and flat deposits, while, at 2000 amp/m^2, Fig. 14, the deposit was clearly "flat."

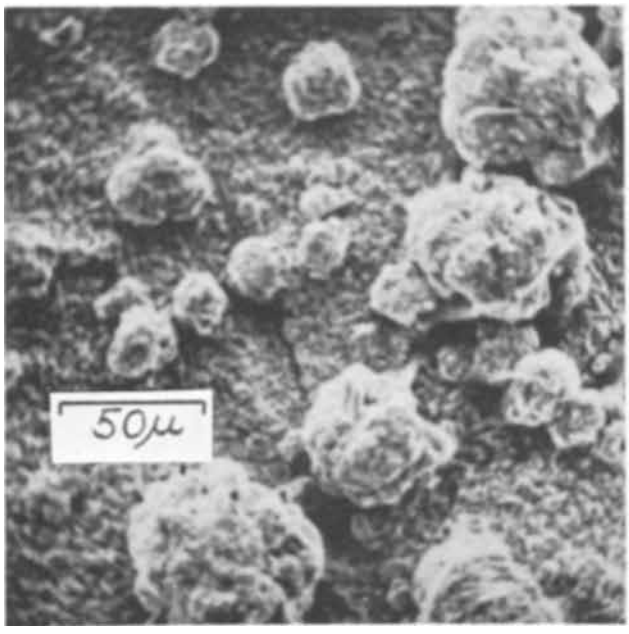

Fig. 13. Scanning electron micrograph of morphology at Re = 13,500, 1 min at 4000 amp/m² viewed at 10° (X400).

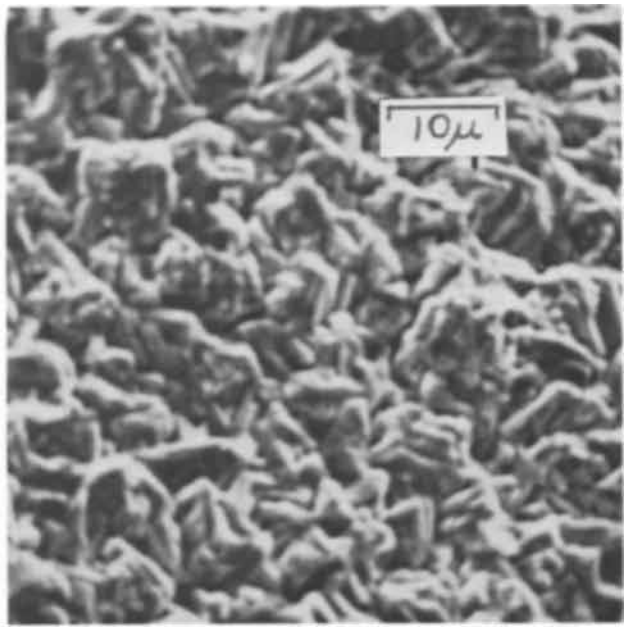

Fig. 14. Scanning electron micrograph of morphology at Re 13,500, 2 min at 2000 amp/m² viewed at 45° (X1500).

The effect of Re on the uniformity of the deposit is shown in Table I in which the maximum protuberance height estimated from the electron micrographs is compared with the theoretical thickness of deposit assuming a current efficiency of 100%.

Discussion

Levich (7) has considered the effect of flowing electrolyte on limiting currents under both turbulent and laminar flow conditions and has calculated that under turbulent conditions the diffusional flow to a plate is approximately proportional to the 0.8-0.9 power of the fluid velocity. For laminar flow, the index is in the region 0.5-0.3. In the present experiments, the "phase" boundary delineating the flat to bulbous transition is a curve in which, approximately, the current density is proportional to $(Re)^{1.0}$. In the case of the bulbous to dendritic transition the current density is proportional to $(Re)^{1.1}$ for $Re > 2000$ and proportional to $(Re)^{0.7}$ for $Re < 2000$. It therefore seems likely, in the light of Levich's theory, that one or other of these curves is in fact the locus of the onset of diffusion-limited current as a function of Re.

The results at 0.5×10^3 amp/m² illustrate the change in morphology produced by flow which is certainly laminar. The dendritic deposit at Re = 0 has been modified to a bulbous deposit at Re = 1100 and it is flat by Re = 1600. This change in morphology produced by flowing conditions which are wholly laminar is not surprising because there is a large amount of microturbulence during the deposition of zinc primarily due to density changes in the electrolyte and to hydrogen evolution. For the same reasons, a sharp transition in morphology when the electrolyte flow changes from laminar to turbulent would not be expected.

Table I

Re	Current, density, amp/m²	Time, min	Theoretical thickness of deposit, μm	Maximum protuberance height estimated from micrographs, μm (±30%)	Ratio (protuberance height / deposit thickness)
0	120	20	6.8	290	43
0	358	8	8.2	33	4.0
0	500	12	17	140	8.2
0	1000	4	12	200	18.0
1570	1000	4	12	120	10.0
3000	1000	4	12	47	4.0
7900	2000	3	17	67	0.6
7900	3000	2	17	50	2.9
7900	6000	1	17	34	2.0
7900	8000	1	23	100	4.4
13500	2000	3	17	7.2	0.4
13500	4000	1	12	32	2.7
13500	12000	1	36	100	2.8
13500	16000	1	46	150	3.3

Previous workers (8-10) have stressed the examination of electrodeposits *in situ* and a number of cells suitable for optical microscopic examination of growing electrodeposits have been used by them. However, even though these cells employed a flowing electrolyte at the surface of the electrode, the flowing conditions were not specified. Indeed the possibility of hydrodynamic conditions affecting the deposit was not considered. The present results show clearly that even flowing conditions which appear to be laminar can affect the deposit morphologies and thus the hydrodynamic condition of the electrolyte is an important factor in the control of the morphology of electrodeposits.

Acknowledgment

This paper is published by permission of the Electricity Council.

Manuscript submitted Nov. 4, 1968; revised manuscript received Jan. 6, 1969.

Any discussion of this paper will appear in a Discussion Section to be published in the December 1969 JOURNAL.

REFERENCES

1. J. E. Oxley, NASA Contract Report CR-377, Contract No. NAS 5-3908 by Leesona Moos Labs., Feb. 1966.
2. R. D. Naybour, *Electrochim. Acta*, **13**, 763 (1968).
3. R. W. Powers, Paper 33 presented at ECS Meeting, Chicago, Oct. 15-19, 1967.
4. S. A. Roote, F. F. Blurton, and H. G. Oswin, Paper 34 presented at ECS Meeting, Chicago, Oct. 15-19, 1967.
5. V. V. Romanov, *Zh. Prikl. Khim.*, **34**, 2692 (1961).
6. R. Yu Bek, N. T. Kudryavtsev, *ibid.*, **34**, 2020 (1961).
7. V. G. Levich, "Physicochemical Hydrodynamics," Prentice Hall, Englewood Cliffs, N. J. (1962).
8. R. W. Powers, *Electrochem. Technol.*, **5**, 429 (1967).
9. J. O'M Bockris and A. Damjanovic, "Modern Aspects of Electrochemistry," No. 3, p. 224, Butterworths (1964).
10. A. Damjanovic, T. H. V. Setty, and J. O'M Bockris, *This Journal*, **113**, 429 (1966).

The Electrochemical Behavior of Molybdenum

L. L. Wikstrom*, [1] and Ken Nobe*

School of Engineering and Applied Science, University of California, Los Angeles, California

ABSTRACT

The anodic and cathodic polarization of molybdenum in 1*N* H_2SO_4 was investigated. In deaerated solutions, two stable rest potentials, 0.368 and —0.020v *vs.* NHE, were observed, depending on the activation procedure. In aerated solutions, only the rest potential of 0.368v was observed. From the more noble rest potential, an anodic Tafel slope of 44 ± 4 mv and a corrosion current of 1.5 ± 0.8 μa/cm^2 were obtained. For the h.e.r., a Tafel slope of 70 ± 3 mv and an exchange current of 0.10 ± 0.04 μa/cm^2 were obtained. Two distinct active-passive transitions were observed between the two rest potentials. The short-time galvanostatic transients exhibited two linear regions in the potential-time responses and could be represented by an electrical model of two R-C networks in series. Capacitance values were determined from the slopes of the two linear regions. The first capacitance was attributed to MoO_2 at the Mo-MoO_2 interface and was a constant value of 3.75 μf/cm^2 throughout the potential region investigated. The second capacitance was surmised to be a pseudocapacitance and ranged from 200 to 600 μf/cm^2. However, for sufficiently large polarization from the more noble rest potential, the second capacitance was too large to be measured.

Few investigations have been made of the electrochemical behavior of pure molybdenum. Some early work (1-3) indicated that molybdenum passivated easily and that the end product of its electrochemical oxidation was hexavalent molybdenum. In acidic solutions, experimental rest potentials of 0.390v *vs.* NHE (4), 0.368v *vs.* NHE (5), and 0.000-0.058 *p*H v *vs.* NHE (6) have been reported. Anodic Tafel slopes of 70 mv (7) and 45 mv (4, 5, 8) have been determined for the dissolution reaction and cathodic Tafel slopes of 76-104 mv (6, 9, 10) have been reported for the h.e.r. on molybdenum. More recently, the anodic passivation (11) and the mechanism of the dissolution reaction (8) have been studied.

As indicated above, two different stable rest potentials of molybdenum in acidic solutions have been reported. The anodic region above the more noble rest potential and the cathodic region below the more active rest potential have been investigated previously. It seems appropriate that one laboratory group investigate the electrochemical behavior of molybdenum in the region between these two stable rest potentials and in the potential regions previously investigated.

Experimental

The test cell was a conventional one and made from Pyrex glass with a nominal capacity of 1 liter. The test solution was 1*N* H_2SO_4. Prior to introduction of a molybdenum electrode, the test solution was either aerated or deaerated (Air Reduction Prepurified N_2, 99.997%) for 24 hr.

Planar (0.005 cm thick sheet, 99.9% Mo) and cylindrical (0.625 cm diameter rod, 99.9% Mo) molybdenum electrodes (Fansteel Metallurgical Corporation) were used. Both types of electrodes had an exposed area of 1 cm^2.

Subsequent to fabrication, the general electrode surface preparation procedure was as follows:

1. Mechanical polishing to 4/0 emery paper.
2. Removal of polishing residue with tissue.
2(a). Masking (planar electrode only) with purified paraffin wax.
3. Wash with distilled water.
4. Degrease with absolute ethyl alcohol.
5. Wash with distilled water.
6. Activate in acid for 5 min.
7. Wash with distilled water.
8. Place electrode in cell while still wet.

Once the electrodes had been polished, care was taken to minimize exposure to the atmosphere. The electrodes were activated in different acids: 5, 8, and 12*N* HCl, 5 and 10*N* H_2SO_4, 5 and 10*N* HNO_3, and a 1-1 mixture of concentrated HNO_3-H_2SO_4.

Both galvanostatic and potentiostatic steady-state polarization techniques were used to determine the potential — log *I* curves. Galvanostatic transient techniques were used to determine the differential capacitance.

The potential of the test electrode was measured with respect to a saturated calomel electrode (SCE), which was connected to the test solution near the test electrode through a Haber-Luggin Capillary. The potential difference between the test electrode and SCE reference electrode was measured with a Keithley electrometer. Wenking and Anotrol potentiostats were employed. A Rutherford Model 585 pulse generator with a cathode follower attachment was used for the short-duration galvanostatic pulses used to determine the differential capacitance. A Tektronix dual beam oscilloscope, Model 555, was used to monitor the initial part of the potential-time response of the test electrode.

Results

All molybdenum electrodes in aerated 1*N* H_2SO_4 had a rest potential of 0.368v *vs.* NHE. Molybdenum electrodes in deaerated 1*N* H_2SO_4, except for the polished cylindrical electrodes activated in HCl, also had a rest potential of 0.368v *vs.* NHE. The polished cylindrical molybdenum electrodes activated in HCl had a rest potential of —0.020v *vs.* NHE.

The polarization data are divided into two separate groups. Group I contains all data taken on electrodes with a rest potential of 0.368v *vs.* NHE and includes data taken in both aerated and deaerated 1*N* H_2SO_4. Group II contains all data taken on electrodes with a rest potential of —0.020v *vs.* NHE.

Group I.—Figure 1 shows the steady-state galvanostatic and potentiostatic polarization data obtained for both planar and cylindrical (tangential velocity, v_t = 6.7 cm/sec) molybdenum electrodes in deaerated and aerated 1*N* H_2SO_4. Cathodic polarization was performed prior to anodic polarization. Subsequent to cathodic polarization, the potential was allowed to return to the rest potential, 0.368v before anodic polarization. Identical polarization behavior was observed for both planar and cylindrical electrodes. The anodic Tafel slope, corrosion current, the h.e.r. cathodic Tafel slope, and exchange current density are given in Table I. During

* Electrochemical Society Active Member.
[1] Present address: New York University, University Heights, New York, New York.

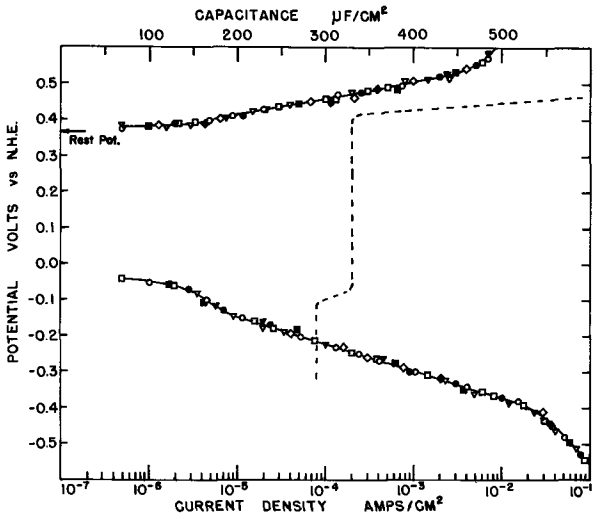

Fig. 1. Cathodic-anodic polarization sequence. E_0 = 0.368v *vs.* NHE. □ galvanostatic, aerated; ■ galvanostatic, aerated; ◇ galvanostatic, deaerated; ◆ galvanostatic, deaerated; ○ potentiostatic, aerated; ● potentiostatic, aerated; ▽ potentiostatic, deaerated; ▼ potentiostatic, deaerated. Open points represent planar electrodes; closed points represent cylindrical electrodes; dashed line represents capacitance data.

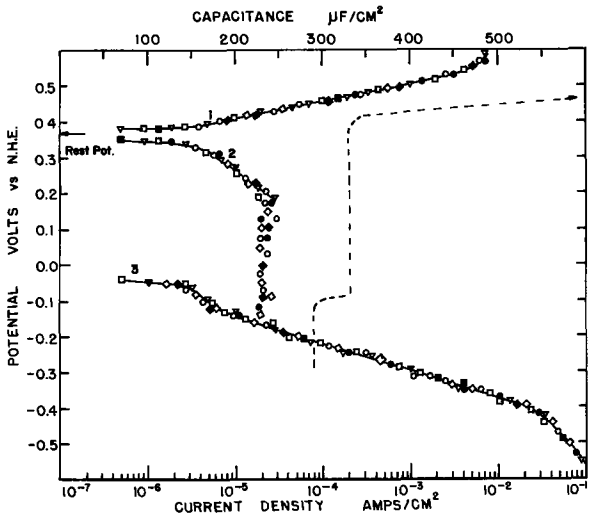

Fig. 2. Polarization sequence. Line 1-2, anodic-cathodic. Line 3-1-2, cathodic-anodic-cathodic. E_0 = 0.368v. □ Galvanostatic, aerated; ■ galvanostatic, aerated; ◇ galvanostatic, deaerated; ◆ galvanostatic, deaerated; ○ potentiostatic, aerated; ● potentiostatic, aerated; ▽ potentiostatic, deaerated; ▼ potentiostatic, deaerated. Open points represent planar electrodes; closed points represent cylindrical electrodes; dashed line represents capacitance data.

anodic polarization, the color of the electrode changed from silver gray to black at a potential of 0.500 ± 0.010v. In addition, the polarization curve started to deviate from the linear Tafel behavior at this potential. Cathodic polarization appeared to be discontinuous between the rest potential, 0.368v, and the beginning of the h.e.r. Initially, a cathodic overpotential greater than 400 mv was observed by the imposition of the lowest cathodic current density.

Figure 2 shows the anodic-cathodic polarization sequence (lines 1 and 2). It is seen that the initial anodic run affects the cathodic polarization. As shown in Fig. 2, there is a gradual decrease in the potential with increasing cathodic current density rather than the abrupt drop in potential as shown in Fig. 1. This gradual decrease in potential continues up to a current density of approximately 25 ± 10 μa/cm² (0.240v $< \Phi <$ 0.340v). At approximately this point, a limiting current density was observed. Beyond this limiting current density, hydrogen gas was evolved and the cathodic polarization was identical to that shown in Fig. 1. Both the stationary planar and rotating cylindrical electrodes exhibited the same limiting current density. The anodic Tafel slope, corrosion current density, cathodic Tafel slope (h.e.r.), and exchange current density (h.e.r.) determined from Fig. 2 were identical to the data in Fig. 1 and presented in Table I. The electrode also turned to a black color at a potential of 0.500 ± 0.01v.

Lines 3, 1, and 2 show the cathodic-anodic-cathodic polarization sequence. The Tafel slopes, corrosion, and exchange current densities were identical to those values obtained for the other two polarization sequences.

Galvanostatic cathodic polarization of the cylindrical electrodes in aerated and deaerated 1*N* H_2SO_4 after different immersion times at the rest potential, 0.368v, is shown in Fig. 3. In the time interval studied, it is

Table I. Electrochemical parameters of molybdenum in H_2SO_4

Group	Rest potential volts *vs.* NHE	Anodic Tafel slope mv	Corrosion current μa/cm²	Cathodic Tafel mv	Hydrogen exchange current density μa/cm²
I	0.368	44 ± 4	1.5 ± 0.8	70 ± 3	0.10 ± 0.04
II	−0.020	—	—	70 ± 3	0.10 ± 0.04

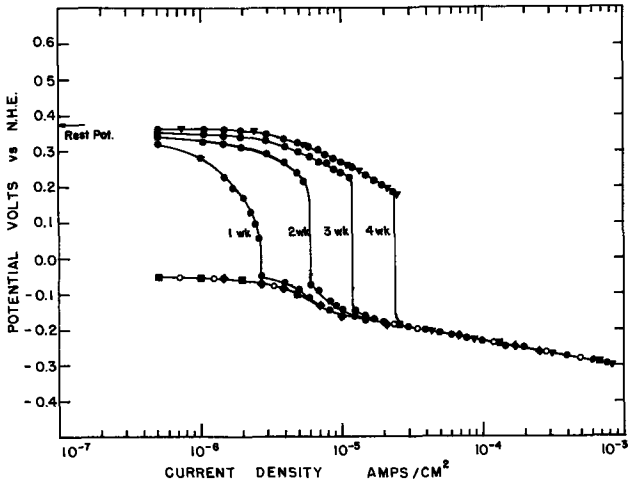

Fig. 3. Cathodic polarization at different immersion times. E_0 = 0.368v. ■ After immersion, deaerated; ○ after immersion, aerated; ◆ after 4 weeks immersion, deaerated; ● after various immersion times, aerated; ▼ after anodic polarization.

seen that the cathodic polarization of molybdenum in the deaerated 1*N* H_2SO_4 did not change with immersion time. However, the cathodic polarization behavior in aerated 1*N* H_2SO_4 did change with immersion time. With increasing immersion time, these cathodic polarization curves approached the curve obtained for electrodes which had previously undergone anodic polarization. These two runs were almost identical when the electrode was immersed in the aerated solution for 4 weeks.

Differential capacitance measurements were obtained with galvanostatic pulses. The potential-time responses exhibited two linear regions as shown in Fig. 4. The initial linear region was attributed to the charging of the metal-metal oxide interface. At open circuit and during polarization, this capacitance remained constant at 3.75 μf/cm². The second linear region was attributed to the charging of the metal oxide-solution interface and showed marked changes with potential. The second capacitance as a function of potential for the different polarization sequences is shown in Fig. 1 and 2. This second capacitance remained constant at

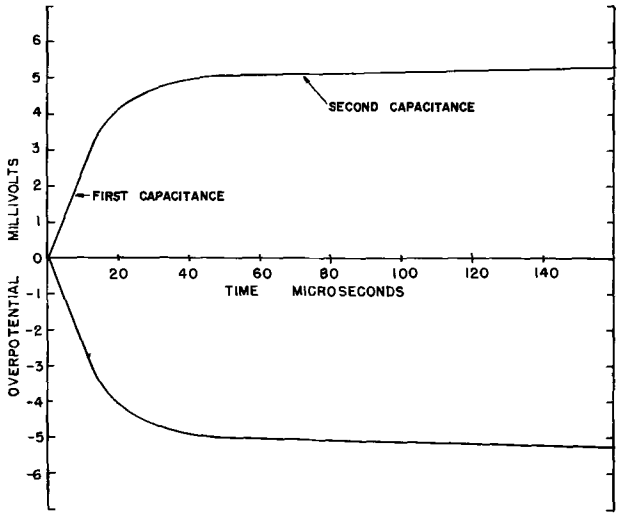

Fig. 4. Potential-time response for galvanostatic pulse. E_0 = 0.368v; 1-hr immersion time. I_p = 1 ma/cm^2.

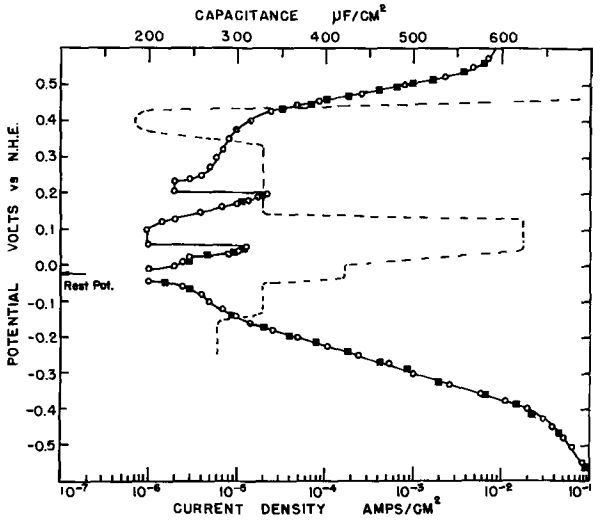

Fig. 5. Polarization of molybdenum in deaerated 1N H_2SO_4. E_0 = —0.020v. ○ Potentiostatic, ■ galvanostatic. Dashed line represents capacitance data.

325 μf/cm^2 at open circuit and during cathodic polarization up to the h.e.r. (except for electrodes which had undergone anodic polarization previously). At the beginning of the h.e.r., the second capacitance decreased sharply to 280 μf/cm^2 and remained constant throughout the h.e.r. Tafel region.

With anodic polarization, the second capacitance increased until it became too large to measure accurately. However, the first capacitance remained constant at 3.75 μf/cm^2. Subsequent to anodic polarization the second capacitance remained at a very high value. Cathodic polarization did not reduce this capacitance value.

In aerated 1N H_2SO_4, the open-circuit second capacitance increased linearly with immersion time until it became too large to measure accurately, while the first capacitance remained constant at 3.75 μf/cm^2. The rate of increase in the open-circuit second capacitance was approximately 14 ± 2.5 μf/cm^2/hr.

Group II. In deaerated 1N H_2SO_4, the rest potential of the polished cylindrical molybdenum electrodes activated in HCl was —0.020v *vs.* NHE. This rest potential stabilized after an immersion time of 2-4 hr. Prior to stabilization, the open-circuit potential fluctuated between 0.080 and —0.160v with potential arrests observed at —0.150, —0.100, and 0.080v. Some electrodes exhibited all three arrests while others exhibited 2, 1, or none. Subsequent to stabilization, the rest potential remained constant for test periods of up to 4 weeks.

The galvanostatic and potentiostatic polarization of molybdenum for the cathodic-anodic polarization sequence and for anodic polarization of a previously unpolarized electrode is shown in Fig. 5. It is seen that cathodic polarization has no apparent effect on the anodic polarization behavior. For current densities greater than 1 μa/cm^2, the cathodic polarization behavior of Group II electrodes was identical to previously unpolarized Group I electrodes.

From Fig. 5, the cathodic Tafel slope and the corresponding exchange current density (h.e.r.) were obtained (Table I). During anodic polarization, two active-passive transitions were observed. The first had a primary passivation potential of 0.035v and a critical current density of 15 μa/cm^2, and the second had a primary passivation potential of 0.190v and a critical current density of 22 μa/cm^2. These values were obtained for experiments on more than six electrodes. Above a potential of 0.390 ± 0.010v, anodic polarization was identical to that observed for Group I electrodes.

In the first active region, the electrode changed from a brilliant silver to a silver-gray color. The silver-gray color was maintained until the potential approached 0.350v. At this potential, the electrode again assumed a brilliant silver color. However, when the anodic Tafel region was reached, the silver-gray color was again observed. The electrode turned black at a potential of 0.500 ± 0.010v.

After anodic polarization to 0.390v, the rest potential changed from —0.020 to 0.368v. The cathodic polarization behavior of this electrode, with the rest potential now at 0.368v, was the same as that of Group I electrodes which had previously undergone anodic polarization.

If potentiostatic anodic polarization of a Group II electrode was discontinued at 0.340v, the rest potential returned to the original value of —0.020v after an arrest at 0.080v. Two types of potential decay behavior were observed. The first was an exponential decay to the potential arrest at 0.080v followed by abrupt decrease in potential to the rest potential of —0.020v. The second was characterized by numerous fluctuations in potential with potential arrests at 0.190v prior to the arrest at +0.080v. Then, as in the first case, the potential abruptly changed from 0.080 to —0.020v.

The anodic polarization of molybdenum subsequent to the above-mentioned decay is shown in Fig. 6. This polarization was not affected by the type of decay observed. In this second anodic polarization run, the first

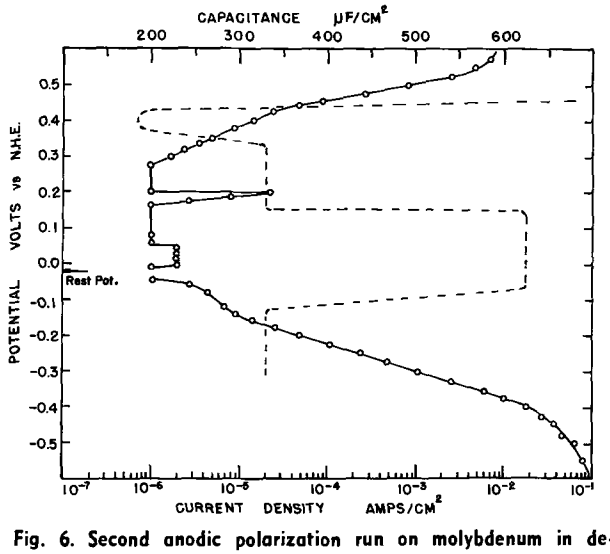

Fig. 6. Second anodic polarization run on molybdenum in deaerated 1N H_2SO_4. E_0 = —0.020v. Dashed line represents capacitance data.

active-passive region almost disappeared. However, the second region exhibited the same primary passivation potential and critical current density as observed for the first anodic polarization run. For the second run, a Tafel region was observed from 0.240 to 0.390v with a slope of 120 mv. Above 0.390v, the anodic polarization behavior was the same for all electrodes. If the second potentiostatic anodic polarization was terminated at 0.340v, the potential did not return to —0.020v but increased to 0.368v and stabilized at this potential.

When short-duration current pulses (10 sec) were utilized for cathodic polarization, the potential-time responses indicated that the passage of 6.4×10^{-4} coulombs/cm^2 was required before a steady-state potential was attained. This result indicates that the surface coverage of hydrogen atoms during the steady-state h.e.r. was about a monolayer.

The anodic transient behavior of molybdenum is shown in Fig. 7. For current pulses (10 sec) less than 150 μa/cm^2, the potential increased monotonically with time. For pulse currents between the range of 150-750 μa/cm^2, it was observed that the potential reached a maximum which was followed by a minimum and then a subsequent monotonic increase with time. Above 750 μa/cm^2, these maxima and minima were not observed and the potential increased monotonically with time. The maximum-minimum phenomena was only observed for electrodes which had not undergone anodic polarization previously. Cathodic polarization prior to the application of anodic pulses had no effect on the potential-time responses. In Fig. 7, the solid lines represent the anodic transients of electrodes which had not been previously anodically polarized. The dashed lines represent anodic transients of electrodes which had previously undergone either pulse anodic polarization (10 sec) above 750 μa/cm^2 or steady-state anodic polarization.

Differential capacitances were obtained at the rest potential, —0.020v *vs.* NHE, and as a function of potential. The potential-time responses were similar to those observed for Group I electrodes. The first capacitance was again constant at 3.75 μf/cm^2 throughout the potential range investigated, while the second capacitance varied with potential as shown in Fig. 5 and 6. It is seen that second capacitance for the first and second anodic polarization runs were identical above

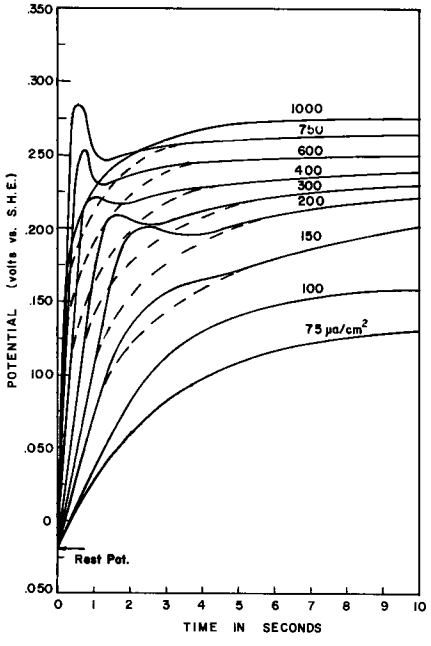

Fig. 7. Anodic transients of molybdenum in deaerated 1*N* H_2SO_4. E_0 = —0.020v. Continuous line—electrodes not previously anodically polarized; dashed line—electrodes previously anodically polarized.

about +0.140v. The open-circuit second capacitance of previously unpolarized electrode was 420 μf/cm^2, while, subsequent to the limited anodic polarization, the open-circuit second capacitance was 625 μf/cm^2. In the h.e.r. Tafel region, the second capacitance of previously unpolarized electrodes was 280 μf/cm^2, while, for electrodes which had undergone limited anodic polarization, it was 330 μf/cm^2. Then, at open circuit, the second capacitance of the former electrodes immediately increased to 330 μf/cm^2 and then slowly increased over a period of 6-8 hr to 420 μf/cm^2. A similar capacitance-time response from 360 $\pm$ 20 to 420 μf/cm^2 was observed after immersion of a fresh electrode and shown in Fig. 8. Electrodes which had undergone limited anodic polarization previously did not exhibit this transient phenomenon. The second capacitance of these electrodes increased from 330 μf/cm^2 to 625 μf/cm^2 at open circuit after cathodic polarization in the h.e.r. Tafel region.

Discussion

The 0.368v rest potential of molybdenum in 1*N* H_2SO_4 (aerated and deaerated) was not changed by repeated anodic and cathodic polarization although the concentration of the oxidation product increased during anodic polarization and in aerated solutions after long immersion times at open circuit. Comparison of the polarization data (Fig. 2, 5, 6) with polarographic data (12) indicates that the product of corrosion and anodic polarization was hexavalent molybdenum. In this potential region, hexavalent molybdenum can be reduced to pentavalent molybdenum (12). These results indicate that rest potential of 0.368v is independent of the concentration of pentavalent and hexavalent molybdenum and oxygen.

The rapid stabilization of the 0.368v rest potential, its independence of Mo (V), Mo (VI), and O_2 concentration, and the differential capacitance data indicate that the molybdenum electrode is covered with an oxide or oxides either before immersion or immediately thereafter. The stoichiometric stable oxides of molybdenum are MoO_2 and MoO_3. The redox reaction involving MoO_2 and MoO_3, $MoO_2 + H_2O = MoO_3 + 2H^+ + 2e^-$, has a redox potential of 0.298v *vs.* NHE. Thus, the 0.368v rest potential is not determined by this redox reaction. However, this reaction may occur as a partial process of a polyelectrode. A process involving this redox reaction must include the reduction of MoO_3 and the formation of MoO_2 since, at open circuit, accumulation of hexavalent molybdenum or increase in differential capacitance was not observed in deareated 1*N* H_2SO_4. A possible mixed process is the following:

$$MoO_2 + H_2O = MoO_3 + 2H^+ + 2e^-$$

$$MoO_3 + 6H^+ + 3e^- = Mo^{+3} + 3H_2O$$

$$Mo^{+3} + 2H_2O = MoO_2 + 4H^+ + e^-$$

In deaerated solutions, molybdenum which has not undergone previous anodic polarization has only a limited amount of hexavalent molybdenum on its surface. Thus, a cathodic current would reduce the hexavalent molybdenum and then shift the potential to the h.e.r.

In aerated solutions, hexavalent molybdenum is continually being formed. However, the rest potential and corrosion current are the same as for deaerated solutions. Since the limiting diffusion current of oxygen reduction to water was not observed, a slower reaction step must determine the rate of production of hexavalent molybdenum. Delahay and Stagg (13), who investigated oxygen reduction on molybdenum, suggested that oxygen reduction involves a peroxyderivative of molybdenum which subsequently reduces to water and a normal oxide state of molybdenum. The formation of the peroxyderivative occurs by the reaction of peroxide with a surface oxide. Thus, the

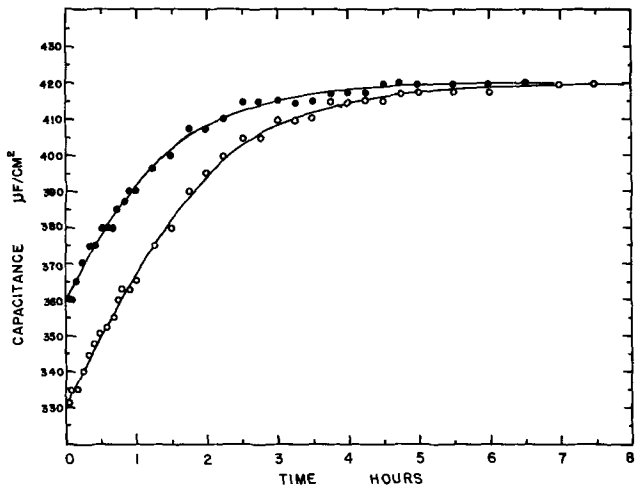

Fig. 8. Open-circuit second capacitance transients. $E_0 = -0.020$v. ● After immersion, ○ after cathodic polarization.

rate of production of the hexavalent molybdenum may be limited by the rate of formation or reduction of this peroxyderivative. The over-all electrode reaction for the formation of hexavalent molybdenum in aerated H_2SO_4 may be as follows:

$$Mo + \frac{3}{2}O_2 + H_2O = HMoO_4^- + H^+$$

As the concentration of hexavalent molybdenum increases, the contribution of the pentavalent/hexavalent redox reaction to the rest potential must be considered. Theoretical cathodic polarization curves for various hexavalent molybdenum concentrations were determined by considering the polarographic studies of Johnson and Robinson (12), the cathodic polarization behavior after anodic polarization, and a limiting current density of 0.5 μa/cm^2 for oxygen reduction. This particular value of the limiting current density for oxygen reduction was arbitrarily chosen to minimize changes in the rest potential and the corrosion current density with changes in the concentration of hexavalent molybdenum. In Fig. 9 are shown the theoretical cathodic polarization curves for hexavalent molybdenum concentrations of 2, 5, and 12.5 μM. It can be seen that the concentration of hexavalent molybdenum has little effect on the rest potential and corrosion current. For example, $E_0 = 0.370$v and $i_{corr} = 1.2$ μa/cm^2 for 12.5 μM, and $E_0 = 0.363$v and $i_{corr} = 0.5$ μa/cm^2 for 0.0 μM Mo(VI). A comparison of the theoretical cathodic polarization curves in Fig. 9 and the experimental curves in Fig. 3 indicate good agreement.

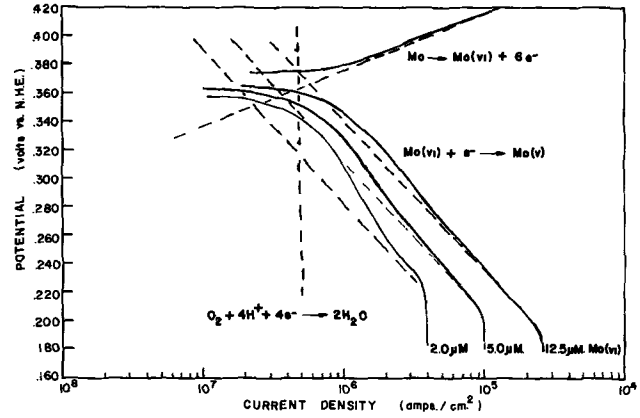

Fig. 9. Partial electrode processes near rest potential of molybdenum in aerated 1N H_2SO_4. $E_0 = 0.368$v. Continuous lines—theoretical polarization curves; dashed lines—single electrode partial process as indicated.

The curves in Fig. 9 represent the following proposed electrode reactions:

$$\text{I.} \quad Mo = Mo(IV) + 4e^- \rightarrow Mo(VI) + 2e$$

$$\text{II.} \quad O_2 + 4H^+ + 4e^- = 2H_2O$$

$$\text{III.} \quad Mo(VI) + e^- = Mo(V)$$

According to Heumann and Hauck (8), the rate-determining step for the anodic dissolution reaction is Mo(IV) → Mo(VI).

The rest potentials of polished cylindrical electrodes activated in HCl were —0.020v which was approximately that of the reversible hydrogen electrode. Prior to stabilization at this steady-state rest potential, potential arrests were observed at 0.080, —0.100, and —0.150v. The arrests occurred at the redox potentials of the reactions (14, 15):

$$Mo + 3\,H_2O = MoO_3 + 6H^+ + 6e^-$$

$$Mo + 2\,H_2O = MoO_2 + 4H^+ + 4e^-$$

and

$$MoO_2 = MoO_2^+ + e^-$$

respectively.

Although the rest potential of —0.020v is the same value as the potential of the reversible hydrogen electrode, there is some doubt as to the actual processes which determine this rest potential. In the potential range in the neighborhood of the rest potential, cathodic polarization indicates a reduction process other than the h.e.r. and anodic polarization indicates oxide growth by the formation of a silver-gray film. Konig and Gohr (11) have concluded that this silver-gray film was MoO_2. Heumann and Hauck (8) have also reported the presence of MoO_2 on the surface of molybdenum in acidic solutions. In addition, the constant value of 3.75 μf/cm^2 for the first capacitance, throughout the entire potential range investigated, suggests the continual presence of MoO_2 on the surface of the molybdenum electrode.

The capacitances determined from the two linear regions in the galvanostatic transients can be interpreted in terms of the electrical model shown in Fig. 10 which describes the charging behavior of molybdenum due to the metal-metal oxide and metal oxide-solution interfaces. The mathematical representation of this model is given as:

$$E = I_p(R_1 + R_2 + R_e - R_1\,e^{-t/R_1C_1} - R_2\,e^{-t/R_2C_2})$$

Where E is the potential, I_p the imposed current, $R_1\,C_1$ refers to the metal-metal oxide interface, $R_2\,C_2$ refers to the metal oxide-solution interface, and R_e is the resistance of the solution. For the potential-time response, the first capacitance is the initial linear region which has the larger slope corresponding to a smaller capacitance value. The second capacitance is determined from the other linear region which has the smaller slope which corresponds to a larger capacitance value. If $R_1\,C_1 << R_2\,C_2$, the capacitance values may be determined independently. Figure 11 shows theoretical $E - t$ curves for $C_1 = 3.75$ μf/cm^2, $R_1 = 5\Omega$, $R_2 \geq R_1$, and various values of C_2 (100, 133, 200, and 400 μf/cm^2). As shown in Fig. 11, the experimental potential-time response for short-time intervals can be very adequately represented by the proposed electrical model. Calculated and experimental potential-time responses for a 1.0 ma/cm^2 current pulse are shown in Fig. 12. The dashed lines represent the upper

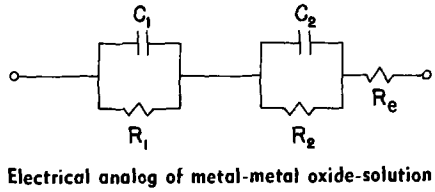

Fig. 10. Electrical analog of metal-metal oxide-solution interfaces

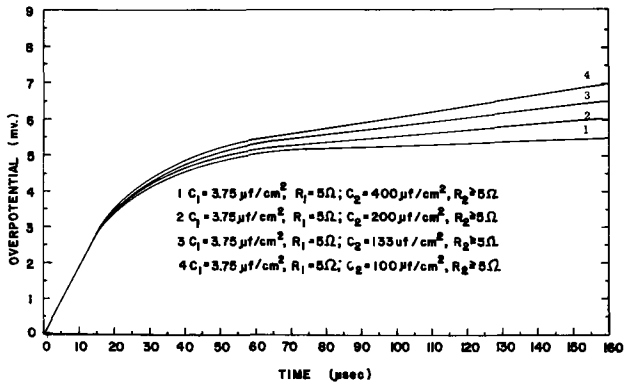

Fig. 11. Calculated potential-time responses for galvanostatic pulses.

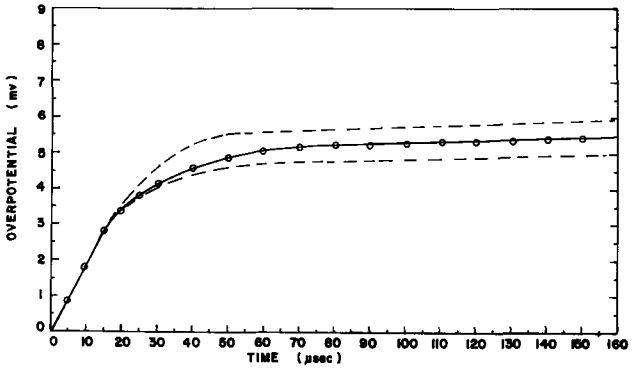

Fig. 12. Calculated and experimental potential-time responses. I_p = 1.0 ma/cm², C_1 = 3.75 μf/cm², R_1 = 5 Ω, C_2 = 420 μf/cm², $R_2 \geq 5$ Ω. Continuous line—calculated data; dashed lines—upper and lower limit of experimental data.

and lower limits of the experimental data (24 runs). The points represent the calculated data.

The first capacitance, 3.75 μf/cm², is ascribed to the MoO_2 at the Mo-MoO_2 interface. Since the first capacitance remained constant throughout the potential range investigated, it seems apparent that MoO_2 was always present on the electrode surface and that the anodic dissolution of molybdenum involves MoO_2. The second capacitance is attributed to the electrical double layer and an adsorption pseudocapacitance which are in parallel and represented by R_2 C_2 in the electrical model. The increase in the open-circuit second capacitance of molybdenum with immersion in aerated solutions and its increase with increase in anodic polarization suggest that the pseudocapacitance may be due to an electroactive intermediate or intermediates produced during the electrochemical oxidation of molybdenum.

Acknowledgments

This work is part of a continuing University of California program on sea water desalination. L.L.W. was recipient of a Standard Oil of California fellowship during this investigation.

Manuscript submitted Aug. 5, 1968; revised manuscript received Dec. 24, 1968. This paper was presented at the Buffalo Meeting, Oct. 10-14, 1965, as Paper 63.

Any discussion of this paper will appear in a Discussion Section to be published in the December 1969 JOURNAL.

REFERENCES

1. W. Muthmann and F. Fraunberger, *Ber. Bayr. Akad.*, **34**, 201 (1904).
2. H. Kuessmer, *Z. Elektrochem.*, **16**, 756 (1910).
3. E. Becker and H. Hilberg, *ibid.*, **31**, 32 (1925).
4. G. Masing and G. Roth, *Werkstoff Korrosion*, **3**, 176 (1952).
5. N. D. Greene and S. B. Greene, *Electrochem. Technol.*, **1**, 276 (1963).
6. J. O'M. Bockris, *Trans. Faraday Soc.*, **43**, 417 (1947).
7. H. J. Booss, *Werkstoff Korrosion*, **13**, 538 (1962).
8. T. Heumann and B. Hauck, *Z. Metallk.*, **56**, 75 (1965).
9. N. Pentland, J. O'M. Bockris, and E. Sheldon, *This Journal*, **104**, 82 (1957).
10. K. Heyepekau and V. Cmendep, *Zh. Fiz. Khim.*, **24**, 865 (1950).
11. M. Konig and H. Gohr, *Ber. Buns. Phys. Chem.*, **67**, 837 (1963).
12. M. Johnson and R. Robinson, *Anal. Chem.*, **24**, 366 (1952).
13. P. Delahay and L. S. Stagg, *This Journal*, **99**, 546 (1952).
14. W. M. Latimer, "Oxidation Potentials," 2nd Ed., p. 250, Prentice Hall, New York (1952).
15. M. Pourbaix, "Atlas of Electrochemical Equilibria," p. 272, Pergamon Press (1966).

Enhancing the Brightness Capability of Color-TV Receivers Through the Use of a Spectrally Selective Tinted Glass

George Ban and H. N. Hersh

Zenith Radio Corporation, Chicago, Illinois

and S. Kaplan

The Rauland Corporation, Chicago, Illinois

ABSTRACT

An ideal picture tube for color TV would have three efficient phosphors with almost spectrally pure (narrow) bands of emission on a faceplate which transmits only at the same wave lengths and is opaque at other wave lengths. This poses an interesting physics problem, for how do you make a narrow-band filter which works simultaneously in three different spectral regions? Working with practical phosphors and available filters, it is interesting to determine what can presently be achieved. A development program, starting out with the well-known didymium glass, led to the present composition. Measurements have been made to determine the characteristics of a 3% neodymium doped glass having some spectral optical properties approximating the specifications. Such a glass would be used to replace the neutral-density safety glass now used. Data are presented showing its optical properties, and the changes in spectra, brightness, and color coordinates of tricolor picture tubes. It is concluded that there are some demonstrable improvements in color, brightness, and contrast.

Every manufacturer of color TV receivers is desirous of obtaining a brighter picture display capability. All other factors being equal, the receiver having a higher brightness capability will understandably out-perform others in a room having high ambient lighting. The manufacturer wants to attain this higher capability at a minimum increase in cost and, certainly, at no sacrifice in over-all performance. Many laboratories are engaged in research, therefore, to develop brighter phosphors, and every year thousands of new phosphors are prepared and tested.

We have investigated an alternate approach to enhance the brightness obtainable with presently used color picture tubes by 30% or more. The approach endeavors to recover most of the loss in phosphor light occurring with the presently used contrast-improving tinted glass in front of the picture tube.

Instead of a neutral tinting of the glass faceplate, as is now the practice, the glass would be tinted only in the spectral regions where the tricolor phosphor emissions are low. The glass would then be highly transmitting to the phosphor light but still retain its contrast-improving capability. Discussions of this approach are given in Ref. (1-4).

Of the materials presently available, the substances found to be most suitable to produce this type of spectrally selective tinting were compounds containing trivalent neodymium. While neodymium-containing glasses tested were found to have most of the desirable characteristics, they have some which are not desirable, and, because of this, the over-all brightness gain was found not to exceed 12%.

Use of Neutral Tinting to Improve TV Picture Contrast

In black-and-white television, tinting or darkening of the faceplate glass is done to permit viewing of the picture in a room having normal ambient lighting. (With neutral tinting, the transmission of the faceplate glass is deliberately reduced. Some manufacturers make the single-pass transmission about 70%; others prefer a transmission as low as 40%.[1] With neutral tinting, also, the optical absorption is approximately uniform throughout the visible spectral range.) The contrast is improved because the ambient light reflected from the phosphor screen is more greatly attenuated than is the phosphor light; this is because it takes two passes through the tinted glass, whereas the phosphor light passes only once.

[1] The practice now is to make the bulb 70% transmitting and the safety windows either 70 or 55%; the final tubes are 52 or 41% transmitting. Some newer tubes do not use a safety window and have a deeper tinted bulb.

Concept of Spectrally Selective Tinting

If the neutral tinting in the faceplate glass of a color-TV screen were replaced by one having high transmissions in the red, blue, and green spectral regions (where the tricolor phosphors emit) and strong absorptions in the blue-green, yellow, and far red regions (where the phosphor emissions are low), it should be possible to realize a substantial gain in the obtainable brightness without degradation of the contrast. In Fig. 1, the shaded areas represent the regions where strong optical absorptions would be permitted; also shown is the emission spectrum of a typical P22 phosphor (in this case, the red-emitting phosphor is a europium-doped yttrium oxysulfide, while the blue and green are both sulfides) (5). If it were possible to obtain 100% optical absorption in the shaded areas

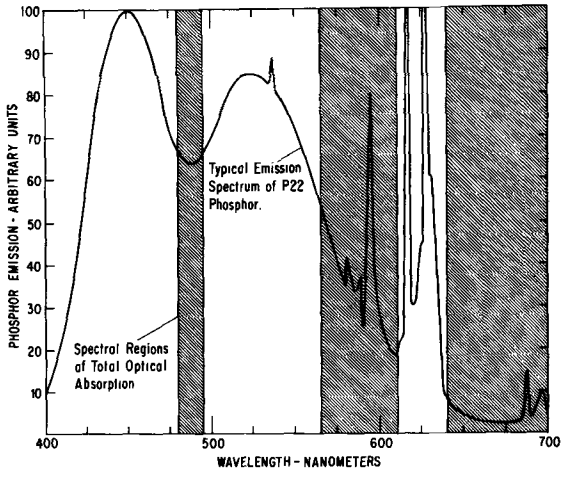

Fig. 1. A selectively tinted glass having total optical absorptions in spectral regions depicted as shaded areas would provide contrast improvement with very little effect on picture brightness. The curved trace describes the emission spectrum of a typical P22 phosphor.

and 100% transmission in the clear areas, the over-all transmission for incandescent light, when viewed by the eye, would be about 53%; for daylight or fluorescent light, it would be about 54%.[2] This is very nearly the same as the double-passage transmission through 70% transmitting neutral tint glass. The amount of reflected light with the spectrally tinted glass would, thus, be the same as with the 70% neutral tint glass. The brightness of the phosphor light, however, for equal beam currents, would be over 30% greater with the spectrally tinted glass.

Of the three desired absorption bands in the spectrally tinted glass, the most effective in improving contrast is that in the yellow region because it is near the peak of the human eye response.

Selection of Material to Produce Spectral Tinting

Unfortunately, a spectrally selective tinting having the desired optical absorbing characteristics is not easily attained. The use of multiple interference-type coatings capable of providing narrow and sharp transmission bands is out of the question; the design of such a filter with three simultaneous spectral regions of transmission (corresponding to the regions of phosphor emissions) is beyond the present state of the art.

Most organic and inorganic tinting materials, incorporable into a glass or plastic, have broad absorption bands with broad edge slope characteristics. Compounds of the lanthanide elements provide spectrally narrow absorption bands at room temperature, but, of these, only Pr and Nd have the desired narrow bands and sharply defined absorption in the yellow spectral region.

The spectral transmissions of water solutions of Pr and Nd nitrates are shown in Fig. 2. The absorptions obtained when the oxides of Pr and Nd are incorporated into glass will be somewhat different in degree and detail but the fundamental absorptive spectral regions will be the same. The shaded areas on the top show the ideal regions depicted in Fig. 1 where absorptions are desired. It may be seen that Pr compounds have an absorption band in the blue region. This would produce an objectionable reduction in the brightness of the blue phosphor. It may also be seen that Nd compounds have undesirable absorption bands in the blue and green regions. However, because of its proportionally greater absorption in the yellow region, it was considered to be the best choice as a tinting material.

Use of Didymium and Neodymium Glasses

At the time of our early measurements and evaluations, a glass with pure Nd_2O_3 was not available as a standard commercial item. However, didymium glass, well known for its yellow-absorbing properties and use in glassblowers' goggles, was available.[3] Didymium is a name given to a group of lanthanide elements, La, Nd, Pr, Sm, and Ce, and is in the extract obtained from monazite sand after most of the Ce is removed. Lanthanum and Nd are the primary constituents, but La compounds do not absorb optically in the visible spectral range.

The spectral transmission of a water solution of didymium chloride solution is shown in Fig. 3. It is identical to the spectral transmission of a Nd chloride solution shown in Fig. 2 except for the greater absorption in the blue spectral region. The latter is attributed to the presence of Pr and Ce.

Figure 4 shows the spectral transmission of a 2-mm thick sample of Corning 5120 glass which contains about 4% of didymium oxide. For comparison, the spectral transmission of 70% transmitting neutral tint glass is also shown. It is shown later that the average double-pass transmission of room light is about the same for the two glasses. Thus, the contrast of a TV picture would be about the same with either tinted glass. The didymium concentration represented in the 2-mm thick glass sample appeared to be optimum for this application. At increasing glass thickness, the attenuations produced by the absorption bands in the blue and green spectral regions increase rapidly. The double-pass attenuation for ambient room light, however, increases only slowly. Thus, a considerable reduction in over-all picture brightness would be experienced without a substantial improvement in contrast.

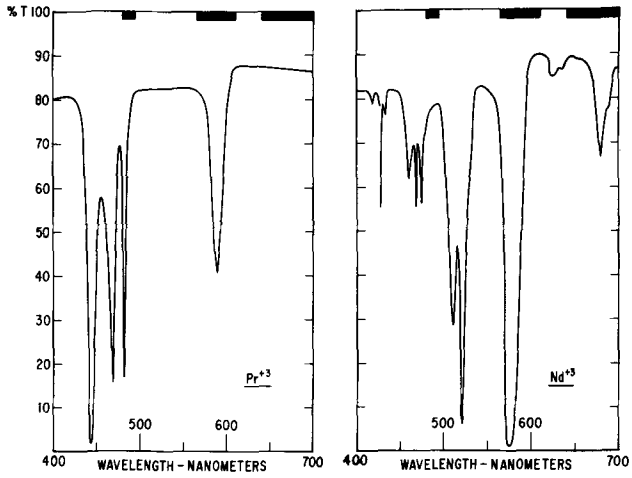

Fig. 2. Relative transmission characteristics of water solutions of $Pr(NO_3)_3$ and $Nd(NO_3)_3$ in the visible spectral range. Shaded areas on top indicate, as in Fig. 1, the spectral regions where total optical absorptions would be desired in a selectively tinted glass.

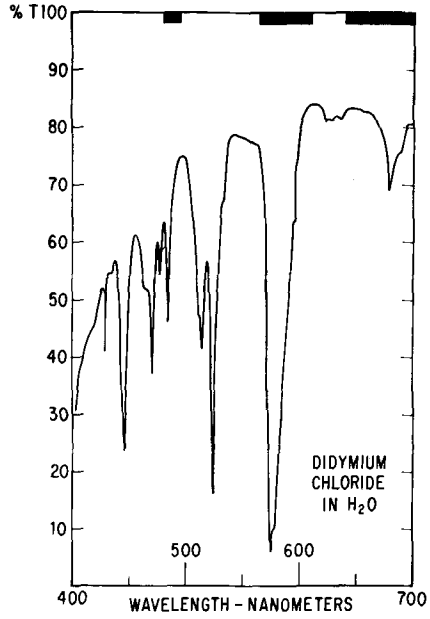

Fig. 3. Relative transmission characteristics of a water solution of didymium chloride in the visible spectral range. Shaded areas on top indicate, as in Fig. 1, the spectral regions where total optical absorptions would be desired in a selectively tinted glass.

[2] These values were computed from the relationship:

$$\overline{T} = \frac{\int_{\lambda = 4000\text{Å}}^{\lambda = 7000\text{Å}} T_\lambda P_\lambda R_\lambda \, d\lambda}{\int_{\lambda = 4000\text{Å}}^{\lambda = 7000\text{Å}} P_\lambda R_\lambda \, d\lambda}$$

where

$\overline{T}$ is the over-all transmission to the room light source (daylight or incandescent)
T_λ is the spectral transmittance of the spectrally tinted glass
P_λ is the spectral distribution of the room light source (daylight or incandescent)
R_λ is the spectral responsivity of the human eye.

[3] Didymium glass is available from Corning Glass Works as their glass number 5120.

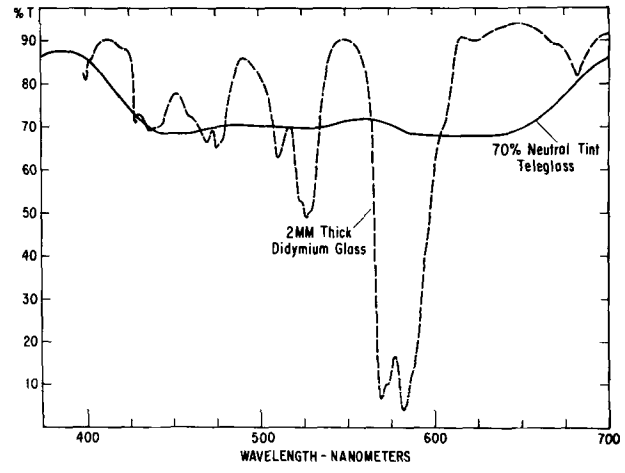

Fig. 4. Spectral transmissions through neutrally tinted and didymium glasses.

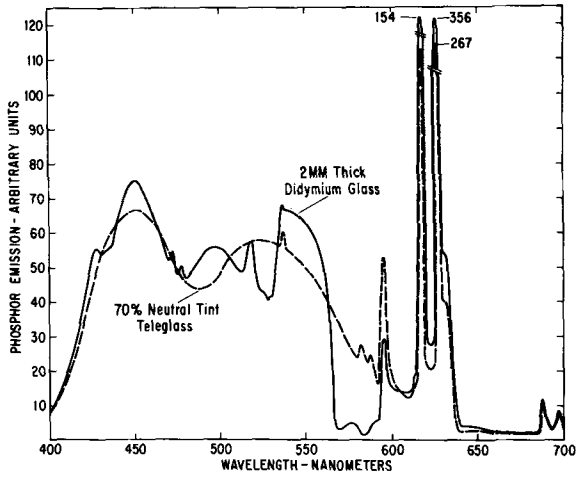

Fig. 5. Computed spectral characteristics of P22 phosphor light through neutrally tinted and didymium glasses. Initial P22 phosphor emission characteristics same as shown in Fig. 1.

The effects of the 70% transmitting neutral tint glass and 2-mm thick didymium glass on the spectral characteristics and intensities of the P22 phosphor emitted light are shown in Fig. 5. The neutral tint glass has no effect on the spectral characteristics of the phosphor light; it acts only to reduce its intensity. The didymium glass, on the other hand, affects both the spectral characteristics and the intensities. Clearly, the red phosphor emission is brighter through the didymium glass than through the neutral tint glass. The yellow component in the red phosphor emission is greatly reduced resulting in a more saturated red color. By the same token, the yellow spectral portion of the green phosphor emission is also reduced, resulting in a more saturated green color as well. Unfortunately, however, some green absorption also occurs which negates any gain in the brightness of the green phosphor emission. In the blue spectral region, some gain in brightness might be realized through the use of the didymium glass.

Glass in which pure Nd_2O_3 was incorporated was available in the latter part of our investigations through the cooperation of the Chicago Dial Corporation.[4] Figure 6 shows the spectral transmission of a glass sample containing 3% Nd_2O_3; the type of glass used as the host is not known. The sample was 3.3 mm thick. It may readily be seen that the absence of Pr and Ce results in greatly reduced absorptions in the blue spectral region. The thickness of 3.3 mm for 3% concentration of Nd_2O_3 appeared optimum in this application, and measurements and observations were made comparing the didymium with the neodymium glass.

[4] Chicago Dial Corp., 1315 North Branch St., Chicago, Ill. 60622.

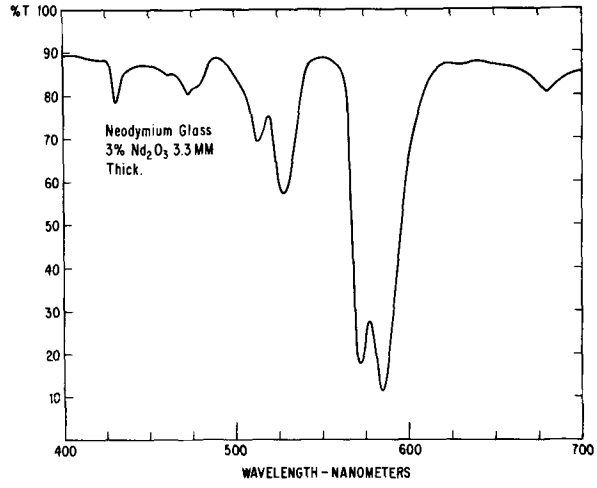

Fig. 6. Spectral transmission through Chicago Dial neodymium glass.

Performance with Didymium and Neodymium Glasses

Measurements were made of the transmissions by the 70% neutral tint, didymium, and neodymium glasses of the emitted light from individual phosphors comprising the P22 screen. The results are shown in Table I. Light intensity measurements required for the determination of these values were made with a Weston Photronic Cell having the spectral response of the human eye. The Nd glass is superior to the didymium glass in the extents of the phosphor emissions transmitted. The increase in transmission of the didymium glass over that of the neutral tint glass for the red oxysulfide type phosphor emission is small, but this is due to the loss of the yellow component which is of appreciable magnitude in this type phosphor. The transmissions by didymium and Nd glasses of the red component of the red phosphor emission (either vanadate or oxysulfide types) is thus greater than that indicated in Table I.

Measurements were also made of the transmissions by the 70% neutral tint, didymium, and Nd glasses of white (9300°K) phosphor light and two types of room lighting. The results are shown in Table II. Again, the light intensities required for the computa-

Table I. Transmission data for light from TV phosphors, transmission %

Phosphor	Through 70% neutral tint glass	Through didymium glass (2 mm thick)	Through neodymium glass (3% Nd_2O_3, 3.3 mm thick)
Red (vanadate type)	72.9	80.7	82.8
Red (oxysulfide type)	72.9	75.5	(Not measured)
Green (sulfide type)	73.4	68.3	76
Blue (sulfide type)	70.5	71.4	84.8

Table II. Transmission data for ambient room light, transmission %

Light source	70% Transmitting neutral tint glass	Didymium glass (2 mm thick)	Neodymium glass (3% Nd_2O_3, 3.3 mm thick)
Averaged transmission for white (9300°K) phosphor light*	72	73.4	81
Illuminant A (60-w incandescent lamp)**	53	54	55
Illuminant C (fluorescent lamp)**	54	51	52

* Single passage through glass.
** Double passage through glass.

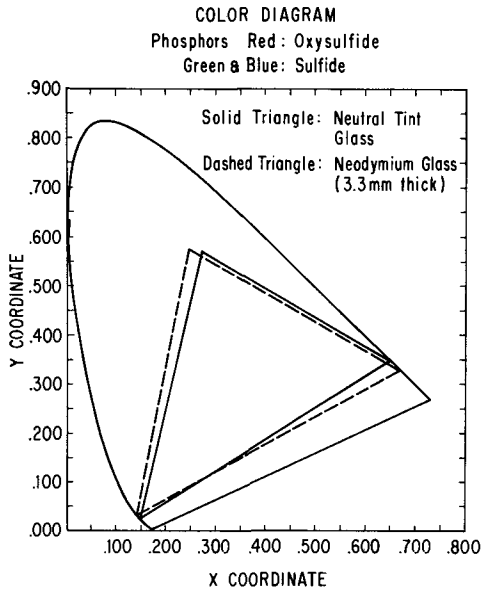

Fig. 7. Trichromatic color coordinates of P22 phosphor light through neutral tint and neodymium glasses.

tion of these values were measured with a Weston Photronic Cell. The double-pass transmissions by all three glasses are about the same for either daylight or incandescent room lighting; for a given TV picture brightness, the reflected light in a room with ambient lighting would, therefore, be the same with either of the three tinted glasses. With identical operating picture tube beam currents, however, the picture on the TV receiver employing the Nd glass was about 12% brighter.

In Fig. 7, we show on a color diagram the change in chromaticity coordinates of the P22 phosphor light resulting from the use of the 3.3-mm thick neodymium glass. The area in the triangle, which shows the gamut of hues obtainable through the mixing of the three primary colors, is larger with neodymium glass. It is possible to generate a greater range of hues, therefore, through the use of neodymium glass. However, the "yellows," which are primarily derived through the excitation of both the red and green phosphors, are somewhat degraded. Visually they appear slightly grayish.

Physical Appearance of Picture Tube Face with Spectrally Selective Tinting

There is a physical appearance attribute evident when using either the didymium or Nd glass. When the TV receiver is off, the face of the picture tube appears to have a bluish cast in a room illuminated by daylight or fluorescent lighting, and a pinkish cast when the room has incandescent lighting. At present, it is considered desirable for the glass to be only neutral-gray. This dichroic effect is a natural consequence of the strong absorption in the yellow spectral region. The effect is not noticeable when the set is on; in this condition, the beneficial effects noted above can probably be maximized by adjusting the color matrixing to match the colorimetric properties of the glass. (This was not done in this investigation.)

Discussion

The use of glasses tinted by Nd compounds in place of neutral tinted glass on the face of a color picture tube has been investigated. Computations indicated that a greater than 30% improvement in brightness capability could be realized, together with the usual reduction in reflected room light, through the use of spectrally selective tinting which would provide total transmission of phosphor light but be opaque in non-emission regions. It was found that Nd compounds come close in providing the desired spectral tinting. Measurements show, however, that the brightness improvement realized with the available Nd glass was only about 12%. The reduced performance is, undoubtedly, due to the undesirable but characteristic Nd^{+3} absorptions in the green and blue spectral regions However, these absorption bands are due to 4f transitions, the probabilities of which are sensitive to the crystal fields surrounding the Nd^{+3} ions.

There is evidence that, when the crystal symmetry is changed, by incorporating the Nd^{+3} ion into different host glasses, the change in the absorption in the green region is not proportional to that in the yellow region. Hirayama and Lewis (6) describe the absorptions of Nd_2O_3 in various host glasses. Comparing their 14.5 Na_2O, 25TiO_2, 60 SiO_2, 0.5 Nd_2O_3 glass with their 33 Li_2O, 66.5 SiO_2, 0.5 Nd_2O_3 glass, it would be seen that, adjusting the thickness to yield the same absorptions in the yellow region, the absorption in the green region will be substantially less in the titanium-containing glass. It is possible, therefore, that through the use of a different host glass brightness improvement closer to 30% might be achieved.

The ideal situation for the ultimate in contrast and brightness would be to have three narrow-band phosphors and one filter with three matching transmission bands. The making of such a filter is an interesting problem in physical optics.

Acknowledgment

The authors wish to thank P. M. Jaffe for his suggestions and criticisms in the preparation of this paper.

Manuscript submitted Oct. 11, 1968; revised manuscript received Jan. 24, 1969. This paper was presented at the Boston Meeting, May 5-9, 1968, as Paper 50.

Any discussion of this paper will appear in a Discussion Section to be published in the December 1969 JOURNAL.

REFERENCES

1. E. W. Herold, *Proc. IRE*, **39**, 1177 (1951).
2. A. J. Torre, RCA Tech. Note No. 61 (1957).
3. J. E. Bridges, U.S. Pat. 3,013,114 (1961).
4. P. S. Schulz and G. Janus, U.S. Pat. 3,078,343 (1963).
5. RCA Specifications on 22UP22 Color Picture Tube (1968).
6. C. Hirayama and D. W. Lewis, *Physics and Chem. of Glasses*, **5**, 44 (April 1964).

Phosphor Screens for High-Current-Density Cathode-Ray Tubes

Vincent D. Meyer and Frank C. Palilla*

The Bayside Laboratory, Research Center of
General Telephone & Electronics Laboratories Incorporated, Bayside, New York

ABSTRACT

Phosphors are evaluated for use in high-current-density cathode-ray tubes. Oxide-based phosphors exhibit a linear increase in brightness with current density, whereas conventional II-VI sulfide phosphors show a less-than-linear increase. At high current densities, the sulfides also exhibit spectral shifts and a decrease in decay times. Selected rare-earth-activated oxide phosphors incorporated in a postdeflection focusing tube demonstrated a substantially linear increase in brightness, improved contrast ratio, and good color balance.

The intensity of the luminescence emitted by a phosphor screen excited by cathode rays increases as the number of electrons per unit area incident upon the phosphor is increased. The linearity of the increase in the intensity of the luminescence is, however, generally limited to low current densities with phosphors used in most color-TV display systems (1-5). At high current densities, the increase is less than linear. This nonlinear behavior is called the "saturation" effect. The most common type of color-TV tube in use today is the shadow-mask version in which a perforated electrode is interposed between the electron guns and the phosphor screen in a unipotential drift space. This electrode severely limits the number of electrons reaching the screen since 85% of the electrons emitted by the guns are not transmitted by the mask (6). Other types of color picture tubes are available which considerably increase the current density at the phosphor screen by providing for finer focusing of the electron beam. One such class of tubes, the post-deflection focusing (PDF) type, produces a focusing action at the screen by replacing the unipotential drift space by a retarding field region created by a grill in close proximity to the screen. The "Chromatron" or "Lawrence" tube (7) are examples of this tube type in which either one or three electron guns are used and in which the current densities on the phosphor screens are several orders of magnitude higher than the current densities in the shadow-mask tube. Recently, another type of tube has been announced (8) which utilizes current densities between those encountered in the shadow-mask and the PDF tubes. In this tube, electron guns with improved focus are used, and a grill system having a higher optical transmittance than that of the shadow mask is placed between the phosphor screen and the electron guns. Conceivably, the development of guns having improved focus could also be utilized in shadow-mask tubes to obtain higher current densities.

The brightness advantage which would be expected from the PDF grill has, however, not been realized in practice. The PDF grill has an electron transmission about six times that of the aperture mask and, in addition, provides a focusing action which delivers a higher current density at the screen. However, the phosphor characteristics preclude full utilization of the higher current density because of the nonlinear response of the phosphors at higher current densities and the decrease in contrast ratio[1] caused by secondary electron bombardment of the screen. This is particularly true of the conventional II-VI sulfide phosphors. Also, some phosphors, especially these sulfides, exhibit color variations with changes in current density which can lead to loss of color balance for colors derived from the combination of two or more phosphors.

In conventional screens for color television, at least one of the three phosphors exhibits a nonlinear increase in brightness as the beam current density is increased. A typical phosphor combination which exhibits this nonlinear effect is the "all-sulfide" screen in which ZnS:Ag serves as the blue primary, (Zn,Cd)S:Ag the green primary, and (Cd,Zn)S:Ag the red primary. All three of these phosphors saturate at current densities well within the operating range of the PDF tube. In more recent screens, the red sulfide is replaced by a Eu^{3+}-activated phosphor (9) which has a substantially linear response; the blue and green sulfide phosphors, however, are nonlinear.

This paper describes a cathodoluminescent screen composed of rare-earth-activated phosphors which exhibits a substantially linear increase in brightness, yields improved contrast ratio, and maintains good color balance over the operating range of the PDF tube.

Experimental

The usual method for studying luminescence intensity as a function of current density is to measure the increase in photomultiplier response as the incident current is increased and the spot size is maintained constant. When the screen operates at high voltage, measurement of the current incident upon the screen becomes difficult and often an indirect measurement is made, *i.e.* the cathode current (current leaving the cathode) is taken as a measure of the screen current. This, however, does not account for those electrons which leave the cathode but do not reach the screen. More reliable measurements can be made by maintaining the cathode current constant while the spot size is changed by defocusing the beam. In this way, the number of electrons which reach the screen remains the same. (By screen current, we mean the total primary current incident upon the screen; this must include electrons backscattered from the screen if a direct measurement of the screen current is attempted.)

When the number of electrons incident upon a phosphor is maintained constant but the current density is varied by changing the spot size, the luminescence output remains constant for a strictly linear phosphor, *i.e.* the efficiency does not change. The magnitude of the change in the emission intensity for a nonlinear phosphor therefore gives a measure of the change in efficiency. Although this method does not provide an absolute measurement of the screen current, the usual errors involved in the measurement of relative screen current are avoided.

Such measurements were made using the following procedure. A Sylvania model VMC-8TV monitor was modified to accept 5F cathode-ray tubes equipped with EM-129 electron guns. The high-voltage supply was variable from 0 to 30 kv. Focusing was accomplished by varying the current to a magnetic focusing coil. A pulse generator pulsed the beam on, by driving G_1 positive, for only a fraction of one scan line (typical

* Electrochemical Society Active Member.

[1] The contrast ratio is defined as $(B_o - B_s)/B_s$, where B_s is the brightness of the screen due to stray electrons, and B_o is the brightness of the screen due to the primary beam and the stray electrons. If $B_s << B_o$, the contrast ratio is approximated by B_o/B_s.

pulse duration, 2 μsec). The pulse was synchronized with the signal to the deflection yoke so that the spot always appeared at the same position on the screen. The screen current was not measured directly. Instead, the current leaving the cathode and the current collected by the first grid, G_1, of the electron gun were measured by using two current probes. These probes were connected to a differential plug-in unit in such a way that the display on the oscilloscope shows the current leaving the cathode minus the current collected by G_1. We found this differential method necessary since a current probe measurement of G_1 alone showed that some current was collected by G_1 during the time that G_1 was driven positive with respect to the cathode. The current collected by G_2 was negligible. (The current collected by the anode of the electron gun was not accounted for and therefore the incident screen current may be less than that measured by our method.) The oscilloscope display was then assumed to be a measure of the instantaneous screen current. A typical value was 1.2 ma. The line width or thickness, which varies with spot diameter, was measured using a cathetometer after the response of a 1P21 photomultiplier equipped with a Wratten 106 filter was recorded. The detector combination therefore gives a measure of the luminosity. The total size of the area bombarded by the electron beam was maintained smaller than the photosensitive area of the photomultiplier tube. Therefore, as the spot size is reduced, since the number of electrons incident upon the screen remains constant, the photomultiplier response should remain constant unless the phosphor "saturates." Typical line widths of 0.5-0.02 cm were obtained by varying the voltage drop across the magnetic focusing coil. With this information, the current density can be calculated if several approximations and assumptions are made.

It is well known that the current distribution across a line is not constant, and it is difficult to determine where the intensity falls to zero. Therefore, any definition of spot size and current density is somewhat arbitrary. We have attempted to use a definition which gives a measure of the current density averaged across the line width. We make the following approximations:

1. The spot is assumed to be circular. Although the spot is actually elliptical, with the same scan speed and raster size, the measurements are consistent.
2. The current falls to zero at the point where the eye perceives a sharp cut-off in brightness contrast. This, in actuality, is the point where the brightness drops to approximately 5% of the peak brightness.
3. Although it is known that the intensity is not equally distributed across a line width (probably a bell-shaped, not quite Gaussian, distribution), the distribution is averaged by dividing the current by the area of the spot. This also yields consistent, although not absolute, values.
4. The effects of backscattered electrons, halation, and light scatter in the phosphor are ignored. These effects may vary from one phosphor to another but it is assumed that they are negligible.

Since the scan speed (and therefore dwell time) and the current distribution across the spot are altered as the tube size is changed, there may be a "scaling-up" effect. Indications of this type of effect were obtained by changing the scan speed and also by studying the effect of pulse duration on the degree of "saturation" for a stationary pulsed spot. To increase the scan speed, the beam was pulsed on during the horizontal retrace. To study the effect of increased pulse duration, the deflection circuit was disconnected and a General Radio Model 1217-C pulse generator was added to the grid circuit. The chassis of the pulse generator was "floating"; its potential was determined by the voltage output from a regulated d-c power supply to give cut-off when the pulsing voltage is zero. The pulsing voltage was then increased to produce a stationary pulsed spot on the screen. The pulse repetition frequency was set at 30 Hz, and the pulse width was varied from 2 to 10 μsec.

In addition to measurements of the intensity of the luminescence as a function of the current density, the spectral distribution was recorded at relatively high and low current densities by interposing a quartermeter Jarrell Ash monochromator between the cathode-ray tube and the 1P21 photomultiplier tube.

Results and Discussion

Figures 1,2, and 3 show the relative luminosity *vs.* current density at constant cathode current for several red-, green-, and blue-emitting phosphors. The value 1.0 in the figures corresponds to 1 amp/cm^2 instantaneous current density (or 6 x 10^{-6} amp/cm^2 averaged over time). In all cases, comparison is made with sulfide phosphors of corresponding emission colors. The blue and green sulfides correspond to the blue and green primaries used in the conventional shadow-mask color-TV display tubes, and the red sulfide corresponds

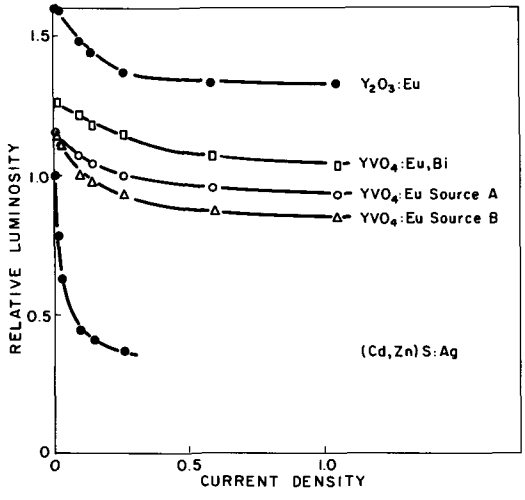

Fig. 1. Relative luminosity *vs.* current density for red-emitting phosphors.

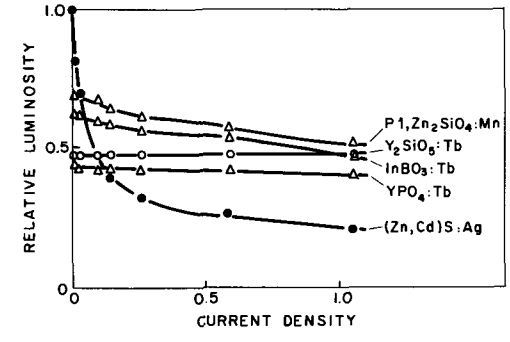

Fig. 2. Relative luminosity *vs.* current density for green-emitting phosphors.

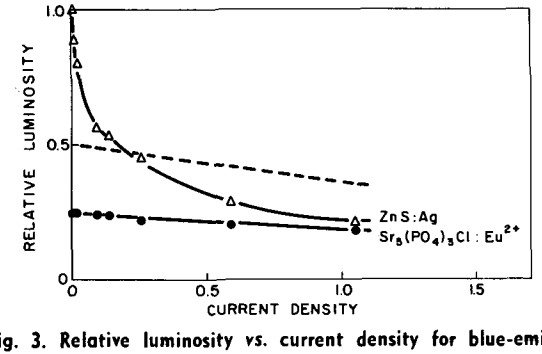

Fig. 3. Relative luminosity *vs.* current density for blue-emitting phosphors. Dashed line represents "effective" efficiency of Eu^{2+} phosphor in producing a white field when mixed with red and green.

to the red primary which had been used prior to its replacement by Eu^{3+}-activated phosphors. It is apparent that the II-VI sulfide phosphors "saturate" (*e.g.*, their efficiencies decrease at high current densities) to a much greater extent than the rare-earth-activated phosphors at the current densities obtainable in a PDF tube. With the red-emitting phosphors of Fig. 1, the Eu^{3+}-activated phosphors are superior to the (Cd,Zn)S:Ag phosphor at both high and low current densities. The Eu^{3+} phosphors show some degree of "saturation," but the effects are not nearly as drastic as with the sulfide phosphor. Therefore, the Eu^{3+}-activated red-emitting phosphors, which are superior to the sulfide red at the low current densities in shadow-mask tubes, show even better relative performance in high-current-density tube designs (Y_2O_2S:Eu behaves similarly to the Eu^{3+}-activated phosphors shown).

Although none of the green-emitting phosphors measured has an efficiency comparable to that of the (Zn,Cd)S:Ag phosphor at low current densities, several phosphors investigated surpass the green sulfide at high current densities (Fig. 2). The Tb^{3+} phosphors (10-12) appear to have an upper limit of 50-60% of the efficiency of (Zn,Cd)S:Ag at low current density, but they maintain their efficiency as the current density is increased and soon exceed the sulfide phosphor at densities above 0.1 amp/cm^2. Other oxygen host systems perform similarly to the Tb^{3+}-activated materials. As an example, Fig. 2 shows the behavior of $Zn_2SiO_4:Mn^{2+}$—a non-rare-earth-oxygen-based phosphor which is closest to the efficiency of sulfide type phosphors. The silicate is, however, characterized by an intrinsically long decay which decreases its utility in color-TV tubes.

In Fig. 3, the response of the phosphor $Sr_5(PO_4)_3Cl:Eu^{2+}$ (13) is shown along with that of the blue-emitting ZnS:Ag phosphor. The measured relative efficiency of the sulfide phosphor is superior to that of the divalent-europium-activated material over the range of current densities studied. However it should be pointed out that the color coordinates of the Eu^{2+} material are $x = 0.152$, $y = 0.032$, and those for the sulfide are $x = 0.145$ and $y = 0.052$. The Eu^{2+} emission is therefore more saturated (more nearly characteristic of a pure spectral color) than the blue emission from ZnS:Ag, and its efficiency requirements for proper color balancing with the other primaries are correspondingly lowered (14). Consequently, $Sr_5(PO_4)_3Cl:Eu$ is more effective, by a factor of 1.9, than ZnS:Ag in producing a white field when it is mixed with red and green. Its "effective" efficiency is indicated by the dashed line which demonstrates that its performance also exceeds that of the sulfide at high current densities.

The magnitude of the deviation from linearity is directly related to the dwell time of the electron beam. This is demonstrated in Fig. 4 and 5 using the test procedures described in the experimental section. Both figures show that the deviation from linearity increases as the dwell time increases either for a stationary or for a scanning spot. The dwell time on the retrace of a scanning spot is about 1/6 that during the normal scan.

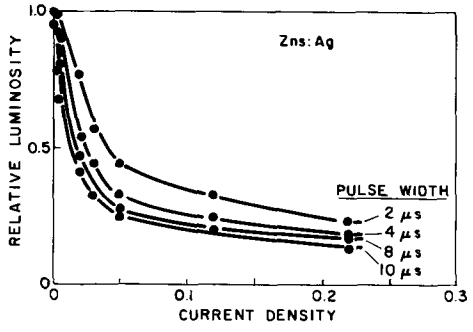

Fig. 4. Relative luminosity *vs.* current density for ZnS:Ag at four different dwell times using a stationary electron beam.

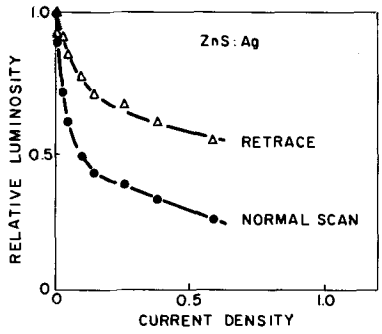

Fig. 5. Relative luminosity *vs.* current density for ZnS:Ag showing the effect of change of dwell time using a scanning spot. The change in dwell time is brought about by pulsing the beam on during normal scan or during retrace.

A limited test of the effect of repetition frequency was made. Using a scanning spot, we were able to pulse the beam on every raster (60 Hz) or alternatively only every eighth raster (7.5 Hz). There was no detectable difference between the saturation effect at 60 and at 7.5 Hz.

For those phosphors which show a drastic deviation from linearity at high current density, we observed a broadening of the emission band and a shift toward shorter wavelength. Figures 6-8 demonstrate the effect. In these figures, the heights of the emission peaks for high and low current densities were set equal by adjusting the gain on the photomultiplier tube. Low current density corresponds to approximately 1 x 10^{-3} amp/cm^2 and high current density to 1.0 amp/cm^2

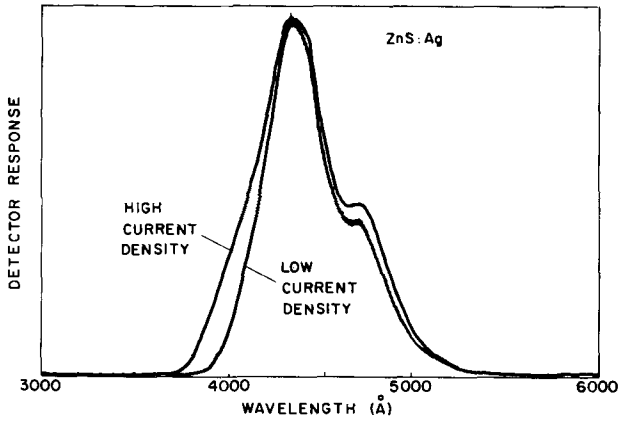

Fig. 6. Spectral shift for ZnS:Ag. The gain was adjusted to equalize the peak heights of the two curves.

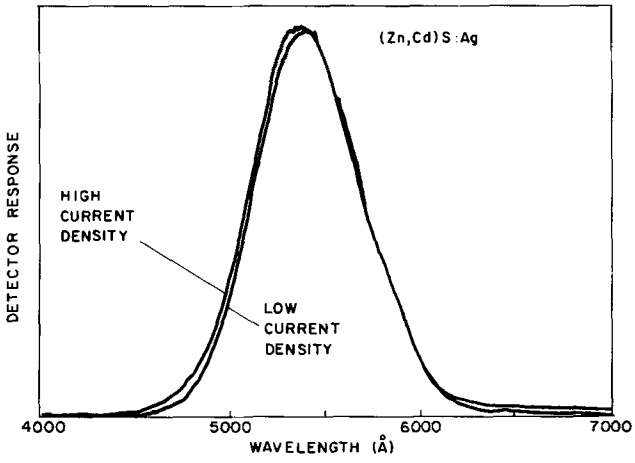

Fig. 7. Spectral shift for (Zn,Cd)S:Ag. The gain was adjusted to equalize the peak heights of the two curves.

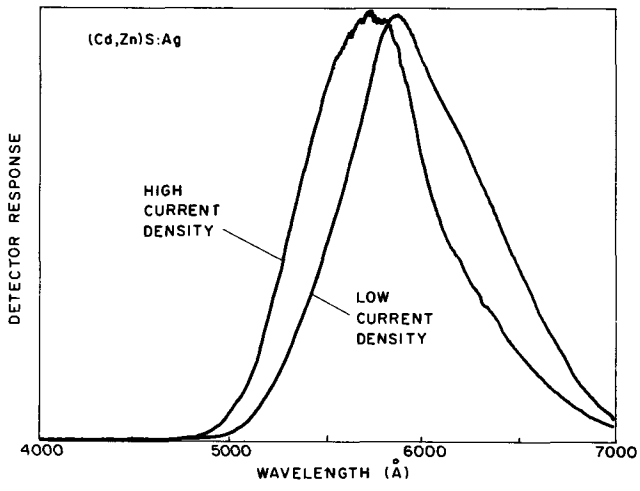

Fig. 8. Spectral shift for (Cd,Zn)S:Ag. The gain was adjusted to equalize the peak heights of the two curves.

according to the definition of spot size discussed previously. No spectral shifts were observed for the other phosphors which showed only small deviations from linearity; that is, the spectral distributions at high and low current density were unchanged.

From our results, we cannot determine if the nonlinearity is due to a true saturation effect (in the sense that the luminescence is limited by the number of luminescent centers available) or due to a temperature increase at high current density.

Inspection of Fig. 2 will show that, while Zn_2SiO_4:Mn is not strictly linear, its nonlinearity is much less pronounced than that of (Zn,Cd)S:Ag. For Zn_2SiO_4:Mn containing 1 m/o (mole per cent) of Mn, we calculate 2 x 10^{20} Mn^{++} ions/cm^3. We can estimate how many Mn^{++} ions are excited by the average incident electron if we use the energy efficiency (8.5%) of Zn_2SiO_4:Mn as measured by Bril and Klasens (15) and assume that the average photon emitted has energy of 2.36 ev (5250Å). If we now estimate the range of primary electrons from that found by Ehrenberg and Frank (16) and by Ehrenberg and King (17) for phosphors with a density nearly the same as Zn_2SiO_4, we can calculate the number of Mn^{++} ions/cm^3 excited by the average electron. For a pulse with a current density of 1 amp/cm^2, we estimate that on the average 4 x 10^{18} Mn^{++} ions/cm^3 are excited per pulse. Therefore a higher current density would be necessary to bring about a very pronounced true saturation effect. By using the same argument for ZnS:0.015 m/o Ag^+ but assuming an energy conversion efficiency of 20%, we estimate that at 1 amp/cm^2 the number of Ag^+ ions/cm^3 excited per pulse is approximately twice the Ag^+ ion concentration. Therefore, at these high current densities, the true saturation effect should be very pronounced for the II-VI sulfide phosphors.

The nonlinearity of the II-VI sulfide phosphors might also result from thermal quenching. Bril and Klasens (15) have shown that thermal quenching for these phosphors begins to set in at about 50°C. We can make a rough estimate of the temperature rise of the phosphor ZnS:Ag by using the thermal properties and the method reported by Archard and Einstein (18). For the case of a stationary pulsed spot, 30 Hz, with a pulse width of 10 μsec and an instantaneous current density of 0.2 amp/cm^2 (Fig. 4), we calculate a temperature of approximately 60°C. We should emphasize that the thermal conductivity of ZnS:Ag and the glass substrate as measured by Archard and Einstein (18) may not be quantitatively appliable to our situation. Therefore, it would not be unreasonable to expect a higher temperature. A higher temperature (about 130°C) would be necessary to attribute all the nonlinearity observed to an increase in temperature alone.

Table I. Decay times for phosphors tested

Phosphor	Time (msec) to decay to 1/10 of initial brightness: Low current density (~5 ma/cm^2)	High current density (~500 ma/cm^2)
(Cd,Zn)S:Ag	0.2*	0.04
$YVO_4:Eu^{3+}$	1.1	0.90
$YVO_4:Eu^{3+}$, Bi	1.1	0.98
$Y_2O_3:Eu^{3+}$	2.5	2.2
(Zn,Cd)S:Ag	0.5*	0.08
YPO_4Tb^{3+}	5.4	5.4
$Y_{1.86}Tb_{0.14}SiO_5$	6.0	6.0
$InBO_3:Tb^{3+}$	19	18
$Zn_2SiO_4:Mn^{2+}$	21	20
ZnS:Ag	0.1*	0.05
$Sr_5(PO_4)_3Cl:Eu^{2+}$	<0.006	<0.006

* These measured values are very sensitive to current density and dwell time.

Table I shows the time in milliseconds for decay to 1/10 of initial brightness for the various phosphors tested. It is obvious that the decay times of the linear phosphors remain constant as the current density is increased, but the decay times of the sulfide phosphors decrease drastically as the current is increased.

Embodiment in PDF tube.—A phosphor screen was fabricated in which phosphors were deposited in vertical stripes across the width of the faceplate. This screen was mated to the grill of the PDF tube after a thin layer of aluminum was evaporated over the phosphor stripes. The phosphors utilized were europium-activated yttrium vanadate, $YVO_4:Eu^{3+}$, terbium-activated yttrium phosphate, $YPO_4:Tb^{3+}$, and divalent-europium-activated strontium halophosphate, $Sr_5(PO_4)_3Cl:Eu^{2+}$. At low current densities, this tube was adjusted to give a white field, and the current was then increased step-wise up to the maximum operating current of the tube. No color shifts were observable, and the brightness increased linearly over the entire operating range.

Figure 9 illustrates the relationship between the luminescence intensity and current density for a hypothetical nonlinear "saturating" cathodoluminescent phosphor and that for a linear phosphor. The contrast ratio for the nonlinear phosphor is B_{on}/B_{sn}, while for the linear phosphor the contrast ratio is B_{o1}/B_{s1}.[2] Since $B_{on} < B_{o1}$ and $B_{sn} > B_{s1}$ it follows that $B_{o1}/B_{s1} > B_{on}/B_{sn}$; that is, the contrast ratio for the linear phosphor is greater than that for the nonlinear phosphor at high current densities. At low current densities, the relative values of the contrast ratio may be reversed because the brightness of the linear phosphor at low current densities is less than that of the nonlinear phosphor. Therefore in cathode-ray tubes such as the shadow-mask tube, which operates at low cur-

[2] The subscript 1 refers to the linear phosphor and n refers to the nonlinear phosphor. The subscripts o and s have the same significance as previously indicated in the definition of contrast ratio.

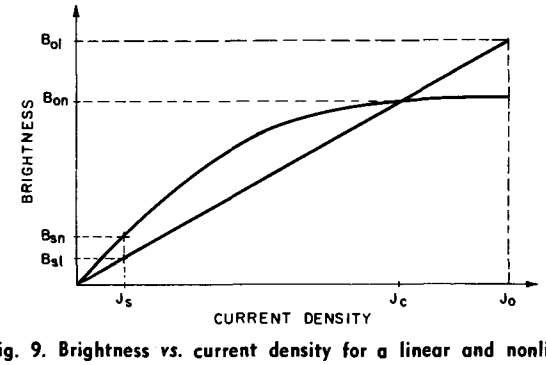

Fig. 9. Brightness vs. current density for a linear and nonlinear phosphor. J_S is the current density of back-scattered electrons, J_0 the current density under operating conditions, and J_c the current density at which crossover occurs.

rent densities, the brighter nonlinear phosphor may perform better than the linear phosphor.

An advantage of the linear phosphor screen over the nonlinear "saturating" phosphor in the PDF type tube is the reduction in the effect produced by electrons scattered back from the screen. Since there is a potential difference between the screen and the grill, electrons which are scattered back from the screen are subjected to a retarding field. Electrons that do not have a large velocity component perpendicular to the plane of the screen follow a parabolic trajectory in the space between the screen and grill and return to the screen with generally less velocity than the primary beam. Since they are distributed over a wider area, the density of these scattered electrons is considerably less than the density of electrons in the primary beam. Therefore, if we again refer to Fig. 9 for the hypothetical linear and nonlinear phosphors, and if we assume that J_s represents the density of back-scattered electrons, it becomes apparent that the brightness due to back-scattered electrons will be greater for the nonlinear than for the linear phosphors. This is true if the nonlinear phosphor is brighter than the linear phosphor at low current densities. For example, this would not be the case where a Eu^{3+}-activated phosphor is compared with (Cd,Zn)S:Ag if the Eu^{3+}-activated phosphor is brighter than the sulfide over the full range of current density.

Conclusion

This paper has described a method by which the "saturation" effect, or the decrease in cathode ray efficiency as a function of current density, can be evaluated. The saturation effect is especially pronounced in conventional II-VI sulfide phosphors. Therefore, although these phosphors have played an important role in the performance of conventional color-TV display systems, their nonlinear performance in high-current-density tubes limits their usefulness. Oxygen-based phosphors, on the other hand, have been found to respond linearly with increase in current density. Specifically, rare-earth-activated phosphors based on Eu^{3+} activation for red, Tb^{3+} activation for green, and Eu^{2+} activation for blue show distinct advantages over the Zn-Cd sulfide phosphors in certain tube designs.

Acknowledgments

The authors would like to express their appreciation to C. Creter for many of the measurements, to H. Dressel and J. Dymon for the fabrication of the PDF tube, and to D. George for helpful discussions.

Manuscript submitted Nov. 7, 1968; revised manuscript received Jan. 24, 1969.

Any discussion of this paper will appear in a Discussion Section to be published in the December 1969 JOURNAL.

REFERENCES

1. A. Bril and F. A. Kröger, *Philips Tech. Rev.*, **12**, 120 (1960).
2. Yu. V. Voronov, Chapter III of "Investigations of the Cathodoluminescence of Zinc Sulfide and Certain Other Cathodoluminophors," by V. L. Levshin *et al. Trans. P. N. Lebedev Phys. Inst.*, Vol. XXIII (1964).
3. P. A. Einstein, *Brit. J. Appl. Phys.*, **8**, 190 (1957).
4. P. H. Dowling and J. R. Sewell, *This Journal*, **100**, 22 (1953).
5. A. Bril, *Physica*, **15**, 361 (1949).
6. V. K. Zworykin and G. A. Morton, "Television," 2nd Ed., p. 793, John Wiley & Sons Inc., New York, (1954).
7. R. Dressler, *Proc. I.R.E.*, **41**, 851 (1953).
8. S. Yoshida, A. Ohkoshi, and S. Miyaoka, *IEEE Trans. Broadcast and Television Receivers*, **BTR-14**, 19 (1968).
9. A. K. Levine and F. C. Palilla, *Electrochem. Technol.*, **4**, 16 (1966); F. C. Palilla, *ibid.*, **6**, 39 (1968).
10. F. J. Avella, O. J. Sovers, and C. S. Wiggins, *This Journal*, **114**, 613 (1967).
11. F. C. Palilla, A. K. Levine, and M. Rinkevics, *Proc. Intern. Conf. Luminescence, Budapest, Hungary*, pp. 1639-1645 (1966).
12. T. Peters, To be published.
13. F. C. Palilla and B. E. O'Reilly, *This Journal*, **115**, 1076 (1968).
14. O. J. Sovers and L. J. Bodi, *J. Opt. Soc.*, **55**, 1643 (1965).
15. A. Bril and H. A. Klasens, *Philips Res. Repts.*, **7**, 40 (1952).
16. W. Ehrenberg and J. Frank, *Proc. Phys. Soc. (London)*, **B66**, 1057 (1953).
17. W. Ehrenberg and D. E. N. King, *ibid.*, **81**, 751 (1963).
18. G. D. Archard and P. A. Einstein, *Brit. J. Appl. Phys.*, **8**, 232 (1957).

Hydrogen Sulfide as an Etchant for Silicon

P. Rai-Choudhury* and A. J. Noreika

Research & Development Center, Westinghouse Electric Corporation, Pittsburgh, Pennsylvania

ABSTRACT

The etch rates for Si by gaseous H_2S are measured as functions of temperature and found to be limited, at temperatures below about 1000°C, by an increasingly stable reaction product, *viz.* SiS_2. Etched surfaces are evaluated by forming carbon replicas which are subsequently examined by transmission electron microscopy. Some epitaxial layers are grown on the etched Si surfaces and are examined optically and by a spreading resistance method. Neither crystallographic (precipitates) nor electrical (doping) anomalies are introduced by the H_2S treatment. All results are compared to equivalent data obtained from controlled etching experiments in which gaseous HCl and H_2O, respectively, are used as etchants. For comparable temperature and flow conditions, etch rates using H_2S have far exceeded those obtained from both HCl and H_2O; *e.g.*, at 1200°C the ratio of etch rates (H_2S::HCl::H_2O) is roughly 2000::15::1. Considerable difference is also observed in the replicas taken from equivalent Si surfaces. Surfaces etched with H_2S show little detail, indicating considerable smoothness. Etching with HCl and H_2O invariably produces patchy or rutlike features.

The role of substrate perfection on the performance of silicon devices has been the subject of a recent review (1). In general, silicon substrates are observed to suffer from two main classes of imperfection, *viz.* (*a*) defects introduced during processing and (*b*) inherent bulk defects. The former, *e.g.* certain surface oxides and films, mechanical damage, *etc.*, can be removed *in situ* by chemical etching. The latter, *e.g.* dislocations, stacking faults, precipitates, *etc.*, are not readily removable.

* Electrochemical Society Active Member.

To date, the most extensively used gaseous etchants for *in situ* etching of silicon are hydrogen chloride (2) and water vapor (3). Hydrogen chloride reacts with the silicon surface at a moderate rate (*see* Table I), the volatile reaction products being removed by the gas flow. At temperatures > 1100°C, hydrogen chloride has the undesirable property of being an excellent transport agent (4). The etched silicon, consequently, is subject to an influx of contaminants from various components, *e.g.* the susceptor, *etc.*

Water vapor, a much slower etchant (Table I), required temperatures > 1200°C before effective cleaning occurred. Unlike hydrogen chloride, water vapor proves a poor transport agent.

Because of a need for a rapid, effective etchant, the present investigation of the etching properties of hydrogen sulfide on silicon was initiated. Some preliminary work on this etchant was done independently by Chu (5) of these laboratories. (Note: thermodynamic calculations indicated that hydrogen selenide might also prove an efficient etchant.)

Experimental

The vapor etching experiments were performed in a conventional horizontal reaction chamber in which substrates were placed on a SiC-impregnated carbon susceptor and heated *via* rf current, the rf coil being externally mounted. Three etchants were used separately, *viz.* anhydrous hydrogen chloride (ultrahigh purity), doubly distilled water, and 10% hydrogen sulfide in ultrapure hydrogen. Desired concentrations of the etchants were obtained by mixing controlled amounts with palladium-purified hydrogen. Si(111) wafers which were to be etched *in situ* were initially chemically polished then split into three parts, thus enabling the effects of the three etches to be evaluated on a given wafer. Carbon replicas of the split Si wafers were made after etching and these were examined by transmission electron microscopy (TEM). The etch rates were determined from weight loss and wafer thickness measurements. All temperatures reported are uncorrected pyrometer readings.

Epitaxial layers were grown on etched substrates by the hydrogen reduction of $SiCl_4$ and provision for doping with B_2H_6 or PH_3 was made. These layers were subjected to optical examinations and spreading resistance measurements (6).

Results and Discussion

Figure 1 shows the variation of etch rate (change in total thickness per unit time) with temperature for a H_2S partial pressure of 5.5 x 10^{-3} atm and a total hydrogen flow of 100 liters/min (linear velocity $\simeq$ 25 cm/sec). The curve indicates a slowing of etch rate as temperature decreases. Appearances of surfaces etched at 800°, 1000°, and 1100° give a clue to the mechanism by which simple mass transfer which would occur *via* the reaction

$$Si(s) + 2H_2S(g) \rightarrow SiS_2(s \text{ or } l) + 2H_2(g)$$

may be inhibited. Substrates etched at 800°C appeared optically smooth although discolored. When examined by reflection electron diffraction, the surfaces were found to be covered by highly insulating amorphous films, most probably SiS_2. The formation of SiS_2 as the prime reaction product is thermodynamically favored over that of SiS in our temperature range of interest 7). It is also substantiated by data which indicate that SiS (the alternate reaction product) may be obtained in significant amounts only through a gas phase reaction between SiS_2 and Si at temperatures greater than 1400°C (8, 9). In the course of Si etching, the reaction product was observed to condense in the cold part of the reaction tube as small yellowish needles. These were subjected to x-ray diffraction examinations and were found to resemble glasslike structures although the compositions could not be ascertained. Since SiS_2 is known to hydrolize readily

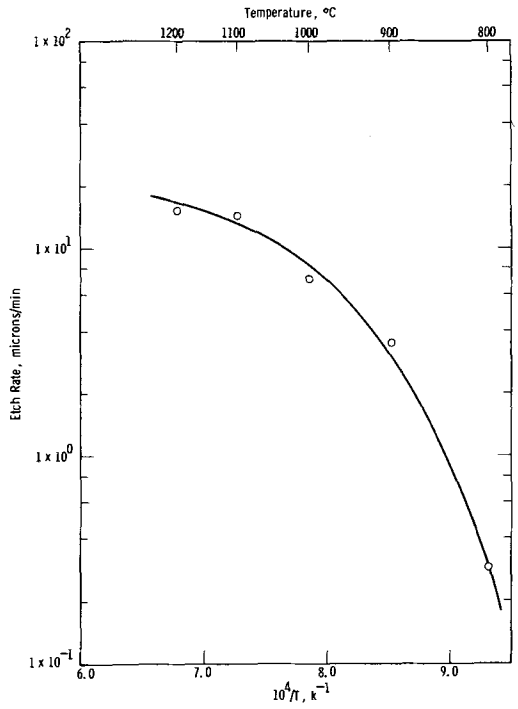

Fig. 1. Effect of temperature on etch rate: $p_{H_2S} = 5.5 \times 10^{-3}$ atm; total flow rate 100 liters/min.

(10), its decomposition to SiO_2 (glassy form) and H_2S is suspected. Substrates subjected to H_2S flow at 1000°C were visibly roughened. The presence of an insulating layer was not detected. At temperatures 1100°C and higher, smooth, highly polished surfaces were prepared, the streaked diffraction patterns being indicative of surface smoothness. The rapidly decreasing slope of the curve for etch rate *vs.* $1/T$, therefore, is most likely due to a surface-limiting activation process. The high- (1100°C) and low-(800°C) temperature results show the respective absence and presence of the amorphous layers. The intermediate temperature ($\sim$ 1000°C) results reflect noncoherent etching due to incomplete removal of the reaction products.

A measure of the relative speed with which H_2S etches at 1200°C is shown in Table I where etch rates of the three etchants are compared. The partial pressures of the HCl and H_2O etchants approximate those used in practice (a higher H_2O pressure, for instance, initiates the formation of SiO_2 and surface pitting). For the pressure and flow parameters chosen, the H_2S etch rate exceeded that of HCl by approximately two orders of magnitude.

The effects of etching at 1200°C on the silicon surfaces are shown by the micrographs of replicated surfaces (Fig. 2). These surfaces were essentially identical, prior to etching, being cut from a single, chemically polished wafer. The results (Fig. 2) indicate a microscopically smoother finish, akin to a rapid nonpreferential chemical etch, for the H_2S etched surface. A total of seven wafers were split and etched, the results being similar.

Although appreciable sulfur doping was not anticipated, the effect of H_2S on doping profiles were investigated. Silicon deposition was initiated on a H_2O etched substrate and a layer of 90μ average thickness

Table I.

Etchant	Etchant partial pressure, atm	Etching temp, °C	Total flow rate, liters/min	Etch rate, μ/min
HCl	1.0×10^{-2}	1200	100	0.183
H_2O	1.3×10^{-4}	1200	100	0.071
H_2S	5.5×10^{-3}	1200	100	15.1

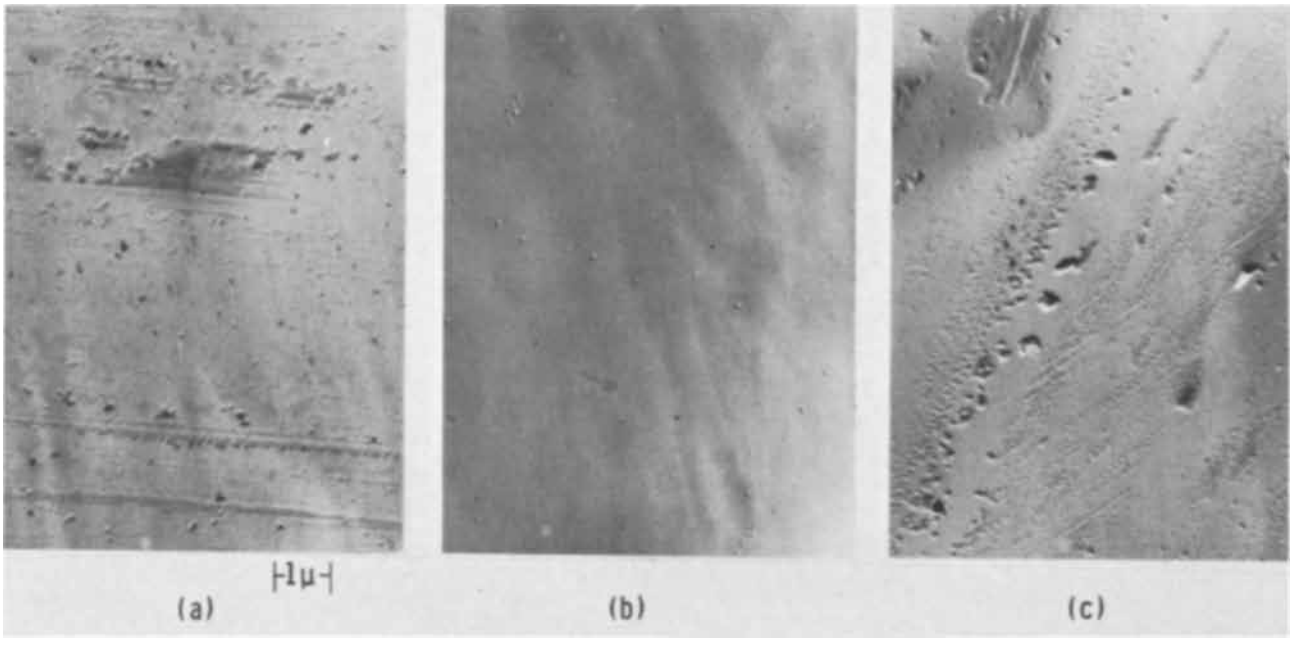

Fig. 2. Transmission electron micrographs of the carbon replicas of silicon surfaces etched at 1200°C using (a) HCl, (b) H_2S, and (c) H_2O.

was formed. Twenty microns of the layer were subsequently removed by etching with H_2S at 1150°C. An additional 75μ of epitaxial silicon were then deposited. These thick epitaxial layers were essentially free from any inclusions and stacking faults, and constitute a severe test of surface cleanliness. Spreading resistance measurements showed no discontinuity in the impurity profile of the combined 145-μ layer, the net donor concentration being 4 x 10^{14} atoms/cm^3 throughout.

Conclusions

Gaseous H_2S is found to be a rapid and nonpreferential etchant for silicon. Sulfur, although a donor impurity in silicon, was not observed to be introduced during the etching cycle.

Acknowledgments

The authors wish to thank J. H. Rieger and W. Cifone for assistance with the experimental work.

Manuscript submitted Aug. 26, 1968; revised manuscript received Dec. 30, 1968. This paper was presented at the Montreal Meeting, Oct. 6-11, 1968, as a Late News Paper.

Any discussion of this paper will appear in a Discussion Section to be published in the December 1969 JOURNAL.

REFERENCES

1. H. F. John, *Proc. IEEE*, **55**, 1249 (1967).
2. G. A. Lang and T. Stavish, *RCA Rev.*, **24**, 488 (1963).
3. T. L. Chu, G. A. Gruber, and R. Stickler, *This Journal*, **113**, 156 (1966).
4. H. Schäfer, "Chemical Transport Reactions," Academic Press, New York, (1964).
5. T. L. Chu, *This Journal*, **115**, 1207 (1968).
6. R. G. Mazur, *ibid.*, **114**, 255 (1967).
7. JANAF Thermochemical Tables, Dow Chemical Co., Midland, Mich., Aug. 1965.,
8. W. C. Schumb and W. J. Bernard, *J. Am. Chem. Soc.*, **77**, 904 (1955).
9. P. Rouquet and M. F. Ancey-Moret, *Bull. Chem. France*, **1954**, 1038.
10. R. Schwarz, *Z. Anorg. Chem.*, **276**, 33 (1954).

Extra-High-Purity Nickel Powder from Nickel Sulfate Solution by Hydrogen Reduction

N. Zubryckyj,[1] W. Kunda, and D. J. I. Evans

Sherritt Gordon Mines Limited, Research and Development Division, Fort Saskatchewan, Alberta, Canada

ABSTRACT

The method described for the preparation of extra-high-purity nickel powder is based on the reduction of nickel sulfate solution by hydrogen under pressure in an autoclave. To obtain the required purity, the nickel sulfate solution must first be thoroughly purified from the elements that are more electropositive than nickel in the Nernst electromotive series and from the elements, the salts of which are susceptible to hydrolysis above a pH of 4. The methods employed for removing the traces of impurities include cementation of the copper, hydrolysis of the iron salts, and chemical precipitation of the cobalt. Unlike commercial practice of the hydrogen reduction process, the reduction of the purified nickel sulfate solution is carried out without a ferrous salt catalyst. To initiate the reduction reaction, a small amount of ammonium carbonate is introduced into the system. Reduction is carried out at a temperature of 350°F under a hydrogen pressure of 350 psi. The ammonium carbonate presumably promotes the formation of a fine suspension of solid basic nickel carbonate which then plays the role of a catalyst and provides the nuclei on which the nickel precipitates. In this way, contamination by the foreign elements originating from the catalysts normally used is avoided. Final "polishing" of the nickel powder is done using a wet hydrogen treatment at a temperature of 800°F to remove traces of carbon from the nickel powder, and a dry hydrogen heat treatment at 800°F to remove oxygen. The purity and some of the properties of the nickel powder produced are given.

Commercial nickel, whether it is produced by electrolysis, by the decomposition of nickel carbonyl, or by precipitation by hydrogen from aqueous systems, is already a high-purity material. Since more than 75% (1967) of the nickel produced is normally incorporated into alloys with iron or copper, the minor contaminants usually present, such as cobalt, copper, iron, sulfur, and carbon, are low enough in commercial nickel to have no effect on the properties of the final products. The remaining 25% of the nickel produced is used directly as the virtually pure metal or as the feed material for the production of catalysts and chemicals. In some of these applications, specific impurities can be harmful; however, these impurities can usually be avoided by careful selection from the commercial forms available.

The purity of commercial forms of nickel is dependent on the starting material and on the refining process used. Table I shows the chemical analyses of commercial nickel produced by various methods and analyzed by the same laboratory. The elements not listed in Table I, namely Ag, Al, Ba, Be, Bi, Ca, Cd, Cr, Ge, Hg, Mn, Mo, Sb, Si, Sn, Ti, and V, are all reported to be less than 0.001% by emission spectrographic analysis.

From time to time, there is a demand for nickel of very high purity for special applications. Such applications include vacuum tubes for submarine cable repeaters (1), electronic equipment (2), special alloys for nuclear reactors (3, 4) and for the study of the mechanical, electrical, and magnetic properties of nickel and nickel-base alloys. With the sophisticated methods presently available for converting metal powders directly into wrought forms, a very-high-purity nickel powder provides a suitable starting material for many of these applications.

The first attempt to prepare a pure nickel powder was made by de Ruolz in 1841 (5) using an electrolytic precipitation method. Since that time, a considerable amount of work has been carried out to improve the purity of the nickel powder produced by essentially the same electrolytic method, by adding intermediate purification steps.

[1] Present address: S. A. Industrias Votorantim, Brazil.

The hydrometallurgical methods developed by Sherritt Gordon Mines Limited for the commercial production of nickel powders from the aqueous ammonium sulfate system (6) or ammonium carbonate system (7) by reduction, at elevated temperatures, with gaseous hydrogen, do yield a relatively high-purity nickel powder. However, to produce an even higher-purity nickel powder for special applications, it is necessary to modify the procedures developed.

The modified method comprises the dissolution of a commercial grade nickel powder in sulfuric acid, purification of the nickel sulfate solution to remove minor metal contaminants, and precipitation of the nickel with hydrogen in a metallic form using a different catalyst from that used conventionally. The product, in the form of a powder, is then decarburized and deoxidized by treatment with hydrogen at elevated temperature. A block flow diagram for the production of extra-high-purity nickel powder is shown in Fig. 1.

Materials and Equipment

In the investigations undertaken to develop the process, the starting material for the preparation of extra-high-purity nickel powder was commercial "S" grade nickel powder.

The reagents used were: C.P. grades of sulfuric acid, ammonium hydroxide, hydrogen peroxide, 1-nitroso-2-

Table I. Analyses of commercially pure nickel produced by various methods

Type of analysis	Element	Method of preparation: Electrolysis	Carbonyl process	H_2 precipitation from Ammonium sulfate system ("S" grade)	H_2 precipitation from Ammonium carbonate system
Chemical	Co	0.07	0.0012	0.07	0.06
	Cu	0.012	0.0011	0.006	0.004
	Fe	0.012	0.015	0.010	0.010
	S	0.004	0.0017	0.016	0.005
	C	0.020	0.013	0.004	0.04
Spectrographic	As	<0.001	<0.001	<0.001	<0.001
	B	0.003	<0.001	<0.001	<0.001
	Li	<0.001	<0.001	<0.001	<0.001
	Mg	0.001	<0.001	<0.001	<0.001
	Pb	0.002	<0.001	<0.001	<0.001
	Te	<0.005	<0.005	<0.005	<0.005
	Zn	<0.005	<0.005	<0.005	<0.005

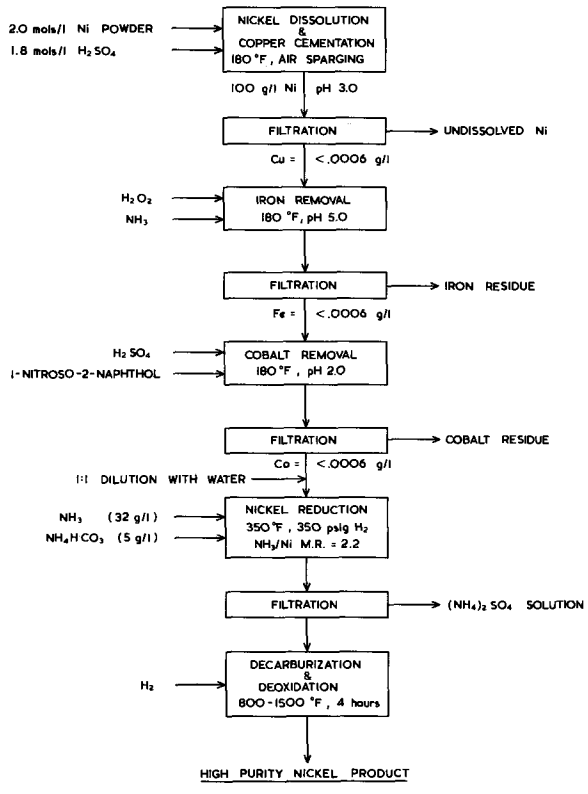

Fig. 1. Flowsheet for preparation of high-purity nickel powder.

naphthol, or 1-naphthol and ammonium carbonate. The 1-nitroso-2-naphthol reagent solution was prepared by dissolving 100g of reagent in 250 ml of a 6% sodium hydroxide solution and mixing with 200 ml of a 20% potassium nitrite solution.

The dissolution of the feed nickel powder and the purification of the nickel sulfate solutions were carried out at temperatures below 200°F at solution *p*H values between 0-6.0. For these operations, glass or polypropylene-lined equipment was used. The precipitation of the nickel by hydrogen was carried out at 350°F from ammoniacal solutions, and stainless steel autoclaves were found to be adequate. The decarburization and deoxidation step was carried out at temperatures in the range of 800°-1500°F in a hydrogen atmosphere, and ceramic or nickel trays were used to hold the nickel powder.

It goes without saying that extreme cleanliness with respect to the equipment had to be maintained throughout all of the process stages. Contamination of the final product by airborne dust particles also had to be avoided.

Process Development Investigations

Preparation of nickel sulfate solution.—Nickel sulfate solution was prepared by leaching commercial "S" grade nickel powder in C.P. sulfuric acid in an agitated vessel into which air or oxygen could be sparged. The essential reaction during leaching was:

$$Ni + H_2SO_4 \rightarrow NiSO_4 + H_2 \qquad [1]$$

However, when oxygen was sparged into the system, the reaction taking place was:

$$Ni + H_2SO_4 + \tfrac{1}{2} O_2 \rightarrow NiSO_4 + H_2O \qquad [2]$$

The rate of dissolution was accelerated by the presence of the sparged oxygen. Cobalt and iron, when present in the nickel powder, dissolved at the same rate as the nickel. Copper did not go into solution in the presence of metallic nickel; however, when the nickel powder was completely leached, copper did dissolve although it was readily cemented out by adding a few grams of fresh nickel powder.

By using a 20-50% stoichiometric excess of nickel powder, a final solution was obtained which contained only a few grams of free sulfuric acid. This solution was suitable for further purification. Although the nickel concentration in the final solution could be built up to about 250 g/liter, it was found preferable to limit the nickel concentration to 100 g/liter for practical considerations.

The rate of nickel dissolution and sulfuric acid consumption is shown in Fig. 2(a) and the behavior of the Co, Fe, and Cu impurities during leaching is shown in Fig. 2(b).

Using an excess of nickel powder, the nickel sulfate solution produced contained less than 0.0006 g/liter Cu and this was considered adequately pure with respect to copper.

Purification of nickel sulfate solution.—Using "S" grade nickel powder, the nickel sulfate solution contained only Fe and Co as impurities. These were necessarily removed before the hydrogen reduction of the nickel from solution.

Iron removal. An effective and convenient method for iron removal is to precipitate the iron as ferric hydroxide and to remove the precipitate by filtration. The completeness of the iron precipitation depends on

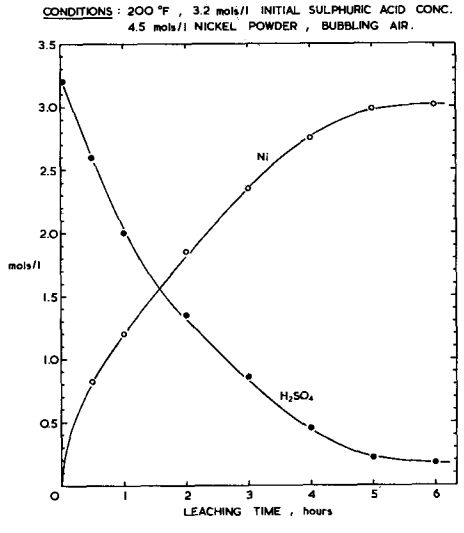

Fig. 2(a). Dissolution rate of nickel powder in sulfuric acid solution.

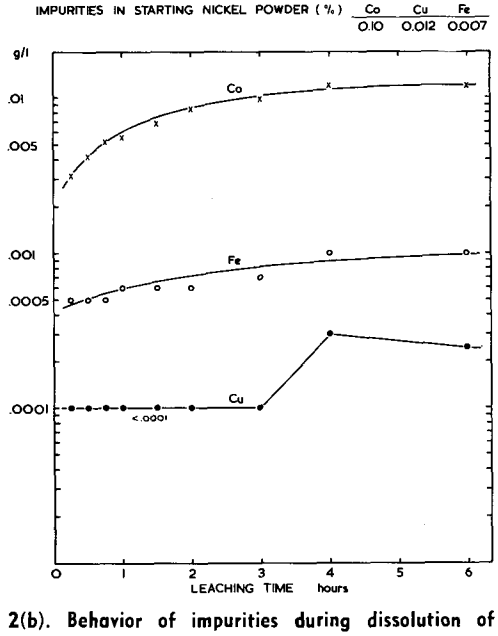

Fig. 2(b). Behavior of impurities during dissolution of nickel powder in sulfuric acid solution.

the iron being present in the ferric form and on the pH of the system. In the above dissolution procedure, the iron in the nickel sulfate solution was present as ferrous sulfate. Two methods were employed to oxidize this iron to the ferric form: (*a*) oxidation with oxygen or air under pressure in an autoclave at elevated temperatures, or (*b*) oxidation with hydrogen peroxide or ammonium persulfate. While the oxidation with air could be carried out at atmospheric pressure, the long retention time made this method impractical.

The important parameters affecting the iron precipitation were the pH of the system and the temperature. The conditions favoring iron precipitation were also conducive to the precipitation of nickel. Oxidation with hydrogen peroxide or ammonium persulfate proved to be more advantageous than oxidation with air under pressure because it could be carried out at lower temperatures. From practical considerations, oxidation using hydrogen peroxide was selected as the preferred procedure.

Under the optimum conditions with hydrogen peroxide and using ammonia for pH control, a nickel sulfate solution was produced containing 0.0002 g/liter Fe as shown in Table II.

The chemical reactions taking place during iron removal were:

$$2FeSO_4 + H_2SO_4 + H_2O_2 \rightarrow Fe_2(SO_4)_3 + 2H_2O \quad [3]$$

$$Fe_2(SO_4)_3 + 6NH_4OH \rightarrow 2Fe(OH)_3 + 3(NH_4)_2SO_4 \quad [4]$$

Filtration was carried out using a diatomaceous earth filter-aid to insure the removal of the very fine ferric hydroxide particles.

Cobalt removal. Because of the similar chemical behavior of nickel and cobalt in solution, a number of procedures had to be investigated for removing cobalt from the nickel sulfate solution. Two promising methods, one using the preferential electrolytic precipitation of cobalt on a high-speed rotating cathode (8) and the other chemical precipitation by sodium ethyl xanthate (9) in an ammoniacal medium, at a pH of 9.5, using 30 times the theoretically required quantity of reagent, have been reported by other workers. Exploratory tests were carried out in the laboratory on acidic nickel sulfate solution using a wide variety of chemical precipitation agents. The most promising results were obtained by precipitating the cobalt with 1-nitroso-2-naphthol or 1-naphthol and these reagents were chosen for systematic investigations to establish the optimum conditions for the precipitation. The work showed that the quantity of reagent and pH were the most important parameters affecting the completeness of the cobalt removal. The effects of these variables are shown in Table III and Fig. 3.

The results of these investigations, as well as those with 1-naphthol shown in Table IV, demonstrated that iron, as well as cobalt, may be removed to a very low level by these reagents.

The reactions taking place during cobalt precipitation can be expressed by the following equation:

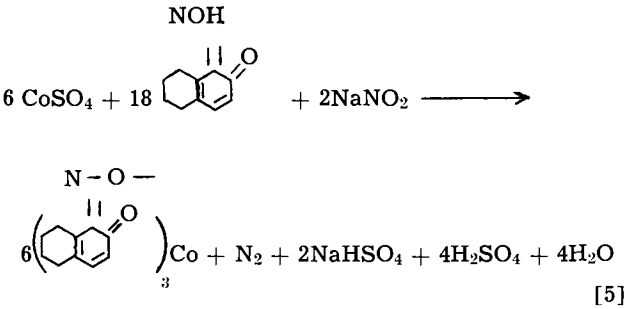

[5]

It is assumed in this reaction that the 1-nitroso-2-naphthol is present in the quinonoid form:

as sugested by Thorne and Roberts (10). The sodium nitrite added with the 1-nitroso-2-naphthol oxidized the cobalt to the cobaltic form. Stoichiometrically, 3 moles of 1-nitroso-2-naphthol are required to precipitate 1 mole of Co. However, for complete precipitation, it was found that a 5-times excess of reagent was required. The completeness of the cobalt precipitation increased with time and a 4-hr reaction time was found to be the optimum. In practice it was found that the filtered nickel solution should be stored for 16 hr and refiltered to remove the very fine particles of cobalt precipitate. The effectiveness of this procedure is shown in Fig. 3.

Nickel reduction.—The reduction of nickel from the aqueous nickel ammine sulfate system by gaseous hydrogen under pressure at elevated temperatures requires a catalyst. In the commercial application of this process, two catalysts are used, ferrous sulfate as a nucleation catalyst and nickel powder as the catalyst in subsequent densifications (11). The procedure used involves a cycle consisting of about 50 densification re-

Table II. Iron precipitation from nickel sulfate solution with H_2O_2 and ammonia at 180°F

	Fe, g/liter	Co, g/liter	pH
Head solution	0.0110	0.042	1.0
Purified solution	0.0002	0.041	5.9

Table III. Precipitation of cobalt from nickel sulfate solution with 1-nitroso-2-naphthol reagent

Conditions: 180°F; pH = 2.0

Variable	Analysis, g/liter Ni	Co	Fe	Excess of reagent × stoichiometric for Co
Head solution	40	0.018	0.012	
pH = 1.0		0.006	0.007	4.7
2.0		0.001	0.008	4.7
3.0		0.001	0.008	4.7
4.3		0.013	0.004	4.7
Quantity of reagent (g/liter)				
0		0.023	0.004	0
0.12		0.010	0.004	0.61
0.24		0.005	0.004	1.25
0.50		0.004	0.002	2.50
1.00		0.001	0.001	5.00

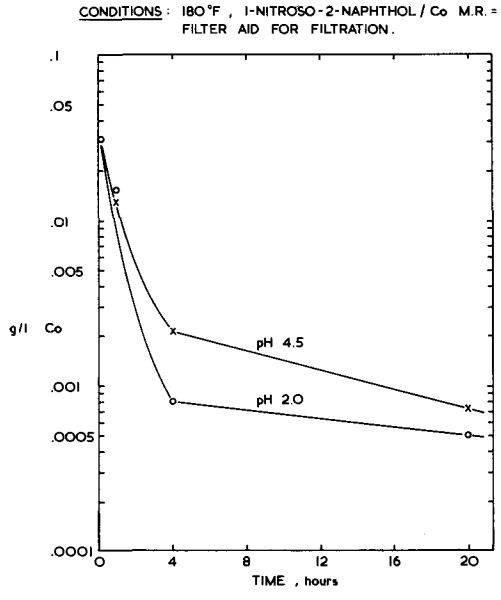

Fig. 3. Effect of time on the precipitation of cobalt with 1-nitroso-2-naphthol at pH 2.0 and 4.5.

Table IV. Purification of nickel sulfate solution with 1-naphthol

Reagents (gpl)	Nickel solution analysis, g/liter Ni	Co	Cu	Fe	Excess of reagent × stoichiometric for Co
Head solution	97	0.100	0.0003	0.016	0
0.88		0.023	0.0002	0.016	1.2
2.64		0.015	0.0002	0.006	3.6
5.28		0.013	0.0003	0.004	7.2
8.80		0.0006	0.0001	0.002	12.0

ductions. The cycle is started with a nucleation reduction using 0.5-1.0 g/liter Fe^{++} in the form of ferrous sulfate as the catalyst. The product of nucleation reduction is a very fine nickel powder with an average particle size of 1-2μ. The subsequent densification reductions are carried out using the nickel powder produced in the previous reduction. The nickel powder becomes coarser as the cycle proceeds and, after about 50 reductions, the cycle is terminated, the nickel product discharged, and a new cycle started.

The following reaction takes place during reduction:

$$Ni(NH_3)_2SO_4 + H_2 \rightarrow Ni + (NH_4)_2SO_4 \qquad [6]$$

In this procedure, about 20% of the iron added as the catalyst in the nucleation reduction, remains with the nickel. During the subsequent densifications, the iron is progressively diluted to less than 0.01% Fe in the final powder and thus does not materially affect the purity of the commercial grades of nickel powder. However, such contamination could not be tolerated if the specifications, arbitrarily set for the extra-high-purity nickel powder, were to be met.

In the search for an alternative catalyst which would not contaminate the final product, it was found that ammonium carbonate was most effective. Ammonium carbonate, added in quantities as low as 5 g/liter, was found to be not only an effective reduction catalyst, as shown in Fig. 4, but its use also resulted in lowering the sulfur content of the final nickel powder from 0.02 to 0.005% S. This finding was a critical advance in the development of the process for the preparation of extra-high-purity nickel powder using hydrometallurgical techniques. Using a similar densification procedure to that in commercial practice, the extra-high-purity nickel powder was prepared from purified nickel sulfate solution in a cycle comprising one nucleation with ammonium carbonate and several densifications. Ammonia was added to the system to give a nickel ammine in solution with an average $NH_{3(free)}$/Ni molar ratio of 2.2/1. In this way, the pH of the system at the end of the reduction was maintained slightly higher than 7.0. With insufficient ammonia, the reduction would finish on the acid side with the

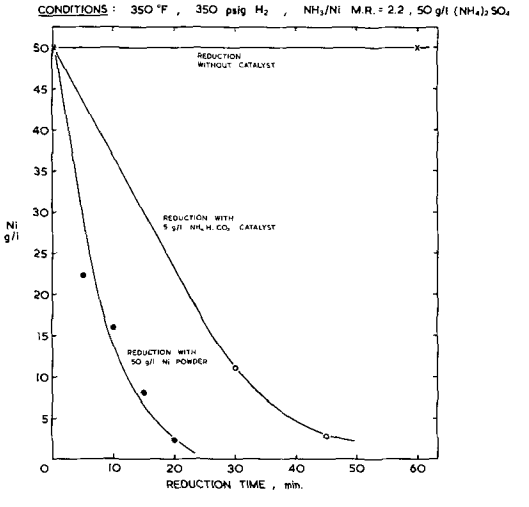

Fig. 4. Rate of nickel precipitation from aqueous ammonium sulfate system with gaseous hydrogen and various catalysts.

possibility of trace contamination of the nickel powder product due to corrosion.

The nickel powder produced by this procedure was superpurity grade with respect to all elements except carbon and oxygen.

Decarburization and deoxidation.—Low carbon and oxygen values in the nickel powder were obtained by subjecting the nickel to treatment with hydrogen at elevated temperatures. Decarburization and deoxidation were carried out at temperatures between 800° and 1500°F. The reactions proceeded at a faster rate at the higher temperatures but the higher temperatures promoted the sintering of powder and the product had to be pulverized. In practice, the temperature was selected on the basis of the particle size of starting material and the required physical properties of the final product. To achieve this final purification without sintering, the nickel powders were treated at 800°F for 2 hr in wet hydrogen followed by an additional 2 hr in dry hydrogen. The wet hydrogen proved most effective for decarburization and the dry hydrogen was necessary for deoxidation. The treated powder was cooled in a dry hydrogen atmosphere and stored in a protective atmosphere of nitrogen if very low oxygen contents were required.

The conditions and procedures worked out in the laboratory were confirmed on a semicommercial scale. The analysis and physical properties of the superpurity nickel powder produced in the semicommercial plant are given in Table V.

Summary

Superpurity nickel powder can be produced by hydrometallurgical methods from the commercial grade nickel. The method developed involves the dissolution of nickel in sulfuric acid under conditions which promote the cementation of copper, purification of nickel sulfate solution from iron and cobalt, and precipitation of a high-purity nickel powder from an aqueous nickel ammine sulfate solution by hydrogen

Table V. Production of extra-high-purity nickel powder on a semicommercial scale; Analyses of starting, intermediate, and final products

Elements	Starting nickel powder	Purified Ni solution (g/liter)	Nickel powder Nucleation, %	Nickel powder After 10 densifications, %
Ag	<0.001		<0.001	<0.001
Al	<0.001		0.001	<0.001
As	<0.001		<0.001	<0.001
B	<0.001		<0.001	<0.001
Ba	<0.001		<0.001	<0.001
Be	<0.001		<0.001	<0.001
Bi	<0.001		<0.001	<0.001
Ca	<0.001		<0.001	<0.001
Cd	<0.001		<0.001	<0.001
Cr	<0.001		<0.001	<0.001
Ge	<0.001		<0.001	<0.001
Hg	<0.001		0.001	<0.001
Li	<0.001		<0.001	<0.001
Mg	<0.001		<0.001	<0.001
Mn	<0.001		<0.001	<0.001
Mo	0.005		<0.001	<0.001
Pb	<0.001		<0.001	<0.001
Sn	<0.001		<0.001	<0.001
Si	<0.001		0.001	<0.001
Sb	<0.001		<0.001	<0.001
Te	<0.005		<0.001	<0.001
Ti	<0.001		<0.001	<0.001
V	<0.001		<0.001	<0.001
Zn	<0.005		<0.001	<0.001
Zr	<0.001		<0.001	<0.001
Co	0.07	0.0001	0.0005	0.0001
Cu	0.006	0.0002	0.0003	0.0003
Fe	0.010	0.0005	0.005	0.0001
S[1]	0.016		0.005[2]	0.003[2] 0.003[3]
C[1]	0.004		0.11[2]	0.056[2] 0.003[3]
Physical properties:				
A.D.	4.2		1.2[2]	3.8[4]
F.N.	100		2[2]	60[4]

[1] Chemical analysis.
[2] Nickel powder as produced in the autoclave.
[3] Nickel powder treated in hydrogen at 1500°F for 4 hr.
[4] After treatment in hydrogen and pulverizing.

using ammonium carbonate as the nucleation catalyst. The autoclave powder is heat treated in hydrogen to remove carbon and oxygen.

Acknowledgments

The authors wish to thank the President, Mr. D. D. Thomas, and the Management of Sherritt Gordon Mines Limited for permission to publish this paper.

Manuscript submitted Oct. 7, 1968; revised manuscript received Dec. 12, 1968. This paper was presented at the Montreal Meeting, Oct. 6-11, 1968, as Paper 558.

Any discussion of this paper will appear in a Discussion Section to be published in the December 1969 JOURNAL.

REFERENCES

1. K. M. Olsen, *Metal Progr.*, **75**, 105 (1957).
2. L. P. Lessing, *Sci. Am.*, **192**, 36 (1955).
3. J. R. Lane, *Metal Progr.*, **75**, 86 (1957).
4. F. C. Langenberg, and F. J. Johnson, *Metal Progr.*, **78**, 69 (1960).
5. H. C. C. de Ruolz, *Berzelius Jahrbericht*, **22**, 410 (1841).
6. V. N. Mackiw, W. C. Lin, and W. Kunda, *J. Metals*, **9**, 786 (1957).
7. W. Kunda, D. J. I. Evans, and V. N. Mackiw, *Blanseeberichte für Pulvermetallurgie*, **12**, No. 3, 153 (Dec. 1964).
8. C. G. Fink and F. A. Rohrman, *Trans. Electrochem. Soc.*, **58**, 403 (1930).
9. K. K. Kershner, F. W. Hoertel, and J. C. Stahl, "Preparation of High Purity Nickel," U.S. Dept. of the Interior, Bureau of Mines, 1961, TN 23.U7 No. 5840.
10. P. C. L. Thorne and E. R. Roberts, "Inorganic Chemistry," p. 368, Oliver and Boyd, London (1954).
11. W. Kunda and D. J. I. Evans, "Controlling the Properties of Nickel Powders Produced by the Hydrogen Reduction of Nickel Ammine Sulphate Solutions," Paper presented at the Second European Symposium on Powder Metallurgy, Stuttgart, May 7-10, 1968.

The Sodium Amalgam-Oxygen Fuel Cell Application to the Chloro-Alkali Industry

J. Adrien LeDuc,* John G. Kourilo*,[1], and Charles Lurie*

The M. W. Kellogg Company, Electrochemical Research Section, Research and Engineering Development Department, Piscataway, New Jersey

ABSTRACT

The ability of the sodium amalgam-oxygen fuel cell to recover power consumed by mercury cells presently employed in the industrial production of chlorine and sodium hydroxide was studied. The effects of temperature, amalgam concentration, current density, as well as the nature of the electrodes, are presented. Results suggest that the power generated by the fuel cell can be supplied directly to the mercury cells on a continuous basis. The sodium amalgam-oxygen cell described operated at voltages up to 1.3v at a current density of 100 amp/ft^2 with special fuel cell cathodes. Utilization of this output would result in a power recovery of up to 35%.

The high conversion efficiencies attainable with fuel cells have stimulated many to consider their application by large energy consumers such as the electrochemical industry.

The production of chlorine and sodium hydroxide by electrolytic methods consumes large quantities of electrical energy. The power demand is becoming increasingly greater with the expansion of the industry. Because power costs represent a large portion of the operating expenses in a chloro-alkali installation, the combination of a sodium amalgam-oxygen fuel cell and a mercury electrolysis cell may become a requirement in the projected expansion of mercury cell plants (1). It is recognized that the extent of industrial application of the fuel cell will be dependent on certain economic factors, principally the power cost in areas where the installations might be considered.

The power recovered by the fuel cell, corrected for products and depreciation, is estimated at 3.5-4.5 mils/kwhr. If variations in local power costs are considered, savings of \$3-\$10/ton of chlorine can be realized.

The sodium amalgam-oxygen fuel cell is an electrochemical device involving the conversion of the free energy of a chemical reaction to useful electrical energy. Its fuel is the sodium of the amalgam, the liquid metal electrode generated continuously in a conventional electrolytic mercury cell. Normally, the amalgam produced by the electrolysis of sodium chloride brine is reacted with steam or water in a physically separated cell, called a denuder or decomposer, to form a sodium hydroxide solution of a concentration of about 50%.

If, however, the sodium amalgam is introduced as the fuel in a fuel cell, up to 35% of the power needed to operate the electrolytic plant may be recovered.

In the early development of mercury cathode cells, it was shown that a decomposer acts as a primary cell in which sodium hydroxide solution is formed as the result of short-circuiting the amalgam to a more noble metal such as iron (2). A simple voltaic cell is thus formed in which the amalgam is the anode and sodium hydroxide is produced. Actually, the mercury acts as a bipolar element: as an anode in the decomposer and as a cathode in the electrolysis cell. The possibility of coupling this primary cell to the electrolysis cell and reducing the voltage requirement on the order of 0.8v presented itself. Such systems are illustrated by Castner and Kellner Short-Circuit and Shunt cells, where large surfaces of iron or graphite are brought into direct contact with the amalgam and alkaline solutions (3). The major difficulty with these systems is that the sodium concentration at the amalgam electrolyte interface drops rapidly to a low value when current is passed and cannot be renewed at a sufficient rate to prevent the emf of the primary cell becoming almost zero.

Dony-Henault effected power recoveries of 13% at a current density of 100 ma/cm^2 and 8% at 200 ma/cm^2 utilizing a similar system (4). In the 1950's, Yeager at

* Electrochemical Society Active Member.
[1] Present address: Aerospace Information Division, Library of Congress, Washington, D. C.

Western Reserve University demonstrated that, when an oxygen half cell is coupled with the sodium amalgam half cell in the presence of low concentrations of alkali, a primary cell is formed capable of generating electrical energy (5).

This primary cell can be run to produce, in addition to the power recovery, 50% sodium hydroxide equivalent to the alkali strength presently made in the decomposer. However, one may elect to operate the fuel cell with 10-20% sodium hydroxide electrolyte (5) to recover higher electrical energy. In most installations, this would be at the expense of evaporation of the caustic liquor to 50% and removal of the heavy metallic impurities. This communication will deal with the 50% electrolyte system.

In a power recovery installation, the liquid sodium amalgam issuing from a mercury cell would constitute the anode, and oxygen or air diffusing through an activated porous electrode would be the cathode. The half-cell reactions of the system are:

Anode $2Na/Hg_x - 2e \rightarrow 2Na^+ + 2Hg_x$ [1]

Cathode $O_2 + 2e + H_2O \rightarrow OH^- + HO_2^-$ [2]

$HO_2^- \rightarrow OH^- + \frac{1}{2}O_2$ [3]

Over-all reaction:

$2Na/Hg_x + \frac{1}{2}O_2 + H_2O \rightarrow 2Na^+ + 2OH^- + 2Hg_x$ [4]

The anticipated performance of the system is calculated from the Nernst equation:

$$E = 1.89\frac{2.30\,RT}{n\mathbf{F}}\log\frac{(A_{Na^+})^2(A_{OH^-})(A_{HO_2^-})}{(A_{O_2})(A_{H_2O})(A_{Na/Hg})^2} \quad [5]$$

Because of the low values of the peroxide ion concentration and the difficulties inherent in its determination, it was of interest to calculate its effect on the oxygen half-cell potential. Figure 1 is a Nernst equation plot and depicts the relationship between cathode potential and peroxide ion concentration (6). The dependence of the amalgam half-cell potential on the sodium activity is shown in like manner in Fig. 2 (5).

Working voltages were calculated by subtracting *IR* drops and electrode polarization from the open-circuit potential estimated from Fig. 1 and 2 and are depicted in Fig. 3. The electrolyte *IR* drop was calculated from a 0.25-in. interelectrode spacing and 50% NaOH electrolyte at 150°F. Electrode *IR* drop assumes a 0.31-in. thick graphite electrode with a resistivity of 0.45 ohm-in. Miscellaneous losses were assigned a value equivalent to 50 mv at a current density of 100 amp/ft^2. The cathodic polarization depicted is the difference between the preceding *IR* losses and the experimental cathodic polarization data reported in Table I.

Experimental

The apparatus used in this investigation (Fig. 4) consists of a horizontal mercury cell (A) of the type currently employed in the industry and an amalgam-oxygen fuel cell (I). The amalgam produced in the mercury cell passes through a flow interrupter (C) to the anode of the fuel cell. The amalgam is depleted in sodium and returned to the mercury cell after flowing through a second interrupter (C). During operation, the mercury was continuously cycled through the system. Conventional steam decomposers (D) provided an alternate route for the amalgam. The fuel cell is composed of a steam-jacketed stainless steel container coated with epoxy resin. This unit contains the elec-

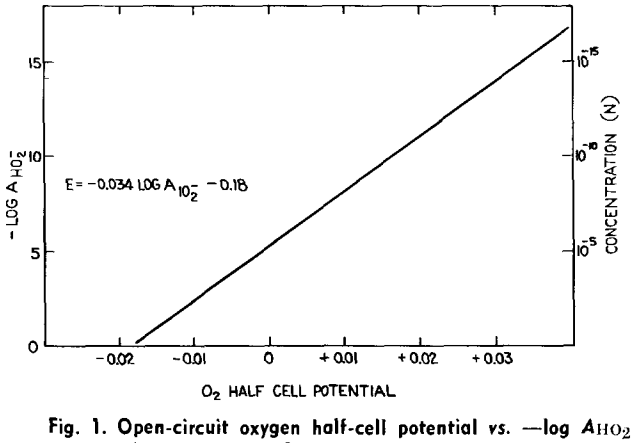

Fig. 1. Open-circuit oxygen half-cell potential *vs.* $-\log A_{HO_2^-}$ assuming: $A_{Na/Hg} = 10^{-2}$M, temperature = 150°F.

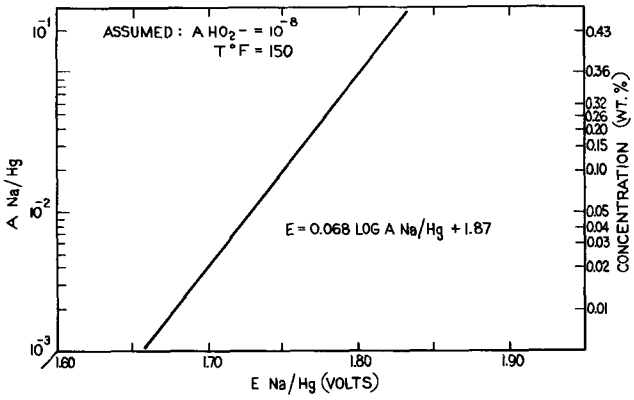

Fig. 2. Open-circuit amalgam half-cell potential *vs.* $A_{Na/Hg}$ assuming: $A_{HO_2^-} = 10^{-8}$M, temperature = 150°F.

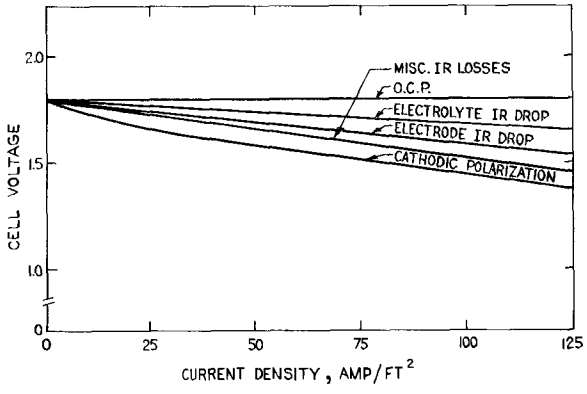

Fig. 3. Polarization and IR losses in the sodium amalgam-oxygen fuel cell assuming: amalgam concentration = 0.15 w/o (weight per cent), $A_{HO_2^-} = 10^{-8}$M, temperature = 200°F.

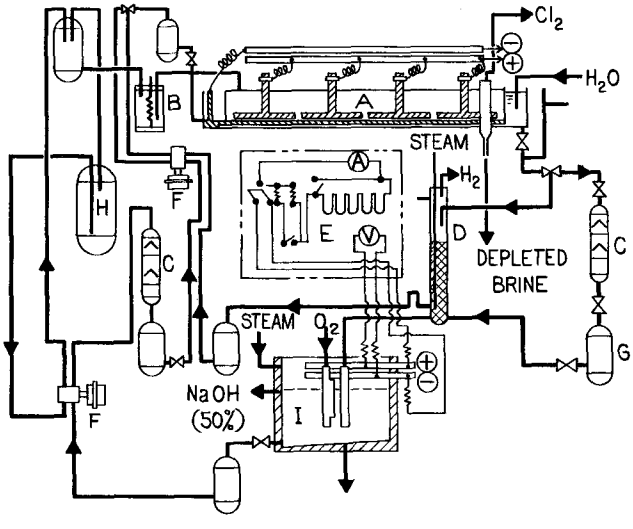

Fig. 4. Laboratory assembly: A—amalgam-producing cell, B—brine preheater, C—amalgam flow interruptors, D—amalgam decomposer, E—load circuit, F—sigma motor pump, G—amalgam preheater, H—brine storage, I—amalgam-oxygen cell.

trolyte and electrodes. The anode consists of a low-carbon steel plate whose surface is grooved and welded to a stainless steel frame. The plate and frame form an enclosure into which the amalgam flows. The amalgam overflows through a series of perforations at the top of the plate and flows downward in a continuous film. A porous electrode mounted on a steel frame similar to the anode structure forms the cathode. Oxygen or air is fed to the back of the cathode. The cathodes selected included plain and activated carbon, a commercial metallic electrode containing silver, and a new gas electrode under development at the M. W. Kellogg laboratories. The electrodes had an apparent area of 0.1-0.15 ft^2. The 48-50% NaOH electrolyte was stirred during certain experiments to assure uniform heating.

Working potentials and currents were measured with a vacuum tube voltmeter (V) and an ammeter (A). The presence of two flow interrupters (C) allowed the measurement of these values to be made independent of the performance of the mercury cell. The load imposed on the fuel cell was controlled with variable resistance (E). Half-cell measurements were made with a Luggin probe connected to a reference cell (Hg/HgO/50% NaOH) which was introduced at a point midway between the anode and cathode.

A rapid and accurate potentiometric method for determining the sodium concentration in the amalgam streams was developed. The details of this method are described elsewhere (7).

Discussion of Results

Electrodes.—Initial evaluation of the power recovery system consisted of determining the voltage-current density relationships for the system with various cathodes. Typical curves for carbon electrodes are depicted in Fig. 5. Curves 2 and 3 were obtained with two different activated porous carbon electrodes. Curve 4 represents untreated carbon and demonstrates the significance of the activating catalysts. Curve 1, which is calculated, assumes $(HO_2^-) = 10^{-8}$ moles/liter and is included for comparison. The open-circuit potentials were reproducible to ± 50 mv for different samples of similar electrodes. It is difficult to compare the experimental voltages with the calculated values because the activity of the peroxide ion is unknown. However, Fig. 1 and 2 indicate that for the activated electrodes the peroxide ion activity would be about 10^{-8} moles which does not seem unreasonable. Kordesch (8) has estimated that, with special peroxide-decomposing catalysts, values of 10^{-10} moles are attainable in KOH electrolyte hydrox systems. The role of the catalysts appears to be, at least in part, to decompose the peroxide ion. This effect has been previously studied and reported (9).

A current density of 100 amp/ft^2 was chosen as a reference point and all working voltages are compared at this current load. Voltages of 1.1 and 1.3v at 100 amp/ft^2 were observed with two different activated carbons. The untreated carbon yielded only 0.23v at 50 amp/ft^2. The calculated voltage assuming a peroxide ion concentration of 10^{-8} moles was found to be 1.4.

Two other types of electrodes were evaluated and the results are depicted in Fig. 6. Curves 1, 3, and 4 refer to specially treated silver electrodes obtained commercially and curve 2 refers to a new type of oxygen electrode under development at The M. W. Kellogg Research Laboratories.

In the course of this investigation, it was observed that when the fuel cell is initially subjected to a direct current from an external source complete wetting of the anode surface by the amalgam is obtained. It was also observed that the open-circuit potential and the working voltages increased. To determine the extent to which this effect is reproducible, a typical activated carbon electrode was tested in the fuel cell prior to current treatment. An open-circuit voltage of 1.55v was obtained. The cell was then subjected to the described treatment and an open-circuit voltage of 2.2-2.3v was observed. This potential was not stable and decayed to 1.55v. Measurements were made with an 11 meg vacuum tube voltmeter. The rate of decay is altered if the duration of the treatment with external current is varied. This phenomenon is depicted in Fig. 7.

One may attempt to explain this behavior by the oxidation of the catalytic species in the cathode; however, similar observations were made with leached, unactivated carbon electrodes whose metallic impurities content was not high enough to allow this explanation. It may be possible that the peroxide ion concentration is reduced drastically, in the immediate vicinity of the cathode, when a current is applied, and that this results in a higher initial cell voltage.

Amalgam concentration and depletion.—The sodium concentration in the amalgam has an effect on the voltage of the cell either at open circuit or under load. The results presented in Fig. 8 show the effect of inlet sodium amalgam concentration on open-circuit voltage. Under load, the inlet and outlet amalgam concentra-

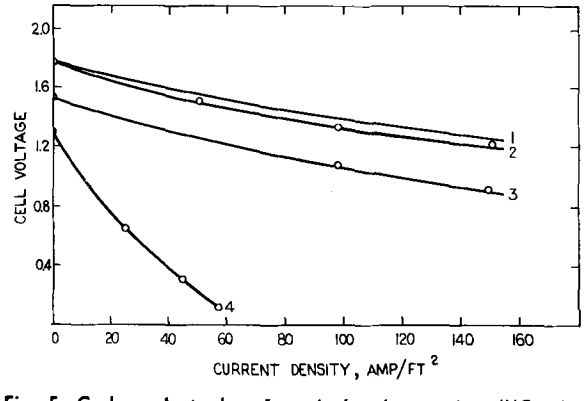

Fig. 5. Carbon electrodes: 1—calculated assuming $(HO_2^-) = 10^{-8}$M, 2—activated, 3—activated, 4—unactivated.

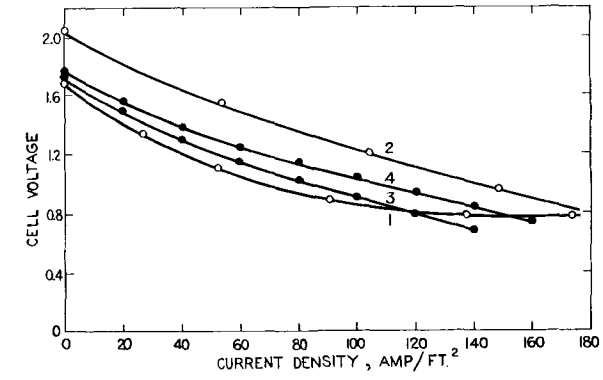

Fig. 6. Metallic electrode: 1—activated silver, 2—activated M. W. Kellogg, 3—activated silver, 4—activated silver.

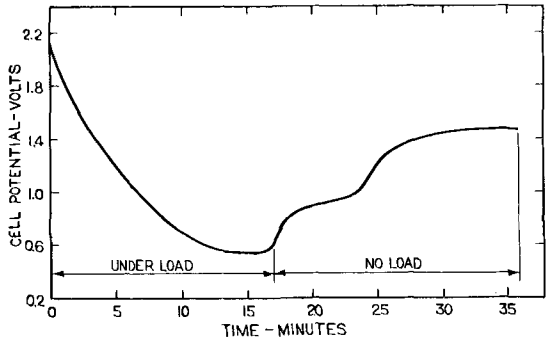

Fig. 7. Effect of current pretreatment on performance

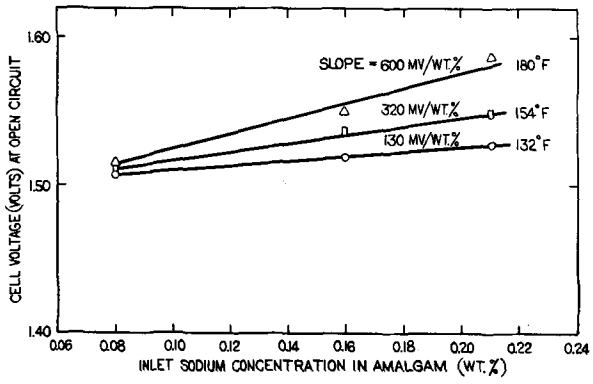

Fig. 8. Open-circuit cell voltage vs. inlet sodium amalgam concentration.

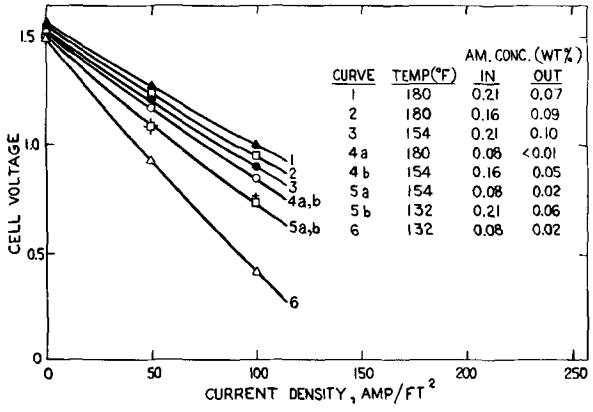

Fig. 9. Effect of amalgam concentration and temperature on performance.

tions may be correlated with the cell voltage. Figure 9 demonstrates the relationship of inlet and outlet amalgam concentrations to performance, particularly when under load. Figure 10 shows a typical effect of sodium depletion.

It was observed that the amalgam should contain a minimum of 0.01-0.02% sodium to promote wettability of the steel or nickel anode surface. This concentration minimum is applicable to the amalgam inlet and outlet streams.

Temperature.—The temperature range of 130°-180°F was investigated. The effect of temperature is shown by Fig. 9 and 10. At a current density of 100 amp/ft², an increase of 10 mv/°F was observed. The upper temperature limit is set by the chemical decomposition of the amalgam in the presence of the aqueous electrolyte.

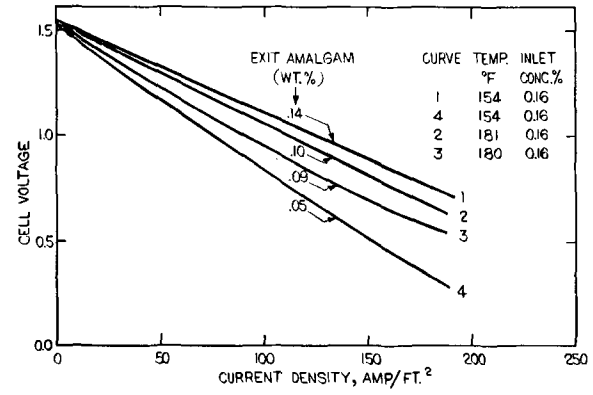

Fig. 10. Effect of amalgam depletion on performance

Table I. Polarization measurements

Cathode = Activated carbon
Electrolyte = 50% NaOH at 150°F
Reference Cell = Hg/HgO/50% NaOH

Current density, amp/ft²	Amalgam half cell, volts	Oxygen half cell, volts	Total cell, volts
2	1.631	−0.063	1.568
5	1.626	−0.087	1.539
21	1.591	−0.168	1.425
41	1.567	−0.213	1.351
117	1.456	−0.366	1.091
142	1.410	−0.453	0.962
200	1.326	−0.578	0.749
263	1.223	−0.729	0.496
309	1.147	−0.839	0.307

The reaction:

$$Na/Hg_x + H_2O \rightarrow NaOH + xHg + \tfrac{1}{2}H_2 \quad [10]$$

is not electrochemical and, therefore, causes low fuel efficiency. Above 180°F, hydrogen evolution becomes evident on the surface of amalgam in contact with the 50% NaOH electrolyte. When the cell was operated at 200°F, an unstable open-circuit potential of about 1.6v was observed.

Half-cell measurement.—It was of interest to determine the extent of anodic and cathodic polarization. A probe from a Hg/HgO/50% NaOH reference cell was inserted midway between the anode and cathode which were 0.25 in. apart. Table I is typical of the data obtained with activated carbon electrodes and demonstrates that oxygen half-cell polarization represents a prime area for system improvement.

Summary and Conclusions

This preliminary study has shown that a sodium amalgam-oxygen fuel cell is capable of generating electric power that can be supplied directly to a mercury cell of the type presently used in the industrial production of chlorine and sodium hydroxide. This cell is capable of delivering a voltage up to 1.3v at a current density of 100 amp/ft² with specially prepared and activated cathodes. The electrical energy recuperated with this type of performance can be equivalent to as much as 23-35% of the power consumed in present-day mercury cells.

Manuscript submitted Dec. 18, 1967; revised manuscript received Dec. 23, 1968.

Any discusson of this paper will appear in a Discussion Section to be published in the December 1969 JOURNAL.

REFERENCES

1. "1965 Chlor-Alkali Report," Presented at the Electrochem. Soc. Meeting, Cleveland, May 1-6, 1966.
2. C. L. Mantell, "Industrial Electrochemistry," p. 347-411, McGraw-Hill Book Co., Inc., New York (1950).
3. F. Foerster, "Elektrochemie Wasserigen Losungen," p. 711, Johann A. Barth, Leipzig (1922); Allmand and Ellingham, "Principles of Electrochemistry," p. 400, Longmans, Green, London (1924).
4. O. Dony-Henault and A. de Jaer, *Compt. Rend.*, **205**, 225 (1937).
5. E. Yeager, H. Dietrick, and F. Hovorka, Tech. Report No. 1, Contract No. Nonr 581(00), Dec. 1951; H. Dietrick, E. Yeager, and F. Hovorka, Tech. Report No. 3 ONR, Contract No. Nonr 581(00), April, 1953.
6. W. G. Berl, *Trans. Electrochem. Soc.*, **83**, 253 (1943).
7. J. A. LeDuc, C. Lurie, and J. Kourilo, *This Journal*, **112**, 870 (1965).
8. K. Kordesch, in "Fuel Cells" Edited by G. J. Young, p. 14, Reinhold Publishing Corp., New York (1960).
9. K. Kordesch and A. Marko, *Oesterr. Chem. Ztg.*, **52**, 125 (1951); W. Vielstich, *Z. Physik. Chem.*, **15**, 409 (1958).

JOURNAL OF THE ELECTROCHEMICAL SOCIETY

REVIEWS AND NEWS

JANUARY 1969

Solid Electrolyte Galvanic Cells

R. T. Foley*

Chemistry Department, The American University, Washington, D. C.

There has been a renewed interest in solid electrolyte galvanic cells during recent years because such cells offer solutions to several problems encountered with aqueous systems. One conspicuous shortcoming of aqueous systems is the limited shelf life of the cell which results from corrosion reactions of the electrode materials in highly conducting electrolytes. A second problem is cell leakage and the need to use special sealing techniques. A third limitation is the rather short temperature range over which these cells can efficiently operate. Finally, there is the need, in many applications, to achieve appreciable miniaturization. These are problem areas in which solid electrolyte galvanic cells offer solutions or the promise of improvement over the present situation.

The renewed interest in this field has coincided with the improvement in certain solid electrolytes and the achievement of a better understanding of the mechanism of transport in these solid ionic materials. Further, in the last decade there have been great advances in techniques whereby thin layers may be vacuum deposited. This has made available methods of fabricating cells with electrolytes with very high area to thickness ratios with resulting high internal conductivity.

The purpose of this review is to appraise the state of the art in this field. Major attention is given to the employment of solid electrolyte cells for energy conversion purposes which explains the detailed discussion of cells utilizing electrolytes such as AgI, one of the better ionic conductors. The study is restricted to low-temperature cells which operate at about 300°C, or lower, as distinguished from cells requiring higher temperatures for (oxide ion) conduction. A further restriction excludes those systems that require water for conduction, such as ion exchange membranes or certain inorganic gels. Raleigh (1) has recently reviewed solid state electrochemistry from the viewpoint of utilizing solid electrolyte galvanic cells for the study of solid state reactions, for the determination of free energies of compound formation, related thermodynamic quantities, and the electronic and ionic conductivity of compounds. These subjects are discussed here only where pertinent to the cell in a power producing capacity.

Historical development.—The fact that solid crystalline compounds could function as electrolytes was recognized early in the development of electrochemistry. Haber and Tolloczko as early as 1904 (2) measured the emf's of the cells

$$Pb/PbCl_2/AgCl/Ag \qquad (I)$$

and

$$Cu/CuCl/AgCl/Ag \qquad (II)$$

over the temperature range of 145°-250°C. The open-circuit voltage of cell I was 0.477v at 145° and 0.500v at 250°C. Cell II gave voltages of 0.150v at 150°C and 0.187v at 240°C. These values were essentially in agreement with what was calculated from thermochemical data for the cell reaction. No current was drawn from these cells. In fact, the experimental arrangement, involving a U-tube with substantial distance between the two electrodes, was such that the internal resistance was too high for appreciable current to pass.

Katayama (3) in 1908 constructed and made measurements on three types of cells utilizing solid electrolytes. These included lead amalgam concentration cells of the type:

$$\text{Amalgam I}/PbBr_2/\text{Amalgam II} \qquad (III)$$

chemical cells such as

$$Pb/PbBr_2/Br_2 \qquad (IV)$$

and

$$Ag/AgCl/Cl_2 \qquad (V)$$

and Daniell type cells as

$$Pb/PbBr_2/AgBr/Ag \qquad (VI)$$

and

$$Pb/PbCl_2/AgCl/Ag \qquad (I)$$

The potential of the AgCl chemical cell (V) was measured over the temperature range of 15°-159°C. The emf was described by

$$E = 1.130 + 0.0006\ (20 - t°)$$

The lead chloride-silver chloride cell gave an emf relationship of

$$E = 0.480 + 0.0001\ (60 - t°C)$$

These relations were in agreement with Haber's earlier results and have been confirmed by present day measurements. Lorenz and Katayama (4) showed that the electrical energy developed by these cells could be calculated from the heat of the chemical reaction. The Gibbs-Helmholtz equation, modified for a constant pressure process, was applicable. At approximately the same time, Beutner (5) used measurements on solid electrolyte galvanic cells to study the reactions of various salts in the solid state.

Significant advances in the understanding of the mechanism of conduction as well as the operation of solid electrolyte cells were made by Tubandt and his co-workers. Tubandt and Lorenz (6) published conductivity data for AgCl, AgBr, AgI, TlCl, TlBr, and TlI over the temperature range 100°-700°C. They also observed (7) that Faraday's laws held in the silver halides and they noted the very high mobility of the Ag ion (1.13×10^{-3} cm sec^{-1}) in AgI in the neighborhood of its melting point. Tubandt and Eggert (8) ex-

* Electrochemical Society Active Member.

tended the test of the applicability of Faraday's law to crystals of AgCl, AgBr, $AgNO_3$, $PbCl_2$, $PbBr_2$, and PbI_2. The problem of dendrite formation and consequent short-circuiting of the cell during deposition of the silver was recognized as a problem. These investigators introduced the technique of measuring transference numbers by the isolation and observation of weight changes in the anode and cathode portion of the cell similar to what had been done in aqueous solutions (Hittorf technique). Tubandt (9) recognized the several different types of conductivity that existed in these crystals. For example, conduction in AgI was mainly due to Ag ions, and in $PbCl_2$ the anion migrated as well. In certain crystals, *e.g.* β-Ag_2S between 150°-170°C, the current was carried by electrons as well as ions.

Reinhold in 1928 (10) studied solid electrolyte cells as thermoelements over the temperature range of 150°-500°C. He investigated solid electrolyte thermoelectric elements, as exemplified by

$$Ag/AgI/Ag \quad (VII)$$

$$Ag/AgCl/Ag \quad (VIII)$$

$$Ag/AgBr/Ag \quad (IX)$$

$$Pb/PbCl_2/Pb \quad (X)$$

$$Cl_2/AgCl/Cl_2 \quad (XI)$$

$$Br_2/AgBr/Br_2 \quad (XII)$$

$$Cl_2/PbCl_2/Cl_2 \quad (XIII)$$

in which the thermoelectric power was generated by the anode and cathode held at different temperatures. It is significant that gas electrodes, which exhibit a higher thermogalvanic voltage and represent the more sophisticated case in thermogalvanic technology, as well as metallic electrodes, were considered as thermogalvanic elements. Reinhold (10) also investigated "solid isothermal" galvanic cells such as

$$Ag/AgCl/Cl_2 \quad (V)$$

$$Ag/AgBr/Br_2 \quad (XIV)$$

$$Pb/PbCl_2/Cl_2 \quad (XV)$$

and

$$Pb/PbCl_2/AgCl/Ag \quad (I)$$

recognized as "chemical" cells and Daniell-type cell, respectively. The emf measurements made on the lead chloride-silver chloride cell (I) were compared by Reinhold to those reported by Haber and Katayama as follows:

Temp, °C	Katayama	Haber	Reinhold
67	0.480	—	0.488
151	0.471	0.480	0.472
200	—	0.492	0.463
250	—	0.500	0.451

The good agreement at the lower temperatures is obvious.

For all of these systems, the Nernst heat theorem applies. Reinhold and Blachney (11) extended the theory and experimental work to cells such as

$$Ag/AgCl/PbCl_2/AgCl/Ag \quad (XVI)$$

and

$$Pb/PbCl_2/AgCl/PbCl_2/Ag \quad (XVII)$$

which involved the transfer of ions across electrolyte/electrolyte interfaces. It was shown that the thermogalvanic emf of a multiple system such as those indicated above was additive from the standpoint of the simpler elements, *e.g.*, $Ag/AgCl/Cl_2$ (V).

At the same time (1934), Reinhold (12) and Wagner (13) used solid electrolyte cells to study tarnishing and corrosion reactions using slightly different techniques. To study the reaction

$$2\,Ag + S = Ag_2S$$

a cell such as

$$Ag/AgI/Ag_2S/Pt(S) \quad (XVIII)$$

was required rather than the simpler cell

$$Ag/Ag_2S/Pt(+S) \quad (XIX)$$

because Ag_2S is a mixed (ionic and electronic) conductor.

Thus, by the early 1930's it had been demonstrated that solid electrolytes could be treated entirely the same as aqueous electrolytes from the viewpoint of the theory of chemical and concentration cells, conduction mechanisms, equilibrium reactions, and thermodynamics.

There was little work reported in this field in the late 1930's and in the 1940's, but studies were revived during the early 1950's with Sator's work (14) on vacuum-deposited films and intensive studies of gas depolarized cells to be discussed below. During the 1950's, a large number of studies were reported in the patent literature, in the open literature, and in reports on government-sponsored research. The major problem holding up substantial development of this type of cell was the relatively low conductance of the electrolyte at room temperature in comparison with aqueous electrolytes and at elevated temperatures in comparison with fused salt systems. Techniques to achieve electrolytes with substantially improved conductivity have been realized during the last decade. A further problem has been one of constructing the solid electrolyte cell so that low internal resistances could be achieved. The employment of vacuum-deposited films has made for improvement in this respect.

Solid Electrolytes

A logical basis for discussing solid electrolytes can be based on the nature of the basic transport process, as suggested by van der Grinten (15). This would distinguish cases utilizing (*a*) Ag^+ transport, (*b*) Cl^- transport, (*c*) Na^+ transport, (*d*) H^+ transport, and (*e*) cases wherein the transport is unknown, *e.g.* the tin sulfate case discussed below.

Solid Electrolytes with Ag^+ Transport.—Most of the work reported on solid electrolyte galvanic cells has been based on the transport of Ag cations through silver halides. This is best understood by considering the unusual structure of AgI and the related compound $Ag_2\,Hg\,I_4$.

The use of the silver halides for current-producing cells was based initially on the conductivity data of Tubandt and Lorenz (6, 7). In the study of the temperature dependence of the specific conductance of the halides of silver and thallium over the range 100°-700°C, the unusual behavior of AgI was noted. Unlike the other halides of silver and thallium, the conductivity of AgI rose sharply as it went from the liquid to the solid state. On further cooling, the conductivity-temperature curve had a slope more characteristic of aqueous solutions than the other solid crystals. In the region of the melting point, the mobility of Ag^+ in AgI was approximately double the mobility of Ag^+ in aqueous solutions. As a result of these findings and their subsequent verification, many galvanic cells were based on AgI as the electrolyte.

AgI undergoes a transition from its low-temperature, low-conductance, beta form to its high-temperature, high-conductance, alpha form at 145.80°C according to Tubandt (16). Jost *et al.* (17) reported $\beta \rightarrow \alpha$ transition temperatures of 143.8°, 144.4°, and 146.7° depending on the rate of heating. Lieser (18) found the transition temperature with certain samples at 153.3° and at 149.3° with a sample that had been heated at 300°-450° for a period of time implying some sort of aging effect. The generally accepted transition temperature is 145°-146°C. A third modification of AgI, with an undefined crystal form, stable above 2940 kg/cm² pressure has also been reported (93).

The alpha form of AgI is stable in the temperature range 146°-552°C. The structure and deficiency order of α-AgI has been the subject of a number of investigations. Lieser (19) made dilatometric measurements and structure (x-ray) measurements on the AgI system from —187°C to above the transition point. He observed a negative dilation coefficient in β-AgI over the temperature range studied, a fact important in the employment of this electrolyte in thermogalvanic cells. Jost *et al.* (20) report similar results and characterized α-AgI as a body-centered cubic structure of I^- ions with disordered cations. Lieser (21) reports a lattice constant of $a = 5.046 \pm 0.02$Å at 150°C. In going from the β-form to the α-form, the conductivity of the crystal increases by a factor of about 4000 (8); the resistivity of α-AgI is 0.38 ohm-cm at 500°C and 0.47 ohm-cm at 350°C (21).

The current in AgI is carried almost exclusively by Ag ions, the transport number of Ag being very close to unity as demonstrated by Tubandt (16). The self-diffusion rate of I^- in α-AgI was measured by Jost and Nölting (22) and their data were expressed by the equation

$$D = (4.41 \times 10^{-4})\, e^{\frac{-16.2}{RT}} \text{ cm}^2/\text{sec}$$

Electronic conductivity is also low. Jost and Weiss (23) reported an electronic transport number of about 10^{-7} at an I_2 partial pressure of 3 mm Hg at 179°C. Ilschner (24) used a direct polarization method to measure electronic conduction. A value for the electron hole conductivity of about 10^{-5}-10^{-6} ohm^{-1} cm^{-1} may be read from the plotted data. At elevated pressure, the conduction mechanism changes, the formation of free silver at pressures of 2 and 4 kilobars being indicated (25). Many similar studies on structure and conduction mechanism have been carried out on the other silver halides, but only the work on silver iodide is discussed here because of the unique electrochemical properties of this compound.

The increased conductivity achieved by working above the transition point, *i.e.*, with the highly conducting α-AgI, was demonstrated by Weininger (26) with batteries composed of a number of gas-activated cells of the type

$$\text{Ag/AgI/I}_2\text{ (Pt)} \qquad \text{(XX)}$$

Temp of cell operation, °C	Open-circuit voltage, v	Short-circuit current, μa
25	6	1
200	6	1000

A number of attempts have been made to improve the conductivity of the silver halides. AgI is highly conducting in its high-temperature form, *i.e.* the form stable over 146°C. It would be desirable to render this highly conductive structure stable at room temperature. Weiss, Jost, and Oel (27) measured the electrical conductivity and phase changes in the systems β-AgI-CdI_2, β-AgI-PbI_2, β-AgI-Ag_2Se, β-AgI-KI, and α-AgI-PbI_2 (and CdI_2). The temperature at which the β-form is converted to the α-form is lowered by the addition of PbI_2, *e.g.* from 144.6° to 100°-101° by the addition of 5 mole % PbI_2. The conductivity of the mixed crystal is lower than that of pure AgI. At 120°, the relative conductivity of the 5 mole % compound is about 18% that of the pure AgI. The mixed crystal system of β-AgI-KI was studied but only at low concentrations (0.5 mole %) of KI. Only in the last decade has this system been fully explored. The use of an electrolyte modified by the addition of lead iodide or cadmium iodide in a vapor-activated cell was proposed by Weininger (28).

According to Lieb and De Rosa, additions of tellurium to the silver halide greatly reduced its resistance (29). For example, the resistance of AgCl at 100°C was reduced from 7.7×10^6 ohms to 2.3×10^3 ohms by the addition of 5% Te. Additions of 3-10% were claimed to give this beneficial effect with 5% being the optimum value. The internal resistance of a cell of the type

$$\text{Ag/AgBr/CuBr}_2\text{(C)} \qquad \text{(XXI)}$$

was decreased from 114 to 18K by the incorporation of 5% Te in the AgBr electrolyte. A 16-μa current was observed with an external load equal to the cell resistance.

Lehovec (30) claimed a galvanic cell in which the improved electrolyte was a crystalline compound possessing lattice defects. An example of this galvanic cell was

$$\text{Ag/AgCl (10\% PbCl}_2\text{)/Pb} \qquad \text{(XXII)}$$

The electrolytes were such crystals as 10% $CdCl_2$ in AgCl, 15% $CaCl_2$ in Hg_2Cl_2, 10% $SbCl_3$ in $PbCl_2$, and 12% $BiCl_3$ in $ZnCl_2$. In addition to cation doping, Lehovec and Smyth (31, 32) cited improvements to be gained in the conductivity of silver halides by the addition of anions such as $Te^=$, $Se^=$, or $S^=$. This improvement occurred for additions low in concentration but greater than 0.1 m/o (mole per cent). The addition of Ag_2S to AgCl in amounts up to 0.1 m/o caused an increase of resistance from 7-10 to 30-40 megohm-cm. However, further additions caused a linear decrease in resistance. The mixture with 1 m/o sulfide had a resistance of 3 megohm-cm, and that with 6 m/o 0.4-0.5 megohm-cm.

In recent years, effort has been devoted to the improvement of the AgI electrolyte by modifying its crystal structure. The preparation of α-Ag_3SI, its crystal structure, and the temperature dependence of the electrical conductivities of the α and β forms were worked out and reported by Reuter and Hardel (34). Takahashi and Yamamoto (33) reported a conductivity of about 10^{-2} ohm^{-1} cm^{-1} for the compound at room temperature with the conduction mechanism similar to that of AgI, *i.e.*, the transference number for Ag^+ was measured as 0.977. This conductance figure agrees approximately with the (extrapolated) value reported by Reuter and Hardel in their early work (34) and confirmed in their recent more complete investigation of the conduction mechanism (94).

A number of widely differing values have been reported for the electronic conduction of Ag_3SI. Takahashi and Yamamoto have reported 10^{-8} (33), 10^{-6} (95), and 10^{-4} ohm^{-1} cm^{-1} (96). An extrapolated figure from Reuter and Hardel's recent work (94) would fall between 10^{-4}-10^{-5} ohm^{-1} cm^{-1}. It is very likely that all of these are correct for the particular samples tested, with the discrepancy caused by the metal/nonmetal ratio in the sample reflecting, in turn, the method of preparation as observed by Takahashi and Yamamoto (96). Values as high as 10^{-4} ohm^{-1} cm^{-1} would be undesirable from the standpoint of tarnish rate and long-term stability. The galvanic cell

$$\text{Ag/Ag}_3\text{SI/I}_2\text{(C)} \qquad \text{(XXIII)}$$

was investigated. The open-circuit voltage was close to that calculated from free energy data and iodine vapor pressure relationships. At 20.0°C, the experimental cell voltage was 0.675v as compared with a calculated 0.687v. The internal resistance of the above cell constructed with an electrolyte thickness of 0.15 cm was 10 ohms and the cell voltage did not decay at 100 μa/cm² current density. The polarization was essentially due to the silver anode, but it was found that this could be considerably improved by amalgamation; *e.g.*, relatively little polarization was observed at 1000 μa/cm² at 25°C. Cathode polarization was improved by the selection of the proper carbon; in the case reported, an acetylene black gave the best results. In the improved cell with the Ag_3SI electrolyte, only slight polarization (less than 10 mv) was observed at a current density of 1000 μa/cm² at 25°C. The cell could be discharged at a 1-ma/cm² rate for 3-4 hr with a relatively flat voltage curve. The polarization

behavior of the silver electrode, amalgamated and unamalgamated, was explained by the degree of reaction polarization (35). Up until this point in the investigation of solid electrolytes, the internal resistance of the solid electrolyte itself had been so high that only resistance polarization had been measured. The rate-determining step accounting for polarization in the cell containing the silver plate anode was established as the reaction between interstitial silver ions and silver-ion vacancies. In the amalgamated silver electrode case, the interstitial silver ion reacted with mercury and the reaction polarization was not observed.

Owens and Argue (36) questioned the long-term stability of cells using the Ag_3SI electrolyte and I_2 as the cathode material. They showed experimentally that the reaction

$$I_2 + Ag_3SI \rightarrow 3AgI + S$$

proceeded readily at 65° and 70°. Therefore, upon standing, the cell described above should convert to a cell

$$Ag/Ag_3SI/AgI, S/I_2(C) \qquad (XXIV)$$

with a corresponding increase in internal resistance. The argument offered by Owens and Argue appears convincing, but it is difficult to reconcile these with the results reported by Takahashi and Yamamoto. A possible explanation might be that the former studies were carried out at 65° and 70° where the reaction rate should be considerably greater than at room temperature. These effects would be expected to show up after several years of storage, however.

Recently, improvements in the AgI electrolyte have been reported by Bradley and Greene (37, 38) and Owens and Argue (39). These involved double salts such as KAg_4I_5 and $RbAg_4I_5$. The quantitative values for the conductivities differed between the two laboratories with Owens and Argue reporting the higher values, *i.e.* 0.21 ohm^{-1} cm^{-1} for both the K and the Rb salts at 20°C. Their explanation, which appears reasonable, was that the English investigators had a high contact resistance in their conductivity specimen. These crystals transformed from the high-temperature, highly conductive, α form to the β form at −136°C (KAg_4I_5) and −155 ($RbAg_4I_5$). Bradley and Greene (37) measured transport numbers and found that the current was essentially all carried by Ag^+ and that there was no change in composition of the anolyte or catholyte after electrolysis. Geller (40) reported on the crystal structure of the highly conductive solid electrolyte, $RbAg_4I_5$, as did Bradley and Greene (41). The latter described the structure of M Ag_4I_5 (where M = K, Rb, NH_4) as consisting of Ag^+ essentially in a liquid state inside of a crystal lattice of I^- and M^+ ions. This explains the high mobility of the Ag^+ ions. The structure that they proposed accounts on a geometrical basis for the experimental fact that the K^+, Rb^+, and NH_4^+ compounds have been found but the Cs^+ and Na^+ compounds have not. The Cs^+ ion is too large and the Na^+ is too small to produce stable structures, while the other three ions are the proper size, the ideal M^+ to I^- distance being 3.62Å.

The electrochemical behavior of the α form of Ag_2HgI_4 is similar in several respects to that of the high-temperature form of AgI. Ketelaar measured the electrical conductivity of this crystal (42) and discussed the relation between conduction and structure (43). He interpreted the high conductivity of α-Ag_2HgI_4 as a result of an averaged structure in which the number of atoms in the crystal was smaller than the number of lattice points among which they were distributed. On an average, every fourth lattice point was unoccupied. Although silver ions and mercury ions are present in the structure, only about 6% of the charge is transferred by mercury ions. The conductivity data reported by Ketelaar for α-Ag_2HgI_4 appear to be too high on the basis of later investigations. Suchow and Pond (44) measured the temperature of phase change and the electrical conductivity of Ag_2HgI_4, Cu_2HgI_4, and their eutectoid. Their transition temperatures are in agreement with Ketelaar's and approximate those reported by Jaffray (45, 46).

Substance	Suchow & Pond	Ketelaar	Jaffray
Ag_2HgI_4	50.0°	50.7°	57°
Cu_2HgI_4	66.6°		72°
$Ag_{1.14}Cu_{0.86}HgI_4$	34.2°		

However, the electrical conductivity data are at variance and, in view of the fact that the data of Suchow and Pond (44) have been substantially confirmed by the recent work of Weil and Lawson (47), the later work is taken as correct. The ionic conductivity has been expressed by the equation

$$\sigma = \sigma_0 e^{-Q/RT}$$

where σ is the specific conductivity at absolute temperature T, σ_0 is a constant, Q is an activation energy, and R the gas constant.

The comparison of the several investigations is as follows:

	Suchow and Pond (44)	Ketelaar (43)	Weil and Lawson (47)
Q (cal/g-atom)	10,200	8600	12,100
σ_0 (ohm^{-1} cm^{-1})	7.5×10^3	4×10^2	

Weil and Lawson (47) investigated the pressure dependence of the electrical conductivity of Ag_2HgI_4 as well as the transport properties. Measurements made at 80°C indicated a low electronic conductivity about 10^{-4} ohm^{-1} cm^{-1}, and an ionic conductivity of about 3×10^{-2} ohm^{-1} cm^{-1}. They pointed out some of the difficulties in making d-c conductivity measurements. As a d-c voltage was maintained on the α-Ag_2HgI_4 crystal between electrodes, silver was deposited at the cathode and HgI_2 and I_2 at the anode. Both the ionic and electronic conductivity dropped and the cell was converted to a galvanic cell with an emf of 0.6v.

In several instances, cells have been constructed wherein two electrolytes were used in a series arrangement. Lehovec and Broder (48) utilized the desirable high ionic conductivity of AgI and Ag_2S at elevated temperatures (about 200°C). They worked with cells of two types. The first was

$$Ag/AgI/Ag_2S/S \qquad (XVIII)$$

the role of AgI being to reduce electronic conductance within the cell. This cell had an open-circuit voltage of 0.2v at 200°C which approximated the value calculated from the free energy of the reaction between Ag and S. A short-circuit current of 0.18 amp/cm^2 and a shelf life of 100 min at 200°C was observed. These operating characteristics were compared to those of a second cell

$$Ag/AgI/I_2\ (C) \qquad (XX)$$

which operated at room temperature at current densities of several hundred microamperes and an emf of 0.7v.

An investigation by Smyth and coworkers (49) dealt with XX which was similar to that previously disclosed by Broder (50). An extensive study of the tarnishing of Ag in I_2 atmospheres was conducted on the basis that the shelf life of the cell was limited by electronic leakage through the electrolyte. The rate of consumption of the electrode material was determined by the reaction of Ag and I_2, which tarnish reaction was governed by the diffusion of cations and electrons through the reaction product film. The tarnish rate was found to be sufficiently rapid so that the $Ag/AgI/I_2$ cell system did not retain sufficient shelf life to be of practical interest in the application of interest to the investigators. To overcome this deficiency, the system

$$Ag/AgCl/AgI/I_2 \qquad (XXV)$$

was taken up. This system offered improvement but only partial solution to certain electrochemical and mechanical problems. The disadvantages of this system were the low emf of 0.684v (20°C) and the requirement that the AgCl film over Ag must be nonporous to prevent attack on the Ag and preserve a long life on open circuit. It was further noted that the I_2 vapor was corrosive to the organic compounds used in sealing the cells.

The tarnishing reaction of silver by bromine and iodine was studied by Weininger (51) in connection with the vapor-activated cell with the respective silver halide electrolyte. This study was conducted from the viewpoint of preparing the solid electrolyte film and also contributed to an understanding of the storage problem discussed above. The halide electrolyte formed at room temperature was relatively impervious as shown by photomicrographs. The rate-determining step was established as the diffusion of defect electrons which migrate in a direction opposite to that of silver ions. In common with many other investigations, the presence of water vapor was found to be important, the tarnish rate being reduced by a factor of two in the presence of water vapor.

In the investigation of cells utilizing silver iodide as an electrolyte, Buchinski *et al.* (52) found that a more adherent silver iodide film was formed on silver if the silver contained low alloying contents of Cu and Si (0.05-0.15% and 0.01-0.15%, respectively).

Solid Electrolytes with Cl^- Transport.—In the halide salts of certain bivalent metals, such as $PbCl_2$ and $BaCl_2$, current is carried by anions as well as cations. For example, in the temperature range of 200°-450°, the transference number of the anion is about unity (53). Data have been reported for elevated temperatures but very little for ambient temperature. For room temperature, the ionic conductivities of these halides are quite low and it is likely that both the cation and anion carry equivalent currents. Cl^- transport is involved in the operation of the rechargeable cell

$$Pb/PbCl_2/AgCl/Ag \qquad (I)$$

studied extensively by Sator (53) and discussed below.

Solid Electrolytes with Na^+ Transport.—Alkaline aluminates of the "beta-alumina" type are examples of structures in which Na^+ (as well as other cations) are transported. Beta-alumina is an example of a solid, relatively low-temperature, electrolyte and for that reason is briefly mentioned here. Its significant employment has not been in a solid galvanic cell but one in which both the anode and the cathode were liquids.

Ridgway *et al.* (54) concluded from their experimental results that beta-alumina was not an allotropic modification of alumina as commonly thought at that time (1936) but rather was an alkaline aluminate with the approximate formula of $Na_2O \cdot 12\ Al_2O_3$ or $K_2O \cdot 12\ Al_2O_3$ depending on the cation involved. The transport properties of beta-alumina were determined by Yao and Kummer (55) who measured the self-diffusion coefficients of Na^+, Ag^+, K^+, Rb^+, and Li^+ in single crystals. Of the ions studied, Na^+ had the highest rate, about 1×10^{-5} cm²/sec at 300°C and 40×10^{-7} cm²/sec at 25°C. The mechanism appeared to be interstitial rather than a vacancy movement. The secondary battery reported by Weber and Kummer (56) utilized an anode of liquid sodium, the sodium aluminate electrolyte, and a liquid sulfur cathode. The electrolyte that they used was a sintered product with a resistance of 3-5 ohm-cm at 300°C and about 250 ohm-cm at 25°C. For this reason as well as the need to maintain the cell products in the molten state to prevent excessive polarization, it was necessary to operate the cell above 250°C. At these temperatures, the cell operated at about 2.0v and a current density of 170 ma/cm² of electrolyte surface.

Solid Electrolytes with H^+ Transport.—Very little experimental work has been reported on proton conduction in (anhydrous) solids although such a mechanism would be of considerable significance in galvanic cells. Proton mobility in ice has been found to be appreciably higher than that of any other ionic mobility in a liquid or solid including that of H^+ in water. The experimental data on mobility and conductivity in ice along with theoretical explanations have been summarized by Eigen and de Maeyer (57). Extrapolated values for the specific conductance of water and ice at 0°C are 1.2×10^{-8} and 0.3×10^{-8} $ohm^{-1}\ cm^{-1}$, respectively. Whereas the proton concentration in ice is lower than that in water by a factor of about 2, the proton mobility is higher by 1 or 2 orders of magnitude. Proton transport in ice is much greater than that of other reported ionic mobilities but it differs by only a factor of 50 from electronic mobilities in semiconductors. Eigen and de Maeyer (57) thus consider the ice crystal as a "protonic semiconductor."

The hydrogen bonded structures represented by water and ice are unique and extreme care must be taken before extrapolating this thinking to other systems. Similar theoretical reasoning was cited in the development of solid electrolytes with proton conduction (58). The solid electrolyte was a mixture of urea or a urea derivative with an organic acid. Typical mixtures were urea and formic acid, thiourea and citric acid, or thiourea and toluene sulfonic acid. A mixture of 100g of urea and 8g of acetic acid yielded a conductivity of 5×10^{-3} $ohm^{-1}\ cm^{-1}$** at ambient temperatures. The conductivity of this solid compound was 10^4 greater than that of silver halides at the same temperature. This electrolyte supposedly could be employed in a galvanic cell with a hydrogen electrode (anode), which might be a catalytic electrode or a metal hydride. The cathode could be manganese dioxide, silver iodide, or oxygen.

Solid Electrolytes with Other Species.—Solid electrolyte cells capable of producing high potentials but limited to low currents were described by Ruben (59-61). Cells of the composition

$$Ni/tin\ sulfate/lead\ peroxide \qquad (XXVI)$$

supplied 1.65v and "several microamperes." A modification of this cell but not an improvement (60) substituted bismuth sulfate or antimony sulfate for the tin sulfate. These were hydrolyzable salts, and cells composed of these electrolytes were capable of holding potentials for long times. However, of the sulfates mentioned, tin sulfate was preferred because it was not hydroscopic (61). It was further pointed out that permanganates such as barium permanganate offered improved cathode depolarization so that a preferred cell was

$$Ni/tin\ sulfate/barium\ permanganate + carbon \qquad (XXVII)$$

This cell operated at 1.42v. These systems, described as "potential producing cells," were characterized by current output in the "several microampere" range. This appears reasonable in view of the fact that there was no apparent allowance for anode depolarization unless a redox reaction involving the electrolyte was involved. Typical cell thicknesses were 0.031 in. with the tin sulfate electrolyte contributing 0.020 in. and the Ni-plated steel anode 0.005 in.

Anodic and Cathodic Reactions

The greater part of the experimental work on solid electrolyte galvanic cells has involved cell reactions between silver and the halogens or sulfur. The anode

** Units of ohm-cm were given in the patent.

was furnished as silver strip, foil, or as a vacuum-deposited layer. As was mentioned above, Buchinski and co-workers (52) found that Cu and Si in low alloying concentrations improved the adherence of the AgI film subsequently formed. But, apparently very little effort has been expended to improve the anode reaction. As was pointed out by Takahashi and Yamamoto (33), anode polarization became obvious as a problem only when electrolytes of greatly improved electrical conductivity became available. The polarization due to the silver anode was effectively countered by amalgamation so that current densities of 1000 μa/cm^2 could be sustained at 25°C. Mrgudich, in an investigation of the conductivity of AgI, also found that electrode polarization could be greatly reduced by amalgamation of the silver electrode (62).

In the investigation of thin films, the interaction of the vacuum-deposited film with the substrate (the anode) was observed by Kostyshin (63). For example, films of PbI_2 and CuCl deposited on metal substrates such as Ag, Pb, or Cu show a greatly enhanced photographic sensitivity over that observed when similar materials are deposited on dielectric substrate. The reaction of the silver anode with halogen vapor upon storage was discussed above in connection with the use of AgCl layers in series with AgI layers.

When the anodic reaction was the oxidation of Ag, the cathodic reaction was usually based on the reduction of sulfur, a halogen, or a halogen-producing compound. The emf for the cell was then derived from the free energy decrease associated with the reaction between Ag and the cathode material. Some of the early work used a sulfur cathode. Lehovec (64) in his patent made a broad claim of a primary cell comprising . . . a solid crystalline electrolyte . . . between two reactive electrodes. His specific example was the cell

$$Ag/AgI/S \qquad (XXVIII)$$

with the sulfur electrode being a compressed mixture of 15% sulfur and 85% carbon, and the AgI a 0.0025-mm tarnish coating produced by I_2 vapor. Such a cell reputedly had an open-circuit voltage of 0.2v and a short-circuit current of 0.22 amp/cm^2 for a single cell. The cell described above is actually better represented by

$$Ag/AgI/Ag_2S/S \qquad (XVIII)$$

as Ag_2S is the product formed immediately after reaction begins.

Whereas the Lehovec patent made the broad claim for a solid electrolyte cell, Broder (50) claimed an improved cell of the type

$$Ag/AgI/I_2 \qquad (XX)$$

in which the Ag and AgI were similar to the Lehovec cell but the cathode material was a pressed mixture of 80% carbon and 20% iodine. This cell yielded an open-circuit voltage of 0.67v and a short-circuit current of 3 ma at room temperature.

Van der Grinten (65) appeared to have been the first to use a gas-depolarized cell as a power-producing unit. In his solid electrolyte cell, he used as a cathode material a permeable solid structure which produced a low pressure of a gas capable of reacting with the anode. Examples were $CuCl_2$, $CuBr_2$, and $FeCl_3$.

The type of performance reported by van der Grinten (66) for the gas activated cell was as follows:

Cell type	Emf (volts)	Flash current (ma)	Optimum load current (μa)
$Ag/AgBr/CuBr_2(C)$	0.74	0.22	2
$Ag/AgBr/Br_2(C)$	0.85	1.5	26

With these cells, coulombic capacities up to 3.6 amp-sec were obtained. One of the rate-limiting factors in these gas-activated cells was the vapor pressure of the cathode depolarizer. The required and obtained gas pressure over the $CuBr_2(C)$ electrode was estimated as 10^{-4}-10^{-7} mm Hg. An improved electrode with Br_2 sorbed on carbon yielded 0.1-10 mm pressure. The Br_2 system approximates Nernst law behavior, while the Cl_2 system does not.

Van der Grinten mentioned vacuum deposition as one possible method of fabrication of the halide electrolyte (65). Van der Grinten and Mohler (67) in further work miniaturized this type of cell to the following dimensions:

$$Ag(0.019\text{ mm})/AgCl(0.025\text{ mm})/Ca(OCl)_2 + C(1.0\text{ mm})$$

This cell produced an open-circuit voltage of 0.9-1.0v and a short-circuit current of 0.03 ma/in.^{2} at room temperature. The problem of internal short circuiting during storage was recognized. This was solved by using an insulating annular washer holding the cathode material in a fixed location. The anode, usually Ag or Pb, was also faced on the side exposed to the solid electrolyte with an impervious electrically conducting material. The gas-activated cell was investigated by Weininger who demonstrated (28, 68) that the iodine gas to activate a cell of the type

$$Ag/AgI/I_2(Ta) \qquad (XX)$$

could be produced by a number of ways depending on the physical structure of the cell. For example, the thermal decomposition of a polyiodide (*e.g.*, CsI_4) or reaction with an oxidizing agent ($KMnO_4$ + CuI) could be utilized.

Vapor-activated cells using silver halide electrolytes were intensively studied by Smyth and his co-workers (49, 69, 70). This study involved cells of the type

$$Ag/AgCl/KICl_4 \qquad (XXIX)$$

Potassium tetrachloroiodide is representative of polyhalide compounds that are reasonably stable at room temperature but dissociate at elevated temperatures to give iodine trichloride (ICl_3), I_2, and Cl_2. A large number of salts of this type and literature on the subject were cited (69). Their general property was that they dissociated rapidly enough to furnish the active cathode component but slowly enough so that the shelf life of the cell was not unduly shortened by the tarnishing of the anode. The cell cited by Smyth and Shirn consisted of a silver anode shaped as a cup, a silver chloride electrolyte 5-50μ thick developed by tarnishing with chlorine gas at 200°-300°C for 30 min, and a cathode composed of 30-50% $KICl_4$, 5-10% carbon black, and 40-60% grease (*e.g.*, a Kel-F) binder. The emf of this cell was 1.04v as compared with a theoretical value of 1.04v. This emf was constant to $\pm$ 5% in the temperature range of —40° to +75°C. The tarnish experiments, which are also a measure of the electronic conductivity in the electrolyte, indicated a shelf life of about 25 yr. The cells constructed on this project had an internal resistance of about 10^5 ohms/cm^2 at 25°C. When loaded with a resistance of 10^6 ohms, a ten-cell battery delivered 1.0 μa for 100 min with a flat discharge curve at about 1.0v. The AgCl film produced by the dissociation of $KICl_4$ was actually a dilute solution of AgI in AgCl (a chloride: iodide atomic ratio of 19.5-1 found by analysis). Of the four types investigated by Smyth and co-workers (49)

1.	$Pb/PbCl_2/AgCl/Ag$	(I)
2.	$Ag/AgI/I_2$	(XX)
3.	$Ag/AgCl/AgI/I_2$	(XXIV)
4.	$Ag/AgCl/KICl_4$	(XXIX)

only the fourth was considered to possess suitable characteristics for further development.

The exact influence of water vapor in supposedly dry solid state cells is not known but it may be re-

lated to the cathode reaction. Van der Grinten (66) had observed that vapor-activated cells stored in a chamber in which the air was less than 1% relative humidity dropped in voltage from 0.73 to 0.4-0.5v. Upon return to the more humid laboratory atmosphere, the original voltage was regained. Smyth and Lehovec (71) noted that the exclusion of all water vapor was detrimental and proposed adding a hydrated salt such as $MgCl_2 \cdot 6H_2O$ to their cathode that contained $KICl_4$ as the active material. They visualized the water vapor as being adsorbed in the cathode side and blocking the electronic current, which, of course, would tend to discharge the cell totally in time. They also pointed out that, in addition to improving the electrochemical behavior of the cell, the tarnish rate of silver in the iodine cell is lowered by a factor of 100. Weininger (51) also observed a reduction in the tarnishing rate of silver in bromine and iodine vapor in the presence of water vapor. The presence of water vapor in these solid electrolyte cells is obviously complex because the possibility then exists of other mechanisms such as proton transfer.

Cathode depolarizers other than halogens have been used in cells in which the electrolyte was the silver halide. Louzos (72) reported on a cell of the composition

$$Ag/AgI/V_2O_5(C) \qquad (XXX)$$

The cathode depolarizers were oxides of polyvalent metals in their higher valence state. In addition to V_2O_5, compounds such as PbO_2, MnO_2, NiO_2, Ni_2O_3, AgO, and CeO_2 were cited. These cells with Ag anodes and AgI electrolytes yielded cell voltages ranging from 0.5 to 0.7v. Cells of this type were able to sustain currents in the 1-10 μa range at cell voltages of 0.45-0.55v over the temperature range of —75° to 200°F. An improved version of the cell was described by Evans (73). By an elevated temperature tarnishing reaction (25 mm I_2 at 230°C), a 15-μ layer of AgI was produced on the Ag strip. Subsequent annealing lowered the electronic conductivity. The cathode current collector was constructed from stainless steel. Cells of this composition gave stable voltages of 0.455v and flash currents of 50 $\mu a/cm^2$ at room temperature. These cells were about 0.625 mm in thickness. A number of improvements were made from standpoint of improving performance or in facilitating production.

Rechargeability

The major effort in the field of solid electrolytes, aside from the use of solid galvanic cells to demonstrate thermodynamic principles, has been in the development of primary cells. Moreover, until recently, such effort has involved only high-voltage and low-current application.

Sator appears to have been the first to utilize thin solid ionic electrolytes in galvanic cells (14, 53, 74) and one of the few to attempt to study reversible systems. Perrot and Sator (74) described a method for measuring the electrical resistance of ionic conductors at room temperature. They vacuum-deposited $PbCl_2$ between silver layers and measured voltage-current curves. Upon passing current, they observed the formation of AgCl at one electrode and Pb at the other. This suggested the development of a reversible galvanic cell. Subsequently (14), vacuum-deposited cells of the type

$$Ag/Pb/PbCl_2/AgCl/Ag \qquad (I)$$

were prepared. These cells were then charged at a constant current of 0.5 μa. The cell equations were

$$PbCl_2 + 2\,Ag \underset{\text{discharge}}{\overset{\text{charge}}{\rightleftharpoons}} Pb + 2AgCl$$

The emf of the cell after charging was 0.523v, which diminished to 0.460v during the first hour and stabilized at this point.

Several different techniques were used by Sator in the preparation of the cells. One method involved starting with a Ag electrode upon which AgCl was formed by chemical attack in chlorine. Upon this substrate, a layer of $PbCl_2$ was vacuum deposited, then a layer of Pb, and finally a layer of Ag to complete the cell. The thicknesses deposited in these experiments were in the range of 10^{-5}-10^{-4} cm. Cells of the

$$Pb/PbCl_2/AgCl/Ag \qquad (I)$$

type were carried through nine charge-discharge cycles and were found to be reversible.

Cells of type I construction were prepared by vacuum deposition techniques by Moulton, Hacskaylo, and Feldman (75). The chloride cell exhibited an open-circuit voltage of 0.47-0.50v and the bromide cell 0.33-0.35v, both values being close to theoretical for the cell reaction. They were not successful in preparing the iodide cell.

The $PbCl_2$-AgCl cell (I) was also investigated by Smyth and co-workers (49). The chlorides of Ag and Pb which furnished the electrolytes were prepared in three ways: (*a*) by evaporation, (*b*) by tarnishing, and (c) by anodically chlorinating. Of these, evaporation appeared to be the most successful. It should be noted that the metal and metal chloride layers were relatively thick as compared to the Sator experiment. A typical cell was constructed as follows:

$$Ag(0.150\text{ mm})/AgCl(0.058\text{ mm})/PbCl_2(0.050\text{ mm}/Pb(0.001\text{ mm})$$

Further, evaporation was carried out from a graphite crucible and the possibility of contamination existed. In some preparations, open-circuit voltages in the range of 0.46v (approximating theoretical) were obtained, but in most cases the voltage was lower. These investigators concluded that the system had a major defect, *i.e.* the tendency for local silver metal deposition at the silver chloride-lead chloride interface. This deposition of free metallic silver which was actually observed at the interface led to inner electronic conduction and cell shorting. For this reason, further investigation of the system was abandoned by Smyth and co-workers.

The reversibility of the iodine-activated cell of the type

$$Ag/AgI/I_2(Pt) \qquad (XX)$$

was investigated by Weininger (76). It was possible to recover some cell capacity, but the charging efficiencies were low. A cell charged immediately after discharge yielded only 73% of the capacity, whereas cells stored for 90 min at —210°, 0°, and 25°C yielded 73, 63, and 15% of capacity on charging. It was postulated that this loss in capacity was related to the loss of iodine by diffusion although it was difficult to correlate the rate of the loss with known diffusion coefficients for I_2 and Br_2 in the appropriate halides. Generally speaking, attempts to recharge the gas-activated type of solid electrolyte cell have been unsuccessful.

A thin-film, rechargeable solid-electrolyte battery was described by Mrgudich *et al.* (77) with the composition

$$Ag/AgI/Pt \qquad (XXXI)$$

Pd was also used as the positive electrode. In typical cells, flash currents of 100 $\mu a/cm^2$ and open-circuit voltages of 0.370v were reported. These cells were subjected to a large number of charge-discharge cycles and apparently rechargeability was demonstrated. The author's description of the mechanism is open to question; *i.e.*, it does not appear reasonable that the experimental observations can be explained in terms of a silver concentration cell. The assumption was made that higher flash currents could be obtained from cells without evident cathode depolarization than those in which the cathode depolarization was provided by the halogen gas. It appears more logical

to explain the results obtained with this cell in terms of the air-depolarization mechanism proposed by Hacskaylo and Foley (78). Recently, Mrgudich (79) has reported some experiments wherein the Ag/AgI/Ag cell has been used as a pressure-sensing device and a temperature-sensing device, in the latter case utilizing the thermogalvanic effort described below.

The reversibility of solid electrolyte cells using silver halides was studied by Andes and Manikowski (80, 81) by charging and discharging in short pulses. Their cell used Pt wire and Ag wire electrodes in halide electrolytes, one of the better being a solution of 80 mole % silver iodide and 20 mole % silver chloride. The cells were charged with single pulses varying from a millisecond to more than a second. Discharging was done by pulses of the same magnitude but of opposite polarity. For example, in a typical experiment, a charge voltage of 45v for a time of 10 msec resulted in a current efficiency of 85% and an energy efficiency of 0.86%, the latter due to the higher charging voltage. The ability to charge reversibly with short pulses argues against Mrgudich's viewpoint that the mechanism involves diffusion of Ag into Pt as the cell operates.

Fabrication and Applications

One of the objectives of many investigations has been to counteract the high internal resistance of the solid electrolyte by using thin layers, *e.g.*, those furnished by vacuum deposition. The possibility of printing the various cell components was suggested. Originally, the idea of making batteries by printing techniques was advanced by Bjorksten (82). In his patent, he described a process that involved, first, printing with an ink containing Fe powder. then orienting the Fe particles so that they touched, and then allowing the resin to dry and cure. This process was repeated with another ink containing a second powder such as Ni. Whereas this may be characterized as a thin-film, printed battery, the electrolyte cited in the patent was a solution such as zinc chloride in the vehicle mainly comprised of linseed oil. Conduction was by mechanisms similar to those in aqueous solution rather than those operating in solid ionic crystals.

The fabrication of solid electrolyte batteries, presumably to minimize internal shorting by surface leakage and to prevent the attack of the anode by corrosive (halogen) vapors, was described by Smyth and Lehovec (83). A design of a galvanic cell intended to produce a high current was described by the same authors (84). In a cell of the type

$$Ag/AgI/I_2(C) \qquad (XX)$$

formed with layer configuration, a battery with a voltage of 0.68v and a short-circuit current of 2.5 ma/cm^2 of active cell was claimed. A battery with 20 cm^2 of effective contact between the foils yielded 50 ma of short-circuit current and operated at 5 ma without "appreciable decrease in cell voltage." It was claimed by these authors that these cells could be recharged although no charging efficiency curves were given. The design and method of manufacturing a cell described by Smyth and Shirm (69) of the type

$$Ag/AgCl/KICl_4 \qquad (XXIX)$$

wherein the cathode reaction involved a gas activation process was claimed by Hutt *et al.* (85). A series arrangement of cup-shaped cells was described.

Richter *et al.* (86) described a process for automatically making the cell described originally by Louzos (72). This cell was of the type

$$Ag/AgI/V_2O_5(C) \qquad (XXX)$$

The gas-activated cell utilizing solid silver halides as electrolytes described above was further developed by Weininger (26, 76). He described a method of fabricating a cell of the type

$$Ag/AgI/I_2(Pt) \qquad (XX)$$

intended to operate at elevated temperatures. In a further improvement (87) of this type of cell, a AgI electrolyte of 2-5μ thickness was developed by chemically tarnishing Ag in I_2 vapor at 150°C. A bimetallic corrugated sheet was used to provide space for the gas to diffuse to the active electrode areas. When the cell was activated by I_2 vapor at 0.306 mm at 25°C, a voltage of 0.67v and a short-circuit current of 200 μa was produced.

Miniature cells of a similar configuration gave short-circuit currents of 6.7 ma at 170°C at which temperature the open-circuit voltage was 0.67v (28).

Galvanic cells using silver iodide in its highly conductive form were utilized as thermogalvanic cells (88). The so-called "silver" thermocell

$$(T_1)\,Ag/AgI/Ag\,(T_2) \qquad (VII)$$

wherein T_1 and T_2 were two different temperatures above 146°C, was investigated and proven feasible as a device for solar energy conversion (89). This cell suffered because of transfer of Ag to the cathode and nonuniform, dendritic build-up as the cell operates. This led to the iodine thermocell

$$(T_1)\,(C)\,I_2/AgI/I_2\,(C)\,(T_2) \qquad (XXXII)$$

using the same electrolyte but gas electrodes (90). In the particular configuration described, with electrodes of 10 cm^2 and an electrolyte thickness of 0.1 cm, with iodine electrodes at 1 atm, with one electrode at 350°C and a second at 550°C, an open-circuit voltage of 112 mv and a short-circuit current of 27 amp was obtained. The voltage approximated that calculated by considering the corresponding entropy transfer within the cell. Whereas the current appears high, it is very close to what would be expected from the configuration of the cell and the reported resistance for the electrolyte, as given above (21). Weininger reports typical operating characteristics for the iodine thermocell for a temperature difference of 280°, a ΔE of 347 mv, equivalent to 1.24 mv/deg, and an internal cell resistance of 91 ohms at a current greater than 1 ma (88).

The first substantial improvement in electrolyte development was made by Takahashi and Yamamoto (33) in their work with the silver sulfide iodide electrolyte, as described above. A miniaturized version of the cell was prepared with a thin film (20μ) of this electrolyte (91). This cell could be discharged at several hundred microamperes per square centimeter at 25°C without significant polarization.

The second improvement was that involving double salts with the alkali halides and the silver halides. Batteries utilizing this type of electrolyte were prepared on a proprietary basis (92). Individual cells were reported to have 0.64v open-circuit voltage and to exhibit flash currents of 900 ma/cm^2. A typical discharge curve of a 100 ma-hr cell at 5.55 ma showed a flat voltage curve approximately at 0.64v out to about 16 hr or 88% of capacity.

As has been pointed out above, the mobile species in this cell is Ag^+ ions. As the cell operates, it would be expected that Ag^+ ions would move to the cathode and form a layer of AgI which would have a comparatively high resistance. Thus, if this passivation is to be prevented, some mechanism to prevent cathode polarization must be built into the cathode reaction. A recent report indicates that this effect is achieved by employing a cathode mixture of RbI_3, carbon, and $RbAg_4I_5$ (97).

Conclusions

For a number of reasons cited above, solid electrolyte galvanic cells as energy conversion devices have been the object of a considerable amount of investigation by electrochemists since the turn of the century.

Solutions to the major battery problems have evolved with the disclosure of highly conductive ionic electrolytes, gas-activated cathodes, and fabrication techniques for eliminating internal short circuiting. In addition, the development of sophisticated vacuum deposition techniques renders the fabrication of thin-film configurations possible.

The question of rechargeability has not been answered satisfactorily as yet, with the experimental work of several investigators furnishing contradictory evidence. However, cells based on lead chloride-silver chloride electrolytes—the so-called Sator-Haber type—offer promise in the development of a secondary battery system.

Acknowledgments

I am pleased to acknowledge the valuable criticism of Dr. Joseph L. Weininger and Dr. W. J. van der Grinten of the General Electric Company, Dr. Charles Feldman of the Applied Physics Laboratory, and Dr. George E. Blomgren of the Union Carbide Corporation. Dr. Weininger brought to my attention several papers on the structure of silver iodide, and Dr. van der Grinten made available government reports on the vapor-activated systems.

Manuscript submitted March 18, 1968; revised manuscript received June 10, 1968.

REFERENCES

1. D. O. Raleigh, in "Progress in Solid State Chemistry," Vol. 3, pp. 83-134, H. Reiss, Editor, Pergamon Press, New York (1967).
2. F. Haber and St. Tolloczko, *Z. Anorg. Chem.*, **41**, 407 (1904).
3. M. Katayama, *Z. Physik. Chem.*, **61**, 566 (1908).
4. R. Lorenz and M. Katayama, *ibid.*, **62**, 119 (1908).
5. R. Beutner, *Z. Elektrochem.*, **15**, 433 (1909).
6. C. Tubandt and E. Lorenz, Nernst's Festschrift (W. Knapp, Halle, 1912) pp. 446-458.
7. C. Tubandt and E. Lorenz, *Z. Physik. Chem.*, **87**, 513 (1914).
8. C. Tubandt and S. Eggert, *Z. Anorg. Allgem. Chem.*, **110**, 196 (1920).
9. C. Tubandt, *Z. Elektrochem.*, **26**, 358 (1920).
10. H. Reinhold, *Z. Anorg. Allgem. Chem.*, **171**, 181 (1928).
11. H. Reinhold and A. Blachney, *Z. Elektrochem.*, **39**, 290 (1933).
12. H. Reinhold, *ibid.*, **40**, 361 (1934).
13. C. Wagner, *ibid.*, **40**, 364 (1934).
14. A. Sator, *Compt. Rend.*, **23**, 2283 (1952).
15. W. J. van der Grinten, Private communication.
16. C. Tubandt, *Z. Anorg. Allgem. Chem.*, **115**, 105 (1921).
17. W. Jost, H. J. Oel, and G. Schniedermann, *Z. Physik. Chem. (Frankfurt)*, **17**, 175 (1958).
18. K. H. Lieser, *Z. Physik. Chem.* [*N.F.*], **2**, 238 (1954).
19. K. H. Lieser, *ibid.*, **5**, 125 (1955).
20. W. Jost, J. Krug, and L. Sieg, Proc. Intern. Symp. *Reactivity Solids, Gothenburg, 1952*, pp. 81-82.
21. K. H. Lieser, *Z. Physik. Chem.* [*N.F.*], **9**, 216 (1956).
22. W. Jost and J. Nolting, *Z. Physik. Chem. (Frankfurt)*, **7**, 383 (1956).
23. W. Jost and K. Weiss, *Z. Physik. Chem.* [*N.F.*] *(Frankfurt)*, **2**, 112 (1954).
24. B. Ilschner, *J. Chem. Phys.*, **28**, 1109 (1958).
25. H. C. Duecker and E. R. Lippincott, *Science*, **116**, 1295 (1964).
26. J. Weininger, U.S. Pat. 2,933,546, April 19, 1960.
27. K. Weiss, W. Jost, and H. J. Oel, *Z. Physik. Chem. (Frankfurt)*, **15**, 429 (1958).
28. J. L. Weininger, U.S. Pat. 3,003,017, Oct. 3, 1961.
29. H. C. Lieb and J. A. De Rosa, U.S. Pat. 2,930,830, March 29, 1960.
30. K. Lehovec, U.S. Pat. 2,696,513, Dec. 7, 1954.
31. K. Lehovec and D. M. Smyth, U.S. Pat. 3,036,144, May 22, 1962.
32. K. Lehovec, U.S. Pat. 3,007,992, Nov. 7, 1961.
33. T. Takahashi and O. Yamamoto, *Electrochim. Acta*, **11**, 779 (1966).
34. B. Reuter and K. Hardel, *Naturwissenschaften*, **48**, 161 (1961).
35. T. Takahashi and O. Yamamoto, *Electrochim. Acta*, **11**, 911 (1966).
36. B. B. Owens and G. R. Argue, Paper presented at Spring 1967 Meeting of American Chemical Society, Miami Beach.
37. J. N. Bradley and P. D. Greene, *Trans. Faraday Soc.*, **62**, 2069 (1966).
38. J. N. Bradley and P. D. Greene, *ibid.*, **63**, 424 (1967).
39. B. B. Owens and G. R. Argue, *Science*, **157**, 308 (1967).
40. S. Geller, *ibid.*, **157**, 310 (1957).
41. J. N. Bradley and P. D. Greene, *Trans. Faraday Soc.*, **63**, 2516 (1967).
42. J. A. A. Ketelaar, *Z. Physik. Chem.*, **B26**, 327 (1934).
43. J. A. A. Ketelaar, *Trans. Faraday Soc.*, **34**, 874 (1938).
44. L. Suchow and G. R. Pond, *J. Am. Chem. Soc.*, **75**, 5242 (1953).
45. J. Jaffray and R. Jouanisson, *Compt. Rend.*, **245**, 40 (1957).
46. J. Jaffray, *J. Rech. Centre Nat. Rech. Sci. Lab. Bellevue (Paris)*, **No. 39**, 125 (1957).
47. R. Weil and A. W. Lawson, *J. Chem. Phys.*, **41**, 832 (1964).
48. K. Lehovec and J. Broder, *J. Electrochem. Soc.*, **101**, 208 (1954).
49. D. M. Smyth, "Final Report on Solid Electrolyte Battery Systems," Contract No. DA-36-039-SC-63151, Period: 1 June 1954 to 30 Nov. 1956.
50. J. D. Broder, U.S. Pat. 2,690,465, Sept. 28, 1954.
51. J. L. Weininger, *J. Electrochem. Soc.*, **105**, 577 (1958).
52. J. J. Buchinski, R. M. Foecking, R. E. Gluyas, and R. A. Powers, U.S. Pat. 2,932,569, April 12, 1960.
53. A. Sator, *Publ. Sci. Univ. Alger, Ser. B.*, **2**, 115 (1956).
54. R. R. Ridgway, A. A. Klein, and W. J. O'Leary, *Trans. Electrochem. Soc.*, **70**, 71 (1936).
55. Y. Y. Yao and J. T. Kummer, *J. Inorg. Nucl. Chem.*, **29**, 2453 (1967).
56. N. Weber and J. T. Kummer, *Proc. Ann. Power Sources Conf.*, **21**, 16 (1967).
57. M. Eigen and L. de Maeyer, *Proc. Roy. Soc. (London)*, **A247**, 505 (1958).
58. Compagnie Industrielle des Piles Electriques, French Pat. 1,395,560, March 8, 1965.
59. S. Ruben, U.S. Pat. 2,707,199, April 26, 1955.
60. S. Ruben, U.S. Pat. 2,816,151, Dec. 10, 1957.
61. S. Ruben, U.S. Pat. 2,852,591, Sept. 16, 1958.
62. J. N. Mrgudich, *J. Electrochem. Soc.*, **107**, 475 (1960).
63. M. T. Kostyshin, E. V. Mikhailovskaya, and P. F. Romanenko, *Soviet Phys.-Solid State*, **8**, 451 (1966).
64. K. Lehovec, U.S. Pat. 2,689,876, Sept. 21, 1954.
65. W. J. van der Grinten, U.S. Pat. 2,793,244, May 21, 1957.
66. W. J. van der Grinten, Final Report on Contract No. DA-36-039-sc-42716, Jan. 1, 1954.
67. W. J. van der Grinten and D. Mohler, U.S. Pat. 2,928,890, March 15, 1960.
68. J. L. Weininger, *J. Electrochem. Soc.*, **106**, 475 (1959).
69. D. M. Smyth and G. A. Shirn, U.S. Pat. 2,905,740, Sept. 22, 1959.
70. D. M. Smyth, *J. Electrochem. Soc.*, **106**, 635 (1959).
71. D. M. Smyth and K. Lehovec, U.S. Pat. 3,346,423, Oct. 10, 1967.
72. D. V. Louzos, U.S. Pat. 2,894,053, July 7, 1959.
73. G. E. Evans, U.S. Pat. 2,894,052, July 7, 1959.
74. M. Perrot and A. Sator, *Compt. Rend.*, **234**, 1883 (1952).
75. C. W. Moulton, M. Hacskaylo, and C. Feldman, *J. Electrochem. Soc.*, **111**, 60C (1964).
76. J. L. Weininger, *ibid.*, **105**, 439 (1958).
77. J. N. Mrgudich, A. Schwartz, P. J. Bramhall, and G. M. Schwartz, *Proc. Ann. Power Sources Conf.*, **19**, 86 (1965).
78. M. Hacskaylo and R. T. Foley, *J. Electrochem. Soc.*, **113**, 1231 (1966).
79. J. N. Mrgudich, *Proc. Ann. Power Sources Conf.*, **21**, 117 (1967).
80. R. V. Andes and D. M. Manikowski, *J. Electrochem. Soc.*, **110**, 66C(1963).
81. Sperry Rand Corp. Belgian Pat. 618,306, Sept. 17, 1962.
82. J. Bjorksten, U.S. Pat. 2,688,649, Sept. 7, 1954.
83. D. M. Smyth and K. Lehovec, U.S. Pat. 2,953,620, Sept. 20, 1960.

84. K. Lehovec and D. M. Smyth, U.S. Pat. 2,954,417, Sept. 27, 1960.
85. S. D. Hutt, D. M. Smyth, and M. F. Stefanski, U.S. Pat. 2,968,687, Jan. 17, 1961.
86. E. W. Richter, D. Shellek, H. E. McMillan, and G. E. Evans, U.S. Pat. 3,004,093, Oct. 10, 1961.
87. J. L. Weininger and H. A. Liebhafsky, U.S. Pat. 2,987,568, June 6, 1961.
88. J. L. Weininger, *J. Electrochem. Soc.*, **111**, 769 (1964).
89. R. T. Foley, "Solar Regenerated Fuel Cell," Contract DA-30-069-ORD-2782, Final Report, Nov. 22, 1960.
90. J. L. Weininger, U.S. Pat. 2,890,259, June 9, 1959.
91. O. Yamamoto and T. Takahashi, *Denki Kagaku*, **34**, 833 (1966).
92. Atomics International, "Solid State Electrochemical Batteries, Timers" (1967).
93. J. W. Mellor, "A Comprehensive Treatise on Inorganic and Theoretical Chemistry," Longmans, Green and Co., Ltd., London (1928).
94. B. Reuter and K. Hardel, *Ber. Bunsenges. Physik. Chem.*, **70**, 82 (1966).
95. T. Takahashi and O. Yamamoto, *Denki Kagaku*, **32**, 610 (1964).
96. T. Takahashi and O. Yamamoto, *ibid.*, **33**, 346 (1955).
97. G. A. Argue, B. Owens, and I. J. Groce, *Proc. Ann. Power Sources Conf.*, **22**, 14 (1968).

Alternating-Current Field-Induced Forces and Their Biological Implications

Herman P. Schwan and Lawrence D. Sher

Biomedical Engineering Department, The Moore School of Electrical Engineering, University of Pennsylvania, Philadelphia, Pennsylvania

ABSTRACT

Steady-state, field-induced forces on particles of microscopic size become significant at field strength values of the order of 100 v/cm. They include "pearl-chain formation," *i.e.* the alignment of particles in the direction of the imposed field, and the orientation of nonspherical particles. The time constant, which describes the speed of these phenomena, depends on field strength, and particle and other parameters. For pulsed fields, a lower level of applied average power can suffice to evoke the phenomena mentioned. Biological implications include the possibility of nonthermal effects of biological significance.

Alternating-current, field-induced force effects have been observed for several decades. However, their detailed understanding in general and field-induced effects on biological material in particular seem not to have been of much interest to the scientific community.

We shall report here about two such effects, which we shall classify as "pearl-chain formation" and "orientation" effects (Fig. 1). Two other effects in this category, a-c electrophoresis and dielectrophoresis, have already been discussed by us (1, 2). "Pearl-chain formation" is the ordered arrangement of small particles in a suspending medium which is observed if an a-c field is applied. "Orientation effects" describe the alignment of suspended particles and micro-organisms as an a-c field is applied, so that their long axes are parallel or perpendicular to the field direction.

Alternating-current, field-induced forces on particles of microscopic size can become significant at field strength values of the order 100 v/cm. They have been observed for a variety of biological cells and the question arose under what circumstances nonthermal effects of rf radiation can be biologically significant.

Background Remarks

Muth (3), by exposing fat-particle emulsions to high-frequency fields, was probably the first to observe the phenomenon of pearl-chain formation. Krasny-Ergen (4) stated that the phenomenon can be explained by considerations of potential theory. However, for mathematical simplicity, he erroneously assumed perfectly conducting biological particles. Liebesny (5) observed pearl-chain formation of erythrocytes in a high-frequency field. Manegold (6), following Muth (3), again demonstrated and discussed pearl-chain formation using fat particle emulsions.

Renewed interest in field effects on biological particles developed in the late 1950's and early 1960's. Heller *et al.* (7, 8) noted not only pearl-chain formation but also orientation and preferential directions of motility of micro-organisms in high-frequency fields. Saito and Schwan (9) provided a theoretical treatment of the problem of how fast pearl-chain formation takes place. Quantitative experiments on pearl-chain formation, studying the threshold field strength of this phenomenon, were probably first carried out by

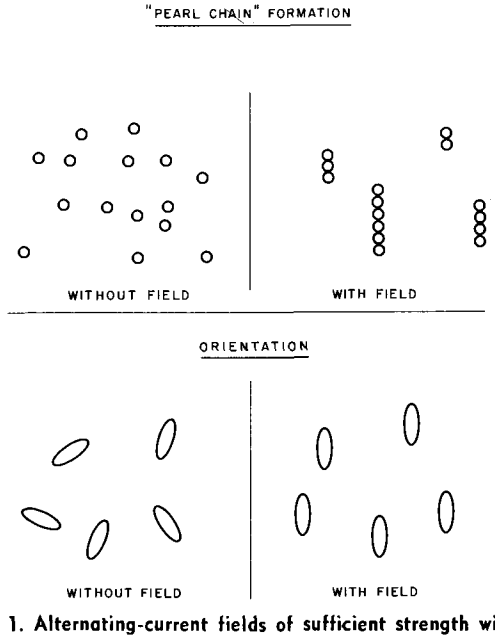

Fig. 1. Alternating-current fields of sufficient strength will cause alignment of particles (pearl-chain formation) and orientation of nonspherical particles parallel or perpendicular to the direction of field.

Sher (10). The results were compared with theoretical equations given by Saito and Schwan (11). A general theory of orientation due to a-c fields was developed by Schwarz, Saito, and Schwan (12). Saito, Schwan, and Schwarz (13) provided a theory of the orientation of biological particles by a-c fields in 1966.

All experimental work so far, with the exception of that done by Sher (10), is not sufficiently quantitative to be suitable for a check against theory. However, Sher's data permit comparison and agree with the theory of pearl-chain formation developed by Saito and Schwan (11). The theory of orientation given by Saito, Schwan, and Schwarz (13) predicts that "turnover" of field-oriented micro-organisms from one direction to another occurs in the high MHz range. This was indeed observed by Heller *et al.*, (7, 8). However, their data are not specific enough to permit a precise quantitative comparison. More experimental work is needed to check fully the orientation theory, even though there appears to be little doubt that the considerations of potential energy by Saito, Schwan, and Schwarz (13) are applicable.

While the response of particles to nonuniform fields is an apparent digression from pearl-chain formation and orientation, both demonstrable in uniform applied fields, it is mentioned here since the individual particles of a pearl-chain do experience nonuniform fields, even when the applied field is uniform. The response of particles to nonuniform fields has been the subject of many investigations. Thus, Debye has proposed a "molecular centrifuge" (14), and separation of biological cells has been achieved by Pohl and Hawk (15) by application of nonhomogeneous fields. The existence of this force and its description for a spherical particle in a d-c field is well-known (16). More recently, Saito and Schwan (11), using the results of Schwarz (17), have shown that pearl-chain formation for complex dielectric media in an a-c field can be described very well by considering each particle of a representative particle pair to be acted upon by the (nonuniform) induced dipole field of its partner. A minimization of their combined potential energy results when the particles are brought to tangency with their line of centers parallel to the field. Pearl-chain formation can thus be considered to be the result of the applied uniform field or, with greater insight, the result of the induced nonuniform fields. The force on single complex dielectric particles in a complex dielectric medium under the influence of an a-c field has been very recently derived and discussed by Sher (2), again basing the derivation on the fundamental work of Schwarz (17).

Pearl-Chain Formation and Orientation

It has been our hypothesis that the above-mentioned effects are manifestations of field-induced forces. We have developed appropriate theoretical concepts by applying potential theory and, in some cases, have conducted experimental work to check the theory. Our group, H. P. Schwan, L. D. Sher, M. Saito, and G. Schwarz, has concentrated on three problem areas which will be described in some detail: Pearl-chain formation and its threshold; time constants of pearl-chain formation; and orientation phenomena and their threshold.

Pearl-chain formation and its threshold.—Pearl-chain formation is the result of attractive forces between induced dipoles on neighboring particles (18). A demonstration of this effect is shown in Fig. 2 (10). Equivalently, it can be considered to occur because, in an electric field, the combined electric potential energy of two particles diminishes with their separation and because any system will move toward that state where its potential energy is minimized. The mathematical treatment of the phenomenon of pearl-chain formation (11) considers the interaction of two spherical particles of complex dielectric constant ϵ_1 and radius R in a medium of complex dielectric constant ϵ_2 under the influence of an alternating field E_0. ($\epsilon = \epsilon' - i\epsilon''$,

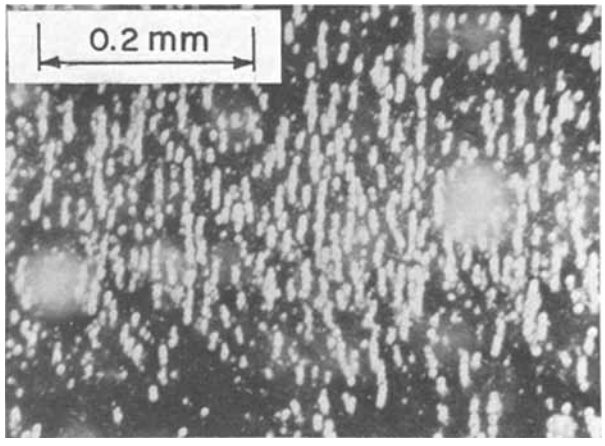

Fig. 2. Demonstration of pearl-chain formation with red blood cells in saline. Field strength is 50 v/cm.

where ϵ' is the real dielectric constant and ϵ'' is electrical, conductivity/angular frequency.) Pearl-chain formation succeeds if the ordering forces, which yield a minimization of potential energy, are greater than the randomizing forces due to Brownian motion. Thus, one anticipates that pearl-chain formation will occur if the change in potential energy due to the particle alignment is greater than kT, *i.e.* if

$$\left[\frac{\epsilon_1 - \epsilon_2}{\epsilon_1 + 2\epsilon_2}\right]^2 \epsilon_2' R^3 E_0^2 > kT \qquad [1]$$

where ϵ'_2 is the real dielectric constant of the suspending phase. In fact, it is found theoretically that the term on the left must be about 9X larger than kT for pearl chains to be observable. Exact numerically evaluated solutions for the minimal, or threshold, field strength needed to cause pearl chains to form have been obtained if the particles are either perfect conductors, perfect dielectrics, or complex dielectrics with any particular set of specified parameters (11). The most general case of complex dielectric constants yields a useful simple closed-form solution (Eq. [2]) if the problem is treated as a dipole-dipole interaction phenomenon, even though the perturbation of a field by a sphere is no longer precisely described by a dipole if there is another sphere in the neighborhood.

For the steady-state case, *i.e.* after the electrical field has been applied for a time which is larger than the time constants characteristic of the process of pearl-chain formation (*see* next section), the following conclusions have been derived:

1. At frequencies for which $\epsilon_1 \approx \epsilon'_1$ and $\epsilon_2 \approx \epsilon'_2$, the threshold value of field strength causing pearl-chain formation is relatively insensitive to changes in the particle concentration but changes rapidly with the real dielectric constant ratio, ϵ'_1/ϵ'_2, of particle and fluid. If the particle's complex dielectric constant becomes identical with that of its environment, the particles cease to be distinguished electrically, and, hence, pearl-chain formation becomes impossible. Thus $E_{th} \to \infty$ as $\epsilon_1 \to \epsilon_2$ (Fig. 3).

2. No frequency dependence for the threshold rf field strength is found in the case where particle and suspending medium have frequency-independent electrical parameters and where either conductive or capacitive currents predominate over the frequency range of interest. This may be recognized from Eq. [2] which gives the threshold field strength E_{th} for pearl-chain formation in complex dielectric media

$$E_{th} = 1.7\, R^{-1.5} \left|\frac{\epsilon_1 + 2\epsilon_2}{\epsilon_1 - \epsilon_2}\right| \sqrt{\frac{kT}{\epsilon_2'}} \qquad [2]$$

Reduction of this general equation to the case where the particle and medium properties are purely conductive or purely dielectric yields equations which

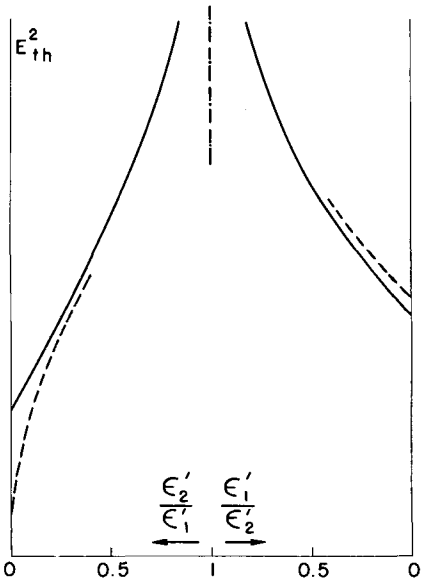

Fig. 3. Threshold field strength E_{th} necessary to cause pearl-chain formation as a function of the ratio of real dielectric constants, if suspended particles (subscript 1) and suspending medium (subscript 2) are pure dielectrics. Notation: – – – – exact value, ——— dipole approximation, – · – – · – asymptote for all curves at the point where $\epsilon'_1 = \epsilon'_2$. The ordinate is linear and is proportional to E^2_{th}. A particle concentration of 1.6% (v/v) was assumed.

predict a frequency-independent threshold value. For example, let us neglect ϵ'_1 and ϵ'_2 which corresponds to the experimental conditions in Fig. 4 ($\epsilon_1' < \epsilon_1''$ due to surface conductance). Then Eq. [2] reduces to Eq. [3]

$$E_{th} = 3.4\, R^{-1.5} \sqrt{\frac{kT}{\epsilon'_2}} \qquad [3]$$

which is independent of frequency, a prediction confirmed experimentally (Fig. 4). The theoretically predicted size dependence of the threshold field strength has also been experimentally confirmed (Fig. 5).

Time constants of pearl-chain formation.—A theory of the transient behavior of pearl-chain formation has been developed. While a complete theory of the speed with which pearl-chains form is difficult, it has been possible to calculate the time constant T if the field strength is at or near zero (in which case T measures the break-up time) or is large in comparison with the threshold value E_{th} (in which case T measures the

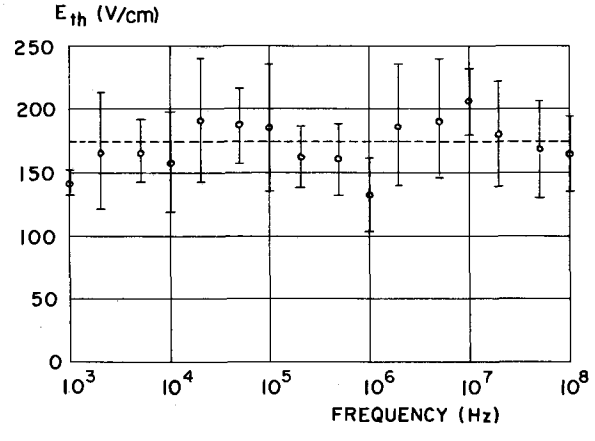

Fig. 4. Experimental threshold field strength values for pearl-chain formation of 1.17μ diameter polystyrene spheres as a function of frequency. Bars indicate ±1 standard deviation. Average of these values is indicated here by a dotted line and in Fig. 5 by the data point and bar numbered "2." Fluctuation of data indicates the experimental difficulty of obtaining precise threshold values, even when the experimental system is very well defined.

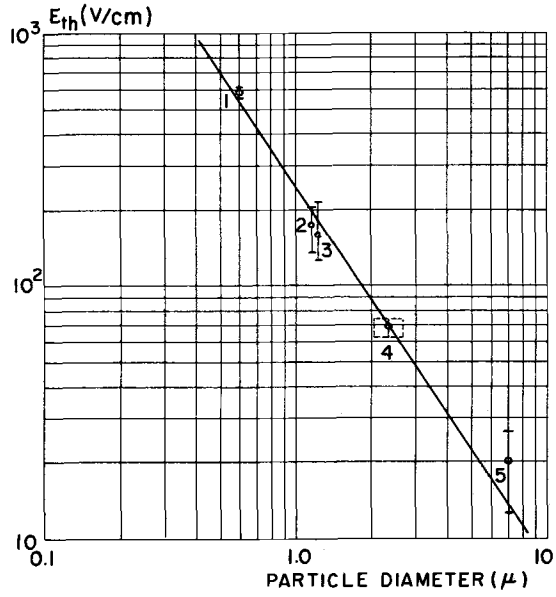

Fig. 5. Threshold field strength for pearl-chain formation vs. particle size. Experimental measurements on five different particle suspensions are shown: 1: 0.6 ± 0.1μ silicone globules; 2: 1.17μ polystyrene spheres; 3: *E. coli* bacteria; 4: 2.3 ± 0.3μ silicone globules; and 5: human erythrocytes. All suspensions are in aqueous media. Vertical bars indicate standard deviations except for 5 in which they indicate the data spread of two (difficult) measurements. Where the E_{th} had a frequency dependence, the values plotted here were the high-frequency limit values. The line is the theoretical prediction using the dipole approximation (Eq. [2]) at its high-frequency limit (where $\epsilon \to \epsilon'$).

formation time). Thus two solutions for small and high values are obtained which, if taken together, indicate the over-all field strength dependence of the time required for pearl chains to form or break up (9). The theory yields the following conclusions:

1. The time constants which characterize how fast pearl-chain formation occurs are proportional to the cube of the radius. For $E \approx 0$, they are of the order of 1 sec for particles of the order of 1μ in radius. For particles of several microns, the time constants become as large as minutes and experimental measurements of the time constants are difficult for such particles.

2. The time constants are not strongly dependent on the field strength when it is small. They are inversely proportional to the square of the field strength when it is large. The transition between the two regions occurs near the threshold field-strength value of pearl-chain formation (Fig. 6). It is apparent from Fig. 6 that appropriately applied pulse trains of high peak field strength can cause pearl-chain formation even though the time average of the field strength applied is less than that needed in the case of continuous fields. To what extent this fact may be utilized to affect biological structures and their function has not yet been studied intensively.

3. However, when the pulse repetition rate is much greater than the reciprocal of the time constant, the pulsed applied field is as effective as is expected from its root mean square value. Personnel hazards due to tissue heating in a radar beam become pronounced at field-strength values smaller than those required for pearl-chain formation for particles smaller than about 20μ in diameter. Thus, with the qualification noted in paragraph 2 above, pearl-chain formation is not likely to be a biological hazard due to microwave irradiation (9).

Orientation phenomena and their threshold.—Positions of stability of nonspherical particles in an rf field were studied theoretically, using a fundamental derivation of Schwarz (17), which gives the potential energy of a complex dielectric body in an a-c field.

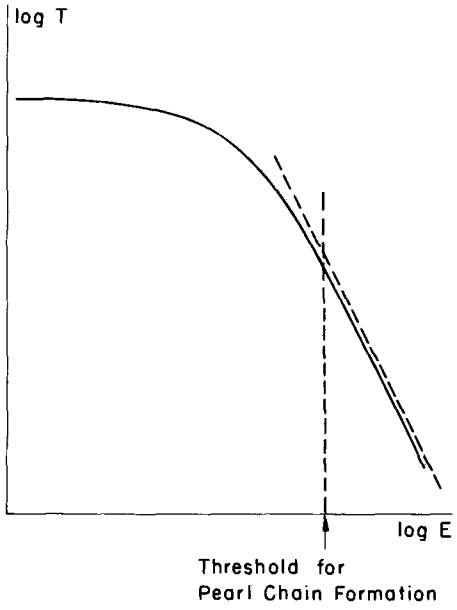

Fig. 6. Field strength dependence of the time constant of pearl-chain formation. The inclined dashed line indicates the $T \propto E^{-2}$ behavior which is approached if E is larger than the threshold field strength for pearl-chain formation.

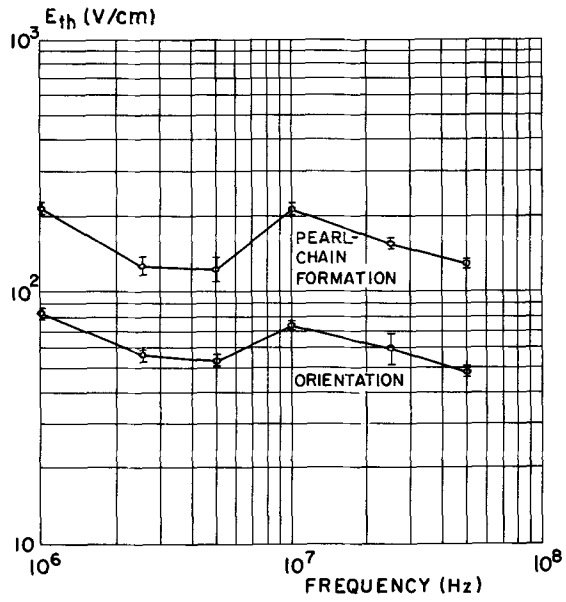

Fig. 8. Comparison of threshold field strengths, E_{th}, for orientation and for pearl-chain formation of *E. coli* in water. Since bacteria possess a highly frequency-dependent complex dielectric constant, the threshold values are frequency dependent. Each point is the average of three measurements whose spread is indicated.

The potential energy of a nonspherical particle of complex dielectric constant in a medium of another complex dielectric constant is found to be a function of frequency, applied field strength, and orientation of the particle. If the particle is free to rotate, then, as the frequency is varied, the particle will rotate from one direction to another in order to maintain a state of minimum potential energy (Fig. 7). A general ellipsoid can assume three possible orientations in the field, while a prolate or oblate spheroid can assume only two, the axis being parallel or perpendicular to the field direction. The transition from one to the other orientation, or "turnover," depends on the frequency and complex dielectric constants of the particle and the suspending medium.

Ellipsoidal particles with and without a shell were treated as special cases. For ellipsoidal particles with parameters of biological interest, the change in orientation with frequency is in the region of 1-100 MHz. In the case where the field intensity is not sufficiently high, the turnover may be blurred by Brownian motion. The threshold field strength necessary to cause a well-defined orientation is usually less than, but of the same order of magnitude as, the threshold for pearl-chain formation (Fig. 8). When both thresholds are exceeded, both phenomena occur simultaneously.

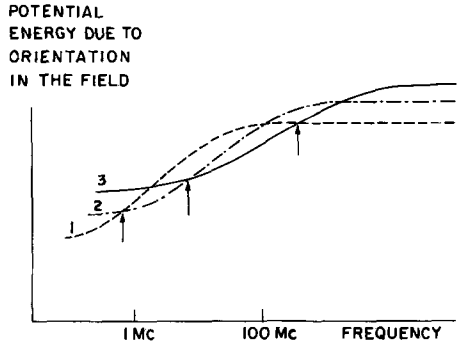

Fig. 7. Each of the curves shown is the potential energy (vs. frequency) of an ellipsoid, one of whose three axes is artificially constrained to be parallel to the field direction. The particle will rotate from one direction to another at the frequencies where curves intersect, as indicated by arrows (see text).

Biological Implications and Conclusions

Biological implications include the possibility of nonthermal effects of biological significance. A phenomenon, which has been reported by several authors, is the direct auditory sensation experienced by persons exposed to pulsed microwave beams. It appears to be related to field-evoked forces (19, 20). The possibility of inducing chromosomal aberrations has been observed (21), but further work appears desirable.

In conclusion, we wish to state that nonpulsed a-c fields are not likely to be biologically significant as a result of nonthermal effects, but that it may be possible to evoke nonthermal biological effects with appropriately designed pulsed fields.

Acknowledgment

This work was supported by ONR contract Nonr-551(52) and NIH grant HE-01253-15.

Manuscript submitted November 28, 1967; revised manuscript received March 25, 1968. This manuscript was presented at the Chicago Meeting, October 15-19, 1967, as Paper 153.

REFERENCES

1. L. D. Sher and H. P. Schwan, *Science*, **148**, 279 (1965).
2. L. D. Sher, *Nature*, **220**, 695 (1968).
3. E. Muth, *Kolloid-Z.*, **41**, 97 (1927).
4. W. Krasny-Ergen, *Hochfrequ. u. Elektroak.*, **48**, 126 (1936).
5. P. Liebesny, *Arch. Phys. Ther.*, **19**, 736 (1939).
6. E. Manegold, *Kolloid-Z.*, **41**, 11 (1950).
7. J. H. Heller, in Digest of the 12th Ann. Conf. on Elec. Tech. in Medicine and Biology, (IRE-AIEE-ISA, Nov. 1959), p. 56.
8. A. A. Teixeira-Pinto, L. L. Nejelski, J. L. Cutler, and J. H. Heller, *Exp. Cell Research*, **20**, 548 (1960).
9. M. Saito and H. P. Schwan, Time Constants of Pearl Chain Formation, in "Biological Effects of Microwave Radiation," Vol. I, p. 85, M. F. Peyton, Editor, Plenum Press, New York (1960).
10. L. D. Sher, Ph.D. Thesis, Dept. of Biomedical Engrg., Moore School, Univ. of Pennsylvania, Philadelphia, Pa. (1963).
11. M. Saito and H. P. Schwan, Unpublished internal report.
12. G. Schwarz, M. Saito, and H. P. Schwan, *J. Chem. Phys.*, **43**, 3562 (1965).
13. M. Saito, H. P. Schwan, and G. Schwarz, *Biophys. J.*, **6**, 313 (1966).

14. P. Debye, *J. Chem. Phys.*, **19**, 589 (1951).
15. H. Pohl and I. Hawk, *Science*, **152**, 647 (1966).
16. M. Abraham and R. Becker, "The Classical Theory of Electricity and Magnetism," 2nd Ed., p. 91, Hafner, N.Y. (1949).
17. G. Schwarz, *J. Chem. Phys.*, **39**, 2387 (1963).
18. H. P. Schwan, "Therapeutic Heat and Cold," S. Licht, Editor, Waverly Press, Baltimore, Md. (1965). Also, "Therapeutic Heat," S. Licht, Editor, Vol. II (1958).
19. A. H. Frey, *Aerospace Med.*, **32**, 1140 (1961).
20. H. C. Sommer and H. E. von Gierke, *ibid.*, **35**, 834 (1964).
21. J. H. Heller, *Nature*, **183**, 905 (1959).

Chemical Behavior of the Components of the $KCN/KAu(CN)_2$ Electroplating System

H. Graham Silver[1]

Bell Telephone Laboratories, Incorporated, Reading, Pennsylvania

ABSTRACT

The chemical reactions occurring within aqueous solutions of potassium cyanide, potassium cyanide and metallic gold, potassium gold cyanide, and mixtures of these compounds with potassium hydroxide have been examined. It was determined that aqueous potassium cyanide solutions are unstable to water and air. The major reaction products formed were the formate and carbonate ions which increased in concentration with time. This increase, which was temperature dependent, was accompanied by a corresponding decrease in the cyanide ion concentration. Analyses confirmed that gold would dissolve, to any extent, only in those aqueous potassium cyanide solutions exposed to air. The reactions of potassium cyanide with water and oxygen within solutions of potassium cyanide and metallic gold produced similar products to those found in pure potassium cyanide solutions.

The addition of potassium hydroxide in concentrations greater than ~0.1M to aqueous potassium cyanide solutions depressed the rate of hydrolysis of potassium cyanide. However, concentrations far in excess of 1M potassium hydroxide would be necessary to prevent the formation of formate ion completely. Analyses confirmed that aqueous potassium gold cyanide solutions are very stable to heat, high concentrations of hydroxide ion and atmospheric oxygen, and show no detectable signs of decomposition. The solutions are likewise stable to acid at room temperature down to a *p*H of ~4.5, below which a slow decomposition to insoluble gold cyanide occurs. At *p*H 1, aqueous potassium gold cyanide solutions remain stable indefinitely at a temperature of 1°C. In mixtures of potassium gold cyanide, potassium cyanide, and potassium hydroxide, which are typical electroplating solution components, the stability of potassium gold cyanide was apparently unaffected. The reactions of potassium cyanide with water and oxygen within these mixtures gave no other products but those detected in a pure potassium cyanide solution. Potassium hydroxide merely decreased the rate of hydrolysis of the potassium cyanide.

Activated charcoal treatment of the cyanide solutions did not remove any of the ionic products of decomposition.

For many years, extensive use has been made of the cyanide-type gold electroplating bath within the electronics industry for processing a wide variety of components, devices, and circuitry. Much empirical information has been accumulated and used to control the many variables associated with the composition and performance of such baths.

For example, it is observed that variations in the brightness, porosity, hardness, impurity, and gas content of the gold electrodeposit depend on the plating bath composition, the nature of the bath additives, the current density, stirring rate, the temperature of the bath, and the final treatments of the material to be coated prior to immersion in the plating bath. However, this information has not been adequate to consistently secure gold deposits with reproducible characteristics, which are essential to electron device applications.

Although there is a great deal of the above empirical data available and although, each year, many patents are granted for new or unique plating bath compositions and for improved techniques of gold electrodeposition, surprisingly enough, very little is known about the basic mechanism of gold electrodeposition and, hence, the latter remains more of an art than a science.

It is apparent that, in order to relate the bath composition with the observable characteristics of the deposit and to establish appropriate techniques of control, an understanding of the basic mechanism of gold electrodeposition during electrolysis is desirable.

As a first step in the solution of this problem, there is a need to explore the inherent behavior of the electroplating solution constituents. Some of the first papers on the chemical reactions occurring within aqueous solutions of potassium cyanide are those of Wick (1) and Angles *et al.* (2), who report on the decomposition of cyanides in plating solutions. Their analyses detect substantial quantities of carbonate, formate, and cyanate ions together with minor amounts of urea and ammonia within the plating solutions.

Accordingly, a careful re-examination of the chemical reactions occurring within aqueous solutions of potassium cyanide, potassium gold cyanide, and mixtures of these compounds with potassium hydroxide, has been undertaken.

Experimental

Twelve Pyrex reaction vessels, each containing 200 ± 20g KCN (DuPont, 98.0% minimum purity) dis-

[1] Present address: General Telephone & Electronics Laboratories Incorporated, Bayside, New York 11360.

Key words: electrodeposition; gold electroplating; cyanide decomposition.

solved in deionized water and made up to 2 liters of solution, were placed upon Fisher combination hotplate and variable-speed magnetic stirrers in a conventional hood. The following experimental conditions were imposed on the reaction vessels: (a) six vessels were maintained at 70° ± 3°C, six maintained at 30° ± 2°C; (b) six solutions were exposed to air, six covered with a Pyrex lid to isolate them, but not hermetically, from air (these latter solutions were prepared using deionized water, which had previously been deaerated by bubbling a stream of nitrogen through the water for 18 hr); (c) four vessels were externally sprayed with flat black enamel paint to prevent visible radiation from penetrating through the walls, four vessels were exposed to laboratory visible radiation, while four were exposed to an intense source of visible radiation, produced by a General Electric Type S-4 lamp, placed about 18 in. above the reaction vessels. A diagram of the arrangement is shown in Fig. 1.

All 12 solutions were continuously stirred for 31 days with Teflon-covered stirring rods. A 50 ml sample from each reaction vessel was withdrawn at approximately the same time every day and sealed in a 50 ml glass bottle, which was then cooled to about 5°C. The following day, each solution was quantitatively analyzed for the components listed below

(a) CN^-	(e) $H.COO^-$ formate
(b) $CO_3^=$	(f) $C_2O_4^=$ oxalate
(c) pH	(g) NH_4^+
(d) CNO^-	(h) $CO(NH_2)_2$ urea

The above experiment was repeated exactly as described, except that a piece of gold, 99.99% pure, obtained from Engelhard Industries, of 16 cm^2 total surface area, was now placed on the bottom of each reaction vessel. The 12 solutions were quantitatively analyzed for the above components plus dissolved gold.

Results and Discussion

Experiment I.—The results of the quantitative chemical analyses, the majority of which were done in duplicate, have been plotted and are shown in Fig. 2-5. The accuracy of these results and subsequent results is ±5%. The graphs drawn for this experiment show that:

1. Those solutions (a) not heated and (b) isolated from air (Fig. 2) show little change in CN^- ion concentration over the period of 1 month.
2. Those solutions (a) not heated and (b) exposed to air (Fig. 3) show a drop in CN^- ion concentration (from ~40 to ~30 g/liter), a build-up of $CO_3^=$ ion concentration (from ~2 to ~9 g/liter) and an increase in $H.COO^-$ ion concentration (from 0 to ~2 g/liter) over the period of 1 month.
3. Those solutions (a) heated and (b) isolated from air (Fig. 4) show a drop in CN^- ion concentration (from ~40 to ~0.8 g/liter) and a build-up of $H.COO^-$ ion concentration (from 0 to ~72 g/liter) over the period of 1 month. Note the absence of $CO_3^=$ ion build-up.

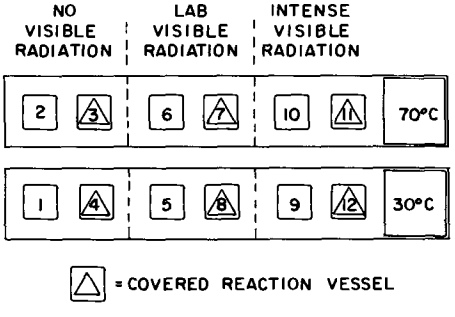

Fig. 1. Solution identification

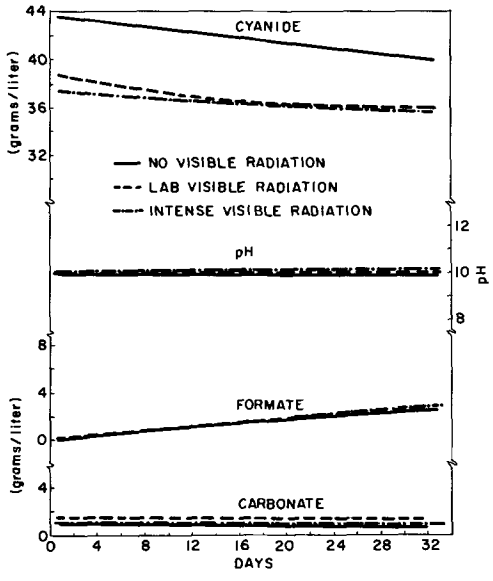

Fig. 2. KCN solution, temperature 30°, no air

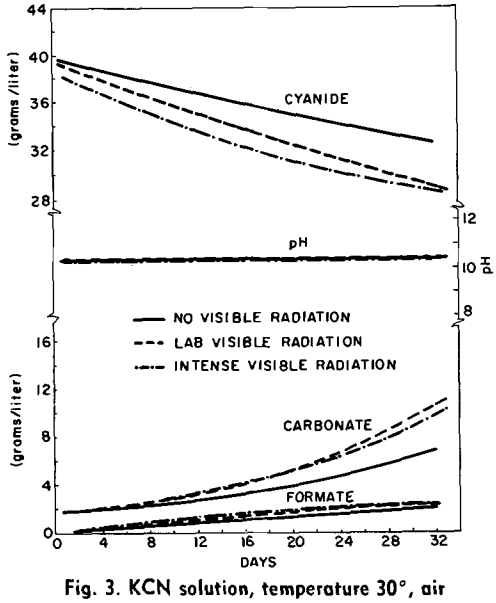

Fig. 3. KCN solution, temperature 30°, air

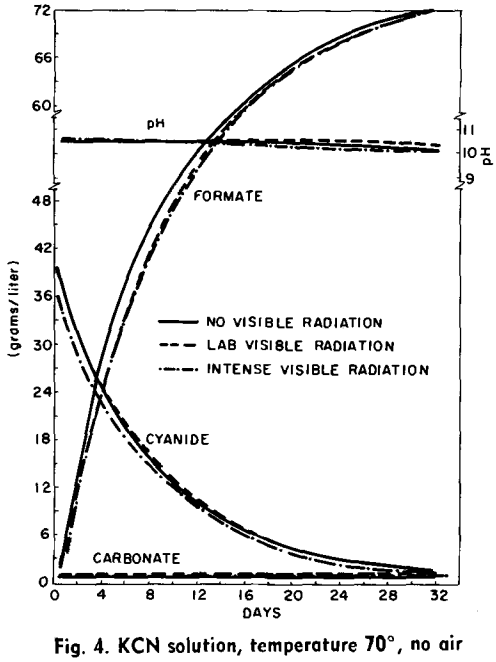

Fig. 4. KCN solution, temperature 70°, no air

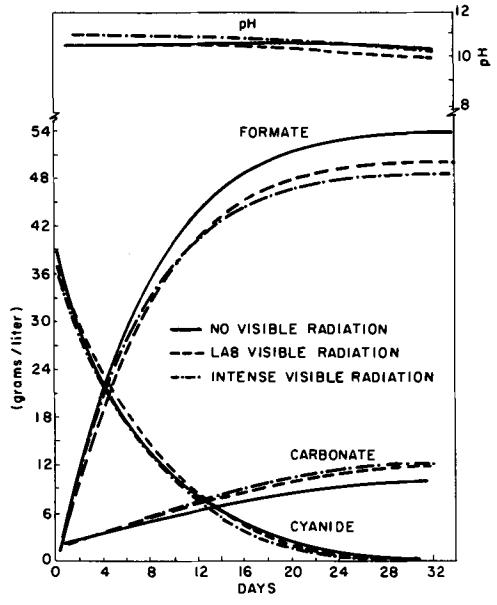

Fig. 5. KCN solution, temperature 70°, air

4. Those solutions (*a*) heated and (*b*) exposed to air (Fig. 5) show a drop in CN^- ion concentration (from ~40 to 0.1 g/liter), a build-up of $CO_3^=$ ion concentration (from ~2 to ~11 g/liter) and an increase of $H.COO^-$ ion concentration (from 0 to ~50 g/liter) over the period of 1 month.

5. The *p*H of all the solutions remains almost constant at 10.3 ± 0.3 over the period of 1 month.

Analytical data which have not been plotted show that:

6. The CNO^- ion concentration in any of the solutions does not exceed ~0.4 g/liter over the period of 1 month.

7. Urea and the $C_2O_4^=$ ion do not form to a concentration greater than 0.5 and 0.2 g/liter, respectively, over the period of 1 month.

8. The NH_4^+ ion is expelled from the solutions as gaseous NH_3. In the heated and covered solutions only (vessels 3, 7, and 11, Fig. 1), its concentration builds up after 7 days to a maximum of ~8 g/liter but then decreases slowly to <0.5 g/liter over the period of 1 month due to gradual escape.

A list of the possible chemical reactions, which may occur between the CN^- ion and atmospheric O_2 and CO_2 in the presence of water and visible radiation, is given below (3, 4)

$$CN^- + 1/2\,O_2 \rightarrow CNO^-$$

$$2CNO^- + 3/2\,O_2 \rightarrow CO_3^= + CO_2 + N_2$$

$$2CN^- + CO_2 + H_2O \rightarrow CO_3^= + 2HCN$$

$$2CN^- + 2H_2O + 2OH^- + O_2 \rightarrow 2CO_3^= + 2NH_3$$

$$HCN + 2H_2O \rightarrow NH_4.OOCH \text{ ammonium formate}$$

$$HCNO + H_2O \rightarrow NH_4.CNO \xrightarrow{H_2O} CO(NH_2)_2 \text{ urea}$$

$$HCN + H_2O \xrightarrow{hv} \begin{matrix} COO.NH_4 \\ | \\ COO.NH_4 \end{matrix} \text{ ammonium oxalate}$$

In the solutions which were heated and isolated from air, the total reaction of the CN^- ion with water to form ammonium formate (Fig. 4), corresponds to an approximate 100% conversion, according to the equations

$$KCN + H_2O \rightarrow KOH + HCN$$

$$HCN + 2H_2O \rightarrow H.COO^- + NH_4^+$$

$$NH_4^+ \rightarrow NH_3\uparrow + H^+$$

The slightly higher, initial *p*H values found for the heated solutions (Fig. 4, 5) probably result from the presence in solution of moderate quantities of NH_3. Since the rate of production of ammonium formate starts to decrease after about the seventh day, but the rate of evolution of NH_3 remains practically constant, the *p*H of the heated solutions also slightly decreases, *e.g.* from 10.3 to 10.1.

In order to determine the free CN^- ion within the solutions, just sufficient $AgNO_3$ solution was added to form the complex ion $Ag(CN)_2^-$. At this point, the *p*H of the solutions was measured, since, then, the CN ion would not contribute to the acid-base equilibrium.

The constant *p*H of ~10.3 observed for all the solutions over the period of 1 month suggests that the bicarbonate-carbonate equilibrium

$$HCO_3^- \rightleftharpoons H^+ + CO_3^=$$

occurring at *p*H 10.25 is responsible for this value. Free hydroxide ion is probably not present since, if it had existed, a higher *p*H would have been expected.

The formation of $CO_3^=$ ion within the solutions exposed to air can occur *via* the reactions

$$CN^- + 1/2\,O_2 \rightarrow CNO^-$$

$$2CNO^- + 3/2\,O_2 \rightarrow CO_3^= + CO_2\uparrow + N_2\uparrow$$

The low concentration of CNO^- ion in all the solutions over the period of 1 month is presumably due to its almost immediate oxidation to $CO_3^=$ ion. Thus, the CN^- ion concentration is reduced.

If the formation were to occur *via* the reaction of CO_2 with the CN^- ion

$$2CN^- + CO_2 + H_2O \rightarrow CO_3^= + 2HCN$$

then regeneration of HCN would result and no drop in the CN^- ion concentration would be observed. This latter prediction is contrary to observation, hence the former reaction path probably predominates.

Similarly, if the formation of $CO_3^=$ ion were to occur *via* the reaction

$$2CN^- + 2H_2O + 2OH^- + O_2 \rightarrow 2CO_3^= + 2NH_3\uparrow$$

then a drop in *p*H of the solutions would be expected owing to the removal of OH^- ions. Since this prediction is again contrary to observation, the first reaction path probably predominates.

Different levels of visible radiation appear to affect only the production of $CO_3^=$ ion from CN^- ion. Those solutions exposed to visible radiation show a concentration of $CO_3^=$ ion 33-50% higher than that in the unirradiated solutions. Thus, it would appear that visible radiation catalyzes the carbonate-producing reaction

$$CN^- + 1/2\,O_2 \xrightarrow{hv} CNO^-$$

$$2CNO^- + 3/2\,O_2 \xrightarrow{hv} CO_3^= + CO_2\uparrow + N_2\uparrow$$

A Kjeldahl test for total nitrogen on one of the solutions indicated that there are no nitrogen-containing compounds present within that solution that are passing undetected. Moreover, a drop in CN^- ion concentration within the solutions may be satisfactorily accounted for by a corresponding increase in the concentration of $CO_3^=$ and $H.COO^-$ ions.

This apparent agreement among the various data gives confidence that all major components of the solutions have been detected.

After the experiment had been run continuously for about 10 days, some crystalline material was observed in those solutions which were heated and exposed to air (reaction vessels 2, 6, and 10, Fig. 1). Approximately a week later, the same crystalline material was observed in those solutions which were heated but isolated from air (reaction vessels 3, 7, and 11). Upon analysis of this material, it was found to consist mainly

of silicon, possibly in the form $K_2SiO_3.(H_2O)_x$, which had been leached out of the Pyrex reaction vessel. Apparently, heating and the presence of air or, more accurately, oxygen, causes an acceleration of the leaching action of the KCN solutions.

A purification procedure widely used throughout the electroplating industry to remove solid material and "organics" from plating baths is to heat and stir the electroplating solutions with a small quantity of activated carbon and subsequently to filter.

In order to assess quantitatively the effect of activated carbon on a KCN solution, two additional samples from reaction vessels 5 and 6 (Fig. 1) were heated and shaken with activated carbon for ½ hr, centrifuged, and finally quantitatively analyzed for the same components as the other 12 regular samples on the final day of the experiment. The results showed that there was essentially no difference in the individual ionic concentrations between the carbon-treated samples 5 and 6 and the untreated samples 5 and 6.

Consequently, activated charcoal is not effective for removing ionic material from cyanide solutions.

A plot of ln[concentration of CN^- ion] *vs.* time for the solutions 3 and 4, 7 and 8, 11 and 12 (Fig. 1), which were isolated from air, gives straight lines, indicative of a first-order or pseudo first-order reaction. The slope of the lines for the solutions maintained at 70°C, 3, 7, and 11, is much greater than for the solutions maintained at 30°C, 4, 8, and 12. In these six solutions, the only reaction occurring was that between the KCN and water

$$(a)\quad KCN + H_2O \rightleftharpoons KOH + HCN$$

$$(b)\quad HCN + 2H_2O = H.COONH_4$$

The absence of air prevented the additional oxidation reaction of CN^- to $CO_3^=$, but, in the remaining six solutions, exposed to air, a deviation from linearity of the ln[CN^-] *vs.* time graphs was observed. Hence, since the hydrolysis reaction (*a*) is very rapid, the rate of formation of ammonium formate (*b*) is directly proportional to the concentrations of HCN and water within the solutions

$$\frac{d[H.COONH_4]}{dt} \propto [HCN]\,[H_2O]^2$$

or

$$\frac{d[H.COONH_4]}{dt} = k[HCN]\,[H_2O]^2$$

where k is the velocity constant for that reaction. Since the water is present in very large excess, its concentration is essentially constant throughout the course of the reaction. The velocity equation, thus takes the form

$$(c)\quad \frac{d[H.COONH_4]}{dt} = k^*[HCN]$$

so that the rate of formation of $H.COONH_4$ is proportional to the concentration of HCN. Thus, this termolecular second-order reaction becomes kinetically of the first order or a pseudo-unimolecular reaction.

Another way of now expressing Eq. (c) would be to state that the rate of disappearance of the CN^- ion is proportional to its concentration at any one instant

$$\frac{-d[CN^-]}{dt} = k[CN^-]$$

This equation upon integration yields

$$-\ln[CN^-] = kt + K$$

where K is the constant of integration.

Thus, the plot of ln[CN^-] *vs.* time for the six previously mentioned solutions yields straight lines of negative slope, as shown in Fig. 6. The gradient of these lines is a measure of the velocity constant k at the temperature chosen for the reaction.

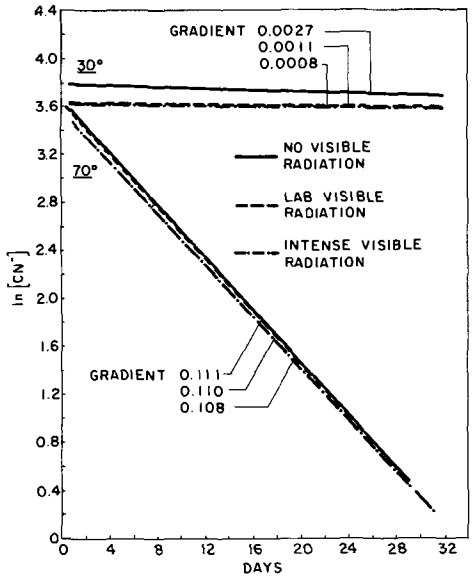

Fig. 6. KCN solution, no air

The half life, $t_{1/2}$, of a first-order reaction may be calculated using the equation $t_{1/2} = 0.693/k$. Hence, for the heated solutions, the half life is calculated to be between 6 and 7 days. This value agrees excellently with the half life observed experimentally for the depletion of the cyanide ion.

Using the integrated form of the Arrhenius equation

$$\ln k = \text{constant} - E/RT$$

where R is the gas constant and T the absolute temperature, the following values for the activation energy E have been obtained

(*a*) $E = 20$ kcal mole^{-1} (k values 0.111 and 0.0027)
(*b*) $E = 24$ kcal mole^{-1} (k values 0.110 and 0.0011)
(c) $E = 26$ kcal mole^{-1} (k values 0.108 and 0.0008)

If any significance can be attributed to the calculated activation energy values and, particularly, the increase in activation energy for the three pairs of solutions exposed to (*a*) no visible radiation, (*b*) laboratory visible radiation, and (c) an intense source of visible radiation, one must conclude that it becomes increasingly difficult for the reaction of HCN with water to occur as the intensity of visible radiation increases.

Experiment II.—Figures 7-10 plotted from the quantitative analytical results obtained for Experiment II

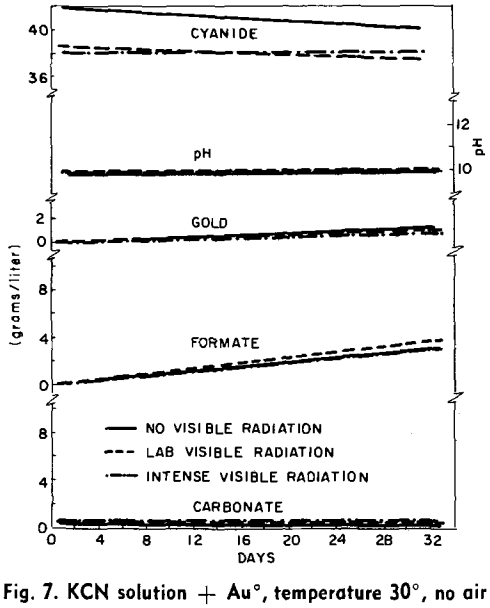

Fig. 7. KCN solution + Au°, temperature 30°, no air

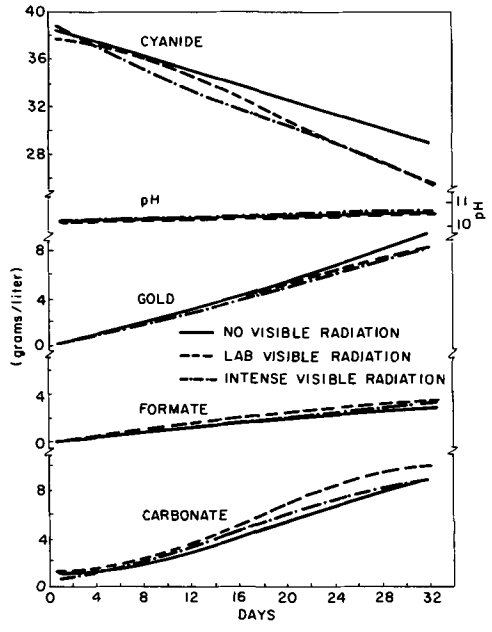

Fig. 8. KCN solution + Au°, temperature 30°, air

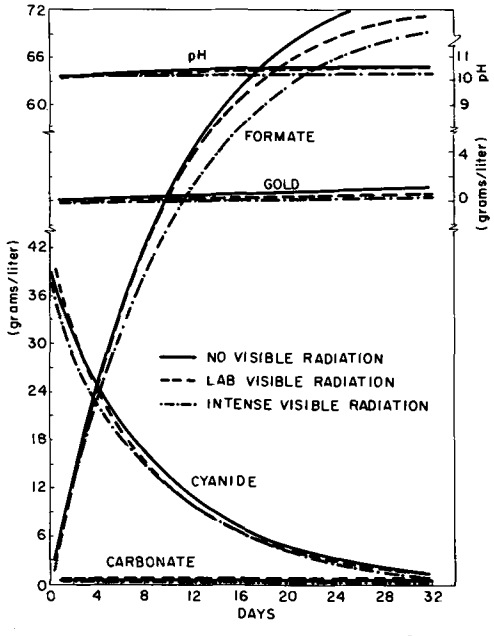

Fig. 9. KCN solution + Au°, temperature 70°, no air

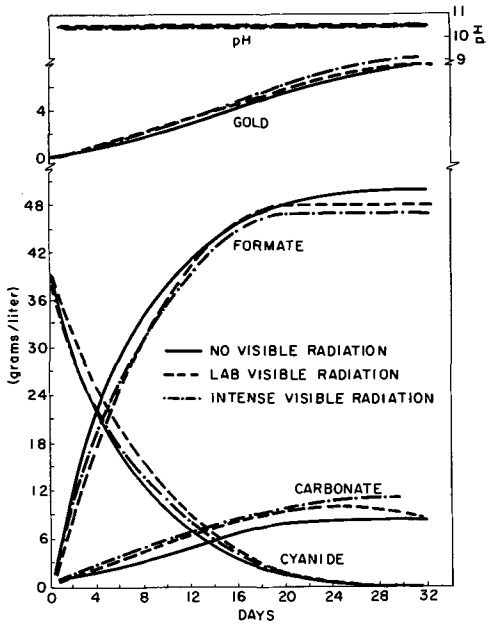

Fig. 10. KCN solution + Au°, temperature 70°, air

reveal a close similarity to those plotted for Experiment I.

1. Those solutions (*a*) not heated and (*b*) isolated from air (Fig. 7) show little change in CN^- ion concentration over the period of 1 month.

2. Those solutions (*a*) not heated and (*b*) exposed to air (Fig. 8) show a drop in CN^- ion concentration (from ~38 to ~27 g/liter), a build-up of Au concentration (from 0 to ~8 g/liter), an increase in $CO_3^=$ ion concentration (from ~1 to 9 g/liter) and a build-up of $H.COO^-$ ion concentration (from 0 to 3 g/liter) over the period of 1 month.

3. Those solutions (*a*) heated and (*b*) isolated from air (Fig. 9) show a drop in CN^- ion concentration (from ~39 to 1.5 g/liter), an increase in Au concentration (from 0 to ~0.8 g/liter), and a build-up of $H.COO^-$ ion concentration (from 0 to ~72 g/liter) over the period of 1 month. Note the absence of $CO_3^=$ ion build-up.

4. Those solutions (*a*) heated and (*b*) exposed to air (Fig. 10) show a drop in CN^- ion concentration (from ~39 g/liter to 0), a build-up of Au concentration (from 0 to ~8 g/liter), an increase in $CO_3^=$ ion concentration (from ~1 to ~10 g/liter), and a build-up of $H.COO^-$ ion concentration (from 0 to ~48 g/liter) over the period of 1 month.

5. The *p*H of all the solutions remains almost constant at 10.3 ± 0.3 over the period of 1 month.

Analytical data which have not been plotted show that:

6. The CNO^- ion concentration in any of the solutions does not exceed ~0.7 g/liter over the period of 1 month.

7. Urea and the $C_2O_4^=$ ion do not form to a concentration greater than 0.5 and 0.2 g/liter, respectively, over the period of 1 month.

8. The NH_4^+ ion is expelled from the solutions as gaseous NH_3. In the heated and covered solutions only (vessels 3, 7, and 11, Fig. 1), its concentration builds up, after 5 days, to a maximum of ~7 g/liter but then decreases slowly to <0.5 g/liter over the period of 1 month, due to gradual escape.

It is immediately apparent from the results that gold dissolves, to any extent, only in those KCN solutions which are exposed to air—oxygen, presumably, being the active ingredient—according to the equation

$$2Au + 4CN^- + 1/2\ O_2 + H_2O \rightarrow 2Au(CN)_2^- + 2OH^-$$

Since the OH^- ion is produced in the above reaction, the *p*H of a solution, in which much gold dissolves, might be expected to rise. This was observed for solutions 1, 5, and 9 (Fig. 1) in which the *p*H rose slightly from ~10.2 at the start of the experiment to ~10.6 at the end of the 1-month period. During this time, ~8 g/liter of gold had dissolved but only ~3 g/liter of $H.COO^-$ ion had been produced.

A similar condition might be expected for solutions 2, 6, and 10 in which ~8 g/liter of gold had also dissolved. But, it was observed that the *p*H of these solutions remained constant at ~10.5 over the 1-month period. A possible reason for this is that the OH^- ion is being neutralized by a small proportion of the 48 g/liter of $H.COO^-$ ion or, rather, the H^+ ion associated with the hydrolysis of formic acid H.COOH, also produced during the reaction. Calculations show that the presence of OH^- ions does not appear to alter the mechanism of formation of $CO_3^=$ ion from CN^- ion, *i.e.*, it proceeds, using oxygen, *via* the CNO^- ion.

An interesting observation made after the third day of the experiment was that the piece of gold, placed on the bottom of reaction vessels 6 and 10, and prob-

ably 2 also (Fig. 1), had become markedly discolored. By the sixth day, on gently shaking vessels 2, 6, and 10 (Fig. 1), thin flakes of gold were seen to become detached from the gold substrate, to float around in the solution for several minutes and then, apparently, to disappear. It was subsequently found that the flakes rejoined the mass of gold, *i.e.*, became reattached to the surface of the gold, which appeared to be "moulting." A bright substrate was visible under the peeling, dark-brown surface film.

Since vessels 2, 6, and 10 were exposed to air, which is required for the dissolution of gold in KCN solution, it was suspected that the dark-brown film observed was a hydrated form of insoluble Au_2O_3 (5) which possibly, is formed as an intermediate in the reaction path to the soluble $Au(CN)_2^-$ ion. After the period of 1 month, an examination of the surface of two different gold pieces by transmission electron microscopy could only detect Au and AuCN diffraction patterns. This failure to detect the diffraction pattern of Au_2O_3 has been commented on previously (5) and a similar problem has been encountered in this work.

Most of the observations and deductions made from the results of Experiment I, in which an aqueous KCN system was alone considered, can be applied to the results of Experiment II. Only those which are different are discussed further.

The production of NH_3 within the solutions does not appear to affect the *p*H of those solutions, as described for Experiment I. Possibly, the formation of the OH^- ion, which is a stronger base than NH_3, overshadows any effect that the NH_4^+ ion may have within the solutions.

Different levels of visible radiation appear not to affect any of the reactions occurring within the KCN/Au solutions, this being contrary, for reasons presently undetermined, to what was observed in Experiment I. The $CO_3^=$ ion concentration in solutions 1, 5, and 9 and 2, 6, and 10 (Fig. 1) are all similar (Fig. 8 and 10). It is also evident that the dissolution of gold in aqueous KCN is not dependent on the catalyzing action of visible radiation (Fig. 8 and 10), but depends solely on the presence of oxygen.

Once again, a drop in CN^- ion concentration within the solutions may be satisfactorily accounted for by a corresponding increase in the concentration of Au, $CO_3^=$ ions, and $H.COO^-$ ions. It would appear that the presence of metallic gold within the KCN solutions adds little more than an extra competitor, along with oxygen and water, for the CN^- ions.

Crystalline material was again observed in reaction vessels 2, 6, and 10 (Fig. 1) after about 10 days and, approximately a week later, the same material became visible in reaction vessels 3, 7, and 11 (Fig. 1). Presumably, it had the same composition and was derived from the same source, the Pyrex reaction vessel, as in Experiment I.

The results of both experiments indicate that visible radiation appears to play a minor role in the majority of reactions occurring within KCN and KCN/Au solutions. From the information gained above, further work was initiated on a less extensive scale to observe the effect of varying quantities of KOH on the reactions of KCN with water; of heat, KOH, and mineral acids on the stability of $KAu(CN)_2$ solutions; and of a low and a high concentration of KOH on the chemical reactions occurring in a solution of KCN and $KAu(CN)_2$.

The experiment performed to observe the effect of varying concentrations of KOH on the hydrolysis of KCN and the reactions of KCN with water and oxygen indicated immediately that the presence of KOH in concentrations greater than ~0.1M depressed the rate of hydrolysis of KCN, and hence the disappearance of the CN^- ion, in proportion to its concentration. A concentration of KOH of 0.1M or less did not appear to affect the hydrolysis of KCN at all, as shown by the following calculations.

A comparison was made between the rate of depletion of CN^- ions in a pure KCN solution, as described in Experiment I, and the rate of depletion in KCN/KOH solutions over the same time interval and under the same conditions. With no air present and over a period of 10 days, a pure KCN solution lost 68% of its CN^- ions. In comparable KCN/KOH solutions, the CN^- ion concentrations dropped (*a*) 68%, (*b*) 64%, and (*c*) 60% for KOH concentrations within the solutions of (*a*) 0.1M, (*b*) 0.5M, and (*c*) 1.0M. With air present and over the same time interval, a pure KCN solution lost 70% of its CN^- ions. In the KCN/KOH solutions, the CN^- ion concentrations dropped (*a*) 70%, (*b*) 64%, and (*c*) 59% for KOH concentrations of (*a*) 0.1M, (*b*) 0.5M, and (*c*) 1.0M.

A drop in CN^- ion concentration within these solutions was satisfactorily accounted for by a corresponding increase in the concentration of $H.COO^-$ and $CO_3^=$ ions, although, at KOH concentrations of 0.5M and 1.0M in those solutions exposed to air, the $CO_3^=$ ion concentrations after 10 days were found to be ~80% and ~120% higher, respectively, than in comparable pure KCN solutions after the same time interval. This increase was attributed to the absorption of CO_2 from the atmosphere. The calculations made above indicated that, as the concentration of KOH increased, so the formation of $CO_3^=$ ion followed the alternative route indicated in the following equation

$$2CN^- + 2H_2O + 2OH^- + O_2 \rightarrow 2CO_3^= + 2NH_3$$

Once again, the CNO^- ion concentration in any of the solutions did not exceed 0.2 g/liter and urea and the $C_2O_4^=$ ion did not form to a concentration greater than 0.5 and 0.2 g/liter, respectively, over the period of 10 days.

The experiment performed to verify the stability of $KAu(CN)_2$ solutions toward heat, alkali, atmospheric oxygen, and mineral acids showed that, for heated aqueous solutions of $KAu(CN)_2$ exposed and isolated from air, a quantitative analysis of the ionic components remained invariant over a period of 10 days.

Treatment of a sample of the above $KAu(CN)_2$ solutions with activated charcoal for ½ hr and subsequent reanalysis for gold showed no change in the gold concentration. This suggests that activated charcoal does not remove gold, as the dicyano complex, from a pure $KAu(CN)_2$ solution which contains no other ingredients.

In solutions of $KAu(CN)_2$ with 1M KOH, a quantitative analysis of the ionic components remained invariant over a period of 10 days, except for the $CO_3^=$ ion, the concentration of which increased from 0 to ~8 g/liter in the solution exposed to air and to 0.8 g/liter in the solution isolated from air. This increase was attributed solely to the absorption of CO_2 from the atmosphere. The above results indicate that $KAu(CN)_2$ solutions are indeed very stable to heat, alkali, and atmospheric oxygen and certainly show no signs of decomposition within the 10 days that the experiment was run.

However, on the addition of dilute HCl, H_2SO_4, or H_3PO_4 to pure unbuffered $KAu(CN)_2$ solutions, yellow AuCN slowly deposited from those solutions which were maintained at room temperature at or below a *p*H of about 4.5, and was first noticed after about 16 hr. The amount of AuCN deposited from the $KAu(CN)_2$ solution, acidified with H_3PO_4, appeared to be less than that observed in the $KAu(CN)_2$ solutions acidified with HCl and H_2SO_4. This could be expected, since H_3PO_4 is a weaker acid than either HCl or H_2SO_4 and therefore may not be able to decompose the $KAu(CN)_2$ as rapidly as the stronger acids. However, by the fifth day of standing, the deposit in the solution containing the H_3PO_4 had increased, while the others remained approximately constant.

A $KAu(CN)_2$ solution acidified with H_3PO_4 to *p*H 1 and left in the refrigerator at 1°C was opalescent after the 16-hr period with only some minor deposition of yellow AuCN. No change in the density of the deposit was observed even after 5 days at this temperature. Thus, the temperature of the solutions plays a large part in determining the rate of breakdown of the $KAu(CN)_2$ to insoluble AuCN. In fact, if any of the above solutions, when freshly prepared, are heated to 65° ± 5°C, AuCN readily precipitates within ½ hr.

The effect of the acids may be similar to the reaction of H_2SO_4 with NaCl, *e.g.*,

$$NaCl + H_2SO_4 \rightarrow NaHSO_4 + HCl$$

so,

$$KAu(CN)_2 + H_2SO_4 \rightarrow KHSO_4 + HAu(CN)_2$$

$$HAu(CN)_2 \rightarrow HCN\uparrow + AuCN\downarrow$$

The acid, $HAu(CN)_2$, is unstable and readily decomposes at elevated temperatures, depositing yellow AuCN and evolving HCN.

The experiment performed to observe the effect of varying concentrations of KOH on the chemical reactions occurring within heated aqueous solutions of KCN and $KAu(CN)_2$ provided results which, as expected, closely paralleled those obtained earlier in this paper. A concentration of, for example, 3 g/liter KOH did not decrease the rate of hydrolysis of KCN, although, at a concentration of 1M KOH, a slight decrease was noted. The gold concentration within the solutions did not change over a period of 10 days, confirming that it was still present as a soluble complex.

A drop in CN^- ion concentration within the solutions was again satisfactorily accounted for by a corresponding increase in the concentration of $HCOO^-$ and $CO_3^=$ ions, although, at the 1M KOH concentration in the solution exposed to air, the $CO_3^=$ ion concentration after 10 days was found to be ~180% higher than in a comparable pure KCN solution after the same time interval. This increase was attributed to the absorption of CO_2 from the atmosphere. From the calculations made above, it appears that, at the 1M KOH concentration, the formation of $CO_3^=$ ion follows the route

$$2CN^- + 2H_2O + 2OH^- + O_2 \rightarrow 2CO_3^= + 2NH_3$$

The CNO^- ion concentration in any of the solutions did not exceed 0.2 g/liter and urea and the $C_2O_4^=$ ion did not form to a concentration greater than 0.5 and 0.2 g/liter, respectively, over the period of 10 days.

Conclusion

In aqueous KCN solutions, isolated from air and maintained at 70°C, the KCN is hydrolyzed to form HCN, which then further reacts with the water to form ammonium formate. This reaction, which is a pseudo first-order reaction with an activation energy of ~24 kcal $mole^{-1}$ and a half life of ~6.5 days, is unaffected by different levels of visible radiation but its rate is much reduced at 30°C.

In aqueous KCN solutions, exposed to air and maintained at either 30° or 70°C, not only is the KCN hydrolyzed, as explained above, to form eventually ammonium formate, but also the CN^- ion reacts directly with atmospheric oxygen to form, *via* the CNO^- ion, $CO_3^=$ ions. This latter reaction appears to be accelerated by visible radiation and by raising the temperature from 30° to 70°C.

The *p*H of aqueous KCN solutions all remain constant at ~10.3, while a Kjeldahl test for total nitrogen and calculations based on the concentrations of reactants and products indicate that all major components of the solutions have been detected and analyzed for.

In aqueous KCN solutions, urea, the CNO^- and $C_2O_4^=$ ions do not form to a concentration greater than 0.5 g/liter and the NH_4^+ ion is expelled eventually from all solutions as gaseous NH_3.

Gold dissolves to any extent only in those KCN solutions which are exposed to air. Its dissolution is not dependent on the catalyzing action of visible radiation but solely on the presence of oxygen.

The reactions of KCN with water and oxygen within the KCN/Au solutions produce similar products to those found in pure KCN solutions.

The addition of KOH to a KCN solution in concentrations greater than ~0.1M depresses the rate of hydrolysis of KCN in proportion to its concentration. The reaction of the HCN produced and of CN^- ions with water and oxygen gives no new products other than those detected in a pure KCN solution. The effect of a 0.1M concentration or less of KOH on the prevention of hydrolysis of KCN solutions would appear to be negligible.

Solutions of $KAu(CN)_2$ are very stable to heat, alkali, and atmospheric oxygen and show no signs of decomposition. However, at room temperature, they slowly decompose over a period of several hours, depositing yellow AuCN at or below *p*H 4.5, while, at 65°C, a thick yellow deposit precipitates well within ½ hr. If the temperature is maintained at about 1°C, solutions of $KAu(CN)_2$ remain stable indefinitely at *p*H 1.

The addition of 3 g/liter KOH to a KCN/$KAu(CN)_2$ solution does not decrease the rate of hydrolysis of the KCN, although, at a concentration of 1M KOH, a slight decrease is noted. The stability of $KAu(CN)_2$ is apparently unaltered in its solutions with KCN and KOH. The reaction of the HCN produced and of CN^- ions with water and oxygen gives no other products but those detected in a pure KCN solution.

Activated charcoal treatment of any of the cyanide solutions does not remove the ionic impurities generated in these solutions by chemical decomposition.

Work is presently in progress to determine the effect of electrolysis on the chemical reactions occurring within aqueous KCN solutions. The results will be reported and discussed in a forthcoming publication.

Acknowledgment

The author wishes to thank Dr. M. J. Elkind for the frequent stimulating discussions, which aided in the interpretation of the results, and the encouragement given to this work. He also acknowledges the technical assistance given by E. W. Hobart, Jr., of Ledoux & Company, in the design of the sample analysis procedure.

Manuscript submitted July 2, 1968; revised manuscript received September 25, 1968.

REFERENCES

1. R. M. Wick, *Proc. Am. Electroplaters' Soc.*, **20,** 113 (1932).
2. R. M. Angles, F. V. Jones, J. W. Price, and J. W. Cuthbertson, *J. Electrodepositors' Tech. Soc.*, **21,** 19 (1946).
3. Sneed, Maynard, and Brasted, "Comprehensive Inorganic Chemistry, Vol. II," Van Nostrand Co., (1954).
4. Moeller, "Inorganic Chemistry," John Wiley & Sons, Inc., (1952).
5. S. Barnartt, *This Journal*, **106,** 722 (1959).

Chlorates and Perchlorates Safety

Carl M. Olson*

Industrial Chemicals Division, Hooker Chemical Corporation, Niagara Falls, New York

ABSTRACT

More than 65 years of American production of sodium chlorate and its use have shown that this oxidant can be handled safely, or that misused it can be extremely hazardous. With any oxidizable substance, it can provide oxygen for fire, or even explosion, if ignited by heat, friction, or pressure unless kept wet. This applies to clothing, including gloves and shoes, buildings, equipment, lubrication, and materials. It is relatively innocuous on body contact, but can be fatally poisonous if ingested in quantities of ½ to 1 oz unless proper medical attention is given. Since it is a source of oxygen, fires involving it cannot be smothered but are extinguished by water. CO_2 snow may provide sufficient cooling to extinguish small fires. Fire blankets and dry powder extinguishers are ineffective.

Potassium chlorate manufacture in the U.S.A. started near the end of the 19th century. Sodium chlorate has been produced in Niagara Falls since 1902. By 1967 there were five U.S. producers of it. Domestic production of potassium perchlorate was begun in 1910. With the increasing number of producers and users, it is quite proper to review the hazards of chlorates and perchlorates and the precautions to be taken in order to work safely with them.

Sodium chlorate by itself is relatively stable; potassium chlorate even more so. Provided the properties are known and given due consideration, chlorates can be and are handled safely. It is very important that this be understood by all persons involved.

There are several good references on chlorates safety. Two are the Manufacturing Chemists' Association Safety Data Sheet SD-42, Sodium Chlorate (1952); and the National Safety Council Data Sheet D-371 (1967). American Potash & Chemical Corp. has a 10½-minute movie in color on the subject.

Walter P. Huhn of American Potash & Chemical Corp. presented a paper covering hazards of sodium chlorate and safe procedures to be used at an ASTME meeting in New York, October 26, 1967. It is a concise, well-organized, up-to-date treatise worth careful study. J. S. Sconce of Hooker Chemical Corp. gave a similar paper at that meeting. Material was drawn from both, as well as forty years of experience with chlorates and perchlorates, in preparing this paper.

Sodium chlorate, $NaClO_3$, is a moderately hydroscopic, white crystalline oxidant, which melts at 248°C and starts to decompose at about 300°C liberating oxygen. Decomposition is exothermic and self sustaining above a critical temperature. The large amounts of oxygen released in case of fire can cause burning of combustible material to be explosively rapid.

Many substances catalyze the thermal decomposition and some form explosive mixtures with sodium chlorate. Such mixtures, particularly those involving organic materials, such as alcohols, solvents, sugars, sawdust, paint and painted metals, lint, vegetable dusts, and oils and greases, or with inorganic materials, such as sulfur, sulfides, ammonium compounds, phosphorus, cyanides, acids, metallic oxides, or reducing agents of any sort, may be extremely sensitive to shock, friction, or heat, and burn or explode spontaneously. Paper, wood, cloth and leather impregnated with chlorate by contact with an aqueous solution are dangerously combustible when dry and may be ignited by friction or heat.

Alkaline chlorate solutions do not exhibit strong oxidizing properties. As the *p*H decreases, the oxidizing activity of chlorate solutions increases. Concentrated acid solutions are vigorous oxidizing agents as a result of formation of chloric acid, a powerful, unstable oxidizing acid known only in solution. In the cold, solutions containing up to about 30% $HClO_3$ are stable in the absence of organic matter and reducing agents. More concentrated solutions decompose spontaneously with the formation of oxides of chlorine, chlorine, oxygen, and perchloric acid. With oxidizable matter, the reaction may be violent, especially at elevated temperatures. Also, chlorine dioxide is an explosive gas in certain concentrations.

Handling Precautions

Clean work clothing must be worn each day and laundered afterwards. It must not be taken home. Clothing wet with chlorate solution should be changed before drying. No smoking can be permitted in chlorate work areas or while wearing work clothes. Deluge-type safety showers should be provided. Some prefer jump tanks (a bath tub old or new, or its equivalent) that will more quickly quench burning trouser legs. Salt can be added to this emergency water to prevent freezing in winter. Rubber shoes must be worn and linings rinsed, if contaminated. Only rubber or rubberized gloves are permitted, and without cloth wristlets. Avoid skin oils, greases, or protective creams. Shower before leaving work.

Clothing fires from smoking have occurred. One October 23, 1967 nearly cost a young worker in Michigan his life. He was permitted to work without a rubber apron or rubber shoes, *etc.* Uncomfortable because his clothing became stiff from dried chlorate solution, he went to the locker room to change. He lit a cigarette, his clothing ignited and he suffered burns on 52% of his body. Warnings had not been heeded or enforced.

A worker with dry chlorate dust on one sleeve used an abrasive wheel grinder in a nearby shop. A spark ignited the sleeve. He convalesced 40 days and has a badly scarred arm. Several farm workers have suffered burns from ignition of chlorate-contaminated clothing, one fatally in 1967. These are but a few cases, all unnecessary if the available information had not been ignored.

Sodium chlorate is not irritating or very toxic by contact or by inhalation. Dust masks are worn only if dusting is excessive. Ingestion of 15-30g may be fatal as it changes hemoglobin to methemoglobin, but August 5, 1957 a research physician at the Buffalo University Medical School survived a measured 40g dose taken by mistake instead of sodium chloride. He was saved by an artificial kidney and massive transfusion of 18 pints of blood, and apparently suffered no ill after-effects. [*JAMA* **180**, 1133 (1962).]

Storage

Sodium chlorate should not be stored close to flammable materials, reducing agents or other substances hazardous with it. Buildings in work areas should be

* Vice-Chairman, National Safety Council Chemical Section.

fireproof. Wood becomes dangerously combustible, so should not be used in any chlorate area. (Treatment with sodium silicate water glass beforehand and periodically thereafter may afford some protection). Chlorate-contaminated wood may ignite from pressure or friction. It must not be left where it could be taken or used, but should be disposed of by burning.

Spillage should be picked up for reuse or disposal, which may be sewering with lots of water. If this is not permissible, bury it in an isolated area away from trees as it is a herbicide. Wash drums with water and carefully burn any paper liners.

Discharge dust ventilating systems to a water scrubber designed for easy flushing with water and clean frequently.

Equipment

Dust control or prevention of contamination by chlorate solution is particularly important where motors are used, since mixtures of sodium chlorate with oil or grease are violently explosive. Hooker now uses totally-enclosed fan-cooled ball bearing type electric motors, not oil-lubricated bearings. Once or twice a year, the end bell is taken off and the area around the fan and the air-cooling passages is cleaned. When motors with outside bearings were used in dusty locations, they were completely protected by enclosure in clean air pressurized cabinets. Open motors in other chlorate service had a steel-plate deflection shield at the back to stop any flame from jetting out in case the motor caught fire. An open motor explosion at a rotary drier blew part of roof off and steel window frames out although doors were wide open. Chunks of motor went through remaining roof and brick wall. About the mid-forties, an explosion of a totally-enclosed motor in chlorate service was reported. There were fatalities.

In his paper, Walter P. Huhn of American Potash & Chemical Corp. says, "TEFC motors with sealed bearings (metallic seals) are acceptable, but the bearings should be cleaned and packed before use with one of the recommended lubricants, fluorolube or halocarbon or Kel-F, and should be changed once a year, whether they need it or not, in areas where contamination is possible. Extreme care should be taken in removing the bearings. They should be pressed off with a steel safety shield between them and the mechanic: bearings sometimes explode if tapped with a hammer. After removal, the bearings should be washed free of any sodium chlorate that may have entered them."

The same hazard exists for pumps and bearings. At Hooker, chlorate liquor pumps have braided Teflon packing surface-lubricated with fluorolube (halocarbon or Kel-F could be used) to be graphite-free and processed for oxygen service. As a second precaution, there is in with the packing, a lantern ring for a flow of water of 2-5 gal/hr measured by a purge meter to maintain a pressure of about 5 psi above the chlorate liquor pressure on the seal.

Shaft flingers keep chlorate solutions from creeping into bearings. A fluorinated lubricant should be used for bearings exposed to chlorate dusts or solutions. And be certain that it is not contaminated with other lubricants. Aluminum (and possibly magnesium) seals, sleeves, and cages must not be used as the fluorinated lubricant may break down and explode if finely divided aluminum and other active metals are present. There are some differences of opinion as to whether fluorinated lubricants are always suitable for high speed applications. Where oxidizable lubricants are still used, they are applied frequently to flush out any contaminated lubricant. However, channeling may permit some contaminated lubricant to remain. Samples of such lubricant are analyzed periodically for oxidants. Bearings should not be run hot and should be armored against explosions by at least ¼-in. steel plate with enough space to contain an explosion.

Several incidents have demonstrated the power of minute quantities of chlorate or perchlorate closely confined with oxidizable material. In 1925 while cleaning an inboard bearing of the grinder he had been operating, a man was decapitated by explosion of the bearing. A change was then made to outboard bearings heavily armored. This and other incidents show the importance of proper bearings procedures.

Special procedures are used repairing bearings and pumps as for all work on chlorate equipment. Hot water or wet steam are used to thoroughly clean before starting work in a special area. If heat is to be applied to a plate-patched steel plate, it is first drilled with running water on the drill to provide a vent for any oxygen released from chlorate inside by thermal decomposition.

The National Fire Protection Association reported seven chemical plant fires in 1957 that each resulted in a loss of more than $¼ million. One of these was a bucket elevator explosion in a chlorate plant. A rubber belt carrying 90 aluminum buckets had jammed with the bottom drive pulley still turning. Undoubtedly it was grinding off rubber and heating the belt. There was an explosion. No trace of the 90 lb of rubber belt was found, and only 4 of the 90 aluminum buckets remained. Aluminum had splattered on the walls and "ingots" of it were on the floor under chlorate. Although rubber belt bucket elevators had been in use at Niagara Falls more than 50 years, bronze or malleable steel chain has been used since for all Hooker chlorate elevator installations.

Fire Fighting and First Aid

Since chlorate provides the oxygen, fires with it cannot be smothered, so dry powder is ineffectual. Carbon dioxide may provide sufficient cooling to extinguish a small fire, but water fog or water usually has to be employed on fires involving chlorate, even electrical fires as it has been found that a stream of tap (pure) water is practically a nonconductor an inch away from a 220v electrical power supply. This is not true of a soda-acid extinguisher stream. Fire blankets are of no use.

For burns, use the cold water treatment as speedily as possible and for as long as necessary. Serious burns should be referred to a physician for treatment. Apply no medications beforehand; only the cleanest cold, moist cloth available.

For ingestion, avoid all stimulants including alcohol. Give an emetic and call a physician immediately. Wash out stomach and follow with demulcent drinks. Keep patient warm. Obtain blood electrolytes immediately and apply adequate intravenous therapy. If large amounts of chlorate have been ingested, it may cause renal failure and require an artificial kidney and transfusions. Such occurrence should be extremely rare.

Manuscript submitted July 22, 1968; revised manuscript received September 15, 1968. This paper was presented at the Boston Meeting, May 5-9, 1968, as Paper 273.

REFERENCES

1. Chemical Safety Data Sheet SD-42 Sodium Chlorate (1952), Manufacturing Chemists' Association, 1825 Connecticut Ave., N.W., Washington, D. C. 20009.
2. Data Sheet D-371 (1968) Chlorates, National Safety Council, 425 North Michigan Ave., Chicago, Ill. 60611.
3. C-62, Chemical Hazards Information Series, Chlorates, American Insurance Association, 85 John St., New York, N. Y. 10038.
4. Hygienic Guide Series, Sodium Chlorate (February 1958), American Industrial Hygiene Association, 14125 Prevost, Detroit, Mich. 48227.
5. Sodium Chlorate Handling Guide, Bulletin No. 99-A (1961), Hooker Chemical Corp., 277 Park Ave., New York, N.Y. 10017.
6. Sodium Chlorate, Data Sheet No. 794-A (May 1962), Hooker Chemical Corp., 277 Park Ave., New York, N.Y. 10017.
7. Sodium Chlorate Safety & Handling for Electrochemical Machining, a paper presented at

ASTME Meeting, October 26, 1967, in New York by Walter P. Huhn, Jr., American Potash and Chemical Corp., 3000 West Sixth St., Los Angeles, Calif. 90054.
8. Sodium Chlorate Safety & Handling for Electrochemical Machining, a paper presented at ASTME Meeting, October 26, 1967, in New York by J. S. Sconce, Hooker Chemical Corp., 277 Park Ave., New York, N.Y. 10017.
9. Sodium Chlorate for Electrochemical Machining, Bulletin No. 24, Hooker Chemical Corp.
10. ASC Monograph No. 146, Perchlorates, Their Properties, Manufacture, and Uses (1960), Joseph C. Schumacher, Editor Reinhold Publishing Corp., Dept. J, 430 Park Ave., New York, N.Y. 10022.
11. Data Sheet 525, Chlorine Dioxide (1967) National Safety Council, 425 North Michigan Ave., Chicago, Ill. 60611.
12. Case History No. 1449, "Fluorochloro Lubricant—Aluminum Detonation Point," Accident Case Histories (January 1968), Manufacturing Chemists' Association, 1825 Connecticut Ave., N.W., Washington, D.C. 20009.
13. C & E News, May 19, 1957, p. 44, "NFPA Reports Major Fires."
14. JAMA, **180**, 1133 (1962). *"Chlorate Poisoning."*

DIVISION NEWS

Battery Division

The Battery Division held its annual business meeting at the Montreal Meeting of the Society on October 8, 1968. The luncheon was well attended by Division members and guests.

The Battery Division Research Award was presented to Dr. Donald Tuomi for his work on the nickel electrode. Dr. Joseph C. White presented a Past-Chairman Pin to Dr. J. J. Lander, honoring his service as Division Chairman.

An election of officers was held for the next two-year term.

The results are as follows:
Chairman—Paul C. Milner, Bell Telephone Laboratories, Inc., Murray Hill, N. J. 07974

Vice-Chairman—Alvin J. Salkind, ESB, Inc., Yardley, Pa. 19068

Secretary-Treasurer—Howard R. Karas, Aerospace Division, Clevite Corp., 540 E. 105 St., Cleveland, Ohio 44108

Howard R. Karas
Secretary-Treasurer

Corrosion Division

The Corrosion Division held its annual business and luncheon meeting in Montreal on October 8, 1968. The following officers were elected to serve the 1968-1969 term.

Chairman—Michael J. Pryor, Olin Mathieson Chemical Corp., Metals Research Division, 275 Winchester Ave., New Haven, Conn. 06511

Vice-Chairman—Z. Andrew Foroulis, Esso Research & Engineering Co., P.O. Box 101, Florham Park, N. J. 07932

Secretary-Treasurer—J. Paul Pemsler, Ledgemont Laboratory, Kennecott Copper Corp., 128 Spring St., Lexington, Mass. 02173

Henry Leidheiser, Jr.
Past Chairman

SECTION NEWS

Boston Section

The sixty-sixth meeting of the Boston Section was held on September 17, 1968 at the Ledgemont Laboratory of The Kennecott Copper Corp., Lexington, Mass.

The speaker was Mr. Mark Nigberg, Market Promotion Manager of Digital Equipment Corp., Maynard, Mass. Mr. Nigberg spoke on "The Application of Dedicated Computers to Laboratory Instrumentation" and pointed out that during the past few years small general purpose computers have become increasingly important tools in analytical laboratories as new instruments lead to increased data rates and more stringent limits of accuracy. In the course of his talk Mr. Nigberg surveyed the areas in which small dedicated systems are currently used and explained some potential applications to laboratory systems.

Raymond G. Donald
Secretary

Chicago Section

The Chicago Section met on October 3, 1968 at the Chicago Engineers Club to hear Prof. E. N. Leith, University of Michigan, Ann Arbor, Mich., present a talk on "Modern Holography."

The following is an abstract of his talk.

The basic theory of holography was presented followed by a discussion of recent ramifications and potential applications. The discussion included multicolor holography, holographic interferometry, data storage on thick recording materials, holomicroscopy, holography at nonoptical wave lengths, "white light" holography, coherence requirements, and holography with incoherent sources as well as transmission of holographic data and techniques for bandwidth reduction.

On November 14 the Section heard Dr. R. P. Frankenthal, U. S. Steel Corp., Monroeville, Pa., present a talk on "Origin of Passivity in Iron-Base Alloys."

The following is an abstract of his talk.

The phenomenon of passivity was discussed in detail for the iron-chromium alloy system. It was shown that two distinct, potential-dependent films are formed during the passivation process. The electrochemical properties of these films were examined at various potentials throughout the passive potential region and changes that occur in these properties were discussed in relation to the effectiveness of the films as passivating agents. The applicability of these results to other systems was also considered.

Metropolitan New York Section

The Metropolitan New York Section held its first meeting of the 1968-1969 season at the Stonehall Inn in New York City with members and guests attending the lecture on "New Aspects of Leclanche Cells Research" presented by Prof. Lou Rozeanu of the Technion Israel Institute of Technology. He reported that comparative tests, of amalgamated zinc vs. pure zinc surfaces, showed that the amalgamated zinc had a higher emf, was more reactive chemically, and gave maximum performance at 4.0 to 4.25 mg Hg/sq in. Impurities in the zinc, such as lead, cobalt, copper, iron, nickel, and antimony were harmful since they were insoluble in mercury. Professor Rozeanu reported that he had developed an accelerated corrosion test for amalgamated zinc, based on rotating a sleeve of zinc at 20,000 rpm for approximately 24 hr in dilute hydrochloric acid, to simulate the results obtained over a period of 6 months of storage.

Dodd S. Carr
Secretary

JOURNAL OF THE ELECTROCHEMICAL SOCIETY

REVIEWS AND NEWS — FEBRUARY 1969

State of the Art of Electrostatic Separation of Minerals

James E. Lawver

Mines Experiment Station, University of Minnesota, Minneapolis, Minnesota

Man's knowledge of electrification of minerals dates back to at least 540 B.C. when Thales of Miletus observed that rubbed amber had the power of attracting small objects. Although the mechanism of Thales' observation of frictional electrification, or triboelectrification as it is now called, is still shrouded with uncertainties, today's engineers are usually able to prevent unwanted static electrification and are often able to use electrical effects as a means of concentrating solids. Materials that have a high surface-area-to-mass ratio readily respond to even weak electrical fields. This is probably the reason that the first electrical concentrator patented in the United States (1880) was a device for purifying ground cereal (1). In 1881 a crude machine (2) was built to concentrate gold ore, and in 1892 Thomas A. Edison also devised an electric machine (3) for the concentration of gold, a sketch of which is shown in Fig. 1. None of these machines was used industrially.

The first commercial process for treating minerals was started in 1908 at Platteville, Wis. (4). This plant, operating under the patents of C. E. Dolbear (5) and the Huff Electrostatic Co. (6), was used to produce lead and zinc concentrates. The process was called the "electrostatic process"—a term often still used for any electrical separation of solids, although such separations rarely are truly static in nature. By about 1914 the electrostatic process had gained considerable favor in the metallurgical industry and was accepted as an industrial process for mineral concentration. It was successfully used on a small scale throughout the world, both as a single process and in conjunction with wet gravity processes. The popularity of concentrating minerals by the electrostatic process, however, was short lived, because about 1912 froth flotation was introduced in the United States as a commercial process. The new flotation process offered numerous advantages over the electrostatic process with respect to both selectivity and cost. As a result, during the following years the flotation process grew with fabulous rapidity, and the electrical method of concentration began to be regarded as little more than a metallurgical curiosity. It was the titanium shortage during World War II that sparked a new interest in the possibility of utilizing electrical separation, and numerous commercial applications using conductivity-type separators were installed to concentrate titanium-bearing, heavy mineral beach sands. Since that time electrical concentration of minerals has steadily increased. Now virtually all physical beneficiation processes producing titanium and tin minerals throughout the world are using conductivity-type electrical concentrators known as "high tension" (7) machines. In 1965 the world's largest electrical concentration plant was installed at Wabush Mines, Que., Canada, to reduce the silica content of a specularite gravity concentrate from 8% to less than 3%. This plant has a "high tension capacity" of over 6 million tons/yr and enjoys a high tension operating cost of about 5¢/ton of dry feed. Figure 2 is a photograph of this modern high tension plant. At present the free world produces about 13 million tons/yr of mineral concentrates (8) by electrical separation. The bulk of this tonnage comes from the beneficiation of iron ore and from the concentration of heavy mineral beach sands.

General Principles

The basic principle of electrical concentration is simply the utilization of body forces acting on charged or polarized solids in an electric field such that a selective sorting of the different species can be ef-

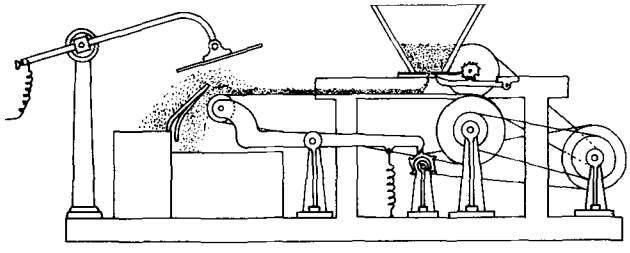

Fig. 1. Thomas A. Edison's electrostatic separator (patented 1892).

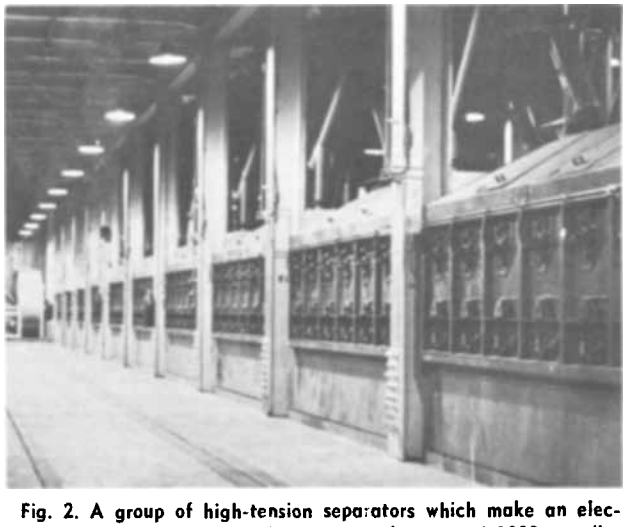

Fig. 2. A group of high-tension separators which make an electrodynamic concentration of iron ore at the rate of 1000 tons/hr.

fected. Both a-c and d-c fields are used at field gradients ranging from about 3 x 10^3 v/m up to the breakdown strength of air (about 3 x 10^6 v/m). Commercial separators use high-voltage power supplies ranging from 5 x 10^3 to 250 x 10^3v. The power requirement is small—rarely exceeding 0.15 kwhr/ton of feed.

The electric body force acting on solid grains in an electric field $\vec{E}$ is:

$$\vec{F}_e = Q\vec{E} + (\vec{p} \cdot \nabla)\,\vec{E}$$

$\vec{F}$ = newtons
$\vec{p}$ = electric moment—coulombs/m^2
Q = total charge on the mineral—coulombs
$\vec{E}$ = electric field—newtons/coulombs

The art and science of electrical concentration depend largely on the ability *selectively* to charge one species differently than the others in the mixture. Once this has been accomplished, they can readily be sorted in an electric field. The important charging mechanisms used commercially for d-c separators are: (*a*) charging by corona discharge; (*b*) charging by conductive induction; and (c) charging by contact electrification. A-C separators usually depend on polarization and shape phenomena to effect a separation.

Charging by corona discharge is effected by passing the solids to be charged through an intense corona glow such as is obtained from needle points or a fine wire charged to a potential exceeding the breakdown strength of air. Special electrodes have been developed for preventing spark-over when treating combustible materials such as coal and grains (9). The corona discharge machine depends almost entirely on the intense electrification caused by a corona wire. Nevertheless, there is a slight tendency to charge conductive particles by the mechanism of conductive induction. The total charge received by conductive induction, however, is very, very slight compared to the corona discharge and is usually unimportant and can be omitted from all calculations.

Charging by conductive induction is accomplished by allowing solids to contact a grounded conductor while the grains are in an electric field whence the conductive particles become charged opposite to the grounded conductor. This type of machine never uses a corona discharge—in fact, the electrodes used are always rather large in diameter and caution is always taken to prevent any sharp edges that might result in corona discharge.

Charging by contact electrification is the same mechanism as is demonstrated by the famous experiment of rubbing hard rubber with catskin. Dissimilar surfaces will always electrify to some extent simply by particle-particle contact. It is sometimes possible to predict the sign of the charge produced from contact electrification on the basis of the band theory of solids. In the usual case, however, contact electrification is controlled by surface films often of unknown composition. For example, quartz and diamonds will strongly electrify by contact electrification at room temperature. According to the band theory, the energy gap for either mineral is such that electrification by contact should be negligible. In this case the transfer of charge is certain to be due to surface films.

Mechanisms (*a*) and (*b*) are invariably used to separate good conductors such as ilmenite, rutile, galena, pyrite, specularite, *etc.*, from poor conductors such as quartz, zircon, monazite, diamonds, *etc.* Mechanism (*c*) is usually used to separate nonconductors such as phosphate rock and quartz from each other.

Commercial Machines

There are virtually hundreds of patents describing various configurations of electrodes and feeding arrangements for making an electrical separation of a mixture of solids. There are, however, only four general types of machines that are used commercially. These are shown in Fig. 3.

The first machine is the corona discharge separator (often called the high tension machine). If a mixture of solids consists essentially of good electrical conductors and good electrical insulators, a high tension machine can separate the conductors from the insulators very efficiently and inexpensively.

Unfortunately, there is very little information in the literature regarding the electrical conductivity of solids. Some insight regarding the conductivity of minerals can be obtained by reference to a Bureau of Mines publication (10) in which 95 minerals have been classified according to the weight per cent that is collected as a conductor (in an electrostatic separator) as a function of the temperature at which the separation was made.

From the standpoint of high tension separation, the criterion used to distinguish conductors from

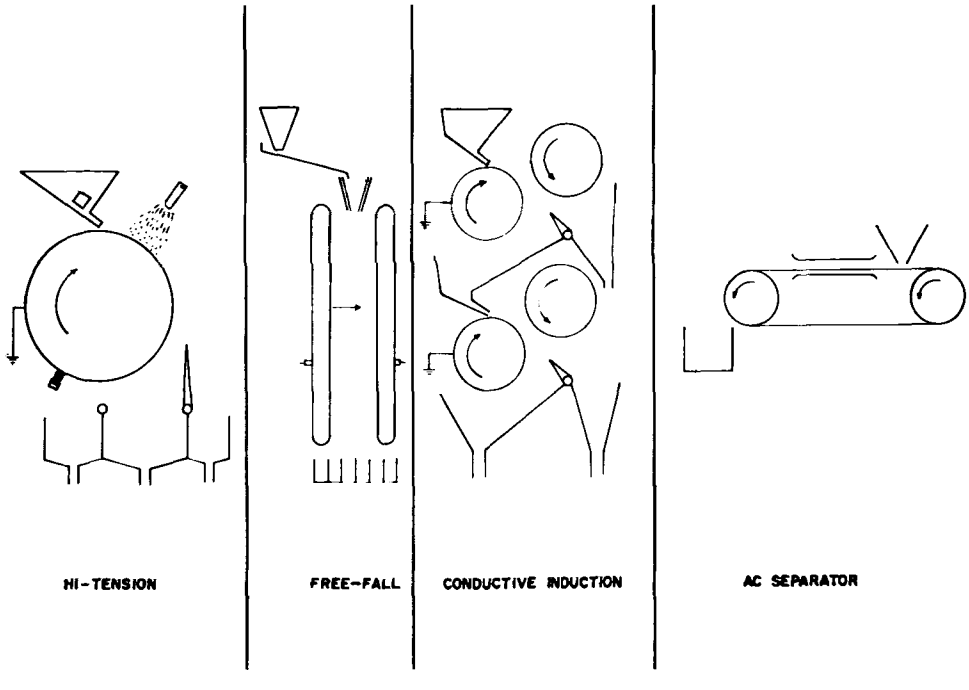

Fig. 3. Common commercial electrical concentrators.

insulators is the relaxation time T_r (11). Relaxation time is defined as the time required for an initial charge density ρ_o to decay to $1/e$ of its original value.

$$\rho = \rho_o e^{\frac{-\sigma}{\epsilon} t}$$

ρ_o = initial charge density
e = charge density at time t
σ = conductivity
ϵ = permittivity

For example, T_r for pyrite is about 10^{-3} sec, while T_r for quartz is about 10^6 sec.

In the high tension machine, conductors and insulators alike are charged as they pass through the corona zone. The limiting charge is a function of the particle radius, the relaxation time, time in the field, and to some extent the permittivity of the particle (12). Particles having a small relaxation time (conductors) share their charge with the grounded rotating cylinder and are thrown free of the cylinder while particles with a large relaxation time (insulators) are held to the cylinder by their image force and must be removed by a scraper. Figure 4 is a photograph of a high tension machine showing the corona discharge.

The capacity of high tension concentrators depends on the particle size distribution and on the electrical properties of the species that are to be separated. The normal range of particle sizes that can be handled is from a coarse value of about 1.5 mm diameter to a fine limit of about 0.03 mm diameter. A good rule of thumb is to estimate capacity at about 175-300 lb/hr/in. of rotor for a particle size distribution that is essentially minus 1 mm plus 0.2 mm. As the mean particle diameter is decreased, the capacity falls rapidly. The capital cost for high tension equipment varies from about $1200 to $1500/ton/hr/pass.

The second most important (conductive-induction) machine (Fig. 3) is a typical twin electrode concentrator. This type of separator can be used to separate conductors from insulators utilizing "charging by conductive induction" or it can be used to separate dielectric particles that have become charged by particle-particle contact or by particle-rotor contact. There are many models available, each with special features of feeding mechanisms, dust control, and

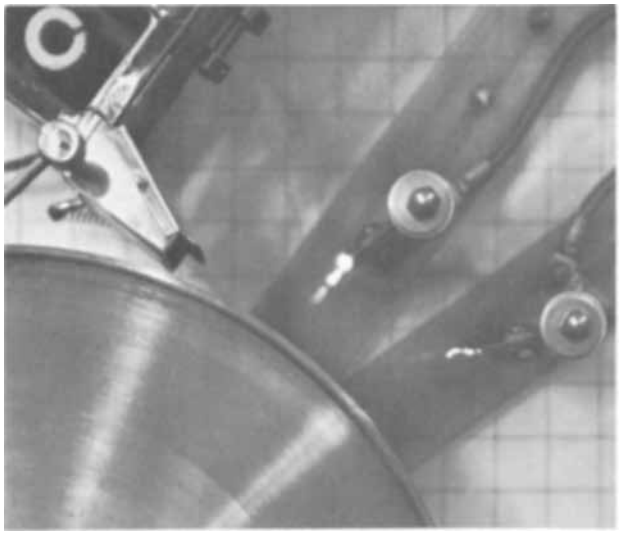

Fig. 4. High-tension machine showing corona discharge

Fig. 5. DF604-Bullock-Simpson electrostatic separator. Double-face unit with 5-ft feed rolls for four stages of separation. Attracting rolls and dividers easily adjusted for most efficient position. Positive or negative polarity to 30,000v. Capacity 3-10 tons/hr. Feed minus 6 to 200 mesh.

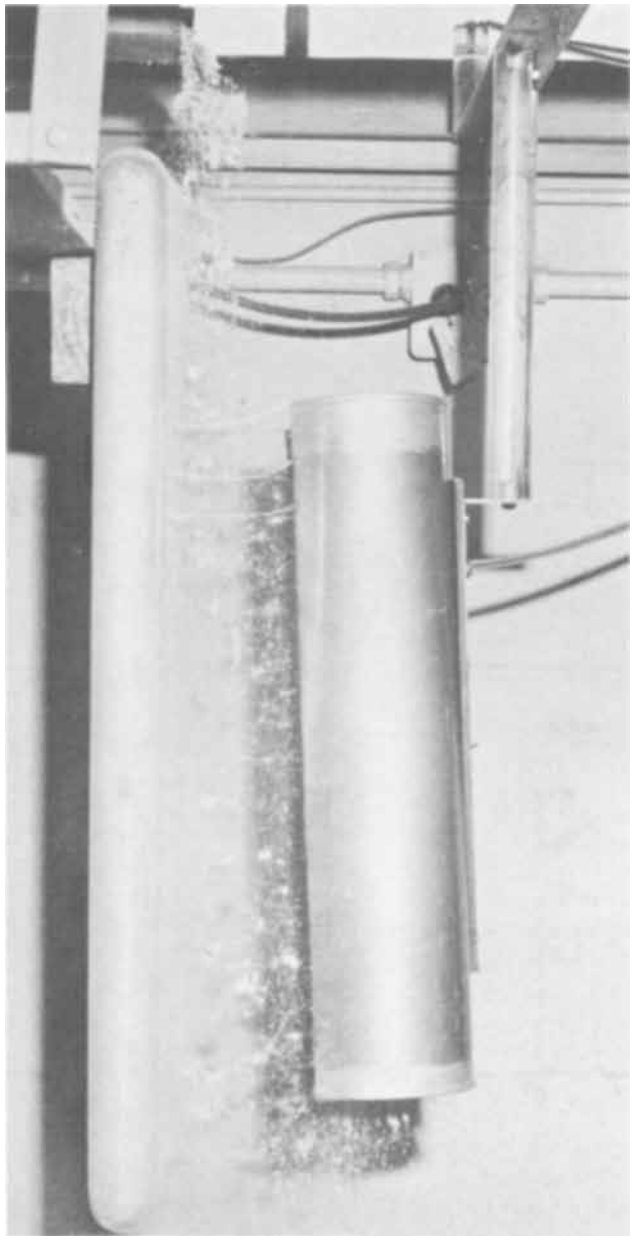

Fig. 6. Carpco Free Fall separator used to concentrate asbestos.

some even having special rotor composition (13) to enhance particle-rotor contact electrification. Figure 5 is a photograph of a Bullock-Simpson electrostatic separator. This is a double-face unit with 5-ft feed rolls for 4 stages of separation. The capacity and capital cost vary widely depending on the material being treated. The approximate capacity ranges from about 85 lb/hr/in. of electrode for fine-grained material to 170 lb/hr/in. of electrode for coarse-grained material. The power cost is negligible.

The free fall machine is used to provide an electric field for separating particles that have become charged by contact electrification. The limiting charge in contact electrification is the electrical breakdown strength of air which limits the charge density on the solids to about 26.6×10^{-6} coulombs/m^2. Several potentially important examples of electrostatic separations based on contact electrification are: separation of Florida phosphate rock from silica sand (14), separation of halite from sylvite (15), and separation of quartz from feldspar (16). The sign and magnitude of the charge obtained from contact electrification depend not only on the electrical properties of the bulk of the material but also on trace quantities of impurities that may be present in the surfaces. It is, thus, impossible to form a meaningful triboelectrification series for minerals since the sample history greatly influences its contact electrification properties. Selective contact electrification is also possible by the addition of a suitable surfactant or cleaning agent (17, 18). The free fall separator has a capacity of about 200 lb/hr/in. of electrode when used to concentrate phosphate rock or feldspar ores. Figure 6 is a photograph of a Carpco Free Fall separator used to concentrate asbestos.

Miscellaneous Separators

There are a variety of a-c machines that have been used for special purposes (19-21) but so far they have not been widely accepted for commercial use. Separations made using a-c fields depend on the fact that conductive and high-permeability particles will oscillate with the field reversals, while nonconductive particles remain stationary (19, 20). Hatfield (22) devised a method for separating minerals on the basis of differences in dielectric constant, but to date the method is restricted to laboratory use since it required the use of dielectric fluids whose cost precluded commercial use.

Applications

At the date of this writing, high tension concentration of iron ore, heavy mineral beach sands, and tin ore accounts for about 95% of the estimated 13 million tons/yr of concentrates produced by electrical methods. The success of the Wabush Plant for concentrating iron ore has aroused considerable interest in the iron and steel industry, and it is likely that corona discharge machines will play an increasingly important part in producing super iron ore concentrates (containing less than 0.5% silica) that can be used for direct reduction processes. Table I lists ten typical applications of the electrical separation processes used throughout the world.

Table I. Ten typical industrial separations

	Mineral combination	Surface treatment	Usual charging mechanism
1.	Specular hematite-quartz	Drying	Corona discharge
2.	Ilmenite and rutile from poorly conducting heavy mineral gravity concentrates (zircon, monazite, *etc.*)	Scrubbing to remove organic slimes Drying (Reducing roast at 650°C)	Corona discharge
3.	Zircon (cleaning)—ilmenite Rutile	Drying	Corona discharge
4.	Cassiterite—scheelite	Drying	Corona discharge or Conductive induction
5.	Feldspar—quartz	Drying HF vapors	Contact electrification
6.	Halite—sylvite	Heating to 340°C or Drying plus 1 lb/ton of fatty acids	Contact electrification
7.	Pyrite—coal	Drying	Corona discharge or Conductive induction
8.	Coal—shale	Humidity control	Corona discharge or Conductive induction
9.	Diamonds—silica	Wet scrubbing in NaCl pulp Drying	Conductive induction
10.	Dry foods and drugs from trash and rodent feces	Drying	Conductive induction

Manuscript submitted Nov. 28, 1967; revised manuscript received Oct. 11, 1968. This paper was presented at the Chicago Meeting, Oct. 15-19, 1967, as Paper 149.

Any discussion of this paper will appear in a Discussion Section to be published in the December 1969 JOURNAL.

REFERENCES

1. T. B. Osborne, U.S. Pat. 224,719.
2. C. H. Hill and E. H. Whited, U.S. Pat. 245,299.
3. T. A. Edison, U.S. Pat. 476,991.
4. H. A. Wentworth, *Trans. AIME*, **43**, 411 (1912).
5. C. A. Dolbear, U.S. Pat. 685,508 and 724,679.
6. C. H. Huff, U.S. Pat. 801,380.
7. Trade name coined by J. H. Carpenter, President, Carpco Research and Engineering, Inc., Jacksonville, Fla.
8. Private communication, J. H. Carpenter, Carpco Research and Engineering, Inc., Jacksonville, Fla.
9. W. Grogg, U.S. Pat. 2,860,276.
10. U.S. Bureau of Mines Bulletin 603, "Electrostatic Separation of Granular Materials," p. 72 (1962).
11. I. Estermann, "Methods of Experimental Physics," Vol. 1, Academic Press, New York (1959).
12. H. J. Lowe and D. H. Lucas, *Brit. J. Appl. Sci.*, Supplement No. 2, pp. 16-19, London (1953).
13. H. L. Bullock, U.S. Pat. 2,225,096.
14. J. E. Lawver, U.S. Pat. 2,805,769.
15. J. E. Lawver, U.S. Pat. 2,805,768.
16. J. E. Lawver, U.S. Pat. 2,805,771.
17. H. Autenrieth, U.S. Pat. 3,217,876.
18. A. Stieler, Aus der Praxis der Elektrostatischen Aufbereitung (Practice of Electrostatic Mineral Dressing), *Zeit. Erz und Met.*, **8**, B127 (1955).
19. H. Comstock, U.S. Pat. 1,110,896.
20. A. Bibolini and P. Riboni, U.S. Pat. 1,154,907.
21. E. M. Benton, U.S. Pat. 3,217,880.
22. H. S. Hatfield, *Trans. Inst. Mining Met. (London)*, **33**, 335 (1924).

Secondary Silver-Zinc Battery Technology

L. Gaines

Tyco Laboratories, Inc., Waltham, Massachusetts

ABSTRACT

A review of the current status of silver-zinc battery technology is presented as part of an attempt to organize, on a fundamental basis, the varied design improvements developed as a result of empirical studies. Past efforts to improve the secondary silver-zinc system have been devoted to (*a*) stabilization of the zinc electrode structure, (*b*) control of zinc dendrite growth, (*c*) increasing the utilization of the silver electrode, (*d*) separator improvements, and (*e*) development of sealed batteries. Improvements that have been suggested in these areas are often mutually exclusive and interdependent. Clarification of the fundamental processes involved is necessary for the creation of an optimum battery configuration.

The conversion of the primary silver-zinc system, as it was originally devised some 25 years ago, into a high energy density rechargeable energy storage device has been a slow and not entirely successful process. Although a high level of performance (in the vicinity of 100 w-hr/lb) is obtainable in primary applications, currently available secondary silver-zinc cells capable of extended cycle life possess energy densities below those of alternative systems which although possessing a lower energy density, are better able to retain their initial capacity on continued cycling.

Past research, both basic and applied, has elucidated many of the problems inherent in the silver-zinc system, and in addition, has indicated methods for their control.

Many of the difficulties in the design of high energy density silver-zinc batteries relate to the solubility of zinc oxide, the anodic discharge material of the zinc electrode, and of silver oxide, the active material of the positive electrode. The high solubility of ZnO causes a gradual degradation of the zinc electrode structure on repetitive cycling at high depths of discharge. Due to the loss of effective surface area, the zinc may plate back on the electrode in a highly structured dendritic form which tends to grow through the cell separators.

The partial solubility of the silver plate ($\approx 10^{-4}$m) allows diffusion of the Ag(I) ion to the zinc electrode where it is reduced to metallic silver causing self-discharge of the cell. In order to prevent the diffusing silver ions from reaching the zinc electrode, and at the same time to prevent deposited zinc from short circuiting the battery plates, separators are required between alternate electrodes. Historically, these separators have been based on cellulosic materials. These materials are satisfactory for limited cycle life, but improved separators have been developed which are more resistant to oxidation by the Ag(I) ions which eventually reduce the effectiveness of cellophane membranes.

In addition to the development of improved separator systems, past efforts to improve the secondary silver-zinc system have been devoted to (*a*) stabilization of the zinc electrode structure to prevent the loss of surface area due to agglomeration of the zinc particles, (*b*) elucidation and control of the conditions which lead to zinc dendrite growth, (*c*) improving the utilization of the silver electrode to assure maximum performance, and (*d*) development of sealed batteries.

Research into these areas of silver-zinc technology, funded principally by DOD and NASA, has been reported in the contract literature. This review attempts to summarize these experiments, and to integrate the results presented with the basic electrochemical and physical principles of battery operation. Since many of the references cited are subject to distribution limitations, this review has the additional purpose of making their contents more readily available in the open literature.

Zinc Electrode Technology

During the past five to ten years a considerable amount of information has been obtained on the cycling characteristics of the silver-zinc system. These tests have been conducted under varying conditions of temperature, depth of discharge, rates of charge and discharge, electrode structure, separator systems, and caustic concentration. The studies indicate that, for the most part, cycle life and performance of silver-zinc cells are limited by the capabilities of the zinc electrode. The negative electrode limits cycle life because of changes in its physical characteristics (particularly porosity) and/or because of the formation during charge of metallic dendrites which can penetrate the cell separators. These mechanisms result in an inability to accept charge efficiently which, in the case of sealed cells, causes a rapid pressure increase due to hydrogen accumulation.

The extent to which each of the above failure mechanisms occurs in a given system depends in large measure on the individual cycle regime and cell structure. Research programs carried out over the period in question have succeeded in large measure in correlating the above failure modes with the electrode reactions occurring at the surface. In addition, empirical studies have indicated several ways in which electrode performance can be significantly improved and cycle life extended.

Theoretical studies—The most recent and comprehensive survey of the electrochemical reactions of the zinc electrode is provided by Dirkse (1). Although the details of the charge transfer reaction are not established, the anodic or discharge process is generally described in three steps:

(*A*) The zinc is oxidized to solid ZnO or $Zn(OH)_2$.
(*B*) The ZnO or $Zn(OH)_2$ dissolves in the electrolyte to eventually yield $Zn(OH)_4^=$.
(C) The electrolyte becomes saturated with zincate, a ZnO or $Zn(OH)_2$ film forms on the surface, and the electrode passivates.

The rate of formation of the oxidized zinc species in step (*A*) is a simple function of current density. Even though the exact composition of the discharge product is unknown, it is apparent that its solubility in KOH is much higher than any of the stoichiometric zinc oxides currently known, since zinc can be anodically dissolved in KOH which has been presaturated with ZnO. The discharge product of the reaction eventually precipitates out as stable ZnO although the rate of this process appears to be slow (1).

The onset of electrode passivation on discharge is a function of electrode surface, caustic concentration, electrolyte volume, and perhaps time. However, at normal temperatures, anodic passivation is not usually the limiting factor in designing cells with zinc electrodes. Properly fabricated porous zinc electrodes,

formed by reduction of compacted zinc oxide of small particle size, are capable of utilizing in excess of 70% of the zinc present (2). It is also well established that this capability is not long maintained under repetitive discharges and charges.

The cathodic behavior of zinc has also been effectively summarized by Dirkse (1). The generally accepted mechanism involves a two-step process:

$$(i) \quad Zn(OH)_4^{=} \rightarrow Zn(OH)_2 + 2\,OH^-$$

$$(ii) \quad Zn(OH)_2 + 2e^- \rightarrow Zn + 2\,OH^-$$

In practical alkaline batteries with zinc electrodes, the problem has been two-fold: loss of capacity on continued cycling and penetration of the cell separators by deposited zinc.

Capacity loss on cycling is usually attributed to an agglomeration of the zinc with a loss in effective surface area as the zinc is deposited from solution according to the above reactions, and to a displacement of active material towards the bottom of the electrode. These two effects are usually denoted by the terms "shape change" and "shedding."

The conditions which lead to and control the growth of zinc dendrites have recently been elucidated (3, 4). In plating zinc from alkaline zincate solutions, it is observed that the deposit can range from short fine whiskers or sponge at low current densities to the longer more highly structured type of branched, dendritic deposits at higher current densities or greater overpotentials. The type of deposit produced is related to the amount of free zincate available at the electrode surface for reduction. If sufficient zincate is present close to the electrode surface, *i.e.*, under conditions of low current density (1 to 5 ma/cm^2), or sufficient agitation is provided to support higher currents, the zinc is deposited under activation control. The growth of this spongy zinc is thus confined to the zinc electrode. There is no tendency to penetrate the separator since sufficient zinc is available for deposition from the free electrolyte.

If the current density is increased or the amount of free zincate surrounding the zinc electrode is reduced, growth of zinc proceeds under diffusion-limited conditions. Zinc dendrites may now enter and grow through (rather than puncture) the cell separators. Under these conditions cell failure is likely to occur by catastrophic shorting or excessive self-discharge.

Empirical studies—Experimental programs have provided most of the design criteria for secondary electrodes. The zinc electrode, formed from a zinc oxide of appropriate particle size, has been improved on through the use of diverse and often unrelated additives, including organic and inorganic binders, surfactants, and solubility depressants.

The process by which the effective surface area of the zinc electrode decreases has not been subjected to the same type of analytical effort as has the dendrite growth mechanism. Although the initially formed electrode can utilize 80% of its theoretical capacity, a substantial excess of zinc oxide must be provided over and above that required to supply the rated capacity. The penalties in terms of cell weight and volume for this extra zinc are clear.

Goodkind (5) has reported extended cycle life capabilities for zinc electrodes prepared with 5 to 10% by weight of Teflon suspension and cured in the vicinity of 275°C. It seems logical to relate the improvement in cycle life to the creation of an inert interlocking matrix which effectively retards shifting of the active material on continued cycling and, in addition, provides for the maintenance of a highly porous structure. The use of cotton fibers and organic binders such as polyvinyl alcohol is discussed by Lander and Keralla (6). The effect of negative grid geometry has also been investigated (10).

Aside from the development of separator materials having greater resistance to penetration than cellophane, efforts to reduce the growth of dendrites have centered in three areas: cell design, use of surfactants, and the use of solubility depressants.

Most presently available silver-zinc cells operate with an excess of ZnO in the negative electrode and with a KOH electrolyte saturated with ZnO prior to cell activation. These steps are taken to reduce the extent of the concentration gradients caused by consumption of $Zn(OH)_4^{=}$ during charge. Depletion of $Zn(OH)_4^{=}$ and the concurrent change in the morphology of the deposited zinc from mossy to dendritic, occurs as the zinc electrodes densify and less ZnO dissolves. Thus, dendrite growth and shape change are often concurrent processes.

The use of surfactants to control the morphology of zinc deposits was first reported by Kryukova (7), who noticed changes in the shape of zinc dendrites penetrating through cellophane when various surface active agents were used. The general usefulness of organic additions to plating baths has long been established in commercial practice (8).

It is unlikely that the addition of surfactants increases the diffusion of zincate, thereby delaying the transfer into diffusion limited conditions. Dirkse (9) has pointed out that the additives significantly increase the viscosity of the electrolyte, and thus should retard diffusion processes. It is possible, however, that adsorption of a surfactant molecule on the zinc surface could alter the deposition process by poisoning active growth sites on the propagating dendrites.

Stachurski (3) measured the adsorption of various surface active agents by double layer capacity measurements on dropping mercury electrodes. At potentials corresponding to a working zinc electrode, only Igepal CO-730 [a polyphenoxypoly (ethyleneoxy) ethanol] remained adsorbed on the electrode surface. The other surfactants tested, Triton X-100 and the fluorochemical surfactants FC-134, FC-19, and FX-161, were desorbed at the same or lower potentials. The above result was given a practical significance by Lander and Keralla (10) and Dirkse (9) who have reported extended electrode life through the incorporation of alkylated poly (ethyleneoxy) ethanols into the zinc electrode structure in amounts from 1-5%. The materials also seem to improve electrode performance when incorporated in the electrolyte alone (11).

The use of zincate solubility depressants, particularly $Ca(OH)_2$, to reduce or eliminate zincate in the cell electrolyte has recently received some degree of attention. Van der Griten (12) has resolved the conflicting experimental results of Romonov (13) and Zhulidov (14) with the observation that zincate trapping only occurs at concentrations of KOH less than 20%, and that the rate of reaction is inhibited by carbonate contamination of the $Ca(OH)_2$ particles. The use of $Ca(OH)_2$ impregnated zinc electrodes in high-rate silver-zinc batteries is complicated by the need to provide sufficient caustic for rapid cell discharge. The low caustic concentrations involved mandate careful cell design to insure adequate amounts of available hydroxide. In addition, the high freezing point of 20% KOH (— 23°C) introduces environmental limitations, particularly when the caustic concentration in the anolyte falls during cell discharge.

Silver Electrode Studies

Theoretical studies—The anodic oxidation of silver in alkaline solutions is basically a two step process. First, a layer of monovalent Ag_2O is produced on the metal. When this layer reaches a critical thickness, mass transfer of oxygen ions to the Ag-Ag_2O interface becomes slow, and the oxidation of Ag_2O to AgO begins. It has been noted (15) that significant additional Ag_2O is also produced on this second plateau. Further anodization leads to evolution of oxygen.

Similarly, discharge of a silver electrode occurs at two distinct potentials. Consequently, discharge of a silver-zinc battery proceeds at two voltage levels: 1.8v

for the reduction of AgO to Ag_2O and 1.55v for the reduction of Ag_2O to metallic silver.

The mechanism of formation and reduction of Ag_2O and AgO is a matter of some controversy, but published x-ray data (16) indicate the following:

(a) Ag_2O nucleates on Ag and grows with random orientations; there is no evidence of a suboxide, solid solution, or alloy of oxygen and silver during charge or discharge.

(b) AgO forms as a distinct second phase and not by distortion or modification of the Ag_2O lattice; similarly, Ag_2O appears on discharge as a distinct separate phase, and not by shrinking of the AgO lattice.

(c) AgO grows on the surface of the Ag_2O layer during charge, and conversely, Ag_2O is formed on the surface of AgO during discharge.

(d) AgO is not reduced directly to Ag.

The sequence of reactions during both charge and discharge thus involves the coating of either the silver or the AgO by a layer of Ag_2O. The argentous oxide is a semiconductor of relatively low electronic conductivity. For these reasons, the voltage and current efficiencies of the silver oxide electrode are dependent to a large extent on the properties of the Ag_2O.

Argentous oxide is also involved in a major mechanism of cell deterioration in the silver-zinc system. Since Ag_2O is appreciably soluble in KOH the dissolved silver can diffuse to the negative electrode where it reacts directly with the zinc. A direct failure mode is the appearance, upon repeated cycling, of dendritic silver growths which may penetrate the cell separators.

AgO is insoluble in KOH, but it is unstable with respect to the reaction:

$$2\,AgO \rightarrow Ag_2O + \tfrac{1}{2}\,O_2 \quad \Delta G = -9512\ \text{cal}$$

The rate of this reaction is inhibited by the high oxygen over-voltage on silver and by the formation of a film of Ag_2O. The reaction results in a self-discharge rate of the silver electrode equivalent to 16% in 1 year at 30°C (17).

The solubility of Ag_2O in KOH was determined by potentiometric titration (17). The results are summarized in Table I.

Empirical approaches to improving charge acceptance—Two general empirical approaches to improving the charge acceptance of the silver-silver oxide electrode have been first, to vary the porous electrode structure by changing the particle size of the silver or the density of the plate, and second, to alloy the silver with small amounts of a second metal in order to alter the properties of the passivating Ag_2O film.

It has been shown that the utilization of silver at the Ag(I) level is improved by the addition of small amounts (~ 1%) of lead or palladium to the silver powder (10, 18, 19). At a discharge current density of 120 ma/in.^{2}, the utilization of silver at the argentous level was approximately 71% in the fifteenth cycle for hot-pressed plates formed from 0.5μ silver. Plates pressed from unalloyed silver powder exhibited only 20% utilization of the silver after the same number of cycles (19).

Recent work has indicated that for alloys of silver with Pd, Pb, Cu, Au, and S the improvement in charge acceptance comes about from a roughening of the silver surface *via* a preferential etching or dissolution of the alloyed metal (20-22). Once the roughening factor has been taken into account, the remaining improvement due to the increase in the electronic conductivity of the Ag_2O is about 10 to 15%.

Table I. Solubility of Ag_2O in KOH

Normality of KOH	Weight per cent KOH	Normality of silver
1	5	1.7×10^{-4}
1.9	10	2×10^{-4}
4.2	20	4.4×10^{-4}
6	27	4.7×10^{-4}
9.7	40	4.5×10^{-4}
13.5	50	3.4×10^{-4}

Lead seems to be the preferred material for use in the positive electrodes of silver-zinc cells, since the contamination of the zinc electrode with palladium leached from the silver electrode is likely to lower the hydrogen overvoltage on zinc and hence cause increased gassing. The use of Pb additives to the zinc electrode has also been shown to have beneficial effects on the morphology of the zinc deposited during charge (4).

The effect of silver particle size and plate fabrication procedures on the performance characteristics of secondary silver-zinc cells is a question of basic interest. Investigation of various silver powders and several different sintering temperatures indicated that the effect of these variables was small (18). Plates were constructed with silver particle sizes in the range 1 to 12μ and sintering temperatures of 800°, 1000°, and 1200°F. In general, the data indicated that even after 1000 cycles at 25% depth of discharge, all the plate efficiencies were comparable. Photomicrographs taken of the electrodes after formation and after 200, 500, and 1000 cycles indicated that the larger particles broke down on cycling, while the smaller particles tended to grow or agglomerate. The tendency was thus for the particle size to become more uniform on continued cycling.

Variation in the density of the silver plates may also be a significant factor in the performance capabilities of the silver-zinc system. From the standpoint of energy density, the use of a dense silver electrode is preferable, since cell pack thickness is thereby reduced. A brief study of the effect of positive plate density has been carried out (19). Plate densities of 3.0, 3.6, 4.2, and 4.8 g/cm^3 were investigated. The corresponding porosities are 71.4%, 65.8%, 60%, and 54.3% based on a silver density of 10.5 g/cm^3. The results indicated that the lower density positives probably increased cycle life, but the results were not statistically significant because of the large error variance. Also tentatively indicated was a decrease in the rate of silver attack on the cellulose separator as the density increased.

The use of a dense electrode structure, while increasing the electronic conductivity of the plate, has the disadvantage of decreasing the utilization of the active material. This capacity loss arises from the fact that ionic transport to the interior of the plate is impeded by the closely packed structure.

Separator Systems

Proper design and functioning of the separator system in alkaline silver-zinc batteries is crucial to successful cell performance. In addition to electronically insulating alternate plates without impeding transport of K^+ and OH^- ions, the separator system must prevent catastrophic dendritic shorting, reduce or eliminate the transport of silver through the cell pack, and be chemically and physically unaffected by the cell environment.

The relationships between the physical properties of membranes and their resistance to penetration by dendrites have been extensively studied by Stachurski (3). As has already been discussed, zinc penetration of the separator can only begin when the zincate concentration in the catholyte becomes too low to sustain the rate of zinc plating. Once penetration commences, however, the rate of growth and the morphology of the deposit will be determined by the diffusion constant and amount of free zincate present in the interior of the membrane.

In addition to the chemical composition of the separator, the concentration of zincate in the external solution was found to influence the amount of free zincate in the membrane. At low external concentrations of zincate (up to 0.2 mole/liter), the apparent concentration of zincate in the absorbed liquid rises

rapidly and is higher than would be expected if no interaction took place between the membrane and the zincate. At concentrations exceeding 0.2M there is a much smaller increase in concentration, and the concentration of zincate inside the membrane is lower than in the external solution. At concentrations of external zincate greater than 1 mole/liter, the amount of absorbed zincate becomes constant.

Based on these observations, zincate present in the membrane was concluded to exist in two distinct forms (3): chemisorbed zincate adsorbed on the microfibers of the membrane material (experimentally indicated at low external concentration), and free zincate in the electrolyte present within the membrane structure.

Since zinc plating within the membrane can only come from this free zincate, it is the concentration of the free zincate which determines whether penetration of the membrane will or will not occur. In order to increase the overpotential for deposition within the membrane, it is desirable that the free zincate concentration be as low as possible. These points are perhaps best illustrated with reference to a specific example.

Regenerated cellophane, both with and without fibers, has been the usual separator material for an extended period. Consequently, it is the one for which the most data, both empirical and theoretical, is available. In saturated zincate, the concentration of zincate outside the membrane exceeds the concentration of free zincate inside the membrane by only a factor of 1.5. In dilute zincate (0.01M), however, the ratio of the outside to the inside concentration becomes 30 (3). The latter case is representative of the situation where the catholyte has become zincate limited. As long as the concentration of free zincate is much lower inside than outside of the membrane, the overpotential for zinc deposition within the membrane will be relatively high, and zinc penetration will be retarded (23).

In addition to eliminating zinc penetration, the cell membrane also functions as a silver barrier. The slightly soluble Ag^+ ion diffuses to the zinc electrode where it is reduced to metallic silver, which decreases charge efficiency (10). Membranes such as cellophane, which reduce the silver ions to silver metal, are initially effective silver barriers but lose their effectiveness as the metallic silver accumulates within their pores and the membrane structure deteriorates.

Nonoxidizable films which retard the diffusion of the silver ions also retard the passage of potassium and hydroxyl ions and thereby increase cell resistance. If a reasonable cell resistance is to be obtained, it is therefore seen to be necessary to accept a finite rate of silver diffusion. The use of multiple layers of both oxidizable and nonreactive films may provide an acceptable set of properties (24).

Table II summarizes the pertinent properties of several representative membrane materials available for use in silver-zinc cells.

The Borden methylcellulose and Permion films are all relatively resistant to oxidation by silver compared with the "standard" cellulosic material. The Permion films, although exhibiting the greatest oxidation resistance, allow the most rapid silver transport of all the films. The use of the Borden 5-9107-21 film which has a low diffusion rate for silver ion is precluded by its high resistance in KOH. For cells which must be sterilized prior to use, several types of inorganic separators have been developed (26). Use of these rigid, relatively thick (25 mil) separators to retain the zinc electrode material mechanically has been reported to result in extended cycle lives (27).

A rational basis for selection among the films just described can only be made with some knowledge of the effect of silver contamination of the zinc electrode. Lander (10) cycled several cells containing silver additions of 0.01, 0.1 and 1.0% to the negative plates. Cell life was significantly reduced due to decreased charge efficiency at the 1.0% silver level. Since the silver powder was dispersed uniformly throughout the electrode, the results are likely to be optimistic when compared with silver deposited on the surface of a working electrode.

The poor recharge capability of zinc electrodes contaminated by unamalgamated silver can result from two distinct processes. By providing sites with relatively low hydrogen overvoltage, the hydrogen evolution reaction can become more favorable than the reduction of ZnO to Zn. In addition, finely divided silver can catalyze the oxidation of zinc by oxygen present in the cell head space or electrolyte.

At 0.1% silver, the silver concentration in a zinc electrode of typical thickness corresponds to 2 mg/sq in. or 2.9×10^{-3} moles/cm^2 (10). The assumption of a silver diffusion rate of 25×10^{-10} moles/cm^2-sec results in a time period on the order of 10^6 sec or 2 months being required to transport the specified amount of silver to the negative plate. Even though this figure is probably conservative, it is apparent that multiple layers of separator material will be required to assure stable performance of the zinc electrode.

In order to retain maximum energy density, it is important that the thickness of the separator layer be reduced to as small a value as is consistent with the cycle life capabilities of the zinc electrode, and with the type and duration of the mission to be encountered. The trade-off between cycle life and energy density requires that the separator system be specifically designed for the mission contemplated.

As of the present time, no separator has been shown to be more effective than those based on cellophane or methylcellulose in preventing dendrite growth, the assumption being that the elevated temperatures required for cell sterilization will not be experienced. However, McBreen (23) reports that the initially higher zincate exclusion properties of the methylcellulose membrane deteriorate after soaking in KOH at temperatures approaching 60°C. In any event, the rapid oxidation of cellulose by Ag^+ makes the use of cellophane in direct contact with the positive plates unattractive for long-term operation. The use of a methylcellulose-based membrane such as Borden 5-9107-23 is therefore a requirement to retard the rate

Table II. Membrane properties (25)

Membrane	Rate of silver diffusion moles Ag/cm^2 sec $\times 10^{10}$	Rate of silver reaction grams Ag/in.^{2}/ hr $\times 10^6$	Resistance Ω-cm^2 40% KOH	Thickness inches	Material
PUDO-300*	35.5	62.7	0.062	0.001	Cellophane
Borden 5-9107-21**	25.1	3.85	2.58	0.0015	Methylcellulose
Borden 5-9107-23 (24)**	23	Comparable to 5-9107-21	0.096 (31%)	0.0015	Methylcellulose and potassium acetate
Borden 5-9107-29**	38.6	13.9	0.048	0.0015	Polyvinyl alcohol
Permion 116***	57.2	0.78	0.161	0.001	Polyethylene acrylic acid graft
Permion 110***	79.9	—	0.135	0.001	Polyethylene acrylic acid graft
Permion 1770 C***	46.6	0.65	0.170	0.001	Chemically grafted polyethylene

* Dupont.
** Borden Chemical.
*** RAI Research Inc.

of silver diffusion and hence slow the oxidation rate of cellophane.

The use of multiple layers of separator material presents some problems in wrapping the electrodes. In the conventional U-wrapping technique (24), two silver electrodes are placed bottom ends opposed across the short dimension of a rectangular separator strip and folded for several wraps (usually 5 or 6). The two electrodes are then folded together to give a U-bend into which the zinc electrode is inserted. When multiple layers of separator are used, the outer layers of separator become stressed at the crease at the bottom of the fold. Small cracks can be produced which may alter the diffusion characteristics of the membrane and allow premature cell failure due to contamination of the zinc electrodes with deposited silver metal, or by dendritic shorting.

Treating the fold area with electrolyte to swell the membrane and make it more resistant to stress cracking has been suggested as a means of eliminating the problem of premature cell failure (24). Alternative methods to eliminate the "U" fold involve changes in the wrapping method.

The use of an "accordian" wrap where a long ribbon of separator is used to wrap the entire cell pack is extensively employed in rectangular nickel-cadmium cells. Its use in silver-zinc cells is precluded by the fact that alternate edges of the silver electrodes are exposed to the free electrolyte, thereby allowing unimpeded diffusion of silver ions to the negative electrodes. The envelope type of wrap, consisting of heat or adhesive sealing of the separator edges around an individual electrode, has also been considered, particularly with regard to the zinc electrode (24).

Sealed Cell Technology

A reliable and predictable method for preventing pressure buildup in sealed silver-zinc cells is a basic requirement. While a pressure relief device is usually included in cell designs to prevent damage to the cell case, frequent venting of excess hydrogen or oxygen on long missions will result in a deterioration of the electrical performance of the cell due to both concentration and volume changes of electrolyte. Four possible methods for recombination of evolved gases have been extensively studied for use in sealed silver zinc cells: internal recombination of gases on the battery plates, use of a third or auxiliary electrode, recombination catalysts placed in the head space of the cell, and finally, the use of externally mounted fuel cells.

Rates of gas evolution and recombination on silver and zinc electrodes.—Zinc is thermodynamically unstable in contact with alkaline solutions, its potential being approximately 0.4v below that required for hydrogen evolution. The rate of gas evolution is strongly influenced by the high hydrogen overvoltage of zinc and by additives which tend to alter the overvoltage, particularly mercury.

Snyder and Lander (28) have studied the rate of hydrogen evolution of zinc electrodes under open circuit conditions. These results indicate that the gassing rate varies inversely with KOH and mercury concentrations and directly with temperature. The presence of ZnO in the electrolyte appeared to have little effect. The use of 2% by weight of HgO dispersed in the ZnO prior to formation was found to yield the lowest gassing rates under most conditions. However, it is not uncommon for increased amounts of HgO (up to 15% by weight) to be employed in applications where it is desirable to maintain the lowest possible gassing rates under a wide range of environmental conditions.

The experimentally observed gassing rate of such an amalgamated electrode (2% HgO) at 100°F in 40% KOH was 1.5×10^{-4} ml/min for each ampere-hour of theoretical capacity. This figure corresponds to a tolerably low self-discharge rate. For a cell containing 20 amp-hours of zinc, this rate of capacity loss corresponds to less than 0.5 ma. For long missions, however, even this low a gassing rate results in an intolerably large pressure buildup in sealed cells, if no provision is made to remove the hydrogen. It is likely that the zinc electrode is always gassing hydrogen at rates similar to the preceding, since the voltage of the electrode always remain close to its open circuit value (assuming the charging potential is closely regulated).

Generation of oxygen at the positive electrode does not present the same degree of difficulty as hydrogen generation at the Zn electrode. The level of free electrolyte in sealed cells is usually maintained at about one-half the plate height to allow any oxygen produced at the silver electrode on stand or overcharge to be reduced by exposure to the high surface area zinc electrodes.

Based on this principle silver-zinc cells are designed to be silver limited so that the silver-electrode reaches full charge and begins to evolve oxygen before rapid hydrogen generation commences at the zinc electrode. In one study a conventional 15 plate, 25 amp-hr cell was shown to be capable of supporting a continuous overcharge current of 0.25 amp without accumulation of excessive oxygen pressure (10). However, buildup of significant oxygen over-pressure has also been reported during initial cycling (29).

The accumulation of hydrogen in sealed cells has presented more of a problem. In addition to the continuous corrosion of zinc as described previously, greater amounts of hydrogen may be evolved as the supply of available ZnO in the negative plate declines during cycling. The zinc and silver electrodes then become mismatched and the zinc electrode must be overcharged to restore full charge to the positive plate.

The extent to which this hydrogen is oxidized to water by AgO is a matter of crucial importance for design of sealed silver-zinc cells. Experimental work has shown that the recombination is fast enough on unwrapped plates to avoid excessive hydrogen accumulation. Completed cells, however, have exhibited the tendency to rupture from excessive hydrogen pressure, particularly at high charge rates.

The existence of the recombination reaction has been shown by both indirect and direct methods. The observation has been made (28) that the pressure buildup in sealed silver-zinc cells on open circuit stand is much slower than would be expected from the amount of hydrogen being generated at the zinc electrode. Rhyne (30) showed that 1g of high surface area AgO moistened with KOH reacts with hydrogen at about 0.008 ml/min at room temperature. Experiments performed on full sized plates (2.5 x 4 in.) have given comparable results (10). Hydrogen recombination rates range from 0.42 ml/min on standard plates to 4.1 ml/min for plates that had been wet-proofed with Teflon to decrease the KOH film thickness and expose more surface area. The total recombination ability of a multiplate, 25 amp-hr battery can be estimated by assuming that ½ the area of each of the 8 positive plates is available for recombination. For the wet proofed electrode the continuous overcharge capability is calculated to be 40 ma (0.039 ma/cm^2) (10).

Sulkes (19) and Lander (10) have both shown that small additions of Pd (about 1%) to the positive plates increase the reaction rate with H_2. However, the rate changes caused by palladium additions were not as great as the changes caused by factors likely to alter the diffusion of H_2 to the electrode surface, *viz.* KOH concentration, choice of separator system, and wetproofing the electrode.

The observed fact that sealed cell failure is due almost universally to hydrogen rather than oxygen accumulation can lead only to the conclusion that the oxidation rate on the positive electrode has a greater kinetic limitation than the oxygen reduction on the zinc electrode. Due to the higher kinetic hindrance for the hydrogen oxidation, it is necessary to provide more surface area for the reaction.

The rate of reaction on the silver positive is thus seen to be more sensitive to factors which may not appreciably affect the reaction rate at the zinc electrode.

In particular, differences in cell pack wrapping or electrode structure which affect either the diffusion of gases through the electrolyte film, or the amount of surface area available for reaction, are more likely to limit the hydrogen rather than the oxygen reaction rate.

Auxiliary electrodes.—The use of AgO electrodes to control hydrogen accumulation has been described previously. Biasing the additional positive plate at a potential lower than that of the working electrodes is not required, since the rate of recombination has been shown to be accelerated by higher potentials (19), and since there is no danger of continuous oxygen evolution from the AgO.

The use of internal fuel cell electrodes to react with evolved hydrogen was investigated by Lander (10). In order for the H_2 electrode to function, it must be connected to the positive plate through a diode to prevent the hydrogen electrode from reaching the oxygen liberation potential.

The electrode investigated consisted of a wetproofed nickel plaque impregnated with a palladium-silver catalyst. Insertion of the electrode into a complete cell required the removal of two plates. Contact of the activated surface with the gas space was maintained by wrapping the electrode in a coarse plastic mesh. The cells were overcharged to an extent limited by a predetermined potential rise. Potential cutoffs in the range 2.00 to 2.19 were investigated. In all cases, cell failure was by dendritic shorting rather than by pressure buildup.

The presence of catalytic materials with low hydrogen overvoltages, *e.g.* palladium, introduces an additional complication. Precautions must be taken to insure that such materials are not transported, either by electrochemical or physical processes, to the surface of the negative electrode, since the result would be to lower the necessarily high hydrogen overvoltage of the zinc. Screening of alternative catalyst materials with relatively high hydrogen overvoltages has indicated that mercury (amalgamated on a silver plaque) has sufficient activity to function as an auxiliary electrode for oxygen reduction (20).

Development of reliable sealed cells with auxiliary electrodes has been hampered by the fact that zinc may plate out on the oxygen electrode. In addition, changes in cell pack dimensions on continued cycling may alter the rates of gas recombinations.

Recombination catalysts.—The use of a recombination catalyst in the head space of the cell has also been investigated (10). Tests indicated that a Pd-Al_2O_3 catalyst was capable of recombining the gases at a significant rate, although some difficulties were experienced. This method can only be successful in recombining stoichiometric amounts of hydrogen and oxygen. A vent of some type is therefore still a requirement.

Externally mounted fuel cells.—The use of an externally mounted device to eliminate the accumulation of gases in sealed cells is attractive since such a device is not exposed to the variable internal cell environment. Programs to evaluate small fuel cells for use in sealed battery operation have been undertaken (29, 31). Fuel cells with from 0.25 to 5.0 sq/cm of electrode area have been investigated.

Successful results have been obtained with commercially available Teflonated platinum black electrodes. Both electrodes are identical and the KOH electrolyte is impregnated in an asbestos matrix.

Since, under most conditions, the internal oxygen recombination reaction has been found to be rapid, the fuel cells are used to oxidize hydrogen. For fuel cells employing two platinum electrodes, an external supply of oxygen is required. Also under investigation is the use of a consumable cadmium or zinc anode for oxygen consumption and a silver or mercuric oxide cathode for hydrogen consumption (31). The results are promising, with efficiencies approaching 90% utilization of the AgO electrodes being obtained at the low current drains required.

Fuel cell operation can be carried out in any of several modes: open end flow without wicking, dead-end flow without wicking, and dead-end flow with wicking of the product water. For long-term operation of the battery and fuel cell system, dead-end flow and return of product water to the cell electrolyte are necessary to assure stable operation.

Since the probable continuous rate of hydrogen evolution is equivalent to less than 1 ma (28), current densities on even the small cells being investigated are quite low. This fact contributes to the maintenance of stable performance. Fuel cells operating in the required mode with an electrode area of 1 cm^2 have exhibited greater than 3000 hr of stable operation at a current density of 5 ma/cm^2.

The implication that the use of external fuel cells is a suitable method for eliminating hydrogen overpressure in sealed silver-zinc cells is clear. If proper formation techniques are followed, and the cells are properly stored while awaiting use, no difficulty should be encountered with oxygen accumulation. The investigation into the gassing rates of silver-zinc cells, which indicated that oxygen pressure became excessive on the first few cycles, employed dry charged batteries which had likely been stored in air prior to their activation (29). Partial surface oxidation of the zinc could have easily occurred, with the result that the oxygen recombination reaction was inhibited for several cycles.

The role of diffusion in sealed cell design.—As has already been pointed out, the reduction rate of oxygen on zinc electrodes is sufficiently rapid to accommodate substantial oxygen evolution from the silver plate. Even though the analogous hydrogen reaction has been shown to occur at the positive electrode, its apparent rate is slower, and in most cases is inadequate to control hydrogen accumulation. Studies on a rotating zinc disk electrode have shown that the rate of oxygen reduction in fabricated cells is limited by the kinetics of the reaction and by the available surface area, rather than by diffusion of the oxygen to the electrode surface (19).

Corresponding studies are not available for the silver electrode. Some conclusions can be drawn from the empirical studies, however, Sulkes (19) has observed that the rate of hydrogen accumulation in sealed cells becomes slower as the temperature is raised. In view of the fact that the rate of gassing at the zinc electrode increases rapidly with temperature (28), it is evident that rate of the hydrogen recombination increases at least as fast as the rate of zinc corrosion. The strong temperature dependence of the recombination rate on silver would thus tend to indicate kinetic rather diffusion control, since diffusion processes would not be expected to exhibit the sensitivity to temperature that has been shown to exist.

Lander (10) investigated the rate of hydrogen recombination on positive plates and found it to be increased by the addition of wet proofing agents such as Teflon and by the use of Pd. Pd has been shown (20-22) to increase the specific surface of the silver electrode and hence provide greater surface area for the recombination reaction. The presence of Teflon would logically have the effect of reducing the thickness of the electrolyte film that the hydrogen must diffuse through in order to react at the electrode surface.

Since the diffusion coefficients of hydrogen and oxygen are of the same order of magnitude, the slow rate of hydrogen recombination on the silver electrode is therefore related to the lower specific surface of the silver-silver oxide plate compared to the zinc plate. The negative electrode has been shown to have a surface area of 200 times its apparent area by double layer capacity measurements (19). In view of this conclusion, the rate of hydrogen recombination may be significantly altered by changes in the porosity and structure of the positive electrode.

Control of hydrogen evolution through the use of externally mounted fuel cells located in the head space of the cell or through internal recombination requires an understanding of the factors which may affect the diffusion of hydrogen from within the zinc electrode. If hydrogen bubbles accumulate in or around the zinc electrode, electrolyte is displaced, the effective current density is increased, and the growth of dendrites is facilitated. In addition, the presence of small discrete pockets of hydrogen may encourage the formation of explosive mixtures due to oxygen diffusing into the bubbles.

The structure of the zinc electrode and the type of electrode-electrolyte interface are the major variables which will determine the amount and size of the generated hydrogen bubbles. Determination of these variables is usually performed on the basis of other performance specifications such as cycle life and zinc utilization. However, many of the design improvements employed for these other reasons have a significant effect on the rate of diffusion of hydrogen from the zinc electrode. In particular, the use of surfactants in the cell electrolyte and of absorbent fibers in the electrode structure may encourage displacement of entrapped hydrogen bubbles by the cell electrolyte.

Summary

A variety of individual improvement factors have been suggested for the zinc electrode. Some of these are mutually exclusive; for example, both hydrophobic and hydrophilic additives are reported to be capable of stabilizing the zinc electrode structure. Some interdependence with factors is to be expected in applying surfactants to control dendrite growth and to prevent zinc agglomeration.

It remains to be determined whether the additives listed above function (*a*) because of their hydrophobic or hydrophilic character, (*b*) because they increase the structural strength of the electrode, (*c*) because they provide for a more uniform structure, or (*d*) through some other mechanism. The appropriate mechanism is, obviously, of concern in choosing the optimum electrode structure.

A number of empirical, factorial studies have related the physical structure of silver oxide electrodes to plate discharge characteristics. These experiments have generally been specific, *i.e.*, related to a single charge-discharge regime; therefore some amplification of work already discussed may be required for use in alternative cycle regimes. Attempts have also been made to improve silver electrode performance by the use of alloyed constituents. It was concluded, for example, that although palladium improved performance, it migrated into the separator. Recent experiments have demonstrated that the effect of many such alloyed constituents is to increase the roughness of the silver electrode and hence to increase the available surface. This same type of basic mechanistic information is required to determine the significance and applicability of individual design features in other areas of battery fabrication.

It is by now apparent that there are several alternative design improvements available in each of the major areas of silver-zinc technology. Selection of any one design procedure must be made so as to insure compatibility with the rest of the cell system and to insure the creation of an optimum cell design.

Acknowledgments

The author wishes to thank his colleagues, Dr. J. Giner and Dr. R. Jasinski for their assistance and guidance in the preparation of this review.

Manuscript submitted June 3, 1968; revised manuscript received October 16, 1968.

REFERENCES

1. T. P. Dirkse, "Electrode Migration and Reaction Processes Occurring Within Alkaline-Zinc Batteries," Contract No. AF 33(615)-3292, Calvin College, Grand Rapids, Mich.
2. O. C. Wagner, "Evaluation of Foreign S-12 Silver-Zinc Cells," Technical Report, ECOM-2884, U.S. Army Electronics Command, Fort Monmouth, N. J.
3. Z. Stachurski, "Investigation and Improvement of Zinc Electrodes for Electrochemical Cells," Contract No. NAS 5-3873, Yardney Electric Corp.
4. S. Arouete and K. F. Blurton, "The Improvement of Zinc Electrodes for Electrochemical Cells," Contract No. NAS 5-9591, Leesona-Moos Laboratories.
5. J. Goodkin, "Long Life Stable Zinc Electrode for Alkaline Secondary Battery," Contract No. DAAB 07-67-C-0185, Yardney Electric Co.
6. J. J. Lander and J. A. Keralla, "Silver-Zinc Electrode and Separator Research," Contract No. AF 33 (615)-3487, Delco-Remy Division, General Motors.
7. T. A. Kryukova, *Soviet Electrochemistry*, **3**, 147 (1961).
8. T. M. Rogers, "Handbook of Practical Electroplating," Macmillan (1959).
9. T. P. Dirkse, "Investigation of the Transport and Reaction Processes Occurring within Silver Oxide-Zinc Batteries," Contract No. AF 33(615)-2297, Calvin College, Grand Rapids, Mich.
10. J. J. Lander, J. J. Keralla, and R. S. Bogner, "Zinc Electrode Investigations," Contract No. AF 33(615)-1583, Delco-Remy Division, General Motors.
11. T. P. Dirkse, U.S. Patent 3,348,973, Secondary Battery.
12. W. J. Van der Griten, "Secondary Electrode with Zincate Trapping," presented at the Chicago Meeting of The Electrochemical Society, October 15-19, 1967.
13. V. V. Romonov, *Zhurnal Prikladnoi Khemii*, **35**, 1293 (1962).
14. N. A. Zhulidov, *Vest. Electroprim.*, **34**, 74 (1963).
15. A. Langer and J. T. Patton, *This Journal*, **114**, 113 (1967).
16. C. P. Wales and J. Burbank, *ibid.*, **112**, 13 (1965).
17. R. F. Amlie and P. Ruetschi, *ibid.*, **108**, 814 (1961).
18. J. J. Lander and J. A. Kerella, "Silver-Zinc Secondary Battery Investigation," Contract No. AF 33(657)-8943, Delco-Remy Division, General Motors.
19. M. Sulkes, "Development of the Sealed Zinc-Silver Oxide Secondary Battery System," Contract No. DA-36-039-AMC-02238(E), Yardney Electric Corp.
20. R. Jasinski, "High Energy Batteries," Contract No. NOw-66-0621, Tyco Laboratories.
21. P. Malachesky and R. Jasinski, *This Journal*, **114**, 1239 (1967).
22. P. Malachesky and R. Jasinski, *ibid.*, **114**, 1258 (1967).
23. J. McBreen, "Study to Investigate and Improve the Zinc Electrode for Spacecraft Electrochemical Cells," Contract No. NAS 5-10231, Yardney Electric Company.
24. H. L. Pfluger and H. E. Hoyt, "Improved Separators for Silver Oxide-Zinc and Silver Oxide-Cadmium Cells for Spacecraft Application," Contract No. NAS 5-9107, Borden Chemical Company.
25. J. J. Kelley and J. A. Szymborski, "Alkaline Battery Separator Characterization Studies," Contract No. NAS 5-10418, ESB, Incorporated.
26. F. C. Arrance, R. Greve, and A. Rosa, "Program to Develop an Inorganic Separator for a High Temperature Silver-Zinc Battery," Contract No. NAS 3-7639, Douglas Aircraft Company.
27. A. Himy, "Improved Zinc Electrode," Contract No. NAS 3-8513, Douglas Aircraft Company.
28. R. N. Snyder and J. J. Lander, *Electrochem. Technol.*, **3**, 161 (1965).
29. H. Frank and M. P. Stries, "Small Fuel Cell to Eliminate Pressure Caused by Gassing in High Energy Density Batteries," Contract No. NAS 5-9594, Douglas Aircraft Company.
30. J. Rhyne, "Silver Oxide-Zinc Battery Program," Contract No. AF 33(600)-41600, Delco-Remy Division, General Motors.
31. H. Frank and M. P. Stries, "Sealing of Silver Oxide-Zinc Storage Cells," Contract No. NAS 5-10409, Douglas Aircraft Company.

A Review of the Electrochemistry and Technology of Chlorates and Perchlorates

Joseph C. Schumacher*

American Potash & Chemical Corporation, Los Angeles, California

Production of chlorates and perchlorates has increased enormously during the past twenty-five years and appears destined to continue to increase at an accelerated rate in the years ahead.

This growing market, as shown in Table I, has brought increased competition among producers and thus has created new demands for better technology and higher standards of production efficiency. A new drive is being made to increase energy efficiency, also to reduce operating and capital costs. These objectives and related goals can be accomplished only through a better understanding of the electrochemical processes and electrode materials constituting the electrolytic cell system.

At the present time, large-scale commercial sodium chlorate cells operate at 80 to 87% current efficiency with an average requirement of 6000 kw hr (DC) of electrical energy per ton (2000 lbs) of product. Potential improvements include increasing current efficiency to 95% or higher and in reducing the electrical energy requirement to 4000 kw hr per ton or less as shown in Fig. 1. Current efficiency losses in the chlorate cell result from losses of hypochlorite, an intermediate in the formation of chlorate. These losses can occur through formation of oxygen at the anode, reduction at the cathode, catalytic decomposition in the electrolyte, or by volatilization of undissociated hypochlorous acid in the cell gases.

Potential improvements lie also in the area of reduced cooling requirements and anode replacement costs. Recovery and use of hydrogen is now not in common practice, but may be so in the future in order to improve production economics.

Commercial perchlorate cells operate at current efficiencies of 95% or higher, but there is a need for and room for further improvement in energy efficiency and reduction of capital and maintenance costs. Improvements of this type can best be achieved through greater knowledge of the electrode processes and materials.

The following chronology of events traces the evolution and development of the electrochemistry and technology of chlorates and perchlorates and points up areas of current interest.

Evolution of Electrochemistry and Technology of Chlorates

1808 Berzelius reports electrochemical preparation of chlorate (1).

1847 Kolbe confirms electrochemical conversion of chloride to chlorate (1).

* Electrochemical Society Active Member.

Table I. Sodium chlorate production

	United States (Short tons)	Sweden (Metric tons)	Japan (Metric tons)
1940	15,000	2000	
1950	22,085	3000	6370 (1958)
1960	91,585	14,000	11,279
1965	132,689	34,000	22,630 (1963)
1966	—	50,000	
1967	151,000		35,000**
1972	220,000**		

** Estimate.

1866 First commercial electrochemical production of chlorate in France with platinum anodes (1).

1894 Carlson reports the use of graphite anodes in chlorate production in Sweden (1).

1898 Müeller reports diaphragm unnecessary when chromate is added to chlorate cell electrolyte (2). Carlson reports the use of magnetite anodes (3).

1899 Foerster and his students postulate mechanism of electrochemical chlorate formation. Discharge of chloride ions is followed by a series of chemical reactions. Current efficiency losses involve oxygen evolution through discharge of hypochlorite (4).

1900's Graphite becomes the standard anode material for chlorate cells. Monopolar and Bipolar cells are used (5).

1911 Müeller and Koppe report relationship of acidity and current concentration to current efficiency (6).

1915 Magnetite anodes are used in chlorate production in Germany (1, 3).

1920 Knibbs and Palfreeman conclude that the discharge of hydroxyl ions or chlorate ions did not contribute significantly to current efficiency losses (7).

1953 de Valera extends Foerster's theory of formation of chlorate by mathematical treatment and describes important role of anode diffusion layer (8, 9).

1954 Wagner explains the effect film has which forms on cathodes when chromate is added to the electrolyte (10).

1956 Nagai and Takei report cathodic losses are controlled by diffusion of hypochlorite toward the cathode surface (11).

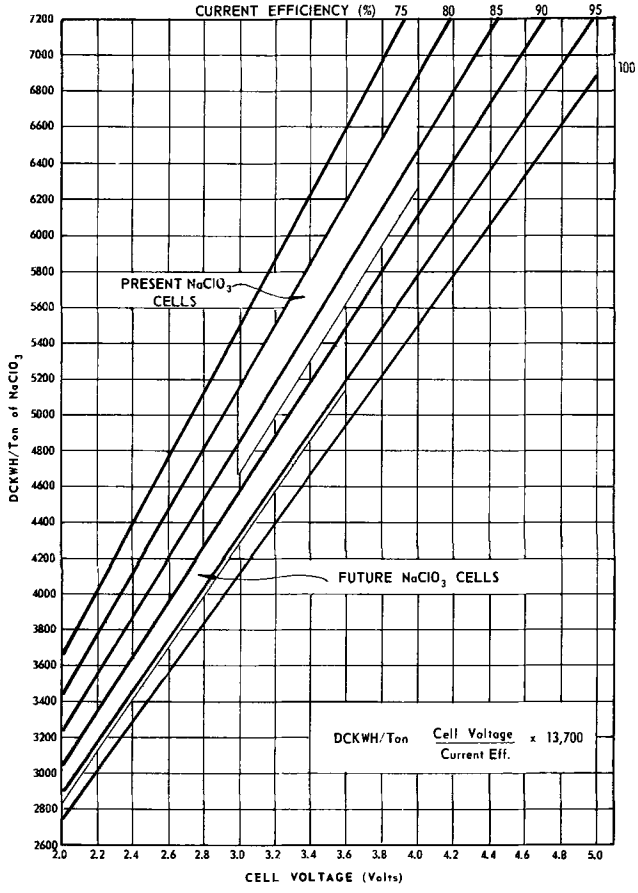

Fig. 1. Current efficiency

1961 Beck's calculations support conclusion that transport of hypochlorite ions from bulk of the solution to the anode is factor which controls rate of reaction (12).

1963 Ibl reports his studies of mass transport during electrolysis in the anodic diffusion layer (13).

Ibl and Landolt postulate chlorine, formed at the anode, is hydrolyzed in diffusion layer. Also diffusion layer is buffered by hypochlorite ion diffusing from bulk of the solution thus maintaining a high *p*H so that chlorine hydrolysis can proceed (14).

1964 de Valera considers hydroxyl ion discharge to be primary step in oxygen evolution anodic reaction (15).

Hammar and Wranglen report their investigations of current efficiency losses in chlorate formation (16).

Evolution of Electrochemistry and Technology of Perchlorates

1816 Von Stadion reports electrochemical preparation of perchlorates (17).

1893 First commercial production of perchlorate in Sweden (18).

1897 Foerster reports studies of electrolytic conversion of chlorate to perchlorate (19).

1903 Oechsli postulates mechanism of perchlorate formation. Discharge of chlorate ions followed by chemical reactions (20).

1916 Bennett and Mack postulate direct oxidation of chlorate by active oxygen at anode (21).

1920 Knibbs and Palfreeman examine losses of current efficiency at the anode. Disagree with Oechsli and Bennett and Mack. Postulate new mechanism involving formation of peroxide followed by rearrangement (22).

1955 Phillip and Morgan postulate direct anodic oxidation of chlorate via high valence platinum oxide (23).

1956 Sugino and Aoyagi report use of lead dioxide anodes. Postulate simultaneous discharge of chlorate and hydroxyl ions followed by combination of radicals (24).

1967 Grotheer postulates direct anodic oxidation of chlorate via oxygen species adsorbed on anode (25).

This historical review shows that reaction mechanisms which occur under operating conditions which exist in industrial electrolytic chlorate and perchlorate cells have not been fully established. Also, the theoretical problems associated with chlorate formation received almost no attention in the published literature during the 33 year period from 1920 until de Valera published his work in 1953. Interest in these problems by other investigators developed rather slowly until approximately 1960. Since then there has been an increasing effort to resolve the mysteries which surround the anode in chlorate cells. Continuing studies along present lines of interest should provide the information required to achieve the previously stated objectives of higher energy efficiencies and lower production costs.

Manuscript submitted September 9, 1968; revised manuscript received October 8, 1968. This paper was presented as an introduction to the Symposium on Chlorates and Perchlorates at the Boston Meeting, May 5-9, 1968.

REFERENCES

1. R. Bauer, *Chemie-Ing. Tech.*, **34**, 376 (1962).
2. Erich Müeller, *Z. Elektrochem.*, **5**, 469 (1899).
3. Genzo Ishi, Address Presented to The Electrochemical Society in Boston, Mass., May 1968.
4. Foerster and Müeller, *Z. Elektrochem.*, **9**, 171 (1903).
5. A. J. Allmand and H. J. T. Ellingham, "The Principles of Applied Electrochemistry," Edward Arnold & Co., London (1931).
6. Müeller and Koppe, *Z. Elektrochem.*, **17**, 421 (1911).
7. Knibbs and Palfreeman, *Trans. Faraday Soc.*, **16**, 402 (1920).
8. V. de Valera, *ibid.*, **49**, 1338 (1953).
9. V. de Valera, *ibid.*, **52**, 250 (1956).
10. C. J. Wagner, *This Journal*, **101**, 181 (1954).
11. T. Nagai and T. Takei, *Denki Kagaku*, **24**, 557 (1956).
12. T. R. Beck, Address Presented to The Electrochemical Society in Indianapolis, Ind., May 2, 1961.
13. N. Ibl, *Chemie-Ing. Tech.*, **5**, 353 (1963).
14. N. Ibl, and D. Landolt, *ibid.*, **39**, 706 (1967).
15. V. de Valera, *Trans. Faraday Soc.*, **60**, 1450 (1964).
16. L. Hammar and G. Wranglen, *Electrochimica Acta*, **9**, 1 (1964).
17. F. von Stadion, *Gilbert's Ann. Phys.*, **52**, 197 (1816).
18. Stockholms Superfosfat Fabriks Aktiebolag, private communication, Nov. 25, 1957.
19. F. Foerster, *Z. Elektrochem.*, **4**, (16), 386 (1897).
20. W. Oeschli, *Z. Elektrochem.*, **9**, 807 (1903).
21. C. W. Bennett and E. L. Mack, *Trans. Electrochem. Soc.*, **29**, 323 (1916).
22. N. V. S. Knibbs and H. Palfreeman, *Trans. Faraday Soc.*, **16**, 402 (1920).
23. W. H. Philipp and L. O. Morgan, Technical Report No. 4 to Office of Naval Research, Contract Nonr 375(04), University of Texas, Department of Chemistry (October 1955).
24. K. Sugino and S. Aoyagi, *This Journal*, **103**, 166 (1956).
25. M. P. Grotheer and E. H. Cook, Paper presented at The Dallas Meeting of the Society, May 7-12, 1967, as Paper 146.

Francis Laurence LaQue

H. H. Uhlig*

Dr. H. H. Uhlig delivers introductory remarks about the Acheson Medalist.

The Acheson Medal was established in recognition of contributions "to the advancement of any of the objects, purposes, or activities, here or hereafter, fostered or promoted by the Society." Our present Medalist has certainly contributed outstandingly to the professional areas fostered by our Society; he has in addition served the Society itself in several capacities, including the office of President. Whatever the place or occasion, he has added luster to what otherwise would be dull or tarnished and, in more ways than one, he has converted rust into useful metal.

During the time I have had the pleasure of knowing Frank LaQue, the characteristics that identify him above all others, to my mind, are both his clarity of thinking and his ability to persuade others that his thinking is clear. The combination, as you might suspect, is a reasonable formula for success. It has carried him to the top ranks of his profession, to the top echelons of his company, to the top office of three technical societies, and to important advisory and consulting positions in government.

Throughout all of his crowded professional and business responsibilities, Frank has retained an inimitable sense of humor which fits the occasion and which he often uses to drive home his point. For variation or for emphasis he is furthermore not averse to, or perhaps I should say he is not shy about, expressing his thoughts of the moment in verse. He is the Poet Laureate of corrosion engineers and the "Robert Frost" of the Sea Horse Institute. Each year, members of the Sea Horse Institute receive a Christmas card, attractively designed by his daughter Mary, on which is printed one of Frank's delightful contributions to rhyme and jingle. I wish there were time to read several of his poetic creations; I know you would enjoy hearing them. Here are some excerpts:

The time has come the Sea Horse said to talk of
many things . . .
Of ships and rigging and deep ocean pinging
That can sound even better than bar-room singing.

Offshore platforms that are much more stable
than political ones seem ever to be able.

Nodules of manganese, a new kind of ore
never even dreamed of in days of yore.

Houses for people who have the odd notion
they would like to live way down in the ocean.
Vessels designed for deep-sea submergence
with reasonable hope of later emergence.

And another:

Novices may feel they must be quite smart
In knowing so much, right after they start.
But, sooner or later, they may have to confess
What they know for sure becomes less and less.

As time goes on, the wise will discover,
The best thing to do is trade with each other.
Like all good Sea Horses who take their turn
In passing along the new facts they learn.

For relaxation, Frank plays golf and bridge, or he goes fishing or sailing. The latter activities center around his summer home in the Thousand Islands where he was born at Gananoque, Canada. He attended public schools there, demonstrating very early a scholarly ability which insured his eventual admission to Queens University. By remaining at the top of his class, he made himself eligible for local scholarship aid which was essential to the furtherance of his education. He also worked in industry during college years in order to supplement available scholarships. It was during one of his summer jobs at Chatham, Canada, that he met Kate Clark who professed an interest in knowing more about science and mathematics and in particular how to use a slide rule. Frank impressed her with his patient ability as a teacher, a characteristic that has carried through all of his subsequent professional activities. More important, she was impressed with Frank. They were married in Gananoque in 1930 and have two daughters. Kathy is an occupational therapist at the Massachusetts General Hospital in Boston, presently on assignment in California, and Mary, who is now Mrs. Gerard McMartin, is married to a teacher and lives with their four sons near Toronto, Canada.

At college, Frank decided to major in metallurgy, both because of the broad challenge which this field offered, and because of the many job opportunities in Canada in the metals and minerals industry. Upon graduation in 1927, a personal appraisal by his classmates appeared in the college yearbook, "Tricolor," which on reading today, impresses one with its terse accuracy. After describing where Frank came from, the scholarships he won and his interim jobs during college years, the "Tricolor" account closes with: "His specialty is metallurgy and he is particularly interested in steel. Brilliant, witty and good, his success in life is assured." The account, I suppose, might also have mentioned nickel, but iron and nickel, after all, are in the same group of the Periodic Table. Thirty-seven years later, his Alma Mater confirmed the "Tricolor" prediction by conferring on him the honorary degree of Doctor of Laws. The college authorities could by then well afford to describe their distinguished alumnus at greater length and with unrestrained approbation. The citation reads, "Native son of the Thousand Islands, graduate and devoted alumnus of this University, metallurgist extraordinary, more than thirty-five years a vital, creative force within the International Nickel Company, whose sustained work and leadership in the study of corrosion on metals have advanced us towards a secular paradise where rust does not corrupt, and who has given unstintingly of his great knowledge

* Introductory remarks by H. H. Uhlig on the occasion of the presentation of the Acheson Medal Award to F. L. LaQue on October 8, 1968 at the Montreal Meeting.

and experience in helping this University to educate a new generation of engineers for the needs of a changing world." I would personally have retained in this description the earlier term "witty" because somehow it belongs in the record. This characteristic has happily remained with Frank, undiminished since his college days. It would be an omission at this point not to mention Kate LaQue's wit which charmingly supplements that of her husband.

Shortly after graduation and a brief job with the Deloro Smelting and Refining Co., Frank was employed by the International Nickel Co. at their office in New York City. Since the company's products, nickel and nickel alloys, are useful in large part because of their corrosion resistance, the company wanted to employ someone who could help develop corrosion information of value to both its established and its potential customers. Frank had had heretofore no experience, nor special interest in corrosion, but typical of a procedure carried out in many companies even today, he was promptly appointed "corrosion engineer." He explored the subject, finding it to be more than ordinarily fascinating, and learned it thoroughly. On his visits to industries besieged with corrosion problems, he offered them unslanted advice on the proper solution, whether or not this advice entailed the sale of nickel. His perspicacity in diagnosing corrosion problems, plus his surprising candor and honesty, won the complete confidence of managers and engineers wherever he went, and in the long run he probably sold much more of the company's products than a dozen men would have sold using any other approach.

In 1938 he was made Assistant Director of Technical Service and in 1940 he was placed in charge of the Corrosion Engineering Section. This was followed in 1954 by the further promotion to Vice-President and Manager of the Development and Research Division. Since 1962, he has been Vice-President and Special Assistant to the President of the company.

On reviewing Frank's career with the International Nickel Co., we go back to 1935 when he was busily spelling out prescriptions for corrosion maladies. One of the industries he visited was the Bromine Plant of the Ethyl-Dow Chemical Co. at Kure Beach near Wilmington, N. C. He immediately recognized that the company's continuous intake of ocean water made the canal leading to the plant an ideal place in which to immerse corrosion test specimens. He persuaded both his own management and that of Dow to make the necessary arrangements, and at first the Dow Co. personnel took care of the test site. Several other companies in addition to the International Nickel Co. became interested in exposing samples, so that eventually the site was expanded and a permanent staff was employed. Inspection of test specimens took place usually on an annual basis at which time a small group of interested people discussed the meaning of the results, with Frank as discussion leader. More corrosion information passed hands at these meetings than at a multiple of classrooms or technical society meetings; I know because I was one of those who benefited.

The reputation of the Kure Beach test site grew, and with it the number of visitors who were anxious to learn the latest performance of alloys, coatings, galvanic couples, cathodic protection, stress corrosion cracking, and a host of related subjects. In order to distinguish the employees, who acted as guides, from the visitors, Mrs. Paterson, wife of the test station manager, supplied red hats trimmed with green sea horses. Spontaneously, the meeting became known as the Sea Horse Institute and Frank arranged to have made appropriate certificates of membership accompanied by small nickel lapel pins of sea horses. The pins were distributed to visiting corrosion engineers so that as they converged on Wilmington by train or plane, they could identify themselves as members of the friendliest corrosion fraternity in the world.

In 1950, Frank persuaded his company to invest considerable money in a permanent test site up the coast at Harbor Island which was much more secure against the damage inflicted by occasional hurricanes and which provided permanent buildings for test equipment and for a museum where test specimens could be adequately displayed and catalogued. The atmospheric test racks were retained at Kure Beach.

The annual corrosion sessions at the new site were attended by several hundred persons, requiring that the local movie house be taken over for adequate space. At these corrosion clinics, Frank stimulated everybody assembled to exchange data and information which he supplemented by incontrovertible data from the array of test specimens exposed at Harbor Island and Kure Beach. Any misinformation, or superstition, or exaggerated claims for proprietary products were apt to be shattered early in the proceedings. Frank held the reins of discussion with a firm diplomatic hand, not quite avoiding stepping on the toes of those whose products or ideas were suspect, but later healing wounded feelings by apologizing for bringing out the truth which on further thought he wished he had not mentioned. His complete aplomb in handling controversial issues amazed both those who agreed with him as well as those who disagreed.

The Corrosion Laboratory and its adjoining facilities at Harbor Island now constitute the largest sea water test station in the world. Any materials considered for use in sea water, such as for desalination equipment, sea water distillation apparatus, marine structures, condenser tubes, *etc.*, are subjected to a complete going over by systematic tests of all kinds. The atmospheric test results are similarly used to survey materials suitable for use in marine atmospheres. At any one time there are as many as 3000 test specimens immersed in sea water, and 30,000 test specimens exposed to the air. Over 100 companies, research institutions, technical societies, and government agencies from the U.S., and also from abroad, participate in carrying out this tremendous evaluation program.

The Harbor Island Laboratory which reflects so much credit to the International Nickel Co. is one of Frank LaQue's great achievements. Another achievement along the same lines involved the establishment of the International Nickel Co.'s modern research facilities at Sterling Forest, N. Y. As long ago as 1956, he and W. Wesley campaigned to have the company's laboratory moved from the original location in Bayonne to a more suitable suburban area. The new building, formally opened on October 29, 1964, is one of the most modern and most attractive metallurgical research laboratories in the country. It is a tribute to Frank's life-long interest in research and development.

Professional Society, Government and Related Activities

Frank's active interest in many professional societies is matched by his numerous invitations to speak at local, national, and international meetings. I would judge there are very few places remaining in this country, or in Mexico or Canada, wherever technical society meetings are held, where Frank has not appeared as speaker one or more times. This fall, for example, he is invited to be Plenary Lecturer at the Australasian Corrosion Conference in New Zealand. His discerning remarks and forthright appraisals, combined with a keen sense of humor have made him a popular lecturer. I recall a technical society meeting some years ago in Schenectady at which Frank talked. As chairman, I asked the audience if there were any questions. Before the usual quiet preceding the storm of inquiries, Frank whispered into my ear, "Tell them that the peculiarity

of my subject allows me to give some sort of answer to any question that is asked."

He was elected president of the National Association of Corrosion Engineers in 1948-1949 and president of the American Society of Testing and Materials in 1959-1960. He says, with a twinkle in his eye, that his Presidential Address to the corrosion engineers was written by his daughter who was then of school age. Kathy learned at the dinner table that her father was going off again to give another of his corrosion talks. She arose from the table and solemnly announced that she knew exactly what he was going to say: "Are we just going to stand around and let metals corrode?" Frank thought that was the most concise reason for the existence of the National Association of Corrosion Engineers so he used it as the sum total of his remarks.

Frank has been active over the years on many government committees, including those of the Materials Advisory Board, the National Research Council, and the National Bureau of Standards. He was recent chairman of the Department of Commerce Panel on Engineering and Commodity Standards, and he is at present chairman of the Advisory Committee on Ocean Resources of the U.S. Department of Interior. I am told that his activities in government extend as far as Canada where he has been known to argue at length with the authorities on the urgent need to change regulations that make it difficult for U.S. citizens to obtain Ontario fishing licenses.

He is a member of the Board of Directors of the William F. Clapp Laboratories in Duxbury, Mass., now a division of the Battelle Memorial Institute. Frank's close association with the Clapp Laboratories goes back to 1938 when the late Bill Clapp, a colorful, world-renowned expert on marine organisms, found that the corrosion test site at Kure Beach was an excellent place to study the various flora and fauna which attach themselves to, or bury themselves in, various materials exposed to sea water. Frank and Bill's combined studies led to jointly authored papers, and inevitably to such unofficial antics as growing hair-like organisms on billiard balls as proof that natural sea water is a good hair tonic.

In our own Society he has contributed outstandingly to each office he has held. He is a former Chairman of the Membership Committee, Business Manager of the *Journal* at a time when income was of essence, and Chairman of the Sustaining Membership Committee. In connection with the latter appointment, Frank's personal acquaintance with a large cross section of administrative heads and research directors made his letters invaluable for gaining additional corporate friends and supporters of the Society. His campaign brought many gratifying replies and an occasional surprise. One unexpected response came from one of the directors of a large aluminum producer whose primary product, of course, is all made electrochemically. The director regretted he was unable to recommend support of The Electrochemical Society in light of the fact that his company's activities were not primarily concerned with electrochemistry. Frank was tempted to ask permission to frame the letter and display it as an example of how much some top managements know about their own business.

He served on the Executive Committee which organized the "Corrosion Handbook" sponsored by the Corrosion Division. Not only were the chapters he contributed outstanding portions of the final book, but his advice to the Editor was also invaluable in choosing the right author for the right chapter. He served as President of our Society in 1962-1963 and continues to contribute his valued counsel to several committees.

Publications

Despite his occupation with a wide range of activities, Frank somehow found time to write more than 150 papers on corrosion, on metals in general, and on a few miscellaneous subjects related to neither, for example a paper in *Metals Review* for 1961 entitled "The Care and Feeding of Librarians." He co-edited with Harry Copson in 1963 a sizeable monograph "Corrosion Resistance of Metals and Alloys," which is a major reference source for corrosion engineers. His many papers on corrosion of metals in sea water combine to form the chief source of authentic information on this subject. The titles of his remaining papers range from down-to-earth subjects such as "Corrosion in the Home" and "Corrosion of Auto Bodies" to "Corrosion Testing," and "Metals for Space Travel." He wrote a fascinating article in the *1968 Yearbook of the Encyclopedia of Science and Technology* on the design of our present sandwich coins. His expert advice was drawn upon to specify the proper electrical conductivity and density of the nickel alloy-copper laminates making it possible for 15 million coin-operating machines in the U.S. to continue operating normally instead of automatically rejecting the new coins as counterfeit.

Perhaps his paper on "A Critical Look at Salt Spray Tests" is the one which received widest notice, debunking as it does a corrosion test that was used ritualistically for many years by industry and government without a true understanding of what the test implied. LaQue, in typical fashion, has verbally summed up the salt spray test as one which "can be used to provide a recordable reason for accepting or rejecting something, and is valuable for this purpose if the reason does not have to be sound." He wrote furthermore: "One of the characteristics of the salt spray test is its inconsistency. This extends as well to some of the people who make the greatest use of it." But his paper was much more than a witty exposure of careless specification. He presented a variety of data, many of which were obtained at the Harbor Island Laboratory by his own staff, to show that the salt spray test could hardly be called reliable for evaluating the merit of metal performance in other than perhaps a spray of NaCl solution. The results certainly did not accord with the performance of metals exposed to rural or industrial atmospheres, or when immersed in fresh or salt waters, or even necessarily when exposed to atmospheres along the sea coast. The journal *Metaux Corrosion-Industries* translated his paper for the benefit of French-speaking engineers and I daresay that engineers in many other parts of the world quickly learned of it through one source or another. Largely because of LaQue's efforts, this test, once a universal hand-me-down, is now specified with greater caution and with greater respect for its limitations.

Educational Activities

In addition to Frank's many talks to technical societies, his corrosion clinics at Harbor Island meetings of the Sea Horse Institute established his reputation as a patient teacher. Early in his career at the International Nickel Co., he taught sales and technical personnel some of the elements of corrosion so that they could better understand the alloys with which they were dealing. This led eventually to the three-reel educational film "Corrosion in Action" which, with the accompanying book, was completed in 1955 with T. P. May's help and some advice from me. The film has been in great demand ever since it was first issued. With sound track available in any of the major foreign languages, it has been shown to thousands of students and technical society audiences all over the world.

Frank has served as a member of the Visiting Committees of the Departments of Metallurgy at M.I.T. and at the Case Institute of Technology, and of the Division of Electrochemistry at the University of Pennsylvania. In 1964 he published results of a survey he conducted on the education of corrosion engineers in which he proposed various recommendations to meet current needs, emphasizing that basic

research should be supported as a stimulant to participation of teachers and students in the many fundamental and practical corrosion problems begging for some solution. His Presidential Address to our Society at Pittsburgh in 1963 included an evaluation of the present education of students in electrochemistry. He concluded that, despite present trends and obvious changes of emphasis, the education of future members of our Society is in good hands.

Honors

He received the F. N. Speller Award of NACE in 1949, the Howard Coonley Medal of the American Standards Association in 1962, and he delivered the Edgar Marburg Lecture of ASTM in 1951. His Honorary Doctorate, conferred by Queen's University in 1963, has already been mentioned. He well deserves, as I am sure you agree, the added recognition by our Society which is provided by the Acheson Medal Award. His name adds further distinction to an already distinguished list of Acheson Medalists. It has been a pleasure and a privilege for me to outline briefly Frank LaQue's impressive career and accomplishments which make him so deserving of the honor he receives tonight. The tremendous influence he has made on his professional area, on the over-all community within which all of us live, and on The Electrochemical Society, continues to evoke our admiration, our respect, and our continuing good wishes for a long career which I expect will more than adequately project the marked successes already in the record.

At this moment in the evening's proceedings, Frank would have an appropriate poem to recite. Perhaps the best I can do is to quote one of his, which has nothing to do with my previous remarks, but which may nevertheless strike a note of sympathy among many of you who have been attending technical sessions:

> We are gathered from all over the nation
> For studying polarization
> And calomel cells that don't ring any bells
> But provide an excuse for oration.

Electrochemistry and Corrosion

(Research and Tests)

F. L. LaQue[1]

Francis L. LaQue accepts Acheson Medal from ECS President Ivor E. Campbell.

Members of this Society and particularly of its Corrosion Division are not likely to require much persuasion that most corrosion processes are electrochemical in nature. Stemming from this fact, research related to corrosion as a phenomenon has become more and more a series of experiments in electrochemistry dealing with what happens when a metal or an alloy is placed in contact with an electrolyte. The significance of such experiments will vary through wide limits, depending on how corrosion is approached and defined by whoever wishes to make some practical use of the results.

In Dr. Uhlig's "Corrosion Handbook," sponsored by the Corrosion Division of this Society, corrosion is defined as "destruction of a metal by chemical or electrochemical reaction with its environment."

In this definition, the order of the words gives priority to the results of the corrosion reactions rather than to the reactions themselves. Otherwise, the definition would presumably have been written as "chemical or electrochemical reaction causing destruction of a metal by its environment."

This difference in wording of the definition of corrosion has probably in some partly subconscious fashion had a strong influence on how the study of corrosion has been approached. Investigators can be divided into two broad classes. One group must deal with corrosion as an engineering problem. The other is principally concerned with corrosion as an interesting subject for electrochemical experimentation.

What is described as "Corrosion Research" undertaken by these groups may have very little in common. Corrosion engineering research, often more properly described as corrosion tests, may do no more than put selected metals and alloys in a proper order of apparent merit in resisting attack by the environment to which test specimens are exposed. No effort may be made to understand the mechanisms of the corrosion reactions or why one metal performed better than another. Generally, the results are expressed in quantitative terms that are likely to be more useful in giving an impression of the order of magnitude of corrosion rates than as a reliable basis for estimating how long the metals will last in the intended service. The numbers also facilitate placing the metals in an order of rank.

On the other hand, a good deal of what is called basic corrosion research represents no more than exercises in the study of electrochemical phenomena employing combinations of metals and environmental conditions chosen mainly to facilitate experiments for the convenience of the investigator. They also may enable him to make use of equipment and experimental techniques with which he is familiar or which are currently in vogue. This leads to the accumulation and publication of data on combinations of metals and environments rarely if ever encountered in practice and of no real significance with respect to our first definition of corrosion.

No doubt, dilute solutions of sulfuric acid represent a convenient electrolyte for undertaking electrochem-

[1] Acheson Medal Address delivered October 8, 1968 at the Montreal Meeting of The Electrochemical Society.

ical experiments with a potentiostat. No doubt, also, such experiments are easier to undertake as well as to interpret when oxygen is excluded. Probably, also, in many cases the choice of the metal to be studied is not really critical to the experiment so long as it is not subject to erratic behavior in the test environment. All of these considerations probably account for the great amount of data that may be found in the literature dealing with experiments making use of a potentiostat and involving dilute sulfuric acid, frequently free of oxygen.

A casual survey turned up eight papers along this line published between 1957 and 1965. Because of the fact that, in my forty years of concern with corrosion problems, no practical questions have arisen with respect to the behavior of the metals covered in these papers in oxygen-free, one or two normal sulfuric acid, one is tempted to wonder if the investigators could not have satisfied their scientific curiosity as well by choosing combinations of metals and environments that someone might be really interested in.

It will be recalled that our definition attaches prime importance to "destruction" of a metal when this is not desired rather than "destruction" to a degree that may be of little consequence to the investigator. Under these circumstances, the corrosion reactions that are involved in some corrosion research are frequently made to occur so that they can be observed and studied largely for their own sake.

One should not object to research undertaken for its own sake and to satisfy scientific curiosity. However, in the field of corrosion, such exercises should not be described as being specifically aimed at an improved knowledge of corrosion in terms of the definition in common use. The most that can be expected is that the product of such research may in some unplanned way provide a missing piece to complete a particular area of the perplexing jigsaw puzzle of corrosion.

These remarks do not extend, of course, to corrosion research aimed at an improved understanding of the mechanisms of corrosion and particularly of the types, such as localized pitting and crevice corrosion, intergranular attack, and stress corrosion cracking, that are most troublesome. Even here, some problems arise when methods of test designed to facilitate study of the basic phenomena are applied to qualify materials for particular services.

Many electrochemical techniques, and particularly the use of potentiostats, are valuable in throwing light on why, and to what extent, changes in composition of an alloy are effective. They are useful for screening alloys for service in environments reasonably approximated by the electrolytes used in the experiments. These solutions need not try to simulate the environment of use. They should be chosen to permit systematic modification so as to provide a means for characterizing the ability of an alloy to preserve, or regain, passivity under conditions which are progressively and measurably made more aggressive.

Potentiostatic techniques are useful, also, in a somewhat oblique connection with the primary definition of corrosion in the controlled etching of specimens to disclose details of structure which are likely to affect corrosion behavior.

Some of the points just discussed will be illustrated by examples encountered during my struggles with corrosion over the past forty years.

In spite of occasional assertions by others to the contrary and possible misinterpretation of these present remarks, I am in favor of basic research in corrosion. I served for several years as chairman of the Corrosion Research Council and endeavored with only limited success to persuade industry to provide funds for support of such research in universities. This program did yield some valuable results and did attract to the field several very competent scientists who are carrying on their work with other support and, equally importantly, are educating others to continue scientific attention to corrosion.

At the same time, I have been frequently disappointed by programs described as fundamental research in corrosion.

All too often it seems that what is called fundamental research should be described more accurately as "oversimplified" research. The "oversimplification" stems generally from the apparent unwillingness of the investigator to cope with important factors that may be difficult to control and which, if allowed to exert their influence, would have such a tremendous effect on the results that it is more convenient to eliminate their possible effects than to cope with them in the experiments and in the interpretation of the results.

This point is illustrated very well by effects of dissolved oxygen. One of the too-frequent characteristics of what are claimed to be "fundamental" corrosion research experiments is the rigid exclusion of oxygen from the test environment. It is obviously easier to keep oxygen out of a test solution than to study its effects over a broad range of concentration.

When researchers are challenged on this point, they frequently assert that the oxygen-free solution represents only the beginning of a series of experiments in which effects of controlled amounts of oxygen will be observed systematically. Unfortunately, many, if not most, of these projects never get beyond the oxygen-free stage.

Since oxygen-free environments are the exception rather than the rule in situations where destruction is an important practical problem, it is not too surprising to hear complaints from industrial sources of support for corrosion research that they have found it to be difficult to recognize practical benefits from such research.

The situation illustrated by oxygen extends to such other important factors as temperature and velocity of movement. Here, again, the control of these factors is likely to be determined more by the convenience of the experiment and the limitations imposed by the test apparatus than by the need to extend the results to other conditions of temperature and velocity more likely to be encountered in practical corrosion problems.

Reference was made previously to the inclination of some investigators to approach the study of corrosion by the use of apparatus and techniques that are currently in vogue. A prime candidate for this characterization is the potentiostat.

The potentiostat is well adapted to grinding out data rather easily, which can be displayed in a series of impressive-looking curves relating applied voltage to current flow. These provide ample scope for interpretation and comment which often extends to portions of the curves which have questionable relationship to what goes on in normal corrosion reactions not disturbed by the application of current from external sources. Potentiostats are quite capable of applying potentials very much higher than could ever be encountered in a normal corrosion reaction. The data outside such normal ranges of potential frequently occupy large sections of the curves that are plotted and are given probably much more attention than they should receive in drawing conclusions from the experiments

I have seen reports of experiments with a potentiostat designed to compare the resistance of a number of low-alloy steels to corrosion by a sodium chloride solution (assumed to represent sea water). The curves that were plotted covered a range of potential well over a volt even though the maximum difference in potential of anodic and cathodic surfaces of the steels studied would not exceed about 200 mv.

The investigator concluded, properly, that there was no significant difference in the resistance of the several steels to corrosion by sea water. This confirmed data which I had published about twenty years earlier based simply on long-time exposure of similar steels under

conditions of immersion in sea water under natural conditions. The similarity in the conclusions should be considered to be largely a matter of coincidence rather than as evidence of the value and reliability of the potentiostat approach. The reason the steels behaved alike in the test under natural conditions was that the rate of attack of all the steels was determined, not by the corrosion-resisting characteristics of the steels, but by the rate at which oxygen could diffuse through the thick layers of rust and marine growths that accumulated on all the steels to the same extent. Since no such controlling factors were capable of being introduced into a short-duration experiment with a potentiostat, it could not be expected that such a test would reliably measure resistance to corrosion under the natural conditions to which the results were claimed to apply, and where the major controlling factor was not a characteristic of the steel but rather an external factor involving marine organisms.

One may also question the reliability of studying the two halves of a corrosion reaction separately and then endeavoring to combine the results on the assumption that this approach is equivalent to studying the simultaneous reactions concurrently without distortion by impressed currents. Some investigators appear to be convinced that it will suffice to observe the behavior of a metal only as an anode even though there are many corrosion reactions in which what happens at the cathode has the dominant effect. There are many other instances of mixed control.

There is a quite legitimate and proper use of a potentiostat or galvanostat to provide a basis for the application of electrochemical methods of protection—cathodic or anodic. Such experiments are likely to be most reliable if the expected environmental conditions are reproduced in the test, *e.g.* with proper control of aeration, temperature, and velocity, as well as the chemical composition of the test solution.

Too many corrosion engineers practicing the art of cathodic protection continue to be unconcerned, as well as confused, by a lack of understanding of the electrochemical phenomena by which what they accomplish is achieved and monitored.

Fortunately, the margin for error in this field appears to be broad enough to accommodate imperfections. The economic penalty and possible hazards of overprotection are generally tolerable except when alloys susceptible to attack by alkalis or to hydrogen damage are involved. This latter danger is worthy of much more attention by both electrochemists and metallurgists.

On the other hand, the practice of anodic protection appears to have a more substantial scientific basis and to be much better understood by those who use it. This fortunately permits more precise application and control. Failure to provide for proper monitoring and control of anodic protection could have disastrous consequences.

Attempts may also be made to use a potentiostat technique to study the normal corrosion behavior of a metal in a corrosive solution likely to be encountered. Here there is a frequent difficulty associated with the very short interval over which the measurements will be made as compared with very long periods of time during which accumulation of adherent protective films of corrosion products or environmental deposits may have a controlling effect on behavior.

Metals to be studied for normal corrosion behavior can be divided into two general classes:

Class one includes metals that are not expected to survive for the desired life without benefit of some means of protection, *e.g.* by some sort of coating or some treatment of the environment which would have to be duplicated in the potentiostat experiment. The difficulty of dealing with and interpreting results of tests with coated specimens in a potentiostat setup limits its usefulness in this category.

Class two includes materials that are expected to survive without the benefit of supplementary protection. These materials very rarely fail by general wastage in either the active or passive state in the environments in which they are likely to be used. They fail, when they do so, by such forms of attack as pitting, stress corrosion cracking, corrosion fatigue, intergranular attack, impingement attack, hot spot effects, and so on, not readily disclosed by the results of studies with a potentiostat. This device is, of course, applicable to studies of the mechanisms of such forms of damage under conditions designed to create the damage so that it can be studied. It is less reliable for qualifying metals for service in which these forms of damage may be encountered.

Devices and techniques for using response to polarizing currents as a means for observing corrosion behavior have been found to be very useful for monitoring the effects of changes in the environment on its corrosivity toward a metal. For example, such measurements have been found to be more sensitive than other means for detecting excursions in the oxygen content of brines in sea water distillation plants.

Mainly because of the short time interval involved in such measurements, they are of questionable value in predicting long-time behavior or for more than preliminary screening of a number of metals and alloys as a basis for selection of the most appropriate one for a particular application.

One can be equally critical of attempts to attach quantitative significance, in terms of life expectancy, to corrosion tests under natural conditions or as good a simulation of natural conditions as may be achieved. It is not too difficult to secure excellent reproducibility of results of such tests and excellent agreement among the results for several specimens tested at the same time. Reproducibility should not be taken as qualifying the results as being quantitative in terms of predicting life.

A principal reason for this difficulty is that in many, if not most, cases the results are determined to a major extent by the dimensions of the test specimens.

Where pitting is the principal mode of attack, the results will involve both the number of pits and their depth. Since in most cases the occurrence of a pit is a matter of statistical probability and the chance that a pit will be found increases with the area of surface exposed to attack, a large specimen can be expected to disclose greater susceptibility to pitting than will a small one. And, since the pitting mechanism usually involves a sort of galvanic effect between an anode in a pit and a cathode on the surrounding surface, the chance that an anodic pit will be surrounded by a large cathode will be greater on a large specimen than on a small one. Consequently, pits on large specimens are likely to be deeper than on small ones. If the size of specimen happens to yield a population and depth of pitting that may occur under conditions of actual use, this is most likely to represent coincidence more than a truly quantitative test.

A similar area effect pertains to tests for resistance to corrosion in crevices. Here, too, the depth of attack that may be observed in a test will be determined largely by the ratio of the area of the freely exposed surface outside a crevice to the area within a crevice. This is illustrated by Fig. 1. Test setups are not likely to duplicate these area relationships as they exist in large fabricated equipment.

Another example of an area effect is provided by tests for studying the ability of alloys to resist erosion in sea water by spinning submerged metal disks on a shaft at some appropriate number of revolutions per minute.

There will be a velocity gradient from the center to the periphery of a spinning disk and, by ignoring friction film or boundary layer effects, it is possible to calculate the velocity at any radius of revolution. By measuring the decrease in thickness at any radius point, it is possible to relate the rate of attack to the speed of movement as shown by Fig. 2, Unfortunately,

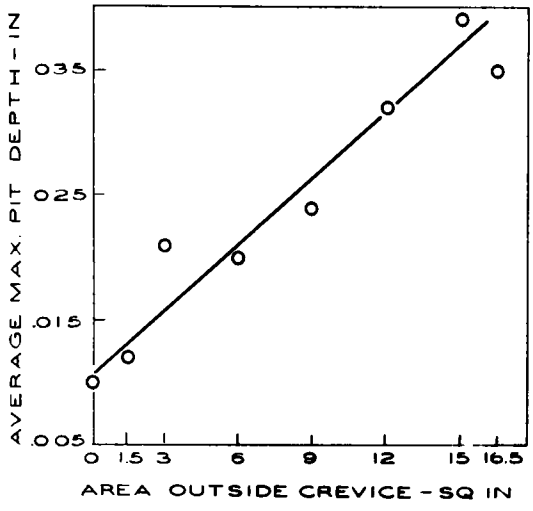

Fig. 1. Average maximum pit depth within the crevice vs. area of specimen outside the crevice.

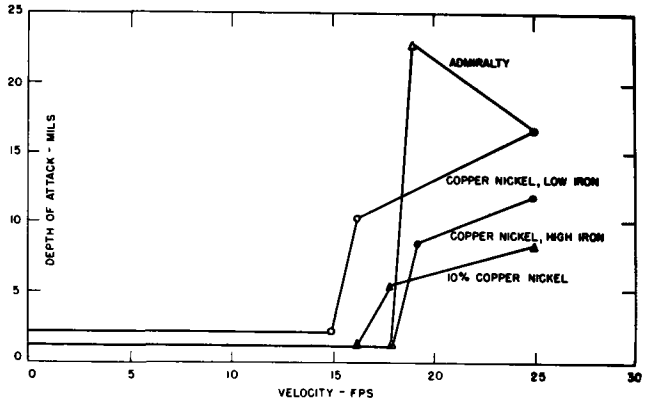

Fig. 2. Effect of velocity on depth of attack in sea water at Kure Beach, N. C., for 60 days.

it has been observed that different rates of attack can be associated with the same velocity depending on the diameter of the disk that is used for the experiment. This is illustrated by a series of tests on copper alloy disks shown in Fig. 3, and the wide spread in rates of attack at the same calculated velocity shown by Table I.

To add further confusion to the interpretation of velocity effect data such as yielded by tests with spinning disks, consider what happens when the materials being tested are iron and its alloys rather than copper and its alloys. Figure 4 shows that, when iron disks are tested, the differential aeration electrochemical phenomena that come into play produce the greatest

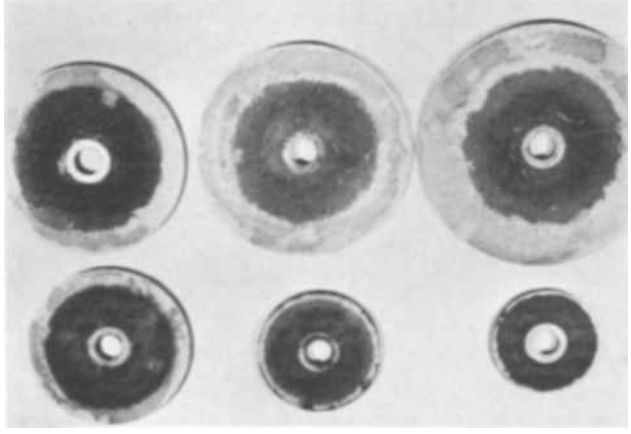

Fig. 3. Distribution of attack on copper alloy disks rotated in sea water at the same speed in revolutions per min.

Table I. Comparison of depths of attack on surfaces of disks of different sizes moving at same speed as periphery of smallest disk

Disk diameter Inches	Cm	Depth of attack at radius of 1.5 in. (3.8 cm) velocity, *15.2 fps 4.5 m/sec In.	Mm
3-1/4	8.3	0.020	0.51
3-3/4	9.5	0.017	0.43
4-15/16	12.5	0.002	0.005
5-21/32	14.2	0.001	0.002
6-5/16	15.9	0.001	0.002
7-3/16	18.3	0.002	0.005

* Calculated from rpm and radius of rotation at point of attack.

attack at the lowest velocity rather than the highest and the size effect becomes as important with iron as it is with copper.

It will be evident also from looking at Fig. 4 that experiments could be conducted that would yield rather amazing and certainly incorrect results. For example, one could decide to study the effects of a range of velocities using small-diameter disks for low velocities and larger disks for higher velocities and measuring the rates of attack at the peripheries of the several disks.

By this means, it would be possible to generate apparently quantitative and reproducible data that would prove that iron is not corroded by sea water at any velocity within the range studied.

Similarly with copper alloy disks, as in Fig 3, it would be just as easy to show that an alloy would be corroded by sea water rather severely at a rate that would be substantially independent of velocity in the range achieved in such a series of tests.

One could also manipulate the choice of size of copper alloy disk to achieve a certain velocity to produce data that would "prove" that one alloy was better than another at the velocity of interest. This would be accomplished by using a larger disk for the alloy one wanted to show to be better and a small disk for the alloy to be downgraded. This would require, or course, that only the velocity achieved, and not the different sizes of disks used to get it, be described in the report of the results.

To make matters worse, the effect of velocity on corrosion is quite different when the method of test achieves a velocity gradient over the surface of the specimen from what it is when the method of test maintains a uniform velocity over the test surface.

A sharp velocity gradient is likely to be more damaging than a high but uniformly distributed velocity. Consequently, any test of velocity effects must be properly related to the expected velocity gradients in the service to which the results of the test are to be applied. It would be reasonable to require the use of both types of test in a search for an alloy that would perform well in the presence of both very high uniform velocities and very high velocity gradients.

Electrochemical measurements including polarization phenomena are not free from the size effects that detract from the quantitative significance of other and more direct means of measuring corrosion behavior. The apparatus generally requires the use of quite

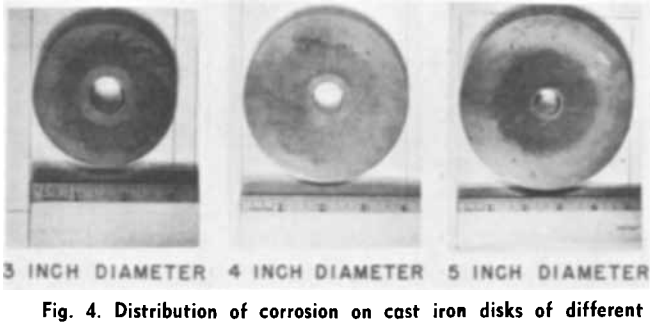

Fig. 4. Distribution of corrosion on cast iron disks of different diameter rotated in sea water at the same speed in revolutions per min: cast iron disks rotating spindle test 30 days at 15°C.

small specimens. Reproducibility is generally favored by making test specimens smaller and smaller. It should be understood, however, that, while reproducibility is a necessary feature of any method of test that gives reliable results, it can also be a characteristic of a procedure that gives consistently wrong answers. One test can be as consistently wrong as another can be consistently right. Either type can be useful once a consistent relationship between the results of the test and performance in the service toward which the test is directed has been established by experience.

Even though the possibility exists that a fundamentally unsound but consistent test can be interpreted properly, one cannot be blamed for preferring the type of test that gives results that point rationally in the right direction.

In summary, I have suggestions for corrosion scientists and for corrosion engineers.

It would be most helpful if electrochemists interested in corrosion phenomena, in their response to scientific curiosity, were more frequently to choose for their experiments combinations of metals and environments that are likely to be encountered in practice, so long as this action does not introduce intolerable or insurmountable experimental difficulties or unduly limit the range of their studies.

Corrosion engineers should develop more scientific curiosity as to the reasons why the metals they test behave the way they do. They should also develop more scientific curiosity about, and a better understanding of, the electrochemical mechanisms of the corrosion reactions responsible for the results they observe. These mechanisms generally determine and frequently restrict the quantitative significance of the data from which they draw their conclusions and on which they make their engineering decisions.

A better understanding of the science of corrosion should lead engineers to abandon improper tests, improve old tests, introduce new tests, make more reliable evaluation and interpretation of results of all kinds of test, good or bad. It would also permit more ready recognition of the faults of a bad or inappropriate test and the merits of a good one.

My friends who know me best will, I am sure, recognize that in making these deliberatively provocative remarks I am, at the same time, hoping that those who feel they have been abused will become determined to demonstrate conclusively that I am mistaken. I shall not be unhappy if they should succeed in such endeavors.

At the same time, there is at least an off chance that one or another of my criticisms has a substantial foundation and that the response to this criticism will show that it has been constructive.

Reports on ECS Summer Assistance Awards and Weston Fellowship Award for 1968

During the summer of 1968, the following graduate students received $800 each, representing three Summer Assistance Awards of The Electrochemical Society.

Karl Doblhofer, Colorado State University, Fort Collins, Colo., was awarded the Edward Weston Fellowship.

Robert A. Bonewitz, Department of Chemistry, University of Florida, Gainesville, Fla., was designated recipient of the Colin Garfield Fink Fellowship.

L. P. Zajicek, University of Hawaii, Honolulu, Hawaii, received the ECS Summer Fellowship Award.

The Summer Assistance Award is made "without regard to sex, citizenship, race, location, or financial need to a fellow or teaching assistant pursuing work between the degree of B.S. and Ph.D. on a subject in a field of interest to The Electrochemical Society." It is intended to cover a period during which the recipient has no financial support for the continuance of his work.

The Edward Weston Summer Fellowship Report

A summary of Mr. Doblhofer's report is given below.

Instrumentation for Interfacial Tension and Differential Capacity Measurements

I am concerned with the measurement of adsorption isotherms of organic materials on mercury electrodes. The amount of adsorbed substance (Γ_O) can be calculated according to the thermodynamic theory of electrocapillarity (1) by means of the equation

$$\left(\frac{\partial \gamma}{\partial \mu_O}\right)_E = -\Gamma_O$$

where γ is the interfacial tension and μ_O is the chemical potential of the sorbate. I am using two experimental methods to investigate the adsorption:

(*A*) Measurement of interfacial tension, using a capillary electrometer.

(*B*) Measurement of differential capacity curves using an a-c bridge.

An improved capillary electrometer was built in our laboratory. It allows the determination of the interfacial tension of the mercury-solution interphase with a standard deviation of approximately 0.02 dynes/cm. Some time last summer was spent evaluating the precision of this instrument. The electrocapillary curves were analyzed by digital computer using the moving fit technique for smoothing and differentiation previously developed in this laboratory (2). As a critical test, double differentiation was performed to obtain the differential capacitance *C*, according to the equation

$$\left(\frac{\partial^2 \gamma}{\partial E^2}\right) = -C$$

The resulting C-E curves for sodium chloride solutions have the characteristic morphology, including the familiar hump (Fig. 1). The general agreement with capacitance values directly determined in our laboratory and also with those reported by Grahame (3) was satisfactory.

A detailed description of the capillary electrometer is being prepared for publication.

The rest of the summer was spent developing the instrumentation for accurate differential capacity measurements. The measurement is carried out with a General Radio type 1615-A transformer ratio-arm capacity bridge. The range of this bridge is not quite wide enough to allow measurement of either capacity or dissipation on the high adsorption-desorption peaks of the differential capacity curves of neutral organic sorbates. However, it was found that satisfactory measurements could be performed by connecting a standard capacitor of 1 μf in series with the electrochemical cell.

Because of the thermodynamic significance of a reference electrode reversible to an ion in the solution [indicator electrode (1)], we wanted to use the very

JOURNAL OF THE ELECTROCHEMICAL SOCIETY

REVIEWS AND NEWS

APRIL 1969

Cahoon and McKinley Take Office in New York

N. Corey Cahoon

Theodore D. McKinley

As a result of the recent annual elections in which the voting was conducted by mail, N. Corey Cahoon has been elected the new President (1969-1970) of The Electrochemical Society and Theodore D. McKinley has been elected Vice-President (1969-1972).

Mr. Cahoon, Senior Scientist, Electrochemical Development Laboratories of the Consumer Products Division of Union Carbide Corp., Cleveland, Ohio, replaces Ivor E. Campbell, who will continue as Past President on the Board of Directors.

Dr. McKinley, Research Supervisor, Du Pont Experimental Station, Pigments Division, E. I. du Pont de Nemours and Co., Wilmington, Del., begins the first year of his three-year term as Vice-President.

The new officers assume their positions in May 1969.

Offices not affected by the election are those of the two other Vice-Presidents, Charles W. Tobias and Cecil V. King; Secretary, Dennis R. Turner; and Treasurer, R. Homer Cherry, respectively.

DIVISION NEWS

Electronics Division

The bylaws of the Electronics Division of The Electrochemical Society require that the Chairman of the Division appoint, at least six (6) months prior to the convention at which the next election is to be held, a Nominating Committee of at least three (3) division members. This committee is required to nominate a slate of officers and members at large of the Executive Committee. At the last Executive Committee Meeting in Montreal, a Nominating Committee was appointed to nominate a slate of officers for the years 1969-1971. It is with pleasure we announce that the Nominating Committee has selected the following candidates for the next term of office.

Chairman-Electronics Division—Roger Newman, Sperry Rand Research Center, North Rd., Sudbury, Mass. 01776

Chairman-Semiconductor Group—Harry Sello, Fairchild Semiconductor Research & Development, 4001 Miranda Ave., Palo Alto, Cal. 94304

Vice-Chairman—General Electronics Group—Erik M. Pell, Xerox Corp., Research & Engineering Science Division, Xerox Square W114, Rochester, N.Y.

Vice-Chairman-Luminescence—Philip Jaffe, Zenith Radio Corp., Research Dept., 6001 W. Dickens Ave., Chicago, Ill. 60639

Secretary-Treasurer—Bertram Schwartz, Bell Telephone Laboratories, Murray Hill, N. J. 07974

The election of officers will be held at a General Electronics Meeting that will be held during the time of the Society Meeting in New York City.

Additional nominations for officers may be made by petition signed by five (5) members of the Division. Such petitions must be in the hands of the Chairman of the Nominating Committee at least ten (10) days before the election, with the assurance of the nominee's willingness to serve if elected.

The officers and members at large shall be elected by a majority vote of those present at the business meeting of the Division that will be held in New York City. Those elected shall take office immediately after adjournment of the New York National Meeting.

D. K. Hartman
Secretary-Treasurer

Electro-Organic Division

The Electro-Organic Division will hold a luncheon and business meeting at the New York Meeting at 12:15 P.M. on Wednesday, May 7, 1969, at the Commodore Hotel. A vote will be taken on adoption of new bylaws for the Division. The new bylaws include provision for changing the name of the group to the Organic Division. Plans for future symposia will also be discussed. Professor Stanley Wawzonek of the University of Iowa, Divisional Editor of the Electrochemical Science Section of the JOURNAL, will present a brief talk on the publication of scientific papers in the JOURNAL.

The Division's Nominating Committee under the Chairmanship of Manuel Bazer have proposed the following

Ion Retention in Cathodes and Precipitates of Silver Chloride-Magnesium Sea Water-Activated Batteries

Duane W. Faletti

Applied Physics Laboratory, University of Washington, Seattle, Washington

Michael A. Gackstetter

University of Minnesota, Minneapolis, Minnesota.

and John A. Arne

Naval Torpedo Station, Keyport, Washington

ABSTRACT

The magnitude of the retention of ions in the reduced portion of the cathodes and in the precipitate formed in AgCl-Mg sea water-activated cells was studied. Both the ions found in the entering electrolyte and those introduced by the electrochemical reaction were retained in significant amounts. Calculations indicate that underestimations in the voltage losses across the interelectrode space as high as 0.05v occur if this retention is neglected. A method to adequately account for retention is suggested.

As part of a continuing study of the silver chloride-magnesium couple in sea water, an investigation was made of the magnitude of the retention of ions in (*a*) the reduced portions of the cathode, and (*b*) the precipitate. This process, referred to as retention, increases the magnitude of the voltage drop across the interelectrode space by its affect on the composition (hence conductivity) of the electrolyte.

The electrochemical reaction for the silver chloride-magnesium couple

$$2AgCl + Mg \rightarrow 2Ag + MgCl_2 \qquad [1]$$

results in the addition of the soluble salt, $MgCl_2$, to the electrolyte and the formation of a porous layer of silver, known as sponge silver, on the AgCl cathode. The void spaces in the sponge silver fill with electrolyte composed of water and dissolved ions from the free electrolyte entering the cell and the Mg^{++} and Cl^- ions generated from reaction [1].

AZ61 magnesium alloy is the commonly used anode material for such batteries as it forms reasonably non-clogging reaction products [ref. (1) and (2)]. Anode efficiencies are reduced to about 75% by the secondary anode reactions with water during discharge to form H_2 and insoluble reaction products, the latter probably containing the hydroxides (along with hydroxy-chlorides and other double salts) of magnesium, aluminum, zinc, and manganese. The anode constituents tied up in these insoluble products are not considered removed or withheld from the free electrolyte since they play no electrochemical role. However, the tying up of chloride ions, etc., via the formation of double (insoluble) salts and/ or the absorption of ions in the precipitate do constitute another source of ion removal (retention) from the free electrolyte.

Basis for Experimental and Calculation Procedure

In order to simplify the chemical analyses, sea water (Table I) was simulated from only three salts: NaCl, $MgCl_2$, and Na_2SO_4. (The resulting solution corresponds to that used in ref. (3) with the substitution, on an equivalent weight basis, of NaCl for the KCl and KBr, and $MgCl_2$ for the $CaCl_2$, and of Na_2SO_4 for the $NaHCO_3$. The remaining salts used in ref. (3), HBO_3, $SrCl_2$, and NaF, are present in such minute concentrations that they were neglected.) Therefore, the retention of four ionic species, Na^+, Mg^{++}, Cl^-, and $SO_4^=$, constituting over 98% of the ions found in sea water, was studied.

The retention of the above ions, with the exception of Na^+, was determined from a material balance by (*a*) determining the flux of each ionic species into and out of the cells by quantitative determinations of the concentration of the ionic species and the flow rate of the electrolyte; (*b*) calculating the amount of Mg^{++} and Cl^- ions generated by reaction [1] from Faraday's law and a knowledge of the current (held constant) flowing through the cell.

The following items were taken into account: (*a*) the amount of water reacting with the AZ61 anode, (*b*) the effect of the weight of the precipitate on the weight of the effluent, and, (*c*) the amount of water entering the sponge silver, calculated by assuming that the water filled 95% of the voids in the sponge silver (the remaining 5% is an allowance for the effects of volume changes resulting from ion retention).

The results were expressed in the form of gram-equivalents per cubic centimeter of sponge silver determined by dividing the equivalents of each ionic species retained per unit time by the volume of sponge silver formed per unit time (calculated from Faraday's law and the current by assuming that no volume change occurred in the over-all dimensions of the cathode on reduction). From electroneutrality one can write

$$R_{\pm} = R_{Cl^-} + R_{SO_4=} = R_{Mg^{++}} + R_{Na^+} \qquad [2]$$

where $R_{\pm}$ is the total retention coefficient, g-equiv/cm^3, and R_{Cl^-}, $R_{SO_4=}$, and R_{Na^+} are the individual ionic retention coefficients for the chloride, sulfate, magnesium, and sodium ions, respectively, g-equiv/cm^3 of sponge silver.

Since no sufficiently accurate analytical technique was available for the direct determination of the retention of Na^+, the retention of sodium ions was obtained from Eq. [2] by subtracting $R_{Mg^{++}}$ from $R_{\pm}$.

Analyses of the effluents of silver chloride-magnesium batteries showed that, except for magnesium,

Table I. Composition of simulated sea water*

Salt	Chlorinity	
	4.5°/oo	19.0°/oo
NaCl	5.695	24.044
$MgCl_2$	1.404	5.926
$NaSO_4$	0.966	4.079

* Concentrations given in g/kg of solution.

negligible amounts (less than 10 ppm) of the constituents of AZ61 alloy remained in solution; hence, only the four above-mentioned ions need be considered.

Apparatus

The apparatus, essentially that used in a former study [ref. (1)], was designed to maintain relatively constant inlet conditions while discharging the cell at constant current and relatively constant flow rate.

The production of H_2 by the secondary reactions at the anode resulted in a two-phase, slugging flow with a relatively long period between slugs of liquid which degraded the accuracy of the flow measurement. To circumvent this problem, nitrogen was passed into the exit line immediately upstream of the exit valve (used to maintain test pressure) in order to reduce the periods of the alternate slugs of liquid and gas to less than one second.

The desired inlet temperature was obtained for the low and the high temperature discharges by passing the incoming electrolyte through a stainless steel coil, placed in a bath kept within ±4°F of the desired inlet temperature. The coil was removed for runs made at or near 75°F.

The current was determined by placing a 0.01 ohm standard resistor (±0.04% accuracy) in series with the constant current load and measuring the voltage drop with a differential voltmeter accurate to 0.05%.

The average flow rate during the sample period was determined by time-weight measurements. The elapsed time, measured with a stop watch, was accurate to about a second; the weight was measured to an accuracy of 0.01%.

Cell Assembly

The cell assembly is the same as described in ref. (1), except that it was modified for use with only one cell.

Cells of two different lengths were used in the study which were fabricated from 0.0215 in. thick silver chloride and 0.013 in. thick magnesium. The cells had active surface areas 2.125 in. wide by 10.75 in. long for discharges conducted at current densities of 1 asi and 2 asi, and 2.125 in. by 6.25 in. for the discharges at 3.4 asi.

Preparation of Electrolytes

Four electrolytes were studied. Two were made according to Table I, having chlorinities of 4.5‰ (parts per thousand) and 19.0‰. The two remaining electrolytes were prepared from simulated sea water with a chlorinity of 4.5‰ by adding, respectively, 17.5 and 35.0g of magnesium chloride per liter (measured at 77°F). The solutions are designated by the notation "chlorinity-added magnesium chloride" (*e.g.*, 4.5-35.0).

Procedure

To complete decontamination of the entire assembly, the battery was flushed with electrolyte for one to two minutes prior to starting the discharge. During the discharge, the current was held constant (±0.05% tolerance) by continual minor adjustments of the constant current load setting.

The outlet valve and nitrogen flow rate were adjusted to maintain a slugging flow with alternating slugs of vapor and gas (exiting at least once per second).

Two samples per run were taken, the first starting one minute after the initiation of current flow (allowing time to flush out the pre-discharge electrolyte). Sample collection times were, for the 1.0 and 2.0 asi discharges, from the 1.0 to the 4.0 min mark for the first sample and from the 4.5 to the 7.5 min mark for the second sample. Sample collection times for the 3.4 asi discharges were from the 1.0 to the 3.25 min mark for the first sample, from the 3.5 to the 5.75 min mark for the second sample. Sample collection times were so chosen as to eliminate the possibility of false results arising from exhaustion of the cathode. At the end of the discharge, a sample of electrolyte was collected at the entrance to the battery assembly as a check on the composition of the entering electrolyte.

The flow rate was held as steady as possible during the discharge with maximum short term variations of 10%, with more typical short term variations of about 3%. Special care was taken to hold the flow steady during the half-minute before the start of the collection period and the half-minute before the end of the collection period as flow variations would have their greatest effect on the results at this time.

After the weight of the effluent sample was determined, the electrolyte was decanted from the precipitate.

Chemical Determinations

Quantitative determinations for chloride, sulfate, and magnesium were made on each of the electrolyte solutions.

The chlorides were determined gravimetrically by precipitation with silver nitrate. The sulfates were determined gravimetrically by precipitation with barium chloride. Two methods were used to determine magnesium: (*a*) gravimetrically by precipitation with dibasic ammonium phosphate (the magnesium was then calculated from the weight of magnesium pyrophosphate), or (*b*) by titrating with EDTA (ethylenediaminetetraacetic acid), using Erochrome Black T as an indicator. The EDTA was standardized by titrating against pure magnesium.

Presentation of Results

The experimental results are presented in Fig. 1 and 2. The values of uncertainty in the total retention coefficient, $R_{\pm}$, shown on Fig. 1 and 2 are derived from a maximum error analysis based on the effects of uncertainties in flow rate and chemical composition (uncertainties in current measurements were negligible in comparison). Levels of uncertainty of 1.0% in flow rate, 0.2% in chloride concentration, and 1.0% in sulfate concentration were used in the error analysis. These estimates of maximum uncertainty are conservative (on the high side). Since the amount of an ion retained was always considerably smaller than the amounts of that ion entering or leaving the cell, the above uncertainties in flow rate and composition resulted in considerably larger (percentagewise) uncertainties in the retention coefficients.

Discussion of Results

The values of the total retention coefficients, $R_{\pm}$, obtained from the first samples collected during the discharges (Fig. 1) were generally about 25% lower than those obtained from the second samples collected

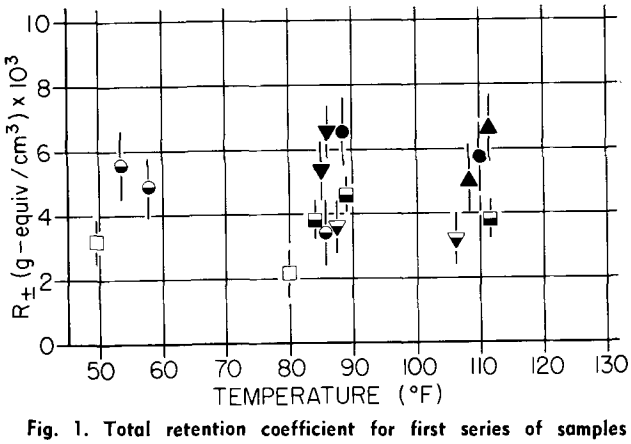

Fig. 1. Total retention coefficient for first series of samples taken during discharge. The symbols designate electrolytes of the following compositions "chlorinity-added magnesium chloride:" □ 4.5-0.0, ○ 19.0-0.0, ▽ 4.5-17.5, and △ 4.5-35.0. Discharges at 1.0, 2.0, and 3.4 asi are designated, respectively, by unshaded, half-shaded, and fully-shaded symbols.

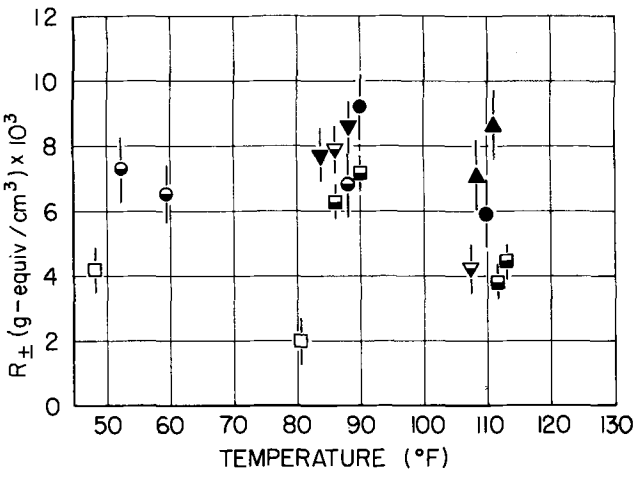

Fig. 2. Total retention coefficient for second series of samples taken during discharge. The symbols designate electrolytes of the following "chlorinity-added magnesium chloride:" □ 4.5-0.0, ○ 19.0-0.0, ▽ 4.5-17.5, and △ 4.5-35.0. Discharges at 1.0, 2.0, and 3.4 asi are designated, respectively, by unshaded, half-shaded, and fully-shaded symbols.

during the discharges (Fig. 2). This result cannot be explained by not allowing adequate time for flushing out the apparatus as this would result in a higher value of $R_{\pm}$, not a lower one. A reduction of the flux of salts leaving the sponge silver as the discharge progresses might explain the increase in $R_{\pm}$ with discharge time; but an increase in the retention due to precipitate effects is unlikely.

The collection time varied from the norm for one discharge at 2 asi in that the first sample was collected between the 3 and 6 min mark, and the second sample was collected between the 6.5 and 8.5 min mark. Though the two values of $R_{\pm}$ obtained with this discharge differ by only 15%, this is not sufficient evidence that the time dependence of $R_{\pm}$ becomes less as the discharge progresses.

For a given collection time, temperature and current density had the greatest effect on the values of $R_{\pm}$; electrolyte composition had no discernible effect. Increased current density caused an increase in $R_{\pm}$, whereas increased temperature caused a decrease in $R_{\pm}$. These results suggest that retention is governed primarily by the diffusion of salt ions from the sponge silver: the effect of higher current density is to increase the rate at which the chloride ions are generated at the sponge silver-silver chloride interface and the effect of temperature is to increase the rate of diffusion.

$R_{SO_4=}$ ranged from 1.6 x 10^{-4} to 1.0 x 10^{-3} g-equiv/cm^3 and ranged from 2 to 20% of the total value of $R_{\pm}$ (note Eq. [2]), except for the case of the two discharges at 1 asi where $R_{SO_4=}$ averaged 35% of $R_{\pm}$. $R_{SO_4=}$ exhibited only a moderate decrease with temperature and had no discernible correlation with current density. However, the ratio of $R_{SO_4=}$ to $R_{\pm}$ was significantly higher at 1 asi than at 2.0 or 3.4 asi, giving weak evidence that $R_{SO_4=}$ was not diffusion controlled to the degree that $R_{\pm}$ (or R_{Cl-}) was.

Of special interest is the fact that the observed values of $R_{SO_4=}$ far exceed those which could be explained by retention in the sponge silver because the only way in which sulfate ion retention in the sponge silver can occur is for the sulfate ion to be carried into the sponge silver by convection via the flow of electrolyte into the void spaces in the sponge silver. Calculations based on convection yield a value of $R_{SO_4=}$ of 1.7 x 10^{-5} g-equiv/cm^3 of sponge silver for the 19.0°/$_{oo}$ chlorinity electrolytes (this value is proportional to chlorinity), which lies far below the values of $R_{SO_4=}$ actually observed (1.6 x 10^{-4} to 1.0 x 10^{-3} g-equiv/cm^3). Molecular diffusion of sulfate ions into the sponge silver is an unlikely explanation for the high observed values of $R_{SO_4=}$ because of the adverse concentration gradient that would be generated. Similarly, electrolytic mobility is ruled out because the electric field inhibits the movement of sulfate ions into the cathode. Therefore, except for precipitation of sulfate ions in the sponge silver, convection is the only method by which the sulfate ion could enter the sponge silver.

The high values of $R_{SO_4=}$ therefore suggest the retention of sulfate ions in the precipitate formed during discharge by the reaction of the AZ61 alloy with water; perhaps by double salt formation or absorption.[1] In order to investigate this hypothesis, samples of electrolyte were collected during discharge of a full-sized battery. The value of $R_{SO_4=}$ calculated from the composition of the clear portion of the electrolyte from the battery was 4.9 x 10^{-4} g-equiv/cm^3 of sponge silver which is well within the range $R_{SO_4=}$ obtained with the single cell discharges. However, when the amount of sulfate ion retained in the precipitate (determined from weight-composition determinations of the precipitate) was taken into account, it was found that essentially all (112 ± 22%) of the sulfate ion retained was retained in the precipitate. The uncertainty value resulted from an error analysis maximizing the effect of experimental errors. The nominal value obtained for the retention of sulfate ions in the sponge silver was of the same order of magnitude (—4.0 x 10^{-5} g-equiv/cm^3 of sponge silver) as that predicted from convection.

The results of a similar full-scale battery test to determine the relative roles played by the precipitate and the sponge silver on the retention of chloride ion showed that 88 ± 1.2% of the chloride ion, produced by reaction [1] was retained in the sponge silver. Two likely mechanisms of chloride retention in the precipitate are: (*a*) the formation of magnesium hydroxychlorides and (*b*) formation of regions of high concentration in the void spaces of the precipitate. The first hypothesis is supported by x-ray diffraction studies which have shown evidence of the presence of magnesium hydroxychlorides in the precipitate; the second hypothesis is supported by an apparent transfer of chloride ions from the precipitate to the electrolyte with time. Whether this transfer is the result of (*a*) molecular diffusion from electrolyte trapped in the pores of the precipitate, (*b*) equilibration between double salts and the surrounding electrolyte, or (*c*) a change in the composition and size of the precipitate particles (*e.g.*, the corrosion of small pieces of magnesium in the precipitate) is not known.

As stated above, the value of R_{Na+} was determined by subtracting R_{Mg++} for $R_{\pm}$. Since the estimated maximum error of the magnesium determination was 1½%, resulting in large uncertainties in R_{Mg++} (see Presentation of Results), and since the values of $R_{\pm}$ exhibit a fair degree of uncertainty (see Fig. 1 and 2), the values of R_{Na+} exhibit a large degree of uncertainty. However, the values of R_{Na+} and R_{Mg++} are of the same order of magnitude and in most cases values overlap when the uncertainties are taken into account. Consequently these results indicate that both the sodium and magnesium ions enter the sponge silver under the influence of the electric field or take part in double salt formation and therefore, one can assume that in a sea water-activated battery, significant amounts of the salts found in the entering sea water and of the $MgCl_2$ formed from the battery reaction are retained.

Effect of Retention on Voltage Losses

In order to estimate the maximum effect of retention on the voltage losses in a sea water-activated battery, two hypothetical and extreme cases were considered: (*a*) only the ions found in the entering elec-

[1] The term "precipitate" will henceforth refer to the precipitate found in the free flowing electrolyte.

Table II. Effect of retention on voltage drop across interelectrode spacing[a]

Chlorinity of electrolyte entering cell (‰)	Temperature electrolyte entering cell (°F)	Temperature increase of electrolyte (°F)	Voltage drop with no retention[b] (volts)	Increase in voltage drop due to: Only magnesium chloride retained (volts)[c]	Only sea water salts retained (chlorinity reduced)[d]
4.5	40	30	0.53	0.048	0.064
19.0	40	30	0.27	0.011	0.012
19.0	85	30	0.17	0.005	0.008
4.5	40	80	0.17	0.020	0.023
19.0	40	80	0.12	0.008	0.009
19.0	85	80	0.09	0.006	0.008

[a] Voltage drop across the electrolyte passage at the point in the cell where temperature of the electrolyte has increased by the indicated amount. Calculated on the basis of cell spacing of 0.022 in., and a current density of 2.00 asi.
[b] For a hypothetical cell with no retention.
[c] The retention of ions is considered to reduce the amount of $MgCl_2$ added by the cell reaction to the electrolyte without affecting the chlorinity of the electrolyte.
[d] The retention of ions is considered to reduce the chlorinity of the electrolyte without affecting the amount of $MgCl_2$ added to the electrolyte by the cell reaction.

trolyte are retained, *i.e.*, the chlorinity of the electrolyte is reduced, and (*b*) only the magnesium chloride generated in the battery is retained. Voltage losses for the two cases are compared to those that would occur in the absence of retention of any form.

A retention coefficient consistent with the data, 6.3 x 10^{-3} g-equiv/cm^3 of sponge silver was assumed. Also, in order to relate retention to the temperature and composition of the electrolyte, which determine its electrical conductivity, the following assumptions were made: (*A*) The cell is adiabatic. (*B*) The thermal energy released by the cell is independent of electrolyte conditions and current density and is 2.4 times as great as the electrical energy produced at 1.065v (the assumed cell emf). This ratio of thermal to electrical energy has been observed in discharges of a typical full-size high-drain battery. Though this ratio cannot be applied to all such batteries it is adequate for the purposes of this calculation. (*C*) The density and heat capacity of the electrolyte are constant at 1.0 g/ml and 1.0 cal/g°C, respectively. (*D*) The effect of ion retention on flow rate is negligible.

The relevant conductivity data were taken from a prior study [ref. (3)]; and the current density and interelectrode spacing were chosen to reflect current design practice; 2.0 asi and 0.022 in., respectively.

The results of the calculations are presented in Table II. The two entering temperatures were 40° and 85°F. The two electrolytes used were of 4.5 and 19.0‰ chlorinity (the former the lowest chlorinity found in the world's oceans, the latter the "normal" chlorinity of the world's oceans). Two temperature rises, 30° and 80°F, were studied.

The results given in Table II show that the increases in voltage losses caused by retention are relatively small at a current density of 2.0 asi for entering electrolytes of 19.0‰ chlorinity, but become significant (0.05v) for electrolytes of low chlorinity. The use of either of the two methods given in Table II to estimate the effects of retention gives results within 0.02v of each other.

Since the two approaches used in Table II are really boundary conditions, and since both sea water salts and the magnesium chloride from reaction [1] are retained in a battery, perhaps the best estimate of the correction needed to account for retention would be obtained by basing the relative amounts of magnesium chloride and sea water salts undergoing retention on the ratio of normality of the salt under consideration (either sea water salts or magnesium chloride) to the sum of the normality of the sea water salts and the normality of the magnesium chloride.

Conclusions

A study of the retention of the four major ions found in silver chloride-magnesium, sea water-activated batteries (Cl^-, $SO_4^{=+}$, Na^+, and Mg^{++}) indicated that the major locus of chloride ion retention was in the pores of the sponge silver formed on the cathode during discharge whereas the major locus of retention of the sulfate ion was in the precipitate formed by secondary reactions at the anode. Both magnesium and sodium were retained in significant amounts indicating that both the salts found in the sea water and the magnesium chloride formed by the battery reaction are retained in significant quantities.

The evidence available suggests that retention in the sponge silver is primarily determined by diffusion as the retention increases with current density and decreases with temperature. Sulfate retention, which occurs primarily in the precipitate, does not appear to be as strongly controlled by diffusion.

A brief study of the effects of retention on battery voltage indicated that increases in voltage losses of 3 to 15% above those predicted without compensating for retention are to be expected. Adequate corrections can be made by use of the retention coefficients presented in Fig. 1 and 2, the method presented herein.

Acknowledgments

The contributions of Dr. William R. Davis, Assistant Director of the Applied Physics Laboratory, Mr. Rodney Lipp, Mr. William Felton, and Mr. Gary Schwartz are gratefully acknowledged. This work was supported by the Naval Ordnance Systems Command, U.S. Navy, under Contract NOw 65-0207-d.

Manuscript submitted Sept. 5, 1968, revised manuscript received Jan. 6, 1969.

Any discussion of this paper will appear in a Discussion Section to be published in the December 1969 JOURNAL.

REFERENCES

1. D. W. Faletti, and L. F. Nelson, *Electrochem. Technol.*, **3**, 98 (1965).
2. D. W. Faletti, *ibid.*, **4**, 456 (1966).
3. D. W. Faletti and M. A. Gackstetter, *This Journal*, **114**, 299 (1967).

The Performance of Direct Ammonia Fuel Cells

E. L. Simons,* E. J. Cairns*,[1] and D. J. Surd[2]

General Electric Research and Development Center, Schenectady, New York

ABSTRACT

Direct ammonia-oxygen or air cells were operated between 25° and 140°C with aqueous potassium hydroxide as electrolyte and with Teflon-bonded electrodes containing either unsupported platinum black or platinum supported on graphite. The effect of platinum on the performance of ammonia, oxygen, and air electrodes was investigated. Power densities of 50 mw/cm^2 at 0.5v (IR-included) were achieved in ammonia-air cells at 120°C with only 2.5 mg Pt/cm^2 on each electrode.

The many advantages of hydrogen as an electrochemical fuel are largely offset, for commercial fuel cell application, by the need to store and distribute it either as a liquid at temperatures below —240°C or as a compressed gas at higher temperatures, *e.g.*, 2000 psi at room temperature. Consequently, much work has been done to develop fuel cell systems in which the hydrogen is generated as needed from fuels that are cheaper and easier to handle than the pure element, such as metal hydrides, ammonia, methanol, and common hydrocarbons. These fuels, except metal hydrides, can also be oxidized directly in fuel cells equipped with the proper combination of electrodes and electrolyte, but power densities at a given voltage are lower than those obtainable by electrochemical oxidation of the hydrogen derived from these fuels.

In a recent review of government-sponsored research on fuel cells, Austin (1) concluded that "ammonia is relatively inert as an electrochemical reactant and requires very active electrodes or high temperatures." Subsequently, Cairns, Simons, and Tevebaugh (2) found that Teflon-bonded platinum black electrodes (3) provided the necessary electrocatalytic activity. The performance levels they observed in a direct ammonia-oxygen fuel cell, operated in the range 100°-200°C with aqueous potassium hydroxide electrolyte, exceeded those reported for any fuels other than hydrogen or hydrazine. More detailed results on ammonia-oxygen and ammonia-air cells are presented in this paper.

The anodic oxidation of ammonia on a platinized platinum surface in contact with aqueous potassium hydroxide has been shown by earlier workers to occur with 100% coulombic efficiency according to the overall stoichiometry (4-7)

$$NH_{3(g)} + 3\,OH^-_{(aq)} \rightarrow \tfrac{1}{2}\,N_{2(g)} + 3\,H_2O_{(liq)} + 3\,e^- \quad [1]$$

The thermodynamic reversible potential ($E°_{298}$) for reaction [1], calculated from free energy data (8), is —0.77v, only 0.06v less negative than the value of —0.83v for a reversible hydrogen electrode in alkaline solution. Experimental open-circuit potentials, however, are 0.2-0.4v less negative than the reversible potential, and calculated exchange current densities range from 10^{-12} amp/cm^2 (9) to 10^{-8} amp/cm^2, compared to about 10^{-3} for hydrogen (5). From attempts that have been made to elucidate the details of reaction [1], it has been suggested that the reaction proceeds by the step-wise oxidation of hydrogen atoms from nitrogen-hydrogen species adsorbed on the catalyst surface (5, 6, 9).

In a complete ammonia-oxygen fuel cell, reaction [1] is accompanied by the cathodic reduction of oxygen, which, in the absence of peroxide formation is represented by (8)

$$3/4\,O_{2(g)} + 3/2\,H_2O_{(liq)} + 3e- \rightarrow 3\,OH^-_{(aq)};\ E°_{298} = 0.40v \quad [2]$$

Performance data for complete gaseous ammonia-oxygen fuel cells are scanty. Wynveen (7) has published a few voltage-current curves for such a cell operating in the range 30°-80°C with the concentrated aqueous potassium hydroxide electrolyte immobilized in a porous matrix. Most other reported work (10, 11) has been performed at temperatures between 140° and 750°C, using fused alkali hydroxide mixtures, usually in a sintered magnesium oxide matrix, as the electrolyte. All cells have used porous flow-by electrodes made of carbon or nickel with platinum as the anode catalyst. Some results have also been reported for cells in which the feed to the anode was a solution of ammonia in aqueous potassium hydroxide (11, 12). The maximum current densities reported for operation below 150°C were about 40 ma/cm^2 at a cell voltage of about 0.4v (11). Current densities of 120-130 ma/cm^2 were achieved only above 200°C (10, 11).

Experimental

Fuel cell assembly.—The fuel cell used in these experiments was like that shown in exploded view in Fig. 1 except that the spacer (electrolyte compartment) was either 1/8 or 1/16 in. thick and the thermocouple well (added to the cell after the first series of runs) did not extend into the electrolyte compartment but ended about 1/32 in. from the circumferential wall. In most experiments the working fuel cell was mounted below an identical reference cell whose gas compartments were kept filled with hydrogen, and the entire system was assembled in a forced convection air thermostat as shown in Fig. 2. Electrolyte flowed under gravity from an upper Teflon reservoir through the working and reference cells into a lower reservoir. Electrolyte was returned by an all-Teflon bellows pump (not shown) from the lower to the upper reservoir, in which the maximum height of electrolyte was set by an overflow pipe through which excess electrolyte was returned to the lower reservoir. The total volume of the electrolyte in the system was 190 cc, of which only 3.6 or 1.8 cc were between the two electrodes of the cell (11.38 cm^2 circular cross section; 0.32 or 0.16 cm thick).

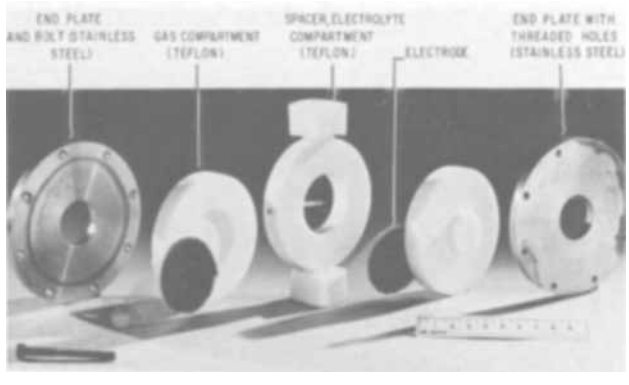

Fig. 1. Exploded view of fuel cell assembly

* Electrochemical Society Active Member.
[1] Present address: Argonne National Laboratory, 9700 South Cass Avenue, Argonne, Illinois.
[2] Present address: Georgetown University, Washington, D. C.

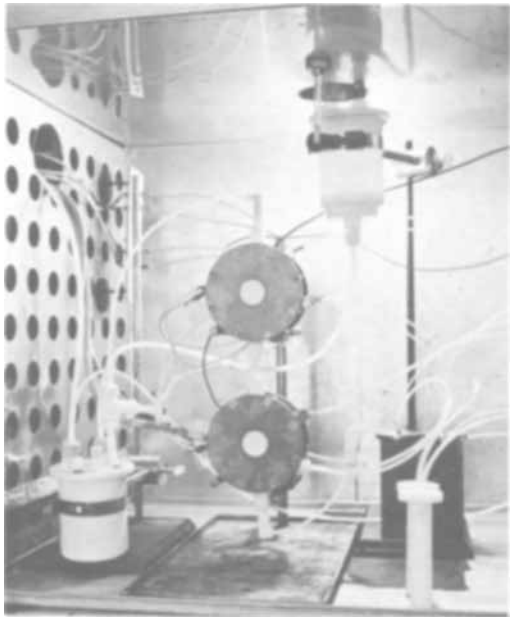

Fig. 2. Fuel cell assembly in air thermostat

In some experiments the total volume of electrolyte was reduced by eliminating the reference cell, electrolyte reservoirs, and bellows pump and installing in their place the electrolyte loop shown in Fig. 3. Thin Teflon tubes (1.7 mm OD) inserted into the upper and lower branches of the electrolyte loop were connected to manually operated syringes and were used to remove gas bubbles that sometimes accumulated in the loop and impeded circulation of electrolyte.

Electrolyte solution and gases.—The electrolyte solution [54 w/o (weight per cent) KOH] was prepared by direct weighing from USP grade KOH pellets and distilled water. Dry gases were fed from tanks into the fuel cell at essentially atmospheric pressure. The air contained 0.035 v/o (volume per cent) carbon dioxide. Ammonia flow rates were 2-3 times stoichiometric and air flow rates 3-4 times stoichiometric.

Electrodes.—Teflon-bonded electrodes (3) were prepared with catalysts that were either unsupported platinum black (Englehard Industries, Inc.) or 10 w/o platinum-on-graphite (American Cyanamid Company designation S-7547-48). The supporting screen was 45-mesh platinum (8-mil wire), and the electrodes were covered on the gas side by a pre-cast film of Teflon containing from 0.04 to 0.22 mg Teflon/cm^2 (~0.2 to ~1.1μ thickness). The amount of catalyst used in preparing the electrodes was chosen to give platinum loadings of 0.9, 1.0, 2.0, 2.4, and 2.5 mg/cm^2 supported on graphite and 51 mg/cm^2 of unsupported platinum black; the total content of Teflon binder was 14-15 w/o. A platinum-free electrode was prepared from Cyanamid 99% graphite. The reference electrodes were made with unsupported platinum black. To obtain reproducible measurements with supported platinum electrodes, the assembled cells were allowed to remain for 24 hr at temperature with electrolyte in the liquid compartment and nitrogen in the gas compartments.

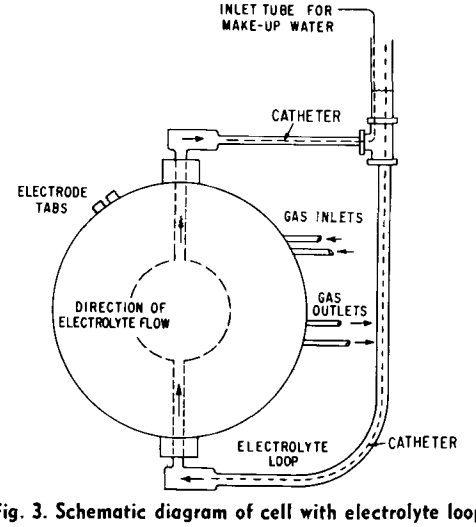

Fig. 3. Schematic diagram of cell with electrolyte loop

Electrical measurements.—Preset currents, measured on a multi-range ammeter, were passed through the cell from a modified 60-cps Kordesch-Marko interrupter bridge (13, 14), and the resulting cell voltage, including resistive losses across the electrodes and electrolyte, was continuously monitored on a Varian strip-chart recorder or measured with a potentiometer. When the cell voltage had reached a constant value for each (average) current, a potentiometer connected to the bridge was used to measure the IR-free voltages between the anode and cathode and between each and the hydrogen reference electrode.

Niedrach and Tochner (14) have shown that a low-frequency interrupter bridge can give erroneous values for IR-free voltages of cells in which the electrodes contain low loadings of supported platinum catalyst because nonresistive voltage changes occur along with the resistive changes during the nonconducting portion of the bridge cycle. Results presented in this paper show similar behavior for low loadings of platinum on carbon in alkaline electrolytes. For cells with low platinum loadings the voltages between anode and cathode and between each and the hydrogen reference electrode were measured while constant currents were being sent through the cells from a d-c power source. In series between the cell and power source was a Clare mercury-wetted relay switch (No. HG2A3033). Additional voltage taps were connected from the cell to the input of a Type H plug-in unit on a Tektronix Type 545 oscilloscope, and the triggering input of the scope was connected in parallel across the coil of the Clare relay. When the coil was energized, by operation of a manual switch, a known current flow through the cell was interrupted in synchronization with a preset oscilloscope sweep rate (usually 10-100 μsec/cm). The voltage step on the oscilloscope screen, resulting from decay of the IR-component of overvoltage, was photographed and measured, the cell resistance calculated from it, and the appropriate correction applied to obtain IR-free values of the cell voltages.

Results and Discussion

Effect of Temperature

The preliminary results already reported (2) for the performance of an ammonia-oxygen cell with platinum black (51 mg/cm^2) electrodes in the range 100°-200°C were confirmed and extended by runs made at ambient temperatures of 140°, 120°, 80°, 60°, and 25°C. The performance data from the runs at 140° and 60°C are presented in Fig. 4 as voltage-current density curves obtained with a Kordesch-Marko bridge. (The data for 120° and 80°C fall between these limits.)

The effect of temperature upon the IR-free performance of the cell in the range 60°-140°C is primarily a reflection of the effect of temperature on the anode performance. The potential-current density curve for the anode at 60°C is roughly parallel to that at 140°C and is displaced upward by about 80 mv. The maximum spread among the four cathode-reference curves is only about 30 mv. No limiting current density was observed up to about 700 ma/cm^2.

The effect of temperature on cell performance is more pronounced when the IR-losses are included in the measurements, because the specific resistivity of the electrolyte increases markedly with a decrease in temperature. The variation of specific conductivity of 54 w/o KOH with temperature is shown in Fig. 5, from which the extrapolated value at 60°C is 0.672 ohm^{-1}

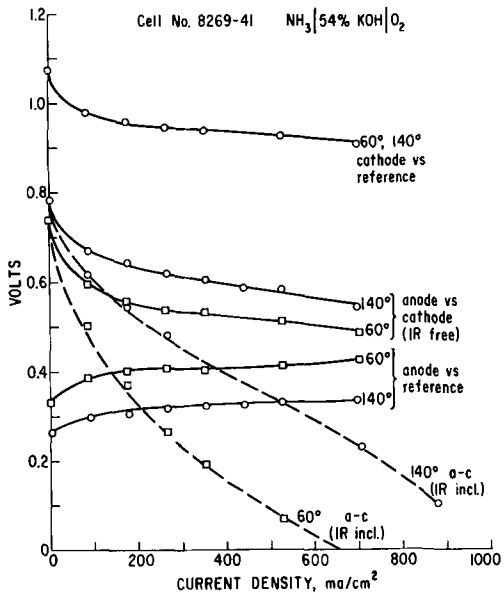

Fig. 4. Effect of temperature on ammonia-oxygen cell No. 8269-41. ——— IR-free data; - - - - - IR included data; Pt black catalyst, 51 mg/cm^2; Teflon coating, 0.22 mg/cm^2.

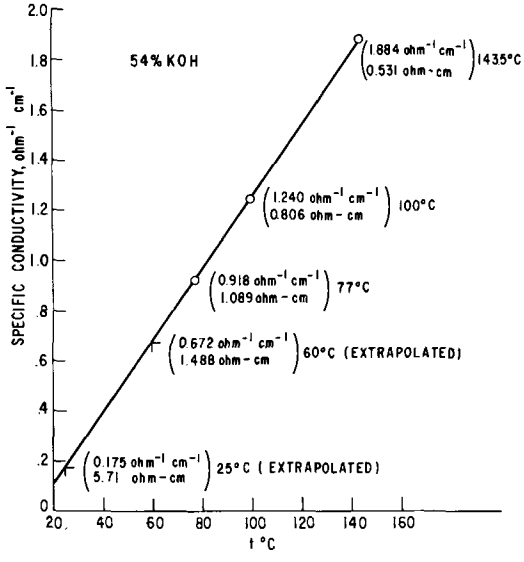

Fig. 5. Effect of temperature on specific conductivity of 54% aqueous KOH.

cm^{-1}, corresponding to a specific resistivity of 1.49 ohm-cm. Thus in the range from 140° to 60°C the specific resistivity increases by a factor of about 2.8. This temperature dependence is in reasonable agreement with that observed by Klochko and Godneva (15) for other aqueous KOH solutions in the range 150°-200°C.

A careful examination of the IR-included anode-cathode voltage curves in Fig. 6 reveals a qualitative as well as quantitative difference between the results at 140°C and those at 120°, 80°, and 60°C. The curve at 140°C shows a change in slope from concave upward at lower current densities to concave downward at higher current densities. The curves at the other temperatures, however, are concave upward over their entire course. In other words, the slope of the voltage-current density curve at each of the lower temperatures decreases continuously with increasing current density in the range covered by these experiments. Furthermore, a comparison of the IR-free and IR-included cell voltages showed that the cell resistance decreased significantly with increasing current density, particularly at 60° and 80°C, indicating that the electrolyte temperature had increased above ambient during operation.

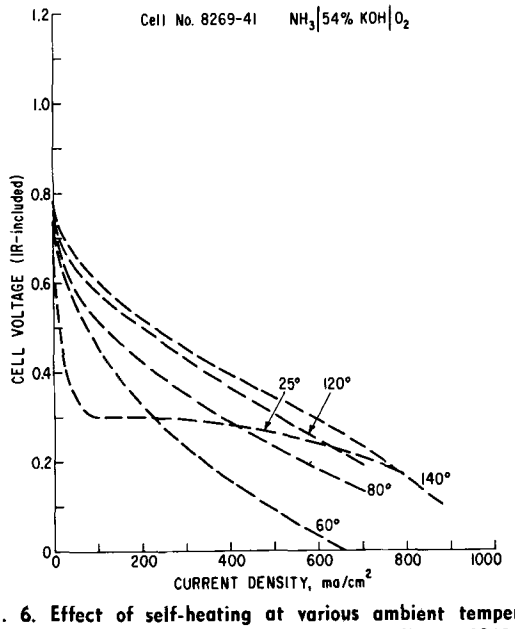

Fig. 6. Effect of self-heating at various ambient temperatures on voltage (IR-included) of ammonia-oxygen cell No. 8269-41. Pt black catalyst, 51 mg/cm^2; Teflon coating, 0.22 mg/cm^2.

The effects of self-heating are dramatically illustrated in Fig. 6 by the performance of a cell whose operation was started at room temperature. The IR-included cell voltage dropped sharply at low current drains, but then remained at about 0.3v over the range 100-300 ma/cm^2. A thermocouple mounted on the outside wall of the anode gas compartment registered ~45°C when the cell was operated at ~800 ma/cm^2, at which point the cell voltage was the same as that observed in the run made at an ambient temperature of 140°C.

The comparison of the performance curves in Fig. 6 can be only qualitative because cell operation was obviously not isothermal at ambient temperatures of 80°C and below. The results, nevertheless, have a two-fold significance: (*i*) They are the first demonstration that a fuel cell operating on a fuel other than hydrogen or hydrazine can be started at room temperature without an external heat source. If room temperature start-up can be achieved in a single cell, such start-up should be even more feasible in a battery designed to reduce initial heat losses; (*ii*) Because of the high electrochemical reactivity of ammonia, which is revealed by these experiments, it should be possible to reduce significantly the amount of platinum catalyst used in the electrodes.

Effect of Platinum Loading

Comparison of 60-cps interrupter bridge and steady d-c drain.—A cell was assembled in which one electrode contained 51 mg platinum/cm^2 as unsupported platinum black and the other contained 6.2 mg platinum/cm^2 supported on Cyanamid graphite. In one run the graphite-based electrode was used as the anode (NH_3); in the other as the cathode (O_2). For both runs, oscilloscope tracings were made of the voltage changes that occurred between anode and cathode during 60-cps operation at several values of the time-average current density. At current densities above 40 ma/cm^2 the tracings from both runs were like that shown in Fig. 7, which is identical in form to those reported by Niedrach and Tochner (14) for a hydrogen-oxygen cell in which the cathode was made with platinum supported on tantalum. The tracings show clearly that at no time in the K-M bridge cycle did the cell voltage reach an IR-free plateau and that significant decay of overvoltage occurred during the zero current portion of the cycle. The magnitude of this decay increased

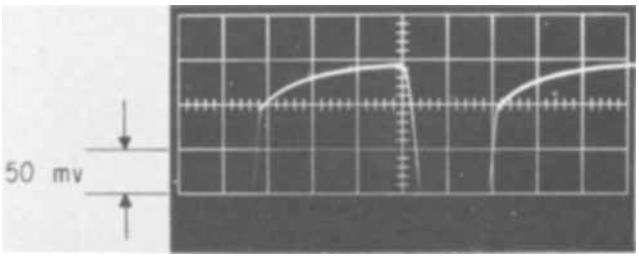

Fig. 7. Cell voltage transient during Kordesch-Marko bridge cycle. If both electrodes had been platinum black, the rapid voltage changes as the current flow was interrupted and then resumed would have been separated by a plateau of constant voltage during the nonconducting portion of the cycle. In this experiment a slow decay of almost 50 mv occurred during the nonconducting portion of the cycle. Run 8446-43-3: $NH_3|54\%\ KOH|O_2$; T = 120°C. Anode, Pt black, 51 mg/cm²; cathode, Pt on C, 6.2 mg/cm²; current density, 88 ma/cm².

with increase in current density to ~150 mv at ~1 amp/cm².

Four pairs of runs were then made with four combinations of high (unsupported) and low (supported) platinum loadings in ammonia-oxygen cells with 54 w/o potassium hydroxide at 120°C. For each combination performance data were obtained both by K-M bridge operation and by steady d-c drain. The voltage-current density relationships are summarized in Table I and Fig. 8, to which the following comments apply:

1. In col. 6. the symbol E_T^{DC} denotes the terminal cell voltage during steady d-c discharge at a constant current (I); the symbol E_T^{KM} denotes the time-average terminal cell voltage during operation of the cell with a K-M bridge at a constant time-average current ($I = I$). The numbers listed in col. 6 are the minimum and maximum values of the difference, $E_T^{KM} - E_T^{DC}$, observed between the members of each pair of runs over the range of current densities from 0 to 350 ma/cm². These values are not significantly different from the differences between duplicate runs made with a given mode. Thus, either mode of operation gives essentially the same values for the IR-included terminal cell voltage of ammonia-oxygen fuel cells with either platinum black or platinum-on-carbon electrodes.

2. By contrast, the four pairs of curves in Fig. 8 show that the relationship between the IR-free voltage *vs.* current density curves obtained by the two modes of operation does depend on the composition of the electrodes. The voltage readings designated as E_{A-C}^{KM} were obtained directly from operation of the K-M bridge. Those designated as E_{A-C}^{DC} were obtained by subtracting from the measured values of E_T^{DC} the appropriate IR-component as calculated from the voltage transients recorded during interruption of the cell at several current levels.

For each pair of runs, the E_{A-C}^{KM} curve lies above the E_{A-C}^{DC} curve; *i.e.*, the K-M bridge gives too high a value for the IR-free anode-cathode voltage. The magnitude of this difference between E_{A-C}^{KM} and E_{A-C}^{DC} is not experimentally significant for cells in which both electrodes are made with unsupported

Table I. Comparison of Kordesch-Marko bridge and d-c discharge

$NH_3|54\%\ KOH|O_2$
$T = 120°C$

(1) Run No.	(2) Mode	(3) Mg Pt/cm² Anode	(4) Mg Pt/cm² Cathode	(5) Estimated cell resist., ohms	(6) $E_T^{KM} - E_T^{DC}$ v
8593-34-1A	K-M	51	51	0.025	−0.010 to
8593-34-1B	D.C.	51	51	0.023	+0.010
8593-46-A	K-M	2.5 on C	51	0.034	−0.011 to
8593-46-B	D.C.	2.5 on C	51	0.024	+0.030
8593-46-D	K-M	51	2.5 on C	0.037	−0.005 to
8593-46-C	D.C.	51	2.5 on C	0.024	+0.014
8446-148-2B	K-M	2.5 on C	2.5 on C	0.047	−0.012 to
8446-148-2A	D.C.	2.5 on C	2.5 on C	0.024	+0.010

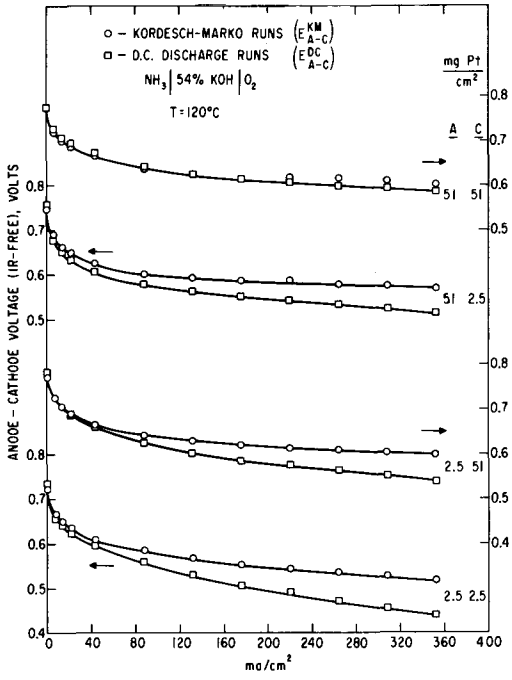

Fig. 8. Comparison between E_{A-C} values obtained from operation of ammonia-oxygen cells with Kordesch-Marko bridge and with d-c discharge. Platinum loadings for each pair of runs are tabulated along right-hand border of figure. Arrows indicate the voltage scale that applies to each pair of curves.

platinum black. The difference is significant for cells in which one of the platinum black electrodes is replaced by a platinum-on-carbon electrode; it is immaterial whether the substitution is made at the anode or cathode. The difference is even greater for cells in which both electrodes contain 2.5 mg platinum/cm² supported on Cyanamid graphite.

3. This difference between the IR-free voltages obtained by the two modes of operation is also summarized in col. 5 of Table I, which lists the estimated values of the cell resistances. Those for the d-c mode were estimated by the interrupter method already described. Those for the K-M mode were calculated from the relationship

$$R = \frac{E_{A-C}^{KM} - E_T^{KM}}{\bar{I}}$$

and were found to be essentially independent of current.

Effect of platinum loading on individual electrode performance.—In addition to the cells described in the preceding section, three were assembled in which the pairs of electrodes were

Cell No.	Electrode pairs	Total mg Pt/cm²
8446-132	2.5 *vs.* 0.0	2.5
8593-4-2	2.5 *vs.* 0.9	3.4
8593-8-2	2.0 *vs.* 1.0	3.0

Altogether, several runs were made on each of seven different cells in order to test the effect of each level of platinum loading on electrode performance with ammonia, oxygen, and air.

For all runs, the d-c interruption method provided reproducible and internally consistent values for IR-free cell voltages, but not for IR-free values of the individual electrode potentials with respect to the hydrogen reference electrode. Single electrode comparisons have, therefore, been made without correcting for the IR-component of overvoltage. Although these IR-included comparisons cannot provide a basis for quantitative electrochemical calculations, they do

show differences in performance, particularly among ammonia anodes of different platinum contents, that are greater than can be attributed to differences in IR-losses between different electrodes or to the scatter of points in replicate runs.

The effects of platinum loading on the performance of an electrode as an anode or cathode are illustrated by the curves of Fig. 9, in which the voltages relative to a common hydrogen electrode are plotted against current density over the range 0-180 ma/cm^2. Although most electrodes could sustain current densities well beyond this range, the curves were distorted by the effects of internal heating at cell currents above 2 amp.

The ammonia oxidation curves (Fig. 9A) for electrodes made with unsupported platinum black and with 2-2.5 mg platinum/cm^2 on graphite are essentially parallel. At 1 mg/cm^2 the performance of the anode and its reproducibility were poorer, and at zero platinum loading the electrode showed negligible catalytic activity. The cathode curves for the graphite electrodes are virtually parallel, and there is no evidence for a limiting current density with pure oxygen out to 176 ma/cm^2 even for the zero platinum loading; with air the platinum-free electrode could not sustain more than 138 ma/cm^2.

The solubility of ammonia in the alkaline electrolyte is high enough (16) so that in the absence of a barrier to its diffusion some fuel is oxidized at the cathode, with a consequent increase in the overvoltage of that electrode, as illustrated in Fig. 9B. The uppermost curve is for a platinum black cathode run in a hydrogen-oxygen cell; the one immediately below it is for a platinum black cathode run in an ammonia-oxygen cell.

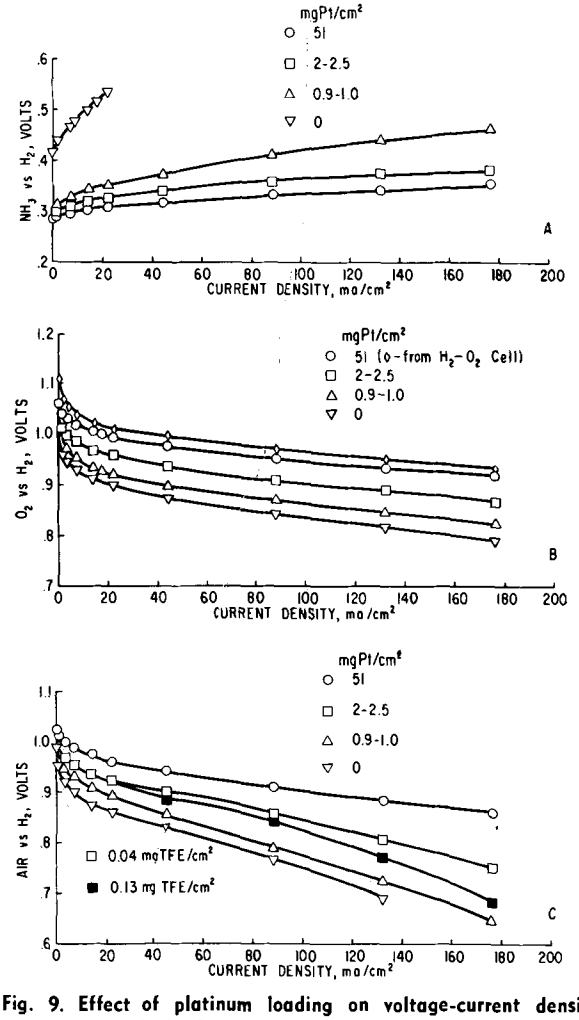

Fig. 9. Effect of platinum loading on voltage-current density curves for individual electrodes (vs. reversible H_2) in cell with 54% KOH (1/15-in. electrolyte space) at 120°C (all voltages include IR component). Except as noted, all measurements were made with ammonia as the anode gas. 9A. Ammonia. 9B. Oxygen. 9C. Air (including two different TFE films).

The performance of an air cathode is affected both by platinum loading and by the thickness of the Teflon film on the gas side. In Fig. 9C the family of air cathode curves includes two at the level of 2-2.5 mg Pt/cm^2. The upper of the two curves is for an electrode with 0.04 mg Teflon/cm^2 ($\sim$0.2μ thickness); the lower, 0.13 mg/cm^2 ($\sim$0.5μ). A similar effect of Teflon thickness was observed with another pair of air electrodes at this platinum level, one with 0.18 and the other with 0.05 mg Teflon/cm^2. No such relation between performance and film thickness was observed when the electrodes were used as oxygen cathodes or ammonia anodes.

Performance of Complete Ammonia-Air Cells

The effects of platinum loading and Teflon film thickness on the IR-included performance of the complete ammonia-air cells used in this investigation are presented in Fig. 10A and B as curves of cell voltage *vs.* current density and power density, respectively.

The upper curve of each figure is for a cell in which both electrodes contained 51 mg of unsupported platinum black per square centimeter. The middle curve is drawn through the points obtained from the cells in which each electrode contained 2.4 mg platinum/cm^2 supported on graphite and in which the film on the gas side of the cathode contained 0.05 mg Teflon/cm^2. One cell was operated in conjunction with a reference cell and electrolyte reservoir (Fig 2); the other was operated with the small electrolyte loop (Fig. 3).

The lower curve is for a cell with virtually the same platinum content (2.5 mg/cm^2) as those for the middle curve, but with a much thicker film on the gas side of the cathode (0.18 mg Teflon/cm^2). This is a reflection of the effect of Teflon film thickness on the performance of the air cathode (see Fig. 9C).

The internal resistances (electrodes plus electrolyte) for the four cells represented by Fig. 10 were 0.023, 0.030, 0.024, and 0.026 ohms, respectively, so even at the highest current density used (176 ma/cm^2 $\equiv$ 2 amp) differences in performance attributable to differences in IR-losses are not more than 14 mv.

Although the total cell performance is diminished by a change from unsupported platinum black to plati-

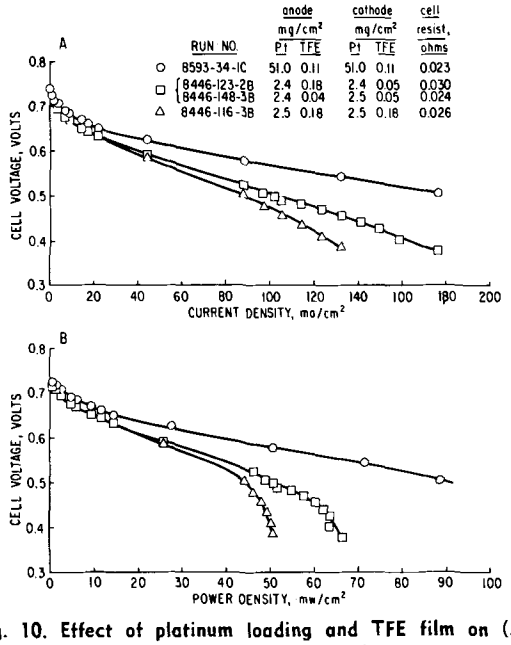

Fig. 10. Effect of platinum loading and TFE film on (A) cell voltage *vs.* current density, and (B) cell voltage *vs.* power density for ammonia-air cell with 54% KOH (1/16-in. electrolyte space) at 120°C. Run No. 8446-148-3B was made with the experimental arrangement shown in Fig. 3.

num-on-graphite, the power density per unit weight of platinum, at 0.5v, is greater with the supported catalyst. For the air cells represented by the middle curves in Fig. 10, the power density of 51 mw/cm^2 at 0.5v was achieved with a catalyst loading in each electrode of 2.5 mg platinum/cm^2, or a total of about 95g of platinum per kilowatt.

Effect of carbon dioxide on air operation.—All of the performance data presented in this paper were obtained during individual runs that lasted no more than a few hours. During the series of experiments reported earlier (2), some cells were operated continuously for periods up to 168 hr with air on the cathode. Cell failures were preceded by sharp decay in performance, and postmortem analyses of the cathodes showed evidence for precipitation of potassium carbonate in the pores of the electrodes. Other experiments showed that aqueous cesium hydroxide is as good an electrolyte as aqueous potassium hydroxide for operation of a cell with oxygen (17) and is better for operation with air because the cesium carbonate that forms does not precipitate in the pores of the cathode but remains in solution, where a steady-state level of carbonate to hydroxide ratio is reached. Although the cell is still operable at this steady state, the performance level is lower than that for a cell with a carbonate-free electrolyte. The most practical solution to the carbonate problem may be to remove the carbon dioxide by scrubbing the incoming air.

During prolonged operation of some cells, droplets of electrolyte appeared on the initially hydrophobic gas-face of the Teflon-bonded electrodes, particularly the cathode. This "weeping" is not caused by cracks in the electrode, but appears to result from a gradual increase in the wettability of the entire electrode by the hot, concentrated alkali solution. If extensive enough, "weeping" can also cause a marked decay in electrode performance.

Conclusions

Most studies that have been made of possible fuel cell power plants for the utilization of ammonia have been based on the thermal dissociation of this gas to provide hydrogen as the electrochemical fuel (18-21). The laboratory experiments described in this paper suggest the feasibility of fuel cell power systems for the direct electrochemical oxidation of ammonia. The direct ammonia-air laboratory cells generated more power per unit weight of noble metal catalyst than laboratory cells using any other fuels except hydrogen and hydrazine. Furthermore, subsequent work on catalyst development (22) has shown that iridium and alloys of iridium and platinum are even more active than platinum alone for the anodic oxidation of ammonia, thus making possible cells with even higher performance than herein reported.

Acknowledgment

The authors appreciate the encouragement and support given to this work by H. A. Liebhafsky.

Manuscript submitted Sept. 6, 1968; revised manuscript received Jan. 20, 1969. This paper was presented at the Montreal Meeting, Oct. 6-11, 1968, as Paper 349.

Any discussion of this paper will appear in a Discussion Section to be published in the December 1969 JOURNAL.

REFERENCES

1. L. G. Austin, "Fuel Cells" (NASA SP-120), p. 21, National Aeronautics and Space Administration, Washington, D.C. (1967).
2. E. J. Cairns, E. L. Simons, and A. D. Tevebaugh, *Nature*, **217**, 780 (1968).
3. L. W. Niedrach and H. R. Alford, *This Journal*, **112**, 117 (1965).
4. T. Katan and R. J. Galiotto, *ibid.*, **110**, 1022 (1963).
5. H. G. Oswin and M. Salomon, *Canadian J. Chem.*, **41**, 1686 (1963).
6. D. Spahrbier and G. Wolf, *Z. Naturforsch.*, **19a**, 614 (1964).
7. R. A. Wynveen in "Fuel Cells," vol. 2, p. 153, G. J. Young, Editor, Reinhold Publishing Co., New York (1963).
8. W. M. Latimer, "The Oxidation States of the Elements and Their Potentials in Aqueous Solutions," 2d Edition, Prentice-Hall, New York (1952).
9. A. R. Despic, D. M. Drazic, and P. M. Rakin, *Electrochim. Acta*, **11**, 997 (1966).
10. Electrochimica Corp., "Direct Ammonia-Air Fuel Cell," Final Report Contract No. DA36-039-AMC-03245(E), U.S. Army Electronics Laboratory, 1 July 1963-31 August 1964.
11. Lockheed Missiles and Space Co., "Basic Studies on Fuel Cell Systems," Final Report Contract NOW 60-0738-d, Navy, Bureau of Weapons, 19 May 1961-19 July 1963.
12. L. G. Austin, P. Palasi, and R. R. Klimpel, in "Fuel Cell Systems," p. 35, R. F. Gould, Editor, Am. Chem. Soc., Washington, D. C. (1965).
13. K. Kordesch and A. Marko, *This Journal*, **107**, 480 (1960).
14. L. W. Niedrach and M. Tochner, *Electrochem. Technol.*, **5**, 270 (1967).
15. M. A. Klochko and M. M. Godneva, *Russian J. Inorg. Chem.*, **4**, 964 (1959).
16. T. Katan and A. B. Campa, *J. Chem. Eng. Data*, **8**, 574 (1963).
17. General Electric Co., British Patent Specification 1,082,575, Improvements in Fuel Cells, Sept. 6, 1967.
18. Allis-Chalmers Manufacturing Co. and Air Products & Chemicals, Inc., "Energy Depot System Study, Liquid Hydrogen and Ammonia Fuels," ACNP-64501, distributed by Clearinghouse for Federal Scientific and Technical Information, Institute for Applied Technology, National Bureau of Standards, U.S. Department of Commerce.
19. Pratt and Whitney Aircraft, "Ammonia-Air Fuel Cell System for Vehicle Propulsion," Final Technical Report, Contract No. DA-44-009-AMC-747(T), USAERDL, 27 July 1964 to 27 July 1965.
20. ASEA, Brevet d'Invention No. 1.365.393 (France), 25 May 1964.
21. O. Lindstrom, *Tek. Tidskr.*, **96** (18), 439 (1966).
22. D. W. McKee, A. J. Scarpellino, Jr., I. F. Danzig, and M. S. Pak, *This Journal*, **116**, 562 (1969).

Improved Electrocatalysts for Ammonia Fuel Cell Anodes

D. W. McKee, A. J. Scarpellino, Jr.,[1] I. F. Danzig,[2] and M. S. Pak

General Electric Research and Development Center, Schenectady, New York

ABSTRACT

Electrocatalysts containing iridium and platinum-iridium alloys have shown very encouraging levels of performance when used as anodes in ammonia fuel cells. These materials were appreciably more active than platinum alone, and the open-circuit voltage and polarization under load generally improved with increasing iridium content. Data are presented for ammonia/oxygen cells at 100°-120°C using 54% potassium hydroxide as electrolyte and platinum-iridium blacks and Pt/Ir supported on boron carbide and graphite as anodes. The observed electrochemical activity of iridium appears to be related to the unique activity of this metal in the gas phase catalytic decomposition of ammonia. Supported iridium catalysts were also found to be effective in an external cracking unit maintained at 350°-450°C and coupled to a hydrogen fuel cell system. In this case enhanced performance was observed when small amounts of oxygen were introduced with the ammonia into the catalytic reactor.

During the course of investigations into the electrocatalytic activity of noble metals and alloys in fuel cells, it has become evident that the platinoid metals are highly specific in their behavior toward fuels of different types and also that alloys can often show higher intrinsic activities than those of the constituent metals alone. Thus, platinum-ruthenium alloys have been found to be much more active than platinum alone in the electrochemical oxidation of methanol (1), and platinum-ruthenium, platinum-iridium, and platinum-rhodium alloys have demonstrated substantial improvements over platinum as anode electrocatalysts for the oxidation of reformer gas (2). Similar synergistic phenomena have often been observed in gas phase catalytic reactions (3), and it is likely that cooperative electronic effects are responsible in both cases.

This work was extended to include studies of the noble metals and their alloys both as anode electrocatalysts in ammonia/oxygen fuel cells and as catalysts for the gas phase decomposition of ammonia. Although ammonia has frequently been considered as a cheap source of hydrogen in fuel cell applications (4), its oxidation at a platinum anode is generally far less reversible than hydrogen. In spite of the improvements recently reported in the performance of ammonia/oxygen cells with platinum catalysts (5, 6), the major overvoltage loss is still observed at open circuit. It has been found, however, that iridium has a unique ability to dissociate ammonia in the gas phase and that fuel cell anodes containing iridium are capable of oxidizing ammonia electrochemically at distinctly lower overpotentials than those observed with platinum electrodes.

In spite of the many studies of the kinetics and mechanism of ammonia decomposition on the transition and noble metals (7), iridium seems to have been almost completely neglected. In this paper the results of electrochemical and catalytic measurements on this metal are presented.

Experimental

Preparation of electrocatalysts.—Unsupported Pt-Ir alloys and iridium black were prepared by a modification of the Adams procedure (8). Appropriate quantities of chloroplatinic acid and iridium trichloride were intimately mixed with an excess of sodium nitrate and the mixture fused in a silica dish at 500°C for 3 hr. After thorough washing the resulting suspension of mixed oxides was reduced at room temperature by hydrogen bubbling through a fritted disk. The product was then allowed to settle and, after removal of the supernatant liquid, was dried slowly under a heat lamp. Finally the catalyst powder was ground and sieved through a 400 mesh nylon screen.

Platinum and iridium were also deposited together on boron carbide and graphite substrates by thermal decomposition of mixed solutions of platinum "P" salt, $Pt(NH_3)_2(NO_2)_2$, and iridium chloride, $IrCl_3$. Commercial boron carbide ("Norbide" abrasive, Norton Company, Worcester) which had been acid leached to remove iron impurity, and Cyanamid graphite powder were used as support materials. Samples of these substrates, previously ground and sieved to 400 mesh, were intimately mixed with aliquots of the mixed salt solution and the paste evaporated to dryness under a heat lamp. The catalysts were then reduced in flowing hydrogen at 125°C for 3 hr and then cooled in a stream of nitrogen.

Catalysts for the indirect ammonia system were prepared by impregnating ⅛ in. alumina pellets (Harshaw Al 0104T) with appropriate quantities of iridium chloride solution. After evaporation to dryness, the catalyst was reduced at 500°C in flowing hydrogen for 3 hr. Supported iridium catalysts were also prepared using activated carbon (Girdler Company, G-32C, 8-30 mesh granules), silica gel (Davison Company, 40 mesh granules) and 5A type molecular sieve (Linde Company, 1/16 in. pellets) as substrates.

Electrode preparation.—Platinum-iridium powdered catalysts were mixed with Teflon suspension and pressed into thin electrodes of the Niedrach-Alford type (9), the quantity of catalyst being adjusted to give approximately 34 mg of noble metal/cm² of geometrical area. A porous film of Teflon was sprayed on the gas side of the electrode to give about 1.6 mg Teflon/cm².

Supported catalysts were mixed into a stiff paste with Teflon and then painted on the platinum screen current collector according to the method described by Grubb and Michalske (10). The loading of noble metal in this case was generally in the range 2-10 mg/cm² of electrode area.

Fuel cell measurements.—The activity of the electrodes was evaluated in the fuel cell assembly described previously (2), which provided a working electrode area of 5.07 cm². A counterelectrode, containing 34 mg of platinum black/cm² was included with oxygen as the reactant, and a similar but smaller cell containing a single hydrogen electrode served as a reference.

The electrodes were normally tested with 54% potassium hydroxide at 100°-120°C, the cell assembly

[1] Present address: Pratt & Whitney Aircraft, East Hartford, Connecticut.

[2] Present address: Direct Energy Conversion Business Section, General Electric Company, 930 Western Avenue, West Lynn, Massachusetts.

being mounted in an air thermostat with a thermocouple inserted directly into the electrolyte chamber of the cell. Most measurements of IR-free and IR-included voltages were made with a Kordesch-Marko interrupter bridge (11), although in some cases IR-included voltages were measured directly across the cell during steady d-c discharge through an external load. The measured cell resistance with supported catalysts was found generally to be smaller than that determined by means of the Kordesch-Marko bridge (6). Cell resistances were about 0.3-0.35 ohm for boron carbide anodes and 0.2-0.25 ohm for graphite anodes, using a ½ in. electrolyte gap. Anhydrous ammonia was supplied to the anode chamber at a constant inlet flow rate of 30 ml/min, corresponding to 3-4 times stoichiometric at the highest current densities used.

Measurement of catalytic activity.—For measurements of the activity of iridium black in the gas phase decomposition of ammonia, catalyst samples weighing 1.5g were sealed into the vacuum system described previously (12), where they were evacuated and reduced at 200°C with pure hydrogen admitted into the apparatus by diffusion through a palladium thimble. After this treatment and further evacuation to 1×10^{-6} Torr, the residual surface area of the catalyst, as determined *in situ* by the BET method, was about 5 m^2/g. No further change in surface area was detected during the subsequent measurements.

Measurements of NH_3-D_2 exchange and NH_3 decomposition were then carried out on the reduced catalyst by admitting samples of NH_3, NH_3-D_2, and NH_3-H_2 mixtures and following the rates of the subsequent reactions as functions of time and temperature by means of a mass spectrometer (Consolidated Electrodynamics Model 21-610), connected through a capillary leak to the gas space over the sample. The temperature of the catalyst was kept constant to within ± 0.5°C by means of a furnace and Honeywell controller.

The activities of supported iridium catalysts for ammonia decomposition were measured in a flow system at approximately 1 atm pressure. The reactor was a quartz tube, 30 cm long and 2.5 cm ID, mounted inside a tube furnace. The catalyst pellets were packed in the central section of the reactor and were confined with glass wool plugs. A thermocouple well was inserted radially into the center of the catalyst bed. The inlet flow of ammonia was adjusted by means of micrometer needle valves and calibrated flow meters. The effluent gas was passed into calibrated gas burettes and the undecomposed ammonia absorbed in 1*N* sulfuric acid. By this means the decomposition of the ammonia was studied as a function of flow rate and catalyst temperature.

Indirect ammonia fuel cell system.—Tests were also carried out of the activity of iridium-based catalysts in an indirect ammonia fuel cell system, that is with a separate catalytic cracking unit coupled to a standard hydrogen fuel cell. The catalytic reactor was a 1 in. diameter quartz tube, filled with 100g of a 4% iridium-alumina catalyst (⅛ in. pellets) and mounted inside a tube furnace. Ammonia was passed through this cracking unit at a constant flow rate and the effluent admitted directly to the anode compartment of a standard fuel cell with platinum black electrodes. This cell used 54% KOH as electrolyte and was maintained at 35° or 100°C throughout. The performance of the cell was studied at different temperatures of the catalytic cracking unit.

In later experiments provision was made for introducing small amounts of air or oxygen into the ammonia feed to the reactor. Controlled rates of addition of these gases was achieved by means of sensitive micrometer needle valves and flow meters.

Results

Fuel cell measurements.—Unsupported platinum iridium black anodes.—The performances of anodes having the composition Pt-21.3% Ir and Pt-51% Ir and containing 34 mg noble metal/cm^2 are compared with that of a standard platinum black anode with 51 mg Pt/cm^2 in Fig. 1A. In this figure the anode polarization (*vs.* H_2 reference) is plotted as a function of current density at 120°C. The polarization of these anodes containing iridium was 100-120 mv less than that of the pure platinum electrode and this improvement was maintained up to current densities of at least 300 ma/cm^2. In addition, the open-circuit potential is within 0.15v of the thermodynamic reversible potential ($E^o_{298} = -0.77$v).

In general the anode polarization with ammonia decreased with increasing iridium content of the electrocatalyst. Difficulty was experienced, however, in preparing satisfactory electrodes with pure iridium black, probably as a result of poor wetting of the powder by the Teflon suspension. Performance data (anode *vs.* cathode, anode *vs.* H_2 reference, IR-free) for an iridium black anode at four different temperatures are presented in Fig. 2. Because of the wetting problem, however, these data may not represent optimum performance.

Supported platinum-iridium anodes.—Figure 1B shows anode-H_2 reference data for Pt/Ir-graphite anodes with noble metal loadings in the range 6-7 mg/cm^2. Similar data for a Pt-graphite anode containing about the same loading of noble metal are also included. The improvement resulting from the addition of iridium is again evident, and increasing proportions of iridium result in lower open-circuit potentials and reduced polarization under load, the improvement over platinum in the best case being over 0.1v at 50 ma/cm^2.

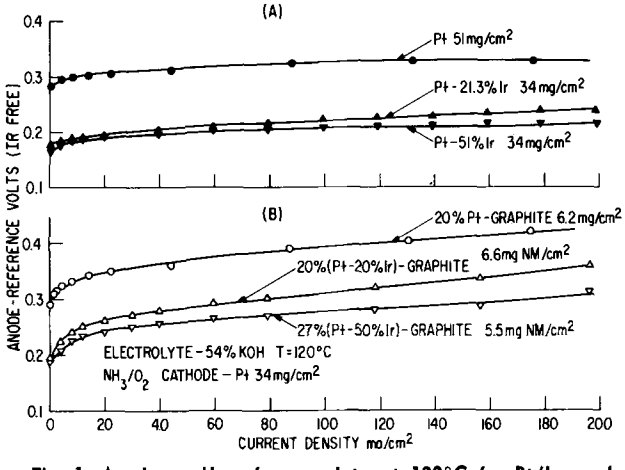

Fig. 1. Anode *vs.* H_2 reference data at 120°C for Pt/Ir anodes for NH_3 oxidation: (A) unsupported blacks; (B) catalysts co-deposited on graphite.

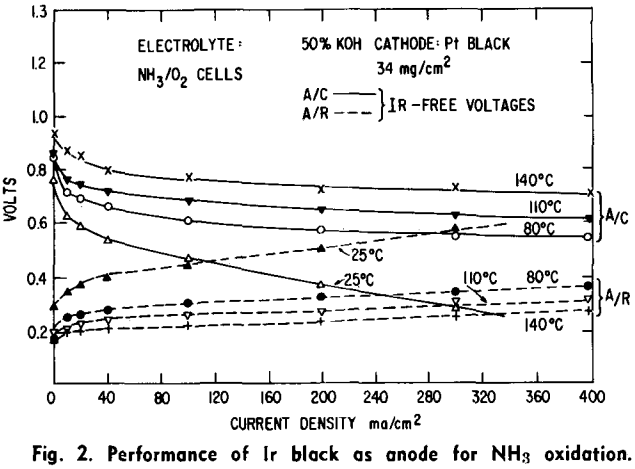

Fig. 2. Performance of Ir black as anode for NH_3 oxidation. Ir-free voltages; H_2 reference.

Satisfactory electrodes were also obtained using boron carbide as the catalyst substrate. Anodes containing iridium again showed less polarization than those with platinum alone. A typical [Pt-20% Ir] $-B_4C$ anode containing 6.8 mg noble metal/cm^2 showed an open-circuit voltage of 0.180v *vs.* SHE and an anode-H_2 reference voltage of 0.255 at a current density of 200 ma/cm^2. Boron carbide-based anodes were, however, generally less reproducible than those prepared from graphite.

Measurements of catalytic activity.—Following the observation of the unexpectedly high activity of iridium in ammonia fuel cell anodes, it appeared logical to inquire whether this metal is superior to platinum in the gas phase decomposition of ammonia. Measurements of the rates of NH_3-D_2 exchange and ammonia dissociation were therefore carried out over iridium black, and subsequently the cracking of ammonia over supported iridium catalysts was studied.

Ammonia-deuterium exchange.—The exchange of ammonia with deuterium took place at a rapid rate over the iridium black at 25°C, the initial rate of formation of the deuteroammonias decreasing with deuterium content. A typical exchange experiment is illustrated in Fig. 3, where the percentage concentration of the isotopic ammonias are plotted against time. In this case a mixture containing equal amounts of NH_3 and D_2 was admitted to the activated catalyst. By analogy with the treatment developed by Kemball (13), the initial rate of substitution of H by D in 100 molecules of NH_3, k_α, was evaluated from the relation

$$-\log_{10}(X_\infty - X) = \frac{k_\alpha\, t}{2.303\, X_\infty} - \log_{10} X_\infty$$

where X is defined by

$$X = \sum_{i=1}^{3} i\, n_i$$

n_i being the percentage of the $NH_{3-i}D_i$ species present at time t, and X_∞ is the equilibrium value of X. Similarly, the rate of removal of NH_3 was calculated in terms of a second rate constant, k_β, defined by the equation

$$-\log_{10}(Y - Y_\infty) = \frac{k_\beta\, t}{2.303(100 - Y_\infty)} - \log_{10}(100 - Y_\infty)$$

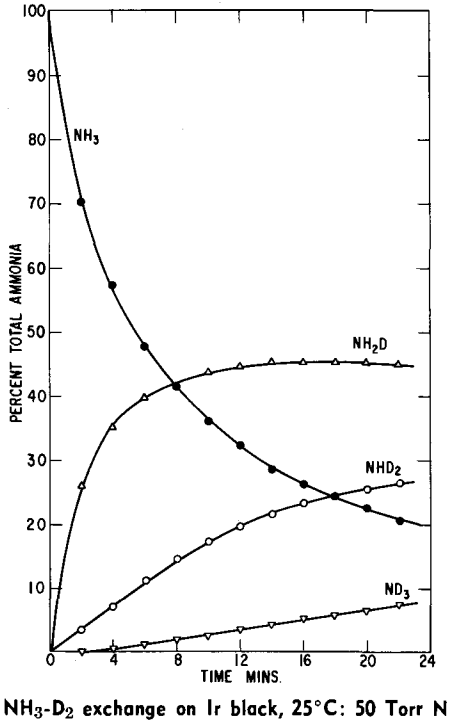

Fig. 3. NH_3-D_2 exchange on Ir black, 25°C: 50 Torr NH_3 + 50 Torr D_2 initially, 1.5g Ir; gas volume = 20.1 ml.

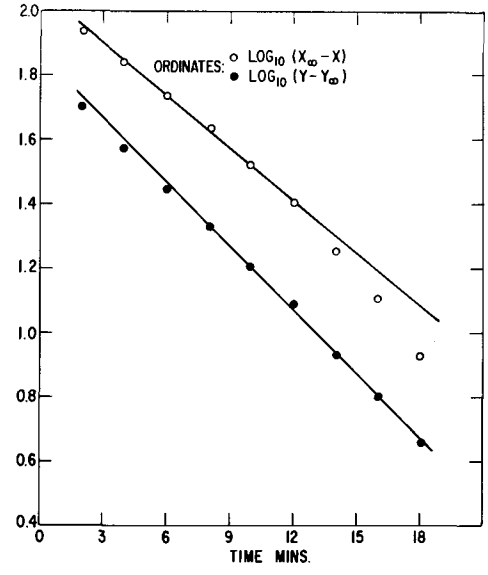

Fig. 4. Plots of $\log_{10}(X_\infty - X)$ and $\log_{10}(Y - Y_\infty)$ *vs.* time for NH_3-D_2 exchange on Ir at 25°C.

Y and Y_∞ being in this case the percentages of NH_3 at time t and at equilibrium. Application of these equations to the exchange data of Fig. 3 is shown in Fig. 4. Good straight lines were obtained over most of the course of the reaction. It is likely that the slight deviation from linearity shown by the lower plot is due to the initial rapid physical adsorption of ammonia on the glass envelope of the apparatus, causing the NH_3 concentration to decrease more rapidly than expected from the exchange reaction. The ratio of the rate constants k_α/k_β is a measure of the average number of hydrogen atoms being replaced by deuterium. The value of this ratio was found to be 1.2 at 25°C, indicating that on the iridium catalyst the hydrogen atoms of the ammonia were being replaced one by one in successive stages.

Ammonia decomposition on iridium black.—Ammonia decomposed rapidly over the iridium black catalyst at temperatures in the range 100°-200°C. Using an initial ammonia pressure of about 50 Torr, the progress of the reaction was followed as a function of time at various temperatures. Figure 5 shows a plot of log (initial rate of formation of N_2) *vs.* 1/T°K. The linear portion of this Arrhenius plot gave an apparent activation energy of 38.5 kcal/mole and a frequency factor, $\log_{10} A = 38.3$, A being in molecules/min.

The initial rate of formation of nitrogen was found to increase with increasing initial ammonia pressure in the range 5-100 Torr, as shown in Table I. A plot of log P_{NH_3} *vs.* log (rate) gave a value for the exponent of ammonia pressure of 0.85 by the method of least squares. The initial rate of nitrogen formation was also found to be strongly retarded by added hydrogen. Figure 6 shows the effect of increasing pressure of hydrogen in premixed NH_3-H_2 mixtures on the initial rate at 160°C. A least squares computation gave a value of -1.4 for the hydrogen exponent. The over-all rate expression was therefore of the form

$$\frac{d[N_2]}{dt} = k\, P_{NH_3}{}^{0.85} \cdot P_{H_2}{}^{-1.4}$$

A few experiments were carried out using platinum black prepared by the same method and having an equivalent surface area to that of the iridium black. It was found that the decomposition of ammonia over platinum was undetectable below 250°C.

Ammonia decomposition on supported iridium catalysts.—In experiments carried out in the flow system, the decomposition of ammonia over supported iridium catalysts was measured as a function of flow rate and temperature.

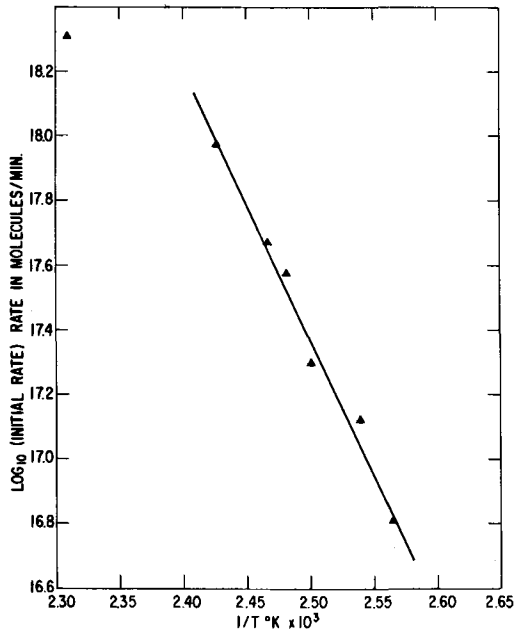

Fig. 5. NH_3 decomposition on Ir black. Plot of $\log_{10}$ (initial rate of N_2 formation) *vs.* 1/T°K.

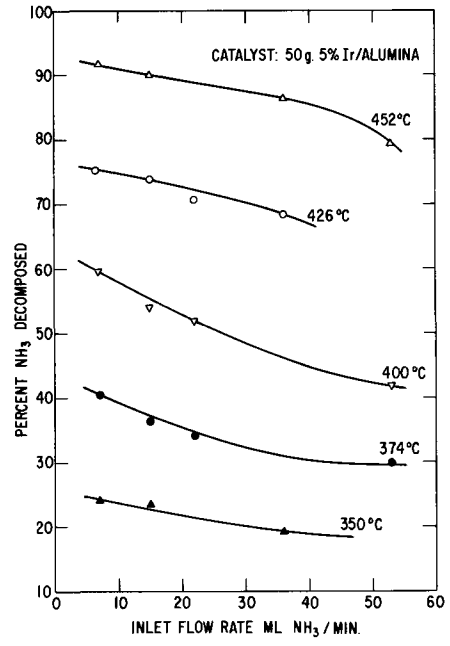

Fig. 7. Decomposition of NH_3 on 5% Ir/alumina (⅛ in. pellets). Conversion *vs.* inlet flow rate.

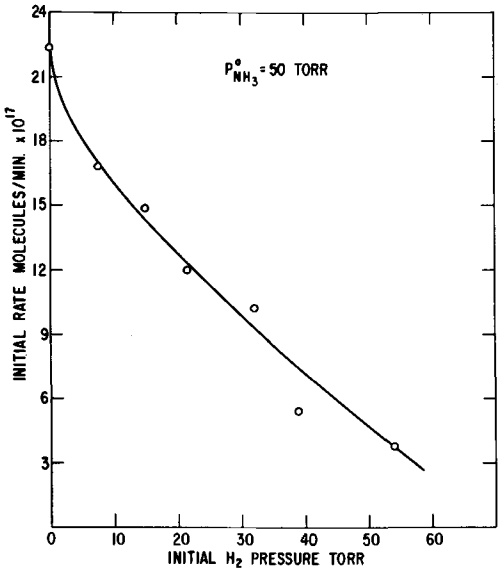

Fig. 6. Effect of added H_2 on initial rate of N_2 formation from NH_3 on Ir black, 160°C.

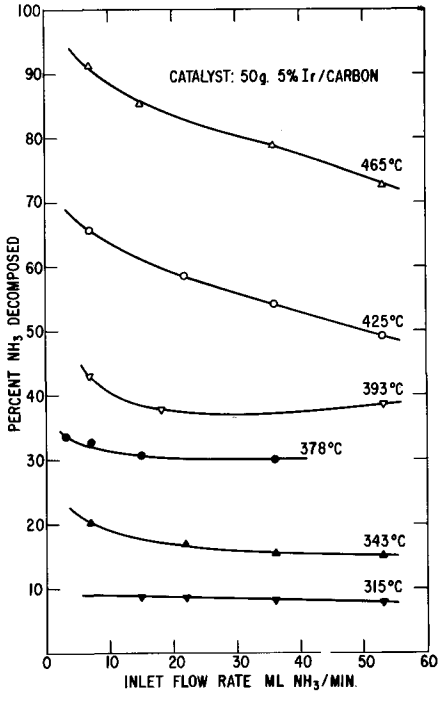

Fig. 8. Decomposition of NH_3 on 5% Ir/carbon (8-30 mesh granules). Conversion *vs.* inlet flow rate.

Figure 7 shows conversion data for a 5% iridium/alumina catalyst in the temperature range 350°-450°C. 50 g of catalyst (⅛ in. pellets) were used in these experiments, and an inlet flow rate of 50 ml NH_3/min corresponded to a space velocity of about 130 hr^{-1}. With this catalyst at low flow rates over 90% of the ammonia was decomposed at a temperature of 450°C. Similar data for a 5% iridium/carbon (8-30 mesh granules) are shown in Fig. 8. For comparison purposes samples of commercial ammonia cracking catalysts were tested under the same conditions. Both nickel/silica-alumina (Harshaw Company, Ni-0901S) and iron/alumina (Harshaw Company, Fe 1401-S) pellets gave much lower levels of activity than the supported iridium catalyst, the per cent NH_3 decomposed at 420°C with a 20 ml/min flow rate being about 15% for both commercial catalysts. The effect of iridium content on the activity of the alumina-based catalysts is shown in Fig. 9. Optimum activity was found with a 2% iridium catalyst, a concentration which may result in a maximum effective metal area. However, even the 0.5% iridium catalyst showed a much higher activity than that previously reported for 0.5% ruthenium/alumina catalyst (14).

The equilibrium percentages of ammonia, extrapolated from the data of Larson and Dodge (15), at 350°, 400°, and 450°C are approximately 1.8, 0.8, and 0.3, respectively, so that equilibrium is not achieved even with the most active catalysts.

Table I. Effect of NH_3 pressure on initial rate of N_2 formation

Temperature = 130°C, 1.5g Ir, gas volume = 69.6 ml

P^{NH_3} init, Torr	Rate N_2 formn, Torr/min	Initial rate, molecules/min	$\log_{10}$ (rate)
22.0	0.115	2.57×10^{17}	17.409
51.2	0.171	3.81×10^{17}	17.581
68.2	0.279	6.22×10^{17}	17.794
82.3	0.297	6.62×10^{17}	17.821
108.0	0.330	7.36×10^{17}	17.867

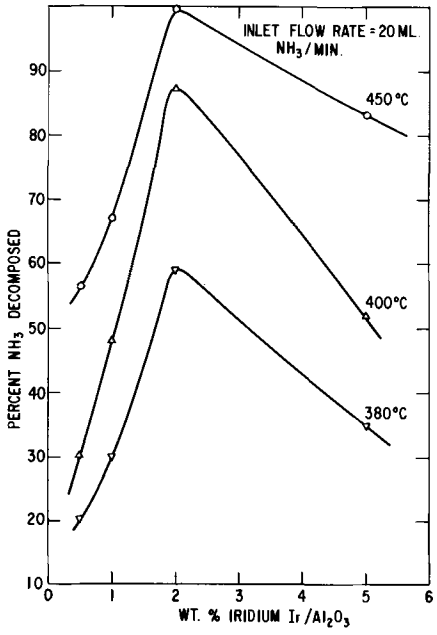

Fig. 9. Decomposition of NH_3 on Ir/alumina (⅛ in. pellets). Effect of Ir loading.

Satisfactory catalysts were also prepared by depositing 5% iridium on silica gel and molecular sieve 5A pellets. These supports generally gave somewhat lower activities than alumina, and large amounts of ammonia were physically adsorbed before steady-state conditions were achieved.

A 5% platinum/alumina, prepared from chloroplatinic acid, was tested after reduction at 500°C under the same conditions as those used for the iridium catalysts. At 480°C less than 15% ammonia was decomposed by the platinum catalyst at the lowest flow rates, whereas below 400°C no decomposition could be detected.

Indirect ammonia fuel cell system.—The results of experiments in which a separate reactor, containing supported iridium catalyst, was coupled to a fuel cell with platinum electrodes, are shown in Fig. 10. Anode-H_2 reference data using pure hydrogen, pure ammonia, and ammonia after passage through the catalytic reactor at various temperatures are indicated. A marked decrease in anode polarization was shown as the cracker temperature increased, the performance being equivalent to that of pure hydrogen at catalyst temperatures of 400°C and above. Figure 11 shows the effect of cracker temperature on the cell voltage under three different conditions, the effect of the cracking

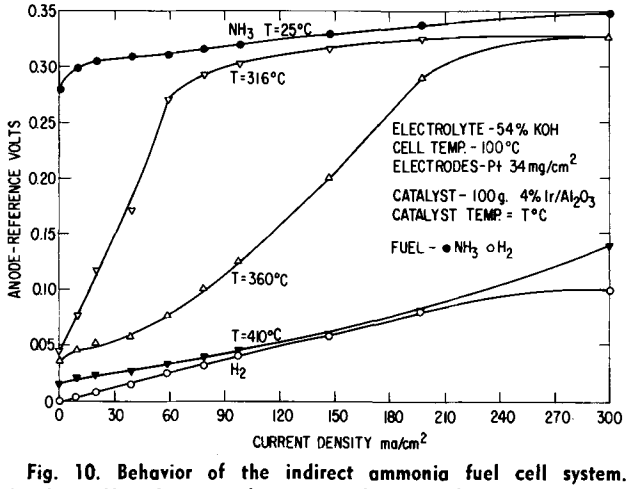

Fig. 10. Behavior of the indirect ammonia fuel cell system. Anode vs. H_2 reference voltages as a function of cracking catalyst temperature.

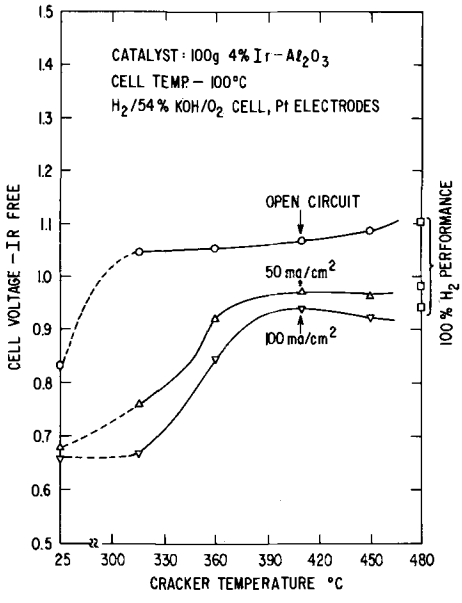

Fig. 11. Indirect NH_3 fuel cell system. Variation of cell voltage (IR-free) with cracker temperature.

catalyst on the open-circuit voltage being especially marked. These results indicate that ammonia acts as an inert diluent in the presence of hydrogen which is more strongly adsorbed on the electrode surface. The fuel cell is thus a reliable indicator of hydrogen concentration in the fuel stream.

The effect of oxygen added to the ammonia inlet of the catalytic cracker on the performance of the fuel cell is shown in Fig. 12. In this case the fuel cell assembly was maintained at 100°C, and the catalytic cracker kept at 367°C initially. The increase in performance shown with added oxygen is a reflection of the heating of the catalyst bed as a result of the exothermic ammonia oxidation reaction: $4NH_3 + 3O_2 = 2N_2 + 6H_2O$. Addition of 19% oxygen to the input ammonia gave fuel cell performance identical with that of pure hydrogen, and the equivalent temperature rise of the catalyst was about 90°C. All the added oxygen was reduced in the reactor unit and none was carried into the anode chamber of the fuel cell.

Figure 13 shows comparable data with the fuel cell maintained at room temperature (about 35°C due to internal heating). In this case, ammonia itself (in the absence of cracking catalyst) showed very poor performance in the cell, although considerable improvement was observed after passage of the fuel through the cracker at 380°C. Additional and marked increase in cell performance was again found when oxygen was introduced into the inlet stream. It appeared to be necessary to preheat the catalyst to around 200°C to

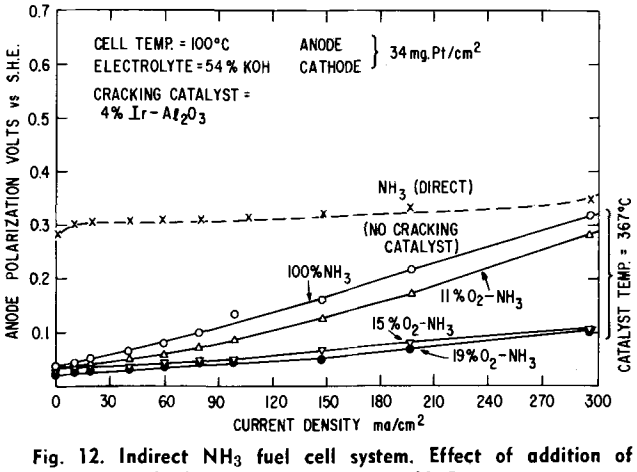

Fig. 12. Indirect NH_3 fuel cell system. Effect of addition of oxygen to NH_3 feed; fuel cell temperature 100°C.

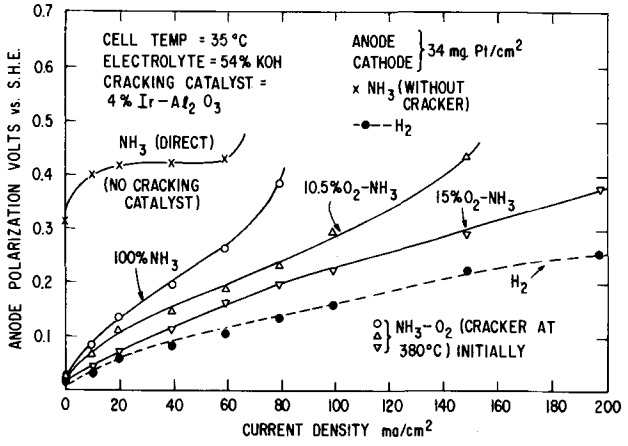

Fig. 13. Indirect NH_3 fuel cell system. Effect of addition of oxygen to NH_3 feed; fuel cell temperature 35°C.

initiate the ammonia oxidation reaction. However, this requirement and the minimum concentration of oxygen needed to produce a given temperature rise, could certainly be improved by optimization of the reactor design and iridium catalyst activity.

Discussion

The high level of activity of iridium and its alloys in the anodic oxidation of ammonia in the fuel cell appears to be directly related to the unusual ability of this metal to dissociate the NH_3 molecule. This analogy between the electrochemical and gas phase decomposition of ammonia has been noted previously by Oswin and Salomon (16). From an analysis of the slopes of the Tafel plots observed with platinized platinum anodes, these authors conclude that the reaction proceeds by a sequence of steps involving the progressive dissociation of ammonia into amine and imine radicals

$$NH_3 + M + OH^- \rightarrow M{-}NH_2 + H_2O + e^- \quad \text{(i)}$$

$$M{-}NH_2 + OH^- \rightarrow M{=}NH + H_2O + e^- \quad \text{(ii)}$$

$$M{-}NH + OH^- \rightarrow M{\equiv}N + H_2O + e^- \quad \text{(iii)}$$

$$M{\equiv}N + M{\equiv}N \rightarrow 2M + N_2 \quad \text{(iv)}$$

It is suggested that at low current densities, reaction (ii) is rate-determining, whereas at high current densities, nitrogen recombination and desorption (iv) may be the slow step. The latter reaction is often regarded as the rate-determining step in the gaseous dissociation of ammonia on active catalysts (17).

Previous studies of the exchange of ammonia with deuterium on evaporated films of platinum, rhodium, and palladium (18) have shown that these metals are very active for this reaction at low temperatures, stepwise exchange being the only mechanism observed. Platinum is the most active metal, the rate of exchange being rapid even at 0°C. By contrast, the decomposition of ammonia on the metals of group VIII requires much higher temperatures, generally in excess of 300°C, and the activity decreases in the order Ru > Rh > Pd (14). Osmium has also been reported to be quite active (19), although the behavior of iridium does not appear to have been investigated previously.

Attempts have frequently been made to correlate the catalytic efficiencies of the group VIII metals for ammonia decomposition with their ability to chemisorb nitrogen and with the number of unfilled d-orbitals in the metal (7). As it is felt that the dissociative chemisorption of nitrogen is the slow step in ammonia synthesis, only those metals which are capable of dissociating N_2 molecules should be active catalysts for the synthesis reaction. Metals which form stable nitrides are not, however, good catalysts, and a weak adsorption of nitrogen atoms is believed to be the most important requisite for high activity in ammonia synthesis and decomposition. Although the ability to chemisorb nitrogen is generally considered to increase on passing from right to left across the group VIII metals, information on the properties of iridium is lacking.

As with the other noble metals, the decomposition of ammonia on iridium appears to be strongly inhibited by hydrogen. Hydrogen is thus more strongly adsorbed than ammonia, a fact that is reflected in the performance of the fuel cell anode, where open-circuit potentials approaching that of hydrogen were observed with NH_3-H_2 fuel mixtures containing only small amounts of hydrogen.

The ratio $(-y/x)$ of the exponents in the rate equation

$$\text{Rate} = k\ P^x_{NH_3} \cdot P^y_{H_2}$$

was observed to be 1.65 approximately. This is in good agreement with the value of 1.7 obtained by Logan and Kemball for evaporated films of platinum and ruthenium (20). Although the Temkin-Pyzhev mechanism, based on nitrogen desorption as the rate-determining step, predicts a value of $(-y/x) = 1.5$, significantly higher values have often been obtained, especially for the metals of the platinum group. It has been suggested (20) that this result is due to the influence of chemisorbed hydrogen atoms which compete with nitrogen atoms for the surface. As the ability to chemisorb nitrogen is expected to decrease in the order Os > Ir > Pt, hydrogen atoms may compete for the surface of iridium more successfully than in the case of osmium. With the latter metal, values of $(-y/x)$ close to 1.5 have been reported (19).

Although the kinetics of ammonia decomposition over iridium agree well with those observed for the other platinum group metals, the high level of activity of iridium is somewhat unexpected. It is interesting to note that iridium and ruthenium, the most active metals for this reaction, have recently been shown to form stable complexes containing molecular N_2 as a ligand (21), in which nitrogen shares two loosely bound electrons with the metal. The corresponding compounds of platinum are very unstable. It is possible, therefore, that the high activity of iridium for the dissociation of ammonia results from an acceleration of step (iv) above, involving the recombination of nitrogen atoms on the metal surface.

Conclusions

In summary it appears that substantial improvements in ammonia fuel cell performance can be achieved by using iridium as the dissociating element. The iridium catalyst can be incorporated directly into the anode structure or used in an external catalytic unit coupled to a hydrogen cell. In the former case, open-circuit voltages of up to 0.934v have been achieved at 100°C with an oxygen cathode, a potential which is at least 0.1v greater than that obtained with the best platinum anodes under the same conditions (5, 6). In the case of an external cracker, the supported iridium catalyst can be maintained at a temperature several hundred degrees lower than that necessary with conventional ammonia dissociators which employ nickel or iron based catalysts.

Acknowledgments

The authors are indebted to E. L. Simons for many useful suggestions and to H. A. Liebhafsky for his continued support of this work and for helpful discussions which led to the experiments on oxygen injection.

Manuscript submitted Sept. 6, 1968; revised manuscript received Jan. 29, 1969. This paper was presented at Montreal Meeting, Oct. 6-11, 1968, as Paper 350.

Any discussion of this paper will appear in a Discussion Section to be published in the December 1969 JOURNAL.

REFERENCES

1. H. Binder, A. Köhling, and G. Sandstede, "Hydrocarbon Fuel Cell Technology," B. S. Baker,

Editor, p. 91, Academic Press, New York (1965).
2. L. W. Niedrach, D. W. McKee, J. Paynter, and I. F. Danzig, *Electrochem. Techol.*, **5**, 318, 419 (1967).
3. J. S. Campbell and P. H. Emmett, *J. Catalysis*, **7**, 252 (1967); D. W. McKee, *Trans. Faraday Soc.*, **64**, 2200 (1968).
4. K. R. Williams, Editor, "An Introduction to Fuel Cells," p. 151, Elsevier Publishing Co., New York (1966).
5. E. J. Cairns, E. L. Simons, and A. D. Tevebaugh, *Nature*, **217**, 780 (1968).
6. E. L. Simons, E. J. Cairns, and D. J. Surd, *This Journal*, **116**, 556 (1969).
7. G. C. Bond, "Catalysis by Metals," p. 378, Academic Press, New York (1962).
8. R. Adams and R. L. Schiner, *J. Am. Chem. Soc.*, **45**, 2171 (1923).
9. L. W. Niedrach and H. R. Alford, *This Journal*, **112**, 117 (1965).
10. W. T. Grubb and C. J. Michalske, *ibid.*, **111**, 477 (1964).
11. K. Kordesch and A. Marko, *ibid.*, **107**, 480 (1960).
12. D. W. McKee, *J. Catalysis*, **8**, 240 (1967).
13. C. Kemball, *Adv. in Catalysis*, **11**, 226 (1959).
14. A. Amano and H. Taylor, *J. Am. Chem. Soc.*, **76**, 4201 (1954).
15. A. T. Larson and R. L. Dodge, *ibid.*, **45**, 2918 (1923).
16. H. G. Oswin and M. Salomon, *Can. J. Chem.*, **41**, 1686 (1963).
17. M. I. Temkin and V. Pyzchev, *Acta Physicochim. USSR*, **12**, 327 (1940).
18. C. Kemball, *Proc. Roy. Soc. (London)*, **A214**, 413 (1952).
19. S. Kiperman and V. Granovskaya, *Zhur. fiz. Khim.*, **25**, 557 (1951).
20. S. R. Logan and C. Kemball, *Trans. Faraday Soc.*, **56**, 144 (1960).
21. J. P. Collman and J. W. Kang, *J. Am. Chem. Soc.*, **88**, 3459 (1966); A. D. Allen and C. V. Senoff, *Chem. Comm.*, 621 (1965).

Inhibition Mechanism of Medium-Sized Polymethyleneimine

Kunitsugu Aramaki*[1] and Norman Hackerman*

Department of Chemistry, The University of Texas at Austin, Austin, Texas

ABSTRACT

The inhibitive effect of medium-sized polymethyleneimines on the corrosion of iron in HCl solution is particularly good, and this effective inhibition is closely related to the angle of C-N-C bond or to strain in the ring as has been observed previously. The inhibition mechanism of the cyclic imines is developed further in this paper. Comparative studies on inhibition effectiveness of dimethylpolymethyleneammonium chlorides, N-phenylpolymethyleneimines, and the cyclic imines were carried out. Synergistic effects of iodide ion on the inhibition by cyclic imines and cyclic ammonium chlorides were also studied. Corrosion rate measurements on pure iron were made in HCl solution by polarization, hydrogen evolution, and weight loss. From the results, it was concluded that good inhibition of medium-sized polymethyleneimine is caused by donation of the unshared π-electron pair of its nitrogen atom to the metal.

The inhibition effectiveness of medium-sized polymethyleneimines, $(CH_2)_n NH$, with 9 to 12 methylene groups, is markedly high, especially with 10, for iron corrosion in HCl solution (1). It was concluded (1) that this was closely related to the angle of C—N—C bond or to strain in the ring.

In this paper the inhibition mechanism of C_{10} inhibitor is developed further by studying inhibition effects of polymethyleneimine derivatives.

Some factors in the enhanced inhibition of medium-sized cyclic imines[2] are:

1. Because of strong strain in the ring, the angle of C—N—C bond in the C_{10} imine molecule is believed to be near 120°, which means sp^2 hybrid orbital geometry of the nitrogen atom (1). This geometry provides π-electron character on the nitrogen atom. The high inhibition of C_{10} imine may be attributed to adsorption via enhanced metal-nitrogen bonding, including π-electron bonding (1-3).

2. If the cyclic imine is adsorbed on the metal by π-electron bonding, the relative molecular area, the effective area of the metal surface covered by inhibitor molecule (1, 2), is presumed to increase. This may result in a high inhibition effect.

3. Polymerized inhibitors may be produced by decomposition of the cyclic imine caused by ring strain, *e.g.*

$$m\,(CH_2)_{10}NH \rightarrow \left[\,(CH_2)_{10}NH\,\right]_m$$

In fact, formation of resinous matter during distillation of medium-sized cyclic imines suggests the likelihood of this reaction. The polymerized compound may well favor the inhibition effect (4, 5).

In order to confirm these factors, three groups of experiments were carried out. The first was a comparative study of inhibition effectiveness between the series of cyclic imines and cyclic ammonium chlorides. The latter, $(CH_2)_n N^+ (CH_3)_2\ Cl^-$, contained 5 and 8 to 14 methylene groups in the ring.

In the second group of experiments, a synergistic effect of these inhibitors and iodide ion was sought. Hackerman, Snavely, and Payne (6) reported on the synergism between C_8 imine and iodide ion in inhibiting iron in HCl solution. Here, adsorption of medium-sized cyclic imine on the iron surface is studied by comparing the cyclic imine-iodide system with the cyclic ammonium chloride-iodide.

The third was a comparative study of inhibition between cyclic imines and phenyl cyclic imines. In the latter compound, $(CH_2)_n NC_6H_5$ containing 5, 8, 10, 12, and 14 methylene groups in the ring, were tested as corrosion inhibitors. Inhibition effectiveness of N,N-dipentylaniline, $C_6H_5N(C_5H_{11})_2$, a phenyl derivative of dipentylamine (C_{10} secondary amine), was also measured.

Three kinds of measurements were carried out for determining corrosion rates of pure iron wire in 6.1M HCl solution with and without the inhibitors at 30°C.

* Electrochemical Society Active Member.
[1] Present address: Department of Engineering, Keio University, Yokohama, Japan.
[2] The terms "cyclic imine," "cyclic ammonium chloride," and "phenyl cyclic imine" used here are, respectively, for polymethyleneimine, for dimethylpolymethyleneammonium chloride, and for N-phenylpolymethyleneimine. Also used are C_n imine, C_n ammonium chloride, and phenyl C_n imine. For example, C_{10} imine for decamethyleneimine, C_{10} ammonium chloride for dimethyldecamethyleneammonium chloride, and phenyl C_{10} imine for N-phenyldecamethyleneimine.

They were made by polarization, hydrogen evolution, and weight loss.

Approximate areas of metal surfaces effectively covered by each inhibitor molecule in the adsorbed position were also determined with properly arranged scale molecular models.

Experimental

Corrosion inhibitors.—Cyclic imines containing 9 to 14 methylene groups were synthesized by known procedures (1). Piperidine and octamethyleneimine were obtained as high-grade commercial reagents. They were all repeatedly purified by fractional distillation or by recrystallization.

N-methylpolymethyleneimines derived from the corresponding cyclic imines with formaldehyde and formic acid (7) were converted to their methiodides. The latter were carefully alkalized with silver oxide and then neutralized with hydrochloric acid. Cyclic ammonium chlorides thus produced were purified by recrystallization. Infrared spectra showed the absence of impurities except for traces of water. They were extremely hygroscopic and melted with decomposition at the following temperatures: C_5,[3] 343°C; C_8, 229°C; C_9, 219°C; C_{10}, 216°C; C_{11}, 243°C; C_{12}, 211°C; C_{13}, 223°C; C_{14}, 217°C.

Phenyl cyclic imines containing 5, 8, 10, 12, and 14 methylene groups in the imine ring were synthesized by reaction of the corresponding cyclic imine with bromobenzene in the presence of sodium amide (8). These imines were purified by fractional distillation and/or by recrystallization. Their purity was verified by infrared spectra and by nuclear magnetic resonance spectra. They have physical constants as follows: C_5, bp 133° C/19 mm Hg; C_8, bp 174° C/16 mm Hg; C_{10}, bp 125° C/1 mm Hg; C_{12}, bp 148° C/1 mm Hg, mp 51°C; C_{14}, 176° C/1 mm Hg, mp 47°C. N,N-dipentylaniline was similarly synthesized from dipentylamine and then purified by fractional distillation at 116°C under 1 mm Hg.

Inhibitor solutions were prepared by dissolving the inhibitors in constant boiling (107°C) HCl solution (6.1M) made from reagent grade material. The solutions containing iodide ion, which was added in 6.1M HCl solution as reagent grade sodium iodide, were stored for short periods under N_2 atmosphere and in a dark cold place. Before use they were refluxed under N_2 for removing traces of iodine produced during the storage.

Corrosion rate measurements.—Corrosion rates of pure iron wire (99.5%, Mallinckrodt Analytical Reagent Grade, 0.36 mm diameter) were determined in 6.1M HCl solution at 30°C by the three kinds of measurements.

Polarization was carried out galvanostatically by supplying current with a coiled Pt wire, a 90v battery, and high variable resistors. Potential of the iron wire was measured with a saturated calomel electrode and an electrometer.

Hydrogen evolution measurements were carried out volumetrically with a graduated gas buret for 120 min. Weight loss measurements were made simultaneously. The details of the experimental equipment and the procedures have previously been given (1).

Relative molecular areas were determined by arranging Stuart-Brieglieb models on a plane in a position corresponding to the appropriate configuration of the molecule adsorbed on the metal surface by formation of a given metal-nitrogen bonding. For example, the nitrogen geometry of cyclic imine molecule adsorbed via the π-electron coordinated bonding was based on the sp^2 hybrid orbitals. The configurations of imine rings were assumed to be analogous to those represented by Dunitz and Prelog (9). All of these molecular areas were compared with that of piperidine. Details of this measurement have also been given (1, 2).

[3] Carbon number in the imine ring.

Results

Corrosion current, i_{corr}, was obtained by the intersection of extrapolated anodic and cathodic Tafel lines. The reproducibility of i_{corr} was good to within less than $\pm$ 4%.

Corrosion currents for cyclic ammonium chlorides are shown as a function of inhibitor concentration in Fig. 1. The results show a regular decrease of i_{corr} with increase of carbon number in the ring.

Hydrogen evolution rates, R_v, were determined by using the average slopes of hydrogen volume versus time curves between 30 and 120 min after the wires were dipped in the solution. Reproducibility was within $\pm$ 4%.

Corrosion rates, R_w, were also measured by weight loss of iron wire in HCl solution. These data were also reproducible to within $\pm$ 4%.

The hydrogen evolution and weight loss rates for cyclic ammonium chlorides are not shown here but are in good agreement with those of Fig. 1. The data for each inhibitor showed the same inhibition efficiencies by all three experimental methods.

Corrosion currents in HCl solution inhibited with iodide ion and either C_{10} imine or C_{10} ammonium chloride were measured as were those inhibited with only iodide ion. Two concentrations of the cyclic inhibitors, 3 x 10^{-3} and 10^{-2} M, were chosen for iodide concentrations at 10^{-4} to 10^{-1} M. Figure 2 gives the log i_{corr} *vs.* iodide ion concentration for the C_{10} imine-iodide system and for the C_{10} ammonium chloride-iodide system, and for the iodide ion alone.

The synergistic effect is evident in these systems since the corrosion currents with the cyclic inhibitors were decreased on increase in iodide concentration.

The synergistic effect was detected with the cyclic imines and with the cyclic ammonium chlorides. The i_{corr} values at 1 x 10^{-2} M of the cyclic compounds and 1 x 10^{-3} M of iodide ion is shown *vs.* ring carbon number in Fig. 3. For comparison, i_{corr} is also given for the system without iodide ion. Both curves for both series are much alike.

Corrosion rate measurements for the phenyl cyclic imine series and for phenyl C_{10} imine were made by polarization, hydrogen evolution and weight loss procedures. Typical curves of log i_{corr} *vs.* concentration of phenyl cyclic imines in imine ring shown in Fig. 4. The trends of the corrosion rates by hydrogen evolution or weight loss were in agreement, all showing rate decrease with increase of carbon number in the imine ring.

In the polarization measurements, anodic oxidation of phenyl cyclic imines was observed at higher concen-

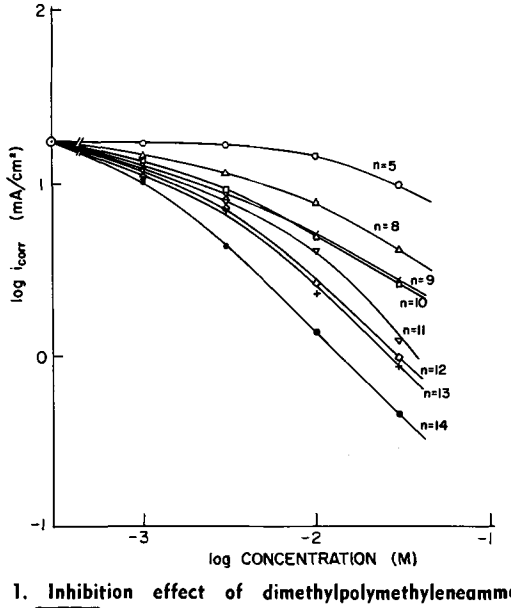

Fig. 1. Inhibition effect of dimethylpolymethyleneammonium chloride, $(\overbrace{CH_2)_n}\,\overbrace{N}^{+}(CH_3)_2\,Cl^-$.

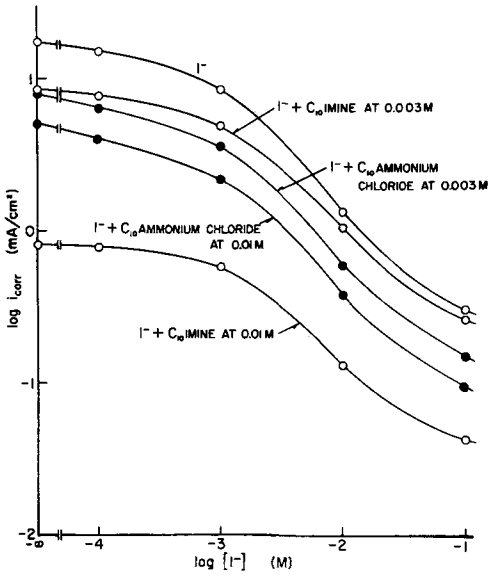

Fig. 2. Synergistic inhibition effect for C_{10} *imine-iodide* ion system and for C_{10} ammonium chloride-iodide ion system.

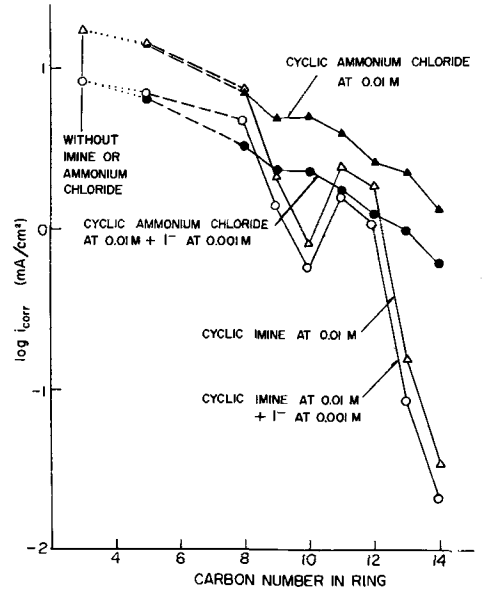

Fig. 3. Synergistic effect of iodide ion on inhibition effectiveness of cyclic imines and cyclic ammonium chlorides.

trations as formation of a red product around the Pt anode. This product is probably a mixture of complex polymers as has been reported for anodic oxidation of dimethylaniline (10). It was found to enhance the inhibition effectiveness of the phenyl cyclic imines. For example, the corrosion current, 0.599 ma/cm^2 for phenyl C_{10} imine at 3 x 10^{-3} M, decreased to 0.300 ma/cm^2 in the first run and to 0.105 ma/cm^2 in the second. Therefore, the i_{corr} values for these inhibitors are reliable at low concentration.

Hydrogen evolution rates with phenyl C_{10} amine are shown in Fig. 5 along with those of phenyl C_{10} imine, C_{10} amine, and C_{10} imine. The data indicate that inhibition effectiveness ability of phenyl C_{10} amine is about the same as with phenyl C_{10} imine. Similar results were also obtained by polarization and weight loss measurements.

Relative molecular areas of cyclic imines adsorbed on the metal by virtue of π-electron bonding are shown in Fig. 6. This also includes those held via σ-electron metal-nitrogen bonding as previously reported (1). Since sp^2 hybrid orbital geometry of the nitrogen atom relaxes the ring strain, there is no irregularity in the relation of molecular area via π-electron bonding to

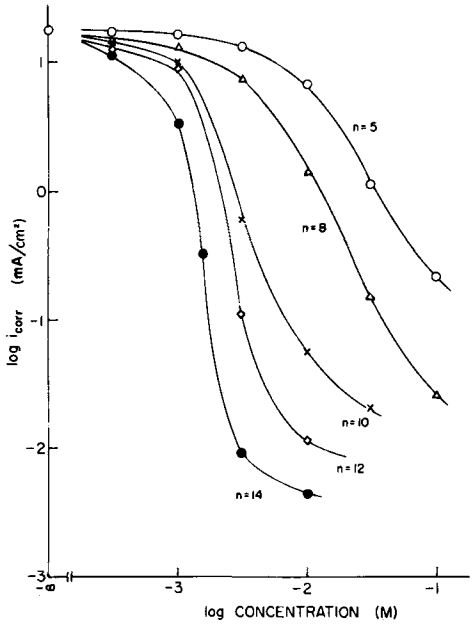

Fig. 4. Inhibition effect of N-phenylpolymethyleneimine, $(CH_2)_n NC_6H_5$.

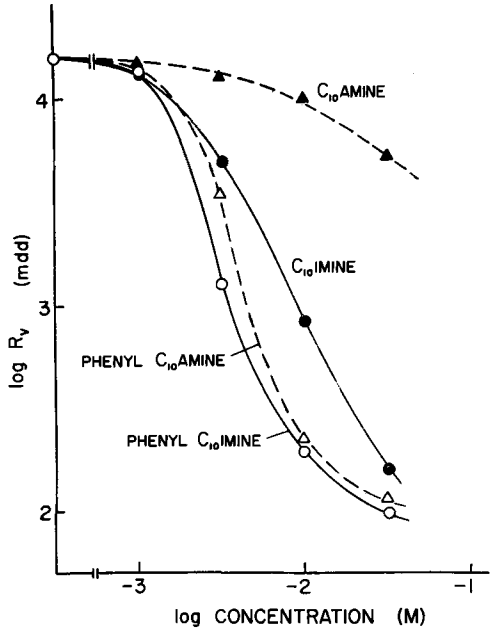

Fig. 5. Rates of hydrogen evolution (R_v) for phenyl C_{10} imine, phenyl C_{10} amine, C_{10} imine, and C_{10} amine.

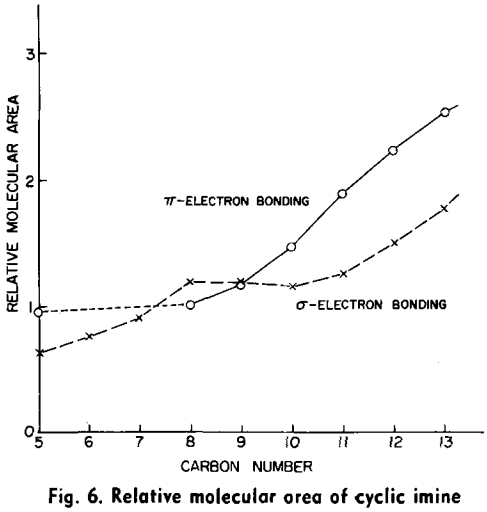

Fig. 6. Relative molecular area of cyclic imine

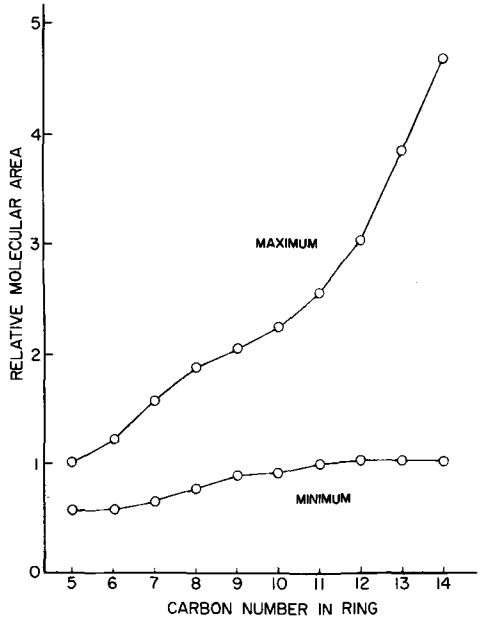

Fig. 7. Relative molecular area of cyclic ammonium ion

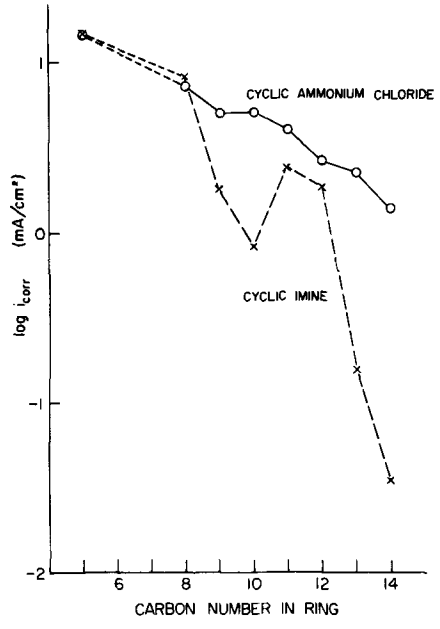

Fig. 8. Relation between corrosion current and carbon number of cyclic ammonium chloride at 10^{-2}M.

carbon number. The two areas differ little from each other at carbon numbers 8 to 10.

Relative molecular areas of the cyclic ammonium ions were also determined. Because there are no unshared electron pairs in these ions, they are adsorbed on the metal surface via coulombic bonding which does not restrict direction. Therefore, simple areal comparison is unavailable even if configuration of hydrocarbon groups are assumed as have been described (9). The maximum and minimum relative molecular areas for cyclic ammonium ions are shown in Fig. 7.

Discussion

To repeat, three effective factors for the enhanced inhibition of medium-sized cyclic imines were considered. To verify the second one, relative molecular areas of cyclic imine molecules adsorbed on the metal by virtue of π-electron bonding were compared with those via σ-electron bonding. The two areas are relatively close to each other at carbon numbers 9 and 10, but not at 11 and 12 (Fig. 6).

C_9 imine, one of the enhanced inhibitors, has almost identical areas by either of the two bonding types. The area of C_{10} imine via π-electron bonding is slightly greater than that by σ-bonding. The i_{corr} value for C_{10} imine remains lower than the value for strain-free cyclic imines,[4] regardless of which area is used. Therefore, increase of the relative molecular area for C_{10} imine is not sufficient to account for the enhancement of inhibition. It is thus concluded that the enhanced inhibition of C_9 and C_{10} imine does not depend on their relative molecular areas while it still might for C_{11} and C_{12} imine.

To decide between the first and third possibilities, corrosion currents for the cyclic ammonium chloride series were compared with those for the cyclic imine series. The rate data for both series, plotted against carbon number in the ring, are shown in Fig. 8. The concentration of each inhibitor was 10^{-2} M.

Comparison of these curves indicates that enhanced inhibition of medium-sized cyclic imine was diminished by converting to cyclic ammonium chloride since there is no peak on the curve for the ammonium chloride series.

Figure 9 shows i_{corr} *vs.* relative molecular areas for cyclic ammonium chlorides. Since the configuration of these inhibitor molecules adsorbed on the metal surface is uncertain, the maximum and minimum areas were used. General consideration of hydrocarbon configuration in adsorbed particles suggest the area is close to the minimum at high inhibition.

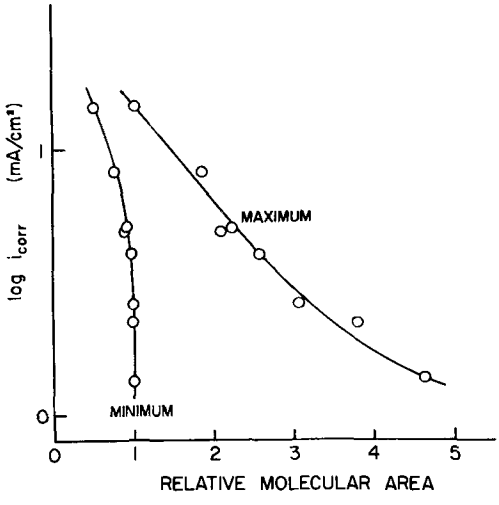

Fig. 9. Log i_{corr} *vs.* relative molecular area of cyclic ammonium chloride at 10^{-2}M.

The curve for cyclic imines is complicated with marked irregularity at the position of the medium-sized compounds (1), whereas Fig. 9 shows a smooth relation with little scattering. The irregularity is the basis in the conclusion relating to strain in the cyclic imine ring.

The difference in this relation between the two inhibitor series thus appears to depend on differences in their molecular structures. Since the unshared electron pair on the nitrogen atom of cyclic imine is blocked by methyl groups, adsorption of cyclic ammonium chloride by means of electron donation to the metal is not likely. However, there is the possibility of polymerization both in cyclic imine and in ammonium chloride because the ring strain persists.

It is concluded, therefore, that the difference in log i_{corr} *vs.* relative molecular area relation is not attributed to polymerization. This leaves donation of the electron pair on the nitrogen atom to the metal as the applicable inhibition mechanism for the medium-sized cyclic imines.

The effect of halide ion on inhibition was studied for developing the inhibiting mechanism of cyclic imines. Synergistic effects between halide ion and amine have been observed and explained by a mechanism which

[4] Refer to Fig. 10 in ref. (1).

includes specific adsorption of the halide ion on the metal (6, 11-13). Iodide is the most adsorbable of the halide ions on iron (14). It enhanced inhibition of both cyclic imine and ammonium chloride in 6.1M HCl solution as shown in Fig. 2.

Murakawa, Nagaura, and Hackerman (13) have expressed synergistic inhibition efficiency, $\eta_{A^+ + X^-}$, of amine and halide ion as

$$\eta_{A^+ + X^-} = \eta_{A^+} + \eta_{X^-} \quad [1]$$

where η_{A^+} and η_{X^-} are inhibition efficiencies due to ammonium ion and halide ion, respectively. The inhibition efficiency, η, is defined here as

$$\eta = \frac{R_o - R}{R_o} \quad [2]$$

where R_o is the uninhibited and R the inhibited corrosion rate.

In this paper, for the cyclic compound and iodide ion not interacting with each other, this relation was expressed with a little modification as

$$\frac{R_{I+I^-}}{R_o} = \frac{R_I}{R_o} \cdot \frac{R_{I^-}}{R_o} \quad [3]$$

where R_I, R_{I^-}, and R_{I+I^-} are, respectively, the corrosion rate of iron in the HCl solution with cyclic compound, with iodide ion, and with both, or

$$\eta_{I+I^-} = \eta_I + \eta_{I^-} - \eta_I \eta_{I^-} \quad [4]$$

where η_I, η_{I^-}, and η_{I+I^-} are, respectively, the inhibition efficiencies of cyclic inhibitor, of iodide ion, and of both.

The efficiency $\eta_{A^+ + X^-}$ can be more than one in Eq. [1] while η_{I+I^-} is limited to less than one.

The R_{I+I^-} value calculated from Eq. [3] was compared to the measured one, R_{I+I^-} by s, defined as

$$s = \frac{R_{I+I^-}}{R_{I+I^-}} \quad [5]$$

This shows the extent of synergism in the cyclic compound and iodide ion system. When there is no interaction between them, s should approach one.

Figure 10 shows the s values calculated from the data in Fig. 2. The s values for C_{10} ammonium chloride plus iodide were almost one and did not change with concentration of either inhibitor. Since these inhibitors are cationic and anionic and are likely to be adsorbed on the metal separately, *i.e.*, the cyclic ammonium ion on the cathode and the iodide ion on the anode, the results are believed to be reasonable. Moreover, there is slight enhancement of the synergism in this system as shown by the values exceeding one at low iodide concentration. This probably arises from stabilization by diminishing coulombic repulsion between charges of the adsorbed ions, as described by Iofa (11), Conway (12), and Murakawa (13).

For the C_{10} imine and iodide ion system, s decreased with increase in concentrations of each. This indicates that adsorption of these inhibitors interferes with each other at high concentrations.

Iodide ion is adsorbed on the anode of the metal surface. Cyclic imine is believed to be adsorbable not only on the cathode areas by coulombic attraction using charge of the protonated molecule, but also on the anode areas by virtue of donation of the electron pair on the nitrogen atom of the unprotonated molecule (15). Therefore, interference adsorption can take place at the anode. Adsorption of C_{10} imine by means of electron donation is probably blocked by the adsorbed iodide ion especially at higher concentrations. Stabilization of the molecules on the metal adsorbed is not likely because the unprotonated imine lacks a charge.

The s values for the cyclic imine series and for the cyclic ammonium chloride series were calculated by using the data in Fig. 3 and are shown in Fig. 11. All the values for cyclic ammonium chlorides are near one. As stated above, there is no interference of their adsorption with iodide ion, but stabilization by diminishing the coulombic repulsion enhances their synergism.

The curve of s *vs.* carbon number for cyclic imines shows a minimum at carbon number 10. This suggests that iodide adsorption on the anode interferes with C_{10} imine adsorption there. Since cyclic imine is adsorbed on the anode by virtue of electron donation, this adsorption is probably blocked by adsorbed iodide. Enhanced inhibition of C_{10} imine is thus again shown to be due to donation of an unshared electron pair to the metal.

The possible effect of chloride ion adsorption on the inhibition of cyclic imine must be considered. In the absence of iodide, chloride ion adsorption on the anode may interfere with cyclic imine adsorption. However, adsorption of chloride ion on iron or steel in acid solutions is less than that of iodide ion (6, 14). Therefore, iodide replaces chloride (16)

$$I^- + Cl^-_{ad} \rightarrow I^-_{ad} + Cl^-$$

Taking into account the high inhibition of cyclic imine in the HCl solution, a similar reaction is possible for cyclic imine, *e.g.*,

$$Cl^-_{ad} + (\overbrace{CH_2)_n NH} \rightarrow [(\overbrace{CH_2)_n NH}]_{ad} + Cl^-$$

But the above results indicate that adsorbed iodide is not replaced by cyclic imine. Therefore, the effect of

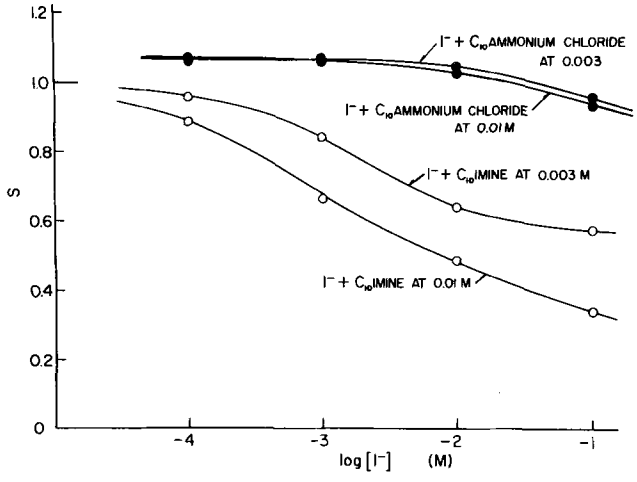

Fig. 10. The s value for iodide ion-C_{10} imine system and for iodide ion-C_{10} ammonium chloride system.

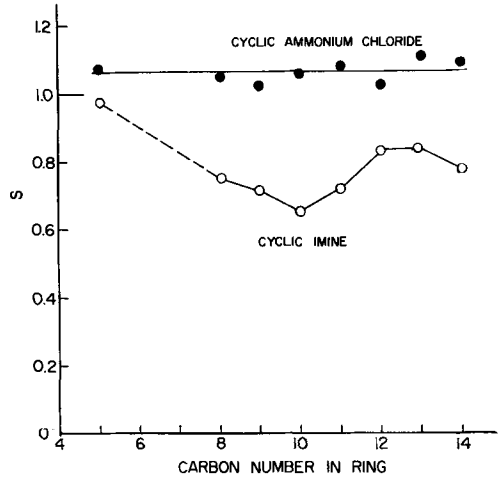

Fig. 11. The s value for cyclic imine-iodide ion system and for cyclic ammonium chloride-iodide ion system.

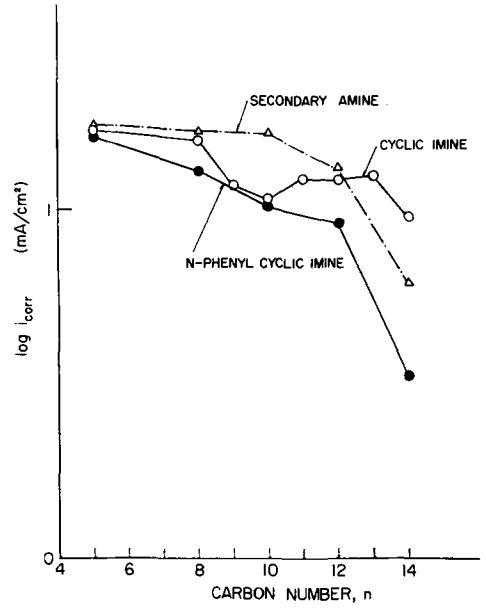

Fig. 12. Inhibition effects of phenyl cyclic imine, $(CH_2)_n N C_6H_5$, cyclic imine, $(CH_2)_n NH$, and secondary amine, $(C_{n/2}H_{n+1})_2 NH$ at 10^{-3}M.

chloride on the synergism discussed here is not believed to be important.

To verify further the effect of π-electrons in C_{10} imine nitrogen on its inhibition, the effectiveness of phenyl cyclic imines was studied. Because the corrosion currents at high concentrations may be in error due to oxidized inhibitor, the data obtained at 10^{-3} M were plotted *vs.* carbon number in the imine ring as shown in Fig. 12, together with those for cyclic imines and for symmetric secondary amines. The curve for phenyl cyclic imine shows no peak at carbon number 10 as is shown for the cyclic imine.

To explain the electron structure of phenyl cyclic imines, phenyl C_5 imine and phenyl C_{10} imine were chosen as typical examples. Because of the ring strain, the geometry on the nitrogen atom of the latter is believed to be sp^2 hybrid orbital, which provides π-electrons on the nitrogen atom, while unshared electrons of the former are σ-type in sp^3 hybrid orbital nitrogen. These unshared electrons are stabilized by participation in resonance with π-electrons of the phenyl group. Electron-delocalized structures of phenyl C_{10} imine are supposed to be stable because of the unshared π-electrons on its nitrogen atom. The π-electrons in phenyl C_{10} imine nitrogen are therefore stabilized more by the resonance than are the unshared σ-electrons in phenyl imine.

Ultraviolet absorption spectra of these compounds agreed with this suggestion. Absorption bands, based on π-π* transition of the phenyl group, shift to longer wavelengths by participation of unshared electrons on a nitrogen atom in resonance of the phenyl group (17). Wavelengths at peak of the E_2 and B band (18) for phenyl cyclic imines measured in cyclohexane are listed in Table I.

The data show a maximum wavelength at carbon number 10. This suggests that the unshared electron pair on phenyl C_{10} imine nitrogen is the most attracted and stabilized by the phenyl group. Therefore, adsorption of phenyl C_{10} imine by virtue of the π-electron metal-nitrogen bonding is weaker than that of phenyl C_5 imine by the σ-electron bonding. This results in no peak on the curve of log i_{corr} *vs.* carbon number as is shown in Fig. 12. This curve and that for secondary amines which are free from the ring strain are similar.

Table I. Ultraviolet absorption spectra of phenyl cyclic imine and phenyl C_{10} amine

	Wavelength, mμ	
	E_2 band	B band
phenyl C_5 imine	253	287
phenyl C_8 imine	263	303
phenyl C_{10} imine	263	304
phenyl C_{12} imine	260	302
phenyl C_{14} imine	258	303
phenyl C_{10} amine	258	303

In order to detect delocalization of unshared electrons in phenyl cyclic imine, other approaches were made by infrared spectra (19) and by nuclear magnetic resonance spectra (20). However, they were not successful except that the electron delocalization in phenyl C_{10} imine was shown to be increased more than in phenyl C_5 imine.

Although the degree of the electron donation to the metal is diminished by the phenyl group, the inhibition effectiveness for phenyl cyclic imine is higher than for cyclic imine. This may be due to increase of the effective molecular area and to bifunctional adsorption via both the nitrogen atom and the phenyl group. Formation of a surface complex (21) would be possible for this inhibitor. Inhibition by cyclic imine is thus concluded to be enhanced by donation of the unshared π-electron pair of the nitrogen atom to the metal.

To confirm this, the inhibition difference between phenyl C_{10} amine and phenyl C_{10} imine was compared with that between C_{10} amine and C_{10} imine. Because of lack of ring strain, there is no unshared π-electrons in the C_{10} amine nitrogen. Therefore, the unshared electrons of phenyl C_{10} amine should be attracted less by the phenyl group than in phenyl C_{10} imine. This agrees with the ultraviolet spectra. Wavelength at the peak of absorption bands for phenyl C_{10} amine is shorter than that for phenyl C_{10} imine as shown in Table I. Thus, adsorption ability of the latter should be decreased more in comparison to that of the former. In fact, as can be seen in Fig. 5, corrosion rates, R_v, for phenyl C_{10} amine and for phenyl C_{10} imine are alike, while R_v for C_{10} amine is much higher than that for C_{10} imine. This result shows that inhibition by phenyl C_{10} imine is decreased by electron delocalization, thereby diminishing the ability of donating unshared π-electrons to the metal.

Conclusion

It is concluded that enhanced inhibition by medium-sized polymethyleneimines on corrosion of iron in HCl solution is caused by donation of the unshared π-electron pair on its nitrogen atom to the metal.

The adsorption of this cyclic imine is improved by formation of coordinated metal-nitrogen bonding via π-electrons. However, there is no evidence for explaining how this bonding enhances the adsorption quality of cyclic imine.

The sp^2 geometry in the nitrogen atom of medium-sized cyclic imine may be changed to the sp^3 geometry to form the metal-nitrogen bonding by chemisorption. However, strong adsorption cannot arise from formation of unstable, deformed sp^3 geometry (1). Formation of stable metal-nitrogen bonding, in which the sp^2 geometry of nitrogen atom remains, may be required for strong adsorption. Little insight into the geometry of adsorbed species by virtue of π-electron bonding is provided by infrared spectra on ethylene adsorbed on metals (22). Direct measurement of adsorption spectra derived from the π-electron metal-nitrogen bonding are needed to confirm this suggestion.

Acknowledgments

The authors are grateful to The Robert A. Welch Foundation of Houston, Texas, and the Office of Naval Research under Contract NONR-375(15) for financial support of this work.

Manuscript received Dec. 11, 1968. This paper was presented at the Montreal Meeting, Oct. 6-11, 1968, as Paper 384.

Any discussion of this paper will appear in a Discussion Section to be published in the December 1969 JOURNAL.

REFERENCES

1. K. Aramaki and N. Hackerman, *This Journal*, **115**, 1007 (1968).
2. N. Hackerman, R. M. Hurd, and R. R. Annand, *Corrosion*, **18**, 37t (1962).
3. N. Hackerman and R. M. Hurd, "First International Congress on Metallic Corrosion," p. 166, Butterworths, London (1962).
4. R. R. Annand, R. M. Hurd, and N. Hackerman, *This Journal*, **112**, 134, 144 (1965).
5. G. W. Poling, *ibid.*, **114**, 1209 (1967).
6. N. Hackerman, E. S. Snavely, Jr., and J. S. Payne, Jr., *ibid.*, **113**, 677 (1966).
7. A. W. Ralston, D. N. Eggenberger, and P. L. DuBrow, *J. Am. Chem. Soc.*, **70**, 977 (1948).
8. J. F. Bunnett and T. K. Brotherton, *J. Org. Chem.*, **22**, 832 (1957).
9. J. D. Dunitz and V. Prelog, *Angew. Chem.*, **72**, 896 (1960).
10. F. Fichter and E. Rothenberg, *Helv. chim. Acta*, **5**, 166 (1922).
11. Z. A. Iofa, V. V. Batrakov, and Cho-Ngok-Ba, *Electrochim. Acta*, **9**, 1645 (1964).
12. B. E. Conway and R. G. Barradas, "Transactions of the Symposium on Electrode Processes," p. 299, John Wiley & Sons, New York (1961).
13. T. Murakawa, S. Nagaura, and N. Hackerman, *Corrosion Sci.*, **7**, 79 (1967).
14. T. Murakawa, T. Kato, S. Nagaura, and N. Hackerman, *ibid.*, **7**, 657 (1967).
15. N. Hackerman, *Corrosion*, **18**, 332t (1962).
16. K. Komiyama, K. Kudo, and N. Sato, *Corrosion Engineering*, **16**, 208 (1967).
17. R. M. Silverstein, G. C. Bassler, "Spectrometric Identification of Organic Compounds," p. 163, John Wiley & Sons, New York (1967).
18. E. A. Brause, *Ann. Repts. Progress Chem.*, **42**, 105 (1945).
19. R. M. Silverstein and G. C. Bassler, "Spectrometric Identification of Organic Compounds," p. 96, John Wiley & Sons, New York (1967).
20. P. L. Corio and B. P. Dailey, *J. Am. Chem. Soc.*, **78**, 3043 (1956).
21. F. M. Donahue, A. Akiyama, and K. Nobe, *This Journal*, **114**, 1006 (1967).
22. L. H. Little, "Infrared Spectra of Adsorbed Species," p. 100, Academic Press, London (1966).

Anodic Polarization of Some Ferritic Stainless Steels in Chloride Media

E. A. Lizlovs* and A. P. Bond*

Research Laboratory, Climax Molybdenum Company of Michigan, Ann Arbor, Michigan

ABSTRACT

Potentiodynamic polarization experiments were performed in 0.1*N* hydrochloric acid with 17% chromium ferritic stainless steels containing up to 3% molybdenum and with 18% Cr-2% Mo ferritic stainless steels containing 0-2% nickel and 0-2% titanium. Potentiodynamic polarization studies with the 17% chromium alloys were also performed in 1*N* hydrochloric acid and in 1*N* sulfuric acid + 0.1*N* sodium chloride media. The critical current densities were significantly decreased with an increased molybdenum content. The pitting potentials were increased with increased molybdenum and titanium contents, whereas nickel additions had no effect. All materials were sensitive to crevice corrosion. Sulfate ions in the $SO_4^=:Cl^-$ molar ratio of 5:1 inhibited pitting corrosion and suppressed crevice corrosion.

The effects of molybdenum on anodic polarization of 17% chromium stainless steels in sulfuric acid have previously been studied in this Laboratory (1). Because of the well-established usage of molybdenum alloying for increasing the resistance of stainless steel to pitting corrosion, interest developed in extending anodic polarization studies to chloride media. It was envisioned that the anodic polarization in acidic chloride media would not only provide information concerning the effect of molybdenum additions on the pitting potential of ferritic stainless steels, but would also provide some information concerning the active-passive transition of stainless steels in the presence of chlorides.

Experimental Procedures

Two sets of laboratory-prepared ferritic alloys and two commercial ferritic stainless steels (Types 430 and 434[1]) were investigated. The high-purity 17% chromium, 17% Cr-1% Mo, and 17% Cr-3% Mo laboratory alloys were prepared by melting and casting in vacuum. The resulting ingots were hot-rolled to 0.64-cm-thick sheet, which was cold-rolled to a 0.32-cm thickness, annealed for 1 hr at 815°C, and water-quenched. The 18% Cr-2% Mo alloys modified by titanium and nickel additions were produced by induction melting in an argon atmosphere, using the split-heat technique. In this technique, the base composition is melted, and part of the melt is poured off to produce an ingot; then to the balance of the melt, the required alloying additions are made and the next ingot is cast. This process is repeated until a series of the desired compositions is cast. The 18% Cr-2% Mo ingots were hot-forged, hot-rolled to 0.76-cm-thick strips, and cold-rolled to 0.38-cm-thick strips. The 18% Cr-2% Mo alloys containing titanium were annealed for 1 hr at 1040°C, the minimum temperature that prevented formation of a second phase in the high titanium alloy, and then water-quenched. The rest of the 18% Cr-2% Mo materials and the hot-rolled, commercial Types 430 and 434 steels were annealed at 815°C for 1 hr and water-quenched. The chemical compositions of all the materials are given in Table I.

The electrodes for the potentiodynamic studies were mounted in acrylic plastic, the exposed surface (0.5 by 0.6 cm) always being a longitudinal section parallel to the rolled surface. A more detailed description of the electrode can be found elsewhere (1). The exposed surface was polished using standard metallographic techniques, ending with a distilled water slurry of 0.3μ alumina. For the pitting potential measurements, the electrode surface was masked with electroplaters

* Electrochemical Society Active Member.

[1] Type 434 is the proposed designation for stainless steel containing 17% chromium and 1% molybdenum.

Table I. Compositions of alloys studied

Alloy	Chemical composition, % C	Cr	Mo	Ni	Ti	Mn	Cu	Si	P	S	N
Type 430	0.046	16.30	—	0.33	—	0.70	0.10	0.60	0.018	0.008	—
Type 434	0.069	16.52	0.99	0.30	—	0.42	0.11	0.54	0.016	0.007	—
High-purity 17% chromium alloys	0.003	17.08	0.03	—	—	—	0.00	0.06	0.009	—	0.0065
	0.002	16.93	1.04	—	—	—	0.00	0.05	0.007	—	—
	0.003	16.68	2.99	—	—	—	0.00	0.06	0.007	—	0.0048
18% Cr-2% Mo nickel series	NA[a]	NA	NA	0.11	—	—	—	NA	—	—	NA
	NA	NA	NA	0.62	—	—	—	NA	—	—	NA
	0.031	18.53	1.95	1.08	—	—	—	NA	—	—	NA
18% Cr-2% Mo titanium series	0.034	18.45	1.97	0.11	0.47	—	—	0.13	—	—	0.045
	0.035	NA	NA	NA	1.86	—	—	NA	—	—	0.023
18% Cr-2% Mo nickel-titanium series	0.032	18.70	1.97	0.57	0.91	—	—	NA	—	—	—
	NA	NA	NA	2.08	1.75	—	—	NA	—	—	—

[a] NA = not analyzed, but assumed to be in the range of the series.

tape (Scotch 470), except for a circular area 0.36 cm in diameter.

The potentiodynamic polarization experiments were performed using standard equipment and techniques. Potentials were measured with respect to a saturated calomel electrode. The auxiliary platinum electrode was isolated from the test solution by a glass frit. All materials were tested in argon-saturated 0.1*N* hydrochloric acid (HCl). The high-purity alloys and commercial steels were tested in argon-saturated 1*N* HCl, 1*N* sulfuric acid (H_2SO_4), and 1*N* H_2SO_4 + 0.1*N* sodium chloride (NaCl). Potential scanning rates for most polarization experiments were 600 mv/hr for the 18% Cr-2% Mo series, and 540 mv/hr for the rest of the materials. For determination of the pitting potentials, the electrode potential was scanned at the rate of 600 or 540 mv/hr up to potentials of about 0.1-0.2v less noble than the expected pitting potential. At this potential the scanning rate was decreased tenfold, *i.e.*, to 60 or 54 mv/hr. Scanning was continued until the pitting potential was reached. The onset of pitting was marked by a sharp and sudden increase in polarization current. The potential scanning was stopped at the pitting potential, and the electrode was allowed to pit for 20 to 30 min. It was then removed from the solution, the tape was stripped, and its surface was examined for pitting and possible crevice corrosion. The potential scanning was usually started at —0.7 to —0.6v, with respect to the saturated calomel electrode (SCE); the scanning was always into the passive potential region. In some experiments, the potential of an actively corroding electrode was changed almost instantaneously to a selected potential in a passive range by switching on a potentiostat, with a potential preset at a desired value.

The experiments with the 18% Cr-2% Mo series of alloys were performed at 24° ± 1°C. All the other materials were tested at 29.6° ± 0.1°C.

Results

Experiments in 0.1N hydrochloric acid.—Typical anodic polarization curves for the Types 430 and 434 stainless steels in 0.1*N* HCl are shown in Fig. 1. The active region for the Type 430 steel exhibited two current maxima, one peak at —0.50v and another at —0.38v. Considerable variations in peak heights were observed for different Type 430 samples, and in some samples the second peak was higher than the first peak. However, the corresponding potentials remained approximately within ± 10 mv of the values given above.[2] The single critical current density peak, shown by the Type 434 steel, was always lower than the corresponding peak for the Type 430 steel.

The passive region for the Types 430 and 434 stainless steels terminated at potentials considerably less noble than the normal transpassive transition range, +0.85 to +0.95v. This passivity breakdown for the unmasked electrodes was characterized by a gradual increase in polarization current. A considerable amount of polarization current could usually be sustained at selected potentials without visible pitting or general corrosion. However, after a long potentiostatic polarization time, microscopic examinations revealed some corrosion at the boundary of the sample and at the acrylic mount. This observation was in accord with the results obtained by Schwenk (2). Thus, in all the potentiodynamic polarization experiments with unmasked electrodes in HCl, the apparent passivity breakdown was not due to pitting corrosion, but was a result of the passivity breakdown inside the extremely fine crevice between the electrode and plastic mount. The presence of crevices with the electrode mounted in metallographic materials was also indicated by Greene *et al.* (3).

The differences in polarization behavior between an unmasked and a masked electrode in the passive state are illustrated in Fig. 1. For the masked electrode the current density beyond the primary passivation potential gradually decreased to the level of 10^{-6} amp/cm^2 or lower, depending on the potential scanning rate, and remained at this level until either pitting or a normal transpassive breakdown occurred. The current density for unmasked electrodes, however, first decreased and then increased gradually, indicative of the onset of crevice corrosion.

Typical anodic polarization curves for the high-purity 17% chromium alloys in 0.1*N* HCl are shown in Fig. 2. As the molybdenum content increased, the critical current density decreased. The primary passivation potential, however, tended to become more noble at higher molybdenum content. A second peak in the active-passive transition region was observed only for the 17% Cr-3% Mo alloy. Critical current density for the 17% chromium alloy varied from 1 to 6 ma/cm^2 for different samples. These variations in critical current density were accompanied by changes in primary passivation potential between —0.49 and

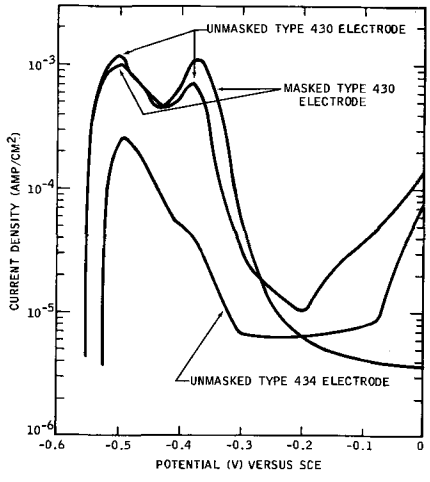

Fig. 1. Anodic potentiodynamic polarization curves for unmasked Types 430 and 434 electrodes and for masked Type 430 electrode in 0.1*N* hydrochloric acid at 29.6°C.

[2] Henceforth, the current density peak at the least noble potential will be referred to as the critical current density, and the corresponding potential as the primary passivation potential.

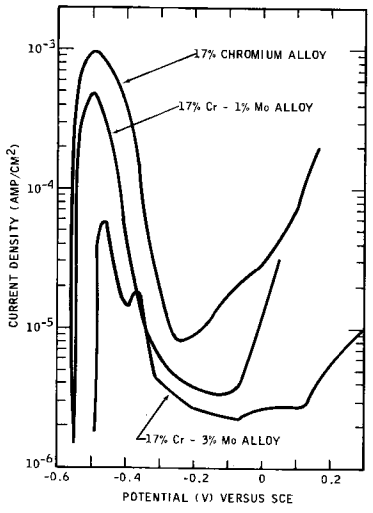

Fig. 2. Anodic potentiodynamic polarization curves for 17% chromium, 17% Cr-1% Mo, and 17% Cr-3% Mo alloys in 0.1*N* hydrochloric acid at 29.6°C (unmasked electrodes).

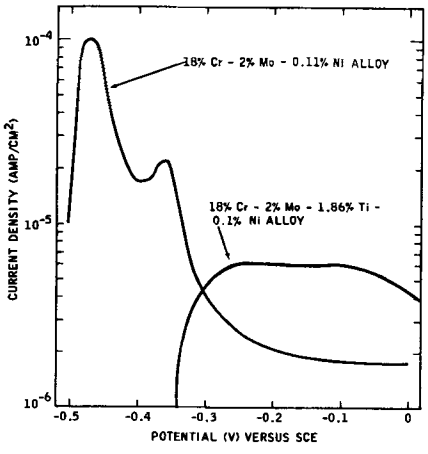

Fig. 3. Anodic potentiodynamic polarization curves for the 18% Cr-2% Mo-0.11% Ni and 18% Cr-2% Mo-1.86% Ti-0.11% Ni alloys (masked electrodes) in 0.1*N* hydrochloric acid at 24°C.

—0.43v; in general, the more noble the primary passivation potential, the higher the critical current density. The passive region for the unmasked electrodes again terminated at potentials less noble than pitting potentials. However, crevice corrosion did not influence the critical current density of the materials, so that unmasked electrodes could be used for the anodic polarization studies in the active region. Furthermore, the minimum current densities, reached in the passive region with unmasked electrodes, appeared to depend on the molybdenum content for both commercial and high-purity alloys. The steels with the highest molybdenum content had the lowest current minima in the passive state (Fig. 1 and 2). Thus, molybdenum appears to improve the resistance of ferritic stainless steels to crevice corrosion in chloride media. However, since the crevice geometry was not intentionally controlled on the electrodes, further experimental work is needed to obtain more quantitative information concerning the effect of alloying additions on crevice corrosion. Representative values of critical parameters for the commercial steels and high-purity alloys are summarized in Table II.

Table III. Current density maxima and corresponding potentials in argon-saturated 0.1*N* hydrochloric acid for 18% Cr-2% Mo ferritic stainless steels

Alloy addition to 18% Cr-2% Mo base, % Ti	Ni	Critical current density, ma/cm²	Primary passivation potential *vs.* SCE, v	Secondary current density maximum, ma/cm²	Potential corresponding to the secondary current density maxima vs. SCE, v
—	0.11	0.11	−0.475	0.014	−0.350
—	0.62	—	—	0.04	−0.340
—	1.08	—	—	0.018	−0.380
0.47	0.11	0.10	−0.480	0.006	−0.350
1.86	~0.1	—	—	—	—
0.91	0.57	0.002	−0.455	0.002	−0.330
1.75	2.08	—	—	0.005	−0.300

Table IV. Average pitting potentials in 0.1*N* hydrochloric acid

Alloy	Average pitting potential, *vs.* SCE, v
Type 430	0.18
Type 434	0.19
17% Chromium	0.26
17% Cr-1% Mo	0.32
17% Cr-3% Mo	>0.80
18% Cr-2% Mo-0.11% Ni	0.31
18% Cr-2% Mo-0.62% Ni	0.35
18% Cr-2% Mo-1.08% Ni	0.34
18% Cr-2% Mo-0.47% Ti	>0.8
18% Cr-2% Mo-1.86% Ti	0.63
18% Cr-2% Mo-0.91% Ti-0.57% Ni	>0.8
18% Cr-2% Mo-1.75% Ti-2.08% Ni	0.62

Representative anodic polarization diagrams in 0.1*N* HCl for 18% Cr-2% Mo alloys are shown in Fig. 3. Table III gives the critical parameters for these alloys. Table III also shows that an increase in nickel content, from 0.11% to 0.62%, results in complete suppression of the active region. Although the addition of 0.47% titanium had no effect on critical behavior, an increase in titanium level to 1.86% resulted in a complete disappearance of the active region. In addition to the normal critical current density peaks, considerably lower secondary peaks were observed for most of the 18% Cr-2% Mo alloys in the —0.38 to —0.30v region.

Average pitting potentials for all the materials are summarized in Table IV. A typical polarization run with a masked electrode, exhibiting termination of the passive range due to onset of pitting, is shown in Fig. 4. The onset of pitting corrosion was always marked by a sharp current rise over several orders of magnitude, but crevice corrosion was marked by a gradual current increase. Under the experimental conditions used, the materials that could be scanned beyond the threshold of transpassivity (+0.80v) ought to be considered resistant to pitting corrosion. However, exploratory studies showed that potentiostatic pitting could be achieved with materials that exhibit a full

Table II. Current density maxima and corresponding potentials in argon-saturated hydrochloric acid for commercial ferritic stainless steels and high-purity 17% chromium alloys

Alloy	0.1*N* Hydrochloric acid				1.0*N* Hydrochloric acid	
	Critical current density, ma/cm²	Primary passivation potential *vs.* SCE, v	Secondary current density maximum, ma/cm²	Potential corresponding to secondary current density maximum	Critical current density, ma/cm²	Primary passivation potential *vs.* SCE, v
Type 430	1.2	−0.502	0.77	−0.380	—[a]	—
Type 434	0.26	−0.490	—	—	18[a]	−0.310 to −0.305
17% Chromium	0.95	−0.495	—	—	140[a]	−0.230
17% Cr-1% Mo	0.48	−0.500	—	—	46	−0.310
17% Cr-3% Mo	0.058	−0.463	0.018	−0.368	13	−0.340

[a] No true passive state attained for these materials.

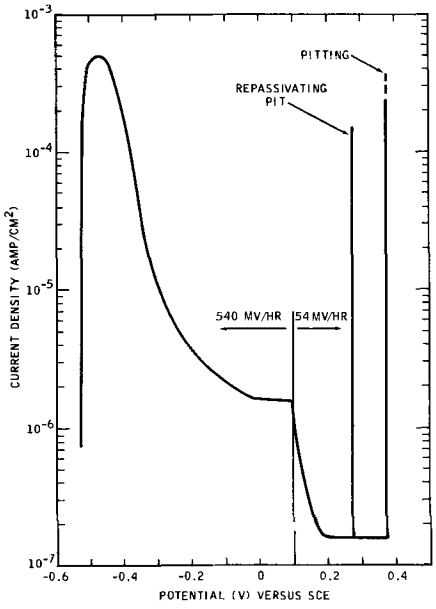

Fig. 4. Anodic potentiodynamic polarization curve for masked 17% Cr-1% Mo electrode in 0.1*N* hydrochloric acid at 29.6°C.

passive range under potentiodynamic conditions. This occurred under conditions of nearly instantaneous potential switch from an active corrosion potential to a sufficiently noble passive potential. Thus, the 17% Cr-3% Mo alloy was pitted at +0.40v under these conditions.

A repassivation phenomenon was also observed during several potentiodynamic pitting experiments. This phenomenon was usually indicated by current blips at potentials that were lower than those at which continuous pitting occurred (Fig. 4). However, the pitting corrosion was sometimes sustained for 15 to 20 min, and then followed by complete repassivation of the pits. Examination of the electrode revealed visible pits inside the free electrode area, but revealed no evidence of corrosion under the masking tape.

Experiments in 1.0N hydrochloric acid.—Anodic polarization curves for the commercial and high-purity alloys in 1.0*N* HCl are shown in Fig. 5 and 6 (unmasked electrodes). Table II gives the critical current densities and primary passivation potentials. Type 430 stainless steel did not passivate at all in 1.0*N* HCl. Type 434 steel did exhibit a current peak at the expected position for the primary passivation potential,

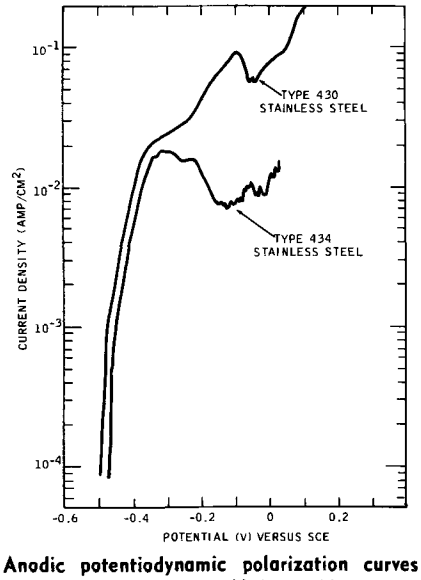

Fig. 5. Anodic potentiodynamic polarization curves for Types 430 and 434 stainless steels in 1*N* hydrochloric acid at 29.6°C (unmasked electrodes).

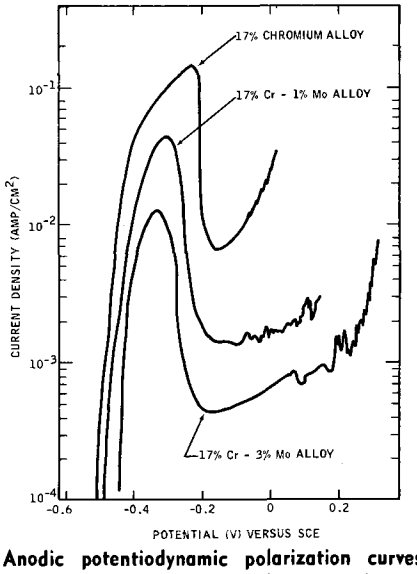

Fig. 6. Anodic potentiodynamic polarization curves for 17% chromium, 17% Cr-1% Mo, and 17% Cr-3% Mo alloys in 1*N* hydrochloric acid at 29.6°C (unmasked electrodes).

—0.310v; however, current densities beyond the critical peak remained quite high. All the high-purity alloys exhibited a critical current density peak, but the current densities at potentials approximately 100 mv more noble than the primary passivation potentials were several orders of magnitude higher than the corresponding current densities in 1*N* H_2SO_4 (1). The potentiostatic passivation experiments, performed in 1*N* HCl with masked electrodes, showed than 17% Cr-1% Mo and 17% Cr-3% Mo alloys could be completely passivated in the —0.20 to —0.10v region. The resulting polarization current densities in the passive state were of the same order of magnitude as those observed in H_2SO_4, 10^{-6} amp/cm² (1). Thus, the apparent high-current densities obtained with unmasked electrodes are an outcome of crevice corrosion, which is much more severe in 1.0*N* than in 0.1*N* HCl.

At any passive potential under potentiostatic conditions, the polarization current densities for the masked 17% chromium alloy and for commercial Types 430 and 434 steel were several orders of magnitude above the 10^{-6} amp/cm² level. Furthermore, the potentiostatic experiments with an unmasked 17% chromium electrode at —0.15v showed that at this potential, the electrode corroded uniformly at a rate corresponding to approximately 10 ma/cm². Thus, for the straight chromium steels and for Type 434 steel, the high current densities in a passive range are primarily the result of the uniform corrosion, but for the 17% Cr-1% Mo and 17% Cr-3% Mo alloys, the relatively high current in the passive range is largely the result of crevice corrosion.

The elimination of the crevice by the use of masking tape was considerably more difficult in 1*N* than in 0.1*N* HCl; in fact, many experiments were invalid because the mask loosened, and crevice corrosion resulted. Therefore, neither the potentiostatic maintenance of the passivity over prolonged periods of time, nor the potential range over which the steels would retain their passivity was investigated.

The critical current density for all materials again decreased with the increase in molybdenum content, and at the same time the primary passivation potentials became more negative. The relationship among molybdenum content, critical current density, and primary passivation potential is shown in Fig. 7.

Potentiodynamic studies in sulfuric acid + sodium chloride solution.—Typical potentiodynamic polarization curves for ferritic stainless steels in the 1*N* H_2SO_4 medium and the 1*N* H_2SO_4 + 0.1*N* NaCl medium are given in Fig. 8, which shows that the critical current density is increased by the addition of the chloride ion

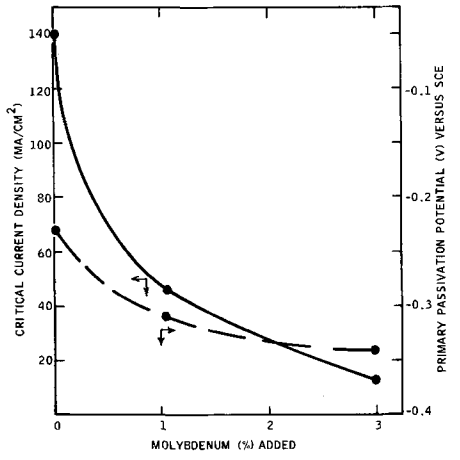

Fig. 7. Effect of molybdenum additions to the 17% chromium alloy on the critical current density and primary passivation potential in 1*N* hydrochloric acid at 29.6°C.

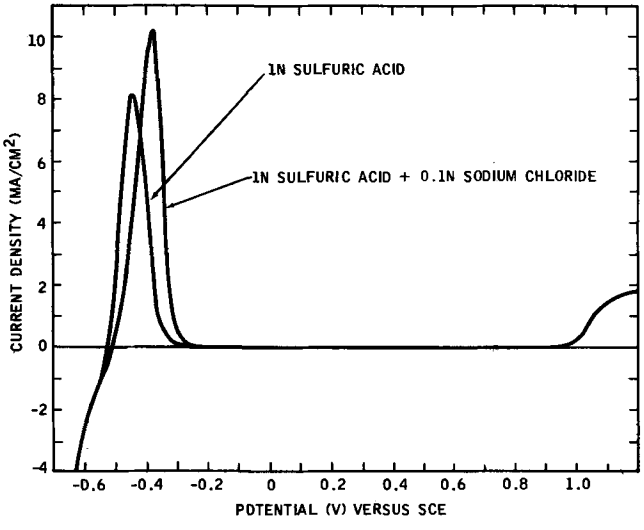

Fig. 8. Potentiodynamic polarization curves for Type 430 stainless steel in 1*N* sulfuric acid and in 1*N* sulfuric acid + 0.1*N* sodium chloride at 29.6°C (unmasked electrodes).

to sulfuric acid; however, this increase is caused by the shift of the primary passivation potential in a noble direction due to the activation effect of the chloride ions. At a given potential up to the primary passivation potential for pure acid, the dissolution rates of Type 430 stainless steel were lower in the chloride-containing acid than in pure acid. This inhibiting effect of chloride ions on anodic dissolution was similar to that reported by Bockris *et al.* (4) for pure iron. Furthermore, in the 1*N* H_2SO_4 + 0.1*N* NaCl solution, the passive range terminated at the same potentials as in the 1*N* H_2SO_4. Similar polarization behavior was observed for Type 434 and all 17% chromium alloys.

Discussion

Pitting potentials in 0.1N hydrochloric acid.—The examination of the average pitting potentials for the 17% chromium alloys (Table IV) discloses that, as the molybdenum content is increased, pitting potentials become more noble (*i.e.*, the resistance toward pitting corrosion increases with the molybdenum content). Since a normal transpassive transition was obtained for the 17% Cr-3% Mo alloy, this material should be immune to pitting corrosion under the experimental conditions. However, Types 430 and 434, which are commercial counterparts of the 17% chromium and 17% Cr-1% Mo alloys, have significantly lower pitting potentials. This difference in pitting potentials is probably the result of the higher carbon levels and impurity contents of commercial steels, as compared with the vacuum-melted laboratory alloys. Furthermore, the average pitting potential for the Type 434 steel is only slightly higher than the pitting potential for the Type 430 steel. The difference in pitting potential was much more in the 17% chromium and 17% Cr-1% Mo alloys. Since the carbon level for the Type 434 sample used in this investigation was considerably higher than that for the Type 430 sample [*i.e.*, 0.069 as compared with 0.046% (Table I)], it may be concluded that the higher carbon level obscured the effect of molybdenum on pitting potential. Higher carbon content in a ferritic matrix will result in more precipitated chromium and molybdenum carbides and in a depletion of the matrix of chromium and molybdenum. Consequently, the ferritic steels with higher carbon contents will probably have a greater sensitivity to pitting corrosion.

The examination of the pitting potentials for the 18% Cr-2% Mo ferritic alloys, with a carbon content of about 0.03%, leads to the conclusion that small nickel additions (up to 1%) do not affect the pitting potentials of these alloys. In contrast to the insensitivity to small additions of nickel, small additions of titanium have a very pronounced effect on pitting potentials. Titanium contents of 0.47 and 0.91% raised the pitting potential above the transpassive transition. A further increase in titanium to about 1.8% reduced pitting potential. Pitting potentials for titanium-modified alloys, however, are still more noble than for titanium-free alloys. This effect of titanium could be indirect. The titanium ties up carbon and nitrogen, preventing the formation of chromium and molybdenum carbides and nitrides and, consequently, prevents the formation of zones depleted in chromium and molybdenum. With larger titanium additions, the considerable amount of second phase that develops might be the preferred site for pitting attack.

The pitting potential for the 18% Cr-2% Mo-0.03% C alloy was about the same as that for the high-purity 17% Cr-1% Mo-0.002% C alloy, and was significantly more noble than that for either Type 430 steel or the high-purity 17% chromium alloy. Thus, in the 17% chromium steels with commercial carbon levels, the increase of molybdenum content to 2% should result in considerably improved resistance to pitting corrosion.

The values of pitting potentials are significantly influenced by experimental techniques (5, 6). In work with molybdenum-containing austenitic stainless steels, a fast potential scanning rate was a more severe experimental condition than a slow scanning rate (7). Consequently, the instantaneous potential rise from the active corrosion potential to a selected passive potential would be one of the most severe experimental conditions for the potentiostatic pitting studies. That the 17% Cr-3% Mo alloy could be pitted by the above method implies that all the materials investigated would pit under conditions of instantaneous potential jump. Thus, the results from the potentiodynamic pitting studies would at best predict only a relative order of resistance to pitting corrosion, but would not necessarily determine the immunity to pitting at a given chloride ion concentration and temperature.

Polarization studies in hydrochloric acid.—The results of the critical current density and primary passivation potential determination in 0.1*N* and 1.0*N* HCl are consistent with previous measurements in H_2SO_4, *i.e.*, molybdenum decreases the critical current density required to produce passivity and, to a lesser extent, shifts the primary passivation potential to more active potentials (1). Thus, molybdenum additions facilitate the attainment of the passive state for ferritic stainless steels in HCl. This effect was especially pronounced in 1*N* HCl for high-purity alloys (Fig. 6). In this series, only alloys containing molybdenum could be completely passivated in 1*N* HCl, *i.e.*, the current densities for masked electrodes decreased to between 10^{-6} and 10^{-7} amp/cm² at some potential beyond the pri-

mary passivation potential. In contrast to such pure alloys as 17% chromium alloy, the commercial Type 430 did not show a critical behavior in 1*N* HCl, and Type 434 showed little tendency to passivate (Fig. 5). This behavior is probably the result of the depletion of the ferritic matrix of chromium and molybdenum by the precipitation of carbides.

Small nickel additions to 18% Cr-2% Mo alloys were somewhat beneficial to the attainment of passivity in 0.1*N* HCl, since these additions depressed the critical current density to the point where no active region was displayed. However, results from work on austenitic stainless steels (7) showed that an 18% Cr-16% Ni alloy free of molybdenum could not be completely passivated in 1*N* HCl, but a similar alloy containing molybdenum could be. Thus, the beneficial effects of small nickel additions to ferritic stainless steel in HCl may be limited to the molybdenum-containing grades.

Polarization studies in HCl solutions revealed that HCl is an effective medium for the potentiodynamic investigation of the effects of alloying elements on the corrosion and passivation properties of stainless steels. The effects of molybdenum additions are very dramatically shown by polarization curves in 1*N* HCl; it is expected than any alloying addition which has a strong effect on the passive film will also have a pronounced effect on the active-passive transition in HCl. Polarization curves in 0.1*N* HCl, especially with the 17% chromium alloy, were characterized by considerable variations in critical current density and primary passivation potential. Such behavior would probably result from the competition of the normal tendency of the alloy to passivate in a weakly acidic medium with the activating effect of the chloride ions. Stainless steels with relatively weak passivation tendencies would therefore be expected to have a more prominently variable passivation behavior than steels with a strong passivation tendency. The active-passive transition region in 0.1*N* HCl was often complicated by the presence of two current density maxima. Since measured current is the difference between the total oxidation and total reduction current, the small secondary current maxima might arise from the changing hydrogen evolution kinetics, which are the result of the passivation of the electrode surface. However, large secondary peaks observed with Type 430 steel could not be explained. Since the potential for either peak is fairly reproducible, the double-peak phenomenon for the Type 430 steel might result from the chromium segregation and different passivation behavior of chromium-rich and chromium-depleted regions. For the Type 434 steel, which has a stronger passivation tendency, the second peak is only slightly indicated (Fig. 1). Some support for the above speculation is given by the work of Voeltzel and Plateau (8) who observed a double-peak phenomenon for sensitized austenitic 18% Cr-8% Ni stainless steel. The double-peak phenomenon was ascribed to chromium depletion along the grain boundaries.

None of the ferritic stainless steels studied was immune to crevice corrosion in HCl, not even those which had a high resistance to pitting.

Polarization studies in sulfuric acid-sodium chloride solution.—Since a complete passive range was obtained for all the materials studied, the results from potentiodynamic polarization studies in 1*N* H_2SO_4 + 0.1*N* NaCl indicate that sulfate ions in the $SO_4^{=}:Cl^-$ molar ratio of 5:1 inhibit pitting corrosion. The inhibiting effect of sulfate ions on chloride pitting of austenitic steels has been described in the literature (5, 9). This investigation showed that pitting corrosion of ferritic stainless steel can also be inhibited by sulfate ions. Furthermore, since crevice corrosion was very prominent in 0.1*N* HCl, it may be concluded that sulfate ions suppress the crevice corrosion to the extent that a normal transpassive transition can be obtained with a potential scanning rate of 0.540 v/hr.

Summary

Molybdenum additions to ferritic stainless steels facilitated the attainment of passivity in 0.1 and 1*N* HCl.

The pitting potential in 0.1*N* HCl became more noble with increased molybdenum content for high-purity 17% chromium alloys and with increased titanium content for 18% Cr-2% Mo-0.03% C alloys. An increase in carbon content generally resulted in less noble pitting potentials, whereas small nickel additions (up to 1%) did not change the pitting potential significantly.

All the ferritic stainless steels studied were very sensitive to crevice corrosion in HCl.

The sulfate ions, in a molar ratio of $SO_4^{=}:Cl^-$ of 5:1 not only inhibited pitting corrosion but also suppressed crevice corrosion for all the steels investigated.

Manuscript submitted Sept. 16, 1968; revised manuscript received Feb. 3, 1969. This paper was presented at the Chicago Meeting, Oct. 15-19, 1967, as Paper 60.

Any discussion of this paper will appear in a Discussion Section to be published in the December 1969 JOURNAL.

REFERENCES

1. E. A. Lizlovs, *Corrosion*, **22**, 297t (1966).
2. W. Schwenk, *2nd International Congress on Metallic Corrosion*, NACE, Houston, Texas, 256 (1966).
3. N. D. Greene, W. D. France, Jr., and B. E. Wilde, *Corrosion*, **21**, 275 (1965).
4. J. O'M. Bockris, D. Drazic, and A. R. Despic, *Electrochim. Acta*, **4**, 325 (1961).
5. G. Herbsleb, *Werkstoffe und Korrosion*, **16**, 929 (1965); **17**, 649 (1966).
6. H. P. Leckie and H. H. Uhlig, *This Journal*, **113**, 1262 (1966).
7. A. P. Bond and E. A. Lizlovs, *ibid.*, **115**, 1130 (1968).
8. J. Voeltzel and J. Plateau, *Compt. rend.*, **254**, 1791 (1962); **256**, 2156 (1963).
9. C. Trabanelli and F. Zucchi, *Corrosion et Anticorrosion*, **13**, 207 (1965).

On the Passivity of Iron-Chromium Alloys

II. The Activation Potential

Robert P. Frankenthal*

Edgar C. Bain Laboratory For Fundamental Research, United States Steel Corporation, Research Center, Monroeville, Pennsylvania

ABSTRACT

Precise potential control and measurement have permitted the determination of the primary activation potential, E_a, of an Fe-24% Cr alloy in 2*N* H_2SO_4 to within ± 0.5 mv and the determination of the kinetics of passivating film growth at this potential, as well as at other potentials. Small changes in potential give rise to large differences in film thickness. From the time dependence of the anodic current and the film thickness during passivation, a theory for the primary passivation process is proposed based on different rates of dissolution and different degrees of passivation at various types of surface sites, *e.g.*, kinks, ledges, and terraces; these differences arise from distinct activation energies for anodic dissolution and distinct adsorption energies associated with each type of site. The steady-state film thickness at the activation potential, as measured by cathodic reduction, is 0.36 ± 0.03 mC/cm² and corresponds to between one and three monolayers of film depending on the assumed model of a monolayer and the reduction product. Finally it is shown that secondary film formation can occur at the activation potential after sufficiently long times of passivation.

In an earlier paper (1) it was shown that on an Fe-24% Cr alloy in H_2SO_4 at least two distinct, potential-dependent films are formed during the passivation process. It was concluded that the primary passivation process is phenomenologically reversible; that the primary film is responsible for the initial passivation and is stable only within a few millivolts of the primary activation potential, E_a, defined as the reversible minimum in the cathodic loop (Fig. 2); and that the thickness of the primary passivating film corresponded to no more, and probably less than one $O^=$ ion per surface metal atom. The secondary film, on the other hand, forms at more positive potentials, grows to a thickness greater than 10^{-7} cm and, with increasing time and potential, becomes very stable and resistant to reduction. In this paper we consider in more detail the passivation process and the passivating film at the primary activation potential. We also emphasize the importance of controlling and measuring potentials very precisely (at least to ± 0.5 mv) to obtain reliable and meaningful mechanistic data. It will also be shown that the primary activation potential and the Flade potential (2) are not synonymous as is frequently assumed (3) and that the Flade potential is strictly a kinetic potential and not a thermodynamic one as is frequently assumed (3).

Experimental

The alloy investigated was a high-purity, vacuum-melted, ferritic Fe-24% Cr alloy which has the following analysis: Cr, 23.8%; C, 0.0075%; N, 0.0068%; O, 0.050%; P, <0.005%; S, 0.004%; Si, <0.01%; Al, <0.005%; Cu, <0.01%; Mg, <0.001%; no other elements were detected. The electrodes were machined as previously described (4) and then annealed for a week at 800°C and quenched in water. To remove any scale and to obtain a uniform surface, they were electropolished according to Sewell *et al.* (5).

The glass cell had two concentric compartments connected by four 2-mm diameter fine porosity frits. The outer compartment housed the auxiliary electrode and the inner compartment, the test electrode. A Luggin capillary connected the inner compartment to a hydrogen reference electrode. A solution reservoir was connected to the cell so that fresh de-aerated solution could be introduced into the cell whenever desired. This vessel, as well as both compartments of the cell, was fitted with a bubbler through which helium was continuously passed. The helium was prepurified by passing it over CuO at 440°C, through a liquid nitrogen cold trap, through an activated charcoal cold trap also at liquid nitrogen temperature, and through a bubbler containing doubly distilled water.

The electrolyte was 2*N* H_2SO_4 (*p*H 0.02) prepared from reagent-grade acid and doubly distilled water (resistivity >4 Mohm-cm). In certain experiments the solution was further purified by passing it over activated charcoal as described by James (6) and Barnartt (7). All experiments were conducted at 24°C.

A schematic circuit diagram is shown in Fig. 1. A Wenking potentiostat was used with an external potential programmer. For rapid switching from one potential to another, mercury-wetted contact relays (C. P. Clare & Company HG-1002) with switching times in the microsecond range were used. Potential measurements were made with an Orion pH-meter, the output of which was connected to a Honeywell Electronik 19 recorder, *vs.* a hydrogen electrode in the same solution and are reported relative to the standard hydrogen electrode (SHE). Current was followed by measuring the potential drop across a precision resistor (0.1%) with an oscilloscope or recorder. All potentials were controlled and measured to better than ± 0.5 mv.

Film thicknesses were measured by coulometric reduction with a standard amperostatic circuit consisting

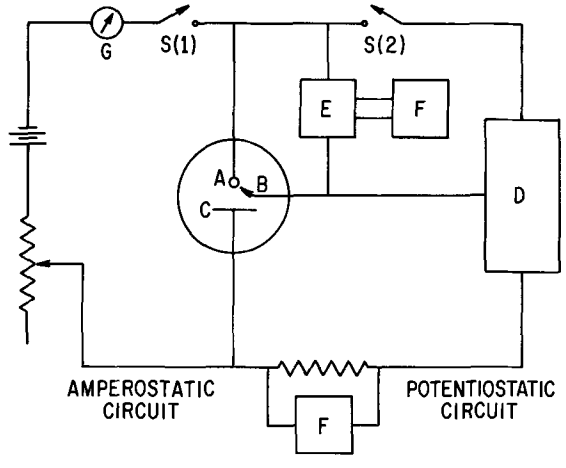

Fig. 1. Schematic circuit diagram: A, test electrode; B, reference electrode; C, auxiliary electrode; D, potentiostat; E, pH-meter; F, recorder; G, ammeter; S, switch.

* Electrochemical Society Active Member.

of a 45v battery and a high resistance to give a constant current density of 1 μa/cm^2 for film reduction. In practice switch S-1 would be closed before S-2 was opened, the potentiostat compensating for the cathodic current introduced by the reduction circuit; this insured that when S-2 was opened, reduction of the film would begin instantaneously with no possibility of side reactions during time at open circuit. The end point for the reduction was taken as the inflection point in the potential-time (E-t) curve. The total current used consisted of the film reduction current plus the hydrogen evolution current at E_a[1] (1). The film reduction potential lies 15 mv negative of E_a and the correction for the hydrogen evolution current should have been slightly greater. As a result the film thicknesses reported may be slightly high.

The real surface area of an electrode was determined by measuring its capacitance at +0.300v and comparing it to the capacitance of an electropolished and cathodically reduced specimen at the same potential, the surface roughness factor of which is assumed to be 1.0. Measurements were made with an a-c bridge (8) at frequencies between 5 and 10 kHz, a region free of frequency dispersion effects. The measured roughness factors were generally between 1.1 and 1.4. All calculations in this paper are based on the real surface area determined in this manner.

The normal operational sequence for any one experiment was as follows. The surface was cathodically reduced at —0.5v and then anodically dissolved at the potential corresponding to the maximum anodic current density, —0.205v; the electrolyte solution was flushed out by fresh solution; the specimen was put on open circuit and allowed to come to its corrosion potential, which normally required about 5 sec; finally the potential was switched to that to be studied. This procedure gave the most consistent and reproducible results. It was found that the cathodic reduction step could be omitted in between experiments in which the specimen was not exposed to the air or to very positive potentials at which thick films grew. Satisfactory cleaning was evidenced by an anodic current density of 28 ma/cm^2 during the dissolution step and by a corrosion potential of —0.261 ± 0.001v. In those experiments in which no secondary film growth was expected, reproducibility of the film reduction potential to within 1 mv was also used as a criterion for an initially clean surface. For a surface that had not been cleaned satisfactorily, the reduction potential was always more negative.

Changing the electrolyte solution between passivation and cathodic reduction was found to have no effect on either the measured film thickness or on the E-t curves for film reduction.

Results

The potentiostatically determined steady-state polarization curve (E-i curve) for this system is shown in Fig. 2. If the potential is not permitted to exceed the primary activation potential, E_a, by more than 5 mv, that section of the E-i plot given by the solid line is measured and exhibits no hysteresis. However, the dashed section always shows a hysteresis (1); the curve in Fig. 2 was measured by changing the potential from negative to positive values. The negative current (cathodic loop, indicated by the discontinuities in the curve) is due to the evolution of hydrogen. The primary activation potential has previously (1) been defined as the potential at which the first increase in the anodic current is observed in going from the passive region into the anodic loop under conditions of reversibility. This corresponds to the minimum in the cathodic loop and lies between —0.108 and —0.109v for this system.

Behavior on open circuit.—If the specimen is potentiostated at a potential slightly negative of E_a, *e.g.*, at —0.111v, until a steady-state current is reached and

[1] 2.3 μA/cm^2.

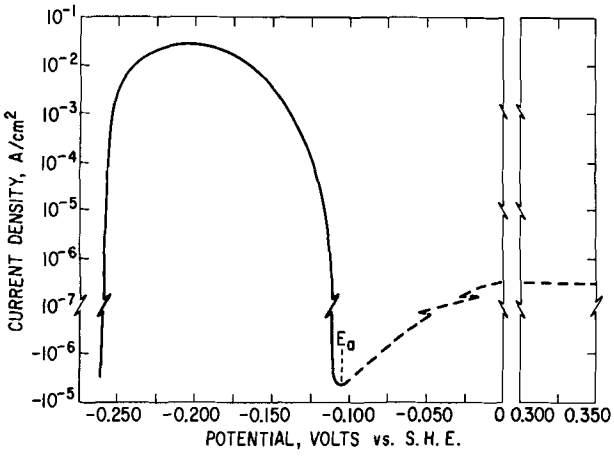

Fig. 2. Potential-current curve for Fe-24% Cr in 2N H_2SO_4. E_a is the primary activation potential. Solid line is region of reversibility; dashed line is region of irreversibility.

then the potentiostat is disconnected so that the specimen is on open circuit, the potential decays to the active state exhibiting a classic Flade potential (2, 9) at the potential at which the specimen had been potentiostated. However, if the specimen is held at a potential positive to E_a until a steady-state current is achieved and then is put on open circuit, the specimen will remain passive and the potential will slowly drift to a value between —0.05 and —0.08v. After passivation at E_a the potential will drift in neither direction on open circuit. At first it appeared that this may provide another definition of the activation potential; however, when these experiments were repeated in the solution purified by passing it over charcoal, the potential corresponding to no drift on open circuit shifted a few millivolts in the negative direction. However, the activation potential as determined by the minimum in the cathodic loop was unaffected by the purification.

Transient phenomena during passivation.—The anodic current-time (i-t) transient (Fig. 3) was obtained by subtracting the steady-state hydrogen-evolution current from the observed i-t curve after switching the potential from the corrosion potential to E_a. Due to iR-drops between the specimen surface and the tip of the Luggin capillary, the potential at the surface differed from E_a by more than 1 mv during the initial half second. At any time during the transient, the thickness Q (in mC/cm^2) of the film formed up to that time could be measured by cathodic reduction. Typical cathodic reduction curves (E-t plots) are shown in Fig. 4 for different times of passivation. The thickness-time (Q-t) transients calculated from the reduction curves are shown for three potentials in Fig. 5. None of the curves shown in Fig. 3-5 was affected by the charcoal

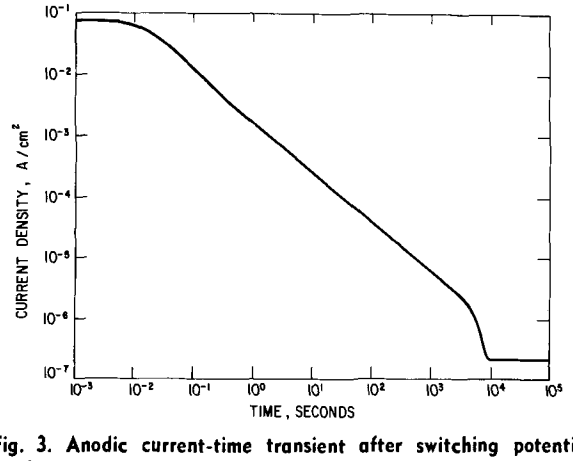

Fig. 3. Anodic current-time transient after switching potential from the corrosion potential to E_a.

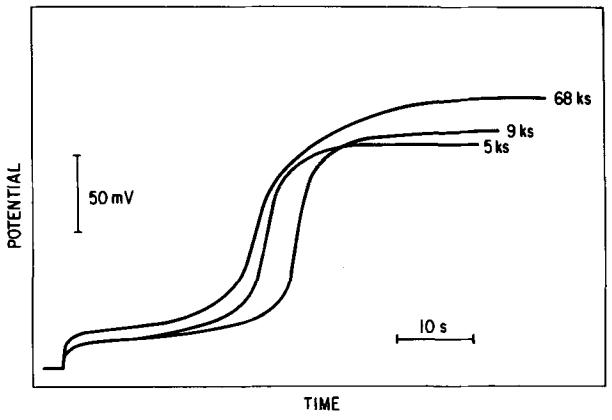

Fig. 4. Cathodic reduction potential-time curves after passivation at E_a for different periods of time. Time of passivation is given next to each curve.

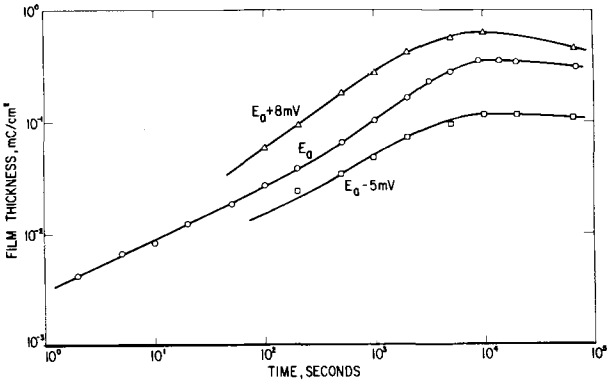

Fig. 5. Film thickness-time transients at three potentials, illustrating large effect of a small potential change on the film thickness. Passivation potential is indicated on each curve.

purification procedure so it was generally omitted. A complete material balance between the quantity of metal going into solution and that going into the film was not made because the former quantity is 10^2 to 10^3 times greater than the latter quantity.

To determine whether perhaps more than one reducible film was formed at E_a, the cathodic reduction was allowed to proceed for a time equivalent to the passage of 54 mC/cm^2. No additional break in the E-t curve was observed, indicating that no other reducible species was present on the surface. In an experiment to determine whether all the film formed during the passivation process was being reduced, the potential was switched to E_a immediately after film reduction was completed, as evidenced by the E-t curve, and the i-t transient was recorded. There was essentially no difference between this i-t transient and that obtained after the normal cleaning procedure.

The film reduction potential, the initial potential on the first plateau at which the E-t curve is linear, was measured after passivating the specimen for 9000 sec at E_a as a function of the cathodic current density for reduction and a plot of these data is shown in Fig. 6. The extrapolation to $i = 0.00$ μa/cm^2 intersects the abscissa at —0.107v, or within 1 to 2 mv of E_a.

Discussion

Activation potential.—The previously determined value of the primary activation potential (1) has been confirmed in this study in which more careful potential control and measurements were accomplished. When the surface was carefully prepared, as described, E_a was always within the limits indicated, namely, —0.108 to —0.109v; deviations from this could always be traced to improper surface treatment. The reproducibility of this value over many experiments also indi-

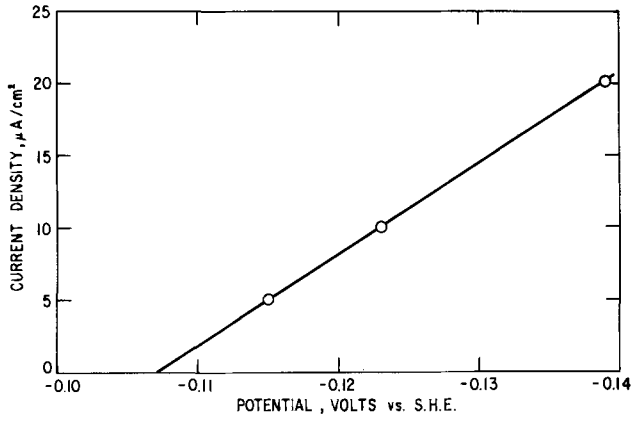

Fig. 6. Plot of film reduction potential against the current density for reduction, illustrating linear polarization kinetics.

cates that the surface composition of the specimen remained constant. To illustrate this point better, it may be pointed out that an Fe-19% Cr alloy has an activation potential of —0.036v in the same solution, a 72 mv difference for a 5% change in Cr content.

The results of the experiments in which the potential decay was followed on open circuit show that in this system the primary activation potential and the Flade potential are not the same. Furthermore, the variation of the Flade potential with purity of the solution indicates that this potential is a kinetic one and not a thermodynamically reversible potential, contrary to what is frequently stated, *e.g.*, ref. (3).

Validity of film thickness measurements.—Before the data can be interpreted, it is necessary to establish that the cathodic reduction procedure measures all the film present. If it is assumed that no film is present at the corrosion potential, then no reducible film other than that measured can be present at potentials between the corrosion potential and E_a because only one break is observed in the E-t curves even when the reduction was permitted to continue for long times. A film with a more negative reduction potential than the hydrogen evolution potential, *i.e.*, the final potential plateau after all film is reduced (Fig. 4), can also be discounted because the hydrogen evolution potential is approximately equal to the corrosion potential at the current densities used for reduction; also if the film were formed at a potential positive of the corrosion potential, but reduced at a more negative potential, we would not observe the reversibility reported, especially in the experiment in which the potential was switched to E_a immediately after film reduction and the i-t transient was observed to be the same as with a clean surface. This same experiment also eliminates the possibility of the formation of a nonreducible film.

A prepassive film, such as might be formed by a dissolution-precipitation mechanism as suggested by Bockris, Reddy, and Rao (10), also does not appear reasonable for this system for several reasons: (*i*) if the prepassive film is converted entirely into the passivating film, then the former must also be of monomolecular dimensions, which is most unlikely for a precipitate; (*ii*) if only part of it is converted, the remainder must either be reducible or nonreducible, possibilities which have been discussed above; (*iii*) after polarizing the specimen at —0.205v, a potential at which the prepassive film would exist, and then putting the specimen on open circuit, the corrosion potential is stabilized within ± 0.1 mv in 5 sec, hardly sufficient time for a film to dissolve and all concentration effects to disappear.

We cannot exclude the possibility that a film forms at potentials negative to the corrosion potential. If so, this film would be present at the corrosion potential prior to the transient experiments. However, it is of no importance because it does not appear to prevent anodic dissolution at potentials in the anodic loop. It

cannot be argued that this film may cover part of the surface and that the passivating film covers the rest because electron microscope examination of the surface shows that it etches uniformly in the region of anodic dissolution (1). Thus we must conclude that it is most unlikely that any film other than that measured is involved in the passivation process at E_a. We also believe that the only cathodic side reaction occurring during film reduction is hydrogen evolution, for which a correction has been made, and hence the remaining current goes solely for film reduction with 100% efficiency because (*i*) the *E-t* reduction curves are very sharp and (*ii*) a linear relationship between the reduction current and potential is observed (Fig. 6) and the extrapolation to zero current comes within 1 mv of E_a. It is highly unlikely that this linear relationship would be followed if side reactions were occurring (11). Self-activation has previously (1) been shown not to be a factor. This was again confirmed in this study when it was found that the film thickness is independent of the current density for cathodic reduction.

Steady-state film thickness.—The limiting film thickness at the primary activation potential is 0.36 ± 0.03 mC/cm² (Fig. 5). The time to achieve this thickness is the same as the time to reach the limiting passive current density (Fig. 3). The apparent decrease in film thickness at longer times at all potentials (Fig. 5) is not real but due to secondary film formation to be discussed below. The deviation of ± 0.03 mC/cm² represents the measured extremes and not the standard deviation, which is much less. We believe this deviation to be due primarily to poor potential control which was generally to within 0.2 to 0.3 mv, although as much as 0.5 mv was tolerated. As may be seen from the curves in Fig. 5, small deviations in potential can give rise to large differences in film thickness. The coulombic equivalent of a monolayer depends on the model chosen for the structure of that monolayer. Assuming the film to be composed primarily of Cr^{+++} and $O^{=}$ ions, reasonable limits for the thickness of a monolayer are 0.4 to 0.7 mC/cm². Inclusion of H_2O, $SO_4^{=}$, or HSO_4^{-} in the film would reduce these values slightly, again depending on configuration. If the passivating film is reduced to the metallic state, *i.e.*, $Cr^{+++} \rightarrow Cr^0$, the measured coulombic film thickness would represent about one monolayer. The reduction to the metallic state seems unlikely because the standard potential for this reaction is —0.74v (12). It is more reasonable to assume that the reduction product is chromous ion soluble in solution.[2] In that case the measured coulombic film thickness corresponding to a monolayer would be 0.13 to 0.23 mC/cm². From this we conclude that the measured limiting film thickness at E_a, 0.36 mC/cm², is equivalent to between 1 and 3 monolayers of film.

Since the reduction potential of the film is constant for thicknesses from 0.02 to 0.36 mC/cm², the structure and composition of the film must be the same throughout this thickness range from fractional to full coverage. Therefore, in the following section on transient behavior we will treat film formation at E_a as an adsorption process, realizing that at complete coverage the film may be thicker than one monolayer.

Transient behavior.—We assume that the limiting thickness of 0.36 mC/cm² represents complete coverage of the surface, *i.e.*, $\theta = 1$, where θ is the fraction of the surface covered. By combining the *i-t* curve from Fig. 3 with the *Q-t* curve from Fig. 5 and converting the coulombic thickness to fractional coverage, a plot of current *vs.* coverage is obtained (Fig. 7). It is seen that a very small coverage affords a high degree of protection. For example, for $\theta = 0.011$ the current is

[2] If the reduction product is chromous chromium, it must be soluble in solution because a corrosion product on the surface is inconsistent with the reproducibility of the *i-t* curve on rapid switching back to E_a after cathodic reduction, as well as for other reasons mentioned in the section on the validity of the film thickness measurements.

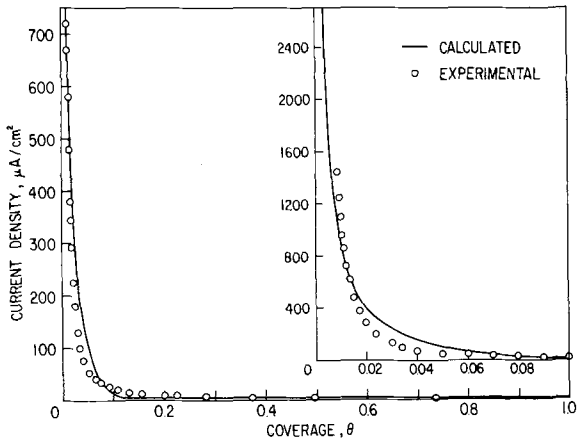

Fig. 7. Effect of surface coverage on the anodic current density at E_a, illustrating large drop in current density with initial coverage. ——— calculated from theory; o - experimental data. Insert is expanded plot of low coverage region.

reduced to 1% of its initial value of 85 ma/cm². This may be explained on an atomistic and kinetic basis.

Anodic dissolution occurs with different rates at different types of surface sites, *e.g.*, kinks, ledges, and terraces (*k*, *l*, and *t*) (13), the rate being governed by the activation energy for the anodic process at that type of site and by the potential, which is independent of the type of site. The current, *i*, may be expressed as the sum of the currents from the different types of sites

$$i = Af(E) \sum_j i_j \, (n_j, \Delta G_j^{\ddagger}) \qquad [1]$$

where $f(E)$ is an exponential function of the potential E, i_j is the current from the *j*th type of site which is a function of the number n_j of that type of site available for anodic dissolution and the activation free energy $\Delta G_j^{\ddagger}$ for anodic dissolution from that type of site, and A is a constant. The passivation process is the deactivation of these sites due to adsorption of, or chemical reaction[3] with, the passivating species; the extent of passivation of any one type of site relative to another type of site depends on the relative adsorption energies of the passivating species at these types of sites. Thus to calculate the variation of i with θ, we must first determine the variation of n_k, n_l, and n_t with θ. We will now treat these ideas quantitatively.

From Parsons (14) we can express the anodic current by

$$i = A \exp\left[-\frac{\Delta G^{\ddagger}}{RT} \right] \exp\left[\frac{(1-\beta) z\mathbf{F}}{\nu RT} E \right] \qquad [2]$$

where $\Delta G^{\ddagger}$ is the activation free energy for the dissolution process, β is the transfer coefficient, ν is the stoichiometric number, and R, T, z, and $\mathbf{F}$ have their usual significance.

Consider a surface atom in a terrace position to be in the standard state. An atom in a ledge position possesses greater free energy and an atom at a kink site still greater free energy, because they form fewer bonds with the substrate. Conversely, the order of the activation energies for dissolution $\Delta G^{\ddagger}$ is

$$\Delta G_k^{\ddagger} < \Delta G_l^{\ddagger} < \Delta G_t^{\ddagger}$$

since the activated state is the same for dissolution from all sites. Combining Eq. [1] and [2] we obtain

$$i = A \exp\left[\frac{(1-\beta) z\mathbf{F}}{\nu \, RT} E \right] \sum_j n_j \exp\left[-\frac{\Delta G_j^{\ddagger}}{RT} \right] \qquad [3]$$

The most prevalent sites on a surface are kink, ledge, and terrace positions. Since $\Delta G^{\ddagger}$ is expected to increase with increasing number of nearest and second-nearest

[3] In this treatment we assume chemisorption, although a completely analogous treatment would follow if we assumed chemical reaction. In that case reaction free energies would be substituted for adsorption free energies.

neighbors and since for each type of site these vary with the orientation of the surface (15), the number of terms in the summation will be larger than three. As an approximation, however, we will consider only one term for each k, l, and t.

Next we evaluate the variation of the n_j's with coverage, θ. Initially at $\theta = 0$, $n_j = n_j^o$ and we assume $n_t^o = 10^{15}/cm^2$, $n_l^o = 10^{14}/cm^2$, and $n_k^o = 10^{11}/cm^2$ (16). As θ increases, the ratio of $n_t : n_l : n_k$ will change due to the different adsorption energies of the passivating species at the different types of sites.[4] Since almost all the passivation occurs during the first few per cent surface coverage (Fig. 7), we can neglect interactions between adsorbed passivating species and assume that the Langmuir adsorption isotherm is obeyed for each type of site. We then define the activity of the passivating species adsorbed on a site of type j as

$$a_j = \frac{\theta_j}{1 - \theta_j} \qquad [4]$$

where θ_j is the fraction of j-sites covered, with the standard state, $a_j = 1$, being $\theta_j = \frac{1}{2}$. Assuming equilibrium between the adsorbed species regardless of the site, so that $\Delta G_k = \Delta G_l = \Delta G_t$ and remembering that

$$\Delta G_j = \Delta G_j^o + RT \ln a_j \qquad [5]$$

where ΔG_j and ΔG_j^o are the free energy of adsorption and standard free energy of adsorption, respectively, of the passivating species on the j-sites, we have

$$\frac{a_k}{a_l} = \exp\left[\frac{\Delta G_l^o - \Delta G_k^o}{RT}\right] \qquad [6a]$$

and

$$\frac{a_k}{a_t} = \exp\left[\frac{\Delta G_t^o - \Delta G_k^o}{RT}\right] \qquad [6b]$$

With

$$\theta = \frac{n_k^o\theta_k + n_l^o\theta_l + n_t^o\theta_t}{n_k^o + n_l^o + n_t^o} \qquad [7]$$

and using Eq. [3], [4], and [6], the i-θ relationship can be calculated if $\Delta G_j^\ddagger$ and ΔG_j^o are known, the constant A in Eq. [3] being evaluated from the measured current at time $t = 0$, when $\theta = 0$. It is not necessary to know the absolute values of the $\Delta G_j^\ddagger$'s but only the differences $(\Delta G_t^\ddagger - \Delta G_k^\ddagger)$ and $(\Delta G_l^\ddagger - \Delta G_k^\ddagger)$ since the value of $\Delta G_k^\ddagger$ can be subtracted from each $\Delta G_j^\ddagger$, taken outside the summation sign in Eq. [3] and included in the constant A. Neglecting changes in entropy which are small (13), the difference between $\Delta G_l^\ddagger$ and $\Delta G_k^\ddagger$ should to a first approximation be equal to the strength of a nearest neighbor bond, or about 12 kcal/mole. The actual difference will probably be lower because H_2O will adsorb more strongly at a kink site than at a ledge site, thereby lowering the free energy of initial state of a kink site more than that of the ledge site. Similarly the difference between $\Delta G_t^\ddagger$ and $\Delta G_l^\ddagger$ should also be less than the energy of a nearest-neighbor bond. For this reason both $(\Delta G_t^\ddagger - \Delta G_l^\ddagger)$ and $(\Delta G_l^\ddagger - \Delta G_k^\ddagger)$ were chosen equal to 9 kcal/mole, and $(\Delta G_t^\ddagger - \Delta G_k^\ddagger)$ then equals 18 kcal/mole. The differences $(\Delta G_l^o - \Delta G_k^o)$ and $(\Delta G_t^o - \Delta G_k^o)$ are more difficult to estimate. Fortunately, however, the results are not very sensitive to variations in these differences, and we arbitrarily chose $(\Delta G_l^o - \Delta G_k^o) = 4$ kcal/mole and $(\Delta G_t^o - \Delta G_k^o) = 8$ kcal/mole. Using the above values the i-θ relationship was calculated as indicated at E_a and compared to the experimentally determined relationship (Fig. 7). The agreement is considered very good.

For $\theta = 0.00$ the anodic current arising from dissolution at kink sites accounts for essentially all the current, *i.e.*, 85,000 $\mu a/cm^2$. The dissolution rate from ledge sites is only 25 $\mu a/cm^2$ and from terrace sites it is only 7.5×10^{-5} $\mu a/cm^2$ or for practical purposes nil. From this it is apparent that the values chosen for the parameters $(\Delta G_t^\ddagger - \Delta G_k^\ddagger)$ and $(\Delta G_t^o - \Delta G_k^o)$ are essentially of no consequence. These calculations were made for the potential E_a. However, even at $E = E_a + 0.2$v, the current from each type of site is increased by a factor of only 55 and the current from terrace sites is still essentially zero.

[4] The concept of preferential adsorption of impurities at active sites is not new (17, 18).

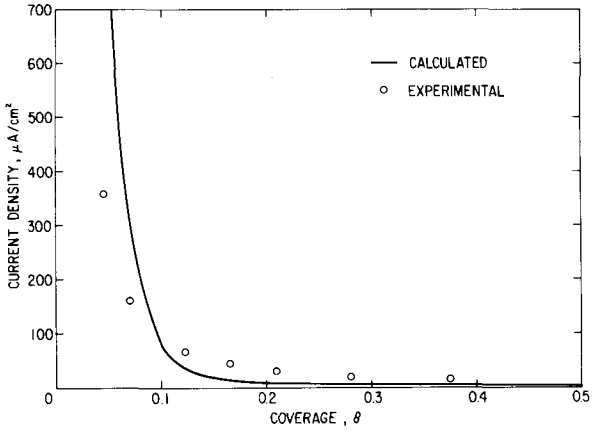

Fig. 8. Effect of surface coverage on the anodic current density at E_a + 100 mv. ——— calculated from theory; o - experimental data.

The effect of potential on the i-θ relationship arises through the factor $\exp\left[\frac{(1-\beta)\, z\mathbf{F}}{\nu RT} E\right]$ in Eq. [3]. Assuming $\beta = 0.5$ and $z/\nu = 1$, and keeping all other parameters constant, we have calculated the i-θ relationship at E_a + 100 mv. This relationship, as well as the experimental data at this potential, is shown in Fig. 8. The agreement between theory and experimental data is satisfactory. At potentials greater than E_a + 20 mv, this theory holds only up to coverages of about $\theta = 0.4$. At higher coverages secondary film formation occurs (19). At potentials above E_a + 200 mv there no longer is any agreement between the theory and the experimental data.

We realize that with the possibility of fixing four parameters $[(\Delta G_l^\ddagger - \Delta G_k^\ddagger), (\Delta G_t^\ddagger - \Delta G_k^\ddagger), (\Delta G_t^o - \Delta G_k^o)$, and $(\Delta G_l^o - \Delta G_k^o)]$, it is not too difficult to get a good fit. However, we have indicated above that the values chosen for two of these parameters are unimportant, and we point out that the same basic shape of the i-θ curve is obtained over a wide range of values of all these parameters. What is important is the basic shape, namely that the maximum decrease in the current occurs with very little coverage. This is a direct consequence of this theory in so far as it requires that almost all the current originates from a small fraction of the surface, the kinks, and that these same kinks are the sites for the initial and strongest adsorption. So while the exact values of the parameters may not be the best ones, the basic theory is in complete agreement with the experimental facts and the values chosen for the parameters have been justified.

Secondary film formation.—It was previously concluded (1) that secondary film formation only occurred at potentials greater than the activation potential. However, the more precise measurements made in the present study indicate that secondary film formation can occur at the primary activation potential and even at slightly lower potentials. This is evidenced by both the E-t curves for cathodic reduction (Fig. 4) and the Q-t curves for film growth (Fig. 5). In Fig. 4 it is observed that the film reduction potential is independent of the time of passivation up to 9000 sec, the time to achieve complete passivation. At longer times, however, the reduction potential increases and the apparent film thickness decreases (Fig. 4 and 5). This is due to the formation of the secondary film which cannot be completely reduced

(1, 19). These changes in reduction potential and film thickness are much more pronounced at higher potentials (19). At E_a the shift in the reduction potential is only about 4 mv at 65,000 sec, and the corresponding reduction in film thickness is about 0.05 mC/cm^2. While these changes are small, they are reproducible and always go together. This, together with the heightening of this effect at higher potentials, leads us to the conclusion that it is a real effect and due to secondary film formation. This will be discussed in more detail in a subsequent paper (19).

Conclusions

The primary activation potential for an Fe-24% Cr alloy in $2N$ H_2SO_4 has been determined to within ± 0.5 mv. It has been shown that the thickness of the passivating film in the potential neighborhood of E_a is very sensitive to small changes in the potential and that, therefore, very precise potential measurements and control are essential if meaningful kinetic measurements are to be made. The time dependence of both the anodic current and the film thickness has been measured, and a theory is proposed to account for the observed behavior. This theory considers different rates of anodic dissolution from kink, ledge, and terrace sites due to differences in the activation free energy associated with different numbers of nearest neighbors; these sites are also passivated to different extents due to different energies of adsorption. The steady-state film thickness of 0.36 mC/cm^2 at the primary activation potential corresponds to between one and three monolayers of film depending on the assumed model and the reduction product. Finally it is shown that secondary film formation occurs at E_a at long times.

Acknowledgments

The author wishes to thank Mrs. A. C. Broz for skillfully performing many of the experiments and Dr. S. Barnartt and Dr. R. A. Oriani for many helpful discussions.

Manuscript submitted Nov. 21, 1968; revised manuscript received ca. Feb. 6, 1969. This paper was presented at the Montreal Meeting, Oct. 6-11, 1968, as Paper 418.

Any discussion of this paper will appear in a Discussion Section to be published in the December 1969 JOURNAL.

REFERENCES

1. R. P. Frankenthal, *This Journal*, **114**, 542 (1967).
2. F. Flade, *Z. physik. Chem.*, **76**, 513 (1911).
3. K. J. Vetter, "Electrochemical Kinetics," English Edition, pp. 748-754, Academic Press, New York (1967).
4. H. W. Pickering and R. P. Frankenthal, *This Journal*, **112**, 761 (1965).
5. P. B. Sewell, C. D. Stockbridge, and M. Cohen, *Can. J. Chem.*, **37**, 1813 (1959).
6. S. D. James, *This Journal*, **114**, 1113 (1967).
7. S. Barnartt, *Can. J. Chem.*, May 1969.
8. H. W. Pickering, *This Journal*, **115**, 690 (1968).
9. U. F. Franck, *Z. Naturforsch.*, **4a**, 378 (1949).
10. J. O'M. Bockris, A. K. N. Reddy, and B. Rao, *This Journal*, **113**, 1133 (1966).
11. C. Wagner and W. Traud, *Z. Elektrochem.*, **44**, 391 (1938); S. Barnartt, *Corrosion Sci.*, in press.
12. W. M. Latimer, "Oxidation Potentials," 2nd ed., p. 247, Prentice-Hall, Inc., Englewood Cliffs, N. J. (1952).
13. W. K. Burton, N. Cabrera, and F. C. Frank, *Phil. Trans. Roy. Soc.*, **A243**, 299 (1951).
14. R. Parsons, *Trans. Faraday Soc.*, **47**, 1332 (1951).
15. J. F. Nicholas, "An Atlas of Models of Crystal Surfaces," Gordon and Breach, Inc., New York (1965).
16. D. A. Vermilyea, *This Journal*, **115**, 162 (1968).
17. J. J. Gilman, W. G. Johnston, and G. W. Sears, *J. Appl. Phys.*, **29**, 747 (1958).
18. M. B. Ives, *J. Phys. Chem. Solids*, **24**, 275 (1963).
19. R. P. Frankenthal, To be published.

A Capacitive Divider Technique for Fast Interface Capacitance Measurement

D. E. Aspnes

Bell Telephone Laboratories, Incorporated, Murray Hill, New Jersey

ABSTRACT

A fast method of measuring interface capacitance in electrolyte-semiconductor systems is presented and discussed. The interface capacitance is determined from the voltage response of the interface to a driving voltage applied across the interface and a small series capacitor which form a capacitive voltage divider. In particular, the differential capacitance, related to the derivative of the constant-current charging curve, is obtained directly if a pulse or square-wave driving voltage is used. A further advantage is that capacitance can be determined in shorter time intervals than required by previous methods. Experimental results which demonstrate the method are given for the intrinsic Ge-aqueous electrolyte system, and it is also shown that semiconductor surface fields can be determined in the presence of rapid modulations. Applications to electroreflectance are discussed.

Rapid measurement of the capacitance of semiconductor-electrolyte interfaces has yielded much useful information about processes which occur in both the space charge region of the semiconductor and in the response of slow and fast surface states on the semiconductor (1-6). The recent development of electroreflectance (7-8), in which the optical properties of a semiconducting crystal are modulated by a periodic, rapidly varying electric field in the space charge region (SCR), has placed new demands on capacitance measurement as a means for determining the surface field for the semiconductor in that capacitance measurements must now be performed in the presence of perturbations of the order of volts, repeating at kHz rates, if detailed information about the field variation during a modulation cycle is to be obtained. Various fast capacitance measuring methods have been developed. The first of these (9, 1, 2) utilized square wave current pulses which resulted in a linear charging curve to the extent that the interface could be represented as a constant capacitance. The constant current pulse technique has since been adapted to potentiostatic control (4), and voltage pulses have also been used successfully (5). The use of continuous sinus-

oidal potentials (10) or currents (11) is well-known. These methods are all adequate for capacitance measurement when the interface potential is changing relatively slowly in time (less than 1000 v/sec), but fail under the usual conditions of electroreflectance. In order to meet electroreflectance requirements, a simple method has been developed which permits the direct measurement of differential capacitance at frequencies in the megacycle range, appreciably higher than previously possible. It is easily adapted to either potentiostatic or galvanostatic control of the interface potential. In addition, the short-term time dependence of the interface differential capacitance can be obtained directly, in contrast to other methods which give an averaged value over a measurement cycle. The method and theory are discussed and followed by an application to the particular case of an intrinsic Ge-aqueous electrolyte interface.

Method and Theory

Measurement principle.—Interface capacitance can be obtained by constructing a capacitative voltage divider with the interface capacitance as one branch, as illustrated in Fig. 1. A typical electrolytic cell configuration is shown, with the control circuit at top center. The new features are shown at the left, and consist of a pulse or fast-rise square wave generator $V_i(t)$ driving a small injection capacitor C_i. The principle of the method is straightforward. Let the effective capacitance which describes the interface be denoted as C. Then the injection capacitor C_i and C form a capacitive voltage divider, and if $C_i << C$, a change ΔV_i in $V_i(t)$ injects a charge $\Delta Q \cong C_i \Delta V_i$ into C causing a voltage change $\Delta V_p \cong \Delta Q/C$ to appear at the probe. Therefore

$$C \cong C_i \frac{\Delta V_i}{\Delta V_p} \qquad [1]$$

Although any waveform $V_i(t)$ may be used, a pulse or square-wave time dependent source has particular advantages which will be discussed later. These follow from the fact that the total interface charge remains constant except when $V_i(t)$ is changing levels, at which time charge is injected into the interface [C_i is a high-pass filter element which differentiates $V_i(t)$]. The terminology "charge injection" refers to the capacitive divider technique when such sources are used. Before proceeding with a more detailed analysis, we note that the charge injection technique is closely related to the coulostatic method introduced and developed by Delahay (12), with the difference that the charge is injected into the interface as a result of a rapid potential change across the capacitive divider rather than by discharging a capacitor into the interface. In the limit of long pulse durations, charge injection and the coulostatic method are basically identical. Charge injection is also directly related to constant-current pulse methods (2, 4, 9), since in the linear approximation, the probe response is the derivative of the constant current charging curve, as will be shown.

Detailed treatment.—Having outlined the method, we now analyze it in detail with the objective of relating the probe output $V_p(t)$ to the interface parameters. For the purpose of obtaining interface capacitance, short pulse duration (<10 μsec) or high-frequency square-wave operation (>100 kHz) is preferred, hence we consider only the high-frequency behavior of Fig. 1. The approximate high-frequency equivalent circuit of Fig. 1 is given in Fig. 2. The source $V_i(t)$ is represented with an effective output impedance R_i. The injection capacitor C_i charges the interface effective capacitance C through the electrolyte and sample resistances R_e and R_s. The interface leakage is described by a conductance G, and the control circuit is represented by its high-frequency equivalent impedance Z_c.

The circuit of Fig. 2 can be simplified since the impedance levels of the various elements in general differ appreciably. With proper line termination, R_i will be one-half the generator output resistance, corresponding to the parallel combination of the generator output resistance and the equal line termination resistance (typically, $R_i = 25$ ohms). Either potentiostatic or galvanostatic control may be used, provided Z_c is sufficiently large (or well-determined) at high frequencies. Z_c is always large with galvanostatic control, and can be made large at high frequencies with potentiostatic control by inserting a large resistance R_o in series with the amplifier output (as indicated in Fig. 1) and reducing the response time τ_a of the control amplifier sufficiently, whence from simple circuit theory

$$Z_c \cong \frac{R_o}{1 + i\dfrac{g_o}{\omega_{\min}\tau_a}}, \quad \omega_{\min}\tau_a >> 1 \qquad [2]$$

where $\omega_{\min}$ is the lowest frequency component of $V_i(t)$ and the gain of the control amplifier is

$$g(\omega) = g_o/(1 + i\omega\tau_a)$$

Therefore, Z_c is neglected throughout. The cell resistance R_e and the bulk sample resistance R_s can usually be made of the order of ohms. R_s may include

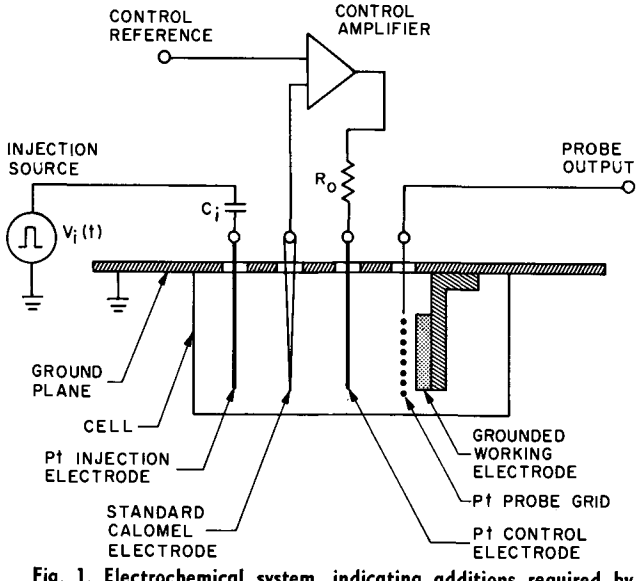

Fig. 1. Electrochemical system, indicating additions required by the capacitive divider technique at left. C_i is the injection capacitor, driven by the source $V_i(t)$. The working electrode is insulated to contact the electrolyte only in the region desired.

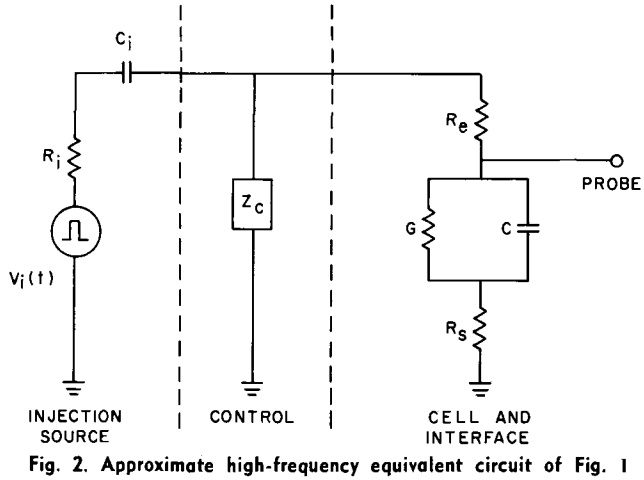

Fig. 2. Approximate high-frequency equivalent circuit of Fig. 1 for calculating the probe response. R_e = electrolyte resistance, R_s = sample resistance, Z_c = control circuit effective impedance; G and C describe the interface and space charge region admittance.

part of the electrolyte resistance, since the probe cannot be located arbitrarily close to the interface.

The interface admittance, represented in Fig. 2 as the parallel combination G and C, is quite difficult to treat in detail, depending on the constituents of the interface as well as on interface biasing conditions, history, and time. Although the following discussion applies in general to any interface, we will discuss explicitly only the semiconductor-electrolyte interface since the objective is to apply the results to these systems. Numerous complicated equivalent circuits have been proposed to describe the admittance of the semiconductor-electrolyte interface (1, 13). However, the problem is simplified considerably for frequencies in the megacycle range, since the most rapid dispersion in C generally occurs at appreciably lower or much higher frequencies, and the leakage conductance G becomes relatively less important. If the charge leakage through G is small, *i.e.*, if $G/C << \omega_{min}$, G is effectively zero and can be neglected. This relation is satisfied in usual capacitance measuring conditions, except when rapid electrochemical reactions occur at the interface. G can be measured independently, since it is approximately the slope of the low-frequency I-V characteristic (1).

The capacitance C is nearly equal to C_{scr}, the capacitance of the semiconductor space charge region (SCR). The Helmholtz capacitance C_h between the semiconductor and electrolyte and the Gouy capacitance C_g of the electrolyte space charge region are in series with C_{scr} so that

$$\frac{1}{C} = \frac{1}{C_{scr}} + \frac{1}{C_h} + \frac{1}{C_g} \qquad [3]$$

but since $C_h \sim 10$ to $20\ \mu f/cm^2$ is typically an order of magnitude larger than C_{scr}, and C_g for aqueous solutions of the order of 0.1M concentration is several times larger than C_h, it follows that $C \cong C_{scr}$. C_{scr} is frequently dependent, and also depends on the SCR potential unless $|\Delta V_{scr}(t)| << kT$, which is easily achieved experimentally. For intrinsic semiconductors, dispersion in C_{scr} occurs when the frequency becomes comparable to the reciprocal of the space charge relaxation time, $\tau_r \sim \epsilon/\sigma$ (14). At lower frequencies C_{scr} is equal to its equilibrium (15, 16) value. If a well-defined minority carrier is present, low-frequency dispersion results from the diffusion of the minority carrier between SCR and bulk, which has a relaxation time $\tau' = L_d^2/D_{min}$, where L_D is the minority carrier diffusion length and D_{min} is the minority carrier diffusion coefficient. If $\tau' >> 1/\omega_{min}$ the capacitance is approximately dispersion-free and may be obtained by dropping the minority carrier contribution to the equilibrium expression, provided an appreciable inversion region is not present (17, 18). Detailed treatments of dispersion in C_{scr} can be found in the literature (17, 18). It is sufficient to point out here that $C \cong C_{scr}$ can be related to SCR parameters such as surface field over a wide range of bulk properties, with the relation determined by the bulk properties. Fast surface states cause complications, but in many cases are not present and in any event can be detected since they produce an additional capacitance which tends to be much larger than the theoretical minimum capacitance of the SCR (17).

Neglecting Z_c and G, the time-dependent probe response $\Delta V_p(t) \cong \Delta V_{scr}(t)$ to a step change in driving potential $V_i(t) = V_o + \Delta V_i u(t)$, where $u(t)$ is the unit step function, is

$$\Delta V_p(t) = \Delta V_i \left\{ \frac{C_i}{C_i + C} + \left[\frac{R_s}{R_s + R_e + R_i} - \frac{C_i}{C_i + C} \right] e^{-t/\tau_c} \right\} \cong \Delta V_i \left\{ \frac{C_i}{C_{scr}} + \frac{R_s}{R_s + R_e + R_i} e^{-t/\tau_c} \right\} \qquad [4]$$

where $\tau_c = [(C_i C)/(C_i + C)](R_s + R_e + R_i)$ describes the decay of the charging transient not included in Eq. [1]. If G is not negligibly small, charge leaks from C_{scr}. This decay can be approximately represented by multiplying the right-hand side of Eq. [4] by $\exp(-Gt/C_{scr})$, where the decay time constant is $\tau_d = C_{scr}/G$.

An actual response $V_p(t)$ is shown in Fig. 3. This signal was obtained from an intrinsic Ge crystal in an aqueous electrolyte, biased near the flat band condition, and represents the response to one cycle of a 1.0 MHz square wave driving voltage $V_i(t)$ of peak-to-peak amplitude 2.6v. Further details of the cell, crystal, and electrolyte are given later. The circuit parameters are $C_i = 100$ pf, $R_i = 25$ ohms, $R_s \cong 5$ ohms, and $R_e \cong 20$ ohms. The small amount of decay following the initial transient in each half of the cycle indicates that G is small and C is independent of time, both to a good approximation. The space charge capacitance C_{scr} can be calculated by measuring ΔV_p as the voltage difference between the baseline defined by the value of $V_p(t)$ at the moment of level change in $V_i(t)$, at $t = 0$ and $t = 500$ nsec in Fig. 3, and the extrapolation of the flat portion of the response past the transient back to the time of level change. We find $\Delta V_p \cong 13$ mv, whence by Eq. [1], $C_{scr} = 0.020\ \mu fd/cm^2$ at this bias condition for the Ge crystal of 1.0 cm^2 apparent surface area [the theoretical minimum value of C_{scr} for intrinsic Ge at 295°K is

$$C_{min} = e\sqrt{\frac{2\epsilon n_i}{kT}} \cong 0.017\ \mu f/cm^2$$

using $n_i = 1.7 \times 10^{13}\ cm^{-3}$ at 295°K (19)]. By Eq. [4], the initial transient should become negligible after a time

$$t_o \cong \tau_c \ln \frac{R_s \cdot C_{scr}}{(R_s + R_e + R_i)C_i} \qquad [5]$$

determined by requiring the time-dependent term to be smaller than the constant term. Using the values relevant to Fig. 3, we have $\tau_c \cong 5$ nsec and $t_o \cong 15$

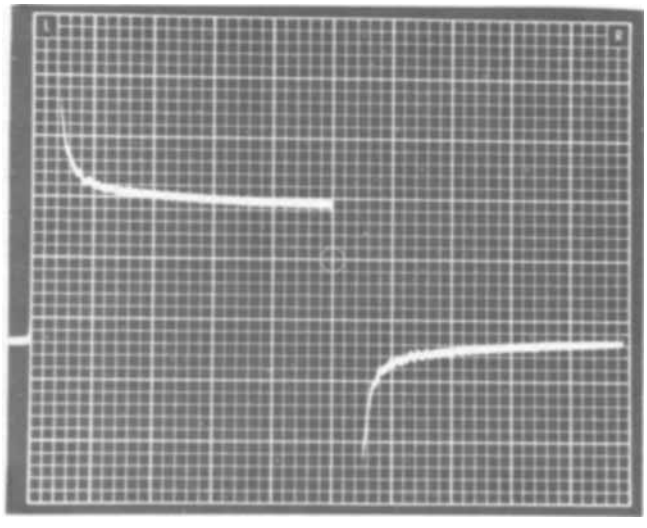

Fig. 3. Probe response to a 2.6 vpp square wave at 1 MHz for intrinsic Ge, biased to approximately the flat-band condition. The horizontal scale represents 100 nsec per large division; the vertical scale 5 mv per large division. The injection capacitor $C_i = 100$ pf.

nsec. C_{scr} can therefore be measured in principle by using a 30 MHz (approximate reciprocal of $2t_o$) repetitive square wave $V_i(t)$, and the magnitude of the response implies measurement capability in the presence of interface voltage changes of the order of 5 mv/50 nsec, or 10^5 v/sec. The actual limit of 100 nsec in Fig. 3 is a result of the measuring instrument recovery time from the initial transient overload, and is appreciably longer than the calculated value (a Tektronix 547 oscilloscope with Type 1A1 preamplifier was used to obtain the experimental results in this paper).

In the linear response limit, where $|\Delta V_{scr}| \cong |\Delta V_p| << kT$, a close connection exists between charge injection and constant current pulse methods of capacitance determination. In this approximation, the space charge response equations can be linearized (17, 18) and the complex admittance $Y(\omega) = G(\omega) + i\omega C(\omega)$ in Fig. 2, including dispersion effects and conductance, can be written as a transfer function $Y(\omega) = 1/Z(\omega)$. After initial transients have dissipated, *i.e.*, by the time that the dependence of the probe output is determined completely by $Y(\omega)$, the time-dependent probe response $\Delta V_p(t)$ can be obtained directly from the input current $I_i(t)$ produced by the source $V_i(t)$ through Fourier analysis

$$\Delta V_p(t) = \frac{1}{2\pi}\int_{-\infty}^{\infty} d\omega\ e^{i\omega t} Z(\omega) \left[\int_{-\infty}^{\infty} dt'\, e^{-i\omega t'} I_i(t') \right] \quad [6]$$

It follows immediately from Eq. [6] that if two time-dependent current sources $I_{i1}(t)$ and $I_{i2}(t)$ bear a derivative relationship to each other such that $I_{i2}(t) = d/dt\ I_{i1}(t)$, then their responses also satisfy the same relationship

$$\Delta V_{p2}(t) = \frac{d}{dt}\Delta V_{p1}(t) \quad [7]$$

Now the approximate current waveform for charge injection, $I_2(t) \cong I_{20}\delta(t)$, is just the derivative of that of a constant-current pulse, $I_1(t) \cong I_{10}u(t)$, to within a constant. Therefore, the respective probe responses relate as in Eq. [7], and the response to the charge injection pulse is proportional to the derivative of the constant current charging curve. This result follows even if G is not negligibly small or C is dispersive. If G is negligibly small, the derivative of the constant current charging curve gives the inverse of the instantaneous differential capacitance. The charge injection response gives this inverse directly, differentiation is not required, and in addition the average capacitance obtained by the total change of V_{scr} for a finite constant current pulse (2, 9), or by sinusoidal methods, is avoided.

We conclude this section by noting that even though charge injection and constant-current methods are closely related, it is generally advantageous to use the former. To the extent that conductance and dispersion are negligible, $V_p(t)$ is the image of $V_i(t)$ for charge injection. Shape-distorting effects such as dispersion and finite interface conductivity are much more easily detected in the nominally square wave image $V_p(t)$ than in its integral, the nominally linearly increasing potential of the constant-current response, where distortions only result in deviations from linearity. The change ΔV_p for determining C_{scr} can be established in a shorter time interval than necessary for obtaining the slope of the constant-current charging curve. In single-pulse operation, charge injected on the leading edge is extracted on the falling edge leaving the system unchanged; constant-current methods require two pulses of opposite polarity to accomplish this. It should be pointed out, however, that the derivative relationship between the charge injection and constant current methods fails for $|\Delta V_{scr}| > kT$, in which case the nonlinearities in the system must be explicitly taken into account in calculating the charging curve, and no simple relation between the two methods exists (20). Also, the separation of dispersion in C from discharging through G cannot be done by either pulse method, but requires both amplitude and phase determination which only sinusoidal methods can give. The lack of a suitable phase-sensitive detector for the megacycle region has restricted the use of sinusoidal methods to much lower frequencies.

Experimental Results and Discussion

The method is illustrated by application to a particular case, the measurement of the space charge capacitance of the (111) face of an intrinsic Ge sample, having an apparent surface area of 1.0 cm^2, in a 0.1M aqueous solution of K_2SO_4 (2) buffered with 0.025M KH_2PO_4 and 0.025M Na_2HPO_4 to a pH of 6.86 (21). The sample was prepared by an optical polish ending with ¼μ diamond grit, followed by an anodic etch in solution. The sample and mount were masked with Apiezon black wax. To eliminate impurities which would react with the surface, particularly heavy metals, the electrolyte was previously gettered with Ge crushed in solution. Both potentiostatic and galvanostatic control were used, and the high-frequency output impedance of these control sources was at least $R_o = 20$ kohms. The effective impedance in series with the injection capacitor C_i was $R_i = 25$ ohms, and $C_i = 100$ pf. A Pyrex cell, Pt electrodes, and a standard calomel electrode (SCE) isolated through a capillary tube and stopcock (200 kohms impedance) completed the electrolytic system. The SCE drove an Analog Devices Model 148A operational amplifier having an input impedance of 10^{11} ohms shunted by 3.5 pf. Potentiostatic control was obtained through a second such amplifier, provided with a feedback loop which limited its response time to 2 msec. The probe response shown in Fig. 3 was obtained using this system.

The capacitance of the interface as a function of bias is presented in Fig. 4, in order to test the capacitive divider method against well-known results (2, 22). Figure 4 shows the probe a-c response to an applied square wave of 2.78 vpp at 1.0 MHz, where the interface potential is swept potentiostatically at 100 mv/sec from anodic bias toward cathodic bias, as indicated in the figure caption. The sweep generates two curves which are simply 10^7 repetitions of the square wave response shown in Fig. 3, but each cycle highly compressed and at slightly different bias conditions given by the abscissa voltage. C_{scr} as a function of bias is then obtained by using Eq. [1], where ΔV_p is the separation between the inner edges of the upper and lower curves. This separation is inversely proportional to C_{scr}, and with the 1.0 MHz square wave driving voltage, yields directly the differential capacitance 500 nsec after the charging pulse as discussed earlier. The two curves of Fig. 4 approximately form the outline of the oscilloscope pattern which one would obtain from a constant-current pulse charging technique, as a comparison with Fig. 2 of ref. (2) shows immediately, except that the constant-current technique gives the average capacitance over the pulse duration.

The capacitance determined from Fig. 4 is plotted in Fig. 5, together with the theoretical equilibrium curve (15, 16) which applies to the intrinsic sample. The theoretical minimum capacitance value $C_{min} = 0.0173$ $\mu f/cm^2$ fits the measured minimum exactly, so only an alignment along the abscissa was required. We note, however, that all quantities used in calculating C_{min} are sufficiently uncertain so that no particular meaning should be attached to this minimum fit; a surface roughness factor of 20-30% is typically obtained (2).

The fit is fairly good, but a deviation is observed on the cathodic side where the slope of the plot is about 70 mv, instead of the theoretical 2 $kT \cong 52$ mv. This deviation is consistently observed in other mea-

surements, and is due to the potential drop across the Helmholtz region (2, 22). The deviation also becomes severe for large anodic bais, where Ge passes into solution at the expense of holes from the SCR and the effective leakage conductance G is no longer negligible (23). The fit between theory and experiment in Fig. 5 is comparable to that obtained in other methods (2, 22) and demonstrates the validity of the charge injection method for determining space charge capacitance.

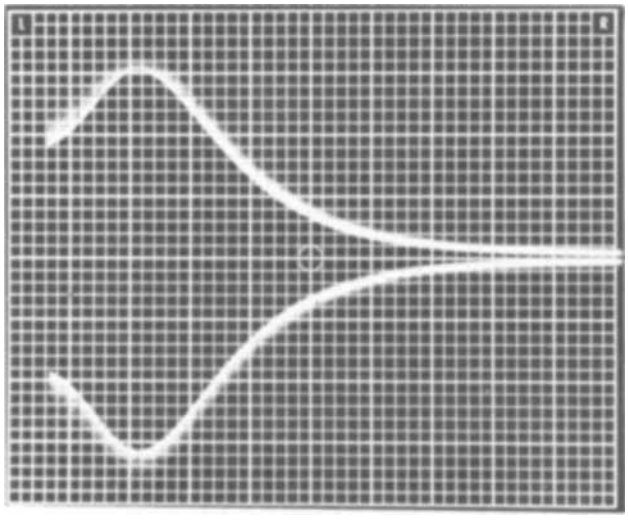

Fig. 4. A-C response of the probe to a 2.78v p-p square voltage wave at 1.0 MHz for the intrinsic Ge sample used in Fig. 3. The interface potential is swept at 100 mv/sec, anodic (left) toward cathodic. The vertical scale is 2.5 mv/large division; the horizontal scale 50 mv/large division. The horizontal scale gives the potential of the Ge electrode with respect to the reference electrode; the left edge corresponds to —100 mv, the right edge, —600 mv. The zero-current (quiescent) potential is —630 mv. The entire curve is taken with the sample biased anodically.

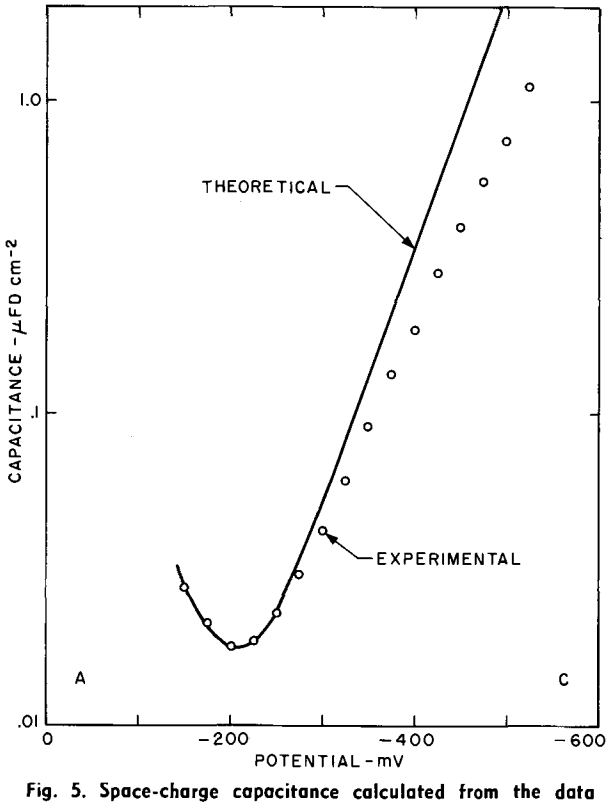

Fig. 5. Space-charge capacitance calculated from the data of Fig. 4, plotted against the theoretical curve for intrinsic Ge. The theoretical curve was normalized for coincidence at the capacitance minimum. The horizontal axis is the potential of the Ge electrode with respect to the reference electrode.

In order to obtain a flat baseline in Fig. 4, the probe output was filtered by a simple L-section high pass RC circuit inserted between the probe and the oscilloscope, with elements $R_f = 100$ kohm and $C_f = 0.01$ μf, having a low-frequency cutoff $\tau_f = R_f C_f = 1$ msec. The low-frequency cutoff was chosen sufficiently long so that the charge

$$\Delta Q_f \cong \frac{\Delta V_i R_s}{R_s + R_c + R_p} \cdot \frac{\tau_c}{R_f} \qquad [8]$$

accumulated on C_f during the initial transient resulted in a voltage change

$$\Delta V_f = \frac{\Delta Q_f}{C_f} \cong \Delta V_i \frac{R_s}{R_s + R_c + R_p} \cdot \frac{\tau_c}{\tau_f} \qquad [9]$$

such that $|\Delta V_f| << |\Delta V_p|$. The sign of ΔV_f is opposite that of ΔV_p and can also occur if a potentiostatic control amplifier is isolated inductively.

We now consider an application to an actual situation arising in electroreflectance, where a relatively large perturbation repeats at high frequency, and it is necessary to determine the surface field as a function of time during a cycle of the perturbation. A 1.0 kHz current square wave was used to drive the intrinsic Ge sample at anodically directed current levels of 90 and 330 μa/cm^2, respectively, for this measurement. Figure 6 shows the resulting probe response, without the high-pass filter used for Fig. 4. The left half of the trace corresponds to $I = 330$ μa/cm^2, and the right half to $I = 90$ μa/cm^2 (flat band). The response of the interface to the 1.0 kHz perturbation alone would be the average of the upper and lower curves. The upper and lower curves correspond to the two curves of Fig. 4, except for being superimposed on the interface response to the 1 kHz current drive. The capacitive divider drive $V_i(t)$ was a 1.0 MHz square wave of amplitude 3.1 vpp. C_{scr} is obtained by measuring the separation of the upper and lower curves of Fig. 6 and using Eq. [1].

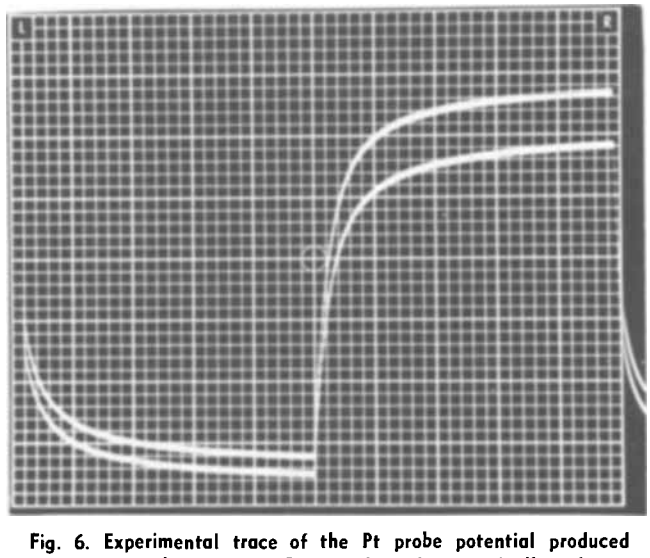

Fig. 6. Experimental trace of the Pt probe potential produced by modulating the intrinsic Ge sample galvanostatically using a 1 kHz current square wave at anodic levels of 90 μa/cm^2 (right half, flat band) and 330 μa/cm^2 (left half). The horizontal time scale of 100 μsec/large division covers one modulation cycle. The vertical scale is the d-c coupled Pt probe voltage at 20 mv/large division, with respect to the grounded Ge electrode. The lower edge is equivalent to +80 mv, the upper edge +240 mv.

Figure 7 shows the calculated surface field E_s as a function of time over one period of the 1 kc current modulation, obtained from point-by-point measurements of expanded portions of the trace of Fig. 6, assuming the intrinsic relation between C_{scr} and E_s applies (15, 16) and that the maximum value of the separation of the upper and lower curves, which occurs over the right half of Fig. 6, corresponds to the flat-band condition where $E_s = 0$ (the sweep was expanded using the Tektronix oscilloscope in the "B intensified by A" time base mode; a type W differential preamplifier was used for this measurement). The last assumption is probably not completely correct, and the true flat band position should be determined experimentally by more sensitive techniques such as photovoltage (15, 24) or electroreflectance (25) response. Notwithstanding this possible uncertainty, Fig. 6 and 7 demonstrate that the surface field as a function of time in the presence of rapid modulations can be obtained relatively easily by charge injection.

The ability to measure the surface field during a rapid modulation cycle has a direct application to electroreflectance, where a comparison of theory and experiment requires the knowledge of the electric field variation over a modulation cycle. Conversely, the capacitance divider or charge injection technique can be used to determine the proper control waveform to obtain the ideal field-on field-off time variation, which would allow a direct comparison of experimental electroreflectance results with theory (26). The simple experimental requirements are compatible with existing electroreflectance technology, which is important for the continuous monitoring of surface field and detection of drifts due to electrochemical reactions during actual measurement. The determination of the true field time dependence in electroreflectance has been almost without exception neglected and as a result serious doubt can be raised about conclusions drawn from the detailed shape of electroreflectance spectra (27). Experiments for more accurately measuring electroreflectance are in progress.

Conclusion

A capacitive divider technique of measuring interface capacitance in electrolytic cells is presented and discussed. A small capacitance in series with the interface acts as a differentiator of pulse or square wave driving voltages and in effect injects charge into the interface during level changes of the driving voltage. The resultant potential response is easily interpreted to give the interface capacitance. The method is analyzed with respect to the semiconductor-electrolyte system and its relation to other capacitance measuring techniques outlined. In particular, it is demonstrated that charge injection produces directly the derivative of the constant-current charging curve in the linear response limit, from which the differential capacitance is obtained. Being faster than other methods, it permits the experimental determination of space charge capacitance in the presence of rapidly changing interface potentials, which is demonstrated by an experimental application to intrinsic Ge. The applications to electroreflectance measurements are discussed.

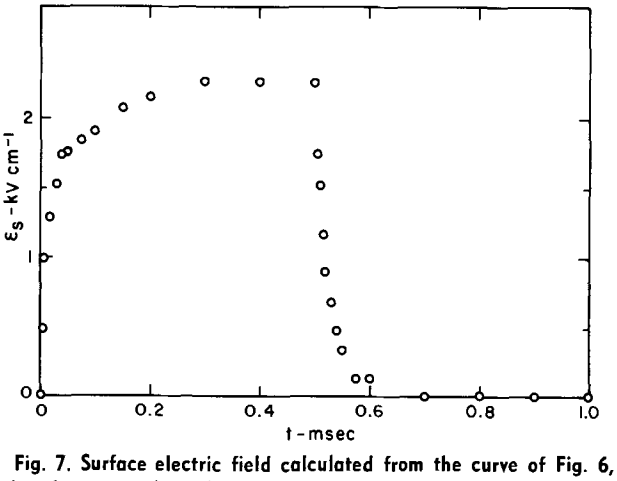

Fig. 7. Surface electric field calculated from the curve of Fig. 6, using the assumptions given in text.

Acknowledgment

It is a pleasure to acknowledge discussions with P. J. Boddy, who suggested the use of pulse methods for capacitance measurement, additional helpful discussions with J. D. E. McIntyre, C. G. B. Garrett, and W. E, Mindt, and the technical assistance of A. A. Studna.

Manuscript submitted Nov. 26, 1968; revised manuscript received Jan. 31, 1969.

Any discussion of this paper will appear in a Discussion Section to be published in the December 1969 JOURNAL.

REFERENCES

1. W. H. Brattain and P. J. Boddy, *This Journal*, **109**, 574 (1962).
2. P. J. Boddy and W. J. Sundburg, *ibid.*, **110**, 1170 (1963).
3. H. Gobrecht, O. Meinhardt, and B. Reinicke, *Ber. Bunsenges. Physik. Chem.*, **67**, 493 (1963).
4. L. Ramaley and C. G. Enke, *This Journal*, **112**, 943 (1965).
5. C. C. Krischer and R. A. Osteryoung, *ibid.*, **112**, 735 (1965); H. Gobrecht, M. Schaldach, F. Hein, R. Blaser and H.-G. Wagemann, *Ber. Bunsenges.*, **70**, 646 (1966).
6. The enormous amount of work done in this area has been well covered by V. A. Myamlin and Yu. V. Pleskov, in "Electrochemistry of Semiconductors," Plenum Press, New York (1967). See particularly Chap. 1 and 3, and references therein.
7. B. O. Seraphin and R. B. Hess, *Phys. Rev. Letters*, **14**, 138 (1965); B. O. Seraphin and N. Bottka, *Phys. Rev.*, **145**, 628 (1966).
8. K. L. Shaklee, F. H. Pollak, and M. Cardona, *Phys. Rev. Letters*, **15**, 883 (1965); M. Cardona, K. L. Shaklee, and F. H. Pollak, *Phys. Rev.*, **154**, 696 (1967).
9. B. D. Cahan and P. Ruetschi, *This Journal*, **106**, 543 (1959); J. S. Riney, G. M. Schmid, and N. Hackerman, *Rev. Sci. Instr.*, **32**, 588 (1961).
10. M. Proskurnin and A. N. Frumkin, *Trans. Faraday Soc.*, **31**, 110 (1935); T. F. Retajczyk and D. K. Roe, *J. Electroanal. Chem.*, **16**, 21 (1968).
11. M. W. Breiter, *J. Electroanal. Chem.*, **7**, 38 (1964).
12. P. Delahay, R. de Levie, and A.-M. Giuliani, *Electrochim. Acta*, **11**, 1141 (1966) and references therein; P. Delahay, *J. Phys. Chem.*, **66**, 2204 (1962).
13. K. Lehovec and A. Slobodskoy, *Solid State Electronics*, **7**, 59 (1964); ref. (6), p. 317.
14. This relaxation time is of the order of 10^{-11} sec in intrinsic Ge [see ref. (6), p. 40]. The relaxation time of 0.1M aqueous electrolytes is longer, of the order of 10^{-9} sec [see H. Falkenhagen, "Electrolytes," pp. 211 ff, Clarendon Press, Oxford, (1934)] but still sufficiently fast as to have negligible effect in the applications to be discussed.
15. C. G. B. Garrett and W. Brattain, *Phys. Rev.*, **99**, 376 (1955).
16. R. H. Kingston and S. F. Neustadter, *J. Appl. Phys.*, **26**, 718 (1955).
17. C. G. B. Garrett, *Phys. Rev.*, **107**, 478 (1957).
18. F. Berz, *J. Phys. Chem. Solids*, **23**, 1795 (1962); **25**, 859 (1964); ref. (6), pp. 285 ff.
19. R. A. Smith, "Semiconductors," p. 359, Cambridge University Press, (1961).
20. V. A. Tyagai and Yu. Ya. Gurevich, *Fiz. Tverd. Tela*, **7**, 12 (1965). English translation: Soviet *Physics—Solid State*, **7**, 7 (1965).

21. "Handbook of Chemistry and Physics," 45th ed., p. D-72, The Chemical Rubber Co., Cleveland (1964).
22. C. C. Krischer and R. A. Osteryoung, *This Journal*, **112**, 938 (1965).
23. W. H. Brattain and C. G. B. Garrett, *Physica*, **20**, 885 (1954); *Phys. Rev.*, **94**, 750 (1954); F. Beck and H. Gerischer, *Z. Elektrochem.*, **63**, 500 (1959); numerous references in ref. (6), Chap. 1 and 2.
24. P. J. Boddy and W. Brattain, *Ann. N. Y. Acad. Sci.*, **101**, 683 (1963); ref. (6), pp. 100 ff.
25. B. O. Seraphin, *Surface Sci.*, **8**, 399 (1967).
26. References to the theory of electroreflectance of the Franz-Keldysh type may be found in D. E. Aspnes, P. Handler, and D. F. Blossey, *Phys. Rev.*, **166**, 921 (1968). Ferroelectric crystal electroreflectance theory has been developed by J. R. Brews, *Phys. Rev. Letters*, **18**, 662 (1967), and G. D. Zook and T. N. Casselman, *Phys. Rev. Letters*, **17**, 960 (1966).
27. Notable exceptions include the work of B. O. Seraphin, R. B. Hess, and N. Bottka, *J. Appl. Phys.*, **36**, 2242 (1965), and F. Evangelisti and A. Frova, *Solid State Comm.*, **6**, 921 (1968), who used a dry sandwich construction and determined the surface field by surface conductivity measurements, and H. Gobrecht, M. Schaldach, F. Hein, R. Thull, and H. J. Kos (to be published), who obtained the surface field through capacitance measurements using lower frequency sinusoidal techniques with a waveform eductor.

Gas Content of Gold Foils Deposited from Polymer-Saturated Electroplating Solutions

H. Graham Silver[1]

Bell Telephone Laboratories, Incorporated, Reading, Pennsylvania

ABSTRACT

A study of the reactions of the cyanide ion at the anode of a potassium gold cyanide electroplating solution containing free potassium cyanide has revealed that a brown polymeric material is generated there which not only discolors, but also codeposits with the gold electrodeposit. This polymer is responsible for the gaseous impurities evolved from the gold deposit on subsequent heating. However, electroplating solutions, formulated without the addition of free potassium cyanide, produce gold deposits containing only low levels of gaseous impurities.

In a recent publication (1), an evaluation of the chemical behavior of typical cyanide electroplating solution components was described. Quantitative evidence was obtained to show that potassium cyanide solutions, or gold electroplating solutions containing free potassium cyanide, are unstable to water and air, the major reaction products formed being the formate and carbonate ions.

Studies of the effect of electrolysis on aqueous KCN solutions have already been performed (2-4). In the most recent of these (4), the authors reported that the passage of current through the aqueous KCN solution, using Pt electrodes, resulted in the formation at the anode of $(HCN)_x$, which precipitates in high concentration. Polymer formation was inhibited in more strongly alkaline KCN solutions.

This work was repeated and experimentally fully confirmed. In addition, it was found that the production of the brown polymer was independent of the anode material chosen and was most readily observable when oxygen was copiously evolved. Activated carbon treatment readily removed the brown polymer from hot aqueous KCN solutions.

Polymerization of HCN can also occur if the pH of the alkaline KCN solution is less than about 10, particularly in the presence of the NH_4^+ ion (5).

Infrared absorption and dipole moment measurements (6-8), chemical (9) and x-ray diffraction (10, 11) studies of the HCN polymer in the solid state have established that it is a tetramer, existing as diaminomaleonitrile

$$\begin{array}{l} H_2N—C—CN \\ \quad\quad\| \\ H_2N—C—CN \end{array}$$

It is generally accepted that organic compounds, intentionally added to or unintentionally generated by a gold electroplating solution, have an important effect on the physical characteristics of the gold electrodeposit (12, 13), although most of the data available is of a qualitative nature. In order to determine whether the presence of this brown polymer $[HCN]_4$ in gold electroplating solutions is potentially deleterious, an observation was made of the effect of the polymer, artificially generated within the electroplating solution, on the color and gas content of gold foils obtained from that solution.

Experimental

A $KCN/KAu(CN)_2$ electroplating solution of formulation

(68% min. Au)	$KAu(CN)_2$	9 g/l	± 0.1 g/l
	KCN	45 g/l	
	KOH	3 g/l	
	pH	13	

and a conventional dibasic ammonium citrate/$KAu(CN)_2$ electroplating solution of formulation (14)

(68% min. Au)	$KAu(CN)_2$	20 g/l	± 0.1 g/l
dibasic ammonium citrate		50 g/l	
	pH	5.5	

were prepared, without boiling, in deionized water. Using a stainless steel plate cathode[2] of total surface area 8 in.^{2}, placed between flat gold anodes of total surface area 50 in.^{2}, a gold foil was plated from each solution at a current density of 20 ± 5 ma/in.^{2} for 45 min after a "flash" of 1 amp for 1 min to facilitate the initial plate. The temperature of the solutions was maintained at 65° ± 3°C. To both solutions was added a total of 5, 15, 25, 50, 75, and 100 ± 0.1 g/l formate ($H{\cdot}COO^-$) ion in the form of ammonium formate.

[1] Present address: General Telephone & Electronics Laboratories Incorporated, Bayside, New York 11360.

Key words: Electrodeposition, gold electroplating, polymeric impurity, gas content.

[2] All stainless steel plates, used for this purpose in this experiment, were degreased in the vapor of boiling trichloroethylene for 5 min, immersed in acetone for 15 min, acid-cleaned in hot 1:1 HCl for 1 min, and finally rinsed in deionized water.

After each addition of the ammonium formate, a gold foil was plated, as explained above, from each solution, using a fresh stainless steel plate cathode. The thickness of the gold deposits varied slightly, but averaged about 100 mg/in.^{2}.

The seven gold foils thus obtained from each solution were stripped from the substrate, carefully washed and dried, and finally mass spectrometrically analyzed for the evolved gases after vacuum fusion at 1300°C.

The entire process, as explained above, was repeated, but substituting potassium formate and then ammonium sulfate for the ammonium formate. Once again, a total of 5, 15, 25, 50, 75, and 100 ± 0.1 g/l formate ($H{\cdot}COO^-$) ion and sulfate ($SO_4^=$) ion, respectively, were added to both the cyanide and citrate electroplating solutions.

Results and Discussion

The results of the mass spectrometric analyses of the gases evolved from the three series of gold foils on vacuum fusion at 1300°C are shown in Fig. 1, 2 and 3. It is immediately apparent that the gold foils plated from the dibasic ammonium citrate/$KAu(CN)_2$ electroplating solution contain low levels of gaseous impurities, which do not increase in concentration as the concentrations of the ammonium formate, potassium formate and ammonium sulfate salts increase. This observation, of course, would be true for any gold electroplating solution, which does not contain free KCN.

However, on the addition of the ammonium salts of $H{\cdot}COOH$ and H_2SO_4 to the KCN/$KAu(CN)_2$ electroplating solution, a rise in the gaseous impurity level within the gold foils is observed to occur. Also, not shown on the figures as a curve, liberal amounts of HCN and cyanogen (C_2N_2) are also detected. On the other hand, the KCN/$KAu(CN)_2$ electroplating solution containing potassium formate does not show this rise in the gaseous impurity level within the gold foils, as the concentration of the salt increases. In fact, the gaseous impurity levels in the latter solution compare very closely with those found in the dibasic ammonium citrate/$KAu(CN)_2$ electroplating solutions.

It is clear that the hydrolysis of ammonium formate and ammonium sulfate reduces the pH of the solutions below pH 10 where it has been shown that $[HCN]_4$ forms (5). Potassium formate, an alkaline salt, reduces the pH only very slightly, so that little, if any, polymer forms.

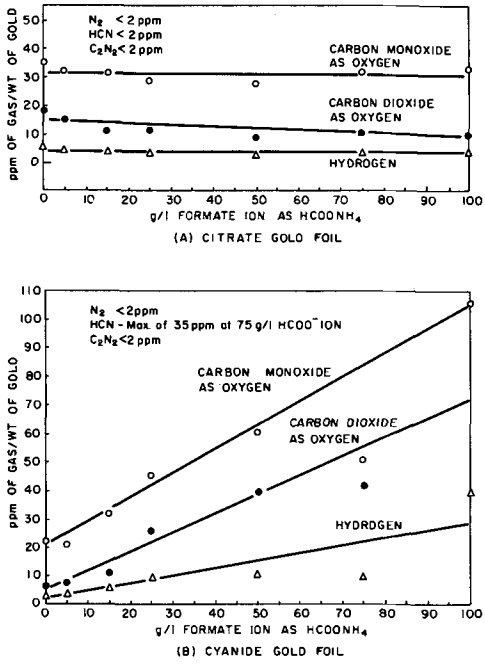

Fig. 1. Gas analysis of gold foils obtained from ammonium formate-rich electroplating solutions.

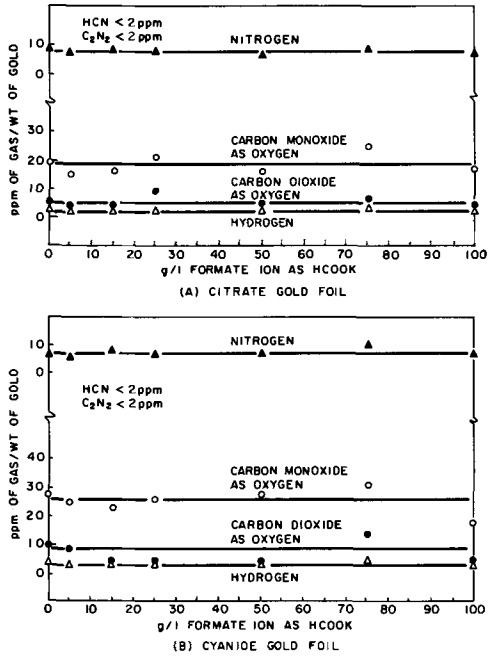

Fig. 2. Gas analysis of gold foils obtained from potassium formate-rich electroplating solutions.

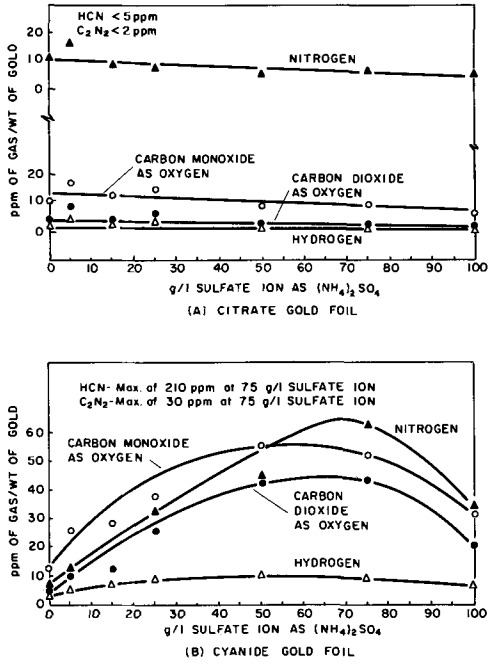

Fig. 3. Gas analysis of gold foils obtained from ammonium sulfate-rich electroplating solutions.

The gold electrodeposits, obtained from those electroplating solutions in which no HCN polymer generation occurs, are all bright yellow and matte. Conversely, those gold deposits obtained from polymer-containing electroplating solutions, progressively become browner and darker as the concentration of polymer absorbed with the gold, increases. The values in ppm of the total gaseous impurity concentration, which correspond to Fig. 3B, are reported in Table I as a function of the concentration of sulfate ion dissolved in the electroplating solution. The gaseous impurities include the following: H_2, CO, CO_2, N_2, CH_4, C_6H_6, HCN, Ar, C_2N_2.

At zero g/l ammonium sulfate in the electroplating solution, the gold deposit is bright yellow and matte in color. This corresponds to the lowest total gaseous impurity concentration (28 ppm), *i.e.*, the sum in ppm of all the gaseous impurities reported in the foil, of

Table I. Total gaseous impurity concentration, ppm

g/l Sulfate ion as $(NH_4)_2SO_4$						
0	5	15	25	50	75	100
28	56	66	171	306	408	149

any of the seven foils. As the concentration of each individual impurity, and hence the sum total of the impurities, increases within the gold foil at any one concentration of the $SO_4^=$ ion, so the color of the foil progressively deepens to a maximum around 75 g/l $SO_4^=$ ion, at which point the total impurity concentration also reaches a maximum of 408 ppm. A similar discoloration of the gold deposits is observed in the $KCN/KAu(CN)_2$ electroplating solution when ammonium formate is added.

For reasons undetermined at present, the polymer was apparently not absorbed to such a high degree on the next gold foil obtained from the $KCN/KAu(CN)_2$ electroplating solution containing 100 g/l $SO_4^=$ ion. This is immediately apparent from the drop in the individual concentrations of H_2, CO, CO_2, and N_2, (Fig. 3B), the resultant drop in the total concentration of the gaseous impurities to 149 ppm and the slight lightening of the gold foil. Thus, the relative discoloration of the gold foils could be used as a qualitative test of the amount of contamination of the foil by the HCN polymer.

It has been postulated that the $H{\cdot}COO^-$ ion, produced as a reaction product of KCN with water (1), is responsible for the large increase of CO, CO_2, and H_2 observed in the gold foils, when the ammonium salts are purposely added to the $KCN/KAu(CN)_2$ electroplating solution (Fig. 1B and 3B). Since the addition of $H{\cdot}COO^-$ ion did not affect the gas content of the gold foils obtained from the dibasic ammonium citrate/$KAu(CN)_2$ electroplating solution (Fig. 1A), it was assumed that the HCN polymer was responsible for entrapping or adsorbing the $H{\cdot}COO^-$ ion or maybe the acid $H{\cdot}COOH$, in some manner not determined, as the polymer codeposited with the gold. However, there is the possibility that monomeric HCN absorbed with the HCN polymer within the gold foil, slowly reacts with water to provide an additional, *in situ* source of the $H{\cdot}COO^-$ ion by the reaction discussed elsewhere (1).

It would appear therefore that, within certain limits, the amount of gaseous impurities evolved from an electrodeposited gold foil is proportional to the concentration of the HCN polymer within the foil, which in turn is proportional to the concentration of polymer within the electroplating solution. The concentration of polymer within the electroplating solution increases as the pH is decreased by the hydrolysis of an acidic ammonium compound or by liberation of oxygen at the anode. It has been found experimentally that another source of gaseous impurities, mainly H_2, is derived from the substrate of the device upon which gold has been electrodeposited. The amount of H_2 evolved is usually dependent on the pretreatment of the substrate and can be several times that evolved from the gold deposit alone. Since an examination of the absorptive properties of different substrates was not within the scope of the present work, it will not be discussed further.

A check to reveal whether continual electroplating from a $KCN/KAu(CN)_2$ solution containing some HCN polymer at a current density less than that required to liberate oxygen at the anode, would ultimately result in the elimination of the polymer, due to its codeposition with the gold, was rather disappointing in that no drastic brightening of the gold deposit was observed even after six successive electroplatings from the same solution. It was hoped that eventually a bright yellow matte gold deposit would result. There is the possibility, however, that many more than six electroplatings would be required to clear the solution of the polymer, which was present in abundance.

It has frequently been observed that gold anodes, used continually in $KCN/KAu(CN)_2$ electroplating solutions, become covered with a dark brown coating, somewhat reminiscent of the brown gold deposit obtained from electroplating solutions heavily contaminated with the HCN polymer. In order to clarify the nature of this brown coating, two gold rod anodes, 99.99% pure, were sent for vacuum fusion and electron diffraction studies of the coating on that part of the anode which had been repeatedly immersed over a period of several months in the plating solution.

The vacuum fusion study revealed that the dark brown coating contained at least 100% and up to about 400% more oxygen than any area of the gold anode uncovered by the dark-brown coating. Moreover, the results of the electron diffraction measurements, shown in Table II are consistent, although not identical, with those obtained from the surface of gold heated in an oxygen atmosphere at 500°C (15). This compound was indexed as hexagonal with lattice parameters $a = 5.28$ and $c = 6.75$ and assigned the formula Au_3O_2. This, however, has been disputed (16) and the patterns assigned to spinels formed from impurities in the gold.

Difficulties in the detection of the diffraction pattern of gold oxide have also been experienced by another worker (17).

Since the gold anodes were used in a standard $KCN/KAu(CN)_2$ electroplating solution and never allowed to remain in contact with the solution for any length of time without electrolysis, the source of the oxygen-containing layer is probably electrolytic. It would appear that, as well as gold being dissolved from the anode, oxygen is also being formed, if not evolved.

On aging, in air at room temperature, the brown layer so formed is particularly resistant to a concentrated solution of KCN, a 1:1 HCl solution, and even to prolonged heating in air at about 600°C. This behavior is contrary to what is usually assumed to be a weak gold compound. Only on prolonged usage in a $KCN/KAu(CN)_2$ electroplating solution will the dark brown material disappear, presumably an electrolytic dissolution reaction to form the soluble $Au(CN)_2^-$ ion.

Since the chemical stability of $KAu(CN)_2$ in solution with compounds other than KCN is an extremely important parameter to be considered in these electrochemical studies, it was decided to determine how stable the standard solution of $KAu(CN)_2$ and dibasic ammonium citrate (14) is, before and after boiling. Thus, a solid sample of $KAu(CN)_2$, Engelhard Industries, was analyzed for total cyanide and gold. A solution was made up by mixing 20 ± 0.1 g/l $KAu(CN)_2$ and 50 ± 0.1 g/l dibasic ammonium citrate in deionized water. An aliquot was removed and analyzed for total cyanide and gold. The solution was then boiled for ½ hr, cooled and after volume-loss corrections, an aliquot removed and analyzed again for total cyanide and gold.

The results of the analyses for total cyanide and gold are shown in Table III, together with calculated theoretical values.

Within experimental error, the results obtained for total cyanide and gold in each case lie very close to the calculated theoretical values. The data present evidence of the stability of $KAu(CN)_2$ to decomposition and that, in particular, no new complex of gold is formed with the citrate ion (14, 18, 19, 20). The gold

Table II. Results of electron diffraction measurements

h, k, l	Calculated d-spacings for Au_3O_2 (15)	Observed d-spacings
100	4.56	4.5
101	3.16	3.0
110	2.54	2.47
102	1.95	1.90
300	1.52	1.54
301	1.43	1.44
310	1.26	1.24

Table III. Analyses for cyanide and gold

Ion	Calculated composition, %	Solid $KAu(CN)_2$, %	Unboiled $KAu(CN)_2$ and ammonium citrate, %	Boiled $KAu(CN)_2$ and ammonium citrate, %
Cyanide	18.03	17.95	18.10	18.55
Gold	68.40	68.05	69.25	70.25

is present as the gold dicyanide ion, whether the electroplating solution is boiled or unboiled. A similar opinion has recently been expressed from observations made during a study of plating conditions on the porosity in gold electrodeposits (21).

Conclusion

Potassium gold cyanide electroplating solutions containing free KCN are subject to contamination not only by $H{\cdot}COO^-$ and $CO_3^=$ anionic impurities, but also by a brown polymeric material of formula $[HCN]_4$, generated at the soluble gold anode when the *p*H in its vicinity is reduced on the occasional anodic evolution of oxygen. This polymer codeposits with the gold, discoloring the latter, and is the agent responsible for the major proportion of the gaseous impurities found residing within the gold deposit. However, gold deposits obtained from electroplating solutions containing no free KCN, for example the dibasic ammonium citrate/$KAu(CN)_2$ electroplating solution, contain only low levels of gaseous impurities.

Electron diffraction and vacuum fusion studies have shown that the dark brown coating formed occasionally on gold anodes is high in oxygen and may be similar to a compound claimed to be Au_3O_2, but believed by others to be a spinel formed from impurities in the gold. When freshly prepared, this material readily dissolves in an aqueous KCN and a 1:1 HCl solution, but, on aging in air at room temperature, becomes particularly resistant to chemical and thermal attack.

No new complex of gold is formed with the citrate ion within a dibasic ammonium citrate/$KAu(CN)_2$ electroplating solution. The gold is invariably present as the $Au(CN)_2^-$ ion, whether the electroplating solution is boiled or unboiled.

Acknowledgment

The author wishes to thank Dr. M. J. Elkind for helpful discussions concerning this work. He also acknowledges the assistance provided by J. J. Chick in the performance of the experiments.

Manuscript submitted Sept. 25, 1968; revised manuscript received Feb. 3, 1969.

Any discussion of this paper will appear in a Discussion Section to be published in the December 1969 JOURNAL.

REFERENCES

1. H. G. Silver, *This Journal*, **116**, 26C (1969).
2. W. Hittorf, *Z. Physik Chem.*, **10**, 616 (1892).
3. J. S. Fitzgerald, *Chem. and Ind.*, **17** (1955).
4. H. Schmidt and H. Meinert, *Z. Anorg. Chem.*, **293**, 214 (1957).
5. J. D. F. Marsh and M. J. Martin, *J. Appl. Chem.*, **7**, 205 (1957).
6. R. L. Webb, S. Frank, and W. C. Schneider, *J. Am. Chem. Soc.*, **77**, 3491 (1955).
7. H. Bredereck, G. Schmötzer, and H. J. Becher, *Ann.*, **600**, 87 (1956).
8. H. Bredereck and G. Schmötzer, *ibid.*, **600**, 95 (1956).
9. P. S. Robertson and J. Vaughan, *J. Am. Chem. Soc.*, **80**, 2691 (1958).
10. B. R. Penfold and W. N. Lipscomb, *Tetrahedron Lett.*, **6**, 17 (1960).
11. B. R. Penfold and W. N. Lipscomb, *Acta Crystallogr.*, **14**, 589 (1961).
12. E. A. Parker, *Plating*, **38**, 1134 (1951).
13. F. I. Nobel, R. B. Kessler, D. W. Thomson, and R. F. Ostrow, *ibid.*, **54**, 926 (1967).
14. R. A. Ehrhardt, *Proc. Am. Electroplaters' Soc.*, **47**, 78 (1960).
15. N. A. Shishakov, *Kristallografiya*, **2**, 686 (1957).
16. D. Clark, T. Dickinson, and W. N. Mair, *Trans. Faraday Soc.*, **55**, 1937 (1959).
17. S. Barnartt, *This Journal*, **106**, 722 (1959).
18. British Pat. No. 922,098, March 27, 1963.
19. For example; Chap. 9, "Electrodeposition of Gold" by Martin Frant from "Gold-Recovery, Properties, and Applications," E. M. Wise, Editor, Van Nostrand Co., New York (1964).
20. R. M. Finne and W. R. Bracht, *This Journal*, **113**, 551 (1966).
21. J. M. Leeds and M. Clarke, *Trans. Inst. Metal Finishing*, **46**, 1 (1968).

Stabilized Zirconia as an Oxygen Pump

D. Yuan and F. A. Kröger

Department of Materials Science, University of Southern California, University Park, Los Angeles, California

ABSTRACT

Electrolytic cells based on stabilized zirconia as a solid electrolyte may be used to remove oxygen from stationary or streaming gas. The minimum pressures (activities) that can be accurately measured are limited by the onset of electronic conduction in the electrolyte. In buffered gases, the lowest pressure that can be attained either by the capacity of the buffer or by the decomposition kinetics of the buffer molecules. Typical values of the oxygen pressures that can be reached when using commercial high-density sintered stabilized zirconia tubes as an electrolyte, are $\approx 10^{-38}$ atm at 530°C, 3×10^{-30} atm at 700°C, and 3×10^{-27} atm at 800°C.

Stabilized zirconia of the composition $Zr_{0.85}\ Ca_{0.15}\ O_{1.85}$ crystallizes in the CaF_2 type structure with the Ca^{+2} and Zr^{+4} occupying metal sites and oxygen occupying the nonmetal sites. The presence of 15% Ca gives rise to 7.5% vacant oxygen ion sites (1, 2). Electrical conduction in $Zr_{0.85}\ Ca_{0.15}\ O_{1.85}$ at high temperatures in air or oxygen is primarily due to the migration of oxygen ions through the movement of doubly charged oxygen vacancies (1, 3). At lower oxygen pressures electronic conduction sets in (4, 5). The value of the oxygen pressure at which the ionic transference number $t_i = 0.5$ is a function of temperature (6) and varies from sample to sample, possibly as a result of the presence of donor impurities in different concentrations (6, 7).

Stabilized zirconia can be used as a solid electrolyte in a galvanic cell with platinum contacts. Such cells, when operated with different oxygen pressures at the

two sides in the range of pressures where $t_i = 1$, can be used as a fuel cell (8), the voltage being given by

$$E = -\frac{RT}{4F} \ln (p_{O_2})_r/(p_{O_2})_1 \qquad [1]$$

On the other hand, operating with a known oxygen pressure at one side and an unknown one at the other, and again using Eq. [1], the cell can be used to measure the unknown pressure (4). Similar cells can be used to measure gas equilibrium constants or free enthalpies of formation of oxides (9).

In the range where stabilized zirconia is an ionic conductor, the passing of current transfers oxygen from the cathode side to the anode side. This has been used to adjust the stoichiometric composition of uranium oxides (10, 11). It has also been used to pump oxygen gas from the cathode side to the anode side, thus reducing the oxygen pressure at the cathode side in a known way. In experiments carried out by Heyne (12) the oxygen is removed from a closed system. It has been indicated, however, that the same principle can be used to remove oxygen from streaming gas in an open system (13). Strickler *et al.* (14), recognizing the dependence of the ionic current on the presence of oxygen gas at the cathode, used this dependence to determine t_i, but did not remove oxygen by passing current.

It is the object of the work reported in this paper to investigate the effectiveness of stabilized zirconia as an oxygen pump. As we shall see, it is possible to reach oxygen pressures as low as 10^{-38} atm at a flow rate of 4.6 cm³/sec at 530°C.

Experimental

The zirconia tubes used in the experiments were high density sintered calcia-stabilized zirconia, obtained from the Zirconium Company of America. It has the composition $(ZrO_2)_{0.9}(CaO)_{0.1}$ and x-ray analysis shows it to consist of two phases, the major phase being calcia-stabilized cubic zirconia, the minor one being monoclinic zirconia. One of the tubes had an inner diameter of 5 mm, the other of 12 mm, both having a wall thickness of 0.5 mm.

Inner and outer electrodes were made with the aid of Hanovia platinum paste. This is a fluxless mixture of 0.1μ platinum powder and resinous material suspended in an organic solvent; it is marketed in the United States by Engelhard Industries, East Newark, New Jersey. The inner electrode (I) is a continuous porous layer, a few microns thick, extending over $\approx$ 22 cm. It was made by pulling a cotton wool plug, wetted with Pt paste, through the tube, followed by heating to 500°C in air. This procedure leaves only platinum metal particles on the zirconia surface. This inner electrode is grounded. The outer electrode consists of three sections. One (II), the "pump" section, made again with the aid of Pt paste in the manner described above, is 14 cm long. The others (III, IV) are $\approx$ 0.5 cm. long and consist of platinum foil and 0.05 in. platinum wire wound around it, placed, respectively 2 and 6 cm away from the edge of II. Figure 1 shows the electrode arrangement. An additional Pt-Rh wire welded to the Pt contact wire at contact III forms a thermocouple which makes it possible to measure the temperature. The whole assembly is placed in an electric furnace, the temperature of which is kept constant to $\pm$ 2°C. Tank nitrogen is led through the tube at measured flow rates. The outside of the tube is kept in air. Application of a positive voltage at II relative to I leads to the removal of O_2 from the inside of the tube. The effectiveness of this "pumping" is determined by measuring the emf E_m of the cells III-I and IV-I, one being further removed from the pumping cell than the other. This is done with the object of determining whether pumping affects the gas over the entire cross section, or only over a thin layer near the surface. Currents are measured with a Simpson meter, and voltages with a Keithley 610 B high impedance voltmeter.

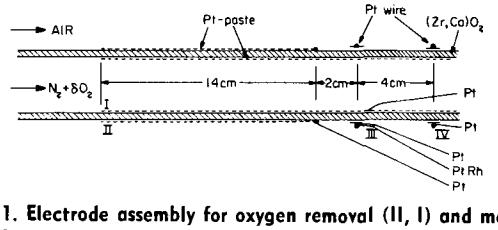

Fig. 1. Electrode assembly for oxygen removal (II, I) and measurement of oxygen pressure (III, I and IV, I).

Results

Initial experiments with no externally applied voltage, using Eq. [1] for E_m, showed that the tank nitrogen contained 2 x 10^{-5} atm O_2. The cell showed the temperature dependence as required by Eq. [1]. No appreciable emf was observed in symmetrical situations, *i.e.*, with nitrogen, air, or oxygen both in and outside the tube.

The results of pumping experiments at 530°C, using the narrow tube with a nitrogen flow rate of 4.6 cm³/sec inside and air outside, are shown in Fig. 2.

The values of the voltage E_m over the measuring cells III-I and IV-I are stationary state values, measured with the Keithley voltmeter without compensation. E_m is seen to increase with increasing current passed through the pumping section II-I. A sharp increase of E_m occurs at pumping currents J_{pump} between 0.7 and 2 ma. In this current range the removal of oxygen from the nitrogen passing through the tube approaches completion. The current at which complete oxygen removal is expected at the given flow rate and the oxygen content of 2 x 10^{-5} atm as determined at $J_{pump} = 0$, should the ionic transference number of the zirconia remain 1, is $J_{pump} = 0.6$ ma. The measuring cells III-I and IV-I, placed at different distances downstream from the pumping section give similar results, but the values of IV-I are systematically $\approx$ 3% lower than those of III-I. The fact that the two voltages are so close indicates that the oxygen is not just removed from a thin layer at the inner surface, maintained by laminar flow, but that there is depletion of oxygen over the entire cross section of the tube. This view finds support in an estimate of the diffusion length l. For oxygen at 530°C, the diffusion coefficient, $D \approx 0.9$ cm² sec^{-1}, and using a transit time $t = 0.1$ sec given by the time it takes the gas to flow from the right-hand edge of II to III at a flow rate of 4.6 cm³/sec in the tube with $d = 0.5$ cm, we find $l \approx (Dt)^{1/2} \approx 0.3$ cm $\approx r$, the radius of the tube. Since diffusion starts well before the edge of II is reached, t may be 2-4 times larger. Accordingly diffusion will

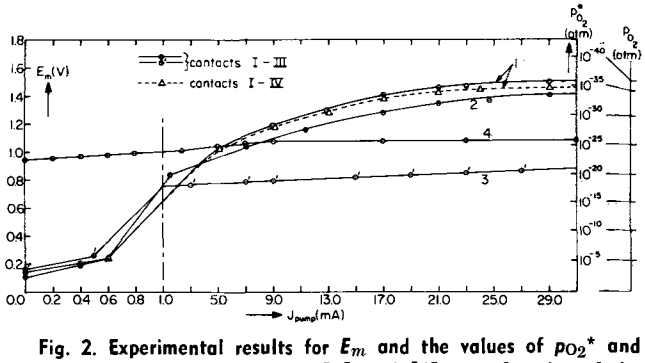

Fig. 2. Experimental results for E_m and the values of p_{O_2}* and p_{O_2} calculated from it with Eq. [1] and [4] as a function of the pumping current, with air as the outside atmosphere and an inner atmosphere consisting of: *1.* $N_2 + 2 \times 10^{-5} O_2$ passed through a liquid nitrogen trap; *2.* $N_2 + 2 \times 10^{-5} O_2$ direct from the tank; *3.* $N_2 + 2 \times 10^{-5} O_2$ passed through water at 25°C; and *4.* wet or dry $N_2 + 4 \times 10^{-5} CO_2$. Inner diameter of tube: 5 mm; flow rate 4.6 cm³/sec. Temperature: 530°C. Note the difference in scale for $J <$ and $>$ 1 ma.

effectively even out the oxygen concentration over the cross section. As we shall see, the small difference between cells III-I and IV-I is probably due to back diffusion from the end of the tube, contact IV being closer to the end than III. Curves 1-4 correspond to different conditions of the experiment. For curve 1 the nitrogen was dried by passing it through a liquid air trap. This leads to the highest voltage (= lowest residual oxygen pressure) attained: E_m = 1.5v, corresponding to $(p_{O_2}^*)_{min} = 10^{-36}$ atm. (Here and below, $p_{O_2}^*$ indicates pressure values calculated from Eq. [1]. As we shall see later, more correct values, given as p_{O_2} without asterisk, are calculated using a more general equation.) Using nitrogen directly from the tank (curve 2) gives E_m = 1.4v, $(p_{O_2}^*)_{min} = 10^{-34}$ atm. Since this suggests a dependence on the water pressure, a third experiment was carried out with nitrogen saturated with water at 25°C (curve 3). Now the minimum pressure obtained is considerably higher, $\approx 10^{-20}$ atm. In the fourth and fifth experiment the oxygen present in the nitrogen was transformed into a mixture of CO_2 and CO by passing the tank nitrogen over graphite at 650°C. For the fourth experiment, tank nitrogen was used as such. For the fifth experiment the gas was predried by means of a liquid air trap. No difference was observed (curve 4). The removal of oxygen in this manner leads to a relatively high E_m without pumping. On the other hand, pumping has little effect on E_m. The no-pumping value of E_m is considerably lower than is expected, should the mixture of CO_2 formed by passing the $N_2 + O_2$ over carbon at 600°C correspond to thermodynamic equilibrium. We shall return to this point later.

Instead of plotting E_m as a function of J_{pump} as shown in Fig. 2, we might plot E_m as a function of the pumping voltage, E_{pump}. There are, however, complications resulting from a time dependence of the current voltage characteristic: J_{pump}-E_{pump} curves obtained by measuring J_{pump} at different times after application of the voltage, are different for $E_{pump} \geqq 4$v. This is demonstrated in Fig. 3, where 1-2-3-4 and 1'-2'-3'-4' represent two different current-voltage sequences. In the first sequence E_{pump} is increased rapidly to 6v and held for 2 hr before decreasing the voltage to 3v. In the second sequence, E_{pump} is kept for 5 min at 9v. In both cases, but especially in the second sequence, lowering the voltage to 3v leaves a small excess current as compared to that in the cell in its initial state.

The change of J_{pump} with time indicates that at these voltages the zirconia of the pumping section is irreversibly changed. This effect is also indicated by the recovery time of the signal of the measuring cell. This recovery time is the time it takes the measuring cell to come back to its original, low, no-pumping value after interruption of the pumping current, indicating that the gas in the tube is again of the original composition. As shown in Fig. 4 for $E_{pump} > 4$v, this time depends on the time during which the pumping has taken place, the recovery time increasing with increasing pumping time. This dependence is stronger for larger E_{pump}. The semipermanent changes in the zirconia of the pumping section are related to its decomposition by electrolysis and/or its becoming polarized when no oxygen is available at the cathode. Thermodynamic data for ZrO_2 and CaO indicate, respectively, decomposition voltages for formation of the pure metals and oxygen at 1 atm of 2.52 and 2.84v at 530°C; in the solid solution employed, the value may be expected to be somewhat higher. The values given correspond to thermodynamic equilibrium. If currents are drawn, the applied voltage will be higher by the ohmic voltage drop. This brings the expected value for the voltage at which electrolysis occurs close to $\approx$ 4v. At voltages smaller than that required for electrolysis, polarization occurs, which gives rise to a change in the stoichiometric composition in the direction of metal excess at the nonreversible electrode. This in turn represents a change in the activity of the components of the compound at this electrode, the metal activity being increased, the oxygen activity being decreased. Note that polarization and electrolysis are closely related: electrolysis occurs when the polarization is so strong that the metal activity reaches the value at which pure metal may be formed. In the strongly polarized state the zirconia assumes a dark color (15, 16) and becomes partly electronically conductive (4-6). The theory of the polarization process and its consequences as far as electronic conduction is concerned is essentially the one given by Wagner for AgBr (17, 18). Phase diagram studies show that tetragonal zirconia saturated with zirconium may contain up to 3 x 10^{-2} excess Zr per molecule ZrO_2 at 1500°C, and probably < 10^{-2} at 530°C. Cubic zirconia, on the other hand, may contain up to 5.5 x 10^{-2} at 1500°C, and a similar value may be expected for calcia-stabilized zirconia. At 530°C this will be reduced to $\approx$ 2 or 3 x 10^{-2}. Although this is still an appreciable concentration, and the building up of this concentration will involve some time, it is doubtful whether it can account for the slow semipermanent changes observed.

A decision as to whether polarization and electrolysis both occur, or whether only polarization occurs, can be reached on the basis of the time dependence of the pumping current. Electrolysis should give a continuously increasing current. Polarization, on the other hand, requires a current approaching asymptotically a certain final value. Our data for voltages > 4v, indicate that electrolysis occurs.

On the basis of these arguments we expect a situation in which we have ionically conductive zirconia in the outer and central sections of the tube, electronically and ionically conducting zirconia, below the inner surface, and zirconium (and calcium) metal at the inner surface. Since application of a strong field tends to give rise to polarization as well as electrolysis, an initial concentration of the field at certain points,

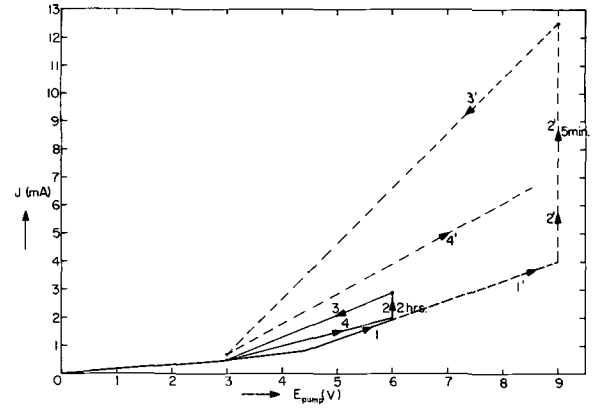

Fig. 3. Current voltage sequences 1-2-3-4 and 1'-2'-3'-4' of the pumping cell (II-I) for different times of operation.

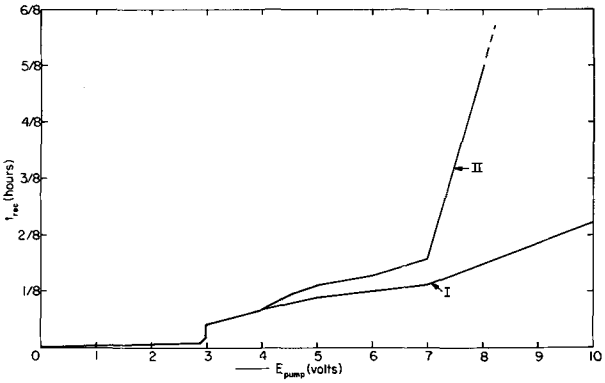

Fig. 4. The time (t_{rec}) needed by the measuring cell (III-I) to revert back to its pre-pumping emf. 1. For interruption of the pumping current immediately after its being established; and 2. for interruption of the pumping current 30 min after its being established.

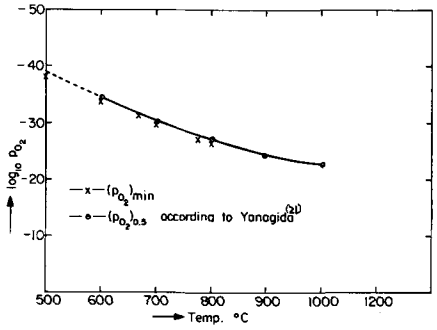

Fig. 5. $(p_{O_2})_{min}$ as $f(T)$ compared to the oxygen pressures $(p_{O_2})_{0.5}$ at which stabilized zirconia is 50% electronic conductor according to Yanagida (21).

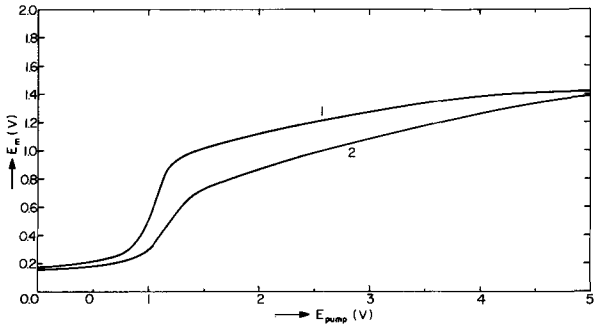

Fig. 6. E_m as $f(E_{pump})$ for a gas flow of 4.6 cm³/sec at 530°C for tubes with different inner diameter d: 1. d = 0.5 cm; 2. d = 1.2 cm.

e.g., at grain boundaries or dislocations, tends to give rise to the local formation of metal and electronically conducting zirconia which in turn tends to strengthen locally the field across the less affected part of the cross section. Thus both effects favor dendrite formation. Such dendrites have been observed with zirconia used in an electrode in magnetohydrodynamic power generators (15, 16).

Electrolysis occurs only at the pumping section which is affected directly by the pumping current. The oxygen-poor, partly decomposed inner surface goes on acting as a pump after interruption of the pumping current until it is reoxidized by the oxygen of the gas. If the oxygen content of the gas is low, as in our experiments, this may take a long time. This explains the long recovery time (measured with the measuring cell) plotted in Fig. 4.

The material of the measuring cell is affected only through the reduced oxygen activity in the gas. If this activity is sufficiently low, it will lead to an oxygen poor, electronically conducting material over part of the cross section. Decomposition with the formation of metallic zirconium will not occur: the lowest oxygen pressure that can be reached corresponds to the coexistence of oxygen-poor zirconia and metallic zirconium, and this does not represent a driving force for the nucleation and formation of metallic zirconium required for electrolysis.

Normally, E_m was measured with the Keithley voltmeter without compensation. Practically the same results are obtained for measurement of E_m with compensation, using the Keithley meter as a zero indicator. This indicates that the small current drawn by the meter does not upset the measurement.

In Fig. 5 the maximum values of E_m reached by pumping are compared with $E_{0.5}$, the emf of the ZrO_2-CaO diffusion cell calculated from Eq. [1] for $(p_{O_2})_{0.5}$; the latter represents the low oxygen pressure at which zirconia has equal ionic and electronic conductivities, Schmalzried's p_θ (20).

It is seen that the values of E_m are close to the values of $E_{0.5}$ found by Yanagida (21) for a tube of the same material as used by us.[1] At 800°C Yanagida's and our values for $E_{0.5}$ correspond to $(p_{O_2})_{0.5} \approx 5 \times 10^{-20}$ atm. Other reported values are considerably lower. Schmalzried's data (20) lead to $(p_{O_2})_{0.5} = 1.6 \times 10^{-32}$ atm. Patterson *et al.* (6) found values of 10^{-34} atm from conductivity measurements, and 10^{-39} atm from polarization experiments. These differences are partly due to differences (and possibly errors) in the measuring techniques, but differences may also result from differences in the composition of the zirconia used. This point deserves further study.

Figure 6 compares E_m as $f(E_{pump})$ for the wide tube (curve 2) and the narrow tube (curve 1) at equal flow rates. As expected, the wide tube is less efficient, although the performance is still satisfactory.

Attempts to measure the pumping efficiency at higher flow rates were complicated by temperature changes, fast flowing gas tending to cool the tube. Although pumping still takes place, uncertainties in the temperature make a quantitative evaluation more difficult. For this reason this line of investigation was not pursued any further.

Instead of removing oxygen from the gas in the tube, we can add oxygen by passing current through the pumping section in the opposite direction. Due to the relatively small pumping currents employed, for flowing gas the effect of oxygen addition is not very spectacular. Figure 7 shows the complete J-E characteristic including both types of operations. As mentioned before, the right-hand part of the characteristic at $E \geq 4$v is time dependent; the curve given corresponds to $t \leq 1$ min. The characteristic differs from that measured on a point electrode [Kleitz (13)] because the various sections of the pumping cell operate in different oxygen pressures. At voltages where the cell acts as a pump, the section near the edge where the flowing gas enters operates in the original oxygen pressure, whereas sections further down operate in an oxygen free environment. Since a change of the oxygen pressure shifts the zero current point of a cell, the total characteristic arises as the sum of contribu-

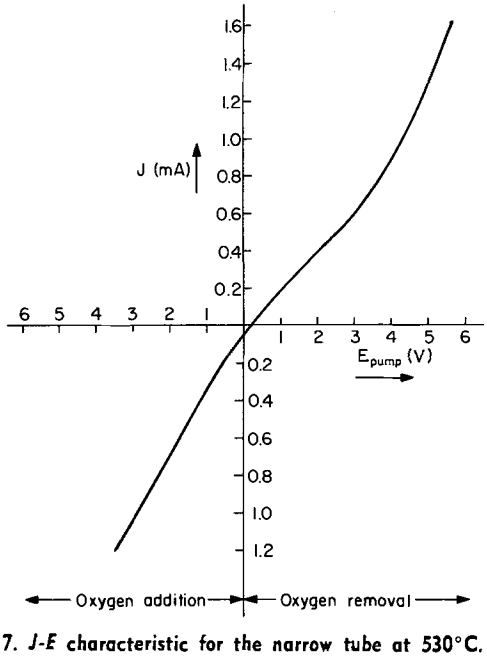

Fig. 7. J-E characteristic for the narrow tube at 530°C. Oxygen addition and removal refer to the inside of the tube.

[1] These values were arrived at by comparing the emf of the cell

$$Al, Al_2O_3 | (Zr, Ca)O_2 | O_2$$

with the theoretical emf calculated from the Gibbs free energy of formation of Al_2O_3 from Al and O_2

$$\frac{E}{E_{th}} = \ln (p_{O_2})_{0.5} \Big/ (p_{O_2})_{Al, Al_2O_3}$$

$(p_{O_2})_{Al, Al_2O_3}$ being the pressure of oxygen over Al in equilibrium with Al_2O_3.

tions from cells, the characteristics of which are shifted relative to each other. As a result the marked S-character of the individual characteristics is largely lost, although some is still observable.

Discussion

It has been shown that under favorable conditions (narrow pumping tube and reasonably low flow rates) stabilized zirconia may be used to reach extremely low oxygen pressures in flowing as well as stationary gases. Two points need closer examination. The first is that, as has been found, the value of $(p_{O_2}{}^*)_{min}$ attained by pumping is dependent on the presence of water vapor and or CO_2, high partial pressures of these gases limiting the lowest oxygen pressures that can be attained. The second point that needs examination is that values of E_m corresponding to values of p_{O_2} as low as reported can be measured at all.

The first effects are due to the capacity of H_2O and CO_2 to produce oxygen by dissociation

$$H_2O \rightarrow H_2 + \tfrac{1}{2}\,O_2 \qquad p_{O_2}{}^{1/2} = K_{H_2O} \cdot p_{H_2O}/p_{H_2}$$

$$CO_2 \rightarrow CO + \tfrac{1}{2}\,O_2 \qquad p_{O_2}{}^{1/2} = K_{CO_2} \cdot p_{CO_2}/p_{CO}$$

with

$$(K_{H_2O})_{530°C} = 6\text{x}10^{-14}\ \text{atm}^{1/2} \quad \text{and}$$

$$(K_{CO_2})_{530°C} = 1.2\text{x}10^{-14}\ \text{atm}^{1/2}$$

After the removal of the free oxygen originally present, dissociation of H_2O and CO_2 establishes a certain residual oxygen pressure. This residual pressure is lowered as more oxygen is removed and as more H_2 or CO is formed. The value actually attained in the relatively short time that the gas passes through the pumping cell depends on the rate of oxygen removal, on the rate of decomposition of the buffer molecules, or on the buffering capacity of the gas for oxygen removal. This buffering capacity must be expected to be greater when more H_2O or CO_2 is present. In the case of water-saturated gas, in which water (and thus oxygen) has been added to the gas, it may well be the increased buffering capacity that is responsible for the decreased pumping efficiency. For the gas mixture made by passing the oxygen-containing nitrogen over graphite at 650°C, no additional oxygen was added. Therefore, in this case the rate of decomposition of the buffer molecule (CO_2) must limit the pumping rate. This view is supported by results obtained by Kleitz (13) with stabilized zirconia in contact with Pt in a mixture of oxygen and CO_2 (Fig. 60, p. 97 of that reference).[2] Oxidation of graphite at $T < 1000$°C leads to partial pressures of CO_2 and CO determined by the kinetics of oxidation rather than by equilibrium (23). The emf of the measuring cell when no pumping is taking place indicates $p_{O_2} = 10^{-22}$ atm, corresponding to $p_{CO_2}/p_{CO} \approx 10^3$. Hence, $p_{CO_2} \approx 2 \times 10^{-5}$ atm (the original oxygen pressure) and $p_{CO} \approx 2 \times 10^{-8}$ atm.

The buffering capacity, but now against oxygen addition, must also be involved to explain why we can measure, without compensation, pressures as low as the ones found in the measurements. The main difficulty lies in the possibility of oxygen leaking back into the tube. There are three ways in which this may occur, *viz.*, (*i*) by counterstream diffusion from the open end of the tube, (*ii*) by diffusion through the tube wall, and (*iii*) as a result of the measuring current. Let us look at these three processes a little more closely.

Counterstream diffusion.—An estimate of the importance of counterstream diffusion may be made by calculating the oxygen pressure, built up a certain distance l up-stream away from the end in the time t required by the flowing gas to cover the distance l, if we start at $t = 0$ with an oxygen pressure step profile with $p_{O_2} = 0$ inside the tube, and $p_{O_2} = 0.2$ atm outside.

$$(p_{O_2})_{l,t} = 0.2\left[\,1 - \text{erf}\left(\frac{l}{2\sqrt{Dt}}\right)\right]$$

For the distances as shown in Fig. 1, with contacts III and IV respectively 6.7 and 2.7 cm from the end, the times involved are ≈0.33 and 0.14 sec. Taking again $(D_{O_2})_{530°C} \approx 0.9$ cm^2 sec^{-1} we find $(p_{O_2})_{III} \approx 2 \times 10^{-17}$ atm and $(p_{O_2})_{IV} \approx 10^{-8}$ atm. These figures have been arrived at with the aid of the tables of error functions given in ref. (24). The relatively large leak at electrode IV due to this mechanism can be largely removed by the use of a somewhat longer tube.

Diffusion through the tube wall.—In the well-sintered tube as used in our experiments, diffusion by neutral species is negligible. The only diffusion of importance involves charged species, moving through the bulk of the crystals. Such diffusion requires the simultaneous diffusion of ionic and electronic defects, *e.g.*, vacancies and electrons and/or holes. If the permeation is diffusion controlled, its rate is given by an expression similar to the one describing the rate of oxidation of a metal according to Wagner's theory of oxidation (12, 25).

$$j = \frac{RT}{8F^2d}\int_{p_{O_2}(\text{inside})}^{p_{O_2}(\text{outside})} \sigma t_i t_{el}\ d\ln\ p_{O_2}\ \text{g-moles/cm}^2\text{, sec} \qquad [2]$$

Here σ is the total conductivity, $t_{el} = 1 - t_i = t_e + t_h$, the total transference number for electrons (t_e) and holes (t_h) and d the thickness of the wall of the tube. Heyne (12) measured the permeation of stabilized zirconia (15% CaO) at 730°C from oxygen to vacuum, conditions under which only t_h is appreciable. Interpretation on the basis of the formula given above gave $t_h = 3 \times 10^{-4}$, smaller by a factor 7 from the value 2×10^{-3}, arrived at by extrapolating to this temperature the conductivity data by Patterson *et al.* (6). A second check can be made by comparing calculated values of $j\,d$ and experimental results by Smith *et al.* (26). At 800°C, from 25 Torr to high vacuum, $(j\,d)_{calc} = 2 \times 10^{-12}$ g-mole/cm, sec whereas $(j\,d)_{obs} = 10^{-14}$ g-mole/cm, sec. Thus in both cases the calculated value is smaller than the observed one. This indicates that the permeation is not entirely diffusion controlled, but is determined to some extent by surface processes. In any case, the formula may be used to find an upper bound to the permeation. Carrying out the integration with

$$\sigma_{el} = \sigma_e + \sigma_h = 4.6 \times 10^7\ p_{O_2}{}^{-1/4}\ \exp\ (-4.3\ \text{ev}/kT) + 8.8 \times 10^4\ p_{O_2}{}^{-1/4}\ \exp\ (-2.12\ \text{ev}/kT) \qquad [3]$$

as found by Patterson *et al.* (6), with outer and inner oxygen pressures of 0.2 and 10^{-38} atm, and $T = 530$°C, we find

$$j = j_e + j_h = 5.2 \times 10^{-17} + 2.6 \times 10^{-17} = 7.8 \times 10^{-17}\ \text{g-mole/cm}^2\text{, sec}$$

Permeation occurs through the wall section between the pumping section and the measuring electrodes with an area of 3.14 cm^2 for contact III and 9.42 cm^2 for contact IV. The times involved are 0.1 sec for III, 0.3 sec for IV. At a gas flow rate of 4.6 cm^3/sec, the permeated gas flows into gas volumes of 0.46, and 1.38 cm^3 respectively for the two cases and gives rise to $(p_{O_2})_{III} \approx 3 \times 10^{-12}$ atm and $(p_{O_2})_{IV} \approx 9 \times 10^{-12}$ atm. Since these are upper bounds, the actual values may be somewhat smaller.

Permeation as a result of the measuring current.—The Keithley 610B electrometer used for the measurements has an entrance impedance of $\geq 10^{14}$ ohms. Therefore a current of 10^{-14} amp flows at $E_m = 1$v. It flows in a direction opposite to that required for pumping, and represents a back flow of oxygen into the system of 2×10^{-20} g-moles/sec. At the rate of flow

[2] Note that Karpachev *et al.* (22), investigating the working of the Pt/zirconia electrode in CO, found rate limitation of the opposite process, the oxidation of CO to CO_2.

Table I. Effect of estimated oxygen leaks

	Electrode III, atm	Electrode IV, atm
Counterstream diffusion	2×10^{-17}	10^{-8}
Permeation	3×10^{-12}	9×10^{-12}
Monitor current	2×10^{-16}	2×10^{-16}

Table II. Combination of partial pressures of H_2O and H_2 in equilibrium with $P_{O_2} = 10^{-38}$ atm at 530°C and the corresponding initial water pressures (units: atmospheres)

p_{H_2O}	$p_{H_2} \approx (p_{H_2O})_{initial}$
10^{-10}	3×10^{-5}
10^{-12}	3×10^{-7}
10^{-13}	3×10^{-8}
10^{-14}	3×10^{-9}
10^{-16}	3×10^{-11}

of 4.6 cm³/sec this corresponds to a partial pressure of 2×10^{-16} atm of oxygen added to the gas in the tube.

Table I summarizes the effect of the various estimated oxygen leaks at electrodes III and IV. The fact that in all cases appreciably lower values are indicated by the voltage of the measuring cells must be due to the removal of the back diffusing oxygen by a buffer. Actually, the emf measured indicates an oxygen activity maintained by the buffer system rather than a real oxygen pressure. We use pressures only as a convenient way to express these activities. For the water system, the buffering action consists of the reaction of oxygen with H_2; for the CO_2/CO system it involves reaction with CO. In the latter case, the calculated p_{CO} is well in excess of the oxygen back flow so that the measurement will not affect the results. In the water system the buffering capacity depends on the presence of H_2. If no H_2 is present in the N_2 initially, all the H_2 active in the measuring section must be formed by decomposition of H_2O in the pumping period. The pressures required, though large relative to the extremely low oxygen pressures involved, are small when considered on an absolute basis; therefore formation of the required amount of H_2 during pumping is not unacceptable. Figure 8 shows the relation between p_{O_2} and possible values of p_{H_2} and p_{H_2O} at 530° in the gas after it has passed the pumping section, calculated under the assumption that equilibrium is attained. Oxygen pressures of $\leq 10^{-38}$ atm are seen to be possible for $p_{H_2} \geq 10^{-11}$ atm and p_{H_2O} between 10^{-8} and 10^{-16} atm. If the hydrogen has been created by the pumping, the initial water pressures must have been equal to $(p_{H_2O})_{initial} = (p_{H_2O})_{residual} + p_{H_2}$.

Table II shows a few combinations of partial pressures p_{H_2O} and p_{H_2} giving $p_{O_2} = 10^{-38}$ atm and the corresponding $(p_{H_2O})_{initial}$. A clue to which of these combinations was actually present when $p_{O_2} = 10^{-38}$ atm was measured at contact III lies in the increase of the measured oxygen pressure to $p_{O_2} \approx 10^{-36}$ atm at contact IV which must result from the countercurrent diffusion leak of $\approx 10^{-8}$ atm. Such an effect is to be expected if the hydrogen pressure, which determines the buffering capacity, is of the same order as the back flow leak, *e.g.*, $p_{H_2} \approx 2 \times 10^{-8}$ atm, $(p_{H_2O})_{residual} \approx 7 \times 10^{-14}$ atm, and thus $(p_{H_2O})_{initial} \approx 2 \times 10^{-8}$ atm. This last value is much higher than the equilibrium pressure of ice at liquid air temperature. However, it is probable that a single stage trap does not remove water vapor down to this theoretical limit, and a residual water pressure of $\geq 10^{-8}$ atm is not unlikely. Under these conditions, all the other leaks are small relative to the buffering capacity and therefore the buffering is practically complete.

Values of E_m actually measured are affected and ultimately limited by the occurrence of electronic conduction in the solid electrolyte at low oxygen pressures. The transition from $t_i = 1$ to $t_i = 0$ is a gradual one. For, whereas the ionic conductivity σ_i is approximately constant, the electronic conductivity $\sigma_e \propto p_{O_2}^{-1/4}$ (4-6). As a consequence $t_i = \dfrac{\sigma_i}{\sigma_i + \sigma_e} = \dfrac{1}{1 + \sigma_e/\sigma_i}$ requires a range of ≈ 10 orders of magnitude in p_{O_2} to change from $t_i = 0.95$ to $t_i = 0.05$. Figure 9 demonstrates this for $(p_{O_2})_{0.5} = 10^{-36}$ atm as observed at 530°C by Yanagida (21) and σ_e as given by Eq. [3]. The variation of t_i in turn affects the value of the measured emf which is given by (20)

$$E_m = -\frac{RT}{4F} \int_{p_{O_2}(\text{outside})}^{p_{O_2}(\text{inside})} t_i \, d\ln p_{O_2} \qquad [4]$$

Equation [4] is equivalent to [1] only if $t_i = 1$. If we apply [4] to our case in which $(p_{O_2})_{outside} = 1/5$ atm, under which condition $t_i = 1$, we find E_m as a function of p_{O_2} by carrying out the integration using t_i as a function of log p_{O_2} as shown in Fig. 9. The result is given in Fig. 10. The shape of the curve is as discussed by Schmalzried (20), the slope at each point

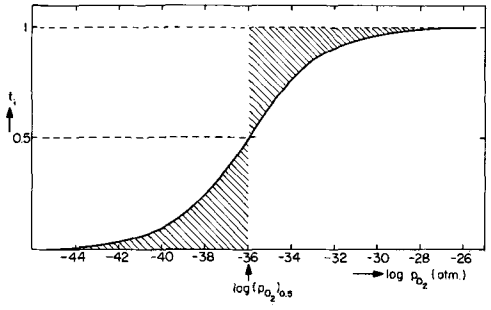

Fig. 9. t_i as a function of log p_{O_2} for σ_i = constant, $\sigma_e \propto p_{O_2}^{-1/4}$ and $(p_{O_2})_{0.5} = 10^{-36}$ atm.

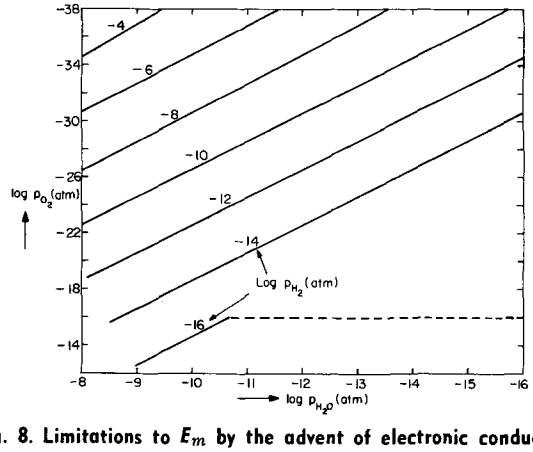

Fig. 8. Limitations to E_m by the advent of electronic conduction in the zirconia and the buffering capacity of various mixtures of H_2O and H_2.

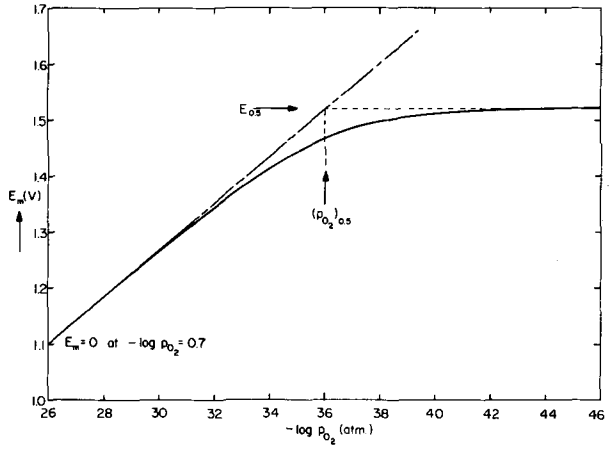

Fig. 10. E_m as a function of log p_{O_2} for the electrolyte characterized by Fig. 9 with $(p_{O_2})_{outside} = 1/5$ atm and $T = 530$°C.

being equal to 2.3 $\frac{RT}{4F}$ t_i. Since the curve t_i *vs.* log p_{O_2} shows inversion symmetry with respect to the point $t_i = 0.5$, the maximum contribution to the integral [4] from the range with $t_i < 0.5$ is just equal to the loss of voltage in the range where $1 > t_i > 0.5$ (the two contributions being proportional to the shaded areas in Fig. 9). Therefore, when the oxygen pressure inside the tube approaches zero, E_m approaches asymptotically the value calculated from [1] at $(p_{O_2})_{0.5}$.

Evidently for $p_{O_2} << 10^{-30}$ atm, the point where t_i starts to drop, values of the oxygen pressure p_{O_2}* deduced from E_m using [1] are considerably too high. The actual oxygen pressures reached in our pumping experiments may be found with the aid of Eq. [4] or Fig. 10. In Fig. 2 these are given as p_{O_2}; the minimum value, $(p_{O_2})_{min} = 10^{-38}$ atm is indeed markedly lower than the corresponding p_{O_2}*. Obviously the nonlinearity of E_m *vs.* log p_{O_2} near $(p_{O_2})_{0.5}$ has to be taken into account when the oxygen pump is used in experiments where the oxygen pressure must be exactly known. It should be pointed out that the results for $(p_{O_2})_{min}$ shown in Fig. 10 and 2 are based on $(p_{O_2})_{0.5}$ as measured by Yanagida (21) on a tube similar to ours, but with $\sigma_e \propto p_{O_2}{}^{-1/4}$ as reported in the literature (6). In case such pumps are to be used in applications where exact knowledge of p_{O_2} is necessary, it is prudent to either restrict the application to the range where [1] holds, or to measure $(p_{O_2})_{0.5}$ and σ_e as f (p_{O_2}) for the tube used and deduce a curve of the type of Fig. 10 for this tube.

Conclusion

Electrolytic cells based on stabilized zirconia as a solid electrolyte may be used to remove oxygen from streaming or stationary gas. Minimum oxygen pressures that can be accurately measured are limited by the onset of electronic conduction in the zirconia at low oxygen pressures. Typical values for the minimum oxygen pressure, reached when using commercial zirconia tubes, were 10^{-38} atm at 530°C and 3×10^{-27} atm at 800°C.

Acknowledgments

The authors had fruitful discussions with Dr. R. J. Brook and Dr. H. Yanagida and wish to thank them for their interest and advice. This work was supported by the Air Force Office of Scientific Research, Directorate of Chemical Sciences, under grant AF-AFOSR-68-1045.

Manuscript submitted Oct. 17, 1968; revised manuscript received Jan. 27, 1969.

Any discussion of this paper will appear in a Discussion Section to be published in the December 1969 JOURNAL.

REFERENCES

1. C. Wagner, *Naturwissenschaften*, **31**, 265 (1943).
2. F. Hund, *Z. physik. Chem.*, **199**, 142 (1952).
3. W. D. Kingery, J. Pappis, M. E. Doty, and D. C. Hill, *J. Am. Ceram. Soc.*, **42**, 393 (1959).
4. H. Schmalzried, *Z. Elektrochem.*, **66**, 572 (1962).
5. R. W. Vest and N. M. Tallan, *J. Appl. Phys.*, **36**, 543 (1965).
6. W. Patterson, E. C. Bogren, and R. A. Rapp, *This Journal*, **114**, 752 (1967).
7. F. A. Kröger, *J. Am. Ceram. Soc.*, **49**, 215 (1966).
8. J. Weissbart and R. Ruka, *This Journal*, **109**, 723 (1962).
9. J. Weissbart and R. Ruka, *Rev. Sci. Instruments*, **32**, 593 (1961).
10. S. Aronson and J. Belle, *J. Chem. Phys.*, **29**, 151 (1958).
11. T. L. Markin and L. E. J. Roberts, Symposium on the Thermodynamics of Nuclear Materials, Intern. Atomic Energy Agency, Vienna (1968).
12. L. Heyne, Nat. Bur. of Standards Special Publication No. 296 (1968), J. B. Wachtman, Jr. and A. D. Franklin, Editors.
13. J. Besson, C. Deportes, and M. Kleitz, Brevet Francais, No. provisoire 128327 (Nov. 1967); M. Kleitz, "Electrode Reactions in Solid Oxide Electrolytes," Thesis, Grenoble, 1968, p. 49.
14. D. W. Strickler and W. G. Carlson, *J. Am. Ceram. Soc.*, **47**, 120 (1964).
15. M. Guillou, J. Millet, M. Asquiedge, N. Busson, M. Jacquin, and S. Palous, *Compt. Rend. Ac.Sc., Paris*, **262**, 616 (1966).
16. J. Millet, C. Deportes, and M. Guillou, *Rev. Gen. Elec.*, **76**, 45 (1967).
17. C. Wagner, *Z. Electrochem.*, **60**, 4 (1956); B. Ilschner, *J. Chem. Phys.*, **28**, 1109 (1958); and D. O. Rayleigh, *J. Phys. Chem. Solids*, **25**, 329 (1965).
18. F. A. Kröger, "The Chemistry of Imperfect Crystals," Chap. 22, Interscience Publishers Inc., New York (1964).
19. R. Ruh and H. J. Garrett, *J. Am. Ceram. Soc.*, **50**, 257 (1967).
20. H. Schmalzried, *Z. physik, Chem. Frkf.*, **38**, 87 (1963).
21. H. Yanagida, Private communication.
22. S. V. Karpachev, A. T. Filjaev, and S. F. Pal'guev, *Electrochem. Acta*, **9**, 1681 (1964).
23. T. F. E. Rhead and R. V. Wheeler, *J. Chem. Soc. London*, **101**, 846 (1912).
24. Mathematical Tables Project, "Table of Probability Functions," Vol. I, Federal Works Agency, Works Project Administration, New York, 1941.
25. Ref. 18, Chap. 21, p. 837.
26. A. W. Smith, F. W. Meszaros, and C. D. Amata, *J. Am. Ceram. Soc.*, **49**, 240 (1966).

Erratum

An error has been discovered in Table I, p. 611, of the Technical Note "A Study of the Dissipation Factor (Tan δ) of Corrosion Product Films Formed on Aluminum Alloys in Hot Sodium Chloride Solutions" by W. H. Anthony which was published in the June 1968 issue of the Journal, Vol. 115, No. 6, p. 610.

The first row of this table reads:

Alloy	Silicon	Iron	Copper	Manganese	Magnesium	Chromium	Zinc	Titanium
5454H16	0.11	0.22	0.04	0.84	3.90	0.09	0.02	0.009

Subsequent analysis of this alloy has shown that the magnesium content and the zinc content were in error.

The correct analysis is as follows:

5454H16	0.10	0.21	0.04	0.76	2.70	0.10	0.06	0.01

The Formation of Chlorine Pentafluoride in an Electrochemical Cell

I. From Chlorine Trifluoride

Howard H. Rogers,* Sheldon Evans,* and Julian H. Johnson

Rocketdyne, A Division of North American Rockwell Corporation, Canoga Park, California

ABSTRACT

Coulometric experiments undertaken with chlorine trifluoride in anhydrous hydrogen fluoride resulted in the formation of chlorine pentafluoride in a divided or an undivided electrolytic cell. The yields of chlorine pentafluoride, based on current, in the undivided and the divided cell were of the order of 25 and 50% respectively. Fluorine, nickel fluoride, and small quantities of chlorine-oxygen-fluorine compounds were also formed at the anode. At the cathode, hydrogen, hydrogen chloride, and chlorine were formed depending on the degree of mixing of anolyte and catholyte. Nickel electrodes were used almost exclusively; however, chlorine pentafluoride was also formed at a Glassy Carbon anode. The rate of formation of chlorine pentafluoride was found to be a function of the concentration of chlorine trifluoride in the electrolyte. From an analysis of polarization data, it was concluded that the mechanism involved the anodic oxidation of fluoride ion to some form of active fluorine, followed by its reaction with chlorine trifluoride to form chlorine pentafluoride.

Anodic oxidations of oxygen- and/or nitrogen-containing compounds in hydrogen fluoride have shown that nearly complete fluorination generally results. For example, oxygen difluoride was formed from the oxidation of water (1), and nitrogen trifluoride was formed from the oxidation of ammonia (2). In this laboratory, nitroxy fluoride, nitrogen trifluoride, and oxygen difluoride were formed by the oxidation of nitrous oxide at a nickel anode (3). Therefore, it seemed reasonable that chlorine pentafluoride (4), would result from the anodic oxidation of chlorine trifluoride dissolved in anhydrous hydrogen fluoride. Vapor pressure measurements (5) have shown that the vapor pressure of the system, 14 m/o (mole per cent) chlorine trifluoride-86 m/o hydrogen fluoride, at 0°, was 527 mm.

This paper deals with a study of the electrochemical synthesis of chlorine pentafluoride from the hydrogen fluoride-sodium fluoride-chlorine trifluoride system.

Experimental

Electrolytic cell and associated apparatus.—A portion of this study was carried out in an undivided cell which was previously described (6). The divided cell (Fig. 1) was utilized in an effort to gain a better understanding of the anodic and cathodic reactions. The cell was divided in both the liquid and gaseous phases to minimize mixing of both anolyte and catholyte reactants and products. The liquid phase divider was an open end tube of porous Teflon (Pall Corporation, Glen Cove, New York). The bottom end of the tube was closed by a disk of solid Kel-F. The walls of the tube were ¼ in. thick and the mean pore opening was specified by the manufacturer to be 9μ. Since the pore size was relatively large, and since hydrogen fluoride wets Teflon, relatively free flow of electrolyte through the Teflon occurred as a result of slight shifts in electrolyte level or thermal gradients in the cell. The wall temperature in the cathode compartment was about −16°, while the anolyte temperature was 10° during electrolysis. With the exception of the reference electrode and level detection system, the other features of this cell were similar to the undivided cell.

The level detection system consisted of a sight tube and two probes, one of which was also a thermocouple well, while the other probe also supported a mercurous fluoride reference electrode. The probes were connected to an a-c-operated electrical alarm to indicate when the level rose or fell below the indicated maximum or minimum. A mechanical refrigeration system was used to supply chilled (−16°) methanol to the condensers and cell jacket. The anolyte was not cooled directly because of the cell geometry.

The design of the mercury reference electrode (Fig. 2) was based upon the work of Koerber and DeVries (7), except that mercurous fluoride was not added intentionally to the electrode. It was found to maintain its potential within 0.1v even after being made anodic to the normal anode and after passage of several milliamperes of current.

The schematic of the anodic product handling system and electrolytic cells is shown in Fig. 3. A separate cathodic product handling system (not shown) is similar to the anodic system.

Electrical apparatus.—The power supply, constant current regulator, and associated recorders have been described (6). Electrode potentials against the reference electrode were read with either a Keithley Model 621 Electrometer or with a transistorized instrument (8).

Polarization curves were taken automatically with the aid of a potentiostat and ramp generator (9). With this equipment, a linearly increasing and decreasing

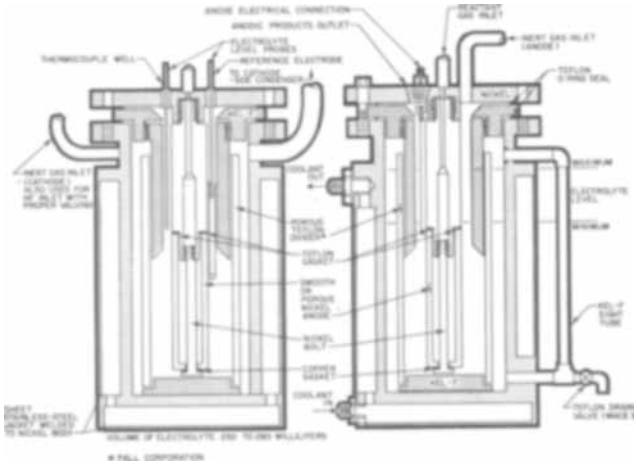

Fig. 1. Divided electrolytic cell (cylindrical)

* Electrochemical Society Active Member.

Key words: chlorine pentafluoride, electrolysis, hydrogen fluoride, electrochemical synthesis, chlorine trifluoride.

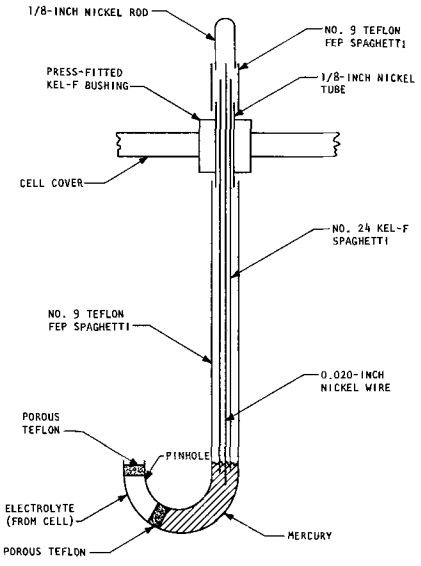

Fig. 2. Mercury reference electrode

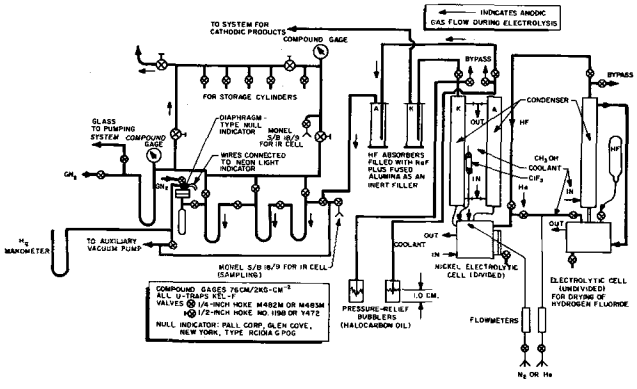

Fig. 3. Electrolytic cells and system for anodic products

anodic or applied voltage (0.17 v/sec usually) could be applied to the electrolytic cell, while the voltage and the logarithm of the current were plotted on an Electro Instruments, Inc., Model 500 X-Y Recorder.

Chemicals.—The Matheson "anhydrous" hydrogen fluoride (99.9% min. purity) was dried overnight in the undivided electrolytic cell (Fig. 3) by periodic reversal of current (6), and then distilled into the divided cell. J. T. Baker Company Reagent Grade sodium fluoride was used after drying at 110° for 16 hr. Matheson chlorine trifluoride (98.0% min. purity) was used directly from the cylinder.

The hydrogen fluoride absorption columns were packed with Harshaw sodium fluoride pellets, No. 0202 T ⅛, mixed with alumina spheres, Norton Alundum Size 8F, E-163, with all particles removed which passed a 12 mesh screen.

Electrolysis procedure.—After electrolytic drying of hydrogen fluoride, about 250 ml were distilled into the divided cell, which contained the dried sodium fluoride, used as a conductivity additive. The dissolution of the sodium fluoride resulted in the formation of a 3 m/o solution. Streams of inert gas (nitrogen or helium) at constant flow rates between 20 and 50 cc/min were fed into the gas space of both the anode and cathode compartments. Up to 6 m/o of liquid chlorine trifluoride was then added to the anolyte (anolyte volume *ca.* 130 ml). When the cell was to run for sustained periods, periodic additions of chlorine trifluoride were necessary to replace that lost by volatilization, anodic oxidation, and diffusion to the catholyte. All electrolyses were carried out at constant current.

After passage through the hydrogen fluoride absorption column, the mixture of anodic products, volatilized chlorine trifluoride, and inert gas (at a known flow rate) passed through the remainder of the anodic system, as indicated in Fig. 3. This product stream was sampled periodically and infrared spectra were taken. The partial pressures of chlorine pentafluoride were then calculated with the aid of the following formulas, where ΔA is the difference in absorbance.

$$P_{mm(ClF_5)} = \Delta A\ (104) \qquad \text{at } 786\ cm^{-1}$$

$$P_{mm(ClF_5)} = \Delta A\ (1.25) \qquad \text{at } 732\ cm^{-1}$$

The data for the above equations were obtained with chlorine pentafluoride which was prepared electrochemically and purified by fractionation through a —112° trap. The only contaminant was a trace of chloryl fluoride. The data (precision ±20%) was in good agreement with that from chlorine pentafluoride prepared by a different route (4). Although more precise analytical procedures were available, they were not required for the purposes of this study. This infrared method was used because it was rapid and convenient, thereby permitting a large number of determinations in a reasonable period of time.

The determination of fluorine in the anode gas stream was carried out by first removing condensable product by passing the stream through —78° and —183° traps. The partial pressure of the fluorine which was mixed with the inert carrier gas, was found by observing the volume change on shaking the mixture with mercury.

Analysis of cathodic products was also carried out by periodic sampling of the gas stream. Mass spectrometry was used for the analysis of hydrogen, chlorine, and hydrogen chloride. Infrared spectrometry was used for fluorine compounds. All yields were based on the amount of current passed.

Anode considerations.—Both smooth and porous nickel anodes of the same outside dimensions, corresponding to an apparent surface area of 66 cm^2, were used for synthesis. Anodic polarization curves indicated that the porous anode had an effective surface area approximately 3½ times greater than the smooth anode. Allowable cell current was limited by heat generation in the anode compartment. Generally, the smooth anode was operated at a constant current of 1 amp, while 2 amp were used with the porous anode. Measured applied voltages ranged from 5 to 7, and anode potentials (against the mercury reference electrode) were about 1½v less.

Results

Results of electrolyses of the hydrogen fluoride-sodium fluoride-chlorine trifluoride system are described below.

Anodic products.—Chlorine pentafluoride yields in the divided cell were larger than 50% for over 2 hr even though no additional chlorine trifluoride was added to the initial 6 m/o. Other gaseous products were fluorine, chloryl fluoride, and occasionally chlorine dioxide and perchloryl fluoride. Large quantities of chlorine trifluoride were entrained with the effluent chlorine pentafluoride. However, yields of chlorine pentafluoride of about 12%, substantially free of chlorine trifluoride, were obtained directly by starting with 0.6 m/o rather than 6 m/o of chlorine trifluoride. Conventional vacuum fractionation was used to remove the by-products.

Cathodic products.—Cathodic products were hydrogen, hydrogen chloride, and chlorine. When 0.6 m/o chlorine trifluoride was used as the starting anolyte, analysis of the products of a typical experiment gave a mole ratio for the above products of 1:0.1:0.02 (82% total cathodic yield). However, when 6 m/o chlorine trifluoride was used, the mole ratio found for a typical experiment was 1:20:6 (85% total cathodic yield). In this latter experiment, chlorine pentafluoride was also found in the cathodic gas stream, in an amount corresponding to an anodic yield of 8%. The chlorine pentafluoride was accompanied by chlorine trifluoride.

Table I. Effect of ClF_3 concentration on yield (current), divided cell

Mole % ClF_3 added to anolyte	% Yield ClF_5 (max.)	% Yield F_2
0.6	12-17	43-52
1.2	17	*
3	36	*
6	51	*

* Not analyzed.

Effect of concentration of chlorine trifluoride.—The yield of chlorine pentafluoride (from the anode compartment) as a function of chlorine trifluoride concentration in the anolyte is shown in Table I. The yield of fluorine obtained when small concentrations of chlorine trifluoride were present in the anolyte is also indicated.

Nickel dissolution.—Nickel was used almost exclusively as an anode material. During electrolysis in the undivided cell, in the hydrogen fluoride-sodium fluoride electrolyte, the current equivalent of the nickel weight loss was 9.5 ma/cm². Such electrolyses were routinely carried out during the electrolytic drying of HF; the equivalent current of the nickel weight loss was highly reproducible. Under the same conditions, but in the presence of 0.6 or 1.2 m/o of chlorine trifluoride, the current equivalents of the anode weight loss were about 4 ma/cm² or 2 ma/cm², respectively.

Studies of other anode materials.—Polarization curves of many materials[1] indicated that only one, Glassy Carbon (Tokai Electrode Manufacturing Company, Tokyo, Japan), had electrical characteristics close enough to nickel to be considered for use as an anode. Electrolysis in the divided cell with a Glassy Carbon anode substituted for nickel resulted in a 35% yield of chlorine pentafluoride after 3 m/o of chlorine trifluoride was added to the anolyte. Although no carbon tetrafluoride was found as an anodic product, complete disintegration of the anode into granular carbon occurred after several hours of operation.

Effect of impurities.—Chlorine pentafluoride was prepared using hydrogen fluoride drawn directly from the cylinder; however, smaller amounts of the oxygen-containing impurities chloryl fluoride, perchloryl fluoride, and chlorine dioxide resulted when the hydrogen fluoride was dried first. In either case, continued electrolysis oxidized the impurities more rapidly than the chlorine trifluoride, so that the quantity of oxygen-containing by-products decreased as a function of time.

Electrochemical data.—Representative anodic polarization curves determined on nickel in the divided cell in the hydrogen fluoride-sodium fluoride and hydrogen fluoride-sodium fluoride-chlorine trifluoride systems are shown in Fig. 4. The low-current portions of the curves are presented to focus attention on the potential region below that corresponding to the oxidation of the solvent. The higher current portions of the curves were not significantly different in the presence or absence of chlorine trifluoride. Polarization curves determined on sheet nickel electrodes in the undivided cell under steady-state conditions were similar to those presented in Fig. 4.

Discussion

Conditions are favorable in the hydrogen fluoride-sodium fluoride system (*e.g.*, indifferent electrolyte, high mobility of fluoride ion) for finding species which would be oxidized below the decomposition potential of hydrogen fluoride. It can be seen (Fig. 4) that, in the hydrogen fluoride-sodium fluoride-chlorine trifluoride system, no substantial oxidation process occurred below the potential corresponding to the oxidation of fluoride ion. During coulometric experiments chlorine

[1] Cu, Au, Zn, Cd, Al, Sn, Pb, Ti, Zr, Nb, Cr, Mo, W, Mn, Fe, Co, Monel, Carbon 371A, Graphite 8826, Pyrographite, Glassy Carbon, Si, and SiC.

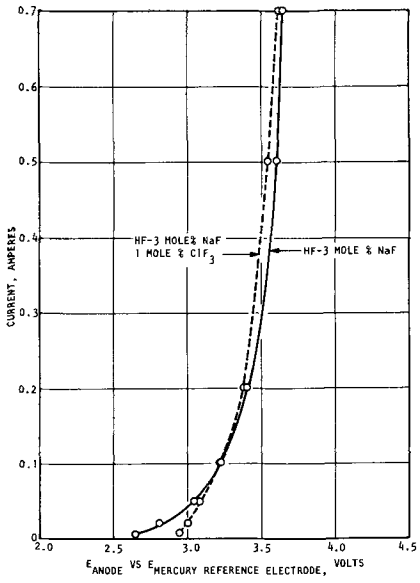

Fig. 4. Polarization curves, HF-NaF and HF-NaF-ClF_3 systems, porous nickel anode (area 66 cm²), divided cell, linear anodic scan rate, 0.17 v/sec, electrolyte temperature, *ca.* 0°C.

pentafluoride was not found at potentials below the decomposition potential of HF. It is concluded that ClF_3 is not electrochemically oxidized below the decomposition potential of HF. The rate of production of ClF_5 increased with increasing anode potentials above the decomposition potential for HF_2^-. Thus, while it may be possible that ClF_3 is directly oxidized at potentials near this decomposition potential, the similarity of the polarization curves (Fig. 4) suggests a common electrochemical reaction, namely the oxidation of fluoride ion.

In one series of experiments, fluorine was bubbled past a nickel anode under conditions which closely approximated those used during electrosynthetic runs, except that no current was passed from an external source. Chlorine pentafluoride was not found among the products. Both short circuit current, and potential measurements, gave no evidence for any electrochemical reaction.

It is postulated that the formation of chlorine pentafluoride results from a reaction at the anode, between chlorine trifluoride and electrochemically generated active fluorine.[2] The basic electrochemical step is shown as Eq. [1].

$$HF_2^- \rightarrow F\cdot + e^- + HF \qquad [1]$$

Subsequent steps are hypothesized which involve reactions of active fluorine with chlorine trifluoride, another active fluorine, or in the case of a nickel anode, with the metal.

$$ClF_3 + F\cdot \rightarrow [ClF_4\cdot] \qquad [2a]$$

$$[ClF_4\cdot] + F\cdot \rightarrow ClF_5 \qquad [2b]$$

$$F\cdot + F\cdot \rightarrow F_2 \qquad [3]$$

$$2F\cdot + Ni \rightarrow NiF_2 \qquad [4]$$

It is obvious from Eq. [2a] and [2b] that an increase in chlorine trifluoride concentration should cause an increase in the rate of formation of chlorine pentafluoride as observed (Table I). At the same time, since the rate of formation of active fluorine should be constant at constant cell current, less active fluorine should have been available for side reactions (Eq. [3] and [4]). Hence the observed large decrease in the extent of nickel dissolution would have been expected.

The participation of complex compounds of nickel has been suggested for the electrochemical fluorination

[2] For convenience, F· is used to represent active fluorine, but does not imply that the form of active fluorine is known.

of organic compounds (10). Since the synthesis of chlorine pentafluoride has been successfully demonstrated at a Glassy Carbon anode, the formation of complex nickel compounds as a necessary condition for the synthesis can be ruled out in this case.

In another investigation in this laboratory, it was found (4) that the following reaction (Eq. [5]) took place when small amounts of water reacted with chlorine pentafluoride dissolved in anhydrous hydrogen fluoride, in an all plastic system. Perchloryl fluoride

$$ClF_5 + 2H_2O \rightarrow ClO_2F + 4HF \quad [5]$$

and chlorine dioxide were also found when the reaction was carried out in metal. The presence of chloryl fluoride, perchloryl fluoride, and chlorine dioxide as products from the metal electrolytic cell could, therefore, easily have been a result of hydrolysis of the primary electrolysis product, chlorine pentafluoride.

Chlorine dioxide, also found as an impurity in the starting material, chlorine trifluoride, would be expected to have been oxidized at the anode during electrolysis, possibly according to the following equation. While Eq. [5] and [6] probably caused reduced

$$ClO_2 + F\cdot \rightarrow ClO_2F \quad [6]$$

yields of chlorine pentafluoride, oxygen-containing impurities were consumed so that the yields of oxygen-containing products decreased during the course of electrolysis.

A negligible degree of mixing occurred in the cell during electrolysis with low concentrations of chlorine trifluoride in the anolyte. Under these conditions, the cathodic product was essentially hydrogen, as expected. At higher concentrations of chlorine trifluoride, significant quantities of chlorine trifluoride were present in the catholyte. The cathodic products were then primarily hydrogen chloride and chlorine.

Acknowledgment

The research described in this paper was supported by the Office of Naval Research under Contract Nonr 1818(00). The suggestion of Dr. Emil A. Lawton that chlorine pentafluoride might be formed by the anodic oxidation of chlorine trifluoride was instrumental in initiating this work.

Manuscript submitted Oct. 2, 1968; revised manuscript received Jan. 20, 1969.

Any discussion of this paper will appear in a Discussion Section to be published in the December 1969 JOURNAL.

REFERENCES

1. J. H. Simons, *This Journal*, **95**, 47 (1949).
2. O. Ruff, *Z. anorg. allgem. Chem.*, **172**, 417 (1928).
3. H. H. Rogers, S. Evans, and J. H. Johnson, *This Journal*, **111**, 704 (1964).
4. D. Pilipovich, W. Maya, E. A. Lawton, H. F. Bauer, D. F. Sheehan, N. N. Ogimachi, R. D. Wilson, F. C. Gunderloy, Jr., and V. E. Bedwell, *Inorg. Chem.*, **6**, 1918 (1967).
5. M. T. Rogers, J. L. Speirs, and M. B. Parrish, *J. Phys. Chem.*, **61**, 366 (1957).
6. H. H. Rogers, S. Evans, and J. H. Johnson, *This Journal*, **111**, 701 (1964).
7. G. C. Koerber and T. DeVries, *J. Am. Chem. Soc.*, **74**, 5008 (1952).
8. H. H. Rogers, *Rev. Sci. Instruments*, **34**, 250 (1963).
9. H. H. Rogers, *ibid.*, **36**, 866 (1965).
10. J. Burdon and J. C. Tatlow, in "Advances in Fluorine Chemistry," M. Stacey, J. C. Tatlow, and A. G. Sharp, Editors, Vol. I, Academic Press, New York (1960).

The Formation of Chlorine Pentafluoride in an Electrochemical Cell

II. From Chlorine

Howard H. Rogers,* Rudolf Keller,* and Julian H. Johnson

Rocketdyne, A Division of North American Rockwell Corporation, Canoga Park, California

ABSTRACT

Galvanostatic experiments were performed at electrolyte temperatures near 0°C with chlorine in anhydrous hydrogen fluoride. Chlorine pentafluoride formed at current yields of up to 18%, and chlorine monofluoride, chlorine trifluoride, fluorine, nickel fluoride, and chloryl fluoride were also found. Both divided and undivided electrolytic cells were used, and the formation of hydrogen and hydrogen chloride at the cathode depended on the degree of mixing of anolyte and catholyte. While the most satisfactory anode was porous nickel, chlorine pentafluoride and chlorine monofluoride were also formed at sheet nickel anodes and at a Glassy Carbon anode. The rate of formation of chlorine monofluoride was found to be a function of the concentration of chlorine at the anode while the rates of formation of chlorine pentafluoride and chlorine trifluoride were not. The addition of chlorine at a nickel anode during electrolysis at constant current above a minimum current density caused a gradual rise in anodic potential. This rise was attributed to the formation of, or a change in, an anodic film. The polarization data were consistent with a mechanism that involved the anodic oxidation of fluoride ion to some form of active fluorine. Chlorine monofluoride, chlorine trifluoride, and chlorine pentafluoride were apparently formed by the stepwise reaction of the active fluorine with chlorine.

The oxidation of chlorine trifluoride during electrolysis in anhydrous hydrogen fluoride has been shown (1) to result in the formation of chlorine pentafluoride. It was of considerable interest to determine whether elementary chlorine also would react at the anode and be oxidized to the plus five state. This paper describes a study of the oxidation of chlorine during electrolysis in anhydrous hydrogen fluoride.

Experimental

Equipment including the electrolytic cells, procedures, experimental conditions, and analytical techniques were almost the same as those previously em-

* Electrochemical Society Active Member.

Key words: chlorine pentafluoride, electrolysis, hydrogen fluoride, electrochemical synthesis, chlorine.

ployed in the synthesis of chlorine pentafluoride from chlorine trifluoride (1). All yields were calculated on the basis of current, which was maintained constant during all electrolyses. Although both divided and undivided cells were used, most of the experimental work was carried out in the divided cell using a porous nickel anode (Kwikset Powdered Metal Products, Anaheim, California). Chlorine (Matheson High Purity Grade, 99.5% min.) was passed through the porous metal into the anolyte.

Cleaning of the anode was accomplished by washing with water and then heating to approximately 600° in a hydrogen atmosphere for several hours. Nickel fluoride hydrates that had not been removed by washing with water were converted to nickel, water, and hydrogen fluoride.

A Glassy Carbon anode (Tokai Electrode Manufacturing Company, Tokyo, Japan) was also used. Since this material is impervious, chlorine was passed through a series of small holes drilled into a Teflon plug placed in the lower end of the tubular carbon anode. This arrangement sufficed to test the effectiveness of the Glassy Carbon in the hydrogen fluoride-sodium fluoride-chlorine system.

Early experiments were carried out in the undivided electrolytic cell using a sheet nickel anode (2). This system was similar to those of Schmeisser (3) and Sartori (4). The chlorine was fed to the anode surface from a short length of pierced Teflon spaghetti tubing, attached along the bottom edge of the anode.

Partial pressures of chlorine monofluoride and chlorine trifluoride were calculated with the aid of the following formulas, where ΔA is the difference in infrared absorbance. The baseline method was used to obtain the data for Eq. [1]. More satisfactory results

$$P_{mm(ClF)} = \Delta A\ (500) + 10 \qquad \text{at } 788\ cm^{-1} \qquad [1]$$

were obtained when the difference in absorbance from the background was used to obtain the data for Eq. [2].

$$P_{mm(ClF_3)} = \Delta A\ (78) + 2 \qquad \text{at } 761\ cm^{-1} \qquad [2]$$

Results

Products.—The gaseous anodic products of the electrolysis of the system consisting of anhydrous hydrogen fluoride, 3 m/o (mole per cent) sodium fluoride and chlorine were found to be chlorine pentafluoride, chlorine monofluoride, chlorine trifluoride, fluorine, and chloryl fluoride. The oxygen-containing compounds resulted from impurities in the chemicals used. Typical yields in the divided cell were chlorine pentafluoride 12%, chlorine monofluoride 49%, and chlorine trifluoride 2%, at a current of 2 amp (30 ma/cm^2) and a flow rate of chlorine through the anode of 50 cc/min.

The primary gaseous cathodic product was hydrogen. However, hydrogen chloride was also found as a cathodic product as a result of mixing of anolyte and catholyte. Mole ratios of hydrogen to hydrogen chloride of 19:1 and 9:1 were found when chlorine flow rates through the anode were 10 and 25 cc/min, respectively.

Effect of chlorine flow rate.—The yield of chlorine pentafluoride was determined in the divided cell as a function of the flow rate of undiluted chlorine through the porous anode. It was found that the yield of chlorine pentafluoride increased as the flow of chlorine was increased from 10 cc/min to 60 cc/min. From 60 cc/min to the largest flow used, 100 cc/min, there was no further change in the yield.

Changing the flow rate of chlorine through the anode could have caused changes in the concentration of chlorine in the anolyte. In addition, the efficiency of the anode as a gas electrode could also have been affected because of changes in diffusion conditions. To isolate the effect of changes in chlorine concentration, the partial pressure of chlorine was varied in a chlorine-nitrogen mixture. The total gas flow was kept constant to minimize variations in the diffusion conditions at the gas electrode. In a separate experiment, nitrogen was found to be unreactive at the anode during electrolysis.

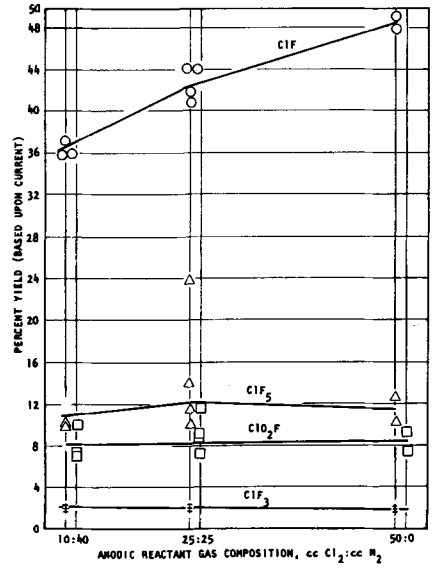

Fig. 1. Effect of partial pressure of Cl_2 on yield, electrolyte temperature, *ca.* 0°C.

The results (Fig. 1) show that the amount of chlorine monofluoride produced increased with increasing partial pressure of chlorine, whereas the chlorine pentafluoride yield remained constant. Furthermore, the amount of chlorine trifluoride determined in the gaseous products did not vary significantly.

After electrolysis had been carried out at a constant flow rate of a 1:4 chlorine-nitrogen mixture for 2½ hr, the chlorine flow was stopped and the nitrogen flow was increased to maintain a constant total gas flow. The yield of chlorine monofluoride decreased drastically from 37 to 15%, whereas the yields of the other products were unaffected (Fig. 2) during the period of measurement. Similar results were obtained when starting with undiluted chlorine.

Effect of impurities.—As with previous work when the starting material was chlorine trifluoride (1), oxygen impurities caused the yield of chlorine pentafluoride to decrease. The oxygen-containing by-product was primarily chloryl fluoride (Fig. 1), although small amounts of perchloryl fluoride and chlorine dioxide were occasionally found. As the amount of chloryl fluoride decreased during electrolysis in the divided cell, the yield of chlorine pentafluoride increased (Fig. 2). In another set of experiments when impurity levels were lower, 18% yields of chlorine pentafluoride were observed.

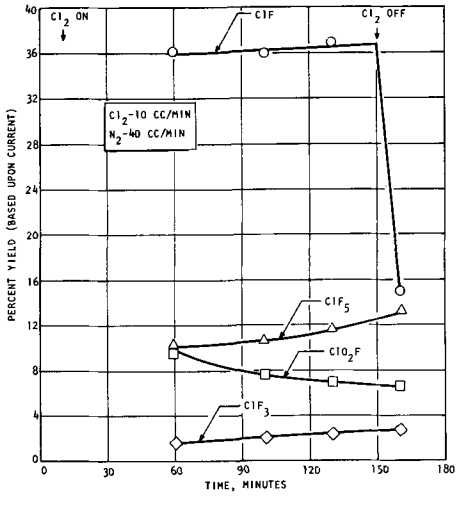

Fig. 2. Effect of Cl_2 on yield (total flow: Cl_2 + N_2 = 50 cc/min), electrolyte temperature, *ca.* 0°C.

Analysis of the anolyte at a time when the yields of chlorine pentafluoride and chloryl fluoride were approximately equal showed 0.015 m/o of chlorine dioxide.

Solubility of chlorine in hydrogen fluoride.—The anolyte was analyzed both before and after the addition of chlorine through the anode at a rate of 10 cc/min for 30 min. The concentration of chlorine at an anolyte temperature of —16° was 0.002 m/o. At —64°, the solubility of chlorine in hydrogen fluoride was found to be at least 2 m/o.

Electrochemical data.—Typical steady-state conditions for the formation of chlorine pentafluoride were: applied cell voltage, 7v at 2 amp (30 ma/cm^2) in the divided cell using a porous nickel anode, or 1 amp (15 ma/cm^2) in the undivided cell using a sheet nickel anode. Variations of the cell voltage as great as ±2v were observed in steady-state operating conditions.

Electrolysis (undivided cell) in the hydrogen fluoride-sodium fluoride-chlorine system with a nickel anode was accompanied by a characteristic, gradual rise in measured anode potential from about 4 to 6v. This rise was obtained only when the current was sufficiently large (Fig. 3), and only after the introduction of chlorine (Fig. 4); inert gas was ineffective. Chlorine pentafluoride was not found as a product unless the anodic potential had risen to the 6v level.

Representative anodic polarization curves determined on nickel in the divided cell in the hydrogen fluoride-sodium fluoride and the hydrogen fluoride-sodium fluoride-chlorine systems are shown in Fig. 5 and 6. As in the previous paper (1), the low-current portions of the curves (Fig. 5) are presented to focus attention on the potential region below that corresponding to oxidation of the solvent. The higher current portions of the curves (Fig. 6) are shown to illustrate the effect of the characteristic rise in potential on the polarization curves.

Polarization curves taken in the undivided cell with sheet nickel electrodes were similar to those taken in the divided cell with a porous nickel anode (Fig. 5 and 6). It was found, however, that a current of at least 2 amp was required to initiate the characteristic rise in potential at the porous anode compared to a current of 0.5-1.0 amp found for the sheet nickel anodes. The electrochemical data obtained from the divided cell with a smooth nickel anode were similar to that obtained in the undivided cell with sheet nickel electrodes.

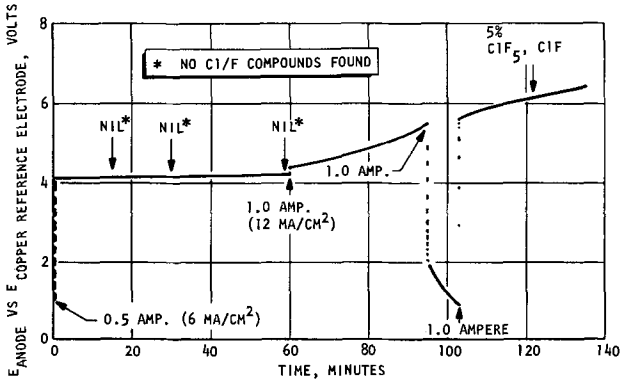

Fig. 3. Behavior of anode potential during a typical run with HF-NaF-Cl$_2$ system, undivided cell, electrolyte temperature, *ca.* 0°C.

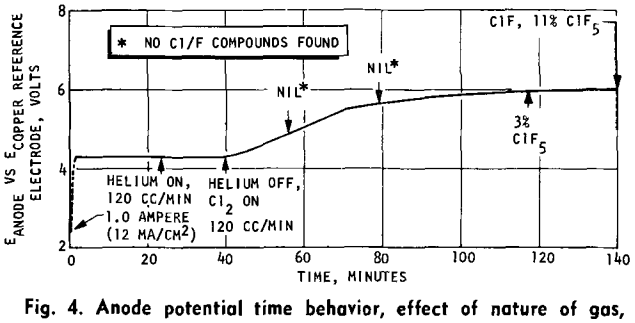

Fig. 4. Anode potential time behavior, effect of nature of gas, electrolyte temperature, *ca.* 0°C.

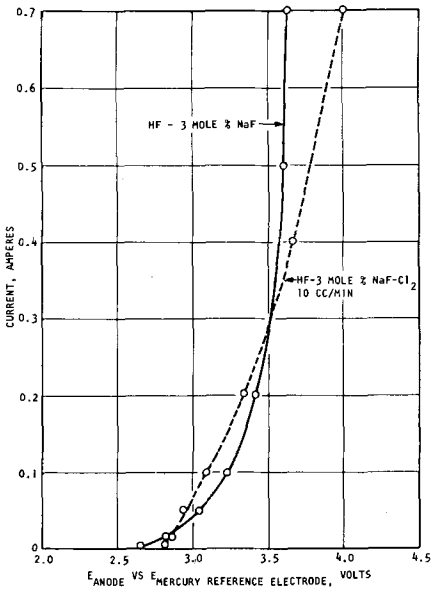

Fig. 5. Polarization curves, HF-NaF and HF-NaF-Cl$_2$ systems, porous nickel anode (area 66 cm^2), divided cell, linear anodic scan rate, 0.17 v/sec, low current region, after several hours electrolysis at 3.2 amp, electrolyte temperature, *ca.* 0°C.

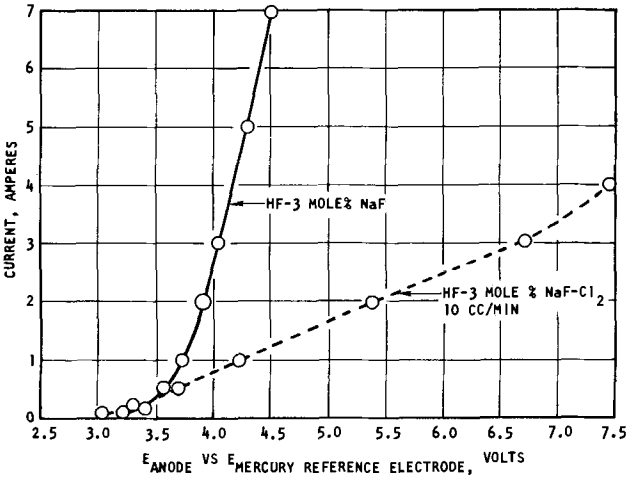

Fig. 6. Polarization curves, HF-NaF and HF-NaF-Cl$_2$ systems, porous nickel anode (area 66 cm^2), divided cell, linear anodic scan rate, 0.17 v/sec, high current region, after several hours electrolysis at 3.2 amp, electrolyte temperature, *ca.* 0°C.

When a Glassy Carbon anode was substituted for a nickel anode in the divided cell, yields of chlorine pentafluoride of 3.5% and of chlorine monofluoride of 4.3% were obtained at a constant current of 2 amp, an applied voltage of 8v, and a chlorine flow rate of 50 cc/min. The gradual rise in potential, which was characteristic of nickel, was not observed with Glassy Carbon. Instead, a rapid 1.5v increase was observed 3 min after the introduction of chlorine. However, potentials at the Glassy Carbon anode were erratic during the first 40 min of electrolysis.

Discussion

The oxidation of chlorine at the anode in a hydrogen fluoride-sodium fluoride electrolyte seems to take place by a mechanism generally similar to that proposed (1) for the anodic oxidation of chlorine trifluoride. Examination of the polarization curves (Fig. 5) for the

hydrogen fluoride-sodium fluoride-chlorine system shows that no substantial oxidation process occurs below the potential corresponding to the oxidation of fluoride ion. As in the oxidation of chlorine trifluoride (1), the similarity of the polarization curves (Fig. 5) again suggests a common electrochemical reaction (Eq. [3]).

$$HF_2^- \rightarrow F\cdot + e^- + HF \quad [3]$$

Subsequent steps probably involve the reaction of active fluorine with chlorine-containing species, as shown below.

$$Cl\text{-}Cl + F\cdot \rightarrow ClF + Cl\cdot \quad [4]$$

$$Cl\cdot + F\cdot \rightarrow ClF \quad [5]$$

$$F\cdot + F\cdot \rightarrow F_2 \quad [6]$$

$$Cl\cdot + F_2 \rightarrow ClF + F\cdot \quad [7]$$

$$\left.\begin{aligned} ClF + F\cdot &\rightarrow [ClF_2\cdot] \\ [ClF_2\cdot] + F\cdot &\rightarrow ClF_3 \end{aligned}\right\} \quad [8]$$

$$\left.\begin{aligned} ClF_3 + F\cdot &\rightarrow [ClF_4\cdot] \\ [ClF_4\cdot] + F\cdot &\rightarrow ClF_5 \end{aligned}\right\} \quad [9]$$

$$Ni + 2F\cdot \rightarrow NiF_2 \quad [10]$$

Chlorine monofluoride and chlorine trifluoride appear as intermediate products in this reaction sequence. Chlorine trifluoride, as the most soluble compound, accumulates in the electrolyte and its concentration directly affects the yield of chlorine pentafluoride (1). Chlorine monofluoride is soluble to a much lesser extent and its concentration in the electrolyte may be the limiting factor in the formation of chlorine pentafluoride from chlorine.

A change in chlorine partial pressure is equivalent to a change in the concentration of chlorine at the anode and thereby affects the yield of chlorine monofluoride (Fig. 1 and 2), according to Eq. [4], [5], and [6]. The yields of the other products are unchanged, apparently because the electrolyte is saturated with chlorine monofluoride so that its concentration is constant.

When oxygen-containing impurities (*e.g.*, water) are present, they compete with the intermediate products and are apparently preferentially fluorinated. The primary by-product is chloryl fluoride, which appears to be formed at the expense of chlorine pentafluoride. The yields of chlorine pentafluoride and chloryl fluoride are approximately inversely proportional.

Anodic polarization curves in the hydrogen fluoride-sodium fluoride-chlorine system with a nickel anode showed higher potentials at high currents than had been found for the hydrogen fluoride-sodium fluoride system alone (Fig. 6). At constant current, a characteristic gradual potential rise with time was observed above a minimum current density (6 ma/cm², Fig. 3) and only on the introduction of chlorine (Fig. 4). It was found that neither chlorine pentafluoride nor chlorine monofluoride was generated until the potential had reached 6v (Fig. 3 and 4). A possible explanation for the increase in potential is an increase in resistance at the nickel anode seen as a change in the slope of the polarization curves (Fig. 6). This increase in resistance may be attributed to the formation of, or a change in, a film at the anode.

It is of significance that the formation of chlorine-fluorine compounds is not dependent on the chemical nature of the anode material (nickel). Both chlorine monofluoride and pentafluoride were formed at a Glassy Carbon anode which had operating potentials close to that of nickel.

Acknowledgment

This research was carried out with the sponsorship of the Office of Naval Research under Contract Nonr 1818(00). The assistance of Dr. C. J. Schack and the advice and encouragement of Dr. E. A. Lawton are gratefully acknowledged.

Manuscript submitted Oct. 2, 1968; revised manuscript received Jan. 20, 1969.

Any discussion of this paper will appear in a Discussion Section to be published in the December 1969 JOURNAL.

REFERENCES

1. H. H. Rogers, J. H. Johnson, and S. Evans, *This Journal*, **116**, 601 (1969).
2. H. H. Rogers, S. Evans, and J. H. Johnson, *ibid.*, **111**, 701 (1964).
3. M. Schmeisser and P. Sartori, *Chem. Ing. Techn.*, **36**, 9 (1964).
4. P. Sartori, *Angew. Chem., internat. Edit.*, **2**, 261 (1963).

Electrochemical Behavior of Sulfide in Fused LiCl-KCl Eutectic

F. G. Bodewig* and James A. Plambeck**

Department of Chemistry, University of Alberta, Edmonton, Alberta, Canada

ABSTRACT

Liquid sulfur has been reduced coulometrically in fused LiCl-KCl eutectic at 420°C. Nernstian behavior is observed for the cell C, S(l)/$S^=$, LiCl-KCl// Pt^{++}, LiCl-KCl/Pt. The standard potentials of the sulfur/sulfide couple at 450°C with respect to the appropriate standard platinum reference electrode are —1.008, —1.039, and —1.219v on the molar, molal, and mole fraction scales, respectively. Voltammetric studies showed an anodic wave at +0.03v ascribed to $2S + 2Cl^- \rightarrow S_2Cl_2 + 2e^-$ and a cathodic wave at —0.92v ascribed to $S + 2e^- \rightarrow S^=$. The diffusion coefficient of the (poly)sulfide ion was found to be 3.12×10^{-6} cm²/sec at 420°C by chronopotentiometric measurements. The observed blue color of sulfur-sulfide solutions is ascribed to polysulfide ions.

Solutions of heavy metal sulfides in fused chlorides are believed to be ionic (1-3), and a reversible sulfur vapor electrode has been used in a recent study (3) of the cell Ag/AgCl, Ag_2S/C, S_2(g) over the temperature range 490°-860°C. Kiukkola and Wagner (4) have measured the emf of the cell Ag(s)/AgI(s)/Ag_2S(s), S(l), C to obtain the standard molar free energy of formation of Ag_2S. A large body of emf data now exists in the fused LiCl-KCl eutectic at 450°C (4, and references cited therein); it therefore appeared de-

* Electrochemical Society Student Member.
** Electrochemical Society Active Member.

sirable to obtain comparable data for the sulfur-sulfide couple. Sulfide has been studied voltammetrically in fused halides by Delarue (6, 7) and Rempel and Malkova (8), Delarue's work being in the LiCl-KCl eutectic. Potentiometric, voltammetric, and chronopotentiometric techniques were used in the present study.

Experimental

Apparatus.—Potentials were measured with a digital voltmeter (Model 3440A, Hewlett-Packard). Coulometric generations employed a Model IV Coulometric Current Source (E. H. Sargent and Company). An Anotrol Model 4100 Potential Controller modified to operate with a Model 4510 linear scan unit (Magna Electronics) was used for voltammetric investigations. Chronopotentiometric investigations employed a Model 6824A power supply-amplifier (Hewlett-Packard) in a constant current configuration controlled by appropriate mercury-wetted relay switching circuitry; measurements were recorded on a Hewlett-Packard Model 175A oscilloscope equipped with 1750B and 1781B plug-in units and a Model 196B camera using ASA 3000 Polaroid film.

The temperature of the 3 in. diameter vertical tube furnace was controlled by a Model 3120-SCR-477 temperature controller (Marshall Products Company). Temperatures were measured with a chromel-alumel thermocouple calibrated at the melting point of zinc.

The electrolytic cell and glassware preparation have been described previously (9).

Solvent.—The LiCl-KCl eutectic solvent [59.5 m/o (mole per cent) LiCl, mp 352°C] was prepared by the method of Maricle and Hume (10) modified as described below.

A total of 600g of the component salts was mixed and melted without previous drying. Chlorine gas dried over magnesium perchlorate was bubbled through the melt for 2 hr. After purging the melt with nitrogen for 4 hr, magnesium ribbon was introduced to displace any heavy metal ions. Subsequently, chlorine was again introduced to oxidize any magnesium metal that may have dissolved in the melt, followed by nitrogen. The molten eutectic was transferred to large test tubes in charges of 120-140g inside a glovebox purged with nitrogen. The test tubes were sealed and stored for future use.

Chemicals.—Reagent grade LiCl (Fisher Scientific Company) and KCl (Shawinigan Chemicals) were used. The sulfur (sublimed; Fisher Scientific Company) was dried at 100°C prior to use. Graphite electrodes were Special Spectroscopic Electrodes ⅛ in. in diameter (National Carbon Company). Nitrogen was purified over hot copper turnings and dried by passage through a magnesium perchlorate column.

Procedure.—The crucible containing the frozen eutectic and isolation compartments with electrodes was placed inside the outer glass jacket of the electrolytic cell which could be connected to a vacuum pump. Transfers of frozen eutectic to the jacket were made inside the glovebox. The outer jacket could also be closed off with a machined Teflon stopper with holes for up to five isolation compartments, a thermocouple, and a nitrogen inlet tube. The isolation compartments were made of Pyrex sealing tubes with 10-20μ frits (D porosity; Ace Glass Inc.) and protruded through the Teflon stopper. A hole below the Teflon stopper allowed entry of nitrogen into the otherwise closed compartments to equalize pressure. The temperature of the cell was then raised slowly to 420°-430°C under vacuum in order to dry thoroughly the glass equipment and electrodes before fusion of the eutectic. The compartments were allowed to fill with eutectic during a further 8 hr at this temperature. Finally, purified nitrogen was introduced and allowed to pass over the melt during all experiments.

A reference electrode based on the Pt(II)/Pt couple (about 0.04M) was generated coulometrically for each experiment by anodization of a 3 cm^2 Pt foil sealed into Pyrex tubing; a current density of 7 ma/cm^2 was employed. All potentials were measured against this reference electrode and are reported with reference to the Pt(II) (1.0M)/Pt standard molar platinum electrode (SMPE) (11), conforming to the IUPAC "Stockholm" sign convention. The counter and indicator electrodes each consisted of a graphite rod.

The boiling point of sulfur (444°C) being very close to the temperature of 450° at which the emf data were desired, it was necessary to work either with a vapor electrode or a liquid electrode and extrapolate from higher or lower temperatures to 450°. The liquid electrode appeared simpler [ref. (3) then not being available], and the sulfur electrode used consisted of an isolation compartment with a pool of liquid sulfur floating on the melt. Electrical contact with the pool was made by a graphite rod attached to Nichrome leads well above the sulfur pool. Sulfide was initially added to the compartment as Li_2S, but this proved unsatisfactory due to hydrolysis and the difficulty in transferring known amounts to the compartment. The addition of sulfide by cathodic coulometric reduction of the sulfur pool proved more satisfactory and was used for all experiments reported here. Precautions were taken to ensure that an excess of liquid sulfur was always present, and more was added as necessary.

The sulfide electrode emf was measured against the same reference electrode for each run which normally included three different sulfide compartments. During the course of one run the sulfide concentration in each of the compartments was successively increased by coulometric reduction of sulfur. The reduction product was blue in color (see below). The graphite electrode had a geometric area of about 2.5 cm^2 and a current density of 8 ma/cm^2 was employed. The thermoelectric potential between the graphite and platinum electrodes was found to be +1.5 mv with respect to the platinum electrode in the temperature range of 400°-450°C. All emf values were corrected accordingly.

The electrodes used in the chronopotentiometric investigations were gold wires (0.05 cm in diameter) suspended in the melt or rhenium wires sealed in glass. Other metals such as tungsten or platinum were unsatisfactory because they became coated, presumably with insoluble sulfide. The geometric area of the gold electrode was calculated from its diameter and depth of immersion, that of the rhenium electrode from its diameter and the length of metal exposed. The carbon rods used in the emf studies were also used as the voltammetric indicator electrodes.

The amount of solvent in each isolation compartment was determined by a potentiometric chloride analysis. When necessary, sulfide was removed from aqueous solution as H_2S by addition of nitric acid and purging with nitrogen. The concentrations of $S^=$ and Pt^{++} ions were determined from the coulombs passed and the solvent volume as described previously (11).

Least square calculations were carried out on the University of Alberta IBM System/360 computer.

Results

Standard potential of the sulfur-sulfide couple.—Five runs were carried out with new compartments, electrodes, and eutectic charge used in each. A total of 89 concentration-potential data points were taken over the range 400°-440°C, each point the mean of two potentials measured 15 min apart. In general the emf became constant, to within 0.5 mv, 15-30 min after coulometric reduction of sulfur had been terminated and did not change more than 1 mv over a period of several hours. The temperature of the melt was recorded at the time of each potential measurement. The effect of temperature on the emf was determined for various sulfide ion concentrations with both increasing and decreasing temperature. Plots of measured potential against temperature were linear over the range 400-440°C for a fixed sulfide ion concentration. Plots of $\Delta E/\Delta T$ against the logarithm of the molar con-

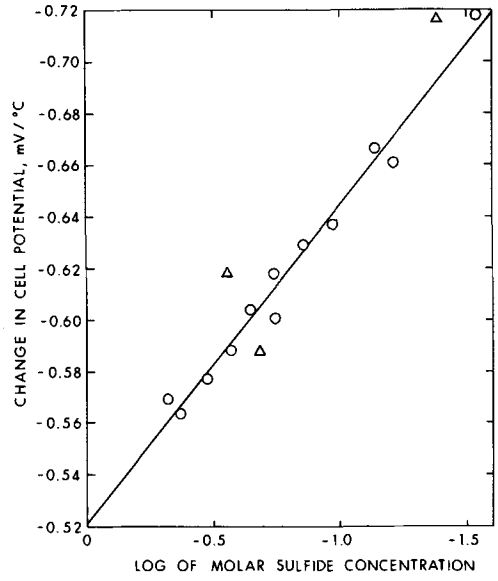

Fig. 1. Temperature dependence of potential as a function of sulfide ion concentration. Line is that given by least-squares analysis. Points indicated by triangles not included in least-squares analysis.

centration of sulfide were linear over the concentration range 0.03-0.5M as shown in Fig. 1. Least square analysis gave, for the temperature dependence of the cell (—)C, S(l)/$S^=$, LiCl-KCl//Pt^{++}, LiCl-KCl/Pt (+), $\Delta E/\Delta T = +0.124 \log [S^=] - 0.520$ mv/°C with a relative standard error of 4.4% in the slope and of 1% in the intercept. This equation was used to extrapolate all measured potentials to 450°. Linear Nernst plots were obtained for these extrapolated potentials over the concentration range 0.03-0.5M sulfide. Less stable potentials were obtained at lower sulfide concentrations. A typical plot of potentials against the logarithm of sulfide concentration (Fig. 2) shows that Henry's law is obeyed over the concentration range studied. A summary of all runs is given in Table I. Least square analysis of all points gave a standard potential (molarity scale) at 450°C of —1.008v with a standard deviation of 0.002v. This corresponds to values of —1.039v and —1.219v with the same standard deviation on the molality and mole fraction scales, respectively (11), all potentials being with respect to the appropriate standard platinum electrode. The slope of the Nernst plot was —0.0772 v/log unit with standard deviation of 0.0015, corresponding to a value of 1.86 ± 0.04 for the number of electrons taking part in the reaction. This is in good agreement with the theoretical value of 2 expected for $S + 2e^- \rightarrow S^=$.

Table I. Standard emf determinations for the $S/S^=$ couple*

Sulfide molarity	No. of points	E°(v) M	Standard deviation (mv)	Exper. n
0.093-0.15	6	−1.010	1.3	1.81
0.095-0.15	6	−1.008	6.7	1.80
0.054-0.25	7	−1.012	0.7	1.75
0.037-0.21	7	−1.012	0.8	1.80
0.045-0.20	7	−1.015	1.3	1.72
0.045-0.22	6	−1.007	0.4	1.98
0.036-0.18	6	−1.009	1.6	2.02
0.071-0.43	7	−1.004	0.2	2.09
0.055-0.20	5	−1.007	0.9	2.03
0.19-0.48	5	−1.006	0.3	2.19
0.092-0.28	5	−1.007	0.2	2.13
0.035-0.26	7	−1.004	0.9	1.79
0.030-0.32	8	−1.002	0.6	1.83
0.046-0.31	7	−1.004	1.3	1.72
Least square analysis of all points	89	−1.008	1.5	1.86

* Two emf readings taken at each point 15 min apart, except for run 1; temperature converted to 450°C; all potentials given with respect to SMPE; each entry is a separate compartment, the first two being run 1 and the remainder, other runs with three compartments per run.

Voltammetric results.—Voltammetric scans of the pure eutectic melt with a graphite electrode gave the curve denoted by circles in Fig. 3. The potential was increased in the reduction direction and the current was measured after it had become constant (generally 5-10 sec). After addition of sulfur to the compartment, the curve denoted by triangles in Fig. 3 was obtained. For the cathodic rise, which we ascribe to the reaction S (l) + $2e^-$ → $S^=$, extrapolation of the lower part of the curve to zero current gave —0.92 ± 0.02v for the "decomposition" potential (mean and standard deviation of 5 experiments), in agreement with the potentiometric measurements cited above. We ascribe the anodic wave to the reaction 2S(l) + Cl^- → S_2Cl_2 + $2e^-$ which Delarue (7) estimated to occur at about —0.05v. The "decomposition" potential determined in this study is +0.03 ± 0.02v (mean and standard deviation of 5 experiments). These measurements were carried out at 420° ± 2°C as were all other voltammetric and chronopotentiometric studies reported here.

Voltammetric curves were also obtained in compartments in which sulfur was present and sulfide had been generated coulometrically at concentrations ranging from 0.1 to 0.5M. Two typical curves are shown in Fig. 4, obtained from two different concentrations in the same compartment. Identical straight lines were always obtained regardless of the direction of voltage change as long as precautions were taken to prevent significant change in the sulfide concentration between measurements. These precautions included stirring and, when necessary, oxidation or reduction such

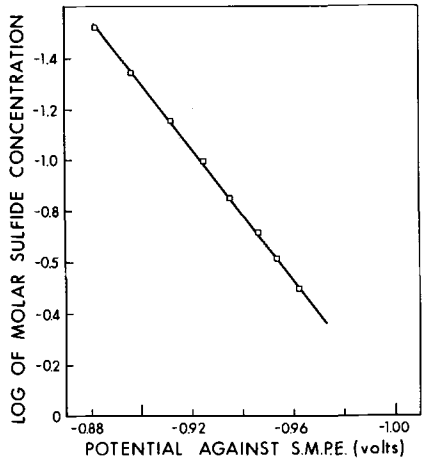

Fig. 2. Electromotive force of sulfide electrode (vs. SMPE) as a function of sulfide concentration in a typical run. Temperature (extrapolated) 450°C.

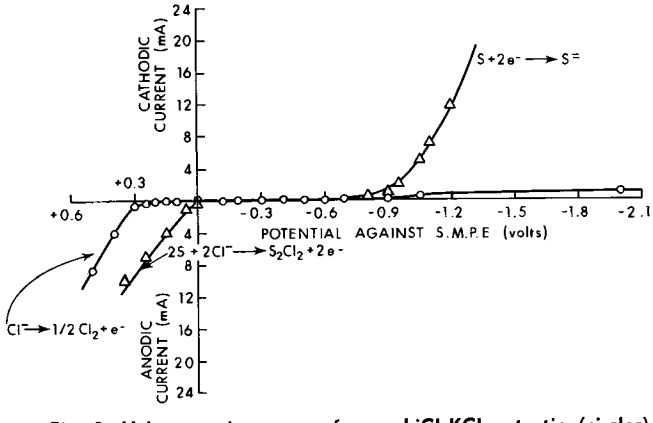

Fig. 3. Voltammetric curves of pure LiCl-KCl eutectic (circles) and of eutectic with sulfur present (triangles). Temperature 420°C, graphite electrode area 2.5 cm^2, reference potential SMPE.

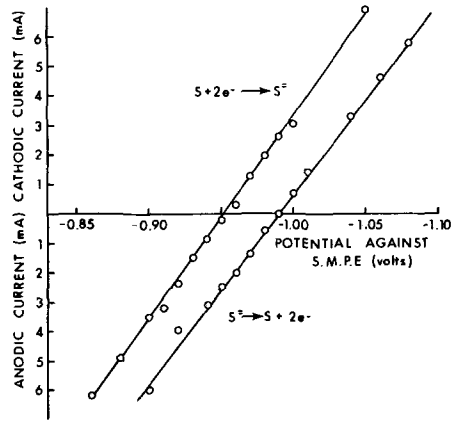

Fig. 4. Current-potential curves for different sulfide concentrations in the same compartment. Reference potential SMPE, temperature 420°C.

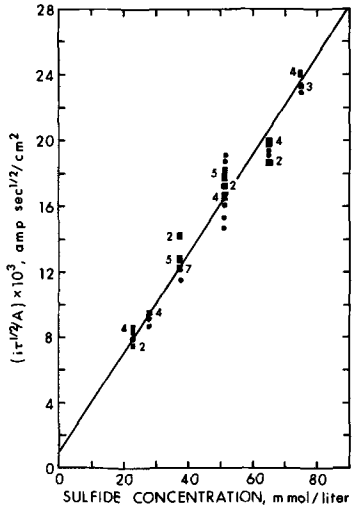

Fig. 5. Variation of chronopotentiometric constant $i\tau^{1/2}/A$ with sulfide concentration, showing obedience to Sand equation. Solid circles, single points; solid rectangles, multiple points, with number given.

that the zero-current potential remained within 3 mv of its original value. The slopes of these lines ranged from 10-15 ohms and represent the cell resistance. These curves show the sulfur/sulfide couple to be reversible under these conditions.

Chronopotentiometric results.—One set of measurements was made with an uninsulated gold wire indicator electrode (diameter 0.055 cm, area 0.43 cm^2), others with rhenium wire (diameter 0.062 cm, area 0.34 cm^2) sealed in Pyrex so as to isolate it from the liquid sulfur pool. A total of 67 anodic chronopotentiograms were obtained. Each contained a single transition whose $E_{\tau/4}$ (corrected for *IR* drop) was within 30 mv of the equilibrium emf for that sulfide concentration. The times for this transition, which we ascribe to $S^= \rightarrow S + 2e^-$, were measured and the results are summarized in Table II. All separate values of $i\tau^{1/2}/A$, except those obtained at 93.6 mmol/l sulfide, were subjected to least square analysis; this produced the linear plot of $i\tau^{1/2}/A$ against concentration shown in Fig. 5. This linearity indicates that the transition is diffusion-controlled and that the Sand equation $i\tau^{1/2} = \frac{1}{2}\pi^{1/2}nFACD^{1/2}$ is obeyed by the sulfur/sulfide system with both rhenium and gold electrodes. From the slope of the line in Fig. 5 and the Sand equation, the diffusion coefficient of the diffusing sulfide species was calculated to be 3.12, standard deviation 0.11, x 10^{-6} cm^2/sec at 420° ± 2°C. This value is almost an order of magnitude smaller than the smallest value reported for a divalent metal ion, Pb^{++}, which we calculate as 1.3 ± 0.2 x 10^{-5} cm^2/sec at 420°C from literature data (12), indicating that the diffusing species is a somewhat larger entity, perhaps a polysulfide ion $S_X^=$. There appears to be a trend towards smaller $i\tau^{1/2}/AC$ values with increasing sulfide concentration (Table II), but it is doubtful whether any significance can be attached to this in view of the standard deviations of these values.

Some of the curves indicated a very ill-defined second transition whose $E\tau/4$ was estimated as —0.08 ± 0.05v and which we therefore ascribe to $2S + 2Cl^- \rightarrow S_2Cl_2 + 2e^-$. No measurements of the transition time were possible due to poor definition and the proximity of chlorine evolution.

Some difficulty was encountered with deposition of sulfur on the electrode. It was necessary to strip off the sulfur produced in each chronopotentiogram cathodically and wait 10 min between polarizations for the solution to become uniform. Erratic results (extremely short transition times, probably due to blocking of electroactive surface) were sometimes obtained, apparently due to attachment of sulfur from the pool to the electrode. A small residual transition time was observed (intercept, Fig. 5), but it was much less than that reported by others (13) in fused salt media and can be ascribed to trace impurities and/or double layer charging.

Table II. Chronopotentiometric study of sulfide*

Sulfide concentration, mmole/l	No. of points	Mean $i\tau^{1/2}/AC$, amp cm $sec^{1/2}$ $mole^{-1}$	Standard deviation
23.2	7	349	20
27.9	6	335	12
37.2	8	331	6
51.1	9	321	20
65.1	8	299	10
37.4**	7	348	25
51.5**	7	352	13
74.8**	8	316	6
93.6**	7	281	9

* Medium, fused LiCl-KCl eutectic at 420° ± 2°C; current density range, 26-101 ma/cm^2; each point taken at a different current density.
** Rhenium electrode; otherwise, gold electrode.

Discussion

It is unfortunately not possible to compare the potential data for the cell Ag/AgCl, Ag_2S/C, S_2 (g) studied by Thompson and Flengas (3) with the results of this work since Ag_2S is completely miscible with AgCl but practically insoluble in the LiCl-KCl eutectic.

The standard potential of the $S^=$/S couple cannot be used to calculate thermodynamic functions of formation of metal sulfides in the LiCl-KCl solvent since metal sulfides (with the exception of lithium sulfide) have neither an anion nor a cation in common with the solvent (14). In the cell M/MCl_n, LiCl-KCl/LiCl-KCl, Li_2S/S (1), C employed in this study, the formation of M^{n+} and $S^=$ takes place in two separate cell compartments.

The present voltammetric studies appeared to be in disagreement with those of Delarue (6), who attributed an anodic wave in sulfide solutions at $E_{1/2}$ = — 0.45v to the reaction $S^= \rightarrow S + 2e^-$. His melt was not purified nor was an inert atmosphere used, and the sulfide was added as $Na_2S \cdot 9H_2O$ and an alkaline earth chloride. The necessity of scrupulously anhydrous and oxide-free melts has been discussed (10, 15), and it originally appeared that impurities in his melt might account for the discrepancy. On duplicating his experiment with a purified melt and a platinum stationary microelectrode, it was found that the voltammetric curves were not reproducible, but that waves of $E_{1/2}$ near —0.45v were sometimes obtained. The poor reproducibility was unaffected by addition of sulfur, $CaCl_2$, and/or water. The equilibrium potential at the microelectrode was always near —0.9v. The platinum surface immediately became dark on immersion in a melt containing sulfide. The discrep-

ancy between our work and that of Delarue appears to be due to formation of a surface layer, probably PtS, on the platinum electrode in his work. We have been unable to obtain reproducible voltammetric results with platinum electrodes in melts containing sulfide.

Delarue (6) has observed the formation of S_2Cl_2 in this solvent when a strong oxidizing agent was added to melts containing sulfur. We therefore ascribe the anodic wave, which we observe voltammetrically and, with less reproducibility, in the chronopotentiometric studies, to the reaction $2S(l) + 2Cl^- \rightarrow S_2Cl_2 + 2e^-$. From the data of Lewis and Randall (16) we calculate ΔG for this reaction as -12.6 kcal/mole at 420°C, while from our voltammetric curves we calculate -12.4 ± 0.9 kcal/mole at the same temperature, in excellent agreement. Our attempts to trap and identify the gaseous S_2Cl_2 product were, however, unsuccessful.

It has long been known that sulfur produces a blue color in certain solvents. This has been observed in fused KSCN (17, 18) and fused LiCl-KCl (19). The nature of the colored sulfur species has not been established, and the following experiment was therefore performed.

Chlorine was generated in a compartment on a graphite electrode to remove any remaining traces of impurities which could reduce sulfur to sulfide ion. The chlorine was then removed by repeated alternation of vacuum and nitrogen purging. Sulfur pieces, obtained by heating sublimed sulfur to 200°C and cooling under vacuum, were added to the melt. No blue color developed even after 1 hr. When sulfide was then generated by cathodic coulometry the blue color developed close to the electrode surface. On stirring the color spread throughout the compartment and was clearly visible at a concentration of about 10^{-5}M calculated as sulfide ion. Further cathodic generation intensified the color. The color disappeared when chlorine was generated or when the potential of the graphite electrode was held at -0.3v with respect to the SMPE, both resulting in oxidation of sulfide to sulfur. The color also disappeared under vacuum after about 2 hr and reappeared on addition of sulfur to the melt. We are unable to explain these results, which indicate that both sulfide and sulfur are necessary to produce the blue color, other than by postulating that the color is due to a polysulfide ion formed by sulfur and sulfide, *i.e.*, $S^= + xS \leftrightarrows S_{x+1}^=$ (blue). The molar extinction coefficient is so high, 16,600 (17), that a small amount of trace impurities present in the fused LiCl-KCl (19) could reduce enough sulfur to sulfide to produce the color. The situation in the fused KSCN system is more complex (17, 18, 20) but both sulfur and sulfide could well be present. Spectrophotometric studies of sulfur species in the LiCl-KCl system are now in progress.

Acknowledgment

The authors are grateful to the National Research Council of Canada for financial assistance in the form of an Operating Grant (to J. A. P.).

Manuscript submitted Sept. 23, 1968; revised manuscript received Feb. 4, 1969. This paper is taken from the thesis of one of the authors (F. G. B.) submitted to the Faculty of Graduate Studies, University of Alberta, in partial fulfillment of the requirements for the Ph.D. degree. The paper was present at the New York Meeting, May 4-9, 1969, as Paper 199.

Any discussion of this paper will appear in a Discussion Section to be published in the December 1969 JOURNAL.

REFERENCES

1. M. C. Bell and S. N. Flengas, *This Journal*, **111**, 569, 575 (1964).
2. M. C. Bell and S. N. Flengas, *ibid.*, **113**, 27, 31 (1966).
3. W. T. Thompson and S. N. Flengas, *Can. J. Chem.*, **46**, 1611 (1968).
4. K. Kiukkola and C. Wagner, *This Journal*, **104**, 379 (1957).
5. J. A. Plambeck, *J. Chem. Eng. Data*, **12**, 77 (1967).
6. G. Delarue, *Bull. Soc. chim. France*, 906 (1960).
7. G. Delarue, *ibid.*, 1654 (1960).
8. S. I. Rempel and E. M. Malkova, *J. Appl. Chem. USSR*, **25**, 631 (1952).
9. H. A. Laitinen and J. A. Plambeck, *J. Am. Chem. Soc.*, **87**, 1202 (1965).
10. D. L. Maricle and D. N. Hume, *This Journal*, **107**, 354 (1960).
11. H. A. Laitinen and C. H. Liu, *J. Am. Chem. Soc.*, **80**, 1015 (1958).
12. C. E. Thalmayer, S. Bruckenstein, and D. M. Gruen, *J. Inorg. Nucl. Chem.*, **26**, 347 (1964).
13. H. A. Laitinen and H. C. Gaur, *Anal. Chim. Acta*, **18**, 1 (1958).
14. K. Kiukkola and C. Wagner, *This Journal*, **104**, 308 (1957).
15. H. A. Laitinen, W. S. Ferguson, and R. A. Osteryoung, *ibid.*, **104**, 516 (1957).
16. G. N. Lewis and M. Randall, "Thermodynamics," 2nd ed., p. 684, McGraw-Hill Book Co., New York (1961).
17. H. Lux and H. Anslinger, *Chem. Ber.*, **94**, 1161 (1961).
18. R. E. Panzer and M. J. Schaer, *This Journal*, **112**, 1136 (1965).
19. J. Greenberg, B. R. Sundheim, and D. M. Gruen, *J. Chem. Phys.*, **29**, 461 (1958).
20. G. Metzger, Report CEA-2566, Commissariat à l'Energie Atomique, Centres d'Etudes Nucléaires, Saclay, France; Nucl. Sci. Abstr. **19**, 1333 (1965).

On Dissolved Oxygen in Bulk Platinum

James P. Hoare*

Electrochemistry Department, Research Laboratories, General Motors Corporation, Warren, Michigan

ABSTRACT

The hydrogen overvoltage was determined on the front side of a bright Pt foil in $2N$ H_2SO_4 solution while the solution on the back side was stirred with H_2, N_2, or O_2. No change in the η was detected when the foil was connected as a diaphragm and when H_2 stirring was replaced with O_2 stirring on the back side. With the foil connected as a bielectrode, the η increased after an induction period depending on the thickness of the foil when H_2 stirring was replaced with O_2 stirring on the back side. These results indicate that under anodic polarization, oxygen can be dissolved in Pt. The dissolved oxygen can penetrate to the front side of the Pt foil where its presence as dermasorbed oxygen modified the catalytic activity of the Pt surface for the H_2 evolution reaction. In the absence of anodization, oxygen sorbed from solution can penetrate the Pt lattice no further than the dermasorbed region.

From a survey of the literature (1), it becomes obvious that the noble metals are not inert to oxygen. When oxygen is adsorbed from solution on a "bare" platinum surface a dissociative adsorption process takes place (2) resulting in the formation of a hydrated, adsorbed layer of oxygen atoms.

It is likely that the adsorbed oxygen can diffuse into the metal. Kalish and Burshtein (3) reported that the work function increased when oxygen was adsorbed on a Pt surface because of the presence of the negative dipoles of the adsorbed oxygen atoms. This effect was also observed by Giner and Lange (4). After about 11 hr, they (3) found that the work function decreased, which was interpreted to mean that some adsorbed oxygen had dissolved in the Pt. From repeated cathodic stripping determinations (3), the equivalent of about 3 or 4 monolayers of sorbed oxygen were detected. Rapid dissolution of oxygen in Pt was reported by Schuldiner and Warner (5), but this oxygen penetrated no further into the Pt surface than the first 2 or 3 atomic layers (5, 6). The term "dermasorption" was suggested (5, 6) to describe this form of occluded oxygen and to distinguish it from oxygen (known as absorbed oxygen) which had penetrated deeper into the metal lattice.

It is possible that anodization causes a penetration of oxygen into the metal lattice deeper than the dermasorbed layer. Supporting evidence for two kinds of sorbed oxygen is obtained from the results of stripping the adsorbed oxygen films with H_2 (7), from the hysteresis effects observed in potentiostatic polarization curves (8) and from triangular sweep traces (9-11).

Treatment with concentrated HNO_3 (12) causes even more oxygen to be dissolved in the Pt lattice to such an extent that it is referred to (13) as a Pt-O alloy. X-ray diffraction data (14) support this conclusion.

As noted in the literature (15-19), a preanodized Pt electrode has different electrochemical properties than one not preanodized, and this effect was explained (20) by the presence of dissolved oxygen in the Pt metal. The dissolved oxygen concept offers a possible explanation [ref. (20) p. 43] for the observation (21-24), that for charging curves obtained on Pt under certain circumstances, the amount of charge, Q_a, required to form a monolayer of adsorbed oxygen anodically is not equal to that, Q_c, required to remove it cathodically; but after a number of cycles of anodic and cathodic polarization, $Q_a = Q_c$.

To determine whether it is possible for oxygen to penetrate the Pt lattice more deeply than the dermasorbed region, an investigation of the diffusion of oxygen through thin platinum foils was undertaken. An account of the results of this work is presented in this report.

Experimental

Platinum lead wires were spot welded to small pieces of Pt foil about 1 cm square. The Pt foil was cleaned by repeatedly heating it to white heat in a burning H_2 jet followed by quenching in concentrated HNO_3. After cleaning, the foil was mounted with polyethylene washers between the compartments of a clean dual Teflon cell (7) in place of the usual glass frit. A Pt gauze counterelectrode, a small Pt gauze reference electrode, gas entrance and exit tubes through the cell tops, and a removable Pt wire preelectrolysis electrode are in each compartment. After the cell was assembled it was soaked in triply distilled water (with numerous changes of water) for at least 72 hr to leach out impurities. The cell was then filled (~20 cc per compartment) with $2N$ H_2SO_4, sealed, and preelectrolyzed for about 16 hr.

Purified hydrogen was bubbled through each compartment until virtually zero v was recorded between all pairs of Pt electrodes. Finally the steady-state, hydrogen-overvoltage curve was determined for stepwise increasing and decreasing current density on the front side of the foil with purified H_2, N_2, or O_2 bubbling in the back-side compartment. Note that H_2 is always bubbled in the front-side compartment. A constant current interrupter (25, 26) was used to correct for the solution iR and to monitor the cleanliness of the system by observing the pseudocapacitance of the H_2 reaction on the Pt foil (27). It was necessary to determine the iR correction for each reading because gas bubbles forming over the Pt surface caused large variations in the value of the solution iR, chiefly in the high current density region. To minimize mass transfer effects, the gases were bubbled through the electrolyte at rates above 300 cc/min.

Two electrical hookups were investigated; the Pt diaphragm (Fig. 1) and the Pt bielectrode (Fig. 2). In the diaphragm case only the front side of the foil was polarized while the back side was unpolarized. Both the front and the back sides of the foil were polarized when the foil was connected as a bielectrode. Since

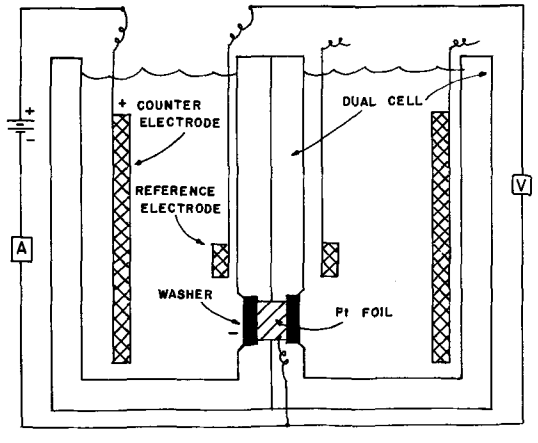

Fig. 1. Dual Teflon cell with Pt foil connected as a diaphragm

* Electrochemical Society Active Member.

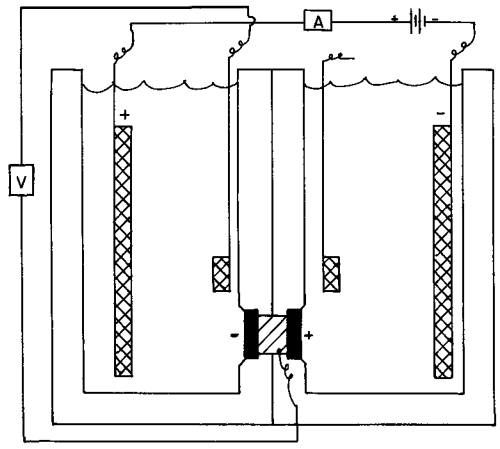

Fig. 2. Dual Teflon cell with Pt foil connected as a bielectrode. Notation same as in Fig. 1.

the iR correction cannot be determined in the bielectrode setup, the overvoltage was determined only over the low current density range where bubble formation on the cathode surface did not interfere with the iR readings and when the iR values obtained with the diaphragm set up could be used.

The hydrogen overvoltage, η, was studied on three thicknesses of Pt (99.9+% pure) foil; 0.00127, 0.00254, 0.00762 cm. Examination for pinholes was made by observing the foil with an intense light behind it. The temperature of this work was 24° ±1°C, and the potential was read on a General Radio Electrometer, Model 1230A.

Results

A plot of the hydrogen overvoltage as a function of the log of the apparent current density is given in Fig. 3 for a 0.00127-cm Pt diaphragm. It is seen that the data do not depend on the nature of the gas bubbled in the back-side compartment since they are the same for H_2, N_2, and O_2. The data points are the average values of at least four complete cycles of increasing and decreasing cathodic polarization on the front side of the diaphragm. Although the spread of data at the higher current densities extended over about 2 mv, the data at the lower current densities could be reproduced within ±0.3 mv. These data are in agreement with hydrogen overvoltage data recorded

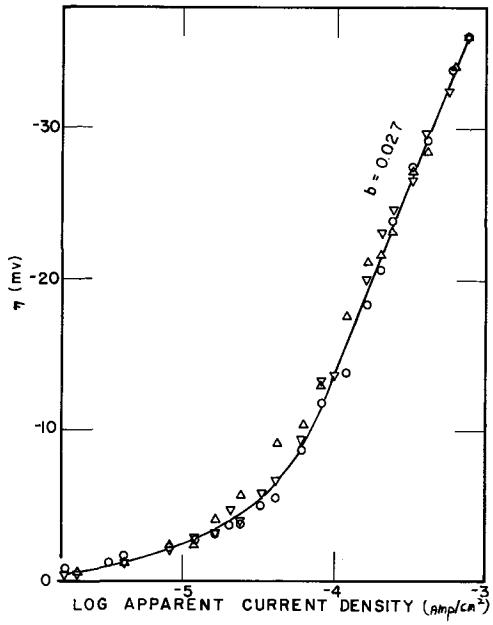

Fig. 3. Hydrogen overvoltage on the front side of a 0.00127-cm thick Pt diaphragm in 2N H_2SO_4 with H_2 (⊙), N_2 (△), and O_2 (▽) bubbling on the back side. Data points are the average of 4 complete cycles of increasing and decreasing polarization.

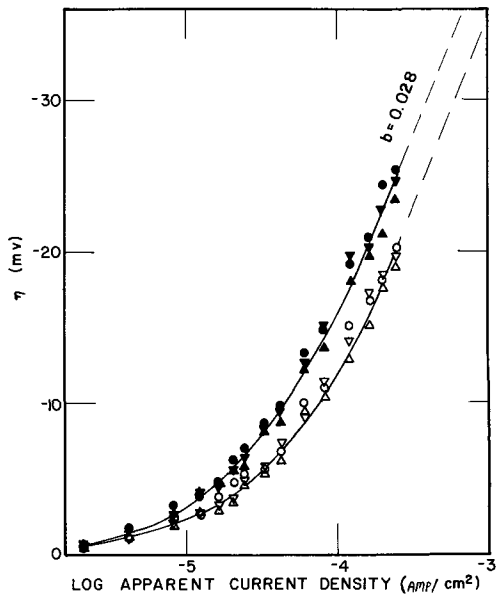

Fig. 4. Hydrogen overvoltage on the front side of Pt bielectrodes with thicknesses of 0.00127 cm (⊙), 0.00254 cm (△), and 0.00762 cm (▽) in 2N H_2SO_4. Open symbols are data with H_2 and filled with O_2 bubbling on the back side. Data points are the average of 4 complete cycles of increasing and decreasing polarization.

in the literature (28) for bright Pt in sulfuric acid electrolytes.

For the Pt bielectrode, Fig. 4, the η is higher with O_2 bubbling in the back-side compartment than with H_2, and although a thickness effect was not observed, a time effect was. After the H_2 in the back-side compartment was replaced with oxygen, the cell had to be polarized at the highest current density studied for a certain time before a change in the η could be observed on the front side of the Pt bielectrode. This induction period was independent of the time during which O_2 was bubbled through the back-side compartment before the polarization procedure was begun. It was difficult to determine exactly the length of the induction period since the change in η was a gradual process. However, at a current density of 0.25 ma/cm², it was estimated that it required a polarization time of about 20-30 min for the 0.00127-cm foil, about 90 min for the 0.00254-cm foil, and about 3-4 hr for the 0.00762-cm foil, before reproducible H_2-η data could be obtained. These data were reproducible within ±1 mv of the average value.

When the O_2 bubbling on the back side of the 0.00127-cm foil was replaced with H_2 again, the η on the front side did not return to the original curve until polarization was continued for several hours.

Discussion

When Pt is placed in contact with O_2-saturated acid solution, a partial monolayer of adsorbed oxygen atoms (Pt-O) is formed on the surface by a dissociative adsorption mechanism (2). Once this partial layer is formed, a local cell can be set up (1, 17) between the O_2/H_2O reaction

$$O_2 + 4H^+ + 4e \rightleftarrows 2H_2O \qquad [1]$$

and the Pt/Pt-O reaction

$$Pt\text{-}O + 2H^+ + 2e \rightleftarrows Pt + H_2O \qquad [2]$$

A steady state is reached after about 24 hr, and the system exhibits a mixed potential of 1.06v.

Schuldiner and co-workers (29) found that above about 1v, oxygen can be dissolved in the surface layers of the Pt metal. Ellipsometric studies (30) have shown that no changes in the platinum-oxygen system are observed until a potential greater than 0.98v is reached. Consequently, a Pt surface in contact with O_2-saturated

acid solution could, in time, dissolve oxygen in the metal derma (first 2 or 3 atom layers) under the driving force of the local cell action.

The data in Fig. 3 are consistent with this viewpoint since no effect was observed on the η on the front side of the Pt diaphragm when H_2 was replaced with O_2 on the back side. Because the back side is not polarized, O_2 is dissolved in the metal no deeper than the dermasorption region and cannot affect any process occurring on the front side of the Pt foil.

As noted by Schuldiner *et al.* (29), the dissolved oxygen penetrated more deeply than the derma when Pt was anodized at 1.7v because the effects of the dermasorbed oxygen could be detected for extended periods of time after the potential had been lowered below 1v. This observation was explained by diffusion of absorbed oxygen from the metal interior into the dermasorbed region.

In the bielectrode case, the front side of the Pt foil is cathodized while the back side is anodized. At a current density of 0.25 ma/cm^2, the potential of bright Pt in O_2-saturated acid solution is in the vicinity of 1.9v (31). It is possible for dissolved oxygen to penetrate into the interior of the Pt metal. As demonstrated in Fig. 4, the oxygen can diffuse all the way through the Pt foil to the dermasorption region of the front side where its presence is detected by catalytic effects on the H_2 evolution kinetics. When H_2 is replaced with O_2 on the back side of the Pt bielectrode, the hydrogen η on the front side increases after a certain induction period depending on the thickness of the foil. Since the value of the Tafel slope did not change, the electrode mechanism is the same whether the back-side compartment is stirred with H_2 or with O_2. The change in i_o, however, indicates that the catalytic nature of the cathode surface does change.

It has been reported (5, 32) that the presence of dermasorbed hydrogen or oxygen in Pt can exert catalytic effects on certain electrode reactions. In the present case, a similar explanation may account for the results shown in Fig. 4.

The rate-determining step for the cathodic evolution of H_2 on bright Pt is assumed to be the combination of adsorbed hydrogen atoms (Tafel mechanism) to form H_2 molecules (33)

$$H + H \rightarrow H_2 \qquad [3]$$

which gives a Tafel slope of $RT/2F$ (28)[1]. If the presence of dermasorbed oxygen in the cathode surface makes a tighter bond between the adsorbed hydrogen and the metal surface, this effect would slow down the hydrogen combination reaction with the resultant inincrease in η and decrease in i_o. The data in Fig. 4 are consistent with such an explanation.

This viewpoint also affords an explanation for the observation that replacement of the O_2 by H_2 on the back side did not lower the η on the front side immediately to the original value but only after an extended period of cathodic polarization (several hours) had been applied. Although dermasorbed oxygen is eventually removed by migrating to the surface to react with hydrogen, it can be replaced by the absorbed oxygen migrating from the interior of the metal. Under these conditions, it would require long periods of time before all of the dissolved oxygen could be removed by reaction with hydrogen. Once all of the dissolved oxygen is removed, the η falls to its original value as observed experimentally.

From the results of this work, it is possible to distinguish between two situations. In the first case, oxygen sorbed from solution penetrates the Pt lattice no deeper than the dermasorption region. In the second case under the influence of anodic polarization, the sorbed oxygen penetrates to much deeper levels of the Pt lattice than the dermasorbed region, and, in fact, oxygen may be made to pass completely through thin Pt foils. The presence of dermasorbed oxygen can modify the catalytic activity of the Pt surface for the hydrogen evolution reaction. Similar observations appear in the literature [*e.g.*, (5), (12), (15-19), (32)].

Other possible explanations for these observations involving the diffusion of hydrogen from the cathode to the anode side are not considered favorably because it was shown (34) that hydrogen would not diffuse through Pt foils which had clean surfaces. The high degree of cleanliness of the Pt surfaces used in this work was confirmed by the large pseudocapacitance observed on the pulses obtained from the current interrupter (28, 35).

[1] A H_2 diffusion-controlled process should show no dependence on the catalytic nature of the electrode surface.

Manuscript submitted Oct. 14, 1968; revised manuscript received Feb. 13, 1969. This paper was presented at the New York Meeting, May 4-9, 1969, as Paper 256.

Any discussion of this paper will appear in a Discussion Section to be published in the December 1969 JOURNAL.

REFERENCES

1. J. P. Hoare, in "Advances in Electrochemistry and Electrochemical Engineering," P. Delahay, Editor, Vol. VI, p. 201, Interscience Publishers, New York (1967).
2. A Damjanovic, M. L. B. Rao, and M. Genshaw, ASTIA Report No. AD405675, Nov. 1962.
3. T. V. Kalish and R. Kh. Burshtein, *Doklady Akad. Nauk SSSR*, **81**, 1093 (1951); **88**, 863 (1953).
4. J. Giner and E. Lange, *Naturwiss.*, **40**, 506 (1953).
5. S. Schuldiner and T. B. Warner, *This Journal*, **112**, 212 (1965).
6. T. B. Warner and S. Schuldiner, *ibid.*, **112**, 853 (1965).
7. J. P. Hoare, *ibid.*, **109**, 858 (1962); **111**, 232 (1964).
8. J. P. Hoare, *ibid.*, **113**, 846 (1966); *J. Electroanal. Chem.*, **12**, 260 (1966).
9. F. G. Will and C. A. Knorr, *Z. Elektrochem.*, **64**, 258 (1960).
10. V. I. Luk'yanycheva, V. I. Tikhomirova, and V. S. Bagotskii, *Elektrokhim.*, **1**, 262 (1965).
11. V. I. Tikhomirova, A. I. Ohse, V. S. Bagotskii, and V. I. Luk'yanycheva, *Doklady Akad. Nauk SSSR*, **159**, 644 (1964).
12. J. P. Hoare, *This Journal*, **110**, 1019 (1963); **112**, 849 (1965).
13. J. P. Hoare, *Nature*, **204**, 71 (1964).
14. J. P. Hoare, S. G. Meibuhr, and R. Thacker, *This Journal*, **113**, 1078 (1966).
15. F. C. Anson, *J. Am. Chem. Soc.*, **81**, 1554 (1959).
16. F. C. Anson and J. J. Lingane, *ibid.*, **79**, 1015, 4901 (1957).
17. B. B. Baker and W. M. MacNevin, *ibid.*, **75**, 1473 (1953).
18. D. G. Davis, *J. Electroanal. Chem.*, **1**, 73 (1959); *Talanta*, **3**, 335 (1960).
19. I. M. Kolthoff and E. R. Nightingale, *Anal. Chim. Acta*, **17**, 329 (1957).
20. J. P. Hoare, "The Electrochemistry of Oxygen," p. 174, Interscience, New York (1968).
21. J. A. V. Butler and G. Armstrong, *Proc. Roy. Soc.*, **A137**, 604 (1932).
22. S. W. Feldberg, C. G. Enke, and C. E. Bricker, *This Journal*, **110**, 826 (1963).
23. H. A. Laitinen and C. G. Enke, *ibid.*, **107**, 773 (1960).
24. K. J. Vetter and D. Berndt, *Z. Elektrochem.*, **62**, 378 (1958).
25. S. Schuldiner and R. E. White, *This Journal*, **97**, 433 (1950).
26. C. H. Presbrey and S. Schuldiner, NRL Report 5472, Washington D. C., July 14, 1960.
27. S. Schuldiner and J. P. Hoare, *J. Chem. Phys.*, **26**, 1771 (1957).
28. S. Schuldiner, *This Journal*, **99**, 488 (1952).
29. S. Schuldiner, T. B. Warner, and B. J. Piersma, *ibid.*, **114**, 343 (1967).
30. A. K. N. Reddy, M. Genshaw, and J. O'M. Bockris, *J. Electroanal. Chem.*, **8**, 406 (1964).
31. J. P. Hoare, *This Journal*, **112**, 602 (1965).
32. S. Schuldiner *et al.*, *ibid.*, **114**, 1121 (1967); **115**, 28, 362 (1962).
33. K. J. Vetter, "Elektrochemische Kinetik," p. 414, Springer Verlag, Berlin (1961).
34. J. P. Hoare and S. Schuldiner, *This Journal*, **103**, 237 (1956); *Can. J. Chem.*, **37**, 228 (1959).
35. S. Schuldiner and J. P. Hoare, *J. Chem. Phys.*, **26**, 1771 (1957).

Technical Notes

Cathodic Crossed Hydrocoupling of Acetone with Pyridine

Tsutomu Nonaka and Kiichiro Sugino*

Department of Applied Electrochemistry, Tokyo Institute of Technology, Ookayama, Meguro-ku, Tokyo, Japan

In previous works (1), cathodic crossed hydrocoupling of acetone with activated olefinic compound was accomplished by using acrylonitrile and maleic acid as starting materials. In the case of acrylonitrile, more than 70% current efficiency was obtained, but in the case of maleic acid the current efficiency was only about 10%. A proposed mechanism for the crossed hydrocoupling and the reason for the difference in current efficiency in two cases were described there.

Further investigation of the cathodic process of acetone with other activated olefines has led to the discovery of the occurrence of a similar crossed hydrocoupling between acetone and pyridine. The current efficiency was as high as 70%. The reaction could be obtained at a potential of −1.30v *vs.* SCE at mercury. The product was a mixture of [2-(1,2,3,6-tetrahydro)-pyridyl]dimethylcarbinol, [2-(1,2,5,6-tetrahydro)pyridyl]dimethylcarbinol, and a small amount of 2-piperidyldimethylcarbinol.

Proof for the formation of the tetrahydro derivatives was the catalytic reduction of the products to the known 2-piperidyldimethylcarbinol and the oxidation with potassium permanganate to a mixture of β-alanine, glycine, α-hydroxyisobutyric acid, and oxalic acid.

Experimental

Electrolysis was carried out in an H-type cell with a sintered glass diaphragm similar to that described earlier (2) using a mercury cathode (area 12.6 cm^2) and a platinum disk anode. The catholyte consisted of a mixture of 14.2g (0.08 mole) of pyridine sulfate, acetone (40g) and 20% sulfuric acid (by weight) (40g); the anolyte was 20% sulfuric acid. The amperage varied from 0.82 to 1.02 amp and gave a cathodic current density of 6.5-8.1 amp/dm^2 (average 6.7 amp/dm^2). The electrolysis was carried out at about 20°C with a controlled cathode potential of −1.30v *vs.* SCE. The amount of current used was 4.23 amp·hr (0.158**F**).

After the electrolysis the catholyte was neutralized with 30-40% aqueous sodium hydroxide and the resulting solution was extracted with ether. Analysis by v.p.c. of the ether extract showed the formation of isopropyl alcohol (0.062g) and pinacol (0.008g).

The aqueous layer was concentrated under reduced pressure and made alkaline with 30-40% sodium hydroxide. The resulting oily layer was extracted with ether and analyzed v.p.c. using Triton 305X on Flusin T6 column at 160°C. The products were [2-(tetrahydropyridyl)]dimethylcarbinol (4.03g) and 2-piperidyldimethylcarbinol (0.42g). These migration times were 10.5 and 8.8 min, respectively, when the flow rate of carrier gas (hydrogen) is 40 ml/min (column diameter, 5 mm; length, 2m). These amounts represent current efficiencies of 73 and 11%, respectively. No piperidine could be detected, but the formation of propane was observed in the electrolysis.

Separation and identification of products was performed as follows. The ether extract containing the basic substances was dried over anhydrous potassium carbonate and gave a brownish oil after removing the solvent. By repeated distillation of the oil at reduced pressure, a fraction boiling at 102.5-103.5°C/19 mm was obtained as the main product; n_D^{30}, 1.4929.

Anal. Calcd. for $C_8H_{15}NO$: C,68.04; H,10.71; N,9.92
Found: C,69.02; H,10.86; N,9.95.

The picrate (recrystallized from benzene) melted at 129°-132°C.

Anal. Calcd. for $C_{14}H_{18}N_4O_8$: C,45.41; H,4.90; N,15.13
Found: C,45.50; H,5.10; N,15.61.

The nitrate (recrystallized from absolute alcohol) melted at 85.5°-86.5°C.

Anal. Calcd. for $C_8H_{16}N_2O_4$: C,47.05; H,7.90; N,13.72
Found: C,46.63; H,8.04; N,14.13.

The N-benzoate (recrystallized from benzene) melted at 101°-103°C.

Anal. Calcd. for $C_{15}H_{19}NO_2$: C,73.44; H,7.81; N,5.71
Found: C,73.25; H,7.81; N,5.60.

This product is a mixture of [2-(1,2,3,6-tetrahydropyridyl)]dimethylcarbinol and [2-(1,2,5,6-tetrahydropyridyl)]dimethylcarbinol since it absorbed one mole of bromine in acidic medium and absorbed one mole of hydrogen using a nickel catalyst and gave 2-piperidyldimethylcarbinol; bp, 107°-107.5°C/26 mm; $n_D^{28.5}$, 1.4777. The picrate melted at 138.5°-139°C. These properties and the infrared spectrum were identical with those of an authentic sample (3).

The location of the double bond in the 2-tetrahydropyridyldimethylcarbinol was indicated by the oxidation products obtained using potassium permanganate. 2-Tetrahydropyridyldimethylcarbinol (0.18 mole) purified by repeated distillation was oxidized with aqueous potassium permanganate (0.97 mole) in basic medium at 25°-32°C. The reaction mixture was concentrated and, then acidified with hydrochloric acid, gave an evolution of carbon dioxide. The resulting solution was again concentrated to a syrupy mass. After esterification with methanol, the syrup was subjected to distillation and gave dimethyl oxalate and a yellow viscous oil. The latter was found to be a mixture of the amides of α-hydroxyisobutyric acid with β-alanine methyl ester and glycine methyl ester, since it gave α-hydroxyisobutyric acid, β-alanine and glycine by hydrolysis with hydrochloric acid; bp 135°-138°C/2 mm, yield, about 20%. The oxidation reaction and the hydrolysis reaction were presumed to proceed as follows:

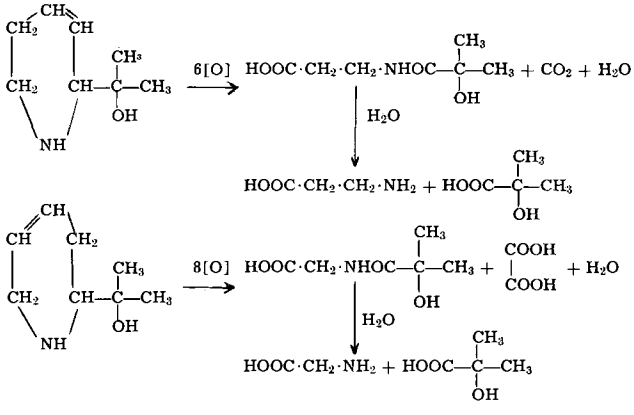

* Electrochemical Society Active Member.

(2-Piperidyl)dimethylcarbinol itself was also present, although in minor quantity, in the reduction product; it could not be separated from the main product by fractional distillation. The amount was determined however by gas chromatography.[1]

Acknowledgment

This investigation was supported in part by a grant for fundamental and development scientific research from the Ministry of Education of Japan and also a grant from Nippon (Japan) Carbide Industries Inc., for which the authors wish to express their deep appreciation.

Manuscript submitted Sept. 12, 1968; revised manuscript received ca. Feb. 4, 1969.

Any discussion of this paper will appear in a Discussion Section to be published in the December 1969 JOURNAL.

[1] Triton 305X at 160°C.

REFERENCES

1. K. Sugino and T. Nonaka, *This Journal*, **112**, 1241 (1965). *Electrochim. Acta*, **13**, 613 (1968).
2. K. Sugino, K. Shirai, and T. Nonaka, *Bull. Chem. Soc. Japan*, **37**, 1895 (1964).
3. W. Sobecki, *Ber.*, **41**, 4103 (1908).

Two-Dimensional Electric Field between Elliptical and Wire Electrodes

G. N. Ellison

The National Cash Register Company, Electronics Division, Hawthorne, California

Continuous wire plating processes frequently require the use of single or multiple electrodes distributed around a substrate for electropolishing and electroplating operations. An asymmetric distribution of these electrodes around the substrate wire may result in an electric field symmetry which is enhanced or diminished by the substrate geometry. The current distribution resulting from this electric field is the "primary current distribution," *i.e.*, the current distribution for vanishing polarization. The following calculation treats the electric field from which the primary current results and is exact only when polarization phenomena are absent.

The theoretical analysis of the electric field is performed for the electrode geometry shown in Fig. 1. A grounded, conducting substrate with an elliptic cross section is used to provide the field asymmetry due to the substrate. A charged double wire electrode is placed above and below the substrate to test the possibility of compensating for the substrate asymmetry. The length and cross-sectional dimensions of the electrodes used in continuous wire plating processes are such that only the two-dimensional field in the x-y plane needs to be considered. Numerical results are given for the points P and Q on the ellipse.

Formulation of the Problem in Elliptical Coordinates

The transformation from the cartesian coordinates x, y to the elliptic coordinates μ, θ is given by (1)

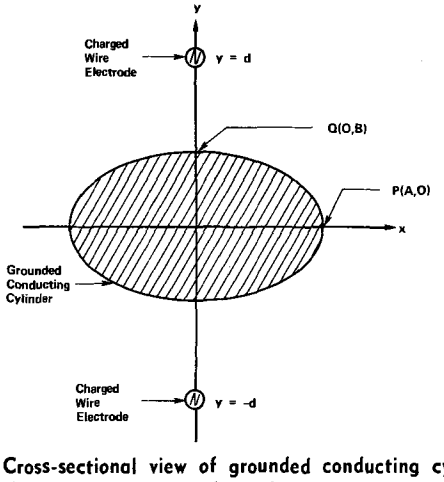

Fig. 1. Cross-sectional view of grounded conducting cylinder in presence of two charged wire electrodes.

$$x = (a/2)\cosh\mu\cos\theta,\ y = (a/2)\sinh\mu\sin\theta \quad [1a]$$

The coordinate μ is an ellipse with semimajor and semiminor axes given by

$$A = (a/2)\cosh\mu,\ B = (a/2)\sinh\mu \quad [1b]$$

respectively. The coordinate θ is measured in a counter clockwise direction from the positive x-axis.

The electric field $E\ (\mu_o, \theta)$ at the surface of the grounded conducting cylinder is given by the gradient of the potential ϕ in the direction normal to the surface μ_o defined by the conducting cylinder

$$E\ (\mu_o,\theta) \propto \frac{2/a}{(\cosh^2\mu_o - \cos^2\theta)^{1/2}}\left(\frac{\partial\phi}{\partial\theta}\right)_{\mu=\mu_o} \quad [2]$$

The potential ϕ is just the solution to Laplace's equation in elliptic coordinates. The potential is calculated in the following sections by superposition of the potential for the two line charges and the potential for the grounded conducting cylinder.

Potential Due to Two Line Charges

The potential of a single charge at μ_1, θ_1 is (2)

$$\phi = -2\mu - 2\ln a + 4\sum_{n=1}^{\infty}\frac{1}{n}e^{-n\mu_1}(\cosh n\mu\cos n\theta\cos n\theta_1 + \sinh n\mu\sin n\theta\sin n\theta_1)$$

A multiplying constant $\lambda/(\pi\epsilon_o)$ containing the line charge density λ and the free space permittivity ϵ_o has been eliminated by setting it equal to one. The potential due to the two line charges at $\mu = \mu_1$ and $\theta = \pi/2$, $-\pi/2$ is found by superposition to be

$$\phi = -4\mu_1 - 4\ln a + 4\sum_{n=1}^{\infty}\frac{(-1)^n}{n}e^{-2n\mu_1}\cosh 2n\mu\cos 2n\theta$$

Total Potential for Two Line Charges and Conducting Cylinder

The θ dependence of the potential due to the conducting cylinder can be written down immediately by noting that the symmetry about $\theta = 0$, $\pi/2$, $-\pi/2$ must be maintained. Clearly the angular dependence is then $\cos 2n\theta$.

The μ dependence is determined by the boundary conditions $\phi = 0$ at $\mu = \mu_o$, ϕ is finite or zero for $\mu_o = 0$, and

$$\frac{2/a}{(\cosh^2\mu_o - \cos^2\theta)^{1/2}}\left(\frac{\partial\phi}{\partial\theta}\right)_{\mu=\mu_o} = 0$$

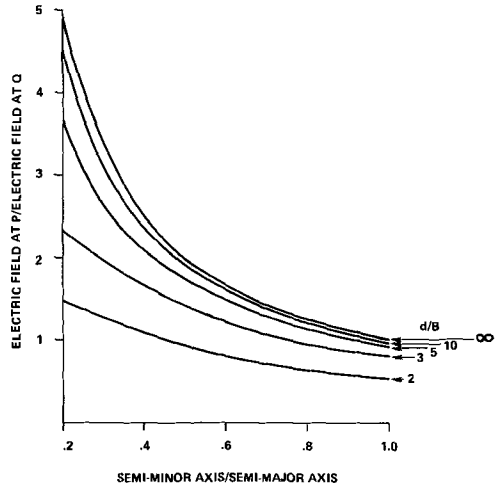

Fig. 2. Ratio of electric fields at points P and Q (see Fig. 1) of elliptic cylinder in presence of double wire electrode.

The multiplicative and additive constants are determined from the requirement that the potential due to both the cylinder and line charges is zero at $\mu = \mu_o$.

The potential ϕ_c due to the elliptical cylinder only is therefore

$$\phi_c = -4(\mu - \mu_o) + 4\mu_1 + 4\ln a - 4\sum_{n=1}^{\infty} \frac{(-1)^n}{n} e^{-2n\mu_1} \cosh 2n(\mu - \mu_o) \times \cosh 2n\mu_o \cos 2n\theta.$$

The total potential of the two line charges and the conducting cylinder is then

$$\phi = -4(\mu - \mu_o) + 4\sum_{n=1}^{\infty} \frac{(-1)^n}{n} e^{-2n\mu_1} \sinh 2n\mu_o \times \sinh 2n(\mu - \mu_o) \cos 2n\theta \qquad [3]$$

Electric Field at Extreme Points of Ellipse

The evaluation of the electric field requires the substitution of Eq. [3] into [2]. The infinite series in the final expression for the electric field at $\mu = \mu_o$ can be summed by writing the hyperbolic and trigonometric functions in their exponential form such that each term of the infinite series may be recognized as a term of a binomial expansion. The electric field at $\mu = \mu_o$ and any angle θ is then

$$E(\mu_o,\theta) = \frac{-2/a}{(\sinh^2\mu_o + \sin^2\theta)^{1/2}} \times \left\{1 - \left[\frac{(1+\tan^2\theta)\tanh(\mu_o - \mu_1)}{1+\tan^2\theta\tanh^2(\mu_o - \mu_1)} + \frac{(1+\tan^2\theta)\tanh(\mu_o + \mu_1)}{1+\tan^2\theta\tanh^2(\mu_o + \mu_1)}\right]\right\}$$

It is sufficient to compare the electric field at the two points P and Q (see Fig. 1) on the surface of the cylinder. The ratio of the electric fields is

$$\frac{E(P)}{E(Q)} = \frac{A}{B}\left[\frac{\tanh(\mu_o - \mu_1) + \tanh(\mu_o + \mu_1) - 2}{\tanh(\mu_o + \mu_1) + \tanh(\mu_o - \mu_1) - 2\tanh(\mu_o - \mu_1)\tanh(\mu_o + \mu_1)}\right] \times \tanh(\mu_o - \mu_1)\tanh(\mu_o + \mu_1)$$

where A/B is the ratio $E(P)/E(Q)$ for $d/B = \infty$. The coordinates μ_o and μ_1 can be determined in terms of A, B, and d using Eq. [1a] and [1b]. Figure 2 is a graph of $E(P)/E(Q)$ *vs.* the ratio B/A for several values of d/B. It is noteworthy that the double wire electrode has only a small effect on the electric field at the substrate for values of d/B greater than 10.

Manuscript submitted Dec. 16, 1968; revised manuscript received Jan. 17, 1969.

Any discussion of this paper will appear in a Discussion Section to be published in the December 1969 JOURNAL.

REFERENCES

1. P. M. Morse and H. Feshbach, "Methods of Theoretical Physics," Part II, p. 1195, McGraw-Hill Book Co., Inc. (1953).
2. P. M. Morse and H. Feshbach, *op. cit.*, p. 1202.

Stress in Thin Films of Silane Vapor-Deposited Silicon Dioxide

Richard Lathlaen and Donald A. Diehl

Philco-Ford Corporation, Microelectronics Division, Research and Development Department, Blue Bell, Pennsylvania

ABSTRACT

The stress in thin films of silane vapor-deposited SiO_2 on Si substrates was measured by an optical technique which is sensitive to changes in focal length. The optical method requires only a single measurement for each value of stress determined and, therefore, is suitable for processing a large number of samples. The equipment used to build the focal length measuring stand was inexpensive. The vapor-deposited films exhibited tensile stress which: (*i*) increased linearly as a function of film thickness, (*ii*) was a linear function of the logarithm of the SiO_2 deposition rate, and (*iii*) increased asymptotically to a constant value as a function of the volume ratio of oxygen to silane, for a constant deposition rate. A typical value for the stress of a 7500Å layer, plated at 4000 Å/min and 400°C, was 2.5 x 10^9 dynes/cm^2.

The low-temperature deposition of SiO_2 by the oxidation of silane is a relatively economical method of coating a microcircuit device with an insulating material which is chemically inert, electrically stable and physically strong. The method was reported by Evitts *et al.* (1), and a detailed description of the process was given by Goldsmith and Kern (2) and by Hammond and Bowers (3).

Vapor-deposited films can be used as the deposited dielectric in multilevel metallized integrated circuits.

Since the elastic condition of silane vapor-deposited SiO_2 was of interest, a sensitive, rapid, and easy to implement method of measuring the stress in thin films on silicon substrates was devised. The stress in thin films of chemically deposited SiO_2 was studied and was observed to be sensitive to the deposition parameters.

The study showed that it was practical to characterize empirically the effect of realistic permutations of the reaction ingredients on the elastic properties of the chemically deposited SiO_2 films.

Stress is a mutual force between contiguous surfaces, which in films is manifested by elastic deformation of the film-substrate pair. The chemical deposition of SiO_2 on a silicon substrate results in an imbalance of forces which deforms the composite Si-SiO_2 system until equilibrium is established. Therefore, the stress of the SiO_2 layer is reflected by the amount of deformation which the substrate must undergo to establish equilibrium. The rigorous mathematical expression for the stress of thin films on thick plates has been derived by Davidenkov (4).

Several authors have described methods by which the deformation of a thin, flexible, rectangular substrate which is clamped rigidly along one edge and free to deflect at the other can be measured (5-7). The edge deflection has been measured using a microscope (5), using a mechanical transducer (6), and as a function of the capacitance between the substrate and a nearby fixed metal plate (7). In general, either the methods were not amenable to the study of a large number of samples within a reasonable period of time or they required the use of expensive equipment. The calculations presented by Glang *et al.*, (8) were used as the framework for an experiment which permitted the stress of vapor-deposited SiO_2 films to be measured without the forenamed limitations.

According to Glang, the stress, σ, in films on thin circular single-crystal substrates can be written as follows

$$\sigma = \frac{1}{3}\frac{E}{1-\nu}\frac{t_s^2}{t_f}\frac{\delta}{r^2} \qquad [1]$$

Key words: thin film stress, vapor deposited SiO_2.

where E and ν are Young's modulus and Poisson's ratio, respectively, for the substrate; t_s is the substrate thickness, and t_f is the deposited film thickness. The quotient of the substrate deflection, δ, divided by the square of the distance r from the center in Eq. [1] may be considered as a functional unit and, consequently, be rewritten in a new form with an arbitrary parameter f. The term $1/4f$ can, therefore, be substituted for δ/r^2, where f is equivalent to the optical focal length of the paraboloid of revolution with a cross-sectional profile defined by the equation

$$4f\delta = r^2$$

Equation [1] may be rewritten in the form

$$\sigma = \frac{1}{12}\frac{E}{1-\nu}\frac{t_s^2}{t_f}\frac{1}{f} \qquad [2]$$

where $(E/1-\nu) = 2.30 \times 10^{12}$ dynes/cm^2 for <111> oriented Si substrates.

The technique which is described in the next section measures f in Eq. [2] instead of the deflection of the substrate at the edge.

Experimental Procedure

The silane vapor deposition system used to prepare the samples for this investigation has been described by Hammond and Bowers (3). The substrates that were used were 2-3 mils thick, <111> oriented Si single-crystals which were supplied by the Monsanto Company. The substrates were close to 3 cm in diameter and were chosen so that any inherent curvature was not measurable using the focal length measuring system described below. The substrates were held flat by a vacuum chuck inside the substrate pedestal of the hotplate to preclude their deformation during deposition.

The stress in the thin films of chemically deposited SiO_2 was determined by measuring the focal length of the substrates on which the films were deposited. A high intensity mercury arc lamp was used to illuminate a pinhole which was then optically positioned at infinity by a collimator. The exit pupil of the collimator could be varied between 1 mm and 1 cm. The collimated illumination was reflected by a front surface mirror on the substrate which was positioned horizontally on a microscope leveling stage. When the source and substrate were properly aligned, the light reflected from the substrate was directed along the optical axis of the system and viewed on a ground glass screen, with the aid of a partially reflecting surface inserted in the path of the illuminating beam of light. The components were rigidly mounted to a calibrated optical bench which enabled measure-

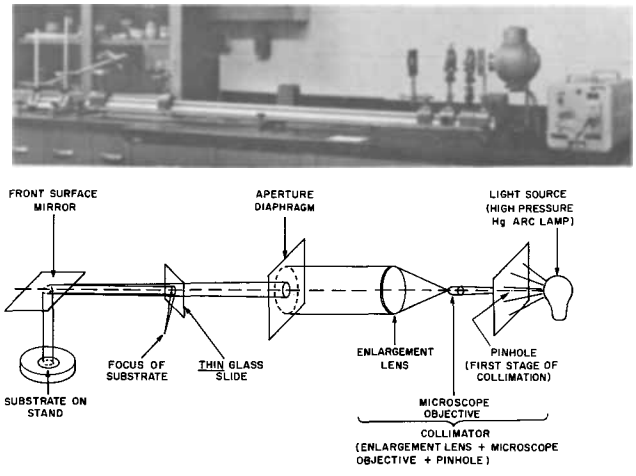

Fig. 1. Top, focal length measuring stand; bottom, path of the light relative to the components of the stand.

ments of the position of the focus of the substrate to be made accurately and reproducibly. Figure 1 shows a photograph and a schematic diagram of the optical stand.

Stress was measured as a function of three parameters of the SiO_2 film: (*i*) film thickness, (*ii*) deposition rate, and (*iii*) volumetric ratio of oxygen to silane. The films were deposited at 400°C and the stress measured at room temperature.

Each sample of vapor plated SiO_2 was prepared by one of two different ways for the measurement of stress as a function of film thickness.

1. An initial thickness of SiO_2 was deposited on a substrate, and subsequent thicknesses were obtained by selectively etching away the initial deposit.
2. A fresh layer of SiO_2 was deposited for each measurement of σ.

In both cases the deposition parameters were constant: 23 cc/min of silane was diluted by 7.6 l/min of N_2, then oxidized by 75 cc/min of O_2.

A fresh layer of SiO_2 7500Å thick was deposited for each measurement of stress as a function of the deposition rate and volume ratio of oxygen to silane.

The film thickness was calculated from the number of interference fringes of yellow light in a wedge formed using a chemical etchant. The deposition rates were calculated from the film thicknesses and deposition times, and the gas volume ratios were monitored by standard gas flow meters.

Results and Discussion

The chemical vapor-deposited SiO_2 films warped the substrates concave upward, thereby forming a real image of the light source; that is, the films were in tension. A typical value for the tensile stress of a 7500Å thick SiO_2 layer deposited at 4000 Å/min was between 2.4×10^9 and 2.7×10^9 dynes/cm^2.

Figures 2, 3, and 4 summarize the quantitative results of the work. Figure 2 is a plot of the stress *vs.* the thickness of the SiO_2 film for a constant deposition rate of 4000 Å/min and a constant volume ratio of oxygen to silane of 3.25 to 1. The range of SiO_2 thicknesses tested was from 3000 to 26,000Å. The graph shows that the stress was consistently higher for the freshly prepared films than for the films prepared by chemical etching. The stress was a linear function of the deposited film thickness for both cases.

Figure 3 is a plot of the stress *vs.* the deposition rate of the SiO_2 film for a constant film thickness of 7500Å and for three different volume ratios of oxygen to silane.

Figure 4 is a plot of the stress *vs.* the volume ratio of oxygen to silane for a constant film thickness of 7500Å and for three different deposition rates.

Figures 3 and 4 were obtained from the same body of data. Figure 3 shows the stress to be a linear function of the logarithm of the deposition rate. Figure 4 shows that the stress increases asymptotically to a constant value, as a function of the volume ratio of oxygen to silane, for a constant deposition rate.

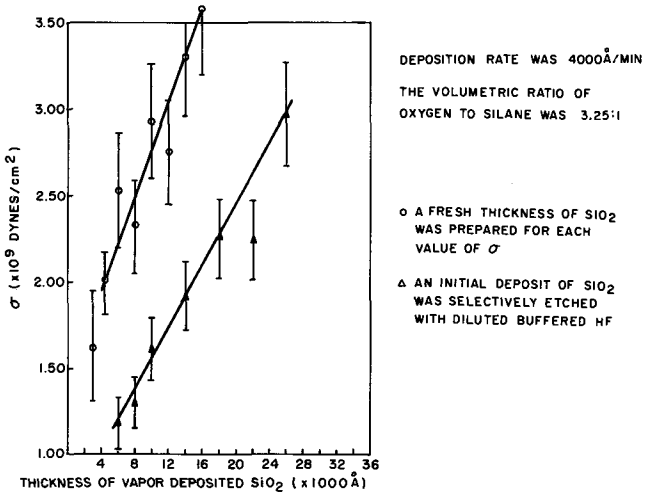

Fig. 2. Stress *vs.* thickness of the SiO_2 film. The deposition rate was 4000 Å/min and the volume ratio of oxygen to silane was 3.25 to 1. ○ A fresh thickness of SiO_2 was prepared for each value of σ. △ An initial deposit of SiO_2 was selectively etched with diluted buffered HF.

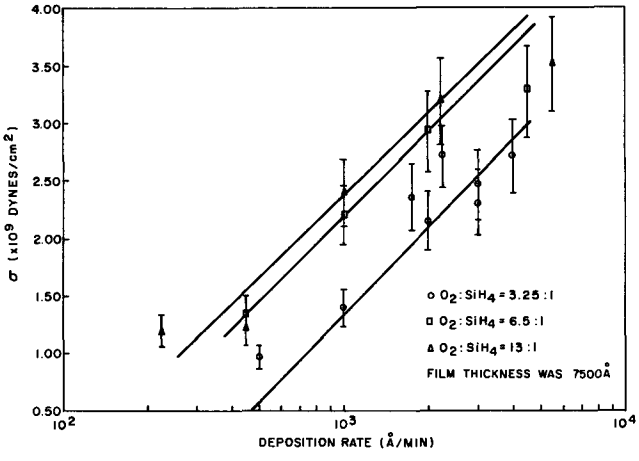

Fig. 3. Stress *vs.* deposition rate for constant oxygen to silane ratios. The film thickness was 7500Å. ○ O_2:SiH_4 was 3.25 to 1. □ O_2,SiH_4 was 6.5 to 1, △ O_2:SiH_4 was 13 to 1.

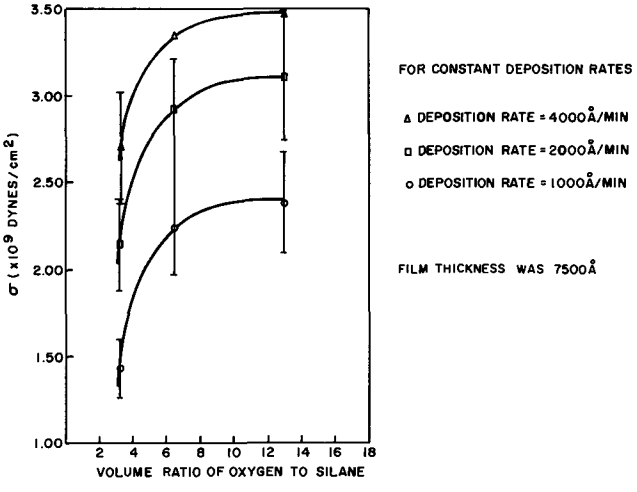

Fig. 4. Stress *vs.* volume ratio of oxygen to silane for constant deposition rates. Film thickness was 7500Å. △, The deposition rate was 4000 Å/min; □, deposition rate was 2000 Å/min; ○, deposition rate was 1000 Å/min.

Experimental errors and limitations.—Stress is a function of three independent variables in Eq. [2]: the substrate thickness, t_s, the film thickness, t_f, and the focal length, f. The error involved in the stress measurement is dependent on the uncertainty associated with each of the independent variables, and was calculated to be typically ±10%, but always less than ±17%.

The following uncertainties were estimated for each of the independent variables in Eq. [2], and for the abscissae shown in Fig. 2, 3 and 4:

1. The substrate thickness was measured gravimetrically, and had an error of less than 1%.
2. The uncertainty in the values of the film thickness was less than ±10%.
3. The error associated with the measurement of the focal length was governed by the factors sketched below and was typically ±10%.
4. The deposition rate errors were governed by the same factors which influenced the film thickness errors, and were, therefore, less than ±10%.
5. The error for the volumetric ratio of oxygen to silane did not exceed ±5%.

The boundary limits for the calculation of the stress are set by factors involving the measurement of the focal length.

The lower detection limit for stress was determined by the unevenness of the substrate. The measurement of the focal length involves the discrimination of the focus from neighboring regions of the reflected light beam. An uneven substrate distorts the geometry of the focus, so that the uniqueness of the focus with respect to neighboring regions of the reflected light beam is compromised. Consequently, the decreased maximum convergence angle of the reflected light at long focal lengths significantly influences the identification of the focus when the substrate is uneven. For example, at about 6 x 10^8 dynes/cm^2, the focal lengths for 2-mil thick substrates were approximately 100 cm, with a corresponding uncertainty of 50%. This was considered to be the lower limit of measurable stress.

The upper measurement limit of stress was fixed by the substrate thickness and the aperture of the collimated light beam. Equation [1] and, therefore, Eq. [2] are valid only when the maximum deflection measured is much less than the substrate thickness. Therefore, since the focal length is directly proportional to the ratio of the square of the beam diameter to the deflection at the perimeter of the illumination, an upper limit of permissible deflection impresses an upper limit to the stress that can be measured with a given substrate thickness and beam diameter. The upper stress limit for 2-mil thick substrates and a 1-cm beam diameter is 3.5 x 10^9 dynes/cm^2.

The upper measurement limit of stress could be raised by decreasing the aperture of the collimator and/or increasing the thickness of the substrate. However, since the aperture should be several times larger than the size of the average abberation in the surface contour of the substrate, the minimum useful aperture is determined by substrate unevenness. On the other hand, the sensitivity of measuring low values of stress decreases sharply by increasing the thickness of the substrate. Therefore, for a given film thickness, the maximum thickness of the substrate which can be used is determined by the minimum value of stress to be measured.

The optimum substrate thickness, t_s, for this experiment was found using Eq. [1] and letting r = beam diameter/2, $\delta = t_s/10$, and assigning realistic values to σ and t_f (see Fig. 2). The 2-mil thick substrates used in this experiment were approximately half the optimum substrate thickness calculated according to the procedure outlined above.

A constant uncertainty of ±10% was observed in locating the position of the focus. The error cannot be accounted for by the same factors which influenced the boundary limits of the stress. However, the eye is relatively insensitive to changes in brightness, which introduces a calculatable error into the judgment of the position of the focus. It is therefore likely that a large portion of the uncertainty can be accounted for by the lack of sensitivity of the eye.

The flatness of the substrate was characterized by two properties: (*i*) the focal length for zero stress, and (*ii*) the unevenness of the surface. The unevenness was given by the maximum possible normal component of the set of vectors connecting any two points of the surface, for zero stress. The focal length of all substrates used in this experiment was much longer than the detectable limit of the 200-cm long optical bench, and the unevenness was less than 1250Å when the stress was zero.

Conclusions

The optical method used to measure stress in this experiment required only a single measurement for each determination, and therefore was effective in processing a large number of samples. The equipment used to build the measurement apparatus was inexpensive.

In general, the stress of deposited films has two components: (*i*) the intrinsic stress, which is independent of the substrate onto which the films are deposited, and (*ii*) the thermal stress, which is due to different thermal expansion coefficients for film and substrate, and which results whenever the measurement temperature differs from the deposition temperature. The thermal stress is compressive because the thermal coefficient of expansion of Si is an order of magnitude higher than for SiO_2. An extrapolation of the data presented by Jaccodine and Schlegel (9) indicates that the thermal stress would not exceed 1.0 x 10^9 dynes/cm^2 for a layer 8000Å thick. Since the deposition temperature was constant in the experiment, the relative shapes of the curves in Fig. 2, 3, and 4 were not influenced by the thermal stress, and the curves can be considered to be characteristic of the intrinsic stress.

No theoretical model was suggested at this time by the observed dependence of the intrinsic stress on the deposition parameters.

Acknowledgment

The authors gratefully acknowledge the contributions of G. L. Schnable, M. M. Schlacter, and R. Keen. G. L. Schnable and M. M. Schlacter reviewed the paper for technical content and were responsible for many of the ideas used to initiate the study. R. Keen supervised the use of the vapor deposition system used to make the samples.

Manuscript submitted July 3, 1968; revised manuscript received Dec. 23, 1968. This was a Recent News Paper presented at the Boston Meeting, May 5-9, 1968.

Any discussion of this paper will appear in a Discussion Section to be published in the December 1969 JOURNAL.

REFERENCES

1. H. C. Evitts, D. L. Tolliver, and K. R. MacKenzie, Technical Report AFML-TR-285 for Contract AF33(657)-11268 by Motorola, Inc., (1968).
2. N. Goldsmith and W. Kern, *RCA Rev.*, **28**, 153 (1967).
3. M. L. Hammond and G. M. Bowers, *Trans. Met. Soc. AIME*, **242**, 546 (1968).
4. N. N. Davidenkov, *Soviet Phys.-Solid State*, **2**, 2595 (1961).
5. H. P. Murbach and H. Wilman, *Proc. Phys. Soc. (London)*, **B66**, 905 (1953).
6. D. S. Campbell, "Vacuum Symposium Transactions 1962," 29, MacMillan, New York (1963).
7. H. Blackburn and D. S. Campbell, "Vacuum Symposium Transactions 1961," 943, Pergamon Press, London (1962).
8. R. Glang, R. A. Holmwood, and R. L. Rosenfield, *Rev. Sci. Instrum.*, **36**, 7 (1965).
9. R. J. Jaccodine and W. A. Schlegel, *J. Appl. Phys.*, **37**, 2429 (1966).

Phosphors Based on Rare Earth Phosphates

II. Reflection Spectra of Rare Earth Phosphates

R. C. Ropp*

Westinghouse Electric Corporation, Bloomfield, New Jersey

ABSTRACT

Because PO_4 does not absorb at wavelengths longer than about 2000Å, the rare earth phosphates, $LnPO_4$, where Ln is any rare earth (other than La, Pm, or Lu), represent an ideal system for the study of rare earth absorption. Reflectance spectra of all compounds are presented for wavelengths between 2000 and 8000Å. Only $TbPO_4$ and $EuPO_4$ produce luminescence when excited by the proper wavelength. Major, broad absorption bands are catalogued but not identified, except for that of Eu^{+3} and Tb^{+3}, where $Eu(III)O_n^{-2n} \rightarrow Eu(II)O_n^{-2n+1}$ and $4f^8 \rightarrow 4f^75d$, respectively, are the probable mechanisms.

A number of prior studies of rare earth absorption spectra have been reported (1), including infrared spectra (2), visible spectra (3), and ultraviolet spectra (4). Perhaps the most extensive of these was published by Jørgensen and co-workers (5). Most of their studies concentrated on the pure and mixed oxides which begin to show strong absorption bands around 2600-2800Å. It would have been desirable to extend their absorption studies at least to 2000Å, particularly in view of the assignments made by Jørgensen *et al.* (5) for the 4f → 5d transition bands and those made for charge transfer bands of the several rare earths. Their results were obtained by correlation of the expected positions of the 4f → 5d bands and also by the observed absorption edge of the oxides.

Because PO_4^{-3} does not absorb appreciably for wavelengths longer than 2000Å and because the peak absorption occurs close to 1800Å, as shown recently by Halmann and Platzner (6), one would hypothesize that rare earth phosphates should represent an ideal system for the study of far-ultraviolet spectra of the rare earths. Any absorption, (1 — R) observed for $LnPO_4$ compounds for wavelengths longer than about 2000Å could only be attributed to rare earth absorption.

A prior paper (7) has already shown that it is possible to obtain resolution of the order of 1-2Å in powder reflectance spectroscopy.

The rare earths occur in nature as xenotime, and monazite (orthophosphates) and as bastnasite and euxenite (fluorocarbonates and complex oxides, respectively). The synthesis of rare earth orthophosphates has been described previously. Fusion methods (8), hydrothermal crystallization from aqueous solutions (9), and chemical reactions (10) are some of the methods to be found. However, there are no previous reports on the absorption properties of the rare earth phosphates.

Experimental Methods

Method of preparation.—The rare earth phosphates were prepared by precipitation from an H_3PO_4 solution, as described previously (11). Since the solubility of the rare earth phosphates is an inverse function of precipitation temperature and a direct function of phosphoric acid concentration, it is possible to prepare crystalline materials of controlled particle size (see Fig. 1) by carefully adjusting the conditions of precipitation. Note that the distribution is size-limited, as would be expected for a chemical growth process. Crystalline materials can be obtained as mono- and hemi-hydrates as shown in Fig. 2, for YPO_4 and $LaPO_4$, respectively. Firing at 1200°C in air then gave crystalline materials with unit cells, as determined from x-ray powder diffraction patterns, whose values matched very closely with published data (12).

Chemical purity.—Commercial raw materials were employed, rare earth oxides having a stated purity of 99.9%, or better, while the H_3PO_4 employed was of reagent grade quality. The oxides were analyzed by spectrographic means and found to contain no detectable amounts of transition element impurities, minor amounts of Al and Si, and several parts per million of alkaline earths. Thus, the only major impurities were rare earths. Since the maximum was only about 1:1000 in ratio, the spectral properties measured are regarded as typical and not affected by the impurities

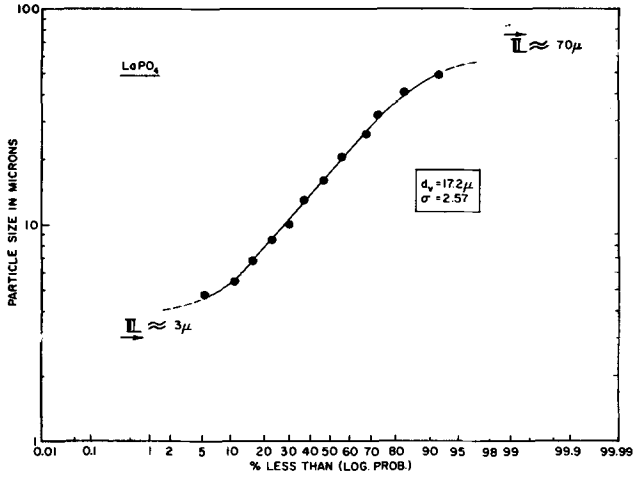

Fig. 1. Particle size distribution produced by precipitation

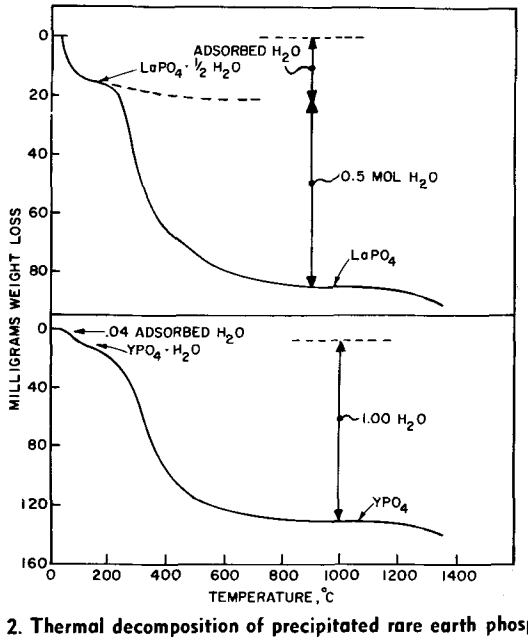

Fig. 2. Thermal decomposition of precipitated rare earth phosphates

* Electrochemical Society Active Member.

present. In addition, the method of preparation effects a further purification (with the exception of other rare earths) since both alkaline-earths and transition elements are complexed, not precipitated, by H_3PO_4 and tend to remain in solution.

Spectral measurements.—Excitation and emission spectra were obtained with the aid of a commercial instrument (13) having two monochromators. The excitation monochromator provided a constant energy excitation beam over the range of 20,000-50,000 cm^{-1} (5000-2000Å). Either monochromator could be programmed separately to provide excitation or fluorescence spectra directly, the former automatically corrected to constant energy, the latter compensated for instrumental energy losses. Resolution in the instrument varied from a few angstroms in the ultraviolet to about 10Å in the red region of the spectrum.

Reflectance measurements were made employing a double-beam Model 15 Cary spectrophotometer equipped with two diffuse reflectance heads, coated with $BaSO_4$. The method was described in detail previously (7).

Resolution.—Resolution of the absorption bands obtained in this work was sufficient to determine that, in most rare earth phosphates, the individual half-widths of the Stark components vary between 55 and 15Å.

However, in order to present a complete reflectance spectrum, as seen below, it was necessary to plot the experimental data on a compressed scale and just to indicate the number of Stark components observed, so as to show the broad bands observed more clearly.

Experimental Results

Structure.—Powder reflectance spectra were obtained for all rare earth phosphates, except for $CePO_4$, which could not be prepared in a pure form by the method. No broad band absorption was observed for YPO_4, and $GdPO_4$ up to 1980Å, the beginning of the phosphate absorption band. Transitions within the $4f^7$ multiplet of Gd^{+3} were observed, however. Various structures are formed by the rare earths, the lighter rare earths being monoclinic (monazite structure) and the heavier rare earth phosphates being tetragonal (zenotime structure). The x-ray diffraction pattern results determined in this study agreed very closely with those already published for the rare earth phosphates (10, 12). Mooney has already shown (10) that certain rare earth phosphates can exist in a low temperature hexagonal modification. Transition from the low to the high temperature form generally occurs below 1000°C (14). The materials studied herein all had the high temperature form, including $TbPO_4$, which is dimorphic.

Reflectance spectra.—$PrPO_4$.—Two broad absorption bands occur in the visible region of the spectrum as shown in Fig. 3, giving rise to the green body color of $PrPO_4$. The figures given in the parentheses in Fig. 3 show the number of individual Stark components observed. In Fig. 3, it is evident that the transition $^3H_4 \rightarrow {}^1D_2$ is greatly broadened in relation to the other transitions which form the band near to 4500Å. This latter band is composed of at least four separate

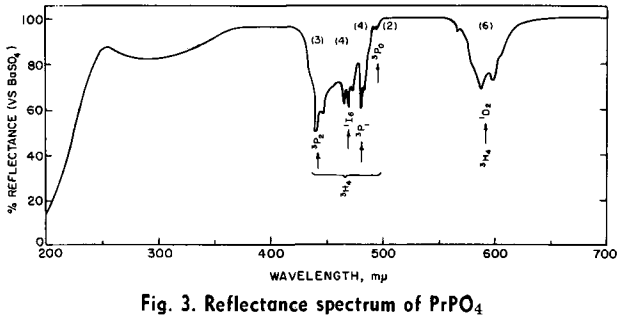

Fig. 3. Reflectance spectrum of $PrPO_4$

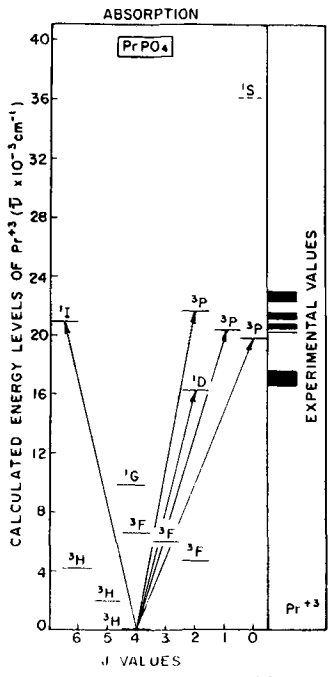

Fig. 4. Transitions found for Pr^{+3} absorption

transitions between $4f^2$ electron states. The average band width was estimated, from the chart, to be about 15Å, nearly three times those of the other phosphates. In Fig. 4 is presented a Grotrian diagram showing the transitions assigned for Pr^{+3}. Note that transitions from the ground state, $^3H_4$, to all known Pr^{+3} states were observed. Undoubtedly transitions to the other ^3H, ^3F, and ^1G states occur in the infrared region of the spectrum, a region not measured in the present work because of lack of instrumental capability. Table I shows the lines observed, transitions between Stark states, the transitions identified, and a comparison of the baricenters of the observed and calculated absorption bands.

There is another broad band which occurs around 3000Å and another whose peak lies below 2000Å. While identification cannot be certain for these bands, they are probably caused by transitions from the ground state to upper state configurations. Jørgensen *et al.* (5) have calculated the positions of these upper state levels to be about 32,000 cm^{-1} for the $4f \rightarrow 5d$ transition and 55,000 cm^{-1} for the charge transfer transition of Pr^{+3}. These values agree very well with those of the present work. However, Sugar (15) has also calculated the configurational levels of Pr^{+3} and surprisingly enough, a transition such as $4f \rightarrow 4f^{n-1}6p$ can occur as low as 3000Å even though the transition is partly forbidden. Apparently, the 4f ground state has a certain percentage of 6s character admixed with the 4f state, thereby raising the transition probability somewhat. At the present time, the broad bands cannot be positively identified.

$NdPO_4$.—$NdPO_4$ absorbs strongly in the green and yellow regions of the spectrum as shown in Fig. 5. Up

Table I. Reflectance spectrum of $PrPO_4$

Transition	Baricenters of absorption bands, cm^{-1} Observed	Calculated*	Lines observed, Å					
$^3H_4 \rightarrow {}^1D_2$	17,007	16,973	5680	5720	5793	5853	5975	6020
$^3H_4 \rightarrow {}^3P_0$	20,243	20,407	4928	4946				
$^3H_4 \rightarrow {}^3P_1$	20,747	20,984	4809	4828	4842	4872		
$^3H_4 \rightarrow {}^1I_6$	21,322	20,898	4659	4698	4729	4748		
$^3H_4 \rightarrow {}^3P_2$	22,212	22,211	4350	4404	4467			

* J. R. Margolis, *J. Chem. Phys.*, 35, 1367 (1961).

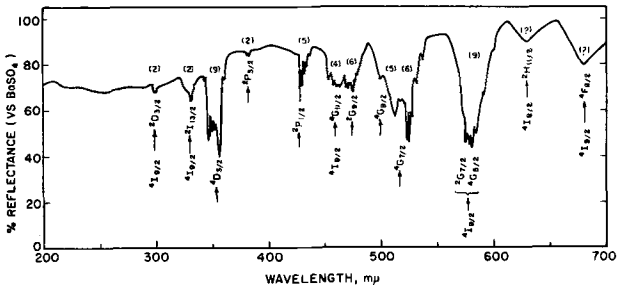

Fig. 5. Reflectance spectrum of $NdPO_4$

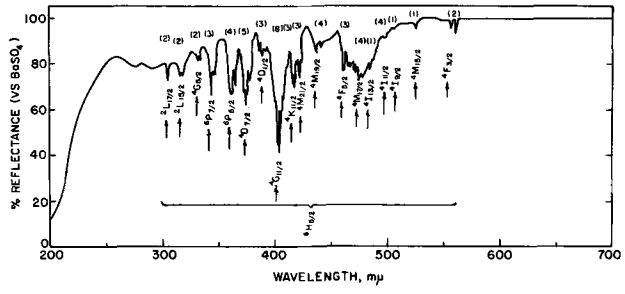

Fig. 6. Reflectance spectrum

to nine components were observed in some of these transitions. However, no broad band was observed in contrast to the results for Pr^{+3}. Neither did a band appear which could be considered the beginning of the phosphate absorption band. Table II gives the spectral data observed for $NdPO_4$.

$SmPO_4$.—$SmPO_4$ absorbs weakly in the blue and blue-green regions of the spectrum as shown in Fig. 6. The strongest absorption band occurs about 4000Å and is caused by transitions to a ^4G level. The numbers given in the parentheses are the number of components observed for each band. Table III gives the spectral data observed. Much of the complexity of Sm^{+3} arises from the fact that the $4f^5$ free-ion configuration of Sm^{+3} is characterized by 198 SLJ states involving sextet, quartet, and doublet states. In the presence of the crystal field (C_1 symmetry) each SLJ state splits into a maximum of J + ½ crystal sublevels (the Kramers degeneracy) to give rise to as many as 2002 crystal states. However, not all of these may participate in the absorption. Polarization data are required to unravel the crystal states which are responsible for the transitions observed.

In addition, there are also two weak, but broad, absorption bands near 2750 and 2900Å whose identity remains uncertain. Since these bands are broad, it is not believed that they can represent 4f →4f transitions. More likely they are upper-state transitions or phosphate absorption bands. The broad band at 2000Å cannot be identified with the present data.

$EuPO_4$.—The reflectance spectrum of $EuPO_4$ is given in Fig. 7. It is characterized by a very strong and broad absorption band occurring around 2300Å with a number of 4f → 4f transitions occurring in the near ultraviolet region of the spectrum. Of all the rare earth phosphates, the strong absorption band of $EuPO_4$, whose width is about 800-1000Å at the 50% point, appears at the lowest energy. The absorption bands representing 4f → 4f transitions were fairly narrow (about 4Å in width) with those from the ground-state to ^5D, ^5L, ^5G, ^5F multiplets being represented. It is interesting to note that, although transitions from the ground state, $^7F_6$, to all of the ^5D states do occur, transitions from an upper-state, $^7F_1$, to all of the same states were

Table II. Reflectance spectrum of $NdPO_4$

Transition	Baricenters of absorption bands, cm⁻¹ Observed	Calculated*		Lines observed, Å							
$^4I_{9/2} \rightarrow {}^4F_{7/2}$	14,706	14,903		Loss of resolution							
$^4I_{9/2} \rightarrow {}^2H_{11/2}$	15,873	15,985		Loss of resolution							
$^4I_{9/2} \rightarrow {}^2G_{7/2}$ }	17,240	17,354		5725	5752		5780	5914			
$^4I_{9/2} \rightarrow {}^4G_{5/2}$ }		17,356		5806	5842		5875	5954	6006		
$^4I_{9/2} \rightarrow {}^4G_{7/2}$	19,084	19,320	5268	5310	5381	5205	5227	5250			
$^4I_{9/2} \rightarrow {}^4G_{9/2}$	19,763	19,620	4995	5060	5102	5125	5165				
$^4I_{9/2} \rightarrow {}^2G_{9/2}$	21,186	21,255	4702	4717	4730	4756	4773	4795			
$^4I_{9/2} \rightarrow {}^4G_{11/2}$	21,786	21,826	4543	4584	4615	4635					
$^4I_{9/2} \rightarrow {}^2P_{1/2}$	23,202	23,146	4288	4301	4326	4347	4372				
$^4I_{9/2} \rightarrow {}^2P_{3/2}$	26,110	26,348	3820	3828							
$^4I_{9/2} \rightarrow {}^4D_{1/2}, {}^4D_{3/2}, {}^4D_{5/2}, {}^2I_{11/2}$	28,571	28,641	3478	3486	3505	3518	3537	3557	3565	3574	3616
$^4I_{9/2} \rightarrow {}^2I_{13/2}$	30,211	30,070	3246	3310							
$^4I_{9/2} \rightarrow {}^2D_{3/2}$	33,333	33,771	2996	3005							

* B. G. Wybourne, *J. Chem. Phys.*, 32, 640 (1960.)

Table III. Reflectance spectrum of $SmPO_4$

Transition	Baricenters of absorption bands, cm⁻¹ Observed	Calculated*		Lines observed, Å						
$^6H_5 \rightarrow {}^4G_{5/2}$	17,828	17,643	5609							
$^6H_5 \rightarrow {}^4F_{3/2}$	17,963	18,059	5567							
$^6H_5 \rightarrow {}^4M_{15/2}$	18,974	19,049	5270							
$^6H_5 \rightarrow {}^4I_{9/2}, {}^4G_{7/2}$	19,802	19,762	5050							
$^6H_5 \rightarrow {}^4I_{11/2}$	20,134	20,190	4933	4956	4976	5002				
$^6H_5 \rightarrow {}^4I_{13/2}$	20,670	20,735	4838							
$^6H_5 \rightarrow {}^4M_{17/2}$	20,912	20,868	4782	4756	4720	4703				
$^6H_5 \rightarrow {}^4F_{5/2}$	21,542	21,742	4668	4650	4609					
$^6H_5 \rightarrow {}^4G_{9/2}, {}^4M_{19/2}, {}^4I_{15/2}$	22,556	22,353	4370	4415	4450	4500				
$^6H_5 \rightarrow {}^4M_{21/2}$	34,697	34,676	4190	4210	4224					
$^6H_5 \rightarrow {}^4K_{11/2}, {}^4P_{5/2}$	24,038	23,933	4141	4154	4174					
$^6H_5 \rightarrow {}^4G_{11/2}, {}^6P_{3/2}$	24,820	24,786	3960	3991	4008	4022	4040	4050	4068	4095
$^6H_{5/2} \rightarrow {}^4D_{1/2}, {}^4K_{13/2}$	25,700	25,705	3862	3890	3920					
$^6H_{5/2} \rightarrow {}^4D_{7/2}, {}^4F_{9/2}$	26,617	26,674	3730	3745	3754	3776	3782			
$^6H_{5/2} \rightarrow {}^4K_{15/2}, {}^6P_{5/2}, {}^4D_{3/2}$	27,640	27,694	3601	3610	3618	3644				
$^6H_{5/2} \rightarrow {}^6P_{7/2}$	28,952	29,008	3436	3457	3470					
$^6H_{5/2} \rightarrow {}^4G_{5/2}$	29,940	29,838	3313	3335						
$^6H_{5/2} \rightarrow {}^2L_{15/2}$	31,605	31,139	3148	3164	3180					
$^6H_{5/2} \rightarrow {}^2L_{17/2}, {}^4F_{9/2}$	32,820	32,662	3047							

* B. G. Wybourne, *J. Chem. Phys.*, 36, 2301 (1962).

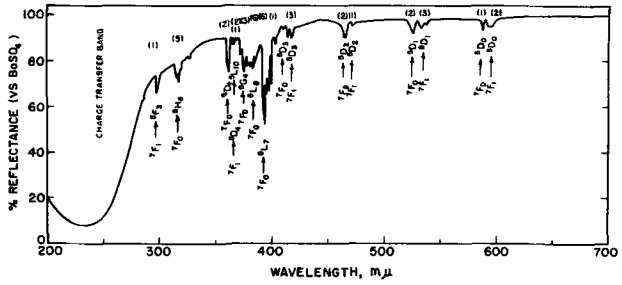

Fig. 7. Reflectance spectrum of $EuPO_4$

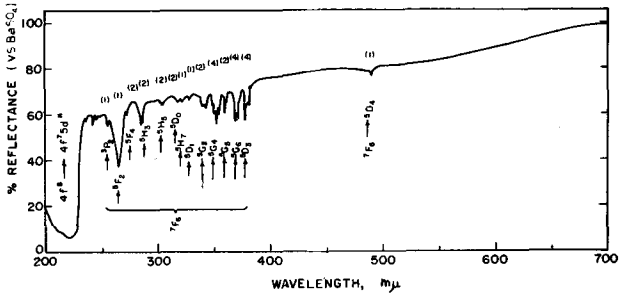

Fig. 8. Reflectance spectrum of $TbPO_4$

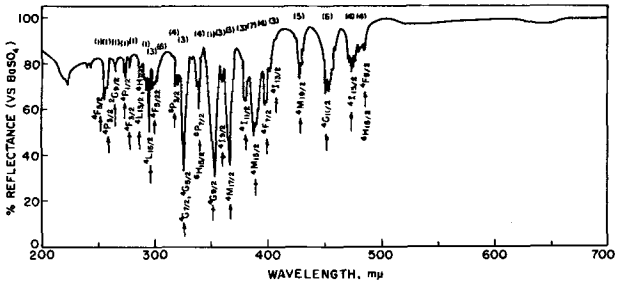

Fig. 9. Reflectance spectrum of $DyPO_4$

also noted. There is little doubt that these transitions do take place and can be proved by comparing the number of Stark components observed, with those possible, as shown in Table IV. Thermal energy at 293°K is sufficient to populate the $^7F_1$ state. Since these levels produce fluorescence, their apparent intensity appears to be low and loss of resolution must certainly have occurred. However, experimental bands involving the lowest ^7F and ^5D states allow unequivocal assignment of transitions between these states. Table V presents the spectral data observed.

The broad absorption band observed in $EuPO_4$ is certainly much different than any observed, or described below, both in position and in apparent width. This is the charge transfer band for Eu^{+3} as asserted by Jørgensen (16) and Borchardt (17) for which substantiating data have been published by the author (18). The mechanism can be postulated as follows

$$Eu(III)O_n^{-2n} \rightarrow Eu(II_n^{O-2n+1})$$

There are probably a number of 4f states which are masked by the charge transfer band.

$TbPO_4$.—The body color of $TbPO_4$ is an off-white. A continuous decrease in the reflectance was seen as a function of shorter wavelengths as shown in Fig. 8 irrespective of the 4f →4f transitions of Tb^{+3} and may be due to the presence of Tb^{+4}. Table VI presents the assignments for Tb^{+3} transitions.

Table IV. Comparison of predicted and observed transitions

	States predicted (C_1 symmetry)	States observed
$^7F_0 \rightarrow {}^5D_0$	1	1
$^7F_1 \rightarrow {}^5D_0$	3	2
$^7F_0 \rightarrow {}^5D_1$	3	2
$^7F_1 \rightarrow {}^5D_1$	5	3
$^7F_0 \rightarrow {}^5D_2$	5	2
$^7F_1 \rightarrow {}^5D_2$	8	1
$^7F_0 \rightarrow {}^5D_3$	7	1
$^7F_0 \rightarrow {}^5D_3$	7	1
$^7F_1 \rightarrow {}^5D_3$	11	3

Table V. Reflection spectrum of $EuPO_4$

Transition	Baricenters of absorption bands, cm^{-1} Observed	Calculated*	Lines observed, Å					
$^7F_1 \rightarrow {}^5D_0$	16,835	17,000	5934	5948				
$^7F_0 \rightarrow {}^5D_0$	17,036	17,374	5878					
$^7F_1 \rightarrow {}^5D_1$	18,692	18,571	5328	5332	5373			
$^7F_0 \rightarrow {}^5D_1$	19,048	18,945	5253	5260				
$^7F_0 \rightarrow {}^5D_2$	21,505	21,508	4644	4655				
$^7F_1 \rightarrow {}^5D_2$	21,186	21,134	4710					
$^7F_1 \rightarrow {}^5D_3$	24,038	24,082	4142	4151	4178			
$^7F_0 \rightarrow {}^5D_3, {}^5L_6$	24,396	24,456	4107					
$^7F_0 \rightarrow {}^5L_7$	25,381	25,340	3939	3954	3975	3998	4043	4064
$^7F_0 \rightarrow {}^5L_8$	26,247	26,220	3783	3797	3818	3892	3850	3864
$^7F_0 \rightarrow {}^5G_2, {}^5G_3$	25,496	26,564	3730	3747	3758			
$^7F_0 \rightarrow {}^5L_{10}$	27,473	27,386	3673	3691				
$^7F_0 \rightarrow {}^5D_4$	27,781	27,747	3612	3617				
$^7F_1 \rightarrow {}^5D_4$	27,367	27,373	3654					
$^7F_0 \rightarrow {}^5H_6$	31,348	31,248	3162	3172	3178	3190	3197	
$^7F_1 \rightarrow {}^5F_3, {}^5I_5$	33,557	33,581	2982					

* G. S. O'Felt, *J. Chem. Phys.*, 38, 2171 (1963).

There is also a broad band occurring around 2100Å, which is the $4f^8 \rightarrow 4f^7 5d$ transition as noted by Jørgensen (6).

$DyPO_4$.—The ivory body color of $DyPO_4$ arises because of the lack of strong absorption in the visible region of the spectrum, as shown in Fig. 9. A great number of near ultraviolet bands were noted due to 4f → 4f transitions. Table VII gives the spectral data observed. It is notable that no broad bands were observed in this reflectance spectrum.

$HoPO_4$.—The body color of $HoPO_4$ is beige. A great number of absorption bands occurs in the visible region of the spectrum and throughout the ultraviolet with a large number of Stark components observed as shown in Fig. 10. Table VIII presents the spectra data measured. No broad bands were observed.

$ErPO_4$.—The pink body color of $ErPO_4$ can be attributed to the strong absorption bands occurring in the green region of the visible spectrum as shown in Fig. 11. A Grotrian diagram of the transitions assigned is shown in Fig. 12. Transitions to ^4F and ^4G multiplets were identified as well as those to individual ^2K, ^2H, ^2L, and ^2P states. Note that a broad band, was also observed. Table IX presents the spectral data observed.

Table VI. Reflectance spectrum of $TbPO_4$

Transition	Baricenters of absorption bands, cm^{-1} Observed	Calculated*	Lines observed, Å					
$^7F_6 \rightarrow {}^5D_4$	20,408	20,455	4890					
$^7F_6 \rightarrow {}^5D_3$	26,385	26,216	3770	3783	3795	3807	3817	3844
$^7F_6 \rightarrow {}^5G_6$	27,027	27,263	3684	3697	3708	3725		
$^7F_6 \rightarrow {}^5G_5$	27,778	27,659	3596	3607	3617			
$^7F_6 \rightarrow {}^5G_4, {}^5D_2$	28,409	28,365	3496	3510	3522	3537	3556	
$^7F_6 \rightarrow {}^5G_3$	28,969	28,960	3542					
$^7F_6 \rightarrow {}^5G_2$	29,274	29,411	3404	3428				
$^7F_6 \rightarrow {}^5D_1$	30,460	30,400	3283					
$^7F_6 \rightarrow {}^5H_7$	31,056	30,953	3192	3200	3217			
$^7F_6 \rightarrow {}^5D_0$	31,447	31,649	3177	3185				
$^7F_6 \rightarrow {}^5H_5, {}^5H_6$	33,000	32,995	3040	3064				
$^7F_6 \rightarrow {}^5H_3$	34,843	34,414	2832	2850	2869			
$^7F_6 \rightarrow {}^5F_4$	36,563	36,223	2735					
$^7F_6 \rightarrow {}^5F_2, {}^5F_3$	37,523	37,563	2665	(90Å wide)				
$^7F_6 \rightarrow {}^3P_2$	39,216	39,295.	2550					
Unknown	40,469	—	2489	2453				
Unknown	41,468	—	2423	2400				
Unknown	42,221	—	2363	2374				

* G. S. O'Felt, *J. Chem. Phys.*, 38, 2171 (1963).

Table VII. Reflectance spectrum of $DyPO_4$

Transition	Baricenters of absorption bands, cm^{-1} Observed	Calculated*	Lines observed, Å							
$^6H_{15/2} \rightarrow {}^4F_{9/2}$	20,704	20,216	4802	4812	4831	4852				
$^6H_{15/2} \rightarrow {}^4I_{15/2}$	21,097	21,427	4723	4738	4754	4771				
$^6H_{15/2} \rightarrow {}^4G_{11/2}$ ($^4M_{21/2}$)	22,075	22,442	4510	4522	4536	4544	4568	4600		
$^6H_{15/2} \rightarrow {}^4M_{19/2}$ ($^4K_{17/2}$)	23,310	23,903	4270	4278	4291	4302	4325			
$^6H_{15/2} \rightarrow {}^4I_{13/2}$	24,661	24,296	4040	4052	4072					
$^6H_{15/2} \rightarrow {}^4F_{7/2}$	24,962	24,720	3980	3994	4020	4028				
$^6H_{15/2} \rightarrow {}^4M_{15/2}$ ($^4I_{11/2}$)	25,707	26,170	3859	3869	3383	3890	3900	3913	3922	
$^6H_{15/2} \rightarrow {}^4I_{11/2}$	26,281	26,224	3784	3799	3814					
$^6H_{15/2} \rightarrow {}^4M_{17/2}$	27,248	27,662	3658	3669	3693					
$^6H_{15/2} \rightarrow {}^4I_{9/2}$ ($^4F_{5/2}$)	27,778	27,772	3586	3596	3603					
$^6H_{15/2} \rightarrow {}^4G_{9/2}$	28,369	28,582	3525							
$^6H_{15/2} \rightarrow {}^6P_{7/2}$ ($^4P_{5/2}$)	29,499	29,400	3334	3381	3395	3425				
$^6H_{15/2} \rightarrow {}^4G_{7/2}$, $^4G_{5/2}$	30,628	30,106, 30,839	3230	3265	3295					
$^6H_{15/2} \rightarrow {}^6P_{3/2}$	31,250	31,478	3166	3182	3193	3208				
$^6H_{15/2} \rightarrow {}^4F_{5/2}$	33,222	33,147	2987	2997	3007	3025	3035	3053		
$^6H_{15/2} \rightarrow {}^4L_{15/2}$	34,130	34,451	2919	2927	2958					
$^6H_{15/2} \rightarrow {}^4L_{13/2}$	34,702	34,733, 34,762	2882							
$^6H_{15/2} \rightarrow {}^4F_{3/2}$	35,907	36,116	2792							
$^6H_{15/2} \rightarrow {}^4P_{1/2}$	36,496	36,498	2740	2750	2758					
$^6H_{15/2} \rightarrow {}^2G_{9/2}$	37,736	37,668	2651							
$^6H_{15/2} \rightarrow {}^4P_{3/2}$	38,711	38,566	2584							
$^6H_{15/2} \rightarrow {}^4F_{5/2}$	38,956	39,210	2567							
Unknown	40,950	—	2442							
Unknown	41,665	—	2405							
Unknown	45,065	—	2360	2290	2240	2195	2175			

* B. G. Wybourne, *J. Chem. Phys.*, 36, 2301 (1962).

Table VIII. Reflection spectrum of $HoPO_4$

Transition	Baricenters of absorption bands, cm^{-1} Observed	Calculated*	Lines observed, Å									
$^5I_8 \rightarrow {}^5F_5$	15,385	15,403	6444	6550								
$^5I_8 \rightarrow {}^5F_4$, $^5S_2$	18,450	18,479	5345	5374	5396	5414	5429	5447	5457	5493	5508	
$^5I_8 \rightarrow {}^5F_3$	20,575	20,568	4859	4878	4897	4909	4917					
$^5I_8 \rightarrow {}^5F_2$, $^3K_8$	21,090	21,113	4682	4689	4703	4724	4734	4752	4764	4781	4800	4810
$^5I_8 \rightarrow {}^5G_6$ ($^5F_1$)	22,080	22,192	4451	4494	4512	4536	4552	4569	4588			
$^5I_8 \rightarrow {}^5G_5$	23,868	24,104	4150	4163	4169	4181	4199	4212	4225	4231		
$^5I_8 \rightarrow {}^5G_4$, $^3K_7$	25,907	26,070	3818	3824	3847	3866	3880	3890	3901	3909	3917	3922
$^5I_8 \rightarrow {}^3H_5$	27,701	28,040	3537	3547	3601	3615	3630	3636	3649	3664		
$^5I_8 \rightarrow {}^5G_3$ ($^5G_2$)	28,968	28,953	3449	3462	3472	3483						
$^5I_8 \rightarrow {}^3K_6$	30,120	30,261	3332	3338	3346	3351	3362					
$^5I_8 \rightarrow {}^3F_4$	30,817	30,726	3245									
$^5I_8 \rightarrow {}^3P_1$ ($^3D_3$)	34,015	33,973	2908	2936	2950	2967						
$^5I_8 \rightarrow {}^5D_4$	34,780	35,125	2848	2878	2897							
$^5I_8 \rightarrow {}^1L_6$ ($^3F_3$)	36,230	36,267	2720	2728								
$^5I_8 \rightarrow {}^3P_0$ ($^3F_2$)	36,710	36,700	2743	2749	2757	2781	2788	2794	2804			
$^5I_8 \rightarrow {}^3I_7$	38,315	38,521	2586	2594	2608	2613						
$^5I_8 \rightarrow {}^3I_5$, $^3F_4$	39,216	39,216	2540	2552								
$^5I_8 \rightarrow {}^3I_6$	39,840	39,654	2507	2514	2424							
$^5I_8 \rightarrow {}^3F_4$	41,667	41,858	2396	2417	2425							
$^5I_8 \rightarrow {}^5D_0$	42,735	42,671	2339									
$^5I_8 \rightarrow {}^3H_4$	45,350	45,314	2203									

* M. H. Crozier and W. A. Runciman, *J. Chem. Phys.*, 35, 1392 (1961).

$YbPO_4$.—The $4f^{13}$ configuration of Yb^{+3} is the "one-hole" conjugate of $Ce^{+3}(4f^1)$ and, with the exception of a $^2F_{5/2}$ level near 10,000 cm^{-1}, has no energy states much below 50,000 cm^{-1} (2000Å). Figure 13 shows the reflectance spectrum measured for $YbPO_4$. Only one broad band near 2200Å was seen which may be a charge transfer band (19).

Fluorescence.—Only two of these phosphates produced fluorescence when irradiated by ultraviolet. This is shown in Fig. 14 for $EuPO_4$ and $TbPO_4$.

$EuPO_4$.—Essentially the same emission spectrum was obtained as for Eu^{+3} in $LaPO_4$ [see Fig. 3, Part I (11)]. In the excitation spectrum, the band at 38,500 cm^{-1} (2580Å) can be identified as the charge transfer band, particularly since the relative intensity of this band changes with Eu^{+3} concentration in the $LaPO_4$:Eu phosphor, eventually showing that presented in Fig. 14, as the Eu^{+3} becomes 100%.

This excitation spectrum may be compared to the absorption spectrum (Fig. 7). One notes that $EuPO_4$ is not an efficient phosphor probably because of concentration quenching.

$TbPO_4$.—The emission spectrum of $TbPO_4$ is quite similar to that of Tb^{+3} in $LaPO_4$ ($LaPO_4$, $EuPO_4$, and $TbPO_4$ all have the same structure; YPO_4 does not). Thus, one concludes that emission occurs from the $4f^8$ energy levels of Tb^{+3} (21). In the excitation spectrum of $TbPO_4$, several separate bands appear which are not as distinct in the absorption spectrum (Fig. 8). In comparing the figures, it becomes apparent that the excitation band at 39,000 cm^{-1} (2550Å) could be assigned to the transition, $4f^8(^7F_6) \rightarrow 4f^8(^5F_2)$ while the

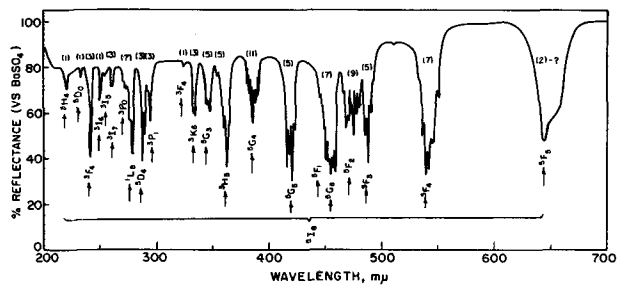

Fig. 10. Reflectance spectrum of $HoPO_4$

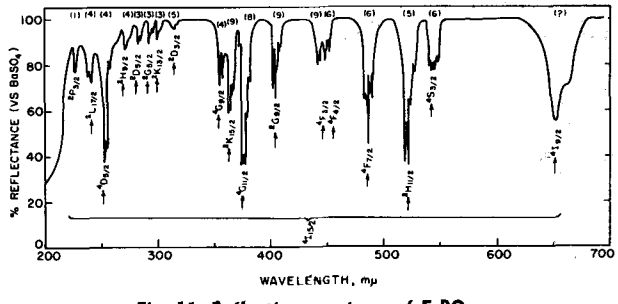

Fig. 11. Reflection spectrum of $ErPO_4$

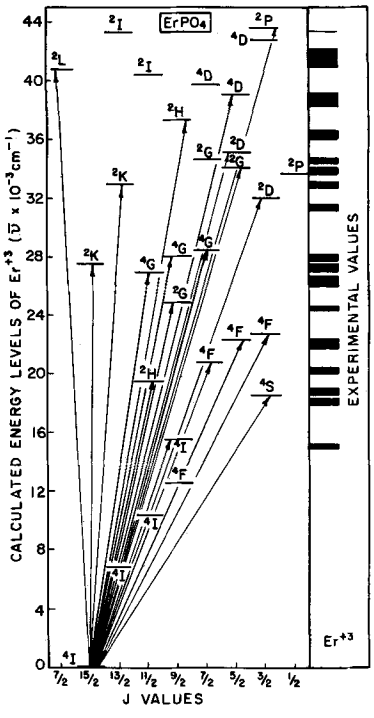

Fig. 12. Transitions found for Er^{+3} ion

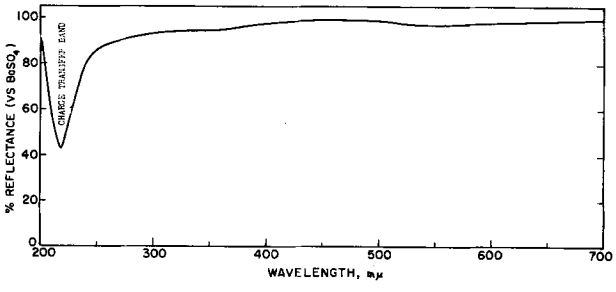

Fig. 13. Reflectance spectrum of $YbPO_4$

bands at 43,000 cm^{-1} cannot be identified with the present data.

Laser application.—It is apparent that several of these materials should be possible candidates for fabrication of lasers. Those materials which absorb in the visible region ($ErPO_4$, $HoPO_4$, and $NdPO_4$) could be used in conjunction with a high intensity xenon arc lamp, with selected activators such as Tm^{+3} and Pr^{+3}. Since the phosphate does not absorb, one should have a rare earth coupled system with host-sensitization as the main excitation process. Such systems should then

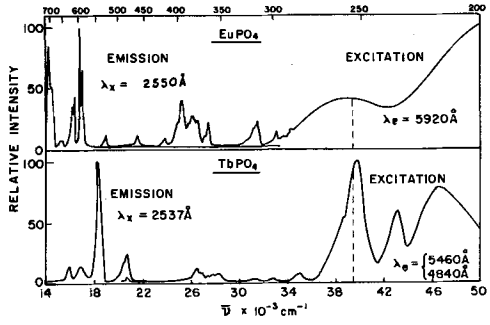

Fig. 14. Spectra of some rare earth phosphates

depend only on the coupling of the two rare earths. For such systems, low threshold values would be expected. In addition, fabrication of single crystals of rare earth phosphates has already been reported (14).

Conclusions

The absorption spectra (1 — R) of the rare earths, as phosphates, have been presented. It is interesting to note that 4f → 4f transitions were identified for all compounds except the $4f^{13}$ configuration ($YbPO_4$). Note that this ion has 4f energy levels between 10,000 and 12,000 cm^{-1} and that sharp line spectra would be expected only below 8000Å, a region not measured because of instrumental incapability.

In regard to luminescence, rare earth ions having ^7F ground states do not interact as strongly with their environment as those with H or I ground-states (21). Thus, only $EuPO_4$ and $TbPO_4$ would be expected to produce luminescence, as noted experimentally. In examining reflectance and excitation data, it becomes clear that excitation is a much more sensitive method of observing energy transitions, although the combination and comparison of both excitation and absorption data leads to conclusions not tenable with just one method of measurement. It has already been noted that only Eu^{+3} and Tb^{+3} produce broad excitation bands (11). It is of interest to summarize the origin of these bands. For Eu^{+3}, the band arises from a charge transfer transition involving nearest oxygen neighbors

$$Eu(III)O_n^{-2n} \rightarrow Eu(II)O_n^{-2n+1}$$

Thus, the efficiency should be dependent on the polarizability of the oxygen atoms. For the rare earth phosphates, where the oxygen atoms are covalently bonded within the phosphate group, phosphor efficiencies should be much lower because of the inherently higher saturation of charge within the PO_4 groups as compared to an individual oxygen atom whose 2p shells remain unfilled in an ionic matrix. This effect on efficiency has already been noted in a prior paper (11).

Table IX. Reflectance spectrum of $ErPO_4$

Transition	Baricenters of absorption bands, cm^{-1} Observed	Calculated*	Lines, observed, Å								
$^4I_{15/2} \rightarrow {}^4I_{9/2}$	15,244	15,449	6550	6660							
$^4I_{15/2} \rightarrow {}^4S_{3/2}$	18,349	18,525	5436	5449	5465	5478	5508	5522			
$^4I_{15/2} \rightarrow {}^2H_{11/2}$	19,237	19,407	5218	5244	5273	5308	5355				
$^4I_{15/2} \rightarrow {}^4F_{7/2}$	20,576	20,717	4872	4881	4894	4923	4941	4957			
$^4I_{15/2} \rightarrow {}^4F_{5/2}$	22,272	22,321	4510	4516	4526	4538	4544	4577			
$^4I_{15/2} \rightarrow {}^4F_{3/2}$	22,624	22,701	4436	4453	4465	4484					
$^4I_{15/2} \rightarrow {}^2G_{9/2}$	24,691	24,893	4057	4062	4072	4076	4083	4092	4099		
$^4I_{15/2} \rightarrow {}^4G_{11/2}$	26,667	26,889	3737	3781	3785	3794	3801	3807	3818	3824	
$^4I_{15/2} \rightarrow {}^2K_{15/2}$	27,397	27,408	3630	3647	3653	3658	3667	3674	3679	3684	3694
$^4I_{15/2} \rightarrow {}^4G_{9/2}$	27,918	27,940	3567	3574	3588	3598					
$^4I_{15/2} \rightarrow {}^2D_{3/2}$	31,949	32,061	3168	3174	3181	3192	3200				
$^4I_{15/2} \rightarrow {}^2K_{13/2}$	32,981	32,857	3022	3032	3042						
$^4I_{15/2} \rightarrow {}^2G_{5/2}$	33,864	33,974	2940	2952	2967						
$^4I_{15/2} \rightarrow {}^2D_{5/2}$	35,089	34,910	2875	2883	2896						
$^4I_{15/2} \rightarrow {}^2H_{9/2}$	37,037	37,217	2740	2752	2766						
$^4I_{15/2} \rightarrow {}^4D_{5/2}$	38,700	39,151	2598	2614	2553	2569					
$^4I_{15/2} \rightarrow {}^2L_{17/2}$	41,152	40,737	2370	2407	2422	2437					
$^4I_{15/2} \rightarrow {}^2P_{3/2}$	43,422	43,626	2303								

* B. G. Wybourne, *J. Chem. Phys.*, 32, 641 (1960).

For Tb^{+3}, the primary band in $TbPO_4$ arises from a perturbed 4f → 4f transition ($^7F_6 \rightarrow {}^5F_2$) whereas in $LaPO_4$:Tb, the primary transition is probably $4f^8 \rightarrow 4f^75d$ in nature, with transitions involving other upper states not identified.

Acknowledgment

The author is indebted to Dr. C. K. Lui Wei for x-ray measurements and to E. Chen and G. Grasso for phosphor preparation.

Manuscript submitted Nov. 21, 1968; revised manuscript received *ca.* Jan. 20, 1969. This paper was presented at the Cleveland Meeting, May 1-5, 1966, as Abstract 33.

Any discussion of this paper will appear in a Discussion Section to be published in the December 1969 JOURNAL.

REFERENCES

1. D. C. Stewart, AEC Report ANL-4812, Argonne National Lab., Chicago (1952); W. J. Baun and N. T. McDevitt, *J. Am. Ceram. Soc.*, **46**, 294 (1963); J. Hoogschagen and C. J. Gorter, *Physica*, **14**, 197 (1948).
2. F. Varsanyi and G. H. Dieke, *J. Chem. Phys.*, **36**, 835 (1962).
3. J. W. Adams, *Am. Mineral.*, **50**, 356 (1965).
4. D. C. Stewart, AEC Report ANL-5642, Argonne National Lab., Chicago (Oct. 1965).
5. C. K. Jorgensen, R. Rappalardo, and E. Rittershaus, Cyanimide European Research Institute Report. CERI-TIC60 (1964); C. K. Jorgensen, R. Pappalardo, and E. Rittershaus, *Z. Natur Wissen.*, **19**, 424 (1964); *ibid.*, **20**, 54 (1965).
6. M. Halmann and I. Platzner, *J. Chem. Soc.*, **1965** 1440.
7. R. C. Ropp, *Appl. Spectroscopy*, To be published.
8. M. F. Radominski, *Compt. Rend.*, **80**, 304 (1875); M. A. Duboin, *loc. cit.*, **107**, 622 (1888).
9. M. K. Carron, C. R. Naeser, H. J. Rose, and F. A. Hildebrand, U.S. Geol. Survey *Bull. 1036N*, 253 (1958); see also: M. K. Carron, M. E. Morse, and K. J. Murata, *Am. Mineral.*, **43**, 985 (1958).
10. R. C. L. Mooney, *J. Chem. Phys.*, **16**, 1003 (1948); R. C. L. Mooney, *Acta Cryst.*, **3**, 337 (1950); H. Schwarz, *Z. Anorg. Allegem. Chem.*, **323**, 44 (1963).
11. R. C. Ropp, *This Journal*, **115**, 841 (1968).
12. F. Weigel, V. Scherer, and H. Henschel, *J. Am. Ceram. Soc.*, **48**, 383 (1965).
13. Perkin-Elmer Corp., Norwalk, Conn. Recording Spectrofluorimeter Model 195.
14. R. S. Feigelson, *J. Am. Ceram. Soc.*, **47**, 257 (1964).
15. J. Sugar, *J. Opt. Soc.*, **55**, 1058 (1965).
16. C. K. Jorgensen, "Proceedings of the Fifth Rare Earth Conference", p. 1, Ames, Iowa (1965), To be published.
17. H. J. Borchardt, *loc. cit.*, p. 65, To be published.
18. R. C. Ropp, E. E. Gritz, P. H. Haberland, and D. E. U. Ridout, *Electrochem. Technol.*, **4**, 24 (1966).
19. B. W. Bryant, *J. Am. Opt. Soc.*, **55**, 771 (1965).
20. E. Loh, *Phys. Rev.*, **147**, 332 (1966).
21. G. H. Dieke and L. A. Hall, *J. Chem. Phys.*, **25**, 465 (1957).

Eu^{2+} Luminescence in the Ternary EuO-Al_2O_3-SiO_2 System

P. M. Jaffe*[1]

Westinghouse Electric Corporation, Bloomfield, New Jersey

ABSTRACT

A study has been made of the ternary EuO-Al_2O_3-SiO_2 system. Several phosphors activated by divalent Eu were found, some of which are very efficient under u.v. excitation. Several new compounds containing divalent Eu are reported. Some of these are fairly efficient photoluminescent phosphors. The materials studied are Al_2O_3:Eu; SiO_2:Eu, Al_2O_3:Si,Eu; SiO_2:Al,Eu; $(1-x)Al_2O_3 \cdot xSiO_2$:Eu; $EuAl_2Si_2O_8$; $Eu^{3+}AlO_3$:Eu^{2+}; $Eu_2Al_2SiO_7$, and $Eu_6Al_{18}Si_2O_{37}$. All but the last two are luminescent.

An attempt to prepare Eu^{2+} activated sillimanite (Al_2SiO_5) by firing a 1:1 Al_2O_3:SiO_2 mixture containing 1 a/o (atom per cent) Eu in NH_3 resulted in a bright blue-white band emitting phosphor. X-ray analysis showed this phosphor to be mainly a mixture of Al_2O_3 and SiO_2 plus a trace of sillimanite and mullite ($3Al_2O_3 \cdot 2SiO_2$). In an attempt to identify the phosphor matrix, the ternary EuO-Al_2O_3-SiO_2 system was studied. As a result of this study, several other phosphors activated by Eu^{2+} were found. In addition, some new compounds containing Eu^{2+} were synthesized, some of which were luminescent.

Experimental Procedure

All phosphors were prepared from mixtures of Eu_2O_3 (Lindsay, 99.8%) and Mallinckrodt's SL $Al(OH)_3$ and SiO_2. The mixtures were slurried, dried at 110°C, and ball milled. Firings were done in silica crucibles for samples high in SiO_2 and in alumina crucibles for samples high in Al_2O_3. The firing atmosphere used was NH_3; somewhat similar results were obtained in H_2 or H_2-N_2 mixtures. Except where otherwise noted, the firings were done at 1250°-1350°C.

Emission spectra were obtained with a Bausch and Lomb 1/2 meter grating monochromator equipped with a wavelength drive. The spectra were corrected for spectral sensitivity of the photomultiplier and instrument transmission. The exciting sources were a 2537Å Germacidal lamp and a 3650Å 100w Hg lamp. Excitation spectra were taken with the same apparatus using a 150w d-c Xenon lamp. The excitation spectra are given relative to a 0.2% fluorescein solution which has a constant quantum efficiency from 250 to 500 nm (1). Diffuse reflectance spectra were obtained with a Beckman DU spectrophotometer equipped with a diffuse reflectance attachment. The data are reported as absorption spectra, using the relationship % absorption = (100 − % reflectance). Brightness measurements were made with a Spectra brightness spot meter.

Experimental Results

Al_2O_3:Eu^{2+} and SiO_2:Eu^{2+}.—Since the x-ray analysis indicated the main components in the 1:1 Al_2O_3:SiO_2 phosphor to be α-Al_2O_3 and SiO_2, these materials were first examined to see if one or the other was the primary phosphor matrix

Eu^{2+} activated SiO_2.—These samples were activated with 0.01-1.0 a/o Eu. They were given two 2-hr firings at 1250°C. After the first firing, the samples developed a strong electrostatic charge on grinding. This charge disappeared after the second firing. X-ray examination

* Electrochemical Society Active Member.
[1] Present address: Zenith Radio Corporation, Chicago, Illinois.

of these samples showed that increasing Eu caused an increase in crystallinity but no apparent compound formation. The body color varied from white to yellow and the emission shifted from blue to yellow with increasing Eu. The maximum blue emission was obtained with 0.05 a/o Eu. Figure 1 shows the emission spectra of samples containing 0.01, 0.1, and 0.5 a/o Eu excited by 2537Å u.v. The 3650Å u.v. excited spectra are similar but the emission peaks are shifted about 15 nm to longer wavelengths.

The absorption spectrum of the SiO_2:1 a/o Eu sample is shown in Fig. 2A. It consists of a broad band peaking around 275 to 300 nm, the intensity of which increases with increasing Eu. The excitation spectrum is shown in Fig. 3A. There are three peaks, increasing in intensity in the order 270, 300, and 330 nm.

Eu^{2+} *activated* Al_2O_3.—The effect of Eu concentration was examined over the range of 0.01-10 a/o. The body color of samples having 1 a/o Eu or less was white; the luminescence was weak blue. The 10 a/o Eu sample had a pale yellow body color and a green-yellow emission.

X-ray examination of the 0.1, 1, and 10 a/o Eu samples gave the following results:

0.1 a/o Eu	α-Al_2O_3 (S),	θ-Al_2O_3 (W)
1 a/o Eu	α-Al_2O_3 (S),	θ-Al_2O_3 (W), unknown (VW)
10 a/o Eu	α-Al_2O_3 (S),	$EuAlO_3$ (W)

(S = strong; W = weak.)

Most likely, the unknown material in the 1 a/o Eu samples is $EuAlO_3$. This compound will be discussed later.

The emission spectra from the Al_2O_3 phosphors containing 0.1, 1, and 10 a/o Eu are shown in Fig. 4. For 0.1 and 1 a/o Eu, the emissions are similar for 2537Å excitation but show a slight long wave broadening with 10% Eu. Under 3650Å excitation, the emission from the 0.1 a/o Eu phosphor is similar to that of the 2537Å excited phosphors. However, as the Eu concentration increases, there is a shift of the emission to longer wavelengths. This shift is due to emission from $EuAlO_3$:Eu^{2+} which is present as a separate phase.

The absorption spectrum of the Al_2O_3:1 a/o Eu phosphor is shown in Fig. 2A. There are several weak bands and one strong one all due to Eu^{2+}. The main band peaks at 275 nm. The excitation spectra of the blue emission is shown in Fig. 3A. It consists of three bands, two major ones at 310 and 350 nm, respectively, and one minor one at 270 nm.

The brightness of the best Eu activated Al_2O_3 and SiO_2 phosphors was much lower than the original 1:1 Al_2O_3:SiO_2 preparation (see also Table I).

Eu *activated* Al_2O_3 *with silica and silica with alumina.*—Since the Eu activated Al_2O_3 and SiO_2 were of low brightness, the possibility of limited solid solutions of Al_2O_3 in SiO_2 and vice versa was investigated. This was done by preparing the following two series of samples: (*a*) Al_2O_3:$x$$SiO_2$,1 a/o Eu where x = 0, 0.01, 0.05, 0.1, and 0.5 m/o; (*b*) SiO_2:xAl,0.05 a/o Eu where x = 0, 0.01, 0.05, 0.1, 0.5, and 1 a/o.

The Al was added as the hydroxide which was freshly precipitated from the nitrate.

After two 2-hr firings, the Al_2O_3:SiO_2,Eu phosphors had a fairly uniform emission. Increasing SiO_2 additions resulted in a shift of the emission, for 3650Å excitation, from blue to blue-green; for 2537Å excitation, the emission was blue for Eu concentrations below 0.05 a/o and blue-white for concentrations above. The intensity of the blue emission, measured through the blue Spectra spot meter filter, had a minimum at about 0.01% SiO_2.

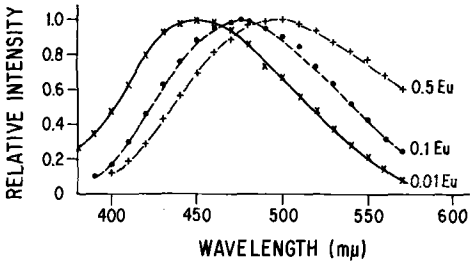

Fig. 1. Emission spectra for SiO_2:xEu^{2+} for 2537Å excitation. The 3650Å excited spectra are similar to the corresponding 2537Å excited spectra but are shifted about 15 nm to longer wavelengths.

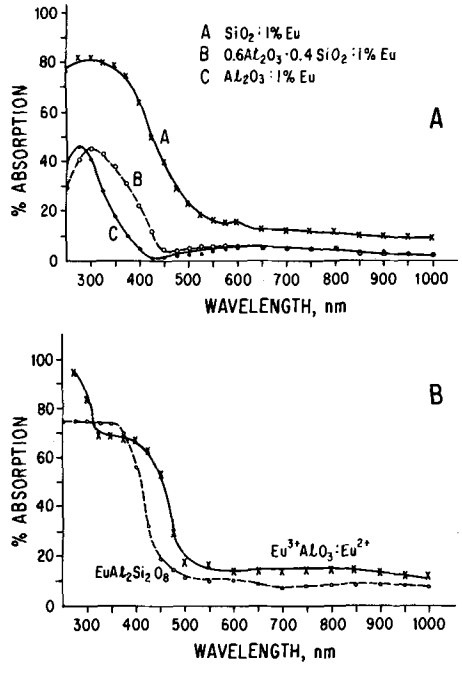

Fig. 2. Absorption spectra for (A) SiO_2, Al_2O_3 and $0.6Al_2O_3 \cdot 0.4SiO_2$; (B) $Eu^{3+}AlO_3$:Eu^{2+} and $EuAl_2Si_2O_8$, all containing 1 a/o Eu^{2+}.

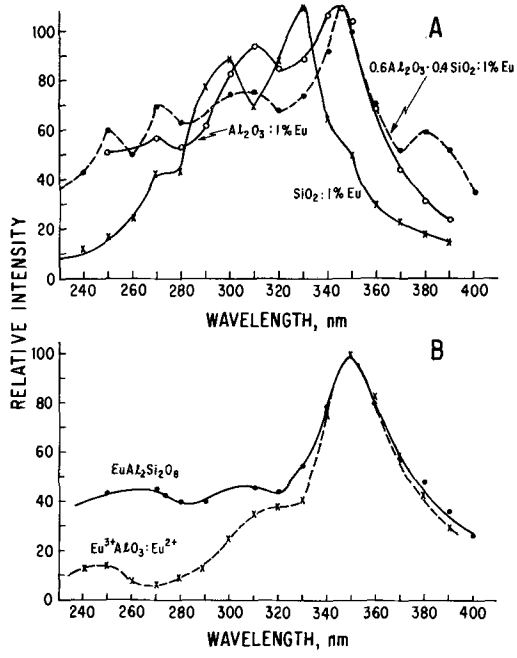

Fig. 3. Excitation spectra for (A) blue emission of SiO_2, Al_2O_3, and $0.6Al_2O_3 \cdot 0.4SiO_2$; (B) green emission of $Eu^{3+}AlO_3$:Eu^{+2} and green-yellow emission of $EuAl_2Si_2O_8$, all containing 1 a/o Eu^{2+}. The ordinate is proportional to the relative number of fluorescent quanta.

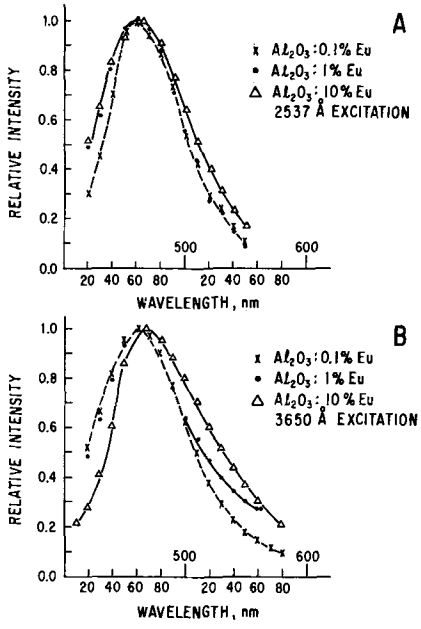

Fig. 4. Emission spectra of Al_2O_3:x a/o Eu^{2+}. (A) For 2537Å excitation; (B) for 3650Å excitation.

The emission of the SiO_2:xAl, Eu samples shifted from blue-green under 3650Å excitation and from blue-white under 2537Å excitation for zero Al to blue with increasing Al additions. The intensity of the blue emission progressively decreased with increasing Al.

In no case was the blue emission from these phosphors as bright as the original Eu^{2+} activated 1:1 Al_2O_3:SiO_2 or the mixed $Al_2O_3 \cdot SiO_2$ phosphors discussed in the next section.

The Al_2O_3-SiO_2 *system* (2).—Since the phosphor obtained by firing a 1:1 Al_2O_3-SiO_2 mixture was found to contain mainly Al_2O_3 and SiO_2 plus some mullite, no further attempts were made to prepare the 1:1 compound.

A sample of almost pure mullite activated by Eu^{2+} was obtained by a series of firings at 1250°C for a total time of 100 hr. The resultant phosphor was much less bright than a sample having the same raw mix composition but having two 2-hr firings. X-ray analysis of the latter phosphor showed it to be primarily a mixture of α-Al_2O_3 and SiO_2 plus a trace of mullite. The emission spectra of these two phosphors, however, were similar.

Since these data indicated that mullite was not needed to give a bright phosphor, no further work was done with it.

The effects of compositional variations, at constant added Eu (= 1 a/o), on the mixed Al_2O_3-SiO_2 system, were examined. Samples having the raw mix composition $(1-x)Al_2O_3 \cdot xSiO_2$ where x varied from 0 to 1 were prepared by firing at 1250°C for 2 hr. X-ray examination of this series showed them all to be essentially the same, namely a mixture of Al_2O_3, SiO_2, and a trace of mullite.

The intensity of the blue emission from this series is shown in Fig. 5. There is a maximum around the composition $0.3Al_2O_3 \cdot 0.7SiO_2$. The brightness of several of these phosphors relative to ZnS·Ag and $CaWO_4$:Pb is shown in Table I. It must be pointed out that even though these phosphors have not been optimized, they have high brightness.

The effect of Eu concentration was examined for both the $0.6Al_2O_3 \cdot 0.4SiO_2$ and $0.3Al_2O_3 \cdot 0.7SiO_2$ raw mixes. The Eu concentration was varied from 1.7 x 10^{-3} to 2.2 a/o. The results for both compositions are similar and are shown in Fig. 6. For both 2537 and 3650Å excitation, the optimum Eu concentration is about 1 a/o.

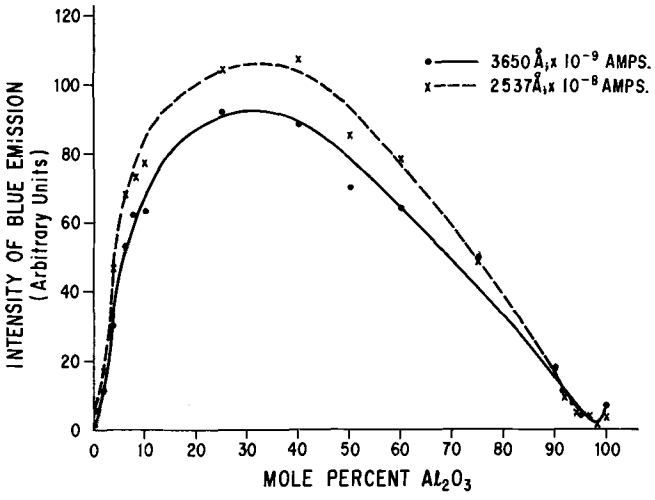

Fig. 5. Intensity of the blue emission from $(1-x)Al_2O_3 \cdot xSiO_2$:1 a/o Eu^{2+}. Data given for excitation by 2537 and 3650Å radiation.

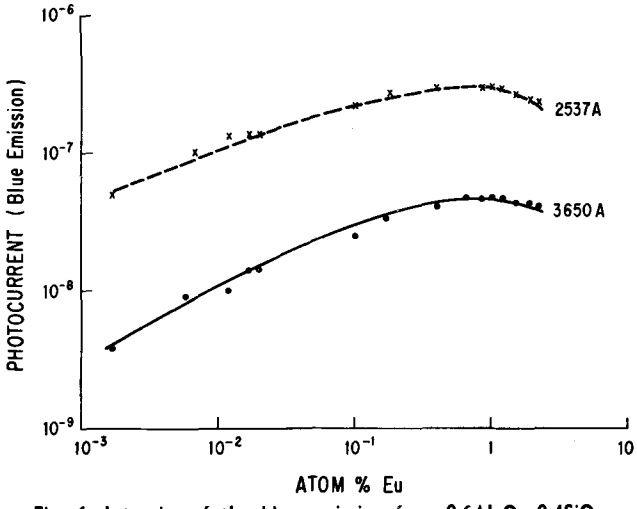

Fig. 6. Intensity of the blue emission from $0.6Al_2O_3 \cdot 0.4SiO_2$ as a function of Eu^{2+} additions. Data given for excitation by 2537 and 3650Å radiation.

The emission spectrum of the $0.6Al_2O_3 \cdot 0.4SiO_2$,1 a/o Eu phosphor is shown in Fig. 7. The spectrum of similar phosphors having the Al_2O_3 to SiO_2 ratio varying between 1:5 to 9:1 is essentially the same. The absorption spectrum of the $0.6Al_2O_3 \cdot 0.4SiO_2$:1Eu is shown in Fig. 2A. There is only one strong absorption band, peaking at about 300 nm. The excitation spectrum of this phosphor is shown in Fig. 3A. It consists of five main peaks which are at 346, 305, 270, 250, and 380 nm (in order of decreasing intensity).

The EuO-Al_2O_3-SiO_2 *system* (3).—During the study of the $(1-x)Al_2O_3 \cdot xSiO_2$ system, x-ray analysis of phosphors having 10 a/o Eu indicated the presence of a new phase, $EuAl_2Si_2O_8$, isomorphous with $SrAl_2Si_2O_8$. Test preparations yielded a bright green-yellow emitting phosphor excited by 2537 and 3650Å. The body color was green-yellow.

Table I. Relative brightness of several blue emitting Eu^{2+} activated Al_2O_3-SiO_2 phosphors

Composition	Eu conc., a/o	Brightness 2537A	Brightness 3650A
SiO_2	0.05	0.85	1.7
Al_2O_3	1	0.85	2.58
$0.6Al_2O_3 \cdot 0.4SiO_2$	1	3.9	20.0
$0.4Al_2O_3 \cdot 0.6SiO_2$	1	4.0	22.0
$0.3Al_2O_3 \cdot 0.7SiO_2$	1	4.3	20.0
$CaWO_4$:Pb	—	4.9	—
ZnS:Ag	—	—	22.5

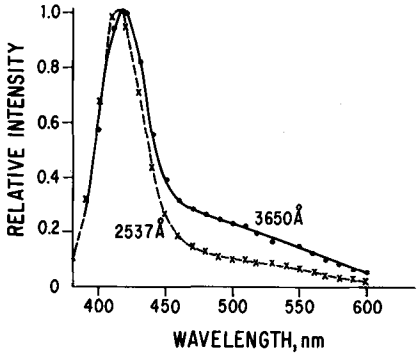

Fig. 7. Emission spectra of $0.6Al_2O_3 \cdot 0.4SiO_2$:1 a/o Eu^{2+} excited by 2537 and by 3650Å ultraviolet.

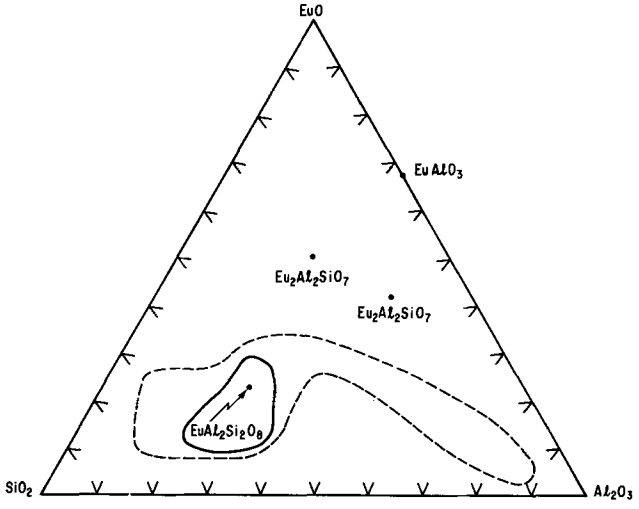

Fig. 8. Approximate phase diagram of the ternary EuO-Al_2O_3-SiO_2 system showing the compounds prepared in this system. The area around $EuAl_2Si_2O_8$ bounded by the solid line is single phased. The area bounded by the dashed line is multiphased but contains some $EuAl_2Si_2O_8$.

The effect of varying the ratio of EuO, Al_2O_3, and SiO_2 on the luminescence was examined over a wide range around the stoichiometric point. Based on visual observation of the emission and body colors and x-ray examination, it appears that $EuAl_2Si_2O_8$ can tolerate a slight excess of Al_2O_3, SiO_2, or EuO. The solid line in Fig. 8 shows the region where x-ray indicates the presence of only one phase, $EuAl_2Si_2O_8$. The region within the dashed line is multiphase but still contains some $EuAl_2Si_2O_8$.

Brightness measurements of samples lying within the area bounded by the solid line of Fig. 8 were made. The results show that the brightness varies with Eu concentration for the basic composition $Eu_xAl_2Si_2O_{(7+x)}$ over the range $x=0.1$ to 2 with a maximum at $x=0.4$. For an Eu concentration of 0.4, there are two regions of maximum brightness, namely $Eu_{0.4}Al_2Si_{(1.5\text{-}1.8)}O_{(6.4\text{-}7)}$ and $Eu_{0.4}Al_{(2.0\text{-}2.2)}Si_2O_{(7.4\text{-}7.7)}$. Phosphors lying within this region are brighter than the stoichiometric compound, Table II. Also shown in Table II are the brightnesses of a (ZnCd)S:Ag phosphor having a similar emission color and a standard Zn_2SiO_4:Mn phosphor.

Table II. Relative brightness of some $Eu_xAl_ySi_2O_{(x\ -\ 1.5y\ +\ 2z)}$ phosphors

Phosphor composition	Brightness 2537Å	Brightness 3650Å
$EuAl_2Si_2O_8$	0.066	25
$Eu_{0.4}Al_{2.1}Si_2O_{7.55}$	0.073	36
$Eu_{0.4}Al_2Si_{1.65}O_{6.7}$	0.078	37
Zn_2SiO_4:Mn	0.92	—
(ZnCd)S:Ag (green-yellow)	—	36

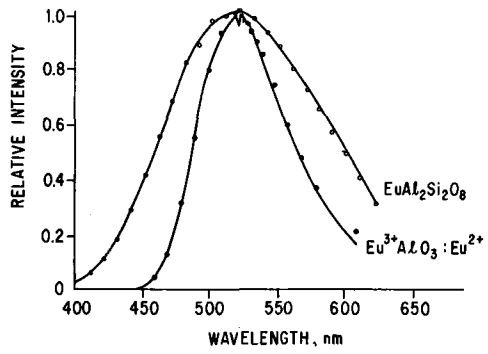

Fig. 9. Emission spectrum of typical $EuAl_2Si_2O_8$ and $Eu^{3+}AlO_3$:-Eu^{2+} phosphors. The lines on the $EuAlO_3$ curve are due to absorption by Eu(III). There are also weak lines, not shown in this figure, at 390 and 470 nm.

The emission spectrum of a typical $EuAl_2Si_2O_8$ phosphor is shown in Fig. 9. It consists of a broad band peaking at 520 nm. Phosphors within the area bounded by the solid line of Fig. 8 have essentially the same emission. The absorption spectrum of these phosphors is shown in Fig. 2B. It consists of a broad band in the u.v. and extending slightly into the visible. The excitation spectrum is shown in Fig. 3B and is the same for the stoichiometric compound and the compositions in the region of maximum brightness. It consists of three peaks. The major one is at 350 nm and the other two are at 265 and 310 nm.

Two other compounds were found in the EuO-Al_2O_3-SiO_2 system, *viz.*, $Eu_2Al_2SiO_7$ and $Eu_6Al_{18}Si_2O_{37}$. They have the same structure as the corresponding Sr analogs. These two compounds have a gray-green body color and are nonluminescent.

The $EuAlO_3$ *system.*—It was mentioned earlier in the section on Al_2O_3:Eu that NH_3-firing a sample with 10 a/o Eu resulted in a phosphor having a green emission. X-ray showed the presence of another compound. Since Eu^{2+} and Sr^{2+} have similar ionic sizes, 1.10 and 1.13Å, respectively, Eu^{2+} may have formed a compound similar to one of the compounds in the SrO-Al_2O_3 system. Those that have been reported are $4SrO \cdot Al_2O_3$, $3SrO \cdot Al_2O_3$, $SrO \cdot Al_2O_3$, $Sr \cdot O \cdot 2Al_2O_3$, and $SrO \cdot 6Al_2O_3$ (4). Firing stoichiometric compositions of Eu_2O_3 and Al_2O_3 corresponding to these Sr analogs at 1000°-1500°C in NH_3 resulted in samples containing mixtures of Al_2O_3, $EuAlO_3$, and $EuO \cdot 6Al_2O_3$. $EuAlO_3$ was the main component in these preparations. Two 2-hr firings of the $Eu_2O_3 \cdot Al_2O_3$ composition at 1300°C resulted in almost pure $EuAlO_3$. However, a slight excess of Al_2O_3 was needed to compensate for Al_2O_3 lost during the firing. A sample of $EuAlO_3$ fired in O_2 was white and nonluminescent. The NH_3 fired samples had a pale yellow body color and a green emission. This phosphor is relatively efficient under 3650Å excitation. Compared to a (Zn,Cd)S:Ag phosphor of about the same color, it is 75% as bright. However, the $EuAlO_3$ phosphors have not been optimized.

The emission spectrum of $EuAlO_3$ is shown in Fig. 9. It consists of a band with a peak at 520 nm plus some superimposed absorption lines. The absorption spectrum is shown in Fig. 2B. It consists of two strong bands and one weak one.[2] The excitation spectrum is shown in Fig. 3B. It consists of three peaks located at 250, 310, and 350 nm with the amplitudes increasing in the order given.

Discussion

The goal of this investigation was to identify the matrix responsible for the bright blue-white fluorescence obtained when mixtures of Al_2O_3 and SiO_2 containing 1% Eu are fired in a reducing atmosphere. Analysis of the x-ray results of various compositions

[2] The absorption lines found in the emission spectrum, Fig. 10, are due to the Eu^{3+}. They do not show up in the absorption spectrum, Fig. 2B, because the former was measured by a continuous scan and the latter was point by point.

of Al_2O_3 and SiO_2, after firing, shows that Al_2O_3, SiO_2, and a trace of mullite ($3Al_2O_3 \cdot 2SiO_2$) are present. Activation of these three compounds by Eu^{2+} results in materials whose emission is much weaker than fired mixtures of Al_2O_3 and SiO_2. Even phosphors containing limited solid solutions of Al_2O_3 in SiO_2 and SiO_2 in Al_2O_3 result in weak emission. An examination of the optical properties of all of these phosphors shows them to be different from the mixed "$Al_2O_3 \cdot SiO_2$:Eu" phosphors. The only conclusion that can be reached is that both Al_2O_3 and SiO_2 are necessary for phosphor formation but the specific host is not known. Subsequent to this work, Wachtel (5) also worked on this system. He believes that the Eu^{2+} is located at the interface between mullite and a second phase which may be Al_2O_3 or SiO_2.

The band emission of these phosphors is due to the presence of Eu^{2+} since Eu^{3+} causes line emission (6). Further evidence for the presence of Eu^{2+} is the need for firing in a reducing atmosphere, the body color in the case of $EuAlO_3$ and $EuAl_2Si_2O_8$ and the lack of luminescence or line emission when fired in O_2.

Normally Eu^{2+} emission is blue. However, in $EuAl_2Si_2O_8$ and in $EuAlO_3$, the Eu^{2+} emission is green-yellow and green, respectively. Note, however, Fig. 9, that both of these phosphors peak at the same wavelength. Their visual color difference is due to the wider emission band of the $SrAl_2Si_2O_8$ phosphor. The difference in emission color, blue *vs.* green, is most likely due to a different lattice environment of the Eu^{2+} ion.

There are other Eu^{2+} activated phosphors that have green emissions, for example, some of the alkaline earth silicates (7), $Na_2B_4O_7$ (8), and Al_2O_3-AlN (9). In fact, it appears that almost any emission color can be obtained with divalent Eu. For example, Jaffe and Banks have obtained yellow, orange, and red band emissions with the alkaline earth sulfides (6).

The interesting thing about the $EuAl_2Si_2O_8$ phosphor is that even with such high Eu concentrations, the phosphor is very efficient, Table II. At these concentrations, one would expect concentration quenching to occur, resulting in relatively low efficiency. The $EuAlO_3$:Eu^{2+} phosphor is interesting in that Eu is present in both the +2 and +3 oxidation states. Examination of Fig. 3B shows that the excitation spectra of Eu^{3+} AlO_3:Eu^{2+} and $EuAl_2Si_2O_8$ are somewhat similar. The main peak at 350 mn is most likely due to a $4f^7$ to $4f^6$ $5d^1$ transition of the Eu^{2+}.

Acknowledgments

The writer would like to thank Mr. G. Scanlon, Mr. F. Escudero[3] and Miss K. Wolejko[3] for their aid in sample preparation and for performing some of the measurements, and Drs. C. K. Lui Wei and G. Arai[3] for the x-ray measurements.

Manuscript submitted Nov. 18, 1968; revised manuscript received Jan. 24, 1969. This was Recent News Paper 331 presented at the Boston Meeting, May 5-9, 1968.

Any discussion of this paper will appear in a Discussion Section to be published in the December 1969 JOURNAL.

[3] Zenith Radio Corporation.

REFERENCES

1. J. F. Hammann, *Z. Angew. Phys.*, **10**, 187 (1958).
2. P. M. Jaffe, U. S. Pat. No. 3,359,211, Dec. 19, 1967.
3. P. M. Jaffe, U. S. Pat. No. 3,359,210, Dec. 19, 1967.
4. E. M. Levin, C. R. Robbins, and H. F. McMurdie, "Phase Diagrams for Ceramists," Fig. 294, Am. Ceramic Soc., Columbus, Ohio (1964).
5. A. Wachtel, *This Journal*, **116**, 61 (1969).
6. P. M. Jaffe and E. Banks, *ibid.*, **102**, 518 (1955).
7. H. McKeag and A. Ranby, *ibid.*, **97**, 415 (1950).
8. H. Gobrecht and R. Tomaschek, *Ann. Phys.*, **28**, 673 (1937).
9. I. Adams, T. R. Au Coin, and G. A. Wolff, *This Journal*, **109**, 1050 (1962).

$LiYO_2$:Eu as a Red Phosphor

Philip M. Jaffe* and John D. Konitzer*

Zenith Radio Corporation, Chicago, Illinois

ABSTRACT

$LiYO_2$ can be activated by Eu(III) to give an efficient red emitting phosphor under cathode-ray and under 2537Å excitation. This phosphor has optical properties which indicate its possible use as the red component in color television screens. Unfortunately, during tube fabrication, the phosphor decomposes to Y_2O_3:Eu. The main cause of this deterioration has been found to be hydrocarbons which are present during tube manufacture.

The search for new and efficient red cathodoluminescent phosphors over the past several years has resulted in a number of interesting host materials activated with rare earth elements. Among these hosts are compounds having the general formula $LiMO_2$ where M is a rare earth element. Hoppe (1), Vorres (2), Bertaut and Gondrand (3) have described the preparation of the pure undoped hosts while Blasse (4) and Brixner (5) have described the luminescent properties of some of the Eu activated compounds.

We have investigated $LiYO_2$:Eu for possible use in color television screens. Cathodo and photoluminescent properties of this phosphor as well as some problems involving its use in CR tubes are presented here.

Experimental Procedure

Phosphor preparation.—The preparation of the host has been most completely described by Bertaut and Gondrand. They fired a mixture of the rare earth oxide with an excess of Li_2CO_3 for two days at 900°C in an alumina crucible in air.

We prepared the compound $LiYO_2$, without prior knowledge of the papers listed, by firing a mixture of Li_2CO_3 and $Y_2(C_2O_4)_3$ at 1000°C for 2 hr in an oxygen atmosphere. We found that the materials attacked platinum and that recrystallized alumina crucibles should be used. Following a procedure which was similar to that of Bertaut and Gondrand, we fired samples in an excess of Li_2CO_3 in order to force the reaction to completion. X-ray diffraction patterns for these samples were much stronger and better resolved than for similar samples without excess Li_2CO_3.

Bertaut and Gondrand state that firing above 900°C results in a room temperature metastable tetragonal structure which, after some time, changes to the monoclinic form, while firing at 900°C or below results in the stable monoclinic form. We fired our charges at

* Electrochemical Society Active Member.

temperatures up to 1200°C for 2 hr and obtained only the monoclinic form. This difference might be due to Bertaut and Gondrand's long firing time and/or may also be due to the incorporation of europium in our samples. We have found that the europium doped monoclinic form results in a bright red phosphor while Eu doped samples which were fired at temperatures high enough and for times long enough to form the tetragonal structure were not luminescent.

In our procedure, firing time is critical. If the materials are fired for periods much longer than 2 hr we obtain mixtures of $LiYO_2$:Eu and Y_2O_3:Eu as evidenced by the presence of Y_2O_3:Eu lines in the emission spectra.[1]

Our phosphors were prepared by ball milling a water slurry of the freshly coprecipitated oxalates of yttrium and europium with about a 1.2 fold excess of Li_2CO_3. This was dried and fired for 1 hr at 1000°C in oxygen. After cooling, the sample was ground finely in a mortar and refired an additional hour. The resultant phosphors have a white body color and are efficiently excited by both 2537Å uv rays and cathode rays. The determined density of the phosphor is 4.29 ± 0.032 g/cc. The maximum solubility in water was 0.06% by weight. The pH of this material was determined to be 12.2. After several washings with boiling water to remove the excess Li_2CO_3, the pH was about 9. After about 1 hr, however, the pH rose to 10 indicating either that some hydrolysis of the sample occurred or that all the Li_2CO_3 was not removed.

Preparations using freshly coprecipitated hydroxides of europium and yttrium mixed with Li_2CO_3 result in even better yield of the phosphor than those obtained using the oxalates. The phosphors resulting from the two methods have the same spectral properties, but the hydroxide method results in a purer and a brighter product.

Measurements.—Emission spectra were obtained with a Jarrell-Ash 1/4 meter grating monochromator equipped with a wavelength drive and a photomultiplier whose output was recorded on a B&L VOM 7 recorder. The spectra were corrected for spectral sensitivity of the photomultiplier and instrument transmission. For the photoluminescent emission, the exciting source was a 2537Å Mineralight while excitation spectra were taken under a 150w d-c Xenon lamp. All spectra are given relative to a 0.2% fluorescein solution which has constant quantum efficiency over the range of 250-500 nm (6). Diffuse reflection spectra were obtained by attaching a Beckman diffuse reflectance unit to the output of the Jarrell-Ash monochromator. The reflected light was detected by a Hitachi 913B photomultiplier and its output recorded on the B&L recorder. The reflection spectra were taken relative to $MgCO_3$. Absorption spectra are reported using the relationship: % absorption = (100 — % reflectance).

The cathodoluminescent data were taken using a demountable cathode-ray tube.

Discussion of Experimental Results

Figure 1 shows the brightness of $LiYO_2$ as a function of europium concentration for both 2537Å and cathode-ray excitation relative to a commercial batch of YVO_4:Eu. The optimum europium concentration occurs in the vicinity of 4-5 a/o (atom per cent) for both modes of excitation although the actual intensities are quite different. This curve represents a larger number of points than is indicated and agrees with the data reported by Brixner (5). However, our data, not shown here, indicate that a small dip occurs at about 5½ to 6 a/o europium. Our original hypothesis was that this dip represented differences in preparation and purity of our samples and so the curve is drawn smoothly through this region ignoring this dip.

[1] The emission spectrum of a sample was much more indicative of the presence of Y_2O_3:Eu than x-ray analysis. The latter technique cannot detect less than 3-5 w/o Y_2O_3:Eu. The former method could detect less than 1%.

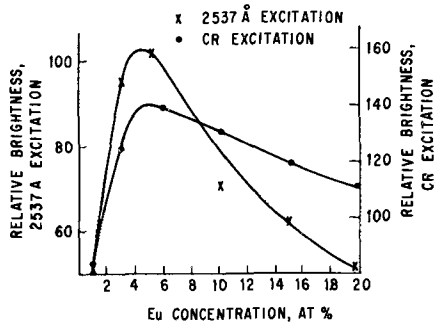

Fig. 1. Emission intensity of $LiYO_2$:Eu relative to YVO_4:Eu under cathode-ray excitation and 2537Å excitation.

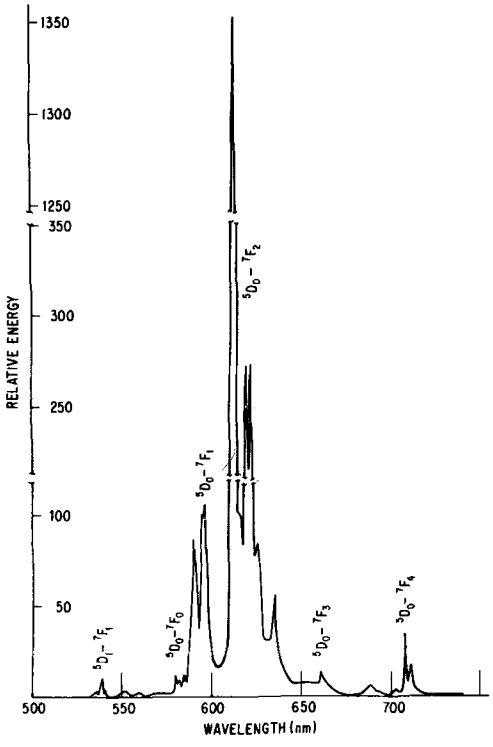

Fig. 2. Expanded scale emission spectrum of $LiYO_2$:Eu under 2537Å excitation. The same spectrum is obtained with cathode-ray excitation.

More recent work indicates that this dip may be real, but if so, we do not know the reason for it.

The emission spectrum of $LiYO_2$:3 a/o Eu is shown in Fig. 2 for uv excitation. The same spectrum is obtained with cathode-ray excitation. It consists primarily of a very strong line at 613 nm and a weaker doublet at 620 and 622 nm.

The transitions shown in Fig. 2 are derived from El'Yashevich (7). According to Blasse, the splitting of these lines should be such that two lines appear for each of the $^5D_0 \rightarrow {}^7F_1$ and the $^5D_0 \rightarrow {}^7F_2$ transitions. It seems that the 613 and 620 nm lines may represent the $^5D_0 \rightarrow {}^7F_2$ transition except that the 620 nm line is further split into two lines. Blasse reports that $LiYO_2$ has a distorted unit cell (4). This may be the cause of the additional splitting. Evidence for the 620 nm lines being due to additional splitting of the $^5D_0 \rightarrow {}^7F_2$ transition and not to an impurity is found by measurement of its persistence. The persistence of the 5920, 6118, 6132, 6200, and 6217 nm lines is the same as that of the 620 lines indicating that all these lines originate from the same $^5D_0$ level, Fig. 3.

Under both uv and cr excitation, $LiYO_2$:Eu shows a slight color shift as a function of the europium concentration as shown in Fig. 4. This is an enlarged view of the lower right side of the chromaticity diagram. Also shown, for comparison, are the color shifts for

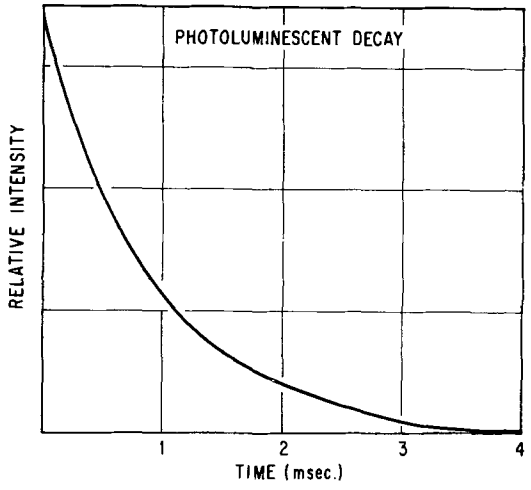

Fig. 3. Relative decay of the 5919, 6118, 6132, 6200, and 6217Å lines from LiYO$_2$:Eu for 2537Å excitation. Identical curves are obtained with europium concentrations of 2 and 10 a/o.

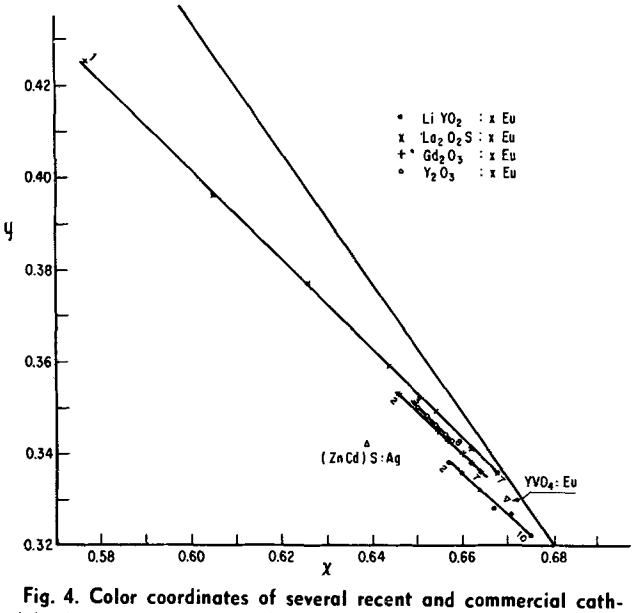

Fig. 4. Color coordinates of several recent and commercial cathodoluminescent phosphors. This figure is a greatly expanded portion of the lower right corner of the C.I.E. chromaticity diagram.

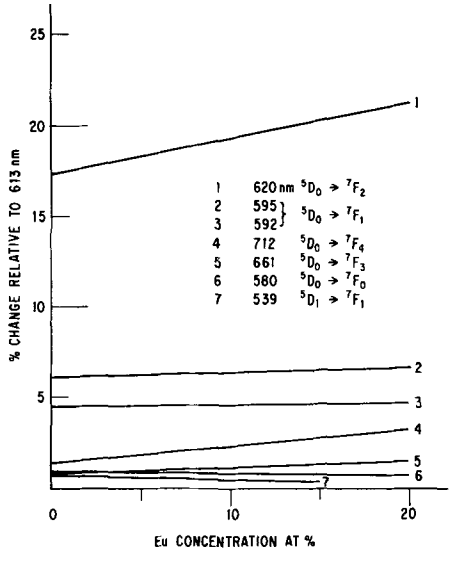

Fig. 5. Ultraviolet excited emission intensities of selected lines from LiYO$_2$ as a function of europium concentration compared to the emission intensity of the 613 nm line. This diagram shows the emission lines which are responsible for the color change as a function of the europium concentration.

La_2O_2S:Eu, Y_2O_3:Eu and Gd_2O_3:Eu and the color coordinates for YVO_4:5 a/o Eu and P22 (ZnCd)S:Ag. Figure 5 shows a least-squares plot of the per cent intensities of selected spectral emission lines from LiYO$_2$: 5 a/o Eu relative to the 613 nm line. From Fig. 5 it can be seen that the color shift is due to a combination of a decrease in the $^5D_1 \rightarrow {}^7F_{1,2}$ and $^5D_0 \rightarrow {}^7F_0$ emissions and an increase in the $^5D_0 \rightarrow {}^7F_{3,4}$ emissions as well as in the doublet at 620 and 622 nm (hereafter called the 620 nm lines).

Figure 6 shows the absorption and excitation spectra of LiYO$_2$ containing 0, 2, and 10 a/o Eu, respectively. The undoped sample exhibits no excitation spectrum. Its absorption spectrum has no structure, but shows a weak band below 240 nm. The absorption and excitation spectra of the Eu containing samples show a strong band lying below 280 nm plus fine structure above 280 nm. The fine structure is due to direct excitation or absorption in the Eu centers (f → f transitions). The band below 280 nm is most likely due to a charge transfer process (8). Blasse (4) reports similar data.

Figure 7 compares the phosphorescent decay of LiYO$_2$:4 a/o with a YVO_4:5 a/o Eu production phosphor under cathode-ray excitation at ambient temperature. Both phosphors show an exponential decay. The LiYO$_2$:Eu has a decay time of 1.08 msec which is twice that observed for YVO_4:Eu, but still well within the limits necessary for use in color television.

Figure 8 shows the brightness of LiYO$_2$:Eu as a function of electron beam current density under an

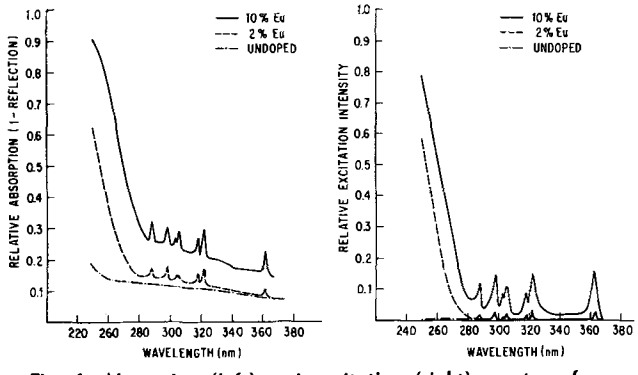

Fig. 6. Absorption (left) and excitation (right) spectra of pure undoped LiYO$_2$ and of europium doped LiYO$_2$.

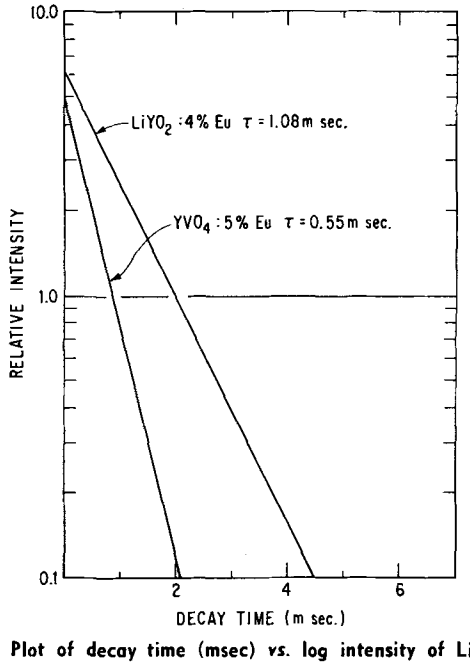

Fig. 7. Plot of decay time (msec) vs. log intensity of LiYO$_2$:Eu compared to YVO_4:Eu. The time constant of the LiYO$_2$:Eu is about twice that of YVO_4:Eu.

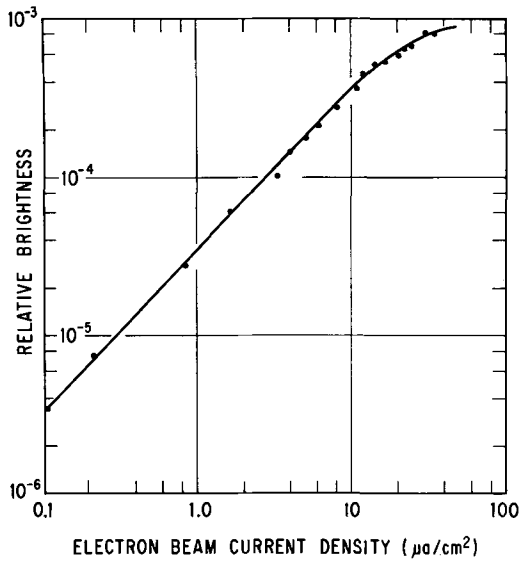

Fig. 8. Relative brightness of $LiYO_2$:Eu phosphor as a function of electron beam current density for a constant accelerating potential of 20 kv. Linear portion indicates usable range of current densities. Saturation of the phosphor is indicated by the deviation from linearity.

accelerating potential of 20 kv. Below 10 μa/cm^2 the curve is linear; above this value the phosphors start to saturate. This saturation occurs above the normal operating current density of 0.8 μa/cm^2. Since we were able to reproduce this curve on the same sample we conclude that the phosphor is stable under cathode-ray bombardment.

In Table I we list some of the luminescent properties of $LiYO_2$:Eu which are important for evaluating the phosphor for possible use in color television tubes. The relative luminosity compares the brightness of $LiYO_2$:Eu and YVO_4:Eu assuming 100% for YVO_4:Eu. The luminosity factors were calculated from the cathode-ray spectra of both phosphors. The fact that the luminosity factors are the same implies that the emission spectra are quite similar. This is also apparent from the color coordinates listed in Table I and the data in Fig. 4. The last column of Table I, relative luminous conversion efficiency, also indicates that the $LiYO_2$:Eu is about 1.5 times brighter than the commercial YVO_4:Eu phosphor.

Experimental Tube Production

All of the data so far presented indicate that $LiYO_2$:Eu should be a successful color television phosphor. However, our attempts to produce a monochrome tube were very disappointing. The resultant tube was low in brightness and showed the emission spectrum of Y_2O_3:Eu indicating that the $LiYO_2$:Eu decomposed during the tube fabrication process.

Table II lists some of the steps in tube fabrication processes which could cause decomposition of the phosphor. Table III shows the actual observations that we made under simulated conditions.

Examination of Table III shows that heating of the phosphor in the presence of hydrocarbons, *i.e.*, pump oil, polyvinyl alcohol, polymethylmethacrylate, but not benzene, resulted in complete degradation to low brightness Y_2O_3:Eu.

Conclusions

The phosphor $LiYO_2$:Eu is a very efficient one which could be used as the red component in cathode-ray tubes, but is not compatible with present tube fabrication processes. Coating the phosphor with silicate could help to stabilize the phosphor in production methods.

Table I. Cathodoluminescent data for $LiYO_2$:Eu and YVO_4:Eu

Phosphor	Relative luminosity	C.I.E. color coordinates x	y	Luminosity factor	Luminous efficiency lumens/rad. watt	Relative luminous conversion efficiency
$LiYO_2$:4 a/o Eu	155	0.664	0.332	0.493	335	1.54
YVO_4:6 a/o Eu	100	0.661	0.336	0.493	335	1.00

Table II. Steps in CR tube manufacture in which $LiYO_2$ could decompose

a. Vacuum heat-treatment;
b. Water washing;
c. Air or vacuum heating in contact with metallic Al;
d. Vacuum heating in the presence of organic materials such as polyvinyl alcohol or polymethylmethacrylate;
e. Air heating in the presence of the above organics.

Note: All heating done at 400°-500°C.

Table III. Effects of various tube fabrication procedures on the $LiYO_2$:Eu phosphor

Treatment	Observation
Heat in vacuum	no change
Heat in O_2, N_2, air, H_2	no change
Wash with water	slight change over long time
heat in vacuum in	
a. presence of carbon	no change
b. vacuum pump oil	degradation
c. contact with aluminum foil	degradation of portion in contact with the aluminum
d. presence of polyvinyl alcohol	degradation
e. presence of polymethylmethacrylate	degradation
f. presence of benzene	no change

Our attempts to do this did not appear to help. Perhaps a dusting process would help, but there still remains the problem of decomposition after deposition of the aluminum film. Because the phosphor is unstable in the presence of the organic materials currently used, a new process of applying it to a screen and a means to prevent its contact with aluminum would have to be developed. In view of these difficulties and the difficulties which new processes would generate, it is concluded that $LiYO_2$:Eu has no immediate application to color television tubes.

Acknowledgments

The authors wish to thank Mrs. H. Stanczyk and Miss K. Wolejko for their assistance in preparing these compounds, Mr. L. Flemming for the cathodoluminescent data, Dr. G. Arai for the x-ray data, and Dr. A. Liberman for the chemical tests performed.

Manuscript submitted Dec. 30, 1968; revised manuscript received *ca.* Feb. 1, 1969. This paper was presented at the Boston Meeting, May 5-9, 1968, as Paper 43.

Any discussion of this paper will appear in a Discussion Section to be published in the December 1969 JOURNAL.

REFERENCES

1. R. Hoppe, *Angew, Chem.*, **71**, 457 (1959); *Z. anorg. u. allgem. Chem.*, **339**, 130 (1965).
2. K. Vorres, Proceedings, Third Conf. Rare Earth Research (1963).
3. F. Bertaut and M. Gondrand, *Compt rend.*, **255**, 1135 (1962).
4. G. Blasse and A. Bril, *J. Chem. Phys.*, **45**, 3327 (1966).
5. L. Brixner, *This Journal*, **114**, 252 (1967).
6. J. F. Hammann, *Z. Angew. Phys.*, **10**, 187 (1958).
7. M. A. El'Yashevich, "Spectra of the Rare Earths," AEC-TL-4403C Chemistry, 1953.
8. G. Blasse and A. Bril, *This Journal*, **115**, 1067 (1968).

The Origin of Secondary Phases in Melt-Grown Fluorapatite Crystals

R. H. Hopkins and W. E. Kramer

Westinghouse Research Laboratories, Pittsburgh, Pennsylvania

ABSTRACT

Czochralski-grown fluorapatite boules contain inclusions identified as CaF_2 and $Ca_3(PO_4)_2$. The morphology and composition of the inclusions depends on the fluoride content of the melt from which a crystal is pulled. Evidence of precipitation in these crystals suggests that some solid solution occurs in fluorapatite at high temperatures. Both inclusions and precipitates promote cleavage of the pulled crystals.

Neodymium-doped fluorapatite (Nd:FAP) was shown to be a promising laser material by Mazelsky *et al.* (1, 2). Most efficient lasing action obtains in crystals free from color centers, dislocation arrays, and inclusions of additional phases. We have investigated the occurrence of such defects in synthetic fluorapatite and reported the results on point and line defects elsewhere (3, 4); in this paper we describe our observation and interpretation of included phases in melt grown FAP crystals.

"Opalescent" inclusions (presumably a second phase) were seen by Johnson (5) in the first large single crystals of FAP produced directly from the melt. Similar feathery inclusions were observed in Czochralski-grown Nd:FAP by Mazelsky *et al.* (1) who noted that their occurrence was minimized by slow growth rates (3-5 mm/hr). These authors sugested that some relation existed between the inclusions and fluoride-ion vacancies in the apatite structure.

We observe two types of inclusions in synthetic FAP and find that they markedly enhance fracturing of the melt grown crystals.

Crystal Growth and Analysis

The ideal composition of fluorapatite, $Ca_5(PO_4)_3F$, lies on the pseudobinary join CaF_2-$Ca_3(PO_4)_2$ at 25 m/o (mole per cent) CaF_2 (6). The inclusions in our crystals strongly suggest that departures from the ideal apatite composition occur during crystal growth. We investigated this possibility by ranging melt composition from 20 to 30 m/o CaF_2 along the join thus producing fluoride-rich or deficient crystals with respect to the ideal FAP composition.

We employed the same materials and methods of crystal growing reported previously (1, 3); no Nd doping was used here. Pull rates were between 2 and 6 mm/hr; $<0001>$ and $<10\bar{1}0>$ were the growth axes. After slow cooling of the crystals to room temperature, sections were cut longitudinal and transverse to the growth axes and prepared for optical examination either by mechanical polishing ending with 6μ diamond paste or by chemical polishing in 1:5 HCl/H_2SO_4 (4). Immersion of samples for 15 sec in 50% HCl/H_2O produces clear dislocation etch pits (and associated "tails") (4, 7) on most crystal planes in FAP.

Observations

Crystal morphology.—When grown from melts of ideal composition and at slow rates, $<0001>$ crystals of FAP exhibit circular cross sections having smooth surfaces marred only by small $\{10\bar{1}0\}$ facets. Boules grown parallel to $<10\bar{1}0>$ have a characteristic paddle shape displaying large basal and smaller prism facets (3). As the melt composition is shifted from $Ca_5(PO_4)_3F$ the surface of a growing crystal becomes quite wrinkled and feathery inclusions like those seen in previous studies (1, 5) become obvious regardless of the crystal growth direction. Crystals grown from both fluoride-rich and fluoride-poor melts contain these feathery inclusions. However, at a given growth rate, *e.g.*, 4 mm/hr, a 3% deficiency of CaF_2 is necessary to induce the inclusions while less than 1% excess CaF_2 is sufficient to produce a similar result. At any composition deviating from the ideal inclusions form when some critical growth rate is exceeded.

Fracture characteristics.—Natural fluorapatite has imperfect basal and $\{10\bar{1}0\}$ cleavage (8); Prener (9) observed no easy cleavage in solution-grown crystals. Melt-grown FAP crystals sometimes fracture by cleaving during growth or cooling to room temperature. We determined from Laue photographs of cleavage surfaces that $<0001>$ crystals cleave on both basal and $\{1\bar{2}10\}$ planes, while $<10\bar{1}0>$ crystals cleave on both prism planes of the hexagonal lattice. The tendency toward cleavage was enhanced by conditions which also favored inclusion formation, *i.e.*, high growth rates and off-ideal composition melts. Some relation then probably exists between the propensity of FAP to cleave and the inclusion content of the crystals. This possibility is discussed further below.

Inclusion morphology.—Optical examination of sections cut from FAP crystals reveals that two types of inclusion are present depending on the growth conditions.

Typically we observe tubular inclusions (type I) in crystals grown from fluoride rich melts, Fig. 1, while crystals grown from CaF_2 deficient melts contain smaller jagged particles (type II), shown in Fig. 2. Both these photomicrographs were taken of unetched longitudinal sections of $<0001>$ crystals grown at 4 mm/hr. The c axis (growth direction) is vertical in each photograph. The highest concentration of defects in these 2 m/o off composition samples is nearest the center of the pulled crystal. Note also that type I inclusions lie parallel to the c axis (Fig. 1) while the long dimension of type II inclusions is normal to c.

The morphology of type I inclusions in CaF_2-rich $<10\bar{1}0>$ crystals is somewhat different from that observed in $<0001>$ samples grown under the same conditions. The photograph of a longitudinal section from a $<10\bar{1}0>$ shown in Fig. 3 illustrates this difference. The inclusions though still tubular are now "T" shaped. However, the longer bar of the "T" is parallel to the c axis of FAP.

The $<10\bar{1}0>$ crystals grown from 1-3% CaF_2-deficient melts contain a general distribution of particles very similar to that illustrated in Fig. 2. Again, the long axes of the inclusions lie normal to $<0001>$. However, as the deficiency of CaF_2 exceeds about 3%, tubular inclusions parallel to c and having a morphology very similar to the type I inclusions shown in Fig. 3 develop in $<10\bar{1}0>$ crystals. Some small jagged type II particles are also distributed within the crystals. Recall from the section on Crystal morphology that inclusions visible to the naked eye in fluoride-poor

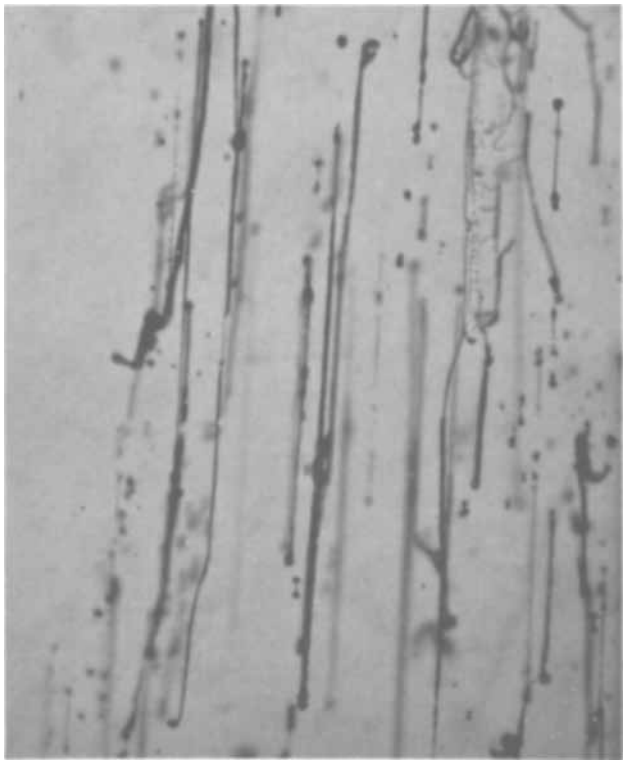

Fig. 1. Type I tubular inclusions in a FAP crystal grown from a fluoride rich melt. <0001> growth direction vertical. Transmitted light. Magnification approx. 50X.

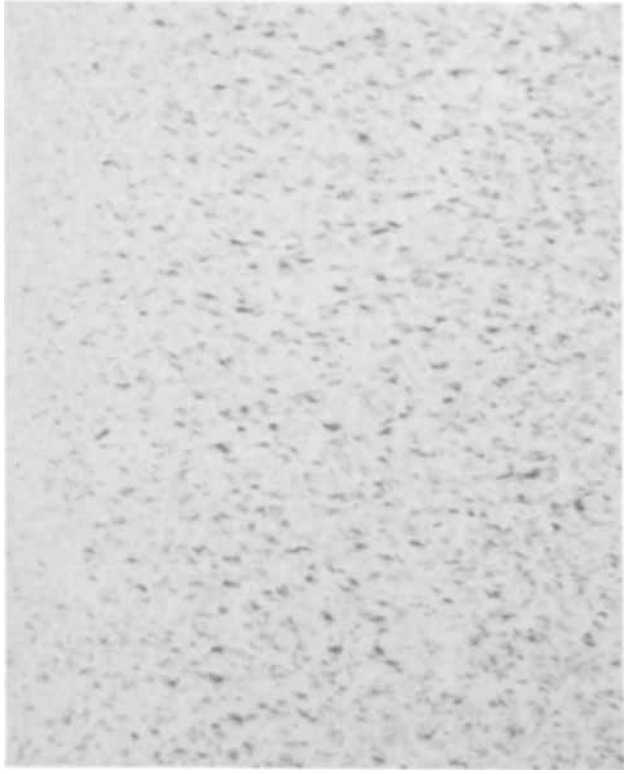

Fig. 2. Jagged type II inclusions in a crystal grown from a fluoride deficient melt. <0001> growth direction vertical. Transmitted light. Magnification approx. 50X.

samples did not develop until a 3% deviation from the ideal FAP composition was exceeded.

Another important observation is that both <0001> and <10$\bar{1}$0> crystals grown from melts of ideal FAP composition contained small amounts of particles with the same morphology as type II inclusions. In this case, however, particles were not randomly distributed

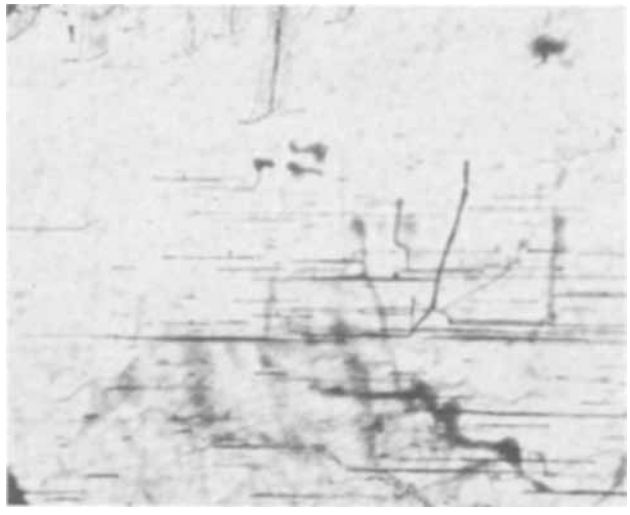

Fig. 3. "T" shaped type I inclusion. Crystal growth direction from top to bottom parallel to <10$\bar{1}$0>. c axis horizontal. Transmitted light. Magnification approx. 36X.

but were localized along dislocation lines. This has been verified by x-ray topographical analysis (4).

Inclusion analysis.—To successfully eliminate the inclusions detected in FAP we must characterize their chemical composition as well as the conditions under which they form. From the phase diagram (6) we expect CaF_2 to be present in fluoride-rich crystals and $Ca_3(PO_4)_2$ to co-exist with FAP in fluoride-poor crystals.

We analyzed type I inclusions by electron microprobe finding that they contained no oxygen or phosphorus within experimental error. The measured fluorine and calcium contents of the inclusions confirmed that they were CaF_2.

The analysis of type II inclusions was slightly complicated by the small size of these particles and their chemical similarity to fluorapatite. The chemical composition of type II inclusions determined by microprobe analysis appears in Table I. The computed amounts of Ca, P, F, and O in fluorapatite and $Ca_3(PO_4)_2$, assuming ideal chemical formulas, are also given for comparison in the table. We conclude from this data that type II inclusions are $Ca_3(PO_4)_2$. The compositions of all other calcium phosphates give poorer agreement than $Ca_3(PO_4)_2$ with the measured composition of the inclusions. We cannot explain the small amount of fluorine found in the inclusions but speculate that either the microprobe beam penetrated the particles thus exciting x-rays from the FAP matrix or that $Ca_3(PO_4)_2$ can hold small amounts of fluorine in solution.

Discussion

We have termed the second phases found in FAP crystals inclusions. However, type II $Ca_3(PO_4)_2$ inclusions are really discrete euhedral particles (seen end on in Fig. 2). This morphology (10, 11) and the tendency of these particles to form along dislocation lines (12) suggests that the origin of type II "inclusions" is through precipitation rather than mechanical

Table I. Experimental and ideal composition of type II inclusions

Element	Inclusion analysis, microprobe	$Ca_3(PO_4)_2$, theoretical	FAP, theoretical
P	19.3* ± 0.2†	20.0	18.4
Ca	38.3 ± 0.1	38.7	39.7
F	0.9 ± 0.1	0.0	3.97
O	44.6 ± 2.8	41.2	37.9

* Compositions are in weight per cent.
† Deviations indicated are variation from sample to sample not instrumental error.

entrainment as the term inclusion implies. The morphology of type I particles is typical of CaF_2 inclusions in solution grown FAP crystals (9) and inclusions in other materials (13).

The evidence of $Ca_3(PO_4)_2$ precipitation in crystals grown from ideal FAP composition melts indicates that CaF_2 vaporizes during crystal pulling thus enriching the melt in $Ca_3(PO_4)_2$. Johnson has also suggested this possibility (5). Our x-ray powder analysis of the white residue condensed on the colder portions of the growth system during a run confirms this hypothesis; the residue was mainly CaF_2. These observations coupled with the findings of Mazelsky *et al.* (3) that the maximum melting point in the vicinity of the composition $Ca_5(PO_4)_3F$ lay at 23% CaF_2, not 25%, lead us to believe that the phase diagram (6) is in error and that FAP can contain an as yet undetermined amount of second component in solution.

Assuming this reasoning correct we can now understand several aspects of second phase formation in pulled FAP crystals. CaF_2 exhibits little solubility in FAP and when it is present to excess in the melt forms a diffusion controlled boundary layer at the growing crystal interface. At high growth rates or high CaF_2 concentrations the planar crystal-liquid interface becomes unstable (14) and CaF_2 is entrapped as inclusions in the growing crystal. Since $Ca_3(PO_4)_2$ is partially soluble in FAP, slight excesses (<3%) of this component result only in precipitation of a second phase, type II inclusions, while larger composition deviations from ideal again lead to interface instability and true second phase entrainment as observed.

We pointed out above that crystal fracture and inclusion formation were both promoted by high growth rate and off-composition melts. It is well known that large stresses can be generated by differential rates of thermal contraction between a particle and its surrounding matrix. In ductile materials these stresses are relieved by dislocation generation and movement (15); this mode of stress relief is difficult in a brittle material. Preliminary studies[1] indicate FAP is highly plastic above about 1375°C but brittle below this temperature. At temperatures above this ductile-to-brittle transition the stress generated between particle and matrix produces dislocation generation. The high etch pit concentration surrounding the CaF_2 inclusion in Fig. 4 demonstrates this fact. However, if all stress cannot be relieved in this manner before a crystal cools below 1375°C then cracks are nucleated at the particle-matrix interface. This is strikingly illustrated in Fig. 5. Here cleavage cracks initiate at many precipitates and propagate into the brittle apatite along {0001} planes.

Conclusions

Our results indicate that the published pseudobinary join between CaF_2 and $Ca_3(PO_4)_2$ is in error; fluorapatite may exist over a solid solution range on the CaF_2 deficient side of the ideal composition. Included phases in pulled fluorapatite crystals form under conditions of constitutional supercooling in the melt and should be suppressed by slow growth rates, high thermal gradients, and stable melt composition. Precipitates of $Ca_3(PO_4)_2$ develop in FAP when CaF_2 volatilizes during crystal growth. The fracture of FAP crystals is caused primarily by cleavage cracks which nucleate at the inclusion (precipitate)-apatite interface then propagate rapidly through the brittle apatite matrix. Cleavage is greatly reduced by removing harmful second phases from pulled crystals.

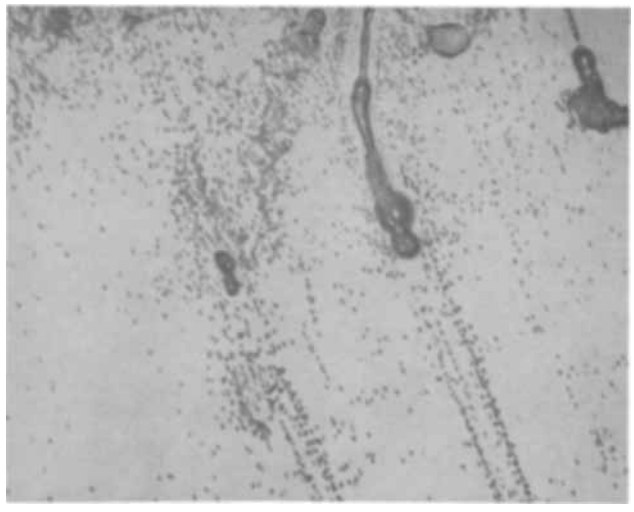

Fig. 4. Dislocation etch pits concentrated in areas surrounding tubular type I inclusion. <0001> growth direction parallel to etch pit rows. Reflected light. Magnification approx. 150X.

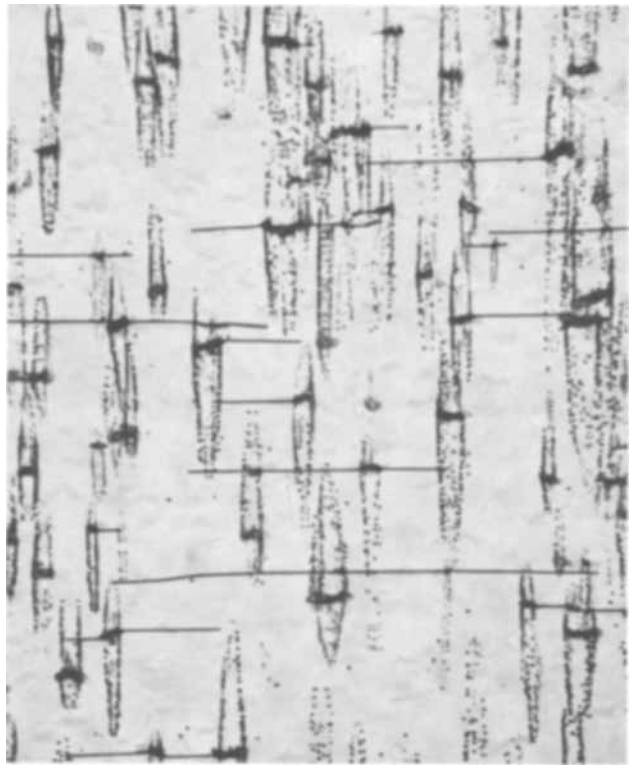

Fig. 5. Nucleation of cleavage cracks at the crystal-precipitate interface. <0001> growth direction vertical. Dark etched precipitates are surrounded by vertical rows of etch pits. Reflected light. Magnification approx. 100X.

Acknowledgments

Mr. P. J. Walitsky, Westinghouse Electric Corporation, Bloomfield, New Jersey, carried out the microprobe analysis. We also gratefully acknowledge the capable technical assistance of Mr. A. M. Stewart and the many helpful comments of Dr. G. W. Roland during preparation of the manuscript. This work was supported by the AF Avionics Laboratory under contract F33615-C-68-1550.

Manuscript submitted Dec. 16, 1968; revised manuscript received Jan. 20, 1969.

Any discussion of this paper will appear in a Discussion Section to be published in the December 1969 JOURNAL.

[1] Prismatic single crystal bars of FAP 1 × 3 × 15 mm were loaded in three point bending at various temperatures. Above about 1375°C these bars could be bent plastically into a "V" shape; below this temperature bars fractured in a brittle manner immediately on loading.

REFERENCES

1. R. Mazelsky, R. C. Ohlmann, and K. B. Steinbruegge, *This Journal*, **115**, 68 (1968).
2. R. C. Ohlmann, K. B. Steinbruegge, and R. Mazelsky, *Appl. Optics*, **7**, 905 (1968).
3. R. Mazelsky, R. H. Hopkins, and W. E. Kramer, "Proceedings of the ICCG," *J. Crystal Growth*, **3**, 260 (1968).

4. G. M. McManus, R. H. Hopkins, and W. J. Takei, *J. Appl. Phys.*, **40**, 180 (1969).
5. P. D. Johnson, *This Journal*, **108**, 159 (1961).
6. R. Nacken, *Zentr. Mineral. Geol.*, **1912**, 545 (1912).
7. L. C. Lovell, *Acta Met.*, **6**, 775 (1958).
8. E. S. Dana, "A Textbook of Mineralogy," John Wiley & Sons, New York (1963).
9. J. S. Prener, *This Journal*, **114**, 77 (1967).
10. A. F. Rodgers and P. F. Kerr, "Thin Section Mineralogy," p. 108, McGraw-Hill, Inc., New York (1933).
11. R. F. Decker and S. Floreen in "Precipitation from Iron Base Alloys," G. R. Speich and J. B. Clark, Editors, p. 69, Gordon and Breach, Inc., New York (1965).
12. J. W. Mitchell in "Direct Observation of Imperfections in Crystals," J. B. Newkirk and J. H. Wernick, Editors, p. 13, Interscience Publishers, New York (1962).
13. R. Brooks, A. T. Horton, and J. L. Torgesen, *J. Crystal Growth*, **2**, 279 (1968).
14. B. Chalmers, "Principles of Solidification," Chap. 5, John Wiley & Sons, New York (1964).
15. D. A. Jones and J. W. Mitchell, *Phil. Mag.*, **3**, 1 (1958).

Phase Studies Using the Traveling Solvent Method of Crystal Growth: The Bismuth-Tellurium System

John Strassburger

Research Division, Carrier Corporation, Syracuse, New York

ABSTRACT

The traveling solvent method (TSM) of crystal growth was evaluated as a means of determining the solidus in a phase diagram, by investigating a portion of the bismuth-tellurium phase system. Sections of ingots grown by TSM were chemically analyzed and these results, combined with the crystallization temperatures of the same sections, were used to define equilibrium solidus lines. A comparison of these results with those obtained from long-term annealing experiments performed by another investigator essentially showed agreement between the two techniques. Much less time and effort is required to obtain the same information if TSM is used. An ingot was grown across a peritectic reaction temperature in the Bi-Te system to demonstrate the ability to prepare a peritectic compound and a congruently melting compound in the same ingot.

Inconsistencies in much of the available phase diagram data probably stems first from the inability to obtain equilibrium conditions, and second from the method of analysis. The importance of obtaining semiconductor materials at their "equilibrium" composition is becoming recognized more every day in the study of phase diagrams and, in general, annealing techniques are being used for studying "equilibrium" phase relationships. These methods are laborious and necessitate the preparation and analysis of a large number of samples. Glatz (1) showed the importance of long-term annealing of fine powders for obtaining "true" equilibrium in the bismuth-tellurium system and pointed out that the phase data presented by Hansen (2) for this system is in error apparently because thermodynamic equilibrium was not attained. Because of the availability of Glatz's data, a direct comparison can be made which shows that crystal growth by the traveling solvent method (TSM) is as good a method, if not better, for elucidating specific portions of an equilibrium phase diagram. Complete solidus lines can be elucidated in much less time and equilibrium seems to be more closely approached.

Although crystal growth by the traveling solvent method was first referred to by Pfann (3) as temperature gradient zone melting (TGZM), we prefer the former name suggested by Mlavsky (4).

Although the theory for preparing compounds by a traveling zone (5, 6) or "controlled solidification" (7) technique is similar in many respects to TSM, the conditions for recrystallization by TSM seem to be more favorable than zone leveling methods for obtaining "equilibrium" compositions. In TSM, all systems are static and the driving force (concentration gradient across the molten zone) for travel of the molten zone is strictly governed by the equilibrium phase diagram, whereas in zone leveling methods the rate of travel of a heater or ingot can regulate purity and repeated passes are usually required because of this limitation. Utilizing TSM one can elucidate a complete solidus line of varying composition by a single pass through one ingot. To obtain similar information by zone leveling techniques seems to require extreme care in manipulation of experimental conditions such as mixing (7) or cooling rate, etc.

Goodman (5) and Pfann (6) forsaw various uses for zone refining such as purification of the elements and the preparation of compounds, both congruently melting as well as those from peritectic reactions. Many investigators have utilized zone refining to study phase relationships. McHugh and Tiller (8) studied the pseudobinary system Bi_2Te_3-Bi_2Se_3 and Umeda *et al.* (9) studied the Sn-Te system.

With a stationary temperature gradient, Pfann (3) used TSM to fabricate semiconductive devices, grow single crystals and measure diffusivities in liquids. More extensive diffusivity studies have since been made by Wernick (10). Because of the interest in semiconductor research, extensive investigations (11-13) have been conducted to determine the solid solubility of various metals in silicon and germanium. Trumbore (14) summarized much of the available solubility data and observed that "over the years there has been a pronounced tendency for the accepted equilibrium solid solubilities to decrease." An interesting case in point has since been brought out by McCaldin and Wittry (15) when they showed that the "Ga concentration in a TSM specimen was reduced some 27 percent from that in the 'regrowth' specimen."

Mason and Cook (16) prepared the peritectic compound $CdIn_2Te_4$ by employing a traveling heater and Armstrong *et al.* (17) studied the compound $AgSbTe_2$ by a similar method. Since then, others (18-22) have used this or a static temperature gradient to prepare congruently melting compounds.

Experimental

Apparatus.—The furnaces used for growing crystals by the traveling solvent method were fabricated from Vycor glass and produced a linear temperature gra-

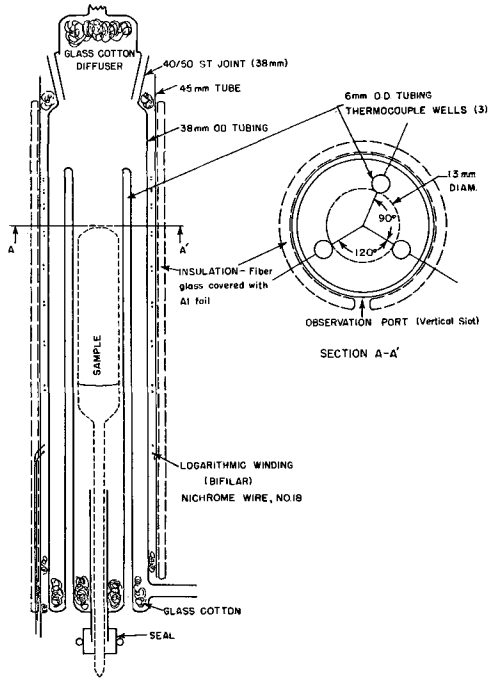

Fig. 1. Furnace for crystal growth by TSM

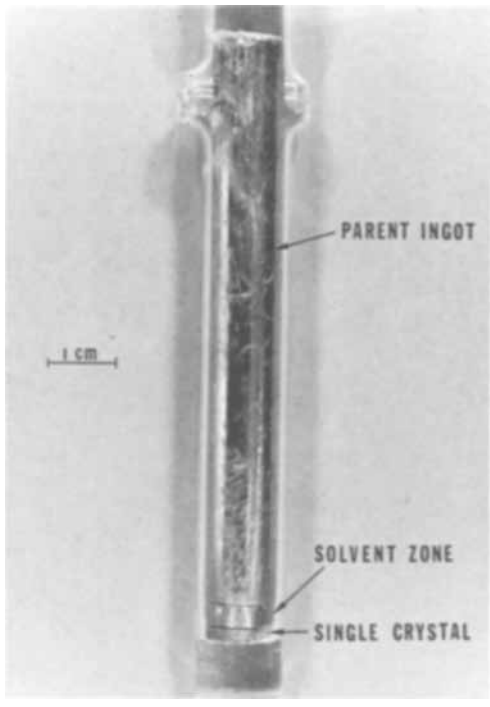

Fig. 2. Crystal growth ampoule before recrystallization

dient of approximately 10°C/cm. As seen in Fig. 1, nichrome wire No. 18 was bifilar wound about the inside furnace tube with logarithmic spacing to produce the desired temperature gradient at the center of the furnace. This furnace was placed inside a glass tube and packed at the ends with glass cotton to form a dead air space. The entire furnace was then insulated with Fiberglass covered inside and outside with aluminum foil except for a long, narrow vertical opening used as an observation port, which was helpful for monitoring the process of the liquid zone. The furnace was designed to be sealed so that crystal growth could be carried out in an inert atmosphere if desired. Three thermocouple wells, which extended essentially the length of the furnace, were placed as close to the sample as possible.

Vertical temperature profiles of the furnace were taken with the specimens in place and also by substituting a fourth thermocouple in place of the sample held in place by a heavy walled glass tube. When three thermocouples were placed as in Fig. 1, Section A-A' and a fourth in the center, the radial temperature distribution across any given horizontal was within 2°C. With an ingot in place, the three outside thermocouples again read within 2°C although it is recognized that the radial temperature distribution could change due to the added heat capacity of the sample.

Originally attempts were made to grow the crystal in a dynamic argon atmosphere but this resulted in volatilization of the solvent zone, and the ingots were consequently sealed in evacuated ampoules, as shown in Fig. 2. A single crystal wafer was placed at the bottom of the ampoule to be used as a deposition site on top of which the solvent zone was placed. The parent material to be recrystallized was placed on top of the solvent zone and supported near the top (hot end) by a glass rod as shown. This was necessary to keep it from falling when the solvent zone melted, thus forcing the solvent up the sides of the ampoule. The ampoule was sealed with a minimum void volume and supported with a glass rod attached to one end.

Materials.—The bismuth metal shot and the tellurium used for preparing the samples were not purified further after being obtained from the manufacturers. The bismuth metal (99.9999+%) was obtained from Cominco Products, Inc., and the tellurium (99.999+%) from the Kawecki Chemical Company.

Crystal growth procedure.—It becomes helpful, when choosing starting compositions for both parent ingot and solvent zone, to have some knowledge of the phase diagram in which one is working. For this reason, the data presented by Glatz (1) for this system was utilized. The solvent chosen for growing Bi_2T_3 (γ-phase, mp = 585°C) was material of tellurium-eutectic composition ($Bi_{10}Te_{90}$) which has a melting point of 414°C. The temperature varied along the polycrystalline ingot between 425° and 530°C; so that when the ingot was recrystallized (solvent zone passed completely through the ingot) its composition followed the tellurium-rich solidus line of Bi_2Te_3 from 425° to 530°C, as is represented in the bismuth-tellurium phase diagram (Fig. 3). The initial thickness of the solvent zone was about 4 mm.

Solvent zones were passed upward through three Bi_2Te_3 ingots with an elapsed time for each of about one month. The zones passed through the entire length of the ingots in about a week or less and the remain-

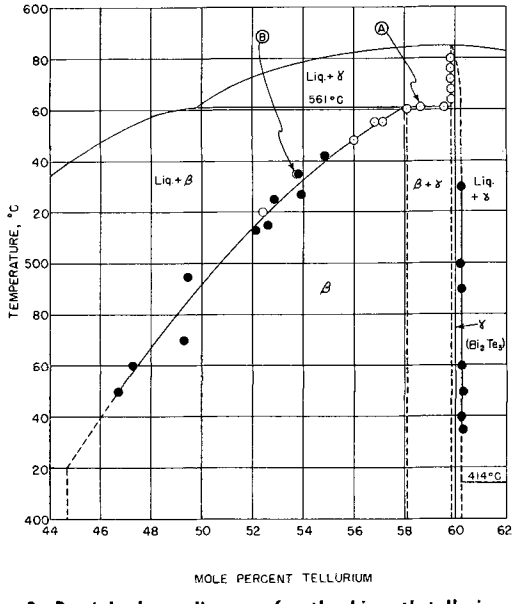

Fig. 3. Partial phase diagram for the bismuth-tellurium system. Open and closed circles are equivalent.

ing time was given to allow possible liquid entrapments to diffuse to the top. The lengths of the resulting ingots varied between 2½ and 3 in., since the liquid zone usually disconnected before reaching the top of the original ingot (3½-4 in.). The diameter of all of the ingots grown was 11 mm.

In an effort to produce a single crystal ingot, a single crystal seed was used as a deposition-site. This seed crystal was cut from an ingot pulled from a Czochralski-type furnace. This configuration was later varied by using an ampoule with a constriction near the bottom. The bulb formed by the constriction was filled with solvent zone and then run through the procedure described above. Although large crystallites were obtained in some ingots, no ingot was grown as a single crystal.

The existence of a peritectic compound (β-phase) on the Bi-rich side of Bi_2Te_3 was reported by Glatz (1) as well as by Abrikasov and Bankina (23). Glatz used long-term annealing of fine powders and established the peritectic invariant point at 562°C and 55 m/o (mole per cent) tellurium. This information was used as a guide in choosing the starting composition for the preparation of the β-phase by TSM. The procedure was the same as that for the preparation of the congruently melting γ-phase except different starting compositions were required. The parent material was a rapidly quenched ingot of composition $Bi_{47}Te_{53}$ and the zone had the composition $Bi_{80}Te_{20}$. Due to the large single-phase region of the β-phase, pure bismuth metal was also used as a zone to furnish enough Bi to reach the saturation point. A starting zone of about 5 mm thickness was used. No seed was used since no parent β-phase material was available as was the case with the γ-phase preparation. The crystallization temperatures of the ingots prepared varied between a minimum of 425° and a maximum of 550°C, except in the unique case described in the next paragraph.

In one case an effort was made to prepare both the β-phase peritectic and the congruently melting γ-phase in one ingot. This ingot could be used to determine the solubility of Bi in Bi_2Te_3 above 562°C as well as an added proof for the existence of the β-phase. A sharp change in the composition of Bi noted as one analyzes along this ingot will be strong evidence for the existence of a peritectic reaction. Quenched Bi_2Te_3 was used as a starting ingot and pure Bi metal was used for the solvent zone. Again no deposition-site was used. The temperature varied from 505°C (cold end) to 580°C (hot end) thereby crossing the peritectic temperature (562°C). Almost a week was necessary for the zone to travel to the top of the 3-in. ingot, and two extra weeks were allowed for annealing.

Analysis of ingots.—After cooling to room temperature, each ingot was cut into representative horizontal slices for chemical, microscopic, and differential thermal analysis (DTA). DTA was used to determine the melting point (first formation of liquid) of a given segment which had also been analyzed chemically.

The DTA thermograms were obtained by plotting the difference in temperature between an aluminum oxide reference standard and the sample on a Honeywell X-Y recorder (Model 153X33). The reference and the sample (ground into powder) were sealed in Vycor ampoules containing thermocouple wells and placed symmetrically in a high thermal capacity Kanthal furnace. The heating rate of the furnace was 5°C/min controlled with a Honeywell cam-type program controller (Model 152). Using sodium chloride as a calibration standard, melting points could be determined well within an accuracy of ±2°C. The melting point defined the ordinate and chemical analysis the abscissa for locating one point on a given solidus. A 4 mm segment was necessary to obtain enough material for duplicate chemical analyses and one 0.75g DTA sample. DTA was also used to determine the presence of any eutectic solvent which may have been trapped in grain boundaries. This was also checked by mounting slices for microscopic inspection. Representative sections, usually near both ends and the middle, were polished so that eutectic phases could be observed under polarized light. Eutectic material must be absent in order to validate the chemical analyses used for determining the equilibrium solidus lines.

The chemical analyses performed by our analytical section were essentially the method of Reed (24) with minor modifications. The analyses were always performed by the same chemist and the accuracy checked by periodically inserting knowns along with the TSM samples. The known standards were prepared by sealing carefully weighed metals of at least 5 9'S purity in an evacuated ampoule. The samples were then melted, rocked, and quenched to insure uniformity. The entire ingot was ground, mixed, and sectioned. The results of a representative analysis is shown in Table I.

The results of other analyses were always approximately the same. One sees that the accuracy for the Te analysis is well within the one to two parts per thousand claimed by Reed and is at least ±0.05 w/o (weight per cent) Te, but the Bi analyses are high. Since the Te analyses were consistently reliable, the %Bi was always taken by difference.

Results

Congruently melting Bi_2Te_3 *(γ-phase).*—Three ingots of γ-phase Bi_2Te_3 were recrystallized by TSM, all of which were tellurium-rich as determined by chemical analyses. All three ingots prepared contained crystallites varying from about 1 to 3 mm in cross-section.

The first ingot grown was removed from the furnace immediately after the solvent zone traveled the length of the parent ingot. Twelve days were required for growth. Differential thermal analyses of sections of this ingot showed the presence of anywhere from 0.1 (near the bottom) to 1.0% (near the top) uncombined tellurium eutectic (solvent), thereby invalidating the chemical analyses for determining the solubility of Te in Bi_2Te_3. Because of these entrapments, it became necessary to anneal the samples past the time for complete zone passage. Microscopic inspection showed that more than 90% of the eutectic material present was located in the outer skin of the ingot and the remainder in grain boundaries.

This distribution was also found in the next two ingots (annealed three weeks) but the total quantity of solvent was at least an order of magnitude less. Separate DTA's were made on sections along the ingots of both the interior and exterior portions. In the thermograms of the sections where the outer skin was concentrated, a very small eutectic peak was seen; and on sections where only the inside of the ingot was used no peak was visible.

The outer skin is a distribution of eutectic material in the outside layer of the ingot and might be as thick as 0.1 mm in some locations. A radial temperature distribution in the furnace is one explanation for the formation of this "skin" since it is quite likely that a slightly cooler temperature exists in the center of the ingot than on the outside on a given horizontal plane. The amount of Te-eutectic located in the grain boundaries (disregarding outer skin) was negligible. The results of all the slices from both ingots were

Table I. Results of representative analysis of known Bi_2Te_3 standard

	Section	Te, w/o	Bi, w/o
Bi (w/o) added = 52.19 (Bi_2Te_3)	A	47.81	52.28
		47.81	52.32
	B	47.83	52.34
		47.83	52.30
Te (w/o) added = 47.81 (Bi_2Te_3)	C	47.82	52.27
		47.83	52.36

Note: w/o is weight per cent.

essentially the same. Chemical analyses of the inside sections of these two ingots indicate a solubility of 0.22 m/o tellurium in Bi_2Te_3 above 420°C, and also indicate that the composition of the equilibrium solidus varies very little (if at all) between 430° and 530°C. The Te concentration variation *vs.* temperature approached the reliability of the chemical analyses (±0.05), therefore, the tellurium concentration was considered invariant over the temperature range studied. The Te-rich solidus is depicted in the partial phase diagram (Fig. 3) as a vertical straight line at the composition 60.22 ± 0.05% Te. The line is solid only where data points were taken. Each segment taken from the two ingots was analyzed in duplicate and considered to be independent. The DTA thermograms for all of these segments were identical, all showing initial melting at about 565°C. The traces showed gradual breaks at the melting point indicative of a solidus transformation. Since the first sign of melting appeared at 565°C, we can draw the Te-rich solidus vertical up to this temperature.

Since the most likely source of error in the chemical analysis is that due to Te-rich eutectic material in the samples, the phase boundary could only be closer to the stoichiometric composition than the value 60.22 ±0.05% Te. Close inspection of the DTA's showed that the Te-eutectic peak was always larger on the cooling cycle (after sample has been completely melted) than on the heating cycle and if no peak was seen on the heating curve, one was usually seen on the cooling curve. The equilibrium solubility of Te in Bi_2Te_3 is apparently disrupted when the sample melts and not restored when refrozen.

Peritectic β-phase.—Four ingots of β-phase bismuth telluride were grown with no variations necessary from the original procedure. The crystalline size obtained from these ingots was markedly larger than those obtained when growing the congruently melting γ-phase. Crystallites up to five or six millimeters in two dimensions were observed and up to one or two centimeters in length. The entrapment of an eutectic phase (including outside skin) was essentially nonexistent as evidenced by microscopic inspection and also DTA. No bismuth-eutectic peak was noted on the heating curve on any of the thermograms obtained. Back reflection x-ray Laue photographs were taken of single crystal sections of one of the β-phase ingots grown and showed very good crystalline perfection. This was also evidenced by the good cleavage obtained with these crystals.

The data obtained from the first three ingots defining the equilibrium solidus are tabulated in Table II and plotted as closed circles in Fig. 3 and those obtained from the last ingot (discussed in the next section) as open circles.

Again, each data point is an average of two chemical analyses plotted *vs.* temperature of first melting as seen on a DTA thermogram. The thermograms of all alloys between 50 and 58% Te showed double peaks indicating that the 561°C peritectic tieline is essentially correct as drawn, meeting the liquidus boundary at about 50 m/o Te. This is in agreement with data found by Glatz (1). The solidus curve calculated by the least squares method was found to follow the equation

$$T(°C) = -0.0031792x^3 + 0.11351x^2 + 24.202x - 604.59$$

where x = m/o Te. The standard deviation for this curve is 5.6°C.

Table II. Melting points of β-phase as obtained from DTA, with corresponding chemical analysis

Melting point, °C	Te, m/o
450	46.71
460	47.27
470	49.29
493	49.48
512	52.21
515	52.62
525	52.97
527	53.96
533	53.83
541	54.86

Along this curve the points obtained from four ingots agree well with each other except for a pair of points at approximately 50 m/o Te. The observed temperature difference of about 25° is much greater than the estimated reliability in the melting point determination. Therefore, there exists the possibility that this pair of points indicates a discontinuity in the solidus line. On close inspection of the DTA's an apparent small peak was seen at about 500°-510°C partially masked by the larger liquidus peak. Another interesting fact was noted. On thermograms of all compositions below 50 m/o Te a bismuth-eutectic peak (268°C) was observed on the cooling curve only, after the sample had been melted. This is evidence that equilibrium solubility is not easily attained in this region. Using annealing techniques to study the same region of the phase diagram, Glatz (1) found difficulty obtaining equilibrium below 52 m/o Te. Whether an actual compound or reaction occurs at this composition necessitates further investigation.

Peritectic jump (β- and γ-phase in same ingot).—The results obtained from the one ingot grown across the peritectic reaction temperature are shown as open circles in Fig. 3. All thirteen data points were obtained from consecutive 4 mm segments starting immediately below the solvent zone which was clearly outlined on the frozen ingot. The chemical analyses showed no temperature dependence of solubility of Bi in Bi_2Te_3 (γ-phase) between 561° and 580°C, but a constant solubility of 0.17 ± 0.05 m/o bismuth. All of the first five samples (crystallized above 561°C) showed sharp melting points at 585° ± 2°C, which is indicative of a vertical solidus line. Since the melting points for these first five samples were essentially the same, and their crystallization temperatures were known to lie from 560° to 580°C, they defined the Bi-rich γ-phase solidus and were plotted as such in Fig. 3. A representative DTA of these five segments is shown in Fig. 4 accompanied by the average chemical composition of each of the five ingots.

The next two segments had a sharp thermal arrest at 561°C followed by the large peak due to γ-phase melting (Fig. 5). This clearly defined the peritectic reaction temperature in agreement with the value (562°C) reported by Glatz (1). The fact that the peritectic reaction was seen in two segments (although very small in one) is explained by assuming that a nonhorizontal or nonplanar isotherm existed in the ingot at the peritectic temperature because of temperature variations within the furnace. When horizontal slices were made, the alloy corresponding to the 561°C crystallization composition was found in two segments.

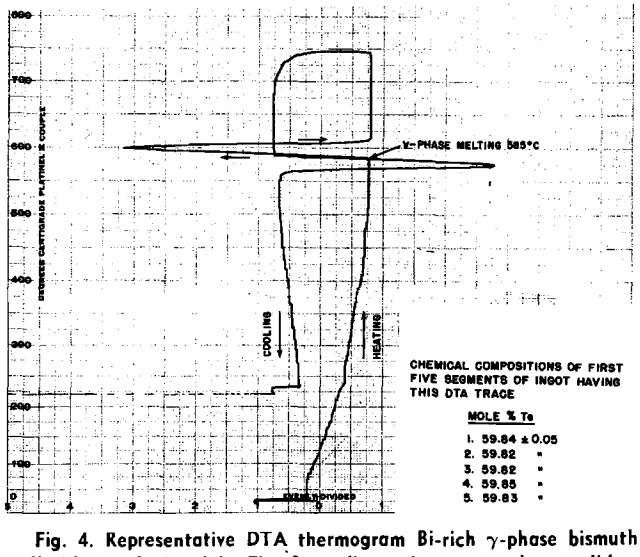

Fig. 4. Representative DTA thermogram Bi-rich γ-phase bismuth telluride as depicted in Fig. 3 as five points on γ-phase solidus.

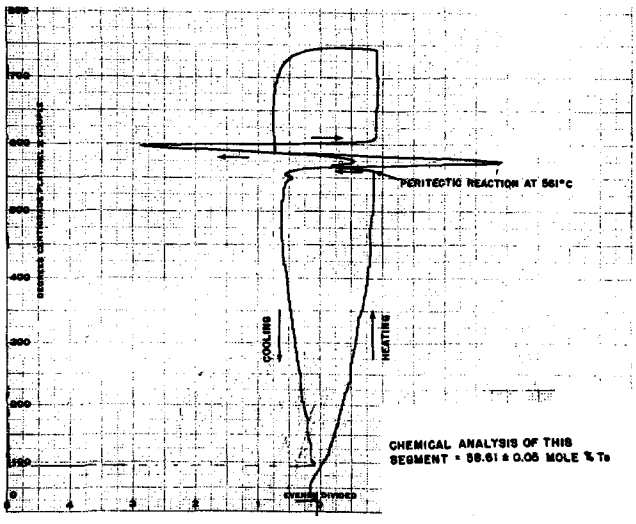

Fig. 5. DTA thermogram showing peritectic reaction at composition A in Fig. 3.

The remaining points tail off to define the β-phase solidus and the lower points are shown overlapping results from the other ingots. The overlapping data are in very good agreement with each other, and two of the points are essentially superimposed. A representative DTA depicting β-phase melting is shown in Fig. 6 from which point B was obtained in Fig. 3.

The calculated β-phase solidus is seen to intercept the peritectic reaction temperature (561°C) at 58.1 m/o Te, thereby defining the peritectic invariant point. Although not as certain, extrapolation at the lower end of the solidus to the 420°C peritectic tieline shows the β-phase region extending to 44.7 m/o Te.

Discussion and Conclusions

The remainder of the partial phase diagram (Fig. 3) is drawn in broken lines. Exactly where the Bi- and Te-rich solidus lines combine on the liquidus might still remain debatable, although the evidence favors a bismuth-rich maximum melting point and was drawn as such. This would agree with Glatz (1), Offergeld and Van Cakenberghe (19), and with Satterthwaite and Ure (20). The evidence favoring a bismuth-rich maximum melting composition is: (I) The data points show a bismuth-rich solidus up to 580°C, whereas data points on the tellurium-rich solidus were taken only to 530°C. (II) The bismuth-rich DTA thermograms show very sharp breaks (Fig. 4) at the melting point, while the tellurium-rich samples show a more gradual break at 565°C which is indicative of incongruent melting of the type shown in Fig. 6 at 535°C. One must therefore conclude that the Te-rich phase boundary slopes toward the Bi-rich side of Bi_2Te_3 above 565°C and the maximum melting composition occurs at 59.83 ± 0.05 m/o tellurium.

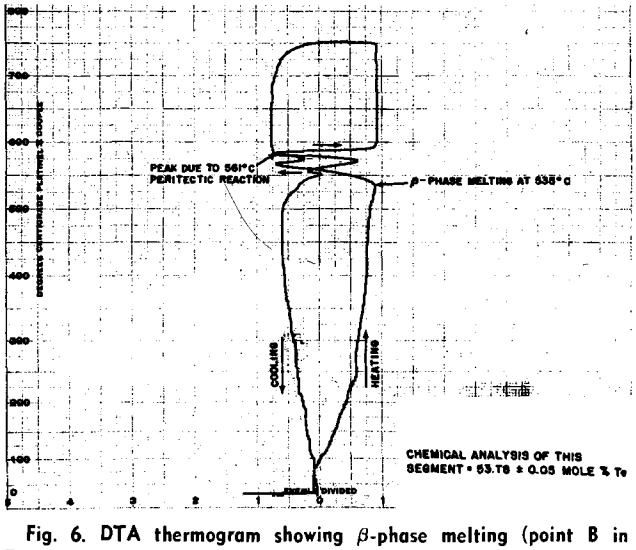

Fig. 6. DTA thermogram showing β-phase melting (point B in Fig. 3) and peritectic transformation.

It must be kept in mind that all data points in Fig. 3 are average values obtained from 4 mm slices. Since the temperature varies continuously across an ingot during crystal growth, a sample with a finite crystallization temperature cannot be chosen and chemically analyzed. Across 4 mm the crystallization temperature may vary as much as 4°C and the concentration as much as 0.4 m/o tellurium, where the slope of the curve is small.

It becomes expedient at this point to compare our results with those obtained by Glatz (1) who used a completely different approach (long-term annealing of fine powders) to define the equilibrium phase relationships for the Bi-Te system. Table III compares significant points and, in general, good agreement is seen except for the peritectic point where Glatz (1) used visual examination of photomicrographs to determine this value.

One concludes that, although either technique is satisfactory for determining equilibrium phase relationships, the advantages for TSM are: (*i*) the results can be obtained in a shorter time; (*ii*) the resulting material is in a condition for practical applications, and (*iii*) the complete solidus curve can be defined from one or two ingots, whereas much more time and effort is necessary when using annealing techniques to obtain the same information. Annealing techniques, however, must be used to study solid-solid equilibria while TSM becomes practical only where the solid phase of interest is in equilibrium with a liquid.

Although fairly large (5 x 5 x 20 mm) single crystals were obtained by TSM crystal growth, an ingot containing only one crystal was not. It is believed that this could be realized by decreasing the temperature gradient across the ingot thereby slowing the crystal growth process and eliminating spurious nucleation. The fact that some Te-eutectic was found in the grain boundaries after two to three weeks of annealing is evidence for an oxide or other high energy barrier at the grain boundaries which prohibited diffusion. Another less likely possibility might be vertical channeling of eutectic phase.

Summary

TSM has been found to be a valuable technique for the preparation of equilibrium binary compounds, both peritectic and congruently melting. The extension into ternary and more complicated systems should be relatively simple. It has been relatively easy to prepare the β-phase peritectic bismuth-telluride from a quenched ingot of Bi_2Te_3. The problem of preparing large single crystals of bismuth telluride by TSM apparently necessitates better control of crystal growth parameters.

From a single ingot of bismuth telluride grown across a peritectic reaction temperature, the following information was obtained: (*i*) the Bi-rich γ-phase solidus was well-defined above the peritectic temperature; (*ii*) the peritectic temperature was easily derived from sharp breaks on DTA thermograms: (*iii*)

Table III. Comparison of results obtained by long-term anneal experiments [Glatz (1)] with those obtained from TSM crystal growth (Strassburger)

	Long-term anneal	TSM
Te-rich γ-phase Solidus limit (% Te)	60.35 ± 0.15	60.22 ± 0.05
Bi-rich γ-phase Solidus limit (% Te)	59.70 ± 0.10	59.83 ± 0.05
Peritectic point (% Te)	55.0	58.1
Lower limit of β-phase (% Te)	~45.0	44.7
Maximum melting of γ-phase (% Te)	59.8	59.83

the peritectic (β-phase) solidus was defined within the temperature range covered, and (*iv*) the peritectic invariant point was found by slight extrapolation of the least squares β-phase solidus curve to the peritectic temperature.

Acknowledgments

The author is indebted to Dr. A. C. Glatz for his many helpful discussions and to Mr. James Endress, Jr. for his skillful fabrication of the crystal growing furnaces.

Manuscript submitted Sept. 9, 1968; revised manuscript received Jan. 6, 1969.

Any discussion of this paper will appear in a Discussion Section to be published in the December 1969 JOURNAL.

REFERENCES

1. A. C. Glatz, *This Journal*, **112**, 1204 (1965).
2. M. Hansen, "Constitution of Binary Alloys," First Supplement, p. 201, McGraw-Hill Book Co., New York (1965).
3. W. G. Pfann, *Trans. AIME*, **203**, 961 (1955).
4. A. I. Mlavsky, *This Journal*, **108**, 263C (1961).
5. C. H. L. Goodman, *Research* (London), **7**, 168 (1954).
6. W. G. Pfann, *J. Metals*, **4**, 747 (1952).
7. W. A. Tiller, *Trans. AIME*, **215**, 555 (1959).
8. J. P. McHugh and W. A. Tiller, *ibid.*, **215**, 651 (1959).
9. J. Umeda, M. Jeong, and T. Okada, *Japan, J. Appl. Phys*, **1**, 277 (1962).
10. J. H. Wernick, *J. Chem. Phys.*, **25**, 47 (1956).
11. F. A. Trumbore, *This Journal*, **103**, 597 (1956).
12. F. A. Trumbore, C. R. Isenberg, and E. M. Probansky, *J. Phys. Chem. Sol.*, **9**, 60 (1958).
13. F. A. Trumbore, E. M. Probansky, and A. A. Tartaglia, *ibid.*, **11**, 239 (1959).
14. F. A. Trumbore, *Bell Syst. Tech. J.*, **39**, 205 (1960).
15. J. O. McCaldin and D. B. Wittry, *J. Appl. Phys.*, **32**, 65 (1961).
16. D. R. Mason and J. S. Cook, *ibid.*, **32**, 475 (1961).
17. R. W. Armstrong, J. W. Faust, Jr., and W. A. Tiller, *ibid.*, **31**, 1954 (1960).
18. A. I. Mlavsky and M. Weinstein, *ibid.*, **34**, 2885 (1963).
19. J. D. Broder and G. A. Wolff, *This Journal*, **110**, 1150 (1963).
20. L. B. Griffiths and A. I. Mlavsky, *ibid.*, **111**, 805 (1964).
21. G. A. Wolff and H. E. LaBelle, Jr., *J. Am. Ceram. Soc.*, **48**, 441 (1965).
22. M. A. Wright, *This Journal*, **112**, 1114 (1965).
23. N. Kh. Abrikasov and V. F. Bankina, *Zh. Neorg. Khim.*, **3**, 659 (1958).
24. J. F. Reed, *Anal. Chem.*, **32**, 662 (1960).
25. G. Offergeld and J. VanCakenberghe, *J. Phys. Chem. Sol.*, **11**, 310 (1959).
26. C. Satterthwaite and R. Ure, *Phys. Rev.*, **108**, 1164 (1957).

Control of Boron Diffusion from a Pyrolitic Borosilicate Glass Source

K. M. Whittle and G. L. Vick

Instrument/Controls Division, Conrac Corporation, Duarte, California

ABSTRACT

A diffusion system is described for the diffusion of boron into silicon which is independent of deposition parameters over wide ranges of values. The diffusion depends only on diffusion time and temperature. A pyrolytically deposited boron-doped oxide is used as the impurity source. Wet oxygen is used to control the diffusion of boron from the oxide into the silicon.

Diffusion systems which use pyrolytically deposited doped oxides as diffusion sources have been discussed by several authors (1, 2). Diffusion from such a source may be performed in either an oxidizing or nonoxidizing atmosphere. For diffusion in a nonoxidizing atmosphere the resulting diffusion profile will depend on the composition of the doped oxide, the segregation coefficient, the diffusion coefficients of the dopant in the oxide and the semiconductor, and the thickness of the oxide. For diffusion in an oxidizing atmosphere, the diffusion profile will depend on all of the above parameters in addition to others relating to the kinetics of oxide growth compared to the diffusion rate of the dopant through the oxide. The diffusion may be carried out in two steps: (*i*) diffusion in a nonoxidizing atmosphere to provide a thin highly doped layer of semiconductor followed by (*ii*) a redistribution cycle in which an oxidizing atmosphere inhibits further doping from the oxide while diffusion continues until the desired junction depth and surface concentration are achieved. The diffusion profiles obtained, in general, depend on a high degree of control over the parameters relating to the deposition of the doped oxide.

This paper describes a system which minimizes or eliminates the dependence on deposition parameters. It does this by satisfying two conditions: (*i*) an oxide of sufficient impurity concentration and thickness that throughout the doping cycle, the diffusion of impurities from the oxide into the semiconductor depends only on the solid solubility and diffusion coefficient of the impurity in the semiconductor, and (*ii*) an oxidizing atmosphere sufficiently effective that oxidation will occur at the semiconductor-oxide interface faster than the impurities can diffuse through it, thus completely preventing further doping during the redistribution cycle. (The doped oxide could be removed by chemical etching eliminating this requirement on the oxidizing atmosphere. It is often undesirable, however, to introduce this step into the diffusion cycles.) The work of Pliskin and Gnall (3) shows that thermal oxidation does proceed at the oxide-silicon interface, but it is not obvious from this work that doping will be prevented at diffusion temperatures (*e.g.*, 1150°C) or in the presence of thick (*e.g.*, 4000Å) doped oxides.

Key words: diffusion, boron, silicon, pyrolysis.

Deposition and Diffusion Systems

The experiment described deals with diffusion of boron into silicon from a borosilicate glass film deposited on the silicon by pyrolysis of tri-n-propyl borate and tetraethyl orthosilicate.

The borosilicate glass film is deposited on the wafers in the system shown in Fig. 1. The wafers are deposited five at a time lying flat on a boat. The quantity of borate and silicate introduced into the deposition

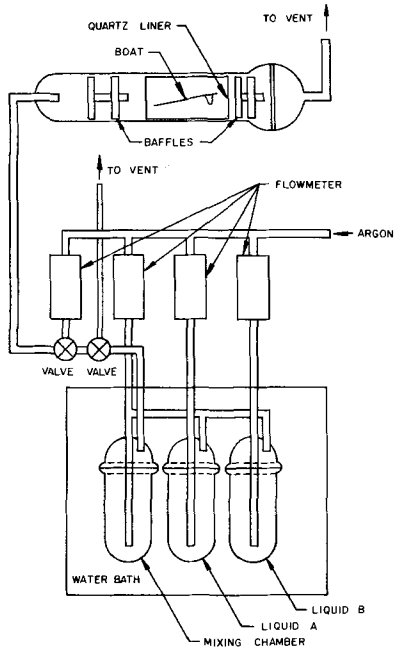

Fig. 1. Deposition system. Liquid A, tetraethyl orthosilicate; liquid B, tri-n-propyl borate.

furnace is determined by the temperature of the water bath and by the flow rate of carrier gas bubbled through the borate and the silicate. It is assumed that the geometry of the bubblers is such as to ensure that the carrier gas is saturated with the dopants. The temperature of the borate and silicate is maintained at 32° ±0.5°C. The furnace temperature is 688°C. Deposition time is 10 to 25 min and gas flow is 600 cc/min through the borate, 47.2 cc/min through the silicate with a diluting flow of 15 SCFH of argon. In this experiment, the deposition parameters were varied one at a time about these values to determine the dependence of the final V/I on the deposition parameters.

The diffusion furnace is operated at 1151° ±2°C and is provided with sources for dry nitrogen and for wet or dry oxygen. The wet oxygen is obtained by bubbling through water at 85°C. Flow rates are 1420 cc/min for the nitrogen and for the oxygen. The diffusion consists of a doping period during which nitrogen flows through the furnace followed by a drive-in period during which the nitrogen is turned off and wet or dry oxygen is introduced into the furnace. The total diffusion time (doping plus drive-in) is held constant at 180 min.

Figure 2 shows the calibration curves of sheet resistivity *vs.* doping time. The curve labeled nitrogen only is plotted for wafers which were removed from the diffusion furnace after the doping time indicated. The wafers for the other two curves were left in the furnace for the drive-in cycle for a total diffusion time of 180 min. It may be seen from these curves that for a dry oxygen drive-in cycle the sheet resistivity continues to decrease during the drive-in, indicating that the dry oxygen is not "turning off" the boron source. This is also indicated by the fact that the sheet resistivity for zero doping time is only 9 ohms/square. The wet oxygen on the other hand turns off the boron source so completely that for zero doping time, the surface of the silicon is not converted from n to p type. (The wafers were originally 3 to 6.5 ohm-cm, phosphorous-doped silicon.) The increase in sheet resistivity during the wet oxygen drive-in results from some of the boron-doped layer being converted to SiO_2 and also some segregation of boron back into the newly grown oxide. It should be pointed out that the doped oxide film used with the dry oxygen is only half as thick as that used with the wet oxygen.

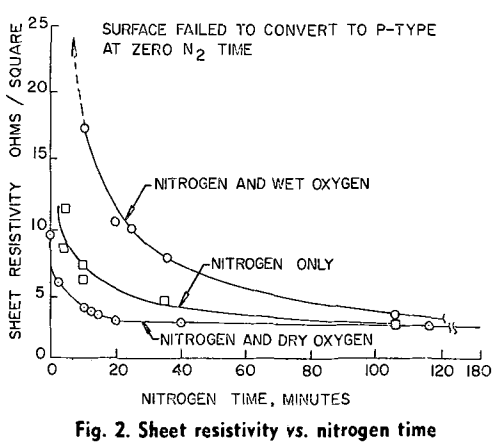

Fig. 2. Sheet resistivity *vs.* nitrogen time

Deposition Parameters

The deposition parameters were varied one at a time about the values given above. The dependence of the resulting sheet resistivity on these parameters for diffusions using wet oxygen to stop the doping process is compared with diffusions using dry oxygen. In Fig. 3 through 7 diffusions of 105 min in N_2, 75 min wet O_2 are compared to the diffusion in dry oxygen which gives roughly the same total number of diffused impurities, namely 30 min N_2, 150 min dry O_2.

Figure 3 shows the dependence of sheet resistivity on deposition time. The curve for diffusion in wet oxygen indicates an approach to an infinite source as the slope approaches zero for a deposition time of 25 min. The curve for diffusion in dry oxygen continues to drop rapidly because of the failure of the dry oxygen to stop the doping reaction. The dependence of final V/I on deposition time is 0.47%/min of deposition time for wet O_2 diffusion and 3.3%/min for dry O_2.

Figure 4 shows the dependence of sheet resistivity on deposition temperature. The two curves compare a 10-min deposition with dry oxygen diffusion to a 25-

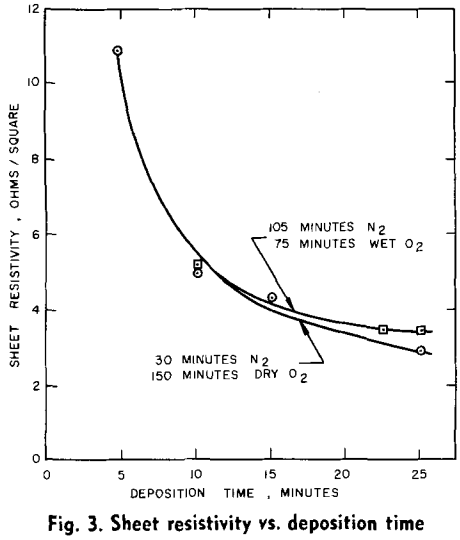

Fig. 3. Sheet resistivity vs. deposition time

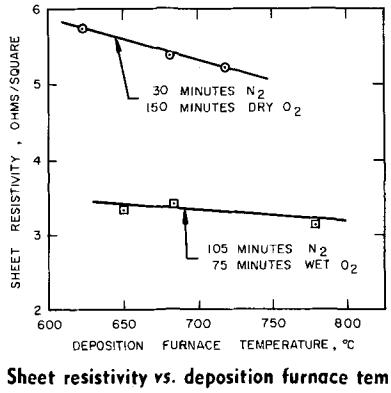

Fig. 4. Sheet resistivity *vs.* deposition furnace temperature

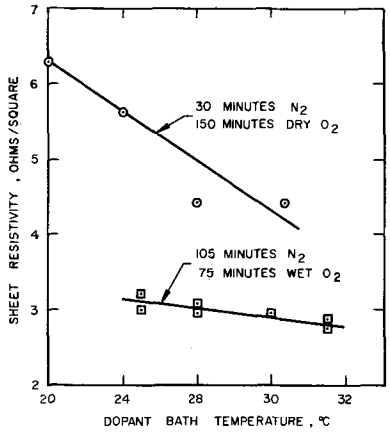

Fig. 5. Sheet resistivity vs. dopant bath temperature

min deposition with wet oxygen diffusion. The latter is found to be insensitive to deposition temperature.

A comparison of the dependence of sheet resistivity on dopant source temperature for dry as opposed to wet diffusion is made in Fig. 5. The 10-min deposition followed by the dry oxygen diffusion cycle is found to show a strong dependence on dopant source temperature, while the 25-min deposition with wet oxygen diffusion is nearly independent of this parameter.

Figure 6 shows the effect of changes in carrier flow through the borate source.

Figure 7 shows the effect of variations in silicate carrier flow rate.

Results

Table I shows the repeatability of sheet resistivity in wafers diffused in accordance with the wet oxygen

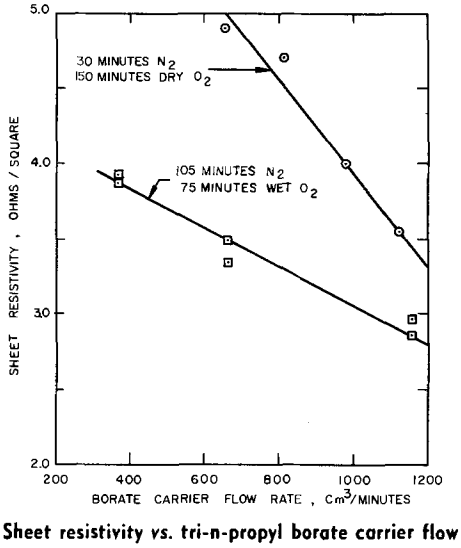

Fig. 6. Sheet resistivity vs. tri-n-propyl borate carrier flow rate

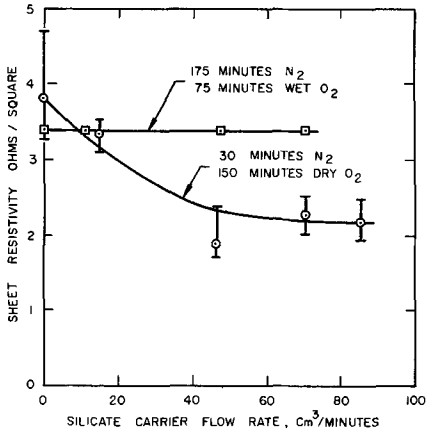

Fig. 7. Resistivity vs. tetraethyl orthosilicate carrier flow rate

Table I. Repeatability of sheet resistivity

Run No.	Wafer No.	Date	ρ_s ohm/square	$\Delta\rho_s$ Over wafer, %
109	1	10/27	3.72	±1.2
	2		3.72	±0.6
110	1	10/30	3.56	±0.6
111	1	11/2	3.56	±0.6
	2		3.55	±0.6
	3		3.33	±1.2
113	1	11/7	3.30	±1.5
114	1	11/15	3.55	±0.7
	2		3.55	±0.7
115	1	12/1	3.26	±0.6
118	1	12/5	3.55	±0.7
	2		3.55	±0.7
120	1	12/26	3.69	±1.5
148	1	4/2	3.33	±0.6
150	1	4/8	3.33	±0.6
151	1	4/11	3.24	0

control described above. The repeatability from run to run is ±6.5%. However, this spread is nearly within the tolerance (6%) to be expected from diffusion temperature variations of ±2°. The repeatability of sheet resistivity over a single wafer is ±1.5%. The resistivities were measured with a four-point probe. The run numbers listed are not consecutive; those omitted were experimental runs not done in accordance with this process or were subjected to inadvertent departures from the process, the most common being water contamination in the dopant bubblers. The deposition tube was cleaned between runs 112 and 114 by etching away the accumulation of deposited glass with a 1:1 solution of hydrofluoric and nitric acids. The consistency of results before and after this cleaning indicates that the process is not dependent on reaching a steady state or equilibrium condition where the walls of the deposition tube are saturated with dopant.

It has been found that the surface concentration after the nitrogen cycle is independent of nitrogen time over periods ranging from 20 to 105 min lending strong support to the assumption that the concentration is limited by solid solubility. The final diffusion profile indicates that significant quantities of boron have segregated out into the oxide during the wet oxygen drive-in cycle, resulting in a maximum concentration at 1.5μ depth.

Staining of the diffused areas resulting from formation of suboxides of boron and silicon (4) or a boron-rich phase (5) which commonly occurs in highly doped boron diffusions did occur on wafers subjected to the

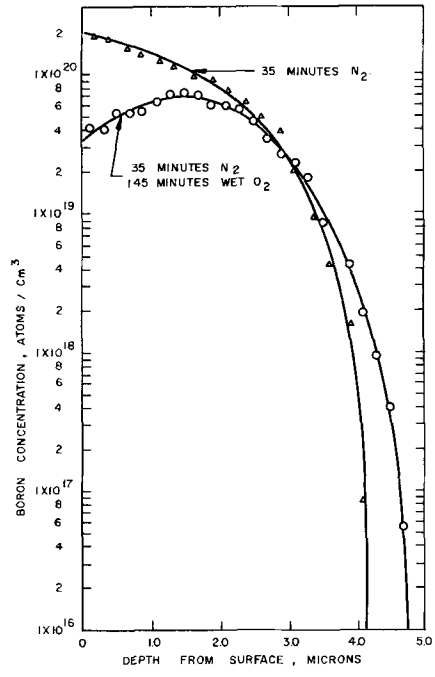

Fig. 8. Boron concentration vs. depth from surface

dry oxygen diffusion, but was eliminated by diffusion in wet oxygen.

Conclusion

It has been shown that a deposition-diffusion system for boron in silicon can be made to be highly independent of the deposition parameters. This is accomplished by using highly doped pyrolytic oxide as an impurity source together with an atmosphere of wet oxygen to control the diffusion of boron from the oxide into the silicon.

Manuscript submitted June 24, 1968; revised manuscript received Dec. 27, 1968. This paper was presented at the Boston Meeting, May 5-9, 1968, as Paper 94.

Any discussion of this paper will appear in a Discussion Section to be published in the December 1969 JOURNAL.

REFERENCES

1. J. Scott and J. Olmstead, *RCA Rev.*, **26**, 357 (1965).
2. M. L. Barry and P. Olafsen, *Solid State Technology*, 39 (1968).
3. W. A. Pliskin and R. P. Gnall, *This Journal*, **111**, 872 (1964).
4. M. S. R. Heynes, *Electrochem. Technol.*, **5**, 25 (1967).
5. K. M. Busen, W. A. Fitzgibbons, and W. K. Tsong, *This Journal*, **115**, 291 (1968).

Zinc Diffusion into Gallium Phosphide under High and Low Phosphorus Overpressure

S. F. Nygren[1] and G. L. Pearson

Stanford Electronics Laboratories, Stanford University, Stanford, California

ABSTRACT

The acceptor zinc has been diffused into n-type single crystal gallium phosphide at temperatures between 700° and 1000°C from diffusion sources which lie in two different regions of the Ga-P-Zn phase diagram. One source (pure zinc) provides low phosphorus overpressure and leads to p-n junctions which are distinctly nonplanar. The other (zinc plus excess phosphorus) provides high phosphorus overpressure and leads to smaller diffusion coefficients and considerably more planar p-n junctions. These effects are consistent with the interstitial-substitutional model for diffusion of zinc in GaP. With either source, diffusion induced dislocations are formed throughout the diffused layer after an incubation time. The p-n junction depth corresponding to the first appearance of the induced dislocations is found to be greater when the high phosphorus pressure source is used.

Zinc diffusion into gallium phosphide has generally been described as anomalous. Concentration profiles cannot be fitted by complementary error functions, and the diffusion coefficient is found to be dependent on zinc concentration as well as temperature (1). Moreover, p-n junctions formed by diffusion from a pure zinc source are usually quite nonplanar.

Recent results from experiments with GaAs (2-4) suggest that the nature of zinc diffused junctions in GaP may be changed and perhaps even improved by using a diffusion source other than pure zinc. Hence, it is the purpose of this study to examine the depth and planarity of zinc diffused junctions in GaP, using temperature, phosphorus overpressure, and time as independent variables. It is found that substantial changes can be made in the diffusion results by changing the diffusion source. Diffusion sources which provide high phosphorus overpressures lead to diffusion coefficients which are smaller than those associated with low phosphorus pressures, and they also lead to considerably more planar p-n junctions. However, with any diffusion source, diffusion induced dislocations appear throughout most of the diffused layer after the p-n junction has reached a critical depth. The onset of these dislocations increases the diffusion coefficient considerably and provides sites on which the zinc can precipitate. Nevertheless, when the induced dislocations are taken into account, the relation among phosphorus overpressure, junction depth, and junction planarity is described quite adequately by the interstitial-substitutional model that was first proposed for Zn diffusion in GaP by Chang and Pearson (1).

The Ga-P-Zn System

In order to understand the relationship among the thermodynamic variables that control diffusion properties, the Ga-P-Zn system must be examined. Figure 1 presents the relationship among the condensed phases at 900°C, as determined by Panish (5). The diagram has this general shape for all temperatures between 700° and 1040°C, the only differences being slight movements of the liquidus lines as temperature changes. Within the temperature range of 700°-1040°C, two regions of the phase diagram are of special interest for diffusion studies. They are labeled regions 1 and 2. In either region, the system contains 4 phases: solid GaP doped with Zn, solid Zn_3P_2 doped with Ga, a liquid ("a" in region 1, "b" in region 2), and a vapor which is discussed below. Both regions are monovariant; that is, within either one the diffusion conditions are fixed as soon as a single variable such as temperature is fixed. This means that reproducible diffusions can be carried out even though rather loose control of the diffusion source is allowed.

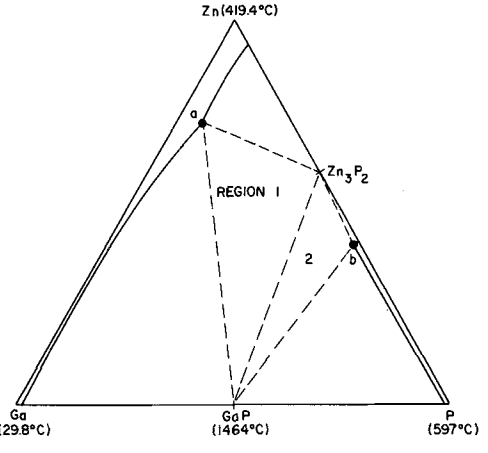

Fig. 1. Ga-P-Zn phase diagram at 900°C (after Panish)

[1] Present address: Bell Telephone Laboratories, Reading, Pennsylvania.

Before diffusion sources for regions 1 and 2 can be prepared, it is necessary to know the vapor pressures that exist in equilibrium with liquids "a" and "b" at the temperatures of interest. Since these pressures are not available in the literature, they must be calculated. From thermodynamic considerations,

$$P_{Zn} = X_{Zn}\ \gamma_{Zn}\ P^{o}_{Zn} \quad [1]$$

$$P_{P_4} = (X_P\ \gamma_P)^4\ P^{o}_{P_4} \quad [2]$$

where P_i, X_i, and γ_i are the vapor pressure, mole fraction, and activity coefficient of substance i for a given liquid, and P^{o}_i is the vapor pressure of substance i over pure liquid i. The values of P^{o}_i are given by the JANAF Tables (6) in the case of phosphorus, and by averaging the data of Barrow *et al.* (7) and Nesmeyanov (8) in the case of zinc. The X_i may be read or extrapolated from Panish's phase diagram (5), and the γ_i are calculated by the regular solution method of Furukawa and Thurmond (9).

Results of the calculations are shown in Fig. 2. It is seen that P_{Zn} is somewhat lower over liquid b than over liquid a, and that P_{P_4} is considerably higher over liquid b than liquid a. Similar calculations show that P_{Ga} is negligible and that other phosphorus species can be neglected over liquid b. The accuracy of these calculations is somewhat difficult to determine, but it can be shown that they give values which are within 25% of those reported by Thurmond (10) for P_{P_2} and P_{P_4} over the GaP binary liquidus.

Experimental Procedure

The GaP single crystals used in this study were grown by an open tube chloride transport process similar to that described by Oldham (11). Epitaxial GaP layers were grown on (111)Ga faces of GaAs seeds. The 50-100 μm of GaP closest to the seed contained about 1 x 10^8 dislocations/cm^2. The remaining portions of the layers were fairly uniform, having about 10^6 dislocations/cm^2 and a density of stacking faults and microtwins of 300-500 cm^{-1}. The layers were n-type with carrier concentrations of 1-5 x 10^{15} cm^{-3}. Samples were prepared for diffusions by lapping away the heavily dislocated portions of the GaP crystals and then mechanically polishing both faces in Linde A 0.3 μm alumina. Each sample was loaded into a clean, evacuated (1 x 10^{-5} Torr) quartz ampoule along with a diffusion source which was located in a quartz container designed to minimize contact between the sample and the ternary source liquid. The net internal volume of the ampoule was 0.170 $\pm$ 0.025 cm^3.

Two different diffusion sources were used. For diffusions in region 1 the source was 1.0 mg of a pulverized mixture of 75% undoped vapor epitaxial GaP and 25% 5 nine's pure Zn. The mixture was annealed at 1000°C for 24 hr before it was pulverized (12). One milligram of this mixture is sufficient to provide a diffusion source in region 1 yet small enough to minimize the amount of liquid in the system.

For diffusion in region 2, the source was 2.7 mg high purity phosphorus, 3.4 mg zinc, 0.87 mg of 7 nine's pure gallium, and 5 mg crushed GaP. These amounts were calculated to provide a diffusion source in region 2 for all temperatures between 750° and 1000°C even if the pressure calculations were in error by 40%. As a check, a diffusion was carried out at 900°C with less than 2.7 mg phosphorus. The resulting sample had almost no surface damage, suggesting that no liquid had been present in the system. The junction depth after 1 hr was 16 μm. When a diffusion was carried out at 900°C using the full 2.7 mg phosphorus, some damage had been done to the sample surface, indicating that liquid had been present in the system, and the junction depth after 1 hr was 10.6 μm. Comparison of these two results suggests that the full 2.7 mg of phosphorus provides a system which is in region 2.

In this study p-n junctions were revealed by cross sectioning diffused samples on (111)Ga planes that are inclined to the surfaces of the samples, and then etching the cross sections in the dislocation etchant 8g $K_3Fe(CN)_6$:12g KOH: 100g H_2O (13). This etchant reveals both the p-n junction and crystal defects so that irregularities in the p-n junction may be correlated with the defects. As shown in Fig. 3, three depths are typically measured: the minimum p-n junction depth, x_j; the minimum p^+-p junction depth, x_j'; and the average depth of a diffusion spike, x_s. The spike depth is measured at a fault that extends from the surface of the sample beyond the p-n junction. Such diffusion spikes have a rather consistent depth, and comparison of x_j and x_s is a good measure of junction planarity. Each of the measured depths is corrected for the thickness of the surface layer that had been removed by the etchant, typically 1-2 μm per side.

Experimental Results

Diffusion with low phosphorus overpressure.—Diffusion of zinc into GaP with liquid a in the diffusion system (region 1 of the phase diagram) typically results in moderate damage to sample surfaces and in p-n junctions that are very irregular. Figure 4 shows a highly magnified picture of a p-n junction and associated crystal defects as revealed by etching a 5° beveled surface on a sample that had been diffused in the presence of liquid a at 1000°C for 15 min. The p-n junction is seen to be quite irregular, and there are two regions where particularly enhanced diffusion is seen. One region is associated with a stacking fault or microtwin (center of the figure) and the other is associated with a cluster of dislocations (right).

The correlation between junction depth and dislocation density is further illustrated by observing how junction depth changes with diffusion time. All samples for this experiment were cut from the same GaP crystal (n = 1.3 x 10^{15} cm^{-3}) so that the initial dislocation and fault densities would be roughly the same in each sample. The results of four diffusions at 800°C and four diffusions at 900°C are shown in Fig. 5. For either temperature, the junction depth is proportional to the square root of time for shallow diffusions. For

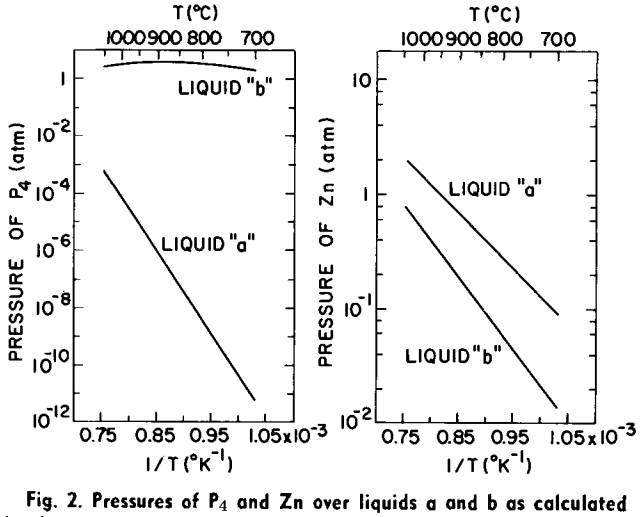

Fig. 2. Pressures of P_4 and Zn over liquids a and b as calculated by the regular solution method.

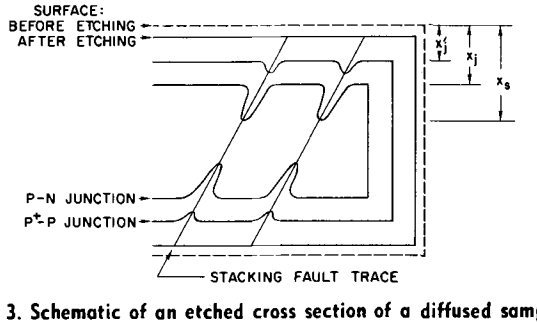

Fig. 3. Schematic of an etched cross section of a diffused sample, showing the various depths that are measured.

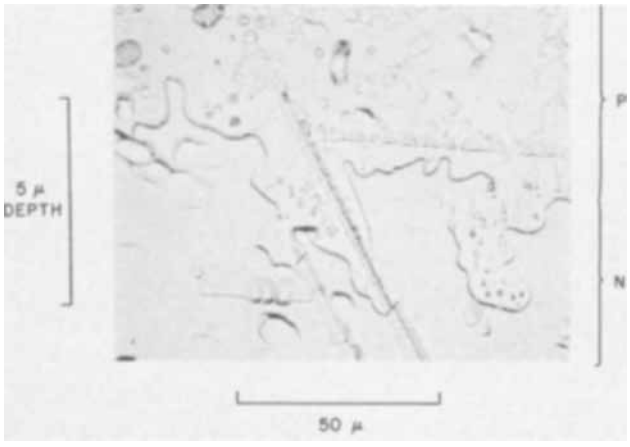

Fig. 4. Zinc diffused (1000°C, 15 min, liquid a) p-n junction in GaP as revealed by etching a 5° beveled surface.

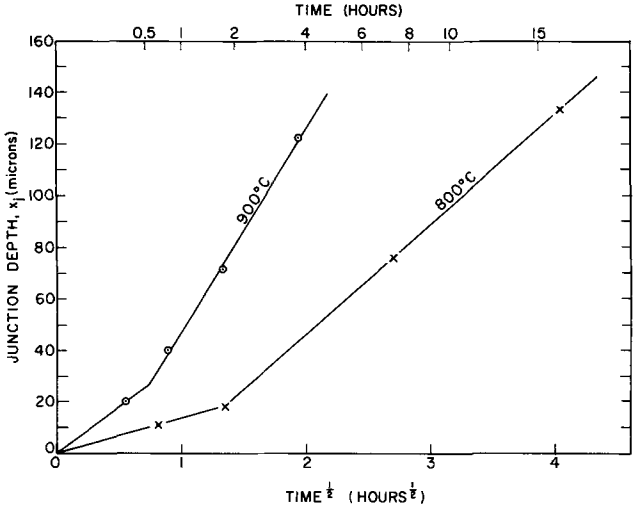

Fig. 5. p-n junction depth vs. the square root of diffusion time for samples that were diffused at 800° and 900°C with liquid a.

diffusions deeper than 20-25 μm, however, the diffusion depth is considerably deeper than would be predicted by proportionality to the square root of time. Previous workers (14) concluded that junction depth is proportional to the square root of time for all depths at 1000°C.

The knee in the curve is a demarcation between two very different diffusion conditions. First, as mentioned above, the diffusion coefficient is smaller below the knee than above. Second, samples with shallow junctions have no diffusion induced defects, while samples that are diffused beyond the knee have diffused layers containing about 1 x 10^8 induced dislocations/cm^2 which are distributed almost uniformly throughout the layer. Only the region within a few microns of the p-n junction escapes the induced dislocations. This is illustrated in Fig. 6, where etch patterns are shown on samples that were diffused below and beyond the knee. Third, samples with shallow junctions remain transparent, while the diffused layers of samples diffused beyond the knee become opaque. Since undiffused samples containing 10^8 dislocations/cm^2 are transparent, the opaqueness is attributed to zinc precipitation. Lastly, Ting (15) has shown that a knee in the x_j *vs.* $\sqrt{t}$ curve also exists for zinc diffusion in GaAs. In that case shallow diffusions have zinc concentration profiles which decrease smoothly with increasing distance; diffusions beyond the knee have concentration profiles which stay relatively constant near the surface and then decrease sharply. It is reasonable to assume that the same effect occurs in GaP. It should be noted that the depth corresponding to

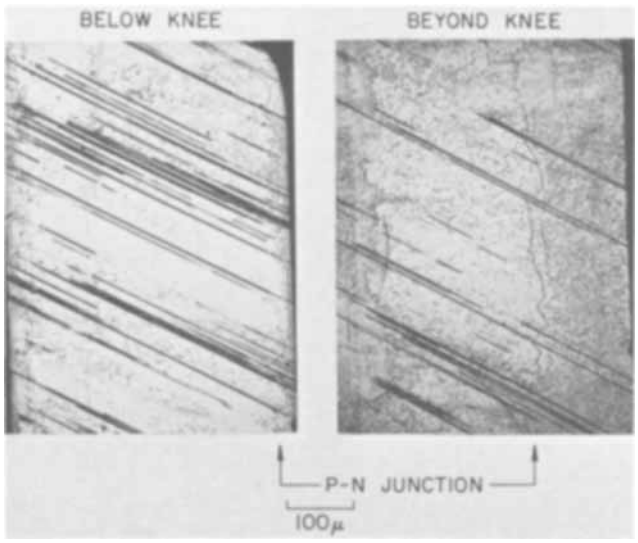

Fig. 6. Etched cross sections of samples that were diffused to different depths at 900°C with liquid a. The sample diffused below the knee in the x_j vs. $\sqrt{t}$ curve (t = 0.31 hr) has no induced defects; the sample diffused beyond the knee (t = 3.75 hr) has a heavily dislocated diffused layer.

the knee in the GaP curve varies slightly from crystal to crystal.

The relationship between diffusion temperature and p-n junction depth has also been measured. Again, all samples were cut from the same crystal. Table I summarizes the results, and both $x_j/\sqrt{t}$ and $x_s/\sqrt{t}$ are plotted against reciprocal temperature in Fig. 7. For the 998°C sample, the diffusion time was so short that warm-up time was appreciable; in this case an effective time was found by fitting $x_j(998°C)/\sqrt{t}$ to the straight line defined by the other points. In view of the fact that x_j is not proportional to $\sqrt{t}$, Fig. 7 should not be used to predict the junction depth that would be reached for specific diffusion temperatures and times. However, the relationship between $x_j/\sqrt{t}$ and $x_s/\sqrt{t}$ does provide a good measure of the irregularity of the junction. At 1000°C, the spikes penetrate 1.5 times as far into the crystal as the shallowest part of the junction. Due to the smaller activation energy associated with the spikes, they become more pronounced at lower temperatures; and at 700°C, they penetrate 5.5 times as deep as the shallowest part of the junction.

Diffusion with high phosphorus overpressure.—Diffusion of zinc into GaP in the presence of liquid b (region 2 of the phase diagram) differs in detail, but not in principle, from diffusions done with liquid a. Liquid b diffusions generally give better results, the sample surfaces being somewhat less damaged, and the p-n junctions being considerably more planar. A comparison of junction irregularity in samples that were diffused to similar depths at 900°C is shown in Fig. 8. (The surface damage on these samples and on the samples shown in Fig. 10 occurred when the samples were cross sectioned and was not present during diffusion.)

As with liquid a diffusions, the relation between junction depth and induced dislocations was studied

Table I. Minimum p-n junction depth and spike depth for samples diffused with liquid a at temperatures between 700° and 1000°C

T, °C	Sample	t, hr	$t^{1/2}$, hr$^{1/2}$	x_j, μm	x_s, μm
715	1	47.17	6.88	31.9	160
761	2	11.88	3.45	31.0	129.5
813	3	3.29	1.185	31.4	96
907	4	0.309	0.556	26.6	42.6
998	5	0.0256*	0.160	18.2	26.6

* Effective time.

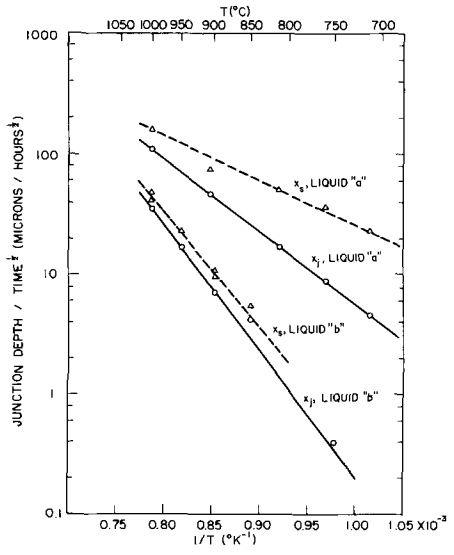

Fig. 7. Minimum p-n junction depths, x_j, and average spike depths, x_s, for diffusions from systems containing liquids a and b between 700° and 1000°C.

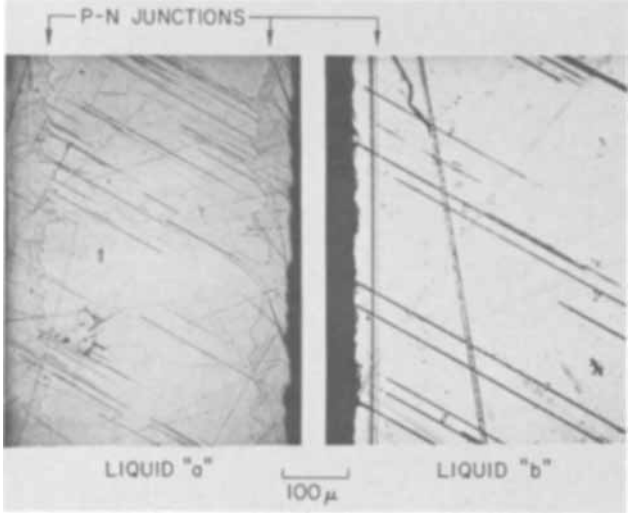

Fig. 8. Etched cross sections of crystals comparing junction planarity of samples that were diffused to approximately the same depth at 900°C with liquids a and b.

by observing how the p-n junction depth changes with time. All samples were cut from the same GaP crystal (n = 2.1 x 10^{15} cm^{-3}), and the diffusions were performed at 900°C. Results are summarized in Fig. 9, where the 900°C curve from liquid a has been included for comparison. For liquid b, both x_j and x_j' are proportional to the square root of diffusion time for medium depths. However, for times greater than about 60 hr, both are deeper than would be expected from proportionality to the square root of time, and for short times the junctions seem too shallow. The shallowest point in Fig. 9 was checked by diffusion into two different crystals; the same junction depth was found in each.

The knee in the curve provides the same demarcation with liquid b as with liquid a. Here again faster diffusion, zinc precipitation, and diffusion induced dislocations occur beyond the knee. It is seen, however, that the knee in the curve does not occur until a considerably greater depth than it does with liquid a. This is consistent with the Zn diffusions performed in GaAs by Black and Jungbluth (16). They found that the use of a high arsenic pressure diffusion source increased the diffusion depth necessary for diffusion induced defects to occur. It is also seen that the diffusion induced defects produced by liquid b do not appear to be as uniformly distributed as those produced by liquid a.

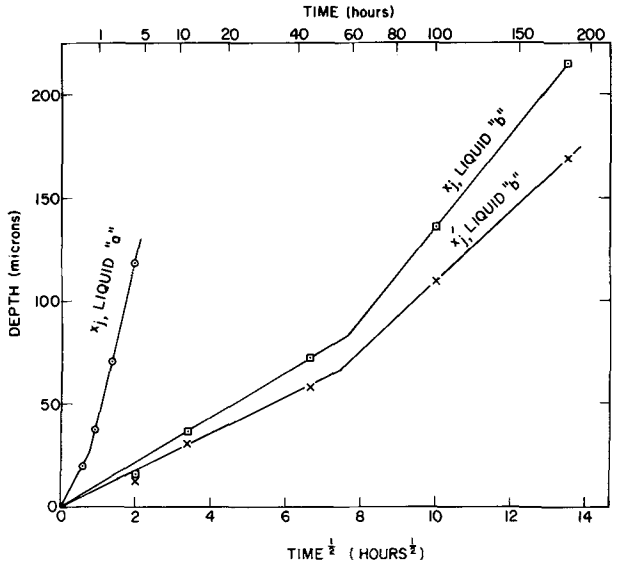

Fig. 9. p-n junction depth x_j, and p^+-p junction depth, x_j', vs. the square root of diffusion time for samples that were diffused at 900°C with liquid b. Data from liquid a are included for comparison.

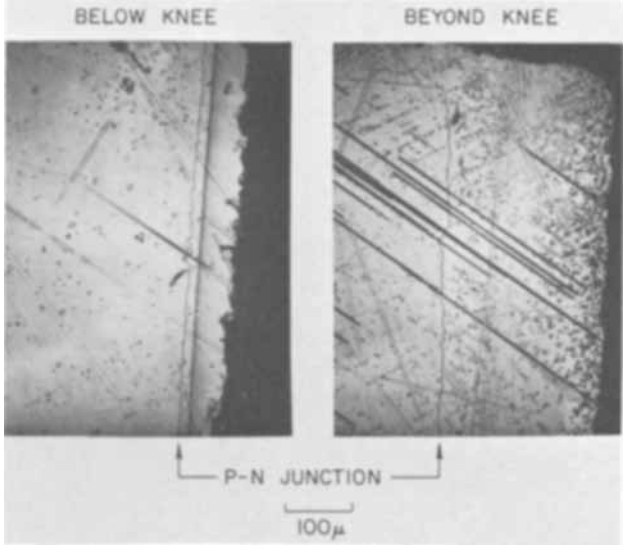

Fig. 10. Etched cross sections of samples that were diffused at 900°C with liquid b. The sample diffused below the knee in the x_j vs. $\sqrt{t}$ curve (t = 45.7 hr) has no induced defects; the sample diffused beyond the knee (t = 182 hr) has a heavily dislocated diffused layer.

A comparison of samples diffused above and below the liquid b knee at 900°C is given in Fig. 10.

For liquid b diffusions, the relationship between junction depth and temperature was measured in an undoped crystal with n = 3.1 x 10^{15} cm^{-3}. Table II summarizes the results, and $x_j/\sqrt{t}$ and $x_s/\sqrt{t}$ are plotted in Fig. 7. Again, since x_j is not proportional to $\sqrt{t}$, the interpretation of these curves must be restricted. Still, it is clear that liquid b diffusions have a smaller diffusion coefficient than liquid a diffusions, and that liquid b diffusions are considerably more planar. The

Table II. Minimum p-n junction depth, minimum p^+-p junction depth, and spike depth for samples diffused with liquid b at temperatures between 750° and 1000°C

T, °C	Sample	t, hr	$t^{1/2}$, hr$^{1/2}$	x_j', μm	x_j, μm	x_s, μm
750	1	118.0	10.85	3.6	4.8	6.6
850	2	10.20	3.20	10.9	14.2	17.5
900	3	3.70	1.92	11.0	13.8	18.5
950	4	1.30	1.14	15.9	19.6	25.9
1000	5	0.575	0.759	21.6	27.3	31.6

spikes go only about 1.3 times as far into the sample as the shallowest part of the junction, and since the activation energy for the spikes is almost the same as the activation energy for diffusion in the bulk, junction irregularity is hardly any worse at low temperatures than at high.

Discussion

Because the diffusion coefficient of zinc in GaP is concentration dependent, the diffusion equation cannot be solved analytically. Nevertheless, it has been shown (14) that the p-n junction depth obtained under such conditions is

$$x_j = \sqrt{D_o t}\, f\left(\frac{C_d}{C_o}\right) \qquad [3]$$

where D_o and C_o are the diffusion coefficient and concentration of zinc at the surface of the sample, t is the diffusion time, C_d is the background donor concentration, and f is an unknown function. In the case of zinc in GaP, the zinc concentration changes very rapidly near the p-n junction so that x_j is only weakly dependent on f. In fact, f may be taken as a constant, f_o, for most purposes.

Diffusion of zinc into GaP is viewed as a parallel mode process, with the zinc existing as both interstitial and substitutional species (1). Casey *et al.* (17) have given the effective diffusion coefficient for this process as

$$\overline{D} = \left(2 + \frac{C_s}{\gamma_p}\frac{d\gamma_p}{dC_s}\right)(K_1^{-1} D_i C_s^2\ \gamma_p^2\ P_{P_4}^{-1/4} + D_s) \qquad [4]$$

where D_i is the interstitial diffusion coefficient, C_s and D_s are the concentration and diffusion coefficient of substitutional zinc, γ_p is the hole activity coefficient, P_{P_4} is the overpressure of P_4, and K_1 is an equilibrium coefficient which is dependent only on temperature. In deriving this equation it was assumed that the interstitial zinc atoms are fully ionized single donors, and that the concentration of interstitial zinc is orders of magnitude smaller than that of substitutional zinc. Expressions for the substitutional diffusion coefficient and the surface concentration of zinc may be obtained from the chemical equilibrium relating gallium vacancies to phosphorus pressure, and from the equilibrium relating zinc in the vapor to zinc in the crystal:

$$1/4\, P_4(g) \rightleftarrows V_{Ga}^{+u} + P_s + ue^- \qquad [5]$$

$$Zn(g) + V_{Ga}^{+u} \rightleftarrows Zn_s^{o} + ue^+ \rightleftarrows Zn_s^{-} + (u+1)e^+ \qquad [6]$$

Here Zn_s^o and Zn_s^- are un-ionized and ionized zinc atoms in substitutional sites in the gallium sublattice, and P_s is a phosphorus atom in a substitutional site in the phosphorus sublattice. V_{Ga}^{+u} is a vacancy in the gallium sublattice which is given an arbitrary charge of $+u$. Applying the law of mass action to the above equations gives

$$C_{V_{Ga}} = K_2\ C_s^u\ \gamma_p^u\ P_{P_4}^{1/4} \qquad [7]$$

and

$$C_s = (K_3\ P_{Zn}\ P_{P_4}^{1/4}/\gamma_p)^{1/2} \qquad [8]$$

where $C_{V_{Ga}}$ is the concentration of gallium vacancies, P_{Zn} is the overpressure of zinc, and K_2 and K_3 are equilibrium coefficients. The substitutional zinc is assumed to be fully ionized so that $C_s = p$. By making the common assumption that the substitutional diffusion coefficient is proportional to the concentration of gallium vacancies, Eq. [3], [4], and [7] may be combined to give an expression for p-n junction depth as predicted by the interstitial-substitutional model

$$x_j = f_o\sqrt{t}\left\{\left(2 + \frac{C_o}{\gamma_p}\frac{d\gamma_p}{dC_s}\bigg|_{C_o}\right)(K_1^{-1}D_i\ C_o^2\gamma_p^2\ P_{P_4}^{-1/4} + K_4 C_o^u \gamma_p^u P_{P_4}^{+1/4})\right\}^{1/2} \qquad [9]$$

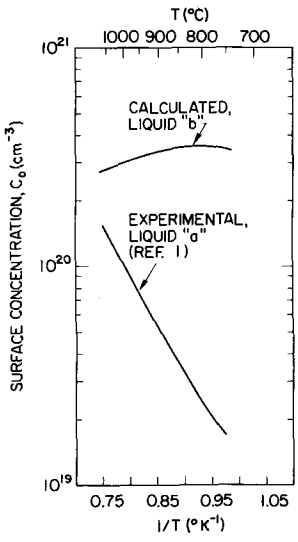

Fig. 11. Surface concentration of zinc in samples that were diffused between 750° and 1000°C with liquids a and b. Values for liquid b were calculated from the experimental values for liquid a.

where γ_p is given by Panish and Casey (18) and the factors inside the square root are evaluated at the surface of the sample in accordance with Eq. [3]. Values of C_o are shown in Fig. 11; the values for liquid a are given by Chang and Pearson (1), and the values for liquid b have been calculated using Eq. [8].

Equation [9] states that, for a fixed time, the junction depth will be determined by the two factors within the second square root. The first factor contains the effects of the built-in electric field and the concentration dependence of the hole activity coefficient. In the second factor, the first term is due to interstitial zinc, and the second term is due to substitutional zinc. In the range where the interstitial zinc is dominant, the junction depth will be proportional to $\gamma_p\ C_o\ P_{P_4}^{-1/8}$; in the range where substitutional zinc is dominant, the junction depth will be proportional to $\gamma_p^{u/2}\ C_o^{u/2}\ P_{P_4}^{1/8}$. In either case, the dominant factor is $P_{P_4}^{\pm 1/8}$ (unless $u < -4$, which seems highly unlikely). Since the experimental evidence shows that the junction depth is decreased by an increase in phosphorus pressure, it is concluded that the interstitial diffusion mode is dominant for all liquid a diffusions in the temperature range studied, and that it is also dominant for at least most of the range between liquid a and liquid b.

Previous workers (1) have shown that Zn diffusions into GaP at 800°, 850°, and 900°C give concentration profiles which decrease smoothly with increasing distance, while diffusions at 950°, 1000°, and 1100°C give profiles which stay relatively constant near the surface and then decrease sharply. This was taken as evidence that the interstitial diffusion mode was dominant only at temperatures above 950°C. However, the low-temperature diffusions of ref. (1) are all shallow, about 45 μm at 900°C, less than 25 μm at 800° and 850°C, while the high-temperature diffusions are all deeper than 75 μm. In light of the present work and that of Ting (15), it seems likely that the low-temperature diffusions involved no diffusion-induced dislocations, while the high-temperature diffusions had created induced dislocations. Thus, the difference seen in the two sets of profiles in ref. (1) is probably due to the differing numbers of dislocations present, and not to the relative importance of the interstitial mode.

It is clear from Fig. 4 that the diffusion of zinc is enhanced in regions near dislocations in GaP. This fact is the basis of a model which is proposed here to

explain why the p-n junction depth is not proportional to the square root of time as predicted by Eq. [3]. Initially, due to some unknown nonequilibrium process, the diffusion proceeds more slowly than expected, as seen in Fig. 9. Before long, however, the junction depth begins following the square root of time law according to the interstitial-substitutional model. As diffusion proceeds, stress is built up within the crystal because of the size difference between Zn and Ga atoms. [The tetrahedral covalent radius of Zn is 1.31Å; of Ga, 1.26Å (19).] During the early stages of diffusion this stress is simply tolerated within the crystal. Finally, at some critical junction depth, the internal stress within the sample exceeds the yield stress of the crystal, and dislocations are formed. These dislocations appear throughout the diffused layer so that almost the entire layer has a uniformly high concentration of diffusion induced dislocations. Moreover, as the diffusion front continues to move into the crystal, new dislocations are formed so that the dislocated layer continues to be almost the same thickness as the diffused layer. The interstitial diffusion coefficient, D_i, is higher in the dislocated region of the diffused layer than it is in the undisturbed bulk, and most of the diffusion now takes place in the dislocated layer. This increases the rate of diffusion, but otherwise the diffusion is the same as before. The junction depth now follows

$$x_j = f_o\sqrt{D_o t_o + D_1(t - t_o)} \qquad [10]$$

where D_1 is the new effective diffusion coefficient, and t_o is the time at which the induced dislocations were formed. For $t >> t_o$

$$dx_j/d\sqrt{t} = f_o\sqrt{D_1} \qquad [11]$$

For times not much greater than t_o, $dx_j/d\sqrt{t}$ is different from that given by Eq. [11]. In the cases presented in Fig. 5 and 9, however, the changes in the diffusion coefficient are relatively small, making the deviations from Eq. [11] too small to be seen experimentally.

According to this model, Eq. [9] should apply to the two time periods in which the x_j *vs.* $\sqrt{t}$ plot is a straight line, and it turns out that the model is in good quantitative agreement with experiment. For example, at 900°C, taking the interstitial mode to be dominant for all phosphorus pressures, the equation predicts that the ratio between liquid b junction depths and liquid a junction depths will be

$$\{x_j/\sqrt{t}\ \text{(liq. b)}\}/\{x_j/\sqrt{t}\ \text{(liq. a)}\} = 0.37$$

Using Fig. 9, the experimentally determined value of this ratio in the shallow, straight line portions of the curves is 0.30. For deep diffusions, beyond the knee in the curves, the experimentally determined slopes of the curves are applicable to Eq. [9] and at 900°C the result is

$$\{\Delta x_j/\Delta\sqrt{t}\ \text{(liq. b)}\}/\{\Delta x_j/\Delta\sqrt{t}\ \text{(liq. a)}\} = 0.31$$

In view of the approximations involved in calculating the pressure over the Ga-P-Zn system, this correspondence between calculated and experimental values is very good. The change in junction depth between liquid a diffusions and liquid b diffusions is correctly predicted within 10%. The fit would not have been as good if the interstitial zinc had been taken as doubly charged, a suggestion that has appeared in the literature (1). This is taken as additional evidence that the appropriate charge state of an interstitial zinc atom is +1.

Several features of this model must be discussed in more detail. It might be argued that the zinc precipitation occurs while the sample is at the diffusion temperature and that the precipitates cause the stress that results in dislocations. However, Panish and Casey (18) have effectively argued against this. They point out that if precipitation occurs during diffusion, then the zinc solubility would be expected to change with time. Moreover, the surface concentration of zinc in a diffused sample would be expected to be different from the zinc concentration found in a solution grown sample. Neither of these effects occur, so it is more reasonable to assume that the presence of unprecipitated zinc can cause dislocations. Calculations similar to those of Black and Lublin (20) suggest that zinc diffusion into GaP may indeed generate sufficient internal stress to cause plastic flow which results in misfit locations (21). The precipitation is then taken to occur on cooling, using the existing dislocations as nucleation sites.

The mechanism that defines the p-n junction depth at which induced dislocations are first nucleated is not clearly understood. The change in critical depth with diffusion source indicates either that diffusions done with liquid b initially place less stress on the crystal or that crystal yield strength near the surface is increased by the use of high phosphorus pressure. The first possibility seems unlikely. For equal p-n junction depths a liquid b diffusion would be expected to have a steeper concentration gradient than a liquid a diffusion since liquid b gives a higher surface concentration. This suggests that a liquid b diffusion would create more, not less, strain in the lattice. Taking the other possibility, Maruyama (22) has suggested that high phosphorus pressure will cause interstitial phosphorus atoms to precipitate onto dislocations, rendering them immobile, and increasing the yield stress of that part of the surface layer with which the phosphorus comes into equilibrium. Since the zinc surface concentration associated with liquid b is substantially larger than that associated with liquid a, the change in yield stress would have to be quite large. Unfortunately, there is no data to suggest how large a change in yield stress might be obtained by this effect.

It was noted above that liquid b diffusions are considerably more planar than liquid a diffusions. This is consistent with the interstitial-substitutional diffusion model. For diffusions with liquid a the interstitial mode is dominant, and the diffusion coefficient is strongly concentration dependent. In this case, any crystal defect that causes a local change in the zinc concentration also causes a local change in the diffusion coefficient, resulting in an irregular diffusion front. When the phosphorus pressure is increased and the diffusion is performed in the presence of liquid b, two effects occur. First, the gallium vacancy concentration in the crystal is increased so that clusters of vacancies near crystal defects are no longer so different from the rest of the lattice. Second, the substitutional diffusion mode increases in importance, decreasing the dependence of the diffusion coefficient on zinc concentration (providing the charge on a gallium vacancy is 0 or ± 1). Both effects would reduce the influence that crystal defects have on diffusion. However, the interstitial diffusion mode appears to have remained dominant for all phosphorus pressures used in these experiments. Thus, the second effect has negligible importance in this particular set of experiments.

Conclusion

The results of zinc diffusions into GaP were found to be strongly dependent on the diffusion sources that were used. When the diffusion source was a sufficient amount of pure zinc, the resulting diffusion system was monovariant, containing a liquid which was mostly gallium and zinc and a vapor which had low phosphorus pressure. Diffusions from this source resulted in highly irregular p-n junctions since the diffusion coefficient was highly sensitive to crystal defects. A second monovariant system could be obtained by using a diffusion source that contained proper proportions of zinc and excess phosphorus; the resulting system contained a liquid that was mostly phosphorus and zinc and a vapor with high phosphorus pressure. Diffusions from this source had smaller diffusion coefficients than the previous source and resulted in p-n junctions that were consistently more planar since the diffusion coeffi-

cient was much less sensitive to crystal defects. Both of these effects can be explained quite adequately by the interstitial-substitutional model for zinc diffusion in GaP.

The results of zinc diffusion were also strongly dependent on diffusion time. Regardless of the diffusion source, short times resulted in diffused layers which had no induced crystal defects. However, if diffusion was continued beyond an incubation time which was dependent on the diffusion source, the stress generated within the diffused layer by the incorporation of zinc into the crystal lattice exceeded the yield stress, and almost the entire diffused layer became filled with a high concentration of dislocations. When this happened, the diffusion coefficient within the diffused layer was suddenly increased, causing a corresponding increase in $dx_j/d\sqrt{t}$. Again, the high phosphorus pressure source resulted in more desirable diffusion properties, allowing a greater junction depth to be reached before the induced dislocations appeared.

Acknowledgments

This project was supported by the National Aeronautics and Space Administration and the Advanced Research Projects Agency through the Center for Materials Research at Stanford University. One of the authors (SFN) also acknowledges financial support from the National Science Foundation and the Institute of Electrical and Electronics Engineers.

Manuscript submitted Nov. 12, 1968; revised manuscript received Jan. 30, 1969.

Any discussion of this paper will appear in a Discussion Section to be published in the December 1969 JOURNAL.

REFERENCES

1. L. L. Chang and G. L. Pearson, *J. Appl. Phys.*, **35**, 374 (1964).
2. H. C. Casey, Jr., and M. B. Panish, *Trans. Met. Soc. AIME*, **242**, 406 (1968).
3. J. C. Marinace, *This Journal*, **110**, 1153 (1963).
4. K. K. Shih, J. W. Allen, and G. L. Pearson, *J. Phys. Chem. Solids*, **29**, 379 (1968).
5. M. B. Panish, *This Journal*, **113**, 224 (1966).
6. JANAF Thermochemical Tables, Thermal Laboratories, Dow Chemical Company (1961).
7. R. F. Barrow, P. G. Bodsworth, A. R. Downie, E. A. N. S. Jeffries, A. C. P. Pugh, F. J. Smith, and J. M. Swinstead, *Trans. Faraday Soc.*, **51**, 1354 (1955).
8. An. N. Nesmeyanov, "Vapor Pressure of the Elements," Academic Press, New York (1963).
9. Y. Furukawa and C. D. Thurmond, *J. Phys. Chem. Solids*, **26**, 1535 (1965).
10. C. D. Thurmond, *ibid.*, **26**, 785 (1965).
11. W. G. Oldham, *J. Appl. Phys.*, **36**, 2887 (1965).
12. M. Gershenzon, R. A. Logan, and D. F. Nelson, *Phys. Rev.*, **149**, 580 (1966).
13. M. I. Valkovskaya and Yu. S. Boyarskaya, *Sov. Phys.-Solid State*, **8**, 1976 (1967).
14. L. L. Chang, *Solid State Electronics*, **7**, 863 (1964).
15. C. H. Ting, To be published.
16. J. F. Black and E. D. Jungbluth, *This Journal*, **114**, 181 (1967).
17. H. C. Casey, Jr., M. B. Panish, and L. L. Chang, *Phys. Rev.*, **162**, 660 (1967).
18. M. B. Panish and H. C. Casey, Jr., *Bull. Am. Phys. Soc.*, **13**, 375 (1968).
19. L. Pauling, "The Nature of the Chemical Bond," p. 246, Cornell University Press, Ithaca, N. Y. (1960).
20. J. Black and P. Lublin, *J. Appl. Phys.*, **35**, 2462 (1964).
21. D. B. Holt, *J. Phys. Chem. Solids*, **27**, 1053 (1966).
22. M. Maruyama, *Jap. J. Appl. Phys.*, **7**, 476 (1968).

Epitaxial Films of Germanium Deposited on Sapphire via Chemical Vapor Transport

R. F. Tramposch*

Airco Speer, Research Laboratory, Niagara Falls, New York

ABSTRACT

Single crystal films of germanium have been deposited on sapphire (α-alumina) by chemical vapor transport using a disproportionation reaction involving water vapor and a technique in which the source and substrate are closely spaced. The heteroepitaxial process was found to be sensitive not only to substrate orientation and temperature, but also to impurities in the source material. Monocrystalline films were only obtained on substrates oriented in the (0001) or basal plane when heated to 800° ± 10°C, and only when using source wafers heavily doped ($\sim 10^{19}$ at./cc) with arsenic. Under identical growth conditions, polycrystalline films invariably resulted if the source materials used were either undoped, or doped with gallium, indium, or antimony in a wide range of concentrations. In addition to a high density of dislocations and low angle grain boundaries, the films also contained stacking faults of the single-line type, believed to occur primarily as a consequence of lattice mismatch. The electrical characteristics, as well as crystalline perfection, approach that of bulk material as film thickness increases; however, p-n junctions fabricated in these films were inferior to those formed in bulk material.

Heteroepitaxial films of germanium on single-crystal aluminum oxide appear to offer a real potential in microcircuit applications requiring high-speed, minority-carrier active film devices (1). Growth and perfection have been studied as part of an effort to obtain the crystalline quality essential in the fabrication of useful bipolar devices.

* Electrochemical Society Active Member.

Single-crystal films of germanium were deposited on sapphire wafers at 800°C by chemical vapor deposition, using a disproportionation reaction and water vapor as the reactant. The process

$$Ge + H_2O \rightleftharpoons GeO + H_2$$

was first investigated by Lever and Jona (2) and applied to germanium epitaxy using a closed-tube

system and slightly higher temperatures. Employing an open-tube flow system and an arrangement in which the source and substrate are closely spaced, similar to the technique used by Nicoll (3) to deposit epitaxial GaAs films, we obtained films of uniform thickness on sapphire at growth rates several orders of magnitude higher. It is believed that the increased growth rate and uniform film deposition are important factors in obtaining good heteroepitaxial films.

Experimental Technique

The vapor growth apparatus consisted essentially of a gas purification train, a means of introducing the water vapor into the carrier gas, and a deposition chamber (20 mm diameter). In the latter, as detailed in the lower portion of Fig. 1, a source wafer and substrate are sandwiched between two graphite blocks inductively heated by rf. Quartz spacers were used to maintain a parallel separation between the source and substrate. For most film depositions the surfaces were separated by about 0.5 mm. The substrate was heated in the temperature range of 750°-850°C. By differential rf coupling and the relative size difference between the heater elements, the source could be heated 25°-50°C higher. In this temperature gradient the disproportionation reaction as indicated is assumed to occur. At the surface of the source, the reaction proceeds to the right, forming a volatile oxide for temperatures above 700°C. Germanium is transported to the cooler substrate via the oxide as the reaction proceeds in the opposite direction.

The source temperature was maintained by a controller and sensing element inserted in a hole in the side of the heater. Prepurified, dry hydrogen was employed as the carrier gas at flow rates of 10-60 cc/min. After the temperature of the source was stabilized, the hydrogen was diverted to pass over a small volume of distilled water. Provisions were made for heating or cooling the water to control vapor pressure; however, best results were obtained with the water bubbler at room temperature.

Source materials used were wafers sliced from single crystal ingots of Ge grown in the (111) or (110) direction, and doped with As, P, Ga, In, or Sb to concentrations of 10^{16} to 3 x 10^{20} at./cc, or the solubility limit. The wafers, nominally 0.025 in. thick, were lapped and etched in CP-4 prior to use and could be used for a number of film depositions.

The sapphire substrates were obtained commercially in the form of 20 mils thick, mechanically polished disks, ⅜ in. or ½ in. in diameter, sliced from Verneuil or Czochralski-grown boules, and oriented in the (0001), near the (11$\bar{2}$3), or (11$\bar{2}$0), *i.e.*, pole directions of 0°, 60°, or 90° with respect to the c-axis. The pulled material, having a lower dislocation density and no visible subgrains, was used to examine the effect of substrate perfection on film quality. For the most part, the substrates were used as received without further surface treatment, except for the usual predeposition cleanup. In a few instances, films were deposited on chemically polished sapphire by wet chemical (4) or gas phase etching techniques (5) to investigate the effect of surface preparation. An evaluation of film quality was made by comparing the electrical characteristics of thick films with that of bulk single-crystal material. Conductivity and Hall effect measurements were performed on the films at room temperature using the van der Pauw technique (6).

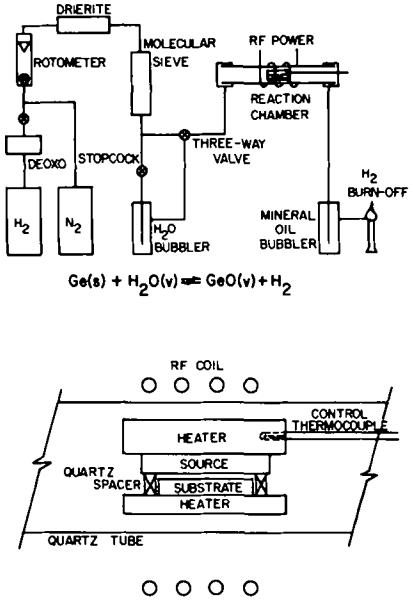

Fig. 1. Schematic of vapor growth apparatus

Results and Discussion

Film growth.—We have found that at least three conditions must be satisfied to obtain perfect heteroepitaxy: (*i*) the substrate must be oriented in the (0001) or basal plane; (*ii*) it must be heated to a temperature of 800° ± 10°C; and (*iii*) the source material must be heavily doped with As (~ 10^{19} at./cc).

Highly oriented films resulted when Ge wafers used as source materials were heavily doped with phosphorus; or the substrate surface was oriented in the (11$\bar{2}$3) plane, *i.e.*, 60° with respect to the c-axis, if the other two conditions were satisfied.

Polycrystalline films having no preferred orientation were obtained consistently for all growth conditions in which the Ge wafers used were doped with Ga, In, Sb, or lower concentrations of As; or the substrates used were oriented in the (11$\bar{2}$0) plane, *i.e.*, 90° with respect to the c-axis.

Substrate orientation had little effect on film growth rate. Films grown under ideal conditions as stated were deposited at a rate of 0.3 to 0.5 μm/min. Deposits grown at lower rates by reducing water vapor pressure and/or source temperature, or at higher rates by increasing these parameters, were invariably polycrystalline or composed of large individual crystallites.

Typical examples of perfect heteroepitaxial, highly oriented, and polycrystalline films of Ge on sapphire, all deposited under identical conditions of substrate temperature and source doping, are shown in Fig. 2, illustrating the effect of substrate orientation on film crystallinity. The film thickness of these and other films described in this work is of the order of 30-50 μm. In the film deposited on the 0°-oriented substrate, the growth features characteristic of epitaxy and the x-ray diffraction pattern in the Laue back reflection photograph are evidence of its single-crystal orientation. The structure and the x-ray diffraction pattern of the surface of a film deposited on a 60°-oriented substrate indicate a high degree of preferred orientation. Films grown on 90°-oriented sapphire exhibit growth facets which are randomly oriented, as is further evidenced by the ring diffraction pattern in the Laue photograph.

Film perfection.—Characteristic growth defects that have been observed in films deposited on 0°-oriented substrates under optimum growth conditions are shown in Fig. 3. The surface was etched lightly in a warm ferricyanide solution to reveal the crystalline imperfections. In addition to stacking faults which appear principally as single and intersecting etched lines along the (110) direction, there is also present a large density of etch pits typical of dislocations and low-angle grain boundaries. The stacking faults have the appearance of the single line type reported by Mendelson (7) as observed in epitaxial silicon films deposited on mechanically polished substrates. We have observed similar effects in epitaxial Ge films.

Substrate perfection and surface treatment.—The effect of using mechanically polished sapphire was ex-

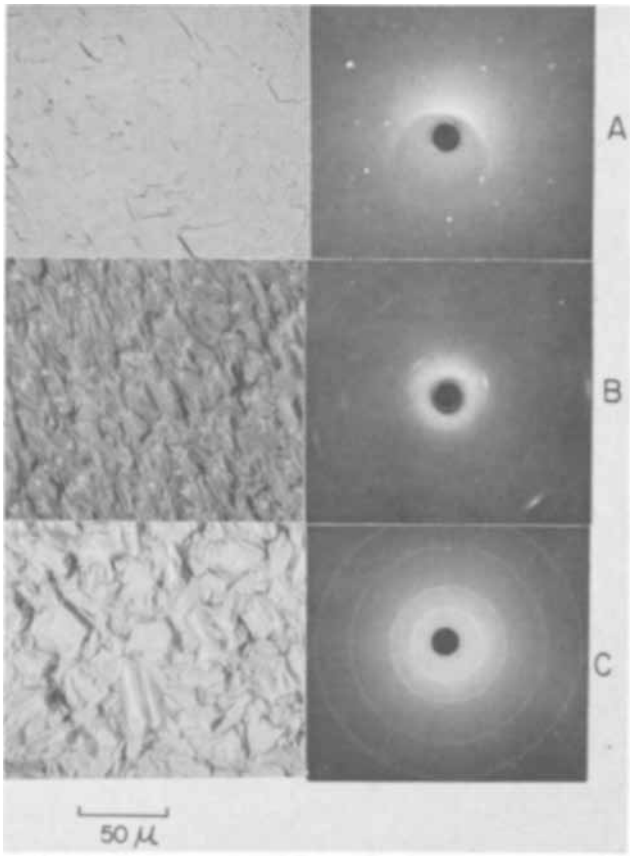

Fig. 2. Films of germanium on sapphire oriented in the (a) 0001, (b) near the $11\bar{2}3$, or (c) $11\bar{2}0$ directions. Magnification approx. 225X.

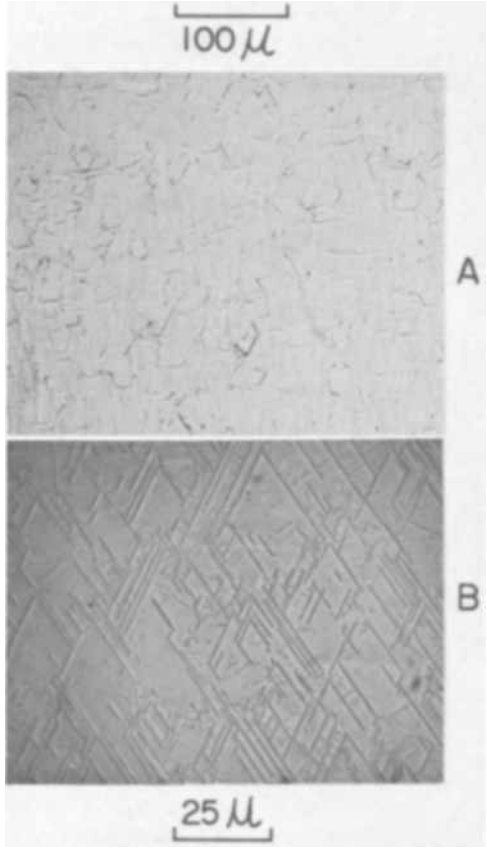

Fig. 3. Defect structure in a Ge film on a (0001) oriented sapphire substrate: (a) as-deposited (175X), and (b) etched surface. Magnification approx. 400X.

amined in a number of ways. Films of Ge were deposited on Ge substrates mechanically polished with different abrasives and the defects produced in these epitaxial films were compared with those found in heteroepitaxial films on sapphire. Figure 4 shows that the defects are indeed similar and appear to result from using mechanically polished substrates. However, in several films deposited on sapphire polished by wet chemical and gas phase etching techniques, the crystalline perfection was found to be as poor as that of films deposited on unetched substrates. In addition, films deposited on etched sapphire under identical growth conditions were generally found to be poorly oriented, multicrystalline, exhibiting only a few single-crystal regions. It was also found impossible to grow well-oriented films on used substrates, *i.e.*, substrates from which previously deposited films were removed by etching. In some cases mechanically polishing these used substrates with 0.25 μm diamond lapping compound seemed to assist in promoting epitaxy; however, the results were not entirely satisfactory.

With regard to the crystalline perfection of the sapphire, it has been noted that films deposited on better quality substrates, *i.e.*, Czochralski-grown material, were more uniformly oriented due to the absence of subgrains, or regions of slight misorientation found in the poorer quality, Verneuil-grown material. The surface of a typical film grown on this latter material is shown in Fig. 5. As a result of perfect epitaxy, subgrains present in the substrate are propagated in the Ge deposit. The darker regions of the etched surface are those having a higher density of stacking faults. The difference in density in adjacent areas is evidence that the stacking faults are produced by lattice mismatch, since these areas differ only in orientation and not in surface treatment.

Although the dislocation density in the better quality substrates was a factor of 10^3-10^4 lower than the standard, Verneuil-grown material, we could find no evidence of film perfection being related to the dislocation density of the substrate.

These results apparently confirm that crystalline defects observed in films of germanium on sapphire are not related primarily to substrate perfection and surface treatment, but rather are a consequence of lattice mismatch inherent of heteroepitaxy, or film deposition on a foreign substrate.

Electrical Characteristics

A comparison of the electrical characteristics of thick films with that of bulk single crystal material is given in Fig. 6, a plot of Hall mobility as a function of excess charge carrier density. The smooth curves represent bulk values and were obtained from both published and unpublished Hall effect data. A pronounced substrate orientation dependence is evident. Films deposited on 0°-oriented substrates have the highest mobilities and, in fact, closely approach bulk values. These data relate electrical characteristics to film crystallinity, *i.e.*, films deposited on 0°-oriented substrates are more highly ordered than those deposited on 60°-oriented substrates, have less structural defects and consequently a higher charge carrier mobility. All films represented here were heavily doped with arsenic, except those indicated otherwise. Films doped with Sb, or low concentrations of arsenic, exhibit low mobilities, are polycrystalline and p-type. Gallium-doped films, on the other hand, exhibit very high hole mobility, approaching that of single crystal material, even though these films are all polycrystalline. This apparent anomaly has been reported by other investigators in vacuum deposited Ge films on alumina (8), glass (9), and GaAs (10).

The effect of arsenic concentration in the source wafer on the film crystallinity and Hall mobility is shown in Table I. The table lists typical results of a large number of film depositions on 0°-oriented sapphire under identical and optimum growth conditions in which the sources used were doped to various

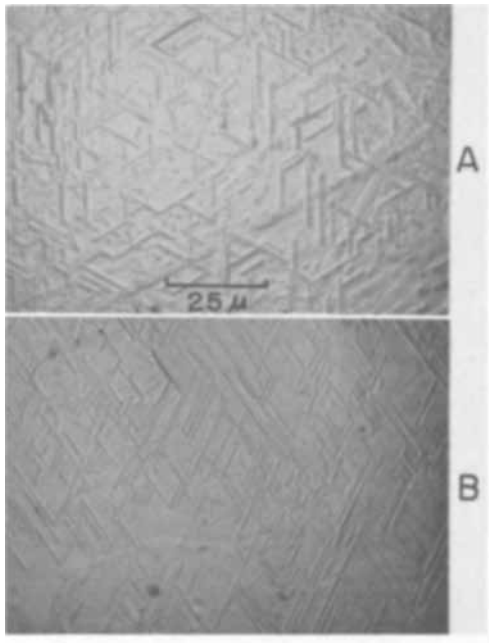

Fig. 4. Stacking fault generation in films of Ge deposited on: (a) polished Ge substrate, and (b) polished sapphire substrate.

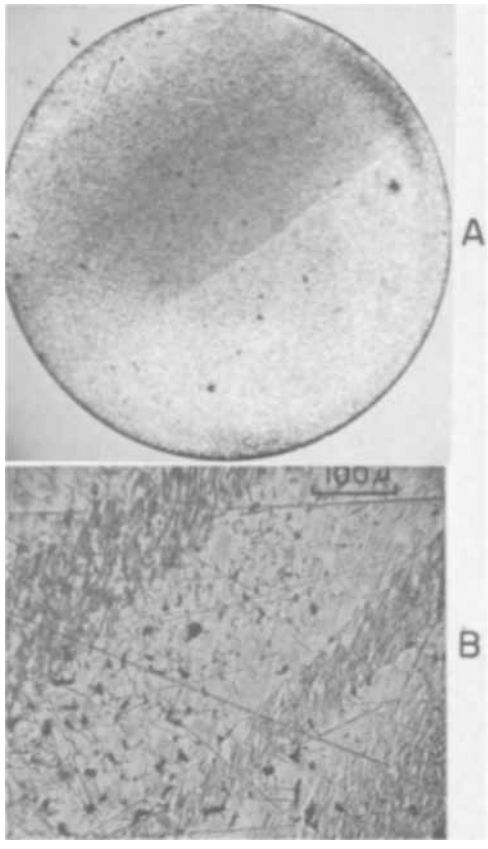

Fig. 5. Effect of substrate perfection on film crystallinity: (a) as-grown surface of a Ge film deposited on a sapphire containing subgrains, (b) same surface, mechanically polished and etched.

levels of arsenic concentration. The mobility in the films is compared to values in bulk material of equivalent excess charge carrier density. There is apparently an optimum arsenic concentration for which good quality films can be obtained, *i.e.*, about 10^{19} at./cc. It is interesting to speculate on the role of arsenic in promoting oriented growth. It may be that As bonds to Al on the reduced surface of the aluminum oxide, forming an interfacial or intermediate layer of

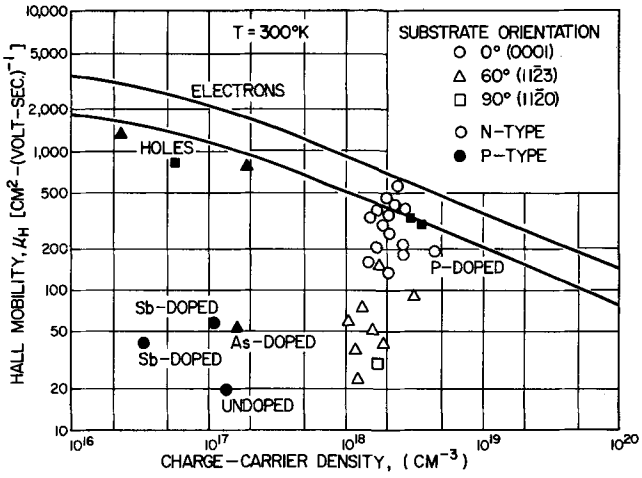

Fig. 6. Hall mobility as a function of excess charge-carrier density in Ge films on sapphire.

AlAs from which a single-crystal film of Ge could propagate, since it has the same crystal structure and a lattice parameter that matches to within a half a per cent (Ge = 5.65Å; AlAs = 5.62Å). Other III-V compounds which could also form an intermediate layer if source materials were doped with P or Sb, *i.e.*, AlP and AlSb, apparently do not promote oriented growth to any great extent because their a spacings differ from that of Ge by 4 and 9%, respectively.

Effect of film thickness.—We have found that film crystallinity and perfection improve with thickness. As film thickness increases, the number of stacking faults appearing in the etched surface are reduced. A correlation was made of the electrical characteristics and crystallinity as a function of film thickness from room temperature measurements of the Hall effect and from x-ray diffraction studies.

The electrical measurements were performed on films that were etched to reduce their thickness in increments, the average charge carrier density and mobility determined for each thickness. A plot of the data for a film exhibiting high electron mobility is shown in Fig. 7. For comparison, the Hall mobility of electrons in bulk material having equivalent charge carrier density is also plotted. Both the number of charge carriers, N, and their mobility, μ_F, increase with increasing film thickness, the latter approaching bulk values. The difference in film and bulk mobility appears to be due to the presence of structural defects, probably dislocations associated with stacking faults, since they are found in increasing numbers as film thickness decreases. The variation in the average excess charge carrier density, *i.e.*, the difference in the density of donor and acceptor levels, $(N_D - N_A)$, indicates that the density of acceptors is decreasing with increasing film thickness, assuming of course, films are uniformly doped with donor atoms. Since dislocations behave as acceptors in Ge, one might conclude that the variation in the electrical characteristics with thickness

Table I. Effect of arsenic concentration in source wafer on the characteristics of Ge films deposited on 0°-oriented sapphire

Concentration cm^{-3}	Film crystallinity	Hall mobility cm^2/v-sec	% Bulk mobility
3×10^{19}	Polycrystalline (highly preferred orientation)	192	37
9×10^{18}	Single-crystal	560	83
9×10^{18}	Single-crystal	385	50
9×10^{18}	Single-crystal	335	44
5×10^{18}	Polycrystalline (preferred orientation)	110	14
5×10^{18}	Polycrystalline (preferred orientation)	82	10
5×10^{16}	Polycrystalline (random orientation)	110	3

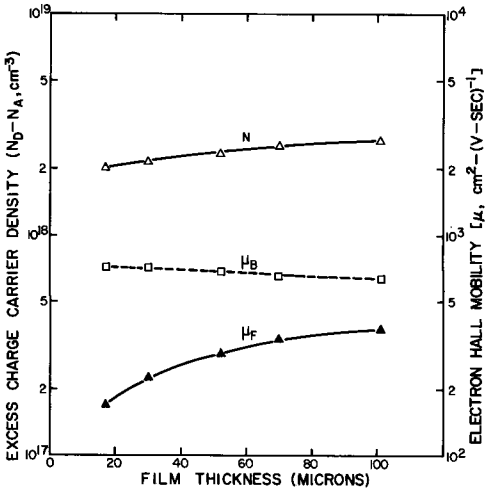

Fig. 7. Electron Hall mobility and charge-carrier density as a function of film thickness of Ge on 0°-oriented sapphire.

is due to dislocations associated with stacking faults which introduce acceptor levels in sufficient concentration to compensate films doped to donor levels in excess of 10^{18} at./cc.

One might speculate that films are being contaminated by the substrate. The presence of aluminum in silicon films deposited on sapphire has been reported by Dumin and Robinson (11). However, they observed that the aluminum diffusion only becomes appreciable at temperatures above 1250°C. For the deposition temperature used and the growth conditions under which Ge films are deposited on sapphire, contamination of films by aluminum from the substrate should be negligible. Similar conclusions have been reported for Ge deposits on spinel (12).

A correlation between film thickness and crystallinity was determined by comparing the x-ray diffraction pattern of a single film grown to various thicknesses. The film was grown to the desired thickness, a Laue back-reflection photograph was made, and then the film thickness was increased by continuing its growth. Results of interrupting its growth at various thicknesses are shown in Fig. 8. At a thickness of 8μ, the film appears to be twinned and highly strained. The diffraction pattern consists of reflections from both the substrate and the film. At a thickness of 35μ, the film is predominantly (111)-oriented, with only a few misoriented regions. The diffraction pattern now shows only three-fold symmetry. At a final thickness of 52μ, the film is well oriented having no misoriented regions.

Device aspects.—Mesa diodes fabricated in these thick Ge films, both by diffusion and by epitaxial techniques, exhibited current-voltage characteristics that were generally inferior to those of p-n junctions formed in simultaneously processed bulk material. This is evidenced by a high reverse leakage current, and lack of a well-defined breakdown voltage, *i.e.*, very soft junction characteristics, due presumably to the high defect density in the heteroepitaxial layer.

Recent results suggest that it may be possible to form reasonably good p-n junctions in epitaxial layers of Ge deposited on the heteroepitaxial films. Using a low-temperature chemical vapor deposition process, the epitaxial films were found to be free of stacking faults, although the substrate film contained high densities of these defects. Details of these results will be reported in a subsequent paper.

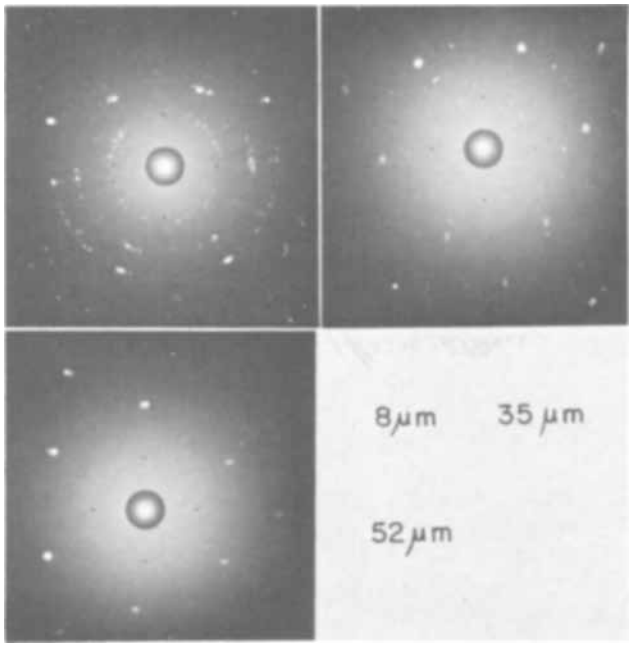

Fig. 8. Laue back-reflection photographs of a Ge film on a (0001)-oriented sapphire showing film crystallinity as a function of thickness.

Summary

In depositing single-crystal films of germanium on sapphire using a wet hydrogen process and close-spacing technique, we have found that, in addition to substrate temperature and orientation, heteroepitaxy is dependent on the presence of high concentrations of arsenic in the source wafer. The films contained many crystalline defects that were characteristic of heteroepitaxy or lattice mismatch, rather than due to surface treatment of the substrate. Although the crystalline perfection and electrical properties were found to improve markedly with thickness, diodes fabricated in thick films were inferior to those formed in bulk material.

Manuscript submitted Nov. 8, 1968; revised manuscript received Jan. 30, 1969. This paper was presented at the Chicago Meeting Oct. 15-19, 1967, as Paper 164.

Any discussion of this paper will appear in a Discussion Section to be published in the December 1969 JOURNAL.

REFERENCES

1. R. F. Tramposch, *Appl. Phys. Letters*, **9**, 83 (1966).
2. R. F. Lever and E. Jona, *J. Appl. Phys.*, **34**, 3139 (1963).
3. F. H. Nicoll, *This Journal*, **110**, 1165 (1963).
4. P. H. Robinson and C. W. Mueller, *Trans. AIME*, **236**, 268 (1966).
5. H. M. Manasevit and F. L. Morritz, *This Journal*, **114**, 204 (1967).
6. L. J. van der Pauw, *Phillips Tech. Rev.*, **20**, 220 (1959).
7. S. Mendelson, "Single Crystal Films," p. 251, M. H. Francombe and H. Sato, Editors, Macmillan Co., New York (1964).
8. M. C. McKinnon and B. A. MacIver, *J. Appl. Phys.*, **38**, 4924 (1967).
9. P. Chartraine and B. Dreyfus-Alain, *J. Phys. Chem. Solids*, **27**, 239 (1966) (in French).
10. J. E. Davy, *Appl. Phys. Letters*, **8**, 164 (1966).
11. D. J. Dumin and P. H. Robinson, *This Journal*, **113**, 469 (1966).
12. D. J. Dumin, *ibid.*, **114**, 749 (1967).

Oxidation Studies on Zirconium Alloys in High-Pressure Liquid Water at 360°C

E. A. Gulbransen* and K. F. Andrew*

Westinghouse Research Laboratories, Pittsburgh, Pennsylvania

ABSTRACT

Corrosion studies were made on 22 zirconium alloys in liquid water at 360°C and 2708 psi for time periods up to 112 days. These alloys include dilute alloys of Zr with V, Cr, Ni, Fe, Sn, and Cu, intermetallic alloys of Zr with V, Cr, Ni, Fe, Sn, and Cu, intermediate alloys of Zr with V, Cr, Ni, Fe, Cu, and Zircaloy-2 and -4. Weight gain and hydrogen contents were determined.

The corrosion of zirconium alloys in liquid water at high pressure and at a temperature of 360°C is a subject of both scientific and technical interest since the corrosion behavior is determined by both oxidation processes and by the hydrogen pick-up and its effect on the metal structure.

This paper presents the results of autoclave corrosion tests on 20 alloys in liquid water at 360°C and 2708 psi for time periods up to 112 days. Alloys were chosen on the basis of the hydrogen reaction of the alloying element's intermetallic phases (1-3). Many of the alloying elements were chosen from the first long period of the periodic table where a wide variation in the hydrogen reaction occurs. These include V, Cr, Fe, and Ni. Cu, Nb, and Sn alloys were also included. Copper forms an intermetallic which breaks down on reaction with hydrogen; Nb does not form intermetallic phases with zirconium. Two separate Zr and Nb rich phases exist in Zr-Nb alloys. Tin is of particular interest since it forms the major alloying element in the Zircaloy alloys.

Types of Hydrogen Reaction of Zirconium Alloys

Four types of hydrogen reaction have been found for the intermetallics (1-3). 1. Hydrogen reacts to breakdown the intermetallic to form δ-$ZrH_{1.4}$ and another metallic or intermetallic phase depleted in Zr after first saturating the alloy. ZrCu and Zr_2Cu are examples. 2. New and unique hydride phases form when the intermetallic is reacted with hydrogen after first saturating the alloy. ZrNi and Zr_2Ni are examples. 3. Solid solution of hydrogen occurs in the intermetallic over an extended composition range. $ZrCr_2$, ZrV_2, and Zr_4Sn are examples. 4. No appreciable reaction with hydrogen is found. $ZrFe_2$ and $ZrCo_2$ are examples.

Zirconium reacts with hydrogen to form δ-$ZrH_{1.4}$ and ϵ-$ZrH_{1.98}$ after saturating the metal. For multiphase alloys, such as the Zr-Nb alloys where no intermetallics form, the hydrogen reactivity depends on the hydrogen stability of each phase. β-Nb absorbs hydrogen only at relatively high hydrogen pressures and after zirconium has taken up large quantities of hydrogen as δ-$ZrH_{1.4}$.

Literature

A complete survey of the literature will not be given. Many papers exist on the effects of alloying, specimen preparation, and heat-treatment on the reaction of zirconium alloys in high-temperature water and steam. Excellent reviews have been given by Wanklyn (4, 5), Coriou (6), and Hillner (7). Douglas (8) has reviewed the physical metallurgy of zirconium alloys.

Preparation of Alloys

High-purity metals were levitated, melted, and cast into a copper mold under purified argon atmosphere to assure homogenous specimens and minimum of contamination. Table I shows the procedures used in the preparation of the alloys while Table II shows the composition of the metals used in preparing the alloys. Many of the alloys were extremely brittle and difficult to cut in 20 mil thick slices. We found it impossible to cast the intermetallic $ZrCr_2$ without cracking of the ingot.

Table III shows a list of the alloys prepared. They can be classified in four major groups: 1, the dilute alloys having compositions at or near the eutectoid composition and containing two phases; 2, the 10 w/o (weight per cent) alloys containing two phases; 3, the intermetallics containing one phase; and 4, the niobium alloys containing two phases, *i.e.*, α-Zr and β-Nb.

Table III shows the annealing treatments used in preparing the alloys. Annealing was done at 10^{-6} to 10^{-7} Torr in Ta and Zr containers. The temperatures were chosen from considerations based on the phase diagrams of the respective systems.

The composition of each ingot was determined by the initial weights of the respective metals. In each case the weight after melting and casting was determined to check for volatilization of the more volatile metals. The final weights of the 10g cast ingots checked within a few milligrams of the weight of the components taken initially. Chemical analysis was made of the alloys and standards set up for x-ray fluorescence analysis. In this way the composition of each sample could be determined before testing. X-ray diffraction patterns were taken of each alloy to check the melting and heat treatment procedures. Light micrographs were taken of each alloy to evaluate the phases present and to compare where possible with photomicrographs in the literature.

Table I. Procedures for preparation of alloys

Crystal bar zirconium	Alloying metal
Sliced under benzene	Sheared or cut into small pieces (air)
Sheared into small pieces (air)	
Cleaned with petroleum ether and alcohol	Cleaned with petroleum ether and alcohol

Compacted under pressure into button for melting

Levitation melted in purified argon atmosphere

Cast into copper mold

Vacuum annealed in Ta or Zr container at 10^{-6}-10^{-7} Torr

Cut into specimens, soft samples with SiC wheel, hard specimens by electric discharge machine

Polish through ¼μ diamond paste

Cleaned using acetone, petroleum ether, and alcohol

Weighed and specimen area measured

Composition checked by x-ray fluorescence analysis

X-ray diffraction and micrographs taken

Reacted

* Electrochemical Society Active Member.

Table II. Material for alloy and specimen preparation

Metal	Metal content, w/o	Major impurities, ppm	Source
Zr (alloy preparation)	>99.8	Fe<100, O<100, Hf-290, Si<25	Numec Corporation
Zr (specimens)	>99.94	Fe-183, O-190, Hf-70, Si-40	Numec Corporation
Cu	>99.999		American Smelting and Refining Company
Fe	99.999		Materials Research Corporation
Cr	>99.99	Fe-200, O-150, N-100, Si-200	Union Carbide Corporation
Sn	>99.999		Vulcan Materials Company
Nb	>99.94		Materials Research Corporation
V	High-purity grade	C-500, O-900, H-100, N-500	Union Carbide Corporation
Zircaloy-2	98.+	Sn-1.45, Fe-0.135, Ni-0.055, Cr-0.100, N-0.038, H-0.002, O=0.14, Hf-0.055, Al-0.0045 *	Westinghouse Electric Corporation
Zircaloy-4	98.+	Sn-142, Fe-0.22, Ni-0.0015, Cr-0.09, N-0.0043, H-0.002, O-0.14, Al-0.0045, Hf-0.0055 *	Westinghouse Electric Corporation

* Weight per cent basis.

Table III. Alloy characterization

Composition, w/o	Phases	Annealing treatment	Composition	Phases	Annealing treatment
Zr-2.2 Fe	α-Zr + $ZrFe_2$	A	Zr-1.3 Ni	α-Zr + Zr_2Ni	A
Zr-54.8 Fe*	$ZrFe_2$	A	Zr-10 Ni	α-Zr + Zr_2Ni	A
Zr-6.4 Nb	α-Zr + β-Nb	B or D	Zr-24.4 Ni*	Zr_2Ni	A
Zr-50 Nb	α-Zr + β-Nb	C	Zr-39 Ni*	ZrNi	A
Zr-5 V	α-Zr + ZrV_2	A or E	Zr-1.6 Cu	α-Zr + Zr_2Cu	A
Zr-10 V	α-Zr + ZrV_2	A	Zr-10 Cu	α-Zr + Zr_2Cu	A
Zr-52.8 V*	ZrV_2	A	Zr-25.8 Cu*	Zr_2Cu	A
Zr	α-Zr	None	Zr-41.0 Cu*	ZrCu	A
Zr-2.5 Sn	α-Zr + Zr_4Sn	F	Zr-1.0 Cr	α-Zr + $ZrCr_2$	A
Zr-23.5 Sn*	Zr_4Sn	G	Zr-10 Cr	α-Zr + $ZrCr_2$	A

* Intermetallics. The exact composition of Zr_4Sn is Zr-24.55 Sn.
A. 900°C-24 hr + 750°C-48 hr + quench
B. 700°C-24 hr + 575°C-96 hr + quench
C. 900°C-24 hr + 575°C-96 hr + quench
D. 1500°C-48 hr + 500°C-120 hr + quench
E. 1300°C-48 hr + 1 day slow cool—750°C-24 hr + quench
F. Cold work 10% + 800°C-72 hr + quench
G. 900°C-72 hr + quench

High-Pressure Autoclave Test Apparatus

A high-pressure autoclave at the Westinghouse Atomic Power Laboratory was used for reacting the zirconium and zirconium alloys in high-purity liquid water at 2708 psi and 360°C. This apparatus had been used previously, and its operation had been checked and qualified.

The autoclave is 12.5 cm inside diameter, 50 cm long, constructed of stainless steel. The volume is 6.6l. The test specimens were supported from a special frame constructed from Ni-Cr alloy sheet using small sections of platinum wire. The frame was placed on a stainless steel tree and then lowered into the autoclave. Before using the autoclave, the tree and supporting specimens were preoxidized. Before each run the autoclave was cleaned with alcohol.

The water was demineralized water having a pH of 6.5-7.5 and a resistance of 1-2.5 x 10^6 ohms cm. The samples and support tree were placed in the autoclave and 3.2l of water were added. The cover was then bolted on to the vessel. The air space was evacuated for 10 min before heating. After heating to 120°-150°C, 100 cc of water was withdrawn as steam to eliminate air from the space over the H_2O. A period of 6 hr was used to heat between 25° and 360°C. Although the initial volume of water was 3.2l this volume expanded to 4.8l at 360°C and 2708 psi.

The test cycle was 28 days after which the heaters were turned off and the system allowed to cool for 8 to 9 hr before opening. Samples were carefully removed and dried. All operations were carried out using platinum tipped tweezers and clean cotton gloves.

Hot Extraction Method for Hydrogen Analyses

The method (9) was designed to use samples of 0.01-0.2g and to determine hydrogen contents of zirconium and zirconium alloys with a sensitivity of 10^{-7} g of H_2 or 1 ppm on an 0.1g sample. The hydrogen was extracted by heating the sample to 1200°C and condensing the gas into a liquid helium cooled trap. The hydrogen was then vaporized and the pressure measured by a sensitive capacitance manometer.

Results

Preliminary oxidation study.—Twenty-two standard size specimens of about 1 cm^2 area and two large control specimens of about 10 cm^2 area of Zircaloy-4 were reacted for 28 days at 2708 psi and 360°C in high-purity water. Table IV shows the alloys, the oxygen weight change calculated from the total weight

Table IV. Preliminary autoclave test results.
28-day, 2708 psi and 360°C ≈ 1 cm^2 specimens

Alloy w/o	Phases	O_2 gain μg	H_2 gain μg	H_2 gain % Theory	Alloy w/o	Phases	O_2 gain μg	H_2 gain μg	H_2 gain % Theory
Zr-5 V	α-Zr + ZrV_2	Disintegrated			Zr-1.6 Cu	α-Zr + Zr_2Cu	2,258	265	94
Zr-10 V	α-Zr + ZrV_2	Disintegrated			Zr-10 Cu	α-Zr + Zr_2Cu	3,331	>230	>55
Zr-52.8 V	ZrV_2	Disintegrated			Zr-25.8 Cu	Zr_2Cu	Disintegrated		
Zr-1.0 Cr	α-Zr + $ZrCr_2$	328	0	0	Zr-41.0 Cu	ZrCu	Disintegrated		
Zr-10 Cr	α-Zr + $ZrCr_2$	11,436	>253	>18	Zr-6.4 Nb	α-Zr + β-Nb	1,562	7.3	3.7
Zr-2.2 Fe	α-Zr + $ZrFe_2$	467	20	35	Zr-50 Nb	α-Zr + β-Nb	1,241	26.7	17.2
Zr-54.8 Fe	$ZrFe_2$	>75% reacted			Zr	α-Zr	139	2.7	15.5
Zr-1.3 Ni	α-Zr + Zr_2Ni	397	52	104	Zr-2.5 Sn	α-Zr + Zr_4Sn	223	1.0	3.6
Zr-10 Ni	α-Zr + Zr_2Ni	6,056	>250	>30	Zr-23.5 Sn	Zr_4Sn	Disintegrated		
Zr-24.4 Ni	Zr_2Ni	Disintegrated			Zirc-2	α-Zr + others	358	2.0	4.5
Zr-39 Ni	ZrNi	Disintegrated			Zirc-4	α-Zr + others	330	2.7	6.5

change and the hydrogen uptake, the increase in hydrogen content of the alloy, and the per cent of theoretical hydrogen taken up by the alloy. The theoretical hydrogen value was calculated from the oxygen weight gain using the weight ratio of H_2/O of 1/8.

Table IV shows that all the tested intermetallic alloys, *i.e.*, Zr_2Ni, ZrNi, Zr_2Cu, ZrCu, $ZrFe_2$, ZrV_2, and Zr_4Sn were reacted to 75% or more. All of the vanadium alloys were disintegrated in the 28-day cycle. The dilute alloys Zr-1.3 Ni, Zr-1.0 Cr, Zr-2.2 Fe, the two Zircaloy alloys, and Zr showed low oxygen weight gains. The hydrogen taken up by the alloys varies greatly from 0 μg for the Zr-1.0 Cr alloy to greater than 250 μg for the Zr-10 Ni and the Zr-10 Cr alloys. This was the approximate upper detection limit for the hydrogen analysis apparatus used in these early tests. The sample sizes used in the later tests were reduced so the complete hydrogen content could be measured.

Multiple cycle oxidation study.—Four 28-day oxidation tests were conducted. The total accumulated oxidation time for some samples was 112 days. On the basis of the preliminary oxidation study all of the intermetallic alloys and the three vanadium alloys were eliminated from the longer period oxidation studies.

Seven samples of each of eight alloys listed in Table V were placed in the high-pressure 360°C autoclave. After 28 days of reaction all samples were weighed. One sample of each of the alloys was removed from the series for hydrogen analysis. The remaining samples were brushed to remove loose corrosion products and reweighed. The weight after brushing was taken as the initial weight for the second 28-day oxidation run. This procedure was repeated for the 3rd and 4th oxidation cycles except duplicate samples were removed for hydrogen analysis on the 3rd cycle.

Tables V and VI show a summary of the experimental data and calculations made on the various alloys for the 28, 56, 84, and 112 day oxidation tests. Table V shows the results on the dilute alloys, and Table VI shows the results on the 6.4 to 50 w/o alloys. Zircaloy-2, Zircaloy-4, and crystal bar zirconium were included with the dilute alloys.

Table V. Autoclave test dilute Zr alloys, 2708 psi — 360°C

Alloy	Time, days	O_2, μg	O_2, $\mu g/cm^2$	H_2, μg	H_2 % theory
	28	279	239	2.6	7.4
	56	402	351	2.4	5.0
Zircaloy-2	84	419	362	3.8	7.3
	84	423	368	2.7	5.1
	112	537	479	14.1	21.0
	28	247	206	3.6	12
	56	202	180	2.3	9
Zircaloy-4	84	259	213	5.2	16
	84	501	414	3.1	5
	112	497	424	3.8	6.1
	28	5473	6,159	89	13.2
Zr-2.5 Sn	56	6931	7,876	132	15.2
	84	9740	11,499	163.3	13.4
	28	441	397	59	107
	56	483	429	68.4	109
Zr-1.3 Ni	84	609	564	74.8	98
	64	675	614	92.5	110
	112	607	557	100.4	132
	28	4033	3,398	367	73
	56	6380	5,968	901	113
Zr-1.6 Cu	84	7824	7,618	984	101
	84	5863	5,306	824	112
	112	5362	5,063	807.7	120
	28	234	226	0.2	0.7
	56	209	281	−0.6	0
Zr-1.0 Cr	84	351	325	0	0
	84	335	327	0	0
	112	538	476	0	0
	28	412	427	19	36
	56	536	550	30	45
Zr-2.2 Fe	84	632	584	40.4	51
	84	652	652	44.5	55
	112	671	709	51.5	61.4
Zr etched	28	6954	7,096	396	46
Zr-5.0 V	28		Disintegrated		

Table VI. Autoclave tests.
Zr + 6.4 — 50 w/o alloying element, 2708 psi — 360°C

Alloy	Time, days	O_2, μg	O_2, $\mu g/cm^2$	H_2, μg	H_2, % theory
	28	7,541	6,207	1453	154
Zr-10 Ni	56	9,564	8,647	3154	263
	84		Disintegrated		
	28	3,660	3,453	628	137
	56	6,977	6,430	1082	124
Zr-10 Cu	84	7,918	7,435	1410	142
	84	10,756	10,176	1661	124
	112	13,718	13,280	2096	122
	28	8,462	8,067	275	26
	56	16,737	16,062	635	30
Zr-10 Cr	84	21,420	21,947	1056	39.4
	84	21,510	20,924	1360	50.6
	112	26,682	24,569	1149	34.4
	28	2,266	2,087	10	3.4
	56	3,570	3,269	18	4
Zr-6.4 Nb	84	4,481	3,971	22	4
	112	4,637	4,476	27.5	4.7
	28	1,633	1,439	27	13
Zr-50 Nb	56	1,463	1,272	35	14
	84	3,285	3,062	30	7.4
	84	2,669	2,530	32	9.5
Zr-10 V	28		Disintegrated		

Tables V and VI show the alloys tested, the oxygen weight gain calculated from the total weight change and the hydrogen uptake, the oxygen weight gain/cm², the increase in hydrogen content resulting from the reaction, and the per cent of theoretical hydrogen produced in the reaction which was taken up by the alloy.

Both Zircaloy-2 and Zircaloy-4 showed low oxygen weight gains and hydrogen pickup with Zircaloy-4 showing the lower values. Of the other tested alloys, only Zr-1.0 Cr showed low oxygen weight gain and low hydrogen absorption.

The oxidation tests on the Zr-2.5 Sn alloy in contrast to the other dilute alloys showed a wide variation in reactivity. Two of the seven samples showed a low reactivity during the first 28-day cycle while the other five samples showed a large amount of reactivity. One of the five samples showing a large amount of reactivity is shown in Table V. The 56-day tests show that all of the Zr-2.5 Sn specimens have large weight gains even though several of the specimens in the first 28-day cycle showed very low total weight gains. One unusual feature of this alloy is the low hydrogen uptake values for the large amount of reactivity.

Zr-5.0 V showed complete reaction for the 28-day test cycle while the Zr-1.6 Cu alloy showed a large amount of reaction and a large hydrogen uptake. In fact, the hydrogen uptake was greater than that expected from the oxygen weight gain. This fact suggests that the Zr-1.6 Cu specimens were gettering hydrogen from the hydrogen produced by the other samples reacting with water.

Zr-1.3 Ni and Zr-2.2 Fe react at a fairly low rate with water. The Zr-2.2 Fe samples have the lower hydrogen uptake values. The Zr-1.3 Ni alloys take up 98-132% of theoretical hydrogen while the Zr-2.2 Fe take up 36-61.4% of theoretical hydrogen. Zr-1.0 Cr alloy has the lowest oxygen weight gain of all of the alloys tested and near zero hydrogen pickup.

High-purity zirconium showed erratic-corrosion behavior in liquid water. Thus, the preliminary screening 28-day test showed a low corrosion rate while seven samples of the same sheet showed complete reaction after 28 days in the first cycle of the multiple cycle tests. All of the specimens had been mechanically polished through 1/4μ diamond paste and cleaned. A second set of seven samples was mechanically polished and reacted in the second cycle of the multiple cycle test. All were completely reacted. Two additional sets of seven samples each were cut from two high-purity crystal bars of zirconium and etched in a solution containing 50 cc of 30% H_2O_2, 30 cc of HNO_3, and 2 cc of HF. Both sets of samples showed a high level of corrosion. A hydrogen analysis was made on the heavily reacted zirconium samples. The unreacted

metal showed a hydrogen content of 46% of theoretical.

Table VI shows the results and calculations for the 6.4-50 w/o zirconium alloys. The Zr-10 Ni, Zr-10 Cu, and Zr-10 Cr showed large oxygen weight gains for the 28, 56, 84, and 112 day oxidation periods. The Zr-10 Ni alloy showed hydrogen uptakes of 154 to 263% of theoretical. The Zr-10 Cu also showed hydrogen uptakes greater than theoretical. Although the Zr-10 Cr alloy showed the highest oxygen weight gains, the hydrogen uptakes were 26-50.6%.

The Zr-6.4 Nb shows oxygen weight gains of 2266-4637 μg. However, the hydrogen uptake values were 3.4-4.7% of theoretical. The Zr-50 Nb alloy showed oxygen weight gains of 1463-3285 μg and hydrogen weight gains of 8.5-14% of theoretical. Considering the extent of reaction the two Zr-Nb alloys show very low hydrogen uptake values.

None of the more concentrated zirconium alloys showed good corrosion behavior in liquid water under the given reaction conditions. The Zr-10 V and Zr-10 Cr alloys showed the highest corrosion rates.

Discussion

Corrosion results.—Our results show that crystal bar zirconium exhibits variable but usually extensive reactivity in liquid water at 360°C and 2708 psi under static conditions. The preliminary 28-day test showed zirconium to have a low corrosion rate while later tests showed poor corrosion resistance. Earlier studies (10, 11) at 375°C using a water vapor plus helium gas mixture in a flow reactor showed zirconium to have a consistently low rate of corrosion. In these experiments the hydrogen formed in the corrosion reaction was removed by gas flow from the reaction interface. In the autoclave tests the hydrogen produced and not absorbed remains in the autoclave atmosphere to be absorbed by other alloys.

Many elements have harmful effects on the corrosion of zirconium as shown by the extended studies (12) which led to the development of Zircaloy-2 and -4. Nitrogen in concentrations above 130 ppm causes rapid corrosion in liquid water at 360°C. Tin was found to reduce the harmful effects of nitrogen (12) although too much tin is harmful. An autoclave test on a Zr-2.5 Sn alloy shown in Table V shows that the Zr-2.5 Sn composition is not a good corrosion resistant alloy. This is in agreement with the conclusions reported by Hillner (7).

Table V shows the excellent corrosion resistance and zero hydrogen pickup of the Zr-1.0 Cr alloy. The Zr-1.3 Ni alloy showed low oxygen weight gains and a hydrogen pickup greater than theory. We conclude that this alloy was gettering hydrogen from the autoclave atmosphere. The Zr-1.6 Cu alloy reacted at a rapid rate with water and had hydrogen pickups greater than theoretical. The Zr-1.0 Cr alloy was less reactive than the two Zircaloy alloys, both in oxygen weight gain and in hydrogen pickup.

The concentrated zirconium alloys Zr-5 V, Zr-10 V, and Zr-10 Ni alloys disintegrated after 28 to 56 days in the autoclave tests. Both the Zr-10 Cr alloy and the Zr-10 Cu alloy reacted rapidly in the autoclave over the 112-day test with the Zr-10 Cu alloy absorbing more hydrogen than theoretical. The most interesting concentrated alloys are the Zr-6.4 Nb and the Zr-50 Nb alloys where β-Nb is present as a second phase in the α-Zr matrix. Both alloys reacted with liquid water at moderate rates of corrosion. Only small amounts of hydrogen were absorbed. Hydrogen absorption experiments on a Zr-25 Nb alloy (3) showed that β-Nb does not absorb appreciable hydrogen until high hydrogen pressures were reached.

The single phased zirconium alloys ZrV_2, $ZrFe_2$, Zr_2Ni, ZrNi, Zr_4Sn, Zr_2Cu, and ZrCu all showed high corrosion rates in liquid water compared to the dilute zirconium alloys containing the intermetallics as second phases. Zr_2Cu and ZrCu were studied earlier by us using a water vapor reactor at 375°C (10). Both alloys reacted rapidly when compared to the dilute alloys.

Differences do exist between the reactivities of the several intermetallics in liquid water corrosion. These differences were not shown in the 28-day liquid water experiments since the alloys were completely reacted. Comparison of the rates of corrosion of the dilute alloys, the 10 w/o alloys, and the intermetallics show that the rates of corrosion were a function of the amount of intermetallic in the alloy.

The following points will be considered in discussion of the mechanisms of corrosion of zirconium alloys in liquid water at 360°C and 2708 psi: 1, the crystal structure and thermodynamic stability of the intermetallic phase; 2, the type and extent of the hydrogen reaction and the stability of hydrogen in the several phases; 3, the distribution of hydrogen between the several metal phases and the hydride phase; 4, the size and distribution of the particles of the several phases in the zirconium matrix; and 5, the nature of the oxide film over the several phases and the transport of oxygen, hydrogen and metal ions through the oxide film.

Crystal structure and thermodynamic stability of the intermetallic compounds.—Table VII shows a summary of the structure types, lattice parameters, ratios of ionic radii of zirconium to the alloying element, electronic structures of the outer shell electrons, elec-

Table VII. Summary of data and calculations on crystal structure, electronic structure, and thermochemical stability of intermetallic compounds of zirconium

Compound AB	Structural data intermetallic compounds: Structure type‡	Lattice parameter, Å	r_A/r_B[17]	Electron structure: Electrons outer shell	Electron/atom ratio	Thermochemical data: L_B* kcal/g at.	L_A/L_B	$-\Delta H_f$ kcal/mole
$ZrCo_2$	C_{15},$MgCu_2$ Cubic	6.954	1.28	$3d^74s^2$	7.3	101.5 ± 4	1.40	16.2
$ZrFe_2$	C_{15},$MgCu_2$ Cubic	7.04	1.25	$3d^64s^2$	6.7	99.5 ± 0.4	1.49	12.5
$ZrCr_2$	C_{14},$MgZn_2$ Hexagonal	5.107 8.272	1.24	$3d^54s^1$	5.3	94.8 ± 0.5	1.49	7.5†
ZrV_2	C_{15},$MgCu_2$ Cubic	7.44	1.19	$3d^34s^1$	4.7	123.0 ± 4	1.16	4.6
$ZrMo_2$	C_{15},$MgCu_2$ Cubic	7.596	1.15	$4d^54s^1$	5.3	158.2 ± 0.8	1.00	2.2
ZrW_2	C_{15},$MgCu_2$ Cubic	7.615	1.17	$5d^46s^2$	5.3	203.4 ± 1.5	0.70	−0.7
Zr_2Ni	C_{16},$CuAl_2$ b.c. tetragonal	6.477 5.241	1.29	$3d^84s^2$	6.0	98.5 ± 4	1.44	11.8
Zr_2Cu	C_{11}, $MoSi_2$ b.c. tetragonal	3.22 11.183	1.16	$3d^{10}4s^1$	3.3	81.0 ± 0.5	1.76	(2.7)
Zr_4Sn	f.c. tetragonal	7.645 12.461	1.02	$3d^84s^2$	4.0	72.0	2.02	—

* L_A, L_B Latent heats of sublimation L_A(Zr) = 145.4 ± 0.4 kcal/g atom (14, 15, and 16).
† Calculation based on high-temperature form, i.e., $C_{15}MgCu_2$ with a_o = 7.20Å.
‡ C_{14} and C_{15} are Laves phases.

tron to atom ratios, latent heats of sublimation of the alloying elements, ratios of the latent heats of sublimation to that for zirconium, and estimates of the heats of formation of the intermetallic compounds. The heats of formation were calculated for us by Kubaschewski (18) and checked by us (3) using an independent analysis of the data. The values given are our calculated values.

The basic hypothesis of the method (19) is that the stability of a metallic multicomponent phase is due to a decrease in heat content from an increase in coordination on formation from the component metals. The coordination numbers are not those used by crystallographers since mutual attraction occurs also between atoms some distance beyond the first shell of nearest neighbors. The heats of formation are estimated from the change in coordination of the alloy when compared to the metals and from the heats of sublimation of the component metals alone. The electronic contribution is neglected.

Table VII shows that $ZrCo_2$, $ZrFe_2$, $ZrCr_2$, and ZrV_2 intermetallics have varying number of electrons in the 3d shell, crystallize in the C_{14} and C_{15} structure of varying lattice parameter, have varying electron to atom ratios and widely varying heats of formation. Zr_2Ni and Zr_2Cu do not crystallize in the C_{14} and C_{15} structures. Zr_4Sn could not be calculated since the structure has not been determined.

All of the intermetallics which crystallize in the C_{14} and C_{15} structures do not react appreciably with hydrogen or they react to take up hydrogen in solid solution. The intermetallics which crystallize in less stable structures react with hydrogen to form hydrides after saturating the metal. Zr_2Cu and Zr_2Ni are examples of these structures. We conclude that the type of hydrogen reaction and the stability of hydrogen in solid solution is a function of the crystal structure, lattice parameter, and the heat of formation of the intermetallic compound.

Correlation of corrosion reaction with thermochemistry of the hydrogen reactions of zirconium and its intermetallics.—Table VIII shows a summary of the important thermochemical data on zirconium and its intermetallics (1-3). The partial molal free energies of formation of hydrogen in the solid solution phase ($\bar{G}_H^\circ - 1/2\ G_{H_2}$), Sievert's law constant, k_H, the terminal solubility, n_H/n_{Zr}, and the hydrogen pressure, p_{H_2}, are tabulated. Positive values of ($\bar{G}_H^\circ - 1/2\ G_{H_2}$) and small values of k_H indicate weak bonding for hydrogen in the metal or alloy. This occurs for hydrogen in the intermetallics $ZrCr_2$ and $ZrFe_2$. Negative values of ($\bar{G}_H^\circ - 1/2\ G_{H_2}$) and large values of k_H indicate strong bonding for hydrogen. Column 6 of Table VIII shows the equilibrium hydrogen concentration in the several intermetallics at 360°C and at the hydrogen concentration where zirconium precipitates $\delta - ZrH_{1.4}$. Column 9 shows values of the partial molal free energy of formation, ($\bar{G}_H^\circ - 1/2\ G_{H_2}$), for the first hydride phase at 360°C when hydrides are formed.

The values of k_H in Table VIII show that Zr_2Cu takes up about 1/2 as much hydrogen in solid solution as does α-Zr at the same hydrogen pressure. In contrast Zr_2Ni takes up 2½ times as much. The calculated value for the hydrogen concentration of α-Zr at the terminal solubility at 360°C is 143 ppm. $ZrCr_2$ and $ZrFe_2$ for the same conditions take up less than 0.5 ppm of hydrogen. Zr_4Sn for these conditions would take up about 8 times as much hydrogen as α-Zr.

Zirconium forms the most stable hydride of the three hydride formers Zr, Zr_2Cu, and Zr_2Ni. With Zr_2Cu or Zr_2Ni as second phases in α-Zr hydrogen reacts with the alloy to first saturate the α-Zr and the intermetallics. Above a hydrogen concentration of $X_H = 0.013$ for α-Zr at 360°C δ-$ZrH_{1.4}$ forms with an equilibrium hydrogen pressure of 2.3×10^{-5} Torr. Zr_2Cu will not form δ-$ZrH_{1.4}$ until a hydrogen pressure of 6.3×10^{-4} Torr is reached while Zr_2Ni requires a hydrogen pressure of 1.59×10^{-4} Torr. Local kinetic conditions involving the permeability of the oxide film over the several phases could lead to hydriding of the intermetallic phases rather than α-Zr.

The corrosion data of Tables V and VI suggests that the intermetallic compounds are a critical factor in the corrosion process. This could occur if the oxide film over the α-Zr matrix were resistant to the penetration of hydrogen. The fact that the Zr-1.0 Cr alloy does not absorb hydrogen suggests that both α-Zr and the intermetallic are resistant to hydrogen. Since larger quantities of second phase makes a poor alloy, *e.g.*, Zr-10 Cr, we propose that stresses exist in the alloy at the phase boundaries between intermetallic and α-Zr where more rapid reaction can occur.

We would predict that Zr-1.0 Fe and Zr-1.0 Co also may have good corrosion properties. The Zr-2.2 Fe alloy tested here is too concentrated to compare its corrosion behavior with that for the Zr-1.0 Cr alloy.

On the basis of Table VIII we would predict that copper and nickel are not good alloying elements since hydrogen is not only taken up in solid solution but both alloys contain hydride forming intermetallics.

Table VIII shows us that tin and vanadium form intermetallics which are strong hydrogen absorbers in solid solution. Lattice parameter changes occur on adsorption of the large amounts of hydrogen with the development of additional stresses between the zirconium and the intermetallic lattices. However, permanent changes in the intermetallic lattice through the formation of hydrides does not occur as was the case for the copper and nickel intermetallics. We would predict that both Sn and V should have fair corrosion resistance at the 1 w/o level. The good corrosion resistant properties of Zircaloy-2 and -4 support this interpretation.

Experimental corrosion data are not extensive enough to make exact correlations between the thermochemical data on the hydrogen reaction and the corrosion reactivity. The critical importance of the amount of second phase on the corrosion properties was not recognized in choosing our alloy compositions. In addition close control must be given to the size and distribution of the second phase particles in the various alloys. There is the difficult problem of characterizing the large number of alloys which need to be studied.

Table VIII. Hydriding calculations zirconium and zirconium alloys at 360°C solid solution region

$$k_H = 10^{\frac{-(\bar{G}_H^\circ - \frac{1}{2} G_{H_2})}{4.575\ T}},\quad X_H = k_H P_{H_2}^{1/2},\quad X_H = n_H/n_{Zr}$$

	Solid solution region					1st plateau
Alloy	$(\bar{G}_H^\circ - \frac{1}{2} G_{H_2})$ 360°C kcal/g at. of H	Sievert's law constant, k_H	Terminal solubility 360°C, n_H/n_{Zr}	P_{H_2} (Torr) 1st plateau 360°C	$p = 2.34 \times 10^{-5}$ (Torr) Zr(H) ⇄ δ-$ZrH_{1.4}$	$(\bar{G}_H^\circ - \frac{1}{2} G_{H_2}^\circ)$ 360°C kcal/g at. of H_2
Zr	−5.66	73.5	0.013	2.34×10^{-5}	term. soly. 0.013	−12.139
Zr_2Cu	−4.73	36.3	0.033	6.3×10^{-4}	6.4×10^{-3}	−8.53
Zr_2Ni	−6.86	182	0.083	1.59×10^{-4}	3.2×10^{-2}	−9.94
$ZrCr_2$	+1.88	0.22	none	—	3.9×10^{-5}	—
ZrV_2	−7.61	324	none	—	5.7×10^{-2}	—
Zr_4Sn	−8.47	617	none	—	1.1×10^{-1}	—
$ZrFe_2$	>2.6	<0.1	—	—	$<1.7 \times 10^{-5}$	—

We can conclude that the thermochemical behavior of hydrogen in α-Zr and in the intermetallic phase is of major importance in the alloys corrosion reactivity. Other factors such as the transport of oxygen, hydrogen, and metal ions through the oxide films over the α-Zr and the intermetallics and the stresses developed between the intermetallics and α-Zr and between the oxide and metal phases also are of major importance.

Manuscript received Jan. 27, 1969. This work was supported in part by the United States Atomic Energy Commission under Contract AT(30-1)-3203.

Any discussion of this paper will appear in a Discussion Section to be published in the December 1969 JOURNAL.

REFERENCES

1. A. Pebler and E. A. Gulbransen, *Electrochem. Technol.*, **4**, 211 (1966).
2. A. Pebler and E. A. Gulbransen, *Trans. AIME*, **239**, 1593 (1967).
3. E. A. Gulbransen, K. F. Andrew, S. A. Jansson, and A. R. Pebler, Westinghouse Electric Research Laboratories, WERL-3203-10, Final Report AEC Contract No. AT(30-1)-3203, June 1, 1963-June 1, 1967.
4. J. N. Wanklyn and P. J. Jones, *J. Nucl. Mat.*, **6**, 291 (1962).
5. J. N. Wanklyn, *Electrochem. Technol.*, **4**, 81 (1966).
6. H. Coriou, *Corrosion et Anticorrosion*, **14**, 351 (1966).
7. E. Hillner, Westinghouse Bettis Atomic Power Laboratory Report WAPD-TM-411, November 1964.
8. D. L. Douglass, *Atomic Energy Rev.*, **1**, 71 (1963).
9. E. A. Gulbransen and K. F. Andrew, *Electrochem. Technol.*, **5**, 471 (1967).
10. E. A. Gulbransen and K. F. Andrew, *ibid.*, **4**, 99 (1966).
11. E. A. Gulbransen and K. F. Andrew, *Corrosion*, **23**, 231 (1967).
12. S. Kass, The Development of the Zircaloys, ASTM Special Technical Publication No. 368 (1964), 41-57.
13. JANAF Thermochemical Tables, Dow Chemical Co., Midland, Mich.
14. H. L. Schick, "Thermodynamics of Certain Refractory Compounds," Academic Press, New York (1966).
15. O. Kubaschewski and E. D. Evans, "Metallurgical Thermochemistry," John Wiley & Sons, Inc., New York (1956).
16. M. E. Kirkpatrick, D. M. Bailey, and F. T. Smith, *Acta Cryst.*, **15**, 252 (1962).
17. W. B. Pearson, "Lattice Spacings and Structure of Metals and Alloys," Pergamon Press, New York (1958).
18. O. Kubaschewski, Private letter, June 13, 1966.
19. O. Kubaschewski, in "The Physical Chemistry of Metallic Solutions and Intermetallic Compounds," p. 346, Chemical Publishing Co., Inc., New York (1960).

The Structure of Thin Oxide Films Formed on Nickel Crystals

J. V. Cathcart,* G. F. Petersen, and C. J. Sparks, Jr.

Metals and Ceramics Division, Oak Ridge National Laboratory, Oak Ridge, Tennessee

ABSTRACT

A study was made of the structural details of thin oxide films formed on the (100), (111), (110), and (311) of nickel. Oxidation temperatures ranged from 400° to 600°C, and the oxide films produced were between 25 and 500Å thick. An x-ray technique was utilized to measure the average strain in the films, the mosaic spread, the thickness, and the epitaxial relationships between oxide and metal. The oxide films on all crystal planes studied were observed to contain large numbers of short circuit diffusion paths. A change in the extent of these diffusion paths in the oxide on a given crystal plane produced a corresponding change in the oxidation rate. Furthermore, there was a variation in the extent and efficiency of the short circuit diffusion paths as a function of crystallographic orientation of the substrate, and this variation correlated directly with the marked oxidation rate anisotropy exhibited by nickel.

Our previous studies (1-6) of the thin-film stage of the oxidation of copper led us to the conclusion that thin Cu_2O films, with thicknesses ranging up to a few hundred angstroms, are subject to large epitaxial forces which give rise to the development in the films of extensive arrays of paths of easy diffusion. We found several correlations between the extent and efficiency of these paths of easy diffusion and the oxidation rates exhibited by the copper specimens. In fact, there was a correspondence between the oxidation rate anisotropy of copper and the anisotropy of the extent of paths of easy diffusion in the oxide films. Other investigators, *e.g.*, Lawless and Gwathmey (7), Smeltzer and coworkers (8), Ali and Wood (9), and Gibbs (10), have also called attention to the potential significance of such structural defects in oxide films.

This paper describes a study of the thin-film stage of oxidation of bulk nickel. Some significant differences were found between the oxidation of nickel and copper especially with regard to the magnitude and nature of the strains which develop in the oxide films. However, there were broad areas of similarity between the two systems. For example, high concentrations of paths of easy diffusion also exist in the NiO films, and we observed that for those crystal planes where the extent of paths of easy diffusion in the oxide was large, the rate of oxidation was high, and vice versa.

* Electrochemical Society Active Member.

Experimental Procedures

Specimen preparation.—All our work was done on single crystals of nickel. Single crystal disks with (100), (111), (110), or (311) surfaces were cut from cylindrical rods with a spark cutter. After mechanical polishing, the specimens were either chemically or electrolytically polished. Just prior to oxidation the specimens were annealed in hydrogen at the oxidation temperature for 10-15 min. The oxidation chamber was then pumped down to a pressure of about 10μ with a mechanical pump, and oxygen was admitted to the system at a pressure slightly less than 1 atm. Oxidation temperatures investigated ranged from 400° to 600°C with most of our work being done at 500°C. The time of oxidation was varied from a few minutes to several hours in order to produce film thickness of 25 to 500Å.

A comment is in order concerning this experimental procedure. Our main concern in this investigation was to establish procedures which yielded reproducible results, and the oxidation methods outlined do that fairly

well. Obviously, however, we have been studying crystals with "dirty" surfaces. Hydrogen was a major impurity in our system, and we know from our own experience as well as that of Gwathmey's group (11) several years ago that the presence of hydrogen can influence the oxidation characteristics of nickel. Surface impurities from the polishing solutions may also have had an effect on our results. Throughout the work we have felt that the important thing was to try to explain the marked oxidation rate anisotropy exhibited by nickel under a given, if arbitrary, set of conditions.

Measuring techniques.—In attempting to characterize these oxide films, we used many of the same methods we employed in our study of copper. X-ray diffraction techniques (12, 13) represented our major research tool in determining the structure of the films. We also used electron microscopy and electron diffraction in investigating other properties of the films.

The x-ray method is a very sensitive one; *e.g.*, we could study a 20Å film with little difficulty. Its success depended on the oxide film being sufficiently well oriented so that, when the specimen was set at the appropriate Bragg angle, virtually all the oxide was in position to diffract.

The x-ray results yielded a variety of information about the films. The 2θ scans allowed us to measure the average d-spacing (and, hence, the average strain) in a direction normal to the surface of the film. The relative line broadening of a pair of first and second order Bragg peaks yielded an estimate of the film thickness and the magnitude of any microstrains in the film. Rocking curves gave a measure of the mosaic spread of the films, and the determination of the area under these curves produced an independent estimate of the average film thickness. Of course, x-ray measurements also permit one to investigate the details of the epitaxial relationships between the oxide and the metal.

Results

Oxidation rate anisotropy.—We used single crystal spheres of nickel to obtain a qualitative measure of the oxidation rate anisotropy. The major crystallographic planes in the order of decreasing oxidation rates were (110), (100), (111), and (311). For a specimen oxidized 30 min at 500°C, the oxide film thickness varied from about 50 to 500Å between the (311) and (110). The film thickness on the (100) was about half that of the (110). For reasons discussed below, the oxidation characteristics of the (111) were quite sensitive to the effects of surface contaminants. Under "standard" conditions the oxidation rate of the (111) was roughly twice that of the (311), but in some experiments the rate increased to a value only slightly less than that for the (100). Thus we characterize the (110) as a high rate plane, the (100) and (111) as intermediate rate planes, while the (311) is a slow-rate orientation.

X-ray Results

Average strain in films.—Figure 1 shows the difference between the average d-spacing observed for the NiO films and that of bulk NiO plotted as a function of thickness for the four major planes of nickel investigated. Previously published data (6) for the oxide on the (110) and (111) of copper is also included for comparison. In every case the thin NiO films exhibited a d-spacing equal to that of the bulk oxide with the exception of very thin films on the (311). There the d-spacing values were slightly smaller than bulk. These results were surprising since the lattice parameter of NiO is about 18% larger than that of Ni (see Table I for the epitaxial relationships). One would expect that the forces arising from this misfit would tend to compress the films in the plane of the metal surface and produce a corresponding expansion normal to the surface (*i.e.*, in the direction in which the d-spacings were measured). As may be seen, the Cu_2O films were, in general, expanded in just this fashion relative to their bulk properties.

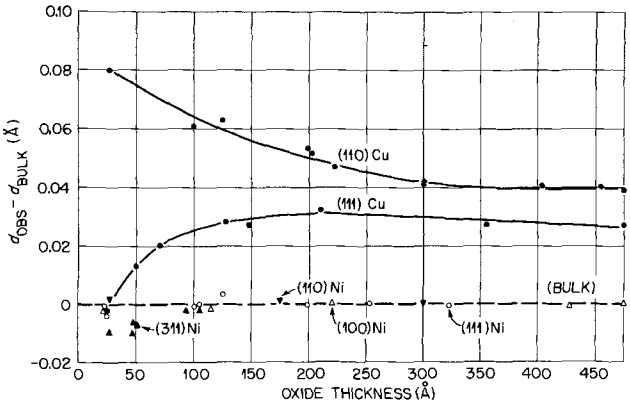

Fig. 1. Deviation of the observed, average d-spacing from bulk values plotted as a function of thickness for oxide on several crystallographic planes of Cu and Ni. In all cases the d-spacing was measured normal to the surface of the oxide film.

Line shape analysis.—Despite the fact that the average lattice parameter of the NiO films was essentially equal to that of bulk material, an analysis of the line shapes of the Bragg maxima for the films indicated that substantial strains existed in the films. X-ray line broadening can result from two general effects: small particle size and the presence of strain gradients (17). Small particle size (in our case, film thickness) causes the widths of first and second order peaks, expressed in terms of sin θ, to broaden equally. Strain effects, on the other hand, produce a greater broadening of the second order than the first order peak. We did, in fact, observe an excessive broadening of second order peaks, a result which we interpret as indicating that strain effects of some sort are important in the NiO films.

These data were analyzed in terms of the model developed by Borie (2, 12) for Cu_2O films in which it is assumed that the strain varies approximately linearly across the oxide film. On the basis of this model, a 2% variation of d_{111} from one interface to the other was indicated for a NiO film formed on the (111) of Ni. The results are shown in Fig. 2 along with comparable data for the oxide on the (110) of copper. Note that the strain gradient in the two films is of the same order of magnitude; however, the fact that the average d-spacing for the NiO films was that of the bulk oxide forced us to conclude that part of the film was in compression and part in tension.

We rationalized the strain gradient in the oxide on the (110) of copper in terms of the development of an array of growth dislocations which permitted a

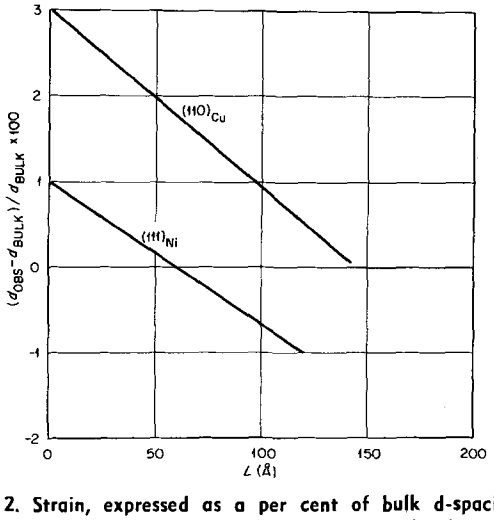

Fig. 2. Strain, expressed as a per cent of bulk d-spacing, vs. position within the oxide for films formed on the (111) of Ni and the (110) of Cu. The d-spacings were measured normal to the film surface, and "L" is the position parameter within the oxide film.

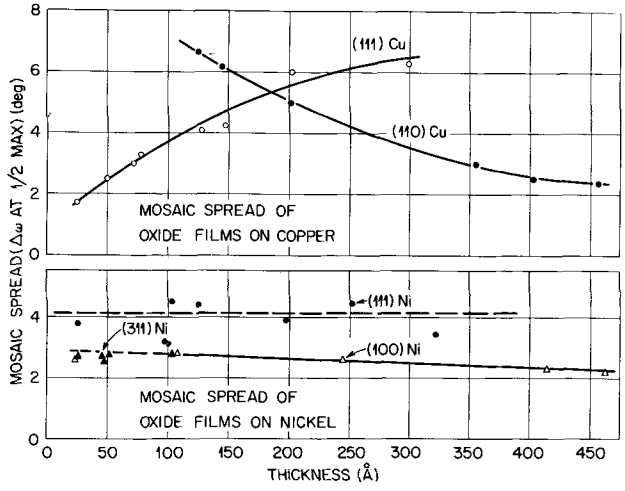

Fig. 3. Mosaic spread vs. film thickness for oxide films formed on several crystallographic planes of Cu and Ni.

relaxation of the epitaxial strains as the film grew (2). In this model, however, the lattice parameter of the Cu_2O, measured normal to the film surface, was never less than that of bulk Cu_2O (see Fig. 2). A situation comparable to that observed for NiO occurred in the Cu_2O films only when they were stripped from the copper surface. The strain gradient in the stripped film was essentially the same as before stripping, but the average strain dropped to zero, reflecting the removal of the epitaxial constraint imposed by the copper surface. Thus, if the dislocation model developed for Cu_2O films is to be applicable to the NiO films, one must assume that a mechanism exists by which the epitaxially induced strain in the oxide at the oxide-metal interface can relax either during film growth or during cooling after oxidation. Conceivably this relaxation could be triggered by the small change in lattice parameter which accompanies the phase transformation NiO undergoes at about 250°C (18, 19). For the present, however, it is not clear what the precise explanation is for the substantial strain effects which exist in the NiO films.

Mosaic spread.—Figure 3 shows the mosaic spread of a series of NiO and Cu_2O films plotted as a function of film thickness. We defined mosaic spread in terms of the width at half-maximum intensity of the rocking curves for the films. Except for the (110) films, which were essentially polycrystalline, the NiO films were better oriented than corresponding Cu_2O films. Note that, in contrast to the Cu_2O, the mosaic spread of the NiO films was approximately constant with thickness.

Epitaxy.—The last of the x-ray results has to do with the epitaxial relationships between the oxide and metal. Except for the formation of polycrystalline oxide on the (110), we found that NiO-Ni exhibited the same epitaxial relationships as Cu_2O-Cu. These data are summarized in Table I, and, with the exception of the results for the (110), are in agreement with the data of Lawless *et al.* (11).

Table I. NiO-Ni epitaxial relationships

Planes $(hkl)_{Ni}$ // $(hkl)_{NiO}$		Directions $[hkl]_{Ni}$ // $[hkl]_{NiO}$	
(100)	(111)	[011]	[0$\bar{1}$1]
		[011]	[01$\bar{1}$]
		[0$\bar{1}$1]	[0$\bar{1}$1]
		[0$\bar{1}$1]	[01$\bar{1}$]
(111)	(111)	[01$\bar{1}$]	[0$\bar{1}$1]
		[0$\bar{1}$1]	[01$\bar{1}$]
(311)	(110)	[011]	[$\bar{1}$10]
(110)	Polycrystalline oxide		

Note that these epitaxial relationships serve as a basis for dividing the NiO films into three general categories. At one extreme is the oxide on the (311). These films are pseudosingle crystals, and while they have a mosaic structure, the mosaic boundaries are all low-angle boundaries (see Fig. 3). On the other hand, the oxide on the (110) is essentially polycrystalline and contains, therefore, a high concentration of high angle boundaries.

The oxide films on the (111) and (100) fall into a third category. These films consist of arrays of small crystallites which may be present in two or more orientations, orientations which bear a twin relationship to one another. The first oxide orientation indicated for the (111) (see Table I) is one in which the oxide and metal lattices are essentially parallel to one another (parallel orientation); the second orientation may be derived by a 180° rotation of the oxide lattice about its surface normal to produce the so-called antiparallel orientation.

Two sets of these twin-related orientations[1] exist in the oxide on the (100). The first pair of orientations shown in Table I form one set, the latter pair the other.

Discussion

Films on the (100) and (111)

Incoherent twin boundaries.—An assessment of the nature of the boundaries between oxide crystallites in the films on the (100) and (111) is essential to an estimate of their importance as paths of easy diffusion. It is not known (*i*) whether actual twinning occurs within a given oxide crystallite as the film grows or (*ii*) whether each oxide crystallite extends untwinned completely through the thickness of the film, maintaining either the parallel or antiparallel orientation throughout its growth. As discussed at greater length in ref. (5), there is some evidence in the case of Cu_2O films that the latter condition prevails; however, as our diffraction data show, if true twinning does occur within the oxide crystallites, the twinning plane is always the (111), *i.e.*, the plane parallel to the film surface. Thus any coherent twin boundaries that develop in the oxide are parallel to the film surface. On the other hand, the boundaries which have a component perpendicular to the film surface and which separate oxide nuclei of different orientations must be incoherent twin boundaries.

Therefore, in either of the two cases just described, regions of incoherent twin boundaries will exist within the films. Such boundaries constitute paths of easy diffusion which are almost as efficient as high angle boundaries (20, 21). Thus if incoherent twin boundaries are present in the oxide film in sufficiently large numbers, they could play a very important role in mass transport processes across the oxide.

The factors which determine the total area of incoherent twin boundaries in the oxide are (*i*) the size of the oxide crystallites, (*ii*) the distribution relative to one another, of oxide crystallites having differing orientations, and (*iii*) the relative amounts of oxide in each possible orientation.

Crystallite size and distribution.—Dark field electron microscopy of stripped NiO films showed the films to have a mosaic structure, the diameter of the mosaic blocks (or oxide crystallites) varying from about 200 to 500Å. This value did not appear to vary with substrate orientation or with film thickness in the range of thicknesses considered in this study. Furthermore, as nearly as we could tell on the basis of electron diffraction experiments, the distribution across the specimen surface of oxide crystallites having a given orientation was essentially random. We concluded, therefore, that films containing sizable quantities of the various possible oxide orientations should be rich in incoherent twin boundaries; *i.e.*, rich in efficient paths of easy diffusion.

[1] For the sake of brevity we shall hereafter refer to the multiple, twin-related orientations described above simply as "twins' or "twin orientations."

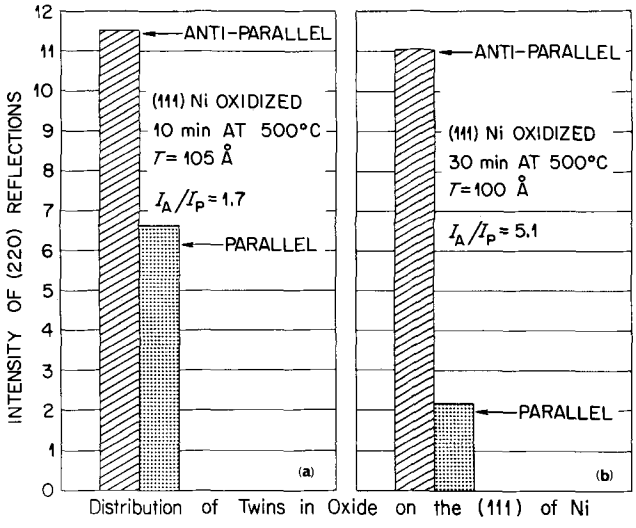

Fig. 4. Bar graphs showing the relative quantities of oxide present in the parallel and antiparallel orientations in oxide films grown on the (111) of Ni. Figure 4a shows results typical of those obtained for chemically polished specimens, while the data in Fig. 4b are characteristic of electropolished specimens.

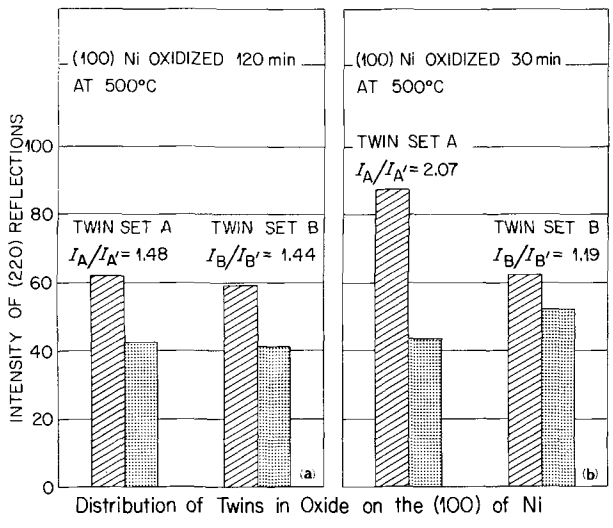

Fig. 5. Bar graphs showing the relative quantities of oxide in the four possible orientations present on the (100) of Ni. The results in Fig. 5a are typical; the results in Fig. 5b are atypical and probably reflect a subtle variation in the degree of the initial surface contamination of the specimen.

Relative quantities of different oxide orientations.— Since, as outlined above, the "twinning plane" in the oxide was parallel to the metal surface, we could not detect the presence of twins in the oxide by x-ray techniques as long as the specimen was kept in the normal diffraction geometry. However, by tilting the specimen so as to bring the (220) planes into diffracting position, we could measure the relative amounts of the twins present in a given oxide film. The mosaic spread for these (220) peaks was the same for all peaks, thus making the peak height proportional to the amount of oxide in a given twin orientation. The results for the (111) are summarized in Fig. 4. The intensity of the (220) reflection is shown for each twin orientation in bar graph form. In all cases investigated we found the antiparallel orientation to predominate in the (111) oxide, but the relative amount of each twin was dependent on the surface treatment given the specimen. The results shown in Fig. 4a are typical of chemically polished specimens, and the ratio of I_a/I_p was 1.7, where I_a and I_p are the (220) peak intensities for the antiparallel and parallel twin orientations, respectively. An electropolished crystal was used to obtain the data shown in Fig. 4b, and I_a/I_p was about 5.

Note the difference in the oxidation rates for the two specimens. The crystal for which I_a/I_p was larger (Fig. 4b) required an oxidation period three times longer than the other in order to attain the same oxide thickness. Obviously, the specimen with the more nearly equal quantities of the parallel and antiparallel orientations of oxide and, thus, with the oxide film containing the greatest extent of incoherent twin boundaries, exhibited the higher rate of oxidation.

The twin distribution in two different (100) films is shown in Fig. 5. The (220) intensity is plotted for each of the four orientations (*i.e.*, for each of the two sets of twins) occurring in the film. Generally the twin ratio was the same for both sets of twins, the results in Fig. 5a with ratios of about 60/40 being typical. Occasionally, however, we found a variation in the twin ratio between the two sets of twins as shown in Fig. 5b where the ratio for the A set was about 2/1 while that for the B set was almost 1/1. This rather atypical result probably reflects a slight difference in the degree of the initial surface contamination of the specimen.

These results for the (100) and (111) may be summarized as follows:

1. The size of the crystallites of which the oxide films are composed ranges from 200 to 500Å and is constant.

2. Crystallites having any one of the orientations observed are distributed essentially randomly through the film.

3. The relative quantities of the oxide crystallites having different orientations vary according to the precise conditions of oxidation. The maximum extent of paths of easy diffusion in the oxide, *i.e.*, of incoherent twin boundaries, is realized when the quantities of oxide of various possible orientations are equal. As this condition was approached in the oxide on the (111), the rate of oxidation was observed to increase.

Analysis of the Oxidation Rate Anisotropy of Nickel

These general observations make clear the important structural aspects of NiO films. In many ways the properties of NiO films are similar to those of comparable Cu_2O films, and it is possible on the basis of these results to propose an explanation for the oxidation rate anisotropy of nickel which is consistent with that already suggested for copper (1, 6). The pattern which emerges is as follows:

1. The oxide films, while generally well oriented, consist of large numbers of small mosaic blocks, 200 to 500Å in diameter in the case of NiO. Assuming a grain boundary width of approximately 10Å, this means that 5 to 10% of the transverse area of the films is associated with mosaic boundaries.

2. Depending, of course, on the exact nature of these boundaries, one expects that the diffusion coefficient, D_{gb}, in such regions will be different from the volume diffusion coefficient, D_v. For the case of the diffusion of Ni along high angle boundaries in NiO, Smeltzer and Perrow (8) have estimated that D_{gb} exceeds D_v by a factor of 10^2-10^4. Such a large value for D_{gb}/D_v is consistent with measured values of this ratio for materials such as silver (14), NaCl (15), and Al_2O_3 (16). Therefore, we feel justified in assuming that at 500°C, D_{gb} for NiO is at least a few orders of magnitude greater than D_v. If that be the case, given the large fraction of oxide area associated with the grain boundaries in the NiO films, one can easily imagine situations where short circuit diffusion in the NiO might swamp out volume diffusion.

3. The numbers cited above apply for high angle boundaries, and obviously not all the mosaic boundaries in the NiO films are high angle boundaries. Our x-ray data indicate that the character of these boundaries varies with crystal plane. Very low angle boundaries exist in the oxide on the (311), and for these films we would expect $D_{gb} \approx D_v$. The resulting oxidation rate of the (311) should be relatively small, as indeed, we observe.

The oxide on the (110) is at the other extreme, the mosaic boundaries being for the most part high angle boundaries. For these films $D_{gb} >> D_v$, and we expect and observe a relatively large rate of oxidation.

The oxide on the (111) and (100) is characterized by the presence of incoherent twin boundaries which in metals, at least, have interfacial energies 50-80% as high as high angle boundaries (21). For these films, therefore, we would predict that $D_{gb} > D_v$, and that, as a consequence, the oxidation rates for these two faces would be significantly greater than that for the (311) but less than that for the (110).

The differences in rate between the (111) and (100) can be rationalized in terms of the fact that the ratio of the amounts of each twin orientation in the (100) oxide tends to approach unity more closely than is the case for the (111) oxide. For that reason one would expect the extent of incoherent twin boundaries to be greater in the (100) oxide. There is also the added factor on the (100) that there are two sets of twin-related orientations rotated at 90° to each other, thus producing two kinds of "incoherent twin" boundaries in the (100) oxide.

We have already reported a similar correlation between the oxidation rate and the extent of short circuit diffusion paths in the oxide on the major planes of copper (1, 6). Only the (110), which is a "slow-rate" plane on copper, deviates from the order of oxidation rates reported for nickel. The reason for this difference lies in the fact that the oxide formed on the (110) of copper, in contrast to that of nickel, is well oriented with but a single orientation. Paths of easy diffusion through it are confined largely to low angle boundaries; hence one expects its oxidation rate to be small.

We conclude, therefore, that for nickel as for copper, paths of easy diffusion in the oxide play an important role in determining the rate of oxidation. Furthermore, a strong correlation exists between the oxidation rate anisotropy exhibited by nickel and copper and the anisotropy of the extent of paths of easy diffusion in the oxide films.

Acknowledgment

This research was sponsored by the U.S. Atomic Energy Commission under contract with the Union Carbide Corporation.

Manuscript submitted Nov. 6, 1968; revised manuscript received Jan. 8, 1969.

Any discussion of this paper will appear in a Discussion Section to be published in the December 1969 JOURNAL.

REFERENCES

1. J. V. Cathcart, G. F. Petersen, and C. J. Sparks, Jr., *Memoires Scientific Ref. Metallurg.*, **62**, 11 (1965).
2. B. S. Borie, C. J. Sparks, Jr., and J. V. Cathcart, *Acta Met.*, **10**, 691 (1962).
3. J. V. Cathcart, J. E. Epperson, and G. F. Petersen, *ibid.*, **10**, 699 (1962).
4. J. V. Cathcart and G. F. Petersen, *Proc., Symposium on Ellipsometry in the Measurement of Surfaces and Thin Films*, p. 201, Natl. Bur. Standards Misc. Pub. No. 256, U.S. Gov. Printing Office, Washington, D.C., 1964.
5. J. V. Cathcart and G. F. Petersen, *This Journal*, **115**, 595 (1968).
6. J. V. Cathcart, G. F. Petersen, and C. J. Sparks, Jr., *Proc., Sagamore Conference on Physical and Chemical Characteristics of Surfaces and Interfaces*, 1967, Univ. of Syracuse Press, Syracuse, New York.
7. K. R. Lawless and A. T. Gwathmey, *Acta Met.*, **4**, 153 (1956); A. T. Gwathmey and K. R. Lawless, "The Surface Chemistry of Metals and Semiconductors," p. 483, John Wiley and Sons, New York (1960).
8. W. W. Smeltzer, R. R. Haering, and J. S. Kirkaldy, *Acta Met.*, **9**, 880 (1961); J. M. Perrow, W. W. Smeltzer, and R. K. Ham, *ibid.*, **15**, 577 (1967); J. M. Perrow, W. W. Smeltzer, and J. D. Embury, *ibid.*, **16**, 1209 (1968).
9. S. I. Ali and G. C. Wood, *Corrosion Sci.*, **8**, 413 (1968).
10. G. B. Gibbs, *ibid.*, **7**, 165 (1967).
11. K. R. Lawless, F. W. Young, Jr., and A. T. Gwathmey, *J. Chim. Physique*, **53**, 667 (1956).
12. B. S. Borie, *Acta Cryst.*, **13**, 542 (1960).
13. B. S. Borie and C. J. Sparks, Jr., *ibid.*, **14**, 569 (1961).
14. D. Turnbull and R. E. Hoffman, *Acta Met.*, **2**, 419 (1954).
15. L. W. Barr, I. M. Hoodless, J. A. Morrison, and R. Rudham, *Trans. Faraday Soc.*, **56**, 697 (1960).
16. Y. Oishi and W. D. Kingery, *J. Chem. Phys.*, **33**, 480 (1960).
17. B. E. Warren and B. L. Averbach, *J. Appl. Phys.*, **21**, 595 (1950).
18. H. P. Rooksby, *Acta Cryst.*, **1**, 226 (1948).
19. K. Kohn and S. Iida, *J. Phys. Soc. of Japan*, **19**, 344 (1964).
20. D. Whitwham and P. Lacombe, *Fourth Metallurgy Colloquium*, France (1960), p. 161.
21. R. L. Fullman, *J. Appl. Phys.*, **22**, 456 (1951).

Technical Notes

Effect of Kilovolt Electrons on the Etch Rate of Al_2O_3 and Ta_2O_5

B. H. Hill

Advanced Electronic Devices Branch, Air Force Avionics Laboratory, Wright-Patterson Air Force Base, Ohio

It has been established recently that the chemical etch rate of thermally grown SiO_2 is enhanced (~3 times) when the sample is bombarded with energetic electrons. This process is called the bombarded enhanced etch rate (BEER) effect and is a function of electron dose. In fact, this new and highly promising technique has been used to fabricate planar silicon transistors without the use of conventional photoresist by opening holes in the SiO_2 diffusion mask for subsequent diffusion and contacting. Process resolution is very high, and windows as small as 0.6 x 5μ have been obtained (1).

In order to determine whether the BEER effect would open discretionary windows in other dielectric materials, electron irradiation studies were conducted on films of Al_2O_3 and Ta_2O_5. The Westinghouse Model 504 Scanning Electron Microscope (SEM) was selected as the source of kilovolt electrons (15 kv). Precise electron-bombarded patterns could be generated since the SEM allowed direct observation of the oxide surface during the irradiation. The characteristic area of the patterns was on the order of 1 mil^2 since exposure time for larger areas would take too long, *e.g.*, $\sim 10^8$ sec for a 1 cm^2 total exposure area using typical SEM operating conditions of a 0.1μ-diam beam at 10^{-8} amp beam current. First, the primary beam current was measured (2); then, this value and the predetermined area to be irradiated were used to calculate the exposure time required to produce the desired electron bombardment dose

$$Q = tI_p/A$$

where Q is electron dose in coulombs/cm^2, t is exposure time in sec, I_p is primary beam current, and A is area in cm^2.

The 0.6-cm^2 specimen was mounted on a TO-5 header at the same height as and adjacent to the Faraday cup using silver print as an adhesive (3). In order to prevent charging of the oxide deposited on the glass microscope slides, the same silver print was used to form a conductive path from the oxide to the specimen holder. All irradiations were conducted in an oil-pumped system at 5 x 10^{-6} Torr with the sample surrounded by a cold finger at liquid nitrogen temperature. This cold finger protected the specimen surface from pump-oil vapor which otherwise would be polymerized by the electron beam.

Films of evaporated Al_2O_3 and anodic Al_2O_3 and Ta_2O_5 were used because of their ease of fabrication and interest to this Laboratory. Table I summarizes the types of films studied, the substrates, and the methods used to produce the films (4). The BEER effect experiment in SiO_2 was repeated in order to develop a standardized experimental technique and to determine the effectiveness of the cold finger. If oil were being polymerized under the beam, then a retardation effect would be obtained on the SiO_2; however, this was not the case.

The unbombarded etch rates and oxide thickness were obtained by masking a portion of the specimen surface with paraffin, etching the specimen for a specified time, and then measuring the step with a Zeiss interference microscope. Films of Al_2O_3 formed by both evaporation and anodization were etched in phosphoric acid (85%) at 70°C. The evaporated films etched at the rate of 500 Å/min and the anodic ones at approximately 1200 Å/min. The etchant for Ta_2O_5 was a solution of 200 cc of hydrofluoric acid (48%), 80g ammonium fluoride, and 20 cc deionized water (5). The etch rate at room temperature was 300 Å/min.

Table I. Sample preparation

Film	Substrate	Method of formation	Etch result
SiO_2	Si wafer	Thermal oxidation	Enhancement
Al_2O_3	Si wafer	Evaporative deposition of sapphire	Retardation
Al_2O_3	Microscope slide	Evaporative deposition of sapphire	Retardation
Anodic Al_2O_3	Microscope slide	Evaporative deposition of Al and anodization	Retardation
Anodic Ta_2O_5	Microscope slide	Triode sputtering of Ta and anodization	Retardation

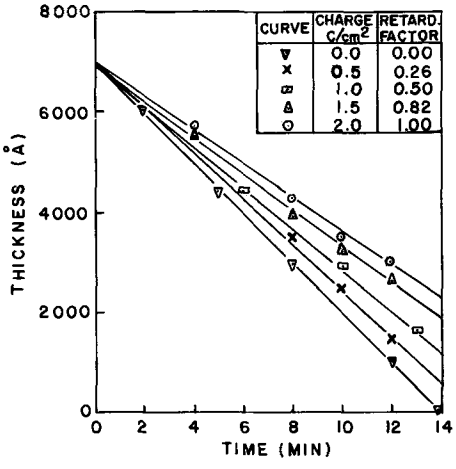

Fig. 1. Etch curves for evaporated Al_2O_3

In a series of irradiations made on samples of evaporated Al_2O_3, the accumulated electron doses ranged from 0.5 to 10 coulombs/cm^2. After a series of etch cycles, a very distinct line of hillocks remained where the surface had been irradiated. Each hillock corresponded to an area which had been irradiated. Exposure to the electron beam had retarded the etch rate, which is an opposite effect to that observed in SiO_2. Figure 1 shows the etching behavior of a 7000Å-thick evaporated Al_2O_3 layer after bombardment by 15 kv electrons, with electron dose as a parameter. The inset summarizes the results with the retardation factor normalized at the value where saturation occurs (2 coulombs/cm^2), *i.e.*, continued bombardment above 2 coulombs/cm^2 produces no further decrease in the etch rate. Any effect of dose below 0.5 coulombs/cm^2 could not be measured with the Zeiss interference microscope and was, therefore, considered negligible.

Films of Al and Ta were electrolytically anodized to form Al_2O_3 and Ta_2O_5, but samples with oxide thickness greater than ~2500Å could not be fabricated due to equipment limitations. The thinness of the samples and the fact that the measurements were hampered further by somewhat uneven etching of the surface resulted in qualitative data only. However, observation of the interference color changes of the bombarded and unbombarded regions after each etch cycle showed that the colors of the bombarded region followed one or two etch cycles behind the unbombarded region. From this observation, and the fact that the oxide on the unbombarded portion of the substrate etched away first leaving a hillock where the oxide had been irradiated, it could be concluded that the etch rate of both anodic films had been definitely retarded after bombardment.

Manuscript submitted Oct. 8, 1968; revised manuscript received Jan. 27, 1969.

Any discussion of this paper will appear in a Discussion Section to be published in the December 1969 JOURNAL.

REFERENCES

1. T. W. O'Keeffe and R. M. Handy, *Solid State Electronics*, **11**, 261 (1968).
2. B. H. Hill, *Rev. Sci, Instr.*, **39**, 1369 (1968).
3. Silver Print, No. 21-1, G C Electronics, Rockford, Ill.
4. J. A. Howard, "Effect on Etch Rate of Oxide Surfaces after Electron Bombardment," Unpublished Thesis, Air Force Institute of Technology, Wright-Patterson Air Force Base Ohio (March 1968).
5. J. Pringle, Private communication.

Determination of Mobility and Its Profile in n/n$^+$ Silicon Epitaxial Layers

Dinesh C. Gupta*[1]

Sylvania Electric Products, Inc., Woburn, Massachusetts

Current needs of achieving good quality epitaxial silicon for applications in integrated circuits and microwave devices make it desirable to know the mobility in epitaxial layers. Hall measurements can be made on layers deposited on substrates of opposite conductivity type such as p on n or n on p (1) or on layers deposited on insulating substrates such as silicon films grown epitaxially on sapphire (2). However, most applications require high resistivity layers on low resistivity substrates of the same conductivity type in which case Hall measurements cannot be made.

There is an increasing interest in depositing thin silicon layers at low temperatures (3, 4) because of the need of achieving controlled doping impurity gradients. At very low temperatures, however, the crystallinity of the layers deteriorates, enhancing the surface (5) and defect scattering (6) and, thus, reducing the carrier mobility. Recently, the MOS capacitance method has been used to measure epitaxial layer resistivity (7) and the effective mobility (8). The mobility of the carriers calculated by this method is usually less than the bulk mobility because it depends on the physical structure of the silicon-insulator interface, which introduces another scattering process.

The spreading resistance probe method (9) has been used to measure the electrical resistivity and the resistivity profile in n/n$^+$ and p/p$^+$ epitaxial layers and the diode voltage-capacitance method (10) has been used to determine the impurity density profile in these layers. These two methods are independent of each other and can be used to determine the carrier mobility in the layer.

Method and Results

In a semiconductor, the conductivity is approximately given by

$$\sigma = q\mu \mid N_D - N_A \mid \qquad [1]$$

if the impurities are fully ionized.

For an uncompensated n-type semiconductor

$$\mu_n \approx \sigma/qN_D \qquad [2]$$

Equation [2] enables one to calculate the majority carrier mobility if independent measurements of the electrical conductivity, σ, and the majority carrier impurity density, N_D, are available. Kennedy *et al.* (11) have pointed out recently that the diode voltage-capacitance method establishes the distribution of majority carriers rather than the impurity atoms. Thus, this technique together with the spreading resistance probe method can be used to determine a value for the majority carrier mobility in an epitaxial layer.

Table I gives the comparison of mobility data calculated by the above measurements and from Hall measurements on n-type bulk silicon. Hall measurements were made by the Van der Pauw method (12). The same specimens were measured by the spreading resistance probe. Diffused junctions were then formed and the impurity densities were calculated from diode voltage-capacitance measurements. The calculated mobility is dependent on the impurity density because of impurity scattering (13) and correlates well with the values calculated from the Brooks-Herring equation at 300°K (14).

Figure 1 shows the mobilities determined in n-type epitaxial layers of about 5 μm in thickness deposited on n$^+$ As-doped (111)-oriented substrates of resistivity about 0.002 ohm-cm by different processes such as hydrogen reduction of $SiCl_4$, SiH_4 pyrolysis and two temperature deposition cycle using SiH_4 in hydrogen. The results are plotted on the curve calculated from the Brooks-Herring equation. Each data point in Fig. 1 is the average of measurements on five layers deposited by the process shown. The spread in the values of mobility was found to be 8-12% and the spread in the values of impurity density was 3-5%.

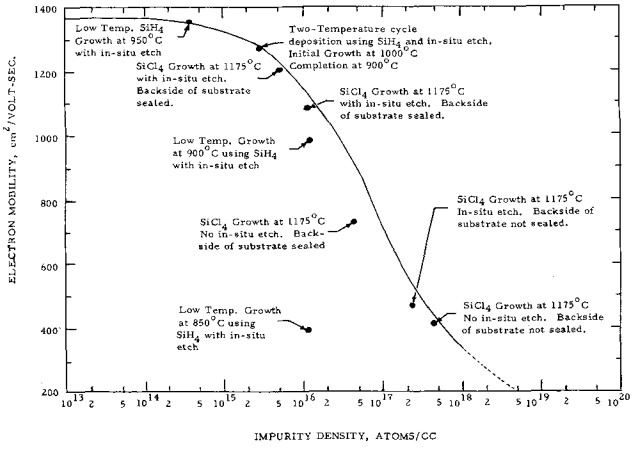

Fig. 1. Electron mobilities in various n/n$^+$ silicon epitaxial layers. Solid line is calculated from Brooks-Herring equation at 300°K for constant activation energy of 0.039 ev and uncompensated n-type silicon.

Figure 2 gives the mobility profile of two epitaxial layers, one deposited by the hydrogen reduction of silicon tetrachloride and the other deposited by the pyrolysis of silane on (111)-oriented substrates of resistivity about 0.002 ohm-cm. Each specimen was scribed into two pieces; one was successively etched in a modified CP_4 etch (60 ml 48% HF, 400 ml acetic acid and 100 ml HNO_3)[2] and measured by the spreading resistance probe; diffused diodes were made on the other half and the diode voltage-capacitance measurements were taken. From the resistivity and impurity density profiles, the carrier mobility was calculated.

Discussion

Results plotted in Fig. 1 show that the same carrier mobilities can be obtained as those reported in bulk semiconductors. However, these values depend on the deposition process used. This may be because the

[2] For small layer thicknesses, a modified pyrocatechol etch (170 ml or 98% ethylenediamine, 30g pyrocatechol and 80 ml water) can be used (15). The temperature of the bath should be kept constant at 100°C during etching.

Table I. Comparison of mobility by Hall and spreading resistance measurements on n-type bulk silicon

Impurity density, atoms/cc	Hall mobility, cm²/v-sec	Mobility calculated from spreading resistance probe measurements, cm²/v-sec
1.55×10^{15}	926	890
5.04×10^{15}	920	1020
5.80×10^{15}	920	905
3.25×10^{16}	540	577
3.50×10^{16}	860	870
5.30×10^{18}	390	372

* Electrochemical Society Active Member.

[1] Present address: General Telephone and Electronics Laboratories, Inc., 100 Sylvan Road, Woburn, Massachusetts 01801.

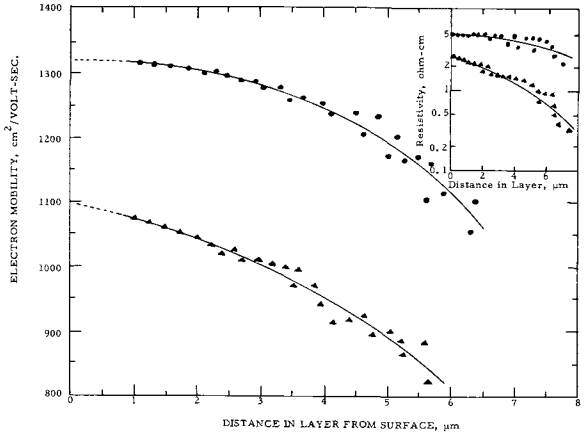

Fig. 2. Mobility profiles in n/n$^+$ silicon; •—SiH_4 deposition at 950°C with *in-situ* etch, ▲—$SiCl_4$ deposition at 1175°C with *in situ* etch. Thickness of these epitaxial layers is about 8 μm. The graph in the upper right corner is a direct resistivity profile from spreading resistance probe measurements.

layers deposited by some processes have greater amounts of surface or defect scattering or both. Layers processed with *in situ* HCl vapor etch yield a higher mobility than those processed without *in situ* etch which may suggest that stacking faults or stair-rod dislocations also give rise to scattering. The mobility in layers deposited at low temperatures with a two-temperature cycle seem to be approaching those obtained in bulk semiconductors. Layers whose surfaces are visibly free of misoriented growth and in which dislocation density readings are fairly low (<1000/cm^2) also have mobility approaching the maximum attained at a given impurity density. A detailed analysis on the dependence of the mobility on defects is not possible at this time.

The data in Fig. 2 show some scattering, probably because of the accuracy limitation in spreading resistance probe measurements. Because the layers were successively etched, the etched surfaces might have caused the variation in the total contact resistance measurements.

Conclusion

Measurements of mobility in n-type silicon epitaxial layers deposited on n$^+$ substrates show that it is possible to obtain values in layers comparable to those in bulk semiconductors. However, the values depend on the deposition process used. A two-temperature cycle yields higher mobilities. *In situ* etch also helps in obtaining higher mobility in layers. The accuracy of the technique is dependent on the accuracy of the spreading resistance probe and diode voltage-capacitance measurements. The technique could also be used on p/p$^+$ silicon epitaxial layers as well as on gallium arsenide epitaxial layers.

Acknowledgments

The author wishes to express his thanks to J. Chan and P. Keating for taking Hall measurements and C-V data, to P. Parekh for diodes fabrication, to V. Lyn for taking dislocation readings, and to P. Wang for helpful suggestions.

Manuscript submitted Dec. 10, 1968; revised manuscript received *ca.* Feb. 3, 1969.

Any discussion of this paper will appear in a Discussion Section to be published in the December 1969 JOURNAL.

REFERENCES

1. W. J. Patrick, *Solid-State Electronics*, **9**, 203 (1966).
2. D. J. Dumin and D. H. Robinson, *J. Appl. Phys.*, **39**, 2759 (1968).
3. D. C. Gupta and Roy Yee, Paper Presented at the Boston Meeting of the Society, May 5-9, 1968, as Paper 75.
4. D. C. Gupta and Pei Wang, *Solid State Technol.*, **11**, 48 (Oct. 1968).
5. J. R. Schrieffer, *Phys. Rev.*, **97**, 641 (1955).
6. R. A. Logan, G. L. Pearson, and D. A. Kleinman, *Bull. Am. Phys. Soc.*, **3**, 261 (1958).
7. D. C. Gupta and N. G. Anantha, *Proc. IEEE*, **55**, 1108 (1967).
8. R. F. Pierret and C. T. Sah, *Solid-State Electronics*, **11**, 279 (1968).
9. R. G. Mazur and D. H. Dickey, *This Journal*, **113**, 255 (1966).
10. D. C. Gupta, *Solid State Technol.*, **11**, 31 (Feb. 1968).
11. D. P. Kennedy, P. C. Murley, and W. Kleinfelder, *IBM J. Res. Develop.*, **12**, 399 (1968).
12. L. S. Van der Pauw, *Philips Research Repts.*, **13**, 1 (1958).
13. E. M. Conwell and V. F. Weisskopf, *Phys. Rev.*, **77**, 388 (1950).
14. W. R. Runyan, "Silicon Semiconductor Technology," p. 166, McGraw-Hill Book Co., New York (1965).
15. P. Wang, Private communication.

Brief Communications

Comments on the Paper "Optical Properties by Far Infrared Ellipsometry"

B. Rao and R. A. Griffin

Department of Chemistry, University of Toronto, Toronto, Ontario, Canada

An infrared ellipsometric method to measure the thickness of thin epitaxial layers of silicon and germanium has been described recently by Jones and Hilton (1, 2). Optical constants derived using their method were compared with those calculated from the Lyden expression (3) for free carrier and lattice absorption in semiconductors. The differences were ascribed as due to surface (ellipsometric technique) rather than bulk (electrical method) optical properties. An alternative explanation which considers the fundamental aspects of the ellipsometric method in the far infrared is proposed.

Ellipsometry (4) relates changes in the phase Δ and amplitude ψ components of monochromatic polarized radiation after reflection at a surface, as a function of wavelength λ of the radiation, optical constants of surface and environment, and the angle of incidence θ. The optical constants so determined depend very much

Table I. Penetration depth for various materials for radiation in different regions of the spectrum

Material	Electrical conductivity, sec^{-1}	Penetration depth in A units for radiation at 1μ	10μ	100μ
Copper	5.14×10^{17}	20	62	193
Pure silicon	9.0×10^{16}	46	145	460
n-type silicon (0.016 ohm cm)	5.62×10^{13}	1800	5800	18,000
Germanium	1.96×10^{10}	100,000	311,000	1,000,000

on the surface preparation (5). This phenomenon has been elucidated by Mott and Jones (6), in attempting to explain the widely different optical constants obtained by different workers for ostensibly the same specimen, as due to the limited penetration of the radiation into the material medium. The extent to which the optical constants are a characteristic of the bulk specimen depends, therefore, primarily on the penetration depth of the radiation into the material medium.

The penetration depth d is defined according to the equation

$$d = \frac{1}{4\pi}\sqrt{\frac{c\lambda_0}{\mu\sigma}}$$

where c is the velocity of light, λ_0 the wavelength in vacuum, μ the magnetic permeability, and σ the electrical conductivity (7). Some typical values of d for $\mu = 1$ are shown in Table I. Considering 0.016 ohm cm n-type silicon, the optical constants measured in the far infrared by the ellipsometric method will be essentially independent of the surface properties, as the penetration depth is of the order of 10,000Å in this region. The differences in optical constants observed by electrical methods (1) (A, B, and C) in comparison with the ellipsometric method (2) (D and E), as shown in Table II, must therefore be due to other factors.

The independence of optical constants with the angle of incidence is assumed in the ellipsometric method. The generality of this statement has been doubted by several workers (4, 7). In Table II, the refractive index and adsorption coefficient of n-type silicon determined by ellipsometric method (1, 2) at two different angles of incidence are compared with those derived from the electrical methods. A wide range of values of the absorption coefficient is found in both electrical and ellipsometric observations of the same silicon surface. The different values of optical constants observed at two angles of incidence may be due to systematic errors in the technique of ellipsometric measurement used in the far infrared.

Table II. Optical constants of n-type silicon obtained by different methods

Method		Angle of incidence	Refractive index, n	Absorption coefficient, k
Electrical (1)	A		2.18	2.44
	B		2.48	2.18
	C		2.21	1.49
Ellipsometry (2)	D	50°	2.59	1.38
	E	70°	2.34	2.64

The Lyden expression (3) is based on a theoretical model of single carrier conduction with attendant assumptions regarding the total dispersion attributable to a lattice contribution and the infrared reflectivity minimum. In mobility measurements, n and k are observed at a frequency different from that employed in the ellipsometric method. Thus, coincidence in optical constants for both methods should not be expected. Other workers and ourselves find that the intensity ratio method (8-10) (which involves the measurement of relative intensities for different azimuthal positions of the analyzer, the polarizer being held at a fixed azimuth) without a quarter wave plate is superior to the technique of visible ellipsometry at these wavelengths.

Acknowledgment

The authors wish to thank Dr. M. J. Dignam for helpful discussions.

Manuscript submitted Dec. 3, 1968; revised manuscript received Jan. 29, 1969.

Any discussion of this paper will appear in a Discussion Section to be published in the December 1969 JOURNAL.

REFERENCES

1. C. E. Jones and A. R. Hilton, *This Journal*, **115**, 106 (1968).
2. A. R. Hilton and C. E. Jones, *ibid.*, **113**, 472 (1966).
3. H. A. Lyden, *Phys. Rev.*, **134**, A1106 (1964).
4. E. Passaglia, R. R. Stromberg, and J. Kruger, Editors, "Ellipsometry in the Measurement of Surfaces and Thin Films," Symposium Proceedings. Washington, D.C. (1964).
5. N. Thomson, *Phil. Mag.*, **18**, 140 (1934).
6. N. F. Mott and H. Jones, "Theory of Properties of Metals and Alloys," p. 116 Dover, N.Y. (1958).
7. A. Vasicek, *Czech. J. Phys.*, **1**, 190 (1952).
8. J. R. Beattie and C. K. T. Conn, *Phil. Mag.*, **46**, 222 (1955).
9. S. Roberts, *Phys. Rev.*, **114**, 104 (1959).
10. S. Roberts, *ibid.*, **118**, 1509 (1960).

Identification of the (0001) and the (000$\bar{1}$) Surfaces of Silicon Carbide

J. M. Harris,* H. C. Gatos,* and A. F. Witt*

Department of Metallurgy and Materials Science, Massachusetts Institute of Technology, Cambridge, Massachusetts

An alkaline solution of $K_3Fe(CN)_6$ has been employed at its boiling temperature (somewhat above 100°C) for differentiating reliably and reproducibly between the (0001) or silicon and the (000$\bar{1}$) or carbon surfaces of α-silicon carbide. Bubbling oxygen or air through the solution during etching enhances the differentiating action of the etchant and decreases the etching time from approximately 20 min down to a few minutes.

In a typical etching test the silicon carbide platelet, polished with 3μ diamond powder, is placed in approximately 50 cc of the etchant which consists of equal volumes of aqueous solutions of $K_3Fe(CN)_6$ and NaOH, both saturated at 22°C. The etchant is then brought to a boil in an open beaker of 200 cc capacity. Isolated etch figures begin to appear on the silicon surface in about 20 min (Fig. 1). They increase in number and intensity with time.

Approximately 15 min of etching without gas bubbling and 10 min with gas (O_2 or air) bubbling could

* Electrochemical Society Active Member.

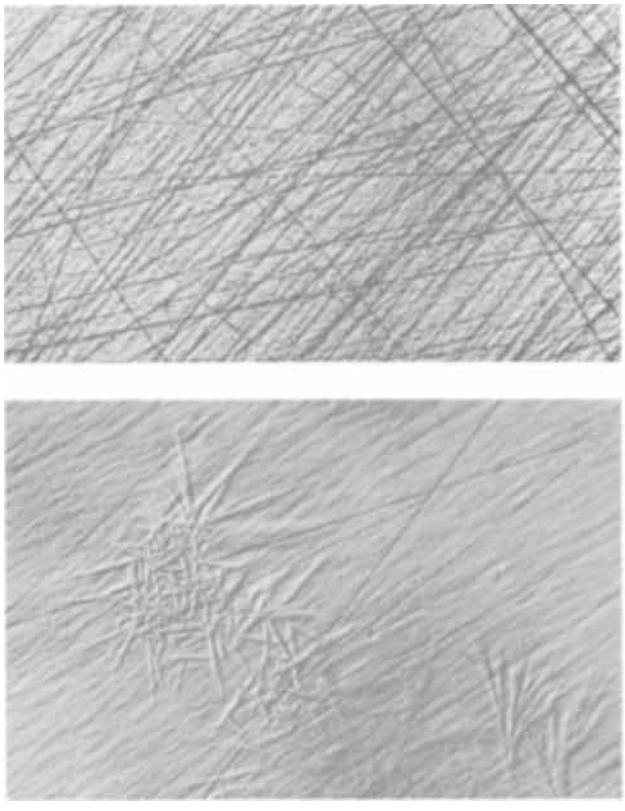

Fig. 1. Carbon surface, $(000\bar{1})$, (upper) and silicon surface, (0001), (lower) after etching for 22 min in the alkaline $K_3Fe(CN)_6$ solution. Both sides were polished with 3μ diamond past prior to etching; the scratch lines on the carbon surface are accentuated during etching but no etch figures develop. Magnification 90X.

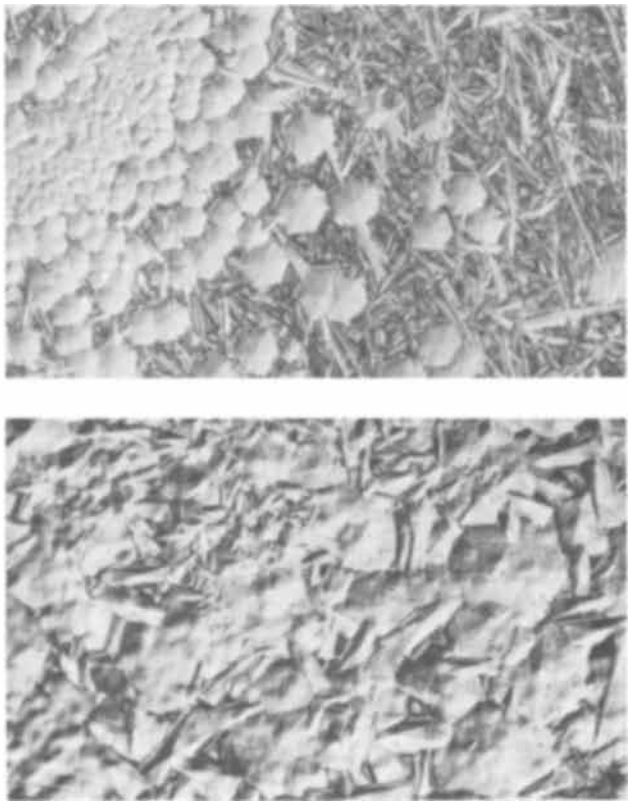

Fig. 2. Silicon surface of SiC exhibiting fully developed etch patterns (upper part). The lower part depicts a typically over-etched condition. Magnification 90X.

be sufficient for the identification of the two surfaces. The silicon surface develops a brownish tint (before any etch figures develop) whereas the carbon surface is not detectably attacked. [Twinned regions of (0001) orientation on the carbon $(000\bar{1})$ surface have typical (0001) appearance.] After about 25 min of boiling (in the open beaker) the solution becomes quite viscous and the silicon surface shows general attack. Representative cases of etched silicon carbide surfaces are shown in Fig. 1 and 2. It is seen that the final etch pattern is dependent on the etching time and concentration of the solution. The particular method of preparation of the surfaces prior to etching (polishing with a diamond abrasive, etching in molten KOH, or high-temperature etching in hydrogen) has no detectable effect on the etching process.

Since in the above described etching process (without gas treatment) the concentration of the etching solution constantly increases with time (boiling in an open beaker) a number of experiments were carried out to examine the effect of concentration. The concentration of the solution was maintained constant by employing a reflux system. Under these conditions it was found that in the solution saturated at room temperature (boiling point 104°C) no etching action is detectable within 35 min. In solutions saturated at 48°C (boiling point 113°C) and at 70°C (boiling point 115°C) etching action became detectable in about 25 and 5 min, respectively. No change in the general features of the etch patterns was observed in the various concentrations. Among a large number of oxidizing agents tested, $K_3Fe(CN)_6$ gave by far the best results in differentiating between the two types of surfaces. The only others which in boiling alkaline solutions exhibited some preferential attack of the silicon surfaces were $KMnO_4$ and $K_3Co(CN)_6$. While evidence of attack could be observed, no clear etch figures developed under these conditions.

It is apparent from the present results that the silicon and carbon surfaces of α-SiC retain to a large extent the characteristics of the surfaces of the corresponding elements silicon and carbon. Indeed, elemental silicon samples exhibited similar etching patterns in the above solutions whereas graphite was not attacked. The detailed mechanism of this process should be of special relevance to the over-all behavior of the surfaces of compounds with a crystallographic polarity.

Solutions of $K_3Fe(CN)_6$ have been used for some time as a cleaning solution for silicon carbide (1) but not for identifying the (0001) and the $(000\bar{1})$ surfaces. The methods usually employed for such identification involve etching at temperatures in excess of 300°C or electrolytic action (2). The present etching process has the distinct advantage of employing aqueous solutions (rather than molten salts) and relatively low temperatures (approximately 110°C) at which ordinary Pyrex glass containers are suitable.

Acknowledgment

The authors wish to acknowledge the Advance Research Projects Agency under contract SD-90 for sponsoring this research. One of them (J.M.H.) wishes to acknowledge IBM for an IBM Resident Study Fellowship.

Manuscript submitted Dec. 20, 1968; revised manuscript received *ca.* Jan. 20, 1969.

Any discussion of this paper will appear in a Discussion Section to be published in the December 1969 JOURNAL.

REFERENCES

1. A. Addamiano, Private communication.
2. J. W. Faust, in "Silicon Carbide," J. R. O'Connor and J. Smiltens, Editors, p. 403, Pergamon Press, New York (1960); R. W. Brander and A. C. Boughey, *Brit. J. Appl. Phys.*, **18**, 905 (1967); C. B. Camport, E. A. Trickett, and G. A. Wolff, Paper presented at the Boston Meeting, May 5-9, 1968, as Paper 67; K. Brack, *J. Appl. Phys.*, **36**, 3560 (1965).

A New Etchant for Thin Films of Tantalum and Tantalum Compounds

J. Grossman* and D. S. Herman

Westinghouse Electric Corporation, Aerospace Division, Solid State Technology Laboratory, Baltimore, Maryland

The etchants for thin films of tantalum and tantalum compounds, *i.e.*, tantalum nitride and tantalum pentoxide, usually contain hydrofluoric acid as one of the constituents. If the thin film of tantalum (or a tantalum compound) is deposited on a substrate which contains silica, *i.e.*, glass, glazed ceramic, or SiO_2 coated silicon, the etchant will also attack the substrate once it has penetrated through the film. This difficulty either requires great care in etching the film or the use of other methods such as depositing an underlayer of Ta_2O_5 or aluminum (1-3). The Ta_2O_5 does not etch as rapidly as TaN or Ta in HF and therefore acts as a protection for the substrate surface. Aluminum acts as a rejection mask, *i.e.*, it can be etched with an aluminum etch which will remove the tantalum overlayer from portions of the substrate where it is unwanted. These methods require additional processing steps with inherent reliability problems.

The use of TaN and Ta_2O_5 in hybrid and monolithic applications as resistor and capacitor elements where the substrate contains silica has presented us with the usual etching difficulty. This problem was extensively examined, and a new etchant found which attacks thin films of tantalum (or one of the tantalum compounds) at a rate equal to, if not faster, than the etches containing HF. It also attacks silica but at a much slower rate than the etches containing HF.

Because the new etchant is highly reactive, it also attacks negative photoresists. Therefore, gold is used as a mask to etch the tantalum (or tantalum compound) thin films. The desired pattern is delineated, using standard photoengraving techniques, in a gold film deposited over the tantalum (or tantalum compound) thin film. After the photoresist is removed the etchant is used to remove the tantalum (or tantalum compound) thin film from portions of the surface where it is not wanted. The gold can then be removed from the entire surface using any of the gold etches. However, the gold can also be selectively removed from the surface using photoengraving techniques. The gold left on the surface makes an ideal contact to resistors or an excellent capacitor electrode. Thus, the deposited gold can perform two functions.

The etchant is made up of a very highly concentrated solution of 30% sodium (or potassium) hydroxide and 30-35% hydrogen peroxide. The proportion is about 9 or 10 to 1 of NaOH to H_2O_2. A small Pyrex beaker (~50 ml) is filled half full of the NaOH solution. The solution is heated to 90°C and the H_2O_2 is added. The substrate is then etched in the mixture. Fresh reactants are used for each substrate; otherwise an insoluble residue remains on the substrate. Sodium or potassium peroxide can also be used for etching, but they leave an insoluble residue on the substrate similar to the one previously mentioned.

This mixture etches tantalum and tantalum nitride at the rate of 1000-2000Å/min and tantalum pentoxide at the same rate. No etching of the silica substrate has been noted after the etching of the tantalum (or tantalum compound) thin film has been completed.

The figures are for tantalum sputtered onto a thermally oxidized silicon wafer followed by a gold deposition. The tantalum is 1500Å thick. Figure 1 is a photograph of the tantalum film exposed through openings in the gold film. The width of the smallest set of gold lines is 1 mil. Figure 2 shows the tantalum etched away down to the oxide and the gold removed in this region. No attack of the oxide surface was noticed. Undercutting occurs, but the amount is very small.

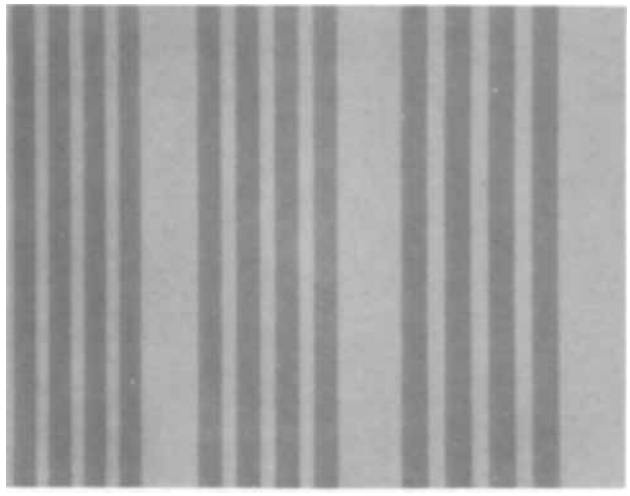

Fig. 1. Gold (3000Å) and tantalum (1500Å) deposited onto a thermally oxidized silicon wafer. The gold has been etched to expose the tantalum, dark on the photograph.

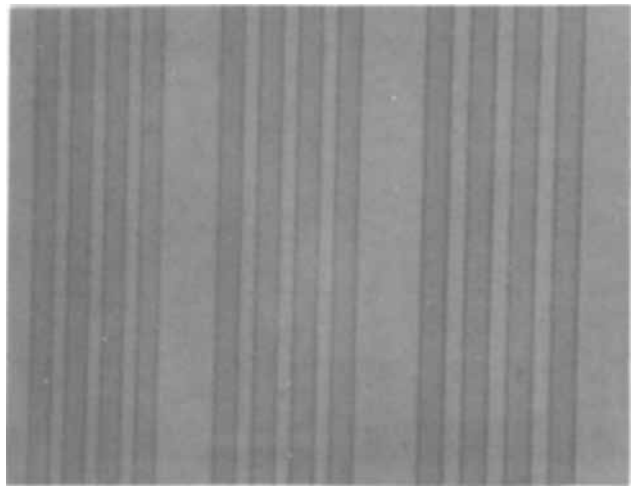

Fig. 2. Same wafer with the tantalum etched and the gold removed.

Manuscript received Jan. 16, 1969.

Any discussion of this paper will appear in a Discussion Section to be published in the December 1969 JOURNAL.

REFERENCES

1. M. J. Walker, *IEEE Trans. Electron Devices*, **ED-13**, 471 (1966).
2. D. A. McLean, N. Schwartz, and E. D. Tidd, *Proc. IEEE*, **52**, 1450 (1964).
3. D. A. McLean and W. H. Orr, *Bell Lab. Record*, **44**, 304 (1966).

* Electrochemical Society Active Member.

Key words: tantalum, thin films, etching, capacitors, resistors.

Calculation of Current Density Distribution and Terminal Voltage for Bipolar Electrolyzers; Application to Chlorate Cells

I. Rousar

Department of Inorganic Technology, Technical University, Prague, Czechoslovakia

ABSTRACT

Criterion equations are derived to enable the calculation of voltage and local current densities in one cell of a bipolar chlorate electrolyzer. For the cell system, expressions for current losses due to parasitic currents are derived for two models (with common bubble separator channel or with bubble separator channels for each cell). The calculation includes also the determination of the circulation rate of electrolyte in the cell system. Finally, the influence of specific parameters on the terminal voltage, parasitic currents, and circulation rate of electrolyte is discussed.

The importance of bipolar electrolyzers in chlorate production is indicated by new patent applications (1, 2) and especially by three installations put in operation recently (3-5). In the present paper, we carry out the chemical engineering calculations for this type of electrolyzer, *i.e.* for a bipolar, diaphragmless flow electrolyzer with the formation of a gas phase in the interelectrode space and with recirculating electrolyte. The present work is a continuation of a series of studies devoted to electrolyzers for chlorate production (6-8).

The Model System

The bipolar electrolyzer consists of a series of identical cells (Fig. 1 and 2). Each cell is in the form of a vertical channel of a rectangular cross section. Two channel walls that are opposite to each other are formed by the electrodes; the other two are made of an insulating material. The electrolyte is led into the cell at the bottom; a mixture of bubbles and electrolyte leaves the cell at the top and enters the bubble-separation channel or channels located along the side of the cells.

All bipolar plane electrodes of the height L and width w are made of a single material of thickness $S_A + S_K$ (from symmetry it follows that $S_A = S_K$). The mutual distance of the electrodes is d. Insulating walls of height L_1 and thickness $S_A + S_K$ lengthen the interelectrode channel to the total height L_T ($= L + 2L_1$). The system of n-interelectrode channels in one row is located in the electrolyzer tank in the distance L_2 from the bottom and from the cover of the tank.

Between two rows of interelectrode channels, there is a common bubble separator channel of width w_1 (model Q). The bubble separator space can be divided using n insulating walls of thickness d_2 into n small bubble separator channels (model W).[1] The connecting inlet electrolyte channels (of length L_{SB} and cross section F_{SB}) are placed on the side of the tank. Outlet connecting channels of length L_{ST} and cross section F_{ST} lie on the cover of the electrolyzer.

Similar arrangements for one-row systems can be seen in Fig. 3 and 4.

The cell is situated in a rectangular system of coordinates x, y, and z with the origin located at the bottom of the cell. Q(O, O, O); Fig. 1 and 2.

Supposing that all cells in the system are identical, we derive first the equations for the j-th cell. Unknown quantities included in these equations are the current load I_j(amp) in the j-th cell and the inlet volume flow rate of the electrolyte V_E (cm³/sec). Both quantities depend on the arrangement of the whole system and will be determined later. The calculation of the temperature of the electrolyte is given in the Appendix.

[1] Equations that refer only to the model Q or only to W are denoted with numbers combined with Q or W, respectively. Other equations are denoted with numbers.

Mathematical Description of the j-th Cell

We suppose that the cell is isothermal with the temperature t_{EB} and that processes on both electrodes are controlled by the rate of the electrode reaction. If the electrodes are large, the distance between them is small, and b_A and b_K in the Tafel equations are large, we can assume that the lines of force in the electrolyte and in the electrodes are perpendicular to the electrode surface. Then the current density in a given height y is the same at both electrodes. The voltage distribution in the j-th cell is given by

$$U = \epsilon_A - \epsilon_K + U_A + U_K + U_M \qquad [1]$$

where U means terminal voltage, U_M ohmic voltage drop in the electrolyte in the x-direction, U_A and U_K ohmic voltage drops in the bipolar electrode (anode

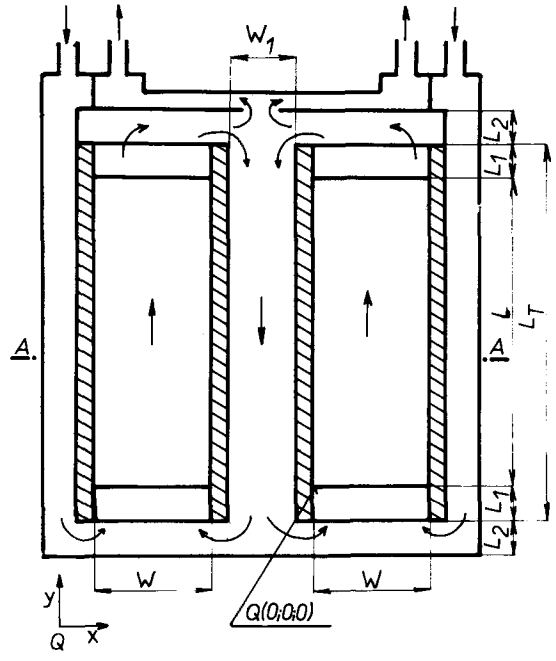

Fig. 1. Model electrolyzer (side view), two-row system: w—width of the bipolar electrode, L—height of the bipolar electrode, L_1—height of the insulating walls, L_2—height of the channel connecting interelectrode channel with bubble separator channel, W_1—width of the bubble separator channel, Q(O, O, O)—origin of the coordinates x, y, z. Arrows indicate the direction of the electrolyte flow.

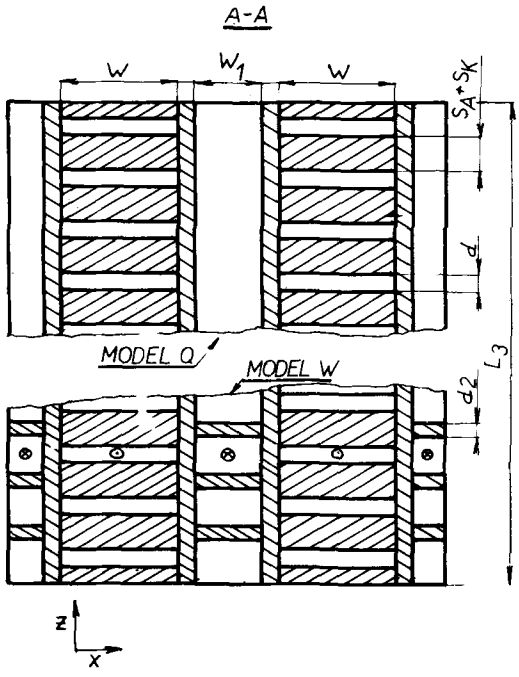

Fig. 2. Model electrolyzer (top view), two-row system: d—distance between electrodes, S_A, S_K—thicknesses of the anode and cathode plates, w—width of the bipolar electrode, w_1—width of the bubble separator channel.

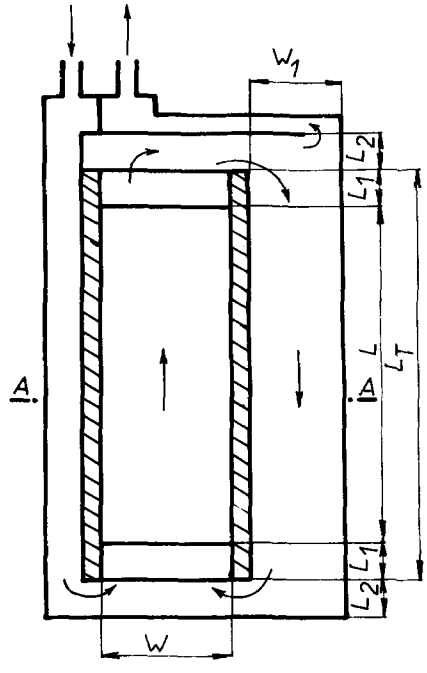

Fig. 3. Model electrolyzer (side view), one-row system. The description is given in Fig. 1.

and cathode, respectively), ϵ_A and ϵ_K local electrode potentials at the anode and cathode, respectively. All parameters except U depend on the distance from the origin of coordinates Q(O, O, O), hence they are functions of y.

The dependence of the local electrode potentials ϵ_A and ϵ_K on the local current density i is given by equations:

$$\epsilon_A = a_A + b_A \ln i, \qquad -\epsilon_K = a_K + b_K \ln |i| \qquad [2a,b]$$

In order to solve Eq. [1] analytically, Eq. [2a,b] must be linearized. For small deviations of i from mean current density in the j-th cell ($\bar{i}\,\eta_{Sj}$),

$$\epsilon_A = a_A' + b_A' i, \qquad -\epsilon_K = a_K' + b_K' i \qquad [3a,b]$$

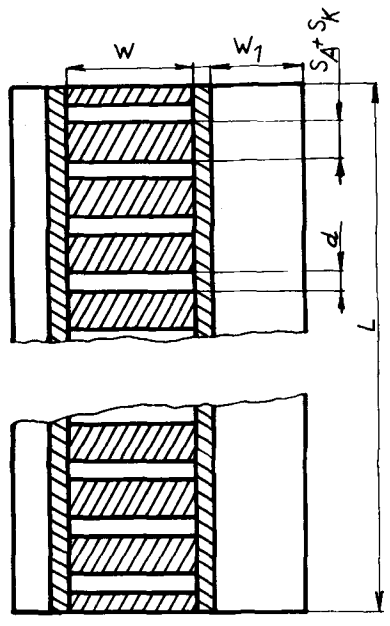

Fig. 4. Model electrolyzer (top view), one-row system. The description is given in Fig. 2.

where

$$a' = a_A - b_A + b_A \ln (\bar{i}\,\eta_{Sj}),$$

$$a_K' = a_K - b_K + b_K \ln (\bar{i}\,\eta_{Sj})$$

$$b_A' = b_A/\bar{i}\,\eta_{Sj}, \qquad b_K' = b_K/\bar{i}\,\eta_{Sj}$$

mean current density $\bar{i}$ is given by $\bar{i} = I_o/wL$, where $I_o = I_T/n_R$ is the input current load for one row, and the current efficiency (dependent on the flow of parasitic current) is defined as

$$\eta_{Sj} = I_j/I_o \qquad [4]$$

The ohmic voltage drops in the anode and cathode are given by Ohm's law,

$$U_A = i\,S_A\,\rho_A, \qquad U_K = i\,S_K\,\rho_K \qquad [5a,b]$$

The voltage drop in the electrolyte is given by the equation

$$U_M = i\,d\,\rho_M$$

in which ρ_M is the specific resistance of the electrolyte containing bubbles. This quantity can be simply calculated from the modified Maxwell (6) equation

$$\rho_M = \rho_E(1 + 1.5F_G/F_E) \qquad [7]$$

where F_G and F_E are hypothetical cross sections of the interelectrode channel corresponding respectively to gas and electrolyte, and

$$F_E = wd(1-\alpha), \qquad F_G = wd\alpha \qquad [8a,b]$$

where α means the fraction of bubble volume (void fraction).

For laminar two-phase flow in vertical channels (9, 10), the relation between the linear velocities of gas (v_G), electrolyte (v_E), and velocity of small bubbles (in the presence of surface active compounds) due to buoyancy (v_R) is

$$v_G = v_E + v_R(1-\alpha)^{3.5} \qquad [9]$$

Equation [9] can be simplified for small void fractions ($\alpha \to 0$) (6-8) to $v_G = v_E + v_R$, or for large bubble volume fractions ($\alpha \to 1$) (11) to $v_G = v_E$.

Using volume rates of gas flow or electrolyte flow and Eq. [8a,b], we obtain

$$v_G = (V_G + V_{GBS})/wd\alpha, \quad v_E = V_E/(1-\alpha)wd \qquad [10a,b]$$

The volume rate of recirculating gas (V_{GBS}) must be determined experimentally. The volume rate of gas

flow V_G in a given height y in the cell can be calculated from Faraday's law and from the equation of state of an ideal gas as

$$V_G = V_{GT} P_r \int_0^{y_r} i_r \, dy_r \quad [11]$$

where

$$V_{GT} = (RT/(P_o - P_S))\,(I_o \eta_{Sj}/\mathbf{F})\,(\eta_A/n_A + \eta_K/n_K) \quad [12]$$

$$P_r = (P_o - P_S)/(P - P_S) \quad [13]$$

$$i_r = i/\bar{i}\,\eta_{Sj} \quad [14]$$

$$y_r = y/L \quad [15]$$

In Eq. [12], the current efficiencies η_A and η_K refer to the evolution of a gaseous phase in the anodic and cathodic processes, respectively. P_o denotes the pressure on the top of the electrolyzer, P the pressure in a given height, and P_S water vapor pressure in the given system.

Substituting linear velocities from [10a,b] into [9] and rearranging, we obtain for α at a height y

$$\alpha = (V_G + V_{GBS})/(V_G + V_{GBS} + V_E + w d v_R (1-\alpha)^{4.5}) \quad [16]$$

and for the ratio F_G/F_E

$$F_G/F_E = \alpha/(1-\alpha) = K_3 P_r F_3 \int_0^{y_r} i_r \, dy_r + K_3' F_3 \quad [17]$$

where (setting α_T for α at $y = L$)

$$K_3 = V_{GT}/(V_E + w d v_R (1-\alpha_T)^{4.5}) \quad [18a]$$

$$K_3' = V_{GBS}/(V_E + w d v_R (1-\alpha_T)^{4.5}) \quad [18b]$$

$$F_3 = (V_E + w d v_R (1-\alpha_T)^{4.5})/(V_E + w d v_R (1-\alpha)^{4.5})$$

The functions P_r and F_3 are generally dependent on y but we can assume that $P_r \approx F_3 \approx 1$.

Assuming that the mean bubble diameter D_G is known and that $s_E >> s_G$, the v_R value can be calculated as

$$v_R = g D_G^2/18\nu \text{ for } Re_G \leq 1.9$$

or

$$v_R = (4/3)^{5/7} (g D_G/18.5)^{5/7} (D_G/\nu)^{3/7}$$

for

$$Re_G = D_G v_R/\nu \; \epsilon < 1.9; 505>$$

Substituting the expressions [3a,b], [5a,b], [6], [7], and [17] into [1], we obtain the equation describing the potential distribution in the electrode-electrolyte system in the following integral form:

$$U = a_A' + a_K' + i(b_A' + b_K' + \rho_A S_A + \rho_K S_K + d\rho_E(1 + 1.5K_3')) + id\rho_E 1.5K_3 \int_0^{y_r} i_r dy_r \quad [19]$$

Since the U value is unknown, we need a boundary condition, which may be written as

$$\int_0^1 i_r \, dy_r = 1 \quad [20]$$

Using following definitions for criteria $K_1 - K_4$

$$K_1 = (U - a_A' + a_K')/\bar{i} d \rho_E \eta_{Sj} \quad [21]$$

$$K_2 = (b_A' + b_K')/d\rho_E \quad [22a]$$

$$K_4 = (\rho_A S_A + \rho_K S_K)/d\rho_E \quad [22b]$$

we obtain from Eq. [19]

$$K_1 = i_r(1 + K_2 + 1.5K_3' + K_4) + 1.5K_3 i_r \int_0^{y_r} i_r dy_r \quad [23]$$

Solving Eq. [23] together with [20] leads to the expressions for K_1 and i_r

$$K_1 = 1 + K_2 + 1.5K_3' + K_4 + 0.75K_3 \quad [24]$$

$$i_r = (K_5 + 0.5)/(K_5^2 + 2K_5 y_r + y_r)^{1/2} \quad [25]$$

Table I. Influence of K_3 on K_1 for Model Q

$K_2 = 0.8266$-0.8360; $K_4 = 0.000447$; $\bar{i} = 0.09$ amp/cm²

K_3	K_1	w_1 (cm*)	V_E (cm³/sec)	U_S (v)
0.1003	1.9118	20	1107	3.092
0.1079	1.9158	10	1028	3.093
0.1377	1.9360	5	796	3.097
0.2438	2.0122	2	439	3.111
0.3620	2.0986	1	293	3.125

* The change of K_3 is due to the change of w_1.

where

$$K_5 = (1 + K_2 + 1.5K_3' + K_4)/1.5K_3 \quad [26]$$

Calculated K_1 values for several K_3 values are summarized in Table I. K_3 depends on V_E; the influence of K_3 on the distribution of the relative current density i_r is shown in Fig. 7. An increase of K_3 results in an increase of the difference between local (i) and average current densities ($\bar{i}\,\eta_{Sj}$).

The terminal voltage U of the j-th cell is then found by substituting [24] into [21] and rearranging as

$$U = A + B\,\eta_{Sj} \quad [27]$$

where $A = a_A' + a_K'$, $B = (1 + K_2 + 1.5K_3' + K_4 + 0.75K_3)\bar{i} d\,\rho_E$. The values of A and B are slightly influenced by changes of η_{Sj}. Nevertheless, we suppose

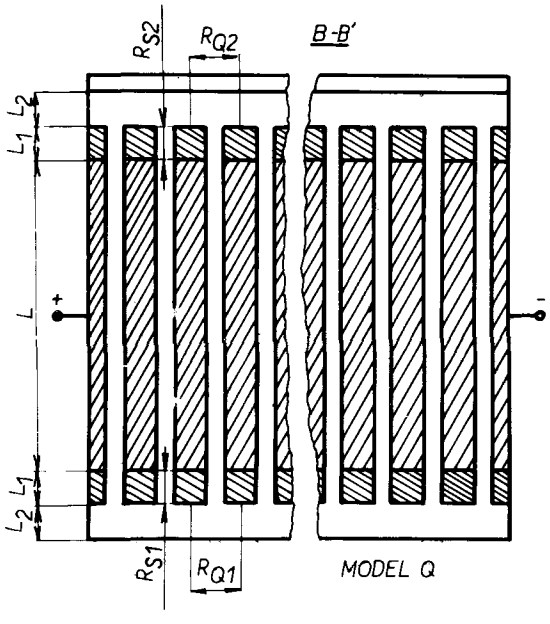

Fig. 5. Model electrolyzer, side view: R_{S1}, R_{S2}—resistances of the electrolyte in the interelectrode channel with insulating walls of the height L_1. R_{Q1}, R_{Q2}—resistances of the electrolyte including bubbles in the connecting channels between two cells of the height L_2.

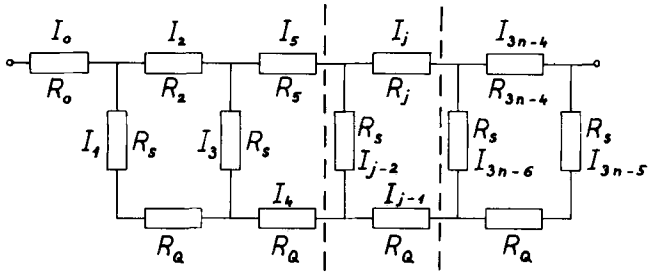

Fig. 6. The electrical basic circuit equivalent to Fig. 5: R_o, R_2, R_5, R_j, R_{3n-4}—bipolar cell resistances, R_S—resistance in the interelectrode channel with insulating walls, R_Q—resistance in the connecting channels between two cells.

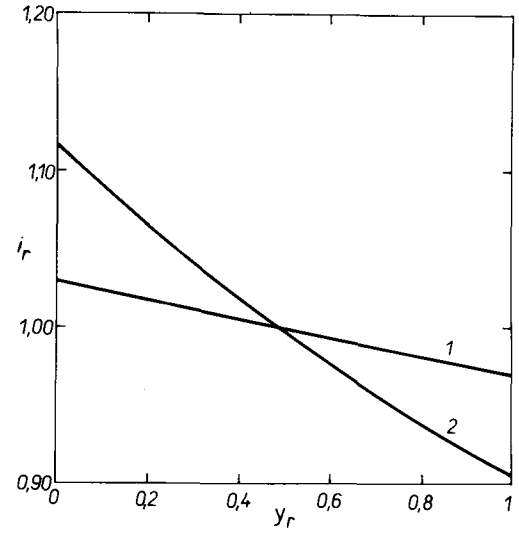

Fig. 7. Dependence of local relative current density i_r on the dimensionless distance y_r from the bottom of the cell for Model Q. K_2 = 0.8266-0.8360; K_4 = 0.000447; Curve 1—K_3 = 0.1003, Curve 2—K_3 = 0.3620.

that for $\eta_{Sj} \to 1$ it is possible to calculate A and B for the mean value of η_{Sj}, which is defined by

$$\eta_S = (1/n) \sum_{j=1}^{j=n} \eta_{Sj} \qquad [28]$$

Calculation of the Parasitic Current

The parasitic current flows through the electrolyte between inlet and outlet channels, which form electrical shunts to the cells.

According to Wilson (12), we can describe such a system by a network of three types of resistances R_j, R_S, and R_Q. R_j denotes the resistance of the j-th cell (more properly, it is the resistance of the j-th bipolar electrode with one half of the electrolyte resistance in the interelectrode channel at each side). The cell resistance R_j is equal to the cell voltage U, Eq. [27], divided by the current I_j. From this point of view, the first and last electrode form a cell loaded by the total current (I_o). R_S is the resistance of the electrolyte in the inlet (R_{S1}) and outlet (R_{S2}) parts of the cell channel(s). R_Q denotes the resistance of the electrolyte in the channel connecting two neighboring cells (on the bottom R_{Q1}, on the top R_{Q2}). We suppose that all resistances of the type R_S are equal and that the same applies for R_Q. This simplification leads to the expressions

$$R_S = ((1/R_{S1}) + (1/R_{S2}))^{-1},$$

$$R_Q = ((1/R_{Q1}) + (1/R_{Q2}))^{-1}.$$

Equations for R_{S1}, R_{S2}, R_{Q1}, and R_{Q2} depend on the model used. Equations leading to the lowest η_S value are as follows.

Model Q:

$$R_{S1} = \rho_E(1 + 1.5K_3 + 1.5K_3')\,(L_1/wd) \qquad [Q\text{-}29a]$$

$$R_{S2} = \rho_E(1 + 1.5K_3')\,(L_1/wd) \qquad [Q\text{-}29b]$$

$$R_{Q1} = \rho_E(1 + 1.5K_3 + 1.5K_3')\,(S_A + S_K + d)/(L_2(w + w_1) + (L + 2L_1)w_1/2n_R) \qquad [Q\text{-}30a]$$

$$R_{Q2} = \rho_E(1 + 1.5K_3')\,(S_A + S_K + d)/(L_2(w + w_1) + (L + 2L_1)w_1/2n_R) \qquad [Q\text{-}30b]$$

Model W:

$$R_{S1} = \rho_E(1 + 1.5K_3 + 1.5K_3')\,((L_1/wd) + 0.5(w + w_1)/L_2d) + \rho_E(1 + 1.5(V_{GT}/V_p))\,(L_{ST}/F_{ST}) \qquad [W\text{-}29a]$$

$$R_{S2} = \rho_E(1 + 1.5K_3')\,((L_1/wd) + 0.5(w + w_1)/L_2d) + \rho_E(L_{SB}/F_{SB}) \qquad [W\text{-}29b]$$

$$R_{Q1} = \rho_E(1 + 1.5(V_{GT}/V_p))\,(S_A + S_K + D)/F_{QT} \qquad [W\text{-}30a]$$

$$R_{Q2} = \rho_E(S_A + S_K + d)/F_{QB} \qquad [W\text{-}30b]$$

Using Kirchhoff's law for the electrical basic circuit (Fig. 6) equivalent to the described system of cells (Fig. 5), we obtain $3n - 4$ linear equations (for n-cells), which can be simplified by introducing the dimensionless parameters $I_{Rj} = I_j/I_o$, $\alpha_R = A/I_oR_S$, $\beta_R = B/I_oR_S$, and $\gamma_R = R_Q/R_S$.

Table II contains coefficients for the dimensionless current and for the right-hand side of the mentioned $3n - 4$ linear equations. It is obvious from Table II that the transition from n-cell system to $n + 1$ cell system is connected with expansion of the matrix by three rows (j, $j + 1$, $j + 2$).

The Thomas method (13) for calculating this tridiagonal matrix leads to the desired values for η_{Sj} and consequently to η_S.

$$\eta_S = (1/n)\left(1 + \sum_{j=1}^{n-1} I_{R(3j-1)}\right)$$

The total voltage U_T for the n-cell system is then given by

$$U_T = n(A + B\,\eta_S) \qquad [30]$$

and the total consumption of energy W for the desired reaction

$$W = n\,\eta_I I_o(A\,\eta_S + B\,\eta_p) \qquad [31]$$

where

$$\eta_p = (1/n)\left(1 + \sum_{j=1}^{n-1} I_{R(3j-1)}{}^2\right)$$

The mean cell voltage U_S is defined by $U_S = U_T/n$. Energy efficiency $\eta_w = W/U_TI_o$ is given by

$$\eta_w = \eta_I(A\,\eta_S + B\,\eta_p)/(A + B\,\eta_S) \qquad [32]$$

and the specific consumption of energy E_{sc} in kilowatt-hours per ton of product can be calculated as

$$E_{sc} + (A + B\,\eta_S)/3.6p\,\eta_I\,\eta_S \qquad [33]$$

where p is gram-equivalents of the product (p = 17.741 g-equiv. for $NaClO_3$).

Table II. Coefficients and right-hand sides of $3n$-4 equations describing the electrical basic circuit in Fig. 6

	I_{R1}	I_{R2}	I_{R3}	I_{R4}	I_{R5}	$I_{R(j-2)}$	$I_{R(j-1)}$	I_{Rj}	$I_{R(3n-6)}$	$I_{R(3n-5)}$	$I_{R(3n-4)}$	Right-hand side
1	$1 + \gamma_R$	$-\beta_R$	−1									α_R
2	1		1	−1								0
3		1	−1		−1							0
4			1	γ_R	$-\beta_R$	−1						α_R
5				1		1	−1					0
j-2					1	−1		−1				0
j-1						1	γ_R	$-\beta_R$	−1			α_R
j							1		1	−1		0
3n-6								1	−1		−1	0
3n-5									1	$1 + \gamma_R$	$-\beta_R$	α_R
3n-4										1	1	1

Calculation of the Volume Flow Rate of the Electrolyte

The value of the volume flow rate of the electrolyte V_E is involved in calculating K_3 and η_I. The latter quantity depends considerably on the volume flow rate (1, 14) and its dependence on V_E (or on the Reynolds criterion) must be found experimentally.

The calculation of V_E is based on the pressure balance for the j-th cell with bubble separation channel or channels situated along the side of the cell row(s). The driving force of the flow is buoyancy acting on the bubbles in the interelectrode space; pressure losses are due to friction in the interelectrode space (Δp_M), in the inlet and outlet channel of the cell (Δp_C), and in the bubble separator channel (Δp_{BS}). Neglecting the acceleration of the electrolyte with rising bubbles and assuming a linear dependence of α on y, we have

$$gL_T s_E(1-\alpha_{BS}) - gL_T s_E(1-0.5(\alpha_T+\alpha_0) = \Delta p_M + \Delta p_{BS} + \Delta p_C \quad [34]$$

The left-hand side of Eq. [34] represents the difference between the pressure at the bottom in the bubble separator channel and in the interelectrode channel; on the other side are friction losses in the recirculation circuit.

The relation between V_E and α_T is given by Eq. [16]. In the bubble separator channel, the buoyancy acts on the bubbles in the direction opposite to the electrolyte flow; hence

$$v_{GBS} = v_{EBS} - v_R(1-\alpha_{BS})^{3.5} \quad [35]$$

where α_{BS} is known from experiments. Substituting the two following equations for v_{GBS} and v_{EBS}

$$v_{GBS} = V_{GBS}/F_{BS}\,\alpha_{BS} \quad [36a]$$

$$v_{EBS} = V_{EBS}/F_{BS}(1-\alpha_{BS}) \quad [36b]$$

where

$$F_{BS} = w_1 L_3/n\,n_R \quad [Q\text{-}37]$$

$$F_{BS} = w_1(S_A+S_K+d-d_2)/n_R \quad [W\text{-}37]$$

into [35] we obtain for V_{GBS}:

$$V_{GBS} = \alpha_{BS}V_{EBS}/(1-\alpha_{BS}) - \alpha_{BS}F_{BS}v_R(1-\alpha_{BS})^{3.5} \quad [38]$$

Using V_{GBS}, we can evaluate the inlet gas volume fraction at the bottom of the interelectrode channel α_0:

$$\alpha_0 = V_{GBS}/(V_{GBS}+V_E+wdv_R(1-\alpha_0)^{4.5}) \quad [39]$$

Equations [16], [39], and

$$V_E = V_{EBS} + V_p \quad [40]$$

express the dependence of α_0 and α_T on V_E or V_{EBS}.

Pressure loss due to friction in the interelectrode channel is given by

$$\Delta p_M = \lambda_M(L_T/D_M)(s_E/2)(V_E/wd)^2/(1-0.5(\alpha_T+\alpha_0)) \quad [41]$$

where λ_M and D_M depend on the shape of the channel cross section; for $w >> d$, we use the relations

$$\lambda_M = 96/Re_M \text{ for } Re_M < 2300$$

or

$$\lambda_M = 0.316/Re_M^{0.25} \text{ for } Re_M > 2300$$

According to Zuber (10), in the calculation of the Reynolds number the dynamic viscosity μ for the two-phase flow has to be replaced by $\mu(1-0.5(\alpha_T+\alpha_0))^{2.5}$, so that

$$Re_M = (V_E D_M/wd\nu)(1-0.5(\alpha_T+\alpha_0))^{2.5}$$

for

$$s_G << s_E$$

where

$$D_M = 2wd/(w+d)$$

Pressure loss in the bubble separator channel is given by

$$\Delta p_{BS} = \lambda_{BS}(L_T/D_{BS})(s_E/2)(V_{EBS}/F_{BS})^2/(1-\alpha_{BS}) \quad [42]$$

λ_M, λ_{BS}, and D_{BS} for

$$L_3 = n(S_A+S_K+d) >> w_1 \text{ (model Q)}$$

or for

$$w_1 >> S_A+S_K+d-d_2 \text{ (model W)}$$

are defined as

$$\lambda_{BS} = 96/Re_{BS} \text{ for } Re_{BS} < 2300$$

and

$$\lambda_M = 0.316/Re_{BS}^{0.25} \text{ for } Re_{BS} > 2300$$

with

$$Re_{BS} = (V_{EBS}\,D_{BS}/F_{BS}\,\nu)(1-\alpha_0)^{2.5}$$

and

$$D_{BS} = 2w_1(S_A+S_K+d-d_2)/(w_1+S_A+S_K+d-d_2) \quad [W\text{-}43]$$

$$D_{BS} = 2w_1L_3/(w_1+L_3) \quad [Q\text{-}43]$$

Pressure losses due to the change of the electrolyte velocity and of its direction in the connecting parts between interelectrode channel and bubble separator channel can be derived from the velocities in the cross section L_3L_2 (model Q) or L_2d (model W). Friction coefficients at the top and at the bottom are denoted as ξ_1 and ξ_2, respectively. Thus, we get

$$\Delta p_C = \xi_1(s_E/2)(V_E/F_C)^2/(1-\alpha_T) + \xi_2(s_E/2)(V_{EBS}/F_C)^2/(1-\alpha_{BS}) \quad [44]$$

where

$$F_C = L_2L_3/n \quad [Q\text{-}45]$$

$$F_C = L_2d \quad [W\text{-}45]$$

Setting [41], [42], [44] together with [16], [39], and [40] into [34], we obtain an implicit formula for evaluating V_{EBS} or V_E.

Discussion of the Influence of Several Parameters on V_E, η_S, U_S, and E_{sc}

The influence of the change of F_{BS} (or w_1) on V_E is given in Table I for model Q. V_E decreases with decreasing w_1 (F_{BS}); this is due to the increase of pressure loss in the bubble separator channel.

The values of V_E, K_3, and U_S depending on the thickness of the insulating wall in the bubble separator channel (d_2) are summarized in Table III for model W. V_E decreases with decreasing F_{BS} (increasing d_2).

The influence of the height of the insulating channel walls L_1 on η_S and η_w for various numbers of cells n for model Q can be seen from Table IV whence the great influence of the increasing number of cells on η_S and E_{sc} is comparable with the influence of L_1. The dependence of η_{Sj} on the cell number j is visualized in Fig. 9. As shown in Fig. 8, η_{Sj} becomes larger with increasing L_1.

Table III. Influence of d_2 on V_E and U_S for Model W

$\bar{i}$ = 0.09 amp/cm²

d_2 (cm)	V_E (cm³/sec)	K_3	U_S (v)
0.2	723	0.158	3.113
0.4	655	0.174	3.116
0.6	578	0.196	3.118
0.8	495	0.228	3.122
1.0	407	0.275	3.128
1.2	319	0.349	3.136

Table IV. Influence of L_1 and n on η_S, U_S, and E_{sc} for Model Q

η_I = 1

L_1 (cm)	n	η_S	U_S (v)	E_{sc} (kwhr/ton)	$\bar{i}\,\eta_S$
10	15	0.9125	3.081	5101	0.0821
20	15	0.9512	3.093	4920	0.0856
40	15	0.9741	3.100	4808	0.0876
60	15	0.9824	3.103	4772	0.0884
20	5	0.9942	3.107	4721	0.0895
20	25	0.8844	3.072	5247	0.0796
20	35	0.8144	3.049	5655	0.0733
20	45	0.7529	3.028	6076	0.0677

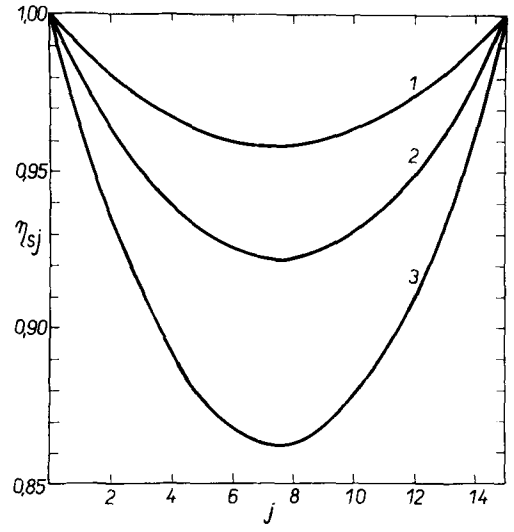

Fig. 8. Dependence of η_{Sj} on the cell number j for Model Q. Curve 1—L_1 = 40 cm; Curve 2—L_1 = 20 cm; Curve 3—L_1 = 10 cm.

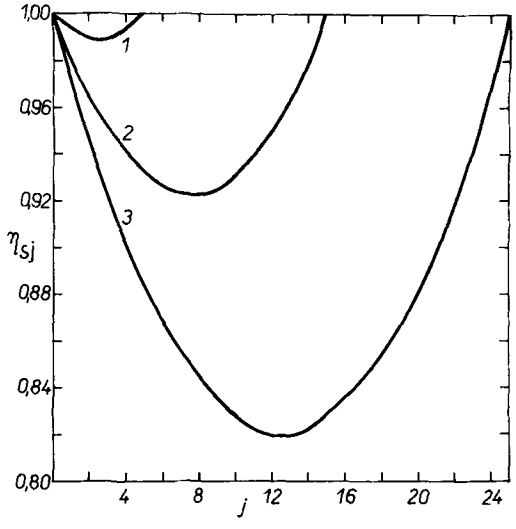

Fig. 9. Dependence of η_{Sj} on the cell number j for Model Q. Curve 1—n = 5; Curve 2—n = 15; Curve 3—n = 25.

The models Q and W can be compared in terms of η_S and E_{sc} values (η_I = 1) using the data in Table V. These parameters are nearly the same for both models with a small number of cells in one row.

With increasing n (25-45), the decrease of η_S for model Q is much greater than for model W. Therefore, the latter shows only a small increase of E_{sc} with rising n.

From the practical point of view, it is necessary to know the time dependence of U_S and E_{sc}, which is due to corrosion of graphite anodes. Supposing that the corrosion rate is constant, we can introduce the parameter

Table V. Influence of the number of cells (n) on η_S and E_{sc}
η_I = 1

η_I = 1	Model Q		Model W	
n	η_S	E_{sc} (kwhr/ton)	η_S	E_{sc} (kwhr/ton)
5	0.9942	4721	0.9999	4726
15	0.9512	4913	0.9995	4728
25	0.8844	5247	0.9986	4731
35	0.8144	5655	0.9975	4736
45	0.7529	6076	0.9960	4742

$C(\leq 1)$ which gives us the ratio of the final thickness of graphite anode to the initial one. The distance between the electrodes changes from d to $d_1 = d + (S_A + S_K)(1 - C)$ and the thickness of the graphite plate changes from $(S_A + S_K)$ to $(S_A + S_K)C$.

The dependence of η_S, U_S, and E_{sc} on C (hence on time) for both models is given in Table VI. For η_I = 0.9, the mean E_{sc} value for model Q is ~5809 kwhr/ton of $NaClO_3$, whereas for model W only ~5619 kwhr/ton of $NaClO_3$, in accord with the published (5) value 5400 kwhr/ton.

APPENDIX

Calculation of Electrolyte Temperature in the Electrolyzer

The previous considerations were made with the assumption that the temperature of the recirculating electrolyte t_{EB} in the electrolyzer was known. Nevertheless, this quantity can be evaluated from the inlet electrolyte temperature t_p using the following procedure.

The enthalpic balance will be made for the interelectrode channel. The heat evolved in this channel as a result of the electrochemical reaction is $T(\Delta S_{rev} + \Delta S_{irrev})$:

$$Q_1 = \left(U - \sum_K (\Delta H_K \eta_{IK}/\eta_{KK})/0.239\mathbf{F} \right) \cdot 0.239\, \bar{i}\, \eta_S w L \qquad \text{[A-1]}$$

where $\Delta H_K \cdot \eta_{IK}$ and η_{KK} refer to partial electrochemical reactions with the enthalpy change ΔH_K (cal/mole) and with current efficiency η_{IK}. The number of equivalents per mole for the k-th electrochemical reaction is η_{KK}.

A part of the heat is absorbed during saturation of the gas phase with water vapor:

$$Q_2 = (\bar{i}\, \eta_S w L/\mathbf{F})\ (P_S/(P_o - P_S))\ ((\eta_A/\eta_A) + (\eta_K/\eta_K))r \qquad \text{[A-2]}$$

where r is the heat of water evaporation (cal/mole) in the given system.

A part of the heat is evolved in the electrolyte by the passage of parasitic current:

$$Q_3 \approx \alpha_H\, 0.239\, U(1 - \eta_S)\, \bar{i}\, w L \qquad \text{[A-3]}$$

and another portion is led off through the side walls of the electrolyzer:

$$Q_4 \approx (t_p - t_F)(S_A + S_K + d)(L_T + 2L_2) \qquad \text{[A-4]}$$

Table VI. Influence of corrosion of the anode plate on η_S, U_S, and E_{sc}

η_I = 1, $\bar{i}$ = 0.09 amp/cm²

		Model Q			Model W		
$C(S_A + S_K)$*	d_1** (cm)	η_S	U_S(v)	E_{sc} (kwhr/ton)	η_S	U_S(v)	E_{sc} (kwhr/ton)
1.2	0.4	0.9512	3.093	4913	0.9995	3.128	4728
0.96	0.64	0.9489	3.185	5071	0.9995	3.238	4894
0.72	0.88	0.9472	3.279	5229	0.9995	3.346	5058
0.48	1.12	0.9456	3.372	5387	0.9994	3.452	5219
0.24	1.36	0.9440	3.465	5544	0.9994	3.556	5376
Mean value				5229			5057

* Thickness of the anode plate.
** Distance between electrodes.

Table VII. Influence of recirculation rate on t_{EB} and t_V at $V_p = 200$ cm³/sec, $t_p = 40°C$ for Model Q

w_1 (cm)	V_B (cm³/sec)	t_{EB} (°C)	t_V (°C)
20	1107	41.42	41.73
10	1028	41.39	41.73
5	796	41.29	41.73
2	439	40.94	41.74
1	293	40.55	41.75

The temperature of the outlet electrolyte rises to t_V:

$$Q_5 = -V_p S_E C_{PE}(t_V - t_p) \qquad [A\text{-}5]$$

The heat balance in the steady state takes the form

$$\Sigma Q_i = 0 \qquad [A\text{-}6]$$

On substituting [A-5] into [A-6] and rearranging, we get

$$t_V = t_p + (Q_1 + Q_2 + Q_3 + Q_4)/(V_p S_E C_{pE}) \qquad [A\text{-}7]$$

In calculating the electrolyte temperature at the inlet into the interelectrode channel, we assume that the temperature of the electrolyte passing through the separating channel is t_V. The enthalpic balance at the channel inlet with the assumption that the electrolyte density is independent of temperature is:

$$V_p t_p + V_{EBS} t_V = (V_1 + V_p) \cdot t_{EB} \qquad [A\text{-}8]$$

The electrolyte temperature at the inlet of the interelectrode channel is found by combination of Eq. [A-7] with [A-8]. Since $V_{EBS} >> V_p$ in practical cases, it follows that $t_{EB} \approx t_V$ and the system can be considered as isothermal.

Diminution of the cross section of the inner separating channel causes an increase of t_V and of the difference between t_{EB} and t_V (Table VII).

On introducing the temperature coefficients of certain quantities used in the calculation (*e.g.*, a_A, b_A, a_K, b_K, ρ_E), we can obtain the values at the temperature t_{EB} instead of t_p and use them in further calculations. The temperature coefficients δ_i are defined by equations of the type

$$f_i = f_{i,p}[1 + \delta_i(t_{EP} - t_p)] \qquad [A\text{-}9]$$

Experimental work is under way to test these calculations.

Acknowledgment

The author is indebted to Professor Dr. A. Regner Dr.Sc. for his continuous interest, stimulating discussions, and critical comments.

Manuscript submitted June 10, 1968; revised manuscript received *ca.* Feb. 13, 1969. This paper was presented at the Chlorates and Perchlorates Symposium at the Boston Meeting, May 5-9, 1968, as Paper 255.

Any discussion of this paper will appear in a Discussion Section to be published in the December 1969 JOURNAL.

REFERENCES

1. G. O. Westerlund, (to Chemech Engineering Ltd.), East German Pat. 55,935 (1967).
2. Imperial Chemical Industries Ltd., Brit. Pat. 905,749 (1961); Norwegian Pat. 110,921 (1967).
3. *Can. Chem. Process.*, **50**, 85 (1966).
4. R. Ramirez, *Chem. Eng.*, **74**, 136 (1967), No. 17, and **72**, 152 (1967), No. 2.
5. D. G. Elliott, "The Production of Sodium Chlorate Using a New Tape Bipolar Cell," 4th International Pulp Bleaching Conference, Toronto (1967).
6. I. Rousar, V. Cezner, and A. Regner, *Coll. Czech. Chem. Comm.*, **31**, 4193 (1966).
7. I. Rousar and V. Cezner, *ibid.*, **32**, 1137 (1967).
8. I. Rousar, V. Cezner, and J. Hostomsky, *ibid.*, **33**, 808 (1968).
9. V. G. Levitch, "Physico-chemical Hydrodynamics," Russ. Ed., p. 447, Moscow (1959).
10. N. Zuber, *Chem. Eng. Sci.*, **19**, 897 (1964).
11. R. B. MacMullin, *Electrochem. Technol.*, **1**, 5 (1963).
12. J. R. Wilson, "Demineralization by Electrodialysis," Butterworths, London (1960).
13. L. H. Thomas, "Elliptic Problems in Linear Difference Equations over a Network," Watson Scientific Lab., Columbia Univ., New York (1949).
14. I. Rousar, V. Cezner, M. Vender, M. Kroutil, and J. Vachuda, *Chemicky prumysl*, **17/42**, 468 (1967).

NOMENCLATURE

		Values used for calculation
a_A	Tafel constant a for anode (v)	1.7*
a_K	Tafel constant a for cathode (v)	1.54*
b_A	Tafel constant b for anode (v)	0.061*
b_K	Tafel constant b for cathode (v)	0.065*
a_A', a_K'	Constants of the linearized Tafel Eq. (v)	
A	Constant in Eq. [27]	
b_A',b_K'	Constants of the linearized Tafel Eq. (ohm-cm²)	
B	Constant in Eq. [27]	
C	Fraction of the thickness of the corroded graphite plate with respect to original thickness	1
C_{PE}	Specific heat of electrolyte (cal/g °C)	
d	Electrode distance (cm)	0.4-1.36
d_1	Electrode distance after corrosion of the graphite plate (cm)	
d_2	Thickness of the insulating wall in the bubble separator channel (cm)	
D_G	Average diameter of bubbles at a pressure P (cm)	0.05
D_M, D_{BS}	Equivalent diameters for interelectrode and bubble separator channels (cm)	
E_{sc}	Specific consumption of energy for $\eta_I = 1$ (kwhr/ton)	
$\mathbf{F}$	One Faraday; 96496°C	
F_C	Cross section of the connecting channel (cm²), *cf.* Eq. [45]	
F_G, F_E	Cross sections of the interelectrode channel effective only for the gas, and for the electrolyte (cm²)	
F_{ST}	Cross section of the connecting inlet channel (cm²)	25
F_{SB}	Cross section of the connecting outlet channel (cm²)	25
F_{QT}	Cross section of the inlet channel (cm²)	200
F_{QB}	Cross section of the outlet channel (cm²)	200
F_3	Function of the criterion K_3	
g	Acceleration of gravity, 981 cm/sec²	
H_K	Reaction enthalpies of the partial electrochemical reaction (cal/mole)	
I_o	Current flowing through one row of bipolar electrodes = I_T/n_R (amp)	
I_T	Total current (amp)	1800
i	Local current density (amp/cm²)	
i_r	Reduced local current density = $i/\bar{i}\,\eta_{Sj}$	
$\bar{i}$	Average current density = I_o/Lw	
j	Cell number	
K_1	Criterion, *cf.* Eq. [21]	
K_2	Criterion, *cf.* Eq. [22a]	
K_3	Criterion, *cf.* Eq. [18a]	
K_4	Criterion, *cf.* Eq. [22b]	
K_5	Criterion, *cf.* Eq. [26]	
L	Height of the bipolar electrode, (cm)	100
L_1	Height of the insulating wall in the interelectrode channel (cm)	5-60

L_2	Height of the connecting channel between interelectrode channels and bubble separator channel (cm)	3
L_3	Width of the electrolyzer (cm)	
L_{ST}	Length of the connecting channel at the top (cm)	100
L_{SB}	Length of the connecting channel at the bottom (cm)	100
n_R	Number of rows in the electrolyzer	2
n_A	Number of equivalents/mole for the anodic process	2
n_K	Number of equiv./mole for the cathodic process	2
n_{KK}	Number of equiv./mole for the partial electrochemical reaction	
p	Gram-equivalent (g-equiv.)	17.741
Δp_M	Pressure loss due to friction in the interelectrode channel (dynes/cm²)	
p_C	Pressure loss due to friction in the connecting channels (dynes/cm²)	
p_{BS}	Pressure loss due to friction in the bubble separator channel (dynes/cm²)	
P	Local pressure (dynes/cm²)	
P_o	Pressure at the top of the cell (dynes/cm²)	9.81×10^5
P_R	Reduced pressure, cf. Eq. [13]	
P_S	Pressure of water vapor in equilibrium with electrolyte (dynes/cm²)	5.88×10^4
$Q_1 \ldots Q_5$	Auxiliary parameters	
r	Heat of water evaporation (cal/mole)	
R	gas constant; erg/mole °C	8.314×10^7
Re_G	Reynolds number for bubbles	
Re_M, Re_{BS}	Reynolds numbers calculated for interelectrode and bubble separator channels	
S_A	Thickness of the anode (cm)	0.6
S_K	Thickness of the cathode (cm)	0.6
s_E	Specific gravity of the electrolyte (g/cm³)	1.43
t_{EB}	Temperature of the electrolyte at the bottom of the interelectrode channel (°C)	40*
t_F	Ambient temperature (°C)	
t_D, t_V	Inlet, outlet electrolyte temperature (°C)	
T	Absolute temperature = t_{EB} + 273.16°	
U	Cell voltage (v)	
U_S	Mean cell voltage ($=U_T/n$) (v)	
U_T	Terminal voltage of the electrolyzer (v)	
U_A, U_K	Ohmic voltage drops in the anode and cathode (v)	
U_M	Ohmic voltage drop in the gas emulsion between the electrodes (v)	
v_E	Rate of flow of the electrolyte in the interelectrode channel (cm/sec)	
v_G	Rate of flow of the gaseous phase in the interelectrode channel (cm/sec)	
v_{EBS}	Rate of flow of the electrolyte in the bubble separator channel (cm/sec)	
v_{GBS}	Rate of flow of the gaseous phase in the bubble separator channel (cm/sec)	
v_R	Velocity of bubbles corresponding to buoyancy (cm/sec)	
V_E, V_{EBS}	Volume flow rates of the electrolyte in the interelectrode and bubble separator channels (cm³/sec)	
V_G, V_{GBS}	Volume flow rates of the gaseous phase in the interelectrode and bubble separator channels (cm³/sec)	
V_{GT}	Volume flow rate of the gaseous phase in the interelectrode channel at the top (cm³/sec)	
V_p	Inlet volume flow rate of the electrolyte for one channel (cm³/sec)	
w	Bipolar electrode width (cm)	100
w_1	Bubble separator width (cm)	10
W	Energy consumption, cf. Eq. [31]	
x, y, z	Coordinates (cm)	
y_r	Reduced distance parallel to the y-axis = y/L	
$\alpha, \alpha_o, \alpha_T$	Bubble volume fractions at a height y, at the bottom and at the top of the interelectrode channel	
α_{BS}	Bubble volume fraction in the bubble separator channel	
α_H	Heat transfer coefficient (cal/cm² sec °C)	
$\alpha_R, \beta_R, \gamma_R$	Reduced parameters for electrical basic circuit	
δ_i	Temperature coefficients, cf. Eq. [A-9]	
ϵ_A, ϵ_K	Potentials of the anode and cathode (v)	
η_A	Anodic current efficiencies for gas evolution	0
η_K	Cathodic current efficiencies for gas evolution	1
η_I, η_{IK}	Current efficiency, current efficiency of the partial electrochemical reaction	
η_p	Dimensionless parameter	
η_S	Average current efficiency	
η_{Si}	Local current efficiency	
η_w	Energy efficiency, cf. Eq. [32]	
λ_M, λ_{BS}	Friction coefficients for interelectrode and bubble separator channels (dynes/cm²)	
μ	Dynamic viscosity of the electrolyte (dynes/cm²)	
ν	Kinematic viscosity of the electrolyte (cm²/sec)	0.0154*
ξ_1, ξ_2	Coefficients of friction resistance, cf. Eq. [44]	
ρ_A	Specific resistance of the anode (ohm-cm)	0.00066*
ρ_K	Specific resistance of the cathode (ohm-cm)	0.00066*
ρ_E	Specific resistance of the electrolyte (ohm-cm)	4.42*
ρ_M	Specific resistance of the gas electrolyte mixture between the electrodes (ohm-cm)	

* The composition of the electrolyte was 600g $NaClO_3$ + 120g NaCl + 10g Na_2CrO_4 in 1 liter; both electrodes were made from impregnated graphite (BAE).

Studies on Chlorate Cell Process

IV. Effect of Neutral Salts on Conversion of Available Chlorine to Chlorate

M. M. Jaksić,* B. Z. Nikolić, I. M. Csonka,[1] and A. B. Djordjević

Electrochemistry Department, Institute of Chemistry, Technology and Metallurgy, Beograd, Yugoslavia

ABSTRACT

It has been shown that neutral salts, such as NaCl and $NaClO_3$ and their mixtures, cause an apparent increase in the thermodynamic dissociation constants of weak acids and bases. The pH value of aqueous salt solutions at fixed hydrogen ion concentration decreases linearly with increasing content of neutral salt and represents a linear function of the salt's heat of hydration (12). The hydrogen ion activity coefficient and, hence, the thermodynamic dissociation constants of weak acids and bases apparently follow a corresponding dependence. In solution for the electrolytic chlorate formation, the dissociation constant of hypochlorous acid is thus apparently enlarged by one order of magnitude. As a consequence, in solutions for the electrolytic chlorate production the optimal pH region for the conversion of available chlorine is shifted toward lower values (pH 5.7-6.1), as shown both in theory and practice. The same phenomenon is shown to be of some importance for what happens in the anode diffusion layer, where chlorine hydrolysis may hence be affected.

The conversion of hypochlorous acid and hypochlorite ion, in other words the total available chlorine, into chlorate was investigated by Foerster (1, 2), who pointed out that it follows the equation:

$$2\ HOCl + OCl^- + 2\ H_2O \xrightarrow{k_1} ClO_3^- + 2\ H_3O^+ + 2\ Cl^- \ldots \quad [1]$$

The conversion kinetics is defined by the following kinetic equation (1, 2, 3):

$$v_1 = -\frac{d\{[HOCl] + [OCl^-]\}}{dt} \cdot V = 3V \cdot \frac{d[ClO_3^-]}{dt} = 3f^2 \cdot k_1 \cdot [HOCl]^2\,[OCl^-] \cdot V \ldots \quad [2]$$

where f is the activity coefficient of hypochlorous acid; k_1, the rate constant for reaction [1]; and V, total volume of the electrolyte.

More recent investigations by Skrabal (4), Imagawa (5), D'Ans and Freund (7), and Jaksić *et al.* (8) in concentrated chloride and chlorate solutions, characteristic for the electrolytic production of the latter, confirmed the mechanism suggested by Foerster.

Lister (9) showed that the formation of chlorite is the slow step in the available chlorine conversion to chlorate, while further oxidation proceeds extremely fast, so that it is practically impossible to identify the presence of chlorite in the solution [*cf.* (7)].

On this account it is not unjustified, at least theoretically, especially for the slightly alkaline region, in which the conversion of available chlorine still proceeds at a sufficiently measurable rate, to assume the possibility of the presence of the following mechanism

$$HOCl + 2\ OCl^- + H_2O \xrightarrow{k_2} ClO_3^- + H_3O^+ + 2\ Cl^- \ldots \quad [3]$$

Namely, for the subsequent fast step of oxidation of chlorite ions to chlorate, it is quite the same, from the theoretical point of view at least, whether it is done by hypochlorous acid or hypochlorite ions. Therefore, two theoretically possible mechanisms have to be considered (Eq. [1] and [3]).

Flis (10, 11) pointed out that the oxidizing ability and character of the oxidizing action of available chlorine to a very large extent depends on the hydrogen ion activity, whereby, with the decrease of pH value of the solution, the oxidation potential becomes proportionately more positive. This can be ascribed to the fact that such changes favor the predominant presence of hypochlorous acid. Therefore, for a long time it has been a common belief that, owing to a considerably higher positive potential, hypochlorous acid oxidizes hypochlorite ion in the process of disproportionation of available chlorine to chlorate. From this point of view, there is no doubt that the mechanism suggested by Foerster (1, 2) is the more plausible one, particularly if one has in mind that, in the highly alkaline region and especially at lower temperatures, the conversion of available chlorine fully ceases.

In a closed-loop system for electrolytic chlorate production, in which the electrolyte is circulated between the cells and a holding volume at any point of the cycle at steady-state conditions, the amount of available chlorine (C_s)

$$C_s = [HOCl] + [OCl^-] \ldots \quad [4]$$

remains practically constant during the operation.

On the other hand, the thermodynamic dissociation constant (K_a) of hypochlorous acid

$$K_a = \frac{a_{H_3O^+} \cdot f_{OCl^-} \cdot [OCl^-]}{f \cdot [HOCl] \cdot a_{H_2O}} \ldots \quad [5]$$

can be expressed in a form more suitable for our consideration, *i.e.*

$$K^* = \frac{a_{H_3O^+} \cdot [OCl^-]}{[HOCl]} = K_a \cdot \frac{f \cdot a_{H_2O}}{f_{OCl^-}} \ldots \quad [6]$$

By substituting the values from Eq. [4] and [6] in Eq. [2], and also in the corresponding kinetic equation relating to Eq. [3], one obtains the rates for two possible mechanisms of available chlorine conversion as a function of hydrogen ion activity

$$v_1 = -\frac{dC_s}{dt} \cdot V = 3 \cdot f^2 \cdot k_1 \cdot V \cdot \frac{K^* \cdot (a_{H_3O^+})^2 \cdot C_s^3}{[K^* + (a_{H_3O^+})]^3} \ldots \quad [7]$$

or

$$v_2 = -\frac{dC_s}{dt} \cdot V = 3 \cdot \beta \cdot k_2 \cdot V \cdot \frac{(K^*)^2 \cdot (a_{H_3O^+}) \cdot C_s^3}{[K^* + (a_{H_3O^+})]^3} \ldots \quad [8]$$

where β represents a kinetic activity factor.

Finally, by differentiating the rates with respect to hydrogen ion activity, pH values are obtained which

* Electrochemical Society Active Member.

[1] Present address: "Jugovinil," Kastel Sućurac, Split, Yugoslavia.

provide maximal conversion for the two theoretically considered mechanisms [for the condition $(dv/d(a_{H_3O^+}) = 0)$]

$$pH_M = pK^* - \log 2 \ldots \quad [9]$$

or

$$pH_M = pK^* + \log 2 \ldots \quad [10]$$

Thus, by applying the thermodynamic value of dissociation constant ($\sim 5.10^{-8}$), one would expect the maximal conversion rate of available chlorine at pH 7.0 for the Foerster mechanism, and 7.6 for the other theoretically possible kinetic path (Eq. [3]).

In dilute solutions, Flis and Byniaeva (11) obtained the maximal conversion rate in the middle of the range defined by the optimal pH values (Eq. [9] and [10]) for the two possible mechanisms and thermodynamic value of dissociation constant, which would in a way be a confirmation of the assumption that the reaction simultaneously proceeds by both theoretically possible kinetic paths.

Critchfield and Johnson (12) showed that, at a fixed constant hydrogen ion concentration, the pH value of an aqueous salt solution is a linear function of ionic strength, *i.e.* of the concentration of neutral salts and of their heats of hydration; that is

$$pH = -\log [H_3O^+] - J)\,(0.18 + 6 \cdot 10^{-3} \cdot \Delta H_s) \ldots \quad [11]$$

where $J = n/2 \times M$, and M the molarity, n the number of ions composing the salt, and ΔH_s the heat of hydration. Thus, in a mixture of NaCl and $NaClO_3$ in concentrations characteristic for chlorate production, the pH value of the electrolyte should be decreased by more than one pH unit (*cf.* [13]), compared to that at zero ionic strength, or, in other words, *hydrogen ion activity coefficient should be larger by one order of magnitude.* Considering that activity coefficients of other components constituting the HOCl dissociation equilibrium (HOCl, OCl^-, and H_2O) are close to each other and close to unity (3, 5, 6, 14),[2] one could conclude that the apparent dissociation constant, K*, should be larger by one order of magnitude, at least, than the one found in dilute solutions. As a direct consequence, the maximal conversion rates of available chlorine into chlorate for the two possible mechanisms should be in the pH range between 6.0 and 6.5, rather than between 7.0 and 7.5, as suggested by some authors (3, 15, 16).

Imagawa (6) also recently found the same phenomenon of the pH decrease in the acid region of sodium chloride solutions containing available chlorine. Such a pH value decrease was explained by the effect of an analogous change of elemental chlorine activity coefficient with increasing neutral salt concentration (6). However, in the alkaline region and in the absence of chlorine, the same pH decrease has also been observed (12, 13). It is, hence, quite evident that such behavior is caused by the presence of neutral salt and depends mainly on its concentration.

Experimental

In a closed-loop system, recently described (8) and consisting of a cell with platinum gauze electrodes and a holding volume, both acting as back mix flow reactors, the effect of pH value of the electrolyte on the degree of conversion of available chlorine inside the latter was investigated. The cell was kept at 25°C so that, apart from the anodic oxidation, the available chlorine consumption was predominantly taking place in the holding volume by chemical conversion to chlorate. Namely, the cell was acting as a steady-state available chlorine generator, and subsequent conversion to chlorate inside a gas-tight holding volume was followed as a function of pH (*cf.* [8]).

The electrolyte was 300 g/liter NaCl and 2.0, 4.0, and 8.0 g/liter of sodium dichromate. Electrolysis was carried out to 30 g/liter of sodium chlorate, whereupon the electrolyte was renewed.

pH values in the holding volume were varied between 4.20 and 10.0, and currents of 2.0-8.0 amp, or current densities of 2.94-11.76 amp/dm^{-2}, were used.

Two quantities were measured simultaneously: the pH values and the total available chlorine of the inflowing and outflowing electrolyte of the holding volume.

The holding volume used was 2.2 liters, and the flow rate, provided by a suitable diaphragm pump, could be varied from 1 to 4 liters/hr, while the temperature was varied between 40° and 60°C.

Results and Discussion

Available chlorine conversion to chlorate inside the holding volume as back mix flow reactor, according to Foerster (1, 2) and Eq. [2] and [7], is given as follows

$$-\left(\frac{dC_{sh}}{dt}\right) \cdot V_h = 3 f^2 \cdot k_1 \cdot V_h \cdot [HOCl]_h^2 \cdot [OCl^-]_h = 3 \cdot f^2 \cdot k_1 \cdot V_h \frac{K_h^* (a_{H_3O^+})_h^2 \cdot C_{sh}^3}{[K_h^* + (a_{H_3O^+})_h]^3} \ldots \quad [12]$$

where all values have a previous meaning, but the subscript h refers here and throughout to the quantities relating to the holding volume.

At the same time, available chlorine conversion inside the holding volume (V_h) is given by the following relationship

$$-\left(\frac{dC_{sh}}{dt}\right) \cdot V_h = q\,(C_{sc} - C_{sh}) \ldots \quad [13]$$

where q is electrolyte flow rate (liters/sec), and C_{sc} and C_{sh} are the total available chlorine concentrations (moles/liter) of inflow and outflow of the holding volume, respectively.

In a previous paper (8), it was shown that current efficiency, t_1, in the case of negligible conversion of available chlorine inside the cell, may be expressed by the equation

$$t_1 = \frac{2}{3} + \frac{2}{3} \cdot \mathbf{F} \cdot \left(\frac{q}{I}\right) \cdot (C_{sc} - C_{sh}) \ldots \quad [14]$$

where **F** is the Faraday constant, and I the load in amperes. Hence, the second term in Eq. [14] defines the yield of the conversion inside the holding volume to the over-all current efficiency of the system.

The effect of hydrogen ion activity on the degree of available chlorine conversion under the actual conditions of industrial chlorate production is represented by the functional relationship of the pH value of the electrolyte inside the holding volume and the second term in Eq. [14], as illustrated in Fig. 1 for temperatures in the range between 40° and 60°C.

It can be clearly seen that the maximum appears in the pH region which has previously been theoretically predicted and expected. Namely, from Eq. [12], [13], and [14], one finds that maximal yields to the over-all current efficiency due to an available chlorine conversion inside a holding volume result at the same optimal pH value [for the condition $dt/d(a_{H_3O^+}) = 0$], which provides maximal reaction rates (Eq. [9]).

[2] According to Imagawa (6), activity coefficient of hypochlorite ion (f_{OCl^-}) in 5.43M NaCl solution is 1.064. Weiss (14) gives activity coefficients of hypochlorous acid for 4.986M NaCl : 1.304, and for 5.468M NaCl : 1.404. Finally, activity of water was recently calculated by Gazith (23): for 5.0M NaCl, $a_{H_2O} = 0.8068$; for 5.4M, $a_{H_2O} = 0.7883$; and for 6.0M NaCl, $a_{H_2O} = 0.7598$; cf. [3]. Therefore,

$$\frac{f \cdot a_{H_2O}}{f_{OCl^-}} \to 1$$

and, from Eq. [6], it follows

$$K^* = \frac{a_{H_3O^+} \cdot [OCl^-]}{[HOCl]} = K_a \cdot \frac{f \cdot a_{H_2O}}{f_{OCl^-}} \to K_a$$

or, apparent dissociation constant of hypochlorous acid, K*, is a linear function of activity coefficient of hydrogen ion, which increases with increasing concentration of neutral salt, NaCl and $NaClO_3$.

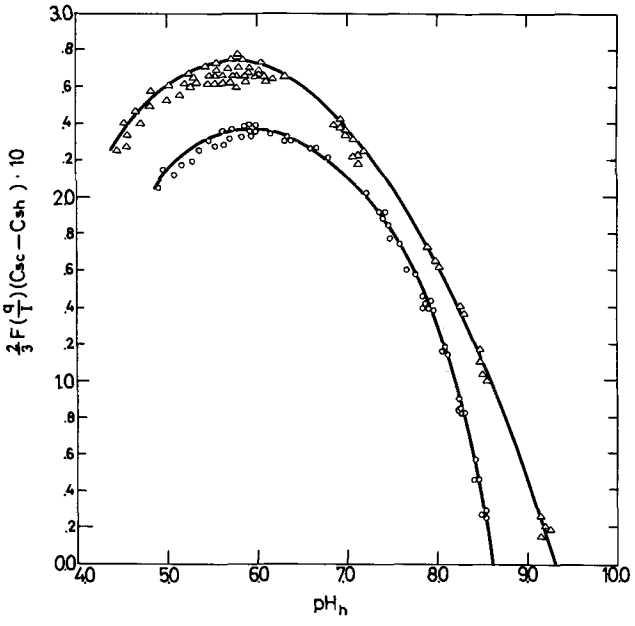

Fig. 1. Contributions of available chlorine conversion to chlorate inside a holding volume to the over-all current efficiency as a function of pH of the holding volume, pH_h: ○ and △ represent curves for temperatures in a holding volume of 40° and 60°C, respectively.

In addition, it has been shown experimentally that in the presence of 5*N* NaCl all the usual buffer solutions show a decrease in pH values for more than one pH unit as compared to the values characteristic for pure aqueous solutions. On this ground, one would also expect an apparent change in the dissociation constants of various acids as a function of ionic strength of neutral salts. Namely, if one has in mind that the maximal buffer capacity is obtained at pH = pK, and that this pH region is changed, it would be reasonable to expect that the dissociation constant itself follows the same dependence.

By titrating solutions of hydrochloric acid and sodium hydroxide of known concentrations, each containing 5*N* NaCl in order to keep the ionic strength unchanged during the titration at 25°C, the ratio $a_{H_3O^+}/[H_3O^+] = f_{H_3O^+}$ was determined for each point of titration and, by the least-squares method, the conversion factor was obtained, $f_{H_3O^+} = 10.0$.

Filippov (17) experimentally showed that losses of graphite anodes in the chlorate production are lowest at pH 6.0, which might be interpreted by the effect of maximal available chlorine conversion in this region, since it has previously been shown that these losses are proportional to the amount of available chlorine present inside the cell (18).

Filippov (19) also pointed out without entering into theoretical considerations, that, in a closed-loop flow system for chlorate production, the maximal efficiency is achieved when the pH value of the cell is 6.0-6.1. Since the whole system was operated at one and the same temperature, the total volume of the electrolyte could be considered integrally, and the results obtained be brought into agreement with the theory presented here and serve as its additional confirmation.

Wranglen (15) recently suggested that current efficiency of the chlorate cell is independent of the pH value of the electrolyte. However, in his experiments the current efficiency was evaluated from the gas analysis and in more alkaline solutions the evolved carbon dioxide was absorbed by the electrolyte. This we consider as a possible source of error that may have led to dubious conclusions (15).

The authors (24) pointed out earlier that the pH value inside the cell directly contributes to the current efficiency by affecting the equilibrium inside the anodic diffusion layer, thus determining the conditions for the hydrolysis of chlorine inside it. On the other hand, it has been shown here that the pH value constitutes a measure of the available chlorine conversion through the system. Therefore, the control of this value at main points of a closed-loop system for the electrolytic chlorate production is of particular importance. From this consideration and taking into account the figures obtained elsewhere (24), it can be concluded that the optimum conditions for chlorate production are provided in the pH value range of 5.7-6.1 and 6.5-6.8 at the point of outflowing the holding volume and the cell, respectively.

It could easily be shown using the usual engineering considerations (20) that a steady-state plug flow reactor under identical working conditions provides higher degrees of conversion than the back mix flow reactor of identical dimensions, so that the former constitutes a more favorable holding volume for industrial chlorate production. Nevertheless, depending on the working cell conditions, the herein previously defined optimal pH value should be maintained at the exit of the reactor, by successively adding hydrochloric acid or caustic soda through it.

The above-described effect of neutral salts also provides for the maximal buffer capacity of the system (HOCl) and (NaOCl) to be just in the pH region which provides maximal conversion of available chlorine. Wagner (21) earlier showed that only minimal and limited chromate reduction at the cathode makes it possible to suppress completely the cathode reduction of hypochlorite ions. Thus, it was here pointed out that it is possible to reduce the presence of dichromate in the electrolyte under the concentration of 1 gpl in order to achieve all the necessary effects (buffering effect and OCl^- cathodic reduction to be suppressed enough). This facilitates pure crystalline chlorate to be obtained in the absence of chromate.

The formerly derived general equation for current efficiency in electrolytic chlorate production (8) has been confirmed under the practical conditions of operation and found to hold only if the values of the apparent thermodynamic dissociation constant are applied, which is another confirmation of the theory (8).

Further Consequences

By analogy, one might expect an apparent change in the equilibrium constant for the hydrolysis of chlorine

$$Cl_2 + 2H_2O \rightleftharpoons HOCl + H_3O^+ + Cl^- \qquad [13]$$

in agreement with the increase in the hydrogen ion activity coefficient, caused by the presence of neutral salts under the conditions of electrolytic chlorate production. Namely, by applying the thermodynamic values which hold for dilute aqueous solutions, Ibl (22) came to the conclusion that, for current densities of practical importance, the hydrolysis of chlorine is not accomplished inside the diffusion layer, but extends into the bulk of solution.

However, by using the apparent values of the equilibrium constants for the hydrolysis of chlorine, corresponding to the actual conditions of the chlorate production and, in agreement with our consideration, by one order of magnitude higher than the known thermodynamic values, it may be shown that the hydrolysis of chlorine in the diffusion layer may be complete. This has actually been confirmed by the experimental and operating practice of chlorate production.

At the same time, one comes to the conclusion that neutral salts, by causing dehydration of the ionic shell of hydrogen ions in aqueous solutions, bring about, on the one hand, a considerable increase in the hydrogen ion activity coefficient and acidity at all, and, on the other, an adequate apparent increase of the value of the thermodynamic dissociation constant of weak acids and bases, as compared to the values pertaining to dilute solutions. The magnitude of this effect is a function of the concentration and heat of solution of the salt (12). Salts with the highest positive heat of

hydration produce the greatest change in pH, hydrogen ion activity coefficient, and apparently in thermodynamic dissociation constant. In this way, the values for thermodynamic dissociation constants, which are constant for any given ratio of components constituting the dissociation equilibrium itself, are no longer invariable with an increased variable composition of neutral salts, as foreign ionic species having a predominant and specific effect on hydrogen ion activity coefficient.

Our measurements and results (Fig. 1) could also be considered as further confirmation of Foerster's (1, 2) mechanism (Eq. [1] and [9]) between two possible ones, including, in equations for one order of magnitude, apparently increased values of the hypochlorous acid dissociation constants.

Acknowledgments

This work has been carried out at the Electrochemistry Department of the Institute of Chemistry, Technology and Metallurgy of Belgrade, and was supported by the Faculty of Chemical Technology of Split.

The authors gratefully acknowledge and are greatly indebted to Professor Dr. A. R. Despić of Belgrade for his personal interest in this work, useful advice, and contributions to the direct preparation of the present paper.

Manuscript submitted Sept. 20, 1968; revised manuscript received *ca.* Feb. 13, 1969. This paper was presented in part at the Chlorates and Perchlorates Symposium at the Boston Meeting, May 5-9, 1968, as Paper 257.

Any discussion of this paper will appear in a Discussion Section to be published in the December 1969 JOURNAL.

REFERENCES

1. F. Foerster and E. Müller, *Z. Elektrochem.*, **9**, 171, 195 (1903).
2. F. Foerster, *Trans. Am. Electrochem. Soc.*, **46**, 23 (1924).
3. V. de Valera, *Trans. Faraday Soc.*, **49**, 1338 (1953).
4. A. Skrabal, *Monatsh.*, **84**, 102 (1953); **70**, 168 (1937); **71**, 251 (1938).
5. H. Imagawa, *Denki Kagaku (J. Electrochem. Soc. Japan)*, **18**, 382 (1950); **19**, 271 (1951); **20**, 25, 571 (1952); **21**, 520 (1953).
6. H. Imagawa and Y. Tanaka, *Bull. Fac. Eng., Yamaguchy Univ.*, Special Printing, Series 10, No. 1, p. 147 (1967).
7. J. d'Ans and H. E. Freund, *Z. Elektrochem.*, **61**, 10 (1957).
8. M. M. Jaksić, A. R. Despić, I. M. Csonka, and B. Z. Nikolić, Paper 257 presented at Electrochem. Soc. Meeting, Boston, May 5-9, 1968.
9. M. W. Lister, Can. *J. Chem.*, **30**, 879 (1952); **34**, 465 (1956).
10. B. P. Nikoljskij and I. E. Flis, *Zh. Obshch. Khim.*, **22**, 1298 (1952).
11. I. E. Flis and M. K. Bynyaeva, *Zh. Priklad. Khim.*, **30**, 339 (1957).
12. F. E. Critchfield and J. B. Johnson, *Anal. Chem.*, **31**, 570 (1959).
13. K. Schwabe, *Electrochim. Acta*, **12**, 67 (1967).
14. J. J. Weiss, *Z. Anorg. Chem.*, **192**, 97 (1930).
15. L. Hammar and G. Wranglen, *Electrochim. Acta*, **9**, 1 (1964).
16. N. V. S. Knibbs and H. Palfreemen, *Trans. Faraday Soc.*, **16**, 402 (1920).
17. T. S. Filippov, V. I. Eberil, R. A. Agapova, and G. W. Razygraeva, *Zh. Prikl. Khim.*, **40**, 2488 (1967).
18. M. M. Jaksić and I. M. Csonka, *Electrochem. Technol.*, **5**, 473 (1967).
19. V. A. Shliapnikov and T. S. Filippov, *Elektrokhimia*, **2**, 1273 (1966); **4**, 20 (1968).
20. O. Lewenspiel, "Chemical Reaction Engineering, An Introduction to the Design of Chemical Reactors," pp. 99-157, John Wiley & Sons, New York (1962).
21. C. Wagner, *This Journal*, **101**, 181 (1954).
22. N. Ibl, *Chem. Ing.-Tech.*, **39**, 706 (1967); D. Landolt "Über den Mechanismus der anodischen Chloratbildung," Ph.D. thesis, Prom. Nr. 3673, Eidgenösischen Technischen Hochschule, Juris-Verlag, Zürich (1965).
23. M. Gazith, "Molal Osmotic Coefficients and Water Activities for Various Electrolytes," p. 19, Israel Atomic Energy Commission, Soreq Nuclear Research Center (1965).
24. M. M. Jaksić, A. R. Despić, and B. Z. Nikolić, To be published.

Statistical Studies of Rechargeable Battery Systems

J. P. Elder*, [1] and E. M. Jost**

Research and Development Department, Metallurgical Materials Division, Texas Instruments Incorporated, Attleboro, Massachusetts

ABSTRACT

The application of the 2^n factorial experiment to the study of the factors influencing the behavior of hermetically sealed, rechargeable Ni-Cd cells is discussed. The characteristic cell parameters may be expressed as logarithmic functions of the pertinent charge-discharge conditions. Data fitting is accomplished by means of a linear regression analysis. Both primary and factor interaction effects contribute to the behavior of the cells. The magnitudes of the effects are dependent on the cell operating conditions. The effects resulting from a cobalt addition to the positive electrode are primarily related to the kinetics of the charge and discharge reactions.

Numerous investigations, aimed at elucidating the effect of process and other experimental variables on the parameters characterizing the operation of a rechargeable battery system, have been performed. In many cases, a meaningful interpretation of the data is difficult, since one cannot separate the effects of the various factors controlling the over-all operational behavior. The term "factor" will be employed to describe any independent variable of the system under the control of the investigator, with the exception of those pertaining to the operating conditions, *i.e.* the charge-discharge routine.

Generally, factors may be of a qualitative or quantitative nature. For example, in a sealed Ni-Cd cell, the nature of the separator material is a qualitative factor, while the electrode thicknesses and the total volume of electrolyte are quantitative factors. In many cases, the composite effect of two or more factors is synergistic; the factors are said to interact. Considerable advantage is gained if the experimental design is such that the effect of changing any one factor can be stud-

* Electrochemical Society Active Member.
** Electrochemical Society Active Member Representative of a Sustaining Member Company.
[1] Present address: Research and Development Division, Whittaker Corporation, San Diego, California.

ied independently of the others. Furthermore, it is of considerable importance to be able to assess the significance of both primary factor effects and factor interaction effects separately. Of the various planned statistical procedures available, the factorial experiment affords a promising method of achieving these objects. It must be noted that the magnitudes of the various factor effects will vary according to the charge-discharge conditions to which the cell is subjected. Thus, a factor, such as an electrode additive, may affect the charge acceptance capabilities of the electrode but show little or no effect on the charge delivery characteristics. By performing a series of cell behavior studies over a range of operating conditions, it should be possible to predict the conditions under which a factor or combination of factors will exert a dominant effect. The results of such studies should prove useful to the battery manufacturer in designing and fabricating cells to be operated under a specific charge-discharge routine.

Factorial Experiments

The reader is referred to Cochran and Cox (1), Davies (2), and Ostle (3) for detailed discussions of this statistical procedure. In this experiment, the effects of a number of factors, set at two or more levels, are examined. For example, in one experiment one may wish to examine two types of separator material, four positive electrode thicknesses, and three electrolyte concentrations. Such an experiment is referred to as a $2^1.3^1.4^1$ factorial. Twenty-four cells are required, each containing a different combination of the three factors at the different levels. Generally, the number of factor combinations required for a complete study is given by $\pi_i L_i^{n_i}$, where L_i is the number of levels of each of the n_i factors. The term "factorial" refers to the manner in which the various factor combinations are formed and not to any basic type of design (3). As can be seen, when one is considering setting up a laboratory-scale experiment with a number of factors at more than two levels, the number of combinations can very easily become prohibitive. It is possible to gain insight into the effect of the various factors by employing only a fraction of the maximum number of combinations. The reader is referred to Davies (2) for a discussion of fractional factorial experiments. The most simple factorial experiment is one in which n factors are examined at two levels only, *i.e.*, the 2^n factorial. The particular factor arrangement for this type of experiment will be elaborated on at a later stage. The procedure is as follows. Having chosen the type of factorial, the various factor-level combinations are incorporated into the requisite number of systems under study. A parameter, characteristic of the system, is measured for each member of the factorial set. An effect is then calculated for each member. Each effect is a measure of the deviation of the parameter value from the set average taking into account the specific factor-level combination contributing to the deviation. In the case of the 2^n factorial, one calculates the effect due to changing a factor from one level (low) to the second level (high) averaged over the two levels of the remaining factors. With a knowledge of the experimental error associated with each measurement for each member of the set, the significance of each calculated factor or factor combination effect is then estimated by means of the statistical F-test.

Factorial experiments have been widely and successfully employed in many fields. However, to the knowledge of the authors, applications of this procedure in electrochemical research, and in particular battery research, have been sparse. Resnic (4) employed a $2^4.4^1$ half factorial in a study of the effect of charge rate and charge level on the faradaic capacity of sealed Ni-Cd cells of various types at various ambient temperatures. Cupp (5) examined the effects of various factors, including positive electrode additives and electrolyte additives, in a $3^4.2^4$ factorial experiment pertaining to the performance of both sealed and vented Ni-Cd cells. The experimental design, referred to as the basic plan for factors was not described in any detail and, furthermore, a literature reference was not given. Panzer and Schaer (6) employed a fractional 2^5 factorial experiment in an optimization study relating to the performance of molten alkali thiocyanate cells. Very recently, Blickwedel (7) has reported on the results of a 2^4 and a 2^3 full factorial experiment performed on Ni-Fe and Ni-Zn cells, respectively. The factors included electrode geometry, electrolyte concentration, electrolyte additive, and separator material. The faradaic capacity was expressed as a linear function of the primary factors and first-order factor combinations. Data fitting was accomplished by means of a multilinear regression analysis. Each partial regression coefficient was used as an indicator of the effect of its associated factor or factor combinations on the capacity independent of the other factors. The computed t-values were used to rank the order of importance of the various factor combinations in affecting the capacity.

Although the limitations of the factorial experiment should not be minimized, the disadvantages are outweighed by the advantages, which may be summarized as follows:

1. Maximum efficiency in the statistical evaluation of a minimal quantity of data.
2. Information on factor interaction effects is obtained, necessary to preclude misleading conclusions.
3. Latent replications inherent in the factorial arrangement result in a comprehensive study over a range of experimental conditions.

There are three main requisites for a successful battery 2^n factorial experiment:

1. The parameter response should be a linear function of the factor level between the chosen limits.
2. The parameter response should be reproducible under identical experimental conditions.
3. The sample cells should have the capability of withstanding a variety of charge-discharge conditions.

It is difficult to realize the first condition. In the case of quantitative factors, one can assume that it is approximated by selecting close limits for the two levels. One of the most significant problems plaguing the battery industry has been the lack of reproducibility of electrodes and cells fabricated under identical conditions. In this laboratory, a great deal of effort has been devoted to determining the causes of these variances, and eliminating them. As indicated by Jost and Popat (8), with the present state of our art, these variances have been reduced to a point where a factorial experiment becomes meaningful. Such experiments have been carried out in this laboratory only after achieving this close uniformity and reproducibility. As indicated in the experimental section, the third condition has been met.

A number of factorial experiments, pertaining to the effect of various factors on the performance of sealed, sintered plate, Ni-Cd cells, have been carried out in this laboratory. This paper deals with the findings of one such study.

Ni-Cd Cell 2^4 Factorial Experiment

The effect of the presence of cobalt on the behavior of the positive electrode in the sealed Ni-Cd cell has been studied relatively extensively in comparison with other metallic ion species. While Yamashita (9) and Doran (10) indicate that this additive improves charge retention, Januszkiewicz (12) indicates little or no effect. Doran (11) reports that the effect of a cobalt addition is to raise the positive electrode potential during discharge and, with up to 20% addition, the efficiency is enhanced (12). During impregnation with hot, concentrated nickel nitrate solution, the sintered nickel plaque corrodes. The extent of corrosion is markedly affected by replacing from 0 to 15% of the nickel content of the impregnation liquor with cobalt (13). Furthermore, the extent of corrosion is dependent on the physical nature of the carbonyl nickel employed to

Table I. Physical characteristics of carbonyl nickel and sintered plaque

INCO designation	Avg particle diameter (μ)	Avg density (g/cc)	Plaque porosity (%)	Weight per cent plaque corroded 0% Co	5% Co
#287	2.9-3.6	0.88	90	18.7	26.5
#255	2.6-4.3	0.59	93.3	25.5	27.0

Table II. Ni-Cd cell, 2^4 factorial experiment

Designation	Factors Description	Levels Low (0)	High (1)
		INCO	INCO
A	Carbonyl nickel plaque material	#255	#287
B	Ratio $Cd/Cd(OH)_2$ at 100% charge level	1.73	6.9
C	Percentage pore filling with 30% KOH	64	82
D	Percentage cobalt in positive plate	0	4.4

fabricate the sintered plaque. As a result of these observations, it is pertinent to reconsider the role of cobalt. Two positive electrode factors were chosen for study: 1—cobalt additive, 2—sintered plaque physical characteristics. The relevant physical parameters of the two types of carbonyl nickel powder used are shown in Table I. As can be seen, sintered plaque fabricated with INCO #255 powder corrodes more than that made from the more coarse-grained #287 powder. However, 5% cobalt in the impregnation liquor only increases the extent of corrosion of the #255 plaque by 6%, whereas a 40% increase is effected in the case of the #287 plaque.

The electrolyte distribution is an important factor in governing the cell behavior. It will be influenced both by the structure of the positive plate and the total amount of electrolyte. Turner (14) has shown that the rate of oxygen recombination in sealed Ni-Cd cells is directly proportional to the state-of-charge of the negative electrode. However, the rate will also be governed by the oxygen diffusion rate through the separator, which will be highly dependent on the amount of electrolyte available for distribution within the separator. These two facts formed the basis for the choice of the remaining factors: 3—volume of 30% potassium hydroxide added to the cell, and 4—ratio of cadmium to cadmium hydroxide in the negative electrode at full charge. The two levels chosen for the four factors are summarized in Table II. A four-digit code, which must not be confused with a number written in binary notation, is employed to describe the cells comprising the factorial set. The digits 0 and 1 are assigned to the low and high levels, respectively, of each factor. The 16 factor combinations are shown in their specific order in the second column of Table III.

Experimental

Cell theoretical capacities.—Weight gain data cannot be used to calculate the theoretical capacity of an electrode, prepared by impregnation of a sintered nickel plaque with nickel or cadmium nitrate solution, since it does not correctly account for the Ni^{2+} produced as a result of plaque corrosion. Analytical procedures have been developed in this laboratory, whereby the total amount of Ni^{2+} may be determined in the presence of Co^{2+} and/or metallic nickel. Similar analytical techniques have been developed for the selective determination of metallic cadmium and Cd^{2+} in the presence of metallic nickel and Ni^{2+}. The theoretical capacity of the positive electrode is calculated on the basis of the total amount of $Ni(OH)_2$. Since there is no evidence that cobaltic ion, which is more stable than nickelic, takes part in the discharge reaction, the amount of $Co(OH)_2$ in the "cobalt additive" plates is not included in the capacity calculation. The theoretical capacities of both electrodes are given by $N\ A\ L\ X$, where N is the number of plates, each of geometric area, A in.^{2}; L is the plate loading, *i.e.* grams of $Ni(OH)_2$ or $Cd(OH)_2$ per in.^{2}; and X is the appropriate conversion factor, 0.292 AH/g $Ni(OH)_2$ and 0.367 AH/g $Cd(OH)_2$. The electrodes, following production, are charged at the 3-hr rate and discharged at the 2-hr rate in the flooded condition. The delivered capacities agree very closely with those calculated from the analytical data.

Experimental cells.—Prismatic cells, of nominal capacity, 1 *AH*, were used for this study. Replicate cells were not assembled. Nylon separators (Pellon) were used throughout. The electrolyte was carbonate-free 30% (6.9M) potassium hydroxide. All cells were filled under vacuum with the requisite volume of electrolyte. The 16 cells were positive limited, and remained so during the entire course of the experiment. No electrical shorts, electrolyte leakages, or excessive cell pressures developed during the various charge-discharge routines.

Data acquisition and test routines.—The factorial sets were located on individual series-connected test stations. All tests were performed under constant current conditions, using a 36v-5 amp regulated power supply (Hewlett-Packard, Harrison model 6266A). Each station was equipped with an adjustable level, voltage and pressure switch, whereby any cell could be electrically bypassed independently of its neighbors. Cell voltage data were automatically recorded, using the DYMEC data acquisition system (Hewlett-Packard, model 2010F), coupled to an IBM card punch. Internal resistances were measured by means of the superimposed a-c technique. Elapsed time meters (Cramer,

Table III. Ni-Cd cell 2^4 factorial experiment

Test routine: 150% Charge level C/10 Charge rate C/2 Discharge rate Ambient temp. 22°C

Cell #	Factor code A	B	C	D	Effcy. data	Factor effect	Variance ratio V	Significance level P	E.C.V. data	Factor effect	Variance ratio V	Significance level P	O.C.V. data	Factor effect	Variance ratio V	Significance level P
1	0	0	0	0	0.6482				1.424				1.388			
2	1	0	0	0	0.6186	−0.0396	5.86	0.940	1.423	0.0059	9.23	0.971*	1.388	0.0030	9.23	0.971*
3	0	1	0	0	0.6555	0.0128			1.423	0.0016			1.388	−0.0003		
4	1	1	0	0	0.6223	−0.0216	1.75	0.757	1.426	0.0031	2.61	0.833	1.389	−0.0003		
5	0	0	1	0	0.7223	0.0742	20.59	0.994*	1.424	0.0059	9.23	0.971*	1.393	0.0063	40.07	0.999*
6	1	0	1	0	0.7112	0.0005			1.429	0.0029	2.21	0.803	1.397	0.0003		
7	0	1	1	0	0.6926	−0.0319	3.82	0.892	1.420	−0.0004			1.390	−0.0030	9.23	0.971*
8	1	1	1	0	0.7037	−0.0037			1.438	0.0031			1.394	0.0005		
9	0	0	0	1	0.5195	−0.0717	19.25	0.993*	1.411	−0.0059	9.23	0.971*	1.376	−0.0052	28.27	0.997*
10	1	0	0	1	0.5195	−0.0239	2.13	0.796	1.418	−0.0004			1.383	0.00075		
11	0	1	0	1	0.6524	0.0194	1.41	0.711	1.416	−0.0001			1.383	−0.0010	1.03	0.642
12	1	1	0	1	0.5547	−0.0263			1.419	−0.0011			1.386	−0.0005		
13	0	0	1	1	0.6640	0.0029			1.424	0.0021	1.21	0.678	1.390	0.0010	1.03	0.642
14	1	0	1	1	0.6328	−0.0152			1.424	−0.0024			1.392	−0.0015		
15	0	1	1	1	0.6913	−0.0199			1.418	−0.0011			1.386	−0.0013		
16	1	1	1	1	0.5663	−0.0027			1.430	0.0009			1.389	0.0008		
					Mean = 0.6359 E.V. = 0.00107				Mean = 1.423 E.V. = 0.000015				Mean = 1.389 E.V. = 0.0000039			

* Significant factor effects.

type 636Y, Giannini Controls Corporation) were employed to measure discharge times to the 1v cut-off, from which faradaic capacities were calculated. Bourdon gauges (Ashcroft #1850, Manning, Maxwell and Moore, Inc.) were attached directly to each cell. Following the automatic recording of voltage data, internal pressure, and discharge time data, test routine information and cell factor-level codes were manually punched. For each charge-discharge routine, two cards per cell were required to record all pertinent information. The IBM s/360, model 30 computer was employed to analyze all data. The analysis of variance and multilinear regression analysis programs were written in Fortran IV.

Thirty-two separate test routines, covering the ranges: 70-150% charge input level, C/50-C/1 charge rate, and C/10-2C discharge rate, were performed at random. During each test, cell voltages were measured at end of charge, E.C.V., on open circuit, O.C.V. following a 2-hr stand period, and at 25, 50, and 75% depth of discharge, based on the theoretical capacity. The cell internal resistances and pressures were measured at end of charge (E.C.R. and E.C.P.). During the stand period, pressure decay data were recorded. There was no capacity degradation after the completion of the entire test routine.

Results

For each test routine, factor effects were calculated for each type of data, with the exception of cell voltages, at 25 and 75% depth of discharge. The Yates sum and difference iterative technique (15) was employed for this purpose. The reader is referred to Davies (2) for an account of this procedure. There are two means whereby an estimate of the experimental error may be made. One or more replicates of each cell of the factorial set may be assembled and tested. The second method, which does not involve the use of replicates, is based on the assumption that true high-order interaction effects are insignificant; *i.e.*, the effects calculated for those cells with three or four high-level factor combinations are due to experimental error. The error variance is then given by the mean square effects for these combinations in the factorial set. It is the opinion of the authors that the uniformity of the cells produced in this laboratory justifies the use of this second method in this factorial experiment. As an example, the efficiency, end-of-charge, and open-circuit voltage data, measured under the conditions 150% charge input level, C/10 charge rate, and C/2 discharge rate, are shown in Table III. Since the analysis calculates only the effect of one or more high-level factors on the parameter value, no effect is calculated for cell #1. The error variance is the mean-square effect for cells #8, 12, 14, 15, and 16. These estimates of error are comparable with those measured from an independent source in this laboratory (8). The variance ratio is given by:

$$V = \frac{2^{n-2}\,(\text{Effect})^2}{\text{Error variance}} \qquad [1]$$

If $V > 1$, then the level of significance of the effect is calculated from the relationship:

$$P = \int_v^\infty F(x, \phi, \theta)\, dx \qquad [2]$$

where $F(x, \phi, \theta)$ is the F-distribution function for ϕ and θ degrees of freedom (3). It has been decided that no significance should be attached to an effect if $P \leq 0.95$. Thus, under the charge-discharge conditions shown in Table III, only three primary effects can be considered significant.

As the experiment proceeded, certain patterns emerged as regards the primary and interaction effects of the four factors on the several parameters. Over the entire range of test conditions, the presence of the INCO 287 more coarse-grained and highly corroded carbonyl nickel substrate resulted in an increase in E.C.V., E.C.R., and E.C.P. The cell voltage at 50% depth of discharge is lowered by this factor, and the efficiency decreased. The high ratio of $Cd/Cd(OH)_2$ emerged as a significant factor only when the cells were overcharged at a relatively high rate. Under these conditions, the E.C.V. is raised. At high charge rates, the presence of this factor tends to effect a reduction in E.C.P. The effect of the high-percentage pore fill was consistent throughout the series of tests. On overcharge, the E.C.V. is raised. The O.C.V., the cell voltage at middle of discharge, the E.C.P., and the efficiency are raised, and the E.C.R. reduced. The effects of the cobalt additive were the most interesting feature of this study. The direction of the effect of this factor on the several parameters is highly dependent on the charging conditions, and to a lesser extent on the discharging conditions. This additive primarily affects the E.C.V., E.C.P., O.C.V., and the efficiency.

During the course of the tests, it was observed that for a constant charge input the faradaic capacity increased linearly with the logarithm of the charging current, when discharged at a constant rate. Similarly, under constant charge and discharge current conditions, the delivered capacity increased linearly with the logarithm of the charge input. A similar dependency between delivered capacity and discharge current, following constant charging conditions, was indicated, although not so well defined. Based on these observations, an attempt was made to fit the predischarge parametric data to an equation of the form:

$$\text{Parameter} = K_0 + K_1 \log_{10}(C.L.) + K_2 \log_{10}(C.R.) \qquad [3]$$

and all other data to an equation of the form:

$$\text{Parameter} = K_0 + K_1 \log_{10}(C.L.) + K_2 \log_{10}(C.R.) + K_3 \log_{10}(D.R.) \qquad [4]$$

where the charge level, charge rate, and discharge rate are given by

$$C.L. = C.T./C.R. \quad [5], \qquad C.R. = T.C./C.C. \quad [6],$$

$$D.R. = T.C./D.C. \quad [7]$$

$T.C.$ is the theoretical cell capacity, calculated on the basis of a chemical analysis of the active material in the positive plates, as previously indicated, $C.C.$, $D.C.$, and $C.T.$ are the charging current, discharging current, and charging time, respectively. The data fitting was accomplished with the aid of a multilinear regression analysis program. In Tables IV and V are shown the regression coefficients and associated statistical data for the E.C.V. and efficiency for each cell in the factorial set. The efficiency is the ratio of the faradaic capacity to the theoretical capacity. Each independent variable is separately correlated with the dependent variable; r_i^2 is the square of the correlation coefficient, corrected for degrees of freedom, of the ith independent variable, $i = 1$, 2, and 3; S_i is the standard error associated with the coefficient, K_i; t_i is the absolute value of the ratio, K_i/S_i; $S.E.E.$ is the standard error of the estimate; $M.C.C.$ is the multiple correlation coefficient; F is the statistical F-value. As can be seen, both the E.C.V. and the efficiency data correlate well with the logarithms of the charge level and the charge rate. The values of r_3^2 indicate a low dependency of the efficiency on the discharge rate. The values of t_i for each cell give a relative measure of the importance of each independent variable in governing the magnitude of the dependent variable. Thus, the E.C.V. is more dependent on the charge rate than on the charge level. For most cells, the charge rate and the charge level are of equal importance in determining efficiency. It is to be noted that certain factors markedly affect the relative r_i^2 and t_i values. Thus, for example, with reference to the E.C.V. data, Table IV, compare t_1 and t_2 for cells 9 and 10 in relation to the values for the remaining cells.

Table IV. Ni-Cd cells. 2^4 Factorial experiment. E.C.V. $= K_0 + K_1 \log_{10}(C.L.) + K_2 \log_{10}(C.R.)$
Regression coefficient and associated statistical data. 32 Observations. $\phi = 2$, $\theta = 29$

Cell No.	Factor code A	B	C	D	K_0	K_1	r_1^2	S_1	t_1	K_2	r_2^2	S_2	t_2	S.E.E.	M.C.C.	F
1	0	0	0	0	1.507	0.1386	0.084	0.0337	4.11	−0.0641	0.683	0.0063	10.18	0.020	0.890	60.36
2	1	0	0	0	1.526	0.1294	0.040	0.0408	3.17	−0.0775	0.717	0.0076	10.16	0.024	0.884	56.70
3	0	1	0	0	1.505	0.1584	0.127	0.0308	5.14	−0.0620	0.665	0.0058	10.76	0.018	0.905	71.14
4	1	1	0	0	1.532	0.1444	0.051	0.0436	3.31	−0.0796	0.695	0.0082	9.77	0.026	0.878	53.22
5	0	0	1	0	1.503	0.1872	0.185	0.0324	5.77	−0.0594	0.593	0.0061	9.79	0.019	0.897	64.66
6	1	0	1	0	1.515	0.2015	0.186	0.0334	6.03	−0.0636	0.606	0.0062	10.30	0.020	0.905	71.23
7	0	1	1	0	1.509	0.2047	0.192	0.0368	5.56	−0.0623	0.564	0.0069	9.06	0.022	0.884	56.50
8	1	1	1	0	1.561	0.3309	0.239	0.0578	5.73	−0.0857	0.489	0.0108	7.94	0.034	0.867	47.94
9	0	0	0	1	1.513	0.0670	0.012	0.0321	2.08	−0.0803	0.837	0.0060	13.36	0.019	0.924	91.46
10	1	0	0	1	1.521	0.0904	0.003	0.0324	2.79	−0.0824	0.829	0.0060	13.62	0.019	0.928	96.75
11	0	1	0	1	1.537	0.2194	0.106	0.0504	4.25	−0.0880	0.637	0.0094	9.34	0.030	0.877	52.66
12	1	1	0	1	1.514	0.1198	0.038	0.0326	3.68	−0.0759	0.778	0.0061	12.47	0.019	0.918	84.61
13	0	0	1	1	1.514	0.1923	0.153	0.0297	6.47	−0.0708	0.686	0.0056	12.74	0.018	0.931	102.21
14	1	0	1	1	1.523	0.1967	0.137	0.0322	6.11	−0.0764	0.699	0.0060	12.69	0.019	0.929	99.26
15	0	1	1	1	1.521	0.2283	0.178	0.0345	6.62	−0.0768	0.650	0.0065	11.91	0.021	0.925	92.87
16	1	1	1	1	1.555	0.2919	0.186	0.0491	5.95	−0.0929	0.602	0.0092	10.13	0.029	0.903	69.09
		Mean			1.522	0.1810				−0.0749						

Table V. Ni-Cd cells. 2^4 Factorial experiment. Efficiency $= K_0 + K_1 \log_{10}(C.L.) + K_2 \log_{10}(C.R.) K_3 \log_{10}(D.R.)$
Regression coefficient and associated statistical data. 32 Observations. $\phi = 3$, $\theta = 28$

Cell No.	Factor code A	B	C	D	K_0	K_1	r_1^2	S_1	t_1	K_2	r_2^2	S_2	t_2	K_3	r_3^2	S_3	t_3	S.E.E.	M.C.C.	F
1	0	0	0	0	0.818	0.894	0.359	0.103	8.69	−0.190	0.448	0.019	9.82	0.092	−0.026	0.049	1.88	0.061	0.920	57.94
2	1	0	0	0	0.710	0.663	0.258	0.087	7.65	−0.164	0.475	0.016	10.07	0.136	0.001	0.041	3.32	0.052	0.917	55.67
3	0	1	0	0	0.820	0.967	0.407	0.107	9.07	−0.183	0.397	0.020	9.14	0.089	−0.027	0.051	1.77	0.063	0.917	55.92
4	1	1	0	0	0.717	0.668	0.301	0.090	7.40	−0.156	0.447	0.017	9.23	0.129	−0.001	0.043	3.01	0.054	0.906	48.61
5	0	0	1	0	0.836	1.043	0.477	0.100	10.44	−0.172	0.343	0.019	9.15	0.093	−0.025	0.047	1.96	0.059	0.928	65.05
6	1	0	1	0	0.792	0.877	0.429	0.095	9.27	−0.157	0.371	0.018	8.86	0.083	−0.025	0.045	1.86	0.056	0.917	55.53
7	0	1	1	0	0.803	0.955	0.450	0.104	9.18	−0.161	0.340	0.020	8.26	0.090	−0.024	0.049	1.82	0.062	0.911	51.56
8	1	1	1	0	0.793	0.895	0.430	0.098	9.15	−0.159	0.365	0.018	8.68	0.087	−0.024	0.046	1.87	0.058	0.914	53.77
9	0	0	0	1	0.694	0.453	0.102	0.086	5.28	−0.203	0.664	0.016	12.55	0.158	0.004	0.041	3.88	0.051	0.927	64.62
10	1	0	0	1	0.705	0.434	0.098	0.087	5.02	−0.198	0.679	0.016	12.17	0.130	−0.010	0.041	3.18	0.051	0.922	59.44
11	0	1	0	1	0.807	0.778	0.295	0.100	7.82	−0.191	0.498	0.019	10.20	0.106	−0.022	0.047	2.25	0.059	0.917	55.96
12	1	1	0	1	0.723	0.476	0.133	0.079	6.01	−0.190	0.661	0.015	12.77	0.126	−0.010	0.038	3.35	0.047	0.931	68.34
13	0	0	1	1	0.821	0.804	0.314	0.094	8.59	−0.192	0.499	0.018	10.90	0.105	−0.022	0.044	2.36	0.056	0.928	65.24
14	1	0	1	1	0.808	0.743	0.285	0.090	8.24	−0.190	0.534	0.017	11.23	0.088	−0.027	0.043	2.07	0.054	0.928	65.37
15	0	1	1	1	0.839	0.897	0.373	0.094	9.50	−0.188	0.447	0.018	10.59	0.103	−0.023	0.045	2.30	0.056	0.931	68.46
16	1	1	1	1	0.786	0.647	0.252	0.087	7.41	−0.178	0.558	0.016	10.85	0.069	−0.030	0.041	1.68	0.052	0.920	58.01
		Mean			0.780	0.762				−0.179				0.105						

The introduction of cobalt into the positive plate causes the E.C.V. to be much more dependent on the charge rate than in the cells not containing cobalt in the nickel hydroxide electrode. Although not so marked, a similar effect is observed with regard to the efficiency data, Table V. The high values of *M.C.C.* indicate that only a small percentage of the experimental data over the entire range of charge-discharge conditions was removed by the regression. The high *F* values indicate that the data fit the proposed equations very well. For the E.C.V. equation, with 2 and 29 deg of freedom, an *F* value exceeding 8.85 is significant at the 0.999 level. For the efficiency equation, with 3 and 28 deg of freedom, an *F* value exceeding 7.19 is significant at the 0.999 level. From the values of the standard error of the estimate, it is seen that, over the operating range covered, the experimental and calculated value of E.C.V. agree to within 1-2%. Similarly, efficiencies are predictable to within 5%. Similar analyses have been performed for the other parametric data recorded. In all cases, the experimental data have been shown to fit the proposed equations.

The factor effects causing the variations in the values of the various regression coefficients may be calculated and tested for significance in the same manner as previously described. For the constant term, K_0, there is no independent estimate of the error. Again, it is assumed that high-order interactions are insignificant and, therefore, the calculated effects for the cells with the second- and third-order interaction factor combinations may be employed to estimate the error variance. In the case of the remaining coefficients, K_i, the regression analyses result in independent estimates of error, S_i. For each cell in the factorial set, the error variance is given by S_i^2. The effects are calculated by the Yates technique, and the significance level, *P*, is given by Eq. [2] with $\phi = 1$ and $\theta = 5$ for the analyses of variance pertaining to K_0. For the analyses of variance pertaining to the K_i coefficients, θ is given by

θ = Number of observations
— Number of independent variables — 1

In Table VI are summarized the findings of the analyses of variance for the following cell parametric data, E.C.V., O.C.V., E.C.R., E.C.P., the cell voltage at mid-discharge and the efficiency. Only *P* values ≥ 0.95 are shown. The signs in parentheses show the direction of the effect on changing the factor from the low to the high level. It has been shown in this laboratory that, if a 50% charged positive plate is employed in a Ni-Cd cell as a reference electrode, then the electrode potentials with respect to this reference, at various stages of the charge-discharge routine, may be correlated with the cell operating conditions by equations of the types [3] and [4].

Discussion

The method of summarizing experimental Ni-Cd battery data, obtained under a variety of operating conditions, by means of the logarithmic parametric equation has proved very successful. First, it allows one to present a large amount of data in a highly compact form. Second, the independent correlation coefficient data, resulting from the regression analyses, indicate the relative importance of the three operational conditions, charge input level, charge rate, and discharge rate, in governing the over-all performance.

For the particular cells employed in this study, the cell efficiency is determined primarily by factors which affect, and conditions associated with, the charge acceptance capabilities of the positive electrode. The end-of-charge voltage and pressure, and to a certain extent the open-circuit voltage and the end-of-charge resistance, serve as useful indicators of this capability, which is governed by the electrode structure and the availability of the electrolyte. The effects produced by the incorporation of certain factors, specifically *A* and *C*, into the cell design, were, to a certain extent, predictable. However, as indicated in the introductory

Table VI. Ni-Cd cell. 2^4 Factorial experiment. Significant factor effects on parametric equation coefficients

Factor code A	B	C	D	E.C.V. K_0	K_1	K_2	O.C.V. K_0	K_1	K_2	E.C.P. K_0	K_1	K_2	E.C.R. K_0	K_1	K_2	Effects Primary	Interaction
0	0	0	0														
1	0	0	0	0.955(+)		0.973(+)					0.997(+)	0.999(+)	0.990(+)			*A*	
0	1	0	0		0.999(+)	0.954(+)						0.953(+)				*B*	
1	1	0	0					0.996(+)				0.999(+)					*AB*
0	0	1	0		0.999(+)		0.999(+)				0.999(+)	0.984(−)	0.999(−)	0.999(−)	0.999(+)	*C*	
1	0	1	0		0.968(+)								0.966(−)		0.963(+)		*AC*
0	1	1	0														
1	1	1	0														
0	0	0	1			0.999(+)	0.979(+)		0.999(+)		0.999(+)					*D*	
1	0	0	1								0.968(+)						*AD*
0	1	0	1														
1	1	0	1								0.996(+)						*ABD*
0	0	1	1														
1	0	1	1														
0	1	1	1														
1	1	1	1														

Factor code A	B	C	D	Cell voltage at mid-discharge K_0	K_1	K_2	K_3	Efficiency (%) K_0	K_1	K_2	K_3	Effects Primary	Interaction
0	0	0	0										
1	0	0	0	0.992(−)	0.999(−)	0.999(+)		0.982(−)	0.999(−)			*A*	
0	1	0	0										
1	1	0	0										
0	0	1	0	0.970(+)				0.991(+)	0.999(+)			*C*	
1	0	1	0	0.986(+)									*AC*
0	1	1	0										
1	1	1	0										
0	0	0	1						0.999(−)	0.992(+)		*D*	
1	0	0	1										
0	1	0	1										
1	1	0	1										
0	0	1	1	0.984(−)									*CD*
1	0	1	1										
0	1	1	1										
1	1	1	1										

paragraphs, their inclusion was considered necessary in order to be able to interpret the cobalt effect.

Factor A.—Cells containing positive electrodes, produced by impregnating the more dense, less porous, sintered #287 carbonyl nickel plaque, are significantly less efficient over the entire range of operating conditions. The correlation coefficient data show that this factor causes the efficiency and the cell voltage data to become less dependent on the charge level, and more rate dependent. However, the opposite effect results for the end-of-charge pressure. The E.C.V. and E.C.R. are increased by this high-level factor, while the cell voltage at mid-discharge is decreased. In the overcharge region, the E.C.P. is raised by this factor.

Factor B.—The negative electrode, high state-of-charge factor shows little effect on the parametric data. In the overcharge region, it does manifest itself in contributing to an increase in both the end-of-charge voltage and pressure. The pressure decay data, although not presented, have been shown to follow the logarithmic relationship (14), $p_t/p_o = \exp(-t/\tau)$. The presence of the excess amount of metallic cadmium at full charge has no significant effect on the oxygen recombination relaxation time constants. Although there is no substantiating evidence, it appears that the higher pressures developed, in the presence of this high-level factor, are due to enhanced hydrogen evolution.

Factor C.—As is fully expected, the effect of the higher percentage pore fill is beneficial to the over-all cell performance. The correlation coefficient data indicate that this high-level factor causes the efficiency, the end-of-charge voltage, and pressure to be more dependent on the charge input level than on the charge rate. However, the end-of-charge cell resistance becomes markedly more dependent on the charge rate than on the charge level. The open-circuit voltage, cell voltage at mid-discharge, and the efficiency are raised, and the end-of-charge resistance is markedly decreased. The oxygen diffusion rate through the cell is impaired by the relative increase in the amount of electrolyte. This is mirrored in the significant increase in the end-of-charge pressure, and a significant decrease in the relaxation time constant for oxygen recombination.

Factor D.—As is indicated in Table I, the inclusion of cobaltous ion in the impregnation liquor causes the two types of nickel plaque to be corroded to the same extent. Thus, the effect of the cobalt additive is to oppose the primary effect of factor *A*. This is further emphasized by the efficiency data for cells #9 and #10 (*see* Table V). Irrespective of the original nature of the substrate, the efficiency regression coefficient data for the electrodes containing the cobalt additive are very similar. The primary effect of the cobalt additive is to enhance the kinetics of the charge acceptance and charge delivery reactions. Thus, the correlation coefficients associated with the charge level regression coefficients of the efficiency and cell voltages are markedly decreased, while the correlation coefficients associated with rate dependency are greatly increased. The fact that there is a cobalt effect *per se*, independent of the positive electrode structure modification effect, is shown by the significant primary factor *D* effects shown in Table VI. Following charge at a high rate, the end-of-charge and open-circuit voltages and the efficiency are raised. Thus, under certain operating conditions, a cobalt additive can enhance the efficiency. However, under other conditions, cobalt can exert a detrimental effect. By considering the relative values of the four terms in the efficiency equation, in the absence and presence of a cobalt additive, one can predict the over-all effect of this additive under different test routines. The predicted effects agree very well with those actually observed, which may be summarized as follows:

1. At or below the 100% charge level, the effect of cobalt is to increase efficiency, especially after charging at high rates.
2. At medium to low discharge rates, C/5-C/50, cobalt contributes to an increase in efficiency.
3. When the positive electrode is overcharged, the presence of a cobalt additive is detrimental to the efficiency.

Conclusion

Provided that high uniformity in cell fabrication and operation can be maintained, the 2^n factorial experi-

ment is a very useful tool whereby the effects of factors on the behavior of a battery system may be examined. The significance of factor interaction effects in determining the performance characteristics of Ni-Cd cells should not be overlooked. The combination of the two statistical techniques has proved highly useful as a cell performance optimization procedure. Thus, it allows one to establish the most favorable choice of factors which should be incorporated into a cell designed for operation according to a prescribed charge-discharge routine.

Manuscript submitted May 10, 1968; revised manuscript received Jan. 16, 1969. This paper was presented in part at the Philadelphia Meeting, Oct. 9-14, 1966 as Paper 19.

Any discussion of this paper will appear in a Discussion Section to be published in the December 1969 JOURNAL.

REFERENCES

1. W. G. Cochran and G. M. Cox, "Experimental Design," 2nd Ed., Chap. 5-8, John Wiley & Sons, New York (1962).
2. O. L. Davies, "Design and Analysis of Industrial Experiments," Hafner Co., New York (1954).
3. B. Ostle, "Statistics in Research," 2nd Ed., Iowa State University Press (1963).
4. B. Resnic, *Proc. Ann. Power Sources Conf.*, **17**, 107 (1963).
5. E. B. Cupp, *ibid.*, **18**, 44 (1964).
6. R. E. Panzer and M. J. Schaer, *This Journal*, **112**, 1136 (1965).
7. T. W. Blickwedel, R&D Tech. Report, ECOM-0102-1, G.T.&E. Labs., Inc., Bayside, N. Y.
8. E. M. Jost and P. V. Popat, *Proc. Ann. Power Sources Conf.*, **20**, 137, (1966).
9. D. Yamashita, *J. Electrochem. Soc. Japan*, **31**, 47 (1963).
10. R. J. Doran, *Proc. 1st Intern. Symp. Batteries*, paper Y (1958).
11. R. J. Doran, *Proc. 2nd Intern. Symp. Batteries*, paper 26 (1960).
12. S. Januszkiewicz, *Proc. Ann. Power Sources Conf.*, **13**, 75 (1959).
13. K. J. Johnson and O. A. Nietzel, Paper 17 presented at Electrochem. Soc. Meeting, Philadelphia, Oct. 9-14, 1966.
14. D. R. Turner, *Electrochem. Technol.*, **2**, 1 (1964).
15. F. Yates, *Imp. Bur. Soil Sci. Tech. Comm.*, **35** (1937).

Secondary Cadmium-Air Cells

O. C. Wagner*

Power Sources Division, Electronic Components Laboratory, United States Army Electronics Command, Fort Monmouth, New Jersey

ABSTRACT

Cadmium-air cells have been developed that deliver 45-50 whr/lb at the C/5 rate of discharge. The major failure modes of the cadmium-air system are: loss of capacity by the cadmium anode, shorting by cadmium penetration, poisoning of the air-cathode by a soluble cadmium species, loss of electrocatalytic activity by the air-cathode during prolonged cycling, and water loss by evaporation through the cathode pores and/or cell vent. It has been determined that loss of capacity by the cadmium anode can be prevented by the addition of Fe_2O_3 or TiO_2 extender into the active structure and by the removal of CO_2 from the influent air stream. It was found that cadmium penetration through the separator wrap can be avoided by preventing carbonate build-up in the electrolyte and by placing a wettable, inert interseparator between the anode and main separator. Poisoning of the air-cathode by soluble cadmium can be overcome by saturating the electrolyte with zincate or aluminate ions. Deactivation of the air-cathode is a problem that requires further investigation, and drying out of the cadmium-air cell can be prevented by providing the cell with an electrolyte sump.

The cadmium-air battery is of interest to the battery technologist in that: 1—it has a theoretical energy density of 202 whr/lb, 2—the stability and cycle life of the alkaline cadmium anode are excellent in nickel-cadmium and silver-cadmium batteries, and 3—the cadmium anode has a very low self-discharge rate.

In order to attain maximum energy density from the cadmium-air system, sponge cadmium electrodes were developed under a USAECOM internal program. The air-cathodes were supplied by General Electric Company and Leesona Moos Laboratories. The separators were supplied by Douglas Aircraft Company, R.A.I. Research Corporation, Pellon Corporation, and E. I. du Pont de Nemours & Company. No auxiliary charging electrodes were employed since the air-cathodes were bifunctional; *i.e.*, they were charging and discharging electrodes.

Experimental Procedure

The sponge cadmium anodes were prepared in the following manner: (*a*) cadmium oxide (Fisher Certified, Cat. No. C-16) was homogeneously blended with 5% by weight of carbonyl nickel powder (International Nickel Company, Type 255) and 5-10% by weight of ferric oxide extender (Fisher Certified, Cat. No. I-116) or titanium oxide extender (Fisher Certified, Cat. No. T-315), and (*b*) 44g of the cadmium oxide mix were mold pressed into an electrode containing an Aldex paper wrap (Aldine Corporation), a 5 Ni-15-2/0 nickel Exmet grid (Exmet Corporation), and a nickel tab. The electrode dimensions were: 0.095 in. in thickness, 3½ in. in height, and 2⅜ in. in width, and the electrode porosity (in the fully charged state) was 62.5%.

The unit cadmium-air cells were constructed as follows: The sponge cadmium anode was inserted into a heat-sealed polyamide Pellon bag of 6 mils thickness (2506K, Pellon Corporation). Around this, one or two layers of main separator material were laterally wrapped. The wrapped negative was then inserted into another Pellon bag (2506K) which completed the separator system for the unit cell. The electrode pack was finally inserted into a bicell containing state-of-the-art bifunctional air-cathodes. Nylon mesh air spacers of 100 mils thickness were placed on the gas side of the air cathodes, and the complete unit cell was secured between lucite supports.

Key words: electrochemistry, energy storage, batteries, cadmium-air, cadmium electrodes, air-cathodes, extenders.

* Electrochemical Society Active Member.

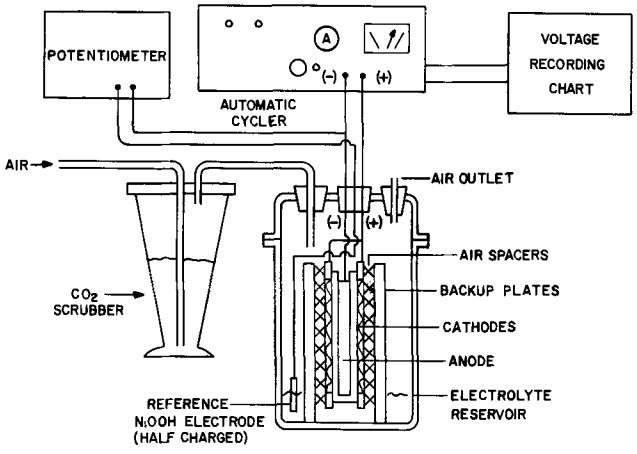

Fig. 1. Instrumentation

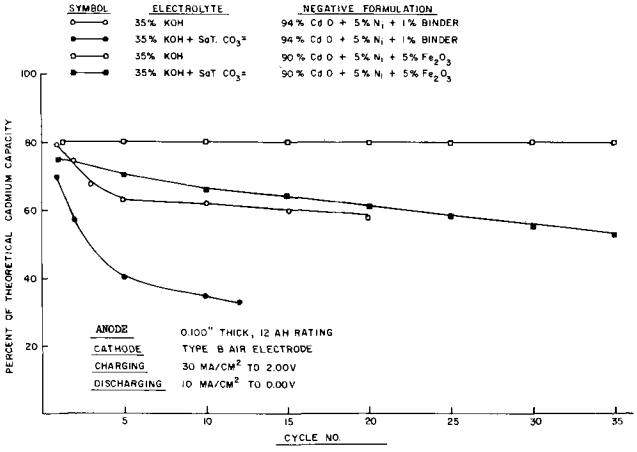

Fig. 2. Capacity maintenance as a function of cadmium mix and CO_2 exposure.

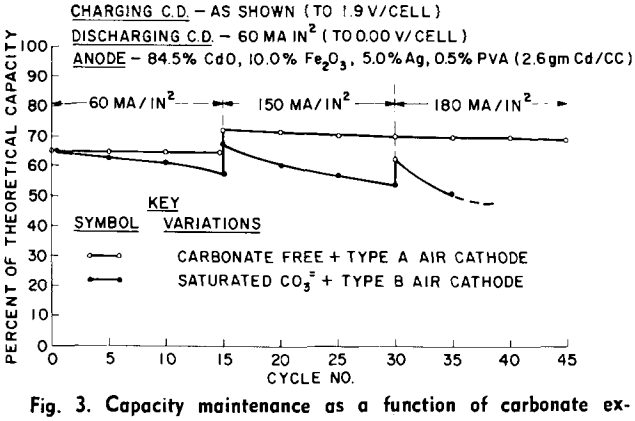

Fig. 3. Capacity maintenance as a function of carbonate exposure and charging current density.

The instrumentation employed in this program is shown in Fig. 1. The unit cadmium-air cell was contained in a reaction kettle. An electrolyte reservoir provided electrolyte to the electrodes by means of the wicking action of the Pellon wraps. The cell was cycled using an automatic cycler with the voltage cut-off set to zero volts on discharge and 1.9v on charge (C/5 rates of charge and discharge). Reference readings were taken with a potentiometer using a partially charged nickel-hydroxide reference electrode. Charge-discharge curves were automatically recorded by a Honeywell-Electronik voltage recorder. When desired, carbon dioxide was removed from the incoming flow of air by means of a scrubber which contained KOH solution. All tests in this program were run at room temperature ambient.

Results

The major failure modes of the cadmium-air system are: loss of capacity by the cadmium anode, shorting by cadmium penetration, poisoning of the air-cathode by a soluble cadmium species, loss of electrocatalytic activity by the air-cathode during prolonged cycling, and water loss by evaporation through the cathode pores and/or cell vent.

Loss of capacity by the cadmium anode.—When an alkaline cadmium electrode is continuously cycled on a deep discharge regime, it gradually loses capacity. This phenomenon is often observed with nickel-cadmium and silver-cadmium batteries when the cells become cadmium limiting on discharge.

The problem of capacity loss by the cadmium anode was to a large extent overcome by the introduction of alpha ferric oxide into the active cadmium powder and by removal of CO_2 from the influent air to the unit cell. Figure 2 shows that a control cadmium-air cell with a sponge negative containing no extender, and which was exposed to CO_2 (black circles), lost 37% of its initial capacity in 12 cycles. A test cell (open squares) with a negative containing 5% ferric oxide, and where CO_2 was removed from the unit cell, delivered 80% of theoretical capacity without any loss in capacity for 35 cycles. The combination of 5% ferric oxide extender and CO_2 exposure (black squares) resulted in the loss of 30% capacity in 35 cycles, while the combination of no extender and no CO_2 exposure (open circles) resulted in a capacity loss of 25% in 20 cycles. From these data, it is seen that the loss in capacity by the cadmium anode can be prevented by the addition of ferric oxide extender to the active cadmium powder and by the removal of CO_2 from the influent air to the unit cell. Recent test results show that 5-10% titanium dioxide also acts as an extender for the cadmium anode, the results being equivalent to that of ferric oxide.

The carbonate effect is further illustrated in Fig. 3. The figure shows the capacity of the sponge cadmium anode (containing 10% Fe_2O_3) as per cent of theoretical capacity *vs.* cycle number. The prime variables were cycling of the cell in carbonate free electrolyte (open circles) and in carbonate saturated electrolyte (solid circles). No data are available for intermediate concentrations of carbonate-KOH solutions. From the figure, it is seen that carbonate exposure decreased the capacity of the anode by 30% in 35 deep cycles, while the anode in a carbonate-free electrolyte lost only 3% of its initial capacity in the same number of cycles. Later cycling data of the test cell containing the ferric oxide extender and where the influent air was scrubbed free of CO_2 show that 75-80% of the theoretical capacity was attainable after 100 deep discharge cycles. These anode efficiencies yield energy densities of 45-50 whr/lb for optimumly designed cadmium-air unit cells of nominal 10 amp-hr capacity.

Cadmium penetration.—Cadmium, like zinc, has been known to build up crystals which can penetrate separators and cause shorting of batteries. Table I shows the effects of carbonated electrolyte, overcharge, and the separator system on shorting by cadmium penetration. Group A separator wraps were employed in a carbonate-saturated cadmium-air cell containing a sponge anode. Group B separator wraps were with a carbonate saturated cell containing a sintered cadmium anode. Group C separator wraps were with a CO_2 scrubbed cell containing a sponge anode.

From the data in Table I, it can be seen that cadmium penetration can be prevented by: (*a*) eliminating carbonate from the unit cell (compare Group C with Groups A and B), (*b*) minimizing overcharge, and (*c*) placing a layer of polyamide Pellon between the anode and main separator (compare A1 and A2). In addition, sintered-nickel cadmium anodes appear

Table I. The effect of overcharge, carbonate, and separator system on cadmium penetration

	Separator system	Cycles to short	Total amp-hr of overcharge
A	Sponge cadmium-air cell ($CO_3^=$ saturated)		
A1	(+) 1×0.001 in. Cellophane/1×0.006 in. Pellon (−)	58	48
A2	(+) 1×0.006 in. Pellon/2×0.001 in. cellophane (−)	9	5
A3	(+) 1×0.006 in. Pellon/2×0.002 in. Astroset /1×0.006 in. Pellon (−)	75	76
B	Sintered nickel cadmium-air cell ($CO_3^=$ saturated)		
B1	(+) 1×0.006 in. Pellon (−)	98	56
C	Sponge cadmium-air cell (no $CO_3^=$ in electrolyte)		
C1	(+) 1×0.006 in. Pellon/2×0.002 in. Astroset /1×0.006 in. Pellon (−)	120+ (still cycling)	180+
C2	(+) 1×0.006 in. Pellon/1×0.0015 in. RAI P300 /1×0.006 in. Pellon (−)	20+ (still cycling)	20+

more resistant to shorting than sponge anodes (compare Group B with Group A).

Cadmium poisoning of the air-cathode.—Both types of air-cathodes evaluated in this program (from General Electric and Leesona Moos) became severely polarized toward the end of discharge in cells discharged at current densities greater than 10 ma/cm². On subsequent recharge, the cathodes were reactivated and exhibited normal E-I discharge responses *vs.* fully charged cadmium anodes. However, *vs.* nearly fully discharged cadmium anodes, the air-cathodes become inactive during discharge. Even when a fresh uncycled air-cathode was discharged against a nearly fully discharged cadmium anode, the cathode became inactive.

Spectrographic analysis shows the presence of 0.1 mg/cm² cadmium in the air-cathode after cycling in a cadmium-air bicell. The poisoning of the air-cathode by the cadmium anode occurred in KOH electrolytes which were free of carbonate ions or other impurities. In these experiments, the influent air had been CO_2 scrubbed.

Figure 4 shows that when the electrolyte is saturated with carbonate ions, deactivation of the air-cathode will not occur. For comparison, the figure includes the discharge curves of the air-cathodes and cadmium anodes (*vs.* an Hg/HgO reference cell) in pure 7 normal KOH (open circles) and 7 normal KOH saturated with carbonate (solid circles). From these data, it appears that the cadmium anode forms a soluble species which poisons the air-cathode, but in the presence of carbonate ions the poisoning effect is prevented. However, as was shown in Fig. 2, carbonate severely decreases the capacity of the cadmium anode (after 20 cycles). Therefore, carbonate is not a desirable additive in a cadmium-air cell to prevent poisoning of the air-cathode. Consequently, a search was

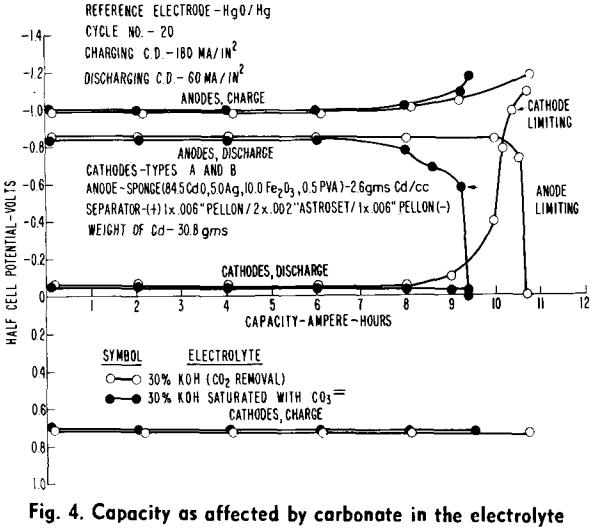

Fig. 4. Capacity as affected by carbonate in the electrolyte

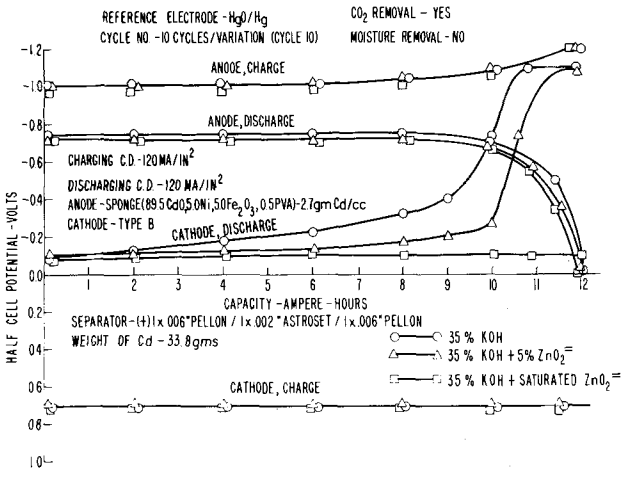

Fig. 5. Capacity as a function of zincate ion content

made for electrolyte additives which would: (*a*) prevent poisoning of the air-cathode by cadmium ions, and (*b*) be innocuous to the cadmium anode. One such additive has been found. As shown in Fig. 5, when the electrolyte was saturated with zincate ions, the air-cathode did not deactivate at the end of discharge. In addition, the electrical efficiency of the cadmium anode was not impaired after 10 deep discharge cycles. Since overcharge did not show a zinc deposition step, it apparently is safe to saturate the electrolyte with zincate in a rechargeable cadmium-air cell. It should be pointed out that aluminate ions have also been found to prevent cathode poisoning. At present, cadmium-air cells with zincate electrolyte are being life cycled and other additives are being screened in an effort to understand and better control the poisoning effect of the air-cathode.

Deactivation of the air-cathode on prolonged cycling.—Another failure mode encountered in the cadmium-air cell program was deactivation of the air-cathode after prolonged cycling. Figure 6 shows the performance of a cadmium-air cell during 300 deep discharge cycles. The air-cathode was manufactured by the Leesona Moos Laboratories in 1966 for a prototype mechanically rechargeable zinc-air battery. The anode was a sintered cadmium anode, and the influent air was *not* CO_2 scrubbed. The upper curve in the figure shows the capacity maintenance of the cell. The cell

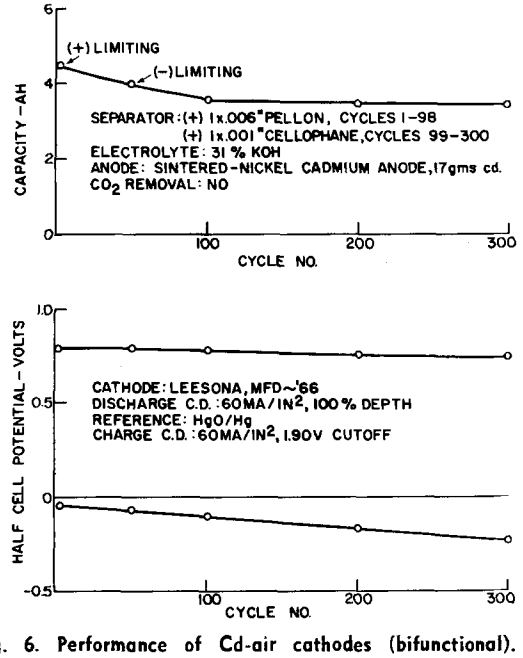

Fig. 6. Performance of Cd-air cathodes (bifunctional). (CO_2 exposure; 31% KOH.)

lost 25% of its initial capacity during the first 100 cycles and was negative-limiting in each discharge cycle. Since the electrolyte became saturated with carbonate ions, the anode lost capacity by carbonate contamination and the air-cathode never became limiting on discharge.

The lower curves in the figure show the half-cell potentials of the anode and cathode *vs.* cycle number (using an Hg/HgO reference cell). At a discharge current density of 10 ma/cm^2, the anode half cell potential decreased from 800 to 750 mv in 300 cycles, while that of the air-cathode decreased from minus 50 to minus 220 mv. The drop in anode potential is probably caused by carbonate contamination and the drop in cathode potential is attributed to a loss in electrocatalytic activity of the platinum catalyst.

Figure 7 shows the performance of cadmium-air cells which were constructed with state-of-the-art air-cathodes manufactured by General Electric and Leesona Moos Laboratories. The cells were charged at 20-ma/cm^2 to a 2.0v cutoff and discharged at 10 ma/cm^2 to a zero volt cutoff. The cells were given 50 deep discharge cycles (without overcharge); the influent air was CO_2 scrubbed; the electrolyte was pure 30% KOH; and the anodes were sponge cadmium electrodes containing 5% ferric oxide extender. From the figure, it is seen that: (*a*) the half-cell potential of the air-cathodes decreased from minus 50 to minus 100 mv in 50 cycles, (*b*) the cells were positive-limiting for each discharge cycle, (c) the electrical capacity decreased by about 10% for each cell in 50 cycles, and (*d*) the negative half-cell potential remained constant at 800 mv during the 50 cycles. In this experiment, the poisoning effect of the air-cathode by soluble cadmium again was very evident. Therefore, the deactivation effect of the cathodes was not very apparent.

To demonstrate more clearly the deactivation effect of the air-cathodes, the preceding experiment was repeated by using similar cells but employing 30% KOH electrolyte saturated with zincate ions. In this case, the cadmium poisoning effect would not be a factor. Figure 8 shows the performance of these cells during 50 deep discharge cycles. It should be noted that the cells were given large overcharges on an intermittent basis. This resulted from failure of the automatic cyclers to cut off on charge during several cycles. The following results were noted: (*a*) one cell failed by cathode flooding after overcharge on

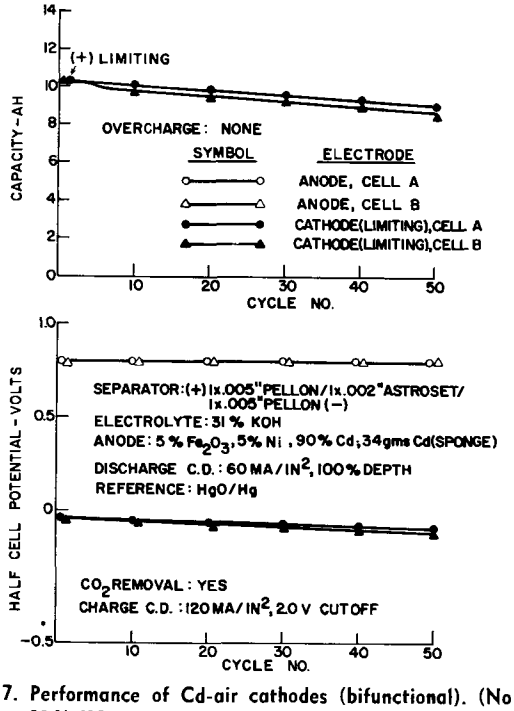

Fig. 7. Performance of Cd-air cathodes (bifunctional). (No CO_2 exposure; 31% KOH).

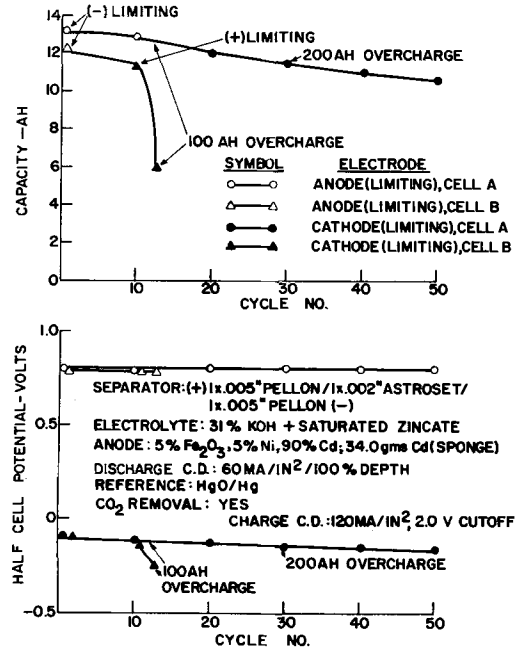

Fig. 8. Performance of Cd-air cathodes (bifunctional). (No CO_2 exposure; 31% KOH + saturated zincate.)

cycle 12, (*b*) the other cell was negative-limiting during the first 20 cycles and became positive limiting during the remaining 30 cycles, (c) the half-cell potential of the air-cathode decreased from minus 100 to minus 160 mv in 50 cycles, and (*d*) the half-cell potential of the cadmium anode remained constant at 800 mv during the 50 cycles.

The slow deactivation of the air-cathode is indicated by the test results of these experiments. The performance characteristics of these state-of-the-art air-cathodes indicate that further developmental work is required to prevent a loss in electrocatalytic activity by the platinum catalyst.

Water loss and unit cadmium-air cell design.—The 10 amp-hr unit cadmium-air cells employed in the USAECOM program lost about 0.5 cc of water per cycle at the C/5 rate of charge and discharge. This water loss primarily resulted from transpiration of water vapor through the pores of the air-cathode and cell vent. As shown in Fig. 9, an optimumly designed cadmium-air cell of nominal 10 amp-hr capacity includes a sump at the base of the cell which contains

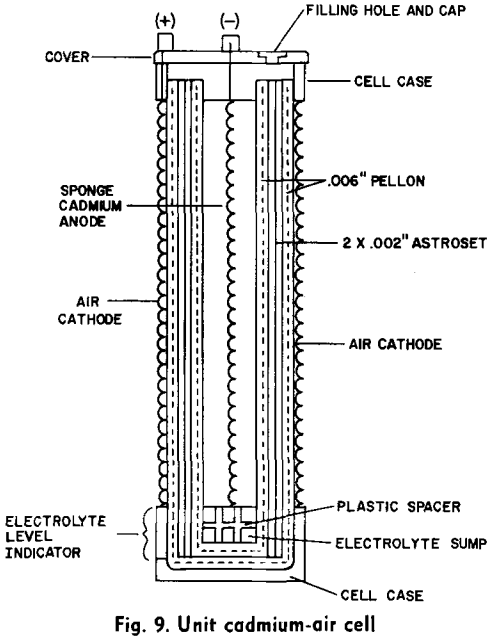

Fig. 9. Unit cadmium-air cell

5 cc of reserve electrolyte (as water). The excess water would prevent drying of the cell for approximately 10 cycles (the unit cells cycled in this program had an electrolyte reservoir of 100 cc of excess electrolyte). The cells could be watered every 10 cycles through a filling hole in the cover, after unscrewing the sealing plug. The required amount of water could be indicated by constructing the cell with a transparent or translucent plastic frame through which the electrolyte level can be seen and adjusted.

Electrolyte absorbent polyamide Pellon is placed in both the anolyte and catholyte compartments to transport electrolyte from the sump to the electrodes. The main separator consists of two layers of a nonoxidizable and nondegradable membrane, such as Astroset 3420-09 (an inorganic membrane from Douglas Aircraft Corporation) or Radiation Applications Inc. P-300 (a grafted polyethylene membrane). The cadmium anode is 100 mils thick, with an apparent porosity of 62%, and contains 5% ferric oxide extender and 5% carbonyl nickel conductor. The air-cathodes are state-of-the-art and bifunctional (with a platinum loading not exceeding 6 mg/cm^2). The electrolyte is 30% KOH saturated with zincate, and CO_2 is removed from the influent air by means of ascarite or soda-lime columns contained within the battery case.

The energy densities on the basis of weight and volume for the 10 amp-hr cadmium-air cell are tabulated in the top of Table II. The weights of the cell components are listed in the bottom of the table. From the data, it is seen that an energy density of 51 whr/lb is attainable at the C/10 rate and 43.5 whr/lb at the C/2 rate.

An actual 24v, 25 amp-hr cadmium-air battery was constructed by General Electric for the U. S. Army Electronics Command. The battery was built according to the design parameters derived from the USAECOM program. The unit test cells had an energy density of 45 whr/lb at the 2-amp rate and the battery plus case hardware had an energy density of 35 whr/lb. Unfortunately, electrolyte leakage from the cells and cathode flooding after prolonged charged stand prevented further testing of the battery. Serious as these problems are, they should not be difficult to correct in future cadmium-air battery designs.

Discussion

The loss in capacity by the cadmium anode is attributed to a loss in real surface area by the growth of cadmium crystals and by the subsequent blockage of the electrode pores (1-3). At moderate and elevated temperatures, the charge and discharge of the cadmium electrode are reported to be controlled by the reaction between a soluble cadmiate ion species [$Cd(OH)_3^-$] and the active lattice sites (4). It is believed that the function of the extender is to provide lattice sites for the formation of cadmium hydroxide and metal cadmium via the soluble cadmiate ion species. As the number of lattice sites, or nuclei, increases, there should then be a greater tendency to form finely divided metal cadmium or cadmium hydroxide. It is possible that any metal oxide, which (*a*) is insoluble in alkali, (*b*) is electrochemically inert, and (c) possesses crystal lattice dimensions similar to those of cadmium hydroxide, could serve as a beneficial extender for the cadmium electrode.

Table II. Energy density calculations for a 12 amp-hr cadmium-air cell

Energy density (cycles 1-50)

Rate	Capacity, amp-hr	CCV, v	Whr/lb	Whr/in.^{3}
C/10	13.5	0.86	51.0	4.05
C/5	12.5	0.83	47.2	3.80
C/2	11.5	0.73	43.5	3.50

Weight of cell components

Cathodes	17.5g
Anode	39.8g
Separator	3.0g
Electrolyte + 5 cc of water	22.0g
Cell case, sump, cover, and other	22.0g
Total	104.3g (0.30 lb)

Volume of cell (including 0.100 in. air spacer) 47.0 cc

The fact that carbonate increases the rate of capacity loss by the cadmium anode may be explained by (*a*) the formation of electrochemically inactive cadmium carbonate and/or (*b*) the accelerated growth of cadmium crystals by a soluble cadmium carbonate species [$Cd(CO_3)_3^{-4}$] (5, 6). The reason that carbonate causes cadmium to penetrate the separator wraps may be due to a dendritic type of electrodeposited metallic cadmium during the reduction of soluble cadmium carbonate. Finally, the fact that carbonate prevents poisoning of the air-cathode by the soluble cadmiate species [$Cd(OH)_3^-$] may be due to a preferential formation of soluble cadmium carbonate by the cadmium anode toward the end of discharge, the soluble cadmium carbonate species being innocuous to the air-cathode. Some of these phenomena are of interest in that they also relate to the performance of nickel-cadmium and silver-cadmium batteries. Basic studies of the effects of carbonate on the electrochemical performance of the cadmium anode are therefore warranted.

The effect of zincate or aluminate ions on the performance of the air-cathode in the presence of cadmiate ions is not understood. Possibly the cadmiate concentration is reduced when the electrolyte is saturated with zincate or aluminate and/or the latter ions prevent chemisorption of cadmiate ions on the electrocatalytic sites of the air-cathode. A study of this phenomenon on a fundamental basis is required.

The loss of electrocatalytic activity by the platinum catalyst after prolonged cycling of the air-cathode may be due to a recrystallization of the platinum and/or loss of hydrophobicity at the three phase interface. Further study and development of the air-cathode is undoubtedly warranted.

Conclusions

1. Loss of capacity by the cadmium anode can be prevented by the addition of ferric oxide or titanium dioxide extender into the active structure and by removal of carbon dioxide from the influent air stream to the unit cells.

2. Cadmium penetration through the separator wrap can be prevented by removal of CO_2 from the cell, minimizing overcharge and placing an inert electrolyte absorbent interseparator between the cadmium anode and main separator.

3. Poisoning of the air-cathode by soluble cadmium can be overcome by saturating the electrolyte with zincate or aluminate ions.

4. Further development work is required on the air-cathode to prevent electrocatalytic deactivation after the prolonged cycling.

5. Water loss can be compensated by providing unit cell with an electrolyte sump.

6. Unit cadmium-air cells have been developed which show a cycle life capability of 300 cycles and an energy density in the range of 45-50 whr/lb.

Manuscript submitted Oct. 16, 1968; revised manuscript received Jan. 17, 1969. This paper was presented at the Montreal Meeting, Oct. 6-11, 1968, as Paper 360.

Any discussion of this paper will appear in a Discussion Section to be published in the December 1969 JOURNAL.

REFERENCES

1. J. P. Harivel, B. Morignat, and J. Migeon, "Investigations on the Negative Electrode of Nickel-Cadmium Cells with Sintered Plates," SAFT, Fourth International Symposium on Batteries, Brighton, England, October 1964.

2. Y. Okinaka, Paper 50, Extended Abstracts of Electrochem. Soc. Meeting, Chicago, Oct. 15-20, 1967.
3. E. Lifshin and J. Weininger, *Electrochem. Technol.*, **5**, 5 (1967).
4. M. Fleischmann, K. S. Rajagopolan, and H. R. Thirsk, *Trans. Faraday Soc.*, **59**, 741 (1963).
5. Y. Okinaka and D. Turner, Paper 28, Extended Abstracts of Electrochem Soc. Meeting, Buffalo, Oct. 10-14, 1965.
6. P. E. Lake and J. M. Gooding, *Can. J. Chem.*, **7**, 1089 (1958).

The Heat Capacity of Electrolytes Simulating Those Found in Silver Chloride-Magnesium Water-Activated Batteries

Duane W. Faletti

Applied Physics Laboratory, University of Washington, Seattle, Washington

and Ivan W. Herrick and Mark F. Adams

College of Engineering, Research Division, Washington State University, Pullman, Washington

ABSTRACT

The heat capacities of magnesium chloride-sea water solutions with chlorinities varying from 4.5 to 19.0 parts per thousand and with 0-70g of magnesium chloride per liter of solution were determined over a temperature range from 5° to 85°C. These solutions simulate the electrolyte conditions found in silver chloride-magnesium water-activated batteries using sea water. An empirical equation was developed which successfully predicts, within 1.5%, the heat capacities of such solutions over a range of chlorinity from 0 to 19 parts per thousand.

Work is in progress to develop an improved design technique for silver chloride-magnesium water-activated batteries based on a semiempirical mathematical model (1). To determine battery performance, heat capacity values accurate to a few per cent are required to calculate the temperature of the electrolyte circulating in flow passages and cells.

AZ61 magnesium alloy is commonly used as the anode in silver chloride-magnesium batteries and sea water is the common electrolyte (though it is possible to operate such batteries on fresh water). Since the primary effect of the battery reaction is to add magnesium chloride to the entering electrolyte, sufficiently accurate results for the purposes of battery design can be obtained from a study of the heat capacity of solutions of magnesium chloride in sea water and in water. Secondary effects include the formation of precipitates of the hydroxides of magnesium, aluminum, zinc, and manganese, and the removal of some of the salts found in the entering electrolytes by, among other things, retention in the sponge silver formed by the reduction of the silver chloride. The solutions studied cover the range of composition and temperature of interest. They were prepared by the method given in Ref. (2).

Experimental Method

The heat capacity was determined by a method commonly applied to static systems: electrical energy was converted to heat at a constant, known rate within the confines of the solution for a known length of time.

Temperature measurements were taken prior to and after the heating period for determining the temperature rise caused by the heat input. The above information plus a knowledge of the heat capacity of the calorimeter and the mass of the fluid in the calorimeter was sufficient to allow a calculation of the heat capacity using the equation

$$Cp = \frac{\dfrac{E^2 t}{4.184\, R \Delta T} - CpCal}{W_{soln}} \qquad [1]$$

Key words: heat capacity, sea water-magnesium chloride solutions, silver chloride-magnesium battery electrolytes.

where Cp is the heat capacity of the solution, Cal/g °C, E is the potential across the heater in volts, t is the length of the heating period in seconds, R is the heater resistance in ohms, ΔT is the temperature rise resulting from the heat input, CpCal is the "heat capacity" (note units) of the calorimeter in Cal/°C, and W_{soln} is the mass of the solution under study.

Apparatus.—Two types of calorimeters were used in this study. One type which worked satisfactorily at 5° and 25°C was simply a 1-liter Dewar flask capped by a cork into which the thermometer, heater, and glass stirrer were mounted, an arrangement which can be operated rapidly and easily. However, there appeared to be no effective way of heating the space in the calorimeter above the liquid while still maintaining calorimetric conditions. The resulting condensation of vapor in this space caused significant errors at temperatures above 45°C.

In order to circumvent these problems, a cavity calorimeter was constructed for use at temperatures of 45°, 65°, and 85°C (Fig. 1). Though agreement between the two calorimeters was acceptable at 45°C, only the results obtained with the cavity calorimeter arrangement are presented for temperatures above 25°C.

A Beckman differential thermometer accurate to 0.002°C was used for the temperature measurements. The heaters were glass coils filled with silicone oil with a nominal 60-ohm length of Nichrome C resistance wire running through them. The resistance wire ended below the liquid level and was connected to copper leads which extended to the outside of the calorimeter.

Electrical energy to the heater was supplied by a stable power supply of 60v. The resistance of the heater was measured immediately before and after the heating period, and the potential drop across the heater was measured during the heating period. The accuracy of the thermometer, electrical components, and balance weights was checked periodically.

Procedure.—All heat capacity determinations were made with a minimum void space above the liquid so that evaporation effects could be ignored.

To eliminate condensation on the upper portion of the calorimeter jar (which occurred at 45°C and

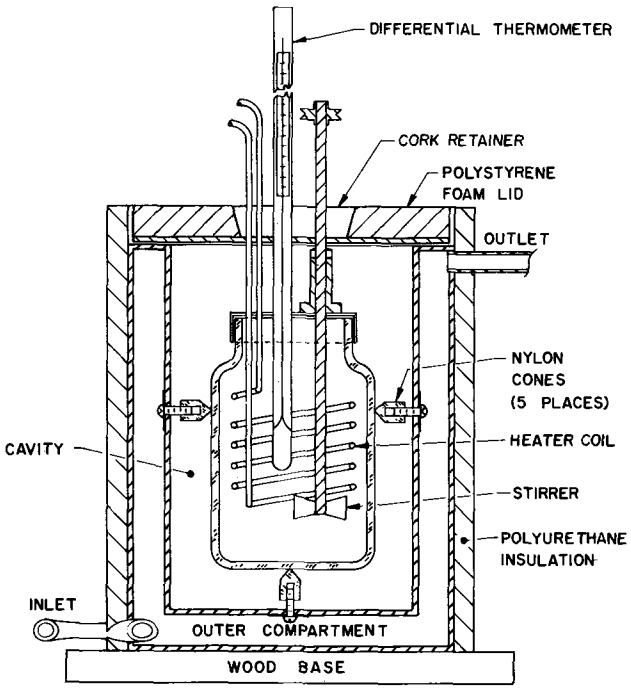

Fig. 1. Schematic of cavity calorimeter; for measuring heat capacity of electrolytes with temperatures ranging from 45° to 85°C.

above), the following procedure was used with the cavity calorimeter: Samples were preheated to about 1°C below the test temperature in a preheating bath, whereupon the top of the calorimeter jar was heated with a hot air blower to evaporate any condensate which may have accumulated there. The calorimeter jar was then placed in the calorimeter with the water circulating through the outer compartment held at 1°C above the test temperature during the entire test.

After the calorimeter was allowed to equilibrate for 20 min, seven temperature readings were taken at 50-sec intervals, whereupon the heater resistance was measured and the heater was started. The voltage of the heater (held constant to 0.01v or better) was measured at least three times during the 150-sec heating interval and the results averaged. Upon completion of the heating period, the heater resistance was measured along with an additional seven temperature readings taken at 50-sec intervals.

Data reduction and error analysis.—The temperature rise in the calorimeter was determined as follows: Separate temperature-time curves were drawn through the two sets of temperatures recorded prior to and following the heating period. This could be done with a maximum deviation of 0.002°C or less by excluding the first point taken after the end of the heating cycle. The temperature rise from the heat input was taken to be the difference of these two temperature-time curves at a time 80 sec after the start of the heating period.

The time chosen to take the temperature rise, using Challoner's Method (3), was based on (*a*) an observed 10-sec time lag between the start of the heating and the first indication of a temperature rise, and (*b*) the apparent linearity of the temperature rise with time during the heating period. This process yields temperature rises with maximum uncertainties of 0.4% (0.008°C) with about two thirds of the uncertainty resulting from the extrapolation process.

The heat capacities of both calorimeters were determined from experiments with water using the techniques described above but solving for the heat capacity of the calorimeter by rearranging Eq. [1] and adding the known value of the heat capacity of water (4). The values of calorimeter heat capacity obtained should at least partially compensate for systematic errors in temperature extrapolations, etc. Five values of calorimeter heat capacity were determined at each temperature level studied from which the average values of calorimeter heat capacity were calculated.

An error analysis based on the values of maximum uncertainties in the five parameters of the experiment (Table I) and the uncertainty values calculated for the heat capacity of the calorimeter (using the values of the same five parameters) gives a maximum uncertainty value of ± 1.25% for the heat capacity results. If the uncertainty value of the calorimeter heat capacity is excluded, a maximum uncertainty value of ± 0.7% results. The latter value is of some interest since the values of the calorimeter heat capacities were subjected to averaging.

As a check on the experimental technique, the heat capacity was determined for four solutions with known heat capacities. Two of these solutions were sea water; the agreement obtained is discussed later. Of the two remaining solutions, one was of 2.44 m/o (mole per cent) sodium chloride solutions which was run through at 45°C. The heat capacity obtained was 0.33% greater than that found by interpolating ICT data (5).

The other check was made with a 0.405 molal sodium chloride solution studied at 85°C. The heat capacity obtained was 0.55% lower than that obtained by Eigen and Wicke (6).

Presentation and Discussion of Results

Three determinations of the heat capacity were made for each solution at each temperature. These three values were averaged and are presented in Table II and Fig. 2. The total spread in the three determinations made at a given point never exceeded 0.7% and was typically 0.3%. Values of the heat capacity of solutions with zero chlorinity, *i.e.* magnesium chloride-water solutions, over a temperature range of 10°-85°C were obtained by crossplotting the results of Eigen and Wicke (6) and Rutskov (7) and are shown in Fig. 2.

An additional check on the accuracy of the results is provided by the values of heat capacity for artificial sea water solutions. The heat capacities determined at 5°C for a solution with a chlorinity of 4.5 parts per thousand (‰) and for a solution at 25°C with a chlorinity of 19.0‰ were, respectively, 0.39% and 0.27% lower than values obtained by Cox and Smith (8).

The empirical equation,

$$Cp = 0.9960 - 0.001259\ (CM) - 0.002174\ (CHL) + 0.000009526\ (CM)\ (CHL) \quad [2]$$

Table I. Estimates of maximum uncertainties

Parameter	Estimated maximum uncertainty, %
Potential (E)	0.03
Resistance (R)	0.05
Mass (W)	0.01
Time (t)	0.07
Temp rise (ΔT)	0.29

Table II. Values of heat capacity of simulated electrolytes for silver-chloride-magnesium sea water-activated batteries (cal/g°C)

Chlorinity (‰)	Added $MgCl_2$ g/liter	5°C	25°C	45°C	65°C	85°C
4.5	0.0	0.987				
4.5	10.0	0.978	0.972	0.984		
4.5	20.0		0.957	0.966	0.961	
4.5	35.0			0.947	0.944	0.945
4.5	50.0				0.926	0.925
4.5	70.0					0.898
9.0	10.0	0.958	0.966	0.970		
9.0	35.0			0.930	0.935	
19.0	0.0		0.953			
19.0	10.0	0.937	0.939	0.957		
19.0	20.0		0.932	0.939	0.934	
19.0	35.0			0.914	0.918	0.916
19.0	50.0				0.899	0.900
19.0	70.0					0.881

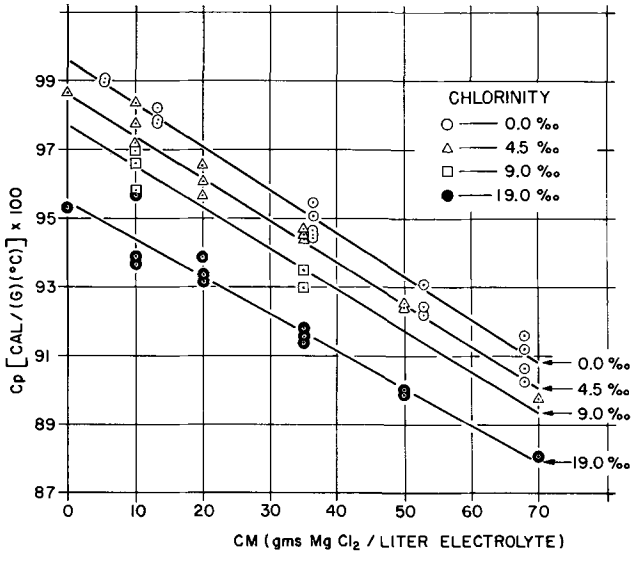

Fig. 2. Heat capacity as a function of added $MgCl_2$. Lines show values of heat capacity as predicted by Eq. [2] for the levels of chlorinity shown, in parts per thousand.

was developed where *CM* is added $MgCl_2$ in g/liter of sea water or fresh water, and *CHL* is chlorinity in parts per thousand. This equation successfully predicts the heat capacity as a function of chlorinity (0.0-0.19°/₀₀) and added magnesium chloride (0-70 g/liter) to within 1%, with two exceptions: The first is a 1.1% deviation with a solution of 4.5°/₀₀ chlorinity and 10 g/liter added magnesium chloride at 45°C; the second is a solution of 19.0°/₀₀ chlorinity and 10.0 g/liter added magnesium chloride at 45°C with a deviation of −1.4%.

The chlorinity of sea water in the world's oceans varies from about 4.5 to 22.5°/₀₀. Since Eq. [2] is based on a linear interpolation between 0.0 and 19.0°/₀₀ chlorinity, the use of Eq. [2] to extrapolate to a chlorinity of 22.5% appears justified.

The electrolyte temperatures and compositions covered in this study are typical of those found in high-drain silver chloride-magnesium sea water-activated batteries. The observed 10% variation in heat capacity (*see* Table II) indicates that corrections for this variation in heat capacity (*i.e.*, Eq. [2]) should be incorporated into design techniques which make use of material and energy balances (such as the design techniques under development at Applied Physics Laboratory, University of Washington).

Acknowledgments

Dr. William R. Davis, Assistant Director of the Applied Physics Laboratory, and Engineering Assistant Mr. Rodney Lipp contributed to the success of this effort. Their contributions are gratefully acknowledged. This work was supported by the Bureau of Naval Weapons, United States Department of the Navy.

Manuscript submitted July 5, 1968; revised manuscript submitted Jan. 27, 1969.

Any discussion of this paper will appear in a Discussion Section to be published in the December 1969 JOURNAL.

REFERENCES

1. D. W. Faletti and M. A. Gackstetter, *This Journal*, **115**, 1210 (1968).
2. D. W. Faletti and M. A. Gackstetter, *ibid.*, **114**, 209 (1967).
3. R. A. Challoner, H. A. Gundy, and R. A. Meetham, *Phil. Trans.*, **A247**, 553 (1955).
4. N. S. Osborne, H. F. Stimson, and D. C. Ginnings, *J. Res. Nat. Bur. Std.*, **23**, 238 (1939).
5. "International Critical Tables," **V**, 122 (1953).
6. M. Eigen and E. Wicke, *Z. Elektrochem.*, **55**, 354 (1951).
7. A. P. Rutskov, *Zh. Prikl. Khim.* (*J. Appl. Chem.*), **21**, 820 (1948).
8. R. A. Cox and N. D. Smith, *Proc. Roy. Soc.* (*London*), **A252**, 51 (1959).

Mechanisms of Oxidation of Ta-10W Alloy Coated With Tungsten Disilicide

Joan B. Berkowitz-Mattuck*

Arthur D. Little, Incorporated, Cambridge, Massachusetts

ABSTRACT

Continuous oxygen consumption measurements have been made on two commercially available W/Si type coatings, the TRW duplex coating and Solar's TNV-13, at temperatures between 1000° and 1800°C and an oxygen partial pressure of 150 Torr in helium. The coatings were applied by the vendors to small cylindrical pellets of Ta-10 a/o W. It was shown that the coated samples undergo significant changes in properties if preheated in non-oxidizing atmospheres. Although the as-received TRW and TNV-13 samples are both nominally similar, they exhibit totally different oxidation behavior under the conditions investigated. Oxidation of the TNV-13 coated samples is parabolic between 1000° and 1700°C, and the parabolic rate constant increases with temperature. Oxidation of the TRW coated samples is logarithmic, and the extent of oxidation in a 1-hr time period decreases as the temperature is increased from 1000° to 1250° to 1500°C. At 1700°C, the TNV-13 coating provides protection, while the TRW coating fails catastrophically. The results of electron microprobe analysis suggest that the basic differences in oxidation mechanism between the two coating systems may be ascribed to the presence of a small amount of titanium in the TNV-13 coating.

The poor oxidation resistance of refractory metals and alloys severely limits their usefulness in oxidizing environments at high temperature. Since the metals themselves are attractive for many projected applications due to their high melting points and good high-temperature strengths, considerable effort has been devoted in recent years to the development of oxidation-resistant coatings. This paper examines the basic oxidation mechanism of two commercial coating sys-

* Electrochemical Society Active Member.

tems, both based on tungsten disilicide, which were developed for improving the oxidation resistance of Ta-10W. The coating systems, while similar from a chemical standpoint, differ both in precise formulation and in over-all oxidation behavior.

Materials

Annealed Ta-10W rod, 0.312 in. in diameter, was supplied by National Research Corporation, Newton, Massachusetts. A certified heat analysis of the material is reproduced in Table I. The principal impurity is seen to be Nb and the W concentration is somewhat lower than the nominal 10%. The as-received rod was machined into cylindrical pellets approximately 0.3 in. in height, a size suitable for the oxidation tests described in Table I. The material analyzed 9.2 w/o (weight per cent) W with the balance Ta.

The coating systems selected for study were the Solar TNV-13 duplex coating (1) and the TRW (Thompson Ramo-Woolridge) silicon-tungsten coating (2). The coatings were applied by the manufacturers to the cylindrical test pellets described above. The basic steps in the respective coating fabrication processes are summarized in Table II. Both coating systems are duplex in nature. The TRW system has a chemically vapor deposited layer of W, applied by Westinghouse, adjacent to the Ta-10W alloy surface. The TNV-13 system starts with a slurry coat of 95W-5Ti. The silicon is diffused into the TRW coating in a vacuum pack, and into TNV-13 in a high-pressure pack. Finally, TNV-13 is impregnated with glass frit, while the TRW coating receives no further treatment.

Oxidation Kinetics Measurements and Results

For both as-received and coated samples, measurements were made of the rate total oxygen uptake as a function of time at temperature. A diagram of the oxidation apparatus is shown schematically in Fig. 1 and has been described previously (3). Briefly, a mixture of helium and oxygen of known composition flows through a thermal conductivity cell (TC-I) containing a thermistor bead detector, and over an inductively heated pellet, where some of the oxygen is lost from the stream by reaction. The oxygen depleted stream passes through a second thermal conductivity cell (TC-II) similar to the first. The two cells, TC-I and TC-II, form two arms of a Wheatstone bridge, whose recorded output at any time is directly proportional to the rate at which the sample is reacting at that time. The recorded rate curve is automatically integrated to give the net extent of reaction over a given time period. The test environment for the oxidation studies reported here was 760 Torr, with 150 Torr oxygen and the remainder helium.

Table I. Certified heat analysis of Ta-10W rod

Impurity	Concentration (ppm)
O	14
N	17
C	48
Al	<25
Cr	<5
Cu	<1
Fe	20
Mo	30
Nb	125
Ni	<5
Si	11
Ti	<10

Table II. Basic steps in coating application

TNV-13 (Solar) (1)	TRW (2)
1. Slurry coat with 95W-5Ti and sinter	1. Chemically vapor deposit W (Westinghouse)
2. Pressure pack silicide in argon near 1 atm	2. Vacuum pack silicide (TRW)
3. Impregnate with glass frit	

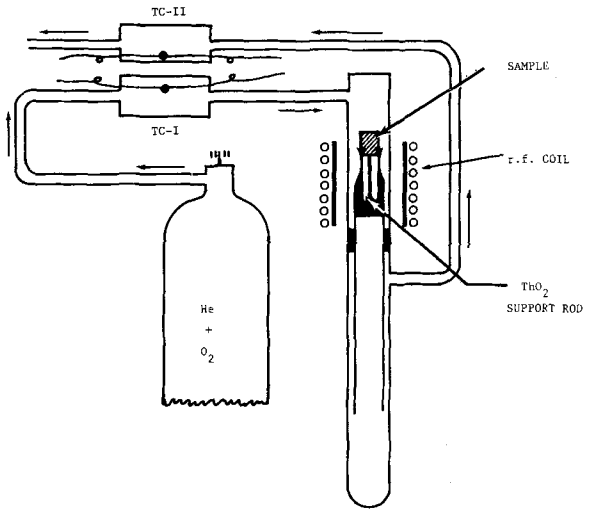

Fig. 1. Schematic drawing of apparatus for monitoring rates of oxygen depletion.

In previous oxidation studies with the present apparatus, it was routine to preheat specimens in pure helium at the planned oxidation temperature to remove any residual permanent gasses. This degassing procedure was found to degrade seriously the coated systems under investigation here, and was ultimately abandoned. Oxidation results for degassed and undegassed TRW samples are compared in Fig. 2 for temperatures of 1000°, 1250°, and 1500°C, respectively. At 1000° and 1250°C, the extent of oxidation at all times is significantly higher for the degassed samples, although the form of the oxidation *vs.* time curves is similar. At 1500°C, the oxidation mechanism may change, and the degassed sample initially oxidizes less rapidly than the undegassed one. Eventually, however, the degassed sample fails catastrophically, while the undegassed one retains excellent protective characteristics. Thus, the oxidation behavior of a coated sample is critically dependent on prior history. Furthermore, coated specimens will not tolerate prolonged exposure at high temperatures in nonoxidizing atmospheres without significant changes in properties. It may be noted that permanent gas evolution, as monitored with the thermal conductivity cell, proved to be negligible in all cases.

In Fig. 3, oxidation results for undegassed TRW coated samples are compared as a function of temperature. Over a 1-hr period, the extent of oxidation decreases as the temperature is increased from 1000° to 1250° to 1500°C. The improvement of oxidation resistance with increasing temperature over the protective range is characteristic of both monolithic molybdenum and tungsten silicides (4). The rate of formation of the protective silica film is probably more rapid at higher temperature and hence protection is established earlier. At 1700°C initial rates are exceedingly high, but a protective oxide is never established and a catastrophic oxidation failure occurs.

In contrast to the data in Fig. 3 for the TRW coating, oxygen consumption *vs.* time curves for the undegassed Solar TNV-13 coating are shown in Fig. 4 for temperatures of 1000°, 1250°, 1500°, 1700°, and 1800°C. The TNV-13 coating clearly shows a declining rate of oxidation with time, characteristic of a good oxidation-resistant material, up to the highest temperatures. Even up to 1500°C, where both the TNV-13 and the TRW coatings are protective, the fundamental mechanism of oxidation appears to be different. The curves of Fig. 4 are approximately parabolic, as seen in the plots of oxygen consumption squared (g^2/cm^4) *vs.* time in Fig. 5. Near 1500°C, where the protective properties of the TRW coating seem to be optimum, the oxidation curve is logarithmic, and the final *rate* of oxidation at long times is lower than for the paraboli-

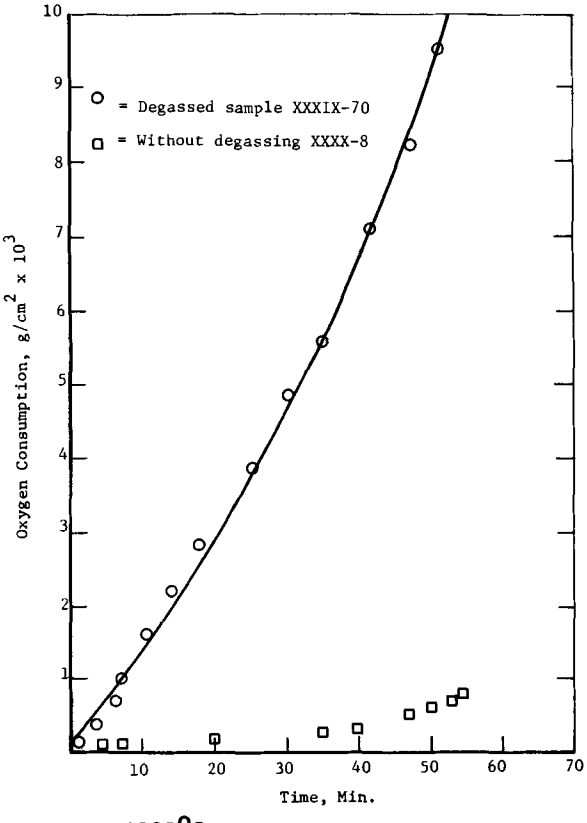

a. 1000°C

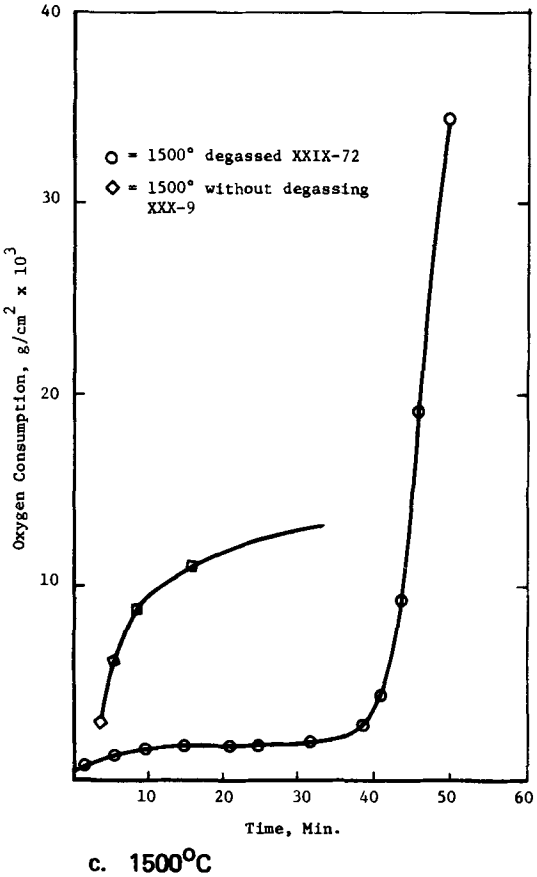

c. 1500°C

Fig. 2. Oxidation of TRW coated Ta-10W

cally oxidizing TNV-13. The total oxygen consumed in a 1-hr time period at 1500°C is also lower for the TRW than for the TNV-13 coating, 1.2 x 10^{-4} g/cm² for TRW compared to 9.4 x 10^{-4} g/cm² for TNV-13. However, at 1700°C, the TNV-13 coating is vastly superior, still retaining good protective properties with

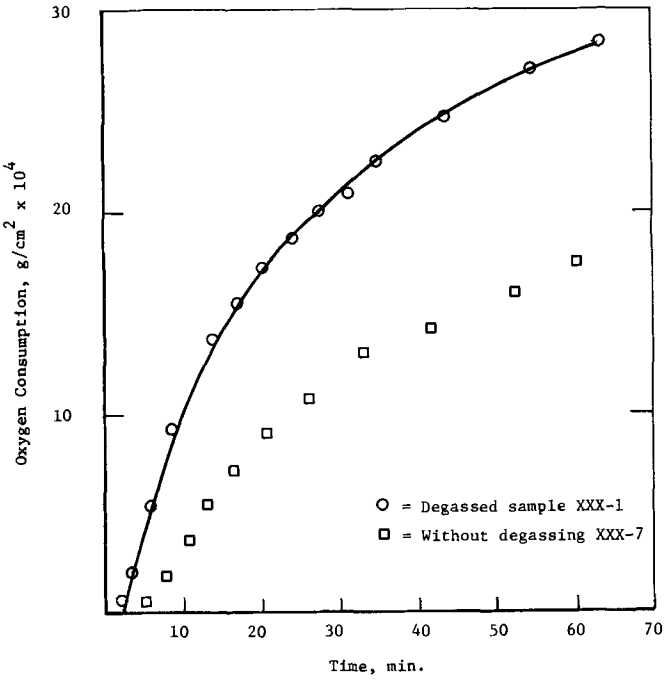

b. 1250°C

parabolic oxidation, while the TRW coating has failed completely. At 1800°C (observed brightness temperature), the TNV-13 coating is seen to have failed catastrophically within 6 min. An experiment conducted at gradually rising temperatures with TNV-13 led to irreparable coating degradation near 1740°C.

For purposes of comparison, a number of runs were made on the uncoated alloy, previously heated in pure helium at the oxidation temperature for about ½ hr. The kinetic results for 150 Torr oxygen partial pressure are summarized in Fig. 6 for temperatures of 1000°, 1250°, 1500°, and 1700°C. At 1000°C, although the rate of oxidation decreases with time for at least 40 min, the rate law is not parabolic. The data at 1250°C show very clearly the breakaway behavior characteristic of tantalum and its alloys. If the 1000°C runs were extended to longer times, sharp increases in rate might become apparent. At 1500°C, the very rapid oxidation precluded a long run. For the first 12 min, oxidation proceeded linearly. Note that at 1250°C the total oxy-

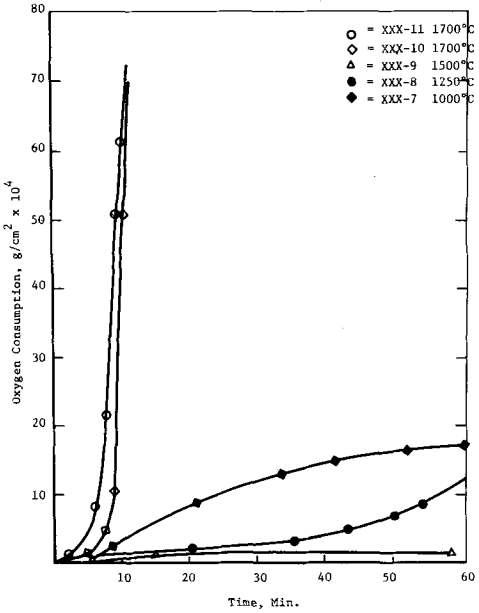

Fig. 3. Oxidation of TRW coated Ta-10W as a function of temperature.

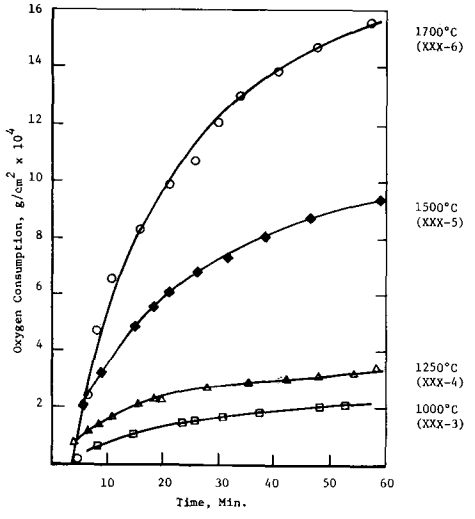

Fig. 4. Oxidation of Solar TNV-13 coated samples as a function of temperature.

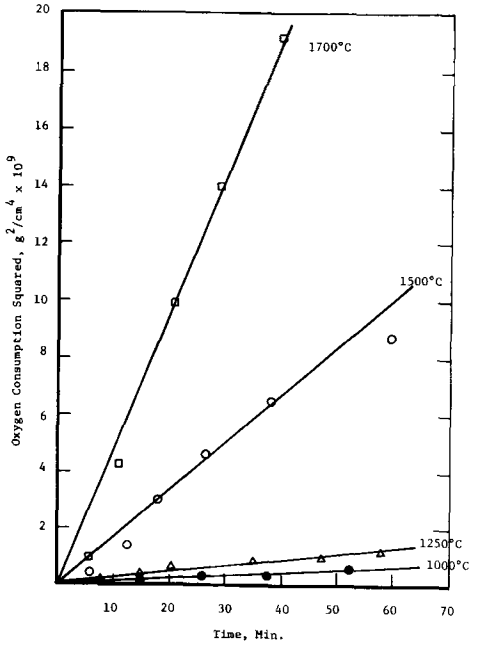

Fig. 5. Parabolic plot of oxidation data for Solar TNV-13 coated samples.

gen consumed over a 45-min period was 0.248 g/cm², with breakaway occurring at an oxygen pick-up close to 0.07 g/cm². At 1500°C, the oxygen pick-up reached 0.248 g/cm² in a period of a little over 9 min. At 1700°C, there is an abrupt increase in oxidation rate after 3 min at temperature, followed by a period of apparent decrease in rate. Thus in these experiments the total oxygen consumed, or equivalently the alloy recession, was comparable after 12 min at both 1500° and 1700°C. Further kinetic measurements for longer times on larger samples, and detailed structural analyses, would be required to determine whether different mechanisms are operative.

Metallography and Microprobe Analysis

Photomicrographs of the oxidized uncoated samples of Ta-10W are shown in Fig. 7. In Fig. 7(a) and 7(b), macrographs (magnification of 10X before reproduction) are shown for uncoated samples oxidized at 1000° and 1250°C, respectively. In Fig. 7(b), the Maltese-cross type cracks visible in the oxide layers are indicative of a highly stressed oxide film. Even at 1000°C, dissolution of oxygen into the tantalum gives rise to an extensive network of internal oxide pre-

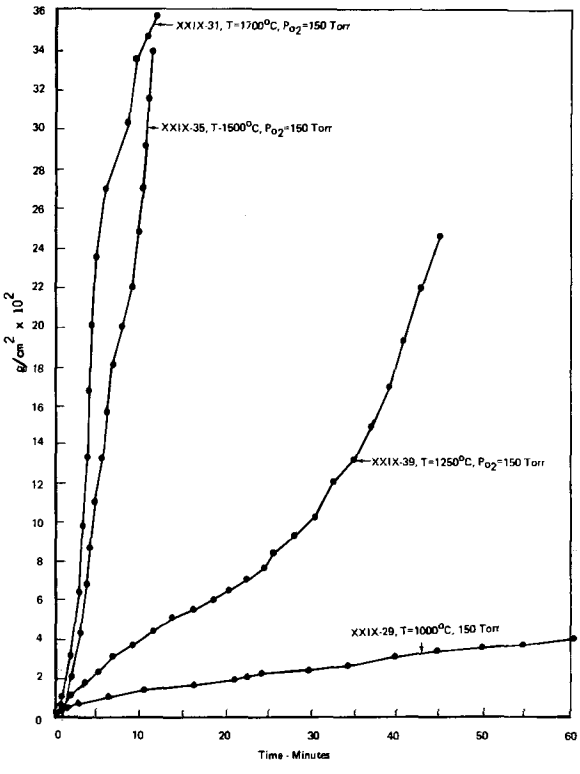

Fig. 6. Oxidation of Ta-10W

cipitate in the alloy immediately adjacent to the outer oxide film [Fig. 7(c)].

Metallographic sections of the as-received TRW coated samples are shown in Fig. 8 under normal and polarized light. The bright outermost layer that appears under polarized light for both coating systems is an artifact, probably due basically to the roughness of the coating surface. The TRW coating is described by the manufacturer as a duplex W/Si-W two-cycle coating (2). A tungsten layer is deposited by chemical vapor deposition, and a Si-W coating is then formed by a vacuum-pack process. The pack typically contains 99% Si, 0.5% W, and 0.5% NaF activator. Silicon is diffused into the tungsten precoat at temperatures near 2200°F for times of the order of 3 hr. A layer of WSi_2 purportedly grows inward from the external surface. The two layers are plainly visible in Fig. 8(a)—a grey band of tungsten adjacent to the alloy substrate, and a crystalline outer layer of silicide.

The Solar TNV-13 coating, shown in Fig. 9, is quite different from the TRW, both in method of preparation and in final microstructure. TNV-13 is described as a duplex (95W-5Ti)-Si composition. It is prepared in three steps. First, a 95W-5Ti slurry, in an organic vehicle, is applied and then sintered in vacuum at 2760°F. Second, a silicide coating is formed by high-pressure pack cementation; *i.e.*, the slurry coated alloy is imbedded in a mixture of silicon and a small amount of NaF activator, and heated in argon at pressures slightly above atmospheric for about 7 hr at 2150°F. Finally, the coating is impregnated with an aqueous slip of finely milled barium borosilicate glass frit, and air-fired for 10-14 min at 1800°F. The duplex nature of the final coating is clear in Fig. 9. A comparison of the TNV-13 coating in Fig. 9 with the TRW coating in Fig. 8 seems to suggest that the 95W-5Ti precoat, applied as the first step in fabricating TNV-13, is silicided almost completely during subsequent steps. The inner layer of TNV-13 has a similar microstructure to the outer layers of the TRW coating system, and was later shown to consist mainly of tantalum silicides. The outer layer of the TRW coating is, of course, WSi_2. Table III indicates the Ti and Ta distribution in the TNV-13 coating system, as determined by electron microprobe analysis. The Ti is seen to be concentrated

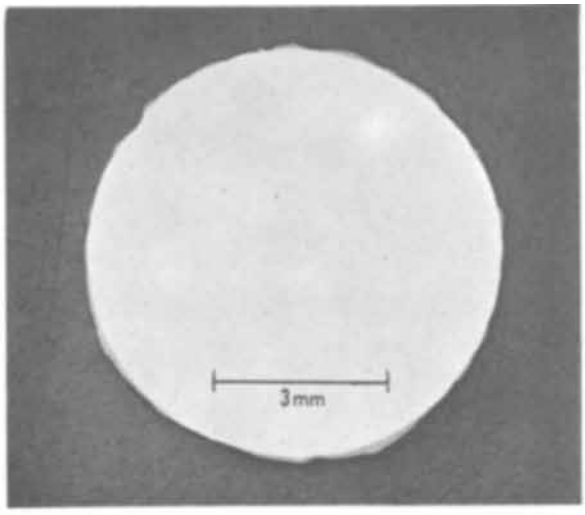

(a) 1000° C

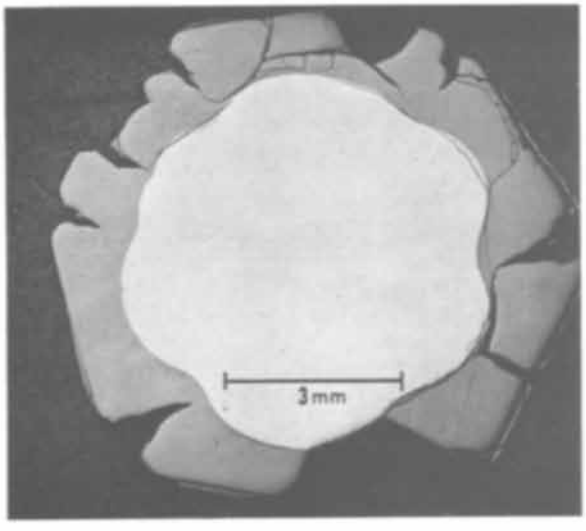

(b) 1250° C

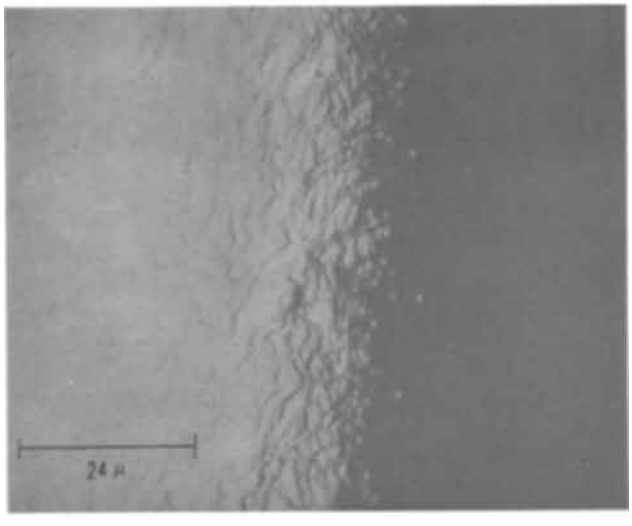

(c) 1000° C; Alloy-Oxide Interface — Higher Magnification

Fig. 7. Oxidized uncoated Ta-10W

near the center of the inner crystalline tantalum silicide band [position 0.5 in Fig. 9(b)]. In this case, the analytical measurements were somewhat crude, and the absolute numbers are of less significance than the relative trends displayed.

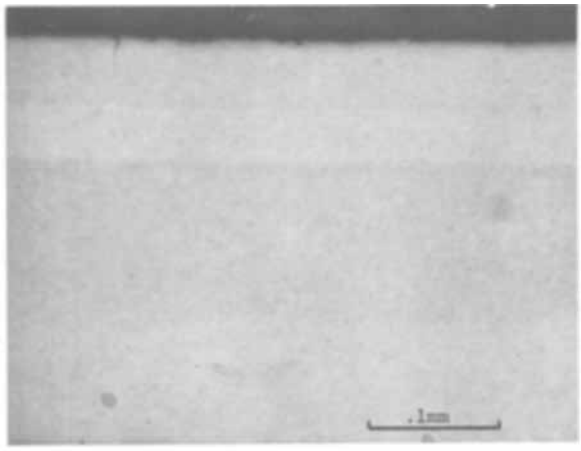

(a) Axial Section

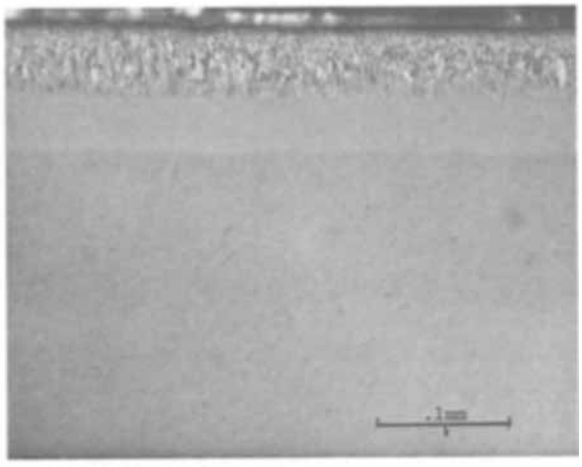

(b) Axial Section; Polarized Light

Fig. 8. TRW coated samples of Ta-10W (as received)

The microstructure of the TNV-13 and TRW coatings after oxidation for 1 hr at 1500°C are compared in Fig. 10. Both coating systems are characterized by the growth of a surface layer with a rough uneven structure at the interface with the coating. The nature of the surface layer, however, is quite different in the two cases. In the Solar coating, the surface layer that develops is a smooth dense oxide with no apparent structure. Microprobe analysis, discussed below, shows the oxide to contain silicon and titanium, but essentially no tungsten. Comparison of Fig. 10(b) with Fig. 9(b) reveals the substantial crystal growth and recrystallization of the coating that appears to occur simultaneously with high-temperature oxidation. While the coating structure of the as-received material shown in Fig. 9(b) appears to be amorphous, the structure in 10(b) after oxidation displays an equiaxed grain structure. Microprobe results for the TRW sample after oxidation at 1500°C are summarized in Table IV. The tungsten and tungsten disilicide layers are identified unambiguously. The outer layer that develops during oxidation is seen to contain both Si and W, and presumably oxygen as well. It is possible that protection is actually conferred by a very thin layer of silica which is not detected in the photomicrograph. It is interesting to note the absence of a W_5Si_3 phase at the W/WSi_2 interface, as well as the absence of interdiffusion between the chemically vapor deposited tungsten layer and the tantalum in the alloy. Unfortunately, adherence at the W/Ta-10W interface may be inadequate. Delamination, as shown in Fig. 10(e), was actually seen to have occurred over most of the surface of the oxidized sample.

In Fig. 11, photomicrographs are shown for coated samples oxidized at 1700°C and 150 Torr oxygen pres-

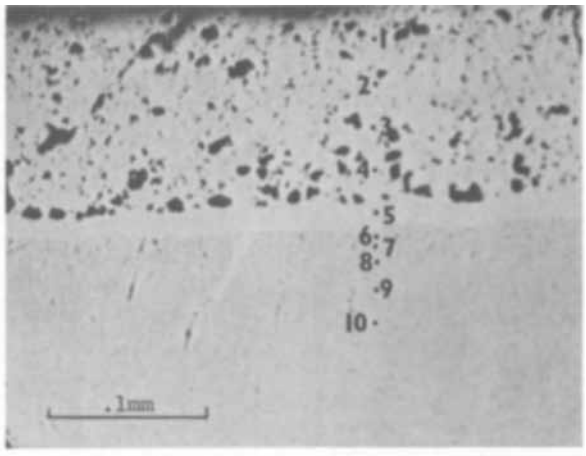

(a) Axial Section

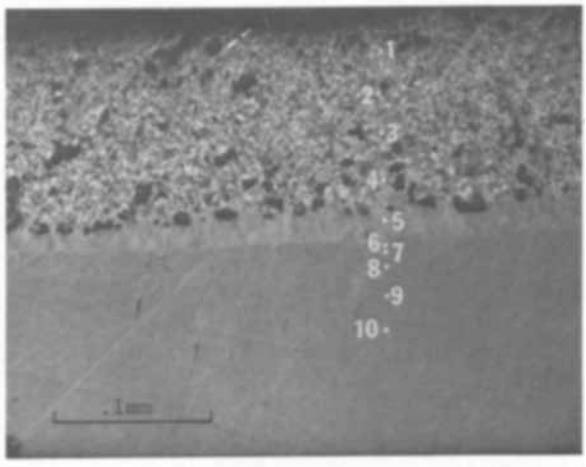

(b) Axial Section; Polarized Light

Fig. 9. Solar TNV-13 coated samples of Ta-10W (as received)

sure. The TNV-13 coating is seen to be intact, with a smooth glassy outer oxide similar to that obtained at 1500°C [*cf.* Fig. 10(a) and (b)]. The oxide is also observed to bridge a crack. Comparison of Fig. 11(b) with 10(b) shows grain growth and recrystallization in the area beneath the surface oxide to have proceeded to a greater extent at 1700° than at 1500°C, as might be expected. Two bands are visible in Fig. 11(b) between the recrystallized zone and the alloy substrate, whereas only one is apparent in Fig. 10(b). Results of electron microprobe analysis of the oxidized coated structure for TNV-13 coating are summarized in Table V. The outer oxide is in all likelihood silica, containing substantial quantities of titanium, probably as the oxide. The new band at the alloy/coating interface appears

Table III. Electron microprobe analysis of solar sample

Point	Area	Ti	Ta
	Coating	w/o	
1	~30μ from surface	0.2	<0.08
2	~60μ from surface	0.2	<0.08
3	~90μ from surface	0.4	<0.08
4	~120μ from surface	0.2	0.2
5	Center of band	0.8	63.7
	Matrix		
6	5μ from coating interface	0.3	90.1
7	10μ from coating interface	0.07	92.0
8	20μ from coating interface	<0.01	91.3
9	40μ from coating interface	<0.01	92.7
10	60μ from coating interface	<0.01	91.5
11	Matrix (way in)	<0.01	92.3

to be Ta_2Si, formed by interdiffusion of silicon from the coating. The extensively recrystallized region is WSi_2 containing some Ti. Beneath this is a band containing W_5Si_3 near the interface with WSi_2, and Ta_5Si_3 (having the same hexagonal crystal structure as W_5Si_3) near the interface with Ta_2Si. It is particularly noteworthy that Ti in the oxidized structure is concentrated in the protective oxide. The TRW sample, shown in Fig. 11(c), (d), and (e) failed at an edge *via* tungsten delamination. The attack on the unprotected substrate is similar to that discussed above for uncoated Ta-10W. The three layers visible in Fig. 10 may also be seen within the light band of Fig. 11(e)—the W, WSi_2, and W-Si-O layers. Failure therefore appears to be basically mechanical in nature.

The TNV-13 specimen that failed at 1800°C is shown in Fig. 12. The very thick oxide that covers most of the surface has the characteristics of the Ta_2O_5 that forms on the uncoated alloy. The conversion of the alloy substrate to oxide results in such a large increase in volume that the oxide grows out to envelop partly the original coating.

Discussion

Both the TRW and TNV-13 coatings have been extensively tested in other laboratories, with results that differ in several aspects from those reported here. Perhaps the most significant difference lies in the upper temperature limit of the coating systems. In this work, catastrophic failure of the TRW coating at 1700°C (3090°F) was noted in less than 10 min; protective lifetimes of 0.5-3.0 hr at 3500°F have been reported by TRW. The TNV-13 coating was found here to provide reliable protection for at least 1 hr at 1700°C, but to show signs of failure near 1730°C (3150°F). The same coating tested by TRW displayed variable edge failures at times of 0.5, 2.0, and 8.50 hr at 3000°F, and general failure after 5 min at 3500°F. Tests of the TNV-13 and TRW coatings at McDonnell are cited by Solar (1) and protective lifetimes reported are as follows: at 3200°F, 10 and 6.5 hr, and, at 3600°F, 0.8 and

Table IV. Microprobe results for TRW sample oxidized at 1500°C

Point	Area	Si	W	Ta	Ti	
		w/o				
	Coating					
1	Surface oxide	16.5	57.8	<0.08	<0.01	W-Si-O
2	White metal in gray surface oxide	23.4	76.6	<0.08	<0.01	WSi_2
3	Band (30μ from surface)	24.8	75.2	<0.08	<0.01	WSi_2
4	Band (50μ from surface)	24.8	75.2	<0.08	<0.01	WSi_2
5	Band (70μ from surface)	0.04	~100	<0.08	<0.01	W
6	Mottled band (90μ from surface)	0.03	~100	<0.08	<0.01	W
	Matrix					
7	~3-5μ from coating interface	<0.02	9.5	90.5	<0.01	
8	10μ from coating interface	<0.02	9.5	90.5	<0.01	
9	20μ from coating interface	<0.02	9.5	90.5	<0.01	
10	40μ from coating interface	<0.02	9.4	90.6	<0.01	
11	60μ from coating interface	<0.02	9.5	90.5	<0.01	
12	100μ from coating interface	<0.02	9.9	90.1	<0.01	
13	Matrix (way in)	<0.02	10.0	90.0	<0.01	

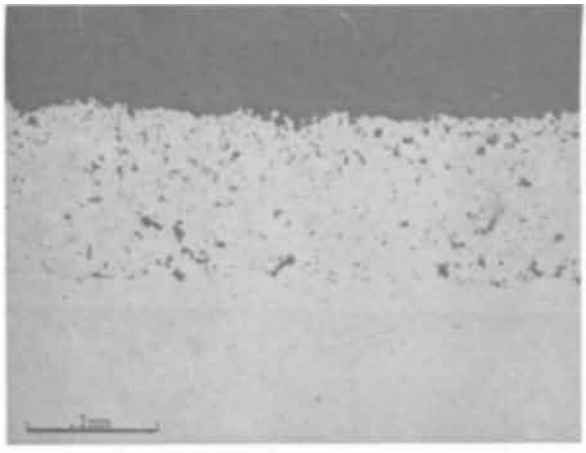

(a) Solar TNV—13; Axial Section

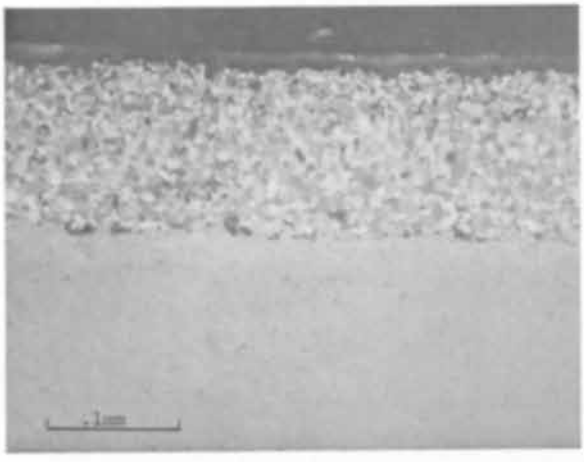

(b) Same as (a), but under Polarized Light

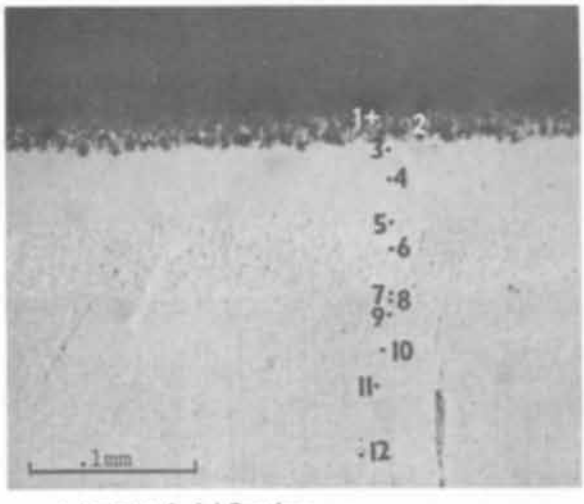

(c) TRW; Axial Section

Fig. 10. Coated sample of Ta-10W after 1 hr oxidation; 1500°C and 150 Torr oxygen pressure.

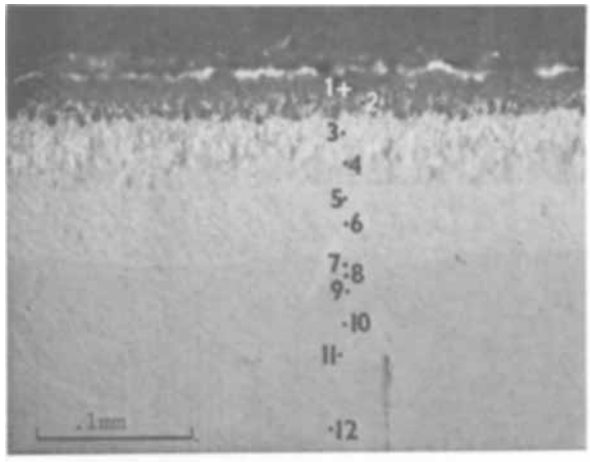

(d) Same as (c), but under Polarized Light

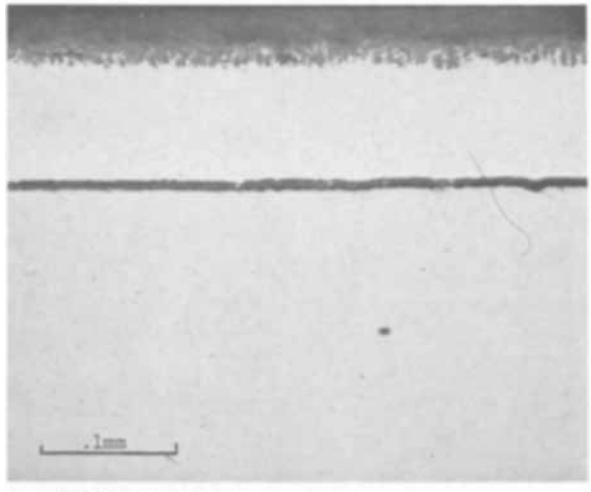

(e) TRW; Axial Section

1.5 hr for TNV-13 (Solar C) and TRW, respectively. On the basis of the present results, useful coating lifetimes could not be predicted above 3090°F for TRW or above 3150°F for TNV-13. The difficulty may lie in the different methods of testing, and/or inaccuracies of temperature, introduced by lack of knowledge of the proper emittance corrections for each test. Further work on temperature measurement is clearly required, and the present experiments serve to confirm the existence of a problem, rather than to provide a solution.

No quantitative data were found in the literature for comparison with results reported here on extent of oxidation as a function of temperature. At 2400°F (1315°C), weight gains of 1 and 5 mg/cm^2 are reported for TNV-13 after 50 hr in static air (5). The measurements described above are of total oxygen consumption, rather than weight gain. Since some tungsten may be lost from the coating in the form of volatile tungsten oxides, total oxygen consumption should be larger than net weight gain. Extrapolating the oxygen consumption data given above for a 1-hr time period at 1250° and 1500°C, to 50 hr on the basis of a parabolic rate equation, oxygen values of 2.4 and 6.65 mg/cm^2 are predicted at 1250° and 1500°C, respectively. While the extrapolation is certainly over too wide a range to be very reliable, the agreement with the Solar results (5) is gratifyingly good nonetheless. Since nitrogen influences the behavior of some materials, the test data reported here for helium oxygen may not be strictly comparable to air oxidation test data. This point might be checked experimentally.

Comparing the oxidation behavior of the TRW and TNV-13 coatings as shown in Fig. 3, 4, and 5, we are led to the conclusion that the oxidation mechanism must be quite different for the two coating systems, in spite of the similarity in basic chemical composition. The TNV-13 coating oxidized parabolically; the TRW coating oxidizes logarithmically. Between 1000° and 1800°C and an oxygen pressure of 150 Torr, the rate of oxidation of the TNV-13 coating increases with increasing temperature and the coating remained protective at 1700°C. In contrast, the rate of oxidation of the TRW coating decreases as the temperature is increased from 1000° to 1250° to 1500°C and then increases catastrophically at 1700°C. The metallographic and microprobe results reported above identify im-

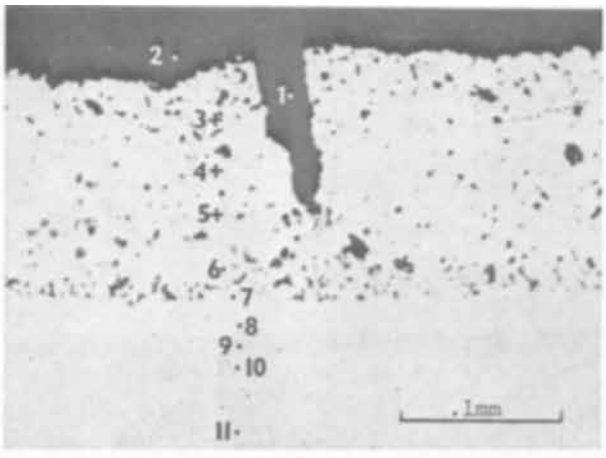

(a) TNV–13; Axial Section

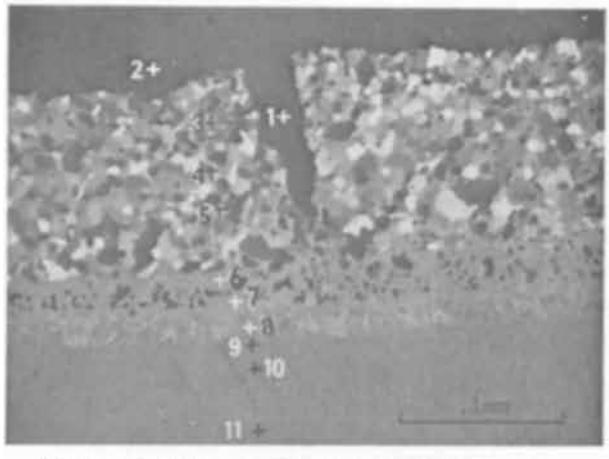

(b) Same as (a), but under Polarized Light

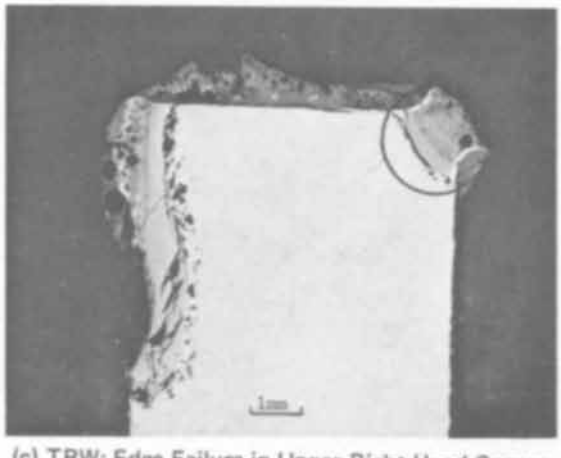

(c) TRW; Edge Failure in Upper Right Hand Corner

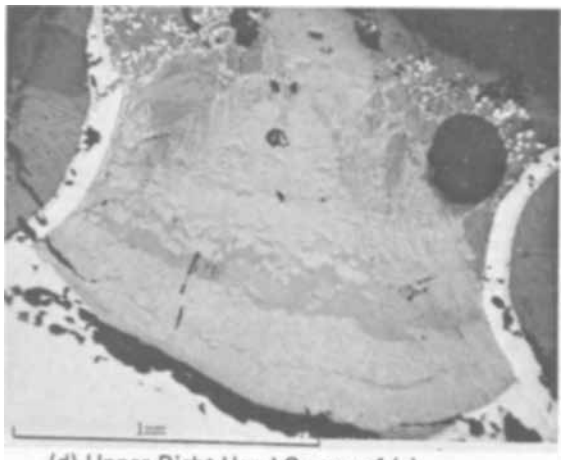

(d) Upper Right Hand Corner of (c)

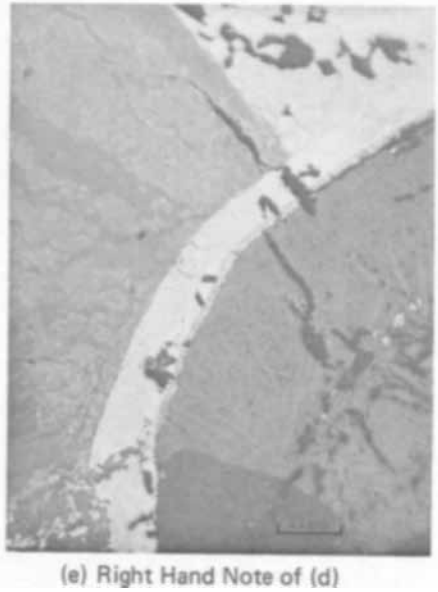

(e) Right Hand Note of (d)

Fig. 11. Coated samples of Ta-10W after oxidation at 1700°C and 150 Torr oxygen pressure.

portant structural differences in the two coating systems that may account for the very different oxidation mechanisms observed.

The protective oxide that develops on TNV-13 is a relatively thick silica glass, containing 4-10 w/o of titanium. The SiO_2-TiO_2 phase diagram is of the simple eutectic type, with a eutectic composition and temperature near 10 w/o TiO_2 and 1540°C (6). The melting point of silica is reported as 1713°C (7). No oxygen pickup was detected in the WSi_2 layer beneath the protective oxide. However, the WSi_2 layer was originally porous and extensive grain growth and recrystallization were observed as a result of the high-temperature exposure. The outer layer observed in the TRW coating was a microcrystalline W-Si-O phase, although the kinetic data suggests that an external silica skin might have been formed as well. The presence of titania in the TNV-13 coating is almost certainly beneficial. It may act as a catalyst for the rapid nucleation and growth of silica, or may improve the protective properties of the glass.

A major problem with the TRW coating is delamination of the chemically vapor deposited tungsten layer during exposure. In the TNV-13 system, although a 95W-5Ti slurry is laid down initially, siliciding is very deep and the final layer left in contact with the alloy is not tungsten but a tantalum silicide. Here, too, it may be that titanium promotes coating adherence.

The oxidation of the TRW coating in the protective range, 1000°-1500°C, is logarithmic, and oxidation resistance improved with increasing temperature. The oxidation of TNV-13 is parabolic. The parabolic rate constants for total oxygen consumption are plotted *vs.* reciprocal absolute temperature in Fig. 13. Between 1250° and 1700°C, the calculated activation energy is 42 kcal/mole. This is significantly higher than the 27 kcal/mole reported both for oxygen diffusion in silicon (8) and for parabolic oxidation of both silicon (9) and silicon carbide (10). This, too, suggests that the titania acts to modify the structure of the outer protective silica glass.

Acknowledgments

The electron microprobe analysis was performed by Frank Kiluk, George Bruno, and Sheldon Moll of

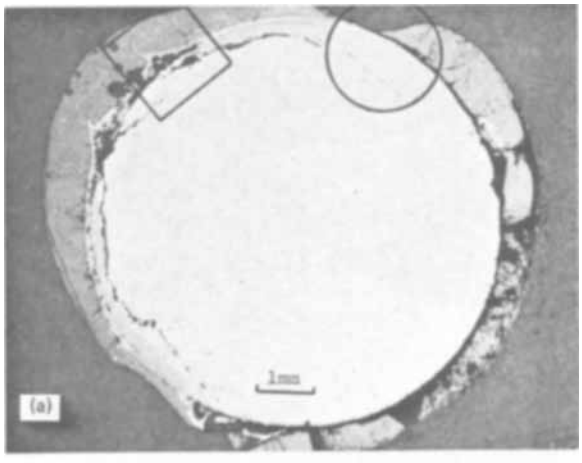

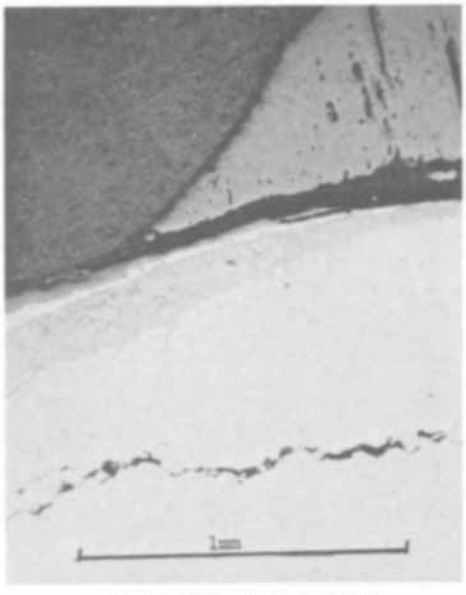

(b) (Circled Area In (a))

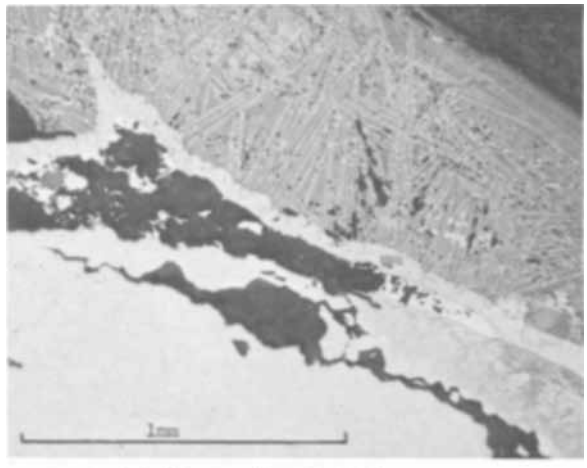

(c) (Square Area in (a))

Fig. 12. Failure of TNV-13 at 1800°C

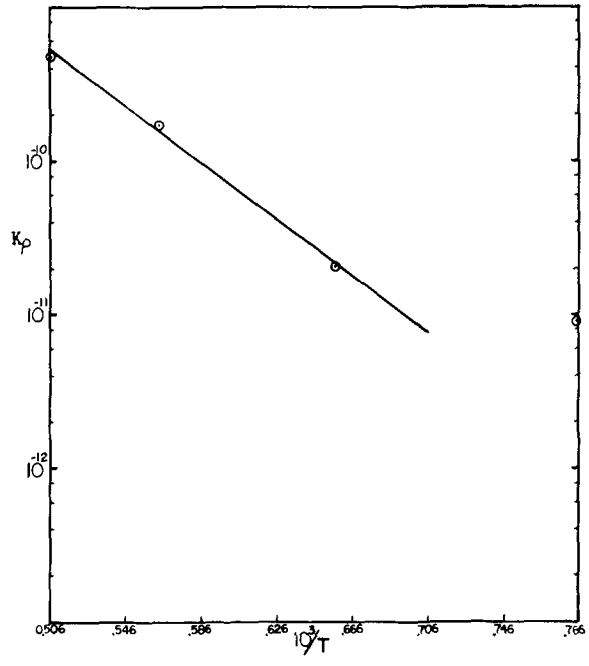

Fig. 13. Arrhenius plot of the parabolic rate constants for oxidation of TNV-13 coated Ta-10W.

Advanced Metals Research Corporation, Burlington, Massachusetts.

The author is indebted to Frank Galligani for the metallography and to David Harlow and John King of the Antioch College work-study program for the oxidation measurements.

This work was supported by Army Materials Research Agency, Watertown, Massachusetts, under DAAG46-67-C-0125(X). Many helpful suggestions were provided by Mr. Milton Levy, who served as project monitor.

It is a pleasure to acknowledge the cooperation and assistance of J. D. Gadd, TRW, and A. R. Stetson, Solar, in expediting delivery of the coated samples, in providing reports and background information, and in criticizing the final manuscript.

Manuscript submitted Sept. 26, 1968; revised manuscript received *ca.* Jan. 17, 1969.

Table V. Microprobe results for solar sample oxidized at 1700°C

Point	Area	w/o Si	W	Ta	Ti	
	Coating					
1	Large oxide	30-40	<0.01	<0.08	4-10	SiO_2
2	Surface oxide	30-40	<0.01	<0.08	4-10	SiO_2
3	Coating (50μ from surface)	22.7	75.7	<0.08	1.4	WSi_2
4	Coating (80μ from surface)	22.4	77.0	<0.08	0.7	WSi_2
5	Coating (110μ from surface)	22.2	77.7	<0.08	0.4	WSi_2
6	Band (150μ from surface)	8.8	81.5	7.9	1.7	W_5Si_3
7	Band (165μ from surface)	8.0	12.4	78.7	0.9	Ta_5Si_3
8	Band (180μ from surface)	6.0	9.0	85.0	0.04	Ta_2Si
	Matrix					
9	~5-7μ from coating interface	<0.02	10.5	89.4	0.1	
10	20μ from coating interface	<0.02	10.5	89.5	<0.01	
11	40μ from coating interface	<0.02	10.5	89.5	<0.01	
12	80μ from coating interface	<0.02	10.2	88.8	<0.01	
13	120μ from coating interface	<0.02	10.4	89.6	<0.01	
	Matrix (way in)	<0.02	10.1	89.9	<0.01	

Any discussion of this paper will appear in a Discussion Section to be published in the December 1969 JOURNAL.

REFERENCES

1. A. R. Stetson and R. T. Wimber, Solar, 2200 Pacific Highway, San Diego, Calif. 92112, "Slurry Applied Duplex Coatings for Tantalum and Columbium Alloys," presented at the 13th Meeting of Refractory Composites Working Group, Seattle, Wash., July 18-20, 1967.
2. W. T. Ebihara and K. C. Lin, TRW, Inc., 23555 Euclid Ave., Cleveland, Oho 44117, "Development and Characterization of High Temperature Coatings for Tantalum Alloys," Second Interim Progress Report, Contract AF33(615)-5011, Jan. 16, 1967.
3. J. B. Berkowitz-Mattuck, *This Journal*, **111**, 908 (1964).
4. J. B. Berkowitz-Mattuck and R. R. Dils, *ibid.*, **112**, 583 (1965).
5. R. T. Wimber and A. R. Stetson, "Development of Coatings for Tantalum Alloy Nozzle Vanes," NASA Cr-54529, RDR 1396-3, Contract NAS3-7276, July 1967.
6. E. M. Levin, H. F. McMurdie, and F. P. Hall, "Phase Diagram for Ceramists," Am. Ceram. Soc. (1956).
7. R. C. DeVries, R. Roy, and E. F. Osborn, *Trans. Brit. Ceram. Soc.*, **53**, [9], 531 (1954).
8. F. J. Norton, *Nature*, **171**, 701 (1961).
9. B. E. Deal and A. S. Grove, *J. Appl. Phys.*, **36**, 3770 (1965).
10. K. Motzfelt, *Acta Chem. Scand.*, **18**, 1596 (1964).

Technical Note

Contact Resistances of Several Metals and Alloys to GaAs

Haruhiro Matino and Makoto Tokunaga

Central Research Laboratory, Tokyo Shibaura (Toshiba) Electric Company, Limited, Kawasaki, Japan

Low-resistance ohmic contacts are essential in the fabrication of GaAs devices, particularly for the demands of high-frequency operation and/or small device geometry required in microwave diodes and transistors. Resistance data have been reported by several investigators on ohmic contacts to n-type GaAs using metal halide fluxes (1) and Ag-In-Ge alloys (2), and to p-type GaAs using Ag-Mn alloys (3).

It is further hoped for planar structure that the contact metals have good adherence to SiO_2 surface. However, no data on the ohmic contact between the metals Mo, Ti and Cr, and GaAs are available in the existing literature.

In this report, the specific contact resistances are quantitatively investigated for a variety of metals (Ag, Au, Mo, Cr, and Ti) and alloys (Sn-Ag, In-Ag, Sn-Ge-Ag, Ge-Au-Ag, In-Ge-Ag) on both n- and p-type GaAs of a wide resistivity range.

Most of the GaAs materials used in this investigation were boat-grown single crystals; epitaxially grown n-type crystals were used for the lower carrier concentrations of 1 to 5 x 10^{15} cm^{-3}. For the n-type studies, the carrier concentrations ranged from 1 x 10^{15} to 6 x 10^{18} carriers/cm^3 and from 1 x 10^{18} to 6 x 10^{19} carriers/cm^3 for p-type samples. All of the metals used in this investigation were of 99.99% purity. After lapping the (100)-oriented wafers, both surfaces of the wafer were chemically etched in a solution of $8H_2SO_4$:$1H_2O_2$:$1H_2O$. The thickness of the etched wafers is about 200μ. On both etched surfaces heated at 300°C, the elemental metals were evaporated to a thickness of 1000Å or more, and were further covered with gold when necessary, under background pressure of 10^{-6} mm Hg or lower. In the case of alloys, *e.g.* In-Ag, the film is formed by sequential evaporation of In and then Ag in the proportion of 25:75 w/o (weight per cent) In:Ag, to a total thickness of 3000Å or more. After evaporation, the wafer was heated to 500°C for 10 min in a hydrogen atmosphere in order to form the contact. The consecutively evaporated metals will alloy in a very short time (minutes or seconds) when exposed to temperatures near the recrystallization temperature of the metal of higher melting point or at a lower temperature (4).

On one side of the wafer, circular dots of 25 or 100μ diameter were formed by a photoengraving technique with the use of a suitable etching solution for each metal or alloy. The smaller contact was used for lower specific resistance measurements in order to raise the accuracy. When this contact of 25μ diameter was used, the error was less than 50% even for 1 x 10^{-7} ohm-cm^2 resistance contacts.

After scribing, chips were mounted on TO-5 headers. Two leads were bonded to each dot: one is for a current feed and the other is used for a voltage drop measurement. No influence of the lead resistance was introduced by this double lead method. The specific contact resistance is obtained from total resistance measured, and the resistivity and the thickness of the wafer. The contact is considered to be ohmic when I-V characteristics are completely linear over several orders of magnitude of current range.

The results obtained are listed in Table I. Ag contacts provide good ohmic contacts to both n- and p-type materials with the carrier concentrations of 1 x 10^{18} cm^{-3} or higher, and of 6 x 10^{18} cm^{-3} or higher, respectively. Au contacts are good only to n-type of 6 x 10^{18} cm^{-3} and p-type of 1 x 10^{19} cm^{-3} or higher. Mo, Ti, and Cr, which are widely known to have good adherence to SiO_2, yield good ohmic contact to p-type materials with carrier concentration of 6 x 10^{18} cm^{-3} or higher. Specific contact resistances of Mo and Cr contacts to the p-type material of 6 x 10^{19} carriers/cm^3 are both one order of magnitude lower than those reported by Nuese and Gannon on Ag-Mn contact to p-type material of 8.5 x 10^{19} carriers/cm^3 (3). The resistivity of the Ti contact was slightly less than that of Ag-Mn. These active-metal (Mo, Cr, and Ti) contacts, however, were found not to be good to n-type materials of 6 x 10^{18} carriers/cm^3, even when a sintering temperature was chosen as high as 700°C. The Ag-alloys containing In, Sn, and/or Ge provide good ohmic contacts to n-type materials with carrier concentration of 1 x 10^{15} cm^{-3} or higher as is shown in

Table I. Contact resistance in ohm-cm^2 of sintered metal contacts to GaAs[a] (300°K)

Carrier concentrations and conduction type	Ag	Au	Sn-Ag (25:75)[d]	In-Ag (25:75)	Ge-Au-Ag (10:10:80)	Sn-Ge-Ag (10:10:80)	In-Ge-Ag (10:10:80)	Mo	Cr	Ti
								Rectifying[b]		
6×10^{18} n-type	2.9×10^{-4}	2.8×10^{-4}	0.3×10^{-6}	3.0×10^{-5}	3.6×10^{-6}	1.2×10^{-6}	7.5×10^{-6}			
1×10^{18} n-type	6.5×10^{-3}	Nonohmic	6.5×10^{-6}	5.5×10^{-5}						
1×10^{17} n-type	Nonohmic		8.0×10^{-6}	9.6×10^{-5}	3.8×10^{-5}	2.3×10^{-5}	9.5×10^{-5}			
5×10^{16} n-type			4.0×10^{-5}							
1×10^{16} n-type			3.4×10^{-4}	2.2×10^{-2}	1.6×10^{-4}		2.3×10^{-4}			
5×10^{15} n-type			3.6×10^{-3}	1.1×10^{-2}						
1×10^{15} n-type			5.5×10^{-2}		7.6×10^{-3}	1.0×10^{-3}	9.0×10^{-4}[c]			
6×10^{19} p-type	3.8×10^{-6}	4.0×10^{-6}		1.3×10^{-6}				1.0×10^{-6}	2.1×10^{-6}	7.2×10^{-6}
1×10^{19} p-type	6.2×10^{-6}	1.1×10^{-5}		1.5×10^{-5}				4.3×10^{-5}	2.7×10^{-5}	
6×10^{18} p-type	2.9×10^{-4}	Nonohmic		2.4×10^{-4}				7.3×10^{-4}	1.9×10^{-4}	
1×10^{18} p-type	Nonohmic			5.3×10^{-4}				Nonohmic	Nonohmic	

[a] The sintering was performed at 500°C for 10 min.
[b] Ohmic contacts cannot be obtained even at 700°C after 60 min sintering.
[c] 1×10^{-3} ohm-cm^2 or less was reported by Cox and Strack (2).
[d] This and other ratios shown in the case of the alloys are the mean of weight per cents.

Table I. Their magnitude is comparable with that of Ag-In-Ge contacts to 0.6-2.6 ohm-cm n-type GaAs reported by Cox and Strack (2).

It is seen in the table that the contact resistance is highly dependent on the carrier concentration. The contact resistances of Mo, Cr, and In-Ag to p-GaAs and of some alloys to n-GaAs are plotted as functions of square root of carrier concentration in Fig. 1. Following the theory of ohmic contact given by Mead (5), this suggests that carrier tunneling through a finite potential barrier of the contact is dominant in governing the contact resistance, even at room temperature. In the case of n-GaAs samples, whose carrier concentrations are relatively lower, the linearity does not hold except in the higher concentration region and, thus, another carrier transport mechanism such as thermionic emission should be present.

Metallurgical features of these contacts have been microscopically examined. Figure 2(a) shows a surface of the Mo contact to GaAs after sintering at 500°C for 10 min; the surface is seen to be extremely smooth. In contrast, the Au contact usually yields a spotty regrown region on the GaAs surface by a sintering at 341°C or higher, as is shown in Fig. 2(b). This would be because of Au-GaAs eutectic formation at 341°C (6). Note that the photograph in Fig. 2(b) was taken after the contact was formed at 500°C for 10 min and Au was etched off by Metex Aurostrip (supplied by McDermid Incorporated of Waterbury, Connecticut). We have been using the Mo or Cr contacts covered with gold in the fabrication of GaAs p^+n planar diodes with a reasonably shallow junction less than 0.5μ without any noticeable degrading of device performances.

In conclusion, Mo and Cr contacts to p-type GaAs of 1 x 10^{18} carriers/cm^3 or higher are recommended, especially for planar structures. For high-purity n-type GaAs, Ag-In-Ge and Ag-Sn-Ge alloys contacts

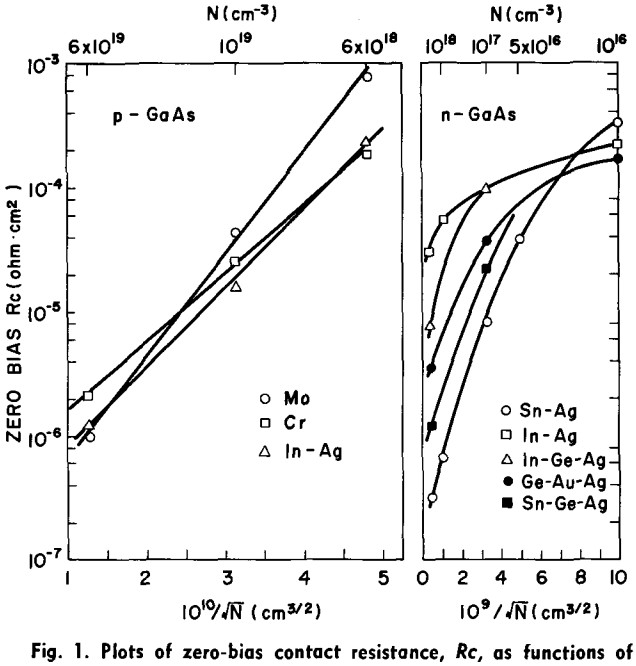

Fig. 1. Plots of zero-bias contact resistance, *Rc*, as functions of square root of carrier concentration, *N*; 300°K.

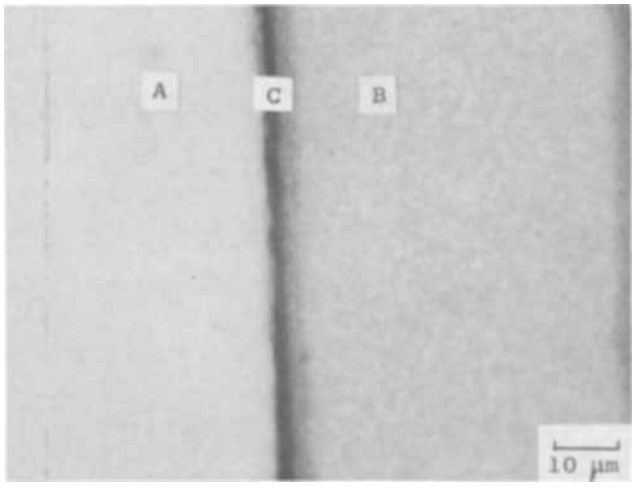

Fig. 2(a). A photomicrograph of a surface of Mo contact after sintering at 500°C for 10 min. (A) GaAs, (B) Mo, (C) mesa-etched region.

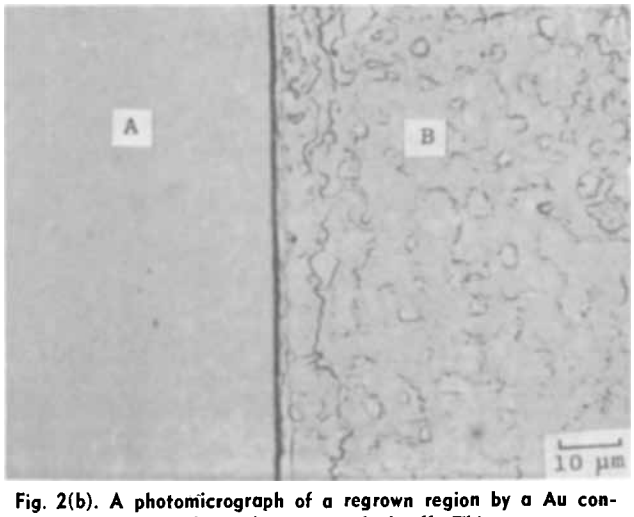

Fig. 2(b). A photomicrograph of a regrown region by a Au contact on a GaAs surface. Au was etched off. This contact was formed at 500°C for 10 min. (A) GaAs, (B) regrown region.

are good. Ag-In alloy contacts are especially recommended to both n- and p-type GaAs of 1 x 10^{18} carriers/cm^3 or higher. This is very advantageous for transistors and integrated circuits which should have both n- and p-type regions.

Manuscript submitted Oct. 9, 1968; revised manuscript received Jan. 27, 1969.

Any discussion of this paper will appear in a Discussion Section to be published in the December 1969 JOURNAL.

REFERENCES

1. B. Schwartz and J. C. Sarace, *Solid-State Electron.*, **9**, 859 (1966).
2. R. H. Cox and H. Strack, *ibid.*, **10**, 1213 (1967).
3. C. J. Nuese and J. J. Gannon, *This Journal*, **115**, 327 (1968).
4. R. B. Belser, *J. Appl. Phys.*, **31**, 562 (1960).
5. C. A. Mead, Paper 491 presented at Electrochem. Soc. Meeting, Montreal, Oct. 6-11, 1968.
6. M. B. Panish, *This Journal*, **114**, 516 (1967).

Addendum

The following Note was added in proof to the Technical Paper "Oxygen Doping of Solution-Grown GaP" by L. M. Foster and J. Scardefield which was published in the April 1969 issue of the JOURNAL, Vol. 116, No. 4, pp. 494-498:

In recent private communication with P. J. Dean, it was pointed out that the estimate of oxygen content from Zn-O pair emission could differ from that determined by electrical compensation by perhaps a factor of two lower, and the perfect agreement reported here is thus somewhat fortuitous. However, it was also pointed out that the local field correction that enters the formula connecting concentrations, oscillator strength, and absorption [J. D. Cuthbert, C. H. Henry, and P. J. Dean, *Phys. Rev.*, **170**, 739 (1968)] might have been sufficiently in error to restore the agreement.

Anodic Oxidation of Cyclic Hydrocarbons at Fuel Cell Electrodes

M. L. Savitz*[1] and A. L. Hubbard*[2]

U. S. Army Mobility Equipment Research & Development Center, Fort Belvoir, Virginia

ABSTRACT

The anodic oxidation of cyclohexane and benzene has been studied with potentiostatic-gas chromatographic techniques on commercially available fuel cell electrodes at 107°C in 85% H_3PO_4. The cathodic desorption products were identified and studied as a function of potential and reactant. Possible mechanisms for over-all oxidation of benzene and cyclohexane are discussed.

The practical application of fuel cell power plants is related to the performance which can be achieved at an electrode surface. Reaction paths and the rate-limiting steps must be understood for aliphatics, olefins, aromatics, naphthenes, and oxygenated compounds if versatile electrode structures are to be devised. Luksha (1) found that there was a 50 mv increase in polarization from that of pure octane when a fuel containing up to 5% olefins, 1% aromatics, 5% six-ringed naphthenes, 15% five-ringed naphthenes, and the remainder saturated normal or isooctane was reacted at a Niedrach-Alford Teflon bonded 35 mg/cm^2 platinum electrode with phosphoric acid electrolyte. Grubb (2) had shown earlier that cyclohexane and benzene were ¼ as reactive as hexane and ⅛ as reactive as the most reactive hydrocarbon, propane. Benzene was slightly less reactive than cyclohexane. Several investigators (3-6) obtained evidence for several types of intermediates adsorbed on the electrode surface when normal saturated hydrocarbons or ethylene were the reactants. Part of the adsorbate designated CH-α (3) can be cathodically desorbed and is thought to contain only C and H. Another C-H material (CH-β) is unreactive toward both reduction and oxidation at reasonable potentials and may be a polymer. The third species is a more highly oxidized material thought to contain at least one C-O bond (O-type). Previously (7) we examined the composition of the steady-state adsorbed residues on platinum wire with benzene or cyclohexane as the reactant using cathodic and anodic desorption techniques developed by Brummer (3). Much of the adsorbed species was removed at 0.01v *vs.* RHE, and this species (CH-α) for both cyclohexane and benzene appeared to be in the same state of oxidation. That part of the adsorbate which was not cathodically desorbable was in a highly oxidized state similar to O-type.

The electrochemical measurements on a wire electrode did not indicate (*i*) whether the cathodically desorbable species is a composite of several entities; (*ii*) whether the relative amounts of the possible constituent species are dependent on the potential maintained during adsorption; and (*iii*) whether these species are the same for benzene and cyclohexane. In order to clarify this situation, gas chromatographic methods were used to study the cathodically desorbable products obtained from the reaction of cyclohexane or benzene at a fuel cell electrode. In prior efforts using this type of technique with propane, Grubb (8) and Barger and Savitz (9) found that on cathodic desorption methane and ethane were identified gas chromatographically and that the relative amounts of these two constituents were very potential dependent.

Experimental

The experimental set-up was similar to that which has been described previously (9). Briefly, a commercially available American Cyanamid type AA-25 electrode, containing 25 mg/cm^2 platinum black and 25 w/o (weight per cent) Teflon pressed together on a tantalum screen with a Teflon coating on the gas side and with an active geometric area of 20.3 cm^2, was mounted into a cell wherein the Teflon backed side was exposed only to the fuel which entered through a 1/16 in. gas space milled out of Teflon block and the other side of the electrode was exposed to 85% H_3PO_4. The counter electrode, in a compartment separated from the working compartment by a glass frit, had a geometric area of 58.2 cm^2 and a platinum loading of 35 mg/cm^2. The reference electrode was the autogeneous type developed by Giner (10). The benzene or cyclohexane (Phillips Research Grade 99.91 mole per cent purity) was introduced into the cell via a liquid capillary pressure system (11) so that reactants were fed at a flow rate no greater than 0.1 cc/min. The liquid was vaporized before entering the cell which was maintained in an oven at 107°C ± 1°. The exit of the working compartment was connected with heated lines directly to the sampling valve of a dual column F&M 5750 research gas chromatograph containing flame ionization and thermal conductivity detectors. A 6 ft, ⅛ in. gas chromatographic column packed with UCON LB550-X on chromosorb W had a retention time of 2.1 min for cyclohexane and 3.2 min for benzene at 90°C. Normal hydrocarbons were retained for only a few seconds and were not well separated; therefore a Poropak T column was used in separate experiments to identify the lower boiling hydrocarbons. Standards of known compounds were run and identification accomplished by comparison of retention times.

In order to obtain a reproducible surface, potentiostatic procedures were used similar to those used by Brummer (12) and Gilman (13) for platinum wire and adapted by us (9) for porous electrodes. Figure 1 shows the schematic of the procedure used. Cyclohexane or benzene could be admitted to the system either

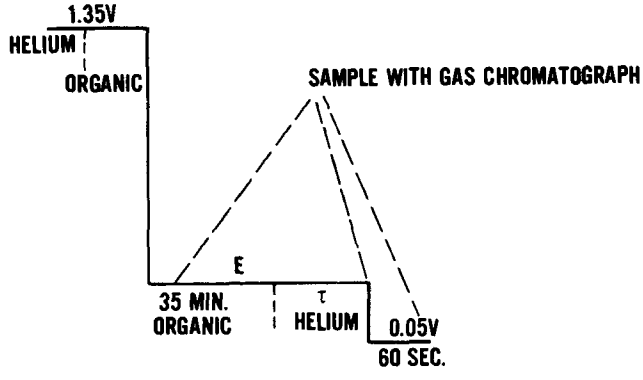

Fig. 1. Schematic of procedure used for gas chromatographic studies.

* Electrochemical Society Active Member.
[1] Present address, Federal City College, Washington, D. C.
[2] Present address, Rockefeller University, New York, N. Y.

at 1.35v or at the potential of adsorption with no change in the results. In most previous hydrocarbon studies, the platinum oxide formed at potentials above 1.0v was usually reduced at a more cathodic potential, *e.g.*, 0.05v, before going to the potential of adsorption. This step was omitted in these studies because in some preliminary experiments at a porous electrode with benzene as the reactant some of the benzene could be hydrogenated to cyclohexane at the more cathodic potentials. With cyclohexane, omission or inclusion of the 0.05v step did not affect the results. When the current no longer changed at the potential of interest, usually after about 35-min total adsorption time, the electrode was swept with helium (high purity 99.995%) at a flow rate of about 6 cc/min. During the helium sweep the effluent from the fuel side of the electrode was sampled periodically with the gas chromatograph. After varying lengths of time at potential under helium, the potential was stepped to 0.05v. The helium effluent was then sampled three times at 15-sec intervals after being at 0.05v for 45 to 60 sec. This time was critical since the maximum amount of desorption products appeared in this interval. The time reflects the length of the line between the cell exit and the gas chromatograph and the rate of the helium sweep. Quantitative determinations of the hydrocarbon species desorbed from the electrode were determined by calculating the area under the curve with the height times the width at half height method (14). This method of area determination gives reasonable accuracy provided the peaks are symmetrical, as was the case with the hydrocarbons on the columns used in this study. No direct normalization of areas corresponding to hydrocarbon concentrations was made. When standard solutions containing 90-10, 50-50, 10-90 mixtures of cyclohexane and benzene were injected on the column, the relative percentage of the areas under the curve corresponded to the prepared composition within ±2%. Five different sample injections of each standard solution gave similar results. Experiments at each potential and under each helium sweep with cyclohexane and benzene as reactant were repeated at least three times. For the same electrode, the value of areas or peak heights for benzene, cyclohexane and C_1 to C_6 hydrocarbons agreed to within 15% in separate experiments.

The electrode area was measured daily to determine whether the results were related to a decrease in surface area. The surface area of the electrode was determined by measuring the charge associated with galvanostatic reduction of a surface oxide formed at a fixed potential (15). Hydrogen adsorption methods could not be used due to extensive hydrogen evolution in the potential range of interest during analysis of hydrogen coverage. The electrode was held at 1250 mv *vs.* RHE for 2 min to form oxide layers. At this point, a cathodic galvanostatic pulse of 2 amp was applied to the electrode [400 μcoul = 1 cm^2 of area (16)]. Galvanostatic reduction of oxygen deposited at constant potential gave reproducible values for a particular electrode at a specific potential. Figure 2 shows how the area of the electrode decreased with time. The electrode decreased the most rapidly the first few days and then leveled off. When benzene was used on the same electrode, the decay rate of the electrode did not increase from that found with cyclohexane. When new electrolyte was added, the area increased temporarily and then decreased to its previous value. The decay of the electrode area was also followed by examining the oxidation of the electrode in the presence of helium at 0.4v. The electrode was held at 1.35v for 20 min and maintained at 0.4v for 30 min. Then the surface of the electrode was examined with an anodic galvanostatic pulse. Although the charge obtained is different by the two methods, the decay is similar. Although the area of the electrode decreases by a factor of three during a 40-day period and the absolute values for the areas corresponding to the desorbed species are different, the relative amounts of C_1 to C_6 compounds agree to within 10% regardless of the age of the electrode.

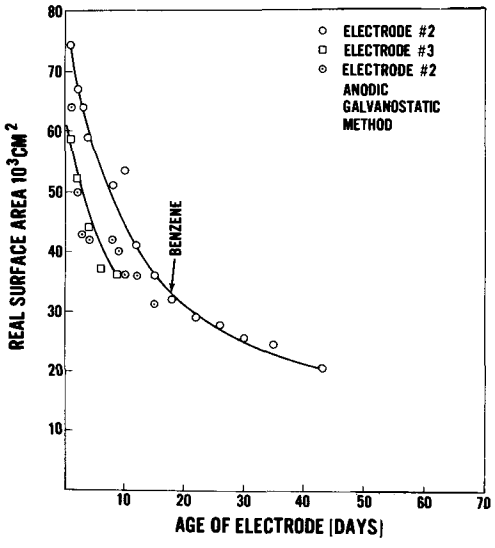

Fig. 2. Change of area of electrodes with time

Results and Discussions

In studies with platinum wire electrodes (7), we found that when cyclohexane or benzene was adsorbed at potentials from 0.1 to 0.4v *vs.* RHE 70% (±5%) of the final adsorbate was CH-α. At 0.5 to 0.7v *vs.* RHE about 60% (±5%) of the adsorbate was CH-α. Since the residue for both cyclohexane and benzene appeared to be in the same state of oxidation, the possibility of a benzene-cyclohexane equilibrium was suggested (7). To determine whether the oxidation reaction proceeds from cyclohexane to benzene to C_1-C_6 species to O-type and CO_2 (Eq. [1], whether conversion of cyclohexane to benzene is a equilibrium reaction with each proceeding via individual paths to CO_2 (Eq. [2]), or whether conversion of cyclohexane to benzene is an equilibrium reaction with a common path to CO_2 (Eq. [3]), the adsorption and desorption of benzene and cyclohexane on a fuel cell electrode was studied at representative potentials.

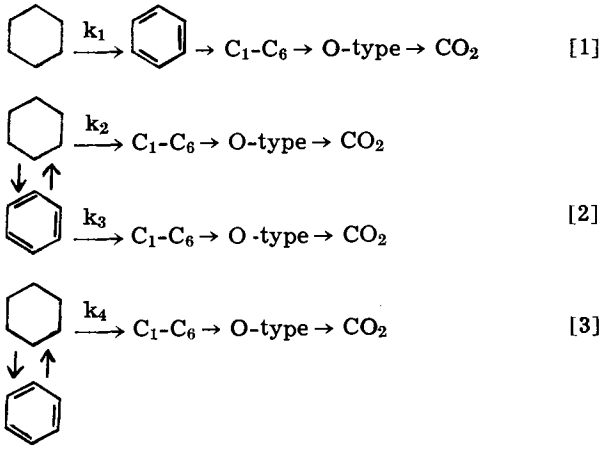

In the above possible reaction paths it has been assumed that O-type is in the main reaction path. There might be parallel paths (Eq. [4]) with any one of the cyclohexane and benzene reactions from Eq. [1] to [3] to form CH-α.

Hydrocarbon → Eq. [1], [2], or [3] → CH types → CO_2
Hydrocarbon → Eq. [1], [2], or [3] → O-types → CO_2 [4]

If some of the cyclohexane is converting to benzene and parallel reaction paths are pursued, and the oxi-

Table I. Variation of benzene formation with time and potential

Time, min	0.2v Cyclohexane/ Benzene	Benzene[a] (8×10^3)[c]	0.4v Cyclohexane/ Benzene	Benzene[b] (8×10^3)[c]
1.25	890	1.05	1650	0.4
6	1140	0.77	2200	0.3
16	1350	0.65	3300	0.2
27	1510	0.55	3300	0.2

[a] Cyclohexane height is constant 880 (8×10^3).
[b] Cyclohexane height is constant 660 (8×10^3).
[c] Represents attenuation of gas chromatographic area. For actual area multiply each area by 8×10^3.

dation of benzene is slow compared to cyclohexane ($k_3 < k_2$) benzene formation would be an undesirable side reaction which could reduce the over-all fuel cell performance. The dehydrogenation of cyclohexane need not necessarily lead to benzene unless there were six Pt atoms involved directly in adsorption and a planar configuration would result. If cyclohexane were to exist in planar form, there would be angle strain and instability. Stereochemically, cyclohexane can exist in a chair or boat conformation. The chair conformation is the more stable form (17) and would lead to 1 site adsorption; the boat form would lead to 4 or 2 site adsorption with preference for the former.

Cathodic desorption products with cyclohexane as reactant.—When cyclohexane was adsorbed on an electrode at a fixed potential, excess removed under helium sweep, and the potential then stepped to 0.05v to remove the cathodically desorbable species (Fig. 1), varying amounts of methane, ethane, propane, n-butane, n-pentane, n-hexane, benzene and cyclohexane were observed in the effluent gas stream.[3] No branched chain hydrocarbon or compounds containing 7 or more carbon atoms were obtained; thus there appears to be no dimerization of species. At 1.35v no material other than cyclohexane appeared in the effluent. When the potential was lowered from 1.35v to 0.05v (no intermediate adsorption potential) with cyclohexane as reactant, neither benzene nor the C_1-C_6 compounds were observed; thus the cathodic desorption step caused no cracking of cyclohexane. However, after 1 min of cyclohexane adsorption at potentials from 0.25 to 0.40v, the gas chromatographic analysis indicated the presence of benzene. The total amount of benzene decreased both with time at potential and with increasing potential as shown in Table I. The amount of benzene was reproducible within 10% for four different experiments with the same electrode. At potentials above open circuit (0.45v) no benzene was observed. Under helium sweep at the potential of adsorption, the benzene disappeared completely, and the excess cyclohexane decreased at least by a factor of 10, depending on the length of helium sweep. When the potential was stepped to 0.05v, benzene was again observed in the effluent. The fact that some benzene desorbed at adsorption potential below 0.4v and more was removed at 0.05v indicates that the benzene formed may be adsorbed in two different ways, may be adsorbed on two different types of sites or that the site energies change with potential. It also appears that benzene is not as tightly bound as has been previously thought (18), may not lose aromatic character, and may be more loosely bound than cyclohexane.

Benzene formed is also competing for sites with the cyclohexane reactant. When the electrode was lowered to 0.05v the maximum amount of benzene desorbed from the electrode was always observed on the chromatograph 15 sec before the maximum cyclohexane peak. This was true at all potentials and length of helium sweep; *e.g.*, at 0.3v adsorption, 60 min. helium sweep, maximum benzene was seen after 60 sec at 0.05v, maximum cyclohexane after 75 sec at 0.05v; at 0.5v adsorption 60-min helium sweep, maximum benzene was seen after 75 sec at 0.05v, maximum cyclohexane after 90 sec at 0.05v. This behavior was not a column effect, as when standards containing 90-10, 50-50, 10-90 mixtures of cyclohexane and benzene were injected on the column, the retention times were independent of relative amount of material in the samples. There was no conversion of benzene to cyclohexane in the 15-sec period as cyclohexane increased to a greater amount than the maximum amount of benzene decreased and there was still benzene coming off the electrode after 75 or 90 sec. If the diffusion coefficients of benzene and cyclohexane in helium were different, benzene would move from the electrode to the gas sampling valve faster. (Air-benzene at 0°C is 0.077 cm²/sec atm; air-cyclohexane at 45°C is 0.086 cm²/sec (19)).

The benzene observed at potentials of adsorption from 0.25 to 0.4v could result from initial dehydrogenation of cyclohexane to benzene (11). When the potential was changed from 1.35 to 0.4v the current became more anodic for 15 sec before becoming cathodic. At potentials anodic to 0.45v where no benzene was observed until desorption, anodic current was always observed during initial adsorption.

In Fig. 3 the cyclohexane and benzene desorbed as a function of potential are presented. Figure 3 shows the actual heights obtained for cyclohexane and benzene as a function of potential after 10- and 60-min sweeps. The cyclohexane which was still in excess in the lines after 10 or 60 min of helium sweep has been subtracted from the total amount of cyclohexane to give that quantity attributed to the cyclohexyl species on the electrode. The quantity attributed to excess cyclohexane in the line was obtained by sweeping with helium at the potential of adsorption for up to 65 min and sampling for cyclohexane at 15-sec intervals. At every potential there was more of the cyclohexyl type species than benzene. At 0.4v, the largest amount of benzene relative to cyclohexane was observed (ratio of benzene to cyclohexane at 0.4v was 1:25, at 0.3v was 1:80, and at 0.5v was 1:130). The area attributed to benzene at 0.4v accounted for only 4% of the total area attributed to desorbed six carbon ring species. The amount of cyclohexane was constant and high at 0.25 and 0.3v regardless of length of helium sweep (10 or 60 min). This is to be expected since in the region of hydrogen deposition any benzene formed could be hydrogenated. At

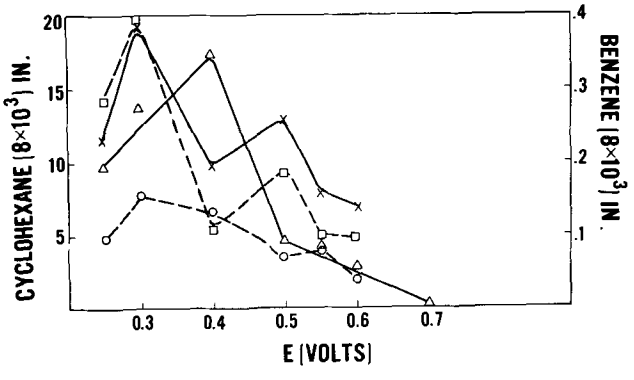

Fig. 3. Desorbed benzene and cyclohexane for 10- and 60-min helium sweeps. Area can be obtained by multiplying the height x 10^{-2} in. (width) x 8 x 10^3 (attenuation factor). Thus, the area of cyclohexane at 0.3v, 10-min sweep would be 20 x 10^{-2} x 8 x 10^3 or 1600 in.². X, Cyclohexane, 10 min He sweep; □, cyclohexane, 60 min He sweep; △, benzene, 10 min He sweep; ○, benzene, 60 min He sweep.

[3] It must be remembered that when C_1, C_2, C_3, cyclohexyl, etc., intermediates are mentioned, the methane, ethane, propane, cyclohexane, etc., are not necessarily the adsorbed compounds. The C_1 might be thought of as a methine, methylene, or methyl fragment representing three, two, or one bond between carbon and the surface. Desorption at 0.05v could hydrogenate the normal species. It does not hydrogenate all of the benzene, as evidenced by presence of benzene in effluent sampled at 0.05v.

potentials positive to open-circuit potential of 0.45v, the total amount of cyclohexane decreases with time and potential. At potentials positive to open circuit the amount of benzene rapidly decreases during the 10-min helium sweep. At 0.7v, no benzene was observed on the 0.05v step within limits of detection of flame ionization using a UCON column. The benzene which is not seen at higher potentials might be an undesirable side product at lower potentials or that which is formed might react directly to CO_2 (Eq. [2]) with k_3 and subsequent steps very fast. Reaction of benzene has been studied to clarify this and is discussed later in the paper.

In addition to benzene and cyclohexane being observed on cathodic desorption, varying amounts of normal chained C_1-C_6 hydrocarbons were observed. Table II indicates the relative amount of each species at several potentials and the total area attributed to the compounds on a gas chromatograph. At most potentials, C_3 and C_4 species were predominant. The relative amounts of C_1 and C_2 species were small although the relative amount of C_1 species increased slightly with potential. In Table II it can be seen that the total amount of C_1-C_6 hydrocarbon increased with increasing potential and was largest at the most anodic potential considered (0.7v). The areas in Table II represent those of an electrode two days old. Total areas on a 17-day old electrode were 50% less, but the relative amounts of C_1 to C_6 material were within ±8%. At all potentials, the total amount of C_1 to C_6 was greater than the benzene. At 0.3v, benzene was 26% of total material excluding cyclohexane. At 0.5v benzene was 8.5% of total material excluding cyclohexane. The amount of cyclohexane found in the desorbable mixture also decreased with potential. At 0.3v 96% of the desorbable species was cyclohexane; at 0.5v, 90%, cyclohexane and at 0.7v, 73%, cyclohexane.

Results from the adsorption of cyclohexane have indicated that any one of the paths mentioned earlier (Eq. [1]-[4]) might occur. The adsorption and desorption of benzene has been studied at representative potentials to provide additional information for choosing a specific path.

Gas chromatographic results with benzene as reactant.—Procedures for pretreatment, adsorption, and helium sweep were the same for benzene as those for cyclohexane. With cyclohexane as reactant, desorption was performed at 0.05v in order to minimize hydrogenation of benzene to cyclohexane during pulsing. When benzene was admitted to the electrode at 1.35v for 30 min, helium swept through for 10 min to remove some of the excess, potential lowered to 0.05v with sampling every 15 sec with the chromatograph, there was a 1:2500 ratio of cyclohexane to benzene after 45 sec at 0.05v, a 1:1625 ratio after 60 sec and 1:180 ratio after about 5 min at 0.05v. During a normal desorption the maximum amount of material is removed after 45 to 60 sec at 0.05v. When benzene is the reactant, hydrogenation of the excess as it passes over the electrode does not appear to occur during the time of interest. Thus any cyclohexane observed during a run would result from desorption of some 6 ring species adsorbed on the electrode and not as a result of hydrogenating excess benzene in the line. Also the amount of cyclohexane that appeared when benzene was adsorbed at potential and then removed at 0.05v was always greater than the corresponding decrease in benzene peak. Whether the cyclohexane which is seen originates from a cyclohexyl species and/or benzene on the electrode and hydrogenated at 0.05v is difficult to distinguish.

Benzene is more difficult to handle chromatographically than cyclohexane. The peaks are broader and not as well defined even though benzene remains on the column only 3 min. With cyclohexane, it was possible to continue sampling at the potential of adsorption to note how cyclohexane would decrease during the time at 0.05v. When cyclohexane was the reactant and the potential was lowered to 0.05v, the area of cyclohexane would increase; thus cyclohexane area originating from excess in line could be subtracted from that total area. When benzene was reactant, the peak after the cathodic pulse would sometimes increase and sometimes decrease.

In spite of the problems with chromatographic analysis for benzene, there were very definite trends as shown on Fig. 4. Each point was repeated at least three times. The areas of desorbed cyclohexane were reproducible to ±18%. The area of cyclohexane changed by 20% as a result of length of helium sweep (*e.g.*, 30-min sweep instead of 10 min at 0.3v). When the experiment was repeated a few days later, the area for 10-min helium sweep at 0.3v decreased 16% and the area for the 30-min helium sweep was still 20% less than the 10-min sweep performed on the same day. The total amount of cyclohexane, as determined by measuring the peak area from the chromatograph, was greatest for 0.3v regardless of time at potential under helium. After 30 min under helium sweep, the value decreased 20% and remained constant. A maximum of cyclohexane might be expected in the region of hydrogen adsorption, as adsorbed benzene could be easily hydrogenated. At 0.5 and 0.7v there was less cyclohexane. At 0.5v the amount of cyclohexane remained fairly constant with time under helium. At 0.7v there was a 40% decrease in cyclohexane during the 30-min helium sweep and then it was fairly constant. If helium was swept through for over 16 hr at the potential of adsorption, there was little benzene left in the line; however a relatively large amount of benzene desorbed at 0.05v. Figure 5 shows the area of cyclohexane and benzene. In the results shown in Fig. 5, the benzene is from the electrode with the small amount of background subtracted out. It can be seen that behavior is similar after 16 hr as 60 min. These results were obtained on

Table II. Percentage C_1-C_6 hydrocarbons, cyclohexane as reactant, helium sweep for 10 min

Potential, v	Total area, in.[2]	C_1	C_2	C_3	C_4	C_5	C_6
0.3	64.2	7.0	7.9	30.7	17.1	23.3	12.4
0.5	131.1	8.9	4.1	24.2	29.2	17.8	17.5
0.6	178.5	6.7	3.6	22.8	20.2	26.9	20.9
0.6	206.5[a]	10.5	4.8	34.6	26.2	16.9	6.6
0.7	258.8	12.5	3.6	31.3	22.1	18.6	12.9
0.7	405.3[b]	9.0	5.4	27.6	28.0	19.0	10.5

[a] Helium sweep for 60 min.
[b] Helium sweep for 30 min.

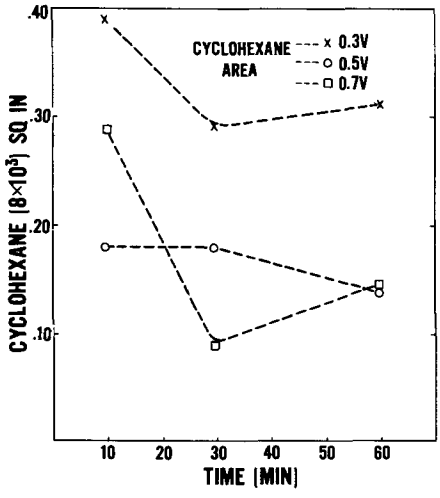

Fig. 4. Area of cyclohexane, desorbed with benzene as a reactant, as a function of time under helium sweeps at various potentials. Number 8 x 10^3 represents attenuation on gas chromatograph.

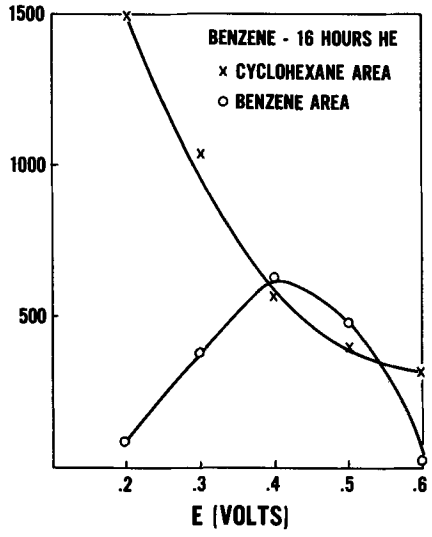

Fig. 5. Areas in square inches, cyclohexane and benzene as a function of potential for 16-hr helium sweep; benzene, the reactant.

a different electrode, but the 10-min results from each electrode were similar in both cases. From the long sweep, it can be seen that there is a maximum amount of cyclohexane desorbed at 0.3v. The amount decreases at the more anodic potentials. There is less benzene at 0.2 and 0.6v than at the intermediate potentials. When cyclohexane was reactant, there was a maximum of benzene at 0.4v; with benzene there is a maximum of benzene relative to cyclohexane at this potential. This might lead to the conclusion that there was an equilibrium between the two species (Eq. [3]) with the relative amount very potential dependent. With cyclohexane, the maximum amount of benzene was still only 4% of the total material from the electrode. When benzene is reactant, at least 50% of the species is cyclohexane. This could be a result of hydrogenation of some of the adsorbed benzene during the 60 sec at 0.05v. Deuterated experiments in progress should give some information concerning this.

If the cyclohexyl species which is desorbed at 0.05v is from a cyclic intermediate species similar to that when cyclohexane is reactant and not just from hydrogenation of adsorbed benzene at 0.05v, the relative amounts of C_1-C_6 species should be similar at the various potentials to those obtained with cyclohexane (Eq. [1] or [3]). This does not prove to be the case. Even though the same C_1-C_6 hydrocarbons were observed on cathodic desorption the relative amounts were different. Table III shows relative percentage of each species at the various potentials. The relative amount was independent of time under helium sweep at potential of adsorption. At 0.3v, there was a minimum of C_1 species. This species increased with potential and was the predominant species at 0.5 and 0.7v. There was also less C_6 species at the lower potentials. At each potential, there was a relatively equal amount of C_3-C_5. It appears that at potentials above open circuit (0.45v) longer chain hydrocarbons convert to C_1 species more readily than at 0.3v. When cyclohexane was reactant, there was no relative increase of C_1 species and the total amount of C_1-C_6 species increased with potential. However with benzene as reactant, there was a maximum of lower boiling material at 0.3v and a minimum at 0.5v which is also where the maximum and minimum amount of cyclohexane is observed on desorption. The distribution of C_1-C_6 was quite different than for cyclohexane, and the total amount of C_1-C_6 was much less when benzene was reactant than when cyclohexane was reactant except at 0.3v. Also, the origin of the species appears to be quite different. Although the C_2 species appears as ethane for both cyclohexane and benzene, the amount of time for the maximum amount of C_2 species to be seen depends on the reactant. This indicates that the C_2 species may be a different C_2 species (a more unsaturated species when benzene is reactant) or bound on different types of sites. Deuterated experiments should clarify the first point.

Table III. Percentage C_1 to C_6 hydrocarbons, benzene as reactant, helium sweep for 10 min

Potential, v	Total area, in.²	C_1	C_2	C_3	C_4	C_5	C_6
0.3	101.1	2.7	19.4	22.4	24.2	20.4	10.7
0.5	22.8	20.1	10.7	15.0	23.8	19.4	10.6
0.7	53.9	26.4	11.0	15.5	15.4	14.4	16.7

The fact that the amounts of C_1-C_6 are so different for benzene and cyclohexane indicates that there is not just a simple consecutive step (Eq. [1]) or equilibrium between cyclohexane and benzene (Eq. [3]), but probably an equilibrium and then different steps to CO_2 (Eq. [2]). To further determine whether the reaction proceeds through O-type (Eq. [2]) or there are parallel paths (Eq. [4]), the rate of oxidation of the two compounds is being studied and will be reported later.

Conclusions

On the basis of gas chromatographic data, benzene and cyclohexane react via different paths. Both compounds yield methane, ethane, propane, n-butane, n-pentane, n-hexane, cyclohexane, and benzene on cathodic desorption. The amount of each species, however, depends on the reactant and potential of adsorption.

Manuscript submitted Aug. 22, 1968; revised manuscript received Feb. 20, 1969. This paper was presented at the Montreal Meeting, Oct. 6-11, 1968, as Paper 330.

Any discussion of this paper will appear in a Discussion Section to be published in the December 1969 JOURNAL.

REFERENCES

1. E. Luksha and E. Y. Weissman, Preprint of papers presented ACS, Miami, Fla., April, 1967, Vol. 11, No. 1, p. 247.
2. W. T. Grubb and C. J. Michalske, Proceeding from the 18th Annual Power Sources, May, 1964, p. 17.
3. S. B. Brummer and M. J. Turner, *J. Phys. Chem.*, **71**, 2825 (1967).
4. S. B. Brummer and M. J. Turner, *ibid.*, **71**, 3494 (1967).
5. S. Gilman, *Trans. Faraday Soc.*, **61**, 2561 (1966).
6. L. W. Niedrach and M. Tochner, *This Journal*, **114**, 17 (1967).
7. M. L. Savitz and R. L. Carreras, Preprints of papers presented ACS Biennial Fuel Cell Symposium, Chicago, Sept., 1967, p. 143, Adv. in Chem., in press.
8. W. T. Grubb in General Electric Report No. 6 on Contracts DA-44-009-AMC-479(T) and DA-44-009-ENG-4909.
9. H. J. Barger and M. L. Savitz, *This Journal*, **115**, 686 (1968).
10. J. Giner, *ibid.*, **111**, 376 (1964).
11. E. Luksha and E. Y. Weissman, Preprints of papers presented ACS Biennial Fuel Cell Symposium, Chicago, Sept., 1967, p. 152.
12. S. B. Brummer, J. I. Ford, and M. J. Turner, *J. Phys. Chem.*, **69**, 3424 (1965).
13. S. Gilman, *ibid.*, **67**, 78 (1963).
14. E. Gremer and R. Muller, *Mikrochem. Acta*, **36/37**, 553 (1951).
15. J. Giner, J. M. Parry, and S. M. Smith, Tyco Laboratory, Inc. Report on Contract DAAE15-67-C-0048, Jan., 1968.
16. A. H. Taylor and S. B. Brummer, *J. Phys. Chem.*, In press.
17. J. D. Roberts and M. C. Caserio, "Basic Principles of Organic Chemistry," pp. 103 ff, W. A. Benjamin, Inc., New York (1965).
18. W. Heiland, E. Gileadi, and J. O'M Bockris, *J. Phys. Chem.*, **70**, 1207 (1966).
19. Chemical Engineers Handbook, R. H. Perry, C. H. Chilton, S. D. Kirkpatrick, Editors, 4th ed., p. 14-22, McGraw-Hill Co., New York (1963).

The Anodic Dissolution and Passivation of Zinc in Concentrated Potassium Hydroxide Solutions

R. W. Powers* and M. W. Breiter*

General Electric Research and Development Center, Schenectady, New York

ABSTRACT

In this study, mainly two sets of experiments were carried out to obtain a better understanding of the tendency of the alkaline zinc electrode to passivate. Either photomicrographs of the electrode surface were taken *in-situ* at different potentials during an anodic voltage sweep or the two components of the electrode impedance were measured with a small signal of superimposed 1000 Hz A.C. The course of the passivation was found to depend strongly on the convective conditions in the electrolyte near the zinc electrode. The conditions for the formation of two different types of solid films have been defined and their effects on the current-potential curve have been determined. Type I film is white, loose, and flocculent. It forms in the absence of convection by precipitation from a supersaturated layer of zincate near the surface. When the conditions for supersaturation are largely removed by stirring, the formation of the type II film can be observed. The latter is more compact and appears to form directly at the surface rather than by precipitation. Its color can range from light gray to black depending on the potential and time of formation. The type II film is considered responsible for the transition from the active to the passive state of zinc in alkaline solution.

Three kinds of studies have been carried out in recent years on the kinetics and mechanism of the zinc electrode in alkaline media: (*a*) measurements near the equilibrium potential of the zinc electrode in solutions containing zincate or other zinc complexes (1-9); (*b*) anodic dissolution and formation of passivating layers (10-41); and (c) cathodic studies with emphasis on the morphology of the electrodeposit. The latter are outside the scope of the present paper.

In this communication, new results on the anodic dissolution and passivation of zinc in KOH solutions are described and discussed. A combination of techniques was used to supplement past work and to gain a better understanding of the processes taking place. Mainly two kinds of experiments were carried out. In one set, an anodic voltage sweep, starting at the rest potential of the zinc electrode, was applied potentiostatically at a slow constant rate and photomicrographs of the electrode surface were taken *in-situ* at different potentials. In the second set of experiments, the ohmic and capacitive components of the electrode impedance, in addition to the current-potential curve, were measured using voltammetry with superimposed 1000 Hz A.C.

Previous work.—There seems to be nearly universal agreement that at anodic potentials near the equilibrium value, the oxidation product of zinc in concentrated alkaline solutions is the soluble zincate ion. By emf measurements, Dirkse has shown that this species is the complex tetrahydroxyl anion, $Zn(OH)_4^{--}$, an interpretation supported by recent Raman and infrared, as well as NMR, studies (2, 4, 5).

Gerischer was the first to study the discharge mechanism of the zinc electrode (1). From impedance measurements on zinc amalgams he concluded that reaction [1] of the following sequence is rate-determining

$$Zn + 2\,OH^- \rightarrow Zn(OH)_2 + 2e^- \qquad [1]$$

$$Zn(OH)_2 + 2\,OH^- \rightarrow (Zn(OH)_4)^{--} \qquad [2]$$

The exchange current density of reaction [1] was about 0.1 amp/cm² in 5M KCl containing various concentrations of hydroxyl ions with a total concentration of zinc ions of 0.1M. Gerischer's results have been confirmed very recently by Farr and Hampson, using however $NaClO_4$ as the supporting electrolyte (9).

Lorenz suggested the subsequent scheme on the basis of the frequency dependence of the electrode impedance of a solid zinc electrode in 2M KCl + 0.5M $ZnCl_2$ at pH values of 7 and 1.5 (3).

$$Zn^{++}{}_{\text{bulk electrolyte}} \rightarrow Zn^{++}{}_{\text{surface}} \qquad [3]$$

$$Zn^{++}{}_{\text{surface}} + 2e^- \rightarrow Zn_{ad} \qquad [4]$$

$$Zn_{ad} \rightarrow Zn \qquad [5]$$

Zinc ions that diffuse to the surface in step [3] are discharged in step [4] to adsorbed atoms. Step [5] includes the surface diffusion of these so-called ad-atoms and their incorporation into the lattice. Surface diffusion was found to be the hindered step. The exchange current density of the discharge step was about the same as for the zinc amalgam electrode. This result suggests that the discharge steps are similar on solid zinc and on zinc amalgams.

Impedance measurements and measurements by the double-pulse technique were made on polycrystalline zinc electrodes, on the cleavage plane of zinc single crystals, *i.e.*, on (0001), and on heavily cold-worked electrodes in different alkaline solutions (6-8). The independence of the exchange current of the discharge step on the zincate concentration indicates the adsorption of intermediates. A two-step discharge mechanism was considered the most probable one

$$Zn_{kink} + OH^- \rightarrow (Zn_{ad}OH)^- \qquad [6]$$

$$(Zn_{ad}OH)^- \rightarrow Zn(OH) + e^- \qquad [7]$$

$$Zn(OH) + OH^- \rightarrow Zn(OH)_2 + e^- \qquad [8]$$

$$Zn(OH)_2 + 2\,OH^- \rightarrow (Zn(OH)_4)^{--} \qquad [9]$$

Step [6] includes the formation and surface diffusion of ad-atoms which may be stabilized by attachment of OH^- ions. It is considered the slowest step and leads to low values of the diffusion flux (6). Step [7] was suggested as the discharge step which determines the value of the exchange current in measurements with the double-pulse technique (7).

Several groups of workers have studied the passivation of zinc in concentrated alkali using the constant current technique (10-19). For a rather wide range of conditions, equations of the type

$$(i - i_l)\, t^{1/2} = k$$

* Electrochemical Society Active Member.

were found to describe the relationship between i, the applied constant current density, and t, the time required for passivation. Here the quantities, i_1 and k, are constants for a given electrolyte concentration, temperature, and convective conditions. The form of the above equation indicates the important role of diffusional processes in the passivation of zinc. However, there is a minimum amount of charge per unit area required for passivation, corresponding to at least the formation of a monolayer. This requirement leads to the replacement of the inverse square root law given above by an inverse linear law at current densities in excess of about 0.2 amp/cm^2. On the other hand, at low current densities the inverse square root law also fails to describe the experimental data if modes of mass transport, other than pure diffusion, become important. Thus, it was found that longer passivation times are required for vertical electrodes than for horizontal ones due to the onset of natural convection (13, 16, 18).

Unlike the experimentally simpler constant current technique, the potentiostatic method permits measurement of the current density at all potentials within a range of interest and hence study of intermediate stages of passivation. The first comprehensive potentiostatic study of solid zinc electrodes in alkaline solutions in both active and passive regions was carried out by Sanghi and Fleischmann (23). They observed that the concentration of zincate ion has a small effect on the dissolution rate in the active region. The maximum dissolution rate (at the peak of the potentiostatic current-potential curve) is only a fraction of the limiting diffusion current of hydroxyl ions at bulk concentrations greater than 0.01M. Stirring increases the current at a given potential in both the active and passive regions. Saturation with zincate decreases the current at a given potential in the passive region. The passivation of the zinc electrode was attributed to precipitation and formation of a new oxide phase that is less soluble than the one formed at lower anodic potentials. The outer portion of this oxide phase is nonetheless converted to a soluble species in the passive region.

Vozdvizhenskii and Kochman found that, in both 2M and 5M KOH solutions, the potentiostatic current-potential curve had two peaks before the electrode became passive (25). The relative heights of these peaks depended on the sweep rate of the voltammetric measurement. According to their visual observation of the surface, a white film, that appears almost from the start of the experiment, covers the surface at the onset of passivation. This film gradually darkens with increasing potential in the passive region, turns brown, and is finally converted to a completely black color, presumably due to the presence of finely dispersed zinc within it. The two peaks were attributed to the formation of oxides with different hydration, structure, and solubility.

The behavior of the zinc electrode in the passive region was thoroughly investigated by Kabanov and co-workers (26-28). In solutions saturated with zincate in the potential range $-1.0 < U < 0.2$v with respect to a mercury-mercuric oxide electrode, the direct dissolution reaction

$$Zn \rightarrow Zn^{++} + 2e^- \qquad [10]$$

was suggested to occur to a large extent in addition to the chemical dissolution of zinc oxide

$$ZnO + 2\,OH^- + H_2O \rightarrow (Zn(OH)_4)^{--} \qquad [11]$$

The independence of current on potential at U less than 0.2v was attributed to the limiting rate of diffusion of zinc atoms through the oxide layer.

Ashton and Hepworth established that the rate of dissolution of zinc single crystals in 0.5M NaOH in the active region decreases slightly at constant potential with an increase in the planar packing density (29). This latter quantity increases in the order

$$(0001) < (10\bar{1}0) < (11\bar{2}0)$$

for zinc and other hexagonal close-packed metals. Their polycrystalline electrodes showed a dissolution behavior similar to that for the $(10\bar{1}0)$ plane.

There is a considerable literature on the structure and properties of the solid products formed during the anodization of zinc in alkali (18, 30-38). Thus Fischer and Budiloff identified the dark, 3-4μ thick layers formed in 2% NaOH at a constant current of 50 mamp/cm^2 as zinc oxide by means of both x-ray and electron diffraction (30). Very extensive studies of anodic coatings formed at anodic potentials corresponding to oxygen evolution in NaOH solutions of various concentrations have been carried out by Huber (31-33, 35, 36). The coloration of such coatings was attributed to an excess of zinc in zinc oxide since they are bleached on heating in air and colored again on heating in zinc vapor (33). Fry and Whitaker established that anodic films formed in 0.145M NaOH + 0.027M Na_2CO_3 at potentials in excess of 3.5v against saturated calomel were white. By both chemical and x-ray diffraction analyses, these films, as well as darker films formed at lower potentials, were identified as zinc oxide (38). Hampson, Tarbox, Lilley, and Farr identified zinc oxide by electron diffraction on specimens in KOH solutions subjected to potentials slightly below that for oxygen evolution. Very weak lines due to γ-zinc hydroxide were also noted (18).

On the other hand, Huber reported that γ-zinc hydroxide and a very small amount of colorless zinc oxide precipitate on an active zinc electrode in 1M NaOH after continued electrolysis. Such findings were obtained by electron diffraction of thinner coatings and by x-ray diffraction of thicker ones (35). Nikitina made an extensive study by means of microscopy as well as by x-ray diffraction of the precipitate formed on a zinc anode as well as the product precipitated in the bulk of the electrolyte. She worked with KOH solutions from 3 to 10M and at different temperatures between —20° and 20°C (37). Prismatic γ-zinc hydroxide, rhombic ϵ-zinc hydroxide, as well as zinc oxide were identified depending on the KOH concentration and the temperature. The less stable γ form of the hydroxide was observed with lower alkali concentrations and at the lower temperatures. The most stable hydroxide, the ϵ modification, appeared under intermediate conditions. Zinc oxide, which is slightly more stable than the ϵ-hydroxide, was observed in the more concentrated KOH solutions at higher temperatures. For instance in 10M KOH, ZnO was found at 20°C, but ϵ-$Zn(OH)_2$ with a small amount of γ-$Zn(OH)_2$ at 0° and —20°C. Nikitina's results are in general agreement with those of Jofa, Mirlina, and Moiseeva (34). Vozdvizshenskii and Kochman reported that after the evolution of oxygen on a zinc anode in 2M KOH, the surface was black but coated on the outside by a white gelatinous coating which readily washed off (25).

Experimental Procedure

Two kinds of zinc electrodes were used in this study. The first was obtained by cleavage from single crystal rods grown from zinc 99.9995% pure. Specimens, about 0.3 cm thick, were produced by the rapid insertion of a needle into the crystal while it was immersed in liquid nitrogen contained in a thermally insulated box. Rewarming to room temperature was carried out in an inert atmosphere. The specimen surface so-produced lies in the (0001) plane. It is mirror-like and marred by only a few cleavage steps. Such specimens were put into the test cell without further pretreatment. Experiments were started after an equilibration time of about 10 min, during which the zinc electrode stayed at open circuit potential in a 7M KOH + 0.25M ZnO solution saturated with purified argon. Both sets of measurements (current density i *vs.* electrode potential U with photomicrographs and $i - U$ curve with determination of the components of the electrode impedance) were made on the single crystal specimens.

Polycrystalline electrodes were cut from rolled zinc sheet, designated as Mix 60 by the supplier, the New Jersey Zinc Company. It was about 99.99% pure. The polycrystalline electrodes were pretreated by dipping them for a short time in concentrated nitric acid followed by thorough rinsing in a stream of distilled water. It took about 2 min to mount an electrode and to transfer it to the test cell. A polycrystalline electrode was connected to a potentiostat and immersed in electrolyte at −1.6v in the absence of zincate and at the rest potential in the presence of zincate. Measurements were started 5 min after immersion. A cathodic current transient was observed during and after immersion of the specimen electrode in KOH solutions without zincate. This cathodic current decays with time and tends toward a steady state value.

Throughout this study, the electrode potential was measured against and is referred here to a mercury-mercuric oxide electrode in pure KOH of the same concentration as that in the test cell. In addition, a secondary potential scale, one referred to the zinc rest potential, is also shown on the various $i - U$ curves presented in this paper. Such a scale facilitates the detailed examination of the shapes of the various experimental curves, an important part of the analysis carried out in this study.

The experimental work was carried out in KOH solutions prepared from reagent grade chemicals and distilled water. The solutions were either freshly prepared before the experiments or were stored under argon with exclusion of air in special apparatus.

The viewing cell and techniques for microscopic observation of zinc electrodes under polarization as well as most of the auxiliary instrumentation were described in detail previously (42). The zinc electrode potential was controlled by a Jaissle potentiostat and was programmed using either a Type 255 or a Model 504 Exact function generator. The current was recorded as a function of potential on a Moseley Model 2D-2A X-Y recorder. In this cell, designated here as cell I, the specimen surface is positioned horizontally facing upward. Impedance measurements on both cleaved and polycrystalline electrodes were also made in it. In addition, a second Teflon vessel, designated here as cell II, was used in which a polycrystalline sheet electrode was positioned vertically. A Teflon block with a cylindrical hole, 1 cm in diameter by 1.5 cm long, was pressed against the zinc sheet to affect a uniform current distribution over the zinc electrode. A fine hole in the block, 0.3 cm from the electrode surface, led to a separate reference electrode compartment.

Both the voltage sweep and the a-c signal were applied to the test electrode by the potentiostat during the impedance measurements as described previously (43). The manually triggered voltage for the sweep was taken from a Type 255 Exact Electronics function generator. It was necessary to keep the amplitude of the a-c signal as small as possible in order not to perturb the shape of the $i - U$ curve. An amplitude of 1 mv between the test and reference electrodes was used as the $i - U$ curve was not affected by the a-c component at this low amplitude. The ohmic ($1/R_p$) and capacitive (ωC_p) components of the electrode impedance in an analog parallel circuit were obtained simultaneously. The a-c signal between test electrode and reference electrode was fed to the reference input of the circuit which resolves the two components of the impedance (44, 45). The a-c voltage across a standard resistor, through which flowed the cell current between test and counter electrodes, was applied to the other input of this circuit. Both components of impedance were recorded as a function of the electrode potential on a Moseley Model 136A X-Y-Y recorder. The d-c current was obtained by amplifying the total voltage across the standard resistor by an operational amplifier, filtering out the a-c component, and feeding the d-c voltage to the Y input of another X-Y recorder. The electrode potential was always recorded on the X axis of the recorders.

Experimental Results

The current-potential curve shown in Fig. 1 was measured on a cleaved single crystal electrode at 0.55 mv/sec in 7M KOH + 0.25M ZnO at 23°C. The photomicrographs A to J shown in Fig. 2 were taken at the corresponding points marked on the $i - U$ curve in Fig. 1. The micrographs, obtained with dark field objectives at a total magnification of 90X, show the changes in the surface structure of the same area during the anodic potential sweep. Representative traces of the two components of the electrode impedance measured in an analog parallel circuit at 1000 Hz on similar cleaved single crystal electrodes in 7M KOH + 0.25M ZnO are shown in Fig. 3. The measurements were made under similar experimental conditions of assembling, sweep rate, and quiescent electrolyte as for those shown in Fig. 1 and 2. The $1/R_p - U$ and the $\omega C_p - U$ curves display characteristic waves which are discussed in a later section.

Because of the low impedance of the zinc electrode, a correction was necessary to take account of the resistance R_{EI} of the electrolyte between the test electrode and the opening to the capillary leading to the reference electrode compartment. This resistance was determined by applying a-c voltages with frequencies between 100 and 10,000 Hz from a function generator across cell I and a multiple decade resistance box in series with this test cell. For this determination, the cell was filled with 0.1M KCl, the zinc electrode was replaced with a platinized platinum sheet, and the Hg/HgO electrode with a platinized platinum wire. Using a dual beam oscilloscope, the series resistance was adjusted so that the amplitude of the a-c signal measured between the platinum sheet and the platinum wire equalled that across the resistance box. When the two signal amplitudes were equal, the electrolyte resistance equalled that of the adjustable series resistance. The distance from the test electrode to the center of the capillary opening, measured with a microscope equipped with a filar eyepiece, amounted to 0.76 mm. This value can be compared with one, 0.77 mm, calculated from the measured electrolyte resistance, the measured cross-sectional area of the cell, and the known specific resistivity of the electrolyte. The electrolyte resistance correction for the cell filled with 7M KOH + 0.25M ZnO was computed with this information and the known specific resistivity of the

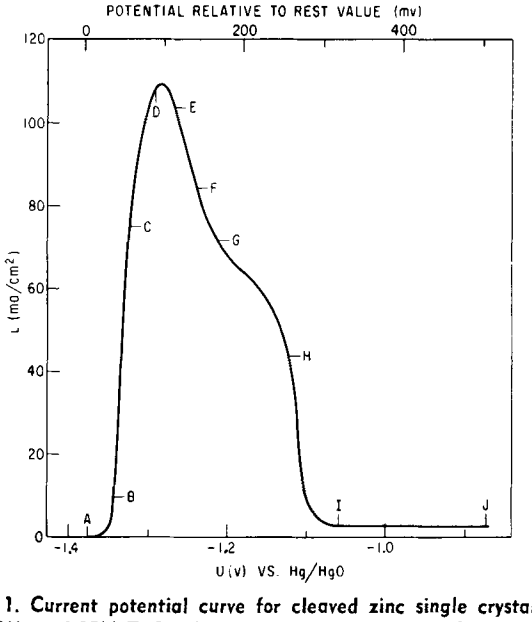

Fig. 1. Current potential curve for cleaved zinc single crystal in 7M KOH + 0.25M ZnO taken during anodic sweep at 0.55 mv/sec in cell I. Quiescent condition.

solution (46). It amounted to only 0.14 ohm cm^2. After converting the data in Fig. 3 to those for an analog series circuit, the electrolytic resistance, R_{EL}, was subtracted from the ohmic component R_s in the series circuit. Then the corrected ohmic value ($R_s - R_{EL}$) and the capacitive component $1/\omega C_s$ were used for a final conversion back to a parallel circuit consisting of the components R'_p and C'_p. This is the regular procedure for the treatment of impedance data (47, 48).

The $1/R'_p - U$, $C'_p - U$, and $i - U$ curves are plotted on Fig. 4 for the cleaved single crystal electrode and on Fig. 5 for the polycrystalline electrode in 7M KOH + 0.25M ZnO. The experimental conditions for the measurements shown on the two figures were the same except for the pretreatment of the electrodes as described in the preceding section.

A large number of voltammetric experiments were carried out on polycrystalline electrodes in cell II. Typical curves of $i - U$, $1/R_p - U$, and $\omega C_p - U$ obtained at a 1 mv/sec sweep rate in 7M KOH + 0.25M ZnO are shown on Fig. 6. Curves for the anodic sweep are represented by solid lines while those for the return cathodic sweep are indicated by broken ones. Still other $i - U$ curves and photomicrographs appear in Fig. 7-13.

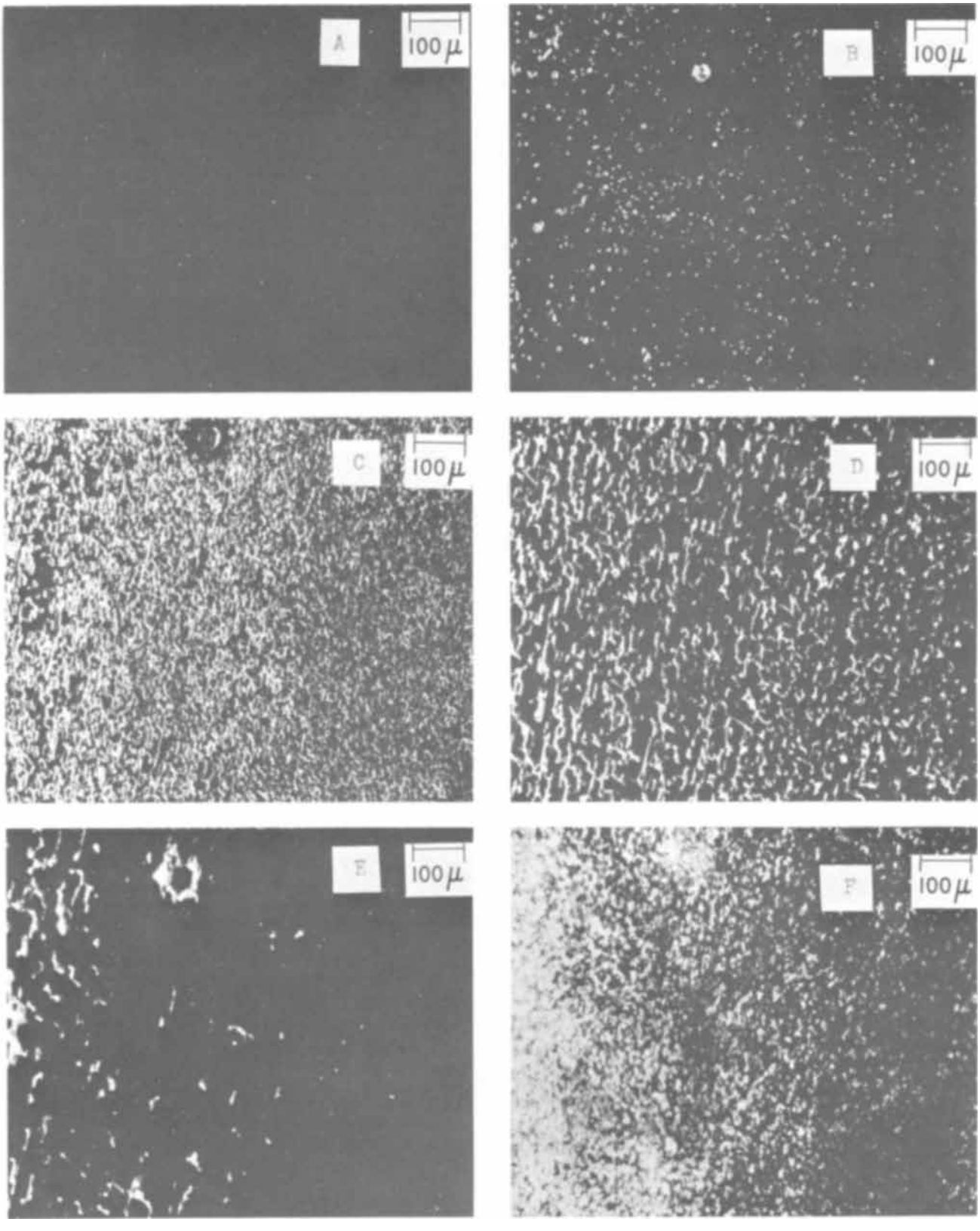

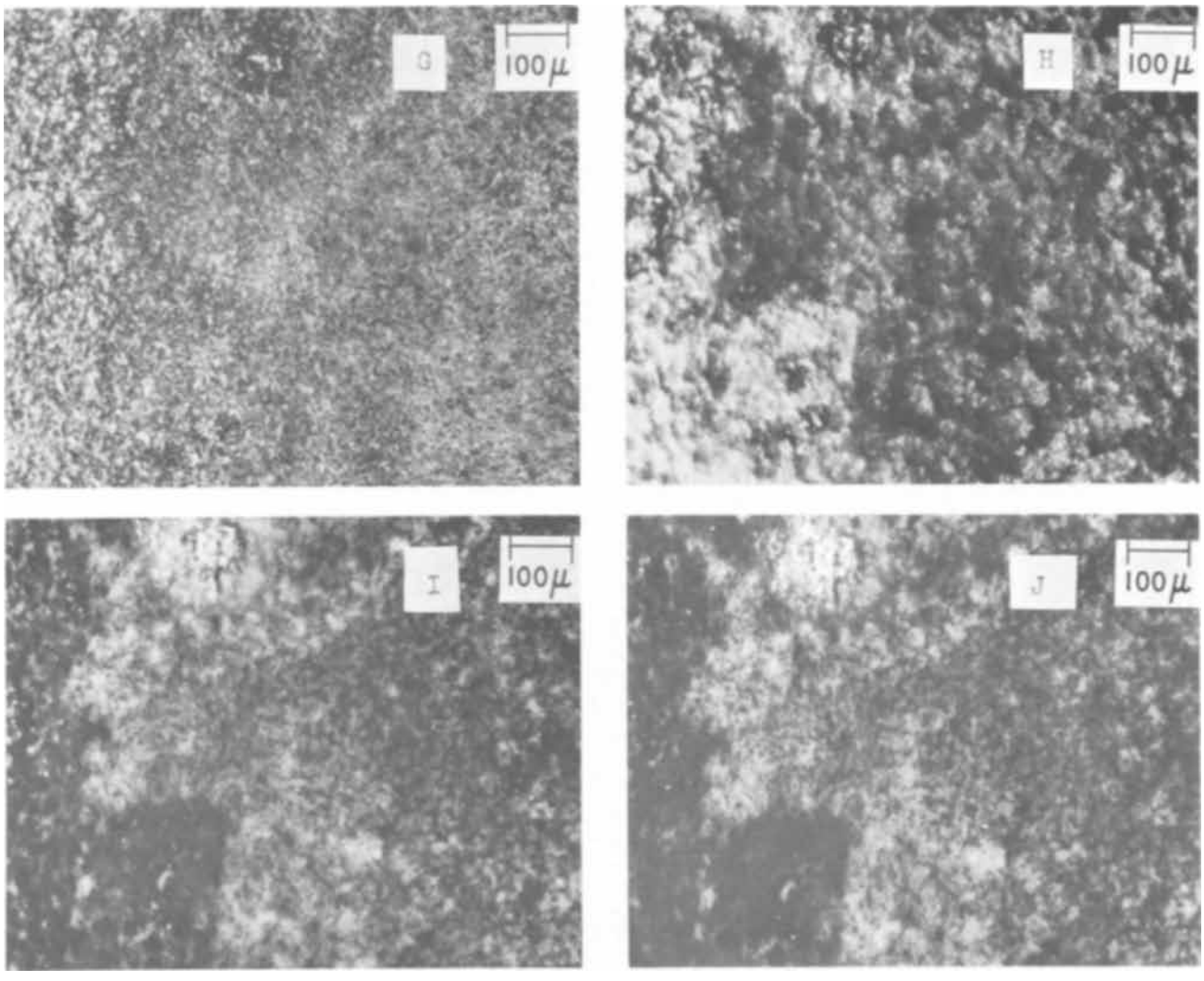

Fig. 2. Changes in the optical morphology of a zinc electrode observed during the anodic sweep shown in Fig. 1. Dark field 90X. Letters correspond to potentials indicated on Fig. 1.

Discussion

Different shapes of the i — U, $1/R_p$ — U, and ωC_p — U curves.—Probably the most interesting feature of the data presented in Fig. 1-6 is that the shapes of the i — U, $1/R_p$ — U, and ωC_p — U curves measured in cell I are very different from those measured in cell II. There is a very large peak in the i — U curve from cell I at a potential of —1.27v that is completely absent on the curve obtained in cell II. As will be discussed in more detail below, double peaks in the i — U curves

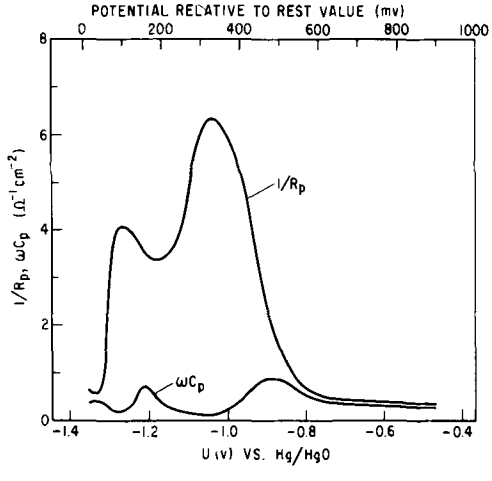

Fig. 3. Parallel conductance ($1/R_p$) and capacitive susceptance (ωC_p) *vs.* U for cleaved zinc single crystal in 7M KOH + 0.25M ZnO taken during anodic sweep at 0.55 mv/sec in cell I. Quiescent condition.

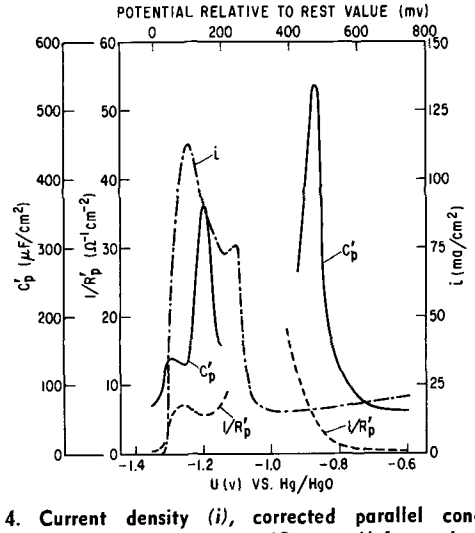

Fig. 4. Current density (i), corrected parallel conductance ($1/R'_p$), and corrected capacitance (C'_p) *vs.* U for a cleaved zinc single crystal in 7M KOH + 0.25M ZnO taken during anodic sweep at 0.55 mv/sec in cell I. Quiescent condition.

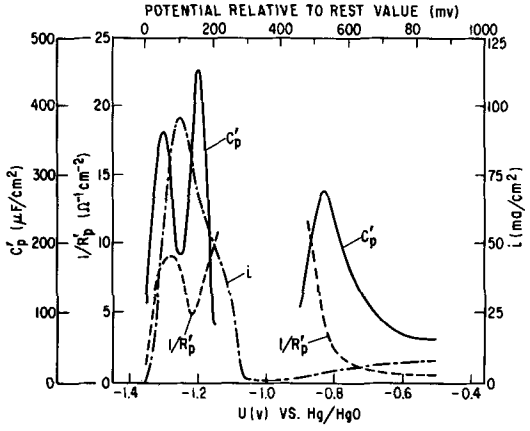

Fig. 5. Current density (i), corrected parallel conductance ($1/R'_p$), and corrected capacitance (C'_p) vs. U for polycrystalline zinc in 7M KOH + 0.25M ZnO taken during anodic sweep at 0.55 mv/sec in cell I. Quiescent condition.

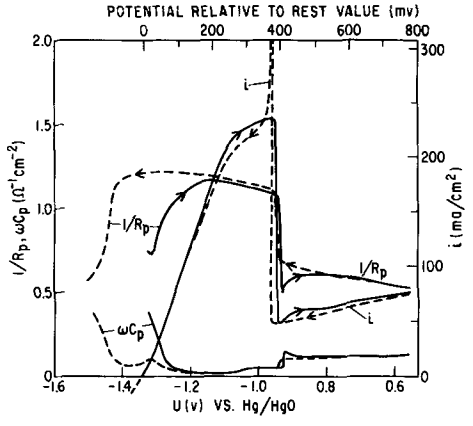

Fig. 6. Current density (i), parallel conductance ($1/R_p$), and capacitive susceptance (ωC_p) vs. U for polycrystalline zinc in 7M KOH + 0.25M ZnO taken during triangular sweep at 1 mv/sec in cell II.

were usually observed only in the former cell. The current densities measured in cell II were usually larger and the width of the active region greater by about 100 mv as can be seen on comparing Fig. 1 with Fig. 6.

The differences in data obtained in the two cells are accentuated in the resolved component measurements. The traces of the two components of the electrode impedance measured in an analog parallel circuit at 1000 Hz as shown in Fig. 3 were representative of data obtained in cell I. They were obtained under similar experimental conditions of assembling, sweep rate, and quiescent electrolyte as for those shown in Fig. 1 and 2. Similar results from numerous runs demonstrated that the characteristic shapes of the $1/R_p - U$ and $\omega C_p - U$ curves shown in Fig. 3 can be correlated with that shape of the $i - U$ curve shown in Fig. 1. When measured data such as shown in Fig. 3 were corrected for the electrolyte resistance by the method described previously, double peaks appeared in the $C'_p - U$ curves in the potential range between —1.37 and —1.07v which correspond qualitatively to the double peaks in the $i - U$ curves. These are shown in Fig. 4 and 5.

Numerous experiments showed that the characteristic shapes of the $1/R_p - U$ and $\omega C_p - U$ curves obtained in cell II, as shown on Fig. 6, are to be associated with that shape of the $i - U$ curve also shown on the same figure. Both components of impedance display a rapid change with U near the potential where the $i - U$ curve undergoes an initial rise. In contrast to data obtained in cell I, neither resolved component changes much with potential between —1.25 and —1.00v. The onset of passivation is correlated with an abrupt decrease in $1/R_p$ and a small increase in C_p. The increase of C_p with increase in potential for potentials less than —1.3v is in general agreement with recent results of Dirkse and Shoemaker (49).

While these measurements of the resolved components of impedance were very useful in pointing up differences between the two experimental cells, a quantitative study of impedance variations is very difficult because the impedance of the zinc electrode in strong alkaline solutions is so low. Even though the electrolyte resistance correction is very small by ordinary standards, amounting to only 0.14 ohm cm^2, it constituted such a relatively large correction on the measured values that presentation of data as $1/R'_p$ and C'_p over a range of potential, roughly between —1.15 and —0.9v, did not seem worthwhile. Although the resistance correction at the beginning of the experiment is probably known to within a per cent, uncertainties arise from the change of the electrolytic conductance during the potential sweep because of the enrichment of the electrolyte film near the surface with zincate as a result of the anodic zinc dissolution. Detailed correlations between the different peaks become difficult since their locations are affected by the uncertainties mentioned.

Most of the variations in the shapes of the curves measured in the two cells arose from very different hydrodynamic conditions. In cell I there was little natural convection as the test electrode was arranged horizontally facing upward. In contrast, in cell II the electrolyte near the vertical test electrode was undoubtedly stirred (50). That stirring due to natural convection is the important difference was shown by mechanically stirring the electrolyte in cell I using both single crystal and polycrystalline specimens. A lift pump operated by ultra-pure hydrogen was used for this purpose. In Fig. 7, the $i - U$ curve for a single crystal electrode with stirred electrolyte is presented and should be compared with Fig. 1 for the unstirred condition. Although these results are strong evidence of the influence of processes in the diffusion layer on some aspects of film formation, additional evidence is presented below.

Formation of a loose white coating under quiescent conditions.—The relationship between the potential and the kind of film formed will be considered first for quiescent conditions. Up to about —1.28v, under which conditions the current increases monotonically with increasing potentials, faceting of the initially very smooth single crystal surface takes place. Such facets grow coarser with time as shown in Fig. 2A-D. As no evidence of anodic film formation is seen in this region, presumably only a soluble oxidized zinc species is formed. The faceting was sufficiently coarse in this experiment that the specimen retained its mirror-like quality reasonably well. A mirror-like surface, which appears dark with dark field microscope objectives,

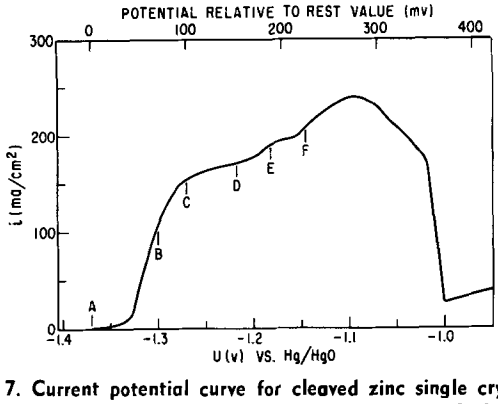

Fig. 7. Current potential curve for cleaved zinc single crystal in 7M KOH + 0.25M ZnO taken during anodic sweep at 0.50 mv/sec in cell I. Solution stirred.

is of course the most suitable background against which to view the formation of a whitish film that occurs at a slightly higher potential. In some runs, for reasons we do not yet understand, the faceting occurred on a smaller scale, with the result that the detection of the beginning of filming was made more difficult.

A coating or film on the electrode is first evident very near that potential at which the current density is maximum, *i.e.*, at about —1.27v as shown on Fig. 2E. This film spreads out and gradually covers the surface (Fig. 2F and G). Although it perhaps cannot be discerned from the photomicrographs, the film that forms near —1.27v is loose, flocculent, and white. At higher potentials, it may cover the electrode to a depth of 50-100μ in some places. This coating likely results from precipitation from a layer of electrolyte close to the electrode surface that is supersaturated with zincate ions. In "channels" between "islands" of film, it is often possible to see small white particles in motion under the microscope. This agitation is an indication of small scale convective motion associated with phase separation as precipitation should leave a less dense solution below a more dense one. This brings out the point that the word "quiescent" is used throughout this paper in a relative sense to distinguish hydrodynamic situations in which natural convection is small from others in which a solution is either pumped or subject to considerable natural convection. At still higher potentials, the anodic coating darkens as shown in Fig. 2G and H. The point I on Fig. 1 at the onset of passivation corresponds to almost complete coverage of the zinc electrode with film.

As shown on Fig. 7, the —1.27v peak in the $i - U$ curve is absent if the electrolyte is stirred. In Fig. 8, photomicrographs are presented which were taken at various potentials as indicated on Fig. 7. A white coating was not observed near —1.27v in this experiment. These results provide negative evidence that this peak is associated with a precipitated film. By stirring, the mass transfer of zincate ions is presumably increased sufficiently that a supersaturated layer of zincate does not form close to the zinc electrode.

When the potential scan rate is reduced to about one-tenth of that used to obtain Fig. 1, other experimental conditions remaining the same, a second peak in the $i - U$ curve near an anodic potential of —1.15v becomes fully developed as shown on Fig. 9. This peak appears only as an inflection point in Fig. 1. The overall reduction in the heights of the anodic peaks at the very slow scan rate should be noted. Double peaks in the anodic polarization curve for zinc in concentrated alkali were reported previously by Vozdvizhenskii and Kochman (25). These authors pointed out that the resolution of the second peak was improved by decreasing the potential scan rate, although they did not state quantitatively the scan rates used in their experiments. In our experience, very low rates of the order of a fraction of a millivolt per second are required. Vozdvizhenskii and Kochman used horizontal test electrodes as did we in cell I. It is important to point out that the horizontal electrode arrangement is not the only experimental situation in which double peaks can be observed. They also appeared with vertical electrodes in contact with a separator. We assume that the natural convection which usually occurs near a vertical zinc electrode under polarization is suppressed by the separator. This reduces sufficiently the rate of mass transport of zincate away from the electrode that the formation of a supersaturated layer of zincate occurs.

The formation of dark compact films.—The shape of the $i - U$ curve is altered greatly by stirring as shown in Fig. 6 for a vertical electrode subject to natural convection and in Fig. 7 for a horizontal electrode with forced convection. Instead of obtaining a peak near —1.27v, the current density continues to rise with increasing potential. However, the rate of rise varied considerably from run to run. In some, the current increased very slowly up to a potential of —0.97v, at which it dropped abruptly and complete passivation ensued. This behavior is very similar to that reported recently by Ashton and Hepworth for the anodization of zinc in 0.5M NaOH (29). A more rapid increase of current density with potential is shown on Fig. 6. In other runs the rise was gradual up to a potential of about —1.22v when fluctuations in the current density occurred as shown on Fig. 7. These fluctuations are often much larger than those indicated on the latter figure. At higher potentials, the current increased more steeply, passed through a maximum, and then dropped precipitously.

The stirring action permits the observation of a second, very different kind of film by preventing the formation of a supersaturated layer of zincate with subsequent precipitation of a loose white layer. The fluctuations in the current mentioned above are associated with the buckling and tearing of this second type. This behavior is shown on Fig. 8E and F. This type II film appears to be much more compact than the first type and is transparent to a greater or lesser degree. It is generally more adherent and seems to form directly on the surface of the zinc electrode. As discussed in more detail below, its color can range from very light gray to black. Other photomicrographs of buckled films, taken during a run under conditions similar to those used for Fig. 7 and 8, are shown in Fig. 10A and B.

There is another technique which facilitates the observation of type II film without interference from the first type. This involves the use of a potential jump from the rest value to a potential ranging usually from —0.5 to 0.5v in a quiescent solution. As discussed in the section on previous work, the application of a large constant current leads to passivation with a minimum, nearly constant, amount of charge per unit area and minimizes the formation of a supersaturated layer of electrolyte near the electrode. With potentiostatic experiments, after jumping the potential, for instance to 0.5v, an initially very high current density is noted which saturates the potentiostat. The current declines with time, amounting after 1 min to about 76 ma/cm^2, after 5 min to 56 ma/cm^2, and to 38 ma/cm^2 after 10 min. With time, surface features on the single crystal zinc electrode surface become obliterated due to the presence of type II film which becomes increasingly opaque. It is interesting to note however that even when the electrode is covered with film so as to appear very black to the eye, underlying surface features on the electrode surface may be viewed microscopically merely by increasing the intensity of illumination. If the potential is reduced after a certain time of formation, *e.g.*, to —0.5v after 10 min, fissures often appear in the film and some portions of the surface become denuded of film as shown on Fig. 11A. On other portions of the surface, the type II film is piled up several layers deep as shown in Fig. 11B.

Interpretation of impedance data.—As discussed previously, the general shape of the $1/R_p - U$ and $\omega C_p - U$ curves reflects the convective conditions under which the measurements were made. The gradual decrease of current with potential between —1.2 and —1.0v on the single crystal and the polycrystalline zinc surface in cell I (see Fig. 4 and 5) and the sudden decrease at about —0.95v on the polycrystalline surface in cell II (see Fig. 6) are accompanied by similar changes in the resolved components. The latter behavior is attributed to the completion of the coverage of the surface with type II film. Further conclusions of a qualitative nature may be derived from the impedance measurements in cell I for which a R_{EI} correction was made under the simplifying assumption that $R_{EI} \approx$ constant. A corresponding correction was not applied to the data obtained in cell II since the convective conditions did not guarantee a uniform current distribution.

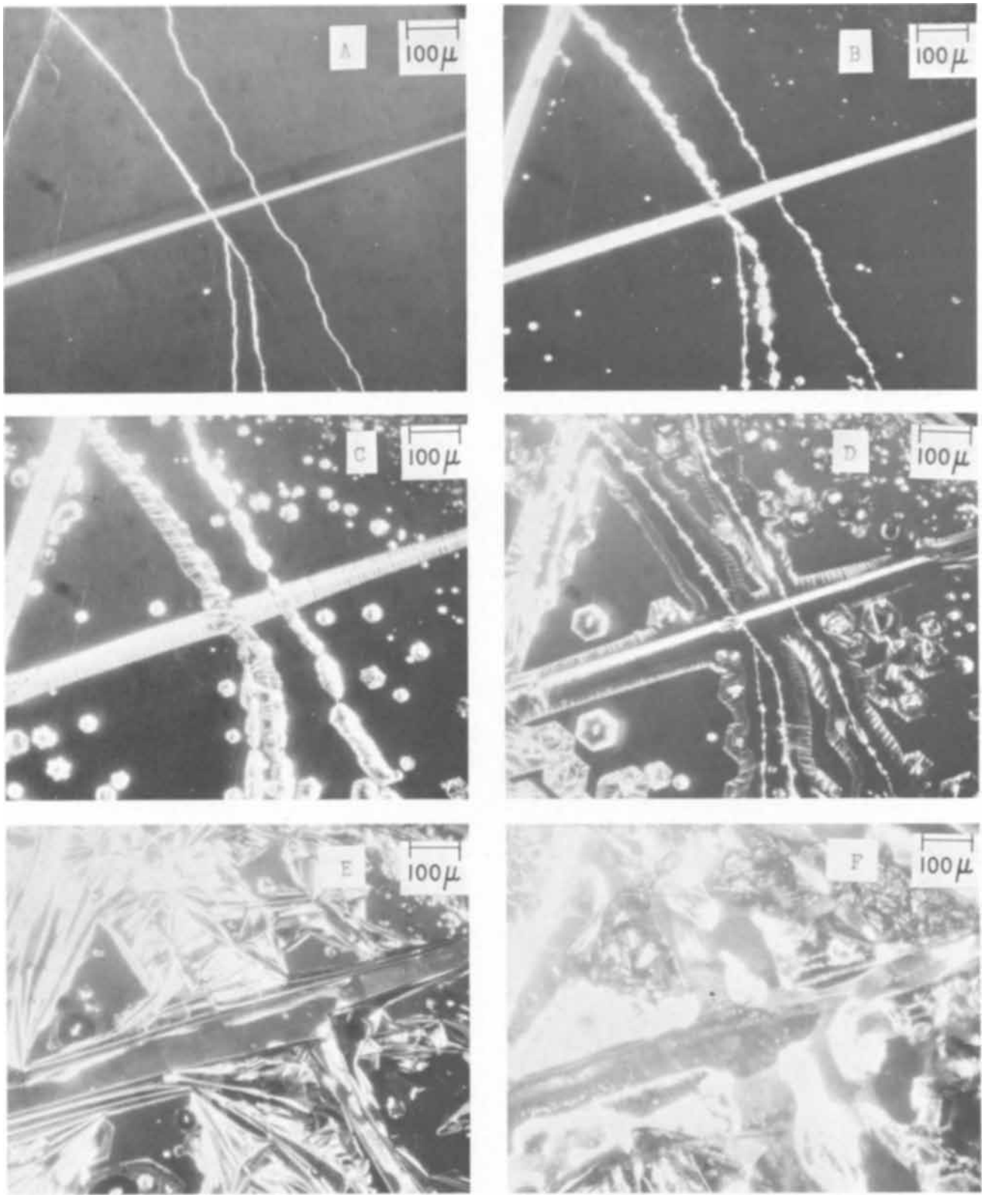

Fig. 8. Changes in the optical morphology of a zinc electrode observed during the sweep shown on Fig. 7. Dark field 90X.

The $C'_p - U$ curves in Fig. 4 and 5 show C'_p values larger than 60 $\mu F/cm^2$ between —1.35 and —1.15v and between —0.90 and —0.70v. The peak values are several hundred $\mu F/cm^2$. Such C'_p values cannot represent the double layer capacitance on zinc which is of the order of 20 $\mu F/cm^2$ (48). Large values of C'_p were also found by impedance measurements at the equilibrium potential of the zinc/zincate electrode and were attributed at high frequencies to a capacitance resulting from the presence of (Zn_{ad}-OH^-) (6). Our capacitance data in the two potential regions defined above have to be interpreted in a similar way. The adsorption reactions in question cannot be specified yet on the basis of the available data. However, it is considered likely that the formation of OH_{ad} is involved in the appearance of one or possibly of the two capacitance peaks in the region between —1.35 and —1.15v. Since the first peak is small on the single crystal plane and larger on the polycrystalline surface, the same adsorption reaction on different planes may have been observed. Since the second potential region is separated by about 0.4v from the first one, an adsorp-

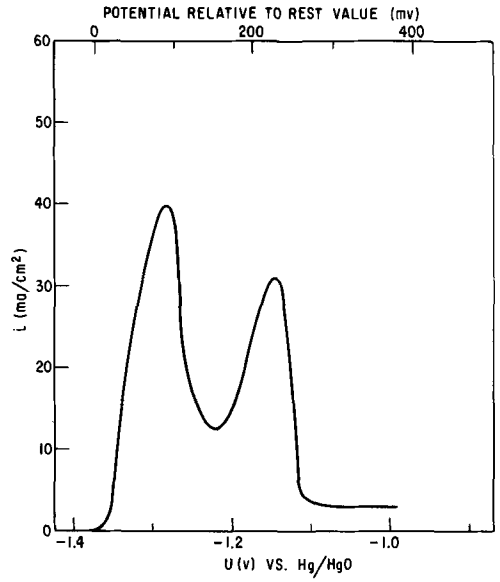

Fig. 9. Current potential curve for cleaved zinc single crystal in 7M KOH + 0.25M ZnO taken during anodic sweep at 0.05 mv/sec in cell I. Quiescent condition.

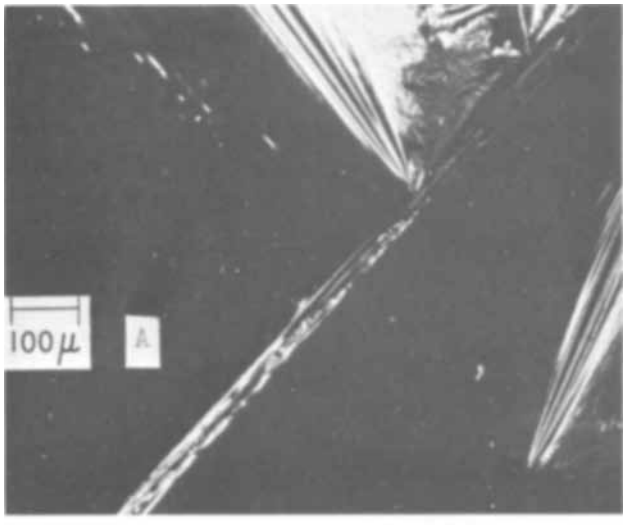

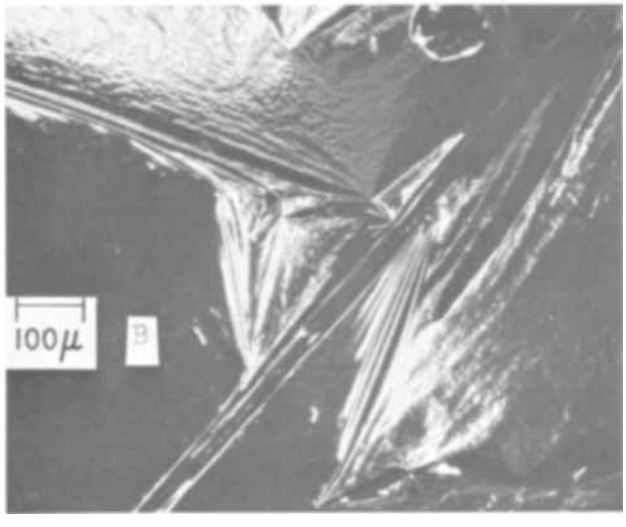

Fig. 10. Additional illustrations of ripped and buckled type II film. Dark field 90X.

tion reaction different from that in the first region has to be postulated as the cause of the capacitance peak between —0.90 and —0.70v.

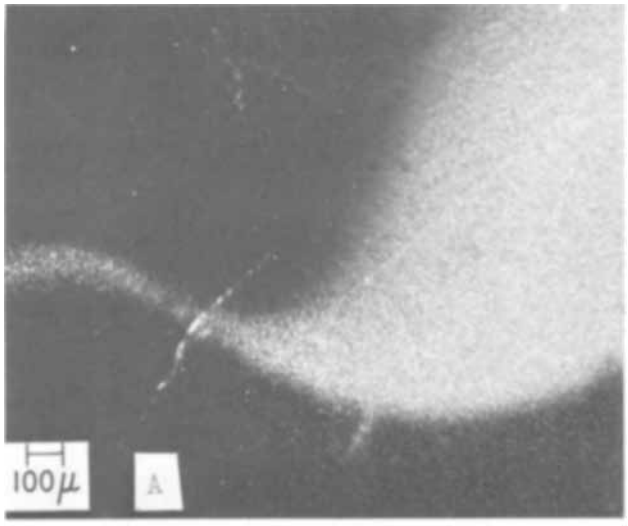

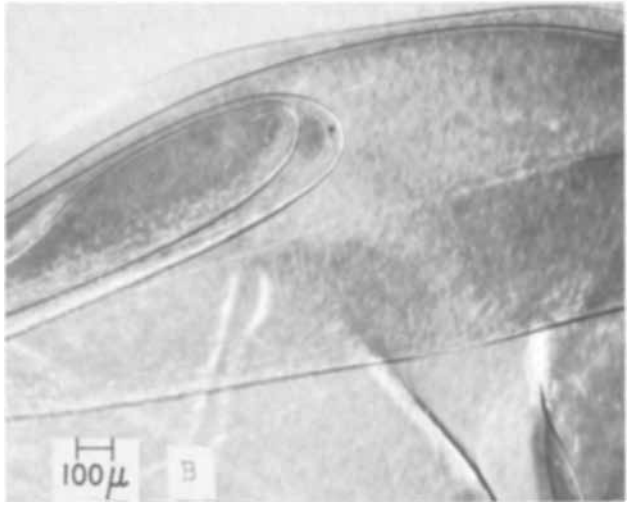

Fig. 11. Torn and piled-up type II film. Formed at 0.5v and torn by reducing potential to —0.5v. Dark field 48X.

Concluding Remarks

In the preceding sections, we have attempted to describe experimental conditions wherein one of the two different kinds of film involved in zinc passivation could be observed without interference from the other type. Both kinds of film were described previously by numerous authors. It appears likely from this prior work that type I film is either a form of zinc hydroxide or of zinc oxide while type II film is zinc oxide. An important part of the present contribution is a better delineation of the conditions for their formation. The electrode potential and the hydrodynamic conditions in the electrolyte near the zinc electrode mainly determine which film is observed.

An intriguing question, for which we have as yet no definitive answer, is the potential at which the type II film first forms. A thin, compact, nearly transparent coating that forms directly atop the surface of the zinc electrode is very difficult to detect. As shown on the photomicrographs in this report, it is probably most easily observed when buckled and torn. In our experience, the films formed by jumping the potential anodically from the rest value were capable of various shades of darkness depending largely on the forming potential and the elapsed time. Type II films formed during stirring at potentials near —1.2v are of a still lighter color. If the darkening of a filmed zinc electrode can be attributed entirely to the type II film, then the film that forms on a zinc electrode under quiescent conditions at potentials in excess of —1.22v must be of a duplex character. A porous, white precipitated film (type I) must cover type II. The dark-

ening of a filmed zinc electrode undergoing anodization under quiescent conditions is evident in that series of photomicrographs shown in Fig. 2 beginning with H, and possibly even in G. Darkening was determined quantitatively in another experiment. The potential of a single crystal zinc electrode was changed rapidly from the rest value by 200 mv in the anodic direction and the intensity of diffusely reflected light from the specimen was sensed using a photometer placed in one of the eyepiece tubes of the Leitz Ortholux microscope used to observe the zinc electrode under polarization. A recording of the intensity variation with time is shown in Fig. 12. The intensity of incident light upon the specimen was held constant throughout the experiment. There was a delay of 20-30 sec during which time the specimen retained its mirror-like character and appeared black. As type I coating formed and spread over the surface, the intensity increased. After about 110 sec, however, as the filmed electrode became dark because of adsorption of incident light, the recorded intensity fell. If the film formed after such an experiment is dissolved by stirring for 10-30 min at open circuit, a black web-like structure is observed under the microscope. It is often one of great delicacy and beauty. These so-called "zinc cobwebs," which we assume to form from an underlying compact type II film, are described elsewhere (51).

The rather different behavior of the two kinds of film substances involved in zinc passivation is brought out in yet another way on considering the curves shown on Fig. 6 and 12. Use was made of triangular sweeps wherein the potential was changed at a constant rate from the rest value to about —0.5v and then back again to the rest value. On Fig. 6, one can see that the current obtained with decreasing potential on the return part of the sweep duplicated rather well that obtained with increasing potential. This conclusion applies particularly well to data obtained at the more negative potentials. These data were obtained in cell II (vertical zinc electrode) where because of natural convection only small amounts of the first type film would be expected to form. Curves demonstrating these points have also been obtained with cell I (horizontal zinc electrode) with stirred electrolyte. In contrast, the very different behavior encountered with a horizontal electrode without stirring (quiescent condition) is brought out in the i — U curves shown on Fig. 13. Here the current at the lower potentials obtained during the cathodic sweep is very much less than that obtained during the anodic sweep. Microscopic observations readily indicate that the type I film which formed gradually with increasing potential (probably with some type II film beneath it) remained on the electrode for the entire return sweep. It thus appears that, whereas type II film substance is of predominant importance in controlling the active to passive transition between —1.07 and —0.97v, type I film can greatly influence the current level at lower potentials.

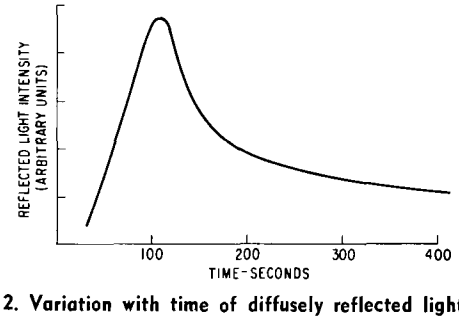

Fig. 12. Variation with time of diffusely reflected light intensity from zinc anode.

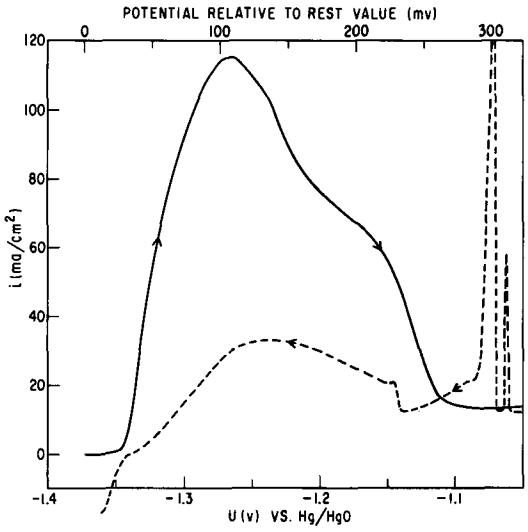

Fig. 13. Current potential curve for cleaved zinc single crystal in 7M KOH + 0.25M ZnO taken during triangular sweep at 0.50 mv/sec in cell I. Quiescent condition.

Acknowledgment

Partial financial support for the work of one of us (R.W.P.) was provided by the International Lead Zinc Research Organization, Inc., New York, New York.

Manuscript submitted Nov. 1, 1968; revised manuscript received March 13, 1969.

Any discussion of this paper will appear in a Discussion Section to be published in the December 1969 JOURNAL.

REFERENCES

1. H. Gerischer, *Z. physik. Chem.*, **202**, 302 (1953).
2. T. P. Dirkse, *This Journal*, **101**, 328 (1954).
3. W. Lorenz, *Z. physik. Chem. N.F.*, **19**, 37 (1959).
4. J. S. Fordyce and R. L. Baum, *J. Chem. Phys.*, **43**, 843 (1965)
5. G. H. Newman and G. E. Blomgren, *ibid.*, **43**, 2744 (1965).
6. J. P. G. Farr and N. A. Hampson, *Trans. Faraday Soc.*, **62**, 3493 (1966).
7. J. P. G. Farr and N. A. Hampson, *J. Electroanalyt. Chem.*, **13**, 433 (1967).
8. J. P. G. Farr, N. A. Hampson, and M. E. Williamson, *ibid.*, **13**, 462 (1967).
9. J. P. G. Farr and N. A. Hampson, *ibid.*, **18**, 407 (1968).
10. R. Landsberg, *Z. physik Chem.*, **206**, 291 (1957).
11. R. Landsberg and H. Bartelt, *Z. Electrochem.*, **61**, 1162 (1957).
12. S. E. S. El Wakkad, A. M. Shams El Din, and H. Kotb, *This Journal*, **105**, 47 (1958).
13. M. Eisenberg, H. F. Bauman, and D. M. Brettner, *ibid.*, **108**, 909 (1961).
14. B. Kabanov, *Electrochim. Acta*, **6**, 253 (1962).
15. T. I. Popova, V. S. Bagotskii, and B. N. Kabanov, *Zhur. Fiz. Khim.*, **36**, 1432 (1962); *Russ. J. Phys. Chem.*, **36**, 766 (1962).
16. N. A. Hampson and M. J. Tarbox, *This Journal*, **110**, 95 (1963).
17. H. Bartelt and R. Landsberg, *Z. Phys. Chem.*, **222**, 217 (1963).
18. N. A. Hampson, M. J. Tarbox, J. T. Lilley, and J. P. G. Farr, *Electrochem. Technol.*, **2**, 309 (1964).
19. M. A. V. Devanathan and S. Lakshmanan, *Electrochim. Acta*, **13**, 667 (1968).
20. R. Landsberg, H. Fürtig, and L. Müller, *Z. physik. Chem.*, **216**, 199 (1961).
21. R. Landsberg and H. Fürtig, *ibid.*, **216**, 212 (1961).
22. J. Euler, *Electrochim. Acta*, **11**, 701 (1966).
23. I. Sanghi and M. Fleischmann, *ibid.*, **1**, 161 (1959).
24. T. I. Popova, V. S. Bagotskii, and B. N. Kabanov, *Zhur. Fiz. Khim.*, **36**, 1440 (1962); *Russ. J. Phys. Chem.*, **36**, 770 (1962).
25. G. S. Vozdvizhenskii and E. D. Kochman, *Zhur. Fiz. Khim.*, **39**, 657 (1965); *Russ. J. Phys. Chem.*, **39**, 347 (1965).

26. T. I. Popova, N. A. Simonova, and B. N. Kabanov, *Elektrokhim.*, **2**, 1476 (1966); *Soviet Electrochemistry*, **2**, 1347 (1966).
27. T. I. Popova, G. L. Vidovich, N. A. Simonova, and B. N. Kabanov, *Elektrokhim.*, **3**, 970 (1967); *Soviet Electrochemistry*, **3**, 860 (1967).
28. T. I. Popova, N. A. Simonova, and B. N. Kabanov, *Elektrokhim.*, **3**, 1419 (1967); *Soviet Electrochemistry*, **3**, 1273 (1967).
29. R. F. Ashton and M. T. Hepworth, *Corrosion*, **24**, 50 (1968).
30. H. Fischer and N. Budiloff, *Z. Metallk.*, **32**, 100 (1940).
31. K. Huber, *Z. Electrochem.*, **48**, 26 (1942).
32. K. Huber, *Helv. Chim. Acta*, **26**, 1037 (1943); **26**, 1253 (1943).
33. K. Huber, *ibid.*, **27**, 1443 (1944).
34. Z. A. Jofa, S. Ya. Mirlina, and N. B. Moiseeva, *Zhur. Priklad. Khim.*, **22**, 983 (1949).
35. K. Huber, *This Journal*, **100**, 376 (1953).
36. K. Huber, *Z. Electrochem.*, **62**, 675 (1958).
37. Z. Ya. Nikitina, *Zhur. Priklad. Khim.*, **31**, 218 (1958); *J. Appl. Chem. (USSR)*, **31**, 209 (1958).
38. H. Fry and M. Whitaker, *This Journal*, **106**, 606 (1959).
39. M. E. Prostakov, A. I. Levin, and V. P. Kochergin, *Zhur. Fiz. Khim.*, **35**, 420 (1961); *Russ. J. Phys. Chem.*, **35**, 202 (1961).
40. T. P. Dirkse, D. DeWit, and R. Shoemaker, *This Journal*, **115**, 442 (1968).
41. A. Langer and E. A. Pantier, *ibid.*, **115**, 990 (1968).
42. R. W. Powers, *Electrochem. Technol.*, **5**, 429 (1967).
43. J. L. Weininger and M. W. Breiter, *This Journal*, **111**, 707 (1964).
44. M. W. Breiter, *J. Electroanalyt. Chem.*, **7**, 38 (1964).
45. M. W. Breiter, *This Journal*, **112**, 845 (1965).
46. C. T. Baker and I. Trachtenberg, *ibid.*, **114**, 1045 (1967).
47. P. Dolin and B. Ershler, *Acta Physicochim. USSR*, **13**, 747 (1940).
48. Tsa Chuan and Z. A. Jofa, *Doklady Akad. Nauk USSR*, **131**, 137 (1960).
49. T. P. Dirkse and R. Shoemaker, *This Journal*, **115**, 748 (1968).
50. N. Ibl, "Advances in Electrochemistry and Electrochemical Engineering," Vol. 2, Chap. III, P. Delahay and Ch. W. Tobias, Editors, Interscience Publishers, New York (1962).
51. R. W. Powers, Abstract No. 369, Montreal Meeting of the Society, Oct. 6-11, 1968.

The Microstructure of Sintered Silver Electrodes

I. During Discharges at the 1-Hour Rate

Charles P. Wales*

Naval Research Laboratory, Electrochemistry Branch, Washington, D. C.

ABSTRACT

Silver electrodes that had been manufactured for Ag-Zn storage batteries were cycled in 35% KOH at 25°C. The electrodes were examined by optical microscopy. The initial Ag_2O formation during a discharge at the 1-hr rate usually occurred on the surfaces of AgO clumps at many scattered areas throughout the electrode. After discharge potential fell to the Ag_2O/Ag plateau, Ag formation occurred on the electrode surface and then gradually spread to the interior as a discharge was continued. When a slow (20-hr) discharge rate was used, however, Ag formed at the surface and at the interior of an electrode simultaneously.

The use of silver-zinc and silver-cadmium storage batteries is limited by several factors, including the gradual loss of capacity often observed with use, the short life of some models, and the difficulty of recharging the batteries to full capacity in a short time. The present investigation concerns the structure of the silver electrode that is used as positive electrodes in silver-zinc and silver-cadmium storage batteries. Microscopic examination of electrodes at various stages of charge and discharge has been of considerable value in understanding the processes which occur. The three phases Ag, Ag_2O, and AgO can be seen and differentiated from each other by using optical microscopy. The progressive decrease in capacity of a sintered silver electrode that was discharged at a low (20-hr) rate has been shown to be the result of a gradual change in electrode structure as large Ag particles formed during the slow discharges in place of the small particles originally present (1).

The present paper describes structural changes that occur during discharges of sintered silver electrodes in the first 30 cycles of an electrode. These electrodes were always discharged at the 1-hr rate and charged at the 20-hr rate. Structures present in these electrodes at the end of discharges and structural changes during charges that followed the 1-hr rate discharges are to be the subject of later papers.

* Electrochemical Society Active Member.
Key words: silver electrode, silver oxides, microstructure.

Experimental Procedure

The silver electrodes used for the microscopic examination had been manufactured commercially for use in Ag-Zn storage batteries. The electrodes were all of the same size and had been designed to discharge at comparatively low rates, requiring one or more hours for a complete discharge. The electrodes consisted of sintered Ag particles with a grid of expanded sheet Ag that was close to one electrode surface. The structure of these electrodes has been illustrated (1). Electrode dimensions were 41.5 mm wide by 38.0 mm high by 0.8 mm thick. The theoretical capacity of an electrode, based on the weight of sintered Ag present, was approximately 2.9 amp-hr.

An electrode which was to be examined was charged and discharged between two other sintered Ag electrodes of the same size and construction. All three electrodes were wrapped individually with treated cellulose separator to slow the diffusion of soluble Ag species. The cell containing these electrodes, which has been described in more detail in ref. (1), was so constructed that the middle electrode could be removed readily from the separator when it was desired to cut an electrode sample for microscopic examination. The cell also contained a Ag/Ag_2O reference electrode. All work was done at approximately 25°C in an excess of 35% KOH solution.

The removable electrodes were charged at the constant current which required approximately 20 hr for

a complete charge. A charge was ended when electrode potential stopped changing rapidly after oxygen began to evolve. These electrodes were discharged at the constant current which required 1 hr for potential to drop to —500 mv *vs.* the reference electrode, a potential equivalent to an endpoint of approximately 1.0v for a typical Ag-Zn cell. Progressively lower values of charge and discharge current were used as the electrode capacity gradually declined with cycling, so that the actual hours usually varied less than 3% from the desired 20 hr for charge and 1 hr for discharge. An exception was the first two cycles of an electrode, where capacity fluctuated and variation from the desired times averaged 9.6%. Samples approximately 19 x 21 mm were cut from a removable electrode at various times, for microscopic examination. The remainder of the electrode was then returned to the cell and placed within the separator as before. Current was lowered by an amount sufficient to compensate for the removal of each sample, so that current density on the remainder of the electrode was unchanged.

Each sample from an electrode was handled separately to avoid unnecessary delay in microscopic examination. Sample treatment was changed from that used earlier (1). The wet-polishing step was omitted and a different impregnation plastic was used. Porous electrodes cannot be ground and polished successfully in preparation for microscopic examination unless the voids within the electrode are filled with a solid material. Several polyesters were tested as the impregnation material but all reacted slowly with Ag_2O and AgO before solidifying. Epoxy resins are available that are less reactive with silver oxides, but most epoxy resins have high viscosity and need to be heated for curing. A little decomposition of AgO seemed to occur even when an electrode sample was heated at the relatively low temperature of 40°C for 8 hr. This agrees with the recent report of slow AgO decomposition taking place at 25°C, while at 50° the AgO decomposition had increased greatly (2). The majority of the samples in the present work were impregnated with an epoxy resin that required several days at room temperature before the epoxy resin hardened sufficiently that it could be ground and polished successfully. The most recent samples were impregnated with a transparent epoxy resin[1] that is less viscous and will harden overnight at room temperature.

Note that an exothermic reaction takes place after the components of an epoxy resin or polyester are mixed. Dangerously high temperatures can occur when a large volume of the liquid plastic is prepared. The temperature may increase sufficiently that the plastic will ignite spontaneously. A particularly hazardous situation can occur if a large quantity of plastic is used to impregnate large battery electrodes consisting of an oxide, because the oxide will decompose when heated and the released oxygen will speed combustion of the plastic. In the present work only a small quantity of epoxy was needed for a sample. The temperature of the aluminum mold that held a sample did not rise noticeably above room temperature.

After a sample was cut from an electrode, the sample was immediately washed in 4-6 changes of distilled water to remove the KOH solution. Then the sample was dried in a vacuum for 1 hr. A dried sample was placed in the cylindrical cavity of an aluminum mold. The cavity was then filled with Lucite pellets to hold the sample upright. While under a vacuum, the sample was impregnated with the epoxy resin. Only 15-20g of epoxy were needed to fill the void spaces between the pellets and in the electrode. The impregnated sample was returned to atmospheric pressure while the plastic was still liquid, and the plastic was cured at room temperature. Then a cross section of the sample was prepared by grinding the sample successively on 120, 240, 400, and 600 mesh silicon carbide papers. Finally the sample was dry polished on a sponge rubber lap charged with 0.3μ alumina powder. The sample was then examined by optical microscopy and the appearance of significant areas recorded by photography.

[1] EPO-TEK 301 (Epoxy Technology Inc., 65 Grove Street, Watertown, Mass. 02172).

Results of Microscopic Examinations

Figure 1 gives typical potentials measured during discharges at the 1-hr rate and for comparison also includes two discharges at the 20-hr rate. The potential in the first portion of a discharge was the potential of AgO being reduced to Ag_2O, and then the remainder of the discharge took place at the potential of Ag_2O being reduced to Ag. Electrodes showed the AgO/Ag_2O potential during the first 11-15% of cycle 1 discharges at the 1-hr rate. A smaller proportion of the following discharges took place at the AgO/Ag_2O potential, and from cycle 3 to cycle 30 this potential lasted for only the first 6-12% of discharges at the 1-hr rate. (No electrodes were given more than 30 cycles in the present work.) The shape and length of this higher potential portion of a discharge varied from cycle to cycle. When the 20-hr rate was used, a larger proportion of a discharge took place at the AgO/Ag_2O potential. The first discharge at the 20-hr rate showed less of this higher potential than the later cycles. After the first cycle, the higher potential plateau resembled that of E in Fig. 1. It can be seen in Fig. 1 that the total capacity delivered during discharge decreased gradually as an electrode was cycled at the 1-hr rate and capacity decreased more rapidly when the 20-hr rate was used, although the slower discharge gave a larger capacity on the first cycle.

At the end of a charge to oxygen evolution at the 20-hr rate over half of the Ag in an electrode had been oxidized to AgO, with much smaller amounts of an electrode consisting of metallic Ag or of Ag_2O. Figure 2 illustrates an electrode at the end of the first charge, as well as can be done in one photograph. This and all subsequent figures are photographs of cross sections through an electrode and, therefore, also show cross sections through individual particles or crystals of which the electrode is composed. The charged electrode had variation from one area to another. At some areas more AgO was present than was in the area shown in Fig. 2, while elsewhere larger amounts of Ag and Ag_2O were present. Large Ag particles did not oxidize completely during charge, but many of the small Ag particles had oxidized completely to AgO. It could be seen under polarized light that what appeared to be large AgO crystals actually consisted of several smaller AgO crystals that had grown together. The AgO crystals tended to fill some of the voids originally present in the unused electrode.

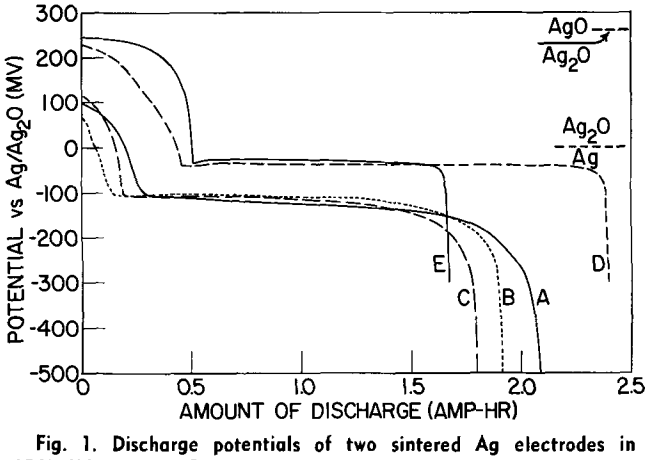

Fig. 1. Discharge potentials of two sintered Ag electrodes in 35% KOH at 25°C following charges at 20-hr rate. A, cycle 1; B, cycle 15; and C, cycle 30 of electrode always discharged at 1-hr rate. D, cycle 1; and E, cycle 6 of another electrode always discharged at 20-hr rate.

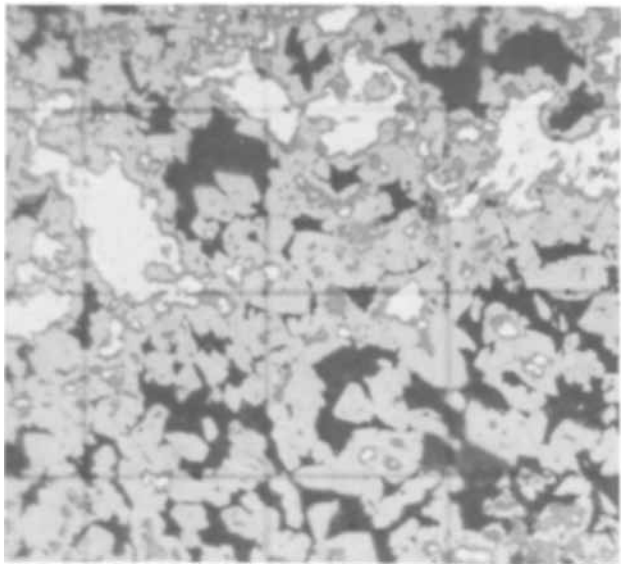

Fig. 2. Previously unused electrode at the end of the first charge to oxygen evolution. Metallic Ag particles are the lightest shade. Groups of AgO crystals are shown by the medium gray that predominates. Ag_2O (darker gray) is present in small patches within the AgO and also is present as a thin layer separating Ag particles from the AgO. Void areas are the darkest shade. Lines forming the squares are 30μ apart.

The appearance of the electrode at the end of the first charge and during the first discharge was different from the appearance when charged or discharged equivalent amounts in subsequent cycles. One area of an electrode that was discharged over 90% at the Ag_2O/Ag potential plateau using the 1-hr rate at cycle 1 is shown in Fig. 3. All areas of an electrode did not discharge simultaneously. In the area illustrated by Fig. 3, the surface of all AgO clumps had been reduced to Ag_2O during the discharge. The Ag_2O was present as very small crystals in a layer that was more porous than the AgO. The Ag present in the area shown in Fig. 3 was Ag that had not been oxidized during the initial charge of the electrode. During the partial discharge no Ag had been formed in this area. Comparison with Fig. 2 indicates the changes that had occurred as Ag_2O formed during an incomplete discharge at cycle 1. The angular shapes of AgO clumps had been retained.

Most of the Ag particles that formed during the first discharge at the 1-hr rate were much smaller than the Ag particles originally present. The formation of Ag from Ag_2O is shown in Fig. 4. During the first discharge the Ag formation took place more often below the surfaces of the small clumps of active material than at their surfaces. Comparison of Fig. 3 to Fig. 4 suggests that the Ag had nucleated from the smaller Ag particles that had remained at the end of the first charge. Ag began to form before all AgO was reduced to Ag_2O. As the Ag_2O coating on a clump of AgO was reduced to Ag, additional AgO was reduced to Ag_2O with the result that Ag never contacted AgO. Almost all of an electrode had been reduced to Ag by the end of a discharge at the 1-hr rate, although a few small areas of oxides usually remained.

The Ag particles produced by a discharge at the 1-hr rate formed into larger clumps than were present in the unused electrode. As an electrode was cycled, these clumps gradually became larger and large void spaces developed. During charge of an electrode that contained clumps of small Ag particles produced by one or more discharges at the 1-hr rate, larger AgO clumps were formed than those shown in Fig. 2 for the initial charge of a sintered Ag electrode. As discharges at the 1-hr rate and charges at the 20-hr rate were repeated, the AgO clumps in a charged electrode became larger. These large AgO clumps contained many particles of Ag that had not been oxidized during the charge. The remaining figures show structures present during discharges of electrodes that had developed clumps of active material after an electrode had been cycled. The appearance of an electrode during cycle 5 discharge will be illustrated as being typical after clumps have formed. Electrodes given 30 cycles differed only in having larger clumps, larger void spaces between the clumps, and in having slightly more Ag remaining unoxidized at the end of a charge.

During the early part of a typical discharge at the 1-hr rate, the first Ag_2O formation was on the surface of AgO clumps. This is illustrated in Fig. 5 by an electrode that was discharged until potential had just reached the Ag_2O/Ag plateau. No Ag had formed during this incomplete discharge. In some areas of this electrode, such as the area shown in Fig. 5, relatively

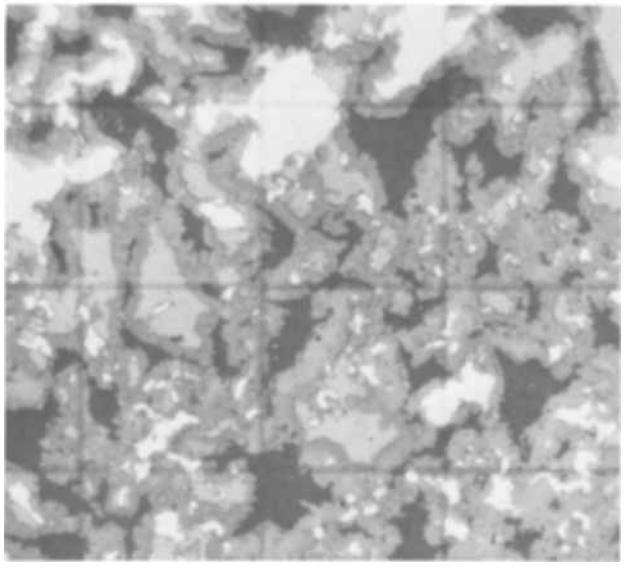

Fig. 3. Incompletely discharged electrode at cycle 1, showing an area where a thick Ag_2O layer has formed on the outside of AgO particles but where Ag has not yet formed during the discharge at the 1-hr rate. Ag present in this area was Ag that had failed to oxidize during the charge. Compare with Fig. 2 at the same magnification.

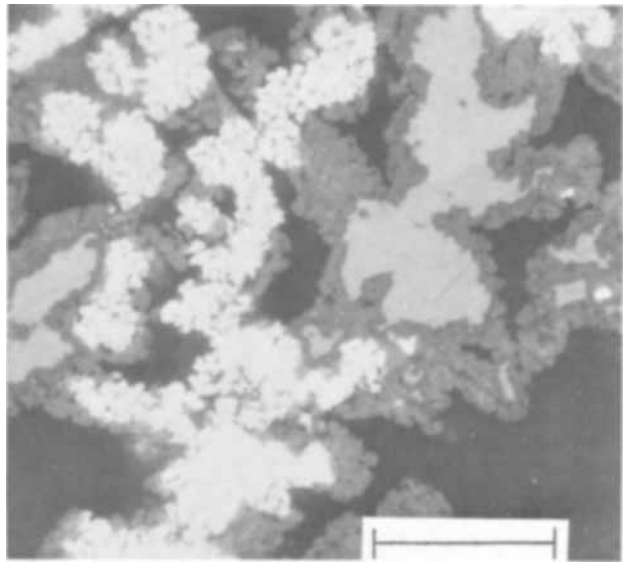

Fig. 4. Electrode incompletely discharged at cycle 1 using the 1-hr rate showing formation of small Ag particles (white). AgO is medium gray, Ag_2O darker gray, and void areas are black. Marker indicates 15μ. Compare with Fig. 3 but note different magnification.

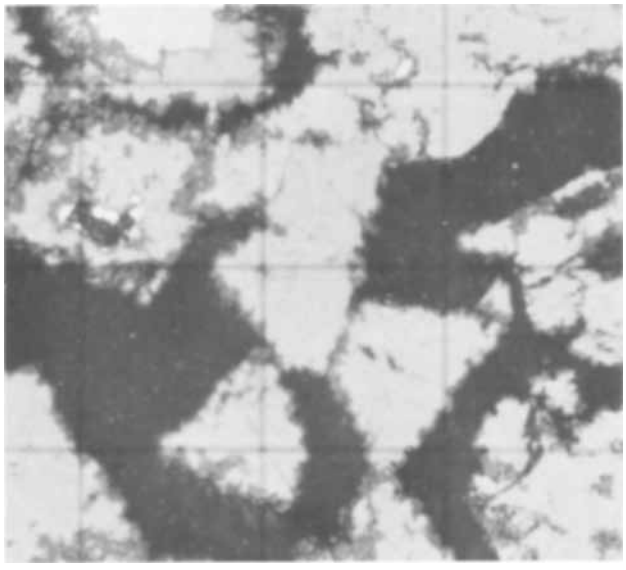

Fig. 5. Electrode discharged at the 1-hr rate just to Ag_2O/Ag potential plateau at cycle 5, illustrating that Ag_2O formed initially on the surface of AgO clumps. Approximately 11% of capacity had been removed during discharge. Most areas of this electrode had more Ag_2O present than is shown here. Lines forming squares are 15μ apart.

little Ag_2O had formed and the shape of the AgO clumps present at the end of the previous charge could be recognized despite penetration of Ag_2O at many points along the AgO surfaces. A more common area is the one shown in Fig. 6, where Ag_2O formation has been extensive in many places. Areas that were predominantly Ag_2O were scattered at random throughout areas of AgO. Ag_2O had formed at both the center and the surface of the electrode, and AgO still remained in both places. AgO remained near most of the Ag grid in the electrode, however, although Ag_2O predominated at a few of the grid members.

Ag began to form during a discharge after potential reached the Ag_2O/Ag plateau. This Ag formed first on the surface of the electrode when the 1-hr discharge rate was used, in contrast to the more random formation of Ag_2O in the earlier part of a discharge. Figure 7 illustrates this Ag formation in an electrode that had been discharged 0.50 hr. Instead of the bright-field vertical illumination used for all other photographs, oblique illumination was used for Fig. 7

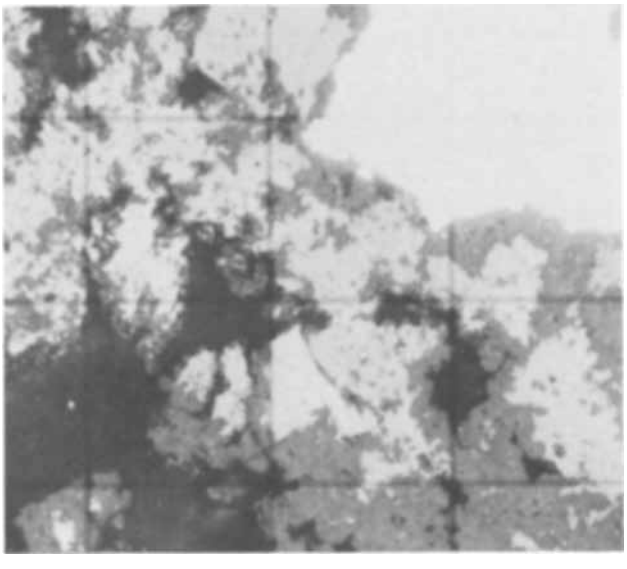

Fig. 6. Typical Ag_2O formation in the discharged electrode shown in Fig. 5. Lines forming squares are 15μ apart.

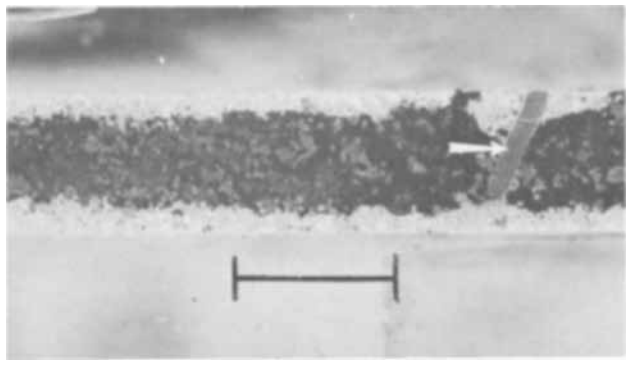

Fig. 7. Cross section of an electrode that was discharged 50% at the 1-hr rate at cycle 5, showing that Ag formed first at the surfaces. Arrow points to cross section of a grid. Large Ag particles that have been cross sectioned and polished appear as medium gray in this photograph using oblique illumination, but most Ag particles were too small to be visible at this low magnification. Reflections of light from the surfaces of Ag particles below the polished cross section appear as white. Oxide regions are the darkest shade. Marker indicates 1 mm.

in order to emphasize the areas where Ag had formed during discharge. Many small black areas remained on the surface in places where Ag had not yet formed during this partial discharge. One such area is visible in Fig. 7 at a small distance to the left of the grid. Less than 5% of the surface of this half-discharged electrode consisted of these oxide areas. The formation of Ag in the electrode is shown in Fig. 8 at higher magnification. In the center of this electrode that was 50% discharged the oxides seemed unchanged from those in an electrode 12% discharged (Fig. 5 and 6), with some areas being predominantly AgO and others Ag_2O.

Figure 9 shows Ag that had formed next to an area where AgO had already been reduced to Ag_2O. Small Ag particles that probably had been formed during the partial discharge were often found in Ag_2O areas such as the top of Fig. 9, but not in AgO areas. Ag formation next to an area that contained AgO with a coating of Ag_2O on its surface is shown in Fig. 10. Areas such as this were more common in the half-discharged electrode than areas where Ag_2O predominated, such as the one shown in Fig. 9.

By the end of a discharge at the 1-hr rate an electrode consisted almost entirely of clumps of Ag par-

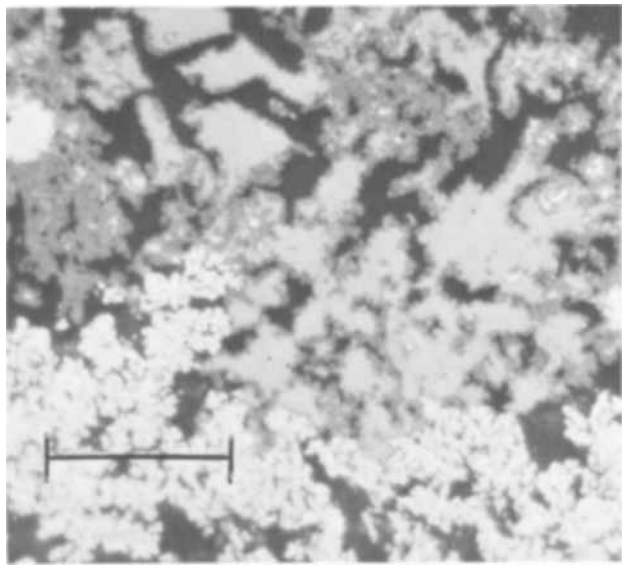

Fig. 8. Higher magnification view of electrode shown in Fig. 7. Boundary was fairly sharp between oxides in the middle of the electrode (top) and Ag that had been formed from the surface inwards (bottom) during discharge. Marker indicates 30μ.

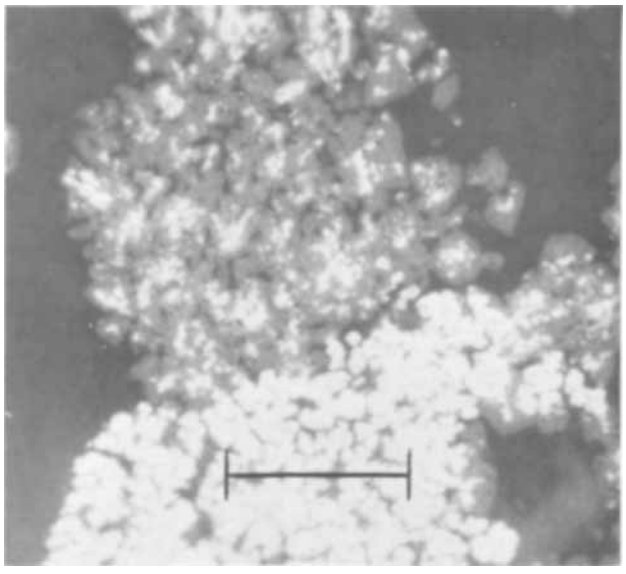

Fig. 9. Ag that formed during discharge (bottom) in a region that was predominantly Ag_2O and Ag (top). Same electrode as Fig. 7 and 8. Marker indicates 15μ.

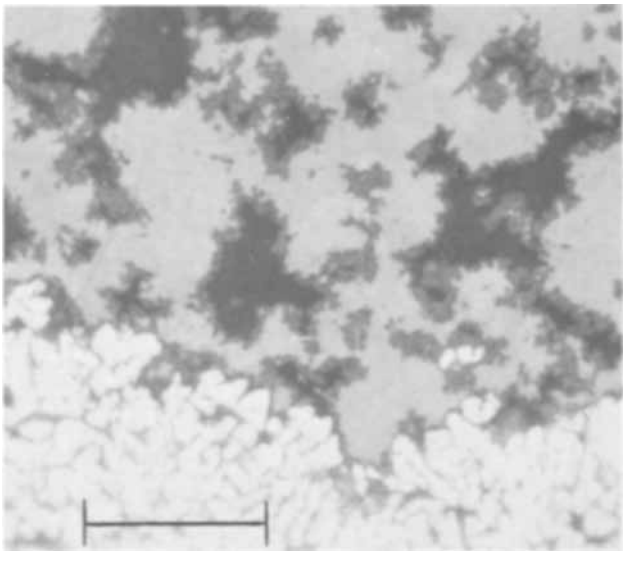

Fig. 10. Boundary between Ag that formed during discharge (bottom) and AgO clumps that were covered with Ag_2O (top). Same electrode and magnification as Fig. 9.

ticles, such as those shown at the bottom of Fig. 8-10. A few small areas of oxides were usually present also. The appearance of discharged electrodes and the gradual changes that occur with cycling will be discussed in detail in the next paper in this series.

Discussion

When the 20-hr rate of discharge was used, it has already been shown that the Ag particles which formed during this slow reduction were larger than the Ag particles originally present in an unused electrode (1). This increase in particle size was the cause of the rapid capacity decrease when slow discharges were used (compare D and E in Fig. 1) because the large Ag particles that had formed did not oxidize completely during charges. When the 1-hr rate of discharge was used, however, most of the Ag particles that formed were smaller than those originally present. Since these small particles oxidized readily during charges, the capacity did not decrease nearly as rapidly when the 1-hr discharge rate was used as when the 20-hr rate was used.

During a discharge, the first Ag_2O was usually formed at the AgO-electrolyte interface and was not formed using as nuclei the Ag_2O that separated Ag particles from AgO (Fig. 3, 5, and 6). The Ag_2O formed an uneven coating on the surfaces of AgO clumps, and penetrated at some points. This penetrating formation resembled the way that Ag_2O formed on Ag during a charge. Since 11% of the capacity had been removed from the electrode shown in Fig. 5 and 6, and this capacity all came from the reduction of AgO, over 22% of the AgO present at the end of the previous charge had been reduced to Ag_2O. The exact amount of AgO that had been reduced is uncertain, because a small part of the capacity of the charged electrode was present as Ag_2O. Judging by the photographs, the surface of all AgO clumps was covered with Ag_2O before discharge potential reached the Ag_2O/Ag plateau. When the discharge was interrupted to cut the electrode sample shown in Fig. 5 and 6, the open-circuit potential rose rapidly and reached the AgO/Ag_2O potential in 1.5 min, which was not surprising considering the large amount of AgO that remained.

Comparison showed many differences between electrodes that were discharged at the 1-hr rate until potential reached the Ag_2O/Ag plateau and electrodes discharged to the same plateau at the 20-hr rate. When the 20-hr discharge rate was used, approximately 30% of the electrode capacity was removed by the time that the Ag_2O/Ag plateau was reached, a value 3 to 5 times greater than the capacity removed when the 1-hr rate was used. As a result, much more Ag_2O was present in an electrode that was discharged slowly to the Ag_2O/Ag plateau, and areas where AgO predominated were relatively uncommon. In an electrode discharged at the 20-hr rate, in contrast to an electrode discharged at the 1-hr rate, the Ag_2O layer which separated Ag particles from AgO had thickened during a partial discharge, and Ag_2O (presumably newly formed) was present within AgO areas. The Ag_2O that was formed during a discharge at the 1-hr rate retained more of the angular shape of AgO clumps than did the Ag_2O formed at the 20-hr rate.

Although most of a discharge at the 1-hr rate took place at the Ag_2O/Ag potential plateau (Fig. 1), much AgO remained in electrodes until potential fell at the end of a discharge. Examples of this AgO were shown in Fig. 8 and 10 for an electrode discharged 50%, and in Fig. 3 and 4 for an electrode discharged over 90%. A few small patches of AgO and Ag_2O could usually be found in an electrode even after a discharge at the 1-hr rate reached the endpoint of —500 mv *vs.* the Ag/Ag_2O reference electrode. At the 20-hr discharge rate the AgO was reduced more readily, with the result that only a small amount of AgO remained by the time that a discharge was two-thirds completed. At the end of a discharge to —300 mv at the 20-hr rate it was unusual to find any AgO or Ag_2O remaining. This difference in the amount of oxide remaining at the end of a discharge was the reason for cycle 1 of an electrode giving a smaller capacity when the discharge was done at the 1-hr rate than when done at the 20-hr rate. Figures 4 and 10 show that a solid AgO clump at the end of a charge becomes a clump of Ag particles at the end of a discharge and that the Ag particles in a discharged electrode occupied less volume than the oxides.

Not only the size of Ag but also the distribution of Ag in the electrode varied with discharge current density. When an electrode was discharged part way along the Ag_2O/Ag potential plateau at approximately the 20-hr rate, some Ag had formed and some oxide remained in areas throughout the electrode, although a little more Ag was found near the surface. In contrast, during the first half of a discharge at the 1-hr rate the Ag started forming at the surface of the electrode and none was formed in the interior (Fig. 7). The width of oxide in the center of the elec-

trode shown in Fig. 7 approximately equalled the sum of the widths of areas without oxide on the surface of this electrode, confirming that the discharge was approximately 50% complete. The Ag had not formed preferentially at the Ag grid, although the grid was connected directly to the electrical leads. Conductivity, therefore, was not the factor that determined in which areas Ag would form. Diffusion in the electrolyte was probably the controlling factor. The formation of Ag_2O from AgO must occur by a different mechanism because Ag_2O areas were formed at scattered sites throughout the electrode. The reduction of AgO seems to have stopped temporarily in the central areas of an electrode after Ag began to form on the surface. The reduction reaction was then concentrated near the surfaces, moving inward after oxide nearer the surface was reduced to Ag. Since AgO areas, such as are shown in Fig. 8 and 10, were commonly found next to Ag areas while Ag_2O areas were less common (Fig. 9), probably Ag_2O areas were reduced preferentially to Ag and the formation of Ag stopped temporarily when AgO regions were reached.

Summary

Sintered Ag electrodes, that had been manufactured commercially for use in Ag-Zn storage batteries, were charged at the 20-hr rate and discharged at the 1-hr rate in 35% KOH solution at 25°C. Samples were cut from an electrode at various times and cross sections were prepared for microscopic examination.

Ag_2O was formed on the surface of AgO clumps during the early part of a discharge. The Ag_2O formation took place at many areas scattered throughout an electrode. Some AgO clumps were completely or almost completely reduced to Ag_2O, while others were only reduced on their surfaces. Discharge potential fell to the Ag_2O/Ag plateau after a coating of Ag_2O had formed on the surface of all AgO clumps. AgO was reduced much less readily at the 1-hr rate than at the 20-hr rate. Comparing discharges at the 1-hr and 20-hr rates, during the more rapid discharge the potential fell to the Ag_2O/Ag plateau after less capacity had been withdrawn from the electrode, the proportion of AgO present in an electrode discharged beyond this point was greater, and noticeable amounts of AgO remained at the end of a discharge.

Ag began to form after discharge potential fell to the Ag_2O/Ag plateau. In contrast to the formation of Ag_2O at scattered sites, Ag formed first on the surface of an electrode when the 1-hr discharge rate was used and then gradually spread from the surface to the interior. During a discharge at the 20-hr rate Ag formed at both the surface and the interior, with a slight preference being shown for areas at or near the surface. The formation of Ag must be limited by a different step in the mechanism than is the formation of Ag_2O during discharge.

Acknowledgment

The author wishes to thank Mr. A. C. Simon for the help and advice that he has given during this work.

Manuscript received Jan. 31, 1969.

Any discussion of this paper will appear in a Discussion Section to be published in the December 1969 JOURNAL.

REFERENCES

1. C. P. Wales and A. C. Simon, *This Journal*, **115**, 1228 (1968).
2. E. M. Otto, *ibid.*, **115**, 878 (1968).

Influence of Oxygen Pressure on the Oxidation Kinetics of Copper in Dry Air at Room Temperature

P. K. Krishnamoorthy and S. C. Sircar

Metallurgical Engineering Department, Indian Institute of Technology, Kharagpur, India

ABSTRACT

The effect of oxygen pressure in the range of 0.01-0.21 atm O_2 pressure on the oxidation behavior of annealed copper at room temperature was investigated. The results have been analyzed with reference to the Cabrera-Mott theory of growth of very thin oxide films on metals. The alteration in the rate of oxidation has been explained on the basis of the cationic vacancy concentration of the oxide, as it is well established that the oxygen pressure on a p-type oxide semiconductor surface has an influence on the cationic vacancy concentration of the semiconductor. A correlation of rate constant with pressure has been obtained which is in conformity with the theoretical treatment of the kinetics by Grimley and Trapnell assuming the destruction of cation vacancies at the metal oxide interface to be the rate controlling step.

It is well known that the oxygen pressure exerts a great influence on the vacancy concentration of p-type semiconductor oxides. Hence it is expected that the pressure should exert an effect on the oxidation kinetics of copper at low temperatures as the cuprous oxide is a metal deficit one. In the thin film range, *i.e.*, at temperatures above 60°C, where the logarithmic, cubic, and parabolic laws are obeyed, a pressure dependent rate has been observed by William and Hayfield (1), Lustman and Mehl (2), etc. At low temperatures, of the order of room temperature, Germer and White (3) found that the rate of oxidation at 4 and 20 mm mercury of oxygen pressure were identical. But Jennings and Stone (4) and Lanyon and Trapnell (5) observed the rates to be pressure dependent.

The present work was taken up to cover the pressure effect in the very thin film range where Cabrera and Mott's (6) inverse logarithmic law leading to a limiting thickness is obeyed. The influence of an applied field, addition of lithium, and cold working were first investigated and have been reported earlier (7-10). These studies have established quantitatively the validity of Mott's theory, and the influence of pressure was then taken up to confirm the hypothesis further.

Experimental Details

The material used contained 0.23% nickel and 0.003% silver. The specimens used were in the form of sheets 2.5 x 1 x 0.05 cm with a hole of 1 mm diameter drilled at one end for hanging purposes. All speci-

mens were thoroughly annealed at 600°C for 2 hr before exposure. Surface preparation was done first by mechanically polishing on emery papers followed by electropolishing in phosphoric acid bath under conditions suggested by Allen (11). To overcome any surface contamination by any phosphate or oxide film the specimens were cathodized in a NaH_2PO_4 and Na_2HPO_4 buffer solution at a current density of 50-100 $\mu A/cm^2$ for a few seconds. They were then thoroughly cleaned and dried in acetone before exposure. The surface obtained was reproducible. The initial air-formed film, before exposure, was the same in all the cases and was small.

Oxidation was carried out at five different pressures, *viz.*, 0.0135, 0.027, 0.068, 0.1227, and 0.21 atm O_2 partial pressure. Different pressures were obtained by first hanging the specimen in a chamber containing silica gel (for drying the air inside) provided with arrangements for evacuation. The chamber was evacuated to a pressure of a few mm of mercury, and then a controlled amount of air was admitted to the system until the desired pressure was reached. The system was quite leak proof. The fall in mercury level even during long exposures was of the order of 1-2 mm only. Only one specimen was used at a time for a particular exposure.

The thickness estimations were done electrometrically by cathodic reduction in a NaH_2PO_4-Na_2HPO_4 buffer solution at a current density of 5 $\mu A/cm^2$. This was done in a setup designed for the purpose similar to that of Mills and Evans (12) with arrangement for evacuation under reduced pressures. An accuracy of $\pm$ 1 Å could be achieved.

Results and Discussions

Results are discussed with reference to the Cabrera-Mott (6) theory of growth of very thin oxide films on metals at low temperatures. They derived their equation by considering the process as follows:

1. Adsorption of oxygen on oxide surface.
2. Ionization of this by capture of electrons from the metal by the quantum mechanical tunnel effect.
3. Creation of cationic vacancies at the oxide/gas interface.
4. Subsequent migration of cations under the action of the electric field set up or, in other words, the migration of cationic vacancies toward the metal/oxide interface.
5. Destruction of these vacancies at the metal/oxide interface.

On the above basis they arrived at an equation of the form

$$\frac{dx}{dt} = K \exp\left(\frac{x_1}{x}\right) \qquad [1]$$

where

$$K = N\Omega\nu \exp\ (-W/kT)$$

and

$$x_1 = \frac{1}{2}\frac{qa}{kT} \cdot V$$

x being the thickness at time t, where the different quantities have the usual significance.

The equation may be rewritten in the form

$$\log\frac{dx}{dt} = \log K + x_1/2.3x \qquad [2]$$

so that a plot of log dx/dt *vs.* $1/x$ should yield a straight line.

The results of oxidation at different pressures are presented in Fig. 1. The log dx/dt *vs.* $1/x$ plot computed by taking the slopes of the curve at different thickness values is shown in Fig. 2. The straight line plot of these seems to obey Mott's equation quantitatively.

Further, the parallelism of these plots indicates that the x_1 term is independent of pressure, or in other words V, the potential difference between the metal/oxide and the oxide/gas interface, stays constant as the other terms in x_1 are constants at a fixed temperature. For the atmospheric pressure case calculations have shown earlier (10) that the V term, and the K term calculated on the basis of slope and intercept on dx/dt axis, respectively, are of the same value as predicted theoretically by Mott (6).

From the plots shown in Fig. 2, it can be concluded that pressure mainly affects the N term (or K term, W being constant at a fixed temperature). This value has been computed at the different pressures and is shown in Table I. The next step, hence, was to find the nature of variation of N with pressure. For this let $K \propto p^n$, where p = partial pressure of oxygen in the system and n = constant.

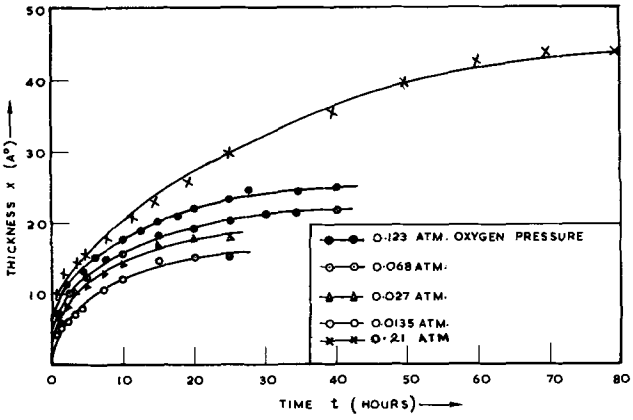

Fig. 1. Oxidation at 30°C at different oxygen pressures

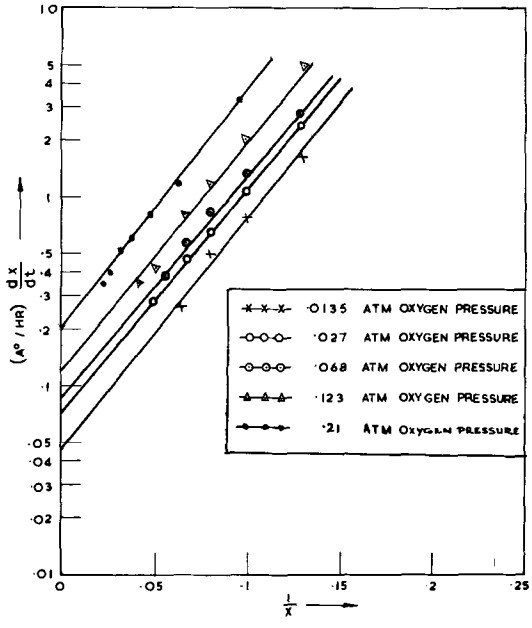

Fig. 2. Effect of oxygen pressures on oxidation at 30°C. Log $\frac{dx}{dt}$ *vs.* $\frac{1}{x}$ plot.

Table I. Variation of N (concentration of cation vacancies in the oxide) with oxygen pressure

Partial pressure of oxygen—p atm	K, A/hr.	$N\Omega\nu$, A/hr.	N, No./cm²
0.0135	0.045	0.2×10^{16}	0.32×10^{15}
0.027	0.07	0.316×10^{16}	0.51×10^{15}
0.068	0.085	0.38×10^{16}	0.608×10^{15}
0.123	0.12	0.55×10^{16}	0.88×10^{15}
0.21	0.20	0.632×10^{16}	1.01×10^{15}

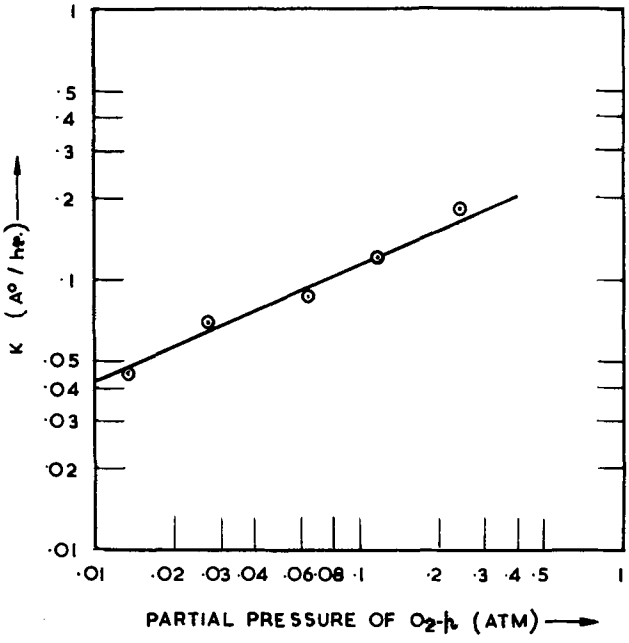

Fig. 3. Log K *vs.* log p plot at 30°C

Hence a plot of log K *vs.* log p should be a straight line with n = slope. This plot is shown in Fig. 3. The curve shows that $n = 0.3$ or $K \propto p^{1/3-1/4}$.

The term N according to Mott and Cabrera is the number of ions/unit area of the oxide ready to migrate or, in other words, the concentration of mobile species/unit area of the oxide. This can be taken equal to the cationic vacancy concentration according to Hauffe (13) that the diffusion in case of defect structures is actuated essentially by the vacancies. This has been further confirmed by the influence of addition of a little lithium to the metal which was found to block the vacancies and thus retard the rate (8).

The observed relationship can be arrived at theoretically by considering Mott's kinetics as has been done by Trapnell and Grimley (14). For very thin films they have formulated two equations for a p-type semiconductor oxide growth based on two different assumptions. According to them, if the rate-controlling step is the destruction of cation vacancies at the metal/oxide interface, then they replace the N term of Mott's equation by a new term involving the concentration of vacancies and a pressure$^{1/4}$ term, whereas if the rate-controlling step is the formation of vacancies at the oxide/gas interface, they have not included any pressure term but define N as the number of adsorption sites/unit area of the oxide surface, which is obviously dependent on pressure to the saturation value. Close observation of Grimley and Trapnell's (14) equation indicates that it is same as Mott's (6) equation with better significance of the parameters V and W. For example, the $\Delta\mu_0$ term in Grimley's equation, *i.e.*, the free energy change of the reaction forming the cationic vacancies at the oxide/gas interface is equivalent to the Wi term, *viz.*, the energy of solution of an ion in the oxide. Again this treatment shows that even though Mott has not specifically talked of pressure effect, the N term obviously includes this.

Rhodin (15) mentioned that in the thin and very thin film range the process is rather insensitive to pressure. This is presumably because he has worked in the pressure range beyond the saturation value (since adsorption dependence on pressure shows a saturation) or because that in the high-pressure range, as the rate is dependent on one-fourth power of pressure, it may be difficult to detect the effect.

The increase in the value of N with pressure is in conformity with the well-known fact that increase in oxygen pressure on a p-type semiconductor oxide surface tends to increase the vacancy concentration of the oxide.

The value of the power n (0.3) is slightly higher than 0.25. This probably shows that, in the pressure range studied, the surface is not fully saturated with oxygen ions and some of them may be present as (O^-/ads) and majority as (O_2^-/ads). At the moment, since the exact nature of the adsorbing species is not well established, the above explanation probably accounts for the deviation in the value of n from 0.25.

The present study also confirms the importance of the interface reaction rate-determining step for very thin film growth as suggested by Grimley and Trapnell (14), Hauffe (13) etc.

Acknowledgment

The authors are grateful to Professor P. R. Dhar, Head, Department of Metallurgical Engineering, Indian Institute of Technology, Kharagpur, for his keen interest and lively discussions.

Manuscript submitted Sept. 19, 1968; revised manuscript received *ca.* Feb. 17, 1969. This paper is part of a Ph.D. thesis submitted by one of the authors (P.K.K.) to the Indian Institute of Technology.

Any discussion of this paper will appear in a Discussion Section to be published in the December 1969 JOURNAL.

REFERENCES

1. E. C. William and P. C. S. Hayfield, "Vacancies and Other Point Defects in Metals and Alloys," Institute of Metals, Monograph No. 23, 131 (1957).
2. B. Lustman and R. F. Mehl, *Trans. AIME*, **143**, 246 (1941).
3. A. H. White and L. Germer. *Trans. Electrochem. Soc.*, **81**, 305 (1942).
4. T. J. Jennings and F. S. Stone, *Advances in Catalysis*, **9**, 441 (1957).
5. M. A. H. Lanyon and B. M. W. Trapnell, *Proc. Roy. Soc.*, **A227**, 387 (1955).
6. N. Cabrera and N. F. Mott, *Rept. Prog. Phys.*, **12**, 163 (1949).
7. P. K. Krishnamoorthy and S. C. Sircar, *Acta Met.*, **16**, 1461 (1968).
8. P. K. Krishnamoorthy and S. C. Sircar, *Scripta Met.*, **2**, 255 (1968).
9. P. K. Krishnamoorthy and S. C. Sircar, *Corrosion*, **24**, 407 (1968).
10. P. K. Krishnamoorthy, Ph.D. thesis, I.I.T., Kharagpur, India, Dec. 1967.
11. J. A. Allen, *Trans. Faraday. Soc.*, **48**, 273 (1952).
12. U. R. Evans and T. Mills, *J. Chem. Soc.*, **1956**, 2182.
13. K. Hauffe, "The Surface Chemistry of Metals and Semiconductors," H. C. Gatos, Editor, p. 439 (1959).
14. T. B. Grimley and B. M. W. Trapnell, *Proc. Roy. Soc.*, **A234**, 403 (1956).
15. T. N. Rhodin, *J. Am. Chem. Soc.*, **72**, 5102 (1950); *ibid.*, **73**, 3143 (1951).

Processes Involved in Reattainment of Steady-State Conditions for the Anodizing of Aluminum Following Formation Voltage Changes

J. W. Diggle*

The Electrochemistry Laboratory, The University of Pennsylvania, Philadelphia, Pennsylvania

T. C. Downie

Department of Chemistry and Metallurgy, Rutherford College of Technology, Newcastle-upon-Tyne, England

and C. W. Goulding

Department of Material Science, Sunderland Technical College, Sunderland, County Durham, England

ABSTRACT

The dissolution processes involved in the formation of porous films in sulfuric acid have been studied by suddenly lowering the formation voltage and observing changes in the current flowing and the barrier layer capacitance as steady-state conditions are re-established. It was found that current changes always follow capacitance changes, and that the dissolution processes involved are (*a*) initially a short time region of chemical dissolution is found up to some point where the minimum electric field strength required for ionic migration is approached, and (*b*) a second stage dissolution assisted by the presence of this electric field. The change from one dissolution rate to the other is continuous as this minimum electric field is approached. On the basis of the Keller model, the required pore base orientation is proposed to occur during the second stage field-assisted process.

The structure of porous anodic oxide films on aluminum has been investigated for many years, the results of which have produced essentially two main proposals: (a) the classical structure of the cylindrical pore proposed by Keller *et al.* (1), this cylindrical pore generally being regarded as being an ideal structure. Proposed variations have included the truncated cone-shaped pore (2), the slanting pore axis (3), twisting and distortion of the pores (4), and the fibrous (5) rather than the regular porous structure. The second model (b) was proposed by Murphy and Michelson (6, 7) in which the structure is seen as a combination of submicrocrystallites of alumina and hydrated alumina, the ratio of the latter to the former increasing as the distance from the metal surface increases (this model has been described as the triple layer model consisting essentially of layers of low, moderate, and high degree of hydration moving from metal outwards).

Model (b), however, lacks the presence of discrete pores, unlike the Keller model (1), and consequently lacks experimental verification since the presence of pores appears to be well established, especially from the excellent photographs of Wood, O'Sullivan, and Vaszko (8). Despite the apparent validity of the Keller model, several phenomena associated with the behavior of porous films have yet to be explained satisfactorily. This paper is concerned with one of these phenomena, *i.e.*, the behavior of the porous films when the anodizing steady-state conditions are changed, particularly when the voltage of formation is reduced.

Since the dimensions of the Keller model are controlled largely by the voltage of formation (the oxide cell size increasing with increasing voltage), changes in the voltage during anodizing would seemingly require a re-orientation of the film dimensions, *i.e.*, as the voltage is reduced new pores should be initiated and the oxide cell size should decrease. Some evidence has been presented to show that this re-orientation takes place (8). The role played by the barrier layer during this re-orientation process is, as yet, uncertain, and it is with this specific problem that this paper is concerned.

From a study of this voltage decrease phenomenon, Michelson (9) has shown that, initially, the processes involved do not produce any significant changes in barrier layer capacitance before substantial current begins to flow. This, it was argued, indicated the barrier layer re-orientation was initially a matter of proton space charge rearrangement (which produces no capacitance change); only later did dissolution occur and, therefore, produce changes in current. It was concluded that the Keller model was incapable of accounting for these experimental observations, which were in agreement with the triple layer model. However, the center of the argument lies in the observation that no barrier layer capacitance, *i.e.*, the thickness, changes were observed before the current began to increase. In the present study, the authors have examined the voltage decrease phenomenon by measuring the rate of reattainment of steady-state thickness for the barrier layer, and the rate of reattainment of the steady-state current density, as functions of the voltage decrease increment and the recovery temperature of the electrolyte.

Experimental

A suitable length of 99.98% superpurity grade fully annealed aluminum in the form of ⅛ in. diameter wire was chemically polished in a solution containing 125 ml concentrated sulfuric acid, 350 ml orthophosphoric acid, and 25 ml concentrated nitric acid at 90°-95°C for 5 min [this time being chosen as that necessary to produce a reproducible surface finish (15)]. Following this treatment, the specimen was washed in distilled water for 1 min, rinsed in acetone and air-blown dry and immediately immersed in 15% w/w sulfuric acid in a cell thermostated at the required temperature. Anodizing was performed by applying the required voltage of formation between the specimen anode and a large area aluminum cathode. Capacitance values were obtained by applying a 100 Hz

* Electrochemical Society Active Member.

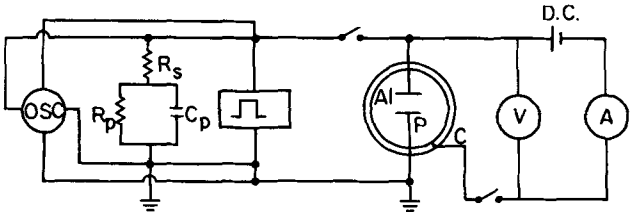

Fig. 1. Circuit, cell and analogue circuit used in this study. Al, aluminum anode; P, platinum gauze subsidiary electrode; C, aluminum cathode; D.C. is stabilized voltage supply, A, a micro-milliammeter, and V is a voltmeter measuring cell voltage.

square wave signal (amplitude < 5 mv) to the test anode and a reference capacitance electrode (25 times the test area platinum gauze electrode) and to an R-C parallel analogue (10) circuit simultaneously. The responses of the two systems were displayed on a twin beam oscilloscope, and a balance obtained by selecting the correct values of R_s, R_p, and C_p (see Fig. 1). The values of R_p and C_p are then taken as being representative of the resistance and capacitance of the barrier layer lying adjacent to the metal surface (after Hoar and Wood) (11).

Following the immersion of the specimen in the 15% w/w sulfuric acid, the capacitance value increased to a constant value (10 μf cm^{-2}). A formation voltage of 5v was then applied from a constant d-c stabilized voltage supply and steady state was allowed to be attained. C_p and the current i, were then measured and noted. The formation voltage was then increased to either 10 or 15v, and steady-state conditions were again allowed to be attained. Following this, the formation voltage was reduced to 5v, and the reattainment of the 5-volt values of C_p and i were observed with respect to time. This procedure was repeated for the 15 to 5v and the 10 to 5v reductions as a function of electrolyte temperature and the mode of change of the formation voltage; the effect of the voltage change mode was studied on a single electrode, and the effect of voltage reduction increment on separate electrodes.

Results

As observed previously by Michelson (9) the rate of reattainment of the 5v values of C_p and i from either the 15 or 10v voltage was strongly dependent on the mode of voltage change; this, itself, suggests some field-assisted dissolution process is involved in the dissolution processes being studied. Consequently, two modes of voltage change were adopted:

(*a*) A relatively slow change in voltage, the current density being maintained above an arbitrary minimum of 1 ma cm^{-2}, *i.e.*, the current flowing was maintained at ionic magnitudes and hence the electric field was maintained about the minimum field required for ionic motion (*ca.* 7.2 $\times$ 10^6 v-cm^{-1}).

(*b*) An instantaneous decrease in voltage in order to induce a large instantaneous decrease in the field strength. The current decreases suddenly to those values typical of electronic magnitude, and hence further oxide growth ceases.

Table I shows the times required for the reattainment of the steady-state cell current and capacitance values for 5v for the voltage change 10 to 5v, as a function of the sulfuric acid electrolyte temperature and the voltage mode of change.

Table II shows the same times for the 10 to 5v compared with times for a 15 to 5v change, employing voltage change mode (b) in each case.

Figure 2 shows the behavior of the cell current with respect to time, during the reattainment process for the voltage change 10-5v employing voltage change mode (b), as a function of electrolyte temperature. Figure 3 shows the change in the cell current correlated to the changes in capacitance for the 10 to 5v change employing voltage change mode (b) at 26°C. This figure clearly shows that a substantial change in capacitance does occur before an appreciable current increase is observed, in exact opposition to that reported by Michelson.

Table I. Reattainment times for the voltage decrease 10-5v as a function of electrolyte temperature and voltage mode of change

Voltage change, v	Electrolyte temperature, °C	Reattainment time, sec, employing the voltage change mode (a)	(b)
10-5	26	45	1080
	35	22	600
	45.5	9	150

Table II. Comparison of the reattainment times for the two voltage changes 10-5v and 15-5v using voltage change mode (b) as a function of electrolyte temperature

Voltage change, v	Electrolyte temperature, °C	Reattainment time, sec, employing voltage change mode (b)
10-5	26	1080
	35	600
15-5	26	3840
	35	1620

Figure 4 illustrates the corrrelation of current and capacitance changes for the two voltage changes 15-5v and 10-5v employing voltage change mode (b) at 35°C electrolyte temperature; the conclusion concerning which parameter changes first, current or capacitance, obtained from Fig. 3, is confirmed in this figure.

Discussion

It would appear from Table II, when comparing the reattainment times required for the 10 to 5v and 15 to 5v changes that, whatever the mechanism of barrier layer dissolution, it does not seem chemical in nature. However, this conclusion is not new. Novakovsky (12, 13) first in a general discussion of passivity and then in a mechanistic study of the passivation of iron has indicated that the film theory of passivity taken with a chemical dissolution process is untenable with the known facts concerning passivating oxide phenomena. Engell (14) has reported that the dissolution of oxides can be strongly potential dependent, *e.g.*, the dissolution rate of oxides of iron falls exponen-

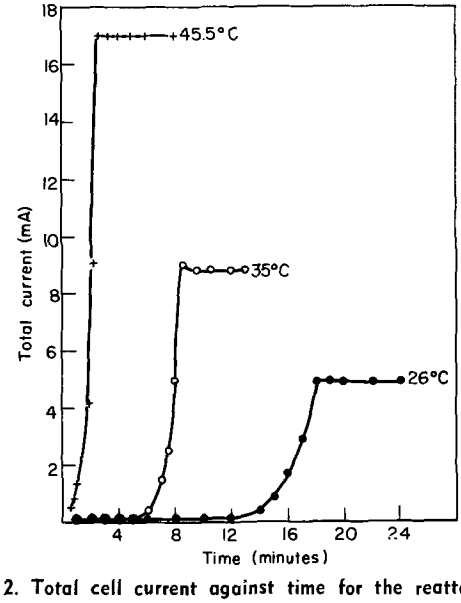

Fig. 2. Total cell current against time for the reattainment of steady-state anodizing conditions for the 10 to 5v change employing voltage change mode (b), as a function of the electrolyte temperature.

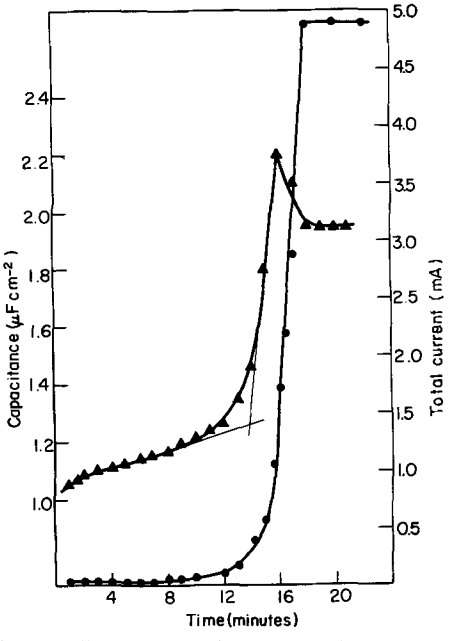

Fig. 3. Total cell current (circles) and barrier layer capacitance (triangles) changes following the voltage reduction 10 to 5v employing voltage change (b) at 26°C electrolyte temperature.

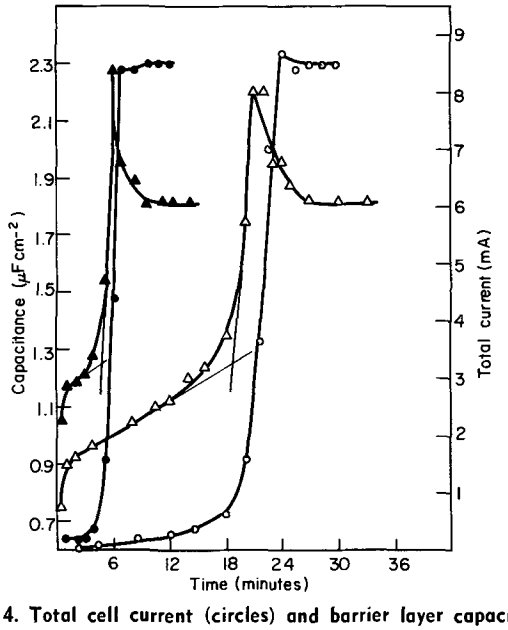

Fig. 4. Total cell current (circles) and barrier layer capacitance (triangles) changes following the voltage reductions, 15 to 5v (empty symbols) and 10 to 5v (filled symbols) at 35°C electrolyte temperature.

tially with increasingly positive potentials. Engell concluded from this that anions, in the oxide lattice, leave the lattice more easily than cations.

If purely chemical dissolution of the barrier layer were involved, and assuming that such dissolution follows zero order kinetics, as has been previously reported (15), then the time of dissolution of 100Å would be double that required for 50Å. However, Table II shows that 100Å required 3.6 times that required for the 50Å dissolution. Figures 3 and 4, which effectively show the change in barrier layer thickness with time, indicate that the rate of dissolution undergoes a sharp increase following a linear C-t change. This may indicate that the nature of the dissolution process changes during the course of dissolution, and consequently a time-basis comparison with purely chemical kinetics would be invalid (Table IV).

Table I provides further apparent evidence that simple chemical dissolution is not involved. When the electric field is maintained above the minimum field required for ionic motion, the reattainment times are between 15 and 25 times less than that required when the field is instantaneously decreased to below the minimum field. Nagayama and Tamura (16) have deduced that the temperature increase due to local Joule heating, in the presence of current flow, is very small (< 1°C) and therefore it can be concluded that the presence of a passage of current cannot account for the wide difference in the dissolution times between voltage change modes (a) and (b).

The influence of the electrolyte temperature can also be seen from Table I as being in the ratio 5:2.5:1 for increasing temperature with voltage change mode (a), and 7:4:1 for increasing temperature with voltage change mode (b). These ratios can be compared with work reported by Hunter and Fowle (17) in which the dissolution action of 15% w/w sulfuric acid was doubled for every 8.5°C rise in temperature, and increased fivefold by a 10°-20°C rise in temperature.

Michelson (9) has proposed the barrier layer dissolution to be the result of the passage of current, and not the cause of the passage of current; however, Fig. 2 and 3 clearly show that initially the capacitance increases rapidly, this rapid increase being followed by an appreciable linear region of increase which, in turn, is followed by a second very rapid increase leading to capacitance overshoot. The greatest change in capacitance and the capacitance overshoot occurs approximately at the point at which the greatest change in the current occurs; this is to be expected if the current is the result of barrier layer dissolution.

If the barrier layer has to dissolve to a thickness which corresponds to the presence of the minimum field required for ionic motion before any appreciable current increase can occur, can one calculate this thickness and perhaps obtain proof of this statement from Fig. 3 and 4? From Table I it was concluded that the presence of a field, in excess of the minimum field, produced a 15-25 times increase in the dissolution rate; therefore, as the field increases from an instantaneously low field to the minimum field, appreciable changes in the dissolution rate should occur and this should be reflected by a rapid change in capacitance at some point. Figures 3 and 4 show this to be true; extrapolation of the linear region to the intersection of the extrapolation of the rapid increase slope produces the capacitance value, at which this minimum field is established, of 1.25 μf cm^{-2} for the three cases reproduced here.

A simple calculation shows that, if the minimum field is assumed as 7.2×10^6 v-cm^{-1}, the thickness of barrier film across which 5v is applied will be 70Å when this minimum field is achieved. The capacitance value of this 70Å film is assumed to be given by the parallel-plate condenser equation, *i.e.*, $\epsilon A/4\pi d$, where ϵ is the dielectric constant [assumed as 10 from the work of Hoar and Wood (11) and Vermilyea (18)], A is the barrier layer surface area [assumed as equal to the metal surface area and not the pore base area, following Dekker and Urquhart (19)], and where d = 70Å. Calculation shows the capacitance to be equal to 1.26 μf cm^{-2}, in excellent agreement with the experimental value.

Therefore, it would appear that the minimum electric field is present at the point the current begins to increase above ionic magnitudes; prior to this point substantial changes in the barrier layer thickness do occur, being the greater the higher the initial voltage of formation.

Table III shows an analysis of the reattainment times from Fig. 3 and 4. The time required up to the minimum field is dependent on the thickness that has to be dissolved, and on the electrolyte temperature for any one voltage change. The dissolution rates above and below the minimum field can now be calculated (Table IV). The dissolution time above the minimum field was corrected for time spent in, and recovering from, barrier layer thickness overshoot.

Table III. Reattainment times from Table II divided into the time spent above and below the minimum electric field strength required for ionic migration

Voltage change, v	Electrolyte temperature, °C	Reattainment time, sec Below minimum field	Above minimum field
10-5	26	840	240
	35	270	330
15-5	35	1080	540

Table IV. Mean dissolution rates calculated above and below the minimum field

Voltage change, v	Electrolyte temperature, °C	Dissolution rate, A min^{-1} Below minimum field: Time averaged	Below minimum field: From linear C-t section	Above minimum field
10-5	26	2.2	1.1	20.0
	35	6.7	3.1	40.0
15-5	35	4.4	1.8	10.0

Prior to the attainment of the minimum electric field, the dissolution rate is a function of temperature and appears to be a function of the voltage change at the temperature of 35°C, being the smaller the greater the voltage decrease to 5v involved, *i.e.*, the lower the instantaneous new field at 5v. However, the rates reported in Table IV, prior to the attainment of the minimum field required for ionic migration, are strictly mean values calculated over the time required to reach this point, and thus may be invalid, as mentioned earlier. Figures 3 and 4 show that initially the capacitance changes rapidly, then is relatively linear for a short while, then changing rapidly finally to produce the overshoot. This observation indicates that a time-averaged dissolution rate is invalid. Applying the equations from an earlier paper (15) to the initial capacitance changes, the rates of dissolution derived from 1/C-time plots were calculated (column 4, Table IV). Values obtained at 25° and 35°C can be compared with the values of 1 and 2Å min^{-1}, respectively, previously reported (15, 17) for dissolution of alumina films in sulfuric acid. Thus, although the first indications were that chemical dissolution was not involved in these steady-state reattainment processes, on closer examination there would appear to be a chemical dissolution process for a short interval below the minimum field. As the minimum field is approached, the dissolution rate increases progressively in an exponential manner, *i.e.*, dissolution rate is field-assisted approaching and exceeding the minimum field. The exponential nature of the increasing dissolution rate, and the fact that when the barrier layer reaches 50Å, insufficient oxide is being produced to balance dissolution, capacitance overshoot occurs. The formation rate of the oxide, *i.e.*, the current, continues to increase, and, at some point during overshoot, exceeds the dissolution rate, thereby producing a decrease in barrier layer capacitance. Finally, balance between the oxide formation rate and the dissolution rate is attained; thus, the barrier layer capacitance remains constant.

Conclusions

The dissolution processes occurring at barrier layer surfaces, following voltage reductions, are seen as processes in which current changes follow capacitance changes, *i.e.*, the opposite to that reported previously (9). The nature of the dissolution process is seen as essentially chemical (apart from some initial unexplained phenomenon) for a short period up to a point where the minimum electric field for ionic migration is approached; following this, dissolution increases exponentially and is seen as a field-assisted process. It is during this latter period that reorientation of the pore base structure is considered to occur. Since this period is not totally taken up with barrier layer dissolution, but with the regrowth of barrier layer following overshoot during dissolution, reorientation of the pore base structure is seen as a process requiring a few minutes when the minimum electric field is achieved (the greater this reorientation, the longer the time that is required).

This evidence concerning the processes which occur when voltage reductions are performed during anodizing can, it is considered, be explained most easily in terms of a model derived from the "ideal" Keller model (1), or one of its derivatives (2). It is further suggested that the capacitance overshoot and the barrier layer regrowth serve to demonstrate the "dynamic equilibrium:" which exists between barrier oxide formation and the ensuing dissolution processes leading to a conversion of barrier to porous oxide. Whenever these two processes, *i.e.*, formation and dissolution, are in nonequilibrium, some phenomenon will occur in an attempt to regain the "equilibrium," *e.g.*, reduction of voltage reduces the formation to a negligible level, and, therefore, the dissolution will predominate (the barrier layer will become thinner) until an "equilibrium" is achieved.

Manuscript submitted Sept. 23, 1968; revised manuscript received Jan. 28, 1969.

Any discussion of this paper will appear in a Discussion Section to be published in the December 1969 JOURNAL.

REFERENCES

1. F. Keller, M. S. Hunter, and D. L. Robinson, *This Journal*, **100**, 411 (1953).
2. G. Paolini, M. Massero, F. Sacchi, and M. Paganelli, *ibid.*, **112**, 32 (1965).
3. R. W. Franklin and D. J. Stirland, *ibid.*, **110**, 262 (1963).
4. P. Csokan, *Trans. Inst. Metal Finish.*, **41**, 51 (1964).
5. H. Ginsberg and K. Wefers, *Metall.*, **17**, 202 (1963).
6. J. F. Murphy and C. E. Michelson, Conference on Anodizing Aluminum, p. 83, Aluminum Development Assoc., Nottingham (1961).
7. J. F. Murphy, *Plating*, **54**, 1241 (1967).
8. G. C. Wood, J. P. O'Sullivan, and B. Vaszko, *This Journal*, **115**, 618 (1968).
9. C. E. Michelson, *ibid.*, **115**, 213 (1968).
10. J. J. McMullen, Jr., and N. Hackerman, *ibid.*, **106**, 345 (1959).
11. T. P. Hoar and G. C. Wood, *Electrochim. Acta*, **7**, 333 (1962).
12. V. M. Novakovsky, *ibid.*, **10**, 353 (1965).
13. V. M. Novakovsky and Y. A. Likhachev, *ibid.*, **12**, 267 (1967).
14. H. J. Engell, *Z. Phys. Chem. (N.F.)*, **7**, 158 (1956).
15. J. W. Diggle, T. C. Downie, and C. W. Goulding, *Electrochim. Acta*, In press.
16. M. Nagayama and K. Tamura, *ibid.*, **13**, 1773 (1968).
17. M. S. Hunter and P. E. Fowle, *This Journal*, **101**, 515 (1954).
18. D. A. Vermilyea, *This Journal*, **104**, 427 (1957).
19. A. J. Dekker and H. M. A. Urquhart, *Can. J. Research*, **28B**, 541 (1950).

Analysis of Gold Foils and Electroplating Solutions for Metallic and Anionic Impurities

H. Graham Silver[1]

Bell Telephone Laboratories, Inc., Reading, Pennsylvania

ABSTRACT

A comparison made between an "acid" citrate gold electroplating solution and an alkaline free potassium cyanide-containing gold electroplating solution demonstrates that both are susceptible to metallic impurity contamination. However, except for silver which is also codeposited from the alkaline electroplating solution, only the acid solution readily releases these impurities to codeposit with the gold. The alkaline solution, on the other hand, immediately becomes contaminated with anionic impurities, such as the formate and carbonate ions, which rapidly build up to a high concentration.

Potassium gold cyanide electroplating solutions containing free KCN are subject to contamination not only by $H.COO^-$ and $CO_3^=$ anionic impurities (1), but also by a brown polymeric material (2) of formula $[HCN]_4$. This polymer is generated at a soluble gold anode when the *p*H in its vicinity is reduced on the occasional anodic evolution of oxygen. The polymer codeposits with the gold, discoloring the latter, and is the agent responsible for the major proportion of the gaseous impurities evolved from the gold deposit on subsequent heating (3). However, gold deposits obtained from electroplating solutions containing no free KCN, for example, the dibasic ammonium citrate/$KAu(CN)_2$ electroplating solution, contain only low levels of gaseous impurities.

It is widely known that, even with careful periodic maintenance, the extended use of all types of $KAu(CN)_2$ electroplating solutions (4, 5) often results in a deterioration of the color, purity, and other physical properties of the gold deposit. Thus, it was deemed instructive to observe and directly compare the increase in metallic and anionic contaminants, by suitable analysis, in heavily used dibasic ammonium citrate/$KAu(CN)_2$ and KCN/$KAu(CN)_2$ electroplating solutions and in the gold foils obtained therefrom. The choice of these particular electroplating solutions was made owing to their immediate availability and the fact that the former solution, as opposed to the latter solution, did not contain free KCN and was operated at a *p*H below 7.

Experimental

A gold foil was plated on a stainless steel substrate[2] from a dibasic ammonium citrate/$KAu(CN)_2$ electroplating solution of formulation (6)

(68% min Au)	$KAu(CN)_2$	20 g/l	± 0.1 g/l
dibasic ammonium citrate		50 g/l	± 0.1 g/l
	*p*H	5.5	
Anodes	Platinized titanium (insoluble)		

which had been used steadily for a period of about six months with periodic maintenance. The foil was analyzed by emission spectroscopy for metallic impurities. Two 50-ml samples of the electroplating solution were withdrawn, one of which was analyzed for total metallic impurities by emission spectroscopy, while the other was analyzed for the following components: (*a*) Free CN^-; (*b*) $CO_3^=$; (*c*) *p*H; (*d*) CNO^-; (*e*) $H.COO^-$ formate; (*f*) $C_2O_4^=$ oxalate; (*g*) $CO(NH_2)_2$ urea.

Key words: electrodeposition, gold electroplating, metallic impurities, anionic impurities.

[1] Present address: General Telephone & Electronics Laboratories Incorporated, Bayside, New York.

[2] All stainless steel substrates, used for this purpose in this experiment, were degreased in the vapor of boiling trichloroethylene for 5 min, immersed in acetone for 15 min, acid-cleaned in hot 1:1 HCl for 1 min, and finally rinsed in deionized water.

A gold foil was plated on a stainless steel substrate from a KCN/$KAu(CN)_2$ electroplating solution of formulation:

(68% min. Au)	$KAu(CN)_2$	9 g/l	± 0.1 g/l
	KCN	45 g/l	± 0.1 g/l
	KOH	3 g/l	± 0.1 g/l
	*p*H	13	
Anodes		Gold (99.99%)	

which had been used continually for a period of about six weeks with periodic maintenance. The foil was analyzed by emission spectroscopy for metallic impurities. In the same manner as above, two 50-ml samples of the electroplating solution were withdrawn and analyzed for total metallic, anionic, and organic impurities.

Finally, in order to act as a reference point, two solid samples of $KAu(CN)_2$, one obtained from Engelhard Industries, 68.31% gold, and one obtained from Technic Inc., 68.2% gold, were analyzed for the following components, (*a*) metallic impurities, (*b*) free CN^- ion, and (*c*) $H.COO^-$ ion.

Results and Discussion

A comparison of the metallic and anionic impurities present in the two solid samples of $KAu(CN)_2$ is shown in Tables I and II.

The results indicate that both the Engelhard and Technic $KAu(CN)_2$ salts have a somewhat high level of silver contamination, which is rather to be expected, owing to the close chemical similarity between silver and gold. However, compared with the results reported below for the heavily used electroplating solutions, the concentration of other metallic impurities and anionic contaminants in the $KAu(CN)_2$ salts is indeed very low and may be considered negligible for most electroplating purposes. This is also true for the metallic impurities present in the soluble gold anodes (99.99%) used in the KCN/$KAu(CN)_2$ electroplating solution.

Table I. Comparison of metallic impurities

Metallic impurity	Fe	Cu	Ag	Si	Pb	Pd	Al	Mg	Ca
Engelhard salt, ppm	5	1	20	2	2	3	1	3	5
Technic salt, ppm	7	1	40	20	<1	<1	4	3	5

Table II. Comparison of anionic impurities

Anionic impurity	Free CN-	H.COO-
Engelhard salt, w/o	<0.03	0.46
Technic salt, w/o	<0.03	0.48

Table III. Metallic impurities

Impurity	Fe	Cu	Ag	Ni	Cd	Si	Pb	Pt	Au
ppm	50	1000	<10	40	500	30	30	10	Major

Table IV. Metallic impurities

Impurity	Pt	Sn	Fe	Cu	Ag	Ni	Cd	Si	Pb
ppm	20	70	400	250	2	900	30	300	20
Impurity	Sr	Ca	Al	B	Mn	Mg	Cr	Ba	Na
ppm	10	400	200	30	200	100	100	200	High

Table V. Anionic and organic impurities

Impurity	Free CN⁻	$CO_3^=$	H.COO⁻	CNO⁻	$C_2O_4^=$	Urea	pH
g/l	0.6	0.4	0.4	0.4	<0.2	<0.5	5.7

The gold foil plated from the six-month-old dibasic ammonium citrate/$KAu(CN)_2$ electroplating solution contained the metallic impurities listed in Table III. The dibasic ammonium citrate/$KAu(CN)_2$ electroplating solution contained the metallic impurities shown in Table IV after the sample was heated to dryness, and the same solution contained the anionic and organic impurities given in Table V. Of the metallic impurities present in the gold foil, copper and cadmium appear to be the ones most easily plated out of the electroplating solution. It is instructive to note that cadmium, although present at a concentration of 30 ppm in the solution, occurs in the foil at a concentration of 500 ppm. Although such a comparison between the concentration of metallic impurities within both the electroplating solution and the gold foil is not strictly valid and quantitative, it is commonly stated that a "concentration" effect has taken place, in that the cadmium appears to be preferentially plated out of the electroplating solution. The same observation applies to the behavior of copper. On the other hand, iron and nickel, present at a concentration of 400 and 900 ppm, respectively, in the solution, occur in the foil at a concentration of only 50 and 40 ppm, respectively.

Presumably, the concentration of the metallic contaminants Cd and Cu within the solution would be even higher if they were not so easily plated out with the gold. In fact, metallic contamination of a dibasic ammonium citrate/$KAu(CN)_2$ electroplating solution is very easily detected, since its color changes to yellow on the dissolution of small amounts of iron (7). This color deepens as the concentration of iron increases, which also usually signifies that other metallic contaminants, such as nickel, cobalt, and copper present in Rodar[3] and copper parts, are also increasing.

Contrary to the ease with which metallic contamination of a dibasic ammonium citrate/$KAu(CN)_2$ electroplating solution can occur, the level of anionic impurity remains remarkably low considering the length of time, about six months, that the solution was used. This is true, even if it is assumed that the levels detected now are no different from those present at the solution make-up, which is unlikely. The pH of the solution, 5.7, precludes too great an increase in concentration, within the solution, of the free CN^- ion, obtained on the electrodeposition of the gold, since HCN is evolved in acidic solution. There is the possibility that some polymerization of the HCN will occur at this pH (2), but owing to the low concentration of HCN present in the solution, the amount of polymer produced is very small and may readily be removed by treating the electroplating solution with activated carbon, upon which the polymer is adsorbed, and filtering. Thus, with a low concentration of the CN^- ion present at any one time, its reaction products with water and air (1), the $CO_3^=$, $H.COO^-$, CNO^- ions, etc., do not form at any appreciable rate.

The gold foil plated from the six-week-old KCN/$KAu(CN)_2$ electroplating solution contained the metallic impurities listed in Table VI.

The KCN/$KAu(CN)_2$ electroplating solution contained the metallic impurities listed in Table VII after the sample was heated to dryness; and the same solution contained the anionic and organic impurities listed in Table VIII. Of the metallic impurities present in the gold foil, silver and iron appear to be the ones most easily plated out of the electroplating solution. All the other impurities are effectively held at a concentration of < 10 ppm within the gold foil. The low concentration of silver in the electroplating solution, on the other hand, may be due to a "concentration" effect, which preferentially plates silver out of the solution. The free KCN present in the electroplating solution combines with many of the metallic impurities to form complex anions, *e.g.*, $Fe(CN)_6^{3-}$, $Cu(CN)_2^-$, $Ni(CN)_3^{2-}$, $Cr(CN)_6^{3-}$, etc., thus altering the redox potentials of the metal ions sufficiently to prevent their codeposition with the gold. This complexation mechanism effectively keeps the metallic impurities dissolved in the electroplating solution, which also slowly turns yellow as the concentration of several of the impurities, notably iron, nickel, and chromium, increases. This color change may be difficult to distinguish from that due to an increase in concentration of the HCN polymer within the electroplating solution (2). Thus, care should be taken in ascribing such a color change exclusively to a polymeric or metallic impurity.

Contrary to the low level of metallic impurities present in the gold foil obtained from a KCN/$KAu(CN)_2$ electroplating solution, the increase of anionic impurities, particularly the $CO_3^=$ and $H.COO^-$ ions, within the electroplating solution, over the period of about six weeks that it had been used, is rather disturbing. The drop in pH of the electroplating solution from 13 to 10.6 is probably partly due to the absorption of CO_2 from the atmosphere, but mainly due to the electrolytic propagation within the solution of CO_2, as will be explained shortly. Thus, an electroplating solution containing free KCN readily

Table VI. Metallic impurities

Impurity	Fe	Cu	Ag	Ni	Si	Pb	Pt
ppm	20	<10	40	<10	<10	<10	<10
Impurity	Cr	Al	Mg	Pd	As	P	Au
ppm	<10	<10	<10	<10	<10	<10	Major

Table VII. Metallic impurities

Impurity	Fe	Cu	Ag	Ni	Si
ppm	100	100	<10	50	20
Impurity	Ca	Al	Mg	Cr	Na
ppm	400	30	<10	<10	200

Table VIII. Anionic and organic impurities

Impurity	$CO_3^=$	H.COO⁻	CNO⁻	$C_2O_4^=$	Urea	pH
g/l	27.2	41.8	0.14	0.30	1.10	10.6

[3] Rodar: 29% Ni, 17% Co, 0.3% Mn, balance Fe.

becomes contaminated with anionic impurities, derived mainly from the side reactions of the KCN with water and air. Moreover, a comparison of the results of this work and those of a previous work (1) would indicate that electrolysis has an effect on the relative concentrations of the $H.COO^-$ and $CO_3^=$ ions present within a $KCN/KAu(CN)_2$ electroplating solution.

The ratio of $CO_3^=$ ion to $H.COO^-$ ion in Table VIII is approximately 0.65. Yet, in an aqueous KCN solution maintained at 70°C and exposed to air (1), in which no electrolysis is being conducted, the ratio is closer to 0.2. The higher $CO_3^=/H.COO^-$ ratio observed for the used electroplating solution probably results from the electrolytic oxidation of the $H.COO^-$ ion at the anode to CO_2 (8, 9), which is retained in the alkaline KCN solution.

Conclusion

Dibasic ammonium citrate/$KAu(CN)_2$ and $KCN/KAu(CN)_2$ electroplating solutions are both susceptible to metallic impurity contamination. These impurities do not plate out of the $KCN/KAu(CN)_2$ solution with the gold as readily as they do from the dibasic ammonium citrate/$KAu(CN)_2$ solution. However, the $H.COO^-$ and $CO_3^=$ ionic impurities build up to a high concentration in the $KCN/KAu(CN)_2$ electroplating solution, but are barely present in the dibasic ammonium citrate/$KAu(CN)_2$ electroplating solution. There is evidence that some of the $H.COO^-$ ion is oxidized at the anode to CO_2, which is retained in the alkaline electroplating solution.

Acknowledgment

The author wishes to thank Dr. M. J. Elkind for his helpful discussions during the course of this work.

Manuscript submitted Oct. 16, 1968; revised manuscript received Feb. 19, 1969.

Any discussion of this paper will appear in a Discussion Section to be published in the December 1969 JOURNAL.

REFERENCES

1. H. G. Silver, *This Journal*, **116**, 26C (1969).
2. H. Schmidt and H. Meinert, *Z. Anorg. Chem.*, **293**, 214 (1957).
3. H. G. Silver, *This Journal*, **116**, 591 (1969).
4. E. A. Parker, *Plating*, **38**, 1134 (1951).
5. "Electrodeposition of Gold" by Martin Frant from "Gold-Recovery, Properties and Applications," Chap. 9, Edmund M. Wise, Editor, Van Nostrand Co., New York (1964).
6. R. A. Ehrhardt, *Proc. Am. Electroplaters' Soc.*, **47**, 78 (1960).
7. F. I. Nobel, R. B. Kessler, D. W. Thomson, and R. F. Ostrow, *Plating*, **54**, 926 (1967).
8. B. J. Piersma, T. B. Warner, and S. Schuldiner, *This Journal*, **113**, 841 (1966).
9. B. E. Conway, N. Marincic, D. Gilroy, and E. Rudd, *ibid.*, **113**, 1144 (1966).

Electrolytic Reductive Coupling

XVI. A Study of 1,2-Diactivated Olefins. Part I, Voltammetry

John P. Petrovich, Manuel M. Baizer,* and Morris R. Ort

Central Research Department, Monsanto Company, St. Louis, Missouri

ABSTRACT

Representative 1,2-diactivated olefins XCH=CHY, in which X and Y are electron-withdrawing groups not themselves reduced in the course of the electrolyses, were studied in polarography, cyclic voltammetry, electron spin resonance spectroscopy, and macroelectrolyses. This first of three papers deals with the voltammetry of these compounds and the evidence it affords that a major pathway to the cathodic formation of reduced dimeric products at the first reduction wave is the nucleophilic attack of the intermediate anion radical on starting material rather than radical dimerization of the anion radicals. The rates of disappearance of the anion radicals were measured as a function of olefin concentration as well as the concentration of proton source and Michael-type acceptor. In each case a linear dependence of observed rate on concentration was noted. The implications for directed synthesis and for anionic polymerization are discussed.

Previous papers in this series (1) have been concerned mainly with delineating the scope of electrolytic reductive coupling of activated olefins as a method for synthesizing bifunctional compounds (2). Within the limits discussed previously the generality of the reactions summarized in Eq. [1] and [2] has been demonstrated when R = H or

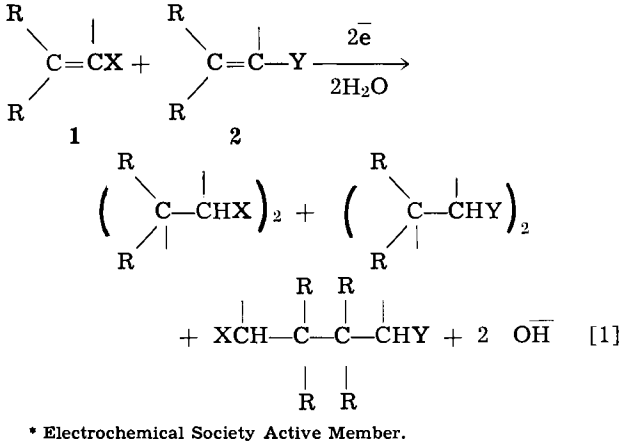

[1]

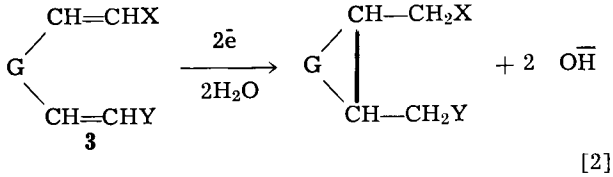

[2]

alkyls, X and Y are electron-withdrawing groups, not themselves reduced under the conditions of the electrolysis, and G is a bridging group, *e.g.*, $(CH_2)_n$. When X = Y (Eq. [1]), the process has been called electrohydrodimerization; the process of [2] is electrohydrocyclization (3).

A working hypothesis which has been very useful in rationalizing the synthetic results previously obtained and, indeed, in predicting the scope of the method has been the proposal (4) that an anionic intermediate is formed by electroreduction of **1** or **2** (depending on which is more easily reduced) and that this intermediate nucleophically attacks the β-position of the unreduced but polarized acceptor molecules to form the coupled product(s) (5). Mechanistic studies (8) relating to Eq. [1] have been concerned mainly with one or another aspect of acrylonitrile hydrodimer-

* Electrochemical Society Active Member.

ization (Eq. [3]) and have not thus far resulted in a

$$2CH_2{=}CHCN \xrightarrow[2H_2O]{2\bar{e}} NC(CH_2)_4CN + 2\,O\bar{H} \quad [3]$$

completely satisfactory detailed elucidation of the reaction. Concerning process [2] evidence has been presented (9) in support of the proposal that concerted one-electron transfer-ring closure occurs followed by a second reduction step

Now olefins **1** and **2** show only one polarographic wave; the limiting diffusion current corresponds to two or fewer electrons per molecule depending on the concentration and type of proton donor available (10). The major mechanistic problems concerning the reactions of **1** and **2** arise then from the fact that the presumed anion radical intermediate reacts with monomer, proton source, or possibly another anion radical before its presence can be verified by available instrumental methods.

The 1,2-diactivated olefins XCH=CHY **4**, however, possess two electron-withdrawing groups and do produce observable (11) anion radicals on one-electron reduction. While the nature of the first intermediate formed from **4** is, within certain limitations, more definable than that from **1**, the analysis of the subsequent steps by which **4** is converted to products via **5** is complex (Chart I) because several reasonable alternate pathways may be

CHART I

$$\underset{\mathbf{4}}{XCH{=}CHY} + \bar{e} \rightarrow \underset{\mathbf{5}}{(XCHCHY)^{\cdot-}}$$

$$\xrightarrow[\text{dimerization}]{k_d} \text{Prod. ec}$$

$$\xrightarrow[\text{olefin}]{k_o} \text{Prod. ece}$$

$$\xrightarrow[\text{water}]{k_H} \text{Prod. ec or ece}$$

$$\xrightarrow[\text{acrylonitrile}]{k_{AN}} \text{Prod. ece}$$

formulated. Processes may be encountered that are ec (an electrochemical step followed by a chemical step, *e.g.*, radical anion formation and dimerization, k_d), eec (formation of a dianion followed by reaction of this species with substrates), ecc (radical anion protonation, k_H, followed by dimerization of neutral radicals), ece (radical anion attack upon substrate followed by a second reduction, k_o and k_{AN}, and ecec. . .c (polymerization). The first objectives therefore, after proving the intermediacy of **5**, were to determine by established electrochemical techniques the most probable modes of decomposition of **5** through chemical reactions with each of the several components of the substrate under electrolysis conditions.

On a microscale olefins **4** were examined by polarography, cyclic voltammetry, and electron spin resonance spectroscopy. On a macroscale olefins **4** were reduced at the first polarographic wave in a divided cell either alone or in the presence of **1** at different levels of proton donor concentration. The polarographic and cyclic voltametric results are reported in this paper. The electron spin resonance spectroscopy and macro electrolysis will be given in subsequent papers.

Experimental

Materials.—Solvent. Dimethylformamide (Dupont, technical grade) was stored at least 24 hr over potassium carbonate, distilled at atmospheric pressure from barium oxide (lumps), distilled under reduced pressure from anhydrous copper sulfate, passed through Linde Type 4A molecular sieve, and stored under nitrogen until used.

Tetraethylammonium perchlorate (Southwestern Analytical Chemicals) was recrystallized from water and dried in a vacuum oven.

Activated Olefins.—Cinnamonitrile, fumaronitrile, ethyl cinnamate, diethyl fumarate, stilbene, and ethyl α-cyanocinnamate were obtained commercially and used without further purification.

Dibenzoylethylene (29), β-benzoylacrylonitrile (30), ethyl β-benzoylacrylate (31, 32), benzalacetophenone (33), β-carbethoxyacrylonitrile (34), 3-(4-pyridyl) acrylonitrile (35), ethyl 3-(4-pyridyl) acrylate (36), N,N-dimethyl β-carbethoxyacrylamide (34), N,N,N',N'-tetramethylfumaramide (37), ethyl 4,4,4-trifluorocrotonate (38), ethyl 4,4,4-trifluoro-3-trifluoromethylcrotonate (39, 40), and ethyl α-cyanosorbate were prepared by minor modifications (41) of literature methods.

N,N-dimethylcinnamamide was prepared from cinnamoyl chloride (185g, 1.11m, Eastman) and dimethylamine (100g, 2.22m). Three recrystallizations of the solid from benzene gave 104g of the desired amide, mp 99°-101°.

Anal. Calcd. for $C_{11}H_{13}NO$: C, 75.32; H, 7.48; N, 8.00. Found: C, 75.43; H, 7.42; N, 8.03.

Ethyl β-trifluoromethylcrotonate. A solution of β-trifluoromethylcrotonic acid (32.8g, 0.21m, Aldrich Chemical Company), 200 ml of ethanol and 0.5 ml of concentrated sulfuric acid was refluxed for 8 hr. The reaction mixture was poured into water, dissolved in dichloromethane, washed with dilute sodium bicarbonate, water, dried over anhydrous sodium sulfate, and the solvent was removed by distillation. The liquid residue was distilled to give 21.5g of ethyl β-trifluoromethylcrotonate, bp 128°, $n^{25}D$ 1.3746.

Anal. Calcd. for $C_7H_9F_3O_2$: C, 46.16; H, 4.98; F, 31.29. Found: C, 46.25, 46.36; H, 5.01, 5.39; F, 31.33, 31.65.

Polarography.—All polarograms were obtained with a Sargent Model XXI polarograph. The dropping mercury electrode constants were m = 1.58 mg/sec., t = 4.20 sec., $m^{2/3}t^{1/6}$ = 1.725. Standard polarographic H cells were used throughout. The polarograms were recorded against a saturated calomel electrode as the reference using 0.1*M* tetraethylammonium perchlorate in dimethylformamide as solvent. Cell resistances were around 1000 ohms and no correction was made for i_r drop in the cell.

Cyclic voltammetry.—The cyclic voltammograms were obtained using a Wenking Model 66TA1 potentiostat and an Exact Model 505 function generator. Recording of the current-voltage curves was accomplished with a Tektronix 502-A Dual Beam Oscilloscope and a C-27 camera attachment. The cell used for these experiments was a three-compartment cell; the reference and auxiliary electrode compartments were separated from the working electrode compartment by glass frits. The working electrode was a mercury drop suspended on a mercury-coated platinum wire. The reference electrode was a saturated calomel electrode connected to the electrolysis vessel by a cotton-plugged glass capillary. The auxiliary electrode was a platinum wire. The solutions analyzed were 1. to 5. x $10^{-3}M$ depolarizer with 0.1*M* tetraethylammonium perchlorate in dimethylformamide as solvent. Typical peak-to-peak separations were between 0.06 and 0.15v for scan rates of between 3 and 360 v/min.

Results and Discussion

Polarography.—The polarograms of a series of diactivated olefins, Tables I and II, were obtained in dimethylformamide (DMF) solution containing 0.1*M* tetraethylammonium perchlorate (TEAP). Both anhydrous DMF and DMF containing 1*M* water were used. Among this group of olefins two distinctive behaviors were observed. For olefins XIII and XVII two one-electron waves were obtained which coalesced into a single two-electron wave with the addition of a sufficient amount of water. This type of polarographic behavior has frequently been reported (12). On the other hand, for olefins III, VI, IX, and X only a single reduction wave was observed using anhydrous DMF as solvent. In these cases a decrease in the limiting current is observed in approximately the expected position for the second reduction wave, and the limiting current (I_d) for the first wave is very small, *e.g.*, 0.80 for olefin III.

Table I. Polarographic reduction of diactivated olefins. X—CH=CH—Y[a]

Compound	X[c]	Y	$-E_{1/2}$[b] with anhy. DMF Wave I	Wave II	I_d[c] Wave I	Wave II	$-E_{1/2}$[b] with 1M water Wave I	Wave II	I_d Wave I	Wave II
I	C_6H_5CO	C_6H_5CO	1.08	1.73	1.51	0.30	0.93	1.37	1.19	0.65
II	C_6H_5CO	CN	1.11	—	0.44	—	1.06	1.64	0.54	0.16
III	C_6H_5CO	$CO_2C_2H_5$	1.23	1.8[d]	0.80	dec.	1.20	1.72	0.89	0.16
IV	C_6H_5CO	4-Py	1.39	2.02	1.47	0.61	1.37	1.86	1.52	0.37
V	C_6H_5CO	C_6H_5	1.59	2.21	1.50	0.61	1.55	2.01	1.52	1.24
VI	CN	$CO_2C_2H_5$[g]	1.45	2.4[d]	1.01	dec.	1.40	2.36	1.24	1.20
VII	CN	4-Py	1.64	2.25	1.62	0.44	1.63	2.00	1.72	1.75
VIII	CN	C_6H_5	1.99	2.58	1.65	1.22	1.94	2.42	1.85	1.64
IX	CN	CN	1.36	2.3[d]	1.10	dec.	1.36	2.25	1.16	0.34
X	$CO_2C_2H_5$	$CO_2C_2H_5$	1.54	2.1[d]	1.27	dec.	1.54	2.27	1.91	1.18
XI	$CO_2C_2H_5$	4-Py	1.71	2.36	1.78	1.10	1.68	1.98	1.95	1.51
XII	$CO_2C_2H_5$	C_6H_5	2.00	2.49	1.72	1.62	1.96	2.35	1.72	1.70
XIII	$CO_2C_2H_5$	$CON(CH_3)_2$	1.76	2.62	1.56	0.53	1.68	1.95[h]	1.53	1.31
XIV	$CO_2C_2H_5$	CF_3	1.74[f]		1.97		1.73[f]		3.08	
XV	C_6H_5	$CON(CH_3)_2$	2.16	2.58	1.74	1.67	2.15	2.38	1.71	1.22
XVI	C_6H_5	C_6H_5	2.36	2.76	1.68	1.21	2.43	2.75	1.76	1.25
XVII	$CON(CH_3)_2$	$CON(CH_3)_2$	1.97	2.28	1.75	1.40	1.99[f]		3.23	

[a] All transconfiguration. [b] $E_{1/2}$ *vs.* SCE in dimethylformamide (DMF) with 0.1*M* tetraethylammonium perchlorate. [c] Concentration of olefins ~1 × 10^{-3}*M*. [d] A dip in the curve indicating the approximate position of the second wave. [e] All of the benzoyl ketones showed 2 additional waves at $E_{1/2}$ −2.3 and −2.5v for the reduction of the keto group. [f] Polarogram changes slope but does not split into two defined waves. [g] The waves in 0.1*M* LiOH solution at −1.57 and −1.94v observed by Karchener *et al.*, *Zh. Obshch. Khim.*, 29, 1364 (1959) we found are due to the reduction of anion of β-cyanoacrylic acid. [h] Collapsed at 3*M* water.

Table II. Polarographic reduction of miscellaneous activated olefins

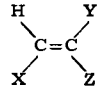

Compound	X	Y	Z	$-E_{1/2}$ with Anhy. DMF Wave I	Wave II	I_d Wave I	Wave II	$-E_{1/2}$, 1M Water Wave I	Wave II	I_d Wave I	Wave II
XVIII	C_6H_5	CN	$CO_2C_2H_5$	1.32	2.05	1.67	0.18	1.35	2.01	1.54	0.45
XIX	$CH_3CH=CH$	CN	$CO_2C_2H_5$	1.37	—	1.00	—	1.37	—	0.84	—
XX	$CO_2C_2H_5$	CH_3	CF_3	1.91	—	2.79	—	1.94	—	4.64	—
XXI	$CO_2C_2H_5$	CF_3	CF_3	1.35	2.57	1.37	3.28	1.34	1.84	1.43	0.89

$$4 \xrightarrow[\text{1 st wave}]{e^-} 5 \xrightarrow[\text{2 nd wave}]{e^-} (XCH—CHY)= \quad [6]$$

6

With olefins I, V, VII, XIII the second wave is considerably smaller than expected for a one-electron process. From the measured rate constants, *vide infra*, it is clear that the generated anion radicals **5** react with incoming depolarizer within the lifetime of the mercury drop.

Under the anhydrous conditions employed here, the reaction can form trimers or higher oligomers as well as dimers, thereby exhibiting a diffusion current somewhat less than one electron per molecule (10, 26). Since the dianion **7** has two negative charges in the same molecule, it would be expected to react even more rapidly with incoming depolarizers than the anion radical **5**, initiating oligomerization and thereby causing the observed decrease in the limiting current at the potential of the second reduction (13). The addition of 1*M* water to these systems affects the first wave only slightly, but eliminates the oligomerization initiated by the dianion, thereby increasing the diffusion current. The second wave is then observed at a slightly more positive potential than the potential at which the decrease in the limiting current is observed in the anhydrous system; *e.g.*, for olefin III in anhydrous DMF the decrease is at −1.8v, and in aqueous DMF the second wave is at −1.72v (Fig. 1). These observations again point out the caution which must be observed in interpreting polarographic data on active systems, especially when proton sources are absent.

The reaction of **5** with sufficient water yields a neutral radical α to an activating group. Since no additional polarographic wave is observed under conditions where this reaction occurs, this radical must be reduced either at the same or at a more positive potential than the olefin (14). Further, no additional reduction waves are observed using conditions under which **5** reacts with the olefin. The product of this reaction is a dimeric anion radical in which the radical site is insulated from the negative charge by a two-carbon bridge. This dimeric anion radical must also consequently be reduced at the same or at a more positive potential than the original olefin. It is clear, therefore, that attempts to trap a dimeric anion radical of this type by chemical methods (15) are difficult since the intermediate is unstable to reduction by the reducing agent, such as an alkali metal, and even the monomeric anion radical.

It is interesting, incidentally, to compare the polarograms of olefin VI, Table I, and olefin XIX, Table II. These two olefins have the same two activating groups, carbethoxy and nitrile, but in 1,2 and 1,1 positions, respectively. The effect of placing both activating groups on the same carbon atom shifts the first wave slightly in the anodic direction and also completely eliminates the second wave below —2.5v. This points

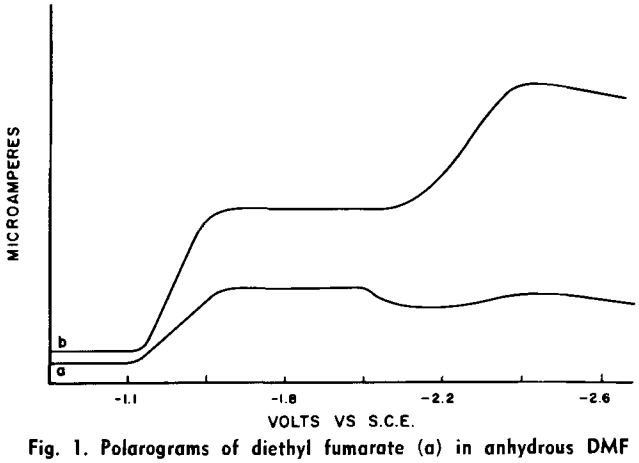

Fig. 1. Polarograms of diethyl fumarate (a) in anhydrous DMF and (b) in DMF with 1M water.

Table III. Cyclic voltametric data for representative diactivated olefins[a]

Compound	Scan rate v/sec	$i_p/v^{1/2}$	i_r/i_f	E_p[b]
		Curve 1, Fig. 2		
II	0.12	6.3	—	1.05
	0.48	6.9	0.30	1.06
	1.2	7.3	0.42	1.07
	4.8	8.6	0.54	1.06
	12.	8.6	0.65	1.09
III	0.12	24	0.34	1.11
	0.24	25	0.38	1.12
	0.72	26	0.55	1.14
	2.4	24	0.80	1.15
	7.2	22	0.97	1.18
		Curve 2, Fig. 2		
XI	0.072	36	0.43	1.67
	0.24	33	0.59	1.68
	0.96	30	0.80	1.70
	1.2	30	0.84	1.71
	2.4	29	0.92	1.73
XIII	0.024	19	0.47	1.64
	0.072	17	0.55	1.65
	0.48	15	0.83	1.65
	1.2	13	0.94	1.66
	2.4	13	0.96	1.67

[a] $2 \times 10^{-3}M$ depolarizer, 0.1M TEAP in DMF; hanging mercury drop electrode. [b] In volts *vs.* SCE.

out the importance of charge separation in the formation of a dianionic species.

Several attempts were made to correlate these polarographic $E_{1/2}$ values with published σ values. Numerous successful correlations for other classes of compounds have appeared in the literature (16). However, the diactivated olefins discussed here do not lend themselves to such treatment.

A qualitative order can be drawn from our data for the stabilizing effects as measured by $E_{1/2}$ values of the activating groups on the anion radical intermediates:

$$\phi CO > CN \geq CO_2C_2H_5 > 4\text{-Py} > CF_3 > CON(CH_3)_2 > \phi > H$$

The most easily reduced diactivated olefin of those studied is dibenzoylethylene (I); the most difficult to reduce is stilbene (XVI).

Attempts to correlate polarographic $E_{1/2}$ values for monoactivated olefins with reactivity as measured by anionic polymerizability have had limited success (17). The rates of polymerization of these olefins depend importantly on the steric requirements of the propagation step. It is clear from the data in Table I that the polarographic data depend overwhelmingly on the number and nature of the electron-withdrawing groups in conjugation with the olefin and only slightly if at all on the bulkiness of the groups, *cf.* I and IX.

The high I_d value for compound XXI is probably due to fluoride ion elimination followed by reduction. Fluoride elimination has been observed in the bulk electrolysis of ethyl β-trifluoromethylcrotonate.[1]

Cyclic voltammetry.—The cyclic voltammograms of a series of diactivated olefins were obtained in anhydrous DMF solution containing 0.1M TEAP. The dependence of the peak current, i_p, on the voltage scan rate was obtained. Representative data are given in Table III. Two types of behavior were noted (Fig. 2). Curve 1, Fig. 2, is typical of the behavior observed for olefins II, III, IV, VI, VII, IX, *i.e.*, olefins which are very reactive and easily polymerizable, while curve 2 was typical of the behavior of the other olefins studied, *i.e.*, I, V, VIII, X, XI, XII, XIII, XV, XVI, XVII. Neither of these curves corresponds to the "linear" dependence of $ip/V^{1/2}$ with $V^{1/2}$ expected for an ec mechanism (18). Curve 2 is, however, typical of the behavior expected for a reversible electron transfer followed by a fast chemical reaction and a subsequent electron transfer (ece) (18). Curve 1 probably corresponds to an ece

[1] See Part II, Experimental Section. J. P. Petrovich, M. M. Baizer and M. R. Ort, *This Journal*, 116, 749 (1969).

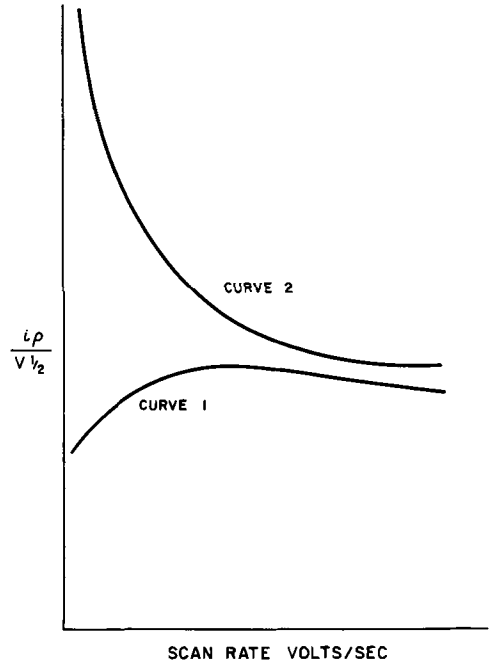

Fig. 2. Plot of $i_P/V^{1/2}$ *vs.* scan rate for curve 1, ethyl cinnamate and curve 2, ethyl β-cyanoacrylate.

mechanism when the slow scan region is complicated by a polymerization reaction. In all cases a 20-40 mv shift in peak voltage was noted for a ten-fold change in sweep rate.

In order to gain some knowledge of the nature of the chemical reaction involved, the rate constants for the decomposition of the electrochemically generated anion radicals were calculated from the cyclic voltammograms using the simplified method of Nicholson (19), Eq. [8], and a numerical plot of $k_f \tau$ *vs.* i_r/i_f as given by Nicholson and Shain (20); where i_r/i_f is the ratio of the reverse to the forward

$$i_r/i_f = \frac{i_{ap}}{i_{cp}} + \frac{0.485\ (i_{sp})}{i_{cp}} + 0.086 \qquad [8]$$

current, i_{ap} is the anodic peak current, i_{cp} is the cathodic peak current, i_{sp} is the current at the switching potential, τ is the time from $E_{1/2}$ to the switching potential and k_f is the first-order rate constant for the disappearance of the intermediate ion radical. When there is no further electron exchange, a plot of $k\tau$ *vs.* τ has been shown to be linear and to pass through zero (21).

For the diactivated olefins, a plot of $k\tau$ *vs.* τ deviates from linearity significantly for values of i_r/i_f of <0.75, but is fairly linear above this value. The region of the curve representing 5-20% chemical reaction was used for all of the rate constants reported here. In this region the contribution from the second electron transfer to i_{cp} and i_{sp} is small. Therefore, the equation derived for an ec mechanism would also apply to an ece mechanism. The rate constants calculated in this manner, Tables IV, V, and VI, were reproducible to $\pm$ 10%.

The half-lives, $^{0.69}/_{k_{obs}}$, varied from 15 sec for dibenzoylethylene to 0.0096 sec for ethyl β-cyanoacrylate at 2 x $10^{-3}M$ depolarizer. In general, the symmetrically substituted olefins are the least reactive indicating that the ground-state dipole contributes to the reactivity. It is interesting to note that the nitrile function contributes significantly more to the reactivity of the anion radical than does the benzoyl function, *e.g.*, the intermediate from olefin VI reacts nearly 30 times as rapidly as does the corresponding intermediate from olefin III. The anion radical from cinnamonitrile (VIII) reacts 9 times as fast as the anion radical from ethyl cinnamate (XII).

The rate constants for the disappearance of the anion radicals by any route were determined for six

Table IV. Pseudo-first-order rate constants[a] for the disappearance of anion radicals electrochemically generated from diactivated olefins at 25°C

$$XCH{=}CHY \xrightarrow{e^-} \dot{X}CH\text{-}CHY \xrightarrow{k} \text{Product}$$

Compound	X	Y	$10^3 M$[b]	k_{obs}[c] sec^{-1}	$t_{1/2}$[d], sec
I	C_6H_5CO	C_6H_5CO	2.01	0.045	15.3
II	C_6H_5CO	CN	2.00	37.	0.018
III	C_6H_5CO	$CO_2C_2H_5$	1.97	2.3	0.3
IV	C_6H_5CO	4-Py	2.04	3.5	0.19
V	C_6H_5CO	C_6H_5	1.96	12.	0.057
VI	CN	$CO_2C_2H_5$	2.15	72.	0.0096
VII	CN	4-Py	1.96	6.9	0.10
VIII	CN	C_6H_5	1.96	2.2	0.31
IX	CN	CN	1.96	—[e]	
X	$CO_2C_2H_5$	$CO_2C_2H_5$	1.99	0.31	2.2
XI	$CO_2C_2H_5$	4-Py	2.34	0.27	2.6
XII	$CO_2C_2H_5$	C_6H_5	2.00	0.24	2.9
XIII	$CO_2C_2H_5$	$CON(CH_3)_2$	2.00	0.24	2.9
XIV	$CO_2C_2H_5$	CF_3	2.02	—[e]	
XV	C_6H_5	$CON(CH_3)_2$	1.95	0.15	4.6
XVI	C_6H_5	C_6H_5	2.00	0.069	10.
XVII	$CON(CH_3)_2$	$CON(CH_3)_2$	2.00	0.11	6.3

[a] Calculated by the method of Nicholson and Shain, *Anal. Chem.* 36, 706 (1964). [b] In DMF solvent with 0.1*M* TEAP. [c] ±10%. [d] $t_{1/2} = 0.69/k_{obs}$. [e] Too fast to measure.

Table V. Pseudo-first-order rate constants for the disappearance of anion radicals electrochemically generated from diactivated olefins as a function of the concentration of olefin, water, and acrylonitrile (AN) at 25°C

Compound	10^3 *M* Olefin[a]	*M* Water	*M* AN	k_{obs}[b]
III	1.00	—	—	1.62
	1.97	—	—	2.25
	4.08	—	—	3.74
	2.38	1.03	—	5.4
	2.25	—	1.01	2.3
VI	1.12	—	—	22.
	2.15	—	—	72.
	2.01	1.0		71.
	2.13	—	1.05	73.
X	0.92	—	—	0.19
	1.99	—	—	0.31
	4.28	—	—	0.53
	2.18	0.99	—	1.28
	2.98	—	1.04	0.52
XI	1.13	—	—	0.30
	2.34	—	—	0.56
	4.18	—	—	0.97
	2.15	1.04	—	3.75
XII	0.98	—	—	0.12
	2.00	—	—	0.24
	4.57	—	—	0.32
	1.85	1.04	—	0.62
XIII	0.89	—	—	0.13
	2.00	—	—	0.24
	4.18	—	—	0.41
	2.98	1.02	—	2.58
	3.59	—	1.04	1.51

[a] In DMF solvent with 0.1*M* TEAP. [b] Reproducibility ± 10%.

Table VI. Rate constants for the reactions of anion radicals electrochemically generated from diactivated olefins with diactivated olefins, k_o, water, k_w, and acrylonitrile, k_{AN} at 25°C

Compound	k_o	k_w	k_{AN}
III	690	2.8	0
VI	40,000	0	0
X	101	0.96	0.12
XI	230	3.1	—
XII	69	4.2	—
XIII	82	2.2	1.2

of the olefins, III, VI, X, XI, XII, XIII, as a function of the bulk concentration of the olefin. The effect of adding water and acrylonitrile to the system was also examined. For each diactivated olefin studied, a plot of the observed rate constant, k_{obs}, *vs.* the bulk concentration of olefin was linear but did not pass through zero. This is the type of behavior expected for competitive reactions following Eq. [9]. The quantity used to calculate k_o

$$k_{obs} = k + k_o\,[\text{olefin}] \qquad [9]$$

was the bulk concentration of olefin. This introduces an error in the calculation of k_o since, under electrolysis conditions, the concentration of the olefin in the area of the electrode is less than but proportional to the bulk concentration. However, since all of the diffusion coefficients for the olefins studied are probably of similar magnitude, the relative values of k_o are sufficiently accurate for comparisons. Since one of the activating groups for each of the olefins studied is a carbethoxy group, the relative reactivity of these olefins is a measure of the contribution to the over-all reactivity from each of the other activating groups. The order and relative reactivity is C_6H_5, 1 ≤ CON$(CH_3)_2$, 1.2 < $CO_2C_2H_5$, 1.5 < 4-pyridyl, 3.3 < C_6H_5CO, 10 < CN, 580.

Three possible reaction paths can be written for the disappearance of these anion radical intermediates **5**, Eq. [10], [11], and [12]. The measured rate constants for the reaction of the anion

$$\underset{\mathbf{4}}{XCH{=}CHY} + e^- \rightarrow \underset{\mathbf{5}}{XCH(\dot{-})\text{—}CHY}$$

$$\mathbf{5} + \text{proton source} \rightarrow \underset{\mathbf{7}}{(XCHCHY)(\cdot)}H \rightarrow \text{dimer} \qquad [10]$$

$$\mathbf{5} + XCH{=}CHY \rightarrow \text{dimeric anion radical} \qquad [11]$$

$$\mathbf{5} + \mathbf{5} \rightarrow \text{dimeric dianion} \qquad [12]$$

radical **5** of representative olefins, Table V, with water clearly indicate that Eq. [10] is not a major path for the reaction of the anion radicals and, therefore, for the formation of dimeric products, *e.g.*, for olefin X, k_o/k_w = 105. The yield of dimeric products is, however, dependent on the concentration of water in the electrolysis mixture (9). In general, the more water present in the electrolysis mixture, the lower the yield of dimeric products and the higher the yield of saturated monomer. It is hard to explain how or why water would interfere with a free radical reaction. Water is an extremely poor free-radical inhibitor. If the formation of dimer products involved the dimerization of the free radicals **7**, Eq. [10], an increase in the water concentration should result in an increase in dimeric products, in contrast to what is observed experimentally.

In addition, the protonation of the anion radical **5** would most likely lead to the resonance stabilized, secondary α-radical, rather than the primary β-radical. The α-radical would lead to branched-chain dimers rather than the linear dimers that are observed. In special cases, small yields of α, β coupled dimers have been observed (7), but no α, α dimers have been obtained.

Concerning the second and third paths, our interpretation of the data obtained in studying cyclic polarograms of **4** at several concentrations and sweep rates as well as the determination of the effect of water on the rate of disappearance of **5** leads to the conclusion that [11] rather than [12] is the major route to the dimeric species.

It is clear that the observed rate constant for the reaction of the electrochemically generated anion radical **5** with the olefin (Eq. [11]) should be a linear function of the bulk concentration of the olefin. On the other hand, the dependence of the observed rate constant for anion radical dimerization (Eq. [12]) on the bulk concentration of olefin is not easily determined. It may also be linear. A rigorous mathematical solution for this kind of system has not been accomplished (22), so that an argument for [10] and [11] based on concentration dependence alone is not at present unequivocal. However, our data (Table V), when coupled with the observed dependence of $i_p/V^{1/2}$ and the peak potential on the sweep rate (Table III), argue strongly in favor of an ece mechanism (Eq.

[11]) rather than an ec mechanism (Eq. [12]). The coupling reaction, therefore, does not involve the dimerization of two electrochemically generated anion radicals to any appreciable extent. In certain nonelectrochemical systems this same conclusion based on electrostatic considerations has been stated by Szwarc (23) in a general discussion of anion radical dimerization. Calculated equilibrium constants (24) for the dimerization of two anion radicals for 1,2-diactivated systems highly favors the monomeric species, *e.g.*, for stilbene anion radicals, log $K = -53$.

The rate constants for the reaction of the anion radicals with water, k_w, as well as with acrylonitrile, k_{AN}, were calculated assuming a simple kinetic expression for competitive pseudo-first-order reaction paths, Eq. [13]. The reactivity of

$$k_{obs} = k + k_o[\text{olefin}] + k_w[H_2O] + k_{AN}[\text{acrylonitrile}] \quad [13]$$

these anion radicals toward the parent olefin was found to be much greater than toward either water or acrylonitrile. In particular, the relative rates for the reactions of the anion radicals from diethyl fumarate (X) and from N,N-dimethyl β-carbethoxyacrylamide (XIII) with the parent olefin, water, and acrylonitrile are 840:8:1 and 39:2:1. In a typical homogeneous reaction, one would expect from polymerization data and their effectiveness as Michael acceptors (25) the relative reactivities toward an anion to be water > acrylonitrile > parent olefin. The apparent "low reactivity" of water in the electrohydrodimerization reaction has been rationalized (26) on the basis of a large difference in the concentration of water in the bulk of the solution and at the electrode surface due to the hydrophobic nature of the tetraalkylammonium ion. Let us examine the result, however, of analyzing the situation from the point of view of electric field effects alone.

Just prior to electron transfer when the depolarizer is oriented in the electric field, one would expect it to have a very strong induced dipole, almost to the extreme of charge separation. All of the molecules in the vicinity of the electrode would be subjected to some kind of polarization. The degree of the polarization at a given electrode potential should be different from each reactant, *e.g.*, diethyl fumarate, acrylonitrile and water, depending on its individual polarizability. The net effect of this polarization should be an "induced reactivity" which may be very different from the respective "normal" reactivity in nonelectrochemical systems (27). This induced reactivity would be quite similar to induced electron density discussed by Hoijtink (28) to rationalize the reduction products of polynuclear hydrocarbons as a function of the applied electric field. The extent of the polarization of the olefins in question should be qualitatively related to their polarographic reduction potentials.

From the rate constants measured for olefins X and XIII an interesting trend is apparent. At their respective reduction potentials (—1.54 and —1.76v) the two anion radicals show similar reactivities toward their respective olefins and yet show different reactivities toward water and acrylonitrile. The reactivities of both water and acrylonitrile are higher at the higher electrode potential. The reactivity of water changes by a factor of 2, while that for acrylonitrile shows a tenfold increase. Extrapolating these very limited data, which is always dangerous, to couplings occurring in similar electrolyte systems, one would predict that the reactivity of acrylonitrile would be about 15 times that of water toward an anion radical generated at ca. —2.0v, the reduction potential of acrylonitrile.

Conclusions Concerning Mechanisms

From the above results as well as the observed rate constants, Tables III and IV, we conclude that the initial chemical step in the electrolytic reduction of activated olefins occurs at the electrode surface. A

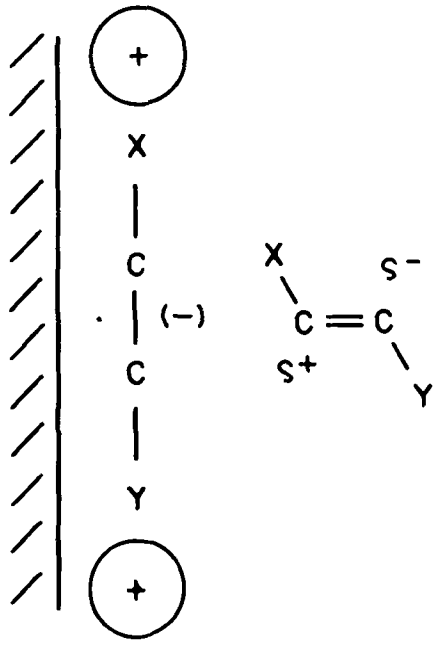

Fig. 3. Mechanistic picture of results

mechanistic picture consistent with these results presents the anion radical lying on the electrode surface within the plane of the adsorbed tetraalkylammonium ions and reacting with a polarized acceptor molecule or proton source as depicted in Fig. 3. The results of the reaction with an acceptor is a coupled species with an anionic site outside of the polarizing field and a radical site at the electrode surface. This radical probably reduces rapidly either by the electrode or by relay through a monomeric anion radical, thus yielding a new anion which is repelled from the electrode surface. Once the final reduction product, either the dimeric or monomeric anion, leaves the influence of the electric field, normal solution reactions can occur. This mechanism is consistent with the mechanism proposed previously for the electrohydrocyclization reaction (9) since the upper limit of a rapid reaction is a concerted process. It is also consistent with the basic suggestions as to the mechanism of the electrohydrodimerization of monoactivated olefins (8) with the exception that the relatively low reactivity of water may be due at least partially to polarization effects rather than exclusively to concentration effects. These three systems, monoactivated olefins, diactivated olefins, and bisactivated olefins, give the full spectrum of reactivities for the electrolytic reductive coupling reaction. The diactivated olefins show the lowest reactivity, *i.e.*, the anion radicals are observable. The bisactivated olefins react by a concerted path, and the monoactivated olefins are intermediate in reactivity.

Manuscript submitted Oct. 22, 1969; revised manuscript received *ca.* Feb. 1, 1969.

Any discussion of this paper will appear in a Discussion Section to be published in the December 1969 JOURNAL.

REFERENCES

1. M. M. Baizer and J. P. Petrovich, *This Journal*, **114**, 1023 (1967).
2. M. M. Baizer, J. D. Anderson, J. H. Wagenknecht, M. R. Ort, and J. P. Petrovich, *Electrochim. Acta*, **12**, 1377 (1967).
3. J. D. Anderson, M. M. Baizer, and J. P. Petrovich, *J. Org. Chem.*, **31**, 3890 (1966).
4. M. M. Baizer, *Tetrahedron Letters*, 973 (1963).
5. The participation of the α-carbon atom is involved in oligomerizations (6) and to a minor extent in certain hydrodimerizations (7).
6. M. M. Baizer and J. D. Anderson, *J. Org. Chem.*, **30**, 1351 (1965).
7. G. L. Jones and T. H. Ledford, *Tetrahedron Letters*, 615 (1967).

8. S. Lazarov, A. Trifonov, and T. Vitanov, *Z. Phys. Chem.*, **226**, 221 (1964); F. Beck, *Chem.-Ing. Tech.*, **37**, 607 (1965); M. Figeys, *Tetrahedron Letters*, 2237 (1967); M. J. S. Dewar in *This Journal*, **111**, 215 (1964) footnote 18.
9. J. P. Petrovich, J. D. Anderson, and M. M. Baizer, *J. Org. Chem.*, **31**, 3897 (1966).
10. M. Murphy, M. G. Carangelo, M. B. Ginaine, and M. C. Markham, *J. Polymer Sci.*, **54**, 107 (1961); I. G. Sevast'yanova and A. P. Tomilov, *Zh. Obshch. Khim.*, **33**, 2815 (1963); A. V. Finkel'shtein and V. I. Klyaer, *Tr. Sibirsk Teknol. Inst.*, **36**, 106 (1963).
11. The details of the esr study are to be reported separately.
12. I. A. Korshunov, Yu V. Vodzinskii, N. S. Vyazankin, and A. I. Kalinin, *Zhur. Obshch. Khim.*, **29**, 1364 (1959); S. Wawzonek and D. Wearring, *J. Am. Chem. Soc.*, **81**, 2067 (1959).
13. In both cases limiting currents of the type that have recently been mentioned (14) are involved.
14. Radical dimerization yields the same results but is ruled out by the evidence for an ece mechanism. J. H. Wagenknecht and M. M. Baizer, *This Journal*, **114**, 1095 (1967).
15. K. F. O'Driscoll and A. V. Tobolsky, *J. Polymer Sci.*, **31**, 123 (1958); K. F. O'Driscoll, R. J. Bondreau, and A. V. Tobolsky, *ibid.*, **31**, 115 (1958).
16. P. Zuman, "Substituent Effects in Organic Polarography," Plenum Press, New York (1967).
17. T. Fueno, T. Tsuruta, and J. Furukawa, *J. Polymer Sci.*, **40**, 499 (1959).
18. R. S. Nicholson and I. Shain, *Anal. Chem.*, **37**, 178 (1965).
19. R. S. Nicholson, *ibid.*, **38**, 1406 (1966).
20. R. S. Nicholson and I. Shain, *ibid.*, **36**, 706 (1964).
21. R. S. Nicholson and I. Shain, *ibid.*, **37**, 190 (1965).
22. A study of these systems is under way. Private communication Professor A. J. Bard, University of Texas.
23. M. Szwarc, *Makromol. Chem.*, **35**, 132 (1960).
24. B. J. McClelland, *Chem. Rev.*, **64**, 301 (1964).
25. A. N. Nesmeyanov, M. I. Rybinskaya, and L. V. Rybin, *Russ. Chem. Rev.*, **36**, 453 (1967).
26. L. G. Feoktistov, A. P. Tomilov, and I. G. Sevast'yanova, *Soviet Electrochem.*, **1**, 1165 (1965); I. E. Gillet, Abstracts 17th Meeting of CITCE, Tokyo-Kyoto, September 1966, p. XXV.
27. The polarization of the reactants is analogous to the Wien effect as shown by the increased conductivity of electrolytes and the changes in ionization constants of weak acids due to polarization in a strong electric field.
28. G. J. Hoijtink, *Rec. Trav. Chim.*, **76**, 885 (1957).
29. R. E. Lutz, "Organic Synthesis," Coll. Vol. III, p. 248, John Wiley & Sons, Inc., New York (1955).
30. A. N. Nesmeyanov and M. I. Rybinskaya, *Dokl. Akad. Nauk. SSSR*, **120**, 793 (1958).
31. N. H. Cromwell and R. Benson, "Organic Synthesis," Coll. Vol. III, p. 105, John Wiley & Sons, Inc., New York (1955).
32. R. Delaby, P. Chabier, and S. Dantor, *Compt. rend.*, **232**, 2326 (1951).
33. E. P. Kohler and H. M. Chadwell, "Organic Synthesis," Coll. Vol. I, p. 78, John Wiley & Sons, Inc., New York (1941).
34. I. A. Korshunov, Yu V. Vodzinskii, N. S. Vyazankin, and A. I. Kalinin, *Zhur. Obs. Khim.*, **29**, 1364 (1959).
35. M. Strell and E. Kopp, *Chem. Ber.*, **91**, 1621 (1958).
36. R. Lukes, J. N. Zvonkova, A. F. Mironov, and M. Ferles, *Collection Czech. Chem. Commun.*, **25**, 2668 (1960).
37. F. A. Marchetti, *Gazz. Chim. Ital.*, **84**, 816 (1954).
38. E. T. McBee, O. R. Pierce, and D. D. Smith, *J. Am. Chem. Soc.*, **76**, 3722 (1954).
39. I. L. Knunyants and Yu A. Cheburkov., *Izv. Akad. Nauk. SSSR Otd. Khim. Nauk.*, 678 (1960).
40. I. L. Knunyants and Yu A. Cheburkov., *ibid.*, 2168 (1960).
41. Detailed descriptions are available on request.

Electrolytic Reductive Coupling

XVII. A Study of 1,2-Diactivated Olefins. Part II. Macro-electrolyses

John P. Petrovich, Manuel M. Baizer,* and Morris R. Ort

Central Research Department, Monsanto Company, St. Louis, Missouri

ABSTRACT

The electrolytic reductive coupling of a variety of diactivated olefins, XCH=CHY, has been studied. The reduced dimeric products have been isolated and carefully identified. Both symmetrical and unsymmetrical dimers were observed. The dimeric products are formed by two paths: the first involves the attack of the electrochemically generated anion radical on unreduced olefin; the second involves the protonation of the anion radical followed by reduction to an anion and subsequent attack on the olefin. The isomer distribution in the dimeric product obtained by the first route is rationalized on the basis of the relative anion stabilizing ability of the activating groups in the acceptor molecule and the relative ability toward stabilizing a radical site in the donor molecule. The possibility of forming cross-coupled products (between a diactivated olefin and a Michael acceptor) is limited to systems in which the electrochemically generated anion radical is relatively stable toward its parent olefin or in which the reduction potentials of the pair are similar, *i.e.*, $\Delta E_{1/2} < 0.4$v.

Part I (1) described the voltammetric study of olefins XCH=CHY, **1**, in which X and Y are electron-withdrawing groups not themselves reduced under the conditions of electrolysis. It was established that anion radicals **2**, were the intermediate species produced by

$$\underset{\mathbf{1}}{\text{XCH—CHY}} \xrightarrow{\bar{e}} \underset{\mathbf{2}}{(\text{XCH—CHY})^{-}}$$

* Electrochemical Society Active Member.

the first one-electron reduction. Strong evidence was presented that **2** reacts anionically at the electrode surface with **1**, water, or nonreduced electrophiles added to the catholyte. The results of macroelectrolyses (at the first reduction wave) designed to obtain simple coupled products are reported here. The interpretation of the results is complicated (Charts I and II) because (*a*) each of the above initial ec reactions initiates a separate route to products; (*b*) water or some other proton donor must be included in the

catholyte lest the **1** oligomerize/polymerize; (c) as a consequence of (*b*), some e-water-e contribution to the total reaction scheme will lead to products formed from anions reacting not in the vicinity of the electrode (Eq. [4]); and (*d*) symmetrical as well as unsymmetrical hydrodimeric products may be formed. From a careful analysis of the coupled products obtained and a consideration of the facts summarized in Part I a rational scheme is proposed for the routes (Chart II) whereby **1** leads to products. A conclusion concerning the most probable path(s) leading to each coupled product is included in the presentation of the Results; the supporting arguments are presented in the Discussion.

Chart I: Over-all reduction coupling reactions of $XCH{=}CHY$

$$2 + 1 \xrightarrow[H_2O]{} \underset{\mathbf{3}}{XCHCH_2Y\ \ XCHCH_2Y} + \underset{\mathbf{4}}{XCHCH_2Y\ \ YCHCH_2X} + \underset{\mathbf{5}}{XCH_2CHY\ \ XCH_2CHY} \quad [1]$$

$$+ XCH_2CH_2Y + \text{polymer}$$

6

$$2 + R_2C{=}CHZ \xrightarrow[H_2O]{1} (3,4,5,6) + \underset{\mathbf{7}}{XCHCH_2Y\ \ R_2CCH_2Z} + \underset{\mathbf{8}}{XCH_2CHY\ \ R_2CCH_2Z} \quad [2]$$

Chart II: Reaction paths for reductive couplings of $XCH{=}CHY$

$$\mathbf{1} \xrightarrow{1e^-} \mathbf{2}$$

Path A $2 + \text{olefin} \rightarrow \text{dimer} \xrightarrow[2H_2O]{e^-} \text{hydrodimers}$ [3]

Path B $2 + H_2O \rightarrow (XCHCHY)H \xrightarrow{e^-} (XCHCHY)H \xrightarrow{-H_2O} XCH_2CH_2Y$ [4]

Path C $2 + CH_2CHCN \rightarrow (XCHCHY)CH_2\overset{-}{C}HCN \xrightarrow[H_2O]{e^-} \text{cross-coupled products}$ [5]

Experimental

Materials.—Solvent.—Dimethylformamide (Dupont, technical grade) was stored at least 24 hr over potassium carbonate, distilled at atmospheric pressure from barium oxide (lumps), distilled under reduced pressure from anhydrous copper sulfate, passed through Linde Type 4A molecular sieve, and stored under nitrogen until used.

Electrolytes.—Tetraethylammonium p-toluenesulfonate (Aldrich Chemical Company) was recrystallized twice from acetone and dried in a vacuum oven.

Activated Olefins.—Cinnamonitrile, ethyl cinnamate, and diethyl fumarate were obtained commercially and were used without further purification. Dibenzoylethylene (19), β-benzoylacrylonitrile (20), ethyl β-benzoylacrylate (21), β-carbethoxyacrylonitrile (24), N,N-diethyl β-carbethoxyacrylamide (22), N,N-dimethyl β-carbethoxyacrylamide (22), N,N-dimethylcinnamide (1), and ethyl 4,4,4-trifluorocrotonate (23) were prepared by literature methods.

α,β-Disubstituted ethanes.—Hydrocinnamonitrile, ethyl hydrocinnamate and diethyl succinate were obtained commercially and used as vpc standards without further purification.

β-Benzoylpropionitrile (24), ethyl β-benzoylpropionate (25), ethyl β-cyanopropionate (26), and dibenzoylethane (27) were prepared by adaptations of literature methods.

N,N-dimethylhydrocinnamamide was prepared from dimethylamine and hydrocinnamoyl chloride, bp 110°-112° (0.8m), $n^{25}D$ 1.5308.

Anal. Calcd. for $C_{11}H_{13}NO$: C, 74.50; H, 8.54; N, 7.89. Found: C, 74.22; H, 8.51; N, 7.65.

N,N-dimethyl β-carbethoxypropionamide.—A suspension of N,N-dimethyl β-carbethoxyacrylamide (23g, 0.134m), 0.5g of 10% palladium on charcoal and 100 ml of ethanol was treated for 30 min with hydrogen at 40 psi in a Parr shaker at room temperature. The solvent was removed by distillation at reduced pressure. Distillation of the oily residue at reduced pressure gave 18.9g of the desired compound, bp 90°-91° (0.1 mm), $n^{25}D$ 1.4527.

Anal. Calcd. for $C_8H_{15}NO_3$: C, 55.50; H, 8.73; N, 8.07. Found: C, 55.03; H, 8.85; N, 8.40.

N,N-Diethyl β-carbethoxypropionamide was prepared by hydrogenation of the olefin as described above, bp 95°-96° at 0.6 mm, $n^{25}D$ 1.4502 [lit. (28) bp 102°-104° (0.8 mm)].

Preparative electrolysis.—The apparatus used for the preparative electrolysis has been described previously (29). A mercury cathode, area 55 cm^2, was used throughout.

General electrolysis method.—The anolyte consisted of a saturated aqueous solution of tetraethylammonium p-toluene-sulfonate. The catholyte consisted of 0.1-0.2m of the depolarizer, 20g of tetraethylammonium p-toluenesulfonate, and 3-20g of water depending on the reactivity of the depolarizer. This mixture was diluted to 150 ml total volume with a cosolvent, either dimethylformamide or acrylonitrile. The electrolysis was conducted to about 80% conversion, assuming 1 electron per mole of depolarizer. The pH of the catholyte was maintained around 8 by the addition of acetic acid. When the electrolysis was completed, the catholyte was diluted, poured into methylene chloride, washed with water, and the organic phase was dried over anhydrous sodium sulfate. The solvent was removed by distillation and the product distribution (olefin, saturate and dimer) was estimated by vpc on appropriate columns.

Electrolysis of ethyl β-cyanoacrylate.—The catholyte contained 16g of water, 24.0g depolarizer with DMF as solvent. A 6-ft XE-60 on Chromosorb W column was used for product identification. It was programed from 120° to 240°. The yields were 16% ethyl β-cyanopropionate and 84% hydrodimers. Two hydrodimeric products were apparent by vpc: peak A 95%, peak B 5%. The hydrodimer was distilled at reduced pressure, 21.0g, bp 159°-160° at 0.4 mm, $n^{25}D$ 1.4535.

Anal. Calcd. for $C_{12}H_{16}N_2O_4$: C, 57.13; H, 6.39; N, 11.11; mol wt 252. Found: C, 56.82; H, 6.70; N, 11.36; mol wt 250.

The nmr spectrum of this mixture had a triplet at τ 8.67, a slightly split doublet at τ 7.12, multiplet at τ 6.51, and a quartet at τ 5.73, a very small triplet at τ 8.65, and a very small quartet at τ 5.68 in a ratio of 3:2:1:2.

The copper I chloride complex (30).—Sulphur dioxide was bubbled for 5 min through a solution of 2.52g (0.01m) of the hydrodimers and 1.34g (0.01m) of copper II chloride in 20 ml of 95% ethanol. The reaction mixture was placed in a refrigerator for 2 days, during which time the product separated from solution. The product was isolated by filtration under nitrogen, washing on the filter with ethanol and drying under vacuum. The product, 1.15g, had an indefinite mp. The original dimer could be regenerated with hydrochloric acid.

Anal. Calcd. for $C_{12}H_{16}CuClN_2O_4$: C, 41.03; H, 4.59; Cu, 18.09. Found: C, 40.49, 40.55; H, 4.43, 4.17; Cu, 17.97, 17.96.

The nmr spectrum of the complex in d_6 acetone as solvent had a single triplet at τ 8.63, a slightly split doublet at τ 6.94, a multiplet at τ 6.27 and a quartet at τ 5.68.

The saponification of the hydrodimer with 10% sodium hydroxide gave quantitatively a dicarboxylic acid, mp 173°-174°.

3,4-Dicyanoadipic acid.—cis-4-Cyclohexene-1,2-diamide was prepared as described by Ficken and Linstead (31). This diamide was dehydrated to form cis-1,2-dicyano-4-cyclohexene by the action of p-toluenesulfonyl chloride by the method of Stephens, Biance, and Pelgrim (32). The 1,2-dicyano-4-cyclohexene was oxidized to 3,4-dicyanoadipic acid (mp 174°-175°) by $KMnO_4$ in acetone solution. The nmr spectrum of this

material was identical to that of the acid isolated from the saponification of the electrolysis product of ethyl β-cyanoacrylate. Diethyl 3,4-dicyanoadipate was prepared from the acid, and it was found to have the same vpc retention time as the electrolysis product.

Electrolysis of ethyl β-benzoylacrylate.—The catholyte contained 10 ml of water and acrylonitrile as solvent. Only 5g of the ethyl β-benzoylacrylate was added to the catholyte at the start of the run. The remainder was added dropwise as necessary to maintain the working electrode potential below —1.0v *vs.* sce (total 20.4g, 0.1m). After electrolysis and extraction, the low-boiling materials, ethyl β-benzoylacrylate and ethyl β-benzoylpropionate, were removed by distillation at reduced pressure. The 13.0g of residual dimeric products was chromatographed on aluminum oxide (Taylor Company 80-200 mesh). Two main fractions were isolated; the first product was a yellowish oil which was washed with hexane and recrystallized from ethanol, 2.9g, mp 105°-115°.

Anal. Calcd. for $C_{24}H_{26}O_6$: C, 70.23; H, 6.39; mol wt 410. Found: C, 70.32; H, 6.23; mol wt 416.

The second major fraction diluted was a white solid which was recrystallized from ethanol, 1.2g, mp 119°-120°.

Anal. Calcd. for $C_{24}H_{26}O_6$: C, 70.23; H, 6.39; mol wt 410. Found: C, 69.90; H, 6.07; mol wt 408.

The nmr spectrum of the first sample, mp 105°-115°, with carbon tetrachloride as solvent had 2 triplets at τ 8.82 and 8.76 in a ratio of 1:10, a poorly defined multiplet at τ ~ 7.2 (very small), a slightly split singlet at τ 6.32, a quartet at τ 5.78, a multiplet at τ 2.4, and a multiplet at τ 1.95 in a ratio of 3:6:2:3:2 for the major signals. The second isolated solid, mp 119°-120°, had a much cleaner nmr spectrum with only the major peaks listed above in a ratio of 3:6:2:3:2. The mother liquors from all of the recrystallizations were combined and analyzed by nmr. The presence of an unsymmetrical isomer was indicated by a triplet at τ 8.91, a doublet at τ 7.36, a multiplet at τ 6.6, and considerable broadening of the phenyl hydrogens.

Electrolysis of β-benzoylacrylonitrile.—The catholyte contained 20 ml of water and acrylonitrile as solvent. The olefin was dissolved in acrylonitrile, 23.5g diluted to 100 ml, and 10 ml of this solution was added to the catholyte at the start of the run. The remainder was added dropwise as necessary to maintain the working electrode potential below —1.0v *vs.* SCE. The organic extract was concentrated by distillation and cooled. A white solid separated, was filtered and washed with methylene chloride. Recrystallization from acetonitrile gave 6.1g of a white solid, mp 197°-198°.

Anal. Calcd. for $C_{20}H_{16}N_2O_2$: C, 75.93; H, 5.09; N, 8.86; mol wt 316. Found: C, 75.62; H, 4.86; N, 8.99; mol wt 314.

The nmr spectrum of this material in d_6-dimethylsulfoxide showed a singlet at τ 6.66, a multiplet at τ 2.13, and a multiplet at τ 1.80 in a ratio of 3:3:2. The mother liquor from above was concentrated, triturated with hot ethanol to remove the β-benzoylpropionitrile, 13.1g, (compared to an authentic sample by nmr and vpc) and the residue was recrystallized from acetonitrile, 4.8g, mp 183°-193°. The nmr spectrum of this material was identical to that of the isomer, mp 197°-198°. These two isomers are meso and dl 1,4-dibenzoyl-2,3-dicyanobutane.

Electrolysis of dibenzoylethylene.—The catholyte contained 3 ml of water, 23.6g dibenzoylethylene (0.1m) and dimethylformamide as solvent. The electrolysis products were chromatographed on alumina with methylene chloride as eluant. Four compounds were isolated, dibenzoylethane (10.2g), mp 144°-145°, from ethanol [lit. (33) mp 144°-145°]; dl 1,2,3,4-tetrabenzoylbutane (6.1g), mp 164°-165°, from ethanol [lit. (33) mp 167°-168°]; meso 1,2,3,4-dibenzoylbutane (1.8g), mp 198°-201°, [lit. (33) mp 202°-203°], and the hydrotrimer, 1,2,3,4,5,6-hexabenzoylhexane (2.4g), mp 285°-286°, probably dl and meso mixtures.

Anal. Calcd. for $C_{48}H_{38}O_6$: C, 81.10; H, 5.38; mol wt 710. Found: C, 81.56; H, 5.42; mol wt 690.

Electrolysis of N,N-dimethyl β-carbethoxyacrylamide.—The catholyte contained 3 ml of water, dimethylformamide, and 44g of depolarizer. The crude electrolysis product was analyzed by vpc. Five hydrodimeric products were observed on 2% silver nitrate, 18% Carbowax 4000, on Chromosorb W 6-ft column at 225°. One of the isomeric products was quantitatively precipitated by treating the oily mixture with acetone, 6.5g, mp 146°-148°.

Anal. Calcd. for $C_{16}H_{28}N_2O_6$: C, 55.79; H, 8.19; N, 8.14; mol wt 344. Found: C, 55.89; H, 8.32; N, 8.21; mol wt 330.

Distillation of the thick, oily residue gave 2.8g, bp 85°-87°, (0.1 mm) of N,N-dimethyl β-carbethoxypropionamide and 26.3g, bp 177°-191°, (0.15-0.3 mm) of a mixture of hydrodimeric products.

Anal. Calcd. for $C_{16}H_{28}N_2O_6$: C, 55.79; H, 8.19; N, 8.14. Found: C, 55.71; H, 8.31; N, 8.52.

A second electrolysis of N,N-dimethyl β-carbethoxyacrylamide was run using 10g of water and dimethylformamide as solvent. The electrolysis products were analyzed as above.

Electrolysis of N,N-diethyl β-carbethoxyacrylamide.—The catholyte contained 20g of water and dimethylformamide as the solvent. The electrolysis products were distilled at reduced pressure. The product distribution based on distilled material was 34% N,N-diethyl β-carbethoxypropionamide, bp 96°-104°, (0.3-0.5 mm) and 66% of a mixture of hydrodimers, bp 162°-171°, (0.3-0.4 mm). The hydrodimer fraction was found to contain about 3% of N,N,N′,N′-tetraethyl-3,4-dicarbethoxyadipamide by vpc comparison with an authentic sample prepared as described below.

N,N,N′,N′-tetraethyl-3,4-dicarbethoxyadipamide.—To a solution of 1,2,3,4-butanetetracarboxylic acid anhydride (158g, 0.8m) in 200 ml of acetone was added dropwise diethylamine (116g, 1.6m) at 25°-35°. The mixture was stirred at room temperature for 2.5 hr, and the solvent was removed. To the residue was added 200 ml of acetic anhydride and the mixture was refluxed for 4 hr. The acetic acid and the excess acetic anhydride were removed by distillation. The residue was taken up in acetone, cooled and 19.6g of 1,2,3,4-butanetetracarboxylic dianhydride was recovered. The filtrate was concentrated and cooled. The desired product crystallized out. Recrystallization from acetone gave 29.6g of 3,4-bis(N,N-diethylcarbamoylmethyl) succinic anhydride, mp 115°-116°. Infrared bands at 1850-1780 cm^{-1} are consistent with a 5-membered anhydride.

Anal. Calcd. for $C_{16}H_{26}N_2O_5$: C, 58.87; H, 8.03. Found: C, 58.34, 58.11; H, 7.84, 7.92.

A solution of 17.7g (0.05m) of this anhydride in 150 ml of ethanol and 0.5 ml of concentrated sulfuric acid was refluxed for 4 hr. The reaction mixture was cooled, poured into water, extracted with benzene, and the organic layer washed with water. The benzene was removed by distillation and the product isolated by preparative vpc. A 12% silicone grease on Chromosorb W column, 8 ft x ¾ in., at 275° was used for the isolation, $n^{25}D$ 1.4728.

Anal. Calcd. for $C_{20}H_{36}N_2O_6$: C, 59.97; H, 9.06; N, 7.00. Found: C, 59.19; H, 9.01; N, 6.78.

Electrolysis of cinnamonitrile.—The catholyte contained 0.25m of depolarizer, 5g of water, 37g depolarizer, and DMF as solvent. The electrolysis products were analyzed by vpc (6-ft 5% XE-60 cm Chromosorb W column programed from 125°-250°) and found to contain 20% hydrocinnamonitrile and 80% hydrodimeric products (7 and 28.2g, respectively). Of the hydrodimeric products, 4 components (A, B, C, and D) were apparent in a ratio of 9:22:57:12%. The crude electrolysis product was treated with methylene chloride whereupon a white solid crystallized. The solid contained only components B and C (vpc). The solid was chromatographed on alumina and the components were separated, B, mp 165°-167° from acetone and C, mp 214°-215° from acetone. The nmr spectrum of C in a 1:1 mixture of methylene chloride and d_6-benzene has a multiplet at τ 8.13, a multiplet at τ 7.08, and a broad singlet at τ 2.80. Therefore C is 3,4-diphenyladiponitrile, lit. (18) mp 215°. The nmr spectrum of B in 1:1 methylene chloride and d_6-benzene has two doublets at τ 7.91 and 7.88, a broad multiplet at τ 6.86, a multiplet at τ 3.33, and a multiplet at τ 2.93. This spectrum is consistent with the expected spectrum of 2-benzyl-3-phenylglutaronitrile. The isomer A was not obtained pure but as a mixture with B. The nmr spectrum of A, eliminating the resonance due to B, showed a doublet at τ 7.75, a multiplet at τ 7.13, and

a broad singlet at τ 2.98. This isomer we believe to be 2,3-dibenzylsuccinonitrile.

Electrolysis of N,N-dimethyl cinnamide.—The catholyte contained 5g of water, 35g of depolarizer and dimethylformamide as solvent. Vpc analysis of the crude electrolysis mixture, 36.2g, 6-ft, XE-60 on Chromosorb W at 200°, showed 18% N,N-dimethyl hydrocinnamide and 82% of a single hydrodimer. Crystallization of the crude electrolysis product from benzene-hexane gave a single hydrodimer, mp 134°-136°. The nmr spectrum of this material in 1:1 d_6-benzene and d_6-acetone as solvent showed a multiplet at τ 7.35, a broad triplet at τ 6.25 and a singlet at τ 3.02. This spectrum is consistent with that expected for N,N,N',N'-tetramethyl-2,3-dibenzylsuccinamide.

Anal. Calcd. for $C_{22}H_{22}N_2O_2$: C, 79.96; H, 6.71; N, 8.48. Found: C, 74.54; H, 8.23; N, 7.92.

Electrolysis of ethyl cinnamate.—The catholyte contained 10g of water, 49.2g of depolarizer and DMF as solvent. Vpc analysis (XE-60 on Chromosorb W column programed from 150° to 225°) of the crude electrolysis mixture, 48.7g showed 41% ethyl hydrocinnamate and 59% of a hydrodimeric mixture (two isomers by vpc analysis). The ethyl hydrocinnamate and ethyl cinnamate were removed by distillation at reduced pressure, bp 65°-75° (0.1 mm). The residue was treated with ethanol and cooled. A white solid crystallized. Recrystallization from ethanol gave product A, a single compound by vpc, mp 105°-107°. The nmr spectrum of the material, in carbon tetrachloride as solvent, had a triplet at τ 9.10, a triplet at τ 8.83, a multiplet at τ 7.20, a triplet at τ 6.46, a pair of quartets at τ 5.88, and a singlet at τ 2.88, slightly split at the base. The IR spectrum of this material has 2 carbonyl frequencies at 1730 and 1700 cm^{-1}. These data are consistent with 2-carbethoxy-3,4-diphenyl cyclopentanone.

Anal. Calcd. for $C_{20}H_{20}O_3$: C, 77.90; H, 6.54. Found: C, 78.00; H, 6.74.

A second product was isolated from the residue by concentration of the ethanol solutions, mp 117°-119° from ethanol [lit. (5) mp for diethyl 3,4-diphenyl adipate 116°]. The nmr spectrum of this material in carbon tetrachloride as solvent showed a triplet at τ 8.75, a broad doublet at τ 7.30, a broad triplet at τ 6.47, a quartet at τ 6.04, and a singlet at τ 2.93. The nmr spectrum of the liquid dimer indicates the presence of a third compound, namely, diethyl 2-benzyl-3-phenylglutarate.

Electrolysis of ethyl 4,4,4-trifluorocrotonate.—The catholyte contained 36g of depolarizer, 5g of water, and DMF as solvent. The electrolysis products were distilled. The products were ethyl 4,4,4,-trifluorobutyrate, 23g, bp 110°-115° (atmospheric pressure) and a dimer fraction, 3g, bp 58°-61° (0.2 mm). The nmr analysis showed ~85% of the dimer mixture was diethyl 3,4-di(trifluoromethyl)adipate; the remaining 15% was probably the unsymmetrical isomer. The mixture was analyzed.

Anal. Calcd. for $C_{12}H_{16}F_6O_4$: C, 42.60; H, 4.73. Found: C, 42.59; H, 4.78.

Electrolysis of ethyl β-trifluoroethylcrotonate.—The catholyte contained 46g of depolarizer, 10g of water, and acetonitrile as solvent. The electrolysis products were distilled, bp 128°-130° (atmospheric pressure). This main cut, 41.6g, contained the depolarizer, 17%, ethyl 3-trifluoromethylbutyrate, 21%, and a third component, 62%. This last component was purified by preparative vpc, 5% silicone rubber on Chromosorb W, 8 ft column, and was identified as ethyl 3-difluoromethylenebutyrate by its i_r spectrum, bands at 1340 and 1760 cm^{-1} for $CF_2 = C$, and nmr spectrum.

Anal. Calcd. for $C_7H_{10}F_2O_2$: C, 51.22; H, 6.14; F, 22.62. Found: C, 50.11, 50.24; H, 6.33, 6.67; F, 23.49, 23.76.

Mixed coupling of N,N-dimethyl-β-carbethoxy acrylamide and acrylonitrile.—The catholyte had 10 ml of water and acrylonitrile as the solvent. Only 5g of the olefin was added to the catholyte at the start of the run. The additional 25g was added as needed to maintain the working electrode potential below −1.4v. The thick electrolysis products were distilled at reduced pressure. Three main cuts were separated: The first, 8.0g, bp 27° (0.6 mm), was shown to be N,N-dimethyl-β-carbethoxypropionamide by vpc comparison with an authentic sample; the second cut, 20.5g, bp 90.92° (0.5 mm), contained 2 isomers in 2:1 ratio by vpc. The infrared and nmr spectra were consistent with a 1:1, N,N-dimethyl-β-carbethoxyacrylamide, acrylonitrile addition product. The minor component was shown to be N,N-dimethyl-3-carbethoxy-5-cyanopentanamide by comparison of vpc retention times on several columns with an authentic sample prepared as described below; the third cut, 2.4g, bp 185°-191° (0.3 mm), was a mixture of hydrodimeric products as discussed above.

N,N-dimethyl-3-carbethoxy-5-cyanopentanamide.—To a solution of chloroacetyl chloride (125g, 1.11m) in 500 ml of dry benzene was added dimethylamine (*ca.* 100g). The solution was stirred for 1 hr, filtered, and the solvent was removed by distillation at reduced pressure. Distillation at reduced pressure gave 115g of N,N-dimethylchloroacetamide, bp 57°-59° (0.3 mm). To a slurry of NaH (40g, 55% dispersion in mineral oil, 0.94m) in 375 ml of dimethylformamide was added diethyl malonate (150g, 0.94m) at a sufficient rate to maintain a reaction temperature between 40° and 50°. After the addition was complete, the yellow solution was stirred until hydrogen evolution ceased. To this solution was added N,N-dimethylchloroacetamide (115g, 0.94m) at a sufficient rate to maintain a reaction temperature of 75°. The slurry was stirred overnight, poured into water, and extracted two times with methylene chloride. The organic layers were combined, dried over sodium sulfate, and the solvent was removed by distillation. Distillation at reduced pressure gave 171g of N,N-dimethyl-diethylmalonylacetamide, bp 140°-143° (0.9 mm).

Anal. Calcd. for $C_{11}H_{19}NO_5$: C, 53.86; H, 7.81; N, 5.71. Found: C, 53.25; H, 7.72; N, 5.75.

Vpc analysis on a 6-ft Ucon. W98 column at 200° showed only one peak.

To a solution of 0.4g of sodium metal in 70 ml of ethanol was added N,N-dimethyl-diethylmalonylacetamide (171g, 0.74m). To this solution was added acrylonitrile (44.5g, 0.8m) dropwise keeping the reaction temperature below 40° by means of an ice bath. The solution was then heated to 50° for 3.5 hr. Sufficient acetic acid was added to neutralize the solution. The solution was poured into water and extracted two times with ether. The ether extracts were combined, dried over anhydrous sodium sulfate, and the solvent was removed by distillation. Recrystallization of the residue from ether gave 114g of N,N-dimethyl-3,3-dicarbethoxy-5-cyanopentanamide, mp 70°-72°.

Anal. Calcd. for $C_{14}H_{22}N_2O_5$: C, 56.35; H, 7.43; N, 9.39. Found: C, 56.36; H, 7.68; N. 9.38.

N,N-dimethyl-3,3-dicarbethoxy-5-cyanopentanamide, (114g, 0.38m) was saponified in the cold with one equivalent of potassium hydroxide in 50% aqueous ethanol as solvent. The neutral solution was acidified with hydrochloric acid, and the solvent was removed by distillation at reduced pressure. The crude acid was dissolved in 750 ml of pyridine. Copper powder (40g) was added, and the slurry was refluxed for 4 hr. The solvent was removed by distillation at reduced pressure. The residue was dissolved in methylene chloride, washed with dilute hydrochloric acid, water, dried over sodium sulfate, and the solvent was removed by distillation. Several recrystallizations of the residue from hexane-ethanol gave 24g of N,N-dimethyl-3-carbethoxy-5-cyanopentanamide, mp 43°-45°.

Anal. Calcd. for $C_{11}H_{18}N_2O_3$: C, 58.39; H, 8.02; N, 12.38. Found: C, 58.36; H, 8.10; N, 12.11.

Ethyl 3,5-dicyanopentanoate was prepared as described above from ethyl bromoacetate and ethyl cyanoacetate, bp 160° (0.9 mm). This material was shown to contain about 6% of an impurity.

Anal. Calcd. for $C_9H_{12}N_2O_2$: C, 59.98; H, 6.71; N, 15.55. Found: C, 59.35; H, 6.85; N, 14.44.

Michael reaction.—The olefin (0.1m) was dissolved in 50 ml of t-butanol with 0.2m of diethyl malonate. Potassium t-butoxide (10 ml of 0.1M solution) was added, and the mixture was stirred about 72 hr. The mixture was then acidified with acetic acid, dissolved in methylene chloride, washed with water, dried over sodium sulfate, and the solvent was removed by distillation. The residue was either distilled or recrystallized to obtain the addition product.

From ethyl p-benzoylacrylate.—The product was distilled, bp 188°-192° (0.35 mm), $n^{25}D$ 1.4943. The nmr spectrum of this material had a pair of doublets at τ 2.10, a multiplet at τ 2.58, a pair of quartets at τ 5.90 and 5.94, a multiplet at τ 6.2 and 6.6, and a pair of triplets at τ 8.78 and 8.83. Vpc analysis on several columns showed only one component.

Anal. Calcd. for $C_{19}H_{24}O_5$: C, 62.65; H, 6.64. Found: C, 62.84; H, 6.60.

From benzalacetophenone.—The product was recrystallized from ethanol, mp 71°-72°. It had a single component (by vpc analysis on several columns).

Anal. Calcd. for $C_{22}H_{24}O_5$: C, 71.72; H, 6.57. Found: C, 71.49; H, 6.71.

From ethyl β-cyanoacrylate.—The product was distilled, bp 138°-140° (0.5m).

Anal. Calcd. for $C_{13}H_{19}NO_6$: C, 54.95; H, 6.37; N, 4.99. Found: C, 54.90; H, 6.37; N, 4.99.

Vpc analysis showed 2 components in a 78:22 ratio. The isomers were separated by preparative vpc. The isomers were saponified with one equivalent of sodium hydroxide and decarboxylated. The two possible products were prepared independently. Diethyl 3-cyanoglutarate was prepared by heating the reaction product of sodium salt of t-butyl cyanoacetate and ethyl chloroacetate with *p*-toluenesulfonic acid, bp 106°-110° (0.2m).

Anal. Calcd. for $C_{10}H_{15}NO_4$: C, 56.32; H, 7.09; N, 6.57. Found: C, 56.34; H, 7.10; N, 6.44.

Diethyl cyanomethylsuccinate was prepared by saponification and decarboxylation of the addition product of ethyl cyanoacetate and diethyl fumarate, bp 115°-117° (0.4m).

Anal. Calcd. for $C_{10}H_{15}NO_4$: C, 56.32; H, 7.09; N, 6.57. Found: C, 56.26; H, 7.30; N, 6.29.

From ethyl β(4-pyridyl)acrylate.—The product was distilled, bp 138°-140° (0.3m).

Anal. Calcd. for $C_{17}H_{23}NO_6$: C, 60.75; H, 6.58; N, 4.14. Found: C, 61.08; H, 7.26; N, 4.68.

Vpc analysis showed 2 components. The isomer distribution was obtained from the nmr spectra.

From N,N-dimethyl-β-carbethoxyacrylamide.—The product was distilled, bp 158° (0.05 mm).

Anal. Calcd. for $C_{15}H_{25}NO_7$: C, 54.50; H, 7.61; N, 4.23. Found: C, 54.37; H, 7.69; N, 4.21.

Vpc analysis showed only one component on four different columns. The material was saponified and decarboxylated. The product of this reaction showed a single ester group in the nmr.

Results

The data obtained from bulk electrolysis at the first polarographic wave of various representative diactivated olefins **1** are summarized in Table I.

The electrolysis of dibenzoylethylene **I** yields four products, dibenzoylethane, meso-1,2,3,4-tetrabenzoylbutane, dl-1,2,3,4-tetrabenzoylbutane and a small amount of 1,2,3,4,5,6-hexabenzoylhexane. In view of the relative stability of the anion radical, $t_{1/2}$ = 15.3 sec at 2 x $10^{-3}M$ toward reaction with the parent olefin (1), it is not surprising that a relatively large amount of the ethane derivative was obtained. Only 3 ml of water could be used in the catholyte in order to get even a 40% yield of the hydrodimer. The hydrodimer in this case is probably formed by a combination of paths A and B.

In contrast, path A is the predominant route to products from β-benzoylacrylonitrile (II). In the electrolysis of II, 20 ml of water was used, and the pH was maintained as near 7 as possible by the frequent addition of acetic acid. Under these conditions 55% of the hydrodimer was isolated. (Using less water resulted in the exclusive formation of trimers and higher oligomers of the olefin.) Two crystalline isomers were isolated from the electrolysis. The nmr spectra of these isomers were identical. The positions of the resonance of the phenyl hydrogens as well as the shape of the signal are identical for the hydrodimers and for β-benzoylpropionitrile. The most likely structure for these products are meso and dl-1,4-dibenzoyl-2,3-dicyanobutane (XI).

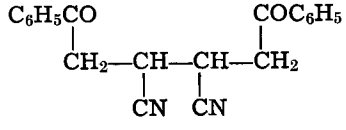

(XI)

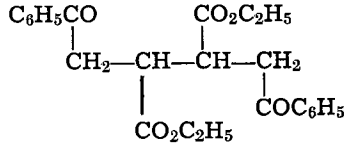

(XII)

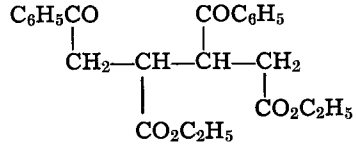

(XIII)

No cross-coupled products were obtained even when acrylonitrile was used as the solvent.

Another example which probably involves paths A and B but not C is the electrolysis of ethyl β-benzoylacrylate (III) in acrylonitrile. Two solid products and a liquid mixture were obtained. The nmr spectra of the solids were nearly identical. The position of the resonance of the phenyl hydrogens are identical for the hydrodimers and for ethyl β-benzoylpropionate.

Table I. Electrolytic reductive coupling of diactivated olefins

$$2XCH{=}CH{-}Y \xrightarrow[2H_2O]{2e^-} [(XCH{-}CHY)H]_2$$

$$XCH{=}CHY \xrightarrow[2H_2O]{2e^-} XCH_2CH_2Y$$

Compd.	X	Y	% Yield[a,g]	Product dist.[b] Dihydro[c]	Hydrodimer[c]	CHYCH$_2$X[c] / CHYCH$_2$X	CHYCH$_2$X[c] / CHXCH$_2$Y	CHXCH$_2$Y[c] / CHXCH$_2$Y
I	C_6H_5CO	C_6H_5CO	76	56[f]	44	—	—	—
II	C_6H_5CO	CN	87	45[f]	55	100	—	—
III	C_6H_5CO	$CO_2C_2H_5$	67	4	96	77	23[f]	—
IV	CN	$CO_2C_2H_5$	89	16	84	—	5[d]	95
V	CN	C_6H_5	92	20	80	22	57	9
VI	$CO_2C_2H_5$	$CO_2C_2H_5$	85	17	83	—	—	—
VII	$CO_2C_2H_5$	C_6H_5	90	41[f]	59	68	32	—
VIII	$CO_2C_2H_5$	$CON(CH_3)_2$	84	4	96	66	31	2
			81	7	93	56	40	4
IX	$CO_2C_2H_5$	CF_3	71	90	10	85	15	—
X	C_6H_5	$CON(CH_3)_2$	94	18	82	100	—	—

[a] % Yield based on current; [b] based on vpc analysis without standards; [c] based on vpc analysis and nmr analysis to identify products; [d] not isolated; [e] dihydro + hydrodimer is 100%; [f] acetic acid was added to control pH and to prevent polymerization; [g] dihydro + hydrodimer.

The nmr spectrum of the liquid mixture indicated the presence of *ca.* 80% of the solid isomers and *ca.* 20% of a third compound which has a carbethoxy group in a different environment. The nmr spectrum of the solid isomer is consistent with the expected spectrum from 1,4-dibenzoyl-2,3-dicarbethoxybutane (XII), while the shifted methylene and methyl resonances in the nmr spectrum of the liquid indicate an unsymmetrical structure, *i.e.*, 1,3-dibenzoyl-2,4-dicarbethoxybutane (XIII) possibly arising through path B. No cross-coupled product was obtained.

Ethyl β-cyanoacrylate on electrolysis gives through path A at least 95% diethyl 3,4-dicyanoadipate (XIV) with a small amount of the unsymmetrical isomer. The nmr spectrum of (XIV) is consistent

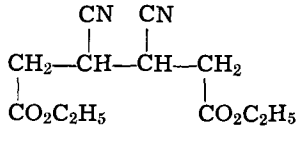

(XIV)

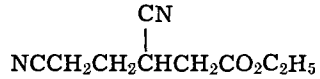

(XV)

with this structure. The nmr spectrum of the copper (I) complex of (XIV) shows the most highly shifted protons are the methylene protons. This type of complex is formed with nitrile groups and is very sensitive to the ring size being formed (2). Saponification of (XIV) gave 3,4-dicyanoadipic acid which was identified by comparison with an authentic sample synthesized from 3,4-dicyanocyclohexene.

Four isomers were indicated by the vpc analysis of the electrolysis products of cinnamonitrile (V) (3). One of the isomers (22%) was the previously reported 3,4-diphenyladiponitrile (XVI). The nmr spectrum of the second isomer showed two different phenyl

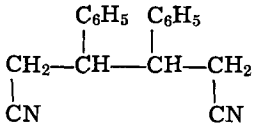

(XVI)

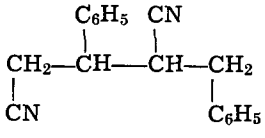

(XVII)

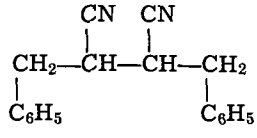

(XVIII)

groups and 2 doublets for the methylene hydrogens. This spectrum is consistent with that expected for 2-benzyl-3-phenylglutaronitrile (XVII). The third isomer had a single phenyl group and a single methylene group both significantly different from the phenyl group of (XVI). It is, therefore, probably 2,3-dibenzylsuccinonitrile (XVIII). The nmr spectra of the fourth isomer showed two different phenyl groups, and therefore the compound is probably an isomer of (XVII). Paths A and B are probably used here. Path C was not tested. Similarly, paths A and B are indicated in the electrolysis of ethyl cinnamate which yielded two solid products and a liquid mixture. One of the solids is the previously reported meso-diethyl 3,4-diphenyladipate (5). The second isomer is a cyclized ketone. The nmr spectrum of this compound has a broad singlet at τ 2.91. Of the two possible ketone products, only 2-carbethoxy-3,4-diphenylcyclopentanone would be expected to have nearly equivalent phenyl groups. The nmr spectrum of the liquid mixture shows two different carbethoxy groups and a broad multiplet for the phenyl group. The mixture probably consists of some dl-diethyl 3,4-diphenyladipate (*ca.* 20%) and diethyl 2-benzyl-3-phenylglutarate.

The electrolysis of N,N-dimethylcinnamide (6) gave only N,N,N',N'-tetramethyl 2,3-dibenzylsuccinamide, probably through path A. The nmr of this material showed a single phenyl group identical to the phenyl group of N,N-dimethylhydrocinnamamide, and the amide-methyl groups were significantly shifted.

A very poor yield of dimeric products was isolated from the electrolysis of ethyl β-trifluoromethylacrylate. The dimeric product appears to be a mixture of *ca.* 85% of diethyl 3,4-trifluoromethyladipate and 15% of diethyl 2-trifluoromethyl-3-(2,2,2-trifluoroethyl) glutarate. Similarly, the electrolysis of ethyl β-trifluoromethylcrotonate gives no dimeric products, but does give the fluoride elimination product, ethyl 3-difluoromethylenebutyrate, in 70% yield. The steric effects on the dimerization reaction are apparent in this case. A methyl group in the position β to the carbethoxy group, the position through which the dimer of olefin (IX) forms, blocks the dimerization reaction and, therefore, affords the intermediate the opportunity to eliminate a fluoride ion.

All three paths are operative in the electrolysis of N,N-dimethyl β-carbethoxyacrylamide. Product analysis by vpc showed 5 hydrodimeric isomers. One solid isomer was isolated, and the nmr spectrum was consistent with diethyl 3,4-(N,N,N',N'-tetramethylcarbamoyl) adipate (XIX). The structures of other isomers were assigned by a comparison of the nmr spectrum of the mixture with the spectra of (XIX) and N,N,N',N'-tetraethyl-3,4-dicarbethoxyadipamide synthesized independently. In this case, the product distribution was sensitive to the amount of proton donor added to the catholyte (1). The second run contained 10 ml of water, while the first run contained only 3 ml of water in the catholyte. No acetic acid was added during the electrolysis. The pH was controlled as uniformly as possible for each run simply by allowing the ester to saponify.

Of the possible paths available for the reaction of the anion radical 2 only path E [Eq. (4)] is sensitive to the water concentration. The protonation of 2 yields a radical α to either X or Y depending on their individual ability to stabilize the radical. This radical is rapidly reduced, yielding the most stable anion. The attack of this anion on the parent olefin yields an unsymmetrical product since the attack would result in the most stable anion (Eq. [6]). Path B can lead to a different isomer than path A and in fact, from olefin VIII.

$$\overset{(-)}{\mathrm{YCH_2\dot{C}HX}} + \mathrm{YCH=CHX} \rightarrow \mathrm{YCH_2CHXC\dot{H}YCHX} \overset{(-)}{} \qquad [6]$$

does as evidenced by the change in isomer distribution with water concentration.

Only diethyl fumarate (—1.54v) and N,N-dimethyl-β-carbethoxyacrylamide (VIII) gave cross-coupled products with acrylonitrile in sufficient yield to be isolated. A trace of cross-coupled product between ethyl β-cyanoacrylate (—1.45v) and acrylonitrile was indicated by vpc analysis after many unsuccessful experiments. The only successful technique for obtaining the cross-coupled products was to add the depolarizer dropwise to the electrolysis solution using acrylonitrile as the solvent. Even using this technique, no cross-coupled products were obtained from olefins II (—1.11v) and III (—1.23v). The cross-coupled products from olefins (VIII) were ethyl 3-(N,N-dimethylcarbamoyl)-5-cyanopentanoate (XX) and N,N-dimethyl-3-carbethoxy-5-cyanopentanamide (XXI) in a 2:1 ratio. The cross-coupled product from olefin IV was ethyl 3,5-dicyanopentanoate (XV). These products were identified by comparison of vpc retention

times and nmr spectra with authentic samples prepared independently.

$$NCCH_2CH_2CHCH_2CO_2C_2H_5$$
$$|$$
$$CON(CH_3)_2$$

(XX)

$$NCCH_2CH_2CHCH_2CON(CH_3)_2$$
$$|$$
$$CO_2C_2H_5$$

(XXI)

Discussion

Reaction sequences and alternate routes to products.—From consideration of the energetics and the nature of the products obtained we conclude that the attack of **2** on the substrate is nucleophilic rather than free radical. This type of reaction leaves the radical site on the electrode surface where it is available for further rapid reduction without reorientation of the molecule. Chart II outlines the detailed subsequent reaction paths. By paths A and C coupled products are formed at the electrode: A leads exclusively to hydrodimers; C leads exclusively to cross-coupled products. Path B, which involves coupling probably away from the electrode surface, can lead to hydrodimers, dihydroproduct, and cross-coupled products. The distribution of total products depends then critically on the extent of participation of reagents by path A, B (7), or C. This, in turn, depends on (*a*) the inherent reactivities of the species involved, (*b*) their availability at the electrode surface, (c) their steric requirements, and most of all (*d*) their polarizability in the electric field.

The influence of each of these factors is best illustrated by an analysis of the situation that obtains, when **1** is undergoing reduction, in the presence of an acceptor like acrylonitrile:

1. The reactivity of **2** toward **1** (path A) is roughly proportional (1) to the reduction potential of **1**. (Deviations from this relationship appear to be due to steric factors.) In all types of current macrocells employed unreduced **1** is always available for reaction with **2** at the electrode. When **2** is formed at a much more positive potential (*e.g.*, —1.23v, compound III) than is required for acrylonitrile (—1.9v), the sequence through path A overwhelms any possibility of obtaining mixed coupled products.

2. The reactivity of **2** toward acrylonitrile (in the unavoidable presence of **1** at the electrode surface) increases as required potential for forming **2** (*e.g.*, —1.76v, compound VIII) becomes more negative probably due to the increased polarization of acrylonitrile at the higher potential. Simultaneously, as indicated above (1), the reactivity of **2** toward **1** decreases, so that mixed coupled products can be formed (path C competing with path A). The limit of separation of the potentials of the donor and acceptor appears to be *ca.* 0.4v. This is a similar potential spread to that observed by Höfelmann *et al.* (8), for the anionic copolymerization of activated olefins.

3. Reaction of **2** with water as the first c reaction leads to products derived from **3** (path B). The extent of participation of water to a much lesser extent than that of acrylonitrile also increases (1) with increasing negative potential requirements of **1**. The distribution of products obtained from **3** is what might be expected from a Michael reaction in which **1**, acrylonitrile, and a proton source compete for a carbanion. In particular the amount of coupled product derived from **3** is sensitive to the bulk water concentration.

Activating group effect; role in isomer distribution.—Since the initial addition products formed by path A are dimeric anion radicals [(Eq. 3)] having a complete separation of the anion and the radical sites, the distribution of the isomeric products obtained should depend on three considerations: (*a*) the relative stabilizing effect of the activating groups for an α-anion in the "acceptor" half of the dimer, (*b*) the relative stabilizing effect of the activating groups for an α-radical in the "donor" half of the dimer, and (*c*) some steric effects similar to those encountered in ordinary Michael reactions. By contrast the major factor that need be considered in rationalizing the distribution of the isomeric Michael adducts obtained from XCH=CHY **1** (9) and a typical donor such as diethyl malonate anion is the relative ability of X and Y to stabilize an adjacent anion (Table II).

By comparing the distribution of isomeric products obtained electrochemically from individual monomers, an order of relative stabilizing effects can be obtained; *e.g.*, from the structure of the dimeric product from olefin (II), it is clear that the benzoyl group is more effective at stabilizing both the anionic and radical sites than is the nitrile group. Similarly, the structure of product from olefin (IV) indicates that the carbethoxy group is more effective than the nitrile group at stabilizing both; the product from olefin (X) indicates that the phenyl group is more effective than the amide for stabilizing both the anionic and radical sites. A comparison of the products from olefins (IV), (V), and (VII) indicates that the relative stabilizing effects for an anionic site are $CO_2C_2H_5 > CN > C_6H_5$, while for the radical site they are $CO_2C_2H_5 \geq C_6H_5 > CN$. The remaining activating groups can be assigned ratings of activating influences in this series on the basis of product distribution from individual olefins. Therefore, the relative stabilizing effects are: for an anionic site, $C_6H_5CO > CO_2C_2H_5 >$ 4-pyridyl $> CN > CF_3 > C_6H_5 > CON(CH_3)_2$ (10), and for the radical site, $C_6H_5CO > CO_2C_2H_5 \geq$ 4-pyridyl $\geq C_6H_5 > CF_3 > CN > CON(CH_3)_2$. These "stabilizing" orders necessarily include steric effects since no attempt was made to eliminate them. It is not clear whether these stabilizing orders reflect kinetic or thermodynamic control of the product distribution. Since the addition of the anion radical **2** to the olefin is very rapid (Eq. [3]), the products which are formed by path A probably exhibit kinetic control. On the other hand, no conclusion on this point can be drawn with regard to the reaction of the monomeric anion with the olefin (Eq. [4]).

With this reservation in mind, some comments concerning the orders of stabilizing ability as derived from this work and its relation to reported work can be made. The predominant ability of the benzoyl group to stabilize both an anion and a radical is as expected (11). The finding that the carboxylic ester dominates over a competing nitrile group is unusual (12). However, recently, Lentz and Weiss (13) have shown that the major adduct obtained from a 1:1 mixture of acrylonitrile and ethyl acrylate catalyzed by trialkylphosphine was ethyl α-cyanoethylacrylate. This reaction has been postulated as going through a series of equilibria (14) one of which in this case would involve a direct competition between an anion α- to the carbethoxy or α- to the nitrile group. The predominance

Table II. Product distribution from the Michael reaction of selected diactivated olefins with the potassium salt of diethyl malonate in t-butanol solution

$$R^- + XCH{=}CHY \rightarrow \xrightarrow{H^+} RCHXCH_2Y + CH_2XCHRY$$

Compound	X	Y	RCHXCH$_2$Y[a]	CH$_2$XCHRY[a]
III	C_6H_5CO	$CO_2C_2H_5$	—	100
XI	C_6H_5CO	C_6H_5	—	100
IV	CN	$CO_2C_2H_5$	78	22
V[b]	C_6H_5	CN	100	—
VII[c]	C_6H_5	$CO_2C_2H_5$	100	—
VIII	$CO_2C_2H_5$	$CON(CH_3)_2$	—	100

[a] Per cent of adduct product; [b] ref. (9); [c] ref. (10).

of this crossed product indicates the greater stabilizing ability of the carbethoxy group over the nitrile group for the anionic site. Both the nitrile (15) and the carbethoxy (16) groups have been shown to be better for stabilizing an anion than the phenyl group. Very limited data are available regarding the relative stabilizing effects of these activating groups on a radical. The data of Knunyants (17) from the amalgam dimerization of cinnamate derivatives in acid media and of Huang and Singh (18) from the generation of hydrocinnamate radicals by t-butyl peroxy radicals indicate that the phenyl group is better than the carbethoxy, nitrile and amide groups for stabilizing a radical. No comparisons in this regard have been reported among the latter three groups.

An attempt to obtain a quantitative reactivity order from our data was unsuccessful. As pointed out previously, the dimeric products can arise by either path A or B (Eq. [3] and [4]) probably yielding different isomeric products. It is difficult to ascertain the relative contribution of each path. Obviously, the concentration of proton source in the catholyte is critical. Hydronium ions must pass through the membrane separating the anolyte and catholyte during the electrolysis to maintain electrical neutrality. Since the porosity of the membrane can not be rigorously controlled, the concentration of proton source in the catholyte varies to a small but significant extent not only during a particular electrolysis but more importantly from one electrolysis to the next. Therefore, only a qualitative order of relative stabilizing effects under these electrochemical conditions can be drawn.

All of these conclusions are based on the use of the tetraalkylammonium cation. The effect of using an alkali metal cation on the product distributions as well as on the reactivity of anion radicals is being investigated.

Acknowledgment

The authors wish to express their appreciation to John L. Chruma for excellent technical assistance and to Dr. Donald A. Tyssee for devising and executing the synthesis of 3,4-dicyanoadipic acid.

Manuscript submitted Oct. 22, 1968; revised manuscript received *ca.* Feb. 1, 1969.

Any discussion of this paper will appear in a Discussion Section to be published in the December 1969 JOURNAL.

REFERENCES

1. J. P. Petrovich, M. M. Baizer, and M. R. Ort, *This Journal*, **116**, 743 (1969).
2. Y. Kmoshita, I. Mutsulara, and Y. Saito, *Bull. Chem. Soc. Japan*, **32**, 741, 1216, 1221 (1959).
3. The electrolysis of cinnamonitrile was reported (33) to yield 2 isomers. The first isomer was correctly identified as 3,4-diphenyladiponitrile; however, the second reported isomer is really a mixture of XXVIII and XXIX.
4. W. Baker and A. Lapworth, *J. Chem. Soc.*, **1924**, 2333.
5. M. P. Oammen and A. I. Vogel, *ibid.*, **1930**, 2148.
6. The structure of the previously-reported products from N,N-diethylcinnamamide was in error; M. M. Baizer and J. D. Anderson, *This Journal*, **111**, 223 (1964).
7. A further complication arises from the fact that the most stable free radical (eq. [4]) does not on reduction necessarily lead immediately to the most stable anion. Therefore, the point of attachment of acceptor to the mono-anion (α- to X or α- to Y) can be subject to either kinetic or thermodynamic factors.
8. V. K. Höfelmann, R. Sattelmeyer, and K. Hamann, *Makromol. Chem.*, **112**, 300 (1968).
9. A. N. Nesmeyanov, M. I. Rybinskaya, and L. V. Rybin, *Russ. Chem. Rev.*, **36**, 453 (1967).
10. F. Arndt, H. Scholz, and E. Frobel, *Ann.*, **521**, 111 (1936).
11. A. N. Nesmeyanov, M. I. Rybinskaya, and L. V. Rybin, *Izv. Akad. Nauk. SSSR*, **11**, 2152 (1961).
12. E. D. Bergmann, D. Ginsburg, and R. Pappo, "Organic Reactions," Vol. 10, p. 205, John Wiley & Sons, Inc., New York (1950).
13. A. Lentz and F. Weiss, French Pat. 1,463,853; *C. A.*, 6873 (1967).
14. M. M. Baizer and J. D. Anderson, *J. Org. Chem.*, **30**, 1357 (1965).
15. C. F. Koelsch, *J. Am. Chem. Soc.*, **65**, 2459 (1943).
16. C. K. Ingold and W. J. Powel, *J. Chem. Soc.*, **1921**, 1976.
17. I. L. Knunyants and N. P. Gamlaryan, *Vspekki Khim.*, **23**, 781 (1954).
18. R. L. Huang and S. Singh, *J. Chem. Soc.*, **1958**, 891.
19. R. E. Lutz, "Organic Synthesis," Coll. Vol. III, p. 248, John Wiley & Sons, Inc., New York (1955).
20. A. N. Nesmeyanov and M. I. Rybinskaya, *Dokl. Akad. Nauk. SSSR*, **120**, 793 (1958).
21. W. Koga, *Nippon Kagaku Zasshi*, **76**, 1053 (1955); *C. A.*, 51, 17823.
22. I. A. Korshunov, Yu V. Vodzinskii, N. S. Vyazankin, and A. I. Kalinin, *Zhur. Obs. Khim.*, **29**, 1364 (1959).
23. E. T. McBee, O. R. Pierce, and D. D. Smith, *J. Am. Chem. Soc.*, **76**, 3722 (1954).
24. C. E. Maxwell, "Organic Synthesis," Coll. Vol. III, p. 305, John Wiley & Sons, Inc., New York, (1955).
25. H. Adkins and C. Seanley, *J. Am. Chem. Soc.*, **73**, 2854 (1951).
26. J. W. Lynn, *J. Org. Chem.*, **21**, 578 (1956).
27. C. Paal and H. Schulze, *Ber.*, **33**, 3795 (1900).
28. A. W. D. Avison, *J. Appl. Chem. (London)*, **1**, 469 (1951).
29. M. M. Baizer, *This Journal*, **111**, 215 (1964).
30. The method used for preparation of the copper complex was a private communication from R. J. Kern.
31. G. E. Ficken and R. P. Linstead, *J. Chem. Soc.*, **1952**, 4846.
32. C. R. Stephens, E. J. Biance, and F. J. Pelgrim, *J. Am. Chem. Soc.*, **77**, 1701 (1955).
33. R. G. Harvey and E. V. Jensen, *Tetrahedron Letters*, 1801 (1963).

The Electrochemical Behavior of Zinc in Alkaline Media

John P. Elder*[1]

Metals & Controls, Inc., a corporate division of Texas Instruments Incorporated, Attleboro, Massachusetts

ABSTRACT

The electrochemical behavior of horizontally disposed planar zinc in 30% (6.9M) potassium hydroxide, alone and saturated with zinc oxide at 25°C, has been investigated in a controlled manner, using both galvanostatic and potentiostatic techniques. The anodic characteristics have been interpreted in terms of a kinetically controlled process preceding a diffusion step. The cathodic behavior of oxidized zinc has been interpreted in terms of a complex two-state process, involving the formation of a bound zinc hydroxide, followed by a reduction of both the adsorbed species and the soluble zincate to zinc metal.

Of the several sophisticated energy conversion devices investigated in the last two decades, there is strong evidence of the increasing predominance of rechargeable alkaline battery systems. Within this field, there is an ever-increasing interest in the use of zinc as the favored anode material. One of the main disadvantages in the use of zinc as the negative electrode in silver-zinc and nickel-zinc cells lies in the fact that zinc hydroxide is highly soluble in the strongly alkaline aqueous electrolytes employed in these systems. Any study of the electrochemical behavior of zinc in alkaline media must consider the mechanism and kinetics of the complex electrode reactions in relation to the nature of the electrolyte at the electrode interface and in the bulk of the solution.

Potentiometric (1, 2), spectral (3) and P.M.R. (4) investigations indicate that the predominant zincate species existing in highly alkaline media is $Zn(OH)_4^{2-}$. Jost (5) and Okinada (6) do not preclude the presence of $Zn(OH)_3^-$, specially in more dilute solutions. Detailed physicochemical data pertaining to solubility (5, 7-9), conductivity (7-9), and vapor pressure (9) is available. Kober and West (10) indicate that the nature of the species present in solution is dependent on the hydroxyl ion activity, which is itself governed by the zincate ion concentration. As one approaches saturation, negatively charged colloids tend to form (2) which further complicates the situation. Under certain conditions, notably during anodization of zinc, supersaturation can occur (11). However, little is known concerning the nature of such solutions, which are localized in the anolyte layer. Practical, porous zinc battery electrodes investigated singly, or in the cell environment, in the laboratory, are normally charged and discharged under constant current conditions. Although it is argued that when such a highly active electrochemical system as this is investigated using the galvanostatic technique, certain transient features of the electrode phenomena will be overshadowed (14), there are reasons why such a technique should be employed. By studying the behavior of planar zinc under such conditions, it is hoped that the observations will assist in the interpretation of the behavior of the more complex practical system. A number of studies of the anodic behavior of planar zinc in highly concentrated aqueous alkali have been performed (12-20). As Hampson *et al.* (17) state, the common feature of galvanostatic investigations is the difficulty in obtaining reproducible results. Eisenberg *et al.* (15) emphasize the importance of considering the disposition of the zinc anode and the resulting effects of convection on passivation phenomena. Using the rotating disk electrode to control mass transfer, Popova *et al.* (18-19) have investigated the anodic dissolution of passivated zinc using both potentiostatic and galvanostatic control. Sanghi and Wynne-Jones (13) concluded that insufficient electrode pretreatment was a major cause of irreproducibility and error in such passivation experiments. Most investigations of this system have employed some form of mechanical polishing, although there is some disagreement as to the correct method. Farr and Hampson, who employed both faradaic impedance measurements (21) and the double pulse galvanostatic technique (22) in attempting to elucidate the mechanisms associated with the anodic oxidation of zinc, have stressed very high metal purity in their studies with micro-electrodes.

The relationship of anodic current density and zinc passivation time has very often been expressed by the empirical equation (12, 15-17) $i - i_{lim} = k \cdot t^{-1/2}$. The purpose of the present investigation was to test the validity of this relationship over a wider range of current densities than has hitherto been studied, with special emphasis on accuracy and reproducibility. The major part of this paper deals with the findings of the chronopotentiometric study. The anodic oxidation of horizontally disposed zinc in 30% (6.9M) potassium hydroxide, and in the zinc oxide saturated electrolyte at 25°C, and the cathodic reduction of the oxidized electrode under galvanostatic control, have been studied. The slow cyclic voltammetric technique was also employed and some of the resulting data are presented.

Experimental

Electrolytic cell.—In Fig. 1 is shown a cross-sectional diagram of the cell used in this investigation. It consists of a 6.5 x 3.5 x 3.5 in. double-walled Lucite container with two compartments. Water from a constant temperature bath is continually circulated through the double-walled spacing, maintaining the temperature at 25°±0.2°C. The mercury-mercuric oxide reference electrode system was set up in the right-hand compartment. The working-counter electrode system consists of a fixed platinum gauze disk and a 1.08 cm^2 area planar zinc disk, embedded in a removable Lucite disk, both mounted on a Lucite support.

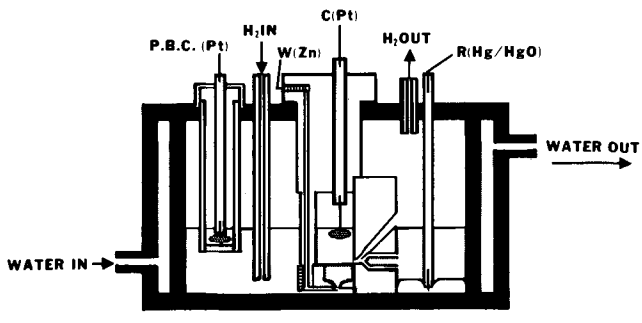

Fig. 1. Electrolytic cell, cross-sectional diagram: C, counter electrode; W, working electrode; R, reference electrode; P.B.C., pre-bias counter electrode.

* Electrochemical Society Active Member.
[1] Present address: Electrochemistry Department, Whittaker Corporation, 3540 Aero Court, San Diego, California.

99.999% zinc (A. D. Mackay, Inc., New York) was used throughout. The electrode support, when introduced into the major compartment, fits rigidly into a position adjacent to the compartment separating wall, in such a manner that the periphery of the zinc disk lies within 0.5 mm of a 0.4 mm diameter, 45° channel through part of the wall. This channel serves as a Luggin capillary. It opens into a wider channel packed with compressed nylon fiber, soaked with cell electrolyte, acting as a salt bridge. The continuation of the open channel as shown, allows for the escape of any gas bubbles which otherwise might become entrapped in the Luggin. A fourth platinum gauze disk electrode, suspended in a cylindrical nylon chamber with a base of compressed nylon fiber located in the major compartment, is employed during potentiostatic prebiasing of the working electrode. Solution and gas inlets and outlets and a thermometer well complete the cell.

Electrode Pretreatment.—Sanghi *et al.* (13, 14) mechanically polished zinc with alcohol-lubricated emory, followed by Selvyt cloth. Hampson *et al.* (16, 17) preferred an acid dip, followed by polishing with moist filter paper. Popova *et al.* (18-20) polished zinc with moist glass powder. It has been observed repeatedly in this laboratory that, if mechanically polished zinc is cathodically polarized in a hydrogen-saturated, concentrated aqueous alkali, finely divided zinc forms on the electrode surface. However, such a deposit, resulting from the reduction of a thin surface layer of oxide, does not form if the mechanically polished zinc is chemically polished prior to immersion in the electrolyte. Chemical polishing was chosen since the suggested laboratory electropolishing procedure for zinc is time-consuming (23). Three solutions were studied. Chromic-sulfuric acid proved unsuccessful, immersion in this solution yielded a white film. Although a 50% hydrogen peroxide—50% acetic acid solution may be used, it is not advised since one must control the temperature and immersion time rigidly and the anolyte layer must be quiescent. A 1-sec immersion in 50% nitric acid at room temperature proved very successful and was used throughout this investigation. Prior to each experiment, the following procedure was followed: The zinc disk was mechanically polished on three grades of water-lubricated silicon carbide emory, followed by a 0.3μ micropolish on Selvyt cloth. The disk, then mounted on the Lucite support, was chemically polished, washed successively in hydrogen-saturated deionized water and 30% potassium hydroxide, and then rapidly inserted into the cell. At the moment of insertion, the zinc was held at the appropriate prebias potential (see Results section) prior to initiating the charging study. Under these conditions, reproducible data were obtained.

Electrical circuitry.—Conventional circuitry was employed for the programmed charging studies. A simplified block diagram is shown in Fig. 2. The potentiostatic-galvanostatic sequence control unit incorporates time-delay circuits and the necessary mercury-wetted switching relays. Philbrick solid-state operational amplifier circuitry was used throughout. The voltage followers, VF1 and VF2, were a P.85 and a P.65AU, respectively. An SP.656 was employed for the integrator, I. P.65AU amplifiers were employed for the differentiator, D, and the voltage comparator, VC, sensitive to ± 1 mv. In conjunction with a potentiostat (Wenking, standard model #61 TRS) and two independent constant current units, of the type described by Bockris *et al.* (24), a variety of operational sequences may be applied to the working electrode system. During potentiostatic prebiasing, the Osteryoung (25) four-electrode technique was employed in order to obtain clean switching to the galvanostatic mode. Switching from the first to the second galvanostat may be accomplished either when the working electrode has attained a given potential level, VF1-VF2-VC network, or when a given charge input has been reached, VF1-I-VC network. The Wenking motor potentiometer, MP. 165, was employed to drive the potentiostat for the slow cyclic voltammetric studies. A Tektronix #565, dual-beam oscilloscope with type 2A63, differential amplifier vertical plug-in units was used to record fast charging curves. Slow chronopotentiometric and cyclic voltammetric data were recorded with a Hewlett-Packard, Moseley, 136AM, dual-pen recorder.

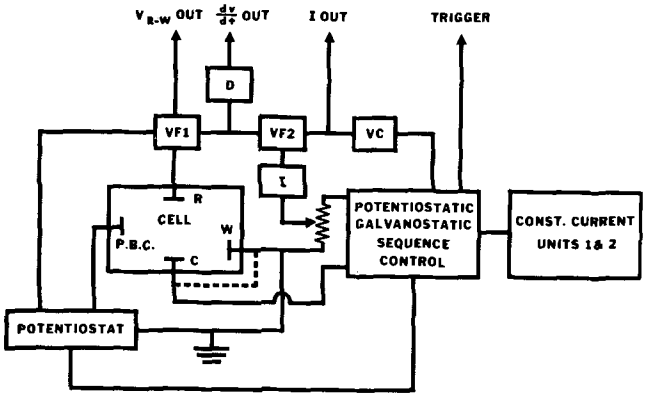

Fig. 2. Simplified electrical circuitry: VF1, VF2, voltage followers; VC, voltage comparator; I, integrator; D, differentiator.

Results

A steady equilibrium potential is not observed when freshly polished zinc is immersed in 30% potassium hydroxide. At —1.400v (—1.302v *vs.* NHE), a very small cathodic current flows. In all subsequent studies in this media, the zinc was prebiased at this potential prior to initiating either the galvanostatic charging program or the slow linear potential sweep. In the zinc oxide saturated electrolyte, zinc initially exhibits a potential of —1.345v (—1.247v *vs.* NHE). This slowly drifts to —1.352v where it remains steady. This final value was employed in this media as the prebias potential.

In Fig. 3 is shown a tracing of an oscillographically recorded potential-time curve, typical of the electrochemical behavior of zinc in 30% potassium hydroxide at 25°C undergoing the following charging program, anodic oxidation at 500 ma (462 ma/cm^2) for 15 sec, *i.e.*, a charge input of 7.5 coulombs, followed by cathodic reduction at 100 ma (93 ma/cm^2). While the zinc was prebiased at —1.400v, the oscilloscope was triggered, point a. Approximately half a second later, anodic charging was initiated, point b. The potential jumped very quickly to point c, *circa* —1.2v where the anodic transition commences. The potential rises linearly to point d, *circa* —1.0v in 6.7 sec. Differential measurements confirmed that this transition exhibits

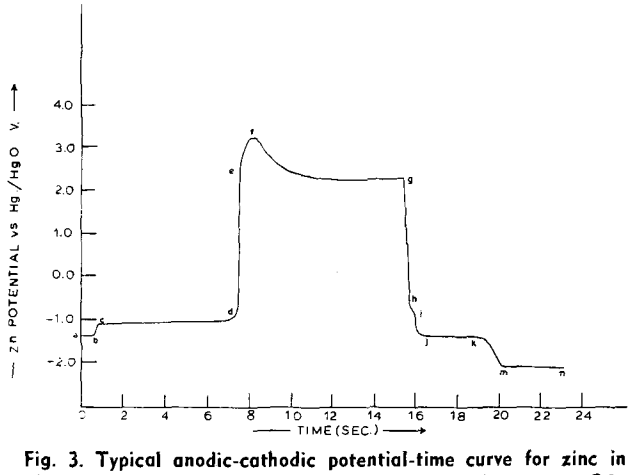

Fig. 3. Typical anodic-cathodic potential-time curve for zinc in 30% potassium hydroxide at 25°C. Prebias —1.400v, anodic C.D. 462 ma/cm^2, cathodic C.D. 93 ma/cm^2.

no discontinuities. At point d, passivation is complete, as indicated by the large increase in impedance. The potential rises extremely rapidly to point e, *circa* +2.2v, where the galvanostatic overshoot commences. The potential peaks at +3.2v, point f, and then levels at +2.25v, where oxygen evolution proceeds. Current reversal was initiated at point g. The potential falls rapidly to *circa* —0.5v, point h, where there is a relatively short-lived transition to point i, *circa* —0.9v. (The time scale of this region has been magnified in the diagram to show the transition.) The potential drops rapidly to point j, *circa* —1.35v, where a larger cathodic transition is observed. Like the anodic transition region, c-d, this transition is well-defined and shows no discontinuities, as indicated by differential measurements. The potential falls linearly to *circa* —1.37v, point k, in 2.1 sec. The potential finally falls to *circa* —1.9v, point m, where vigorous hydrogen evolution occurs. In the zinc oxide saturated electrolyte, the potential-time characteristics are very similar to that described above. Following prebias at —1.352v, on charging, a well-defined continuous passivation region is observed, followed by a galvanostatic overshoot. On cathodic polarization from the oxygen evolution potential, the first cathodic transition is observed. This is more well defined than that observed in potassium hydroxide alone. The potential then falls to the final value, —1.35v. On continuous polarization, a mossy deposit of zinc results, and the potential never falls to that indicative of the H.E.R. The anodic transition region has been studied over a wide range of current densities in both electrolyte media at 25°C. In order to study the cathodic current density-transition time characteristics, zinc was anodically oxidized under constant conditions (potassium hydroxide alone, 462 ma/cm^2, zinc oxide saturated electrolyte, 342 ma/cm^2) to 7.5 coulombic input, prior to initiating cathodic polarization. The resulting chronopotentiometric data for regions c-d, h-i and j-k are shown in Table I.

Anodic characteristics.—Zinc exhibits a steady anodic potential when charged at low current densities. As the limiting current density is approached, the potential commences to drift with time to less negative values. At any given current density in the range, 10^{-4} — 10^{-1} amp/cm^2, the anode potential is less negative in the zinc oxide saturated electrolyte than in potassium hydroxide alone. Furthermore, there is no linear Tafel region. In the zinc oxide saturated media only, two anodic transitions were observed at high current densities. The first transition was very short lived, and the potential was relatively close to the equilibrium value. The second, main transition, was of much longer duration and at a less negative potential, *e.g.*, at an anodic current density of 740 ma/cm^2, the first transition at —1.27v lasted for 3 msec, while the second transition at —0.7v lasted for 0.37 sec before passivation and the ensuing overshoot. With decrease in current density, the potential of the short-lived transition approached the equilibrium value, and the time decreased to such a value as to be extremely difficult to measure with any accuracy.

Table I. Anodic and cathodic chronopotentiometric data, planar, horizontally disposed zinc

30% KOH, 25°C						ZnO saturated 30% KOH, 25°C			
Region c-d		Region h-i		Region j-k		Region c-d		Region h-i	
i_a ma/cm^2	τ_a sec	i_c ma/cm^2	τ_c sec	i_c ma/cm^2	τ_c sec	i_a ma/cm^2	τ_a sec	i_c ma/cm^2	τ_c sec
109.0	1012.0	0.46	0.70	9.3	104.0	60.0	1500.0	0.46	5.0
111.0	655.0	0.92	0.68	13.9	51.0	65.0	1278.0	0.92	4.8
120.0	452.0	1.85	0.62	18.5	21.5	74.0	331.0	1.85	3.25
129.0	259.0	3.70	0.56	27.7	10.8	83.0	225.0	3.7	1.9
139.0	216.0	5.60	0.46	37.0	6.95	93.0	181.0	5.6	1.3
148.0	129.0	7.40	0.43	46.2	4.8	102.0	75.0	7.4	1.05
157.0	112.0	9.30	0.37	55.5	3.65	111.0	61.0	9.3	0.86
166.0	93.0	13.90	0.27	64.7	2.7	139.0	40.0	13.9	0.69
176.0	82.0			74.0	2.5	162.0	27.4	18.5	0.5
185.0	77.0			83.2	2.2	185.0	19.3	27.7	0.26
203.0	64.0			92.5	2.1	208.0	16.7	37.0	0.22
222.0	51.0					231.0	13.8	46.2	0.16
240.0	44.0					254.0	9.8		
277.0	31.0					277.0	7.2		
324.0	19.4					324.0	4.5		
370.0	14.0					370.0	3.8		
416.0	10.5					416.0	2.4		
462.0	6.7					462.0	2.1		
555.0	4.3					509.0	1.7		
647.0	3.0					555.0	1.1		
740.0	1.95					601.0	0.85		
832.0	1.4					647.0	0.7		
925.0	1.05					693.0	0.49		
						740.0	0.37		
						832.0	0.17		
						925.0	0.13		
						1020.0	0.12		
						1200.0	0.11		

Cathodic characteristics.—The potential-time curves characteristic of the cathodic behavior of oxidized zinc were monitored in the following manner. After prebias and anodization, the oscilloscope was triggered just prior to point g (see Fig. 3). The appropriate time base was selected to study either region h-i or j-k. The first cathodic transition region h-i was observed on potential decay as well as during cathodic polarization. On potential decay in potassium hydroxide alone, the transition time was 0.72 sec. In the zinc oxide saturated media, the transition time was 5 sec. On cathodic polarization, the transition times were reduced considerably and, furthermore, the region became increasingly ill defined. In potassium hydroxide alone, it became impossible to measure transition times with any accuracy above 15 ma/cm^2. In the zinc oxide saturated electrolyte, this limit was extended to 45 ma/cm^2. This characteristic region is observed only if, in the preceding oxidation, the potential has attained a certain value. If, by means of the voltage level switch, anodic charging is interrupted at any potential between points d and e, region h-i is not observed. An example of this behavior is shown in Fig. 4. Following prebias at — 1.4v, the oscilloscope was triggered and the zinc oxidized at 462 ma/cm^2. At —0.75v, the potential decay curve was initiated. The potential fell instantaneously to —1.35v where it remained steady. If the voltage cut-off is raised from e to f, the characteristics of the first cathodic transition region become more well defined. Once the peak of the galvanostatic overshoot has been attained, region h-i characteristics remain unaffected on further anodic polarization. The second cathodic transition region j-k, which can only be studied in potassium hydroxide alone, was observed irrespective of the voltage level at which cathodic polarization was initiated.

In Fig. 5 are shown cyclic voltammograms characteristic of the behavior of zinc in 30% potassium hydroxide (full line) and the zinc oxide saturated

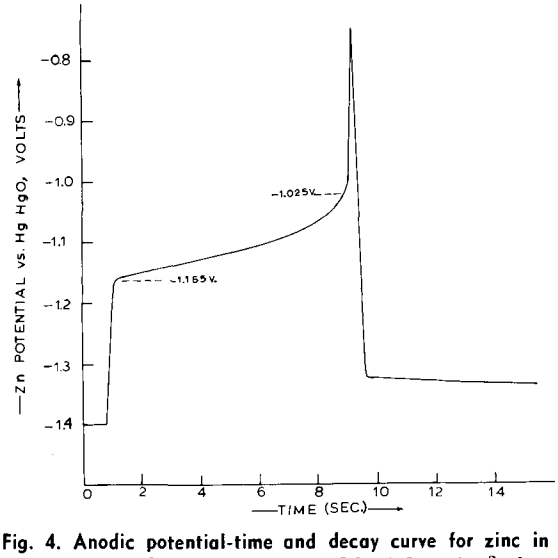

Fig. 4. Anodic potential-time and decay curve for zinc in 30% potassium hydroxide at 25°C. Anodic C.D. 462 ma/cm^2, decay initiated at 0.75v vs. Hg/HgO.

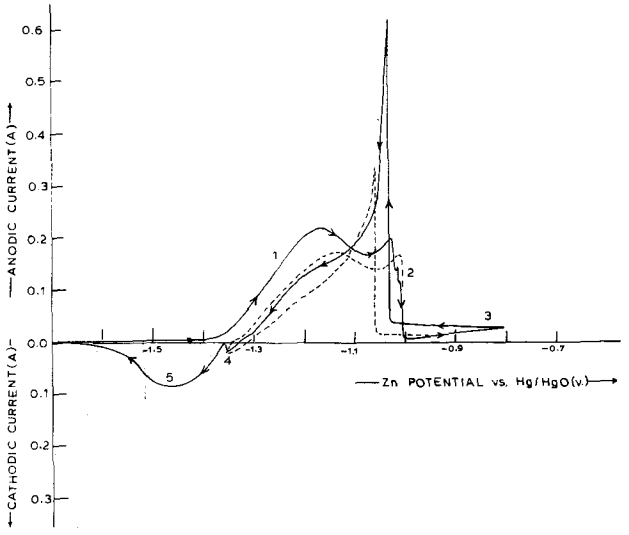

Fig. 5. Cyclic voltammograms for zinc in 30% potassium hydroxide at 25°C. Sweep rate 2.78 mv/sec; full line, potassium hydroxide alone; dashed line, zinc oxide saturated media.

electrolyte (dashed line) at 25°C. The sweep rate was 2.78 mv/sec. In potassium hydroxide alone, following an initial prebias at —1.4v, the applied potential was lowered to —1.7v and the slow linear potential sweep initiated. The sweep was reversed manually at —0.8v and continued to —1.7v. In the zinc oxide saturated media, the forward sweep was initiated from the prebias potential, —1.352v, reversed at —0.8v and stopped at —1.352v. If the sweep was continued to more negative potentials in this electrolyte, the cathodic current density increased linearly and a mossy zinc deposit resulted. At very low sweep rates, marked current oscillations were observed in region 2. Visual observation showed the growth of an oxide film in region 3. On the reverse pass, this film disappeared in region 2, with an instantaneous increase in anodic current. Irrespective of the sweep rate, this anodic spike occurred at the same potential, —1.03v in potassium hydroxide alone, —1.06v in the zinc oxide saturated media. With increase in sweep rate, the character of regions 1, 2, and 4 became less well defined, whereas region 5 remained unaffected. A study of the variation of the peak currents and potentials of regions 4 and 5 with sweep rate yielded inconclusive results. However, on the forward pass, consistent results were obtained relating the region 1 anodic peak current and potential with sweep rate. For both electrolyte media, the potential shifted to less negative values, and the current increased with increase in sweep rate. The majority of the data recorded pertained to the zinc oxide saturated electrolyte. The relevant data over the range, 0.56-139 mv/sec are summarized in Table II. The potential data was reproducible to ±5 mv and the current density to ±2 ma/cm². On continued cycling at any particular sweep rate, the over-all voltammetric character remained essentially the same. However, the anodic region 1 broadened and lost character. The peak, which became increasingly difficult to identify, tended to move to more negative potentials, and the current density decreased in value, ultimately approaching a limit. When cycling was interrupted at the conclusion of a complete pass, the system immediately reverted to its initial state, as indicated by the character of the first voltammogram recorded after the interruption. On continued cycling, the above behavior was repeated.

Table II. Cyclic voltammetric data, zinc in ZnO saturated potassium hydroxide, 25°C

Sweep rate, V_t, mv/sec	Anodic peak C.D., i_p, ma/cm²	Peak potential, E_p vs. Hg/HgO, volts
0.56	116	−1.155
1.11	127	−1.160
1.39	136	−1.140
2.78	161	−1.125
5.6	201	−1.080
11.1	253	−1.030
13.9	275	−1.007
27.8	341	−0.950
56.5	423	−0.887
139.0	537	−0.810

Discussion

The anodic polarization data obtained at low charging current densities in this study is in good agreement with that reported by Dirkse *et al.* (26). The limiting current density data obtained in this investigation is compared with selected pertinent published data in Table III. The magnitude of the values reported for differently oriented electrodes examined after various pretreatments in the several media tend to cast doubt on the value reported by Hampson and Tarbox (16). In general, a working electrode potential is a function of both the current density and the electrolyte interfacial concentration of the electroactive species (27). Since Dirkse (11) and Eisenberg *et al.* (15) have established a concentration build-up in the anolyte layer during the anodic oxidation of zinc, it is not surprising that the working potential data cannot be analyzed in terms of the charge transfer kinetic equation (28). $i - \tau$ data for the anodic oxidation of zinc in highly alkaline media has traditionally been correlated by means of Eq. [1]

$$(i - i_{lim})\tau^{1/2} = k \qquad [1]$$

The data obtained in this investigation (Tables I and III) has shown that k is a function of the current density. For both electrolyte media, with increase in current density, k increases to a maximum (KOH, k_{max} = 1 amp sec$^{1/2}$/cm² at 425 ma/cm², KOH-ZnO, k_{max} = 0.65 amp sec$^{1/2}$/cm² at 230 ma/cm²), and then gradually decreases. The conventional method of treating chronopotentiometric data, characteristic of electrochemical phenomena involving at least one electrolyte soluble species, is to study the characteristics of $i\tau^{1/2}$ *vs.* i plot. Such plots are shown in Fig. 6 for A, potassium hydroxide, B, zinc oxide saturated potassium hydroxide. When the limiting current density has been exceeded, $i\tau^{1/2}$ decreases linearly with increase in current density, ultimately attaining a limiting value. Between the linear plot current density limits, the data has been fitted to a general equation of type [2] by means of a least squares fit regression analysis program (IBM S/360 computer).

$$i\tau^{1/2} = k_0 - k_1 \cdot i^m \qquad m = 1, 2, 3, \ldots \qquad [2]$$

In Table IV are shown the calculated values of k_0 and k_1 for m = 1, and the associated statistical data. The high value of the correlation coefficient, C.C., and

Table III. Summary of limiting current density data, anodic oxidation of zinc

Reference	Electrolyte	Electrode	Orientation	i_{lim}, ma/cm²
(12)	4.0M NaOH, 20°C	Zn plated Cu wire	Vertical	55
(17)	5.0M KOH, 20°C	Zn disk	Vertical	84
(17)	7.0M KOH, 25°C	Zn disk	Vertical	150
(16)	6.5M KOH, 25°C	Zn disk	Horizontal face up	0.118
This work	6.9M KOH, 25°C	Zn disk	Horizontal face up	115
This work	6.9M KOH, 25°C ZnO sat'd.	Zn disk	Horizontal face up	60
(15)	6.9M KOH, 25°C ZnO sat'd.	Zn rectangular plate	Horizontal face up	67
(15)	6.9M KOH, 25°C ZnO sat'd.	Zn rectangular plate	Horizontal face down	143
(26)	6.9M KOH, 25°C ZnO sat'd.	Zn microdisk	Horizontal face down	62

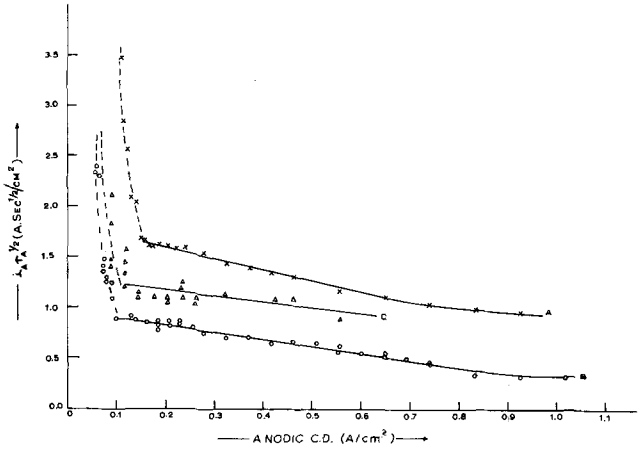

Fig. 6. Anodic chronopotentiometric curves for zinc in 30% potassium hydroxide at 25°C. Region c-d. A (x) potassium hydroxide, this investigation; B (o) zinc oxide saturated media, this investigation; C (△) zinc oxide saturated media, Eisenberg *et al.* (15).

the low values of the standard error, S.E., and the standard error of the estimate, S.E.E., confirm the accuracy and reproducibility of the data and the validity of Eq. [2]. With increase in m, C.C. decreases indicating that $m = 1$ is the correct value. For comparison, the data of Eisenberg *et al.* (15) in zinc oxide saturated potassium hydroxide are shown plotted in Fig. 6, Curve C, and the calculated coefficients of [2] are given in Table IV. The greater scatter in this data is mirrored in the associated statistical data. The anodic oxidation of zinc shows all the characteristics of a complex mechanism involving a kinetically controlling step preceding the diffusion of a soluble species through the boundary layer. Theory (27) indicates that, if the concentration of a soluble diffusing species is dependent on the kinetics of a preceding process, then the chronopotentiometric parameter is related to the current density by Eq. [3].

$$i^{1/2} = \frac{n\mathbf{F}(\pi D)^{1/2}\Delta C}{2} - \frac{i\pi^{1/2}}{2K(k_f + k_r)^{1/2}} \qquad [3]$$

ΔC is the concentration difference between the bulk and the interface, D is the diffusion coefficient of the soluble species. $K = k_f/k_r$ is the equilibrium constant of the preceding kinetically controlling step. This equation is valid provided that $(k_f + k_r)^{1/2}\tau^{1/2} \geq 2$. At sufficiently high current densities, when τ is small, [3] reduces to [4].

$$i\tau^{1/2} = \frac{K}{K+1} \cdot \frac{n\mathbf{F}(\pi D)^{1/2}\Delta C}{2} \qquad [4]$$

Farr and Hampson (21, 22) indicate the possibility of kinetically controlling reactions preceding a solution diffusion stage. Dirkse *et al.* (26) have summarized the possible mechanistic steps involved in the anodic oxidation. Following the stabilization of zinc adatoms by hydroxyl ion adsorption, a rapid two-electron charge transfer process is postulated with an exchange current density of 224 mA/cm² in a zinc oxide saturated 7M potassium hydroxide solution (22). The very short-lived potential plateau, observed at high current densities, may well be indicative of this step. This stage is followed by equilibria

$$Zn(OH)_{2ad} \rightleftharpoons Zn(OH)_{2diss} \qquad [5]$$

Table IV. Anodic oxidation of horizontally disposed zinc facing up at 25°C

Electrolyte	C.D. limits, ma/cm²	$i\tau^{1/2}{}_{lim}$, amp sec$^{1/2}$/cm²	k_0	k_1	C.C.	S.E.	S.E.E.
6.9M KOH	148-555	0.913	1.825	1.121	0.989	0.043	0.031
6.9M KOH ZnO sat'd.	102-740	0.345	0.967	0.696	0.982	0.024	0.032
6.9M KOH (15) ZnO sat'd.	117-555	—	1.286	0.544	0.463	0.224	0.133

$$Zn(OH)_{2diss} + n\,OH^- \rightleftharpoons Zn(OH)_{2+n}^{n-} \qquad [6]$$

If either [5] or [6] is rate controlling, and if a first-order process, then, assuming the validity of [3] and [4], k_f and k_r may be calculated using the data of Table IV. In potassium hydroxide, $k_f = 0.98$, $k_r = 0.9$ sec^{-1}. In the zinc oxide saturated media, $k_f = 0.02$, $k_r = 0.06$ sec^{-1}. Although no great emphasis should be placed on these absolute values, relatively they appear plausible. Utilizing the values for the bulk and interfacial concentrations of zincate given by Eisenberg *et al.* (15), a value of 1.0 x 10^{-5} cm²/sec is calculated for the apparent diffusion coefficient of the zincate ion in the zinc oxide saturated media. This value is slightly greater than 0.85 x 10^{-5} cm²/sec reported by Stachurski (29) from polarographic measurements (temperature not given). Further experimentation in varying concentrations of potassium hydroxide and zincate over a range of temperatures is required before it is possible to state which of the two processes, [5] zinc dissolution or [6] the complexing step, is rate determining.

The findings of the cyclic voltammetric study qualitatively confirm the conclusions regarding the complexity of the anodic process. The region 1 anodic peak current density and IR-free peak potential data, shown in Table II, obey the relationships

$$i_p = 123.4\ V_t^{0.3}\ (\text{ma/cm}^2) \qquad [6]$$

with a correlation coefficient of 0.996. The standard error of the index is 0.002.

$$E_p = -1.177 + 0.1565 \log_{10} V_t\ (\text{volts}) \qquad [7]$$

with a correlation coefficient of 0.975. The standard error of the estimate is 24 mv.

$$E_p = -0.701 + 0.5246 \log_{10} i_p\ (\text{volts}) \qquad [8]$$

with a correlation coefficient of 0.987. The standard error of the estimate is 17 mv.

For a purely diffusion-controlled process, i_p should be a linear function of the square root of the sweep rate. Equation [8] shows that the anodic peak corresponds with the initial potential of the anodic plateau, point c, Fig. 3. Region 2 corresponds with the onset of passivation, point d. The potential at which the anodic spike is observed agrees with the peak potential reported by Popova *et al.* (18-19). These workers have been primarily concerned with the electrode phenomena associated with region 3. They have shown that, when zinc is deeply passivated, 80-90% of the total current is associated with the direct electrochemical dissolution of zinc. The remaining current is associated with the growth of the oxide film. Impedance data (20) has been employed to support the conclusion that the kinetically controlling stage in the zinc dissolution is the rate of diffusion of zinc atoms through the thickening oxide film. The situation is further complicated by the chemical dissolution of this film, the rate of which is dependent on the nature of the electrolyte. The rate decreases linearly with increase in the zincate concentration, ultimately ceasing in supersaturated solutions. It would appear, therefore, that the cathodic behavior of passivated zinc is dependent not only on the prior anodic history of the electrode, but also on the nature of the electrolyte.

It is pertinent first to consider the second cathodic transition region, j-k. The data for this region, observed in potassium hydroxide alone, have been analyzed in a manner similar to that for the anodic region, c-d. $i\tau^{1/2}$ (amp sec$^{1/2}$/cm²) increases linearly with i (amp/cm²) according to Eq. [9].

$$i\tau^{1/2} = 0.0736 + 0.602\,i \qquad [9]$$

The very high correlation coefficient, 0.98, and the low standard error of the estimate, 0.003, confirm the validity of this relationship. General theory of coupled adsorptive-diffusive phenomena (30) predicts that the chronopotentiometric parameter should increase linearly with the polarizing current density. As is often

the case, the data fits the three Lorenz models (30), (*i*) adsorbate reduced first, (*ii*) adsorbate reduced last, (*iii*) simultaneous reduction of adsorbate and diffusing species. Furthermore, quantitative estimations of the diffusion coefficient of the soluble species and of the surface concentration of the adsorbate are precluded because of the lack of knowledge of the catholyte concentration gradient and the true surface area of the electrode.

The findings of this investigation regarding the appearance and characteristics of region h-i are in general agreement with those of Popova *et al.* (18). They find that this region becomes increasingly well defined if the zinc is passivated at increasingly positive potentials. Since this region is observed on potential decay, it would appear to be a spontaneous reduction. Since it is also observed even if the anodic overshoot is incomplete, prior to the O.E.R., it is thought not to be due to the reduction of adsorbed oxygen molecules. Popova *et al.* (18) propose that this region is the result of the reduction of excess oxygen in the zinc oxide film. If this indeed is true, then one may speculate that the hydroxyl ion so produced reacts with the zinc ion, continually produced as a result of the direct electrochemical oxidation of diffusing zinc atoms, forming a surface bound zinc hydroxide. Since the growing oxide film is thicker in the zinc oxide saturated electrolyte, there is a relative increase in the amount of excess oxygen available for reduction. Therefore, the amount of charge associated with this reduction will be greater in the zinc oxide saturated media than in potassium hydroxide alone. An examination of the data pertaining to this region in Table I shows that as the cathodic current density is increased, $i\tau$ approaches a limiting value, 4 millicoulombs/cm^2 in potassium hydroxide, 8 millicoulombs/cm^2 in the zinc oxide saturated media.

Acknowledgments

The author wishes to thank Mr. Y. Trenkler and Mr. S. Ostrach for their assistance in performing the experimental work described herein.

Manuscript submitted Sept. 6, 1968; revised manuscript received Jan. 27, 1969. This paper was presented at the Chicago Meeting, Oct. 15-19, 1967, as Paper 29.

Any discussion of this paper will appear in a Discussion Section to be published in the December 1969 JOURNAL.

REFERENCES

1. T. P. Dirkse, *This Journal*, **101**, 328 (1954).
2. G. Schorsch, *Bull. Soc. Chim. France*, **7**, 1456 (1964).
3. J. S. Fordyce and R. L. Baum, *J. Chem. Phys.*, **43**, 843 (1965).
4. G. H. Newman and G. E. Blomgren, *ibid.*, **43**, 2744 (1965).
5. E. Jost, Paper presented at the Philadelphia Meeting of the Society, Oct. 9-14, 1966 as Paper 49.
6. Y. Okinada, *ibid.*, Paper 48.
7. T. P. Dirkse, *This Journal*, **106**, 154 (1959).
8. C. T. Baker and I. Trachtenberg, *ibid.*, **114**, 1045 (1967).
9. W. H. Dyson, L. A. Schreier, W. P. Sholette, and A. J. Salkind, *ibid.*, **115**, 566 (1968).
10. F. P. Kober and H. West, Paper presented at the Chicago Meeting of the Society, Oct. 15-19, as Paper 28.
11. T. P. Dirkse, *This Journal*, **102**, 9 (1955).
12. R. Landsberg and H. Bartelt, *Z. Elektrochem.*, **61**, 1162 (1957).
13. I. Sanghi and W. F. K. Wynne-Jones, *Proc. Indian Acad. Sci.*, **47A**, 49 (1958).
14. I. Sanghi and M. Fleischmann, *Electrochim. Acta*, **1**, 161 (1959).
15. M. Eisenberg, H. F. Bauman, and D. M. Brettner, *This Journal*, **108**, 909 (1961).
16. N. A. Hampson and M. J. Tarbox, *ibid.*, **110**, 95 (1963).
17. N. A. Hampson, M. J. Tarbox, J. T. Lilley, and J. P. G. Farr, *Electrochem. Technol.*, **2**, 309 (1964).
18. T. I. Popova, N. A. Simonova, and B. N. Kabanov, *Soviet Electrochemistry*, **2**, 1347 (1966).
19. T. I. Popova, G. L. Vidovitch, N. A. Simonova, and B. N. Kabanov, *ibid.*, **3**, 860 (1967).
20. T. I. Popova, N. A. Simonova, and B. N. Kabanov, *ibid.*, **3**, 1273 (1967).
21. J. P. G. Farr and N. A. Hampson, *Trans. Faraday Soc.*, **62**, 3493 (1966).
22. J. P. G. Farr and N. A. Hampson, *J. Electroanal. Chem.*, **13**, 433 (1967).
23. W. J. M. Tegart, "The Electrolytic and Chemical Polishing of Metals," Pergamon Press, London (1956).
24. J. O'M. Bockris, H. Wroblowa, E. Gileadi, and B. J. Piersma, *Trans. Faraday Soc.*, **61**, 2531 (1965).
25. R. A. Osteryoung, *Anal. Chem.*, **37**, 429 (1965).
26. T. P. Dirkse, D. DeWit, and R. Shoemaker, *This Journal*, **115**, 422 (1968).
27. P. Delahay, "Advances in Electrochemistry and Electrochemical Engineering," Vol. 1, P. Delahay and C. W. Tobias, Editors, Interscience, New York (1961).
28. J. P. Elder and A. Hickling, *Trans. Faraday Soc.*, **58**, 1852 (1962).
29. Z. O. J. Stachurski, NASA Report 617-65, p. 8, December 1968.
30. W. H. Reinmuth, *Anal. Chem.*, **33**, 322 (1961).

A Study of the Anodic Oxidation of Tantalum Using Open-Circuit Transients

J. L. Ord*
Department of Physics, University of Waterloo, Waterloo, Ontario, Canada
and D. J. DeSmet*
Department of Physics, University of Alabama, University, Alabama

ABSTRACT

The anodic oxidation of tantalum in sulfuric acid has been studied by analyzing open-circuit transients applied at intervals along galvanostatic oxidation transients. The dependence of the oxidation current density, i, on the overpotential, V, is expressable in an equation of the form $i = i_o \exp(V/V_o)$, where i_o and V_o are parameters determined from the data analysis. The parameter V_o is found to vary linearly with the potential during galvanostatic oxidation, while i_o depends on the applied current density. Using this equation relating current density and potential, together with a knowledge of the behavior of the parameters i_o and V_o, one can predict both the steady-state and transient behavior of this system.

In studies of the anodic oxidation of valve metals such as tantalum, the overpotentials observed, because of their magnitude, are generally assumed to appear across the oxide layer and the parameters measured are usually expressed in terms of the electric field in the layer. In studies of the anodic oxidation of other metals, in particular the passive metals such as iron,

* Electrochemical Society Active Member.

the overpotentials observed are much lower. In these systems there is no general agreement as to whether the overpotential appears across the oxide layer, across the double layer in the electrolyte, or even whether this potential can be called a true overpotential. As a result, measurements on the anodic oxidation of the passive metals are interpreted in a wide variety of ways, thus underlining the fact that the determination of an equation relating current density to overpotential from electrical measurements is not a unique process.

A striking illustration of this fact is provided by two careful studies of anodic oxidation which used similar techniques, yielded similar data, but from which quite different conclusions were drawn: Young's study of the anodic oxidation of tantalum (1), and Sato and Cohen's study of the anodic oxidation of iron in neutral electrolyte (2). Both of these investigations yielded data on the dependence of dV/dQ on log i. This dependence, which is generally linear, may be written in the form $dV/dQ = B \log (i/A)$ by introducing the two parameters A and B. Both sets of data showed only a slight dependence of dV/dQ on log i. Sato and Cohen took what might be called the logical approach to their data and ignored this slight variation by setting $B = 0$. In their proposed model the current density depended on both the overpotential and the layer thickness, but not explicitly on the electric field in the layer. Young, following the work of Güntherschulze and Betz (3), expected the field in the layer to affect the conduction process, and hence expected dV/dQ to vary linearly with log i. He decided that the variation he detected experimentally was significant, accounted for its magnitude by making A a very small number, and concluded that the electric field in the layer controlled the current through the layer. Thus, although the experimental data obtained in these two studies were quite similar (as are most features of the anodic oxidation of iron and tantalum with the exception of the range of potentials which can be studied), the two systems were described in the literature as behaving quite differently.

Over the past few years the work carried out in our laboratory (at the University of Waterloo) has been aimed at determining which features of the anodic oxidation process are dependent on the particular substrate or electrolyte used, and which features are more characteristic of the process itself. In an earlier paper (4) data were presented which showed that if open-circuit transients (5) were used to study the anodic oxidation of iron in sulfuric acid and in neutral electrolyte, similar results were obtained. The data in both cases indicated that the current through the layer was controlled by the electric field in the layer.

In the present work we present the results of open-circuit transient measurements taken during the anodic oxidation of tantalum. The parameters arising from the analysis of open-circuit transients provide a different starting point for setting up an equation relating current density to overpotential and can be used as basic parameters to describe the response of the system to other types of transients. Perhaps the most important use of these parameters is in the comparison of the anodic oxidation of the valve metals and the passive metals.

Experimental

Electrodes were prepared from single crystals of tantalum (purchased from Semi-Elements Inc. of Saxonburg, Pennsylvania). Hollow cylindrical samples of length 0.3 in. and diameter 0.2 in. were machined from this material. The samples were then etched to remove the cold-worked layer, or to remove the anodic oxide in subsequent experiments, and then chemically polished (6). The final surface treatment consisted of a brief immersion in hydrofluoric acid (6 to 8 sec), followed by a rinse in distilled water. The sample was then dried and mounted between Teflon washers in the electrode assembly (7). All the data

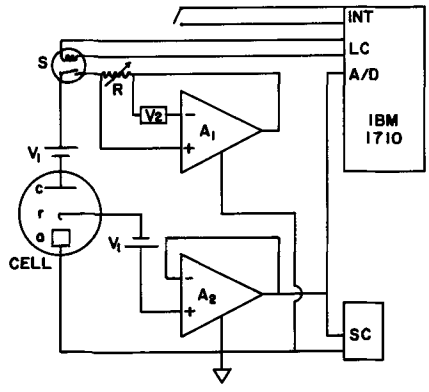

Fig. 1. Circuit schematic: A_1, A_2, operational amplifiers; SC, strip chart recorder; INT, computer interrupt switch; LC, latching contact; A/D, analog to digital data line; S, computer operated relay; V_1, blocking batteries; C, cathode; r, reference electrode; a, anode.

presented in this work were obtained using the same sample. Current densities were computed by dividing the applied current by the macroscopic surface area, assuming a roughness factor of unity.

The cell consisted of a 500 ml jacketed five-necked flask fitted with standard taper joints through which the electrode assembly, a mercurous sulfate reference electrode, a platinum cathode, a gas dispersion tube, and a thermometer were inserted, the electrode surface under study being vertical. The electrolyte used was 0.2N H_2SO_4 which was bubbled with argon for at least 12 hr prior to the beginning of an experiment in order to remove traces of other dissolved gases. The bubbling was continued throughout the course of an experiment. The cell was maintained at a temperature of 25.0° ± 0.1°C.

A schematic diagram of the circuitry used is shown in Fig. 1. High input impedance differential operational amplifiers (Philbrick SP2A) were used for the galvanostat and follower. These amplifiers normally operate over a ±10v range, therefore biasing batteries (V_1) were used to provide an operating range of 0-20v. Potentials were monitored on a strip chart recorder (Sanborn 7700), and open-circuit transients were recorded using the analog to digital converter of an IBM 1710 Process Control Computer. The computer was used rather than a fast recorder simply because our laboratory was linked to the computer and the analysis of open-circuit transients was greatly simplified by storing the data in digital form in the computer.

An open-circuit transient was initiated by closing an interrupt switch. The computer sensed the closure of this switch, recorded the potential, started an internal clock with a 4.8 msec time interval, and set a latching contact which energized a relay which opened the circuit. The potential was then sampled every 4.8 msec, and, when the sampled potential differed from the last stored potential by more than 100 mv, it was stored along with the corresponding time. The transient was terminated by a second closure of the interrupt switch. The computer then stopped sampling the potential, opened the latching contact to reclose the relay, transferred the values of potential and time to a disk memory, and was ready to record another transient.

Results

Open-circuit transients (in which the potential of the electrode was recorded as a function of time as the layer capacitance discharged through the layer) were used to determine the values of i_o and V_o in the equation

$$i = i_o \exp (V/V_o) \qquad [1]$$

which is used to relate the current density through the layer, i, to the overpotential of the electrode, V. Here i_o and V_o are parameters which have the same dimensions as i and V, respectively. Since the charge stored

on the layer capacitance is small when compared to the charge necessary to cause an appreciable change in the thickness of the layer, these transients may be considered as taking place at fixed layer thickness. The analysis of this type of transient has been described by Grahame (8), and transients of this type have been used to study the anodic oxidation of passive iron (4, 5, 9, 10).

Using Eq. [1] for the relation between the overpotential and the current density through the layer, the differential equation of the circuit under study is

$$C\,dV/dt + i_o \exp(V/V_o) = i_1 \qquad [2]$$

where C is the layer capacitance and i_1 the measured current in the external circuit. When the circuit is opened the external current immediately becomes zero and Eq. [2] takes the form

$$C\,dV/dt + i_o \exp(V/V_o) = 0 \qquad [3]$$

with the initial condition that the current flowing immediately before the circuit was opened is known.

If i_o, V_o, and C are considered constant during the open-circuit transient (or during some initial portion of the transient), then, by solving Eq. [3], the potential will have a time dependence during the transient given by

$$V = V_o \log(CV_o/i_o) - V_o \log(t + \theta) \qquad [4]$$

where $\theta = CV_o/i_1$. Thus V_o, i_o, and C can be determined directly by the analysis of such a transient.

Experimental open-circuit transients fit expressions of this form extremely well for suitably chosen values of θ. Transients were analyzed either graphically, by plotting V *vs.* log $(t + \theta)$, or with the aid of a digital computer. In either case θ was varied until the best fit to a straight line was obtained for an initial portion of the transient. The transient would not necessarily be expected to fit Eq. [4] for large values of time since complicating factors may enter as the current density becomes extremely small and Eq. [1] may no longer be valid. Experimentally, the fit to a straight line was found to be good to a point where dV/dt (or the current through the layer) had decreased by a factor of at least 25 from its initial value. From this we conclude that the exponential form of Eq. [1] is valid with constant parameters during an open-circuit transient. A typical set of data gave straight lines for V *vs.* log $(t + \theta)$ by the method of least squares with the standard deviation in the slope less than $2 \cdot 10^{-3}$ for slopes of the order of unity. For the least squares analysis points separated by equal potentials rather than equal times were used in order to have equally spaced data points on a semilogarithmic plot. The fit to a straight line is relatively insensitive to small variations in θ; hence the values found for θ cannot be considered very accurate, and the values of the capacitance found in this way may not be as accurate as those determined by other techniques.

A series of open-circuit transients was recorded at intervals along a galvanostatic oxidation transient and analyzed to determine the values of V_o and θ. In what follows we will use the term formation current density to designate the current density of the galvanostatic oxidation transient, and the term formation potential to designate the overpotential at which the circuit was opened. Figure 2 shows the values of V_o obtained from these transients as a function of the formation potential for two values of the formation current density, 3 and 100 μa/cm^2. For each value of the formation current density the plot of V_o *vs.* formation potential is linear, and both lines pass through the zero of formation potential. At 3 μa/cm^2 the slope of the straight line is 0.0938 with a standard deviation of 0.0008 and at 100 μa/cm^2 the slope is 0.0865 with a standard deviation of 0.0013. The difference between the slopes is statistically significant.

The corresponding values of the reciprocal capacitance, calculated from $1/C = V_o/(i_1 \cdot \theta)$, are shown in Fig. 3 for formation current densities of 3 and 100 μa/cm^2. This result shows that the reciprocal capacitance varies linearly with formation potential, but it does not show the slight dependence on the oxidation current density reported by others (1).

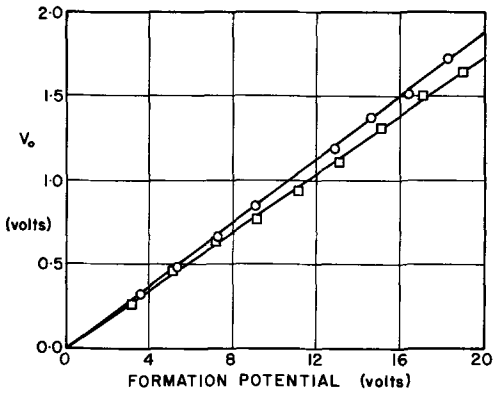

Fig. 2. Dependence of V_o on formation potential. The formation current density is 3 μa/cm^2 for the data represented by the circles and 100 μa/cm^2 for the data represented by the squares.

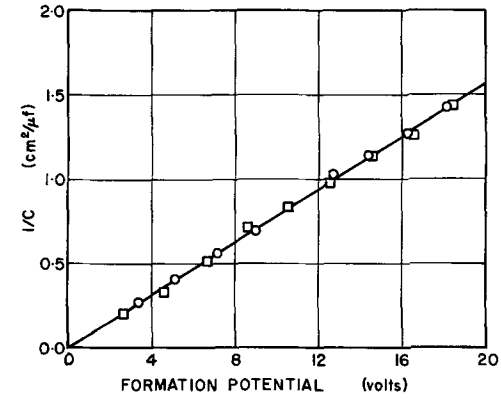

Fig. 3. Dependence of the reciprocal capacitance on formation potential. The formation current density is 3 μa/cm^2 for the data represented by the circles and 100 μa/cm^2 for the data represented by the squares.

A value for i_o can be calculated for each open-circuit transient; however, since values of V_o are proportional to the formation potential for a fixed formation current density, i_o will have the same value for all transients from the same formation current density. For example, at 100 μa/cm^2 the value of i_o may be found by setting log $(100/i_o)$ equal to 1/0.0865, giving $i_o = 93.5 \cdot 10^{-5}$ μa/cm^2. Figure 4 shows i_o plotted *vs.* formation current density, i_f, on logarithmic scales for five sets of open-circuit transients with formation current densities ranging from 3 to 300 μa/cm^2. (The straight line is a least squares fit to these points.) From this figure, assuming that the relation between log i_o and log i_f is linear over this range of formation current densities, one may write

$$i_o = k(i_f)^\alpha \qquad [5]$$

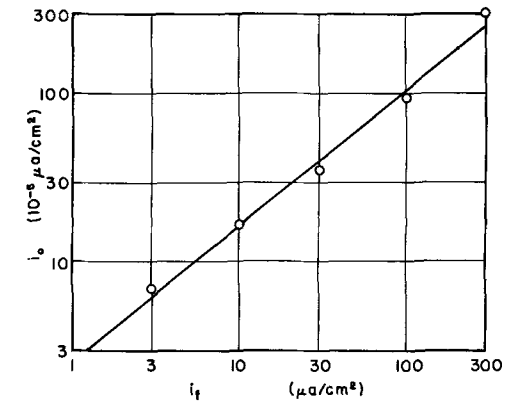

Fig. 4. Dependence of i_o on the formation current density

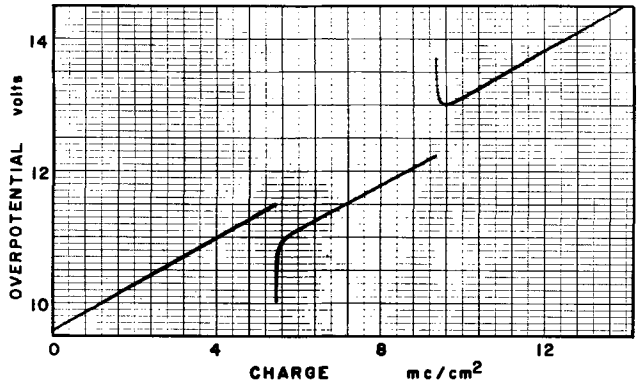

Fig. 5. Recorder trace of overpotential vs. charge for an oxidation transient in which the current density was switched from 200 to 40 μa/cm^2 and then back to 200 μa/cm^2.

The values of k and α obtained from this figure are $2.7 \cdot 10^{-5}$ and 0.8, respectively, if both i_o and i_f are expressed in μa/cm^2. The errors in k and α cannot be given quantitative estimates with any degree of confidence, but errors of 25% would not be surprising. It should be noted that if there were no dependence of the slope of V_o *vs.* formation potential on the formation current density then i_o would be directly proportional to the formation current density.

In order to facilitate the discussion of the difference between the parameters found here and those found by other methods (11,12) a transient in which the current density was switched from 200 to 40 μa/cm^2 and then back to 200 μa/cm^2 is shown in Fig. 5. The speed of the strip chart recorder was slowed by a factor of five when the current density was switched back to 200 μa/cm^2, producing a plot of potential *vs.* charge. Reference is made to this figure below.

Discussion

In general an exponential dependence of current density on overpotential can be interpreted in terms of a process controlled by an activation energy using the relation

$$i = \kappa\lambda \frac{ekT}{h} a_1 \exp(-U/kT) \exp(\beta\lambda e\eta/kT) \quad [6]$$

This expression is valid provided η, the overpotential across the barrier, is large enough to inhibit the reverse current across the barrier. Here κ is the transmission coefficient, λ the valence of the charge carriers, a_1 the activity of carriers moving across the barrier in the forward direction, U the activation energy at the reversible potential, and β the fraction of the overpotential aiding motion in the forward direction. The other symbols have their standard meanings.

The parameter V_o can be interpreted in terms of this equation using a simple Mott-Cabrera model (13). The data plotted in Fig. 2 show that V_o is proportional to the formation potential, V_f. In this model the overpotential appears across a layer of thickness D, setting up an electric field V/D in the layer. The product of this field and the half jump distance, a, gives the overpotential which aids the forward current, $\beta\eta$. Thus

$$V_o = (kT/\lambda ea)D \quad [7]$$

and is directly proportional to the layer thickness.

The experimental data strongly support a model of this type in which the electric field in the layer controls the current density through the layer. The parameter V_o varies over a wide range of values, and the fit to a linear proportionality to formation potential for fixed formation current density is quite good. Data taken at different formation current densities fall on lines with slightly (but significantly) different slopes. Since V_o and Q are both proportional to the layer thickness, dV/dQ is proportional to dV/dV_o. The difference in the slopes in Fig. 2 is essentially the experimental data from which the high-field models are deduced in the dV/dQ measurements. In terms of the open-circuit measurements, the high-field model is deduced from the first-order proportionality of V_o to V_f, and the second order dependence of the V_o *vs.* V_f slope on the formation current density is related to the behavior of the parameter i_o.

The behavior of the parameter i_o cannot be interpreted in terms of a simple Mott-Cabrera model since this model assumes that all of the factors in Eq. [6] except the exponential factor containing the overpotential are constants. The dependence of i_o on the formation current density detected experimentally can be made consistent with Eq. [6] by choosing a more complicated model in which at least one of these factors can vary. The Frenkel-defect model (14) used to interpret transient Tafel slopes in theories based on dV/dQ data is one such model in which the activity factor is given an explicit field dependence. We do not feel that we can deduce a meaningful model to account for the i_o variation from present experimental data. In Fig. 4, i_o is plotted *vs.* the formation current density, i_f, both of which parameters have the same dimensions. The data in Fig. 4 could equally have been given in terms of the formation field. Had the parameter i_o been found experimentally to be independent of the formation current density, the open-circuit parameters would have been identical to the parameters determined by dV/dQ measurements, and the dV/dQ data would have predicted transient Tafel slopes.

The data in Fig. 3 show that the reciprocal of the capacitance which is discharged through the layer during an open-circuit transient is proportional to the formation potential and, therefore, is proportional to the layer thickness. It might be expected that the reciprocal capacitance data would show the same dependence on the formation current density that is shown by V_o, a result which has been obtained by other workers (1). One explanation of the lack of dependence on formation current density found here is that the parameter θ from which the reciprocal capacitance is calculated is far less sensitive to the fitting process than is V_o. This explanation must be rejected on the basis of the experimental evidence in Fig. 3, which shows very little scatter in the reciprocal capacitance data. The explanation we propose for this behavior is based on data obtained in our laboratory (16) on the effect of the electric field in the layer on the low-frequency dielectric constant and the refractive index of the layer. It was found that at fixed layer thickness the reciprocal capacitance of the layer decreased appreciably when the current density through the layer was lowered, and it exhibited an overshoot of similar duration to the potential overshoot. The data obtained by other workers which detected the dependence of the slope of the reciprocal capacitance *vs.* formation potential on current density were taken with the formation current disconnected. We suggest that the reciprocal capacitance plotted in Fig. 3 is the reciprocal capacitance with the formation current flowing and that $1/C$ retains its initial value over the initial portion of an open-circuit transient, as does i_o. Our data on the field dependence of the dielectric constant predicts that this reciprocal capacitance should show very little dependence on the formation current density.

The equation usually used to describe the steady-state (constant growth rate) current density through the oxide layer during the anodic oxidation of tantalum is

$$i = A \exp(BE) \quad [8]$$

where E is the electric field in the layer and A and B are constants with the values $0.5 \cdot 10^{-12}$ μa/cm^2 and $5 \cdot 10^{-6}$ cm/v, respectively. The transient presented in Fig. 5 can be used to illustrate the way in which the parameter A can be determined. The slope of the curve in Fig. 5 is about 5% lower at a formation current density of 40 μa/cm^2 than it is at 200 μa/cm^2.

Since dV/dQ is proportional to E, and E is in turn proportional to log (i/A), log (i/A) must also change by 5% when the formation current density is switched between these two values, implying that $A = 2 \cdot 10^{-12}$ μa/cm^2. This estimate agrees reasonably well with the accepted value given above.

The steady-state equation (Eq. [8]) can also be obtained from the open-circuit transient data as a special case of Eq. [1]. In the steady state, Eq. [5] can be substituted into Eq. [1], giving

$$i_f = k\ (i_f)^{\alpha} \exp\ (V_f/V_o)$$

or

$$i_f = (k)^{1/(1-\alpha)} \exp (V_f/(1-\alpha)V_o) \qquad [9]$$

For the parameters in Eq. [9] to have the same values as the parameters in Eq. [8], α must have a value of 0.63. This value falls within our estimate of the error in α. (This error estimate takes into account the fact that V_o is determined from the slope of V *vs.* log $(t+\theta)$, i_o from the slope of V_o *vs.* V_f, and α from a third successive slope, the slope of log i_o *vs.* log i_f.)

The parameter α can be estimated much more accurately with the aid of Fig. 5 by extrapolating the linear portion of the potential transient at 200 μa/cm^2 back to the point where the current density was switched from 40 μa/cm^2. The potential at this point is found to be 12.9v. Thus when the current was switched the change in the formation potential (ignoring the potential overshoot) was from 12.2v to 12.9v. Using

$$V = V_o \log (i/i_o) = V_o \log (i/k(i)^{\alpha})$$

one obtains

$$\Delta V = V_o\ (1-\alpha)\Delta \log\ (i) = V_o\ (1-\alpha)\ \log\ (i_2/i_1)$$

With $i_1 = 40$ μa/cm^2, $i_2 = 200$ μa/cm^2, $V_o = 1.1$v (at $V = 12.2$v), and $\Delta V = 0.70V$ (from Fig. 5) one finds that $\alpha = 0.61$, which is consistent with the value of 0.63 necessary for the numerical comparison of Eq. [8] and [9].

We have stated that i_o is a function of the formation current density, but so far the only statement we have made about the manner in which i_o changes when the formation current density is changed is that i_o changes very little during the initial portion of an open-circuit transient. We would now like to outline briefly one way in which potential overshoot may be treated using the parameters derived from open-circuit transients.

The general equation used to relate the total current in the circuit to the currents charging the layer capacitance and flowing through the layer was given in Eq. [2]. The differential equation describing this type of galvanostatic transient can be obtained in much the same manner as Eq. [3] was obtained, with the exception that here V, C, i_o, and V_o are all functions of time. The time dependence of V_o can be taken care of quite simply by setting V_o proportional to Q. The capacitance may be considered a constant because the capacitive term is only important when dV/dQ is large. Therefore it is only necessary to specify the time dependence of i_o in order to solve the differential equation. One such time dependence is a relaxation time approximation for the change in i_o when the formation current density is changed from $i_{f,i}$ to $i_{f,f}$

$$i_o = i_{o,f} + (i_{o,i} - i_{o,f}) \exp\ (-t/\tau) \qquad [10]$$

where τ is a relaxation time. Since the experimental evidence shows that the overshoot involves an approximately constant amount of charge, the relaxation time can be made inversely proportional to the current density, the proportionality constant being the only unknown parameter which must be fit to experimental data. The foregoing discussion is in no sense an explanation of potential overshoot; it is merely one way of fitting overshoot transients using the parameters V_o and i_o determined from open circuit transients.

The discussion of overshoot given above predicts a long relaxation time for open-circuit transients for which the only current flowing through the layer is the rapidly decreasing current which discharges the layer capacitance. This prediction is consistent with our assumption based on the fitting of open-circuit transients that i_o does not change appreciably over the initial portion of an open-circuit transient. If an extended open-circuit transient is analyzed, a deviation from a log $(t + \theta)$ fit is found for large values of t. The direction of this deviation is such as to produce a slower decrease of V with t than predicted by log $(t + \theta)$. This deviation is consistent with our prediction that any change in i_o over an open-circuit transient must be a decrease produced by the decreasing current density through the layer. A deviation in the other direction is observed with poorly prepared samples with appreciable leakage currents. Reclosing the circuit produces a slight overshoot whose magnitude increases with the duration of the open-circuit transient. We interpret this overshoot as the recovery of i_o to its initial value. A larger overshoot is observed if, instead of opening the circuit, the current density is lowered by a factor of two for the same length of time before reapplying the initial current density. Greater potential changes (and hence field changes) are produced during the open-circuit transient than during this transient, but we interpret the smaller overshoot as indicating that the open-circuit transient creates a smaller perturbation of the system. It is for this reason that we prefer open-circuit transients for studying the system. We feel that they come closest to determining the true field dependence of the current density, *i.e.*, the partial derivative of the current density with respect to electric field with all other variables constant.

If an equation relating current density to overpotential, deduced from experimental data, is considered to be no more than a compact way of summarizing the experimental results, then the exact form of the equation is not important. If, on the other hand, the equation is considered to have sufficient general validity to enable it to be compared with a theoretical equation such as Eq. [6] in order to deduce a model for the conduction process, then the form of the equation becomes very important, since it is generally the model and the deduced values of parameters and not the experimental data on which they are based which are referred to when describing a system. For example, it has been stated that one of the basic differences between the behavior of the valve metals and that of the passive metals is the vast difference between the value of A quoted for the valve metals and the value of i_o quoted for the passive metals. We have shown that this vast difference between the values arises because of different approaches to the data analysis. When the two systems are studied using open-circuit transients, their behavior is found to be quite similar.

We have stated that the parameters obtained from open-circuit transients provide a basis for the comparison of the anodic oxidation of tantalum with that of iron in a neutral electrolyte. It has been previously mentioned that both of these systems show a slight dependence of dV/dQ on log i. It is also well known that both systems show potential overshoot when the current density is abruptly changed. By comparing the open-circuit transient data for iron in a neutral electrolyte presented by Ord (4), several more quantitative similarities become evident. The potential decay during an open-circuit transient fits Eq. [4] for both systems, implying that the dependence of overpotential on current density may be described by Eq. [1] for both systems. Both systems show a linear dependence of V_o on V_f at constant formation current density. The value of the slope of this line is comparable in the two systems (for tantalum it is about 0.09 while for iron it is 0.2). Both systems show a slight dependence of the slope of V_o *vs.* V_f on the formation current density; in both cases the slope increases with decreasing current density. Thus the

parameter i_o will depend on the current density in roughly the same manner for both systems. Values of i_o for comparable formation current densities are $7 \cdot 10^{-5}$ μa/cm^2 for tantalum and $5 \cdot 10^{-3}$ μa/cm^2 for iron [this latter number was calculated from data presented in ref. (4)].

Because of the many similarities between iron and tantalum it is our opinion that many general features of the anodic oxidation process may be independent of the metal involved, even when the metals are as dissimilar as iron and tantalum. Therefore we believe that any theory devised to apply to one of these systems should be equally applicable to the other. For this reason we feel that theories of the passivity of iron which place the entire overpotential across the electrical double layer are not tenable. Likewise, any theory of the anodic oxidation of tantalum should be applicable to a film only 10Å thick.

Acknowledgment

The authors are indebted to Mr. P. Freeman for his assistance in performing the experiments, and to Mr. P. Isaacs and Mr. A. Weerheim of the University of Waterloo Computing Centre for their work with the process control computer. This work received partial support from the National Research Council of Canada under Grant No. A-1151, and from the Office of Naval Research under Contract No. N00014-66-C0200.

Manuscript submitted Sept. 12, 1966; revised manuscript received Sept. 30, 1968.

Any discussion of this paper will appear in a Discussion Section to be published in the December 1969 JOURNAL.

REFERENCES

1. L. Young, *Trans. Faraday Soc.*, **53**, 841 (1957).
2. N. Sato and M. Cohen, *This Journal*, **111**, 512 (1964).
3. A. Guntherschulze and H. Betz, *Z. Phys.*, **92**, 367 (1934).
4. J. L. Ord, *This Journal*, **113**, 213 (1966).
5. J. L. Ord., *ibid.*, **112**, 46 (1965).
6. W. J. McG. Tegart, "The Electrolytic and Chemical Polishing of Metals," Pergamon Press, London (1956).
7. H. G. Feller and J. Osterwald, *This Journal*, **111**, 119 (1964).
8. D. C. Grahame, *J. Phys. Chem.*, **57**, 257 (1953).
9. J. L. Ord and J. H. Bartlett, *This Journal*, **112**, 160 (1965).
10. J. L. Ord and D. J. De Smet, *ibid.*, **113**, 1258 (1966).
11. L. Young, *Trans. Faraday Soc.*, **50**, 153 (1954).
12. D. A. Vermilyea, *Acta Met.*, **1**, 282 (1953).
13. N. Cabrera and N. F. Mott, *Rept. Prog. Phys.*, **12**, 163 (1948-49).
14. J. F. Dewald, *J. Phys. Chem. Solids*, **2**, 55 (1957).
15. C. P. Bean, J. C. Fisher, and D. A. Vermilyea, *Phys. Rev.*, **101**, 551 (1956).
16. J. L. Ord, *This Journal*, **114**, 57C, Abstract No. 42 (1967).

Effects of Oxidizable Anion Adsorption on the Anodic Behavior of Platinum

Sigmund Schuldiner*
Naval Research Laboratory, Washington, D. C.

ABSTRACT

The retardation of the hydrogen oxidation reaction which commences at about 0.7v (NHE) in sulfuric acid solution can be modified by the presence of formate ions. Steady-state, potentiostatic measurements were made in formic acid and formic acid plus sulfuric acid solutions both in the presence and absence of hydrogen. The work showed that at potentials under 1.5v passivity was due to adsorbed anions rather than adsorbed oxygen atoms, Pt oxides, or free radicals formed by the oxidation of water. Pure formic acid solutions were not passivated below 1.5v; however, formate ion did retard hydrogen oxidation, but not as strongly as does sulfate ion. The oxidation of formic acid in solutions containing sulfuric acid was affected by adsorption of both sulfate and formate ions. The retardation of the net oxidation of hydrogen and formic acid in formic acid-sulfuric acid mixtures was less than that of hydrogen in sulfuric acid. In the presence of dermasorbed oxygen, both formate and sulfate ions strongly retard the oxidation of added species. The effect of potential on reaction rate appears to depend on the particular organic species adsorbed and may reflect the potential of zero charge.

Several recent papers (1-3) from this Laboratory have indicated that under steady-state, potentiostatic conditions, the retardation of the hydrogen oxidation reaction at potentials more anodic than 0.7v may be caused by anion adsorption rather than adsorbed oxygen atoms, oxides, or oxygen containing radicals. The possibility of this passivation being due to adsorbed oxygen atoms, oxides, or oxygen-containing free radicals was shown to be improbable because of the very rapid reaction of such oxygen species with hydrogen.

To provide further evidence to support the author's opinions concerning anion adsorption, experiments were designed to determine the effects of reactable (oxidizable) anions. Such oxidizable anions should compete with inert anions adsorbed at anodic potentials and may affect reaction rates. In addition the total replacement of an inert anion with a readily oxidizable anion should eliminate or appreciably reduce passivation due to anion adsorption.

It was felt that an ideal oxidizable anion for this work would be formate ion. This is the simplest type of organic anion. It should be easily adsorbed at positive potentials and is fairly easily oxidized. Formate ions and formic acid could be dissociated on a Pt electrode and neutral products such as atomic hydrogen, carbon monoxide, and carbon dioxide, could be formed. However, if formate ion can adsorb on the surface (or highly polarizable formic acid, free radicals or similar species), competition with inert anions are possible and information concerning the effects of such adsorbed species[1] on the rate of anodic reactions would be available.

Experimental

The experimental high-purity, gas-tight setup and conditions were the same as previously used (1, 4). The solutions were 1M formic acid, and 0.1M and 1M formic acid in 1M sulfuric acid solution. Each solution was investigated under both helium and hydrogen saturated conditions (atmospheric pressure). The formic acid was reagent grade. An initial run through the

* Electrochemical Society Active Member.

[1] No attempt was made in this work to determine the actual organic species which were adsorbed or oxidized and the terms formic acid and formate ion are not used in a strict sense.

potential range up to 2v was made before data were recorded. The concentrations of formic acid given are the initial values; losses in concentration due to electrochemical reaction, decomposition, and vaporization during each experiment did occur. Titrations of acid content after termination of a run (some lasted for over a month) showed decreases in the order of 25-40% of formic acid. However, changes in the potentiostatic current density *vs.* voltage relations were not appreciable during a series of runs. In several cases, formic acid was added during a run to approximately approach the initial concentration. This made little difference.

It should be emphasized that this work was designed to determine the steady-state potentiostatic behavior of formic acid oxidation and oxidation of hydrogen and formic acid mixtures with especial interest in the influence of the formic acid (or a derivative) on the passive behavior of platinum in the potential region above 0.7v (NHE). No attempt was made to correct for IR losses in the low conductivity, pure formic acid solutions, to conduct a mechanistic or kinetic study which involved the various by-products of formic acid, or, indeed, to determine what the reaction steps or products were. The goal was the effects of formate ion adsorption (or other oxidizable by-products), in particular the effects of such species on the adsorption of an inert anion (sulfate ion) and on the reactability of oxidizable species on a Pt anode.

The two bright Pt bead (99.99%) working electrodes used were about 0.5 cm^2 in true area (5) and the temperature was 25° ± 2°C. The gas flow into the cell was about 40 ml/min until a steady-state current density was reached. The time necessary to attain this steady-state current density varied from a few minutes to more than a day, depending on both the set potential and the previous sequence of potentials. The gas flow rate was then increased to well over 1000 ml/min, and the constant current density was recorded. Potentiostatic control was accomplished with a Pt wire reference electrode for one series of runs and with a Pd wire reference in a side arm for another series. The presence of a Pd wire made no apparent difference in the potentiostatic measurements. When hydrogen flowed either a Pt/H_2 reference electrode or a miniature glass electrode was used to monitor the potential. The results were the same in either case. In helium saturated solution the potential monitoring reference was always a miniature glass electrode. All potentials are referred to the normal hydrogen electrode (NHE) with the exception of the data in pure formic acid solutions (Fig. 2 and 3) where the reference electrode is the hydrogen electrode, same solution (HESS). To change the scale for these formic acid solutions to NHE would require a reduction of the HESS values by about 0.1v.

Cyclic current fluctuations usually ranging from about 10 to 20% were observed in the potential region between 0.3 and 1v and on the decreasing potential sequence from 1.3 to 0.9v. Values shown in the figures are average values. The scatter of points was essentially the same as found for pure hydrogen [Fig. 1, ref. (1)]. At least three increasing and decreasing potential sequences were determined and wherever critical changes occurred, many additional checks were run. Figure 1 demonstrates the current density *vs.* time relation typically found when the potential was changed in regions where slow changes occurred.

Results and Discussion

Figures 2 and 3 show the potentiostatic current density *vs.* potential relations obtained in 1M formic acid both in helium- and hydrogen-stirred solution. Figure 2 is for the increasing potential sequence, whereas Fig. 3 is for the decreasing potential sequence. The broken line in Fig. 2-7 is either the increasing or decreasing potential sequence for the oxidation of water in helium-saturated 1M sulfuric acid solution (4) and the dotted line in each figure is either the increasing or decreasing potential sequence for the oxidation of hydrogen (1) in 1M H_2SO_4.

The 1M HCOOH curve in Fig. 2 shows that although the rate of oxidation of formic acid is much slower than hydrogen oxidation there is no passivation of the Pt electrode to the formic acid oxidation below 1v. Indeed, the rate of oxidation of formic acid increases with potential or remains constant in several potential regions until a potential of 1.6v (HESS) or about 1.5v (NHE) is reached. From about 1.0 to 1.8v the rate of formic acid oxidation is about one order of magnitude faster than the rate of hydrogen oxidation in sulfuric acid solution.

The mixture of formic acid and hydrogen, as illustrated in Fig. 2, shows a great increase in the rate of oxidation at potentials below 1.0v. This shows that the primary reaction in this region is the oxidation of hydrogen. The formic acid under these potential conditions retards the hydrogen oxidation reaction. There is a retardation of the oxidation reaction at about 0.8 to 1.2v, but it is not as sharp as for pure hydrogen in sulfuric acid solution. At potentials more noble than 1.2v, the rate of oxidation of the formic acid-hydrogen mixture is essentially the same as for formic acid alone.

The data in Fig. 2 clearly show that passivation of platinum for formic acid oxidation does not occur

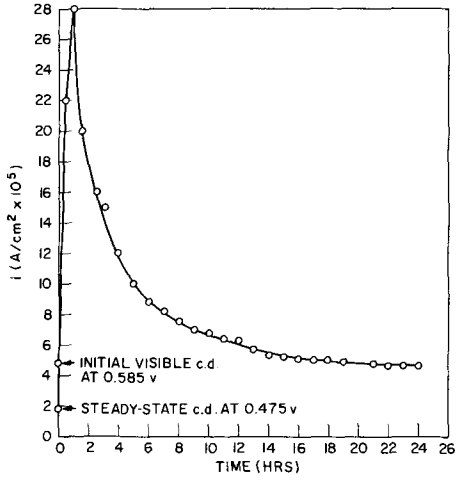

Fig. 1. Typical current density *vs.* time relation found when the potential was changed in a region where slow processes occurred. Potential was increased from 0.475 to 0.585v 0.1M HCOOH + 1M H_2SO_4.

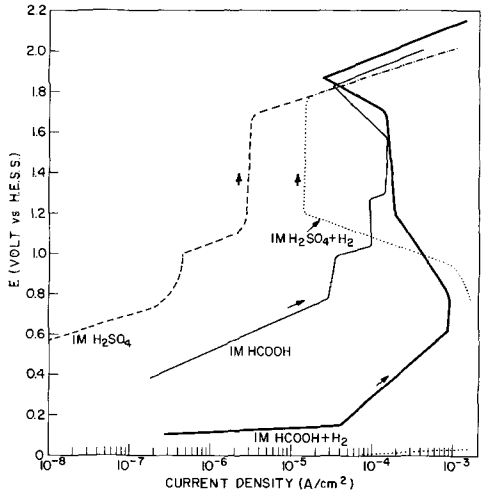

Fig. 2. Potentiostatic anodic current density *vs.* potential relation on a bright Pt electrode for increasing potential sequence. Solid lines, 1M HCOOH in helium- and hydrogen-saturated solutions (1 atm); broken line, 1M H_2SO_4 in helium-saturated solution; dotted line, 1M H_2SO_4 in hydrogen-saturated solution. HESS is hydrogen electrode, same solution.

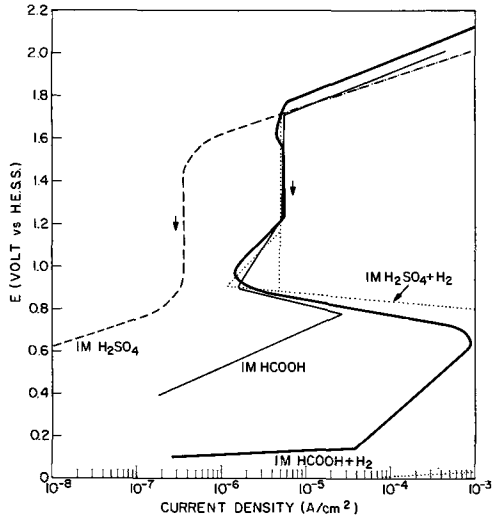

Fig. 3. Potentiostatic anodic current density vs. potential relation on a bright Pt electrode for decreasing potential sequence. Solid lines, 1M HCOOH in helium- and hydrogen-saturated solutions (1 atm). See legend in Fig. 2. for meaning of broken and dotted lines. HESS is hydrogen electrode, same solution.

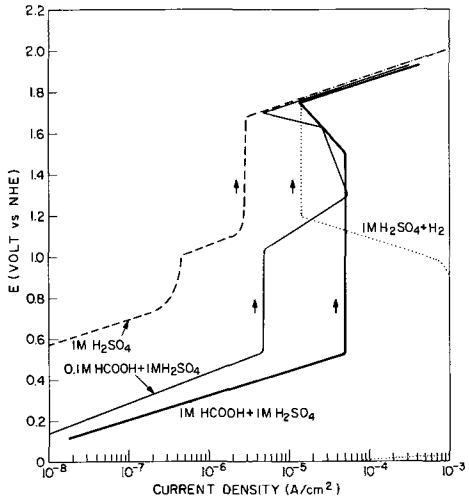

Fig. 4. Potentiostatic anodic current density vs. potential relation on a bright Pt electrode for increasing potential sequence. Solid lines, 0.1 and 1M HCOOH in 1M H_2SO_4 in helium-saturated solution. See legend in Fig. 2 for meaning of broken and dotted lines.

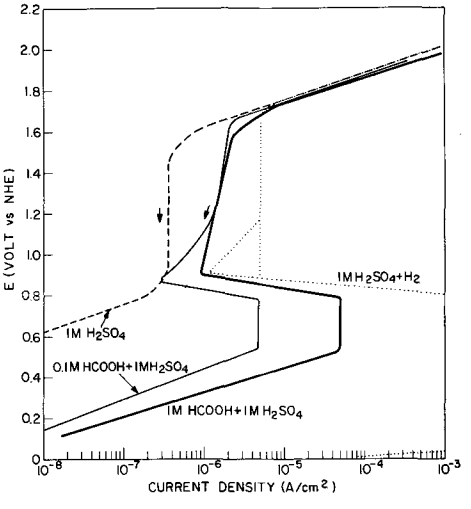

Fig. 5. Potentiostatic anodic current density vs. potential relation on a bright Pt electrode for decreasing potential sequence. Solid lines, 0.1 and 1M HCOOH in 1M H_2SO_4 in helium-saturated solution. See legend in Fig. 2 for meaning of broken and dotted lines.

below 1.6v. Hence the formation of either oxides or adsorbed oxygen atoms which passivate the electrode is not possible. In the case of the formic acid-hydrogen mixture, formate ion most likely is being adsorbed, which in fact retards the hydrogen oxidation reaction, even though the formate ion itself can be oxidized but at a much slower rate. Determinations of the over-all rate of oxidation of a monolayer of $Pt\text{-}O_{ad}$ with formic acid gave reaction rates of about 5×10^{-4} amp/cm². Thus the rate of reaction of adsorbed oxygen atoms with formic acid is well over two to three orders of magnitude faster than the oxidation of water in the potential range from 0.7 to 1.6v. Hence, significant amounts of oxygen cannot remain on the surface below 1.6v.

Data for the decreasing potential sequence, Fig. 3, clearly show that, from 1.7 to 0.9v, the behavior of formic acid, formic acid + hydrogen, and hydrogen in sulfuric acid solution is virtually identical. Evidently, the formation of dermasorbed oxygen decreases the catalytic activity of the platinum so much that the rate of oxidation of formic acid is identical to that of hydrogen in the presence of sulfate ion. However, the rate of water oxidation under similar potential conditions is still significantly slower. It should be mentioned that the presence of dermasorbed oxygen also considerably reduces the reaction rate of adsorbed oxygen with oxidizable species such as hydrogen (6). However, it is doubtful that adsorbed oxygen is an important factor under these conditions. This is because the reduced reaction rate between adsorbed oxygen and hydrogen or formic acid would still be well above the rate of water oxidation.

Potentiostatic polarization curves (increasing potential sequence) for a mixture of formic acid and sulfuric acid at two nominal concentrations of formic acid (0.1 and 1M) are shown in Fig. 4. Here again, even though, at lower potentials, the rate of oxidation of formic acid is considerably slower than that of hydrogen; no passivation occurs at 0.7v. Passivity is evident at about 1.6v only. Furthermore, in the potential range between 1.2 and 1.6v, the rate of oxidation of formic acid is greater than that of hydrogen. At potentials above 1.7v, where the principle reaction is the oxidation of water to oxygen, formate ions slightly increase the net oxidation current.

For the potential decreasing sequence shown in Fig. 5, in the potential range from 1.7 to 0.9v the rate of the oxidation of formic acid mixed with sulfuric acid is well below that of either formic acid, formic acid + hydrogen, or hydrogen in sulfuric acid solution (Fig. 3). This shows that sulfate ion adsorption on the Pt electrode containing dermasorbed oxygen retards the formic acid oxidation considerably more than the hydrogen oxidation. Thus under similar conditions of sulfate ion plus dermasorbed oxygen, hydrogen is more readily oxidized than is formic acid. This indicates that even though formate ions may be present, the bulk of the coverage of the electrode is with sulfate ions and that under similar surface conditions and at high positive potentials the electrostatic attraction of formate ions does not have as great a bearing on the rate of oxidation as does the presence of a neutral but more easily oxidizable species such as hydrogen. This is in contrast with the case of the increasing potential sequence (Fig. 4) where formate ions do effectively compete with sulfate ions. The difference is most likely due to the reduction in catalytic activity owing to dermasorbed oxygen. The dermasorbed oxygen affects the rate of formic acid oxidation much more than that of hydrogen.

The data shown in Fig. 6 and 7 show the potentiostatic behavior in formic acid + sulfuric acid in the presence of hydrogen for the increasing and decreasing potential sequence, respectively. Figure 6 shows that in the active low potential range, high concentrations (1M) of formic acid in the presence of sulfate ion retard the hydrogen oxidation rate considerably more than in the absence of sulfuric acid (Fig. 2). At low

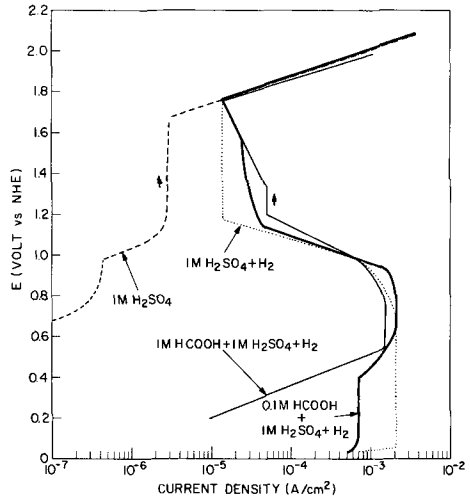

Fig. 6. Potentiostatic anodic current density *vs.* potential relation on a bright Pt electrode for increasing potential sequence. Solid lines, 0.1 and 1M HCOOH in 1M H_2SO_4 in hydrogen-saturated solution. See legend in Fig. 2 for meaning of broken and dotted lines.

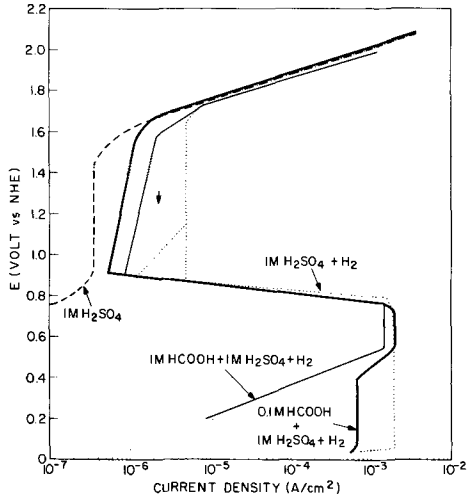

Fig. 7. Potentiostatic anodic current density *vs.* potential relation on a bright Pt electrode for decreasing potential sequence. Solid lines, 0.1 and 1M HCOOH in 1M H_2SO_4 in hydrogen-saturated solution. See legend in Fig. 2 for meaning of broken and dotted lines.

concentrations of formic acid (0.1M), however, oxidation of hydrogen is affected only moderately.

In the potential range from 0.7 to 1.6v, passivation does occur as in the case of pure hydrogen; however, the presence of formic acid has a moderating effect and significantly increases the rate of the net oxidation reaction. This is believed to be due to the competitive adsorption of formate ions which can be oxidized and can contribute to the net anodic current. Figure 7 again shows that the presence of formic acid considerably retards the hydrogen oxidation reaction when dermasorbed oxygen is present. In the low current density regions shown in both Fig. 5 and 7, water oxidation may contribute significantly to the net current density.

Investigations of formic acid oxidation [see Conway (7) and Piersma and Gileadi (8) for reviews] offer only a limited amount of information on the steady-state, potentiostatic oxidation of formic acid at potentials positive to 0.9v. Gilroy and Conway (9) refer to data from Conway's laboratory which indicate a passivation of formate ion oxidation in aqueous solution at about 1v. They attribute this passivation to the presence of a passivating "oxide." For pure formic acid-potassium formate solutions, Conway, *et al.* (10) indicated passivation by the formation of intermediates. The results reported here (Fig. 2) indicate no passivation in aqueous formic acid solution up to 1.6v. The data obtained in this investigation verify previous findings (1-3) that passivation in the vicinity of 0.7v is due to sulfate ion adsorption rather than the formation of adsorbed oxygen, an oxide, or other oxidation products of water. Water oxidation is too slow below 1.6v, and the oxidation products of water on a Pt surface react so rapidly with oxidizable species in solution that the possibility of the build-up of a passive layer by such oxygen species is most unlikely. Only at high noble potentials is the combined effects of anion adsorption and sorbed oxygen adequate to retard the oxidation of hydrogen and formic acid effectively. At sufficiently noble potentials the rate of water oxidation exceeds the rate of hydrogen and/or formic acid oxidation.

The data can therefore be reasonably explained by attributing passivity to anion adsorption. As shown in Fig. 2, formate ion can cause passivation of the hydrogen oxidation reaction, but the retardation of reaction rate is much less than for inert sulfate ions. Since formic acid is more difficult to oxidize than hydrogen it would tend to increase the retardation if oxygen passivated the Pt electrode, but the reverse is obtained.

One may argue that some formate ion attracted to the positive surface in the passive region may cause a partial breakdown of a passive oxygen layer and, thereby, increase the rate of oxidation. However, this is not borne out by the behavior observed in the decreasing potential sequence curves (Fig. 3, 5, and 7). Figure 3 shows that in the presence of dermasorbed oxygen the formate ion retards the rate of hydrogen oxidation just as much as does sulfate ion. The data in Fig. 5 and 7 show that in the presence of dermasorbed oxygen and both sulfate and formate ions, the rate of oxidation of hydrogen is less than in the presence of only sulfate or formate ion (Fig. 3). Figure 2 clearly shows that, even though formate ion does not passivate its own oxidation below 1.6v, it passivates hydrogen oxidation at 0.8v. In addition, a breakdown in passivity due to formate ion adsorption assumes a complete oxygen coverage of the Pt surface at potentials in the vicinity of 0.7v. Data previously given (2) show that such a complete oxygen film is not obtained. The 1M HCOOH + 1M H_2SO_4 curve in Fig. 4 shows that a limiting current density is reached at 0.5v and passivation does not occur until 1.5v. Contrasting this with the results for 1M HCOOH shown in Fig. 2, the initial limiting current density occurs at 0.8v. These results show that sulfate ions do play an important role in the oxidation of formic acid.

One may speculate on the potential of zero charge (pzc) and the region in which adsorption of formic acid species are at a minimum. This effect is best seen in Fig. 6 in the 0.1M HCOOH + 1M H_2SO_4 + H_2 curve. These data show a current density maximum between 0.6 and 0.8v. Below 0.6v the rate of hydrogen oxidation is moderately retarded by formic acid, but in the potential range from 0.6 to 0.8v a current density of 2×10^{-3} amp/cm^2 is reached. This is exactly the maximum current density found for pure hydrogen oxidation in high purity sulfuric acid solution (1). This may indicate that the potential of zero charge is in the vicinity of 0.6-0.8v because at the pzc the adsorption of a highly polarizable species, such as formic acid or of formate ion, should be at a minimum. The maximum current density of 2×10^{-3} amp/cm^2 does not decrease until a potential of 0.8v. Contrast this to the 1M H_2SO_4 + H_2 curve which starts decreasing at 0.7v. This also shows that formate ion does compete with sulfate ion in the passivation of the Pt surface.

Conclusions

This work verifies that, at potentials negative to 1.5v, passivation of a Pt electrode to the oxidation of hydrogen is not due to the adsorption of species from

the oxidation of water or to the formation of Pt oxides. Such passivity is caused by anion adsorption.

If the oxidizable material exists as an adsorbable anion, which can oxidize faster than water, then no passivation will occur. If a species is present which is oxidized more rapidly than the adsorbable anion, then the oxidation of that species will be retarded when the potential is noble enough to significantly adsorb such anions.

In the presence of dermasorbed oxygen, passivation in a combination of sulfuric and formic acids is much more pronounced than in the presence of either acid alone. The oxidation reaction rates may give a clue as to the potential of zero charge in the presence of an organic species which is both easily polarized and ionized.

Manuscript submitted March 22, 1968; revised manuscript received Jan. 13, 1969.

Any discussion of this paper appears in the Discussion Section of this issue, p. 824. Additional discussion will be published in the December 1969 JOURNAL.

REFERENCES

1. S. Schuldiner, *This Journal*, **115**, 362 (1968).
2. S. Schuldiner, *ibid.*, **115**, 897 (1968).
3. S. Schuldiner and C. M. Shepherd, *ibid.*, **115**, 916 (1968).
4. S. Schuldiner, T. B. Warner, and B. J. Piersma, *ibid.*, **114**, 343 (1967).
5. S. Schuldiner and R. M. Roe, *ibid.*, **107**, 452 (1960).
6. S. Schuldiner and T. B. Warner, *ibid.*, **112**, 212 (1965).
7. B. E. Conway, in "Progress in Reaction Kinetics," Vol. 4, pp. 430-437, G. Porter, Editor, Pergamon Press, Oxford (1967).
8. B. J. Piersma and E. Gileadi, in "Modern Aspects of Electrochemistry," No. 4, pp. 102-114, J. O'M. Bockris, Editor, Plenum Press, New York (1966).
9. D. Gilroy and B. E. Conway, *J. Phys. Chem.*, **69**, 1259 (1965).
10. B. Conway, E. Gileadi, and M. Dzieciuch, *Electrochim. Acta*, **8**, 143 (1963).

The Electrical Properties of Lanthanum Oxide-Calcium Oxide Solid Electrolytes

T. H. Etsell and S. N. Flengas*

Department of Metallurgy and Materials Science, University of Toronto, Toronto, Ontario, Canada

ABSTRACT

Electrical conductivity measurements have been made in the La_2O_3-CaO system as a function of composition, temperature, and oxygen pressure. At 1600°C, La_2O_3 can dissolve about 16 m/o CaO which leads to the creation of anion vacancies. These defect solid solutions behave as oxygen anion conductors below an oxygen pressure of 10^{-7} atm. Above this pressure, the appearance of p-type conductivity, proportional to $P_{O_2}^{1/4}$, produces a region of mixed conduction. No evidence of n-type conductivity was observed. Even La_2O_3 exhibits predominantly ionic conduction at intermediate oxygen pressures. Several transport numbers were verified by emf measurements. The results of this investigation are compared with those obtained previously for other oxide electrolyte systems.

For certain substitutional solid solutions of oxides having cations of different valences, the condition of electrical neutrality requires the appearance of oxygen anion vacancies. Within specified ranges of temperature and oxygen pressure, such systems exhibit exclusively ionic conduction arising from the motion of oxygen anions through lattice vacancies. However, outside these ranges, the solid solutions cease to function satisfactorily as electrolytes due to the appearance of either p- or n-type conductivity.

Most of the previous studies of the electrical conductivities of these electrolytes have dealt with mixtures of various di- and trivalent metal oxides (MgO, CaO, SrO, Sc_2O_3, Y_2O_3, and the rare earth oxides) with the group IV oxides ZrO_2 (1-9), ThO_2 (10-17), HfO_2 (5, 18, 19), and CeO_2 (20, 21). For solid solutions based on trivalent metal oxides, only a limited number of measurements have been reported (22-24), and the potentiality of such systems as solid electrolytes cannot be properly evaluated. Particularly, for the La_2O_3-CaO system, results have been given (23) for only two oxygen pressures.

In the present investigation, the electrical properties of La_2O_3-CaO solid solutions containing from 0 to 50 m/o (mole per cent) CaO have been measured over the temperature interval 400°-1100°C, under oxygen pressures varying between 1 and 10^{-21} atm at 1000°C. Care was taken to ensure that equilibrium was achieved during the preparation of the specimens since several authors (25, 26) have denied any significant solubility of CaO in La_2O_3, although Foex (27) determined that 16 m/o CaO could be dissolved during fusion in a solar furnace.

Normally, La_2O_3 has the hexagonal A-type rare earth oxide structure. The cubic C-type can only be prepared by decomposing lanthanum compounds below 550°C (28-30). Other forms may be stable above 2040°C (31), although these phases could not be retained by rapid quenching to room temperature. In A-type La_2O_3, each cation is seven-coordinated with six of the oxygen anions in an octahedral arrangement which is distorted to accommodate the seventh. The cations have four oxygen neighbors at 2.42Å and three at 2.69Å (32). Both four- and five-coordinated oxygen anions exist in the lattice.

During the formation of solid solutions in the La_2O_3-CaO system, substitution of La^{3+} ions with Ca^{2+} ions on the cation sublattice will cause the formation of either anion vacancies or cation interstitials. For the anion vacancy model, the fraction of vacant oxygen sites x_{V_O} will be given by

$$x_{V_O} = \frac{x_2}{6x_1 + 3x_2} \qquad [1]$$

where x_1 and x_2 are the mole fractions of La_2O_3 and CaO, respectively. Even for small additions of CaO,

* Electrochemical Society Active Member.

the composition-controlled vacancy concentration will far exceed that arising from thermal disorder. In a system of this kind, the ionic conductivity σ_i may be expressed as

$$\sigma_i = [V^{\cdot\cdot}_O]2eu \quad [2]$$

where $[V^{\cdot\cdot}_O]$ is the charge carrier concentration in vacancies per cubic centimeter, $2e$ is the charge in coulombs, and u is the mobility in square centimeter/volt-second. Therefore, there will be a large increase in the ionic conductivity accompanying the addition of CaO to La_2O_3 which could result in an oxygen pressure region of almost exclusively ionic conduction.

According to the theory of Kiukkola and Wagner (33), at high oxygen pressures some of the anion vacancies may dissolve gaseous oxygen according to the reaction

$$\tfrac{1}{2}\, O_{2(g)} + V^{\cdot\cdot}_O = O_O + 2h^{\cdot} \quad [3]$$

where $V^{\cdot\cdot}_O$ is a doubly ionized oxygen vacancy, O_O is an oxygen anion on a normal lattice site, and $h^{\cdot}$ is an electron hole. Assuming that the concentration of electron holes p is low, the equilibrium constant for this reaction may be written as

$$K = \frac{p^2}{P_{O_2}^{1/2}\,[V^{\cdot\cdot}_O]} \quad [4]$$

Since $[V^{\cdot\cdot}_O]$ is large and essentially unaffected by Eq. [3], the p-type conductivity σ_p will be proportional to $P_{O_2}^{1/4}$. Similarly, at low oxygen pressures, oxygen will be lost from the lattice via the reaction

$$O_O = \tfrac{1}{2}\, O_{2(g)} + V^{\cdot\cdot}_O + 2e' \quad [5]$$

where e' is an excess electron. The resulting n-type conductivity σ_n will vary as $P_{O_2}^{-1/4}$ providing that the excess electrons do not mutually interact. Equation [2] indicates that the ionic conductivity should be independent of oxygen pressure. Hence, the oxygen pressure dependence of the electrical conductivity should describe the type of charge carriers present in these oxide systems.

Experimental

The oxide mixtures were prepared by an oxalate coprecipitation method, which was found superior to both evaporation of nitrate solutions and direct mixing of the constituent oxides. Initially, appropriate amounts of 99.99% La_2O_3 and 99.95% $CaCO_3$, whose analyses are given in Table I, were dissolved in a slight excess of nitric acid. Prior to this, the "La_2O_3" had been heated to 1000°C to remove H_2O and CO_2. After neutralization with ammonium hydroxide, precipitation was effected by the rapid addition of the near-boiling nitrate solution to a boiling solution containing a 25-40% excess of ammonium oxalate. After filtering immediately, the oxalates were washed, dried at 125°C, and decomposed at 950°-1050°C in a porcelain crucible.

Subsequently, the oxides were reacted in a Pt crucible held in air for 24 hr at 1400°-1450°C. The caked products were ground to obtain —300 mesh particles. Next, the light brown oxide powders were compacted at 100,000 psi in a tungsten carbide die into disks ½ in. in diameter and about ⅛ in. thick. Most of these pellets were sintered in air for 36 hr at 1600°C in a platinum-wire-wound furnace, while being supported by prefired 1 in. diameter pellets of a similar composition. Several were treated in air for 3 hr at 1900°C in a gas-fired furnace or in vacuum (10^{-3} Torr) at 1500°C.

Table I. Impurities in La_2O_3 and $CaCO_3$

Impurity	La_2O_3 ppm	Impurity	$CaCO_3$ ppm
CeO_2	10	$SO_4^=$	70
Pr_6O_{11}	100	Ba	100
Other rare earths	20	Sr	200
Fe	1	Mg	<50
		Fe	10
		Pb	10
		K	<50
		Na	50

Prior to conductivity measurements, the faces of the samples were platinized by applying a 10% chloroplatinic acid solution which was subsequently decomposed at 600°-700°C to yield an adherent, black Pt film. They were then transferred to the high-temperature press shown in Fig. 1. The Inconel tube (76% Ni, 16% Cr, 7% Fe) was 24 in. long with an inside diameter of 1.35 in. With this apparatus, 0.002 in. Pt foil electrodes could be pressed against the samples at 12,000 psi and 1000°C. After this operation, the measured conductivities became independent of the applied pressure and, indeed, the electrodes could not be separated from the ceramic disks. A second method of electrode application consisted of pressing —200 mesh Pt powder onto the faces of the pellets before they were removed from the carbide die. These electrodes (~0.003 in. thick) adhered extremely well after sintering. Both methods effectively eliminated contact resistance. The conductivity measurements were taken in either the high-temperature press or a quartz cell, in which the samples were held between an alumina rod and the bottom of a quartz tube.

High oxygen pressures (1-10^{-5} atm) were achieved using Ar-O_2 mixtures analyzed with either a mass spectrograph or an electrochemical oxygen analyzer. Intermediate and low oxygen pressures (10^{-6}-10^{-18} atm at 1000°C) were controlled with CO-CO_2 mixtures analyzed with a gas chromatograph. In addition, highly reduced conditions (10^{-18}-10^{-21} atm at 1000°C) were obtained using H_2-H_2O mixtures. The appropriate gases were dried with either $Mg(ClO_4)_2$ or P_2O_5, passed through calibrated rotameters, and mixed in a one-liter Pyrex bulb. All of the expected oxygen pressures were verified with an oxygen concentration cell involving a commercial ZrO_2 + 10 m/o CaO closed-end tube as the electrolyte and at Pt,O_2 reference electrode. The gases were passed at a total pressure of 1 atm and room temperature linear speeds of about 0.9 cm/sec.

The two-probe a-c conductivity readings were taken at 3000 cps with a conductivity bridge equipped with

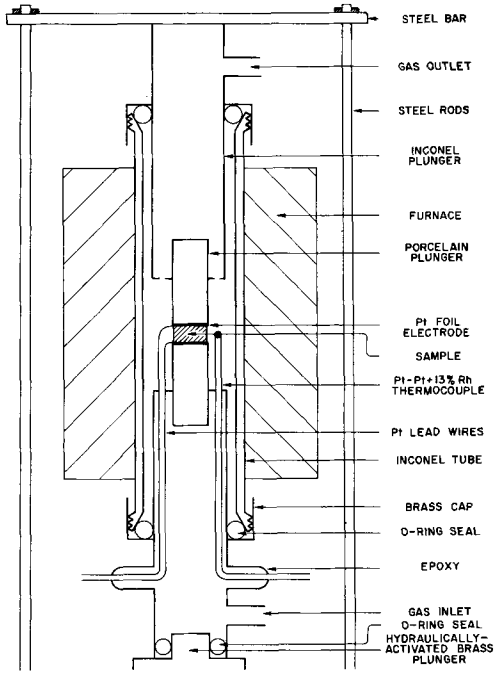

Fig. 1. High-temperature press for electrical measurements

a Wagner ground and a cathode ray oscilloscope and having an accuracy of ±0.1% in the range 500-50,000 ohms. Usually, measurements were made by holding the temperature constant until the entire oxygen pressure range had been traversed in both directions.

Emf measurements were conducted on the cells

(—) Ni,NiO/La_2O_3-CaO/Cu,Cu_2O (+)

and

(—) Fe,Fe_xO/La_2O_3-CaO/Ni,NiO (+)

at 600°-1100°C in the high-temperature press shown in Fig. 1. The metal-metal oxide electrodes were prepared by mixing the appropriate powders, pressing them at 80,000 psi, and sintering *in situ*. With this arrangement, the three pellets could be pressed tightly together in order to minimize any harmful effects from the surrounding atmosphere which could give rise to mixed potentials (34). After evacuating the system, argon, dried with $Mg(ClO_4)_2$ and P_2O_5 and deoxygenated with Cu turnings at 500°C and Ti pellets at 850°C, was admitted into the cell. Readings were taken at increasing and decreasing temperature using a Radiometer Universal *p*H meter connected to a scale expander which could be read to ±0.1 mv.

Results and Discussion

Physical properties.—Unfortunately, La_2O_3 is very hygroscopic due to weak bonding between hexagonal layers (27) and insufficiently screened cations (35). In the present study, x-ray diffraction analysis indicated the presence of only hexagonal La_2O_3 with a = 3.937Å and c = 6.130Å. If the oxide was handled in air for more than 2-3 hr, lines of $La(OH)_3$ were observed. However, the addition of CaO markedly improved the stability of La_2O_3 towards hydration. Foex (27) reported that the addition of 15 m/o CaO decreased the hydration speed by about 25 times.

Room temperature x-ray analysis indicated that about 16 m/o CaO [3.2 w/o (weight per cent)] could be dissolved in La_2O_3 at 1600°C. Sintering at 1900°C did not affect the solubility limit. The lattice parameters of La_2O_3 were almost independent of the CaO content on account of the limited solubility and the similarity of the radii of the cations (r_{La3+} = 1.14Å, r_{Ca2+} = 0.99Å). For specimens containing from 17.5 to 50 m/o CaO, lines of hexagonal La_2O_3 and CaO were observed. Therefore, no compound formation occurs in this system, a finding which is substantiated by a previous study (36) and predictable from cation field-strength considerations (37). The solubility limit was verified by gravimetric analyses on samples having more than 16 m/o CaO since the free lime could be separated from the solid solution phase by preferential dissolution in distilled water. Also, two phases could be seen under a microscope when more than 20 m/o CaO was present.

For temperatures below 1600°C, the solubility limit shifts to lower CaO contents. For instance, heating a pellet containing 15 m/o CaO at 1000°-1200°C for 20 hr resulted in the appearance of free CaO.

After sintering, the densities of the pellets were determined by carefully measuring their dimensions. All of the ceramic disks underwent a linear shrinkage of 5-7% of their original ½ in. diameters. Theoretical densities were calculated using the oxygen vacancy model for the solid solutions and the measured lattice parameters. Past the solubility limit, the theoretical densities were determined by accounting for the volume fractions of the two phases. These values are compared with the measured ones in Fig. 2. The measured densities range from 95-100% of theoretical. The agreement between the two sets of data from 10-17.5 m/o CaO, combined with an almost complete absence of porosity evidenced from observations made with a microscope, lends support to the anion vacancy model for the solid solutions. Sintering at 1900°C did not lead to any improvement in the densities of the pellets.

Although La_2O_3 pellets were white, the solid solutions were brown and reached a maximum color intensity at the solubility limit. The colors were not as intense after sintering in vacuum, indicating that color centers are created in the crystals when they are exposed to high oxygen pressures. In order to observe the microstructure of the pellets, they were etched with a hot HF + 20% HNO_3 solution. Grain sizes increased with the CaO content and were approximately 2.5-5, 10, and 25μ for samples containing 0-2.5, 5, and 15 m/o CaO, respectively. Grains in the order of 2000μ resulted from the heat treatments at 1900°C. The pressed Pt electrodes, adhering to the faces of the pellets, were never observed to penetrate to a depth greater than 25μ.

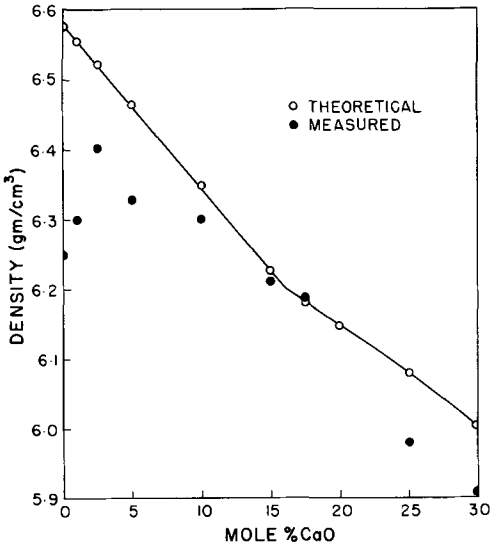

Fig. 2. Measured and theoretical densities in the La_2O_3-CaO system.

Electrical conductivity measurements.—All of the reported measurements were taken at 3000 cps. Increasing the frequency from 1000 to 3000 cps caused resistance decreases of less than 1% at high oxygen pressures and less than 2% at low pressures. Upon changing the oxygen pressure, the time required to attain equilibrium varied from 10-15 min at 1000°-1100°C to several hours at 600°-700°C.

To illustrate the oxygen pressure dependence, four conductivity isotherms for the La_2O_3 + 15 m/o CaO composition are plotted in Fig. 3. The solid lines define the oxygen pressure range covered with Ar-O_2 and CO-CO_2 mixtures, while the dotted lines continue to the lowest pressures imposed by the H_2-H_2O mixtures. An analysis of these curves indicates that the conductivity is solely ionic below 10^{-7} atm and, above this pressure, mixed p-type and ionic conductivity is present. The oxygen pressure dividing the two regions is essentially independent of temperature. No trace of n-type conductivity was detected.

The effect of the CaO content on the ionic conductivity is shown in Fig. 4. The corresponding vacancy concentrations, calculated from Eq. [1], are also given. Among nominally identical samples, the conductivity results were reproducible to about ±10%. The ionic conductivity increases rapidly up to 3 m/o CaO and is proportional to the vacancy concentration, as predicted by Eq. [2] for a dilute solution of defects. From 3 to 16 m/o CaO, the conductivity increases only slightly making any decomposition that may occur during the measurements difficult to detect. In the two-phase region past 16 m/o CaO, the conductivity decreases very little. However, in samples containing 30 and 50 m/o CaO, free CaO only occupies 7 and 20% of the volume, respectively. The conductivity at 50 m/o CaO is 25-30% lower than the maximum value. Since the conductivity of CaO is only about 10^{-6} $ohms^{-1}cm^{-1}$ at 1000°C (2, 5), a rapid decrease in con-

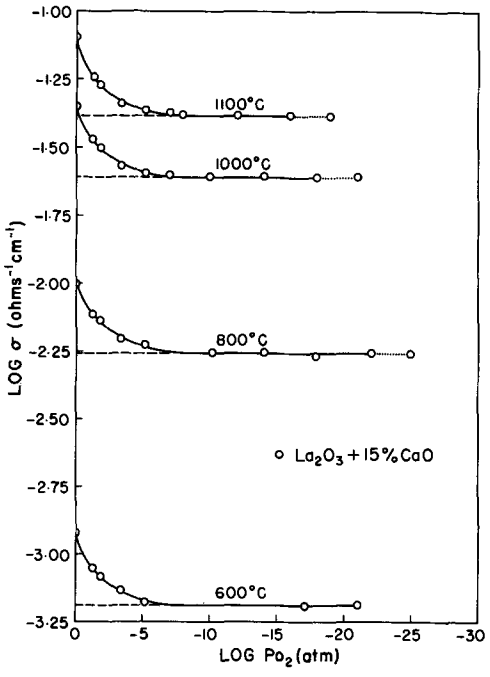

Fig. 3. Conductivity isotherms for La_2O_3 + 15 m/o CaO

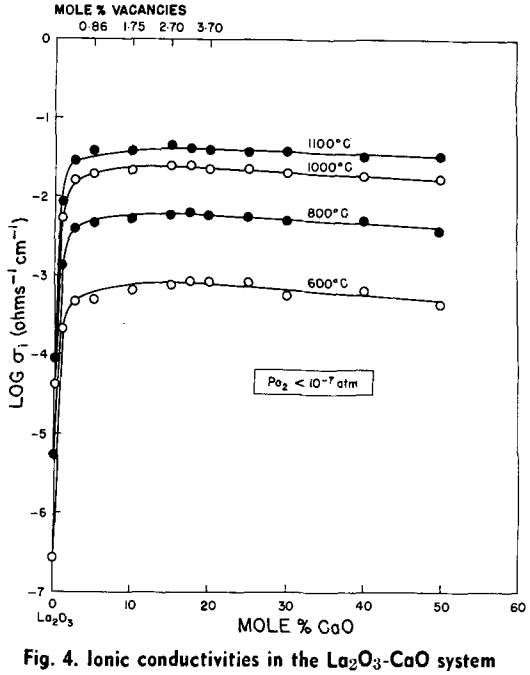

Fig. 4. Ionic conductivities in the La_2O_3-CaO system

ductivity should occur when the continuity of the solid solution phase is destroyed.

The variation of p-type conductivity with oxygen pressure and composition is presented in Fig. 5 and 6 for temperatures of 1063° and 895°C. The p-type contribution was determined by assuming that the ionic conductivity remained independent of oxygen pressure above 10^{-7} atm. The slopes are in reasonable agreement with the value of 0.250 predicted from Eq. [4]. Hence, the electron holes produced via Eq. [3] are free to conduct and the assumption of doubly ionized anion vacancies appears to be true. The reaction

$$V^{\cdot}_O = V^{\cdot\cdot}_O + e'$$

will go to the right at high oxygen pressures where the concentration of excess electrons is low. The p-type conductivity increases as the oxygen vacancy concentration increases. If the electron hole mobility and the activity coefficient for the anion vacancies are independent of the CaO concentration, Eq. [4] predicts that

$$\sigma_p \propto [V^{\cdot\cdot}_O]^{1/2}$$

at a constant oxygen pressure. This relationship, previously discussed by Bauerle (15) and Lasker and Rapp (16), was obeyed up to about 5 m/o CaO.

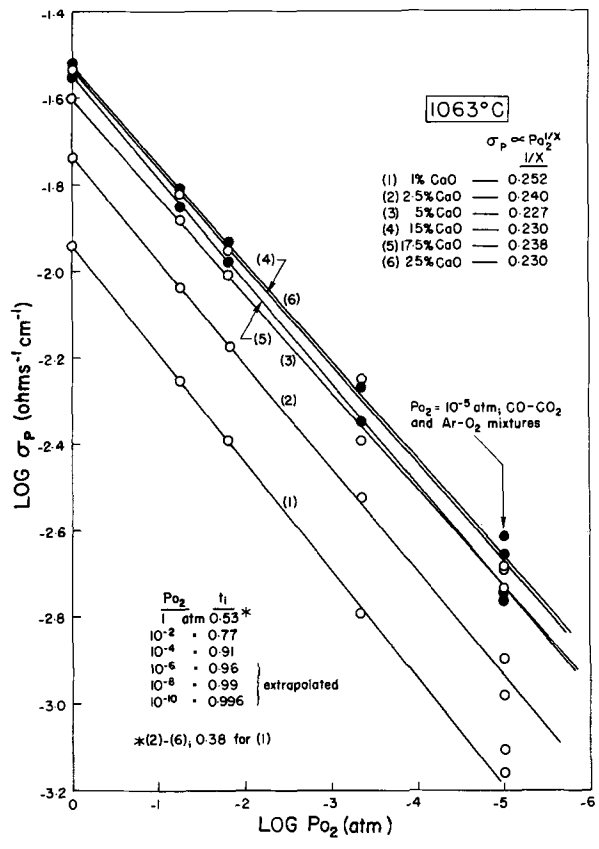

Fig. 5. P-type conductivity at 1063°C as a function of oxygen pressure and m/o CaO.

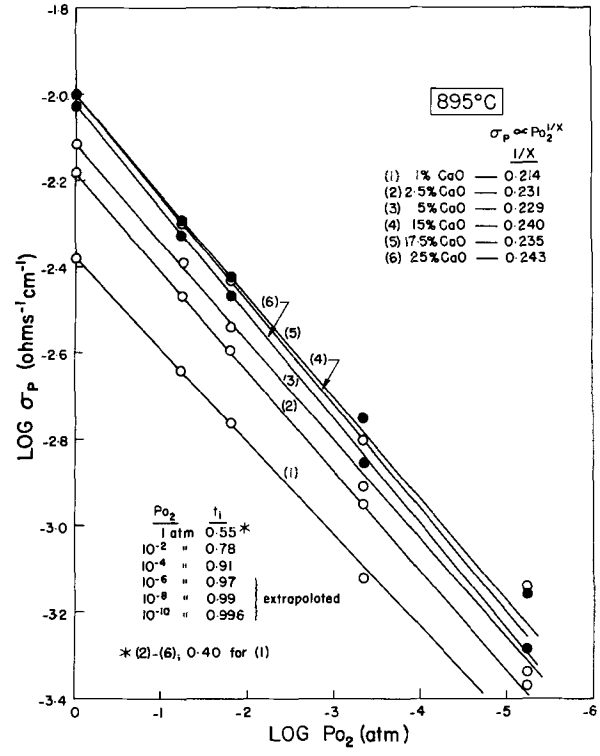

Fig. 6. P-type conductivity at 895°C as a function of oxygen pressure and m/o CaO.

Also given in Fig. 5 and 6 are several ionic transport numbers t_i, calculated from the expression $t_i = \sigma_i/\sigma$ where σ is the total conductivity. The transport numbers at oxygen pressures below 10^{-5} atm must be obtained by extrapolation of the log σ_p *vs.* log P_{O_2} plots. For compositions from 2.5 to 25 m/o CaO, the electronic contribution reaches nearly 50% at an oxygen pressure of 1 atm, while pressures below 10^{-8} atm are required to reduce it below 1%. The ionic transport numbers are somewhat lower for the 1 m/o CaO composition, in agreement with the dilute solution model proposed by Lasker and Rapp (16) for ThO_2-Y_2O_3 solid solutions. The transport numbers are approximately independent of temperature from 600°-1100°C.

The total conductivity of La_2O_3 over a much wider range of oxygen pressures than previously reported (38-42) is shown in Fig. 7 for 1032°C. A broad minimum occurs between 10^{-9} and 10^{-12} atm. The σ *vs.* $P_{O_2}^{1/4}$ plot in Fig. 8 illustrates that this minimum is essentially ionic conductivity. The intercept at $P_{O_2}^{1/4} = 0$ is in close agreement with the minimum conductivity of 4.5 x 10^{-5} ohms^{-1} cm^{-1} in Fig. 7. Assuming that the ionic conductivity is independent of oxygen pressure, both σ_p and σ_n may be determined and are also plotted in Fig. 7. Extrapolation of these lines

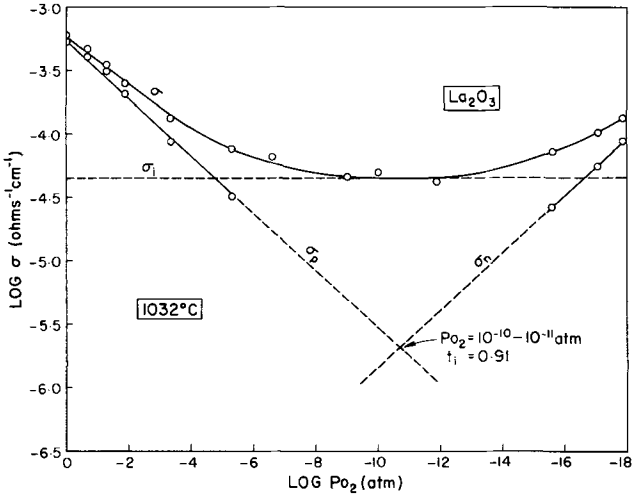

Fig. 7. Total and partial conductivities of La_2O_3 at 1032°C

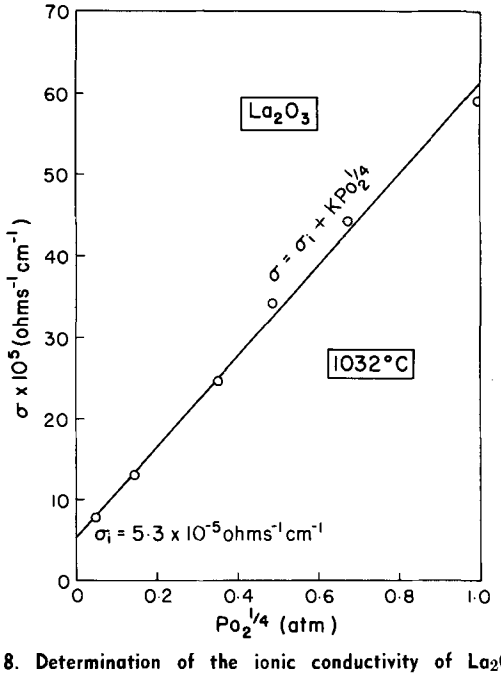

Fig. 8. Determination of the ionic conductivity of La_2O_3 at 1032°C.

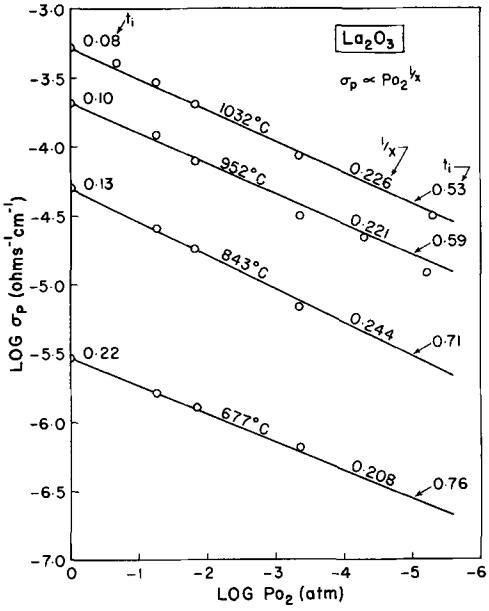

Fig. 9. P-type conductivity isotherms for La_2O_3

indicates that the smallest electronic contribution is found between 10^{-10} and 10^{-11} atm. Lower temperatures shifted the p-n transition point to somewhat lower pressures. At this point, the ionic transport number was calculated to be 0.91 at 1032°C.

Four p-type conductivity isotherms for La_2O_3 are presented in Fig. 9. Similar to the La_2O_3-CaO solid solutions, the data appear to be best represented by a $P_{O_2}^{1/4}$ dependence. The slope at 677°C may be low on account of the difficulty experienced in achieving equilibrium with the surrounding atmosphere below 700°C. Ionic transport numbers are given in Fig. 9 at oxygen pressures of 1 and 10^{-5} atm. The conduction is almost entirely electronic at 1 atm and the ionic transport numbers increase markedly with decreasing temperature.

Regarding the conduction mechanisms in La_2O_3, the questions remain as to what type of lattice defects are present and which ions (La^{3+}, $O^{=}$, or impurity ions) are transporting the ionic current. The hexagonal A-type structure of La_2O_3 is closely related to the low-temperature, cubic C-type form which, in turn, is obtained from the fluorite structure by removing ¼ of the anions and slightly rearranging the remainder. Therefore, anion interstitials might reasonably be expected. From Table I, the major impurities in the La_2O_3 used in this investigation were Pr^{4+} and Ce^{4+} cations. Their presence on the cation sublattice could also create anion interstitials. Also, the possibility of Schottky defects cannot be ignored. On account of the large charges and radii of the cations, cationic conductivity appears unlikely. Thus, the ionic conduction in La_2O_3 undoubtedly resulted from the migration of oxygen anions through either vacancies or interstitial positions. The intrinsic or extrinsic origin of these defects cannot be determined from the preceding discussion. However, the analysis of Chebotin *et al.* (43) of Rudolph's results (39) for La_2O_3 (1000 ppm impurities) indicates that the ionic transport number is 0.31 at 1000°C and an oxygen pressure of 1 atm. In the present study involving purer La_2O_3 (100 ppm impurities), the corresponding value is 0.09. This difference lends support to the possibility of impurity-controlled ionic conduction.

At high oxygen pressures, oxygen may enter the lattice by filling anion vacancies, creating cation vacancies, or occupying interstitial positions. The anion vacancy case has been treated in Eq. [4] and [5]. The cation vacancy and anion interstitial mechanisms may be represented by the reactions

$$3/4\ O_{2(g)} = 3/2\ O_o + V'''_{La} + 3h^{\cdot} \qquad [6]$$

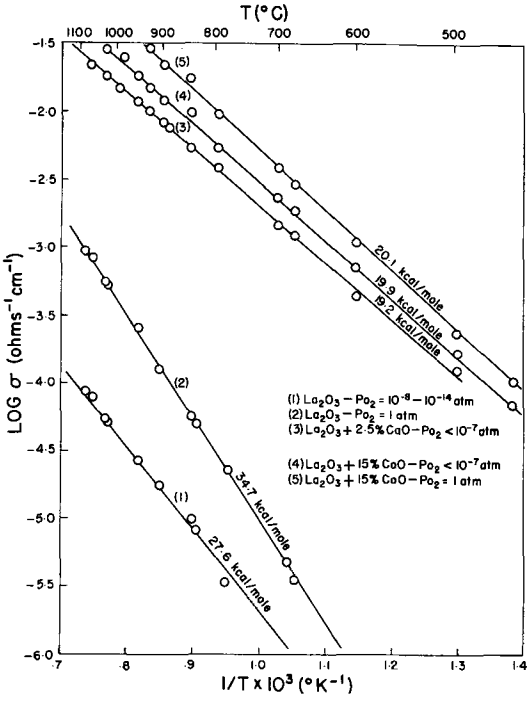

Fig. 10. Arrhenius plots of the total conductivity. Apparent activation energies are shown. Compositions are in terms of m/o CaO.

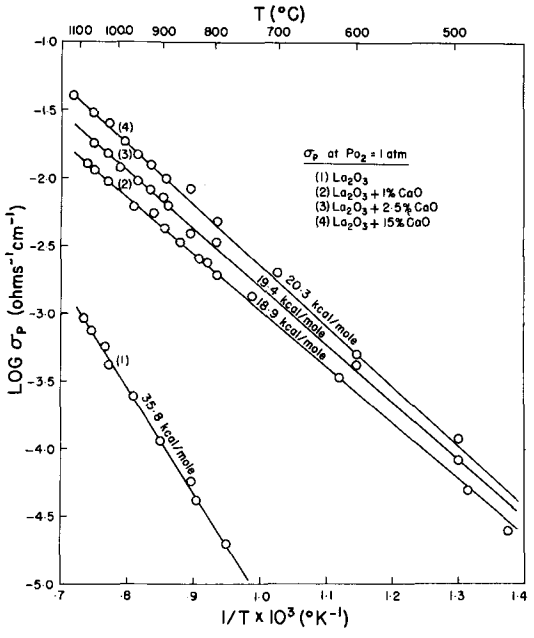

Fig. 11. Arrhenius plots of the p-type conductivity at an oxygen pressure of 1 atm. Apparent activation energies are shown. Compositions are in terms of m/o CaO.

and

$$1/2\ O_{2(g)} = O''_i + 2h^{\cdot} \qquad [7]$$

where V'''_{La} is a triply-ionized cation vacancy and O''_i is an interstitial oxygen anion. It is evident that, regardless of which mechanism is assumed, a $P_{O_2}^{1/4}$ dependence for p-type conductivity will always be derived, providing that only small deviations from stoichiometry occur. Since electronic defects are much more mobile than ionic defects, this should be true near an oxygen pressure region where $t_i \sim 1$. Equation [5] describes a possible mechanism which would lead to the appearance of n-type conductivity at low oxygen pressures. In the present instance, this onset may have been aided by the ease of reduction of the Pr^{4+} and Ce^{4+} impurity ions.

The temperature dependence of the total conductivity for both La_2O_3 and La_2O_3-CaO solid solutions is presented in the form of Arrhenius plots in Fig. 10. Curves 1, 3, and 4 represent mainly ionic conductivity, curve 2 represents mainly p-type conductivity, and curve 5 represents approximately equal amounts of both types. Arrhenius plots for p-type conductivity are given in Fig. 11. For La_2O_3, the apparent activation energy for ionic conduction Q_i and for p-type conduction Q_p are somewhat lower than the values determined by Chebotin *et al.* (43). Since $Q_p > Q_i$, ionic transport numbers increase with decreasing temperature as shown in Fig. 9. For the solid solutions, $Q_p \sim Q_i$ and both are approximately independent of composition. However, for La_2O_3 + 1 m/o CaO, $Q_i \sim 17$ kcal/mole. The apparent activation energy for p-type conduction may be related to the enthalpy change of Eq. [3].

Least squares analyses have been made on the equation

$$\log \sigma = \log A - B/T$$

where $B = Q/2.303R$ and the results are recorded in Table II. Both the conductivities and the apparent activation energies were more difficult to reproduce for solid solutions rich in CaO than for those dilute in CaO. Several times, the conductivities of samples containing more than 10 m/o CaO decreased irreversibly around 1000°C. However, two La_2O_3 + 2.5 m/o CaO samples were cycled over the temperature range 600°-1100°C for 3 weeks. During this time, no detectable changes in their Arrhenius plots were observed.

Emf measurements.—Some of the transport numbers of these electrolytes were determined by emf measurements. Results for several runs are plotted in Fig. 12. The solid lines define values recently measured with a stabilized zirconia electrolyte (34), a purely ionic conductor. Agreement to within ±1 mv was obtained with the La_2O_3-CaO electrolytes. At 1000°C, the Cu-Cu_2O, Ni-NiO, and Fe-Fe_xO electrodes impose oxygen pressures of $10^{-6.2}$, $10^{-10.3}$, and $10^{-14.8}$ atm, respectively (34). Verification has, therefore, been obtained for the assumption that the pressure-independent conductivities in Fig. 3 define a region of solely ionic conduction. The low value for the Cu/Ni cell in Fig. 12 at 1000°C may have resulted from the appearance of p-type conductivity in the electrolyte because of the relatively high oxygen pressure associated with the Cu-Cu_2O mixture. The cell

Table II. Constants for the equation $\log \sigma = \log A - B/T$

Mole % CaO in La_2O_3	Conductivity type	log A, ohms⁻¹ cm⁻¹	B, °K	Standard deviation, ohms⁻¹ cm⁻¹	Q, kcal/mole	Reproducibility of Q,* kcal/mole	Temperature range, °C
0	p-type**	2.613	7,710	±0.044	35.3	±1.5	700-1100
0	Ionic	0.323	6,010	±0.035	27.5	±1.5	700-1100
1	Ionic	0.654	3,740	±0.037	17.1	±0.5	400-1100
2.5	Ionic	1.498	4,200	±0.030	19.2	±0.2	400-1100
15	Ionic	1.864	4,440	±0.027	20.3	±1.0	400-1100

* The deviation from the mean of the apparent activation energies for nominally identical samples.
** At P_{O_2} = 1 atm.

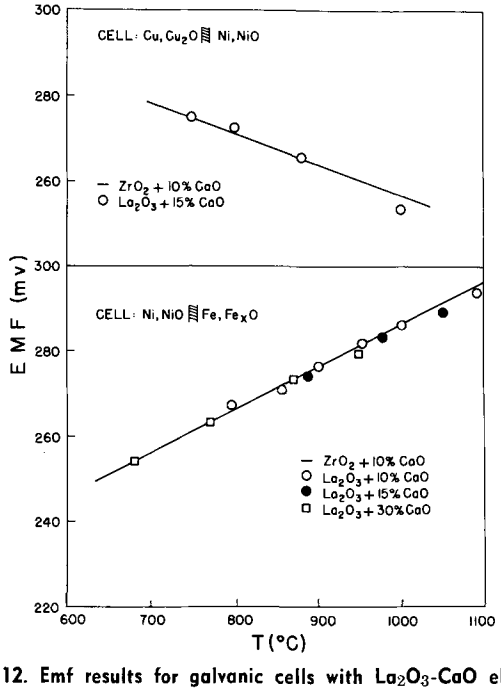

Fig. 12. Emf results for galvanic cells with La_2O_3-CaO electrolytes. Compositions are in terms of m/o CaO.

$$(-)\ Fe, Fe_xO/La_2O_3/Ni, NiO\ (+)$$

we also investigated. For an electrolyte exhibiting mixed conduction, $\bar{t}_i = E_{meas}/E_{thermodyn}$ where $\bar{t}_i$ is the average ionic transport number between the oxygen potentials defined by the electrodes and $E_{thermodyn}$ is calculated for the case where $t_i = 1$. If the electrodes do not remain reversible because of electronic conduction in the electrolyte, low values for E_{meas} will result. Application of this equation to the measurements on the above cell gave $\bar{t}_i \sim 0.9$ from 800°-1050°C, in good agreement with the results in Fig. 7.

Comparison with other oxide electrolytes.—The maximum ionic conductivities reported in several solid oxide electrolyte systems are presented in Table III. The data have been averaged where more than one reference is used. For the ZrO_2-based electrolytes, the maximum conductivities occur at compositions which coincide with the minimum amount of the additives necessary to fully stabilize the cubic phase (1, 3-7). Although the conductivity of the La_2O_3-based electrolyte is comparable to the other oxide systems, the concentration of anionic vacancies is somewhat lower. However, the shape of the curves in Fig. 4 indicates that the limited solubility of CaO in La_2O_3 has not restricted the maximum ionic conductivity to any appreciable extent.

The La_2O_3-based electrolytes can be more easily compared to ThO_2-based ones since similar vacancy concentrations can be considered. Although the ionic conductivities of La_2O_3 and ThO_2 (15, 16) are similar, the addition of CaO to La_2O_3 causes a much more rapid increase in conductivity than the addition of either Y_2O_3 or CaO to ThO_2. For instance, the ionic conductivity of La_2O_3 + 1.5 m/o CaO is one to two orders of magnitude greater than it is for ThO_2 + 0.5 m/o Y_2O_3 (12, 15, 16). These two compositions have equivalent vacancy concentrations of 0.25 m/o. In addition, the ionic conductivity of La_2O_3 + 6 m/o CaO (1 m/o vacancies) is about two orders of magnitude higher than values reported for the Sc_2O_3-CaO, Y_2O_3-CaO, and Sm_2O_3-CaO systems at a similar vacancy concentration (24). The oxygen anions are very mobile in the hexagonal A-type rare earth oxide structure of La_2O_3. Perhaps, the three large La^{3+}-$O^{=}$ interionic distances and the low coordination numbers for the anions cause them to be weakly held in their lattice positions. Also, there may be relatively large gaps between the cations through which the anions can move.

Table III. Conductivities of solid oxide electrolytes

Composition, m/o	Anionic vacancies, m/o	σ_i at 1000°C, ohms^{-1} cm^{-1}	Q_i, kcal/mole	References
ZrO_2 + 13% CaO	6.5	5.2×10^{-2}	26.2	3, 4, 6, 9
ZrO_2 + 8% Y_2O_3	3.7	11×10^{-2}	17.8	3, 7
ZrO_2 + 8% Sc_2O_3	3.7	25×10^{-2}	15.2	7
ThO_2 + 8% Y_2O_3	3.7	0.5×10^{-2}	25.4	12, 16
HfO_2 + 12% CaO	6.0	0.4×10^{-2}	33.0	5
HfO_2 + 8% Y_2O_3	3.7	2.9×10^{-2}	25.8	19
La_2O_3 + 15% CaO	2.7	2.4×10^{-2}	20.3	This study

Nevertheless, in the La_2O_3-CaO system, the conductivity-composition curves shown in Fig. 4 level off much more rapidly than they do in the ThO_2-Y_2O_3 (12, 16) or ThO_2-CaO (12) systems. Possible reasons for this include lattice distortion introduced by the Ca^{2+} cations, defect interactions between Ca^{2+} cations and anion vacancies, vacancy clustering, and vacancy ordering, a phenomenon previously found to reduce the ionic conductivity in the ZrO_2-CaO (4, 9, 44) and ZrO_2-Y_2O_3 (6) systems. Vacancy ordering might occur at relatively low defect concentrations since all the La^{3+}-$O^{=}$ interionic distances are not equal and, accordingly, all the oxygen positions are not equivalent.

The marked stability of the La^{3+} and Ca^{2+} valence states could render La_2O_3-CaO electrolytes useful to extremely low oxygen pressures. From Eq. [5], σ_n varies as $[V^{\cdot\cdot}_O]^{-1/2}P_{O_2}^{-1/4}$ at low defect concentrations. Combining this expression with the proportionality between σ_p and $[V^{\cdot\cdot}_O]^{1/2}P_{O_2}^{1/4}$ leads to the result that, at constant temperature, $\sigma_p\sigma_n$ is constant. For La_2O_3 at 1000°C, $\sigma_p\sigma_n = 7 \times 10^{-13}$ ohms^{-2} cm^{-2}. Providing that the mobilities of the electron holes and excess electrons do not change appreciably, this product may be extended to La_2O_3-CaO solutions, dilute in CaO. Application of this relationship to the La_2O_3 + 5 m/o CaO composition means that $\sigma_i = \sigma_n$ ($t_i = 0.50$) at $P_{O_2} = 10^{-35}$ atm and 1000°C.

Conclusions

Solid electrolytes, permeable only to oxygen anions below an oxygen pressure of 10^{-8} atm ($t_i > 0.99$), may be formed in the La_2O_3-CaO system. The oxalate coprecipitation method permits solid solutions to be formed at relatively low temperatures. Although 16 m/o CaO will dissolve in La_2O_3 at 1600°C, only 2 to 3 m/o CaO is required to achieve a high level of ionic conductivity. Conditions favoring ionic conduction in La_2O_3 are low temperatures, intermediate oxygen pressures, and, perhaps, the presence of impurity ions. The electrolytes are extremely resistant to reduction and may be useful for measuring the thermodynamic properties of systems which exert very low oxygen potentials.

Acknowledgment

Financial aid from the Defense Research Board and the National Research Council of Canada is gratefully acknowledged.

Manuscript submitted Dec. 2, 1968; revised manuscript received Feb. 28, 1969.

Any discussion of this paper will appear in a Discussion Section to be published in the December 1969 JOURNAL.

REFERENCES

1. F. Trombe and M. Foex, *Compt. rend.*, **236**, 1783 (1953).
2. Z. S. Volchenkova and S. F. Pal'guev in "Electrochemistry of Molten and Solid Electrolytes," Vol. 1, p. 97, Consultants Bureau, New York (1961).
3. J. M. Dixon, L. D. LaGrange, U. Merten, C. F Miller, and J. T. Porter II, *This Journal*, **110**, 276 (1963).

4. T. Y. Tien and E. C. Subbarao, *J. Chem. Phys.*, **39**, 1041 (1963).
5. H. A. Johansen and J. G. Cleary, *This Journal*, **111**, 100 (1964).
6. D. W. Strickler and W. G. Carlson, *J. Am. Ceram. Soc.*, **47**, 122 (1964).
7. D. W. Strickler and W. G. Carlson, *ibid.*, **48**, 286 (1965).
8. J. W. Patterson, E. C. Bogren, and R. A. Rapp, *This Journal*, **114**, 752 (1967).
9. R. E. Carter and W. L. Roth in "Electromotive Force Measurements in High-temperature Systems," p. 125, C. B. Alcock, Editor, Institution of Mining and Metallurgy, London (1968).
10. Z. S. Volchenkova and S. F. Pal'guev in "Electrochemistry of Molten and Solid Electrolytes," Vol. 1, p. 104, Consultants Bureau, New York (1961).
11. Z. S. Volchenkova and S. F. Pal'guev in "Electrochemistry of Molten and Solid Electrolytes," Vol. 2, p. 53, M. V. Smirnov, Editor, Consultants Bureau, New York (1964).
12. B. C. H. Steele and C. B. Alcock, *Trans. AIME*, **233**, 1359 (1965).
13. C. B. Alcock and B. C. H. Steele in "Science of Ceramics," Vol. II, p. 397, Academic Press, London (1965).
14. E. C. Subbarao, P. H. Sutter, and J. Hrizo, *J. Am. Ceram. Soc.*, **48**, 443 (1965).
15. J. E. Bauerle, *J. Chem. Phys.*, **45**, 4162 (1966).
16. M. F. Lasker and R. A. Rapp, *Z. physik. Chem. (N.F.)*, **49**, 198 (1966).
17. J. M. Wimmer, L. R. Bidwell, and N. M. Tallan, *J. Am. Ceram. Soc.*, **50**, 198 (1967).
18. Z. S. Volchenkova and S. F. Pal'guev, *Trudy Inst. Elektrokhim., Akad. Nauk S.S.S.R., Ural. Filial*, **5**, 133 (1964); *C.A.*, **62**, 8472d.
19. J. Besson, C. Deportes, and G. Robert, *Compt rend.*, **262**, 527 (1966).
20. S. F. Pal'guev and Z. S. Volchenkova, *Trudy Inst. Elektrokhim., Akad. Nauk S.S.S.R., Ural. Filial* **2**, 157 (1961); *C.A.*, **59**, 12267d.
21. A. D. Neuimin and S. F. Pal'guev, *ibid.*, p. 185; *C.A.*, **59**, 8186a.
22. A. D. Neuimin, L. D. Yushina, Yu. M. Ovchinnikov, and S. F. Pal'guev in "Electrochemistry of Molten and Solid Electrolytes," Vol. 2, M. V. Smirnov, Editor, p. 92, Consultants Bureau, New York (1964).
23. S. F. Pal'guev and Z. S. Volchenkova, *Trudy Inst. Elektrokhim., Akad. Nauk S.S.S.R., Ural. Filial* **9**, 133 (1966); *C.A.*, **67**, 47754x.
24. B. C. H. Steele, B. E. Powell, and P. M. R. Moody, *Proc. Brit. Ceram. Soc.*, **10**, 87 (1968).
25. A. Rabenau, *Z. anorg. allgem. Chem.*, **288**, 221 (1956).
26. T. L. Barry, V. S. Stubican, and R. Roy, *J. Am. Ceram. Soc.*, **49**, 667 (1966).
27. M. Foex, *Bull. soc. chim. France*, 109 (1961).
28. K. Loehberg, *Z. physik. Chem.*, **28**, 402 (1935).
29. P. N. Mehrotra, G. V. Chandrashekar, C. N. R. Rao, and E. C. Subbarao, *Trans. Faraday Soc.*, **62**, 3586 (1966).
30. V. B. Glushkova and E. K. Keler, *Dokl. Akad. Nauk S.S.S.R.*, **152**, 611 (1963).
31. M. Foex and J. Traverse, *Bull. Soc. Franc. Mineral. Crist.*, **89**, 184 (1966).
32. L. Pauling, *Z. Krist.*, **69**, 415 (1929).
33. K. Kiukkola and C. Wagner, *This Journal*, **104**, 379 (1957).
34. G. G. Charette and S. N. Flengas, *ibid.*, **115**, 796 (1968).
35. M. W. Shafer and R. Roy, *J. Am. Ceram. Soc.*, **42**, 563 (1959).
36. T. L. Barry and R. Roy, *J. Inorg. Nucl. Chem.*, **29**, 1243 (1967).
37. K. S. Vorres, *J. Am. Ceram. Soc.*, **46**, 410 (1963).
38. M. Foex, *Compt. rend.*, **220**, 359 (1945).
39. J. Rudolph, *Z. Naturforsch.*, **14**, 727 (1959).
40. W. Noddack and H. Walch, *Z. Elektrochem.*, **63**, 269 (1959).
41. W. Noddack, H. Walch, and W. Dobner, *Z. physik. Chem.*, **211**, 180 (1959).
42. A. D. Neuimin and S. F. Pal'guev, *Trudy Inst. Elektrokhim., Akad. Nauk S.S.S.R., Ural. Filial* **3**, 133 (1962); *C.A.*, **59**, 9417g.
43. V. N. Chebotin, Z. S. Volchenkova, and S. F. Pal'guev in "Electrochemistry of Molten and Solid Electrolytes," Vol. 4, p. 123, A. N. Baraboshkin and S. F. Pal'guev, Editors, Consultants Bureau, New York (1967).
44. E. C. Subbarao and P. H. Sutter, *J. Phys. Chem. Solids*, **25**, 148 (1964).

The Effect of Overpotential on the Electrolytic Hydrogen-Deuterium Separation Factor on Bright Platinum Electrodes in 1.2*N* HCl-10% D_2O

M. Hammerli, J. P. Mislan, and W. J. Olmstead

Atomic Energy of Canada Ltd., General Chemistry Branch, Chalk River Nuclear Laboratories, Chalk River, Ontario, Canada

ABSTRACT

The electrolytic hydrogen-deuterium separation factor, S_D, was studied on bright platinum as a function of overpotential in 1.2*N* HCl-10% D_2O at 25°C. S_D increased from 4.1 ± 0.21 at —50 mv to 6.5 ± 0.35 at —400 mv, and remained virtually constant between —400 mv and —1.2v applied overpotential. Results agree with published work with H_2SO_4 but not HCl as electrolyte. Only because there is a plateau in the S_D *vs.* overpotential curve are the ohmic potential drop corrections of little significance. The high degree of reproducibility in results achieved, namely ±5%, is believed to be due to (*a*) effective exclusion of Cl_2 (anode gas) from the cathode compartment, (*b*) relatively short (1-60 min) electrolyses, and (c) removal of the large pre-electrolysis cathode from the cell prior to an electrolysis. A leaching-distillation process was also employed as the pretreatment, and is shown to be as effective as pre-electrolysis. Tafel plots obtained before and after electrolysis showed no hysteresis, and are in agreement with recent work on copper cathodes, where cathodic saturation currents are observed.

Many investigators (1-7) have studied the effect of cathode materials, current density, temperature, and the nature and concentration of the electrolyte on the electrolytic hydrogen-deuterium separation factor, S_D,[1] usually in an attempt to distinguish between different mechanisms of the hydrogen evolution reaction. More recently, several workers (8-12) have studied the separation factor as a function of the applied electrode potential.

To date, very little agreement exists between results of various workers. Thus, for example, the deuterium separation factor for platinum in acid solution has been reported as low as 2 (14) and as high as 9 (11) by different workers. Moreover, even investigators from the same laboratory have obtained different results on the same cathode-electrolyte system (12, 15). Theoretical predictions as to the magnitude of the separation factor are at present conflicting, because of the complexity of the calculations and their inherent assumptions, as Salomon and Conway (16) have pointed out.

The present work was undertaken in an attempt to obtain more consistent experimental data. Potentiostatic rather than galvanostatic control was chosen for the work reported here, because it has been shown (17, 18) that the potential at a solid metal electrode can vary with time under constant current conditions. It will be shown that we have achieved some measure of success in our aim, and that the dependence of the separation factor on overpotential is not greatly altered when the applied overpotential has been corrected for ohmic potential drop in the electrolyte.

Experimental

The cell.—The separation factor measurements were made under potentiostatic conditions in a three-compartment cell, (see Fig. 1 and 2) whose temperature was controlled to 0.1°C by a circulating water bath. Each compartment could be isolated by solution-wetted stopcocks. The reference electrode was connected to the cathode compartment by a Luggin capillary. The solution volume of the cathode compartment is about 80 ml, and the gas volume about 60 ml. The gas exit on the cathode compartment head was fitted with a water-cooled condenser for future experiments to be carried out at higher temperatures. Presaturators for the argon sweep gas were connected to the anode and cathode compartment with O-ring joints. Viton O-rings were used for all such joints.

A leak-tight fit of the electrode into the cathode holder (Teflon) was achieved with a Teflon plug which had a tapered thread and a center hole just large enough to accept the exposed stem of the electrode. The cathode holder was designed to fit into a 10 ml Pyrex syringe barrel (uniform bore) blown onto the cathode compartment head. A good seal between the

Fig. 1. Electrolysis cell; A, anode; C, cathode; R, reference electrodes.

Key words: hydrogen, deuterium, isotope separation, electrolysis, water, heavy water.

[1] S_D is defined as the H/D ratio in the evolved gas divided by the H/D ratio in the electrolyte.

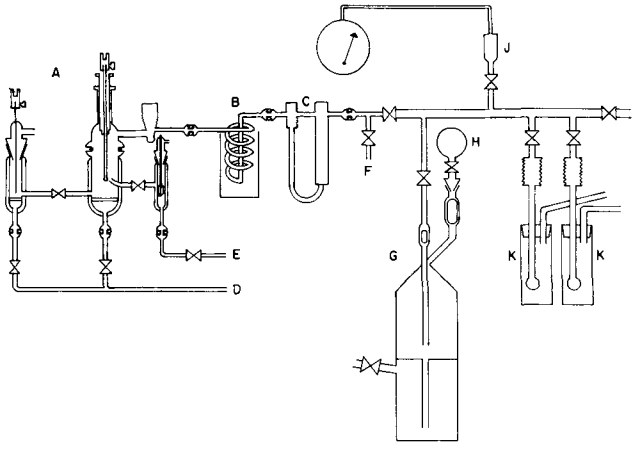

Fig. 2. Semischematic diagram of the electrolysis cell and gas collection system; A, electrolysis cell; B, solid CO_2-acetone trap; C, Cartesian manostat; D, argon inlet; E, hydrogen inlet; F, purge vent; G, Toepler pump; H, sample flask; J, Pirani gauge; K, solid N_2 trap.

barrel and Teflon holder was obtained with an O-ring, and yet the holder could readily be moved for the purpose of positioning the cathode with respect to the Luggin capillary. Later, the O-ring seal was replaced by a seal formed by expanding the polished surface of a new Teflon holder against the syringe barrel by screwing a stainless steel cylinder with a tapered thread into the holder.

Reference electrodes.—Two reference electrodes, one for potential control and the other for potential measurements, were used in the same solution at the same temperature. Apart from some early measurements which were based on quinhydrone reference electrodes with gold as the metallic phase, hydrogen reference electrodes were employed. The design of the hydrogen electrode half-cell was such that no hydrogen gas from it was ever detected in the cathode compartment. An electrolytic hydrogen generator, (Matheson of Canada Ltd., model R-152) was the source of pure hydrogen gas for the reference electrodes, and the reduction of the cathodes described later. Prior to an experiment the emfs of the hydrogen reference electrodes were checked against a saturated calomel electrode as well as each other.

Chemicals.—Analytical grade concentrated HCl was doubly distilled in an all-quartz still. The 1.2*N* (unit activity) HCl solutions containing 10% D_2O by volume were made up with triply distilled H_2O and D_2O each of which had been preirradiated with Co^{60}-γ-rays, and then refluxed with alkaline permanganate to destroy any peroxides formed before the final distillation. The distilled electrolyte was stored in a liter quartz flask.

Cathodes.—Two types of electrodes were employed as cathodes. A platinum tube electrode (diameter = 1.27 mm, wall thickness = 0.254 mm), sealed at one end in the shape of a hemisphere,[2] was used as received from Engelhard Industries Ltd. after it had been cleaned in a hot H_2SO_4-HNO_3 bath. Heat shrinkable Teflon tubing was pushed over the open end until the desired geometric surface area at the closed end remained exposed to the electrolyte. Thus, the electrolyte was in contact only with the outside of the tube electrode.

Smooth platinum bead electrodes were formed by melting the tips of 1.27 mm diameter (0.050 in.) platinum wires in a gas-oxygen flame. They were reduced in a hydrogen atmosphere for a few hours in a quartz oven either at 800° or 1050°C. The system was then evacuated through a grease free vacuum line before reducing the oven temperature. Heat shrinkable Teflon tubing, which had been treated in the hot H_2SO_4-HNO_3 bath, was then pushed over the electrode stem until only the bead and the upper part of the stem, where electrical contact was made, was exposed. As a final pretreatment the electrode was extracted with warm electrolyte overnight in a Soxhelet extractor.

Anode.—The anode consisted of a strip of platinum gauze, 15 cm long and 4.5 cm wide (Johnson, Matthey and Mallory Unimesh #Q2050, 48 mesh x 0.006 in.). This strip was wound into a roll, 0.5 cm in diameter and 4.5 cm wide, to which a platinum wire, 0.127 cm in diameter, was fastened at one end.

Pre-electrolysis pretreatment.—For all the experiments on the platinum tube electrode, the electrolyte was pre-electrolyzed, *in situ,* overnight with the aid of a platinum gauze cathode identical to the anode just described. This pre-electrolysis cathode could be raised from, or lowered into the electrolyte, by means of double O-ring seal contained in a Pyrex sleeve, which was mounted vertically on the cathode compartment head.[3] The current used was 10-15 mA. After pre-electrolysis was completed, the platinum gauze cathode was pulled out of the electrolyte, but not removed from the cathode compartment. This procedure led to difficulties which will be discussed later.

Leaching-distillation pretreatment.—For all experiments on the platinum bead cathodes, the pretreatment was as follows. Prior to a series of runs, the cell was treated in a hot H_2SO_4-HNO_3 mixture, baked in a 525°C oven overnight, and leached with freshly redistilled electrolyte for at least 24 hr. Meanwhile, the selected cathode was extracted with warm electrolyte overnight in a Soxhelet extractor as already mentioned. Another aliquot of electrolyte was then totally distilled in an all-quartz still immediately before filling the cell and mounting the bead electrode into the cathode holder.

Argon sweep gas.—Once the cell system had been assembled, argon gas entering the anode and cathode compartments at the bottom of each through glass frits, specially selected for their uniform porosity, served to sweep the hydrogen gas and/or air out of the cell. The Matheson ultra high purity argon used for this purpose received no further purification. Mass spectrometric analysis of argon samples in which the impurities had been concentrated about a thousandfold by freezing most of the argon in a solid N_2 trap, confirmed the low levels of impurities claimed by the manufacturer. The hydrogen concentration was found to be about 0.1 ppm.

Potential control.—The desired overpotential was controlled to ±2 mv by a sensitive potentiostat (Magna Corporation, model 4700M), and continuously monitored on one channel of a Moseley dual-channel strip chart recorder, (model 7100B-11-19 with two plug-in modules 17501A); the current passed between the counter (anode) and working (cathode) electrodes was continuously recorded on the other channel. The time of electrolysis varied from 1 to 60 min depending on the overpotential applied.

Temperature measurements.—For a few runs a platinum-10% rhodium 90% platinum thermocouple was placed a few millimeters from the Pt-bead electrode in order to measure possible temperature increases in the vicinity of the electrode during electrolysis, and to check on the efficiency of the thermostating facilities described previously.

Gas collection.—After completion of an electrolysis, the cathode compartment was isolated from the anode and reference compartments, and the H_2, HD, and D_2 gases swept into the collection system (see Fig. 2) with high-purity argon. The collection system consisted of a glass spiral trap cooled to —80°C with solid

[2] This electrode configuration was obtained with another experiment in mind.

[3] This particular cathode compartment head is not shown in Fig. 1.

CO_2-acetone, a Cartesian manostat (Edwards High Vacuum Canada Ltd., model 6), and a solid N_2 trap in which the hydrogen isotopes were concentrated by freezing down some of the argon. After about 15 min, the solid N_2 trap was isolated so that the gas in the rest of the system could be transferred into a gas flask with a Toepler pump without appreciably diluting the gas sample with argon (vapor pressure about 3 mm Hg, and volume of trap: volume of system ::1:60). The remaining gas in the trap was then expanded into the system, the trap isolated again, and the gas added to the flask. Experience showed that one expansion was enough to collect essentially all the hydrogen. This procedure increased the hydrogen concentration in argon sufficiently to permit accurate analyses of samples from electrolyses as short as 1 min.

H/D analyses.—All samples were analyzed mass spectrometrically. A CEC (Consolidated Electrodynamics Corporation) model 21-610 mass spectrometer was first used. Later, the work load on this instrument became too great, and a CEC model 21-130 mass spectrometer was employed. Both instruments were carefully calibrated over a range of ionizing currents and sample pressures, as well as different hydrogen to argon ratios from 30% hydrogen: 70% argon to 2% hydrogen: 98% argon. Carefully prepared heavy water standards were reduced in a uranium furnace previously equilibrated with the same standard, and the gas mixtures withdrawn at the reduction temperature (500°C). Complete reduction required several hours. An appropriate quantity of argon was then added to the hydrogen isotopes. From the equilibrium constant data (12) for the reaction

$$H_2 + D_2 \rightleftharpoons 2HD$$

at 500°C, the isotopic composition of the hydrogen was calculated and this, in turn, allowed the sensitivity factors for HD and D_2 relative to H_2 to be determined for each instrument. Each gas sample was analyzed three times with a reproducibility of ±1%.

The deuterium content of the electrolyte was determined before and after a series of runs on a Thomson-Houston model THN-202B hydrogen-deuterium mass spectrometer (13).

Ohmic potential drop measurements.—The ohmic potential drop between the tip of the Luggin capillary and the cathode was measured galvanostatically. Current supplied by a galvanostat (Northeast Scientific Corporation, model RI-234) to the cell was interrupted at the anode with a mercury relay (C.P. Clare and Company, type HG 2A-1004). The energizing current to the relay coil was also used to trigger the time base of an oscilloscope (Tektronix type 556, vertical plate amplifier type L). For meaningful measurements of the ohmic potential drop, a 50 μsec/div or faster sweep rate was necessary, but the switching time of the relay was about 5 msec or ten times slower than the required oscilloscope sweep. This problem was solved by delaying the triggering pulse from the relay coil to the oscilloscope with the variable delay time of a pulse generator (Datapulse, type 101). The change in the potential difference between the cathode and reference electrode was recorded photographically.

Tafel plots.—Steady-state Tafel plots were obtained periodically in the usual manner at both increasing and decreasing successive overpotentials before, and sometimes after a set of electrolyses.

Results and Discussion

S_D as a function of η.—The main result of our experiments concerning the relation between overpotential and the separation factor, S_D, on platinum electrodes immersed in 1.2*N* HCl-10% D_2O aqueous electrolyte is that S_D increases as the applied cathodic overpotential, $\eta_{applied}$, increases from zero to about |— 400 mv|, and then remains virtually constant with increasing overpotential.

Figure 3 shows this dependence of S_D on $\eta_{applied}$ for (*a*) the platinum tube electrode at two different exposed areas with the quinhydrone electrode as the reference electrode and pre-electrolysis as the electrolyte pretreatment, and (*b*) two platinum bead electrodes in two series of runs with the hydrogen electrode as the reference electrode and the leaching-distillation process as the pretreatment.

It must be pointed out that, although stringent precautions were taken to keep quinhydrone out of the cathode compartment, no claim is made that this aim was achieved. For this reason two experiments were carried out, one with the hydrogen reference electrode, and the other with the quinhydrone electrode plus deliberate additions of quinhydrone (approx. 10^{-3}M) to the catholyte. The values of S_D were experimentally the same in both cases, but it was observed that the hydrogen gas in the catholyte containing quinhydrone was liberated in smaller and more uniform bubbles from the electrode surface, suggesting that quinhydrone was probably adsorbed on the cathode surface.

For the S_D determinations on the platinum tube electrode several aliquots of electrolyte were used over a period of several days. For the S_D determinations on the platinum bead electrodes only one aliquot of electrolyte was used for each electrode and all electrolyses (whose corresponding S_D values are numbered in Fig. 3 in the order in which the electrolyses were obtained) were carried out over a period of about 14 hr. Because of our sensitive hydrogen isotope measurement technique, it was possible to keep the electrolysis time ≤5 min for $\eta_{applied} \geq$ |—100 mv| thereby minimizing time effects on S_D due to electrode surface aging (9, 20, 21) and/or changes in concentrations of electroactive impurities in the electrolyte with time.

As Fig. 3 shows, the data obtained on the tubular electrode system show good reproducibility contrary to expectations based on the above discussion, and are in excellent agreement with the results shown in Fig. 4 to be discussed later. While the scatter in the data obtained on the bead electrode systems is much greater, the over-all reproducibility of the results of Fig. 3 is still within that obtained by previous workers [*e.g.* see ref. (11)].

Reproducibility of S_D measurements.—The dilemma of why the more stringent electrode and electrolyte pretreatments used for the bead electrode system should yield the less reproducible results, was at least partially resolved, when it was realized that Cl_2 could reach the cathode, and that this possibility was greatly enhanced by the very time-saving techniques designed

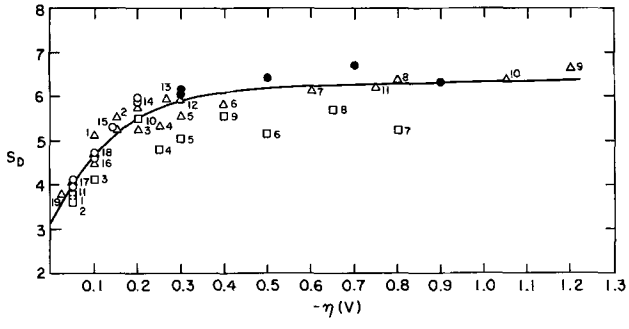

Fig. 3. Electrolytic separation factor as a function of applied overpotential for bright platinum in 1.2*N* HCl-10% D_2O at 25°C; ● and ○, hollow platinum tube electrode with geometric surface areas of 0.063 and 0.51 cm², respectively; electrolyte was pre-electrolyzed and the quinhydrone reference electrode was used. □ i and △ i, two platinum bead electrodes, each with geometric surface area = 0.06 cm²; the leaching-distillation pretreatment and the hydrogen reference electrode were used; i = i'th consecutive electrolysis on a given electrode.

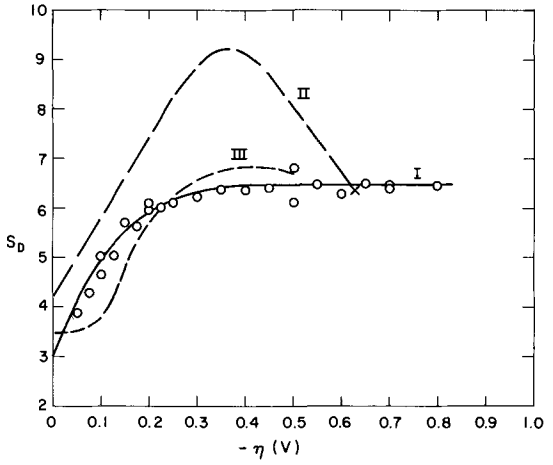

Fig. 4. Electrolytic separation factor as a function of applied overpotential for bright platinum. Curve I, this work in 1.2*N* HCl-10% D_2O at 25°C; curve II, average values for 1.0*N* HCl-10% D_2O at 25°C from ref. (11); curve III, average values for 1.0*N* H_2SO_4-10% D_2O at 15°C from ref. (12); x and o, with galvanostatic and potentiostatic control, respectively.

to reduce impurity build-up. When some Cl_2 was deliberately added to the catholyte, the separation factor from the subsequent electrolysis was always depressed as Table I shows, although the results in Table I are qualitative only. In order to prevent chlorine contamination of the catholyte, the anode compartment was thereafter continuously purged with argon rather than only for a few minutes between successive electrolyses. S_D determinations utilizing this improvement are shown in Fig. 4.

The results in Fig. 4 were all obtained from a single electrode and one aliquot of electrolyte. Successive overpotentials were chosen at random as before. The results obtained here without pre-electrolysis are in excellent agreement with those of Fig. 3 with pre-electrolysis. Our leaching-distillation pretreatment therefore appears to be as effective as pre-electrolysis in yielding reproducible results, at least as far as S_D determinations are concerned. A pretreatment other than electrolysis is to be preferred, provided it is effective, in any system where the electrolyte concentration is being changed as a result of electrolysis (Cl_2 evolution at the anode in this work). One value of S_D was obtained under controlled current conditions and, as shown, is in good agreement with the potentiostatic data. This behavior was also observed by Yokoyama (12) and suggests that the importance of potentiostatic control may very well have been over emphasized in steady-state applications such as electrolysis at high current densities, where large ohmic potential drops cannot be avoided. Ohmic potential drop measurements are discussed in a later section.

The results presented in Fig. 4 are within a ±5% reproducibility range. This degree of reproducibility, not achieved before, is believed to be due to several factors. The relatively short duration of an electrolysis, the exclusion of Cl_2 from the cathode compartment, and the electrode and electrolyte pretreatments

Table I. Effect of chlorine on the H/D separation factor on platinum at 50°C

Run No.	S_D at −600 mv: Chlorine added to cathode compartment	S_D at −600 mv: Chlorine purged from cathode compartment
1		5.50
2	4.26	
3		5.47
4		5.57
5	4.81	
6		5.41
7		5.32

Table II. Values of S_D based on successive aliquots of gas from a single electrolysis

Aliquot No.	S_D
1	4.11
2	3.99
3	3.84
4	3.51
5	2.78
6	2.17

have already been mentioned. Two additional factors will now be discussed.

It was observed that H-D analyses of successive aliquots of gas, removed from the cell 30 to 90 min apart following one electrolysis period, yielded different values of S_D. Typical results are shown in Table II. It is obvious that the first aliquot was relatively richer in hydrogen (S_D larger) than the mean value, and *vice versa* for the last aliquot. Under the same electrolysis conditions, a value of S_D close to the mean value was obtained from analyses made on the total gas produced. This effect disappeared entirely when the large surface area pre-electrolysis cathode was removed from the cathode compartment prior to an electrolysis. We believe the effect was due to slow effusion of absorbed hydrogen gas with an isotopic ratio significantly different from that of the electrolysis gas, and time dependent. The pre-electrolysis electrode would be expected to occlude apreciable quantities of the hydrogen isotopes after a 24-hr pre-electrolysis (22-25). Nevertheless, since the cell was always thoroughly purged with argon for at least an hour after completion of the pre-electrolysis, it was surprising to find this effect. Part of the scatter in published S_D values, where pre-electrolysis was employed, might be explained if the pre-electrolysis electrode were left in the cathode compartment and H/D analyses were based on aliquots of the electrolysis gas. All S_D measurements reported here are based on analyses of the total electrolysis gas. The pre-electrolysis electrode was removed from the cathode compartment when that technique of purification was used.

The second factor is that mass spectrometric analysis results for samples of pure hydrogen isotopes are pressure dependent due to H_3^+ formation, which is also dependent on composition and the ion source characteristics of the mass spectrometer. With our instruments the pressure effect was only about 3% over a decade change in analyzer pressure, but could be more significant in other systems. In our work this difficulty was circumvented by diluting the hydrogen isotopes with argon, and also by working over a small range of inlet pressures at a constant ionizing current of 80 μA. This resulted in analyses of such mixtures being independent of pressure.

Comparison with published results.—Our results in Fig. 4 have been compared with the AVERAGE values of S_D on platinum obtained by Salomon and Conway (11) for 1.0*N* HCl-10% D_2O at 25°C, and those obtained by Yokoyama (12) for 1.0*N* H_2SO_4-10% D_2O at 15°C. Our results agree well with Yokoyama's when his experimental error of about 25% and lower temperature are taken into account. However, our results disagree with those of Salomon and Conway who found a maximum in the curve. Lewis and Ruetschi (8) observed maxima on Pt electrodes, but in 6*N* KOH. No explanation of the disagreement can be given except that electrode surface conditions could have been different. Nevertheless, some doubt now exists as to the validity of Salomon and Conway's co-anion hypothesis (11) to explain their HCl and $HClO_4$, and Fukuda and Horiuti's (15) H_2SO_4 results.

Temperature control.—Temperature measurements with the thermocouple near the cathode during electrolysis at high overpotentials (current density approx. 2A cm^{-2}) indicated that no significant in-

crease in temperature occurred in our system and that temperature control inside the cathode compartment was within ±0.1°C. It may be significant that no decrease in S_D was observed here at the higher overpotentials. Such a decrease could conceivably be due to local heating of the electrode and solution in its immediate vicinity, for it is well established [see (26) for example] that S_D decreases with increasing temperature.

Ohmic potential-drop measurements.—A typical oscillograph of the ohmic potential drop between the cathode and the Luggin capillary is shown in Fig. 5. The ohmic potential drop was measured from the horizontal line at the top, representing $\eta_{applied}$ just before the anode circuit was broken, to the point where the intensity of the display increased sharply, but where the potential decay was still almost vertical on the 50 μsec cm^{-1} sweep rate used. Reproducible results were obtained in this manner up to $\eta_{applied} = |-500$ mv|, beyond which the relay failed to produce a sharp break, as evidenced by noise signals in the oscillographs. The magnitude of the ohmic potential drop, for electrode placements of about 1 mm from the capillary tip, is displayed in Fig. 6 and seen to be a large "correction" at the higher applied overpotentials. For example, at $\eta_{applied} = |-400$ mv| the ohmic potential drop = 107 ± 5 mv. The current density is ~0.7A cm^{-2}, and "R" is thus ~0.15 ohm cm^2.

Although the ohmic potential drop correction can be large, its effect on the dependence of S_D on overpotential is relatively small as seen in Fig. 7. Because S_D reaches a plateau at about $\eta_{applied} = -400$ mv, the ohmic potential drop correction has no further effect on the shape of the curve (Fig. 7) for $\eta_{applied} \geq |-400$ mv|. The experimental limitations of the relay are thus irrelevant for this special case. However, the importance of the ohmic potential drop correction will increase with increasing cathodic overpotential for all such curves which do not exhibit a plateau. Comparison of results of different workers must therefore be made with the ohmic potential drop correction in mind. The appropriate curve in Fig. 7 should be employed when comparing the results of our work with results of other workers. Any theoretical treatment should be based on the corrected S_D *vs.* η curve.

Tafel plots.—A typical Tafel plot, corrected for ohmic drop, is shown in Fig. 8. The data were obtained after the series of electrolyses whose corresponding S_D values are given in Fig. 4 and 7. The linear portion at the lower current densities, based on the geometric area, always had a slope of −30 ± 1.5 mv regardless of whether the data were obtained before or after S_D measurements. Moreover, the Tafel

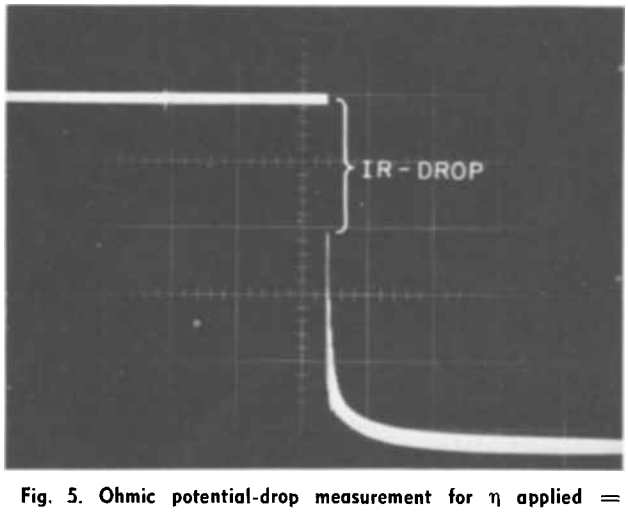

Fig. 5. Ohmic potential-drop measurement for η applied = −350 mv using the galvanostat;* IR-drop = −100 mv and η corrected = −250 mv; ordinate = 50 mv/division, abscissa = 50 μsec/division.

*The constant current was adjusted such that η applied = −350 mv just prior to an IR-drop measurement.

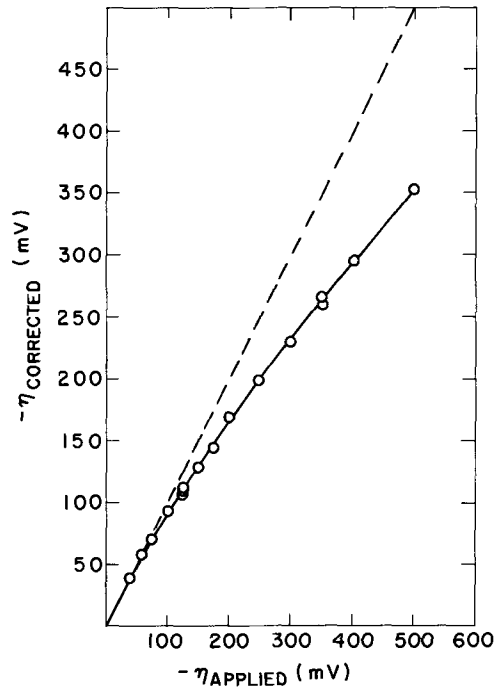

Fig. 6. Effect of ohmic potential drop on the applied overpotential; - - - -, slope = 1.

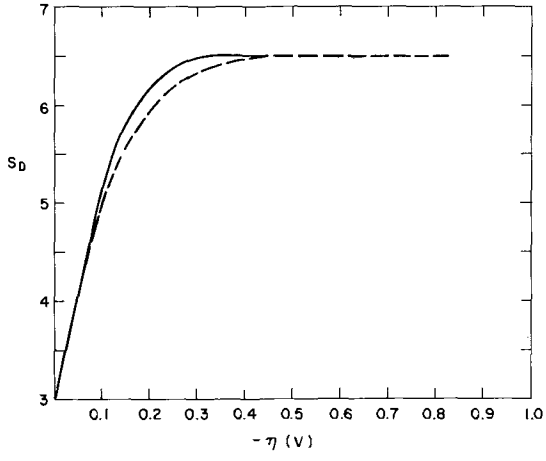

Fig. 7. Average values of S_D from Fig. 4 *vs.* η; ————, corrected for ohmic potential drop; - - - - - -, uncorrected for ohmic potential drop.

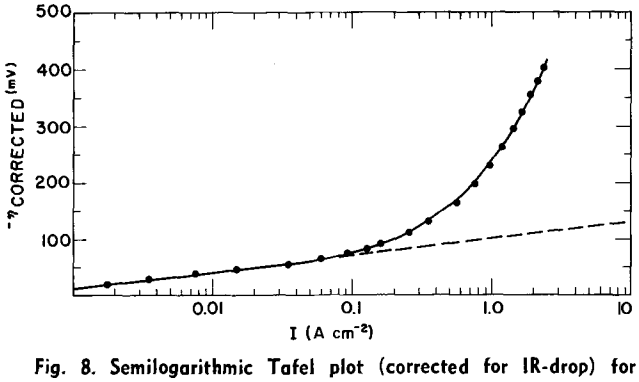

Fig. 8. Semilogarithmic Tafel plot (corrected for IR-drop) for platinum bead electrode at 25°C; data obtained after the series of electrolyses whose corresponding S_D values are depicted in Fig. 4, curve I; - - - -, slope = −29 mv; current density based on geometric surface area.

plot showed no hysteresis [*cf.* ref (27)]. Our Tafel plot resembles closely that recently published by Nomura and Kita (28) for the hydrogen evolution reaction on copper cathodes. They argue that the large deviation from the Tafel slope at the higher current densities is due to the existence of a cathodic saturation current, which they regard as evidence for the catalytic mechanism for the hydrogen evolution reaction; that is

$$2MH_{ads} \rightarrow 2M + H_2$$

(where M denotes the metal adsorption site) is the rate-determining step of the over-all reaction,

$$2H_3O^+ + 2e \rightarrow 2H_2O + H_2$$

Whether their arguments are applicable or not to the hydrogen evolution reaction on platinum, no evidence was obtained under the present experimental conditions for the second Tafel region of 100-120 mv (27, 29), which has been attributed (27) to a slow electrochemical atom-ion desorption step, *viz.*

$$MH_{ads} + H_3O^+ + e \rightarrow M + H_2O + H_2$$

At first sight, it appears that our Tafel data are inconsistent with those of Bockris and Azzam (27), and Schuldiner (29). This is not so for the following reasons. Although Bockris and Azzam obtained their data employing a flow technique, thereby minimizing concentration polarization effects, and they applied an IR-drop correction, their results on Pt are in some doubt. It is particularly difficult to explain the pronounced hysteresis in their Tafel plot without invoking adsorption of some inorganic impurity(ies) on their electrodes as Schuldiner (30) has pointed out. Furthermore, our results do not disagree with those obtained by Schuldiner (30) at about the same *p*H. Schuldiner observed the Tafel slope of about 110 mv only in systems of higher *p*H (>1), and in systems with added salts (29), also at higher *p*H.

Acknowledgments

The authors thank Dr. W. H. Stevens for suggesting this study and Professor B. E. Conway of the University of Ottawa for several profitable discussions and for reading the manuscript. They are also grateful to Mr. J. G. Wesanko who so willingly undertook the difficult task of constructing electrolysis cells.

Manuscript submitted Dec. 23, 1968; revised manuscript received Feb. 19, 1969. This paper was presented at the New York Meeting, May 4-9, 1969, as Paper 212.

Any discussion of this paper will appear in a Discussion Section to be published in the December 1969 JOURNAL.

REFERENCES

1. R. P. Bell, *J. Chem. Phys.*, **2**, 165 (1934).
2. G. Ogden and C. Bawn, *Trans. Faraday Soc.*, **30**, 432 (1934).
3. A. Eucken and K. Bratzler, *Z. physik. Chem.*, **A174**, 273 (1935).
4. F. P. Bowden and H. F. Henyon, *Nature*, **135**, 105 (1935).
5. J. H. Wolfenden and H. F. Walton, *Trans. Faraday Soc.*, **34**, 436 (1938).
6. J. Brun and Th. Varberg, *Kgl. Norske Videnskab. Selskabs. Forh.*, **26**, 19 (1953) [*C.A.* 49: 11468e].
7. B. E. Conway, *Proc. Roy. Soc. (London)*, **A256**, 128 (1960).
8. G. P. Lewis and P. Ruetschi, *J. Phys. Chem.*, **66**, 1487 (1962).
9. W. Vielstich, T. H. Schuchardt, and M. Von Stackelberg, *Ber. Bunsenges.*, **67**, 645 (1963).
10. H. von Buttlar, W. Vielstich, and H. Barth, *ibid.*, **67**, 650 (1963).
11. M. Salomon and B. E. Conway, *J. Phys. Chem.*, **68**, 2009 (1964).
12. T. Yokoyama, *J. Res. Inst. Catalysis, Hokkaido Univ.*, **15**, 84 (1967).
13. G. Nief and R. Botter, *Advances in Mass Spectrometry*, **1**, 515 (1959).
14. J. Horiuti and M. Fukuda, *Shokubai*, **3** (2), 115 (1961).
15. M. Fukuda and J. Horiuti, *J. Res. Inst. Catalysis Hokkaido Univ.*, **10**, 43 (1962).
16. M. Salomon and B. E. Conway, *Ber. Busenges.*, **69**, 669 (1965).
17. J. O'M. Bockris and B. E. Conway, *Trans. Faraday Soc.*, **45**, 989 (1949).
18. J. O'M. Bockris and D. F. A. Koch, *J. Phys. Chem.*, **65**, 1941 (1961).
19. A. Farkas, "Orthohydrogen, Parahydrogen and Heavy Hydrogen," p. 177, Cambridge University Press (1935).
20. M. Rome and C. F. Hiskey, *J. Am. Chem. Soc.*, **76**, 5207 (1954).
21. Y. Takahashi, S. Oka, and M. Oikawa, *Bull. Chem. Soc. Japan*, **31**, 220 (1958).
22. D. P. Smith, "Hydrogen in Metals," p. 79, University of Chicago Press (1948).
23. D. J. BenDaniel and F. G. Will, *This Journal*, **114**, 909 (1967).
24. S. Schuldiner, *ibid.*, **114**, 916 (1967).
25. F. G. Will and J. J. BenDaniel, *ibid.*, **114**, 1271 (1967).
26. M. S. Raman, R. Kumar, and R. L. Datta, *Z. Naturforg.*, **18a**, 347 (1963).
27. J. O'M. Bockris and A. M. Azzam, *Trans. Faraday Soc.*, **48**, 145 (1952).
28. O. Nomura and H. Kita, *J. Res. Inst. Catalysis Hokkaido Univ.*, **15**, 35 (1967).
29. S. Schuldiner, *This Journal*, **101**, 426 (1954).
30. S. Schuldiner, *ibid.*, **99**, 488 (1952).

Mechanism of the Electrochemical Reduction of Persulfates and Hydrogen Peroxide

R. Memming

Philips Zentrallaboratorium GmbH, Laboratorium Hamburg, Germany

ABSTRACT

Electrochemical studies have shown that the reduction of persulfate and hydrogen peroxide is a two step mechanism, the first step occurs by electron transfer with the conduction band and the second step by hole injection with the valence band. It could be concluded from corresponding measurements performed with a semiconductor electrode (GaP) that the electrochemical properties of these oxidizing agents have to be described by two instead of one redox (normal) potential. One normal potential is much lower (ϵ^0_1) and the other much larger (ϵ^0_2) than the theoretical value (ϵ^0) determined from thermodynamic data. These values are estimated as

$$\epsilon^0_1 \leqq 0.6\text{v};\ \epsilon^0_2 \geqq 3.4\text{v};\ \epsilon^0 = 2\text{v for } S_2O_8^{2-}$$

and

$$\epsilon^0_1 \leqq 0.6\text{v};\ \epsilon^0_2 \geqq 2.9\text{v};\ \epsilon^0 = 1.77\text{v for } H_2O_2.$$

Redox reactions with persulfates and hydrogen peroxide have been subject of several investigations. Especially the electrochemical behavior of H_2O_2 was of interest in connection with the electrochemical reduction and formation of oxygen. Bagotzky and Jablokowa (1) and Weiss (2) determined the reaction order in the reduction process of H_2O_2 on a dropping Hg-electrode and assumed a two step mechanism

$$H_2O_2 + e^- \rightarrow OH + OH^-$$

$$OH + e^- \rightarrow OH^-$$

R. and H. Gerischer (3) and Winkelmann (4) obtained the same results with a Pt-electrode and assumed also the same mechanism. Chemical properties of persulfate also are reported in the literature (5). The reaction kinetics, however, have not been studied in detail. Frumkin (5) has only postulated a possible reduction process which is similar to that of H_2O_2.

In the present paper investigations on the reduction mechanism using a semiconductor electrode (GaP) are reported. As is shown such a GaP-electrode with a large energy gap makes it possible to obtain fundamental information about the corresponding charge transfer in the reduction process.

Experimental

The electrochemical measurements were performed with single crystals of GaP as electrode material. These crystals were oriented in the <111> direction. The best results were obtained with Ga planes. In all cases the density of free carriers was about $10^{17}/cm^3$. The solutions (Merck, p.a.) were buffered to the proper pH values using standard phosphate and borate buffers. The electrodes were glued in araldit (CIBA) sockets (exposed area ~ 0.2 cm^2). A saturated calomel electrode was used as a reference electrode. (In the figures, however, values are plotted against the potential of the normal hydrogen electrode.)

All measurements were performed under potentiostatic conditions. In the medium pH range, measurements could be carried out only at cathodic potentials since $Ga(OH)_3$ layers are formed during anodic polarization (8). The interfacial capacity was determined at 250 kc by measuring the phase angle between a-c current and a-c voltage (6). The experimental arrangement for the luminescence measurements has been described previously (7).

Reduction of Simple Redox Systems

Charge transfer processes on GaP electrodes may occur via the valence or the conduction band of the crystal. As was reported (8) previously the anodic dissolution proceeds via the valence band, whereas for the cathodic hydrogen evolution conduction electrons are consumed. In the latter case a charge transfer across the interface can only occur if sufficient electrons in the conduction band are available. Consequently, in the case of n-type GaP the interfacial current rises rapidly with increasing cathodic potential, whereas with p-type GaP a very small saturation current of less than 1 μa was found (Fig. 1). Illumination of such a p-type electrode, *i.e.*, optical excitation of electrons from the valence band into the conduction band, leads to an increase of the cathodic current. The saturation current is only determined by the number of electrons excited by light. As shown in Fig. 2 it increases linearly with the light intensity.

Moreover, it was observed (8) that the charge transfer during the reduction of certain redox systems on GaP proceeds via the conduction band and in others via the valence band. This is demonstrated in Fig. 3 for ceric and ferricyanide ions in acid solutions using a p-type electrode. In the first case the current density is quite large and is not determined by the diffusion of minority carriers toward the surface, *i.e.*, the reduction of ceric ions proceeds via the valence band. In the case of ferricyanide ions the cathodic current is much smaller. Since this current may be increased by illumination of the p-type electrode it has to be concluded that electrons from the conduction band are consumed for the reduction of $[Fe(CN)_6]^{3-}$ in acid solutions.[1]

As proved by investigations with a variety of semiconductor electrodes the probability for a charge

[1] It should only be mentioned here that in alkaline solutions the reduction of $[Fe(CN)_6]^{3-}$ proceeds via the valence band. This effect is not of interest here, it was discussed elsewhere (8).

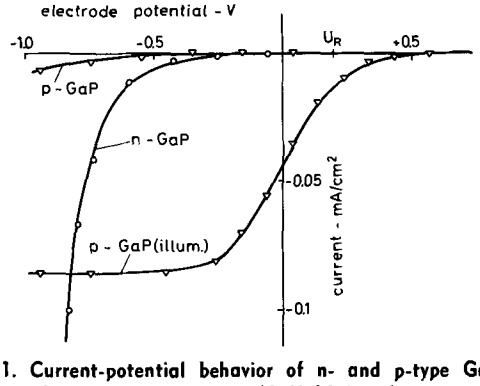

Fig. 1. Current-potential behavior of n- and p-type GaP electrodes in the cathodic region (1*N* H_2SO_4) (electrode potential against normal hydrogen electrode, NHE).

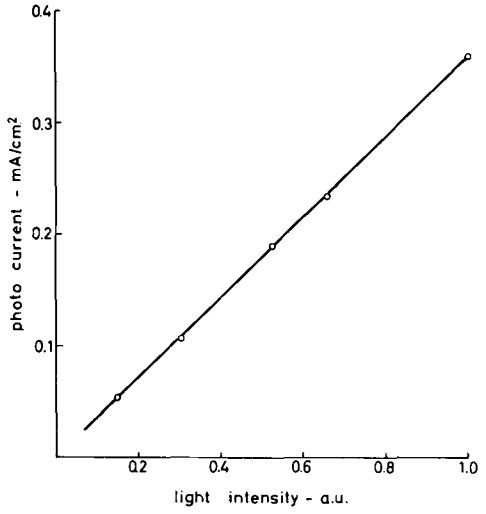

Fig. 2. Cathodic photocurrent vs. light intensity for a p-GaP electrode (1N H_2SO_4).

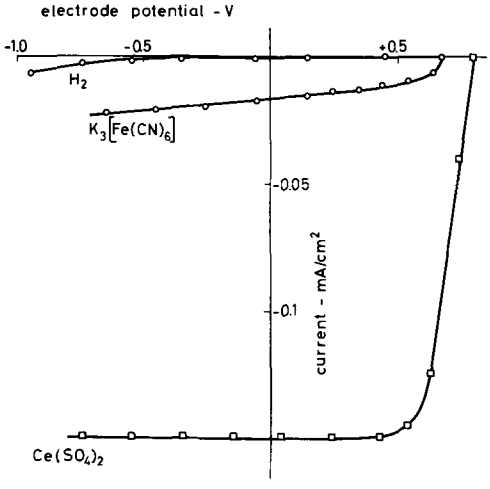

Fig. 3. Current-potential (NHE) behavior of a p-type GaP electrode in various oxidizing agents (10^{-2}M) in 1N H_2SO_4.

transfer via the conduction or the valence band depends on the redox potential of the corresponding systems (9). It was always found that the valence band process is preferred for systems with a high redox potential. This result may be qualitatively understood by the fact that an oxidizing agent is an electron acceptor. This property can be described energetically by deep lying energy levels. If we have, *e.g.*, a redox reaction of the type

$$A^{(z+1)+} + e^- \rightarrow A^{z+}$$

then the $A^{(z+1)+}$ ions represent the unoccupied and, A^{z+} the occupied electron levels. According to Gerischer's theory (10) the position of those energy levels is influenced by the solvation shell of the corresponding ions. Since the structure of the solvation shell depends on the charge of such an ion in its oxidized ($A^{(z+1)+}$) or reduced state (A^{z+}) the energy levels of $A^{(z+1)+}$ and A^{z+} differ considerably from each other. This is schematically shown in Fig. 4. According to the basic concept of this model electrons can be exchanged only between states on the same energy level (10), *i.e.*, the tunneling of an electron occurs without energy exchange with the surrounding molecules. As further shown by Gerischer the Fermi level in the semiconductor and of the redox system are equal at equilibrium conditions. Since generally we do not have an inert electrode no equilibrium is achieved, *i.e.*, one observes a corrosion potential which differs considerably from the redox potential. This

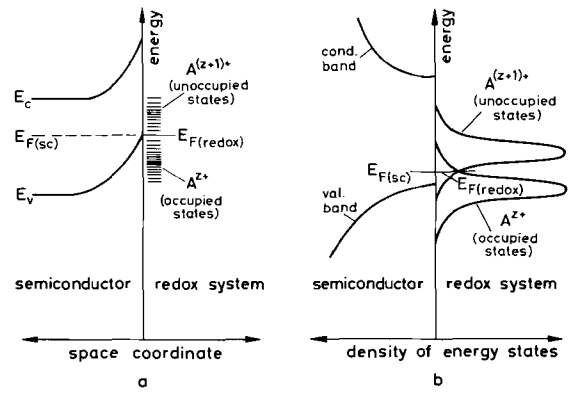

Fig. 4. Schematic energy diagram of the interface semiconductor-redox system.

model proposed by Gerischer (10) is the basis of all further considerations.

In Fig. 4 we have shown schematically a situation where the energy levels of the redox system only overlap with the valence band. In this case the electron transfer only occurs via the valence band as it was observed with ceric ions on gallium phosphide electrodes. The normal potential of this redox system amounts to 1.4v. The energy levels of redox systems with a higher normal potential have a much lower position in Fig. 4 (strong electron acceptors), *i.e.*, in this case the electron transfer is expected even more to proceed via the valence band.

We have performed corresponding measurements with persulfates and hydrogen peroxide which have a normal potential of 2.0 and 1.77v, respectively. As discussed above the reduction of these systems should occur via the valence band, *i.e.*, the reduction current should not be limited by minority carriers in p-type GaP. In contradiction to this postulation, however, we did observe a cathodic current diffusion limited by minority carriers. The results obtained with persulfates and hydrogen peroxide and the corresponding reduction mechanism are discussed next.

Reduction Mechanism of Persulfate and Hydrogen Peroxide

In Fig. 5 the current-voltage behavior is shown for a p-type GaP electrode in sulfuric acid before and after addition of $(NH_4)_2S_2O_8$ of various concentrations. It should be noted that the current scale is considerably enlarged compared with Fig. 1. As shown in Fig. 5a only a very small current increase occurs after addition of a large amount of $S_2O_8^{2-}$ ions. Similar results were also obtained with H_2O_2. As shown in Fig. 5b the cathodic current may be increased by illumination of the electrode. In this figure it is quite striking that at large cathodic potentials the current obtained for the reduction of $S_2O_8^{2-}$ is twice as large as that measured during the hydrogen evolution in H_2SO_4. As discussed in the previous section and demonstrated in Fig. 1 and 2 the saturation value of the photocurrent for the hydrogen evolution is only determined by the number of electrons excited by light from the valence band into the conduction band. Provided that this argument still holds for the reduction of persulfate we have to assume that only half of the electrons necessary for the reduction is produced by light excitation. This is possible principally because two electrons are necessary for the reduction of one persulfate ion according to

$$S_2O_8^{2-} + 2e^- \rightarrow 2SO_4^{2-} \qquad [1]$$

Actually, this result leads to a very simple model assuming that reaction [1] is a two step process. We can then assume that only for the first reaction step an electron from the conduction band is consumed, whereas an electron from the valence band is transferred across the interface in the second step. Conse-

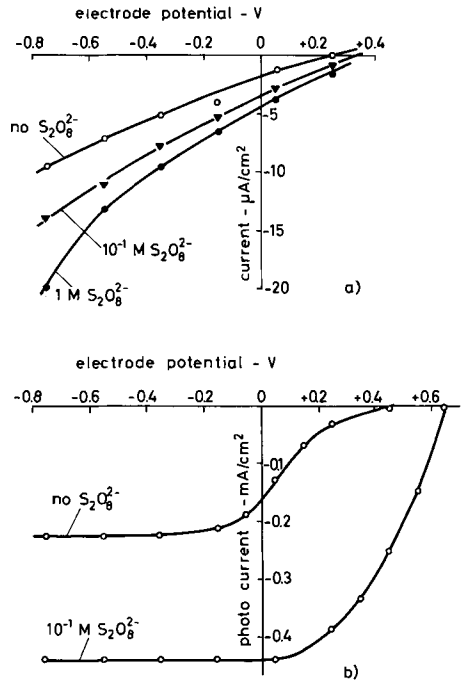

Fig. 5. Interfacial current vs. electrode potential (NHE) of p-type GaP in 1*N* H_2SO_4 with various concentration of $(NH_4)_2S_2O_8$. (a) Without illumination, (b) during illumination.

quently reaction [1] may be split up into

$$S_2O_8^{2-} + e^- \rightarrow SO_4^- + SO_4^{2-} \quad [1a]$$

$$SO_4^- \rightarrow SO_4^{2-} + p^+ \quad [1b]$$

In these equations e^- indicates an electron from the conduction band whereas p^+ is a hole injected into the valence band. Such a hole is created if an electron from the valence band is transferred to the redox system. A similar equation can be postulated for the reduction of hydrogen peroxide

$$H_2O_2 + e^- \rightarrow OH + OH^- \quad [2a]$$

$$OH \rightarrow OH^- + p^+ \quad [2b]$$

Such a current-doubling was also observed by Morrison and Freund (11, 12) for the oxidation of formic acid on ZnO. These authors also postulated a two step mechanism in which both valence and conduction band are involved. This interpretation of the current doubling, of course, is only an assumption. In the case of GaP electrodes, however, it is possible to prove this model as follows:

As mentioned above holes are injected if electrons from the valence band are consumed in the second reaction step ([1b] and [2b]). Using n-type GaP instead of p-type as the electrode material, these holes diffuse into the interior of the crystal and recombine somewhere with an electron from the conduction band. As we reported recently (7) this recombination process corresponds to a radiative transition, *i.e.*, luminescence occurs if holes are injected into an n-type GaP electrode. Such an experiment can only be performed with n-type material in order to have sufficient electrons in the conduction band for the recombination with injected holes. In the case of persulfate or hydrogen peroxide an n-type electrode has also the advantage in the luminescence experiment that the first reaction step ([1a] or [2a]) is not limited by minority carriers.

As we reported recently (7) we did observe luminescence which can only be explained by injection of holes. The same spectral distribution was also obtained with hydrogen peroxide. This result proves indeed that the second reaction step proceeds via the valence band.

pH dependence.—In a further experiment we also measured the *p*H dependence of the current doubling, as shown for hydrogen peroxide in Fig. 6 and for persulfate in Fig. 7. As a standard value we used again the cathodic photocurrent for the H_2 evolution which is independent of the *p*H value. In the case of H_2O_2 current doubling always occurs in alkaline solutions, whereas in acid solutions it depends on the H_2O_2 concentration (Fig. 6).

This *p*H dependence may obviously be related to the degree of dissociation of this molecule. Since the *p*K value of H_2O_2 is about 12 it may be concluded that the OOH^- ion is more easily reduced on a GaP electrode than the undissociated molecule itself. The *p*H dependence for $S_2O_8^{2-}$ as shown in Fig. 7 is much more difficult to understand. One possible explanation for the drop of the current doubling above about *p*H = 2 would be the assumption that hydrogen persulfate ions ($HS_2O_8^-$) exist below *p*H = 2. In general ions with a lower negative charge are more easily reduced than those with a higher charge for electrostatic reasons. Unfortunately the corresponding *p*K value is not known. Only the corresponding *p*K value for SO_4^{2-} (HSO_4^-) is tabulated which would fit to the experimental results (*p*H ~ 2). It seems to be reasonable to assume the *p*K value for persulfate to be similar. This is supported by the fact that the reduction current (saturation value) of persulfate on a Pt electrode varies in the same way in the corresponding *p*H range and remains constant at higher *p*H values. On the other hand the photocurrent on a GaP electrode increases slowly again at higher *p*H values. This may be due to the fact that $S_2O_8^{2-}$ is not very stable in alkaline solutions and decomposes partly to H_2O_2 (via Caro acid).

It would be interesting to study the *p*H dependence in the reduction of persulfate or peroxide also with n-type electrodes since then sufficient electrons are available in the conduction band. Current voltage curves have shown, however, that with n-type material practically no increase of the cathodic current

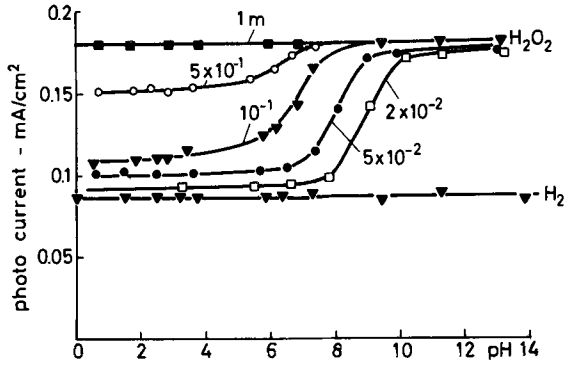

Fig. 6. *p*H dependence of the photocurrent for p-type GaP in various H_2O_2 concentrations.

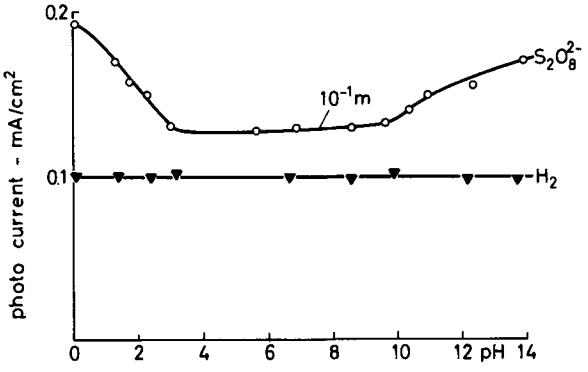

Fig. 7. *p*H dependence of the photocurrent for p-type GaP and 10^{-1}M $(NH_4)_2S_2O_8$.

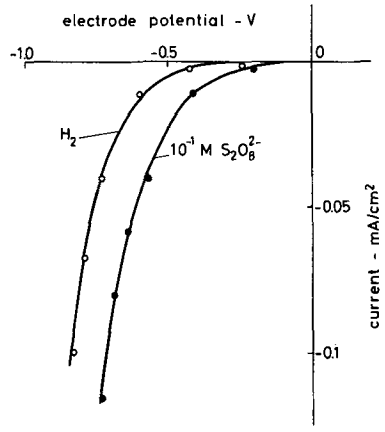

Fig. 8. Current potential (NHE) behavior of an n-type GaP electrode in 1*N* H_2SO_4 and 10^{-1}M $(NH_4)_2S_2O_8$.

occurred after addition of persulfate to H_2SO_4 (pH = 0.5) (see Fig. 8). On the other hand we did already mention in connection with the luminescence experiments that holes are injected if $S_2O_8^{2-}$ ions were present in the electrolyte. From this we may conclude that obviously the reduction of $S_2O_8^{2-}$ does occur at higher cathodic potentials than for p-type electrodes. Actually, in the case of n-type electrodes the reduction of persulfate sets in at about the same potential as the hydrogen evolution. This result implies that also with n-type electrodes the rate determining step is not determined by the redox system but by charge carriers within the electrode. This prediction may easily be proved by capacity measurements as follows:

In Fig. 9 the experimental values of the space charge capacity C_{sc} are plotted *vs.* the electrode potential for n- and p-type GaP. According to this figure $1/C_{sc}^2$ varies linearly with the electrode potential, *i.e.*, the space charge capacity follows the Schottky-Mott law

$$\frac{1}{C_{sc}^2} = \frac{2kT}{e^2\,\epsilon\epsilon_0\,N_{D(A)}}\left(\frac{e\,U_{sc}}{kT} - 1\right)$$

where U_{sc} = potential drop across the space charge layer, $N_{D(A)}$ = density of donor or acceptor states within the semiconductor, ϵ = dielectric constant, ϵ_0 = 8.854 x 10^{-12} amp·sec·v^{-1}·meter^{-1}). Such a relationship is always obtained for a depletion layer (6). Extrapolating the curves to $1/C_{sc}^2 = 0$ one obtains roughly flat band position, *i.e.*, $U_{sc} = 0$. The band bending is zero for n-type at —0.9v and for p-type at +1.2v. The difference between the two flat band positions is then 2.1v, *i.e.*, it is slightly less than the energy gap of GaP (2.25 ev). This result is expected for highly doped semiconductors provided that the potential difference applied across the interface occurs only within the space region of the electrode. From this result the band bending at the rest potential U_R = +0.35v (see Fig. 9) can be determined (13). One obtains an upward bending of 1.25v for n-type and downward bending of 0.85v for p-type as shown schematically in Fig. 10. Consequently the electron density at the surface of an n-type electrode is so small that any charge transfer from the conduction band into the electrolyte is only determined by number of electrons available at the surface. This behavior makes it also impossible to obtain any further information about the reduction of persulfate from current voltage curves with n-type GaP-electrodes.

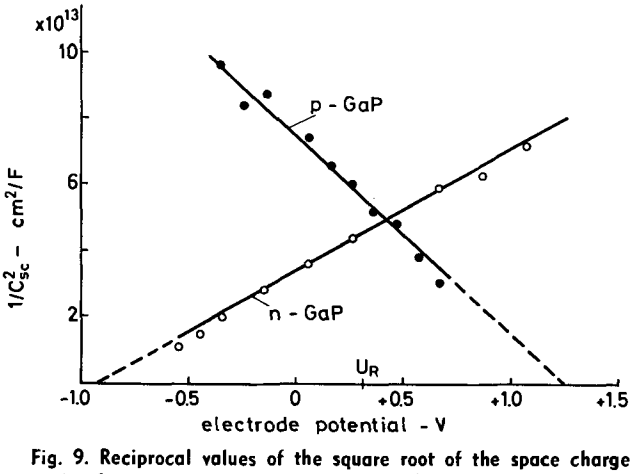

Fig. 9. Reciprocal values of the square root of the space charge capacity for n- and p-GaP electrodes in 1*N* H_2SO_4. Potential *vs.* NHE.

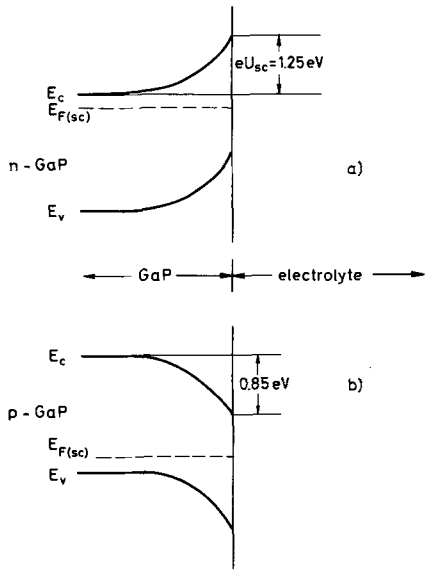

Fig. 10. Energy band bending at the rest potential U_R; (a) n-GaP, (b) p-GaP.

Normal potentials of persulfate and hydrogen peroxide.—As described in the first part of our discussion in this paper it depends on the normal potential of a redox system whether the charge transfer occurs via the conduction or via the valence band. Since the reduction of $S_2O_8^{2-}$ and H_2O_2 is a two-step mechanism in which both energy bands of the electrode are involved it follows directly from Gerischer's model (10) that the properties of these redox systems can only be described by two instead of one normal potential. This can be demonstrated again by an energy diagram (Fig. 11a) which is similar to that shown in Fig. 4b. In the case of persulfate, for example, we have now three energy states. The energy position of the

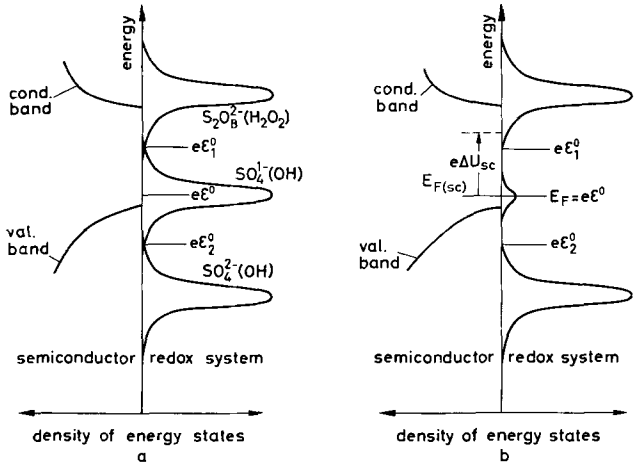

Fig. 11. Schematic energy diagram of the interface semiconductor-persulfate (hydrogen peroxide) (at equilibrium). Concentration of SO_4^{1-}: (a) large, (b) small.

intermediate state SO_4^- is just between the unoccupied $S_2O_8^{2-}$ and the occupied state SO_4^{2-}. According to Gerischer's model the density of the unoccupied ($S_2O_8^{2-}$) and of the intermediate state (SO_4^-) are equal at normal potential ϵ^0_1 for the first reaction step provided that the concentrations of $S_2O_8^{2-}$ and SO_4^- are equal. The latter condition is more or less trivial because, according to Nernst law, the redox potential is only identical with the normal potential if the concentrations are equal. In the same way also the normal potential for the second step ϵ^0_2 is determined. The effective redox potentials depend on the concentrations of the three species. The corresponding Nernst equations are given by[2]

$$e\epsilon_1 = e\epsilon^0_1 + kT \ln \frac{C_{S_2O_8^{2-}}}{C_{SO_4^-}\, C_{SO_4^{2-}}} \qquad [3]$$

$$e\epsilon_2 = e\epsilon^0_2 + kT \ln \frac{C_{SO_4^-}}{C_{SO_4^{2-}}} \qquad [4]$$

where e = elementary charge, and k = Boltzmann's constant. The free enthalpy of the complete reversible electrochemical reaction is given by $\Delta G = zF\epsilon^0$. For a two-step mechanism this free enthalpy may be split up into two values

$$zF\epsilon^0 = (z_1\epsilon^0_1 + z_2\epsilon^0_2)F \qquad [5]$$

According to [1a] and [1b] $z_1 = z_2 = 1$ and $z = 2$ so that

$$\epsilon^0 = \frac{\epsilon^0_1 + \epsilon^0_2}{2} \qquad [6]$$

i.e., the normal potential ϵ^0 of the total system is just the mean value of the normal potentials ϵ^0_1 and ϵ^0_2 defined for each reaction step (see Fig. 11a). Under equilibrium conditions the concentrations of the three species have to arrange themselves in such a way that the redox potentials are equal, *i.e.*,

$$\epsilon_1 = \epsilon_2 = \epsilon \qquad [7]$$

Since the intermediate state SO_4^- is a very unstable species its concentration is very low. Using an electrolyte containing $S_2O_8^{2-}$ and SO_4^{2-} ions in concentrations of the same order of magnitude then the effective redox potential ϵ of the complete system is almost identical with the corresponding normal potential ϵ^0 according to

$$\epsilon = \epsilon^0 + \frac{kT}{2e} \ln \frac{C_{S_2O_8^{2-}}}{C^2_{SO_4^{2-}}} \qquad [8]$$

In this case the redox potential ϵ ($\approx \epsilon^0$) is just halfway between the two normal potentials ϵ^0_1 and ϵ^0_2 and the density of energy states for the intermediate species (SO_4^{1-}) is very low as indicated in Fig. 11b.

Moreover, at equilibrium the Fermi level $E_{F(sc)}$ in the semiconductor and the Fermi level $E_{F(redox)}$ in the redox system (which is defined as $e\epsilon$) are equal (10) (Fig. 11b). Values of the normal potential ϵ^0 in this energy scale are not known. Only the corresponding normal potential ϵ^0_h relative to the hydrogen normal potential can be generally measured or calculated from thermodynamic data. In the case of persulfate $\epsilon^0_h = +2.0$v (14). Consequently, at equilibrium one would also measure an electrode potential of +2.0v provided that no corrosion etc. occurs. This is a very large potential and according to capacity measurements the energy bands even for p-type GaP would be bent upward very strongly. Consequently the electron density at the semiconductor surface would be very low, *i.e.*, at an electrode potential of +2.0v the Fermi level at the surface of the semiconductor is quite close to the valence band. This leads to the conclusion that the upward band bending has to be decreased considerably by varying the electrode potential into the cathodic direction before sufficient electrons are available in the conduction band for a charge transfer across the interface. In the energy distribution picture (Fig. 11b) this is equivalent to an upward shift of the Fermi level in the semiconductor (dotted line for $E_{F(sc)}$). According to the current voltage curves (Fig. 5b) a reduction current was actually measured below +0.75v, *i.e.*, Fermi level $E_{F(sc)}$ has to be shifted upward relative to the equilibrium value by at least 1.5v.

It is important to note that this behavior of persulfate or hydrogen peroxide not only occurs on semiconductor electrodes but exhibits a general property of these redox systems. Using a platinum instead of a semiconductor electrode a cathodic reduction current is also only observed below about +0.8v, although sufficient electrons are available even at large anodic electrode potentials. On the other hand it is also a necessary condition for a charge transfer that occupied energy states in the metal overlap with the empty states ($S_2O_8^{2-}$) in the redox system. In the case of a metal its Fermi level is also equal to that of the redox system at equilibrium. Since only energy states up to Fermi level are occupied and no higher energy levels can be filled, the overlapping between the occupied states and the $S_2O_8^{2-}$ states is very poor (Fig. 13a). Applying an external voltage ΔU the Fermi level in a metal (in contradiction to a semiconductor) cannot be shifted relative to its energy states. In this case only the potential difference across the Helmholtz double layer can be changed (Fig. 12b), *i.e.*, the energy states in the metal are shifted relative to those of the redox system as shown schematically in Fig. 13b. Since the energy difference between the unoccupied ($S_2O_8^{2-}$) and the occupied state (SO_4^{2-}) is quite large (see below) the electrode potential has to be varied considerably into the cathodic direction before a current flow is discernible.

Comparing the results obtained with $S_2O_8^{2-}$ and H_2O_2 with those of other redox systems it is possible to get a rough estimate for the values of the two normal potentials ϵ^0_1 and ϵ^0_2. This does not mean that we obtain absolute values of the potentials. We can only determine corresponding values of the normal poten-

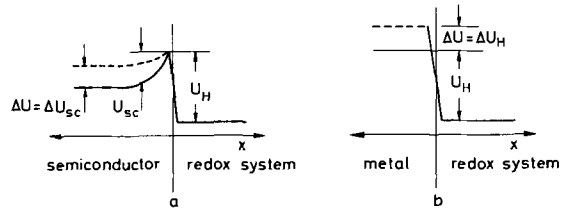

Fig. 12. Potential distribution for (a) semiconductor and (b) metal electrolyte interface. Dotted line: at cathodic polarization.

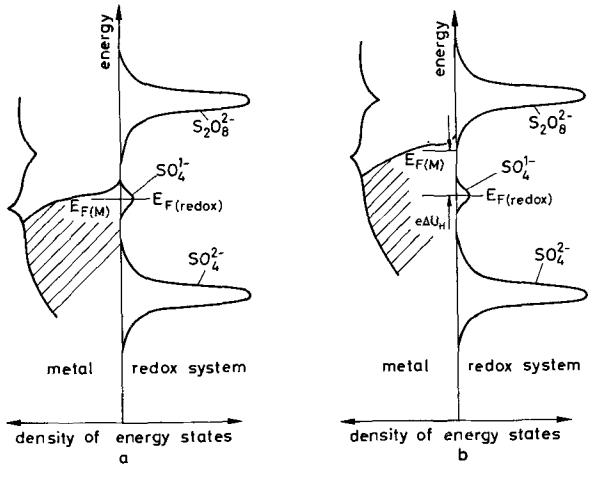

Fig. 13. Schematic energy diagram of the interface metal-persulfate. (a) At equilibrium, (b) during cathodic polarization.

[2] The reference point for the normal potentials $\epsilon^0_{1,2}$ is here not the standard hydrogen electrode. The point of zero energy is the free electron energy at infinity which is zero by definition.

tials $\epsilon^0_{1,h}$ and $\epsilon^0_{2,h}$ *vs.* a normal hydrogen electrode. As mentioned before it depends on the normal potential whether the charge transfer in a certain redox reaction occurs via the conduction or the valence band. According to Fig. 3 the reduction of Fe^{3+} proceeds already via the conduction band. Since the normal potential of the Fe^{2+}/Fe^{3+} amounts to 0.6v we have to conclude that also the normal potential $\epsilon^0_{1,h}$ for the first reaction step of persulfate and hydrogen peroxide is equal or smaller than this value. The normal potential $\epsilon^0_{1,h}$ can immediately be calculated using Eq. [6] since the normal potential of the complete system is known from thermodynamic data. One obtains for persulfate

normal potential:	ϵ^0_h	$= +2.0$v (complete system)
	$\epsilon^0_{1,h}$	$\leqq +0.6$v (1. reaction step)
	$\epsilon^0_{2,h}$	$\geqq +3.4$v (2. reaction step)
and for H_2O_2:	ϵ^0_h	$= +1.77$v
	$\epsilon^0_{1,h}$	$\leqq +0.6$v
	$\epsilon^0_{2,h}$	$\geqq +2.94$v

In the case of persulfate, *e.g.*, the difference between the two normal potentials is

$$\Delta\epsilon = |\epsilon^0_1 - \epsilon^0_2| \geqq 2.8\text{v}$$

Consequently, the energy difference between the unoccupied and occupied states is also larger than 2.8 ev.

Acknowledgments

The author is indebted to Dr. Beckmann, Dr. Möllers, and Dr. Schwandt for many helpful discussions and to Mr. G. Kürsten for performing the measurements. Thanks are also due to Ir. Peters from the Philips Laboratories in Eindhoven for supplying the single crystals of GaP.

Manuscript submitted Nov. 19, 1968; revised manuscript received Feb. 18, 1969.

Any discussion of this paper will appear in a Discussion Section to be published in the December 1969 JOURNAL.

REFERENCES

1. V. S. Bagotzky and I. E. Jablokowa, *J. Phys. Chem. USSR*, **27**, 1665 (1953).
2. J. Weiss, *Trans. Faraday Soc.*, **31**, 1547 (1935).
3. R. and H. Gerischer, *Z. Phys. Chem. N.F.*, **6**, 178 (1956).
4. D. Winkelmann, *Z. Elektrochem.*, **60**, 731 (1956).
5. A. N. Frumkin, *ibid.*, **59**, 807 (1955); *J. Chem. Phys.*, **26**, 1552 (1957).
6. R. Memming, *Philips Research Repts.*, **19**, 323 (1964).
7. K. A. Beckmann and R. Memming, *This Journal*, **116**, 368 (1969).
8. R. Memming and G. Schwandt, *Electrochim. Acta*, **13**, 1299 (1968).
9. H. Gerischer in "Advances in Electrochemistry," Vol. 1, p. 139, P. Delahay, Editor, International Publishers, New York (1961).
10. H. Gerischer, *Z. Phys. Chem. N. F.*, **26**, 223, 325 (1960), **127**, 48 (1961).
11. S. R. Morrison and T. Freund, *J. Chem. Phys.*, **47**, 1543 (1967).
12. S. R. Morrison and T. Freund, *Electrochim. Acta*, **13**, 1343 (1968).
13. R. Memming and G. Schwandt, *Surf. Sci.*, **5**, 97 (1966).
14. W. M. Latimer, "Oxidation Potentials," Prentice-Hall Inc., New York (1959).

Capacities of Zinc-Potassium Hydroxide Interfaces

R. A. Myers[1] and J. M. Marchello

University of Maryland, College Park, Maryland

ABSTRACT

A galvanostatic pulse current technique was employed to measure the capacitance of flat and porous zinc electrodes in 32 w/o KOH solution at 25°C. The data were obtained by operating near the hydrogen evolution potential. The electrode capacities were used to obtain the wet surface area of the zinc-KOH interface. Some exchange currents were obtained and average pore cross sections were calculated for porous zinc electrodes.

The metal-electrolyte interface exhibits a double layer capacitance which can be used to calculate the surface area. The objective of this investigation was to obtain a better understanding of the properties of the zinc electrode in the zinc-air battery. Unpublished results of investigations conducted on zinc electrodes at the Naval Ordnance Laboratory indicated that porous zinc electrodes do not seem to passivate as readily as flat zinc electrodes. Performance data is usually based on current density in terms of projected geometric area without regard for the physical structure of the surface. Since performance is dependent on the surface characteristics, the double layer capacitance technique was employed to determine the wet surface area of the zinc electrode.

Grahame (1) states that the charges (once the conditions equilibrate) do not cross the double layer because they lack the tendency to do so. The metal electrode is infinitely polarizable either (+) or (—) at the interface. The distribution of charge in the electrolyte phase at the interface may be calculated using the Gouy-Chapman theory. The original theory assumed point size charges, but this has been modified by Stern to account for finite size particles. In this theory, two double layers are assumed; the compact double layer (Helmholtz or inner double layer) is separated by the distance of closest approach from the outer or diffuse double layer.

The double layer capacity is usually measured by a galvanostatic pulse or an a-c bridge technique. The total capacitance is made up of two double layer capacitances in series. If the bulk of the capacitive nature of the interfacial system is very close to the interface then $C_{diffuse}$ is large and the total capacitance is equal to the compact capacitance. This is usually the case in strong electrolytes. It is also assumed that there is no specific adsorption of impurities which would alter the double layer. The capacitance is a function of potential. The electrode-electrolyte interface exhibits a minimum capacitance with respect to some particular potential, often referred to as the

[1] Present address: Harry Diamond Laboratory, Washington, D. C.

zero-point. This minimum usually occurs when the interface capacitance equals the compact capacitance.

The true surface area is obtained by dividing the capacitance measured by some standard capacitance density. The standard that has been used is liquid mercury for which the geometric and interfacial area are the same. Liquid mercury behaves as an ideally polarizable electrode (no charge transfer). Specific adsorption effects can be prevented by using a dropping mercury electrode (4). In strong electrolytes, mercury exhibits only a compact double layer for which the minimum capacitance is 16 μf/cm^2 (1, 2). This capacitance minimum can be used as a standard because the compact double layer is independent of metal, electrolyte, and temperature (2).

Single pulse techniques, similar to the one used in this investigation, are described theoretically and experimentally in the literature. McCallum *et al.* (2, 3) report capacitance data for the following: flat platinum, nickel, and silver; porous carbon and nickel: and nickel screen in aqueous electrolytes. They also report results for porous lithium in propylene carbonate electrolyte. Mercury-electrolyte interface capacitance techniques are reported by McMullen and Hackerman (4). They also report values for platinum, silver, copper, aluminum, and tantalum.

McCallum *et al.* (3) report an attempt to measure the capacitance of zinc electrodes in KOH. Their conclusion was that it was impossible to obtain meaningful results under the conditions they used due to faradaic effects. However, Dirkse *et al.* (5) recently report measurements for flat zinc.

Experimental

In galvanostatic pulse techniques the capacitance, C_T, or the electrode surface is calculated from the equation

$$C_T = i_p \Big/ \frac{dv}{dt} \qquad [1]$$

where i_p is the pulse current in amperes and dv/dt is the slope of the voltage response curve.

The technique used for double layer capacitance determination, Myers (6), was adapted from the work of McCallum and Hardy (3, 4). The cell used in the determination of the double layer capacitance is shown in Fig. 1. It was fabricated from Pyrex and Teflon. No grease was used in any joint because of contamination. The body was a standard tapered joint, 5 in. high, with a capacity of 250 ml. Two provisions were made for bubbling argon gas through the cell. A 2 cm gas dispersion tube rested in the bottom of the cell for deoxygenating the KOH. A surface level opening introduced an argon blanket over the KOH. These openings were connected to the gas washing bottle shown on the left. The male end of the joint was fashioned into a top for the cell. It contained four female joints for electrode connections and a ball joint and stopper for KOH addition. Teflon stoppers with a small hole down the center were used in the female joints. Two of these held the nickel wire which was connected to a 65 cm^2 platinized platinum counter electrode; one held the nickel wire connected to the working electrode, and the fourth was for optional leads to a Teflon sheathed copper-constantan thermocouple.

Fig. 1. Double layer capacitance measurement cell configuration

The reference electrode shown on the far right of Fig. 1 in a separate compartment connected to the cell by an electrolyte bridge was a saturated calomel electrode (SCE). While the mercury-mercuric oxide electrode is recommended to avoid liquid junction potentials, the SCE was found to be adequate for this study (6). Preliminary experiments gave liquid junction potentials of 3.5 mv which is well below the $\pm$ 10 mv accuracy of the electrometers used here.

A wire diagram of the double layer circuit appears in Fig. 2. It is similar to the diagram appearing in the report by McCallum (3). The circuit is divided into two sections. The right half was the polarizing circuit. The power source (battery and/or power supply) applied a voltage between the working electrode and counter electrode in the cell. The 10,000 ohm precision adjustable resistance controlled this voltage so that the desired voltage, between the working and reference electrodes, could be established. The two reversing switches allowed polarization in either direction. The milliammeter measured the faradaic current. The two 45-henry inductor coils prevented pulsing through the polarization circuit.

The left side of Fig. 2 shows the pulsing circuit. The Tektronix 160 series instruments provided a known constant square wave pulse across the working electrode and counter electrode with the pulse generator operating in "negative pulse out" mode. Pulse durations could be adjusted from 0.01 to 100 msec, pulse heights from 0.5 to 50v, and pulse repeat intervals between 0.1 and 10,000 msec, each independently. The pulse size and the voltage response of the working electrode were separately indicated on the oscilloscope through the dual-trace plug-in unit. A permanent record of these traces was obtained on polaroid film with a C-12 Polaroid Camera Unit mounted on the oscilloscope.

The pulse current was obtained by dividing the height of the pulse on the lower trace by 10,000 (R_s-series resistance). The dv/dt was measured directly on the upper trace. The capacitance of the electrode surface was calculated from Eq. [1].

An electrolyte of 32 w/o (weight per cent) KOH was used throughout. It was prepared from reagent grade KOH pellets and purified water. Distilled water was passed through an acid-leached activated carbon bed and redistilled, using a small Pyrex distillation apparatus, from an alkaline permanganate solution.

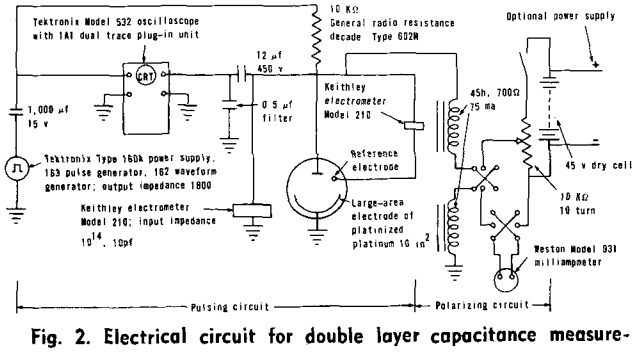

Fig. 2. Electrical circuit for double layer capacitance measurements.

Distillation was carried out at atmospheric pressure. Vapors passed through a 4 ft insulated column to prevent mechanical carry over. The final water had a conductivity of 8 x 10^{-7} mhos/cm. This water was used to make up the electrolyte. The final procedure was to pre-electrolyze the KOH solution for 48 hr at 50 ma employing two platinum electrodes just before use.

All zinc electrodes studied were less than 2 cm^2 projected area and weighed less than 0.6g. The size and weight were restricted due to limitations in detecting slopes of the dv/dt response during the double layer capacitance measurements.

Flat zinc electrodes were cut from acetone washed 99% pure zinc metal strips, 0.016 in. thick, to an area of 1 cm^2 with a 4 in. extension of the same piece of metal. Only zinc metal contacted the KOH. The area of extension that contacted the KOH was taken into account for apparent area determinations. Before making the capacitance measurement, the electrode was placed in pure KOH and cathodically cleaned at 50 ma for 30 min to remove any oxide film. The counter electrode during cleaning was a 14 cm^2 platinum electrode. At the end of the cleaning period, the electrode was rapidly transferred to the Pyrex cell for the double layer capacitance measurements.

Porous zinc electrodes were prepared by electrochemical deposition of zinc onto a silver X-mat screen from a saturated ZnO-KOH solution. The silver X-mat was pure silver, weighed 0.2 g/in.^{2} and was 0.005 in. thick. For each zinc electrode 1 cm^2 of this screen was cut out and spot-welded to a 6 in. piece of nickel wire. The rate of deposition was controlled at values between 0.1 and 0.5 amp/cm^2 for a period of 1-2 hr at about 2.0v. By knowing the rate and time of deposition, the amount of zinc on the screen was determined. Zinc is known to deposit under these circumstances at a rate of 1.1833 g/amp-hr. The electrode was then pressed to a thickness of between 0.03 and 0.05 in. and cleaned the same as the flat zinc described above. This procedure produced pure mossy type porous zinc electrodes.

The controlling parameters studied for effect on surface area were time and rate of deposition and applied pressure after deposition. A few electrodes were prepared by depositing zinc onto flat zinc to obtain surface area data between flat zinc and porous zinc. This procedure followed the same outline.

At the beginning of a capacitance measurement the cell was assembled and purged with argon for 30 min. Then the argon flow was stopped and the stopcocks closed. The polarizing switch was closed, and the polarizing voltage was applied across the cell. The voltage between the working and reference electrodes was observed until it reached the desired value. The signals on the oscilloscope were centered and a picture was taken of these signals. A series of pictures was taken at various voltages for several electrodes in order to obtain the zero-point capacitance. This was the point that corresponded to the true surface area. The minimum capacitance occurred where the response trace had a maximum slope which made it easy to find the approximate voltage range by scanning first and then working step by step across the range recording the responses. Plots of capacitance *vs.* reference voltage defined the zero-point which was used in later runs as the operating point. A slightly negative overpotential had to be established on the zinc during the argon purge to prevent zinc from going into solution. Also, the establishment of the desired zinc-reference voltage (saturated calomel electrode) on the porous electrode required a longer time than for the other electrodes.

Posey *et al.* (7) developed an expression for the charging of ideally porous structures. For charging times greater than the characteristic time constant τ, his results simplify to

$$v(x,t) = ipR_o\left[\frac{t}{\tau} + \frac{1}{3} + \frac{x}{L}\left(\frac{x}{2L} - 1\right)\right] + V_o \quad [2]$$

where $v(x,t)$ = potential in electrolyte at point x and time (v), $R_o = \rho L/A$ total axial pore resistance (ohms), A = normal pore cross sectional area (cm^2), ρ = electrolyte resistivity (ohm-cm), i_p = current pulse (amp), $\tau = R_oC_T$ time constant (sec), C_T = total capacitance (farads), L = electrode thickness (cm), t = pulse time (sec), and V_o = initial voltage on porous structure (v).

Differentiation of Eq. [2] with respect to time results in Eq. [1] which shows that for charging times greater than τ the potential response will be a constant. A preliminary estimate showed that the pulse current had to be greater than 1.0 msec to allow for the total zinc pore to be charged and less than 12 msec in order to minimize faradaic effects. Therefore, a pulse time of 5 msec was chosen for this work. The smallest setting on the vertical deflection of the oscilloscope was 0.005 v/cm. On this setting, the smallest detectable voltage deflection (which corresponded to the change in the zinc electrode potential resulting from the galvanostatic pulse) was about 0.25 mv. For a pulse current of 1.2 x 10^{-4} amp for a duration of 5 msec this would correspond to a capacitance of about 30,000 μf according to Eq. [1]. Based on the standard of 16 $\mu f/cm^2$, this capacitance would correspond to a double layer area of about 2000 cm^2. Therefore, this was the limit for the area determination on the porous electrodes.

Sixteen standard electronic capacitors with rated values in the range from 12 to 250 μf were tested on several occasions. This was done by removing the cell from the system and connecting the capacitor across the working electrode-reference electrode panel connections. The rest of the procedure was the same. Several voltages were placed on each capacitor for tests. As before, the oscilloscope traces were evaluated, and the capacitance was calculated. In all cases, the results were within 2% of the rated values, and repeated results checked within 0.5%.

Results

In the course of the experimental work, about 350 pictures were taken of the double layer responses of electrode surfaces and response of electrodes to load changes during discharge. This entailed the study of over 75 electrodes. About one half of these electrodes were of metals that were reported in the literature (1, 2, 4) and were used to establish the limitations of the procedure used here. The other half of the electrodes were either flat or porous zinc on which the experimental data were the main concern of this research. All of the data were taken in 32% KOH at a temperature between 25° and 27°C.

Before measuring zinc the values for platinum, nickel, silver, and mercury were measured to check with reported literature values. These are summarized in Table I. Sample oscilloscope traces are shown in Fig. 3.

Table I. Summary of double layer capacitance measurements on standard metals

Metal	Description	E_{min} (v)	Current (ma)	Geometric area (cm^2)	Specific capacitance ($\mu f/cm^2$)
Nickel	0.012 in. thick sheet	−0.70	0.006	12.9	20.65
		−0.70	0.004	12.9	20.60
		−0.70	0.0	12.9	26.30
Silver	0.025 in. thick sheet	−0.44	0.0	13.5	61.4
		−0.335	0.0	13.5	70.0
	0.003 in. thick foil	−0.70	0.0	12.9	38.3
Platinum	0.002 in. thick foil	−0.77	0.004	14.1	62.2
		−0.77	0.002	2.0	29.6
Mercury	Triple distilled liquid	−0.81	0.035	0.952	17.3
		−0.84	0.037	0.952	18.4
		−0.84	0.036	0.952	18.4

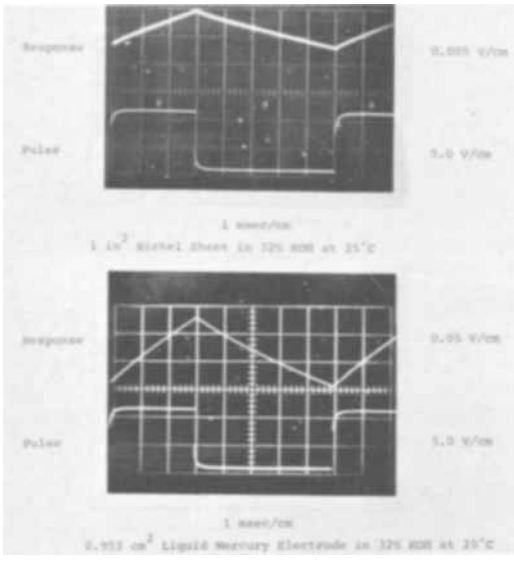

Fig. 3. Oscilloscope traces from double layer capacitance measurements on nickel and mercury.

The first successful results were obtained on flat zinc plates near the hydrogen evolution potential. With small surface areas in comparison to porous zinc, it was easier to traverse the current-voltage curve of flat zinc in KOH. The rest voltage for zinc was —1.60 *vs.* SCE. Figure 4 shows current density (based on geometric area) voltage characteristics for a flat zinc electrode under current producing conditions. However, the current producing reaction at the interface disrupts the double layer. In fact any faradaic current involving the metal ions at the surface decreases the capacitive nature of the surface so that the double layer can not be readily measured. Therefore, attempts to measure the double layer capacitance at voltage less negative than —1.60 (*vs.* SCE) were unsuccessful. As positive polarization was applied more current flowed as indicated by Fig. 4 until a current of about 375 ma/cm² was obtained. At this point passivation occurred. Passivation is the result of a zinc oxide coating forming on the surface which inhibits the flow of current. Oscilloscope traces photographed in this current-voltage region showed extreme curvature.

Thus polarization was applied to make the zinc voltage more negative. The current went to zero and then became negative below —1.64v, Fig. 5. The net current was flowing onto the zinc electrode. The oscilloscope response curve straightened at about —1.75v. More negative operating voltage caused the response to become curved again. Linear voltage responses indicate a minimum faradaic current and capacitance at the interface. Therefore, an apparent zero-point ex-

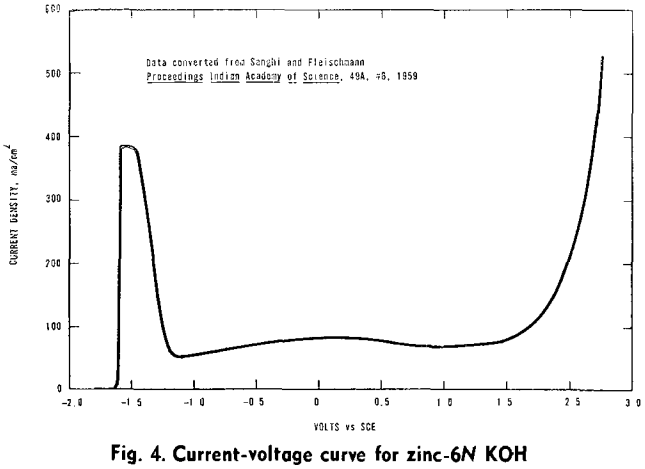

Fig. 4. Current-voltage curve for zinc-6*N* KOH

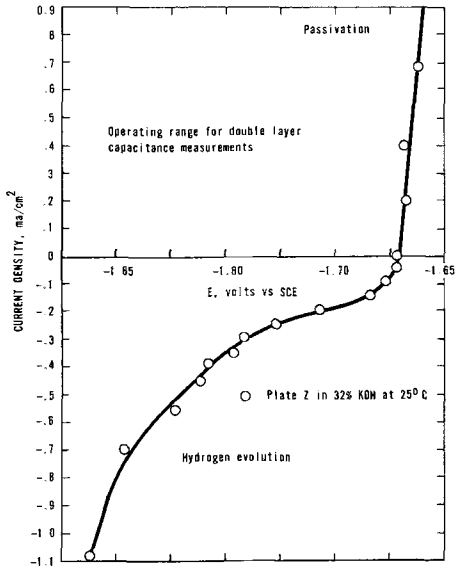

Fig. 5. Current-voltage characteristics for flat zinc

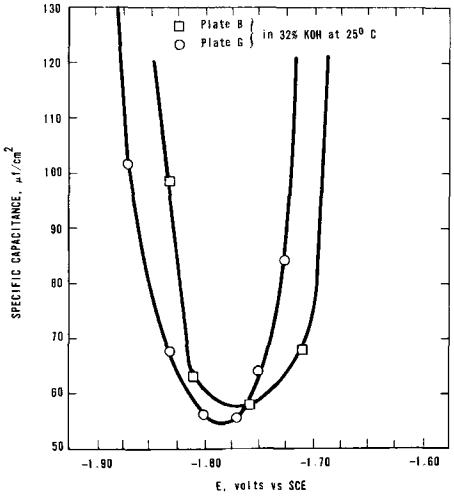

Fig. 6. Double layer capacitance measurements for flat zinc

ists in this voltage range. Several flat zinc electrodes were measured in this range to define the exact minimum. Figure 6 shows two sets of data taken to show the capacitance obtained. The zero-point is found to be at —1.76v. Figure 7 shows example oscilloscope traces for flat and porous zinc at the minimum.

The current-voltage characteristics were measured potentiostatically in the operating range on flat zinc since this data was not reported by Sanqhi and Fleischman (9). A sample of these results is shown in Fig. 5. This figure also shows production of current and a trend toward passivation which was shown in Fig. 4. More negative voltages are the results of adding current which eventually results in hydrogen evolution. There is an inflection point near the measured zero-point capacitance. The slope of this curve (di/dv) in the operating range has a smaller magnitude. The magnitude of the current is less than 0.2 ma/cm² (based on geometric area) and is not the result of the zinc electrode reaction.

Once the zero-point capacitance range and current-voltage range were obtained for zinc, the data taking procedure was simplified for the remaining electrodes studied. It was only necessary to establish the zero-point voltage on an electrode and photograph the traces at that point, since this is the only one corresponding to the double layer area.

Equation [1] was used with the oscilloscope readings to calculate the capacitance. The double layer

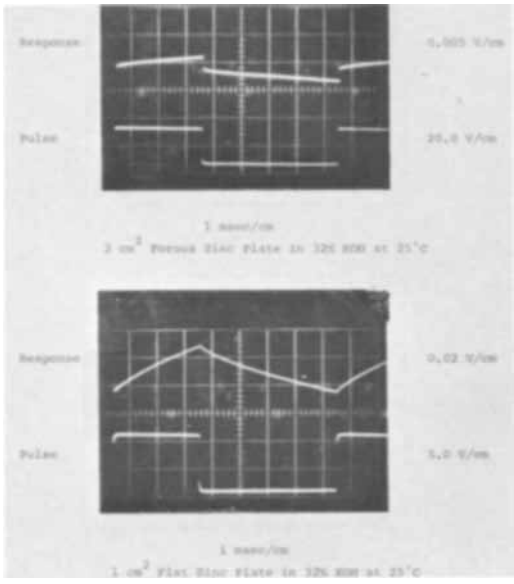

Fig. 7. Oscilloscope traces from double layer capacitance measurements on zinc electrodes.

area (DLA) in square centimeters was obtained from Eq. [3], according to ref. (2).

$$DLA = \frac{C(\mu f)}{16(\mu f/cm^2)} \quad [3]$$

where C is the capacitance measured.

Thirty-two zinc electrodes were studied in the course of experimental work. Double layer areas were measured from 3.82 cm² on flat zinc to 824.0 cm² on porous zinc. If a roughness is defined as the ratio of double layer area (DLA) to geometric areas (GA), then the range of roughness obtained was 3.0 to 212 cm²/cm². Based on the weight of zinc on the electrode, these compared to about 20.0 to 2100 cm²/g. The faradaic current effect was obtained by dividing the total current at the zero-point by the DLA. These values ranged from 0.02 to 0.17 ma/cm². A summary of results of the double layer measurements on zinc are listed in Table II.

According to McCallum (3), the oscilloscope trace data used to determine the double layer capacitance can be used to determine an exchange current according to Eq. [4].

$$I_o = \frac{nF}{RT}\left(\frac{\eta_{act}}{I}\right) \quad [4]$$

where I_o is the exchange current density. η_{act} is the voltage change due to the pulse current I. However, because of the large negative polarization (1.60 mv) the nature of the species involved in the exchange current reaction will be different. This polarization should prevent zinc from taking part in the exchange reaction.

Equation [4] held for $\eta_{act} < 50$ mv, and in most cases this voltage change was less than 5 mv. For a pulse of 5 msec duration the resulting voltage change

Table II. Summary of double layer capacitance measurements on zinc

Zero-point voltage	−1.76 ± 0.1v *vs.* SCE
Pulse currents, amp	4 and 12 × 10^{-4}
Geometric area, cm²	2.0-4.0
Double layer area, cm²	Flat zinc 4.0-10.0 Electroplated 20-40 Porous 100-800
Roughness	Flat 3.0-4.0 Electroplated 20-25 Porous 40-200
Double layer area/gram of zinc	20.0-2100.0
Exchange current, μa/cm²	Flat 34 Electroplated 29 Porous 20
Average pore diameter	0.05-0.10 cm

Table III. Exchange current values

Plate zinc		Electrodeposited flat zinc		Porous zinc	
I_o	I_o'	I_o	I_o'	I_o	I_o'
114.0	37.0	290.0	33.0	2026.0	19.0
124.0	36.0	430.0	24.0	2188.0	21.0
137.0	34.0	831.0	33.0	2568.0	19.0
122.0	32.0			1430.0	20.0
157.0	34.0			1162.0	19.0

I_o μa/cm² based on geometric area.
I_o' μa/cm² based on double layer area.

can be assumed to be activation controlled, which is a requirement of Eq. [4]. For these calculations η_{act} was not the electrode overpotential which was equal to 1.76-1.60v or 160 mv. The I_o values obtained in this way are tabulated by the type of zinc electrode in Table III. I_o is based on geometric area, and I_o' is based on the DLA. Similar results were obtained by Farr and Hampson (8) in the potential range for zinc going to zincate.

Two electrodes of the same physical characteristics were discharged up to 95% of their theoretical capacity. One was mounted vertically and the other horizontally in the cell to study the gravitational effect. There was some zinc left on the electrodes at 95% discharge which indicated that the method used to calculate weight of zinc was accurate. The two sets of data are plotted in Fig. 8.

Equation [2] can also be solved for the response at the outside edge at the beginning of the pulse

$$V(O,O) = \frac{i_p R_o}{3} + V_o \quad [5]$$

The pore resistance according to Eq. [2] is equal to $\rho l/A$, where A is the normal average pore cross sectional area. The range of the average pore diameters obtained in this equation are reported in Table II.

Discussion

This investigation measured the surface area and pore structure of porous zinc electrodes. The area measurement was made by a single pulse galvanostatic measurement of the double layer capacitance of zinc metal in potassium hydroxide electrolyte. Extensive work has been done by McCallum *et al.* (2) on this particular approach to measuring the double layer area of metals. Their conclusion was that pH, temperature, and agitation had little effect on the capacitance values. If temperature is controlled within ±5.0°C the change in capacitance will not be detected. Graham (1) calculated that capacitance minimum only changed 1.5 μf for an 85°C change in temperature.

The effect of concentration was also considered by McCallum. The only effect occurred in dilute solutions. There are two double layers according to the theory of Gouy and Chapman: the compact and diffuse double layers. In dilute solutions, a second minimum occurred because the diffuse double layer was controlling. They recommended using concentrated electrolyte to avoid ambiguous results, since these

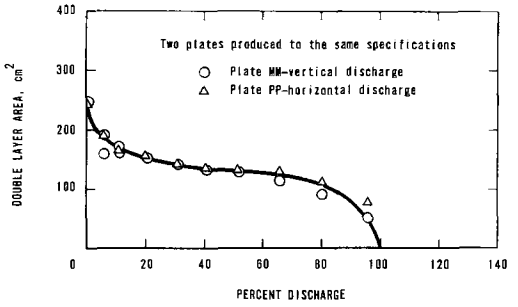

Fig. 8. Porous zinc double layer area = *f* (per cent discharge)

minima might occur very close in some cases and also to avoid high resistances in the cell that could introduce curvature in the *dv/dt* trace for the porous zinc.

The results for nickel, platinum, and silver in Table I agree well with those reported by McCallum *et al.* (2) both in the zero-point voltage and the capacitance.

Mercury in aqueous systems has received the attention of many workers. Grahame showed that theoretically the minimum should be 16 μf/cm^2. Until only recently, the best data published was about 20 μf/cm^2. Table I lists three values of mercury obtained in this work of 17.5, 18.4, and 18.4 μf/cm^2.

The oscilloscope traces in Fig. 4 and 6 show a voltage gap at the beginning of each pulse. This is the IR component of the polarization between the working and counter electrode due to the pulse. The size of the IR component depends on the relative position of these electrodes in the cell.

An operating voltage was found at which the capacitance of zinc could be measured. The approximately parabolic like curves in Fig. 5 are similar in shape to ones obtained for the other metals. The capacitance values at the minimum for the various types of zinc are consistent with the method of production. The relative areas seem reasonable. The surface of flat zinc was viewed under a microscope, and it appeared slightly more rough than the other metals. The minimum capacitance obtained on zinc was about 56-64 μf/cm^2 or a roughness of 3.5-4.0. The faradaic current was larger than it was for the other metals, and hydrogen evolution was noted at the minimum of -1.76v *vs.* SCE. But because the amount of hydrogen evolution was small and the surface area was large, the evolution was not believed to alter the double layer significantly.

Dirkse *et al.* (5) reported values for zinc which approached the values obtained in this work for the minimum capacitance. Their plots of capacitance *vs.* voltage do not show a minimum which is because they were not at the minimum voltage found in this work (6). It is felt that this point (-1.76v *vs.* SCE) is the zero point for zinc because it was the same for the three types of zinc: flat, electroplated, and porous; and the *dv/dt* response was linear in each case. In this work electrodes of about 1 cm^2 area were measured. The specific capacitance (in μf/cm^2) would not differ greatly from the total capacitance so that small errors in the area had little effect on the specific capacitance. However, Dirkse's electrodes had an area of only 0.02 cm^2 so that a small error could change the specific capacitance by 10-20 μf/cm.

The zinc reaction in KOH during discharge is

$$Zn + 4(OH)^- \rightarrow Zn(OH)_4^= + 2e^- \qquad [6]$$

For the double layer measurements, a negative overpotential was placed on the zinc which eliminates this reaction and any oxide present is converted to zinc. Current is forced in the opposite direction which results in hydrogen evolution at the zinc metal surface according to the reaction

$$2H^+ + 2e^- \rightarrow H_2 \qquad [7]$$

The current is small, in the order of μa/cm^2 at the operating voltage, and the rate of hydrogen evolution is also small.

The hydrogen reaction stabilizes the double layer. Without this reaction, the oxide and electrolyte exist in both a compact and diffuse double layer. The hydrogen reaction eliminates the effect of the diffuse layer. Hydrogen exists either as (H^+) or (H_3O^+) since this species has to exist with a positive charge in the electrolyte phase of the double layer and the chemisorbed species on zinc at the other side of the double layer. The electrons (e^-) in the zinc redistribute at the metal side of the interface. The controlling reaction is

$$H^+ + e^- \rightleftarrows Zn\,(H)_{chem} \qquad [8]$$

It is this hydrogen equilibrium reaction that stabilizes the double layer. The small current is the result of a second reaction causing the hydrogen evolution

$$2Zn\,(H)_{chem} \rightleftarrows 2Zn^o + H_2 \qquad [9]$$

The above interpretation of the double layer structure on zinc is consistent with the theory of the structure of the double layer and the particular operating point for zinc.

The determination of the exchange current from the oscilloscope pictures resulted in values that are almost constant. The exchange current should be a constant value for a metal. Values reported for other metals are usually in the order of 1 ma/cm^2 based on the geometric area. The zinc data are less than 1 ma/cm^2 and dependent on the type of zinc surface, but they are constant based on the DLA. The average values are about 34, 29, 20, ± 2 μa/cm^2. These values are not likely to be the true exchange currents for the zinc electrode as described by Eq. [6], but rather an exchange current due to Eq. [8] and [9].

Double layer measurements were attempted in KOH saturated with ZnO. As would be expected, it was not possible to obtain the proper polarization voltage for the measurement. Instead of the hydrogen evolution reaction, which was necessary to establish the compact double layer, zincate ion was being converted to zinc.

In order to confirm the fact that the double layer area was being measured in the study, several electrodes were discharged to obtain the DLA as a function of the per cent of discharge. Electrodes were discharged in a separate Lucite cell with an excess of 32% KOH in order to prevent any precipitation of ZnO. Precipitation of ZnO would result in ZnO trapped in the porous structure which could alter the capacitance measured. Then at various percentages of total discharge the electrodes were switched into the Pyrex cell containing fresh KOH that was not contaminated with zinc species for the double layer capacitance measurements. In this way, zincate ion would not be available to interfere with the capacitance determination. Two sets of data are presented in Fig. 8. The DLA drops about 40% in the first 10% of discharge, maintains a slower rate of change up to about 60% of discharge and then drops off. The initial change in DLA is due to reaction of the many small dendrites resulting from the method of electrodepositing and pressing. Once this large, rough surface is reacted, the remaining uniform internal structure reacts away slowly. Therefore, the DLA must be the total wet surface area available to the KOH, but it is not the reaction area.

Porous electrodes fail by passivation but only at much higher current densities. This is because the reaction surface is greater so that there is more space available for diffusion of $Zn(OH)_4^=$ and for saturation to occur.

Acknowledgment

The authors wish to express their appreciation to the Naval Ordnance Laboratory in Silver Spring, Maryland, for the loan of the electronic equipment and materials. R. A. Myers was an NDEA fellow during the course of this study.

Manuscript submitted Aug. 12, 1968; revised manuscript received Jan. 13, 1969.

Any discussion of this paper will appear in a Discussion Section to be published in the December 1969 JOURNAL.

REFERENCES

1. D. C. Graham, *Chem. Rev.*, **41**, 441 (1947).
2. J. McCallum, R. W. Hardy, and R. F. Redmond, Contract No. TR—AFAPL-TR-66-31, Battelle Memorial Institute (April, 1966).
3. J. McCallum, D. E. Semones, and C. L. Faust, Contract No. TR-AFAPL-TR-67-13, Battelle Memorial Institute (Feb., 1967).
4. J. J. McMullen, and N. Hackerman, *This Journal*, **106**, 341 (1959).

5. T. P. Dirkse and R. Shoemaker, *ibid.*, **115**, 784 (1968).
6. R. A. Myers, Ph.D. Thesis, University of Maryland (1968).
7. T. A. Posey and T. Morozumi, *This Journal*, **113**, 176 (1966).
8. J. P. G. Farr and N. A. Hampson, *ibid.*, **113**, 433 (1967).
9. I. Sanqhi and M. Fleischman, *Proc. Ind. Aca. Sci.*, **49A**, 6 (1959).

Interfacial Electrical Effects Observed during the Freezing of Dilute Electrolytes in Water

Alan W. Cobb[1] and Gerardo Wolfgang Gross

New Mexico Institute of Mining and Technology, Socorro, New Mexico

ABSTRACT

Dilute solutions of about 50 typical salts, acids, and bases in the concentration range 10^{-6} to $10^{-3}M$ were frozen at nonequilibrium rates. The freezing potential, charge separation across the phase boundary, and chemical composition of the phases were measured. The charge separation is a function of ionic species present in the solution, their concentration, and the freezing rate. It is caused by a differential transfer of ion constituents across the phase boundary. Hydrogen and hydroxyl ions neutralize the charge as the phase boundary advances. The solution pH greatly affects the charge separation, other conditions held constant.

In 1950, Workman and Reynolds (1) suggested that thunderstorm electricity may be produced by an electrical effect that they had found to occur during controlled freezing of dilute ionic solutions. Depending on the ions present and their concentration, they measured potential differences that could exceed 200v between an electrode placed wholly within the ice and an electrode in the unfrozen solution. Workman and Reynolds showed that these potentials are not merely electrostatic in nature, that is, contact potentials, but that charge is actually transferred across the advancing phase boundary. The rate of charge transfer is dependent on the rate of phase transformation (2), and the amount of charge transferred is proportional to the mass, or volume, of the solid phase. For a given experimental configuration and freezing rate, sign and magnitude of the potential difference and rate and quantity of charge transfer depended on the kind and amount of contaminants in solution. Thus, for a $2 \times 10^{-4}M$ NaF solution, Workman and Reynolds measured a transfer of 530,000 esu or 1.8×10^{-4} coulombs/cm^3 of ice formed. Working in a helium atmosphere with a $7 \times 10^{-5}M$ NaCl solution, these investigators found that the pH of the solid phase, when melted and brought back to room temperature, was lower than that of the liquid phase. They interpreted this as being caused by selective trapping of chloride ions in the solid phase and rejection of sodium ions into the supernatant liquid. They found a rough agreement to exist between the charge transfer calculated from the pH change and that based on the electrical measurements. Workman and Reynolds suggested that the incorporation of solute ions may be a means for reducing the surface energy of a freshly formed ice surface.

Subsequently, other investigators made experimental (3, 4) and theoretical (5, 6) studies of the charge transfer mechanisms, the effects of specific solutes (7-12), the effect of electrode materials and electrode treatment on the charge separation (13), the connection between freezing rate and preferential ion incorporation (14), the relation between interface processes during ice growth and d-c conductivity characteristics of the bulk ice (15), solute partition coefficients (16), and spontaneous freezing of supercooled solutions (17). These studies have recently been discussed by one of us (18). Partial reviews are also found in ref. (19) and (20).

The purpose of the present paper is a systematic investigation of typical solutes, grouped according to their chemical characteristics and studied over a large range of concentrations. The pH effect has been investigated in detail, and charge separation measurements have been compared to the solute content of the phases.

Experimental Procedures

Aqueous solutions.—Solutions in the range 10^{-6} to $10^{-3}M$ were tested. The water was first carefully distilled and then passed through an ion exchange column of Amberlite MB-1 resin just before using. Typical resistivity range for the freshly prepared water stock was 3 to 10×10^6 ohm-cm. Control experiments with freshly distilled water of 1 to 2×10^6 ohm-cm not subjected to ion exchange yielded results indistinguishable within experimental error from those where deionized water was used. The reagents used to make up the test solutions were of the best grade commercially available. All glassware, plastic materials, and metal parts used in contact with the samples were carefully cleaned and stored in purified water.

Freezing arrangement.—A small cylindrical sleeve of Teflon (0.25-0.50 mm wall thickness, 34 mm diameter, and 52 mm height) was pressed onto a metal base, usually platinum, to make a water-tight container (see Fig. 1). This "freezing cup" was filled with approximately 35 ml of the solution to be frozen and put in contact with a heavy block of copper maintained at about −12° to −14°C (except where noted otherwise). Thermal contact was improved by having the bottom of the cup base wet as it was hand-pressed to the cold copper. With this procedure, ice forms within a few seconds on the inside surface of the metal base and grows upward with the c-axis approximately normal to the refrigerating surface. In order to avoid the formation of large concentration gradients in the ice, freezing was customarily halted when 10-15% of the solution had frozen. Typically, the initial freezing rate (after 1 sec) was of the order of $1.9\text{-}2.5 \times 10^{-2}$ cm/sec, and the average freezing rate for the first 5 min of freezing was about one-tenth of the initial

[1] Present address: California State Polytechnic College, San Luis Obispo, California.

Key words: interfacial electrical effects, ice/water system, freezing potentials, differential solute incorporation in ice, ice/water interface potentials, charge separation at the advancing ice/water interface.

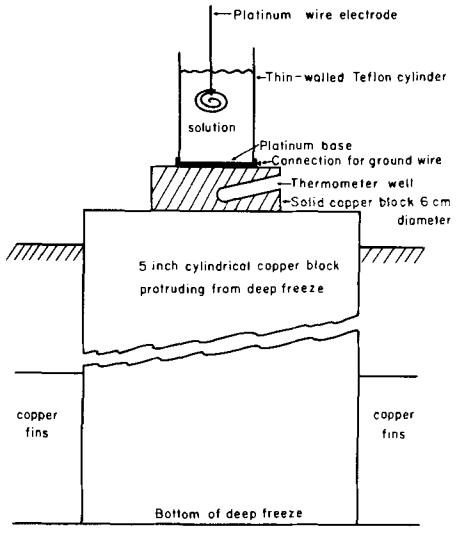

Fig. 1. Experimental arrangement used for studying electric charge separation during the freezing process.

rate. Runs were terminated after 5 to 6 min unless otherwise stated.

Electrical measurements.—The platinum base also served as the ice electrode and was electrically grounded. The solution electrode was a platinum wire with a flat Teflon-tipped spiral formed at one end. The other end was connected to the input terminal of an electrometer through a movable Lucite arm connected to a micrometer. When the Teflon tip made contact with the ice surface, the electrical continuity was interrupted, causing a deflection on the electrometer. The corresponding level of the ice surface could be read off the micrometer and recorded. In this way, it was possible to measure the freezing rate and the volume frozen.

A General Radio model 1230A d-c electrometer was used to measure either the potential difference or the charge flow between the solution and ice electrodes. Since the highest full-scale deflection of this instrument was 10v, potentials exceeding this value were measured either with a bucking potential from a dry cell connected between the solution electrode and the electrometer input or with an electrostatic voltmeter.

The input impedance of the GR 1230A electrometer is variable from zero to "infinity" ($> 10^{12}$ ohms). Freezing potentials were measured across an "infinite" input impedance called "open-circuit" arrangement in this paper. The rate of charge transfer (freezing current) was measured with an input impedance of 10,000 ohms. This effectively provided a low-resistance electrical shunt between the water and ice electrodes. Either freezing potential or current were recorded on a strip chart recorder (Varian Model G-10) running at a speed of 4 ipm. The freezing current was integrated over 5 min (unless otherwise indicated). From the total charge thus obtained, the average concentration of transferred charges was derived and compared with the chemically determined difference between solute cations and anions.

The type of material used for the cup base (and for the solution electrode) was not critical provided that comparable freezing rates could be maintained and the electrodes were not attacked by the solutions. For charge-transfer determinations, however, the metal used for the base must be resistant to electrolytic oxidation; platinum, palladium, gold, purified graphite, and stainless steel were found to be satisfactory.

The dimensions of the freezing cup, as well as the electrode distances (and shapes), did not in our experience affect freezing potentials and transferred charge concentrations, as long as comparable freezing rates were maintained. Theoretically, the interface potential is independent of the area of a flat, smooth interface (Eq. [2]).

The freezing potential was measured under experimental conditions essentially precluding charge neutralization except through the phase boundary itself which can be characterized by an "interface resistance" (6, 14). The bulk resistances of the phases had no direct effect on the measurements.

The cell resistance was estimated from the average of the ratio of a small change in freezing-cell emf to a small change in current when an external source of emf was applied in both the positive and negative directions. For many solutes, notably those yielding a larger incorporation of the negative ion constituent, this is essentially the ice resistance. To convert cell resistance to ice resistivity it would be necessary to evaluate the external circuit resistance, the two electrode resistances, the solution resistance, and the ice/solution interface resistance, subtract these from the cell resistance and multiply the result by a cell geometry factor of about 23. Data on ice resistivity and interface resistances for samples of a few solutions grown under comparable experimental conditions are found in the literature (6, 14-16).

Exclusion of atmospheric gases.—Most experiments were carried out in the normal atmosphere. Freezing of deaerated solutions under vacuum often led to supercooling and disorderly freezing and therefore was not practical as a routine. Of gases occurring in the atmosphere, carbon dioxide and ammonia were found to have specific effects which will be discussed later. No specific effect was detected from atmospheric oxygen. Since the solubility of air in ice is smaller than in water, air bubbles may form at the interface and, in escaping, cause convection. This reduces the interface concentration below the theoretical level.

Analysis methods.—After completing a freezing run, the unfrozen liquid was separated, and the ice was immediately washed several times with high-purity water. After removing excess water, the ice was melted. Analyses for alkali and alkaline earth metal ions were made with a Beckman D. U. flame photometer. The pH was determined with a Beckman model G pH meter, and the fluoride and chloride determinations were made by standard colorimetric methods (21) using a Bausch and Lomb Spectronic 20 spectrometer. For ammonium ion or ammonia determinations, the Jackson modification of Nessler's method was used (22). For a given element or radical, analysis results are expressed as concentrations (in moles per liter) of ion constituent in the melted ice at room temperature. The use of the terms "ion" or "ion transfer" does not imply judgment concerning the state of the impurities in the phases.

Freezing rate and interface concentration.—Assume that heat flow is perpendicular to and through the base only of the freezing cup (that is, the interface is horizontal, flat, and smooth), that the solute concentration far from the phase boundary remains constant, and that no convection takes place. Under these ideal conditions, the freezing rate diminishes according to the relation (Ref. 23, p. 285, Eq. [12])

$$\frac{dx}{dt} = at^{-1/2} \qquad [1]$$

a is the heat-flow parameter (see List of Symbols), which is numerically equal to the freezing rate one unit time after the beginning of freezing.

For this freezing mode, Wagner (24) has shown that the concentrations of a solute atom at the interface (on the solid and on the liquid side) are independent of freezing rate and, indeed, constant if the solute partition coefficient is constant. Thus, these concentrations are uniquely related to the concentration of the initial solution. For ionic impurities in ice, however, the distribution coefficient may be concentration-dependent (12, 18, 25, 26). While it thus appears probable that Wagner's relation is not strictly applicable to

ionized solutes in water, it is a useful first-order approximation.

Results

The Freezing Potential

The potential difference developed during the freezing of dilute ionic solutions depends in sign and magnitude on the ionic species present. The magnitude also depends on concentration and on the freezing rate. Only salts gave consistent freezing potential differences of more than 1 or 2v. The typical potential curve exhibits a relatively steep initial rise leading to a peak, and a much more gradual decline. Table I lists for a number of salts in unbuffered solutions the highest peak potential obtained and the corresponding concentration. For each salt, a considerable number of concentrations was tested, and for each concentration the data of three or more consistent freezing runs were averaged. With care, freezing potentials could be duplicated within plus or minus 10%. The major causes of variation were (*a*) poor thermal contact of the freezing cup with the cold block (potentials too low), (*b*) partial supercooling of the solution before the onset of orderly freezing (very sharp initial rise to an unusually high peak), and (*c*) insufficient recovery of the heat sink between runs (potential too low).

The effect of concentration on the magnitude of the potential peak is illustrated in Fig. 2 for solutions of five typical salts. All curves exhibit a maximum of varying sharpness. The maximum-peak concentration increases in the order: ammonium salts (except ammonium fluoride); lead salts and fluorides; chlorides; and ammonium fluoride (Table I).

The fluorides tested typically showed a maximum freezing potential of 30-45v (ice negative) at a concentration of approximately $2 \times 10^{-5}M$. Sodium salts showed a somewhat greater freezing potential than potassium salts and usually more of the sodium ions were carried into the ice.

Every pure uncontaminated hydroxide solution yielded an insignificant freezing potential (*e.g.*, 0.1v for a fresh ammonium hydroxide solution, $5 \times 10^{-6}M$), whereas the presence of carbonates, either by design or not, caused the development of high potentials (*e.g.*, 165v for a similar solution prepared from old stock and in contact with the atmosphere).

Table I. Highest freezing potentials for various salts. Concentrations given in units of 10^{-6}M. Sign of potential difference refers to the ice.

Mother solution			Solid ice		Melted ice analysis	
Species	Conc.	[H+]	Max. pot., v	Cell res., 10^6 ohms	Salt	[H+]
$(NH_4)_2CO_3$	15	0.5	+214	1000	—	1.0
$NH_4C_2H_3O_2$	5	0.4	+151	1000	—	1.6
NH_4Cl	5	0.7	+92	1000	1	1.3
NH_4CHO_2	15	2.0	+84	10,000	—	—
$Pb(C_2H_3O_2)_2$	11	—	+102	100	—	—
$Pb(NO_3)_2$	15	—	+68	10,000	—	—
K_2SO_4	20	1.1	+8	5000	<1	1.3
Na_2SO_4	20	1.0	+22	4000	1	1.4
$NaHSO_4$	20	20	+8	3000	<1	2.4
$NaC_2H_3O_2$	50	1.2	+16	1000-10,000	2	1.6
Li_2SO_4	100	1.3	+9	3000	2-4	1.6
NH_4F	2000	2.0	−9	5-9	1600	1.6
KF	20	1.4	−40	2	6	3.2
KCl	250	—	−37	2	7	3.2
KBr	180	—	−35	2-3	6	1.3
KI	750	2.0	−25	5-9	18	4.0
$KCHO_2$	100	1.5	−28	2	5-7	1.6
KNO_3	250	—	−31	2-4	2	3.2
$KHCO_3$	250	0.03	−41	100-1000	5	0.3
$KHCO_3$ plus CO_2 (sat'd.)	200	0.2	−13	15	—	1.0
KCN	25	0.002	−90	1000-10,000	—	—
NaF	20	2.4	−44	1.5	5-7	3.2
NaCl	250	2.0	−43	3-5	8-16	2.0
$NaCHO_2$	200	1.0	−28	2-3	25	1.6
$NaHCO_3$	200	0.02	−55	100-1000	10	1.0
Na_2CO_3	50	0.05	−70	1000-10,000	1	1.3
NaN_3	170	—	−27	0.9	50	0.8
LiF	10	0.1	−45	—	—	3.5
$CaCO_3$	28	—	−40	200	—	—
$Ca(HCO_3)_2$	100	—	−30	6	—	—
NiF_2	20	—	−32	2	—	—
ZnF_2	20	—	−28	5	—	—
$(C_2H_5)_2NH_2F$	12	—	−23	2-3	—	—
$(C_2H_5)_2NH_2Cl$	150	—	−16 (?)	1-3	—	—
$(C_2H_5)_4NF$	10-30	—	−31	0.6-2	—	—

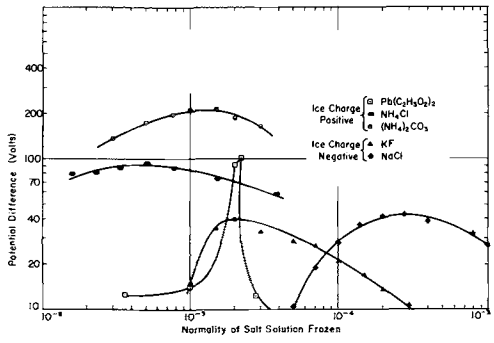

Fig. 2. Effect of solute concentration on the freezing-potential peak. The ammonium salts yield the largest potential differences. The concentration dependence is relatively weak. The ice is positively charged with respect to the liquid phase. Lead acetate also gives a positively charged ice, but the maximum potential is sharply peaked between 1 and 2 x 10^{-5}M. A less rapid decline is shown by the fluorides which (except the ammonium fluoride) also peak around 2 x 10^{-5}M. In the fluorides the ice is negatively charged.

Solutions of the acids HF, HCl, and H_2SO_4 gave insignificant potentials.

Solutions of various nitrates, oxalates, and sulfates, with a few exceptions (lead nitrate) gave maximum potential differences not exceeding 25v (ice positive) and poorly reproducible. In some cases this may have been due to a rise time exceeding the duration (typically 5-6 min) of our runs.

Qualitatively, these results are typical, but quantitatively they may differ for different investigators or for the same investigator at different times. The reasons are several: different samples of a reagent-grade salt may yield solutions of different *p*H even when made up with water of the same degree of purity; a reagent may contain traces of interfering impurities; a lack of care during the handling of a solution prior to and during freezing may cause the absorption of carbon dioxide or of ammonia from the atmosphere, or of other impurities from different sources.

Effect of pH on the freezing potential.—The maximum freezing potential of a $2 \times 10^{-5}M$ NaF solution varied from 90 to 6v as the *p*H was lowered from 7.7 to 4.8. Detailed results are presented in Table II. The optimum solution *p*H for the highest freezing potential, regardless of sign, was usually between 7 and 8. A number of the salt solutions tested, especially those containing anions of the stronger acids, were slightly acidic (*p*H near 6). An adjustment to a *p*H 7.5 in these cases would probably have resulted in a higher maximum freezing potential than shown in Table I. For example, the *p*H of a $5 \times 10^{-6}M$ NaF solution was adjusted to 7.85 by means of $1 \times 10^{-5}M$ NaOH. This solution gave successive maximum freezing potentials of 240 and 225v (ice negative); a freezing potential of under 10v was the rule when the *p*H was not adjusted.

Typically, the fluorides show a rapid decrease with concentration of the freezing-potential maximum on the low-concentration side of the peak (Fig. 2). The fluoride concentration in the ice at the point where the maximum freezing potential had fallen to 25% of the

Table II. Effect of *p*H on the freezing potential of a 2 x 10^{-5}M NaF solution

Acid or base added	*p*H Solution	Freezing potential	Cell res., 10^6 ohms	*p*H Melted ice
$1 \times 10^{-6}M$ NaOH	7.68	90	30-70	6.17
None	5.62	46	1.5	5.38
$1 \times 10^{-6}M$ HF	5.07	14	0.6	5.10
$2 \times 10^{-5}M$ HF	4.82	6	0.3	4.82

peak was in the narrow range of 6×10^{-7} to $1.5 \times 10^{-6}M$ for seven different fluorides tested. This was approximately the hydrogen-ion concentration of the solutions frozen. At these very low solute concentrations the availability of hydrogen ions from the solution may be sufficient to keep pace with the incorporation of solute anions, thus leading to a sharp reduction of the observed freezing potential.

In general, a reduction of the hydrogen ion concentration in a given solution reduces the slope of the potential decay curve and allows the development of much higher maximum potentials.

An increase in the hydrogen-ion content of the freezing solution invariably increases the proton content of the ice as measured by the *p*H of the melted ice or by an increased conductivity of the solid (Table II).

Effect of the freezing rate on the freezing potential.—In one series of experiments the temperature of the heat sink was varied from −47° to 0°C. This resulted in initial freezing rates (after 1 sec) of 4.2 to 0.7×10^{-2} cm/sec. The observed maximum freezing potential for a $4.3 \times 10^{-5}M$ NaF solution appeared to saturate at initial freezing rates above 2.4×10^{-2} cm/sec (Fig. 3). The saturation value lay between −45 and −50v. The impurity concentration in the ice was in direct proportion to the initial freezing rate.

Effect of ammonia and atmospheric carbon dioxide.—Ammonia may be a residue in distilled water, or it may be absorbed from tobacco smoke, floor waxes, or fertilizers. In the presence of carbon dioxide it impresses a positive potential on an advancing ice/water phase boundary and therefore tends to counteract negative potentials such as those caused by halides.

Atmospheric carbon dioxide, by itself, produces two distinct effects. In solutions of salts producing a negatively charged ice, it lowers the *p*H and therefore the freezing potential difference. In basic solutions, on the contrary, it increases the freezing potential difference. Both of these effects have been discussed above.

Volatile organics from various sources (*e.g.*, insecticides used to spray garden plants) appear to have an inhibiting effect on freezing potentials.

Location and width of the charged layer.—A freezing cup was equipped with several small wire probes imbedded horizontally in the insulated side of the cup above the base. As the advancing ice front covered a probe completely, the probe potential became the same as that of other more deeply imbedded probes, or of the base itself. Therefore, the freezing potential is generated close to the growing ice surface.

Net Charge Transport

Purpose.—Because of the specific relation, experimentally observed, between freezing potentials and

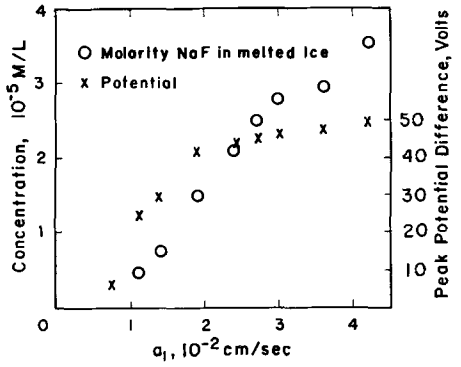

Fig. 3. Freezing-potential peak and solute concentration in the melted ice as a function of the freezing rate 1 sec after start of freezing (a_1) for a $4.3 \times 10^{-5}M$ NaF solution. The difference between solute cation and anion constituents was below the detection limit.

types of solute species present, Workman and Reynolds (1) concluded that charge transfer is related to a selective incorporation into the solid phase of ions of one sign. Actually, in many cases a considerable number of the "less favored" ion constituents are also taken into the solid, so that it is more accurate to speak of differential rates of transfer of the solute species across the phase boundary. Workman and Reynolds (1) presented evidence that, as the phase boundary advances, charge balance is being restored by hydrogen and hydroxyl ions, respectively. The charge separation ceases when the interface ceases to advance or when it advances very slowly. Theoretically, the quantity of charge transferred should be directly and simply related to the chemical composition of the phases. In practice this relation is difficult to demonstrate in a quantitative manner: the phenomenon is observed in rather dilute solutions, the solute fraction incorporated into the ice is frequently small, and differences between species are typically of second-order magnitude (Ref. 14, Table II).

For some solutes (those favoring incorporation of the anion), the charge separation effect can be demonstrated by shunting the phase boundary with an external resistance of known value. In this case a fraction of the charge transferred appears as a current that can be measured and recorded as a function of time. Workman and Reynolds (1), using shunts of 10^6 to 10^8 ohms, measured a maximum charge transfer of about 500,000 esu/cm³ of ice frozen from dilute fluoride solutions. Because this is too low for chemical detection (see Table III, Footnote), we arbitrarily chose a shunt resistance of 10,000 ohms. This is at least two orders of magnitude lower than the typical interface resistance but high enough to allow accurate electrical

Table III. Charge separation and differential incorporation for KF solutions (3×10^{-5} to $2 \times 10^{-3}M$). (Concentrations are given in units of $10^{-6}M$.)

Mother solution		Solid ice	Melted ice				Supernatant analysis			
				Analysis		Computed				
[KF]	[H+]	Charge transfer*	[H+]	[K+]	[F−]	[F−]	[K+]	[F−]	[H+]	Remarks
30	1.0	13	13	1.6	15	15	35	—	0.4	10KΩ shunt
45	1.1	19	18	3.2	20	21	61	—	0.3	Compare Fig. 4a
70	1.3	28	32	4.6	30	37	86	—	0.3	
100	1.3	37	32	6.2	40	38	120	—	0.3	
150	1.6	41	32	22	50	54	190	—	0.3	
300	1.3	37	32	69	100	110	380	—	0.3	
450	1.3	28	28	110	130	140	550	—	0.5	
700	1.3	11	16	200	200	220	830	—	0.5	
1000	1.3	10	10	260	250	270	1,400	—	0.6	
20	—	—	3.0	5.6	10	—	29	28	1.4	Open-circuit
60	0.005 (?)	—	2.0	20	25	—	75	83	2.0	Compare Fig. 4b
200	—	—	(?) 0.3	43	50	—	280	310	0.03 (?)	
600	2	—	4	280	260	—	660	710	3.1	
2000	8	—	18	880	800	—	2,300	2,100	9.0	

* In units of 10^{-6} moles of elementary charges per liter of solid formed. This unit is approximately equivalent to 6×10^{14} elementary charge units, 1×10^{-4} coulombs, or 3×10^{6} esu/cm³ of ice formed.

measurements, and the charge separation is increased from five to thirtyfold over Workman and Reynolds' results.

Experimental.—In Table III and Fig. 4, we present data on the charge transport and differential ion transfer. Potassium fluoride solutions were frozen in a freezing cup much larger than the one described before. The base was made of stainless steel (interior diameter 11.2 cm) and the solution electrode of pure nickel. 500 ml of solution were placed into this cup and about 100-120 ml of this were frozen in about 30 min (average freezing rate about 1×10^{-3} cm/sec). Thus, enough melt water was obtained to analyze for solute cation, solute anion, and hydrogen ions. Both shunt and open-circuit data are presented. For the shunt experiments, the solute cation concentration of the melted ice is considerably smaller than the anion concentration at the most dilute concentrations. The fractional difference becomes smaller as the mother solution concentration increases. The difference between solute cations and anions is made up by hydrogen ions. There is good agreement between the hydrogen-ion transfer derived from charge transfer data and results computed from *p*H measurements. The sum of hydrogen-ion concentration and potassium-ion concentration agrees fairly well with the measured fluoride concentration. For the open-circuit runs, the differences between cations and anions are much smaller and difficult to measure accurately, therefore the agreement of the difference with the hydrogen-ion concentration is poor. At smaller freezing rates, however, larger differences were obtained (Ref. 14, Table II). NaF solutions gave similar results.

Chlorides of sodium and potassium (Fig. 5 and 6) showed trends similar in general to the fluorides, but at a given solution concentration the fraction incorporated into the ice was generally smaller for the chlorides.

The contrast in cation constituents between shunt and open-circuit samples grown from the same solutions is illustrated in Fig. 7.

The maximum charge transfer for a number of representative compounds is given in Table IV along with the concentration required for maximum transfer. The concentration dependence of the charge transfer is shown in Fig. 8. These charge transfer data were obtained with the small freezing cup (see Experimental Procedures). Typically, the solution concentration for maximum charge flow is from five to ten times the concentration that gives a maximum freezing potential. A current of more than 10 μa/cm^2 of interface surface was obtained with fluoride solutions at the concentration and at the freezing rate specified.

With the exception of ammonium fluoride (see below), all the fluorides tested (those of Cs, K, Na, Li, Mg, Ca, Ba, Ni, Zn, Ag, di- and tetraethylammonium)

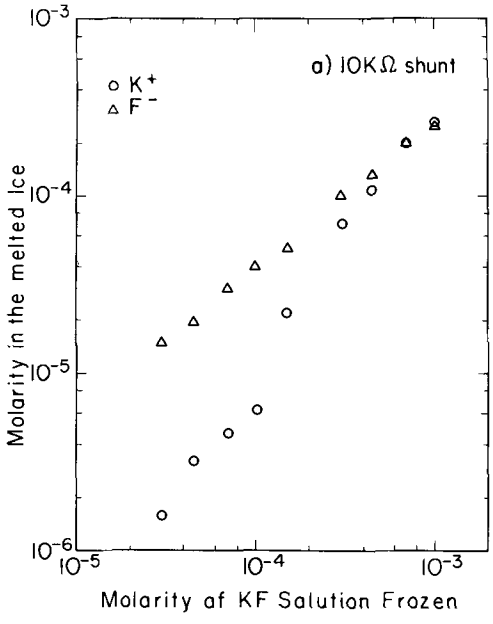

Fig. 4a. Differential incorporation of the ionic constituents of potassium fluoride as a function of concentration. Data taken from Table III, 10 kohm shunt.

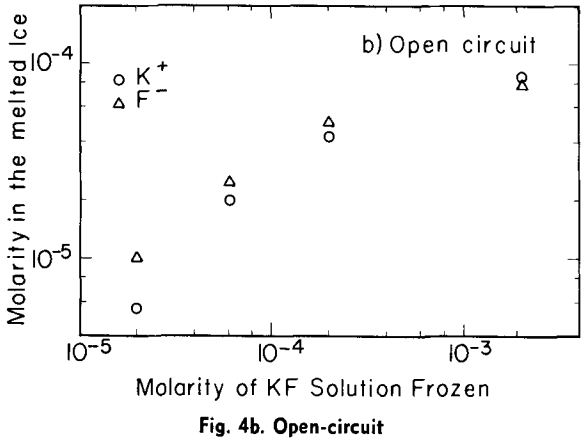

Fig. 4b. Open-circuit

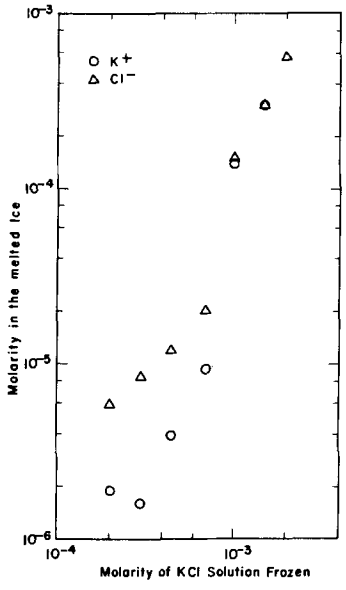

Fig. 5. Differential incorporation of the ionic constituents of potassium chloride as a function of concentration, 10 kohm shunt.

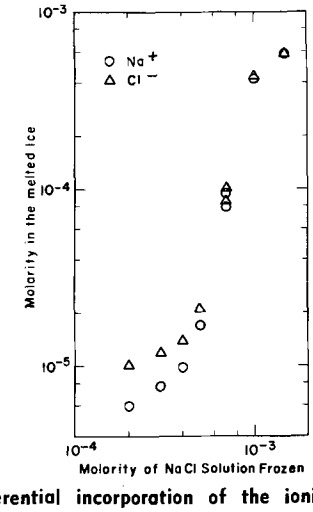

Fig. 6. Differential incorporation of the ionic constituents of sodium chloride solutions as a function of concentration, 10 kohm shunt. The difference between sodium and chloride at low concentrations is appreciably smaller than for potassium and chloride (Fig. 5).

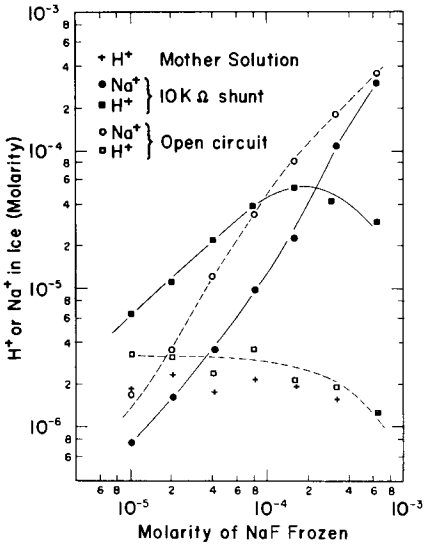

Fig. 7. Cation constituents in ice samples grown from dilute NaF solutions with and without a shunt. In the melted "shunt" ice, Na^+ content is lower, H^+ content higher than in the "open-circuit" ice. Hydrogen-ion concentration of open-circuit ice follows closely but is consistently a little higher than that of the original solutions.

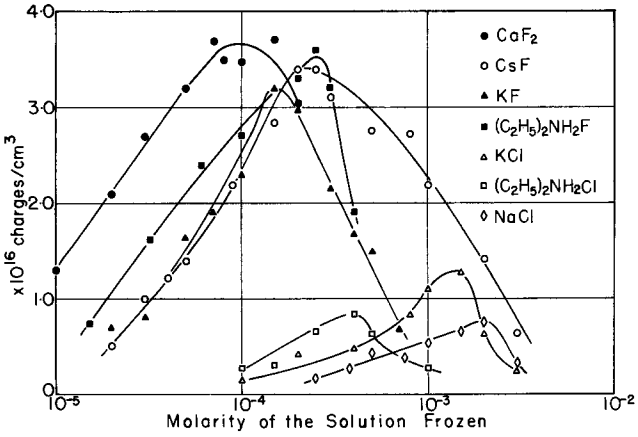

Fig. 8. Transferred charge concentration for several typical solutes (type I) as a function of concentration of the freezing solution. The curves are clustered in two groups (fluorides and chlorides, respectively) because the anion is preferentially incorporated and therefore determines the charge transfer.

showed a maximum charge transport of 3-4 x 10^{16} elementary charges per cubic centimeter of ice formed at solution concentrations of 2 to 3 x $10^{-4}M$. The nature of the positive ion (excluding ammonium) had only a small effect on the charge transfer in contrast to salts of other negative ions.

Among the potassium salts, the fluoride gave the highest interphasial charge transfer, followed by the formate, the azide, the chloride, the bromide, the nitrite, and the iodide. Solutions of salts that on freezing gave a cell resistance of more than 10^7 ohms (see Tables I and IV) showed only a small charge transfer (10^{15} or less charges/cm^3) at any concentration.

The freezing current through an external circuit is accompanied by electrolytic production of oxygen and hydrogen at the electrodes. The formation of oxygen on the base (visible as a uniform white deposit of minute bubbles) was demonstrated in a clear Lucite freezing cell with a stainless steel base. A KF solution (2 x $10^{-4}M$) within the airtight cell was first boiled under vacuum to flush the cell free of all atmospheric gases. The oxygen identity was verified by Winkler's method (27) on the gas collected on repeated freezing and melting under shunt conditions.

The charge transfer through an external circuit is greatly dependent on the condition of the metal surface on which freezing takes place (13) and can be enhanced by conditioning the metal base prior to freezing. Two methods were used: Hydrogen was electroplated onto the base by applying —3v from a battery while allowing a very thin layer of ice to form on the base. The ice was removed prior to freezing the desired solution. Alternatively, a small charge was passed through the cell applying + 1.5v to the base for a few seconds and cutting off when freezing started. These procedures assured an immediate release of hydrogen ions to the ice from the base, greatly lowering the electrical resistance of the ice as well as the ice/metal contact resistance (Fig. 9). The open-circuit freezing potential was not influenced by these preparations of the base.

As in the case of potential measurements, the hydrogen-ion content of the freezing solution has an effect on the measured charge flow since these ions provide a neutralizing or countercurrent at the interface. When the proportions of a mixture of 2 x $10^{-4}M$ KF and 2 x $10^{-4}M$ HF were adjusted to a *p*H of 4.5 and this mixture was frozen in the usual manner, no appreciable charge flow was observed through an external shunt, nor did a measurable potential develop

Table IV. Maximum charge flows obtained with a 10,000-ohm shunt, with or without treatment of the base. (Concentrations are given in units of $10^{-6}M$)

Species	Mother solution Conc.	[H+]	Solid ice Charge transfer*	Solid ice Cell res., 10^4 ohms	Melted ice analysis Solute cation	Melted ice analysis [H+]
KF	150-300	2.5	50-80	8-9	40-80	30-60
KCl	2000-3000	—	50	6-8	200-1000	50
KBr	1500-3000	—	50	6-13	100-400	40-50
KI	800-1500	2.5	7	40-50	200	10
$KCHO_2$	400-1000	—	30-70	7-30	5-200	20-30
KN_3	500	—	50-70	8	—	—
KNO_3	1500	—	15	20	300	10
K_2SO_4	100	1.7	0.004	200,000	<1	1.5
NaF	160	2.0	50-70	10	20-60	30-60
NaCl	800-1500	2.0	30	10-20	100-600	30
Na_2CO_3	20	0.2	0.2	70,000	—	1.4
$NaHCO_3$	100	0.04	0.7	6,000	3	1.6
Na_2SO_4	40-100	1.5	0.004-0.006	300,000	3	1.5
LiF	100	—	50	—	—	—
Li_2SO_4	1000	1.4	0.03	600	590	2.0
NH_4F	450	2.0	3-7	50-100	300-400	—
$(C_2H_5)_2NH_2F$	250	—	50-70	10	—	—
$(C_2H_5)_2NH_2Cl$	400	—	10-20	40-80	—	—
$(C_2H_5)_4NF$	150	—	60	10-20	—	—
CaF_2	90-100	—	60-70	—	—	—
MgF_2	20-30	—	30-60	—	—	—
BaF_2	100	—	50-70	—	—	—
NiF_2	140	—	50	10	—	—

* In units of 10^{-6} moles of elementary charges per liter of solid formed. See Footnote, Table III.

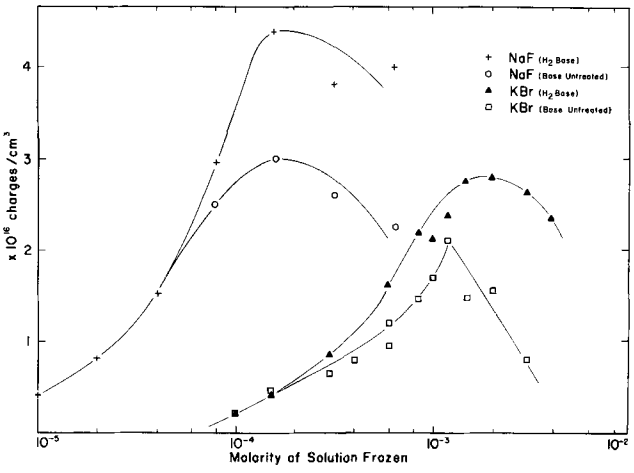

Fig. 9. Effect of electroplating the freezing base with hydrogen. Charge transfer during freezing with a shunt. The effect is greatest near the concentration of maximum charge transfer.

at the ice surface. The composition of the ice was the same as though a 2 x $10^{-4}M$ KF solution had been frozen under maximum charge flow conditions.

Ammonium Salts

A salt composed of ammonium and fluoride ions, both of which are preferentially incorporated into ice when they are constituents of other salts, might be expected to show a rather unusual behavior. NH_4F concentrations below 5 x $10^{-5}M$ gave freezing potentials under 1v (ice negative). Above this concentration, the potential difference increased to a maximum of —9v at 2 x $10^{-3}M$. Since other ammonium salts tested (chloride, bromide, formate) gave very high positive potentials, the ammonium radical has a greater tendency to enter the solid phase than any anion constituent except the fluoride. The quantity of NH_4F transported into the ice during the usual freezing procedure was higher than that of any other salt (Table I). The concentration for maximum freezing potential (2 x $10^{-3}M$) was 100 or more times the concentration for maximum freezing potential of any other fluoride and ammonium salt, and from 3 to 10 times higher than that of any other salt studied. Furthermore, the maximum charge transfer, of only 0.25 x 10^{16} charges/cm^3 of ice, was measured at a solution concentration more dilute, 4.5 x $10^{-4}M$, than the solution giving the maximum potential. The cell resistance during the freezing experiments was higher than that observed for other salts giving negative freezing potentials (Table I), and it passed through a minimum value for a solution concentration of 2.5 x $10^{-5}M$ [see also ref. (15), Fig. 4]. The cell resistance of ice prepared with other ammonium salts, those giving positive potentials, was always very much higher (Table I). The substituted ammonium salts, diethyl ammonium and tetraethyl ammonium fluorides, performed like the metallic fluorides, that is, they exhibited moderate negative freezing potentials and a large charge transfer.

Discussion

The experimental work discussed above leads to a broad classification of solutes into three types according to their electrochemical characteristics during freezing of an aqueous solution (18). This classification is summarized in Table V.

Differential Incorporation of Ion Constituents

The electrical effects discussed above are specifically related to ion-forming solutes. From this, it does not necessarily follow that in the solid phase these solutes exist in the ionic state, or even that they cross the phase boundary as ions. As to the first point, it has been postulated on the basis of conductivity measurements that impurities in the ice lattice ionize according to the law of mass action (28-30). If this is true, then a certain fraction must be nonionized. Seidensticker's semiconductor model of ice (31) postulates that impurities also affect the orientational and translational lattice defect states in the ice structure itself, and these states may produce a potential in addition to ionized impurities. Therefore, electrical effects could occur even if a given solute atom or radical crosses the phase boundary in a nonionized state, that is, effectively shielded by a hydrogen or hydroxyl ion. The fact, however, that dilute salt solutions may show high freezing potentials which are absent with all concentrations of either the corresponding acid or the appropriate base alone (even if solute incorporation proceeds at comparable rates) lends some justification to the view that it is indeed the ionic charge, unshielded by hydrogen or hydroxyl ions, that gives rise to the freezing potential.

The preferential inclusion of foreign atoms or radicals into the ice lattice appears to be based on size and structure so that a minimum readjustment of the ice lattice will afford accommodations. This may explain the high acceptability of the ammonium radical and the fluorine atom. The large anions, such as Cl^-, Br^-, CN^-, are less acceptable. Some of the still more complex anions (SO_4H^-, SO_4^{--}, NO_3^{--}, $C_2H_3O_2^-$) are not preferentially incorporated into the ice structure, and the same holds true of the simple cations, NH_4^+ and Pb^{++} excepted. The results obtained with ammonium fluoride and other ammonium salts (Fig. 10) indicate, however, that the acceptability of a given ion (its distribution coefficient) is coupled to that of its counterion. This greatly complicates the picture.

Variables That Determine the Freezing Potential Peak

LeFebre (6) has given an analytical expression of the freezing-potential peak as a function of the ionic incorporation rates and the neutralizing interface current. We are specifically interested in his expressions for the amplitude and time (after start of freezing) of the freezing-potential peak

Table V. Generalized electrochemical classification of solutes tested for this report

Type & Species	Charge separation: Sign of freez. pot.*	Dependence on: Concen.	Freez. rate	Shunt	Interface dischg**	Solute incorporation: Magnitude***	pH of melted ice	Supernatant
I. Alkali halides, NH_4F	Neg.	Strong	Strong	Strong	Large	A	Acid	Alk.
II. Ammonium salts (except NH_4F). Sulfates, nitrates, oxalates, acetates	Pos.	Weak	Weak	Weak or none	Small (?)	S	Alk. (?)	Acid (?)
IIIa. Acids	Pos. (<1v)	—	—	—	—	A	Acid	Acid
IIIb. Bases (carbonate-free, solub. hydroxide)	Neg. (<1v)	—	—	—	—	S	Alk.	Alk.

* Ice with respect to liquid.
** Estimated from difference between anion and cation constituent in the ice grown without a shunt.
*** Arbitrarily defined as appreciable (A) if solute content of solid phase was typically high enough to be measured with fair to good accuracy; small (S) if solute was close to or below detection limits.

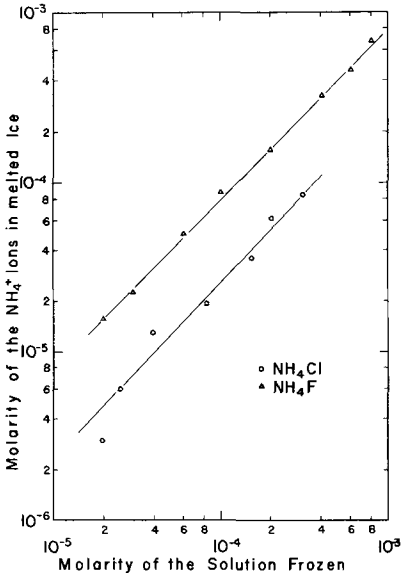

Fig. 10. Incorporation of ammonium ion constituent during the freezing of ammonium fluoride and of ammonium chloride. The incorporation of a given ion constituent is coupled to that of its counterion.

$$V_{max} = K_1 I_g' A (aR_s/C_s)^{1/2} = K_1 I_g' d_s (a\rho_s/\epsilon_s)^{1/2} \quad [2]$$

$$t_{max} = K_2 C_s R_s \quad [3]$$

K_1 and K_2 are empirical constants, depending on experimental conditions; I_g' is a parameter characterizing the charging current, defined below; A is the surface area of the interface; a is the heat-flow parameter defined in Eq. [1]; R_s, the interface resistance, and C_s, the interface capacitance, determine the discharge current; ρ_s, ϵ_s, and d_s are, respectively, the interface resistivity, dielectric constant, and thickness.

The charging parameter

$$I_g' = |z^+q^+|k^+c_l^+ - |z^-q^-|k^-c_l^- \quad [4]$$

where the superscript refers to the anion or cation respectively, z is the valence and q the effective ionic charge. The charging parameter is a function of the difference between two products involving interface concentrations (on the liquid side), c_l, and distribution coefficients, k.

This expression accounts in a general way for the concentration dependence of the maximum potential peak amplitude in different solutes. In particular, we compare KF and KCl (Table I). The maximum potential peak is of about the same amplitude but the corresponding concentrations are 2 x $10^{-5}M$ and 2.5 x $10^{-4}M$, respectively. Equation [2] gives this result if in Eq. [4] the distribution coefficient for the chloride ion is about an order of magnitude smaller than for the fluoride. The distribution coefficient for chloride is indeed smaller (16, 18) although there is no certainty at present about the magnitude of the difference. Discharge currents may also be different for these two cases and affect the potential, but this possibility is not at present experimentally verifiable.

The concentration dependence of the potential amplitude peak for the same solute can also be explained by this model through the concentration dependence of the distribution coefficients.

Since the freezing potential, according to this model, is produced by the sum of several ion currents, it is not in any simple way related to the work of building a solute into the ice lattice.

Other possible models have been reviewed elsewhere (18).

Effect of Interface Potential on the Solute Content of Ice

The relationship between interface potential and ice composition was studied for fluorides of potassium (14) and sodium. The amount of fluoride ion constituent incorporated into the ice was not appreciably affected by either the potential differences naturally present or artificially imposed during freezing. Incorporation of the cation constituent, on the other hand, was highly sensitive to the potential difference between ice and solution. Reduction of this potential difference by an external shunt resulted in a considerable reduction of solute cation incorporation into the ice (Fig. 7). The shunt permits an electrolytic reaction that produces an abundant supply of neutralizing hydrogen ions. Conversely, it has been seen that adding hydrogen ions to a freezing solution decreases the potential.

If both solute anion and cation were equally acceptable to the ice structure, the shunt should not make an appreciable difference with respect to either the cation or the anion constituents in the ice. This case is approximately realized for ammonium fluoride, and indeed results of a shunted sample differ little from the open-circuit case.

The effect of the interface potential on the solute distribution is also related to the problem of the thickness of the charged interface layer which has been discussed elsewhere (18).

Role of Hydrogen Ions in Interface Processes and Bulk Ice Conductivity

The migration of hydrogen ions into the ice as a mechanism for making possible the preferential incorporation of certain anion constituents (type I) was substantiated in this work by (*i*) the large increase of the freezing potential and of the ice resistance when the hydrogen ion content of the solution was lowered (*ii*) the rapid decline of the freezing potential when the freezing was lowered or suddenly terminated; (*iii*) the absence of a freezing potential, regardless of the kind and concentration of solute anion constituent, at high hydrogen-ion levels ($\geq 10^{-4}M$); and (*iv*) the high ice resistance when type II solutes were incorporated and therefore no "demand" existed for hydrogen ions.

With the exception of the shunt case, where the ice resistance is connected in series-parallel with the interface resistance, the bulk resistance of ice has no appreciable effect on the interface processes. The following experimental evidence supports this conclusion. First, the polarity and magnitude of the freezing potential is not affected by the conductivity of a substrate ice of different composition. Thus, when a cold type I solution is substituted for a freezing type II solution, the ice of which is characterized by a high positive potential and low conductivity, the potential difference reverses its sign and acquires the characteristics of the new solution. If a cold type II solution is poured onto a highly conductive type I (or type III) ice, a similar reversal is observed in the opposite sense (3, 18). (In performing this experiment, it is important to avoid mixing of the two solutions, or remelting of the substrate ice.)

Second, ice is grown from a type I solution at a uniform freezing rate (16). The potential curve typically exhibits a more or less pronounced peak and then declines very slowly. In this stage, the solution is briefly stirred vigorously. The potential sharply declines as new ice ceases momentarily to form but, as the freezing rate recovers, the potential sharply rises to a value considerably higher than before stirring. A slow decline begins from this new and higher value. This process may be repeated at will. The freezing potential is primarily a function of the interface concentration in the liquid but not of the bulk resistance of the ice column.

Since ice is a proton conductor (28-30), those solutes (types I and IIIa), freezing rates, and interface conditions (shunt) favoring a large hydrogen-ion transfer into the solid will also produce an ice with a high electrical bulk conductivity.

Summary and Conclusions

Experimental techniques were described to measure the charge transfer across the phase boundary during nonequilibrium freezing of dilute solutions and to relate this charge transfer to the difference between the concentrations of anionic and cationic solute constituents in the phases. The maximum measured charge transfer was of the order of 10^{16} elementary charge units per cubic centimeter of ice formed. This appears to be an upper limit.

Because hydrogen and hydroxyl ions restore the charge balance, the solution pH drastically affects the freezing-potential difference; its largest values (of more than 200v) were observed in the pH range between 7 and 8.

The charge separation effect is specific in magnitude, sign, and rates of growth and decay with respect to type (acid, base, salt), species, and concentration of solutes. It is also a function of freezing rate. For a given solute, the concentration giving the maximum charge transfer through a shunt is, in general, roughly ten times the concentration giving the highest potential difference.

Acknowledgment

This work was undertaken at the behest of Dr. E. J. Workman who also designed much of the experimental equipment and suggested some of the experiments. The authors acknowledge many valuable suggestions from Dr. R. G. Seidensticker in connection with this paper. This work was supported in part by the Office of Naval Research under contract Nonr 815(05) and by Project Themis under contract N00014-68-A-0157.

Manuscript submitted Aug. 19, 1968; revised manuscript received ca. Feb. 4, 1969.

Any discussion of this paper will appear in a Discussion Section to be published in the December 1969 JOURNAL.

LIST OF SYMBOLS

a heat flow parameter, cm-sec$^{-1/2}$; $a = a_o\sqrt{\Delta T}$, in which:

$$a_o = \left(\frac{c_i K_i}{2Q}\right)^{1/2} \simeq 6.04 \times 10^{-3}\,\Delta T^{-1/2}\ \text{cm sec}^{-1/2}$$

where c_i = specific heat of ice (0.505 cal/g-C° at 0°C); K_i = thermal diffusivity of ice (0.0115 cm^2/sec; Q = latent heat of fusion (79.7 cal/g); ΔT = difference between temperature of heat sink and of ice melting point

a_1 freezing rate 1 sec after start of freezing, cm-sec^{-1}

c_1^+, c_1^- solute cation or anion concentration, respectively, on the liquid side of the phase boundary, cm^{-3} or moles 10^{-3} cm^{-3}

C_s interface capacitance, farads

D diffusion coefficient, cm^2 sec^{-1}

d_s thickness of the interface, cm

ϵ_s dielectric constant of the interface, dimensionless

I_g' charging parameter, coul-cm^{-3}

k^+, k^- distribution coefficients of a positive or negative ion constituent, respectively (ratio of solute concentration on the solid side of the phase boundary to that on the liquid side)

q^+, q^- effective charges of ions as they cross the phase boundary, coul or coul/mole

R_s interface resistance, ohms

ρ_s interface resistivity, ohm-cm

t_{max} time, after freezing begins, at which the freezing-potential difference reaches its maximum value (without regard to sign), sec

V_{max} maximum freezing-potential difference (without regard to sign), volts

REFERENCES

1. E. J. Workman and S. E. Reynolds, *Phys. Rev.*, **78**, 254 (1950).
2. J. Costa Ribeiro, *Anais Acad. Brasil. Cienc.*, **22** (3), 325 (1950).
3. S. E. Reynolds, M. Brook, and M. F. Gourley, *J. Meteorol.*, **14**, 426 (1957).
4. M. Brook, in: "Recent Advances in Atmospheric Electricity," pp. 383-389, Pergamon Press, New York (1959).
5. B. Gross, *Phys. Rev.*, **94**, 1545 (1954).
6. V. LeFebre, *J. Coll. Interface Sci.*, **25** (2), 263 (1967).
7. E. W. B. Gill and G. F. Alfrey, *Nature*, **169**, 203 (1952).
8. E. W. B. Gill, *Brit. J. Appl. Phys.*, Suppl. 2, 16 (1953).
9. J. P. Lodge, M. L. Baker, and J. M. Pierrard, *J. Chem. Phys.*, **24**, 716 (1956).
10. F. Heinmets, *Trans. Faraday Soc.*, **58**, 788 (1962).
11. H. C. Parreira and A. J. Eydt, *Nature*, **208**, 33 (1965).
12. L. Levi and O. Milman, *J. Atmospheric Sci.*, **23**, 182 (1966).
13. J. T. Carlin, M. S. Thesis, New Mexico Institute of Mining and Technology, Socorro (1956).
14. G. W. Gross, *J. Geophys. Res.*, **70**, 2291 (1965).
15. G. W. Gross, *Ann. N. Y. Acad. Sci.*, **125**, 380 (1965).
16. G. W. Gross, *J. Coll. Interface Sci.*, **25**, 270 (1967).
17. H. R. Pruppacher, E. H. Steinberger, and T. L. Wang, *J. Geophys. Res.*, **73**, 571 (1968).
18. G. W. Gross, *Adv. in Chemistry Series*, **73**, 27 (1968).
19. L. B. Loeb, "Static Electrification," Springer, Berlin (1958).
20. W. Drost-Hansen, *J. Coll. Interface Sci.*, **25**, 131 (1967).
21. D. M. Zall, D. Fisher, and M. Q. Garner, *Anal. Chem.*, **28**, 1666 (1956).
22. Snell and Snell, "Colorimetric Methods of Analysis," Vol. 2, 3rd ed., p. 815, D. Van Nostrand & Co., New York (1949).
23. H. S. Carslaw and J. C. Jaeger, "Conduction of Heat in Solids," Clarendon Press, Oxford (1959).
24. C. Wagner, *Trans. AIME*, **200**, 154 (1954).
25. C. Jaccard and L. Levi, *Z. Angew. Math. Phys.*, **12**, 70 (1961).
26. Chen-Ho Wu, M. S. Thesis, New Mexico Institute of Mining and Technology, Socorro, 1968.
27. ASTM Water Manual No. 148-C, p. 257, 1957.
28. A. Steinemann, and H. Gränicher, *Helv. Phys. Acta*, **30**, 553 (1957).
29. C. Jaccard, *Helv. Phys. Acta*, **32**, 89 (1959).
30. G. W. Gross, *Science*, **138**, 520 (1962).
31. R. G. Seidensticker and R. L. Longini, *J. Chem. Phys.*, **50**, 204 (1969).

The Transport Entropy of Hydrogen Ion in the Water-Ethanol System

I. The Initial Thermoelectric Powers of the Hydrogen-Hydrogen Ion Thermocell, and the Cation Transport Number of HCl in the Water-Ethanol System

J. Lin and James J. De Haven

Department of Chemistry, Boston College, Chestnut Hill, Massachusetts

ABSTRACT

The initial thermoelectric powers $\epsilon_0(X)$ of the thermocell $(T)Pt/H_2$ (1 atm)/HCl (0.01M), H_2O (100-X), $C_2H_5OH(X)/H_2$(1 atm)/$Pt(T + \Delta T)$ [X w/o (weight per cent)], and the cation transport numbers $t_{H^+}(X)$ of HCl in the H_2O-C_2H_5OH system were measured at 25°C. These experiments were undertaken in connection with a thermoelectric study of the mechanism of the transfer of hydrogen ion across a temperature gradient. The dependence of $\epsilon_0(X)$ and $t_{H^+}(X)$ on X is discussed in terms of the structure of the solvent system.

The exceptionally high mobility of the hydrogen ion under an applied electric field in water has long attracted interest. In spite of the view of Darmois (1) regarding proton mobility on the Lorenz-Drude model as an electronlike metallic conductivity involving the bare proton, existing evidence seems to suggest overwhelmingly that the small size of the proton could not itself be responsible for the high mobility, since the proton is strongly hydrated in aqueous solution as a distinct chemical species $H^+(H_2O)_n$, where n = 1,2,3. . . Since the formation of hydrogen bonds is involved, the structure of the solvent itself is particularly relevant to the problem. Indeed, the transfer of proton with help from another water molecule as a possible mechanism for the abnormally high hydrogen ion mobility, has been developed more explicitly in recent years by utilizing modern ideas concerning the structure of water and the nature of hydrogen ions in the solution (2a). The point of view here is that when water contains an acidic substance, the H_3O^+ ions that are formed may be considered to fit into the structure just as well as in pure water and that interatomic distances can be regarded as approximately unchanged. When an electric potential is applied, it is supposed that the hydrated protons migrate to some extent through the solution in the ordinary diffusion manner from one equilibrium position to another; at the same time a proton can transfer from the hydronium ion to an adjacent water molecule which is favorably oriented. This latter process can be very rapid. The exchange takes place within a hydrogen bond, and the actual distance an individual proton moves is quite small (≈1Å) (2a), but the center of charge has moved an oxygen-oxygen distance which is the order of 2.5Å (2a). In this way the positive charge will be transferred a considerable distance in a short time, and as a consequence the hydrogen ion acquires an exceptionally high mobility.

The familiar experimental data on ion mobility, conductance, transport number, conductance-viscosity product, and activation energy for ionic mobility (4) all point to the fact that the migration of the hydrated hydrogen ion through aqueous solution involves a mechanism different from that applicable to other ions. Recently in a study of the entropies of aqueous ions, Breck and Lin (3) have observed that the ionic entropies of transport for H^+ and OH^- are also exceptionally large for univalent ions. For example at infinite dilution the standard "absolute" ionic entropies of transport $S^{*\circ}_i$, as determined by these authors (3) are: (in e.u.) Cl^-, 0.7; H^+, 10.2; OH^-, 14.2; Na^+, 2.2; K^+, 1.5; Br^-, 0.6; I^-, —0.9. Since both H^+ and OH^- ions have a unique relation to the solvent, it was also suggested that the behavior of both ions under the influence of a temperature gradient might be exceptional. Thus, the alternate ordering and disordering effect of the ionic field on the water structure arising from the simple migration of these ions may not be the only contribution to the transport of entropy. There may be a much more significant contribution from the entropy of reaction as hydrogen bonds are alternately made and broken. The heats of transport involved here are of the order 3-4 kcal/mole while the experimental value of the hydrogen bond energy in water is approximately 3.1 kcal/mole (5).

The present work is motivated by the above considerations and is concerned with the mechanism of the transfer of hydrogen ion under a temperature gradient. Experimentally this may be approached by studying the solvent effect on the thermoelectric power of thermocells. For indeed, if a considerable part of the heat of transport of H^+ comes from the fact that hydrogen bonds are alternatively made and broken, then $S^*_{H^+}$ should exhibit a distinct dependence on the structure of the solvent. In fact in a recent study of the heats of transport of $CdSO_4$, $AgNO_3$, $BaCl_2$, and KI in H_2O and D_2O, Becsey and Bierlein (6) found that heats of transport in H_2O are considerably higher than in D_2O. This is attributed by the authors to the fact that D_2O has more "structure" than H_2O. A more randomly constituted liquid will experience a greater degree of orderliness while under the influence of the electrostatic field of an ion and hence will exhibit the greater heat of transport. Furthermore, by a proper choice of solvents it should be possible to diminish to a great extent the contribution from alternative formation and breakage of hydrogen bonds to the heats of transport. One good example of this solvent system is the H_2O-ROH system where R is an alkyl group. If we represent the reaction which is mainly responsible for the transfer of additional (besides the simple migration) aqueous H^+ as

$$H_3O^+ + H_2O \rightarrow H_2O + H_3O^+ \qquad [1]$$

then at a point where enough alcohol has been added to the water reaction, [1] is replaced by

$$H_3O^+ + ROH = H_2O + ROH_2^+ \qquad [2]$$

However, [2] is favored chemically in the backward

direction (equilibrium constant for the reverse reaction is ≈250 for R = C_2H_5) and therefore the additional proton transfer process should be retarded substantially. Under these circumstances, a simple migration mechanism should be operative and if the suggestion by Breck and Lin is correct, S^*_{H+} should then be of the order of magnitude of that of an ordinary univalent ion, *i.e.*, around —1 to +2 e.u.

Hydrochloric acid in the H_2O-C_2H_5OH solvent system was investigated first. The system H_2O-C_2H_5OH as a solvent is particularly convenient for present purposes. First, the physical constants of the solvent system have been studied and are fairly complete (7). Second, thermodynamic properties and the structural aspects have been reviewed admirably by Franks and Ives (8). An attractive feature of the solvent system is that, at about 20 w/o ethanol, it exhibits a very strong solvent structure quite sharply. This is very interesting, since we have found that t_{H+} shows a maximum, and ϵ_0 shows a minimum at this particular solvent composition. Detailed discussions of this observation are given in the Discussion section.

In any solvent study the problem of standard states is always a formidable one. If we wish to compare our study with the available results in aqueous solution, the results of heats or the corresponding entropies of transport obtained at each X, where X is the weight per cent of alcohol in the solvent mixture, must be converted to the same reference state as that of the aqueous solution (whether this is on a conventional or on an "absolute" basis). Therefore, in order to have quantitative results from the thermocell study, we need to know the cation transport number at a given X, $t_{H+}(X)$, for HCl in H_2O-C_2H_5OH system, initial and final thermoelectric powers[1] $\epsilon_0(X)$ and $\epsilon_x(X)$ of a thermocell of the form

$$\underset{T}{A/HCl(m),\ H_2O(100\text{-}X)\text{-}C_2H_5OH(X)/}\underset{T+\Delta T}{A} \quad [3]$$

where A is the electrode system reversible to H^+, and finally the standard partial molar entropy of H^+, $S^o_{H+}(X)$, at each solvent composition. The cation transport number $t_{H+}(X)$ at concentration greater than 0.1m has been studied by Wear, Curtiss, and Amis (9) by the Hittorf method; also at infinite dilution it is readily calculated from Spivey and Shedlovsky's (10) conductance result. However, data for $t_{H+}(X)$ at the concentration of present interest (0.01m) are lacking. Although theoretical interpolation may be used to give the desired value at 0.01m, we have preferred not to do so and we have measured $t_{H+}(X)$ at 0.01m using the moving boundary method. In this paper, we report the observed $t_{H+}(X)$ and $\epsilon_0(X)$ of cell [3] at an average temperature of 25°C (T = 20°C and ΔT = 10°) using hydrogen electrodes at m = 0.01 and X ranging from 0 to 92%. The hydrogen electrode is popular and has served as a reference electrode in isothermal cells; however, data on the hydrogen electrode in thermocell study appear to be rare. For example, the work by Goyan (11) which is frequently referred to dates back to 1937. A comparison (even though only at X = 0) with the result of Goyan would also seem interesting. Results of $\epsilon_x(X)$ of [3] and $S^o_{H+}(X)$ which may be calculated referring to $S^o_{H+}(X = 0)$ by studying the isothermal temperature coefficient of the emf of the cell Pt/H_2/HCl(m), H_2O//HCl(m), H_2O-$C_2H_5OH(X)$/H_2/Pt, where // represents a salt bridge, will be reported in a future paper.

Experimental

Preparations of the solutions.—Baker's analyzed HCl was used throughout the experiments. 95% commercial ethanol was used after distilling twice. The specific gravity of the purified ethanol was found to be d^4_{25} = 0.8058 which, by the interpolation of the density data given by the Handbook of Chemistry (7), was found to correspond to a composition of 92.0% ethanol. Solutions used in the thermocells and the transport number measurements were then prepared by mixing proper amounts of concentrated HCl and the purified ethanol to give 0.01m solution at a desired solvent composition. Densities, molality (m), and molarity (C) of the solutions along with solvent compositions are given in Table I.

[1] The initial and final thermoelectric powers ϵ_0 and ϵ_∞ refer to the thermocell before thermal diffusion has occurred and after it has reached its steady state, respectively.

Table I. Observed cation transport number $t_{H+}(X)$ and initial thermal emf $\epsilon_0(X)$ of 0.01m HCl in ethanol (X)-water (100-X) mixtures at a mean temperature of 25°C. X = Weight per cent

X	d_4^{25}	C_{HCl}	M_{HCl}	t_{H^+}	$\epsilon_0(X)$ mv/deg
0	0.9970	0.01033	0.01040	0.826	0.150
4.9	0.9855	0.01002	0.01017	0.824	0.156
17.9	0.9676	0.009366	0.00968	0.854	0.140
34.2	0.9429	0.009806	0.01040	0.823	0.163
48.7	0.9126	0.008812	0.00966	0.795	0.202
63.4	0.8785	0.008856	0.01008	0.756	0.243
77.8	0.8457	0.008560	0.01013	0.700	0.348
92.0	0.8079	0.008200	0.01015	0.576	0.551

Measurement of the transport numbers.—A moving boundary method described by Shoemaker and Garland (12) was used to measure the transport numbers of HCl in the H_2O-C_2H_5OH system. Fisher certified grade Cd stick was used as the anode and Ag/AgCl, prepared by the thermal method (13), as cathode. The current source used was a General Radio Type 1203B unit power supply. The graded transference cell was calibrated at 25°C so that accurate volume displacements could be obtained. The IR drop over a constant standard resistance (General Radio Type 500-A) was recorded with a Sargent MR recorder; the amount of total electricity passed through the transference cell was calculated by integrating the potential-time curve obtained in the recorder. Methyl orange was used as indicator up to X = 80. For X higher than 80% it was found necessary to use Gramacey Universal Indicator to give a better view of the boundary. The results of the measurements are given in Table I.

Measurements of $\epsilon_0(X)$.—A modified N-type cell (14) to accommodate the improved Hildebrand type hydrogen electrode (13) was used to measure $\epsilon_0(X)$. Glass joints were used where needed to prevent access of air to the electrode. As is well known the purity of the hydrogen gas used is critical to the accuracy of the measurement, and it is necessary that gas supplied to the electrode be of adequate purity. The gas used in this investigation is Matheson ultrapure hydrogen and is analyzed to contain less than 5 ppm N_2 and less than 1 ppm O_2. To avoid introducing any impurities, a stainless steel regulator (Matheson Model 18) was used. General instruction concerning the plating of the electrode given by Hills and Janz (13) was followed. The hydrogen gas was presaturated with the cell solution before supplying to the cell. A few experiments were carried to study the sensitivity of the electrode to the flow rate of the hydrogen gas. In some cases, it was found that for flow rates lower than one bubble per second, the thermal emf would fluctuate considerably (over a range of about 0.1 mv) and would almost take an hour to reach a steady value. For over two bubbles per second, the electrode was found to be quite insensitive to the flow rate and was fast to reach a steady value (≈10 min). For example, between two bubbles per second and continuous stream of hydrogen gas (approximately six bubbles per second), the thermal emf observed was in difference of about 10 μv. For the data reported here, a flow rate of about three bubbles per second was used. The electrodes so prepared were very reproducible and gave a residual emf of about 30 μv over a period of about a week. The temperature of each electrode compartment was measured by a copper-constantan thermocouple, and the emf of the thermocell was recorded

by the MR recorder. The recorded reading was frequently checked by the L&N K3-type potentiometer. A L&N constant current supply (L&N No. 0,99034) was used for the K3 potentiometer. A Guildline enclosure Type 1149 standard cell and Type 9450 galvanometer were used. Residual emf readings were taken both before and after the measurement of ϵ_o, and the average of the two readings, which was within 15 μv of each of the readings, was then subtracted from the value of the measured ϵ_o. The initial thermoelectric powers ϵ_o observed are listed in Table I.

Discussion

By virtue of the high solubility of alcohols in water, the alcohol-water system has been used frequently as a solvent. However, alcohol-water mixtures often show abnormalities which are as yet inadequately understood; for instance the viscosity-composition maxima and the negative partial molal volumes (18). Although attempts may be made to study these solvent systems directly, it may often be more profitable to use ions as a kind of internal indicator which reflect the electrochemical properties of the solvents, *e.g.*, the study of ionic Walden product of H^+ ion in ethanol-water system. Many thermodynamic, transport, and structure data (8) indicate that the addition of a small amount of simple alcohols to water initially enhances the structure of the solvent. For the case of ethanol, this structure enhancement reaches its maximum at around $X = 20\%$. Further addition of ethanol to increase its concentration tends to reduce the structure progressively. This structure-composition variation is also indicated by the sharp maximum of the ionic Walden product of H^+ ion at about $X = 20\%$. According to Spivey and Shedlovsky (10) the position of the maximum Walden product is the point where the probability of the occurrence of the hydrogen bonded path required for the hydrogen ion transfer is the highest. Thus, it is implied that the solvent has more structure at this composition.

The structure-composition variation of the solvent system seems to be also in line with our results on the transport number of H^+. It is noticed from Fig. 1 that t_{H+} also has a maximum at around $X = 20\%$. The capacity of our transference cell is 1 ml, and the unit of the graded scale is 0.01 ml; therefore, it is likely that our results may have an inherent error of about 0.5%. At around $X = 5\%$ the t_{H+} has a slight decrease, and it is not known whether this bears any significance in the ion solvent interaction or whether this is due to the experimental error. Just to see how the present measurement compares with other studies, we have calculated t_{H+} from the conductance data of Spivey and Shedlovsky obtained at infinite dilution. The equation used for this calculation comes from a simple Debye-Hückel consideration and is given by Robinson and Stokes (15). Denoting η as the viscosity

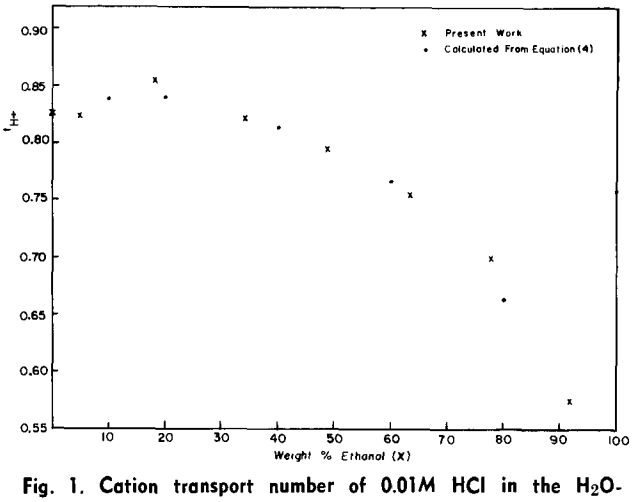

Fig. 1. Cation transport number of 0.01M HCl in the H_2O-ethanol system.

of the solvent, N the Avogadro number, e the electronic charge, and D the dielectric constant, the equation reads

$$t_{H+} = \frac{\lambda^o_{H+} - 0.5\,AC^{1/2}_{HCl}/\,(1 + \kappa\mathring{a})}{\Lambda^o_{HCl} - AC^{1/2}_{HCl}/\,(1 + \kappa\mathring{a})} \qquad [4]$$

where λ^o_{H+} and Λ^o_{HCl} are the equivalent conductance of H^+ and HCl, respectively, at infinite dilution and $A = 82.5/\eta(DT)^{1/2}$, $\kappa = (8\pi Ne^2/1000DkT)^{1/2}\ C^{1/2}_{HCl}$, and $\mathring{a}$ is the distance of closest approach which is taken from Scatchard (16) to be 4.05Å. The result of this calculation is compared with the experimental results in Fig. 1. It is interesting to see that the calculated t_{H+}'s seem to fit in well with the observed t_{H+}'s except at X around 10 ~ 20%. However, it is worth mentioning that the conductance data at $X = 10\%$ is an estimated value (10) and therefore subject to a slight uncertainty. The fact that the calculated t_{H+} at $X = 100\%$ is large, deserves some comment. If, indeed, transfer of protons occurs according to [1], then it is not surprising that t_{H+} at $X = 100\%$ should be higher than that of X around 90%. Since at about $X = 90\%$, the percentage of protons present as H_3O^+ is close to 100 (17) and therefore, $ROH_2^+ + ROH \rightarrow ROH + ROH_2^+$ at $X = 100\%$ should be more effective than the case expressed in Eq. [2]. While the general agreement of the observed and calculated points is good, the over-all shape of the curve does not as yet permit the tracing of a curve through the points especially in the domains X = 0-20% and 90-100%.

In measuring the initial thermoelectric power, instead of measuring the residual emf and applying this correction, measurements may also be done by the so-called reversal technique described by Goyan (11). For 0.01*m* HCl in aqueous solution ($X = 0$) Goyan's ϵ_o value is 0.142 mv/deg which is somewhat lower than our value, 0.150 mv/deg. Since for aqueous 0.01*m* HCl the activity coefficients λ_{HCl} and the relative partial molal heat content $\bar{L}_{HCl}$ are known it is interesting to see how the present measurement compares with other thermocell studies. The equation which governs the initial thermoelectric powers when a hydrogen electrode is used may be written as

$$\mathbf{F}\,\epsilon_o = \frac{1}{2}S_{H_2} - \bar{\bar{S}}_e - S_{H+} - t_{H+}S^*_{H+} + t_{Cl-}S^*_{Cl-} \qquad [5]$$

where $\mathbf{F}$ is the Faraday constant, $\bar{\bar{S}}_e$, the transported entropy of the electron in the metal leads (Cu leads were used in this study) and S_{H+}, the partial molal entropy of the hydrogen ion. If instead of the hydrogen electrode, other electrodes such as Ag/AgCl or Hg/HgCl are used, then the other initial thermoelectric powers ϵ'_o may be written as

$$\mathbf{F}\,\epsilon'_o = S_M - S_{MCl} - \bar{\bar{S}}_e + S_{Cl-} - t_{H+}S^*_{H+} + t_{Cl-}S^*_{Cl-} \qquad [6]$$

where M denotes the metal and MCl, its chloride. By subtracting [5] from [6]

$$\mathbf{F}(\epsilon'_o - \epsilon_o) = \left(S_M - S_{MCl} - \frac{1}{2}S_{H_2}\right) + S_{HCl}$$

$$= \left(S_M - S_{MCl} - \frac{1}{2}S_{H_2}\right) + S^o_{HCl} - 2\left(\mathrm{R}\ln m_{HCl} + \mathrm{R}\ln\gamma_{HCl} + RT\frac{\partial}{\partial T}\ln\gamma_{HCl}\right)$$

$$= \left(S_M - S_{MCl} - \frac{1}{2}S_{H_2}\right) + S^o_{HCl} - 2\mathrm{R}\ln m_{HCl} + 2S'_{HCl} \qquad [7]$$

Using the familiar expression in terms of the relative partial molal enthalpy of the solute $\bar{L}_{HCl}$, we may

Table II. Ionic activity coefficients, $\gamma_{H+}(X)$, nonideal entropy, $S'_{H+}(X)$, and the thermal diffusion potential, TDP

X	0	4.9	10	17.9	20	34.2	40	48.7	60	63.4	79.8	80	92.0	100
γ^{obs}_{HCl}	0.905		0.891		0.883									0.632
$\gamma^{Cal}_{H^+}$	0.905		0.895		0.883		0.851		0.803			0.729		0.629
$-T\frac{\partial \ln D}{\partial T}$	1.37		1.51		1.60		1.68		1.70			1.78		1.90
S'_{H^+} (cal'd)	0.31	0.36	0.39	0.45	0.47	0.59	0.65	0.74	0.89	0.95	1.36	1.36	1.79	2.17
S'_{H^+} (obs)	0.22													
TDP	−0.117	−0.110		−0.123		−0.093		−0.048		−0.007	+0.125		+0.346	

S'_{H^+} (cal'd); In e.u., from Eq. [10]. Those other than $X = 0$, 10, 20, 40, 60, 80, and 100% are interpolated results.
S'_{H^+} (obs); In e.u., from γ_{HCl} and $\bar{L}_{HCl}$ given in ref (18).
γ^{obs}_{HCl}; From ref. (18).
$T\frac{\partial \ln D}{\partial T}$; Calculated from D at 0, 25, 35°C.
TDP; In mv/deg = $\mathbf{F}^{-1}(t_{Cl^-}S^*_{Cl^-} - t_{H^+}S^*_{H^+})$, based on conventional value $S^o_{H^+}(X) = 0$.

write the nonideal terms S'_{HCl} as

$$S'_{HCl} = -R\left(\ln \gamma_{HCl} + T\frac{\partial \ln \gamma_{HCl}}{\partial T}\right) = -R\left(\ln \gamma_{HCl} - \frac{\bar{L}_{HCl}}{2RT}\right) \quad [8]$$

Taking $\gamma_{HCl} = 0.905$ (18), $\bar{L}_{HCl} = 15.86$ cal/mole (18), for 0.01M HCl from [8] we have, $S'_{HCl} = 0.22$ e.u. With $S_{Ag} = 10.206$ e.u., $S_{AgCl} = 22.97$ e.u., $S_{Hg} = 18.5$ eu., $S_{HgCl} = 23.4$ eu., $\frac{1}{2}S_{H_2} = 15.61$ e.u., $\bar{\bar{S}}_e = -0.045$ e.u. and $S^o_{HCl} = 13.16$ e.u. we have from [7]

$$\mathbf{F}(\epsilon'_o - \epsilon_o) = \begin{cases} 3.53 \text{ e.u. for M} = \text{Ag} \\ 11.39 \text{ e.u. for M} = \text{Hg} \end{cases}$$

Since ϵ'_o for Ag/AgCl electrode at 0.01m HCl is reported to be 0.288 (19) mv/deg and that of Hg/HgCl, 0.638 mv/deg (20), we obtained the calculated initial thermoelectric powers for H_2-electrode as

$$\epsilon_o = \begin{cases} 0.135 \text{ mv/deg, based on Ag/AgCl electrode} \\ 0.144 \text{ mv/deg, based on Hg/HgCl electrode} \end{cases}$$

Thus it is seen that both Goyan's and our results seem to be consistent with other existing thermocell studies.[2]

It is worth mentioning that the thermocell studies could be an effective way of measuring the standard partial molal entropies of electrolytes. This is seen in Eq. [7] from which all thermal diffusion potentials and transport entropy have been eliminated. If one wishes to calculate the standard partial molar entropy of an electrolyte, say HCl, one could study the isothermal temperature coefficient of the cell Pt/H_2/HCl/AgCl/Ag at infinite dilution; however, in a thermocell study one would only have to measure the initial thermoelectric powers using the two electrodes at an average temperature of interest. Thus, as far as entropy is concerned, what may be accomplished by several temperature measurements in an isothermal cell may be equally well accomplished with the measurements of two thermocells at a given average temperature.[3]

There is, at present, no way of cross checking the consistency of the other $\epsilon_o(X)$ values for which X is not 0%. It is interesting to note that the variation of $\epsilon_o(X)$ values with X shows behavior opposite to that of the transport numbers. In view of the correlation between the transport numbers and the structure of the solvents, the behavior of $\epsilon_o(X)$ *vs.* X must be more than just a coincidence. However, there appears no satisfactory way of explaining the correlation between $\epsilon_o(X)$ and the solvent structure, at the present time.

Assuming that standard partial molar entropy of the hydrogen ion, $S^\circ_{H+}(X)$, is known, it is possible to compute S^*_{H+} on a conventional basis of $S^*_{Cl-} = 0$ at 0.01m provided that the nonideal contribution S'_{H+} is known. Since the solution is dilute enough, S'_{H+} may be estimated within the frame of Debye-Hückel theory. For this purpose, we have computed "ionic" activity coefficients γ_{H+} at X=0, 10, 20, 40, 60, 80, and 100% by the equation

$$\ln \gamma_{H+} = -\frac{\alpha m^{1/2}_{H+}}{1 + \kappa\mathring{a}} + \beta m_{H+} \quad [9]$$

where, using d as the density of the solvent, at 25°C, $\alpha = 816.147 \times \left(\frac{d}{D^3}\right)^{1/2}$. The constant β is known to vary with D^{-2} (16) and we have taken $\beta = 2000/D^2$. The results of this calculation are compared with experimental (18) activity coefficients of HCl at X=0, 10, 20, and 100% in Table II. By neglecting the coefficient of thermal expansion and from the dielectric constant at 0°, 25°, and 35° given by Spivey and Shedlovsky, $S'_{H+}(X)$ may finally be calculated by the following formula (21)

$$S'_{H+} = +\frac{3}{2}R\left(T\frac{\partial \ln D}{\partial T} + \frac{1}{3}\right)\ln \gamma_{H+} \quad [10]$$

Results of S'_{H+} are also entered in Table II. It is interesting to see that for X=0, the observed S'_{H+} and the calculated values are in a good agreement. Based on the calculated S'_{H+}, and taking $S^\circ_{H+}(X=0) = -5.5$ e.u. the conventional S^*_{H+} (0.01m, X=0) is found to be 9.98 e.u. The value reported by Snowdon and Turner (22) is 10.22 e.u. For other solvent compositions it is not possible to perform the same analysis since $S^\circ_{H+}(X)$ is not known. However, the thermal diffusion potential (TDP), TDP = $1/\mathbf{F}(t_{Cl}-S^*_{Cl-} - t_{H+}S^*_{H+})$ using a conventional value of $S^\circ_{H+}(X) = 0$ may be calculated and is shown in the last row of Table II. It is interesting to note that TDP's also exhibits a minimum at around X=20%. Further discussion will be reserved until the determination of $S^\circ_{H+}(X)$ and $\epsilon_\infty(X)$, to be published in another paper.

Acknowledgment

The authors wish to thank Mr. John Griffin for supplying them with the silver-silver chloride electrode used. They also wish to express their thanks to Professor Andre J. de Bethune for his interest in this work and his reading of the manuscripts. This work was supported by the Office of Saline Water, United States Department of the Interior, under Grant No. 14-01-0001-1466.

Manuscript submitted Sept. 3, 1968; revised manuscript received *ca.* Feb. 10, 1969.

[2] By making a correction on concentration from 0.01040 to 0.0100M, our result becomes 0.147 mv/deg.

[3] Equation [7] may be rewritten as $P = \mathbf{F}(\epsilon'_o - \epsilon_o) + 2R \ln M_{HCl} = \left(S_M - S_{MCl} - \frac{1}{2}S_{H_2}\right) + S^o_{HCl} + 2S'_{HCl}$. Since $S'_{HCl} = 0$ at infinite dilution S^o_{HCl} may be evaluated by extrapolating P to infinite dilution.

Any discussion of this paper will appear in a Discussion Section to be published in the December 1969 JOURNAL.

REFERENCES

1. E. Darmois, *J. Phys. Radium*, **2**, 2 (1941).
2. For a general review, see for example; (a) B. E. Conway, "Modern Aspects of Electrochemistry," No. 3 p. 43, Butterworths, London (1964); (b) B. E. Conway, *Ann. Rev. Phys. Chem.*, **17**, 481 (1966).
3. W. G. Breck and J. Lin, *Trans. Faraday Soc.*, **61**, 2223 (1965).
4. S. Glasstone, K. J. Laidler, and H. Eyring, "Theory of Rate Processes," McGraw-Hill Book Co., New York (1941).
5. The experimental values of the hydrogen bond energy varied considerably according to different authors. Present value is quoted from ref. (2b), p. 484.
6. J. G. Becsey and J. A. Bierlein, *J. Chem. Phys.* **46**, 391 (1967).
7. Handbook of Chemistry, N. A. Lange, Editor, Handbook Publishing Inc., Sandusky, Ohio (1949).
8. F. Franks and D. J. G. Ives, *Quart. Rev.*, **20**, 1 (1966).
9. J. O. Wear, J. I. Curtis, and E. S. Amis, *J. Inorg. Nucl. Chem.*, **24**, 93 (1962).
10. H. O. Spivey and T. Shedlovsky, *J. Phys. Chem.*, **71**, 2165 (1967).
11. F. M. Goyan, Thesis, University of California (1937).
12. D. P. Shoemaker and C. W. Garland, "Experiments in Physical Chemistry," McGraw-Hill Book Co., New York (1962).
13. G. J. Hills, and D. J. G. Ives, in "Reference Electrodes," D. J. G. Ives and G. J. Janz, Editors, Academic Press, New York (1961).
14. W. G. Breck, *Trans. Faraday Soc.*, **59**, 729 (1963).
15. R. A. Robinson and R. H. Stokes, "Electrolytic Solutions," Butterworths, London (1959).
16. G. Scatchard, *J. Am. Chem. Soc.*, **47**, 2098 (1925).
17. Ref. (2a) p. 82.
18. R. G. Parsons, "Handbook of Electrochemical Constants," Butterworths, London (1959).
19. J. C. Goodrich, Thesis, University of California, 1941.
20. Average value from M. B. Young, Thesis, University of California, 1935 and J. C. Goodrich, F. M. Goyan, E. E. Morse, R. G. Preston, and M. B. Young, *J. Am. Chem. Soc.*, **72**, 4411 (1950).
21. G. N. Lewis and M. Randall, "Thermodynamics," revised by K. S. Pitzer and L. Brewer, McGraw-Hill Book Co., New York (1961).
22. P. N. Snowdon and J. C. R. Turner, *Trans. Faraday Soc.*, **56**, 1409 (1960).

Technical Notes

Preparation of Uniform Pore Structures for Porous Electrode Studies

Richard C. Alkire,* Edward A. Grens II,* and Charles W. Tobias*

Lawrence Radiation Laboratory and Department of Chemical Engineering, University of California, Berkeley, California

In many experimental studies using porous materials it is desirable to have highly regular pore structures where the local porosity and specific surface area are determinable to a much greater accuracy than would be possible with random pore configurations. In these cases knowledge of the pore geometry reduces the number of unknown parameters of the system thereby permitting a more quantitative assessment of experimental results. Some investigators have used porous bodies composed of bundles of fine tubes (1) or beds of small spheres (2) to accomplish this purpose, but the former approach is limited to pores of quite large dimensions ($>300\mu$) while the latter gives structures of insufficient regularity for many purposes.

In connection with studies of anodic dissolution of porous metal electrodes a technique has been developed for fabrication of porous structures possessing highly uniform porosity and having individual pores of nearly identical and uniform size and shape (3). These structures are formed from fine wires sintered in parallel close-packed configuration.

In principle, the method may be used to fabricate porous bodies from any material which may be sintered and which is available in wire form. A bundle of straight wires is assembled in such a way that the wires lie in a hexagonal close-packed array. The bundle is then sintered under appropriate conditions of temperature and duration. The resulting mass has parallel individual pores passing through it which correspond to the original void spaces between wires. If the assembly of the bundle is carefully accomplished, all of the pores will have very nearly the same size and shape. This method of assembling wires in a hexagonal close-packed array is an extension of the work of Alexander and Balluffi (4) to the formation of porous bodies on a considerably larger scale.

Proper choice of sintering conditions will allow complete fusion of adjacent wires along lines of contact and elimination of the narrow fissures bordering these contact lines without distortion of the over-all structure. An array of straight wires can be closely approximated by sections of a large wire coil where the radius of curvature of windings is much greater than any pore length of interest. This technique has been successfully applied to fabrication of porous copper electrodes with pores of about 35μ diameter.

Experimental

Porous structures were fabricated from 0.010 in. diameter copper wire (BS No. 30, 99.9% Cu) formed in a coil of 6 5/8 in. ID. In order to promote good sintering conditions, the wire was first cleaned three times in trichloroethylene solvent. The degreased wire was wound in hexagonal close-packed array on a stainless steel spool (3 ¾ in. width). The first layer of wire was wound in such a way that on each turn the wire was in contact with the neighboring wire, wound on the previous turn. Each subsequent layer of wire was wound in the same direction and placed in the crack between wires of the preceding layer. In this manner 83 layers of wire were placed on the spool (a 1.04 cm

* Electrochemical Society Active Member.

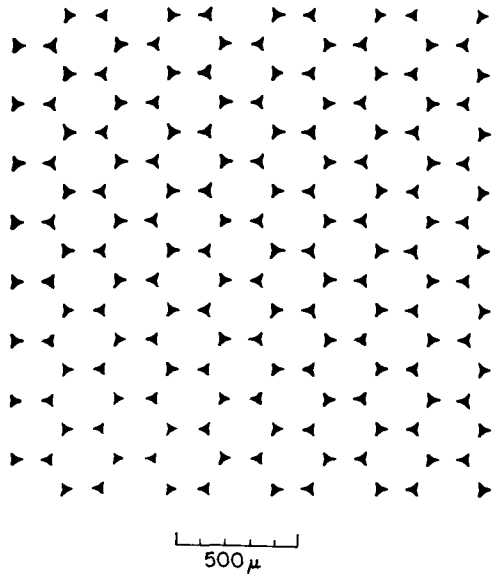

Fig. 1. Porous electrode structure; enlarged cross section parallel to electrode face.

thickness). During the winding, the tension in the wire was maintained at approximately 130g force.

After completion of winding, the air contained in the coil was evacuated and replaced with nitrogen. The coil was then stored in nitrogen until sintering. At that time the nitrogen was removed under vacuum and replaced with hydrogen. The coil was then placed in furnace with a hydrogen atmosphere and sintered for 60 hr at 1050° ± 10°C. These conditions were determined by the results of test sinterings made with small coils of the same wire for temperatures of from 980° to 1070°C and for sintering times of from 4 to 64 hr. After sintering the temperature was reduced at the approximate rate of 100°C/hr.

Individual porous blocks were cut from the sintered coil. The first cut, of two used to remove a block, was made such that the exposed surface was parallel to and about 0.04 cm off a radial plane bisecting the coil. The second cut was made parallel to the first to give a rough piece about 0.57 cm thick. The pieces were then machined to final dimension, with removal of about 0.04 cm from the faces (first and second cuts). The pores then intersected the face at approximately right angles. This machining did not damage the pore structure although it wiped or smeared a thin film of copper over the surface, largely closing over the pores. The smeared film was then removed by electrochemical dissolution in dilute sulfuric acid at current densities sufficiently high (~0.8 A/cm^2) to prevent penetration of the reaction appreciably into the pores; about 3 min of such electrolysis was required to give clean surfaces with open pores.

Results and Discussion

A typical cross section of the resulting structure is shown greatly enlarged in Fig. 1. From photographic enlargements, measurements of individual pore cross-sectional areas and perimeters yielded mean values, at the 95% level of

$$1.964\ (\pm 0.101) \times 10^{-5}\ \text{cm}^2, \text{ and}$$

$$2.22\ (\pm 0.05) \times 10^{-2}\ \text{cm}$$

respectively, and thus a specific surface area of

$$1{,}130\ \text{cm}^2/\text{cm}^3$$

based on void volume. The porosity was 3.5%.

Porous materials fabricated by the method outlined above have a highly uniform porosity. This property is particularly advantageous in such applications as the study of the rate of dissolution at various locations within porous bodies. If the porosity is initially uniform, measurement of the porosity distribution throughout the porous piece after dissolution immediately gives the time-averaged reaction rate during dissolution. This type of porous body has a further advantage. Should a large part of the sintered contact region be removed by a process such as dissolution, the material will still retain its essential structure. Further, analyses of many experiments involve a parameter which contains the product of the specific surface area and the reaction rate constant, and often neither of these is known with confidence. Thus use of porous bodies such as those described here having a known and uniform specific surface area facilitates the theoretical interpretation of experimental data. Finally, the structures formed by this method possess a regular geometry readily described mathematically. They thus lend themselves well to experimental investigation of theories based on well characterized pore configurations.

Acknowledgment

This work was supported by the United States Atomic Energy Commission.

Manuscript submitted Jan. 31, 1969; revised manuscript received *ca.* Feb. 17, 1961.

Any discussion of this paper will appear in a Discussion Section to be published in the December 1969 JOURNAL.

REFERENCES

1. M. Guillou and R. Buvet, *Electrochim. Acta*, **8**, 489 (1963).
2. T. Katan, S. Szpak, and E. A. Grens, *This Journal*, **112**, 1166 (1965).
3. R. Alkire, Reaction Distribution in a Dissolving Porous Anode, Ph.D. Thesis, UCRL-18425, Lawrence Radiation Laboratory, University of California, Berkeley, Calif. September, 1968.
4. B. H. Alexander and R. W. Balluffi, *Acta Met.*, **5**, 666 (1957).

On the Formation of Growth Twins in Electrodeposited Silver

T. Kilner[1] and A. Plumtree

Materials Science Laboratory, Department of Mechanical Engineering, University of Waterloo, Waterloo, Ontario, Canada

Faust and John (1) have reported twinned boundaries in electrodeposited dendrites of aluminum, copper, gold, lead, and silver. The presence of twinned boundaries has also been reported in metals grown by vapor deposition (2) and semiconductors solidified from the melt (3). The importance of twin boundaries lies in their ability to provide re-entrant grooves or two-dimensional nucleation sites, which are self-perpetuating when two or more twin planes are present in a dendrite of a material crystallizing in

[1] Present address: Ryerson Institute of Technology, Toronto, Ontario, Canada.

the diamond-centered cubic or face-centered cubic systems.

This present investigation reports some observations on the origin of twinned boundaries in silver electrodeposited from an unstirred aqueous solution (1M $AgNO_3$ + 2M NH_4NO_3). The cathode was made from 99.98% Ag wire of 0.030 in. diameter and was subsequently melted to increase the available surface area, producing a bead of about 1/16 in. in diameter. The cathode was then annealed at 900°C for 7 hr to produce excessive grain growth, resulting in the bead containing only about 10-20 grains. To prevent deformation due to handling during x-ray work and also to ease removal from the electrolyte, the cathode was contained in an open-ended capillary tube normally used for powder pattern x-ray diffraction work. The anode was also prepared from 99.98% Ag wire.

The electrodeposition conditions ranged from 15 μA and 0.210v up to 200 μA and 0.700v a room temperature. Voltage measurements included the IR drop between cathode and anode. No reference electrode was used. The current density was estimated from the total current and the area of the cathode which showed deposition, thereby giving average values which ranged from 4 x 10^{-3} A/in.^{2} to 50 x 10^{-3} A/in.^{2} Outside this range, higher current densities produced nonadherent deposits, and lower current densities resulted in impracticably slow growth rates (0.001 in./day). Throughout the range of current densities used in this investigation, two basic growth morphologies were observed. The first consisted of a small needlelike form and the second, a thin flat angular form in the shape of a three- or six-sided lozenge[2] on which the present work was carried out.

These lozenge-shaped dendrites were studied metallographically by mounting in a cold setting resin and mechanical polishing on emery papers. Final mechanical polishing was carried out using 6 and 1μ diamond paste. The specimens were then chemically polished with the chromic acid-based solution of Gilpin and Worzala (4) and etched in the manner described by Kilner and Plumtree (5). This technique revealed that the dendrites possessed several twinned boundaries running parallel to the major flat surfaces of the dendrite as seen in Fig. 1 which shows a longitudinal cross section of a dendrite electrodeposited at 300 mv. Laue x-ray back-reflection photographs revealed that the boundaries were {111} twin planes and that the growth direction was $[2,\bar{1},\bar{1}]$. Faust and John have discussed the ramifications of the growth direction of twinned dendrites (1,6).

Careful examination showed twin boundaries appearing within the deposited metal as shown in Fig. 2, indicating that these growth twins formed out of a faulting sequence which occurred during deposition itself rather than from epitaxial growth on the substrate and also in the absence of polycrystalline growth. The presence of secondary twinning branching out from the main twinned planes was also observed, and an example is shown in Fig. 3. However, the incidence of secondary twinning was not marked. As with the main twins, growth accidents or faulted stacking sequences occurring at the re-entrant groove may well account for the origin of the secondary twins. Once this twinned region is formed, the current density or driving force for crystal growth by the secondary twinning mechanism will be the same as that for growth by the main twin boundaries and therefore both parts of the crystal will grow at the same rate. Since the main twinned bands have a greater component of growth in the growth direction, (*i.e.*, $[2,\bar{1},\bar{1}]$ direction) than the secondary twin bands, then the secondary twin bands will be outgrown, leaving the dendrite dominated by twinned boundaries lying parallel to the main growth direction (in this case, $[2,\bar{1},\bar{1}]$ direction) as seen in Fig. 1

[2] Since in cross section these logenze-shaped growth forms exhibited branching, they will be referred to as dendrites. This is in keeping with the nomenclature of previous authors (1).

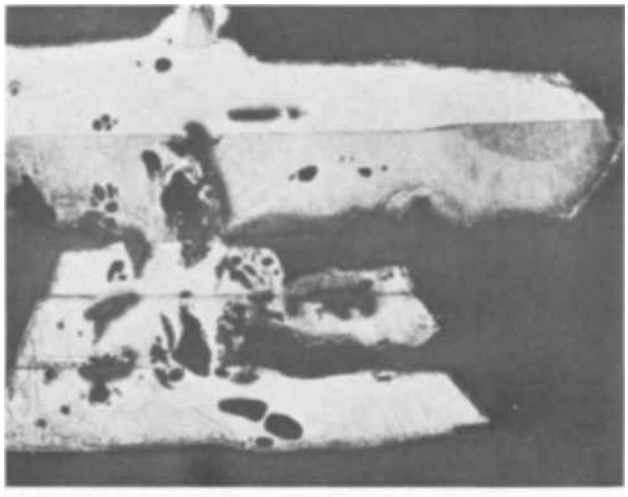

Fig. 1. Lozenge-shaped dendrite. Cell voltage 300 mv, etched. Magnification approximately 60X.

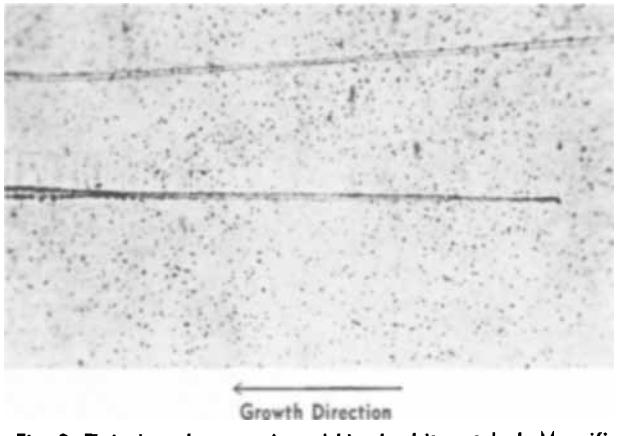

Fig. 2. Twin boundary starting within dendrite, etched. Magnification approximately 820X.

Fig. 3. Secondary twin branching out from main twin, etched. Magnification 600X.

Acknowledgment

This investigation was supported by the National Research Council of Canada (Grant No. A-2770).

Manuscript submitted April 11, 1968; revised manuscript received Feb. 17, 1969.

Any discussion of this paper will appear in a Discussion Section to be published in the December 1969 JOURNAL.

REFERENCES

1. J. W. Faust, Jr., and H. F. John, *This Journal*, **108**, 109 (1961); **110**, 463 (1963).
2. P. B. Price, *Phil. Mag.*, **4**, Series 8, 1229 (1959).
3. E. Billig and P. J. Holmes, *Acta Met.*, **5**, 53 (1957).
4. C. B. Gilpin and F. J. Worzala, *Rev. Sci. Inst.*, **35**, 229 (1964).
5. T. Kilner and A. Plumtree, *Trans. Met. Soc., AIME*, **239**, 129 (1967).
6. J. W. Faust, Jr., and H. F. John, *ibid.*, **233**, 230 (1965).

The Field-Effect Transistor as a Constant Current Source in Electrochemical Investigations

R. B. Davidson and M. A. Hopper*

Department of Physics, University of Alabama, University, Alabama

The well-known application of the field-effect transistor to current control (1, 2) has received no attention in electrochemical investigations. Circuits employing the field-effect transistor are simply and inexpensively constructed, in addition offering excellent control of current. These advantages, combined with the moderate operating voltage of the device, make a field-effect transistor galvanostat more practical than the usual constant current circuit of a source of emf in series with a high impedance. In comparison to operational amplifier based galvanostats the circuits using a field-effect transistor require fewer components, thus being more economical to construct.

Electrical circuit schematics for a galvanostat using only a field-effect transistor, a resistance and a power supply (battery) are shown in Fig. 1. For the circuits shown a maximum current is maintained in the load resistance (the electrochemical cell) when the feedback resistance is small. The maximum controllable current depends on the particular transistor, but is generally between 1 and 10 mA. The load current is decreased by increasing the feedback resistance. With a feedback resistance of 10 megohms the current is reduced to about 0.1 μA. Generally, no current smaller than this is required in electrochemical applications.

The load current will be held constant provided that the voltage between the drain and source of the field-effect transistor is less than the breakdown voltage but greater than the so-called "pinch-off" voltage of the device. In our studies we have used the Motorola HEP 802 field-effect transistor (priced at under $2). This transistor has a rated breakdown voltage of 25v, but certain transistors were found to have actual breakdown voltages of almost 50v. Employing a power supply with an output slightly less than the breakdown voltage of the transistor, it was found that load currents between 0.1 μA and 5 mA could be controlled to better than 0.1% provided that the voltage drop across the transistor was greater than 3v (the "pinch-off" voltage). The current remains constant, subject to the above conditions, even though the voltage appearing across the load may vary over a fairly wide range (approximately 20v for the transistors used in this study).

As a check on the operation of the circuit of Fig. 1 the galvanostatic oxidation of bismuth in a sodium carbonate solution was studied up to an overpotential of 20v. The results obtained in this study were in excellent agreement with the investigation of the anodic oxidation of bismuth using an operational amplifier galvanostat (3).

The variable feedback resistance in Fig. 1 may be replaced by the combination of a potentiostat and a fixed resistance; a modified circuit using this technique is shown in Fig. 2. The potentiostat controls the voltage between the gate and the source of the field-effect transistor, thus controlling the load current. By varying the potentiostat output, the load current may be altered to any desired value. Replacement of the potentiostat of Fig. 2 with a potential sweep generator transforms the circuit into a current sweep generator.

The disadvantage of the simple field-effect transistor circuit (Fig. 1) is that a maximum current of the order of only 5 mA may be controlled. Many electrochemical applications require more current than this upper limit. An extension of the current range

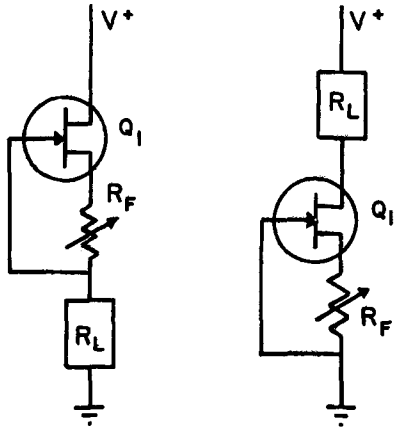

Fig. 1. Schematic diagrams for field-effect transistor galvanostats: Q_1, field-effect transistor; R_L, load resistance; R_F, variable feedback resistance; V^+, d-c power supply.

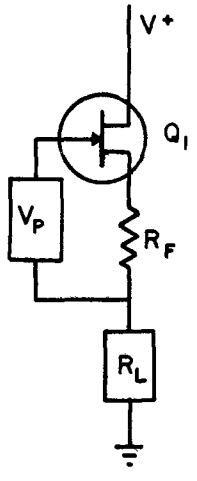

Fig. 2. Schematic diagram for potentiostatic control of galvanostat: Q_1, field-effect transistor; R_L, load resistance; R_F, feedback resistance; V_P, potentiostat; V^+, d-c power supply.

* Electrochemical Society Active Member.

Any discussion of this paper will appear in a Discussion Section to be published in the December 1969 JOURNAL.

REFERENCES

1. J. W. Faust, Jr., and H. F. John, *This Journal*, **108**, 109 (1961); **110**, 463 (1963).
2. P. B. Price, *Phil. Mag.*, **4**, Series 8, 1229 (1959).
3. E. Billig and P. J. Holmes, *Acta Met.*, **5**, 53 (1957).
4. C. B. Gilpin and F. J. Worzala, *Rev. Sci. Inst.*, **35**, 229 (1964).
5. T. Kilner and A. Plumtree, *Trans. Met. Soc., AIME*, **239**, 129 (1967).
6. J. W. Faust, Jr., and H. F. John, *ibid.*, **233**, 230 (1965).

The Field-Effect Transistor as a Constant Current Source in Electrochemical Investigations

R. B. Davidson and M. A. Hopper*

Department of Physics, University of Alabama, University, Alabama

The well-known application of the field-effect transistor to current control (1, 2) has received no attention in electrochemical investigations. Circuits employing the field-effect transistor are simply and inexpensively constructed, in addition offering excellent control of current. These advantages, combined with the moderate operating voltage of the device, make a field-effect transistor galvanostat more practical than the usual constant current circuit of a source of emf in series with a high impedance. In comparison to operational amplifier based galvanostats the circuits using a field-effect transistor require fewer components, thus being more economical to construct.

Electrical circuit schematics for a galvanostat using only a field-effect transistor, a resistance and a power supply (battery) are shown in Fig. 1. For the circuits shown a maximum current is maintained in the load resistance (the electrochemical cell) when the feedback resistance is small. The maximum controllable current depends on the particular transistor, but is generally between 1 and 10 mA. The load current is decreased by increasing the feedback resistance. With a feedback resistance of 10 megohms the current is reduced to about 0.1 μA. Generally, no current smaller than this is required in electrochemical applications.

The load current will be held constant provided that the voltage between the drain and source of the field-effect transistor is less than the breakdown voltage but greater than the so-called "pinch-off" voltage of the device. In our studies we have used the Motorola HEP 802 field-effect transistor (priced at under $2). This transistor has a rated breakdown voltage of 25v, but certain transistors were found to have actual breakdown voltages of almost 50v. Employing a power supply with an output slightly less than the breakdown voltage of the transistor, it was found that load currents between 0.1 μA and 5 mA could be controlled to better than 0.1% provided that the voltage drop across the transistor was greater than 3v (the "pinch-off" voltage). The current remains constant, subject to the above conditions, even though the voltage appearing across the load may vary over a fairly wide range (approximately 20v for the transistors used in this study).

As a check on the operation of the circuit of Fig. 1 the galvanostatic oxidation of bismuth in a sodium carbonate solution was studied up to an overpotential of 20v. The results obtained in this study were in excellent agreement with the investigation of the anodic oxidation of bismuth using an operational amplifier galvanostat (3).

The variable feedback resistance in Fig. 1 may be replaced by the combination of a potentiostat and a fixed resistance; a modified circuit using this technique is shown in Fig. 2. The potentiostat controls the voltage between the gate and the source of the field-effect transistor, thus controlling the load current. By varying the potentiostat output, the load current may be altered to any desired value. Replacement of the potentiostat of Fig. 2 with a potential sweep generator transforms the circuit into a current sweep generator.

The disadvantage of the simple field-effect transistor circuit (Fig. 1) is that a maximum current of the order of only 5 mA may be controlled. Many electrochemical applications require more current than this upper limit. An extension of the current range

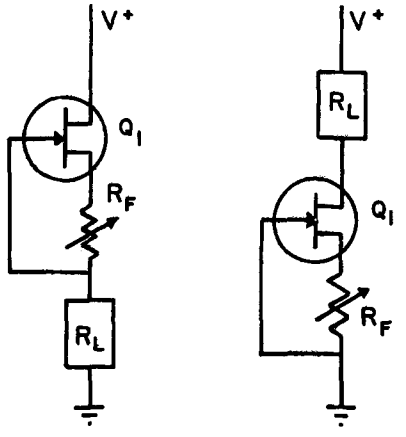

Fig. 1. Schematic diagrams for field-effect transistor galvanostats: Q_1, field-effect transistor; R_L, load resistance; R_F, variable feedback resistance; V^+, d-c power supply.

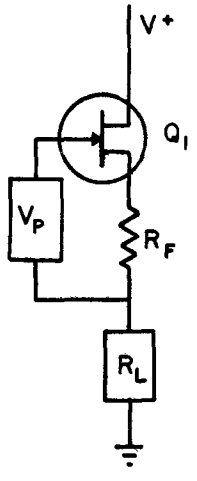

Fig. 2. Schematic diagram for potentiostatic control of galvanostat: Q_1, field-effect transistor; R_L, load resistance; R_F, feedback resistance; V_P, potentiostat; V^+, d-c power supply.

* Electrochemical Society Active Member.

may be achieved by the addition of a single or multiple transistor current amplifier to the basic circuit.

Manuscript submitted Jan. 9, 1969; revised manuscript received March 4, 1969.

Any discussion of this paper will appear in a Discussion Section to be published in the December 1969 JOURNAL.

REFERENCES

1. L. J. Sevin, "Field-Effect Transistors," McGraw-Hill Book Co., New York (1965).
2. J. Sherwin and N. Matzen, "FET Applications Handbook," J. Eimbinder, Editor, Chap. 7, Tab Books, Blue Ridge Summit, Pa. (1967).
3. D. J. DeSmet and M. A. Hopper, Submitted for consideration.

Measurement of Electrical Conductivity in Molten Fluorides. A Survey[1]

G. D. Robbins*

Reactor Chemistry Division, Oak Ridge National Laboratory, Oak Ridge, Tennessee

Investigation of the electrical conductivity of molten salt systems has been an area of lively research in recent years, and a number of articles have appeared which deal with this aspect of transport phenomena (1-3). It is the intent of this survey to limit itself to the subject of conductance measurements in molten fluorides. The containment problems encountered with these materials set them apart from the other molten halides with respect to experimental difficulties and consequent precision of measurement which can be expected. By considering only fused fluorides, it is hoped that sufficient details may be presented to permit workers in the field to obtain a comprehensive overview of the experimental techniques employed covering the period 1927 to 1967, to indicate possible sources of error in the light of electrode process concepts, and to present a recommended procedure for the measurement of electrical conductance in highly corrosive molten salts. To our knowledge, no such survey exists which addresses itself to these questions.

Many investigations in the past have been concerned with cryolite-containing melts because of their relevance to the aluminum industry, and a review of these systems has been given by Grjotheim and Matiasovsky (4). Renewed interest in the transport properties of fused fluorides in general has resulted from their use as fuel, blanket, and coolant materials in molten salt reactors (5).

This survey consists of a tabulation of fluoride systems investigated over the last forty years, followed by a discussion of experimental techniques noted in the tabulation and a critical analysis of their relation to the principles of measurement of electrical conductance in molten salts. Emphasis is placed on cell and electrode design and material, on measuring bridges, and on frequency ranges employed and frequency dispersion of the measured resistance. Values of specific and equivalent conductance for many of the systems reported here may be found in tabular form in Janz's "Molten Salts Handbook" (6).

Tabulation

Table I is a tabulation of electrical conductance investigations ordered by system and within each system, chronologically. Where similar experimental techniques have been employed for more than one fluoride system a cross reference is given. In the column headings, (R) and (l/a) refer to approximate values of measured resistance and cell constant, respectively. V_{pp} is the peak-to-peak value of voltage applied to the bridge. The logic of the table headings and the significance of the large number of "not stated" (abbreviated "N.S.") entries will become apparent in the discussion which follows.

* Electrochemical Society Active Member.

[1] Research sponsored by the United States Atomic Energy Commission under contract with the Union Carbide Corporation.

Discussion

Materials.—Because of the high specific conductance of most molten salts (1-6 ohm^{-1} cm^{-1}) (7), experimental approaches have tended to fall into two groups (1): (I) use of capillary-containing cells, which results in a cell constant of several hundred cm^{-1}, the capillaries being constructed from electrically insulating materials; or (II) use of metallic cells in which the container is usually one electrode, with a second electrode positioned in the melt. The latter type of cell has cell constants of the order of a few tenths cm^{-1}, requiring quite accurate measuring bridges and determination of lead resistances. Since the value of measured resistance in such cells is less than 1 ohm, errors due to temperature gradients, changes in cell constant with temperature, and polarization become a significant problem. Hence, cells of type (I) are clearly desirable for use in molten salts. However, electrically insulating materials for capillary construction which are resistant to attack by molten fluorides are scarce.

Boron nitride (15) and single-crystal magnesium oxide (19-21) have been employed in capillary construction in cells of type I, while metallic cells of type II have been fabricated from platinum (8, 13, 14, 16-21, 26-28) and platinum-20% rhodium (9, 22, 23). Hot-pressed beryllium oxide (28), fused magnesium oxide (25), and graphite (15, 24, 32) also have been used in cell construction.

In addition to the above-mentioned metallic conductors, electrode materials have ranged from graphite (25, 32) to Inconel (11, 12), molybdenum (15, 24), and molten aluminum (25, 32).

Bridges.—Figure 1 shows the basic circuits of bridge types listed in Table I. By far the most commonly employed type of measuring bridge is some form of the basic Wheatstone bridge circuit (Fig. 1A), such as the Jones bridge (33, 34) (Fig. 1B), in which the two upper arms are matched, standard resistances, and the impedance of the cell in one lower arm is balanced by a variable impedance in the fourth arm. A sinusoidal potential source and a null detector complete the circuit. The balancing impedance is usually a variable resistance, R_p, and capacitance, C_p, connected in parallel. However, the solution resistance, R_s, and solution-electrode interfacial capacitances, C_s, in the cell are considered to be in series (35) (Fig. 2a). The capacitance resulting from the electrode leads is in parallel, across the representation shown in Fig. 2a, but at frequencies ordinarily employed, and with some care in positioning, the relatively low resistances encountered in molten salts usually permit this capacitance to be neglected.

At applied potentials sufficiently small that no electrochemical reaction occurs, the equivalent circuit of Fig. 2a is approximately valid (C_s is potential

Table I. Electrical conductance investigations of molten fluoride systems

No.	System	Ref.	Cell, (R) or (l/a)	Electrodes	Bridge (Detector)	f (kHz) of Measurement	R vs. f	Vpp (v)
1	LiF	8	Pt crucible (R) $\cong$ 0.1 Ω	Pt crucible and platinized Pt foil (3 × 4 mm)	Wheatstone (telephone)	6	N.S. = Not stated	N.S.
2	LiF	9	Two Pt(80%)-Rh hemispheres (d = ¾" and 2"). These are also current electrodes.	Two Pt(80%)-Rh rods (d = 0.01"). These are potential-measuring electrodes.	Specially developed by E. Fairstein (10) f range = 0.2-6 kHz; R range = 0.01-10 Ω (oscilloscope)	N.S.	N.S.	N.S.
3	LiF	11 12	Hot-pressed BN cylinder (id = 3/16") surrounded by graphite, (R) $\simeq$ 3-6 Ω. (l/a) = 17-39 cm^{-1}	Inconel rod and Inconel plate across ends of BN cylinder.	Wheatstone, no capacitors (oscilloscope)	2	"Did not vary appreciably between 1 and 20 kHz."	N.S.
4	LiF	13 14	Pt crucible (vol. = 39 cm^3), (l/a) $\simeq$ 0.28 cm^{-1}	Two platinized Pt foils (10 × 10 mm)	Thomson-type (oscilloscope)	50	f-dependency at lower f, independent at 50 kHz	~0.05
5	LiF	15	Graphite crucible (id = 3.5", 5" deep) containing 2 BN cylinders (id = 3/16") encased in graphite and enlarged at top to accommodate electrodes, (l/a) ~ 100 cm^{-1}	Two ¼" Mo tubes fitting into upper portions of BN cylinders	Jones (null detector)	10	f independent 1-20 kHz	N.S.
6	NaF	16 17	Pt crucible (400 ml), (l/a) = 0.0835 cm^{-1}	Hemispherical Pt electrodes, platinized originally.	Kelvin	0.6 to 4	$R \propto f^{-1/2}$ extrapolated to $f = \infty$	10
7	NaF	18	Pt crucible (0.2 mm wall), (R) = 0.02 Ω	Crucible and a Pt cylinder, (area = 2 cm^2), both platinized	N.S.	0.15 to 8	N.S.	N.S.
8	NaF	11 12	Same as No. 3	No. 3	No. 3	No. 3	No. 3	No. 3
9	NaF	13 14	Same as No. 4	No. 4	No. 4	No. 4	No. 4	No. 4
10	NaF	15	Same as No. 5	No. 5	No. 5	No. 5	No. 5	No. 5
11	KF	8	Same as No. 1	No. 1	No. 1	No. 1	No. 1	No. 1
12	KF	9	Same as No. 2	No. 2	No. 2	No. 2	No. 2	No. 2
13	KF	11 12	Same as No. 3	No. 3	No. 3	No. 3	No. 3	No. 3
14	KF	13 14	Same as No. 4	No. 4	No. 4	No. 4	No. 4	No. 4
15	KF	19 20 21	MgO, single crystal, dip cell; Pt container	Container and Pt electrode	Jones	0.5 to 10	Varied <0.3% over f range	N.S.
16	CsF	9	Same as No. 2	No. 2	No. 2	No. 2	No. 2	No. 2
17	CsF	20 21	Same as No. 15	No. 15	No. 15	No. 15	No. 15	No. 15
18	AgF	13 14	Same as No. 4	No. 4	No. 4	No. 4	No. 4	No. 4
19	BeF_2	22 23	Pt-Rh(20%) crucible (id = 2", ht. = 2½") (l/a) = 0.11 or 0.28 cm^{-1}	Crucible and Pt-Rh (20%) bob	"Wheatstone R-C Bridge" (scope or VTVM)	2-10	f independent 2-10 kHz	N.S.
20	CaF_2	24	Carbon crucible	Mo electrodes	N.S.	N.S.	N.S.	N.S.
21	MnF_2, CuF_2, ZnF_2, PbF_2, KBF_4, Na_2TaF_7, K_2TiF_6, K_2TaF_7	13 14	Same as No. 4	No. 4	No. 4	No. 4	No. 4	No. 4
22	Li_3AlF_6	11 12	Same as No. 3	No. 3	No. 3	No. 3	No. 3	No. 3
23	Na_3AlF_6	25	Fused MgO tube (d = 0.99, l = 10.3 cm) (l/a) = 0.0752 cm^{-1}	Graphite plates across ends of tube	Wheatstone $\vec{R}$ and $\vec{C}$ in parallel (telephone)	Two f's	N.S.	N.S.
24	Na_3AlF_6	17	Same as No. 6	No. 6	No. 6	No. 6	No. 6	No. 6
25	Na_3AlF_6	18	Same as No. 7	No. 7	No. 7	No. 7	No. 7	No. 7
26	Na_3AlF_6	11 12	Same as No. 3	No. 3	No. 3	No. 3	No. 3	No. 3
27	Na_3AlF_6	13 14	Same as No. 4	No. 4	No. 4	No. 4	No. 4	No. 4
28	Na_3AlF_6	26	Pt hemisphere (od = 4 cm), (l/a) = 0.386 cm^{-1}	Container and Pt rod (d = 3 mm)	Thomson plus phase indicator	5	N.S.	N.S.
29	K_3AlF_6	11 12	Same as No. 3	No. 3	No. 3	No. 3	No. 3	No. 3
30	LiF + ThF_4	15	Same as No. 5	No. 5	No. 5	No. 5	No. 5	No. 5
31	LiF + UF_4	15	Same as No. 5	No. 5	No. 5	No. 5	No. 5	No. 5
32	NaF + CaF_2 (67 w %)	27	Pt crucible (R) $\simeq$ 0.1 Ω	Crucible and Pt rod, both platinized originally	Carey-Foster	1	N.S.	N.S.

33	$NaF + SrF_2$ (67 w %)	27	Same as No. 32	No. 32	No. 32	No. 32	No. 32	No. 32	No. 32
34	$NaF + BaF_2$ (67 w %)	27	Same as No. 32	No. 32	No. 32	No. 32	No. 32	No. 32	No. 32
35	$NaF + ZrF_4$	28	Hot-pressed BeO tube in a cylindrical Pt crucible (l/a) = 24 cm^{-1}	Wheatstone, R and C in parallel (oscilloscope)	1	N.S.	N.S.	N.S.	N.S.
36	$NaF + ThF_4$	15	Same as No. 5	No. 5	No. 5	No. 5	No. 5	No. 5	No. 5
37	$NaF + UF_4$	15	Same as No. 5	No. 5	No. 5	No. 5	No. 5	No. 5	No. 5
38	$NaF + NaBF_4$	29	Described in Ref. 30, not readily available	Wheatstone, with balancing R (oscilloscope)	5	N.S.	N.S.	N.S.	N.S.
39	$NaF + Na_3AlF_6$	16 17	Same as No. 6	No. 6	No. 6	No. 6	No. 6	No. 6	No. 6
40	$KF + KBF_4$	29	Same as No. 38	No. 38	No. 38	No. 38	No. 38	No. 38	No. 38
41	$MgF_2 + Na_3AlF_6$	31	Pt cell	Wheatstone, R and C in parallel (oscilloscope)	N.S.	N.S.	N.S.	N.S.	N.S.
42	$CaF_2 + Na_3AlF_6$	32 25	Graphite crucible (R) $\simeq$ 0.5 Ω	Wheatstone, R and C in parallel (telephone)	Two f's	N.S.	N.S.	N.S.	N.S.
43	$CaF_2 + Na_3AlF_6$	16 17	Same as No. 6	No. 6	No. 6	No. 6	No. 6	No. 6	No. 6
44	$CaF\text{-}Na_3AlF_6$ (81 m%)	11 12	Same as No. 3	No. 3	No. 3	No. 3	No. 3	No. 3	No. 3
45	$AlF_3\text{-}Na_3AlF_6$	31	Same as No. 41	No. 41	No. 41	No. 41	No. 41	No. 41	No. 41
46	$AlF_3 + Na_3AlF_6$	16 17	Same as No. 6	No. 6	No. 6	No. 6	No. 6	No. 6	No. 6
47	$LiAlF_6 + Na_3AlF_6$ (40 w %)	11 12	Same as No. 3	No. 3	No. 3	No. 3	No. 3	No. 3	No. 3
48	LiF-NaF-KF (46.5-11.5-42 m%)	28	Hemispherical Pt crucible (l/a) = 0.162	Current electrodes; crucible and Pt sphere; potential electrodes; crucible and Pt cylinder surrounding sphere	0.5	No bridge; VTVM and ammeter	N.S.	N.S.	N.S.
49	$NaF + ZrF_4 + UF_4$	28	Same as No. 48	No. 48	No. 48	No. 48	No. 48	No. 48	No. 48

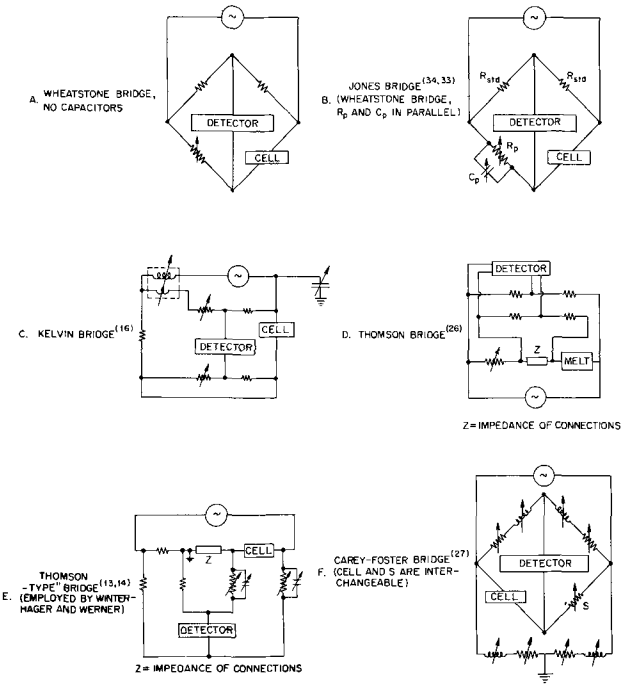

Fig. 1. Basic types of impedance bridges employed with molten fluorides.

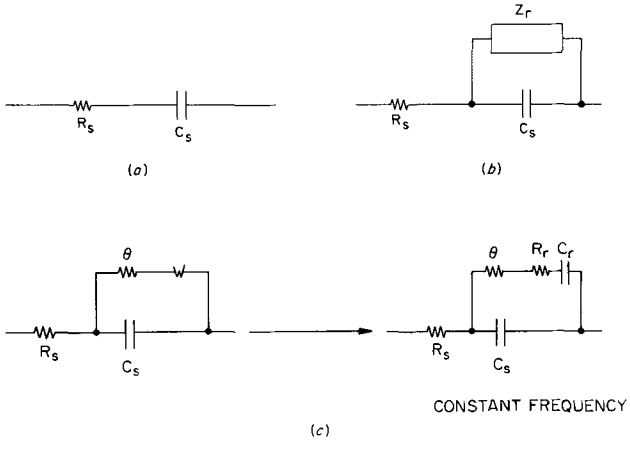

Fig. 2. Equivalent circuit representations for a conductance cell: (a) no electrochemical reaction, (b) generalized electrochemical reaction, (c) electrochemical reaction according to Faradaic admittance theory.

dependent), and the interfacial capacitance is charged and discharged during each half-cycle through the solution resistance. Substituting this equivalent circuit representation for the cell into Fig. 1B and performing a circuit analysis reveals that the two conditions which must obtain at balance are

$$\frac{R_s}{R_p} + \frac{C_p}{C_s} = \frac{R_{std}}{R_{std}} = 1 \qquad [1]$$

and

$$R_s R_p C_s C_p (2\pi f)^2 = 1 \qquad [2]$$

f is the frequency of the sine wave. Equations [1] and [2] may be combined to yield

$$R_p = R_s [1 + R_p^2 C_p^2 (2\pi f)^2] \qquad [3]$$

or

$$R_p = R_s + \frac{1}{R_s C_s^2 (2\pi f)^2} \qquad [4]$$

It is often the practice to equate R_p (the reading on the bridge dials) to R_s (the true solution resistance). (In the case of unmatched standard resistors, their ratio is used.) Yet as Eq. [4] demonstrates, this is

really an approximation in which the additive term $1/R_sC_s^2(2\pi f)^2$ has been neglected. The approximation is usually valid in dilute aqueous solutions where R_s is large. However, in molten salts, particularly in cases where capillaries are not used to increase the conducting path (such as in most fluorides), considerable error can result from the neglect of this term.

As an example, in a dilute aqueous solution reasonable values of R_s, C_s, and f might be 1000 ohms, 20 μf, and 1000 Hz, respectively. In which case the neglected term is 0.06 ohm (compared to 1000 ohms). In molten salts in cases where capillaries are not used to increase resistance, R_s is often less than 5 ohms. For such a value of resistance, and assuming values of C_s (36) and f as above, the neglected term becomes 12 ohms (compared to 5 ohms).

Although this approximation was pointed out by Jones (34) forty years ago and has been discussed more recently (37), in none of the nine groups of investigations employing this type of bridge (Table I) is it apparent that the effect of the approximation has been considered. R_s can be calculated from R_p and C_p (the resistance and capacitance readings on the bridge) via Eq. [3] provided the bridge has been demonstrated to obey Eq. [1] and [2] by first testing it with a dummy cell consisting of a known resistance and capacitance connected in series.

It is not possible to assess the extent to which neglect of the additive term in Eq. [4] may have contributed to an error in the published results (using Eq. [3]) because no author reported the values of capacitance required for bridge balance. However, such an error would be frequency dependent in magnitude, and the frequency independence of some results (15, 19-23) indicates no error from this source.

Use of Eq. [3] to calculate R_s is limited by the accuracy with which the values of the variable capacitance and the frequency are known and by the demonstrated ability of the bridge to satisfy the balance equations using dummy components. These difficulties can be avoided by employing a bridge in which the balancing components are in series (38). Then in the case of no electrochemical reaction, the value of R_s is well represented by the reading on the balanced bridge; however, this method does require the use of large capacitors.

Frequency response.—As seen in Table I, of the sixteen independent groups of investigators, over half do not state whether or how measured resistance varied with measuring frequency. Jones and Christian (39) considered this question in their investigations in aqueous electrolytes, measured resistances at a series of frequencies, and extrapolated measured resistance to infinite frequency employing the functional form $f^{-1/2}$. The theoretical basis for their experimental procedure was the work of Warburg (40, 41) and Neumann (42) who, on the basis of Fick's laws of diffusion, predicted that the polarization resistance (that part of the measured resistance due to electrode polarization) was inversely proportional to $f^{1/2}$. Thus the measured resistance, R_m, was considered to be composed of a true solution resistance, R_s, and a polarization resistance, R_z.

$$R_m = R_s + R_z \qquad [5]$$

Frequency dispersion of the measured resistance has been observed in organic solvents (43) and in molten salts. Often the form of the frequency dispersion was not $f^{-1/2}$. Nichol and Fuoss (43) observed f^{-1} frequency dependence in methanol solutions, while De Nooijer (44) reported that in molten nitrate melts plots of measured resistance *vs.* $f^{-1/2}$ were not linear, but approached linearity as the frequency approached infinity. His values of measured resistance at 20 kHz only differed from values extrapolated to infinite frequency by about 0.1%. Winterhager and Werner (13, 14) have considered frequency dispersion in molten nitrate, chloride, and fluoride melts and have mathematically (45) analyzed their results obtained with a Thomson-type bridge. They conclude that at sufficiently high frequencies measured resistance becomes independent of frequency, and they employ a measuring frequency of 50 kHz.

It should be emphasized that, while one can measure resistance at a series of frequencies and extrapolate to infinite frequency, one cannot make measurements at frequencies which approach infinity. In fact, very high-frequency measurements (in the megahertz range) are to be avoided because of the increased admittance of the leads and the fact that at very high frequencies one ceases to measure a property associated with ionic mobility and observes properties associated with dipole moments and polarizabilities. Hence the question of concern is what functional form of the frequency should be employed to extrapolate the measured resistance to infinite frequency.

Applying the concepts resulting from electrode process studies (46-48), when a sufficiently large a-c potential is impressed on the cell that charge is transferred across the solution-electrolyte interfaces during part of each half-cycle, corresponding to an electrochemical reaction, one may envision the equivalent circuit shown in Fig. 2b. Z_r represents the impedance associated with the reaction, which is in parallel with the solution-electrode interfacial capacitance. Under the exacting assumptions of faradaic admittance theory, Z_r may be represented by a frequency-independent resistance, θ, in series with a frequency-dependent impedance, $-W-$, the Warburg impedance (Fig. 2c). The latter is conveniently represented as a resistance and capacitance in series, R_r and C_r, at constant frequency, while both are predicted to vary as $f^{-1/2}$. Although this is the functional form sometimes observed in conductance measurements, the assumptions on which faradaic admittance theory are based are sufficiently restrictive (*e.g.*, that the amplitude of the sine wave approach zero) as to render equivalent circuit 2c of marginal applicability to most conductance apparatus. However, during that part of each half-cycle in which reaction is occurring at the electrodes, equivalent circuit 2b is a useful concept, and it is interesting to examine this representation in the light of experimental practices commonly employed to eliminate R_z (Eq. [5]). In the practice of extrapolating the measured resistance to infinite frequency, it can be seen that at very high frequencies the impedance of the capacitance path across the interface decreases relative to that of the reaction path, so that the equivalent circuit approaches that of Fig. 2a. The practice of platinizing the electrodes results in greatly increasing their surface area, increasing C_s and the relative admittance of this path. Thus, the effect of R_z is diminished.

Robinson and Stokes (49) have considered the question of frequency dispersion in terms of electrode process concepts as applied to aqueous media and give balance equations for a bridge with a parallel-component balancing arm, assuming various relative magnitudes for R_s, θ, and R_r. Under the conditions employed by Jones and Christian (39), $f^{-1/2}$ dependence is predicted. Hills and Djordjevic (50) analyzed frequency response in terms of an equivalent circuit representation similar to that of Fig. 2c and demonstrated possible errors which may result from extrapolation *vs.* $f^{-1/2}$. The largest error encountered in molten salts was 0.04 ohm. Robinson and Stokes conclude that one should measure resistance as a function of frequency and extrapolate to infinite frequency in accordance with the observed behavior. This is also the conclusion of Nichol and Fuoss (43), who had observed a f^{-1} frequency dependence of resistance in methanol solutions. Buckle and Tsaoussoglou (51) have found that measured resistance *vs.* frequency plots show a plateau in the range 10-100 kHz in aqueous potassium chloride and molten potassium bromide. They suggest that extrapolation of resistance *vs.* $f^{-1/2}$ would lead to erroneous conductances and

that one should study frequency dispersion in a particular apparatus and select a frequency-independent region for performing conductivity experiments.

Thus, it seems clear that *a priori* prediction of the functional form which should be employed for elimination of polarization resistance (via Eq. [5]) is not possible, and one must determine experimentally the frequency response with a particular apparatus and under a given set of experimental conditions. However, before resorting to this empirical approach, there are several steps which may be taken to reduce frequency dependence of the measured resistance: 1. A test of the bridge circuit by substituting a calibrated resistance and capacitance, connected in series, having values similar to those expected from the conductance cell indicates within what limits the bridge reading represents the series resistance (cf. Eq. [4]). 2. Reduction of the sine wave amplitude to the smallest possible value compatible with the detector (preferably below 100 mv) reduces effects associated with any electrode reactions. That over half of the investigators represented in Table I do not address themselves to the question of frequency dispersion justifies, the author feels, the foregoing discussion.

The lower the applied voltage, the less should be the contribution from any electrochemical reaction since during each half-cycle the time during which reaction occurs is less. The last column of Table I lists the peak-to-peak voltage applied to the bridge. Two authors (13-14, 16-17) contributed this information.

Summary

A survey of electrical conductivity measurements in molten fluoride systems covering the period 1927 to 1967 has been presented. Particular emphasis is placed on cell and electrode material and design, on measuring bridges, and on the frequency dispersion of the measured resistance. It is pointed out that the common practice of measuring resistance with a Wheatstone-type bridge having a parallel resistance and capacitance, R_p and C_p, in the balancing arm can result in considerable error if the relation $R_p = R_s[1 + R_p^2C_p^2 (2\pi f)^2]$ is not employed in determining the solution resistance R_s. The frequency dependence of the measured resistance and the practice of extrapolating measured resistances to infinite frequency *vs.* $f^{-1/2}$ is examined in terms of electrode process concepts. Recommendations are presented for reducing frequency effects, and a summary of experimental approaches of 16 groups of investigators for 56 molten fluoride systems is given.

Manuscript submitted April 22, 1968; revised manuscript received *ca.* Feb. 10, 1969.

Any discussion of this paper will appear in a Discussion Section to be published in the December 1969 JOURNAL.

REFERENCES

1. G. J. Janz and R. D. Reeves, "Molten-Salt Electrolytes—Transport Properties," in "Adv. in Electrochem. and Elec. Eng.," Vol. 5, C. W. Tobias, Editor, John Wiley & Sons, Inc., New York (1967).
2. B. R. Sundheim, "Transport Properties of Liquid Electrolytes," in "Fused Salts," B. R. Sundheim, Editor, McGraw-Hill Book Co., New York (1964).
3. A. Klemm, "Transport Properties of Molten Salts," in "Molten Salt Chemistry," M. Blander, Editor, John Wiley & Sons, Inc., New York (1964).
4. K. Grjotheim and K. Matiasovsky, *Tidsskr. Kjemi Bergv. Metallurgi*, **26**, 226 (1966).
5. W. R. Grimes, "Materials Problems in Molten Salt Reactors," in "Materials and Fuels for High Temperature Nuclear Energy Applications" by M. T. Simnad and L. R. Zumwalt, the M.I.T. Press, Cambridge (1964).
6. G. J. Janz, "Molten Salts Handbook," Academic Press, New York (1967).
7. I. S. Yaffe and E. R. Van Artsdalen, *J. Phys. Chem.*, **60**, 1125 (1956).
8. E. Ryschkewitsch, *Z. Elektrochem.*, **39**, 531 (1933).
9. I. S. Yaffe and E. R. Van Artsdalen, Chemistry Division Semiannual Progress Report for Period Ending June 20, 1956, ORNL-2159, p. 77.
10. E. Fairstein, Instrumentation and Controls Semiannual Progress Report for Period Ending July 31, 1955, ORNL-1997, p. 9.
11. E. W. Yim and M. Feinleib, *This Journal*, **104**, 622 (1957).
12. *Ibid.*, 626 (1957).
13. H. Winterhager and L. Werner, *Forschungsber. des Witschafts-u. Verkehrsministeriums Nordrhein-Westfalen*, No. 438 (1957).
14. *Ibid.*, No. 341 (1956).
15. E. A. Brown and B. Porter, U.S. Department of Interior, Bureau of Mines, I28.23:6500 (1964).
16. J. D. Edwards, C. S. Taylor, L. A. Cosgrove, and A. S. Russell, *This Journal*, **100**, 508 (1953).
17. J. D. Edwards, C. S. Taylor, A. S. Russell, and L. F. Maranville, *Ibid.*, **99**, 527 (1952).
18. G. J. Landon and A. R. Ubbelohde, *Proc. Royal Soc.*, **A240**, 160 (1957).
19. H. R. Bronstein and M. A. Bredig, Chemistry Division Annual Progress Report for Period Ending June 20, 1959, ORNL-2782, p. 59.
20. *Ibid.*, *J. Am. Chem. Soc.*, **80**, 2077 (1958).
21. H. R. Bronstein, A. S. Dworkin, and M. A. Bredig, Chemistry Division Annual Progress Report for Period Ending June 20, 1960, ORNL-2983, p. 65.
22. J. D. Mackenzie, *J. Chem. Phys.*, **32**, 1150 (1960).
23. *Ibid.*, *Rev. Sci. Instr.*, **27**, 297 (1956).
24. T. Bääk, *Acta Chem. Scand.*, **8**, 1727 (1954).
25. J. W. Cuthbertson and J. Waddington, *Trans. Faraday Soc.*, **32**, 745 (1936).
26. J. Bajcsy, M. Malinovsky, and K. Matiasovsky, *Electrochim. Acta*, **7**, 543 (1962).
27. M. deK. Thompson and A. L. Kaye, *Trans. Electrochem. Soc.*, **67**, 169 (1935).
28. N. D. Greene, ORNL-CF-54-8-64 (1954).
29. V. G. Selivanov and V. V. Stender, *Russian J. Inorg. Chem.*, **4**, 934 (1959).
30. G. A. Meerson and M. P. Smirnov, "Khimiva Redkikh Elementov, Akad. Nauk SSSR," **2**, 133 (1955).
31. E. Batslavik and A. I. Belyayev, *Russ. J. Inorg. Chem.*, **3**, 324 (1958).
32. T. G. Pearson and J. Waddington, *Discussion Faraday Soc.*, **1**, 307 (1947).
33. P. H. Dike, *Rev. Sci. Instr.*, **2**, 379 (1931).
34. G. Jones and R. C. Josephs, *J. Am. Chem. Soc.*, **50**, 1049 (1928).
35. D. C. Grahame, *J. Am. Chem. Soc.*, **63**, 1207 (1941).
36. C. H. Liu, K. E. Johnson, and H. A. Laitinen, in "Molten Salt Chemistry," p. 715, M. Blander, Editor, Interscience Publishers, New York (1964).
37. F. S. Feates, D. J. G. Ives, and J. H. Pryor, *This Journal*, **103**, 580 (1956).
38. G. D. Robbins and J. Braunstein, Reactor Chemistry Division Annual Progress Report for Period Ending December 31, 1967, ORNL-4229, p. 57.
39. G. Jones and S. M. Christian, *J. Am. Chem. Soc.*, **57**, 272 (1935).
40. E. Warburg, *Wied. Ann. Physik.*, **67**, 493 (1899).
41. E. Warburg, *Drude Ann. Physik.*, **6**, 125 (1901).
42. E. Neumann, *Wied. Ann. Physik.*, **67**, 500 (1899).
43. J. C. Nichol and R. M. Fuoss, *J. Am. Chem. Soc.*, **77**, 198 (1955).
44. B. De Nooijer, "The Electrical Conductivity of Molten Nitrates and Binary Nitrates," Thesis, University of Amsterdam, The Netherlands, 1965.
45. G. Oberdorfer, *Lehrbuch der Elektrotechnik*, Bd. II, 1944, p. 212.
46. D. C. Grahame, *This Journal*, **99**, 370C (1952).
47. D. C. Grahame, *Ann. Rev. Phys. Chem.*, **6**, 345 (1955).
48. P. Delahay, "New Instrumental Methods in Electrochemistry," pp. 146-168, Interscience Publishers, New York (1954).
49. R. A. Robinson, and R. H. Stokes, "Electrolyte Solutions," pp. 88-95, Butterworths, London, 2nd ed. (revised), (1965).
50. G. J. Hills and S. Djordjevic, *Electrochim. Acta*, **13**, 1721 (1968).
51. E. R. Buckle and P. E. Tsaoussoglou, *J. Chem. Soc., London*, 667 (1964).

DISCUSSION SECTION

The Discussion Section includes discussion of papers appearing in the *Journal of The Electrochemical Society*, Vol. 115, No. 4, 5, 6, 9, (April, May, June, and September), and in Vol. 116, No. 6 (June 1969).

The Alkaline Manganese Dioxide Electrode II. The Charge Process

David Boden, C. J. Venuto, D. Wisler, and R. B. Wylie
(pp. 333-338, Vol. 115, No. 4)

S. Ghosh[1]: In understanding the mechanism of the charge process in the alkaline medium of the manganese dioxide cell system, a basic question has remained unanswered: whether alkali will dissolve MnO_2 to form manganate solution. During the discharge of the MnO_2 electrode in the alkaline media, it is susceptible to the formation of solution in liquid phase near the electrode. At the time of charging, the quantitative reformation of MnO_2 could not be obtained resulting in loss of initial electrode material. In our study of the depolarization mechanism of gamma MnO_2, we observed that high *p*H was not conducive to obtaining the proper charge and discharge capacity relation with that of the theoretically calculated value, whereas in the acidic range the coulometric capacity has some comparable relations.

In Fig. 5, 7, and 8, the charge and discharge curves were drawn on the basis of constant current charge and discharge. I feel, instead, if the discharge were carried out through a standard resistance and similarly the coulometric values obtained during the charge, it would have been useful for comparison with the theoretical coulometric capacity for a closer understanding of the practical utility of the system. To date a reversible cell system with manganese dioxide electrode has not been a practical proposition. Your study is most enlightening; I hope you will explore further and will be able to establish the proper condition for a reversible alkaline managanese dioxide cell.

Before I close my observations, I would like to inform you about my unpublished work in which I have tried to form a reversible system with manganese dioxide as positive electrode and cadmium as negative. I observed that the alkali was reacting with the stationary electrode and a liquid layer was formed in the neighborhood of it; a considerable dissolution of MnO_2 was observed after a few cycles of charge and discharge. The initial cycling was, no doubt, hopeful but we were restricted by the problem of dissolution and other side reactions, which occurred in the system. In the study on the depolarization mechanism of gamma MnO_2, we observed that high *p*H was not conducive to getting the proper coulometric discharge capacity compared with the medium in acidic or neutral range. It was observed that, if discharge is carried out to the point beyond breakdown of the structure of manganese dioxide, it was difficult to obtain MnO_2 again for discharge process. Up to the point where the lattice dilution of the oxide occurred it was possible to bring them back to the charge condition. In our study we examined those progressively discharged samples of MnO_2 by x-ray diffraction, electron diffraction, and electron microscopy, and found that discharge products of progressively discharged samples are mixtures of manganese dioxide with lower oxide of manganese, and the preparation of lower oxide progressively increased with the discharge.

[1] Indian Standards Institution, Manak Bhavan, 9 B. S. Zafar Marg, New Delhi 1, India.

I am giving the above comments in the hope that they will help to reveal the actual mechanism of this charge and discharge process which is, no doubt, still an open question.

Field Ion Microscopical Studies of Exchange Current Density on Iridium

Leonard Nanis and Philippe Javet
(pp. 509-511, Vol. 115, No. 5)

D. A. Smith[2]: The contrast to be expected from field-ion images of dislocated surfaces has recently been quantified in detail (Pashley, 1965[3]; Ranganathan, 1966[4]; Smith *et al.*, 1968[5]; Brandon and Perry, 1967[6]; Sanwald and Hren, 1968[7]). It is generally agreed that a dislocation will be visible when the component of the dislocation Burgers vector along the normal to the surface where it emerges is not equal to zero. Dislocations are visible as a characteristic spiral contrast which may arise from both edge and screw dislocations. Almost all observations of dislocations can be analyzed in terms of this model. The authors reference to the absence of "spiral dislocations" is imprecise. More importantly, it is worth emphasizing that the perpetual steps postulated in theories of growth both from the vapor phase and by electrodeposition may be produced at emergent edge and mixed dislocations, not just screw dislocations. Any dislocation converts a crystal into a continuous helical ramp (Cottrell, 1964[8]). The geometrical situation in the surface is illustrated in Fig. 1 of Smith *et al.*[5] It may be that consideration of the surface topology around emergent stacking faults can add to knowledge of the reasons for the different behavior of various substrates in growth processes.

It is not justified to suggest that the absence of dislocation spirals in the small image shown as Fig. 5 suggests a growth mechanism which does not involve dislocations; a field-ion tip and the deposit which was observed to develop contain a multitude of the kink sites required for nucleation. Furthermore dislocations might emerge in the areas of the specimen which did not contribute to the image. Dr. G. D. W. Smith of this laboratory has pointed out that the occurrence of only two "spikes" around the tetrad axis of the specimen casts doubt on the crystallographic nature of the build up.

Some Properties of Electroless Cobalt

Allen S. Frieze, Richard Sard, and Rolf Weil
(pp. 586-591, Vol. 115, No. 6)

P. Cavallotti and **G. Salvago**[9]: Interesting information is supplied by Messrs. Frieze, Sard, and Weil on the nucleation and growth of chemically deposited cobalt. The explanation given of their results in terms of growth inhibition by codeposited phosphorus is, however, in contrast with some experimental results obtained in the course of the systematic research work carried out in this Laboratory on the chemical plating

[2] Metallurgy Department, University of Oxford, Parks Road, Oxford, England.
[3] D. W. Pashley, *Rept. Prog. Phys.*, 28, 291 (1965).
[4] S. Ranganathan, *J. Appl. Phys.*, 37, 4346 (1966).
[5] D. A. Smith, M. A. Fortes, A. Kelly, and B. Ralph, *Phil. Mag.*, 17, 1065 (1968).
[6] D. G. Brandon and A. J. Perry, *Phil. Mag.*, 16, 119 (1967).
[7] R. C. Sanwald and J. J. Hren, *Surf. Sci.*, 9, 257 (1968).
[8] A. H. Cottrell, Theory of Crystal Dislocations, Blackie (1964).
[9] Institute of Electrochemistry, Physical Chemistry and Metallurgy, Milan Polytechnic, Milan, Italy, Laboratorio del gruppo di ricerca "Elettroliti e processi elettrochimici" del C.N.R.

of nickel and cobalt. As a matter of fact, x-ray and electron diffraction patterns of the chemical deposits obtained in different conditions showed different preferred orientations corresponding to the most densely packed planes parallel to the base: <0001>, <10$\bar{1}$0> and <11$\bar{2}$0>.[10]

Further experiments were carried out varying the parameters of a bath assumed as standard, of the following composition

$$[CoSO_4] = 0.3 \text{ m/l}$$

$$[NaH_2PO_2] = 0.6 \text{ m/l}$$

$$[C_6H_6O_7^{2-}]/[Co^{2+}] = 1$$

$$[NH_4^+]/[Co^{2+}] = 2$$

$$[NH_2CH_2COOH]/[Co^{2+}] = 1$$

pH = 10.5 adjusted with NaOH.

The deposition usually was carried out at 80°C, on copper specimens chemically plated with acid nickel baths containing $[NiCl_2]$ = 0.15 m/l; $[CH_3CHOHCOOH]$ = 0.5 m/l; $[NaH_2PO_2]$ = 0.3 m/l, at pH = 3.5 and 90°C. Therefore the deposition occurred on a nickel-phosphorus alloy of very high phosphorus content, which could be considered an "amorphous" substrate.[11]

All our deposits were examined to determine possible preferred orientations by taking electron reflection diffraction patterns, as well as by x-ray diffraction, with the method of Clark and Simonsen, mentioned by Frieze, Sard, and Weil, or with a North American Philips Geiger counter x-ray spectrometer.

Results obtained by the three techniques were in agreement; except that the <0001> fiber texture was more markedly observed by x-ray diffraction techniques in the deposits of low phosphorus content.

Deposits from the standard bath showed a strong <10$\bar{1}$0> fiber texture. Varying the operating conditions, by lowering $[NaH_2PO_2]$ to 0.225 m/l or increasing the pH up to incipient precipitation of basic salts or hydroxides in the solution (corresponding to a pH value of about 11.5 at room temperature), we noticed a <0001> fiber texture perpendicular to the base, as we did when the thickness of the deposit was 10μ.

At variance with the results of Frieze, Sard, and Weil a strong <11$\bar{2}$0> preferred orientation was observed varying four different operating conditions:

1. Increasing $[NaH_2PO_2]$ up to 1.5 m/l;
2. Using solutions not containing ammonium ions;
3. Increasing the molar ratio $[C_6H_6O_7^{2-}]/[Co^{2+}]$ up to 2.4;
4. Decreasing the pH value to 8.

Figure 1 shows the electron diffraction patterns obtained from deposits in the above mentioned conditions with <10$\bar{1}$0>, <0001> and <11$\bar{2}$0> fiber axes.

According to the theory followed by Frieze, Sard, and Weil the <11$\bar{2}$0> fiber axis corresponds to the least inhibited outgrowth. If the growth inhibition was to be attributed to codeposited phosphorus, as in those authors' opinion, the occurrence of a <11$\bar{2}$0> fiber axis would correspond to a decrease of the phosphorus content in the deposit. This is not, however, the case, because for deposition at increased $[NaH_2PO_2]$, which lead to the development of a strong <11$\bar{2}$0> preferred orientation, the phosphorus content obviously increased from about 4%, in the deposits from the standard bath with <10$\bar{1}$0> fiber axis, to about 5%. Moreover, the deposits with <11$\bar{2}$0> preferred orientation had different phosphorus content depending on the conditions under which they were obtained.

So, when we increased $[NaH_2PO_2]$ the phosphorus content increased too, as already noted, but deposits

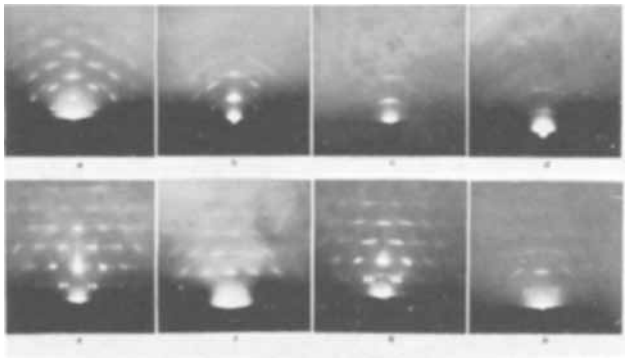

Fig. 1. Electron reflection diffraction patterns of chemical cobalt deposits. Bath conditions: a—$[CoSO_4]$ = 0.3 m/l; $[NaH_2PO_2]$ = 0.6 m/l; $[C_6H_6O_7^{2-}]/[Co^{2+}]$ = 1; $[NH_4^+]/[Co^{2+}]$ = 2; $[NH_2CH_2COOH]/[Co^{2+}]$ = 1; pH = 10.5 adjusted with NaOH; T = 80°C, deposit thickness, 50 μ; b, *idem* a, except pH = 11.7 adjusted with NaOH, deposit thickness: 3μ; c, *idem* b, deposit thickness: 30μ; d, *idem* a, except $[NaH_2PO_2]$ = 0.225 m/l, deposit thickness: 10μ; e, *idem* a, except $[NaH_2PO_2]$ = 1.5 m/l, deposit thickness: 30μ; f, *idem* a, except no ammonium ions in the solution, deposit thickness, 30μ; g, *idem* a, except $[C_6H_6O_7^{2-}]/[Co^{2+}]$ = 2.4, deposit thickness: 10μ; h, *idem* a, except pH = 8 adjusted with NaOH, deposit thickness: 10μ.

from solutions not containing ammonium ions showed nearly the same phosphorus content as in the deposits obtained from the standard solution, and deposits from bath at pH 8 showed a decreased phosphorus content of about 3.5%. An increase in the phosphorus content to about 5% was also observed for deposition from baths at a molar ratio $[C_6H_6O_7^{2-}]/[Co^{2+}]$ value of 2.4. Examining the phosphorus content in the deposits with <0001> fiber axes, a more striking evidence arises of the consequential character of obtaining of the preferred orientations in the deposits on the plating conditions; the phosphorus content does not appear as the cause of the development of preferred orientations but rather as a consequence of the operating conditions. In fact, while the deposits from baths of low $[NaH_2PO_2]$ = 0.225 m/l contain about 2% of phosphorus, the deposits obtained in severe conditions of precipitation at very high pH, with the same <0001> fiber texture of the preceding deposit, contain about 5% of phosphorus, conditions in which the inhibition would be severe according to the above mentioned authors, who affirm that "the {0001} plane should tend to be perpendicular to the surface." Considering the chemical deposition of nickel, it has been shown that only a <111> fiber texture could be observed in most deposits with phosphorus content up to 7%.[12]

According to the theory of Reddy, as reported by Frieze, Sard, and Weil, the {111} plane should tend to be perpendicular to the surface when growth is inhibited. This is in sharp contrast with the experimental evidence, which shows a more marked lamellar structure (*i.e.*, lateral growth according to Reddy) when the phosphorus content increases.

In the case of cobalt chemical deposition a similar tendency toward a more lamellar structure is shown when $[NaH_2PO_2]$ in the solution is increased, and consequently the phosphorus content in the deposits increases; the preferred orientation, however, changes from <0001>, through <10$\bar{1}$0> to a <11$\bar{2}$0> fiber axis. This sequence of preferred orientation is at variance with the explanation given by Frieze, Sard, and Weil. Moreover, Gutzeit[11] attributed the lamellar structure to periodic variations of the phosphorus content in the coating. This would lead, increasing the phosphorus content in the deposited cobalt, to a disorientation of the deposit, as a consequence of the different preferred orientations depending on the amount of

[10] L. Cadorna, P. Cavallotti, and G. Salvago, *Electrochim. Metallorum*, 1, 177 (1966).
[11] G. Gutzeit, *Plating*, 46, 1158 (1959).
[12] A. H. Graham, R. W. Lindsay, and H. J. Read, *This Journal*, 112, 401 (1965); L. Cadorna and P. Cavallotti, *Electrochim. Metallorum*, 1, 93 (1966).

phosphorus codeposited, variable in each lamella. The very strong <11$\bar{2}$0> fiber axis obtained at higher [NaH_2PO_2] is at variance with this conclusion. According to the theory proposed by Reddy[13] to explain the different preferred orientations obtained in the electrodeposition of nickel, the coverage of different faces with adsorbed hydrogen atoms on the cathode is a decisive factor in the development of a preferred orientation. Trying to explain the experimental results by assuming the adsorbed atomic hydrogen as a growth inhibitor, we would observe only the most inhibited fiber textures because of the very high hydrogen concentration on the surface, since a marked hydrogen evolution was always observed in the chemical plating of nickel and cobalt. This, however, is contradicted by the obtainment of several preferred orientations, among which also the <0001> and <11$\bar{2}$0> fiber texture for chemical deposits of cobalt, corresponding to the less inhibited lateral and outgrowth according to Reddy, as well as the <111> fiber texture for chemical deposits of nickel. Also the sequence <0001>, <10$\bar{1}$0>, <11$\bar{2}$0> of fiber textures, which was observed when increasing [NaH_2PO_2] in the cobalt solutions for chemical plating, with consequent increase of hydrogen evolution, cannot be explained by this theory.

Frieze, Sard, and Weil have also underlined the similarity between the microstructures of chemical and electrodeposited cobalt with <10$\bar{1}$0> fiber axes. An analogous relationship is valid between electrodeposits and some chemical deposits with <11$\bar{2}$0> fiber axes, *viz.*, from baths without ammonia or at low *p*H. When [NaH_2PO_2] or [$C_6H_6O_7^{2-}$]/[Co^{2+}] are increased to a high value with corresponding development of a <11$\bar{2}$0> fiber axis, the coating shows a mamelonar structure, typical of deposits containing inclusions. It may be concluded that phosphorus affects the morphology and the grain size of the deposits, without inhibiting the formation of a crystalline structure in the case of cobalt deposits.

Deposits with <0001> fiber axes were observed at low [NaH_2PO_2] and high *p*H, *i.e.*, in a range of possible inhibition conditions, with a decrease of the deposition rate. These conditions can be related to a too great stabilization of the hydrated and hydrolyzed cobalt ions in the layer adjoining the surface, on which the reaction occurs.

Deposits with <0001> fiber axes were also obtained in our laboratory by electrodeposition.[14] In this case the <0001> fiber texture is favored by high temperature, high c.d., and eventual presence of surface-active substances. This is substantially in agreement with the results of several authors.[15] The addition of boric acid has a negative influence on the development of this preferred orientation; *e.g.*, from a bath containing [$CoSO_4$] = 1 m/l, at *p*H = 5.5, T = 80°C, c.d. = 1500 amp/m^2, the deposits presented strong <0001> fiber axis.

As in the preceding case, the <0001> preferred orientation can be related to the formation of highly stabilized hydrolyzed species at the cathode. A certain relationship between the microstructures of chemical and electrodeposited coatings with the same preferred orientation can be observed. These results are at variance with the theory of Reddy, which is followed by Sard, Schwartz, and Weil,[16] because, in the given conditions, corresponding to inhibition by hydroxides or basic salts, the less inhibited lateral growth according to Reddy can be observed. If one attributes the inhibition to the hydrogen atom coverage of the surface, the already mentioned objection arises on the possibility of obtaining this preferred orientation in the chemical plating, when the surface coverage by hydrogen atoms is always very high.

The microhardness of the deposits with <0001> fiber axes presented a characteristic behavior for indentation on the cross section: the hardness changed with direction and was greater for indentation parallel to the base (300 HV for electrodeposits, 260 for chemical deposits from baths at low [NaH_2PO_2], while in the perpendicular direction it was 250 for electrodeposits and 230 for the corresponding chemical ones).

Deposits with <11$\bar{2}$0> and <10$\bar{1}$0> fiber axes behaved in the opposite way: indentation parallel to the base was 350 HV from the standard bath, 200 HV from baths without ammonia, 450 HV from baths with high [NaH_2PO_2], while in the perpendicular direction it was 400 HV, 270 HV and the same of that in the parallel direction for baths at high [NaH_2PO_2]. This behavior is in agreement with the crystallographic structure and with the results of the micrographs of the surface and of the cross section of the deposits.

In our last paper on chemical plating of nickel and cobalt by reduction with hypophosphite,[17] we examined the characteristics of the process and evidenced the importance of hydrolysis phenomena in the process. The reactions, by which nickel or cobalt are reduced, involves hydrolyzed species, but with hydroxyl ions not too tightly bonded to the nickel or cobalt ion, and the possibility of bridged intermediates.

The importance of the hydrolysis phenomena cannot be misunderstood taking into account the interpretative scheme of the obtainment of the different preferred orientation. In fact, to obtain a determinate preferred orientation we must consider the possible influence of the substrate and of the particular bath conditions, at which the reactions occur at the surface. We have deposited cobalt on a surface of "amorphous" chemical nickel of high phosphorus content,[11] searching to eliminate the first effect. Examining the conditions at which deposits with <11$\bar{2}$0> fiber axes obtained: low *p*H, high [NaH_2PO_2], high relative citrate concentration, no ammonia in the solution, it appears that all these conditions can be related to a decreased interaction of the hydrolyzed species with the surface, caused either by an increase in the concentration of the concurrent hypophosphite, or, when the *p*H or the complexing agents in the solution are decreased, by a decrease in the concentration of the hydrolyzed species, or else by a decrease of their degree of reactivity in respect to the considered reduction reactions. It is not possible to extend the consideration on the chemical plating to the electrodeposition without taking into account the differences between the two processes. The intervention of the hydrolyzed species on the anodic dissolution as well as on the cathodic deposition of the iron-group metals has been outlined in a number of papers (*e.g.*, [18]). This influence can also be acknowledged, when considering the modes of electrocrystallization of cobalt. As a matter of fact, by increasing the c.d. some influence may be observed toward changing the preferred orientation from <11$\bar{2}$0> to <10$\bar{1}$0>. The influence of increasing chloroanions concentration is the opposite.[16] The influence of the *p*H is complicated by the possible formation of cubic cobalt, which favors the <110> + <11.0> fiber axes.[14]

By obtaining a <11$\bar{2}$0> fiber axis, rather than a <10$\bar{1}$0> fiber texture, the substitution of the hydroxyl ions in the coordination sphere of the metal ions by

[13] A. K. N. Reddy, *J. Electroanalyt. Chem.*, 6, 141 (1963).
[14] L. Cadorna and P. Cavallotti, *Electrochim. Metallorum*, 1, 364 (1966).
[15] N. A. Pangarov and S. Rashkov, *Comp. Rend Acad. Bulg. Sci.*, 13, 555 (1960); R. Breckpot, *Anal. Real Soc. Espan Fix. Quim (Madrid)*, Ser. **B61**, 517 (1965); N. A. Pangarov and S. D. Vitkova, *Electrochim. Acta*, 11, 1733 (1966); K. E. Heusler and R. Knodler, *Ber. Bunsenges. Phys. Chem.*, 71, 1085 (1967).
[16] R. Sard, C. D. Schwartz, and R. Weil, *This Journal*, 113, 424 (1966).
[17] P. Cavallotti and G. Salvago, *Electrochim. Metallorum*, 3, 239 (1968).
[18] K. E. Heusler, *Ber. Bunsenges. Phys. Chem.*, 62, 582 (1958); 66, 177 (1962); 71, 620 (1967); K. E. Heusler and L. Gaiser, *Electrochim. Acta*, 13, 59 (1968); R. Piontelli, B. Rivolta, B. Mazza, and F. Magnoni, *Ist Lomb. (Rend. Sc.)*, A97, 282 (1963); R. Piontelli, B. Rivolta, M. Lazzari, and A. La Vecchia, *ibid.*, A98, 372 (1964); H. Dahms, *J. Electronal. Chem.*, 8, 5 (1964); H. Dahms and I. M. Croll, *This Journal*, 112, 771 (1965).

chlorides, and more precisely in the hydrolyzed layer adjoining the surface, may be considered. By increasing the concentration of the hydrolyzed species in this layer, the preferred orientation of the deposit would change to the $<10\bar{1}0>$ fiber axis and to the $<0001>$ in the most pronounced conditions, where hydroxides or basic salts begin to precipitate. This suggestion, although still lacking decisive experimental evidence, allows one to explain and predict several results, while by "using the concepts of free and inhibited outgrowth" this "was not possible."

A. S. Frieze, R. Weil, and **R. Sard:** We fail to see where our experimental results are "at variance" with those of Cavallotti and Salvago, when the fact is considered that their bath compositions, plating conditions, and deposit thicknesses were considerably different from ours. We did not observe the $<11\bar{2}0>$ fiber axis because the conditions under which it occurs were not investigated.

Cavallotti and Salvago seem to feel that, because the $<11\bar{2}0>$ fiber axis was observed in deposits with higher phosphorus contents than those where $<10\bar{1}0>$ was found, the whole concept of free and inhibited growth is negated. We disagree with this conclusion. Deposits with both fiber axes have the most densely packed plane perpendicular to the surface. The difference between the axes is that the $<11\bar{2}0>$ direction is more closely packed. As the plane is the governing factor, there is, therefore, not a significant difference in the degree of inhibition between the deposits with the two fiber axes. The work of Pangarov and Vitkova[19] illustrates this fact. The phosphorus contents reported by Cavallotti and Salvago is probably the average over the entire thickness. It is conceivable that in deposits as thick as those used by them, the phosphorus content near the surface where the electrodiffraction patterns were taken was considerably different from the average. Therefore, it is necessary to show that the phosphorus content in the surface layer, where the $<11\bar{2}0>$ fiber axis was determined, was higher than where the grains have the $<10\bar{1}0>$ preferred orientation.

The statement "it may be concluded that phosphorus affects the morphology and the grain size of the deposits, without inhibiting the formation of a crystalline structure in the case of cobalt deposits," appears to be a contradiction. Also, Cavallotti and Salvago appear not to have performed the necessary experiments to determine grain size, which obviously[20] cannot be done by optical microscopy.

We also disagree that a lamellar structure constituted lateral growth. Earlier work[21] has shown that lamellar structures consist of alternating layers of columnar and more equiaxed crystallites. A columnar structure is outgrowth.

Cavallotti and Salvago criticized the lateral and outgrowth concepts, claiming that they do not predict the results. The theory put forth by them is also a phenomenological one and gives no reason why certain plating variables should produce a certain order of crystallographic orientations. Their interpretation follows from a different point of view, namely, that of chemists, while ours is that of physical metallurgists. The argument that hydrolysis at the surface accounts for all observations is far from compelling. It appears that the chemical and metallurgical approaches must be reconciled if a satisfactory understanding of electroless deposits is to be reached.

[19] N. A. Pangarov and S. D. Vitkova, *Electrochim. Acta*, 11, 1733 (1966).
[20] R. Weil and H. C. Cook, *This Journal*, 109, 295 (1962).
[21] R. Weil and W. N. Jacobus, *Plating*, 53, 102 (1966).

Charge-Transfer Complexes and Electrochemical Cells—Coal Batteries

R. A. Friedel
(pp. 614-615, Vol. 115, No. 6)

F. Gutmann,[22] A. M. Hermann,[23] and A. Rembaum[24]: With reference to the recent paper by R. A. Friedel, we wish to offer the following comment.

Dr. Friedel maintains that the operation of the solid-state primary cells based on charge transfer complexes reported by us[25,26] is based on the presence of liquid water which acts as a reactant and not merely as a catalyst. He substantiates this by experiments using Mg anodes.

We wish to point out that his experiments, as well as his conclusion regarding the presence of water, agree with our own work as long as magnesium anodes are employed. A parasitic corrosion reaction between Mg and I_2 which occurs without drawing current causes the poisoning of the Mg surface with insulating MgI_2 and thus stops the reaction unless sufficient water is present to dissolve it. The presence of water, of course, then causes the evolution of gaseous hydrogen, as reported by Dr. Friedel.

However, we have already pointed out[26] that water as such is by no means essential, even using Mg anodes, and have shown that a number of nonaqueous, organic liquids, serve at least equally well. Moreover, later, so far unpublished experiments using Ag anodes in place of the Mg, support our above contention that the presence of water is associated with a parasitic reaction of the Mg: primary cells were prepared and assembled in a dry box under dry argon, using a 1:2 phenothiazine:iodine complex, and Ag anodes. Some of these were then assembled in nickel formers, spot-welded together, and potted in epoxy while still in the dry box. A further coat of epoxy was then applied immediately after removal from the dry box. These cells gave open-circuit voltages of 0.65-0.68v and short circuit currents of the order of 100 $\mu a/cm^2$, so far for about 4 weeks after preparation.

Other cells were assembled in a Teflon insulated C-clamp and then sealed, still in the dry box, in a glass jar containing P_2O_5. These cells gave the same voltage and a short circuit current density of about 8 ma/cm^2 and thus far have lasted for several weeks under the above conditions. The higher current densities are probably due to a better mechanical contact between the cell components; in the case of the Ni-formers it is very difficult to maintain sufficient positive pressure to ensure uniform contact over the entire electrode area.

Still other cells prepared under like dry conditions, using a highly iodinated ionene[27] complex salt behaved likewise: no significant current with Mg anodes, and 0.8 ma/cm^2 sealed over P_2O_5 thus far for several days.

As to the merits of containing the iodine in the form of a charge transfer complex rather than in its elemental form, it might be apposite to point out that the current obtainable from a cell is determined *inter alia* by the cell's effective internal series resistance. Room temperature resistivity of commercial, chemically pure, iodine is usually about 10^5 to 10^6 ohm-cm; zone refined iodine has a resistivity[28] of 1.3 x 10^9 ohm-cm, while, *e.g.*, the phenothiazine:iodine complex has a resistivity of 3-10 ohm-cm at room temperature. The resulting improvement by 5 to 6 orders of magnitude

[22] Institute for Direct Energy Conversion, University of Pennsylvania, Philadelphia, Pa.
[23] Tulane University, New Orleans, La.
[24] Jet Propulsion Laboratory, California Institute of Technology, Pasadena, Calif.
[25] F. Gutmann, A. Hermann, and A. Rembaum, *This Journal*, 114, 323 (1967).
[26] F. Gutmann, A. Hermann, and A. Rembaum, *This Journal*, 115, 359 (1968).
[27] A. Rembaum, W. Baumgartner, and A. Eisenberg, *J. Polymer Sci.*, B6, 159 (1968).
[28] E.G., "Handbook of Physics and Chemistry," 48th ed., p. F-132, Chemical Rubber Co., Cleveland (1967-1968).

in the ohmic series resistance of the cell caused by storing the iodine in the form of a charge transfer complex, is thus by no means negligible.

R. A. Friedel: With reference to the discussion by Gutmann *et al.* I wish to offer the following comment:

The above discussion principally concerns new work and work that had not been published at the time of my paper. I wish to congratulate the authors on the development of their new Ag-anode charge-transfer battery that operates without any trace of water or other high permittivity solvents.

There is only one point that perhaps needs clarification, the degree of importance of having a charge-transfer complex as the source of iodine. In the above discussion Gutmann *et al.* state that the storing of iodine in the form of a charge-transfer complex is important because the effective internal resistance of a cell is thereby lowered to a practicable range of values. But the preparation of complexes by mechanical grinding was reported in the original paper to be as good as a chemically prepared complex.[25] The two "complexes', must differ greatly; it seems questionable, therefore, whether a *bona fide* charge-transfer complex is vitally important. Perhaps the new battery with Ag anode requires a true, chemically prepared complex. In any case the batteries with Mg anodes apparently attain low resistance values in the first few moments of operation, for the uptake of water or solvent vapors and the production of MgI_2 and probably other compounds must lower drastically the internal resistance of chemically pure iodine and thus reduce the importance of having a charge-transfer complex.

We are indebted to Gutmann, Hermann, and Rembaum for their discovery of these batteries which led to our use of coals as battery components. Work on coal-iodine batteries will continue; water will be involved as it is a constituent of all coals. Work will be carried out also on anthracite batteries; pieces of some anthracites as the cathode, with a magnesium anode, produce open-circuit voltages under one volt and short-circuit current densities in the range of 100 $\mu a/cm^2$.

The Direct Observation of Barrier Layers in Porous Anodic Oxide Films

G. C. Wood, J. P. O'Sullivan, and B. Vaszko
(pp. 618-620, Vol. 115, No. 6)

A. La Vecchia,[29] **G. Piazzesi,**[30] **F. Siniscalco**[29]: The beautiful electron micrographs of the anodic oxide cross section presented by the authors improve our knowledge about oxide morphology and restrict the very subtle discussions grown up on this subject to a sound model supported by the most complete evidence.

Regarding Fig. 1, we observe that the lack of details in the cell section does not allow one to discover fine structure such as those observed by other experimenters[31] and ourselves.[32]

We systematically found a sort of graininess on cell surface, both from the Al and the oxide side, working with different replica techniques such as two-stage cellulose acetate-carbon or direct carbon replicas. Even with the purest single crystal samples such irregularities were discovered, and this fact led us to think of a probable subpore mechanism of ion transfer in the barrier layer. Instead of considering the barrier layer as a bulk homogeneous material, one may imagine a further subpore structure consisting of microchannels spreading radially from the pore bottom toward the cell surface. Those channels may not be considered as ordinary pervious channels, but

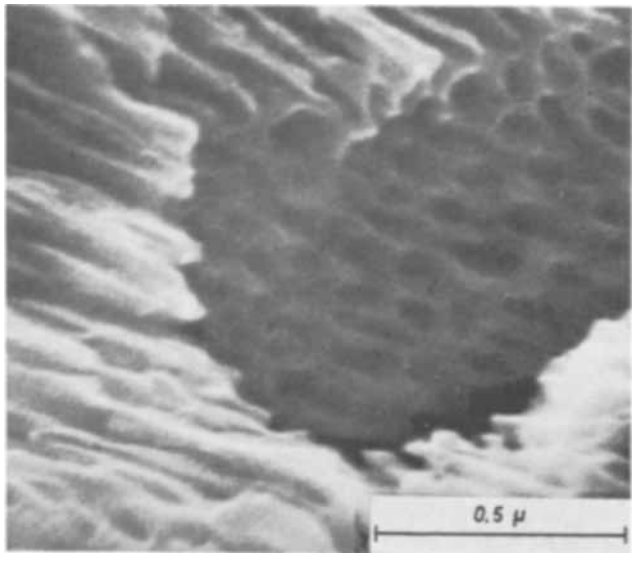

Fig. 1. Electron scanning micrograph of a fracture surface

rather as easy paths of peculiar structure, such as chains of more hydrated nearly amorphous alumina, in which charge carriers flow preferentially. So we arrive to a sort of Murphy-type mechanism confined in the barrier layer. A more detailed observation of the layer morphology will give useful contribution to support or to disregard this hypothesis.

Observing oxide microfractographs we found that pore channels grow up approximately perpendicular to the mean metal surface, but with a memory of the previous metal crystal structure and orientation; very often the fracture surface does not contain pore axes but is slightly tilted giving a low angle section of pore channels. For this reason we could not make extensive observations along single pore sections that appeared limited in length, such as those shown by the authors in Fig. 3.

An Electron Scanning Microscope Stereoscan II[33] enabled us to remove doubts: there was no artifact introduced by the replica technique and fracture surfaces appeared highly irregular and not everywhere parallel to pore axes such as shown in Fig. 1. For this reason, we would ask the authors if they used a particular technique to obtain fracture surfaces or if they have further experimental evidence supporting the proposed mechanism for redistribution of pores and cells during transient assessment of the barrier layer after having changed the external electrical conditions.

Transient electrical response constitutes another important source of information about the oxide formation processes, although in our experience such results must be handled with great care. We performed several tests on samples of various purity (from commercial grade to 99.9995% Al single crystals) anodized in sulfamic acid baths (7.5% Hσ) at different temperatures, and we noted the essential influence on such behavior of the actual time-gradient of the imposed electrical variable and of the stirring of the bath. The electrical transient behavior of our layers was rather complicated, and we could observe three essential stages: a very rapid departure from the stationary value of one of the electrical parameters depending on the time-gradient imposed to the other; the layer behaves as a condenser with a large apparent capacity, the major contribution to which may be ascribed to the electrical space charge build up by protons. The second stage consists in a slower subsequent recovery toward the stationary values, mainly due to thermal and diffusional phenomena and strongly

[29] Istituto di Chimica Fisica, Elettrochimica e Metallurgia del Politecnico di Milano, Italy.
[30] Centro di Microscopia Elettronica del Politecnico di Milano, Italy.
[31] M. Paganelli, *Alluminio*, 27, 3 (1958).
[32] A. La Vecchia, G. Piazzesi, and F. Siniscalco, *Electrochim. Metall.*, 2, 71 (1967).
[33] Observations at the Electron Scanning Microscope were performed with the kind collaboration of Cambridge Scientific Instruments Ltd., England.

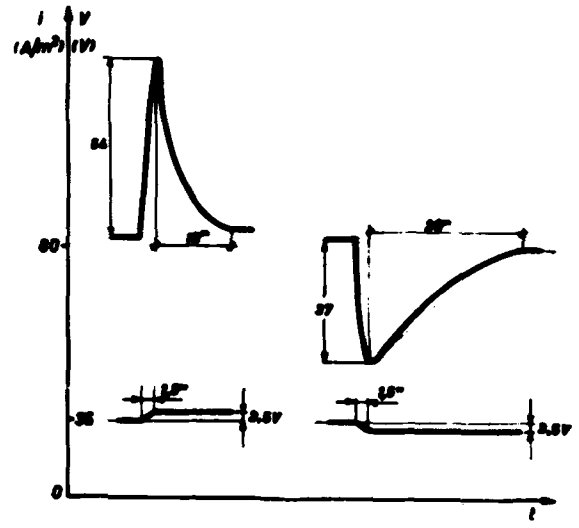

Fig. 2. Current transient response to a linear voltage variation

influenced by the amount of stirring or by the rate at which fresh solution can be supplied at the anode. Finally, depending on the magnitude of the impressed variation, there may be a slow drift toward final values of the observed electrical parameter determined by the actual value at which the other electrical variable is constrained. In this stage we recognize a plausible change in the oxide geometrical structure to fit the imposed electrical conditions. We studied systematically the effects of small linear variations around steady-state values, acting with an anodization cell already described.[34] An example of recorded curves is shown in Fig. 2. Detailed description, results and discussion will be given in a later paper.

Observing the curves reported by the authors in Fig. 2, we wonder, because we never found that behavior, that, after a voltage change, current always increases reaching the steady value.

This fact seems to us very interesting; unfortunately, more information about the experimental conditions is needed to evaluate the importance of such results, and we also would ask to the authors if they have formulated some thermodynamical interpretation. Clearly, in both cases the system is evolving, through a transient structure, toward a more organized state showing an increase in energy dissipation.

A tentative explanation, based on the theory of the local potential of Prigogine and Glansdorff[35] in analogy with the work done for other organized structures such as the cell pattern arising in the Bénard convection, will be of remarkable interest.

G. C. Wood, J. P. O'Sullivan, and **B. Vaszko:** We thank the authors of the discussion for their kind remarks on our electron micrographs and for their interesting comments.

The lack of "graininess" in oxide sections shown in our paper was reproducible throughout the experiments described and also in subsequent extensive work. Replicas taken from the metal after removal of the oxide film, as well as those from the cell bases themselves, showed even less structure, apart from the cell arrangement itself. It is our experience that simple scanning electron micrographs add little information in this area although it is conceivable that careful experimentation, *e.g.*, special precautions to avoid "charging up" of the specimen in the electron beam, might improve the situation. It should be noted that to draw conclusions concerning the chemical or electrical nature of the barrier oxide from electron microscopical data alone is not advisable, without reference to other techniques. Without necessarily denying the existence of hydrogen bonding, anion incorporation, proton space charges, etc., in anodic films we consider that their use in explaining the development of pores, etc., has been overemphasized. Our results support a very simple model which we intend to publish shortly.

Concerning the nature of the fracture surfaces, the observation that fracture often occurs at an angle to the direction of pore growth is in line with our experience, although occasionally the two planes correspond. No special technique was used to achieve this.

Our transient electrical measurements are different from those by the discussors, our changes being much greater. Thus the system is removed much further from equilibrium in our case. Generally, we find that the changes observed were much less reproducible at smaller values of the change in the applied voltage. We have formulated an explanation showing the importance of the general film structure prior to the voltage change in determining the nature of the electrical fluctuations observed. This explanation does not involve thermodynamics directly.

[34] A. La Vecchia, G. Piazzesi, and F. Siniscalco, *Electrochim. Metall.*, 3, 71 (1968).

[35] R. J. Donnelly, R. Herman, and I. Prigogine, Editors, "Non-equilibrium Thermodynamics, Variational Techniques and Stability," University of Chicago Press, Chicago (1965).

Analysis of the Uhlig Defect Model of Oxidation Kinetics

A. T. Fromhold, Jr.
(pp. 882-890, Vol. 115, No. 9)

Dennis B. Matthews[36]: The recent paper by Fromhold in this journal analyzes the kinetics of electron tunneling processes in a way which fails to take into account several factors which significantly affect the conclusions reached.

It is fundamental that the rate of a reaction is controlled by the activation energy rather than the energy change accompanying the reaction, but it is not obvious that under certain circumstances the two may be equal. Such a situation can occur when the reaction involves electron tunneling. The word "involves" is important because, in general, the actual tunneling process is preceded by an activation process, wherein the electron in its ground state absorbs energy which raises the electron to some excited energy level. The need for such an activation process is brought about by the fact that the electron in its ground state is not always in a state conducive to tunneling owing to the absence of empty acceptor states at the same energy level. To undergo a radiationless transition the electron often has to undergo thermal excitation. For an electron in a metal this thermal excitation is described by the Fermi distribution function. The mechanism under discussion is best described as "thermally excited electron tunneling." Such a mechanism cannot, within the framework of absolute rate theory, be divided into two steps, thermal excitation and tunneling, one of which becomes rate determining, just as one cannot divide other reactions into distinct steps comprising thermal excitation to the top of a barrier and electronic arrangement to form the product nuclei.

Utilizing the Uhlig model as given in Fig. 2(c) of Fromhold's paper it is seen that in order for electron transfer to occur the electron has to be thermally excited either to the level of the oxide conduction band (top of the barrier) or to the O^- energy level which then permits electron tunneling with nonzero probability to the O^- site. For thin films where the electron tunneling probability is high, the latter mechanism is more probable while for very thick films the former mechanism is the more probable. Naturally, for intermediate thicknesses both mechanisms will be operative, and in general the rate is proportional to $\int n(E) \cdot W(E) \cdot dE$ where $n(E)$ is the number of elec-

[36] Union Carbide Australia Ltd., Research and Development Laboratories, Marquet St., Rhodes, N. S. W., Australia.

[37] But *c.f.* below for a corrected version of this Uhlig model.

trons at the energy level E, $W(E)$ is the probability of electron tunneling at the energy level E, and integration is over all energy levels E. The possibility of an absence of O^- sites at the energy level E is accounted for by $W(E)$, which would then be zero. $W(E)$ is a function of oxide film thickness.

The concept of electron tunneling described above does not necessarily result in a fast electron transfer step (*i.e.*, nonrate determining) since the thermal activation term $n(E)$ still remains even if $W(E)=1$. Under conditions of easy electron tunneling the activation energy of the electron transfer step is given by footnote 37 Φ-A where Φ is the metal/oxide electronic work function and A is the electron affinity of oxygen at the oxide-oxygen interface.

Thus it is seen that there is a distinctive feature of electron transfer during oxide formation as compared to electron emission, namely, the availability of acceptor states, which introduces a thermal excitation term into the rate expression. The distinction is actually not so clear cut when one considers that, in order to measure the number of electrons emitted, we need a collector electrode biased with respect to the emitter electrode in such a way as to provide an electron sink for all the emitted electrons. In this sense then the adsorbed oxygen acts like an electron sink or as a collector of the emitted electrons.

Regarding the relative energies of the metal and O^- electron levels, one must take into account all energy terms. Thus if the reaction step under consideration is

$$O\ (ads.) + e^-\ (M) \rightarrow O^-\ (ads.) \qquad [1]$$

then the standard enthalpy change is given by

$$\Delta H_o = \Delta H_o\ (O^-\ ads.) - \Delta H_o\ (O\ ads.) + \Phi\text{-}A \qquad [2]$$

where ΔH (O^- ads.) and ΔH (O ads.) are the standard enthalpies of O^- and O adsorption, respectively. The electronic work function is potential dependent according to

$$\Phi = \Phi(V = 0) + V \qquad [3]$$

so that when the metal/oxide interface is positively charged with respect to the oxide-air interface then V is positive and $\Phi > \Phi(V = 0)$.

The energy change ΔH_o defines the differences in energy of the O^- and metal electron states. For the thermally excited electron tunneling mechanism the standard enthalpy of activation ΔH_o is equal to $\Delta H_o^{\neq}$ hence from Eq. [2] and [3]

$$\Delta H_o = \Delta H_o\ (O^-\ ads.) - \Delta H_o\ (O\ ads.) + \Phi \qquad [4]$$

$$= \Delta H_o^{\neq}\ (V = 0) + V \qquad [5]$$

and a linear dependence of log (rate) on potential, V, is predicted.

As a concluding remark, it is noted that if one allows for the thermal distribution of electrons in the metal, one should also allow for the thermal distribution of adsorbed oxygen states, *i.e.*, the oxide — O^- bond can have a Boltzmann distribution of vibrational-rotational energy levels. At first sight, for thin films this will lead to an approximately equal distribution of current between all energy levels extending from just above the Fermi level up to the O^- level.

A. T. Fromhold, Jr.: Dr. Matthews makes a statement in his opening paragraph which is entirely unsupported by the remainder of his discussion. The principal point of the discussion appears to be that rate processes limited by tunneling can have activation energies equal to the energy change accompanying reaction, a point that is made explicitly in the section "On the Possibility of Obtaining the Direct-Logarithmic Law" of the paper which he says does not consider this factor. That the tunneling process is not in actuality directly relevant to the Uhlig theory[38] is a fact which has apparently missed his attention also; no attempt is made in his discussion to explain the relevance of the equations to any theory of metal oxidation.

It should be pointed out that Eq. [3] underlying the derivation of the final result embodied in Eq. [5] in his discussion is valid only when the potential V is impressed over a barrier thickness so thin ($\simeq$ 50 or 100Å) that electron tunneling has a nonnegligible probability of occurring. In addition, a positively charged metal-oxide interface, such as mentioned by Dr. Matthews, clearly precludes electronic emission processes (including thermally-activated tunneling) from being rate limiting in thermal oxidation; instead, this would generally indicate that ionic transport is rate limiting. Furthermore, no attempt is made in his discussion to deduce the film thickness dependence of V, which is the critical step in ascertaining the resulting kinetics of thermal oxidation.

It thus appears that my recent paper serves as an opportunity for Dr. Matthews to present his views on the complexities of thermally activated tunneling whenever no single step is completely rate limiting. For an authoritative account of this matter, the reader is referred to the excellent article by Murphy and Good[39] entitled "Thermionic Emission, Field Emission, and the Transition Region", which is ref. (26) in the paper Dr. Matthews uses as a basis for his remarks.

[38] H. H. Uhlig, *Acta Met.*, 4, 541 (1956).

Effects of Oxidizable Anion Adsorption on the Anodic Behavior of Platinum

Sigmund Schuldiner

(pp. 767-771, Vol. 116, No. 6)

K. J. Vetter and **J. W. Schultze**[40]: Schuldiner's assumption that the retardation of hydrogen oxidation on platinum at potentials above 1v is due to adsorbed anions[41, 42] rather than to adsorbed oxygen atoms or platinum oxides is essentially based on the following experimental results and hypotheses: (*i*) The unstationary rate of the reaction of platinum oxide with dissolved hydrogen, measured on open circuit, is adequate to a current density of $0.4\text{-}8\cdot10^{-3}$ amp/cm^2.[43] During this reduction of the platinum oxide the coverage of PtO and the potential decrease, whereas the reaction rate remains constant.[43] From this Schuldiner concludes that this reaction is a potential independent reaction of zero (or first) order in the PtO-coverage.[42, 43] The reaction rate of the platinum oxide with formic acid is stated to be $5\cdot10^{-4}$ amp/cm^2.[41] (*ii*) The rate of the electrochemical formation of the oxide layer is assumed by Schuldiner to be equal to or less than the stationary measured current density of 10^{-7} to 10^{-6} amp/cm^2 in the absence of hydrogen (see Fig. 2, footnote[41] curve 1M H_2SO_4). Since the rate of the reaction of PtO with H_2 or HCOOH according to hypothesis (*i*) at potentials below 1.6v is much more rapid than the rate of the electrochemical formation of PtO as given by hypothesis (*ii*), Schuldiner concludes that significant amounts of oxygen cannot remain on the surface below 1.6v.[41]

Hypotheses (*i*) and (*ii*) are not compatible with other experimental results. As shown below, the chemical reaction

$$PtO + H_2 \rightarrow Pt + H_2O \qquad (I)$$

has to be subdivided into an anodic reaction

$$H_2 \rightarrow 2H^+ + 2e^- \qquad (Ia)$$

and a cathodic reaction of equal rate

$$PtO + 2H^+ + 2e^- \rightarrow Pt + H_2O \qquad (Ib)$$

The current densities of reactions (Ia) and (Ib) as a function of potential E and coverage θ are plotted in

[39] E. L. Murphy and R. H. Good, Jr., *Phys. Rev.*, 102, 1464 (1956).
[40] Institut fur Physikalische Chemie der Freien Universitaet Berlin, Berlin-Dahlem, Germany.
[41] S. Schuldiner, *This Journal*, 116, 767 (1969).
[42] S. Schuldiner, *This Journal*, 115, 362 (1968).
[43] T. B. Warner and S. Schuldiner, *This Journal*, 115, 28 (1968).

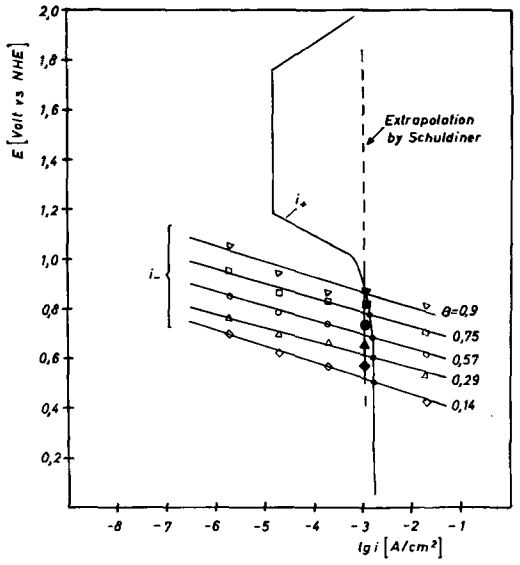

Fig. 1. i_+ anodic current density of reaction (Ia); i_- (open symbols) cathodic current density of reaction (Ib);[44] θ = coverage of PtO. Full symbols, experimental rate of over-all reaction (I) by Schuldiner and Warner.[43] Full circles, estimated values of the rate of over-all reaction (I) obtained from partial current densities i_+ and i_-.

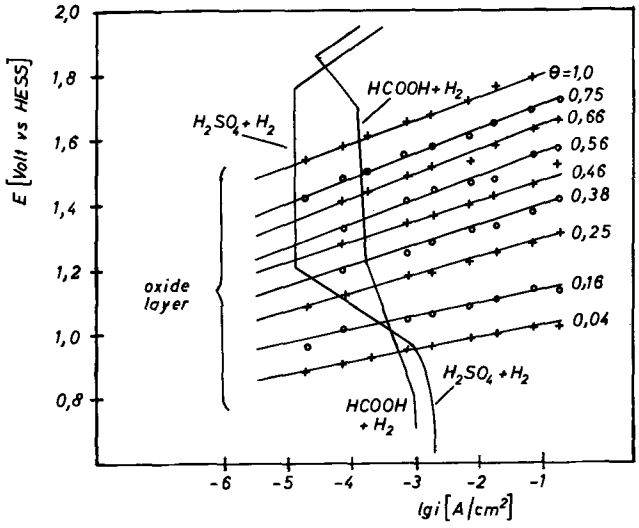

Fig. 2. Anodic current density of the oxide layer formation[44] and the current-potential curves of the systems $H_2SO_4 + H_2$ and HCOOH + H_2 (41, 42). θ = coverage of PtO. HESS = hydrogen electrode same solution.

Fig. 1. The anodic current density i_+ of reaction (Ia) is taken from Fig. 1 of Schuldiner's paper.[42] The cathodic current density i_- of the reaction (Ib) was determined by Vetter and Schultze[44] through galvanostatic pulse experiments as a function of θ, E, and pH. In Fig. 1 the current-potential curves are shown for different values of coverage of PtO at pH 0.3 (1N H_2SO_4). The experimental values of footnote[44] are given by the open symbols. From these measurements follows

$$i_- = k_- \cdot c_{H^+} \cdot \exp\left(a_-\theta - \frac{2.3\,E}{b_-}\right) \qquad [1]$$

with a_- = 13.8, b_- = 60 mv, k_- = constant, c_{H^+} = concentration of hydrogen ions. If reaction (I) is a combination of reactions (Ia) and (Ib), the rate of (I) on open circuit is given in Fig. 1 by the points of intersection of the curves of i_+ and of i_-. i_+ is independent of the potential in the range of 0.4v < E < 0.9v, whereas i_- is dependent on E and θ. It can be seen that the resulting rate given by the full circles in Fig. 1 is nearly constant and independent of E and θ because a drop in θ is compensated by a decreasing potential. This conclusion can be verified by the experimental results obtained by Schuldiner and Warner.[43] The mean value of the reaction rate is stated to be $1.2 \cdot 10^{-3}$ amp/cm^2,[42,43] Potential E related to this current density and coverage θ, stated in Fig. 1, are taken from Fig. 4 of the paper by Schuldiner and Warner.[43] These points are shown in Fig. 1 by full symbols. The agreement of the intersection points (dots) estimated from [42] and [44] and the experimental points (full, large symbols) taken from [43] is excellent. Hence, the reaction of PtO with H_2 is an electrochemical process combining (Ia) and (Ib). This conclusion is in agreement with conceptions of Breiter.[45] An extrapolation of the reaction rate constant in the range of 0.4v < E < 0.9v, to higher potentials E > 0.9v as shown by the dotted line of Fig. 1 is not allowed. The same conclusion may be valid for the reaction of PtO with formic acid; for this reaction Schuldiner does not give any experimental details.[41]

If chemical reaction (I) would take place besides the electrochemical oxidation of hydrogen, the reaction rate should be equal to or less than the current density of $1.5 \cdot 10^{-5}$ amp/cm^2 in the potential range 1.2v < E < 1.7v. In this case an equivalent current density is consumed to substitute the PtO which has been reduced by chemical reaction. To calculate the resulting coverage, the anodic current density of the oxide formation as a function of θ and E must be given. This was measured by Vetter and Schultze[44] and is shown in Fig. 2. The resulting equation is

$$i_+ = k_+ \cdot c_{OH^-} \cdot \exp\left(-a_+\theta + \frac{2.3\,E}{b_+}\right) \qquad [2]$$

In the case of pure chemical oxidation of the hydrogen, the coverage of PtO is determined by the intersection points of the current-potential curves of the oxide-layer formation and the current-potential curve of the system $H_2SO_4 + H_2$ measured by Schuldiner. The PtO-coverage is 0.4 for a potential of 1.2v, and 1 for 1.5v. These are minimum values for a pure chemical oxidation mechanism which is not proved. In the case of minor participation of the chemical reaction, the coverage values are higher, i.e. about 0.6 and > 1 for the pure electrochemical mechanism.

As for formic acid solutions with or without hydrogen, it can be seen from Fig. 2 that the minimum coverage of PtO is 0.36 at 1.2v and 1.0 at 1.6v provided that the chemical reaction of PtO with formic acid is rate determining. If not, even higher coverages of 0.6 and > 1 result.

These values of PtO coverages are sufficient to change the electrochemical and electronic[46] properties of the platinum surface and to cause the retardation of the hydrogen oxidation reaction.

[44] K. J. Vetter and J. W. Schultze, To be published; J. W. Schultze, Thesis. Freie Universitaet Berlin 1966.
[45] M. W. Breiter, *This Journal*, 109, 425 (1962).
[46] H. Shimizu, *Electrochim. Acta*, 13, 27 (1968).

Stress Generation during High-Temperature Oxidation

I. Oxygen Solution Effects[1]

R. E. Pawel* and J. J. Campbell

Metals and Ceramics Division, Oak Ridge National Laboratory, Oak Ridge, Tennessee

ABSTRACT

The flexure of thin rectangular specimens of tantalum and niobium oxidizing on one side at 800°C was measured at several oxygen pressures. In these experiments, the oxygen pressure and oxidation time were generally kept small enough to prevent excessive oxide formation, and the oxygen diffusion distances were of the same order as the specimen thickness. For both oxidation and annealing experiments, the observed flexure behavior under these conditions could be correlated with that predicted on the basis of changes in the oxygen concentration gradients in the specimen. The results have helped to establish further some of the important characteristics of stress generation due to the dissolution of oxygen into the surface layers of a metal during oxidation.

The influence of mechanical stresses during gaseous oxidation has been a subject of intuitive importance for some time. However, the measurement and characterization of these effects have only recently been attempted on a quantitative and systematic basis. Stress systems which arise as a consequence of the oxidation process itself have now been shown in several instances to be the primary trigger for dramatic kinetic and morphological responses. Events such as wrinkling, cracking, and spalling of comparatively thick oxide films on either a macro- or microscopic scale furnish the more obvious bases for several types of changes in reaction rates. However, especially in the thin-film stage of oxidation, stresses may act in less spectacular ways while still playing a large role in the determination of the reaction kinetics and mechanism. For example, studies of the first stages of gaseous oxidation of copper (1) and nickel (2, 3) emphasize the importance of structural defects in such films on the rate of oxidation. It follows that the existence of stresses within the films may in large measure determine the extent of such defects as well as their behavior during continuing film growth.

In systems where the solution of oxygen into the metal is an important factor during oxidation, it has been predicted (4, 5) and shown (6, 7) that large stresses (of the order of the yield stress) in the surface layers of the metal can arise from this source. There are several ways in which these stresses in the metal might be expected to affect the oxidation rate. Although few definitive experiments have been made, a clear example where the normal reaction sequence has been drastically changed by the presence of stress in the metal is furnished in the initial stages of the gaseous oxidation of tantalum at temperatures in the range of 350°-550°C, where platelets of oxide grow into the metal along certain crystallographic planes. The unusual morphology in this particular case is very probably a result of a shear or martensitic type of transformation (8, 9), a process which would take place more readily under the influence of the high biaxial stress which exists.

The refractory metals tantalum and niobium are cases where stresses due to both oxygen solution and film effects might be expected to arise. Our previous work with these metals has shown that in the temperature range 350°-550°C the stress system is initially dominated by oxygen solution effects which give way later in the process (after the "breakaway" increase in the oxidation rate) to film effects. We are continuing our investigation of the details of stress generation in these metals a higher temperatures where it appears more feasible to separate the two major stress sources by varying the oxygen pressure. The present paper presents data for oxidation at 800°C under conditions which emphasize oxygen solution effects and further establishes some of the important phenomena during the dissolution of a reactant into the surface layers of a solid.

Experimental Procedure

We have continued to use the flexure technique (6) to follow stress development during oxidation. In this method, the curvature exhibited by a thin rectangular specimen is measured as it oxidizes on one side only. Thus, if the dimensions and physical properties of the specimen are known, the elastic bending stresses which exist can be computed. While the measurement is basically a simple one, its accuracy depends critically on maintaining pure cylindrical elastic bending of the specimen, a condition requiring specimen uniformity and very close tolerances on dimensions.

The equipment and procedures for these basic measurements have been described in detail previously (6, 7). Tantalum and niobium coupons approximately 1 x 4 cm were cut from 0.020, 0.030, and 0.050 in. sheet and annealed in vacuum at 1600° and 1000°C, respectively.[2] They were carefully mechanically and electrolytically polished and furnished with a Nichrome support yoke to facilitate mounting in the oxidation apparatus. Finally, a thin layer of a protective material was deposited on one side of each specimen by vacuum evaporation. Aluminum proved to be effective for this purpose for oxidation temperatures up to 550°C; however, for experiments at 800°C, a 2 parts gold, 1 part aluminum alloy was used. The specimen was affixed to the support in the apparatus and brought to the oxidation temperature in vacuum. The oxygen pressure was then adjusted to the desired value by a controlled leak, and the flexure of the specimen followed as a function of time by measuring the deflection of a fiber "transducer" with a cathetometer. The amount of flexure exhibited by the specimen per unit of strain energy supplied by the oxidation reaction depends on the thickness of the specimen. Thus, some additional degree of control was available with respect to the sensitivity of the measurements as well as the ability to insure that the bending stresses remained within the elastic limit throughout most of the experiments. The maximum elastic bending stress was computed from the simple beam formula

$$\sigma_s = \pm \frac{Eh}{2\rho_x} \qquad [1]$$

* Electrochemical Society Active Member.

[1] Research sponsored by the U.S. Atomic Energy Commission under contract with the Union Carbide Corporation.

[2] Nominal analysis: 99.8-99.9 w/o with Ta, Nb, Fe, and W major metallic impurities; typical oxygen content after anneal was about 200 ppm.

where E is Young's modulus for the metal, h is the specimen thickness, and ρ_x is the radius of curvature of the specimen in its long dimension. It is recognized that the equation is an approximation which, for coupon-shaped specimens, generally yields slightly conservative bending stress values (6).

Results

It is important to remember that the flexure of the specimen is the mechanical result of a process that takes place on one side of the specimen. Thus, in order to be able to use bending stress values to determine the complete stress distribution in a quantitative fashion, it is necessary to establish either the mechanism of stress generation and/or the general shape of the stress-distance curve. If such information is not immediately available, it is possible to use the bending stress data themselves to point out or to evaluate the consistency of a given model.

In our present work, the flexure of tantalum and niobium specimens was followed during oxidation at 800°C at oxygen pressures from about 10 to 100μ. A few experiments were conducted at higher pressures in order to observe the influence of film stresses on the total strain behavior. Additionally, strain measurements made during annealing after short oxidation periods were useful in corroborating the oxidation model.

Method of analysis.—Previous work (10) has indicated that under the conditions of our experiments, the solution of oxygen into the metal would be expected to account for a significant fraction of the total oxygen consumed, at least during the first stages of the reaction. Thus, since an oxygen concentration gradient exists, a corresponding stress gradient will also exist.[3] The relation between the surface stress and the measured bending stress can then be determined by employing the conditions of mechanical equilibrium; that is, the sum of the forces and moments for the system must be equal to zero. The stress in the reaction layer is assumed to be a function of depth, x, and time, t, given by

$$\sigma_1(x, t) = K[C(x, t) - C_o] \quad [2]$$

where $C(x, t)$ is the oxygen concentration as a function of position and time, C_o is the residual oxygen concentration, and K is a proportionality constant, the form of which depends on the boundary conditions of the experiment. This stress, (σ_1), on one side of the specimen, will result in a set of bending stresses given by

$$\sigma_2(x, t) = \sigma_B + \left[\frac{2\sigma_s(t)}{h}\right]x \quad [3]$$

where σ_B is the component of bending stress at the reacting surface, $\sigma_s(t)$ is the measured maximum bending stress as a function of time from Eq. [1], and h is the specimen thickness. Thus, the equilibrium equations are

$$\int_o^h K[C(x, t) - C_o]dx + \int_o^h \left[\sigma_B + \left(\frac{2\sigma_s}{h}\right)x\right]dx = 0 \quad [4]$$

and

$$\int_o^h K[C(x, t) - C_o]x\,dx + \int_o^h \left[\sigma_B + \left(\frac{2\sigma_s}{h}\right)x\right]x\,dx = 0 \quad [5]$$

In our earlier paper, it was shown that, for conditions where the surface oxygen concentration quickly reached its final value, and the depth of oxygen penetration was small compared to the thickness of the specimens, an approximate "working equation" could be derived by simultaneous solution of Eq. [4] and [5]. For these conditions

$$\sigma_1(x, t) = \sigma_I\frac{C(x, t) - C_o}{C_s - C_o} = \sigma_I \operatorname{erfc}\frac{x}{2\sqrt{Dt}} \quad [6]$$

where σ_I is the surface stress due to oxygen solution, D is the diffusivity of oxygen in the specimen, and C_s is the oxygen concentration at the surface. For the steep concentration gradients which existed, the complementary error function could be approximated by a linear function of x, resulting in a simple relationship between the surface stress and the measured maximum bending stress

$$\sigma_I = 2\sigma_s(t)\frac{h^2}{d(3h - 2d)} \quad [7]$$

where d is the effective penetration distance, $2.3\sqrt{Dt}$. Similarly, when other simple boundary conditions are applicable along with semi-infinite geometry, analytical expressions can be used to obtain the stress distribution parameters under the terms of the model. However, the rate of oxygen diffusion is sufficiently high at 800°C so that for most specimens the condition of a limited diffusion zone is met only for the very early stages of reaction. When diffusion distances begin to approach the specimen thickness, the relation between total stress and bending strain is not direct, and particular attention must be paid to differences in stress behavior between free specimens, constrained specimens, or specimens oxidizing on both sides.

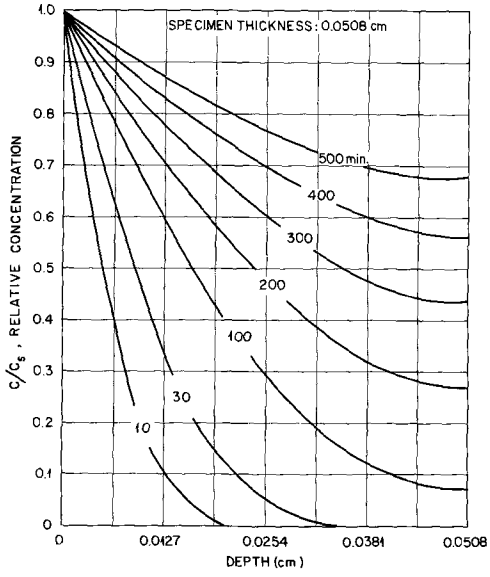

Fig. 1. Oxygen concentration profiles for diffusion at 800°C in 0.020 in. (0.0508 cm) thick tantalum sheet.

Data and interpretation.—In order to interpret flexure data in terms of oxygen-solution effects, it is necessary to define the oxygen concentration profiles in the specimen as a function of time.[4] A typical set of such profiles for a simple oxidation experiment on a 0.020 in. (0.0508 cm) thick tantalum specimen is shown in Fig. 1. Since the specimen thickness must be considered finite rather than semi-infinite when solving the diffusion equation in this case, these profiles, and the others used in this work, were obtained from distance-time arrays produced by a computer program based on finite-difference techniques. This approach was sufficiently accurate for the purposes of these experiments and, in addition, furnished an exceptional versatility in allowing us to vary the boundary conditions to test several details of the oxygen solution model. These tests would have been virtually impossible to make by analytical means. The profiles in Fig. 1 were computed on the assumption that a constant

[3] Unless the concentration gradient is completely linear and the specimen is not constrained.

[4] Diffusion coefficients based on the expressions $D = 0.019 \exp(-27{,}500/RT)$ for diffusion of oxygen in tantalum and $D = 0.015 \exp(-26{,}300/RT)$ for diffusion of oxygen in niobium were used in this work (11).

surface oxygen concentration, C_s, existed during the diffusion time. While this assumption is probably incorrect in detail for short diffusion times, the computer results obtained by the methods referred to above indicated that the shape of the profiles would not be altered significantly for diffusion times greater than about 20 or 30 min. As is seen in the figure, oxygen penetrates rapidly and after about 100 min the oxygen level on the protected side of the specimen starts to increase. According to the oxygen-solution model for stress generation, this behavior should result in flexure or bending stress components that should first increase, then decrease as the specimen "fills up" with oxygen. The resulting "ideal" behavior of the maximum bending stress, expressed as a fraction of the surface stress developed, was computed on this basis and is presented in Fig. 2. The bending stresses are seen to increase to a maximum and then to decrease at a slower rate. Unlike the case for which the reaction is limited to a shallow region, it is noticed that for experiments in which the thickness of the diffusion zone is comparable to the specimen thickness, the maximum bending stress will be a significant fraction of the surface stress, σ_I. However, it must be remembered that for specimens undergoing flexure, the stress at the surface due to oxygen solution will be reduced by the component of the bending stress at the reacting surface. Thus, the resultant stress at the surface may approach zero even as the specimen goes through its maximum flexure.

The measured maximum bending stresses for a tantalum specimen being oxidized on one side at 800°C at a pressure of approximately 10μ are shown in Fig. 3. Metallographic examination at the conclusion of the experiment did not reveal any significant changes in the appearance of the polished specimen surface, indicating that little, if any, oxide film or platelet formation occurred. The behavior is similar enough to the ideal to lead us to believe that oxygen is indeed the principal stress source under these conditions. However, the behavior of the apparent surface stress, computed via Eq. [7], in the initial stages of flexure show that the ideal model, which assumes a constant surface oxygen concentration, is not sufficiently accurate to permit quantitative values to be obtained. The most probable reason for this is that the effective oxygen concentration at the surface is increasing with time during this part of the reaction. For example, if it is assumed in this experiment that the surface oxygen concentration increases to its maximum value at a decreasing rate (parabolically) over the first 30 min, a more consistent result is obtained which correlates the oxygen concentration with stress very closely. Values of the surface stress thus computed for this

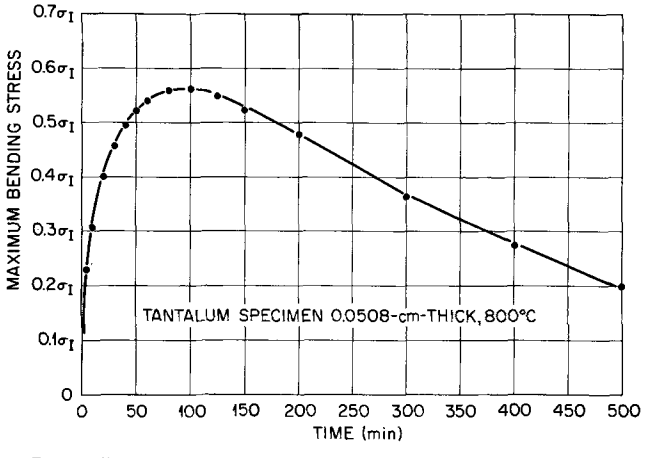

Fig. 2. "Ideal" flexure behavior for 0.020 in. (0.0508 cm) thick tantalum specimen computed from concentration profiles shown in Fig. 1. The maximum bending stress is expressed here as a fraction of the surface stress due to oxygen solution, σ_I, assumed to be a constant.

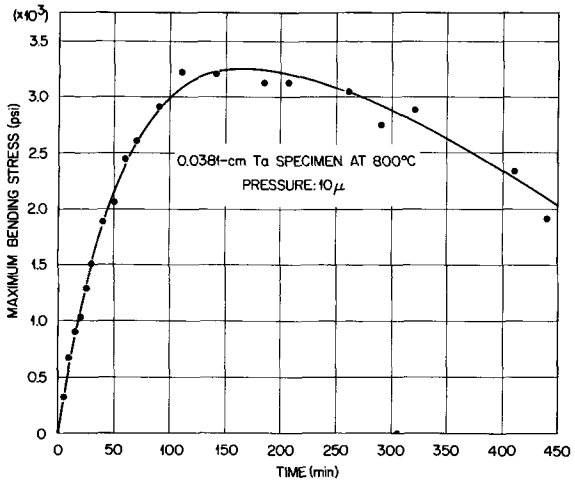

Fig. 3. Experimental flexure behavior for 0.0381 cm thick tantalum specimen at 800°C at an oxygen pressure of approximately 10μ.

experiment reached approximately 4000 psi. Such computations necessitate the use of Eq.[4] and [5], including computer solutions for $C(x,t)$ for the unusual conditions imposed to obtain surface stress values.

An interesting sidelight which was made evident from such experiments was the possibility of using flexure behavior to estimate diffusion coefficients for oxygen in the metal in a manner which does not require quantitative strain measurements. To a first approximation, the specimen should start to "unbend" during a flexure experiment shortly after the effective penetration distance equals the specimen thickness. Thus, for these conditions

$$D \cong \frac{h^2}{5.3\, t_m} \qquad [8]$$

where D is the diffusion coefficient, h is the specimen thickness, and t_m is the time at which the specimen flexure starts to decrease. For the experiment represented by the data of Fig. 3, the flexure reversal occurred at approximately 150 min. Thus, Eq. [8] leads to a diffusion constant for oxygen in tantalum at 800°C of 3×10^{-8} cm²/sec, a value which compares very favorably with the accepted value of 4.75×10^{-8} cm²/sec (11). A similar experiment with a niobium specimen yielded $D = 8 \times 10^{-8}$ cm²/sec which also compares well with the accepted value of 6.6×10^{-8} cm²/sec. This agreement is taken as additional evidence that volume diffusion rather than grain boundary diffusion controls the strain effects observed in these specimens.

At intermediate pressures for tantalum and niobium specimens, flexure effects due to both oxygen solution and oxide film sources are seen. However, if the oxygen is pumped out of the system before large quantities of oxide have formed, the unbending of the specimen observed during the anneal can then be correlated satisfactorily with the changes in the oxygen concentration gradient alone. Figure 4 shows maximum bending stress data for a niobium specimen held at 800°C. For the first 16 min, the oxygen pressure was maintained at about 15μ; then the oxygen was removed and the specimen allowed to anneal in vacuum at the same temperature. The measured bending stresses (solid circles) are seen to have increased to about 16,000 psi during the oxidation period, and then to have virtually disappeared after an hour's vacuum anneal. The oxygen concentration profiles pertinent to this experiment are presented in Fig. 5. Linear approximations of these profiles were then used in the mechanical equilibrium equations (Eq. [4] and [5]) to obtain bending stress changes during annealing. These computed bending stresses, normalized with

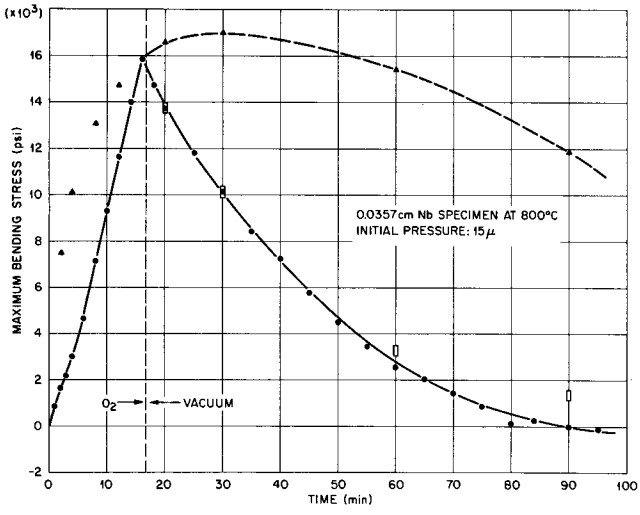

Fig. 4. Flexure behavior for 0.0357 cm thick niobium specimen held at 800°C. For the first 16 min, the oxygen pressure was held at about 15μ. • Experimental values; ▲ calculated values (normalized at t = 16 min) on the basis of a constant oxygen concentration at the surface; □ calculated values (normalized at t = 16 min) on the basis of oxygen redistribution by volume diffusion during anneal.

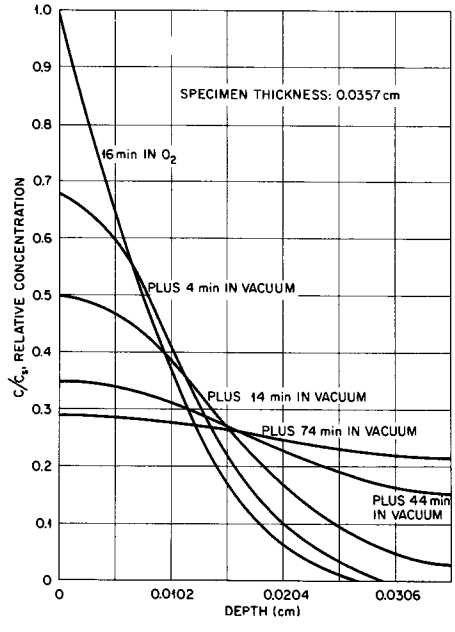

Fig. 5. Oxygen concentration profiles in niobium specimen pertinent to oxidation-annealing experiment described in text and in Fig. 4.

respect to the measured value at t = 16 min, are shown by the open rectangles in Fig. 4. The agreement with the actual values is good. The flexure behavior that would be expected if the oxygen concentration at the surface of the specimen were maintained constant, perhaps by dissolving oxide, is shown in this figure by the solid triangles. Clearly, in this experiment, the latter case does not apply, oxide dissolution was a slow step, or insufficient oxide was present. Metallographic examination of this specimen after the experiment revealed only a few isolated small patches of NbO with a limited superficial film, which may have formed during cooling. A similar result was obtained for flexure of tantalum specimens as shown in Fig. 6. In this case, the specimen was held for 65 min at about 45μ O_2 pressure before starting the anneal. The bending stresses during annealing, computed on the basis of oxygen redistribution, again

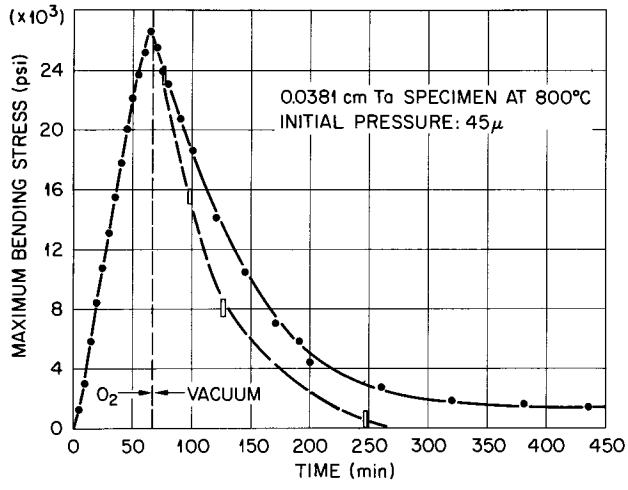

Fig. 6. Flexure behavior for 0.0381 cm thick tantalum specimen held at 800°C. For the first 65 min, the oxygen pressure was held at about 45μ. • Experimental values; □ calculated values (normalized at t = 65 min) on the basis of oxygen redistribution by volume diffusion during anneal.

agreed reasonably well with the observed values. The divergence between the observed and predicted values, as well as the residual curvature of the specimen is thought to be due mainly to the presence of a small amount of plastic strain induced during the oxidation period, since virtually no film or platelet growth could be found at the conclusion of the experiment. Surface stresses of about 20,000 psi due to oxygen solution were estimated in the manner discussed previously, allowing for a finite time over which the surface oxygen concentration increased.

At still higher pressures, the formation of oxide products along with oxygen dissolution led to a very rapid stress build-up which resulted in extensive plastic bending and distortion unless the oxidation time was limited. Of course, if plastic deformation occurs, the maximum bending stresses calculated from the observed flexure by Eq. [1] will be excessive by an amount proportional to the depth in the specimens over which the yield stress was exceeded. Figure 7 illustrates flexure behavior for a tantalum specimen under such conditions. In only a few minutes, a maximum bending stress of over 20,000 psi was indicated. The oxygen was removed from the apparatus, but then instead of unbending in strict accordance to oxy-

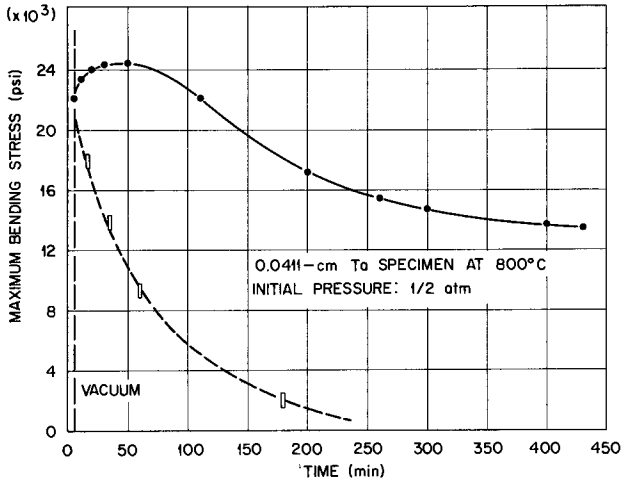

Fig. 7. Flexure behavior for 0.0411 cm thick tantalum specimen held at 800°C. For the first 5 min, the oxygen pressure was held at 0.5 atm. • Experimental values; □ calculated values (normalized at t = 5 min) on the basis of oxygen redistribution by volume diffusion during anneal.

gen redistribution effects, the specimen continued to bend. Finally, the maximum bending stresses were observed to decrease sluggishly to some constant value. There are several possible explanations for this behavior; however, it seems reasonable to postulate that oxygen from dissolving oxide is responsible for the postoxidation time flexure changes which are similar to those shown by the dashed curve in Fig. 4. The tendency for the maximum bending stresses to approach a constant value is probably due to a combination of (*i*) stresses which exist in the remaining thin oxide film and (*ii*) plastic deformation which occurred as the bending stresses went through their maximum.

Summary

The flexure of tantalum and niobium specimens oxidizing at 800°C on one side was measured at several oxygen pressures. The large mechanical strains observed in these experiments during the early stages of the oxidation reaction were found to be due to the presence of oxygen concentration gradients, in agreement with both prediction (4, 5) and previous results (6, 7). Annealing experiments, in which the changes in bending stresses were correlated directly with the redistribution of the oxygen which was present were particularly definitive in this respect. Since the effective oxygen concentration at the surface of an oxidizing specimen changed as a function of both time and oxygen pressure, the exact form of the oxygen concentration gradient, and thus the stress gradient, was difficult to compute. However, reasonable approximations regarding this behavior permitted at least semiquantitative values of the surface stresses to be obtained. For example, for the experiment depicted in Fig. 3, the component of stress at the tantalum surface due to oxygen reached a maximum of only 4000 psi; at higher pressures, *e.g.*, Fig. 6, the stress values reached about 20,000 psi.

These experiments have shown the usefulness of the flexure technique to test models for stress development during oxidation and, despite the approximations involved, have contributed to a more complete characterization of the nature and extent of these effects.

Acknowledgment

The authors are indebted to J. V. Cathcart for many helpful suggestions during the course of this research and during the preparation of the manuscript.

Manuscript submitted Dec. 9, 1968; revised manuscript received *ca.* Feb. 20, 1969. This paper was presented at the Chicago Meeting, Oct. 15-19, 1967, as Paper 87.

Any discussion of this paper will appear in a Discussion Section to be published in the December 1969 JOURNAL.

REFERENCES

1. J. V. Cathcart, G. F. Petersen, and C. J. Sparks, "Surfaces and Interfaces, I Chemical and Physical Characteristics," p. 333, Syracuse University Press (1967), and references contained therein.
2. J. M. Perrow, W. W. Smeltzer, and J. D. Embury, *Acta Met.*, **16**, 1209 (1968), and references contained therein.
3. J. V. Cathcart, G. F. Petersen, and C. J. Sparks, *This Journal*, **116**, 664 (1969).
4. J. D. Eshelby, "Solid State Physics 3," pp. 112-3, Academic Press, New York (1956).
5. O. Richmond, W. C. Leslie, and H. A. Wriedt, *Trans. Am. Soc. Metals*, **57**, 294 (1964).
6. R. E. Pawel, J. V. Cathcart, and J. J. Campbell, *This Journal*, **110**, 551 (1963).
7. R. E. Pawel and J. J. Campbell, *Acta Met.*, **14**, 1827 (1966).
8. R. E. Pawel, J. V. Cathcart, and J. J. Campbell, *ibid.*, **10**, 149 (1962).
9. J. Van Landuyt and C. M. Wayman, *ibid.*, **16**, 803, 815 (1968).
10. P. Kofstad, "High Temperature Oxidation of Metals," John Wiley & Sons, Inc., New York, 1966. particularly Chap. VI.
11. The activation energies were taken from J. W. Marx, G. S. Baker, and J. M. Sivertsen, *Acta Met.*, **1**, 193 (1953). Pre-exponential factors were taken from C. Y. Ang, *Acta Met.*, **1**, 123 (1953). While based on internal friction measurements, these expressions lead to *D* values in reasonable agreement with the limited high-temperature diffusion data which exist.

Rare Earth Bismuth Titanates

R. W. Wolfe and R. E. Newnham

Materials Research Laboratory, The Pennsylvania State University, University Park, Pennsylvania

ABSTRACT

Ferroelectric compounds in the family $Bi_{4-x}R_xTi_3O_{12}$ (R = rare earth) have been prepared as ceramics and single crystals. The solid solution limit increases with ionic radius: x_{max} exceeds 2 for La^{3+} and Pr^{3+} and approaches zero for the smaller Yb^{3+} and Lu^{3+} ions. The larger rare earth ions also stabilize the paraelectric phase. The dielectric properties and crystal chemistry of the bismuth titanates are discussed with reference to related structures, and the results of preliminary optical and electrical measurements are given.

Twenty years ago Aurvillius (1) discovered a family of mixed bismuth oxides with composition $M_{n+1}R_nO_{3n+3}$ where M = Bi^{3+}, Pb^{2+}, Na^+, K^+, Sr^{2+}, Ca^{2+}, Ba^{2+}; R = Ti^{4+}, Nb^{5+}, Ta^{5+}, Fe^{3+}, Ga^{3+}; and n = 2, 3, 4, 5. The crystal structures consist of Bi_2O_2 layers interleaved with $M_{n-1}R_nO_{3n+1}$ layers containing n perovskite-like units. The pseudotetragonal unit cell of $Bi_4Ti_3O_{12}$, with n = 3, is illustrated in Fig. 1.

Most, if not all, of these compounds are ferroelectric (2-5) with high transition temperatures and large spontaneous polarizations. X-ray patterns indicate orthorhombic symmetry, but recent electrical and optical measurements on $Bi_4Ti_3O_{12}$ (5) show that the true symmetry is monoclinic, point group m. A change in the sense of polarization produces a large change in the optical properties of bismuth titanate, making it unique among ferroelectrics and stimulating several device proposals (6). Bismuth titanate has a high transition temperature (675°C) resulting in large switching fields; to lower the voltages, it is desirable

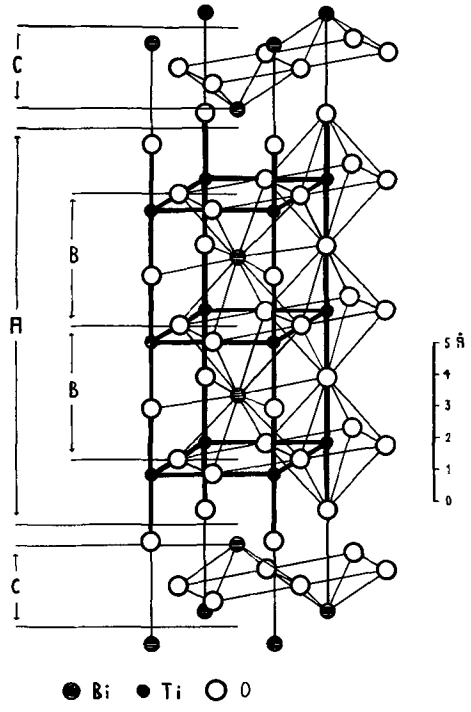

Fig. 1. Crystal structure of $Bi_4Ti_3O_{12}$ after Aurvillius (1). Dimension A delineates the $Bi_2Ti_3O_{10}$ layers with its three perovskite units, B, and C denotes the bismuth oxide layers.

to lower T_c. We have attempted to do this by substituting trivalent rare earth ions for bismuth, forming the solid solution series $Bi_{4-x}R_xTi_3O_{12}$.

Ceramic specimens of the rare earth-bismuth titanates were prepared by sintering reagent grade oxides in air at 1150°C. Weight losses never exceeded 1%. Solid solution limits were determined to an accuracy of 3%, using x-ray diffractometer patterns and the disappearing phase method. In all cases the major exsolved phase was a rare earth pyrochlore ($R_2Ti_2O_7$), possibly containing bismuth in solid solution. The results of these experiments are shown in Fig. 2, where the maximum value of x in $Bi_{4-x}R_xTi_3O_{12}$ is plotted against rare earth ionic radius. The larger ions from La to Eu fill 50% or more of the Bi sites; Gd substitutes 35%, and x_{max} descends rapidly to near zero for the smallest ions, Yb and Lu.

X-ray intensity calculations showed that the rare earth ions do not substitute randomly for bismuth. There are two different bismuth positions in the unit cell: half are coordinated to twelve oxygens in the perovskite layers, while the remainder are closely bonded to four oxygens in the bismuth oxide layer. Possible ordered configurations for composition $Bi_2R_2Ti_3O_{12}$ are illustrated in Fig. 3. Structure factors

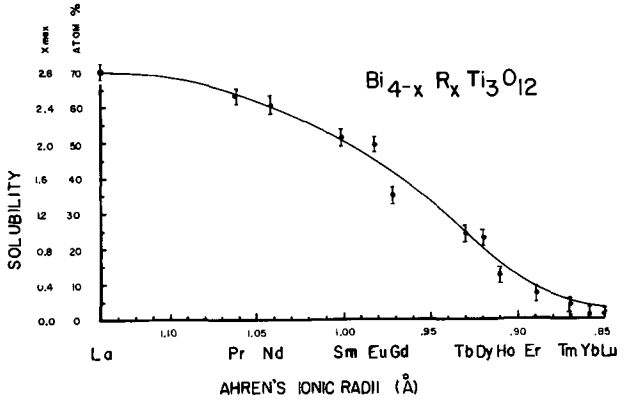

Fig. 2. Solubility of the rare earth elements in bismuth titanate at 1150°C.

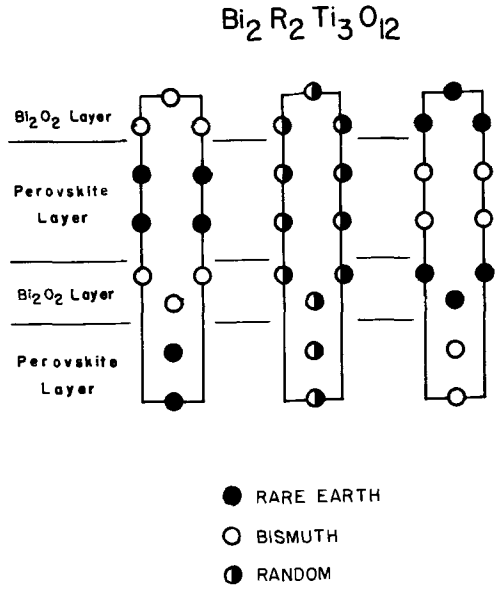

Fig. 3. Possible ordered configurations for the rare earth bismuth titanates of composition $Bi_2R_2Ti_3O_{12}$. The large cation sites in the perovskite and Bi_2O_2 layers are equal in number. ●, Rare earth; ○, bismuth; ◑, random.

were computed for the three models and compared with the structure amplitudes measured from x-ray diffractometer patterns. The results for $Bi_2La_2Ti_3O_{12}$ given in Table I are typical of the rare earth-bismuth titanates. The rare earth ions show marked preference for the perovskite-layer position, with bismuth in the more asymmetric interlayer site. Similar results have been reported for $CaBi_2Nb_2O_9$ (1) and $Na_{0.5}Bi_{4.5}Ti_4O_{15}$ (7).

The observed ordering explains the stability ranges presented in Fig. 4 for the $Bi_{4-x}R_xTi_3O_{12}$ solid solution series. $Bi_2R_2Ti_3O_{12}$ compositions are stable for R^{3+} ions larger than Gd^{3+}. Since rare earth ions occupy perovskite sites up to $x = 2$, their ionic radii must satisfy the requirements for twelve-coordination. In divalent-ion titanates (M TiO_3), the perovskite structure forms when the M^{2+} radius exceeds that of Cd^{2+}, with ilmenite structures predominating for smaller cations. Since the ionic radii of Gd^{3+} and Cd^{2+} are identical on the Ahrens' scale, it appears that the same stability criteria apply. Compounds such as $Bi_2Lu_2Ti_3O_{12}$ are unstable because the Lu^{3+} ion is too small for the perovskite layer site. For larger ions like La^{3+}, the Bi_2O_2 layer limits substitution. Only an atom with an asymmetric electron cloud, such as the lone-pair configuration of Bi^{3+} or Pb^{2+}, will promote the stability of the bismuth oxide layer. Hence x_{max} never exceeds 2 by very much.

Lattice parameters were determined from x-ray diffractometer patterns using CuKα radiation and a silicon standard. The pattern of pure $Bi_4Ti_3O_{12}$ was indexed on an orthorhombic unit cell out to $2\theta = 120°$. Having observed no monoclinic splitting in appropriate high-angle reflections, we conclude that the angle β differs from 90° by less than 0.15°.

Table I. Typical results of structure factor calculations for the three ordering models in Fig. 3

hkl	$\lvert F_o \rvert$	F_c		
		La in perovskite	random	La in $(BiO)_2$ layer
006	25	26	29	32
113	14	−16	−9	−20
115	28	27	15	5
026	21	−24	−26	−29
226	20	−20	−23	−25
111	21	22	24	27
131	14	18	21	22
133	12	−10	−7	−15
	R Factor	9%	19%	31%

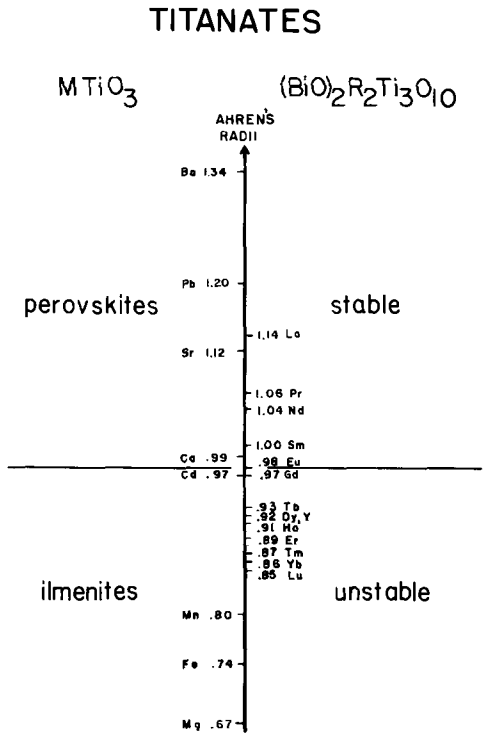

Fig. 4. Stability fields of the divalent-ion titanates and the rare earth bismuth titanates of composition $Bi_2R_2Ti_3O_{12}$.

Orthorhombic cell dimensions for a few rare earth bismuth titanates are given in Table II. Comparing cell volumes, it appears that the radii of Bi^{3+} and La^{3+} are nearly equal, contrary to the Ahrens' scale which gives Bi^{3+} 0.93Å, and La^{3+} 1.14Å. The axial ratio b/a is a measure of the orthorhombic distortion; b/a decreases when any rare earth is substituted for bismuth, suggesting that the ferroelectric transition temperature is lowered.

Curie temperatures of the rare earth bismuth titanates were determined by differential thermal analysis using Al_2O_3 as a reference material, and the α- to β- quartz transition as a calibrant. As shown in Fig. 5, T_c decreases linearly with increasing rare earth concentration x. The effect is more pronounced with large ions like La^{3+}, showing that T_c depends on rare earth ion radius r as well as composition x. Analytically, the straight lines in Fig. 5 are given by

$$T_c = 660° - A(r)x$$

To determine the dependence of T_c on radius r, the slopes $-A(r)$ are plotted against r in Fig. 6. This too yields a straight line

$$-A(r) = M(r - r_o)$$

where $M = 5.47°C$ and $r_o = 0.83Å$. Thus the transition temperature depends linearly on the product $(r - r_o)x$

$$T_c = 660° - 5.47\ (r - 0.83)x \qquad [1]$$

This equation is plotted in Fig. 7 along with a number of experimental points. The agreement verifies that Eq. [1] is valid for any rare earth R and any composition $Bi_{4-x}R_xTi_3O_{12}$.

Table II. Orthorhombic cell dimensions for several rare earth bismuth titanates

Composition	a	b	c	a/b	Cell volume
$Bi_4Ti_3O_{12}$	5.411	5.449	32.82	1.007	968.7
$Bi_{3.6}La_{0.4}Ti_3O_{12}$	5.421	5.439	32.88	1.003	969.5
$Bi_{3.6}Nd_{0.4}Ti_3O_{12}$	5.407	5.433	32.83	1.005	965.5
$Bi_{3.8}Y_{0.2}Ti_3O_{12}$	5.407	5.442	32.81	1.006	965.4
$Bi_{3.2}Y_{0.8}Ti_3O_{12}$	5.400	5.434	32.78	1.006	961.9
$Bi_{3.8}Dy_{0.2}Ti_3O_{12}$	5.403	5.439	32.78	1.006	963.3
$Bi_{3.2}Dy_{0.8}Ti_3O_{12}$	5.398	5.431	32.77	1.006	960.7

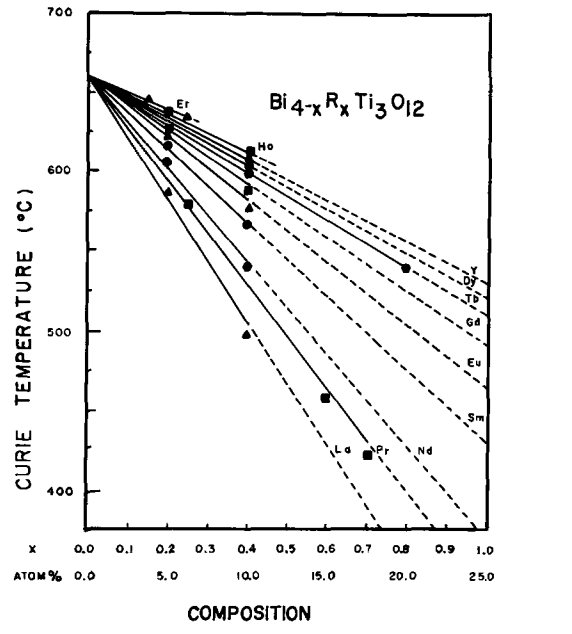

Fig. 5. Curie temperatures of the rare earth bismuth titanates as determined by differential thermal analysis.

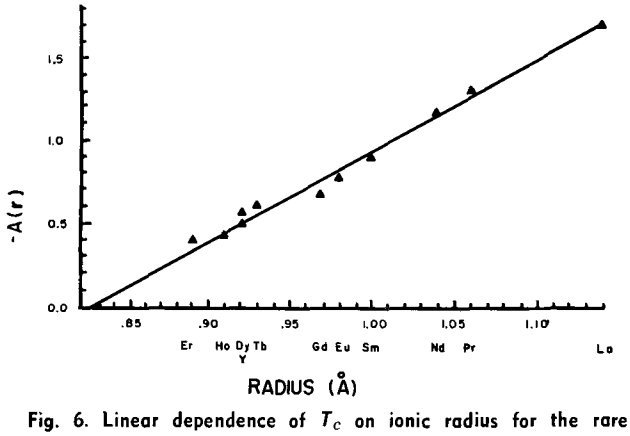

Fig. 6. Linear dependence of T_c on ionic radius for the rare earth bismuth titanates.

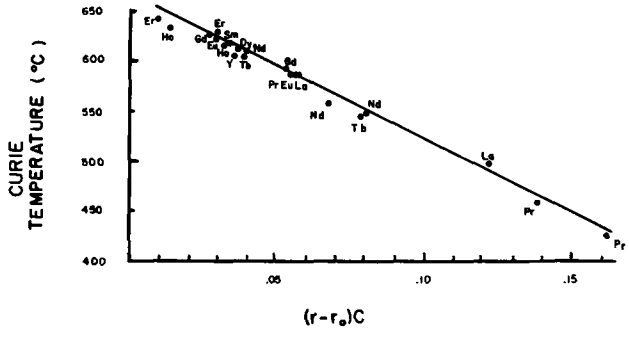

Fig. 7. Linear dependence of T_c on the product of radius and composition. All the experimental points in Fig. 5 are plotted here.

The one-dimensional models shown in Fig. 8 can be used to explain the dependence of T_c on x and r.

Figure 8a shows a polar chain which is schematically representative of bismuth and oxygen atoms in ferroelectric $Bi_4Ti_3O_{12}$. Because of its nonspherical electron configuration, Bi^{3+} prefers an asymmetric arrangement of oxygen neighbors. This is true in many oxides of trivalent bismuth and isoelectronic Pb^{2+}. In $Bi_4Si_3O_{12}$, for example, each bismuth is coordinated to six oxygens, three on one side at 2.15Å and three on the other at 2.62Å, a marked difference in bonding.

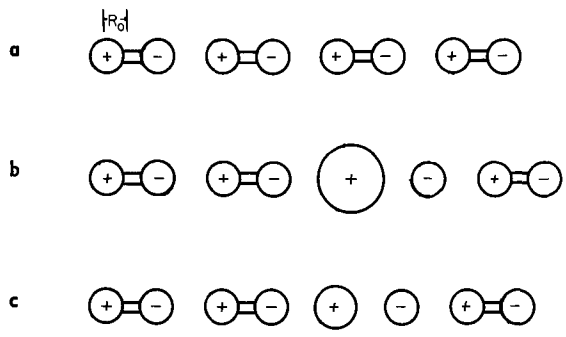

Fig. 8. One-dimensional model of bismuth and oxygen atoms in $Bi_4Ti_3O_{12}$ showing the effects of rare earth substitution.

Using 1.32Å as the ionic radius of oxygen, the shortest distance yields a Bi^{3+} radius of 0.83Å, very close to the critical radius r_o in Eq. [1].

Figure 8b shows the polar chain with a large rare earth atom replacing a bismuth atom. The substitution has two effects on the polar chain. First, the introduction of a symmetrical atom into the chain weakens the ferroelectric interactions of the bismuth atoms simply by reducing their number; this is the compositional dependence. Second, the large effective size of the substituting atom separates the bismuth atoms even further; this is the radius effect. Figure 8c shows a polar chain in which a small rare earth ion has replaced a bismuth atom. The compositional effect is the same, but the radius contribution to the depression of T_c is decreased. Ultimately, as r approaches r_o (the effective bismuth radius in the direction of its shortest bond length), the radius contribution goes to zero, and T_c becomes independent of composition.

Permittivity measurements as a function of temperature were made on ceramic disks of the rare earth bismuth titanates as a check on the Curie points determined by DTA.

Figure 9 shows some typical curves. The transition temperature observed for ceramic $Bi_4Ti_3O_{12}$ was 676°C, with a peak dielectric constant of 375, slightly lower than the value reported by Subbarao (8). Peak dielectric constants for all the compositions tested were in the range 300-500. The dielectric measurements consistently yielded T_c values 20° higher than those observed by DTA.

Single crystal measurements were needed to determine the true symmetry of the solid solutions since x-ray powder patterns are insensitive to the monoclinic distortion in $Bi_4Ti_3O_{12}$. The crystals were grown by the flux growth technique in which titania, rare earth oxide, and excess Bi_2O_3 were melted in a platinum crucible, brought to a peak temperature of 1250°C for 8 hr, and then cooled at a programmed rate of 2°-5°C/hr. The crystals were removed from the flux with a platinum sieve suspended in the melt. The largest plates measured 7 mm on edge and 0.5 mm thick. Crystals of composition $Bi_{3.4}La_{0.6}Ti_3O_{12}$ were chosen for optical and electrical studies.

The technique devised by Cummins and Cross (5) was used to prepare thin sections of $Bi_{3.4}La_{0.6}Ti_3O_{12}$ with the a or b axis normal to the thin section. When the crystal sections were viewed under polarized light, both a and b sections showed uniform parallel extinction. This observation strongly suggested that the

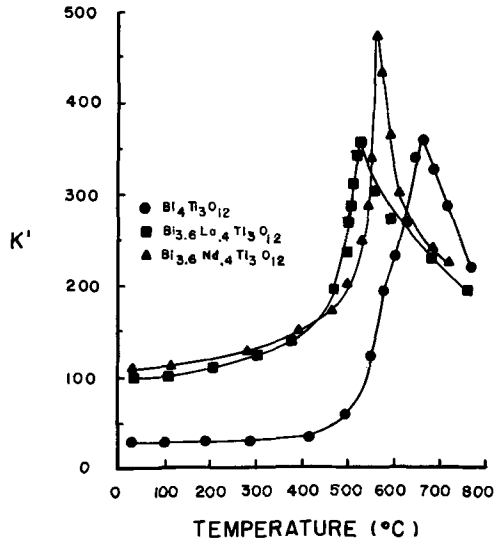

Fig. 9. Dielectric constant as a function of temperature for some rare earth bismuth titanates.

crystals possessed orthorhombic symmetry, point group mm2. Hysteresis measurements in the c direction supported this conclusion. Fields as high as 150 kv/cm failed to produce a noticeable hysteresis loop for a small single crystal; if a spontaneous polarization along c does exist it must be smaller than 0.4 $\mu C/cm^2$. This result is unfortunate since it is the component of polarization along the c direction that gives rise to the interesting electrooptical properties of $Bi_4Ti_3O_{12}$.

When the same crystal was subjected to an alternating current pyroelectric test, a small but definite signal was observed, an indication that the crystal symmetry may yet be monoclinic. Further work is underway in an attempt to determine the true symmetry of the rare earth bismuth titanates.

Acknowledgment

This work was supported by the Advanced Electronic Devices Branch, Air Force Avionics Laboratory, Wright-Patterson Air Force Base, Ohio, under Contract No. F33615-67-C-1427.

Manuscript received Jan. 22, 1969. This paper was presented at the Montreal Meeting, Oct. 6-11, 1968, as Paper 439.

Any discussion of this paper will appear in a Discussion Section to be published in the December 1969 JOURNAL.

REFERENCES

1. B. Aurvillius, *Arkiv Kemi*, **1**, 499 (1949); **2**, 463 (1949); **1**, 519 (1950).
2. E. C. Subbarao, *J. Amer. Ceram. Soc.*, **45**, 166 (1962).
3. E. C. Subbarao, *J. Phys. Chem. Solids*, **23**, 665 (1962).
4. I. G. Ismailzade, *Sov. Phys.-Cryst.*, **8**, 686 (1964); **12**, 400 (1967).
5. S. E. Cummins and L. E. Cross, *J. Appl. Phys.*, **39**, 2268 (1968).
6. S. E. Cummins, *Proc. IEEE*, **55**, 1536 (1967); **55**, 1537 (1967).
7. R. E. Newnham, *Mat. Res. Bull.*, **2**, 1041 (1967).
8. E. C. Subbarao, *Phys. Rev.*, **122**, 1804 (1961).

Effect of Polarizing Temperature on the Characteristics of SR_{10} Vinyl (PVC) Electrets

P. K. C. Pillai, V. K. Jain, and G. K. Vij

Department of Physics, Indian Institute of Technology, New Delhi, India

ABSTRACT

The results of an experimental investigation on the charge formation and decay characteristics of SR_{10} vinyl (PVC) electrets prepared at different temperatures are presented in this paper. The results show that the polarity of the final charge on either side of the electrets is positive irrespective of the polarizing conditions. It is also shown that polarizing temperature has a major influence on the behavior of vinyl electrets.

A permanently polarized dielectric, which exhibits electrical charges of opposite sign on its sides, is known as an electret (1). Recently there has been a considerable increase in the study of electret effect in solids, because of its various applications in electronics and electrical devices (2-5). The literature on electrets has been reviewed by Gutmann (6), Johnson (7), and Gross (8). Properties of electrets are known to be dependent on the properties of the electret material and also on the polarizing conditions under which the sample is fabricated (9-14).

Experimental Details

The object of this paper is to describe the effect of polarizing temperature on the decay characteristics of SR_{10} vinyl electrets. SR_{10} vinyl is a PVC compound (manufactured by Rajasthan Vinyl & Chemical Industries, Kota, India) which is found to be a good electret-forming material. This material is available in powder form. Although it does not show any definite melting point, most of the ingredients of this compound are molten at about 140°C. Above 140°C it becomes reddish in color, and at about 210°C it becomes very brittle and completely carbonized.

A special technique has been developed for the preparation of plastic electrets (9). A small quantity of this plastic powder was kept in a mica cavity of 1.0 cm^2 area and 1.0 mm thickness between two aluminum electrodes. This electret gadget with the sample was then kept in a regulated thermostat for thermal and electrical treatment. A polarizing field of 10 kv/cm was applied for 6 hr. After 3 hr of heating, the sample was allowed to cool down to room temperature while under the influence of the polarizing field. The electret molded in the mica cavity in this way was then taken out for charge measurement. The surface charge measurement was carried out by means of a Lindemann electrometer using the method of induction. After measurement the sample was short circuited by means of metallic foil and preserved in a desiccator for further studies.

Results and Discussions

The charge decay characteristics of the electrets prepared at different temperatures (30°-170°C), but with all other parameters constant, have been studied for about 30 days and the charge decays of these samples are shown in Fig. 1 to 6. It can be seen that, for the anode side of the samples prepared in the temperature range 30°-110°C, the initial charge was hetero, which reversed to homo in a few days' time except for those electrets prepared at 30° and 80°C. For the cathode sides of those samples prepared at 30°-110°C, the initial charge was hetero, which gradually decayed to a more or less permanent value in about a month without showing any charge reversal. In the second temperature range (120°-170°C), the anode side initially showed a high homocharge which gradually decayed to a constant value in about 30 days without showing any reversal of charge. But it is interesting to note that the cathode sides of these samples first possessed a homocharge which eventually reversed to a final heterocharge unlike many other electret forming materials.

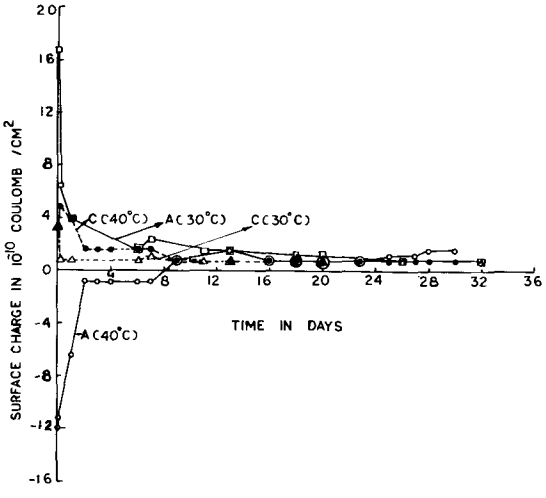

Fig. 1. Surface charge density vs. time for SR_{10} vinyl electrets prepared at 30° and 40°C with 10 kv/cm field strength in 6 hr time. Symbols used: A means anode side, and C means cathode side.

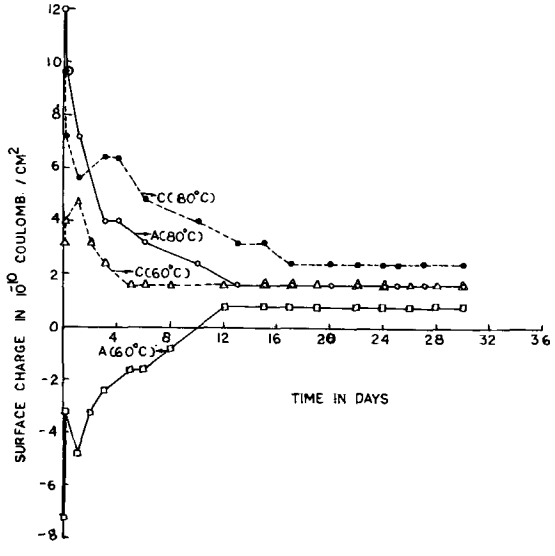

Fig. 2. Surface charge density vs. time for SR_{10} vinyl electrets prepared at 60° and 80°C with 10 kv/cm field strength in 6 hr time.

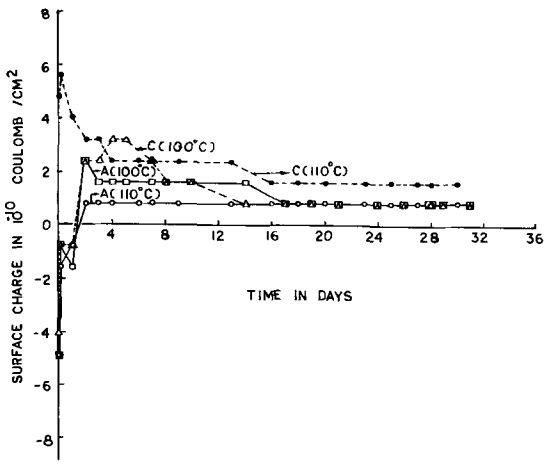

Fig. 3. Surface charge density vs. time for SR_{10} vinyl electrets prepared at 100° and 110°C with 10 kv/cm field strength in 6 hr time.

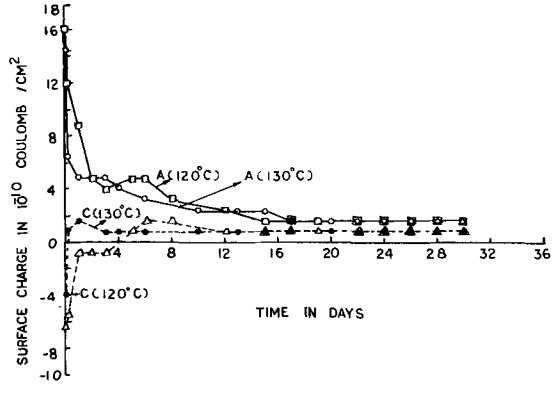

Fig. 4. Surface charge density vs. time for SR_{10} vinyl electrets prepared at 120° and 130°C with 10 kv/cm field strength in 6 hr time.

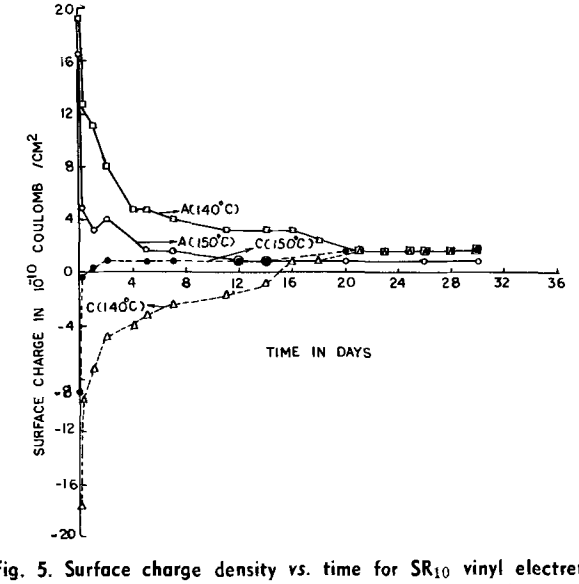

Fig. 5. Surface charge density vs. time for SR_{10} vinyl electrets prepared at 140° and 150°C with 10 kv/cm field strength in 6 hr time.

Figure 7 shows the final charge after 30 days *vs.* polarizing temperatures. These curves indicate that the final charge on either side of the various electrets has the same polarity (positive) irrespective of the forming conditions. In most of the electret forming materials, the final charges on either side are found to have opposite polarity.

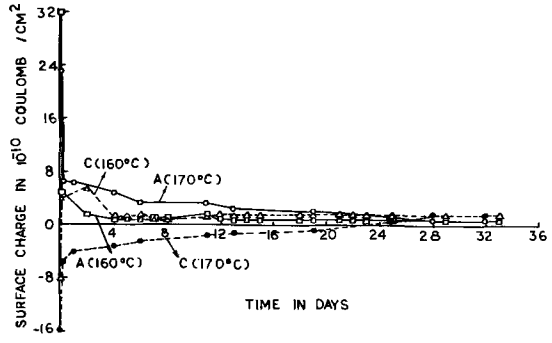

Fig. 6. Surface charge density vs. time for SR_{10} vinyl electrets prepared at 160° and 170°C with 10 kv/cm field strength in 6 hr time.

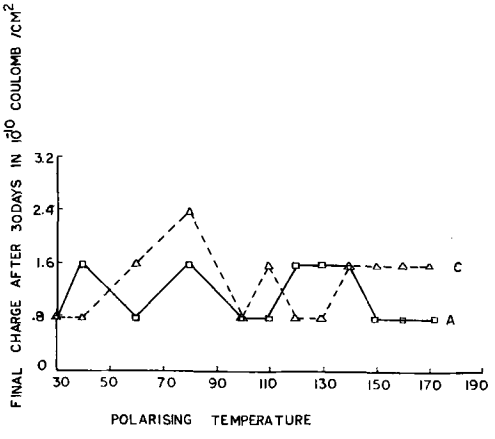

Fig. 7. Final charge density after 30 days vs. polarizing temperatures for SR_{10} vinyl electrets prepared with 10 kv/cm field strength in 6 hr time.

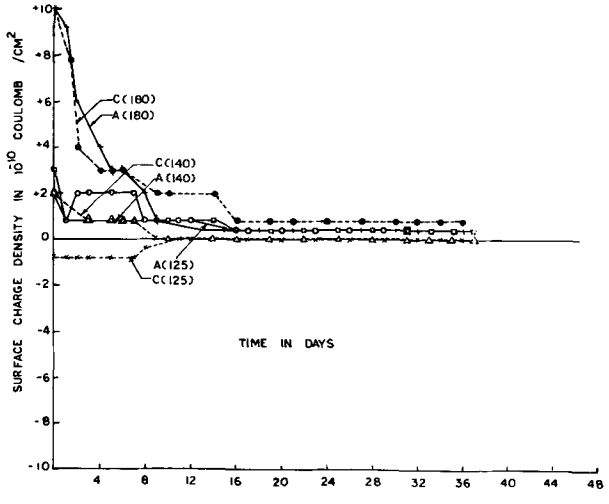

Fig. 8. Surface charge density vs. time for SR_{10} vinyl electrets formed without polarizing voltage at 180°, 140°, and 125°C.

Figure 8 shows the charge decay curves of dummy samples prepared at 125°, 140°, and 180°C without the application of polarizing field. The sample prepared at 180°C gives an initial charge of 10×10^{-10} coul/cm^2 on either side which gradually decays to a constant value of about 1.0×10^{-10} coul/cm^2 in about 15 days. The sample prepared at 140°C shows only a smaller value of about 2 to 3×10^{-10} coul/cm^2 initially and decays to about 0.75 coul/cm^2 in 15 days. But the sample prepared at 125°C did not show a permanent charge. The anode side of this sample initially showed about 2.0×10^{-10} coul/cm^2 which decayed to zero in 10 days' time. But the cathode side showed an initial homocharge of about 1.0×10^{-10} coul/cm^2 which also decayed to zero in about eleven days without any reversal of

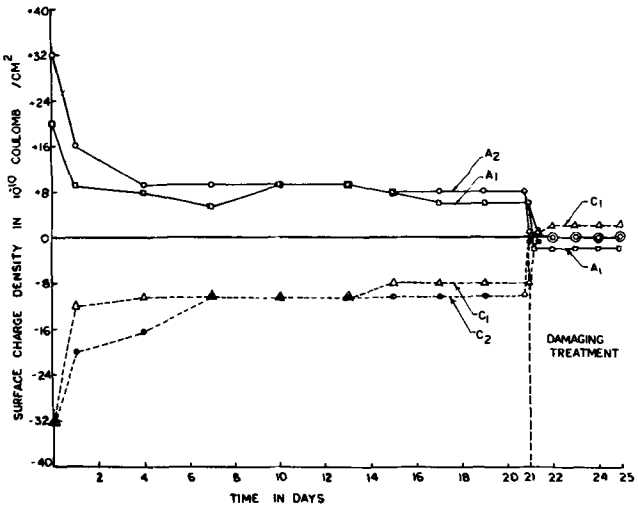

Fig. 9. Surface charge density vs. time for SR_{10} vinyl electrets prepared directly from powder at 200°C with the application of 12 kv/cm field strength. Damaging treatment *(i)* by heating and *(ii)* by dipping in water for 2 min were done on the 21st day. □ A_1, △ C_1 } corresponds to heat-treated sample; ⊙ A_2, ⊗ C_2 } corresponds to water-treated sample.

charge. It has also been noted that samples prepared at 100° and 80°C exhibited no stripping charge from the very beginning. This may be due to the lack of close contact between the dielectric and the electrode below the softening point of the electret material. These results thus show that stripping charge phenomena is temperature dependent and the magnitude is more at higher temperatures particularly above the molten state of the material.

Figure 9 shows the charge decay curves for two electrets prepared from SR_{10} vinyl. The samples were prepared directly from the powder by heating at 200°C for 3 hr under an electric field of 12 kv/cm, and then cooled down to room temperature in about 3 hr. When the charge becomes permanent, the following two types of damaging treatments were performed on the 21st day to see whether the SR_{10} electrets are good at recovering their charge after damaging treatment.

One of the samples was heated for an hour in a thermostat at 140°C and, when the sample cooled down to room temperature, the charge on either side was measured for a few days. The charges on either side were found to be reversed, and the magnitudes of charge were also reduced considerably. With time the charges gradually increased to about $2.0\text{x}10^{-10}$ coul/cm^2 after reversal (Fig. 9).

The second electret was dipped in water for 2 min, and then it was allowed to dry. On measurement for a few days, no surface charge was obtained from this sample (Fig. 9). It indicated that penetration of water into the sample damaged the electret almost permanently without regaining either hetero or homocharge. The same result was obtained with another sample after performing the same type of damaging treatment.

The above experiments show that recovery of heterocharge is possible at least partially for the sample treated at high temperature. But for the other sample, water penetration seems to have spoiled both the internal and the external polarizations, and no recovery of charge was detected for four days.

Dummy samples were also prepared without any metallic electrode and without the application of polarizing field at 145°C, and it was found that such samples did not show any charge. These experiments indicate that the presence of a metallic electrode is highly essential for obtaining a molding charge and also for the formation of an electret.

Comparing the charge decay characteristics of the zero field samples to those with field at low and high temperatures, it can be seen that polarizing field has played a major role in the formation and characteristics of SR_{10} vinyl electrets. Charge formation below 100°C is mainly due to the influence of polarizing field as zero field samples did not show any final charge at these low temperatures. However, contribution due to molding charge plays an important role at and above the molten state of the electret material.

It can be seen from Fig. 5 that the anode side of electret prepared at 140°C with 10 kv/cm field gives an initial charge of $18\text{x}10^{-10}$ coul/cm^2 in comparison to $3\text{x}10^{-10}$ coul/cm^2 of the dummy sample (Fig. 8) prepared without field. The zero field sample gives a final charge of about $0.75\text{x}10^{-10}$ coul/cm^2 after 30 days whereas the other one gives about $2.0\text{x}10^{-10}$ coul/cm^2. But the cathode side of the sample without field gives an initial heterocharge of $2\text{x}10^{-10}$ coul/cm^2 whereas the sample with field shows about $18\text{x}10^{-10}$ coul/cm^2 homocharge initially which reversed to hetero with time and assumes the final value of about $2.0\text{x}10^{-10}$ coul/cm^2. But the anode side does not show such reversal of charge. This indicates that the polarizing field and polarizing temperature have major influence on the formation and characteristics of SR_{10} vinyl electrets. It also shows that the charge obtained with both zero field samples and the samples with field are not merely due to the contact electrification between the induction electrode and the dielectric surface as indicated by Donald (16) during measurement.

The curves in Fig. 7 again show that the cathode side always gives a final heterocharge whereas the anode side shows a final homocharge. It would be difficult to explain these typical charge formation characteristics of the SR_{10} vinyl electrets on the basis of the two-charge theory of Gross (15) alone. Since the cathode side always shows a final heterocharge, it can be assumed that this material contains more positive ions which under the influence of the electric field must have collected on the cathode side and produced an excessive positive charge on that surface. Charge due to dielectric polarizations as well as various mechanisms for transferring charge across the electret-electrode gap may also be simultaneously existing and the observed charge may be the resultant of all these contributions. Thus the effective charge of electret at any instant can be expressed analytically by the following equation.

$$\sigma_E = \sigma_D + \sigma_i + \sigma_{\text{Homo}} + \sigma_M$$

where σ_E is the effective surface charge of the electret; σ_D is the contribution of charge due to dipolar orientation; σ_i is the component due to ionic polarization produced by opposite displacements of positive and negative ions in the material; σ_{Homo} is the contribution of charge due to external polarizations; and σ_M is the charge due to molding and stripping. The sign, magnitude, and the time constants of each of these components decides the magnitude and sign of the effective charge of an electret.

Summary and Conclusions

From this investigation the following conclusions can be drawn.

(i). SR_{10} vinyl is found to be suitable for electret preparation.

(ii). 80° and 140°C are found to be good polarizing temperatures for the fabrication of vinyl electrets with stable surface charge characteristics.

(iii). The cathode sides of all the electrets prepared above 120°C give an initial homocharge which eventually reverses to a permanent heterocharge, a fact which is not observed normally with other electret forming materials. But the cathode sides of all the samples prepared below 120°C show a high initial heterocharge which slowly decays to a permanent value without any reversal of charge. This result indicates the influence of polarizing temperature on the

behavior of electrets, especially in determining the polarity of the final charge.

(*iv*). The initial charge on the anode side of all the samples is found to be more than that of the cathode side. This may be due to the fact that charge measurements on the anode side was carried out first, and, as the charge decay is very rapid initially, some charge on the cathode side must have been decayed before the actual measurement on that surface has been made. This effect could also be partially due to contact electrification which can occur when the polarizing electrode is removed from the electret.

(*v*). The polarity of the final charge on either side of all the electrets is found to be positive irrespective of the polarizing conditions.

(*vi*). The charge decay characteristics of electrets prepared directly from powder under an electric stress (Fig. 9) is found to be very much different from those prepared from a molded sample (Fig. 1-6).

(*vii*). It is again shown in Fig. 8 that charged samples can be prepared by thermal treatment alone without the application of a polarizing field. But the magnitude and stability of charges of these samples are not as good as those obtained from the electrets prepared with a forming field. This result thus clearly shows that polarizing field plays an important role in the formation of a stable electret.

Acknowledgments

The authors are thankful to Professors S. C. Jain and M. S. Sodha of the Department of Physics, Indian Institute of Technology, Delhi, for the encouragement given to them during the course of this investigation. Thanks are also due to the Council of Scientific and Industrial Research, Government of India, for the research grant for carrying out this work.

Manuscript submitted Aug. 12, 1968; revised manuscript received *ca.* March 10, 1969.

Any discussion of this paper will appear in a Discussion Section to be published in the December 1969 JOURNAL.

REFERENCES

1. M. Eguchi, *Phil. Mag.*, **49**, 178 (1925).
2. A. N. Gubkin and V. Kopanyev, *V. Radio*, **54** (1960).
3. G. M. Sessler and J. E. West, *J. Acoust. Soc. Am.*, **34**, 1787 (1962).
4. H. H. Wieder and S. Kaufman, *J. Appl. Phys.*, **24**, 156 (1953).
5. H. H. Wieder and S. Kaufman, *Elect. Eng.*, **72**, 411 (1958).
6. F. Gutmann, *Rev. Mod. Phys.*, **20**, 457 (1948).
7. V. A. Johnson, "Electrets, A State of The Art Survey," Part I, p. 48; Part II, A Bibliography, p. 124, Office of Technical Services, U.S. Department of Commerce, Publications AD 299259 and AD 299256 (1962).
8. B. Gross, "Charge Storage In Solid Dielectrics," Elsevier Publishing Co., Amsterdam/London/New York (1964).
9. V. K. Jain and P. K. C. Pillai, *Phys. Stat. Sol.*, **28**, 415 (1968).
10. S. Mikola, *Zis. Phys.*, **32**, 476 (1925).
11. A Gemant, Direct Current (Sept. 1953).
12. G. G. Wiseman and G. R. Feaster, *J. Chem. Phys.*, **26**, 521 (1957).
13. N. P. Baumann and G. G. Wiseman, *J. Appl. Phys.*, **25** (1954).
14. J. W. Wild and J. D. Stranathan, *J. Chem. Phys.*, **27**, 1055 (1957).
15. B. Gross, *ibid.*, **17**, 866 (1949).
16. D. K. Donald, *This Journal*, **115**, 270 (1968).

Characteristics of $Ba_2NaNb_5O_{15}$ for Optical Switching and Harmonic Generation

R. R. Rice,[1] H. Fay, H. M. Dess,[2]* and W. J. Alford

Union Carbide Corporation, Electronics Division, Crystal Products Department, San Diego, California

ABSTRACT

The optical quality of large single crystals of $Ba_2NaNb_5O_{15}$ grown by the Czochralski process has been studied. Crystals pulled along the a axis appear more attractive than those pulled along the c axis for both electrooptic and nonlinear applications. The 0.528μ second-harmonic beam divergence is slight in a-axis crystals, but is severe in c-axis crystals. Using a-axis crystals, extinction ratios of 13-17 db were obtained over apertures on the order of 1 mm. The extinction is limited by inhomogeneity in the passive birefringence due to slight gradients in the refractive indices.

Several ferroelectric niobates of the tungsten bronze structure have been synthesized as single crystals by Rubin, Van Uitert, and Levinstein (1). Compositions such as $Ba_2NaNb_5O_{15}$ that have filled A-sites are said to be resistant to the type of optical damage observed in $LiNbO_3$. The properties of $Ba_2NaNb_5O_{15}$ have been investigated by Geusic and co-workers, and it was reported that $Ba_2NaNb_5O_{15}$ crystals suffered no optical damage even under intense irradiation at 0.53μ (2). The useful nonlinear coefficients of $Ba_2NaNb_5O_{15}$ crystals are approximately twice those of $LiNbO_3$. The conversion efficiency for second harmonic generation has been found to approach 100% under optimum conditions, and continuous parametric oscillation has also been observed (3-5). The half-wave retardation voltage for optical switching was found to be conveniently low, the field distance product being about 1500v in the optimum direction (6).

Since $Ba_2NaNb_5O_{15}$ ideally has such interesting properties, a great deal of effort at various laboratories has been devoted to its growth, characterization, and improvement. This paper describes the authors' efforts to grow and characterize single crystal $Ba_2NaNb_5O_{15}$. The most serious problem in the growth and application of $Ba_2NaNb_5O_{15}$ has been that of obtaining good optical quality. The authors have attempted to improve the optical quality of this material by using various growth procedures and to characterize the performance of optical components fabricated from existing material.

* Electrochemical Society Active Member.
[1] Present address: McDonnell Douglas Corporation, St. Louis, Missouri.
[2] Present address: National Lead Company, Highstown Laboratory, Highstown, New Jersey.

Growth and Preparation

Large single crystals of $Ba_2NaNb_5O_{15}$ can be grown from the melt by the Czochralski technique. The melting point is approximately 1450°C (uncorrected pyrometer reading) and is essentially unaffected by slight changes in melt composition or gross changes in ambient atmosphere. The melt can be established and maintained in platinum crucibles by inductive coupling of the crucible to an r-f generator. Single crystals are grown by nucleation on a seed crystal and pulling the seed from the melt. In a typical growth run, the crystal is pulled into a neutral or oxidizing atmosphere at a rate of 5-15 mm/hr with a rotation rate of about 30 rpm. An electrically heated afterheater is located over the melt so that the crystal can be cooled slowly after termination of the growth, in order to reduce cracking. Crystals can be pulled along either the a or c direction by approximately the same technique, although the a-axis crystals have a somewhat greater tendency to crack. Figure 1 shows two representative a-axis and c-axis boules. Typical boule dimensions are 1 x 5 cm.

Boules of $Ba_2NaNb_5O_{15}$ consist of many ferroelectric domains as shown by the earlier studies (7). The domain structure in both a- and c-axis crystals consists of stacked concave disks in which the polarization is oppositely directed. The domain structure in c-axis $Ba_2NaNb_5O_{15}$ can be readily observed by polishing or lightly etching with HF normal to the growth direction. The domains may be detected similarly in a-axis boules, but they are more difficult to observe. The domain thickness in both a- and c-axis crystals varies from approximately two to ten microns. To be useful as an active optical component a crystal must first be converted to a single ferroelectric domain by an appropriate poling procedure. Both a- and c-axis crystals can be completely poled by the same procedure which consists of applying a field in excess of 100 v/cm along the c direction near the Curie temperature. The field can be applied a few degrees below the Curie point for a sufficient period, or the crystal can be cooled through the Curie point under field. The authors prefer the latter procedure.

Since $Ba_2NaNb_5O_{15}$ is an orthorhombic crystal (2 mm) below about 300°C, it becomes finely twinned whenever the boule is cooled below this temperature. Detwinning is accomplished after poling by applying a compressive mechanical stress along one of the principal orthorhombic directions (a or b) perpendicular to the tetragonal c direction, to reorient the undesired twins. As in the case of $LaAlO_3$ (8), detwinning can be accomplished at room temperature by the application of sufficient stress. It can also be accomplished by the application of a milder stress at elevated temperatures. Typical stress requirements are 30,000 to 50,000 psi at 25°C, 10,000 psi at 175°C, or less than 100 psi at 300°C. The detwinned crystal is sufficiently stable so that it can be subsequently cut and polished without reintroducing the twins. However, reheating the crystal to 300° will cause the twins to recur.

Characteristics

The dielectric properties of many $Ba_2NaNb_5O_{15}$ boules have been measured from room temperature to 600°C. The real part of the dielectric constant along the c direction rises from about 50 at 25°C to as high as 70,000 at the Curie point, as shown in Fig. 2. The imaginary part also rises with temperature and attains a maximum at the Curie point. There appears to be no dielectric anomaly at the orthorhombic-tetragonal transition near 300°C. Figure 2 shows the dielectric constant at 10 kHz along the c direction as a function of temperature for one particular specimen. The reciprocal is also plotted to show how well the Curie-Weiss law is obeyed above T_c. The value of T_c can be reproduced to within 1°C and is probably accurate to within a few degrees.

The Curie point was found to be sensitive to composition. When spectroscopic grade $Ba(NO_3)_2$ and $NaNO_3$ were used as starting materials, the authors found the Curie point to be near 560°C, as reported by Van Uitert. However, when reagent grade nitrates were used, the Curie point rose to 580°C. In both cases, the same source of Nb_2O_5 was used. Analysis of the powders used are reported in the Appendix.

The effects of doping stoichiometry and growth orientation were studied. Ta_2O_5 was added up to 5 w/o, and excesses of up to 10 a/o Na_2O, BaO, and Nb_2O_5 were made in various melts. The Curie point is depressed about 8° per m/o Ta_2O_5 added to the melt, indicating the formation of a continuous solid solution as in the case of KTN. The Curie point was found to be slightly depressed in crystals pulled from off-stoichiometry melts. Chemical analyses did not reveal any significant variations in the stoichiometry of crystals pulled from melts of different compositions. This is similar to the results found for $LiNbO_3$ (10).

There are four types of optical aberration in $Ba_2NaNb_5O_{15}$ which tend to restrict the usefulness of crystals for electrooptic or nonlinear applications. The most persistent defects are growth striations which appear to some extent in all crystals. A second more subtle optical defect is a refractive index variation parallel to the growth direction which is observable as bands parallel to the growth axis. A third type of defect is a slow variation of refractive index which produces interference fringes when a crystal with flat and parallel faces is used as a Fabry-Perot etalon in a laser beam. A fourth type of defect, seen only occasionally, is a gross localized refractive index anom-

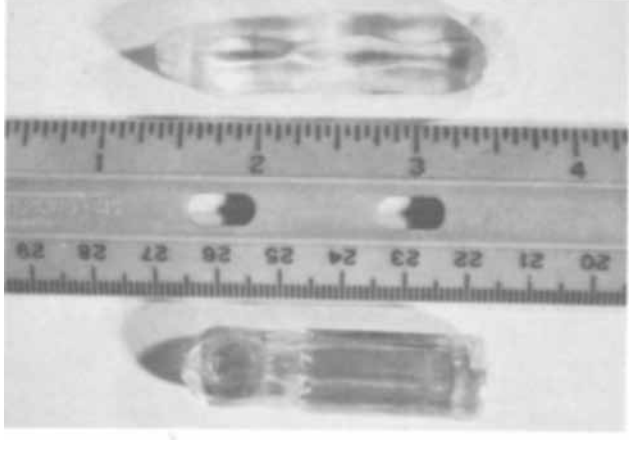

Fig. 1. Typical boules of Czochralski-grown $Ba_2NaNb_5O_{15}$ pulled along the a axis (top) and along the c axis (bottom).

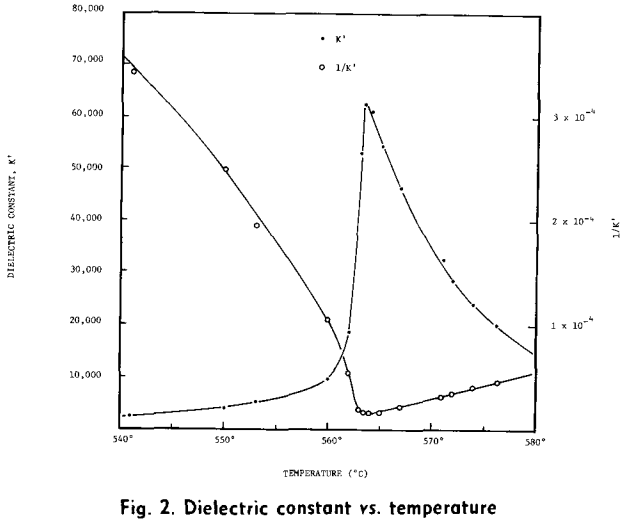

Fig. 2. Dielectric constant vs. temperature

aly which may appear quite different when viewed under different polarizations.

The growth striations are periodic variations of refractive index normal to the growth direction. Under certain growth conditions, the spacing of the striations is perfectly regular and is usually between 5 to 10μ. The growth striations appear to be identical in crystals pulled along either the a axis or the c axis. The appearance of the growth striations and other refractive anomalies in the crystal is strongly dependent on the polarization of the transmitted light. The striations appear in sharpest relief when the light is propagating along the a or b axis and is polarized along the c axis. The striations nearly vanish when viewed in light propagating along a, polarized along b, or *vice versa*.

In both electrooptic and nonlinear applications the incident beam is directed normal to the c axis. This requires that the light pass along or between the growth striations in a c-axis crystal and normal to the striations in an a-axis crystal. Light is refracted and diffracted by these index variations, and the aberration can be appreciable in a c-axis crystal when the beam passes parallel to the striations. This may cause a deleterious affect on the performance of an optical component. In an a-axis crystal, the beam passes normal to the striations, and the aberration is much less severe.

Optical defects cause an increase of beam divergence when a collimated beam of light is transmitted through the crystal. The beam divergence introduced by a-axis crystals differs markedly from that produced by c-axis crystals. Figure 3 shows the effect of inserting optically finished crystals of both orientations into a He-Ne laser beam. In all cases the light was propagated perpendicular to the c axis. For the c-axis crystal this direction is along the striations, and the beam is degraded appreciably by diffraction in the crystal. In the a-axis crystal the beam is propagated in the growth direction, thus, normal to the striations, and the beam divergence is much less. The incident light is polarized along c on the right, at 45° to c in the center, and along a on the left. The photographic plate was at a distance of 3m from the crystal. The most severe effect is seen for light polarized along c, which is the polarization direction of the harmonic wave in second-harmonic-generation experiments when the incident wave is polarized normal to c. Figure 4 shows actual 0.528μ second-harmonic spots obtained with a- and c-axis crystals at a distance of 3m from the crystal with a lens after the crystal to collimate the harmonic beam. The harmonic beam generated by the c-axis crystal suffers severe distortion, and the spot is degraded into a line. The spot obtained with the a-axis crystal shows some loss of definition, but the effect is not nearly so severe as in the c-axis crystals.

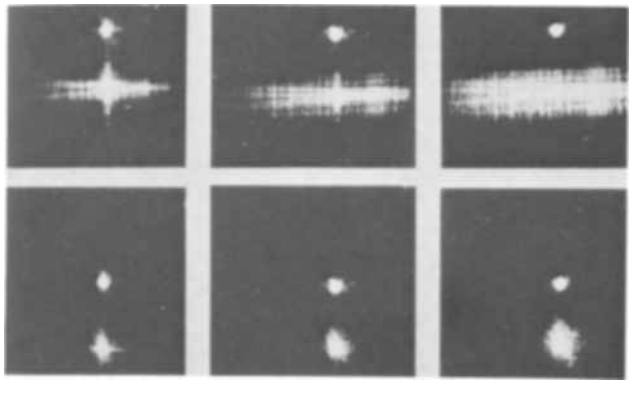

Fig. 3. Distortion of He-Ne laser beam by transmission through c-axis crystals (upper) and a-axis crystals (lower) of $Ba_2NaNb_5O_{15}$. The uppermost spot in all photographs is that produced by the laser alone; the lower image is the beam after passing through the crystal. The c axis is horizontal. The incident light is polarized parallel to c (right), at 45° to c (center), and normal to c (left).

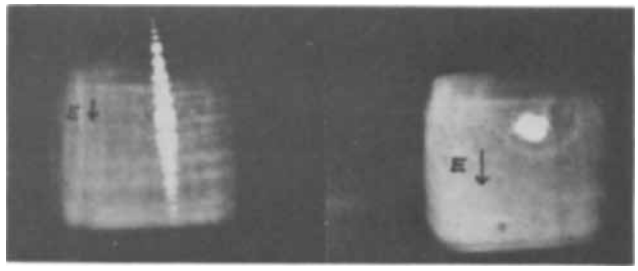

Fig. 4. Photographs of 0.53μ harmonic beam generated by passing 1.06μ laser beam into c-axis (left) and a-axis (right) crystals of $Ba_2NaNb_5O_{15}$. A lens was used to collimate the harmonic beam. The distortion of the spot indicates the beam divergence at the plane of the lens.

Crystals of $Ba_2NaNb_5O_{15}$ are very good harmonic generators for 1.06μ Nd:YAG laser radiation. About 20 mw of 0.528μ second harmonic radiation was produced in an early experiment using a rather poor a-axis crystal without antireflection coatings. No optical damage was induced in the crystal at this power level, nor was damage reported by Geusic for the much higher power levels obtained with selected crystals. Some differences have been observed in the phase-matching temperature (PMT) of crystals studied at this laboratory. Some crystals have a PMT as high as 125°C, while others grown from purer melts have a PMT as low as 80°C. The PMT and the Curie point show a definite correlation. Crystals having a Curie point near 580°C have a PMT near 80°C. The precise PMT obtained for a given crystal is very sensitive to the presence of slight impurities in the starting materials.

In a typical electrooptic experiment the incident collimated light propagates down the a or b axis polarized at 45° to the c axis, and the switching field is applied along the c axis. The field distance product for half wave retardation has been reported as 1570 and 1720v for light propagating along a and b, respectively (2). This compares favorably to the 2800-3000v obtained with $LiNbO_3$ and $LiTaO_3$. The authors have obtained a lowest value of about 1250v for light propagating down the a axis for the best crystals examined.

To be useful for electrooptic applications, $Ba_2NaNb_5O_{15}$ crystals must show a high extinction ratio over a reasonable aperture. An indication of the useful aperture can be obtained by an examination of the passive interference patterns observed when an optically finished crystal is illuminated by parallel coherent light between polarizing prisms. Figure 5 shows three such interference patterns obtained for a typical a-axis crystal. The b axis, which

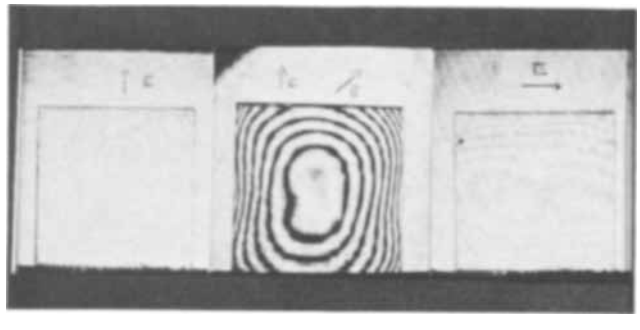

Fig. 5. Interference patterns produced by a crystal of $Ba_2NaNb_5O_{15}$ illuminated by parallel coherent light between polarizing prisms. The direction of the E field and the c axis are indicated. The outer images show etalon fringes due to variations in n_z and n_x, respectively. The central image shows fringes due to variations in the birefringence, n_z-n_x.

for this crystal is the growth direction, is the direction of light propagation for the three cases shown. On the left the prisms are set parallel to c, and the interference pattern results from a spatial variation in n_z. On the right the prisms are set parallel to a, and here the interference pattern is the result of a spatial variation in n_x. The variations in n_x and n_z combine to produce a net spatial variation in birefringence B_y across the face of the crystal, which is observed directly when the prisms are set at 45° to c, as shown in the center photograph.

The birefringence interference pattern shows high contrast, but the interference patterns due to variations of n_x and n_z are faint. This is because the birefringence pattern is formed by waves which make a single transit through the crystal, whereas the interference patterns observed for polarizations along a and c are formed by waves which are incompletely reflected from the crystal faces an odd number of times. The wave amplitude decreases with each reflection, hence complete cancellation does not occur. The crystal is a Fabry-Perot resonator or "etalon." The interference patterns shown in Fig. 5 are rather typical of good a-axis crystals viewed down the growth axis. Note that, while the spatial variation in n_z and n_x is different, the birefringence exhibits a nearly radial variation. The birefringence patterns observed for c-axis crystals, viewed normal to the growth axis, show fringes which are broken up by the growth striations.

The electric field dependence of n_x and n_y can be measured directly. The intensity an etalon fringe will go from maximum to minimum as the optical length of the crystal changes by one-quarter wavelength. The applied field necessary to change the optical length of the crystal by $\lambda/4$ can be easily calculated from the crystal dimensions and the electrooptic coefficients. When the light propagates down b polarized parallel to c, one has

$$2\epsilon_o n_z^3 z_{33}^o = \lambda_o/(E_3 \cdot l_2) \quad [1]$$

Likewise, when the light propagates down b polarized parallel to a, one has

$$2\epsilon_o n_x^3 z_{13}^o = \lambda_o/(E_3 \cdot l_2) \quad [2]$$

Here z_{ij}^o is defined as $\partial\beta_i/\partial E_j$, where β_i is a principal optical impermeability coefficient, λ_o is the free space wavelength of the light, and l_2 is the length of the crystal in the b direction. The quantity $(E_3 \cdot l_2)$ is the field-distance product that induces a change in optical length of $\lambda/4$. A change in relative retardation of one halfwave is required to change the intensity of the fringes in the birefringence interference pattern from maximum to minimum and *vice versa*. For light propagating down b polarized at 45° to c, the halfwave field-distance product obeys the equation

$$\epsilon_o(n_z^3 z_{33}^o - n_x^3 z_{13}^o) = \lambda_o/(E_3 \cdot l_2) \quad [3]$$

By measuring these three different values of $(E_3 \cdot l_2)$ one can independently determine z_{13}^o and z_{33}^o from Eq. [1] and [2] and determine their relative signs from Eq. [3].

The three values of $(E_3 \cdot l_2)$, for a particular crystal of $Ba_2NaNb_5O_{15}$, have been measured to be 535, 1400, and 1600v, respectively. The corresponding electrooptic coefficients are

$$\begin{aligned} \epsilon_o n_x^3 z_{13}^o &= 2.3 \times 10^{-10} \text{ m volt}^{-1} \\ \epsilon_o n_z^3 z_{33}^o &= 5.9 \times 10^{-10} \text{ m volt}^{-1} \\ \epsilon_o(n_z^3 z_{33}^o - n_x^3 z_{31}^o) &= 3.9 \times 10^{-10} \text{ m volt}^{-1} \end{aligned} \quad [4]$$

The latter value has been determined from Eq. [3] but can be computed using the results of applying Eq. [1] and [2]. This procedure leads to a value of 3.7 x 10^{-10} m volt^{-1}, which agrees well with the directly measured value and shows that z_{13}^o and z_{33}^o have the same relative sign. The values given in Eq. [4] agree within the limits of experimental uncertainty with those reported by Geusic *et al.* (2) on crystals of $Ba_2NaNb_5O_{15}$ synthesized by them.

The extinction ratio for electrooptic switching has been measured for a number of crystals. The values obtained depend strongly on the aperture used for the measurement. The highest values are obtained when the beam passes through the central region of the passive birefringence pattern shown in Fig. 5. With an effective aperture of 1 mm^2, extinction ratios of 13-17 db have been measured in this central region. When larger apertures are used, or the aperture is moved to a different region of the crystal, the extinction ratio degrades rapidly due to the nonuniformity of the passive birefringence. By observing the entire crystal with the d-c halfwave voltage applied, or by applying an a-c signal with a peak-to-peak voltage corresponding to a full wave of retardation, it may be shown that the electrically induced birefringence is essentially homogeneous throughout the crystal. The extinction ratio is determined by the inhomogeneity of the passive birefringence and thus could be improved greatly if these variations could be compensated by special wave plates or other means.

Summary

The quality of $Ba_2NaNb_5O_{15}$ crystals produced by Czochralski pulling along the crystallographic a- and c-axis directions has been compared. Both types of crystal exhibit striations and slight variations in index of refraction, Curie temperature, and phase-matching temperature. The optical behavior of a-axis crystals is superior to c-axis crystals since the light is propagated normal to the striations and thus suffers less beam divergence. The Curie and phase-matching temperatures and the electrooptic coefficients have been measured and found to agree with previously reported values. With a 1 mm^2 aperture extinction ratios of 13 to 17 db have been measured in the central region of the interference pattern. The extinction is limited by the inhomogeneity of the passive birefringence.

Manuscript submitted Nov. 18, 1968; revised manuscript received *ca.* Feb. 10, 1969. This was Paper 107 presented at the Boston Meeting, May 5-9, 1968.

Any discussion of this paper will appear in a Discussion Section to be published in the December 1969 JOURNAL.

APPENDIX

The chemical analyses for the reagents used are as follows:

Nb_2O_5	Kawecki Chemical Company	
		ppm
	Ta_2O_5	250
	Fe	< 3
	Ta, Cr, Co, Ni, Cu, Mn, V	< 1 each
	Loss on ignition	200
$NaNO_3$	Spectroscopic grade, United Mineral and Chemical Company	
		ppm
	Ba	3
	Ca	5
	Fe	2
	Mg, K	1 each
$Ba(NO_3)_2$	Spectroscopic grade, United Mineral and Chemical Company	
		ppm
	Fe	3
	Ca	1
	Al	< 1
	Mg	< 1
$NaNO_3$	Reagent grade, Baker Chemical Company	
		%
	Cl	0.001
	IO_3	< 0.0005
	NO_2	< 0.001
	PO_4	0.0001
	SO_4	0.001
	Ca, Mg, and R_2O_3 precipitate	0.0003
	Heavy metals (as Pb)	0.0003
	Fe	0.0001

$Ba(NO_3)_2$	Reagent grade, Baker Chemical Company	
		%
	Cl	0.0002
	Ca	0.025
	Heavy metals (as Pb)	0.0001
	Fe	0.0001
	Sr	0.050

REFERENCES

1. J. J. Rubin, L. G. Van Uitert, and H. J. Levinstein, *J. Crystal Growth*, **1**, 315 (1967).
2. J. E. Geusic, H. J. Levinstein, J. J. Rubin, S. Singh, and L. G. Van Uitert, *Appl. Phys. Letters*, **11**, 269 (1967).
3. J. E. Geusic, H. J. Levinstein, S. Singh, R. G. Smith, and L. G. Van Uitert, *ibid.*, **12**, 306 (1968).
4. R. G. Smith, J. E. Geusic, H. J. Levinstein, J. J. Rubin, S. Singh, and L. G. Van Uitert, *ibid.*, **12**, 308 (1968).
5. R. C. Smith, J. E. Geusic, H. J. Levinstein, S. Singh, and L. G. Van Uitert, *J. Appl. Phys.*, **39**, 4030 (1968).
6. S. Singh, D. A. Draegert, J. E. Geusic, H. J. Levinstein, R. G. Smith, and L. G. Van Uitert, International Quantum Electronics Conference (1968).
7. H. J. Levinstein, Private communication.
8. Homer Fay and C. D. Brandle, *J. Appl. Phys.*, **38**, 3405 (1967).
9. R. R. Rice and H. Fay, *ibid.*, **40**, 909 (1969).
10. H. Fay, W. J. Alford, and H. M. Dess, *Appl. Phys. Letters*, **12**, 89 (1968).

The Epitaxy of ZnSe on Ge, GaAs, and ZnSe by an HCl Close-Spaced Transport Process

H. J. Hovel* and A. G. Milnes*

Carnegie-Mellon University, Pittsburgh, Pennsylvania

ABSTRACT

The epitaxial growth of ZnSe is described on (111) oriented substrates of Ge, GaAs, and ZnSe, using a close-spaced HCl transport process. Single-crystal layers of 1-350μ in thickness were obtained at growth rates of 0.5-160 μ/hr and substrate temperatures of 550°-680°C. Both the surface appearance and the growth rate were found to depend strongly on the substrate material. For ZnSe layers grown on Ge, cracking caused by temperature coefficient differences may occur, but can generally be suppressed by using a slow cooling process. Resistivities of 10^3 ohm-cm were obtained using Ga as the n-type dopant accompanied by a zinc-rich ambient.

Description of the Growth System

Several vapor phase processes have been used for the epitaxy of ZnSe, including open tube transport in pure H_2 (1) and iodine disproportionation (2). An open tube HCl process has also been described (3); however, relatively large HCl concentrations (10-15%) were required to produce the desired growth rates, while secondary constituents such as iodine were used to prevent substrate etching.

A close-spaced epitaxy technique (4) using HCl was chosen for this work because of its inherent high efficiency and flexibility. A diagram of the growth system is shown in Fig. 1. The "close-spaced" term refers to the area encircled at the lower center, where the source and substrate are held rigidly between oxidized Si blocks and separated by a quartz spacer of 10-12 mils. The upper and lower blocks are heated independently by infrared lamps and the temperatures regulated by thermocouples, enveloped inside quartz fingers, which are inserted into the blocks and lead out to SCR (Thyristor) controllers. During growth, 620°-760°C is established at the source and 550°-680°C at the substrate, with a maximum obtainable temperature difference of approximately 120°C.

High-purity HCl (Precision Gas Company) and palladium-diffused H_2 are mixed at flow rates of about 20 and 1000 cc/min, respectively. A large fraction (98-99%) of this mixture is "dumped" (exhausted out of the system) and the remainder admitted into the growth tube, bypassing the zinc to prevent reaction with the HCl. (The zinc is used in the doping procedure after the layer has been grown.) A second H_2 input introduces H_2 at 100-200 cc/min, diluting the final mixture in the tube to HCl concentrations of 0.01%; even lower concentrations are possible at the cost of higher flow rates. Low HCl concentrations were necessary to prevent etching of Ge substrates. The system was run at just slightly greater than atmospheric pressure, as determined by the height of H_2SO_4 and H_2O in the exhaust line.

In order to eliminate possible sources of contamination resulting from reaction with HCl, all parts of the system coming into contact with it were constructed of Pyrex, quartz, and inert plastics, such as Teflon and Kel-f. Many of the glass connections were made into solid pieces by glass working techniques, and the remaining intersections were made with Teflon fittings (Beckman Company). The use of H_2O, H_2SO_4, and a cold trap in the output sections prevented the diffusion of contaminants into the system from the atmosphere

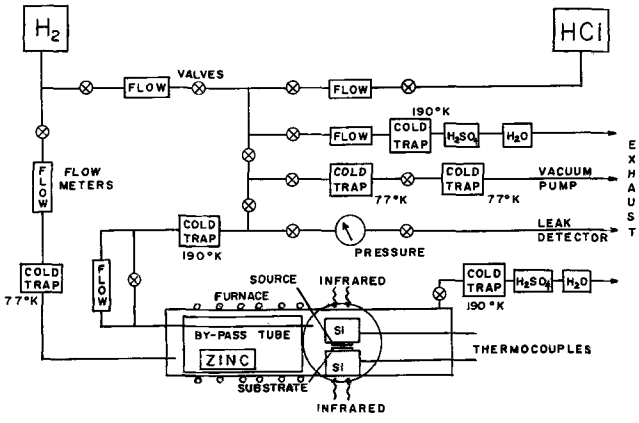

Fig. 1. ZnSe growth system

* Electrochemical Society Active Member.

and eliminated the corrosive gases from the exhaust line. Just prior to growth, all connections were checked for leaks using helium leak detection techniques. H_2 was then passed through the system at high flow rates, while heating the quartz reaction tube and zinc to 350°C, to eliminate water vapor and oxygen. These precautions minimized the possibility of unwanted impurities in the growths.

Source Preparation

The ZnSe used as the source material was purchased in the form of high resistivity (10^8-10^9 ohm-cm) ingots of large crystal grain size (Eagle-Picher Company). Doping of the sources was performed by cutting the ingot to 0.050-in. thick slices and sealing these under vacuum (10^{-6} mm Hg) in an ampoule containing zinc and an n-type dopant such as high-purity aluminum, gallium, or indium. (Contact with molten zinc during doping suppresses zinc vacancies and may also getter metallic impurities from the ZnSe.) The ampoule was then held at a temperature in the range 900°-1050°C for a period of 4-7 days. After cooling to 700°C the sealed ampoule is tipped upside down to pour off the zinc and allowed to cool. Any traces of zinc remaining on the ZnSe may be etched off with HCl.

For aluminum as the dopant the ZnSe showed electron concentrations in the low 10^{18} cm^{-3} and mobilities (300°K) in the range 100-200 cm^2/volt-sec. For gallium the concentrations were typically from 2 x 10^{16} to 10^{17} cm^{-3}, depending on the doping temperature, and the mobilities were 300-500 cm^2/volt-sec; the lower mobilities were associated with the higher doping densities. For indium the concentrations were usually about 2 x 10^{16} cm^{-3} and the mobilities about 400 cm^2/volt-sec. Zinc with no Al, Ga, or In present produced electron concentrations of just under 10^{16} cm^{-3} with mobilities of 350-550 cm^2/volt-sec.

For use as a source the ZnSe slice was mechanically lapped, followed by cleaning in acetone and methanol. Just prior to loading the slice was etched for several minutes in bromine-methanol solution and quenched in methanol.

Substrate Preparation

Germanium substrates were cut and mechanically lapped to a 1μ finish, then mounted on quartz disks and polished to scratch-free, mirror smoothness using an NaOCl process (5). The samples were then cleansed in boiling trichloroethylene, acetone, and methanol and finally etched in modified Superoxol (1HF: $1H_2O_2$: $4H_2O$): (20 H_2SO_4) in a rapidly rotating beaker in order to remove several microns from the Ge surface, removing any shallow surface damage and providing an initially clean surface.

Substrates of GaAs were polished satisfactorily by mechanical lapping to 0.05μ, then heating in 10 H_2O: 1NaOCl for 1 hr at 60°-70°C, removing about 0.5 mils of material and producing mirror smooth surfaces. ZnSe substrates were prepared by the same mechanical lapping followed by a 10-15 min etch in a rapidly rotating beaker of bromine-methanol solution. The amount of material removed by this etch is determined by the bromine concentration, and can be varied over a wide range.

ZnSe *Epitaxial Layers*

Single-crystal layers of ZnSe have been grown on (111) oriented substrates of ZnSe, GaAs (B face), and Ge using both pure H_2 and H_2-HCl atmospheres. Strong dependence of the growth rate on the substrate material was observed; the rates were typically 10-40 times higher on Ge than on either of the other two materials. This can probably be attributed to a chemical reaction occurring between the Ge and the reaction products from the ZnSe etching.

Figure 2A shows the surface of a 15μ ZnSe layer grown under "fast" conditions, *i.e.*, high growth rates and high HCl concentrations. A large density of irregular stacking faults is apparent. The reason for this

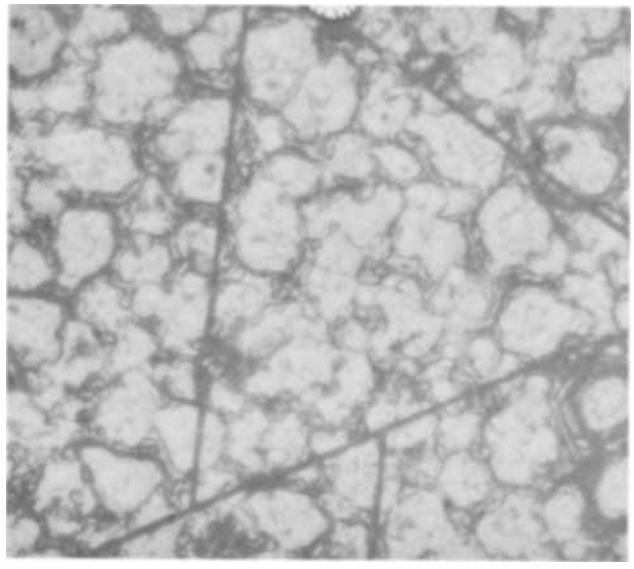

Fig. 2A. ZnSe surface under fast growth conditions: source temperature 640°C; substrate temperature 570°C; 15 μ/hr; 0.2% HCl; Magnification 300X.

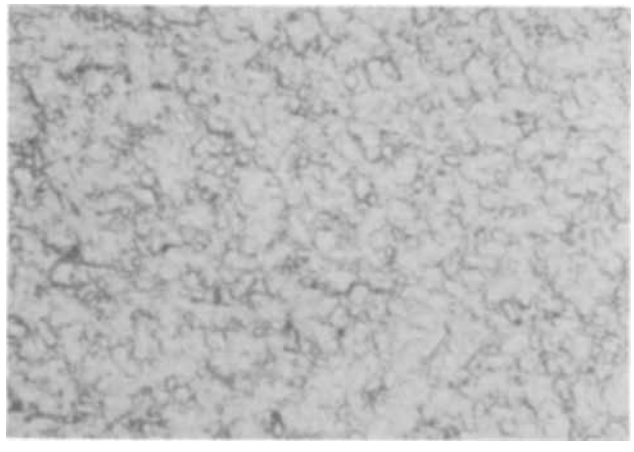

Fig. 2B. Ge surface after removal of ZnSe layer in Fig. 2A, showing deteriorated surface. Magnification 300X.

is revealed in Fig. 2B, which shows the Ge surface after removal of the ZnSe layer by bromine-methanol solution, which does not affect the Ge. The Ge has been severely etched (½ mil, roughly, in depth) by the simultaneous action of HCl and H_2Se (one of the ZnSe-HCl reaction products) during the initial stages of the ZnSe growth.

The situation is greatly improved by lowering the concentrations of these etching gases. Figure 3A shows the surface of a ZnSe layer grown under "slow" conditions, an order of magnitude reduction in both the growth rate and HCl concentration. The layer is well oriented, single-crystal material, although a relatively high density of triangular stacking faults is observed. The Ge surface after removal of the ZnSe is shown in Fig. 3B; the surface has been unaffected by the epitaxial growth, and retains the mirror smooth polish with which it started.

Figure 4 shows the surface of a ZnSe layer on GaAs (B face), in which a Ge substrate was also present (adjacent to the GaAs) during the growth in order to obtain reasonable growth rates. The surface has a cobblestone appearance, 4A, made by a high density of triangular pyramids. In 4B the same surface is shown at a different position, demonstrating larger pyramids extending about 2μ out of the surface. The GaAs surface beneath the ZnSe layer generally retained the high polish (comparable to Fig. 3B) with which it started. Occasionally however, slight pre-

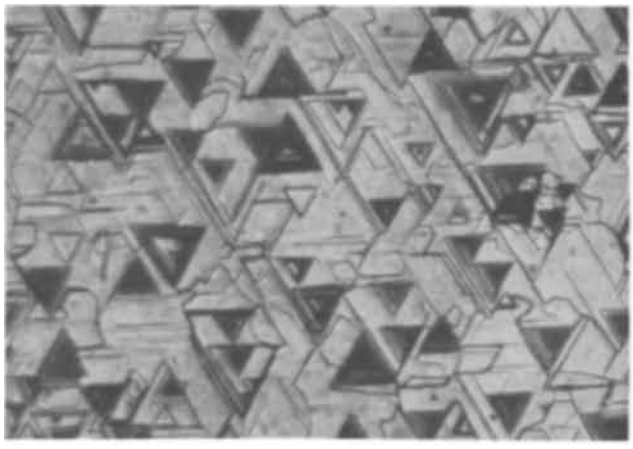

Fig. 3A. ZnSe surface under slow growth conditions: source temperature 700°C; substrate temperature 580°C; 2 μ/hr; 0.02% HCl; Magnification 300X.

Fig. 3B. Ge surface after removal of ZnSe layer in Fig. 3A, showing that the original mirror polish is retained. Magnification 300X.

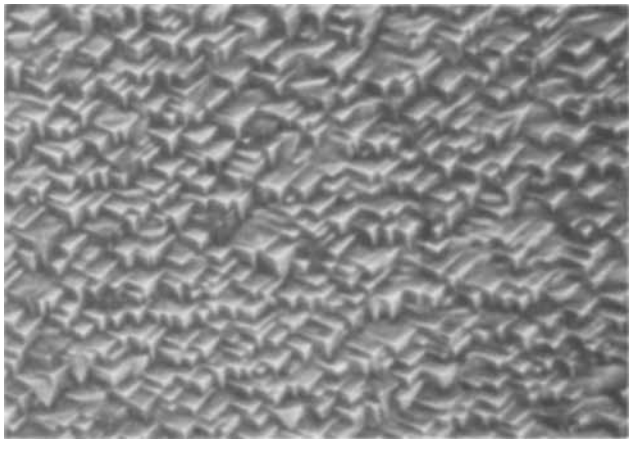

Fig. 4A. ZnSe grown on GaAs under slow conditions, with Ge substrate also present: ZnSe surface; source temperature 700°C; substrate temperature 580°C; 1 μ/hr; 0.02% HCl; Magnification 300X.

growth etching was noted; this etching occurred whenever leakage was introduced into the system either intentionally or unintentionally, and is presumably due to reaction with oxygen or water vapor. This slight etching did not occur whenever such leaks were reduced to their practical minimum, roughly 10^{-8} cc/sec per fitting.

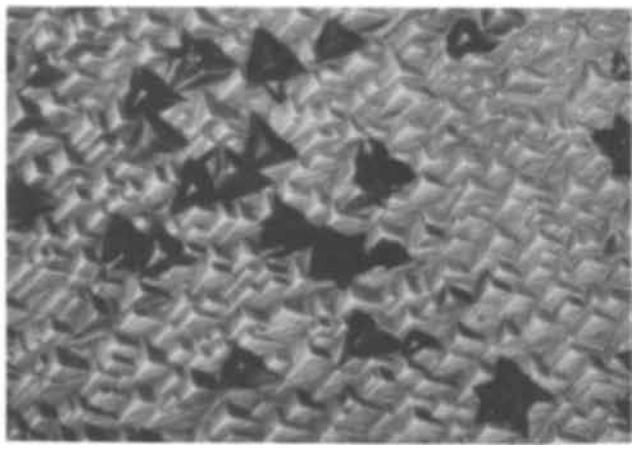

Fig. 4B. Same surface as in Fig 4A, different position, showing growth irregularities.

ZnSe layers grown on ZnSe substrates had mirror smooth surfaces over most of the grown region. The presence of twin bands usually found in ZnSe single crystals allowed an orientation dependence to be observed; the growth rate on one twinned region was 3 or 4 times that on the other twin, giving alternately high and low plateaus, each with mirror finishes.

The quantitative results for the growth of ZnSe on ZnSe, Ge, and GaAs under various operating conditions are presented in Table I. For a given substrate temperature and HCl concentration, the growth rate increased with increasing source temperature; however, there was no appreciable change in the nature of the epitaxial layers. (The efficiency, defined as the amount of ZnSe grown divided by the amount etched from the source, was 45-60% and was independent of the substrate and growth rate.) Rows 1 and 2 describe the results for relatively high HCl concentrations; the growth rate on Ge seeds is seen to be many times higher than on ZnSe substrates for essentially equal conditions. Rows 3 and 4 demonstrate similar enhancement with Ge for growth in pure H_2 atmosphere. A comparison of 1 and 2 with 3 and 4 demonstrates the much higher growth rates using HCl as the transport agent instead of pure H_2. Rows 5 through 7 describe the situation using low HCl concentrations; the rates on GaAs substrates were approximately the same as on ZnSe ones. When ZnSe-GaAs devices grown at low substrate temperatures (560°-580°C) were desired, adjacent Ge and GaAs substrates were used simultaneously; the presence of Ge increased the ZnSe growth rate on GaAs to a practical value.

The enhanced rates of growth on Ge substrates are probably caused by a chemical reaction between the Ge and the ZnSe reaction products

$$2HCl + ZnSe \rightleftarrows ZnCl_2 + H_2Se \qquad [1]$$

Table I. Growth of ZnSe on ZnSe, Ge, and GaAs

All substrates were (111) oriented, with total flow rate of 200 cc/min (reaction tube 43 mm diameter). Source to substrate spacing is 12 mils.

	Growth conditions	Source temp, °C	Substrate temp, °C	Growth rate, μ/hr
1.	ZnSe upon ZnSe	760	660	8
	0.2% HCl	620	580	0
2.	ZnSe upon Ge	760	620	160
	0.2% HCl	620	570	8
3.	ZnSe upon ZnSe pure H_2	760	660	0.05
4.	ZnSe upon Ge pure H_2	760	660	0.3
5.	ZnSe upon Ge 0.02% HCl	680	570	1
6.	ZnSe upon GaAs (B)	750	640	0.5
	0.02% HCl	700	590	0
7.	ZnSe upon GaAs (B) (0.02% HCl with Ge seed also present)	700	580	1.0 on GaAs 3.0 on Ge

$$Ge + xH_2Se \rightleftarrows GeSe_x + xH_2 \quad [2]$$

The Ge vapor species then produces a feedback effect by greatly increasing the etch rate at the ZnSe source. It is not known, however, whether the Ge acts as a catalyst for reaction [1] or produces a second reaction at the ZnSe source. Since the upper Ge surface is gradually covered by the growing ZnSe layer, less Ge surface is available for reaction [2]. The sides and bottom of the wafer, however, do not become covered and remain available for the reaction.

A second possibility, reaction between the Ge and HCl

$$y\,HCl + Ge \rightleftarrows GeCl_y + \frac{y}{2}H_2 \quad [3]$$

to produce the chloride as the feedback species, can be largely ruled out. When layers of GaAs were grown on Ge in an identical system at the same HCl concentration, temperature, and growth rate, no etching of the Ge substrate comparable to Fig. 2B was ever observed (6). The surface in Fig. 2B is therefore attributed to reaction of the Ge with H_2Se rather than HCl.

A Laue back-reflection pattern of a 20μ ZnSe layer grown on Ge at 5μ/hr is seen in Fig. 5. Since the ZnSe layer is relatively thin, a certain portion of the pattern may be due to the Ge beneath. The fraction F of the scattered beam intensity contributed by a layer of thickness x is given by (7)

$$F = 1 - e^{-\alpha x[1+1/\sin(2\theta-90°)]} \quad [4]$$

where α is the x-ray absorption coefficient at a particular wavelength, and 2θ is the angle between the incident and back-reflected beams. Since tungsten targets yield a variety of wavelengths, an exact analysis of the scattering would take into account an integration over all the wavelengths present. Values of α range from 300 to 1500 cm^{-1} for ZnSe; taking 800 cm^{-1} as an example, and using $x = 20\mu$ and $\theta = 75°$, the fraction [4] of the scattering due to the ZnSe is 0.97 at this wavelength. The pattern of Fig. 5 therefore demonstrates the single crystallinity and (111) orientation of the ZnSe layer and is typical of all the patterns taken.

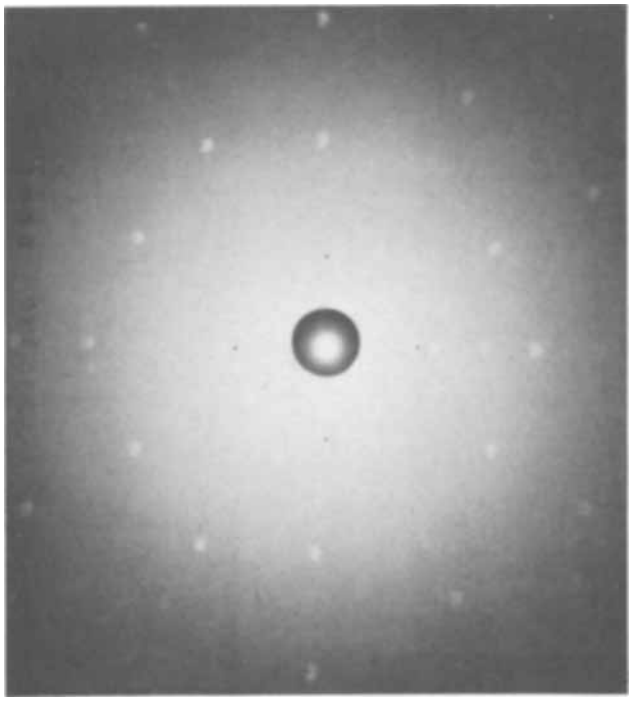

Fig. 5. Laue x-ray back reflection pattern of a 20μ ZnSe layer on Ge (tungsten target).

Fig. 6A. Cracks in ZnSe layers grown on Ge: layer 30μ thick, cooled from growth temperature at 10°C/min, showing crack formation. Magnification 300X.

Fig. 6B. Layer 3μ thick, cooled from growth temperature at 0.8°C/min, showing absence of cracks. Magnification 100X.

Crack Formation

After heterojunction layers have been grown, problems may arise from the thermal expansion mismatch of the two materials. Figure 6A shows a 30μ layer on Ge which was cooled from the growth temperature of 600°C at the rate of 10°C/min. Severe cracking has resulted, extending completely through the ZnSe and partly into the Ge. Such cracking has been observed in other heterojunction structures, notably Ge-Si where the lattice mismatch at room temperature is about 4%. The thermal expansion coefficient of ZnSe has been measured (8) up to 520°C; the lattice mismatch between ZnSe and Ge at the growth temperature is approximately 0.6% compared to 0.15% at room temperature. Although this is considerably less than the 4% of Ge-Si, it is apparently sufficient to cause cracking.

By restriction of the ZnSe growth to thinner layers however, and cooling from the growth temperature at very slow rates, a process of annealing is introduced. Figure 6B shows a 3μ ZnSe layer cooled at 0.8°C/min; under these conditions cracking apparently does not occur. For ZnSe-GaAs the lattice and expansion mismatches are higher, and here also no cracking is observed for thin layers and slow cooling.

Doping of ZnSe *Layers*

Difficulties are encountered in doping II-VI compounds such as ZnSe because of the self-compensation which occurs. For each intentionally added n-type impurity a corresponding zinc vacancy may be formed, which being acceptor-like, compensates the donor. Such compensation may be almost exact (9), so that

the number ($N_d - N_y$ (Zn)) is orders of magnitude less than N_d. It is therefore necessary to provide Zn atoms to the crystal ambient in order to control the Zn vacancy density and allow the donors to become electrically active.

The best method available is to surround the ZnSe with liquid Zn at temperatures of 800°-1100°C for times dependent on the size of the sample (10). In addition to reducing Zn vacancies, this has the additional advantage of gettering other p-type impurities from the ZnSe. It cannot be used for ZnSe on Ge directly, however, since the Ge dissolves completely in Zn at these temperatures. This problem does not arise with ZnSe on GaAs, since the GaAs does not dissolve, but Zn is a fast diffuser in GaAs and drastically changes its resistivity, therefore leading to poor control.

The method adopted here is the diffusion of Zn from the vapor phase. A zinc-filled quartz boat is placed near the input end of the tube (see Fig. 1) and kept at room temperature during the growth period. The zinc is therefore inactive during the growth, but is heated to temperatures of 700°-800°C after the growth has finished, establishing a Zn partial pressure of 10-150 mm Hg in the vicinity of the grown layer. Zinc may then diffuse into the layer from the vapor while the Ge or GaAs is protected by its contact with the SiO_2-covered Si block.

The donor impurity itself can be added in a variety of ways. The most successful method has been to use source ZnSe material heavily doped with Ga or Al, prepared by heat-treating in liquid Zn-Ga or Zn-Al alloy (10). The dopant contained in the source is presumably transported to the growing ZnSe layer. In this way 10^3-10^4 ohm-cm layers were obtained from 5 x 10^{16} Ga doped sources and 10^5-10^6 ohm-cm from 10^{18} Al doped sources, in conjunction with the Zn diffusion step mentioned above. These low substrate-to-source doping ratios are probably due to dopant transport factors, rather than inefficiencies in the Zn step, since consistent differences are observed in the use of Ga doped versus Al doped source material.

Doping was also attempted by adding elemental Ga or Al into the bypass tube (see Fig. 1) and heating it to 300°-500°C, so that all the HCl is converted to Ga or Al chloride. The etching reaction at the ZnSe source then proceeds via this chloride, releasing large amounts of Ga or Al in the growth region. Although there was some evidence that more highly doped layers were obtained by this method (about 500 ohm-cm), the ZnSe layers tended to be of poor quality and the conditions (growth rate, surface appearance, etc.) could not be well controlled. It is thought, however, that this method of doping holds promise of success with the use of Ga if better steps are developed to introduce the $GaCl_x$. The use of Al is less promising because of reactions between the $AlCl_x$ and quartz.

The Hall mobility was measured for a number of Ga doped ZnSe layers (10^3-10^4 ohm-cm) grown on Ge, and generally ranged between 50 and 100. Since the electron mobility of bulk material is 300-400 $cm^2v^{-1}s^{-1}$, this does not represent a serious difference between the bulk and epitaxial materials. Lower mobilities are expected for such epitaxial layers because of the stacking faults, twin bands, and other defects which can occur. It is also possible that a significant amount of Ge could be incorporated in the growing layer due to the presence of the Ge vapor species. The resulting Ge scattering centers would then have the effect of lowering the mobility of the epitaxial material.

The V-I characteristic of an nZnSe (10^3 ohm-cm)-p^+Ge heterojunction is shown in Fig. 7 (ohmic contact is made to both materials by the alloying of pure In). In the forward direction the conduction is moderate with most of the voltage dropped across the bulk

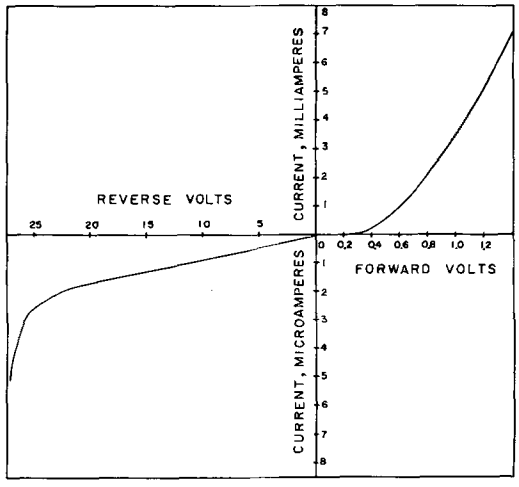

Fig. 7. Volt-ampere characteristics of an nZnSe-p^+Ge heterodiode

ZnSe. The reverse currents are quite low, and rectification ratios of several thousand are common. The diode action involves injection of electrons from the ZnSe into the Ge, and transistors with ZnSe emitters and Ge base-collector junctions with common emitter current gains of 50, or more, have been fabricated (11).

Conclusions

An HCl close-spaced transport process has been described suitable for the growth of single crystal epitaxial layers of ZnSe on several types of semiconductor substrates. The growth rates were found to be considerably higher on Ge than on GaAs or ZnSe, and rates of several mils per hour were easily achieved; however, in order to prevent unwanted etching of the Ge and maintain flat metallurgical interfaces for useful device fabrication, low HCl concentrations and subsequent low growth rates (1-10 μ/hr) were necessary. The cracking due to lattice mismatch was eliminated by growing thin layers and cooling very slowly. Resistivities of 10^3 ohm-cm were routinely achieved using Ga and a zinc over-pressure after the growth to eliminate compensating zinc vacancies.

Acnowledgments

This work was supported by the Air Force Cambridge Research Laboratories under Contract AF 19(628)-5811. The authors are indebted to K. Sleger for his assistance in portions of this study.

Manuscript submitted Sept. 3, 1968; revised manuscript received Feb. 27, 1969. This was Paper 165 presented at the Chicago Meeting, Oct. 15-19, 1967.

Any discussion of this paper will appear in a Discussion Section to be published in the December 1969 JOURNAL.

REFERENCES

1. G. Galli and F. L. Morritz, *This Journal*, **113**, 62C (1966).
2. T. Arizumi, T. Nishinaga, and M. Kakehi, *Jap. J. Appl. Phys.*, **5**, 588 (1966).
3. A. Baczewski, *This Journal*, **112**, 577 (1965).
4. F. H. Nicoll, *ibid.*, **110**, 1165 (1963).
5. A. Reisman and R. Rohr, *ibid.*, **111**, 1425 (1964).
6. G. O. Ladd, Private communication.
7. B. D. Cullity, "Elements of X-ray Diffraction," Addison-Wesley, Reading, Pa. (1956).
8. H. P. Singh and B. Dayal, *Phy. Stat. Sol.*, **23**, K93 (1967).
9. R. L. Longini and R. F. Greene, *Phys. Rev.*, **102**, 992 (1956).
10. M. Aven and R. E. Halsted, *ibid.*, **137(A)**, 228 (1965).
11. H. J. Hovel and A. G. Milnes, *IEEE Trans. Electron Devices*, To be published.

Diffusion of Nickel and Chlorine into Lead Telluride

II. Diffusion at the Phase Limits

T. D. George[1] and J. B. Wagner, Jr.*

Department of Materials Science, Northwestern University, Evanston, Illinois

ABSTRACT

The diffusion of nickel and chlorine has been studied at the limit of solid solubility of both lead and tellurium in PbTe at 700°C. When nickel and chlorine are diffused simultaneously in a lead atmosphere there is an interaction between chlorine and the lattice such that the concentration profile of nickel exhibits a minimum. The same type of minimum in the nickel distribution is produced when lead is diffused under a lead concentration gradient into or out of a nickel-doped crystal. No minimum in the concentration of nickel was observed when a tellurium atmosphere is maintained above the crystal. The diffusion of chlorine indicates that there are anti-Frenkel defects on the anion sublattice.

Recently we reported (1) on the diffusion of nickel and chlorine into p-type lead telluride at 700°C. In that paper all of the diffusion anneals were carried out on material initially containing approximately 2×10^{18} holes/cm^3. A mechanism was suggested by which nickel redistributed in p-type PbTe during the in-diffusion of chlorine. The nickel was said to redistribute behind the advancing front of chlorine because the chlorine disturbed the local electronic equilibrium necessitating an increase in the lead vacancy concentration.

It is the purpose of the present paper to report further studies on the diffusion of nickel and chlorine into lead telluride pre-equilibrated at both of the limits of solid solubility of PbTe. At the lead telluride/lead phase limit PbTe contains excess lead and is n-type with an electron concentration of 9.7×10^{17} electrons/cm^3. With excess tellurium PbTe is p-type and contains 6.4×10^{18} holes/cm^3 at the phase limit.

Experimental

Single crystals of lead telluride were grown by the Bridgman technique from the melt. Wafers 2-3 mm thick were sawed from the ingot with a jewelers saw and lapped on 500 A silicon carbide paper and polished using 0.1μ alumina on felt.

Wafers were equilibrated either at the lead telluride-lead phase boundary or at the lead telluride/tellurium phase boundary. Several wafers were encapsulated together with powdered lead telluride and an excess of either lead or tellurium and annealed for at least 100 hr at 700°C. They were quenched by allowing the capsule to drop directly out of the vertical furnace into a bath of ice and water. Hall measurements indicated carrier concentrations of 9.7×10^{17} electrons/cm^3 at the lead phase boundary and 6.4×10^{18} holes/cm^3 at the tellurium phase boundary. The respective absolute Seebeck coefficients were -285 and $+150$ μv/°C. The carrier concentration of the lead phase boundary is in agreement with that of Brebrick and Gubner (2). The carrier concentration at the tellurium phase boundary is lower (6.4×10^{18}/cc compared to 8×10^{18}/cc) than that reported by Brebrick and Gubner. From etch pit counts we estimate the dislocation density of these crystals to be 2×10^5/cm^2.

Before applying the radiotracer, each wafer was again polished with alumina on felt to remove surface roughness produced during equilibration. Both the nickel-63 and chlorine-36 were obtained as acid solutions (pH $\sim$ 1) of $NiCl_2$ and contained 2.8×10^{-2} mg Ni/ml. The tracer was applied to one face of the wafer as before (1) with one exception. It was found experimentally that if nickel-63 was deposited on the wafer by allowing an acid solution of $^{63}NiCl_2$ (pH $\sim$ 1) to evaporate to dryness on the surface of a wafer, instead of using a neutralized solutions (pH $\approx$ 7), the diffusion results were identical with those in which nickel-63 was electroplated onto one surface. That is, the chlorine atoms from the $NiCl_2$ did not appear to diffuse into the crystal. As a further test, $Ni^{36}Cl_2$ was deposited from an acid solution. Virtually all of the chlorine evaporated. Whereas the initial surface activity of chlorine-36 was approximately 80,000 counts/min when evaporated from a neutralized solution, the initial surface activity dropped to about 80 counts/min when an acid solution of $Ni^{36}Cl_2$ was used. Crystals left in HCl for 24 hr showed no surface attack. When the behavior of nickel in the absence of chlorine from the $NiCl_2$ was to be studied, a drop of $^{63}NiCl_2$ acid solution was placed on one face of a wafer and allowed to evaporate to dryness. When the wafer was dry, the surface remained bright and there was no evidence of attack. It is suggested that nickel may be chemisorbed from the acid solution in a manner similar to that observed for a number of other metals with gallium arsenide (3).

When the effect of chlorine on the diffusion and distribution of nickel was to be studied, $^{63}NiCl_2$ was deposited from a neutralized solution onto one face of a PbTe wafer. This provided a source of both nickel and chlorine atoms which diffused into the crystal simultaneously. Chlorine-36 was always deposited onto one face of a wafer from a neutralized solution of $Ni^{36}Cl_2$.

Diffusion anneals were carried out at 700°C in sealed quartz ampoules of about 2 cm^3 total volume. When it was desired to establish the composition corresponding to one of the phase limits, the appropriate two-phase mixture of lead telluride/tellurium or lead telluride/lead was added to the ampoule with the diffusion specimen. For some experiments the wafer was sealed without the two-phase mixture.

The counting and grinding procedures were identical with those previously described (1) A semiquantitative determination of the nickel concentration was made by comparing the count rate of our samples with calibrated standards of nickel-63. Three nickel-63 standard sources were obtained from New England Nuclear Corporation. The activity of the sources covered the range of count rates encountered here, and the standard sources were approximately the same size as the diffusion wafers. Each standard source was mounted in a stainless steel ring identical to those used for mounting the diffusion samples (1). From the relationships given by Libby (4, 5), the linear absorption coefficient for the β-radiation of nickel-63 (E_{max} = 0.067 mev) in PbTe has been calculated as 18,700 cm^{-1}. This value of the linear absorption coefficient gives a half-thickness of 0.38μ. That is, half of the

* Electrochemical Society Active Member.
[1] NASA Trainee. Present address, Central Analysis and Characterization Laboratory, Texas Instruments, Incorporated, Dallas, Texas.

radiation is absorbed in passing through 0.38μ of PbTe. It has been assumed that the radiation reaching the detector comes from a depth of twice the half-thickness or 0.76μ. Taking this value and the diameter of the wafers (5.34 mm), the volume giving rise to the detected radiation was computed. Calibration curves were constructed for the nickel-63 solution used, and these were used to convert count-rate to nickel concentrations. No determinations have been made for the chlorine concentrations.

Results

Diffusion in crystals initially equilibrated at the PbTe/Pb phase limit.—The following series of experiments employed PbTe wafers pre-equilibrated at the lead telluride/lead phase limit. The crystals were initially n-type having an electron concentration of 9.7 x 10^{17} electrons/cm^3.

If nickel alone is allowed to diffuse into these crystals, nickel penetrates the crystals completely in a very short time. Based on the shortest diffusion time used, 1 hr, we estimate that the diffusion coefficient of nickel must be at least 16^{-6} cm^2/sec at 700°C. When the diffusion of nickel was carried out in the presence of excess lead, the crystal remained n-type at the end of the diffusion anneal. If the diffusion anneal was carried out in an evacuated ampoule without a lead reservoir, the crystal converted to p-type in from 3 to 5 hr. In both cases the concentration of nickel was higher near both the source surface and also the surface of the opposite side of the crystal analogous to the behavior reported previously (1). In the present studies the nickel concentration in the bulk was 2 x 10^{17}/cc. Crystals pre-equilibrated at the lead telluride/lead phase boundary and annealed in an evacuated ampoule at 700°C with no tracer also showed a conversion from n-type to p-type conductivity. Depending on the crystal size, conversion to p-type conductivity was again noted in from 3 to 5 hr.

When nickel and chlorine were diffused into the crystal simultaneously, the nickel concentration profile again contained a minimum. The results of two sets of experiments are shown in Fig. 1 and 2. The profiles for chlorine-36 are also shown in these figures. If the diffusion anneal was carried out in the presence of a lead atmosphere, the results shown in Fig. 1 were obtained. The minimum in the nickel concentration corresponds to about 1 x 10^{17} nickel at./cm^3, while the

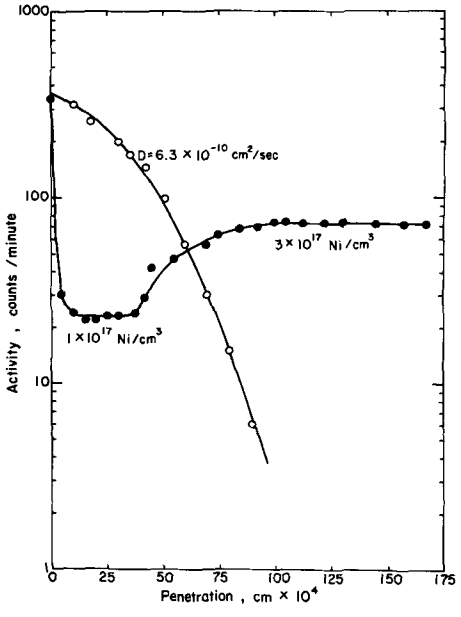

Fig. 1. Simultaneous diffusion of nickel and chlorine into a crystal pre-annealed at PbTe/Pb and diffusion annealed under the same conditions for 2 hr. —○— Chlorine-36 (determined in a separate experiment); —●— nickel-63.

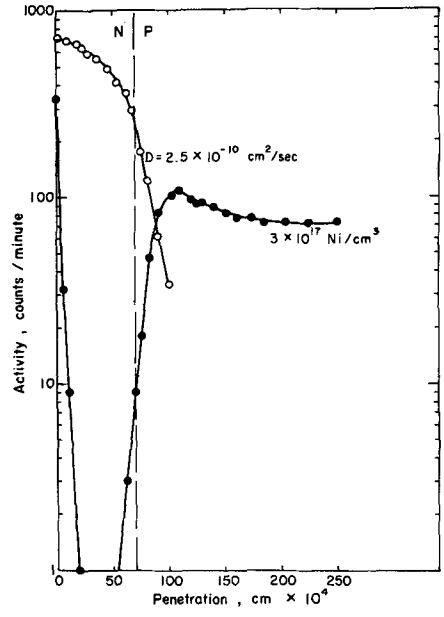

Fig. 2. Simultaneous diffusion of nickel and chlorine into a crystal pre-annealed at PbTe/Pb and diffusion annealed in evacuated ampoule for 6 hr. —○— Chlorine-36 (determined in a separate experiment); —●— nickel-63.

constant region beyond the minimum corresponds to about 3 x 10^{17} nickel at./cm^3.

If the same experiment was repeated without the lead reservoir, typical results as shown in Fig. 2 were obtained. The minimum in the nickel concentration profile is much deeper in this case, and there appears to be an appreciable region containing no nickel at all. An n-type layer was found near the surface of these crystals, but the bulk of the crystal was p-type. As already noted, crystals pre-equilibrated at the lead phase boundary and annealed in an evacuated ampoule turn p-type in a few hours. The n-type layer at the surface must be produced by the in-diffusing chlorine. The p-n junction migrates linearly with the square root of time. However, plots of $x_{p\text{-}n}$ *vs.* $\sqrt{t}$ do not extrapolate back to the origin (see Fig. 3). In these experiments a similar nickel distribution profile was found near the opposite face of the wafer, and the nickel concentrations were the same as near the plated surface.

In order to investigate the effect of lead on the distribution of nickel, the following experiment was conducted. A crystal was pre-equilibrated at the lead tel-

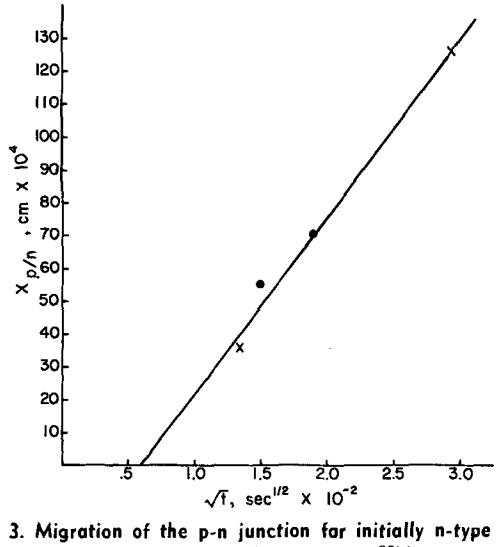

Fig. 3. Migration of the p-n junction for initially n-type crystals diffused in an evacuated ampoule. ● From ^{63}Ni curves; x from ^{36}Cl curves; corresponding to Fig. 2.

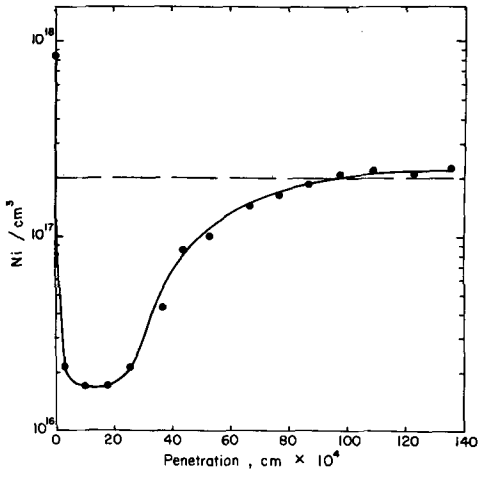

Fig. 4. Redistribution experiment. The effect of diffusing lead into an initially p-type nickel-doped crystal. - - - Nickel concentration before re-anneal in Pb atmosphere; –●– nickel distribution after 5 hr in Pb atmosphere.

luride/lead phase boundary. Next, nickel tracer (without chlorine) was applied to the wafer, and it was annealed in an evacuated quartz ampoule for 5 hr during which time the crystal converted from n- to p-type. The crystal was counted and lapped on both faces until the concentration of nickel was the same (2×10^{17} Ni/cm³). It was then placed in an evacuated ampoule containing excess lead but no additional nickel tracer and again annealed for 5 hr. The results are shown in Fig. 4. The nickel concentration increased at the surface, and there is a deep minimum located 15μ below the surface. In addition, the crystal turned n-type again indicating that lead had diffused into the lattice.

The reverse of this experiment was also carried out. Nickel was diffused into n-type PbTe in the presence of a lead reservoir. Nickel completely penetrated the crystal, and the crystal remained n-type. This crystal was lapped on both faces until the concentrations were the same on each face. The crystal was reannealed for 5 hr in a closed vacuum. The crystal was converted to p-type, and the nickel redistributed in a manner similar to that of Fig. 4 although the minimum in the nickel profile was not as deep.

Diffusion in crystals initially equilibrated at the PbTe/Te *phase limit.*—The results of diffusion experiments on crystals pre-equilibrated at the lead telluride/tellurium phase limit can be divided into two categories. The first series of experiments were carried out in the presence of excess tellurium to maintain the partial pressure over the crystal. When nickel alone was allowed to diffuse into PbTe, the resulting profile could be fit to the plane source solution of the diffusion equation

$$C(x) = C_o \exp(-x^2/4Dt) \qquad [1]$$

where C_o is the nickel concentration at the surface following the diffusion anneal, $C(x)$ is the concentration at distance x below the surface, D is the diffusion coefficient, and t is the time of the diffusion anneal. These results are shown in Fig. 5. The value of C_o shown in Fig. 5 is the one obtained by extrapolating the ln C *vs.* x^2 plot to the surface. The actual C_o measured at the surface at the end of the diffusion anneal was usually 5 or 6 times this extrapolated value. The diffusion coefficient for nickel is 4.5×10^{-10} cm²/sec.

When this experiment was repeated using $^{63}NiCl_2$ as the source of nickel, so that nickel and chlorine simultaneously diffused into the crystal, similar results were obtained, but the apparent diffusion coefficient for nickel was 2×10^{-11} cm²/sec. These results are also shown in Fig. 5. The diffusion time of

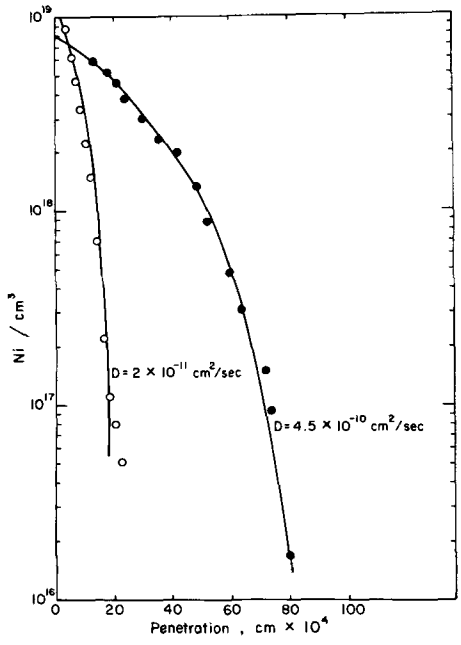

Fig. 5. Diffusion of nickel into crystals pre-annealed at PbTe/Te and diffusion annealed under the same conditions. –●– Nickel-63, 2 hr; –○– nickel-63 simultaneously diffused with chlorine, 23 hr (plotted on a reduced scale).

this experiment was 23 hr. In plotting the data, the curve has been normalized to correspond to a 2-hr anneal. This was accomplished by taking each data point and applying the relation

$$\frac{x}{t^{1/2}} = \frac{x[23]}{(8.28 \times 10^4)^{1/2}} = \frac{x[2]}{(7.2 \times 10^3)^{1/2}}$$

where x is the penetration distance, t the time, and the numbers in brackets denote the different annealing times in hours. The normalization was done so that the differences in the diffusion coefficients would be more obvious.

If nickel and chlorine are simultaneously diffused into a crystal in the absence of a tellurium reservoir, the nickel profile again exhibits a minimum, and nickel completely penetrates the crystal in a matter of 6 hr, the shortest diffusion time used. The nickel profile and corresponding chlorine profile are shown in Fig. 6. The minimum in the nickel profile is nearer the surface for equivalent diffusion times in crystals pre-equilibrated at the tellurium phase limit (6.4 x

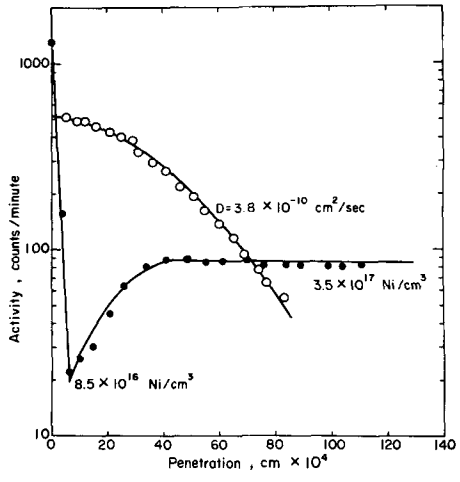

Fig. 6. Simultaneous diffusion of nickel and chlorine into a crystal pre-annealed at PbTe/Te and diffusion annealed in an evacuated ampoule for 6 hr. –○– Chlorine-36 (determined in a separate experiment); –●– nickel-63.

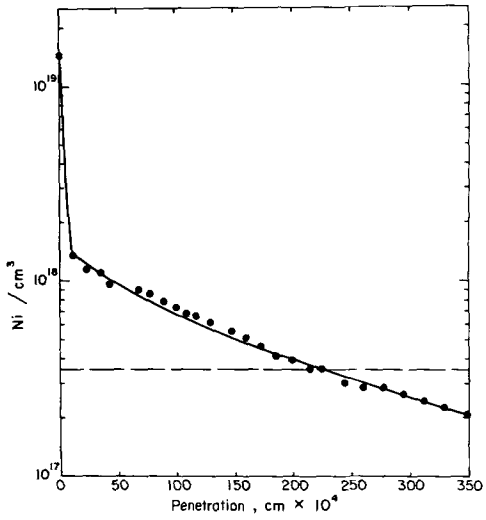

Fig. 7. Effect of tellurium on an initially p-type nickel-doped crystal for 5 hr. - - - Uniform concentration before re-anneal; -●- nickel distribution after re-anneal in Te.

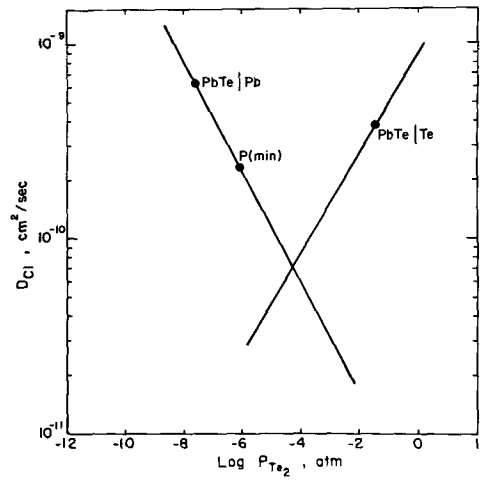

Fig. 8. Diffusion coefficient of chlorine as a function of tellurium pressure. The lines are drawn with slopes = ± ¼.

10^{18} holes/cm^3) than for crystals treated at the minimum total pressure (2 x 10^{18} holes/cm^3).

There was no conversion to n-type conductivity in any of the crystals pre-equilibrated at the tellurium phase limit. All of the crystals were p-type at the end of the diffusion anneal whether or not a tellurium reservoir was used during the diffusion anneal. Several crystals were annealed without radiotracer in evacuated sealed ampoules for times up to 26 hr. No change was noted in either the carrier concentration as determined from Hall measurements or in the Seebeck coefficient.

The effect of tellurium on the distribution of nickel was established in the following way. A crystal pre-equilibrated at the tellurium phase limit was simultaneously diffused with nickel and chlorine for 6 hr in an evacuated ampoule without a tellurium reservoir. Both surfaces were ground down and counted until the nickel activity was the same on both surfaces. This was beyond the depth where any chlorine activity could be detected. The crystal was then sealed in an evacuated ampoule containing excess tellurium but no additional radiotracer and annealed at 700°C for 5 hr. The resulting nickel distribution is shown in Fig. 7. The dashed line represents the nickel concentration before the crystal was subjected to the tellurium treatment. There is a general increase in nickel concentration near the surface with a very sharp increase at the surface.

Diffusion of chlorine.—In those experiments where chlorine from the $NiCl_2$ entered the crystal, the penetration profiles of chlorine were also determined. These have already been presented with the appropriate nickel profiles. The diffusion coefficients for chlorine have been measured, and the results are tabulated in Table I along with the crystal characteristics. These diffusion coefficients represent those obtained under thermodynamically stable conditions. That is, the partial pressure of one of the components was fixed during the experiment. It should be noted, however, that nickel was always present in these crystals. A graph of D_{Cl} *vs.* log P_{Te_2} is shown in Fig. 8. The diffusion coefficient for chlorine appears higher at both phase limits than under conditions of minimum total pressure. The tellurium partial pressure corresponding to the minimum total pressure was obtained from the relation given by Fujimoto and Sata (6)

$$P_{Te_2}(\min) = 2^{-2/3}K^{-2/3} \qquad [2]$$

where K is the equilibrium constant for the formation of PbTe from monatomic Pb and diatomic Te_2 vapor. At 700°C $1/K = 1.6 \times 10^{-9}$ (atm)$^{3/2}$.

Discussion of Results

The diffusion of nickel and chlorine, their interaction with each other and with the lattice have now been examined at the extremes of solid solubility of both lead and tellurium in lead telluride. The results are summarized in Table II. This study, combined with a similar investigation at an intermediate composition defined by the minimum total pressure over lead telluride (1), provides a more complete picture of the interaction of nickel and chlorine with PbTe.

Two limiting cases are to be considered, one in which only nickel is diffusing and the other in which both nickel and chlorine are diffusing simultaneously. In the previous paper (1), it was shown that when nickel alone was diffused into a p-type crystal of fixed composition [pre-annealed under an inert atmosphere corresponding to p(min) and then diffusion-annealed under the same conditions], there was no minimum in the resulting penetration profile for the concentration of nickel. On the other hand, the re-arrangement studies of both the previous study [Fig. 7 of ref. (1)] and of the present work (Fig. 4) show that when nickel is distributed homogeneously in a crystal and this crystal is then annealed under conditions to change the stoichiometry, a minimum in the nickel concentration is formed near the surface of the wafer. These data lead to the first conclusion that the production of a minimum is associated with crystals whose composition or concentration of lattice defects is changing during the migration of nickel.

When chlorine diffuses simultaneously with nickel, more pronounced minima are found in the penetration profiles. These findings confirm the first conclusion because chlorine diffuses into the lead telluride, acts as a donor, and creates cation vacancies. These newly created cation vacancies disturb the local defect equi-

Table I. Diffusion coefficients for chlorine in PbTe at 700°C

D_{Cl}, cm²/sec	Position	P_{Te_2}, atm	log P_{Te_2}	log D_{Cl}	Carrier concentration, cm^{-3}	Seebeck coefficient, μv/°C
6.3 x 10^{-10}	PbTe/Pb	2.4 x 10^{-8}	−7.620	−9.200	1 x 10^{18} n	−285
2.3 x 10^{-10}	P(min)	8.7 x 10^{-7}	−6.060	−9.638	2 x 10^{18} p	+230
3.8 x 10^{-10}	PbTe/Te	3.9 x 10^{-2}	−1.410	−9.420	6 x 10^{18} p	+150

Table II. Summary of diffusion studies

Diffusion elements	Prediffusion conditions	Diffusion conditions	Summary of results
1. Lattice defects in PbTe. No tracer.	Equilibrated at PbTe/Pb. n = 9.7 × 10^{17}/cc	Annealed in evacuated ampoule without lead reservoir [corresponding to p(min)].	Crystals, 2-3 mm thick, convert from n- to p-type [p = 2 × 10^{18}/cc] in 3 to 5 hr. Chemical or interdiffusion coefficient, $\tilde{D} \cong 10^{-6}$ to 10^{-7} cm²/sec estimated from time to equilibrate.
2. Nickel (alone). Thin source on surface.	Same as 1.	Same as prediffusion anneal.	Complete penetration of crystal by nickel. $D_{Ni} \geq 10^{-6}$ cm²/sec. Crystal remains n-type.
3. Nickel (alone). Thin source on surface.	Same as 1.	Annealed in an evacuated ampoule without a lead reservoir.	Complete penetration of crystal by nickel. Crystal converts to p-type.
4. Nickel and chlorine. Thin source on surface.	Same as 1.	Same as prediffusion anneal.	Minimum in nickel profile. Crystal remained n-type (Fig. 1).
5. Nickel and chlorine. Thin source on surface.	Same as 1.	Annealed in an evacuated ampoule without a lead reservoir.	Minimum in nickel profile. Crystal exhibits n-p boundary (Fig. 2). Bulk of crystal remains n-type.
6. Nickel (alone) homogeneously distributed in crystal.	p-type crystal lapped until uniform nickel concentration = 2 × 10^{17}/cc	Annealed in evacuated ampoule containing excess lead. Redistribution experiment.	Nickel concentration increases at surface and minimum in profile found near surface. Crystal converts to n-type (Fig. 4).
7. Nickel (alone) homogeneously distributed in crystal.	n-type crystal lapped until uniform nickel concentration = 2 × 10^{17}/cc	Annealed in evacuated ampoule without excess lead.	Nickel concentration increases at surface and minimum in profile found near surface. Crystal converts from n to p type. [p = 2 × 10^{18}/cc].
8. Nickel (alone). Thin source on surface.	Equilibrated at PbTe/Te. p = 6.4 × 10^{18}/cc	Same as prediffusion anneal.	"Conventional" penetration profile $D_{Ni} = 4.5 \times 10^{-10}$ cm²/sec crystal remains p-type (Fig. 5).
9. Nickel and chlorine. Thin source on surface.	Same as 8.	Same as prediffusion anneal.	"Conventional" penetration profile $D_{Ni} = 2 \times 10^{-11}$ cm²/sec crystal remains p-type (Fig. 5).
10. Nickel and chlorine. Thin source on surface.	Same as 8.	Annealed in an evacuated ampoule without excess tellurium.	Minimum in nickel profile. Crystal remains p-type (Fig. 6).
11. Nickel (alone) homogeneously distributed in crystal.	p-type crystal lapped until uniform nickel concentration = 2 × 10^{17}/cc	Annealed in evacuated ampoule containing excess Te. Redistribution experiment.	Nickel concentration increases at surface with no minimum in profile near surface. Crystal remains p-type.

librium, and the lead atoms from the sites where the cation vacancies were created must migrate out. In the previous paper (1) it was suggested that the cause of these minima in the penetration profiles was due to the "pile up" of the lead atoms trying to migrate outward to the surface while the chlorine front moved inward. Because the diffusion coefficient of chlorine (in the presence of nickel) is of the order of 10^{-10} cm²/sec (see Table I) while the diffusion of cation vacancies is estimated to be of the order of 10^{-6} to 10^{-7} cm²/sec from the time necessary to equilibrate the specimens in an inert atmosphere (see Table II), this explanation is not correct. Nevertheless, the migration of atoms must occur as stated, *i.e.*, the chlorine ions move in creating cation vacancies while the lead atoms move in the opposite direction.

It is assumed that the nickel migrates interstitially (except under high tellurium pressures as will be discussed below) and that it meets and occupies lead vacancies in accord with the mechanism first suggested by Bloem and Kröger (8) for nickel diffusing into lead sulfide. The minima in the penetration profiles of nickel observed in the present study must therefore be a direct consequence of a low concentration of available cation vacancies and correspondingly a high concentration of interstitial lead atoms ($K_F = [V'_{Pb}][Pb_i^{\bullet}]$) so that the sites available for nickel atoms are decreased from the concentration of sites in the bulk crystal.

Next consider the production of the p to n boundary within the crystal. Because minima in the nickel penetration profiles occur both with and without a corresponding apparent change in carrier, the second conclusion is that a change from p to n type, or conversely, is not necessary for the migration of nickel nor for the formation of the minima. However, there is an interaction between the electrons and the migration of the minima because the defect equilibrium must be preserved.

The position of the minimum in the nickel concentration profile is displaced further from the surface of the crystal as the hole concentration decreases or as the electron concentration increases for equal diffusion times. The region of the minimum in the nickel concentration profile is wider, or extends further into the crystal, in PbTe containing excess lead than in material containing excess tellurium. The region of the minimum in the nickel concentration is expected to be wider the slower the out-diffusion of lead or the faster the in-diffusion of chlorine. In other words the greater the difference in the diffusion coefficients of lead and chlorine, the wider will be the region where a nonequilibrium defect concentration exists. The chlorine diffusion coefficient is higher at both phase limits than at an intermediate composition (see Fig. 8). If all other parameters were fixed, then it is to be expected that the minimum in the nickel profile would be the widest and be found farthest into the crystal in highly n-type material. Furthermore, the minimum should be the narrowest and lie closest to the surface at the intermediate composition studied, because the chlorine diffusion coefficient is lowest here. As already noted, however, this trend is not the one observed. The trend from broad minima well away from the surface of the crystal on the lead rich side to narrow minima located nearer the surface on the tellurium rich side suggests that the diffusion coefficient of lead changes continuously and in the same direction across the phase field.

While no quantitative arguments can be made because of the changing chlorine diffusion coefficient across the phase field, it appears that the diffusion coefficient of lead increases in going from the lead telluride/lead phase boundary to the lead telluride/tellurium phase boundary. The faster the out-diffusion of lead when chlorine is diffusing into the lattice, the more narrow will be the region where there is a transient excess of lead relative to the equilibrium value. A simple cation defect structure which has the property of increasing the cation diffusion coefficient with increasing hole concentration is vacancies on the cation sub-lattice. The cation vacancy concentration would be expected to increase in going from the lead rich side of the phase field to the tellurium rich side.

When crystals pre-equilibrated at the tellurium phase limit were diffused with nickel in the presence of a tellurium atmosphere, the nickel penetration profiles were unlike those obtained under any other experimental conditions (see Fig. 5). In the absence of chlorine the penetration profile of nickel could be fit to Eq. [1] with $D = 4.5 \times 10^{-10}$ cm²/sec, with the exception that C_o obtained from a plot of ln C *vs.* x^2 was only about one-fifth of the observed value of the nickel concentration at the surface after the diffusion anneal. When nickel and chlorine were simultaneously diffused under the same conditions, similar results were obtained except that the apparent diffusion coefficient of nickel was 2×10^{-11} cm²/sec. Again the

value of C_0 obtained from a plot of ln C *vs.* x^2 was considerably less than the observed value.

The fact that the observed C_0 was always higher than the extrapolated value implies that nickel is being trapped on the surface. Such behavior is indicative of some sort of surface reaction. Since nickel appears to diffuse very rapidly in the absence of a tellurium atmosphere, the data suggest that nickel reacts at the surface to form nickel telluride. This reactive behavior of tellurium was confirmed by exposing a nickel-doped crystal of PbTe to a tellurium atmosphere. Nickel is withdrawn from the crystal with the nickel concentration increasing near the surface and decreasing in the bulk of the crystal (see Fig. 7). There is almost a discontinuity in the nickel concentration profile very near the surface. Such a concentration profile can be explained if the chemical potential of nickel at the surface of the crystal is less than that in the bulk as was first suggested by Bloem and Kröger (8) for the behavior of nickel in lead sulfide. This would be the case if nickel reacted with tellurium vapor at the surface of the crystal to form a second phase of nickel telluride. Nickel is known to form several compounds with tellurium. (7).

It is possible to speculate why the nickel concentration profiles obtained in tellurium atmospheres show completely different characteristics than otherwise found. If reaction at the surface were simply trapping part of the nickel, then one would expect that only a small amount of nickel would enter the crystal, but nickel would diffuse rapidly as observed under other experimental conditions. Instead, the diffusion of nickel itself appears to be much slower. It may be that the concentration profiles of nickel obtained under tellurium atmospheres are not representative of nickel diffusing into the lattice but may be instead a measure of some interpenetration of nickel telluride and lead telluride.

This same sort of behavior is observed with nickel in lead sulfide. Bloem and Kröger (8) found nickel diffusion coefficients in PbS on the order of 7×10^{-6} cm^2/sec at 500°C under inert atmospheres, whereas Seltzer and Wagner (9) found nickel diffusion coefficients on the order of 3×10^{-13} cm^2/sec at 700°C in sulfur atmospheres. Further, it was found (9) that the diffusion coefficient at 700°C was not particularly affected by varying the partial pressure of sulfur between 0.1 and 3×10^{-6} atm, and that in the region 200°-500°C nickel diffused out of PbS when nickel-doped PbS was exposed to an H_2S atmosphere (8). Both of these results suggest that nickel reacts with sulfur at the surface of PbS to form nickel sulfide.

In the present study an additional effect has been observed, however. When nickel and chlorine are simultaneously diffused into PbTe at 700°C under a tellurium atmosphere, the apparent diffusion coefficient of nickel is much smaller than when nickel alone is diffused under the same experimental conditions. If nickel is forced to diffuse via a vacancy mechanism when a tellurium atmosphere is present, the results can be explained in terms of the availability of cation vacancies. Under a tellurium atmosphere nickel appears to have a diffusion coefficient of 4.5×10^{-10} cm^2/sec in the absence of any chlorine. This value is about the same as found for chlorine under the same conditions, 4.2×10^{-10} cm^2/sec. Since it is believed that chlorine creates lead vacancies, the out-diffusing excess lead should affect the diffusion of nickel in the manner observed, *i.e.*, decrease the apparent diffusion coefficient. While the data suggest a definite interaction between nickel, chlorine and the crystal under tellurium atmospheres, it has not been possible to ascertain the exact mechanism. It is suggested that the diffusing nickel species is different in an oxidizing atmosphere (tellurium) than in an inert or reducing atmosphere (vacuum or lead), and is thereby forced to diffuse via a vacancy mechanism rather than interstitially.

While the behavior of nickel under various experimental conditions has been the main focus of this investigation, some information has been collected on the diffusion of chlorine. Even though the diffusion of chlorine has always been carried out in the presence of nickel, certain trends seem apparent. The diffusion coefficient of chlorine varies across the phase field of lead telluride in a manner which suggests a Frenkel defect structure on the anion sublattice. The diffusion coefficient of chlorine is higher at both phase limits than at the intermediate composition studied (see Fig. 8). Anion vacancy migration should predominate on the lead rich side of the phase field, while interstitial migration will predominate near the tellurium rich phase limit.

The change in the diffusion coefficient with a change in tellurium partial pressure on the lead rich side of the phase field can be given by

$$D_{Cl} \propto P_{Te_2}{}^{-0.245} \cong P_{Te_2}{}^{-1/4} \qquad [3]$$

This value is calculated on the basis of only two experimental points and, therefore, is only an approximation. Nevertheless, a $-\frac{1}{4}$ dependence on the tellurium partial pressure is the dependence one would expect if anion migration occurred via a singly charged anion vacancy, $V^{\bullet}_{Te}$. The line through the point located at the lead telluride/tellurium phase boundary has been drawn with a $+\frac{1}{4}$ slope. While there is no experimental verification of this dependence, this is the expected dependence for diffusion via singly charged interstitials.

The suggestion made here that a Frenkel disorder is present on the anion sublattice of lead telluride is in agreement with most of the anion diffusion work on the lead chalcogenides and on the II-VI compounds (10-12). The first indication that anion diffusion in compound semiconductors was of sufficient magnitude to be of importance was made by Seltzer and Wagner (10) in their study of sulfur-35 diffusion into PbS. Their results indicated that not only was anion migration an appreciable component of diffusion in PbS, but also that the predominant disorder on the anion sublattice was a Frenkel defect, anion vacancies in lead rich PbS and anion interstitials in sulfur rich PbS. The anion Frenkel disorder has also been inferred for PbSe by diffusion of Se-75 into PbSe (11). Woodbury (12) has established that an anion Frenkel disorder also exists in II-VI compounds, although anion migration in chalcogenide rich materials seems to occur via a neutral interstitial.

Summary and Conclusions

The diffusion of nickel and chlorine has been studied at the limit of solid solubility of both lead and tellurium in lead telluride at 700°C, and the results compared with those previously reported (1) on PbTe equilibrated at the minimum total pressure composition. With the exception of diffusion anneals in a tellurium atmosphere, the diffusion of nickel at 700°C is very rapid. We estimate D_{Ni} to be greater than 10^{-6} cm^2/sec.

The minimum which is produced when chlorine is diffused into nickel-doped lead telluride or is simultaneously diffused with nickel is also produced when lead is diffused into or out of nickel-doped PbTe. Any condition which causes the migration of lead through the lattice of a nickel-doped crystal produces a minimum in the nickel distribution. This supports our earlier conclusion concerning the minima in the nickel concentration profile (1). Contrary to the interpretation by Peart *et al.* (13) and by Larrabee and Osborne (14) in their studies of impurity interaction in GaAs, it is not believed that amphoteric behavior of nickel in PbTe is the reason for the minimum. For such to be the case, it seems likely that there would be only one combination of crystal stoichiometry and electronic state which would yield a solubility minimum. Instead we observe the phenomena in both n- and p-type PbTe.

The results of diffusion experiments carried out in a tellurium atmosphere suggest that nickel reacts with tellurium vapor forming a second phase at the surface. The effects on the distribution of nickel in PbTe on exposure to a tellurium atmosphere confirm this result as do diffusion studies in the absence of a tellurium atmosphere. These results also suggest an explanation for differences observed in the diffusion of nickel into PbS at low temperatures (8) in an inert atmosphere and those obtained in the 700°C region under sulfur atmosphere (9). It is also suggested that the diffusing nickel species is different in a tellurium atmosphere than under inert or reducing conditions.

The implications of these results on general doping experiments and practice in the lead salts are also of interest. If other impurities in the lead salts behave to change in the crystal stoichiometry as does nickel, methods of doping the lead salts must be reinvestigated. Changes in the crystal composition brought about by changes in the atmosphere above the crystal could induce changes in an impurity distribution which will not return to equilibrium in the time normally assumed reasonable to properly equilibrate crystals. The result will be a nonuniform doping concentration which will obviously affect other measurements.

The analysis of the chlorine diffusion data suggest that migration on the anion sublattice occurs via a Frenkel defect, anion vacancies being responsible for motion in lead rich PbTe and anion interstitials in tellurium rich material.

Manuscript submitted June 5, 1968; revised manuscript received March 17, 1969. This was Paper 629 presented at the Montreal Meeting, Oct. 6-11, 1968. Work on this paper was supported by the Army Research Office—Durham.

Any discussion of this paper will appear in a Discussion Section to be published in the December 1969 JOURNAL.

REFERENCES

1. T. D. George and J. B. Wagner, Jr., *This Journal*, **115**, 956 (1968).
2. R. F. Brebrick and E. Gubner, *J. Chem. Phys.*, **36**, 1283 (1962).
3. G. B. Larrabee, *This Journal*, **108**, 1130 (1961).
4. A. D. Suttle, Jr., and W. F. Libby, *Anal. Chem.*, **27**, 921 (1955).
5. W. F. Libby, *ibid.*, **29**, 1566 (1957).
6. M. Fujimoto and Y. Sato, *Jap. J. Appl. Phys.*, **5**, 128 (1966).
7. H. Reiss, Editor, "Progress in Solid State Chemistry," Vol. I, p. 83, Pergamon Press, New York (1964).
8. J. Bloem and F. A. Kröger, *Philips Research Repts.*, **12**, 303 (1957).
9. M. S. Seltzer and J. B. Wagner, Jr., *J. Chem. Phys.*, **38**, 2309 (1963).
10. M. S. Seltzer and J. B. Wagner, Jr., *J. Phys. Chem. Solids*, **26**, 233 (1965).
11. Y. Ban and J. B. Wagner, Jr., Unpublished data.
12. H. Woodbury and R. B. Hall, *Phys. Rev.*, **157**, 641 (1967).
13. R. F. Peart, K. Weisner, J. Woodall, and R. Fern, *Appl. Phys. Letters*, **9**, 200 (1967).
14. G. B. Larrabee and J. F. Osborne, *This Journal*, **113**, 564 (1967).

Doped Oxides as Diffusion Sources

I. Boron into Silicon

M. L. Barry* and P. Olofsen*

Fairchild Semiconductor Research and Development Laboratory, Palo Alto, California

ABSTRACT

A model is presented describing the diffusion of dopants from a deposited oxide into a semiconductor substrate, and simple methods are developed for measuring directly the physical constants required to describe the diffusion. Experimentally determined values of these constants for the case of boron diffusing into silicon are given for wide ranges of temperature and concentration.

Diffusion of dopants into semiconductors, particularly silicon, from a doped oxide which has been deposited at low temperatures appears to hold several advantages over standard high-temperature predeposition and diffusion processes; these advantages include better over-all process control and increased flexibility in choosing diffusion schedules, doping levels, and device configurations. Diffusion from deposited doped oxides has been reported (1-7), but these reports deal primarily with device applications and the stress effects from low-level doping. Owen and Schmidt (8) described diffusion of phosphorus from thin doped anodic oxides, but their analysis is complicated by uncontrolled experimental conditions in their early work with these oxides. In this paper, we first develop a simple model for diffusion from a doped oxide into a semiconductor, use this model to interpret experimental data for the case of boron diffusing into silicon, and then discuss improvements to the model in light of these data. Subsequent reports will treat the cases of other dopants diffusing into silicon.

* Electrochemical Society Active Member.

Theory

The most general one-dimensional case for diffusion of a dopant from a uniformly doped oxide into a semiconductor substrate is shown in Fig. 1. Here region I is the deposited doped oxide, with initial concentration C_o and thickness $x_o - x_B$, region II is the semiconductor substrate, and region III is an undoped barrier oxide of thickness x_B. Subscripts 1, 2, and 3 denote these regions, respectively. For normal device application of this type of diffusion, x_B is reduced to a minimum, of course, but the inclusion of a barrier oxide in the model illustrates several useful points and allows us to measure some diffusion parameters of the dopant in the oxide. The diffusion equations in each region are

$$\frac{\partial C_1(x,t)}{\partial t} = D_1 \frac{\partial^2 C_1(x,t)}{\partial x^2}, \quad -x_o < x < -x_B, \; t > 0 \qquad [1]$$

$$\frac{\partial C_2(x,t)}{\partial t} = D_2 \frac{\partial^2 C_2(x,t)}{\partial x^2}, \quad x > 0, \; t > 0 \qquad [2]$$

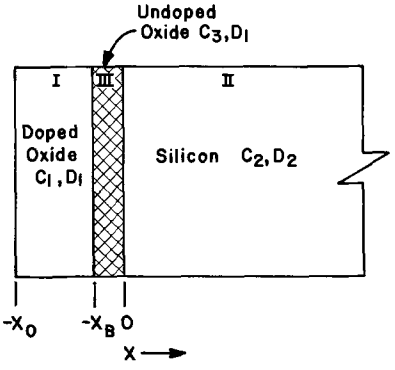

Fig. 1. Diffusion from a deposited doped oxide through a barrier oxide into a semiconductor substrate.

$$\frac{\partial C_3(x,t)}{\partial t} = D_3 \frac{\partial^2 C_3(x,t)}{\partial x^2} = D_1 \frac{\partial^2 C_3(x,t)}{\partial x^2}, \quad -x_B < x < 0, t > 0 \quad [3]$$

assuming the diffusion coefficients are not functions of concentration, and ignoring any field-aided diffusion terms operating on ionized dopants. The conditions under which these assumptions appear valid and the corrections to be made when they are not will be discussed in a later section. These equations also implicitly assume that the diffusion is a fixed-boundary problem; that is, silicon oxide is not formed at the oxide-silicon interface by oxidizing species from the ambient diffusing through the deposited oxide or by the transfer of the doping species from the oxide to the silicon (for example, boron oxide being reduced by silicon to form elemental boron and silicon oxide). The first condition can be assured either by performing the diffusion in an inert atmosphere or by using a thick deposited oxide, and it will be shown that the thickness of the oxide arising from the second factor is small compared to the diffusion length of the dopant in the oxide.

In most cases, the thickness of the substrate is very large compared to the diffusion depth in the substrate, so region II may be considered semi-infinite with little loss of generality. Other boundary conditions are

$$C_1 = C_o, C_2 = C_3 = 0 \text{ at } t = 0 \quad [4]$$

$$C_1 = 0 \text{ at } x = -x_o, t > 0 \quad [5]$$

$$C_2 \to 0 \text{ as } x \to \infty, t > 0 \quad [6]$$

$$C_3 = C_1 \text{ at } x = -x_B, t > 0 \quad [7]$$

$$D_1 \frac{\partial C_1}{\partial x} = D_1 \frac{\partial C_3}{\partial x} \text{ at } x = -x_B, t > 0 \quad [8]$$

$$C_2 = mC_3 \text{ at } x = 0, t > 0 \quad [9]$$

$$D_1 \frac{\partial C_3}{\partial x} = D_2 \frac{\partial C_2}{\partial x} \text{ at } x = 0, t > 0 \quad [10]$$

Boundary condition [5] implies that mass transfer of the dopant in the gas phase at the outer surface is very fast compared to diffusion in the oxide to the surface, and therefore, the concentration of dopant at the outside interface is vanishingly small. This assumption may not be entirely correct, but it appears physically more realizable than that of an impermeable boundary, and it is no more arbitrary than is estimating a suitable mass transfer coefficient; also, as will be shown later, under most conditions of operation this outside boundary condition is largely irrelevant. Boundary conditions [7] and [8] imply equilibrium exists at the boundary between the doped and undoped oxide, that the activity coefficients of dopant in the oxides are independent of concentration, and that all the dopant is free to diffuse, that is, there is continuity of flux at the interface. Conditions [9] and [10] again imply equilibrium and continuity of flux at the oxide-semiconductor interface, but here the segregation coefficient, m, defines the ratio of the activity coefficients of the dopant in the silicon and in the oxide; here again it is assumed that the activity coefficients in both phases are independent of concentration.

Equations [1] through [3] may be solved using boundary conditions [4] through [10], giving

$$C_1(x,t) = C_o \left[1 - \sum_o^\infty \frac{\alpha^n}{2} \left(\text{erfc} \left[\frac{2nx_o - x - x_B}{2\sqrt{D_1 t}} \right] + \alpha \text{erfc} \left[\frac{2nx_o - x + x_B}{2\sqrt{D_1 t}} \right] + 2\text{erfc} \left[\frac{(2n+1)x_o + x}{2\sqrt{D_1 t}} \right] - 2\alpha \text{erfc} \left[\frac{(2n+1)x_o - x}{2\sqrt{D_1 t}} \right] - \text{erfc} \left[\frac{(2n+2)x_o + x - x_B}{2\sqrt{D_1 t}} \right] - \alpha \text{erfc} \left[\frac{(2n+2)x_o + x + x_B}{2\sqrt{D_1 t}} \right] \right) \right] \quad [11]$$

$$C_3(x,t) = \frac{C_o}{2} \left[\sum_o^\infty \alpha^n \left(\text{erfc} \left[\frac{2nx_o + x_B + x}{2\sqrt{D_1 t}} \right] - \alpha \text{erfc} \left[\frac{2nx_o + x_B - x}{2\sqrt{D_1 t}} \right] - 2\text{erfc} \left[\frac{(2n+1)x_o + x}{2\sqrt{D_1 t}} \right] + 2\alpha \text{erfc} \left[\frac{(2n+1)x_o - x}{2\sqrt{D_1 t}} \right] + \text{erfc} \left[\frac{(2n+2)x_o - x_B + x}{2\sqrt{D_1 t}} \right] - \alpha \text{erfc} \left[\frac{(2n+2)x_o - x_B - x}{2\sqrt{D_1 t}} \right] \right) \right] \quad [12]$$

$$C_2(x,t) = \frac{C_o \sqrt{D_1/D_2}}{(1+k)} \sum_o^\infty \alpha^n \left(\text{erfc} \left[\frac{2nx_o + x_B + mkx}{2\sqrt{D_1 t}} \right] - 2\text{erfc} \left[\frac{(2n+1)x_o + mkx}{2\sqrt{D_1 t}} \right] + \text{erfc} \left[\frac{(2n+2)x_o - x_B + mkx}{2\sqrt{D_1 t}} \right] \right) \quad [13]$$

where

$$k = \frac{1}{m} \sqrt{D_1/D_2} \quad [14]$$

and

$$\alpha = \frac{1-k}{1+k} \quad [15]$$

These equations can be considerably simplified if we take the case where the doped oxide thickness is large compared to the diffusion length of the dopant in the oxide, that is, when

$$x_o - x_B \cong 4\sqrt{D_1 t} \quad [16]$$

as will be illustrated by experimental data, this condition is easily achieved for the case of boron. If inequality [16] holds, then terms containing x_o dominate the arguments of the functions in Eq. [11]-[13] and we can restrict the solutions to those terms for which $n = 0$. Then, the concentration of dopant in the silicon becomes

$$C_2(x,t) = \frac{C_o \sqrt{D_1/D_2}}{(1+k)} \text{erfc} \left[\frac{x_B + mkx}{2\sqrt{D_1 t}} \right] \quad [17]$$

For the case of no undoped barrier oxide ($x_B = 0$), this reduces to the simple case of diffusion from a semi-infinite source into a semi-infinite sink, or a complementary-error-function diffusion with an equivalent surface concentration, C_s

$$C_s = \frac{C_o\sqrt{D_1/D_2}}{(1+k)} \quad [18]$$

Thus, the surface concentration for this simple case is independent of time and depends on both the square root of the ratio of the diffusion coefficients and the segregation coefficient.

If we integrate expression [17] from $x = 0$ to $x = x_j$ (the junction depth in the semiconductor), we can determine Q, the total quantity of dopant per unit area which has diffused into the semiconductor and which is proportional to the sheet conductivity, or the inverse of the V/I commonly measured with a four-point probe:

$$I/V = 4.53Q\bar{\mu}q = 4.53\bar{\mu}q\left(\frac{2C_o\sqrt{D_1t}}{(1+k)}\left[\text{ierfc}\left[\frac{x_B}{2\sqrt{D_1t}}\right] - \text{ierfc}\left[\frac{x_B + mkx_j}{2\sqrt{D_1t}}\right]\right]\right) \quad [19]$$

where $\bar{\mu}$ is the effective mean mobility of carriers, q is the electronic charge, and 4.53 is $\pi/\ln 2$, the spreading-current factor for the 4-point probe. If the substrate resistivity is high enough (greater than 2 ohm-cm for most cases), the second term in Eq. [19] can be ignored. Then, for the simple case of no undoped barrier oxide

$$I/V = 8.15 \times 10^{-23}\bar{\mu}C_s\sqrt{D_2t} \quad [20]$$

or

$$\sqrt{D_2} = \frac{1.23 \times 10^{22}}{\bar{\mu}C_s}\frac{d(I/V)}{d(\sqrt{t})} \quad [21]$$

where $\bar{\mu}$ is in units of cm²/sec-V, C_s in atoms/cm³, I/V in mhos, t in hours, and D_2 in μ^2/hr. In addition, it can easily be shown that for this simple case the junction depth can be written

$$x_j = 2\sqrt{D_2t}\,\text{argerfc}\left[\frac{C_b}{C_s}\right] \quad [22]$$

or

$$\sqrt{D_2} = \frac{\frac{d(x_j)}{d(\sqrt{t})}}{2\text{argerfc}\left[\frac{C_b}{C_s}\right]} \quad [23]$$

where C_b is the bulk concentration of the semiconductor substrate. Thus, if we plot the sheet conductivity and the junction depth as functions of the square root of the diffusion time, we should obtain straight lines whose slopes are functions of the surface concentration[1] and are directly proportional to the square root of the diffusivity of the dopant in the semiconductor. If the surface concentration is high enough, it is possible to measure C_s independently, either by anodic oxidation profiling of the sheet conductivity (9) or by determining the plasma frequency (10, 11); when either or both of these techniques are used, it is possible to determine two independent values of D_2 from sheet conductivity and junction depth data. When the surface concentration is too low to be measured accurately, it is still possible to combine Eq. [21] and [23] and determine self-consistent values of D_2 and C_s from the above data.

Once the diffusion coefficient of the dopant in the semiconductor has been measured, it is possible to determine the diffusion coefficient, D_1, of the dopant in the oxide by comparing wafers with and without a thin undoped barrier oxide which have been coated and diffused simultaneously. If the subscript "B" refers to the wafer with a thin, undoped oxide of thickness x_B, and the subscript "N" refers to the wafer with no such barrier oxide, then manipulation of Eq. [17], [19], and [21] results in

$$\sqrt{D_1} = \frac{x_B}{2\sqrt{t}\,\text{argierfc}\left[\frac{\bar{\mu}_N(I/V)_B}{\bar{\mu}_B(I/V)_N\sqrt{\pi}}\right]} \quad [24]$$

$$\sqrt{D_1} = \frac{x_B}{2\sqrt{t}\,\text{argerfc}\left[\frac{(C_s)_B}{(C_s)_N}\right]} \quad [25]$$

$$\sqrt{D_1} = \frac{x_B\sqrt{D_2}}{(x_j)_N - (x_j)_B} \quad [26]$$

That is, if we measure the sheet conductivities, the surface concentration, and the junction depths for diffused wafers with and without a barrier oxide, we can obtain three independent measurements of the diffusivity of the dopant in the oxide.

The segregation coefficient, m, can be determined once the diffusion coefficients are known, from the following relationships derived from Eq. [17] for a wafer with no barrier oxide

$$m = \frac{1}{8.15 \times 10^{-23}\bar{\mu}(V/I)C_o\sqrt{D_2t} - \sqrt{D_2/D_1}} \quad [27]$$

$$m = \frac{1}{\frac{C_o}{C_s} - \sqrt{D_2/D_1}} \quad [28]$$

$$m = \frac{1}{\frac{C_o}{C_b}\text{erfc}\left[\frac{x_j}{2\sqrt{D_2t}}\right] - \sqrt{D_2/D_1}} \quad [29]$$

Thus, we can determine the constants of the diffusion by determining surface concentrations, sheet conductivities, and junction depths, and then, in turn, calculate concentration profiles from this model for any given diffusion time, diffusion temperature, and initial dopant concentration in the oxide.

Experimental

The substrates used in this work were all (111) silicon wafers, sliced from Czochralski-grown crystals, lapped on both sides, and mechanically and chemically polished on one side. The boron doped oxides were deposited by oxidation of silane and diborane at a substrate temperature of 400°C, and the diffusions were performed in dry nitrogen ambients. The thickness of the doped oxide was normally 0.5μ, although several experiments were done with thicker films. The boron concentration of the films was determined by flame photometric analysis of films deposited simultaneously with those used for diffusion (13). The sheet conductivity was measured with a four-point probe in an 18-position array on each wafer; earlier studies have shown that the distribution of these values across the wafer is normal; a typical standard deviation was less than 5% of the mean. Junction depths were measured using the Nomarsky interfer-

[1] Actually the slope of the sheet conductivity curve is a function of the product of the surface concentration and the mean mobility of the carriers, defined as

$$\bar{\mu} = \frac{\int_o^{x_j}\mu(C)\,C(x,t)\,dx}{\int_o^{x_j}C(x,t)\,dx}$$

It can be shown that if $C_2(x,t)$ has the form of a complementary error function, $\bar{\mu}$ is independent of diffusion time and depends on the surface concentration only. Using this assumption, we have calculated $\bar{\mu}$ as a function of C_s by numerical integration of Irvin's conductivity mobility data (12), assuming complete ionization.

ence technique after delineation by grooving and staining with a nitric-hydrofluoric acid solution (70% HNO_3:49% HF:H_2O = 0.1:50:50, by volume). The surface concentration, as mentioned above, was determined either from a profile (normal to the surface) of the sheet conductivity or from the minimum in the infrared reflection spectrum (plasma-frequency technique). Ellipsometric methods were used to measure the thickness of the barrier oxides used for measurements of the diffusivity of boron in the oxide.

Results

That these diffusions actually do follow the behavior predicted above is evidenced by Fig. 2 and 3 where the results of diffusions of boron into silicon at 1100°C from three different initial doping concentrations are shown. In addition, as predicted by Eq. [18], the surface concentrations remain constant in time, with the possible exception noted below. The concentration profile for a typical diffusion is shown in Fig. 4; the solid dots are the values measured by a sheet-conductivity profiling technique (9), and the bars are estimates of the uncertainty of the measurement, reflecting primarily a ±2% accuracy in measuring the sheet conductivity. The data follow a complementary-error-function curve satisfactorily, although at this level of accuracy it is probably impossible to distinguish between this profile and a Gaussian profile.

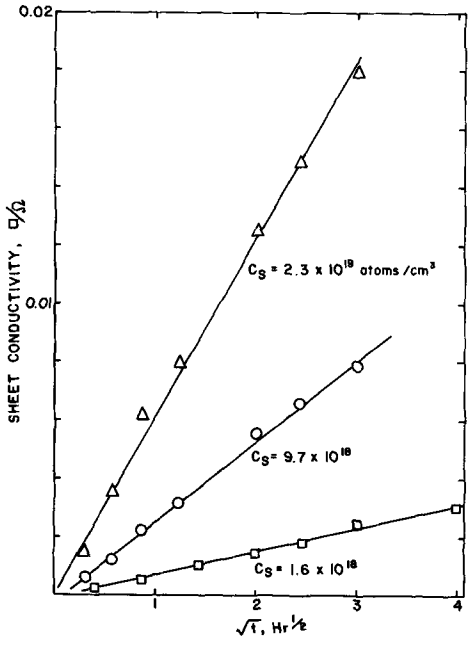

Fig. 2. Sheet conductivities resulting from diffusion of boron into silicon at 1100°C from deposited oxides with different initial boron concentrations.

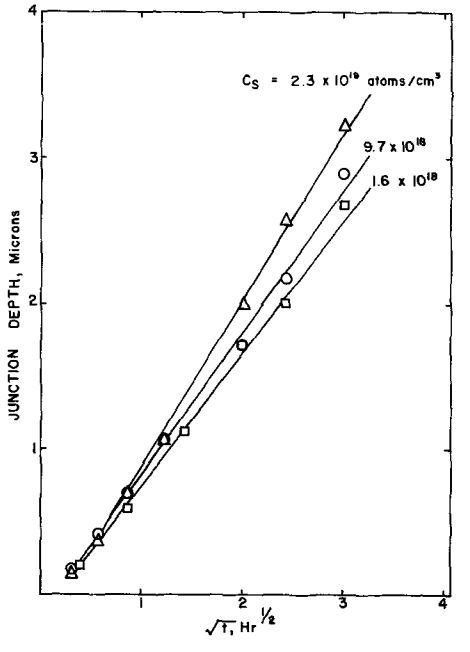

Fig. 3. Junction depths resulting from diffusion of boron into silicon at 1100°C from deposited oxides with different initial boron concentrations.

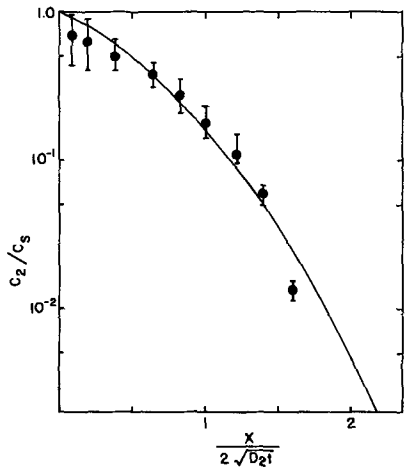

Fig. 4. Concentration profile of boron diffusing into silicon from a deposited oxide.

At temperatures below 1100°C, we find experimentally that the sheet conductivity and junction depth curves are shifted slightly along the positive time axis from the origin; we explain this as the effect of a thin, irremovable oxide which always exists at the silicon surface and which acts as a diffusion barrier. Calculations based on our diffusion model yield an estimated thickness of this oxide of about 50Å, and this is corroborated by ellipsometric measurements. At high temperatures this thickness is normally small compared to the diffusion lengths of dopant in the oxide, and the effect disappears.

At high surface concentrations (about 1 x 10^{20} at./cm³), a more serious deviation from our simple model occurs: the $I/V - \sqrt{t}$ curve becomes distinctly concave downward at diffusion times of about 2-3 hr, as shown in Fig. 5. There also may be a slight decrease in the surface concentration at this point, although the decrease is about the same size as the estimated accuracies of the measuring techniques used. At higher temperatures this behavior begins at lower

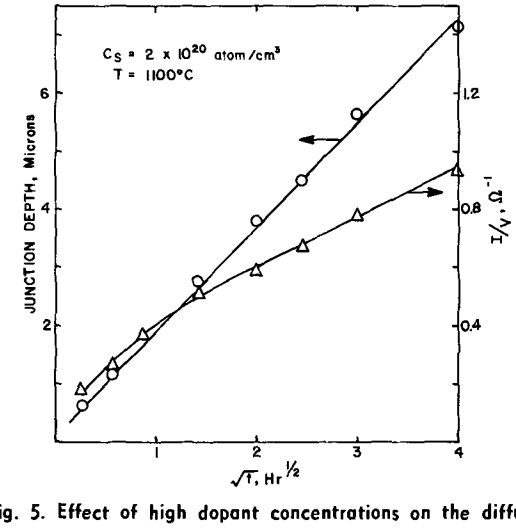

Fig. 5. Effect of high dopant concentrations on the diffusion of boron into silicon from a deposited oxide.

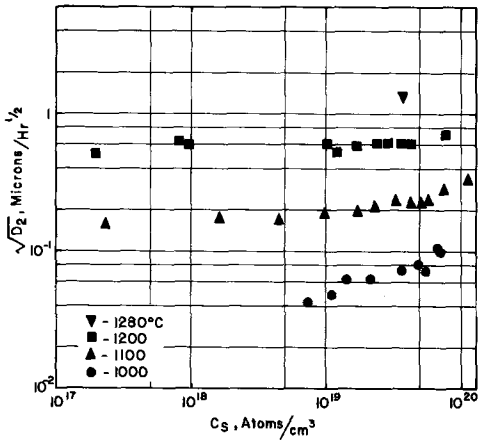

Fig. 6. Diffusion coefficients of boron in silicon at various temperatures and surface concentrations.

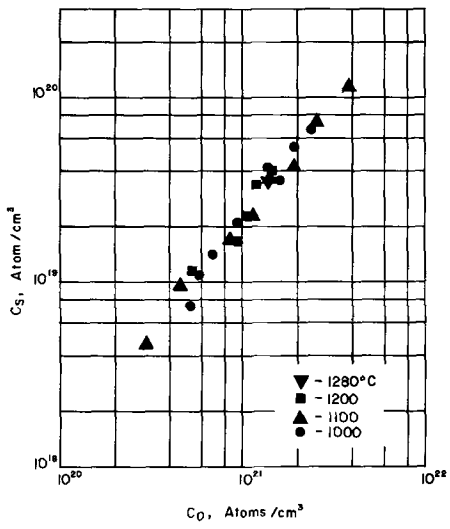

Fig. 7. Surface concentrations of boron in silicon resulting from various concentrations of boron in the deposited oxide.

surface concentrations, and conversely at lower temperatures. The junction depth remains a linear function of $\sqrt{t}$ for all conditions as is also shown in Fig. 5. This effect at high surface concentrations is quite reproducible, and effective diffusion coefficients calculated from the junction depth measurements are in agreement with predicted values.

The square roots of the diffusion coefficients of boron in silicon measured using all the above techniques at surface concentrations from 2 x 10^{17} to 1 x 10^{20} at./cm^3 and for temperatures from 1000° to 1280°C are shown in Fig. 6. Results of measurements of the diffusivity of boron in the oxide and the segregation coefficient at various temperatures are shown in Table I; the three different methods cited for the diffusivity measurements refer to Eq. [24], [25], and [26], respectively, while the values for the segregation coefficient were calculated from surface concentration data using Eq. [28].

The surface concentrations resulting from various concentrations of boron in the deposited oxide are shown in Fig. 7. Surface concentrations greater than 2.5 x 10^{19} at./cm^3 were measured using the techniques described earlier, while those less than this figure were calculated. The overlapping of the points at different temperatures reflects the relative insensitivity of the ratio of the diffusion coefficients to temperature.

Reliability of the Data

The data presented above fall into two general classifications: In some cases it has been possible to measure the same parameter with more than one technique; for example, at relatively high surface concentrations we can measure the diffusivity of boron in silicon by either the sheet-conductivity method (Eq. [21]) or by the junction-depth method (Eq. [23]). The validity of the model is then directly related to the agreement between these independent values, and these values can be legitimately compared to diffusivities and segregation coefficients measured by other techniques. Data which fall in the other class comprise those cases where independent values of one parameter are not readily measurable; then the parameters calculated can only be self-consistent and cannot be used directly to test the validity of the model, but can be used to make predictions of experimental behavior within the range of the model. In discussing the reliability of the data, then, it is important to distinguish between the accuracies involved in establishing the model as valid and the reliability which can be claimed (based on self-consistent data) for predicting experimental behavior from this model.

The reliability of the values reported above has been estimated by a geometrical combination of deviations for each of the factors entering in the calculations. For example, the diffusivity of boron in silicon as calculated by the sheet-conductivity method (Eq. [21]) is a function of the slope of the $I/V - \sqrt{t}$ curve, the effective mean mobility, and the surface concentration. The sheet conductivity data have been fitted to a least-squares straight line assuming no uncertainty in the diffusion time values; the relative standard deviations of the slopes of these lines are typically well under 5%. The uncertainty in the measured surface concentration can be as high as 25% in some cases, while the uncertainty of the mean mobility is close to 10%; these combine to yield an expected relative standard deviation in $\sqrt{D_2}$ of about 28%. In similar fashion, $\sqrt{D_2}$ calculated from junction depth measurements (Eq. [23]) has a relative standard deviation of only about 6%, primarily because argerfc (C_b/C_s) is insensitive at values of C_b and C_s normally encountered. Table II shows values of $\sqrt{D_2}$ for boron in silicon at various temperatures, as determined by these two methods. In general, there is excellent agreement between these two methods, much better than predicted from the relative accuracies of the measurements, and this agreement indicates the model is applicable under these diffusion conditions.

On the other hand, the uncertainties in the self-consistent data are much smaller than predicted above because a direct measurement of the surface concentration is not involved. For example, analyses similar to that above result in expected deviations of about 15% for $\sqrt{D_2}$ and about 12% for calculated values of

Table I. Diffusion parameters of boron in oxide

Temp, °C	C_o, at./cm^3	$\sqrt{D_1}$ ($\mu/\sqrt{hr}$), by method of: Sheet conductivity	Surface concentration	Junction depth	m
1000	1.4 x 10^{21}	—	—	0.0011	—
1100	1.4 x 10^{21}	0.01	0.01	0.006	0.2
1200	1.4 x 10^{21}	0.02	0.03	0.015	0.06
1280	1.4 x 10^{21}	0.04	0.06	0.02	0.06

Table II. Diffusion coefficients of boron in silicon by junction-depth and sheet-conductivity methods

Temp, °C	C_s	$\sqrt{D_2}$ ($\mu/\sqrt{hr}$), by method of: Sheet conductivity [21]	Junction depth [23]
1000	8 x 10^{19}	0.1	0.098
1100	5 x 10^{19}	0.2	0.22
1200	4 x 10^{19}	0.6	0.60
1280	4 x 10^{19}	1.3	1.41

C_s; in these cases, the major uncertainty is in the mobility data used.

The uncertainties in the measurements of the diffusion coefficient of the dopant in the oxide and the segregation coefficient are generally larger than those mentioned above. Normally in these calculations we are using either small differences between measured values or functions which are very sensitive to the ratios of experimentally determined values; in either case, slight errors can be magnified into large relative deviations. As a result, values of $\sqrt{D_1}$ are probably good only within ±50%, while values of m (which reflect the total of all the uncertainties listed above plus a 10% deviation in the determination of C_o, lumped into one calculation) are reliable only within a factor of 3.

Discussion of Results

Any test of the validity of a simple model such as that formulated above must indicate how well experimental data within the specified range of the model agree with its predictions and how severely the model must be modified to cover cases falling outside this specified range. With this in mind, we will discuss, first, the over-all behavior of the data and, then, in more detail, the deviations which appear at high surface concentrations.

Inspection of the results shown in Fig. 6 shows that the diffusion coefficient of boron in silicon is not strictly independent of the concentration, as is assumed in our simple model. Much of this concentration dependence can be explained by including effects of the self-induced field acting on the ionized dopants or, in other words, considering the electrochemical potential as the driving force, rather than just the chemical potential. Then an effective diffusion coefficient can be written as shown by Smits (14) and Kurtz and Yee (15):

$$D_{\text{eff}} = D_2\left(1 + \frac{C_2}{\sqrt{C_2^2 + 4n_i^2}}\right) \qquad [30]$$

where n_i is the intrinsic carrier concentration in the substrate at the diffusion temperature. The effective diffusion coefficient then varies between D_2 at low surface concentrations and twice this value at high surface concentrations. The transition regions should extend roughly from 3 x 10^{18} to 9 x 10^{19} at./cm^3 at 1000°C, from 5 x 10^{18} to 2 x 10^{20} at./cm^3 at 1100°C, and from 1 x 10^{19} to 3 x 10^{20} at./cm^3 at 1200°C. Within these concentration limits the diffusivities we have reported are actually values averaged over the range of concentration extending from the surface to the lower value of the limits given above. Since the majority of dopant atoms in these diffusions are at high concentrations near the surface, it is a reasonable approximation to report the diffusion coefficients as a function of surface concentration.

A more serious problem, both in terms of validating our diffusion model and in terms of making accurate predictions of diffusion behavior, is the divergence of the sheet conductivity $-\sqrt{t}$ curve from a straight line at high surface concentrations. The reason for this behavior is not known at the present time, but several hypotheses which have been advanced are discussed in some detail below:

1. formation of an oxide barrier at the doped oxide-silicon interface;
2. nonuniform concentration of the dopant in the oxide;
3. excessive out-diffusion of dopant from the oxide;
4. dependence of the diffusivity of the dopant in the oxide on concentration;
5. nonequilibrium at the interface.

If it is assumed that boron is transferred across the oxide-silicon interface by a reaction such as

$$2B_2O_3 + 3Si \rightarrow 3SiO_2 + 4B$$

then it can be shown that the ratio of the thickness of SiO_2 grown (x_o') to the diffusion length of boron in the oxide is

$$\frac{x_o'}{2\sqrt{D_1 t}} = \frac{1.8 \times 10^{-23} C_o}{1 + 1/m\sqrt{D_1/D_2}} \qquad [31]$$

where C_o is in units of at./cm^3. Even in heavily doped oxides, where C_o may be 3 x 10^{21} at./cm^3, the oxide formed is only a few per cent of the diffusion length of the dopant in the oxide and will not interfere significantly with the course of the diffusion.

The anomalous results shown above in Fig. 5 can also be explained by a nonuniformly doped oxide with a high surface concentration of dopant close to the oxide-silicon interface (see Appendix A). However, in our particular deposition system, a change in the deposition rate greatly magnifies any concentration gradient existing in the oxide, and we have seen no change in the anomalous behavior described above over a twentyfold deposition rate increase. Therefore we conclude that this behavior is not a result of a concentration gradient in the oxide. In addition, we have found that depositing a 1.5μ doped oxide, rather than the normal 0.5μ film, has no effect on the shape of the sheet conductivity curve at high surface concentrations. This confirms our assumption, based on the data given in Table I, that excessive out-diffusion of dopant from the oxide into the ambient is not the cause of this anomaly.

We have not been able to measure the diffusion coefficient of the dopant in the oxide accurately enough to test its independence of concentration. It is not unlikely, however, that the diffusion coefficient of boron becomes dependent on its concentration in the oxide at the relatively high levels where our discrepancies appear (16), and variations in the diffusion coefficient as large as those noted in Table I would be sufficient to cause the behavior shown in Fig. 5.

It has also been proposed that equilibrium does not always exist at the silicon-oxide interface; that in the initial stages of the diffusion, perhaps because of high stresses at the surface or because of specific boron-silicon compound formation (17), a large quantity of dopant is transferred across the interface and then diffuses normally into the substrate. At the present time, we have not been able to devise experimental means of discriminating between this behavior and that listed directly above.

It should be emphasized here that the deviations which have been discussed above occur only over a very limited range of surface concentrations, and that in the majority of cases of interest, the model presented above is quite adequate to describe the experimental behavior. A comparison is made in Fig. 8 of some of our data with that reported by other workers. Our values for the diffusivity of boron in silicon at surface concentrations near 3.5 x 10^{19} at./cm^3 are slightly lower than those of Fuller and Ditzenberger (18) at high surface concentrations, but agree well with those of Kurtz and Yee (15) and Maekawa and Oshida (19) at comparable concentrations. Our values for m agree with those estimated by Grove *et al.* (20).

Conclusions

The technique of diffusing from doped oxides deposited at low temperatures is very attractive, primarily because of complete and independent control of the surface concentration. The solution of the diffusion equations, with appropriate simplifications, predicts that the diffusion profile in the semiconductor substrate will follow a simple complementary error function if the thickness of the doped oxide is sufficient, and that the effective surface concentration depends directly on the initial concentration of dopant in the oxide, the ratio of diffusivities of the dopant in the oxide and in the semiconductor, and the segregation coefficient. The model also predicts simple techniques for measuring these parameters. We have shown ex-

perimentally that this model is followed for surface concentrations less than 1 x 10^{20} at./cm^3, and we have determined values of the diffusion coefficients of boron in silicon over wide ranges of temperature and concentration. We have not been able to explain certain deviations from this model at surface concentrations greater than 1 x 10^{20} at./cm^3, but diffusions in this range are reproducible and thus useful.

Acknowledgment

The authors are indebted to Mrs. J. Bien and Mrs. B. Tyson for their assistance in the experimental part of this work and to Dr. W. H. Shepherd for many technical discussions.

Manuscript submitted Nov. 27, 1968; revised manuscript received Jan. 27, 1969. This paper was presented at the Chicago Meeting, Oct. 15-19, 1967, as Paper 169.

Any discussion of this paper will appear in a Discussion Section to be published in the December 1969 JOURNAL.

APPENDIX A

Diffusion from a continuously varying concentration of dopant in the initial deposited oxide can be approximated by the case of diffusion from a series of oxide increments parallel to the silicon interface, the dopant concentration being constant within any increment but varying from increment to increment. The first order solution[2] given here is for one increment, x_i thick, with a uniform concentration C_{oi} adjacent to the silicon, with the remainder of the oxide $x_o - x_i$ thick, having a uniform concentration C_o. The concentration in the substrate is

$$C_2(x,t) = \frac{mk}{1+k}\sum_0^\infty \alpha^n \left[C_o \left(\operatorname{erfc}\left[\frac{2nx_o + x_i + mkx}{2\sqrt{D_1 t}}\right] - 2\operatorname{erfc}\left[\frac{(2n+1)x_o + mkx}{2\sqrt{D_1 t}}\right] + \operatorname{erfc}\left[\frac{(2n+2)x_o - x_i + mkx}{2\sqrt{D_1 t}}\right]\right) + C_{oi}\left(\operatorname{erfc}\left[\frac{2nx_o + mkx}{2\sqrt{D_1 t}}\right] + \operatorname{erfc}\left[\frac{(2n+2)x_o + mkx}{2\sqrt{D_1 t}}\right] - \operatorname{erfc}\left[\frac{2nx_o + x_i + mkx}{2\sqrt{D_1 t}}\right] - \operatorname{erfc}\left[\frac{(2n+2)x_o - x_i + mkx}{2\sqrt{D_1 t}}\right]\right)\right] \quad [A\text{-}1]$$

If x_o is large, this reduces to

$$C_2(x,t) = \frac{mk}{1+k}\left(C_{oi} \operatorname{erfc}\left[\frac{x}{2\sqrt{D_2 t}}\right] - C_{oi} - C_o) \operatorname{erfc}\left[\frac{x_i + mkx}{2\sqrt{D_1 t}}\right]\right) \quad [A\text{-}2]$$

The sheet conductivity then has the form

$$I/V = 9.06\,\bar{\mu}q\left(\frac{mk}{1+k}\right)\left(\frac{C_{oi}}{\sqrt{\pi}} - (C_{oi} - C_o)\ \text{ierfc}\left[\frac{x_i}{2\sqrt{D_1 t}}\right]\right)\sqrt{D_2 t} \quad [A\text{-}3]$$

For suitable values of C_{oi} and x_i, this function has the shape of the conductivity curve given in Fig. 5.

[2] This solution and Eq. [11], [12], and [13] are by the method of LaPlace transformation (21).

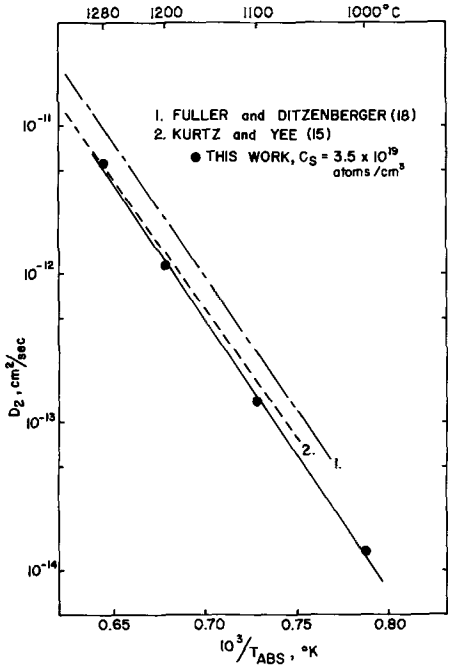

Fig. 8. Effect of temperature on the diffusion coefficient of boron in silicon.

REFERENCES

1. P. F. Schmidt and A. E. Owen, *This Journal*, **111**, 682 (1964).
2. J. Scott and J. Olmstead, *RCA Review*, **26**, 357 (1965).
3. P. F. Schmidt, T. W. O'Keeffe, J. Oroshnik, and A. E. Owen, *This Journal*, **112**, 800 (1965).
4. W. von Muench, *Solid-State Electronics*, 9, 619 (1966).
5. D. L. Tolliver and D. L. Elgon, Paper presented at the Philadelphia Meeting of the Society, Oct. 9-14, 1966, as Paper 183.
6. T. L. Chu and G. A. Gruber, Paper presented at the Philadelphia Meeting of the Society, Oct. 9-14, 1966, as Paper 174.
7. D. B. Lee, *Solid-State Electronics*, **10**, 623 (1967).
8. A. E. Owen and P. F. Schmidt, *This Journal*, **115**, 548 (1968).
9. E. Tannenbaum, *Solid-State Electronics*, **2**, 123 (1961).
10. E. E. Gardner, W. Kappalto, and C. R. Gordon, *Appl. Phys. Letters*, **9**, 432 (1966).
11. T. Abe and Y. Nishi, *Japan. J. Appl. Phys.*, **7**, 397 (1968).
12. J. C. Irvin, *Bell System Tech. J.*, **41**, 387 (1962).
13. The method used was that of J. A. Dean and C. Thompson, *Anal. Chem.*, **27**, 42 (1955), modified for silicon interference by B. Yurash and R. Ceynowa, Fairchild Semiconductor R&D Laboratory, to be published.
14. F. M. Smits, *Proc. IRE*, **46**, 1049 (1958).
15. A. D. Kurtz and R. Yee, *J. Appl. Phys.*, **31**, 303 (1960).
16. S. Horiuchi and J. Yamaguchi, *Japan. J. Appl. Phys.*, **1**, 314 (1962).
17. "Research on Phase Equilibria Between Boron Oxides and Refractory Oxides," P. J. Gielisse, T. J. Rockett, and W. R. Foster, Ohio State University Research Foundation, Report 931 (1961).
18. C. S. Fuller and J. A. Ditzenberger, *J. Appl. Phys.*, **27**, 544 (1956).
19. S. Maekawa and T. Oshida, *J. Phys. Soc. Japan*, **19**, 253 (1964).
20. A. S. Grove, O. Leistiko, Jr., and C. T. Sah, *J. Appl. Phys.*, **35**, 2695 (1964).
21. H. S. Carslaw and J. C. Jaeger, "The Conduction of Heat in Solids," 2nd ed., p. 298, Oxford Press (1959).

Study of the Dissipation Factor of $PbZr_{0.7}Ti_{0.3}O_3$ in the Vicinity of the Curie Point

Donald F. Weirauch[1] and Victor J. Tennery[2]

Department of Ceramic Engineering, University of Illinois, Urbana, Illinois

For most ferroelectric and antiferroelectric phases possessing the perovskite structure the relative permittivity exhibits a maximum at the temperature where the material transforms to a paraelectric phase. Within the phase transformation region the measured dissipation factor or loss tangent usually exhibits an anomaly whose origin is in many cases unclear. In the case of polycrystalline $PbZr_{0.7}Ti_{0.3}O_3$, at audio frequencies the dielectric loss increases with increasing temperature except in the vicinity of the phase transformation from the rhombohedral ferroelectric phase to the paraelectric cubic phase at 340°C. At this temperature the measured loss decreases anomalously before increasing again at higher temperatures. This work reports data which indicated that for this solid solution the decrease in dissipation factor in the vicinity of the transformation temperature is primarily a consequence of the large change in the material's electrical permittivity and not due to an anomaly in the electrical resistivity.

Ceramic specimens of $PbZr_{0.7}Ti_{0.3}O_3$, 1.5 cm in diameter and 0.3 cm thick and possessing densities of 85% of theoretical, were prepared by standard techniques. Gold electrodes were applied to the flat parallel faces of the specimens by a vacuum evaporation method.

Capacitance and dissipation factor measurements were made at a frequency of 10 kHz on specimens enclosed in a small stainless steel holder whose temperature could be controlled to ± 0.2°C (1). A General Radio 1620-A capacitance measuring assembly was used for these measurements. The direct current resistivity of the same specimen was measured in the same holder with a Keithly 610A electrometer. Figure 1 shows the relative permittivity and dissipation factor of a typical specimen as a function of temperature.

It was assumed that the dielectric could be represented by an equivalent parallel circuit consisting of a capacitor in parallel with a resistor. From the measured capacitance and dissipation factor and the specimen's geometry the equivalent parallel resistivity of the specimen could be calculated from the relation

$$D = \frac{1}{2\pi fRC} = \frac{1}{\omega RC} \qquad [1]$$

which is valid for the simple parallel circuit. In this expression D = dissipation factor, f = frequency, C = parallel equivalent capacitance, R = parallel equivalent resistance, and ω = the angular frequency. If the parallel equivalent resistivity were approximately equal to the measured d-c resistivity, then the losses were all essentially conductive in nature. Also, the equivalent circuit represented the dielectric through the phase transformation region if both resistivities had the same value and the same temperature dependence through this region. Figure 2 shows that indeed these two resistivity values are very nearly equal to each other above 200°C and that they have the same temperature dependence above this temperature. Therefore, above about 200°C and at this frequency the parallel equivalent circuit was a reasonable approximation for this dielectric material. The electrical conductivity of the specimen had thus become the major source of dielectric losses in this material at these high temperatures. The observed changes in the a-c and d-c resistivities at the transformation temperature were small and, because of the demonstrated validity of Eq. [1], the decrease in the dissipation factor at the transformation temperature was due to the large observed increase in the permittivity. The rise

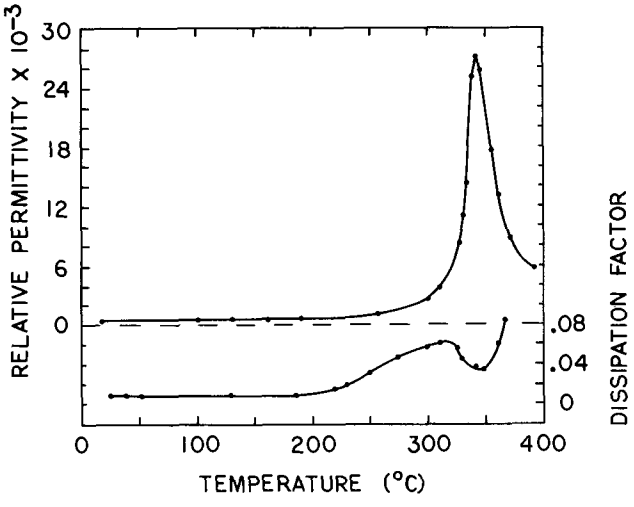

Fig. 1. Relative permittivity and dissipation factor of $PbZr_{0.7}Ti_{0.3}O_3$ as a function of temperature.

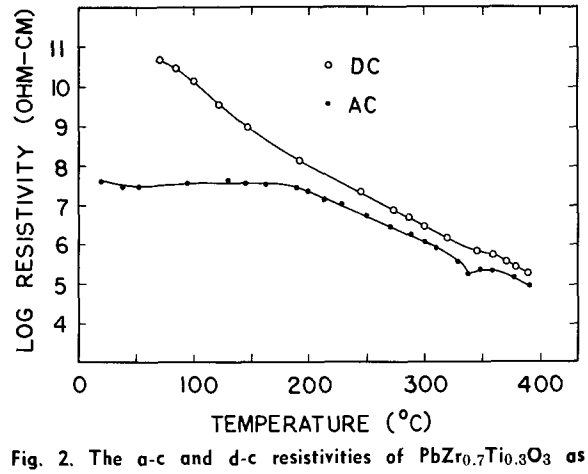

Fig. 2. The a-c and d-c resistivities of $PbZr_{0.7}Ti_{0.3}O_3$ as a function of temperature.

[1] Present address: Texas Instruments, Dallas, Texas.
[2] Present address: Oak Ridge National Laboratory, Oak Ridge, Tennessee.

in dielectric loss just prior to the permittivity peak was due to the increasing conduction losses. The sharp rise in loss at temperatures just above the transformation was due to the ever increasing conduction losses and the sharp decrease in permittivity in the cubic phase region.

Acknowledgment

This work was supported by a fellowship grant from the Speer Carbon Company. This work was a portion of a thesis submitted by D. F. Weirauch in partial fulfillment of the requirements for the degree of Doctor of Philosophy in Ceramic Engineering, University of Illinois, 1968.

Manuscript submitted Jan. 27, 1969; revised manuscript received March 15, 1969.

Any discussion of this paper will appear in a Discussion Section to be published in the December 1969 JOURNAL.

REFERENCE

1. D. F. Weirauch, A Study of Phase Transitions in the Lead Zirconate-Lead Titanate System, Ph.D. Thesis, Dept. of Ceramic Engineering, University of Illinois (1968) 102 pp.

Solid Solution in the Silicon Nitride-Silicon Dioxide System

N. C. Tombs,[1] F. A. Sewell, Jr., and J. J. Comer[2]

Sperry Rand Research Center, Sudbury, Massachusetts

Since the description of a new insulated-gate field-effect transistor using silicon nitride as the diffusion mask and gate dielectric (1), considerable effort has been directed toward the investigation of silicon nitride for semiconductor device applications (2). This note describes investigations of the preparation and properties of the solid solution series which we were able to form between silicon nitride and silicon dioxide as end members.

We have observed that the pyrolytic reaction between silane and ammonia gases can, in the presence of certain oxygen-containing gases, yield amorphous films having compositions intermediate between those of silicon nitride and silicon dioxide (3). This has formed the basis for the controlled preparation of a series of films covering the full range of composition. It is shown by infrared absorption, electron diffraction, and optical studies that these materials are to be regarded as solid solutions rather than multiphase mixtures. The formation of the full range of solid solutions is presumably facilitated by the structural flexibility inherent in the amorphous state. Film characteristics such as etch rate in hydrofluoric acid, maximum field strength, and dielectric constant, are influenced by the solid solution composition in a manner which enables a practical compromise to be achieved for device applications.

Films were deposited on silicon substrates which had been mechanically polished and chemically etched in the conventional manner. Deposition was carried out in all-glass flow system, using an rf-heated graphite susceptor sealed in a quartz envelope. The reaction gases were silane, ammonia, and nitrous oxide at a 1% concentration in argon carrier gas. In order to obtain consistent results, it was found to be essential to minimize contamination of the reaction gases both prior to and during the reaction. Suitable deposition conditions for the entire range of films involved a substrate temperature of 900°C (uncorrected optical pyrometer reading), and a total flow rate of 18-20 liters/min, with an ammonia-silane volume ratio of 80:1.

Film thickness was determined by etching a step, evaporating a reflecting silver layer onto the surface, and measuring the fringes formed in a double-beam interferometer. A reflection spectrum was obtained over the wavelength range 0.5-1.5μ, using a Beckman DKZA spectrometer. The refractive index was obtained from the reflection minimum, the film thickness, and the instrument geometry. The film etch rate was determined at 22°C using buffered HF etch (100 ml saturated ammonium fluoride to 15 ml concentrated HF, 48%). The principal absorption band in the 5-25μ region was determined using a Perkin-Elmer Model 337 Spectrophotometer. The dielectric constant was determined from maximum capacitance *vs.* voltage measurements using 10 mil diameter aluminum electrodes evaporated onto the film.

Figure 1 shows the results obtained, on corresponding samples, for etch rate, IR absorption maximum, refractive index, and dielectric constant, *vs.* mole-per cent ammonia replaced by nitrous oxide in the reaction mixture. It is seen that the results follow a reasonably smooth curve, with the greatest effect of nitrous oxide increments occurring at the lower concentrations, as might be expected. Insofar as a direct comparison is justified, in view of the important effect of the experimental conditions, these results are consistent with other published data (4). It is not certain that these zero per cent N_2O samples do in fact represent entirely oxygen free silicon nitride, and this fact might account for the dielectric constant being close to 6, compared with values of 7 to 8 previously published. It should also be noted that the use of lower ammonia to silane ratios can yield silicon excess samples with increased dielectric constants. Concerning the refractive index, values somewhat less than

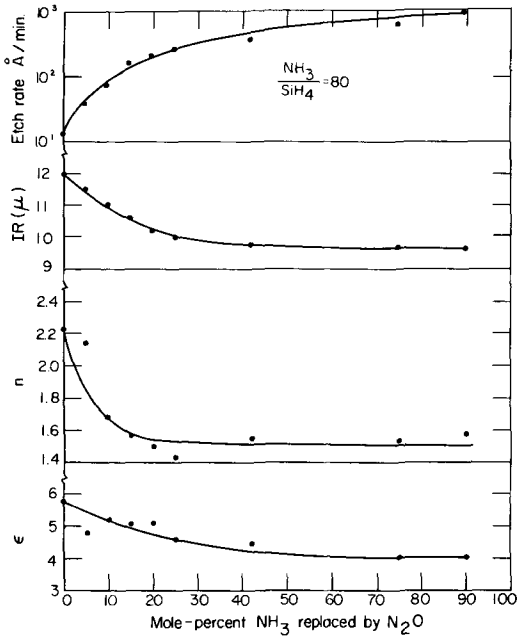

Fig. 1. Measured film properties *vs.* mole-per cent NH_3 replaced by N_2O in the reaction mixture.

Key words: silicon nitride films, silicon oxynitride films, solid solution, electron microscopy.

[1] Present address: National Aeronautics and Space Administration, Electronics Research Center, Cambridge, Massachusetts.

[2] Present address: Air Force Cambridge Research Laboratory, Bedford, Massachusetts.

our value of 2.2 for the end member have been reported. The discrepancy is difficult to explain, especially since our corresponding dielectric constant is about 6.

Information concerning the structure of the films was obtained using selected-area transmission electron diffraction techniques (JEM 6A electron microscope, 100 kv beam). It was necessary to make windows in the silicon substrate, using the jet-chemical etching method of Booker and Stickler (5). Two specimens were usually prepared from each film sample, one film being reduced to about one half of its initial thickness (2000Å) by continuing the etching process after the silicon window had been opened. Both film thicknesses always gave similar diffraction results, so that no variations with depth through the film were apparent. However, the thinner film gave better diffraction contrast. A calibration spot-pattern for silicon could be superimposed on the amorphous film pattern by exposing a thinned edge of the silicon to the electron beam.

All the nitride and oxynitride films gave diffuse ring patterns characteristic of amorphous structures. The positions of the diffraction rings were measured on the photographic plates using a steel rule. Despite the simplicity of the technique, it is felt that the accuracy of the ring diameter measurements was ± 1%. The "d" spacings corresponding to the three most distinct diffraction rings are tabulated in Table I for films prepared using various mole-per cent replacements of ammonia by nitrous oxide. Results for a silicon dioxide film formed by thermal oxidation of silicon are also included. Figure 2 shows a plot of the outermost "d" spacing *vs.* composition. Figure 3 shows diffraction patterns for 0 and 90 m/o replacement of ammonia by nitrous oxide.

The gradual change in "d" values with composition indicates that the silicon nitride and silicon dioxide end members form a continuous series of solid solutions rather than simple mixtures. This evidence forms valuable support for that provided by the corresponding gradual change in the infrared absorption and other characteristics of the films. From the point of view of practical device applications, it is normally desirable to achieve a single-phase film in order to avoid possible inhomogeneous properties associated with mixtures. Previous reports concerning films intermediate in composition between silicon nitride and silicon dioxide (4) have not always clearly distinguished the solid solution and mixture possibilities, and electron diffraction appears not to have been applied to this problem previously. It is, in fact, possible that some preparation techniques will yield mixtures instead of solid solutions. Drum and Rand (6) have applied electron-beam microanalysis to a series of oxynitride films in connection with comparative stress measurements. They find that the atomic fraction of silicon in the various compositions is not consistent with the presence of a mixture of silicon nitride and silicon oxide.

It is of interest that Coleman and Thomas (7) have studied the structure of silicon nitride and silicon dioxide films formed by a glow discharge method. In the case of nitride, compositions ranged from silicon

Table I. The "d" spacings corresponding to the three most distinct diffraction rings for films prepared using various mole-per cent replacements of NH_3 by N_2O

"d" Spacings (Å)								
0% N_2O	5% N_2O	10% N_2O	20% N_2O	25% N_2O	42% N_2O	75% N_2O	90% N_2O	Thermally grown SiO_2
3.60	3.57	3.57	3.66	3.71	3.69	4.02	3.95	4.12
2.28	2.29	2.32	2.33	2.35	2.36	2.36	2.40	2.35
							2.04*	2.00*
1.35	1.33	1.33	1.30	1.30	1.27	1.27	1.24	1.20

* These rings were detectable only for the 90% N_2O sample and the thermal SiO_2 sample.

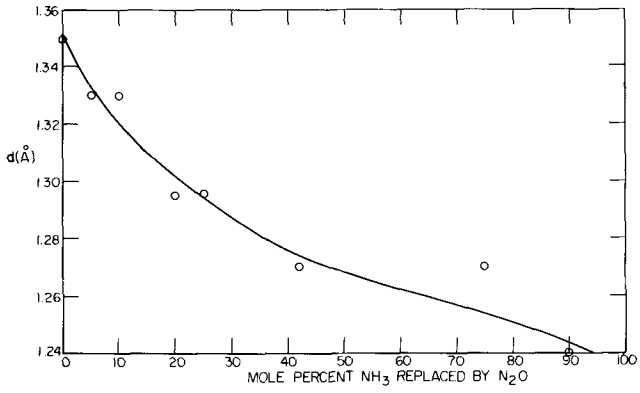

Fig. 2. Outermost "d" spacing *vs.* film composition

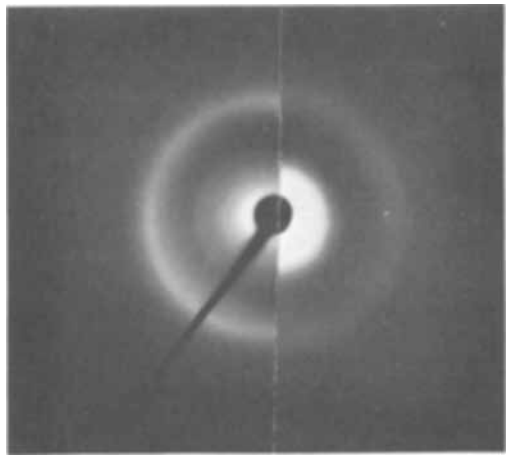

Fig. 3. Comparison of transmission electron diffraction patterns from films prepared with (a) (left) 0% N_2O replacement and (b) (right) 90% N_2O replacement.

to silicon nitride. Using the variation of the scattered intensity of an electron beam with angle, they have deduced the position, number, and type of atoms surrounding a given origin atom. An analogous approach might usefully be applied to the silicon nitride-silicon dioxide films we have described.

Acknowledgment

The research reported in this paper was sponsored in part by Rome Air Development Center under contract No. RADC F30602-67-C-0223.

Manuscript submitted Dec. 23, 1968; revised manuscript received March 7, 1969.

Any discussion of this paper will appear in a Discussion Section to be published in the December 1969 JOURNAL.

REFERENCES

1. N. C. Tombs, H. A. R. Wegener, R. Newman, B. T. Kenney, and A. J. Coppola, *Proc. IEEE (Corres.)*, **54**, 88 (1966).
2. See, for example, V. Y. Doo, D. R. Kerr, and D. R. Nichols, *This Journal*, **115**, 61 (1968); G. A. Brown, W. C. Robinette, Jr., and H. G. Carlson, *ibid.*, **115**, 948 (1968).
3. N. C. Tombs (to Sperry Rand Corporation), U. S. Pat. 3,422,321 (filed June 20, 1966, issued January 14, 1969).
4. D. M. Brown, P. V. Gray, F. K. Heumann, H. R. Philipp, and E. A. Taft, *This Journal*, **115**, 311 (1968).
   T. L. Chu, J. R. Szedon, and C. H. Lee, *ibid.*, **115**, 318 (1968).
5. G. R. Booker and R. Stickler, *Brit. J. Appl. Phys.*, **13**, 446 (1962).
6. C. M. Drum and M. J. Rand, *J. Appl. Phys.*, **39**, 4458 (1968).
7. M. V. Coleman and D. J. D. Thomas, *Phys. Stat. Sol.*, **25**, 241 (1968); *ibid.*, **22**, 593 (1967).

Thermal Expansion of Sputtered Silicon Nitride Films

P. J. Burkhardt* and R. F. Marvel

IBM Components Division, East Fishkill Laboratory, Hopewell Junction, New York

When silicon nitride first came into vogue in the semiconductor industry as a thin film passivating material for silicon planar devices, one of its strong selling points was that its thermal match with silicon was better than that of silicon dioxide. At that time, the best available value for the thermal expansion coefficient was that measured for the bulk crystalline material by Popper and Ruddlesden (1). This was given as 2.5×10^{-6} °C^{-1}. Bean *et al.* (2) have approximated the expansion coefficient of pyrolytically deposited silicon nitride as 4.2×10^{-6} °C^{-1} over a temperature range of 0°-1000°C by measuring the curvature of a silicon-silicon nitride wafer. More recently Tokuyama *et al.* (3) measured the expansion coefficient of pyrolytically deposited silicon nitride by measuring the curvature of a silicon-silicon nitride strip by x-ray diffraction microscopy. Their measurements were made on strips on which nitride had been deposited at 800° and 1000°C and cooled to room temperature. Rather than using the expansion coefficient of silicon, they measured equivalent strips with steam-grown SiO_2 and used the value of 5.5×10^{-7} °C^{-1} for SiO_2 as a reference. The same authors also reported the observation of cracks in the silicon nitride films. Because of the apparently good thermal match of silicon nitride and silicon, they concluded that differences in Young's modulus between silicon and silicon nitride caused the cracking.

We have developed a technique for measuring the thermal expansion coefficient of thin films such as silicon nitride directly without the use of bending beams. In this method, a cathetometer is used to measure the distance between two reference marks as a function of temperature on a freely suspended strip of film. Thus the need for a reference expansion coefficient is eliminated. Furthermore, the effect of any intrinsic interfacial stress of unknown temperature dependence, which may be present in a silicon nitride-silicon beam, is eliminated.

The silicon nitride films with which this study is concerned were produced by rf sputtering (4). This method of deposition on silicon substrates results in large intrinsic compressive stresses. These stresses are isothermally produced and would complicate a beam-type expansion coefficient measurement unless their thermal behavior is known.

For completeness the thermal expansion of a single crystal silicon wafer was also measured in the <110> direction with the same apparatus.

Experimental

Specimen preparation.—The sample films were prepared by sputtering them 1-2μ thick onto a strip of annealed molybdenum metal. The strip was ½ in. wide, 3 in. long, and 0.003 in. thick. Before cutting, the molybdenum sheet was rolled over an edge to provide a lateral curvature (Fig. 1 insert). The purpose of the curvature was to keep the stripped silicon nitride film from curling along its length.

The sequence in preparing the films was as follows: Two fiducial marks were scribed onto the molybdenum strip with a diamond scribe, at a distance no farther apart than the range of the cathetometer. The molybdenum strips were etched briefly in aqua regia. Next the silicon nitride film was deposited. Following deposition, the strips were placed into a furnace at 800°C, where commercial chlorine gas was used to etch away the molybdenum. This etching left intact the straight strips of silicon nitride film, with the scribed fiducial marks replicated on them.

Many attempts were necessary to obtain films that would remain intact after chlorine etching. Successful results were obtained by sputtering at 4μ nitrogen pressure from a Cerac[1] hot pressed silicon nitride target and by using an rf power density of 4.0 w/cm^2. The substrate temperature was 300°C.

Chemical analysis of comparable stripped silicon nitride films showed them to be about 98% Si_3N_4. Impurities detected by electron microprobe were Mo, Cl, O, Ca, and Al.

Measurement.—After stripping, the silicon nitride strips were suspended from a silica clip in a vertical silica tube furnace (Fig. 1). The furnace was wound with Kanthal A-1 wire and contained an optical silica window 4 in. long and 1 in. wide.

A chromel-alumel thermocouple was located in a well directly behind the specimen. It could be raised and lowered for measuring the temperature along the entire length of the specimen. This profiling at several temperatures showed that the variation in temperature along the length of the specimen was always less than 1°. All measurements were made in an air ambient.

The silicon strip was cut from a 2¼ in. silicon wafer and was mounted in the furnace in the same way as the silicon nitride film.

A Gaertner micrometer slide cathetometer was used to measure the distance between the two fiducial marks. The cathetometer itself was provided with aluminum foil reflectors and other heat-shielding devices to prevent expansion of the micrometer from heat radiated by the furnace. The instrument was placed about 1 ft from the furnace. The micrometer slide used

[1] Cerac Inc., Menomonee Falls, Wisconsin.

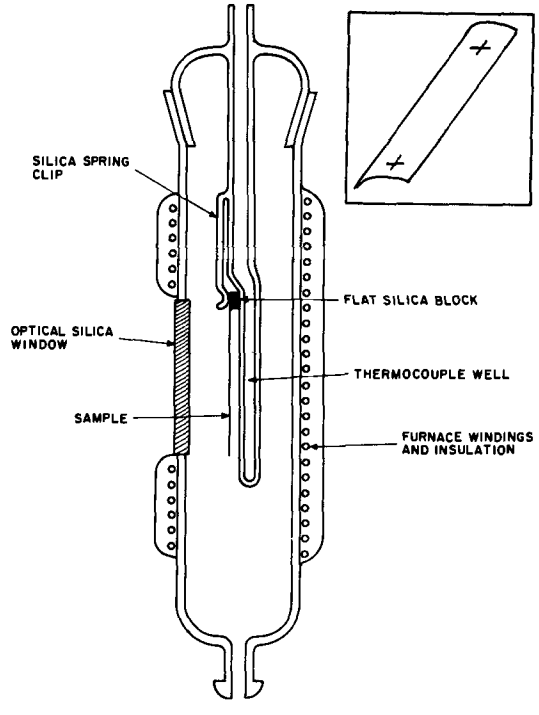

Fig. 1. Vertical tube furnace with optical silica window used for expansion measurements. Insert shows the configuration of the film sample.

* Electrochemical Society Active Member.

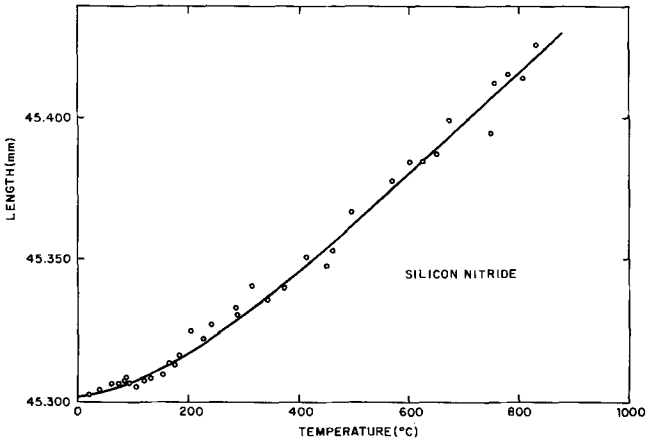

Fig. 2. Variation, with temperature, of distance between fiducial marks for a silicon nitride specimen. Circles represent data points; the line represents the least-squares fit to Eq. [1].

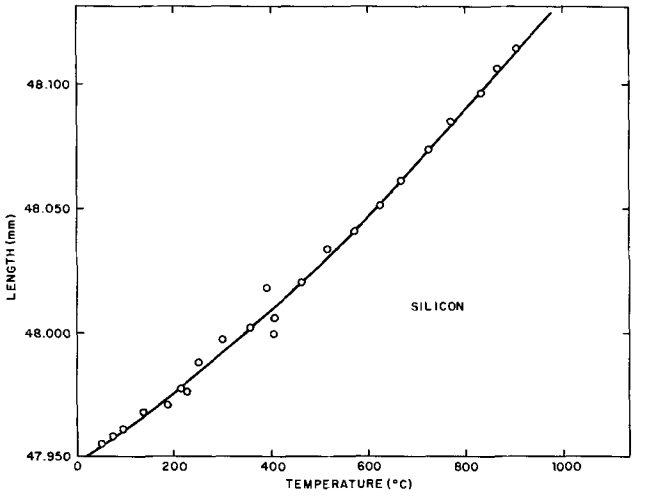

Fig. 3. Variation, with temperature, of distance between fiducial marks for a silicon specimen. Circles represent data points; the line represents the least squares fit to Eq. [1].

for these measurements had a range of 50 mm and a sensitivity of 0.001 mm.

Results and Discussion

The variation in distance between fiducial marks with temperature for the sputtered silicon nitride strip is shown in Fig. 2. These data points represent many temperature cycles on a single sample, to ensure that any annealing effects, at least within the temperature range of the measurements, would be observed. The data were fitted by the method of least squares (by use of an IBM 7090 computer) to the four-parameter equation

$$l = c_1 + c_2 e^{-c_3 t} + c_4 t \qquad [1]$$

where l is in millimeters and t is in degrees centigrade. The computed constants c_1, c_2, c_3, and c_4 of Eq. [1] are given in Table I for silicon and silicon nitride. The data obtained for silicon, along with the least squares fit to Eq. [1], are shown in Fig. 3. Note that over most of the range the scatter is much less than that for the

Table I. Computed constants for silicon and silicon nitride

Parameter	Silicon	Silicon nitride
c_1 (mm)	47.574	45.271
c_2 (mm)	0.3752	3.064×10^{-2}
c_3 ($°C^{-1}$)	6.834×10^{-4}	5.596×10^{-3}
c_4 (mm $°C^{-1}$)	3.745×10^{-4}	1.816×10^{-4}
a_1 ($°C^{-1}$)	-5.35×10^{-6}	-3.78×10^{-6}
a_2 ($°C^{-1}$)	6.83×10^{-4}	5.60×10^{-3}
a_3 ($°C^{-1}$)	7.81×10^{-6}	4.01×10^{-6}

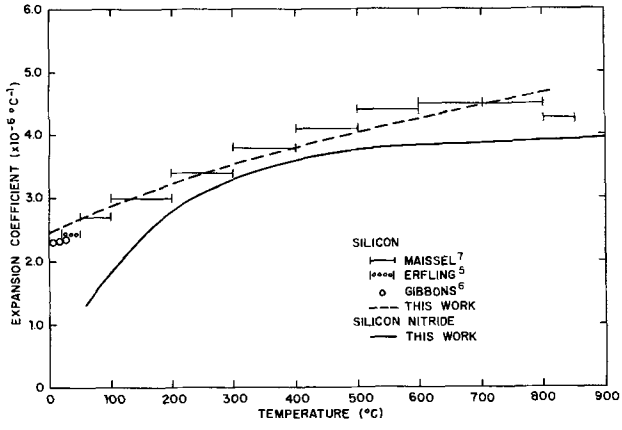

Fig. 4. Variation, with temperature, of the coefficient of thermal expansion of silicon and of a silicon nitride film.

silicon nitride films. The scatter in the thin film measurements is attributed primarily to the relative lack of rigidity of the film in spite of its lateral curvature. The thin films are therefore much more subject to distortion by room vibrations and convection than the rigid silicon strips. Both were observed.

The expansion coefficients can be expressed empirically in terms of the constants in [1] by

$$\alpha = a_1 e^{-a_2 t} + a_3 \qquad [2]$$

The constants a_1, a_2, and a_3 are simple functions of the constants in Eq. [1] and also are given in Table I.

Figure 4 shows the variation of the computed expansion coefficients with temperature, along with some data on silicon published by other authors (5-7). The curve for silicon fits fairly well with the data obtained by other authors except at the low- and high-temperature ends. It is felt that if measurements were made at lower temperatures, say down to —100°C, the fit to the data of Erfling (5), Gibbons (6), and Maissel (7) would be better.

Over the entire temperature range investigated, the thermal expansion coefficient of silicon nitride is lower than that of silicon. Above 200°C the difference between the two is very small. The thermal stresses that result from depositions at elevated temperatures will be compressive.

This result is contrary to the conclusions reached by Bean *et al.* (2). Their value of 4.2×10^{-6} in the range 0°-1000°C presumably is deduced from wafer curvature by assuming that all of the curvature is related to the thermal mismatch. Doo *et al.* (8), as did Bean *et al.*, also found wafer curvature in silicon nitride films deposited pyrolytically from silane-ammonia mixtures. The curvature has been observed to develop during deposition, *i.e.*, isothermally (9). By the same token, reverse curvature has been observed to occur during the deposition of sputtered silicon nitride films at 300°C.

Doo *et al.* (8) have suggested film densification as a possible source of tensile stress. Although this seems to be a plausible explanation for an intrinsic tensile stress, it is puzzling why such stresses could not be relieved by annealing of the silicon substrate at the temperatures of the pyrolytic depositions. In any event, an intrinsic tensile stress dependent on the deposition mechanism could conceivably account for the dependence of curvature on the silane-ammonia ratio observed by Bean *et al.* (2). Furthermore, the cracking phenomena reported by Tokuyama *et al.* (3) is probably caused by just such an intrinsic tensile stress. The inclusion of this tensile stress into the thermal component would naturally lead to an expansion coefficient higher than that of silicon.

The sputtered silicon nitride films we examined have compressive stresses of the order of 10^{10} dynes/cm^2. These are developed isothermally during deposition.

These stresses too are intrinsic and must depend on the deposition mechanism. Indeed they are dependent on the rf power density, but not noticeably on the substrate temperature.

Conclusions

The measurement of the thermal expansion coefficient of silicon nitride over a large temperature range shows it to be compatible with silicon. Efforts to relate residual stress in deposited films to thermal expansion coefficients must take into account intrinsic stresses produced during deposition. These stresses themselves may have temperature dependence that could make them difficult to separate from thermal expansion stresses.

Acknowledgment

This work was sponsored by the United States Air Force Avionics Laboratory, Air Force Systems Command, Wright-Patterson Air Force Base, Ohio, under Contract AF 33(615)-5386.

Manuscript submitted Nov. 25, 1968; revised manuscript received Feb. 14, 1969.

Any discussion of this paper will appear in a Discussion Section to be published in the December 1969 JOURNAL.

REFERENCES

1. P. Popper and S. N. Ruddlesden, *Trans. Brit. Ceram. Soc.*, **60**, 603 (1962).
2. K. E. Bean, P. S. Gleim, R. L. Yeakley, and W. R. Runyan, *This Journal*, **114**, 733 (1967).
3. T. Tokuyama, Y. Fujii, Y. Sugita, and S. Kishino, *Japan J. Appl. Phys.*, **6**, 1252 (1967).
4. P. D. Davidse and L. I. Maissel, *J. Appl. Phys.*, **37**, 574 (1966).
5. H. D. Erfling, *Ann. Physik*, **41**, 467 (1942).
6. D. F. Gibbons, *Phys. Rev.*, **112**, 136 (1958).
7. L. Maissel, *J. Appl. Phys.*, **32**, 211 (1960).
8. V. Y. Doo, D. R. Nichols, and G. A. Silvey, *This Journal*, **113**, 1279 (1966).
9. V. Y. Doo, Private communication.

Evidence of Phosphorus N-skin on Silicon from Vapor Transport

John R. Edwards

Department of Electrical Engineering and Materials Research Laboratory, University of Illinois, Urbana, Illinois

In surface mobility studies it was necessary to obtain diffused N^+ phosphorus doped islands for inversion layer N-channel MOS transistors. When the bulk material was 100 ohm-cm boron doped silicon, it was discovered that a diffused N-type skin layer existed in the channel region of the bulk material. This note reports the results of experiments which were designed to determine the cause of the N-skin layer. It is shown that in addition to furnace contaminations, N-skin can be created by vapor transport of phosphorus from the phosphorus-rich N^+ diffused island to the exposed silicon surface surrounding the N^+ island. The N-skin can be avoided by leaving part of the original masking oxide to protect the channel during subsequent high temperature processes.

As early as 1946, Serin (1) suggested that heat-treatment could cause a reduction in the impurity concentration near the surface of a semiconductor which was the result of a rapid evaporation of the impurity atoms from the surface. Later Lehovec *et al.* (2) presented experimental differential capacitance-voltage measurements for the impurity distribution arising by evaporation of antimony from homogeneously doped germanium.

Also using a differential capacitance-voltage method for determining doping profiles in depth in epitaxial semiconductor films, Kahng, Thomas, and Manz (3, 4) presented experimental results for a proposed model of transfer of dopant from the silicon backside (and the silicon pedestal used in the epitaxial process) into the working gas phase.

Several experiments were performed to determine the source of the N-skin caused during the fabrication of the transistors. Test wafers used were 89-91 ohm-cm boron doped, Czochralski grown silicon wafers oriented in the <111> direction. All wafers were cleaned with organic solvents, deionized water, and then etched with a mixture of 6:1:1 mixture of HNO_3:HF:-CH_3COOH as a pre-etch. Following the pre-etch a chemical-mechanical polish was performed on one side using a 13:1 HNO_3:HF solution in a rotating beaker. After polishing, the wafers were quenched in acetic acid, followed by alternate rinses in hot deionized water and a mixture of 1:1 HNO_3:H_2SO_4 (reagent grade). The deionized water for the final rinse had a resistivity greater than 10^7 ohm-cm.

The results of the experiments are summarized in Table I. Two types of silicon test wafers were used and listed as types A and B. Type A wafers were used as cleaned and placed in the furnaces after drying with blower type drying heater. Type B wafers were further processed to obtain diffused N^+ phosphorus doped islands.

The initial experiments consisted of wafers of type A which were placed in the furnace to determine whether the ambient of the furnace had caused the N skin. The furnace tubes were made of high-purity quartz and the gaseous ambients were obtained from

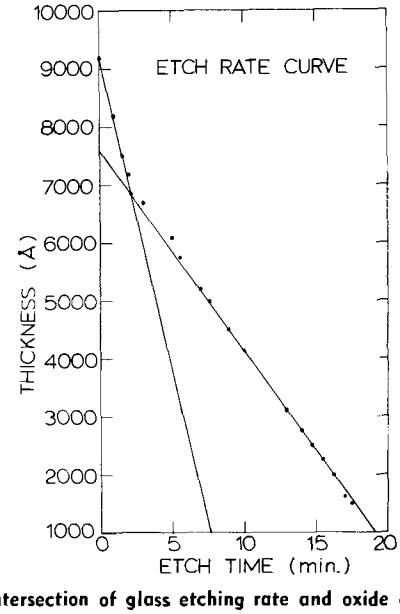

Fig. 1. Intersection of glass etching rate and oxide etching indicates glass thickness.

Table I. Summary of results of experiments

Oxide prior to diffusion		Purpose of experiment	Wafer type	Oxide prior to drive in	Diffusion drive in Temp. °C	Time, min	Ambient	Room temperature leakage resistance ohms/square	Hot point probe test	Stain test
I	placed in furnace alone	Furnace cleanliness	A	0Å	1200	60	Ar		no	no
					1200	60	O_2		no	no
					1000	90	O_2 (wet)		no	no
II-A	9200Å	Determination of N-skin sheet resistance	B	0Å	0	0	0	10^4		no
II-B	1			0	1200	60	Ar	2×10^1		yes
	2 9200Å	Vapor transport	B	0	1200	60	O_2	2×10^3		yes
	3			0	1000	90	O_2 (wet)	5×10^3		yes
II-C	1			1500Å	1000	90	O_2 (wet)	10% of units with sheet resistance greater than 10^4		Partial
	2 9200Å	Vapor transport	B	2700Å	1000	90	O_2 (wet)	90% of units with sheet resistance greater than 3×10^5		no
	3			3100Å	1000	90	O_2 (wet)	94% of units with sheet resistance greater than 5×10^5		no
II-D	9200Å	Surface diffusion into interface region	B	1μ Si removed	1000	90	O_2 (wet)	leaking but probe dependent		yes
III-A	placed on top of 2-B-1	Vapor transport between wafers	A	0	1200	60	Ar		yes	Partial
	placed on top of 2-B-2		A	0	1200	60	O_2		no	no
	placed on top of 2-B-3		A	0	1000	90	O_2 (wet)		no	no
III-B	1 placed along side 2-B-1	Phosphorus rich glass causing a plating action	A	0	1200	60	Ar		no	no
	2 placed along side 2-B-2		A	0	1200	60	O_2		no	no
	3 placed along side 2-B-3		A	0	1000	90	O_2 (wet)		no	no

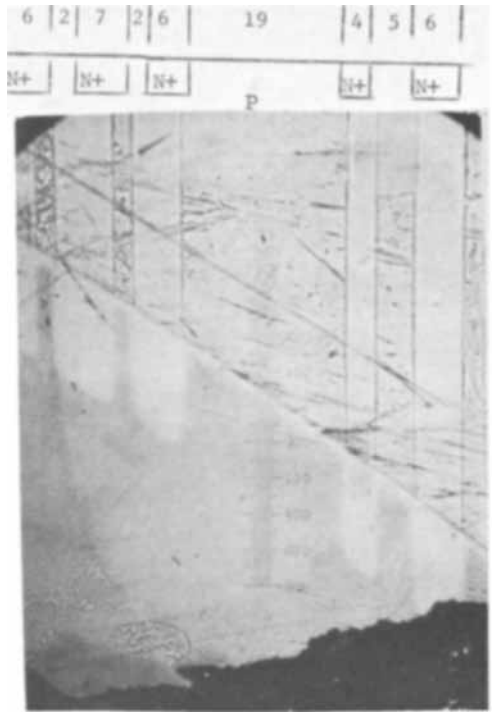

Fig. 2. Stain test result on wafer

liquid sources. The gas was transported from the liquid source through stainless steel tubing and gas purifiers into the furnace tubes with all valving made of quartz and Teflon. The ambient O_2 (wet) in Table I refers to an oxygen ambient bubbled through water whose temperature was 95°C. The results are listed in Table I as group I. These wafers were placed in the furnace under the different time, temperature and ambient conditions listed in the table. The hot-point probe measurement gave no indication of a skin layer nor was there any consistent skin indication from the stain test. (All stain tests were made using a 1:1 H_2O to HF solution with an addition of 0.1g of $Cu(NO_3)_2{:}3H_2O$ added per 100 ml of acid, water solution.)

Group II wafers had N^+ phosphorus diffused islands to allow direct electrical current measurements of the N-skin layer formed on the surface of the p-type substrate between the N islands. These wafers were cleaned and etched as those of group I, then oxidized to an oxide thickness of 9200Å in a wet O_2 ambient for 4 hr at a temperature of 1000°C.

The N^+ junctions were made using the usual photolithographic techniques. Diffusion windows were cut in the oxide and drain source islands were deposited in a two zone, P_2O_5 deposition system (5, 6) for 12 min at a temperature of 1200°C with a 500 cc/min argon carrier gas flow and a 210°C P_2O_5 source temperature.

The group of N^+ P junction wafers were tested by observing the leakage current between the drain and source of an MOS-T structure. This was given as sheet resistance in IIA. Measurements were made with the mask oxide removed using a 1:1 H_2O to HF solution in order to eliminate surface channel leakage due to oxide charge. The predeposited junction leakage resistance was greater than 10^6 ohms/square, as measured using a Tektronix 575 Transistor Curve Tracer. The practical limit of measuring the leakage resistance using the curve tracer is estimated to be about 5×10^5 ohms/square for the particular MOS-T geometry.

The wafers of group IIB were phosphorus deposited wafers which had the masking oxide completely removed by thoroughly rinsing the wafers in 1:1 H_2O to HF, followed by thorough rinsing in deionized water, a 7-min soaking in 1:1 HNO_3 to H_2SO_4, and thorough

rinsing in deionized water. These wafers were then placed in a diffusion drive-in furnace.

A 1-hr diffusion at 1200°C in an argon ambient caused the minimum N-skin leakage resistance of 20 ohms/square between the drain and source islands (II-B-1 in Table I). Under the same time and temperature conditions with oxygen as the ambient, the leakage resistance was increased by two orders of magnitude to a value 2 x 10^3 ohms/square (II-B-2). With the ambient oxygen bubbled through 95°C water, O_2 (wet), the leakage resistance was again increased by a factor of two to three to a value 5 x 10^3 ohms/square (II-B-3). These wafers showed a skin with the stain test as shown in Fig. 2. The skin was of the order of 1-2μ deep for the dry O_2 ambient and ½ to 1μ for the wet O_2 ambient. Above the photograph are the physical dimensions of the structure tested. The regions of skin close to the N^+ islands appear to have a thicker skin. The region separating structures appears to have a skin which tapers to a smaller thickness as the distances from the N^+ region increases.

Consistent with this magnitude of N-skin depth were tests made which showed the leakage considerably reduced by etching part of the silicon in a solution of 6:1:1; HNO_3:HF:CH_3COOH followed by an acetic acid rinse.

In addition a measurement of the leakage resistance which could be increased from 2 x 10^3 ohms/square for wafers II B-2 to a value of 2 x 10^{10} ohms/square (measured by an electrometer) by applying a bias voltage to a gate electrode over the oxide between the two N^+ junctions also demonstrates that the skin depth is small.

Another set of N^+P junction wafers, II-C, had the phosphorus-rich glass removed by etching in a buffered etch of NH_4F and HF, but with the layer of oxide underneath the phosphorus glass left on the silicon surface. The glass removal base solution (buffered solution) was made by dissolving 1 lb of NH_4F in 670 ml of H_2O and filtered through a 7μ millipore filter. One part HF (49%, electronic grade) was added to 20 parts buffered solution. The etching rate was determined to be about 345 Å/min. The glass thickness was determined by plotting the thickness observed optically (7) *vs.* the time left in the etching solution. The intersection of the glass etching rate and the oxide etching indicates a glass thickness of about 2400Å as shown on the etch rate curve, Fig. 1. The oxide remaining on the wafers used in this experiment was between 1500 and 3100Å which was well below the 6000Å oxide thickness indicated by the corner of the etch rate curve, indicating complete removal of the phosphorus rich glass.

The electrical tests showed that no detectable skin existed for wafers with oxide thickness of 2700-3100Å but showed a slight N-skin for the 1500Å thickness used. A stain was inconclusive on one group of devices, sometimes showing a partial skin and not at other times. It is believed that the stain test is the least conclusive and least sensitive of the tests used.

The wafer for experiment II-D had the oxide completely removed and in addition had approximately 1μ of the deposited phosphorus islands removed. This was done to explore the possibility that surface diffusion occurred, instead or in addition to vapor transport. A silicon etch composed of 6:1:1 HNO_3:HF:CH_3COOH was used. The wafer was quenched in acetic acid, rinsed in deionized water, followed by alternate rinses in deionized water and 1:1 HNO_3 to H_2SO_4 with a final rinse in deionized water. The wafer was diffused in a wet O_2 ambient for 90 min at 1000°C. The wafer showed a stain with the stain test and indicated a low leakage resistance, but measurements were probe dependent. Coupled with the absence of skin on wafers of group II-C, it is concluded that surface diffusion into the boron out-diffused region is not an important factor in the formation of the N-skin.

During the tests using N^+P junctions (type B wafers), a second group of wafers of type A were used. One group (III-A) of wafers was placed physically on top of the N^+ diffused junctions to test for vapor transport between wafers during the diffusion drive-in. Both groups were placed in the diffusion drive-in furnace at the same time. One wafer in group III-A showed an N-skin with the hot-point probe which is not completely decisive since there is the possibility of the probe breaking through the N-skin.

The final test was made in order to test the idea that removal of a phosphorus-rich glass in an acid solution might possibly cause phosphorus to plate out of the acid solution onto the bare silicon surface and cause an N-skin. The wafers of group III-B were placed in a solution of 1:1 H_2O to HF at the same time the phosphorus-rich glass was being removed from the wafers of group II. These treated wafers were rinsed thoroughly, soaked in a 1:1 solution of HNO_3 to H_2SO_4 for 7 min, then rinsed thoroughly in deionized water. The results listed in Table I show no N-skin and eliminate plating action during the phosphorous glass removal as a major cause of N-skin.

The conclusion of these experiments is that the major cause of the N-skin on an exposed Si surface must be associated with its proximity to the heavily doped N^+ regions. This can easily be interpreted by a model in which phosphorus is evaporated into the ambient at the drive-in diffusion temperature and transported in the gas phase onto the regions near the N^+ islands. The N-skin layer is formed during the diffusion drive-in cycle. This also means that any total removal of oxide in order to regrow a fresh oxide will result in an N-skin layer before the oxide can be regrown. This is in agreement with previous observations and models (1-4). A protective oxide remaining over the p-regions surrounding the N^+ island is sufficient to prevent the phosphorus from penetrating to the p-region. Since the N-skin measurements were made using channel conductance of MOS-T with the gate oxide removed, surface states and oxide charges do not enter into the interpretation. The phosphorus remaining in the furnace from previous use can also be eliminated as the major contribution since the sheet resistance of the skin was changed by orders of magnitude during tests in the same furnace.

Acknowledgment

The author wishes to thank Laurence L. Rosier for invaluable help during this work and Professor C. T. Sah for suggesting and support of this work which was also supported by the Air Force Office of Scientific Research and the Advanced Research Projects Agency.

Manuscript submitted Dec. 9, 1968; revised manuscript received Feb. 24, 1969.

Any discussion of this paper will appear in a Discussion Section to be published in the December 1969 JOURNAL.

REFERENCES

1. B. Serin, *Phys. Rev.*, **69**, 357 (1946).
2. K. Lehovec, K. Schoeni, and R. Zuleeg, *J. Appl. Phys.*, **28**, 420 (1957).
3. L. O. Thomas, D. Kahng, and R. Manz, *This Journal*, **109**, 1055 (1962).
4. D. Kahng, L. O. Thomas, and R. Manz, *ibid.*, **109**, 1106 (1962).
5. C. J. Frosch and L. Derick, *ibid.*, **104**, 547 (1957).
6. C. T. Sah, H. Sello, and D. A. Tremere, *J. Phys. Chem. Solids*, **11**, 288 (1959).
7. W. A. Pliskin and E. E. Conrad, *IBM Journal*, p. 43, January 1964.

Relations between Thermodynamics of Formation of Point Defects and Integral Thermodynamic Properties of Metal-Oxygen Systems

Per Kofstad

Central Institute for Industrial Research, Blindern, Oslo, Norway

Heats and entropies of formation of point defects in oxides and other inorganic compounds are most commonly determined from studies of the deviation from stoichiometry, electrical conductivity, and diffusion as a function of temperature and partial pressure of oxygen. When the thermodynamics of point defect formation are not known or are difficult to determine experimentally, it would be valuable to be able to correlate or to estimate such properties from other known properties of oxides. In this respect approximate empirical relations between heats of formation of fully ionized cation and oxygen vacancies and thermochemical properties of oxides have been proposed (1). Much work is also being carried out to theoretically calculate heats of formation of point defects in inorganic compounds (2), but at this stage calculations on oxides have not proved successful (3).

The purpose of this note is to point out that the thermodynamics of formation of point defects which predominate at the limits of nonstoichiometry in oxides may be related to integral thermodynamic properties of metal-oxygen systems and knowledge of the metal-oxygen phase diagrams.

Such a relation will be illustrated for an oxygen deficient oxide in which interstitial metal ions predominate at the lower limit of nonstoichiometry. The treatment may be made quite general, but for the sake of simplicity a simple hypothetical oxide system as illustrated in Fig. 1, will be considered. MO_2 is oxygen deficient, and it is assumed that interstitial ions with effective charge q, M_i, are the predominating point defects at the lower limit of nonstoichiometry. In the region at and next to this lower limit the composition of the oxide may thus be written $M_{1+y}O_2$ and the maximum value of y is termed y_m. It is further assumed that MO is essentially stoichiometric.

When the interstitial metal ions predominate, the defect equilibrium, assuming ideal behavior and that concentrations may be substituted for activities, may be written (4)

$$[M_i]\, n^q\, p_{O_2} = K_{M_i} = \exp\,(\Delta S^\circ_{M_i}/R)\, \exp\,(-\Delta H^\circ_{M_i}/RT) \qquad [1]$$

where n denotes the concentration of electrons, K_{M_i}, is the equilibrium constant, and $\Delta H^\circ_{M_i}$ and $\Delta S^\circ_{M_i}$ are the standard enthalpy and entropy terms for the formation of the defect, respectively. The standard state for M_i and the electrons is the infinitely dilute solution.

When intrinsic ionization and effects of impurities can be neglected, the electroneutrality condition requires that $n = q\,[M_i]$, and when further expressing the concentration of interstitial cations in terms of y, *i.e.*, $[M_i] = y$, Eq. [1] can be rewritten to give

$$\ln y = \frac{1}{q+1}\left(\frac{\Delta S^\circ_{M_i}}{R} - \frac{\Delta H^\circ_{M_i}}{RT} - \ln p_{O_2} - q\ln q\right) \qquad [2]$$

At maximum values of y, y_m, the MO_2 phase decomposes to MO, and the corresponding partial pressures of decomposition are $p^*_{O_2}$. In terms of y_m and $p^*_{O_2}$ Eq. [2] can be written

$$\ln y_m = \frac{1}{q+1}\left(\frac{\Delta S^\circ_{M_i}}{R} - \frac{\Delta H^\circ_{M_i}}{RT} - \ln p^*_{O_2} - q\ln q\right) \qquad [3]$$

For the decomposition of MO_2

$$MO_2 = MO + \tfrac{1}{2}\,O_2 \qquad [4]$$

the decomposition partial pressure of oxygen, $p^*_{O_2}$, can also be written

$$\ln p^*_{O_2} = \frac{2}{RT}\,(\Delta G^\circ_{MO_2} - \Delta G^\circ_{MO}) = \frac{2}{RT}\,(\Delta H^\circ_{MO_2} - \Delta H^\circ_{MO}) - \frac{2}{R}\,(\Delta S^\circ_{MO_2} - \Delta S^\circ_{MO}) \qquad [5]$$

where $\Delta G^\circ_{MO_2}$, $\Delta H^\circ_{MO_2}$, and $\Delta S^\circ_{MO_2}$ are the standard free energy, heat, and entropy of formation of MO_2, and ΔG°_{MO}, ΔH°_{MO}, and ΔS°_{MO} are the corresponding properties for MO. The standard state is 1 atm O_2. In Eq. [5] it is assumed as an approximation that the maximum deviation from stoichiometry is sufficiently small so that $\Delta G^\circ_{MO_2} \approx \Delta G^\circ_{M_{1+y_m}O_2}$.

Introducing the value of $p^*_{O_2}$ (Eq. [5]) in Eq. [3], y_m becomes

$$\ln y_m = -\frac{1}{RT(q+1)}\{2\Delta H^\circ_{MO_2} - 2\Delta H^\circ_{MO} + \Delta H^\circ_{M_i}\} + \frac{1}{R(q+1)}\{2\Delta S^\circ_{MO_2} - 2\Delta S^\circ_{MO} + \Delta S^\circ_{M_i}\} - \frac{q}{q+1}\ln q \qquad [6]$$

If the temperature dependence of y_m at the temperature where M_i predominates

$$\ln y_m = \ln A - \frac{\Delta H_{y_m}}{RT} \qquad [7]$$

can be determined from the phase diagram, it is seen by comparing Eq. [6] and [7] that $\Delta H^\circ_{M_i}$ and $\Delta S^\circ_{M_i}$ are given by

$$\Delta H^\circ_{M_i} = -2(\Delta H^\circ_{MO_2} - \Delta H^\circ_{MO}) + (q+1)\Delta H_{y_m} \qquad [8]$$

$$\Delta S^\circ_{M_i} = (q+1)R\ln A + qR\ln q - 2(\Delta S^\circ_{MO_2} - \Delta S^\circ_{MO}) \qquad [9]$$

The same procedure may be followed and relations corresponding to Eq. [8] and [9] may be derived for other defect structure situations, *e.g.*, if oxygen vacan-

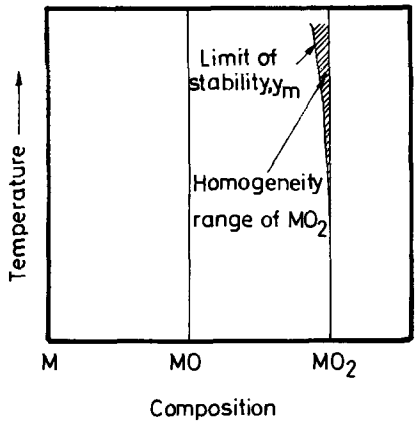

Fig. 1. Hypothetical metal-oxygen phase diagram with MO and MO_2 phases. It is assumed that the MO is essentially stoichiometric and that the MO_2 phase may be nonstoichiometric and that interstitial metal ions predominate at the lower limit of homogeneity.

cies predominate in oxygen deficient oxides or if metal vacancies or interstitial oxygen predominate at the limit of nonstoichiometry in metal deficient oxides.

Examples

Nb_2O_5.—Nb_2O_5 is oxygen deficient (5, 6), and it has been proposed that oxygen vacancies predominate at small deviations from stoichiometry and doubly charged interstitial niobium ions at and close to the lower limit of nonstoichiometry in the temperature range 900°-1200°C (6). When the interstitial niobium ions predominate, the defect equilibrium can be written

$$[Nb_i^{\cdot\cdot}]\, n^2\, p_{O_2}^{5/4} = K_{Nb_i^{\cdot\cdot}} \qquad [10]$$

By following the above procedure and considering, corresponding to Eq. [4], the reaction $Nb_2O_5 = Nb_2O_4 + \frac{1}{2} O_2$ it may be shown that

$$\Delta H^\circ_{Nb_i^{\cdot\cdot}} = -\frac{5}{4}(2\Delta H^\circ_{Nb_2O_5} - 2\Delta H^\circ_{Nb_2O_4}) + 3\Delta H_{y_m} \qquad [11]$$

For the temperature range 900°-1100°C it may be estimated that $\Delta H_{y_m} \simeq$ 6-8 kcal/mole (5, 6). At 1200°K, $\Delta H^\circ_{Nb_2O_5} = -449.2$ kcal/mole and $\Delta H^\circ_{Nb_2O_4} = -377$ kcal/mole (7) and following Eq. [11] this yields a value of $\Delta H^\circ_{Nb_i^{\cdot\cdot}} \simeq 200$ kcal/mole. The very same value of 200 kcal/mole was also estimated directly from the studies of nonstoichiometry as a function of temperature and partial pressure of oxygen (6). It may be noted that the term $-5/4(2\Delta H^\circ_{Nb_2O_5} - 2\Delta H^\circ_{Nb_2O_4})$ is much larger than $3\Delta H_{y_m}$ (Eq. [11]), and as a general trend the heat of formation of defects will increase with increased stability of the oxides.

Cu_2O.—Cu_2O is a metal-deficient oxide and Cu-vacancies are the predominating defects. Figure 2 shows the deviation from stoichiometry, x in Cu_2O_{1+x} as a function of partial pressure of oxygen as determined by Wagner and Hammen (8). (The deviation from stoichiometry may alternatively be written $Cu_{2-y}O$, and when $x << 1$, then $y = 2x$.) The values of $p^*_{O_2}$ represent the decomposition pressures of CuO according to the reaction $2CuO = Cu_2O + \frac{1}{2} O_2$.

Wagner and Hammen interpreted the oxygen pressure dependence of x as $x \propto p_{O_2}^{1/5}$, but, as shown in Fig. 2, it is not unreasonable to suggest the alternative dependence $x \propto p_{O_2}^{1/4}$. This latter relationship may be rationalized assuming that neutral copper vacancies, V^x_{Cu}, predominate. The formation of these defects in Cu_2O may be written

$$\frac{1}{4} O_2 = V^\times_{Cu} + \frac{1}{2} O_0 \qquad [12]$$

and the corresponding defect equilibrium is given by

$$V^\times_{Cu} = K_{V^\times_{Cu}} p_{O_2}^{1/4} \qquad [13]$$

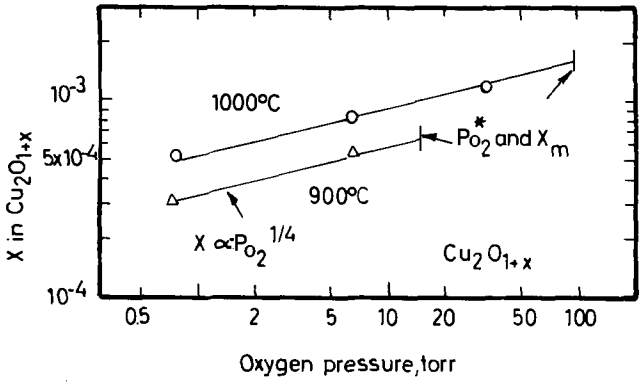

Fig. 2. Nonstoichiometry in Cu_2O (x in Cu_2O_{1+x}) as a function of partial pressure of oxygen at 900° and 1000°C. x_m indicates maximum deviation from stoichiometry and $p^x_{O_2}$ the decomposition pressure in the reaction $2CuO = Cu_2O + \frac{1}{2} O_2$. Experimental results after Wagner and Hammen (8).

When following the above procedure, it may be shown that the heat of formation of neutral vacancies, $\Delta H^\circ_{V^\times_{Cu}}$, is given by

$$\Delta H^\circ_{V^\times_{Cu}} = \Delta H^\circ_{CuO} - \tfrac{1}{2}\Delta H^\circ_{Cu_2O} + \Delta H_{x_m} \qquad [14]$$

where ΔH_{x_m} is the heat term associated with x_m ($x_m = B \exp(-\Delta H_{x_m}/RT)$).

It is, of course, not possible to obtain an accurate value of ΔH_{x_m} for the results in Fig. 2, but an estimate from the two values suggests $\Delta H_{x_m} \simeq 27$ kcal/mole. At 1100°K, $\Delta H^\circ_{CuO} = -35.8$ kcal/mole and $\Delta H^\circ_{Cu_2O} = -38.8$ kcal/mole (7), and from these values and that of ΔH_{x_m} Eq. [14] yields a calculated value of $\Delta H^\circ_{V^\times_{Cu}} \simeq 11$ kcal/mole. From the results in Fig. 2, *e.g.*, at 10 Torr O_2, $\Delta H^\circ_{V^\times_{Cu}}$ may be estimated to be approximately 12 kcal/mole.

General Remarks

The above procedure relates the thermodynamics of formation of defects predominating at limits of nonstoichiometry with integral thermodynamic properties of metal-oxygen system and the maximum deviation from stoichiometry as a function of temperature (*e.g.*, Eq. [8], [9]). The relations will be particularly useful in estimating heats of formation of defects in oxides (or correspondingly in other inorganic compounds) for which such data are lacking or for which such data are difficult to obtain experimentally. The relations are also useful in testing the internal consistency of interpretations of experimental values. Unfortunately values of maximum deviations from stoichiometry and the corresponding value of ΔH_{y_m} (Eq. [7]) are not as yet accurately known for many oxides. However, it may also be noted that for the most stable oxygen deficient oxides ΔH_{y_m} probably makes a relatively small contribution to the heat of formation of the defects (*cf.* Nb_2O_5). If the heat of formation of the defects and integral thermodynamic properties of the oxides are known, the above procedure may conversely be used to construct more accurate details of phase diagrams.

In the procedure it has been assumed that the decomposition pressure of the oxide can be determined from the free energy values of the stoichiometric oxides. This introduces no serious error for small defect concentrations (< about 2%). However, for large deviations in stoichiometry the correct chemical equation (which includes nonstoichiometry in the oxides) has to be written and the corresponding thermodynamic properties of the oxides at the limits of nonstoichiometry has to be estimated and used in evaluating $p^*_{O_2}$. Under these conditions it is also probable that ideal defect equations (*e.g.*, Eq. [1]) must be modified to take into account possible interactions or ordering of defects.

Manuscript submitted Oct. 24, 1968; revised manuscript received Feb. 11, 1969.

Any discussion of this paper will appear in a Discussion Section to be published in the December 1969 JOURNAL.

REFERENCES

1. P. Kofstad, *J. Phys. Chem. Solids*, **28**, 1842 (1967).
2. "Calculation of the Properties of Vacancies and Interstitials," Conference Proceedings National Bureau of Standards, Misc. Publ. 28, 1966.
3. I. M. Boswarva and A. D. Franklin, in "Mass Transport in Oxides," Symposium Proceedings, National Bureau of Standards Special Publication 296, Washington, D. C. (1968).
4. F. A. Kröger, "The Chemistry of Imperfect Crystals," North-Holland Publishing Co., Amsterdam (1964).
5. R. N. Blumenthal, J. B. Moser, and D. H. Whitmore, *J. Am. Ceram. Soc.*, **48**, 617 (1965).
6. P. Kofstad, *J. Less-Common Metals*, **14**, 153 (1968).
7. J. P. Coughlin, "Contributions to the Data on Theoretical Metallurgy," Bull. 542, Bureau of Mines, Washington, 1954.
8. C. Wagner and H. Hammen, *Z. physik. Chem.*, **B40**, 197 (1938).

Brief Communications

The Afterglow of Some Old and New Ce^{3+}-Activated Phosphors

A. H. Gomes de Mesquita and A. Bril

Philips Research Laboratories, N.V. Philips' Gloeilampenfabrieken, Eindhoven-Netherlands

Efficient and very fast, so-called P16 phosphors with decay times of 100 nsec or less are required for some applications such as the one-gun beam-indexing television tube (1) and the flying-spot cathode-ray tube. The decay time, τ, is usually defined as the time during which the intensity of the fluorescent emission decreases from its maximum value I_o to I_o/e; this means that the expression $I = I_o\, e^{-t/\tau}$ is taken to represent the decay of the luminescence at least to a first approximation. For the above applications Ce^{3+}-activated akermanite (2) and gehlenite (3) ($Ca_2MgSi_2O_7$ and $Ca_2Al_2SiO_7$, respectively) are normally used. We found that the decay time of both phosphors is about 50 nsec, using the techniques described in ref. (3) and (4). Ropp (5) recently proposed $Y_{0.8}La_{0.1}Gd_{0.1}PO_4$:Ce ($\tau$ = 40 nsec) as an alternative phosphor.

While applying Ce^{3+}-activated gehlenite it was noticed that the fast initial decay is followed by an afterglow phenomenon of relatively long duration. This was studied on the oscilloscope screen by exciting the phosphor at a 10 kc repetition rate with 10 kev cathode-ray pulses of 20 μsec duration. The intensity of the cathodoluminescence at 80 μsec after the end of an excitation pulse (*i.e.*, just before the next pulse is initiated) was found by us to be of the order of 5-10% of the maximum intensity, I_o. We shall call this quantity δ. If the entire decay were to follow the above exponential law, δ would be 10^{-700}% instead of 5-10%.

The value of δ varies from one gehlenite sample to another. When the samples are cooled from room temperature down to the temperature of liquid nitrogen, the δ-values of some of them increase, those of others decrease. We have not been able to explain this complex behavior, or to correlate it to any known property of this phosphor material.

The afterglow adds considerably to the unwanted radiation background in the aforementioned tubes. We found that akermanite and yttrium phosphate with δ-values of 3 and 1.5%, respectively, are somewhat more suitable phosphors in this respect than gehlenite, but still far from satisfactory.

A search for phosphors with better properties has led to the discovery of the Ce^{3+}-activated yttrium silicates, Y_2SiO_5 and $Y_2Si_2O_7$, which were prepared by firing intimate mixtures of yttrium oxide, cerous oxide, and silicic acid in a slightly reducing atmosphere. The δ-values of these phosphors are an order of magnitude smaller than those of the above-mentioned phosphors, whereas their decay times are about equally short. Their high radiant efficiencies constitute a great additional advantage. In Table I the phosphor properties of the old and these new phosphors are listed together.

In the system Y_2O_3-SiO_2 several compounds occur; moreover, $Y_2Si_2O_7$ is known to exist in a number of crystalline modifications. A more detailed discussion of this complicated system and of the preparation of the desired phases will be given elsewhere.

Table I. Phosphor properties[a]

Phosphor	η, %	τ, nsec	δ, %	λ_{max}, nm
$Ca_2MgSi_2O_7$:Ce	4	45	3	370, 395[b]
$Ca_2Al_2SiO_7$:Ce	4.5	50	5-10	405[b]
YPO_4:Ce	2.5	25[b]	1.5	330[b]
$Y_{1.98}Ce_{0.02}SiO_5$	6	30	0.1	415
$Y_{1.98}Ce_{0.02}Si_2O_7$	8	40	0.1	385

[a] All values were measured by the present authors unless otherwise stated. The meaning of τ and δ is explained in the text. η stands for the radiant efficiency, λ_{max} for the wavelength at maximum emission; both were measured with 20 kev cathode-ray excitation.
[b] Ref. (4).

Acknowledgment

The assistance of Miss M. P. Bol and Mrs. A. Huisman, M. M. H. Janssen, C. J. Loyen, and J. A. de Poorter is gratefully acknowledged.

Manuscript received Feb. 25, 1969.

Any discussion of this paper will appear in a Discussion Section to be published in the December 1969 JOURNAL.

REFERENCES

1. J. Davidse, *Philips Research Repts.*, **19**, 112 (1964).
2. A. L. Smith, *J. (and Trans.) Electrochem. Soc.*, **96**, 287 (1949).
3. A. Bril and H. A. Klasens, *Philips Research Repts.*, **7**, 421 (1952).
4. A. Bril, G. Blasse, and J. A. de Poorter, To be published.
5. R. C. Ropp, *This Journal*, **115**, 531 (1968).

Luminescence of Gallates

W. L. Wanmaker and J. W. ter Vrugt

N.V. Philips' Gloeilampenfabrieken, Eindhoven-Netherlands

A number of luminescent gallium-containing compounds of the self-activated type has been described in the literature, *e.g.*, $YGa_3B_4O_{12}$, $TbGa_3B_4O_{12}$ (1), $Sr_3(PO_4)_2$, and $Ca_3(PO_4)_2$ containing Ga (2). Gallates in the M_2O-Ga_2O_3 and MO-Ga_2O_3 systems and activated with Mn^{2+} were prepared by Hoffman and Brown (3). The same types of gallates were synthesized by us but without the addition of an activator. Luminescence was found in several of these gallates. Some properties of the most efficient of these phosphors are described in this communication.

The phosphor samples were made by standard ceramic methods, with a double firing process in air at temperatures ranging from 900° to 1400°C. Optical

Table I. Some data on gallium containing phosphors

Composition	λ_{max}(nm) Emission, room temp	Refl., %	Efficiency, % q_{UV} (254 nm)	η_{CR} (20 kv)	T_{50}, °K
$(LiGa)_{0.5}Ga_2O_4 = LiGa_5O_8$	400	44	40	8.5	340
$(LiGa)_{0.45}Mg_{0.1}Ga_2O_4$	415	27	55	7	350*
$(LiGa)_{0.36}Mg_{0.28}Ga_2O_4$	420	21	60	6	360*
$MgGa_2O_4$	415	27	35	5	360*
$(LiGa)_{0.26}Zn_{0.48}Ga_2O_4$	460	7	70	4	380*
$ZnGa_2O_4$	465	12	45	4.5	560*
$(MgZn)_{0.5}Ga_2O_4$	460	6	45	4	500*

Refl.—diffuse reflection at 254 nm.
q_{UV}—quantum efficiency (250-270 nm excitation).
η_{CR}—energy efficiency (20 kv cathode-ray excitation).
T_{50}—temperature in °K at which the light output of the phosphor has decreased to 50% of the value measured at room temperature.
* These phosphors have their maximum light output (254 nm excitation) below room temperature.

measurements were performed as previously described (4).

Like that of many phosphors of the zinc-sulfide type the efficiency of most of the gallates depends on the intensity of the exciting radiation. The excitation spectra, when measured in the usual way with a low excitation energy, therefore do not correspond to the wavelength-dependence of the excitation at high intensities. When the excitation spectra are measured with a low constant energy of the exciting radiation, most of the gallates show an excitation maximum between 220 and 250 nm.

With cathode-ray excitation the most efficient phosphors proved to be $LiGa_5O_8$, $MgGa_2O_4$, and $ZnGa_2O_4$, all with the spinel crystal structure (Table I). The energy efficiency of $LiGa_5O_8$ (8.5%) is high for an oxidic phosphor. With cathode-ray excitation the emission peak of $LiGa_5O_8$ is found at a shorter wavelength (about 380 nm) than with ultraviolet excitation (about 400 nm) (see Fig. 1). $LiGa_5O_8$ may find practical application in cathode-ray tubes, *e.g.*, in cascade screens (5). With uv excitation the emission spectrum varies with temperature as we found for $MgGa_2O_4$ and $ZnGa_2O_4$ and also for the MgLi and ZnLi gallates.

We extended the work of Hoffman and Brown (3) by preparing various mixed gallates. It was found that LiZn, LiMg, and MgZn gallates (all with the spinel crystal structure) show both a higher absorption and a higher quantum efficiency (60-70%) with 250-270 nm excitation than the unsubstituted gallates (Table I). It will be seen from Fig. 1 that the most efficient gallate phosphors have a peak height of about 80% with respect to that of a calcium halophosphate.

With cathode-ray excitation $LiGa_5O_8$ shows a non-exponential decay, the decay time depending on the pulse length of the excitation. With uv excitation a very slow rise of the fluorescence and some afterglow were observed both in $LiGa_5O_8$ and in the mixed gallates mentioned above. These phenomena might be ascribed to the presence of traps in the host lattice, *e.g.*, through a small loss of oxygen. We also found luminescence in Ga_2O_3 when it had been heated in air above 1100°C, the most intense luminescence being observed with samples fired at 1500°C (Fig. 1).

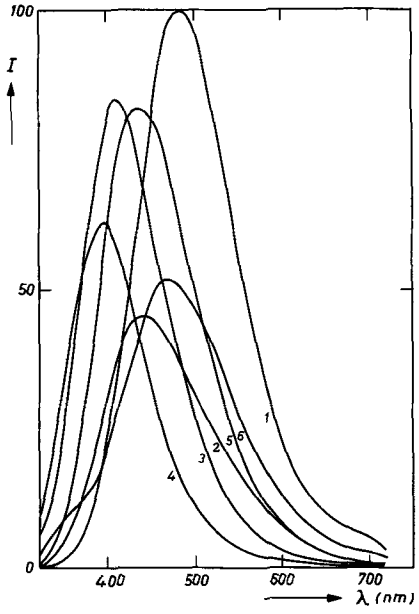

Fig. 1. Emission spectra of Ga_2O_3 and of some gallates in comparison with that of calcium halophosphate-Sb^{3+}, with mainly 254 nm excitation: curve 1, calcium halophosphate-Sb^{3+}; curve 2, Ga_2O_3 twice heated for 2 hr at 1500°C in air; curve 3, $(LiGa)_{0.45}Mg_{0.1}Ga_2O_4$; curve 4, $LiGa_5O_8 = (LiGa)_{0.5}Ga_2O_4$; curve 5, $(LiGa)_{0.45}Zn_{0.1}Ga_2O_4$; curve 6, $ZnGa_2O_4$.

The kind of luminescent center occurring in the self-activated gallates is still obscure, and more work is required in order to elucidate the mechanism of the luminescence found in the gallium compounds described above. Explaining the centers in the gallates and in Ga_2O_3, one should also consider the work of Tippins (6), who observed photoconductivity in single crystals of Ga_2O_3 grown by the Verneuil technique.

Manuscript received March 7, 1969. This was Paper 88 presented at the New York Meeting, May 4-9, 1969.

Any discussion of this paper will appear in a Discussion Section to be published in the December 1969 JOURNAL.

REFERENCES

1. G. Blasse and A. Bril, *J. Inorg. Nucl. Chem.*, **29**, 266 (1967)
2. W. L. Wanmaker, J. G. C. M. de Bres, and J. W. ter Vrugt, Proceedings of the International Conference on Luminescence, Budapest, 1966, p. 1370.
3. C. W. W. Hoffman and J. J. Brown, *J. Inorg. Nucl. Chem.*, **30**, 63 (1968).
4. A. Bril and W. L. Wanmaker, *This Journal*, **111**, 1363 (1964).
5. J. L. Ouweltjes, "Luminescence and Phosphors," Modern Materials, Vol. 5, p. 231, Academic Press, New York (1965).
6. H. H. Tippins, *Phys. Rev.*, **140A**, 316 (1965).

Low-Temperature Epitaxial Growth of Single Crystalline Silicon from Silane

David Richman and Robert H. Arlett

RCA Laboratories, Princeton, New Jersey

Normal techniques for the growth of epitaxial silicon films by the hydrogen reduction of chlorosilane require temperatures of the order of 1200°C. Using silane pyrolysis in hydrogen allows a lowering of the temperature to the 1000°C region. Below this temperature the growth rate falls markedly if epitaxy is to be maintained. A typical reported epitaxial growth rate at 950°C in hydrogen is 0.06 μm/min (1)

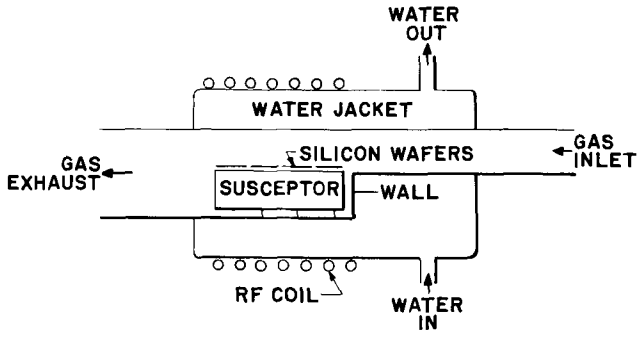

Fig. 1. Schematic diagram of epitaxial growth apparatus

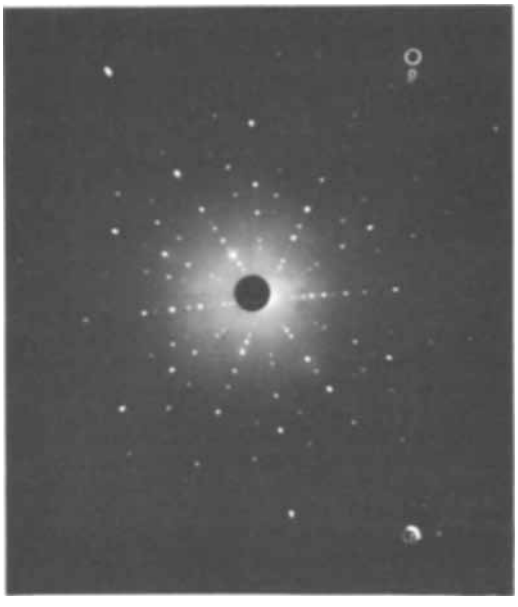

Fig. 2. Laue pattern of an 11μ silicon epitaxial layer grown at 800°C.

Low growth temperatures are of interest in order to minimize impurity diffusion effects which are appreciable at temperatures above 1000°C. However, in this regard, the very slow growth rates at temperatures below 1000°C negate the advantage of a low-temperature process.

This paper reports the results of an investigation of the pyrolysis of silane in a helium ambient. The reason for the choice of a gas other than hydrogen follows from the suggestion of Joyce and Bradley (2) that the desorption of hydrogen from the silicon surface is the rate-limiting process in the epitaxial growth of silicon from silane. It was felt that any steps taken to reduce the hydrogen pressure would increase the desorption rate and hence the epitaxial growth rate, especially at lower temperatures.

A water-cooled reaction chamber was used to prevent premature decomposition of the silane. This chamber provided a streamlined horizontal flow of the entering gas over the RF heated susceptor surface (see Fig. 1). This was intended to prevent the raining of amorphous silicon onto the substrates by minimizing heating of the gas stream away from the susceptor-gas interface thereby minimizing the homogeneous gas phase reaction.

A typical epitaxial growth experiment consisted of initially removing 5-6 μm from the (111) oriented silicon substrate wafers by etching with 1% by volume HCl gas in hydrogen at 1180°C. The temperature was then decreased to the required growth temperature, 910° or 800°C, and the hydrogen replaced by helium

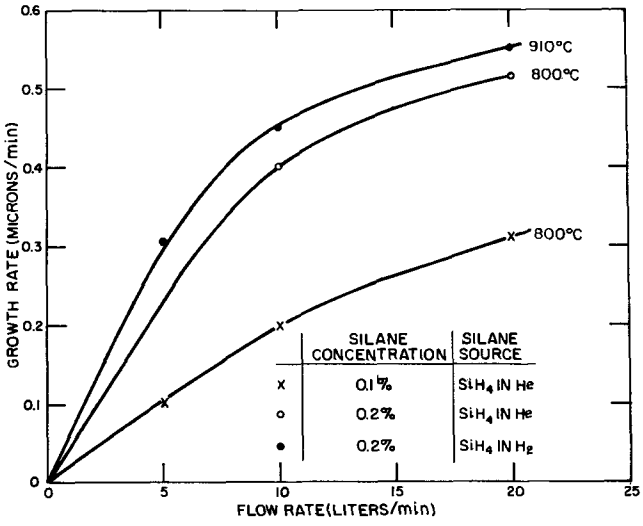

Fig. 3. Dependence of epitaxial growth rate on flow rate as a function of temperature and silane concentration.

which had been passed through two molecular sieves at 77°K and subsequently filtered through a 0.8μ filter. The silane sources were commercial mixtures of 3% silane in hydrogen or 3% silane in high-purity helium. These were mixed with the helium carrier gas to give the requisite silane concentration immediately before entering the reaction chamber. Total gas flow rates of 5, 10, and 20 liters/min were used. These correspond to linear velocities of 15, 30, and 60 cm/sec, respectively. Silane concentrations of 0.1 and 0.2% by volume were used. Growth times varied from 30 to 60 min and film thicknesses were of the order of 5-15 μm.

Using the silane in hydrogen source, epitaxial growth was obtained at 910°C for both silane concentrations and all flow rates. However at 800°C only polycrystalline deposits were obtained. Using the silane in helium source single crystal epitaxial growth was obtained at 800°C. Figure 2 shows a typical Laue pattern for a film grown at 800°C. The high quality of this pattern indicates that growth rates as high as 0.5 μm/min can be achieved at 800°C with no loss of crystallinity. Figure 3 shows the dependence of growth rate on the various experimental parameters. Electrical evaluation of these layers is presently in progress.

In conclusion, these results show that the presence of excess hydrogen inhibits the ability to obtain epitaxial growth of silicon from silane at low temperatures and high growth rates. Replacement of the hydrogen by helium has yielded epitaxy at 800°C at growth rates of 0.5 μm/min. It is noteworthy that at this high growth rate and at such a low temperature, impurity diffusion is virtually negligible.

Acknowledgment

The authors are grateful to E. Miller for excellent technical assistance, and to Dr. J. Dismukes for valuable discussions.

The research reported herein was supported in part by the Air Force Materials Laboratory, Wright-Patterson Air Force Base, Dayton, Ohio 45433 under Contract No. F33615-68-C-1331.

Manuscript received Feb. 28, 1969.

Any discussion of this paper will appear in a Discussion Section to be published in the December 1969 JOURNAL.

REFERENCES

1. S. Nakanuma, *IEEE Trans., Electron Devices*, **ED-13**, 578 (1966).
2. B. A. Joyce and R. R. Bradley, *This Journal*, **110**, 1235 (1963).

DISCUSSION SECTION

This Discussion Section includes discussion of papers appearing in the *Journal of The Electrochemical Society*, Vol. 115, No. 4, 7, and 12 (April, July, and December, 1968).

Effect of Low Pressure on Surface Charge of Electrets

R. A. Draughn and A. Catlin
(pp. 391-394, Vol. 115, No. 4)

Bernhard Gross[1]: The authors present an interpretation of their surface charge measurements based on a formula for the field in the interface between the electret surface and the movable induction electrode and a comparison of the interface field with Paschen's law for the breakdown voltage. In this connection, reference is made to Gubkin and Skanavi.[2]

I should like to point out that I already have established an equation for the interface field of a three-layer electret in my paper "Experiencias com Eletretos, II," Fig. 1 and Eq. [4], [5], and [7].[3] The expression for the field between the dielectric surface and the lifted electrode was discussed and used extensively by me in another paper.[4] In this paper, Paschen's curve has already been used to calculate the conditions for surface breakdown exactly in the same way as now has been done by Draughn and Catlin. I was able to obtain quantitative agreement, at atmospheric pressure, between theory and experiment, which was corroborated by independent evidence from measurements of a-c effects in voids in dielectrics.

The Synthesis and Epitaxial Growth of GaP by Fused Salt Electrolysis

J. J. Cuomo and R. J. Gambino
(pp. 755-759, Vol. 115, No. 7)

R. Monnier:[5] In the discussion section of your article, Yocom's mechanism is suggested to explain the formation of P on the cathode of a cell of fused salts containing sodium metaphosphate:

$$4\ PO_3^- + 5\,e = P + 3\ PO_4^{3-}$$

Thus, this reaction is justified by the formation of sodium orthophosphate in the cathodic compartment.

It seems to me that this phenomenon is better explained by a very weak dissociation of the anion PO_3^- as in:

$$PO_3^- = P^{5+} + 3\ O^{2-}$$

followed by a direct discharge of the ion P^{5+}. Ga should then deposit according to the direct way you mention, *i.e.* Ga^{3+} ions' discharge resulting from Ga_2O_3 dissociation.

A synthesis of these two elements should follow in order to form GaP. It should be noted, however, that the order of discharge you observe during electrolysis, first P, then Ga, agrees with thermodynamics.

In order to support this interpretation, we could add that the formation of sodium orthophosphate can be easily explained. In any case, the rough equation is practically the same in both cases:

$$NaPO_3 = Na_3\,(PO_4)_2 + P + \tfrac{1}{2}\,O_2$$

With a C anode, oxygen would then give a mixture of $CO + CO_2$.

[1] Diretor do Departamento de Pesquisa Científica e Tecnológica, Comissão Nacional de Energia Nuclear, Rua General Severiano 90, Rio de Janeiro, GB, Brazil.
[2] A. N. Gubkin and G. I. Skanavi, *Sov. Phys. Solid State*, 3, 215 (1961).
[3] B. Gross, *Ann. Acad. Brasil. Ci.*, 17, 219 (1945).
[4] B. Gross, *Brit. J. Appl. Phys.* 1, 1259 (1950).
[5] Laboratoire de Chimie et d'Electrochimie Techniques, Case Postale 226, 1211 Geneve 4, Switzerland.

D. Shanefield[6]: The first III-V semiconductor material produced by electrodeposition was gallium arsenide.[7] Germanium crystals have also been grown by fused salt electrolysis.[8] The work of Cuomo and Gambino is certainly a great advance over earlier work because they produced doped single crystals. Their method seems broadly useful, partly because it has been demonstrated that the crystal perfection can improve as the crystal grows during electrodeposition.[9] Possibly the improvement during this process is due to the sidewise growth of dislocations observed with silicon.[10] Also, ultrapurification with respect to certain growth-affecting materials can readily be achieved by various sacrificial electrodeposition means.[11]

Electropolymer Studies, II. Electrical Conductivity of a Polystyrene Sulfonic Acid Membrane

C. S. Fadley and R. A. Wallace
(pp. 1264-1270, Vol. 115, No. 12)

J. A. Kitchener[12]: The authors have remarked that their results and theoretical calculations "disagree with a recent hypothesis that membrane inhomogeneity may seriously disrupt Grotthus conduction chains" (referring to the paper of Block and Kitchener.[13])

Unfortunately, their present argument rests on a theory of doubtful reliability. The mass of earlier work on conductivity of ion-exchange resins has demonstrated the inadequacy of any simple models. In addition to electro-osmotic flow, the universal molecular heterogeneity with even the supposedly "homogeneous" resins cannot be ignored. It must also be recalled that our suggestion of interruption of Grotthus chains in heterogeneous membranes applied to condition of strong electrical polarization.

It is a pity that the authors did not include in their paper some measurements which might well have provided direct evidence for or against the hypothesis —namely, comparative conductivities of H- and Na-form membranes at comparable water contents. It would be extremely interesting to know whether their ratio would be found equal to that of, say, the corresponding homogeneous resins, or, better, the H- and Na-forms of polystyrene sulfonic acid.

M. Block[14]: The authors assume the effect of the polyethylene matrix, constituting 75% by weight of the membrane, to have only an indirect effect on the conductivity. This assumption may be examined more closely in the light of published information on the manufacture and properties of this membrane.

Manufacture.—C.I.T.-T.N.O., The Central Technical Institute of the Organisation for Applied Scientific Research in the Netherlands, developed and marketed the TNO C-60 membrane. Despite the secrecy that obscures details of membrane manufacture,[15, 16] the following methods appear relevant.[17, 18] Commercially available, low-density polyethylene films are swollen

[6] Western Electric Company, Engineering Research Center, Princeton, New Jersey.
[7] "Final Report, Contract AF 19(604)-8490," p. 20, Sept. 1963, AD 427-306. (*See* ASTIA TAB 1 April 64, Div. 25A, p. 204.)
[8] J. O'M. Bockris, J. Diaz, and M. Green, *Electrochim. Acta*, 4, 362 (1961).
[9] P. E. Lighty, D. Shanefield, S. Weissmann, and A. Shrier, *J. Appl. Phys.*, 34, 2233 (1963).
[10] W. C. Dash, Canadian Pat. 713,524 (1965).
[11] D. Shanefield and P. E. Lighty, *This Journal*, 110, 973 (1963).
[12] Imperial College, London, S.W. 7, England.
[13] M. Block and J. A. Kitchener, *This Journal*, 113, 947 (1966).
[14] Unilever Research Laboratory, Isleworth, Middlesex, England.
[15] M. Block, *Chem. Ind. (London)*, 1962, 1882.
[16] M. Block, Ph.D. thesis, University of London (1964).
[17] J. F. A. Hazenberg and B. Knol, Dutch Pat. 95,477 (1960).
[18] J. F. A. Hazenberg, *Dechema Monograph.*, 47, 487 (1962).

at 40°-50°C in styrene containing 2% divinyl benzene (DVB) and 1% benzoyl peroxide, taking up 20-30%. Immersion in saturated sodium sulfate solution at 70°C for 6 hr insures polymerization of the styrene. Sulfonate groups are subsequently introduced with sulfuric or chlorsulfonic acid. Crabtree and Glueckauf believe the chemical initiator to be stannic chloride.[19] The American Machine and Foundry Company developed similar membranes using irradiation to effect grafting in complete or partial replacement of the chemical method.[20] The similarities were so great that patent litigation ensued and A.M.F. purchased the patent rights and manufactured AMF C-60 in Holland, as well as in the U.S.A.

Substrate.—Michaels *et al.*[21] considered polyethylene film a network structure, wherein the crystalline phase serves to cross-link and immobilize chains in the amorphous phase. They point out that crystallites can be destroyed and created by changing the temperature, higher temperatures and gradual cooling favoring the growth of large crystals. Kresser[22] discussed the influence of production variables on film irregularities in greater detail. Hoffman *et al.*[23] found polyethylene films to expand in styrene more in the direction transverse than parallel to the original direction of extrusion. They pointed out that extrusion from the melt would orient polymer chains more in thinner than in thicker films, the material closest to the surface being most oriented. In the central regions of lower stress, larger crystallites could form. Styrene would diffuse first into the amorphous regions and then slowly dissolve crystallites. Antioxidants, antiblocking agents, and catalyst fragments might also be present, complicating the polymer structure.

Cross-linking.—The DVB commercially available contains 45-60% ethyl benzene, which cannot cross-link, as well as isomers of differing reactivities,[24] further complicating the structure of the final polymer. Hazenberg[18] noted that during polymerization 1-2% polyethylene may be extracted and that grafting to polyethylene occurs to a certain extent. Chen and Friedlaender[25] found that under comparable conditions 0.2% benzoyl peroxide induced 32% covalent grafting and γ-radiation 53-83%. The higher rate of grafting in thicker films was attributed to a greater number of swollen, amorphous polyethylene "micelles" but this was not proved. Some polyethylene was cross-linked further by irradiation. Whereas irradiation polymerized styrene to a molecular weight of 47,900, the same material in a polyethylene film attained a molecular weight of 178,000. Selegny[26] pointed out that these membranes largely consist of coiled chains of styrene homopolymer trapped within the interstices of the polyethylene film, corresponding to the snake-cage type.[27]

Membrane heterogeneity.—Chen *et al.*[28] found the electrical resistance 3-5 times greater across the membrane than along the direction of extrusion and believed this to be due to nonhomogeneous distribution of styrene throughout the membrane thickness. Forgacs and Scharf[29] measured the swelling of AMF C-60 in water at 30°-100°C and explained the irregularities found as transitions of the polyethylene substrate from amorphous to crystalline modifications. Arnold and Koch[30] noted an increase in electrical resistance during and just after immersion of the membrane in water in the hydrogen form. This certainly indicates nonuniformity. Arnold[31] recently used acid absorption data to confirm considerable heterogeneity.

Fig. 1. AMF C-60 stained with methylene blue. 45X

The evidence for heterogeneity, as well as large variations in reproducibility, is supported by experiments such as that illustrated in Fig. 1.[32] It shows the uneven uptake of a cationic dye of small dimensions by AMF C-60, easily visible to the naked eye. The regions of high ionic concentration are separated by large regions of different, lower ion-exchange capacities.

Jump distance.—Gregor *et al.*[33] found a volume increase of 175% to occur on transfer of this membrane from 0.1*N* KCl to 0.1*N* H_2SO_4. As this was mainly due to the PSA fraction, its volume increase must have been sevenfold. The small resistance to diffusion shown by the rapid uptake of dyes across large membrane areas[32] is a further indication of the extended nature of this material. Similarly, the doubling in volume on hydration found by Fadley and Wallace indicates an eightfold increase in volume of the PSA polymer. The square of the effective jump distance used in the paper will therefore vary by a factor of up to 16, rather than 4.

In the light of the above evidence, this membrane cannot usefully be compared with the rigid PSA resins discussed by Grubhofer.[34]

Hydration.—Oda and Yawataya[35] considered the water in a membrane to consist of three parts, namely hydration water of the fixed ion, hydration water of

[19] J. M. Crabtree and E. Glueckauf, *Trans. Faraday Soc.*, 59, 2639 (1963).
[20] W. K. W. Chen, M. S. Mintz, and D. G. Conning, *Dechema Monograph.*, 47, 619 (1962).
[21] A. S. Michaels, R. F. Baddour, H. J. Bixler, and C. Y. Choo, *Ind. Eng. Chem., Process Design Develop.*, 1, 14 (1962).
[22] T. O. J. Kresser, Chap. 9 in "High Polymers," Vol. 20, Part 2, Edited by R. A. V. Raff and K. W. Dook, Interscience Publishers (1965).
[23] A. S. Hoffmann, E. R. Gilliland, E. W. Merill, and W. H. Stockmayer, *J. Polymer Sci.*, 34, 461 (1959).
[24] F. Helfferich, "Ion Exchange," McGraw-Hill Book Co., New York (1963).
[25] W. K. Chen and H. Z. Friedlaender, *J. Polymer Sci. C*, 4, 1195 (1963).
[26] E. Selegny, *J. Polymer Sci. C*, 4, 1455 (1963).
[27] M. J. Hatch, J. A. Dillon, and H. B. Smith, *Ind. Eng. Chem.*, 49, 1812 (1957).
[28] K. W. Chen, R. B. Mesrobian, D. S. Ballantine, D. J. Metz, and A. Glines, *J. Polymer Sci.*, 23, 903 (1957).
[29] C. Forgacs and E. Scharf, *Israel J. Chem.*, 34, 269 (1963).
[30] R. Arnold and D. F. A. Koch, *Austral. J. Chem.*, 19, 1299 (1966).
[31] R. Arnold, *Austral. J. Chem.*, 21, 521 (1968).
[32] M. Block, *Chem. Ind. (London)*, 1967, 2099.
[33] H. P. Gregor, R. Kramer, A. Lalik, V. Holmstrom, and T. Saber, Membrane Evaluation Program, New York, Brooklyn Polytechnic (1961).
[34] N. G. Grubhofer, *Makromol. Chem.*, 30, 96 (1959).
[35] Y. Oda and T. Yawataya, *Bull. Chem. Soc. Japan*, 29, 673 (1956).

the counter-ion, and solvent water filling the pores. In a PSA membrane at concentrations of 0-4*N* HCl, they found the electro-osmotic transport of H^+ to be 1 and the water of hydration of the sulfonate groups to be 1.5-3.5.[36] This is confirmed indirectly by measurements of dielectric constant and conductance by Dickel and Bunzl[37] on a PSA resin of 8-10% DVB content. They found that the hydrogen ion begins to dissociate from the sulfonate group on uptake of 2.5 moles of water per mole of valency. The lower cross-linkage of AMF C-60 would permit greater transport of water,[38-42] as indeed found by the authors. However, the fact that such a great variability exists, according to the type of membrane considered,[43] detracts from the authors' thesis that a hydration shell of about seven water molecules requires to be filled around the hydrogen ion in order to reach a maximum conductance.

Conductivity.—The factor of seven difference in conductivity between the sodium and hydrogen forms of this membrane indeed suggests that conduction by the Grotthus mechanism occurs to a considerable extent. The finding is supported by Zapior *et al.*[44] On the other hand, Cooke[45, 46] and Block and Kitchener[47] found a negligible transport of hydrogen ions during electrodialysis at current densities many times above the critical value. Similarly, although a factor of 7.8 difference in conductivity between the hydrogen and sodium forms of Amberplex C-1 was noted,[48] Grubb[49] did not and Block and Kitchener[47] failed to detect abnormal hydrogen transport.

The last-named workers found that commercial membranes containing one resin with reinforcements of different, inert materials gave rise to different electrochemical behavior. Moreover, changes were observed between batches of the same membrane.[16] Gregor *et al.*[33] noted large variations in physical properties of samples of commercial membranes, including differences in conductivity of 300%. In view of these facts and the many variants that could occur in manufacture and that can affect conductivity, it is considered likely that Fadley and Wallace were examining membranes different from those tested by Block and Kitchener under the same generic name, and that the Amberplex membranes of the latter differed from those discussed by Spiegler *et al.* one year earlier.

It could be objected that the conditions used by Block and Kitchener and the six cations tested by Cooke did not include H^+, so that the environment within the membrane was not comparable. However, the fact that anomalous conduction has been observed many times with anion-exchange membranes[16] and at least once with a cation-exchange membrane[50] shows that the appropriate alkaline or acidic loading is not essential to obtain Grotthus conduction.

In cases where anomalous conduction does not occur to an appreciable extent, it is still postulated that the Grotthus chains are interrupted, more or less frequently, by hydrophobic barriers, through which the ions have to migrate by a jump mechanism.

The existence and extent of the Grotthus mechanism of conduction across an ion-exchange membrane could be tested with the simultaneous use of deuterium or tritium and O^{18} in the diluate compartment of a two-chambered cell.[16] While the hydrogen isotope could migrate across a cation-exchange membrane as an ion or as water or both, the oxygen isotope could move only as water. Both could move as ion or solvent across anionic membranes. The simultaneous determination of ionic and electro-osmotic transport would show whether there were a complete physical transport of H^+ or OH^- ions across the membrane or if some of the charge were transferred by a chain process. In the latter case, there would be little electro-osmotic water transfer.

C. S. Fadley and R. A. Wallace: Our conclusion that abnormal conduction takes place in the hydrogen form of this membrane (AMF C-60) is based on our measurement that $\sigma_{H+}/\sigma_{Na+} \approx 7$ for ionic membranes with approximately 15 moles of water/equiv. We refer to these experimental data in our paper. The reliability of our equations for predicting conductivity as a function of water content is thus not important to this conclusion, but rather the theory is qualitatively supported by the conclusion. To further clarify this point, Fig. 1 shows the detailed variation of ionic mobility with water absorption for both sodium and hydrogen forms of the membrane. The data for sodium form are from recent work by Dr. Wallace.[51]

In effect, Fig. 1 answers Dr. Kitchener's request that we provide further experimental proof of the comparative conductivities or ion mobilities of the H- and Na-form of the polystyrenesulfonate membrane as a function of water content. Our data speak for themselves. In addition, Dr. Wallace and J. Ampaya have

[51] R. A. Wallace, "Electrical Properties of Electrodialysis Membranes," Report No. 68-3, Sea Water Conversion Laboratory, University of California, Berkeley, California.

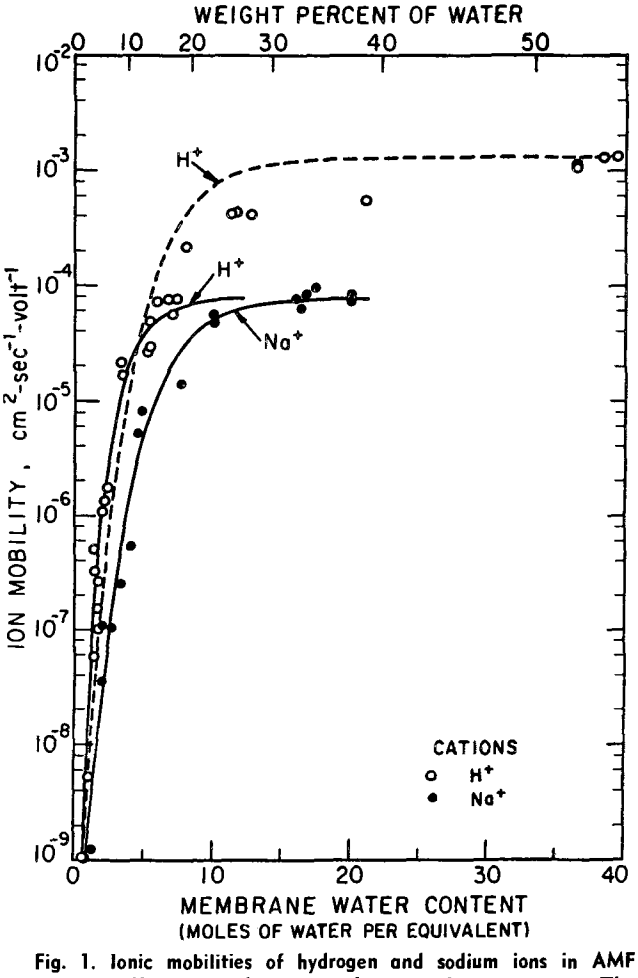

Fig. 1. Ionic mobilities of hydrogen and sodium ions in AMF polystyrenesulfonate membrane as a function of water content. The data for H^+ are from our paper under discussion, and the data for Na^+ are from footnote 51. The curves have been calculated as described in the text.

[33] Y. Oda and T. Yawataya, *Bull. Chem. Soc. Japan*, 30, 213 (1957).
[37] G. Dickel and K. Bunzl, *Makromol. Chem.*, 79, 54 (1964).
[38] F. Helfferich, *Angew. Chem.*, 68, 693 (1956).
[39] W. F. Graydon and R. J. Stewart, *J. Phys. Chem.*, 59, 86 (1955).
[40] E. Blasius and H. Pittack, *Angew. Chem.*, 71, 445 (1959).
[41] D. K. Hale and D. J. McCauley, *Trans. Faraday Soc.*, 57, 137 (1961).
[42] H. Ohtaki, K. Gonda, and H. Kakihana, *Bull. Chem. Soc. Japan*, 34, 293 (1961).
[43] M. Block and K. S. Spiegler, *This Journal*, 110, 577 (1963).
[44] B. Zapior, M. Lesko, and J. Klinowski, *Zesz. Nauk. Uniw. Jagiel. Ser. Nauk. Mat.-Przyrod. Mat., Fiz., Chem.*, 12, 145 (1967). *Chem. Abs.*, 69, 90063z.
[45] B. A. Cooke, *Electrochim. Acta*, 4, 179 (1961).
[46] B. A. Cooke, Private communication (1964).
[47] M. Block and J. A. Kitchener, *This Journal*, 113, 947 (1966).
[48] K. S. Spiegler, *This Journal*, 100, 303C (1953).
[49] W. T. Grubb, *J. Phys. Chem.*, 63, 55 (1959).
[50] H. P. Gregor and M. A. Peterson, *J. Phys. Chem.*, 68, 2201 (1964).

recently submitted to *This Journal* a detailed experimental analysis and theoretical study of anomalous or abnormal ion conduction occurring in both cation- and anion-exchange membranes used in electrodialysis.

The two curves for H^+ correspond to the theoretical curves given in Fig. 9 of our paper. The curve for Na^+ was calculated using the empirical constants $\beta\Delta F_A^\circ = 9800$ cal/mole, $n_o = 2.75$. We have already commented that the solid H^+ curve might approximately represent "normal" (non-Grotthus) conduction. The Na^+ curve agrees quite well with the experimental data from 0 to 20 moles/equiv., and has a high water absorption limit very close to the solid curve for H^+. For approximately 1 mole of water/equiv., the experimental mobilities are equal, indicating no appreciable difference in the effects of absorbing one molecule of water for the two ionic forms.

One might also ask why the normal curve for H^+ does not agree more closely with the curve for Na^+ if transport is substantially the same for the two ions exclusive of Grotthus conduction. The answer is probably twofold. First, the sodium ion interacts less strongly with water molecules during hydration. A reflection of this is the free energy of absorption, which is greater by a factor of ~1.5 for H^+ in PSA of 10% DVB content.[52] From our equation connecting conductivity and free energy of absorption (Eq. [9] of our paper), such a difference in free energy of absorption translates qualitatively into the difference between the normal H^+ curve and the Na^+ curve between 1 and 5 moles of water/equiv. Second, abnormal conduction probably contributes to the experimental conductivity in this region and thus our solid curve overestimates normal conduction.

To be sure, the membrane we have studied has a heterogeneous molecular structure and is subject to variations in property from batch to batch. Our measurements (including those of Fig. 1 on sodium form) were made on samples from the same batch, so the latter difficulty was minimized. As to the former, several comments are in order. Heterogeneity and variations in molecular structure from surface to bulk are almost certainly present, but regardless of this the water-PSA interaction is the dominant one as far as variations in conductivity with water absorption are concerned. As Block has pointed out, PSA in the membrane probably exists as coiled chains in polyethylene interstices.

On the other hand, polyethylene crystallites will probably contain very little PSA and we are thus dealing with a quasi two-phase system. However, the PSA phases must be interconnected in order for spatially continuous conductivity to occur. With regard to the occurrence of abnormal conduction in some instances with a given commercial membrane and not in others, it is possible that the interconnections between groups of PSA molecules for some membranes are made through very dense areas of polyethylene. This spatially restricted, hydrophobic atmosphere would limit Grotthuss conduction. If conduction along the interconnecting PSA molecules is the transport-limiting process between "high-conductivity" regions dense in PSA and water, then the measured conductivity will reflect normal conduction.

For the membrane we have studied, no such hindrance of abnormal conduction was observed. Also, the conductivities at saturation are very near to those of pure phenolsulfonic acid resins of a similar exchange capacity.[53] Thus, it seems that links between any more or less condensed regions of PSA are very complete or that the membrane is more homogeneous than might be imagined from the above model.

As to phase changes of the polyethylene matrix, all our measurements with varying water absorption were made at room temperature, so it is doubtful that such changes affected our results. In view of the above, it seems reasonable to assume that for a given membrane batch at fixed temperature the polyethylene matrix has only a small effect on the variation of conductivity with water absorption.

A more precise theoretical formulation should clarify our assumption that the effective free energy of absorption ($\Delta F^{\ddagger}$) will be appreciably changed by water absorption, but not the effective jump distance (λ). In an exact treatment of conductivity based on absolute reaction rate theory, we must start with the total number of different sites for ionic carriers in the polymer matrix, each denoted by an index j. For each site, there will be various possible jump distances (λ_{ji}) and each λ_{ji} will have associated with it a free energy of activation ($\Delta F_{ji}^{\ddagger}$). The concentration of sites of type j will be denoted by c_j, such that

$$c = \sum_j c_j = \text{total concentration of counterions} \qquad [1]$$

The conductivity of each site will be given by

$$\sigma_j = \frac{c_j q^2}{h} \sum_i \lambda_{ji}^2 \exp(-\Delta F_{ji}^{\ddagger}/RT) \qquad [2]$$

and total conductivity by

$$\sigma = \sum_i \sigma_j = \frac{q^2}{h} \sum_{j,i} c_j \lambda_{ji}^2 \exp(-\Delta F_{ji}^{\ddagger}/RT) \qquad [3]$$

The effective jump distance can be related to these quantities by equating total conductivities. This yields

$$\lambda^2 \exp(-\Delta F^{\ddagger}/RT) = \sum_{j,i} f_j \lambda_{ji}^2 \exp(-\Delta F_{ji}^{\ddagger}/RT) \qquad [4]$$

where f_j = the fraction of sites which are of type j.

Since each λ_{ji} represents a *single-step* process, it is extremely unlikely that λ_{ji} will be greater than a few anion-anion distances or a few water molecule diameters. This will be reflected as a very high ΔF_{ji} for large λ_{ji} values and a correspondingly small contribution of such terms to the sums of Eq. [3]. Experimental evidence for this is indirectly given by the observation of Lapanze and Rice[54] that even PSA in aqueous solution consists of hydrated ions bound to the anionic polymer in a tight sheath. This sheath is responsible for the low effective degree of ionization observed in PSA solutions.[55] Jumps to distances much larger than the sheath diameter will thus be very unlikely upon the application of fields as low as those used in our conductivity experiments.

Therefore, the effective jump distance as we have defined it will have at most a roughly fivefold variation and the comments of Block on changes in jump distance based on macroscopic volume changes of the PSA fraction do not directly relate to this jump distance. Our mention of the work of Grubhofer[56] on PSA molecular structure was merely to indicate that intrachain λ_{ji} will remain very much the same for both wet and dry membrane. Interchain λ_{ji} will no doubt change in magnitude and relative importance, but a factor of 16 increase is very doubtful.

Equation [3] can be simplified if we assume an average site type (counterions near the PSA chain) and if the dominant terms on the right side are taken to be jumps by roughly one anion-anion distance (λ_{aa}) along the PSA chain and also jumps by λ_G due to Grotthus conduction. The conductivity will then be given by

$$\sigma = \frac{cq^2}{h} \{\lambda_{aa}^2 \exp(-\Delta F_{aa}^{\ddagger}/RT) + f_G \lambda_G^2 \exp(-\Delta F_G^{\ddagger}/RT)\} \qquad [5]$$

where f_G = the fraction of sites capable of abnormal conduction. This equation adds the effects of normal

[52] H. P. Gregor, B. R. Sundheim, K. M. Held, and M. H. Waxman, *J. Colloid Sci.*, 7, 511 (1952).
[53] A. O. Jakubovich, G. J. Hills, and J. A. Kitchener, *Trans. Faraday Soc.*, 55, 1570 (1959).
[54] S. Lapanze and S. A. Rice, *J. Am. Chem. Soc.*, 83, 496 (1961).
[55] R. A. Mock and C. A. Marshall, *J. Polymer Sci.*, 13, 263 (1954).
[56] N. Grubhofer, *Makromol. Chem.*, 30, 96 (1959).

and abnormal conduction. The quantities affected primarily by water absorption will be $\Delta F_{aa}^{\ddagger}$ and f_G, whereas λ_G and $\Delta F_G^{\ddagger}$ will be essentially constant and have been determined previously.[57] From Eq. [4] and [5], we see that for f_G small, $\lambda \approx \lambda_{aa}$, $\Delta F^{\ddagger} \approx \Delta F_{aa}^{\ddagger}$, and it is in this approximate form that we have applied Eq. [5] to normal conduction. We should also note here that the additive nature of terms in Eq. [3] and [5] is valid only when different conduction modes (*i.e.*, different λ_{ji}) exist in parallel. For the case just mentioned, this parallel nature is probably a reasonable assumption. However, the situation we have discussed of interconnecting PSA chains passing through strongly hydrophobic surroundings would represent modes in series and only the rate-limiting term(s) need be treated in such situations.

Our conclusions regarding water of hydration are based on a comparison of conductivity results and data on the net volume change per mole of water absorbed (Δv). A negative value of Δv indicates denser over-all packing of molecules in wet membranes than in the reference state of dry membrane-liquid water. Therefore, the minimum in this quantity near 10 moles of water/equiv. indicates a dense structure somehow accommodating approximately 10 molecules/HSO_3 group. The hydration estimates of 7 molecules for the H^+ ion (Stokes and Robinson[58]) and 1.5-3.5 molecules for the sulfonate group (Oda and Yawatawa[59]) would give just such a structure.

The fact that measured conductivity reaches a maximum at the same extent of water absorption probably indicates that conductivity is strongly affected by the hydration water, but only weakly affected by further absorption of essentially free solvent water. We further note that the primary hydration number for H^+ as calculated by Glueckauf[60] is only 4. Oda and Yawatawa[59] assumed this number of water molecules to be rigidly transported with the hydrogen ion as one contribution to electro-osmosis. It is not surprising, however, that some further ordering of water molecules occurs up to approximately a hydration number of 7 and that this added water interaction acts to increase conductivity.

[57] H. Eyring, K. J. Laidler, and S. Glasstone, "Theory of Rate Processes," p. 559, McGraw-Hill Book Co., New York (1941).

[58] R. H. Stokes and R. A. Robinson, *J. Am. Chem. Soc.*, **70**, 1870 (1948).

[59] Y. Oda and T. Yamataya, *Bull. Chem. Soc. Japan*, **30**, 213 (1957).

[60] E. Glueckauf and G. P. Kitt, *Proc. Roy. Soc. (London)*, **A228**, 322 (1955).

Thin-Film Silver Halide Electrolyte Cells

Paul Vouros[1] and Joseph I. Masters

Technical Operations, Incorporated, Burlington, Massachusetts

ABSTRACT

Thin-film solid-state batteries ranging in thickness from 5 to 12μ were prepared on quartz substrates by vacuum-deposition techniques. Silver films ~1000Å thick were used in all cases as the reversible electrode, while platinum and in some cases gold films of a similar thickness were used as the counterelectrode. Electrolyte films consisted of evaporated AgI, evaporated AgBr, and a double electrolyte of AgI evaporated onto a film of AgCl or AgBr. Cells consisting of the above types of electrolytes were rechargeable, and the ones containing pure AgI or AgI + AgBr or AgCl electrolyte exhibited long shelf life. Preliminary conductivity measurements using an a-c bridge method indicate, as expected, that the electrode-electrolyte interfaces rather than the electrolyte films are the principal sources of the high internal resistance exhibited by these batteries.

The use of solid-state electrolytes in electrochemical cells was first demonstrated by Reinhold (1) during his studies of chemical equilibria between solid salts. Ionic conductivity in the solid state has since been studied by a number of workers and an extensive review of the subject has been presented by Lidiard (2). A more recent review by Raleigh (3) deals with the general aspects of solid-state electrochemical techniques and the use of solid-state galvanic cells for various thermodynamic calculations.

Silver iodide, when contained between two metallic electrodes of which one is a reversible silver anode, has long been known to act as a solid electrolyte in which the ionic current is carried almost in its entirety by Ag^+ ions (4). In recent years, several articles have appeared in the literature on the utilization of silver iodide as an electrolyte in solid-state battery applications. A bead cell developed by Weininger (5) consists of a silver anode and a platinum or tantalum cathode embedded into the solid AgI electrolyte. In the presence of iodine vapor, the cell acts as a primary battery, the iodine being reduced at the inert Pt (or Ta) electrode. Mrgudich (6, 7) has recently reported on the performance of AgI pellet batteries in which the AgI electrolyte is compressed between silver and platinum electrodes, and he also suggested that the possibility of making an all thin-film version of the system be explored. The Mrgudich batteries are rechargeable concentration cells in which the cell voltage is a function of the activity of Ag^o on the inert platinum electrode and is given by the Nernst concentration-cell equation

$$E = (RT/n\mathbf{F}) \ln \frac{a_s}{a_p} \qquad [1]$$

Here n is the valence change of silver to silver ions (*i.e.*, unity), R is the gas constant, T is the absolute temperature, $\mathbf{F}$ is the Faraday constant, a_s is the activity of Ag^o in the silver electrode which is constant and essentially unity, and a_p is the activity of Ag^o in the platinum electrode which is variable.

Aside from isolated examples such as the MAg_4I_5 electrolyte cells, where M = K, Rb or Cs (8, 9, 10, 11), a characteristic of solid-state batteries prepared to this date is their generally high d-c internal resistance, due either to the poor ionic conductivity of the electrolyte or to the high resistance of the electrochemical double layer at the electrode-electrolyte interface. The electrolyte problem may be minimized by decreasing its thickness, while a reduction in double-layer boundary effects may be achieved by increasing the interface surface area. For example, the interface structure may be altered by mixing of the electrode and electrolyte materials thus making the mixture both an electronic and an ionic conductor (6).

A solid-state cell in which the electrolyte thickness is of the order of magnitude of a micron, or as thin as possible, represents a goal in miniaturization if high resistance boundary conditions and electronic conductivity of the thin electrolyte film are not a severe limitation. A demonstration of the feasibility of an all thin-film battery produced by conventional vacuum-deposition techniques may eventually encourage a variety of low power applications in microelectronics where evaporation techniques are used, such as in integrated microcircuitry.

Thin-film solid state batteries have been reported in the past (12, 13). In those cases, they involved the use of the more complex solid electrolyte system Pb/$PbCl_2$-AgCl/Ag. We report here on a vacuum-deposited thin-film adaptation of the Mrgudich pellet format Ag/AgX/Pt or Au concentration cell system (where $X = I^-$ or Br^-).

Experimental Procedure

Film deposition and measurement techniques.—Films of silver bromide and silver iodide varying in thickness from 5 to 12μ were vapor deposited at a pressure of 5 x 10^{-5} mm Hg. A tungsten boat was operated at 632° and 560°C for the AgBr and AgI evaporations, respectively. The thickness of the transparent silver bromide film was determined by an interference measurement (14), whereas a gravimetric method based on the bulk density of opaque AgI was used to estimate the thickness of the deposited silver iodide film. The estimate given in this paper for the thickness of the AgI films may be low since the density of evaporated silver halide films is generally lower than bulk density. For example, the density of evaporated AgBr films is 4.55 g/cc as compared with a bulk density of 6.5 g/cc.

The silver metal film electrodes were deposited by evaporation using a tantalum coil source, and a CVC AST-100 sputtering unit was employed for the deposition of the platinum film electrodes. Metal film thickness varied between 700 and 1000Å, and in general the resistance of the 2.5- x 0.4-cm electrode films used (Fig. 1) was 100 ohms or less. Electrical contact with the thin metal films was established with the conductive Eccobond solder No. 56C.

To ensure against loading samples of very high internal resistance, a high input impedance Keithley 610B electrometer was used for open-circuit voltage measurement. Although the original state of charge is disturbed by a small current drain, steady-state internal resistance of charged cells can be estimated by momentarily lowering the Keithley's input impedance until the measured cell voltage is half its open-circuit value (impedance matching). The charge-discharge

[1] Present address: Baylor University, College of Medicine, Institute for Lipid Research, Texas Medical Center, Houston, Texas 77025.

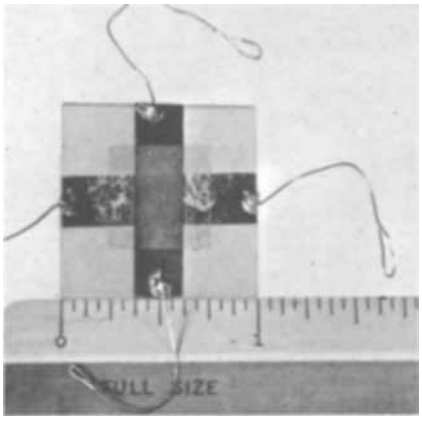

Fig. 1. Typical Pt/AgX/Ag cell in overlapping format

dynamic characteristics of the cells were also monitored by using various loads. For this work, the electrometer output was recorded with a Bausch and Lomb VOM-5 recorder. All discharge curves were taken on cells that had been charged for 1 hr at 0.5v between discharges unless otherwise specified. An a-c bridge was used to avoid polarization effects and thereby approximate (upper bound) the conductance of the electrolyte. The applied a-c voltage was small and of a variable frequency up to 600 kHz.

Cell format.—Two different cell formats were constructed: "overlapping" and "nonoverlapping." The overlapping electrode format is one in which the electrolyte is "sandwiched" between the two electrodes. The procedure used for the fabrication of a typical overlapping cell is as follows. The platinum film is sputtered on a quartz substrate. This is followed by evaporation of silver halide on portions of the substrate covered by the platinum film. Finally, the silver electrode is evaporated by masking off the platinum-covered portions of the substrate. All charge-discharge data reported below were taken with cells in which the total electrode-electrolyte overlap area was approximately 0.4 cm^2. An example of a typical overlapping cell is shown in Fig. 1.

The second, or nonoverlapping electrode format (*see* Fig. 2), is one in which the two electrode films are deposited side by side, separated by 150μ or more. The electrodes and gap between them are then coated with the evaporated silver halide. It is evident that this nonoverlapping format produces a cell of much higher electrolyte resistance than the corresponding overlapping cell because of its longer path and smaller cross-sectional area. It is not, however, subject to shorting if pinholes are present in the electrolyte film, thus allowing the study of other thin electrolyte films which may be prone to a pinhole structure.

Experimental Results

Silver iodide electrolyte thin-film cells.—Overlapping format.—The preparation of a Pt/AgI/Ag thin-film cell in an overlapping format was initially unsuccessful because of a direct short between the platinum and silver electrodes. Electron micrographs of the evaporated silver iodide film when deposited on a substrate whose temperature was 41°C indicate that the silver iodide grains [Fig. 3(a)] do not form a continuous structure and that large breaks exist between grains. Further supporting evidence [Fig. 3(b)] clearly shows that these breaks are actual voids which extend through the silver iodide layer.

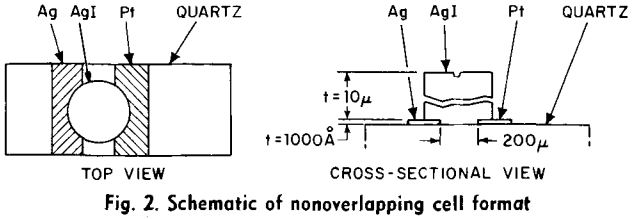

Fig. 2. Schematic of nonoverlapping cell format

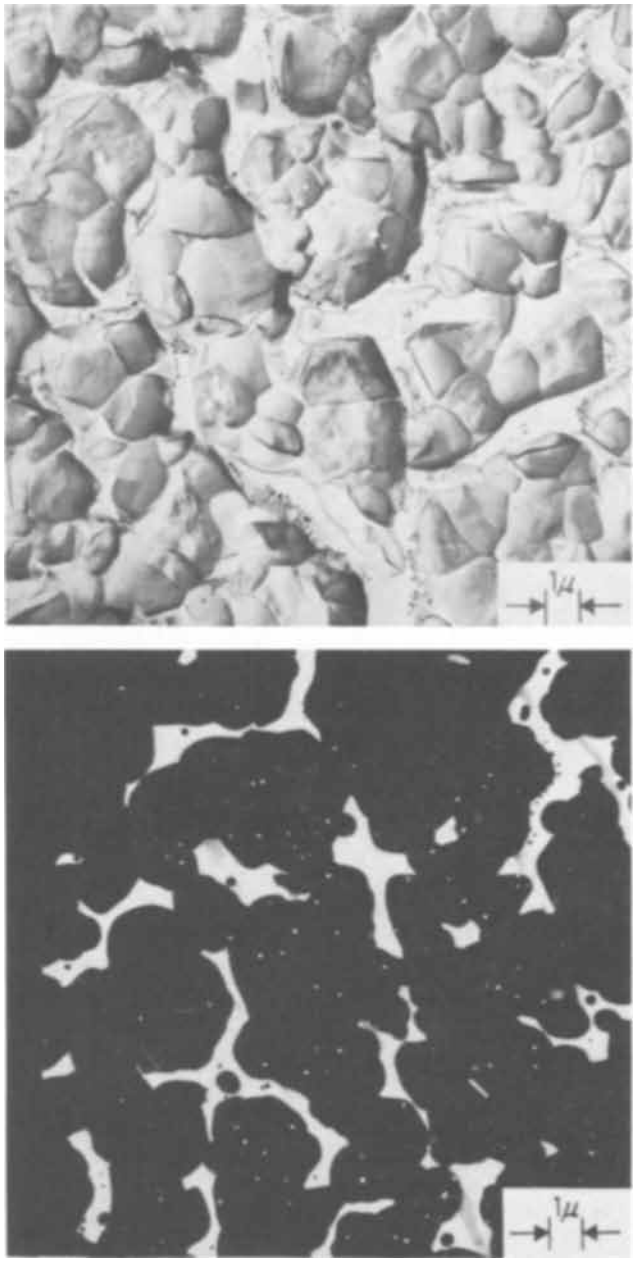

Fig. 3. Electron micrographs of evaporated AgI film deposited at a substrate temperature of 41°C: (a, top) replicated sample and (b, bottom) unreplicated sample. The electron micrographs were taken on silver iodide samples that were evaporated onto thin carbon films which were supported by nickel grids. The evaporation conditions were identical to those used for the deposition on the quartz substrate. The silver iodide film was shadowed at a 3:1 angle ratio with the platinum-imbedded carbon pellet technique. It was then coated at normal incidence with carbon, and the original halide was dissolved with a methanolic KCN solution (0.5g KCN/50 ml CH_3OH). The sample was washed gently for 5 min in three changes of distilled water.

In view of this problem, an additional step for preparation of the electrolyte was introduced, involving the chemical conversion of Ag to AgI. A strip of platinum 2.5 cm x 0.63 cm x 0.1μ was deposited by sputtering on a quartz substrate. This was followed by the deposition of a film of silver (~1000Å) directly over the center of the platinum strip. The system was then placed in an iodine chamber for ~24 hr to ensure the conversion of most of the silver to AgI. A second layer

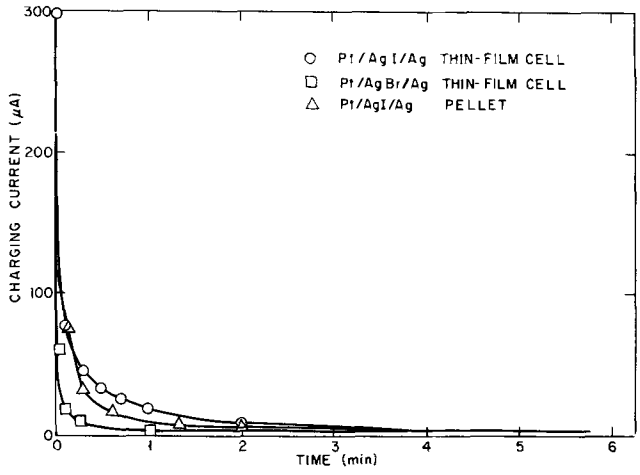

Fig. 4. Typical charging curves of various concentration cells

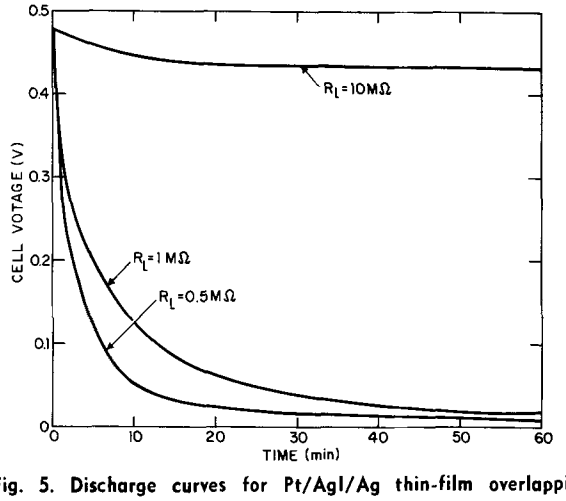

Fig. 5. Discharge curves for Pt/AgI/Ag thin-film overlapping cell using various loads.

of silver iodide was deposited by evaporation over the original ultrathin iodized silver film, which acted as the nucleus for the formation of a uniform and void-free deposit of AgI. This, in turn, was followed by the deposition by evaporation of the silver electrode.[2] The open-circuit cell voltage, which was monitored in vacuum during the deposition of the silver electrode, attained the low value of 0.06-0.10v, presumably due to the presence of some unconverted silver at the platinum electrode surface which lowers a_p in Eq. [1]. The cell was then charged at a voltage of 0.5v. A typical charging curve is shown in Fig. 4, along with those of other thin-film or pellet cells of various formats or electrolytes. Figure 5 shows a series of discharge curves for several large resistance load values. These cells showed no detectable leakage after several months of storage.

Nonoverlapping cell format.—At the outset of the AgI evaporation, the activity of Ag° at the platinum electrode starts from a minimum value, except for the activity that occurs due to diffusion and reduction of Ag^+ ions from the deposited silver iodide, to establish the equilibrium

$$Ag^+ + e^- \rightleftarrows Ag^\circ \ (a_p) \qquad [2]$$

By monitoring the cell voltage in vacuum, it is there-

[2] In addition to the chemical conversion of silver iodide to form a nucleus for the vacuum-deposited AgI film, the problem of structural voids in evaporated AgI films was also overcome by depositing a thin continuous subbing layer of AgCl or AgBr over the platinum electrode prior to the AgI evaporation. Cells consisting of Pt/AgCl or AgBr, AgI/Ag maintained the voltage to which they had been charged for several months with no detectable leakage, but suffered from a high d-c internal resistance (10^7 ohms), presumably due to the presence of high contact resistance between the halide films and the electrode interfaces.

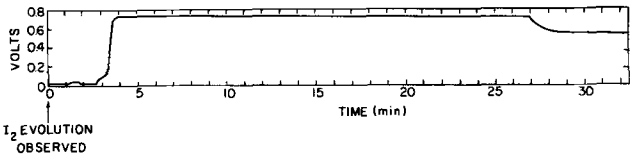

Fig. 6. Nonoverlapping cell OCV as a function of AgI evaporation

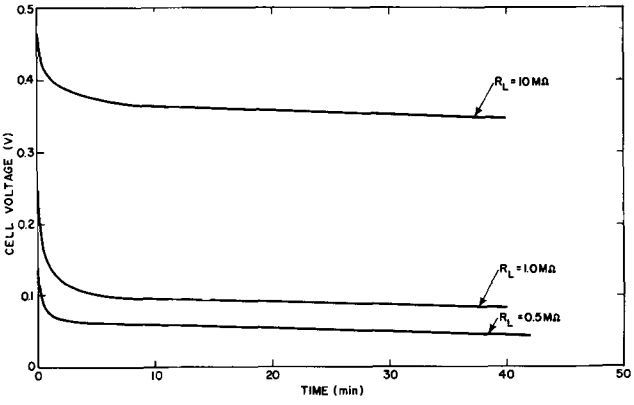

Fig. 7. Discharge curves for Pt/AgI/Ag thin-film nonoverlapping cell using various loads.

fore possible to follow the rate of AgI deposition and study the basic cell properties during the actual cell preparation. As is shown in the open-circuit voltage *vs.* time plot of Fig. 6, there is no significant increase in voltage for about 2.5 min after iodine evolution is first observed. This is followed by a rapid increase in cell voltage, which occurs when the AgI film is thick enough so that its resistance matches that of the electrometer (10^{14} ohms). The cell voltage finally reaches the high value of 0.725v where it remains constant until the evaporation is stopped (approximately 27 min). The drop in boat temperature is followed by a decrease in the cell voltage to a value of 0.550v.

The high open-circuit voltage of 0.725v can be accounted for by the operation of an I_2,Pt/AgI/Ag cell, the I_2 vapors being produced from partial decomposition of the AgI.[3] The observed value of 0.725v is higher than the theoretical value of 0.688v corresponding to the thermodynamic free energy of formation of AgI, this discrepancy occurring because of the heating of the substrate from the AgI boat. In that respect, it is consistent with the results of Weininger (5) who reported open-circuit voltage values as high as 0.75v when an I_2,Ta/AgI/Ag cell was operated at elevated temperatures. The observed voltage drop to 0.550v, typical of a Pt/AgI/Ag concentration cell (6, 7), after the source is turned off, is presumably due to the reduction of the partial pressure of I_2 and the removal of excess iodine.

The performance of a nonoverlapping Pt/AgI/Ag cell when placed under load is shown in Fig. 7. The electrode separation in this case was 750μ and the thickness of the AgI layer was about 4μ, with an overlap area of ~1.8 cm² between the electrolyte and each electrode. The cell output was generally lower than that of its overlapping counterpart which in part is due to the smaller cross-sectional area of the electrolyte and the increased internal resistance. The nonoverlapping Pt/AgI/Ag cells exhibited the same excellent voltage stability as the overlapping cells.

Silver bromide electrolyte thin-film cells.—Because of previous experience in the deposition of AgBr films for photographic applications (14), this material was tested as an overlapping cell electrolyte. Although a thin AgBr film can be deposited more readily than AgI in a continuous void-free electrolyte layer, it is

[3] The iodine evolved during the AgI evaporation is also available at the Ag electrode but it can be postulated that it reacts to form silver iodide.

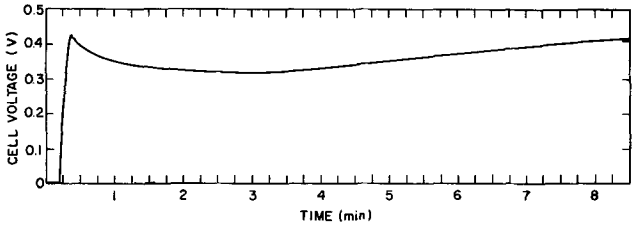

Fig. 8. Overlapping AgBr cell OCV as a function of evaporated Ag deposition.

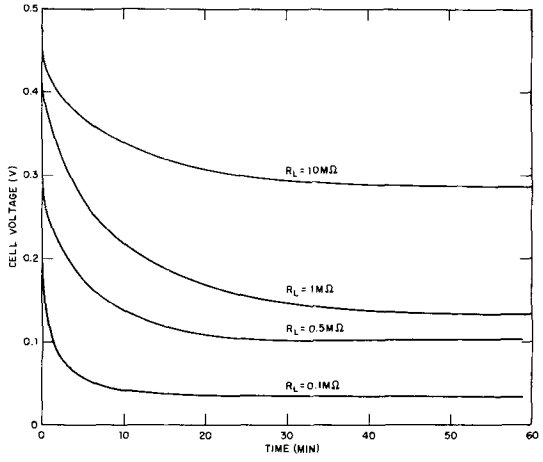

Fig. 9. Discharge curves for Pt/AgBr/Ag thin-film overlapping cell using various loads.

less desirable than AgI because of a noticeably higher electronic conductivity (causing an internal short in a cell) and lower ionic conductivity. Because of the latter, the nonoverlapping format was not considered for AgBr samples.

Silver bromide electrolyte overlapping cells were prepared, as in the case of AgI cells, by the deposition of a strip of sputtered platinum onto a quartz substrate followed by a 5-10μ thick layer of the halide. The silver electrode was then deposited so as to cover the electrolyte. As soon as a continuous layer of silver was established, the open-circuit cell voltage, which was monitored during silver deposition, increased rapidly from zero, as shown in Fig. 8,[4] and decreased gradually to a low of ~0.3v followed by an increase to about 0.4v.

The reasons for this voltage variation are not entirely clear at this point, but it may be due to heat or light radiated from the tantalum coil, the reaction of deposited silver with photolytically produced bromine, the partial diffusion of the initially deposited silver into the AgBr (15, 16), or other undetermined factors. On occasions where the evaporation became erratic, such as when the tantalum filament was overheated, high-energy silver particles or vaporized molecules penetrated through the electrolyte layer and the breakdown of the cell by an internal short was indicated by the sudden drop of the cell voltage to zero.

A typical charging curve of a Pt/AgBr/Ag thin-film cell (of thickness $t = 10\mu$) is shown in Fig. 4 and its discharge characteristics under load are given in Fig. 9. When an evaporated Au film was used as an electrode instead of sputtered platinum, the cell output was generally comparable. As anticipated, the AgBr electrolyte thin-film cells proved less stable than similar AgI cells, losing more than 30-40% of their charge in less than 1 week.

Discussion of Results

The external work done by a cell is the integral

$$W = \frac{1}{R_L}\int_0^t (E - ir)^2\, dt \qquad [3]$$

where $V = E - ir$ is the cell voltage, r is its internal resistance, R_L is the external load resistance, and i is the current. In a concentration cell, power is not delivered at a constant voltage, since during discharge E is a decreasing function of time (Eq. [1]). Therefore, capacity should be rated in terms of watt hours (whr) rather than in the more ambiguous ampere-hours. For optimum performance in such a cell, it is clear that the inert electrode should "soak up" a generous amount of material from the reversible electrode while maintaining an effectively low Ag concentration. In other words, the optimum platinum electrode in an Ag/AgI/Pt cell must have a large Ag absorptivity as well as a large effective surface. Cell output is also limited by the cell's internal resistance since the cell voltage V is reduced by the internal ir drop when under load.

The energy output of the various thin-film cells discussed earlier was roughly estimated during a 1 hr discharge into an appropriate matched load using Eq. [3]. For AgBr and AgI electrolyte overlapping cells of the dimensions discussed above, the total output is on the order of 2 x 10^{-8} whr and about half as much for a AgI electrolyte cell in the nonoverlapping format (Fig. 7). In this respect, thin-film cells had about 4-5 times less output than state-of-the-art pellet cells with thin-film electrodes (6); however, the use of the thin-film format produced approximately a threefold improvement in energy density (whr/lb) over the pellets.

An improved version of the Mrgudich pellet cell involves the replacement of the thin-film electrodes by pulverized platinum and silver compressed on either side of the silver iodide pellet, thus producing a larger overlap surface between electrode and electrolyte. This results in a hundredfold improvement in the cell output, accompanied by a corresponding increase in the amount of silver transferred to the platinum electrode (6). We believe that some improvement in cell capacity could be achieved in a similar manner for thin-film cells by depositing electrodes of larger surface area or by introducing a graded layer of electrode-electrolyte mix between the electrode and electrolyte to increase their total overlap area.

The steady-state internal resistance of the overlapping AgI electrolyte thin-film cells is on the order of 10^4 to 10^5 ohms, while it is close to 10^6 ohms for the overlapping Pt/AgBr/Ag cells and nonoverlapping Pt/AgI/Ag cells. This resistance consists basically of the sum of the resistance of the electrolyte and the resistances at the two electrode-electrolyte interfaces. The latter, however, due to an interface barrier or double layer, is capacitive in nature, and is partially shunted during current transients or during the application of a-c signals of sufficiently high frequency (16). The electrolyte resistance in various AgI and AgBr thin-film cells was thus measured using an a-c bridge with an applied voltage of 60 mv and variable frequency. The electrolyte resistance was generally found to be on the order of 10-30 ohms, depending on film thickness, and the double-layer capacitance was found to be in the 100-1000 μf range.

Table I shows the variation of cell resistance with frequency of applied a-c voltage for a Ag/AgBr/Ag thin-film overlapping system, with an electrode overlap area of 0.4 cm^2 and a AgBr film thickness of 10μ. Resistance values obtained with the same bridge for a 25-ohm resistor, run for calibration purposes, are also given. The interface capacitance appears as a significant reactance at frequencies below 1 kHz, and thus the higher frequency value of 17-18 ohms should be considered as representative of the electrolyte resistance plus any unshunted resistance. On this basis, we were able to calculate an upper bound specific ionic conductance of 1.4 x 10^{-4} ohm^{-1} cm^{-1} for evap-

[4] In addition to recording the cell voltage in vacuum, by monitoring the resistance of the silver electrode film during its deposition, the Ag evaporation may be stopped at the point where the film reaches its desired resistance value.

Table I. A-C resistance values of a Ag/AgBr/Ag system as a function of frequency*

Frequency (kHz)	Resistance (ohms)	
	25-ohm Resistor	AgBr film**
0.01	—	60-70
0.10	26	30
1.0	26	20
10	26	20
100	26	18
200	26	18
500	—	17
600	22	—

* If a cell is charged, it must be prevented from discharging with a suitable d-c bias voltage. In order to avoid the use of such a d-c bias, the measurements given in Table I were made on a symmetrical Ag/AgBr/Ag system.
** The values given in this column have been corrected for any ohmic resistances due to the silver electrode films.

orated AgBr films and 1.1 x 10^{-3} ohm^{-1} cm^{-1} for evaporated AgI films. This compares with bulk conductivities at room temperature of 2 x 10^{-5} —2 x 10^{-7} ohm^{-1} cm^{-1} for AgBr (18) and 1.65 x 10^{-6} ohm^{-1} cm^{-1} for β-AgI (19). Such a comparison, however, of bulk and thin-film conductivity values may be unrealistic at room temperature where the distribution of Frenkel defects is to a large degree a function of sample preparation techniques—unlike the randomized distribution of Frenkel defects exhibited at elevated temperatures.

The above data indicate that the main source of total cell resistance in a thin-film cell lies in the electrode-electrolyte interface and that the electrolyte resistance, as expected, is very small by comparison. Because of the large internal capacitance, discharge curves (*see* Fig. 5, 7, and 9) of thin-film cells show a large transient effect in which an appreciable fraction of the $\sim 10^{-8}$ whr of energy stored in a charged cell is involved in cell polarization or in charging and discharging the interface capacitance.

The AgI thin-film cells discussed above exhibited no detectable current leakage shown by the fact that they retained the voltage to which they had been charged for several months. The overlapping thin-film Pt/AgBr/Ag system, however, showed evidence of considerable electronic conductance after a few days of storage. Occasional failure in storage of silver iodide electrolyte cells, even when stored in the dark, was found to be due to a deterioration of the silver electrode. This may be due to reaction with atomic iodine species trapped in the AgI film during its deposition. Dense iodine vapors were in fact visible throughout the AgI heating and vaporization as stated earlier. Outgassing of the deposited silver halide film for a period of time prior to deposition of the silver film is expected to improve stability.

Improvement of the thin-film concentration cells at this early stage of their development would be expected in the area of increasing capacity and reducing internal resistance. Conductivity measurements have indicated that the principal source of internal resistance is in the electrode-electrolyte interface. Preparation of a cell in which there is a higher over-all surface of contact between electrode and electrolyte, and a greater Ag absorptivity of the blocking electrode is therefore indicated.

Acknowledgment

The authors wish to acknowledge the support of Dr. J. N. Mrgudich of the USAECOM (Contract No. DAAB07-67-C-0339).

Manuscript submitted Aug. 20, 1968; revised manuscript received Jan. 30, 1969.

Any discussion of this paper will appear in a Discussion Section to be published in the December 1969 JOURNAL.

REFERENCES

1. H. Reinhold, *Z. Anorg. Allgem. Chem.*, **171**, 181 (1928).
2. A. B. Lidiard, "Handbuch der Physik," Vol. 20, p. 250, Springer Verlag, Berlin (1957).
3. D. O. Raleigh, "Solid State Electrochemistry" in "Progress in Solid State Electrochemistry," Pergamon Press, New York (1966).
4. C. Tubandt, "Handbuch der Experimentalphysik," Vol. 12 (1), p. 383 (1932).
5. J. L. Weininger, *This Journal*, **105**, 439 (1958).
6. J. N. Mrgudich, P. J. Bramhall, and J. J. Finnegan, *Trans. IEEE*, **AES-1**, 290 (1965).
7. J. N. Mrgudich *et al.*, *Proc. Ann. Power Sources Conf.*, **19**, 86 (1965).
8. G. R. Argue and B. B. Owens, Paper 281 presented at Electrochem. Soc. Meeting, Boston, May 5-9, 1968.
9. B. B. Owens and G. R. Argue, *Science*, **157**, 308 (1967).
10. S. Geller, *ibid.*, **157**, 310 (1967).
11. J. N. Bradley and P. D. Greene, *Trans. Faraday Soc.*, **62**, 2069 (1966); **63**, 2516 (1967).
12. A. Sator, *Compt. Rend.*, **234**, 2283 (1952).
13. C. W. Moulton, M. Hacskaylo, and C. Feldman, Paper 62 presented at Electrochem. Soc. Meeting, Toronto, May 3-7, 1964.
14. A. Shepp, G. Goldberg, J. Masters, and R. Lindstrom, *Phot. Sci. Eng.*, **11**, 316 (1967).
15. T. Evans, J. M. Hodges, and J. W. Mitchell, *ibid.*, **3**, 73 (1955).
16. W. Jost, "Diffusion in Solids, Liquids, Gases," p. 201, New York (1952).
17. R. J. Friauf, *J. Chem. Phys.*, **22**, 1329 (1954).
18. I. Shapiro and I. M. Kolthoff, *ibid.*, **15**, 41 (1947).
19. K. H. Lieser, *Z. Physik. Chem. (n.F.)*, **9**, 302 (1956).

New Methods of Obtaining Fuel Cell Electrodes

IV. Powder Electrode Fuel Cell with Lateral Feeding

D. M. Drazić, R. R. Adzić, and A. R. Despić

Institute of Chemistry, Technology and Metallurgy, Beograd, and Faculty of Technology, University of Beograd, Beograd, Yugoslavia

ABSTRACT

A previously developed powder electrode in combination with lateral feeding with gases has been further improved. A fuel cell without gas chambers and with loose carbon powder electrodes has been constructed and tested with acid and alkaline electrolytes. 0.065 w/cm^2 of power output was achieved with a cell having an over-all thickness of 3 mm at H_2 and O_2 pressures of 0.01-0.02 atm gauge. If a battery of such cells were built, one could expect a specific power ouput of about 250 w/liter or 150 w/kg.

In most low-temperature fuel cells which have been developed in recent years, porous electrodes separating gas and electrolyte chambers have been used. In this way, the necessary gas-electrolyte-catalyst contact is readily obtained. Besides the improvements of sintered metal or porous carbon electrodes achieved up to now, efforts have been made during the last few years to develop electrodes based on some new ideas. Among the more interesting are the rotating and the laterally fed electrodes of Bonnemay *et al.* (1, 2) and Gerischer's suspension electrode (3). The so called "powder electrode", developed in our laboratory (4, 5) appeared to be very convenient for fast determinations of the electrochemical activity of powdered materials which are to be used for fuel cell electrode manufacturing. In two recent papers (6, 7), this type of electrode was used in the investigation of the influence of different kinds of treatment of active carbon on its electrochemical activity. It was shown that carbon powder properly treated and impregnated with very small quantities of platinum can be a good electrode material in powder form for oxygen reduction and hydrogen oxidation, in alkaline as well as in acid electrolytes.

In the present work, the basic concept of the powder electrode was used to develop one employing lateral feeding of the reacting gases. This was achieved by pouring the carbon powder, impregnated with the catalyst, into the approximately 0.5 mm deep hollow of the electron-conducting electrode holder and covering with the porous matrix soaked with the electrolyte. The whole cell was obtained when two such electrodes were pressed together. In Fig. 1, a schematic diagram of the cross section of such a fuel cell is presented.

A novelty of this cell is that the gases have access to carbon powder only through a few small gas feeding holes on the edge of the holder and that the usually existing gas chambers, screens, and similar gas distributing devices are completely omitted. The gas is diffused laterally from the small edge holes through the active carbon layer to the sites of the reaction. In normal type cells with gas chambers, the ratio of the projected electrode surface exposed to the electrolyte and to the gas phase is 1:1. Bonnemay *et al.* (2) realized the lateral diffusion electrode with a hydrophobic carbon powder fixed to a metallic current collector, where a greater part of the electrode was immersed in the electrolyte, while the rest was in gas phase, the reacting gas diffusing through the carbon powder to the place of consumption. The ratio of the surfaces exposed to the electrolyte and to the gas in this case was 6:1 (8). In our case, this ratio is about 1000:1, which results in considerable reduction of total volume of this fuel cell.

A second substantial feature of these electrodes—in which they differ from all other types—is the mode of current collecting. Due to the existence of gas chambers in normal cells, current collecting is often lateral. This introduces problems of great ohmic voltage drops when large electrodes are used, particularly with carbon electrodes, so that metallic nets [*e.g.*, screen electrodes (9)], or sintered metal plates (10) have to be incorporated into the electrodes, losing the substantial advantages of carbon as the electrode material: lightness and resistivity to the attack of acid electrolytes.

In our electrode, since the resistivity of carbon cannot be lowered, the mode of gas feeding and current collecting has been inverted. The gas is fed laterally, while the current is collected normally to the electrode surface (*i.e.*, the shortest way), giving rise only to the practically negligible voltage drops across the resistive carbon. This construction enables us to replace the metals as the electrode holder and electron-conducting material with other acid-resistant materials like electron-conducting plastics (*e.g.*, a polyethylene-graphite mixture produced in our laboratory with $\rho \approx 0.2$ ohm-cm) so that the average specific weight of the complete fuel cell battery can be lowered as much as 1.5 g/cm^3.

Experimental

The voltage-current characteristics of a H_2-O_2 cell were experimentally determined for two sets of electrodes. The cell with electrode area of about 20 cm^2 (diameter 5 cm) had the gas inlet and outlet at two opposite sides on the edge of the electrode. In order to decrease the distance between the inlets and outlets, and in this way the pressure drop in the battery, for the larger-area cell (440 cm^2), the electrodes

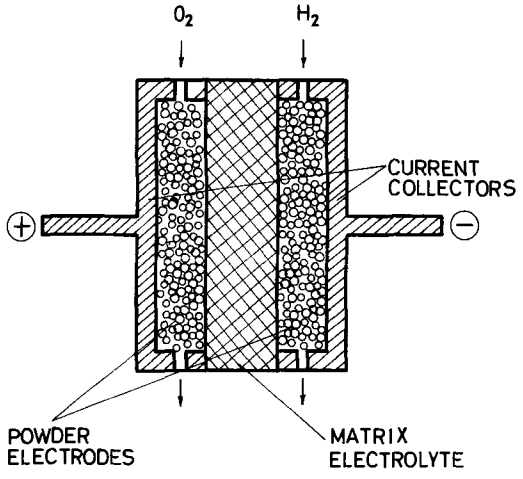

Fig. 1. Schematic cross section of a powder electrode fuel cell unit with lateral feeding.

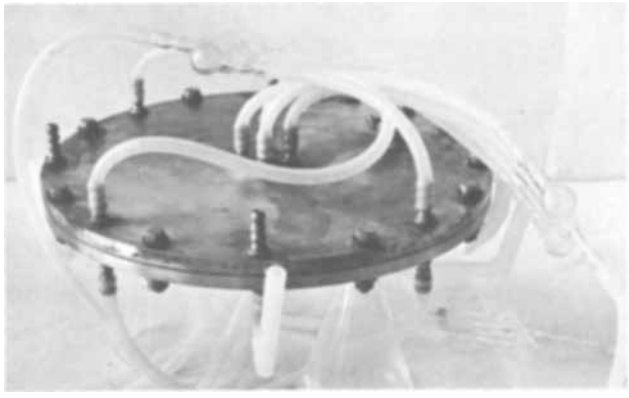

Fig. 2. Photograph of the larger experimental cell

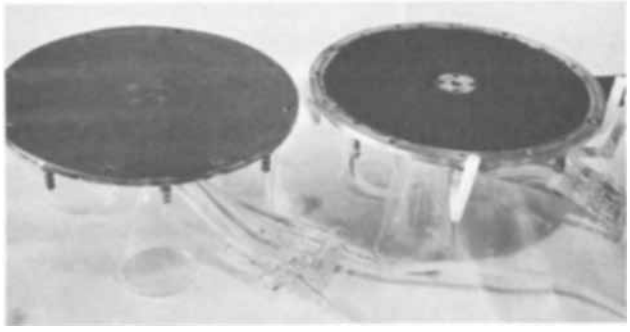

Fig. 3. Photograph of the disassembled cell. Right: electrode holder packed with active carbon. Left: electrode holder covered with porous matrix.

are made in the form of a modified annular electrode. Gases were introduced through several holes at the edge of the electrode, while the excess of gases, if necessary, was collected through the holes in the middle, as can be seen in Fig. 2. A photograph of the disassembled larger experimental cell is shown in Fig. 3. All the details of this construction are given in the patent literature (11).

The smaller cell was tested with three different electrode thicknesses: 0.25, 0.5, and 1 mm (*i.e.*, the hollow on the electrode holder was 0.25, 0.5, and 1 mm deep). Electrode material was pretreated active carbon powder (80-100μ) [for details, *see* (6, 7)] impregnated with platinum (3% by weight). After impregnation, the carbon powder was mixed with Teflon emulsion (Du Pont TFE 30B or FEP 120, 10% by weight).

Porous plastic sheets (Porvic S. Porous Plastic Ltd., England) were used as the matrix for the electrolyte. In order to eliminate the possibility of drying of the matrix, one central and several edge holes filled with electrolyte, and in contact with the porous matrix, were provided. No other gasket material was used. As the electrolytes, 5*N* H_2SO_4 or 6*N* KOH was used. The measurements were done at 25° and 60°C. Gas pressures applied were 0.01-0.02 at. gauge.

Gases used were commercial gases in cylinders. To remove the accumulated impurities and product water, an approximately 3% excess flow of gases was used and allowed to vent from the cell. No effects of water unbalance were observed. Several experiments were done with an ion-exchange membrane (Permutit C.) soaked with KOH.

Results and Discussion

Preliminary investigation of this concept in the small (20 cm^2) and large (440 cm^2) cell showed the direct parallelism between the performance of the cell and the performance of the separate powder electrodes, when the same carbon powder was used. Since in the ordinary powder electrode (4, 5) feeding with gas is normal to the electrode, this indicated

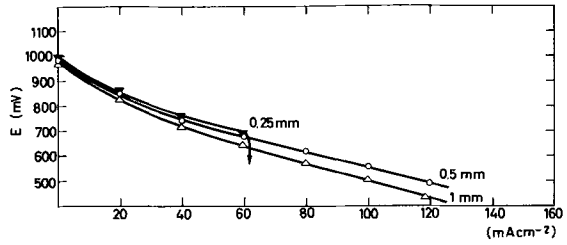

Fig. 4. Voltage-current density curves for small H_2-O_2 fuel cell (20 cm^2) with 6*N* KOH at 25°C for 1.0-, 0.5-, and 0.25-mm thick electrodes.

that practically no limitation was imposed on the cell performance by the lateral diffusion of gases through the carbon layer, at least not when the path is smaller than 15 cm. This comes out also from the fact that practically no pressure drop was achieved when the gas was passed through the electrode between the inlet and outlet holes.

In Fig. 4, voltage-current characteristics of the small cell with alkaline electrolyte at 25°C for 1-, 0.5-, and 0.25-mm thick electrodes are presented. Since in all the experiments the same carbon powder was used, the quantity of platinum, recalculated as the quantity per square centimeter of the projected electrode area was 2, 1, and 0.5 mg Pt/cm^2, respectively. From the diagrams one can conclude that the thickness of the electrode of 0.5 mm gave the best performance of the cell and therefore 0.5 mm was adopted as the optimum thickness in further experiments. The thinner electrodes obviously had much poorer gas feeding, while 1-mm thick electrodes had slightly higher overvoltages, probably due to the higher ohmic drop between the carbon particles.

In Fig. 5, voltage-current characteristics of the small cell with 0.5-mm thick electrodes are presented for acid (dotted lines) and alkaline electrolyte (solid lines) at 25° and 60°C, and power-current density characteristics at 60°C for both types. Power densities of 0.065 and 0.057 w/cm^2 at 100 ma/cm^2 for alkaline and acid types, respectively, were achieved. Since the electrode holder was made of compact nickel, when the acid electrolyte was used the edges at the holder which were in direct contact with the acid matrix were protected with an acid-resistant lacquer, while the bottoms of the hollows were unprotected (to provide the electrical contact). No trace of corrosion was observed in the course of the measurements (about 2 days), probably due to the hydrophobic properties of the carbon-Teflon mixture.

An attempt to replace the rather coarse pore size porous matrix with an ion-exchange membrane gave much poorer results. Even though in principle one can expect better results with an ion-exchange membrane, this result leads to the conclusion that at present a matrix type of fixed electrolyte is the best solution of this problem.

The large cell (440 cm^2) had 0.5-mm thick electrodes. In Fig. 6, a voltage-current curve and total

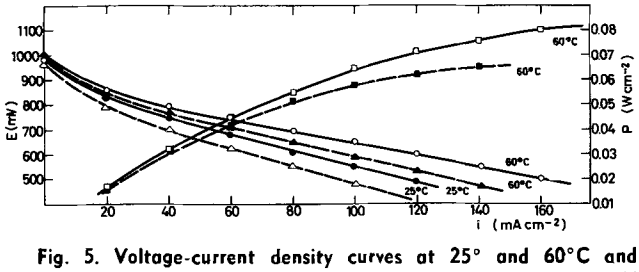

Fig. 5. Voltage-current density curves at 25° and 60°C and power-current density curves at 60°C for small H_2-O_2 cell with 5*N* H_2SO_4 (dotted lines) and 6*N* KOH (solid lines).

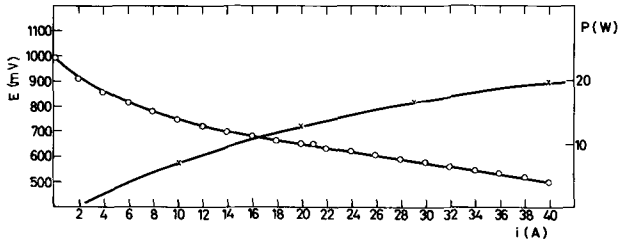

Fig. 6. Voltage-current and power-current curves for larger cell (440 cm^2) with 6N KOH at 25°C.

power-current curve for this cell are presented for 25°C as the ambient temperature.

The real temperature within the cell could not be measured but we estimated that it could not be more than 20° above the ambient temperature. Since the electrochemical activity of carbon for these electrodes can be further increased, particularly for the oxygen electrode, it is to be expected that the cell characteristics can be better than presented here.

If we take 3 mm as the total thickness of one cell, and use electron-conducting plastic for the electrode holders, it is reasonable to expect achievement of very high specific power densities of such fuel cell batteries up to 250 w/liter or 150 w/kg.

It might be concluded, finally, that the powder electrode fuel cell with lateral feeding seems to be very promising for obtaining a compact fuel cell battery.

Acknowledgments

The authors are indebted to the Federal Research Fund of the S.F.R. Yugoslavia and the Research Fund of the S.R. Serbia for financial support.

Manuscript submitted Oct. 28, 1968; revised manuscript received Feb. 13, 1969.

Any discussion of this paper will appear in a Discussion Section to be published in the December 1969 JOURNAL.

REFERENCES

1. M. Bonnemay, G. Bronoël, E. Levart, and A. A. Pilla, Journées Internationales d'Etude res piles à Combustible, Bruxelles, 1965.
2. M. Bonnemay, G. Bronoël, and E. Levart, *Advanced Energy Conversion*, **7**, 159 (1967).
3. H. Gerischer, *Z. Elektrochem.*, **67**, 164 (1963).
4. A. R. Despić, D. M. Drazić, and I. V. Kadija, *Electrochem. Technol.*, **4**, 451 (1966).
5. D. M. Drazić, A. R. Despić, and G. A. Savić-Maglić, *ibid.*, **4**, 453 (1966).
6. D. M. Drazić and R. R. Adzić, *Electrochim. Acta*, In press.
7. D. M. Drazić and R. R. Adzić, *Bull. Soc. Chem. Beograd*, In press.
8. D. Doniat, Thesis (Section IV, "Electrodes à diffusion latérale), Paris (1965).
9. R. Haldeman, W. Colman, S. Langer, and W. Barber, in "Fuel Cell Systems," p. 113, R. Gould, Ed. Adv. Chem. Series No. 47 (1965).
10. M. Clark, W. Darland, and K. Kordesch, *Electrochem. Technol.*, **3**, 166 (1965).
11. A. R. Despić, D. M. Drazić, and R. R. Adzić, Yugoslav. Pat. appl. (1968).

Reactively Sputtered Thin Films in the Vanadium-Oxygen System Using Triode Sputtering

D. H. Hensler, A. R. Ross, and E. N. Fuls

Bell Telephone Laboratories, Incorporated, Murray Hill, New Jersey

ABSTRACT

The technique of reactive triode sputtering has been employed to deposit several of the vanadium oxides in thin-film form. The resistivity, Hall coefficient, and thermoelectric power of the resulting compositions have been measured at room temperature and presented along with the partial pressure of oxygen in the sputtering gas. These data are compared with the literature when possible to categorize the observed films. It is shown that $VO_{1.87}$ and lesser oxides are metallic at room temperature as determined by a small Hall coefficient and small thermoelectric power.

The vanadium-oxygen system contains a very large number of oxide phases as determined by structural studies (1-3). Even though the existence of some of these phases seems to be in question, the occurrence of many apparently stable oxides is of particular interest to thin film investigators, since the technique of reactive sputtering of vanadium in a partial atmosphere of oxygen should readily permit the formation of some of these oxide compounds. In addition, it should be possible to form nonstoichiometric compositions of oxygen and vanadium of which little is known at present. Measurement of the electrical properties of the various oxide phases began with the work of Morin (4) who measured the conductivity of VO, V_2O_3, and VO_2 crystals. Later data on V_2O_3 was provided by Goodman (5) who measured the conductivity of single crystals, and Acket and Volger (6) who measured the resistivity, thermoelectric power, and obtained estimates of the Hall coefficient of sintered samples. The electrical conductivity and thermoelectric power of VO_2 crystals were measured by Bongers (7), and the infrared reflectivity by Barker, Verleur, and Guggenheim (8).

More recently, some studies have been made in nonstoichiometric compositions of vanadium and oxygen. Kawano, Kosuge, and Kachi (9) have measured the conductivity as a function of temperature for a series of compositions ranging from $VO_{0.8}$ to $VO_{1.25}$. These studies are especially interesting in that they indicate that a material of very low temperature coefficient of resistance may exist in this oxygen range.

Compounds in the vanadium-oxygen system have been produced in thin-film form by several techniques. Films of VO_2 have been prepared by reactive evaporation of vanadium in a residual atmosphere of oxygen gas followed by an annealing process (10). Several vanadium-oxygen compounds have been formed by sputtering vanadium and vanadium oxide films followed by suitable heat treatment (11). More recently, a reproducible single-step process for depositing good quality vanadium dioxide films by reactive sputtering was reported by Fuls, Hensler, and Ross (12), and

Table I. Tabulated oxygen partial pressure, Hall coefficient thermoelectric power, and x-ray information for each sample

Sample No.	Oxygen partial pressure, Torr	Hall coefficient, cm^3/coulomb	Thermoelectric power, $\mu v/°K$	X-ray analysis	Comments
1	0	10.7×10^{-5}	5.0	Vanadium	Lattice expanded 2-3% from bulk
2	1×10^{-4}	22.5×10^{-5}	5.8	Vanadium	Lattice expanded 4% from bulk
3	1.8×10^{-4}	13.3×10^{-5}	0.40	$VO_{0.2}$	
4	2.5×10^{-4}	10.7×10^{-5}	−0.47		
5	4.0×10^{-4}	9.2×10^{-5}	+3.2	$VO_{1.2}$	Face-centered cubic pattern of VO type
6	5.0×10^{-4}	12.6×10^{-5}	−18.0	$VO_{1.2}$ and V_2O_3	
7	6×10^{-4}	7.48×10^{-5}	−20.0	$VO_{1.87}$	
8	7×10^{-4}	0.041	−108.0	VO_2	As determined by metal-semiconductor transition
9	8×10^{-4}	0.027	−91.0		
10	1.0×10^{-3}	0.027	−59.0		
11	2.0×10^{-3}	0.035	−50.0		

subsequent transport measurements have been made on these films (13). In this paper, the technique of reactive sputtering has been extended to other compositions of the vanadium-oxygen system. Hall coefficient, resistivity, and thermoelectric power data are presented in an effort to provide basic information on transport properties of these materials in thin-film form.

Experimental

The sample films were deposited on sapphire substrates by sputtering from a vanadium cathode in an atmosphere of argon and oxygen. A 24-in. metal bell jar evacuated by a 6-in. oil diffusion system was used. The amount of oxygen reacting with the vanadium to form the film depends on the partial pressure of oxygen included in the sputtering atmosphere. This was carefully controlled by means of variable leak valves on the argon and oxygen input to the bell jar. The sputtering gas was continually flushed through the bell jar at the rate of 45,000 μliters/min.

The diode sputtering apparatus used earlier to sputter VO_2 films (12) was changed to a triode system in order to increase the deposition rate while at the same time using somewhat lower argon pressure. This was done simply by adding a filament (14) and an anode to the d-c sputtering configuration as shown in Fig. 1. In this configuration, sputtering was done using an argon pressure of 18μ. The filament current was held at 250 ma, with the anode biased at 200v. The vanadium cathode had a negative potential of 4600v with the substrate holder held at ground potential.

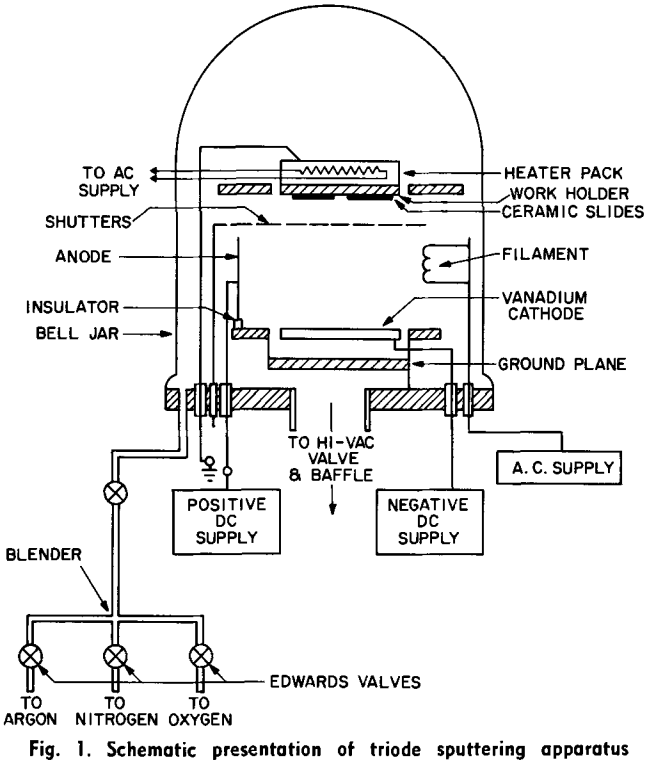

Fig. 1. Schematic presentation of triode sputtering apparatus showing position of anode and filament used to support the sputtering discharge.

The sample films were sputtered on randomly oriented sapphire substrates 0.904 cm by 2.16 cm by 0.81 mm in size after a 15-min presputter to stabilize the sputtering parameters. The substrates were held at 400°C during the sputtering process and for a 30-min postdeposition annealing in vacuum, after which they were allowed to cool slowly over several hours in vacuum.

Standard d-c techniques were used to measure the Hall effect and the resistivity. Data were taken on samples of lower resistivity using a Keithley nanovoltmeter and on higher resistivity samples using a Cary vibrating reed electrometer. Hall bridge patterns were etched in the film and leads were attached using an ultrasonic soldering device and indium solder. The thermoelectric power was measured using a technique outlined by Sidles and Danielson (15).

X-ray studies of the films were made using the Debye-Scherrer technique. Since the films were polycrystalline, Debye-Scherrer rings were obtained on film from which "d" values were measured. The crystal structure was determined by comparing the measured "d" values with those published in the literature. The chemical composition was also estimated from a comparison of the "d" values with the literature. Chemical compositions determined in this way can be considered only as approximate. The results are shown in Table I. In addition, previous studies (16) showed that films deposited on sapphire substrates at oxygen partial pressures greater than 7.0×10^{-4} Torr were highly oriented films of VO_2.

Results

Tables I and II show the variation of the resistivity, Hall coefficient, thermoelectric power, and the temperature coefficient of resistivity with oxygen partial pressure. The resistivity of vanadium sputtered without oxygen is 75 μohm-cm. This value is very close to the resistivity of evaporated vanadium films (17), but it is three times the bulk value of 25 μohm-cm (18) found in the literature. The Hall coefficient of 10.7×10^{-5} cm^3/coulomb is high compared with the value of 8.13×10^{-5} cm^3/coulomb found by Foner (19) for bulk

Table II. Thickness, resistivity, and temperature coefficient of resistivity tabulated for the samples discussed in the text

Sample No.	Thickness, A	Resistivity, ohm-cm	Temperature coefficient of resistivity, $\times 10^{-6}$/°C
1	1970	75.5×10^{-6}	
2	1950	241×10^{-6}	+196
3	5080	395×10^{-6}	0.01
4	3140	400×10^{-6}	−32
5	1135	765×10^{-6}	−105
6	837	1.76×10^{-3}	-1.7×10^{3}
7	685	1.40×10^{-3}	-4.47×10^{3}
8	850	1.43	
9	690	4.2	-3.6×10^{4}
10	1000	2.3	
11	830	1.74	-1.06×10^{5}

vanadium, and the value of 7.0×10^{-5} cm³/coulomb for evaporated vanadium films found by Chander, Howard, and Jain (17) possibly due to the inclusion of residual oxygen in the film during deposition.

The x-ray analysis of samples 3 and 4 is based on the work of Klemm and Grimm (20) and Seybolt and Sumsion (21) who identified the compositions $VO_{0.1}$ to $VO_{0.4}$ containing 13.4 to 26.2 a/o (atomic per cent) of oxygen.

Sample 5 is shown by x-ray analysis to be of the face-centered cubic type. On the basis of a comparison of the "d" values with the literature, the composition is placed at $VO_{1.2}$. Because the structure is face-centered cubic with excess oxygen atoms at interstitial sites, it is felt that comparisons with the literature are justified provided that one keeps in mind the doping effects of the excess oxygen atoms. The resistivity of this film is considerably lower than the value of 10^4 μohm-cm given by Morin (4) and somewhat lower than 2×10^3 μohm-cm given by Kawano, Kosuge, and Kachi for samples of pressed powder (9). Denker (23) has reported values of the Hall coefficient for films of the VO_x type: $x = 0.88$, $R_H = -1.1 \times 10^{-2}$ cm³/coulomb and for values of $x = 1.1$, $R_H = +2.8 \times 10^{-3}$ cm³/coulomb. He also has observed evidence of conduction by positive and negatively charged carriers. The value of $R_H = +9.2 \times 10^{-5}$ cm³/coulomb we have observed is consistent with this model for which

$$R_H = -\left(\frac{\sigma_n}{\sigma_t}\right)^2 \frac{1}{ne} + \left(\frac{\sigma_p}{\sigma_t}\right)^2 \frac{1}{pe}$$

where σ_n/σ_t is the ratio of electron conductivity to the total conductivity, σ_p is the hole conductivity, and n and p are the electron and hole densities, respectively. In the data reported here, the smaller Hall coefficient represents a more nearly equal contribution on the part of the two terms. The temperature coefficient of resistance is approximately -100×10^{-6} $(°C)^{-1}$ for this sample. These results are contrary to the findings of a positive temperature coefficient of resistance by Morin (4) for single crystals of VO. However, measurements of the temperature dependence of the resistivity of pressed powder samples with compositions in the range $VO_{0.8}$ to $VO_{1.25}$ (9) show a negative temperature coefficient of resistivity.

The temperature coefficient of resistivity is progressively more negative for samples 6 and 7. Though a direct comparison with V_2O_3 is not reasonable, it is of interest to note that both Morin (4) and Goodman (5) report a positive temperature coefficient of resistance for V_2O_3. The negative temperature coefficient of resistance in samples 6 and 7 is probably a result of structural damage inherent in the deposition process. It is also interesting to note that for sample 1 through sample 7 the Hall measurements are consistent with the estimate of $R_H < 2 \times 10^{-3}$ cm³/coulomb at 300°K by Acket and Volger (6) for V_2O_3. The composition of sample 7 is identified as $VO_{1.87}$ after the work of Anderson (22).

Conclusions

It has been shown that reactive sputtering using a triode system can be used to deposit some of the compositions in the vanadium-oxygen system. Basic room-temperature transport properties have been measured and compared with available literature. Agreement is fairly good considering the spread in the available data. Much of the data presented herein for thin films are the only data available for the compositions discussed. At oxygen partial pressures below 6×10^{-4} Torr corresponding to $VO_{1.87}$ and lesser oxides, the films are metallic as indicated by the high carrier concentration and small thermoelectric power. Between oxygen partial pressures of 1×10^{-4} Torr and 6×10^{-4} Torr, the Hall coefficient is very small indicating that both electrons and holes contribute to conduction. In our samples, the dominant carriers are holes. In the range 7×10^{-4} Torr to 2×10^{-3} Torr oxygen partial pressure, VO_2 is formed and electrons predominate. The scatter in the data for VO_2 samples is due to impurity band effects in which charge carriers of two bands contribute to conduction (13). Similarly, for $VO_{1.87}$ and lesser oxides, the thermoelectric power is small being both positive and negative, whereas, in the region where VO_2 is formed, the thermoelectric power is somewhat larger and negative.

From Table II it can be seen that a broad range of resistivities occurs in which the temperature coefficient is small. This region may be important in making resistive components in thin-film circuits. The high resistivity may make it possible to use these films as high value resistors supplementing existing thin-film technology.

Acknowledgments

The authors wish to thank Mr. N. Berlinski for his conscientious efforts in film deposition and Mrs. M. Read for performing the x-ray analysis of the films. We also wish to thank Mr. D. McNair for supplying filaments that can be used in a partial oxygen atmosphere.

Manuscript submitted Aug. 8, 1968; revised manuscript received March 12, 1969.

Any discussion of this paper will appear in a Discussion Section to be published in the December 1969 JOURNAL.

REFERENCES

1. J. Stringer, *J. Less-Common Metals*, **8**, 1 (1965).
2. R. Roy, S. Kachi, G. J. McCarthy, O. Miller, and W. B. White, "Second Quarterly Report on Crystal Chemistry Studies," Jan. 1966, Contract No. DA-28-043 AMD-01304 (E).
3. K. Kosuge, *J. Phys. Chem. Solids*, **28**, 1613 (1967).
4. F. J. Morin, *Phys. Rev. Letters*, **3**, 34 (1959).
5. G. Goodman, *ibid.*, **9**, 305 (1962).
6. G. A. Acket and J. Volger, *Physica*, **28**, 277 (1962).
7. P. F. Bongers, *Solid State Communications*, **3**, 275 (1965).
8. A. S. Barker, Jr., H. W. Verleur, and H. J. Guggenheim, *Phys. Rev. Letters*, **17**, 1286 (1966).
9. S. Kawano, K. Kosuge, and S. Kachi, *J. Phys. Soc. Japan*, **21**, 2744 (1966).
10. K. van Steensel, F. van de Burg, and C. Kooy, *Philips Res. Reports*, **22**, 170 (1967).
11. G. Rozgonyi and W. Polito, *This Journal*, **115**, 56 (1968).
12. E. N. Fuls, D. H. Hensler, and A. R. Ross, *Appl. Phys. Letters*, **10**, 199 (1967).
13. D. H. Hensler, *J. Appl. Phys.*, **39**, 2354 (April 1968).
14. D. McNair, *Rev. Sci. Instr.*, **38**, 124 (1967). The authors are indebted to D. McNair for supplying high quality filaments.
15. P. H. Sidles and G. C. Danielson, "Thermoelectricity," Edited by P. H. Egli, p. 270, John Wiley & Sons, New York (1960).
16. G. Rozgonyi and D. H. Hensler, *Journal of Vacuum Science and Technology*, **5**, 194 (1968).
17. R. Chandler, R. E. Howard, and S. C. Jain, *J. Appl. Phys.*, **38**, 4092 (1967).
18. C. A. Hampel, "Rare Metals Handbook," 2nd Ed., Reinhold Publishing Co., London (1961).
19. S. Foner, *Phys. Rev.*, **107**, 1513 (1957).
20. V. W. Klemm and L. Grimm, *Z. Anorg. Allgem. Chem.*, **250**, 42 (1942).
21. A. U. Seybolt and H. T. Sumsion, *J. Metals*, **5**, 292 (1953).
22. G. Anderson, *Acta Chem. Scand.*, **18**, 1599 (1954).
23. S. P. Denker, "Electronic Properties of Refractory Monoxides Having Intrinsic Lattice Vacancy Concentrations," Report #CU-3553-6, AEC Contract No. AT(30-1)-3553.

Phosphorus Diffusion into Silicon Using Phosphine

M. S. R. Heynes*,[1] and P. G. G. van Loon*,[2]

ITT Semiconductors, West Palm Beach, Florida

ABSTRACT

Phosphine (PH_3) was used as a diffusion source under both reducing and oxidizing conditions. Erratic results were obtained under reducing conditions using up to 1% PH_3. In an oxidizing ambient, solid solubility limited results were reproducibly obtained from 750° to 1200°C; PH_3 concentrations from 0.1 to 2.0% were used. The presence of water resulting from the oxidation of PH_3 does not appear to be of significance. No difficulty was experienced in applying phosphine diffusion to device fabrication.

Gaseous compounds are attractive as diffusion source materials for equipment simplicity, minimum maintenance, and ease of control; the gas diborane has found widespread use in boron diffusion processes. In this work, the gas phosphine, which was shown to be a promising source material by Donovan and Smith (1), was evaluated.

Phosphine is available commercially in hydrogen and in inert carrier gases in concentrations from a few parts per million to 15% or more. In this work, source cylinders ranging from 0.1 to 5% phosphine in argon were used.

Equipment

The furnace and gas supply arrangements used are shown in Fig. 1 and 2. (The two input arrangements shown are discussed later.) Good exhaust venting was provided for the input plumbing. Total gas flow rates through the furnace were maintained at 2 liters/min. The quartz furnace tubes were of 54 mm diameter and the quartz boats were of conventional flat slab type.

Runs were made with the wafers lying flat on the boat. The test wafers were of about 1 ohm-cm resistivity boron doped and were mechanically polished. The doping gas stream was turned on 5-20 min before runs were started. If the furnace had not been used for several hours, 15-20 min were allowed but, if only say 1 hr had elapsed since the last run, just sufficient time to flush the tube with doping gas was allowed. The doping gas flowed into the furnace for the full duration of the diffusion runs and was turned off only after the diffused wafers were removed. Evaluation was by a conventional four-point probe kit and angle lapping and staining techniques.

Experimental Conditions

Diffusion experiments were carried out under both reducing and oxidizing conditions.

Under reducing conditions, thermal decomposition of the phosphine occurs above about 400°C releasing elemental phosphorus, and deposits of red phosphorus were formed at the cool ends of the furnace tube.

Experiments were run at 1000°, 1100°, and 1200°C using a source cylinder of 1% phosphine in argon with and without additions of nitrogen and hydrogen, but erratic and high sheet resistance values were obtained for all conditions tried.

It appears that the vapor pressure of phosphorus released even from the undiluted 1% source (which would be in the region of 3 Torr), is too low for much dissolution in the silicon to occur. Solid solubility limited diffusions using an elemental phosphorus source have been reported but these were sealed-tube methods in which high phosphorus vapor pressures would be expected [for example, Fuller and Ditzenberger (2)].

Coupland (3) has studied the use of elemental phosphorus as a diffusion source in a two-zone sealed system. The phosphorus was contained in a limb of the system which was outside the diffusion furnace and the vapor pressure of the phosphorus was controlled by the temperature of this limb. An extrapolation of Coupland's results indicates that a phosphorus vapor pressure of 3 Torr will give a surface concentration of about 10^{20} atoms/cm^3 which is about an order of magnitude below the solid solubility of phosphorus in silicon in the diffusion temperature range. The high sheet resistance values obtained with phosphine under reducing conditions are therefore understandable.

A long extrapolation of Coupland's results indicates that a phosphorus vapor pressure about 100 Torr is required for surface concentrations to reach solid solubility levels.

The prospect of carrying out diffusions with 30% or more of phosphine to check this estimate was unattractive and no further work was done in this direction.

Oxidizing Conditions

Good diffusion characteristics were immediately obtained with oxygen additions to the phosphine mixtures. The phosphine oxidizes immediately in the furnace to P_2O_5 plus $3H_2O$.

It is interesting to note that good results are obtained in this system when, in P_2O_5 systems, great care is taken to exclude moisture. Apparently, the composition P_2O_5 plus $3H_2O$ as formed in the hot zone of the furnace distributes well and forms a uniformly doping glass on the silicon surfaces without causing surface damage or "spiking" at the diffusion front.

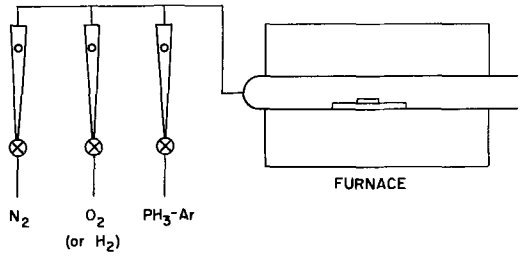

Fig. 1. Gas input and furnace arrangement

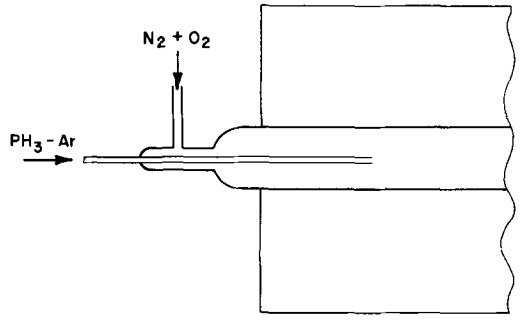

Fig. 2. Alternative gas input arrangement

Key words: phosphorus, diffusion, phosphine.

* Electrochemical Society Active Member.
[1] Present address: Signetics Corporation, Sunnyvale, California.
[2] Present address: Union Carbide Corporation, Electronics Division, San Diego, California.

With the simple furnace input arrangement shown in Fig. 1, a problem of premature reaction between PH_3 and O_2 soon became apparent. The input end of the furnace tube and the glassware near to it was hot enough for some oxidation of the phosphine to occur, particularly for diffusion temperatures above 1000°C. This left a messy deposit of (apparently) phosphorus oxides and acids and even some red phosphorus. In addition to the obvious maintenance problem, this reaction depletes the ingoing doping mixture.

The arrangement shown in Fig. 2 provided a way of minimizing this effect, and most of the results presented below were obtained using this arrangement.

Systematic Study of the Oxidizing System

The most convenient way of achieving uniformity and reproducibility of diffused doping is to operate with conditions which will keep the silicon surface saturated at the solubility limit of the impurity.

If this fundamental controlling factor is used, slight variations in furnace conditions will be unimportant. Only the maintenance of excess doping is required, and the oxidizing system was systematically investigated to find the range of operating conditions which would provide excess doping.

The effect of the systematic variation of phosphine concentration on sheet resistance values for 30-min diffusions at various temperatures is shown in Fig. 3. Oxygen concentrations for these runs were chosen to provide a slight excess over the amount required to oxidize the phosphine completely. (The results shown in Fig. 4 and discussed below indicate that the oxygen concentration is not critical.)

It is observed that the sheet resistance values fall to minimum levels at about 0.2, 0.4, 1, and 1.5% PH_3 at 850°, 1000°, 1100°, and 1200°C, respectively.

It should be noted that the apparent concentrations required to reach these minima depend on the construction of the input plumbing to the furnace. These results were taken with the input arrangement shown in Fig. 2 as discussed above. With the simple arrangement shown in Fig. 1, the premature reaction in the glassware resulted in a need for higher flow rates of PH_3 to achieve the minimum sheet resistances.

These minimum sheet resistance values agree within about 10% with the minimum values we have observed in P_2O_5 and $POCl_3$ diffusion systems for these times and temperatures and are assumed to be controlled primarily by the solid solubility of phosphorus in silicon.

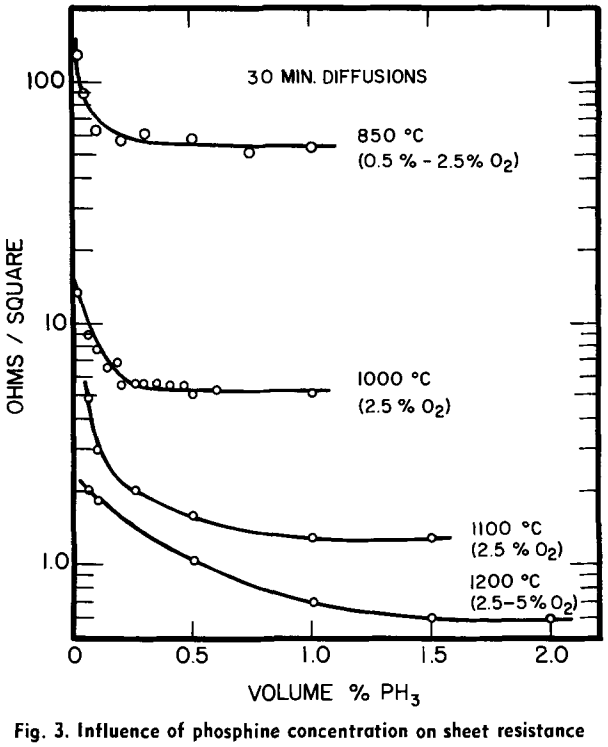

Fig. 3. Influence of phosphine concentration on sheet resistance

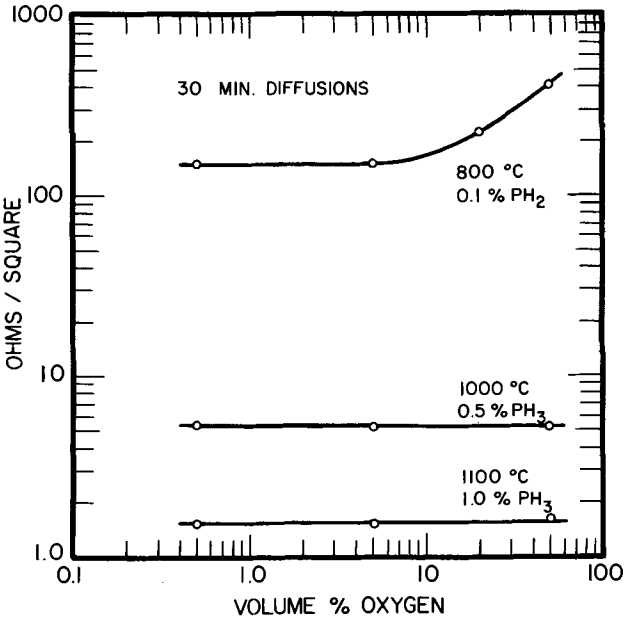

Fig. 4. Influence of oxygen concentration on sheet resistance

It is interesting to compare the concentration of phosphorus compounds present in P_2O_5 and $POCl_3$ systems with the results obtained with phosphine.

In a typical P_2O_5 emitter diffusion (carried out around 1050°C), with P_2O_5 source temperatures in the region of 220°-230°C, the concentration of P_2O_5 in the carrier gas will be in the region of 1.5% if the gas is saturated with the oxide vapor. In $POCl_3$ systems, a typical $POCl_3$ concentration in the input gas is 1% which, on oxidation, will yield a P_2O_5 concentration of 0.5%.

The present phosphine results indicate that about 1% PH_3, equivalent to 0.5% of P_2O_5, is required for solid solubility limited diffusions at 1050°C.

Not surprisingly, about the same phosphorus compound concentrations are required regardless of the particular source material.

The effect of the variation of oxygen content is shown in Fig. 4.

The phosphine concentrations used in these experiments were those found in the earlier experiments to give solid solubility controlled diffusions at relatively low oxygen concentrations.

There is no perceptible variation in sheet resistance with oxygen concentration at 1000°C and above but, at 800°C, the sheet resistance values increase from the saturation value of about 150 ohms/sq to 400 ohms/sq at 50% oxygen.

The probable explanation is that at low temperatures additional oxidation due to extra oxygen causes a significant glass dilution and masking effect but, at high temperatures, phosphorus can still diffuse through the glass rapidly enough to keep the silicon surface saturated.

Having established the conditions necessary for achieving saturation diffusions, sheet resistance and junction depth values were compiled for various times and temperatures. Figure 5 shows the sheet resistance results. These curves agreed within about 10% with those we had generated previously for $POCl_3$ and P_2O_5 diffusions (4). Figure 6 shows the junction depth results which also agree well with those from the other phosphorus systems.

The P_2O_5-H_2O System

The oxidation of PH_3 yields the composition P_2O_5: $3H_2O$. This composition will form orthophosphoric acid at low temperatures:

$$P_2O_5 + 3H_2O = 2H_3PO_4$$

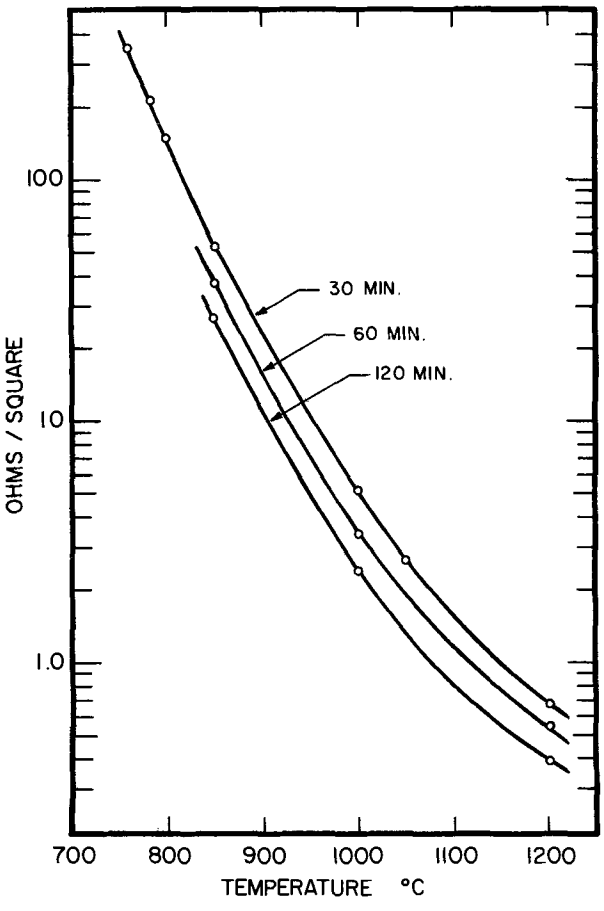

Fig. 5. Variation of sheet resistance with temperature (solid solubility-limited diffusions).

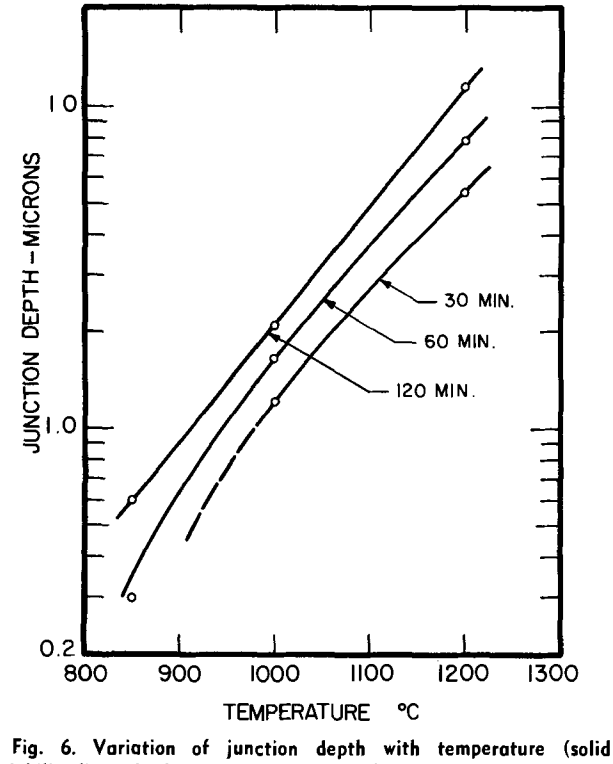

Fig. 6. Variation of junction depth with temperature (solid solubility-limited diffusions in ~ 1 ohm-cm boron-doped test wafers).

As H_3PO_4 is heated, it loses H_2O, decomposing first to pyrophosphoric acid, $H_4P_2O_7$, then at about 260°C, to metaphosphoric acid, HPO_3. At diffusion temperatures, the molecular composition of the vapor is uncertain. Apparent molecular weights for the P_2O_5-H_2O system have been measured by the vapor density method by Tarbutton and Demming (5) and, for the composition P_2O_5:$3H_2O$, the results indicated a mixture of only P_4O_{10} and H_2O molecules but the presence of low molecular weight ultraphosphoric acids was also suspected. However, for the purpose of phosphorus diffusion in silicon, it appears to be of no significance whether or not compounds are formed between P_2O_5 and H_2O. P_2O_5 and the phosphoric acids are all quite volatile and are expected to be equally reactive with a silicon surface. This is in contrast to the case of boron diffusion, where we believe that the presence of water (from doping sources such as diborane, methyl borate, and boron halides with H_2 and O_2) assists in the distribution of doping through the formation of boric acids which are much more volatile than B_2O_3 (6).

The use of what are effectively P_2O_5-H_2O systems for diffusions is not new with the use of phosphine. Lothrop (7) reported the use of the P_2O_5-H_2O azeotrope (92.4% P_2O_5:7.6% H_2O) prepared by heating metaphosphoric acid for several hours at 800°C. Lothrop concluded that reproducible diffusions could be obtained with the azeotrope which provides a source of invariant composition and whose vapor pressure is reproducibly controlled by furnace temperature.

Also, Maekawa (8) described the successful use of a source material prepared by heating orthophosphoric acid at 600°C.

The presence of water in the phosphine system will certainly contribute to oxidation of the silicon. However, with the conditions described here, the water content of the furnace atmosphere will be only 0.3-3% and only slightly more oxide growth is observed in a phosphine diffusion than in a comparable $POCl_3$ diffusion.

Device Fabrication

In the practical application of phosphine diffusion in transistor and integrated circuit fabrication, no processing difficulties were experienced in substituting the oxidizing phosphine diffusions for P_2O_5 and $POCl_3$ methods and no significant differences in device characteristics were noticed.

However, we do not favor the use of phosphine for high concentration diffusions at temperatures above 1000°C because of the high concentrations of the relatively expensive and highly toxic gas which must be used; 0.3-1.5% is required in the furnace tube in contrast to, say, the diborane system where only about 0.01% is required. Also, at these high phosphine concentrations, there is a maintenance problem. Some reaction occurs in the input glassware of the furnace and at the output end of the furnace phosphoric acid is deposited which is even more messy than the initially dry P_2O_5 from $POCl_3$ systems.

Phosphine diffusion is attractive for low temperature applications where very good control and reproducibility have been observed.

Conclusion

Good diffusion characteristics have been observed for the oxidizing phosphine system over a wide range of temperatures but because of toxicity, maintenance, and expense problems it appears unlikely that phosphine will displace existing source materials except perhaps in some low temperature-low concentration applications.

Manuscript submitted Aug. 5, 1968; revised manuscript received Feb. 24, 1969. This paper was presented at the Dallas Meeting, May 7-12, 1967, as Paper 92.

Any discussion of this paper will appear in a Discussion Section to be published in the December 1969 JOURNAL.

REFERENCES

1. R. P. Donovan and A. M. Smith, Paper 150 presented at Electrochem. Soc. Meeting, New York, Sept. 29-Oct. 3, 1963.

2. C. S. Fuller and J. A. Ditzenberger, *J. Appl. Phys.*, **27**, 544 (1956).
3. M. J. Coupland, *Proc. Phys. Soc.*, **73**, 577 (1959).
4. M. S. R. Heynes and J. T. Wilkerson, *Electrochem. Technol.*, **5**, 464 (1967).
5. G. Tarbutton and M. E. Demming, *J. Am. Chem. Soc.*, **72**, 2086 (1950).
6. M. S. R. Heynes, *Electrochem. Technol.*, **5**, 25 (1967).
7. R. P. Lothrop, *J. Appl. Phys.*, **33**, 2656 (1962).
8. S. Maekawa, *J. Phys. Soc. Japan*, **17**, 1592 (1962).

ID-Diamond-Sawing Damage to Germanium and Silicon

Ronald L. Meek and M. C. Huffstutler, Jr.

Bell Telephone Laboratories, Incorporated, Murray Hill, New Jersey

ABSTRACT

The surface damage associated with wafering of germanium and silicon using an ID-saw has been investigated. Well-defined damage layers, which consist principally of microcracks and which have a depth of 25 $\pm 5\mu$ in germanium and 50 $\pm 10\mu$ in silicon, were observed for a range of sawing parameters. In no case was there evidence to suggest bulk damage to the materials. On the basis of vibration studies of the specimen and ID-blade, out of plane blade vibrations and periodic abrasive contact (due to noncircularity of the center hole in the blade) appear to be the important damage mechanisms.

The sophistication of present-day semiconductor device and integrated circuit technology is such that small lattice imperfections may have large enough effects on the material's transport properties and its uniformity of response to subsequent process steps to preclude satisfactory performance (1). It has been found in this laboratory that residual effects of early process steps carry over to produce defective finished devices. The present investigation is part of a continuing effort to optimize processing technology and to control or eliminate the associated defects.

While a nonmechanical method of semiconductor wafering—electrolytic shaping (2) or perhaps a laser knife—might be more desirable, at present only sawing is practical. With respect to surface damage, wire sawing is clearly superior (3) since it is essentially a lapping operation and the damage depth has been shown (4-7) to be of the order of the abrasive size; typically, a few microns. Presently available proprietary wire saws are impractical for large volumes of work, however, and inside-diameter (ID) diamond saws are usually used because of their material-savings advantage.

Little work has been reported on the nature and extent of the damage to semiconductor materials due to the wafering operation; that which is available is somewhat contradictory in that the depth of damage is reported as 12-13 or 40-70μ for what appears, superficially at least, to be the same sawing operation (8). The great depth to which mechanically sawed metal crystals are strained (9) indicates the advisability of investigating not only the surface damage but also the possible incidence of damage to the bulk of the slice.

Presumably, the vibrations of a slice being cut set up stresses analogous to fatigue tests and some of the damage may be related to this mechanism. Unfortunately, fatigue and fracture of homopolar crystals has not received the same attention as has been accorded to metals (10).

Several observations have been made while slicing silicon and germanium which deserve explanation:

1. Sometimes it is not possible to produce a whole (nonshattered), thin ($\sim 200\mu$) slice at saw settings (blade speed and feed rate) for which quite satisfactory, somewhat thicker ($\sim 300\mu$) slices are obtained. Rather, the feed rate must be increased to obtain the thin slice even though the over-all vibration level, as measured at the crystal mount, is considerably increased.

2. Sometimes, thin ($\sim 200\mu$) slices can be obtained from a certain crystal cut on the <111> plane, but the same saw settings do not permit a slice of the same thickness to be cut from seemingly equivalent material on the <100> plane.

3. Even with saw performance well within manufacturer's specifications, and with a saw blade of maximum concentricity (*i.e.*, $\sim 25\mu$ differential), no successful attempts have been made to produce slices of thickness less than about 175-200μ.

4. It appears to be possible to cut thinner germanium slices ($\sim 175\mu$) than silicon slices ($\sim 200\mu$).

These observations (No. 1 in particular) seemed to indicate the possibility of a fatigue mechanism. Although silicon and germanium (and diamond) have essentially no plastic flow domain at room temperature (11-13), the fatigue cracking of diamond has been demonstrated in a preliminary way (11). Furthermore, current information (14-16) indicates that dislocations may exist at the bottom of cracks in silicon and germanium. Repeated opening and closing of the crack might be expected to expand such networks into the bulk of the material. It seemed advisable, therefore, to ascertain not only the extent of gross surface damage but also the incidence, if any, of bulk material damage for ID-sawed semiconductor wafers.

The ID Saw

The basic configuration of the specimen and blade in an ID-saw is shown schematically in Fig. 1. (The coordinate system of Fig. 1 is used for orientation reference throughout this paper.) In principle, the support arm to which the wax-mounted ingot is fastened is an asymmetrically stiffened cantilever mounted on the feed table; y- and z-directional motions for cutting and indexing, respectively, are furnished by devices which operate at a fixed rate of speed (generally, the y- and z-drive mechanisms are powerful enough to be used on heavy-duty surface grinders, and are not equipped with a force-limiting clutch). In the process of cutting a slice, the z-motion is "locked" and the ingot moves in the y-direction at some set speed (typically, 2 cm/min). The true cutting rate is not constant, however, since there are variations due to the shape of the ingot and, what is more important, the blade edge does not move in an exact circle. When the blade edge is viewed from the frame of reference of the crystal, as a first approximation it appears that the rotation of an ellipse (with semimajor and semiminor

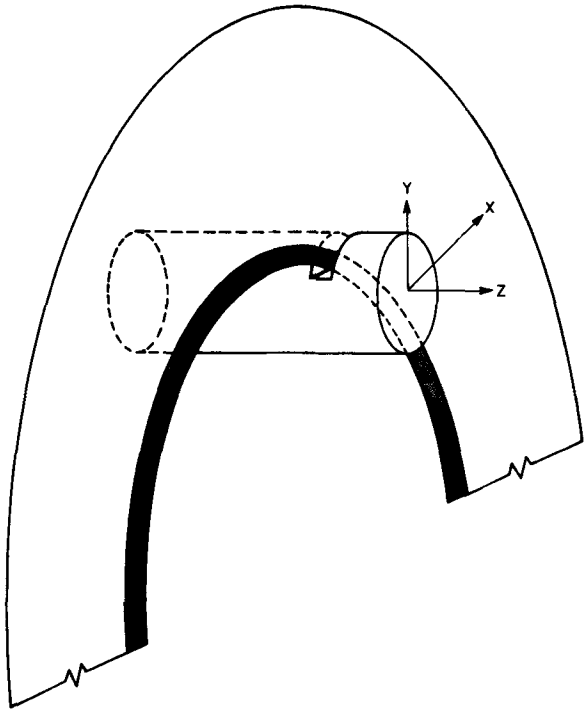

Fig. 1. ID saw schematic

axes differing by 25-50μ) is being viewed. The usual rotational blade speed is about 50 rps when a blade of 10 cm ID is used. That is, the feed rate is about 10μ per blade revolution. The lateral feed rate of the ingot being cut was measured, by means of a transducer which sensed table position as a function of time, and was found to be constant to within the uncertainty of the measurement which was estimated as less than 5%. It is clear then that large variations in cutting rate occur and that, in fact, the blade edge is not even in contact with the crystal part of the time.

In conjunction with the damage studies to be discussed shortly, vibration measurements were made in which a transducer sensitive to y-direction acceleration was placed on the crystal mount on the side opposite the kerf being cut. Frequencies of n x (wheel rotational frequency) were observed with $n = 1, 2, 3, \ldots$. The principal component appears to be at $2n$, that is about 100 Hz, and the amplitude of the vibration is about 1μ. Thus, since the crystal does not flex away from the blade edge, the large variations in cutting rate are quite real.

Typical practice in ID cutting calls for a small, low-pressure jet of water directed on the blade edge immediately before it enters the kerf. Because of the centrifugal force operating on the water film, it forms a tapered layer on the sides of the blade, being thinnest at the cutting edge. It has been found that best results are obtained if the water flow where the blade enters the kerf is sufficient only to wet the blade. The blade edge is then washed of excess cuttings with a larger water stream where it leaves the kerf. Too thick a water film where the blade enters produces tapered wafers, presumably due to ever-increasing hydrodynamic coupling between the blade and the crystal through the thickening water film.

Methodology for Damage Investigation

A number of methods are applicable to damage/defect study (4, 8, 17, 18), but the ease and speed of direct metallographic examination have been employed for the present inquiry. Some studies were carried out by alternately etching and chemically and/or mechanically polishing away the damaged material. Since all silicon/germanium etches are polish-etches, this method has the decided disadvantage that features observed after any etching step are characteristic not only of the final material surface but also the initial material surface and all the layers within the damaged layer. Mechanical polishing and then etching partially, but not totally, avoids perpetuation of the outermost surface irregularities in subsequent etches. Much better results were obtained when the slice under observation was mechanically polished on one side to a depth of about half of the slice thickness. The wafer was then mounted damaged-side-down on a glass slide with acidproof wax, after which the polished face was repeatedly etch/polished, the amount of material removed being determined (by thickness measurement) after each step. This permitted dislocations (or other etchable features) to be observed in the bulk of the material as well as any variation in their character across the slice thickness. Since the damaged surface layers are approached from beneath, their incidence is very clearly defined. The dislocation pattern in the bulk of the slice was compared to the uncut crystal's etched feature characteristics. In order to further assure that any and all flaws were revealed, two etches were used for each material and one-to-one correspondence of etched features was observed. For silicon, a modification of Dash's etch (17, 19), as well as a copper nitrate etch (20), was employed. In the case of germanium, CP-4 and the Westinghouse silver etch were utilized (20). Slices of various thickness cut on <111> and <100> planes were examined for large variations in sawing parameters.

Wafer Damage

Crystals of germanium and silicon were sawed with a stainless-steel ID-blade. The blade stock thickness was 100μ and the diamond grit (~50μ) plus blade thickness was 200μ. The kerf produced was 225μ, the average cuttings size being 2-3μ. The blade concentricity was 25-50μ.

Slices, 20-30 mm in diameter, of silicon and germanium having thicknesses of 190-360μ were cut from <100> and <111> material. Blade speed settings of 50-70 rps and feed rates of 1-4 cm/min were employed. All silicon studied was initially essentially dislocation free, but one germanium sample had a grown-in dislocation density of $7(10)^4$ lines/cm^2.

As-sawed silicon surfaces appear in Fig. 2(a) and 2(b). A profilimeter survey of the surface (Fig. 3) shows it to be chipped and fractured to a depth of about a micron (the profilimeter tip diameter was about a micron). This measurement probably underestimates the surface irregularity.

A silicon wafer which was lightly Syton polished (5μ removed) and then etched appears in Fig. 4. After the polish step, the surface still appeared rough and cracked. The etched features clearly tend to lie in lines along the cutting arc of the saw. A wafer subjected to two polish/etch steps appears in Fig. 5. After the second polish (25μ total material removed) no surface defects were observed at 500 magnification. After a second etch, however, the features of Fig. 5 were revealed. The etched line has the same character and orientation as those of Fig. 5, although there are many fewer such lines. Both etches, and etching from beneath the damaged layer, revealed the same characteristics for all silicon samples studied. The total damage layer for silicon is 50 $\pm$10μ, and in no case did either etch reveal damage to the bulk of the slice beneath the damaged surface layers.

A Syton-polished germanium surface which was etched with the Westinghouse silver etch appears in Fig. 6 from which it is seen that the defect character and orientation is much the same as in silicon. The sawing-damage surface-layer for germanium is 25 $\pm$5μ, in distinction to the relative lapping-damage situation where germanium is damaged to a greater depth than silicon (8).

Examination of germanium wafers having a grown-in dislocation density of $7(10)^4$ lines/cm^2 from beneath the damaged surface is more instructive. Figure 7(a)

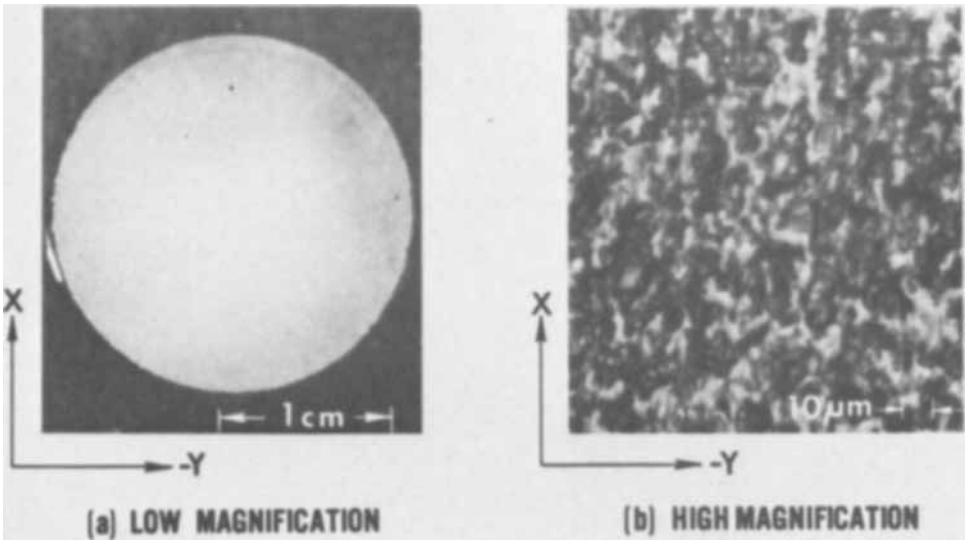

shows a particular slice at a depth of 25μ below the cut surface. The CP-4 etch clearly reveals the grown-in dislocations. In no case did the character or number of these dislocations indicate bulk damage to the slice center. The same slice appears in Fig. 7(b) after 5μ more material was etched away; *i.e.*, 5μ closer to the surface. The same type of features as seen in silicon are revealed. The character of these etch pits is very much different from the dislocation pits of the previous picture [Fig. 7(a)]. It is to be further noted that in the

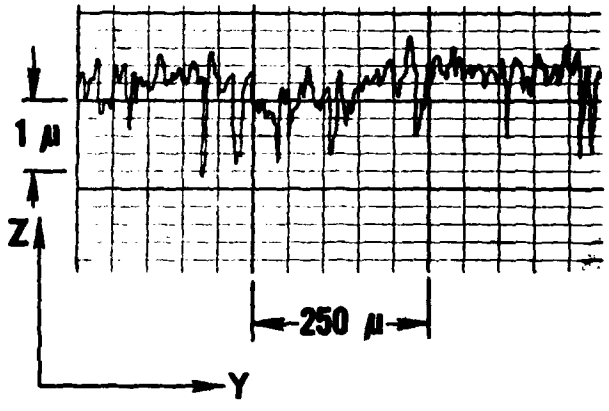

Fig. 3. Profilometer survey of as-sawed surface

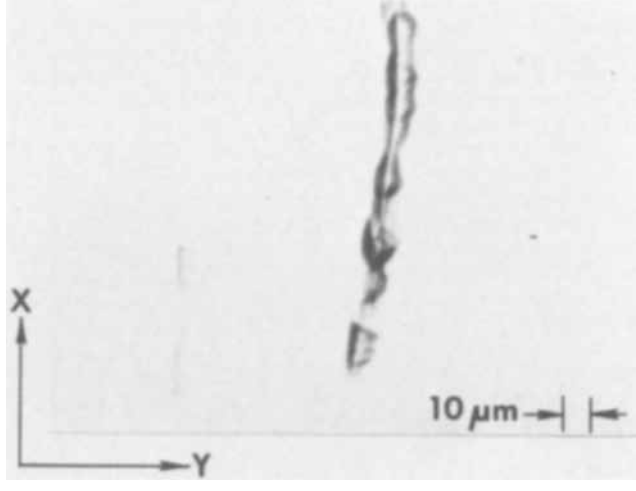

Fig. 5. Etched silicon surface (30 μm depth). Preparation of as-cut surface: 25 μm removed by sequence Syton/Chem polish/-Syton, 5 μm removed by final modified Dash etch.

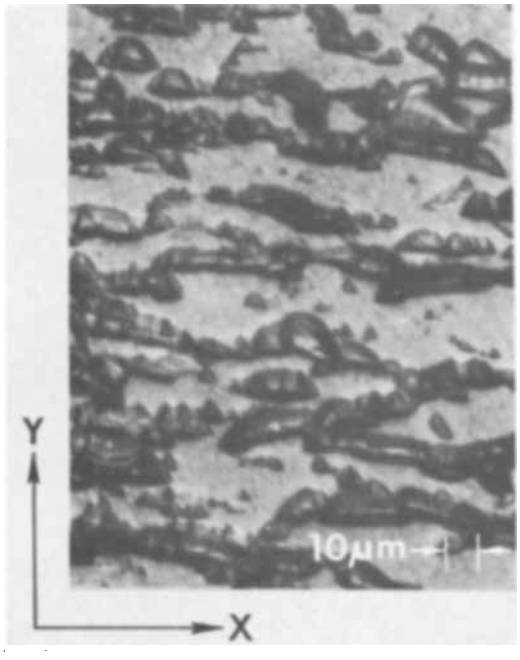

Fig. 4. Etched silicon surface (15 μm depth). Preparation of as-cut surface: 5 μm removed by Syton polishing, 10 μm removed by modified Dash etch.

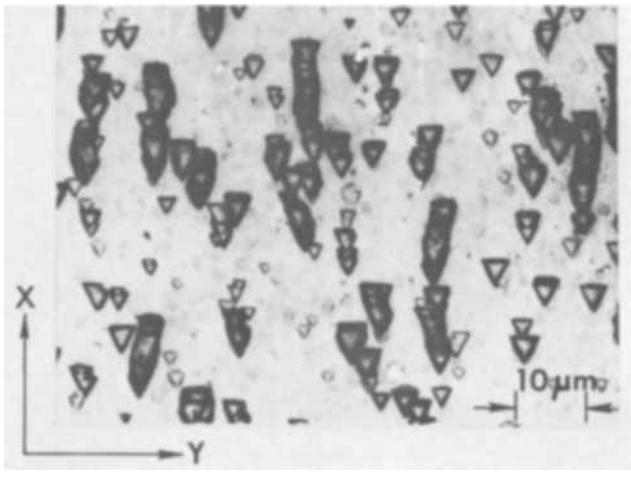

Fig. 6. Etched germanium surface (15 μm depth). Preparation of as-cut surface: 10 μm removed by Syton polishing, 5 μm removed by WAg etch.

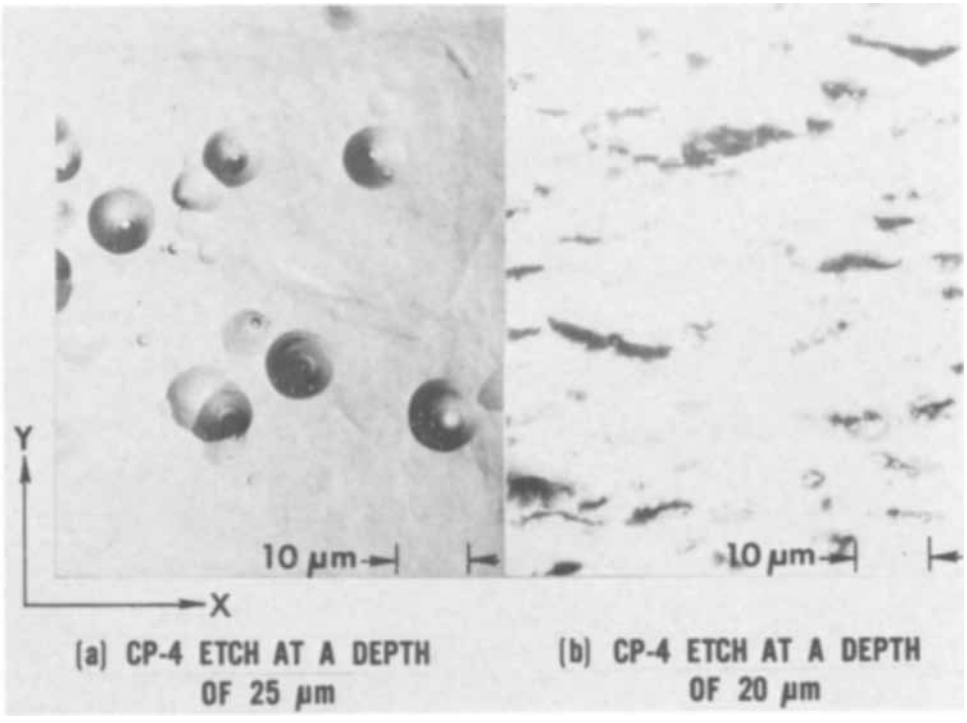

Fig. 7. Etched germanium surface as viewed from below the as-cut surface.

surface layers the damage is so extensive that the dislocations characteristic of the bulk cannot be distinguished at all. Figure 8 shows a germanium sample (well into the slice center) which was first etched with CP-4, in order to reveal the dislocations, and then with the WAg etch. A pyramidal pit was formed in the bottom of each CP-4 pit, as shown in the figure, which can be contrasted to the flat-bottomed WAg pit (Fig. 6) characteristic of the damaged layers. Because of this decided difference in etched feature characteristics, we conclude that the damaged layers consist largely of microcracks rather than dislocations. In support of this position, it is again noted that room-temperature plastic deformation of germanium or silicon is not generally accepted (13). When the presence of the coolant and the total damage depth are taken into account, it is difficult to believe that the cutting action produces local heating sufficient to permit plastic deformation.

Saw Wafer Interaction

In order to gain understanding of the stresses to which the wafer is subjected during cutting, the interaction of the saw blade with the wafer is considered. At least two phenomena are apparent. First, the blade vibrates within the kerf and applies a bending force to the wafer as illustrated in Fig. 9, for which b is the radial diamond grit extent, Δ is the wafer thickness, S is the cutting rate, and t is time as measured from the start of the cut. Second, as the blade cuts into the crystal, some force F_2 is applied at a small angle β to the corner of the kerf as illustrated in Fig. 10. This tends to shear off the crystal wafer along the cleavage plane which lies at an angle α. (This shear force is much greater than that associated with F_1.)

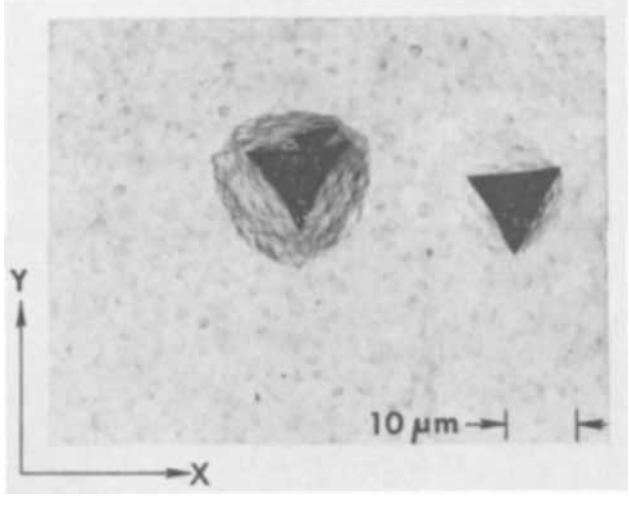

Fig. 8. Etched germanium surface (100 μm depth). Dislocations in ingot as shown by WAg etch pits (pyramidal features) formed in conical pits from previous CP-4 etch.

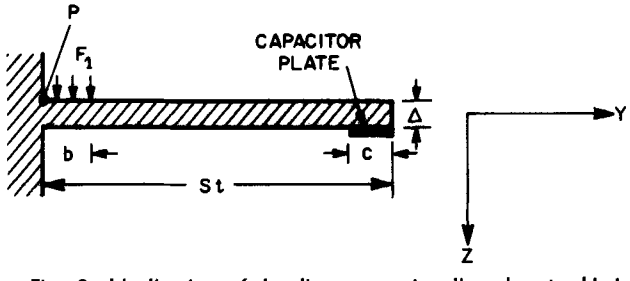

Fig. 9. Idealization of bending stress in slice due to blade vibration.

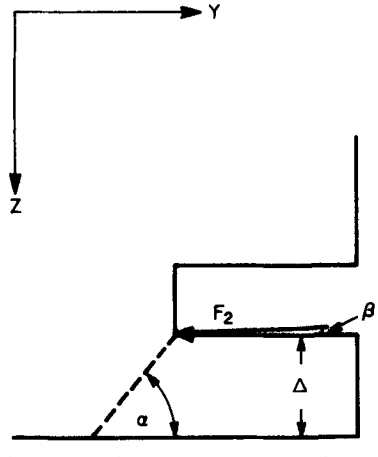

Fig. 10. Idealization of shearing stress in slice due to cutting force

The forces involved were evaluated as follows: A thin metal foil, which functioned as one plate of a capacitor, was placed on the wafer as shown in Fig. 9. A similar plate placed 50μ away was fastened to a massive aluminum support extended from the crystal mount. This capacitor then functioned as a capacitance microphone to measure the slice deflection under cutting conditions. For the situation described, elementary beam-bending theory (21) shows the deflection δ is given by

$$\delta = \frac{F_1 b^2}{2Ew\Delta^3} [4St - 2c - b]$$

where w is the slice width at the kerf and E is the appropriate Young's modulus. Experimental measurements of the slice deflection have shown that F_1/w is nearly constant at about $4(10)^5$ dynes/cm for silicon.

It is difficult to represent the deflections by any one frequency, but it appears that major deflections occur at about 500-1000 times/sec in agreement with estimates of the fundamental frequency of out-of-plane blade vibration at the relevant tension. The maximum tensile stress, at point P of Fig. 9, can then be calculated as a function of slice thickness, by use of elementary beam-bending formulas (21), from

$$\sigma_{t,\max} = \frac{3b}{\Delta^2}\left(\frac{F_1}{w}\right)$$

Values are presented in Table I. Evaluation of F_2 is somewhat more difficult. The angle β must be very small, and so will be neglected, and the cleavage plane will be assumed to intersect the cutting plane along the line of cut. Then the shear stress on the cleavage plane is

$$\sigma_s = \frac{F_2}{w\Delta} \cos\alpha \sin\alpha$$

The cleavage plane will always be a <111> plane (13), (also see later). The average cutting force per unit kerf length is easily measured and from such measurement F_2/w is estimated, with F_2 the average cutting force, as 10^7 dynes/cm when silicon is sawed. Calculated values of σ_s when the cutting plane is <111> or <100> are presented in Table II.

The tensile stress in bending necessary to break silicon and germanium wafers has been measured as illustrated in Fig. 11. The force, F, necessary to break the slice is applied slowly (over a period of about a minute) and uniformly by means of a screw feed operating against a direct-reading, spring-loaded force transducer. It was observed that the force could be maintained at about 95% of the value needed for breakage for at least 15 min without fracture of the slice. Slices were examined with the length l (the beam axis), as shown in Fig. 11, oriented along the y and x axes. In all cases, breakage was on <111> cleavage planes (as determined by observation of the angle between the breakage plane and the known surface plane) and fracture was initiated at the point where the slice entered the wax. When an appropriate cleavage plane lay within about 20° of the wall, the wafer broke along a single line. For greater angles, multiple fracture occurred, the ~25% of the slice closest to the block being shattered into several fragments. Data, in terms of the maximum tensile stress, are summarized in Table III. (The columns x and y under $\sigma_{t,\max}$ are for the beam axis along the x-, y-axes, respectively.) The germanium and all but B-silicon are from the same batches as used for depth of damage study. The B-silicon wafers were cut when saw performance was poor and scratch marks and gross surface damage were much more evident.

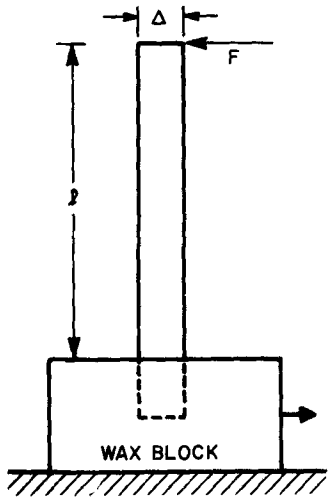

Fig. 11. Experimental slice-breakage-measurement configuration

Several observations can be made:

1. It always takes a larger stress to cause fracture when the beam axis is parallel to the damage cracks than when it is perpendicular to them. That is, the damage effect weakens the slice anisotropically.
2. The stress necessary to cause fracture is considerably increased when the damaged surfaces are removed and the breakage-stress anisotropy disappears.
3. A somewhat greater stress is necessary to break <100> than <111> slices although the difference is small for as-sawed wafers.

Comparison of the measured fracture stress with the calculations of the stresses during sawing (Tables I and II) allows plausible explanation of the observed thin slice breakage:

1. Clearly, the existing interaction stresses limit the possible slice thinness to somewhere in the range 100-

Table I. Maximum tensile stress in bending due to blade vibration for various silicon wafer thicknesses

Wafer thickness, Δ, microns	Maximum tensile stress, $\sigma_{t,\max}$, dynes/cm²
100	$2(10)^8$
150	$8(10)^8$
200	$4(10)^8$
250	$3(10)^8$

Table II. Approximate shear stress on the cleavage plane due to cutting force for various wafer thicknesses

Wafer thickness, Δ, microns	Shear stress on cleavage plane, σ_s, dynes/cm² <111> cut	<100> cut
100	$3(10)^8$	$5(10)^8$
150	$2(10)^8$	$4(10)^8$
200	$2(10)^8$	$3(10)^8$
250	$1(10)^8$	$2(10)^8$

Table III. Tensile stress in bending sufficient to induce wafer fracture

Material	Plane Cut	Condition	Wafer thickness, Δ, microns	$\sigma_{t,\max} \times 10^{-9}$, dynes/cm² y	x
A-Si	<111>	As-sawed	390	1.4	1.6
A-Si	<111>	As-sawed	320	1.3	1.4
A-Si	<111>	As-sawed	330	1.4	1.6
A-Si	<111>	As-sawed	340	1.4	1.7
A-Si	<111>	Polished	280	2.2	2.3
A-Si	<111>	Polished	290	2.3	2.4
B-Si	<111>	As-sawed	480	0.8	1.5
B-Si	<111>	As-sawed	330	0.8	1.7
C-Si	<100>	As-sawed	410	1.6	1.9
C-Si	<100>	As-sawed	410	1.8	2.0
C-Si	<100>	As-sawed	410	1.8	2.1
C-Si	<100>	Polished	260	3.8	3.8
C-Si	<100>	Polished	260	3.9	3.8
Ge	<111>	As-sawed	180	1.0	1.4
Ge	<111>	As-sawed	200	1.0	1.3
Ge	<111>	As-sawed	250	1.0	1.5
Ge	<111>	As-sawed	240	1.0	1.4
Ge	<111>	Polished	260	1.5	1.5
Ge	<111>	Polished	260	1.6	1.5

200μ, for Si and Ge ingots of approximately 25 mm diameter.

2. When the added effect of the shear stress due to the cutting action is taken into account, the minimum possible <100> slice thickness may be greater than for <111> slices, since the shear stress along the cleavage plane is greater for the <100> slice.

3. When a certain thickness slice cannot be cut successfully, increasing the feed rate, and consequently the shear stress, may be desirable if sufficient damping of blade vibration, and reduction of tensile stress, results.

4. Since germanium is not as hard as silicon, the blade/crystal interaction forces are expected to be smaller, and may be enough less to allow lower than critical stresses in thinner slices than is the case for silicon.

At any rate, it is clear that thinner slices having less surface damage are not likely to be produced by diamond ID-saws until devices to damp blade vibrations and smooth out variations in the cutting rate are implemented.

Finally, in support of the microcrack hypothesis, it is interesting to compare the tensile stress at a crack tip necessary to instigate fracture with that calculated from the Griffith formula (10),

$$\sigma \doteq \sqrt{\frac{E\alpha}{c}}$$

for a crack of length c in a material with specific surface energy α. If it is supposed that cracks extend from the surface to the bottom of the damaged layer, then the tensile stress at the crack tip needed to propagate the crack (fracture the slice) is easily calculated from the data in Table III. For silicon this stress is found to be 0.9-1.0 $(10)^9$ dynes/cm^2 and for germanium it is 0.7-0.8 $(10)^9$ dynes/cm^2. The specific surface energy, for the cleavage plane, is estimated (10) as 900 erg/cm^2 for silicon and 700 erg/cm^2 for germanium. Examination of the etch features for a number of slices indicates that, near the bottom of the damaged layer, the crack length is about 50μ. The calculated Griffith stress based on this crack length is 0.6 $(10)^9$ dynes/cm^2 for silicon and 0.5 $(10)^9$ dynes/cm^2 for germanium. The agreement is well within the uncertainties in the formula and the numerical values used.

Conclusions

Damage patterns in ID-sawed, thin (200-400μ) silicon wafers (2-3 cm in diameter) have been analyzed by surface etch/polishing, by material removal from the side opposite the damaged layers, by measurement of the magnitude and anisotropy of the fracture strength, and by use of specialized dislocation etches with the following conclusions:

1. The depth of surface damage as judged by the sudden appearance of etchable structural features is about 50μ.

2. The pattern of the etched damaged material can be described as dense strings of pits coincident with the abrasive path and appears to be mostly microcracks (as substantiated by a sharply decreased and anisotropic fracture strength).

3. The mechanism of damage appears to be largely out-of-plane flexural vibration of the membranelike ID-blade which produces, in turn, oscillating stresses in the wafer being cut.

Comparison studies on germanium (for which the damage depth is about 25μ) further verify that the surface damage is predominantly microcracks oriented parallel to the abrasive path. The length of these cracks is, of course, unchanged during processing so long as the wafer is not subjected to stress (at a sufficient level and appropriately directed) which would extend them. Presumably, an etch immediately after sawing would eliminate some of the most easily extended microcracks which would otherwise spread and deepen the damage during subsequent grinding and polishing operations.

Acknowledgment

The authors are pleased to acknowledge W. J. Rhines for discussions and calculations relevant to blade vibration.

Manuscript submitted Sept. 9, 1968; revised manuscript received Feb. 10, 1969.

Any discussion of this paper will appear in a Discussion Section to be published in the December 1969 JOURNAL.

REFERENCES

1. H. F. John, *Proc. IEEE*, **55**, 1249 (1967).
2. A. Uhlir, *Bell System Tech. J.*, **35**, 333 (1956). S. Sheff, *Electrochem. Technol.*, **5**, 47 (1967).
3. M. C. Huffstutler and B. T. Kerns, *Am. Ceram. Soc. Bull.*, **46**, 1098 (1967). E. W. Jensen and H. R. Jacobsen, *S. S. Technology*, **11**, 53 (1968).
4. T. M. Buck and F. S. McKin, *This Journal*, **103**, 593 (1956).
5. W. C. Dash, *J. Appl. Phys.*, **29**, 228 (1958).
6. E. N. Pugh and L. E. Samuels, *This Journal*, **108**, 1043 (1961).
7. E. N. Pugh and L. E. Samuels, *ibid.*, **109**, 409 (1962).
8. T. M. Buck, "The Surface Chemistry of Metals and Semiconductors," H. C. Gatos, Editor, p. 107, John Wiley & Sons, New York (1960).
9. R. Maddin and W. Asher, *Rev. Sci. Instr.*, **21**, 881 (1950).
10. B. L. Averbach *et al.*, Editors, "Fracture," John Wiley & Sons, New York (1959).
11. R. Berman, Editor, "Physical Properties of Diamond," Clarendon Press, Oxford (1965).
12. J. Friedel, "Dislocations," Addison-Wesley Publishing Co., Reading (1964).
13. H. G. Van Bueren, "Imperfections in Crystals," North Holland Publishing Co., Amsterdam (1961).
14. E. N. Pugh and L. E. Samuels, *This Journal*, **109**, 1197 (1962).
15. R. Stickler and G. R. Booker, *ibid.*, **109**, 734 (1962).
16. R. Stickler and G. R. Booker, *ibid.*, **109**, 1167 (1962).
17. S. Amelinckx, "The Direct Observation of Dislocations," Academic Press, New York (1964).
18. J. Patel, R. Wagner, and S. Moss, *Acta Met.*, **10**, 759 (1962).
19. N. N. Sirota and A. A. Tonoyan, *Proc. Acad. Sci. USSR, P. Chem. Sect.*, **134**, 987 (1960).
20. W. G. Johnstone, "Progress in Ceramic Science," Vol. 2, J. E. Burke, Editor, p. 3 (1962).
21. E. P. Popov, "Mechanics of Materials," Prentice-Hall, Inc., Englewood Cliffs, N. J. (1961).

Liquid Phase Epitaxial Growth of $Ga_{1-x}Al_xAs$[1]

J. M. Woodall*, H. Rupprecht, and W. Reuter

Research Division, International Business Machines Corporation, Yorktown Heights, New York

ABSTRACT

The liquid phase epitaxy method of solution growth has been applied to the ternary compound semiconductor, $Ga_{1-x}Al_xAs$, for nearly the complete solid composition range. Epitaxial deposition of this compound has been achieved on GaAs substrates. Factors which determine the metallurgical and chemical nature of the layers include: the geometry of the crystal growth apparatus, the design of the furnace and its temperature profile, the cooling schedule, the melt composition, and the residual oxygen concentration in the purging gas.

Since its development as a useful epitaxial crystal growth method for GaAs (1), the liquid phase epitaxy technique has been applied to other binary compounds, such as GaP (2). Recently (3), it was found that this method can be used for preparing efficient electroluminescent junctions in $Ga_{1-x}Al_xAs$. In this paper, we describe the necessary conditions for the successful application of the liquid phase epitaxial method to this system and report the resulting morphological and chemical characteristics of the $Ga_{1-x}Al_xAs$ epitaxial layers that are produced.

Apparatus

A vertical dip apparatus, shown in Fig. 1, was used for this study. Except for the graphite substrate holder and the Al_2O_3 crucible, the entire apparatus is made of fused quartz. The dimensions below the gas inlet and outlet ports are 12 in. by 1 in. OD. The Al_2O_3 crucible has a volume of 10 cm^3. The graphite substrate holder is hollow to allow for the insertion of dopants into the melt during growth. The substrate holder is suspended from a quartz tube which in turn is clamped to the main body of the apparatus by Teflon fittings. The quartz tube is normally covered by a gas-tight fitting which contains the dopants which are inserted in the melt during growth.

Fused quartz was found to be an unsuitable material for containing Ga-Al melts. Aluminum vapor and Al alloys react with quartz vessels causing silicon contamination at temperatures as low as 750°C (4). Both Al_2O_3 and graphite can be used for Ga-Al melts for temperatures up to 1150°C without noticeable Si contamination or other crucible and melt reactions occurring.

In order to prevent the preferential oxidation of Al in Ga-Al melts during growth, it is necessary to use an ultrapure inert purging gas. The large residual water vapor and oxygen concentrations in industrial-grade forming gas (10% H_2, 90% N_2) were found to cause nonuniform growth of uncontrolled composition. Also, during heating an oxide scum forms on Ga-Al melts, which, unlike the scum on pure Ga melts, cannot be easily reduced even in an ultrapure hydrogen ambient. This oxide layer hinders wetting between the substrate and melt in the horizontal tip method (1). However, in the vertical system the substrate is inserted through the scum into a clean liquid where wetting will occur.

Even when the purest purging gases are used, an oxide layer will form on the surface of a $Ga_{1-x}Al_xAs$ layer before its insertion into the melt and after its removal from the melt. This oxide, which is neither reduced nor dissolved when dipped into the melt, inhibits further epitaxial growth.

The furnace used for this study provided a maximum cooling rate of 30°C/min at 950°C. The temperature profile measured from the inside bottom of the furnace is shown in Fig. 2. The melt region of the apparatus is normally located between the 0- and 3-cm positions of the profile. Shifting the apparatus along this profile was found to affect the morphologi-

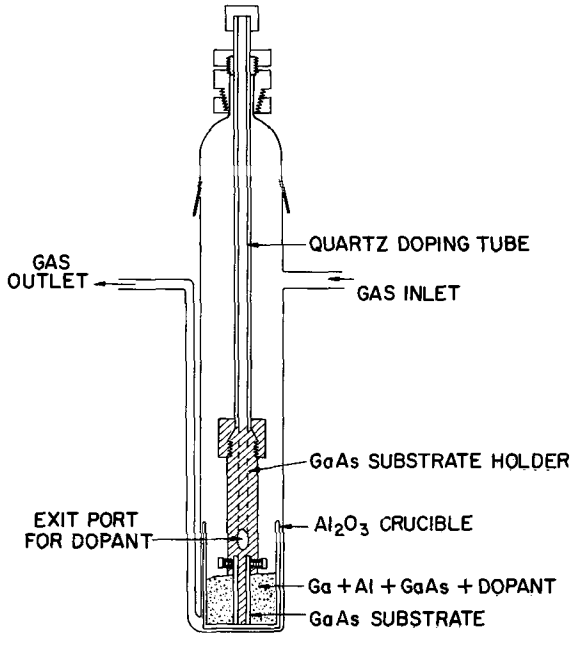

Fig. 1. Liquid phase epitaxy apparatus used for the $Ga_{1-x}Al_xAs$ system.

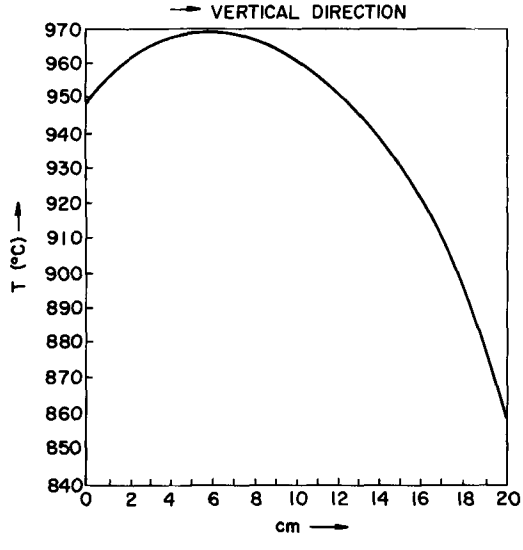

Fig. 2. Temperature profile of the furnace with apparatus in place. The melt is located between 0 and 3 cm.

* Electrochemical Society Active Member.

[1] Sponsored in part by the U.S. Army Electronics Command, Fort Monmouth, New Jersey.

cal characteristics of the epitaxial layers. The temperature is controlled to ± 0.2°C.

Experimental Procedure

The experimental procedure is divided into two operations. First is the preparation of the substrate and melt. The GaAs substrate is prepared by lapping away the sawing damage with 5μ Al_2O_3 powder and then removing the lapping damage by etching in 1:3:4 HF:HNO_3:H_2O for about 45 sec. After rinsing the wafer with H_2O, the surface is blown dry with Freon gas. As is shown below, the manner in which the surface is prepared can have an effect on the quality of the resulting epitaxial growth. Wafers with both (100) and (111) faces were used in this study.

The melts are based on 20g of 99.9999% grade Ga. For all compositions studied, the melts contained at least 90 m/o (mole per cent) Ga. To saturate them with As, an excess of GaAs over that required for saturation at a given growth temperature and Al concentration is added to the melt at room temperature prior to growth. The amount of GaAs required to saturate various Ga-Al melts was determined by measuring the weight loss of a solid piece of GaAs which is soaked in a Ga-Al melt at constant temperature for 90 min. In principle, this technique (5) should not provide equilibrium values for ternary liquidus lines at constant temperature, since pure GaAs cannot equilibrate with a Ga-Al-As melt. However, the observed saturation of the Ga-Al melts with As using this technique implies that the kinetics of saturation are such that a protective layer of solid $Ga_{1-x}Al_xAs$ forms between the melt and the pure GaAs causing an apparent equilibrium to be established. Figure 3 shows the solubility of As in mole fraction as a function of 1/T°K for three melts with starting Al/Ga mole ratios of 0, 0.0097, and 0.0194. Due to the difficulty of measuring the melt temperatures during saturation, melt temperatures were approximated by averaging the furnace temperature profile at the melt region. This approximation creates a melt temperature error of ± 10°C. It is seen that the solubility of As in Ga-Al is strongly dependent on the Al concentration. For a growth temperature of 955°C, the addition of only 0.0194 mole ratio of Al to Ga reduces the solubility of As by a factor of 1/3. The information in Fig. 3 is helpful for determining the temperature ranges which should be used in order to grow epitaxial layers of the same thicknesses for different Al concentrations.

In addition to Ga, Al, and GaAs, the melt can also be charged with dopants. The addition of 0.002-0.005g of Te during initial preparation and of 0.050-0.100g of

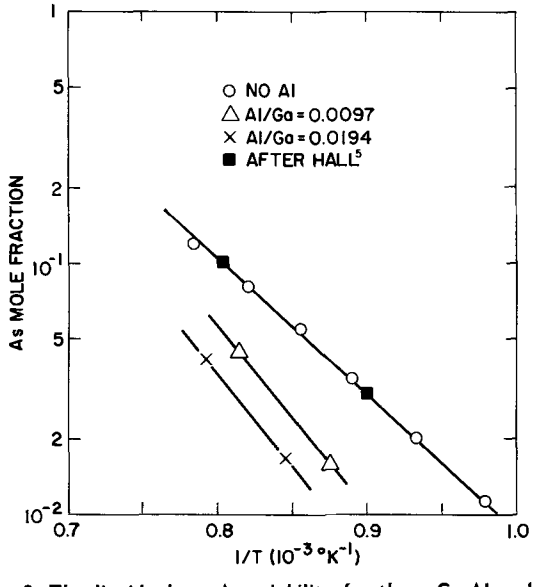

Fig. 3. The liquid phase As solubility for three Ga-Al melts vs. reciprocal absolute temperature.

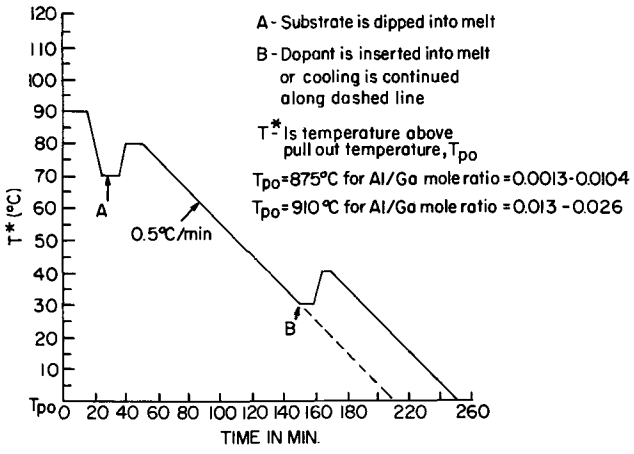

Fig. 4. Cooling and heating schedule for $Ga_{1-x}Al_xAs$ epitaxy

Zn during the middle of the growth schedule results in the formation of efficient electroluminescent p-n junctions for Al concentrations between 0 and 0.0088 mole fraction in the melt (3).

After the melt is composed, the GaAs substrate is mounted on the graphite holder. Next, the apparatus is assembled and purged with ultrapure forming gas at 3 liters/min for 30 min. The flow rate is then lowered 200 cc/min. The apparatus is then placed into the preheated furnace such that the melt region is located in the 0-3 cm position of the furnace. A typical cooling and heating schedule for the liquid phase epitaxial growth is shown in Fig. 4. The solid line is the time-temperature schedule normally used for preparing layers which contain a p-n junction, whereas the solid line to point B and dashed line after point B are the usual schedule for either undoped or singly doped layers. The shifting of the schedule to higher temperatures as the Al concentration in the melt increases compensates for the decrease in As solubility with increasing Al concentrations. Also, as the Al concentration in the melt increases, the time necessary to achieve As saturation at a given temperature increases beyond the 20 min necessary for pure Ga-GaAs melts. This longer saturation time can be effectively reduced by lowering the temperature after the 20-min period. This is the reason for the initial 20°C rapid cooling prior to dipping the substrate into the melt as shown in Fig. 4.

Ten minutes after the substrate is dipped into the melt, the temperature is raised 10°C in order to remove the growth which can occur during the dipping of the cool substrate. This 10°C rise also causes a slight etching of the substrate which assures good wetting prior to growth. The 0.5°C/min cooling rate was chosen because it was a rate below which no effect on growth composition was observed. Higher cooling rates result in lower Al concentrations in the growth. Ten minutes after point B of Fig. 4, the temperature is raised 10°C in order to remove the growth resulting from the insertion of the dopant into the melt. The growth schedule is usually terminated by first withdrawing the substrate from the melt and then removing the apparatus from the furnace. The apparatus can be withdrawn from the furnace before the substrate is removed from the melt. However, this causes the growth of a layer with a somewhat lower Al concentration than that of the layers grown during the slow-cool schedule.

Results and Discussion

Figure 5 shows photomicrographs of an n-type epitaxial layer of $Ga_{1-x}Al_xAs$ grown on the (100) face of a GaAs substrate from a melt with 0.011 mole fraction of Al and 0.050g Te. Figure 5 (top), taken at 5X magnification, shows the surface characteristics of the epitaxial growth. The surface is not as rough as the photomicrograph suggests. This becomes evi-

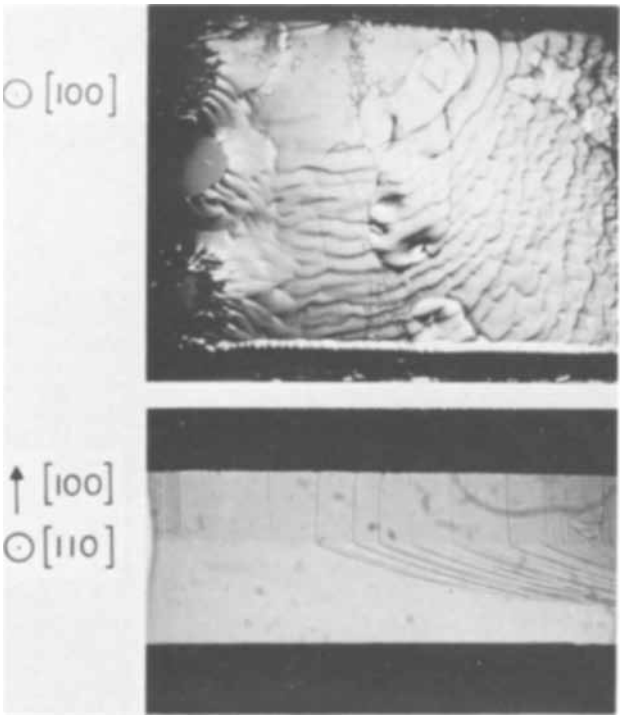

Fig. 5. Top: surface characteristics of $Ga_{1-x}Al_xAs$ layer at 5X magnification. Bottom: The same layer when cleaved along the growth direction at 43X magnification.

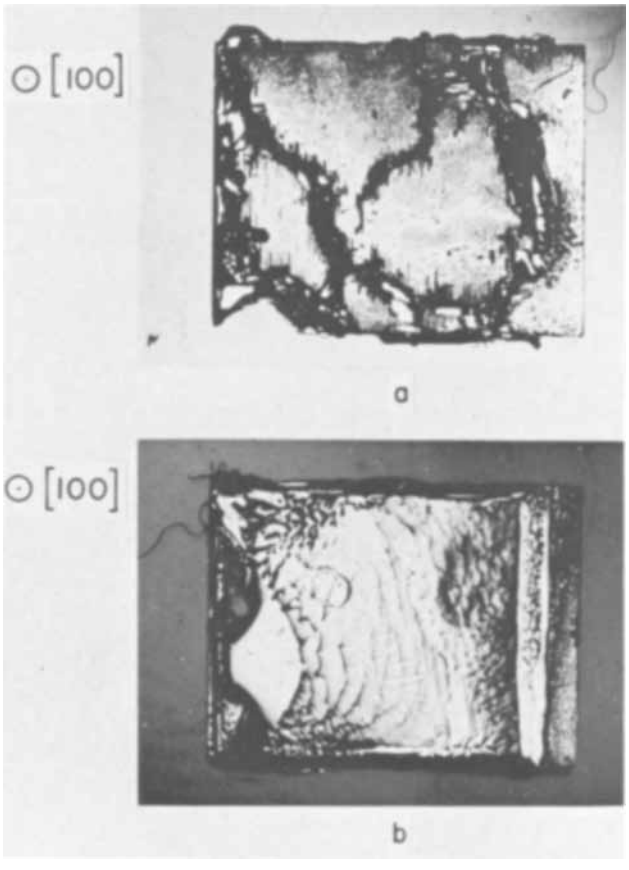

Fig. 6. Effect of wafer preparation on growth characteristics: a—H_2O:H_2O_2:H_2SO_4 1:1:3 polish; b—A lap with 5μ grit plus an etch with 1:3:4 HF:HNO_3:H_2O. Magnification 5X.

dent when viewed at higher magnification on a cleaved surface parallel to the growth axis, as in Fig. 5 (bottom) taken at 43X magnification. It should be noted that there are several areas of Fig. 5 (top) which appear as blotches. This is growth which occurs when the droplets of the melt stick to the substrate when it is removed from the melt. The composition of this layer with respect to the normal growth is discussed at the end of this section. The thickness of the epitaxial layer in Fig. 5 (bottom) is 190μ. This layer was formed by cooling from 955° to 850°C at 0.5°C/min. The epitaxial growth rate was found to be nearly constant for this temperature range and cooling rate. The epitaxial layer does not include all of the material which crystallizes from the melt during the cooling schedule. In addition to epitaxial growth, there is dendritic growth occurring simultaneously throughout the melt.

The morphology of the epitaxial layers changes drastically when the melt region of the apparatus is placed in the constant temperature zone of the furnace. When this is done, the resulting layers are highly tapered with more growth occurring on that portion of the substrate nearest the top of the melt. In addition, the layer is extremely rough with unfilled gorges extending nearly to the substrate interface. The inability to determine accurately temperature distributions of a melt with an inserted substrate holder prevents an explanation of this behavior. However, it is most likely that when the melt region is in the constant temperature zone of the furnace the melt is probably cooler at the surface than at the bottom due to heat sinking by the inserted substrate holder. This condition would be expected to produce tapered growth.

Another parameter which affects the growth of epitaxial layers is the surface preparation of (100) GaAs substrates. Figure 6 shows the effect of different etchants on epitaxial growth. The substrate in Fig. 6a was chemically polished in 1:1:3 H_2O:H_2O_2:H_2SO_4, whereas the substrate of Fig. 6b was prepared by etching 1:3:4HF:HNO_3:H_2O for 45 sec. The reagent concentrations were: HF-50%; HNO_3-70%; H_2SO_4-95%; H_2O_2-30%. Both substrates were cut from the same wafer and were used in the same growth schedule. The dark areas in Fig. 6a are caused by a small amount of fibrous growth. The rest of the wafer was not wetted by the melt. However, as seen in Fig. 6b, the entire substrate exposed to the melt is covered with good-quality epitaxial growth.

An interesting aspect of these liquid phase epitaxial layers of $Ga_{1-x}Al_xAs$ is the nature of the composition profiles along the growth axis. To obtain quantitative information about the chemical composition profiles, an x-ray fluorescent analysis was made using an electron beam probe. This proved to be a very useful technique. The resolution of the beam was such that it sampled a hemisphere of material with a diameter of about 3μ. Since the Al in the crystal matrix does not appreciably absorb the Ga and As fluorescence leaving the matrix, and since As is the constant mole fraction species, it was possible to determine the weight per cent values of each component from the Ga and As counts at each position after small corrections for the absorption due to Al in the lattice. From this, the mole fraction value x for $Ga_{1-x}Al_xAs$ was calculated as a function of position along the growth axis. Figure 7 shows a plot of composition *vs.* position for three layers grown from melts of different compositions. Positions are measured from the GaAs substrate interface. Curve A represents a layer containing a p-n junction grown from a melt with 0.0088 mole fraction Al which was cooled between 955° and 875°C. Curve B shows the profile of the layer described by Fig. 5. Curve C is an n-type layer grown from a melt with 0.017 mole fraction Al which was cooled between 990° and 910°C.

The fact that the Al concentration decreases with distance away from the substrate and that the composition gradient decreases with increasing Al concentrations can be understood in terms of the behavior of the segregation coefficient of Al, k_{Al}. If k_{Al} is defined as the ratio of the mole fraction of Al in the solid in equilibrium with the melt to the mole fraction of Al in the melt, it is found that k_{Al} is > 1 and

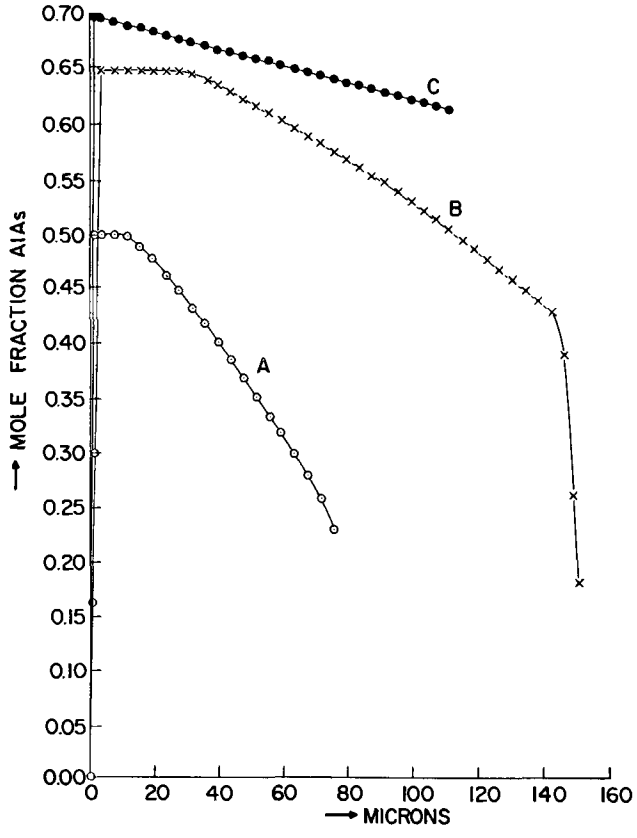

Fig. 7. Composition profiles in mole per cent AlAs along the growth axis of three layers. The zero position is the substrate-growth interface. Profiles A, B, and C represent layers grown from melts and initial growth temperature of 0.0088 mole fraction Al and 955°C, 0.011 mole fraction Al and 955°C, and 0.017 mole fraction Al and 990°C, respectively.

that it decreases with increasing Al concentration at high mole fractions of Al in the solid. Figure 8 shows the variation in k_{Al} with the Al concentration in the melt as determined by the Al concentration in first-to-freeze portions of the layers in Fig. 7 and the Al concentration in the melt. It should be noted that the points corresponding to Al mole fractions of 0.017 represent k values at 990°C, whereas the other points refer to k values at 955°C. The 955°C k value for an Al mole fraction of 0.017 would be expected to be only about 10% larger. It is not surprising that k_{Al} starts to decrease at higher Al concentrations. Since

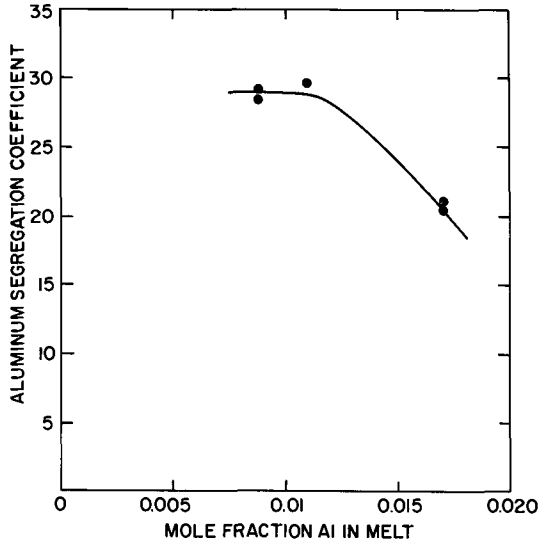

Fig. 8. Segregation coefficient for Al in Ga-Al-As melts vs. Al concentration in mole fraction in the melt.

the mole fraction of Al in the solid cannot exceed 0.5, k_{Al} must decrease as the Al concentration in the melt increases. The fact that $k_{Al} > 1$ explains qualitatively why the profiles of Fig. 7 show a decrease in the Al concentration with distance away from the substrate. The higher k_{Al}, the more melt is depleted of Al for each incremental volume element frozen, and therefore the steeper the profile. Thus, curve C ($k_{Al} = 20$) is not as steep as curve A ($k_{Al} = 28$).

The layer represented by curve A of Fig. 7 has a p-n junction 39μ from the substrate which, when forward biased, emits radiation at a peak energy of 1.83 ev at room temperature. The composition of this junction is 0.40 ± 0.02 mole fraction AlAs. This agrees well with the data of Ku and Black (4).

The electroluminescent diodes prepared from the layer described by curve A exhibit a large amount of emission passing through the surface of the n-type side when the GaAs substrate has been removed. The reason for this is easily understood from an analysis of curve A. The n-type layer extends up to 39μ, where the p-n junction is formed. The p-type layer extends from this junction to the surface. The energy of the radiation emitted at the p-n junction is greater than the band gap energy of the p-type side, since the Al concentration is continuously decreasing away from the p-n junction on the p-type side. Therefore, light traveling toward the surface of the p-type layer will be strongly absorbed. However, since the band gap energy increases (Al concentration increases) away from the p-n junction on the n-type surface, the radiation from the p-n junction traveling to the n-type surface will not be strongly absorbed. Thus, the profile of curve A permits the fabrication of efficient large area surface emitting electroluminescent diodes. To date, quantum efficiencies as high as 6% have been obtained for epoxy-domed diodes emitting at a peak energy of 1.65 ev at room temperature. The brightest visible epoxy coated diodes emit at 1.83 ev with an external quantum efficiency of 0.8%.

Finally, it should be noted that in curve B of Fig. 7 the Al concentration tends to drop rapidly near the surface. This area was formed as the result of the fast cooling of a droplet of the melt which stuck to the layer when it was withdrawn. The fact that this surface layer has a lower Al concentration is further experimental proof that segregation constants go to unity with increasing growth rate (6). This in principle should allow the formation of heterojunctions by variations in the cooling rate, providing that increasing the cooling rate does not cause an instability in the solid-liquid-interface during growth.

Summary and Conclusions

The critical parameters which affect the liquid phase epitaxial growth of $Ga_{1-x}Al_xAs$ on GaAs substrates include: substrate preparation, purity of purging gases, choice of container materials, and the temperature profile across the melt. The compositional characteristics of the layers are determined by: melt composition, growth rates, and the oxygen content of the purging gas. The composition profiles were found to be desirable for the fabrication of efficient, surface emitting electroluminescent diodes.

Acknowledgments

The authors wish to express their appreciation for the technical contributions made by C. J. Lent and V. Garrison.

Manuscript submitted Nov. 12, 1968; revised manuscript received Feb. 11, 1969.

Any discussion of this paper will appear in a Discussion Section to be published in the December 1969 JOURNAL.

REFERENCES

1. H. Nelson, *RCA Rev.*, **24**, 603 (1963).
2. M. R. Lorenz and M. Pilkuhn, *J. Appl. Phys.*, **37**, 4094 (1966).
3. H. Rupprecht, J. M. Woodall, and G. D. Pettit, *Appl. Phys. Letters*, **11**, 81 (1967).
4. S. M. Ku and J. F. Black, *J. Appl. Phys.*, **37**, 3733 (1966).
5. R. N. Hall, *This Journal*, **110**, 385 (1963).
6. W. G. Pfann, "Zone Melting", John Wiley & Sons, New York (1958).

Environmental Factors Affecting the Critical Pitting Potential of Aluminum

H. Böhni and H. H. Uhlig*

Department of Metallurgy and Materials Science, Massachusetts Institute of Technology, Cambridge, Massachusetts

ABSTRACT

The critical pitting potential determined potentiostatically of pure Al in 0.1*N* NaCl is —0.40V (SHE). This value is not greatly sensitive to temperature (0-40°C), to small alloying additions of Mn or Mg, nor to thickness of oxide film produced by anodizing. The value is more active the higher the Cl^- concentration, but becomes more noble with additions to NaCl of nitrates, chromates, acetates, benzoates, or sulfates. The latter act as pitting inhibitors which are effective in the order as listed. Dissolved Cu^{++} in trace amounts deposit on the Al surface as Cu which then acts as an efficient cathode, shifting the corrosion potential of aluminum to the critical pitting potential. Trace amounts of Fe^{+++} and Pd^{++} act similarly. Anodized surfaces effectively retard penetration of the oxide by Cu^{++} thereby delaying onset of pitting, but they are not similarly effective when Al is coupled to Cu. The mechanism of pitting is interpreted in terms of competitive adsorption of Cl^- with oxygen for sites on the metal surface. Extraneous anions compete in turn with Cl^- ions, making it necessary to shift the potential in the positive direction in order for Cl^- to adsorb followed by pit initiation. Similarities in adsorption parameters of various anions other than Cl^- on Al and 18-8 stainless steel are pointed out.

Precise determination of the critical pitting potential of Al was first carried out by Kaesche (1) using both potentiostatic and galvanostatic techniques. He found that the potential above which, but not below, Al undergoes pitting corrosion in 1*M* NaCl is —0.48V [std. H_2 scale (SHE)] which value is independent of *p*H between the interval *p*H 2-11. He also reported that the critical potential becomes more active (more negative) the higher the NaCl concentration between 0.1-4.0*M* NaCl. Bond *et al.* (2) measured the critical pitting potential for zone-refined Al in 0.5*M* NaCl in approximate agreement with the corresponding value reported by Kaesche.

Leckie and Uhlig (3) pointed out that the cathodic protection of aluminum, as usually practiced in aerated saline media, consists of polarizing Al only below the critical pitting potential and not below the open-circuit anode potential as is required for steel. In principle, therefore, zinc is a possible sacrificial anode for this purpose, but not iron. For stainless steels, on the other hand, pitting corrosion can be avoided in saline media such as sea water by coupling either iron or zinc, since either metal succeeds in polarizing the alloy below its critical pitting potential (0.21V).

In view of the importance of the critical potential to the application of Al to saline environments, data are reported herewith on the effect of temperature, of various anions and cations, of some alloying elements and of inhibiting salt concentrations on observed values. In addition, the mechanism of accelerated pitting by traces of Cu^{++} is discussed.

Experimental

For most of the measurements, 99.99% Al electrodes were employed measuring 1.5 cm long and 0.4 cm in diameter. One end of each electrode was drilled and tapped, allowing a threaded member attached to a nickel wire to hold the electrode firmly against a glass tube separated by a water-tight Teflon gasket. Only the electrode surface, totally immersed, Teflon, and glass made contact with the electrolyte. Specimens were polished to 3/0 emery paper followed by pickling in 2*N* NaOH at 80°C for 5 min and then washing in distilled water. A few measurements were also carried out on 99.4% Al and on alloys of 1.3% Mn-Al and 2.4% Mg-Al all of which were supplied by courtesy of the Aluminum Company of America.

The all-glass cell as previously described (3) was placed in an air thermostat maintained at 25° ± 0.2°C. Temperatures could also be maintained at some value above or below room temperature. At 0°C, the glass cell was placed additionally in a water-ice bath. The electrolyte was deaerated before measurements by bubbling through it purified N_2 previously passed over Cu turnings at 400°C.

The procedure was to polarize the electrode anodically within the passive region for 5 min at —0.80V *vs.* saturated calomel electrode (SCE) or —0.56V (SHE) using a Wenking potentiostat in conjunction with a chart recorder. This procedure achieved steady-state conditions before a step-by-step technique was applied by which the potential was increased 50 mV every 5 min and the corresponding current noted. The current remained relatively constant below the approximate critical potential V'_c (<1 $\mu A/cm^2$), but increased sharply above by two or more orders of magnitude. These measurements in turn were supplemented by longer time runs maintaining a given potential near the critical value for at least 12 hr. The least noble value at which pits could not be observed under a low-power microscope was taken as the steady-state critical potential V_c. Reproducibility of steady-state values was better than ±15 mV. All potentials are reported with reference to the SHE.

As a check on some of the critical pitting potentials obtained as described, immersion tests were also run using pickled specimens of 99.4% Al measuring 1½ x ½ x 0.065 in. (3.8 x 1.3 x 0.17 cm). These were suspended by means of a nylon thread through a hole drilled in one end of the specimen and then placed in closed 250 ml flasks for a period of 1-14 days. After the test period, the number of pits on the two main faces of the specimen, visible under a low-power microscope, was counted.

Results

Effect of temperature.—Temperatures between 0° and 40°C were found to have very little effect on the critical potential V_c as results of Fig. 1 show. These data are in contrast to the critical potentials for 18-8 stainless steel in 0.1*M* NaCl which are 0.6V more noble at 0°C than at 25°C (3). In other words, 18-8 stainless

* Electrochemical Society Active Member.

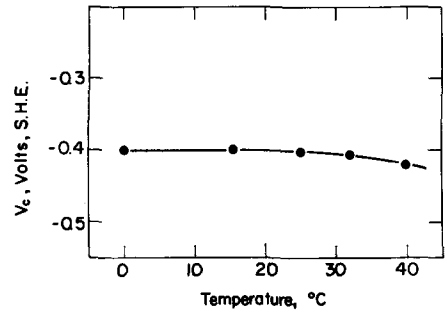

Fig. 1. Critical pitting potentials of 99.99% Al in 0.1M NaCl as a function of temperature.

steel is much more resistant to pitting corrosion at low temperatures compared to room temperature, but susceptibility of aluminum is about the same. This temperature effect refers only to initiation of pits and not to rate of pit growth. Size of pits after a given time depends on the cathodic reaction rate, the latter in turn usually proceeding more rapidly the higher the temperature.

Effect of anion concentration and alloying.—It is known that pitting of Al is pronounced in presence of chloride ions. In sulfates, on the other hand, Al electrodes can be polarized anodically without exhibiting a critical pitting potential or showing any evidence of pitting attack. In perchlorate solutions, however, pitting occurs, as well as in bromide and iodide solutions, although the pitting tendency is less pronounced than in chloride solutions.

The respective steady-state critical potentials in each environment are listed in Table I including the value in 0.5*M* NaCl reported by Bond *et al.* (2) and the nonsteady-state values reported earlier by Kaesche (1). The more active the critical potential, the greater is the tendency for pitting to occur. The effect of temperature is small in either 0.1*M* NaCl or NaBr.

Alloys of Al containing a small amount of Mg or Mn tend to pit more than does pure Al, although the shift of potential is small. For 99.4% Al, the critical potential is the same as for 99.99% Al within experimental error of the measurements. Porter and Hadden (4) reported that immersion tests in various supply waters showed that superpure Al tended to pit somewhat less than did Al alloys, although the final pit depth was almost the same.

Added anions which do not of themselves cause pitting shift the critical potential of Al in halide solutions in the noble direction corresponding to improved corrosion resistance. This was shown previously to be true for stainless steels (3, 5). If extraneous salts are added in amount sufficient to shift the critical potential above the oxygen electrode potential in air approximating 0.8V, it is obvious that aluminum will no longer pit in an aerated solution of the electrolyte mixture since the corrosion potential cannot exceed the open-circuit cathode potential. Pitting could then occur only under conditions where passivity breaks down locally, such as in a crevice due to lack of oxygen and to high concentrations of chloride ion caused by electrochemical transport, or to decrease of *p*H caused by accumulation of $AlCl_3$. Pitting otherwise would not be expected below the critical potential in any period of time for a crevice-free passive surface avoiding environmental gradients of the kind mentioned

Table I. Steady-state critical pitting potentials, V_c, vs SHE

	Electrolyte	25°C	0°C
99.99% Al	0.1*M* NaCl	−0.40 V	−0.41 V
	0.1*M* NaBr	−0.29	−0.32
	0.1*M* $NaClO_4$	0.0	
	0.5*M* NaCl [Bond *et al* (2)]	−0.50	
	1*M* NaCl [Kaesche (1)]	−0.48*	
	1*M* KBr [Kaesche (1)]	−0.35*	
	1*M* KI [Kaesche (1)]	−0.20*	
99.4% Al	0.1*M* NaCl	−0.41	
1.3% Mn-Al	0.1*M* NaCl	−0.45	
2.4% Mg-Al	0.1*M* NaCl	−0.44	

Metal analysis

	%Cu	%Si	%Fe	%Mn	%Mg	%Cr
99.99% Al	0.0039	0.0016	0.0007	—	0.0005	—
99.4% Al	0.1	0.08	0.48	0.004	0.0004	0.002
1.3% Mn-Al	0.006	0.002	0.002	1.3	0.001	—
2.4% Mg-Al	0.04	0.08	0.16	0.02	2.43	0.23

* Values approximate but are not truly steady-state values.

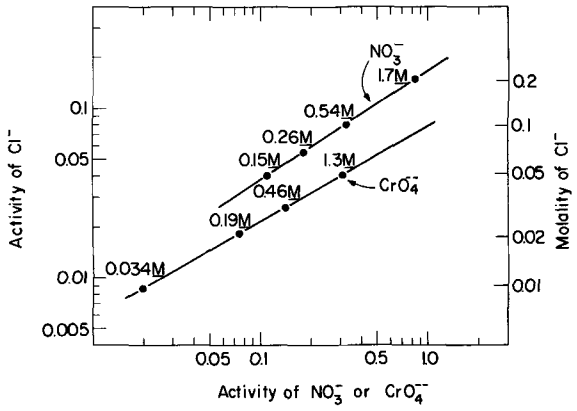

Fig. 2. Relation of minimum activities (or concentrations) of sodium nitrate or of sodium chromate required to inhibit pitting of 99.99% Al in aerated sodium chloride solutions.

It was shown earlier for stainless steels that the logarithm of the activity of an extraneous anion necessary to shift the potential to an arbitrary noble value accompanied by inhibition of pitting in aerated solutions, is linear with the logarithm of the corresponding chloride ion activity. This relation is also found to hold for Al, as is shown by data for sodium nitrate and sodium chromate additions (Fig. 2) and for sodium sulfate, sodium benzoate and sodium acetate additions (Fig. 3), where the critical potential is shifted to 0.8V (SHE) in each case. In calculating ionic activities, the corresponding activity coefficients were taken from Latimer (6) for pure sodium salts omitting corrections for total ionic strength of the solutions. Since activity coefficients for sodium acetate and sodium benzoate were not listed, they were approximated by corresponding values for rubidium acetate at and above 0.1*M* and by NaCl below. Values for Na_2CrO_4 solutions were taken from Robinson and Stokes (7) above 0.1*M* and approximated by values for Na_2SO_4 for the one lower concentration.

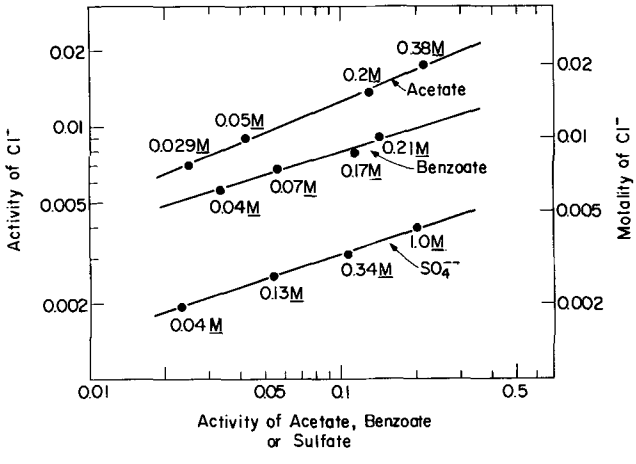

Fig. 3. Relation of minimum activities (or concentrations) of sodium acetate or sodium benzoate or sodium sulfate required to inhibit pitting of 99.99% Al in aerated sodium chloride solutions.

The mixtures of electrolytes were not adjusted to constant pH in view of the fact that both our measurements and those previously reported by Kaesche showed no appreciable effect of pH on the critical potential. Molybdates and tungstates were also tried as inhibiting anions, but these substances were probably reduced to insoluble oxides at the aluminum surface and hence led to irreproducible results. Equations representing inhibiting activities of the various successful anions are as follows:

$$\log (Cl^-) = 0.65 \log (NO_3)^- - 0.78 \quad [1]$$

$$\log (Cl^-) = 0.56 \log (CrO_4^{--}) - 1.11 \quad [2]$$

$$\log (Cl^-) = 0.41 \log (\text{acetate}^-) - 1.50 \quad [3]$$

$$\log (Cl^-) = 0.30 \log (\text{benzoate}^-) - 1.80 \quad [4]$$

$$\log (Cl^-) = 0.31 \log (SO_4^{--}) - 2.19 \quad [5]$$

Accordingly, the efficiency of inhibition within the present chloride concentration range decreases in the order: NO_3^- > CrO_4^{--} > acetate > benzoate > SO_4^{--}.

Effect of heavy metal ions.—It is well known that traces of Cu^{++} greatly accelerate the pitting of Al exposed to potable or industrial waters. Water passing through copper or brass piping, for example, picks up sufficient Cu^{++} to damage Al surfaces downstream. The mechanism of accelerated pitting is apparently, first, the deposition of metallic Cu on the Al surface by a replacement reaction, the sites of which act as pit nuclei. Second, the Cu sites become cathodes for the efficient reduction of dissolved O_2 or of any other suitably reducible species in solution, thereby polarizing Al to the critical potential at which anodic corrosion or pitting takes place. The potential reached is slightly more noble than, but does not appreciably exceed the critical value, however vigorous the pit growth, because of the small anodic polarizability of nonpassive Al within the pits (cathodic control). The time required for the shift from corrosion potential to critical potential is about 30 sec for 5 ppm Cu^{++} additions to 0.1*M* NaCl as shown by data of Fig. 4. For 5 ppm Pd^{++} addition, which behaves similarly, the time required is less, and for 5 ppm Fe^{+++} addition the time is longer, but the same critical pitting potential is reached in each case.

The above facts suggest that a suitable approach to measuring critical potentials in a given saline solution is to determine the corrosion potential in presence of a small concentration of Cu^{++}. The relevance of this technique to measuring critical potentials as a function of NaCl concentration is summarized in Fig. 5. As was shown previously for 18-8 stainless steel (3), the critical potentials for Al are linear with logarithm of Cl^- activity. Comparative data obtained by Kaesche using a different technique are included, showing good accord with present measurements. Either set of data follows the equation

$$V'_c \text{ (volts, SHE)} = -0.124 \log (Cl^-) - 0.504 \quad [6]$$

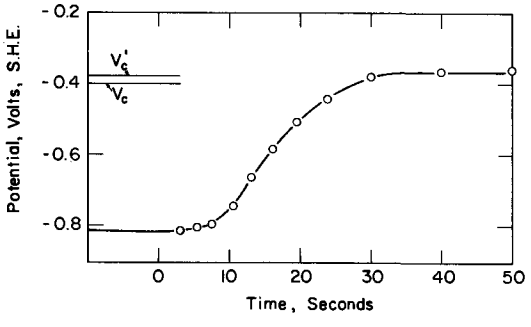

Fig. 4. Change of corrosion potential with time on immersion of 99.99% Al in 0.1*N* NaCl plus 5 ppm Cu^{++}, 25°C. Critical potentials V_c and V'_c are potentiostatic values.

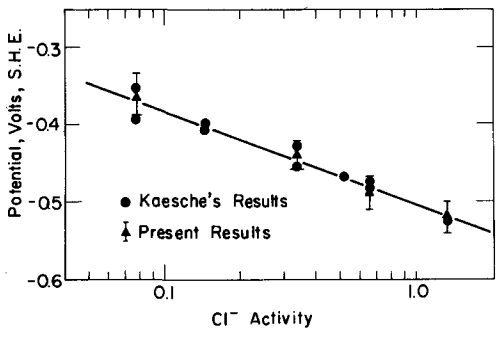

Fig. 5. Corrosion potentials of 99.99% Al in various activities of NaCl containing 5 ppm Cu^{++} in comparison with critical pitting potentials determined by Kaesche.

Since the critical potentials calculated by this equation, for reasons stated earlier, are slightly more noble than the steady state values, they more nearly accord with the continuous polarization values V'_c (continuous shift of potential to more noble values). For example, the critical potential for 0.1*M* NaCl ($\gamma = 0.78$) calculated by the equation is —0.37V compared to the steady-state value —0.40V given in Table I.

The success of the above-described method for measuring critical potentials suggested that the effect of inhibiting anions could also be investigated in like manner. In carrying out such measurements, a higher concentration of Cu^{++} (2.5 x 10^{-3}*M* or 159 ppm Cu^{++}) was found to be advisable in order to stimulate growth of pits that are nucleated at the critical potential, therefore making it easier to count their number. Figure 6, for example, shows that Na_2SO_4 additions to 0.005*M* NaCl shift the resultant critical potentials for Al, as determined potentiostatically, in the noble direction. The equilibrium potential for Cu ⇆ Cu^{++} + 2*e*, on the other hand, corresponding to 2.5 x 10^{-3}*M* $CuSO_4$ is equal to 0.337 + (0.059/2) log (2.5 x 10^{-3} x 0.7) = 0.256V where 0.7 is the approximate activity coefficient of the $CuSO_4$ solution (6). The calculated potential is relatively insensitive to the actual value chosen for the activity coefficient. Hence if the electrolyte is deaerated with nitrogen, Cu^{++} reduction is the only relevant cathodic reaction and pitting is therefore expected only below a SO_4^{--} activity of 0.02 corresponding to 0.035*M* Na_2SO_4. To check this prediction, specimens of 99.4% Al (same approx. critical potential as pure Al) were immersed in 0.005*M* NaCl containing various additions of Na_2SO_4 plus 2.5 x 10^{-3}*M* $CuSO_4$, the results of which are shown in Fig. 7. Many of the pits, when observed after an immersion period of 24 hr, were localized on the speci-

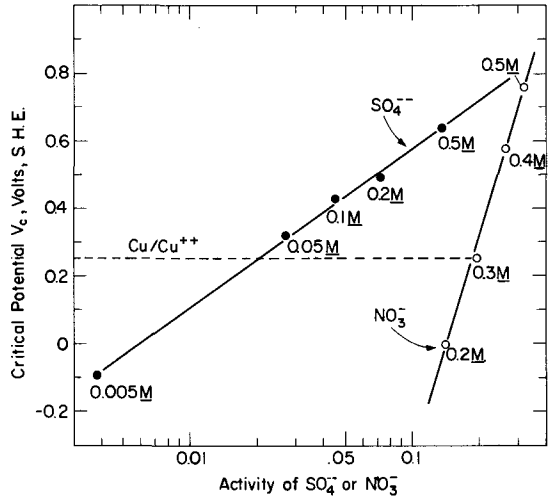

Fig. 6. Critical pitting potentials, determined potentiostatically, of Al in 0.005M NaCl with Na_2SO_4 additions, and in 0.1M NaCl with $NaNO_3$ additions, 25°C.

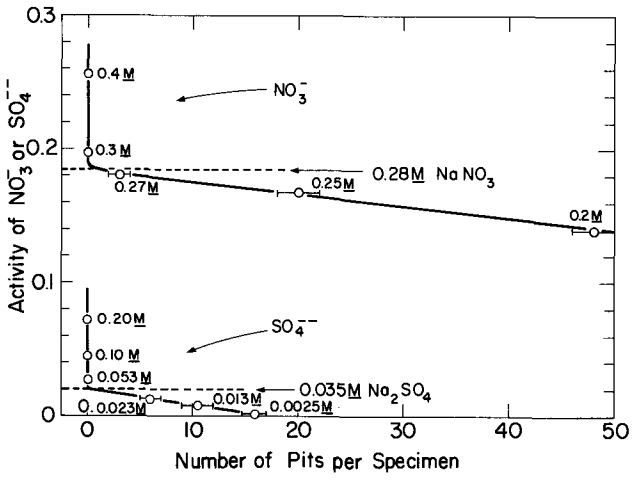

Fig. 7. Number of pits per specimen after immersing 99.4% Al in 0.005M NaCl with Na_2SO_4 additions, and in 0.1M NaCl with $NaNO_3$ additions, 24 hr, 25°C.

men edges, but for convenience only those were counted on the two main faces. When pitting was not observed on either face or edges, the test was usually continued beyond 24 hr to the order of two weeks so as to confirm that no pitting had taken place.

As the results show, the intersection of the line connecting points for the Na_2SO_4 concentrations which induce pitting, with the line for zero pitting occurs at an activity of SO_4^{--} equal to 0.02. This value agrees with the inhibiting activity predicted by data of Fig. 6. Similar good agreement was found between predicted and observed inhibiting concentrations of $NaNO_3$ added to 0.1*M* NaCl (Fig. 6 and 7).

The amount of extraneous salt needed to inhibit pitting depends on the applied potential as data of Fig. 6 show. Hence the amount of sulfate which is required to inhibit pitting in presence of Cu^{++} at a cathode potential of 0.26V is less than that required in presence of dissolved air at 0.8V. The latter situation is described by Fig. 3.

Effect of cations.—Since anions have a large effect on the critical potential, it is of interest to know whether the type and valence of cations also have an influence. The effect of calcium ion was investigated by measuring through continuous potentiostatic polarization curves the critical potentials of 99.99% Al in 5 concentrations of $CaCl_2$ from 0.05 to 1.0*M*. The dependence of the critical potential V'_c on logarithm of chloride ion activity followed the same linear equation within expected experimental variations as that derived for NaCl (Eq. [6]). Hence it is concluded that a divalent cation like Ca^{++} has no special effect on the critical potential compared to a monovalent ion like Na^+. Subsequent measurements were carried out in 0.1*N* KCl, RbCl, CsCl, $SrCl_2$, $BaCl_2$, and $LaCl_3$. Observed steady-state critical potentials corrected to the same approximate Cl^- activity, using the equation cited above, were all the same within less than 20 mV, hence only the Cl^- activity appears to be important. However, continuous polarization runs (50 mV/5 min) gave nonsteady-state critical potentials for $BaCl_2$ and CsCl which were about 70 mV more noble than for the other chlorides listed above. Although this peculiar effect of Ba^{++} and Cs^+ was not investigated further, it is perhaps caused by the double layer reaching its equilibrium structure much slower when large cations like Ba^{++} and Cs^+ are involved compared to the situation for smaller cations.

Discussion

The critical potential has been explained in terms of Cl^- penetrating an oxide film which covers the metal surface (8, 9) or in terms of competitive adsorption of Cl^- and oxygen for sites on the metal surface (3, 5). Aluminum provides an excellent opportunity to evaluate the influence of an oxide film because of the well-established procedure for increasing oxide film thickness by anodizing. The thicker the oxide film, presumably the smaller is the electric field impelling Cl^- to penetrate it and the longer is the diffusion path of Cl^- from electrolyte to metal surface. These factors, if relevant, should combine to produce a more noble critical pitting potential. On the other hand, if competitive adsorption at the metal surface is the mechanism, the thickness of any overlying oxide film would have no bearing on the steady-state potential at which Cl^- displaces adsorbed oxygen.

Aluminum specimens of 99.99% purity were anodized in 15% H_2SO_4 at 25 mA/cm² for specific times, then washed and sealed in distilled water at 90°C for ½ hr. Thickness of oxide produced by anodizing was estimated from values reported by Hoar and Wood (10). Steady-state critical potentials were determined by potentiostatic polarization in 0.1*M* NaCl. Although continuous polarization runs showed a slightly more noble value (—0.33V) for anodized electrodes, the same steady-state value —0.39V was obtained both for an oxide film 0.3 and 1.4μ thick, compared to —0.40V for aluminum not anodized. The latter values are the same within the usual experimental variations of such measurements. They support the view, therefore, that the mechanism of competitive adsorption is in better accord with the facts, and they also provide evidence that any improved resistance of anodized aluminum to pitting corrosion does not result from a shift of the critical potential.

Davies (11) reported improved resistance to pitting corrosion of anodized aluminum immersed in a solution containing 30 ppm Cl^-, 40 ppm Ca^{++}, and 0.2 ppm Cu^{++}. No pits appeared in two weeks time, contrary to unanodized specimens which pitted in a much shorter period. These results suggest that the anodized oxide film is a good diffusion barrier to Cu^{++} ions even though it is not successful in preventing diffusion of Cl^- ions. This matter was checked by anodizing 99.99% Al specimens to a film thickness of 1.4μ and sealing in H_2O at 90°C for 1 hr. They were then immersed in 0.1*M* NaCl containing 2.5 x 10^{-3}*M* Cu^{++} at 25°C. Two specimens were coupled to an equal area of copper; these showed evidence of pitting after 2 hr, with many deep pits visible after 24 hr. Two specimens not coupled were free of pits after 24 hr, in line with Davies' longer time observations.

The above results show therefore that Cu^{++} must penetrate the oxide film in order to deposit suitable cathodic sites of metallic Cu before pitting is observed in short-time tests. To this end, anodized Al is better than unanodized Al. They also show that anodized films have no particular merit in preventing pitting corrosion whenever aluminum is coupled to a more cathodic metal like Cu.

The high-temperature coefficient of the critical potential for austenitic stainless steels reported previously (3, 12) was attributed to sensitivity of the double layer structure to temperature, caused perhaps by variable hydration of the passive film and of ions located within the double layer. A negligible temperature effect for Al suggests that it is not the temperature-sensitive hydration of ions that is important so much as the temperature-sensitive hydration and structure of the passive film in the case of 18-8, and the absence of such an effect for the passive film on Al.

The role played by various cations is not important, probably because characteristically they do not adsorb at prevailing potentials, and hence their effect on the double layer and on passive film structure is minimal. The behavior of extraneous anions to inhibit pitting is similar to the behavior noted previously for 18-8 stainless steel for which inhibiting efficiency, as for Al, decreases in the order $NO_3^- > Ac^- > SO_4^{--}$. The data for inhibition of 18-8 by NO_3^- and SO_4^{--} were previously reported by Leckie and Uhlig (3); for acetates the data were presently obtained using the same

Table II. Ratios of n appearing in Freundlich adsorption isotherm

	Observed ratios			Calc. ratios		
	$n_{Cl^-}/n_{NO_3^-}$	$n_{Cl^-}/n_{SO_4^{--}}$	n_{Cl^-}/n_{Ac^-}	$n_{SO_4^{--}}/n_{NO_3^-}$	$n_{Ac^-}/n_{NO_3^-}$	$n_{SO_4^{--}}/n_{Ac^-}$
18-8	1.88	0.85	1.12	2.21	1.68	1.32
Al	0.65	0.31	0.41	2.10	1.59	1.32

potentiostatic technique and the same stainless steel as was used formerly. The equation representing activity of acetate necessary to inhibit pitting of 18-8 in a given activity of Cl^- ranging from 0.05 to 0.2M NaCl is

$$\log(Cl^-) = 1.13 \log (Ac^-) + 0.06 \quad [7]$$

The above log-log relationship was derived by Matsuda and Uhlig (13) on the basis of the Freundlich adsorption isotherm; $a_1 = k_1$ (Anion)$^{1/n_1}$ where (Anion) is the anion activity in solution, a_1 is the quantity of anion adsorbed per unit area, and k_1 and n_1 are constants. It was shown that the coefficient of the log (Ac^-) term in the above Eq. [7] is then equal to n_{Cl^-}/n_{Ac^-}. The values of this ratio are in general larger for 18-8 than for Al, corresponding to a greater tendency for Cl^- to adsorb on Al than on 18-8. Interestingly, the ratio of n's for any pair of ions not involving Cl^- are similar for both Al and 18-8. This is shown by the derived values listed in Table II. For example, $n_{SO_4^{--}}/n_{NO_3^-}$ obtained by dividing $n_{Cl^-}/n_{NO_3^-}$ by $n_{Cl^-}/n_{SO_4^{--}}$ is 2.21 for 18-8 and 2.10 for Al. The similarity of these ratios for anions other than Cl^- point to the unique adsorption behavior of Cl^- which is also the anion among those presently considered which is responsible for observed pitting corrosion.

Acknowledgment

The authors are pleased to acknowledge support of this research by the Office of Saline Water, U.S. Department of the Interior. One of the author's (H.B.) is furthermore grateful for a travel grant awarded by Stiftungen auf dem Gebiete der Chemie, Basle, Switzerland.

Manuscript submitted Oct. 17, 1968; revised manuscript received *ca.* Jan. 28, 1969. This was Paper 388 presented at the Montreal Meeting, Oct. 6-11, 1968.

Any discussion of this paper will appear in a Discussion Section to be published in the June 1970 JOURNAL.

REFERENCES

1. H. Kaesche, *Z. physik. Chem. N.F.*, **34**, 87 (1962).
2. A. Bond, G. Bolling, and H. Domian, *This Journal*, **113**, 773 (1966).
3. H. Leckie and H. Uhlig, *ibid.*, **113**, 1262 (1966).
4. F. Porter and S. Hadden, *J. Appl. Chem. (London)*, **3**, 385 (1953).
5. Y. Kolotyrkin, *Corrosion*, **19**, 261t (1963).
6. W. Latimer, "Oxidation Potentials," Prentice-Hall, New York (1952).
7. R. Robinson and R. Stokes, "Electrolyte Solutions," p. 486, Academic Press, New York (1955).
8. M. Streicher, *This Journal*, **103**, 375 (1956).
9. T. Hoar, D. Mears, and G. Rothwell, *Corrosion Sci.*, **5**, 279 (1965).
10. T. Hoar and G. Wood, *Electrochim. Acta*, **7**, 333 (1962).
11. D. Davies, *J. Appl. Chem. (London)*, **9**, 651 (1959).
12. J. Horvath and H. Uhlig, *This Journal*, **115**, 791 (1968).
13. S. Matsuda and H. Uhlig, *ibid.*, **111**, 156 (1964).

Electrochemical Ellipsometric Study of Gold

R. S. Sirohi and M. A. Genshaw

Electrochemistry Laboratory, University of Pennsylvania, Philadelphia, Pennsylvania

ABSTRACT

The application of ellipsometry and electrochemical techniques to the oxidation of gold reveals that a chemisorbed species is formed in the potential region 0.2-1.1V *vs.* SCE in acidic solution with gold oxide formed at more anodic potentials. In alkaline solution the chemisorbed species formed in the potential region −0.8 to +0.2V *vs.* SCE with oxide formation at more anodic potentials. Evidence supporting a change in the optical properties of the oxide film with pH and, for alkaline solution, with the presence of chloride ions, is presented.

The electrochemical oxidation of gold has been a topic of interest for many years (1-11). This oxidation leads to the formation of chemisorbed oxygen (1, 5, 7) or gold oxide (1-6, 8-10) with the initial formation of this film occurring about 1.27-1.37V (1, 3, 4, 7-10) *vs.* a reversible hydrogen electrode (RHE). Reduction of the film commences at potentials between 1.2 and 1.37V (4, 6-8, 9, 10) *vs.* RHE. The potential of oxidation and reduction varies by −2.3 RT/F (3-5, 8, 9) per unit pH. The thickness of the film is of the order of a monolayer, but at potentials more anodic than 1.8 (7, 10) −1.95V (8), a thick oxide film forms.

Inflections in charging curves, which could not be reproduced by later workers (5-10), were attributed to successive formation of Au_2O, AuO, and Au_2O_3 (4). Two arrests in film reduction have been attributed to Au_2O_3 and AuOH or AuO (2, 12).

In acidic chloride solutions passivation is observed, with the passivation time dependent on the concentration of chloride (13-17), indicating that passivation occurs when the surface concentration of chloride approaches zero.

An ellipsometric study of gold oxidation in sulfuric acid solutions, some with added oxalate, has been reported (18).

To gain further insight into the nature of the film formed at gold on electrochemical oxidation, this study, which combines optical and electrochemical measurements, was initiated.

Ellipsometry is the measurement of changes introduced in the polarization state of light by reflection from metal or metal oxide surface. The reflected light is analyzed for its polarization state, giving the relative phase retardation Δ and relative amplitude di-

minution ψ. Δ and ψ are related to the complex refractive index n^*_F and thickness L_F of film by the film optics equation (19, 20). The methods of analysis are adequately described by other authors (21-24) and need not be repeated here.

Experimental

Apparatus.—Ellipsometer.—For the steady-state measurements a Gaertner L119 Ellipsometer with horizontal plane of incidence was used along with a He-Ne laser as the source of monochromatic light. The output of the laser was converted to circularly polarized light by a waveplate prior to the polarizer. A quarter waveplate was used in the fixed 45° orientation and was positioned between the polarizer and the cell. A photomultiplier was used as the light detector.

For the transient measurements the source was changed to a 2w tungsten arc lamp (Sylvania Type C2T) filtered at 5500Å (50Å bandwidth) and a phototransistor (Motorola MRD 300) was used as a detector to maximize the signal-to-noise ratio by eliminating photomultiplier noise and minimizing the source noise. The angle of incidence at the electrode surface was 72.53°.

Cell.—The airtight cylindrical cell was made of Teflon. The light passed obliquely through synthetic quartz windows ($n = 1.457$, $\lambda = 6328$Å) which were fitted in the cell. All the connections to the cell were made through Beckman joints. Prepurified nitrogen which was further purified to get rid of organic impurities, etc., was bubbled through the electrolyte.

Electrolyte.—Acidic solutions were made from purified H_2SO_4. The H_2SO_4 was purified by adding a few drops of 30% H_2O_2 in 50 cc of H_2SO_4 and heating it for 10 min around 60°C (25). The alkaline solutions were made from NaOH, and NaCl solution was added for chloride solutions. All solutions were made from conductivity water. The acidic solutions were pre-electrolyzed by two platinized platinum electrodes with an applied potential difference of 1.35V for at least 24 hr. No pre-electrolysis was used with alkaline and chloride solutions. All experiments were carried out at room temperature.

Electrode.—The working electrode used was in the form of a block, which was polished bright and flat with different grades of emery. The counterelectrode was a smooth platinum electrode. A saturated calomel electrode was used as the reference electrode. All potentials are reported with respect to SCE.

Potential staircase measurements.—In these measurements the potential was varied in steps of 0.1V with measurements of Δ and ψ begun after 15 min.

Potential step measurements.—In these measurements the potential was varied in a single step between two values with simultaneous measurement of the intensity time and current time transient or the intensity time and charge time transients.

Potential sweep measurements.—A potential sweep generator (26) was used to vary the potential between two set potentials while the intensity-time and current-time relations were recorded on a Clevite Mark 220 dual channel recorder.

Results and Discussion

Acidic solution.—General behavior in acidic solution.—In acidic solution, the plot of Δ against potential as the potential is made more anodic in a potential staircase measurement exhibits two regions (Fig. 1): a region of slow change between 0.0 and 1.10V, and a region of rapid change anodic to 1.10V as also observed by Reid and Kruger (18). A similar trend is observed in the apparent capacity[1] of the electrode (Fig. 2).

[1] The apparent capacity was estimated from the charging current in the potential sweep measurements. It was corrected for a steady-state background current of 2 μA/cm^2 due to residual oxygen, but will include contributions due to any other faradaic processes. It should not be compared to the differential capacity measurements of other workers (12, 27, 28) whose measurements exclude any effect of faradaic processes.

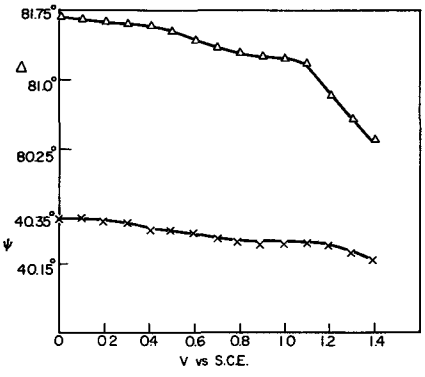

Fig. 1. Δ and ψ vs. potential for gold in 1*N* H_2SO_4 at 6328Å, potential staircase measurements.

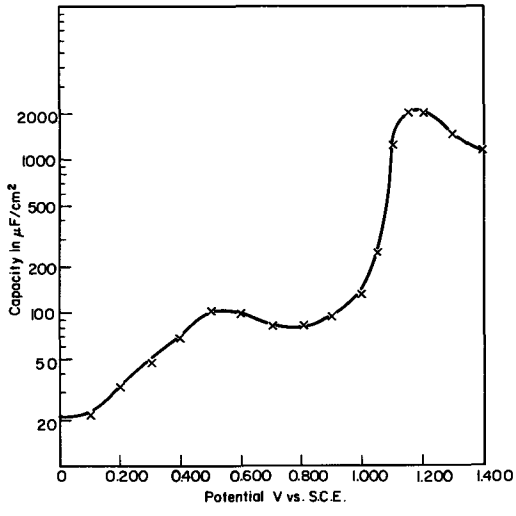

Fig. 2. Apparent capacity for gold in 1*N* H_2SO_4

Accordingly, the discussion will consider each region in turn.

The region between 0.0 and 1.1V.—At the most cathodic potentials the changes in Δ and ψ with potential are the least (cf. also Fig. 5), and the measured apparent capacity of ~20 μF/cm^2 is characteristic of the double layer capacity of a bare surface. Thus, we conclude that the bare gold surface is stable in this potential range. The optical constants calculated for gold at 6328Å are $(0.236 - 3.504i)$, which compare satisfactorily with $(0.18 - 3.48i)$ (29, 30).

As the potential is made more anodic, appreciable changes in Δ (>0.3°) occur. These changes are much greater than the experimental sensitivity (~0.02°) and so must reveal a real phenomenon. The apparent capacity (Fig. 2) shows an appreciable increase over the value observed at more cathodic potentials, indicating that charge is consumed as the potential is changed in this region.

Qualitatively similar results have been obtained in coulometry by other workers (2, 4, 8, 12) as well as changes in differential capacity (12, 27, 28). These have been attributed to the formation of AuOH or AuO (called "chemisorbed oxygen") (12, 27, 31). Thus it seems likely that a chemisorbed oxygen species is formed at gold in this potential region which is "seen" by ellipsometry.

Impurity explanations seem untenable because similar (except for kinetic effects, cf. below) results are obtained in transient and steady-state results with no evidence of diffusion control characteristic of impurities present at low concentrations.

The adsorption of anions which has been determined at other metals (32) is unlikely as a cause for the changes in Δ because the changes in Δ are larger than those characteristic of anion adsorption as observed

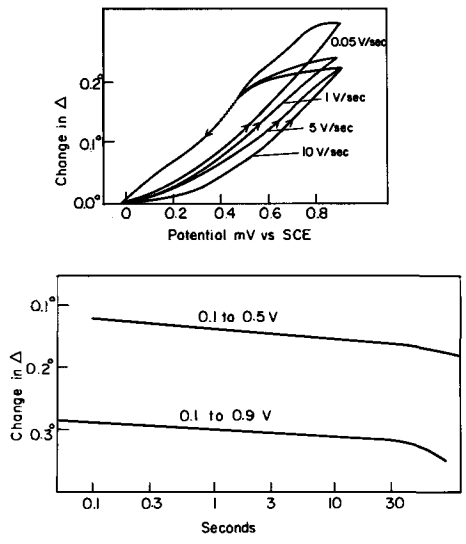

Fig. 3. Kinetics of formation of adsorbed oxygen (5500Å). Potential sweep and potential step measurements.

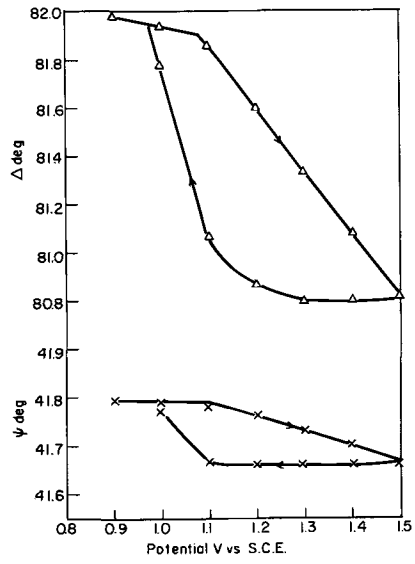

Fig. 4. Δ and ψ vs. potential in oxide region (6328Å), potential staircase measurements.

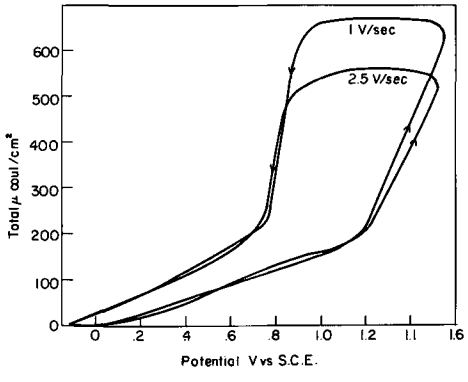

Fig. 5. Charge passed as function of potential in potential sweep measurement.

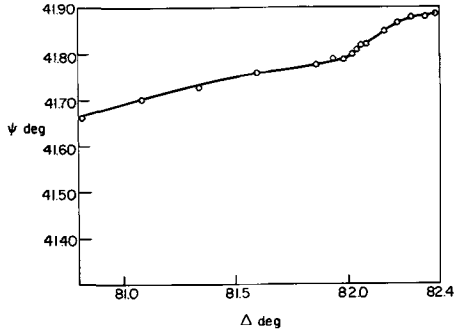

Fig. 6. ψ vs. Δ Plot. Au in H_2SO_4 at 6328Å

for Pt and Hg (32). Also, similar changes (except for a shift due to the *p*H differences) are observed at gold in 0.5*N* NaF which does not give detectable changes in Δ due to anion adsorption at platinum and mercury (32) (Fig. 3).

If one presumes the changes in Δ and ψ observed are due to "adsorbed oxygen," one can calculate the optical constants of the film by using coulometry. Using the relation between charge and potential of Fig. 5 and Δ and potential of Fig. 1, one obtains a charge of 250 μcoul/cm² to produce a change of 1° in Δ. Assuming a roughness factor of 1.7, the true amount of charge required to produce a 1° change in Δ is 150 μcoul/cm². If one takes 190 μcoul/cm² (7) as equivalent to a monolayer (univalent species), a change of 1.26° in Δ is equivalent to a monolayer. Assuming a monolayer is 3Å thick, using the exact ellipsometric equations, the only fit found is for film optical constants of about 0.3 — 0.7*i*. This value of optical constant seems improbable for any adsorbed species and would be more consistent with a metallic layer. Gold has been reported to show changes in optical constants upon application of an electric field (33) and would also be expected to be sensitive to adsorbed layers.

To attribute the observed changes in Δ and ψ solely to field induced changes in the metal optical constants is inconsistent with the observed kinetics in the Δ change. Changes occurring inside the metal should occur in the time required for double layer relaxation, $\sim 10^{-8}$ sec. The relatively slow changes observed are consistent with a slow chemisorption of a species which induces changes in the metallic optical constants producing the observed Δ and ψ changes (34).

Phase oxide growth.—At potentials anodic to 1.10V in acid and 0:200V in alkaline solution, Δ and ψ decrease linearly with potential (Fig. 4). The number of coulombs consumed in oxidation of the surface also increases linearly with potential (7-9) (Fig. 5). A hysteresis loop is observed in the graphs for film formation and reduction by both ellipsometric and coulometric methods.

This film is apparently a phase oxide. Evidence supporting this view is that more than a "monolayer" of film can be formed, that the film reduction occurs in a potential plateau characteristic of a definite phase, and that the potential for initial formation and reduction lies near that observed for the oxide Au_2O_3 (35). Also, at potentials anodic to 2.0V, a thick film forms which has been shown by chemical analysis to be Au_2O_3 or hydrated Au_2O_3 (28).

The oxide film at gold is light-absorbing, as it is not possible to fit the experimental positive slope of $d\psi/d\Delta$ (Fig. 6) for any transparent film. The absorption may arise from one of several factors. The film is probably semiconducting (11) and thus would absorb light by exciting electrons from the valence band to the conduction band. It is also possible that the absorption is due to the presence of charges in the film induced by "double layer" effects (36). It is also possible to have absorption due to the excitation of charges from the conduction band of the metal to the conduction band of the oxide.

For very thin films as observed in this work, if one assumes the film optical constants are independent of thickness, the film thickness is a linear function of Δ within the precision of the measurements. Then, from the measured values of Δ as a function of time, plots of Δ *vs.* log *t* (direct logarithmic law) (Fig. 7) and $1/\Delta$ *vs.* log *t* (inverse logarithmic law) (Fig. 8) may be made. Linearity is observed for the direct

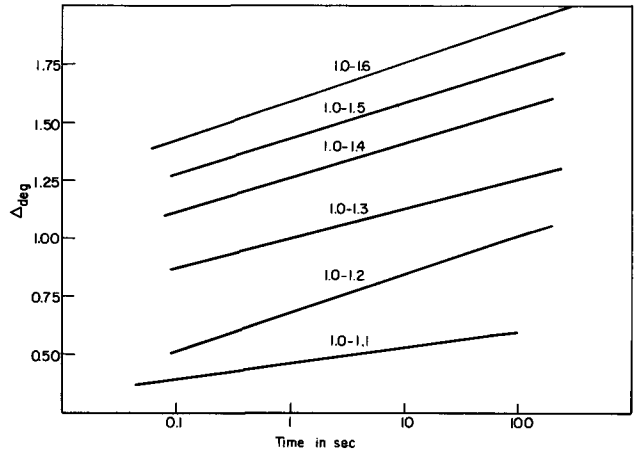

Fig. 7. Direct logarithmic plot of Δ in potential step measurement at 5500Å.

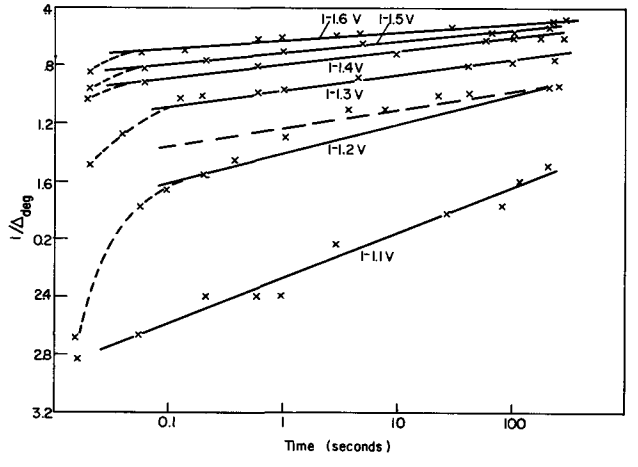

Fig. 8. Inverse logarithmic plot of Δ in potential step measurement at 5500Å.

logarithmic plot. Unfortunately, the data deviate from each growth law so that a distinction between them cannot be made (the slopes of the direct log plot decrease systematically from 0.164 deg/decade at 1.6V to 0.132 at 1.2V to 0.063 at 1.1V). Also, a plot of the value at Δ at time t (Δ_t) after the potential step is applied *vs.* V (Fig. 9) is not linear, as would be expected for mechanisms predicting the direct logarithmic law (as well as the inverse logarithmic law).

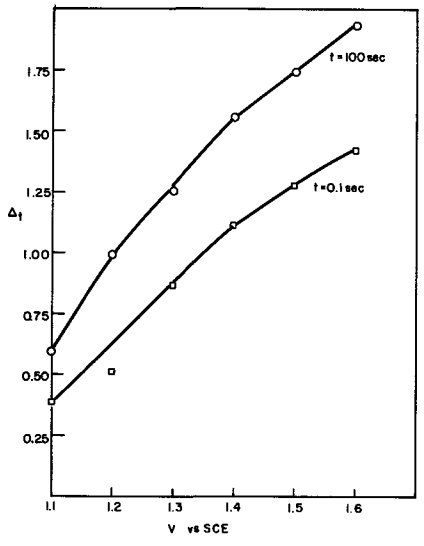

Fig. 9. Plot of Δ at constant time from potential step measurements.

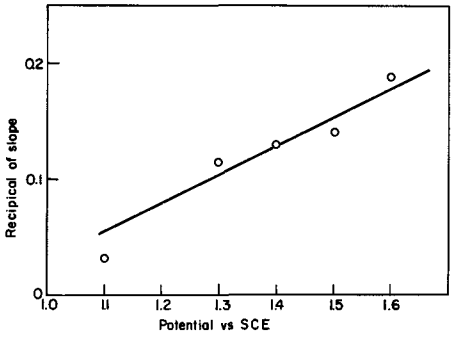

Fig. 10. Plot of the reciprocal of the slope of the inverse logarithmic plots as a function of potential.

Moreover, the fit for the inverse logarithmic law is not good at 1.2V, with considerable curvature observed. However, the reciprocal of the slopes (Fig. 10) does vary linearly with potential, as predicted from growth mechanisms producing the inverse logarithmic law; and the intercepts of Fig. 9 are scattered only 0.1 log units for 1.6-1.3V (a constant is expected for the intercept).

These measurements do not apply to the thick oxide film which forms at more anodic potentials and grows linearly with time (10).

It seems probable that for these films of only a few layers thickness, the kinetic laws suggested either do not apply or the changes in kinetics from a bare surface to a bulk oxide surface are sufficient to mask the true kinetic law.

Results in alkaline solution.—In alkaline solution the general shape of the plots of Δ and ψ against potential (Fig. 11) are similar to those in acidic solution except that the potential of oxide formation is shifted by 0.9V due to the pH change. It may be noted that this is somewhat more than expected from the usually observed change of $(2.3\ RT/\mathbf{F})/p\mathrm{H}$ (= 0.68V) for pH-dependent reactions.

The noteworthy differences are that $d\psi/d\Delta$ for the oxide region is 0.19 ± 0.02 in NaOH solution as compared to 0.12 ± 0.02 in H_2SO_4 and that $d\Delta/dV$ = 2.1 deg/volt in NaOH and 2.60 deg/volt in H_2SO_4. Also the value of $dq/d\Delta$ is not the same with 275 μcoul/deg observed in acidic solution and 170 μcoul/deg observed in alkaline. The changes in $d\Delta/dV$ may be attributed to the formation of a thicker film in alkaline solution than in acidic solution for the same change in potential. The changes in $d\psi/d\Delta$ and $dq/d\Delta$ are not explainable as a difference in film thickness alone. For a thin film with constant optical constants,

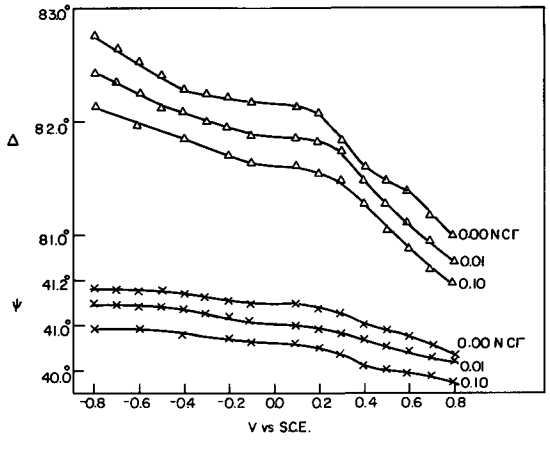

Fig. 11. Plots of Δ and ψ *vs.* potential at 6328Å in chloride containing alkaline solutions. The data in the chloride solutions is displaced vertically for greater clarity.

$d\psi/d\Delta$ is essentially independent of thickness, as shown by computer calculations using the exact ellipsometric equations. Hence, a change in $d\psi/d\Delta$ indicates a change has occurred in the film optical properties. This is supported by the observed changes in $dq/d\Delta$ as a film with constant optical properties should have a constant relation between the amount of film determined coulometrically and the optical thickness, which is not observed for the films in acidic and alkaline solution. The changes in solution refractive index are insufficient to account for the observed changes in $d\psi/d\Delta$ and $dq/d\Delta$. Probably in acid solution the film is Au_2O_3 with a change toward $Au(OH)_3$ occurring in alkaline solution, resulting in a less dense film with a lower refractive index causing a lower $dq/d\Delta$ in alkaline solution. A change in the kinetics of film formation with pH is also observed as the potential of formation is not that expected from a 59 mV/pH dependence and the relation between Δ and potential is different.

Effect of chloride.—In acid solution chloride causes gold dissolution with passivation occurring when the concentration of chloride at the surface approaches zero (13-17). Ellipsometric experiments proved unsuccessful, due to the attack on the surface destroying the reflectivity.

In alkaline solution gold is passive. The ellipsometric measurements show little effect on the trends of the plots of Δ and ψ against potential (Fig. 11). The only appreciable difference is that $d\psi/d\Delta$ for the oxide is lower (0.12) than that obtained without chloride (0.19), possibly showing a change in the optical properties of the film due to incorporation of chloride ions. There is little or no effect in $d\Delta/dV$ or in the potential of oxidation.

Acknowledgment

The authors wish to thank the U.S. Department of the Interior, Office of Saline Water, for their support of this work under Grant No. 14-01-0001-1320. They also thank Professor John O'M. Bockris for encouraging them in this work.

Manuscript submitted Aug. 20, 1968; revised manuscript received *ca.* March 28, 1969.

Any discussion of this paper will appear in a Discussion Section to be published in the June 1970 JOURNAL.

REFERENCES

1. G. Armstrong, F. R. Himsworth, and J. A. V. Butler, *Proc. Roy. Soc.*, **143A**, 89 (1934).
2. G. Deborin and B. Ershler, *Acta Physicochim.*, **13**, 347 (1940).
3. A. Hickling, *Trans. Faraday Soc.*, **42**, 518 (1946).
4. S. E. S. El Wakkad and A. M. Sham El Din, *J. Chem. Soc.*, **1954**, 3098.
5. K. J. Vetter and D. Berndt, *Z. Elektrochem.*, **62**, 378 (1958).
6. D. Clark, T. Dickinson, and W. N. Mair, *Trans. Faraday Soc.*, **55**, 1937 (1959).
7. F. G. Will and C. A. Knorr, *Z. Elektrochem.*, **64**, 270 (1960).
8. H. A. Laitinen and M. S. Chao, *This Journal*, **108**, 726 (1961).
9. S. B. Brummer and A. C. Makrides, *ibid.*, **111**, 1122 (1964).
10. G. Gruneberg, *Electrochim. Acta*, **10**, 339 (1965).
11. F. F. Faizullin and N. P. Nikendrov, *Elektrochim.*, **3**, 988 (1967).
12. G. M. Schmid and R. N. O'Brien, *This Journal*, **111**, 832 (1964).
13. W. J. Shutt and V. J. Stirrup, *Trans. Faraday Soc.*, **26**, 635 (1930).
14. W. J. Shutt and A. Walton, *Trans. Faraday Soc.*, **30**, 914 (1934).
15. G. Armstrong and J. A. V. Butler, *ibid.*, **30**, 1173 (1934).
16. F. P. A. Robinson and F. A. Frost, *Corrosion*, **19**, 115t (1963).
17. G. Just and R. Landsberg, *Electrochim. Acta*, **9**, 817 (1964).
18. W. E. Reid and J. Kruger, *Nature*, **203**, 402 (1964).
19. A. B. Winterbottom, *Kgl. Norske Videnskab. Selskabs Skrifter*, **1955**, 1.
20. J. Kruger and W. J. Ambs, *J. Opt. Soc. Amer.*, **49**, 1195 (1959).
21. E. Passaglia, R. R. Stromberg, and J. Kruger, Editors, "Ellipsometry in the Measurement of Surfaces and Thin Films," Natl. Bur. Stds. Misc. Pub. **256** 1964.
22. J. O'M. Bockris, A. K. N. Reddy, and B. Rao, *This Journal*, **113**, 1133 (1966).
23. A. K. N. Reddy and J. O'M. Bockris, ref. (21), p. 229.
24. J. Kruger and J. P. Calvert, *This Journal*, **114**, 43 (1967).
25. W. Visscher and M. A. V. Devanathan, *J. Electroanal. Chem.*, **8**, 127 (1964).
26. Designed and constructed by B. Cahan.
27. J. P. Hoare, *Electrochim. Acta*, **9**, 1289 (1964).
28. G. M. Schmid and N. Hackerman, *This Journal*, **109**, 243 (1962).
29. C. V. Fragstein and H. Kampermann, *Z. Phys.* (Germany), **173**, 39 (1963).
30. M. Otter, *ibid.*, **161**, 539 (1961).
31. J. P. Hoare, *This Journal*, **110**, 245 (1963).
32. Y. C. Chiu and M. A. Genshaw, To be published.
33. W. N. Hansen, *Anal. Chem.*, **39**, 1057 (1967).
34. W. Hansen, Private communication.
35. F. Jirsa and O. Buryanek, *Z. Elektrochem.*, **29**, 126 (1923).
36. R. C. Plumb, *J. Phys.*, **25**, 69 (1964).

Study of the Lithium Oxide-Nickel Oxide System

I. Thermodynamics of Dilute Solid Solutions

S. Pizzini*, R. Morlotti, and V. Wagner

Reactor Materials Laboratory, Thermochemistry Group, EURATOM CCR, Petten, Netherlands

ABSTRACT

Emf measurements on suitable solid galvanic cells have been carried out to investigate the thermodynamics of solid solutions of Li_2O in NiO. It was shown that in the range of the dilute solutions [0.15-7 a/o (atomic per cent) Li] α — Li_2SO_4 is useful as an intermediate electrolyte. The following cell was operated

$$Pt/NiO,Li_2O(x_2)//\alpha - Li_2SO_4//NiO,Li_2O(x_1)/Pt$$

at temperatures between 570° and 800°C. Results show that the mixture is ideal to 1.5 a/o Li. Deviations from ideality at higher concentrations can be described with purely configurational energy terms.

In spite of many investigations (1-16), the thermodynamic properties of solid solutions obtained by mixing lithium oxide and nickel oxide under a convenient oxidizing gaseous environment are practically unknown. As an extension of our previous work (17) on pure NiO it was indeed felt interesting to investigate these solid solutions over the entire field of their stability.

The solid solutions of Li_2O in NiO are known to be of the substitutional type and have been treated as a binary system, where lithium enters cationic positions and electroneutrality is maintained via an equivalent amount of electron holes.

$$0.5Li_2O + 0.25\,O_2 \rightarrow Li'_{Ni} + O_O + h^{\cdot} \qquad [1]$$

As oxygen gas is needed to maintain the one-to-one ratio between the number of anions and cations, the system is better described by means of the ternary phase diagram of Fig. 1, where NiO, Ni_2O_3, and Li_2O are used as components. It is apparent that the region of the solid solutions with which we deal corresponds to the single-phase field around the line connecting pure NiO with $LiNiO_2$ that expresses a one-to-one correspondence with Li_{Ni} and $Ni^{\cdot}_{Ni}$,[1] *i.e.*, it satisfies the condition for the stoichiometry of the solution. It is also apparent from Fig. 1 and is implied by Eq. [1] that we consider NiO and $LiNiO_2$ as the components of the solid solution.[2] The structure of $LiNiO_2$ derives from that of the solid solution by the substitution of one half of the nickel ions with lithium.

On the line that expresses the stoichiometry within the homogeneity field, dissociation pressures are indicated as p^o_1, p^o_2, and p^o_n and it is apparent that by moving the system on a dissociation path (dotted line B'-B) in the B'-B direction, Li_2O is in equilibrium with the solid solution when the system becomes two phase. By moving the composition of the system in the opposite direction along the same dissociation path we enter a cation deficient region that only at temperatures lower than about 400°C eventually segregates Ni_2O_3, which is unstable at higher temperatures. At higher temperatures we will therefore consider the existence of nickel sesquioxide only fictitious.

In Fig. 1 only a guess is made on the extension of the homogeneity region, as it is only recognized that at room temperature the single phase field extends at least to 20 a/o (atomic per cent) lithium (15) whereas Bade *et al.* (18a) and Toussaint and Vos (18b) demonstrated that the single-phase region extends to at least 33 a/o lithium.

In speculating on the form and the extension of the homogeneity region,[3] we could at first imagine that on the right of the line corresponding to the stoichiometric compositions (cation deficient region) the defects should be cation vacancies and electron holes trapped at cationic positions, according to the equation

$$\tfrac{1}{2}\,O_2 \rightarrow NiO(ss) + V''_{Ni} + 2h^{\cdot} \qquad [2]$$

In the region near the NiO corner we can assume that the value of the equilibrium constant for reaction [2] does not differ greatly from that which holds for pure NiO. A quantitative estimate of the extension of the homogeneity range is therefore possible by using Mitoff's (19) equation

$$n_v = 0.11P_{O_2}^{1/6} \exp(-17800/RT) \qquad [3]$$

which gives the cation vacancy concentration (n_v) for pure NiO in terms of vacancies per ion pair. Results are given in Fig. 2, where the isobars at 760 Torr of O_2 for the vacancy concentration as well as for the equilibrium constant of reaction [2] are reported *vs.* the temperature.

From Fig. [2] it appears that positive deviations from stoichiometry are negligibly small and, therefore, the homogeneity range should be very narrow. This condition is different from that in systems containing iron, where large deviations from stoichiometry are characterisic (20). Moreover, as anion deficient NiO has not been proved to exist, guesses on the understoichiometric region of the homogeneity range are

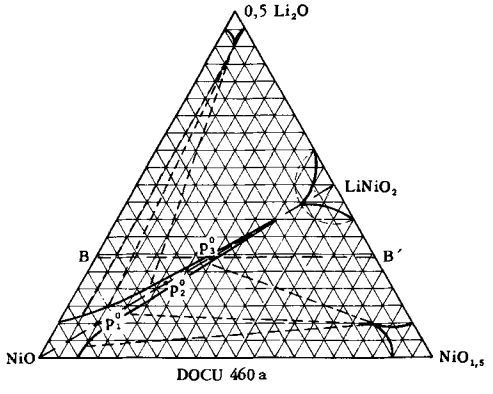

Fig. 1. Phase diagram of the system NiO, Ni_2O_3, and Li_2O (tentative). Solid lines indicate boundaries of single-phase regions. B-B' type paths indicate dissociation paths.

* Electrochemical Society Active Member.

[1] A $Ni^{\cdot}_{Ni}$ site corresponds to an electron hole trapped at a Ni site.

[2] The choice of $LiNiO_2$ as a component of the solid solution results from structural considerations. It is well known that the structure of $LiNiO_2$ is a slightly disordered rhombohedral structure, derived from a superstructure of the NaCl lattice in which the octahedral coordination is conserved (33).

[3] The phase diagram of Fig. 1 contains some symmetry elements (as the form of the homogeneity region) which are only introduced for the sake of simplicity. Actually, at the NiO corner, it is apparent that deviations from stoichiometry are much smaller than those indicated in Fig. 1, and large Li_2O excesses in the homogeneity field are unexpected over the entire composition range.

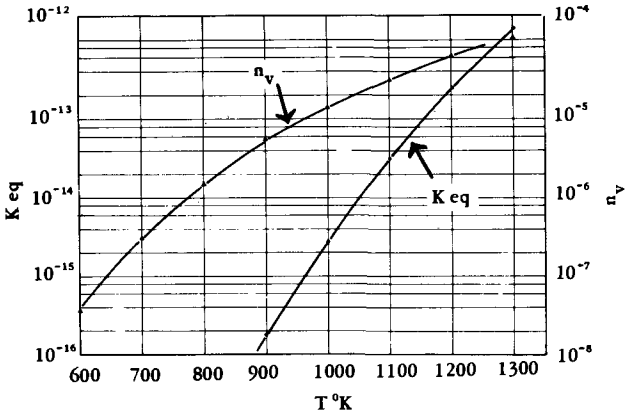

Fig. 2. Plots [from ref. (19)] of the equilibrium constant of reaction [2] and vacancy concentration n_v vs. temperature. n_v is given in terms of vacancies per ion pair and is calculated for $P_{O_2} = 1$ atm.

difficult. We suggest, however, that, in the oxygen deficient region, lithium could enter interstitial positions, the clustering of such interstitials should promote the segregation of Li_2O as the second phase, which is in fact observed when the solid solutions are investigated in reducing atmospheres. As this paper refers only to experiments carried out in the range of dilute solid solutions, we assume that an excess oxygen partial pressure does not greatly affect the composition over the stoichiometric one.

On the Measurements of Thermodynamic Activity of Dissolved Lithium Oxide

Details of the technique and generalities on the determination of thermodynamic functions via solid-state electrochemical measurements have been given recently and exhaustively by Schmalzried (21) and Steele (22), and therefore further remarks can be avoided here.

The determination of the activity ratios of Li_2O dissolved in NiO (*i.e.*, $LiNiO_2$ dissolved in NiO) was carried out by measuring the emf of a cell of the type

$$Pt/LiNiO_2(x_2) \text{ in NiO/interm. electrolyte/} LiNiO_2(x_1) \text{ in NiO/Pt} \quad [4]$$

where the atomic fractions (x_1) and (x_2) of $LiNiO_2$ correspond to those of the LiO_2 dissolved in the oxidic matrix, namely

$$x = \frac{n_{LiNiO_2}}{n_{LiNiO_2} + n_{NiO}} = \frac{n/2_{Li_2O}}{n/2_{Li_2O} + n^\circ_{NiO}} \quad [5]$$

where n_{NiO} equals the total number of moles of NiO, and $n_{NiO} = n^\circ_{NiO} - n/2_{Li_2O}$. The difficulty to be solved in the operation of these cells is the selection of a suitable intermediate electrolyte, and the problem becomes critical in the range of concentrated solutions (23).

Preliminary experiments demonstrated that the voltage of a cell fitted with (lime) zirconia or (lanthana) thoria drops with time to values near zero. Measurements of Li concentration in the solid solution after running the cell for some days at temperatures not higher than 1000°C show that the drop in emf is due to the irreversible migration of lithium from the left-hand compartment to the right-hand one, when $x_2 > x_1$.

Stable and reproducible emf values were, however, obtained when using α-Li_2SO_4 as the intermediate electrolyte, which, according to the transport number determinations of Lunden (24) is a purely cationic electrolyte.[4] Cell [4] could be written as follows

$$Pt/LiNiO_2(x_2)NiO//\alpha\text{-}Li_2SO_4//LiNiO_2(x_1)NiO/Pt \quad [4a]$$

where it is assumed that the $LiNiO_2$ in each compartment is in equilibrium with its proper partial pressure of oxygen p°_2 and p°_1, and therefore the over-all cell reaction could be written

$$LiNiO_2(x_2) + \tfrac{1}{2}\,O_2(p^\circ_1) \rightarrow LiNiO_2(x_1) + \tfrac{1}{2}\,O_2(p^\circ_2) \quad [4b]$$

With a separate experiment,[5] which will be described in a subsequent paper, we demonstrated that a partial pressure of oxygen as high as 1 atm affects neither the concentration nor the activity of $LiNiO_2$ in solid solution. Therefore, we are allowed to use the emf of the cell [4a] when measured under the same partial pressure of oxygen

$$P_{O_2} > p^\circ_1, p^\circ_2$$

at both electrodes, as a measure of the work done by the system when 1 mole of $LiNiO_2$ is transferred reversibly from the left-hand to the right-hand electrode. Thus:

$$\mathbf{F}\,E = -\,[\Delta^M G'_{LiNiO_2} - \Delta^M G''_{LiNiO_2}] \quad [6]$$

where $\Delta^M G_{LiNiO_2}$ is the relative partial molar free energy of mixing of $LiNiO_2$ in a solution of a certain composition x and $\mathbf{F}$ and E have their conventional meanings.

Since

$$\Delta^M G_i \equiv \overline{G}_i - G^\circ_i \quad [7]$$

where $\overline{G}_i$ is the partial molar free energy of mixing of a component i and G°_i is the corresponding molar free energy, the emf of cell [4a] becomes

$$\mathbf{F}\,E = -\,[\overline{G}_{LiNiO_2(x_2)} - \overline{G}_{LiNiO_2(x_1)}] \equiv RT \ln \frac{a^*_{1(LiNiO_2)}}{a^*_{2(LiNiO_2)}} \quad [8]$$

where the stars on the activity terms of Eq. [8] indicate that these activities are measured under a partial pressure of oxygen higher than the equilibrium one. Therefore we use Eq. [8] with the condition that we do not expect, according to Fig. 2, large deviations from stoichiometry when operating both electrodes of cells like [4a] at partial pressures of oxygen $P_{O_2} > p^\circ_1$, p°_2. This last condition will be assumed to hold within the range of the dilute solid solutions. The values of the partial molar free energies of mixing experimentally obtained and their differences can indeed be compared with the corresponding values calculated *a priori* with the aid of a pertinent model of the solution.

Experimental

Preparations of solid solutions.—Lithium doped nickel oxide was prepared according to the method of ref. (25) which consists of the utilization of lithium peroxide instead of lithium carbonate as the lithium dopant. Intimate mixtures of nickel oxide[6] and lithium peroxide[7] were prepared by ball-milling the weighed components in an agate mill with nickel balls. The use of nickel balls was demonstrated to be useful in avoiding contamination with oxidic materials as has been observed when harder ceramic balls were used. Pellets of ½ in. diameter were prepared with standard ceramic methods and sintered at 1000°C in closed Pt crucibles under 1 atm of oxygen. X-ray analysis proved that solid solutions are formed after some hours. It is worth noting here that lithium losses due to the vaporization of lithium oxide [quoted by some authors (16) as the main source of lithium losses during the high-temperature process] must be excluded for our conditions, as the partial pressure of lithium oxide is negligibly small (26). A source of lithium losses could

[4] Transport properties of α-Li_2SO_4 have been studied intensively by Kvist. A summary of his work on this subject is contained in ref. (24bis.).

[5] Which consisted of operating a cell like [4a] with separate compartments at different partial pressures ($0.001 < P_{O_2} < 1$ atm) of oxygen in each compartment and both electrodes at the same $LiNiO_2$ concentration.

[6] Prepared by thermal decomposition of twice-crystallized Ni_2SO_4 (Merck) and by annealing the decomposition product at 1100°C in oxygen.

[7] Obtained from Alfa Inorganics, Inc.

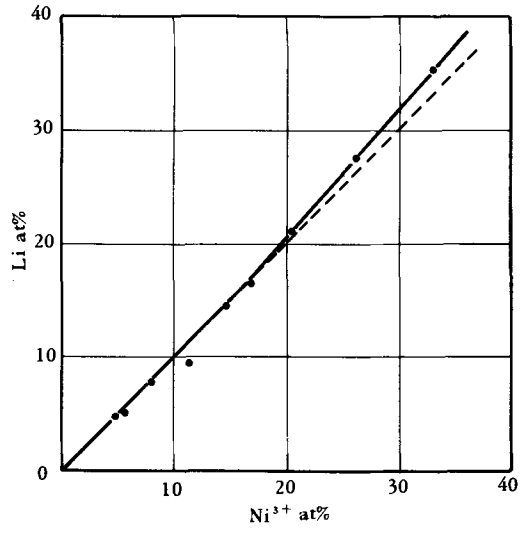

Fig. 3. Plot of the experimental values of atomic ratios of Li^+ (from photometric analysis) and of Ni^{3+} (from electrochemical analysis, see text).

be the hydrothermal decomposition of lithium oxide to lithium hydroxide which has a relatively larger vapor pressure (27).

The lithium content in the solid solution was measured by flame emission photometry as well as by measuring the lattice spacings (18b) at the Analytical Chemistry Division of the CCR EURATOM—ISPRA. The Ni^{3+} content was measured in the chloridic solution of the oxide (28) by the iodometric method and the end point determined with the dead-stop method in a cell fitted with Pt microelectrodes (29). Results are given in Fig. 3. In apparent contrast with the results of Iida and Hayashy (15), at 25 a/o lithium only a slight inflection is obtained from the line which indicates the expected one-to-one correspondence between the dissolved lithium and trivalent nickel (*i.e.*, $Ni^{\cdot}_{Ni}$.

Emf measurements.—Emf measurements on solid galvanic cells of type [4a] have been carried out on cells of conventional design, as illustrated in our previous study (17), but with α-Li_2SO_4 used as the intermediate electrolyte. Directions for the use of Li_2SO_4 in a solid galvanic cell were given in a previous paper (30). As soon as it was demonstrated that, within the range 0.155-0.522 a/o lithium, the experimental emf values fit a Nernst plot, any composition within this range was used as reference composition. The transference number determinations in α-Li_2SO_4 quoted by Lunden (24) indicate that the transport number of Li^+ is one, within the accuracy of the measurements. After a closer inspection of his data, we could quote a figure for the accuracy of about 5% over the entire range of temperature where the cubic modification is stable.

The fact that the electrolyte works as a purely ionic electrolyte was independently and indirectly demonstrated by fitting the emf values with an ideal Nernst plot (see below). Emf values were measured and recorded by a digital voltmeter and digital recorder (Hewlett Packard, Dymec System). Experiments have been carried throughout under one atmosphere of pure oxygen. Within the entire set of experiments described in this paper, the reproducibility of the emf data is better than ±5 to 10 mV.

Results and Discussion

The parameters of the equations which express the linear temperature dependence of the emf at different concentrations of lithium are given in Table I. The number of (E, T) points utilized for computing the a and b values is between 20 and 100.

Table I. Experimental results of the emf measurements

X_1/X_0	Temperature range, °C	$E = a + bT$ (V·10⁻³)
0.235/0.155	570-850	$E = -9.8 - 0.0358T$
0.365/0.155	570-850	$E = -2.0 - 0.0736T$
0.522/0.155	570-850	$E = -45.2 - 0.076T$
1.965/0.155	570-850	$E = -55.8 - 0.260T$
2.874/0.155	570-850	$E = +3.3 - 0.367T$
4.508/0.155	570-850	$E = -85.8 - 0.364T$
5.088/0.155	570-850	$E = -28.1 - 0.403T$
5.265/0.155	570-850	$E = -89.6 - 0.373T$

The equations of Table I have been used for plotting the E *vs.* x isotherms of Fig. 4, 5, and 6. The straight-line represents the Nernst plot calculated by using the equation

$$E = \frac{RT}{\mathbf{F}} \ln \frac{x_1}{x_2} \qquad [8a]$$

where x_1 and x_2 are the atomic ratios of lithium in the electrode compartments calculated according to Eq. [5].

It is apparent that, in the temperature range 600°-800°C the experimental points follow the (ideal) Nernst plot up to about 1.5 a/o lithium. Deviations from the Nernst isotherms, detectable at atomic ratios of lithium higher than 1.5%, over the entire range of temperatures, can be discussed entirely in terms of the entropy of mixing, as the Arrhenius plots of the log γ values[8] indicate negligibly small values of the heat of mixing.

Moreover, it is apparent from Fig. 7 that the plot of the isothermal temperature coefficient ϵ of the emf (from Table I) fits, in the range of the dilute solutions, the theoretical plot calculated from the purely

[8] The deviations from ideality have been computed and are reported in Table II as log γ values, where

$$\ln \gamma = (E - E^0)\, \mathbf{F}/RT \qquad [9]$$

E is the experimental value and E^0 is the Nernst value.

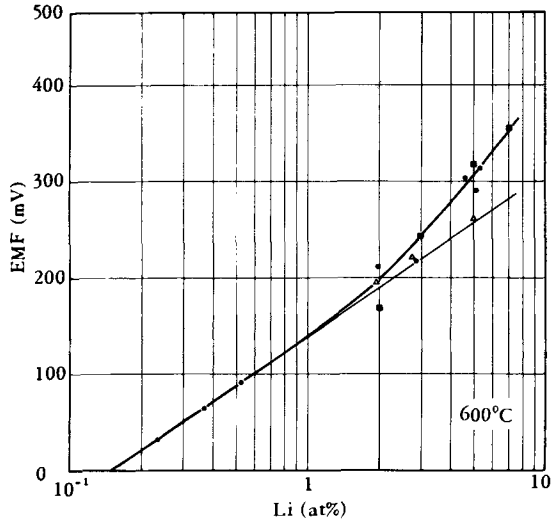

Fig. 4. Plot at 600°C of the experimental and calculated emf values as a function of the atomic ratios of Li^+. ○ Experimental points, △ from Guggenheim's formula (Eq. [11]), □ from Eq. [13]. Straight lines correspond to the Nernst plots.

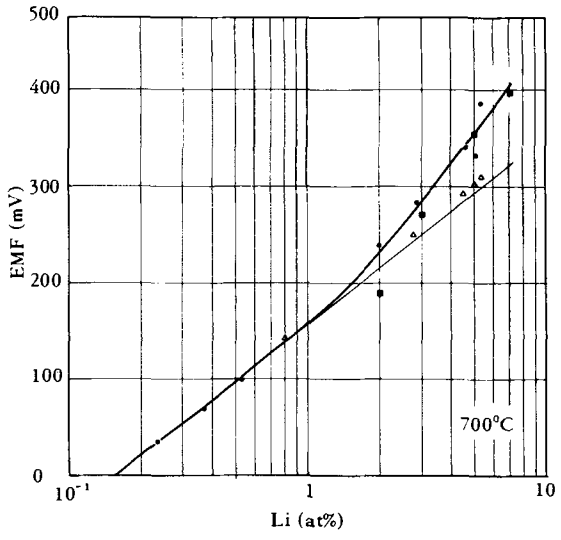

Fig. 5. Same as Fig. 4 at 700°C

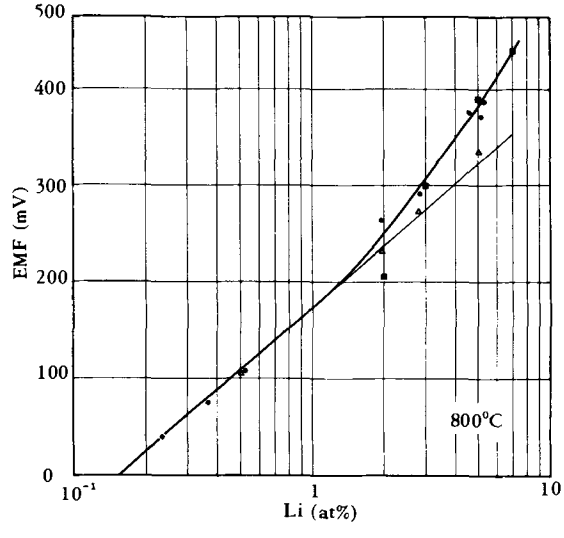

Fig. 6. Same as Fig. 4 at 800°C

configurational entropy function

$$-\epsilon\mathbf{F} = R[\ln x_2 - \ln(1-x_2) - \ln x_1 + \ln(1-x_1)] \quad [10]$$

where x_1 and x_2 are the molar ratios of $LiNiO_2$ in the cell compartments.

To discuss conveniently the experimental fitting of the emf data with Eq. [8a] and [10] in the range of the dilute solid solutions as well as the deviations from this "ideal" behavior observed at higher concentration, let us imagine that[9] between a substitutional lithium site and a positive hole trapped at a nickel position an attraction of coulombic nature exists that gives rise to a nonnegligible concentration of ion pairs $Li'_{Ni} - Ni^{\cdot}_{Ni}$. In order to look at the influence of ion pairing on the thermodynamics of the system, we consider first the mixture as an athermal solution, according to the treatment of Fowler and Rushbrooke (31) for athermal nonideal mixtures. We will, however, use Guggenheim's (32) method to calculate the configurational free energy of mixing and thereafter the log γ values, by assuming that the solution is a mixture of two kinds of molecules (strictly speaking, ions), one ($=Ni^{2+}$) which occupies one single lattice position, and a second one (*i.e.*, Li^+-Ni^{3+}) which occupies two nearest neighbor positions.

[9] So far we could assume that the lithium concentration is so low that we could exclude the presence of a lithium as nearest neighbor or next-nearest neighbor of a nickel ion of a $Ni^{\cdot}_{Ni}$-Li'_{Ni} pair chosen as the center of the system. Only the cationic sublattice is considered here.

Table II. Experimental values of activity coefficient and activity

T = 873°K				
Li a/o	log γ	γ	γx	^{n}tr.*
1	0.014	1.03	0.010	
2	0.088	1.22	0.024	0.021
3	0.147	1.40	0.042	0.043
5	0.279	1.90	0.095	0.099
7	(0.376)	(2.37)	(0.166)	0.157
T = 973°K				
Li a/o	log γ	γ	γx	^{n}tr.*
1	—			
2	0.077	1.19	0.023	0.021
3	0.155	1.43	0.042	0.043
5	0.285	1.93	0.096	0.099
7	(0.389)	(2.45)	(0.171)	0.157
T = 1073°K				
Li a/o	log γ	γ	γx	^{n}tr.*
1	—			
2	0.082	1.20	0.024	0.021
3	0.117	1.31	0.039	0.043
5	0.258	1.81	0.090	0.099
7	(0.353)	(2.25)	(0.158)	0.157

* The triplet concentration ^{n}tr. was calculated according Eq. [13].

The absolute activities ratios which result are

$$\frac{\gamma'}{\gamma''} = \frac{N'_2(N''_2 + N''_1/2)}{N''_2(N'_2 + N'_1/2)} \left[\frac{(N'_2 + N'_1/2)}{(N''_2 + N''_1/2)} \frac{N''_2 + N''_1/2}{N'_2 + N'_1/2}\right]^{\frac{1}{2}nq} \quad [11]$$

where N_1 is the relative number of Ni^{2+} ions, N_2 is the relative number of ($Ni^{3+} - Li^+$) couples, n is the coordination number (which for a face-centered cube is 12) and q could be calculated by the following equation

$$\tfrac{1}{2}\, n(2-q) = 1$$

which strictly holds for a mixture of monomers and dimers. The triangles in Fig. 4, 5, and 6 show the calculated emf values.

It appears that at the lowest and intermediate concentrations the Nernst plot (Eq. [8a]) and the athermal mixture plot (Eq. [11]) practically coincide, whereas at the higher concentration, where the de-

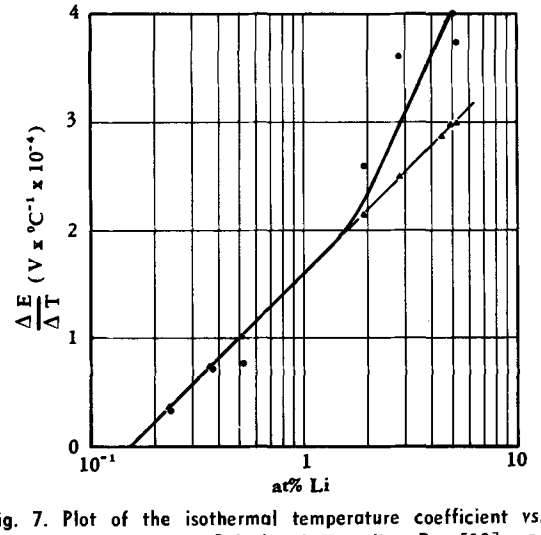

Fig. 7. Plot of the isothermal temperature coefficient vs. the lithium concentration. △ Calculated according Eq. [10], ○ experimental points.

Table III. Ratios of Ni ions

Li a/o	Fraction of nickel atoms having r Li atoms as nearest neighbors		
	$r = 0$	$r = 1$	$r = 2$
0.15	0.98	0.019	0.0002
2.0	0.784	0.194	0.021
3	0.693	0.260	0.043
5	0.540	0.344	0.099
7	0.418	0.381	0.157
10	0.282	0.378	0.231

viations from the "ideal" behavior appear far from negligible, the proposed model accounts only for a part of the deviation. The activity of the solution is therefore not simply determined by the configurational energy terms of Eq. [11].

A closer approach could, however, be obtained by considering that, when the solution becomes more concentrated, it is no longer possible to exclude the presence of other lithium ions as nearest neighbors of a nickel ion in a $Ni^{\cdot}_{Ni}$-Li'_{Ni} pair. To take this fact into account, we have reported in Table III the ratios of Ni ions in solution having zero, one, or two lithium ions as nearest neighbors. The calculations have been accomplished by considering that, for $n = 12$, the coordination number for a fcc structure, the fraction x_A of the nickel ions having 12 nickel ions as nearest neighbors is

$$x_A = (1 - x)^{12} \qquad [12]$$

and the fraction $x_A{}^r$ of the nickel ions having r lithium ions as nearest neighbors is

$$x_A{}^r = \frac{\dfrac{n_B!}{r!\,(n_B - r)!}\,\dfrac{(N - n_B)!}{(n - r)!\,(N - n_B - n + r)!}}{\dfrac{N!}{n!\,(N - n)}} \qquad [13]$$

where n_B is the number of lithium ions in a system of dimension N, (here $N = 1000$), $n = 12$ is the dimension of the sample removed from the system (*i.e.*, the dimension of the first coordination shell), N is obviously the sum of the elements of type A and type B, and r, as before, is the number of elements of type B which are assumed to be contained in a sample of n elements. In Fig. 4, 5, and 6 we have plotted the emf values calculated as

$$E = \frac{RT}{\mathbf{F}} \ln \frac{x'_1}{x^{o}_2} \qquad [8b]$$

where x' is the atomic ratio of the nickel ions having at least two lithium ions as nearest neighbors and x^{o} is the molar ratio of lithium in the reference compartment. It appears that the theoretical points fit the experimental curve quite well in the range of the deviations from the ideal behavior.

Moreover, in Table II, the experimental γ values are used to calculate the fraction of the electroactive species γx.

This fraction is compared with the figures for triplet concentration reported in Table III. It is apparent that there is a reasonable agreement at atomic ratios of lithium higher than 3%. We should therefore conclude that, even at higher concentrations, purely configurational energy terms describe the thermodynamics of the solution. It is out of the scope of this paper to discuss the solution in terms of nonthermodynamic properties and to define the nature of the electroactive species. It appears, however, from our results and others that the presence of Li-Ni-Li triplets affects the thermodynamics of the solution as well as the electrical conductivity and the activation energy for the electrical conductivity. Both functions, in fact, are known (4, 5, 8) to show a sharp discontinuity in the same concentration range where the emf plot deviates from the Nernst plot.

Acknowledgments

The authors are greatly indebted to C. Geel and Dr. G. Monari for skillful assistance and to Dr. G. Sternheim and Professor G. Bianchi for many stimulating discussions. We acknowledge also the contribution of Dr. G. Vos and C. J. Toussaint in the determination of the lattice spacings of the solid solutions.

Manuscript submitted Dec. 9, 1968; revised manuscript received March 3, 1969.

Any discussion of this paper will appear in a Discussion Section to be published in the June 1970 JOURNAL.

APPENDIX

The use of a triplet concentration function as a measure of the $LiNiO_2$ activity does not mean that we identify a particular array of ions in the lattice with a chemical species, such as $LiNiO_2$. We may, however, show that the identity of the functional trends (the experimental emf *vs.* the concentration and that derived from introducing in the Nernst equation the concentration of the triplets) has a physical basis.

Without entering the problem of charge transport in NiO and related oxides (pure and doped), according to Heikes (34, 34bis) and Van Houten and Bosman (35) nickel sites with more than one lithium as nearest neighbor should act as trapping centers for electron holes. At high lithium concentration we quote the relative probability of the occurrence of this configuration with the activity of the solute, whereas at low lithium concentration where only isolated Li'_{Ni}-$Ni^{\cdot}_{Ni}$ pairs exist, we are allowed to quote the atomic ratio of lithium as the activity of the solute.

REFERENCES

1. E. J. Verwey *et al.*, *Philips Research Repts.*, **5,** 173 (1950).
2. A. Bielansky, J. Deren, and M. Volter, *Kinetics and Catalysis*, **55,** 849 (1964).
3a. J. Deren and J. Ziolkowski, *Bull. Acad. Pol. des Sciences*, **XIV,** 7 443 (1966).
3b. E. G. Misynk, *et al.*, *Sov. Electrochem.*, **2,** 3, 311 (1966).
4. W. D. Johnston and R. R. Heikes, *J. Am. Chem. Soc.*, **78,** 3255 (1956).
5. T. P. Janusz, R. R. Heikes, and W. D. Johnston, *J. Chem. Phys.*, **26,** 973 (1957).
6. J. Yamashita, and T. Kurosawa, *J. Phys. Chem. Solids*, **5,** 34 (1958).
7. G. M. Schwab and H. Schmid, *J. Appl. Phys. Suppl.*, **1,** 33, 426 (1962).
8. S. Van Houten, *J. Phys. Chem. Solids*, **17,** 7 (1960).
9. R. R. Heikes *et al.*, *Ann. Phys.*, **8,** 733 (1963).
10. Ya. M. Ksendzov *et al.*, *Sov. Phys. Sol. State*, **5,** 1116 (1963).
11. S. Koide, *J. Phys. Soc. Japan*, **18,** 1699 (1963).
12. S. Koide, *ibid.*, **20,** 123 (1965).
13. A. J. Springthorpe *et al.*, *Sol. State Comm.*, **3,** 143 (1965).
14. M. Roilos and P. Nagels, *ibid.*, **2,** 285 (1964).
15. Y. Iida and N. Hayashi, *Bull. Chem. Soc. Japan*, **37,** [5], 659 (1964).
16. Y. Iida, *J. Am. Ceram. Soc.*, **43,** 171 (1960).
17. S. Pizzini and R. Morlotti, *This Journal*, **114** [11], 1179 (1967).
18a. H. Bade, W. Bronger, and W. Klemm, *Coll. Int. CNRS*, No. 149 (1965).
18b. C. J. Toussaint and G. Vos, *J. Appl. Crystallography*. In press.
19. S. P. Mitoff, *J. Chem. Phys.*, **35,** [3], 882 (1961).
20. P. Reijnen, *Philips Research Repts.*, **23,** 151 (1968).
21. H. Schmalzried, "Thermodynamics," IAEA, Vienna (1966).
22. B. C. H. Steele, "Electromotive Force Measurements in High Temperature Systems," C. B. Alcock, Editor, The Institution of Mining and Metallurgy, London (1968).
23. V. Wagner, H. Langenberg, R. Morlotti, and S. Pizzini, Paper 202 presented at the New York Meeting of the Society, May 4-9, 1969.
24. A. Lunden, *Z. Naturforschg.*, **17** [2], 142 (1962).

24 bis. A. Kvist, "Transport Properties of Solid and Molten Sulfates," Acta Univ. Gotheburgensis, (1967).
25. W. D. Johnston, and R. R. Heikes, *J. Am. Chem. Soc.*, **78**, 3255 (1956).
26. J. Berkowitz, W. A. Chupka, C. D. Blue, and J. L. Margrave, *J. Chem. Phys.*, **63**, 644 (1959).
27. J. Berkowitz, D. J. Meschi, and W. A. Chupka, *ibid.*, **33**, 533 (1960).
28. H. B. Sachse, *Analyt. Chem.*, **32** [4], 529 (1960).
29. C. Geel and G. Monari, Private communication.
30. S. Pizzini, E. Römer, and R. Morlotti, *Electrochim. Metall.*, **III** [2], 151 (1968).
31. R. H. Fowler, and Rushbrooke, *Trans. Faraday Soc.*, **33**, 1272 (1937).
32. E. A. Guggenheim, "Mixtures," Oxford at the Clarendon Press (1952).
33. A. F. Wells, "Solid State Physics," Vol. 7, F. Seitz and D. Turnbull, Editors, Pergamon Press, New York (1958).
34. R. R. Heikes, A. A. Maradudin, and R. C. Miller, *Ann. Phys.*, **8**, 733 (1963).
34. bis. R. Heikes, from "Transition Metal Compounds," page 1, E. R. Schatz, Editor, Gordon and Branch Publishing, New York.
35. S. Van Houten and A. J. Bosman, *ibid.*, page 123.

Diffusion of Radiotracer Ions in a Cation-Exchange Membrane

W. J. McHardy,[1] P. Meares, and J. F. Thain[2]

Chemistry Department, The University, Old Aberdeen, Scotland

ABSTRACT

The tracer diffusion coefficients of Na^+, Cs^+, Sr^{2+}, and Br^- in a homogeneous cation-exchange membrane have been measured in the homoionic counterion states over the external solution concentration range 0.005-1.0 equiv/liter and in the $Na^+ + Cs^+$ and $Na^+ + Sr^{2+}$ heteroionic counterion states over the whole equivalent fraction range at 0.02 and 0.10 equiv/liter total external concentration. Steady- and transient-state permeation and diffusion techniques have been used. The results show that the resin material is essentially uniform apart from a small volume of material of low crosslinking which forms a labyrinthine network interpenetrating the main structure. This labyrinthine network is important mainly in the diffusion of Br^- at low external concentrations. In concentrations above about 0.02 equiv/liter the diffusion coefficient D_{Br} of Br^- does not vary greatly either with concentration or with counterion type. D_{Br} is greatest in the Cs^+ state and least in the Na^+ state. These observations and the way in which D_{Br} varies with the equivalent fraction of the counterions in the heteroionic states can be explained by considering the expected frictional interactions between Br^- coions and the counterions and by the influence of the local variations in electric potential on the movements of the ions.

The diffusion coefficients of all the counterions increase as the external concentration is increased. When these diffusion coefficients are compared with the diffusion coefficients in aqueous solutions Na^+ is seen to be the least retarded in the membrane and Sr^{2+} the most retarded. The observed behavior can be understood qualitatively in terms of the relative roles of "chain" and "volume" diffusion as suggested by Jakubovic *et al.* (20). A quantitative theory of these mechanisms has not been developed, but the relevance of theoretical treatments of the effects of electric potentials on counterion mobilities in polyelectrolyte and micellar solutions is pointed out. When the membrane is in a heteroionic state the diffusion coefficients of both counterions decrease when the equivalent fraction of Na^+, the thermodynamically nonpreferred ion in each mixture, is increased. This behavior is consistent with the mechanism of diffusion discussed above and with the expected distribution of the counterions in a heteroionic state of an exchanger which has the structure deduced from the behavior of the Br^- ions.

Although several studies of the diffusion of radiotracer ions in ion-exchange membranes have been made during the past fifteen years (1) several aspects of diffusion, relevant to electrodialysis, are still incompletely understood. These include the effects of ion valency, solution concentration, and temperature. Furthermore, very few measurements have been made on membranes containing a mixture of counterions although this is the condition most often met in practice.

In the present study, in order to throw some light on these problems, the diffusion of the coions and of a series of three counterions, singly and in pairs, in a so-called "homogeneous" phenol-sulfonic cation-exchange membrane, Zeo-Karb 315, have been examined under strictly comparable conditions.

Another reason for undertaking the work was that when Spiegler (2) published his frictional treatment of transport in ion-exchange membranes he also suggested a simple, though approximate, method of estimating all the frictional coefficients from a limited amount of experimental data which included tracer diffusion coefficients. Spiegler's scheme has never been given a well-defined test although his approximations have been criticized several times (3, 4). The data given in this paper have been obtained in the course of collecting sufficient data to use Spiegler's method. Subsequent papers will deal with the measurement and interpretation of the other transport properties required and with the evaluation of the frictional coefficients.

[1] Present address: Macaulay Institute for Soil Research, Craigiebuckler, Aberdeen, Scotland.
[2] Present address: School of Biological Sciences, University of East Anglia, Norwich, England.
Key words: diffusion, permeation, tracer, radioactive, ion, ion-exchanger, cation, cation-exchanger, charged, membrane.

Experimental Methods

Permeation method.—Most of the data given here were obtained by studying the rates of transfer of radiotracer ions from one solution phase through the membrane into a second solution phase of the same chemical composition as the first and initially at zero specific radioactivity. This permeation method is well known, and an early version of the authors' apparatus has been described already (5). Later developments in the apparatus and technique have also been published (1).

The entire apparatus was enclosed in an air thermostat and, in addition, water at a constant temperature was circulated continuously through coils immersed in the solution reservoirs. In this way the experimental temperature was controlled to ±0.1°C.

A flow-type Geiger-Müller tube was used as the radiation detector to monitor continuously the activity of the outgoing solution when β-emitters were being used. When γ-emitters were used the solution was circulated around an encapsulated scintillation crystal attached to a photomultiplier.

The usual circulation rate of the solutions through the diffusion cell was 1.5 liter/min. This produced a rapid flow across the membrane faces. Increasing and decreasing the flow rate between 2.0 and 1.0 liter/min had almost no effect on the ion fluxes. On this test the ion transport was apparently membrane-controlled, but experiments using several membranes which differed only in thickness showed that corrections were needed for boundary processes in order to obtain the true coefficients of homogeneous diffusion in the membrane. These corrections were made by the well-established method of treating the boundary processes as though they were due to stagnant solution films at the interfaces (6, 7). The effective thickness of the stagnant layers was found to be 16 ± 1μ in one diffusion cell and 20 ± 1μ in another. It appeared to be insensitive to the nature of the counterions and to small variations in the circulation rate of solution.

The thickness of the membrane was an appreciable fraction of its exposed diameter and an edge correction was needed to calculate the effective area available for ion transport. This correction was applied by the method of Barrer, Barrie, and Rogers (8). In our system it amounted to about 2% of the total area.

Three methods were used to evaluate diffusion coefficients from the permeation rates. Whenever possible a pseudosteady state of permeation was established. The rate of permeation was then obtained from the slope of the pen-recorder trace of the radioactivity of the outgoing solution *vs.* time, the volume of that solution and the ratio of the specific activities of the ingoing and outgoing solutions at a known time. This method was especially appropriate when using moderately concentrated solutions.

When a pseudosteady state could be obtained diffusion coefficients could also be obtained from the time-lag method. An equation for calculating D from the time lag in the presence of boundary layers is available (9). The time lag, as measured on the pen-recorder trace of the rate-meter output, was obtained directly in our experiments. This had to be corrected by subtracting from it the integrating time of the rate meter. The method was most accurate for relatively slowly diffusing ions since the time lag was then large compared with the integrating time of the rate meter and also with the operational uncertainty about the zero of time in an experiment.

When using dilute external solutions the amount of diffusate in the solution reservoirs was often smaller than the amount in the membrane on account of its relatively high exchange capacity. A steady state of permeation could not then be approached and an S-shaped permeation curve was obtained. The diffusion coefficient was evaluated from this curve by using an appropriate solution of the diffusion equation (10) which has been discussed in ref. (1). When using this nonsteady method the correction for boundary processes is less well understood. Here the method used was the same as with the steady permeation experiments.

In order to evaluate the diffusion coefficient in the membrane from the permeation rates thermodynamic equilibrium was assumed to exist between the solutions and membrane resin at the faces of contact. Extensive measurements had to be made of the sorption of coions and, in electrolyte mixtures, of the distributions of the counterions to determine these equilibrium conditions. The results of these experiments have been published elsewhere (11).

Nonstationary method.—The permeation method was not suitable for studying the diffusion of multivalent counterions when in very dilute solution and in the presence of a larger amount of univalent counterions because the multivalent ions are so strongly absorbed by the membrane. In these circumstances measurements were made by using an adaptation of the method (12) in which the movement of the tracer along a strip of membrane is followed. It had previously been established by electrical conductance measurements that the membranes were isotropic so that measurements could be made in any convenient direction.

A strip of membrane (4 x 1 x 0.1 cm) was equilibrated with the required solution and mounted on a Perspex sheet so that half of the strip was covered and sealed by plasticine and plastic tape. The edge of the Perspex sheet lay at right angles to and half way along the length of the strip of membrane. The assembly was clamped vertically with the uncovered part of the strip immersed in a beaker of the required solution until equilibrium was assured. The appropriate radiotracer was then added to the solution which was stirred for 2 hr. This was long enough to obtain a uniform distribution of tracer in the uncovered part of the strip without seriously blurring the boundary between the labelled and unlabelled halves of the strip.

The membrane strip was then removed from the Perspex sheet, rinsed quickly with unlabelled solution, blotted, and mounted in a groove in a Perspex block into which it fitted tightly. Small wells in the block at the ends of the membrane groove were filled with the inactive solution so that the ionic concentrations and water activity in the strip remained constant. The Perspex block was then covered by a thin impermeable polystyrene sheet (Polyglaze) to prevent evaporation and set in a closed plastic refrigerator box containing a little of the equilibrating solution so as to provide the correct atmosphere to prevent drying out. This box was then left in the air thermostat for the diffusion profile to develop.

At intervals the Perspex block was removed from the box and the distribution of the tracer determined by placing the block on a carriage driven by a micrometer screw under a well-screened end-window Geiger-Müller tube. Radiation from the strip entered the Geiger-Müller tube through a collimating slit 7 x 0.5 mm in a lead shield 6 mm thick (89 Sr, a pure β-emitter, was used in these experiments). Counting was carried out inside the air thermostat and the activity was determined at a series of well-defined points along the strip.

These nonstationary experiments lasted from four to seven days and a series of radioactivity determinations required about 30 min. The mean time t of the series of determinations was recorded. The spread of the activity observation times about this mean time was insignificant after the run had been in progress for about two days.

If an initially sharp boundary had existed between unlabelled (radiocount rate = 0) and labelled (radiocount rate = m_o) parts of the strip then at a subsequent time t, too short for interdiffusion to have proceeded as far as the ends of the strip, the count rate

m is given as a function of distance x from the initial boundary by

$$\frac{m}{m_o} = \frac{1}{2}\left[1 - \text{erf}\left(\frac{x^2}{4Dt}\right)^{1/2}\right] \quad [1]$$

where D is the diffusion coefficient (13).

In practice the absolute values of t and x were not known with precision. From a series of readings of m/m_o *vs.* the micrometer reading r, where

$$r = x + a \quad [2]$$

and a is a constant of the apparatus, a series of values of $(x^2/4Dt)^{1/2}$ were obtained by using error function tables. These values were plotted against r and a straight line was obtained of slope $(4Dt)^{-1/2}$ from which the apparent D at time t was obtained. As t increases the effect of the uncertainty in the zero time becomes less. Hence a graph was plotted of each apparent value of D against $1/t$ and extrapolated to the D-axis ($1/t = 0$). The intercept on this axis gave the true value of D.

Experimental accuracy.—Since transport and equilibrium data had to be combined and several corrections to be applied, it is not easy to make an estimate of the over-all accuracy of the diffusion coefficients. For various reasons radiocounting under ordinary conditions is not a highly accurate procedure. This factor probably limited the attainable accuracy of our measurements to ±1%. The desirability of keeping the integrating time of the rate meter to a minimum caused wide statistical fluctuations on the pen recorder trace. To eliminate the effect of these a set of mean points was obtained by integrating under sections of the activity *vs.* time trace with a planimeter. Steady-state slopes were determined by drawing a line through this set of mean points. The slope of this line was taken as giving the steady permeation rate relative to the activity of the ingoing solution half way through the experiment. No departure from a linear recorder trace was noticed provided the outgoing activity at the end of a run did not exceed 2% of the ingoing activity.

When the final outgoing activity was greater than 2% of the ingoing activity Crank's method (10) was used to treat the data. In the border-line region both methods of calculation were tried and they gave results which agreed to within ±2%.

The time-lag method was most useful in the study of Sr^{2+} and gave results which agreed satisfactorily with those from permeation measurements.

Measurements on Sr^{2+} in dilute mixtures of NaBr + $SrBr_2$ were mostly made by the strip method. A direct comparison between this and direct permeation measurements in pure $SrBr_2$ at 0.02 equiv/liter gave diffusion coefficients which differed by only 2%. This observation constituted evidence also for the validity of the correction for boundary processes in permeation experiments since such processes do not affect the strip method.

This correction for boundary processes was very important when studying counterions in dilute solutions. In the worst cases it amounted to 25% of D and a small error in the thickness of the hypothetical stagnant layer would have had a serious effect on the corrected value of D. Although the physical picture of stagnant liquid films at the membrane faces is inaccurate, the method of correction is valid provided the boundary regions behave as layers across which transport obeys Fick's first law of diffusion and into which sorption from the stirred solutions obeys Henry's law.

Errors in D would also arise from errors in the equilibrium data relating the composition of the membrane to that of the solution. These errors were probably most serious in measurements on coions in very dilute solutions, where spuriously high sorbed concentrations (the expected direction of any experimental error) would give low values of the diffusion coefficient. Measurements on counterions in mixed electrolytes were most liable to error when the membrane contained relatively little of one kind of counterion because the ion-exchange equilibria were then difficult to study accurately.

In comparison with the errors discussed above the uncertainties in the physical dimensions of the apparatus and membrane and in the concentrations of the solutions were unimportant. It is estimated that diffusion coefficients interpolated from smooth curves drawn through the data on any given membrane + solution system were within 3% of the true values.

Materials and Results

Membranes.—Zeo-Karb 315 (Permutit Company Ltd.) is a phenol + formaldehyde condensate membrane with fixed ions $-CH_2SO_3^-$ on a proportion (about 1/5) of the aromatic rings. The exchange capacity, water content, and swollen dimensions of the membranes were determined in each solution studied. Only a small number of membranes were used and these analytical properties agreed between different membranes to within better than 1%.

Data on the ionic equilibria between the membranes and solutions have been published (11); a few data are given in Table I.

Electrolytes.—Solutions were prepared from dried, pure NaBr, CsBr and $SrBr_2$. They were made up on the molar scale at 25°C using deionized water and regularly checked by titration against standard $AgNO_3$. The radio-tracers $^{22}Na^+$, $^{134}Cs^+$, $^{89}Sr^{2+}$, and $^{82}Br^-$ were obtained from the Radiochemical Centre, Amersham. They were converted when desirable to the appropriate salt by passing through ion-exchange columns.

Diffusion coefficients.—In calculating the diffusion coefficients from the experimental data appropriate allowances were made for dimensional and concentration changes in the membrane which resulted from changes in swelling, coion sorption, and ion-exchange equilibria with the different external solutions. The tracer diffusion coefficients are expressed in $cm^2\ sec^{-1}$ relative to the membrane as fixed reference. Corrections due to differences in mass between the inactive and tracer ions were neglected.

The diffusion of the cation and Br^- were studied with the membrane in equilibrium with NaBr between 0.005 and 1.00M, with CsBr between 0.005 and 0.10M, and with $SrBr_2$ between 0.0025 and 0.50M.

All three mobile ions were studied over the whole equivalent fraction range of mixtures of NaBr + CsBr and of NaBr + $SrBr_2$ at 0.02 and 0.10 equiv/liter total concentration.

Most measurements were made at 25°C, and a few experiments were carried out at 15° and 35°C to determine apparent activation energies for diffusion. Strictly, these were activation energies for permeation because they included also the heat of ion sorption but, within our experimental accuracy, sorption was not affected by temperature in this range (14).

Discussion

Coions.—The coions are electrostatically repelled by the fixed charges. They must be expected to make relatively few direct contacts with the polymeric matrix of the membrane and to diffuse in an environ-

Table I. Properties of Zeo-Karb 315 membranes per gram of Na^+ form fully swollen in water

Exchange capacity, m equiv	Volume, cm^3	Weight of water, g
0.486	0.887	0.665

Details of variations with solution concentration and type of counterion are given in ref. (11).

ment mainly of water molecules. However, because of the bulk and electric potential of the matrix, they may be forced to follow more tortuous paths than those taken by ions diffusing in an aqueous solution of a simple electrolyte.

The coions must also interact with the counterions by which they are electrostatically attracted. The extent of these interactions depends on the nature of the counterions through their size, charge, and degree of hydration, and also on the local concentrations of the counterions and coions. These local concentrations are controlled in part by the extent to which the counterions approach, or are bound by, the polymer chains and fixed charges and in part by the uniformity of the polymer network. The Donnan exclusion effect causes the coions to be most concentrated in those regions of the membrane where the fixed charge density and hence the counterion concentration, are lower than average.

With these considerations in mind it is possible to understand the diffusion characteristics of the coions as shown in Fig. 1-5. In Fig. 1 the diffusion coefficient D_{Br} in the membrane is plotted against the concentration of the external solution. It can be seen that at concentrations above 0.05 equiv/liter the variation of D_{Br} with increasing concentration is slight in each electrolyte and scarcely greater than the experimental uncertainty. Below 0.02 equiv/liter D_{Br} decreases in the Na^+ and Cs^+ forms of the membrane though not, apparently, in the Sr^{2+} form.

If the resin were truly homogeneous, the tortuosity of the diffusion pathways followed by the coions should be scarcely altered by the changes in the swelling of the resin which were very small over the concentration ranges studied. A simple relation between the degree of swelling and the diffusion coefficient in a homogeneous gel has been deduced earlier (15). It is

$$D = D_o \left(\frac{v_w}{2 - v_w} \right)^2 \qquad [3]$$

where v_w is the volume fraction of water in the swollen gel and D_o the diffusion coefficient of the ion in free aqueous solution. This equation takes into account only the effect of the bulk of the polymer matrix on the tortuosity of the diffusion paths. It predicts $\sim 7.5 \times 10^{-6}$ cm^2 sec^{-1} for D_{Br} in the membrane examined here.

Figure 1 shows that above 0.05 equiv/liter D_{Br} lies between 7.5 and 9.3 x 10^{-6}. This suggests that the membrane does not depart greatly from the homogeneous gel structure. The largest value of D_{Br} could be accounted for by setting v_w equal to 0.80 instead of of to its over-all average value of 0.75. This deviation may not be significant in view of the inexact theoretical basis of Eq. [3]. It is in the expected direction because the coions tend to be concentrated into those regions of the resin where the fixed charges are least

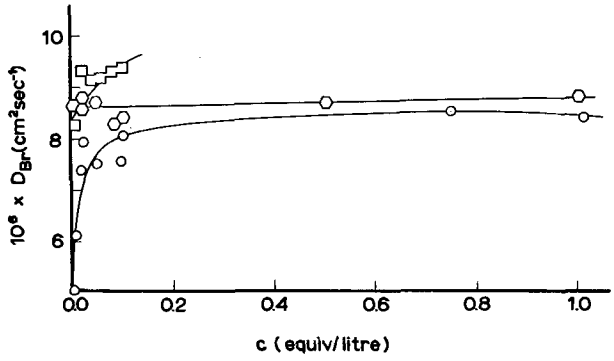

Fig. 1. Diffusion coefficient of Br^-, D_{Br}, in Zeo-Karb 315 at 25°C as a function of external solution concentration, c equiv/liter. □, membrane in Cs^+ form; ○, membrane in Sr^{2+} form; ○, membrane in Na^+ form.

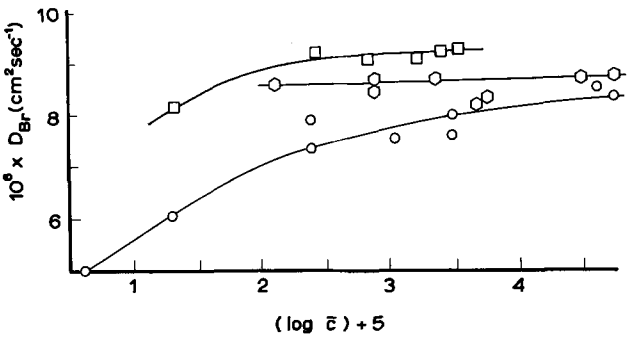

Fig. 2. Diffusion coefficient of Br^-, D_{Br}, in Zeo-Karb 315 at 25°C as a function of logarithmic bromide concentration in the membrane, $\bar{c}$ equiv/liter. □, membrane in Cs^+ form; ○, membrane in Sr^{2+} form; ○, membrane in Na^+ form.

concentrated and these are the regions least obstructed by polymer chains.

The internal concentration of the coions must be the main variable which controls the changes in D_{Br} with the concentration of the external solution. In Fig. 2 D_{Br} is plotted against the logarithm of the concentration of coions in the resin. It may be seen that D_{Br} scarcely alters over the range in which the concentration of Br^- in the resin is decreased from 5 x 10^{-1} to 5 x 10^{-3} equiv/liter. The most extended concentration range was covered with the membrane in the Na^+ form. Here, lowering the coion concentration by a further factor of a hundred from 5 x 10^{-3} to 5 x 10^{-5} equiv/liter lowers D_{Br} by about 30%.

In their cation exchanger Glueckauf and Watts (16) observed a steady decrease in D_{Br} by about fivefold over the concentration range of coions which we have studied. In a detailed analysis of the structure of their resin Glueckauf (17) showed that the distribution of fixed charge density, and hence of the coions, was very nonuniform. By comparing our data qualitatively with theirs the conclusion may be drawn that in our resin the distribution of the coions is not far from uniform and the polymer network structure basically homogeneous. However, there appears to be a small volume of material with a fixed charge density considerably lower than the average. The labyrinthine interconnection of these regions of low fixed charge density throughout the membrane creates a network of channels which interpenetrate the main structure. At low external concentrations the bromide coions are situated mainly in these regions and hence they diffuse along routes of greater than average tortuosity. This view of the resin structure is consistent also with an analysis of the bromide ion uptake data (18). At higher external concentrations the contribution of this low fixed charge density network to the coion transport is small, and its influence on the counterion transport is probably always negligible.

Figure 2 also shows that at any given coion concentration the value of D_{Br} depends on the nature of the cations. It increases in the order $Na^+ < Sr^{2+} < Cs^+$. The Na^+ form of the membrane has the largest volume and water content and the Cs^+ form the smallest. If swelling changes were causing differences between D_{Br} with the different counterions then D_{Br} would be expected to vary in the reverse direction from that observed. However this factor is probably unimportant because the variations in the water content and volume of the swollen resin with its cationic form do not exceed 2%.

It is doubtful also whether differences between the demands of the different cations on the available water for their hydration shells were important. In every case when in dilute solution there were more than seventy water molecules per counterion in the resin whereas D_{Br} scarcely changed in any given cationic form when, with the entry of the sorbed electrolyte at higher concentrations, the number of water molecules per cation was decreased from 70 to 30.

Table II. Energies of activation E for ion permeation and diffusion in Zeo-Karb 315

Ion	Concentration c (equiv/liter)	E kcal/mole
Br^-	0.05 (Na^+ form)	4.2
Br^-	1.0 (Na^+ form)	4.7
Br^-	0.005 (Sr^{2+} form)	4.1
Br^-	0.5 (Sr^{2+} form)	4.0
Na^+	0.1	5.6
Cs^+	0.05	4.8
Sr^{2+}	0.02	4.6
Sr^{2+}	0.1	4.9
Sr^{2+}	1.0	4.0

The order of the cations in which D_{Br} increases is also the order of increasing thermodynamic affinity of the resin for the counterions (11). It seems likely therefore that the frictional interaction between the coions and water does not depend on the nature of the counterions, but the interactions between the coions and counterions do so depend. These interactions produce the differences between D_{Br} in the different cationic forms of the resin.

This dependence could arise in two closely interconnected ways. The thermodynamically more preferred counterions should on the average be found closer to the polymer matrix on account of their stronger interaction with it. Thus they would offer less physical obstruction to the diffusing coions which tend to avoid the fixed charges. If the univalent counterions were paired with the fixed charges, the local electric potential in the regions most freely accessible to the coions would be more nearly uniform than if the counterions and fixed charges were largely independent in location. Such ion-pairing, even on a loose time-average basis, would therefore minimize the electrostatic energy barriers met by the diffusing coions.

Information on energy barriers is frequently sought from energies of activation. Table II lists the apparent energies of activation for diffusion calculated from the data in Fig. 3. The accuracy of these energies of activation is not better than ± 0.2 kcal/mole. The activation energy for Br^- diffusion in the Na^+ form of the membrane appears to be significantly greater than that in the Sr^{2+} form. This observation correlates satisfactorily with the suggested greater interaction between coions and counterions in the Na^+ form, especially at higher concentrations, when the counterions are interacting only weakly with the matrix. In both forms of the membrane the energy of activation for Br^- diffusion is close to that in ordinary aqueous solutions, 4.07 kcal/mole (19). This agreement emphasizes that the diffusion mechanism of Br^- ions in the membrane is essentially the same as in aqueous solutions.

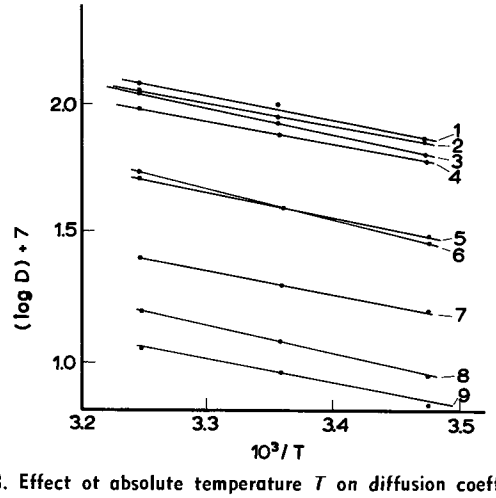

Fig. 3. Effect of absolute temperature T on diffusion coefficient D of various ions in Zeo-Karb 315. Line 1, D_{Br} in Sr^{2+} form at $c = 0.005$ equiv/liter, 2, D_{Br} in Sr^{2+} form at $c = 0.5$ equiv/liter, 3, D_{Br} in Na^+ form at $c = 1.0$ equiv/liter, 4, D_{Br} in Na^+ form at $c = 0.05$ equiv/liter, 5, D_{Cs} at $c = 0.05$ equiv/liter, 6, D_{Na} at $c = 0.1$ equiv/liter, 7, D_{Sr} at $c = 1.0$ equiv/liter, 8, D_{Sr} at $c = 0.1$ equiv/liter, 9, D_{Sr} at $c = 0.02$ equiv/liter.

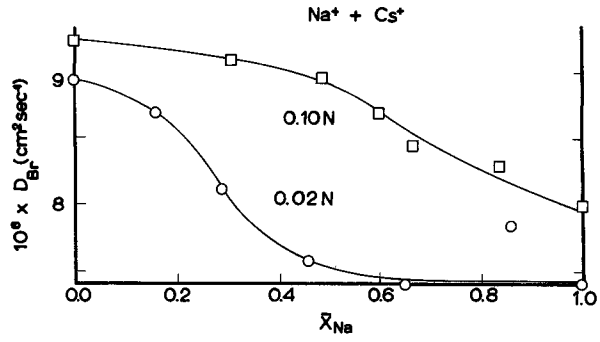

Fig. 4. Diffusion coefficient of Br^-, D_{Br}, in Zeo-Karb 315 at 25°C containing Na^+ and Cs^+ ions plotted against equivalent fraction of Na^+ ions in the membrane, $\bar{X}_{Na}$. ○, 0.02 equiv/liter Br^- in external solution; □, 0.10 equiv/liter Br^- in external solution.

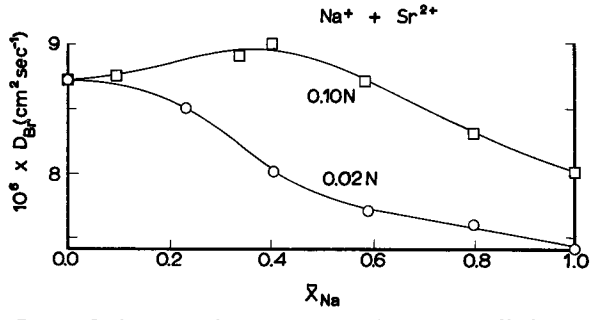

Fig. 5. Diffusion coefficient of Br^-, D_{Br}, in Zeo-Karb 315 at 25°C containing Na^+ and Sr^{2+} ions plotted against equivalent fraction of Na^+ ions in the membrane, $\bar{X}_{Na}$. ○, 0.02 equiv/liter Br^- in external solution; □, 0.10 equiv/liter Br^- in external solution.

The behavior of D_{Br} as Cs^+ or Sr^{2+} counterions are progressively replaced by Na^+ at two different total external solution concentrations and at 25°C is shown in Fig. 4 and 5. In each case D_{Br} fell rapidly in the more dilute solutions (0.02 equiv/liter) as the Na^+ ions were introduced. D_{Br} had reached almost its value in the pure Na^+ form by the time 50% of the counterions were Na^+. Evidently once 50% of the counterions in the resin were Na^+ the counterions which the coions met were almost exclusively Na^+. In such dilute solutions the regions of lowest fixed charge density contributed significantly to the transport of Br^-. Probably the first nonpreferred counterions, Na^+, to enter the resin were also located mainly in these more dilute regions where they balanced the few fixed charges.

At 0.10 equiv/liter the decrease in D_{Br} occurred more smoothly and gently as Cs^+ ions were replaced by Na^+. This behavior is consistent with the almost uniform distribution of the bromide ions which is believed to exist at higher external concentrations. A flat maximum was observed in the curve of D_{Br} in the Na^+/Sr^{2+} mixtures. Its height was scarcely greater than the experimental uncertainty. A real effect of this kind might however arise if a more nearly uniform electrical potential distribution in the resin were achieved once some univalent counterions were introduced in exchange for bivalent ones. This could occur because the detailed balancing and screening of the fixed charges would be more complete in the presence of some univalent counterions.

Counterions.—The diffusion coefficients of the three counterions, Na^+, Cs^+ and Sr^{2+}, are plotted in Fig. 6

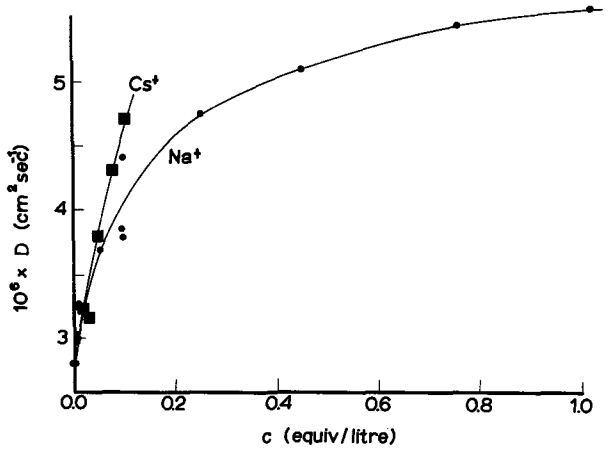

Fig. 6. Diffusion coefficients of Na^+ and Cs^+ in Zeo-Karb 315 at 25°C as functions of external solution concentration, c equiv/liter. ■ Cs^+, ● Na^+.

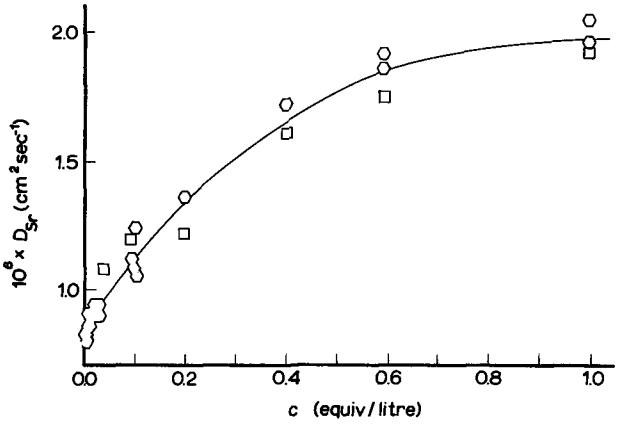

Fig. 7. Diffusion coefficients of Sr^{2+} in Zeo-Karb 315 at 25°C as a function of external solution concentration, c equiv/liter. ○, steady permeation method; □, time-lag method.

and 7 against the concentration of the external solutions. In every case it can be seen that the diffusion coefficient increased with increasing concentration over the whole range. This is in contrast with D_{Br} which was almost constant above 0.1 equiv/liter. The increase in D over the range 0-1 equiv/liter was about twofold for Na^+ and Sr^{2+}.

Although this pattern of behavior has been observed by many workers (1) it has not yet been explained quantitatively. The counterions are attracted by the fixed charges and as a result experience considerable frictional interaction with the polymer matrix. As well they are exposed to the electric field of the fixed charges which fluctuates from point to point in the gel. Jakubovic *et al.* (20) have suggested that the electrical influence may be so great that in a highly swollen resin and in the absence of coions the counterions migrate mainly from fixed ion to fixed ion along the polymer chains. Thus they follow paths of greater tortuosity than required by purely geometrical considerations. To jump from the ionic atmosphere around one chain into that of another involves surmounting the intervening potential barrier. This process, called "volume diffusion" by Jakubovic *et al.*, can take place more readily with counterions of low charge and high hydrated radius because they interact least with the fixed charges. Volume diffusion should be facilitated by increasing the temperature and by increasing the concentration of coions which can act as "electrical bridges" by smoothing the potential peaks between the neighboring fixed charges.

This mechanism is in qualitative agreement with the observed facts. The activation energies for diffusion of Na^+ and Cs^+ ions in the membrane (Table II) are

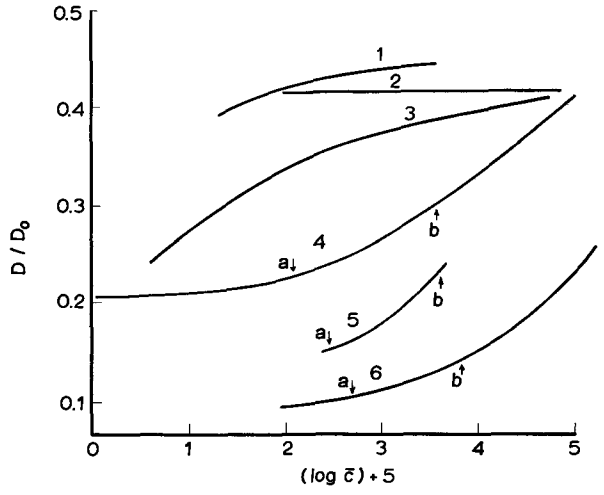

Fig. 8. Ratio of diffusion coefficients in Zeo-Karb 315 to those in dilute solution, D/D_o, as a function of logarithmic bromide concentration in the membrane, $\bar{c}$ equiv/liter. Curve 1, Br^- in Cs^+ form; curve 2, Br^- in Sr^{2+} form; curve 3, Br^- in Na^+ form; curve 4, Na^+ in Na^+ form; curve 5, Cs^+ in Cs^+ form; curve 6, Sr^{2+} in Sr^{2+} form. a, indicates external concentration c = 0.02 equiv/liter; b, indicates external concentration c = 0.10 equiv/liter.

each about 1 kcal/mole larger than in aqueous solution where the values are 4.4 and 3.9, respectively (19). The same is probably true of Sr^{2+}, but no value is available for the activation energy in free solution for comparison. The activation energy appeared to decrease at high concentrations in the Sr^{2+} state, and this would accord with the view that at high concentrations there is a more plentiful supply of coions to lower the electric potential barriers between the chains.

A clearer comparison between the three counterions is seen in Fig. 8 where, for each ion, the ratio of its diffusion coefficient in the resin to that in free solution, D/D_o, is plotted against the logarithm of the coion concentration. Also shown in Fig. 8 are the curves of D/D_o for Br^- ions in each ionic form of the membrane. It can be seen that D for each counterion increases in much the same way on increasing the coion concentration.

Cs^+ and Sr^{2+} are relatively more retarded in the resin than is Na^+. This is consistent with their stronger interactions with the matrix as indicated by the thermodynamic preferences (11). At the highest concentration D/D_o for Na^+ was close to that for Br^-. It may be concluded that at high coion concentrations the migration of highly hydrated nonpreferred counterions such as Na^+ occurs freely by volume diffusion and that the potential barriers favoring chain diffusion are unimportant. With the less hydrated Cs^+ and more highly charged Sr^{2+} counterions the situation in which there were insignificant electrical barriers to volume diffusion was not reached at the concentrations studied (21).

It can be seen that D/D_o for Sr^{2+} was less than for Cs^+ although the thermodynamic equilibrium constants showed a preference for Cs^+ over Sr^{2+} Evidently the electrical potential barriers were greater and volume diffusion less easy for the bivalent ions because a pair consisting of a fixed charge and a bivalent counterion carries a residual positive charge.

Lifson and Jackson (22) and Jackson and Coriell (23) have examined theoretically a similar electric potential barrier phenomenon which controls the diffusion coefficient of the counterions in a salt-free polyelectrolyte solution as a function of concentration. Clifford and Pethica (24) have applied this theory to the diffusion of counterions in micellar solutions and have attempted to take into account the effect of added salt. They predicted and observed an increase in D

as the added salt concentration was increased. Although the results predicted by these treatments of idealized models of polyelectrolytes and micelles are comparable with the effects observed in the ion-exchange membrane, it seems improbable that in the nonuniform and relatively randomly entangled and cross-linked network of the resin matrix the processes of chain and volume diffusion could be distinguished sufficiently clearly to enable a quantitative theory to be developed on this basis.

Data on the diffusion coefficients of the counterions in the heteroionic states of the membrane are shown in Fig. 9-12 where the diffusion coefficients are plotted against the equivalent fraction $\overline{X}_{Na}$ of Na^+ in the membrane. In every case the diffusion coefficients of both ions decreased as $\overline{X}_{Na}$ was increased (the maximum in D_{Na} in the Na^+/Sr^{2+} state at 0.1 equiv/liter seen in Fig. 12 is referred to later). The relative changes were different for the three ions; D_{Cs} was affected by composition more than D_{Na} and D_{Sr} was affected most.

In each mixture the concentration of coions decreased as $\overline{X}_{Na}$ increased and, in the light of the observations with single salts, this would shift both counterion diffusion coefficients in the observed direction. It can easily be seen from Fig. 8 that the effect of these changes in coion concentration would alone

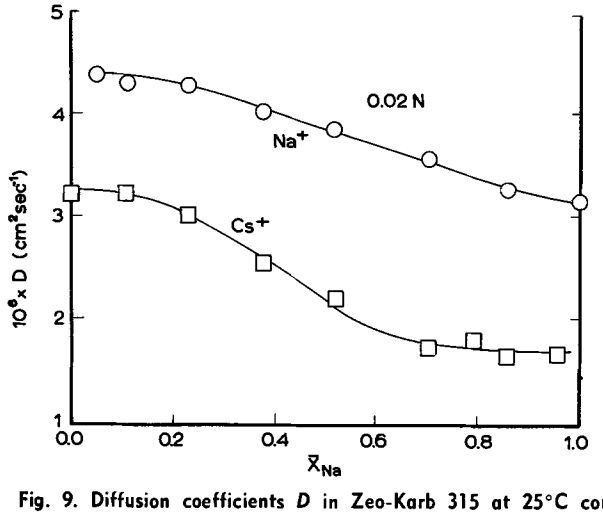

Fig. 9. Diffusion coefficients D in Zeo-Karb 315 at 25°C containing Na^+ and Cs^+ ions plotted against equivalent fraction of Na^+ ions in the membrane, $\overline{X}_{Na}$. Total solution concentration 0.02 equiv/liter. ○ D_{Na}, □ D_{Cs}.

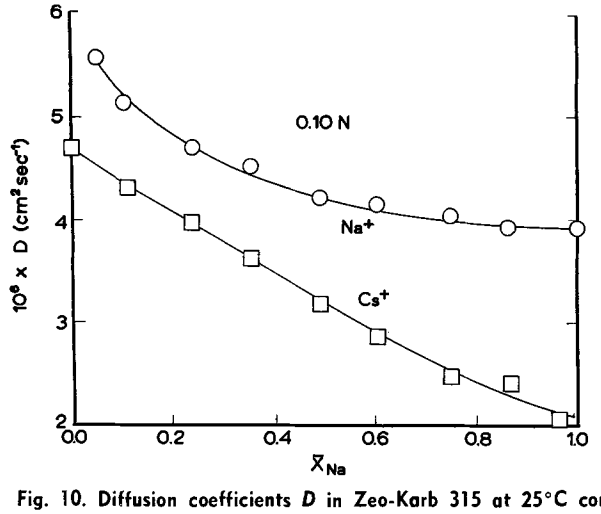

Fig. 10. Diffusion coefficients D in Zeo-Karb 315 at 25°C containing Na^+ and Cs^+ ions plotted against equivalent fraction of Na^+ ions in the membrane, $\overline{X}_{Na}$. Total solution concentration 0.10 equiv/liter. ○ D_{Na}, □ D_{Cs}.

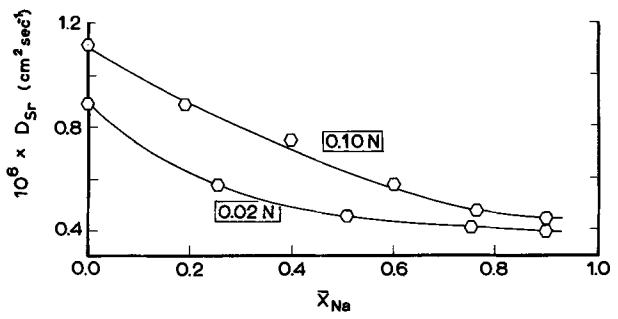

Fig. 11. Diffusion coefficient D_{Sr} of Sr^{2+} ions in Zeo-Karb 315 at 25°C containing Na^+ and Sr^{2+} ions plotted against equivalent fraction of Na^+ ions in the membrane, $\overline{X}_{Na}$. Curve 1, total solution concentration 0.10 equiv/liter; curve 2, total solution concentration 0.02 equiv/liter.

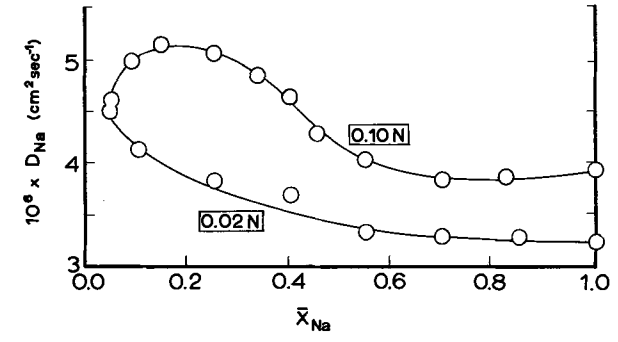

Fig. 12. Diffusion coefficient D_{Na} of Na^+ ions in Zeo-Karb 315 at 25°C containing Na^+ and Sr^{2+} ions plotted against equivalent fraction of Na^+ ions in the membrane, $\overline{X}_{Na}$. Curve 1, total solution concentration 0.10 equiv/liter; curve 2, total solution concentration 0.02 equiv/liter.

be much too small to account for the observed decreases in the diffusion coefficients.

It must be concluded that the observed behavior was connected with the fact that Na^+ was the nonpreferred ion in both mixtures. When the membrane is loaded entirely with preferred ions (*i.e.*, the left-hand sides of Fig. 9-12) these ions take up an equilibrium distribution with respect to the fixed charges and coions. Some will be in any densely cross-linked regions of unusually high fixed charge density, others in the unusually dilute and swollen regions. At any instant some counterions will be close to and interacting strongly with the electric fields of the fixed charges, others will be far away from these charges in regions where the electric field strengths are quite low. The observed diffusion coefficient is an average of the instantaneous mobilities of all these counterions.

When a few Na^+ ions are introduced it may be inferred from the well-known variation of ion-exchange selectivity with cross-linking that these nonpreferred ions mostly will take up positions in the least dense regions of the resin. In these regions the coion concentration is higher than average, and the nonpreferred counterions spend a lower proportion of their time close to the fixed charges than they would in the denser regions. These factors contribute to the high mobility of the first Na^+ ions which enter the Cs^+ or Sr^{2+} forms of the membrane.

At 0.02 equiv/liter the limit of D_{Na} as $\overline{X}_{Na}$ tended to zero was about 4.5×10^{-6} cm^2 sec^{-1} in Na^+/Cs^+ and in Na^+/Sr^{2+} mixtures. At 0.10 equiv/liter in mixtures of Na^+/Cs^+ D_{Na} reached a limit of about 6×10^{-6} cm^2 sec^{-1}. This was slightly greater than the value in the pure Na^+ state at high external solution concentrations.

In the Na^+/Sr^{2+} mixture at 0.1 equiv/liter the behavior of D_{Na} as $\overline{X}_{Na}$ was decreased from 1.0 to 0.3 suggested that it would rise to about 6×10^{-6} cm^2

sec^{-1} as $\overline{X}_{Na}$ tended to zero. Once $\overline{X}_{Na}$ was taken below 0.2 however D_{Na} appeared to decrease. The maximum in D_{Na} did not appear to be due to errors or difficulties in the permeation experiments, and unexpectedly large errors in the equilibrium measurements would be necessary to explain the maximum in D_{Na} in this way. The decrease in D_{Na} when $\overline{X}_{Na} < 0.2$ may be due to less complete screening of the fixed charges when the resin is loaded with only multivalent counterions than is possible when some univalent counterions also are present.

Just as the first Na^+ ions to enter the membrane are concentrated into the regions where mobility is greatest so the Cs^+ and Sr^{2+} ions are displaced from these regions and their average mobilities, *i.e.*, D_{Cs} and D_{Sr}, are decreased. As more and more Na^+ ions enter they penetrate into the denser regions of the network where they spend a greater proportion of their time close to the fixed charges. Also the fixed charges are less well shielded by Na^+ than by the preferred ions. Consequently the average mobility of the Na^+ ions falls continuously as $\overline{X}_{Na}$ increases. D_{Cs} and D_{Sr} also fall continuously and the last Cs^+ and Sr^{2+} ions remaining in the resin are situated mainly in those regions where movement is most difficult.

D_{Cs} and D_{Sr} both decrease by a factor of about 2 at 0.02 equiv/liter and 2.5 at 0.10 equiv/liter when $\overline{X}_{Na}$ is changed from 0 to 1, whereas the change in D_{Na} is only about 1.5 at both concentrations. Thus that part of the membrane transport selectivity which arises from differences between the mobilities of the ions leads to a greater discriminating power when the membrane is richest in the nonpreferred ions.

The most directly comparable results of other workers are those of Ishibashi (25) who measured diffusion coefficients and electrical mobilities in a phenol sulfonic membrane containing Na^+ and Ca^{2+} ions. In agreement with our results on the $Na^+ + Sr^{2+}$ system, he observed that the mobilities of both counterions decreased as $\overline{X}_{Na}$ increased.

Soldano and Boyd (26) examined Na^+ and Cs^+ diffusion in Dowex 50 resin cross-linked with 8% and 16% divinyl benzene and observed that D_{Na} and D_{Cs} decreased as $\overline{X}_{Na}$ increased in agreement with our findings. However in the Na^++Zn^{2+} mixture on the 16% divinyl benzene resin they found that D_{Na} and D_{Zn} increased with $\overline{X}_{Na}$.

Morig and Rao (27) studied rates of exchange between Na^+ and Sr^{2+} on Dowex 50, 8% divinyl benzene, and concluded that the discrepancy between their observations and the theoretical rates of exchange (28) would be explained if D_{Na} and D_{Sr} both increased as $\overline{X}_{Na}$ increased.

The apparent disagreement between these results on Dowex 50 and ours for the $Na^+ + Sr^{2+}$ mixture is probably a consequence of the relatively large deswelling of the Dowex 50 resins when Na^+ is replaced by Zn^{2+} or Sr^{2+}.

Conclusion

It is evident from this discussion that the changes in ionic diffusion coefficients in a cation exchange resin membrane with external solution concentration and with the equivalent fractions of the different counterions in a heteroionic state of the membrane, as well as the differences between the diffusion coefficients of different kinds of ions, can all be understood in terms of the influence of the electric fields surrounding the polymer chains and fixed charges on mobility and of the existence of a few local inhomogeneities in the fixed-charge and cross-link densities. There is no need to invoke fixation of counterions by specific ion-pairing with the fixed charges nor is there any evidence of this in the system studied here.

The relative importance of the electric fields and structural dispersities in determining the observed behavior is harder to assess. If the resin network were completely homogeneous the distances between neighboring chains would average about 25-30Å. This cannot be very different from the mean distance between the fixed charges along the chains. Consequently diffusion along chains should not be greatly favored relative to diffusion across the gaps between chains. This view is consistent with the observations that at high external concentrations the diffusion of Na^+ appears to be little affected by electrostatic fields and the introduction of relatively few coions has a large effect in facilitating the diffusion of Cs^+ and Sr^{2+}. The evidence from the sorption and diffusion of the coions is that the resin consists mainly of relatively uniform material permeated by an interconnecting network of less dense regions which makes up a small part only of the total volume. This has an important function in the diffusion of coions at low external concentrations but has almost no influence on the behavior of the counterions.

Manuscript submitted Dec. 26, 1968; revised manuscript received March 24, 1969. This was Paper 226 presented at the Boston Meeting, May 5-9, 1968.

Any discussion of this paper will appear in a Discussion Section to be published in the June 1970 JOURNAL.

SYMBOLS

a, an apparatus constant, cm.
c, solution concentration, equiv/liter.
$\bar{c}$, coion concentration in membrane, mole/liter.
D, diffusion coefficient in membrane, $cm^2\ sec^{-1}$.
D_o, diffusion coefficient in solution, $cm^2\ sec^{-1}$.
E, energy of activation for permeation, kcal/mole.
m, radio count rate at t and x, count/min.
m_o, radio count rate at $t = 0$, count/min.
r, micrometer reading, cm.
t, time, sec.
v_w, volume fraction of water in membrane.
x, distance from boundary, cm.
$\overline{X}_{Na}$, equivalent fraction of Na^+ in membrane.

REFERENCES

1. For a recent review see P. Meares, "Diffusion in Polymers," Chap. 10, J. Crank and G. S. Park, Editors, Academic Press, London, In press.
2. K. S. Spiegler, *Trans. Faraday Soc.*, **54**, 1408 (1958).
3. R. Caramazza, W. Dorst, A. J. C. Hoeve, and A. J. Staverman, *Trans. Faraday Soc.*, **59**, 2415 (1963); W. Dorst, A. J. Staverman, and R. Caramazza, *Rec. Trav. Chim. (Pays-Bas)*, **83**, 1329 (1964).
4. G. B. Wills, *Trans. Faraday Soc.*, **63**, 579 (1967).
5. P. Meares, *J. Chim. phys.*, **55**, 273 (1958).
6. F. Helfferich, *Discussions Faraday Soc.*, **21**, 83 (1956).
7. D. Mackay and P. Meares, *Kolloid-Z.*, **167**, 31 (1959).
8. R. M. Barrer, J. A. Barrie, and M. G. Rogers, *Trans. Faraday Soc.*, **58**, 2473 (1962).
9. J. A. Barrie, J. D. Levine, A. S. Michaels, and P. Wong, *ibid.*, **59**, 869 (1963).
10. J. Crank, Private communication.
11. P. Meares and J. F. Thain, *J. Phys. Chem.*, **2**, 2789 (1968).
12. K. S. Spiegler and C. D. Coryell, *J. Phys. Chem.*, **57**, 687 (1953).
13. J. Crank, "The Mathematics of Diffusion," Oxford University Press, Oxford (1956).
14. J. S. Mackie and P. Meares, *Proc. Roy. Soc.*, **A232**, 485 (1955).
15. P. Meares, *J. Polymer Sci.*, **20**, 507 (1956).
16. E. Glueckauf and D. C. Watts, *ibid.*, **A268**, 339 (1962).
17. E. Glueckauf, *ibid.*, **A268**, 350 (1962).
18. W. J. McHardy, P. Meares and K. R. Page, To be published.
19. R. Parsons, "Handbook of Electrochemical Constants," Butterworth, London (1959).
20. A. O. Jakubovic, G. J. Hills, and J. A. Kitchener, *J. Chim. phys.*, **55**, 263 (1958).
21. J. Feitelson, *J. Phys. Chem.*, **66**, 1295 (1962).
22. S. Lifson and J. L. Jackson, *J. chem. Phys.*, **36**, 2410 (1962).
23. J. L. Jackson and S. R. Coriell, *ibid.*, **38**, 959 (1963).
24. J. Clifford and B. A. Pethica, *Trans. Faraday Soc.*, **60**, 216 (1964).

25. N. Ishibashi, *Mem. Fac. Engng. Kyuchu Univ.*, **21**, 159 (1962).
26. B. A. Soldano and G. E. Boyd, *J. Am. Chem. Soc.*, **75**, 6107 (1953).
27. C. R. Morig and M. G. Rao, *Chem. Engng. Sci.*, **20**, 889 (1965).
28. F. Helfferich and M. S. Plesset, *J. chem. Phys.*, **28**, 418 (1958).

Electrochemical Processes of the Chlorine-Chloride System on Platinum-Iridium-Coated Titanium Electrodes

G. Faita, G. Fiori, and J. W. Augustynski[1]

Laboratory of Electrochemistry and Metallurgy, University of Milan, Milan, Italy

ABSTRACT

Anodic and cathodic processes of the Cl_2/Cl^- system on Ti/Pt-Ir (30% Ir) in comparison with Ti/Pt electrodes were examined. The anodic Cl_2 evolution follows the same scheme on both the electrodes

$$Cl^- \rightarrow Cl_{ads} + e$$
$$2Cl_{ads} \rightarrow Cl_2$$

but Ti/Pt electrodes undergo a marked passivation for $\eta_{an} > 0.2V$, whereas the passivation on Ti/Pt-Ir electrodes is important only at overvoltages higher than 0.5V. Such a difference in passivation is noted also in the cathodic process: on Ti/Pt-Ir electrodes in fact, at low overvoltages, the process follows the scheme

$$Cl_2 \rightarrow 2Cl_{ads}$$
$$Cl_{ads} + e \rightarrow Cl^-$$

due to the higher catalytic activity of the surface.

The electrochemical behavior of the Cl_2/Cl^- system on Pt electrodes has been studied for 70 years (1, 2) mainly owing to interest in the electrochemical production of chlorine.

From the point of view of theoretical electrochemical kinetics the first important approach was that of Chang and Wick (3) who showed that the shapes of the polarization curves for the anodic Cl_2-evolution conform to the theory of slow discharge.

For anodic Cl_2-evolution Tedoradse (4, 5) found that the maximum kinetic current is (Cl^-)- and pH-dependent according to

$$i_{max} = K\,(Cl^-)\,(pH)^{1/2}$$

He suggested that the rate-determining-step is

$$Cl^- - e \rightarrow Cl_{ads}$$

and that the pH-dependence would be due to passivation of the electrode surface.

Difficulties caused by surface oxide layers and by possible O_2-evolution were pointed out by Toshima and Okaniwa (6), whose results agree with Tedoradse's.

Other authors considered the influence of electrode passivation (7) and its dependence on pH (8), current density (9), anode potential (10, 11), and Cl^- concentration (12).

Fewer papers are available on the cathodic Cl_2 reduction (7, 13). Frumkin and Tedoradse studied the dependence of the rate of Cl_2 ionization on a smooth Pt electrode in strongly acid solution, on the electrode rotation speed, and on Cl^- concentration. These authors interpreted the kinetic mechanism according to the scheme

$$Cl_2 + e \rightleftarrows Cl_{ads} + Cl^-$$
$$Cl_{ads} + e \rightarrow Cl^-$$

both these electrochemical steps being equally rate-determining. It is noteworthy that in the above studies strong acid solutions usually were used to reduce electrode passivation effects. Pt electrodes under these conditions undergo corrosive phenomena with possible changes in surface activity.

The aim of the present work was to investigate both the anodic Cl_2-evolution and the cathodic Cl_2-reduction on a new kind of electrode, which was obtained by thermal deposition of Pt-Ir (30% Ir) alloy on a titanium substrate. Electrodes of this type recently have aroused considerable interest from the industrial point of view as an alternative to graphite anodes in chlorine cells. Such electrodes show no corrosion phenomena even in strongly acid solutions containing Cl^- plus Cl_2 (14) and the surface passivation they may undergo is considerably less than that observed on Pt surfaces.

In the present study electrochemically platinum-coated titanium electrodes also were used to get better comparison with the previous work. Thus pH 3 was chosen because corrosion of platinized titanium takes place below this pH value. All measurements were made using a rotating disk electrode which has been described in detail elsewhere (15).

Experimental Techniques and Results

Deposition of Pt-Ir (30% Ir) alloy on titanium was performed by the thermal method (16). The titanium matrix, previously machined, was heated at 500°C in air, cooled, ground, and degreased. The electrode surface was painted with a mixture of metal chlorides ($PtCl_4 \cdot 5H_2O$ and $IrCl_4$), methanol, and lavender oil and was then dried. The sequence, painting and drying, was repeated five times, until the amount of Pt+Ir as chloride, reached 1 mg/cm^2. The Pt-Ir alloy was obtained by thermal decomposition at 500°C in air (1 hr), followed by cooling in water. The layer formed (about 1μ thick) was bright and adhered well to the support.

Three electrodes were prepared in this way which showed very reproducible behavior. The temperature used during the thermal decomposition strongly affected the catalytic properties of the alloy, the catalytic activity decreasing with increasing temperature above 500°C. An electrode, obtained by decomposition at 650°C, for example, showed a poorer behavior in

[1] Present address: Ecole Supérieure d'Electrochimie et Electrométallurgie, Grenoble, France.

the cathodic reduction of chlorine than galvanic platinum.

Platinum was electrochemically deposited on titanium according to the following procedure. The cylindrical titanium stem, after being turned, was carefully ground, then sandblasted and put into a solution of the following composition (17): 14g Pt $(NH_3)_2(NO_2)_2$, 10g $(NH_4)_2$ SO_4, 50g NH_3 per liter; pH = 10. Electrolysis was carried out at 70 mA/cm², using a Pt sheet as counterelectrode at 1-cm distance with vigorous stirring, at 80°-90°C. Electrolysis was continued until a 30μ Pt layer was obtained.

Both kinds of electrodes were then cold-pressed into polytetrafluoroethylene tubing (Algoflon-Montedison). The Pt surfaces were exposed by polishing with alumina. The diameter of the working electrode was 10 mm, the total diameter (metal + plastic) being 20 mm. Figure 1 shows the measuring circuit and the measuring technique. Required potentials were set up using a 557 AMEL potentiostat and read on a 610B Keithley electrometer. Before each set of measurements the electrodes were activated by 10 polarization cycles in the same test solution. In each cycle the electrode was potentiostated anodically at +1.7V (NHE) for 10 sec then cathodically at −0.4V (NHE) for 10 sec.

The measurements were made potentiostating the electrodes cathodically at −0.4V (NHE) for 3 sec, then at the required potentials; the polarizing current was read after 15 sec. The tip of the reference electrode was placed 10 mm under the working electrode. The ohmic drop, calculated by oscillographic methods, was always <5% of the total overvoltage (η) except for the anodic polarization on Ti/Pt-Ir electrodes, where the ohmic drop was about 10% of the total overvoltage. The question of the distribution of the current on the electrode surface was considered on the basis of Newman's theory (18). In our conditions, when η is <50 mV, the local current density shows a maximum deviation of ± 10% with respect to the average current density. When η is >>50 mV, such a deviation is very small.

Test solutions were made up with reagent grade chemicals ($NaClO_4$ from BDH, NaCl from C. Erba and triply distilled water). Solutions were saturated by Cl_2-N_2 mixtures (1 ± 0.01% to 10 ± 0.1% in Cl_2). Temperature of experiments was regulated to 30° ± 0.2°C by means of a specially designed air-thermostat.

Figure 2 shows typical cathodic polarization curves obtained, at constant rotation speed, for both types of electrodes, whose cathodic behavior was tested as a function of NaCl concentration and rotation speed. Figure 3 shows anodic polarization curves, obtained under various experimental conditions.

Discussion

Chlorine reduction.—On the basis of the rotating disk electrode theory the functional dependence of current density on rotation speed may be written as

$$1/i^{1/p} = 1/i_L^{1/p} + [i^{(p-1)/p} \times B]/\sqrt{\omega} \times C_S$$

where p is the reaction order of the surface reaction with respect to the reactant, i the current density at rotation speed ω, i_L the current density at infinite rotation speed, C_S the bulk concentration of the re-

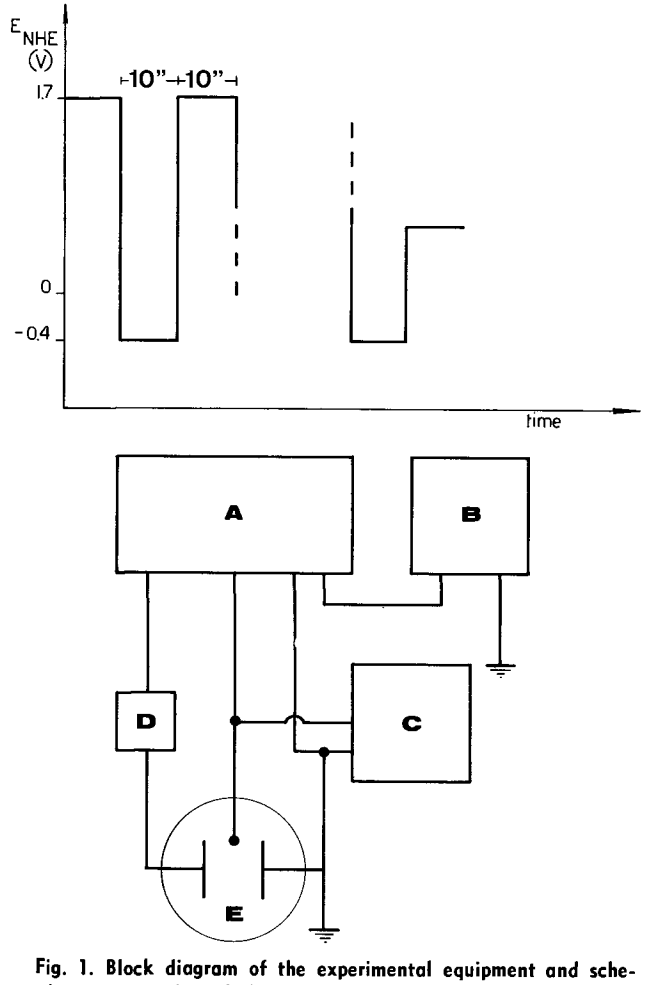

Fig. 1. Block diagram of the experimental equipment and schematic representation of the activation and measurement sequence. A—potentiostat, B—activation circuit, C—valve electrometer, D—amperometer, and E—cell.

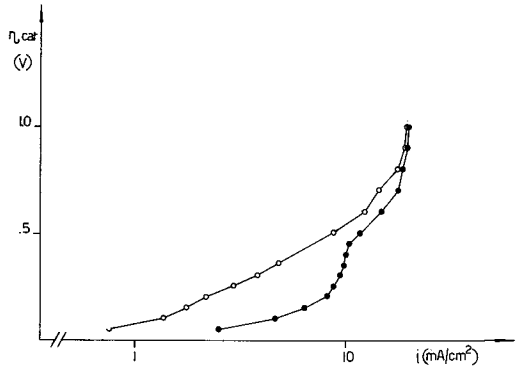

Fig. 2. Cathodic polarization curves. 1M $NaClO_4$; 0.02M NaCl; 1.00% Cl_2; 4100 rpm; 30°C. ○ Ti/Pt. ● Ti/Pt-Ir (30% Ir).

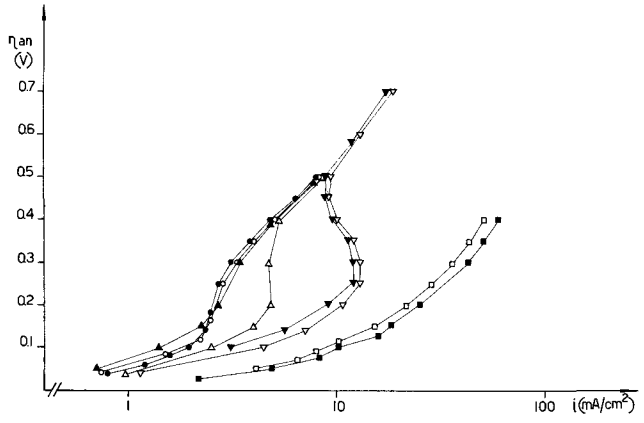

Fig. 3. Anodic polarization curves. 1M $NaClO_4$; 1.00% Cl_2; 30°C.

● 0.02M NaCl	m = 850 rpm electrode: Ti/Pt
○ 0.02M NaCl	m = 2800 rpm electrode: Ti/Pt
△ 0.07M NaCl	m = 850 rpm electrode: Ti/Pt
▲ 0.07M NaCl	m = 2800 rpm electrode: Ti/Pt
▽ 0.14M NaCl	m = 850 rpm electrode: Ti/Pt
▼ 0.14M NaCl	m = 2800 rpm electrode: Ti/Pt
■ 0.07M NaCl	m = 1500 rpm electrode: Ti/Pt-Ir
□ 0.02M NaCl	m = 1500 rpm electrode: Ti/Pt-Ir

actant, and B a factor including all constant terms derived from the analytical treatment.

Plots of $1/i^{1/p}$ against $i^{(p-1)/p}/\sqrt{\omega}$ should be straight lines only if the true value for p is used. The cathodic data were tested against various postulated values for p: a linear plot was obtained in the case $p = 1$, with the exception of the data concerning Pt-Ir electrodes at overvoltages less than 0.2V (Fig. 4 and 5). The intercepts on the $1/i^{1/p}$ axis allow the current densities at infinite rotation speed (i_L) to be computed. Data at high rotation speed (8,000 $\simeq$ 10,000 rpm) would be useful to avoid long extrapolations; unfortunately, in these extreme conditions the currents showed such instability that the accuracy of measurements was strongly affected. It seems likely that at the highest speeds, the surface roughness, although slight, might have produced turbulent conditions close to the electrode.

In order to improve the reliability of the extrapolated data, the experiments at various rotation speeds were repeated at least three times: the data used in the plots of $1/i^{1/p}$ against $i^{(p-1)/p}/\sqrt{\omega}$ for different overvoltages were the average values from the various measurements.

As regards the cathodic data of the Pt-Ir electrodes for overvoltages less than 0.2V, almost linear plots were obtained if a value of 0.5 for p was used. This remarkable result was experimentally checked by carrying out measurements at overvoltages less than 0.2V in the presence of chlorine at concentration of 1 and 10%; the ratio of the current densities, at the same electrode potentials, confirmed the reaction order to be 0.5. Electrode potentials were plotted against the log of the extrapolated i_L at various Cl^- concentrations. Since the i_L values, at the same electrode potentials, were independent of the Cl^- concentration, the reaction order with respect to Cl^- ion should be 0 (13) (Fig. 6 and 7). Experimental kinetic parameters (Tafel b-coefficient, exchange current, charge transfer resistance, stoichiometric number, reaction order) are

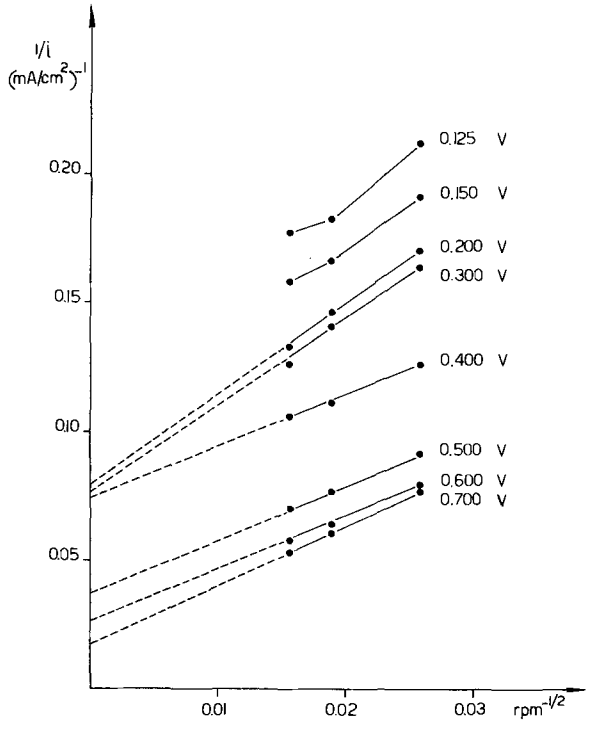

Fig. 4. Dependence of $1/i$ on $1/\sqrt{m}$ at specified values of η_C 1M $NaClO_4$; 0.07M NaCl; 1.00% Cl_2; 30°C; Ti/Pt-Ir(30% Ir).

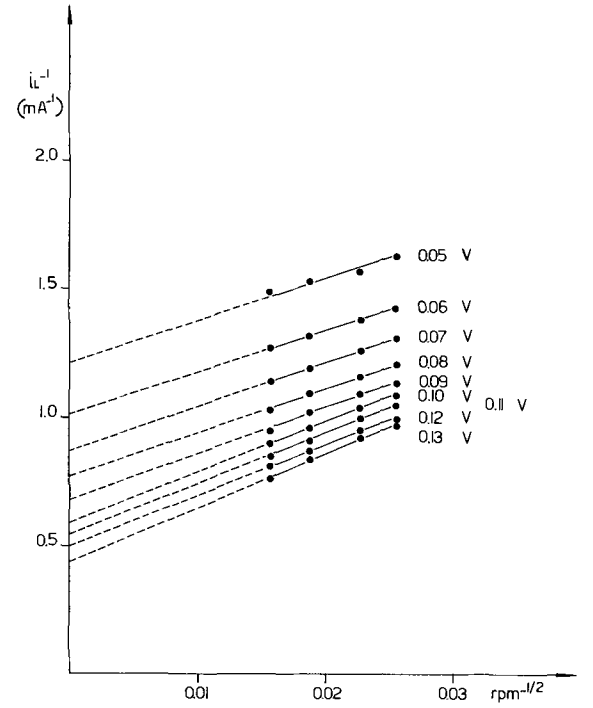

Fig. 5. Dependence of $1/i$ on $1/\sqrt{m}$ at specified values of η_C 1M $NaClO_4$; 0.05M NaCl; 1.00% Cl_2; 30°C; Ti/Pt.

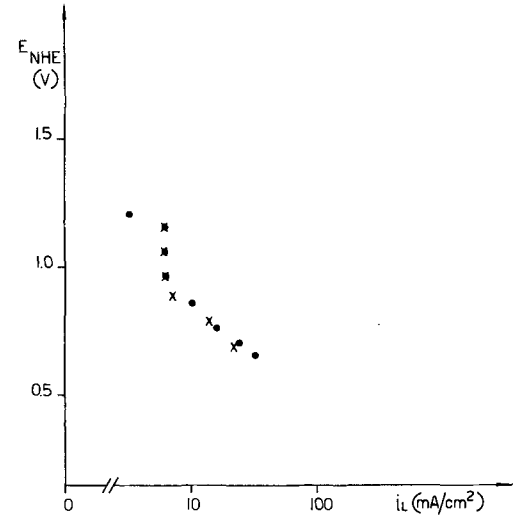

Fig. 6. Dependence of electrode potential on log i_L for two NaCl concentrations. 1M $NaClO_4$; 1.00% Cl_2; 30°C; Ti/Pt-Ir (30% Ir). △ 0.02M NaCl. ● 0.07M NaCl.

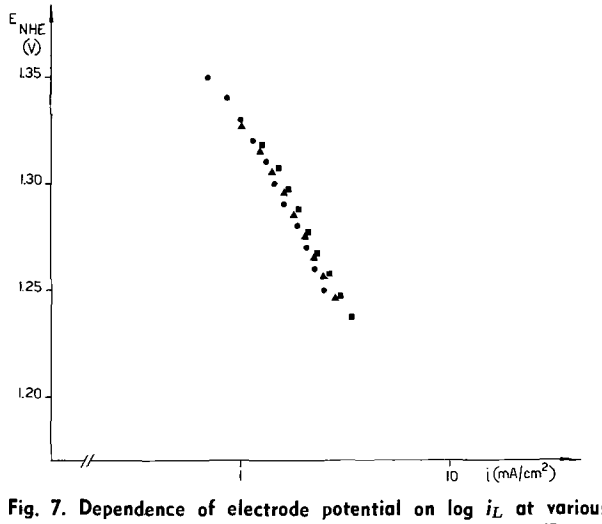

Fig. 7. Dependence of electrode potential on log i_L at various NaCl concentrations. 1M $NaClO_4$; 1.00% Cl_2; 30°C; Ti/Pt. ● 0.02M NaCl. ▲ 0.05M NaCl. ■ 0.08M NaCl.

Table I. Kinetic parameters of the cathodic Cl_2-discharge

Electrode		Ti/Pt-Ir (30% Ir)	Ti/Pt
Tafel coefficient "b"	$\eta_{cat} \leq 0.2V$	0.18	0.2
	$0.25 \leq \eta_{cat} \leq 0.4$	$\rightarrow \infty$	0.4 ÷ 0.5
	$\eta_{cat} > 0.5V$	—	0.4 ÷ 0.5
i_o (mA/cm²)		2.0	0.46
Stoichiometric number		2.0	2.3
$\left(\frac{\Delta\eta}{\Delta i}\right)_{i\to 0}\left(\frac{V\cdot cm^2}{A}\right)$		12	70
Reaction order with respect to Cl_2		0.5 ($\eta < 0.2V$) 1 ($\eta > 0.2V$)	1
Reaction order with respect to Cl⁻		0	0

Table II. Kinetic parameters of the anodic Cl_2-evolution

Electrode		Ti/Pt-Ir (30% Ir)	Ti/Pt
Tafel coefficient "b"	$\eta_{an} < 0.2V$	0.15 ÷ 0.2	0.12
	$\eta_{an} > 0.4V$	0.6	0.6
i_o (mA/cm²)		2.5	0.6
Stoichiometric number		2.0	1.9
$\left(\frac{\Delta\eta}{\Delta i}\right)_{i\to 0}\left(\frac{V\cdot cm^2}{A}\right)$		12	50
Reaction order with respect to Cl_2		0	0

summarized in Table I. Taking into account the ohmic drop, current distributions, and other experimental uncertainties, the accuracy of Tafel b-coefficients and of the exchange currents was about ±5%, that of the charge transfer resistance being ±10%.

A combined knowledge of the reaction orders, stoichiometric numbers, and Tafel coefficients enable the mechanism of the electrode process to be elucidated. In Table III possible mechanisms of the cathodic Cl_2 reduction and related kinetic parameters are summarized. By comparing theoretical with experimental parameters, it is clear that the cathodic chlorine reduction on Ti/Pt-Ir electrodes follows two different schemes depending on the overvoltage range:

$\eta < 0.2V$.—The process follows path C, with C_2 rate determining step (RDS).

$0.25V < \eta < 0.5V$.—The process still follows path C, but now C_1 is the RDS, since the velocity of step C_2 increases with increasing overvoltage. A similar behavior was observed in the case of the kinetics of hydrogen evolution (19).

$\eta > 0.5V$.—Experimental results agree with the parameters theoretically required by both path A [at high overvoltages A_1 is in any case RDS (20)] and B (RDS B_1). Paths A and B have the same first electrochemical step; the second step is again electrochemical in path A, but chemical in path B.

The application of the same analysis to the data of galvanic platinum showed that the cathodic process always follows either path A (steps A_1 and A_2 comparably rate-controlling) or path B (B_1 RDS).

The main difference between the thermal Pt-Ir electrodes and galvanic platinum is described by the behavior at cathodic overvoltages less than 0.5V (Fig. 2): as a matter of fact the Pt-Ir alloy shows more favorable current-voltage characteristics owing to the higher catalytic activity of the surface. The effect of decomposition temperature on the catalytic activity has been pointed out in the section on Experimental techniques and results.

Cl_2 *evolution.*—By comparing the parameters theoretically required (Table IV) with the experimental results (Table II) on Ti/Pt-Ir electrodes, it turns out that the anodic chlorine evolution may follow both path A' (steps A'_1 and A'_2 comparably rate-controlling) and C' (C'_1 RDS), whereas path B' must be rejected because anodic currents are unaffected by P_{Cl_2}. In order to elucidate whether path A' or C' is valid a critical discussion on $(\Delta\eta/\Delta i)_{i\to 0}$ and i_o values is needed. Anodic and cathodic i_o values, obtained from the Tafel slopes, are practically identical. Furthermore, the anodic and cathodic values of $(\Delta\eta/\Delta i)_{i\to 0}$ are also identical: therefore the anodic process seems

Table III. Kinetic parameters theoretically required by different cathodic mechanisms

	Mechanism	RDS	Stoichiometric number	Reaction order with respect to Cl_2	Reaction order with respect to Cl⁻	"b" Tafel coefficient
A	1) $Cl_2 + e \rightarrow Cl_{ads} + Cl^-$	A_1	1	1	0	$RT/\alpha F$
	2) $Cl_{ads} + e \rightarrow Cl^-$	A_2	1	1	−1	$RT/(1+\alpha)F$
		$A_1 \simeq A_2$	2*	1	0	
B	1) $Cl_2 + e \rightarrow Cl_{ads} + Cl^-$	B_1	2**	1	0	$RT/\alpha F$
	2) $2Cl_{ads} \rightarrow Cl_2$	B_2	1**	2	−2	$RT/2F \leq b \leq \infty$
C	1) $Cl_2 \rightarrow 2Cl_{ads}$	C_1	—	1	0	$\rightarrow \infty$
	2) $Cl_{ads} + e \rightarrow Cl^-$	C_2	2	0.5	0	$RT/\alpha F$

Either step A_1 and B_1 could be interpreted as two-stage steps
$Cl_2 + e \rightarrow Cl_{2ads}^-$
$Cl_{2ads}^- \rightarrow Cl_{ads} + Cl^-$ (fast chemical equilibrium)

* The stoichiometric number in this case was obtained following Krishtalik's treatment (22), which requires knowledge of the ratio $\gamma = i_{oA_1}/i_{oA_2}$. This is achieved recalling that extrapolation of the anodic Tafel line to $\eta = 0$ gives $2i_{oA_2}$ as intercept, while extrapolation of the cathodic gives $2i_{oA_1}$.

** Stoichiometric numbers in the case of mechanism B were obtained following Makrides treatment (23).

Table IV. Kinetic parameters theoretically required by possible anodic mechanisms

	Mechanism	RDS	Stoichiometric number	Reaction order with respect to Cl_2	Reaction order with respect to Cl⁻	"b" Tafel coefficient
A'	1) $Cl^- - e \rightarrow Cl_{ads}$	A'_1	1	0	1	$RT/(1-\alpha)F$
	2) $Cl_{ads} + Cl^- - e \rightarrow Cl_2$	A'_2	1	0	2	$RT/[(1-\alpha)+1]F$
		$A'_1 \simeq A'_2$	2	0	1	$RT/(1-\alpha)F$
B'	1) $Cl_2 - 2Cl_{ads}$	B'_1	—	1	0	$\rightarrow \infty$
	2) $Cl_{ads} + Cl^- - e \rightarrow Cl_2$	B'_2	2	0.5	1	$RT/(1-\alpha)F$
C'	1) $Cl^- - e \rightarrow Cl_{ads}$	C'_1	2	0	1	$RT/(1-\alpha)F$
	2) $2Cl_{ads} \rightarrow Cl_2$	C'_2	1	0	2	$RT/2F$ $\theta \rightarrow 0$; $\rightarrow \infty$ $\theta \rightarrow 1$

Either step A'_2 and B'_2 could be interpreted as two-stage steps
$Cl_{ads} + Cl^- \rightarrow Cl_{2ads}^-$ (fast chemical equilibrium)
$Cl_{2ads}^- - e \rightarrow Cl_2$

to be exactly symmetrical to the cathodic process at $\eta < 0.2V$ and probably follows path C'.

For the Pt electrode, at $\eta < 0.2V$, both paths A' and C' are possible. Recalling the cathodic results on the same electrode, the more reasonable conclusions are: (*i*) cathodic and anodic processes are symmetrical (A and A') and (*ii*) the cathodic mechanism is B and the anodic one is C'.

If the anodic and cathodic processes were symmetrical, the exchange currents would fulfill the relation (20)

$$\left(\frac{\Delta\eta}{\Delta i}\right)_{i\to o} = \frac{RT}{2F}\left(\frac{1}{i_{o,an}} - \frac{1}{i_{o,cat}}\right)$$

which is not the case (Table I and II). Therefore on platinum electrodes the cathodic process probably follows path B and the anodic one path C'. This asymmetric behavior is clearly determined by the step $2Cl_{ads} \rightarrow Cl_2$, which is faster than both steps A_2 and A'_2.

The shape of the anodic polarization curves on platinum electrodes shows a surface passivation at $\eta > 0.2V$ [Cl^- diffusion current should be about 10 times higher (21)]. At high Cl^- concentration the passivation is incomplete (8), the currents, read after 15 sec, are not stationary and decrease as rotation speed increases. Such a behavior may be determined by a more efficient mass transport of the passivating species, *e.g.*, ClO^- ions. At $\eta > 0.5V$ the passivation is, however, complete and the anodic current is unaffected by Cl^- concentration and rotation speed. On Pt-Ir the oxide layer formation takes place only at $\eta > 0.4V$. This property, rather than the outstanding catalytic activity, allows the very advantageous anodic voltage current characteristic of thermal Pt-Ir electrode, which seems especially suitable for brine electrolysis. At $\eta > 0.4V$ the b-Tafel coefficients are identical for both electrodes: the surfaces are surely covered with oxide species and the anodic mechanism should then implicate the intermediate formation of oxychlorides (24). Clearly, at such overvoltages, the possibility of chlorate formation and oxygen discharge should be considered.

Conclusions

Anodic and cathodic processes of the Cl_2/Cl^- system were examined.

1. On Ti/Pt-Ir electrodes the cathodic Cl_2 reduction follows the scheme

$$\eta < 0.5V \begin{cases} Cl_2 \rightarrow 2Cl_{ads} \\ Cl_{ads} + e \rightarrow Cl^- \end{cases}$$

$$\eta > 0.5V \begin{cases} Cl_2 + e \rightarrow Cl_{ads} + Cl^- \\ Cl_{ads} + e \rightarrow Cl^- \\ 2Cl_{ads} \rightarrow Cl_2 \end{cases} \text{ concurrent steps}$$

2. On Ti/Pt electrodes the cathodic process follows the scheme

$$Cl_2 + e \rightarrow Cl_{ads} + Cl^-$$
$$2Cl_{ads} \rightarrow Cl_2$$

3. An Ti/Pt-Ir electrodes the anodic Cl_2 evolution follows the scheme (symmetric to the cathodic scheme at low overvoltages)

$$Cl^- \rightarrow Cl_{ads} + e$$
$$2Cl_{ads} \rightarrow Cl_2$$

Passivation on this electrode is important only at overvoltages higher than 0.5V.

4. On the contrary, Ti/Pt electrodes undergo a marked passivation for $\eta_{an} > 0.2V$. Such passivation is diffusion controlled at intermediate and high Cl^- concentrations. The anodic Cl_2 evolution, at $\eta_{an} < 0.2V$ on this electrode, is similar to that on Ti/Pt-Ir electrode; at higher overvoltages, passivation phenomena and formation of oxychlorides may complicate the electrode processes.

Acknowledgments

This investigation has been sponsored by the Consiglio Nazionale delle Ricerche, Rome, Italy. The authors wish to thank Dr. A. Nidola of the O. De Nora Impianti Elettrochimici, Milan, for his assistance in the electrode preparation.

Manuscript submitted Sept. 3, 1968; revised manuscript received Feb. 26, 1969.

Any discussion of this paper will appear in a Discussion Section to be published in the June 1970 JOURNAL.

REFERENCES

1. F. Haber and S. Grinberg, *Anorg. Chem.*, **16**, 198 (1898).
2. H. Wohlwill, *Z. Elektrochem.*, **5**, 52 (1898).
3. F. Chang and H. Wick, *Z. Phys. Chem.*, **172**, 448 (1935).
4. G. A. Tedoradse, *J. Acad. Sci. USSR, HHT*, **250** (1958).
5. G. A. Tedoradse, *Z. Phys. Chem.*, **33**, 129 (1959).
6. S. Toshima and H. Okaniwa, *Denki Kagaku*, **34**, 641 (1966).
7. R. Greef, Ph.D. Thesis, University of Newcastle u.T., GB (1963).
8. E. L. Littauer and L. L. Shreir, *Electrochim. Acta*, **11**, 527 (1966).
9. C. Suzuki, M. Yoshida, H. Onone, and T. Matsuro, *Denki Kagaku*, **34** 165 (1966).
10. M. M. Flisskii, *Elekhtrokhim.*, **2**, 806 (1966).
11. M. M. Flisskii, *Russ. J. Phys. Chem.*, **39**, 97 (1965).
12. B. M. Blavetnik and G. A. Tsiganov, *Corrosion*, **19**, 421 (1963).
13. A. Frumkin and G. A. Tedoradse, *Z. Elektrochem.*, **62**, 251 (1958).
14. G. Faita, P. Longhi, and T. Mussini, *This Journal*, **114**, 340 (1967).
15. G. Faita, G. Fiori and J. W. Augustynski, *Electrochim. Metall.*, **2**, 437 (1967).
16. N. B. Beer, Brit. Pat., 164,913, *C.L. C 23 c* (July 29, 1964).
17. A. Nidola, Paper presented at 1.st CNR Meeting on Electrolytes and Electrochemical Processes, Rome, 1966.
18. J. Newman, *This Journal*, **113**, 1235 (1966).
19. J. O'M. Bockris and A. M. Azzam, *Trans. Faraday Soc.*, **48**, 145 (1952).
20. P. Delahay, "Double Layer and Electrode Kinetic," pp. 178-180, Interscience Publishers, Inc., New York (1965).
21. G. Faita, G. Fiori, and T. Mussini, *Electrochim. Acta*, **13**, 1765 (1968).
22. L. I. Krishtalik, *Elekhtrokhim.*, **1**, 297 (1965).
23. A. C. Makrides, *This Journal*, **109**, 256 (1962).
24. D. G. Peters and J. J. Lingane, *J. Electroanal. Chem.*, **4**, 193 (1962).

Significance of Electrolyte Films for Performance of Porous Hydrogen Electrodes

I. Film Model

Fritz G. Will* and David J. BenDaniel

General Electric Research and Development Center, Schenectady, New York

ABSTRACT

A refined analysis of the electrolyte film model is presented and evaluated on experimental polarization curves of porous hydrogen diffusion electrodes. Simultaneous diffusion and kinetic control and the existence of hydrogen surface coverage are taken into account. The effects of electrolyte film thickness and height on the shape of the polarization curves are analyzed. Polarization curves obtained on various types of partly wet-proofed porous hydrogen electrodes are in very good agreement with the computed curves. A concept of the morphology and the wetting behavior of partly wet-proofed electrodes is developed based on electron micrographs and a comparison between predicted and observed polarization curves. It is concluded that, under often prevailing conditions of diffusion control, the reaction proceeds predominantly on the wetted walls of macro pores, while the much smaller micro pores are mostly flooded and contribute little to the current.

Experiments on foil electrodes partly immersed in aqueous electrolytes have generally established the existence of stable electrolyte films[1] above the intrinsic meniscus (1-5). On electrodes with polished surfaces, films are sometimes unstable and menisci with contact angles larger than zero form (1, 6-9). Under conditions of extreme cleanliness, however, stable films have been shown to exist even on highly polished surfaces (10, 11).

Mathematical analyses of the film model have been presented (12-18) and evaluated by describing polarization curves observed on model electrodes (1, 10, 12, 13, 18). More refined geometric and kinetic models are required to describe polarization curves of actual porous gas electrodes, and very few attempts have been made in this direction (17, 19, 20). In these few cases, discrepancies up to a factor of 4 between predicted and measured curves existed (19) or unlikely kinetic equations or parameters had to be assumed to produce a curve fit.[2]

In this paper we present a refined analysis of the film model for the hydrogen oxidation reaction. We use the well established Heyrowsky-Volmer mechanism to describe the hydrogen oxidation, also taking into account the effects of hydrogen surface coverage and slow hydrogen diffusion on the reaction rate. Experimental polarization curves of actual porous hydrogen electrodes, obtained by other authors (21), are then evaluated in terms of the film model using measured structure parameters of these electrodes.

Model and Analysis

First the polarization behavior of a single pore of uniform diameter is analyzed and then a porous gas electrode as a system consisting of a large number of such pores is described.

Single pore.—The model treated is as follows: (*i*) The film meets the bulk electrolyte at right angles at the pore mouth ($x = 0$). This means that effects due to the meniscus and the electrolyte-filled part of the pore are neglected. (*ii*) The film thickness δ_o is small compared to the pore radius r and the film height H. This allows a treatment in Cartesian coordinates. (*iii*) The electric field in the film perpendicular to the surface (outside the Helmholtz layer), dE/dy, is small compared to dE/dx. (*iv*) The electrolyte concentration in the film stays approximately constant. It has been suggested (18) that water condensation and transport through the film may accomplish this. In fact, it has been shown (12) that in thick films (~1 mm) concentration gradients are very small due to water vapor transport and capillary motion.

We may write the pore current per unit perimeter $W = 2\pi r$ as

$$I/W = -(\delta_o/\rho)\, dE/dx \qquad [1]$$

where ρ is the resistivity of the electrolyte and E the local electrode polarization. The local current density i is given by

$$i = -dI/Wdx \qquad [2]$$

By differentiating Eq. [1] and substituting for dI/dx in Eq. [2] we obtain

$$\delta_o\, d^2E/dx^2 = \rho i \qquad [3]$$

subject to the boundary conditions

$$E(x) = E_a \quad \text{for } x = 0 \qquad [3a]$$

$$dE/dx = 0 \quad \text{for } x = H \qquad [3b]$$

where E_a is the total measured electrode polarization. In order to express i as a function of E, the reaction mechanism has to be known. The oxidation of hydrogen is best described by either the Heyrowsky-Volmer mechanism or the Tafel-Volmer mechanism. The former is more suitable in cases where the coverage of the metal surface with atomic hydrogen is large, the latter is preferred if the coverage is small. In the following analysis we discuss only the Heyrowsky-Volmer mechanism because hydrogen diffusion electrodes are usually made of metals which exhibit large equilibrium coverages with hydrogen and are often operated in a potential region where the coverage remains relatively large. For very small thicknesses and small polarizations, the electron transfer process (Heyrowsky-Volmer) should become rate-determining. In other cases, however, hydrogen diffusion through the film is expected to determine the rate.

* Electrochemical Society Life Member.

Key words: electrochemistry, fuel cells, porous electrodes, hydrogen oxidation, film model.

[1] A film thickness of 1.5μ and a minimum film length of 1 cm was established for the system H_2/Pt-black/8NH_2SO_4 (1, 13) using an electrochemical technique. Applying the same technique, a film of 0.18 to 0.25μ was found for KOH on Ni (3) in close agreement with values between 0.1 and 0.5μ obtained with optical techniques (11).

[2] Thus, the kinetic model assumed for O_2-reduction in (17) predicts that the local current density goes through zero and changes sign in contrast to the actual findings (4, 5). The model proposed in (20) has to assume surface diffusion coefficients 4 to 5 orders of magnitude higher than known bulk electrolyte values.

For a full description we need to consider both processes simultaneously.

The current density due to the diffusion of molecular hydrogen through the film is given by

$$i = i_l(1 - c/c_o) \quad [4]$$

$$i_l = 2FD\, c_o/\delta_o \quad [4a]$$

where **F** is the Faraday constant, D the diffusivity, c the local concentration, c_o the concentration of molecular hydrogen for standard pressure $p_o = 1$ atm, and i_l the limiting diffusion current of H_2. It is assumed that the transport of hydrogen in the gas phase and the dissolution of hydrogen in the electrolyte proceed sufficiently fast such that $c = c_o$ at the gas-electrolyte interface.

The Heyrowsky mechanism

$$H_2 \rightarrow H + H^+ + e^- \text{ (acid)} \quad [5a]$$

$$H_2 + OH^- \rightarrow H + H_2O + e^- \text{ (alkali)} \quad [5b]$$

is described by

$$i = 2i_{oH}\left[\frac{c}{c_o}\frac{1-\theta}{1-\theta_o}\exp(\alpha_H\phi E) - \frac{\theta}{\theta_o}\exp(-(1-\alpha_H)\phi E)\right] \quad [6]$$

where $\phi = \mathbf{F}/RT$ and i_{oH} and α_H are the exchange current density and the transfer coefficient for the Heyrowsky reaction, respectively. θ and θ_o are the hydrogen coverage of the surface for any voltage E and $E = 0$ ($p = p_o$), respectively. The coverage of the surface is defined as that fraction of the surface which is covered with hydrogen atoms.

The Volmer mechanism

$$H \rightarrow H^+ + e^- \text{ (acid)} \quad [7a]$$

$$H + OH^- \rightarrow H_2O + e^- \text{ (alkali)} \quad [7b]$$

is described by

$$i = 2i_{oV}\left[\frac{\theta}{\theta_o}\exp(\alpha_V\phi E) - \frac{1-\theta}{1-\theta_o}\exp(-(1-\alpha_V)\phi E)\right] \quad [8]$$

where i_{oV} and α_V are the exchange current density and the transfer coefficient for the Volmer reaction, respectively. By eliminating c/c_o and θ/θ_o from Eq. [4], [6], and [8], we obtain the current density as a function of the voltage in the form

$$i = (B - \sqrt{B^2 - 4AC})/2A \quad [9]$$

with

$$A = \theta_o \exp[(1-\alpha_V)\phi E]/2i_{oV}i_l \quad [9a]$$

$$B = \theta_o \exp(-\alpha_H\phi E)/2i_{oH} + (1-\theta_o)\exp[(1-\alpha_H)\phi E]/2i_{oH} + \theta_o \exp[(1-\alpha_V)\phi E]/2i_{oV} + (1-\theta_o)\exp(-\alpha_V\phi E)/2i_{oV} + \exp(\phi E)/i_l \quad [9b]$$

$$C = \exp(\phi E) - \exp(-\phi E) \quad [9c]$$

When Eq. [9] (together with Eq. [4a], [9a], [9b], and [9c]) is substituted into Eq. [3], a second order nonlinear differential equation in the variables E and x results. This equation cannot be solved analytically, and, therefore, was programmed in BASIC for numerical solution on a General Electric 265 computer. The output of the computer are E and I as a function of x and, hence, also the total pore current I_t as a function of the total polarization E_a.

Porous gas electrode.—We approximate the complex structure of a gas electrode of known porosity p with an array of nonintersecting macro pores of uniform diameter equal to the measured mean diameter $2r$.

Porous gas electrodes prepared from ultra-fine catalyst powders (22), exhibit a micro pore structure within the system of macro pores. Figure 1 shows an electron micrograph[3] of an electrode cross section taken at a magnification of 100,000X. The average diameter of the catalyst particles is 50Å. Large numbers of these particles form clusters with an average size of 500-2000Å. The individual particles in a cluster form micro pores with diameters between 10 and 50Å. Most of the clusters are linked together and have irregularly shaped voids (macro pores) between them. The macro pores have diameters in the 500-5000Å range and exhibit considerable surface roughness. The Teflon particles (not visible in the micrograph) range from 2000 to 5000Å (22). Since the pore volume increases with the second power of the radius while the internal surface area increases only with the first power, most of the internal pore volume, *i.e.*, the porosity, is due to the large pores, while most of the internal surface area is due to the small pores.

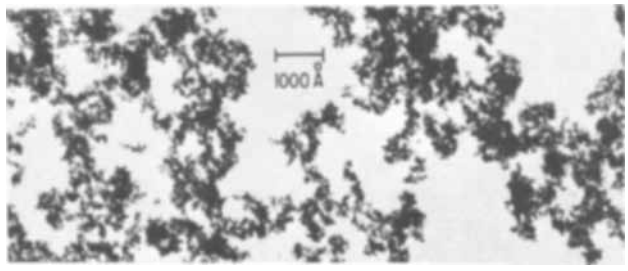

Fig. 1. Electron micrograph of electrode cross section at 100,000X (courtesy Dr. L. W. Niedrach).

We may, therefore, calculate the number of macro pores per unit of projected surface area from the measured values of the macro pore radius and the porosity, *i.e.*

$$n = p/\pi r^2 \quad [10]$$

The apparent current density i_a of the electrode (referred to the projected area) is then given by the current contributed by a single pore times the number of macro pores. In terms of the pore current per unit of circular perimeter, I_t/W, we can write

$$i_a = (2p/r)I_t/W \quad [11]$$

I_t/W contains the parameters H and δ_o which, for a porous electrode, have the significance of a mean film height and a mean film thickness. No reliable measurements of these two quantities are available.

We must also consider that the model assumes smooth pore walls exposing only catalytically active material, while in fact the pore walls are rough, contain micro pores, and expose active and inactive material. The current density referred to the projected area of the macro pore walls is, therefore, changed in proportion to the wall roughness and the catalyst fraction. Both are functions of the current density if the reaction is discharge limited, as the electric field penetrates more into the micro pores when the current density decreases. However, if the reaction is diffusion limited, the wall roughness and the catalyst fraction are constant as long as the film thickness is large compared to the micro pore radii. A treatment in two independent variables would be required to take these effects into account. This is beyond the scope of this paper. We will consider the wall roughness and catalyst fraction as constant and account for them by introducing an adjustable parameter f, changing the local current density i in Eq. [2] and [3] to fi.

Two special cases are amenable to analytical solutions and serve to illustrate the effect of f on the apparent current density of the porous electrode. For the case of diffusion control and electric field penetration $<<$ film height we obtain

$$i_a = (4p/r)\sqrt{\mathbf{F}Dc_of/\rho}\,\sqrt{E_a - (1 - \exp(-2\phi E_a))/2\phi} \quad [12]$$

[3] The loan of the relevant micrograph by Dr. L. W. Niedrach is gratefully acknowledged.

For the case of diffusion control and electric field penetration >> film height we obtain the limiting current

$$i_{al} = (4p/r)\mathbf{F}Dc_o fH/\delta_o \qquad [13]$$

which should commence at the polarization

$$E_l = \mathbf{F}Dc_o\rho f(H/\delta_o)^2 + E_H \qquad [14]$$

E_H is the polarization at the upper film end ($x = H$), and is approximately 50 mv.

Single Pore Polarization

We will now present computed polarization curves of individual pores for various film geometries. Although we have considered only the particular case of sulfuric acid electrolyte with concentrations 8-normal and 1-normal, the analysis can also be applied to other concentrations and other electrolytes.

Electrochemical parameters.—We have made use of the following values for the resistivity (23) of the electrolyte and the diffusivity (24) and solubility (24-26) of hydrogen in the electrolyte: $\rho = 1.21(8N)$ and 4.65 ($1N$) ohm cm, $D = 2.8\cdot10^{-5}$ ($8N$) and $3.7\cdot10^{-5}(1N)$ cm²/sec, $c_o = 4.2\cdot10^{-7}(8N)$ and $7.0\cdot10^{-7}(1N)$ moles/cm³. All values are for 25°C. The values for the diffusivity were extrapolated from measurements at 30°C and may be in error by 20%. The error of the solubility data should be less than 5%, that of the resistivity values less than 1%.

For the kinetic and thermodynamic parameters in Eq. [6] and [8] we have used the following values: $\alpha_V = \alpha_H = 0.5$, $i_{oV} = i_{oH} = 0.1$ A/cm² (27, 28), $\theta_o = 0.98$ (27, 29). α_V and α_H may assume values between 0.4 and 0.6, θ_o values between 0.9 and 1.0 on Pt, smaller on Ni. Depending on the "activity" of the catalyst, i_{oV} and i_{oH} on Pt may assume values an order of magnitude higher. Smaller values than 0.1 A/cm² are likely on Ni and on Pt in systems of limited purity. The effect of these parameters on the polarization curves will be discussed elsewhere.

Effect of H and δ_o.—Figure 2 shows a plot of the pore current I_t per unit perimeter $W = 2\pi r$ as a function of the applied voltage or polarization E_a, both measured at $x = 0$. The plot applies to $1N$ H_2SO_4 and shows the effect of various film heights and thicknesses on the shape of the polarization curve. We note that (*i*) a limiting current of 0.5 mA/cm is obtained for all film heights and thicknesses whose ratios $H/\delta_o = 100$ (curves 4, 5, and 6), (*ii*) the curves exhibit an inflection point

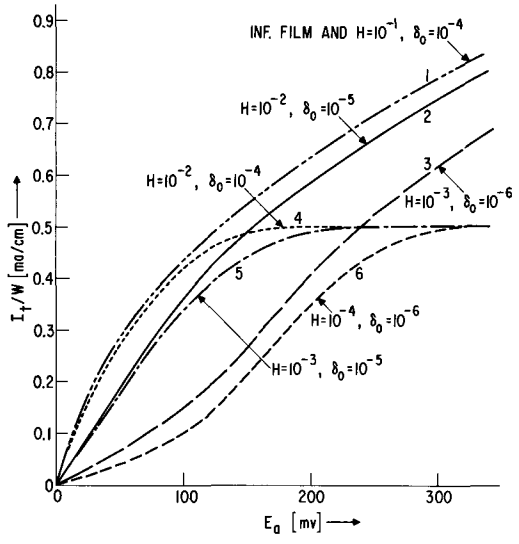

Fig. 2. Effect of film geometry on polarization curves for individual pore in $1N$ H_2SO_4, I_t/W = pore current per unit of pore perimeter, E_a = electrode polarization or applied potential, H = film height, δ_o = film thickness.

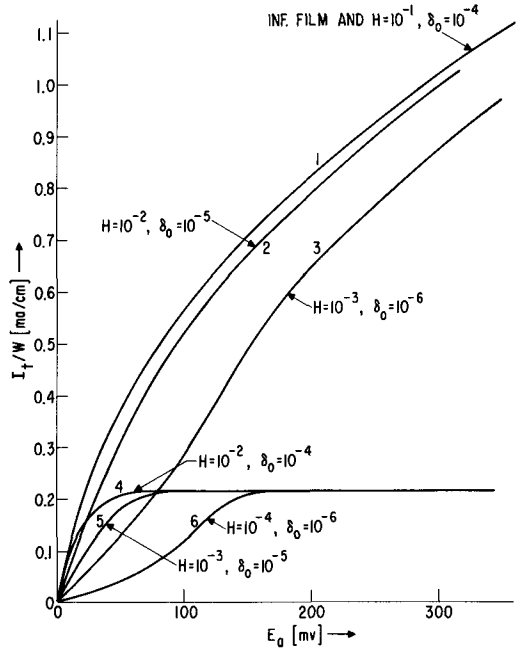

Fig. 3. Effect of film geometry on polarization curves for individual pore in $8N$ H_2SO_4.

and become increasingly concave as the film thickness decreases while for the larger thicknesses the curves are convex throughout, (*iii*) the film height has no pronounced effect on the curves for voltages $E_a < 100$ mv. In fact, in the case of $\delta_o = 10^{-4}$ cm any increase of H beyond 10^{-1} cm has no effect on curve 1 ("infinite film") throughout the voltage range.

The polarization curves for $8N$ H_2SO_4 are shown in Fig. 3. The character of the curves is very similar to that obtained for $1N$ H_2SO_4. However, the magnitude of the currents is different. Thus, the limiting current for $H/\delta_o = 100$ is 0.22 mA/cm instead of 0.5 mA/cm and starts at potentials considerably less anodic. The currents for $H/\delta_o = 1000$, on the other hand, are some 25% larger than for $1N$ H_2SO_4.

For small film thicknesses and small polarizations, the reaction rate is controlled by the charge transfer step, *i.e.*, the Heyrowsky and the Volmer mechanism (Eq. [5] and [7]), and the curves exhibit the characteristic concave shape (curves 3 and 6). As E_a and, hence, $E(x)$ increase, the rate of the transfer reactions Eq. [6] and [8] increases exponentially. Therefore, the regions of the film close to the bulk solution come under diffusion control. Since diffusion control is associated with a convex curve shape, the curves run through an inflection point. For yet larger values of E_a, even the regions of the film close to the upper end come under diffusion control, and we approach the limiting current. Curves 6 in Fig. 2 and 3 are examples for this behavior.

In accordance with Eq. [13] the limiting currents are proportional to H/δ_o and are larger in $1N$ than in $8N$ H_2SO_4. As H/δ_o increases, the onset of the limiting current is delayed according to Eq. [14]. For $\delta_o > 10^{-5}$ cm, diffusion control prevails and H hardly affects the current as long as $I_t << I_l$. For values of i_{oH} and i_{oV} larger than 0.1 A/cm², curves 2, 3, 5, and 6 would be less affected by slow discharge and, hence, approach curves 1 and 4 more closely.

Comparison with Experiments

Source of experimental data.—We have chosen the detailed experimental study of Austin and Almaula (21) with typical data for wet-proofed electrodes as the basis for comparison with our analysis. These authors obtained accurate polarization data on four porous hydrogen diffusion electrodes prepared with different known amounts of platinum, graphite, and

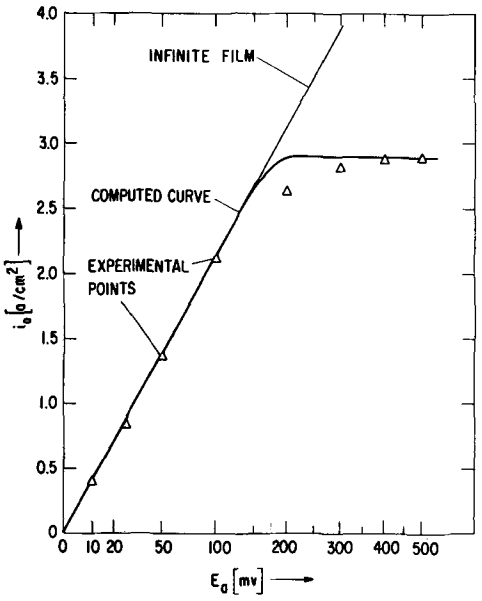

Fig. 4. The values on the abscissa have been calculated from $\sqrt{E_a - (1-e^{-2\phi E_a})/2\phi}$. Experimental data (triangles) for Teflon-bonded electrode SM1 [ref. (21)] and polarization curve computed from film model; $\phi = F/RT$, i_a = current density referred to apparent surface area, E_a = electrode polarization.

Teflon in 1N H_2SO_4. They also determined the porosity p, and the mean macro pore radius r. With the exception of one of the four electrodes, the macro pore radii lie between 0.6 and 3.2μ. This is more than two orders of magnitude larger than the micro pore radii. Hence, most of the internal pore volume is due to the macro pores, and we may calculate the apparent current density i_a from Eq. [11], substituting for p the measured total porosity and for r the macro pore radius.

For the electrochemical parameters the same values were used as for the single pore polarization except for i_{oH} and i_{oV} for which 1 A/cm² was employed. This value is reasonable for platinum electrodes in a high state of activity (27, 28).

Polarization curves of wet-proofed electrodes.— Figure 4 shows experimental points (triangles) for i_a in the case of Austin and Almaula's Teflon bonded platinum electrode SM1 as a function of $\sqrt{E_a - (1 - \exp(-2\phi E_a))/2\phi}$. Up to 100 mv the points lie on a straight line through the origin. A limiting current of 2.9 A/cm² is obtained at polarizations larger than 400 mv. This behavior is characteristic (1, 12, 13) for the existence of electrolyte films. The curve in Fig. 4 was computed by using the measured values for the porosity ($p = 0.72$) and the mean pore radius ($r = 3.2\mu$). The values $H = 11\mu$, $\delta_o = 1030$Å, and $f = 1.2$ were chosen to match the experimental values for curve slope and limiting current.

Good agreement is obtained between the computed curve and the experimental points except for the potential region 100-300 mv where the predicted currents are up to 10% too high. Curves identical to curve 1 are obtained for any set of values $H > 11\mu$, $\delta_o > 1030$Å, as long as $H/\delta_o = 107$, and for any values i_{oH} or $i_{oV} > 0.5$ A/cm². For smaller values of H and δ_o, however, the computed curves would exhibit an increasingly concave shape (looking from above) at potentials smaller than 100 mv. This behavior is not observed and, thence, $H = 11\mu$ and $\delta_o = 1030$Å constitute lower limits for the film height and film thickness for the electrode SM1.

Figure 5 shows a plot of i_a against $\sqrt{E_a - \ldots}$ for a platinized and wet-proofed carbon electrode, labeled FC100 by Austin and Almaula (21). The measured values $p = 0.2$ and $r = 0.25\mu$ (Pure Carbon Company catalogue values) along with the assumed parameters $H = 196\mu$, $\delta_o = 250$Å, and $f = 4.9 \cdot 10^{-4}$ were used for

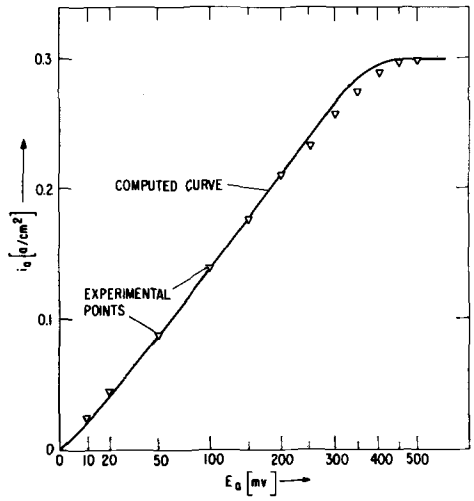

Fig. 5. The values on the abscissa have been calculated from $\sqrt{E_a - (1-e^{-2\phi E_a})/2\phi}$. Experimental data (triangles) for Teflon-bonded electrode FC100 [ref. (21)] and curve computed from film model.

the computations. An excellent fit between the data points (triangles) and the computed curves is obtained with these values. The slightly concave curve shape for $E_a < 150$ mv is an indication of some charge transfer hindrance due to the small film thickness δ_o. Apart from this small deviation, however, the curves in Fig. 4 and 5 follow the behavior predicted by Eq. [12], [13], and [14] for slow H_2 diffusion through a film.

Figure 6 summarizes experimental data (characterized by various symbols) obtained by Austin and Almaula on four different electrodes, SM1, CAA1, SM2, and FC100, in a linear plot of i_a against E_a. The curves were all computed on the basis of the film model. The structure parameters used for electrode CAA1 are $p = 0.73$, $r = 2.8\mu$, $H = 84\mu$, $\delta_o = 2800$Å, and $f = 0.135$, those for electrode SM2 are $p = 0.60$, $r = 0.65\mu$, $H = 117\mu$, $\delta_o = 650$Å and $f = 4.4 \cdot 10^{-4}$. While the curve fit is very good for electrodes FC100 and SM2, the predicted currents for CAA1 and SM1 are some 10-20% larger than observed in the potential range 100 mV $< E_a <$ 300 mV. If much smaller values for H and δ_o had been chosen, the predicted curves would have adopted a concave shape at low potentials. The observed convex shape of all four curves shows that the rate of hydrogen oxidation on these four porous electrodes is overwhelmingly determined by slow H_2 diffusion.

Conclusions

From a comparison between polarization curves predicted by the film model and curves observed on wet-proofed porous hydrogen electrodes coupled with an evaluation of electron micrographs of such electrodes we draw the following conclusions.

1. For large film thicknesses and large charge transfer rates ($\delta_o > 0.5\mu$ for $i_o > 0.1$ A/cm² or $\delta_o > 500$Å for $i_o > 1$ A/cm²) the polarization curves are determined by slow diffusion through the film.

2. For ratios film height to film thickness of several hundred or less, limiting currents are obtained. For ratios of the order of 1000 or more, the curves follow the $i - \sqrt{E_a}$ relation predicted by the infinite film model.

3. As δ_o and/or i_o decrease, charge transfer limitation is introduced, and the curves are concavely shaped at low potentials (< 50 to 150 mV).

4. Polarization curves obtained on various types of partly wet-proofed porous hydrogen electrodes are in very good agreement with the curves predicted from the film model when only the macro pores of known

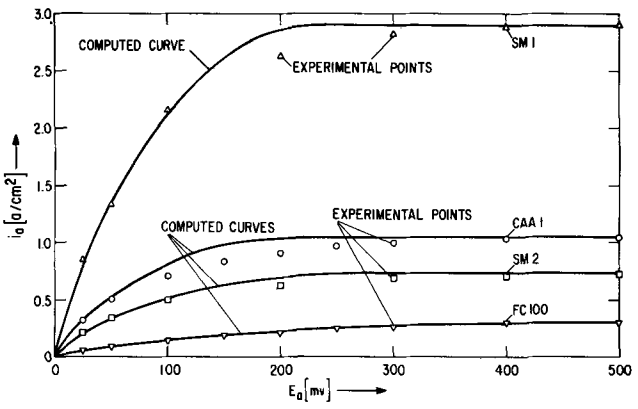

Fig. 6. Experimental data (various symbols) for four different Teflon-bonded electrodes [ref. (21)] and curves computed from film model.

diameter are considered and the micro pores are disregarded. Diffusion control prevails.

5. This indicates that the micro pores are flooded and the walls of the macro pores are covered with an electrolyte film of a thickness large compared to the micro pore diameters (10-50Å).

6. The film thicknesses range from 250 to 3000Å, the film heights from several hundred to several thousand film thicknesses.

7. The presence of hydrophobic particles of 2000-5000Å diameter prevents complete flooding of the macro pores and limits the film height.

Acknowledgment

The authors are obliged to Dr. L. W. Niedrach for the loan of electron micrographs of Teflon-bonded electrodes.

Manuscript submitted Aug. 26, 1968; revised manuscript received March 12, 1969.

Any discussion of this paper will appear in a Discussion Section to be published in the June 1970 JOURNAL.

List of Symbols

c	Concentration of molecular hydrogen
c_o	Standard concentration of hydrogen at standard pressure
D	Diffusivity of molecular hydrogen
E	Local electrode polarization (function of x)
E_a	Electrode polarization, measured at bulk end of film
E_H	Polarization at upper film end
E_l	Electrode polarization for which the limiting current is obtained
f	Adjustable parameter for porous electrode structure
$\mathbf{F}$	Faraday constant
H	Film height
i	Local current density in film (function of x)
i_l	Limiting diffusion current density
i_{oH}	Exchange current density for Heyrowsky mechanism
i_{oV}	Exchange current density for Volmer mechanism
i_a	Apparent current density of porous electrode
i_{al}	Apparent limiting current density of porous electrode
I	Local current in film (function of x)
I_t	Total film current
n	Number of pores per square centimeter
p	Porosity of electrode
r	Median macro pore radius
R	Gas constant
T	Absolute temperature
W	$2\pi r$ = macro pore perimeter
x	Coordinate parallel to pore axis
y	Coordinate perpendicular to pore wall or axis
α_{oH}, α_{oV}	Transfer coefficients of Heyrowsky and Volmer mechanisms
δ_o	Film thickness
ϕ	$\mathbf{F}/RT$
ρ	Resistivity of electrolyte
θ	Hydrogen surface coverage
θ_o	Coverage at standard pressure

REFERENCES

1. F. G. Will, *This Journal*, **110**, 145 (1963).
2. Yu. A. Mazitov, K. I. Rozental, and V. I. Veselovski, *Russian J. Phys. Chem.*, **38**, 234 (1964).
3. A. G. Pshenichnikov, G. I. Shnaider, and R. Kh. Burshtein, *Elektrokhimiya*, **1**, 418 (1965).
4. H. J. R. Maget and R. Roethlein, *This Journal*, **112**, 1034 (1965).
5. D. N. Bennion and C. W. Tobias, *ibid.*, **113**, 589 (1966).
6. H. C. Weber, H. P. Meissner, and D. A. Sama, *ibid.*, **109**, 884 (1962).
7. S. Palous and R. Buvet, *Bull. Soc. Chim. France*, **270**, 1602 (1962).
8. M. Bonnemay, G. Bronoel, and E. Levart, *Electrochim. Acta*, **9**, 727 (1964).
9. B. D. Cahan and J. O'M. Bockris, Paper 202 presented at the Dallas Meeting of the Society, May 7-12, 1967.
10. M. B. Knaster and M. I. Temkin, *Doklady Akad. Nauk.*, **152**, 841 (1963).
11. R. H. Muller, *This Journal*, **113**, 943 (1966).
12. F. G. Will, *ibid.*, **114**, 138 (1967).
13. F. G. Will, *ibid.*, **110**, 152 (1963).
14. R. P. Iczkowski, *ibid.*, **111**, 605 (1964).
15. E. A. Grens, R. M. Turner, and T. Katan, *Adv. Energy Conversion*, **4**, 109 (1964).
16. Yu. V. Alekseev and Yu. A. Popov, *Elektrokhimiya*, **1**, 422 (1965).
17. J. A. Rockett and R. Brown, *This Journal*, **113**, 207 (1966).
18. D. N. Bennion and C. W. Tobias, *ibid.*, **113**, 593 (1966).
19. R. P. Iczkowski, *ibid.*, **111**, 1078 (1964).
20. R. Brown and J. A. Rockett, *ibid.*, **113**, 865 (1966).
21. L. G. Austin and S. Almaula, *ibid.*, **114**, 927 (1967).
22. L. W. Niedrach and H. R. Alford, *ibid.*, **112**, 117 (1965).
23. Gmelins Handbuch der Anorganischen Chemie, "Schwefel," 8, Aufl. B2, Verlag Chemie, Weinheim (1960) p. 703.
24. P. Ruetschi, *This Journal*, **114**, 301 (1967).
25. G. Geffcken, *Z. Physik. Chem.*, **49**, 268 (1904).
26. A. Christoff, *ibid.*, **55**, 627 (1906).
27. M. Breiter, C. A. Knorr, and W. Voelkl, *Z. Electrochem.*, **59**, 681 (1955).
28. A. N. Frumkin, "Advances in Electrochemistry," Vol. 3, pp. 287-392, P. Delahay, Editor, John Wiley & Sons, New York (1963).
29. F. G. Will and C. A. Knorr, *Z. Electrochem.*, **64**, 258 (1960).
30. W. Vielstich, *Z. Physik. Chem. N. F.*, **15**, 409 (1958).

Adsorption and Oxidation of Ethane, n-Butane, and n-Octane on Platinum Electrodes

G. Aronowitz*[1] and R. J. Flannery*

Research and Development Department, American Oil Company, Whiting, Indiana

ABSTRACT

Ethane, n-butane, and n-octane are adsorbed from aqueous sulfuric acid solutions onto platinum electrodes at 0.25-0.55V *vs.* NHE. At potentials higher than 0.30V how fast the surface coverage builds up depends on both the rate of adsorption and the rate of anodic oxidation. At 0.25-0.30V adsorption can be studied independently. Rate data show that adsorption is potential independent and first order in apparent uncovered surface area. Studies of the kinetics of anodic oxidation and studies of hydrogen codeposition indicate that the adsorbed species are similar for ethane and n-octane but differ for n-butane adsorption.

Electrooxidation of hydrocarbons is currently of interest in fuel cell technology. However, the oxidation of a complex hydrocarbon molecule occurs in many successive steps, of which one or more would be expected to involve adsorption. Consequently the development of adequate kinetic models for the process requires a detailed knowledge of the role played by the adsorption of reactants, intermediates, and products.

The build-up of intermediates has been detected during the electrooxidation of methanol and formic acid (1, 2), olefins (3), and, more recently, during the electrooxidation of saturated hydrocarbons (4, 5) on platinum electrodes. But the identities of the adsorbed species and the nature of the adsorption processes remain in doubt.

In this study the build-up of adsorbed intermediates attending electrooxidation of ethane, n-butane, and n-octane on platinum electrodes in aqueous sulfuric acid solution was observed in the potential region of interest in fuel cell technology by constant current and controlled potential methods. Studies of the kinetics of electrooxidation by a potential step method have provided a basis for analyzing the build-up process. Hydrogen codeposition studies have provided useful clues to the nature of the adsorbed species.

Experimental

A Pyrex electrolytic cell of conventional design was employed. The polarizing electrode was a 1.5-in. diameter platinum gauze basket. It was connected to a $Hg/Hg_2SO_4/Hg_2SO_4$(sat'd) + 1.0M H_2SO_4 reference electrode through a salt bridge and Luggin capillary filled with test solution. All electrode potential values cited here are given with reference to a normal hydrogen electrode.

The helium used was Bureau of Mines analytical reagent grade. The hydrocarbons were Phillips research grade.

The electrical apparatus was conventional. A Brinkman Model 61-R fast-rise potentiostat maintained the electrode potential. A galvanostat was constructed using banks of resistors and a 90V "B" battery. Mercury relays provided rapid switching between galvanostat and potentiostat and between reference potential sources. The latter were constructed from ten-turn potentiometers and batteries. The switching arrangement was sufficiently versatile for the potential step sequences employed in these studies. A Tektronix Model 531A oscilloscope with a type D preamplifer, equipped with an oscilloscope camera using Polaroid film, was used to record electrode potential *vs.* time curves.

Test electrodes were sputtered platinum film electrodes supported on bright platinum foils and were prepared following a technique developed in this laboratory (6). Electrical connection was made with a platinum wire spot welded to the foil and sealed in a soft glass tube. Electrodes were degreased in hot acetone and rinsed in conductivity water before being used. True surface areas of these electrodes were calculated from apparent areas and the charge required to strip cathodically the platinum surface oxide which was normalized to unit roughness by comparison with values reported for bright platinum (7). Roughness factors for the sputtered films varied from about 50 to 70. All results are presented on the basis of 1 cm^2 of apparent area but are normalized to an electrode having a roughness factor of 57. Thus Q and i values given per square centimeter can be divided by 57 to obtain Q and i for 1 cm^2 of real area. Twelve electrodes were used with no variation in behavior between electrodes. Electrodes were subjected to a standard activating treatment before being used on any given day. This consisted of cycling the electrode potential between 1.15 and 0.35V 6-8 times. Following this, the electrode was maintained at 1.15V for 2 min. Variation of electrode potential between 1.15 and 1.75V (mild oxygen evolution) made no differences in subsequent experimental results but treatment at potentials less positive (noble) than 1.15V resulted in a loss in activity for hydrocarbon electrooxidation and a general lack of reproducibility.

The test solution was 1.0M H_2SO_4 prepared from water obtained from a Barnstead Model E-1 conductivity water still. The conductivity of the water did not exceed 6.0×10^{-7} ohm^{-1} cm^{-1}. Test solutions were pre-electrolyzed in a separate vessel for at least 72 hr at 2.0 mA/cm^2 on bright platinum electrodes before admittance to the cell. All experiments were conducted at 65° ± 1°C. Helium was bubbled through the cell solution to provide an inert atmosphere and provision was made to switch to hydrocarbon gas flow without admitting air or impurities to the cell. Gases were washed in conductivity water before admittance to the cell and were permitted to contact only Pyrex glass or Teflon tubing to avoid contamination. In the n-octane studies, a large excess of n-octane was added to the cell solution and stirred vigorously until saturation was apparently achieved.

Rates of Build-up of Adsorbed Species

Surface species were detected by anodic charging curves. After an activation treatment, the electrode potential was stepped to a value in the range of 0.20-0.55V and maintained there to permit adsorption. After a given time a constant anodic current was applied, and the potential was followed as a function of

* Electrochemical Society Active Member.
[1] Present address: Pan American Petroleum Corporation, Box 591, Tulsa, Oklahoma 74102.

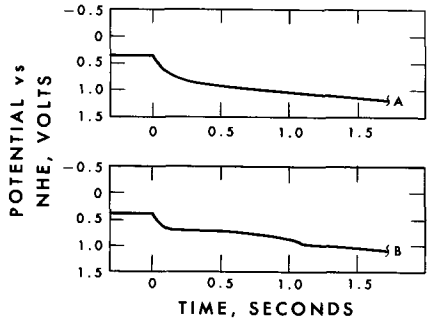

Fig. 1. Potential vs. time curves for the anodic stripping of ethane after a given time of adsorption on Pt at 65°C and 0.35V. Curve A, adsorption time = 0; curve B, adsorption time = 300 sec.

time. If the anodic current is high enough, the charge involved in the arrest is independent of the stripping current and thus reflects only the charge used in the anodic stripping of surface species. This surface charge is denoted as Q.

Oscillograms obtained after adsorption of ethane at 0.35V at various adsorption times are shown in Fig. 1. Trace A is identical to traces obtained with the solution free of hydrocarbons. In trace B a potential arrest appears in the range 0.60-0.75V. The length of the arrest, τ, increases with increasing adsorption time. Solutions saturated with n-butane and n-octane show similar arrests.

Figures 2, 3, and 4 show curves of Q_{ethane}, $Q_{\text{n-butane}}$, and $Q_{\text{n-octane}}$ *vs.* adsorption time, over a range of potentials. The curves show a build-up of adsorbed species with time until steady-state conditions are achieved. The charge at steady state is denoted as Q_s. The net rate of build-up, dQ/dt, decreases with increasing Q. Both dQ/dt at a given adsorption time and Q_s decrease with increasing potential. At potentials of 0.25-0.30V the curves tend to converge, and Q_s approaches a limiting value, $Q_{s,max}$. Below 0.20V, Q declines sharply with potential, and adsorbed hydrogen can be detected. The 0.45 and 0.50V curves for n-octane are unusual. Q decreased with time after apparently attaining Q_s. No evidence for this apparent desorption appears at lower potentials even after several hours of adsorption time.

The above-described behavior strongly suggests that adsorbed species undergo electrooxidation (8). Then

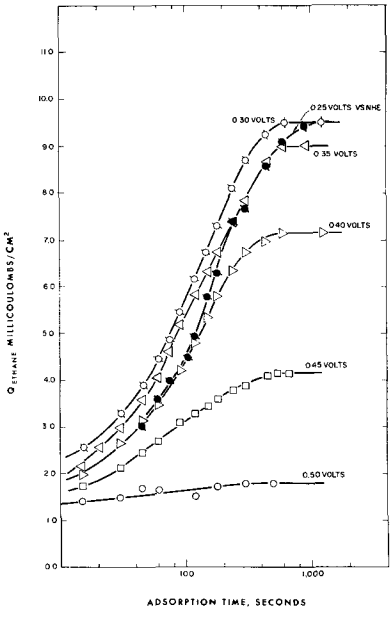

Fig. 2. Q_{ethane} vs. adsorption time

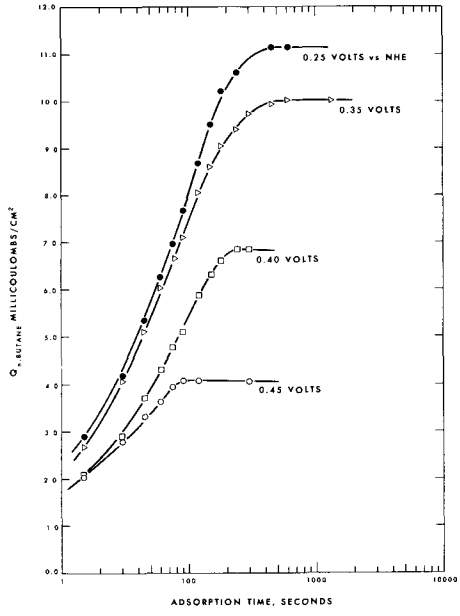

Fig. 3. $Q_{\text{n-butane}}$ vs. adsorption time

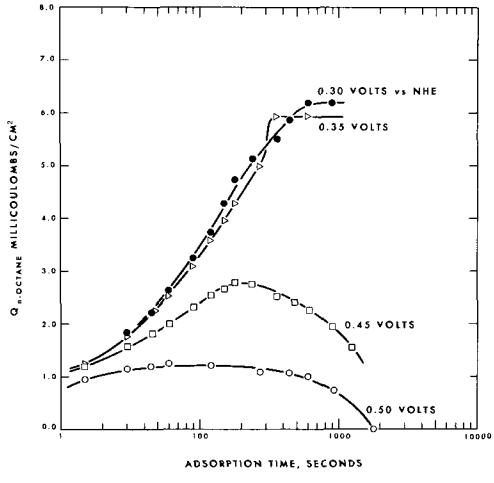

Fig. 4. $Q_{\text{n-octane}}$ vs. adsorption time

dQ/dt must depend on the rate of this electrooxidation as well as on the rate of adsorption. If adsorption occurs via a dissociation mechanism to produce partially dehydrogenated fragments and hydrogen, then recombinative desorption can be discounted because of the rapid anodic oxidation of adsorbed hydrogen in the potential range involved.

The attainment of a maximum value for Q_s at low potentials implies that saturation adsorption occurs. Consequently, $Q_{s,max}$ represents the limiting fraction of surface sites available for adsorption, and the free fraction of available surface is $(Q_{s,max} - Q)/Q_{s,max}$. Assuming that the rate of adsorption is first order with respect to this quantity, the net rate of build-up of adsorbed species can be expressed as follows

$$\frac{dQ}{dt} = k_{ad}\frac{(Q_{s,max} - Q)}{Q_{s,max}} - k_{ox}Q\, e^{\alpha nFE/RT} \qquad [1]$$

where k_{ad} and k_{ox} are constants at constant temperature and hydrocarbon concentration.

At sufficiently low values of E, where the rate of adsorption is proportional to dQ/dt, the second term on the right-hand side of Eq. [1] can be dropped. Integrating the resultant equation and taking logarithms then gives

$$\log (Q_{s,max} - Q) = \log Q_{s,max} - \frac{k_{ad}}{2.303Q_{s,max}}t \qquad [2]$$

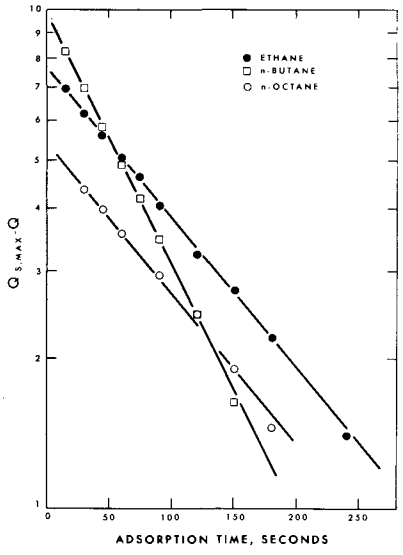

Fig. 5. Log ($Q_{s,max} - Q$) vs. adsorption time

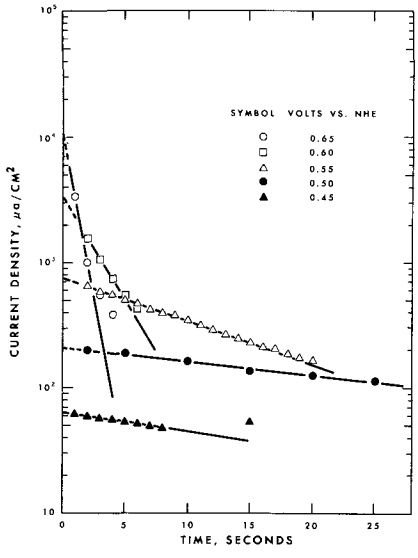

Fig 6. Log i vs. time passed during oxidation of adsorbed ethane at constant potential, E.

Figure 5 shows semilog plots of $(Q_{s,max} - Q)$ *vs.* t for ethane, n-butane, and n-octane adsorption in the range 0.25 — 0.30V. From the slopes of these curves and the values of $Q_{s,max}$, the following values of k_{ad} were computed:

Fuel	k_{ad} millicoulombs/cm²sec
ethane	0.0657
n-butane	0.1285
n-octane	0.0432

Kinetics of Electrooxidation of Adsorbed Species

Values for k_{ox} and $\alpha n\mathbf{F}/RT$, needed to test the validity of Eq. [1], were obtained by the following potential step method:

a. After activation, the electrode was maintained at an adsorption potential of 0.35V long enough to insure attainment of steady-state conditions.

b. The potential was raised to a value, E, in the range 0.425-0.650V, and the resulting anodic currents were measured simultaneously as a function of time.

c. An anodic galvanostatic pulse was applied after a fixed time at E, and Q was determined by the anodic charging curve method.

Anodic currents observed for short times during step *b* are due almost entirely to electrooxidation of adsorbed species and can be related to the instantaneous value of Q as follows

$$i = -\frac{dQ}{dt} = k_{ox}Q\, e^{\alpha n\mathbf{F}E/RT} \qquad [3]$$

The boundary condition was established in step *a*

$$Q = Q_{s,0.35} \text{ when } t = 0$$

where t now refers to the duration of step *b*. Integrating Eq. [3], substituting for Q, taking logarithms, and rearranging terms then gives

$$\log i = \log k_{ox}Q_{s,0.35} + \frac{\alpha n\mathbf{F}E}{2.303RT} - \frac{k_{ox}}{2.303}\, e^{\alpha n\mathbf{F}E/RT}\, t \qquad [4]$$

$$\log Q = \log Q_{s,0.35} - \frac{k_{ox}}{2.303}\, e^{\alpha n\mathbf{F}E/RT}\, t \qquad [5]$$

Figure 6 shows semilog plots of i *vs.* t for ethane at several values of E. Similar results were obtained for n-octane. The curves tend to become nonlinear with time probably because of readsorption of dissolved hydrocarbon and subsequent oxidation on freshly produced sites. Figure 7 shows semilog plots of the slopes $-(k_{ox}/2.303)$ exp $\alpha n\mathbf{F}E/RT$, and intercepts, log $k_{ox}Q_{s,0.35}$ + $\alpha n\mathbf{F}E/2.303\ RT$, of the curves of Fig. 6 and the corresponding n-octane curves plotted as a function of E. Figure 8 is a semilog plot of i for n-butane at t = 0.5 sec *vs.* E. These data represent approximate values of the intercepts of Eq. [4]; they could be slightly low.

Figure 9 shows semilog plots of Q *vs.* t obtained for n-octane in step c. Similar curves were obtained for ethane and n-butane. Figure 10 shows semilog plots of the slopes of the log Q *vs.* t curves, $-(k_{ox}/2.303)\exp \alpha n\mathbf{F}E/RT$, *vs.* E for ethane, n-butane, and n-octane.

The rate constant, k_{ox}, and the Tafel slope, $2.303RT/\alpha n\mathbf{F}$, computed from the data in Fig. 6-10, are shown in Table I.

In Figure 8 the data points of the log i at t = 0.5 sec *vs.* E curve for n-butane break off the Tafel plot at 0.65V. Since mass transfer limitations cannot be a factor, this behavior suggests a change in kinetics. To explore this further, an analysis was made of the anodic charging curves obtained during galvanostatic stripping. By substituting $Q_{t=0}[(\tau - t)/\tau]$ for Q in Eq. [3], integrating, taking logarithms, and using the established relationship $i\tau = Q_{t=0} = Q_{s,0.35}$, we obtain

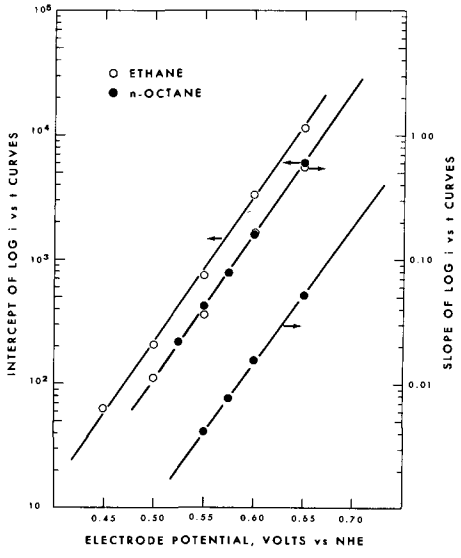

Fig. 7. Log of intercept and slope of Eq. [4] vs. E for ethane and n-octane.

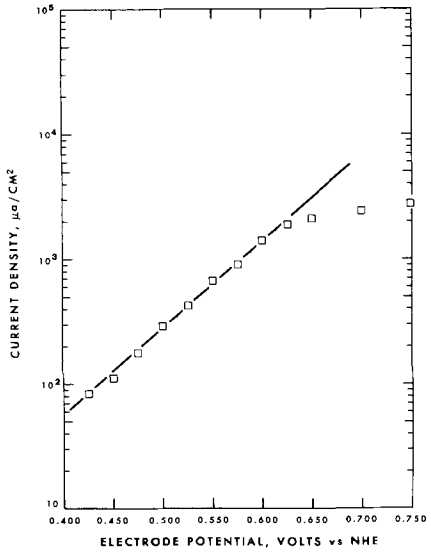

Fig. 8. Log i at $t = 0.5$ sec vs. E for n-butane

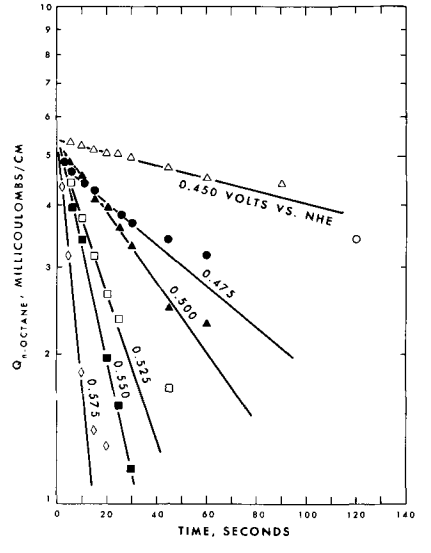

Fig. 9. Log Q vs. time of oxidation of adsorbed n-octane at constant potential, E.

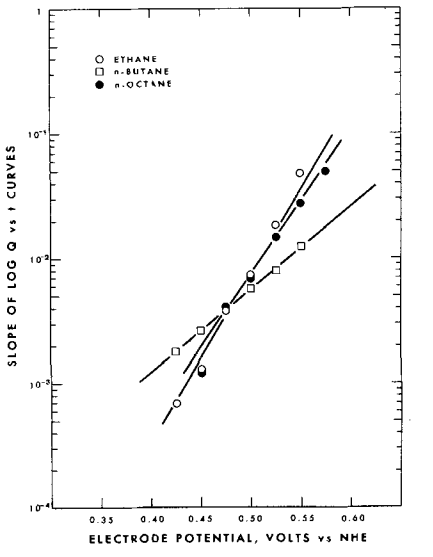

Fig. 10. Log slope of Eq. [5] vs. E for ethane, n-butane, and n-octane.

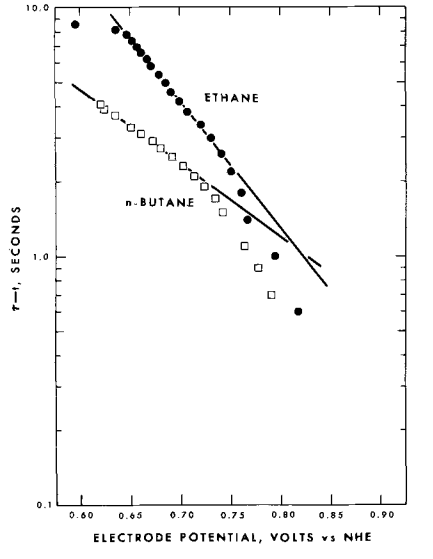

Fig. 11. Time remaining in potential arrest, τ-t vs. E during galvanostatic oxidation of adsorbed ethane and n-butane.

$$-\log(\tau - t) = \frac{\alpha n \mathbf{F} E}{2.303RT} + \log k_{ox} \qquad [6]$$

where τ = length of potential arrest in seconds, and t = time passed during the galvanostatic charging step (step c above).

Figure 11 shows semilog plots of $\tau - t$ vs. E for ethane and n-butane. Tafel slopes and k_{ox} values computed from the slopes and intercepts of the curves in Fig. 11 are

Adsorbate	k_{ox}, sec^{-1}, cm^{-2}	$2.303RT/\alpha n\mathbf{F}$
Ethane	4.00×10^{-4}	0.198
n-Butane	3.50×10^{-3}	0.337

Comparing these values with those in Table I indicates that the mechanism of anodic stripping changes at potentials higher than 0.60V.

Because knowledge of how anodic stripping affects subsequent adsorption should indicate the nature of the products of stripping, the following study was carried out. After adsorption at 0.25 or 0.30V for a time sufficient to attain $Q_{s,max}$, anodic stripping was performed by two methods: (*a*) treatment at 0.575V for 2 to 3 min; (*b*) application of an anodic galvanostatic pulse of sufficient duration just to complete the potential arrest. The electrode potential was then stepped to 0.35V for a time, t, to permit readsorption, and adsorption was measured by the anodic charging method. The Q vs. t curves so obtained were compared with the curves of Fig. 2-4. The two methods of oxidizing the surface species led to identical results. No difference was observed for ethane, but the n-butane and n-octane curves were shifted to lower Q values by some 10-15%. However, a treatment at 1.15V for 10 sec re-established the original Q vs. t behavior.

Although a partially oxidized intermediate, such as CO, would be expected to remain on the surface and block subsequent readsorption, the results suggest that

Table I. Tafel slope and k_{ox} from Eq. [4] and [5]

Fuel	Slope of Eq. [4]	Intercept of Eq. [4]	Slope of Eq. [5]
	Tafel slope, $2.303RT/\alpha$ nF		
ethane	0.086	0.086	0.073
n-butane	—	0.144	0.152
n-octane	0.086	0.086	0.086
	Rate constant, k_{ox}, sec^{-1} cm^{-2}		
ethane	3.82×10^{-8}	3.82×10^{-8}	2.51×10^{-9}
n-butane	—	9.55×10^{-6}	6.68×10^{-6}
n-octane	3.72×10^{-9}	3.02×10^{-8}	2.69×10^{-8}

complete conversion to CO_2 occurs during anodic stripping of adsorbed ethane (9). The stripping at potentials below 1.15V evidently fails to convert 100% of the adsorbed n-butane or n-octane to CO_2, and so leaves a residue which poisons a small portion of the surface available for readsorption.

Analysis of the Net Rate of Build-up of Adsorbed Species

Another limiting case arises when steady-state conditions exist. In this case the conditions $Q = Q_s$ and $dQ/dt = 0$ can be combined with Eq. [1]. Integrating the resulting equation, taking logarithms, and rearranging terms

$$-\log \frac{Q_s}{Q_{s,max} - Q_s} = \frac{\alpha n \mathbf{F} E}{2.303RT} + \log \frac{Q_s k_{ox}}{k_{ad}} \quad [7]$$

Figure 12 is a semilog plot of $Q_s/Q_{s,max} - Q_s)$ *vs.* E for ethane. Using the slope and intercept of this curve along with the previously obtained value of k_{ad}, values of 0.084V for the Tafel slope, and 3.56 x 10^{-8} sec^{-1} for k_{ox} were computed. These agree favorably with values in Table I.

Integrating Eq. [1], taking logarithms, and rearranging terms gives

$$t = -\frac{2.303}{k_{ad}\beta} \log (1 - \beta Q) \quad [8]$$

where

$$\beta = \frac{1}{Q_{s,max}} + \frac{k_{ox}}{k_{ad}} e^{\alpha n \mathbf{F} E/RT}$$

Semilog plots of $(1 - \beta Q)$ *vs.* t were constructed with values of k_{ox} and the Tafel slope averaged from all but three values from Table I. These are presented in Fig. 13 and 14 for ethane and n-octane. Curves for n-butane showed behavior similar to the n-octane curves. Values of the slope, $-2.303/k_a\beta$ were determined from the linear portions of the curves. These data are given in Table II, which also gives, for comparison, the corresponding slope values computed directly from previously calculated k_{ad} values and from the data presented in Table I.

The greatest deviation from linearity occurred at the high potentials and low ordinate values or high Q values. At 0.25 or 0.30V the slopes are nearly equal to the corresponding slope of Eq. [2]; $-2.303Q_{s,max}/k_{ad}$. This behavior is expected since when $E << \alpha n\mathbf{F}/RT$, $\beta\alpha 1/Q_{s,max}$. The ethane data fits Eq. [8] best. The readsorption studies indicate that no residue was formed during anodic stripping of adsorbed ethane. The apparent slowing of the build-up of adsorbed n-butane and n-octane above 0.35V at sufficiently long adsorption times could thus be caused by build-up of a residue which is difficult to remove by anodic treatment at potentials below surface oxide formation. Anodic oxidation could be interfering with adsorption at the more positive potentials.

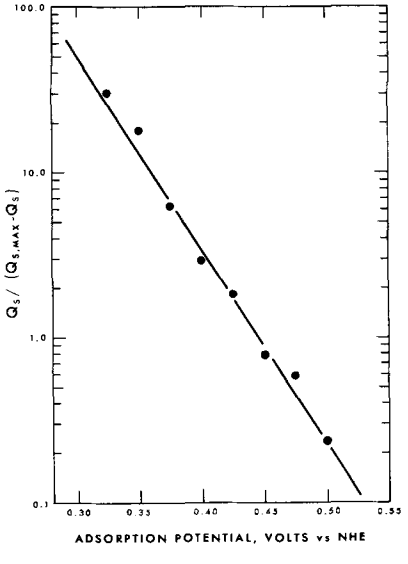

Fig. 12. Log $[Q_s/(Q_{s,max} - Q_s)]$ *vs.* adsorption potential of ethane.

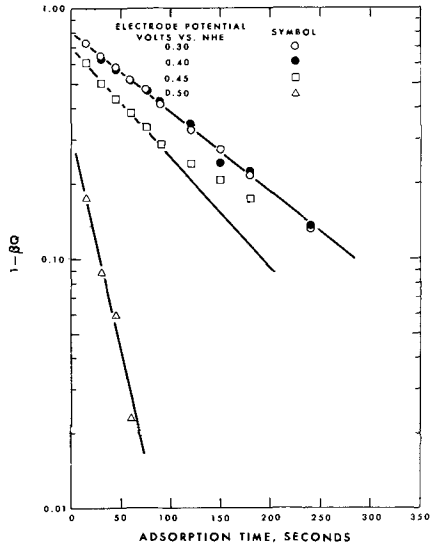

Fig. 13. Fit of adsorption data for ethane to Eq. [8]

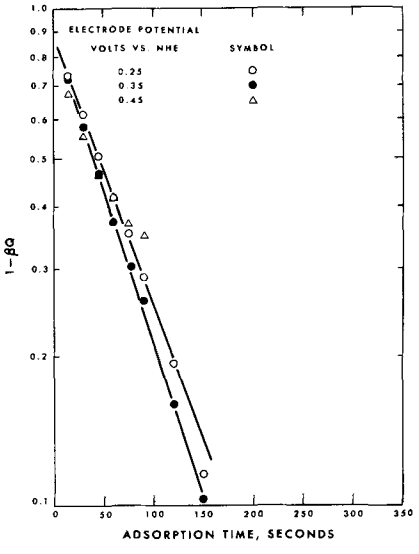

Fig. 14. Fit of adsorption data for n-octane to Eq. [8]

Coverage of Hydrogen Adsorption Sites by Hydrocarbons

The number of hydrogen adsorption sites consumed in the adsorption of the hydrocarbons was estimated by measuring the decrease in cathodic charge required to form an adsorbed hydrogen layer after adsorption of hydrocarbon. The potential step program was used

Table II. Comparison of calculated and observed values of the slope of Eq. [8]

Fuel		E, V *vs.* NHE					
		0.25	0.30	0.35	0.40	0.45	0.50
ethane	observed	—	314	—	314	226	56
	calculated	—	328	—	258	153	63
n-butane	observed	186	—	173	—	—	
	calculated	193	—	172	—	120	
n-octane	observed	—	327	327	—	208	
	calculated	—	327	314	—	198	

with one modification, after adsorption for a fixed time at 0.35V, a constant cathodic current was applied and the electrode potential measured as a function of time. The cathodic charge, Q_H, was computed from the length of the potential arrest occurring in the range 0.05-0.25V. The displaced cathodic charge, $Q_{H,t=0} - Q_{H,t}$ (t = hydrocarbon adsorption time), was compared to the charge required to strip adsorbed hydrocarbons anodically. The ratios of anodic to displaced cathodic charge were: ethane, 1.5; n-butane, 6.5; n-octane, 1.2, with an average deviation less than 6% over a broad range of adsorption times. From these ratios, $Q_{s,max}$, and $Q_{H,t=0}$, the maximum surface coverages of platinum sites, $\theta_{s,max}$, were computed: ethane, 0.44; n-butane, 0.12; n-octane, 0.37.

To determine whether codeposition of hydrogen would affect the state of the adsorbed hydrocarbon or *vice versa*, the following experiments were performed. After adsorption at 0.35V for a time sufficient to attain Q_s, the electrode potential was stepped to 0.1V and maintained for a time $t_{0.1}$, to attain hydrogen coverage free on sites. A constant anodic current was applied and an anodic charging curve obtained. For ethane and n-octane Q_s was unchanged even after a 30-min treatment at 0.1V. The ratios of $Q_{s,0.35}$ to displaced anodic charge for adsorbed hydrogen oxidation, were nearly identical to values cited above for the corresponding ratio of $Q_{s,0.35}$ to displaced cathodic charge. The behavior of n-butane differed from that of ethane and n-octane. The $Q_{n\text{-butane}}$ value obtained after treatment at 0.1V for $t_{0.1}$ = 1 min to $t_{0.1}$ = 30 min dropped to ½ $Q_{s,0.35}$, and the potential arrest for anodic stripping of adsorbed n-butane shifted to less noble values by some 100 mv.

If the potential is stepped from 0.1 to 0.35V and an anodic pulse applied after a time $t_{0.35}$, both $Q_{s,0.35}$ and the form of the arrest for adsorbed butane oxidation revert to their original state (as for no treatment at 0.1V) after $t_{0.35}$ = 5 min, indicating a complete reversal of the adsorbed hydrogen-adsorbed n-butane interaction and readsorption of material desorbed in the hydrogen adsorption region.

One possibility for error in the estimated number of sites covered by adsorbed hydrocarbon could be the occurrence of reversible hydrogenation and dehydrogenation during cathodic hydrogen deposition and subsequent oxidation steps. This would make the maximum θ values observed appear too low.

Two potential arrests of approximately equal length, corresponding to strongly and weakly bound hydrogen, appear in both the anodic and cathodic charging curves. All three hydrocarbons adsorb preferentially on sites otherwise occupied by the strongly bound hydrogen.

Discussion

The fact that only a low number of electrons per site appear to be required for oxidation of adsorbed ethane and n-octane suggests the formation of a C_1 or C_2 partially oxygenated species. The close similarity of the rate constants for electrooxidation indicates the adsorbed species are the same for both ethane and n-octane.

Support for these views is found in the observations of Niedrach (4) during anodic galvanostatic treatment of platinum electrodes in 5*N* H_2SO_4 containing ethane. The adsorbed species failed to undergo cathodic hydrogenation. Niedrach concluded from this and other observations that the adsorbed material was an oxygenated C_1 species.

The behavior of adsorbed n-butane with respect to its oxidation kinetics, its charge requirements of 6.5 electrons/site for anodic oxidation, and its response to cathodic coadsorption of hydrogen contrast markedly with that of adsorbed ethane and n-octane. The lower $Q_{n\text{-butane}}$ value observed after treatment with cathodically generated hydrogen and the readsorption at 0.35V suggest that at least part of the adsorbed butane is dehydrogenated at 0.1V and desorbed. These findings agree with a recent study of n-butane adsorption at platinum electrodes using radiolabelling techniques (6); it showed that butane preadsorbed at 0.3V was partially desorbed during treatment at 0.1V. Apparently a partially dehydrogenated species is formed during n-butane adsorption.

The attainment of maximum coverage at values substantially less than unity during adsorption of hydrocarbons on platinum electrodes was reported by Gileadi *et al.* (10) who measured maximum θ values of 0.35 to 0.45 for ethylene adsorption on platinum electrodes. This could be connected with our observation that adsorption occurs only on strongly bound hydrogen sites. Based on the observed apportionment of the two types of adsorbed hydrogen of roughly 50% of each, the observed maximum coverages of ethane and n-octane of 44% and 36%, respectively, indicate nearly complete coverage of strongly bound hydrogen sites.

The failure to detect adsorption on weakly bound sites indicates that the species adsorbed on these sites cannot be observed in the anodic charging curve. Such species may fail to undergo C-C bond breaking or a surface rearrangement to the precursors of detectable species. The hydrogen coadsorption studies however imply that such species, if they exist, are rapidly desorbed in the hydrogen deposition region with small cathodic charge requirements. The adsorption-rate studies show first-order rate dependence on free available sites over a broad range of coverage for all the hydrocarbons studied and a potential independent rate constant. Apparently a rate-determining surface process occurs between the initial adsorption step and the subsequent oxidation to detectable species.

Acknowledgment

The authors wish to express their gratitude to Mr. Ramsey White for his assistance during the electrochemical measurements. The work was financially supported by the Advanced Research Projects Agency of the Department of Defense as part of Project Lorraine under Contract Nos. DA-11-022-ORD-4023 and DA-49-186-AMC-167(X). The technical guidance of the U.S. Army Research Office (Durham), Harry Diamond Laboratories of the U.S. Army Materiel Command, and the U.S. Navy Marine Engineering Laboratories is acknowledged.

Manuscript submitted July 28, 1966; revised manuscript received Feb. 27, 1969.

Any discussion of this paper will appear in a Discussion Section to be published in the June 1970 JOURNAL.

REFERENCES

1. M. W. Breiter, *Electrochim. Acta*, **7**, 533 (1962).
2. P. R. Johnson and A. T. Kuhn, *This Journal*, **112**, 599 (1965).
3. H. Wroblowa, B. S. Piersma, and J. O'M. Bockris, *J. Electroanal. Chem.*, **6**, 401 (1963).
4. L. W. Niedrach, *This Journal*, **111**, 1309 (1964).
5. S. B. Brummer, J. I. Ford, and M. J. Turner, *J. Phys. Chem.*, **69**, 3424 (1965).
6. R. J. Flannery and D. C. Walker, "Hydrocarbon Fuel Cell Technology," pp. 333-46, Academic Press, Inc., New York (1965).
7. H. A. Laitinen and C. G. Enke, *This Journal*, **107**, 773 (1960).
8. S. Gilman, *Trans. Faraday Soc.*, **61**, 2546 (1965).
9. W. T. Grubb and L. W. Niedrach, Proceedings 17th Annual Power Sources Conference, Atlantic City, N. J., p. 69 (1963).
10. E. Gileadi, B. T. Rubin, and J. O'M. Bockris, *J. Phys. Chem.*, **69**, 3335 (1965).

Overvoltage of Two Stepwise-Proceeding Electrode Reactions under Transient Conditions

I. H. Plonski

Institute for Atomic Physics, Bucharest, Romania

ABSTRACT

General equations are derived for the overvoltage of two stepwise-proceeding electrode reactions for the transient regime under galvanostatic conditions. Two shapes of η-t curves have been found depending on the mechanism and i values: for $i_{o1} > i_{o2}$ and $i > i_{critical}$, the η-t curves are peak shaped; for $i_{o1} > i_{o2}$ and $i \leq i_{critical}$, the η-t curves gave the usual form of monotone increasing η toward the steady-state value. At the same time, the intermediate ion concentration increases, following an S-shape curve: for $i_{o1} = i_{o2}$ and $i_{o1} < i_{o2}$, the η-t curves have the same form as for the $i_{o1} > i_{o2}$ and $i < i_{critical}$ case, but the intermediate ion concentration remains constant and equal to the equilibrium concentration for $i_{o1} = i_{o2}$ and decreases below the equilibrium concentration for $i_{o1} < i_{o2}$. The relationships concerned are of some help in assigning a mechanism and under specific conditions in calculating the exchange currents of both steps by using them in conjunction with experimental results.

The multielectron transfer processes present the possibility of a stepwise proceeding implying a transitory existence of intermediate ion of lower valency oxidation states.

The rates of electrochemical formation and disappearance of intermediate ion are equal under steady-state conditions. The general equations for the kinetics of multielectron stepwise-proceeding electrode processes under steady-state conditions have been derived by Parsons (1), Vetter (2), and Losev *et al.* (3).

In the present paper, a general two stepwise-proceeding electrode reaction is considered and equations are derived for the transient regime under galvanostatic conditions.

In Part I, the overvoltage and intermediate ion concentration equations are discussed, under limited time conditions, that is at the very moment of switching on the current and at the steady-state. In Part II, the overvoltage-time and intermediate ion concentration-time relationships are derived assuming no simultaneous charging of the double layer or a negligible capacitive current. In Part III, the same relationships are derived taking into consideration the simultaneous charging of the double layer.

The following simplifying assumptions have been made:

(*A*) The electrochemical reaction is two stepwise-proceeding.

(*B*) During the pulse current, the final ion concentration and, of course, the metal concentration are constant; only the intermediate ion concentration is changing, but its mass transfer is neglected.

(*C*) The electrode potential and the ion concentrations are unaffected by the electric double layer potential.

(*D*) No competitive chemical or disproportionation reactions accompany the transfer process.

Equilibrium State, the Moment of Switching on the Current, and the Steady-State (Part I)

The over-all electrode reaction

$$M \underset{k_c}{\overset{k_a}{\rightleftarrows}} M^{n+} + ne^-$$

may occur through two consecutive steps

$$M \underset{k_{c1}}{\overset{k_{a1}}{\rightleftarrows}} M^{z_1+} + z_1e^- \qquad [I]$$

$$M^{z_1+} \underset{k_{c2}}{\overset{k_{a2}}{\rightleftarrows}} M^{(z_1+z_2)+} + z_2e^- \qquad [II]$$

where M is metal; M^{z_1+} is the intermediate ion; $M^{(z_1+z_2)+} \equiv M^{n+}$ is the final ion; z_1 and z_2 are the number of electrons involved in the first and second step, respectively; $n = z_1 + z_2$ is the number of electrons involved in the over-all reaction; k_a, k_c, k_{a1}, k_{c1}, k_{a2}, and k_{c2} are the rate constants in the anodic and the cathodic directions for the over-all process, the first and the second step, respectively.

The actual rates of the two steps, expressed in current density terms are given by electrochemical kinetics as

$$i_1 = i_{o1}\left(e^{\alpha_{a1}\eta} - \frac{[M^{z_1+}]}{[M^{z_1+}]_o} e^{-\alpha_{c1}\eta} \right) \qquad [1]$$

and

$$i_2 = i_{o2}\left(\frac{[M^{z_1+}]}{[M^{z_1+}]_o} e^{\alpha_{a2}\eta} - e^{-\alpha_{c2}\eta} \right) \qquad [2]$$

where i_1 and i_2 are the current densities corresponding to the first and second steps, respectively; η is the overvoltage; $[M^{z_1+}]$ and $[M^{z_1+}]_o$ are the intermediate ion concentrations at the time t and at equilibrium ($i=0$); α_{a1}, α_{c1}, α_{a2}, and α_{c2} are the transfer coefficients in anodic and cathodic directions of the two steps. The transfer coefficient expressions are

$$\alpha_{a1} = \beta_1 z_1 \mathbf{F}/RT; \alpha_{c1} = (1 - \beta_1) z_1 \mathbf{F}/RT;$$

$$\alpha_{a2} = \beta_2 z_2 \mathbf{F}/RT; \alpha_{c2} = (1 - \beta_2) z_2 \mathbf{F}/RT$$

where β_1 and β_2 are named symmetry factors, may have values ranging from zero to 1, and depend on the symmetry of the potential energy barrier, being 0.5 for a symmetrical barrier (1); $\mathbf{F}$ is the Faraday number; R is the gas constant; and T is the absolute temperature. The exchange currents of the first step, i_{o1}, and of the second step, i_{o2}, are expressed by

$$i_{o1} = z_1 \mathbf{F} k_{a1} [M] e^{\alpha_{a1}\epsilon_o} = z_1 \mathbf{F} k_{c1} [M^{z_1+}]_o e^{-\alpha_{c1}\epsilon_o}$$

and

$$i_{o2} = z_2 \mathbf{F} k_{a2} [M^{z_1+}]_o e^{\alpha_{a2}\epsilon_o} = z_2 \mathbf{F} k_{c2} [M^{(z_1+z_2)+}] e^{-\alpha_{c2}\epsilon_o}$$

where [M] and $[M^{(z_1+z_2)+}]$ are the metal and the final ion concentrations, respectively, and ϵ_o the equilibrium potential.

Under galvanostatic conditions, that is i = constant, at any moment, the corresponding current densities of the first step, i_1, and of the second step, i_2, satisfy the relation

$$i = i_1 + i_2 \qquad [3]$$

By introducing [1] and [2] into [3], the expression of the ratio $[M^{z_1+}]/[M^{z_1+}]_o$ is obtained as

$$\frac{[M^{z_1+}]}{[M^{z_1+}]_o} = \frac{i + i_{o2}e^{-\alpha_{c2}\eta} - i_{o1}e^{\alpha_{a1}\eta}}{i_{o2}e^{\alpha_{a2}\eta} - i_{o1}e^{-\alpha_{c1}\eta}} \quad [4]$$

as well as the expression of the current density, i

$$i = i_{o1}\left(e^{\alpha_{a1}\eta} - \frac{[M^{z_1+}]}{[M^{z_1+}]_o}e^{-\alpha_{c1}\eta}\right) + i_{o2}\left(\frac{[M^{z_1+}]}{[M^{z_1+}]_o}e^{\alpha_{a2}\eta} - e^{-\alpha_{c2}\eta}\right) \quad [5]$$

Under steady-state conditions, the rate of the appearance of the intermediate ion in the first step, $d[M^{z_1+}]_I/dt$, is equal to the rate of its disappearance in the second step, $d[M^{z_1+}]_{II}/dt$, that is, the rate of the appearance of the final ion, $d[M^{(z_1+z_2)+}]/dt$. This may be written, by taking into account the Faraday law, as

$$\frac{d[M^{z_1+}]_I}{dt} = \frac{i_1}{z_1\mathbf{F}} = \frac{d[M^{z_1+}]_{II}}{dt} = \frac{i_2}{z_2\mathbf{F}} = \frac{d[M^{(z_1+z_2)+}]}{dt} = \frac{i}{(z_1+z_2)\mathbf{F}} \quad [6]$$

that is

$$\frac{i_{o1}}{z_1\mathbf{F}}\left(e^{\alpha_{a1}\eta_\infty} - \frac{[M^{z_1+}]_\infty}{[M^{z_1+}]_o}e^{-\alpha_{c1}\eta_\infty}\right) = \frac{i_{o2}}{z_2\mathbf{F}}\left(\frac{[M^{z_1+}]_\infty}{[M^{z_1+}]_o}e^{\alpha_{a2}\eta_\infty} - e^{-\alpha_{c2}\eta_\infty}\right) \quad [7]$$

where $[M^{z_1+}]_\infty$ and η_∞ denoted the intermediate ion concentration and the transfer overvoltage under steady-state conditions.

By introducing [4] in [7] and rearranging the terms we obtain

$$i = \frac{z_1+z_2}{z_1z_2}i_{o1}i_{o2}\frac{e^{(\alpha_{a1}+\alpha_{a2})\eta_\infty} - e^{-(\alpha_{c1}+\alpha_{c2})\eta_\infty}}{\frac{i_{o1}}{z_1}e^{-\alpha_{c1}\eta_\infty} + \frac{i_{o2}}{z_2}e^{\alpha_{a2}\eta_\infty}} \quad [8]$$

which is the equation deduced by Vetter (2). The explicit solution of η_∞ from Eq. [8] is a rather difficult problem. It may be solved by employing the simplifying assumption of the existence of only symmetrical energy barriers, that is $\beta_1 = \beta_2 = 0.5$, which leads to the equalities: $\alpha_{a1} = \alpha_{c1} = \alpha_1$ and $\alpha_{a2} = \alpha_{c2} = \alpha_2$. For $z_1 = z_2$, then, $\alpha_1 = \alpha_2 = \alpha$, and by substituting $e^{\alpha\eta_\infty}$ by y we obtain a fourth-order algebraic equation. One of the real roots of this equation will give the expression y corresponding to $e^{\alpha\eta_\infty}$. The problem is solved in a similar way for $z_1 = 1$, $z_2 = 2$; $z_1 = 2$, $z_2 = 1$; and $z_1 = z_2 = 2$. The expressions of η_∞ as a function of i deduced in this way are very intricate. When $\beta_1 \neq \beta_2 \neq 0.5$, we must introduce into [8] the corresponding numerical values of α's and calculate η_∞ by means of a computer. It is more convenient to calculate inversely the i values corresponding to certain η_∞ values.

In discussing the following equations, we will choose the case $z_1 = z_2 = 1$; $\alpha_{a1} = \alpha_{c1} = \alpha_{a2} = \alpha_{c2} = \alpha$. In this case, Eq. [8] becomes

$$i = 2i_{o1}\frac{e^{\alpha\eta_\infty} - e^{-3\alpha\eta_\infty}}{1 + \frac{i_{o1}}{i_{o2}}e^{-2\alpha\eta_\infty}} \quad [8']$$

Two particular situations are of interest for the following discussions.

When i is sufficiently large so that the exponential terms concerning negative arguments in Eq. [8] may be neglected, this becomes (2)

$$i = \frac{z_1+z_2}{z_1}\cdot i_{o1}\cdot e^{\alpha_{a1}\eta_\infty} \quad [9]$$

Therefore

$$\eta_\infty = \frac{1}{\alpha_{a1}}\ln\frac{i}{\frac{z_1+z_2}{z_1}i_{o1}} \quad [10]$$

that is for the particular case mentioned above

$$\eta_\infty = \frac{1}{\alpha}\ln\frac{i}{2i_{o1}} \quad [10']$$

For an even more specific case, $i_{o1} = i_{o2}$, the substitution of $e^{\alpha\eta_\infty}$ by y into Eq. [8'] leads to a second-order algebraic equation, the roots of which are

$$y_{1,2} = \frac{i \pm \sqrt{i^2 + 16i_{o1}^2}}{4i_{o1}}$$

We choose for η_∞ the expression given by the positive root

$$\eta_\infty = \frac{1}{\alpha}\ln\frac{i + \sqrt{i^2 + 16i_{o1}^2}}{4i_{o1}} \quad [11]$$

(The root containing a minus sign before the square root has no physical sense because $i_{o1} > 0$, which leads to a negative value of the logarithm argument.)

At the very moment of switching on the current, that is at $t = 0+\epsilon$, where ϵ depends on the edge of the pulse transient current, the intermediate ion concentration is approximately equal to the equilibrium concentration, $[M^{z_1+}]_{0+\epsilon} = [M^{z_1+}]_o$, and Eq. [1] and [2] become

$$i_1 = i_{o1}(e^{\alpha_{a1}\eta_{(o+\epsilon)}} - e^{-\alpha_{c1}\eta_{(o+\epsilon)}}) \quad [12]$$

and

$$i_2 = i_{o2}(e^{\alpha_{a2}\eta_{(o+\epsilon)}} - e^{-\alpha_{c2}\eta_{(o+\epsilon)}}) \quad [13]$$

where $\eta_{(o+\epsilon)}$ is the overpotential value established at the very moment when the current density, i, may be considered constant.

Substitution of [3] into [12] and [13] leads to

$$i = i_1 + i_2 = i_{o1}(e^{\alpha_{a1}\eta_{(o+\epsilon)}} - e^{-\alpha_{c1}\eta_{(o+\epsilon)}}) + i_{o2}(e^{\alpha_{a2}\eta_{(o+\epsilon)}} - e^{-\alpha_{c2}\eta_{(o+\epsilon)}}) \quad [14]$$

For the case $z_1 = z_2 = 1$ and $\alpha_{a1} = \alpha_{a2} = \alpha_{c1} = \alpha_{c2} = \alpha$, we can derive from [14] the expression of $\eta_{(o+\epsilon)}$ as

$$\eta_{(o+\epsilon)} = \frac{1}{\alpha}\ln\frac{i + \sqrt{i^2 + 4(i_{o1}+i_{o2})^2}}{2(i_{o1}+i_{o2})} \quad [15]$$

The ratio of [12] and [13], for the above-mentioned case, leads to

$$\frac{i_{1(o+\epsilon)}}{i_{2(o+\epsilon)}} = \frac{i_{o1}}{i_{o2}} \quad [16]$$

from which, taking into account Eq. [3], we obtain

$$i_{1(o+\epsilon)} = \frac{i_{o1}}{i_{o1}+i_{o2}}i \quad [17]$$

and

$$i_{2(o+\epsilon)} = \frac{i_{o2}}{i_{o1}+i_{o2}}i \quad [18]$$

That is, at the very moment of switching on the current, the latter is divided between the two steps proportionally with the relative values of the corresponding exchange current densities.

Comparing [15] with [11] shows that for $i_{o1} = i_{o2}$ the expressions become identical, that is, at the very moment of switching on the current, the transfer overvoltage springs up to its steady-state value.

In this case, the value of i for which η_∞ becomes 0.01288V gives the value of i_{o1}, because, by replacing i with i_{o1} in Eq. [15] it becomes

$$\eta_\infty = \eta_{(o+\epsilon)} = \frac{1}{\alpha}\ln\frac{1+\sqrt{17}}{4} = 0.01288\text{V}$$

Table I. Comparison of $\eta_{(o+\epsilon)}$ and η_∞ for various i values

i_{o1} (A)	i_{o2} (A)	i (A)	η^∞ (V)	$\eta_{(o+\epsilon)}$ (V)	$\eta^\infty - \eta_{(o+\epsilon)}$ (mV)	$\frac{[M^+]_\infty}{[M^+]_o}$
1×10^{-4}	1×10^{-5}	2.072×10^{-4}	5×10^{-2}	4.367×10^{-2}	+0.633	4.119
		3.1262×10^{-4}	5.98×10^{-2}	5.98×10^{-2}	0*	5.035
		5.3882×10^{-4}	7.5×10^{-2}	8.47×10^{-2}	−9.7	6.44
		8.54×10^{-4}	9×10^{-2}	1.0174×10^{-1}	−11.74	7.625
		1.1223×10^{-3}	1×10^{-1}	1.2128×10^{-1}	−21.28	8.248
		3.453×10^{-3}	1.5×10^{-1}	1.793×10^{-1}	−29.3	9.698
		9.2591×10^{-3}	2×10^{-1}	2.306×10^{-1}	−30.6	9.954
		6.34×10^{-2}	3×10^{-1}	3.307×10^{-1}	−30.7	9.999
		Very large			−31.097†	
1×10^{-3}	1×10^{-3}	6.96×10^{-6}	5×10^{-3}	1.56×10^{-4}	+4.844	8.29×10^{-1}
		5.095×10^{-5}	5×10^{-2}	1.28×10^{-3}	+48.72	1.56×10^{-1}
		1.363×10^{-4}	1×10^{-1}	3.47×10^{-3}	+96.53	3.148×10^{-2}
		9.3×10^{-4}	2×10^{-1}	2.31×10^{-2}	+176.9	1.048×10^{-2}
		2.95×10^{-1}	5×10^{-1}	2.85×10^{-1}	+215	1×10^{-2}

* Calculated by Eq. [34]).
† Calculated by Eq. [20].

A comparison of $\eta_{(o+\epsilon)}$, Eq. [15], with η_∞, Eq. [8'], for $i_{o1} > i_{o2}$ and $i_{o1} < i_{o2}$ at various values of i_{o1}, i_{o2} and i, is given in Table I.

It can be seen from Table I that, in the case of $i_{o1} > i_{o2}$, the $\eta_{(o+\epsilon)}$ is lower than η_∞ when the current density, i, is below a certain critical value, $i_{critical}$, denoted by i_{cr}, which is further explained; $\eta_{(o+\epsilon)}$ is equal to η_∞ for $i = i_{cr}$, and $\eta_{(o+\epsilon)}$ is higher than η_∞ for $i > i_{cr}$. With increasing i, the difference $\eta_\infty - \eta_{(o+\epsilon)}$ tends to the value corresponding to Eq. [20]. When $i_{o1} < i_{o2}$, then $\eta_{(o+\epsilon)}$ is always lower than η_∞.

When $i >> 2(i_{o1} + i_{o2})$, Eq. [15] leads to

$$\eta_{(o+\epsilon)} = \frac{1}{\alpha} \ln \frac{i}{i_{o1} + i_{o2}} \qquad [19]$$

Subtracting [19] from [10] we obtain

$$\eta_\infty - \eta_{(o+\epsilon)} = \frac{1}{\alpha} \ln \frac{i_{o1} + i_{o2}}{2\, i_{o1}} \qquad [20]$$

From Eq. [20] it should be noted that: (*a*) when $i_{o1} > i_{o2}$ and $i >> 2(i_{o1} + i_{o2})$, then $\eta_{(o+\epsilon)} > \eta_\infty$; when $i_{o1} < i_{o2}$, then $\eta_{(o+\epsilon)} < \eta_\infty$. (*b*) The maximum difference, $\eta_\infty - \eta_{(o+\epsilon)}$, should be apparent when i_{o1} is quite different from i_{o2}; when $i_{o1} > i_{o2}$, then the maximum difference is equal to $1/\alpha$ ln 1/2; when $i_{o1} < i_{o2}$, this difference may reach values as high as the i_{o2} value will allow.

Now, by substituting [8] into [4] and by rearranging the terms, we can obtain the expression of the ratio of the intermediate ion concentration under steady-state conditions, $[M^{z_1+}]_\infty$, and at the moment $t = o + \epsilon$, $[M^{z_1+}]_{(o+\epsilon)}$. The $[M^{z_1+}]_{(o+\epsilon)}$ may be considered as equal to the intermediate ion concentration at equilibrium, $[M^{z_1+}]_o$. Thus, we have

$$\frac{[M^{z_1+}]_\infty}{[M^{z_1+}]_o} = \frac{\frac{z_2}{z_1}\frac{i_{o1}}{i_{o2}} e^{\alpha_{a1}\eta_\infty} + e^{-\alpha_{c2}\eta_\infty}}{\frac{z_2}{z_1}\frac{i_{o1}}{i_{o2}} e^{-\alpha_{c1}\eta_\infty} + e^{\alpha_{a2}\eta_\infty}} \qquad [21]$$

When i is sufficiently large for neglecting the terms containing negative argument exponentials, Eq. [21] leads to

(*a*) When $z_1 = z_2 = 1$ and $\alpha_{a1} = \alpha_{a2} = \alpha_{c1} = \alpha_{c2} = \alpha$

$$\frac{[M^+]_\infty}{[M^+]_o} \to \frac{i_{o1}}{i_{o2}} \qquad [22]$$

so that the intermediate ion concentration under steady-state conditions cannot be increased by increasing i. It results from Eq. [21] and [22] that, in the special case of $z_1 = z_2 = 1$ when $i_{o1} > i_{o2}$, the steady-state intermediate ion concentration is larger than the equilibrium intermediate ion concentration. The ratio between the two limiting concentrations, $[M^+]_\infty/[M^+]_o$, increases with increasing i and tends to the limit value given by Eq. [22]. When $i_{o1} < i_{o2}$, the intermediate ion concentration under steady-state conditions is smaller than at equilibrium and their ratio tends, with increasing i, to the value given by Eq. [22].

(*b*) When $z_1 = 1$, $z_2 = 2$ and $\alpha_{a1} = \alpha_{c1} = \frac{1}{2}\alpha_{a2} = \frac{1}{2}\alpha_{c2}$, under the same conditions

$$\frac{[M^+]_\infty}{[M^+]_o} = 2\frac{i_{o1}}{i_{o2}} e^{-\frac{1}{2}\alpha_{a2}\eta_\infty} \qquad [23]$$

that is, the steady-state intermediate ion concentration decreases with increasing i.

(*c*) When $z_1 = 2$, $z_2 = 1$ and $\alpha_{a1} = \alpha_{c1} = 2\,\alpha_{a2} = 2\,\alpha_{c2}$

$$\frac{[M^{2+}]_\infty}{[M^{2+}]_o} = \frac{1}{2}\frac{i_{o1}}{i_{o2}} e^{\alpha_{a2}\eta_\infty} \qquad [24]$$

so that the steady-state intermediate ion concentration increases with increasing i. (The special case of $n = 3$ will be treated in another paper.)

The Transient Regime for C = 0 (Part II)

It has already been mentioned that the relations between the current densities corresponding to the two consecutive charge transfer steps, i_1 and i_2, and the rates of appearance, $d[M^{z_1+}]_I/dt$ (by the first step), and of disappearance, $d[M^{z_1+}]_{II}/dt$ (by the second step) of intermediate ion, M^{z_1+}, are given in accordance with the Faraday law as

$$\frac{i_1}{z_1 F} = \frac{d[M^{z_1+}]_I}{dt} \qquad [25]$$

and

$$\frac{i_2}{z_2 F} = \frac{d[M^{z_1+}]_{II}}{dt} = \frac{d[M^{(z_1+z_2)+}]}{dt} \qquad [26]$$

where $[M^{z_1+}]_I$ is the quantity of M transformed into M^{z_1+} (in concentration terms) at time t, and $[M^{z_1+}]_{II}$ is the quantity of M or of M^{z_1+} transformed into $M^{(z_1+z_2)+}$ (in concentration terms also) at time t. The quantity of intermediate ion, $[M^{z_1+}]$, existing in the system at time t, will be equal to the difference between the quantity of intermediate ion formed up to that time in the first step, $[M^{z_1+}]_I$, and the quantity of intermediate ion that disappeared up to that time in the second step, $[M^{z_1+}]_{II}$. The latter is equal to the quantity of final ion, $[M^{(z_1+z_2)+}]$, appeared as a result of the over-all reaction (not the quantity of $M^{(z_1+z_2)+}$ existing in the system, depending on the initial conditions).

The rate of accumulation of intermediate ion, $d[M^{z_1+}]/dt$, in the system will be equal to the difference in its rate of formation, $d[M^{z_1+}]_I/dt$, and its rate of disappearance $d[M^{z_1+}]_{II}/dt$. Therefore, taking into account Eq. [25], [26], [1], and [2], we obtain

$$\frac{d[M^{z_1+}]}{dt} = \frac{d([M^{z_1+}]_I - [M^{z_1+}]_{II})}{dt}$$

$$= \frac{i_{o1}}{z_1F} e^{\alpha_{a1}\eta} + \frac{i_{o2}}{z_2F} e^{-\alpha_{c2}\eta} - \frac{[M^{z_1+}]}{[M^{z_1+}]_o} \left(\frac{i_{o1}}{z_1F} e^{-\alpha_{c1}\eta} + \frac{i_{o2}}{z_2F} e^{\alpha_{a2}\eta} \right) \quad [27]$$

The substitution of [4] into [27] leads to

$$\frac{d[M^{z_1+}]}{dt} = \frac{i_{o1}}{z_1F} e^{\alpha_{a1}\eta} + \frac{i_{o2}}{z_2F} e^{-\alpha_{c2}\eta} - \frac{i + i_{o2} e^{-\alpha_{c2}\eta} - i_{o1} e^{\alpha_{a1}\eta}}{i_{o2} e^{\alpha_{a2}\eta} - i_{o1} e^{-\alpha_{c1}\eta}} \left(\frac{i_{o1}}{z_1F} e^{-\alpha_{c1}\eta} + \frac{i_{o2}}{z_2F} e^{\alpha_{a2}\eta} \right) \quad [28]$$

Also by differentiation of [4] with respect to time, we obtain

$$\frac{d[M^{z_1+}]}{dt} = [M^{z_1+}]_o \left\{ \frac{(\alpha_{c2} i_{o2} e^{-\alpha_{c2}\eta} + \alpha_{a1} i_{o1} e^{\alpha_{a1}\eta})(i_{o1} e^{-\alpha_{c1}\eta} - i_{o2} e^{\alpha_{a2}\eta})}{(i_{o2} e^{\alpha_{a2}\eta} - i_{o1} e^{-\alpha_{c1}\eta})^2} - \frac{(i + i_{o2} e^{-\alpha_{c2}\eta} - i_{o1} e^{\alpha_{a1}\eta})(\alpha_{a2} i_{o2} e^{\alpha_{a2}\eta} + \alpha_{c1} i_{o1} e^{-\alpha_{c1}\eta})}{(i_{o2} e^{\alpha_{a2}\eta} - i_{o1} e^{-\alpha_{c1}\eta})^2} \right\} \frac{d\eta}{dt} \quad [29]$$

By equating [28] to [29] we obtain

$$\frac{d\eta}{dt} = \frac{(i_{o2} e^{\alpha_{a2}\eta} - i_{o1} e^{-\alpha_{c1}\eta})[(z_1 + z_2) i_{o1} i_{o2} (e^{(\alpha_{a1}+\alpha_{a2})\eta} - e^{-(\alpha_{c1}+\alpha_{c2})\eta}) - i(z_2 i_{o1} e^{-\alpha_{c1}\eta} + z_1 i_{o2} e^{\alpha_{a2}\eta})]}{N} \quad [30]$$

where

$$N = z_1 z_2 F [M^{z_1+}]_o \{ (\alpha_{c1} + \alpha_{a1}) i_{o1}^2 e^{(\alpha_{a1}-\alpha_{c1})\eta} + (\alpha_{c2} + \alpha_{a2}) i_{o2}^2 e^{(\alpha_{a2}-\alpha_{c2})\eta} + i_{o1} i_{o2} [(\alpha_{c2} - \alpha_{c1}) e^{-(\alpha_{c1}+\alpha_{c2})\eta} + (\alpha_{a2} - \alpha_{a1}) e^{(\alpha_{a1}+\alpha_{a2})\eta}] - i(\alpha_{a2} i_{o2} e^{\alpha_{a2}\eta} + \alpha_{c1} i_{o1} e^{-\alpha_{c1}\eta}) \}$$

The solution of Eq. [30] gives the explicit form of η as a function of t, *i.e.*, $\eta(t)$. By further introduction of $\eta(t)$ into Eq. [29] and after integration of the latter we obtain the change of $[M^{z_1+}]$ with time.

By integrating [30], we obtain only the explicit form of t as a function of η, and this one only for the special case of $\beta_1 = \beta_2 = \frac{1}{2}$, when we may substitute $e^{\alpha\eta}$ by y. In other words, the explicit form of η, $\eta(t)$, and of $[M^{z_1+}]$, $M^{z_1+}(t)$, which signify the transient regime, cannot be obtained. The solutions of this kind of equation are numerical only.

One can see, from Eq. [30] that $d\eta/dt = 0$ in two cases, namely:

1. When the first round bracket is equal to zero; hence,

$$i_{o2} e^{\alpha_{a2}\eta} = i_{o1} e^{-\alpha_{c1}\eta} \quad [31]$$

that is, when the transfer overvoltage reaches the value given by the relation

$$\eta = \frac{1}{(\alpha_{a2} + \alpha_{c1})} \ln \frac{i_{o1}}{i_{o2}} \quad [32]$$

Hence, at the value of η given by Eq. (32), either the overvoltage reaches directly its steady-state value or attains a minimum or a maximum value. As the η-t curve given by Eq. [30] does not present maxima and minima, in the mentioned case, the curve reaches its steady-state from the beginning. This corresponds to the condition

$$\eta_{(o+\epsilon)} = \frac{1}{(\alpha_{a2} + \alpha_{c1})} \ln \frac{i_{o1}}{i_{o2}} \quad [33]$$

By substituting [33] into [14], it results that, at a critical value of i, denoted i_{cr}, given by the equation

$$i_{cr} = i_{o1} \left(e^{\frac{\alpha_{a1}}{\alpha_{a2}+\alpha_{c1}} \ln \frac{i_{o1}}{i_{o2}}} - e^{-\frac{\alpha_{c1}}{\alpha_{a2}+\alpha_{c1}} \ln \frac{i_{o1}}{i_{o2}}} \right) + i_{o2} \left(e^{\frac{\alpha_{a2}}{\alpha_{a2}+\alpha_{c1}} \ln \frac{i_{o1}}{i_{o2}}} - e^{-\frac{\alpha_{c2}}{\alpha_{a2}+\alpha_{c1}} \ln \frac{i_{o1}}{i_{o2}}} \right) \quad [34]$$

or, for the special case of $z_2 = z_1 = 1$, $\beta_1 = \beta_2 = \frac{1}{2}$

$$i_{cr} = (i_{o1} + i_{o2}) \left(e^{\frac{1}{2} \ln \frac{i_{o1}}{i_{o2}}} - e^{-\frac{1}{2} \ln \frac{i_{o1}}{i_{o2}}} \right) \quad [34']$$

the overvoltage springs up to its steady-state value, the very moment of switching on the current.

It is obvious that the two values, i given by Eq. [34] and η given by Eq. [33], must satisfy the steady-state equation, [8]; that is,

$$i_{cr} = \frac{z_1 + z_2}{z_1 z_2} i_{o1} i_{o2} \frac{e^{\frac{\alpha_{a1}+\alpha_{a2}}{\alpha_{a2}+\alpha_{c1}} \ln \frac{i_{o1}}{i_{o2}}} - e^{-\frac{\alpha_{c1}+\alpha_{c2}}{\alpha_{a2}+\alpha_{c1}} \ln \frac{i_{o1}}{i_{o2}}}}{\frac{i_{o1}}{z_1} e^{-\frac{\alpha_{c1}}{\alpha_{a2}+\alpha_{c1}} \ln \frac{i_{o1}}{i_{o2}}} + \frac{i_{o2}}{z_2} e^{\frac{\alpha_{a2}}{\alpha_{a2}+\alpha_{c1}} \ln \frac{i_{o1}}{i_{o2}}}} \quad [34'']$$

From Eq. [33] one can see that for $i_{o1} > i_{o2}$, the value of i at which the overvoltage reaches its steady-state value is a positive value (for anodic net current, of course); for $i_{o1} < i_{o2}$, under the same conditions, i should have a negative value; that means that by applying an external anodic current the condition of $\eta_{(o+\epsilon)} = \eta_x$ cannot be satisfied for this mechanism.

2. When the second bracket is zero, that is when

$$i = \frac{z_1 + z_2}{z_1 z_2} i_{o1} i_{o2} \frac{e^{(\alpha_{a1}+\alpha_{a2})\eta} - e^{-(\alpha_{c1}+\alpha_{c2})\eta}}{\frac{i_{o1}}{z_1} e^{-\alpha_{c1}\eta} + \frac{i_{o2}}{z_2} e^{\alpha_{a2}\eta}}$$

The latter equation is identical with Eq. [8] and signifies the steady state. In the case of $i_{o1} = i_{o2}$, it has already been shown (Eq. [11] and [15]) that $\eta_{(o+\epsilon)} = \eta_x$ for all values of current densities, so that the second bracket is zero.

The Transient Regime for $C \neq 0$ (Part III)

Therefore, if in transient regime Eq. [1], [2], and [3] were valid, Eq. [30] would mean the change of the transfer overvoltage with time under galvanostatic conditions. But, just during the transient regime the charging of the double layer, of the capacity, C, occurs. In other words, Eq. [3] becomes

$$i - C \frac{d\eta}{dt} = i_1 + i_2 \quad [35]$$

where $C\frac{d\eta}{dt}$ is the capacitive current density.

The substitution of [1] and [2] into [35] leads to

$$\frac{[M^{z_1+}]}{[M^{z_1+}]_o} = \frac{i - C\frac{d\eta}{dt} + i_{o2}\, e^{-\alpha_{c2}\eta} - i_{o1}\, e^{\alpha_{a1}\eta}}{i_{o2}\, e^{\alpha_{a2}\eta} - i_{o1}\, e^{-\alpha_{c1}\eta}} \quad [36]$$

(instead of [4]). Hence,

$$\frac{d\eta}{dt} = \frac{1}{C}\left[i + i_{o2}\, e^{-\alpha_{c2}\eta} - i_{o1}\, e^{\alpha_{a1}\eta} - \frac{[M^{z_1+}]}{[M^{z_1+}]_o}\,(i_{o2}\, e^{\alpha_{a2}\eta} - i_{o1}\, e^{-\alpha_{c1}\eta}) \right] \quad [37]$$

Equation [37] in conjunction with [27]

$$\frac{d[M^{z_1+}]}{dt} = \frac{i_{o1}}{z_1\mathbf{F}}\, e^{\alpha_{a1}\eta} + \frac{i_{o2}}{z_2\mathbf{F}}\, e^{-\alpha_{c2}\eta} - \frac{[M^{z_1+}]}{[M^{z_1+}]_o}\left(\frac{i_{o1}}{z_1\mathbf{F}}\, e^{-\alpha_{c1}\eta} + \frac{i_{o2}}{z_2\mathbf{F}}\, e^{\alpha_{a2}\eta}\right) \quad [37']$$

forms a system of two first-order differential equations which may be solved numerically.

The special case of $i_{o1} = i_{o2}$ presents the particularity of $[M^{z_1+}]/[M^{z_1+}]_o = 1$, so that Eq. [37] may be solved for the sake of simplifying assumptions of $\alpha_{a1} = \alpha_{a2} = \alpha_{c1} = \alpha_{c2} = \alpha$. The substitution of $e^{\alpha\eta}$ by y leads to a differential equation whose solution allows η to be put into an explicit form. The result is

$$\eta = \frac{1}{\alpha}\ln \frac{\left(\frac{i}{4i_{o1}} + \sqrt{\frac{i^2}{16i_{o1}^2}+1}\right)\left(1 - \frac{i}{4i_{o1}} + \sqrt{\frac{i^2}{16i_{o1}^2}+1}\right) - \left(\frac{i}{4i_{o1}} - \sqrt{\frac{i^2}{16i_{o1}^2}+1}\right)\left(1 - \frac{i}{4i_{o1}} - \sqrt{\frac{i^2}{16i_{o1}^2}+1}\right) e^{-\frac{\alpha}{C}\sqrt{i^2+16i_{o1}^2}\cdot t}}{1 - \frac{i}{4i_{o1}} + \sqrt{\frac{i^2}{16i_{o1}^2}+1} - \left(1 - \frac{i}{4i_{o1}} - \sqrt{\frac{i^2}{16i_{o1}^2}+1}\right) e^{-\frac{\alpha}{C}\sqrt{i^2+16i_{o1}^2}\cdot t}} \quad [38]$$

Limiting Conditions: $\eta_{(o+\epsilon)}$ and η_∞ Expressions

The equivalent electrical scheme of a condenser of capacity, C (representing the electric double layer), connected in parallel with a resistance (the equivalent of the transfer reaction) is currently accepted for an electrode process. This equivalent electrical scheme allows us to write Eq. [35] and means that at $t = o + \epsilon$, for $\epsilon \to o$ all the current, i, is a capacitive current; that is,

$$C\frac{d\eta}{dt} = i \quad [39]$$

Therefore, according to Eq. [35]

$$i_1 + i_2 = 0 \quad [40]$$

from which

$$\eta_{(o+\epsilon)} = 0 \quad [41]$$

The relation $[M^{z_1+}]_{(o+\epsilon)} = [M^{z_1+}]_o$ is valid in this case too.

Also, at steady state $C\frac{d\eta}{dt} = 0$; thus the equations are similar to those derived in Part II.

Discussion

On the grounds of expression [30], theoretical curves of η-t were computed for the special case of $C = 0$, $z_1 = z_2 = 1$, $\beta_1 = \beta_2 = 0.5$, $[M^+]_o = 1 \times 10^{-11}$ M/l, and arbitrary values of i_{o1}, i_{o2}, and i, by the computer CET-501, from I.C.P.U.E.C., Bucharest, Romania. The results are graphically presented in Fig. 1A, 2A, and 3A, the values of i_{o1}, i_{o2}, and i being pointed out on the figures. On figures 1B, 2B, and 3B, the theoretical curves of the case of $C = 30$ μF and the same values of i_{o1}, i_{o2}, and i as before are shown in accordance with Eq. [27] and [37].

From these curves, two observations should be noted as valid for all of the cases:

1. With the increase in time, all the curves tend to their steady-state values.
2. The time necessary to reach the steady state decreases with the increase in the i value.

The other observations will be discussed, separately, for the three particular cases.

The case of $i_{o1} > i_{o2}$—(a) $C = 0$, Fig. 1A.— When $i > i_{cr}$, the η-t curve is decreasing; when $i = i_{cr}$, the η is constant from the beginning and equals η_∞; when $i < i_{cr}$, the η-t curve is increasing. From this figure, it can be seen that for the very large values of i, the difference $\eta_\infty - \eta_{(o+\epsilon)}$ becomes constant in accordance with Eq. [20].

(b) $C \neq 0$, Fig. 1B.

Case I. $i > i_{cr}$. 1. All the curves are peak shaped.

2. The peak overvoltage increases with increasing current density. The change of the peak overvoltage with the logarithm of the current density follows a Tafel law; in this case,

$$\frac{d\eta_{peak}}{d\ln i} \simeq \frac{52.18\ \text{mV}}{\text{decade}}\left(\simeq \frac{\mathbf{F}}{RT}\right)$$

which compared with

$$\frac{d\eta_\infty}{d\ln i} = \frac{50\ \text{mV}}{\text{decade}}$$

leads to the conclusion that, at very large current densities, the Tafel slope given by the peak-overvoltage values is almost equal to the Tafel slope given by the steady-state overvoltage values. At smaller

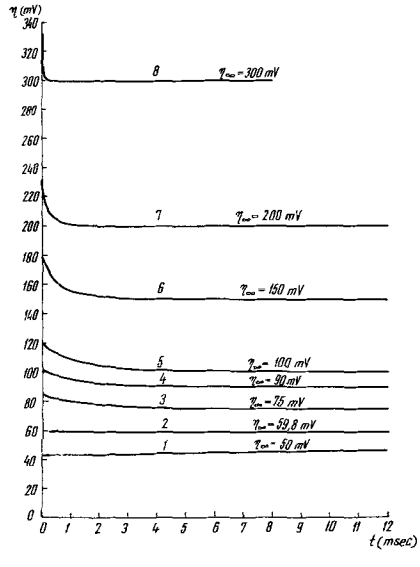

Fig. 1A. The overvoltage, η, as a function of time, t; the case of $i_{o1} = 1 \times 10^{-4}$ (A) $> i_{o2} = 1 \times 10^{-5}$ (A) for $C = 0$ and different values of i (in A).

Curve 1, $i = 2.072 \times 10^{-4}$
Curve 2, $i = 3.1262 \times 10^{-4}$
Curve 3, $i = 5.2882 \times 10^{-4}$
Curve 4, $i = 8.54 \times 10^{-4}$
Curve 5, $i = 1.1223 \times 10^{-3}$
Curve 6, $i = 3.453 \times 10^{-3}$
Curve 7, $i = 9.2591 \times 10^{-3}$
Curve 8, $i = 6.34 \times 10^{-2}$

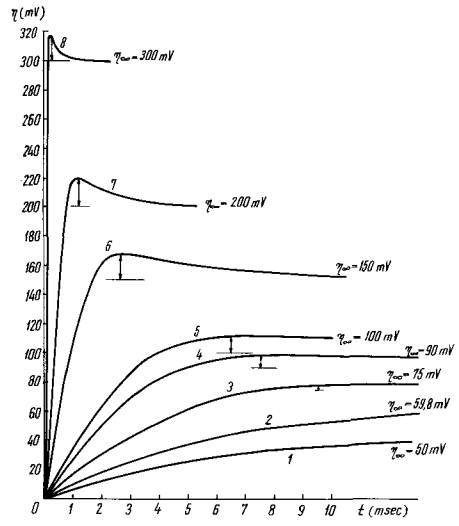

Fig. 1B. The overvoltage, η, as a function of time, t, for C = 3 x 10^{-5}F and the same values of i, i_{o1}, and i_{o2} as in Fig. 1A.

current densities

$$\frac{d\eta_{peak}}{d \ln i} = \frac{47,7 \text{ mV}}{\text{decade}}$$

and

$$\frac{d\eta_{\infty}}{d \ln i} = \frac{33.9 \text{ mV}}{\text{decade}}$$

Therefore, the Tafel slope given by the overvoltage peak values is larger than the Tafel slope given by the overvoltage steady-state values.

3. The difference $\eta_\infty - \eta_{peak}$ first increases, then tends to a constant value. It is obvious that, as C tends to zero, $\eta_\infty - \eta_{peak}$ tends to $\eta_\infty - \eta_{(o+\epsilon)}$.

4. With increasing of the current, the time corresponding to the maxima on the curves, τ peak, tends to zero. In the studied case

$$\frac{d \log \tau_{peak}}{d \log i} = -\frac{0.82}{\text{decade}}$$

Case II, $i = i_{cr}$. The curve η-t increases with increasing time, tending asymptotically to the steady-state value. Hence, the critical current density may be identified as being the maximum value of i for which the peak does not appear. The experimental determination of i_{cr} and corresponding η_∞ allows the calculation of i_{o1} and i_{o2} by means of Eq. [33] and [34], because in this case $\eta_{(o+\epsilon)} = \eta_\infty$.

Case III, $i < i_{cr}$. The curves η-t are of the same shape as in case II.

The case of $i_{o1} = i_{o2}$ (Fig. 2, curves 1-5).—(a) C = 0, Fig. 2.—For all values of i, the η springs up to the steady-state value.

(b) C ≠ 0.—The η-t curves are of the same shape as in the case of $i_{o1} > i_{o2}$ when $i \leq i_{cr}$.

The case of $i_{o1} < i_{o2}$ (Fig. 3).—(a) C = 0, Fig. 3A.

1. All the curves η-t are increasing and S shaped.

2. The time at which the inflection appears tends to zero with increasing current density.

(b) C ≠ 0, Fig. 3B.—The η-t curves are monotone increasing, tending asymptotically to their steady-state values.

The changes of intermediate ion concentration with time for the three cases, namely $i_{o1} > i_{o2}$, $i_{o1} = i_{o2}$, and $i_{o1} < i_{o2}$, and C ≠ 0 are given in Fig. 4.

From this figure it can be seen that for the case of $i_{o1} > i_{o2}$ (curves 1-7) all the curves are increasing and S shaped. The time necessary to reach the steady state as well as the time at which the inflection point appears decreases with increasing current density.

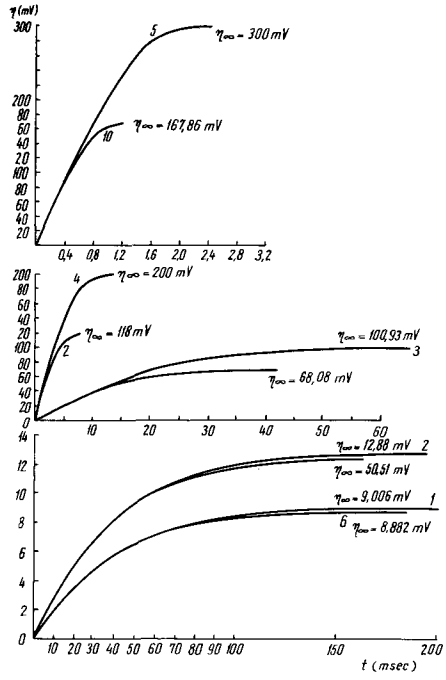

Fig. 2. The overvoltage, η, as a function of time, t, for different values of current density. The case of $i_{o1} = i_{o2} = 1 \times 10^{-5}$ (A), curves 1-5, two step-wise proceeding transfer. The case of $i_o = 1 \times 10^{-5}$ (A), curves 6-10, one step-wise proceeding transfer.
Curves 1 and 6, $i = 6.96 \times 10^{-6}$ (A)
Curves 2 and 7, $i = 1 \times 10^{-5}$ (A)
Curves 3 and 8, $i = 1.363 \times 10^{-4}$ (A)
Curves 4 and 9, $i = 9.3051 \times 10^{-4}$ (A)
Curves 5 and 10, $i = 6.34697 \times 10^{-3}$ (A)

In the case of $i_{o1} = i_{o2}$ (curve 8), the intermediate ion concentration is constant and equal to the equilibrium concentration all the time.

In the case of $i_{o1} < i_{o2}$ (curves 9-12), the intermediate ion concentrations decrease with increasing time, tending asymptotically to the steady-state values.

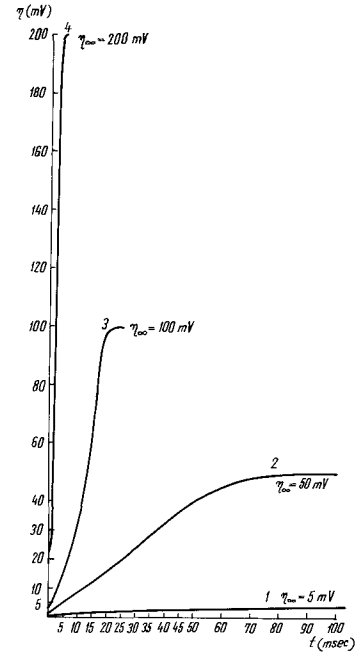

Fig. 3A. The overvoltage, η, as a function of time, t, for the case of $i_{o1} = 1 \times 10^{-5}$ (A), $i_{o2} = 1 \times 10^{-3}$ (A) for C = 0 and different values of current density.
Curve 1, $i = 6.96 \times 10^{-6}$ (A)
Curve 2, $i = 5.195 \times 10^{-5}$ (A)
Curve 3, $i = 1.363 \times 10^{-4}$ (A)
Curve 4, $i = 9.3 \times 10^{-4}$ (A)

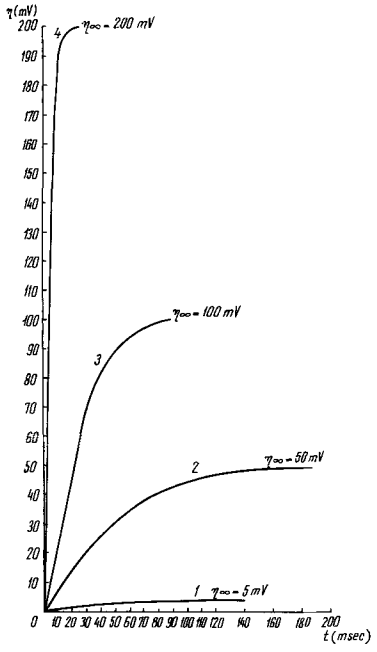

Fig. 3B. The overvoltage, η, as a function of time, t, for $C = 3 \times 10^{-5}$F, and the same values of i, i_{o1}, and i_{o2} as in Fig. 3A.

It is obvious and important that the experimental determination of the change of intermediate ion concentration with time, or at least of the ratio between the steady-state concentration and the equilibrium concentration, would give valuable information on the transfer mechanism.

We find it interesting to present, in the following, the case of the transfer of n electrons in only one step, that is

$$M \underset{k_c}{\overset{k_a}{\rightleftarrows}} M^{n+} + ne^-$$

for comparison with the cases shown before.

The expression of the current density, i, at steady state is

$$i = i_o \left(e^{\alpha_a \eta_\infty} - e^{-\alpha_c \eta_\infty}\right) \qquad [42]$$

where $\alpha_a = \beta n\mathbf{F}/RT$ and $\alpha_c = (1-\beta)n\mathbf{F}/RT$.

The substitution of α_a and α_c by α' and of $e^{\alpha'\eta_\infty}$ by y in Eq. [42] leads to a second order-algebraic equation whose positive root allows η_∞ to be put in an explicit form

$$\eta_\infty = \frac{1}{\alpha'} \ln\left(\frac{i}{2i_o} + \sqrt{\frac{i^2}{4i_o^2} + 1}\right) \qquad [43]$$

In this case, if $C = 0$, then $\eta_\infty = \eta_{(o+\epsilon)}$; that is, the overvoltage springs up readily to its steady-state value.

When $C \neq 0$, that is at transient regime, Eq. [43] becomes

$$i - C\frac{d\eta}{dt} = i_o \left(e^{\alpha'\eta} - e^{-\alpha'\eta}\right) \qquad [44]$$

By substituting $e^{\alpha'\eta}$ by y in Eq. [44] and solving the second-order equation in y, we obtain for η the expression

$$\eta = \frac{1}{\alpha'} \ln \frac{\left(\frac{i}{2i_o} + \sqrt{\frac{i^2}{4i_o^2}+1}\right)\left(1 - \frac{i}{2i_o} + \sqrt{\frac{i^2}{4i_o^2}+1}\right) - \left(\frac{i}{2i_o} - \sqrt{\frac{i^2}{4i_o^2}+1}\right)\left(1 - \frac{i}{2i_o} - \sqrt{\frac{i^2}{4i_o^2}+1}\right) e^{-\frac{\alpha'}{C}\sqrt{i^2 + 4i_o^2}\cdot t}}{1 - \frac{i}{2i_o} + \sqrt{\frac{i^2}{4i_o^2}+1} + 1 - \left(1 - \frac{i}{2i_o} - \sqrt{\frac{i^2}{4i_o^2}+1}\right) e^{-\frac{\alpha'}{C}\sqrt{i^2 + 4i_o^2}\cdot t}} \qquad [45]$$

(It may be noted that Eq. [45] is different from Eq. [38] only in the substitution of i_o by $2i_{o1}$ and n by $z_1 = z_2$ in α's expression.)

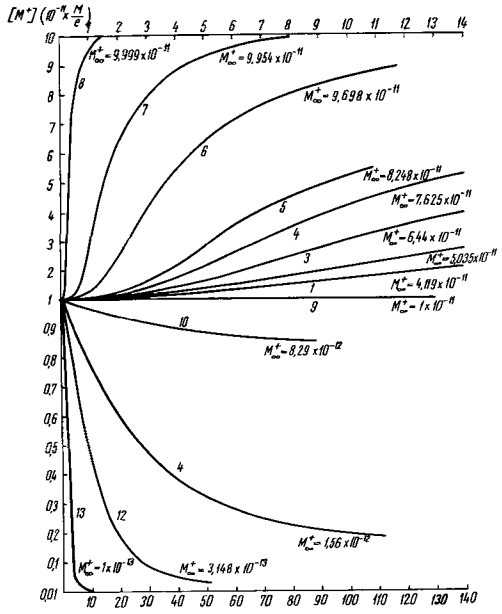

Fig. 4. The intermediate ion concentration, $[M^+]$, as a function of time, t, for the three special cases: case 1, $i_{o1} = 1 \times 10^{-4}$ (A); $i_{o2} = 1 \times 10^{-5}$ (A) (curves 1-7) for different values of current density.

Curve 1, $i = 2.172 \times 10^{-4}$ (A)
Curve 2, $i = 3.1262 \times 10^{-4}$ (A)
Curve 3, $i = 5.3882 \times 10^{-4}$ (A)
Curve 4, $i = 8.54 \times 10^{-4}$
Curve 5, $i = 1.1223 \times 10^{-3}$
Curve 6, $i = 3.453 \times 10^{-3}$
Curve 7, $i = 9.2591 \times 10^{-3}$
Curve 8, $i = 6.34 \times 10^{-2}$

Case 2, $i_{o1} = i_{o2} = 1 \times 10^{-5}$ (A) (curve 9). Case 3, $i_{o1} = 1 \times 10^{-5}$ (A); $i_{o2} = 1 \times 10^{-3}$ (A) (curves 10-13).

Curve 10, $i = 6.96 \times 10^{-6}$ (A)
Curve 11, $i = 5.095 \times 10^{-5}$ (A)
Curve 12, $i = 1.363 \times 10^{-4}$ (A)
Curve 13, $i = 9.3 \times 10^{-4}$ (A)

In Fig. 2, the η-t curves are given for the special case of $n = 2$, $\beta_a = \beta_c = 0.5$ and for the arbitrary values of i_o and i shown on the figure. It can be seen from curves 6-10 that all of them are steadily increasing, tending to the steady state. As the transfer in only one step and the transfer in two steps with $i_{o1} = i_{o2}$ are similar when $C = 0$, because η springs up to its steady-state value, both cases have been represented on the same figure. A comparison between them leads to the observation that for small values of i and the same value of exchange current the curves for both mechanisms almost coincide; with increasing of i, the η_∞ increases for the mechanism in steps more than for the mechanism in only one step, but the slopes of the η-t curves are the same for both cases.

For the sake of comparison, the time $t_{1/2}$ necessary to reach half of the steady-state values of η, denoted by $\eta_{1/2}$, for the treated cases are given in Table II.

Experimental Determination of the Double Layer Capacity

In accordance with Eq. [39]

$$C = \frac{i}{\left.\frac{d\eta}{dt}\right|_{t=o+\epsilon}}$$

the double layer capacity may be obtained from the slope of η-t curves at time t equals $o+\epsilon$. This relation is valid regardless of transfer mechanism.

Table II. Time ($t_{1/2}$) necessary to reach half of the steady-state values of η ($\eta_{1/2}$)

i (A)	i_0 (A)	i_{o1} (A)	i_{o2} (A)	η^∞ (V)	$t_{1/2}$ (sec)
6.96×10^{-6}	2×10^{-5}			4.503×10^{-3}	$13\text{-}14 \times 10^{-3}$
	1×10^{-5}			8.882×10^{-3}	27×10^{-3}
		1×10^{-5}	1×10^{-5}	9.006×10^{-3}	27×10^{-3}
		1×10^{-5}	1×10^{-3}	5×10^{-3}	33×10^{-3}
1×10^{-5}	2×10^{-5}			6.441×10^{-3}	$13\text{-}14 \times 10^{-3}$
	1×10^{-5}			1.2517×10^{-2}	24×10^{-3}
		1×10^{-5}	1×10^{-7}	1.19791×10^{-1}	1070×10^{-3}
		1×10^{-5}	1×10^{-5}	1.2882×10^{-2}	27×10^{-3}
1.363×10^{-4}	2×10^{-5}			5.046×10^{-2}	6.7×10^{-3}
	1×10^{-5}			6.8084×10^{-2}	8.5×10^{-3}
		1×10^{-5}	1×10^{-5}	1.0093×10^{-1}	$13\text{-}14 \times 10^{-3}$
		1×10^{-5}	1×10^{-3}	1×10^{-1}	21×10^{-3}
9.3051×10^{-4}	2×10^{-5}			1×10^{-1}	1.01×10^{-3}
	1×10^{-5}			1.18×10^{-1}	1.05×10^{-3}
		1×10^{-5}	1×10^{-5}	2×10^{-1}	$3.4\text{-}3.5 \times 10^{-3}$
		1×10^{-5}	1×10^{-3}	2×10^{-1}	4.5×10^{-3}
6.34697×10^{-3}	2×10^{-5}			1.5×10^{-1}	$0.36\text{-}0.37 \times 10^{-3}$
	1×10^{-5}			1.67861×10^{-1}	0.40×10^{-3}
		1×10^{-5}	1×10^{-7}	3×10^{-1}	
		1×10^{-5}	1×10^{-5}	3×10^{-1}	0.72×10^{-3}
		1×10^{-5}	1×10^{-3}	3×10^{-1}	

Far from the initial moment, it would be possible to obtain the double layer capacity value by introducing certain t and η values (preferably $t_{1/2}$ and $\eta_{1/2}$ as being more accurately determined from the curves) into the theoretical expression of the double layer capacity, which will be a function of i, i_0 (or i_{o1}, i_{o2}), and t. Unfortunately, this is possible only for the special cases where it was possible to determine η as a function of time, that is for $i_{o1} = i_{o2}$ and for the transfer reaction in only one step. From Eq. [38] we can obtain the expression of C for $i_{o1} = i_{o2}$, that is

$$C = -\frac{\alpha\sqrt{i^2 + 16i_{o1}^2}\cdot t}{\ln\dfrac{\left(e^{\alpha\eta} - \dfrac{i}{4i_{o1}} - \sqrt{\dfrac{i^2}{16i_{o1}^2}+1}\right)\left(1 - \dfrac{i}{4i_{o1}} + \sqrt{\dfrac{i^2}{16i_{o1}^2}+1}\right)}{\left(e^{\alpha\eta} - \dfrac{i}{4i_{o1}} + \sqrt{\dfrac{i^2}{16i_{o1}^2}+1}\right)\left(1 - \dfrac{i}{4i_{o1}} - \sqrt{\dfrac{i^2}{16i_{o1}^2}+1}\right)}} \qquad [46]$$

Similarly, from Eq. [45] the expression of C for transfer in one step is

$$C = -\frac{\alpha'\sqrt{i^2 + 4i_o^2}\cdot t}{\ln\dfrac{\left(e^{\alpha'\eta} - \dfrac{i}{2i_o} - \sqrt{\dfrac{i^2}{4i_o^2}+1}\right)\left(1 - \dfrac{i}{2i_o} + \sqrt{\dfrac{i^2}{4i_o^2}+1}\right)}{\left(e^{\alpha'\eta} - \dfrac{i}{2i_o} + \sqrt{\dfrac{i^2}{4i_o^2}+1}\right)\left(1 - \dfrac{i}{2i_o} - \sqrt{\dfrac{i^2}{4i_o^2}+1}\right)}} \qquad [47]$$

Of course, introducing experimental values of $t_{1/2}$ and $\eta_{1/2}$ for a stepwise-proceeding mechanism into Eq. [47] results in false capacitive values.

Conclusions

The main conclusion of this paper consists in the fact that one can obtain useful information on the transfer mechanism by studying the transient regime. The transient regime offers the possibility of identifying the existence of the step-mechanism and even of specifying the nature of the ratio between the exchange currents of the two steps. The step-mechanism dealt with above gives a new explanation of the peak-shaped η-t curves, frequently encountered in the electrode processes, and an explanation of the discordance between the double layer capacity values determined from the slope of the η-t curves at the initial moment and at a distant one, when a stepwise-proceeding transfer reaction and the over-all reaction may be confused.

Acknowledgments

The author is indebted to Dr. V. V. Losev and Dr. A. Pcelnikov from the Institute of Chemical Physics, L. I. Karpov, Moscow, for helpful criticism of this paper. The work of programming the computer CET 501 performed by Dr. E. Ciupitu, as well as fruitful discussions with several of the author's friends from the Institute of Atomic Physics, Bucharest, are gratefully recorded.

Manuscript received Dec. 27, 1968.

Any discussion of this paper will appear in a Discussion Section to be published in the June 1970 JOURNAL.

REFERENCES

1. R. Parsons, *Trans. Faraday Soc.*, **47**, 1330 (1951).
2. K. J. Vetter, *Z. Naturforsch.*, **7a**, 328 (1952); **8a**, 823 (1953); *Z. Elektrochem.*, **55**, 121 (1951); **59**, 596 (1955).
3. V. V. Losev, V. V. Gorodenski, and A. I. Molodov, *Coll. Czech. Chem. Comm.*, **32**, 2917 (1957).

The Activity Coefficient of Lithium Chloride in Anhydrous Dimethyl Sulfoxide Solutions

Gerhard Holleck, David R. Cogley,* and James N. Butler*

Tyco Laboratories, Inc., Waltham, Massachusetts

ABSTRACT

Activity coefficient measurements of LiCl in dimethyl sulfoxide have been made by the emf method and the cryoscopic method. The emf measurements are in good agreement with similar emf measurements in the literature, but not with cryoscopic measurements in the literature. By applying an empirical correction for temperature gradients resulting from heat transfer in the steady state, agreement is obtained between our cryoscopic measurements and the emf measurements. The systematic errors from heat transfer phenomena in DMSO solutions appear to have been too large thus far for accurate cryoscopic measurements.

The measurement of activity coefficients in nonaqueous solutions is of fundamental importance to a wide variety of investigations. These include the establishment of standard potentials, equilibrium constants, and other thermodynamic data; kinetic studies; and an understanding of ionic solvation and association phenomena. Solutions of lithium chloride in the dipolar aprotic solvent dimethyl sulfoxide (DMSO) have received more attention than any other similar nonaqueous system.

To evaluate the results of our studies (1) of the kinetics of the lithium amalgam-lithium ion electrode in DMSO we required values of the activity coefficient of LiCl over a wide range of concentrations. The values available in the literature at the time (2, 3) were not consistent with each other and did not cover a wide enough range of concentration. After we began our own measurements, two other studies were published (4, 5). Discrepancies between the results of three different studies by the cryoscopic method (2, 3, 5) and by the emf method (4) are much larger than their precision and no critical comparison of all these various data has been made. The LiCl-DMSO system is the only electrolyte solution in an aprotic organic solvent for which sufficient data have been obtained to allow such a critical examination.

This paper reports our measurements of the mean activity coefficient of LiCl in DMSO by both the emf and cryoscopic methods and examines critically the results of other workers.

Experimental

Materials.—Solutions were prepared from anhydrous lithium chloride (Anderson Physics Laboratories, 99.999%) and dimethyl sulfoxide (Matheson, Coleman and Bell, "Spectroquality"). The solvent was dried using molecular sieves (Linde 5-A, washed with triple-distilled water, and dried for 24 hr at 375°C in a stream of dry argon) and filtered through a 10-20μ pore-size glass frit. Analysis was performed by gas chromatography using a column of Porapak Q (Waters Associates) and thermal conductivity detection (6). Water content of the solutions was less than 25 ppm (1.5 mM) and organic impurities were less than 10 ppm.

Amalgams were prepared by weight from triple-distilled mercury (Doe and Ingalls), lithium metal (Foote Mineral Company, 99.96%), and thallium metal (American Smelting and Refining Company, 99.999%). All experiments were performed in a glove-box (Vacuum Atmospheres Corporation) using an atmosphere of argon which was recirculated through a purification train designed to remove water, oxygen, nitrogen, and organic vapors. The oxygen and water content of the atmosphere was estimated to be less than 1 ppm.

* Electrochemical Society Active Member.

Most solutions were prepared by weight, but some solutions were prepared by volume, and conversion to the molal scale was made using values interpolated from measured densities of LiCl-DMSO solutions, together with literature values for the density of pure DMSO (7). The expression

$$d = 1.0946 + 0.015\,C$$

where C is the concentration of the solution in moles/liter, was used for calculations at 25°C.

EMF measurements.—The potential of the cell

$$\mathrm{Li(Hg)/Li^+,\ Cl^-\ DMSO/TlCl(s)/Tl(Hg)}$$

was measured. A two-compartment cell with the compartments separated by a coarse glass frit, with platinum leads sealed through the glass to contact the amalgams, was used. A total of 16 cells of various LiCl concentrations were prepared. For all cells the amalgams contained 0.818 m/o (mole per cent) Li and 6.50 m/o Tl. The cells were filled by first adding approximately 5 ml of each of the amalgams to the compartments of the dry cell, sprinkling approximately 100 mg solid TlCl on top of the thallium amalgam, and then adding the LiCl-DMSO solution to the compartment containing the lithium amalgam. In this way contamination of the lithium amalgam compartment by dissolved thallium ion was reduced.

The potential of each cell was measured as a function of time, using a high impedance differential voltmeter (John Fluke), which was calibrated against a Weston Standard Cell (Eppley Laboratories) and found to be accurate to ± 0.05 mV. Potentials were steady to the nearest 0.1 mV after 1 hr and remained constant (within the uncertainty caused by temperature fluctuations in the drybox) for 24 hr afterward. Because of difficulties in thermostating the drybox, the temperature was not controlled; but it was recorded to ± 0.03°C and ranged from 22° to 26°C.

Cryoscopic measurements.—Two similar 300 ml, partially silvered Dewar flasks were covered with a single ½-in. thick, 4 x 10-in., aluminum plate, insulated with styrofoam, which served as a controlled heat sink. Figure 1 is a diagram of the apparatus. The plate temperature could be measured by copper-constantan thermocouples inserted into holes bored at four different positions. A thermoelectric cooling module (E.G. and G. Model G9-65) was mounted centrally on the aluminum plate and its low-temperature side was cooled by circulating water through a copper coil. To avoid any possible leaks of water into the drybox, the copper tube was installed in a single piece and all joints were made outside the drybox. The temperature sensor was a thermistor bead mounted on the underside of the aluminum plate, opposite the cooling module, and this was connected to an operational am-

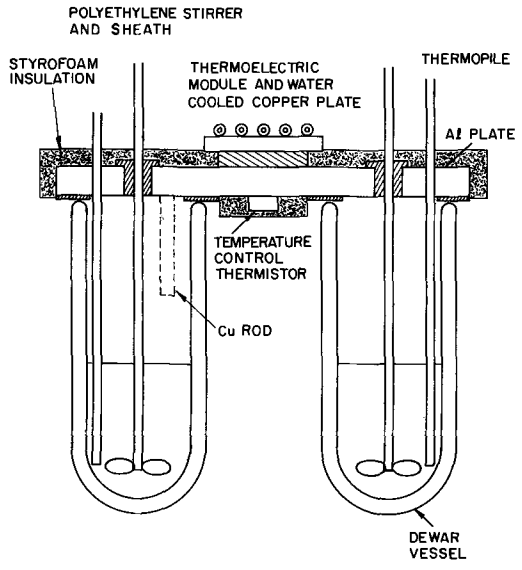

Fig. 1. Apparatus for freezing point depression measurements

plifier (Tyco) which controlled the current through the thermoelectric module so as to maintain the temperature constant (± 0.01°C) at a preset value. An attempt to use a radiative heat sink (to avoid water lines in the drybox) was not successful because of the large amount of heat generated by the resistance of the thermoelectric module. With the low-temperature side of the module cooled by tap water (7°-10°C), the temperature of the plate could be brought to below zero or controlled at temperatures as high as 30°C. At optimum conditions, approximately 7w of heat were pumped by the module.

The solutions in the Dewars were stirred with matched variable-speed stirring motors (Fisher Dyna-Mix) with polyethylene stirrers. These were normally run at approximately 100 rpm.

The temperature difference between the two vessels was measured with a 25-junction copper/constantan thermopile (Science Products Corporation) which had an output of 1.008 mv/°C (as calibrated by the manufacturer), and a resistance of 900 ohms. The thermocouple junctions were enclosed in stainless steel tubes. One arm contained a separate reference thermocouple to determine the absolute temperature. The potential of the thermopile was measured using a microvoltmeter (Keithley Model 150A), and all leads were shielded to avoid spurious currents. The output of the microvoltmeter was read on a potentiometric chart recorder as a function of time. All connections were made between pure copper leads using low thermal emf solder (Science Products Corporation). The noise level was approximately 0.001°C, but temperature differences between the thermopile elements could be estimated with a precision of ± 0.0002°C if the temperature difference was steady.

An attempt to record a simple cooling curve resulted in supercooling by as much as 3°C, which made such a freezing point determination impractical. Therefore, it was necessary to seed the solution with solid DMSO and to attempt to measure a steady-state temperature under conditions as close to equilibrium as possible. Because the mixture of liquid and solid must be stirred to achieve thermal and chemical equilibrium, a certain amount of heat is produced within the solution by the mechanical action of the stirrer. This heat must be removed by external cooling or else the seed crystals will eventually melt. Such a "melting curve" approach was taken by Garnsey and Prue (5) in their cryoscopic studies on DMSO and sulfolane. Our technique was closer to that of Dunnett and Gasser (3) in that we used as a heat sink a cover plate common to both vessels which was maintained at a temperature below the freezing point of the solution, and attempted to achieve a steady state in which a small amount of solid DMSO was present; all the heat generated by the stirrer was being absorbed by the heat sink, and the temperature did not change with time.

With the Dewar vessels each containing 100 ml pure DMSO, the effect of heat transfer on the apparent freezing point was investigated. Both vessels were cooled until solid DMSO appeared, and then the temperature of the plate was raised to approximately one degree below the freezing point of the solvent. The stirrers were operated at the lowest speed which gave a smooth time-dependence of the temperature difference between the vessels. This temperature difference was zero, but an imbalance in the heat transfer between the two vessels (*e.g.*, by changing the shape of the insulation on the aluminum plate) could affect the difference by ± 0.005°C.

We then deliberately made the heat transfer asymmetric by attaching a Teflon-covered copper rod to protrude from the plate into one vessel (this increased the cold surface in this vessel by about 1/3). With the plate temperature at 17.5°C this vessel indicated a freezing point for pure DMSO which was 0.014° ± 0.002°C (constant for at least 10 min) lower than the vessel without the copper rod. With similar Teflon-covered copper rods protruding into both vessels, the temperature difference was again zero. From these tests it was clear that the rate of cooling (even though it was small) had a substantial effect on the observed steady-state temperature of the solid-liquid mixture.

The arrangement with unsymmetrical heat transfer (copper rod protruding into one vessel but not the other) was used to evaluate the heat transfer coefficient of the system, and this coefficient was used in correcting measurements made both with the unsymmetrical arrangement and with the symmetrical arrangement, as described in the next section.

A typical measurement was made as follows: A sample of pure DMSO was placed in each vessel and the plate temperature lowered to approximately 6° or 7°C. As soon as a small amount of solid DMSO appeared, the temperature of the plate was raised until it was less than 1°C below the temperature of the vessel. The temperature difference between the vessels was recorded as a function of time and, although it was not zero, it was usually constant to within ± 0.001°C for 20 min or more.

Then measured amounts of a concentrated, precooled LiCl solution were added through an opening in the cover plate to the vessel into which the copper rod protruded and the temperature difference recorded again until equilibrium was reached. Normally there was only a small amount (less than 1%) of solid present so that this temperature corresponded closely to the freezing point of the dilute LiCl solution. If the concentrated LiCl solution warmed the DMSO too much, the seed crystals melted. The temperature of the solution could be lowered to seed it again, but this resulted in less stable temperature measurements than the method just described.

An earlier set of measurements was made by placing a sample of pure DMSO in one vessel and a solution of LiCl in DMSO in the other vessel and cooling strongly until both solvent and solution produced crystals. The temperature of the plate was then raised to approximately 1°C below the expected freezing point of the solution and the steady temperature was observed. In these experiments the heat transfer arrangement was symmetrical and, thus, this procedure corresponds exactly to that used by Dunnett and Gasser (3). In the dilute solutions this procedure produced less precise results than the addition of LiCl solution to previously seeded pure DMSO.

Results

EMF measurements.—The experimental values of the cell potential E are given in Table I for various concentrations of LiCl. The quantity

Table I. Activity coefficients of LiCl in DMSO at 25° from emf measurements

m, moles/kg	T, °C	E, V	$E^{\circ\prime}$, V	log $\gamma_{\pm}$, molal scale
2.029	22.24	1.4130	1.4381	−0.4485
0.9870	22.32	1.4461	1.4113	−0.4154
0.4870	21.70	1.4749	1.3983	−0.3519
0.4870	25.77	1.4748	1.4003	−0.3511
0.4870	24.37	1.4750	1.3997	−0.3528
0.19323	22.30	1.5146	1.3949	−0.2861
0.09636	23.30	1.5445	1.3954	−0.2367
0.09636	25.80	1.5426	1.3948	−0.2206
0.09636	26.42	1.5429	1.3954	−0.2232
0.09636	24.36	1.5438	1.3952	−0.2308
0.05776	22.31	1.5669	1.3954	−0.2037
0.01923	23.26	1.6138	1.3945	−0.1226
0.01923	25.70	1.6131	1.3950	−0.1167
0.00481	24.31	1.6793	1.3963	−0.0740
0.00481	25.70	1.6789	1.3966	−0.0707

$$E^{\circ\prime} = E + 0.1183\left(\log m - \frac{1.115\sqrt{m}}{1+\sqrt{m}} + 0.282m\right) + 0.511\,(T-25)$$

where m is the molal concentration of LiCl and T is the centigrade temperature, is given for each measurement. This expression contains the Guggenheim-type concentration dependence found by Smyrl and Tobias (4) as well as a temperature coefficient calculated from known temperature coefficients of cells (4, 9).

From Table I it can be seen that $E^{\circ\prime}$ is constant within ±1 mV for concentrations below 0.5M. The average of these twelve points gives the standard potential of our cell at 25°: E° =1.3963 ± 0.001V.

From each point, then, a value of the activity coefficient $\gamma_{\pm}$ was calculated using the expression:

$$\log \gamma_{\pm} = \frac{E^{\circ} - E}{0.1183} - \log m$$

and these values are also listed in Table I.

Cryoscopic measurements.—The results of the cryoscopic experiments are summarized in Table II. $\theta_{obs} = T_{o(obs)} - T_{s(obs)}$ is the observed temperature difference between the solvent and solution at steady state. These include a set of experiments where the heat transfer arrangement was symmetrical (copper rods protruding into both vessels), and a set of experiments where the heat transfer arrangement was unsymmetrical (copper rod protruding only into the solution vessel). For this latter set of experiments the plate temperature was measured and is recorded as T_p in Table II.

Table II. Cryoscopic measurements on LiCl-DMSO solutions

m, moles/kg	T_p[a], °C	θ_{obs}, °C	θ_{corr}[b], °C	ϕ
pure DMSO	6.0	0.180	0.0178	1.0000
pure DMSO	17.5	0.013	−0.0007	1.0000
0.0037	17.5	0.0397	0.0275	0.9132
0.0037	17.6	0.0405	0.0297	0.9862
0.0037	18.1	0.0327	0.0283	0.9397
0.0074	17.3	0.0704	0.0571	0.9481
0.0074	17.7	0.0664	0.0584	0.9697
0.0074	18.1	0.0615	0.0587	0.9747
0.0247	17.3	0.192	0.185	0.9207
0.0280	—	0.199	0.210	0.9220
0.0400	17.3	0.297	0.296	0.9100
0.0474	—	0.337	0.355	0.9212
0.0550	17.2	0.387	0.390	0.8723
0.126	16.6	0.873	0.894	0.8743
0.126	16.9	0.877	0.902	0.8822
0.137	—	0.928	0.979	0.8808
0.191	16.3	1.266	1.305	0.8431
0.217	—	1.429	1.507	0.8576
0.351	—	2.307	2.433	0.8587
0.446	14.7	2.976	3.086	0.8591
0.592	—	3.869	4.081	0.8589

[a] Data for which T_p is given were obtained with the unsymmetrical heat transfer arrangement. If T_p is not given, the heat transfer arrangement was symmetrical.
[b] Corrected for heat transfer effect using Eq. [3] if T_p is listed, and Eq. [5] if T_p is not listed.

From the experiments with unsymmetrical heat transfer it is possible to estimate the heat transfer coefficient and to correct all the measurements for the shift in temperature caused by the displacement from equilibrium. Four of the experiments listed in Table II were performed at two or more plate temperatures and in all cases it was observed that $d\theta_{obs}/dT_p$ = −0.013 ± 0.002 in agreement with our preliminary observations on pure DMSO. This relation between observed freezing point depression and plate temperature holds over a wide range of plate temperatures and concentrations. Even when the plate temperature is 6°C, which is 12.5°C below the freezing point of DMSO, θ_{obs} is 0.180 and $d\theta_{obs}/dT_p$ = −0.0144.

This remarkably consistent behavior led us to a simple empirical correction for the heat transfer effect. Assuming that the difference between the observed temperature and the true equilibrium temperature in each vessel is proportional to the exposed cold surface area of the plate and rod and to the difference between the temperature of this cold surface (T_p) and that of the liquid, we have for the solution

$$T_{s(true)} - T_{s(obs)} = 4Q(T_{s(true)} - T_p) \quad [1]$$

and for the solvent

$$T_{o(true)} - T_{o(obs)} = 3Q(T_{o(true)} - T_p) \quad [2]$$

The factors 4 and 3 are approximately proportional to the cold area in the solution vessel (with the rod) and the solvent vessel (without the rod). These equations can be combined to give an expression for the corrected freezing point depression:

$$T_{o(true)} - T_{s(true)} = \theta_{corr} = \frac{\theta_{obs} - Q(T_{o(true)} - T_p)}{1 - 4Q} \quad [3]$$

The freezing point of pure DMSO (3, 5) ($T_{o(true)}$) is 18.55°C. We have observed that the value of the derivative $d\theta_{obs}/dT_p$ is constant over a wide range of conditions. From Eq. [3] we obtain by differentiation

$$d\theta_{obs}/dT_p = -Q \quad [4]$$

and thus Q = 0.013 ± 0.002.

For the symmetrical heat transfer arrangement where a rod is projected into both vessels, the factor 3 in Eq. [2] is replaced by a factor of 4, and when combined with Eq. [1] this yields

$$\theta_{corr} = \frac{\theta_{obs}}{1 - 4Q} \quad [5]$$

with the same value of Q as derived above.

The data in Table II for which T_p is listed were obtained with the unsymmetrical heat transfer arrangement and were corrected using Eq. [3]; and those for which T_p is not listed were obtained with the symmetrical heat transfer arrangement and were corrected using Eq. [5]. An alternate set of equations, derived using $T_{s(obs)}$ and $T_{o(obs)}$ on the right-hand sides of Eq. [1] and [2], yield the same values of θ_{corr} to within the round-off errors of the table.

Osmotic coefficients were calculated from the values of θ_{corr} using the equation (5, 8)

$$\phi = \frac{T_o\theta}{2\lambda m(T_o - \theta)}$$

with T_o = 18.55°C, and with a cryoscopic constant (5) λ = 4.07°C. These osmotic coefficients are also listed in Table II.

Activity coefficients were not calculated from these cryoscopic measurements because of the large errors inherent in the smoothing and integration required. Instead the cryoscopic and electrochemical measurements were compared in terms of the integration function j, as described in the next section.

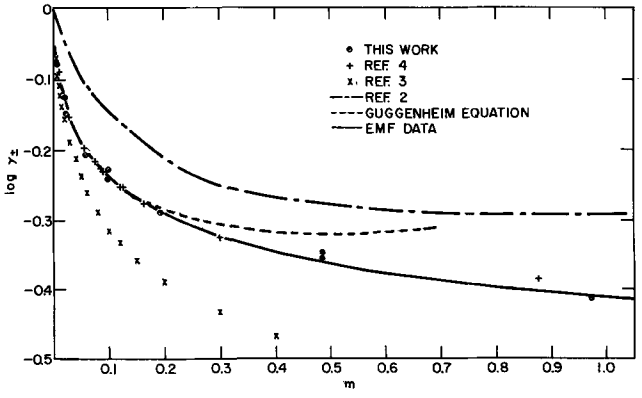

Fig. 2. Activity coefficients of LiCl in DMSO

Discussion

The activity coefficients reported in Table I are in excellent agreement with those obtained by Smyrl and Tobias (4) using the cell

$$\mathrm{Li(s)/Li^+, Cl^-, DMSO/TlCl(s)/Tl(Hg)}$$

where the thallium amalgam contained 0.967 m/o thallium. The comparison is made in Fig. 2 where it can be seen that the deviation corresponds to approximately 1 mV in the cell potential, or 0.01 in log $\gamma_\pm$. Within this same limit of error an equation of the Guggenheim form, obtained by Smyrl and Tobias,

$$\log \gamma_\pm = -\frac{1.115\sqrt{m}}{1+\sqrt{m}} + 0.282m$$

is obeyed for m less than 0.15 mole/kg. At higher concentrations the activity coefficients predicted by the equation are higher than the experimental values, but substantial ion pairing is not indicated.

The results can also be represented by the extended Debye-Hückel equation. With the parameter $B = 0.449$ [see ref. (5)] we calculate from our activity coefficients the ion size parameter $a = 3.8 \pm 0.2$Å. As with the Guggenheim form of the equation, deviations are observed for $m > 0.1$ mole/kg.

By contrast, the agreement between these measurements and those obtained by the cryoscopic method is very poor. In Fig. 2 are also plotted the activity coefficient values given by Dunnett and Gasser (3) and Skerlak *et al.* (2). These are in marked disagreement with each other and with the emf measurements. The results of Garnsey and Prue (5) were given as osmotic coefficients instead of activity coefficients, but they are quite close to those of Dunnett and Gasser. A more direct comparison can be made in terms of the function (8)

$$j = 1 - \frac{\theta}{2\lambda m}$$

which is related to the activity coefficient approximately by the equation

$$j = -\frac{1}{m}\int_0^{\ln\gamma} m\,d(\ln\gamma)$$

In Fig. 3 our results are compared with those of Dunnett and Gasser (3) and Garnsey and Prue (5). By numerical integration we also obtained j as a function of m, corresponding to the best fit to the emf data (Fig. 2 corrected to 18.5°C) and to the extended Debye-Huckel equation used by Garnsey and Prue. All calculations were made using the cryoscopic constant ($\lambda = 4.07$) determined by Garnsey and Prue. (In their paper Dunnett and Gasser used $\lambda = 4.36$.)

The most obvious feature of Fig. 3 is that the shape of the curve of j *vs.* log m is quite similar for both Dunnett and Gasser's data and Garnsey and Prue's data, but there is an almost constant difference between the two sets. This shape, however, is quite different from the shape of the curve obtained by integrating either the emf measurements or an extended Debye-Huckel equation. This discrepancy has been explained (3, 5) in terms of ion-pairing between lithium and chloride ions and both papers give association constants: Dunnett and Gasser (3), 5 kg/mole, Garnsey and Prue (5), 3 kg/mole.

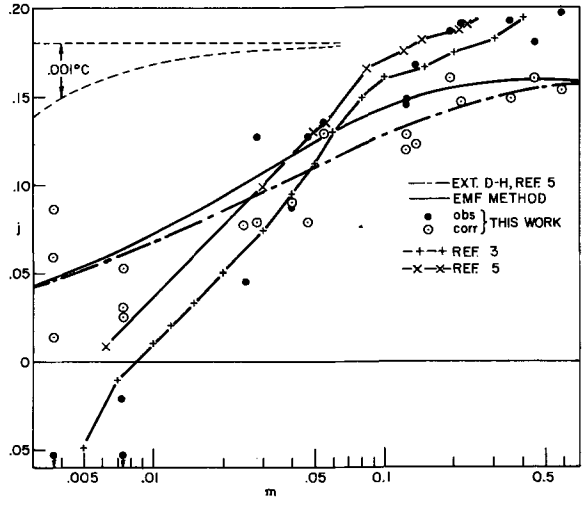

Fig. 3. Cryoscopic integration function j (see text) for LiCl-DMSO solutions.

Although ion pairing seems plausible at first glance, this explanation predicts that the cryoscopic data should approach the Debye-Huckel line at low concentration. It is quite clear from Fig. 3 that this is not the case. The cryoscopic data of Dunnett and Gasser actually give negative values for j at concentrations which are still relatively large ($0.007m$). The data of Garnsey and Prue, although sparse at low concentration, tend in the same direction. These negative values at low concentrations can be removed by adjusting the cryoscopic constant, but such adjustment only moves the data up and down on the plot of Fig. 3 and does not change its slope. No amount of adjustment can give a slope to the data which approximates that of the Debye-Huckel theory at low concentrations.

A more appropriate explanation of the difference between the previous cryoscopic measurements and the emf measurements can be found in the heat transfer phenomena inherent in the cryoscopic method. As we have pointed out in detail in this paper, even though a steady temperature may be measured, there is still heat transfer to the cooling plate from solution and crystals, and this is balanced by the heat generated from stirring the mixture of solution and crystals. Our experiments indicated that a steady temperature can be obtained for periods of up to a half hour even though the heat transfer rate is quite different and, furthermore, that the steady-state temperature of the solution depends quite strongly on the heat transfer rate. We have attempted to correct our data for this effect and, even though our results are not so precise as those of Dunnett and Gasser (3) or Garnsey and Prue (5), they appear to be in general agreement with the emf measurements at high concentrations (slightly better agreement is obtained with $\lambda = 4.12$).

In our experiments, a small quantity ($< 1\%$) of solid DMSO was present in the freezing mixture, and thus the actual concentration was about 1% greater than the value calculated from the known amount of LiCl and DMSO used to make up the solution. This error probably accounts for much of the scatter in our data and also tends to make our measured values of j too low by less than 0.01 units. Although quantitative measurements of the amount of solid DMSO present were not made, a correction for this error would place our results (without any correction for heat transfer) almost exactly in agreement with those of Dunnett and

Gasser. It should also be pointed out here that this 1% error is quite small compared to the errors resulting from the uncertainty in λ.

Our observations lead us to propose that the cryoscopic measurements on DMSO systems may suffer from an inherent systematic error. If both the solution and solvent vessels are cooled by the same heat sink, the heat transfer correction (Eq. [5]) decreases the value of j, which would bring Dunnett and Gasser's data into general agreement with the emf data. Garnsey and Prue used an absolute temperature measurement, but a similar argument could be applied to their data if a larger rate of heating was used in the determination of the freezing point of the pure solvent and dilute solutions than in the determination of the freezing point of concentrated solutions. However, such an argument must also apply to the measurements on benzoic acid solutions, which were made in the same apparatus and from which λ was determined, and thus the errors should cancel out to some extent. The striking parallelism of these two sets of measurements is not simple to explain in view of the quite different experimental setups.

We cannot make a detailed comparison of the data of Skerlak *et al.* (2), since these authors did not give any numerical results for freezing point values but only their graph of $\gamma_{\pm}$ *vs.* m. Furthermore, they did not appear to have taken any precautions to exclude moisture and the description of their experimental method is quite brief: "Beckmann apparatus with the following modifications was used for the cryoscopy. The size of the vessel containing the thermometer was about 50% narrower, wider at the (flat) bottom, and provided with a magnetic stirrer. The cooling was regulated to within 0.2 to 0.3°C with the aid of a pair of aluminum plates half immersed in the solution, suspended by constantan wires through a side arm. On cooling through 0.1°C the plates were rubbed with a thermometer against the wall of the vessel until rapid crystallization took place. Thermostated water was used in place of the cooling mixture." No mention is made of the rate of cooling or the extent to which heat transfer in the vessel was regulated. Because of the deviation of their results from those of other investigations it seems likely that the data of Skerlak *et. al.* are not of sufficient accuracy to be discussed further.

The systematic errors (resulting from heat transfer) in the cryoscopic method seem thus far to have been too great for accurate measurements of activity coefficients in DMSO solutions. To improve the accuracy, one would have to improve the heat distribution within the vessel and to eliminate virtually all heat transfer to the outside. This could probably be best achieved by modification of the apparatus described by Scatchard *et al.* (10). One would have to use a separate cover on each vessel and control its temperature carefully to correspond to that of the solution in the vessel. A metal inner container would help to obtain a more uniform temperature, but it should not be in thermal contact with the cover plate.

In performing the experiment, it would be best to have a large amount of finely distributed solid DMSO yielding a large solid-liquid interface, which would absorb the heat generated by the stirring process. This heat transfer must be minimized, but will of necessity remain at a finite value if equilibrium is to be attained even approximately. After attaining the closest approach possible to thermal and chemical equilibrium, a sample of the liquid phase should be withdrawn for analysis, since the concentration of the solution will have changed due to melting or freezing of the solid DMSO. The accuracy of the final result will depend on success in reducing heat transfer to the outside, improving heat distribution within the vessel, and minimizing the heat generated by stirring.

In conclusion, we believe that the most accurate measurements made thus far of the activity coefficients of LiCl in DMSO are those made by the EMF method. The systematic errors inherent in those measurements have been shown (4) to be negligible, and the agreement between two independent measurements is excellent.

Acknowledgments

The authors thank Dr. W. H. Smyrl for a stimulating discussion and for providing a copy of his thesis and of the translation of ref. (2). This work was supported by the Air Force Cambridge Research Laboratories, Office of Aerospace Research, under Contract No. AF 19(628)-6131, but does not necessarily constitute the opinion of that agency.

Manuscript submitted Oct. 17, 1968; revised manuscript received ca. Feb. 5, 1969.

Any discussion of this paper will appear in a Discussion Section to be published in the June 1970 JOURNAL.

REFERENCES

1. D. R. Cogley and J. N. Butler, *This Journal*, **113**, 1074 (1966); D. R. Cogley and J. N. Butler, *J. Phys. Chem.*, **72**, 4568 (1968).
2. T. Skerlak, B. Ninkov, and V. Sislov, *Glasnik Drustva Hemicara Tehnol. SR Bosne Hercegovine*, **11**, 39, 43 (1962). *C.A.*, **61**, 2496d, 3749f. Univ. California Radiation Laboratory Translation UCRL-1330.
3. J. S. Dunnett and R. P. H. Gasser, *Trans. Faraday Soc.*, **61**, 922 (1965).
4. W. H. Smyrl and C. W. Tobias, *This Journal*, **115**, 33 (1968); W. H. Smyrl, Thesis, University of California, Berkeley, 1966.
5. R. Garnsey and J. E. Prue, *Trans. Faraday Soc.*, **64**, 1206 (1968).
6. R. J. Jasinski and S. Kirkland, *Anal. Chem.*, **39**, 1663 (1967).
7. H. L. Clever and C. C. Snead, *J. Phys. Chem.*, **67**, 918 (1963).
8. R. A. Robinson and R. H. Stokes, "Electrolyte Solutions," Butterworths Scientific Publications, London (1959).
9. D. R. Cogley and J. N. Butler, *J. Phys. Chem.*, **72**, 1017 (1968).
10. G. Scatchard, P. T. Jones, and S. S. Prentiss, *J. Am. Chem. Soc.*, **54**, 2676 (1932).

Correction

In the paper "On the Passivity of Iron-Chromium Alloys, II. The Activation Potential" by Robert P. Frankenthal which was published in the May 1969 issue of the JOURNAL, Vol. 116, pp. 580-585, the current density for film reduction given in the first paragraph on page 581 should be 10 $\mu A/cm^2$ instead of 1 $\mu A/cm^2$.

Infrared Reflection Studies of the Oxidation of Copper and Iron

G. W. Poling[1]*

Research and Technical Department, Texaco, Inc., Beacon, New York

ABSTRACT

Infrared multiple reflectance spectra were used to record the growth of oxide films on copper and iron mirrors. Cuprous oxide and cupric oxide films were readily distinguished since they exhibit intense single bands at 640 cm^{-1} and ~560 cm^{-1}, respectively. Iron oxide films of a single composition also exhibit highly characteristic bands in the 230 to 1100 cm^{-1} region of the reflectance spectra. Spectra of mixed iron oxide films were composed of many highly overlapping bands making quantitative interpretations difficult. The intensities of the infrared bands from the copper oxide and iron oxide films were directly proportional to the oxide film thicknesses. Using a seven reflection-73° incidence optical accessory, sensitivity to detect oxide films as thin as about 5Å was achieved.

Infrared reflection spectra have been used to analyze the structure and thickness of corrosion protective films formed on metal mirrors by organic inhibitors (1). These spectra often contained bands that were attributed to metal oxide layers. The purpose of the present study was to determine whether such infrared spectra could indicate the thickness and composition of metal oxide films.

Prior use of infrared spectroscopy to characterize oxide films on metals has been scant. Hannah (2) reported that he was able to detect 10Å thick aluminum oxide films on aluminum mirrors using a four-reflection accessory. Reflection studies of Babushkin (3) indicated that copper oxide films on copper mirrors produced bands at 1055 and 610 cm^{-1}. He attributed these bands to electronic excitations rather than to lattice vibrational modes.

Interpretations of reflection spectra of surface films are usually based on comparison with transmission spectra of analogous pure compounds. Although reference spectra of several copper and iron oxide compounds are reported in the literature (4-6), most of these are nonquantitative. Therefore, reference transmission spectra of copper and iron oxides are included in this paper. These spectra often differed significantly from the oxide film-reflection spectra because the latter depend on refractive index as well as absorptivity (7, 8). These differences and the complications that they sometimes introduced in interpreting the reflection spectra are discussed.

Copper and iron mirrors were oxidized in air or in oxygen at temperatures up to 700°C. Sequences of infrared multiple reflection spectra recorded the growth of oxide films on these mirrors. Oxide film thicknesses were measured by an optical interferometer and by using interference colors. Infrared oxide band intensities were found to be directly proportional to film thickness over the range of about 0 to 5000Å.

The reflection spectra readily distinguished between cuprous and cupric oxide films on copper. Iron oxide films of a single composition also exhibited characteristic spectra. Spectra of the more common mixed iron oxide films were composed of many strongly overlapping bands that were difficult to interpret quantitatively. The reflectance spectra provided a convenient measure of the kinetics of oxidation of copper and iron.

Experimental

Recording infrared spectra.—Spectra of oxide films formed on copper and iron mirrors were recorded from 230-4000 cm^{-1} on a Beckman IR-12 spectrophotometer using multiple reflectance accessory optics. This accessory has been described in detail in a previous paper (1). To enhance sensitivity a wire-grid polarizer, oriented to transmit the parallel component, was installed in the monochromator section of the spectrophotometer (1). The accessory optics provided seven reflections at 73° incidence from two planar sample mirrors (76 x 38 x 3 mm and 51 x 38 x 3 mm). Similar optics were provided in the reference beam of the double beam spectrophotometer. Spectra of films on the sample mirrors were thereby recorded differentially against a similar set of reference mirrors. Since most spectra were recorded with the mirrors exposed to dry air, the reference mirrors were covered by a film of air-formed oxide.

The intensities of absorption bands in the reflectance spectra were measured in terms of ΔR, the fractional change in reflectivity at a band maximum; *i.e.*, $\Delta R = (R_0\text{-}R)/R_0$ where R_0 = reflectivity in absence of a film and R = reflectivity at band maximum. Spectra were recorded in a linear absorbance (A) mode or in an expanded per cent transmission ($\%T$) mode. ΔR values as low as *ca.* 0.0005 could be measured reproducibly.

Film thicknesses.—Theory predicted that the thickness (d) of an isotropic film was directly proportional to the measured ΔR values. To a good approximation the two were related by the following equation (7) (for 73° incidence angle of the parallel component)

$$d_A \simeq \left(\frac{6.38 \times 10^5 N_1^3}{\nu \cdot K_1}\right) \cdot \Delta R \qquad [1]$$

where N_1 = refractive index of the oxide, K_1 = absorption constant of the oxide = $\alpha\lambda/4\pi$ where α = absorption coefficient in cm^{-1} and λ = wavelength in cm, and ν = position of band maximum in cm^{-1}. Values of K_1 for the several oxides were determined from our reference transmission spectra (see Table I). Refractive indices were based on literature values (9, 10).

Calculations of film thicknesses using Eq. [1] were compared with independent thickness determinations. Progressions of interference colors provided approximate measures of oxide film thicknesses in the eighty to several thousand angstrom range (11-14). Checks on final oxide film thickness were made using a Bausch and Lomb interference microscope and by extracting the oxide films with concentrated mineral acids for quantitative analyses.

Materials and procedures.—Sample mirrors were prepared either by polishing OFHC copper and Armco

* Electrochemical Society Active Member.
[1] Present address: Department of Mineral Engineering, University of British Columbia, Vancouver, British Columbia.

iron plates or by vacuum deposition techniques. Most of the plate-mirrors were prepared by electropolishing the copper in 1:1 H_3PO_4:H_2O electrolyte (15, 16) and the iron in 20:1 glacial acetic acid: 70% $HClO_4$ (17). Following the electropolishing of the copper mirrors they were washed in distilled water, 10% H_3PO_4, boiling distilled water and methanol to ensure that no phosphate remained on the surfaces (16, 18). Some tests were also made on Armco iron plates that were mechanically polished using αFe_2O_3 grit.

Thin film copper and iron mirrors were vacuum deposited on top of gold films on glass flats. This enabled these metal films to be oxidized completely and the gold substrate served as mirror surfaces for recording the final spectra. The thicknesses of the Cu and Fe films were measured before and after oxidation treatments using an interference microscope. A strip along one side of each mirror was masked during film deposition. This resulted in a "step" equal to the copper or iron film thickness. Interference fringe shifts and hence film thicknesses were measured at several locations along each step.

Background reflectance spectra from the freshly prepared mirror surfaces were recorded first. The sample mirrors were then subjected to oxidation treatments and reflectance spectra were again recorded to detect absorption bands due to an oxide film. Oxide growth was monitored by recording sequences of spectra. Infrared band intensities were correlated with independent oxide film thickness determinations.

Most oxidation treatments were conducted in air in a laboratory oven. The metal mirrors were laid on a massive, preheated copper block. After the desired oxidation time the mirrors were cooled rapidly to room temperature in order to record their spectra.

Some tests were conducted with the two sample mirrors installed in a heatable (to ~450°C) infrared vacuum cell (with CsI windows) mounted on the multiple reflectance accessory. This enabled reflection spectra to be recorded continuously as a high temperature oxidation or reduction progressed. The IR-12 spectrophotometer was modified slightly so that the instrument could discriminate against the infrared radiation emitted by the hot sample mirrors. Otherwise, the emission bands from the oxide films tended to cancel out their absorption of the radiation from the instrument's source. The modification involved clutching the beam re-combining mirror of the IR-12 so that it was half way in each of the sample and reference beams. The source radiation reaching the sample mirrors was then chopped while the radiation being emitted from the hot sample mirrors was unchopped. This enabled spectra of the hot sample mirrors to be recorded while still operating in a double beam mode. Although the energy reaching the detector was halved, this did not appreciably impair the quality of the spectra.

Results and Discussion

Reference transmission spectra.—Copper oxides.— Figure 1 shows infrared spectra of (A) cuprous oxide and (B) cupric oxide in KI pellets. The 620 cm^{-1} Cu_2O band and 510 cm^{-1} CuO band were the only significant bands detected for these oxides in the 230 to 4000 cm^{-1} region. Published results indicated that the 620 cm^{-1} Cu_2O band was due to optically active lattice vibrations in this oxide (9, 19, 20). Absorption constants (K_1) for the copper oxide bands shown in Fig. 1 are presented in Table I. The anomalous dispersion effects, seen on the high frequency side of the copper oxide bands in Fig. 1, would be expected to make the observed band intensities slightly less than they should be. Identical absorption constants have however been determined from spectra of Cu_2O and CuO where such dispersion effects were all but absent. Thus the absorption constants given in Table I are thought to be accurate for the reagent grade chemicals used. Both copper oxide bands are strong infrared absorbers.

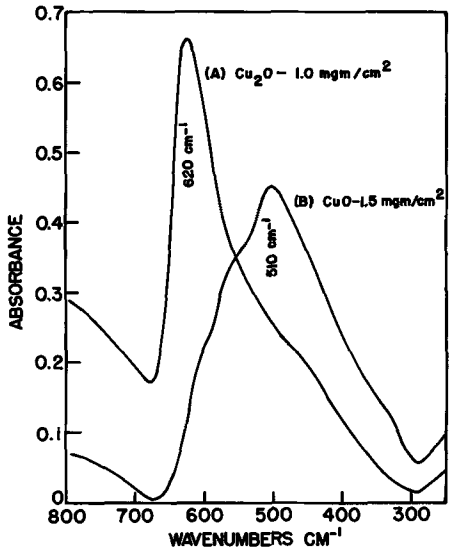

Fig. 1. Transmission spectra of Cu_2O and CuO (in KI pellets)

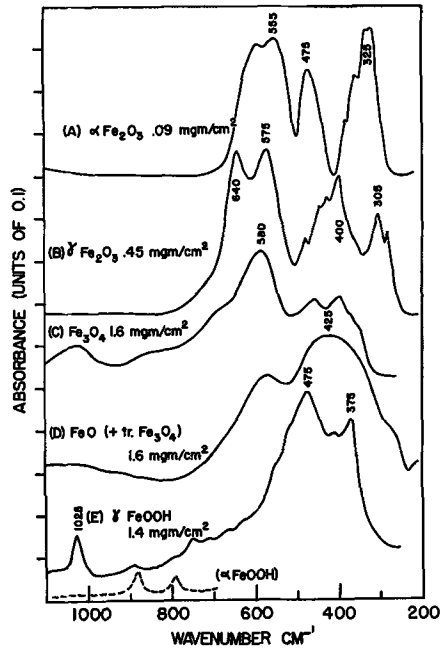

Fig. 2. Transmission spectra of iron oxides

Iron oxides.—Transmission spectra of several iron oxide compounds (in KI pellets) are shown in Fig. 2. The αFe_2O_3, γFe_2O_3, and Fe_3O_4 were all reagent grade chemicals whose compositions were checked by x-ray analysis. Wüstite (FeO) was prepared by a 700°C air oxidation of Armco iron plates. The oxidized plates were quenched in water to retain the FeO structure.

Table I. Absorption constants for copper and iron oxide infrared bands

Compound	Band position, cm^{-1}	$k^{(a)}$, cm^2/molecule	$\alpha^{(b)}$, cm^{-1}	$K_1^{(c)}$
Cu_2O	620	0.13×10^{-18}	7,600	0.93
CuO	510	0.038×10^{-18}	4,300	0.67
αFe_2O_3	555	1.00×10^{-18}	45,000	6.3
γFe_2O_3	640	0.22×10^{-18}	10,000	1.2
Fe_3O_4	580	0.066×10^{-18}	2,100	0.27
FeO	425	0.025×10^{-18}	2,800	0.53
γFeOOH	475	0.045×10^{-18}	2,800	0.46

(a) k = extinction coefficient = absorbance/C, where C = sample thickness in molecules/cm^2.
(b) α = absorption coefficient = 2.303 absorbance/path length in cm.
(c) K_1 = absorption constant = $\alpha\lambda/4\pi$.

X-ray analysis showed that a small amount of Fe_3O_4 was present in the FeO sample used to record spectrum (D) of Fig. 2. Atmospheric weathering of Armco iron plates produced the common rust (γFeOOH) whose spectrum is shown as Fig. 2(E). X-ray analysis of this sample detected a small amount of αFeOOH as well.

Each spectrum shown in Fig. 2 was sufficiently unique to identify the pure iron oxide compounds. The dissimilarities in the spectra of γFe_2O_3 (B) and Fe_3O_4 (C) were noteworthy since these compounds are not readily distinguished by x-ray or electron diffraction techniques. At the oxide thicknesses (mg/cm^2) specified in Fig. 2, no significant bands were detected in the higher wavenumber region (4000-1100 cm^{-1}) that was also scanned. Lepidocrocite (γFeOOH) and geothite (αFeOOH) were the exceptions, since these compounds exhibited O-H stretching bands at about 3400 cm^{-1}. The spectra in Fig. 2 indicate that quantitative infrared analysis of mixed iron oxides would be difficult, since the bands of each oxide overlap strongly.

Absorption constants (K_1) for the most prominent band in the spectrum of each iron oxide are given in Table I. The wide differences in these K_1 values further complicated quantitative analysis since this means that the sensitivity to detect each oxide differs markedly. The K_1 of 6.3 for the 555 cm^{-1} αFe_2O_3 band ranks it among the strongest of infrared absorbers.

Oxide films on copper.—Cuprous oxide, (a) Spectra. —Figure 3 shows a sequence of reflection spectra recorded at stages in the 140°C air oxidation of copper film mirrors. These spectra were traced from spectra recorded using a 0 to 1 absorbance range (*i.e.*, no scale expansion was required). The sample mirrors consisted of 580Å thick copper films on top of gold films on glass. Exposure times are shown on Fig. 3. Growth of the 640 cm^{-1} band terminated after about 60 min of oxidation. Spectrum (D) was typical of several spectra that were recorded after oxidation of the copper films was complete.

Comparison of the reflectance spectra in Fig. 3 with the reference spectra of Fig. 1 indicated that the oxide films were composed of relatively pure Cu_2O. This was the only oxide that was expected to form under the conditions of this oxidation (21). The observed +20 cm^{-1} shift of the absorption band from the transmission spectrum (Fig. 1A) to the reflection spectra (Fig. 3) agreed with a calculated shift. Published optical constants for Cu_2O over the 400-800 cm^{-1} region were substituted into Eq. [1] to produce a calculated reflectance spectrum. This also exhibited a +20 cm^{-1} shift in the band maximum position.

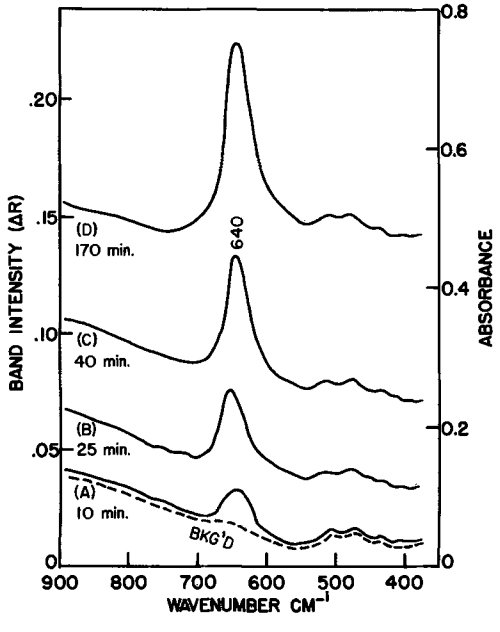

Fig. 3. Reflectance spectra from copper oxidized in air at 140°C

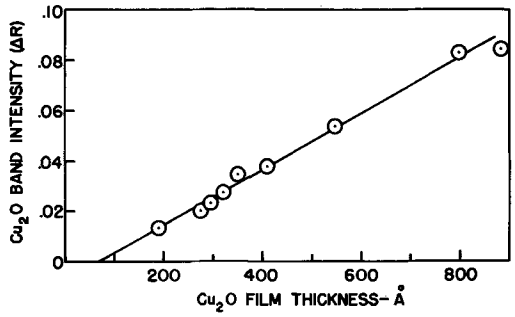

Fig. 4. Relation between Cu_2O film thickness and infrared reflectance spectra.

The reflectance spectra shown in Fig. 3 were typical of many others exhibited by both electropolished copper-plate mirrors and vacuum deposited copper films that were oxidized in air or in oxygen at 25°-200°C.

(*b*) *Film Thickness.*—Figure 4 shows that the intensity (ΔR) of the 640 cm^{-1} Cu_2O band (from Fig. 3) increased linearly with the oxide film thickness. Interference colors indicated oxide film thicknesses as oxidation progressed. The point at maximum ΔR = 0.09 and 900Å thickness represented complete conversion of the Cu film to Cu_2O (see Fig. 5). The plot extrapolated to a 70Å intercept on the abscissa. This was a reasonable value for the initial Cu_2O film thickness on the sample mirrors since they had been stored in clean air for about a month (22). The reference mirrors had been freshly prepared and were expected to have oxide films only 10-20Å thick (15). Since this oxide thickness was effectively cancelled out by recording spectra differentially, the initial films on the sample mirrors were probably *ca.* 80Å instead of 70Å.

The 900Å limiting oxide film thickness indicated in Fig. 4 was confirmed by measurements made with the interference microscope. The initial copper + air-formed oxide films were 580Å thick. These consisted of *ca.* 500Å of Cu and ~80Å of Cu_2O. Conversion of the 500Å of Cu to Cu_2O was expected to produce a Cu_2O film 500 x 1.64 + 80 = 900Å thick [1.64 is the volume ratio of Cu_2O/2Cu (21)]. The accuracy of this 900Å figure was also checked by extracting the Cu_2O from the underlying gold mirrors and analyzing quantitatively for copper.

The slope of the line in Fig. 4 was $d_A/\Delta R_{640\ cm^{-1}} \doteq$ 9000. A similar ratio was obtained from the oxidation of another set of vacuum deposited copper mirrors. Studies of rougher, electropolished copper mirrors gave $d_A/\Delta R_{640\ cm^{-1}}$ values ranging from 9500 to 11,000. Calculation of $d_A/\Delta R_{640}$ by substituting K_1 = 0.93 (Table I) and N_1 = 2.0 [at 640 cm^{-1} (9)] in Eq. [1] gave a ratio of 8600. This calculation assumed a perfectly planar surface. These results therefore suggested that the $d_A/\Delta R$ ratio increased with the roughness of the sample mirrors.

(*c*) *Oxidation kinetics.*—The kinetics of Cu_2O film growth on the copper mirrors were followed by measuring the growth in intensity of the 640 cm^{-1} infrared reflection band. Figure 5 shows results obtained from the oxidation test that resulted in the data shown in Fig. 3 and 4. Inverse logarithmic kinetics appeared to describe the oxidation better than direct logarithmic kinetics. This figure also shows that oxidation was complete after 70 min. Similar oxidation kinetics for copper have been reported in the literature (18, 23). In some of our infrared studies of the oxidation of

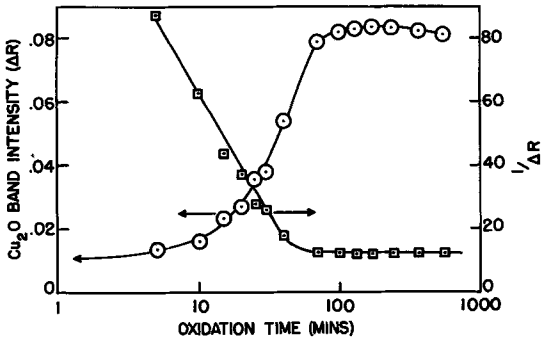

Fig. 5. Kinetics of the air oxidation of copper at 140°C

electropolished copper, linear logarithmic kinetics have provided a better fit to the data. Slight differences in the initial surface preparation are known to cause such discrepancies in the oxidation kinetics.

Cupric oxide, (a) Spectra.—When the air oxidation temperature exceeded about 200°C, CuO was found to grow on top of the Cu_2O films. Evidence for this was growth of a new band at 520-560 cm^{-1} in addition to the 640 cm^{-1} Cu_2O band in the reflectance spectra (see Fig. 1).

Relatively pure CuO films were produced by the complete oxidation of thin film copper mirrors at temperatures above 250°C (24). Figure 6 shows the reflectance spectrum that resulted from such an oxidation. The sample mirrors, consisting of 700Å Cu films on gold on glass, were first oxidized in 100 mm O_2 at 300°C for 17 hr before recording the spectrum shown in Fig. 6. An additional 22 hr oxidation in 100 mm O_2 at 400°C produced no detectable change in the spectrum. Oxidation of the copper was therefore complete when Fig. 6 was recorded.

Comparison of Fig. 6 with the reference spectra in Fig. 1 indicated that the oxide films were composed of CuO. Absence of even a shoulder at 640 cm^{-1} showed that no appreciable Cu_2O was present. The band shift of +50 cm^{-1} from the transmission (Fig. 1B) to the reflectance spectrum (Fig. 6) was in the direction expected. This resulted from the inverse dependence of ΔR on refractive index (N_1) which reached a minimum on the high frequency side of the transmission band. The magnitudes of the observed and calculated shifts could not be compared since insufficient refractive index data for CuO were available.

Comparison of the reflectance spectra shown in Fig. 3 and 6 illustrates that Cu_2O and CuO films could be readily differentiated.

(b) Film thickness.—The CuO films which exhibited the spectrum shown in Fig. 6 had an average thickness

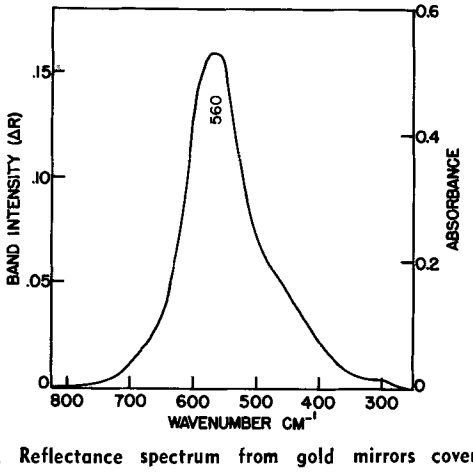

Fig. 6. Reflectance spectrum from gold mirrors covered by 1200Å of CuO.

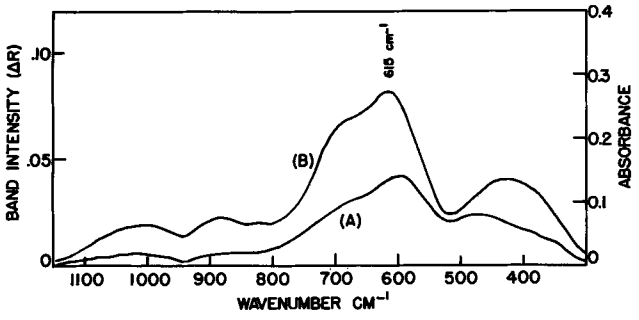

Fig. 7. Reflectance spectra from iron covered by Fe_3O_4 films formed during exposure to boiling water for (A) 21 hr (Ar purged) and (B) +6½ hr (air exposed).

of 1190Å based on measurements with the interference microscope. This checked well with the thickness expected from complete conversion of 700Å Cu films to CuO, *i.e.*, 700Å x 1.72 = 1200Å where 1.72 is the volume ratio of CuO:Cu (21). Based on this test $d_{A\ CuO} \doteq 7700\ \Delta R_{560\ cm^{-1}}$.

Oxide films on iron.—Magnetite.—Figure 7 shows reflection spectra from Armco iron mirrors covered by Fe_3O_4 films produced by exposing the iron to boiling water (25). Spectrum A was recorded after exposing freshly electropolished iron mirrors for 21 hr to boiling, argon purged distilled water. Spectrum B was recorded after an additional 6½ hr exposure to boiling H_2O at *p*H 9.0 that was open to the air. Comparison with the reference spectra in Fig. 2 shows that these reflection spectra most closely resemble the transmission spectrum of Fe_3O_4 (Fig. 2C). The +35 cm^{-1} shift of the 580 cm^{-1} band in the transmission spectrum to 615 cm^{-1} in the reflection spectrum (Fig. 7) was in the direction expected. X-ray analysis showed Fe_3O_4 to be the only iron oxide detected in these films. No correlation of Fe_3O_4 film thickness with the band intensity data was made in this test. The spectra in Fig. 7 indicated that reflection spectra could identify oxide films of a single composition on iron.

Mixed iron oxides, (a) Spectra.—A sequence of reflection spectra that resulted from the 250°C air oxidation of Armco iron mirrors is shown in Fig. 8. Oxidation times are shown with each spectrum. These mirrors were prepared by mechanically polishing the iron with αFe_2O_3. Similar spectra also resulted from the 250°C air oxidation of electropolished mirrors and from oxidation of vacuum deposited iron-film mirrors. No bands other than those shown in Fig. 8 were observed over the 4000 to 230 cm^{-1} spectral range.

The bands exhibited by the oxide films in the earlier stages of oxidation (*i.e.*, spectra A and B) are attributed to Fe_3O_4 and γFe_2O_3 (see Fig. 2). Marked enhancement of the 650 cm^{-1} bands in these spectra cannot be explained by simple additivity of the ref-

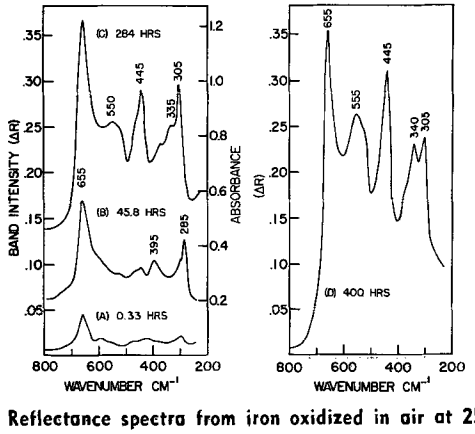

Fig. 8. Reflectance spectra from iron oxidized in air at 250°C

erence transmission spectra (B and C of Fig. 2). Instead, the additional dependence of ΔR on refractive indices (N_1) probably contributed to the intensity of this band in the reflection spectra of these "duplex" films. This is based on the fact that N_1 dips to a minimum on the high frequency side of a strong absorption band and $\Delta R \propto 1/N_1^3$ (see Eq. [1]) (7, 8).

After several hundred hours of oxidation at 250°C, bands attributed to αFe_2O_3 emerged from the reflection band envelope. These new bands are shown at ~560, 440, and 310 to 340 cm^{-1} in spectra C and D of Fig. 8. Comparison with spectrum A of Fig. 2 shows that these bands are in reasonable agreement with the reference spectrum of αFe_2O_3. Thus, the oxide appeared to be composed of Fe_3O_4, γFe_2O_3, and αFe_2O_3 films at this stage. Although the αFe_2O_3 bands became relatively intense in spectrum (D), this oxide probably composed only a small part of the films. Reference to Table I shows that αFe_2O_3 absorption was 4 to 20 times greater than γFe_2O_3 or Fe_3O_4 and Eq. [1] shows that film thickness was inversely proportional to these absorption constants. The infrared evidence for the $Fe_3O_4 + \gamma Fe_2O_3 + \alpha Fe_2O_3$ composition of such oxide films is in qualitative agreement with results in the literature (21, 26).

(b) *Film thickness.*—Oxide films formed by air oxidation of iron at 25°-300°C usually exhibited a linear relation between the intensity (ΔR) of the 650 cm^{-1} band and the film thickness. Figure 9 shows that the relation was reasonably linear from 0-1100Å for the oxide films that exhibited the spectra shown in Fig. 8. The oxide film thicknesses were determined by interference colors (12). The slope of the line in Fig. 8 is $d_A/\Delta R_{650\ cm^{-1}} = 6100$. In several other tests this ratio has varied from 5000 to 8000. Differences in surface roughness of the mirrors appeared mainly responsible for this variation as was described previously for copper mirrors.

Oxidation studies on vacuum deposited iron-film mirrors were used to check the thickness calibration of the infrared $\Delta R_{650\ cm^{-1}}$ data. An interferometer was used to determine film thicknesses as previously described for the oxidation of copper. These measurements indicated that over the range of 0-1200Å, the interference colors provided a reasonably accurate measure of the oxide film thickness.

(c) *Oxidation kinetics.*—Figure 10 shows direct logarithmic (A) and parabolic (B) plots of the infrared iron-oxide band growth from two separate tests. The solid lines show results from the 250°C air oxidation of mechanically polished iron that was also described in Fig. 8 and 9. The dashed lines show results of a similar oxidation using electropolished Armco iron mirrors. These graphs indicate that the oxidation of both sets of specimens obeyed direct logarithmic kinetics in the early stages of film growth and parabolic kinetics in the later stages. The transition occurred when the oxide films were 300-400Å average thickness. Similar transitions in the oxidation kinetics of iron have been attributed to formation of compact oxide barrier layers (21). Such layers made diffusional processes rate controlling and thus resulted in parabolic oxidation kinetics.

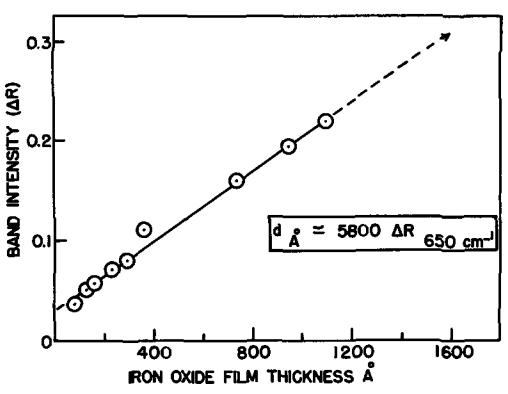

Fig. 9. Relation between iron oxide film thickness and infrared reflectance spectra.

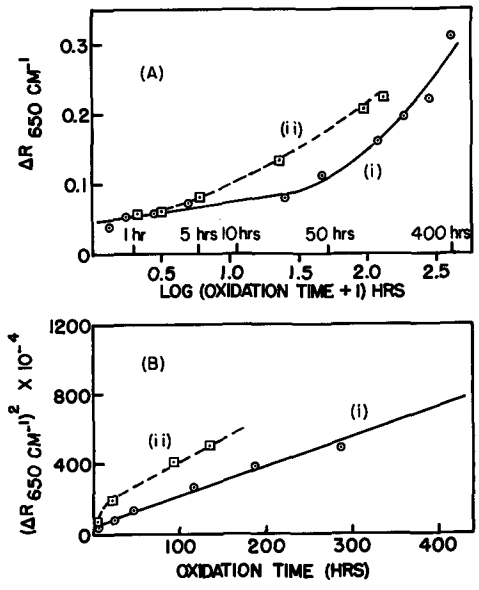

Fig. 10. Kinetics of the air oxidation of iron at 250°C. (i) Mechanically polished, (ii) electrolytically polished.

The kinetics of the oxidation of iron and subsequent hydrogen reduction of the oxide film were studied with the sample mirrors installed in a heatable vacuum cell. By recording rapid sequences of spectra over the 230 to 1100 cm^{-1} range, growth or reduction of oxide films could be followed closely while the sample mirrors were at temperature. In one experiment two 710Å iron-film mirrors were oxidized in 100 mm O_2 at 300°C for 16 hr and then at 400°C for an additional 3 hr. The appearance of the spectral sequences recorded at 300° and 400°C were similar to those shown in Fig. 8A and B. No αFe_2O_3 bands were observed. The 19 hr oxidation resulted in complete conversion of the iron films (on gold mirrors) to $Fe_3O_4 + \gamma Fe_2O_3$ films about 1500Å thick. These iron oxide films were then exposed to flowing Pd-diffused H_2 (40 cc/min) at 250°C.

Rapid sequences of reflection spectra showed that the 650 cm^{-1} iron oxide bands were reduced from a maximum ΔR of 0.30 to zero intensity in a 2 hr period. Such complete reduction of the oxide at the relatively low temperature of 250°C was surprising.

Conclusions

Infrared reflectance spectra of oxide-covered copper and iron mirrors exhibited intense metal oxide absorption bands in the 1100 to 230 cm^{-1} region. Cuprous oxide films exhibited a single strong peak at 640 cm^{-1}. They were readily distinguished from cupric oxide films which produced a slightly weaker band at 560 cm^{-1}. Reflection spectra of oxide films on iron mirrors were usually more complex and more difficult to interpret. The added complexity of these spectra was probably caused by the existence of both tetrahedral and octahedral coordinations of the iron ions in the iron oxide lattices. Thus changes in oxide composition did not produce dramatic changes in the spectra since this involved only redistribution of the iron ions between these two types of sites. In spite of their complexity, the reflection spectra did appear to distinguish between the cubic oxides (Fe_3O_4 and γFe_2O_3) and αFe_2O_3 which has a corundum structure.

The intensities of metal oxide absorption bands, in the reflection spectra, increased in direct proportion to the oxide film thickness. The following approximate relationships were observed

$$d_{A\ Cu_2O} \doteq 10{,}000\ \Delta R_{640\ cm^{-1}}$$

$$d_{A\ CuO} \doteq 7{,}700\ \Delta R_{560\ cm^{-1}}$$

$$d_{A\ Fe_xO_y(cubic)} \doteq 7{,}000\ \Delta R_{650\ cm^{-1}}$$

These linear relationships indicated that effects of any anisotropism on the spectra of the films were small. Use of polycrystalline metal mirrors probably contributed to this by randomizing the molecular orientations in the oxide films. Results using mirrors made from single crystals of metals might be quite different.

The seven reflection accessory used in these studies enabled measurement of ΔR values as low as 0.0005. This meant that copper and iron oxide films as thin as 3-5Å average thickness could be detected. By using only one reflection oxide films up to about 5000Å thickness could be studied.

Most metal oxides exhibit strong lattice bands in the 200 to 1000 cm^{-1} region (4-6). Therefore, infrared reflectance spectroscopy could provide a useful tool for studying either the growth or reduction of oxide films on most metals.

Acknowledgments

The author has appreciated the help of H. Macy and D. Bauer with the experimental work and the discussions with R. P. Eischens. Support of this research by the management of Texaco Inc. has also been appreciated.

Manuscript submitted Jan. 27, 1969; revised manuscript received *ca.* March 16, 1969.

Any discussion of this paper will appear in a Discussion Section to be published in the June 1970 JOURNAL.

REFERENCES

1. G. W. Poling, *This Journal*, **114**, 1209 (1967).
2. R. W. Hannah, *Appl. Spectroscopy*, **17**, 23 (1963).
3. A. A. Babushkin, *Russ. J. Phys. Chem.*, **38** 1004 (Eng. trans.) (1964).
4. N. T. McDevitt and W. L. Baun, *Spectrochim. Acta*, **20**, 799 (1964).
5. F. Vratny, M. Dilling, F. Gugliotta, and C. N. R. Rao, *Indian J. Sci. Ind. Res.*, **20B**, 590 (1961).
6. L. C. Afremow and J. T. Vandeberg, *J. Paint. Tech.*, **38**, 169 (1966).
7. S. A. Francis and A. H. Ellison, *J. Opt. Soc. Amer.*, **49**, 131 (1959).
8. R. G. Greenler, *J. Chem. Phys.*, **44**, 310 (1966).
9. M. O'Keefe, *ibid.*, **39**, 1789 (1963).
10. Handbook of Chemistry and Physics, 43rd Edition.
11. W. E. Campbell and U. B. Thomas, *Trans. Electrochem. Soc.*, **76**, 303 (1936).
12. D. E. Davies, U. R. Evans, and J. N. Agar, *Proc. Roy. Soc. (London)*, **225A**, 443 (1954).
13. F. H. Constable, *ibid.*, **115A**, 570 (1946).
14. A. B. Winterbottom, *Trans. Faraday Soc.*, **42**, 487 (1946).
15. J. A. Allen, *ibid.*, **48**, 273 (1952).
16. N. H. Simpson and N. Hackerman, *This Journal*, **102**, 660 (1955).
17. P. B. Sewell, C. D. Stockbridge, and M. Cohen, *Can. J. Chem.*, **37**, 1813 (1959).
18. F. W. Young, J. V. Cathcart, and A. T. Gwathmey, *Acta Met.*, **4**, 145 (1956).
19. I. Pastrniak, *Optics and Spectroscopy*, **6**, 64 (Eng.) (1959).
20. M. Terada, *Bull. Chem. Soc. Japan*, **37**, 766 (1964).
21. O. Kubaschewski and B. E. Hopkins, "Oxidation of Metals and Alloys," Butterworths (1962).
22. J. Kruger, *This Journal*, **106**, 847 (1959).
23. T. N. Rhodin, *J. Am. Chem. Soc.*, **72**, 5102 (1950).
24. H. Wieder and A. W. Czanderna, *J. Phys. Chem.*, **66**, 816 (1962).
25. U. R. Evans, "The Corrosion and Oxidation of Metals," Edward Arnold, London (1960).
26. P. B. Sewell and M. Cohen, *This Journal*, **111**, 508 (1964).

Electrical Breakdown in Thin Dielectric Films

N. Klein[1]

Bell Telephone Laboratories, Allentown, Pennsylvania

ABSTRACT

Thermal and electric breakdown processes in thin film insulators are discussed. Interpretation of the processes is greatly facilitated by using specimens with self-healing breakdowns, cleared of weak spots. Thousands of breakdown tests can be carried out on such specimens. Thermal breakdown is initiated by an increase in the electrical conductance by joule heat; breakdown occurs at a definite voltage, which can be calculated with good accuracy. Electric breakdown can be initiated by the increase of the electrical conductance in a channel by a pulse, such as an electronic avalanche. Destruction arises by discharge of the electrostatic energy stored in the specimen through the channel. The incidence of breakdown is of a statistical nature. In contrast to concepts which assume a definite breakdown field, electric breakdown can occur in certain oxides over a wide range of fields. Breakdowns occur at a rate which increases quasi-exponentially with field and also with temperature, *e.g.*, in hafnium dioxide. Experimental results are examined in the light of existing breakdown theories. It appears that further theoretical and experimental work is needed for the interpretation of the oxide results.

Investigations on breakdown are greatly facilitated in thin films because test voltages are low. Earlier work on thin films was concerned with the influence of insulator thickness on breakdown field, and dielectrics such as mica (1), NaF and KBr (2), and aluminum oxide were investigated (3). In the investigations problems were encountered with thin films which were known to arise also in thicker insulators. The specimens shorted and the breakdown voltage measured was not that of the bulk but that of the weakest spot. There was often a large spread in the breakdown properties of a batch of specimens. Breakdown caused destruction in the insulator and in the electrodes mainly by melting and by evaporation. The destruction was not only due to the breakdown event, but also due to the follow-up current. These experi-

[1] On Sabbatical Leave from TECHNION—Israel Institute of Technology, Haifa.

mental circumstances made it difficult to interpret breakdown.

Conditions are different when specimens with self-healing breakdown are tested. In such specimens one electrode at least is thinner than 1000 to 2000Å. On breakdown the thin electrode does not melt, but evaporates at the breakdown site. Shorting does not occur, and damage arising from the follow-up current is avoided. Such breakdowns were first observed nearly sixty years ago (4), and use was made of the self-healing property in the making of certain paper capacitors (5, 6).

Breakdown investigations with thin film specimens exhibiting self-healing properties were reported on mylar by Inuishi and Powers (7) and on silicon oxide by Siddall (8). Kennedy (9) observed self-healing breakdowns in aluminum oxide and Young (10) in tantalum pentoxide. It was found that hundreds and often thousands of breakdown tests could be carried out on an individual specimen. Klein and co-workers (11-17) investigated silicon oxide specimens with self-healing breakdowns and found that (*a*) distinction can be made between the properties of weak spots and those of the bulk, (*b*) the processes involved in the destruction can be identified and distinguished, (*c*) the thermal breakdown field can be measured without destruction and can be accurately calculated, (*d*) the electric breakdown can be observed with minimal destruction, and (*e*) the breakdown properties can be ascertained from measurements on one specimen. It appeared from these results that the use of thin film specimens with self-healing breakdowns offers considerable advantages over the use of shorting specimens in investigations on breakdown. This article will therefore be based mainly on experimental results obtained with self-healing breakdowns.

Breakdown can be produced by a number of processes. Several of them, such as electrochemical deterioration, dendrite formation, and gas discharges can considerably decrease the breakdown strength. These processes can be avoided with suitable care and will not be discussed here. The processes which determine the highest breakdown fields are of interest. One of them is electromechanical breakdown (18), which is due to the mechanical collapse of the insulator by the attractive forces of the electrodes. This breakdown is restricted mainly to a few soft polymers, such as polyethylene. Other breakdown processes are the thermal and the electric breakdowns. These are generally observed in insulators and the properties of these two kinds of breakdowns will be described for thin film insulators. For both kinds of breakdowns the destruction occurs mainly by melting and by evaporation. Apart from this aspect, the processes of the two kinds of breakdowns are different. The following discussion will relate to specimens from which the weak spots were eliminated by self-healing breakdowns.

Thermal breakdown has been understood since the investigations of Wagner and Hayden and Steinmetz and information on earlier work can be found in ref. (19-22). Thermal breakdown is initiated by an increase in the electrical conductance by joule heat and/or dielectric heat. In thin films without weak spots the breakdown involves the whole insulator and occurs at a definite voltage. Destruction occurs simultaneously over nearly the whole insulator. It is possible, however, to determine the breakdown voltage without destroying the specimen.

The term electric breakdown relates to events which are known in the literature under various names, such as intrinsic, avalanche, and field emission breakdown. These processes are discussed in detail in ref. (19-22). Electric breakdown in thin films can be initiated by the increase in the electrical conductance by a pulse, such as an electronic avalanche. The breakdown involves a small spot only. The incidence of breakdown is often of a statistical nature. Experimental results will be presented for oxides, showing that electric breakdown does not occur at a sharply defined field, but over a wide range of fields in each of the substances. The breakdown destroys a very small part of the insulator, and this destruction cannot be avoided on testing.

Both thermal and electric breakdown may occur in an insulator, and breakdown is produced by the process which arises at the lower field.

Thermal Breakdown

Investigations for bulk breakdown properties begin with the elimination of weak spots and with the identification of the breakdown process. The identification of the process, whether it is thermal or electric, is relatively simply achieved by measuring the d-c leakage current I *vs.* voltage V characteristic of the insulator. For this purpose the thin film specimen is connected to the power source with a series resistor larger than 10 kohms. Such a resistor is usually small relative to the specimen resistance in the vicinity of breakdown, but it is sufficiently large to prevent propagating breakdowns (11) which destroy relatively large areas at weak spots and in specimens exhibiting electric breakdown.

The following is observed on specimens exhibiting thermal breakdown in the bulk: When increasing voltage is applied, breakdowns are observed to occur at a rate which increases with voltage. When a certain voltage in maintained for a period of 5-30 min, the breakdowns stop. These breakdowns are ascribed to weak spots (11) and the destruction caused is of the single hole type illustrated by Fig. 1. After the elimination of the weak spots a V-I characteristic can be measured as shown schematically in Fig. 2 (13). This characteristic exhibits a maximum voltage V_{dm} and a negative resistance range. At point D current and thermal runaway occur and practically the whole specimen is destroyed simultaneously. This mode of destruction is in sharp contrast to the small single hole destruction which occurs at weak spots and as will be described later, occurs also on electric breakdown.

When currents are restricted to values smaller than at D, destruction is avoided. The V-I characteristic can be repeatedly measured and V_{dm} has a fixed value for a given set of conditions. V_{dm} is the maximum thermal breakdown voltage (13) and destruction arises at this voltage when the series resistance is negli-

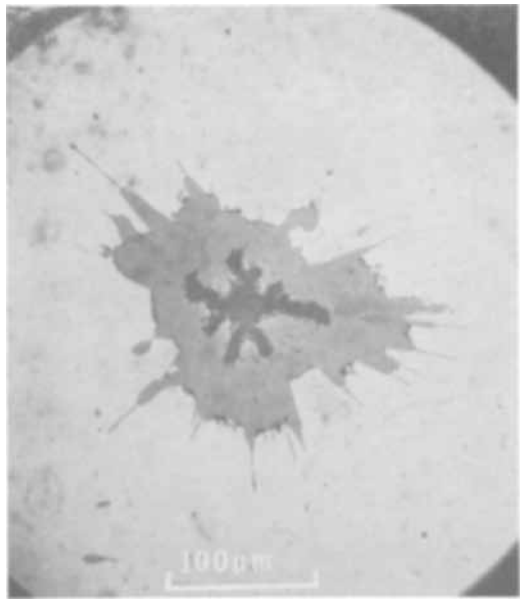

Fig. 1. Microgram of single hole breakdown in a tantalum pentoxide specimen anodized to 130V on sputtered tantalum. The top electrode is gold. The center black area is a hole through oxide and through electrodes, the gray area is oxide bared of gold.

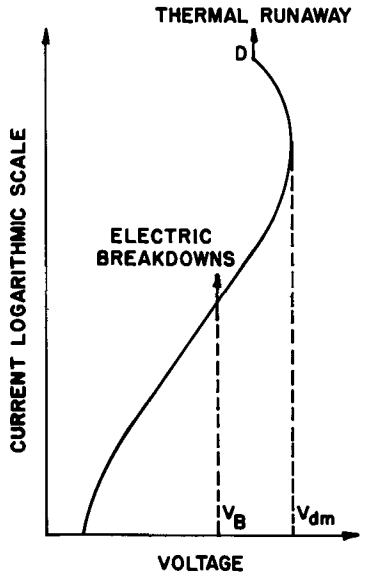

Fig. 2. Identification of the breakdown process with the *V-I* characteristic of the specimen.

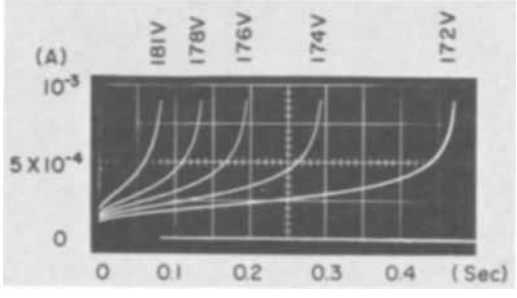

Fig. 3. Current *vs.* time oscillograms of a 5000Å thick, 4 x 10^{-3} cm^2 vapor grown silicon oxide specimen obtained on the application of voltage steps. The parameter is the applied voltage (16).

gibly small. With increasing series resistance the point of destruction D moves upward on the *V-I* characteristic. The nature of thermal runaway is well illustrated by current *vs.* time oscillograms, obtained when step shaped voltage pulses larger than V_{dm} are applied to the specimen. This is shown for a silicon oxide insulator in Fig. 3, with pulse voltage as a parameter (16). Thermal runaway is possible in insulators because above some temperature the electrical conductivity increases exponentially with temperature. An increase in temperature by joule heat increases the conductivity, which in turn increases the joule heat leading to mutual escalation. Runaway arises due to instability, when the joule heat input cannot be balanced by the heat loss of the heat transfer processes.

At the voltage V_{dm} the joule heat in the insulator is significant, a few watt per square centimeter, and the specimen temperature is a few tens of centigrades above ambient. The thermal nature of breakdown is indicated by this joule heat at the onset of the negative resistance range. It can be indicated also by showing that increased cooling increases V_{dm} (13). Negative resistance ranges with insignificant joule heat are observed sometimes in semiconductors (23). In this case, the breakdown is not thermal and may be caused by double injection. The verification of the nature of the process requires the calculation of V_{dm} on the assumption of thermal breakdown and the comparison of the calculated and the observed values of V_{dm}.

The calculation of the thermal breakdown voltage requires the solution of the equation of conduction of heat for the specimen and for the adjacent solids (19-22). For the calculations current continuity is assumed in the insulator and the thermal and electrical conductivity, K and σ are given as functions of temperature T, field F, and occasionally of time t. The equation of conduction of heat is with c the specific heat per unit volume

$$c\frac{\partial T}{\partial t} = \text{div } (K \text{ grad } T) + \sigma F^2 \qquad [1]$$

the equation for current continuity is

$$\text{div } (\sigma \vec{F}) = 0 \qquad [2]$$

and the relations for K and σ are

$$K = K(T) \text{ and } \sigma = \sigma(T,F,t) \qquad [3]$$

where σ may also be an explicit function of time. Solutions of Eq. [1]-[3] are available in thick insulators only for simple cases. Solutions are, however, relatively easily obtained for thin insulators, because use can be made of the following simplifications: the insulator temperature is assumed to be uniform and the insulator is considered as a planar source of heat. The solution of the equations yields the thermal breakdown field F_m as that field for which the temperature in the insulator rises to a destructive value T_c. $T_c \to \infty$ can often be used in the calculation of F_m without any significant error.

The possibility of obtaining simple expressions for F_m depends on the functional form of the relation $\sigma = \sigma(T,F,t)$. Various relations of exponential form were found to fit experimental observations. Sze (24) used for silicon nitride the relation

$$\sigma = \sigma_o e^{-q(\phi - dF^{1/2})/kT} \qquad [4]$$

σ_o, ϕ, and d being constants of the substance, q the electronic charge and k Boltzmann's constant. O'Dwyer used for σ an equation proposed by Hartman *et al.* (25)

$$\sigma = \frac{C_1 h}{F} e^{-(E - \alpha_1 F^{1/2})/kT + \alpha_2 F^{1/2}} \qquad [5]$$

with h the insulator thickness and C_1, E, α_1, and α_2 constants of the substance. These equations are based on an assumed physical mechanism of the electrical conduction in an insulator. The use of Eq. [4], [5] leads to relatively involved relations for the breakdown field.

It appeared that for the calculation of F_m the relation for σ need not be fundamental, but may be empirical, as long as it fits observations accurately. Such a relation is often

$$\sigma = \sigma_o e^{[bF + a(T - T_o)]} \qquad [6]$$

where σ_o, b, and a are determined from the *V-I* characteristics of the specimen, and T_o is the ambient temperature. Calculations with Eq. [6] lead to relatively simple relations for the thermal breakdown field F_m in thin insulators. Such relations for the breakdown fields on d-c F_{dm}, on a-c F_{am}, and on pulses F_{pm} are listed in Table I (13, 15, 16).

Although these relations were derived for infinitesimally thin insulations, their use can be extended to thicker insulations. Whitehead and Nethercot (26) found that for d.c. and a.c. at lower fields the error in F_m using thin film relations is 1.5%, when the thermal resistance across the insulator is one tenth of the thermal resistance from the specimen to ambient.

The use of the relations of Table I in the verification of thermal breakdown will now be illustrated. Figure 4 shows the d.c. *V-I* characteristics of a 4100Å thick, 0.06 cm^2 evaporated silicon oxide specimen with 500Å thick aluminum electrodes in the temperature range 4.2 to 515°K (14). The curves permit calculation of σ using Eq. [6] and determination of F_{dm} as function of the temperature. The observed values of F_{dm} are compared in Fig. 5 with those calculated with Eq.

Table I. Relations for the thermal breakdown field

The d.c. breakdown field F_{dm}:

$$F_{dm} = \frac{1}{b} \log \frac{\Gamma}{eaAh\sigma_0 F^2_{dm}} \quad [7]$$

b, a, and σ_0 are determined from the V-I characteristic, A is the specimen area, h is the dielectric thickness, Γ is the thermal conductance of the specimen, and e the basis of natural logarithms.

The a.c. breakdown field F_{am}:

$$B(bF_{am}) = \frac{\Gamma}{eahA\sigma_0 F^2_{am}} \quad [8]$$

where

$$B(bF_{am}) = I_0(bF_{am}) + I_2(bF_{am}) \quad [9]$$

and I_0 and I_2 are modified Bessel functions.

The pulse breakdown field F_{pm}:

$$F_{pm} = \frac{1}{b} \log \frac{K}{eah\sigma_0 HF^2_{pm}\psi(\bar{\tau})} \quad [10]$$

with

$$\bar{\tau} = K\tau/cH^2 \quad [11]$$

$$\psi(\bar{\tau}) = 1 - \frac{8}{\pi^2} \sum_{n=0}^{\infty} \frac{e^{-K(2n+1)^2\pi^2\tau/4ecH^2}}{(2n+1)^2} \quad [12]$$

where K is the thermal conductivity, c the specific heat per unit volume, and H the thickness of the substrate, respectively, and τ the pulse duration.

For $3.5h^2/\kappa < \tau < 0.5H^2/\kappa$ Eq. [10] simplifies to

$$F_{pm} = \frac{1}{b} \log \frac{\left(\frac{\pi Kc}{4e\tau}\right)^{1/2}}{ah\sigma_0 F^2_{pm}} \quad [10a]$$

For $\tau < 3.5h^2/\kappa$ heat conduction is negligible and

$$F_{pm} = \frac{1}{b} \log \frac{c_e}{a\tau\sigma_0 F^2_{pm}} \quad [10b]$$

where $c_e = (c_i h + c_m h_m)/h$, c_i and c_m being the specific heat of insulator and electrode metal, respectively, and h and h_m the thickness of insulator and of the two electrodes, respectively.

Equations [10]-[12] are based on the assumption that heat is transported from the specimen by conduction through the substrate only. Under experimental conditions heat is transported also by the electrodes and by convection. The effect of the additional heat flow paths is an increase in the value of K. This apparent value of K is calculated with Eq. [10] from one value of V_{pm} observed for one pulse duration τ.

[7]. Figure 5 also presents a curve for tantalum pentoxide obtained by anodizing tantalum sheet (22) (the tantalum was negative) and observations on silicon nitride by Sze (24). The breakdowns in silicon nitride were thermal in the temperature range, where F_{dm} decreases, but were assumed to be electric at 128°K.

Experimental results in silicon oxide on a.c. are presented in Fig. 6 (15). The ratio of the a-c peak and d-c breakdown voltage F_{am}/F_{dm} is by Eq. [7] and [8] a function of the parameter bF_{dm} only. The calculated ratio is given in Fig. 6 by the curve and the experimental results for a number of specimens at room temperature by dots. The F_{am} value of this specimen was not influenced by frequency below 1000 Hz. Above this value F_{am} decreased slowly with frequency due to the added heating associated with dielectric loss.

Breakdown test results obtained on the application of pulses to a 5000Å thick silicon oxide specimen are presented in Fig. 7, where V_{pm}, the thermal pulse breakdown voltage, is plotted *vs.* pulse duration τ (16). The small circles are measured results, and the curve was calculated. Breakdowns in this kind of specimen were observed to be thermal up to about 210-215V. However, above 195V electric breakdowns were observed as well. These occurred after a mean time lag τ_B, which decreased rapidly with increasing voltage (discussed in the following section). There was a large scatter in the time lag around τ_B. Breakdowns were electric when the time lag was less than τ, the pulse duration for thermal breakdown; in the range of 210-215V effectively all breakdowns were electric. The two kinds of breakdown can be distinguished, *e.g.*, by oscillograms, which are shown in Fig. 3 and 15 (16).

The results of Fig. 5-7 verify the thermal nature of the breakdowns in silicon oxide on d.c., a.c., and pulses of longer duration. The agreement of measured and calculated values of the breakdown field is of the order of 1%. Thermal breakdown was observed in silicon oxide in the thickness range of 2900Å to 15 μm (13). Thermal breakdown fields up to about 10^7 V/cm were observed in silicon nitride (24), in evaporated silicon dioxide kind of specimens (13), and in glass (25) 5-100 μm thick. The influence of ambient gas pressure was investigated from 2.10^{-5} Torr to atmospheric pressure (17). A small decrease in the maximum thermal

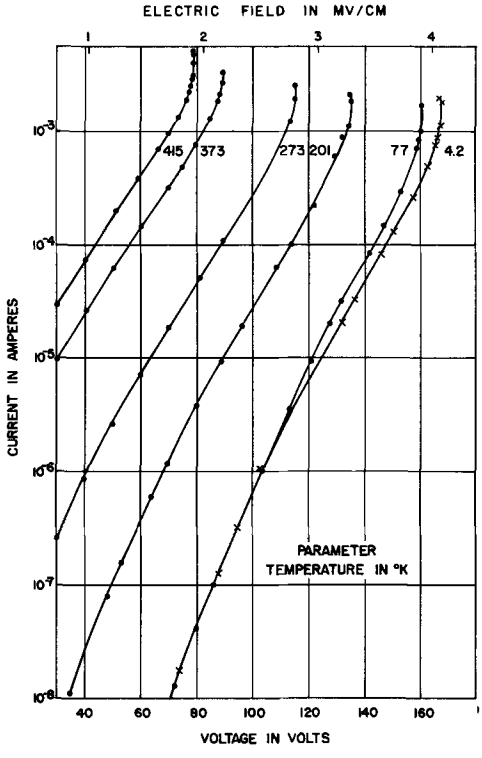

Fig. 4. V-I characteristics of a vapor grown silicon oxide specimen. The parameter is the temperature (14).

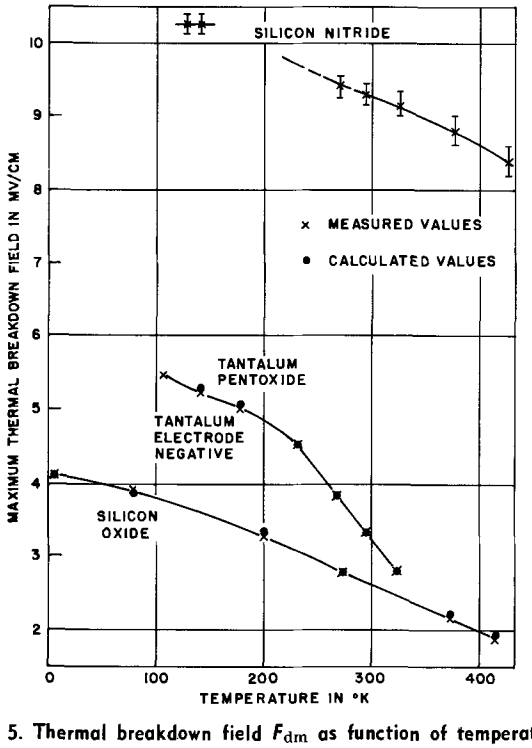

Fig. 5. Thermal breakdown field F_{dm} as function of temperature (a) in vapor grown silicon oxide (14), (b) in anodically grown tantalum pentoxide with the tantalum negative (22), (c) in silicon nitride (24). Crosses measured, dots calculated values.

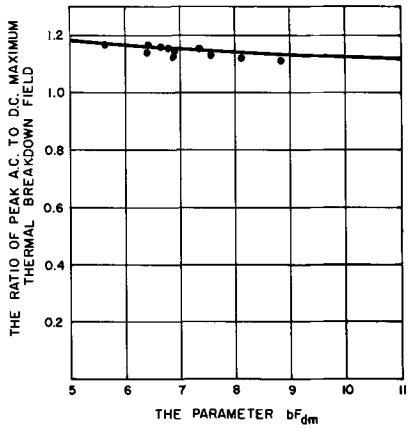

Fig. 6. The ratio of a-c peak to d-c thermal breakdown field in 0.06 cm², 3100-5900Å thick, vapor grown silicon oxide as function of bF_{dm} (15). Dots measured, the curve calculated.

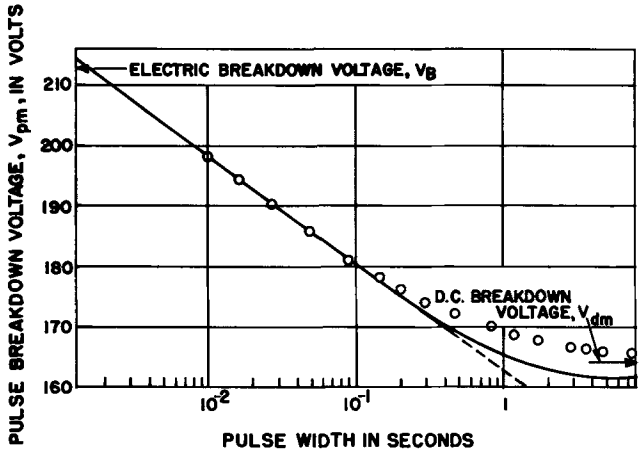

Fig. 7. Thermal pulse breakdown voltage V_{dm} as function of pulse duration τ in a 5000Å thick, 4 x 10^{-3} cm², vapor grown silicon oxide specimen (16). Circles observed, line calculated.

breakdown field was observed with a decrease in pressure. This was found to be caused by the decrease in the thermal conductance due to diminishing heat transport by convection.

The thermal breakdown results can be summarized in breakdown characteristics by plotting F_m *vs.* temperature with pulse duration as a parameter. This is illustrated in Fig. 8 for a 5000Å thick silicon oxide specimen (16).[2] Such results may be obtained on an individual specimen, because the tests are nondestructive.

Electric Breakdown

Experimental observations.—Recent studies on amorphous thin film oxides with self-healing breakdowns produced new results, which enlarge the information on electric breakdown available from shorting specimens. The results do not support accepted concepts and seem to be of interest for the interpretation of breakdown. The subject of this section is developed, therefore, mainly around the observations on the oxides, which were anodically grown on tantalum, hafnium, and aluminum and thermally grown on silicon.

Single hole breakdowns were observed in the oxides above a minimum voltage, the magnitude of which varied from specimen to specimen. On the application of a constant voltage larger than the minimum repetition of breakdown events was observed. The rate of the breakdown events decreased with time to a steady value, and this value was found to increase rapidly

[2] In this case the characteristics were obtained by a combination of measurements and of calculations. The upper end of the curves is presented by broken lines, because in that range the breakdowns were electric.

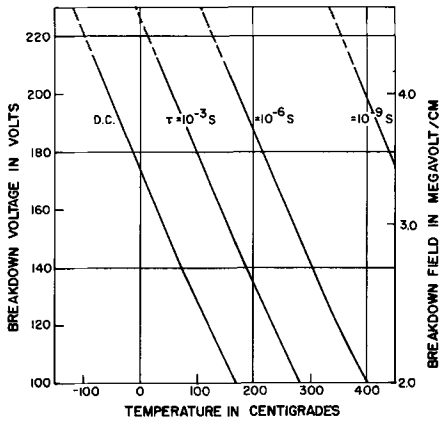

Fig. 8. Thermal breakdown characteristics of a 5000Å thick, 4 x 10^{-3} cm², vapor grown silicon oxide specimen. The parameters are the pulse duration (16)

with voltage. The rate became so large in the vicinity of a voltage V_B (see Fig. 2) that the specimen was completely destroyed by separate single hole breakdowns within a small fraction of a second.

The oxides differed from the specimens with thermal breakdown with respect to the d-c *V-I* characteristic. A maximum voltage V_{dm} and a negative resistance range were not observed (Fig. 2). The characteristic could be measured only to some voltage below V_B, for which the breakdown rate was not yet large. The average joule heat in the specimen was usually insignificant at the voltage V_B. When the maximum thermal breakdown voltage V_{dm} was calculated, it was found that $V_B < V_{dm}$. Thermal breakdown of the bulk therefore could not occur.

The oxides differed from specimens exhibiting thermal breakdown also with respect to the effect of a constant voltage. Single hole breakdowns did not settle down to a steady rate in specimens exhibiting thermal breakdown of the bulk, but stopped after some time. These single hole breakdowns were ascribed to weak spots (11). The question arose, therefore, whether the single hole breakdowns in the oxides were not due to numerous weak spots. To investigate this question the specimen was subjected to a series of breakdowns in sequential tests. In such tests the voltage rises typically within seconds to breakdown, collapses, rises again to breakdown, etc. Results of such tests are illustrated for a 2000Å thick thermally oxidized silicon dioxide specimen in Fig. 9 where the breakdown voltages *vs.* the serial number of the test are plotted (22). The first breakdown voltage at the weakest spot occurred at 38V and the breakdown voltage in the subsequent 150 breakdowns increased to a steady average value of 140V with a scatter of a

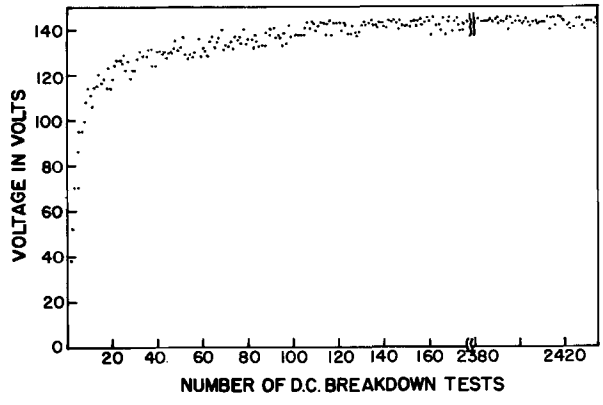

Fig. 9. Breakdown voltages of subsequent breakdown tests on a thermally grown 0.1 cm², 2000Å thick silicon dioxide specimen (22).

few per cent. The results were interpreted that the first 150 breakdowns are due to weak spots, while subsequent breakdowns are characteristic of a bulk property (22). Similar results were obtained with a number of insulators and it is believed that breakdowns at weak spots and in the bulk can be distinguished in these oxides by sequential breakdown testing. Impact ionization and field emission may be instrumental in these breakdowns and it is assumed that electric breakdowns were observed in the oxides.

Breakdowns in the bulk did not occur only at the voltages found by sequential tests, and this is illustrated here by the example of an 0.1 cm^2 tantalum pentoxide specimen with a gold electrode, anodized to 130V. The bulk breakdown voltage on sequential testing averaged 125V when the tantalum was negative. When instead of sequential testing with rising voltages, constant voltage was applied at various magnitudes, breakdowns could be observed from 80 to about 160V. The breakdowns occurred at random sites and at random time intervals. The voltage influenced the rate at which breakdowns repeated and while several hours might have elapsed between breakdowns at 80V, thousands of breakdowns occurred per second at 160V. This kind of behavior was observed also in anodic oxides of hafnium and aluminum, and in thermally grown silicon dioxide and is illustrated for aluminum trioxide in Fig. 10. The dielectric of this specimen was produced by anodization, the oxide thickness was 1700Å, the area 0.1 cm^2 and the counter-electrode was gold. In Fig. 10 the breakdown rate R_B is plotted *vs.* the voltage for room temperature, when either the aluminum, or the gold are negative and for liquid nitrogen temperature, when the aluminum is negative. The breakdown rate appears to rise quasi-exponentially with voltage. There is a very marked polarity effect, which may be related to the electrode material. The breakdown rate decreases sharply with temperature both in the oxides of aluminum and of tantalum and in hafnium dioxide the decrease was found to be quasi-exponential with temperature. It is significant that the breakdown rate usually remains constant with increasing number of breakdowns. This is illustrated for a hafnium dioxide specimen in Fig.

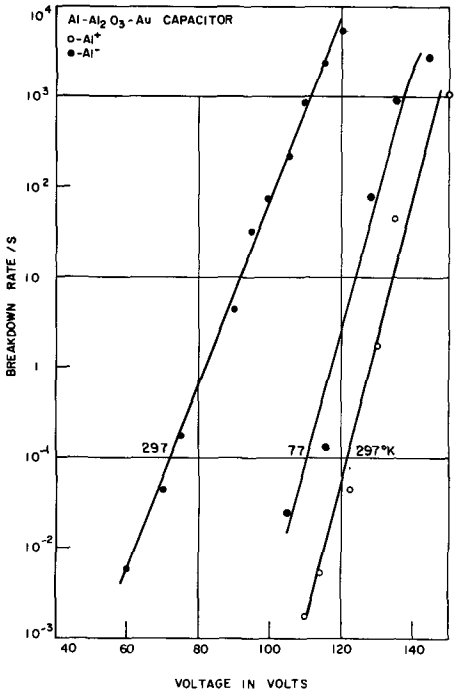

Fig. 10. Rate of breakdown R_B as function of voltage in a 0.1 cm^2 $Al-Al_2O_3-Au$ specimen. Thickness of oxide 1700Å. Curve 1 and 3 at room, curve 2 at liquid nitrogen temperature. Curve 1 and 2 the aluminum negative, curve 3 the gold negative.

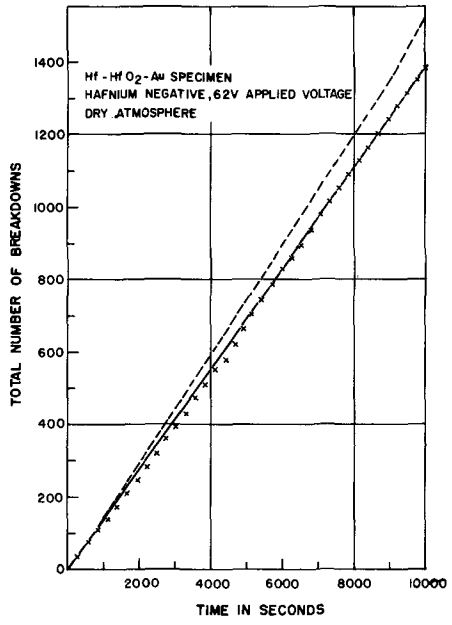

Fig. 11. Number of breakdowns *vs.* time of application of 62V to 3250Å thick, 0.1 cm^2 hafnium dioxide specimen. The hafnium was negative. Crosses indicate batches of about 40 breakdowns.

11, where the number of breakdowns is plotted *vs.* the duration of voltage application. The area of the specimen decreased in the course of this experiment. As the breakdown rate R_B is related to the undamaged specimen area of 0.1 cm^2 in Fig. 10 and 11, the full line was corrected for area decrease in Fig. 11 to the broken line. The gradient of the broken line shows that R_B is mostly constant. An increase in R_B is indicated only after 1000 breakdowns. This slight increase may be due to new breakdowns occurring at the weakened periphery of the earlier breakdowns.

The measurements of R_B extended over 6-7 decades. Extension of the measurements, however, is of interest both to lower and to higher breakdown rates. There is an indication of what happens at low breakdown rates. When fields are low at low R_B values there is a tendency for the R_B curve to bend parallel to the ordinates. This was observed with hafnium dioxide specimens. The extension of the measurement of R_B to higher values is limited by the method of determining R_B. The breakdown rate is determined by dividing the time for which full voltage was maintained by the number of breakdowns. When R_B becomes so large that the voltage rise time on the specimen becomes comparable to the average interval between breakdowns, constant voltage periods become rare, breakdowns occur while the voltage is rising and R_B cannot be determined. The limit for R_B can be increased by decreasing the voltage rise time on the specimen.

The question arises, whether there is an upper voltage limit for electric breakdowns. Evidence on this question is available only for evaporated silicon oxide specimens with self-healing breakdowns (16). A highest average electric breakdown voltage, V_B, was observed with breakdowns occurring while the voltage was rising and a breakdown rate could not be determined. Pulse rise times varied from 5×10^{-8} to 5×10^{-6}s and the peak voltage prior to breakdown was maintained for 10^{-9}s, or less. As shown in Fig. 12 for the silicon oxide specimen V_B slightly increased with decrease in the temperature but was not influenced by pulse rise time. The bars in Fig. 12 denote the standard deviations in the measurements on the specimen. The thermal pulse breakdown data of this specimen were presented earlier in Fig. 7.

The experimental results in the oxides are in conflict with assumptions of a sharply defined breakdown

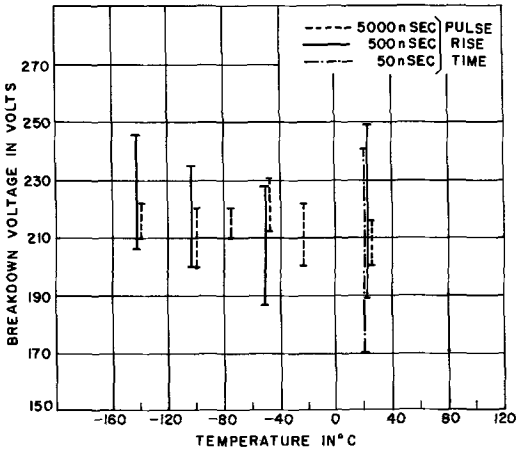

Fig. 12. Highest electric breakdown voltages in an evaporated 5000Å thick silicon oxide film as function of temperature, with voltage rise time as parameter (16). Area of specimen 4 x 10^{-3} cm^2.

field and shed new light on the significance of earlier investigations on statistical time lags. Statistical time lags between the application of voltage and the consequent breakdown have been observed in shorting specimens for a number of substances. The statistical time lag, t_s, is related to the mean interval t_B between self-healing breakdowns in the bulk. t_s is the mean interval to the first breakdown at the weakest spot. Kawamura, Ohkura, and Kikuchi (28) found for about 3 μm thick biotite mica that t_s was a strong function of the applied field. t_s increased from 6 x 10^{-8} to 8 x 10^{-5}s quasi-exponentially, while the field decreased from 8 x 10^6 to 5 x 10^6 V/cm. While these results were obtained on relatively few specimens and while they related to weakest spots in the insulations, they showed the same field dependence as was described here for the bulk of oxides. A rapid decrease in t_s with increasing field was found also in 0.01-0.07 cm thick sodium chloride in a series of detailed observations by Cooper and Smith (29).

The electric breakdown results can be summarized by plotting the electric breakdown voltage *vs.* temperature with $1/R_B = t_B$, the average interval between breakdowns as parameter. This is illustrated in Fig. 13 by the electric breakdown characteristics for a hafnium dioxide specimen.

When both thermal and electric breakdowns occur in the range of observations the thermal and electric breakdown characteristics may be superposed in one figure. This was shown earlier for glass by Vermeer (27). The glass breakdown results were obtained with shorting specimens and electric breakdowns were represented by one curve only. It remains to be ascertained for glass with self-healing specimens whether breakdowns occur over a range of voltages, as found in the oxides.

In addition to observations on breakdown voltages and rates, important information on the breakdown process are obtained from observation of the damage caused and of the voltage changes during the breakdown event. The electric breakdowns, as mentioned earlier, produce single hole type of destruction in thin films (Fig. 1) when the series resistors are larger than about 10 kohms. The magnitude of the destruction expressed by an equivalent diameter of the material removed by the breakdown increases with voltage (11, 12). This is illustrated for the destruction in the top electrode of a thermally grown silicon dioxide specimen in Fig. 14 (12). The voltage changes with time during the breakdown event are determined oscillographically, as shown in Fig. 15, for a silicon dioxide specimen (12). The traces indicate the applied voltage, the voltage collapse on breakdown and the initial phase of the recharge of the specimen from the

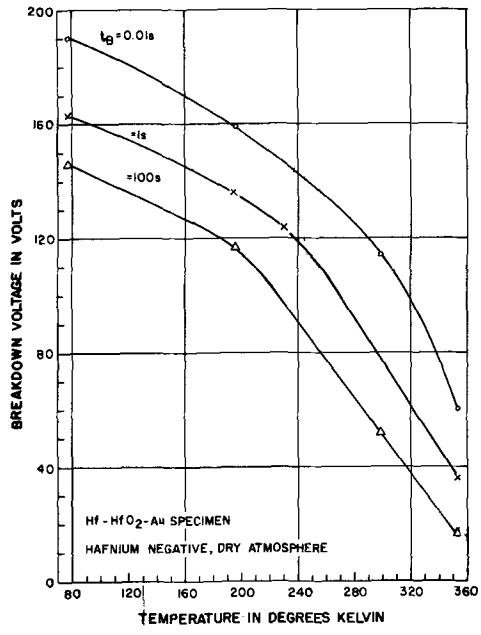

Fig. 13. Electric breakdown characteristics of an anodically grown, 0.1 cm^2 hafnium dioxide specimen. The oxide thickness was 3250Å. The parameters are the average interval between breakdowns, t_B.

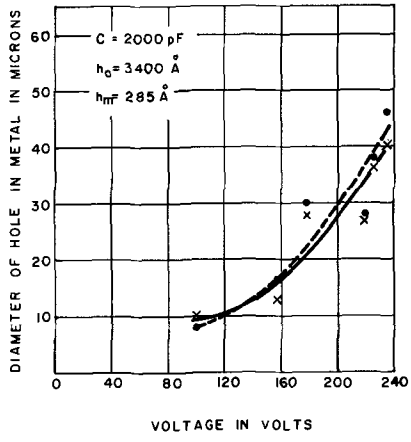

Fig. 14. Diameter of breakdown hole in counterelectrode metal *vs.* voltage in an Si-SiO_2-Al specimen (12). P-type, 1000 ohm-cm substrate, + Si. Crosses and full lines represent measurements; circles and broken lines are calculations.

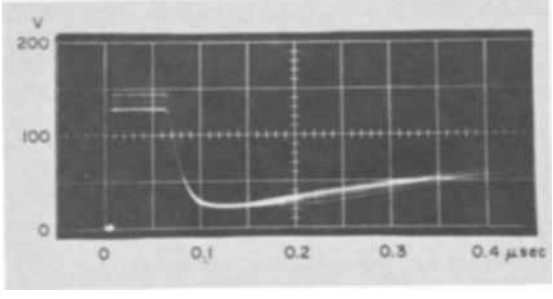

Fig. 15. Specimen voltage *vs.* time oscillogram on single hole breakdown events in a thermally grown silicon dioxide specimen (12). P-type, 0.3 ohm-cm substrate, + Si.

external supply. The voltage collapse was found to occur in thin film specimens of 10^{-10}-10^{-7}F within 10^{-8} to 10^{-5}s, while the recharge time was determined by the product of the series resistor and of the specimen capacitance.

Discussion of the observations.—The discussion of the electric breakdown process is simplified if the processes of destruction are considered first.

The voltage collapse in the oscillogram of Fig. 15 can be interpreted as discharge of the electrostatic energy stored in the specimen into the breakdown spot in a time determined by the resistance of the discharge path and by the capacitance of the specimen. Sträb (6) suggested earlier that the destruction on single hole breakdown is due to this process of discharge. The assumption as to the cause of destruction was investigated in detail in evaporated silicon oxide (11, 16) and in thermally grown silicon dioxide specimens (12). To verify the validity of the assumption, the current in the breakdown spot as function of time and the spreading resistance of the discharge path was calculated from the oscillogram (12). These data permitted the calculation of the magnitude of destruction caused by the joule heat of the discharge process. Results of such calculations were compared with observations, as illustrated by Fig. 14. Calculated and observed single hole breakdown diameters have been found to agree within 10-15% in a number of insulators. Another experimental approach to support the suggested mechanism of destruction was the determination of the temperature of the spark occurring on breakdown. This was determined independently from the rate of vaporization found from the breakdown oscillograms and from the line intensities of spectra of the breakdown events (12). In thermally grown silicon dioxide specimens breakdown temperatures of about 4000°K were ascertained by both methods. It is interesting to remark that during the discharge into the breakdown spot current densities up to 10^{10} A/cm^2 and power inputs up to 10^9 W/cm^2 were found to occur (12).

These results indicated that single hole breakdown consists of two main, consecutive stages: (*i*) a conducting channel is formed by the breakdown process in the insulator, and (*ii*) the electrostatic energy stored in the specimen discharges through the conducting channel, evaporates material and produces a hole much larger than the conducting channel.

Since it appears that the processes during the second stage of the breakdown process can be explained, the main question of electric breakdown is the identification and interpretation of the processes producing the conducting channel.

Since the work of von Hippel, Zener, and Fröhlich electronic avalanche and tunneling processes were believed to cause the conducting breakdown channels. Recently though Budenstein and Hayes (30) suggested for silicon oxide that the conducting channel is formed by decomposition of the insulator caused by the high field. Theoretical considerations based on the avalanche and tunneling processes resulted mostly in relations for a sharply defined breakdown field for insulators. The avalanche theories for single crystal insulators predicted a slow increase in breakdown field with temperature owing to increase with temperature of energy losses of the ionizing electrons by lattice vibrations. Detailed reviews of the theoretical work are given in ref. (19-21), with references to the original papers.

Most of the theories seem to be inapplicable to the interpretation of the oxide results owing to disagreement on the temperature and possible electrode dependence of the breakdown field and owing to the occurrence of breakdowns over a wide range of breakdown fields. Three theories however, Fröhlich's theory for amorphous insulators, von Hippel and Algers' assumption on space charges, and the single electron avalanche theory, predict some of the thin film oxide breakdown properties correctly, and these will be discussed now.

Fröhlich (31) assumed that an amorphous insulator has trapped a large density of electrons, n_2, in excited impurity levels separated by the energy ΔW from the bottom of the conduction band. The density of the free electrons is n_1 and $n_1/n_2 a e^{-\Delta W/kT}$. It is assumed that the free and the trapped electrons are strongly coupled by interelectronic collisions and that energy is lost to the lattice vibrations both by the free and by the trapped electrons. Energy is gained however, only by the free electrons. Breakdown arises at the field, for which the energy gain of the free electrons cannot be balanced by the losses. As the density of the free electrons increases exponentially with temperature, calculations result in

$$F_B = \frac{A}{\Delta W^{1/2}} e^{\Delta W/2kT} \qquad [13]$$

with A being a constant. The exponential temperature dependence of F_B agrees with observations in the oxides. This theory however, results in a sharply defined breakdown field, which is an intrinsic property of the insulator and independent of the electrode material, or polarity. These aspects of the theory do not agree with the observations.

It was assumed by von Hippel and Alger (32) that positive ion migration occurs in the insulator enhancing the field at the cathode. The magnitude of the effect increases with temperature and time of application of voltage. The average field for breakdown should, therefore, decrease with increasing temperature, as was observed in the oxides. On the other hand, time of application of the voltage should increase the breakdown rate, but this was not observed in the oxides.

The single electron avalanche breakdown theory developed by Fröhlich (33) and Seitz (34) has been frequently used for the interpretation of experimental results. The theory connects the formation of an avalanche with destruction. It is assumed that a single electron at the cathode starts an avalanche by impact ionization. When the avalanche reaches the anode, the number of electrons has grown to $2^{t_w/t_i}$ where t_w is the electron transit time through the insulator and t_i is the mean time between ionizing collisions. The avalanche grows to a cross section $4\pi l_p h/3$ at the anode by sideways diffusion. Here l_p is the mean free path for electron-phonon collisions and h is the insulator thickness. The phonon collisions cause a temperature increase in the insulator, and the heat produced is largest at the anode. The breakdown field is calculated with the condition that the joule heat is sufficient to start destruction of the material at the anode. According to the calculations of Seitz, the destruction in a 5000Å thick specimen would be initiated by an avalanche of about 5×10^7 electrons.

The development of a destructive single electron avalanche is a chance event. It depends on the rate of supply P_1 of a free electron in the insulator at the cathode and on the probability P_2 of an avalanche growing in excess of the size required for destruction. The breakdown is supposed to occur after a mean statistical time lag, t_s, which is a function of the field and which is

$$t_s = (P_1 P_2)^{-1} \qquad [14]$$

When many breakdowns are observed on a specimen cleared of weak spots, t_s can be identified with t_B the mean time interval between breakdowns and $t_B = 1/R_B$, the inverse of the breakdown rate.

The breakdowns observed in the oxide films are clearly chance events, both spacially and timewise, as also indicated by the constancy of R_B in Fig. 11 and agree with this aspect of the single electron avalanche theory. It is feasible to assume that many avalanche-like pulses occur constantly in the oxides. The avalanches which reach a critical size cause breakdown.

The original form of the single electron avalanche theory has been subjected to a number of criticisms. The theory assumes that the energy for destruction of the breakdown channel derives from the avalanche. This assumption is in some disagreement with the

two stage model for breakdown, discussed earlier because it was shown, that energy for the destruction is available from the energy stored in the specimen. It is believed, therefore, that the magnitude of the avalanche which causes destruction was overestimated and it was proposed that the breakdown process develops in the following way (16):

The avalanche only triggers the breakdown. It increases the temperature in the breakdown channel from the ambient temperature T_1 by a few hundred centigrades to T_2. The increase in electrical conductivity caused by the temperature rise is such as to make the channel thermally unstable at the temperature T_2. Thermal runaway arises then as shown in the oscillograms of Fig. 3, but in a time many orders of magnitude shorter. The energy for thermal runaway is supplied from the energy stored in the specimen. The avalanche and the thermal runaway produce the conducting channel and the processes of the first stage of the breakdown event. The second stage, as mentioned above, is destructive, with energy supplied by discharge of the specimen.

The number of electrons in an avalanche, N_i, triggering breakdown by increasing the channel temperature to T_2 was found (16)

$$N_i = \frac{c_e A_c}{qaF_B} \log \left[\sigma_o(T_2)/\sigma_o(T_1)\right] \qquad [15]$$

where A_c is the breakdown channel cross section and q is the electronic charge; c_e, a, and σ_o are defined in Table I. It was found also that the magnitude of the triggering charge is smallest when conduction of heat is negligible during most of the thermal runaway process.

The electric breakdown properties of a 5,000Å evaporated silicon oxide film were given in Fig. 12. The peak voltage was maintained on this specimen roughly for 10^{-9}s prior to voltage collapse on breakdown. Identifying the 10^{-9}s with the first stage of the breakdown process in this film, a minimum temperature rise in the channel of about 340°C and a minimum avalanche size of 4.5 x 10^5 electrons was calculated. This avalanche size is by more than two orders of magnitude smaller than that calculated on the earlier assumption that the avalanche has to provide the energy for destruction (34).

Serious difficulties were found recently with the original form of the single electron avalanche theory. Electroluminescence accompanies an avalanche, and the light emission is expected to be largest where the number of free electrons is largest. According to the single electron avalanche theory this should be the case at the anode. Cooper and Elliott (35) observed thick NaCl and KCl crystals between the electrodes prior to the destructive stage of the breakdown and found the largest light emission not at the anode, but at the cathode.

The original form of the single electron avalanche theory considers electrons only and the positive charges are thought to be immobile. O'Dwyer (36) calculated the field produced by the positive charges left behind in the insulator by the electron avalanche. He found that this field opposing the applied field would be 10^{11} V/cm for a destructive avalanche of the size calculated by Seitz.[3] Even the avalanche sizes postulated in ref. (16), which are smaller by two orders of magnitude imply impossible large opposing fields. Under these circumstances a single electron avalanche in its form suggested originally (33, 34) cannot develop.

Cooper and Elliott (35) and also O'Dwyer (36) suggest that the development of an avalanche is not determined by impact ionization in the insulator only but also by field emission at the cathode. When the developing avalanche leaves a positive space charge at the cathode, this space charge greatly enhances field emission of electrons from the cathode into the insulator, ensuring current continuity and making possible the development of an avalanche large enough for breakdown. O'Dwyer (25) recently further elaborated these ideas by assuming that the holes have a finite, although very small mobility and a very small ionization coefficient. These calculations result in a well-defined breakdown field.

It appears from these results that the present forms of the single electron avalanche breakdown theory do not explain yet the oxide observations. Several aspects of this theory may however be useful in interpretations. When the breakdown depends on the availability of a free electron at the cathode and the cathode insulator barrier is less than 1.5 eV, Schottky emission may explain observations. When the breakdown depends on the probability of the growth of an avalanche to a critical size, the breakdown may be explained as a chance event, which is determined by particular transport and trapping properties of the holes and by field emission at the cathode.

As the nature of the avalanche producing breakdown is not yet known, the development of a satisfactory theory requires further experimental work, mainly aimed at the identification of the processes forming a conducting channel. The first problem is, whether the occurrence of the initiating free electron, or the development of a critical size avalanche determine the breakdown event. This may be investigated by the internal photoemission of free charge carriers into the insulator from the electrodes and by observing the influence of these carriers on the breakdown rate. Preliminary experiments in thermally grown silicon dioxide showed that this method is feasible. As no large influence of photoemission on the breakdown rate was observed, the development of the avalanche was assumed to be the process determining the breakdown. When this is the case in an insulator, a second problem is whether the holes have a finite mobility at the breakdown fields. This may also be investigated with internal photoemission as shown by Goodman (37) who estimated that in silicon dioxide $\mu\tau \simeq 10^{-14}$ m²/V, μ being the hole mobility and τ the time before trapping.

[3] Earlier Kawamura *et al.* (28) made a similar observation about the single electron avalanche theory.

Acknowledgments

Thanks are due to F. Huber for the provision of the hafnium dioxide specimens, to F. Rosztoczy for the aluminum trioxide specimens and to R. W. MacDonald for the silicon dioxide specimens. Acknowledgments are due to H. Basseches for detailed and helpful discussions of the manuscript.

Manuscript submitted Dec. 16, 1968; revised manuscript received March 24, 1969. This was Paper 456 presented at the Montreal Meeting, Oct. 6-11, 1968.

Any discussion of this paper will appear in a Discussion Section to be published in the June 1970 JOURNAL.

REFERENCES

1. E. W. Austen and S. Whitehead, *Proc. Roy. Soc.*, **A176**, 33 (1940).
2. K. W. Plessner, *Proc. Phys. Soc.*, **60**, 243 (1948).
3. P. D. Lomer, *ibid.*, **B63**, 818 (1950).
4. W. W. Dean, U.S. Pat. No. 965, 992 (1910).
5. D. A. McLean, *Proc. IRE*, **38**, 1010 (1950); J. R. Weeks, *ibid.*, 1016.
6. Sträb, Ver. Deutscher Elektr., Fachberichte (1954).
7. Y. Inuishi and D. A. Powers, *J. Appl. Phys.*, **28**, 1017 (1957).
8. G. Siddall, *Vacuum*, **9**, 274 (1959).
9. D. R. Kennedy, Electr. Res. Assoc. (Leatherhead, England), Rep. L/T 374 (1958).
10. L. Young, "Anodic Oxide Films," Academic Press, New York and London, (1961).
11. N. Klein, H. Gafni, and H. J. David, *Physics of Failure in Electronics*, **3**, 315 (1965).
12. N. Klein, *IEEE Trans. El. Dev.*, **ED-13**, 788 (1966).
13. N. Klein and H. Gafni, *ibid.*, **ED-13**, 281 (1966).

14. N. Klein and Z. Lisak, *Proc. IEEE*, **54**, 979 (1966).
15. N. Klein and N. Levanon, *J. Appl. Phys.*, **38**, 3721 (1967).
16. N. Klein and E. Burstein, *J. Appl. Phys.*, **40**, June (1969).
17. M. Brestechco (Manor) and N. Klein, *Thin Solid Films, (London)*, **3**, 175 (1969).
18. C. G. Garton and K. H. Stark, *Nature*, **176**, 1225 (1955); R. A. Fava, *Proc. IEE (London)*, **112**, 819 (1965).
19. W. Franz, in Hdb. Physik (S. Flügge, Editor), XVII, p. 155, Springer, Berlin (1956).
20. R. Stratton, *Progr. in Dielectrics*, **3**, 235 (1961).
21. J. J. O'Dwyer, "The Theory of Dielectric Breakdown in Solids," Oxford University Press, London (1964).
22. N. Klein, in "Electrical Breakdown in Solids," Adv. Electr. Electron Physics, L. Marton, Editor, Academic Press, New York, vol. 26, pp. 309-424 (1969).
23. M. A. Lampert, *Rept. Prog. Phys.*, **27**, 329 (1964).
24. S. Sze, *J. Appl. Phys.*, **38**, 2951 (1967).
25. T. E. Hartman, J. C. Blair, and R. Bauer, *ibid.*, **37**, 2468 (1966); J. J. O'Dwyer, *This Journal*, **116**, 239 (1969).
26. S. Whitehead and W. Nethercot, *Proc. Phys. Soc. (London)*, **47**, 974 (1935).
27. J. Vermeer, *Physica (Holland)*, **20**, 313 (1954).
28. H. Kawamura, H. Ohkura, and T. Kikuchi, *J. Phys. Soc. Japan*, **9**, 541 (1954).
29. R. Cooper and W. A. Smith, *Proc. Phys. Soc.*, **78** 734 (1961).
30. P. P. Budenstein and P. J. Hayes, *J. Appl. Phys.*, **38**, 2837 (1967).
31. H. Fröhlich, *Proc. Roy. Soc.*, **A188**, 521 (1947).
32. A. von Hippel and R. S. Alger, *Phys. Rev.*, **76**, 127 (1949).
33. H. Fröhlich, Rep. Brit. Electr. Allied Ind. Res. Assoc. L/T 113, 1940.
34. F. Seitz, *Phys. Rev.*, **76**, 1376 (1949).
35. R. Cooper and C. T. Elliott, *Brit. J. Appl. Phys.*, **17**, 481 (1966); *ibid.* (J. Phys. D.) Ser. 2, **1**, 121 (1968).
36. J. J. O'Dwyer, *J. Phys. Chem. Solids*, **28**, 1137 (1967).
37. A. M. Goodman, *Phys. Rev.*, **152**, 780 (1966).

Influence of Bond Energies of Oxides on the Kinetics of Anodic Oxide Growth on Valve Metals

Ashok K. Vijh*

Research & Development Laboratories, Sprague Electric Company, North Adams, Massachusetts

ABSTRACT

Average bond energy values have been calculated for the oxides of Bi, V, U, Y, Nb, Zr, Ti, W, Ta, Al, Hf, and Si from the appropriate thermochemical data. An attempt has been made to explore the influence of these bond energies on the magnitude of kinetic parameters for the anodic oxide growth on the corresponding metals. It has been concluded that, in general, with increasing bond energy, the field required for sustaining a given ionic current density tends to increase, as also does the "Tafel slope." Further, the magnitude of the "activation dipole" in Dignam's theory, both for the steady-state and the transient kinetics, tends to decrease with increase in bond energy. Interrelationship of these correlations has been briefly pointed out.

For conventional electrode processes, *e.g.*, hydrogen evolution reaction (HER) and oxygen evolution reaction (OER), M-H and M-OH bond energies, respectively, have been related quantitatively to the electrode kinetic parameters (1, 2) of the corresponding metals (represented by M). An attempt has been made here to extend similar approaches to the kinetics of oxide growth on valve metals.

The bond energies (Table I) for the various valve metal oxides have been calculated by the procedure of Howald (3). The procedure essentially involves obtaining heats of atomization per equivalent for various oxides by taking into account spin correlation stabilization energies. The quantity thus obtained is an average bond energy value. In our computations, presence of any coordinate bonds has been ignored since unambiguous estimates of their contribution are not always readily accessible, as discussed by Howald (3).

In the kinetics of HER (1), it has been suggested that the bond energies should be obtained by the procedure of Pauling (4). However, Pauling's method assumes an isolated, *e.g.*, M-H (metal hydride) bond and hence gives the bond dissociation energy (1). In the HER or OER where only a monolayer hydride or a slightly thicker surface oxide is involved, Pauling's procedure is quite valid. In the kinetics of oxide growth, however, much thicker oxides indicating phase growth reactions are involved; hence, the valid values of bond energies are those which give an average M-O (metal oxide) bond energy for the M-O bond as it exists in the environment of the bulk oxide, *i.e.*, not an isolated M-O bond. Such values are given by Howald's method and are shown in Table I and have been used in constructing the various figures in this paper.

Table I. Bond energies

Anodic oxide	Field (V cm^{-1} at an ionic current density of ca. 2 × 10^{-3} A·cm^{-2} (room temp.)	MO bond energy in eV
Bi_2O_3	1 × 10^6 (13)*	2.91
V_2O_5	3.2 × 10^6 (15)	4.56
UO_3	3.6 × 10^6 (16)	4.68
Y_2O_3	4.4 × 10^6 (17)	5.59
Nb_2O_5	4.65 × 10^6 (13, 14)	5.29
ZrO_2	4.76-5.3 × 10^6 (13, 14)	6.16
TiO_2	5 × 10^6 (14)	5.42
WO_3	5.5 × 10^6 (13, 14)	4.76
Ta_2O_5	6.2 × 10^6 (13, 14)	5.34
Al_2O_3	7.9 × 10^6 (13, 14)	5.73
HfO_2	—	6.42
SiO_2	2.6 × 10^7 (11)	5.16

* Note: The numbers in the parentheses refer to the source reference from which a given value of the field has been obtained.

* Electrochemical Society Active Member.

Correlation of Bond Energies to Kinetic Parameters

In Fig. 1 bond energies for various valve metal oxides have been plotted against the logarithm of field required to sustain a moderate value of ionic current density. In general, the higher the bond energy, the higher is the field required for a given steady-state ionic current, *i.e.*, the activation energy for oxide growth increases with the increase in the bond energy of the corresponding oxide.

It may be noted that zirconium departs noticeably from the general trend in Fig. 1. This is probably related to the fact that zirconium shows some anomalous characteristics of fundamental nature in its kinetic behavior. For example, it appears that zirconium is unique among valve metals in that its kinetic behavior depends on the thickness of the film (7), for films thicker than about 100Å. No reliable data, it seems, exist for field strength for the oxide growth on hafnium at moderate current densities, *i.e.*, in the range of mA/cm^2. It may be noted that Si does not follow the trend shown in Fig. 1 (Si as in SiO_2, solid point). The fields required for oxide growth on Si are unusually high (*ca.* 2.6 x 10^7 V cm^{-1}) and current efficiencies are extremely low from the very commencement of oxide growth, thus suggesting quite complex parallel reactions (*e.g.*, OER, dissolution) occurring concomitantly (8). It may be mentioned, however, that Si would follow the trend shown in Fig. 1, if Si-O bond energy (8 eV) as in SiO is used instead of average Si-O bond energy as in SiO_2. For a material like SiO_2 which shows rather pronounced glassy character and three-dimensional bonding network, with the consequent spectrum of melting points (hence "softening" of glass), it is not possible to decide whether the bonding behavior is determined by SiO bonds as they exist in SiO or SiO_2. Indeed, a whole spectrum of bonds would be expected (9), which would not be detected from the stoichiometric evidence on the composition of anodic oxide on Si.

Finally we note that W and Y in Fig. 1 follow the general trend only very approximately.

The intermediate value for ionic current density (*ca.* 2 mA cm^{-2}) has been purposely chosen to obtain fields used in Fig. 1. It is believed that this moderate value is more representative of the anodic behavior than the low ones (*i.e.*, μA cm^{-2}) or the high ones (*ca.* A cm^{-2}). In the microampere region, electronic currents associated with the impurity reactions from the inadvertent redox couples in the solution may vitiate the results. In the high current density region, OER, film dissolution, heating effects, sparking, and other complications may interfere with the significance of the data. Since the relation in Fig. 1 is intended to emphasize the approximate, qualitative trends only, inserting the values of field obtained at any other reasonable (*e.g.*, 1 x 10^{-5} to 1 x 10^{-2} A cm^{-2}) value of ionic current density, in Fig. 1 would not change, substantially, the general significance of the conclusions drawn here.

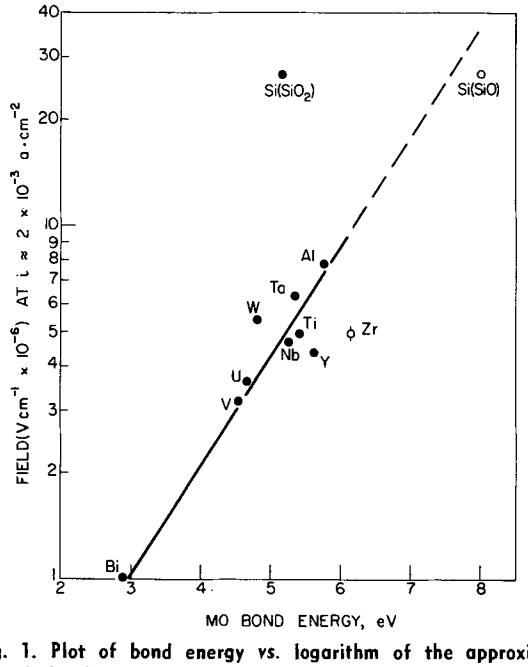

Fig. 1. Plot of bond energy vs. logarithm of the approximate value of the field required to sustain an ionic current density of 2 x 10^{-3} A·cm^{-2} for the anodic oxides of the indicated metals.

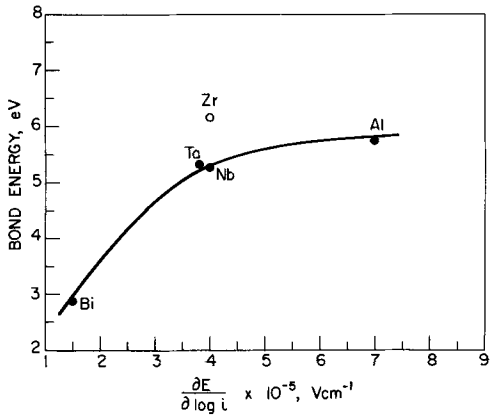

Fig. 2. Plot of Tafel slope for anodic oxide growth vs. bond energy.

In Fig. 2, the values of steady-state Tafel slopes (10-12), $\partial E/\partial \log i$, have been related to the corresponding bond energy values. Departure of Zr from the general trend may again be noted and, of course, is not entirely unexpected for the reasons outlined in the foregoing discussion. No reliable values for Tafel slopes, it seems, are available for valve metals not shown in Fig. 2. The higher the Tafel slope, the higher is the activation energy for ionic conduction since higher Tafel slopes indicate higher values of increments in overfield for given increments of ionic current density. Hence Fig. 2 corroborates the conclusions drawn from Fig. 1.

In Fig. 3, bond energies have been plotted against the corresponding values of the activation dipole (*i.e.*, μ^*), as defined in Dignam's theory, both for the steady-state and transient kinetics. Reliable values of μ^* for valve metals other than those shown in Fig. 3 are not available.

In Dignam's theory (7)

$$\frac{\mu^*}{K} \simeq \text{constant}$$

where K is the dielectric constant. Since μ^* decreases with increasing bond energy (Fig. 3), K must decrease with increasing bond energy, a result which is easily

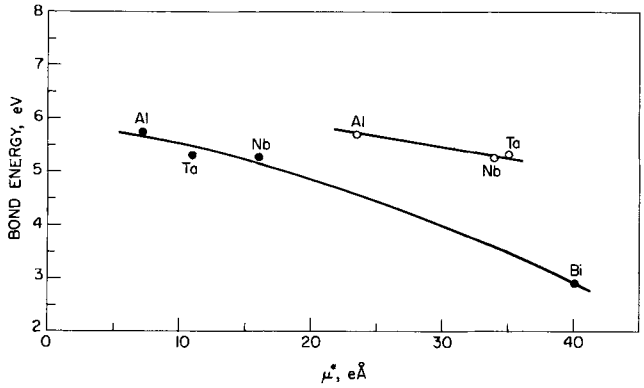

Fig. 3. Plot of bond energy vs. "activation dipole" μ^*, for ○ steady-state kinetics; ● transient kinetics.

verified as regards the rough trend, and has already been shown, directly, to be valid for a number of valve metal oxides, *viz.*, HfO_2, ZrO_2, Ta_2O_5, and Nb_2O_5 (6). Hence Fig. 3 and the related discussion constitutes some confirmation of one of the aspects of Dignam's theory, *i.e.*, $\mu^*/K \simeq$ constant.

Discussion

It follows from the preceding correlations (Fig. 1-3; Table I) that fields (for a given ionic current density) and hence activation energies for anodic growth (Fig. 1), Tafel slopes (Fig. 2), and activation dipoles (Fig. 3) may be related, at least qualitatively, to the corresponding bond energies for a number of valve metal oxides. These three quantities are among the fundamental parameters that describe the kinetics of anodic oxide growth and are, in turn, related to one another as shown below.

In the anodic growth of oxide films on valve metals, ionic current density i is related to the field E by the equation (19)

$$i = \alpha e^{\beta E} \qquad [1]$$

where α and β are constants for a given metal.

Equation [1] may also be written in the form

$$\log i = \log \alpha + 2.3\beta E \qquad [2]$$

Figure 1 illustrates that, for a given value of i, E required to sustain that i increases with increasing bond energy.

Differentiation of [2] gives

$$\frac{\partial \log i}{\partial E} = \beta' \qquad [3]$$

where

$$\beta' = 2.3\ \beta = \frac{qa}{kt}$$

or

$$\frac{\partial E}{\partial \log i} = \frac{1}{\beta'} = \text{Tafel slope} \qquad [4]$$

Figure 2 illustrates the relation of bond energy to the Tafel slope, which is the inverse of the field-coefficient in Eq. [2]. No attempt has been made here to relate α of Eq. [2] with the bond energy since the values of α reported in the literature by various workers under apparently comparable conditions differ by several orders of magnitude. It may be added that α here has the same significance as exchange current density i_o in the conventional electrode processes, *e.g.*, HER and is equivalent to, in terms of absolute reaction rate theory, the rate constant (1). The wide spread in the values of α reported by various workers tends to emphasize that the difficulties involved in obtaining reliable α values (or i_o values) are not restricted only to reactions like HER.

Dignam (7) defines activation dipole as

$$\mu^* = (qa)_{E \to 0} \qquad [5]$$

Ignoring for a moment the field dependence of qa, it may be observed that

$$\frac{\partial E}{\partial \log i} = \frac{kt}{qa} = \frac{kt}{\mu^*} \qquad [6]$$

It follows from Eq. [6] that the Tafel slope would change with bond energy (Fig. 2) in a manner opposite to that in which μ^* changes with bond energy (Fig. 3), a result clearly supported by Fig. 2 and 3.

It may, therefore, be stated that like the case of other electrode processes, *e.g.*, HER and OER, the magnitude of various kinetic parameters for the anodic growth on valve metals is also influenced by the bond energies of the corresponding oxides.

An attempt would now be made to explore the possible origin of the main conclusion of this paper, namely, the activation energy for anodic growth increases with increase in bond energy. For predominantly ionic compounds, *e.g.*, alkali halides, the activation energies for the formation and diffusion of point defects depend on the lattice energy (19). For predominantly covalent compounds, however, the activation energies for the formation and diffusion of point defects would be determined (5), instead, by heat of atomization, *i.e.*, bond energy. For example, if the point defect is assumed to be a hole, the foregoing argument may roughly be developed mathematically on the basis of the following considerations.

The work necessary to form a hole in an ionic crystal (*e.g.*, NaCl), W_H, is given by (19)

$$W_H = W_L - \frac{1}{2} e\phi \qquad [7]$$

where W_L is the lattice energy per ion pair; ($\frac{1}{2}\ e\phi$) factor takes into account the fact that the polarization of the surrounding medium on removal of an ion will set up at the vacant lattice point an electrostatic potential ϕ. For the case of these oxides, the lattice energies per ion pair are extremely high (6) and are the predominant term in the right hand side of Eq. [7]. Hence, Eq. [7] may be approximated as

$$W_H \simeq W_L \qquad [8]$$

The calculation of W_L may be carried out by a Madelung-type procedure based on Born's electrostatic model; alternatively, W_L may be computed by an appropriate Born-Haber cycle as follows.

$$W_L = \Delta H^o_f + \Delta H_{Sub} + \frac{1}{2}\Delta H_{diss.} + I_m + A_X \qquad [9]$$

where, ΔH^o_f is the heat of formation of the oxide;

ΔH_{Sub} is the heat of sublimation of the corresponding metal;
ΔH_{diss} is the heat of dissociation of O_2 into O atoms;
I_m is the sum of successive ionization potentials of the metal needed to produce the requisite ions;
A_X is the electron affinity of O^{-2} ion, *i.e.*, energy needed to form O^{-2} from an O atom.

All quantities in Eq. [9] must be taken as per ion pair.

For a predominantly covalent crystal (*e.g.* Ge), the lattice energy has no significance, *i.e.*, I_m and A_X in Eq. [9] disappear giving

$$W_L = \Delta H^o_f + \Delta H_{Sub} + \frac{1}{2}\Delta H_{diss.} \qquad [10]$$

or

$$W_L = \text{heat of atomization} \qquad [11]$$

or

$$W_L = \text{bond energy} \qquad [12]$$

By comparing Eq. [8] with [12], we write

$$W_L \simeq \text{bond energy} \qquad [13]$$

i.e., the work for hole formation for a covalent crystal is roughly equal to the bond energy. On the basis of similar arguments, one could show that for a covalent crystal, work for the formation or diffusion of any point defect would be determined by the bond energy.

Now we note, as has been shown elsewhere (6), that the various fundamental properties, *e.g.*, mp, bp, of several valve metal oxides increase systematically with increasing bond energy and decreasing lattice energy. These oxides, therefore (5), must be concluded to be predominantly covalent. If these oxides are assumed to be predominantly covalent, the activation energies for the formation and diffusion of point de-

fects would be expected to increase with increasing bond energy; hence, higher activation energies for anodic growth are found to be associated with oxides possessing higher bond energies (Fig. 1-3). This possible relation between bond energies and activation energies for anodic growth was first mentioned by Young (9). He did not pursue the subject in any detail, however.

It may be added that, unfortunately, the considerations developed here do not provide a basis for distinguishing the various possible mechanisms that may be involved in the anodic growth of oxides; *e.g.*, no conclusions can be drawn on the basic validity of Dignam's mosaic model (7) or on the identity of point defects mainly responsible for carrying the current during anodic growth of these oxides (9).

Manuscript submitted Dec. 26, 1968; revised manuscript received March 20, 1969.

Any discussion of this paper will appear in a Discussion Section to be published in the June 1970 JOURNAL.

REFERENCES

1. B. E. Conway and J. O'M. Bockris, *J. Chem. Phys.*, **26**, 532 (1957).
2. P. Ruetschi and P. Delahay, *ibid.*, **23**, 556 (1955).
3. R. Howald, *J. Chem. Ed.*, **45**, 163 (1968).
4. L. Pauling, "The Nature of the Chemical Bond," p. 79 and Appendix XII, Cornell University Press (1960).
5. A. A. Vorobe'v, *Russ. Chem. Rev.*, **36** (6) 440 (English Trans.), 1967, Consultants Bureau, New York.
6. A. K. Vijh, *This Journal*, **116**, 353 (1969); *ibid.*, **115**, 1096 (1968).
7. M. J. Dignam, *ibid.*, **112**, 730 (1965); *Can. J. Chem.*, **42**, 1155 (1964).
8. L. Young, W. S. Goruk, and F. G. R. Zobel in "Modern Aspects of Electrochemistry," Vol. 4, J. O'M. Bockris, Editor, Plenum Press, New York (1966).
9. L. Young, "Anodic Oxide Films," p. 171, Academic Press, New York (1961).
10. Ref. (9) p. 21.
11. J. J. Randall, Jr., W. J. Bernard, and R. R. Wilkinson, *Electrochim. Acta*, **10**, 183 (1965).
12. B. E. Conway, "Theory and Principles of Electrode Processes," Ronald Press, New York (1965).
13. F. J. Burger and L. Young, "Electrolytic Capacitors," in "Progress in Dielectrics," Vol. 5, Heywood and Co., Ltd., London (1962).
14. D. A. Vermilyea, *This Journal*, **110**, 345 (1963).
15. R. G. Keil and R. E. Salomon, *ibid.*, **115**, 628 (1968).
16. Ref. (8), p. 274.
17. R. M. Goldstein and W. J. Pettit, *This Journal*, **115**, 979 (1968).
18. "Handbook of Chemistry and Physics," 45th Ed., The Chemical Rubber Co. (1964-65).
19. N. F. Mott and R. W. Gurney, Electronic Processes in Ionic Crystals, Dover Ed., (1964).

Electrical Conductivity of Potassium Ferrite with the Beta-Alumina Structure

W. L. Roth and R. J. Romanczuk

General Electric Company, Research & Development Center, Schenectady, New York

ABSTRACT

The d-c conductivity of the beta-alumina form of potassium ferrite has been measured in crystals grown from KF flux and in crystals and polycrystalline specimens grown using solid state reactions. Both electronic and ionic conduction was observed. The former depends on the ferrous ion concentration, which can be varied by equilibration with varying partial pressures of oxygen at temperatures above 300°C. Typical conductivities ranging from $\sigma = 1.4 \exp(-3570/RT)$ to $12.3 \exp(-2420/RT)$ ohm^{-1} cm^{-1} were observed in specimens containing 0.22 and 1.6% Fe^{+2}, respectively. The electronic and ionic conductivities are comparable at 300°C and Fe^{2+} ~0.2%; the former becomes dominant at higher ferrous ion concentration and/or low temperature. Transient polarization-type phenomena were observed and tentatively explained by a model based on the coexistence of ionic conduction and electronic conduction due to the presence of Fe^{2+} and Fe^{3+} ions. Some observations are reported on the crystallography, existence range, and chemical composition of hexagonal potassium ferrite.

An isomorphous series of hexagonal compounds $A_2O \cdot nM_2O_3$, where A = Na, K, Rb and M = Al, Ga, Fe^{3+}, with n having reported values ranging from 5 to 11, crystallizes in the beta-alumina structure. The rates of exchange and self diffusion of sodium in beta-alumina (A = Na and M = Al) are very large (1) and comparable large alkali ion mobilities have been observed in hexagonal ferrites where A = Na, K and M = Fe^{3+} (2). The self diffusion coefficients of Na^+ and K^+ is hexagonal ferrites at 300°C are in the range 10^{-5} to 10^{-6} cm^2/sec, similar to ion mobilities in beta-alumina at the same temperature. The atomic arrangement of $NaAl_{11}O_{17}$ was described by Beevers and Ross (3) and Braun reported that $KFe_{11}O_{17}$ crystallized in the same structure (4). Recent investigations have shown the situation is more complex, with at least two crystallographically similar phases having been attributed to beta-alumina. X-ray and magnetic studies (5, 6) showed that the beta-alumina form of potassium ferrite was stable above 1100°C, but that between 900° and 1100° there was a potassium-rich phase with approximate composition KFe_7O_{11}. Scholder and Mannsmann (7) concluded the composition was $K_2Fe_{12}O_{19}$ and that $KFe_{11}O_{17}$ did not exist. A subsequent single crystal investigation by Rooymans *et al.* (8) suggested the formula was KFe_5O_8. It is possible that there are statistically disordered solid solutions which may exist over a broad homogeneity range.

The structure of beta-alumina may be regarded, for the present purposes, as a stack of identical "spinel-like blocks" with composition $\{Fe_{11}O_{16}\}^+$, held together by $\{KO\}^-$ layers. Since the alkali ions move

Table I. Lattice parameters of hexagonal potassium ferrites

N	A_0 (Å)	C_0 (Å)	C_0/N (Å)	Source	Ref.
2	5.929 ± 0.003	23.80 ± 0.03	11.90	Oxides; 1400°C	This work
2	5.932*	23.73*	11.87	Oxides	(9)
2	5.930 ± 0.002	23.80 ± 0.02	11.90	KF flux	This work
2, 3	5.939 ± 0.003	23.78 ± 0.02	11.89	KF flux crystal	This work
2, 3***	5.943 ± 0.003	23.82 ± 0.02	11.91	Oxides	(7)
3	5.927 ± 0.004	35.88 ± 0.04	11.96	Oxides; 1100°C	This work
3	5.939	35.76**	11.92	Oxides	(5)
3	5.925 ± 0.004	35.83 ± 0.04	11.94	KF flux	This work
3	5.94	35.7	11.9	KF flux crystal	This work
3	5.933	35.86	11.95	KF flux crystal	†

* Corrected to Å from kX units.
** Calculated for 3 block cell.
*** The x-ray pattern in Fig. 4 of Ref. (7) contains peaks from both $N=2$ and $N=3$ structures.
† M. Mansmann and M. Rooyman.

preferentially between the spinel blocks, a variable composition in the alkali containing layer may be particularly significant with respect to ionic transport.

Sample Preparation

Dense polycrystalline bars for conductivity measurements were made from cp K_2CO_3 and α-Fe_2O_3 to yield the composition $K_2O \cdot 6Fe_2O_3$. The dry powders were calcined in O_2 at 900°C, crushed and pressed into bars which measured ⅛ x ⅛ x ⅝ in. The bars were surrounded by excess powder from the prefire mix to minimize potassium loss, fired at 1400°C for ½ hr in O_2, then washed in distilled water to remove water soluble impurities. The final bars were about 93% dense, based on a theoretical x-ray density of 4.28 g/cm³ calculated for $K_2O \cdot 11Fe_2O_3$.

Single crystals suitable for conductivity measurements were produced by heating the conductivity bar specimens at 1400°C for 5 hr. The crystals were black and grew as thin hexagonal plates, 2-3 mm in diameter and up to 0.3 mm thick. X-ray photographs showed they were the beta-alumina form of potassium ferrite.

Potassium ferrite crystals also were grown from a 16KF:1Fe_2O_3 melt held in a Pt crucible at 1000°C for 4 hr, cooled at 10°/hr to 746°C, then furnace quenched to room temperature. After dissolving the excess KF in water, three types of crystalline product were found: (*a*) Black, hexagonal crystals, a few as large as 1-2 mm in diameter and 0.05 mm thick. Although x-ray photographs at first indicated they were single crystals identical to those crystallized from the oxides, long exposures revealed weak spots due to a syntactic intergrowth of a second phase, probably the rhombohedral KFe_5O_8 described by Rooymans *et al.* (8) (Fig. 1); (*b*) Transparent, extremely thin (less than 0.02 mm), red crystal plates. The x-ray photographs were of very poor quality, but the crystals appeared to be similar to KFe_5O_8 described above; (*c*) Small black crystals of α-Fe_2O_3. These crystals exhibited parasitic ferromagnetism and could be magnetically separated from the potassium ferrites.

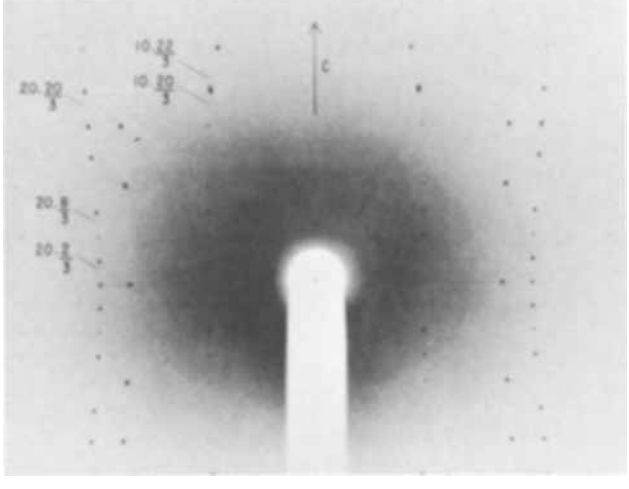

Fig. 1. X-ray photograph showing syntactic intergrowth of the "three block" phase in a "two block" crystal. The designated spots are noncoincident reflections which for convenience have been indexed on a beta-alumina cell. CoK_α rotation photograph.

Lattice Parameters and Existence Ranges

The unit cell parameters of the hexagonal potassium ferrites prepared in this work are compared in Table I with values taken from the literature. There are two structures which, if they have identical composition, may be regarded as polytypes. The unit cells are derived by stacking $N=2$ or $N=3$ hexagonal "spinel-like" blocks with dimensions A = 5.93Å and C = 11.9Å. The atomic arrangements, and consequently the free energies, of the two phases are very similar and some "crystals" contain mixed coherent regions of the $N=2$ and $N=3$ block sequences in which the A and C directions are coincident (Fig. 1). The small differences in unit cell dimensions observed in ferrites prepared in various ways may reflect differences in composition and hence the structures probably are not true polytypes.

The 2-block and 3-block structures were observed in crystals precipitated from KF, and in polycrystalline bars prepared from the oxides at temperatures below 1100°C. The 3-block phase is unstable with respect to 2-block when heated above 1100°C. If the system is open so that potassium may be lost, decomposition into a mixture of 2-block and α-Fe_2O_3 takes place in 4-5 days at temperatures as low as 650°C.

The potassium content of both 2- and 3-block phases is greater than the commonly accepted β-alumina composition $K_2O \cdot 11Fe_2O_3$. Thes chemical analyses of flux and oxide synthesized potassium ferrites are summarized in Table II. The analytical data cannot be interpreted unambiguously because the materials were not necessarily single phase. The composition derived from the analysis of flux grown 2-block crystals probably is the most reliable since α-Fe_2O_3 was separated magnetically and the x-ray patterns gave no indication of 3-block material (<5%). The potassium content of both 2- and 3-block crystals indicates an average composition near K_2O:Fe_2O_3 = 1:7, confirming the stoichiometric ratio 1:7.2 required to complete the chemical reaction.

Table II. Chemical analyses of potassium ferrites

K, %	Fe, %	Fe^{+2}, %	Source	Phases
6.9	63.1	0.22	Flux	2 Block
5.8	63.8	<0.5	Flux	2 + 3 Block
	62.3		Flux	3 Block
6.3	62.3		Oxide*	2 + 3 Block
7.4	63.7		$K_2Fe_{12}O_{19}$	Calculated
6.4	64.5		$K_2Fe_{14}O_{22}$	Calculated

* W. L. Roth and A. S. Cooper (5).

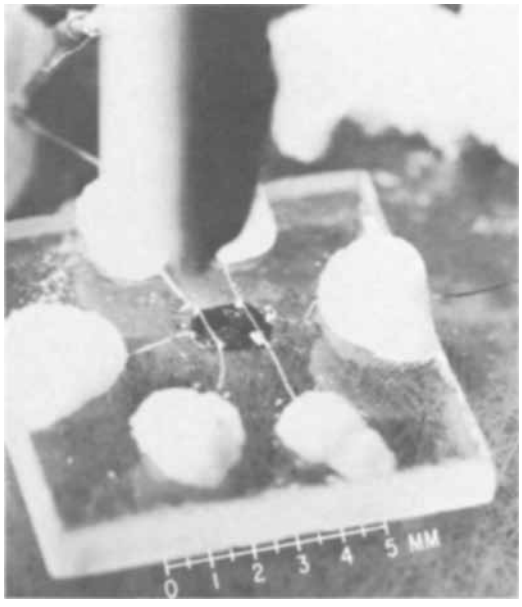

Fig. 2. Crystal-electrode assembly for 4-point conductivity measurements. The crystal is about 1.5 mm long and 0.2 mm thick. Current leads enter horizontally and the voltage probes are doubly soldered.

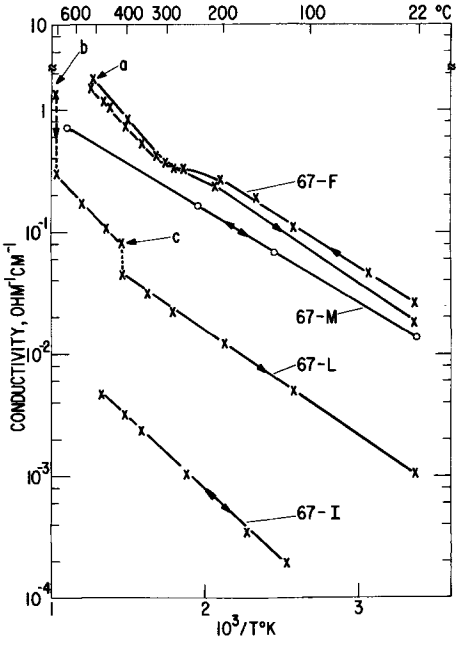

Fig. 3. Conductivity of potassium ferrite polycrystalline bars prepared from the oxides at 1400°C. 67-F, 67-M, and 67-L were fired ½ hr; 67-I for 5 hr. *(a)* Held in air at 500°C for 24 hr; *(b)* held in O_2 at 700°C for 42 hr; *(c)* held in O_2 at 400°C for 64 hr.

Conductivity Measurements

The d-c conductivities of single crystals and polycrystalline bars were measured with the 4-probe technique. Voltages were read with a Keithley model 200B electrometer and currents with an equivalent electrometer in conjunction with a Keithley decade shunt. The specimen-electrode assembly could be inserted in a 1 in. diameter cylindrical furnace.

A typical crystal-electrode assembly is shown in Fig. 2. Electrodes were either 0.002 in. Pt or Pt-Rh, attached to the crystal by In-Hg solder. The electrodes behaved satisfactorily up to 300°C but reaction with the solder occurred at higher temperatures. It was not necessary to support the larger polycrystalline specimens with the silica glass base so they were simply held in the furnace by 0.010 in. Pt wires wrapped around notches filed in the bars.

Conductivity of Polycrystalline Bars

Representative conductivity data for the polycrystalline bars are shown in Fig. 3 and summarized in Table III. At temperatures below 500°C the conductivities were reversible and described by $\sigma=\sigma_0 e^{-E/RT}$. Above 500°C the level of conductivity could be altered fairly rapidly by changing the oxygen partial pressure over the specimen.

Specimens 67-F, 67-L, and 67-M are typical of bars prepared by firing in O_2 for ½ hr at 1400°C. Specimen 67-I was prepared by firing in O_2 for 5 hr, instead of the customary ½ hr. The large decrease in σ is attributed to grain growth. Single crystal grains grew completely across the bar and these specimens were characteristically fragile and of lower density.

The shifts in σ at higher temperatures were shown to be due to oxidation-reduction reactions by isothermal experiments in which the atmosphere was changed and the conductivity then followed as a function of time (Fig. 4). Similar experiments in which the temperature was changed and the atmosphere was held constant were consistent with oxidation-reduction reactions taking place rapidly at temperatures above 450°C. The steady state conductivity depends on both the temperature and oxygen partial pressure, *i.e.*, at higher temperatures, a greater oxygen pressure is required to maintain the oxidized (low σ) state.

The changes in oxidation state were confirmed by chemical analysis. The Fe^{+2} concentration of conductivity bars equilibrated in 1 atm O_2 at 1400°C was 1.61%; after holding in O_2 at 650°C for 4½ days it decreased to 0.18%.

Single Crystal Conductivities

The potassium ferrite crystals grew as thin plates perpendicular to the C-axis and consequently four point conductivities were measured parallel to the C-face only. Representative conductivities of oxide-grown crystals, KF-flux grown crystals, and of crystals aged in O_2 are shown in Fig. 5.

Crystals 67-D and 67-Q were grown from the oxides. Both the magnitude and variation with temperature of the conductivity is the same as observed in the fine-grained polycrystalline specimens (Fig. 4) showing that the effects of grain boundaries and the solder used to attach the electrodes were negligible.

Crystals 2 and 3 were grown from KF flux. The conductivities were an order of magnitude smaller than those of oxide crystals or bars. This is consistent with the lower oxidation state of the latter which were grown at much higher temperature: the Fe^{+2} concentration in flux-grown crystals was 0.22%, compared to 1.41% in conductivity bars. The first experiment with crystal 2 was characterized by a high resistance and activation energy, but thereafter the system behaved reversibly. The same initially high resistance was observed with crystal 3, and subsequent runs indicated a discontinuity near 150°C, which decreased after the first heating cycle, and the σ-T characteristic appeared to be approaching that of crystal 2. In addition, the flux-grown crystals exhibited polarization or transient effects which are described in the next section. Several attempts to grow larger crystals from

Table III. Potassium ferrite conductivities

$$\sigma = \sigma_0 e^{-E/RT}$$

Type sample	No.	σ_0 (ohm-cm)$^{-1}$	E (cal mole^{-1})
Oxide grown bars[a]	3	6.4 ± 2.5	3370 ± 270
Oxide grown crystals	2	12.3 ± 8.2	2420 ± 500
Flux grown crystals[b]	2	1.4 ± 1.2	3570 ± 600

[a] Fe^{+2} = 1.61%.
[b] Fe^{+2} = 0.22%.

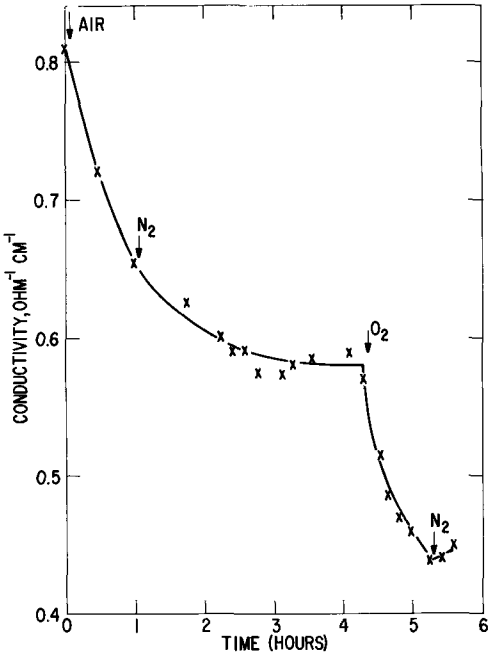

Fig. 4. Conductivity of polycrystalline potassium ferrite at 700°C as a function of oxygen partial pressure. Specimen 67-M, prepared from oxides by firing ½ hr in air at 1400°C. Arrows denote the times at which the gas flowing over the specimen was changed to the designated composition.

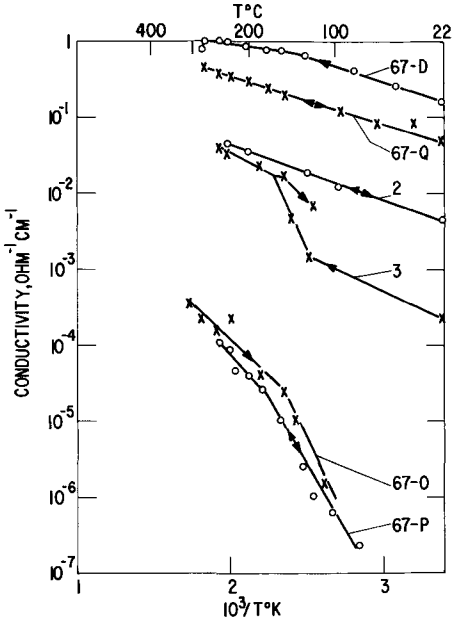

Fig. 5. Conductivity of potassium ferrite single crystals. 67-D and 67-Q, oxide grown crystals (1400°C, 5 hr); 2 and 3, fluoride flux-grown crystals; 67-O and 67-P, oxide grown crystals heated in O_2 at 650°C for 4½ days.

the flux which would be suitable for further conductivity measurements were unsuccessful and the source of these anomalies remains unresolved.

Oxide-grown crystals 67-O and 67-P were heated in oxygen at 650°C for 4½ days. The conductivity decreased as expected due to the reduction of Fe^{+2}, but in addition there was an unanticipated large increase in the activation energy. The x-ray pattern of a crushed crystal showed α-Fe_2O_3 was present, indicating the crystal had partially decomposed into K_2O and Fe_2O_3, or $KFeO_2$.

Transient Effects

The conductivities in Fig. 3, 4, and 5 are the average of instantaneous values, measured in the forward and reverse (current direction reversed) directions through the crystal, which usually agreed within a few per cent. The flux grown crystals, however, exhibited transient effects which were characterized, at constant current, by an increase to saturation, with time, in the voltage measured across the inner electrodes on the crystal.

A typical experiment illustrating this effect is shown in Fig. 6. A potential across the crystal produced an initial rapid rise ($<10^{-1}$ sec) of the probe voltage V_I which then increased to a steady-state value V_F after about 30 sec. The transient was reproducible and was observed in two crystals over a range of temperature and current density. Defining k as the reciprocal of the time t required for the voltage to rise by one-half the difference of the instantaneous value V_I and the steady state value V_F (or fall to $V_D/2$), then

$$1/t = k = k_0\, e^{-E_k/RT}\ \text{sec}^{-1}$$

with k_0 = 16.9 (±10) sec^{-1} and E_k = 4590 (±520) g-cal/mole. The steady state conductivities calculated for KF flux crystal 2 were about 30% less than the instantaneous values and had a slightly smaller activation energy. The magnitude of the voltage rise $\Delta V = V_F - V_I$ was approximately equal to V_D, and did not depend on temperature.

Discussion

The primary mechanisms to consider for electrical transport in alkali ferrites are ionic conduction through the alkali layer, or electronic semiconduction, either by hopping of electrons from Fe^{+2} to Fe^{+3} ions or 3*d* band conduction.

The ionic conductivity resulting from diffusion of potassium ions can be estimated with the Nernst-Einstein equation. According to Hever (2), the self diffusion coefficient of K^{42} in $M_2O{\cdot}7Fe_2O_3$, where M = $0.866K^+ + 0.134Na^+$, is given by $D = 1.05 \times 10^{-3}\, e^{-7210/RT}$ cm^2/sec. Assuming the same diffusion coefficient for pure potassium ferrite, two mobile K^+ per unit cell, and an average temperature 573°K

$$\sigma = D\frac{C\,Z^2\,F^2}{RT} = 9.4\, e^{-7210/RT}\ \text{ohm}^{-1}\,\text{cm}^{-1}$$

The ionic conductivity predicted by this equation at a temperature of 200°C is 4.5×10^{-3} ohm^{-1} cm^{-1}, somewhat smaller but of the same magnitude observed in flux grown crystals and in the polycrystalline bars after low temperature oxidation.

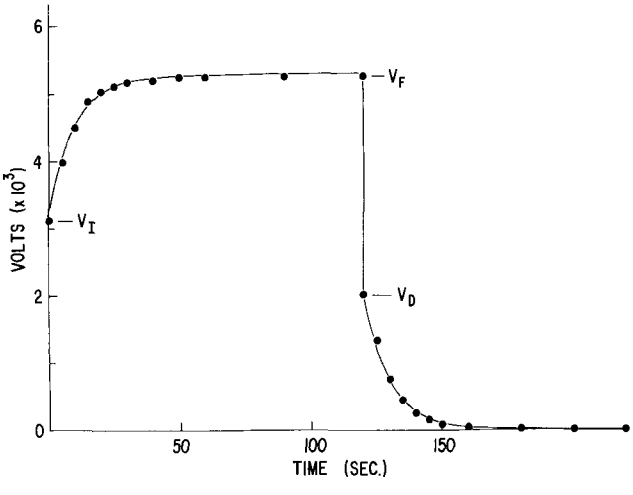

Fig. 6. Typical curve showing voltage build up and decay in fluoride flux-grown potassium ferrite. Crystal 2 at 212°C. V is voltage measured across the inner probes. Solid curve is calculated from Eq. [A], [B] in Appendix for R_1 = 1.11 x 10^4 ohms, R_2 = 6.85 x 10^3 ohms, C = 553 microfarads (see Fig. 8), and R_s = 10^7 ohms, V_0 = 7.7V.

Electronic conduction predominates at larger Fe^{+2} concentrations and the different levels of conductivity summarized in Table III can be explained if the number of carriers is proportional to the Fe^{+2} concentration.

Electrical charge neutrality requires that a reduction in the valence of iron be compensated by either a cation interstitial or an anion vacancy, so the concentration of defects responsible for ionic diffusion also may increase with the concentration of ferrous ion. The co-existence of ionic and electronic conduction suggests a possible explanation for the transients related to the proposal by Hever (2) that potassium ferrite be regarded as a parallel plate condenser in which one set of plates are the K^+ ionically conducting layers and the other set are the semiconducting spinel blocks containing Fe^{++} donors. The transient characteristics are described by the circuit shown in Fig. 7. The system is represented by the ionic resistance R_1 which is in series with capacitance C, both shunted by the parallel electronic resistance R_2. An analysis of the electrical responses for the network is given in the appendix.

The parameters derived from the transients measured in flux-grown crystals are shown in Fig. 8. The activation energy $E_1 = 6100 \pm 1000$ cal/mole determined for the ionic component is in reasonable agreement with the activation energy 7210 cal/mole measured for K^+ ion diffusion. The activation energy $E_2 = 2175$ cal/mole attributed to the electronic component may be compared with the value 2300 cal/mole obtained from the temperature dependence of the resistivity of the structurally similar hexagonal ferrite, $BaFe_2^{2+}\ Fe_{16}^{+3}\ O_{27}$ (Fe_2 IIW) [Fig. 45.5 of ref. (10)].

The apparent absence of a transient in the oxide-grown crystals is explained by R electronic $<<$ R ionic. Assuming the same values for the capacitance and the ionic resistivity, and substituting the observed values for R electronic, time constants of the order of 5 sec and voltage increments of 2×10^{-4}V would be expected. Transients of this magnitude would not have been observed in the present experiments.

The calculated equivalent capacitance of the flux grown crystal was 550×10^{-6} farads. Since the crystal volume was 1.4×10^{-4} cm^3, this corresponds to 3.9 farads/cm^3, in agreement with the capacitances of solid state batteries which ranged from 1.7 to 5.0 farads/cm^3 at 300° and 500°C (2).

The internal consistency of the transient analysis, and the agreement of the parameters derived from it with those obtained from diffusion and electrochemical

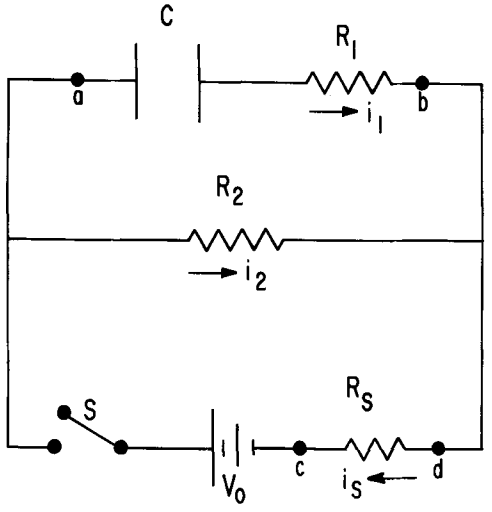

Fig. 7. Equivalent circuit for transient effects observed in flux crystals. V_{ab} corresponds to voltage measured across inner probes on crystal, and V_{cd}/R_s corresponds to current (i_2) flowing through the crystal.

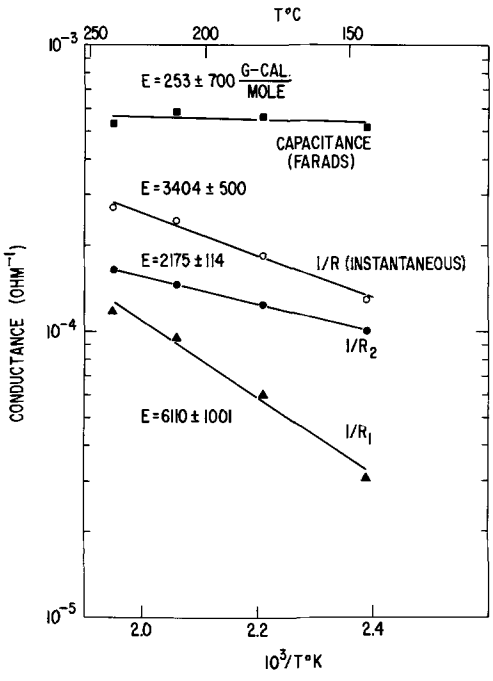

Fig. 8. Log conductance vs. $1/T$ for parameters derived from the transient analysis.

cell measurements, support the theory developed in this paper. However, there are other possible explanations for the origin of the capacitance effects, particularly those based on concentration cells in the vicinity of the electrodes. The possibility that oxide ions were partially replaced by fluoride ions cannot be excluded, although mass spectrographic analysis indicated the fluoride content of the flux grown crystals was negligible. In addition, the flux used to attach the electrodes is a potential source of electron donors, for example, by reactions of the type $Hg \rightarrow Hg^+ + e^-$. Pulse and a-c methods might be used to distinguish some of these alternatives, but such investigations would be severely limited by the size of the crystals presently available.

Conclusions

The electrical conductivity in potassium ferrite crystals with the beta-alumina structure is due to a combination of electronic and ionic conductivity. The electronic portion depends on the Fe^{2+} concentration, which in turn can be controlled by equilibration with varying partial pressures of oxygen. The ionic conductivity is due to diffusion of K^+ ions through the alkali containing layers and its magnitude and temperature dependence agree with the predictions of the Nernst-Einstein equation. At 300°C electronic semiconduction predominates when the Fe^{2+} concentration is greater than 1%, but for Fe^{2+} concentrations of about 0.2%, the electronic and ionic conductivities are comparable.

Acknowledgments

We are indebted to R. C. DeVries and J. F. Fleischer for the crystals grown from $KF\text{-}Fe_2O_3$, and to J. W. Szymaszek for the synthesis of conductivity bars and crystals from the oxides. The authors profited from helpful discussions with R. J. Charles, S. P. Mitoff, D. A. Vermilyea, and F. G. Will.

Manuscript submitted Jan. 13, 1969; revised manuscript received April 3, 1969.

Any discussion of this paper will appear in a Discussion Section to be published in the June 1970 JOURNAL.

APPENDIX

Elementary circuit analysis for the network of Fig. 7 gives the following (at $t = 0$, switch S closed)

$$i_1 + i_2 - i_s = 0$$
$$V_o - i_2 R_2 - i_s R_S = 0$$
$$i_2 R_2 - \frac{q}{C} - i_1 R_1 = 0$$

Combining these equations and remembering that

$$\frac{dq}{dt} = i_1$$

Then

$$V_o = R_A\left(\frac{dq}{dt}\right) + \frac{q}{C} \quad (\Delta)$$

where

$$R_A \equiv \frac{R_1R_2 + R_1R_S + R_2R_S}{R_2}$$
$$\Delta \equiv \frac{R_2 + R_S}{R_2}$$

also

$$q = \frac{V_oC}{\Delta}\left[1 - \exp\left(-t\Delta/R_AC\right)\right]$$

and since $V_{ab} = \frac{q}{c} + i_1 R_1$

$$V_{ab}\ (\text{charging}) = \frac{V_o}{\Delta} - V_o\left[\frac{1}{\Delta} - \frac{R_1}{R_A}\right]\left[\exp\left(\frac{-t\Delta}{R_AC}\right)\right] \quad [A]$$

After the switch has been closed for a long time $\left(t >> \frac{R_AC}{\Delta}\right)$, it is opened. A similar argument yields

$$V_{ab}\ (\text{decaying}) = \frac{V_oR_2}{(R_1 + R_2)\Delta}\left[\exp\left(\frac{-t}{(R_1 + R_2)C}\right)\right] \quad [B]$$

$$V_I \equiv V_{ab}\ (\text{charging } t = 0) = V_o\left\{\frac{R_1R_2}{R_1R_2 + R_1R_S + R_2R_S}\right\} \quad [1]$$

$$V_F \equiv V_{ab}\left(\text{charging } t >> \frac{R_AC}{\Delta}\right) = V_o\left\{\frac{R_2}{R_2 + R_S}\right\} \quad [2]$$

$$V_D \equiv V_{ab}\ (\text{decaying } t = 0) = V_o\left\{\frac{R_2^2}{(R_1 + R_2)(R_2 + R_S)}\right\} \quad [3]$$

Defining time constants

$$t_{c1/2} \equiv t\left(V_{ab} = \frac{V_F + V_I}{2}\right) = \left(\frac{R_1R_2 + R_1R_S + R_2R_S}{R_2 + R_S}\right)C \ln 2 \quad [4]$$

$$t_{d1/2} \equiv t\left(V_{ab} = \frac{V_D}{2}\right) = (R_1 + R_2)\,C \ln 2 \quad [5]$$

REFERENCES

1. Yung-Fong Yu Yao and J. T. Kummer, *J. Inorg. Nucl. Chem.*, **29**, 2453 (1967).
2. K. O. Hever, *This Journal*, **115**, 826, 830 (1968).
3. C. A. Beevers and M. A. S. Ross, *Z. Krist.*, **97**, 59 (1937).
4. E. W. Gorter, *Philips Research Repts.*, **9**, 363 (1954).
5. W. L. Roth and A. S. Cooper, *General Electric Rep.*, **60**, RL2461M.
6. W. L. Roth and F. E. Luborsky, *J. Appl. Phys.*, **35**, 966 (1964).
7. R. Scholder and M. Mansmann, *Z. anorg. u. allgem. Chem.*, **321**, 246 (1963).
8. C. J. M. Rooymans, C. Langerais, and J. A. Schulkes, *Solid State Communications*, **4**, 85 (1965).
9. P. Braun. *Philips Research Repts.*, **12**, 491 (1957).
10. J. Smit and H. P. J. Wijn, "Ferrites," Fig. 45.5, p. 234, John Wiley and Sons, New York (1959).
11. V. Adelskold, *Arkiv Kemi, Min. Geol.*, **12A**, 1 (1938).
12. H. Saalfeld, H. Matthies, and S. K. Datta, *Ber. deut. keram. Ges.*, **45**, 212 (1968).

Polymeric Electron Beam Resists

H. Y. Ku[1] and L. C. Scala

Westinghouse Research Laboratories, Pittsburgh, Pennsylvania

ABSTRACT

Crosslinking polymers may be used as negative acting resists. The product of the minimum charge dose Q required and the weight average molecular weight $\overline{M}_w$ is a constant and is a characteristic of the polymer. At an electron beam voltage of 10 kV, this Q-M product is found experimentally to be 6.3 coul-g/cm^2-mole for polystyrene, 1 coul-g/cm^2-mole for poly(vinyl chloride), and 14 coul-g/cm^2-mole for polyacrylamide. Degrading polymers may be used as positive acting resists. Their average molecular weights have only a very minor effect on their efficiency as positive resists. Their glass transition temperatures T_g are an important factor. It is recommended that these resists be prebaked at $T > T_g$, stored and developed at $T < T_g$, and postbaked at $T > T_g$.

The technology of microelectronics moved from discrete components to integrated circuits and is moving toward monolithic subsystems. The increase in packing density requires reduction in circuit size and, hence, in the component size. The decrease in component size has been limited by the resolution of conventional photoresist operation to about 2-3μ. Electron beam fabrication (1) offers much improved resolution.

Electron beam fabrication requires etch resists which are sensitive to an electron beam. Conventional photoresists, *i.e.*, the family of negative acting resists (KPR, KMER, KTFR) from Kodak and the positive acting resist AZ1350 from Shipley, were found to be exposable by electron beams (1-5). Although Kodak gives no information about the chemical composition of their resists, some of them (KPR) are believed to be vinyl polymers (6) or their derivatives with some sensitizer. Under uv light, the vinyl functions of neighboring chains crosslink forming an insoluble three-dimensional network. Others (KTFR) are believed to

[1] Present address: IBM, Thomas J. Watson Research Center, Yorktown Heights, New York.

be polymerized isoprene dimers. The composition of Shipley's AZ1350 is not revealed, and its action is not known definitely.

Because of the high sensitivity of these resists to uv and even visible light, some crosslinking or insolubilizing chemical reaction occurs on standing. They are not stable, and shelf life is short. These resists are quite satisfactory in fabricating devices of conventional size, but, since their resolution deteriorates with age and varies from batch to batch, they are not satisfactory in the fabrication of devices of very small dimensions.

Electron beam exposure of resists can be done in two ways. One way is to expose the resist with a single beam of electrons in an electron microscope or a similar instrument (1). A more recent development is to expose the complete wafer using a complete pattern of electrons employing a uv sensitive photocathode as an electron source (7). In this case the resist is exposed to the electrons with a background of strong uv light. Photoresists cannot be used and electron beam resists insensitive to uv light are needed.

Etch resists are generally high molecular weight polymers. Haller *et al.* (8) have shown that poly(methyl methacrylate) is a positive acting electron resist of superior resolution. It is not sensitive to uv light and is very stable. This paper describes the general properties of polymeric electron resists, both positive and negative, and reports some results of our investigation of electron resists that are also not sensitive to uv or visible light.

General Characteristics of Electron Resists

High polymers undergo physical and chemical change under ionizing radiation. Physical properties such as color, impact strength, elastic constants, and tensile strength are altered as the radiation dose increases. Gases are liberated indicating a change in the chemical nature of the polymer. The most important fact pertaining to their use as resists is that both crosslinking and scission of polymer chains occur. In many cases one dominates the other, and a polymer either crosslinks or degrades depending on its nature. When a polymer crosslinks, the chains link to each other forming a complex structure, and its average molecular weight increases. A polymer is degraded if the chains undergo random scission resulting in chains of decreasing molecular weights as the dose increases. Eventually, the degraded polymer may dissolve in a solvent in which the original polymer is not soluble. Polyethylene, polyacrylates, polyacrylamide, polystyrene, poly(vinyl chloride), and polysiloxanes are crosslinking polymers; polyisobutylene, polymethacrylates, poly(α-methylstyrene), and cellulose are degrading polymers. For vinyl polymers it is known that when each carbon atom of the polymer chain carries at least one hydrogen atom, the polymer crosslinks, and that if a tetrasubstituted carbon atom is present in the monomer unit, the polymer degrades.

Most of these polymers, without added light sensitizers, are insensitive to uv and visible light. They have much longer shelf life and are much more stable than conventional photoresists.

When a crosslinking polymer film coated on a surface is exposed selectively to an electron beam, the irradiated portion crosslinks. With sufficient dose the crosslinked polymer forms a three-dimensional network and becomes insoluble in the usual solvent for the polymer. The film can be "developed" by immersing it in the solvent for the polymer to dissolve away the unexposed polymer film, leaving the three-dimensional network of the polymer in the exposed area. A crosslinking polymer is a negative-acting electron resist if the crosslinked polymer is unaffected by the etching solution.

When a degrading polymer film is exposed to an electron beam, random scission occurs and the average molecular weight decreases. The film may be developed by the method of fractional solution, *i.e.*, soaking in a poor solvent which dissolves away the molecules of low molecular weight but not the ones of high molecular weight. During development the exposed film is washed away leaving the unexposed film on the wafer. If the original polymer is unaffected by the etching solution, the polymer is a positive-acting resist.

The effect of the radiation on polymer chains is usually measured in terms of the radiation chemical yield G. It is defined as the number of chemical events occurred per 100 eV of energy absorbed. The particular event occurred is usually specified within parentheses following the symbol G. Thus, the expression $G(\text{c.l.}) = 2$ means that two crosslinking events occur for every 100 eV of energy absorbed in the polymer. An electron losing E eV of energy in passing through a crosslinking polymer film will create $E \cdot G(\text{c.l.})/100$ crosslinks involving twice as many crosslinked monomers. Similarly, a scission yield is designated by $G(\text{s})$ and the number of scission events is $E \cdot G(\text{s})/100$. The energy loss E is smaller for a more energetic beam. Hence the efficiency of a 20 kV electron beam is lower than that of a 10 kV electron beam. The yield, $G(\text{c.l.})$ or $G(\text{s})$, is naturally dependent on the nature of the polymer irradiated and on the nature of the bombarding radiation. For electron energy of 10 kV or more and polymer films of 1μ or less, the energy loss may be considered uniformly distributed and the crosslinking or scission events are completely random.

While the average molecular weight $\overline{M}$ of a degrading polymer used as a positive resist has only a minor effect on the efficiency of the system, the efficiency of a crosslinking polymer used as a negative resist is greatly affected by $\overline{M}$.

When a polymer is used as a negative-acting resist, the polymer must be sufficiently crosslinked to form a three-dimensional network insoluble in the solvent for the original linear chain polymer. Assuming no intramolecular crosslinking and only single crosslinking between two molecules, Stockmayer (9) showed that for an arbitrary molecular weight distribution a three-dimensional network occurs when there is on the average one crosslinked monomer per molecule of weight average molecular weight, or one crosslink for two molecules of weight average molecular weight. For a given weight of material the number of crosslinks required is inversely proportional to the weight average molecular weight. The number of crosslinks created by each passing electron is $E \cdot G(\text{c.l.})/100$. The total number of crosslinks per square centimeter of film created by a charge dose density Q coulomb/cm^2 is $Q \cdot E \cdot G(\text{c.l.})/100q$, where q is the electronic charge. The number of weight average molecules per square centimeter is $dA/\overline{M}_w$, where d is the sheet density of the film in grams per square centimeter, A is Avogadro's number, and $\overline{M}_w$ is the weight average molecular weight of the polymer. Therefore, the minimum charge dose required for achieving a three-dimensional network is

$$Q = 50\, q\, dA/EG(\text{c.l.})\overline{M}_w \qquad [1]$$

which is inversely proportional to the crosslinking yield $G(\text{c.l.})$, the molecular weight $\overline{M}_w$, and the energy E absorbed per unit area of the film.

The significant fact is that the minimum dose required for a negative electron resist is inversely proportional to the weight average molecular weight $\overline{M}_w$ of the polymer. In other words, the Q-M product, the product of the minimum charge dose Q and of the molecular weight $\overline{M}_w$, is a constant and is a characteristic of the polymer. For better efficiency, a polymer with smaller Q-M product is preferred over one with a large Q-M product, and a polymer of high $\overline{M}_w$ is preferred over the same polymer of low $\overline{M}_w$.

The case for a degrading polymer used as positive resist is entirely different. We assume that the scission is completely random occurring at the bonds between the monomers of molecular weight M_o. Let $\overline{M}_n$ be the number average molecular weight of the polymer. The number of molecules of molecular weight $\overline{M}_n$ in a film of sheet density d g/cm^2 is $dA/\overline{M}_n$, where A is as before Avogadro's number. Each molecule has $(\overline{M}_n/M_o - 1)$ bonds and the total number of bonds is $dA(1/M_o - 1/\overline{M}_n) \cong dA/M_o$. For an electron dose of Q coul/cm^2, the number of scission events is $Q\,E\,G(s)/100\,q$. Hence the probability of scission at a bond is

$$p_s = Q\,E\,G(s)\,M_o/100\,q \cdot dA \qquad [2]$$

The number of bonds in each molecule of molecular weight of $\overline{M}_n$ is $\overline{M}_n/M_o$, and the number of scission fragments is $p_s\overline{M}_n/M_o + 1$. The number average molecular weight of these fragments is

$$\overline{M'}_n = \overline{M}_n/[p_s\overline{M}_n/M_o + 1]$$

or

$$1/\overline{M'}_n = p_s/M_o + 1/\overline{M}_n \qquad [3]$$

If $p_s\overline{M}_n/M_o >> 1$, then

$$\overline{M'}_n = M_o/p_s \qquad [4]$$

Combining [2] and [4], we get

$$\overline{M'}_n = 100\,q\,d\,A/Q\,E\,G(s)$$

If $\overline{M'}_n$ is small enough so that only the scission fragments, but not the original polymer, dissolve in a poor solvent, then the resist is developed. The value $\overline{M'}_n$ depends on the developer selected and determines the minimum electron dose Q required for exposing the resist given by the equation

$$Q = 100\,q\,d\,A/E\,G(s)\,\overline{M'}_n \qquad [5]$$

The minimum dose Q is independent of the molecular weight $\overline{M}_n$ of the original polymer. Hence, the efficiency of a positive electron resist does not depend on the average molecular weight $\overline{M}_n$ of the polymer used if $\overline{M}_n$ is sufficiently large. Furthermore, the initial molecular weight distribution is also not important. After a few scissions per molecule of $\overline{M}_n$, any distribution will approach closely the "most probable distribution" given by

$$N(x) = Np_s \exp(-p_s x)$$

$$= Np_s \exp(-M/\overline{M'}_n) \qquad [6]$$

where x is the degree of polymerization of the scission product ($x = M/M_o$) and N is the total number of molecules after scission (10). For this exponential distribution, the weight average molecular weight $\overline{M}_w$ is twice the number average $\overline{M}_n$. Equation [4] assumes the relation $p_sM/M_o >> 1$. This inequality simply means that the number of scissions per molecule is large. This is true and will be illustrated later in the case of the positive resist poly(methyl methacrylate). Equations [1] and [5] appear similar, but their meanings are quite different.

An important characteristic of a polymer is its glass transition temperature T_g. Above this temperature the polymer chains can slide over each other and the polymer is soft, pliable, and rubberlike. Below this temperature the atoms can only vibrate about their equilibrium positions at fixed distances from each other, but the chains cannot slide over each other. The polymer is hard, brittle, and glasslike. The glass transition temperature is a second order transition temperature and is usually determined by measuring the temperature at which the volume coefficient of expansion α changes. For polystyrene, α is 2×10^{-4} below T_g (100°C) and is 6×10^{-6} above T_g.

At temperatures above its glass transition temperature T_g, a polymer deforms easily under stress. An exposed and developed film will change its shape if it has some residual stress. The developed film will not maintain its definition, and the film is not suitable for high resolution application. Such loss of resolution due to creep in a polyisobutylene film ($T_g = -70$°C) was noticed by Haller *et al.* (8). The creep may be minimized by prebaking the coated film at a temperature above T_g to relax the stress created in the film during coating and by storing the film at a temperature below T_g.

The development of a resist, either positive or negative, is based on the principle of fractional solution. Flory (11) has shown that $v_1(x)$ is the volume fraction of polymer of degree of polymerization x in the solid phase and $v_2(x)$ is the corresponding volume fraction in the solution phase; then

$$v_2(x)/v_1(x) = \exp(-\sigma x) \qquad [7]$$

where σ is a function of the concentrations of the polymer in the solution, of the number average molecular weight, and of the interaction energy between the polymer molecules and the solvent molecules. The quantity σ is not calculable; however, it is important to note that the ratio $v_2(x)/v_1(x)$ is a continuous function of x. The extracted polymer fraction contains a wide range of molecular weights, with a higher concentration of molecules of low molecular weight than the solid polymer had originally. In developing an exposed positive resist, not only the polymer fragments in the exposed area will be removed but also some smaller molecules in the unexposed area, thus increasing the probability of pin-hole formation. This unwanted solution of smaller molecules from the unexposed area occurs if the development is performed at a temperature above T_g. However, below T_g the polymer chains cannot slide along each other and small molecules are not easily extracted, being held rigidly by other molecules. Similarly, if an exposed negative resist is developed at temperatures above T_g, some smaller three-dimensional network may be extracted away. This extraction will be much less likely if the film is developed at a temperature below T_g. After development, holes or discontinuities may be formed in the film and along the edge of the developed film vacated by the extracted molecules. These holes may be closed if the film is baked at temperatures above T_g. Therefore, a resist film should be prebaked at $T > T_g$, exposed, developed, and stored at $T < T_g$, and postbaked at $T > T_g$. As the resist is usually processed and stored at room temperature, the glass transition temperature of the polymer must be above the room temperature, preferably above 350°K.

The number of known polymers is large: about one thousand are listed in the "Polymer Handbook" (12). Only a small number has been examined for the effect of ionizing radiation. Among those polymers that are known to be crosslinked or degraded by scission, only a few have reasonably high glass transition temperatures. Crosslinking polymers of low T_g such as polybutadiene ($T_g = 180$°K) and polydimethylsiloxane ($T_g = 150$°K) are not good negative resists. Degrading polymers of low T_g such as polyisobutylene ($T_g = 200$°K) and poly(vinylidene chloride) ($T_g = 254$°K) are not good positive resists. The number of polymers that can be used as high resolution electron resists is therefore rather limited.

Negative Electron Resists

Crosslinking polymers have been investigated extensively. There are several known crosslinking polymers that have T_g's above room temperature. Table I lists some crosslinking polymers together with their glass transition temperatures T_g and the crosslinking yield G(c.l.).

Table I. Negative electron beam resists

Polymers	T_g, °K	G(c.l.)	Density, g/cm³
Polystyrene	370	0.04	1.05
Polyacrylamide	>350	0.02	1.06
Poly(vinyl chloride)	354	0.3	1.41

Polystyrene.—Polystyrene is resistant to all alkalis and weak acids, but is attacked slowly by strong oxidizing acids. It dissolves easily in chlorinated hydrocarbons or aromatic hydrocarbons. The density of polystyrene is 1.05 and the crosslinking yield G(c.l.) is about 0.04 (13). For a typical film of 5000Å the sheet density is 5.25×10^{-5} g/cm². The energy loss E by an electron beam passing through a thin film of polystyrene is difficult to estimate. One reason is that the energy loss mechanism is a complicated one; in addition, the dissipation is not uniform through the film. Another known factor is the back scattering of electrons from the oxidized silicon into the resist film. Ehrenberg and King (14) measured the energy loss of 10 kV electrons in bulk polystyrene as a function of penetration depth. Assuming the energy loss in a polystyrene film is the same as that in bulk polystyrene of the same depth and neglecting the difference in back scattering at the resist-substrate interface, we have $E = 800$ eV for a film of 5000Å. As shown by Eq. [1], the minimum exposure dose required is inversely proportional to the weight average molecular weight $\overline{M}_w$. Three lots of polystyrene[2] of $\overline{M}_w$ of 20,000, 35,000, and 230,000 were tested. Toluene was used as a solvent. The concentration was 5% for the highest polymer and 10% for the two lower polymers. The films were exposed by 10 kV electron beams and were developed by soaking in xylene for 30 sec and then by spraying with xylene twice for 2 sec each. The minimum exposure was found to be inversely proportional to the molecular weight $\overline{M}_w$. The experimental values were 3×10^{-4}, 2×10^{-4}, and 2.5×10^{-5} coul/cm², respectively, for the three lots of polystyrene of increasing molecular weight. The observed Q-M products are 6, 7, and 5.8 coul-g/cm²-mole, respectively, giving an average value of 6.3 under 10 kV electron beam. The Q-M product calculated by Eq. [1] is 7.9 coul-g/cm²-mole. Considering the uncertainties in the values of E and G(c.l.) and the difficulties in observing the value Q, the agreement between the observed and calculated values of the Q-M product is remarkable.

The exposed film is a three-dimensional network insoluble in xylene. It can be stripped by heating to about 100°C in the commercial stripper J100.

As stated above, polystyrene of high molecular weight is preferred over polystyrene of low molecular weight. However, the resolution of the polystyrene of $\overline{M}_w$ of 230,000 is not as good as that of $\overline{M}_w$ of 20,000. The edges of the developed polymer film pattern have a sloping bank less than 1μ wide for the polystyrene of $\overline{M}_w$ of 20,000, but they have a sloping bank of 2μ for the one with $\overline{M}_w$ of 230,000. This is due to the wider molecular weight distribution of the higher polymer with respect to that of the lower polymer.

When an electron beam penetrates into a polymer film coated on a surface, scattering increases the beam cross-sectional area in the film. Although the beam density decreases very rapidly along the normal to the edge of the irradiated area, molecules of very high molecular weight become crosslinked and remain on the surface after development, thus creating a wide sloping bank along the edges of the developed film pattern. The resolution can be improved by fractionating the polymer to attain a sharp cut-off in the high molecular weight region of the molecular weight distribution curve. This has been substantiated as follows. A dilute solution of polystyrene of $\overline{M}_w$ of 230,000 in benzene (5% solids) was prepared and ethanol was added. A 56% fraction of the dissolved solid consisting of most of the high molecular weight material was thus removed from the solution. More ethanol was added to the remaining supernatant solution, and a second fraction of 33.8% of the original polymer was separated. The viscosity of this fraction in benzene at 25°C was measured with a Cannon-Fenske viscometer and the intrinsic viscosity was found to be 0.326. Using the equation given by Orofino and Wenger (15)

$$[\eta] = 9.18 \times 10^{-5} M^{0.743}$$

we found that $\overline{M}_w = 60{,}000$. The required minimum charge dose was found to be about 1×10^{-4} coul/cm². The width of the sloping bank along the edge of the developed pattern is less than 1μ.

Molecules of molecular weight much less than M_w are also not desirable. They are less likely to get crosslinked and are dissolved away during development, thus increasing the probability of pinhole formation. Hence, polystyrene of high molecular weight but very narrow molecular weight range is recommended.

Poly(vinyl chloride).—Poly(vinyl chloride), PVC, is resistant to most acids, alkali, and common inexpensive organic solvents. Irradiation in air causes degradation, but irradiation in vacuum induces crosslinking. The crosslinking yield is estimated to be about 0.3 (16). As bought, PVC powders[2] dissolve easily in cyclohexanone. The resist solution used, 10% by weight, has excellent film-forming properties. Uniform films exhibiting brilliant colors can be easily obtained by the usual spin-coating method. The films were exposed to 10 kV electrons and developed in cyclohexanone. The minimum dose Q was found to be about 3×10^{-5} coul/cm².

Measuring the $\overline{M}_w$ by the light scattering method, Moore and Hutchison (17) found that the intrinsic viscosity of PVC in cyclohexanone at 25°C is

$$[\eta] = 174 \cdot 10^{-5} M^{0.55}$$

The intrinsic viscosity of the PVC we used was determined with Cannon-Fenske viscometer and was found to be 0.522. Hence, the average molecular weight of our PVC is $\overline{M}_w = 32{,}000$, and the Q-M product is about 1 coul/cm².

The density of PVC is 1.41 g/cm³. A 5000Å film has a sheet density of 7×10^{-5} g/cm². The energy loss of a 10 kV electron beam in passing through such a film is expected to be larger than that through a polystyrene film but lower than that through a Cu or Au film of the same sheet density. A value of $E = 1200$ eV is taken as the energy loss of 10 kV electron in passing a PVC film of 5000Å. Using [1], we found that the calculated Q-M product is 0.94 coul-g/cm²-mole, in excellent agreement with the observed Q-M product.

Polyacrylamide.—Polyacrylamide is a water soluble polymer. Its solubility in water is low, about 2%. Because of the low concentration and the low vapor pressure of the solvent water, the coating process is time consuming. Nevertheless, uniform films can be obtained. The minimum dose required was about 3×10^{-6} coul/cm². The exposed film was developed in deionized water and then rinsed in methanol, a nonsolvent. The crosslinked polyacrylamide is not soluble in water, but is swelled by aqueous solutions such as buffered HF, dilute acids, and alkalis. Hence, polyacrylamide is not an etch resist for aqueous acids or alkalis. The crosslinked polymer is resistant to concentrated phosphorous acid and is therefore a useful aluminum etch resist. It may also be used as a mask for sputtering etch.

The polyacrylamide[2] we used was not fractionated. The distribution of molecular weight is wide, and the resolution is poor. The edge of the developed re-

[2] Acquired from Monomer-Polymer Laboratories, Borden Chemical Company, Philadelphia, Pa.

sist pattern has a sloping bank of 2μ. Again, the resolution can be improved by removing the high molecular weight fraction of the polymer at the expense of slightly increased dose requirement.

The viscosity of the polyacrylamide used was measured in water at 30°C and the intrinsic viscosity was found to be $[\eta] = 13.6$. Scholtan (18) gave the following viscosity-molecular weight relation for polyacrylamide in water at 30°C

$$[\eta] = 6.31 \times 10^{-5} M^{0.80}$$

Hence, the molecular weight $\overline{M}_w$ of our polyacrylamide is 4.7×10^6 and the Q-M product is 14 coul-g/cm^2-mole.

Polyacrylamide has about the same density as polystyrene. The sheet density for a 5000Å film is 5.3×10^{-5} g/cm^2. Assuming the energy dissipation of 10 kV electrons in polyacrylamide is the same as that in polystyrene, we have $E = 900$ eV. The crosslinking yield G(c.l.) was not known. However, using the experimental values of Q and $\overline{M}_w$ and the estimated values of E, we found that the crosslinking yield of polyacrylamide under 10 kV electron is G(c.l.) = 0.02.

Positive Electron Resists

As discussed above, positive electron resists are long chain polymers which degrade by chain scission under electron bombardment. Degrading polymers have not been investigated intensively, for only a few are known to have a reasonably high glass transition temperature. Table II shows a few of the polymers that are useful as positive electron resists.

Several other styrene derivatives having tetrasubstituted carbon atoms also have high T_g. However, it is well known that a benzene ring will lower scission yield. Therefore, any styrene derivative, even if it is a positive resist, will have a low efficiency.

Poly(methyl methacrylate).—Poly(methyl methacrylate), PMMA, is very stable (unaffected by uv) and is resistant to most acids. Using 95% ethanol (5% water) as a developer, we found that the minimum exposure required for a 10 kV electron beam is 5×10^{-5} coulomb/cm^2 (19). The density of PMMA is 1.2 g/cm^3 and the molecular weight M_o of the monomer is 100.11. For a typical film of 5000Å the sheet density d is 6×10^{-5} g/cm^2. Assuming the energy loss of electron in a PMMA film is the same as that in a polystyrene film, we have $E = 1000$ eV. Assuming G(s) = 1.65 (20), we get from Eq. [2]

$$P_s = 0.014$$

For PMMA of molecular weight 100,000, $P_s\overline{M}_n/M_o = 14$. Each number average molecule has 14 scissions resulting in 15 fragments and the average weight of the scission fragments is, by [3]

$$\overline{M}_n' = 6700$$

If the initial molecular weight $\overline{M}_n$ is infinite, then the last term in [3] is zero and we have $\overline{M}_n' = 7100$. This can be reduced to 6700 by a 6% increase in the electron dose Q from 5×10^{-5} to 5.3×10^{-5} coul/cm^2, which is a very small increase. Hence, the initial molecular weight $\overline{M}_n$ of PMMA has very little effect on the final molecular weight $\overline{M}_n'$ after scission.

The number of scissions per number average molecule is large, and the molecular weight distribution follows Eq. [6]. Figure 1 shows the weight distribution

Table II. Positive electron beam resists

Polymer	T_g, °K	G(s)	M_o	Density, g/cm^3
Poly(methyl methacrylate)	378	1.65	100.11	1.20
Poly(α-methyl styrene)	373	0.25	130.18	0.906
Polymethacrylonitrile	400	1.0	67.09	1.10

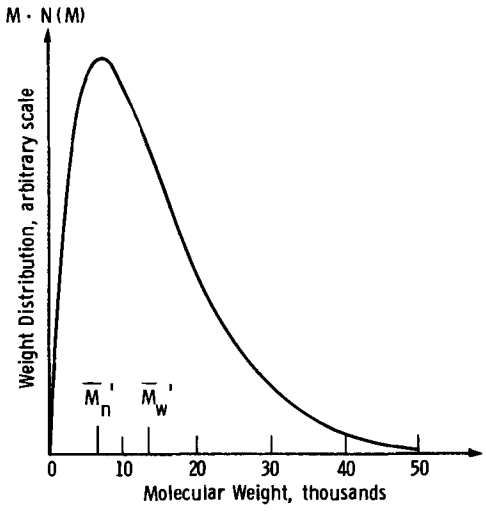

Fig. 1. Molecular weight distribution of polymethyl methacrylate (initial M.W. 100,000) after electron dose of 5×10^{-5} coul/cm^2 at 10 kV.

of PMMA as a function of the molecular weight after an electron dose of 5×10^{-5} coul/cm^2 at 10 kV. It can be seen that the tail of the distribution curve extends appreciably over 6 $\overline{M}_n'$ or 40,000. Since the developer is apparently able to dissolve molecules of such size, it is imperative that the molecular weight $\overline{M}_n$ of PMMA be relatively high, 100,000 or over, and that the fraction of molecules of $M < 50{,}000$ be very low to avoid pin-hole formation during developing. More generally, the distribution curve of the scission fragments must be well separated from that of the original polymer.

Using a 30/70 mixture of methyl ethyl ketone and isopropanol as a developer, Haller *et al.* (8) also found that the minimum exposure at 10 kV is 5×10^{-5} coul/cm^2 which corresponds to our results with ethanol as a developer. This coincidence is rather fortuitous as it is difficult to determine the minimum dose exactly. Nevertheless, it does indicate that the two different developers have about the same solvent power.

Poly(α-methyl styrene).—Poly(α-methyl styrene) has a scission yield G(s) = 0.25 (21), a monomer molecular weight of 130.18, and a density of 0.906. The sheet density of a 5000Å film is $d = 4.53 \times 10^{-5}$ g/cm^2. Assuming the energy loss in this material is the same as that in polystyrene of the same sheet density, then we have $E = 750$ eV. Using a 10/60 mixture of benzene/ethanol as a developer, Haller *et al.* (8) found that the minimum exposure at 10 kV is 1×10^{-4} coul/cm^2, hence we have from [2]

$$P_s = 7 \times 10^{-3}$$

The average molecular weight of the scission product is

$$\overline{M}_n' \approx 140\, M_o$$

$$= 18{,}000$$

For a polymer of molecular weight of 200,000, the number of scissions per molecule is about 10.

The average molecular weight $\overline{M}_n'$ is relatively large. Figure 1 and Eq. [6] imply that generally an appreciable number of the scission fragments has molecular weights over 6 $\overline{M}_n'$ or 100,000. The molecular weight $\overline{M}_n$ of the original polymer must be high, 200,000 or over, otherwise the resolution will be poor and the pin-hole count high.

Conclusion

Although the number of polymers with suitable glass transition temperature is not very large, there

are still several polymers worth investigation, even neglecting the fact that the physical and chemical properties of a polymer may be modified by copolymerization with other polymers. The general characteristics described are those of electron resists. With some modifications, they are also common to photoresists. The efficiency of a negative resist, either photoresist or electron resist, is proportional to the average molecular weight $\overline{M}_w$. Although monodispersity is not required (nor is it obtainable), a narrow range distribution in molecular weight is recommended. In the case of a positive resist, neither the average molecular weight nor its distribution is important as long as the molecular weight distribution curve is well separated from that of the scission fragments.

Manuscript submitted Jan. 22, 1969; revised manuscript received April 2, 1969.

Any discussion of this paper will appear in a Discussion Section to be published in the June 1970 JOURNAL.

REFERENCES

1. M. W. Larkin and R. K. Matta, *Solid State Electronics*, **10**, 491 (1967).
2. O. C. Wells, T. E. Everhart, and R. K. Matta, *IEEE Trans.* **ED-12**, 556 (1964).
3. R. F. M. Thornley and T. Sun, *This Journal*, **112**, 1151 (1965).
4. K. Kanaya, K. Tanaka, and T. Yuasa, Proc. Sixth Intern. Conf. Electron Microscopy, Kyoto (1966).
5. R. K. Matta, *Electrochem. Techol.*, **5**, 382 (1967).
6. J. Kosar, "Light-Sensitive Systems," p. 141, John Wiley & Sons, Inc., New York (1965); Levine *et al.*, "Control of Photoresist Materials," paper in Kodak Photoresist Seminar Proceedings, Vol. 1968.
7. T. W. O'Keeffe and R. M. Handy, Paper 165 presented at the Boston Meeting of the Society, May 5-9, 1968.
8. I. Haller, M. Hatzakis, and R. Srinivasan, *IBM Journal*, **12**, 251 (1968).
9. W. H. Stockmayer, *J. Chem. Phys.*, **12**, 125 (1944).
10. F. A. Bovey, "The Effect of Ionizing Radiation on Natural and Synthetic High Polymers," Interscience Publishers, New York (1958).
11. P. T. Flory, "Principles of Polymer Chemistry," Cornell University Press, Ithaca, N. Y. (1953).
12. J. Brandrup and E. H. Immergut, "Polymer Handbook," Interscience Publishers, New York (1966).
13. A. Chapiro, "Radiation Chemistry of Polymeric Systems," p. 449, Interscience Publishers, New York (1962).
14. W. Ehrenberg and D. E. N. King, *Proc. Phys. Soc.*, **81**, 751 (1963). A detailed curve showing total dissipated energy E as a function of depth in polystyrene for 10 kV electrons is shown in the paper by V. E. Cosslett and R. N. Thomas, *Brit. J. Appl. Phys.* **16**, 791 (1965).
15. T. A. Orofino and F. Wenger, *J. Phys. Chem.*, **67**, 566 (1963).
16. A. Chapiro, *loc. cit.*, p. 469.
17. W. R. Moore and R. J. Hutchison, *Nature*, **200**, 1095 (1963).
18. W. Scholtan, *Makromol. Chem.*, **14**, 169 (1954).
19. R. K. Matta and L. Scala, Paper 550 presented at the Montreal Meeting of the Society, Oct. 6-11, 1968.
20. A. R. Shultz, P. I. Roth, and G. B. Rothmann, *J. Polymer Sci.*, **22**, 495 (1956).
21. A. M. Kotliar, *J. Appl. Polymer Sci.*, **2**, 134 (1959).

Cathodoluminescent $Ln_y(SiO_2)_x$:Tb Phosphors

T. E. Peters*

The Bayside Research Center of General Telephone and Electronics Laboratories, Incorporated, Bayside, New York

ABSTRACT

The synthesis of terbium-activated compounds in Ln_2O_3-SiO_2 system is described and their cathodoluminescence is compared to Zn_2SiO_4:Mn, (ZnCd)S:Ag, and other efficient Tb^{+3}-activated phosphors. The utility of the Tb^{+3} phosphors in tricolor CR tubes is also considered.

The literature affords numerous references (1) to luminescent systems in which the crystalline matricies are silicate compounds of the Group II metals. Typical activators for these systems include Pb and/or Mn, Ce^{+3}, and, more recently, Tb^{+3} (2). In phosphors containing divalent cations and trivalent rare earth activators, it is usually necessary to employ valence compensation by the introduction of a monovalent cation of the appropriate size. This generally improves the crystalline perfection and may also enhance and simplify the emission spectra. The minerals yttrialite $(Y,Th)_2Si_2O_7$ and thortveitite $(Y,Sc)_2Si_2O_7$ have been reported to contain substantial quantities of the rare earths metals as impurities (3) and therefore suggest silicate systems in which charge compensation would not be necessary to achieve maximum emission. Recent research on the phase diagrams of the Ln_2O_3-SiO_2 systems (4, 5) (where Ln = La, Y, Sc, or a rare earth) has suggested a variety of silicates of this type.

Silicates, like the sulfides, seem to be uniquely responsive to excitation by cathode rays, and therefore it was decided to investigate cathodoluminescence in several of these compounds. Of particular interest are the silicates of Y, Gd, and La since these ions possess no incomplete 4f shell, or in the case of Gd, the shell is half filled, and therefore the three are optically inert in the visible and near-ultraviolet regions of the spectrum. Trivalent terbium was chosen as the activator because it has been shown to be effective in silicate matricies, and a few efficient cathode ray phosphors based on this activator have been reported.

Experimental Procedure

The various silicate compounds are given in Table I, together with references to the reporting investigators. It may be seen that these compounds extend from SiO_2/Ln_2O_3 = 0.5 to 2.0 (where Ln = Y, Gd, La). In an effort to encompass all of the previously reported compounds, a series of silicate phosphors were synthesized over the compositional range of SiO_2/Ln_2O_3

Table I. Various silicate compounds

SiO_2/Ln_2O_3	Compound	Designation*	Ref.
0.5	Ln_4SiO_8	—	(6)
1.0	Ln_2SiO_5	Oxyorthosilicate	(4, 5)
1.5	$Ln_4(SiO_4)_3$	Orthosilicate	(4)
2.0	$Ln_2Si_2O_7$	Pyro or diorthosilicate	(4, 5)

* Designations are those used by Toropov *et al.*

* Electrochemical Society Active Member.

from 0.5 to 2.4. In the synthesis procedure, which is somewhat similar to that reported earlier for lanthanum silicate (6), a portion of the cationic oxide or nitrate was replaced by the fluoride which served as a mineralizer. Alternatively, the mineralizing action could also be accomplished by the addition of another fluoride salt such as ammonium fluoride. Pending the elucidation of the most efficient host compounds, the fluoride concentration was held constant at $LnF_3/Ln_2O_3 = 0.22$. Similarly, the terbium concentration was constant at 10 a/o (atomic per cent) of the host cation. These parameters were subsequently optimized for the best phosphors. The high-purity SiO_2 utilized in all syntheses was supplied by Cabot Corporation (Cabosil). The extremely small particle size of this material contributed to the ease of synthesis and uniformity of the product. Usually a slight excess of silica over that dictated by stoichiometry was necessary for the synthesis of the most efficient phosphors. All of the lanthanide components except Gd were of 99.9% purity or higher with respect to other rare earth elements. The principal impurity in the Gd_2O_3 was Eu_2O_3.

In a typical synthesis, the reagents were dry blended and reacted at 1300°C for 4 hr or longer in uncovered quartz crucibles. X-ray diffractometry was employed for the identification of the resulting compounds.

X-Ray Diffractometry

Crystallographically, the oxyortho and pyrosilicates each exhibit three structural subgroups, the particular structure being related to the ionic size of the lanthanide ion (5, 7). The pyrosilicates, in addition, exhibit high- and low-temperature polymorphic modifications (5) with inversion temperatures between 1200° and 1300°C.

The literature describing the orthosilicates is confusing, particularly with respect to the stability of this structure type. A temperature stability minimum has been ascribed to at least the orthosilicates of the larger lanthanides (4a, b) but more recent work indicates that this may not be the case (8). Investigators agree, however, that the orthosilicates are part of the hexagonal crystal system S. G. $P6_{3/m}$ (8, 9). Yttrium orthosilicate is apparently unique since it has been crystallized in both the hexagonal and a cubic (garnet) modification (10).

Identification of these numerous phases by x-ray diffraction was further complicated by the prolific and often conflicting lattice spacings reported by these earlier workers. In the majority of cases, identification was possible by correlating the reported data and eliminating those which were in conflict. The compounds identified in the various phosphor compositions are presented in Table II. The data presented in Table II warrant some further interpretation.

Oxyorthosilicates

All three oxyorthosilicates were obtained as pure phases. Contrary to what has been previously reported, only two structure types were observed. La_2SiO_5 and Gd_2SiO_5 were hexagonal, while Y_2SiO_5 was monoclinic. The compound Ln_4SiO_8 was not detected.

Table II. Compounds identified in various phosphor compositions

SiO_2/Ln_2O_3	Lanthanum silicates	Gadolinium silicates	Yttrium silicates
0.5	$La_2O_3 + A$	$Gd_2O_3 + A$	$Y_2O_3 + A$
1.0	A	A	A
1.2	A	—	A
1.4	A	—	$A + B$
1.6	$A + C$	$A + C^*$	$A + B + C$
1.8	$A + C$	—	$B + C$
2.0	C	C^*	$B + C$
2.4	$SiO_2 + C$	—	$B + C$

$A = Ln_2SiO_5$, $B = Ln_4(SiO_4)_3$, $C = \beta\text{-}Ln_2Si_2O_7$
* Yielded C structure when fired at 1600°C.

Orthosilicates

The orthosilicates of La and Gd were not observed. At SiO_2/Ln_2O_3 values of 1.4-1.8, corresponding to the range in which the orthosilicate might be expected to crystallize, only the oxyortho and β-pyrosilicates were detected. This seems to indicate a temperature stability minimum for these compounds as discussed earlier. Yttrium orthosilicate was observed, but never as a pure phase. Several attempts to crystallize this compound in the pure form were unsuccessful.

Pyrosilicates

Only the β-polymorphs of $La_2Si_2O_7$ and $Gd_2Si_2O_7$ were obtained as pure phases; the low-temperature α-pyrosilicate was absent, presumably because of the high synthesis temperature. The β-$Gd_2Si_2O_7$, however, was not obtained under the usual synthesis conditions; the oxyorthosilicate phase persisted over the entire range of SiO_2/Gd_2O_3 values. The reason for this was not apparent since the Gd_2SiO_5 crystal type persisted at higher flux ratios and proved to be independent of the source or chemical nature of the gadolinium employed. However, it was possible to crystallize the pyrosilicate by refiring the $SiO_2/Gd_2O_3 = 2.0$ composition at 1600°C. Yttrium pyrosilicate, on the other hand, was never obtained as a pure phase even when subjected to higher flux ratios or reaction temperatures as high as 1600°C.

Evaluation of CR Response

The cathode ray response of the phosphors was ascertained by settling them at optimum screen density on 1-in.^{2} sheets of conducting glass and exciting them at 15 kV in a demountable CR tube. A Photovolt Photometer equipped with a 1P21 phototube and a Wratten 106 filter was employed for luminosity measurements. Cathode ray performance data are reported relative to that of (Zn, Cd)S:Ag.

Typical data are presented in Table III for phosphors synthesized at a constant LnF_3/Ln_2O_3 ratio of 0.22 and a Tb^{+3} concentration of 10 a/o.

The CR response of La_2SiO_5:Tb was extremely weak, and luminosity measurements were not possible. During the syntheses of this compound and of Gd_2SiO_5:Tb, the terbium was oxidized to the tetravalent state, resulting in phosphors exhibiting brownish body color and dull green emission. In order to better evaluate these monosilicate hosts, several syntheses were conducted in reducing ambients and/or at reduced Tb^{+3} concentration levels. Under these conditions, the CR response of Gd_2SiO_5:Tb improved but that of La_2SiO_5 remained weak.

The oxyorthosilicates of yttrium and the β-pyrosilicates of lanthanum and gadolinium formed the most efficient phosphors. No attempt was made to optimize the synthesis parameters for β-$Gd_2Si_2O_7$:Tb since the temperatures at which the component oxides reacted were substantially higher than those achievable in conventional phosphor synthesis equipment. The lanthanum and yttrium phosphors, however, were op-

Table III. CR response of Ln^{+3} silicates (relative luminosity)

SiO_2/Ln_2O_3	La	Gd	Y	Compound
1.0	—	19*	64	Ln_2SiO_5
1.6	Comp. not formed		58	$Ln_4(SiO_4)_3$
2.0	28	40*	52	$Ln_2Si_2O_7$

* Refired at 1600°C in H_2 atm.

Table IV. Synthesis parameters for optimum emission

Matrix crystal	x/y	$MF^-/MSiO_2$	a/o Tb	Reaction time & temp
Y_2SiO_5	1-1.2	0.6	7.0	1300°C—4 hr
$La_2Si_2O_7$	2.0-2.2	0.5	10.0	1300°C—4 hr

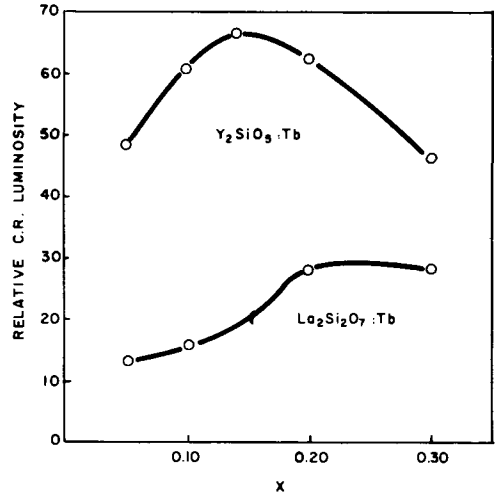

Fig. 1. Relative CR luminosity and Tb concentration in $La_{2-x}Tb_xSi_2O_7$ and $Y_{2-x}Tb_xSiO_5$.

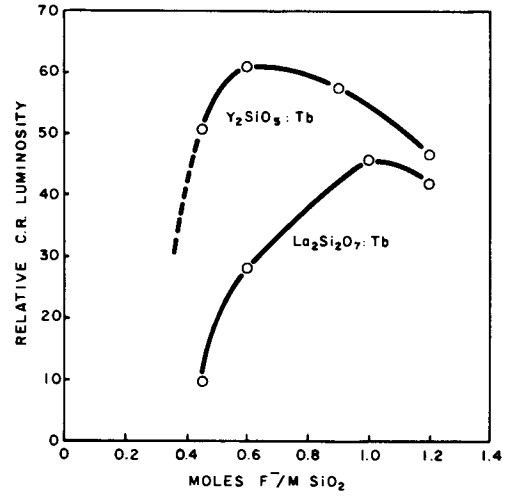

Fig. 2. Relative CR luminosity and flux concentration in Ln silicate phosphors.

timized for CR performance. These data are presented in Fig. 1 and 2, and the optimum parameters are summarized in Table IV.

Cathodoluminescence Spectra

The cathode-ray-excited emission spectra of the optimized phosphors were recorded with a ¾-m Czerny-Turner spectrometer which employed an internal correction function to render the output directly in terms of relative energy. These spectra are presented in Fig. 3 and are noted to be typical of Tb^{+3} emissions in a variety of other host crystals (13). The emission spectra in all cases are dominated by a group of lines which extend from 532 to 564 nm and which are attributed to electronic transitions between $^5D_4$-

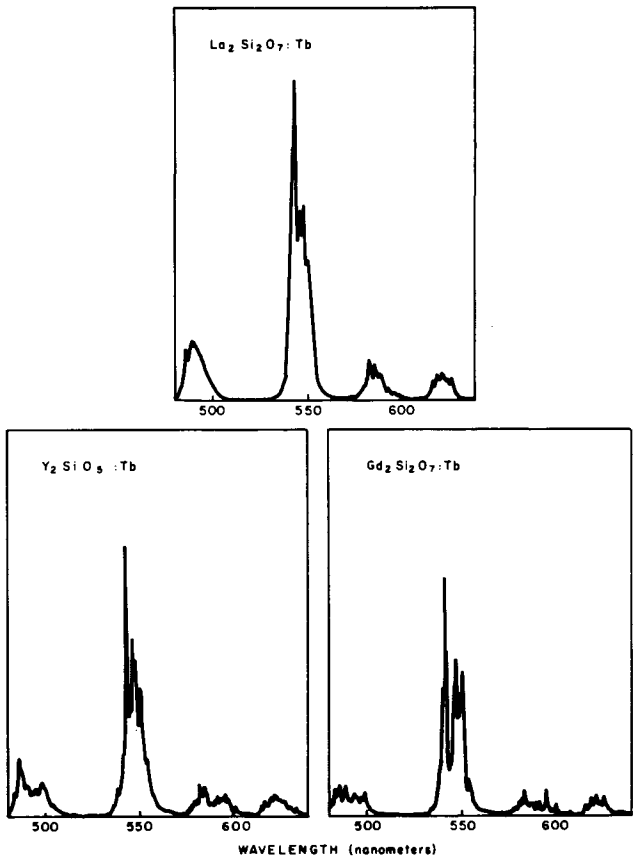

Fig. 3. Cathodoluminescence spectra of Ln silicate phosphors activated with Tb^{+3}.

$^7F_5$ levels. A smaller contribution to the luminosity arises from emissions at 480-508, 576-610, and 614-634 nm. These line groups arise from $^5D_4$-$^7F_{6,4,3}$ transitions. In general, any variation in the observed emission color of the Tb activator is usually due to differences in the relative intensities of these line groups rather than to subtle differences within the line groups. The former can result in an appreciable shift in the chromaticity coordinates on the CIE diagram as is demonstrated and discussed in the following section.

Cathode Ray Performance

The cathode ray performance data for the silicate phosphors are summarized in Table V. Data for other efficient Tb^{+3} phosphors, YPO_4:Tb and $InBO_3$:Tb, have been included for comparison (11, 12). The luminosity and conversion efficiencies for all of the phosphors have been determined relative to (Zn, Cd)S:Ag.

In terms of relative luminosity, Y_2SiO_5:Tb compares favorably with the phosphate and borate phosphors, and all three exhibit a slight improvement over Zn_2SiO_4:Mn. The silicates of La and Gd, although somewhat less efficient than the other Tb systems,

Table V. Cathodoluminescence data for green-emitting phosphors

	Relative luminosity	Decay to Io/10 msec	CIE coordinates x	y	u	v	Lumen equivalent lumen/ radian watt	Relative conversion efficiency	ΔA	% L_R
$Zn_{0.72}Cd_{0.28}S$:Ag*	100	0.05	0.27	0.62	0.11	0.38	500	1.00	0	100
Zn_2SiO_4:Mn	60	15	0.22	0.71	0.08	0.38	540	0.56	—	—
$InBO_3$:Tb	65	15	0.31	0.66	0.12	0.38	610	0.54	−0.4	101
$La_2Si_2O_7$:Tb	45	7	0.32	0.61	0.13	0.38	530	0.42	—	—
$Gd_2Si_2O_7$:Tb	40	7	0.33	0.59	0.14	0.38	519	0.38	—	—
Y_2SiO_5:Tb	65	5	0.33	0.59	0.14	0.38	516	0.62	−8.3	107
YPO_4:Tb	65	5	0.35	0.57	0.15	0.38	504	0.67	−11.9	111

ΔA = Change in color area by replacement of green primary.
% L_R = Required brightness for reproduction of 9300°K white.
* Subscripts denote weight fractions.

still exhibit appreciable CR performance. In their decay characteristics, the terbium-activated systems are intermediate to the Zn_2SiO_4:Mn and (Zn,Cd)S:Ag. Among the Tb^{+3} phosphors, Y_2SiO_5 and YPO_4 have the highest luminous conversion efficiency; they are exceeded only by the sulfide phosphor.

The CIE coordinates and lumen equivalents indicate a steady decrease in the saturation of the green emission color as one moves from $InBO_3$:Tb to YPO_4:Tb. This shift is accounted for by an increase in the $^5D_4$-$^7F_6$ electronic transitions relative to those of the $^5D_4$-$^7F_5$ as the symmetry of the Tb^{+3} lattice site decreases. For $InBO_3$ in which the Tb^{+3} lies in a centrosymmetric site, the $^5D_4$-$^7F_5$ magnetic dipole transitions are allowed, and these are responsible for 75% of the luminous emission. In YPO_4, where Tb^{+3} occupies a noncentrosymmetric site, electric dipole transitions are also allowed, and the contribution to the total luminosity of the $^5D_4$-$^7F_5$ line group falls to 50%. On this basis, it would appear that Tb^{+3} occupies a site of slightly higher symmetry in the silicates than in the phosphate.

Utility of Tb^{+3} Phosphors in Tricolor CR Tubes

In assessing the utility of terbium-activated phosphors in conventional tricolor cathode ray tube applications, it is necessary to consider the effect of the change in chromaticity coordinates on both color reproduction and the luminosity requirements for color mixing.

The effect on color reproduction is best assessed by substituting the chromaticity coordinates of the Tb^{+3} phosphors for those of the green primary (Zn,Cd)S:Ag and evaluating the change in the area of the triangle formed by connecting the u.v. coordinate points of the three primaries on the CIE 1960 McAdam diagram. The luminosity requirements for color mixing, such as in the reproduction of the 9300°K white point on the CIE diagram, can be obtained from a knowledge of the ratio of the lumen fractions and relative luminosities of the green primary and the phosphor under consideration. These calculations have been made for the three most efficient terbium phosphors, and the results are included in Table V. The red and blue primaries are YVO_4:Eu and ZnS:Ag, respectively. The errors encountered in the determination of the chromaticity coordinates are of necessity transmitted to the calculated areas of the resulting triangles and to the green lumen fractions. However, the presented data are sufficiently accurate to permit a qualitative appraisal of the utility of these phosphor compounds in CR tube applications.

From the standpoint of color reproduction, $InBO_3$:Tb is an acceptable replacement for the sulfide primary. Use of the silicate or phosphate, however, would result in a decrease in the gamut of obtainable colors. The silicate phosphor, as indicated, is intermediate to the borate and phosphate in this respect.

At the outset it is observed that all three of the terbium phosphors are deficient in terms of the luminosity required to reproduce the 9300°K white. The $InBO_3$:Tb phosphor appears the most promising but is still some 35% short of meeting this requirement, and the silicate and phosphate are even more deficient in this respect. Until improvements in the luminosity of these phosphor systems are obtained, their application in conventional tricolor shadow mask tubes does not appear likely.

The rare earth phosphors exhibit a distinct advantage over the green sulfide primary in their linear response at high current densities and may therefore find application in novel tube designs. This is demonstrated in Fig. 4 where the cathodoluminescent response of Y_2SiO_5:Tb and (Zn,Cd)S:Ag are presented as a function of current density. The terbium-activated silicate exhibits no saturation effect as the current density is increased while the sulfide begins to saturate and deviates from linearity almost immediately. Thus,

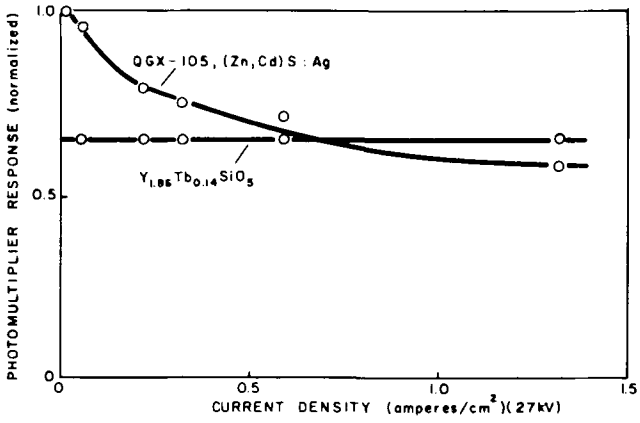

Fig. 4. Current density and CR response of $Zn_{0.72}Cd_{0.28}S$:Ag and $Y_{1.86}Tb_{0.14}SiO_5$ phosphors.

at a current density of 0.65 A/cm² the two phosphors exhibit equal luminosities. The most effective application of these rare earth phosphors, therefore, would lie in cathode ray tubes of the PDF (post deflection focusing) type where the phosphors are subjected to high current densities.

Conclusions

In summary, this investigation has shown that these terbium-activated silicates represent a new family of efficient green-emitting cathode ray phosphors. The most efficient of these, Y_2SiO_5:Tb, is equal to $InBO_3$:Tb and YPO_4:Tb in terms of relative luminosity and intermediate to the two in color and conversion efficiency.

The application of terbium-activated phosphors in tricolor shadow mask tubes has been considered and their utility was found to be limited by the brightness requirements even if some sacrifice in color could be tolerated.

The terbium phosphors were superior to (Zn,Cd)S:Ag in their performance at high current densities, indicating that the most effective application of these materials would lie in cathode ray tubes of the PDF type.

Acknowledgments

The author is indebted to A. Alimonda for assistance in sample preparation and evaluation, to C. Wiggins for the emission spectra, and to V. Meyer for the current response data. Thanks are also due to F.C. Palilla for helpful discussions and suggestions.

Manuscript submitted Jan. 15, 1969; revised manuscript received April 2, 1969.

Any discussion of this paper will appear in a Discussion Section to be published in the June 1970 JOURNAL.

REFERENCES

1. F. A. Kroger, "Some Aspects of the Luminescence of Solids," Elsevier Publishing Co. (1948).
2. W. A. McAllister, *This Journal*, **114**, 226 (1966).
3. N. A. Toropov, I. A. Bondar, G. A. Sedorenko, and L. N. Koroleva, *Izv. Akad. Nauk, Neorg. Mat.*, **1**, No. 2, 218 (1965).
4a. N. A. Toropov and I. A. Bondar, *Izv. Akad. Nauk. SSSR, Otd. Khim. Nauk*, **1960**, 153.
4b. N. A. Toropov. F. Ya. Galakhov, and S. F. Konovalova, *ibid.*, **1961**, 539.
4c. N. A. Toropov and I. A. Bondar, *ibid.*, **1961**, 544.
4d. N. A. Toropov and I. A. Bondar, *ibid.*, **1961**, 739.
5. I. Warshaw, "Phase Equilib. and Cryst. Chem. Rel. in Rare Earth Systems," Doctoral Dissertation, Penn State University (1961).
6. W. L. Wanmaker, W. P. DeGraaf, and H. L. Spier, *Physica*, **25**, 1125 (1959).
7. I. A. Bondar, F. Ya. Galakhov, and N. A. Toropov, *Izv. Akad. Nauk SSSR, Otd. Khim. Nauk*, **1962**, 377.
8. G. T. McCarthy, W. B. White, and R. Roy, *J. Inorg. Nucl. Chem*, **29**, 253 (1967).

9. E. A. Kuzmin and N. V. Belov, *Dokl. Akad. Nauk SSSR*, **165**, 88 (1965).
10. N. A. Toropov, F. A. Bondar, and M. M. Piryutko, *ibid.*, **156**, 619 (1964).
11. F. J. Avella, *This Journal*, **113**, 1225 (1966).
12. F. C. Palilla, A. K. Levine, and M. Rinkevics, *Proc. Intern. Conf. Luminescence*, Sect. D, No. 9, 64-70, Budapest, Hungary (1966).
13. G. Blasse and A. Bril, *Philips Res. Repts.*, **22**, 481 (1967).

CdS-PbS Heterojunctions

Saburo Watanabe and Yoh Mita

Central Research Laboratories, Nippon Electric Company, Ltd., Shimonumabe, Kawasaki, Japan

ABSTRACT

Heterojunctions between n-type CdS and p-type PbS were prepared by chemical deposition of PbS films on CdS single crystals. The PbS films were found to grow epitaxially on CdS crystals. The cubic (111) plane of PbS was parallel to the hexagonal (002) plane of CdS and the cubic (220) plane to the hexagonal (110) plane. The heterojunctions showed a marked photovoltaic effect and distinct rectifying characteristics. The maximum open circuit voltage obtained was 0.4V under irradiation with a tungsten lamp at 0.3 w/cm^2. The spectral sensitivity of the photovoltaic effect showed a sharp maximum at the absorption edge of CdS and a flat plateau extending toward long wavelengths as far as 1μ. The junction capacitance at zero bias and diffusion voltage were measured to be 10 $\sim$ 30 nF/cm^2 and 0.4V, respectively. From these results the energy band diagram was constructed for the heterojunction.

The preparation of the p-n junction of CdS is extremely difficult. Heterojunctions with p-type Cu_2S are used for various applications (1, 2). However, as the electrical and crystallographic properties of Cu_2S are complicated, the investigation of the nature of CdS-Cu_2S heterojunction is difficult to carry out.

In this paper the heterojunction of n-type CdS and p-type PbS, which has a simple structure, is reported. It was found that the heterojunction can be prepared by chemical deposition of PbS on CdS crystals. The preparation of the heterojunctions is described and the results of the examination of crystallographic and electrical properties are given with special attention to the crystallographic structures, photovoltaic effect, and energy band diagram of the heterojunctions.

Fabrication of CdS-PbS Heterojunctions

In order to prepare CdS-PbS heterojunctions, PbS films were deposited chemically on oriented surfaces of CdS single crystals. Procedures for obtaining PbS films were similar to those reported elsewhere for PbS photoconductive films (3, 4). The solution used to grow PbS films contained 0.12 mol-NaOH, 1.2 x 10^{-2} mol-$Pb(NO_3)_2$, 4.4 x 10^{-2} mol-$CS(NH_2)_2$, and 3.4% ethyl alcohol. CdS crystals were cut parallel to their hexagonal (002) and (110) planes and were optically polished. They were immersed in the solution for 20 min at room temperature. After PbS films were formed by deposition, the crystals were taken out and washed with water and ethyl alcohol. Ohmic contacts to CdS were made prior to the growth of PbS by evaporating and alloying indium. Ohmic contacts to PbS were made by simply evaporating gold.

The thickness of the PbS films was determined by means of chemical analysis and was found to be 0.3μ. The electrical conductivity of PbS films was p-type with specific resistivity of 16 ohm-cm. The resistivity of the films decreased to 1 ohm-cm under irradiation with a tungsten lamp at an intensity of 0.3 w/cm^2. In our experiments photoconductive and semiconductive CdS crystals were used. The resistivity of the photoconductive crystals was approximately 10 kohm-cm in the dark and 500 ohm-cm under the light, and the resistivity of most semiconductive crystals was 3.0 ohm-cm.

Crystallographic Properties

Electron diffraction studies were made for several PbS films deposited on various CdS surfaces. Figure 1 (a), (b), and (c) show diffraction patterns of PbS deposited on Cd- and S-surfaces of (002) planes and on (110) planes of CdS crystals, respectively.

From the analysis of the diffraction patterns, the films were found to be cubic and epitaxial with CdS lattices. When PbS films were deposited on the (002)

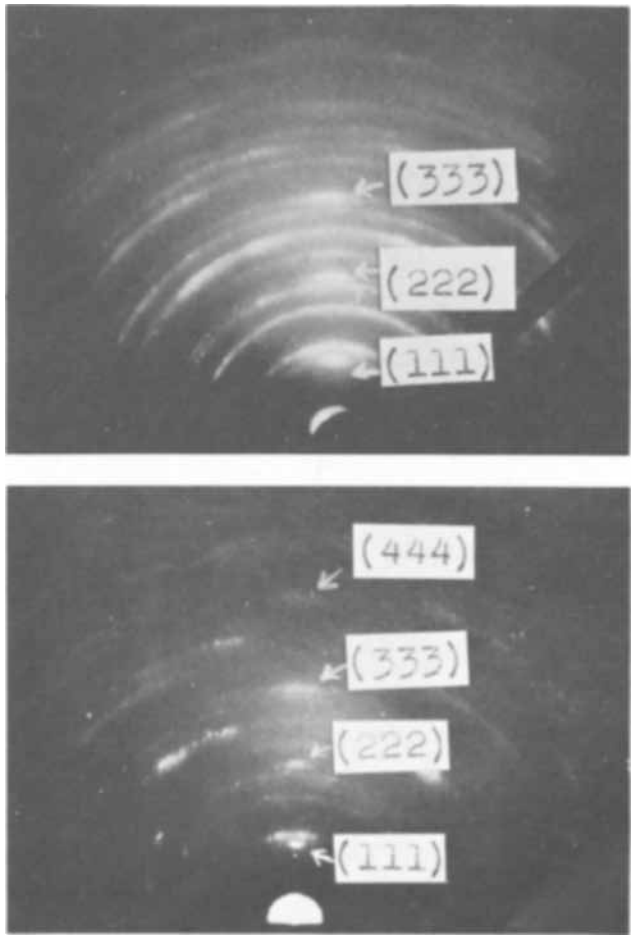

Fig. 1a (top). Electron diffraction patterns of PbS film, deposited on Cd-surface of (002) plane of CdS, Fig. 1b (bottom). deposited on S-surface of (002) plane of CdS.

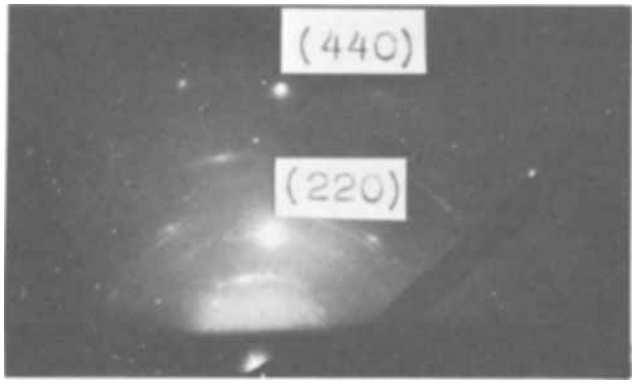

Fig. 1c. Deposited on (110) plane of CdS

planes of CdS, the films grew parallel to their (111) planes. Better crystals were obtained when grown on the S-surfaces of (002) planes than on the Cd-surfaces of the same plane. When PbS films were prepared on the (110) planes of CdS, the films grew parallel to their (220) planes. In this case the spots of the diffraction patterns are so distinct that the films are considered to be in nearly perfect orientation [Fig. 1(c)].

The electron microscope photographs of these three kinds of PbS films are shown in Fig. 2 (a), (b), and (c). It is clear that the surfaces of the films reflect the etching patterns of the CdS crystals.

Electrical and Photoelectrical Properties

The heterojunctions showed clear rectifying characteristics and marked photovoltaic effects. We have measured these properties at room temperature. Representative examples of V-I characteristics are shown in Fig. 3(a) and (b). Figure 3(a) shows the characteristics for (002) planes of semiconducting CdS crystal as the substrates, and Fig. 3(b) shows that of photoconductive CdS crystals.

The maximum values of the open circuit voltage and short circuit current are shown in Table I for various planes of CdS. The rectifying characteristics of the cells cannot be related in general to the photovoltaic effect of the cells. The spectral sensitivity of the photovoltaic effect is shown in Fig. 4, in which the output voltage was normalized with respect to the incident energy. The spectral sensitivity has a conspicuous peak at the absorption edge of CdS. In addition to this peak, there is another low and flat region extending toward longer wavelengths up to 1μ.

The photoconductive spectrum of a CdS crystal is shown in Fig. 5. It has a sharp maximum near the absorption edge and a long tail toward longer wavelength.

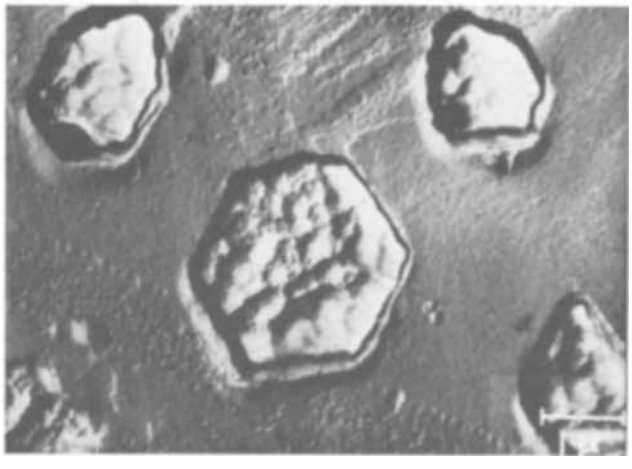

Fig. 2a. Electron microscope photograph of PbS film, deposited on Cd-surface of (002) plane of CdS.

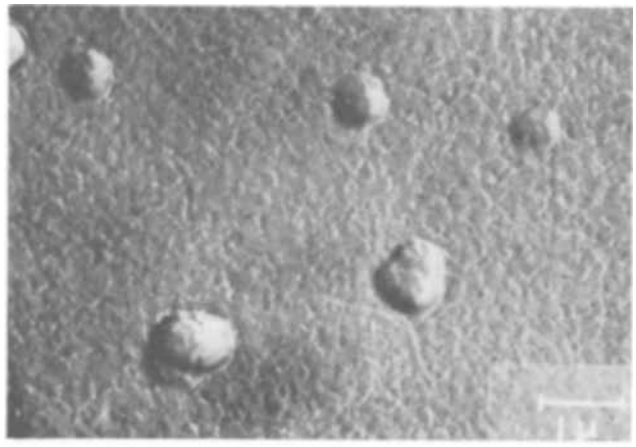

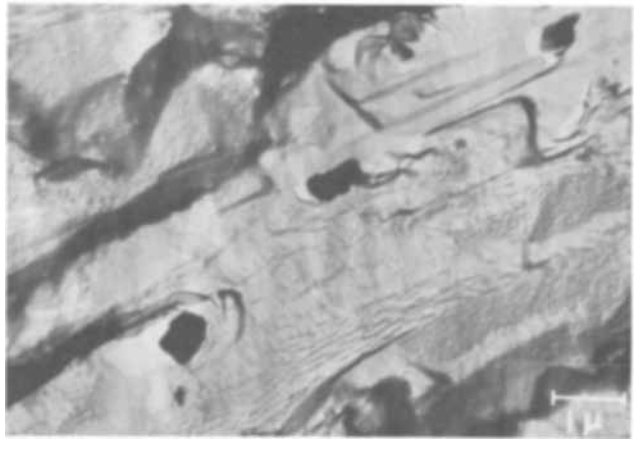

Fig. 2b (top). Deposited on S-surface of (002) plane of CdS, (c, bottom) Deposited on (110) plane of CdS.

The junction capacitance and bias dependence were measured for the heterojunctions between semiconductive CdS and PbS. The measurements were carried out at the frequency of 1 MHz, and the Q value was larger than 10. The zero-bias capacitance ranged between 10 to 30 nF/cm^2. The relation between the junction capacitance and bias voltage is given in Fig. 6. The two lines are the results of two different samples obtained on the same wafer. The inverse square of the capacitance was found to be in linear relation with applied voltage. From the lines in Fig. 6 the diffusion voltage of 0.4V was obtained. The diffusion voltage changed only slightly for different samples, but the slopes of the line differed considerably.

Discussion

PbS films deposited on amorphous substrates do not show noticeable orientations. But is has been known that they have epitaxial relations with such substrates as NaCl or Ge, which have the same or similar crystal structure as PbS (5-7). The present experiments have clearly shown that the PbS films are epitaxially oriented with respect to the hexagonal CdS lattice. The cubic (111) planes of PbS are parallel to the hexagonal (002) planes of CdS and the (220) planes of the former are parallel to the (110) planes of CdS.

In Fig. 7 (a) and (b) the arrangements of cations (or anions) of CdS and PbS are shown with respect to the (002) planes of CdS and (111) planes of PbS. The two crystal lattices closely resemble each other. The

Table I. The relation between orientation of CdS, PbS film and maximum output of photovoltages

CdS orientation	(002)Cd	(002)S	(110)
PbS orientation	(111)	(111)	(220)
Open circuit voltage (V)	0.2	0.4	0.2
Short circuit current (mA/cm^2)	0.02	0.04	0.2

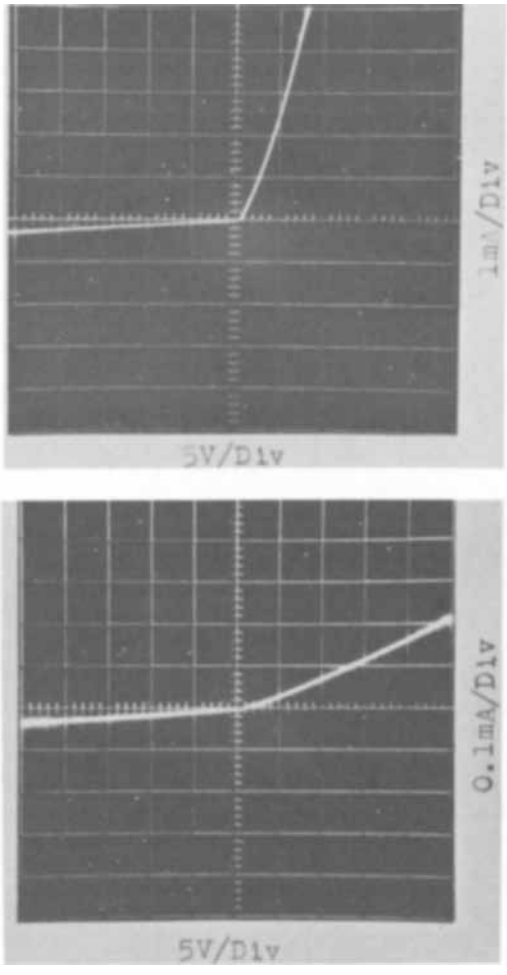

Fig. 3a (top). V-I characteristic of a cell, constructed on semiconducting CdS, Fig. 3b (bottom). Constructed on photoconducting CdS.

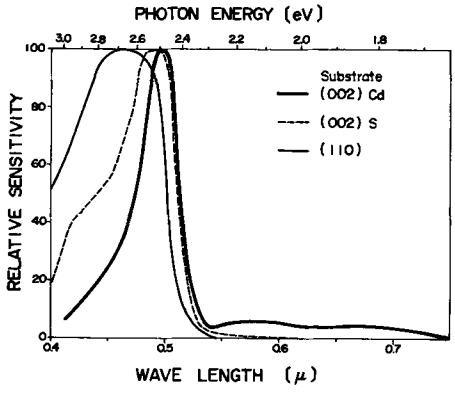

Fig. 4. Spectral sensitivity of photovoltaic effect

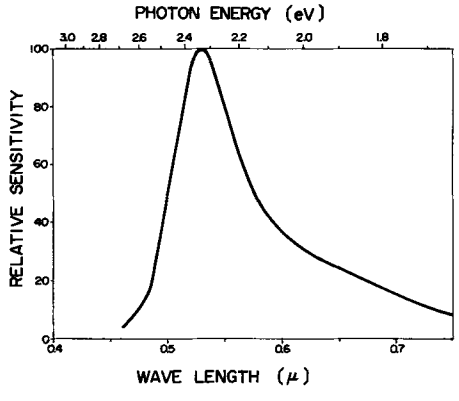

Fig. 5. Spectral sensitivity of photocurrent

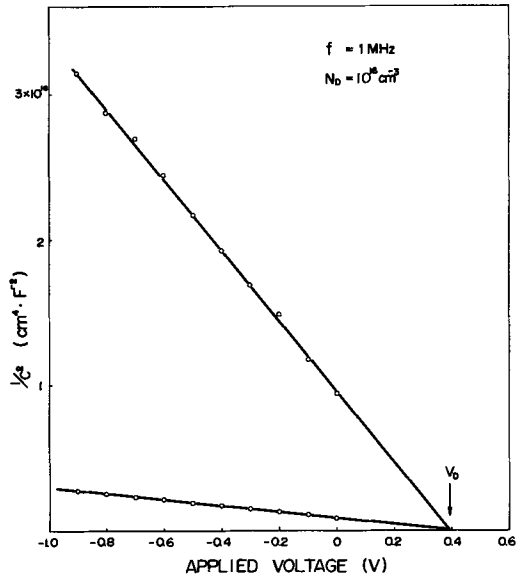

Fig. 6. Bias-voltage dependence of junction capacitance

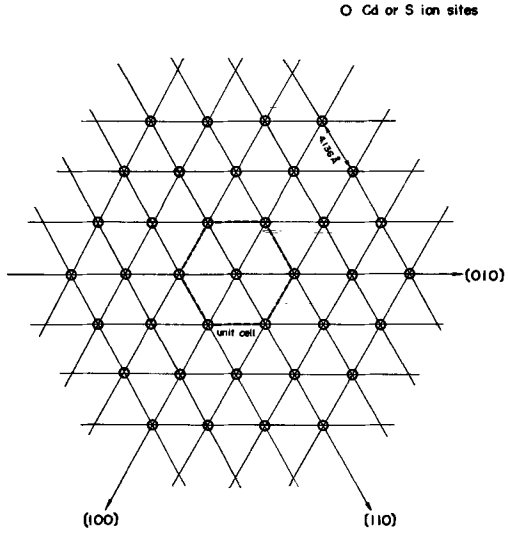

Fig. 7a. Ionic arrangement on (002) plane of CdS and (111) plane of PbS. (002) plane of CdS.

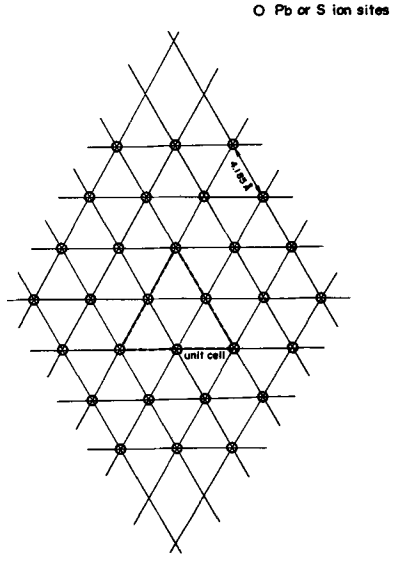

Fig. 7b. (111) Plane of PbS

misfit between two neighboring cations is 1.2%. Figure 8 (a), (b), and (c) show ionic arrangements of cations and anions on the (110) plane of CdS and (220) plane of PbS. Two kinds of planes are laid so that the [001] axis of CdS agrees with the [111] axis of PbS. From Fig. 8(c) it can be shown that the misfit between CdS and PbS lattices is very small in the direction perpendicular to the [111] direction of PbS and the misfit is considerably larger along the [111] direction of PbS. But, if we take a large unit cell as shown in the figure, the two lattices almost coincide. The misfit in neighboring cations (or anions) is 1.2% for the smallest interionic distance and 1.6% for the largest one. The misfit in cation-anion distance amounts to as much as 18%.

The orientations of the PbS films agree with those which are expected from crystallographic considerations. The similarity in atomic arrangement and the smaller misfit indicate that the (111) planes of PbS and (002) planes of CdS are likely to have a better epitaxial relation than another combination. Actually, however, the combination of (220) planes of PbS and

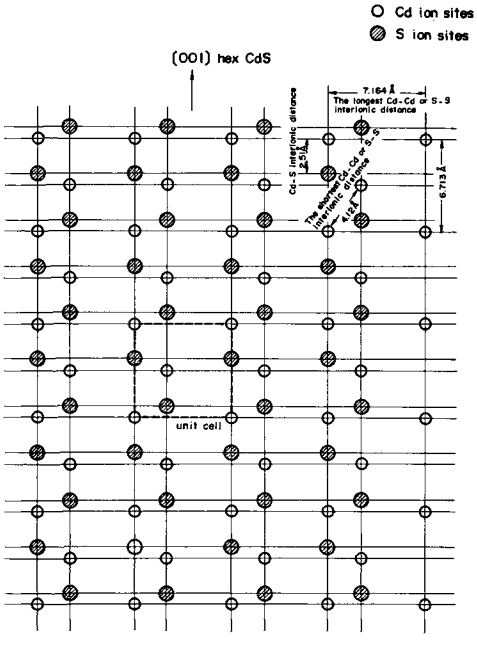

Fig. 8a. Ionic arrangement on (110) plane of CdS

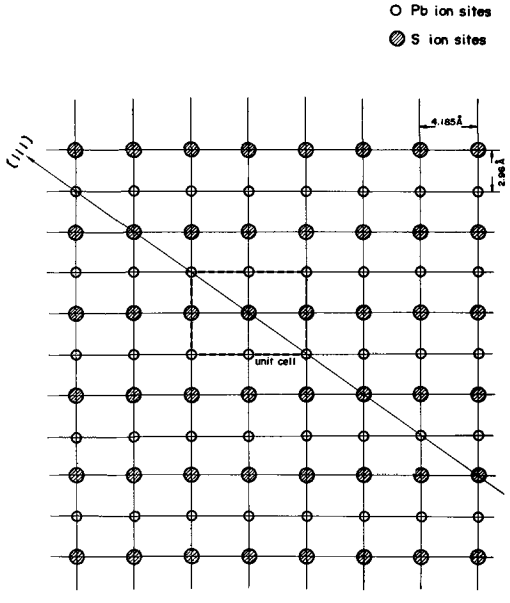

Fig. 8b. (220) Plane of PbS

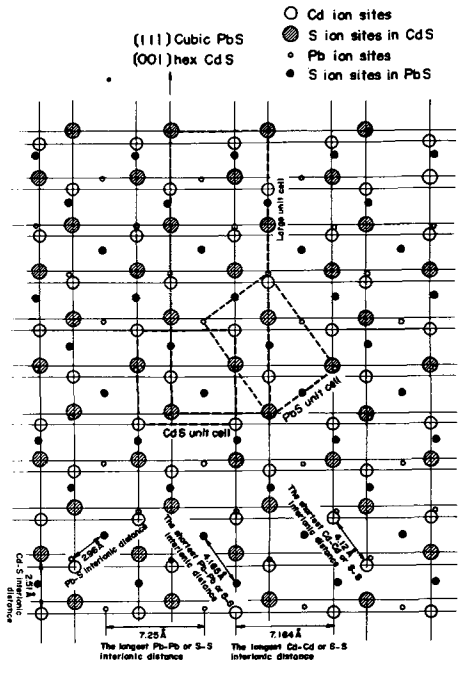

Fig. 8c. (220) Plane of PbS on (110) plane of CdS

(110) planes of CdS shows much better epitaxial growth.

The interface between PbS and CdS shows marked photovoltaic effect and rectifying characteristics. These phenomena can be interpreted as the result of the formation of p-n heterojunctions. But the heterojunctions obtained so far are not ideal. The "n" value obtained from the forward characteristics is considerably larger than 1 to 2, which is expected in an ideal diode. Clear rectifying characteristics are not always observed, particularly when photoconductive CdS crystals are used as substrates.

The heterojunctions show a photovoltaic effect under irradiation of visible and infrared light. The maximum output voltage is about the same order of magnitude as is observed in CdS solar cell. But the conversion efficiency so far obtained is considerable lower than that of the solar cell (1). This is presumably due to a lower conductivity of PbS compared with that of Cu_2S and the lack of long wavelength sensitivity of the CdS used in the experiments. The spectral sensitivity of the photovoltaic effects has a prominent peak near the absorption edge of CdS. The photovoltaic effect is almost exclusively due to intrinsic excitation of CdS and only partially due to PbS and extrinsic levels of CdS.

From the voltage dependence of the junction capacitance the junction seemed to be an abrupt junction. In Fig. 9 a schematic energy band diagram of the heterojunction on the semiconductive CdS is shown which was obtained according to a simple model (8). The interface states and intermediate levels were not taken into consideration. The position of the Fermi levels was calculated using suitable assumptions. The greater part of the diffusion voltage seemed to be supported on the CdS side because of difference in carrier concentrations and in band gaps (10^{16} cm^{-3} for CdS

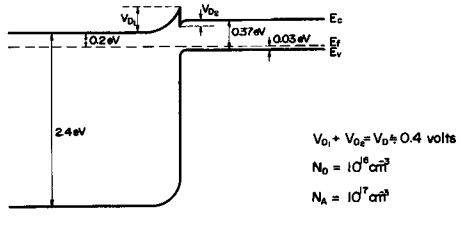

Fig. 9. Schematic energy band diagram of the heterojunction

and 10^{17} cm^{-3} for PbS; in the latter case mobility was assumed to be lower than 10 cm^2/V-sec). The measured junction capacitance was considerably smaller than that expected from the carrier concentration and the diffusion voltage. The thickness of the depletion layer obtained from zero-bias capacitance was 0.3-1μ. The donor concentration was calculated to be less than $6 \cdot 10^{15}$ cm^{-3}, which was considerably lower than that obtained from specific resistivity. So far there is no satisfactory explanation for this difference nor for the relatively large change in slopes of the lines in Fig. 6.

The energy band diagram showed the presence of large energy discontinuities at conduction and valence bands. For this reason the transfer of free electrons from PbS to CdS seemed less probable as well as the transfer of free holes in the same direction.

In conclusion the oriented growth of chemically deposited PbS films on CdS crystals was confirmed and their crystallographic relations were elucidated. The heterojunction between n-CdS and p-PbS showed a marked photovoltaic effect. The schematic energy band diagram was obtained from the results of capacitance measurements.

Acknowledgment

The authors are very grateful to Dr. M. Uenohara, Dr. I. Uchida, and Dr. Y. Nannichi for their suggestions and support of the work. They are also thankful to Mr. Y. Fujino for his discussion and cooperation on the electron diffraction and electron microscope studies.

Manuscript submitted Jan. 2, 1969; revised manuscript received *ca.* March 17, 1969.

Any discussion of this paper will appear in a Discussion Section to be published in the June 1970 JOURNAL.

REFERENCES

1. F. A. Shirland, *Advanced Energy Conversion*, **6**, 201 (1966).
2. P. N. Keating, *J. Phys. Chem. Solid*, **24**, 1101 (1963).
3. F. Kichinski, *J. Soc. Chem. Ind.*, **67**, 54 (1948).
4. H. Pick, *Z. Physik*, **126**, 12 (1949).
5. A. J. Elleman and H. Wilman, *Proc. Phys. Soc. (London)*, **61**, 164 (1948).
6. D. W. Pshley, *Advan. Phys.*, **5**, 174 (1954).
7. J. L. Davis and M. K. Norr, *J. Appl. Phys.*, **37**, 1670 (1966).
8. R. L. Anderson, *Solid-State Electronics*, **5**, 341 (1962).

Gallium Phosphide Double-Epitaxial Diodes

I. Ladany

RCA Laboratories, Princeton, New Jersey

ABSTRACT

The external quantum efficiency of red EL emission in GaP diodes is studied as a function of doping in the p layer. A standardized procedure is used, consisting of liquid phase epitaxial growth of an n layer, followed by similar growth of the p layer. It is found that efficiencies up to 1.4% result from optimizing the Zn and O additions to the p melt, but that efficiencies as high as 3.4% can be obtained if the p melts are compensated by the addition of Te. Arguments are presented showing that a residual donor, probably sulfur, accounts for compensation effects in diodes made by an earlier process. Some other factors which may influence the efficiency are also discussed.

The highest efficiency so far reported for GaP red-emitting diodes was obtained by liquid phase epitaxial (LPE) growth of a Te doped layer onto a solution grown (SG) platelet doped with Zn and O. By following the growth with a heat treatment, Logan *et al.* (1) obtained efficiencies on the order of 2% at room temperature. In fabricating diodes in this way, we encountered considerable variations between platelets from the same growth run and large differences in El efficiencies of the final diodes. We have, therefore, investigated a method of fabrication consisting of successive growth of n and p layers by liquid phase epitaxy. An advantage of such a scheme is that the diode properties are less dependent on the substrate, so that similar results might be obtained for substrates obtained by various methods, such as vapor phase growth, Czochralski growth, or solution growth. All the work reported in this paper used epitaxial growth on SG platelets, however, and it is for this type of substrate that our conclusion apply directly.

Although our main concern is the double-epitaxial diode, that is a diode obtained by successive growth of two LPE layers, we shall be comparing the results to the high efficiency single-epitaxial diode mentioned above. The single-epitaxial diode we call a class I diode, and although we believe that our class I diodes compare to those made at other laboratories, the reader should bear in mind that all the data to be presented have been obtained on units made here. The double-epitaxial diode will be referred to as a class II diode.

An obvious difficulty in the formation of both p and n layers by LPE is the volatility of the dopants. One attempt to solve the doping problem involved the addition of zinc to the gas flow from a separately heated source, and the addition of gallium oxide to the melt, but gave only moderate efficiency, about one fourth of that mentioned earlier (2). Recently a method was described in which the melt is tipped onto the substrate inside a sealed quartz ampoule, which largely prevents the escape of dopants (3). Nevertheless, reported efficiencies were again below earlier values, thus hardly justifying the added complication.

In the present paper we describe a simpler method of p layer growth and discuss some properties of the resultant diodes. We also report on compensation effects in the p layer and their influence on efficiency. We begin, however, with a brief review of our efficiency measurement.

Determination of Efficiency

A vexing question in all work of this kind is the reliability of efficiency measurements. After a certain amount of experience gained using alternate methods, we have found the following to be most useful for room temperature measurements.

The GaP chip to be measured is clamped between small pressure contacts and placed in a box lined with 6 Hoffman N220CG-10L solar cells. The ratio of short circuit current of the cells connected in parallel to the current flowing in the diode is a lower limit to the efficiency. This value would be the true efficiency if the

solar cells were 100% efficient, and if 100% of the emitted light were collected. One may improve on this estimate without doing any calibration by noting that solar cell efficiencies generally run between 70% and 80%, and one may evaluate the collection efficiency by determining the portion of the solid angle not intercepted by solar cells. The estimate so arrived at is not far from the actual multiplication factor we use, equal to 1.3, which was obtained by measuring a diode in this box and in a calibrated integrating sphere.

The measured efficiency as described above is higher than the efficiency of the same chip after alloyed ohmic contacts have been applied. That this is due to absorption in the contact and not degradation can be seen from the recovery of the original efficiency if the contacts are removed by etching. This is, of course, consistent with light absorption in the contact as recently discussed by Bergh (4). If the alloy contact area is kept small, and the chip is coated with a transparent higher index material, the original efficiency is again recovered. Measurements on chips using pressure contacts therefore provide a good indication of what can be obtained from the same material in a carefully made diode. Nevertheless, the values later given in Table II were obtained from mounted diodes with alloyed ohmic contacts and a plastic or wax coating.

Determination of Optimum Doping

The Zn and O concentration required to maximize the photoluminescence efficiency of SG platelets is known (5); because of similarity of SG and LPE it might equally well apply to LPE growth. We do not expect this to be so, however, since the impurity segregation coefficients for epitaxial growth are quite different from those applying to platelet growth. Furthermore, platelet growth is carried out in a sealed crucible, whereas, in the interest of simplicity, we wish to use the standard open tube method (6). The loss of dopants under these conditions is not easily predicted, especially in the case of oxygen whose behavior in a melt is largely unknown.

To gain some idea of the loss of zinc and oxygen in LPE of class II diodes, we carried out preliminary tests using the following procedure:

We grow a Te doped layer onto a SG platelet using the optimum Te doping (7) and follow this without lapping, with the growth of the Zn and O doped p layer. Doping is accomplished by adding to the melt suitable quantities of one or another of the dopants Zn, Te, ZnO, and Ga_2O_3.

The furnace is identical to the one first described by Nelson (6). Forming gas flows over a carbon outer crucible, which is provided with a vitreous carbon liner. Tipping temperatures are in the 1050°-1070°C range, and the cooling rate varies between 20°C/min at the start of growth, and 10°C/min toward the end. About 50 μm of material is grown during one LPE run.

After the second layer is grown, the SG substrate is lapped off, the wafer cleaved into chips, and the efficiency measured.

If only zinc is added to a fresh melt (typically composed of Ga and GaP in the ratio of 10:1) we obtain very weak red emission. In the next use of the same melt, addition of oxygen alone in the P melt gives quite good efficiencies; this shows that enough zinc has remained in the melt from the previous run. If on the next run we add only zinc, the efficiency again drops to very small values, which indicates an almost complete loss of oxygen in the previous run. These observations are summarized in Table I.

Numerous runs with different additions were made in order to determine the joint dopant quantity which will maintain a high efficiency in repeated use of the same melt. The value obtained is 0.2 a/o (atomic per cent) for zinc, and 0.4 a/o for oxygen, which gives efficiencies ranging from 1 to 1.5%.

Table I. Efficiency for either O or Zn addition

Run No.	Additions, a/o		Efficiency, %
1	Zinc	0.6	0.1
2	Oxygen	0.19	0.6-0.8
3	Zinc	0.15	<0.1

Spontaneous Junctions

A noticeable difference between the structure of the p-layers grown by LPE and by SG is the occurrence of spontaneous junctions. During the growth of the p-layer by LPE, we usually obtain another junction, sometimes so close to the surface as to be hardly noticeable, but usually several microns below it. A typical photomicrograph is shown in Fig. 1, which illustrates the various junctions and layers involved.

We remove this extra junction by lapping or etching, as it might interfere with the ohmic contact to the p layer. In agreement with earlier reports (8), we never observe internal junctions in SG platelets doped with Zn and O. The implication of the occurrence of spontaneous junctions is discussed in a later section.

Compensation of the P Melt

Using the previously determined optimum doping, we have made a number of runs in which various amounts of the donor tellurium were added to the P melts. Experience with n layer growth has shown very little Te loss during a run and we therefore assume that a single addition specifies the Te concentration for all subsequent runs using that melt.

Diodes made from such material, which we call class III diodes, can show remarkably high efficiencies (Fig. 2). The scatter in efficiencies is however much greater than in uncompensated material. The spontaneous junction in the P layer is moved in deeper but in a somewhat random way, as shown in Fig. 3 where we plot the distance between the spontaneous and the optically active junction *vs.* the tellurium concentration in the melt.

Heat Treatment

Heat treatment has been shown to produce improvements in class I diodes (1). All of the class III diodes discussed have been given a heat treatment at 600°C (9), whereas class II diodes received none. Unfortunately, we found the effect of heat treatment to be uncertain. Thus, some class I and II diodes could be improved thereby but some could not, whereas some class III diodes did not change on heat treatment and others did.

Comparisons of the Three Diode Classes

Although no careful studies of the electrical properties of these diodes were made, limited measurements of the C-V, I-V, and L-I characteristics showed no clear differences between the three classes. The dependence of the total light intensity on bias has the form exp (eV/nkT) with $n \cong 1$, whereas the current dependence on bias is of the same form with $n = 1.7$. Thus radiative recombination proceeds outside the space charge region (or at shallow centers within it), whereas a good part of the current recombines in

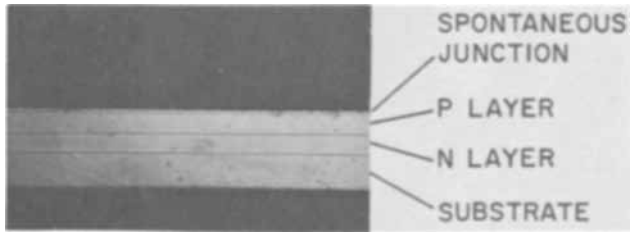

Fig. 1. Delineation of junctions occurring in double epitaxial growth on p-type SG substrates. The total thickness of the wafer is 0.19 mm.

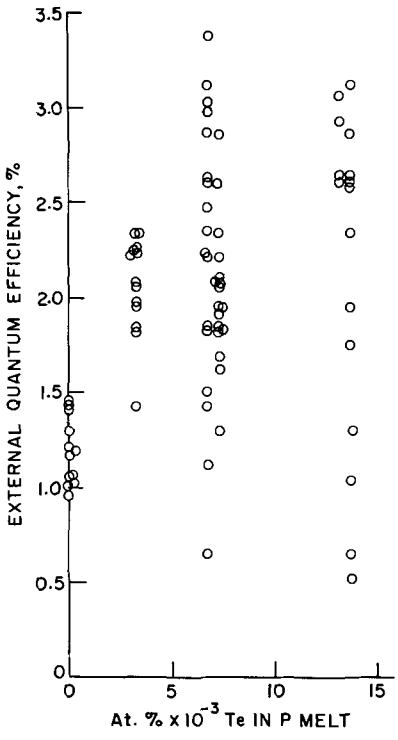

Fig. 2. Efficiencies obtained using tellurium in the p melts

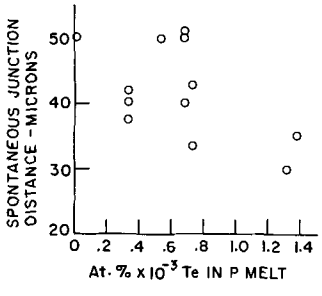

Fig. 3. Distance between the optically active and the spontaneous junction in a group of wafers grown from compensated melts.

the space charge region. This is not much different from previous findings for GaP diodes (10).

There is an indication, however, that the internal absorption in these diodes is related to the presence of the compensating donor on the p side of the junction. A convenient, if crude way of showing this connection is to measure the efficiency of a chip before and after coating it with a bead of glycol phthalate ($n \cong 1.57$), which reduces the optical mismatch to free space. In Fig. 4 we show results of such determinations, each point representing a chip from a different wafer. It can be seen that class II diodes generally show no improvement on coating, which can be taken as indicating very little absorption (11). Class I and III diodes, on the other hand, show a modest increase in efficiency.

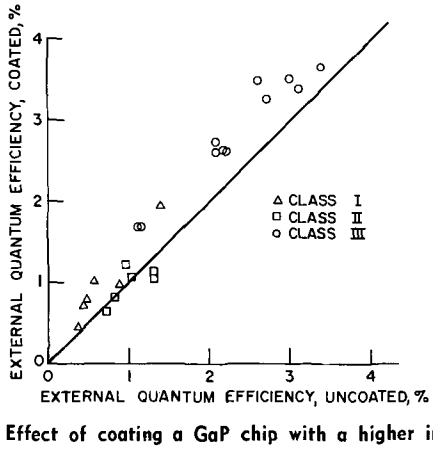

Fig. 4. Effect of coating a GaP chip with a higher index transparent wax. Each point represents a chip from a different wafer.

As mentioned before, epitaxial layers usually have a spontaneous junction near the end of growth, even if no donors are added to the melt. SG platelets grown from similar melts, however, do not yield internal junctions. This can be understood by considering the distribution coefficients for the two processes. In general, one expects impurities with large distribution coefficients such as sulfur, selenium, or tellurium (12), to be present in heavier concentrations when the growth rate is slower. Impurities with distribution coefficients less than 1, such as zinc, on the other hand require a fast growth rate in order to be incorporated into the crystal in concentrations higher than allowed by the equilibrium distribution coefficient. Since our LPE proceeds with a higher cooling rate initially, and a lower cooling rate near the end of growth, we expect to incorporate high concentrations of zinc in the early part of growth and higher concentrations of donors in the later stages. We thus see that pn junctions could arise during LPE, and we also expect a reduced donor concentration, *i.e.*, reduced compensation, in the first part of the LPE layer.

In the case of SG on the other hand, very fast growth from a supersaturated melt implies more nearly uniform doping to concentrations equal to those in the melt. (The lack of deep junctions often found by others may be due to the very high purity of currently available starting material, and the fast cooling rate used in our furnace). We therefore expect SG platelets to be evenly compensated with residual donors.

In Fig. 5 we have sketched a possible doping profile for class I and class II diodes. The left portion of each figure is the substrate (class I) or the LPE n layer (class II), and the LPE layer which defines the junction is on the right. Zinc diffusion during growth shifts the junction into the n layer but does so to a somewhat shorter distance for class II diodes since both dopants reach their maxima at the boundary.

In the case of class II diodes we have some evidence for locating the junction very close to the metallurgical boundary. In a careful search for traces revealed by etching we have seen a faint line somewhat under 1 μm away on the p side of the junction. The junction displacement is thus less than the expected location of the red emission, which may be as much as several microns away in the p layer (13). Radiative recombination in these diodes therefore occurs in the uncompensated p layer. In class I diodes, recombination will occur partly in the n layer compensated by the zinc diffusion, and partly in the p layer compensated by residual donors (7).

We review the three types of diodes in Table II. The main argument presented is that compensation is required in order to achieve the highest external effi-

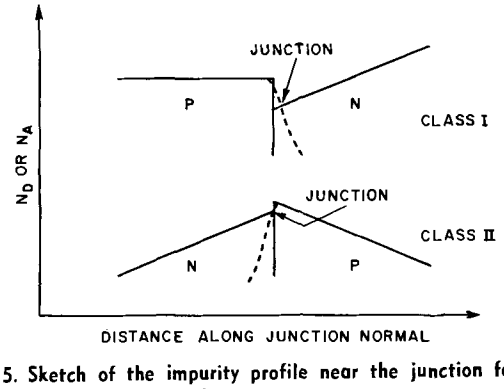

Fig. 5. Sketch of the impurity profile near the junction for two types of diodes discussed in the text.

Table II. Comparison of the three diode classes

Class	I	II	III
Fabrication	n-LPE on p-SG	p-LPE on n-LPE	p-LPE on n-LPE
Compensation	By residual donors	Little if any	Deliberate
Internal absorption	Yes	No	Yes
Maximum efficiency	2%	1.4%	3.4%

ciencies for Zn-O doped diodes. In addition, we find a difference in the internal absorption coefficient connected with the compensation. This is of considerable practical importance because class II diodes cannot be improved by index matching. If better high index coatings become available, class III diodes can be improved a great deal more. In order to arrive at an estimate of the ultimate limit, we have determined the internal efficiency by observing the change in external efficiency when the diode is surrounded by liquids of different refractive indices (11). Our best estimate for the ratio of internal to external efficiency is 3, and the maximum internal efficiency for class III diodes is therefore about 10%.

Discussion

Mass spectrometric analyses carried out at this laboratory[1] have shown the presence of sulfur and silicon in most of our GaP material. It is also found that they are difficult to remove by further recrystallization of GaP from high purity gallium. As regards the choice between the two, Hall measurements and EL spectra both suggest sulfur as the most likely donor present in class I diodes. We have made some runs using sulfur instead of tellurium, for compensation in class III diodes, and we have also fabricated some diodes with sulfur as the n layer dopant as well as the compensating donor. In both cases results were similar to those obtained with tellurium, with similar high efficiencies. Sulfur is, however, exceedingly difficult to control (its distribution coefficient is ≈ 44). Since the effects of sulfur thus are not distinguishable from those of tellurium, we have a ready explanation for the poor correlation between tellurium addition and efficiency. It must also be supposed that forming gas contains not only sulfur, but hydrocarbons as well, which introduce carbon acceptor levels in GaP (14). Uptake of these impurities from the forming gas can easily shift the spontaneous junction in a random way from run to run.

As mentioned earlier, class III diodes received a heat treatment, whereas class II diodes did not. In a number of cases, class III diodes gave high efficiencies without the heat treatment and did not improve very much afterward. Also, class II diodes generally did not improve by the same heat treatment. A few exceptions to this behavior were also noted, but in view of what has been said earlier about sulfur, it is difficult to exclude the possibility of accidental sulfur compensation. In most cases, however, heat treatment for 30 min at 600°C was effective for class III diodes, but not for class II diodes.

[1] We are indebted to W. L. Harrington and E. Botnick for the mass spectrometer studies.

We now raise the question whether structural differences other than the difference in compensation could explain the superiority of class III diodes over class I diodes. One might suppose that further reduction of dislocations by the double growth step would produce more perfect junctions. But as Saul (15) has recently shown, SG platelets are largely dislocation free, which makes this supposition unlikely. Variations between individual diodes from the same wafer, on the other hand, could be due to isolated flaws propagated from the substrate.

No doubt there are impurities besides those mentioned which may influence the Zn-O emission in GaP, some present in the starting material and others picked up from the forming gas. Better control over impurities will certainly give improved reproducibility, and possibly higher efficiency.

Acknowledgments

We are grateful to H. S. Sommers, Jr. for a critical review of the manuscript, to H. Nelson for useful discussions, to H. Kressel for spectral measurements and many helpful discussions, to N. Byer for various measurements, and to D. Redfield for clarifying several problems. The assistance of M. E. Heller, J. Alexander, and D. Marinelli in various phases of this work has been greatly appreciated.

Manuscript submitted Nov. 27, 1968; revised manuscript received *ca.* March 24, 1969. This was Recent News Paper 610 presented at the Montreal Meeting, Oct. 6-11, 1968.

Any discussion of this paper will appear in a Discussion Section to be published in the June 1970 JOURNAL.

REFERENCES

1. R. A. Logan, H. G. White, and F. A. Trumbore, *Appl. Phys. Letters*, **10**, 206 (1967).
2. F. A. Trumbore, M. Kowalchik, and H. G. White, *J. Appl. Phys.*, **38**, 1987 (1967).
3. K. K. Shih, M. R. Lorenz, and L. M. Foster, *ibid*, **39**, 2747 (1968).
4. A. A. Bergh and R. J. Strain, Fall Meeting of the Electrochemical Society, Montreal, Oct. 6-11, 1968, Abstract 499.
5. M. Gershenzon, F. A. Trumbore, R. M. Mikulyak, and M. Kowalchik, *J. Appl. Phys.*, **36**, 1528 (1965).
6. H. Nelson, *RCA Review*, **24**, 603 (1963).
7. H. Kressel and I. Ladany, *Solid-St. Electron.*, **11**, 647 (1968).
8. M. R. Lorenz and M. Pilkuhn, *J. Appl. Phys*, **37**, 4094 (1966).
9. A. Onton and M. R. Lorenz, *Appl. Phys. Letters*, **12**, 115 (1968).
10. R. A. Logan, M. Gershenzon, F. A. Trumbore, and H. G. White, *ibid.*, **6**, 113 (1965).
11. M. R. Lorenz and G. D. Petit, *J. Appl. Phys.*, **38**, 3983 (1967).
12. L. M. Foster, T. S. Plaskett, and J. E. Scardefield, *IBM J.*, **10**, 114 (1966).
13. M. Gershenzon, R. A. Logan, and D. F. Nelson, *Phys. Rev.*, **149**, 580 (1966).
14. P. J. Dean, C. J. Frosch, and C. H. Henry, *J. Appl. Phys.*, **39**, 5631 (1968).
15. R. H. Saul, *This Journal*, **115**, 1184 (1968).

Characteristics of Fast Surface States Associated with SiO_2-Si and Si_3N_4-SiO_2-Si Structures

B. E. Deal,* E. L. MacKenna,* and P. L. Castro*

Fairchild Semiconductor Research and Development Laboratory, Palo Alto, California

ABSTRACT

Characteristics of fast surface states located at the SiO_2-Si interface of thermally oxidized silicon structures (MOS) and structures incorporating vapor-deposited silicon nitride films over thermally oxidized silicon (MNOS) have been investigated. Effects of oxidation and annealing conditions on the formation or reduction of fast surface states, using MOS capacitance-voltage curves, are first discussed. The effects of silicon nitride layers over thermal oxides on the electrical properties of MNOS structures are next presented, with emphasis being placed on the ability of the nitride to prevent or mask the annihilation of fast states which normally occurs during an anneal in dry N_2 at 500°-565°C for 2-5 min after aluminum deposition. Such variables as deposition ambient, flow rate, high temperature anneals, nitride structure, and reactant type are shown to affect the masking ability of the nitride. These results, along with special experiments, help to confirm the postulate that some active species of hydrogen plays an important part in the elimination of fast surface states in MOS and MNOS structures.

Silicon nitride layers, when deposited over semiconductor device structures, have been shown to be an effective mask against the diffusion of impurity ions such as sodium (1-5). Apparently the dense nature of the nitride actually blocks the ion migration, as opposed to the phosphosilicate glass layers, also used for this purpose, which more likely getter or complex the sodium ions (6-7). The silicon nitride layers used for device passivation are generally deposited by a vapor deposition process in which NH_3 is reacted with either SiH_4 or $SiCl_4$ in the temperature range 700°-1000°C, although lower temperature processes involving sputtering or plasma excitation are also being developed (8).

Previous work in this laboratory (9) and by other investigators (8) has demonstrated that the electrical instabilities of the Si_3N_4-Si interface preclude the use of a silicon nitride layer directly on the silicon surface in most cases. On the other hand, satisfactory results have been obtained by depositing a thin nitride layer over thermally oxidized silicon (9-10). Thus, the advantage of the nitride's ability to mask against sodium migration may be combined with the excellent Si-SiO_2 interface characteristics.

It has been shown that four main types of charges are associated with the thermally oxidized silicon structure (11). These are mobile impurity ions, Q_o; fixed surface charge, Q_{ss}; radiation induced charge, N_{ot}; and fast surface or interface states, N_{st}. Of these, the fast states have been most extensively investigated but are still the least understood. However they probably affect many device electrical characteristics to the greatest degree. Examples of attempts to better understand the nature of these states and their effect on device properties, especially metal-oxide semiconductor (MOS) devices are given in ref. (12-17).

One of the interesting but puzzling characteristics of fast surface states (located at the SiO_2-Si interface) is that their density can be reduced to a relatively low level by annealing in an inert ambient such as nitrogen at low temperatures (500°-550°C) *if an active metal such as aluminum is present over the thermal oxide* (18). It has also been found (9) that this annealing or reduction of fast states is greatly retarded by the presence of a silicon nitride layer between the metal field plate and the thermal oxide. Experiments involving the nature of this phenomenon, whereby the fast state reduction is retarded in Si_3N_4-SiO_2-Si structures, are summarized in this paper. Effects of the nitride deposition process as well as subsequent thermal treatments are included. In order that the results may be more easily interpreted, characteristics of fast state formation in the thermally oxidized silicon structure (without the nitride layer) are first presented along with techniques for detecting and measuring surface state densities in MOS structures.

* Electrochemical Society Active Member.

Experimental

Czochralski silicon, sliced and lapped to 250μ thickness, was obtained from the Wacker Chemical Company, Los Angeles, California. Dislocation count was specified to be less than 100 cm^{-2}, while doping impurity concentration was about 1.5×10^{16} cm^{-3}. The silicon slices, either p- or n-type and (111) or (100) oriented, were cleaned in organic and inorganic solvents and chemically etched to 150μ thickness in a 4 HF: 10 HNO_3 solution at 25°C.

The silicon slices were thermally oxidized immediately after etching. The standard oxidation condition was 60 min in dry oxygen at 1200°C with a very rapid cool after pulling into room ambient. This procedure provided an oxide thickness of 0.20μ, a Q_{ss}/q (fixed surface charge) value of 2×10^{11} cm^{-2}, and a medium low N_{st} (fast surface state density), *i.e.* $<5 \times 10^{11}$ cm^{-2} as oxidized. Certain samples received variations in the oxidation ambient and cooling rate as well as subsequent annealing treatments. The oxidation and annealing apparatus was similar to that used in previous work (19-20). All gases were from high purity, liquid sources.

For those structures incorporating a silicon nitride layer, the oxidized silicon slices were placed in the appropriate nitride deposition system. These systems, employing either $SiCl_4$-NH_3 or SiH_4-NH_3 reacting mixtures and H_2 or N_2 carrier gases, were in the form of horizontal, rectangular cross sectional quartz reactors. Heating was accomplished using an R.F. generator. The latter inductively heated a SiC coated graphite susceptor on which the silicon substrates were placed. Deposition temperatures were in the range 700°-1000°C. Thicknesses of the silicon nitride films were generally in the range 500-2000Å. Subsequent annealing of some of the nitride-oxide samples was carried out in nitrogen or hydrogen at temperatures in the 700°-1000°C range. Thickness measurements of both the thermal oxide and silicon nitride layers were carried out using multiple beam interferometry on mechanically polished test slices.

Most of the evaluations reported in this paper involved MOS (metal-oxide-semiconductor) or MNOS (metal-nitride-oxide-semiconductor) capacitor structures. For the metal portion of these structures, high purity aluminum (99.9999%) dots were evaporated over the oxide or nitride layer. Aluminum was also evaporated on the back side for better contact to the silicon. (Any dielectric layer remaining on the back of the slice had previously been removed using hydrofluoric acid and photoresist techniques.) After aluminum evaporation a portion of each sample was annealed in dry nitrogen at 550°C for 2-5 min.

Capacitance-voltage measurements were carried out using techniques and apparatus described earlier (9, 21). The usual measurement frequency was 100 kHz although other frequencies were also used. In addition to room temperature measurements, plots were made at lower temperatures, *i.e.*, —196°C, using encapsulated devices. The nature of these measurements is discussed later. In addition, values of surface recombination velocity, s_o, were obtained using gate-controlled diode structures which have been described earlier (9, 22).

Measurement of Fast Surface States

It will not be the purpose of this paper to determine or even speculate as to the source of fast surface states associated with thermally oxidized silicon. Rather it should be sufficient to state that these states are probably located at the SiO_2-Si interface with a density distribution through the silicon band gap. This distribution may be either discrete or continuous with energy. However, the actual case is more likely to be some combination of these two possibilities. Work at this laboratory and others (16, 23) indicates the density of states is fairly continuous through the middle of the gap with peaks near both band edges. Further, since these states adversely affect many semiconductor device properties, a minimum density is desired, *i.e.*, $<10^{10}$ cm^{-2}.

The presence of fast surface states may be detected in a variety of ways. The simplest way is by comparing an unannealed MOS capacitance-voltage curve with one having a theoretical shape. If the structure contains a relatively large number of fast states, the C-V curve will exhibit particular distortions. These may be broad slope variations (indicating a continuous distribution of states) or specific breaks (indicating single levels) or both. An example of these single levels is shown in Fig. 1. Here a typical C-V plot is shown for 2000Å SiO_2 (produced at 1200°C in dry O_2 and rapidly cooled) on 1.3 x 10^{16} cm^{-3} (111) p-type silicon. The curve is shifted along the voltage axis to compensate for Q_{ss} and ϕ_{MS}. Its shape, for both the high (H.F.) and low (L.F.) frequency cases, is compared with a curve representing no fast surface states, *i.e.*, theory. The distortion labeled Ⓐ is a result of the density of states near the valence band, that labeled Ⓑ is more related to states near the midgap, or the intrinsic level, and that labeled Ⓓ is due to states between the intrinsic level and the conduction band. The width of the low frequency type C-V curve at its midpoint is labeled Ⓒ. The broadening of this curve is a result of the states nearest the conduction band.

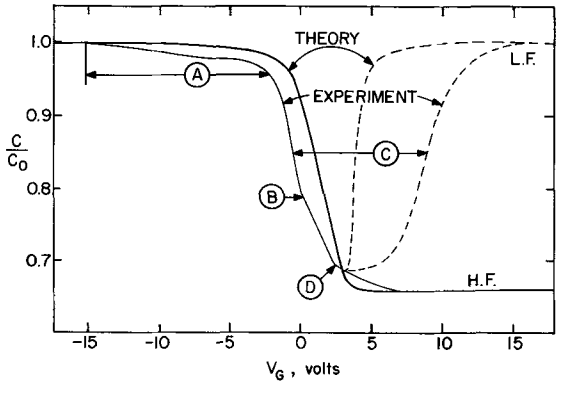

Fig. 1. Comparison of experimental and theoretical MOS C-V curves showing typical distortions in the experimental curve due to fast surface states (labeled Ⓐ, Ⓑ, Ⓒ, and Ⓓ). Unless otherwise indicated all C-V curves plotted from inversion to accumulation voltage. [p-Type (111) silicon; $C_B \cong 10^{16}$ cm^{-3}; $x_o = 0.2\mu$; $Q_{ss} = 0$, $\phi_{MS} = 0$]

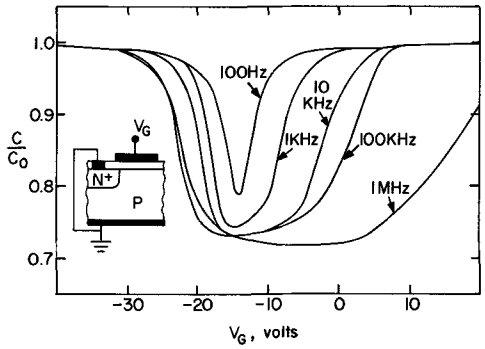

Fig. 2. Dependence of low frequency type C-V curve on measurement frequency for an MOS gate-controlled diode exhibiting medium fast state density. [p-Type (111) silicon; $C_B \cong 10^{16}$ cm^{-3}; $x_o = 0.2\mu$.]

The distortions shown in the C-V plot in Fig. 1 might be confused with nonuniform charge densities often found with contaminated structures. However it has been found through thousands of drift-free MOS runs that the distortions due to fast states are real and reproducible for a given process condition.

Some interesting observations have been made concerning the fast states as indicated in the C-V plot of Fig. 1. First, the amount of the voltage distortion labeled Ⓐ, hereafter called the Ⓐ-state voltage, is always proportional to the Ⓒ-state voltage[1] at a given frequency. As the frequency is changed, the Ⓒ-state characteristics change as indicated in Fig. 2. This effect can be attributed to the time constant required to charge and discharge the states which prevents these states from following the a-c signal as frequency increases. The Ⓐ-state voltage does not appear to vary as greatly with frequency.

Second, the number of fast states obtained in a thermally oxidized silicon structure can be varied over a wide range depending on the moisture content of the ambient used in the final high temperature treatment, *i.e.*, >600°C. As reported by other investigators (16, 17), if the oxidized silicon is cooled from a dry ambient, *i.e.*, N_2 or O_2, a high density of fast states will result. If the cooling ambient contains water (or hydrogen) the fast state density will be greatly reduced as indicated by the Ⓐ- or Ⓒ-state voltage.

A third observation is that certain device characteristics have been correlated with the states indicated in Fig. 1. For instance, the Ⓑ-state is related to noise in MOS transistors (24). Further, the amount of

[1] The low frequency type C-V curve can best be obtained by using the gate-controlled diode structure shown in the insert of Fig. 2. Here, a diffused region, extending into the edge of the MOS capacitor, of impurity type opposite to that of the silicon bulk supplies enough minority carriers to provide the low frequency type C-V curve. If the surface of p-type silicon is inverted by a large positive surface charge, low frequency type C-V curves may also be obtained for MOS capacitors, due to electrons available from the adjacent inversion layer.

Ⓑ-state distortion and thus noise can be increased by large negative fields (24, 25). The Ⓐ- and Ⓒ-states, which are undoubtedly the same as those reported by Gray and Brown (16) to be near the band edges, affect turn-on voltages, of MOS transistors. Surface recombination velocity, which is related to transistor gain, will be shown later in this paper to be correlated with several of the fast surface states. It should be noted that similar C-V curve distortions indicating fast surface states are found for n-type silicon.

Gray and Brown (16, 26) have reported that fast surface state densities may be more readily observed using low temperature (—196°C) C-V plots. As the temperature decreases, the Fermi level moves toward the band edge. Thus, the distortion in the C-V plot due to fast states near the valence band in p-type silicon becomes more pronounced at the low temperaure, resulting in a ledge or plateau in the C-V plot. The number of volts over which this ledge extends can be an indication, or relative measure, of fast state density. This effect is shown in Fig. 3. The larger the number of fast states, the further displaced the flatband voltage and the greater the ledge voltage. A considerable amount of hysteresis and other effects can occur during this low temperature plotting, but reproducible results of the type shown in Fig. 3 can be obtained if the structure is cooled under positive bias and plotted from positive (inversion) to negative (accumulation) bias. For n-type silicon the situation is just the opposite. It can be noted in Fig. 3 that the capacitance minimum of the low temperature plot is higher at the right side of the ledge than the room temperature value. This occurs once the voltage sweep is started, although it does not occur in static measurements. The phenomenon, which is not present in gate-controlled diodes or where a sufficient supply of minority carriers is present, is not completely understood but does not affect the fast state measurement.

The low temperature effect for gate-controlled diodes, where low frequency type C-V curves are obtained, is similar to the capacitors described above. An example is shown in Fig. 4 for such a structure having a medium number of fast states under the gate region. Included in the figure are the effects obtained for different conditions of voltage sweep direction and illumination. Note that if the plot is made from the accumulation side (— bias), nonequilibrium depletion characteristics prevent the measurement of the fast state ledge. Thus, as is also the case for capacitors, low temperature plots must be made from inversion to accumulation. For this plot direction the sweep rate has

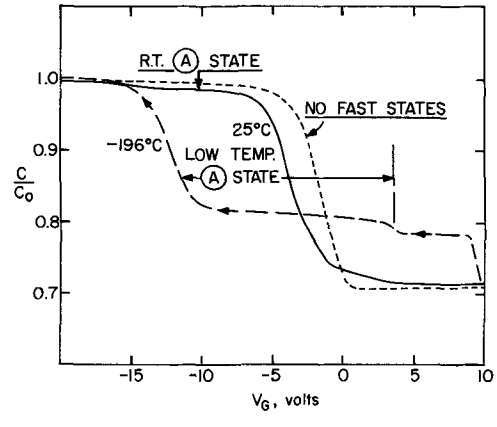

Fig. 3. Example of room temperature (25°C) and low temperature (—196°C) C-V curves for an MOS capacitor exhibiting medium-low fast state density. Thermal oxide was prepared in dry O_2 at 1200°C with rapid cool. Also shown is theoretical C-V curve for same structure with no fast states. [Silicon type, orientation and doping as well as oxide thickness same as Fig. 2 for Fig. 3-8.]

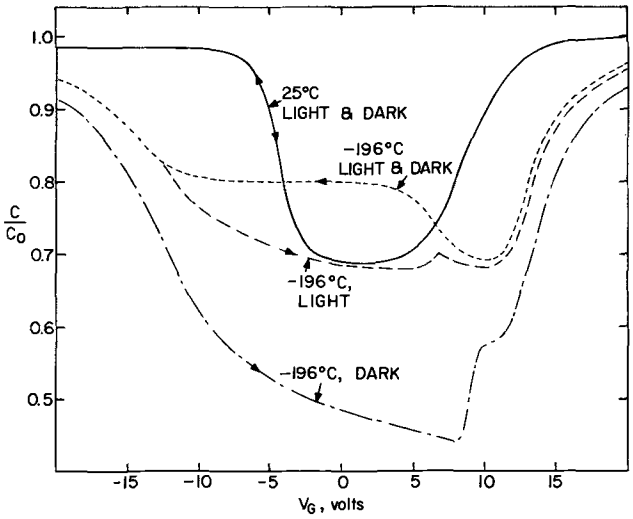

Fig. 4. Effect of plotting conditions on —196° and 25°C C-V plots for an MOS gate-controlled diode with medium fast state density.

not been found to affect the ledge or fast state measurement.

Note from Fig. 4 that the effective inversion point has been shifted to the right or more positive voltage at —196°C. Also the capacitance minimum is that predicted by theory at this temperature, *i.e.*, slightly lower than at 25°C. It should be kept in mind that for low frequency type C-V plots as obtained with gate-controlled diodes the room temperature Ⓒ-state voltage is as good a way to measure fast state density. However, this structure is more difficult to prepare and under many conditions the low temperature plots using MOS capacitors are preferred.

The change of the C-V characteristic shape with temperature is demonstrated in Fig. 5. Here a gate-controlled diode structure was cooled to —196°C. The C-V plot was made and the device allowed to slowly warm to room temperature. At various time intervals additional C-V plots were made, thus providing a series at different temperatures. The change in apparent Ⓐ-state voltage as well as the shift in inversion voltage can be noted.

Annealing of Fast Surface States

In earlier work in this laboratory (21) it was found that fast surface state densities were reduced to a level below the MOS C-V method detection point ($<5 \times 10^{10}$ cm^{-2}) during the heat treatment used to insure back side ohmic contact of aluminum to the silicon. This heat treatment is in the temperature range 500°-565°C

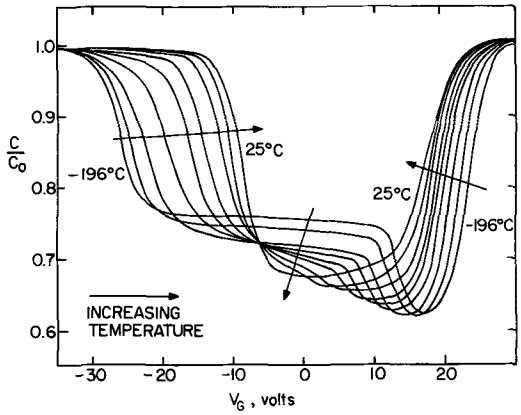

Fig. 5. Change of C-V curve shape with temperature for an MOS gate-controlled diode with medium fast state density.

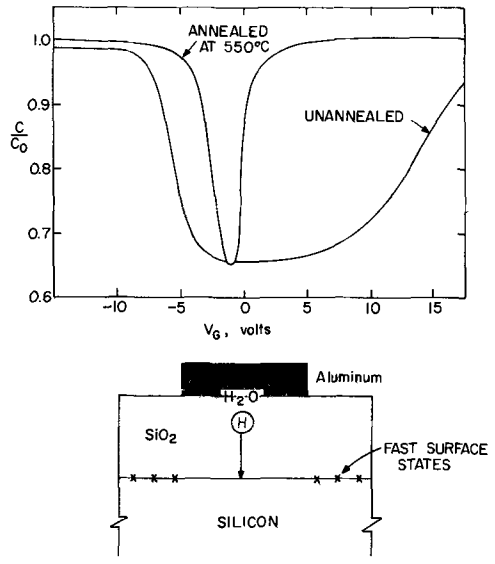

Fig. 6. Effect of post-aluminum anneal on low frequency type C-V curve for an MOS capacitor exhibiting medium fast state density. Lower portion of figure indicates proposed model for the annihilation of fast states by a hydrogen species produced by an Al-H_2O reaction.

for 2-5 min in dry nitrogen. Coincidentally, aluminum field plates are also on the oxide during this alloying step. Balk reported this fast state annealing effect (18) and proposed that during the heat treatment the aluminum reacts with minute amounts of water on the oxide surface to release a hydrogen species. This hydrogen migrates rapidly to the Si-SiO_2 interface and annihilates the fast surface states. Balk's earlier work added support to this model through hydrogen annealing experiments where a similar fast state annealing effect was noted (27).

This annealing effect when aluminum is present over the oxide is demonstrated in Fig. 6. In the upper part of the figure MOS C-V curves of gate-controlled diode structures are shown before and after a 550°C heat treatment for 2 min in dry N_2. Initially, a 0.2μ oxide structure resulted in a Ⓒ-state voltage of nearly 20V at 100 kHz. After the anneal, the theoretical curve shape is approached. If the aluminum were not present over the oxide, annealing for hundreds of hours in dry N_2 would be required to obtain this low number of fast states.

The lower part of Fig. 6 represents Balk's proposed mechanism for the annealing step. Here some hydrogen species is released to eliminate the fast states at the interface.

The effectiveness of the annealing step discussed above for minimizing fast state densities in thermally oxidized silicon structures is indicated in Fig. 7. Here, room temperature C-V plots are shown for both low and high Q_{ss} [2] oxides on p- and n-type silicon at 100 kHz. Corresponding C-V plots taken at —196°C and 100 kHz as well as data obtained at 25°C and 100 MHz are included. Either of these two measurement conditions should be a sensitive indication of fast states. As observed, the fast state density is less than 5 x 10^{10} cm^{-2}. Also, there is no dependence on the value of fixed surface charge Q_{ss}.

A more practical example of the fast state annealing effect is shown in Fig. 8. Current-voltage plots are given for an MOS n-channel transistor before and after annealing at 550°C with the aluminum field plates present on the oxide. The plots are included for three temperatures: 25°,—72°, and —196°C. Before annealing the device turn-on or threshold voltage is

[2] The relationships between N_{ss} (fast surface states) and Q_{ss} (fixed surface charge) are not discussed in this paper. While their dependence on oxidation temperature and silicon orientation are probably similar, the density of each can be independently varied.

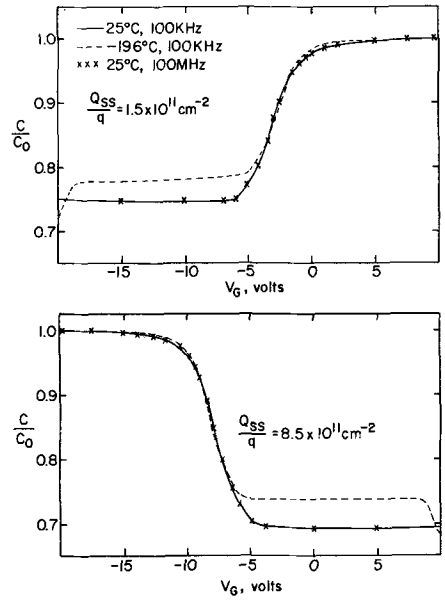

Fig. 7. Example of effectiveness of post-aluminum anneal on reducing fast state density in thermally oxidized silicon. C-V plots taken over wide frequency and temperature ranges on p-type and n-type silicon indicate less than 10^{10} cm^{-2} fast state density for low Q_{ss} (upper curves) and high Q_{ss} (lower curves) MOS capacitors.

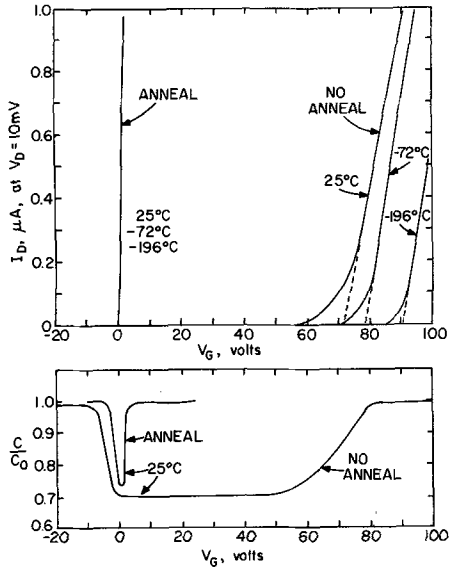

Fig. 8. Effect of temperature on turn-on voltage for an MOS transistor exhibiting a large fast state density before and after post-aluminum anneal. Note the lack of temperature dependence after the anneal. Also shown are the corresponding 25°C C-V plots.

above 70V, even at room temperature. As the temperature decreases this threshold voltage increases as predicted by Fig. 5 and also reported by Brown and Gray (26). After annealing there is no appreciable temperature effect on threshold voltage. Corresponding C-V plots are included in Fig. 8.

Effect of Silicon Nitride Films on the Annealing of Fast States

General effect.—It was reported previously that a silicon nitride layer over thermally oxidized silicon can prevent or retard the reduction of the fast surface state density which normally occurs when aluminum is present over the oxide during a low temperature (550°C) annealing treatment (9). This masking effect was first noted when the distortions of the MNOS C-V curves (attributed to fast states) were not eliminated during the 550°C anneal (see Fig. 6A). The

Table I. Value of V_{FB} and (A)-state voltage for MNOS capacitors*

(After low temperature, post-aluminum nitrogen anneal)

Silicon	V_{FB} (V)	−196°C (A)-state voltage (V)
p-Type (111)	−4.0	10.0
p-Type (100)	−1.7	2.5
n-Type (111)	−4.3	10.0

* Dielectric thickness: 0.1μ Si_3N_4/0.2μ SiO_2.
Oxidation conditions: Dry O_2, 1200°C.
Nitride deposition conditions: $SiCl_4$-NH_3-H_2, 800°C.
Postaluminum anneal conditions: N_2, 550°C, 2 min.
Silicon: $C_B = 1 \times 10^{16}$ cm^{-3}.

presence of the fast states (located at the SiO_2-Si interface) in these double-dielectric structures was confirmed by low temperature C-V plots.

Typical values of the −196°C (A)-state voltage for structures incorporating 0.1μ $SiCl_4$-NH_3-type silicon nitride layers deposited at 800°C over 0.2μ thermal oxides are listed in Table I. These values, as well as flatband voltages V_{FB} were obtained after the conventional 550°C, 5-min heat treatment with aluminum field plates present over the dielectric. This annealing treatment, as mentioned earlier, results in a −196°C (A)-state voltage of less than 0.2V for a thermal oxide of equal thickness but with no nitride layer. The data of Table I indicate that the fast state masking effect due to the nitride layer is the same for p-type and n-type silicon. Furthermore, the resulting fast state density for (100) silicon is less than that for (111) by a factor of one-third, which agrees with data previously reported by Gray and Brown (16).

Additional experiments were carried out involving the effect on fast state annealing by silicon nitride films of varying thicknesses in MNOS gate-controlled diode structures. These thicknesses were 200, 400, 700, and 900A. The reduction of the fast states due to 10 min post-aluminum anneal at 550°C was prevented in all cases except for the 200Å nitride film. It is not clear whether this thin film permitted the reduction effect through the bulk of the nitride or whether pinholes were responsible.

Carrier ambient.—Hydrogen was the carrier gas used for the nitride depositions whose results are summarized in Table I. If this ambient is changed from hydrogen to nitrogen, then an effect on resulting fast state density is obtained which is similar to that previously found for thermal oxides. In other words, a much higher fast state density results for the nitrogen carrier ambient. A typical example of this large increase in fast state density is shown in Fig. 9, where a −196°C C-V plot is compared with that obtained at room temperature for a 0.1μ $SiCl_4$ silicon nitride/0.2μ

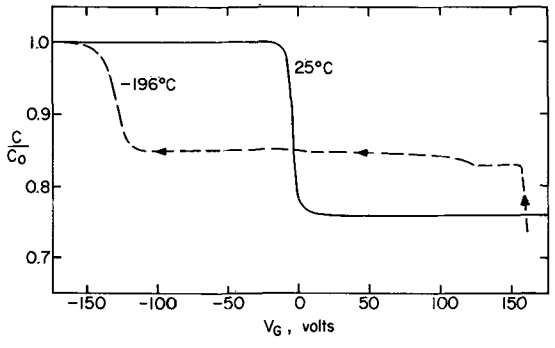

Fig. 9. Room temperature and low temperature (−196°C) C-V plots showing large fast state density induced by postnitride deposition, high temperature anneal in N_2 for 0.1μ Si_3N_4/0.2μ SiO_2 MNOS capacitor. Note that the post-aluminum anneal does not annihilate these fast states.

Table II. Relative values of fast surface states for MNOS gate-controlled diode structures* as a function of nitride deposition carrier ambient

(After low temperature, post-aluminum nitrogen anneal)

Dielectric	−196°C (A)-state voltage (V)	25°C (C)-state voltage (V)	Surface Recombination velocity, s_0 (cm/sec)
Thermal oxide	0.2	3.1 (0.1)	1-5
Silicon nitride (H_2)/thermal oxide	7	7 (4)	5-10
Silicon nitride (N_2)/thermal oxide	200	120 (117)	250
Silicon nitride (5% H_2)/thermal oxide	50	Not measured	Not measured

* Same process conditions as for Table I.
Silicon type: p-type, (111), $C_B = 1 \times 10^{16}$ cm^{-3}.

thermal oxide MNOS capacitor. It was also found that if a small percentage of hydrogen (*i.e.*, 5%) is included in the nitrogen carrier ambient, an intermediate value for the fast state density will be obtained.

Data typifying the above findings using gate-controlled diode structures are summarized in Table II, where values of −196°C (A)-state voltages, (C)-state voltages, and surface recombination velocity are listed. In the case of the (C)-state voltages, the theoretical width of the C-V curves is subtracted, leaving the excess value due to fast states in parentheses. The table provides an indication of the very good correlation among (A)-state and (C)-state voltages and s_0.

Subsequent high temperature annealing treatment.—Samples of the same depositions listed in Table I were subjected to an additional annealing treatment in nitrogen at 1000°C for 15 min prior to metallization. Values of flatband voltage and −196°C (A)-state voltages (obtained after the post-aluminum, 550°C nitrogen anneal) are given in Table III. These results indicate the large increase in fast state density due to this nitrogen treatment and demonstrate the ability of the nitride layer to prevent post-aluminum reduction of the fast states. It should be kept in mind that similar processing of thermal oxide structures alone will result in (A)-state voltages of less than 0.2V after post-aluminum anneal, even though very high fast state densities result after the 1000°C treatment in nitrogen.

Other experiments involved treatment of MNOS structures in 100% hydrogen at 700°-1000°C for 30 min, the structures having previously been deposited using a nitrogen carrier ambient. The very high density of fast states resulting from the deposition process was apparently reduced by the hydrogen to the same value obtained using hydrogen as the carrier ambient during deposition, *i.e.*, an (A)-state voltage of 7-10V for (111) silicon.

Table III. Values of V_{FB} and (A)-state voltage for MNOS capacitors*

(After 1000°C nitrogen anneal and subsequent low temperature post-aluminum nitrogen anneal)

Silicon	V_{FB} (V)	−196°C (A)-state voltage (V)
p-Type (111)	−5.5	200
p-Type (100)	−2.3	25
n-Type (111)	−6.1	200

* Same samples and process conditions as for Table I except for 15 min, slow-pull anneal in N_2 at 1000°C after nitride deposition.

Table IV. Similarity in effects on Ⓐ-state voltage of MNOS capacitors* due to deposition carrier ambient as compared to subsequent anneal in the same ambient at the same temperature

Nitride ($SiCl_2$-NH_3) carrier ambient	Anneal ambient (700°-1000°C)	−196°C Ⓐ-state voltage (V)
H_2	—	7-10
N_2	—	150-200
N_2	H_2	7-10
H_2	N_2	150-200
5% H_2 / 95% N_2	—	25-50

* Same process conditions as for Table I.
Silicon type: p-type, (111), $C_B = 1 \times 10^{16}$ cm^{-3}.

The similarity between the results due to the carrier ambient and subsequent anealing treatments is summarized in Table IV. Ranges in values are tabulated for a number of depositions and samples. It is apparent that for the conditions of these experiments involving $SiCl_4$-NH_3 nitrides, hydrogen results in medium-low values of fast state densities while nitrogen gives high densities, either during the deposition or subsequent anneals. The nitride layer does not permit these states to be annealed or annihilated by the post-aluminum treatment in any case.

It was also shown that when high densities of fast states were produced in $Si_3N_4/SiO_2/Si$ structures incorporating SiH_4-NH_3 nitrides, these states also could not be annealed by the post aluminum 550°C treatment. The nature of differences due to the SiH_4 deposition process will be discussed later.

Structure variations in silicon nitride.—Changes in the structure of the silicon nitride film might be expected to affect its ability to mask against the fast state annealing. It has been reported that several deposition variables such as temperature, reactant compositions, and flow rates can result in nitride films of varying structure or composition (8). These differences can in turn be reflected by variations in etch rates.

Effects of film composition or structure on fast state density are presented in Table V, where three different deposition temperatures resulted in varying etch rates (in concentrated HF) and varying fast state densities after the post-aluminum anneal. For the depositions used to prepare the structures reported in Table V, flow and reactant composition conditions were maintained constant.

Another way to change the silicon nitride structure is to vary total flow rate, *i.e.*, the slower the flow rate, the faster the etch rate. Experiments were carried out in which fast state densities of nitride/thermal oxide structures were determined as a function of etch rate, the latter varied by flow rate changes. Results of these experiments, for $SiCl_4$ nitrides deposited at 900°C, are given in Fig. 10. The correlation between etch rate and fast state density is readily apparent, and results correlate very closely with the values listed in Table V. Thus, the relationship between fast state density and silicon nitride structure (indicated by etch rate) is clearly established.

Table V. Dependence of Ⓐ-state voltage of MNOS capacitors* on nitride etch rate and deposition temperature

Deposition temperature (°C)	Etch rate (conc. HF) (Å/sec)	−196°C Ⓐ-state voltage (V)
760	20	3-4
800-850	12	6-9
900	4	10-14

* Same process conditions as for Table I.
Silicon type: p-type, (111), $C_B = 1 \times 10^{16}$ cm^{-3}.

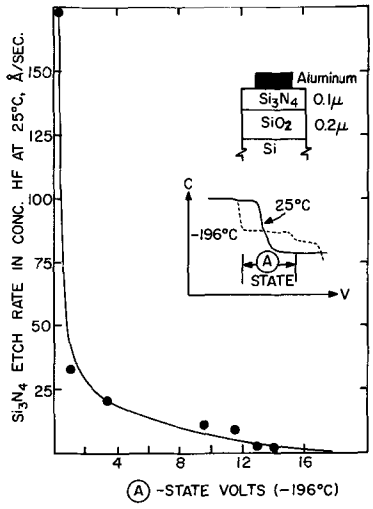

Fig. 10. Relationship of fast state (low temperature Ⓐ-state voltage) density after post-aluminum anneal to Si_3N_4 etch rate for MNOS capacitors.

Silicon nitride type ($SiCl_4$ *vs.* SiH_4).—Most of the results reported thus far have been concerned with silicon nitride films deposited using the $SiCl_4$-NH_3 reaction. While these nitrides prevent the post-aluminum annealing of fast states, they cause a minimum amount of polarization in the MNOS structure either as deposited or after 300°C stress tests.

Differences have been noted, however, for silicon nitride films deposited using the SiH_4-NH_3 reaction as compared with the $SiCl_4$-NH_3 reaction. While similar etch rates in concentrated HF are observed (1 to 10 Å/sec), very low fast state densities are observed for the silane nitride structures even before the post-aluminum anneal. These low values are obtained whether the deposition carrier ambient is nitrogen or hydrogen and over a wide temperature range. If these structures are given a subsequent high temperature anneal in nitrogen, large fast state densities are obtained as is the case for $SiCl_4$ nitrides.

The silane nitrides also cause much more polarization (9) in the MNOS structures both before and after 300°C stress tests. Examples of differences in fast state densities and polarization for the two nitride types are shown in Fig. 11. The C-V curves for the SiH_4 nitrides are of the low frequency type due to inversion of the surrounding silicon for the examples shown. This in-

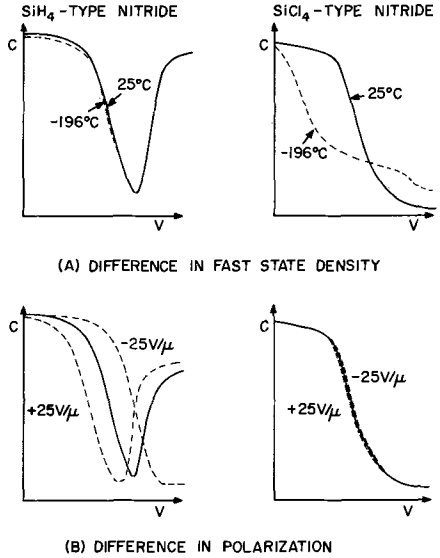

Fig. 11. Difference in electrical characteristics after post-aluminum anneal of MNOS capacitors incorporating either $SiCl_4$ or SiH_4 type silicon nitride layers.

version is prevented in the $SiCl_4$ nitride samples by the fast states.

Fast State Annealing Mechanism

The results reported thus far concerning the ability of certain silicon nitride films deposited over thermal oxides to prevent reduction of fast state densities at the SiO_2-Si interface generate some interesting questions. The first is: How does the silicon nitride film prevent the fast state annealing? In fact, what is the mechanism of post-aluminum annealing of fast states in thermal oxides?

If we accept Balk's proposed mechanism (18) that the fast state reduction in oxides occurs by the action of a hydrogen species produced by the reaction of the metal, *i.e.*, aluminum, with water on the oxide surface, then two possibilities exist for the nitride case: Either the nitride surface prevents the Al-water reaction, or the nitride prevents the migration of the hydrogen species to the SiO_2-Si interface where the fast states are located. The following experiment was conducted to establish the more likely possibility. MIS capacitors were fabricated which included four different combinations of dielectrics. As shown in Fig. 12, they were: I. Si_3N_4 only, II. Si_3N_4 over thermal SiO_2, III. vapor-deposited SiO_2 over Si_3N_4 over thermal SiO_2, and IV. vapor-deposited SiO_2 over thermal SiO_2. All nitrides were deposited using the $SiCl_4$-NH_3-H_2 reaction. The silicon in all cases was p-type (111) and aluminum field plates were deposited on each structure. After the 550°C nitrogen treatment, C-V plots were obtained at 25° and —196°C and are indicated in Fig. 12. Note that for the Si_3N_4-only structure, the high surface charge associated with the nitride-silicon interface results in a low frequency type C-V curve.

If the nitride merely prevents some surface reaction with the aluminum, then structure No. III of Fig. 12 with vapor deposited oxide should allow this reaction to occur and the fast states should be annihilated as happens in structure No. IV (no nitride). However, this did not occur. Thus we assume, as is indicated in the figure, that the hydrogen species is produced by the reaction of aluminum and possibly water, and that the dense Si_3N_4 (structures I, II, III) blocks the hydrogen migration as it also blocks Na^+ ion migration at temperatures up to 550°C. At higher temperatures (700°-1000°C) some amount of hydrogen can penetrate the nitride (28), thus resulting in a decrease of fast states (see Table IV).

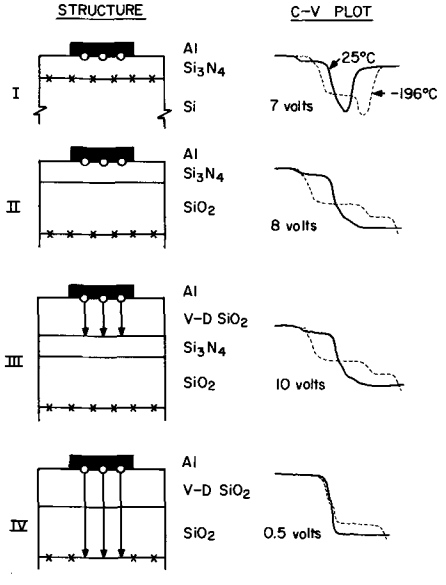

Fig. 12. Results of experiment designed to determine mechanism for nitride masking of fast state annihilation during post-aluminum anneal. Conclusion is that the silicon nitride layer prevents migration of a hydrogen species to the fast states.

A further indication that Balk's model of a metal-water reaction is responsible for fast state annealing was obtained from the results of comparing the effect of a number of metals used as field plates over thermal oxides. The over-all trend for the same postmetallization treatment (550°C, 2 min, N_2) was that the more active metals such as aluminum and magnesium resulted in very low fast state densities, while the less active metals such as gold and platinum permitted very little reduction of fast state densities.

Another question posed by these results concerns the difference between silicon nitrides produced by $SiCl_4$ or SiH_4. While the SiH_4 nitride structures over thermal oxides exhibit much lower fast state densities as deposited than $SiCl_4$ nitrides, very large densities of fast states can be induced by subsequent high temperature annealing of both nitride types in nitrogen. These fast states cannot be annihilated by post-aluminum annealing. Thus, the structural aspects of the two types of nitrides are considered similar, with the probable cause of fast state variations as well as differences in amount of polarization being due to the reactants $SiCl_4$ and SiH_4.

The main difference between SiH_4 and $SiCl_4$ is the hydrogen. However, both processes can involve hydrogen as a carrier gas. Thus, this indicates that a special form of hydrogen, *i.e.*, active or atomic, is produced in the SiH_4 reaction and this is what is required for fast state reduction. An experiment was designed to test out the active or atomic hydrogen theory. Special MNOS structures incorporating a $SiCl_4$ nitride were prepared using palladium field plates. These structures, along with nonmetallized controls, were treated in hydrogen at 800°C for 5 min. Aluminum was then deposited over the palladium for better contact and —196°C C-V plots were obtained. Results indicating relative values of fast state densities as well as amount of polarization are tabulated in Table VI.

It is well known that molecular hydrogen will dissociate into an atomic species on a palladium surface at elevated temperatures (29). This atomic hydrogen will then diffuse through the palladium if the hydrogen pressure is reduced on the other side. This is the basis for one type of hydrogen purifier. The results given in Table VI are remarkable in that the higher fast state density and low polarization of the $SiCl_4$-type silicon nitride/thermal oxide structure has been converted to the SiH_4-type silicon nitride/thermal oxide structure exhibiting no fast states but considerably more polarization. Apparently at 800°C the atomic species of hydrogen produced by a reaction with palladium diffused through the silicon nitride layer and into the silicon oxide. Here this species is free to annihilate the fast states at the SiO_2-Si interface, but at the same time can migrate back and forth in the oxide (30, 31). These results thus lead to the conclusion that the electrical difference between the two types of nitrides might be explained on the basis of atomic or active hydrogen produced by the SiH_4-NH_3

Table VI. Effect of palladium field plate and 800°C hydrogen anneal on electrical properties of MNOS capacitors*

Palladium field plate	Hydrogen anneal	−196°C Ⓐ-state voltage (V)	Polarization ΔV (V)
No	No	5-6	<0.2
No	Yes	5	<0.2
Yes	No	4-5	<0.2
Yes	Yes	<0.2	7.5

* Nitride deposition conditions: $SiCl_4$-NH_3-H_2, 800°C.
Dielectric thickness: 0.1μ Si_3N_4/0.2μ SiO_2.
Hydrogen anneal conditions: 800°C, 5 min.
Final metallization: aluminum field plates over palladium or nitride.
Postmetallization anneal conditions: N_2, 550°C, 3 min.
Test for polarization: 300°C, ±10V, 2 min.
Silicon type: p-type, (111), $C_B = 1 \times 10^{16}$ cm^{-3}.

reaction. This type of hydrogen, not present to any extent in the $SiCl_4$-NH_3 process, reduces the number of fast states but causes polarization in the nitride/oxide structure. It was interesting to note that the medium-low density of fast states in thermal oxide controls (no field plates) was not reduced by the hydrogen annealing at 800°C.

The above experiment involving palladium field plates and hydrogen was also carried out at 550°C. At this temperature no changes in electrical characteristics of the $SiCl_4$-type nitride/oxide structure occurred. This was undoubtedly due to the inability of any hydrogen species to diffuse through the nitride layer and is in agreement with the main finding of this paper, *e.g.*, fast states are not annihilated during the 550°C postmetallization anneal process in Si_3N_4/SiO_2 structures.

Conclusions

The characteristics of fast surface states associated with thermally oxidized silicon structures have been studied using the MOS capacitance-voltage method of analysis along with other device measurements. Process conditions for induction and annihilation of fast states have been established. While the initial fast state density of thermal oxides may be related to the fixed charge Q_{ss}, the presence or absence of a hydrogen-containing species during the cooling process or subsequent thermal treatments may determine the final fast state density. If a hydrogen species is present, a low fast state density results. Furthermore, the common low temperature (550°C), post-aluminum anneal has also been shown to be very effective in reducing fast state densities to low levels in thermal oxide structures.

Thin, silicon nitride layers have been shown to prevent or retard the annihilation of fast states in underlying, thermally oxidized silicon during the post-aluminum annealing treatment. The following effects of process variations on this phenomenon have been noted.

1. The masking or retardation of the fast state annihilation in $Si_3N_4/SiO_2/Si$ structures due to the silicon nitride layer is not dependent on silicon impurity type, concentration, or silicon orientation. Nitride layers thicker than 200Å are effective in retarding fast state reduction.

2. The final density of fast states is a function of the carrier and cooling ambient during silicon nitride deposition where $SiCl_4$ is the reactant. A nitrogen ambient will result in a large fast state density, hydrogen in a medium-low density.

3. Postdeposition annealing treatments at 700°-1000°C in nitrogen will induce large densities of fast states in MNOS structures which will not be reduced by the post-aluminum anneal treatment. A subsequent high temperature anneal in hydrogen at 700°-1000°C of a $Si_3N_4/SiO_2/Si$ structure with a high fast state density will reduce this value back to that originally obtained in $SiCl_4$-NH_3-type deposition involving a hydrogen carrier ambient.

4. The structure of the silicon nitride layer as reflected by its etch rate will influence its ability to mask against fast state annihilation. The faster the etch rate in concentrated HF, the less effective the masking. Deposition variables (such as reactant compositions, flow rates, and temperature) which affect nitride structure also affect the fast state masking property.

5. The type of nitride, $SiCl_4$ or SiH_4, has a very important effect on the fast state densities. Nitrides produced by the $SiCl_4$-NH_3-H_2 reaction result in medium-low fast state densities (5-10 x 10^{11} cm^{-2}). Those nitrides produced by the SiH_4-NH_3-H_2 reaction, on the other hand, provide very low fast state densities (<2 x 10^{10} cm^{-2}) but do cause significant polarization. Neither type of nitride permits fast states induced by post-deposition anneals to be subsequently annihilated by post-aluminum treatments.

From the above results, it is believed that for thermally oxidized silicon MOS structures some type of hydrogen species is produced during postmetallization anneals at 500°-565°C by the reaction of the field plate metal, *i.e.*, aluminum, with water adsorbed on the oxide surface. This hydrogen then migrates to the SiO_2-Si interface where it somehow annihilates the fast states. Silicon nitride layers deposited over the thermal oxide retard this hydrogen migration, however, and any fast states remaining after the nitride deposition or subsequent high temperature annealing treatments are not annihilated by the post metallization anneal. A similar hydrogen species is produced during the deposition of silane-type nitrides which, at the temperatures of deposition, can migrate through the nitride layer. This causes a reduction in fast state density, but also results in a polarization-type of instability.

Acknowledgment

The authors wish to thank Maija Sklar and Philip Fleming for their assistance during the experimental portion of this program, and A. S. Grove for helpful discussions.

Manuscript submitted Jan. 13, 1969; revised manuscript received March 11, 1969. This was Paper 86 presented at the Boston Meeting, May 5-9, 1968.

Any discussion of this paper will appear in a Discussion Section to be published in the June 1970 JOURNAL.

REFERENCES

1. N. C. Tombs *et al.*, *Proc. IEEE*, **54**, 87 (1966).
2. V. Y. Doo, *IEEE Trans. Electron Devices*, **ED-13**, 561 (1966).
3. S. M. Hu, *This Journal*, **113**, 693 (1966).
4. T. L. Chu, C. H. Lee, and G. A. Gruber, *ibid.*, **114**, 717 (1967).
5. S. M. Hu and L. V. Gregor, *ibid.*, **114**, 826 (1967).
6. D. R. Kerr, J. S. Logan, P. J. Burkhardt, and W. A. Pliskin, IBM *J. Res. Develop.*, **8**, 376 (1964).
7. E. H. Snow and B. E. Deal, *This Journal*, **113**, 263 (1966).
8. Electrochemical Society, Joint Symposium (Dielectrics and Insulation and Electronics—Semiconductor Division), on Silicon Nitride, Oct. 12 and 13, 1966, Philadelphia, Pa.
9. B. E. Deal, P. J. Fleming, and P. L. Castro, *This Journal*, **115**, 300 (1968).
10. T. L. Chu, J. R. Szedon, and C. H. Lee, *Solid-State Electronics*, **10**, 897 (1967).
11. B. E. Deal, E. H. Snow, and A. S. Grove, *SCP and Solid State Tech.*, **9**, (No. 11), 25 (1966).
12. A. Many, Y. Goldstein, and N. B. Glover, "Semiconductor Surfaces," John Wiley and Sons, New York (1965).
13. L. M. Terman, *Solid-State Electronics*, **5**, 285 (1962).
14. E. H. Nicollian and A. Goetzberger, *Appl. Phys. Letters*, **7**, 216 (1965).
15. K. H. Zaininger and A. G. Revesz, *ibid.*, **7**, 108 (1965).
16. P. V. Gray and D. M. Brown, *ibid.*, **8**, 31 (1966).
17. E. Kooi, "The Surface Properties of Oxidized Silicon," Philips Technical Library, Springer-Verlag, Netherlands (1967).
18. P. Balk, Paper presented at the Buffalo Meeting of the Society, Oct. 10-14, 1965, Abstract 111.
19. B. E. Deal, *This Journal*, **110**, 527 and 1292 (1963).
20. B. E. Deal and A. S. Grove, *J. Appl. Phys.*, **36**, 3770 (1965).
21. A. S. Grove, B. E. Deal, E. H. Snow, and C. T. Sah, *Solid-State Electronics*, **8**, 145 (1964).
22. A. S. Grove and D. J. Fitzgerald, *ibid.*, **9**, 783 (1966).
23. A. Goetzberger, V. Heine, and E. H. Nicollian, *Appl. Phys. Letters*, **12**, 95 (1968).
24. S. T. Hsu, D. J. Fitzgerald, and A. S. Grove, *ibid.*, **12**, 287 (1968).
25. B. E. Deal, M. Sklar, A. S. Grove, and E. H. Snow, *This Journal*, **114**, 266 (1967).
26. D. M. Brown and P. V. Gray, *ibid.*, **115**, 760 (1968).

27. P. Balk, Paper presented at the San Francisco Meeting of the Society, May 9-13, 1965, Abstract 109.
28. L. V. Gregor, "Study of Silicon Nitride as a Dielectric Material for Microelectronic Applications," Final Report, WPAFB Contract No. AF33-615-5386, Nov. 1967.
29. S. Dushman, "Scientific Foundations of Vacuum Technique," p. 612, John Wiley and Sons, New York (1949).
30. P. J. Burkhardt, *This Journal*, **114**, 196 (1967).
31. S. R. Hofstein, *IEEE Trans. Electron Devices*, **ED-14**, 749 (1967).

Thermal Diffusion of Sodium in Silicon Nitride Shielded Silicon Oxide Films

T. E. Burgess, J. C. Baum,[1] F. M. Fowkes,*[2] R. Holmstrom,[3] and G. A. Shirn*

Sprague Electric Company, North Adams, Massachusetts

ABSTRACT

The ability of silicon nitride layers deposited on silicon oxide-passivated silicon to act as contamination barriers has been measured through the use of a radioisotope, sodium-22. Transport studies at 500°C have shown that the concentration of sodium reaching the silicon oxide-silicon interface was reduced one thousandfold when a 1000Å shield of silicon nitride was present. These nitride films which may be deposited by any one of several techniques act not only as mechanical barriers against sodium penetration, but also as sodium getters. The amount of sodium retained by the silicon nitride film depends mainly on the film deposition temperature. For example, silicon nitride films deposited at 850°C trap more sodium than those deposited at 1100°C. The presence of moisture in the ambient atmosphere during any annealing process of a silicon nitride shielded silicon oxide film will release some of the sodium trapped in the nitride layer and allow it to move to the silicon oxide-silicon interface.

With the change to plastic packages for silicon transistors and microcircuits, silicon dioxide passivated surfaces are more subject than ever before to degradation of insulating properties by mobile charges arising from the incursion of moisture and sodium or similar impurities. Junctions are softer, gain decreases, and nearly all MOS transistor characteristics are degraded (1-3). One potential remedy for these ills is to shield the passivating oxide from moisture and sodium by covering it with an impermeable shielding layer of silicon nitride, which can be deposited by a variety of techniques (4-6). The effectiveness of silicon nitride shields has been assessed and compared by measuring the amount of thermal diffusion of sodium-22 through silicon nitride shielded silicon oxide films. As will be shown, the amount of sodium entering the passivating oxide from the nitride shield is not proportional to the concentration of sodium in the nitride, so simple diffusion studies in nitride films (7) do not necessarily predict their relative effectiveness as contamination shields. This method consists of the deposition of a measured amount of sodium-22 chloride solution on the surface of the film followed by indiffusion of the sodium for 2 hr at 500°C. The sodium-22 concentration profile in the film is used as a measure of the shielding ability of the film.

Experimental

Silicon wafers cut from (100) or (111) single crystal material were oxidized in dry oxygen at 1150°C to produce 2000Å silicon oxide films. The 1000Å silicon nitride films were deposited on this silicon oxide layer by either a pyrolytic chemical vapor deposition (PCVD) (3, 4) or by a RF-reactive sputtering technique (6). The PCVD films were prepared in 1:10, 1:100, or 1:200 silane-ammonia mixtures with the substrate temperature at 850°, 1000°, or 1100°C. The carrier gas in all cases was hydrogen. The RF sputtered silicon nitride films were deposited by reactive sputtering of a silicon target in a nitrogen atmosphere.

A carrier-free sodium-22 chloride solution which contained about 0.03 mc/ml of sodium-22 was used for the indiffusion. The specific activity of such a solution was around 5 x 10^{10} Na atoms/count/minute in the NaI well-type scintillation detector used in this work. This solution was added drop-wise from a dropping pipet to the surface of the sample film and dried at 90°C for 15 min. It was not necessary to cover the entire surface of the film with an even distribution of the radiotracer in this type experiment since comparisons were made between similarly indiffused samples. However, it was important that the same amount of sodium-22 was deposited on each surface. Five drops (approx. 0.25 mil) of the sodium-22 chloride solution gave a significant activity in most films after diffusion, and this amount of the solution was easily and reproducibly deposited on the surface of the films. Autoradiographs of indiffused samples showed that five drops covered about one tenth of the total surface area of the sample. If more sensitivity is desired, then additional sodium-22 could be deposited on the surface; however, this increase in sodium-22 must be taken into account when comparing these samples with those containing smaller amounts of the radiotracer.

After deposition of the sodium-22 chloride on the surface of the film the samples were placed on a quartz boat and annealed at 500°C in a flowing dry nitrogen atmosphere for 2 hr. The sodium-22 contaminated surface was covered during the annealing process with a clean silicon wafer to reduce the loss of sodium-22 by evaporation.

Successive layers of the films were dissolved in an appropriate solvent after indiffusion of the radiotracer was completed. Concentrated hydrofluoric acid (49%) was used as the etchant for the PCVD silicon nitride while a 10:1 solution of water-hydrofluoric acid was used to etch the silicon oxide. Silicon oxide films dis-

* Electrochemical Society Active Member.
[1] Present address: Princeton University, Princeton, New Jersey.
[2] Present address: Chemistry Department, Lehigh University, Bethlehem, Pennsylvania.
[3] Present address: Intel Corporation, Mountain View, California.

solve in this solution at a rate of about 300 Å/min. The solubility of PCVD silicon nitride in concentrated hydrofluoric acid depends on the method of preparation. The etch rate of this film varies betwen 40 to 200 Å/min depending on the density of the film. In order to obtain a sharp boundary in the sodium concentration profile between the silicon nitride and silicon oxide layers the final 400Å of the silicon nitride were always dissolved in hot phosphoric acid. This etchant will not attack silicon dioxide appreciably, but will dissolve PCVD silicon nitride at a rate of about 50 Å/min. The sodium-22 content of each etch solution was determined directly by the well scintillation detector.

Results and Discussion

These sodium transport studies show that a 1000Å silicon nitride film effectively shields an underlying silicon oxide film against sodium indiffusion at temperatures up to 500°C. Table I shows the average value of sodium-22 concentration found at silicon nitride-silicon oxide and silicon oxide-silicon interfaces for several samples indiffused with sodium-22 at 500°C for 2 hr in a dry nitrogen atmosphere. The PCVD silicon nitrides were deposited at three different substrate temperatures 850°, 1000°, and 1100°C using silane-ammonia gas mixtures of 1:10, 1:100, or 1:200. The density of the silicon nitride film deposited by the pyrolytic process depends on the substrate temperature and is greater for films deposited at higher temperatures. The density effects the solubility of these films with the etch rate in concentrated hydrofluoric acid being the slowest for the films prepared at 1100°C. The shielding abilities of the silicon nitride films are demonstrated by comparing the sodium concentration measured at the silicon oxide-silicon interfaces.

Since device performance is influenced by ionic impurities in the oxide film near the silicon surface, sodium concentrations in the oxide within about 300Å of the silicon surface are most important. If in Table I a comparison is made between the unshielded silicon oxide samples and those protected by a silicon nitride layer, it is seen that the presence of a nitride film reduced the amount of sodium-22 reaching the silicon oxide-silicon interfaces by as much as one thousandfold. The RF-sputtered silicon nitride films did not give the protection against the sodium penetration afforded by the PCVD silicon nitride films probably because these films were less dense than the PCVD layers.

Typical sodium-22 concentration distributions in the silicon nitride-silicon oxide films are shown in Fig. 1. The most striking feature of this figure is the shielding ability of the silicon nitride film when compared with the unshielded silicon oxide sodium-22 concentration curve. Further consideration of this figure and the data in Table I brings out another interesting feature of the silicon nitride film. In all of the samples except those prepared by RF sputtering the sodium-22 concentrations in the nitride films after indiffusion are ten to one hundred times larger than the sodium-22 concentrations in the adjacent oxide layers. This sodium distribution indicates that silicon nitride may act not only as a mechanical barrier against sodium penetration, but also as a getter for sodium. In this

Table I. Average values of sodium-22 concentrations at silicon nitride-silicon oxide and silicon oxide-silicon interfaces. Indiffusion at 500°C, 2 hr, N_2 atmosphere, 1000Å Si_3N_4 over 2000Å SiO_2

Si_3N_4 type	Sodium-22 atoms/cm³ Si_3N_4-SiO_2 interface	Sodium-22 atoms/cm³ SiO_2-Si interface	Etch rate Si_3N_4 in HF (Å/min)
PCVD (1:10, 850°C)	9.4×10^{17}	4.5×10^{16}	200
PCVD (1:100, 850°C)	1.1×10^{17}	7.0×10^{15}	200
PCVD (1:200, 850°C)	2.5×10^{16}	2.4×10^{15}	200
PCVD (1:109, 1000°C)	2.2×10^{16}	3.6×10^{15}	40
PCVD (1:100, 1100°C)	4.8×10^{16}	1.2×10^{15}	40
RF Sputtered	2.0×10^{17}	3.2×10^{17}	>>1000
3000Å SiO_2	—	4.8×10^{18}	—

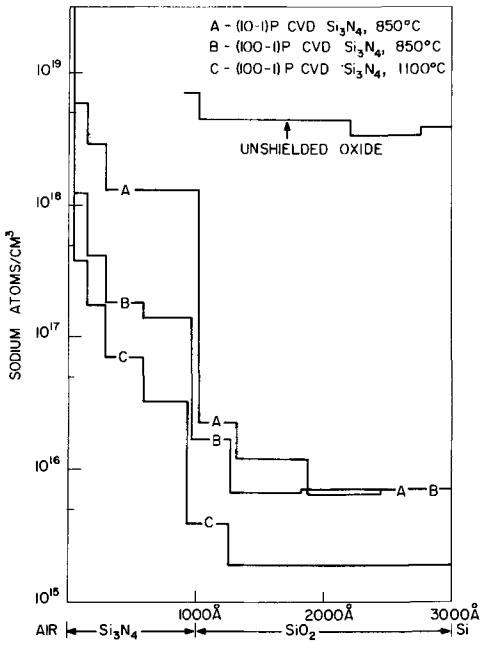

Fig. 1. Concentration of sodium-22 in silicon nitride shielded silicon oxide films after 2-hr indiffusion at 500°C in dry nitrogen.

case it should be possible for sodium originally present in the underlying silicon oxide film to out-diffuse into the silicon nitride layer under the conditions used for deposition of this film. This reaction is demonstrated in Fig. 2. Here, an 850°C PCVD 1:100 silicon nitride film was deposited over a silicon oxide film which contained indiffused sodium-22. After the deposition of the nitride film the sodium-22 originally present in the silicon oxide film was found distributed throughout the silicon nitride-silicon oxide layers. Measurements also showed that the sodium concentration was at least tenfold larger in the silicon nitride layer.

The results indicate that silicon nitride films act as both getters for sodium and physical barriers against sodium penetration. These characteristics are strongly influenced by the method of preparation. Although the physical characteristics of all the silicon nitride films were almost identical, the films produced at the higher temperatures were more dense and prohibited sodium penetration by acting as simple mechanical barriers. However, as Table I and Fig. 1 show, the sodium

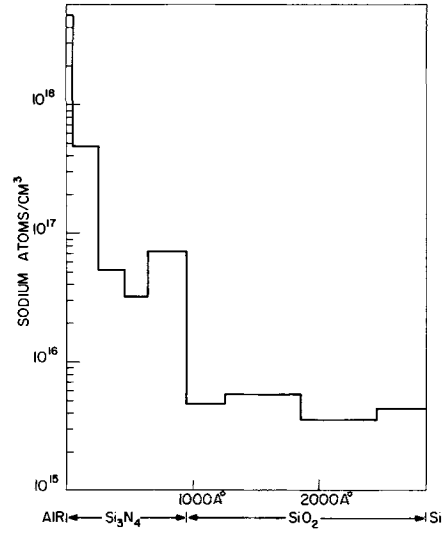

Fig. 2. Gettering of sodium-22 by pyrolytic CVD (100-1) silicon nitride deposited at 850°C on sodium-22 contaminated silicon oxide.

concentration at the silicon nitride-silicon oxide interface was lower in the higher temperature PCVD films, and these films were not as active sodium getters. In fact, the RF sputtered silicon nitride film which had the lowest density of all films listed in Table I and was deposited at the lowest temperature seemed to be the best sodium getter. Although this film retained a large concentration of sodium, considerable amounts of this ion managed to penetrate the low density silicon nitride layer. The sodium-22 profiles observed in all the silicon nitride films are probably related to the structural defects (vacancies) and their ability to immobilize sodium ions by an electron trapping mechanism. A similar sodium mechanism is reported for silicon oxide films (10).

The diffusion of sodium in silicon oxide films is strongly influenced by the presence of water (8). Water neutralizes the E'_1 centers, associated with oxygen vacancies in SiO_2 (9), that tend to trap electrons and immobilize sodium (10). Figure 3 shows that in the presence of water the sodium has less of a tendency to be trapped in the bulk oxide and is more concentrated next to the silicon. The presence of water vapor in the annealing atmosphere was also found to have a considerable effect on the sodium concentration profile in silicon nitride-shielded silicon oxide films. Sodium concentrations at the silicon oxide-silicon interfaces were increased at the expense of the sodium levels at the air-silicon oxide or air-silicon nitride interfaces. Figures 4 and 5 compare the distribution of sodium-22 in the films after annealing sodium-22 indiffused films in either dry or wet nitrogen. For these measurements samples containing these films were indiffused with sodium-22 for 2 hr at 500°C in a dry nitrogen atmosphere. Each wafer was cut in half and one half was annealed for two hours at 500°C in dry nitrogen while the second half was annealed under the same conditions except in an atmosphere of nitrogen saturated with water (at 25°C). The sodium-22 concentration at the silicon oxide-silicon interface increased in all cases when the annealing was done in an atmosphere containing water vapor. This shift occurred even at a temperature of 200°C.

The immobilizing of sodium in silicon nitride films can be attributed to the presence of electron traps (probably nitrogen vacancies) similar to those found in silicon oxide layers. The fact that the sodium gettering ability of these films varies inversely with the film deposition temperature indicates that silicon nitride layers deposited by the PCVD method at 850°C (or by RF sputtering at lower temperatures) contain larger concentrations of these electron traps than those deposited at 1000° or 1100°C. Release of the trapped sodium through the neutralization of these electron trapping centers by moisture would occur in the same manner as it does in the silicon oxide films, and would permit the sodium to move into the underlying silicon oxide film (Fig. 4 and 5). This mechanism suggests that sodium penetration of the silicon oxide layer would be more likely to occur under conditions of high ambient temperature and humidity when the protecting silicon nitride film was a good sodium getter.

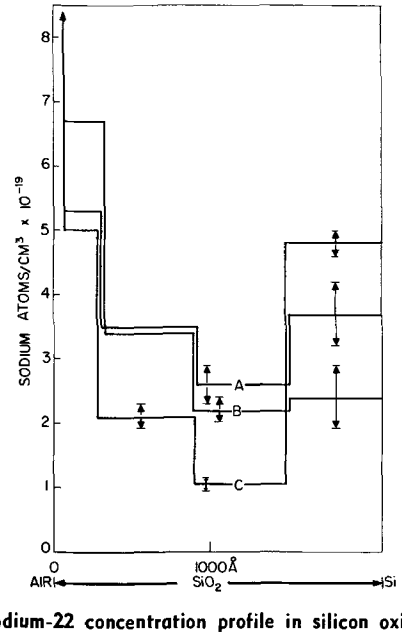

Fig. 3. Sodium-22 concentration profile in silicon oxide film annealed at 500°C: (A) 4 hr, dry nitrogen; (B) 2 hr, dry nitrogen; (C) 2 hr, dry nitrogen plus 2 hr wet nitrogen.

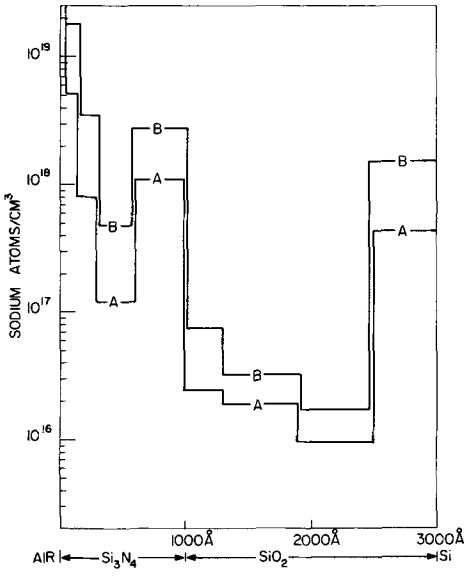

Fig. 4. Sodium-22 concentration profile in silicon nitride shielded silicon oxide annealed at 500°C. (A) 4 hr, dry nitrogen; (B) 2 hr, dry nitrogen plus 2 hr wet nitrogen (pyrolytic CVD (100-1) nitride deposited at 850°C).

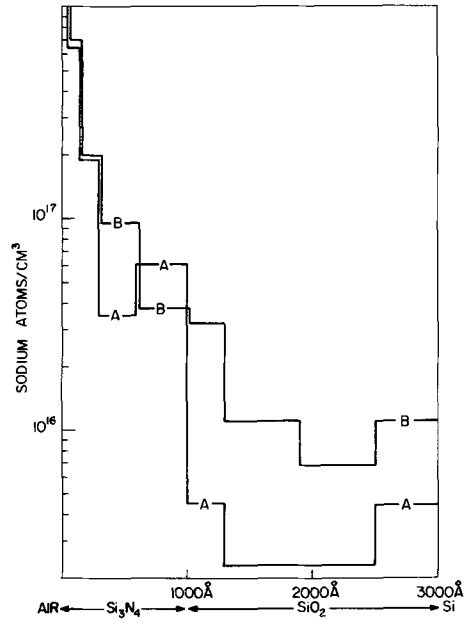

Fig. 5. Sodium-22 concentration profile in silicon nitride shielded silicon oxide annealed 2 hr at 500°C in dry nitrogen plus: (A) 24 hr, dry nitrogen; (B) 24 hr, wet nitrogen. (pyrolytic CVD (100-1) nitride deposited at 850°C).

Summary

Silicon nitride films deposited over silicon oxide layers may be used to shield the passivating oxide film against sodium penetration. These films, deposited

by a variety of techniques, act not only as sodium barriers but also as sodium getters. The film deposition temperature strongly influences the sodium gettering characteristic of the silicon nitride layer. Films pyrolytically deposited at the lower temperature (~850°C) are always better sodium getters than those produced at 1000° or 1100°C, but all the PCVD films give equal protection to the silicon oxide layer against sodium penetration. This fact indicates that the films produced at 1000° or 1100°C are better mechanical barriers than those prepared at 850°C.

The presence of moisture in an annealing atmosphere causes sodium to move into the silicon oxide-silicon interface from the silicon nitride layer. This effect is more pronounced in systems that contain the better sodium gettering silicon nitride films. Consideration must be given for this effect for any test of sodium penetration in either silicon oxide or silicon nitride-silicon oxide film systems.

Manuscript submitted Jan. 16, 1969; revised manuscript received April 7, 1969. This was Paper 87 presented at the Boston Meeting, May 5-9, 1968.

Any discussion of this paper will appear in a Discussion Section to be published in the June 1970 JOURNAL.

REFERENCES

1. J. Lindmayer, *Solid State Electronics*, **8**, 523 (1965).
2. E. H. Snow, A. S. Grove, B. E. Deal, and C. T. Sah, *J. Appl. Phys.*, **36**, 1664 (1965).
3. J. R. Matthews, W. A. Griffin, and K. H. Olson, *This Journal*, **112**, 899 (1965).
4. V. Y. Doo, D. R. Nichols, and G. A. Silvey, *ibid.*, **113**, 1299 (1966).
5. V. Y. Doo and D. R. Kerr, NASA CR-995 (1968).
6. A. R. Janus and G. A. Shirn, *J. Vacuum Sci. and Tech.*, **4**, 37-40 (1967).
7. J. V. Dalton and J. Drobek, *This Journal*, **115**, 865 (1968).
8. T. E. Burgess and F. M. Fowkes, Paper 55 presented at the Cleveland Meeting of the Society, May 1-6, 1966.
9. R. A. Weeks and E. Lell, *J. Appl. Phys.*, **35**, 1932 (1964).
10. F. M. Fowkes and T. E. Burgess, *Surface Sci.*, **13**, 184 (1969).

Preliminary Investigations of Reactively Evaporated Aluminum Oxide Films on Silicon

E. Ferrieu and B. Pruniaux[1]

Laboratoire d'Electronique et de Technologie de l'Informatique, Centre d'Etudes Nucleaires de Grenoble, France

ABSTRACT

Amorphous films of aluminum oxide have been vacuum deposited on silicon substrates by reactive evaporation through a highly localized partial pressure of water vapor. The properties of these films, such as density, dissolution rate, dielectric constant, and electrical breakdown, were determined as a function of deposition parameters. Values of the refractive index and of the infrared absorption of the layers are also reported. Aluminum-aluminum oxide-n-type silicon structures were prepared in various deposition conditions and were characterized by either positive or negative values for flat band voltage. Preliminary investigations of the stability of the structures under thermal, electrical, and radiation stresses are reported. Typical memory behavior of the MIS structure is also reported, which is assumed to be a consequence of a transfer of charges from the semiconductor to trapping levels in the insulator.

For several years, thermally grown silicon dioxide has been used to fabricate MOS (metal-oxide-silicon) structures. However silica films are structurally porous and their permeability toward impurities and ion migration is detrimental in device application (1, 2). Thus, it is desirable to find new amorphous dielectric films, and many investigations on pyrolytic deposition of silicon dioxide and silicon nitride on silicon and gallium arsenide have been reported (3, 4); the silicon dioxide-silicon nitride mixture has also been studied (1). Conduction phenomena in these insulators are beginning to be understood theoretically (5, 6).

The first results concerning preparation and properties of aluminum oxide films were published by Aboaf (7), using thermal decomposition of aluminum alkoxide at 420°C, and by Waxman (8) and Waxman and Zaininger (9) using plasma anodized aluminum. Amorphous alumina was found to be more dense than silica and resulted in electrically stable structures under radiation and thermal stressing. The high dielectric constant of alumina ($\epsilon_r \simeq 8$) allows lower operating voltages or thicker gate insulators than for SiO_2 ($\epsilon_r \simeq 4$) or even Si_3N_4 ($\epsilon_r \simeq 6$).

[1] Present address: Bell Telephone Laboratories, Murray Hill, New Jersey.

Few results of vacuum deposition of alumina have been reported (10-12), and we have found no reference of its use in MIS (metal-insulator-semiconductor) structures. Reactively evaporated "alumina" films, deposited on glass substrates at low temperatures ($\leq$ 300°C) have been used as a dielectric for thin film capacitors (13): ϵ_r ranging from 7 to 8, dielectric strength 3×10^6 V/cm, loss tangent $3 \cdot 10^{-3}$ measured at 55 kHz. In the reactive evaporation process, the substrate may be maintained at a low temperature. This makes the method attractive for the deposition of the insulating film of multilayered structures or of MIS structures on temperature sensitive semiconductors. This paper reports the results of preliminary experiments which have been carried out in order to evaluate the suitability of reactively evaporated alumina films for field effect devices.

Experimental

Experimental process.—(111) surfaces of n-type silicon, 0.5 ohm-cm resistivity, were used in the experiments. The slices were circular, 25 mm diameter. Just prior to deposition of the alumina films, the silicon wafers were cleaned using successive baths of trichlorethylene, methanol, nitric acid, hydrofluoric acid, and deionized water.

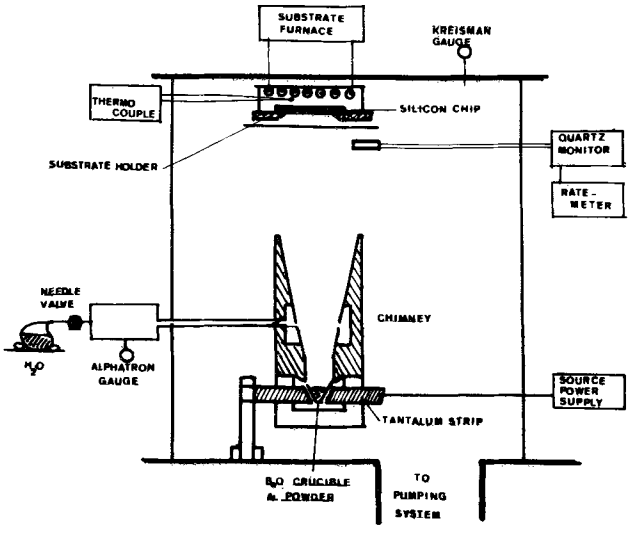

Fig. 1. Schematic of the vacuum deposition system

The silicon wafer was then placed at the top of the vacuum jar (Fig. 1) and outgased under vacuum at 400°C for 2 hr, using a radiative furnace placed above it. The substrate temperature, for deposition of the insulating film, has been varied between room temperature and 300°C and measured using a thermocouple fixed between the silicon slice and the heating furnace. The reactive evaporation of aluminum oxide was performed as follows:

1. Very pure aluminum powder (99.999%) was evaporated from a beryllia crucible heated by a tantalum strip. (The pressure during this preliminary step was better than 5×10^{-6} Torr.)

2. Then, water vapor was injected into the vacuum system through a needle valve.[2] The reaction between evaporated aluminum particles and water vapor was confined in a chimney in order to maintain a high concentration of water vapor molecules only in the evaporation field. Effectively a highly localized water vapor partial pressure was obtained: the pressure measured in the chimney was 2.6×10^{-1} Torr (NRC Alphatron gauge), while pressure in the vacuum system remained at 4×10^{-4} Torr (Ultek Kreisman gauge).

3. Then a shutter was open, and the oxidized aluminum was allowed to deposit on the silicon substrate. Deposition rates (V_{dep}) of aluminum oxide were measured using a quartz crystal monitor from 4 to 20 Å/sec. After deposition, the layer was annealed ½ hr at 300°C.

A number of electrical evaluations involved MIS structures. These were prepared by depositing on the nonheated substrate 5000Å thick aluminum field plates over the insulator. It was done in the same vacuum run, in order to lower the contamination at the Al-Al_2O_3 interface. MIS capacitors (the diameters of the field electrode being 800, 400, and 200μ) were obtained by etching aluminum using conventional photoresist techniques. Seventy-five samples of each area were obtained and tested, on the same silicon wafer, in order to establish the precision of the reported results.

The thickness of the films was measured using a Talysurf (Taylor-Hobson) which gives a ±50Å accuracy down to 200Å thickness. The dielectric constant was measured at 10 kHz with a general radio capacitance bridge. The infrared transmittance curve was taken using a Model 317 Perkin Elmer infrared spectrophotometer. The refractive index of the insulating layer was estimated using a Brewster angle technique. The C(V) curves were recorded using an MOS meter [ref. (25)] at a frequency of 10 kHz.

Discussion.—Defects in the insulating layer can be due either to the reactive process itself or to the materials of the evaporation source. Without claiming any assumptions concerning the reactive process, we can assume that two kinds of defects can be encountered in the as-made films: either noncomplete oxidation (nonstoichiometry) or formation of hydroxides. Contamination by H_2O molecules can also be a consequence of the 4×10^{-4} Torr water vapor environment, close to the substrate (H_2O molecules being adsorbed by the freshly deposited layer).

Contamination can proceed from the source materials, although the source arrangement is such that the substrate can only "see" the molten aluminum part of the source. Reaction between Ta and BeO which forms gaseous TaO, and reaction between Be and H_2O forming volatile BeOH are not believed to be an important source of contamination of the deposits. Furthermore there is no evidence of Be inclusions in the layers from the infrared measurements (Fig. 2) (but only the absence of the 7.2μ absorption peak of BeO can be significant for the 11.8 and 13.7 peak of BeO fall within the broad absorption peak of alumina). Thus, we consider, in the following, that the deposits can contain only two kinds of defects: (*i*) excess of aluminum, or oxygen vacancies, or H^+ ions which are named "positive contamination," and (*ii*) excess of [OH^-] ions which are named "negative contamination."

Results

Physical properties.—Examination of the infrared spectrum (transmission) of the aluminum oxide films (Fig. 2) indicated a broad absorption peak from 11 to 20μ, which is in good agreement with reported values for pure alumina (14).

The refractive index of the deposited alumina was typically 1.71 ± 0.03 (it is 1.765 for pure α-alumina (15)). It is of particular interest to evaluate the homogeneity of the Al_2O_3 layers as a function of deposition parameters. A compactness factor r can be defined as being the ratio

$$r = \frac{d_f}{d_a}$$

where d_f = density of reactively evaporated alumina and d_a = density of pure crystalline alumina ($\simeq$3.97).

The density d_f has been measured: (*i*) by weighing the silicon slice before and after deposition of the alumina layer, using a sensitive microbalance (accuracy for d_f equal to ±5%), and (*ii*) using the quartz crystal monitor. The relation which gives the frequency shift ΔF of the quartz when ΔM material is deposited on it, is

$$\Delta F = k\Delta M$$

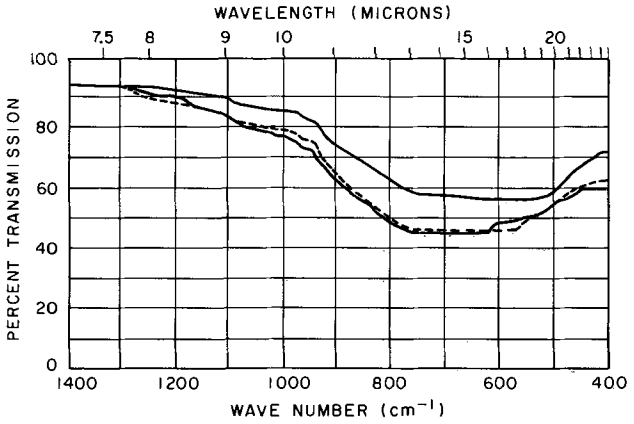

Fig. 2. Infrared absorption spectrum of three Al_2O_3 films deposited on silicon.

[2] Using pure oxygen as the oxidant instead of water vapor, makes the deposition process much more difficult to control. Furthermore the aluminum oxide films obtained were found to be less homogeneous and stable.

Table I. Deposit homogeneity as a function of deposition rate, substrate temperature 300°C

Density						
Quartz monitor	3.49	3.56	3.69	3.81	3.91	3.0
Weight	3.43	3.56	3.72	3.85	3.89	3.55
Average r value	0.87	0.89	0.925	0.967	0.982	0.82
Relative dielectric constant	7.5	7.9	7.95	8	8.05	Not measurable
Deposition rate, Å/sec	3	4	5	7	10	14

so $\Delta F_1 = kd_{al}e$ for pure aluminum deposit of thickness e and $\Delta F_2 = kd_fe$ for aluminum oxide deposit of thickness e. Thus

$$d_f = d_{al} \times \frac{\Delta F_2}{\Delta F_1}$$

This method for measuring d_f gives an accuracy of ±2%. The mechanical homogeneity of the aluminum oxide films can also be evaluated from its dielectric constant ϵ_f (24). If r is the compactness factor defined above and ϵ_a the dielectric constant of pure alumina, then

$$\epsilon_f = \frac{1}{1 - r + r/\epsilon_a}$$

The measured aluminum oxide film densities are reported in Table I. An average value of the compactness factor is given for each deposition rate. The dielectric constant is given for comparison. It can be seen from Fig. 3 that the higher the deposition rate, the better the compactness factor. But, when the deposition rate is increased further (higher than 15 Å/sec), the density strongly decreases indicating that the layer is no longer a pure dielectric film, but contains nonoxidized aluminum particles. The dielectric constant of such a deposit is not measurable, the layer being a cermet (Al_2O_3 + Al) rather than an insulator (13). Similar results are obtained from Fig. 4 where the etching rate of the layers is plotted against the deposition rate.

In order to evaluate the uniformity in depth of the films, a special arrangement was used to prepare nine steps of increasing alumina thickness on the same silicon wafer and in the same vacuum run. The etching rate of the steps was found to be constant (Fig. 5), indicating that the Al_2O_3 films are homogeneous throughout their thickness.

Adhesion of the alumina layers to the silicon substrates was excellent, up to 20,000Å thick films, operating at a substrate temperature higher than 100°C.

Electrical properties.—A reproducible ohmic contact on the silicon wafer was difficult to obtain. Best measurements were made using silver paste at the back of the silicon slice; otherwise a contact diode exists which strongly distorts C-V and dielectric constant measurements.

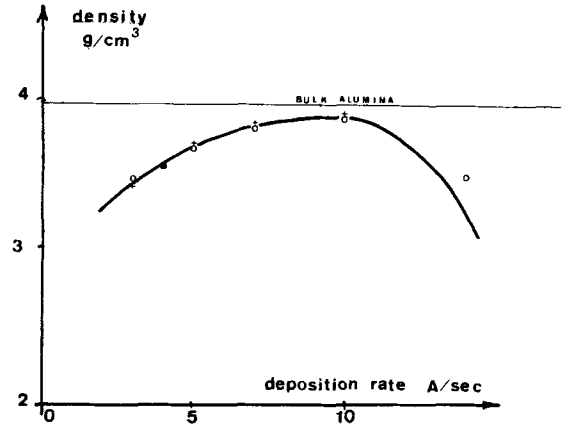

Fig. 3. Density vs. deposition rate of alumina deposited on silicon (substrate temperature 300°C): + quartz monitor measurements, O weight measurements.

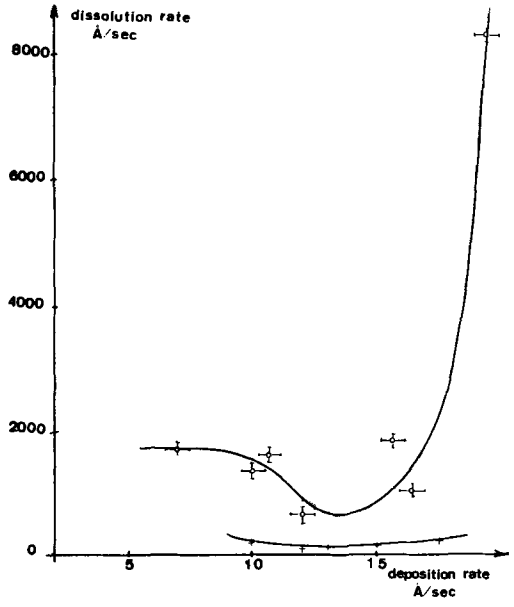

Fig. 4. Dissolution rate of alumina layers vs. deposition rate: + PO_4H_3 etch 55°C, O PO_4H_3 etch 70°C.

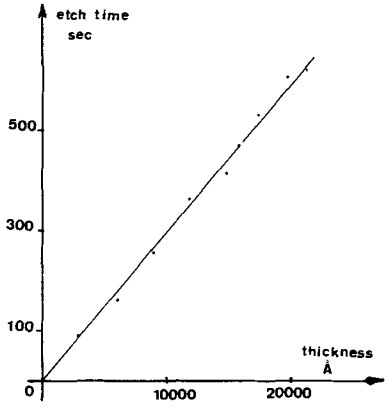

Fig. 5. Etch time vs. deposit thickness

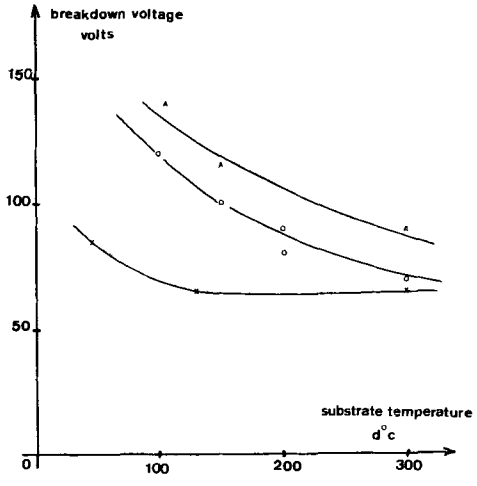

Fig. 6. Breakdown voltage of MIS structures as a function of substrate temperature during deposition (1500Å thick films): + 15 Å/sec deposition rate, O 10 Å/sec deposition rate, △ 7 Å/sec deposition rate.

Figure 6 reports the variation with deposition parameters of breakdown voltage for 1500Å thick alumina films.[3] Highest dielectric strength is obtained for low substrate temperature and deposition rate.

[3] Breakdown voltage was defined as being the voltage at which the current through the insulator was 10 μA (readings were made using a Tektronix I-V tracer); accuracy ±5%.

Unfortunately layers deposited under 100°C are poorly adherent.

Figure 7 shows that, for small probing areas (dot diameter = 200μ), the dielectric strength is constant over all the thickness of the layer. For larger probing areas, the pinhole density (due to surface roughness of the wafer or to particles in the insulating layer) is such that a short occurs for a thickness of the order of 400Å. A similar effect is observed when the dielectric constant is plotted *vs.* the thickness of the insulator (Fig. 8): the decrease of ϵ_r with thickness for large testing areas can be a consequence of mechanical defects in the insulating layer.

C-V measurements on the MIS structures indicate (Fig. 9 and 10) that the best alumina layers (lower flat band voltage) are obtained for low substrate temperatures and low deposition rates. It is evident also that, by changing these two deposition parameters, the flat band voltage can be varied from positive to negative values.

From all the results reported above, we have been able to assume that the insulator is homogeneous throughout its thickness, and to choose the following values for the deposition parameters: substrate temperature = 150°C and deposition rate ranging from 7 to 12 Å/sec (in order to study the positive and negative flat band voltage MIS structures).

MIS Structures

C-V measurements.—Typical C-V curves are shown in Fig. 11. For both curves, hysteresis is "abnormal" with respect to ion migration. According to Snow and Deal (16) this is a result not of the drift of fast ions,

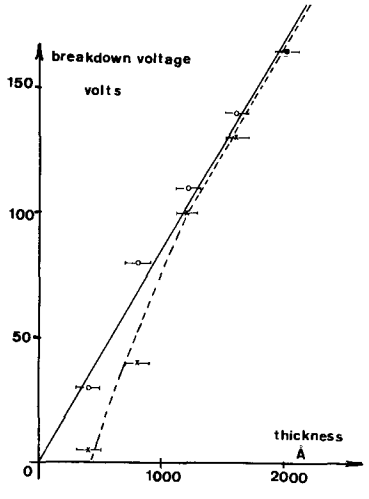

Fig. 7. Breakdown voltage of MIS structures *vs.* thickness of the Al_2O_3 layer: O ϕ = 200μ probe electrode, + ϕ = 400μ probe electrode.

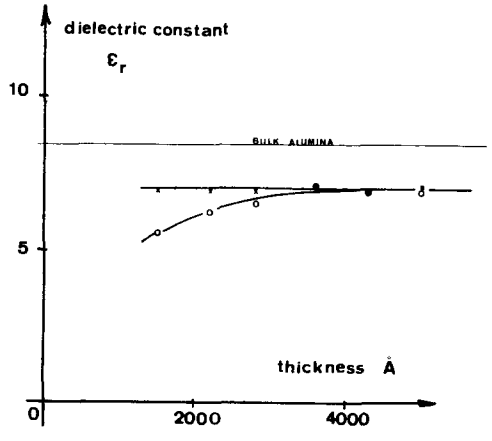

Fig. 8. Al_2O_3 dielectric constant *vs.* thickness of the layer: + ϕ = 400μ probe electrode, O ϕ = 800μ probe electrode.

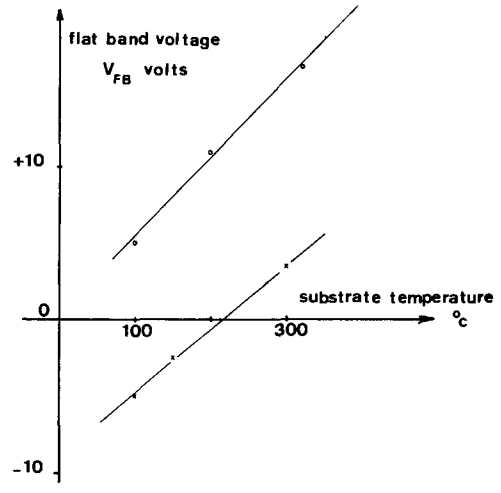

Fig. 9. Flat band voltage of the MIS structures as a function of substrate temperature: + V_{dep} = 7 Å/sec, O V_{dep} = 14 Å/sec.

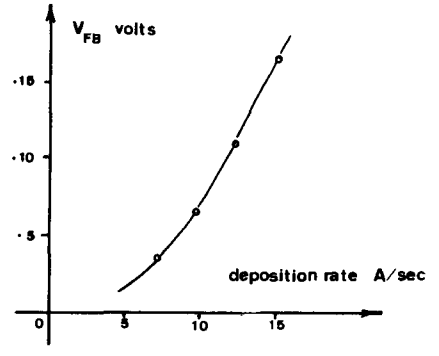

Fig. 10. Flat band voltage of the MIS structures *vs.* deposition rate (substrate temperature 300°C).

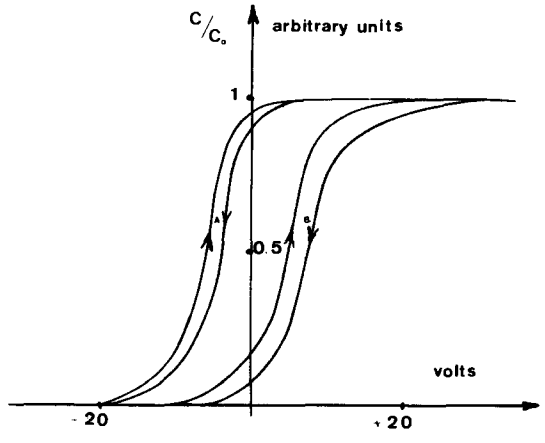

Fig. 11. Typical C(V) curves of the Al-Al_2O_3-*n*Si structures (measuring frequency 10 kHz, substrate temperature 150°C). Curve A, V_{dep} = 7 Å/sec; curve B, = V_{dep} = 12 Å/sec.

but indicates a dominancy of a "trapping polarization" process. The flat band voltages V_{FB}, representative of the total amount of electrical states at the Al_2O_3-Si interface, were calculated using the Goetzberger (18) and Whelan (19) theoretical curves.

It is interesting to note (Fig. 12) that for both positive and negative flat band voltage MIS structures, V_{FB} decreases with alumina thickness. Extrapolating to a zero thickness, for both structures, leads to a limiting positive flat band voltage, ranging between +1 and +5v (the uncertainty being due to the hysteresis effect of the C(V) curves). As a consequence, the structure which shows a negative flat voltage for large oxide thicknesses, goes through a zero flat band voltage for a thickness around 1000Å. The flat band volt-

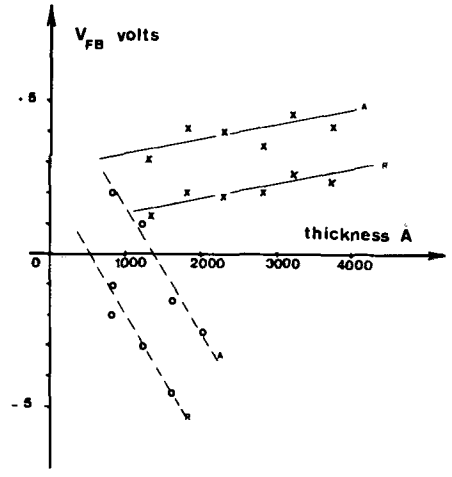

Fig. 12. Flat band voltage vs. Al_2O_3 thickness: O V_{dep} = 7 Å/sec, X V_{dep} = 12 Å/sec. Curve A, bias voltage is applied from positive to negative values; Curve B, bias voltage is applied from negative to positive values.

age can be given by the relation

$$V_{FB} = -\phi_{MS} - \frac{Q_T}{C_o} \quad Q_T = Q_{OX} + Q_{SS}$$

where Q_{OX} stands for the oxide charges (assumed to be at the semiconductor oxide interface) and Q_{SS} for the silicon pure surface charges (assumed usually to be positive charges, due to Na^+ ions).

ϕ_{MS} is the difference between the work function of the metal and the electron affinity of the silicon; in our case $\phi_{MS} = -0.25$V (17).

C_o is the capacitance per square centimeters of the insulator. Thus

$$V_{FB} = 0.25 - \frac{Q_T}{\epsilon_o \epsilon_r} t_{ox}$$

where ϵ_r is the relative dielectric constant of the insulator of thickness t_{ox}.

As shown on Fig. 12, the variation of V_{FB} with t_{ox} seems to be effectively linear. (The limiting value for $t_{ox} = 0$ is greater than 0.25V, because for very low oxide thicknesses a uniform field in the insulator can no longer be assumed, due to the fact that the ratio between the oxide thickness and the extent of the space charge in the oxide approaches one. Thus, the simple expression of V_{FB} given above is no longer valid.)

Both straight lines on Fig. 12 can be interpreted assuming that Q_{OX} are negative charges such that: $Q_{OX} << Q_{SS}$ for V_{dep} = 7 Å/sec and $Q_{OX} >> Q_{SS}$ for V_{dep} = 12 Å/sec. The dominancy of Q_{SS} over Q_{OX} (or Q_{OX} over Q_{SS}) results in a negative (or positive) value for the dV_{FB}/dt_{ox} slopes of the lines. Thus, the purest films, as expected from density and etching rate measurements, are those deposited at the lower deposition rate. "Negative contamination" appears to be the most important defect encountered, and an inversion (p-type) layer was found most of the time at the silicon surface [a similar observation is reported by Aboaf (7)].

Drift of the MIS structures under electrical and radiation stressing.—Figures 13 and 14 show the drift of the C-V curves under various applied bias, before and after annealing (30 min at 410°C, under N_2 gas flow). Annealing of the structure results in a large improvement, *i.e.*, lower drifts and saturation times.

The drifts under positive and negative bias are due to very different phenomena: regardless of the sign of the applied bias V_P, the resulting drift ΔV is positive. Thus, for positive V_P, the product $V_P \cdot \Delta V$ is positive, which [according to (16) and (21)] is now assumed to be the characteristic of carrier injection

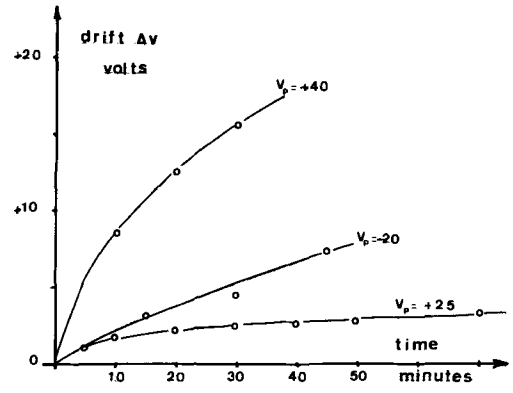

Fig. 13. Drift of C(V) curves with time under various bias voltages, before annealing of the structure.

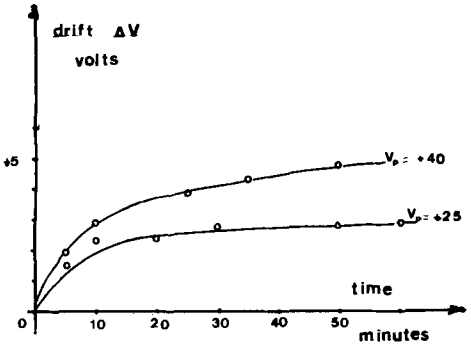

Fig. 14. Drift of C(V) curves with time under various bias voltages, after annealing of the structure 30 min at 410°C under N_2 gas flow.

from the silicon surface toward trapping levels in the insulator. On the other hand, for negative applied bias, $V_P \cdot \Delta V$ being negative, this may indicate a migration of slow negative ions in the insulator ("negative contamination") toward the silicon-insulator interface.

When cycling the structures between —40 and +40V, (after annealing) one obtains the typical hysteresis drift curve of Fig. 15; similar curves have also been reported for Si_3N_4 layers (23) and vapor deposited SiO_2-Si_3N_4 mixtures. This effect is also assumed to be a consequence of trapping effects at the Si-insulator interface.

Figure 16 reports the effect of radiation stressing on the MIS structures. Electrons of 1 mev were used, and the field electrode of the structure under test was shorted. The C(V) curves were measured after each dose. The total induced drift is less than 5V, lower than the drift observed in SiO_2 MOS structures (20)

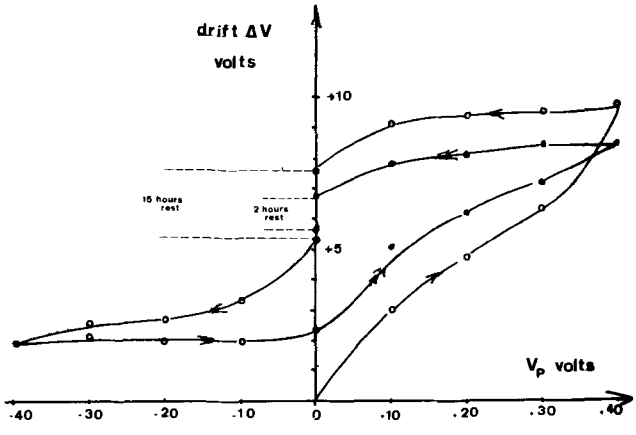

Fig. 15. Drift of C(V) curve as a function of applied bias. Each reported point on the curve was measured after 15 min applied voltage.

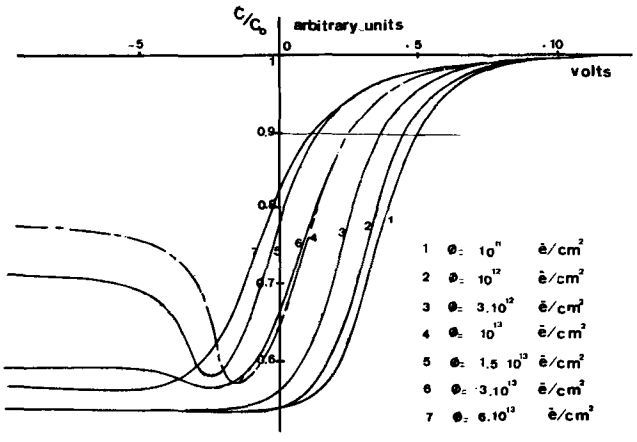

Fig. 16. Drift of C(V) curve for a 1600Å thick Al_2O_3 layer, under irradiation. The measuring frequency is 10 kHz. Each curve is drawn after each reported dose has been applied to the structure.

but similar to that obtained when Si_3N_4 was used as the insulating layer (22).

Table II reports typical observations on the stability of Al_2O_3 MIS structures, after various treatments. The drift is quite low (after annealing) as shown by the "after 6000 hr" measurements. But, it can be seen that the structures are not yet fully stabilized.

Conclusion

More detailed information of the aging behavior of the C-V curves as a function of temperature, time, and frequency are needed to fully identify the processes taking place in the structures. Nevertheless, the results obtained during this preliminary work can lead to the assumption that "negative contamination" (*i.e.*, $[OH]^-$ ions) is the main defect encountered in reactively evaporated alumina films, and to the conclusion that these insulating layers are physically homogeneous and suitable for multilayered structures. We think that a "trapping polarization" process has been identified, which can be in full or in part hidden by ion migration.

Further experiments are being carried out, for a better understanding of the phenomena involved, and to decide whether or not, reactive evaporated alumina is more suitable for field effect devices than the other well known insulators.

Table II. Stability of the structures

Flat band voltage	First measurements, V	After 6000 hr at room temperature	After applied bias: 25V for 5 hr	Drift
Sample N160	−1.7	−0.7	−3.5	Abnormal
Sample 1500 II	−2.3	−2.4	−1.8	Normal

Acknowledgments

The authors wish to thank I. Melnick and the vacuum deposition laboratory for their technical advice, M. Verdone and the integrated circuits laboratory for their constant assistance in silicon and etching processings. We also wish to acknowledge many helpful suggestions from G. Grunberg, J. L. Pautrat, and J. C. Pfister.

Manuscript submitted Sept. 5, 1968; revised manuscript received March 18, 1969.

Any discussion of this paper will appear in a Discussion Section to be published in the June 1970 JOURNAL.

REFERENCES

1. T. L. Chu, J. R. Szedon, and C. H. Lee, *This Journal*, **115**, 318 (1968).
2. B. E. Deal, P. J. Fleming, and P. L. Castro, *ibid.*, **115**, 300 (1968).
3. Y. Sato, *Japanese J.A.P.*, **7**, 595 (1968).
4. M. J. Grieco, F. L. Worthing, and B. Schwartz, *This Journal*, **115**, 525 (1968).
5. D. Meyerhofer in "Field Effects Transistors," Wallmark and Johnson, Editors, Prentice Hall, New York (1966).
6. J. R. Yeargan and H. L. Taylor, *This Journal*, **115**, 273 (1968).
7. J. A. Aboaf, *ibid.*, **114**, 948 (1967).
8. A. Waxman, *Electronics*, **41**, 88 (March 18, 1968).
9. A. Waxman and K. H. Zaininger, *Appl. Phys. Letters*, **12**, No. 3, 109, (1968).
10. E. M. DaSilva and P. White, *This Journal*, **109**, 12, (1962).
11. L. H. Kaplan, *Electrochem. Technol.*, **3**, 335, (1965).
12. B. Pruniaux, Thesis, Grenoble, 1966.
13. B. Pruniaux, G. Grunberg, I. Melnick, and M. Cordelle, *Thin Solid Films*, **1**, 417 (1967/1968).
14. D. W. Sheibley and M. H. Fowler, NASA TND-3750, p. 61.
15. "Handbook of Chemistry and Physics," 49th Edition.
16. E. H. Snow and B. E. Deal, Trans. Met. Soc., AIME, 242, 512 (1968).
17. B. E. Deal, E. H. Snow, and Mead, *J. Phys. Chem. Solids*, **27**, 1873 (1966).
18. A. Goetzberger, *Bell System Tech. J.* **45**, 1097 (1966).
19. M. V. Whelan, *Philips Research Rept.*, **20**, 620 (1965).
20. F. P. Heiman and G. Warfield, *IEEE Trans. ED*, p. 167, April 1965.
21. S. R. Hofstein, *ibid.*, **ED-13**, No. 12, p. 222 (Feb. 1966).
22. C. W. Perkins, *Appl. Phys. Letters*, **12**, 153 (1968).
23. H. C. Pao and M. O'Connell, *ibid.*, **12**, 260 (1968).
24. G. J. Tibol and R. W. Hull, *This Journal*, **111**, 1368 (1964).
25. E. Mackowiak, Note Technique EL/TR/ 402-31-9-1967, Centre d'Etudes Nucleaires de Grenoble.

The Preparation and Properties of Silica Films Deposited from Silane and Carbon Dioxide

R. C. G. Swann* and A. E. Pyne

ITT Semiconductors, West Palm Beach, Florida

ABSTRACT

Silicon dioxide has been deposited from a reaction involving silane and carbon dioxide. Hydrogen and argon were used as carrier gases. Growth rates were measured from 700° to 1100°C. The choice of carrier gas had a pronounced effect on the growth rate at low temperatures. Etch rates, dielectric loss, and infrared spectra are reported. Interface charge properties are shown under certain conditions to be stable and hysteresis free with typical N_{FB} values of 1-3 x 10^{11} charge/cm^2.

The introduction of large-scale integrated MOS circuits has resulted in increased interest in chemical vapor deposition systems. At this time, silicon dioxide remains the most useful dielectric for interfacing with silicon. The advantages of deposited silicon dioxide over thermal or bulk grown oxides are well known. They include the ability to deposit thick layers at high growth rates and low temperatures to avoid movement of diffusion fronts as well as the ability to form oxides on foreign substrates. Many silicon dioxide deposition systems have been investigated, for example, the direct oxidation of silane (1), decomposition of ethyl-triethoxy-silane (2), the reaction of silicon halides with carbon dioxide (3-5), as well as sputtering (6, 7) and glow discharge reactions (8). The literature, however, contains no reference to the investigation of the silane/carbon dioxide reaction.

This system was investigated because silane and carbon dioxide do not react spontaneously at room temperature as, for instance, silane and oxygen do. Furthermore, by using prediluted silane, and argon as carrier gas, no hazardous gases are involved. The system is also highly compatible with the silane/ammonia reaction for the deposition of silicon nitride (9). With the addition of an ammonia source, the authors have deposited sequential layers of silicon dioxide and silicon nitride without removal of the wafer from the reactor.

The silicon oxide-silicon nitride structure is particularly useful as a gate insulator in MOST's because the nitride, in this context, is a poor interfacing material but an excellent sodium barrier. In the field region, thick oxides are often employed to alleviate channeling or inversion under metallizations. Ideally, for P-channel devices, such an insulator needs a high fixed charge as contrasted with the low fixed charge required for the gate regions. The field region therefore could be a layer of silicon nitride over which silicon dioxide is deposited. Because of the slow etch rate of silicon nitride and its higher dielectric constant, only a thin layer (<1000Å) would be used. The film thickness is then built up to typically 10,000Å with silicon dioxide which is also a convenient mask to use for the phosphoric acid etching of the nitride. A suitable gate dielectric would consist of 500Å of silicon dioxide over which is deposited 500Å of silicon nitride.

Experimental

The apparatus used to perform these experiments was a single slice vertical reactor using r.f. heating of a quartz coated graphite susceptor (Fig. 1). The gas manifold was constructed entirely of stainless steel, and the reaction tube was quartz. A rotary shaft was provided for substrate rotation; and contained vacuum seals to enable leak checking with a vacuum pump and pressure gauge. The substrate temperature was measured by a Huggins Infrascope infrared pyrometer placed vertically above the substrate. All temperatures are quoted for a constant emissivity correction of 0.65.

The silicon wafers used in these experiments, except for I.R. studies, were 2 ohm cm phosphorus doped <111> oriented and optically polished to ~250μ thickness. The I.R. wafers were 50 ohm cm <111> oriented phosphorus doped and both sides optically polished to ~1000μ. Slices were degreased and then cleaned in 50% HF and boiled in nitric acid with intermediate and final washes in 18 Mohm deionized water. The slices were dried in a stream of dry nitrogen and pretreated in the reactor at 1200°C for 5 min in hydrogen to remove any residual oxide. After adjustment to the desired substrate temperature the carbon dioxide and silane were admitted. The carbon dioxide used was Coleman grade (99.99% min. purity), the hydrogen was Matheson ultrapure grade (99.999% min. purity), and the argon was Matheson high purity (99.995% min. purity).

Oxide thickness was determined in two ways; for growth rate studies the thickness was measured by comparison with a color chart, but for etch rate determinations the thickness was measured with a Hilger and Watts interferometer.

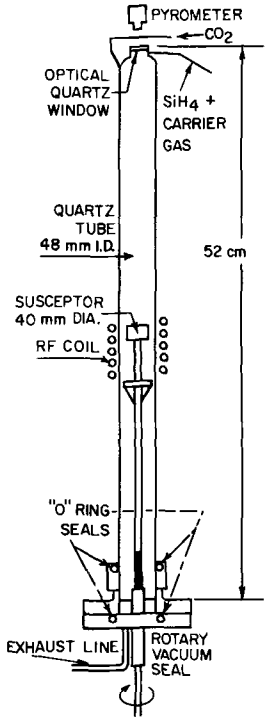

Fig. 1. Single slice vertical reactor

* Electrochemical Society Active Member.

Surface charge measurements were made by depositing aluminum by electron beam evaporation and etching 400μ diameter dots. The electron beam damage was annealed out at 560°C for 5 min in nitrogen. Plots of capacitance *vs.* voltage were then made on an automated C-V plotter.

Results

It is important to emphasize that the results, in particular those of growth rates, will be reproducible only in a reactor of similar geometry and heating method (Fig. 1).

Growth rates.—Growth rates were studied as a function of substrate temperature, percentage silane, percentage carbon dioxide, and total flow rate. Figure 2 shows the deposition rate as a function of percentage silane for a range of substrate temperatures from 700° to 1100°C. In this case, the carbon dioxide:silane ratio was 100:1 and the balance gas was hydrogen. Growth rates vary from 15 to 4000 Å/min over the range explored. It can be seen that the growth rate is less temperature sensitive between 900° and 1100°C than between 700° and 900°C. Figure 3 is a similar graph of deposition rate *vs.* percentage silane except for using argon as balance gas, instead of hydrogen. The salient difference is the significantly higher growth rate at 700°C. At 0.18% silane, is 800 Å/min for the argon case and 100 Å/min for the hydrogen.

From the two families of growth rate curves, plots of deposition rate *vs.* $1/T$ were derived, but no meaningful activation energy could be calculated from the plots that were linear only over a small temperature range. The reason for this nonlinearity was upstream decomposition, which became more pronounced at high substrate temperatures. The susceptor mass and geometry were found to affect the amount of upstream decomposition; and in this work it should be noted that the susceptor was quartz-enclosed graphite.

The effect of carbon dioxide concentration on growth rate was studied at a fixed silane concentration of 0.037% and substrate temperature of 900°C. Figure 4 shows that the growth rate curve, although having a decreasing slope, does not saturate even at a carbon dioxide:silane ratio of 250:1.

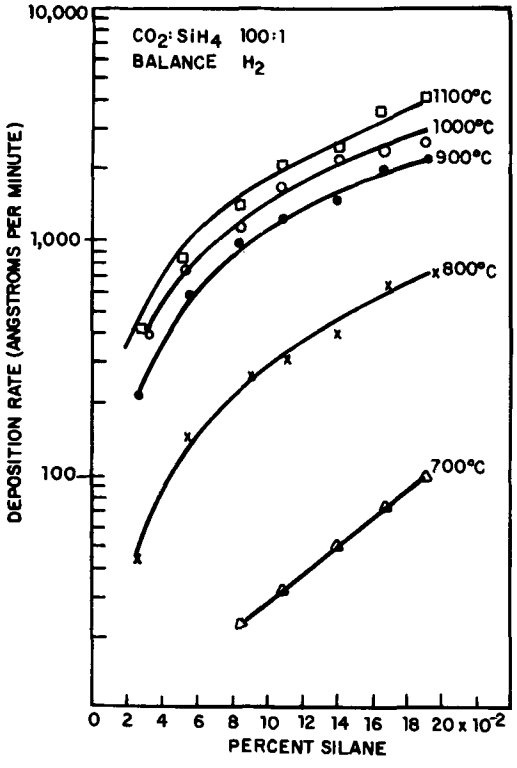

Fig. 2. Deposition rate of SiO_2 *vs.* SiH_4 concentration at different temperatures with H_2 as carrier.

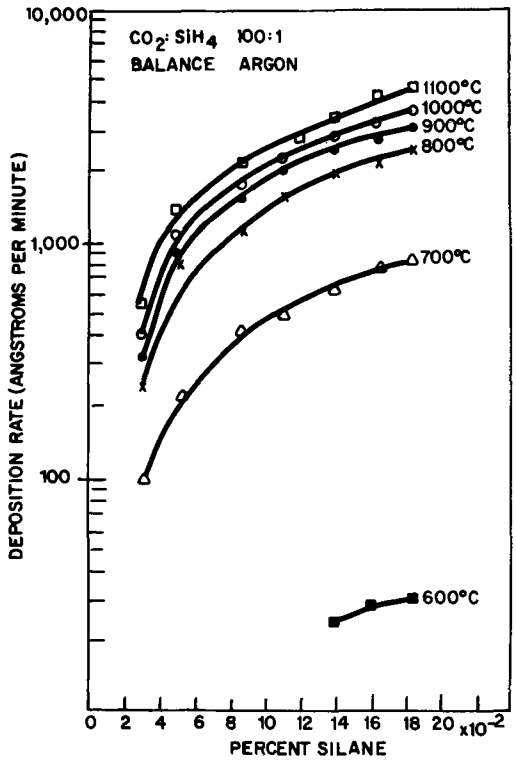

Fig. 3. Deposition rate of SiO_2 *vs.* SiH_4 concentration at different temperatures with argon as carrier.

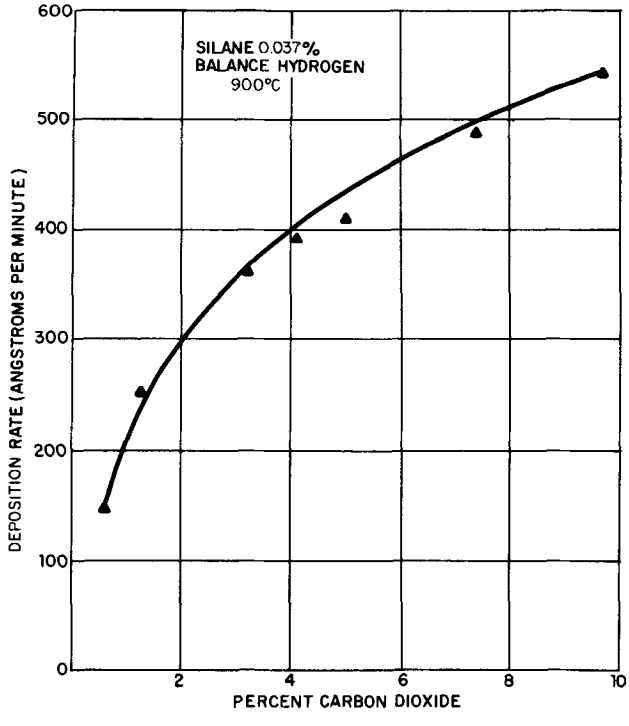

Fig. 4. Deposition rate of SiO_2 *vs.* CO_2 concentration

Growth rates were studied as a function of total flowrate (Fig. 5) at a fixed carbon dioxide:silane ratio (100:1) and the balance gas was hydrogen. All three gases were proportionately increased for each determination of growth rate at a constant substrate temperature of 900°C. The reaction is seen to be transport controlled up to approximately 1.4 l/min and thereafter the growth rate is substantially constant.

Infrared.—Figures 6 and 7 show the extremities of the conditions in this study. There was no obvious difference in the IR spectra for samples deposited using the two different carrier gases. There was, how-

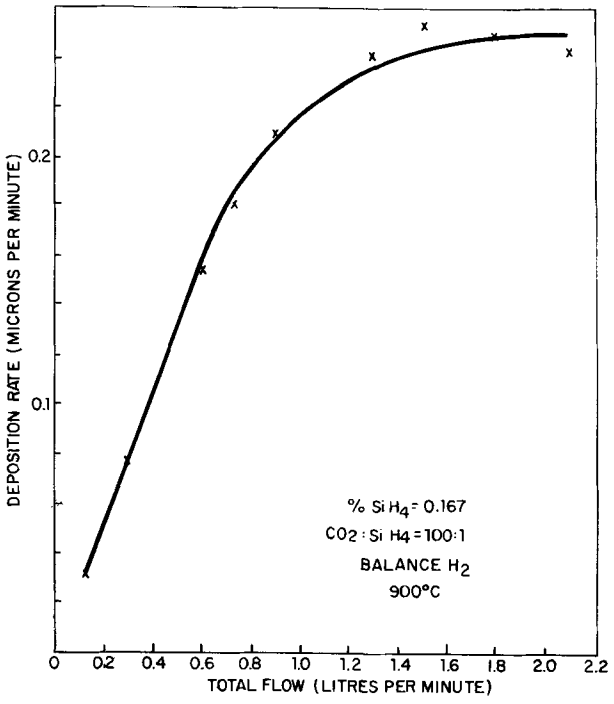

Fig. 5. Deposition rate of SiO_2 vs. total flow rate.

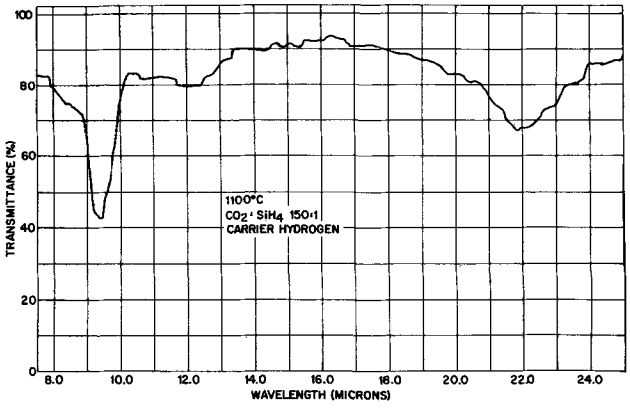

Fig. 6. IR spectra of SiO_2 deposited at high temperature and high CO_2:SiH_4 ratio.

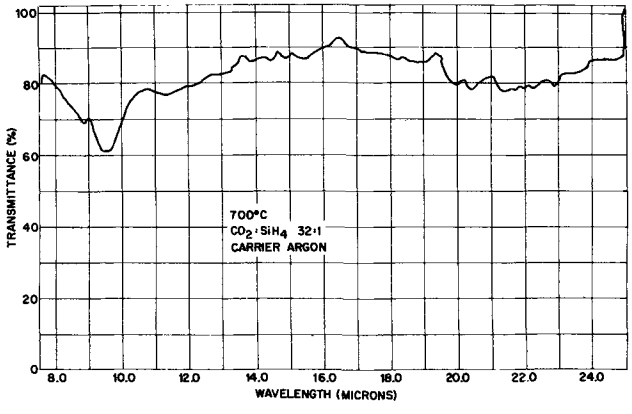

Fig. 7. IR spectra of SiO_2 deposited at low temperature and low CO_2:SiH_4 ratio, showing a shoulder at 8.8 μ.

ever, a dependency on substrate temperature and carbon dioxide/silane ratio. The 9.3μ absorption was more intense at high substrate temperatures and high carbon dioxide/silane ratios. In general these films were comparable to thermally grown oxides, whereas, at low substrate temperatures and low carbon dioxide/silane ratios (Fig. 7) a low intensity 9.5μ peak is observed which has a definite shoulder at 8.8μ. These films are probably silicon rich as is discussed later.

Etch rates.—Controlled etch rate studies were only performed on the oxides produced with hydrogen as carrier gas. Etch rates were not measured on layers deposited in argon as these left a thin brown film on etching. Rates were determined using a P etch solution (20°C) in which dry thermally grown oxides etch at 2 Å/sec (10). The highest etch rate was observed on films grown at 900°C, and this was 6.5 Å/sec. The etch rate fell to 4.5 Å/sec at 1100°C and 4.0 Å/sec at 700°C.

Interface charge properties.—Silicon dioxide was deposited at substrate temperatures between 700° and 1100°C at a carbon dioxide:silane ratio of 100:1 using both carrier gases. The oxides grown in hydrogen showed surface charges typically between 1 and 3 x 10^{11} charges/cm^2. These oxides were very stable under bake bias. An increase of $\sim$1 x 10^{11} in the surface charge for an applied field of 2 x 10^6 V/cm for 30 min at 250°C was a normal result. These surface charge and stability measurements were made over a period of several months and the stability and charge were found to be repeatable. Low-temperature (77°K) C-V plots did not show any fast states around inversion.

The oxides grown in argon behaved differently. The oxide quality depended markedly on deposition temperatures. The C-V curves of the 700°C oxide showed room temperature hysteresis. The curves were very similar to those of silicon nitride, *i.e.*, the amount of hysteresis depended on the applied voltage. At deposition temperatures of 1000°C however, this room temperature hysteresis disappeared and low charge oxides were formed.

Discussion

Steinmaier and Bloem (4), Tung and Caffrey (11), and others, using the $SiCl_4$-CO_2-H_2 reaction have proposed that their reaction proceeded in two steps.

$$H_2 + CO_2 \rightleftharpoons H_2O + CO \quad [1]$$

$$SiCl_4 + 2H_2O \rightarrow SiO_2 + 4HCl \quad [2]$$

The silicon dioxide is therefore formed by the hydrolysis of the halide. These authors recognized that intermediate steps must exist.

Similarly, in the SiH_4-CO_2-H_2 system it is possible for two reactions to coexist, that is the water gas reaction and the direct oxidation of SiH_4 by CO_2 as shown below.

$$SiH_4 + 4CO_2 \rightarrow SiO_2 + 4CO + 2H_2O$$

$$\Delta F + -116 \text{ kcals/mole at } 1200°K \text{ (12)}$$

The water formed by this reaction may hydrolize further SiH_4.

That the reaction does not proceed solely by the water gas reaction was verified by the substitution of argon for hydrogen. In fact the growth rate in argon was considerably greater; for instance, at 800°C the growth rate in argon was approximately four times that in hydrogen. It is thought the different growth rates result from the different thermodynamic properties of the gases, and thus there is less upstream decomposition in the case of argon.

Film properties are certainly modified when using argon, in particular at low temperature the films were much softer and, as mentioned before, a residue not etchable in HF was found at the interface. The loss factor of SiO_2 formed in argon at 700°C was 0.015, but for a film grown in argon at 1000°C the loss factor was 0.005.

These facts together with the infrared data indicate that these low-temperature films deposited in argon contain free silicon. The effect of free silicon on the dielectric loss in silicon nitride has previously been reported. (13)

Conclusions

The silane-carbon dioxide reaction has been characterized for a specific deposition system. The resultant film properties were found to be dependent on the balance gas in that argon gave films that were mechanically soft and nonadherent at low substrate temperatures. On the other hand, the use of hydrogen as balance gas produced films of superior mechanical and electrical properties.

The MOS capacitance-voltage measurements showed that the oxide would make an excellent passivating film for a gate dielectric because of its stable and low interface charge. The charge densites ($\sim$1-3 x 10^{11}/cm on <1-1-1> silicon) were the same as those normally quoted for thermally oxidized films, and it is expected that even lower values would result from using <1-0-0> oriented surfaces.

Deposited silicon dioxide offers a distinct advantage over thermally grown oxide in that the time and temperature of growth can be minimized. For example, at 900°C deposition rates ranging from 200 to >2000 Å/min can be achieved; whereas a dry or wet thermal oxidation would require approximately 8 hr and 20 min, respectively, to grow 1000Å of silicon dioxide.

The chemical compatibility of this reaction with the silane-ammonia reaction offers the capability of depositing sequential layers of silicon nitride and oxide (or *vice versa*) for a variety of semiconductor applications.

Acknowledgment

The authors are indebted to P. Stauffer who prepared the samples and to D. Pitzer who helped with the electrical measurements. The authors also wish to thank Dr. R. M. Warner, Jr. for his many helpful comments.

Manuscript submitted Dec. 9, 1968; revised manuscript received *ca.* March 1, 1969. This was Paper 305 presented at the Boston Meeting, May 5-9, 1968.

Any discussion of this paper will appear in a Discussion Section to be published in the June 1970 JOURNAL.

REFERENCES

1. T. L. Chu, J. R. Szedon, and G. A. Gruber, *Trans. Met. Soc. AIME*, **242**, 532 (1968).
2. E. L. Jordon, *This Journal*, **108**, 478 (1961).
3. C. F. Powell, I. E. Campbell, and B. W. Gosner, "Vapor Plating," p. 141, John Wiley & Sons, Inc., New York (1955).
4. W. Steinmaier and J. Bloem, *This Journal*, **111**, 206 (1964).
5. M. J. Rand and J. L. Ashworth, *ibid.*, **113**, 48 (1966).
6. G. S. Anderson, W. N. Mayer, and G. K. Wehner, *J. Appl. Phys.*, **33**, 2991 (1962).
7. P. D. Davidse and L. I. Maissel, 3rd International Vacuum Congress Stuttgart, June 1965, Germany.
8. H. F. Sterling and R. C. G. Swann, *Phys. Chem. Glasses*, **6**, 109 (1965).
9. V. Y. Doo, D. R. Nichols, and G. A. Silvey, *This Journal*, **113**, 1279 (1966).
10. W. A. Pliskin and H. S. Lehman, *ibid.*, **111**, 872 (1964).
11. S. K. Tung and R. E. Caffrey, *Trans. Met. Soc. AIME*, **233**, 572 (1965).
12. JANAF Thermochemical Tables, Dow Chemical Co., Midland, Mich., 1965.
13. R. C. G. Swann, R. R. Mehta, and T. P. Cauge, *This Journal*, **114**, 713 (1967).

Technical Notes

Effect of Ce^{+3}, Pr^{+3}, and Tb^{+3} on the Brightness of YVO_4:Eu under Cathode-Ray Excitation

E. J. Mehalchick, F. F. Mikus,* and J. E. Mathers*

Sylvania Electric Products Inc., Chemical and Metallurgical Division, Towanda, Pennsylvania

The behavior of YVO_4:Eu when excited by uv was studied extensively (1, 2) and its utility as a red emitting color TV phosphor is well known (3). The effect of Tb^{+3} in alkaline metal rare earth tungstates and in Y_2O_3 was reported by Van Uitert (4) and by Ropp (5). Thompson has reported the effect of Ce^{+3}, Pr^{+3}, and Tb^{+3} in his patent (6). The effect of Ce^{+3} is reported by Kano and Otomo (7). The present work shows the effect of Tb^{+3}, Pr^{+3}, and Ce^{+3} on the brightness of YVO_4:Eu under cathode-ray excitation. Small additions of Tb^{+3} and Pr^{+3} cause significant increases in luminescence while small amounts of Ce^{+3} decrease it.

Experimental

Yttrium oxide of extremely high purity was used in all phosphor preparations. Results of quantitative analysis of the rare earth are shown in Table I. Stock solutions of Ce^{+3}, Pr^{+3}, and Tb^{+3} containing 6.435 x 10^{-4} g Ln/cc of solution were prepared by dissolving a known quantity of the corresponding oxide in nitric acid and diluting to volume. The required volume of solution containing the desired ion was added to a nitrate solution of yttrium and europium from which the rare earths were coprecipitated as oxalates. Am-

Table I. Solids mass analysis of Y_2O_3

Concentration expressed in ppm		
Impurity	Sample A	Sample B
Ce	<1	53
Pr	<1	2
Nd	<1	10
Sm	16	21
La	1	2
Eu	32	20
Gd	<3	12
Tb	<1	6
Dy	<2	129
Ho	<1	65
Er	<2	66
Tm	<1	7
Yb	<2	75
Lu	1	25
Th	<1	13

* Electrochemical Society Active Member.

monium metavanadate was added to the dried oxalate and the mixture was fired at 950°C for 2 hr to produce the YVO_4:Eu (Ln) phosphor. The concentration of Tb^{+3} and Pr^{+3} were varied from 2.5 x 10^{-4} g/g Y_2O_3 to 5 x 10^{-5} g/g Y_2O_3 at Eu concentrations of 1, 3, and 5 m/o (mole per cent). The resultant phosphors, settled on glass slides, were excited with 12 kV electrons at a beam current of 6 μA. The intensity of the emission was measured with a Weston foot lambert meter.

Results and Discussions

Enhancement of the light output of YVO_4:Eu in the red region of the spectra by Tb^{+3} and Pr^{+3} are shown in Fig. 1 and 2, respectively. In Thompson's patent (6) he claims that 200 ppm Tb^{+3} give brilliant luminescence, a vague term since europium activated vanadates are generally brilliant. Our data point out that optimum luminescent efficiency is achieved when 50-75 ppm of Tb^{+3} or Pr^{+3} are added to the yttrium vanadate matrix. We have further evidence to show that the amounts of rare earth dopants he claims produce brilliant luminescence would result in a very inefficient phosphor. This effect increases rapidly from 0 to about 75 μg of Tb^{+3} and Pr^{+3} with gradual tapering off as more of each is added. These lanthanides behave uniquely in YVO_4:Eu in that no emission characteristic of these ions was observed under cathode-ray or uv excitation. A comparison of the excitation spectra of YVO_4:Eu with that of YVO_4:Eu,Tb (Fig. 3) indicates that an additional quenching is obtained with small amounts of these elements. The spectral energy distribution of YVO_4:Eu (0.01), YVO_4:Eu (0.01) Tb^{+3}, and Y_2O_3:Eu (0.01) Pr^{+3} are shown in Fig. 4. The emission of YVO_4:Eu (0.01) in the 430-480 nm and in the 530 and 580 nm range is quenched with both Tb^{+3} and Pr^{+3} under CR excitation. This is also manifested in the shift in the chromaticity coordinates to the more saturated red region. The low value of the x coordinate for the YVO_4:Eu suggests a significant contribution to the color from the lower wavelength emissions.

Addition of the 5 x 10^{-5}g Ce^{+3}/g Y_2O_3 to 5 x 10^{-4}g Ce^{+3}/g of Y_2O_3 decreases the brightness of YVO_4:Eu significantly as shown in Fig. 5. Thompson, in his patent (6), claims that he obtains brilliant luminescence with 100 ppm Ce^{+3}. We disagree very strongly as is shown in Fig. 5. At 100 ppm Ce^{+3} and 3 m/o Eu the luminescent efficiency of YVO_4:Eu would be 20% less as compared to material containing no Ce^{+3}. This statement is borne out further by work completed by Kano and Otomo. They show a significant drop in the cathodoluminescence efficiency when small amounts of Ce^{+3} are present in the phosphor. It was reported earlier that high purity Y_2O_3 is important in the preparation of efficient YVO_4:Eu phosphors. This is again demonstrated in Fig. 6 which shows the washing out

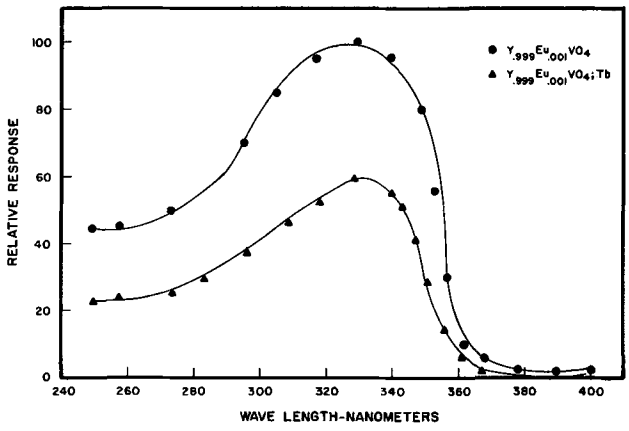

Fig. 3. Excitation spectra for YVO_4:Eu and YVO_4:Eu, Tb

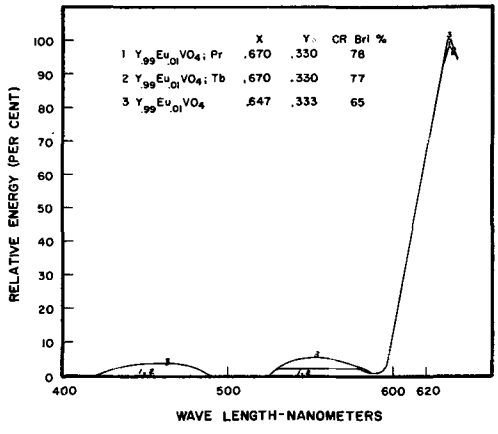

Fig. 4. Spectral energy distribution for 1, YVO_4:Eu; Pr; 2, YVO_4:Eu; Tb; 3, YVO_4:Eu (0.01).

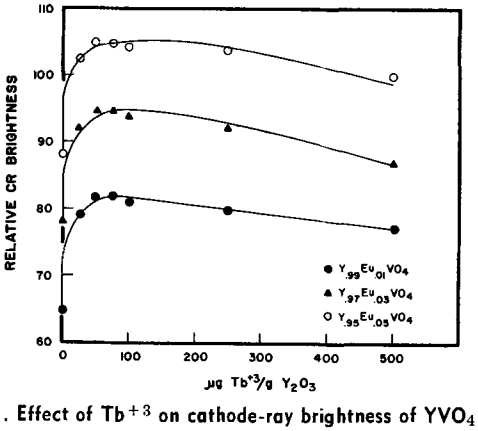

Fig. 1. Effect of Tb^{+3} on cathode-ray brightness of YVO_4:Eu

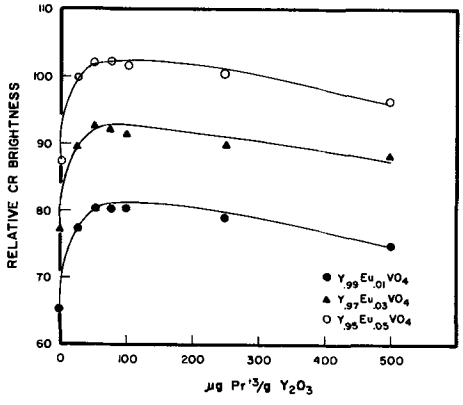

Fig. 2. Effect of Pr^{+3} on cathode-ray brightness of YVO_4:Eu

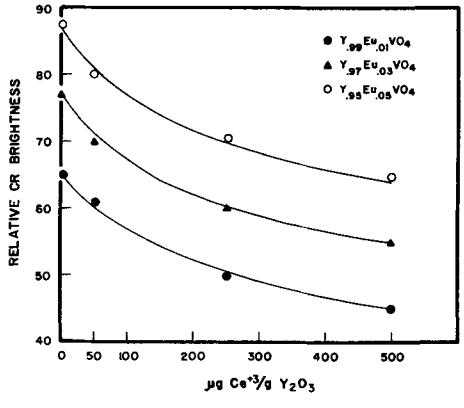

Fig. 5. Effect of Ce^{+3} on cathode-ray brightness of YVO_4:Eu

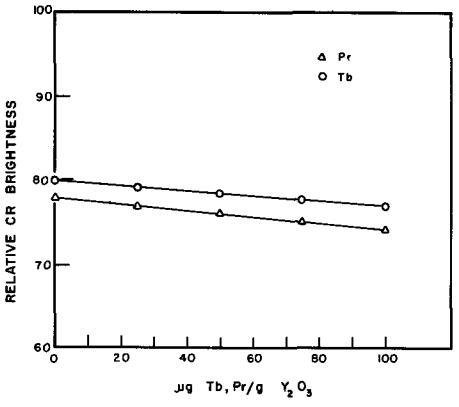

IMPURITY	SAMPLE-B
Ce	53
Pr	2
Nd	10
Sm	21
La	2
Eu	20
Gd	12
Tb	6
Dy	129
Ho	65
Er	66
Tm	7
Yb	75
Lu	25
Th	13

Fig. 6. Effect of Tb^{+3} or Pr^{+3} on cathode-ray brightness of YVO_4:Eu (0.05).

of the beneficial enhancement effect from Tb^{+3} and Pr^{+3}.

In conclusion, it can be said that: 1, with very pure Y_2O_3 as raw material, the brightness of YVO_4:Eu phosphor is increased by additions of Pr^{+3} and Tb^{+3}; 2, Ce^{+3} decreases the brightness of YVO_4:Eu; 3, emissions of Tb^{+3} and Pr^{+3} in the YVO_4:Eu system are not observed under either CR or uv excitation; and 4, addition of Pr^{+3} and Tb^{+3} increase the saturation of a red emission of the YVO_4:Eu at all europium levels tested.

Acknowledgments

The authors wish to express their thanks to D. T. Palumbo and S. Z. Toma for their helpful discussions. They wish also to thank M. Dyer and W. Persun for the phosphor measurements.

Manuscript submitted Dec. 11, 1968; revised manuscript received *ca.* April 7, 1969. This was Paper 52 presented at the Boston Meeting, May 5-9, 1968.

Any discussion of this paper will appear in a Discussion Section to be published in the June 1970 JOURNAL.

REFERENCES

1. L. G. Van Uitert, R. C. Lenares, R. R. Soden, and A. S. Ballman, *J. Chem. Phys.*, **36**, 702 (1962).
2. L. H. Brixner and E. Abramson, *ibid.*, **112**, 70 (1965).
3. A. K. Levine and F. C. Pallila, *Appl. Phys. Letters*, 5 (1964).
4. L. G. Van Uitert and R. R. Soden, *J. Chem. Phys.*, **36**, 1289 (1962).
5. R. C. Ropp, *J. Opt. Soc. Amer.*, **57**, 213 (1967).
6. G. L. Thompson, U. S. Pat. 3,322,682, May 30, 1967.
7. T. Kano and Y. Otomo, *This Journal*, **116**, 67 (1969).

Self-Activated Luminescence of β-Ga_2O_3

William C. Herbert,[1] Henry B. Minnier, and Jesse J. Brown, Jr.[2,] *

Sylvania Electric Products, Incorporated, Chemical and Metallurgical Division, Towanda, Pennsylvania

Gallium sesquioxide, Ga_2O_3, is known to exist in at least two stable crystalline modifications. The stable, low-temperature (α) form has the α-corundum crystal structure in which the oxygen ions approximate a hexagonal close-packed array and all of the Ga^{3+} ions are in octahedral coordination. Foster and Stumpf (1) prepared α-Ga_2O_3 by heating gallium monohydrate in air at about 400°C. Above approximately 600°C, α-Ga_2O_3 transforms to β-Ga_2O_3, the high-temperature polymorph. Since β-Ga_2O_3 is extremely persistent even below the $\alpha \rightleftarrows \beta$ transition temperature, it is the polymorph normally encountered in commercial gallia. Sheka *et al.* (2) discuss three other crystalline modifications of Ga_2O_3, *i.e.* γ, δ, ϵ, with each appearing to have an Al_2O_3 analog. The crystal structure of β-Ga_2O_3 has been investigated by Geller (3) and is monoclinic with $a_o = 12.23$, $b_o = 3.04$, $c_o = 5.80$Å, and $\beta_o = 103.7°$. Four molecules are contained in each unit cell, and the most probable space group is C 2/m. The structure is similar to that of θ-Al_2O_3 and is characterized by two nonequivalent cation sites, one tetrahedrally and one octahedrally coordinated by oxygen.

High-purity (99.9+% pure), commercial Ga_2O_3 normally contains the beta phase and is nonluminescent.

Experimental Procedure

Raw material purity.—99.999+% pure gallium oxide as received from two vendors was analyzed semiquantitatively by spectrographic methods for trace impurities. The results shown in Table I indicate the relatively high purity of starting materials. The only impurities present in both lots that are normally associated with impurity activation are Cu and Mo. (Ca, Mg, and Pb are possible acceptors and could also contribute to luminescence.) Neither of these starting materials showed significant luminescence as received. Elements sought but not detected (detection limits vary depending on elements, but, in all cases, detection limits are less than 10 ppm): As, B, Ba, Be, Bi, Cd, Co, Ce, Fe, Ge, Mn, Ni, P, Sb, Si, Sn, Sr, Ta, Th, Ti, W, Zn, and V.

Sample preparation.—Compositions were heat treated in alumina or fused silica crucibles in electric resistance furnaces. Some reaction with the fused silica crucibles was encountered and, therefore, the outer ¼ in. of exposed sample was routinely discarded before any measurements were made. Noble metal containers were unsatisfactory because of apparent amalgamation between the crucible metal and gallium.

Measurements.—Routine phase identification was achieved using a Norelco x-ray diffractometer which employed nickel-filtered CuKα radiation and operated at 40 kV and 15 ma.

All photoluminescent excitation and emission spectra and peak height measurements were obtained at room temperatures using a Perkin-Elmer spectrofluorimeter as previously described (4). Reflectance spectra were also measured using this instrument. Cathodoluminescent spectra were obtained using a demountable cathode ray tube operating at 12 kV anode potential and 6 μA beam current over a standard scan TV raster of 1-in.^{2} area. Brightnesses under these conditions were measured with an eye-corrected Weston foot-lambert meter.

Table I. Semiquantitative spectrograph analyses of two Ga_2O_3 raw material lots (in ppm)

Vendor	Ag	Al	Ca	Cu	Mg	Mo	Pb
A	<1	1-10	1-10	<1	<1	1-10	1-10
B	—	1-10	1-10	1	1	1-10	—

* Electrochemical Society Active Member.

[1] Present address: Drexel Institute of Technology, Philadelphia, Pennsylvania.

[2] Present address: Department of Metals and Ceramic Engineering, Virginia Polytechnic Institute, Blacksburg, Virginia 24061.

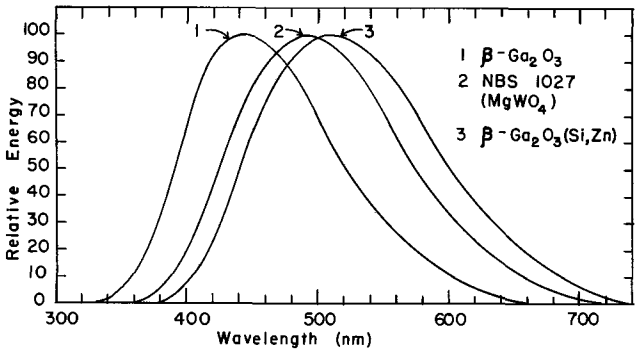

Fig. 1. Fluorescence spectra of β-Ga_2O_3, β-Ga_2O_3 (Si, Zn), and $MgWO_4$.

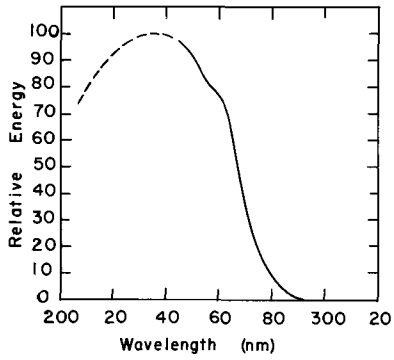

Fig. 2. Excitation spectra of β-Ga_2O_3

Experimental Results

Commercial grades of Ga_2O_3 are normally nonluminescent, although in some cases an extremely weak emission can be detected. Upon heat treatment at high temperatures, *e.g.* above 1250°C, a bright blue luminescence develops. This emission is characterized by the spectrum shown in Fig. 1 and the optical data listed in Table II. Under 253.7 nm excitation, unactivated β-Ga_2O_3 has a peak emission at 456.0 nm and a ½ I_{max} band width of 130 nm. This corresponds to a shorter wavelength of emission and a more narrow band width than that of $MgWO_4$ (NBS 1027) which emits at 501.0 nm and has a band width of 150 nm. Luminescent β-Ga_2O_3, properly prepared, has a more intense peak emission than $MgWO_4$, and, consequently, the integrated area of the emission spectrum of β-Ga_2O_3 is slightly larger than that of $MgWO_4$.

Under cathode ray excitation, β-Ga_2O_3 is about 19% as bright as ZnS:Ag, the conventional blue-emitting, color-television phosphor.

The intensity of the photoluminescence varies considerably depending on the temperature and duration of heat treatment. In addition, the luminescence appears to be very sensitive to low level impurities, including those present in the furnace atmosphere and the fused silica container. It is not possible to describe a given procedure for the preparation of this phosphor, since each lot of Ga_2O_3 appears to behave somewhat differently. Phosphor preparations under mildly reducing conditions, generated by adding a few per cent NH_4Cl and firing in covered crucibles, markedly enhance the luminescence brightness. This modification does not change the other emission characteristics.

Substitutions of Si^{4+} and Zn^{2+} for Ga^{3+} were found to increase the peak emission wavelengths to approximately 510 nm. These substitutions, which can be represented by the formula $(Ga_{0.99}^{3+},Si_{0.005}^{4+},Zn_{0.005}^{2+})_2O_3$

Table II. Comparison of photoluminescence and cathodoluminescence of self-activated β-Ga_2O_3 with standard phosphors

Photoluminescence (λex = 253.7 nm)	β-Ga_2O_3	$MgWO_4$ (NBS 1027)
Peak wavelength (nm)	456.0	501.0
Peak intensity (%)	144	100
Band width at ½ I_{max} (nm)	130	150
Relative areas of emission peak (%)	106	100
Chromaticity coordinates		
x	0.184	0.234
y	0.207	0.320

Cathodoluminescence	β-Ga_2O_3	ZnS:Ag (P-21 Blue)
Brightness (ft-L)	6.2	33.5
Chromaticity coordinates		
x	0.176	0.149
y	0.166	0.043

indicate that the luminescence is sensitive to some chemical additions even when they are present in low concentrations.

The photoluminescence excitation spectrum for luminescent β-Ga_2O_3 obtained in the present study (Fig. 2) is in basic agreement with the optical absorption data of Tippins (4).

Discussion of Results

In view of the high purity and especially the low concentration of potential activator ions present in the Ga_2O_3 raw material, it is unlikely that the observed luminescence arises from absorption of energy by impurity activator ions. The broad, apparently structureless, absorption and emission spectra of luminescent β-Ga_2O_3 substantiate this viewpoint. This does not eliminate the possibility of these ions acting as coactivators or sensitizers.

The most likely explanation of the absorption mechanism has been discussed by Tippins (4) in which he semiquantitatively relates the experimental optical absorption of β-Ga_2O_3 to a $Ga^{3+} + O^{=} \rightarrow Ga^{2+} + O^{-}$ type process. The excitation spectrum for luminescent β-Ga_2O_3 shown in Fig. 2 is in close agreement with the optical absorption spectra measured by Tippins.

Although this appears to be a plausible explanation of the absorption (excitation) mechanism in β-Ga_2O_3, it does not explain why luminescence is observed only when the oxide has been subjected to high-temperature heat treatments. Evidently, energy absorbed by β-Ga_2O_3 is transferred quite freely through the lattice until it is eventually dissipated as heat. Luminescence does not develop until something, either vacancies or impurity ions, is introduced in sufficient concentration into the lattice to disrupt the continuity and serve as energy traps and, subsequently, emission centers. High-temperature heat treatments, therefore, are necessary to form vacancies.

Only recently, Lorenz, Woods, and Gambino (5) have shown by Hall coefficient and resistivity measurements that β-Ga_2O_3 can be an insulator or semiconductor depending on the conditions of preparation. In oxidizing atmospheres, the material exhibits insulating properties, but mild reduction introduces semiconducting characteristics. Semiconduction was attributed to the presence of anion vacancies. Optical absorption spectra obtained from the semiconducting β-Ga_2O_3 is in good agreement with the results of Tippins (4) and those of the present study.

Summary

The preparation of luminescent β-Ga_2O_3 can be achieved by simply heat treating the oxide at high temperatures in a nonoxidizing atmosphere. The resultant broad band emission peaks at 456 nm. As is typical for this type of luminescence, the emission wavelength can be varied somewhat by introducing impurity levels in the normally forbidden band gap.

Acknowledgment

Discussions of this work with Dr. S. Z. Toma were greatly appreciated.

Manuscript submitted Jan. 13, 1969; revised manuscript received ca. March 27, 1969.

Any discussion of this paper will appear in a Discussion Section to be published in the June 1970 JOURNAL.

REFERENCES

1. L. M. Foster and H. C. Stumpf, *J. Am. Chem. Soc.*, **73**, 1590 (1951).
2. S. Geller, *J. Chem. Phys.*, **33**, 676 (1960).
3. W. Slavin, R. W. Mooney, and D. T. Palumbo, *Opt. Soc. Am.*, **51**, 93 (1961).
4. H. H. Tippins, *Phys. Rev.*, **140**, A316 (1965).
5. M. R. Lorenz, J. F. Woods, and Gambino, *J. Phys. Chem. Solids*, **28**, 403 (1967).

Brief Communication

A Chemical Polish for $Sn_xPb_{1-x}Te$

J. Edward Coker

Autonetics Division of North American Rockwell Corporation, Anaheim, California

Single-crystal wafers of $Sn_xPb_{1-x}Te$ for $0 \leq x \leq 1$ have been polished down to a thickness of 3-4 mils. The resulting surface is specular, providing enough material has been removed to remove damage due to cutting or mechanical polishing.

To date, no one has reported a good polish for $Sn_xPb_{1-x}Te$. In an attempt to polish $Sn_xPb_{1-x}Te$, several chemical polish-etches were tried; among those tried was a lead telluride polish consisting of 40 cc saturated $K_2Cr_2O_7$ solution and 9 cc concentrated HNO_3 (1). A tin telluride polish that was used was prepared by dissolving 0.35g I_2 in 40 ml ethanol to which was added 10 ml distilled H_2O and 4.0 ml 49% HF (2). Also tried was $PbSe_{1-x}Te_x$ polish which was made by dissolving 0.5g disodium ethylenediamine tetraacetate in 25 ml distilled H_2O, then adding 50 ml 30% H_2O_2 and 25 ml glacial acetic acid (3). All of these display one or more undesirable properties. The polishes for PbTe and $PbSe_{1-x}Te_x$ leave stains on the surface; the tin telluride polish produces orange peel surfaces if careful control is not maintained.

The problem in polishing compounds of tin and lead lies in the fact that very few compounds of tin are soluble in aqueous solutions. To obtain the desired solubility, it is necessary to oxidize tin to the Sn(IV) state and lead to the Pb(II) state. This can be accomplished with the use of bromine in an acidic solution. A polish-etch has been found which is particularly good for polishing surfaces and/or etching patterns in $Sn_xPb_{1-x}Te$ substrates. The polish-etch contains 6 parts by volume bromine and 100 parts 48% hydrobromic acid which is used at room temperature. The crystals of $Sn_xPb_{1-x}Te$, when immersed in the polish-etch, will form a dark stain which is easily removed by agitating the liquid. The polish lends itself readily to tumbling techniques or the use of a magnetic stirrer. Quenching of the etch is accomplished by successive dilution with either methanol or deionized water. For thinning or etching patterns, wafers can be mounted on glass slides and, while stirring the liquid, etched to the desired thickness with a smooth reflective surface. Investigation indicates the polish-etch works well with a range of from 2 to 12 parts bromine.

The range of etch rates was found to be from 20 to 25 μ/min at 2%, to 80-85 μ/min at 12% concentrations of bromine.

A single sample of $Cd_{0.15}Hg_{0.85}Te$, a related infrared material, was polished with a 2% concentration of bromine in hydrobromic acid. The sample was a saw-cut wafer which had a very rough surface. After removal of the damage introduced by the saw ($\sim$15-20μ), the surface was both smooth and reflective.

Manuscript submitted March 20, 1969; revised manuscript received ca. April 7, 1969.

Any discussion of this paper will appear in a Discussion Section to be published in the June 1970 JOURNAL.

REFERENCES

1. M. R. Lorenz, *This Journal*, **112**, 240 (1965).
2. M. K. Norr, *ibid.*, **113**, 621 (1966).
3. M. K. Norr *et al.*, *ibid.*, **114**, 632 (1967).

Contribution of Spacer Paper to the Frequency and Temperature Characteristics of Electrolytic Capacitors

Robert S. Alwitt*

Research and Development Laboratories, Sprague Electric Company, North Adams, Massachusetts

ABSTRACT

Electrolyte-impregnated capacitor paper has dielectric properties typical of a colloidal dispersion. The parallel capacitance of the paper is substantially enhanced by contact with aluminum oxide. The capacitance loss exhibited by aluminum electrolytic capacitors at low temperatures and/or high frequencies is accounted for by the combined effects of the etch structure of the foil electrodes and the dielectric properties of the impregnated paper.

Foil-type electrolytic capacitors exhibit a capacitance decrease at low temperatures and/or high frequencies that cannot be accounted for by a simple discrete capacitance for the oxide dielectric. Some performance curves for capacitors designed to illustrate this behavior are shown in Fig. 1. This effect has been ascribed to a capacitance of the electrolyte-impregnated spacer paper (1, 2) and to a decrease in the effective area of etched foil electrodes because of a "tuning out" of the interior of the etch structure (2, 3). It has recently been suggested that pores in the anodic oxide may contribute to the capacitance loss (3). Each of these factors is now considered briefly.

Assigning a fixed capacitance to the impregnated spacer paper helps reproduce the impedance *vs.* frequency characteristic of a capacitor (1, 3), but it does not account for all of the capacitance decrease at higher frequencies (3).

The treatment of the electrical properties of a porous capacitor electrode as a distributed network of capacitance and resistance was first presented in a quantitative fashion by Vergnolle (4). The capacitance due to the oxide dielectric was distributed along the pore walls, while the electrolyte resistance was distributed along the pore interior. A detailed consideration of the electrical properties of rough and porous electrodes has been presented by deLevie (5). The mathematical analysis of the electrical properties of etched foil electrodes presented by Broadbent (3) is essentially correct, but his experimental results did not show that characteristically different results were obtained with etched foil compared with plain foil. This was probably the result of not separating out the effect of the impregnated spacer paper that was measured in series with the foils.

Young (6) has shown that pores and microfissures in a dielectric film can be detected by the frequency dependence of the series resistance. If such discontinuities are present, there is a deviation from a linear R *vs.* $1/f$ relationship due to high series resistance at low frequencies. Broadbent (3) found a linear R *vs.* $1/f$ relationship, so it is unlikely that the capacitance loss he ascribes to pores or cracks can be accounted for in that fashion. Moreover, the effect of fissures would be least at those conditions which produce the largest capacitance loss, *i.e.* high frequency and low temperature.

Thus, the low-temperature and high-frequency characteristics of foil-type electrolytic capacitors have not yet been satisfactorily explained. This is due primarily to incorrect interpretations of the dielectric properties of the electrolyte/spacer system. The main purpose of this paper is to describe some electrical properties of impregnated spacer paper. Consideration of these properties, in conjunction with the known characteristics of the oxide dielectric and etch structure, permits a complete operational description of the low-temperature and high-frequency behavior of aluminum electrolytic capacitors.

Properties of Impregnated Spacer Paper

General.—More than 30 years ago, Fricke and Curtis (7) observed that an aqueous suspension of cellulose exhibited a very broad low-frequency dielectric dispersion. The apparent dielectric constant of the suspension was as much as several orders of magnitude greater than that of water and had a strong frequency dependence. Other colloidal systems showed the same effect. This property arises from the motion of ions, under the influence of an external electric field, along the surface of the solid particles. Schwarz (8) showed that the net ionic current tangential to the solid surface would be out of phase with the impressed field so as to give rise to a surface capacitance. He showed that the apparent dielectric constant arising from this effect could account very well for the experimental results.

It might be expected that the cellulose fibers in paper sheet would still retain many colloidal properties. Indeed, we have reported recently that paper sheet exhibits the same kind of dielectric dispersion as cellulose suspensions (9). It was found that the dielectric constant of electrolyte-impregnated spacer paper varied over the range 10^2 to 10^7 and depended on frequency, temperature, and solute concentration (9).

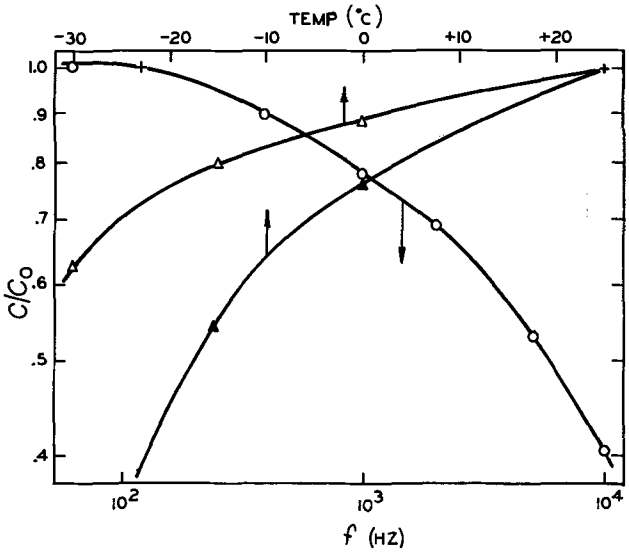

Fig. 1. Capacitance of 5V aluminum electrolytic capacitors made with Benares paper and an 800 ohm-cm glycol electrolyte: (○) = frequency dependence at 25°C; (△) = temperature dependence at 120 Hz; (▲) = temperature dependence at 1000 Hz; (+) = C_0 reference points.

* Electrochemical Society Active Member.

The temperature and solute concentration determine electrolyte resistivity with a particular solvent. The resistance R_p of any one paper type is proportional to electrolyte resistivity (10). The paper capacitance C_p is proportional to the dielectric constant, where C_p is in parallel with R_p. It has now been found that, when the data presented in Ref. (9) are plotted as C_p *vs.* fR_p, all the results with the same paper type fall within a narrow band, independent of the particular temperature or concentration. It should be noted that this is an empirical correlation. No theoretical grounds for the correlation would be expected since C_p is an interfacial property, while R_p is presumably determined by ionic conduction in electrolyte outside the range of surface effects.

The correlations obtained for a 1-mil thick Benares paper and a 2.4-mil Manila paper in electrolytes of sodium salicylate in ethylene glycol are shown by the line marked (a) in Fig. 2. The data were obtained at solute concentrations from 0.015 to 0.5M, temperatures from −24° to +80°C, and frequencies from 60 to 10^4 Hz. Both papers had about the same capacitance over much of the range of fR_p. Paper properties, experimental procedures, and further discussion of these data have been presented elsewhere (9, 10).

Behavior in a capacitor.—The effect of the dielectric properties of the impregnated spacer on the capacitance of an electrolytic capacitor is illustrated in Fig. 3. The fractional capacitance of a 4V smooth aluminum anode is shown as a function of frequency and electrolyte resistivity. Measurements were made at 25°C at frequencies up to 10,000 Hz and in glycol electrolytes with resistivities up to 10,000 ohm-cm. The reference capacitance C_o was about 1 mfd/cm², obtained at 60 Hz in a 12 ohm-cm aqueous electrolyte with no spacer present. Measurements with paper were made using a sandwich consisting of a central aluminum foil anode separated from two platinized electrodes by electrolyte-impregnated spacers (single sheets). The paper had been soaked overnight in electrolyte at 25°C. Care was taken to exclude air from the sandwich. Measurements without paper were made using the apparatus described by Bernard (11), with the aluminum electrode maintained at a separation of about 2 mils from a platinized electrode. The decrease in C/C_o in the absence of a spacer was probably due to residual surface roughness and possibly slight misalignment of the electrodes.

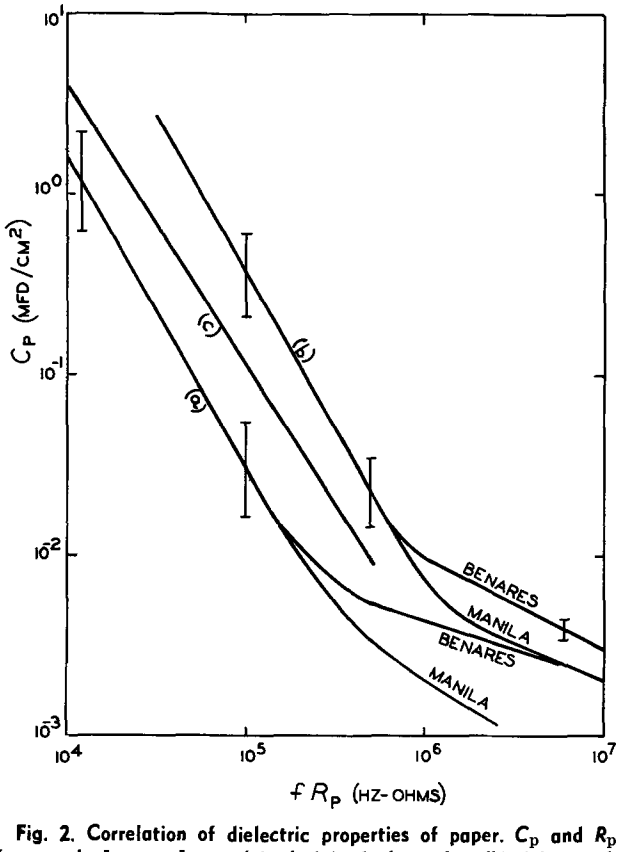

Fig. 2. Correlation of dielectric properties of paper. C_p and R_p for sample 1 cm x 1 cm; (a) platinized electrodes, (b) 4V smooth Al electrode, (c) etched Al electrodes. Vertical lines show range of data. See text for other details.

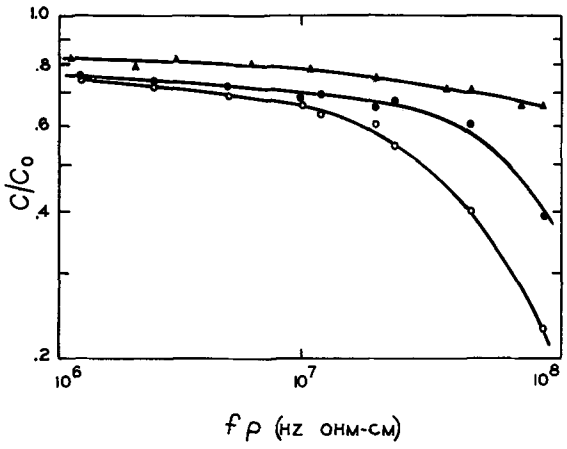

Fig. 3. Dependence of capacitance on frequency and electrolyte resistivity. Smooth, 4V Al at 25°C. (△) = no paper, (●) = Manila paper, (○) = Benares paper.

The capacitance and resistance of the paper in these sandwiches were calculated from the total series C and RC measured on a conventional bridge and the independently measured C and RC of the anodized aluminum foil. The procedure was the same as that used for measurements made between platinized electrodes (9) but with the oxide dielectric substituted for the external capacitor. This calculation treats the total capacitance and resistance as consisting of the oxide C_{ox} and R_{ox} in series with the parallel combination of paper C_p and R_p. Values of C_p and R_p were determined from the data in Fig. 3, and from data obtained over the same ranges of frequency and resistivity but at temperatures down to −24°C.

At any particular condition, the value of R_p was the same as found previously when using platinized electrodes. However, C_p was about an order of magnitude greater with the aluminum electrode. The correlation for these data obtained with a smooth, 4V Al anode is shown in Fig. 2 as line (b).[1]

Measurements of C and RC of some low-voltage miniature aluminum electrolytics were analyzed in a similar fashion and the correlation line for the paper properties is shown in Fig. 2 as line (c). These capacitors were made with etched foils and both Benares and Manila papers. Several electrolytes were used, including glycol/sodium salicylate and glycol/borate electrolytes. The correlation line is intermediate to those obtained with platinized electrodes and with a smooth Al electrode.

The fact that these lines are parallel indicates that the substitution of an oxidized Al electrode for a platinized electrode produced an increase in the magnitude of the dielectric constant of impregnated paper, rather than the introduction of a new dielectric phenomenon. This was made more evident by an examination of the dependency of paper dielectric constant on temperature, solute concentration, and frequency. In each case, the functional dependence was the same for both electrode materials.

Heavy metal cations are known to have a large effect on the surface properties of fibrous materials, including paper pulp (12). It was thought that even slight dissolution of aluminum or aluminum oxide might

[1] To estimate C_p for any particular condition in Fig. 3, one can calculate fR_p from $f\rho$ by using Eq. [4] in Ref. (10), treating R_p as frequency-independent. For the conditions of this study, this gives $R_p = 0.040\rho$ for Benares paper and $R_p = 0.025\rho$ for Manila paper for an area of 1 cm².

have imparted unsuspected properties to the paper, resulting in an increased capacitance. However, the addition of as much as 10^{-2} $Al(NO_3)_3$ to a glycol/sodium salicylate electrolyte did not shift the correlation line for Benares paper measured between platinized electrodes. Thus, dissolved aluminum seemed an unlikely source for the enhanced capacitance.

Contact with aluminum electrodes produced no permanent change in paper as evidenced from the fact that impregnated paper that had been in contact with aluminum for an extended time had the same capacitance, measured between platinized electrodes, as freshly prepared paper.

The following experiment established that it was the paper/Al_2O_3 interface, and not the presence of the aluminum electrode, that produced the enhanced dielectric constant for the impregnated paper. The capacitance of a smooth Al foil anodized to 3V was measured *vs.* platinized electrodes in a 10^4 ohm-cm glycol electrolyte at 25°C under the following conditions:

(*a*) Electrode separation about 25 mils; no paper present.

(*b*) Same electrode separation; one layer of Benares paper pressed against platinized electrodes but not touching Al.

(c) Electrode separation reduced so that paper is in intimate contact with both platinized and Al electrodes.

The decrease in over-all series capacitance with increasing frequency is shown in Fig. 4 for these three cases. The large decrease in equivalent series capacitance for case (c) shows that C_p, the effective parallel capacitance of the paper, was much greater than in case (*b*). The necessity for paper-oxide contact to produce very high C_p is supported by the results with etched foil (Fig. 2). With roughened foil, the actual contact area between foil and paper was reduced, resulting in a smaller C_p than with smooth Al foil.

Evidence that the high capacitance is localized near the oxide/paper interface is that, upon substituting three sheets of Benares paper for a single sheet in a sandwich made with a smooth 4V Al foil, no change in the measured capacitance occurred. A decrease of almost 25% would have been predicted at the particular conditions used if the dielectric properties had been uniformly distributed.

It has been shown elsewhere (9) that the dielectric constant of impregnated paper sheet is dependent on temperature, frequency, fiber dimensions, bulk electrolyte properties, and surface charge density. It would seem that only surface charge density (σ_0) could be affected by proximity to an electrode surface. To a first approximation, $\Delta\epsilon' \propto \sigma_0^3$ (9), so a relatively small change in σ_0 could produce a large change in dielectric constant.

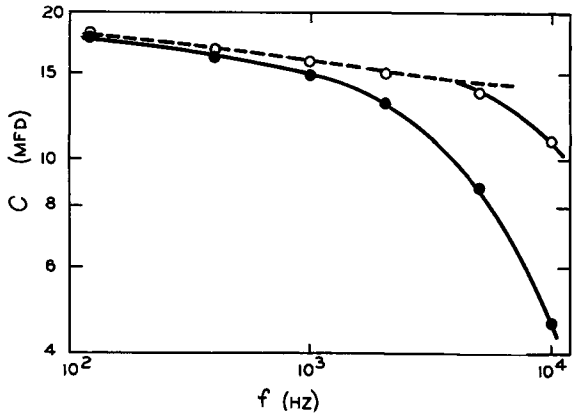

Fig. 4. Effect of paper/oxide interface on capacitance decrease. Dashed line represents results with no paper, (○) = Benares paper not in contact with oxide, (●) = Benares paper in contact with oxide.

Although paper in contact with anodized Al acts as if it had acquired an increased surface charge density, it is not apparent how this process could take place. Furthermore, it has been shown (9) that contact with platinized electrodes imparts no special properties, as evidenced by the fact that $\Delta\epsilon'$ was found to be the same for three sheets as for one sheet of paper. Thus, any explanation of the effect of an Al electrode must account for the difference between a metal and an oxide contact.

Etch Structure

The theory of porous electrodes (5) predicts that the effective capacitance of an oxide-covered electrode depends on the parameter $f\rho C_0$. At a critical value of $f\rho C_0$, the impedance of the furthest regions of the pores becomes sufficiently high, relative to the impedance of the surface regions, that the current and potential lines in the surrounding electrolyte no longer penetrate the full length of the pore. As $f\rho C_0$ increases above this value, the effective surface area, and hence C/C_0, becomes proportional to $(f\rho C_0)^{-1/2}$. The critical value depends on the ratio of pore diameter to length and increases as this ratio becomes larger.

During the course of our investigation of paper properties, it was found that paper impregnated with electrolytes using a mixed solvent of 1:1 water:glycol had no effect on the capacitance of foil sandwiches over a wide range of frequencies and electrolyte resistivities. This provided a convenient tool for studying the effect of etch structure on capacitance. Recent results in this area presented by Broadbent (3) did not exclude the capacitive contribution of the spacer paper.

Sandwiches were made as described under "Behavior in a capacitor," but using an anodized, etched aluminum foil as the central electrode and electrolytes made with the mixed solvent. Measurements were made over a frequency range of 60-1000 Hz at temperatures from —40° to 25°C and with electrolytes with resistivities at room temperature of 2 x 10^3 and 10^4 ohm-cm.

Four different etched aluminum foils were examined; two foils with a fine etch structure used for low-voltage applications, a foil with a coarser structure used for high voltages, and a cathode foil. These were anodized to several voltages up to 30V.

As expected, for each foil the value of C/C_0 was dependent on oxide thickness, temperature, *etc.*, only insofar as it affected the value of $f\rho C_0$. Surprisingly, there was not much difference among the several types of foils. All of the results could be described reasonably well by the single line shown in Fig. 5. The vertical bars describe the total range for the four foils. The points represent results obtained with one of the low-voltage foils. The slope of the line at high values of $f\rho C_0$ is —0.46, close to the theoretical value of —0.50. The gradual approach to this slope, rather than a sharp transition, is due to the presence of a distribution of pore sizes each with their own cut-off point.

The ordinate in Fig. 5 represents the effective surface area of the electrode. The oxide series resistance is inversely proportional to area and so will be inversely proportional to C/C_0.

Discussion

Equivalent circuit.—Based on the considerations in the preceding sections, one can arrive at the equivalent circuit shown in Fig. 6. The anode capacitance and resistance and cathode capacitance are shown as being distributed with the electrolyte resistance in the pores. The electrolyte/spacer system should also be represented by distributed parameters but this cannot be done in a simple fashion. Instead, C_p is depicted as a lumped parameter dependent on frequency and electrolyte resistivity.

If the capacitor section is sufficiently large, the resistance and inductance of the foil electrodes may be-

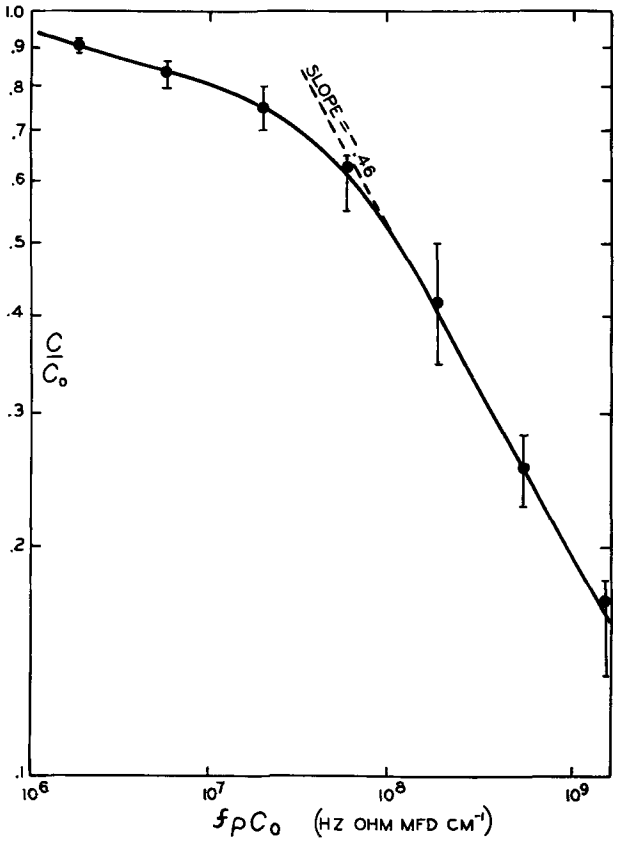

Fig. 5. Capacitance decrease of etched Al foil. Vertical lines show total range for four foils, points are results with a low-voltage foil.

come important. Peekema and Beesley (13) have recently presented an analysis of this situation. In such a case, the circuit in Fig. 6 would represent a unit element of the capacitor to be distributed over the foil resistance and inductance.

An important point of this work, and one emphasized by Peekema and Beesley (13), is that an accurate representation of an electrolytic capacitor requires that all major parameters be treated as distributed rather than lumped. Under certain conditions, some of the parameters can be approximated by discrete capacitance or resistance, but probably only lead and contact resistances can truly be considered as lumped parameters.

Predicting capacitor performance.—In principle, it should be possible to predict the capacitance and resistance of an electrolytic capacitor as a function of frequency and temperature from measurements of the foil, paper, and electrolyte properties by use of the circuit in Fig. 6. The effective capacitance and resistance of the foil-electrolyte system can be found in a straightforward manner. The paper/electrolyte properties in a capacitor are more difficult to assess. The resistance of impregnated paper will depend on the degree of constraint within the capacitor section

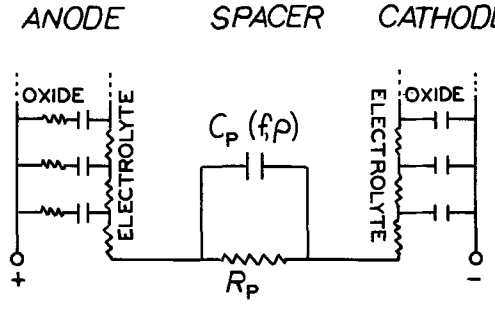

Fig. 6. Equivalent circuit for electrolytic capacitor

and the time-temperature history after impregnation (10). Since the value of C_p used for the calculation will be determined by the value of R_p chosen for use in Fig. 2, any error in selecting R_p is compounded. Our experience has been that with a low-resistance paper, such as Manila, the etched foil properties are dominant and a reasonable estimate of R_p is sufficient to provide good agreement between observed and predicted values of capacitance over a wide range of frequencies and temperatures. With a more resistive paper, such as Benares, the paper properties determine the capacitance loss at the lowest temperatures and/or highest frequencies and, unless an accurate value of R_p is used, there could be a substantial difference between observed and calculated values. Of course, even without an accurate value of R_p, this approach could be used to predict the relative effects of design changes or use of new materials.

An interesting aspect of the localization of the high C_p near the oxide/paper interface is that, when calculating the effect of paper for a capacitor using multilayers of paper, C_p is that corresponding to R_p for a single layer, even though the effective R_p in the capacitor will be that for all the layers.

The correlation between C_p and R_p shown in Fig. 2 can be used with systems other than those discussed here. Results with paper equilibrated with electrolyte at 85°C, as well as at 25°C, fell on line (b). An extensive study with smooth aluminum anodes showed that data obtained with uncalendered Kraft paper fell on line (b), as did results obtained with other electrolyte systems, *e.g.* using dimethylformamide as solvent. Presumably, line (c) would have this same generality though this was not studied in detail.

Conclusions

1. Electrolyte-impregnated capacitor paper exhibits dielectric properties typical of a colloidal dispersion. It can be inferred that the effective capacitance of the paper is increased by contact with aluminum oxide.
2. A correlation between C_p and fR_p exists for several paper/electrolyte systems.
3. The effective capacitance of etched Al foil is essentially that predicted by the theory of porous electrodes.
4. The effect of low temperature and high frequency on the capacitance of electrolytic capacitors can be accounted for by the combined properties of the etched foil and impregnated spacer paper.

Acknowledgment

The author is grateful to Mrs. E. Vigna for obtaining the laboratory results reported here.

Manuscript submitted Sept. 13, 1968; revised manuscript received *ca.* April 8, 1969.

Any discussion of this paper will appear in a Discussion Section to be published in the June 1970 JOURNAL.

REFERENCES

1. I. F. M. Walker, *Radio Electronic Components*, **4**, 25 (1963).
2. S. Boone and R. D. Bügel, *Bull. Assoc. Suisse Elec.*, **54**, 313 (1963).
3. R. H. Broadbent, *Electrochem. Technol.*, **6**, 163 (1968).
4. J. Vergnolle, *This Journal*, **111**, 7 (1964).
5. R. deLevie, *Electrochim. Acta*, **9**, 1231 (1964); *ibid.*, **8**, 751 (1963).
6. L. Young, *Trans. Faraday Soc.*, **55**, 842 (1959).
7. H. Fricke and H. J. Curtis, *J. Phys. Chem.*, **41**, 729 (1937).
8. G. Schwarz, *ibid.*, **66**, 2636 (1962).
9. R. S. Alwitt, *ibid.*, **73**, 1056 (1969).
10. R. S. Alwitt, *Electrochem. Technol.*, **6**, 172 (1968).
11. W. J. Bernard, *This Journal*, **108**, 446 (1961).
12. C. E. Mossman and S. G. Mason, *Can. J. Chem.*, **37**, 1153 (1959); D. A. I. Goring and S. G. Mason, *Can. J. Research*, **28B**, 323 (1950).
13. R. M. Peekema and J. P. Beesley, *Electrochem. Technol.*, **6**, 166 (1968).

Electrodeposition of Molybdenum Coatings

Frank X. McCawley,* Charlie Wyche, and David Schlain*

College Park Metallurgy Research Center, Bureau of Mines, United States Department of the Interior, College Park, Maryland

ABSTRACT

The electrodeposition of coatings of molybdenum from a sodium and lithium metaborate-molybdate-molybdenum oxide fused salt system was investigated. Coatings up to 16 mils thick were deposited on Inconel, Carpenter 20 stainless steel, nickel, copper, and graphite at current densities of 3.1-6.2A dm^{-2} (0.2-0.4A $in.^{-2}$) and 900°C under an argon atmosphere. The composition of the electrolyte is critical; deposits are obtained only when the electrolyte contains between 1.0 and 3.3% molybdenum.

Interest in molybdenum has increased rapidly with the advent of the missile and space industries (1). However, the production methods, such as compact powder sintering and arc casting, are expensive and useful forms of molybdenum metal are difficult to fabricate. The Bureau of Mines undertook this investigation to develop methods for applying coherent coatings of molybdenum on several substrates in order to take advantage of the properties of the molybdenum and to bypass expensive fabrication techniques.

Earlier investigators claimed deposits of molybdenum alloys from aqueous solutions (2, 3) and deposits of molybdenum metal from fused salt systems (4-7). Senderoff and Brenner (8) attempted to repeat some of these experiments and concluded that molybdenum had not been electrodeposited from aqueous, organic, or molten salt systems by the methods described. In 1954, Senderoff and co-workers developed a method for making coherent, dense molybdenum deposits up to 0.02 in. thick from a LiCl-KCl-K_3MoCl_6 fused salt electrolyte (8-11). Later, McCawley (12) and Cummings *et al.* (13) prepared coarse dendritic crystals of high-purity molybdenum by electrodeposition from fused salt mixtures made up with one or more alkali metal or alkaline earth chlorides and molybdenum pentachloride or potassium hexachloromolybdate, respectively. At about the same time, Heinen and Zadra (14, 15) described the electrowinning of high-purity molybdenum from sodium phosphate-borate-halide fused salt baths containing MoO_3. In 1964, Mellors and Senderoff (16-18) described a method for electroforming dense, coherent deposits of molybdenum from molten fluoride baths.

Starting with a 37.5% NaCl-37.5% KCl-25% K_3MoCl_6 fused salt electrolyte, the Bureau of Mines was able to obtain thick coatings. For example, adherent, dense coatings of molybdenum of up to 16 mils in thickness were made from this electrolyte at 900°C on graphite and stainless steel substrates. Cathode current efficiencies were from 80 to 99% for coatings made at current densities (C.D.) up to 9.3A dm^{-2}. However, corrosive vapors diffused through the protective graphite liner, attacked the structural parts of the cell, and contaminated the electrolyte.

The chemical similarity of molybdenum and tungsten and the success in preparing coatings of tungsten from the metaborate electrolyte by Davis and Gentry (19) and the improvement by McCawley *et al.* (20) suggested the use of a similar plating electrolyte for molybdenum. Therefore, this investigation deals mainly with the $NaLiB_2O_4$-$NaLiMoO_4$-MoO_3 fused salt system.

Experimental Equipment and Procedures

A special furnace which allowed visual observation of the cell during the high-temperature electrodeposition process was used in this investigation. The furnace is described in detail in a paper on electroplating thick tungsten coatings (20). However, a short description of the apparatus is given below and an isometric diagram of the apparatus is shown in Fig. 1.

Equipment.—The container used for plating consisted of a 4-in.-diam by 5-in.-high platinum crucible. The cell had one molybdenum anode and a cathode of nickel, Inconel, Carpenter 20 stainless steel, graphite, or copper. The two electrodes usually had the same dimensions, about 1 in. wide, 3-6 in. long, and 0.031-0.125 in. thick. They were spaced 1⅛ in. apart and were generally immersed in the electrolyte to a depth of 1-3 in., giving submerged areas of about 2-6 $in.^2$. The electrodes were attached to Inconel[1] extension rods. The cathode was connected to a d-c power supply by means of a constant low-voltage drop rotating assembly (21) which utilized mercury metal as the electrical contact. A thermocouple encased in ¼-in. OD Inconel tube covered with a 5-mil coating of platinum or molybdenum was used to measure the temperature and activate the temperature-controlling mechanism.

The cell was enclosed in a Pyrex furnace tube, the ends of which were sealed with wax into grooves on the brass end plate. These end plates were water-cooled by means of copper coils silver-soldered to the outside edges. The top end plate had an opening which was sealed with an "O" ring and an aluminum lid. The anode extension rod and the cell thermocouple passed through gastight seals in this lid. A 7-in.-high by 2-in.-diam aluminum interchange chamber was attached to the furnace lid. The cathode extension rod passed up through the interchange chamber lid. A gate valve separated the interchange chamber from the main furnace chamber and deposits were removed and fresh cathodes were introduced without allowing the cell or its contents to come in contact with the outside atmosphere. The bottom end plate was solid except for two gastight fittings. One was the argon gas inlet and the other supported a second thermocouple. The cell was heated by means of a high-voltage, 10-kw, 450-kHz rf induction generator. Cell temperature was maintained within ±5°C.

A resistance furnace was used to fuse and dry the electrolyte salts in a controlled atmosphere. A vacuum oven was used for predrying the salts. A stainless steel dry box was used for crushing, weighing, and mixing the salts under an Ar or N_2 atmosphere.

Bend tests were made using an adjustable bend fixture (Fig. 2) which allowed the specimen to bend as a beam in a three-point loading. This test method is similar to the method used for testing refractory metal sheet (22). The fixture rolls were adjustable to 1.0, 1.25, and 1.75 in. and the radii of the wedge tips were 0.05 in., 0.10 in., and a sharp knife edge. The wedge and rolls were attached to a compression tester and were closed at a controlled rate.

* Electrochemical Society Active Member.

[1] Reference to specific brands is made to facilitate understanding and does not imply endorsement of such items by the Bureau of Mines.

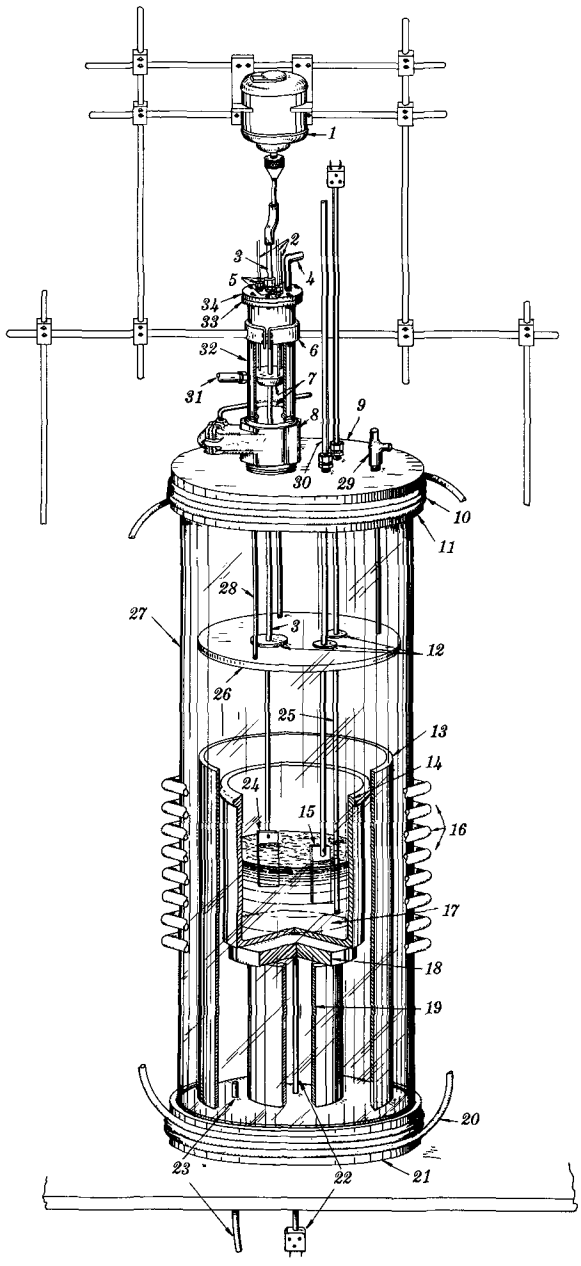

Fig. 1. Isometric cutaway diagram of Pyrex tube furnace with cell and interchange chamber: 1—stirring motor, 2—centering bearing support rods, 3—cathode extension rod, 4—gas outlet, 5—gas tight tube fitting, 6—chamber support clamp, 7—centering bearing and ring, 8—interchange chamber shutoff valve, 9—main lid, 10—top flange cooling coils, 11—top flange, 12—boron nitride bearings, 13—quartz shielding tube, 14—crucible, 15—anode, 16—induction coils, 17—electrolyte, 18—boron nitride table, 19—alumina support tube, 20—bottom cover cooling coils, 21—bottom cover, 22—thermocouple, 23—gas inlet, 24—cathode, 25—thermocouple, 26—baffle plate and heat shield, 27—Pyrex glass tube, 28—baffle plate support rods, 29—gas and vacuum outlet, 30—anode extension rod, 31—gas inlet, 32—interchange chamber body, 33—interchange chamber flange, 34—interchange chamber lid.

Hardness was determined on a Tukon microhardness tester.

Preparation of electrolyte.—The electrolyte was made up of sodium and lithium metaborates ($NaBO_2$ and $LiBO_2$), sodium and lithium molybdates (Na_2MoO_4 and Li_2MoO_4), and molybdenum oxide (MoO_3). The salts were obtained from commercial sources and were of the highest quality available. The $NaBO_2$, which was received with 4 molecules of H_2O, and the $LiBO_2$, which contained only a small amount of H_2O, were predried at 200°C in a vacuum oven at a pressure of < 0.2 mm Hg and then fused at 980° and 900°C, respectively. The Na_2MoO_4 and Li_2MoO_4 were fused and the MoO_3 was dried at 600°C. The salts were always fused under an argon atmosphere and in platinum dishes. Spectrographic analyses of the dried salts are shown in Table I.

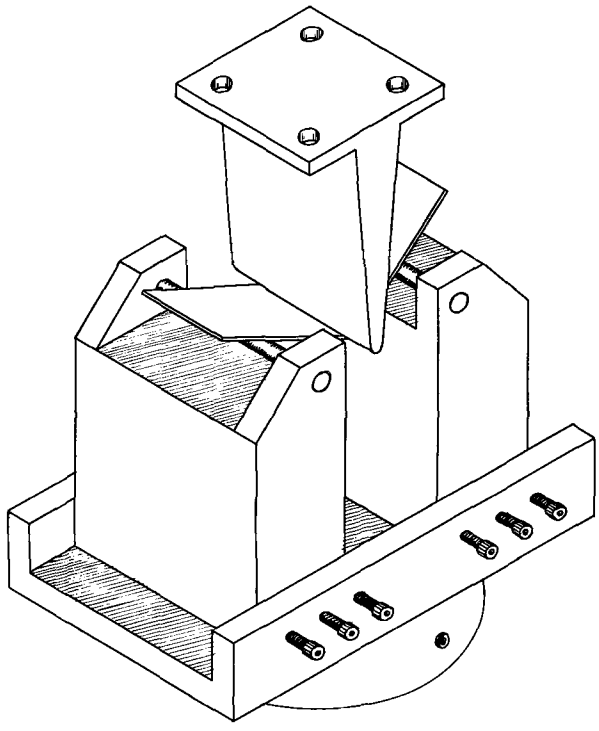

Fig. 2. Adjustable bend vise and wedge assembly, showing three-point loading of a bend specimen.

The fused salts were crushed in the dry box under a dry atmosphere of N_2 or Ar. Proper proportions of the salts were transferred to a bottle; the bottle was tightly sealed, removed from the dry box and tumbled for several hours. The mixture was then transferred to the cell.

Preparation of electrodes.—Anodes were made of cold-rolled molybdenum sheet and had a purity of 99+%. Prior to weighing, they were washed in warm, soapy water, hand rubbed with pumice, rinsed with distilled water, washed with alcohol, and air-dried. The nickel, stainless steel, and Inconel cathodes were wet ground on 80 and 120 grit belts prior to the washing treatment above. Copper and graphite cathode surfaces were hand ground with 3/0 emery paper prior to the washing treatment. Graphite electrodes were oven-dried to remove any water from the internal pores.

Electrolysis.—The dry weight of electrolyte used in the experiments was about 500-1400g. Electrolysis must be performed under an inert atmosphere and the electrolyte must be free of H_2O. Therefore, the replacing of air with argon in the furnace chamber was started immediately after placing the crucible and mixed proportions of electrolyte in the chamber and securing the chamber lid. Argon continuously flowed through the furnace chamber throughout the heating, the electrolysis, and the cooling periods at a rate of 150 cc min^{-1} and at a pressure of about 1½ in. of H_2SO_4. The electrodes were immersed in the molten electrolyte with a small applied potential to eliminate any corrosion of the cathode and contamination of the bath.

The cathode was rotated at 250 rpm during electrolysis to agitate the bath and eliminate stratification of the electrolyte. Cell current and voltage were continuously measured and recorded throughout the experiment. Cell voltages were measured outside the

Table I. Spectrochemical analyses of initial electrolyte materials,* per cent

	Al	B	Ca	Cr	Cu	Fe	K	Li	Mg	Mn	Mo	Na	Ni	Si	W
$NaBO_2$	0.01	>10	0.05	—	0.005	0.01	—	0.03	0.0005	0.005	0.01	>10	0.05	0.01	0.05
$LiBO_2$	0.05	>10	0.05	0.05	0.005	0.05	—	>10	0.001	0.01	0.05	0.1	0.05	0.01	0.05
Na_2MoO_4	—	—	0.001	—	—	0.01	0.05	—	—	—	>10	>10	—	—	—
Li_2MoO_4	—	—	0.005	—	—	0.005	0.05	10	0.001	—	>10	0.05	—	—	—
MoO_3	—	—	—	—	0.001	—	—	—	0.0005	—	>10	—	—	—	—

* After salts were dried and fused.
The following elements were not detected: Ag, As, Ba, Be, Bi, Cd, Co, Cs, Ge, Hg, Nb, P, Pb, Rb, Sb, Sn, Sr, Ta, Ti, Tl, V, Zn, Zr.

cell chamber and included the voltage drops through the connections, the extension rods, and the mercury rotating assembly. The resistance of these was measured at approximately 0.049 ohms and was considered negligible. The quantity of electricity was determined by a copper coulometer.

"Conditioning" of the electrolyte was required for new batches and for electrolytes which had become contaminated with air or water vapor. A "conditioning" run consisted of an electrolysis at a high current density with molybdenum electrodes.

After electrolyses, the electrodes and deposits were washed in warm distilled water for several hours. Loose material was removed at this time. Then the electrodes and deposits were washed in distilled water, rinsed in alcohol, and air-dried. The loose material was collected and treated in the same manner as the adherent deposit. Loose material was usually weighed separately.

Evaluation of the deposits.—Anode and cathode current efficiencies were based on changes in the weights of the electrodes and the weight of copper deposited in the copper coulometer. The thickness of the deposit was calculated from the weight of the adherent deposit and the area of the plate, using the value of 10.2g cc^{-1} for the density of molybdenum.

Samples for metallurgical and microhardness examinations were cut from the "as-plated" deposits and from deposits which had been subjected to the controlled bend tests. The samples were cut from edges of the deposits and from the central areas of the deposit surfaces. The samples were mounted in Lucite in a manner suitable for studies of the substrate and coating cross sections. They were polished to a mirror finish and some were etched with a 3% $K_3Fe(CN)_6$-0.5% NaOH solution. Hardness measurements were made on the mounted samples at points adjacent to the substrate, adjacent to the surface of the coating, and halfway between these two points. In the samples which were bent, the hardness measurements were made on both the tensile-stressed and the compressive-stressed coatings. The hardness indentations were made parallel to the substrate and perpendicular to the columnar structure of the coatings. The average of several indentations was calculated for each microhardness number.

Electron probe analyses were made on samples cut from the corners of the Mo coatings by the X-ray Section of the College Park Metallurgy Research Center. The concentration profiles were made along a path perpendicular to the sample surface. The probe spot was at least 2μ in diameter. Semiquantitative spectrochemical analyses were made on crystals of nonadherent metal scraped from the surfaces of the deposits.

Experimental Results and Discussion

Deposits made under optimum conditions.—During this investigation, the optimum cell conditions for electroplating molybdenum coatings were determined. The optimum initial electrolyte contained, on a dry weight basis, 55.5% $NaBO_2$, 41.9% $LiBO_2$, 1.0% Na_2MoO_4, 0.9% Li_2MoO_4, and 0.7% MoO_3. Hereafter in this paper, this composition of electrolyte is called the standard electrolyte. The optimum cathode C.D. was 3.1-6.2A dm^{-2} (0.2-0.4A $in.^{-2}$) and the cathode was rotated. The optimum bath operating temperature was 900°C and the cell was operated under a dry inert atmosphere.

Coherent, adherent coatings of molybdenum were deposited on nickel, Inconel (Fig. 3), Carpenter 20 stainless steel, copper, graphite, and molybdenum sheet. A smooth, uniform coating of molybdenum was deposited on a stainless steel pipe, tees, elbows, and plugs (Fig. 4). Cathode deposit current efficiencies were above 95%. The apparent anode current effi-

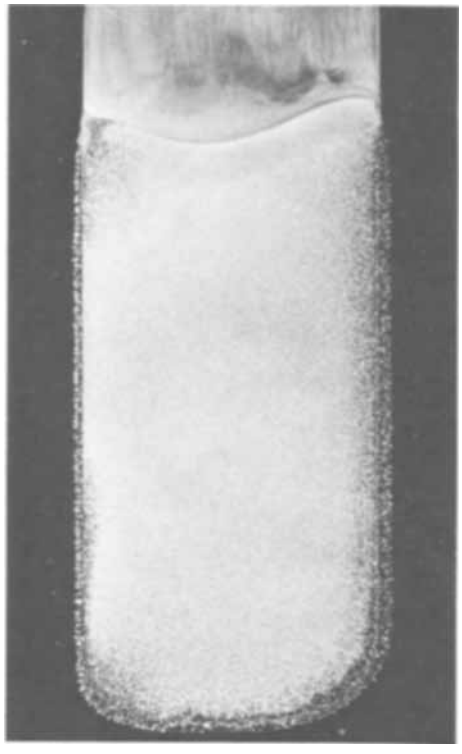

Fig. 3. Molybdenum deposit, approximately 5.6 mils thick, on Inconel sheet. Cathode C.D. 6.2A dm^{-2} (0.4A $in.^{-2}$); temp, 900°C; deposition time, 241 min; cathode rotation, 250 rpm (original mag., 2.5X).

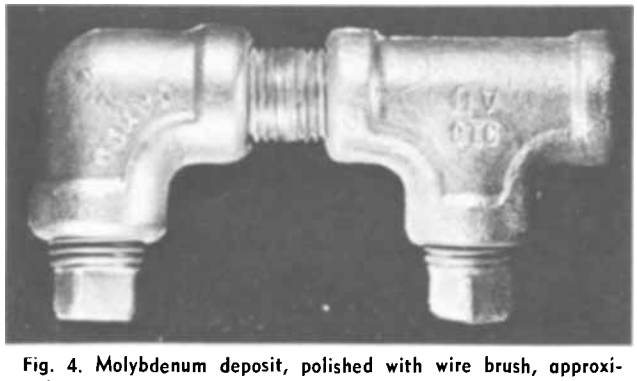

Fig. 4. Molybdenum deposit, polished with wire brush, approximately 3 mils thick, on stainless steel pipe fittings. Cathode C.D., 4.6A dm^{-2} (0.3A $in.^{-2}$); temp, 900°C; deposition time, 182 min, cathode rotation, 250 rpm (original mag., 1.7X).

Table II. Electrodeposition of molybdenum under optimum conditions*

Substrate metal	Deposition time (min)	Current density (A dm^{-2}) Cathode	Anode	Current efficiency (%) Cathode	Anode	Cell voltage (V)	Thickness (calc) (mils)
Mo	300	6.0	6.8	99.0	103.7	0.18	6.8
Inconel	120	6.7	6.2	98.7	101.1	0.25	3.0
Inconel rod	600	6.1	6.1	98.6	101.0	0.42	13.7
Inconel	481	3.1	3.1	98.2	102.7	0.12	5.6
Ni	120	6.2	6.3	95.6	103.3	0.27	2.9
Carpenter 20 SS	120	6.4	6.2	97.1	103.3	0.27	2.9
Carpenter 20 SS	40	6.8	6.7	98.6	103.4	0.26	1.0
Carpenter 20 SS**	60	6.3	6.2	96.1	102.4	0.25	1.4
Cu	120	6.2	5.6	98.4	104.7	0.22	2.8
Graphite	60	6.2	6.3	99.3	105.5	0.30	1.4
SS-pipe	182	4.6	5.5	99.7	101.9	0.26	3.2
Graphite	180	4.7	4.6	99.9	102.3	0.17	3.2

* Standard electrolyte; C.D., 3.1-6.2A dm^{-2} (0.2-0.4A in.$^{-2}$); temp, 900°C; cathode is rotated; cell operated under an inert atmosphere.
** Cathode consisted of a Mo coating on stainless steel from the previous experiments.

ciencies based on total anode weight losses were almost always above 100%. Deposits were up to 13 mils in thickness. A summary of results of typical deposits is given in Table II.

Microscopic examination showed that the coatings were composed of closely packed crystals. X-ray diffraction patterns identified the crystals as cubic with predominantly cubic (100) and dodecahedron (110) faces on the surface of the sample. Metallographic studies showed the crystals have an elongated columnar structure (Fig. 5).

Electrolyte composition.—The borate (BO_2^-) and molybdenum (Mo) contents of the electrolyte must be maintained within definite concentration ranges to obtain satisfactory electrodeposition of molybdenum (23). The concentration ranges can be defined in terms of a BO_2^-:Mo weight ratio and a molybdenum weight percentage. To obtain smooth, adherent, coherent metallic molybdenum coatings, the electrolyte must contain from 1.0 to 3.3% Mo and have a BO_2^-:Mo ratio of 75:1 to 21:1. The initial mixture of the standard or optimum electrolyte contained 1.4% Mo and had a BO_2^-:Mo ratio of 52:1. The BO_2^-:Mo ratio and the molybdenum content of an electrolyte changed slightly with each electrodeposition test owing to the difference between the anode and cathode current efficiencies. One standard electrolyte was still operable after 220 hr of electrodeposition time covering 15 months. If necessary, electrolyte composition can be adjusted by small additions of the proper components.

Deposits made from electrolytes which contained less than 1% Mo and had BO_2^-:Mo ratios of approximately 80:1 were partially in the form of nonadherent powders. When electrolytes contained less than 0.7% Mo and had BO_2^-:Mo ratios of approximately 100:1, only nonadherent powders were obtained; however, the cathode current efficiencies were above 90%. When the initial electrolyte contained only the borate salts, enough molybdenum accumulated in the electrolyte after several hours as a result of anode solution to enable deposition of a nonadherent powder at a low current efficiency.

Deposits made from an electrolyte which contained somewhat more than 3.3% Mo were chiefly in the form of smooth, adherent, and coherent coatings. These were partially covered with dark, flat, hexagon-shaped nonmetallic crystals. Cathode current efficiencies were low. When electrolytes contained 6% Mo and had a BO_2^-:Mo ratio of 9:1, the deposits were entirely nonmetallic crystals. Furthermore, even without a flow of current, these crystals formed in a fused salt mixture which contained 23% Mo and had a BO_2^-:Mo ratio of 18:1. Later, upon the application of d-c current, these crystals were deposited on the cathodes. Chemical analyses of several samples of these crystals showed that they contained 67-69% Mo, 2.5-3.7% Li, and 0.7-0.3% Na; the balance is assumed to be oxygen. X-ray diffraction patterns of the crystals did not correspond to any known compounds.

Cell operation.—Two-hour deposits of molybdenum were made at 900°C on Inconel cathodes at current densities of 3.1 to 12.5A dm^{-2} (0.2-0.8A in.$^{-2}$). The data are summarized in Table III. At C.D. up to 7.7A dm^{-2}, the deposits were smooth; however, the deposits made at C.D. of 9.3A dm^{-2} were rough and had heavy edges (Fig. 6).

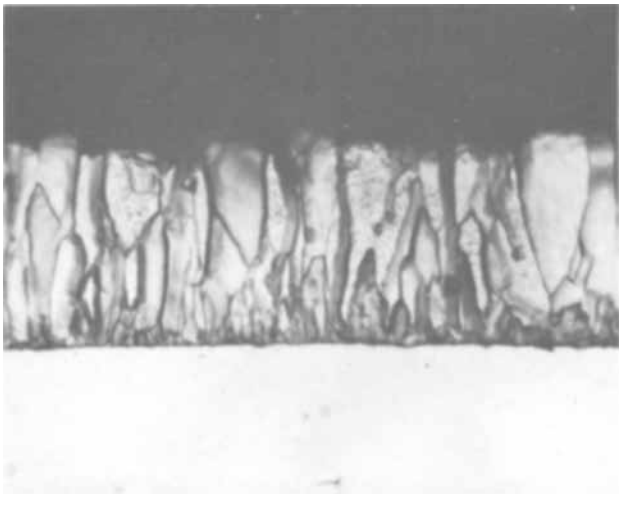

Fig. 5. Molybdenum deposit on Carpenter 20 stainless steel showing columnar structure of molybdenum crystals. Sample etched with 5 g/liter NaOH, 30 g/liter $K_3Fe(CN)_6$ solution (original mag., 500X).

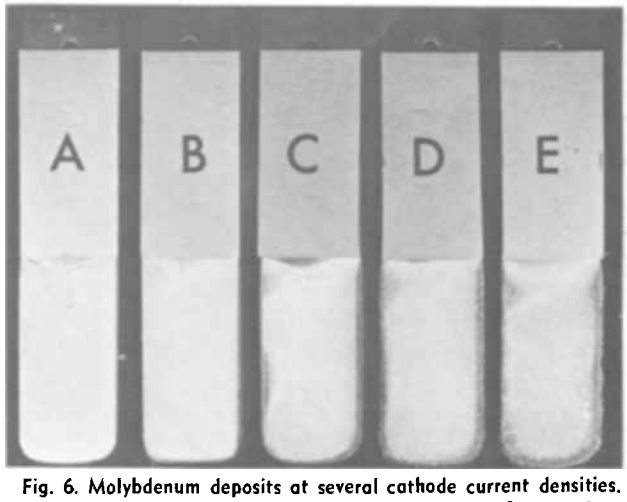

Fig. 6. Molybdenum deposits at several cathode current densities. Cathodes, Inconel; temp, 900°C; cathode rotation, 250 rpm; time, 120 min; cathode C.D.: A—4.7A dm^{-2} (0.3A in.$^{-2}$), B—6.2A dm^{-2} (0.4A in.$^{-2}$), C—7.8A dm^{-2} (0.5A in.$^{-2}$), D—9.3A dm^{-2} (0.6A in.$^{-2}$), E—12.5A dm^{-2}(0.8A in.$^{-2}$).

Table III. Effects of current density on the electrodeposition of molybdenum*

Current density (A dm^{-2}) Cathode	Anode	Time (min)	Current efficiency (%) Cathode	Anode	Cell voltage (V)	Thickness (calc) (mils)	Description of deposits
3.2	3.0	120	98.5	103.4	0.13	1.5	Very smooth, bright, adherent plate
4.7	4.4	120	88.5	101.5	0.20	1.9	Smooth, bright, adherent plate
6.2	5.9	120	98.9	101.2	0.23	2.8	Smooth, bright, adherent plate
7.8	7.3	120	95.2	101.5	0.29	3.4	Smooth, bright, adherent plate
8.9	8.4	120	99.0	101.1	0.33	4.0	Bright, adherent plate
9.3	8.8	120	98.6	100.9	0.33	4.2	Rough, adherent plate; edges heavy
12.5	11.9	120	99.2	100.7	0.45	5.7	Rough, adherent plate; edges heavy
6.2	6.0	240	98.7	101.6	0.24	5.6	Bright, adherent plate; edges heavy
3.1	3.1	480	98.2	102.7	0.12	5.6	Very smooth, bright, adherent plate

* Temp, 900°C; Inconel cathodes rotated 250 rpm.

Table IV. Effects of electrolyte temperature on the electrodeposition of molybdenum*

Temperature (°C)	Current efficiency (%) Cathode	Anode	Cell voltage (V)	Thickness (calc) (mils)	Description of deposit
750	0	100.8	0.43	0	Dark, hexagonal, nonmetallic flakes
825	5.71	101.5	0.32	0.2	Dark, hexagonal, nonmetallic flakes over thin plates
850	90.3	101.1	0.30	2.6	Some dark, hexagonal, nonmetallic flakes over smooth plate
875	99.0	99.0	0.26	2.9	Smooth, bright, consolidated, adherent plate
900	101.8	105.0	0.22	2.8	Smooth, bright, consolidated, adherent plate
925	98.6	102.8	0.22	2.9	Smooth, bright, consolidated, adherent plate

* Current density, 6.2A in.$^{-2}$; Inconel cathodes rotated at 250 rpm.

Three deposits were made to a thickness of 5.6 mils at C.D. of 12.5, 6.2, and 3.1A dm^{-2} for 2, 4, and 8 hr, respectively (Table III). These experiments indicated low-C.D., long-time deposits are smoother and more coherent than high-C.D., short-time deposits of equal thickness.

Two-hour deposits were made on Inconel cathodes at a C.D. of 6.2A dm^{-2} and at electrolyte temperature of 750°-950°C. The results are summarized in Table IV. Cell voltage decreased as the temperature increased. Coatings made at 875°-925°C were bright, adherent, and consolidated. Deposits made at 850°C were partially in the form of dark, hexagonal, flat, nonmetallic crystals which covered a smooth consolidated plate. At 750° and 800°C, the major portion of the deposits was dark flakes. The composition of these crystals was the same as those described in a previous section. Attempts to make deposits at 950°C were abandoned because of excess volatilization of the bath.

Platinum crucibles used in the molybdenum investigation showed no corrosion or deterioration as a result of contact with the bath. Graphite crucibles were found to be unsuitable. The repeated cooling and heating of the electrolyte caused small particles of graphite to break off and float on the surface of the electrolyte. Agitation of the electrolyte with these particles in suspension produced rough, dark deposits. An Inconel crucible, with a weld seam corroded at the weld, caused contamination of the electrolytes and was unsatisfactory for molybdenum deposition.

Examination of deposits on several substrate materials.—One- and 2-hr deposits of molybdenum were made at 900°C on graphite, Inconel, Carpenter 20 stainless steel, and nickel cathodes at current densities of 3.1, 6.2, and 9.3A dm^{-2}. All deposits had cathode current efficiencies of over 95%. The deposits on metal substrates were bright, smooth, consolidated coatings, but those on a graphite substrate were pitted and easily chipped.

Coatings 0.7-4.2 mils in thickness deposited on the Inconel, Carpenter 20 stainless steel, and nickel substrates were bent to angles of approximately 90° on the adjustable bend apparatus. The fixture rolls were spaced 1.0, 1.25, and 1.75 in. for the stainless steel, nickel, and Inconel substrates, respectively. The bend tests did not cause the coatings to separate from the metal substrates; however, examination of the outside surface area of a bent specimen showed small parallel cracks running from edge to edge. Microscopic and metallographic examinations of samples cut from these areas showed the coatings were cracked along the crystal boundaries perpendicular to the substrate on the tensile side (outside) of the bend (Fig. 7), while no such cracking occurred on the compressive side (inside) of the bend. Regardless of the substrate material, the thickness of the deposits, or the specifications of the test, all specimens showed the same types and degrees of failure.

Electron probe analyses were made on cross sections cut from molybdenum coatings deposited on Inconel, Carpenter 20 stainless steel, and nickel substrates. Lα radiation was used for the analysis of molybdenum and Kα radiation was used for the analyses of Fe, Ni, and Cr. Figure 8 is a reproduction of the electron probe chart obtained from the analysis of a molybdenum coating on a nickel substrate. The dip in the nickel line begins as the circular probe beam spot, which is a minimum of 2μ, approaches the molybdenum coating and the line reaches zero when the spot falls completely on the coating. The molybdenum line goes from zero to maximum intensity at the same time. This change in the relative intensities

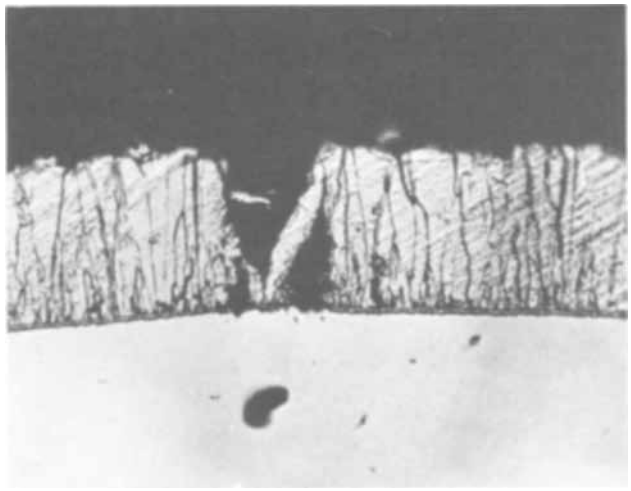

Fig. 7. Molybdenum deposit on nickel substrate, showing crack in molybdenum. Cathode and deposit bent 92° with knife edge between a horizontal distance of 1.25 in.; rate of wedge travel, 1 in. min^{-1}. Sample etched with 5 g/liter NaOH, 30 g/liter $K_3Fe(CN)_6$ (original mag., 500X).

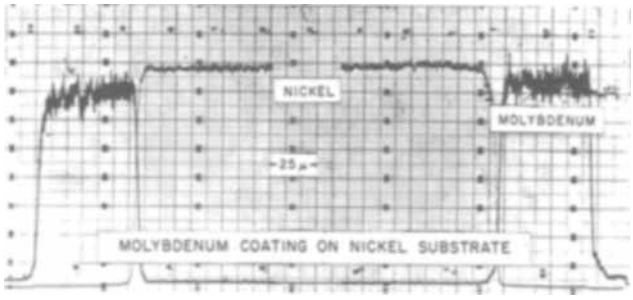

Fig. 8. Electron probe chart of the cross section of a molybdenum coating on nickel substrate. Lα radiation for Mo and Kα radiation for Ni.

in an area of 5-8μ is not evidence of interdiffusion between the molybdenum coating and the nickel substrate. The electron probe analyses of coatings on Inconel and stainless steel substrates gave similar results.

Average microhardnesses for the molybdenum coatings deposited on nickel, Inconel, and Carpenter 20 stainless steel substrates were 250-270 KHN_{100}. The hardness of the molybdenum anode material was 280 KHN_{100}. Spectrochemical analysis did not indicate any noticeable refinement of the molybdenum metal.

Conclusions

Smooth, adherent, consolidated coatings of molybdenum can be electrodeposited from a $NaLiB_2O_4$-$NaLiMoO_4$-MoO_3 fused salt bath. The composition range of the electrolyte was determined and was found to be critical. The optimum conditions of cathode current density and electrolyte temperatures were determined. The process is a true electrodeposition process and not a diffusion process.

Manuscript submitted Jan. 31, 1969; revised manuscript received April 10, 1969.

Any discussion of this paper will appear in a Discussion Section to be published in the June 1970 JOURNAL.

REFERENCES

1. R. W. Holliday, "Molybdenum," from "Mineral Facts and Problems," U. S. Bureau of Mines, Bulletin 630 (1965), p. 595.
2. H. J. Seim and M. L. Holt, *J. (and Trans.) Electrochem. Soc.*, **96**, 205 (1949).
3. L. F. Yntema, U.S. Pat. 2,428,404 (1947).
4. J. W. Beckman, U.S. Pat. 973,336 (1910).
5. A. Krothey and W. Bruckner, German Pat. 263,301 (1911).
6. T. R. Forland, U.S. Pat. 1,305,350 (1919).
7. J. L. Andrieux, *Ann. Chem.*, [10] **12**, 499 (1929).
8. S. Senderoff and A. Brenner, *This Journal*, **101**, 16 (1954).
9. S. Senderoff and A. Brenner, U.S. Pat. 2,715,093 (1955).
10. D. E. Couch and S. Senderoff, *Trans. AIME*, **212**, 320 (1958).
11. J. J. Harwood, Editor, "The Metal Molybdenum," Am. Soc. Metals, Cleveland, Ohio (1958), Chap. 10, p. 210, by S. Senderoff.
12. F. X. McCawley, U.S. Pat. 2,987,390 (1961).
13. R. Cummings, F. Cattoir, and T. Sullivan, Bureau of Mines Report of Investigations 6850 (1966).
14. H. J. Heinan and J. B. Zadra, Bureau of Mines Report of Investigations 5795 (1961).
15. H. J. Heinan and J. B. Zadra, Bureau of Mines Report of Investigations 6444 (1964).
16. G. W. Mellors and S. Senderoff, *Plating*, **51**, 972 (1964).
17. G. W. Mellors and S. Senderoff, Canadian Pat. 688,546 (1964).
18. S. Senderoff, *Metall. Rev.*, **11**, 97 (1966).
19. G. L. Davis and G. H. R. Gentry, *Metallurgia*, **53**, 3 (1956).
20. F. X. McCawley, C. B. Kenahan, and D. Schlain, Bureau of Mines Report of Investigations 6454 (1964).
21. C. Wyche and F. X. McCawley, *Electrochem. Technol.*, **4**, 447 (1966).
22. MAB Report 192-M, Evaluation Test Methods for Refractory Metal Sheet Material (1963).
23. C. Wyche, F. X. McCawley, and D. Schlain, U.S. Pat. 3,369,973 (1968).

Electron Resists for Microcircuit and Mask Production

M. Hatzakis

International Business Machines Corporation, Thomas J. Watson Research Center, Yorktown Heights, New York

ABSTRACT

The properties of poly-(methyl methacrylate), a new electron resist developed at IBM Research, are presented in comparison to commercial photoresists under electron beam exposure. It is shown that methacrylate resist, with suitable processing, presents a means for submicron device fabrication with reasonable speed. Transistors with one- and half-micron emitter stripe widths have been fabricated using this resist as a medium for diffusion masking with SiO_2. Also, a method for producing high-resolution, defect-free masks through methacrylate resist is presented.

The advantages of using electron beam systems rather than light optical systems for the exposure of photoresist layers for microcircuit fabrication are the resolution, power density, and deflection capabilities of electron beams. It is possible to build a practical electron beam system that produces a 10^{-8}A, 2000Å diameter electron beam that can be deflected over a 50- x 50-mil field. This would require a beam deflection over 6250 spot diameters in two dimensions, and a beam convergence angle of approximately 8 x 10^{-3} radians, with the assumption that the aberration contribution is less than 10% of the final spot diameter over the field. The above figures represent only an estimate and are obtained through the uniform field aberration expression, assuming a 1-cm long deflecting field (1). The beam current of 10^{-8}A can be realized by using a LaB_6 electron gun with a brightness of 2 x 10^5 A/cm^2-steradian which is within the range of the long-life cathode reported by Broers (2). Such a system, together with a suitable electron resist, is capable of fabricating submicron geometry devices with extremely high packing densities. Also, it has been shown theoretically and experimentally (3) that a decrease in the size of the transistor active area, and particularly the emitter width, results in an increase in transistor switching speed. Since practical optical

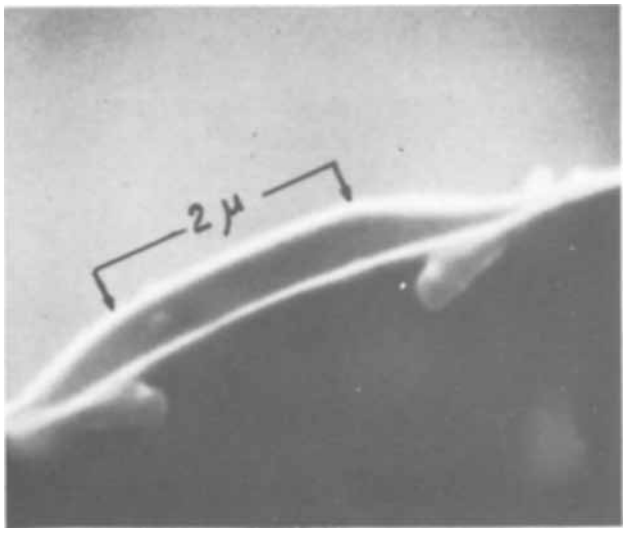

Fig. 1. Cross section of a 2-μ wide line exposed by the electron beam on 5000Å thick KTFR.

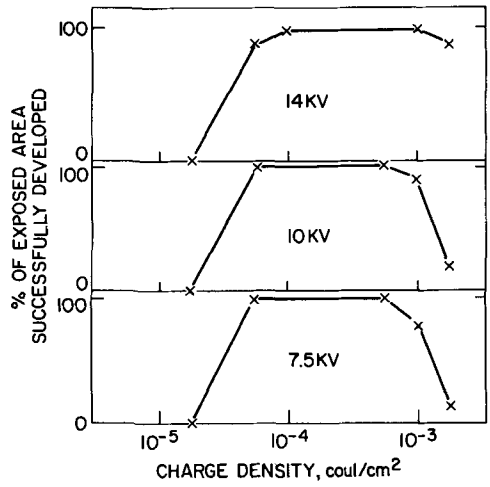

Fig. 2. Exposure characteristics of methacrylate electron resist

systems are ultimately limited in resolution by the wavelength of light, electron beams present the only known means for fabricating submicron structures.

Electron Resist Evaluation

Initially, the resolution of several commercially available photoresists was evaluated under electron beam exposure. The resists tested included KTFR,[1] KOR,[1] KPR,[1] and KMER,[1] all of which have been investigated already for electron beam exposure sensitivity by Thornley and Sun (4) who reported that a charge density of approximately 10^{-5} coulombs/cm^2 at 10-20 kV was required in each case for correct exposure. In order to evaluate edge resolution, lines 2μ wide were exposed with the beam on resist-coated silicon wafers. After exposure, the resists were developed and the substrates broken in a direction perpendicular to the direction of the lines. The cross sections were then observed in a scanning electron microscope with 200Å resolution. These investigations revealed sloping profiles on either side of the lines extending as far as 2μ beyond the edges of the lines. Figure 1 shows a scanning electron micrograph of the cross section of a 2-μ wide line (as indicated by the arrows) with the sloping edge clearly visible. In this typical test, a 5000Å layer of KTFR was exposed with a 1000Å, 12-kV beam which was wobbled to 2μ with a fast scan, while a slow scan swept the beam in the direction of the line. KOR, KPR, and KMER exhibited similar edge effects. The sloping edge profiles (most probably caused by a combination of beam scattering in the resists and substrates as well as the exposure characteristics of the negative photoresists) make these resists unsuitable for high-resolution work (line width 1μ or less).

Shipley resist AZ-1350,[2] was tested next and was found to develop correctly only in a narrow range of exposure around 5×10^{-5} coulombs/cm^2 $\pm$ 50% at 14 kV. For this reason, and also because Shipley resist cannot be used in basic etch baths, it was considered unsuitable for the reliable microcircuit fabrication system.

Poly-(methyl methacrylate) resist, developed at the IBM Watson Research Center through controlled polymerization of the monomer (5) was tested and found to exhibit most of the properties desirable for high-resolution, electron beam exposure. Poly-(methyl methacrylate), henceforth abbreviated to methacrylate, is a positive electron resist, insensitive to light, and only slightly less electron sensitive than commercial photoresists. The exposure characteristics of a 3000Å thick resist layer are shown in Fig. 2 at 7.5, 10, and 14 kV. It can be seen that the exposure latitude of this resist extends over an order of magnitude in charge density from 5×10^{-5} to 5×10^{-4} coulombs/cm^2. Beyond this charge density, cross-linking dominates so that overexposed resist cannot be removed easily.

Resist exposure within the charge density shown above results in random scission of the molecule chains which effectively reduces the average molecular weight of the polymer. Development is based on the change in solubility in the exposed areas due to the molecular weight reduction, and it is accomplished by soaking in a mixture of two liquids, one of which is a solvent and one of which is a nonsolvent of the original polymer. During electron beam exposure of the resist film, a small fraction of the polymer is decomposed into volatile products due to the random scission of the macromolecules, but this was found to reduce the original resist thickness by less than 10% after exposure at 5×10^{-4} coulombs/cm^2.

The methacrylate resist used in all the experiments described below was prepared by dissolving the polymer in methyl ethyl ketone in various concentrations. When spin coated at 5000 rpm on oxidized silicon wafers, 7% polymer concentration produced a dried resist thickness of 3000Å. For a 5000Å resist thickness, a 10% polymer concentration was required.

All resist-coated samples were baked at 170°C for at least 15 min before exposure and were subsequently exposed in a vacuum of approximately 5×10^{-6} Torr. All samples were developed immediately after exposure by soaking in a 3:1 solution of isopropyl alcohol and methyl isobutyl ketone for 1 min followed by a 30-sec spray with the same solution.

In order to study resolution, lines were exposed with an electron beam on silicon wafers coated with this resist. Figure 3 shows a resist pattern with lines 1μ wide separated by 0.5μ. This pattern was generated by a 1000Å diameter electron beam under the control of an optical scanner (6). The scanner (*see* Fig. 4) consists of a 5-in., high-resolution C.R.T., which generates a 1000 line raster that is projected through a lens onto a 8.5- x 11-in. mask. Light transmitted through the clear areas of the mask falls on a photomultiplier, and the resulting electrical signal is used to modulate the beam. Exposure time for the optical scanner system was set at 10 sec as a compromise between electron beam performance and exposure speed.

Chemical etching experiments indicated that 2000Å resist layers can withstand basic or acidic etch baths for as long as 10 min. To study etch characteristics in buffered HF baths, silicon wafers oxidized with 3000Å of SiO_2 were coated with methacrylate resist, baked for 30 min at 170°C to improve resist adhesion and to complete solvent evaporation, exposed to a line pattern by the beam, and developed. Subsequently,

[1] Kodak trade name.
[2] Shipley Company, Inc., Wellesley, Massachusetts.

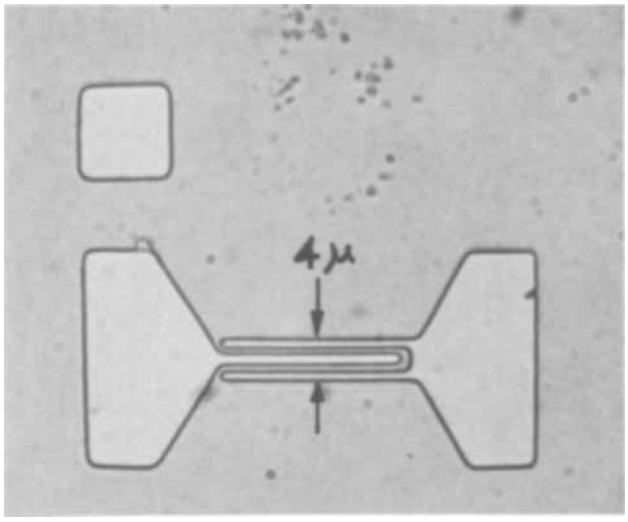

Fig. 3. Electron beam exposed and developed pattern on methacrylate resist.

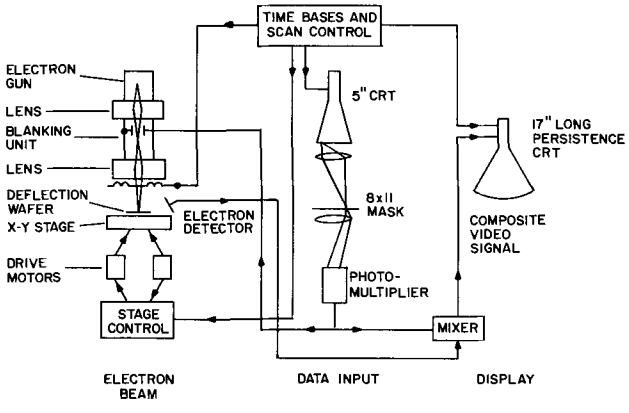

Fig. 4. Schematic of the electron beam machining system

the wafers were etched in buffered HF without agitation until all of the SiO_2 was removed in the lines. It was found with this technique that considerable widening of the lines was taking place during etching. It was also found that the widening effect could be reduced or eliminated if the wafers were baked after resist development and before chemical etching. To study this effect in more detail, a wafer with resist lines was broken in a direction perpendicular to the direction of the lines and three sections of the same line structure were observed in the scanning microscope after processing (*see* Fig. 5). Sample "A" shows the cross section of two 0.5-μ wide lines and one 0.2-μ (2000Å) wide line, exposed and developed in 0.5-μ thick resist layer without postbaking. Of particular interest is the slight undercut in the edges of the two 0.5-μ wide lines. Samples "B" and "C" indicate the effects of postbaking on the edge structure of the lines. If samples "B" or "C" are used in etching the underlying SiO_2, it is clear that the resultant lines would be even narrower than the original lines in sample "A." This phenomenon presents the possibility of adjusting the line width in the etched pattern even after resist development. The resolution of the resist seems to be limited only by the undercut effect which, in a 0.5-μ resist layer exposed at 12 kV, is 2-5°. This means that the bottom of a 0.5-μ deep line in resist is recessed by at most 500Å from the top edge of the line. For thinner resist layers, the effect is considerably reduced. An example of the resolution obtained in SiO_2 etched in HF is presented in Fig. 6. (The fine structure on the edges of the cut is an artifact due to mechanical vibration of the specimen in the scanning microscope.) It is believed that an optimized

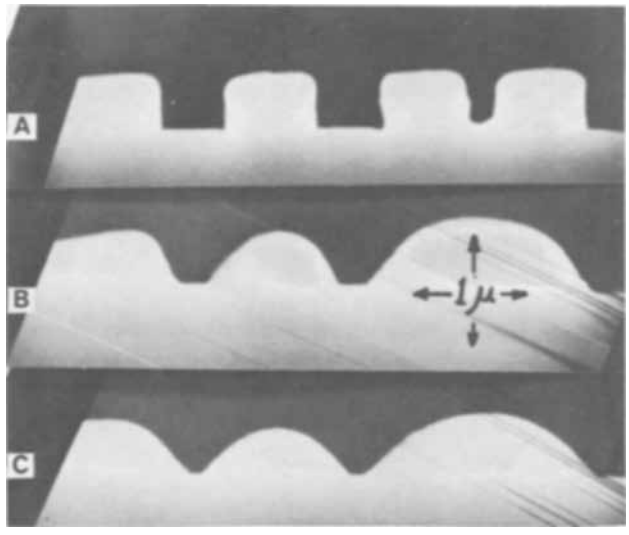

Fig. 5. Cross section of resist lines on SiO_2: A—before baking; B—after baking at 135°C, 5 min; C—after baking at 135°C, 10 min.

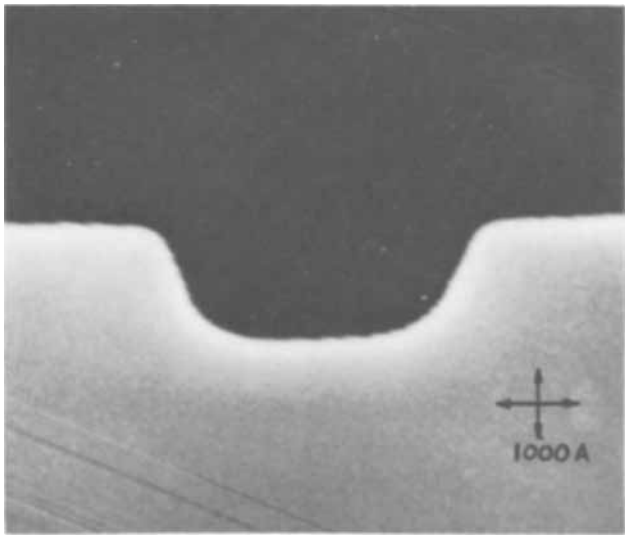

Fig. 6. Profile of a 3000Å wide and 1500Å deep cut in SiO_2 etched in HF through methacrylate resist.

combination of reduction in resist thickness and postbaking can produce even higher resolutions.

Metallization

As can be seen from the above results, methacrylate resist is an excellent medium for submicron diffusion masking with SiO_2. However, metallization presents an additional problem in microcircuit and device fabrication, particularly in the contact area of the base and emitter of submicron transistors. It is well known that aluminum (the most commonly used contact metal) structures produced by chemical etching exhibit edge irregularities of the order of 1μ due mainly to nonuniformity in the evaporated aluminum which causes nonuniform etching rates. These irregularities impose a limitation on the minimum aluminum line width that can be reliably etched that is well over 1μ.

A new method of metallization has been developed through the use of the undercut effect in the methacrylate resist described above. Figure 7 illustrates this method in which the metal is evaporated onto the wafer after the application and exposure of the resist. Note that the undercut in the resist structure results in a discontinuity between metal in the slot and metal on top of the resist, as long as the metal thickness is kept below the resist thickness. This discontinuity allows solvent to penetrate to the unexposed resist

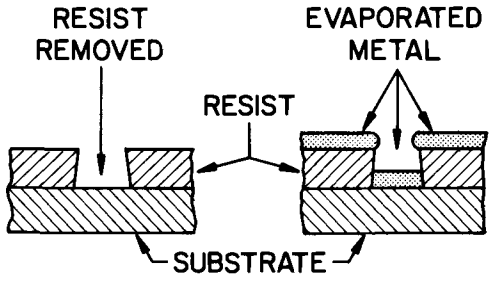

Fig. 7. Metallization through a methacrylate resist mask

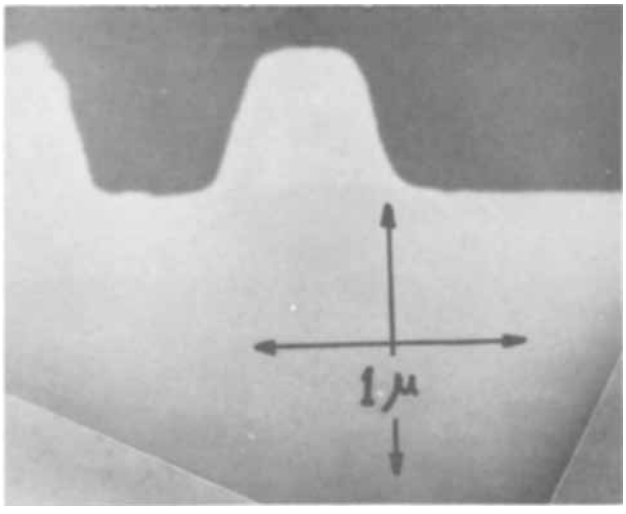

Fig. 8. Cross section of aluminum lines evaporated through a methacrylate resist mask.

layer and remove the resist together with the metal over it. This stripping is accomplished in hot trichloroethylene with moderate agitation. Figure 8 is a scanning electron micrograph of a cross-section of aluminum lines fabricated in this manner. The center line is 0.5μ high and 3000A wide at the top. The excessive tapering of the sides was caused by the resist being overdeveloped before the aluminum evaporation, and by too short a distance between the evaporating source and the sample due to the limited size of the evaporator.

Transistor Fabrication

Planar silicon transistors have been fabricated, with methacrylate resist for base and emitter diffusion masking through HF-etched SiO_2 and aluminum contact metallization, using the process described above (section on Metallization). Figure 9 is a scanning electron micrograph of a typical transistor at a viewing angle of 45°. The base area for this device is 10 x 15μ, the emitter stripe width is 0.8μ, and the metallization stripe width is 1μ. The transistor is one of 32 transistors made on a silicon epitaxial wafer. All of these transistors show very similar characteristics, a beta of 25, and a cutoff frequency (f_T) of 2.2 GHz. This is much lower than the expected value of 10 GHz and is attributed to the lack of an appropriate diffusion process for these dimensions.

Figure 10 is a similar micrograph of a 0.5-μ (metallization stripe width) dummy transistor which contains all the steps required except diffusions.

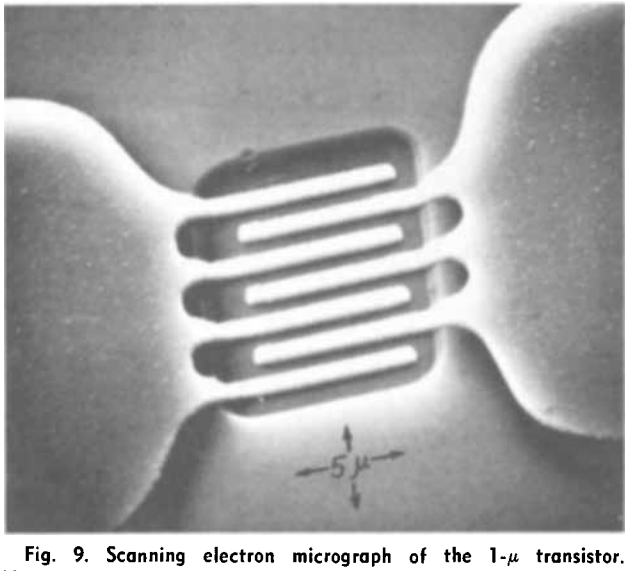

Fig. 9. Scanning electron micrograph of the 1-μ transistor. Viewing angle: 45°.

Mask Fabrication

The metallization process described above can be applied in a slightly modified manner to instances of mask fabrication where more durable masks are re-

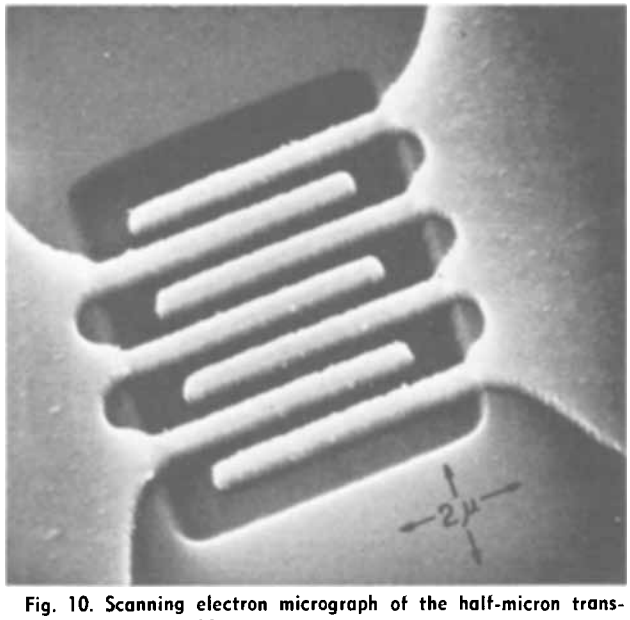

Fig. 10. Scanning electron micrograph of the half-micron transistor. Viewing angle: 30°.

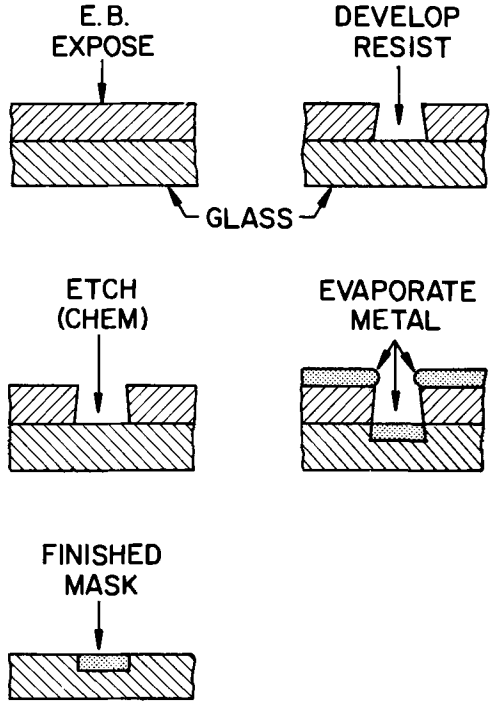

Fig. 11. Mask fabrication steps

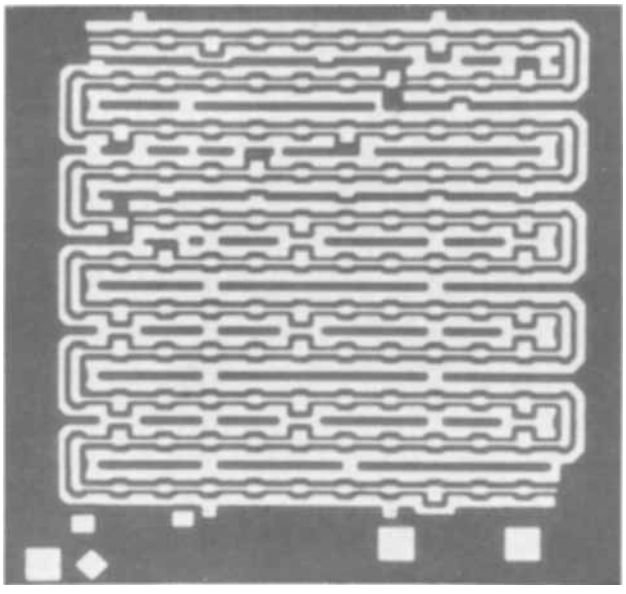

Fig. 12. Reflected light photo of a 10- x 10-mil mask made by evaporation of Al through a methacrylate resist.

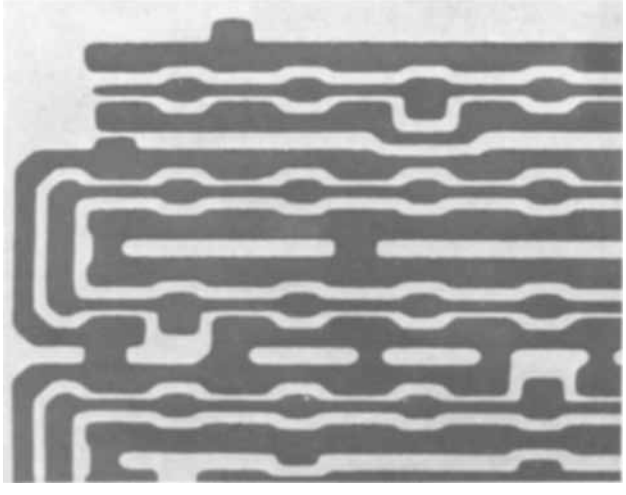

Fig. 13. Transmitted light photo of part of the mask shown in Fig. 12. Minimum line width: 1μ.

quired, free of defects, and with high edge resolution. One solution to the mask problem is the chromium-on-glass mask. Unfortunately, chromium mask fabrication is hampered by two conflicting requirements: the metal layer must be kept very thin in order to obtain good edge resolution, and kept thick in order to avoid pinhole formation. The process presented here eliminates the conflict and makes it possible to produce masks with metal thicknesses as high as 0.5μ (5000Å) while maintaining excellent edge definition. The metal can be on the surface of the glass substrate or it can be completely, or partially, buried in the glass. The fabrication steps are outlined in Fig. 11. One other advantage of this method is that the mask can be made from any opaque material that can be evaporated or plated, so long as the substrate temperature does not exceed 100°C during deposition.

Figure 12 is a reflected light photograph of a 4000Å thick aluminum mask partially buried in a fused quartz substrate. Minimum width of the metal lines is 1μ. Figure 13 is a transmitted light photograph of a section of this mask where, again, the minimum line width is 1μ. This mask was also made from a 8.5- x 11-in. transparency using the optical scanner shown in Fig. 4.

Conclusions

A process has been presented which allows the fabrication of microcircuits and devices with a resolution exceeding that of any previous practical process. Devices have been fabricated with almost 100% yield on several silicon wafers. In addition, a method for fabricating high-resolution, defect-free masks has been outlined. The process presents possibilities for high packing density and high speed integrated circuit fabrication if used with a high-performance electron beam system and pattern generator.

Manuscript submitted Jan. 28, 1969; revised manuscript received *ca.* March 20, 1969. This was Paper 164 presented at the Boston Meeting, May 5-9, 1968.

Any discussion of this paper will appear in a Discussion Section to be published in the June 1970 JOURNAL.

REFERENCES

1. R. F. M. Thornley, A. V. Brown, and A. J. Speth, *IEEE Trans. Electronic Computers,* **EC 13,** 36 (1964).
2. A. N. Broers, *J. Appl. Phys.*, **38,** 1991 (1967).
3. J. M. Early, *Proc. IRE,* **46,** 1924 (1958).
4. R. F. M. Thornley and T. Sun, *This Journal,* **112,** 1151 (1965).
5. I. Haller, M. Hatzakis, and R. Srinivasan, *IBM J. Res. Develop.*, **12,** 251 (1968).
6. R. F. M. Thornley and M. Hatzakis, "Electron-Optical Fabrication of Solid-State Devices," IEEE 9th Annual Symposium on Electron, Ion, and Laser Beam Technology, San Francisco Press, Inc., 94 (1967).

A Contribution to the Theory of Electrolytic Chlorate Formation

T. R. Beck*

Boeing Scientific Research Laboratories, Seattle, Washington

ABSTRACT

Analysis of literature data indicates that anodic discharge of hypochlorite in relatively concentrated salt solutions approximately fits the Ibl-Venczel correlation for mass transport at gas evolving electrodes. In this correlation, the mass transfer coefficient varies as the one-half power of the gas evolution rate. Equations are derived for a model system employing a separate electrolyzer and reactor with circulating flow between them, considering the Foerster mechanism for homogeneous formation of chlorate in solution and the mass transport limited anodic discharge. Efficiency of chlorate formation is related to appropriate dimensionless groups containing the important system parameters. It is proposed that the model provides a basis for economic optimization of an electrolyzer-reactor flow system.

The production of sodium chlorate by electrolysis of relatively concentrated neutral sodium chloride solutions is an old and well-known commercial process (1). Although Foerster and co-workers (2) formulated the cell reactions that to date have not been superseded, the process is still not completely quantitatively understood. Foerster showed that chlorine produced at the anode by discharge of chloride is hydrolyzed to hypochlorite which in turn is converted to chlorate in the bulk solution by auto-oxidation. He also showed that hypochlorite is anodically discharged to form chlorate and oxygen. The latter process leads to a current efficiency of 66.7% for chlorate formation compared to 100% for the solution reaction. The rate constant for the solution reaction was determined by Foerster (2) and by Knibbs and Palfreeman (3). Although Foerster apparently recognized that hypochlorite discharge is mass transport controlled, he did not treat it quantitatively.

The first attempt at quantitative treatment of the mass transport of hypochlorite to the anode was made by de Valera (4). He made an analysis of cell data in which he assumed a constant diffusion layer thickness of 0.05 cm at the anode, which gave an approximate fit to the data. Hammar and Wranglen (5) conducted experiments which showed that hypochlorite discharge at both the anode and cathode (without chromate addition) is mass transport limited. They recognized that gas evolution at the cathode affected the diffusion layer thickness and, at the suggestion of Ibl (6), applied the correlation of Ibl and Venczel (7, 8) which is described later.

Ibl and Landolt (9) have done experiments and analysis for a flowing electrolyte system with well-defined hydrodynamic conditions using dilute sodium chloride solution. They found that in dilute sodium chloride solution, chlorine hydrolysis occurred within the diffusion layer and that a model involving coupling of mass transfer with a first-order chemical reaction for the hydrolysis proceeding in the diffusion layer adequately described their data.

The present paper deals with a treatment of mass transport of hypochlorite to the anode for the concentrations and conditions of commercial electrolysis and with an analysis of a system consisting of a separate cell and reactor. This work was first presented in 1961 (10) and is now modified in accordance with new data available in the intervening period. The whole analysis presented here is based on data available in the literature. Although the analysis is limited to the chlorate system, it is believed that the concepts involved could be applied to other electrochemical systems in which there are simultaneous reactions in solution and mass transport limited electrode reactions.

The reason for considering the system with separate electrolyzer and reactor is that process economics dictates a high current efficiency for chlorate formation and a low cell voltage. The two requirements are contradictory unless the electrolyzer and reactor are separated. A relatively large reactor volume is required to promote the formation of chlorate by the higher-efficiency solution reaction, whereas a minimum anode-cathode spacing is required in the cell to minimize cell voltage. In practice, these requirements are now met by suspending a battery of bipolar graphite electrodes in a large tank and using convection developed by the cell gases to circulate the electrolyte or to use a separate cell and reactor with circulating pump.

A review of cell reactions, kinetics of the solution reaction, and mass transport at the anode is presented as background for the model for separate electrolyzer and reactor.

Reactions

The chlorate cell reactions and stoichiometry proposed by Foerster (2) are used as a basis for the model:

Anode reactions

1. $6Cl^- \rightarrow 3Cl_{2(aq)} + 6e$
2. $6ClO^- + 3H_2O \rightarrow 2ClO_3^- + 4Cl^- + 6H^+ + 3/2\,O_2 + 6e$

Solution reactions

3. $3Cl_{2(aq)} + 3H_2O \rightarrow 3HClO + 3Cl^- + 3H^+$
4. $HClO \rightleftarrows ClO^- + H^+$
5. $ClO^- + 2HClO \rightarrow ClO_3^- + 2Cl^- + 2H^+$

Cathode reaction

6. $6H^+ + 6e \rightarrow 3H_2$

The first anode reaction is discharge of chloride ion to form dissolved chlorine near the reversible potential for this reaction. The dissolved chlorine hydrolyzes in solution to form hypochlorous acid. Ionization of hypochlorous acid gives hypochlorite ion in equilibrium with the acid. Reaction of hypochlorite ion and hypochlorous acid gives chlorate ion in solution. This sequence would give 100% current efficiency for chlorate formation.

Discharge of hypochlorite anodically gives chlorate and oxygen. The potential for hypochlorite discharge is well below the anode potential (2). In slightly alkaline solutions, reactions 1 and 2 predominate and the current efficiency for chlorate formation approaches 66.7%. In neutral or slightly acid solutions with a large cell volume, reactions 1, 3, 4, and 5 predominate and

the current efficiency approaches 100%. There is a limit to the beneficial effect of increasing acidity, however, because gaseous chlorine is liberated.

With chromate inhibitor, cathodic reduction of hypochlorite and chlorate can be minimized and hydrogen is essentially the only cathode product.

Chemical Reaction Rate

Foerster (2) and Knibbs and Palfreeman (3) present reaction rate data for the purely chemical conversion of hypochlorite to chlorate. The rate of change of concentration of hypochlorite ion is first order in respect to ClO^- and is second order in respect to hypochlorous acid concentration, so the reaction rate can be expressed by:

$$\frac{d(C_{ClO-})}{dt} = -k(C_{ClO-})(C_{HClO})^2 \qquad [1]$$

The temperature dependence of the apparent rate constant, k, from 30° to 80°C was determined by Knibbs and Palfreeman (3).

The exact mechanism may be different than that implied by these expressions, as shown by Lister (11), but the expressions provide a suitable description for the present analysis.

Mass Transport of Hypochlorite

The correlation of mass transfer coefficient for hypochlorite discharge *vs.* the anodic gas evolution rate calculated from Foerster's data (2) was first presented in 1961 (10). The correlation was compared to data of Ibl and Venczel (7) developed at about the same time for reduction of Fe^{+3} at a hydrogen evolving platinum electrode. Calculations based on the recent data of Hammar and Wranglen (5) are now added to the correlation. Experimental conditions used by the three sets of investigators are summarized in Table I and the correlation is plotted in Fig. 1.

Ibl and Venczel (7, 8) showed that the mass transfer coefficient is relatively large at a gas evolving electrode compared to usual values for free convection and that it varies as approximately the one-half power of the gas evolution rate. The relatively large value compared to values for natural convection (without gas evolution) is because bulk solution displaces the gas bubbles at the electrode surface as they are released. This in effect short-circuits the diffusion layer. Ibl and Venczel derived an equation for this simple displacement model which gave an exponent of one half and a coefficient in

$$K_L = Bv^{1/2} \qquad [2]$$

that was close to their experimental value.

Mass transfer coefficients for hypochlorite discharge and gas evolution rate at the anode were calculated from the Foerster (2) and the Hammar and Wranglen (5) data using the equations[1]

$$K_L = \frac{i_a \epsilon_2}{C n_a \mathbf{F}} \qquad [3]$$

$$v_a = \frac{i_a R T \epsilon_2}{P n_a' \mathbf{F}} \qquad [4]$$

where ϵ_2 is the current efficiency for reaction 2 (oxidation loss of Hammar and Wranglen), $n_a = 1$ for reaction 2 (one electron per hypochlorite) and $n_a' = 4$ for oxygen. The Foerster data and calculated values of K_L and v are given in Table II. The following equations were used for the cathodic reduction data of Hammar and Wranglen:

$$K_L = \frac{i_K \epsilon_K}{C n_K \mathbf{F}} \qquad [5]$$

[1] Applies when transference is negligible as for the hypochlorite ion considered in this paper because of the excess of supporting electrolyte, NaCl.

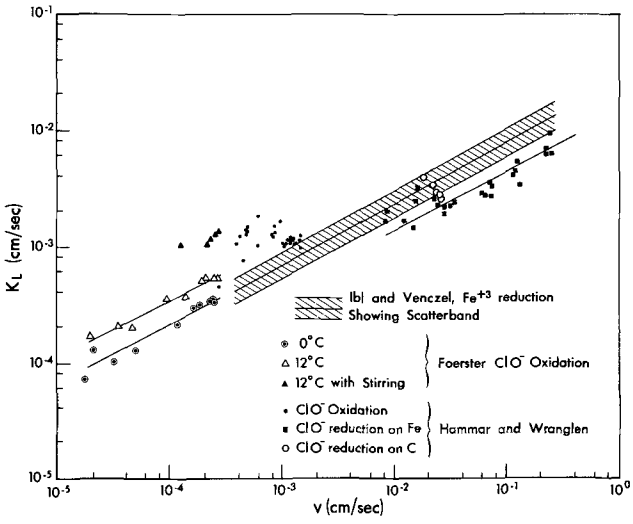

Fig. 1. Correlation of mass transfer coefficient with gas evolution rate.

Table I. Experimental conditions for data plotted in Fig. 1

Investigator	Ibl (7)	Foerster (2)	Hammar and Wranglen (5)
Electrolyte	1M H_2SO_4	4.35M NaCl +0.2% K_2CrO_4	2.56M NaCl (no chromate)
Species oxidized	—	ClO-	ClO-
Species reduced	Fe^{+3}	—	ClO-
Temperature, °C	25°	0°, 12°	25°
Cathode	Cu, C, Ni, Fe, Pt, 1- x 1-cm sheets	Cylinder of small mesh Pt wire gauze inside and concentric to anode	Fe and C cylinders 0.1 to 3.2 cm diam x 6.0 cm length
Anode	(Pt sheet, 4 cm^2)	Cylinder of small mesh Pt wire gauze 4.5 cm diam 5.3 cm length	C cylinder 5.0 cm I.D. 6.0 cm length
Cell	H. Cell, frit diaphragm between compartments	Glass beaker 250 cm^3 of electrolyte	3000 cm^3 flask

Table II. Calculation of K_L and v from Foerster data for 4.35M NaCl at a current density of 0.013 amp/cm^2

	Grams hypochlorite oxygen/ 100 cm^3	ϵ_{O_2}	K_L (cm/sec)	v (cm^3/cm^3 sec)
Temperature = 12°C				
Without stirring	0.034	0.026	1.65×10^{-4}	0.205×10^{-4}
	0.049	0.046	2.03	0.362
	0.064	0.060	2.03	0.473
	0.082	0.133	3.50	1.005
	0.099	0.171	3.74	1.35
	0.106	0.244	5.00	1.92
	0.116	0.282	5.25	2.22
	0.120	0.290	5.22	2.28
	0.126	0.313	5.35	2.47
	0.130	0.327	5.44	2.58
	0.130	0.328	5.45	2.58
With stirring at 1750 rpm	0.032	0.158	10.6×10^{-4}	1.25×10^{-4}
	0.056	0.347	13.4	2.74
	0.056	0.277	10.7	2.18
	0.056	0.300	11.6	2.36
	0.056	0.329	12.7	2.59
Temperature = 0°C				
Without stirring	0.046	0.028	1.32×10^{-4}	0.212×10^{-4}
	0.070	0.023	0.712	0.173
	0.091	0.043	1.02	0.324
	0.112	0.067	1.29	0.505
	0.146	0.154	2.28	1.16
	0.160	0.216	2.92	1.63
	0.176	0.255	3.13	1.91
	0.197	0.311	3.42	2.34
	0.204	0.341	3.62	2.57
	0.202	0.336	3.60	2.53

$$v_K = \frac{i_K(1-\epsilon_K)RT}{Pn_{K'}\mathbf{F}} \quad [6]$$

where ϵ_K is their reduction loss, $n_K = 2$ for $ClO^- + H_2O + 2e \rightarrow Cl^- + 2OH^-$ and $n_{K'} = 2$ for hydrogen evolution.

Observations and tentative conclusions drawn from Fig. 1 are as follows:

1. The mass transfer coefficients calculated from the Foerster anodic oxidation data and the Hammar and Wranglen reduction data appear to fit the one-half power law (Eq. [2]).

2. The Foerster value of K_L when extrapolated to 25°C and the Hammar and Wranglen values of K_L for oxidation of hypochlorite fell above the Ibl and Venczel data, whereas the Hammar and Wranglen values of K_L for reduction fell below the Ibl and Venczel data. The differences are considerably larger than what might be expected for differences in diffusivities of the ions in the respective solutions based on the ratios of mobilities of Fe^{+3} and halide containing ions at infinite dilution[2] and the correction for viscosity of the H_2SO_4 and NaCl solutions.[3] Some other factors are apparently involved. It is possible that the high values of K_L for oxidation of hypochlorite are due to formation of hypochlorite within the diffusion layer by reaction 3 as found by Ibl and Landolt (9) for dilute NaCl solutions.

3. Stirring increases the value of K_L as indicated by the Foerster data at 12°C, where K_L was increased by more than a factor of two with a bent glass stirrer rotated at 1750 rpm inside the concentric gauze electrodes. It is suggested that the mass transfer coefficients resulting from gas bubble disengagement and from the convective diffusion layer are additive as these processes are essentially in parallel (14):

$$K_L = K_G + K_C \quad [7]$$

The flow conditions in the electrolyzer could therefore play an important but secondary role in determining the value of K_L.

Model of Electrolyzer-Reactor System

A schematic of the electrolyzer-reactor system is given in Fig. 2. The basic assumptions used in the model are listed in Table III. Equations describing the Foerster system of reactions are combined with material balances for the steady-state electrolyses system shown in Fig. 2.

Electrolyzer:

Hypochlorite formed by reactions 1 and 3 $= \dfrac{\epsilon_1 I}{2\mathbf{F}}$

Hypochlorite discharged by reaction 2 $= K_L A C_e$ [4]

Hypochlorite reacted by reaction 5 assuming Foerster kinetics $= k(C_{ClO^-})_e\,(C_{HClO})_e^2\,V_e = kf_eV_eC_e^3$ [5]

[2] From "Handbuch der Physik" (12), the ratio of equivalent conductivities at infinite dilution of Cl^- to $Fe^{+3} = 1.12$ and of ClO_4^- to $Fe^{+3} = 0.995$. The ratio of mobilities of ClO- and HClO to Fe^{+3} might also be expected to be near unity.

[3] From "International Critical Tables" (13), the ratio of viscosities of 2.5M NaCl to 1M H_2SO_4 at 25°C is 1.07. The ratio of diffusivities would be approximately the reciprocal, again near unity.

[4] It is assumed that both ClO- and HClO diffuse to anode because, even if only ClO- were discharged, reaction 4 should be fast enough to convert HClO to ClO- at the electrode surface. Hammar and Wranglen (5) show that efficiency for discharge of hypochlorite is independent of pH from pH 6 to 10, in support of this assumption.

[5] Combining $C = C_{ClO^-} + C_{HClO}$ with $\dfrac{(C_{ClO^-})\,(C_{H^+})}{(C_{HClO})} = K_i$

gives $C_{HClO} = \left[\dfrac{C}{1+\dfrac{K_i}{C_{H^+}}}\right]$ and $C_{ClO^-} = C\left[1-\dfrac{1}{1+\dfrac{K_i}{C_{H^+}}}\right]$

$\therefore (C_{ClO^-})\,(C_{HClO})^2 = C^3 f$, where $f =$

$$\left[\frac{1}{1+\frac{K_i}{C_{H^+}}}\right]^2 \left[1-\frac{1}{1+\frac{K_i}{C_{H^+}}}\right]$$

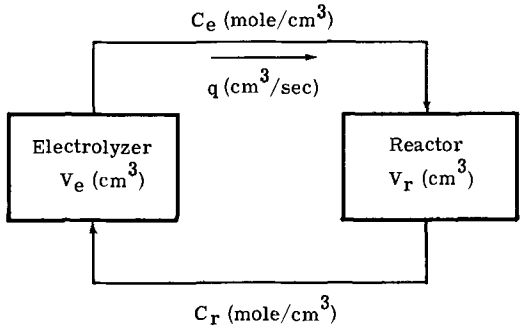

Fig. 2. Schematic of chlorate cell system with separate reactor

Hypochlorite in entering stream $= qC_r$

Hypochlorite in leaving stream $= qC_e$

Material balance gives:

$$qC_r + \frac{\epsilon_1 I}{2\mathbf{F}} = K_L A C_e + kf_eV_eC_e^3 + qC_e \quad [8]$$

Similarly for reactor, material balance gives:

$$qC_e = kf_rV_rC_r^3 + qC_r \quad [9]$$

Equation [3] rewritten:

$$I\epsilon_2 = K_L A C_e \mathbf{F}$$

A Faradaic balance gives:

$$\epsilon_1 + \epsilon_2 = 1 \quad [10]$$

Eliminating C_e, C_r, and ϵ_1 gives:

$$N_r\left[\frac{3/2\,\epsilon_2}{N_q} + \epsilon_2 + \frac{N_e}{N_q}\epsilon_2^3 - \frac{1}{2N_q}\right]^3 + 3/2\,\epsilon_2 + N_e\epsilon_2^3 - 1/2 = 0 \quad [11]$$

where:

$$N_e = \frac{kf_eV_eI^2}{K_L^3 A^3 \mathbf{F}^2}$$

(dimensionless electrolyzer number) [12]

$$N_r = \frac{kf_rV_rI^2}{K_L^3 A^3 \mathbf{F}^2}$$

(dimensionless reactor number) [13]

and

$$N_q = \frac{q}{K_L A}$$

(dimensionless circulation rate number) [14]

The electrolyzer and reactor numbers are essentially the ratios of the rate of the solution reaction in the electrolyzer and reactor, respectively, to the anodic discharge rate. The circulation rate number expresses the ratio of the rate that hypochlorite is carried out of the electrolyzer to the rate that it is anodically discharged.

Equation [11] is plotted in Fig. 3 in the form of ϵ_1 *vs.* $(N_e + N_r)$ with N_q as a parameter. The family of

Table III. Assumptions used in model

1. The system consists of a separate electrolyzer and reactor with circulating loop of electrolyte as shown in Fig. 2.
2. The Foerster reactions 1 to 6 describe the stoichiometry. No cathodic reduction of hypochlorite occurs with suitable addition of chromate. No OH^- or water is discharged at the anode to form oxygen.
3. The pH is high enough to avoid appreciable loss of chlorine or HClO.
4. Reaction 5 is kinetically limited in the bulk solution and can be described by the Foerster kinetics.
5. Reaction 2 is mass transport limited at anode in respect to diffusion of both ClO- and HClO. Electrolytic migration is not important at the high salt concentration.
6. Perfect mixing occurs within the electrolyzer and the reactor.

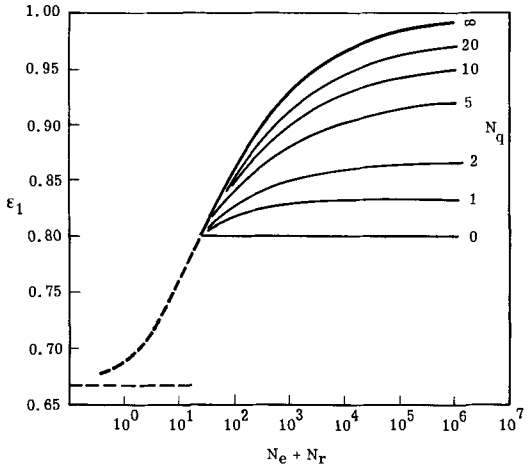

Fig. 3. Plot of current efficiency vs. $(N_e + N_r)$ with N_q as parameter (for $N_e = 25$).

curves for a particular value of $N_e = 25$ is one of many similar families for various values of N_e. It can be seen that a large reactor volume is effective only for a relatively large value of N_q. When $N_q = 0$, the efficiency is limited by the electrolyzer only. When $N_q \rightarrow \infty$ (perfect mixing between electrolyzer and reactor), Eq. [11] reduces to a form similar to that of de Valera (4). However, the form is slightly different because he assumed that only ClO^- ions discharge whereas HClO is also assumed to discharge by reaction 2 in the present model. The diffusion layer thickness of 0.05 cm used by de Valera, combined with a diffusivity of approximately 10^{-5} cm²/sec for hypochlorite, gives a value of $K_L = 2 \times 10^{-4}$ cm/sec which is on the low side of the data exhibited in Fig. 1. The data of Hammar and Wranglen for anodic discharge of hypochlorite give values of K_L nearly an order of magnitude larger, thus emphasizing the need to determine the value of the mass transfer coefficient under the conditions of electrolysis.

Figure 3 clearly indicates the need for economic optimization of a chlorate cell system. For example, high Faradaic efficiency is obtained by providing a larger reactor and a high circulation rate. Within the limits of the assumptions, the model equations provide a means for making economic balances. In making the balance between efficiency and circulation rate, it may also be necessary to consider the second-order effect of flow on K_L at high flow rates as well as the capital and operating costs of pumps.

A limitation of the present analysis is that it was based solely on laboratory cell data. Even a simple laboratory cell, though, may be subject to the limitations due to flow if the electrodes do not bound the whole cell volume and there is less than complete mixing. The derivation was also based on complete mixing within the electrolyzer and reactor and, under certain conditions, plug flow could occur in actual equipment giving somewhat different numerical values. A test of the model with pilot-plant data for a circulating system with separate electrolyzer and reactor will be presented in another paper (15).

Conclusions

1. Examination of literature data on electrolytic formation of chlorate in relatively concentrated salt solutions indicates that anodic discharge of hypochlorite is mass transport limited and that the mass transfer coefficient is determined largely by the gas evolution rate, *i.e.*

$$K_L = Bv^{1/2}$$

2. Equations have been derived relating current efficiency to dimensionless numbers containing the important system parameters for an electrolyzer reactor system for chlorate production.

Acknowledgments

Grateful acknowledgment is given to Dr. Norbert Ibl for his helpful comments relating to the mass transport phenomena and to Mr. Joseph C. Schumacher of American Potash and Chemical Corporation for permission to present the original version of this work.

Manuscript submitted Jan. 27, 1969; revised manuscript received March 19, 1969.

Any discussion of this paper will appear in a Discussion Section to be published in the June 1970 JOURNAL.

NOMENCLATURE

- A = Anode area, cm²
- B = Constant in Eq. [2], $(cm/sec)^{1/2}$
- C = Concentration of total hypochlorite in bulk electrolyte, moles/cm³ (subscripts for ClO^-, HClO, and H^+ concentrations)
- f = Concentration factor, dimensionless (*see* footnote in text)
- $\mathbf{F}$ = Faraday, 96,500 coulombs/equiv.
- i = Current density, A/cm²
- I = Current, amperes
- k = Foerster rate constant, $(mole/cm^3)^{-2}\ sec^{-1}$
- K_i = Ionization constant for Reaction 4, mole/cm³
- K_L = Mass transfer coefficient, cm/sec
- n = Electrons per mole
- N = Dimensionless number (defined in text)
- P = Pressure, atm
- q = Circulation rate, cm³/sec
- R = Gas constant, cm³ atm/deg mole
- t = Time, sec
- T = Temperature, °K
- v = Gas evolution rate cm³/cm²sec
- V = Volume, cm³
- ϵ = Current efficiency, dimensionless

Subscripts

- 1 = Reaction 1
- 2 = Reaction 2
- a = Anodic
- C = Convection
- e = Electrolyzer
- G = Gas
- K = Cathodic
- q = Circulation rate
- r = Reactor

REFERENCES

1. A. J. Allmond and H. J. T. Ellingham, "The Principles of Applied Electrochemistry," p. 384, Edward Arnold & Co., London (1931), and C. L. Mantell, "Industrial Electrochemistry," p. 117, McGraw Hill, New York (1940).
2. F. Foerster, *Trans. Am. Electrochem. Soc.*, **46**, 23 (1924).
3. N. V. S. Knibbs and H. Palfreeman, *Trans. Faraday Soc.*, **16**, 402 (1921). N. V. S. Knibbs, *ibid.*, **16**, 415 (1921).
4. V. deValera, *ibid.*, **49**, 1338 (1953) and **52**, 250 (1956).
5. L. Hammar and G. Wranglen, *Electrochim. Acta.*, **9**, 1 (1964).
6. T. R. Beck and N. Ibl, Unpublished correspondence (1961/1963).
7. N. Ibl and J. Venczel, Paper presented at 11th and 12th CITCE meetings, 1959 and 1961, and at Electrochem. Soc. Meeting, Cleveland, May 1-6, 1966, Paper 94.
8. N. Ibl, *Chem. Ing. Technik*, **35**, 353 (1963).
9. N. Ibl and D. Landolt, *This Journal*, **115**, 713 (1968).
10. T. R. Beck, Paper 125 presented at Electrochem. Soc. Meeting, Indianapolis, April 30-May 3, 1961.
11. M. W. Lister, *Can. J. Chem.*, **30**, 879 (1952); *ibid.*, **34**, 465 (1956).
12. "Handbuch der Physik," Vol. 20, p. 401, S. Flugge, Editor, Springer-Verlag, Berlin (1957).
13. "International Critical Tables," V, p. 12, McGraw-Hill, New York (1929).
14. T. R. Beck, Paper 97 presented at Electrochem. Soc. Meeting, Cleveland, May 1-6, 1966.
15. T. R. Beck and R. Brannland, Paper 253 presented at Electrochem. Soc. Meeting, Boston, May 5-9, 1968.

Multicell Assemblies for Studying Ion-Selective Electrodes at High Pressures

M. Whitfield

CSIRO, Division of Fisheries and Oceanography, Cronulla, N.S.W., Australia

ABSTRACT

Two compact assemblies are described that enable simultaneous measurements to be made on two or three galvanic cells at pressures up to 3 kilobars. One unit, with pressure transmitted by a Teflon piston, is designed for use with Mouquin-Garman (flat membrane) glass electrodes. The second, which uses a mercury trap for pressure equilibration, can be adapted to take a range of ion-selective electrodes. The cells are gastight so that systems sensitive to oxidation or to the partial pressure of dissolved gases can be studied. Mercury or silver-based reference electrodes are used. Examples are given which illustrate the versatility of the system and its application to studies of junction-free cells with a variety of ion-selective electrodes.

Since Distèche first used *p*H-sensitive glass membranes at high pressure (1), the technique has been applied to a variety of problems (2-7) but little effort has been made to refine the method or apply it to a wider range of ion-selective electrodes. The principle of Distèche's method (1) was to use a light, nonconducting fluid (*e.g.*, silicone oil) to equilibrate the pressure on either side of the glass membrane and to act as an insulating layer between the internal and external reference electrodes. The sample solution was held in an open beaker. It is difficult to prevent contamination of the solution in this kind of cell. Even trace quantities of grease or dust can cause erratic behavior, especially in the silver/silver chloride reference electrodes (1, 8). Further problems arise when the cell reaction is sensitive to oxidation or to the presence of carbon dioxide (1).

These problems can be minimized by enclosing the electrode system in a syringe vessel within the pressure vessel itself. This approach has been adopted by Culberson *et al.* (4, 5) who used rubber bungs to transmit the pressure to the solution. Their technique is restricted to robust bulb-type electrodes. Recent investigations (9) indicate that this form of electrode is inferior to the more delicate flat-membrane types in its performance at high pressure. In addition, it is difficult to expel all the air from the kind of cell they describe.

These earlier investigations (1-5) were directed toward problems of oceanographic importance. For these studies, accurate data are needed over a moderate temperature and pressure range (—5° to +30°C, 1 to 1000 bars). When mounted in a thick-walled pressure vessel, the cell may take up to 1 hr to re-equilibrate after a pressure or temperature change. At low temperatures, the situation is aggravated by the slow response of the membrane electrode (10, 11). When the solutions are complex, a large body of experimental data must be gathered before a significant thermodynamic analysis can be made. In consequence, there is considerable advantage in designing high-pressure electrode systems so that several solutions can be investigated simultaneously.

Apparatus

The high-pressure electrode system is suspended from the lead plug of the pressure vessel so that the whole assembly can be removed as a unit. The electrical leads are made from magnesia-insulated triaxial cable and sealed into the lead plug by a modified Bridgman seal so that they can be readily removed and replaced (12). The present assembly can accommodate four such leads.

Key words: electrodes, pressure.

A temperature-comparator bridge gives a time-shared trace on a potentiometric recorder that compares the temperature sensed by thermistors placed inside and outside the pressure vessel. This can be used to reduce by 20-30% the time required for equilibration after a temperature or pressure step (13). The cell potentials are measured by using a precision potentiometer (Leeds and Northrup Type K-4) to back off the input signal to an electrometer (Keithley Model 610BR) which acts as an amplifier and a null detector. All connections are made with noise-free coaxial cable. The output signal from the electrometer is fed to the potentiometric recorder. The pressure is also recorded by a microtorque potentiometer mounted on one of the Bourdon tube pressure gauges. The simultaneous recording of temperature, pressure, and cell potential on a single chart provides a sensitive indication of the attainment of a steady state within the pressure vessel (*see* Fig. 5). The input signals to the recorder could also be used in conjunction with a process programmer to automate the measuring procedure.

Low pH Cells

The Mouquin-Garman (M-G) glass electrode (G, Fig. 1) acts as a combined beaker and sensor and has several advantages that make it particularly suitable for high-pressure work (9, 14). Only Corning 015 glass is at present available in sufficient quantity to make these electrodes. Their use is, in consequence, restricted to low *p*H work or to studies of anion or cation activity using colloidon or protamine coated membranes (15). The low *p*H cell has been designed to accommodate these electrodes.

The pressure is transmitted to the tube containing the electrodes by a gastight stopper (A, Fig. 1). A bleed hole that can be closed by a screw (E) allows gas bubbles to be expelled when the cell is filled. The lead tube (B) is made of precision-bore Pyrex tube (25 mm ID) with four platinum wires sealed into its walls at 90° intervals *via* carefully annealed Housekeeper seals (16). Araldite adhesive placed at the platinum/glass junction on the outside of the test tube prevents the seals from cracking even at high pressures and low temperatures (3 kilobars, —5°C). The external leads are insulated with PVC sleeving and soldered to Teflon insulated sockets (12) set in an annular collar (D).

The lead tube is connected to the electrode holder (C) by a ground-glass joint. Two M-G glass electrodes are held side by side in the holder by a Teflon former (F). The platinum leads are welded to the silver wires which are used as the metal base for the silver/silver chloride reference electrodes (H). These were prepared *in situ* by series electrolysis.

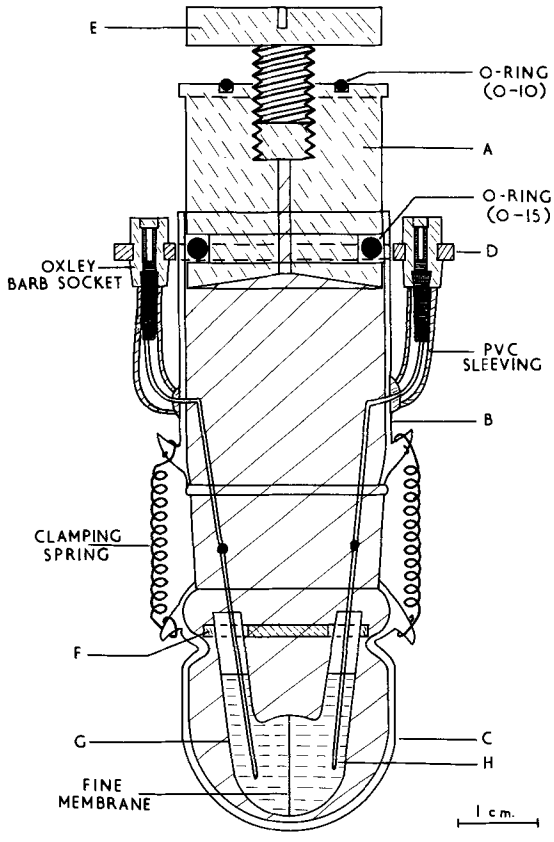

Fig. 1. Low pH cell: A—gastight piston (Teflon), B—lead tube (Pyrex), C—electrode holder (Pyrex), D—fiberglas collar, E—bleed screw (Teflon), F—Teflon former, G—glass electrode (Mouquin-Garman), H—silver/silver chloride electrode. The second glass electrode is stacked alongside the one shown. After the electrodes have been placed in position, the whole cell is filled with n-heptane.

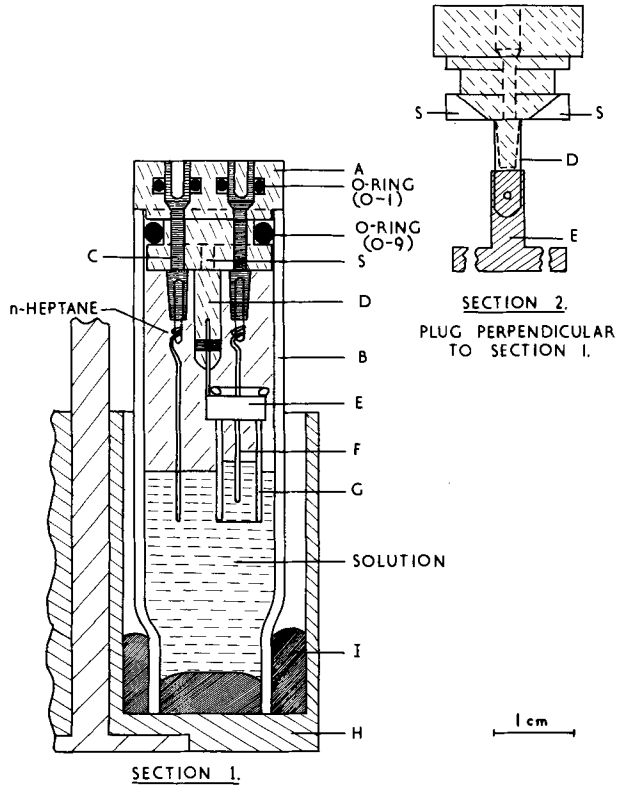

Fig. 2. General-purpose cell: A—Teflon plug, B—cell body (Pyrex), C—platinum contact, D—Teflon rod, E—platinum stirrup, F—silver/silver chloride electrode, G—glass electrode, H—holder, I—mercury trap, S—slots in piston. Redistilled silicone oil (MS 200/5 cs) may be used instead of n-heptane in the insulating layer.

n-Heptane is chosen as the pressure-transmitting fluid because it maintains a low viscosity at high pressures and low temperatures. It has a smaller compressibility than the light silicone oils previously used (1) and this reduces the temperature changes accompanying adiabatic compression. n-Heptane is a good electrical insulator and is available commercially in a pure form. In addition, it is volatile and is readily cleaned off the cell components at the end of the experiment.

General Purpose Cell

This cell consists of an open-ended glass tube sealed at the top by a Teflon cap and at the base by a mercury trap which acts as a pressure-equalizing piston (Fig. 2). The electrode assembly is suspended from the cap which also carries the electrical leads.

The cell body (B, Fig. 2) is formed by a length of precision-bore Pyrex tubing (15 mm ID). The lower end of the tube is restricted slightly to insure a good mercury seal in the space available. Extra insulated leads can be fed through the mercury pool without disturbing the effectiveness of the seal. The mercury can also be used as the metal base for an external reference electrode. In this case, the inside of the tube is given a hydrophobic coating of Teflon (17) or a silicone compound (18). If the mercury seal does not perform any auxiliary function, the base of the tube can be constricted to leave only a pinhole (0.25 mm diam) for pressure equilibration. The cells can then be interchanged without disturbing the contents.

The platinum lead pins (C) are machined to give a force fit in the holes in the Teflon piston. Silicone rubber O-rings were introduced to insure a good seal under all conditions. Pistons made in this way had a leakage rate of only 10 μl/hr under full vacuum.

The silver/silver chloride reference electrodes were prepared by an electrolytic method on a 1-mm diameter platinum or silver base. They were prepared and stored according to the recommendations of Brown and MacInnes (19).

A platinum foil holder (E) for the glass electrode is secured to a Teflon rod (D) which protrudes from the lower surface of the cap. The electrode stem is 3 cm long and the upper centimeter is insulated by a tight-fitting collar of heat shrinkable Teflon. Slots (S) are machined in the base of the piston to allow air bubbles to be expelled from the cell in the final stages of filling.

The mercury reservoir (E, Fig. 3) is machined from a single block of Perspex or Teflon in the form of a beaker divided into three equal segments. The three mercury pools are electrically isolated and are not connected to earth. A locating collar holds the glass tubes vertically in the reservoir during assembly. The cells are clamped lightly against the base of the reservoir by a securing plate (D). This plate is slotted to match a key (F, Fig. 3) which is screwed into the plug carrying the electrical leads into the pressure vessel. The key fits into a recessed slot machined on the underside of the securing plate. This quick release mechanism enables the cell assembly to be exchanged for a new unit in only a few minutes.

So far, three types of cell have been investigated using this assembly. In the first (Fig. 2), silver/silver chloride electrodes are used for reference and a flat-membrane glass electrode is employed. A wide range of glasses can be used to form a membrane of this type on a soda-glass stem. For example NAS 27-4 and LAS 25-10 glasses (20) as well as membranes blown from commercial high pH glass bulbs can be used. In all cases, stable and reliable glass electrodes result. The fineness of the membrane enables good seals to be made between apparently incompatible glasses (21).

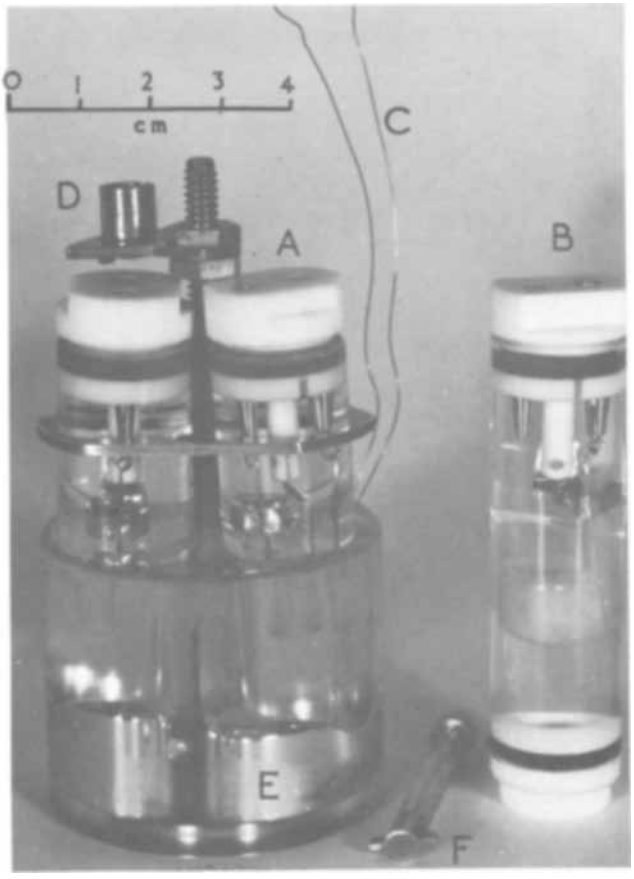

Fig. 3. Cell assembly: A—glass electrode cell (Fig. 2), B—calomel/liquid ion-exchange cell (Fig. 4), C—Thermistor leads, D—securing plate, E—mercury reservoir, F—key.

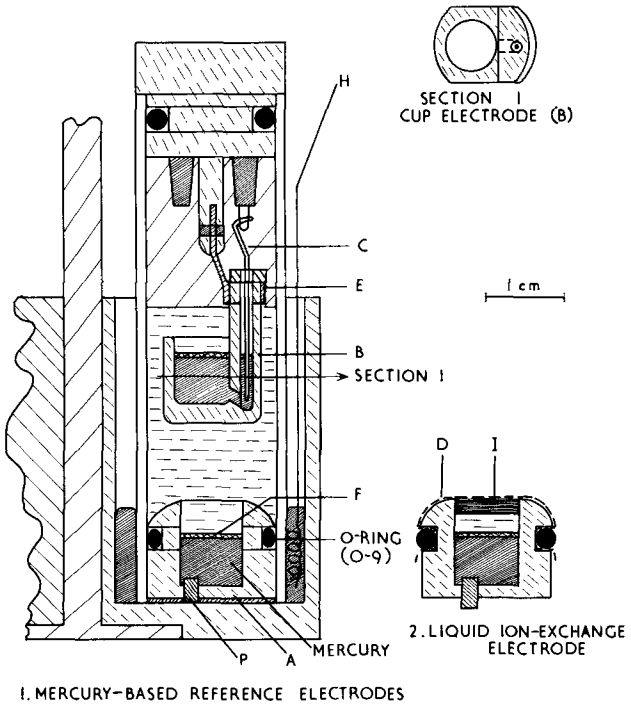

Fig. 4. Calomel/liquid ion-exchange cell (details of cap omitted). 1. Mercury-based: A—combined electrode/piston (FEP polymer), B—cup electrode (FEP polymer), C—contact wire, E—platinum stirrup (see Fig. 2), F—calomel layer, P—platinum, H—contact to mercury reservoir. 2. Liquid ion-exchange: D—sheet of dialysis membrane, I—ion-exchange oil (other components as in 4—1).

The second assembly (Fig. 4—1) was used to investigate the properties of mercury-based reference electrodes at high pressures. Here the pressure is equalized by a piston (A) sealed to the cell walls by an O-ring. The piston is machined in the form of a cup from FEP fluorocarbon polymer (22). This material is as inert as Teflon but it has the added advantage that it can be heat treated and so irregularities introduced by the machining process can be smoothed out. It is translucent to transparent, depending on its thermal history, and it provides a hydrophobic surface that is essential for the proper functioning of mercury-based electrodes (18). A platinum pin (P, Fig. 4) in the base of the cup connects the electrode base to the mercury reservoir which acts as the external lead.

A calomel electrode is prepared by filling the cup to a depth of 6 mm with purified mercury and by adding a relatively thick skin of calomel (F, Fig. 4) according to the instructions of Covington *et al.* (23). A layer of the appropriate halide solution is then added. Other metal/insoluble salt electrodes with mercury or amalgam bases can be prepared in this way. The second electrode in the cell (B, Fig. 4—1 is prepared in a similar way in an FEP holder that is suspended from the platinum stirrup in the cell cap. The completed assembly is shown on the right hand side of Fig. 3.

A third cell (Fig. 4—2) employs a liquid ion-exchange electrode for pressure equilibration. Several distinct problems arise in the preparation of these electrodes (24, 25). A layer of light ion-exchange oil must be held between a reference and an unknown solution. The interfaces between this oil and both solutions must be stable and reproducible. In addition, an equal pressure must be applied to both solutions to maintain the hydrostatic stability of the system. This problem is made more difficult by the high solubility of the ion-exchange oil in organic hydraulic fluids. In the assembly illustrated (Fig. 4—2), a calomel electrode acts as an internal reference. Electrical contact is maintained by a platinum pin (P). The electrode is then filled to a depth of 5 mm with the internal reference solution and a 2-mm layer of ion-exchange oil (I) is floated on top of this. The upper surface of the oil is then trapped by a permeable or semipermeable barrier to complete the electrode. This barrier can consist of a No. 3 grade porous glass plug treated with silicone water-repellent or, more simply, a sheet of cellulose dialysis tubing (D) which is fixed in place by the O-ring that seals the electrode to the wall of the cell. When a porous glass plug is used, a 0.25-mm hole is drilled in the base of the FEP body to improve pressure equilibration across the ion-exchange surface.

Results

The versatility of the system is best illustrated by showing examples of problems that can be investigated using the various cell configurations. In the first example (Fig. 5), the triple cell assembly was used to compare the behavior of silver/silver chloride and calomel reference electrodes. Two symmetrical calomel cells (I and II, Fig. 5) and a symmetrical silver/silver chloride cell (III, Fig. 5) were prepared. The electrodes were immersed in a 0.1M solution of hydrochloric acid. A miniature thermistor was introduced into cell III. Figure 5 illustrates the response of this arrangement to a pressure step of 290 bars at 20°C. The emf of cell I as well as the temperature and pressure profiles were recorded directly on the strip chart. The emf's of cells II and III were measured at regular intervals and are plotted on the same time and potential scales as cell I. This figure illustrates well the amount of data that can be recorded from a single experiment with the multicell system.

Both sets of calomel electrodes show relatively high bias potentials that decay exponentially after the pressure step. Experiments involving calomel reference electrodes therefore require much slower rates of pressure application and release than those employing silver/silver chloride electrodes.

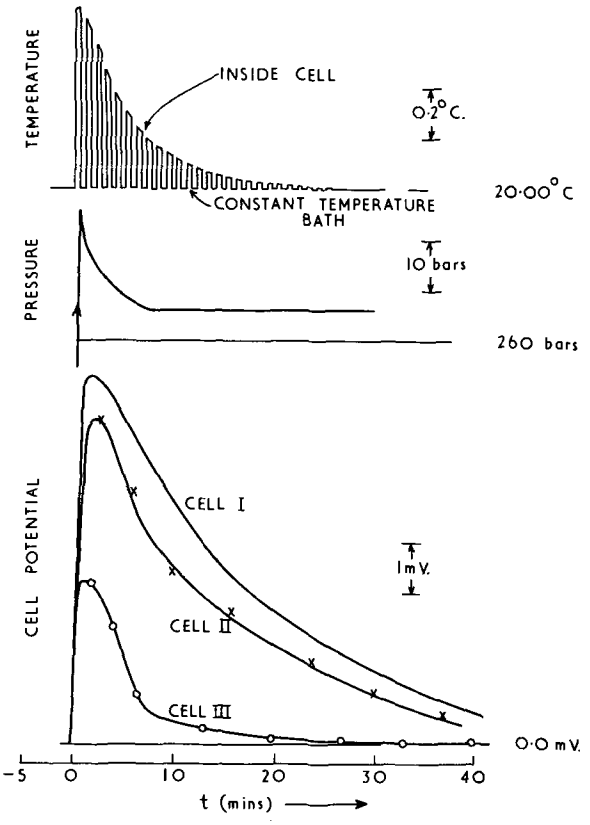

Fig. 5. Response of symmetrical cells to a sudden pressure step. Cells I and II, calomel electrodes (Fig. 4—1); Cell III silver/silver chloride electrode (Fig. 2).

Both assemblies (Fig. 1 and 2) have been used to compare the properties of a range of glass electrodes with different membrane geometries (9). The cells were symmetrical with 0.1M hydrochloric acid on either side of the membrane. In Fig. 6, the asymmetry potentials of three different types of electrodes measured in a single experiment are plotted as a function of pressure. The simple bulb type shows considerable hysteresis that is not exhibited by the other two electrodes. Data for a Mouquin-Garman electrode from a separate experiment using the low *p*H cell are included to illustrate the stable performance of these electrodes.

The reproducibility of three identical cells mounted together is shown in Fig. 7. In this instance, flat-membrane electrodes, prepared by reworking commercial high *p*H bulbs, were mounted in a general-purpose cell (Fig. 2). The internal solution was a potassium chloride/hydrochloric acid buffer and the external solution a carbonate/bicarbonate buffer. The general agreement between the three cells was good (within ± 0.05 mV). The hysteresis exhibited by cell III was traced to the poor performance of the silver/silver chloride electrodes employed. This underlines the need for caution in preparing and handling these electrodes which form the least reliable link in the electrochemical chain. The relationship between cell response and applied pressure deviates from a straight line at pressures above about 1 kilobar. This is in concordance with the data of Distèche (1-3) who worked below 1 kilobar.

The final example (Fig. 8) is taken from work on electrodes sensitive to cations other than hydrogen ions. The electrodes were prepared with a 0.1M filling solution of the appropriate halide. Flat-membrane glass electrodes made from NAS 27-4 glass (20) were used in the sodium chloride cells and liquid ion-exchange electrodes in the calcium chloride cells. A commercial liquid ion-exchange resin (26) was employed. Three electrodes of a given type were mounted

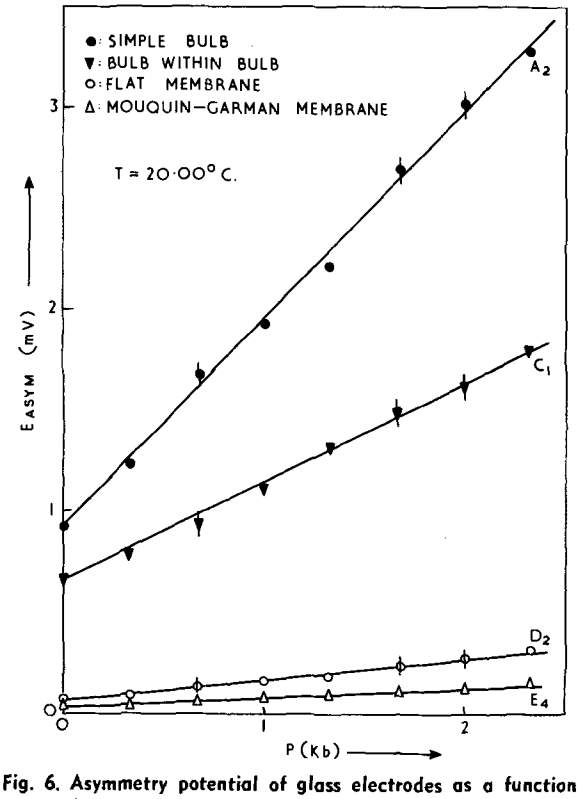

Fig. 6. Asymmetry potential of glass electrodes as a function of pressure. A bar on a symbol indicates a reading taken during the decompression cycle.

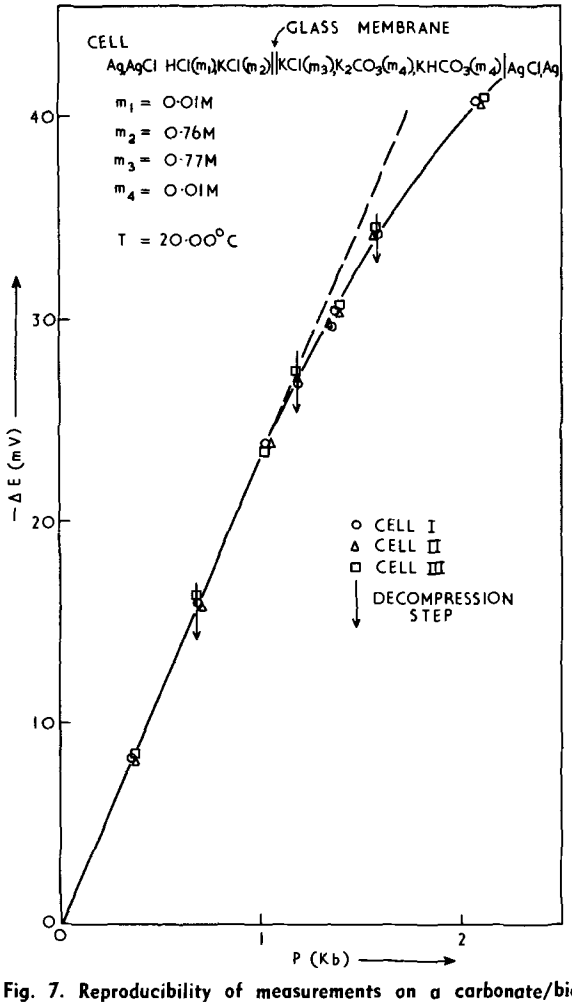

Fig. 7. Reproducibility of measurements on a carbonate/bicarbonate buffer.

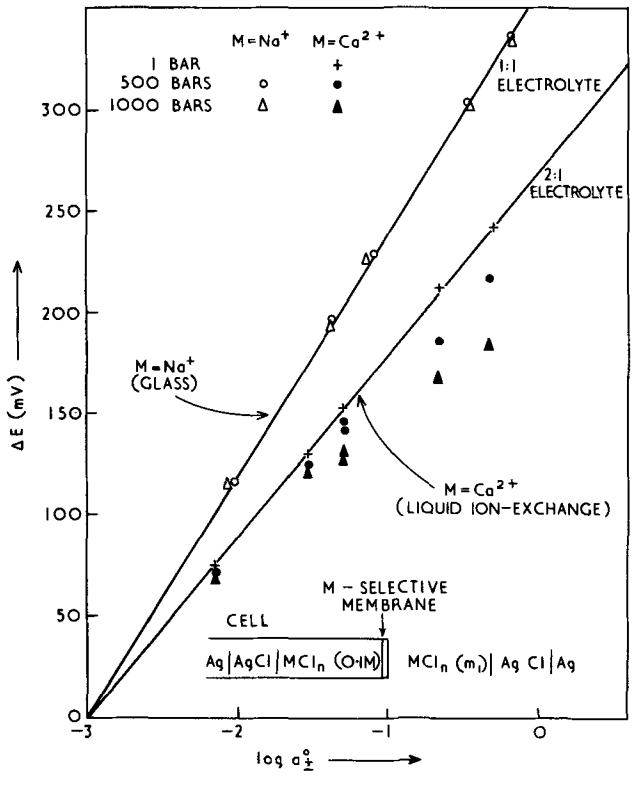

Fig. 8. Response of cation-selective electrodes as a function of pressure at 25°C. Solid lines indicate theoretical slope.

together in the pressure vessel with a different external solution in each. At least one cell in the assembly had a 0.001M external solution. In plotting the data, the potential of this cell was set arbitrarily at zero. The potentials of the other cells were then plotted relative to this point. If a different cell is used each time as the arbitrary reference point, then the composite curve obtained represents a fair picture of the performance of that particular electrode type. Errors caused by asymmetry potentials, irregularities in the individual electrodes, and effects caused by pressure cycling are effectively averaged out. The curves shown in Fig. 8 are composites of three experimental runs on three separate cells.

Pressures up to 1 kilobar have only a small effect on the activity coefficients of simple electrolyte solutions (1, 27). In consequence, a plot of log $a_{\pm}^{\circ}$ (mean ion activity coefficient of electrolyte at 25°C and 1 bar) *vs.* the cell potential relative to the value in the reference solution (ΔE) should give a straight line with the appropriate Nernst slope if the electrodes are behaving ideally. The slope would be 120 mV for each tenfold change in activity for a 1:1 electrolyte and 90 mV for a 2:1 electrolyte if the cell is composed of electrodes selective to both the anion and the cation of the electrolyte.

The sodium chloride cell (Fig. 8) behaves well up to 1 kilobar in agreement with previous work on pH-selective glass electrodes. The liquid ion-exchange cells, although performing well at atmospheric pressure, show poor response at high pressure. A number of interface types have been tried, all with similar results. Further work is being carried out on this problem; in particular, a solid ion-exchange electrode with a high selectivity to divalent ions (28) is being studied.

Manuscript received Feb. 24, 1969.

Any discussion of this paper will appear in a Discussion Section to be published in the June 1970 JOURNAL.

REFERENCES

1. A. Distèche, *Rev. Sci. Instr.*, **30**, 474 (1959).
2. A. Distèche and S. Distèche, *This Journal*, **112**, 350 (1965).
3. A. Distèche and S. Distèche, *ibid.*, **114**, 330 (1967).
4. C. Culberson, D. R. Kester, and R. M. Pytkowicz, *Science*, **157**, 59 (1967).
5. C. Culberson and R. M. Pytkowicz, *Limnol. Oceanog.*, **13**, 403 (1968).
6. S. D. Hamann, *Aust. J. Chem.*, **18**, 1 (1965).
7. S. D. Hamann, *J. Phys. Chem.*, **67**, 2233 (1963).
8. D. J. G. Ives and G. J. Janz, "Reference electrodes," pp. 63, 213-222, Academic Press, New York (1961).
9. M. Whitfield, *Electrochim. Acta*, In press.
10. R. G. Bates, in Ref. (8), p. 253.
11. A. K. Covington, *J. Chem. Soc.*, **1960**, 4441.
12. M. Whitfield, *Rev. Sci. Instr.*, **39**, 1053 (1968).
13. M. Whitfield and D. R. Lockwood, In preparation.
14. H. Mouquin and R. L. Garman, *Ind. Eng. Chem., Anal. Ed.*, **9**, 287 (1937).
15. G. N. Ling, Chap. 10 in "Glass Electrodes for Hydrogen and other Cations," G. Eisenman, Editor, Marcel Dekker, New York (1967).
16. W. G. Housekeeper, *Elec. Eng.*, **42**, 954 (1923).
17. H. C. Berg and D. Kleppner, *Rev. Sci. Instr.*, **33**, 248 (1962).
18. G. J. Hills and D. J. G. Ives, in Ref. (8), pp. 127-178.
19. A. S. Brown and D. A. MacInnes, *J. Am. Chem. Soc.*, **57**, 1356 (1935).
20. G. Eisenman, *Adv. Anal. Chem. Inst.*, **2**, 35 (1965).
21. H. D. Portnoy, Chap. 8 in "Glass Electrodes for Hydrogen and other Cations," G. Eisenman, Editor, Marcel Dekker, New York (1967).
22. M. E. Runner and G. Balog, *Anal. Chem.*, **28**, 1180 (1956).
23. A. K. Covington, J. V. Dobson, and Lord Wynne-Jones, *Electrochim. Acta*, **12**, 513 (1967).
24. J. W. Ross, *Science*, **156**, 1378 (1967).
25. A. K. Mukherji, *Anal. Chim. Acta*, **40**, 354 (1968).
26. Cat. No. 92-20-02, Orion Research Inc., 11 Blackstone Street, Cambridge, Mass. 02139.
27. H. S. Harned and B. B. Owen, p. 504, "Physical Chemistry of Electrolyte Solutions," Reinhold, New York (1958).
28. A. Shatkay, *Anal. Chem.*, **39**, 1056 (1967).

Technical Notes

Properties of Some Selected Europium-Activated Red Phosphors

S. S. Trond,* J. S. Martin, J. P. Stanavage, and A. L. Smith*

Radio Corporation of America, Electronic Components, Lancaster, Pennsylvania

Since the advent of rare earth phosphors, numerous red-emitting, europium-activated materials have been synthesized. For various reasons, the extensive use of these materials has been limited to the yttrium based phosphors listed in Table I.

The materials used in the study described in this paper were the oxide, vanadate, and oxysulfide phosphors of yttrium, gadolinium, and lanthanum. The investigation was made to determine the comparative stability of various europium-activated, red-emitting phosphors under conditions which would show the relative merit of these materials as the red component of color-television picture tubes. The stability of these phosphors during heat treatment, acid washing, and milling was studied. It is pertinent that any commercial phosphor have high stability during heat treatment in the presence of organics to achieve a kinescope product of high quality with respect to light output. Stability during acid washing may be required to facilitate reclamation which is necessary for economical utilization. Reclamation, as referred to in this paper, is the recovery of usable phosphor and not the recovery of rare earth raw materials which must be reworked into new virgin phosphor.

Phosphors Evaluated

All of the phosphors in Table II were prepared from luminescence-grade rare earth oxides by conventional phosphor preparatory techniques. The yttrium vanadate and yttrium oxysulfide phosphor samples were standard RCA phosphor products; the remaining samples were experimental. All efficiency readings are given relative to the RCA yttrium vanadate standard. Although the experimental phosphors may not be optimum with respect to efficiency and color, any discrepancy is slight.

The cathodoluminescent efficiencies of the phosphor powders were measured with a RCA-built spectroradiometer as described by Hardy (1). The spectroradiometer was equipped with an eye-corrected Weston Photronic Cell No. 856RR, whose output was measured with a sensitive, low-impedance galvanometer. The color coordinates were calculated from precise spectral emission data recorded by a General Electric spectroradiometer. All of the phosphors had good efficiencies and reasonable emission colors, except the lanthanum oxide and lanthanum vanadate phosphors. Although these two lanthanum phosphors were quite inefficient and had a desaturated red emission color, they were included in the study. The comparative data of YVO_4:Eu and YVO_4:Eu,Bi agree with Datta's (2) findings that the incorporation of bismuth enhances the brightness and is coupled with an emission color shift. Datta suggested that under cathode-ray excitation, the increased brightness is due to a Bi^{+3} emission (also leading to the color shift) and that there is little effect on the Eu^{+3} emission intensity. The relative brightness, with respect to emission color, of the yttrium oxysulfide and gadolinum oxysulfide phosphors agree with the data reported by Haynes and Brown (3); however, the lanthanum oxysulfide reported in Table II is superior to the respective phosphor discussed by the above authors. Bril (4) and his associates also found that the lanthanum oxide phosphor was significantly less efficient than the oxide phosphors of yttrium or gadolinium.

The median particle size by weight is also listed in Table II. These measurements were made with a Coulter Counter; again, no effort was made to optimize the size of the experimental samples.

All of the phosphors produced sharp, crystalline, and characteristic x-ray patterns. It was carefully noted that all vanadate and oxysulfide samples were free of their respective oxides.

Milling Stability

The stability of the phosphors during milling was determined by use of small samples milled in water in a half-pint mill. Table III shows the per cent efficiency lost by each phosphor as a result of milling in water for 1 and 2 hr.

Within each phosphor type, the lanthanum samples suffered the greatest degradation during milling. The modified yttrium vanadate (YVO_4:Eu,Bi), the gadolinium vanadate, and the yttrium oxide phosphors showed remarkable stability under the test conditions. All of the milled samples retained sharp characteristic x-ray patterns. The milled vanadate and oxysulfide samples remained free of their respective oxides.

Table I. Rare earth red phosphors in commercial use

1. YVO_4:Eu
2. YVO_4:Eu,Bi
3. Y_2O_2S:Eu
4. Y_2O_3:Eu

Table II. Rare earth red-emitting phosphors

Phosphor	Relative brightness	C.I.E. coordinates x	y	Median particle size (μ)
YVO_4:Eu	100	0.667	0.333	7.2
YVO_4:Eu,Bi	111	0.651	0.344	8.1
$GdVO_4$:Eu	91	0.665	0.335	14.5
$LaVO_4$:Eu	12	0.630	0.360	12.0
Y_2O_2S:Eu	148	0.658	0.340	10.0
Gd_2O_2S:Eu	126	0.660	0.340	11.7
La_2O_2S:Eu	130	0.656	0.342	16.4
Y_2O_3:Eu	172	0.642	0.353	8.0
Gd_2O_3:Eu	185	0.640	0.355	6.6
La_2O_3:Eu	36	0.615	0.363	15.6

Table III. % Efficiency loss due to milling in H_2O

Phosphor	Milling time 1 hr	2 hr	Phosphor	Milling time 1 hr	2 hr
YVO_4:Eu	5.2	7.2	Y_2O_3:Eu	1.3	3.7
YVO_4:Eu,Bi	2.0	2.9	Gd_2O_3:Eu	11.4	24.0
$GdVO_4$:Eu	2.0	2.1	La_2O_3:Eu	93.0	93.0
$LaVO_4$:Eu	—	10.0			

Phosphor	Milling time 1 hr	2 hr
Y_2O_2S:Eu	7.6	13.8
Gd_2O_2S:Eu	16.1	22.2
La_2O_2S:Eu	22.4	22.4

* Electrochemical Society Active Member.

The significance of the milling test is to illustrate the effect of attempts to reduce particle size manually, if such reduction were necessary. Obviously, only a few of the materials could withstand such treatment. In most cases, however, the phosphor can be synthesized to the desired particle size and milling is not necessary. It should be noted that milling in the presence of PVA during slurry preparation is an entirely different situation, as is discussed later.

Acid Stability

From an economic standpoint, it is mandatory that any commercial rare earth phosphor must be salvaged either as a usable phosphor or for its rare earth raw materials values. As was pointed out earlier, this paper deals with the reclaim of salvage as usable phosphor because this is felt to be the most economical approach. The use of this salvaged phosphor must yield a finished color picture tube of quality comparable to that of the product fabricated from its virgin phosphor. The salvage recovery procedure requires acid treatment to assure the required quality. Acid treatment is necessary either to control the chromium level in the salvaged phosphor or to remove blue and/or green sulfide phosphor contamination from the salvaged phosphor.

This investigation has shown that, with respect to acid stability, the ten phosphors in question fall into two distinct classes:

I. Phosphors which are quite soluble in mild acid solutions at room temperature. These phosphors suffer in luminous efficiency as a result of acid digestion.

II. Phosphors which have very limited solubilities in mild acid solutions at elevated temperatures and/or very limited solubilities in strong acid solutions at room temperature. These phosphors do not suffer in luminous efficiency as a result of acid digestion.

Table IV lists the effects of digestion on the phosphors of Class I with 5 and 10% nitric acid solutions and with a 10% hydrochloric acid solution. Each sample of virgin phosphor was digested for 30 min at room temperature. The table lists the per cent weight loss of each digestion, as well as the efficiency of the recovered sample relative to its untreated virgin sample.

All three lanthanum-based phosphors are in Class I, as well as the oxide phosphors of yttrium and gadolinium. The latter two phosphors suffered gross losses in luminous energy when exposed to the acid solutions. The table shows the high weight losses of the three most efficient phosphors of this class (Y_2O_3, Gd_2O_3, and La_2O_2S). It should be emphasized that the acid conditions specified do not dissolve blue or green sulfide contaminants; therefore, these phosphors cannot be separated from such contamination by this technique.

The conventional technique for removal of blue and/or green sulfide contaminants from the yttrium vanadate phosphor is to digest the salvaged phosphor in 5-10% nitric acid solution at temperatures of 50°-70°C. The most severe condition (10% HNO_3/70°C) was chosen to evaluate the acid stability of the Class II phosphors. Under this condition, sulfide contamination is dissolved rapidly and completely. Because this condition may not represent optimum acid concentration and temperature, the relative weight losses should be examined rather than the absolute values.

Table IV. Dilute acid digestions of Class I phosphors at 25°C

	Conditions of Digestion					
	5% HNO_3/0.5 hr		10% HNO_3/0.5 hr		5% HCl/0.5 hr	
Phosphor	% Wt loss	% Eff	% Wt loss	% Eff	% Wt loss	% Eff
Y_2O_3:Eu	18.0	61.5	16.4	38.0	18.1	30.3
Gd_2O_3:Eu	98.4	51.8	100		100	
$LaVO_4$:Eu	7.8	83.4	12.2	83.0	—	
La_2O_2S:Eu	76.8	88.5	88.8	57.1	90.8	57.0
La_2O_3:Eu	100		100		—	

Table V. 10% Nitric acid digestions of Class II phosphors at 70°C

	0.5-Hr digestion		1-Hr digestion	
Phosphor	% Wt loss	% Efficiency	% Wt loss	% Efficiency
YVO_4:Eu	4.6	101	7.6	101
YVO_4:Eu,Bi	3.8	105	5.4	104
$GdVO_4$:Eu	18.6	105	38.4	108
Y_2O_2S:Eu	8.1	101	15.6	103
Gd_2O_2S:Eu	13.6	106	25.8	105

Table V lists the per cent weight losses and efficiencies of the recovered samples. The efficiency readings are given relative to the efficiency of each untreated virgin sample. This acid treatment had no detrimental effect on any of the samples with respect to luminous efficiency. The gadolinium vanadate and gadolinium oxysulfide phosphors proved to be much more soluble than the yttrium vanadate and yttrium oxysulfide phosphors. The yttrium oxysulfide phosphor, on the other hand, was significantly more soluble than either of the yttrium vanadate phosphors. The modified yttrium vanadate phosphor was slightly more stable than the bismuth-free yttrium vanadate.

Further investigations revealed that blue and/or green sulfide phosphor contaminants can be removed as efficiently and as rapidly at room temperature by increasing the nitric acid concentration to values greater than 20%. For this study, the Class II phosphors were digested in 25% nitric acid solutions at room temperature.

Table VI lists the results of this test. Again, the acid digestion was nondetrimental to the luminous efficiency in all cases. Under this condition, there was much less deviation in stability within the Class II phosphors. The yttrium oxysulfide phosphor displayed remarkable stability at high nitric acid concentrations at room temperature. Even the gadolinium vanadate and gadolinium oxysulfide phosphors could be treated under this condition if the digestion time was carefully monitored.

Under the same concentration and temperature conditions, hydrochloric acid is as effective as nitric acid in the complete and rapid dissolution of blue and/or green sulfide phosphor contaminants. Yttrium vanadate (nonmodified) and yttrium oxysulfide phosphors were evaluated at room temperature and 70°C with hydrochloric acid. Table VII lists the results. Again, the luminous efficiencies of the Class II phosphors were not affected by acid digestion. At room temperature with 25% solutions, the results were essentially the same as in the nitric acid study. However, at 70°C, the yttrium oxysulfide was much more stable in 10% hydrochloric acid than it was in 10% nitric acid.

For all ten of the rare earth phosphors tested in this study, there was essentially no change in emission color or x-ray pattern as a result of acid treatment.

Table VI. 25% Nitric acid digestions of Class II phosphors at 25°C

	1-Hr digestion		2-Hr digestion	
Phosphor	% Wt loss	% Efficiency	% Wt loss	% Efficiency
YVO_4:Eu	4.0	100	4.2	99
YVO_4:Eu,Bi	2.6	101	4.2	103
$GdVO_4$:Eu	4.8	104	7.6	106
Y_2O_2S:Eu	2.0	101	1.8	103
Gd_2O_2S:Eu	4.2	105	4.0	107

Table VII. HCl digestions of YVO_4:Eu and Y_2O_2S:Eu

	10%/70°C				25%/25°C	
	0.5 Hr		1 Hr		1 Hr	
Phosphor	% Wt loss	% Eff	% Wt loss	% Eff	% Wt loss	% Eff
YVO_4:Eu	2.8	101	3.9	100	1.5	102
Y_2O_2S:Eu	3.2	103	6.8	103	1.8	102

This acid stability study has determined that the phosphors of Class I cannot be recovered by a salvage procedure which requires the removal of sulfide phosphor contaminants by acid treatment; the phosphors of Class II can be recovered readily and efficiently by such a procedure. If the salvaged phosphors have not been contaminated with sulfide phosphors, the residual chromium content can be controlled by treatment with a 3% nitric acid solution. Again, the Class I phosphors are not stable to such a recovery technique.

Heat Treatment Stability

During the fabrication of picture tubes, the phosphor is heat treated in the presence of polyvinyl alcohol (PVA). Some salvage recovery procedures also require baking at temperatures that will remove all traces of PVA. Both situations require temperatures of approximately 450°C.

To study the effect of baking in the presence of PVA on the efficiency of each of these phosphors, pilot slurries were prepared with each phosphor. The slurries were of standard RCA red phosphor formulation, but were unsensitized. The slurry preparation included a milling step in the presence of PVA. The slurries were held with agitation for 25 hr, and then the phosphor from each was salvaged by thoroughly washing in a centrifuge. After drying, the salvaged phosphors were baked at 450°C for 2 hr in air.

Table VIII lists the powder efficiencies of the reclaimed phosphors. The yttrium- and gadolinium-based phosphors proved to be quite stable under these test conditions, while the lanthanum-based phosphors showed severe luminous efficiency losses.

The recovery of these phosphors from sensitized slurries was also investigated. Slurries were again prepared; however, after the milling step, the appropriate amount of ammonium dichromate was added (as in the standard RCA formulation). As with the unsensitized slurries, these sensitized slurries were held with agitation for 24 hr, and then the phosphor from each was salvaged by thorough washing in a centrifuge. The salvaged phosphors were then dried and were measured under simulated tube conditions. Because the spectroradiometer used to measure all previous samples was not capable of the voltages needed for this test (~25 kV), 2- x 2-in. glass slides were water settled with each phosphor to be tested. A control slide of each virgin sample was also prepared as a reference. The slides were then baked at 450°C for 2 hr in air. The slides were measured on a demountable test set. Each salvaged phosphor was measured relative to its control; Table IX shows the results.

The values obtained can actually be regarded as hypothetical conversion factors for each phosphor with regard to the luminous energy retained through tube processing. Of course, the test was modfied with regard to the tube-processing procedures and run under fairly optimum conditions. Still, the results can be reviewed relative to each other with regard to salvageability and luminous energy retention during tube processing.

The vanadate and oxysulfide phosphors of yttrium and gadolinium have remarkable luminous conversion factors. In practice at RCA, tubes prepared with virgin rare earth red phosphor (either yttrium vanadate or yttrium oxysulfide) are indistinguishable from tubes prepared with the respective reclaimed salvage. Both of these phosphors exhibited high conversion factors in this test.

The oxide phosphors of both yttrium and gadolinium have lower luminous conversion factors. The lanthanum phosphors all have low luminous conversion factors. The dichromate was readily adsorbed by the three oxide phosphors and caused a discoloration of these phosphors even after centrifuge washing. This result did not occur with any of the other phosphors.

This conversion factor is extremely important because it allows the rapid rating of materials relative to one another with respect to luminous energy available in a fabricated picture tube. For example, the La_2O_2S phosphor used in this study was 130% of the YVO_4 phosphor; however, when the luminous conversion factor is applied, the red field of the YVO_4 picture tube is actually about 108% of the red field of the La_2O_2S kinescope.

It is believed that the reclaimed salvage of any phosphor which has a low luminous conversion factor will not provide picture tubes comparable to those prepared with its virgin phosphor.

Table VIII. Phosphors recovered from unsensitized slurries

Phosphor	Powder efficiency*
YVO_4:Eu	96.5
YVO_4:Eu,Bi	97.2
Y_2O_2S:Eu	98.6
Y_2O_3:Eu	96.5
$GdVO_4$:Eu	99.0
Gd_2O_2S:Eu	95.0
Gd_2O_3:Eu	94.0
$LaVO_4$:Eu	77.0
La_2O_2S:Eu	84.4
La_2O_3:Eu	39.3

* Efficiency relative to respective virgin sample.

Table IX. Phosphors recovered from sensitized slurries

Phosphor	Plate efficiency*
YVO_4:Eu	98.0
YVO_4:Eu,Bi	97.0
Y_2O_2S:Eu	97.0
Y_2O_3:Eu	93.0
$GdVO_4$:Eu	98.5
Gd_2O_2S:Eu	95.0
Gd_2O_3:Eu	85.0
$LaVO_4$:Eu	79.0
La_2O_2S:Eu	70.0
La_2O_3:Eu	17.0

* Efficiency relative to respective virgin sample.

Summary

When some form of acid treatment is required for the recovery of rare earth salvage as a usable phosphor, the phosphors of Class I are immediately eliminated as desirable red components. The remaining phosphors, the vanadates and oxysulfides of yttrium and gadolinium (Class II), have comparable stability to acid treatment under selected process conditions. From an economic standpoint, the gadolinium-based phosphors become impractical because of Gd_2O_3 raw material cost. Although this cost may be alleviated in the future, these phosphors offer no advantages over their yttrium counterparts. As a result, the yttrium-based phosphors of Class II are the most practical red components for color-television picture tubes at the present time.

It is possible that a technique for the recovery of Class I phosphors as usable phosphors, which does not require acid treatment, could be devised. The lower conversion factors exhibited by these Class I phosphors make continual reclaim and reuse questionable.

The reclaim of salvage of any rare earth phosphor is mandatory to justify its use. If a given rare earth phosphor, which cannot be reclaimed as a usable material, is found to possess certain desirable characteristics, its use should not be discouraged on this factor alone. Any rare earth phosphor salvage can be reclaimed by recovering the rare earth raw materials by standard chemical means and synthesizing into new virgin phosphor. From an economic standpoint, such a reclaim procedure is more expensive than the direct recovery of salvage as usable material. A phosphor which cannot be directly reclaimed must have unusual merit in order to justify the added cost of complete reprocessing.

Acknowledgments

The authors express their thanks to W. G. Rudy and his associates for their determination of the cathodo-

luminescent and spectral data within this paper. Graditude is also extended to M. M. Fornoff and R. H. Woods for their x-ray determinations.

Manuscript received March 14, 1969. This was Paper 53 presented at the Boston Meeting, May 5-9, 1968.

Any discussion of this paper will appear in a Discussion Section to be published in the June 1970 JOURNAL.

REFERENCES

1. A. E. Hardy, RCA Tube Dept. Pub. No. ST-358 (1946).
2. R. K. Datta, *This Journal*, **114**, 1057 (1967).
3. J. W. Haynes and J. J. Brown, Jr., *ibid.*, **115**, 1060 (1968).
4. A. Bril, W. L. Wanmaker, and C. D. J. C. deLaat, *ibid.*, **112**, 111 (1965).

Brief Communication

Technique for a Scanning Electron Microscope Study of Etched Aluminum

C. G. Dunn* and R. B. Bolon

Research and Development Center, General Electric Company, Schenectady, New York

The light microscope has long been used to reveal the surface morphology of aluminum foil etched for electrolytic capacitors (1), but its effectiveness has been partly limited by insufficient depth of focus at high magnifications. The electron microscope with its greater depth of focus and higher resolution has been used to reveal considerable detail in configurations like those produced by tunnel corrosion in a 2S aluminum alloy (2) and tunnel electroetching in aluminum foil of 99.8% purity (3), but the anodic oxide replica samples for this technique have to be relatively transparent to electrons.

The scanning electron microscope (SEM), on the other hand, has neither of these limitations. It has a depth of focus generally 50-100 times that of the optical microscope and samples may be thick and opaque to electrons. Nonconducting samples, however, require the addition of a thin conducting layer such as vapor-deposited carbon or gold. In fact, gold-coated anodic oxide replicas are found to be excellent SEM samples for studying the morphology of etched aluminum. Illustrations have been reported for lightly etched foil (4, 5). The present communication gives a brief description of the preparation of SEM samples for studying both lightly and heavily etched foil.

Lightly etched foil and final oxide replicas were obtained in the following way. A specimen of annealed 99.99% Al foil was given an oxide-removing treatment in a NaOH bath, a 5-sec electroetch at 10 A/in.^{2} in a hot NaCl electrolyte, and a thorough wash in distilled water. An anodic film of about 600Å thickness was then formed in an aqueous solution of ammonium pentaborate. Small sheared pieces were placed in a bromine-methanol solution to dissolve the aluminum matrix and thus free the oxide replicas. Each replica was mounted with the oxide-metal interface up. Vapor deposition of about 500Å of gold in the normal direction completed the preparation of the SEM samples.

Figure 1 shows a region within a single grain of the annealed aluminum where the oxide replica takes a "jungle-gym" configuration. This morphology arises from tunnel etching along <100> directions (6).

Figure 2 shows a region involving three grains of aluminum in a specimen etched 10 sec at 1 A/in.^{2}. The jungle-gym structures, of course, join together at grain boundaries; the details of this and other features are best seen using stereo SEM micrographs.

When tunnel etching extends beyond the midsection of the foil thickness, the final oxide replicas from both surfaces tend to be joined together. They generally can

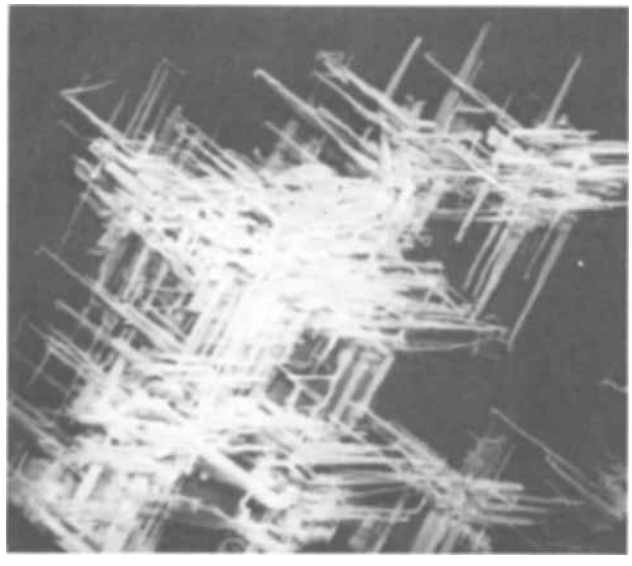

Fig. 1. Tunnel etching in a single aluminum grain seen as a "jungle-gym" structure in the oxide replica. SEM micrograph. X1000.

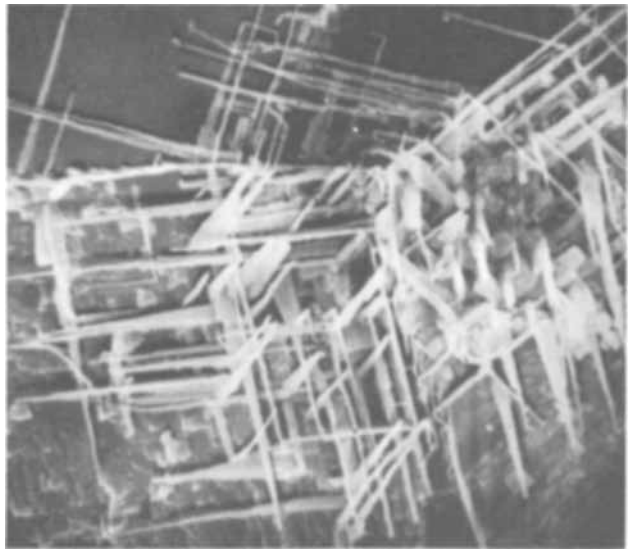

Fig. 2. Tunnel etching in region of three aluminum grains. X1000

* Electrochemical Society Active Member.

be separated, however, and the interior view obtained. Alternatively, one may fracture the joined pair to obtain a cross-section view. A simpler procedure for obtaining a three-dimensional, cross-section (or any other section) view is to prepare the ordinary metallographic section and to finish with an electropolish that removes the aluminum to the desired depth, leaving the oxide replica in relief. Application of a gold coating completes the preparation of the sample.

Manuscript received March 25, 1969.

Any discussion of this paper will appear in a Discussion Section to be published in the June 1970 JOURNAL.

REFERENCES

1. P. McK. Deeley, "Electrolytic Capacitors," The Cornell Dubilier Electric Co., South Plainfield, N. J. (1938).
2. E. C. Pearson, H. J. Huff, and R. H. Hay, *Can. J. Technol.*, **30**, 311 (1952).
3. F. J. Burger, V. F. G. Tull, and P. H. Harris, *Bull. Inst. Metals*, **3**, 6 (1955-1957).
4. W. Morris, E. Lifshin, and R. Bolon, "Improved Microprobe Performance Through a New Scanning Display System," Paper presented at the Third National Conference on Electron Microprobe Analysis, Chicago, 1968.
5. E. Lifshin, "Metallurgical Applications of Scanning Electron Microscopy," AIME Annual Meeting, Washington, D. C., 1969.
6. C. Edeleanu, *J. Inst. Metals*, **89**, 90 (1960-1961).

Electromotive Force Investigation of the Bismuth-Tellurium System

Chung-Chiun Liu[1] and John C. Angus

Chemical Engineering Science Division, Case Western Reserve University, Cleveland, Ohio

ABSTRACT

The bismuth-tellurium alloy system was investigated by electromotive force measurements, coulometric titrations, x-ray diffraction, and differential thermal analyses. The thermodynamic properties of the system have been obtained from the electromotive force measurements. The partial molar free energy, enthalpy, and entropy have been measured as a function of alloy composition at 655°, 700°, and 766°K. The integral thermodynamic properties were computed from the experimental data. The heat of formation of the compound Bi_2Te_3 is estimated at -46 ± 10 kcal/g mole at 766°K. The phase equilibrium diagram was established from experimental data. The results confirm that a very narrow single γ-phase region exists near the compound Bi_2Te_3.

Significant research and development effort has been devoted to thermoelectric materials in recent years. A bismuth-tellurium alloy in the form of Bi_2Te_3, when properly doped, has been found to be one of the most promising thermoelectric materials, especially in the thermoelectric refrigeration applications. However, the thermodynamic properties of the bismuth-tellurium system are only partially known and of questionable accuracy. Also, the exact form of the phase equilibrium diagram of the bismuth-tellurium system is still obscure, and notable discrepancies exist among reported phase diagrams. This paper is a report on the investigation of the bismuth-tellurium system by electromotive force measurements, coulometric titrations, x-ray diffraction, and differential thermal analyses. The first part of this paper covers the thermodynamic properties of the bismuth-tellurium compounds obtained from the emf measurements; the second part discusses the construction of the phase diagram of the system from the results of emf measurements and coulometric titrations.

The reversible galvanic cell used was

$$\text{Bi}(l) \mid \text{BiCl}_3 \text{ in LiCl} + \text{KCl} \mid \text{Bi-Te}$$

The bismuth ions in the melt are trivalent Bi^{3+} throughout our experimental region. This can be shown from the data on the bismuth-gold system by Kleppa (1). Furthermore, the results of our coulometric titrations independently confirm the valence of the bismuth ions in the melt.

When the emf measurements are carried out over a significantly large composition and temperature range, this method gives us, in principle, the data required for an evaluation of the: activity, partial molar free energy, entropy and enthalpy of the constituents. Also integral thermodynamic properties can be calculated from these partial molar quantities.

The basic relationships used to relate the cell potential to the thermodynamic properties are

$$\bar{\mu}_{Bi} - \mu_{Bi}^{\circ} = RT \ln a_{Bi} \qquad [1]$$

$$\bar{\mu}_{Bi} - \mu_{Bi}^{\circ} = -ZFE \qquad [2]$$

In Eq. [1], a_{Bi} refers to the activity of the bismuth in the Bi-Te alloy; the activity of pure bismuth is taken as unity.

Thermodynamic Properties

Experimental Procedure

Preliminary studies indicated that bismuth chloride is highly volatile. Therefore, a closed, isothermal cell was used. Within the cell, the equilibrium between the bismuth existing in different phases could be reached at any desired temperature under isothermal conditions provided a sufficient quantity of the bismuth chloride was present in the molten electrolyte.

The experimental cell used was made of Pyrex glass and is shown in Fig. 1. The cell had an over-all length of 22 cm and an outside diameter of 2.54 cm. Each electrode compartment was approximately 2 cm in length and 0.8 cm in diameter. The leads for the electrodes were made of 0.025 cm diameter platinum wire (99.99+% pure). After fabrication of the cell, the electrodes were prepared, one of pure bismuth, and the second, an alloy of bismuth-tellurium. About 1.5-2.1g of metals for each electrode were used. High-purity (99.999+%) bismuth and tellurium, each in powder form of particle size 20-325 mesh, were used. The correct amount of metal was carefully weighed and packed into the electrode compartments.

The electrodes were then reduced in order to remove any trace of bismuth and tellurium oxide and to have ideal conditions for the melting and forming of the electrodes. A mixture of 90% nitrogen and 10% hydrogen was employed as the reducing gas. The temperature during reduction was gradually increased and was kept at the melting point of the alloy for 3 to 4 hr after the melting temperature was reached in order to obtain complete reduction. The cell was then cooled under the stream of the reducing gas and the electrodes solidified. The diameter of the upper section of the cell was narrowed from 2.54 to 0.6 cm (see the dotted line in Fig. 1). This procedure later aided in making a vacuum seal.

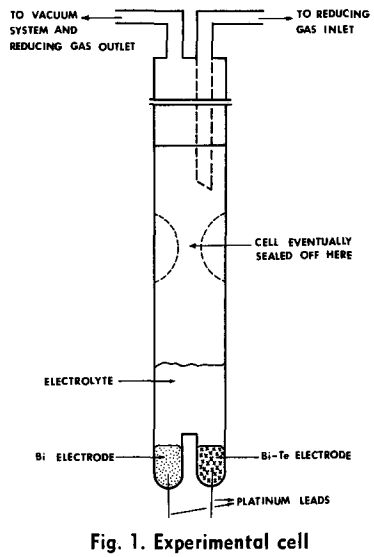

Fig. 1. Experimental cell

[1] Present address: Chemical and Petroleum Engineering Department, University of Pittsburgh, Pittsburgh, Pennsylvania 15200.

Key words: bismuth-tellurium system, thermodynamic properties, phase diagram.

During the preparation of the electrode, a small amount of the tellurium could vaporize. A careful collection of the vaporized tellurium in the upper part of the experimental cell indicated that the loss of the tellurium under the most unfavorable condition, *i.e.*, prolonged annealing at high temperature, was approximately 0.2 m/o (mole per cent) of the tellurium used. Therefore a maximum correction of —0.2 m/o tellurium must be made in the "weighed-in" alloy composition.

A mixture of $BiCl_3$ and LiCl + KCl eutectic was used as electrolyte. The LiCl + KCl eutectic was purified according to the method of Laitinen, Ferguson, and Osteryoung (2). The bismuth chloride used was reagent grade and was dehydrated under vacuum before use.

Approximately 8g of LiCl + KCl eutectic and 1.5g of $BiCl_3$ were used as the electrolyte in each cell. All the material transference was performed inside a high-purity nitrogen-filled dry box in which oxygen was less than 2 ppm and moisture 0.5 ppm. The cell was then sealed under vacuum.

The experimental cell was placed vertically in a 7.62 cm ID split furnace. Glass wool was used as packing material around the cell to assure a firm vertical position. The leads of the cell were connected to a potentiometer. The temperature of the cell was measured with a chromel-alumel thermocouple which was attached to the bottom of the cell.

The temperature of the furnace was gradually brought up to 766°K, the highest desired temperature in this study, in a period of 2 hr. The emf became constant once thermal equilibrium was attained. The emf measurements were recorded every 10-30 min for a period of 12-24 hr. The experimental data show that the fluctuation of these measurements during this period was less than 1 mV. The operating temperature was lowered to 700° and then 655°K. At each temperature the system was held for a period of 12-24 hr, and the emf measurements mentioned above were repeated. Subsequently, the operating temperature was raised again to 766°K in order to observe any hysteresis effect.

Results and Discussion

A summary of the experimental data is presented in Table I. The emf was taken as positive if the bismuth-tellurium alloy electrode was positive. At each temperature, the emf increased as the tellurium composition in the alloy increased. The emf increased as the operating temperature decreased for each alloy having a tellurium composition of 34.9 m/o or more. For alloys which had a tellurium composition less than 34.9 m/o, the emf decreased slightly as the operating temperature decreased.

As mentioned before, the emf for each alloy composition at each temperature was recorded every 10-30 min for a period of 12-24 hr, and the emf's reported in Table I are average values of those recorded during that 12-24 hr period. In each cell, at a fixed temperature, the initial emf and that at the end of the 12-24 hr period were very close. The difference was generally 2% or less of the reading. In each run, the temperature was cycled between 766° and 655°K at least once. In some runs, the temperature was cycled three times. The emf's were always within 2% of those previously recorded, indicating no appreciable hysteresis effect for any alloy composition at any temperature. The reversibility and stability of this galvanic cell with fused salt electrolyte were exceptionally good, as was the reproducibility of the emf measurements. But at lower temperatures, the impedance of the cell increased, which made the emf measurement more difficult and affected the precision of these measurements.

Table I. Summary of experimental emf measurements

Run No.	Composition Bi, mole fraction	Average emf, V 766°K	700°K	655°K
37	0.8217	+0.00512	+0.00440	+0.00246
8	0.7095	+0.00693	+0.00495	+0.00255
9	0.6509	+0.01186		
34	0.5992	+0.01203	+0.01663	+0.01788
10	0.5448	+0.01210		
15	0.4990	+0.01957	+0.02210	+0.02563
12	0.4507	+0.02700	+0.03000	+0.03200
20	0.4170	+0.04420	+0.05445	
28	0.4140	+0.11090	+0.12803	+0.13602
29	0.4140	+0.11071		+0.13628
25	0.4110	+0.11093	+0.12870	+0.13646
18	0.3981	+0.11030	+0.12925	+0.13548
23	0.3942	+0.11031	+0.12933	+0.13766
24	0.3881	+0.11250	+0.12993	+0.13790
30	0.3496	+0.11450	+0.13255	+0.13705
33	0.3008	+0.11420	+0.13340	+0.13696
14	0.2501	+0.1120	+0.13205	+0.13667
32	0.2014	+0.11400	+0.13345	+0.13722
7	0.1088	+0.11400		+0.13703

The activity of the bismuth in the alloy was calculated from the emf measurements. The relation between the activity of the bismuth in the alloy and the composition of the alloy at 766°K is shown in Fig. 2. As expected, the activity of the bismuth in the alloy inclines more toward the ideal solution value as the bismuth atom fraction approaches unity. The activity of the bismuth deviates from Raoult's law considerably when the bismuth content is less than 49.9 m/o.

The activity of the tellurium in the alloy at 766°K was obtained by graphical integration of the Gibbs-Duhem relation

$$\ln a_{Te} = -\int_0^{x_{Bi}} \frac{x_{Bi}}{1 - x_{Bi}} \left(\frac{\partial \ln a_{Bi}}{\partial x_{Bi}} \right) dx_{Bi} \quad [3]$$

The equation above can be integrated by parts, thus

$$\ln a_{Te} = \int_0^{x_{Bi}} \frac{\ln a_{Bi}}{(1 - x_{Bi})^2} dx_{Bi} - \frac{x_{Bi}}{1 - x_{Bi}} \ln a_{Bi} \quad [4]$$

The activity of the tellurium in the alloy at 766°K is also plotted as a function of the alloy composition in Fig. 2. There are two comments which should be made concerning the accuracy of the computed values of a_{Te}.

1. Considerable uncertainty was introduced during the integration of the Gibbs-Duhem relation in Eq. [4], since the measurements of the emf's were not available for alloys having a very high or low bismuth composition. Therefore, at best only fair accuracy in evaluating the activity of the tellurium should be expected.

2. At high tellurium composition, the computed activity of the tellurium has a positive deviation from Raoult's law whereas at low tellurium composition a negative deviation. Similar behavior has been observed in the activity of the aluminum in the silver-aluminum system at 1273°K (3, 4). A physical meaning of this positive and negative deviation from Raoult's law for a component is not readily apparent.

The partial molar free energy, *i.e.*, the chemical potential, of the bismuth in the alloy at 766°K can be

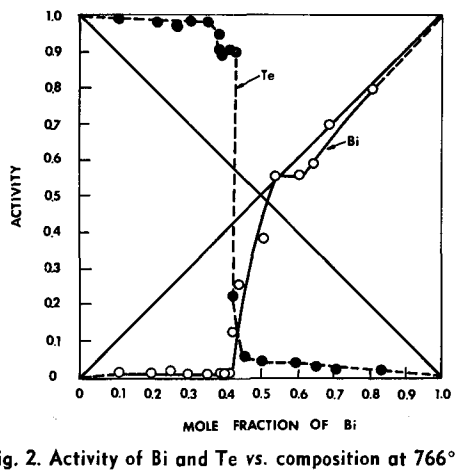

Fig. 2. Activity of Bi and Te vs. composition at 766°K

Table II. Relative partial molar free energy of Bi and Te in the alloy of 766°K

Run No.	Composition Bi, mole fraction	$\bar{\mu}_{Bi} - \mu_{Bi}^{\circ}$, cal/g-at.	$\bar{\mu}_{Te} - \mu_{Te}^{\circ}$, cal/g-at.
37	0.8217	−354.3	−6565
8	0.7095	−479.5	−6082
9	0.6509	−820.6	−5359
34	0.5992	−832.4	−5338
10	0.5448	−837.2	−5298
15	0.4990	−1354	−4755
12	0.4507	−1868	−4308
20	0.4170	−3058	−2250
28	0.4140	−7673	−155.3
29	0.4140	−7660	−155.3
25	0.4110	−7675	−144.7
18	0.3981	−7632	−174.5
23	0.3942	−7633	−173.8
24	0.3881	−7784	−76.2
30	0.3496	−7923	−5.50
33	0.3008	−7902	−2.28
14	0.2501	−7750	−58.01
32	0.2014	−7888	−16.37
7	0.1088	−7888	−10.10

Table III. Temperature coefficient of emf and the relative partial molar entropy of the bismuth and the tellurium in the alloy

Composition Bi, mole fraction	dE/dT in mV/°K	$\Delta\bar{S}_{Bi} = \bar{S}_{Bi} - S_{Bi}^{\circ}$ in cal/g-at. °K	$\Delta\bar{S}_{Te} = \bar{S}_{Te} - S_{Te}^{\circ}$ in cal/g-at. °K
0.8217	+0.01	+0.70	−12.19
0.7095	+0.03	+2.07	−20.65
0.6509			
0.5992	−0.07	−4.80	−9.22
0.5441			
0.4990	−0.04	−2.77	−10.82
0.4507	−0.045	−3.11	−10.30
0.4170	−0.155	−10.72	−2.54
0.4140	−0.260	−18.0	−0.42
0.4140	−0.260	−18.0	−0.42
0.4110	−0.270	−18.7	+0.03
0.3981	−0.286	−19.92	+0.07
0.3942	−0.288	−19.92	+0.06
0.3881	−0.264	−18.27	+0.06
0.3496	−0.273	−18.89	+0.64
0.3008	−0.291	−20.13	+0.65
0.2501	−0.300	−20.75	~0
0.2014	−0.294	−20.34	~0
0.1088	−0.294	−20.34	~0

calculated directly from the experimental measurements. The partial molar free energy of the tellurium was calculated from the activity of the tellurium obtained above. Both the partial molar free energy of the bismuth and the tellurium in the alloy at 766°K, using pure bismuth and pure tellurium, respectively, as the reference states, are presented in Table II. For a binary system, the relative integral molar free energy is defined as

$$G^m = x_{Bi}(\bar{\mu}_{Bi} - \mu_{Bi}^{\circ}) + x_{Te}(\bar{\mu}_{Te} - \mu_{Te}^{\circ}) \quad [5]$$

The relative integral molar free energy of the bismuth-tellurium alloy at 766°K was computed and is plotted as a function of the alloy composition in Fig. 3.

The relative partial molar entropy of the bismuth in the alloy can be calculated using the equation

$$\bar{S}_{Bi} - S_{Bi}^{\circ} = ZF\left(\frac{\partial E}{\partial T}\right)_P \quad [6]$$

The temperature coefficient of the emf in our case was estimated only by measurements between 700° and 766°K. The relative partial molar entropy of the tellurium in the alloy may be obtained by a graphical integration of the Gibbs-Duhem relation in the form of

$$\Delta\bar{S}_{Te} = \int_{x_{Bi}=0}^{x_{Bi}} \left(\frac{x_{Bi}}{x_{Te}}\right) d\Delta\bar{S}_{Bi} \quad [7]$$

The limit of the integration is so chosen that the relative partial molar entropy of the pure tellurium is zero. This choice of limit simplifies the calculation and has been adopted by Lewis and Randall (5), Kleppa (6), and Wagner (7). Both the relative partial molar entropy of the bismuth and the tellurium in the alloy are presented in Table III. The relative integral molar entropy of the bismuth-tellurium alloy at 766°K is plotted as a function of the alloy composition in Fig. 4. The uncertainty in the integration mentioned earlier is, of course, reflected in both $\bar{S}_{Te}$ and S^m. In addition, the slope dE/dT, is somewhat uncertain because of the limited number of points at different temperatures. The estimated value of S^m at the compound, Bi_2Te_3, is −7.8 ± 2.3 cal/g at. °K. The relative integral molar entropy of the bismuth-tellurium alloy, therefore, is negative. There are binary metallic systems which also possess a negative molar entropy such as gold-cadmium, sodium-lead, and iron-silicon, etc. (8). Radcliffe (9) and his co-workers have found that the relative integral molar entropy of iron-aluminum alloy has a negative value. Radcliffe qualitatively associated this negative value with changes in the configurational, magnetic, vibration, and conduction-electron energies of the alloy. In the bismuth-tellurium system, we consider that similar effects may account for the negative value. However, a quantitative discussion of each contribution to the relative integral molar entropy is not possible.

The relative partial molar enthalpy of the bismuth was computed from

$$\bar{H}_{Bi} - H_{Bi}^{\circ} = (\bar{\mu}_{Bi} - \mu_{Bi}^{\circ}) + T(\bar{S}_{Bi} - S_{Bi}^{\circ}) \quad [8]$$

The relative partial molar enthalpy of the tellurium was obtained by a graphical integration of the Gibbs-Duhem relation in a calculation analogous to that of the relative partial molar entropy. Both the relative partial molar enthalpy of the bismuth and the tellurium at 766°K are presented in Table IV. The relative integral molar enthalpy at 766°K is plotted as a function of the alloy composition in Fig. 5. The relative integral molar enthalpy of an alloy corresponding to Bi_2Te_3 is −46 ± 10 kcal/g mole Bi_2Te_3 at 766°K. Using the heat of formation and heat capacity data of Bi_2Te_3 compiled by Kubaschewski and his co-workers (8), we computed the relative integral molar enthalpy of Bi_2Te_3 and obtained a value of −30.06 kcal/g mole at 766°K. This value is significantly smaller than our experimental result. The deviation may be caused by uncertainties in the Gibbs-Duhem integrations and the determination of dE/dT.

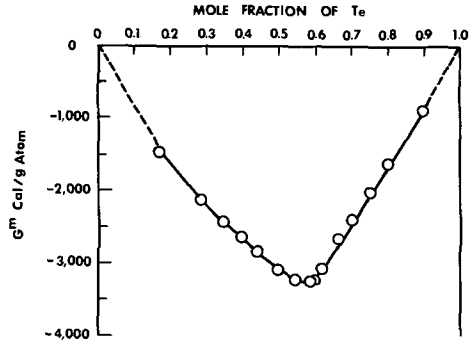

Fig. 3. Relative integral molar free energy vs. composition at 766°K

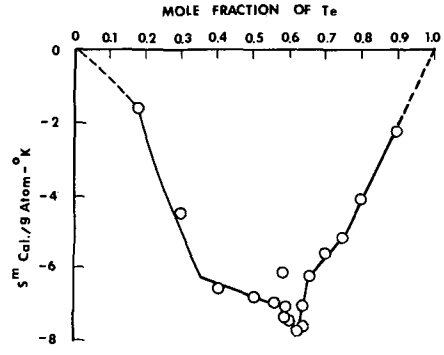

Fig. 4. Relative integral molar entropy vs. composition at 766°K

Table IV. Relative partial molar enthalpies of the bismuth and the tellurium in the alloy at 766°K

Composition Bi, mole fraction	$\Delta\bar{H}_{Bi} = \bar{H}_{Bi} - H_{Bi}^{\circ}$, cal/g-at.*	$\Delta\bar{H}_{Te} = \bar{H}_{Te} - H_{Te}^{\circ}$, cal/g-at.
0.8217	+182	−15900
0.7095	+1130	−21900
0.6509		
0.5992	−4510	−12400
0.5448		
0.4990	−3480	−13100
0.4507	−4250	−12200
0.4170	−11300	−7200
0.4140	−21500	−480
0.4140	−21500	−480
0.4110	−22000	−120
0.3981	−22900	−120
0.3942	−22900	−125
0.3881	−21800	−115
0.3496	−22400	−540
0.3008	−23300	−325
0.2501	−23600	−95
0.2014	−23500	−55
0.1088	−23500	−55

* Value obtained from $\Delta\bar{G}_{Bi} = \Delta\bar{H}_{Bi} - T\Delta\bar{S}_{Bi}$ and rounded to three significant figures.

The thermodynamic data obtained above permit a qualitative understanding of the characteristics of the alloy. For instance, the relative integral molar enthalpy of the alloy gives an estimate of the bonding energies. The relation between the relative integral molar enthalpy and the bonding energies formulated by Herzfeld and Heitler (10), Guggenheim (11), Bethe (12), and Wagner (7) is adopted here

$$H_{Bi\text{-}Te}^{m} = J_{Bi\text{-}Te}[U_{Bi\text{-}Te} - \tfrac{1}{2}(U_{Bi\text{-}Bi} + U_{Te\text{-}Te})] \quad [9]$$

where J designates the number of Bi-Te atom pairs and U the corresponding energy for the individual combination of atom pairs referred to the gaseous state.

In this study, the values of $H_{Bi\text{-}Te}^{m}$ obtained from the experimental results are negative throughout the composition range of $x_{Bi} = 0 - 1.0$. These negative values of $H_{Bi\text{-}Te}^{m}$ indicate that the bonding energy of the pair atoms Bi-Te, $U_{Bi\text{-}Te}$, is greater than the average bonding energy of pair atoms Bi-Bi and Te-Te. This conclusion agrees with the bismuth telluride structure proposed by Drabble and Goodman (13). They suggest that the bonding length between Te atoms (3.57Å) in adjacent layers is greater than that between the bismuth and the tellurium atoms (3.12-3.22Å) in the layer. The large spacing between the Te layers suggests that the layers are held together by weak van der Waals forces between the Te atoms, whereas the bonding between the Bi-Te atoms is predominately covalent.

Also relevant to the constitution of alloys are (*i*) the different electronic states, and (*ii*) the electronic contributions to the thermodynamic properties. From the relation of the electronegativities and the changes in the electron/atom ratio that take place in the alloying process. Wagner (6) has shown, in the silver-tellurium system, how the difference in the electronic states contributes to the thermal properties of the alloys. We have adopted his basic approach and assumed (*A*) that in the bismuth-tellurium system, as in the silver-tellurium system, elemental bismuth releases electrons to form cations and tellurium species take up electrons to form anions, and (*B*) that the valence of the bismuth ions equals +3 throughout the composition range.

The alloys may be characterized at any of the following three states:

1. The mole ratio between Bi and Te is greater than 2:3 ($n_{Bi}/n_{Te} > 2/3$). Thus, there is an excess of bismuth, and the predominant constituents are Bi^{3+} and composite anions with more than two negative charges per atom of tellurium.
2. The mole ratio between Bi and Te is equal to 2:3 ($n_{Bi}/n_{Te} = 2/3$). This is the case of an ideal stoichiometric composition, and the only constituents are Bi^{3+} and Te^{2-}.
3. The mole ratio between Bi and Te is less than 2:3 ($n_{Bi}/n_{Te} < 2/3$). There is an excess of tellurium, and the predominant constituents are Bi^{3+} and composite anions with less than two negative charges per atom of tellurium.

Therefore, two cases may be distinguished in the relative partial molar enthalpy of bismuth.

1. When the bismuth is transferred from its pure state (Bi^{3+}, e^{-}) to an alloy rich in bismuth, a rearrangement of the quasi-free electrons will not occur because there are only Te^{2-} ions saturated with electrons. The corresponding relative partial molar enthalpy of the bismuth will be relatively small.
2. When the bismuth is transferred from its pure state to an alloy rich in tellurium, the electrons introduced will be taken up by the tellurium, since there are tellurium anions with less than two negative charges per atom of tellurium, these will tend to become saturated Te^{2-} ions. The relative partial molar enthalpy will therefore be strongly negative, corresponding to the electron affinity of the unsaturated tellurium anions.

The experimental results of the relative partial molar enthalpy of the bismuth in our study show a behavior exactly as predicted above. $\Delta\bar{H}_{Bi}$ has a slightly positive value of +182 cal/g-mole with a tellurium content of 17.83 m/o, but becomes negative and attains a value of −23500 cal/g-mole with a tellurium content of 89.10 m/o in the alloy. The relation between $\Delta\bar{H}_{Bi}$ and composition of the alloy is shown in Fig. 6. This suggests that the states of the bismuth-tellurium alloys discussed above are reasonable.

Phase Diagram

The phase equilibrium diagram of the bismuth-tellurium system has been studied by different investigators. However, the exact form of the phase equilibrium diagram of this system is still obscure. Hansen (14) summarized earlier work by others and pre-

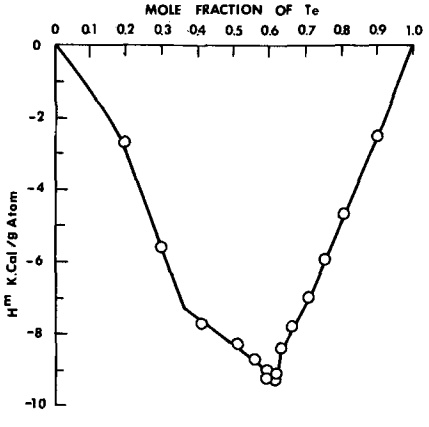

Fig. 5. Relative integral molar enthalpy vs. composition at 766°K

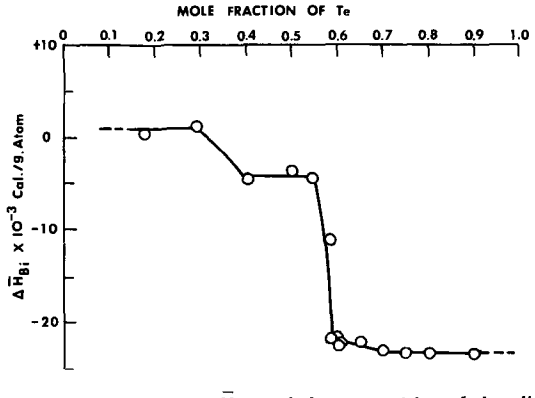

Fig. 6. Relation between $\Delta\bar{H}_{Bi}$ and the composition of the alloy

sented a phase diagram, but the solidus curves were not given. Phase diagrams of the bismuth-tellurium system have been proposed independently by Brown and Lewis (15), Abrikasov and Bankina (16), and Glatz (17). There is remarkable disagreement among these reported phase diagrams, particularly in the region around the compound Bi_2Te_3 (60 m/o Te). Both Brown and Lewis and Hansen report the "compound" Bi_2Te_3 can exist as a single phase over a wide composition range while Abrikasov and Bankina and Glatz report a very narrow range of stability for Bi_2Te_3. These apparent discrepancies indicate that a more detailed investigation of the bismuth-tellurium system is required in order to clarify the phase diagram.

Electromotive force measurements, coulometric titrations, x-ray diffraction, and differential thermal analyses were employed in this study. The experimental procedure and results of each method are discussed below.

Electromotive Force Measurements

The application of emf measurements in determining phase diagrams has been discussed by Chipman (4) and Wagner (7), and the detailed experimental procedure for emf measurements on the bismuth-tellurium system has been described in the previous section. An important advantage of studying phase transitions by this technique is that it permits a horizontal examination of the phase diagram rather than a vertical one. In other words, the emf measurements detect the phase boundaries on a horizontal, constant temperature segment of the phase diagram. Thus, at each specific temperature, a plot of the cell potential as a function of the alloy composition will indicate the phase boundaries. A plot of the potential at 766°K (Fig. 7) shows three regions on the curve with a slope of zero, indicating these three regions are two-phase regions. One region appears between the tellurium composition of 34.8 ± 0.1 and 45.9 ± 0.1 m/o; another, between 58.5 ± 0.1 and 60.5 ± 0.1 m/o; and the third between 61.9 ± 0.1 and 88.9 ± 0.1 m/o. One can compare the discrepancies between previous published phase diagrams and the results of our study. Hansen proposed that there are two two-phase regions existing at 766°K: one, between 35 and 52 m/o tellurium; another, between 61.5 and 83 m/o tellurium. Brown and Lewis suggested that these two-phase regions at 766°K exist between 34 and 56.5 m/o and 61.5 and 83 m/o tellurium. Glatz proposed that, at 766°K, there are three two-phase regions; the first one from an undefined lower boundary up to 46.5 m/o tellurium, the second one between 57.5 and 59.7 m/o, and the third one from approximately 60 m/o tellurium up to an undefined upper boundary. Abrikasov and Bankina gave the boundaries of these two-phase regions at 766°K as 34.0 to 49.0 m/o, 54.7 to 60.2 m/o, and 61.0 to 84 m/o tellurium, respectively.

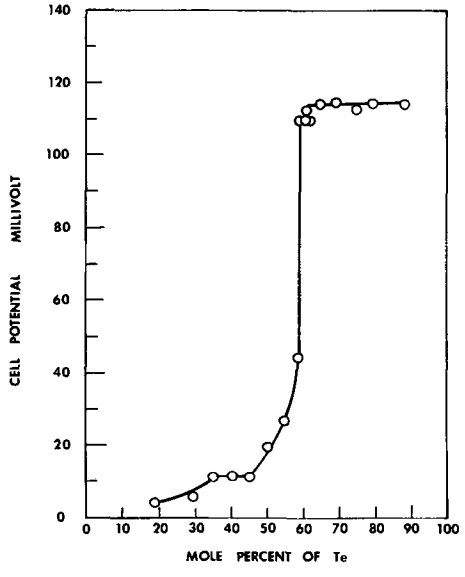

Fig. 7. Cell potential vs. composition at 766°K

Qualitatively, our results agree with those of Glatz and of Abrikasov and Bankina extremely well. This is particularly noticeable in the region near 60 m/o tellurium, namely, near the compound Bi_2Te_3, where our results and those of Glatz and of Abrikasov and Bankina show a narrow single phase region rather than the wide range represented by Hansen and Brown and Lewis. Quantitatively, we find the single β-phase region to exist between the boundaries of 45.9 — 58.5 ± 0.1 m/o tellurium at 766°K. Glatz defines the boundaries as 46.5 — 57.5 m/o at the temperature, and Abrikasov and Bankina, as 49.0 — 54.7 m/o tellurium. Our experimental result confirms quantitatively the boundaries of the β-phase at 766°K postulated by Glatz.

The emf's of each experimental cell were measured at 700° and 655°K as well as 766°K. The relation between the emf and the composition at the two lower temperatures can also be shown analogously to that shown in Fig. 7 for 766°K. However, the impedance of the galvanic cell increased considerably at the lower temperatures and affected the precision of the measurements. Therefore, one cannot rely absolutely on the precision of data obtained at the lower temperatures, particularly at 655°K. Consequently, low-temperature measurements must be complemented with supplementary techniques.

In addition to the insensitivity of the emf measurement at low temperature, the multiplicity of phases in the bismuth-tellurium alloys makes any study on the phase equilibrium of the system very difficult. Establishment of the phase diagram is also complicated by the necessity of excessively long annealing times to obtain thermodynamic equilibrium. Attainment of equilibrium may require annealing for periods in excess of 6 months (17). This problem appears to be more serious for alloys having a tellurium content of 5-50 m/o. Reported phase diagrams may reflect the differences in the alloy preparations, particularly in the range of 5-50 m/o tellurium.

X-Ray Diffraction Study

The Debye-Scherrer powder method of x-ray diffraction was employed. The x-ray radiation of wavelength $\lambda = 2.29092$Å was obtained from a chrome target, and a vanadium filter was used to eliminate the Kβ radiation in the camera. The alloy was converted by filing and grinding into powder which would pass through a 325 mesh screen. The film was exposed from 7 to 10 hr.

Our results of the x-ray powder diffraction study show that the alloy electrodes used in our galvanic cells have a rhombohedral structure. Francombe (18) gives detailed diffraction data on Bi_2Te_3, and his result is in excellent agreement with our investigation.

But our observations indicate no obvious difference in the patterns obtained from alloys in the β-phase region, the $\beta + \gamma$ region, and the γ-phase region. The dimensions of the unit cell of alloys in different phase regions are essentially identical. The average values of the lattice dimensions given by Brown and Lewis are $A_o = 4.38$Å, and $C_o = 30.49$Å, which are in excellent agreement with our values of $A_o = 4.38$Å and $C_o = 30.487$Å. Brown and Lewis give the difference in dimensions of the unit cells between 33 and 60 m/o tellurium as 0.09Å in A lattice and 0.8Å in C lattice. The x-ray study performed by Glatz on the bismuth-tellurium compounds with a tellurium content of 56-62 m/o gives the lattice parameters of the compound Bi_2Te_3 as $A_o = 4.384$Å and $C_o = 30.495$Å which also agree well with those reported by Brown and Lewis and by us. But the differences in the lattice parameters between the compounds in the $\beta + \gamma$ two-phase region and the γ single phase region, namely, between the compounds having a tel-

lurium content of 58.7 and 59.7 m/o reported by Glatz, are extremely small: $A_o = 4.386$Å, $C_o = 30.48$Å for compound with 58.7 m/o tellurium, $A_o = 4.384$Å, $C_o = 30.48$Å for compound with 59.7 m/o tellurium. Thus, the change in lattice dimensions between alloys of varying composition is difficult to detect, especially around the compound Bi_2Te_3, where the change in composition between the β and the γ phases is only 2 m/o.

Differential Thermal Analysis

Differential thermal analysis was used to investigate the phase transitions in the lower temperature range in which the emf measurements became less valid. In our study, a duPont Model 900 analyzer was employed. Alumina was used as the reference material. The sample cell was heated from room temperature up to 873°K at a heating rate of 20°K/min and was then cooled naturally. Differential thermal analyses were performed on various bismuth-tellurium alloys which were all prepared the same as the electrodes in the emf measurements. The tellurium-rich samples lost Te rapidly, and we were unable to obtain any useful information from the samples. For all alloys having a tellurium content up to 65 m/o, a strong endothermic effect was observed at 533°K corresponding to the bismuth-rich eutectic temperature. Glatz also reported that an endothermic effect was observed at 539°K in his differential thermal analyses, and he argued that this phase transition can be eliminated by long time annealing of the alloy. However, the characteristics of the bismuth-tellurium alloy at lower temperature, *i.e.*, below 573°K, in our opinion still have not been fully clarified.

Coulometric Titrations

One of the main interests is to clarify the discrepancy in the phase diagram near the compound Bi_2Te_3; this necessitates an accurate determination of the phase boundaries for the single γ-phase region. To this end, coulometric titrations were performed.

Coulometric titrations were first introduced by Grower (19), and the theory and technique are reviewed elsewhere (20, 21). In our application of the technique, the bismuth ions were transferred from the pure bismuth electrode to the bismuth-tellurium electrode. This method is applicable to a transference of as little as a hundredth of a microgram or even less. This small change in composition allows a close definition of the boundaries of the phase boundaries.

However, the equilibrium potential, *i.e.*, the emf after the titration had been performed, was established very slowly. This low rate of attaining equilibrium was presumably due to the slow rate of diffusion of the bismuth within the alloy. It was unfortunately impractical to increase the rate of attaining equilibrium by increasing the temperature because of the high vapor pressure of $BiCl_3$. Cubicciotti (22) estimated that the vapor pressure of $BiCl_3$ at 850°K might be as high as 70 atm. In this study, coulometric titrations were performed at 766°K, and true equilibrium was successfully established.

The preparation of the experimental cell and the procedure of recording data were similar to those in the conventional emf measurements. The current used in the titration ranged from 0.6 to 70 mA. The emf's of the cell were recorded after the titration had been performed; usually it required 36 hr or more for the system to reach equilibrium. After equilibrium was reached the procedure was repeated. A sequence of titrations performed in the same cell allowed us to scan the concentration easily. The reproducibility of the emf measurements and their agreement with the earlier conventional emf runs is exceptionally good and is shown in Fig. 8. As discussed earlier, a possible loss of up to 0.2 m/o tellurium may occur in the process of preparing the alloy. This loss also may occur in the coulometric titration. From the results obtained, taking into account the loss of the tellurium, the

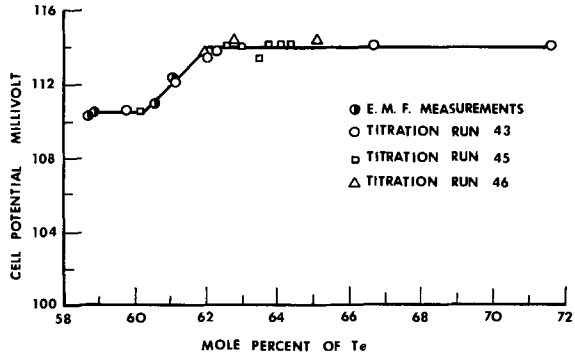

Fig. 8. Relation between cell potential and composition as determined by coulometric titrations and conventional emf measurements.

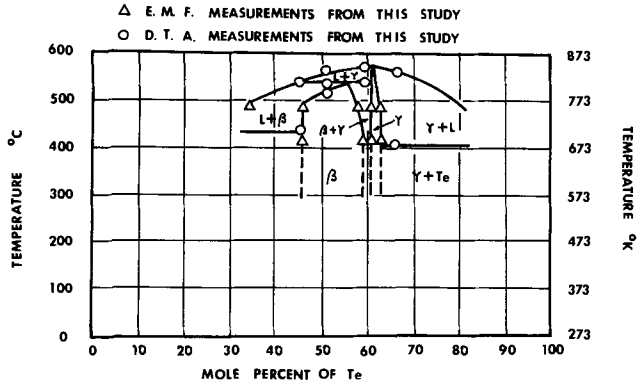

Fig. 9. Proposed phase diagram for the Bi-Te system

boundaries of the single γ-phase region are 60.5 ± 0.1 to 61.9 ± 0.1 m/o tellurium. The close correspondence between the phase boundaries indicated by the coulometric titrations and the conventional emf runs is further confirmation that the bismuth valence is +3. See especially run 43 in which a rather large amount of Bi was transferred.

Proposed Phase Diagrams

Basically, the data obtained from emf measurements, coulometric titrations, and the differential thermal analyses provide sufficient information for the construction of the phase diagram of the bismuth-tellurium system. However, the characteristics of the bismuth-tellurium alloys at lower temperature, *i.e.*, below 573°K, still have not been fully clarified. As mentioned before, an endothermic effect was observed at 533°K, corresponding to the bismuth-rich eutectic temperature, in the differential thermal analyses for all alloys having a tellurium content up to 65 m/o; this phenomenon results in many difficulties in interpreting the data at low temperatures.

In view of the uncertainty in defining the characteristics of the bismuth-tellurium alloys at lower temperature, we restrict our interest to temperatures higher than 673°K and in the composition range of 35-75 m/o tellurium. A phase diagram so constructed is presented in Fig. 9. This phase diagram is based on our emf measurements, coulometric titrations, and differential thermal analyses. Both qualitatively and quantitatively, this phase diagram agrees very well with those proposed by Glatz and by Abrikasov and Bankina. These phase diagrams show a narrow single phase region, the γ-phase region, existing near the compound Bi_2Te_3. At 766°K, the boundaries of this γ-phase region are defined by us as 60.5 ± 0.1 to 61.9 ± 0.1 m/o tellurium, while Glatz defines them as 59.7 to 60.1 m/o and Abrikasov and Bankina give a value of 60.2 to 61.0 m/o tellurium. The differences between the definition of the boundaries is approximately 1 m/o in composition. The agreement between us and Abrikasov and Bankina regarding the location of the boundaries is excellent.

Conclusions

1. The thermodynamic properties of the bismuth-tellurium alloy have been obtained by emf measurements. The activity, relative partial molar free energy, relative partial molar entropy, relative partial molar enthalpy of the bismuth and the tellurium in the alloy, and the relative integral properties of the alloy were obtained. It appears that the electronic state has a significant effect on the thermodynamic properties of the alloy; this effect is similar to that in the silver-tellurium system.

2. The heat of formation of Bi_2Te_3 is -46 ± 10 kcal/g mole at 766°K.

3. The phase diagram of the bismuth-tellurium alloys has been investigated by emf measurements, coulometric titrations, x-ray diffraction, and differential thermal analyses. From these experimental results, the discrepancies between reported phase diagrams of the bismuth-tellurium system have been clarified. We conclude that a very narrow single γ-phase region exists near the compound Bi_2Te_3, in agreement with the work of Glatz and Abrikasov and Bankina. The boundaries of this single phase region have been defined by us as 60.5 ± 0.1 and 61.9 ± 0.1 m/o tellurium at 766°K.

Acknowledgments

One of the authors (JCA) would like to thank R. Fredrick for many long and interesting discussions of the phase equilibrium in the Bi-Te system. Another author (CCL) would like to express his gratitude to The Electrochemical Society for a summer fellowship. The financial support from the Selenium-Tellurium Development Association, Inc. is also gratefully acknowledged.

Manuscript submitted Oct. 1, 1968; revised manuscript received April 10, 1969.

Any discussion of this paper will appear in a Discussion Section to be published in the June 1970 JOURNAL.

NOMENCLATURE

- E Electromotive force, V
- $\mathbf{F}$ The Faraday
- G Gibbs free energy of system, cal/g-atom
- G^m Relative integral molar free energy, cal/g-atom
- H Enthalpy, cal/g-atom
- $\overline{H}_i$ Partial molar enthalpy of component i, cal/g-atom
- H_i^o Molar enthalpy of pure component i at chosen reference state, cal/g-atom
- $\Delta\overline{H}_i$ Relative partial molar enthalpy of component i, cal/g-atom
- H^m Relative integral molar enthalpy, cal/g-atom
- J Number of atom pairs
- R Gas constant per mole
- S Entropy, cal/g-atom
- $\overline{S}_i$ Partial molar entropy of component i, cal/g-at. °K
- S_i^o Molar entropy of pure component i at chosen reference state, cal/g-at. °K
- $\Delta\overline{S}_i$ Relative partial molar entropy of component i, cal/g-at. °K
- T Temperature, °K
- U Bonding energy for the individual combinations referred to the gaseous state
- Z Valency
- a_i Activity of component i
- $\overline{\mu}_i$ Chemical potential of component i, cal/g-at.
- μ_i^o Chemical potential of pure component i at chosen reference state, cal/g-at.

REFERENCES

1. O. J. Kleppa, *J. Am. Chem. Soc.*, **73,** 385 (1952).
2. H. A. Laitinen, W. S. Ferguson, and R. A. Osteryoung, *This Journal*, **104,** 516 (1957).
3. C. Chou and J. F. Elliott, Unpublished work.
4. J. Chipman, *Discussions Faraday Soc.*, **4,** 23, Gurney and Jackson, London (1948).
5. G. N. Lewis and M. Randall, "Thermodynamics," 2nd. ed., pp. 384-389, McGraw-Hill Co., New York (1961).
6. O. J. Kleppa, *J. Am. Chem. Soc.*, **71,** 3275 (1949).
7. C. Wagner, "Thermodynamics of Alloys," pp. 1-30; 67-79, Addison-Wesley Publishing Co., Reading, Mass. (1962).
8. O. Kubaschewski, E. Ll. Evans, and C. B. Alcock, "Metallurgical Thermochemistry," 4th. ed., Pergamon Press Ltd., Oxford, England (1967).
9. S. V. Radcliffe, B. L. Averbach, and M. Cohen, *Acta Met.*, **9,** 169 (1961).
10. K. F. Herzfeld and W. Heitler, *Z. Elektrochem.*, **31,** 536 (1925).
11. E. A. Guggenheim, *Proc. Roy. Soc. (London)*, **A148,** 304 (1935).
12. H. A. Bethe, *ibid.*, **A150,** 522 (1935).
13. J. R. Drabble and C. H. L. Goodman, *J. Phys. Chem. Solids*, **5,** 142 (1958).
14. M. Hansen, "Constitution of Binary Alloys," 2nd. ed., pp. 339-341, McGraw-Hill Co., New York (1958).
15. A. Brown and B. Lewis, *J. Phys. Chem. Solids*, **23,** 1597 (1962).
16. N. Kh. Abrikasov and V. F. Bankina, *Z. Neorg. Khim.*, **3,** 659 (1958).
17. A. Glatz, *This Journal*, **112,** 1204 (1965).
18. M. H. Francombe, *Brit. J. Appl. Phys.*, **9,** 415 (1958).
19. G. G. Grower, *Am. Soc. Testing Materials, Proc. II*, **17,** 129 (1917).
20. S. L. Szebelledy and Z. Somogyi, *Z. Chem.*, **112,** 313, 323, 332, 385, 391, 395, 400 (1938).
21. J. J. Lingane, "Electroanalytical Chemistry," 2nd. ed., pp. 484-610, Interscience Publishers, Inc., New York (1958).
22. D. Cubicciotti, H. Eding, F. J. Keneshea, and J. W. Johnson, *J. Phys. Chem.*, **70,** 2389 (1966).

The Carbon Monoxide, Carbon Dioxide and Carbon Monoxide Electrodes in Molten Alkali Carbonates

P. K. Lorenz* and G. J. Janz*

Rensselaer Polytechnic Institute, Department of Chemistry, Troy, New York

ABSTRACT

The potentials of cells Au|CO,CO_2|$CO_3^=$|CO_2,O_2|Pt and Au|CO|$CO_3^=$|CO_2, O_2|Pt have been determined in the ternary eutectic Li_2CO_3-Na_2CO_3-K_2CO_3 between 510° and 800°C. At 800°C the potential resulting from the Au|CO, CO_2|$CO_3^=$|CO_2,O_2|Pt cell indicated that the reaction occurring at the Au electrode was $CO_3^= + CO - 2e \rightleftarrows 2CO_2$. At 700°C and lower, the cell potential confirmed that the reaction $CO_3^= + C - 2e \rightleftarrows CO_2 + CO$ dominates the high CO partial pressure range. At lower temperatures the reaction $CO + 2\,OH^- \rightleftarrows CO_3^= + H_2$ was observed to proceed to the right, consuming part of the incoming CO stream so that the cell potential appeared to deviate from the Nernst slope (corresponding to the reaction $CO_3^= + CO - 2e \rightleftarrows 2CO_2$). The Nernst slopes and cell potentials follow the thermodynamic prediction for the electrochemical reactions occurring at the Au electrode.

The potentials resulting from the Au|CO|$CO_3^=$|CO_2,O_2|Pt cell were in agreement with the thermodynamically calculated potential for the reaction $CO_3^= + 2C - 2e \rightleftarrows 3CO$ occurring on the Au electrode between 510° and 670°C. At low CO flow rates over the entire temperature range and at all flow rates at higher temperatures the cell potential differed considerably from the predictions for the above reaction. The reaction $CO_3^= + 2H_2 - 2e \rightleftarrows CO + 2H_2O$ is seen as a possible explanation for this behavior.

Reactions occurring in fused alkali carbonates are of interest for their potential applications in (*i*) a practical reference electrode, (*ii*) oxygen regenerative systems, and (*iii*) the carbonate fuel cell.

The Au|CO, CO_2 electrode has been advanced as a reference electrode for the (Li, Na, K)$_2CO_3$ system between 700° and 800°C (1, 2). The behavior of this electrode below 700°C and at high partial pressures of CO is unexplained. Reduction of CO_2 can be utilized to regenerate O_2 from electrolysis in carbonate systems (3, 4). Since the absence of CO is a requirement for most O_2 regenerative systems, it is of interest to establish the temperature regions in which CO is not produced. Relative to the carbonate fuel cell, electrochemical investigations are of interest in order to explore the question of thermodynamic control and to observe possible interfering reactions (5, 6).

The present investigation was undertaken to determine the reactions occurring on a Au electrode immersed in the molten (Li,Na,K)$_2CO_3$ eutectic while the electrode was subjected to CO and mixed CO,CO_2 atmospheres.

Experimental Technique and Apparatus

Chemicals.—Lithium, sodium, and potassium carbonates (reagent grade) were vacuum dried at 250°C under a CO_2 atmosphere. The dried carbonates were stored in a desiccator over $Mg(ClO_4)_2$ until required for use. In order to avoid contamination by H_2O, the eutectic mixture (Li_2CO_3-Na_2CO_3-K_2CO_3, 43.5-31.5-25.0 m/o [mole per cent] mp 397°C) (7) was weighed out in a dry-box. The mixture was then placed in the furnace and melted under a constant atmosphere of predried CO_2. The CO_2 atmosphere above the melt served to minimize the carbonate dissociation and to remove OH^- from the melt by virtue of the reaction (8)

$$CO_2 + OH^- \rightleftarrows CO_3^= + H_2O \qquad [1]$$

Apparatus.—The gastight electrochemical cell assembly is illustrated in Fig. 1. The cell potential was monitored with a high input impedance electrometer which was connected between the test and reference electrodes. The electrometer output was connected through a series of decade resistors to a potential-time recorder. The recorder functioned to indicate when the system had reached equilibrium; the potential registered on the electrometer was then noted.

A Pt wire bathed in a flow of CO_2,O_2 (mol ratio, 2/1) served as the reference electrode. The behavior of this electrode has been thoroughly investigated (9-12). Carbon dioxide and oxygen were passed through drying trains containing $Mg(ClO_4)_2$, monitored on flowmeters, and mixed before entering the reference elec-

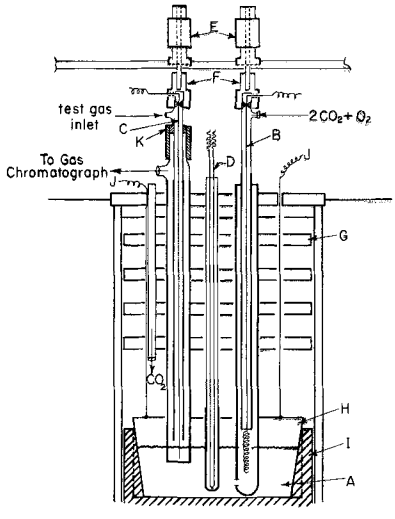

Fig. 1. Electrochemical cell assembly: A, molten carbonate electrolyte; B, reference electrode: Pt wire, 0.5 mm diameter in a Pythagoras porcelain sheath and enclosed in a 10 mm OD Pythagoras porcelain sheath which is pierced by a small hole (0.5 mm diameter) about ¼ in. above the lower end; C, working electrode: Au wire, 0.5 mm diameter housed in two Pythagoras porcelain sheaths as shown; D, thermocouple; E, micrometer depth gauge: (Lufkin, Model 212); F, Insulators; G, baffle; H, crucible: (80% Au, 20% Pd; 50 cc); I, crucible holder; J, auxiliary electrode; K, rubber seal.

* Electrochemical Society Active Member.

trode compartment. Flow rates of 40 and 20 cm³/min were used for CO_2 and O_2, respectively.

The test electrode consisted of a Au wire (0.8 mm diameter) dipping into the melt. The Au wire was housed inside two concentric pythagoras sheaths; the inner served to supply the desired atmosphere over the electrode, the outer contained this atmosphere and exhausted it to the connecting gas chromatograph for analysis.

Periodic analysis of the spent gases, "on-stream," was accomplished with a gas chromatograph. Two columns consisting of silica gel and molecular sieve were connected in series across the detector elements. The purpose of the gas chromatographic determination was to identify the spent gases and to yield the relative ratios so as to compare with input flow measurements.

The furnace temperature was controlled to ±0.6°C over the 2-in. working zone by means of appropriate adjustment of variable resistors connected to each of the five separately wound furnace windings. Two sets of baffle systems, one above and the other supporting the crucible (Fig. 1), functioned to minimize temperature gradients by halting convective currents. The lower baffle system, mounted on a thermocouple rod, could slide freely in the alundum core. The thermocouple rod was seated on a variable platform jack; the melt, thus, could be raised or lowered to any desired position in the furnace. A Pt-Pt 10% Rh thermocouple, insulated with an alumina sheath, was fitted into a Au casing and rested on the bottom of the 80-20 Au-Pd alloy crucible.

Measurements.—The potential resulting from the cell

$$\text{Au} \mid \text{CO},\text{CO}_2 \mid \text{CO}_3^{=} \mid \text{CO}_2,\text{O}_2 \mid \text{Pt} \qquad [2]$$

was monitored over the partial pressure ranges of CO (0.05-0.95 atm) and CO_2 (0.05-0.95 atm). At a constant temperature, the cell potential for a high partial pressure CO_2 stream was recorded. Stepwise, the CO partial pressure was increased at the expense of the CO_2 partial pressure and the potential recorded until the influence of the entire range of partial pressures was investigated. The measurements were then continued to complete the cycle from the high CO to the high CO_2 partial pressure region. At each gas composition, the potential was recorded until the value was invariant with time, and the latter value was noted as the equilibrated value. The results are in Table IA.

In studying the cell

$$\text{Au} \mid \text{CO} \mid \text{CO}_3^{=} \mid \text{CO}_2,\text{O}_2 \mid \text{Pt} \qquad [3]$$

predried and metered flows of CO were passed through the test electrode compartment. The resultant potentials were monitored as a function of the CO flow rates, starting with flows of 230 cm³/min and decreasing to 10 cm³/min in 30 cm³/min decrements. At each flow rate the potential was observed until the equilibrated (time-invariant) value was gained. The measurements were continued with increasing flow rates and the same increments until the initial flow rate (230 cm³/min) was attained. The results of this series of measurements established that the cell potentials were independent of the CO flow rates in the region of higher CO flows. Accordingly the temperature dependence of the cell potential was investigated in the region of high CO flows, with a fixed flow rate of about 200 cm³/min. The equilibrated values thus established are in Table IB, and are shown in Fig. 5 with the limits of uncertainty for each potential given by the double headed arrows.

Results

The electrochemical cell

$$\text{Au} \mid \text{CO},\text{CO}_2 \mid \text{CO}_3^{=} \mid \text{CO}_2,\text{O}_2 \mid \text{Pt} \qquad [2]$$

was investigated over the temperature range 510°-800°C.

The reactions occurring on the Au electrode, predicted from thermodynamic calculations, are

Table IA. Emf of the Au|CO,CO_2 electrode in molten carbonates as a function of partial pressures and temperature, measured against the Pt|CO_2,O_2 (mol ratio 2/1) reference electrode system

P_{CO_2}, atm	P_{CO}, atm	EMF, V	P_{CO_2}, atm	P_{CO}, atm	EMF, V
(a) 510°C			(c) 700°C		
0.049	0.951	0.830	0.044	0.956	1.06
0.055	0.945	0.838	0.060	0.940	1.04
0.072	0.928	0.818	0.106	0.894	1.02
0.096	0.904	0.805	0.170	0.830	1.00
0.141	0.859	0.803	0.266	0.734	0.980
0.141	0.859	0.813	0.358	0.642	0.950
0.225	0.775	0.780	0.530	0.470	0.905
0.235	0.765	0.775	0.628	0.372	0.870
0.326	0.674	0.760	0.791	0.209	0.820
0.489	0.511	0.720	0.871	0.129	0.780
0.586	0.414	0.695	0.908	0.092	0.765
0.735	0.265	0.660	0.960	0.040	0.73
0.813	0.187	0.585			
0.884	0.116	0.535			
0.948	0.052	0.485			
(b) 625°C			(d) 800°C		
0.046	0.954	1.08	0.044	0.956	1.17
0.062	0.938	1.08	0.072	0.928	1.13
0.144	0.856	1.05	0.105	0.895	1.10
0.206	0.794	1.04	0.149	0.851	1.08
0.310	0.690	1.02	0.164	0.836	1.05
0.552	0.448	0.965	0.183	0.817	1.06
0.560	0.440	0.965	0.195	0.805	1.02
0.565	0.435	0.970	0.215	0.785	1.04
0.787	0.213	0.915	0.311	0.689	0.99
0.887	0.113	0.875	0.377	0.623	0.985
0.936	0.064	0.820	0.432	0.568	0.960
0.967	0.033	0.75	0.705	0.295	0.890
			0.785	0.215	0.865
			0.852	0.148	0.815

Table IB. Emf of the Au|CO electrode in molten carbonates, as a function of temperature measured against the Pt|CO_2,O_2 (mol ratio 2/1) reference electrode system

Temp, °C	EMF, V	Temp, °C	EMF, V	Temp, °C	EMF, V
510	0.74	620	0.88	670	0.96
540	0.77	630	1.02	710	1.38
580	0.83	650	1.05	770	1.35
		660	0.98	830	1.27

$$\text{CO}_3^{=} + \text{CO} - 2e \rightleftarrows 2\text{CO}_2 \qquad [4]$$

and

$$\text{CO}_3^{=} + \text{C} - 2e \rightleftarrows \text{CO}_2 + \text{CO} \qquad [5]$$

The Nernst equation for reaction [4], assuming unit carbonate activity, reduces to

$$E = E^{\circ} + 2.303\frac{RT}{2F}\log\frac{P_{CO}}{P_{CO_2}^2} \qquad [6]$$

For reaction [5], the Nernst equation, at unit C and carbonate activity, reduces to

$$E = E^{\circ} - 2.303\frac{RT}{2F}\log P_{CO_2}P_{CO} \qquad [7]$$

The contributions of reactions [4] and [5] to the cell potential can be evaluated by constructing graphs of the cell potential *vs.* log $P_{CO}/P_{CO_2}^2$ and log $P_{CO_2}P_{CO}$. The experimental results were treated in this manner and are illustrated in Fig. 2 and 3. Figure 4 shows the oxidation potentials for reactions [4] and [5], calculated from thermodynamic data (13), as a function of temperature. The experimental and calculated Nernst slopes for reactions [4] and [5] are summarized in Table II.

The electrochemical oxidation of carbonate and C to CO was investigated with cell [3]

$$\text{Au} \mid \text{CO} \mid \text{CO}_3^{=} \mid \text{CO}_2,\text{O}_2 \mid \text{Pt}$$

over the temperature range 510°-830°C. The result of this investigation is illustrated in Fig. 5 where the cell potential is shown as a function of temperature along

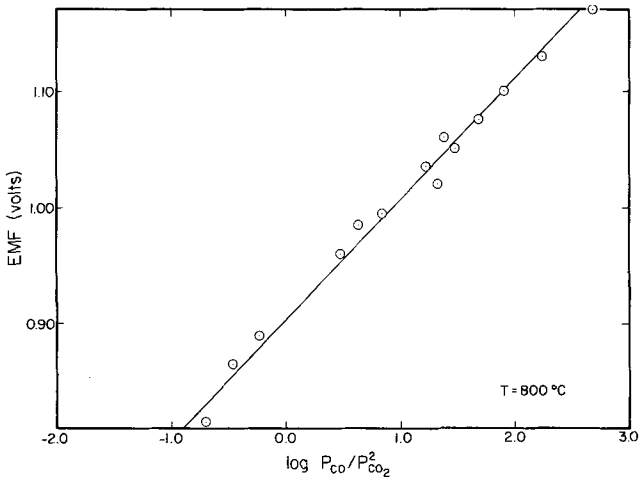

Fig. 2. Potential *vs.* log $\frac{P_{CO}}{P_{CO_2{}^2}}$ for the CO-CO_2 cell at 800°C in the ternary eutectic. The solid line is theoretical prediction for the Nernst equation: $E = E° + 2.303\ RT/2F \log (P_{CO}/P_{CO_2{}^2})$; the circles are the observed values.

with the thermodynamically calculated oxidation potential-temperature curve for the reaction

$$CO_3{}^= + 2C - 2e \rightleftarrows 3CO \qquad [8]$$

Discussion

In using a mixture of CO and CO_2 to supply the Au electrode in the cell

$$Au \mid CO,CO_2 \mid CO_3{}^= \mid CO_2,O_2 \mid Pt$$

due note must be taken of a possible change in the composition of the metered input mixture due to the Deville equilibrium

$$2CO \rightleftarrows C + CO_2 \qquad [9]$$

The maximum rate of CO decomposition to C and CO_2 is known to occur between 500° and 600°C (14, 15). Walker, Rakszawski, and Imperial (16, 17) studied this process [9] extensively, and observed that H_2 plays an important role as a catalytic agent. Neville and Taylor (18) found the forward reaction to be accelerated in the presence of alkali carbonates. This acceleration is undoubtedly due to a series of simultaneous processes possible in molten carbonates, such as: (*i*) CO_2 reacting with the oxide from the dissociated carbonate; (*ii*) CO_2 dissolving in the melt; (*iii*) CO reacting with H_2O vapor yielding CO_2 and H_2; (*iv*) CO reacting with hydroxide in the melt producing H_2 and carbonate; and (*v*) the H_2, thus produced, catalyzing the conversion of CO to CO_2. The contributions of (*iii*), (*iv*), and (*v*) would be the dominating factors after equilibrium has been achieved between the melt and CO_2. The preceding considerations, while somewhat speculative, leave little doubt that the composition of the spent gas stream from the Au electrode should be monitored in order to determine the contribution from reaction [9]. This was investigated accordingly. Gas chromatographic analyses of the spent gas streams for pure CO input streams established that a maximum of 1% CO_2 was formed via reaction [9] at CO flow rates of 10 cc/min. At the more rapid flow rates used for the cell potential studies (150 cc/min), the CO conversion rate was found to be less than 0.5%. The conversion of CO to C and CO_2 due to the Deville equilibrium [9] is thus a slow process under the experimental conditions of the present studies, and, unless otherwise indicated, one may justifiably assume that the compositions of mixtures of CO and CO_2 about the Au electrode were essentially the same as established via the input flowmeters.

Table II. Theoretical and observed Nernst slopes

T, °K	Theoretical Nernst slope	A* observed slope	B* observed slope
783	0.078	0.080	−0.086
898	0.089	0.086	−0.086
973	0.097	0.102	−0.098
1073	0.106	0.104	—

* A: for $CO_3{}^= + CO - 2e \rightleftarrows 2CO_2$.
* B: for $CO_3{}^= + C - 2e \rightleftarrows CO_2 + CO$.

Inspection of Fig. 2 clearly illustrates that reaction [4] controls the cell potential over the entire range of gas compositions at 800°C. As seen in Fig. 3, at temperatures of 700°C and lower, the cell potential deviates from that expected for reaction [4] in the high and low CO partial pressure ranges. The deviation at high CO partial pressures may be due to reaction [5] becoming thermodynamically more favored than reaction [4]. This receives support from the thermodynamic considerations summarized in Fig. 4, where the theoretical oxidation potentials for reaction [4] and [5] are plotted as a function of temperature along with the calculated shift of the cell potentials obtained from the Nernst equations at various CO partial pressures. It is evident, from inspection of the results, that the observed cell potentials follow the thermodynamic predictions. The expected inversion of reaction [4] to reaction [5] at high CO partial pressures is within the experimental accuracy of the measurements at temperatures of 625°C and above. The low cell potential at 510°C and the consequent greater range of CO partial pressure where reaction [4] was observed can be understood as due to possible traces of moisture in the reference gas stream. The deviation of the cell potential from reaction [4] at low CO partial pressures may be due to a loss of CO from the gas stream. The following series of reactions are seen possible

$$2CO \rightleftarrows C + CO_2 \qquad [9]$$

$$CO + 2\ OH^- \rightleftarrows CO_3{}^= + H_2 \qquad [10]$$

$$CO + H_2O \rightleftarrows CO_2 + H_2 \qquad [11]$$

$$CO + H_2 \rightleftarrows C + H_2O \qquad [12]$$

$$CO + 3H_2 \rightleftarrows CH_4 + H_2O \qquad [13]$$

The equilibria for these reactions thermodynamically favor the formation of the products (displacement to the right) at temperatures less than 800°C. Exploratory studies in this laboratory have shown that reaction [10] is the major source of CO consumption. The Au electrode, thus, undoubtedly experienced a CO partial pressure lower than the metered inputs (used for the abscissae in Fig. 2 and 3, respectively). This receives additional support from the results of the gas chromatographic analyses of the spent gas streams. An increase of H_2 at the lower CO partial pressures and the lower temperatures was observed.

Borucka (1, 2) investigated reaction [4] on Au electrodes using a concentration cell of the type

$$Au \mid CO,CO_2 \mid CO_3{}^= \mid CO,CO_2 \mid Au \qquad [14]$$

At 780° and 800°C, the cell potentials were in agreement with Nernst predictions, and use of the Au| CO,CO_2 electrode as a practical reference electrode in the carbonate eutectic in this temperature range was recommended. It was suggested (1, 2) from thermodynamic considerations, that the Deville reaction [9] sets a limit on the application of the proposed reference electrode. The results of the present study show that additional considerations must be taken into account in evaluating the limits of applicability of this reference electrode. Thus it follows from the present study that: (*i*) reaction [9] is kinetically so slow that the potential created by a change in the composition of the dynamic inlet stream is negligible; (*ii*) the dominant CO consuming process appears to be reaction [10] and

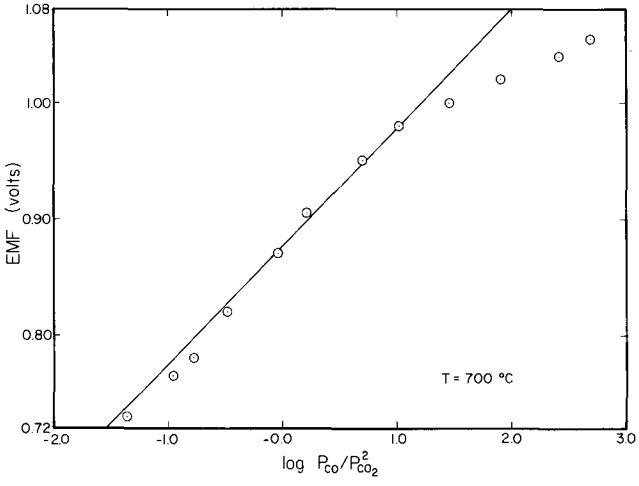

Fig. 3A

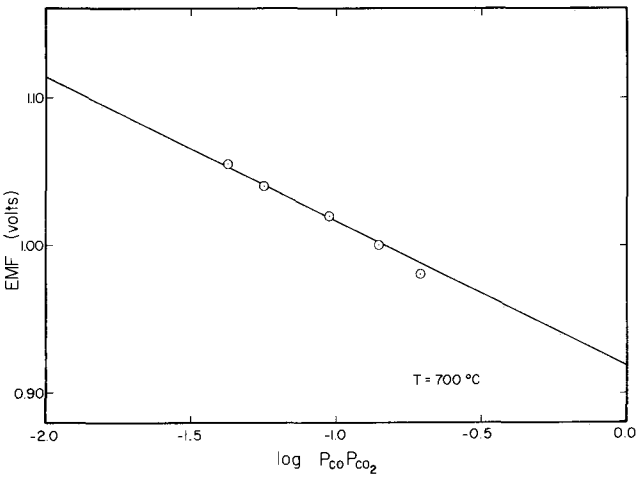

Fig. 3B

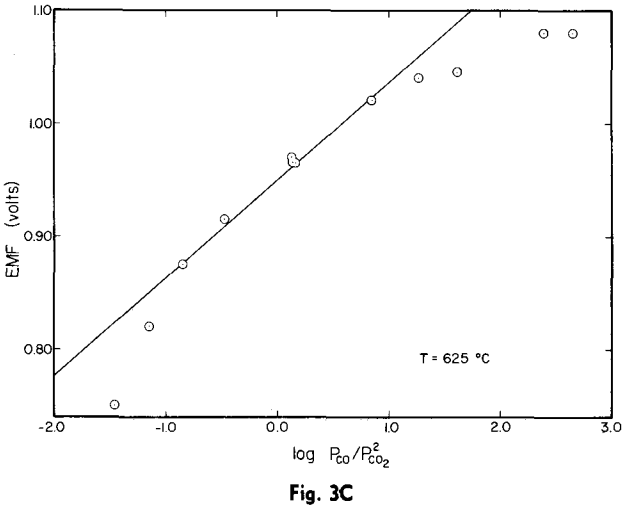

Fig. 3C

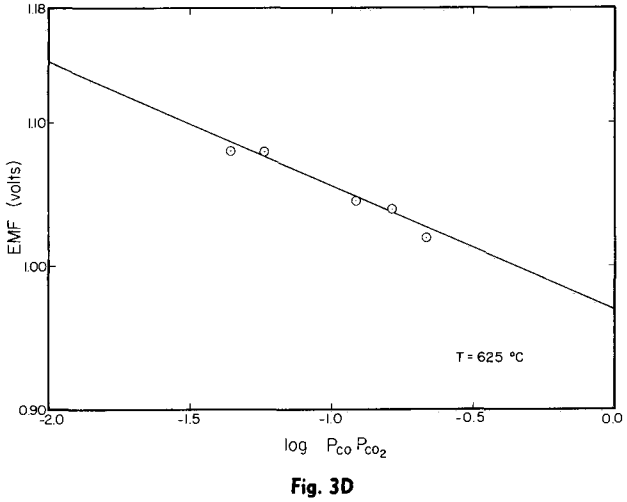

Fig. 3D

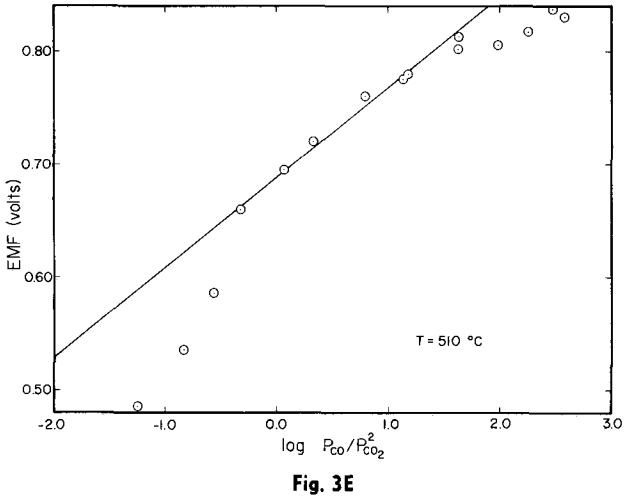

Fig. 3E

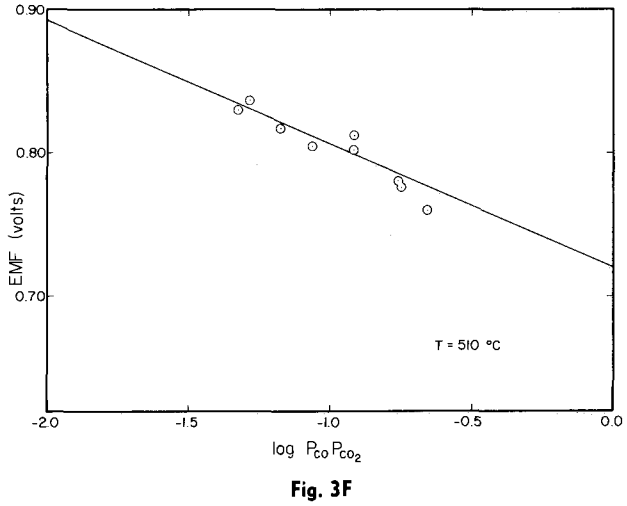

Fig. 3F

Fig. 3. Potential vs. log $\frac{P_{CO}}{P_{CO_2}^2}$ and log $P_{CO_2}P_{CO}$ for the CO,CO_2 cell in the ternary eutectic. The solid lines are the theoretical predictions for the two Nernst equations: $E = E^\circ + 2.303\ RT/2F$ log $(P_{CO}/P_{CO_2}^2)$ and $E = E^\circ - 2.303\ RT/2F$ log $(P_{CO_2}P_{CO})$, respectively, at 700°, 625°, and 510°C; the circles are the observed values.

not the Deville reaction (unless the melt is completely void of moisture, and this is very difficult to attain in practice); and (*iii*) reaction [5] becomes thermodynamically favored at lower temperatures and may overshadow any effect of a shift in the inlet stream composition due to the Deville equilibrium.

The emf from cell [3]

$$Au \mid CO \mid CO_3^= \mid CO_2,O_2 \mid Pt$$

indicated that reaction [5]

$$CO_3^= + 2C - 2e \rightleftarrows 3CO$$

proceeded at the Au electrode between 510° and 670°C. The correspondence between the thermodynamic values and the cell potentials, shown in Fig. 5, is support for this viewpoint. The deviation from the theoretical slope in the higher temperature range (700°-830°) has not been explained, but appears due to other electrochemical processes. Thus it readily follows from thermodynamic considerations the theoretical reduction

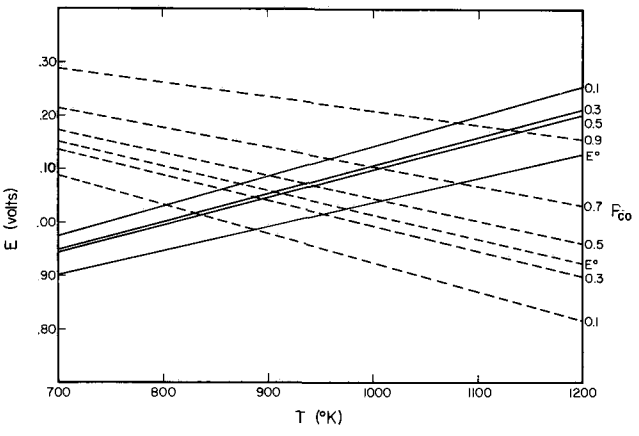

Fig. 4. Theoretical emf temperature dependence of the CO, CO_2|molten carbonate cell at various CO partial pressures. Variation of the thermodynamically predicted oxidation potentials with temperature for the two electrode reactions: $CO_3^= + CO - 2e \rightleftarrows 2CO_2$ and $CO_3^= + C - 2e \rightleftarrows CO_2 + CO$ (solid and dashed lines, respectively).

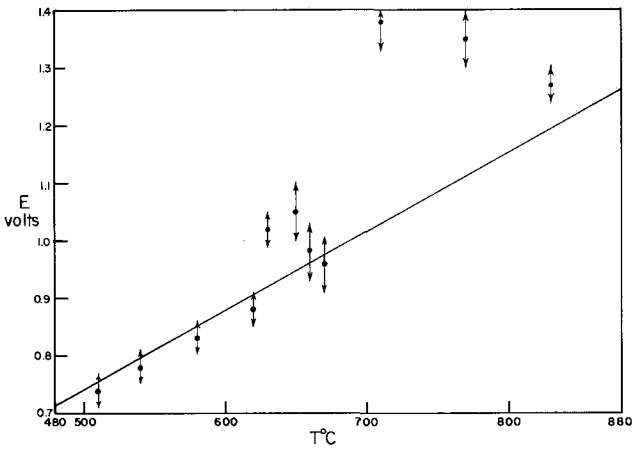

Fig. 5. Graph of the potential vs. temperature for the CO cell in the ternary eutectic. The solid line is the thermodynamically predicted value for the process: $CO_3^= + 2C - 2e \rightleftarrows 3CO$. The limits of uncertainty of the equilibrated potentials are indicated by the double-headed arrows.

potential of reaction [5] can be shown to intersect a number of electrochemical reactions (involving CO_2, CO, OH^-, and H_2) at 670°C. Under appropriate conditions these can become thermodynamically more favorable than reaction [5]. For example, one may use the Nernst equation to calculate the partial pressures of CO, CO_2, and H_2; from this approach it appears that a very plausible explanation for the higher potentials above 700°C is the reaction

$$CO_3^= + 2H_2 - 2e \rightleftarrows CO + 2H_2O \qquad [15]$$

for which the Nernst equation is

$$E = E^\circ + 2.303\frac{RT}{2F}\log\frac{[CO_3^=]\,P_{H_2}^2}{P_{CO}\,P^2_{H_2O}} \qquad [16]$$

The calculated P_{H_2}/P_{H_2O} ratios are 74.0 and 32.5 at 800° and 1100°K, respectively, so that this process, as well as

$$CO + 2\,OH^- \rightleftarrows CO_3^= + H_2 \qquad [10]$$

would contribute directly to deviations (higher values) than would be predicted from a consideration of reaction [5] as the only potential-controlling process in this electrochemical cell.

Acknowledgments

This work was made possible, in large part, by financial support received from the U.S. Office of Naval Research, Division of Chemistry. The award of a Predoctoral Traineeship sponsored by the National Aeronautics and Space Administration to one of the authors (P. K. L.) is gratefully acknowledged. The authors thank D. A. Aikens and M. Breiter for stimulating discussions in the course of this work.

Manuscript submitted Oct. 16, 1968; revised manuscript received March 3, 1969.

Any discussion of this paper will appear in a Discussion Section to be published in the June 1970 JOURNAL.

REFERENCES

1. A. Borucka, Abstract 2.23 CITCE, 16th Meeting, Budapest, September (1965).
2. A. Borucka, *Electrochim. Acta*, **13**, 295 (1968).
3. Research and Development Program for a Combined CO_2 Removal and Reduction System, Hamilton Standard, Division of United Aircraft Corp., Contract NASI-4154, October (1965).
4. W. E. Arnoldi, in "Atmosphere in Space Cabins and Closed Environments," Chap. 4, K. Kammermeyer, Editor, Appleton-Century-Crofts, New York (1966).
5. F. Jones, in "An Introduction to Fuel Cells," Chap. 7, K. R. Williams, Editor, Elsevier Publishing Co., New York (1966).
6. G. H. J. Broers and J. A. A. Ketelaar, in "Fuel Cells," Chap. 6, G. J. Young, Editor, Vol. 1, Reinhold Publishing Co., New York (1960).
7. G. J. Janz and M. R. Lorenz, *J. Chem. Eng. Data*, **6**, 321 (1961).
8. N. Busson, S. Palous, J. Millet, and R. Buvet, *Electrochim. Acta*, **12**, 1609 (1967).
9. G. J. Janz and F. Saegusa, *ibid.*, **7**, 339 (1962).
10. G. K. Stepanov and A. M. Trunov, *Doklady Akad. Nauk. USSR*, **142**, 886 (1962).
11. L. P. Klevtsov, G. G. Arkhipov, and G. K. Stepanov, *Soviet Electrochem.*, **2**, 1170 (1966).
12. Yu. M. Pashkov and G. S. Tyurikov, *ibid.*, **3**, 441 (1967).
13. JANAF Thermochemical Tables, Advance Research Agency Program, U.S. Air Force Contract No. AF33 (616)-6149.
14. B. Fleureau and A. Sancelme, *Compt. rend.*, **235**, 801 (1952).
15. T. F. Berry, R. N. Ames, and R. B. Snow, *J. Am. Ceram. Soc.*, **39**, 308 (1956).
16. P. L. Walker, J. F. Rakszawski, and G. R. Imperial, *J. Phys. Chem.*, **63**, 133 (1959).
17. P. L. Walker, J. F. Rakszawski, and G. R. Imperial, *ibid.*, **63**, 140 (1959).
18. H. A. Neville and H. S. Taylor, *J. Am. Chem. Soc.*, **43**, 2055 (1901).

Concentration Changes in Operating Fuel Cells

J. T. Lundquist, Jr., and W. M. Vogel*

Advanced Materials Research and Development Laboratory, Pratt & Whitney Aircraft, Middletown, Connecticut

ABSTRACT

The high current densities at which fuel cells operate give rise to large concentration changes across the porous matrix employed in most of these cells. These changes were measured in cells especially constructed for these determinations using aqueous potassium hydroxide and phosphoric acid as electrolytes. Part of the resulting voltage losses of the fuel cells, due to pH changes and liquid junction potentials, were measured. A theoretical treatment is presented which accurately describes the experimental data.

The electrolyte in H_2/O_2 fuel cells is frequently a highly concentrated solution of a strong acid or base. In these solutions only one kind of ion participates in the electrode reaction, *i.e.*, either H^+ or OH^- ions. The cells often contain a porous matrix between the electrodes which greatly reduces convection in the electrolyte. A necessary consequence of these conditions is that, in the steady state, an ionic concentration gradient exists which counteracts by diffusion the electrical migration of the inert ions, while it enhances the transport of the reactive ions. This concentration gradient affects the cell operation through changes in the vapor pressure and in gas solubilities. A direct result of the electrolyte variation is the existence of an ionic concentration overvoltage η_d, a liquid junction potential ϵ_D, and a change in the ohmic polarization $\Delta\eta_{ohm}$. The latter two are sometimes combined as resistance polarization (1), but for the purpose of this study this definition is impractical since, although it is possible to measure the sum $\eta_d + \epsilon_D$ and also $\Delta\eta_{ohm}$, it is impossible, even in principle, to accurately determine η_d or ϵ_D separately.

The concentration overvoltage was first considered by Williams and Gregory (2) who measured the total electrode polarization but not the concentration changes. Because of the complex nature of the polarization of porous fuel cell electrodes, one cannot accurately separate the portions due to ionic changes from such data.

In a recent paper Beltzer (3) discussed ionic concentration overvoltages at fuel cell electrodes emphasizing buffer electrolytes. In contrast to our findings the author did not observe any effects of concentration changes in 30% H_2SO_4 or 3M KOH at current densities up to 200 mA/cm^2. Due to the lack of experimental details we cannot speculate as to the reasons for this discrepancy.

While the present paper was being prepared, a paper by Miller and Fornasar (4) appeared, in which actual concentration gradients were measured in KOH fuel cells. The results obtained by these authors were strongly influenced by the flow pattern of the gases in their cells and, therefore, do not lead easily to an understanding of the fundamental process involved.

In view of the incomplete and contradictory nature of these results it was felt that a theoretical and experimental treatment of concentration gradients in fuel cells would be of value. This paper presents the results of studies whereby ionic concentration changes were measured in special fuel cells and the resultant voltage losses were determined with hydrogen concentration cells with liquid junction.

Experimental

The electrochemical cell consisted of four cylindrical Plexiglas sections. The porous membrane and the two fuel cell electrodes were inserted between these sections as shown in Fig. 1. The whole assembly was held together with bolts (not shown) inserted into holes in the Plexiglas walls. Electrolyte leakage through the porous bodies was prevented by means of rubber gaskets and by applying a rubber cement along the outside perimeter of these porous parts. Anolyte and catholyte were stirred separately by means of external pumps.

It was necessary to overcome the large iR drop in the cell with an external power source, for which purpose a potentiostat (Anotrol, Model 4100) was used in galvanostatic circuit.

The electrodes were porous Teflon/platinum black fuel cell electrodes of Pratt & Whitney Aircraft manufacture. The matrix was made of porous hydrophilic Teflon sheet (American Cyanamid, Type TA-1). For the experiments with KOH 10 mil asbestos sheet was used (Johns-Manville, Fuel Cell Asbestos). Both electrodes as well as the membrane had the same effective diameter of 4.15 cm.

Anolyte and catholyte both had the same volume of 95 cm^3. The cell was positioned in a Plexiglas tank with the membrane in horizontal position (any other position leads to liquid circulation through the membrane due to density differences). The temperature in the cell was maintained at 60°C. Reagent grade chemicals were used without further purification.

The hydrogen in the anode was not vented. The oxygen, after being preheated and humidified, was passed through the space behind the cathode and vented to remove the reaction water. The degree of humidification and the flow rate were adjusted to maintain a constant total electrolyte volume in the cell. For this purpose preliminary experiments were done, so that during the main experiment only minor adjustments had to be made. At certain times equal and small electrolyte samples were withdrawn, weighed, and titrated potentiometrically. The experiment was continued in a few cases until no further concentration change was observed. In the majority of the cases

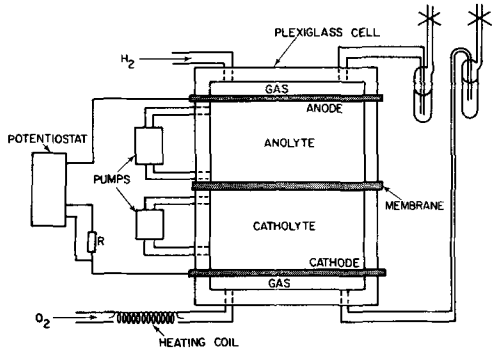

Fig. 1. Apparatus used to simulate a fuel cell under load. (Electrolyte KOH; with acid electrolyte positions of anode and cathode reversed so that more dense electrolyte is always on the bottom.)

* Electrochemical Society Active Member.

the experiment was terminated after the data allowed a sufficiently accurate extrapolation to steady state. This extrapolation was made by plotting log $(1 - \Delta C/\Delta C_\infty)$ *vs.* time according to Eq. [5], where ΔC_∞ was chosen to obtain a straight line. This procedure was checked with the data from those runs where steady state was obtained and found to be actually more accurate (because of the averaging) than the direct determination of ΔC_∞.

The efficiency of the stirring was studied by observing the boundary layer at the membrane when the electrolyte, colored with a dye, was slowly pushed through the matrix into the other half of the cell. This boundary layer was not exactly uniform but it was less than 0.03 cm over more than 90% of the membrane area.

The equilibrium voltage of concentration cells of type Eq. [8] was measured using platinized platinum wires as electrodes around which H_2 was bubbled. Freshly made solutions of electrolyte were used. The two solutions were separated from each other by a porous plug of glass wool or of asbestos. Voltages were measured with a vacuum tube voltmeter with a precision of approximately 1%.

Theoretical

A rigorous theoretical treatment of the experiments would be a matter of considerable complexity. However, by introducing a number of reasonable assumptions an approximate theory can be derived which describes the experiments rather well. The equations are derived for phosphoric acid as electrolyte. Analogous equations for bases are given without derivation.

Let V be the volume of liquid in either of the two chambers of the cell and let C_A and C_C denote the concentrations of anolyte and catholyte, respectively. Before reaching the stationary values these concentrations are continually changed by the migration and back diffusion of electrolyte through the matrix. In the actual experiments liquid flow through the matrix was prevented and the electrolyte in both chambers was stirred, thus confining the concentration gradient to the matrix and the associated liquid boundary layers.

We assume that, because the rate of change in C_A and C_C is very small (see Fig. 2) and because the porous matrix is thin, the concentration distribution in the matrix is at any time very similar to the stationary distribution which would prevail if the momentary values for C_A and C_C were kept constant. We assume further a constant concentration gradient through the matrix and neglect the effect of the liquid boundary layers at the matrix. Under certain conditions this last assumption can introduce serious inaccuracies. The experimental evidence shows, however, that this was not the case (see, *e.g.*, Fig. 6). Assuming finally that the transference numbers n and the diffusion coefficient D of the electrolyte do not depend on the concentration, we have as transport equations for a matrix of area q and thickness l

$$VdC_A/dt = in_-/\mathbf{F} - Dq\Delta C/l \quad [1]$$

$$VdC_C/dt = -in_-/\mathbf{F} + Dq\Delta C/l, \ \Delta C = C_A - C_C \quad [2]$$

The indices A and C refer to anolyte and catholyte, respectively, i is the current through the matrix, and n_- is the effective anion transference number. From the sum of Eq. [1] and [2] we obtain

$$d(C_A + C_C)/dt = 0 \text{ or } C_A + C_C = 2C_O \quad [3]$$

The concentrations are divided symmetrically around the initial concentration C_O. The difference of [1] and [2] yields

$$Vd\Delta C/dt = 2in_-/\mathbf{F} - 2Dq\Delta C/l \quad [4]$$

the solution of which is

$$\Delta C = [1 - \exp(-2Dqt/Vl)]\, in_-l/\mathbf{F}Dq \quad [5]$$

The initial slope is given by

$$(d\Delta C/dt)_{t=0} = 2in_-/V\mathbf{F} \quad [6]$$

and depends on the current but is independent of the particular matrix used. The steady state concentration difference is given by

$$\Delta C_\infty = in_-l/Dq\mathbf{F} \quad [7]$$

and depends on the geometry of the matrix as well as on the current but is independent of the amount of electrolyte V surrounding the electrodes.

The polarization $\eta_C = \eta_d + \epsilon_D + \Delta\eta_{ohm}$ due to concentration changes would be very difficult to measure directly on a fuel cell under load, because of the complicated interaction between it and other kinds of polarizations. A partial measurement of $\eta_d + \epsilon_D$ at $i = 0$ also would be unsatisfactory because of the difficulties encountered in making reversible O_2-electrodes. We, therefore, determined the sum $\eta_d + \epsilon_D$ indirectly from the emf ΔE_t of the cell with junction

$$(Pt)H_2/C_A/C_C/H_2(Pt) \quad [8]$$

which is given by

$$(\Delta E_t)_{H_2/H_2} = n_-RT/\mathbf{F} \ln a_A/a_C \quad [9]$$

where a is the activity of phosphoric acid in anolyte and catholyte, respectively. Writing $(\Delta E_O)_{O_2/H_2}$ for the thermodynamic voltage of the fuel cell at $C_A = C_C = C_O$ and $(\Delta E_t)_{O_2/H_2}$ for $C_A \neq C_C$ we have, for the difference

$$\eta_d + \epsilon_D = (\Delta E_O)_{O_2/H_2} - (\Delta E_t)_{O_2/H_2} =$$
$$RT/2\mathbf{F} \ln (H_2O)_C/(H_2O)_O + n_-RT/\mathbf{F} \ln a_A/a_C \quad [10]$$

Here (H_2O) is the water activity in the catholyte and in the original electrolyte. By combining Eq. [9] with [10] we obtain

$$\eta_d + \epsilon_D = (\Delta E_t)_{H_2/H_2} + RT/2\mathbf{F} \ln (H_2O)_C/(H_2O)_O \quad [11]$$

From data for the emf of cell [8], which can be easily and accurately measured, and vapor pressure data we can determine the direct voltage loss due to ionic concentration changes across the matrix. The total loss of the cell is greater because of the neglected $\Delta\eta_{ohm}$, because of similar effects within the porous electrode structures and because of other effects neglected here.[1]

For KOH as electrolyte an analogous derivation yields

$$\Delta C = [1 - \exp(-2Dqt/Vl)]\, in_+l/Dq\mathbf{F} \quad [5a]$$

$$(d\Delta C/dt)_{t=0} = 2in_+/V\mathbf{F} \quad [6a]$$

$$(\Delta C)_\infty = in_+l/Dq\mathbf{F} \quad [7a]$$

$$\eta_d + \epsilon_D = RT/\mathbf{F} \ln (H_2O)_C^{1/2} (H_2O)_O^{1/2}/(H_2O)_A$$
$$+ 2n_+ RT/\mathbf{F} \ln (a_\pm)_A/(a_\pm)_C \quad [10a]$$

$$\eta_d + \epsilon_D = (\Delta E_t)_{H_2/H_2} + RT/2\mathbf{F} \ln (H_2O)_O/(H_2O)_C \quad [11a]$$

Calculating the voltage losses from pH differences alone (*i.e.*, only η_d), as was done by others [Ref. (2) and (3)], leads to partial results because ϵ_D is being neglected. The data presented below indicate that ϵ_D is rather large but has the opposite sign of η_d.

Results and Discussion

The experimental results are reproduced in Tables I, II, and IIIa (column 3). In Fig. 2 the concentrations of anolyte and catholyte are plotted against time for three typical experiments. We see that, in agreement with Eq. [6], the initial slope is independent of the geometry of the matrix although the steady state values C_∞ are quite different (curves 1 and 2). This initial slope also is approximately proportional to the

[1] *E.g.*, changes in gas concentration overvoltages due to changes in the water vapor pressure.

Table I. Steady state concentrations in O_2/H_2-cell filled with 49% H_3PO_4

Porous Teflon matrix (13.8 cm^2, thickness ~0.056 cm), 60°C, $V_{catholyte} = V_{anolyte} = 95$ cm^3

I [mA/cm^2]	$(C_A)_\infty$ [mole/l]	$(C_C)_\infty$ [mole/l]	$(\Delta E_t)_{H_2/H_2}$ [mV][a]
0	6.55	6.55	0
72	7.35	5.70	−4.8
72[b]	8.16	5.02	—
144	8.44	4.79	−10.2
216	9.13	4.22	−14.1

[a] Equilibrium voltage at 60°C of cells $H_2/H_3PO_4(C_A)/H_3PO_4(C_C)/H_2$.
[b] Matrix of thickness ~0.110 cm.

Table II. Steady state concentrations in O_2/H_2 cell filled with KOH

Fuel cell asbestos (13.8 cm^2, thickness ~0.025 cm), 60°C, $V = 95$ cm^3

I [mA/cm^2]	$(C_A)_\infty$ [mole/l]	$(C_C)_\infty$ [mole/l]
0	6.80	6.80
72	6.14	7.38
144	5.50	8.02
0	4.27	4.27
72	3.66	5.02

Table IIIa. Voltage loss $\eta_d + \epsilon_D$ of $O_2/KOH/H_2$ fuel cell caused by concentration drop across 10 mil asbestos matrix at 60°C

[Data in column 4 according to Eq. [11a] using *emf* data for cells of type Eq. [8] and measured in this work; in column 5 according to Eq. [10a] using activity data from ref. (9)]

C_A/C_C (w/o)	$\frac{RT}{2F}\ln\frac{(H_2O)_C}{(H_2O)_C}$, mV	$(\Delta E_t)_{H_2/H_2}$, mV	$\eta_d + \epsilon_D$ (Eq. [11a]), mV	$\eta_d + \epsilon_D$ (Eq. [10a]), mV
20.7/29.7	1.9	−22.5	−20.6	−20.5
20.7/41.3	6.7	−57.2	−50.5	−51.6
29.9/41.3	1.9	−36.2	−34.3	−31.7
25.0/35.0	2.6	−29.2	−26.6	−24.2
27.1/31.9	1.1	−12.5	−11.4	−11.2

Table IIIb. Voltage loss $\eta_d + \epsilon_D$ of $O_2/H_3PO_4/H_2$ fuel cell caused by concentration drop across 22 mil porous Teflon matrix at 60°C

I [mA/cm^2]	$(C_A/C_C)_\infty$ (mole/l)	$(\Delta E_t)_{H_2/H_2}$, mV	$\eta_d + \epsilon_D$ (Eq. [11]), mV
72	7.38/5.70	−4.8	−5.8
144	8.44/4.79	−10.2	−11.8
216	9.13/4.22	−14.1	−16.3

current i as required by Eq. [6]. The anolyte and catholyte concentrations in Tables I and II approximately average to the initial concentration, as per Eq. [3]. The small remaining difference reflects the accuracy with which we were able to match the water removal rate to the rate of production. (This is rather difficult especially during unattended night runs.)

In Fig. 3 we have plotted log $(1 - \Delta C/\Delta C_\infty)$ against time for three experiments. According to Eq. [5] we have

$$\log (1 - \Delta C/\Delta C_\infty) = -2Dqt/2.3Vl \qquad [12]$$

We see that the slopes in Fig. 3 indeed do not depend on i. The steady state concentrations C_∞ are plotted against the current density I through the matrix (Fig. 4). ΔC_∞ is proportional to I as required by Eq. [7].

One could calculate the transference number $n_\pm$ from the initial slopes of the curves in Fig. 2 using Eq. [6]. A more accurate way of obtaining $n_\pm$ is indicated by combining Eq. [7] and [12]. We thus obtain for the anion in H_3PO_4

$$n_- = -(2.303VF\Delta C_\infty/2i)\, d \log (1 - \Delta C/\Delta C_\infty)/dt \qquad [13]$$

From the slopes of the lines in Fig. 3 and 4 we calculated the values for $n_\pm$ at 60°C given in Table IV. A direct comparison with the published data listed in Table IV is not possible mainly because of the difference in temperature. We feel, however, that, in spite of these differences, these figures afford a check into the validity of our results.

We calculated the voltage loss $\eta_d + \epsilon_D$ from our data using Eq. [11] and [11a]. The values of the water activities were calculated using the well known ther-

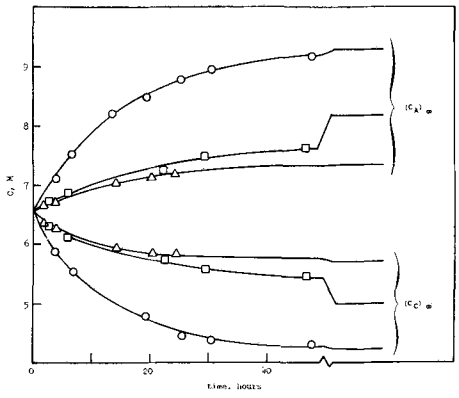

Fig. 2. Variation of C_A and C_C with time 49 w/o H_3PO_4, 60°C. △ TA-1 matrix, l = 0.056 cm, 72 mA/cm^2; □ TA-1 matrix, l = 0.112 cm, 72 mA/cm^2; ○ TA-1 matrix, l = 0.056 cm, 216 mA/cm^2.

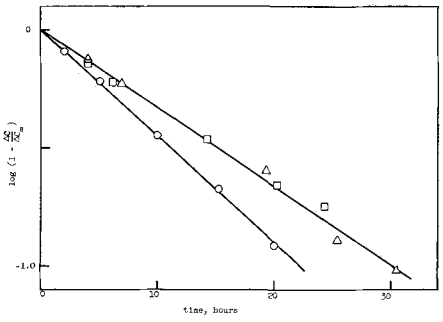

Fig. 3. Variation of log $(1 - \frac{\Delta C}{\Delta C_\infty})$ with time. △ 216 mA/cm^2 and □ 72 mA/cm^2, 49 w/o H_3PO_4, 60°C, TA-1 matrix, l = 0.056 cm; ○ 144 mA/cm^2, 30 w/o KOH, 60°C, asbestos matrix, l = 0.025 cm.

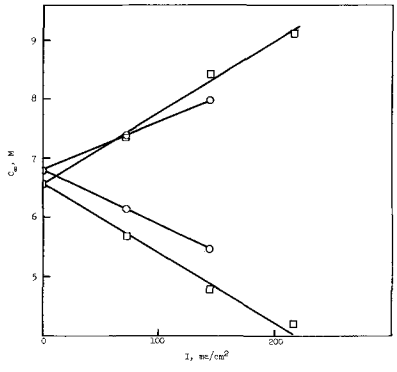

Fig. 4. Variation of C_∞ with current density. □ 49 w/o H_3PO_4, 60°C, TA-1 matrix, l = 0.056 cm; ○ 30 w/o KOH, 60°C, asbestos matrix, l = 0.025 cm.

Table IV. Calculated values for $n_\pm$ at 60°C

Electrolyte	Conc. (mole/l)	n, 60°C	n (lit.)
H_3PO_4/H_2O	~6.5	$n_- = 0.17$	$n_+ = 0.71$ (6m, 25°C) (5)
KOH/H_2O	~6.8	$n_+ = 0.17$	$n_+ = 0.70$ (7m, 25°C) (5) $n_- = 0.78$ (7m, 20°C) (6)

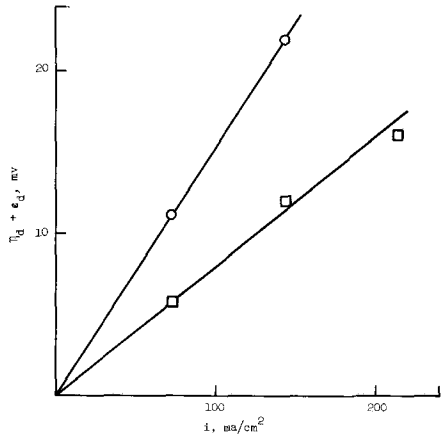

Fig. 5. Variation of electrolyte concentration overvoltage and liquid junction potential with current density. ⊙ 30 w/o KOH, 60°C; □ 49 w/o H_3PO_4, 60°C.

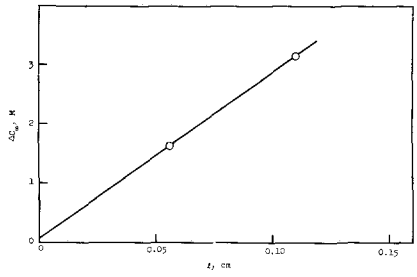

Fig. 6. Variation of ΔC_∞ with matrix thickness, 49 w/o H_3PO_4, 60°C, TA-1 matrix, 72 mA/cm².

modynamic relationship, from vapor pressure data from ref. (7) and (8). The results are given in Table IIIa and IIIb and also in Fig. 5. In Table IIIa results are included which were obtained from activity data for 25°C from ref. (9) using Eq. [10a]. The temperature dependency of the activity ratio in Eq. [10a] is small. For this reason we calculated the losses $\eta_d + \epsilon_D$ for KOH which are plotted in Fig. 5 from the same data (9).

The magnitude of the liquid junction potential ϵ_D could be determined if it were possible to measure thermodynamic pH values of the respective solutions. Although this is not possible, we can estimate some values from the difference between the sums $\eta_d + \epsilon_D$ in Table IIIb and the values for η_d which were calculated from published data according to Eq. [14] for H_3PO_4

Table V. Values calculated from Eq. [14]

C_A/C_C (mole/l)	$\frac{RT}{2F} \ln \frac{(H_2O)_O}{(H_2O)_C}$, mV	$\Delta pH_{25°C}$	$(\eta_d)_{25°C}$ (Eq. [14]), mV	$(\eta_d + \epsilon_D)_{60°C}$ (Table IIIb), mV
7.38/5.70	−1.0	−0.3	−20.8	−5.8
8.44/4.79	−1.6	−0.67	−45.8	−11.8
9.13/4.22	−2.2	−0.92	−62.9	−16.3

$$\eta_d = RT/2F \ln (H_2O)_O/(H_2O)_C + [(pH)_A - (pH)_C]\, 2.3\, RT/F \quad [14]$$

Values calculated in this fashion using data of ref. (8) and pH data of ref. (10), together with those of Table IIIb, are given in Table V.

The increase of ΔC_∞ with the matrix thickness is shown in Fig. 6. The extrapolated line goes almost through the origin, demonstrating that the influence of the liquid boundary layers at the matrix is small. These boundary layers are the essential difference between our cell and actual compact fuel cell. Our results thus can be directly applied to fuel cells.

Manuscript submitted Nov. 1, 1968; revised manuscript received March 7, 1969. This was Paper 335 presented at the Montreal Meeting, Oct. 6-11, 1968.

Any discussion of this paper will appear in a Discussion Section to be published in the June 1970 JOURNAL.

REFERENCES

1. See, *e.g.*, K. Vetter, "Electrochemical Kinetics," p. 386, Academic Press (1967).
2. K. R. Williams and D. P. Gregory, *This Journal*, **110**, 209 (1963).
3 M. Beltzer. *ibid.*, **114**, 200 (1967).
4. M. L. Miller and H. J. Fornasar, *ibid.*, **115**, 330 (1968).
5. C. M. Mason and J. B. Culvern, *J. Am. Chem. Soc.*, **71**, 2387 (1949).
6. S. Lengyel, J. Giber, G. Beke, and A. Vertes, *Acta Chim. Hung. Tomus*, **39**, 357 (1963).
7. Internatl. Crit. Tables, III: 373 (1928).
8. M. M. Striplin, *Ind. Eng. Chem.*, **33**, 912 (1941); see also Technical Bulletin No. P-26, Phosphoric Acid, Monsanto Chemical Company (1946).
9. R. A. Robinson and R. H. Stokes, *Trans. Faraday Soc.*, **45**, 612 (1949). See also B. E. Conway, "Electrochemical Data," p. 82, Elsevier Publishing Co., New York (1952).
10. K. L. Elmore, J. D. Hatfield, R. L. Dunn, and A. D. Jones, *J. Phys. Chem.*, **69**, 3520 (1965).

The Decomposition of AgO in Alkaline Solutions

Aladar Tvarusko[*1]

Research Center, ESB, Inc., Yardley, Pennsylvania

ABSTRACT

The gassing rate, r, of powder AgO samples, made by the chemical oxidation of $AgNO_3$, was measured in gassing pipettes. The mean r of 52 AgO samples at 200 hr (AgO content $\geq 95\%$, $r_{200} \leq 35$ μl/day/g) was 23.0 μl/day/g. Gassing rates at different times and in different solutions, respectively, are correlated. r increased with increasing NaOH concentration, temperature, and pelletizing pressure, and with ball milling. r of AgO samples made in the presence of transition elements (added as compounds) were, in general, larger than r of samples with nontransition elements. The effect of Co and Ni is especially catastrophic. Pb suppressed r of highly gassing AgO samples regardless of the method of addition.

Silver(I)-silver(III) oxide, commonly designated as AgO, is thermodynamically unstable in alkaline electrolytes (KOH, NaOH) but has a reasonable degree of metastability (1). Oxygen evolution is the end result of the decomposition reaction

$$2AgO \rightarrow Ag_2O + \tfrac{1}{2} O_2 \qquad [1]$$

Denison (2), however, claimed that AgO is stable in 20-40% KOH solutions.

Oxygen overvoltage of the local cell action and formation of a protective Ag_2O film on the AgO is thought to be the reason for its metastability (1, 3). The decomposition of AgO (*a*) is light sensitive (4, 1), (*b*) increases with increasing temperature (1, 3, 5-8), and (c) increases with increasing KOH concentration (1, 7, 8). The decomposition of "Ag_2O_3" (a reaction product of $AgNO_3$ and $K_2S_2O_8$) in KOH ($< 1N$) was found by Stehlik (6) to be a first order reaction with an activation energy of 22 kcal/mole.

The stability of AgO seems to depend on its mode of preparation (9) and the various AgO samples were found to decompose at different rates (1, 5, 7). Unoxidized silver metal increased the rate of decomposition of AgO (3, 7) whereas Ag_2O did not affect the stability of AgO (3). Boer and Ormondt (10) found that the incorporation of Mn, Cu, and Co into AgO during its preparation decreased its stability, whereas Cd increased the stability of $(Ag_3O_4)_a \cdot AgSO_4$ (where a varies from 2 to 2.5). The presence of carbon in AgO battery plates is claimed to have no adverse effects (11), whereas CO_2 decomposes AgO (10).

The addition of Al_2O_3 to alkaline electrolytes is said (12) to inhibit the oxygen evolution. The addition of ZnO to KOH electrolytes decreases the decomposition rate of AgO to Ag_2O (1, 5) and prevents the reduction of Ag_2O to Ag (5). According to Amlie and Rüetschi (1), the addition of zincate ions has little influence because the addition of ZnO to KOH electrolyte reduces its OH^- activity and this causes the decrease of the decomposition rate. Cahan (13) showed that the addition of PbO to 40% KOH (and other electrolytes) markedly reduced the gassing rate of AgO; 1% PbO was found to be the optimum.

Yoshizawa and Takehara (14) have shown that the formation of AgO was retarded by Te and Sb which lowered the oxygen overvoltage or made the decomposition of AgO easier.

The effect of intentionally added inorganic additives on the electric resistivity of AgO was described in a previous paper (15). It was found that the AgO content of samples was very low in the presence of small amounts of Co and Ni indicating either an inhibited formation or an accelerated decomposition of AgO during its preparation in alkaline medium. Since AgO is mainly used in sealed cells, it is very important to know its gassing rate in the absence or presence of beneficial or detrimental additives.

The gassing, *i.e.*, decomposition rate of AgO samples (prepared by chemical oxidation of $AgNO_3$) was determined in alkaline electrolytes as a function of time, NaOH concentration, temperature, porosity, surface area, pelletizing pressure, and intentionally added inorganic additives.

Experimental

The AgO samples were prepared by the chemical oxidation of $AgNO_3$ with alkaline $K_2S_2O_8$ (16). The inorganic additives were incorporated into AgO during its preparation (15), initially at one concentration level: 1000 parts (element) per million parts of Ag, *i.e.*, 1000 ppm (Ag). Subsequently, some of the beneficial and detrimental impurities were studied as a function of concentration.

The amount of oxygen evolved in contact with alkaline solutions was determined in a modified Amlie-Rüetschi microvolumetric apparatus (1), "gassing pipette." The ground glass joint of their apparatus was replaced by an 18/7 O-ring joint (Pyrex, Buna N rubber ring) to eliminate "freezing" of the joint. Furthermore, filling of the gassing pipette (0.2, 0.5, or 1.0 ml capacity) with the electrolyte and joining of the two parts is easier with an O-ring than with a ground glass joint. Loose AgO powder (0.5000 $\pm$ 0.0002g) was used for the determinations unless otherwise mentioned.

The assembled gassing pipettes were placed in a constant temperature oil bath and allowed to equilibrate for 1 hr. The position of the meniscus of the electrolyte column after this time is considered as the zero hour reading; at least two parallel measurements were made on each sample at 37.78 $\pm$ 0.02°C (100°F) unless otherwise mentioned. The measurements were made in the presence of light.

The gassing rate is calculated at various time intervals from the volume of the evolved gas. This gassing rate is a cumulative average gassing rate and is not corrected for water vapor pressure.

The decomposition of AgO was measured in two alkaline electrolytes, unless otherwise mentioned. One of them contained 8.6N NaOH and 2.2N Na_2ZnO_2, whereas the other had 9.7N KOH and 2.8N K_2ZnO_2.

The data were subjected to statistical analysis. The "mean" parameter refers to the average of the samples the distribution of which tends to normality. The least square method was used for regression and curve fittings. If the coefficient of correlation, R of linear regression was low, the data were subjected to polynomial regression analysis.

Results and Discussion

Gas evolution as a function of time.—Figure 1 shows the gas evolution and the gassing rate of an AgO sample (98.1% AgO content) as a function of time in

* Electrochemical Society Active Member.
[1] Present address: Engineering Research Center, Western Electric Company, Inc., Princeton, New Jersey.

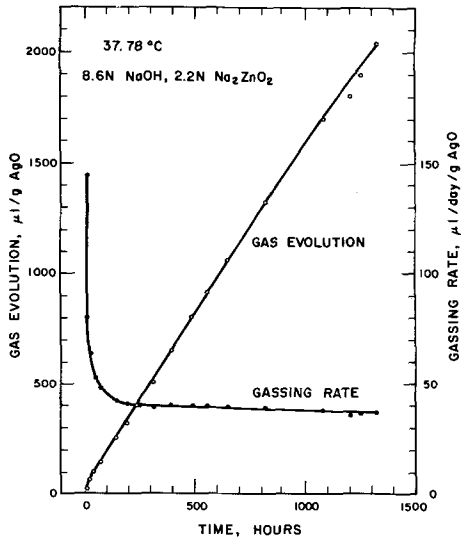

Fig. 1. Gas evolution and gassing rate of AgO as a function of time

8.6*N* NaOH and 2.2*N* Na_2ZnO_2 electrolyte. It can be seen that gas evolved almost linearly with time. The initial nonlinearity shows up clearly in the rapid decrease of the gassing rate. After approximately 200 hr the decrease of the gassing rate is small. On the basis of these results and other considerations, the minimum duration of the gassing test was chosen to be about 200 hr and this is the gassing rate, r_{200}, given, unless otherwise mentioned.

This test is time consuming (200 hr) and the long delay in obtaining the gassing rate is not well suited for routine testing. It was observed that the gassing rate-time curves were more or less parallel to each other. Figure 2 shows an approximately linear relation ($R = 0.896$) between the gassing rates of 114 AgO samples at 20 and 200 hr (samples with $r_{20} > 150$ μl/day/g are not shown in Fig. 2 but were taken into the consideration in the regression analysis). The analysis of variance for a quadratic regression reveals that the linear term is dominating (degree of freedom, $df = 1$, mean square, $MS = 13{,}791$), the increase due to the quadratic term is negligible ($df = 1$, $MS = 24.58$), and the deviation about regression is small ($df = 111$, $MS = 30.18$). Because of low R, the gassing rate at 20 hr (approximately overnight) and the linear regression equation in Fig. 2 can be used only for semiquantitative prediction of the gassing rates of AgO samples. This test, however, may be useful in the production of AgO and in testing a new batch of chemicals for sealed-cell electrolytes.

The mean gassing rates, $\bar{r}_{200}$, of AgO samples (AgO content ≥ 95.0%) were calculated for arbitrarily chosen

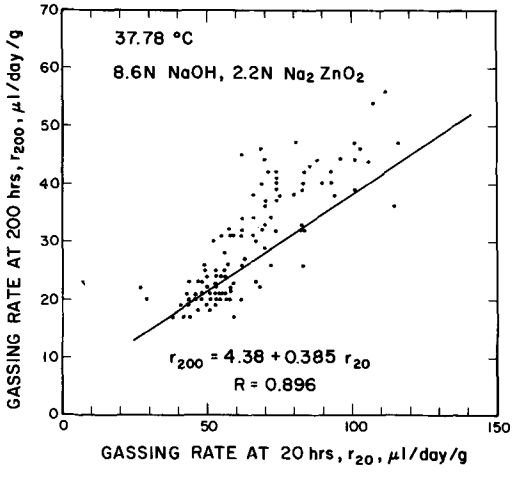

Fig. 2. Gassing rates of AgO samples at 20 and 200 hr.

Table I. The mean gassing rate of AgO samples in 8.6*N* NaOH, 2.2*N* Na_2ZnO_2 solution

r_{200}, μl/day/g	Number of samples	Mean $\bar{r}_{200}$, μl/day/g	Mean AgO content, %	Standard deviation r_{200}, μl/day/g	Standard deviation AgO content, %
≤35.0	52	23.0	98.1	4.62	0.82
≤25.0	37	20.6	98.2	2.32	0.75
≤20.0	15	18.3	98.1	1.23	0.64
≤18.0	5	16.8	97.8	0.82	1.00

levels and are shown in Table I. The majority of the considered AgO samples had $r_{200} \leq 25.0$ μl/day/g which clearly shows up in mean gassing rates. The standard deviation of $\bar{r}_{200}$ becomes smaller mainly due to the narrower gassing rate levels. These results support the observation of several workers (1, 5, 7, 9) that various AgO samples decompose at different rates.

It can be seen in Table I that the mean AgO content of the AgO samples did not change appreciably with the gassing rate. No correlation was found between the gassing rate and AgO content down to 60%.

According to Eq. [1], ½ mole oxygen gas is obtained from 2 moles of AgO at its complete conversion to Ag_2O. Thus, 50,483 μl O_2, a, would evolve per gram AgO (98.1% AgO content) at 37.78°C and 760 mm Hg. If the decomposition is a first order reaction

$$\log \frac{a}{a-x} = \frac{k}{2.303} t \qquad [2]$$

should be linear. In this equation x is the volume of the evolved gas/g AgO at time t and k is the rate constant. Figure 3 shows this to be the case with $R = 0.9988$. The rate constant is calculated from the slope to be 3.09 x 10^{-5}/hr, *i.e.*, 0.271/year in 8.6*N* NaOH and 2.2*N* Na_2ZnO_2 solution at 37.78°C. It should be mentioned that others consider the decomposition to be zero (7, 8), pseudo zero (7), or first order (6) reaction.

Influence of concentration and temperature.—Figure 4 shows the gassing rate of AgO at 42 hr (98.4% AgO content) to increase with increasing NaOH concentration at all temperatures (these solutions do not contain ZnO). This is in agreement with the results in KOH (1, 7, 8). In view of the large gassing rates at 60°C, r_{42} was chosen instead of r_{200} even though some uncertainty may exist (see Fig. 1), mainly at lower temperatures. Linear regression analysis of the data in Fig. 4 ($R \geq 0.983$) yielded physically incorrect nega-

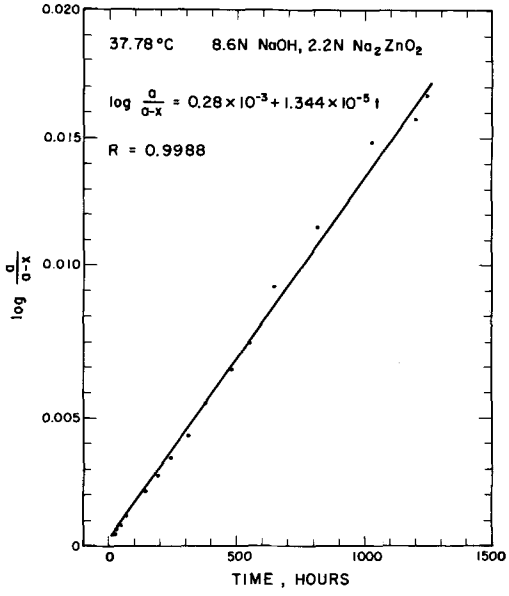

Fig. 3. First-order reaction plot of the decomposition of AgO in alkaline solution.

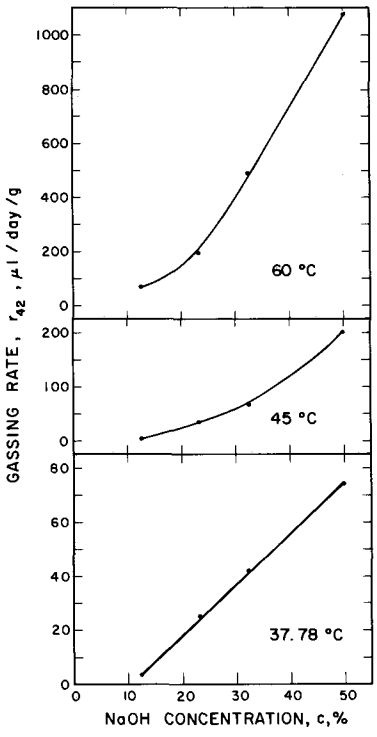

Fig. 4. Gassing rates of AgO as a function of NaOH concentration at various temperatures.

tive intercepts, *i.e.*, no gassing would take place below a certain NaOH concentration. This would be contrary to the results obtained by others in KOH (6-8). Polynomial regression analysis revealed that the curves in the investigated concentration range are predominantly linear and the increase due to the quadratic and cubic terms is slight. The slope of the log r_{42} — log c curve was found to be 2.2, 2.7, and 2.0 at 37.78°, 45°, and 60°C, respectively ($R \geqq 0.973$).

Figure 4 reveals also the known temperature dependence of the gassing rate in alkaline solutions (1, 3, 5-8); the gassing rate increased with increasing temperature. The rate constants, k in various NaOH solutions were calculated by the half-life method from r_{42} and r_x, the gassing rate at the longest available time ($x \geqq 42$ hr). The activation energies, E were calculated from the slopes of log k *vs.* $1/T$ curves. The activation energy of the complex decomposition reaction of AgO (1, 3, 5, 7, 8, 17) was calculated from all data to be 26 kcal/mole. E calculated from r_{42} was found to be 24 kcal/mole whereas E from r_x is 28 kcal/mole. These results are close to the following values obtained by other workers: (*a*) 28.4 kcal/mole in 10-50% KOH solutions (8), it was calculated from gassing rates at approximately 35 hr; (*b*) 22 kcal/mole for "Ag_2O_3" in solutions up to 1*N* KOH (6); and (c) 30 kcal/mole for the decomposition of AgO in air (18).

Calculating E from Otto's gassing rates in 11.6*M* (44%) KOH solution [(7), Table I] through the half-life method, one obtains 18.9 kcal/mole. This is considerably lower than the aforementioned E values for AgO. If the gassing rate at 100°C, *i.e.*, r at approximately 20 hr is neglected, 17.2 kcal/mole is obtained from gassing rates at approximately 200 hr and more. The difference in activation energies of the two groups is probably due to the decrease of gassing rate with time, mainly in the beginning of the test.

Figure 5 shows log k *vs.* $1/T$ in two zincate-containing electrolytes. The E values calculated from their slopes are: 21.0 and 23.6 kcal/mole in 9.7*N* KOH, 2.8*N* K_2ZnO_2 and 8.6*N* NaOH, 2.2*N* Na_2ZnO_2 solutions, respectively. The k values were obtained from gassing rates at 100 hr and more. These lower E values seem to support the aforementioned explanation for the difference of E.

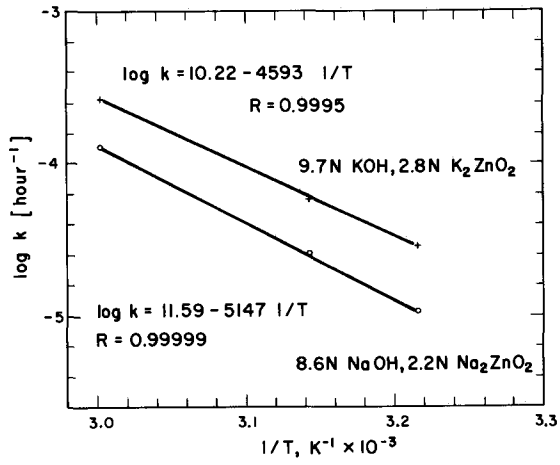

Fig. 5. Rate constants as a function of temperature

Correlation of r in various solutions.—The composition of the electrolyte in AgO cells is varied and the gassing rates are usually determined in each of them. This is, however, time consuming. Figure 6 shows the correlation of the gassing rates (r_{200}) in two frequently used battery electrolytes. It can be seen that the gassing rate in 9.7*N* KOH, 2.8*N* K_2ZnO_2 solution is approximately three times larger than in 8.6*N* NaOH, 2.2*N* Na_2ZnO_2 solution. Even though the data are scattered ($R = 0.887$), the linear relation allows a semi-quantitative prediction of the gassing rate in one of the solutions if r is known in the other one.

Amlie and Rüetschi (1) found that the decomposition rate is larger in 10*N* KOH (40%) solution than even in 13.8*N* (40%) NaOH. This could be explained by the different activities of KOH and NaOH. The activity, a is given by $a = \gamma m$ where γ is the mean molal activity coefficient and m is the molality of the solutions. Since $m_{KOH} = 8.96$, $m_{NaOH} = 12.71$, $\gamma_{KOH} = 4.82$, and $\gamma_{NaOH} = 6.12$ [obtained by linear interpolation of the published values (19)], activities are: $a_{KOH} = 43.2$, $a_{NaOH} = 77.8$. It can be seen that the activities are opposite to the gassing rate values and thus, the activities of KOH and NaOH cannot account for the difference in gassing rates. Unfortunately, the individual ionic activities are not available for correlation.

Effect of pressure.—The gassing rate of loose AgO powder samples is measured in this work. AgO, however, is usually compressed in actual cells and therefore it was of interest to investigate the gassing rate of AgO as a function of pelletizing pressure. Figure 7 shows the increase of the gassing rate with increasing pelletizing pressure in both cases. It is evident that

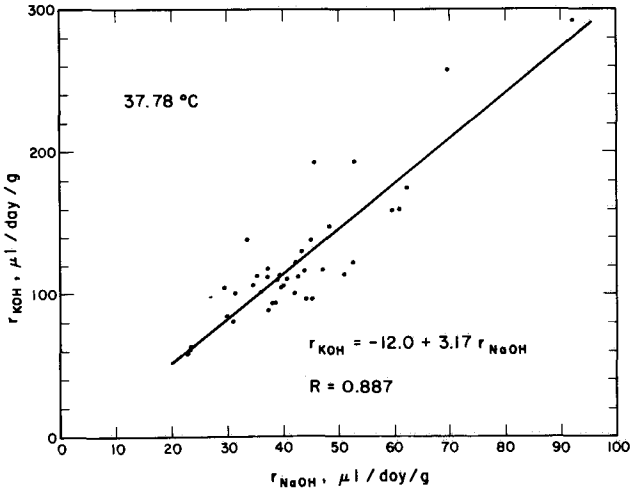

Fig. 6. Gassing rates of AgO samples in 9.7*N* KOH, 2.8*N* K_2ZnO_2 (r_{KOH}) and 8.6*N* NaOH, 2.2*N* Na_2ZnO_2 (r_{NaOH}) solutions.

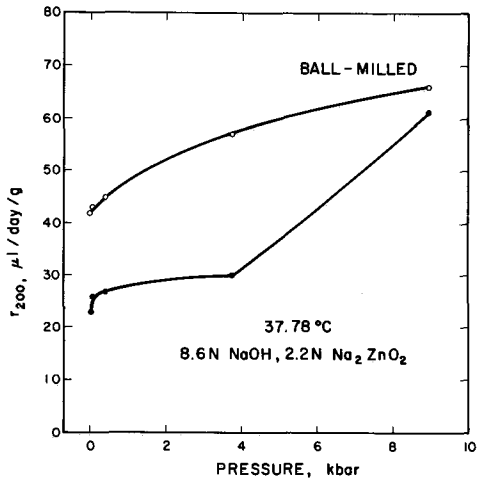

Fig. 7. Gassing rate of AgO as a function of pelletizing pressure

ball-milling of the AgO sample is detrimental. The gassing rate of pellets made from ball-milled AgO was markedly higher than that of unmilled AgO sample at pressures up to approximately 4 kbar; at the highest pressure the difference became small. In view of these results and the pressure dependence of resistivity (15), the pressure of the pelletizing of AgO should be kept to an optimized minimum.

Influence of surface area.—The BET surface area of AgO samples did not correlate with gassing rate of AgO samples contrary to the observation of Amlie and Rüetschi (1) who found a slight correlation. The mean surface area of 13 AgO samples is 1.12 m^2/g (standard deviation, $s = 0.39$) and the $\bar{r}_{200}$ is 22.8 µl/day/g ($s = 3.2$). The surface area increased with decreasing AgO content of the samples (0.86 to 1.79 m^2/g between 98.8 and 71.8%, respectively) and with increasing rate of $AgNO_3$ addition during the preparation of AgO (0.63 to 0.99 m^2/g between 4.25 and 34g $AgNO_3$/min). The surface area increased by *ca.* 50% in the presence of 1000 ppm (Ag) Pb (1.62 m^2/g) but Sn and Hg did not influence it.

The pore volume of AgO samples (determined by mercury intrusion in an Aminco-Winslow porosimeter) showed no correlation with the gassing rate. The mean pore volume of 43 AgO samples ($\bar{r}_{200} \leq 35.0$ µl/day/g) was found to be 0.57 ml/g ($s = 0.05$) at a mean gassing rate of 23.7 µl/day/g ($s = 4.5$). The pore volume (0.525 ml/g) of Otto's AgO sample (7) is close to the mean pore volume. The gassing rates of this section were measured in the 8.6*N* NaOH, 2.2*N* Na_2ZnO_2 solution.

Effect of inorganic additives.—The influence of various inorganic additives on the resistivity of AgO samples was described separately (15). Here, their effect on the gassing rate of AgO samples is described. Tables II and III show the results for the investigated elements (added as compounds) at a concentration of 1000 parts by weight per million parts of silver used for the preparation of AgO, *i.e.*, 1000 ppm (Ag). The AgO content should not decrease due to this small amount of additive unless it is detrimental. The AgO contents of samples made in the presence of nontransition elements varied slightly but all were > 96.0%. Samples with transition elements had, in general, lower AgO contents and Co and Ni caused the largest drop.

AgO samples made in the presence of nontransition elements had, in general, low gassing rates (Table II). Sb leads the list with a gassing rate of 46 µl/day/g and only samples with Mg, Ba, and Sn show gassing rates above 30 µl/day/g. On the other hand, AgO samples with Pb, Al, Cd, and Zn have gassing rates ≤ 20 µl/day/g.

The incorporation of Cd was found (10) to increase the stability of $(Ag_3O_4)_a \cdot AgSO_4$ (where *a* varies from 2 to 2.5) and the addition of Al_2O_3 (12) and PbO (13)

Table II. Effect of nontransition element impurities (added as compounds) on the AgO content and gassing rate of AgO samples in 8.6*N* NaOH, 2.2*N* Na_2ZnO_2

Periodic Table group	Element, 1000 ppm (Ag)	AgO content, %	Gassing rate, µl/g AgO/day
—	—	98.1	$\bar{r}_{200} = 23$*
II A	Mg	97.2	32
	Ca	98.5	23
	Sr	97.8	21
	Ba	97.4	33
II B	Zn	98.5	20
	Cd	97.7	16
	Hg	97.5	22
III	Al	98.5	17
	In	97.1	27
	Tl	96.0	22
IV	Ge	98.3	22
	Sn	97.2	32
	Pb	98.5	17
V	As	98.3	25
	Sb	96.8	46
	Bi	98.4	23

* See Table I.

Table III. Effect of transition element impurities (added as compounds) on the AgO content and gassing rate of AgO samples in 8.6*N* NaOH, 2.2*N* Na_2ZnO_2 solution

Transition element	Elements, 1000 ppm (Ag)	AgO content, %	Gassing rate, µl/g AgO/day
—	—	98.1	$\bar{r}_{200} = 23$*
First series	V	96.0	18
	Cr	97.7	18
	Mn	95.3	60
	Fe	96.4	55
	Co	37.7	8800[1]
	Ni	38.0	9000[2]
	Cu†	97.3	65
Second series	Y	96.5	44
	Zr	88.0	5800[3]
	Mo	98.5	28
	Pd	97.3	174
Third series	Ta	92.2	43
	W	98.5	171
Lanthanides	Ce	95.7	648[4]
	Pr	96.9	24
	Eu	97.5	39
Actinides	Th	96.7	72

* See Table I.
† Considered as transition element, see ref. (15).
[1] At 5.5 hr.
[2] At 5.0 hr.
[3] At 4.0 hr.
[4] At 69.0 hr.

to alkaline electrolyte, to inhibit and markedly reduce, respectively, the oxygen evolution from AgO. The corresponding low gassing rates of Table II support these findings. The decrease of gassing rate of AgO in the presence of large amounts of ZnO (1, 5) is said (1) to be due to the decrease of OH^- activity of the alkaline solution and the zincate ions have little influence (1). The 20 µl/day/g gassing rate in the presence of 1000 ppm (Ag) Zn is only slightly below the mean gassing rate and the addition of Zn seems to have little influence. Yoshizawa and Takehara (14) found that the AgO formation is retarded on a silver alloy anode containing 2% Te or Sb because the oxygen overvoltage is decreased or the decomposition of AgO is easier in their presence. Table II shows that the sample with Sb has the highest gassing rate. According to Amlie and Rüetschi (1), the decomposition rate of AgO must depend on the oxygen overvoltage. Yoshizawa and Takehara (14) measured the anode potential of silver and its alloys (2% alloying element) during oxygen evolution and found the oxygen overvoltage to decrease by *ca.* 100 mV according to following series (20): pure Ag > Cd > Au > Pb > In > Cu > Te > Sb. The corresponding gassing rates are: 16.8,[2]

[2] The lowest $\bar{r}_{200}$ used (Table I).

16, —, 17, 27, 65, —, 46 μl/day/g in 8.6*N* NaOH, 2.2N Na_2ZnO_2 at 37.78°C. It can be seen that the gassing rate increases with decreasing oxygen overvoltage of silver alloys mainly in the second half of the aforementioned series.

Table III shows the gassing rates of AgO samples made in the presence of transition elements (15) to be, in general, larger than the gassing rates of samples with nontransition elements. The presence of 1000 ppm (Ag) Co, Ni, and Zr is catastrophic from the viewpoint of gassing rates. Samples with Ce, Pd, and W have intolerably large gassing rates. On the other hand, AgO samples made in the presence of the common V, Cr, and Mo have low gassing rates because they were oxidized and washed out from the precipitate as meta-vanadate, chromate, and molybdate, respectively. When Mn was incorporated, part of it was oxidized to permanganate (red-wine colored mother liquor) and part of it precipitated with AgO. This supports the similar observation of Boer and Ormondt (10). The large gassing rates support their observation (10) that the incorporation of Mn, Cu, and especially Co into AgO during its preparation decreased its stability, *i.e.*, increased the amount of oxygen evolved at 20°C and 77% relative humidity.

Gassing rate as a function of additive concentration.—In view of the aforedescribed, mainly detrimental, effects of the additives, it was of interest to determine the effect of additive concentration. Their influence on the resistivity of AgO and other pertinent information were described elsewhere (15). It should be emphasized that reagent-grade chemicals and additives were used for the preparation of AgO samples without recrystallization or other purifying treatments.

Figure 8 shows the gassing rate of AgO samples as a function of additive concentration. This concentration represents the metal content of the additive used in the preparation of AgO and does not necessarily correspond to its content in the sample (15). It can be seen that the gassing rate of AgO samples increased with increasing additive concentration. The gassing rate in the presence of Cd (not shown) increased only slightly to 34 μl/day/g at 10^5 ppm (Ag) Cd.

The resistivity of AgO samples decreased in the presence of Pb, Sn, Hg, and Bi (15). The gassing rate increased slowly with increasing Sn concentration and it went through a small minimum in the presence of Pb. The latter supports Cahan's similar observation (13). In the presence of small amounts of Hg, the gassing rate was small but started to rise rapidly above 10^4 ppm (Ag) Hg. The gassing rate of AgO samples with Bi was high already at moderate Bi concentrations. Sb and As yielded samples of high gassing rates without beneficially affecting their resistivity.

Ni and Co, which are common trace impurities in most chemicals, drastically increased the gassing rate

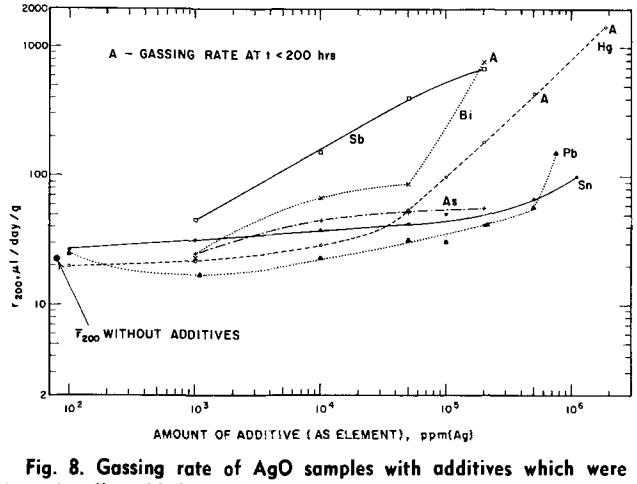

Fig. 8. Gassing rate of AgO samples with additives which were intentionally added in various amounts during their preparation.

Table IV. Gassing rate and AgO content of AgO samples made in the presence of Ni, r_5 in 8.6*N* NaOH, 2.2*N* Na_2ZnO_2 solution

Ni, ppm (Ag)	AgO content, %	r_5, μl/day/g
1000	38.0	8900
100	83.1	8300
10	96.2	1150
1	98.2	176

of AgO samples at 1000 ppm (Ag) concentration (Table III). Therefore, it was of interest to determine the gassing rate at lower Ni concentrations. Table IV shows the gassing rates at 5 hr to be still intolerably high even at 1 ppm (Ag) Ni addition. The volume of the evolved gas increased linearly with time up to 5 hr except at 1 ppm (Ag) Ni where a break occurred after 2 hr.

The explanation of the effect of these inorganic additives cannot be ascertained on the basis of the performed experiments. A correlation of the gassing rates with some meaningful parameters may shed some light on the influence of these additives. This, however, will not be attempted here. The possibilities are numerous. According to Amlie and Rüetschi (1), the gassing rate depends on the oxygen overvoltage and the physical characteristics (structure and porosity) of the surface Ag_2O film. The BET surface area of AgO sample with 1000 ppm (Ag) Pb was *ca.* 50% higher than the mean surface area of AgO samples without additives. In view of the smaller gassing rates in the presence of small amounts of Pb and higher surface areas, the porosity does not seem to be a controlling factor. Cahan (13) ascribed the decrease of gassing rate to the presence of a silver plumbate surface film. The limited number of oxygen overvoltage data on silver alloys (14, 20) seem to correlate with the gassing rates but not without exception.

The effect of transition metal additives, mainly Ni, Co, Zr, and Ce, on the gassing rate seems to point to catalytic action. The thermodynamic, but more likely the kinetic metastability of AgO in alkaline solution can be also affected by their presence. The charge transfer may take place in the bulk or at the surface of AgO by several possible mechanisms (injection, tunneling, transition state).

Suppression of gassing.—In order to determine the effect of beneficial additives (from the viewpoint of resistivity and gassing rate) as gassing suppressors, AgO samples were made in the presence of 5 ppm (Ag) Ni with and without 10^4 ppm (Ag) Hg, Sn, and Pb. The results are shown in Table V. Hg increased the gassing rate by the same amount whether the $Hg(NO_3)_2$ was added to the $AgNO_3$ or to the alkaline persulfate solution. Sn decreased the gassing rate moderately, whereas Pb decreased it markedly neutralizing the affect of Ni to some degree. Replacing part of Pb by Hg, the gassing rate increased indicating the aforementioned detrimental effect of Hg. The resistivity of

Table V. Effect of additives included during the preparation of AgO in the presence of 5 ppm (Ag) Ni

Additive		AgO content, %	ρ, ohm-cm at 2.1 kbar	r_{200}, μl/day/g, 37.78°C, in 8.6*N* NaOH, 2.2*N* Na_2ZnO_2
Element	ppm (Ag)			
—	—	95.7	64.0	280
Hg	10^4	96.7	2.84	405†
Hg	10^4	94.7	3.71	400‡
Sn	10^4	93.4	4.05	222
Pb	10^4	95.5	2.63	84*
Hg Pb	5×10^3 5×10^3	95.8	1.77	122*

† At 117 hr.
‡ $Hg(NO_3)_2$ was added to the alkaline persulfate solution.
* At 165 hr.

Table VI. Effect of additives, incorporated into the 8.6N NaOH, 2.2N Na_2ZnO_2 solution, on the gassing rate of AgO

Additive, 10^4 ppm (Ag) element	Gassing rate, μl/day/g 37.78°C, 8.6N NaOH, 2.2N Na_2ZnO_2	Duration of r determination, hr
—	249	185
HgO	292	161
Na_2SnO_3	246	209
GeO_2	147	209
PbO	105	209

AgO samples containing Pb, Sn, and Hg are lower as found earlier (15). The AgO content of the samples are generally lower due to the presence of Ni. The addition of Pb to AgO during its preparation is beneficial not only from the viewpoint of electric resistivity but also of gassing rate. Thus, it is advantageous to have Pb as one of the components in any combination of beneficial additives.

In view of the aforementioned beneficial affect of Pb, etc. on the gassing rate and Cahan's results with PbO (13), it was of interest to determine their influence on the gassing rate when they are incorporated in the alkaline solution. An AgO sample with high gassing rate was chosen (98.2% AgO content). The results of Table VI show that Hg increased, Sn did not influence, and Ge and Pb decreased the gassing rate of the AgO sample. Since the trend of the gassing rates in Table V and VI is nearly the same, the effectiveness of the additives is due to their presence and is independent of the method of incorporation.

Summary

The volume of the oxygen evolved from AgO samples in contact with alkaline solutions was measured in a modified microvolumetric appartus of Amlie and Rüetschi (1) and the gassing rates (cumulative average) were calculated. The AgO samples were prepared by the chemical oxidation of $AgNO_3$ with alkaline $K_2S_2O_8$ (16) in the absence or presence of intentionally added metal additives (as compounds). The gas evolved almost linearly with time and the decrease of gassing rate, r after 200 hr was small. In view of the approximately linear relation between the gassing rates at 20 and 200 hr, r_{20} can be used for the rapid semiquantitative prediction of gassing rates. The gassing rates varied somewhat and the mean r_{200} of 52 AgO samples (AgO content $\geq 95\%$, $r_{200} \leq 35$ μl/day/g) was 23.0 μl/day/g. Assuming the decomposition of AgO to be a first order reaction, 0.271/year was obtained for the rate constant in 8.6N NaOH, 2.2N Na_2ZnO_2 solution at 37.78°C.

The gassing rate increased with increasing NaOH concentration and temperature. With NaOH concentration, r_{200} increased approximately linearly. The activation energy for the complex O_2 evolution reaction was calculated from all data to be 26 kcal/mole. The correlation of the gassing rates in two solutions of different composition was found to be approximately linear. The gassing rate of AgO powders increased with ball milling and increasing pelletizing pressure. No correlation was found between the gassing rate and surface area or porosity.

The gassing rates of AgO samples made in the presence of transition elements were, in general, larger than the gassing rates of samples with nontransition elements. The presence of 1000 ppm (Ag) Co, Ni, and Zr is catastrophic from the viewpoint of decomposition and samples with Ce, Pd, and W have intolerably large gassing rates. The gassing rate of AgO samples increased with increasing additive concentration with the exception of Pb at small concentration. The addition of Pb is advantageous also from the viewpoint of electric resistivity (15).

Sn, Ge, and especially Pb suppressed the large gassing rates of AgO samples regardless whether they were incorporated with 5 ppm (Ag) Ni during their preparation or only added to the alkaline solutions.

Acknowledgment

The author wishes to thank Dr. R. A. Schaefer for permission to publish this paper and Mr. W. E. Wilson, Jr. for experimental assistance.

Manuscript submitted Dec. 26, 1968; revised manuscript received March 20, 1968. This was Paper 259 presented at the New York Meeting, May 4-9, 1969.

Any discussion of this paper will appear in a Discussion Section to be published in the June 1970 JOURNAL.

REFERENCES

1. R. F. Amlie and P. Rüetschi, *This Journal*, **108**, 813 (1961).
2. I. A. Denison, *Trans. Electrochem. Soc.*, **90**, 387 (1946).
3. T. P. Dirkse and B. Wiers, *This Journal*, **106**, 284 (1959).
4. V. I. Veselovskii, *Zh. Fiz. Khim.*, **22**, 1302 (1948); *C. A.*, **43**, 2503f (1949).
5. F. M. Bowers, R. D. Wagner, N. R. Berlat, and G. L. Cohen, AD-403777 (April 1963).
6. B. Stehlik, *Chem. zvesti*, **15**, 474 (1961).
7. E. M. Otto, *This Journal*, **115**, 878 (1968).
8. P. Rüetschi, Paper No. 290 presented at the Montreal Meeting, Oct. 6-11, 1968.
9. J. Selbin and M. Usategui, *J. Inorg. Nucl. Chem.*, **20**, 91 (1961).
10. J. H. de Boer and J. van Ormondt, *Proc.* Intern. Symposium Reactivity of Solids, Gothenburg 1952, pp. 557-564 (Publ. 1954).
11. J. R. Coleman and T. E. King, "Power Sources 1966," pp. 193-205, D. H. Collins, Editor, Pergamon Press (1967).
12. J. J. Coleman and P. G. Kort, U. S. Pat. 2,829,189, April 1, 1958.
13. B. Cahan, U. S. Pat. 3,017,448, Jan. 16, 1962.
14. S. Yoshizawa and Z. Takehara, *J. Electrochem. Soc. Japan*, **31**, 91 (1963).
15. A. Tvarusko, *This Journal*, **115**, 1105 (1968).
16. R. N. Hammer and J. Kleinberg, "Inorganic Syntheses," Vol. IV, pp. 12-14, McGraw-Hill Book Co., New York (1953).
17. T. P. Dirkse, L. A. Vander Lugt, and H. Schnyders, *J. Inorg. Nucl. Chem.*, **25**, 859 (1963).
18. B. Stehlik, *Chem. zvesti*, **15**, 469 (1961).
19. R. Parsons, "Handbook of Electrochemical Constants," pp. 28-29, Butterworths Scientific Publications, London (1959).
20. S. Yoshizawa and Z. Takehara, *Denki Kagaku*, **32**, 197 (1964).

Electrical Properties of Electrodeposited PbO_2 Films

W. Mindt

Bell Telephone Laboratories, Incorporated, Murray Hill, New Jersey

ABSTRACT

Resistivity, Hall effect, and optical absorption of electrodeposited α- and β-PbO_2 films have been investigated. Films of both crystalline modifications show low resistivities (α-PbO_2: 10^{-3} ohm-cm, β-PbO_2: 10^{-4} ohm-cm) and electron densities of about 10^{21} cm^{-3}. Free electrons are due to nonstoichiometry or to incorporation of hydrogen. As a result of the high carrier densities, the absorption edge is shifted to higher photon energies. The band gaps of intrinsic α- and β-PbO_2 are about 1.4 eV.

Lead dioxide has a high electrical conductivity, comparable with that of some metals. This property is important for its use as positive active material in the lead acid battery as well as for other applications, *e.g.*, as an inert anode material in several electrolytic processes.

In the past two decades, very little experimental work on the electrical properties of PbO_2 has been published. Most of the information we have today originates from papers of Palmaer (1), Kittel (2), and Thomas (3). The latter two authors carried out Hall effect measurements on electrodeposited samples. They found n-type conduction with electron densities between 10^{20} and 10^{21} cm^{-3} and mobilities of the order of 100 cm^2/Vsec. It was assumed that the free electrons are due to an effective deficiency of oxygen, which is generally found in PbO_2 regardless of the method of preparation (4-6). According to Thomas, the temperature coefficient of the resistivity is positive in the temperature range between —200°C and +100°C and the sign of the thermoelectric power negative.

At the time these studies were made, only the tetragonal (β) modification of PbO_2 was known. Conductivity measurements on both orthorhombic (α) and tetragonal PbO_2 were carried out by White and Roy (7) and Aguf *et al.* (8). Unfortunately, pressed powder samples were used, which have the disadvantage of being extremely sensitive to experimental parameters such as grain size and applied pressure, particularly since the thermal instability of PbO_2 does not allow heat treatment of the powder samples. The resistivity values obtained by the two groups of authors differ by more than three orders of magnitude. There are, as far as we could determine, no Hall effect measurements reported on the pure α-PbO_2 phase.

PbO_2 films prepared by reactive sputtering of lead in an oxygen atmosphere were investigated by Lappe (9). The films were several hundred angstroms thick and consisted of a mixture of α- and β-PbO_2. An electron density of 10^{21} cm^{-3} and a relatively low mobility of 0.6 cm^2/Vsec were found. The latter value was probably influenced by the low film thickness. From the optical absorption spectra of these films the band gap of PbO_2 was estimated to be 1.5 eV. At lower photon energies free electron absorption occurs.

In the present work resistivity, Hall effect, and optical absorption of electrodeposited PbO_2 films were investigated. Since α- and β-PbO_2 can be obtained in pure forms by electrodeposition (1-6, 10-16), a separate study of the two modifications was possible. A better knowledge of the difference of their electrical properties is desirable in problems concerning the lead acid battery, in which both crystalline forms occur.

Experimental

Deposition of PbO_2 *films.*—Electrolytic deposition of PbO_2 is possible on electrochemically inert substrate electrodes. In the present investigations, Pt and SnO_2 coated glass were used as anodes.

To obtain a uniform and continuous deposit of PbO_2, it was necessary to nucleate some PbO_2 on the substrate electrode prior to the deposition. This was done by briefly applying a high anodic current density in an acid solution of 10^{-4}M/l lead perchlorate. Electron photomicrographs of a Pt surface treated in this way showed a uniform distribution of PbO_2 clusters with an average diameter of about 100Å. No crystalline structure could be detected in these clusters by electron diffraction. Lead dioxide films subsequently deposited grew uniformly and without leaving uncovered spots or pores visible by electron microscopy. The crystalline modification of the PbO_2 films was not affected by the pretreatment, as could be seen by comparison with PbO_2 deposited on clean, un-nucleated Pt electrodes.

The solutions were prepared by dissolving PbO (yellow, Fisher Certified) in $HClO_4$. It is generally believed that under acid conditions β-PbO_2 is obtained. We found, however, a considerable amount of the α-modification in deposits obtained even from strong acid solutions (pH $\leq$ 0). The intensities of the x-ray lines of α-PbO_2 were in some cases stronger than those of the β-lines. A similar observation has recently been reported by Duisman and Giauque (6). In general, high Pb^{++}-concentrations and low current densities seem to promote the formation of α-PbO_2 in this pH region. The conditions under which a good crystalline and pure β-PbO_2 deposit was obtained involved the use of a solution of 20 mM/l PbO in 0.165 M/l $HClO_4$ (pH 1) and a current density of 0.1 mA/cm^2. α-PbO_2 was deposited from a saturated solution of PbO in 0.2M $HClO_4$ (pH 5.5) at the same current density. Under alkaline conditions, Pb_3O_4 is likely to be formed as a second phase. For this reason, only studies on α-PbO_2 obtained from neutral solutions are reported here. The solutions were slightly stirred. The temperature was always 25°C.

After deposition the samples were rinsed with distilled water and dried at room temperature. The thickness of the films was calculated from the amount of charge passed, using x-ray densities and current efficiencies determined by weight gain measurements on 20 cm^2 Pt electrodes under equivalent conditions of deposition. In most cases the current efficiencies were close to 100%.

Electrical measurements.—The substrate electrode used for the resistivity and Hall effect measurement is shown in Fig. 1. A 500Å Pt film was evaporated on a glass slide with a 200Å Ti underlayer for better adherence. A geometrical form was chosen which is commonly used for Hall effect measurements: Two contacts on the same side are used to measure the ohmic voltage drop, V^R, and two contacts on opposite sides to measure the Hall voltage V^H. The contacts to the Pt were made with silver flake and covered with epoxy to isolate them from the electrolyte during deposition.

The principle of the method was to determine V^R and V^H before and after deposition of the PbO_2 films

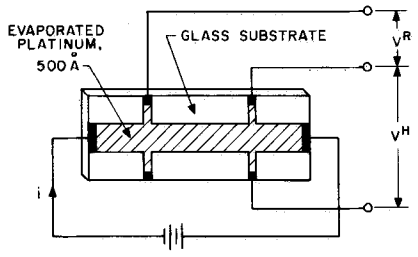

Fig. 1. Electrode arrangement for Hall effect and resistivity measurements.

and to calculate resistivity and Hall coefficient of PbO_2 from these data. To be able to do this, the contact resistance between Pt and PbO_2 must be low and not rectifying. We made, for this reason, some studies of the contact resistance between PbO_2 and Pt as well as some other metals. The current-voltage characteristic of the contacts was nonlinear in most cases where an insulating oxide can be formed between PbO_2 and the metal, *e.g.*, in the case of Ag, Cu, Al, or Ga. On precious metals like Au or Pt the contact resistance was sufficiently low and ohmic.

The Hall voltage of a sandwich type sample as used here, consisting of two conductors with different resistivities ρ_1 and ρ_2 and thicknesses d_1 and d_2, can be derived straightforwardly from elementary considerations of the Hall effect (31) and is given by

$$V^H_{1+2} = -\frac{i \cdot B}{e_0} \frac{\left(\frac{\rho_1^2}{n_2 d_1} + \frac{\rho_2^2}{n_1 d_2}\right)}{\left(\frac{\rho_1}{d_1} + \frac{\rho_2}{d_2}\right)^2 d_1 d_2} \qquad [1]$$

where i is the current, B the magnetic field strength, e_0 the electronic charge, and n_1 and n_2 the carrier densities. The indices 1 and 2 refer to Pt and PbO_2, respectively. Since the Hall voltage of one of the layers, 1, can be measured separately, a simplification is possible. If the same current and magnetic field strength are applied to measure the Hall voltage of layer 1, V^H_1, and of both layers together, V^H_{1+2}, the Hall coefficient of layer 2, $\mathcal{R}^H_2$, is given by the relation

$$\mathcal{R}^H_2 = \frac{-d_2}{B \cdot i}\{(1+\gamma)^2 V^H_{1+2} - \gamma^2 V^H_1\} \qquad [2]$$

γ is the ratio of the resistances, R_2/R_1, which was in most cases smaller than 1. The carrier concentration, n_2, and the mobility, μ_2, can be calculated from the Hall coefficient in the usual way

$$n_2 = \frac{1}{e_0 |\mathcal{R}^H_2|}; \mu_2 = \frac{|\mathcal{R}^H_2|}{\rho_2} \qquad [3]$$

Optical measurements.—As the substrate electrode, commercial tin dioxide coated glass was used (resistance 15 ohms/in.^{2}). Deposition of PbO_2 was carried out in the same way as on Pt, following the nucleation pretreatment described above. The thickness of the PbO_2 films was 3000Å.

Transmission spectra of the systems α-PbO_2-SnO_2-glass, β-PbO_2-SnO_2-glass, and SnO_2-glass were determined in the wavelength interval from 4600 to 15,000Å with a Cary 16 spectrophotometer. The transmission of PbO_2 was calculated from the ratio

$$\frac{\text{transmission of } PbO_2\text{-}SnO_2\text{-glass}}{\text{transmission of } SnO_2\text{-glass}}$$

The error involved by not taking into account reflections at the various interfaces is low in the spectral region in which the transmission of PbO_2 is low.

Results

Electrical measurements.—In Fig. 2, the resistivity of a β-PbO_2 film is plotted against the film thickness.

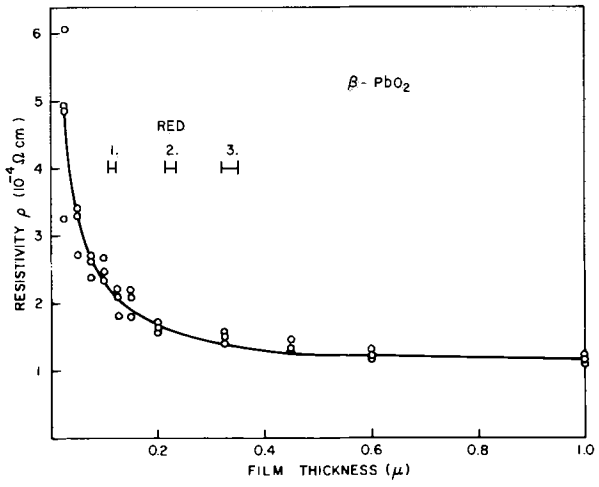

Fig. 2. Resistivity of β-PbO_2 vs. film thickness. The positions of the first three red interference colors are indicated.

The form of the curve is characteristic of metal or semiconductor films. At low values of the film thickness, surface scattering or inhomogeneities in the film are mainly responsible for a higher resistivity. With increasing thickness the resistivity approaches a nearly constant value. In the present case, deposition was continued up to a thickness of 50μ. The resistivity increased slightly but was no more than a factor of 1.2 higher than at 1μ. This shows that the properties of PbO_2 films in the thickness range studied here are very similar to bulk properties of electrodeposited PbO_2. Resistivity values of electrodeposited β-PbO_2 bulk samples reported in the literature (1-3) are mostly close to the value of 10^{-4} ohm-cm obtained here. The films show bright interference colors which can be seen up to the fifth order. The approximate positions of the first three red interference colors are marked in Fig. 2.

A comparison of data obtained on α- and β-PbO_2 is given in Fig. 3. The resistivity of α-PbO_2 films is almost one order of magnitude higher. This is mainly the result of a lower electron mobility in α-PbO_2, which overcompensates the effect of a higher electron concentration in this phase. It may be noted, in the right of Fig. 3, that the electron concentration in α-PbO_2 is only about a factor of 20 smaller than the concentration of lead ions in the lattice.

In general, these curves are fairly reproducible under different plating conditions. In the case of α-PbO_2, a variation of the pH between 4 and 6 and a variation

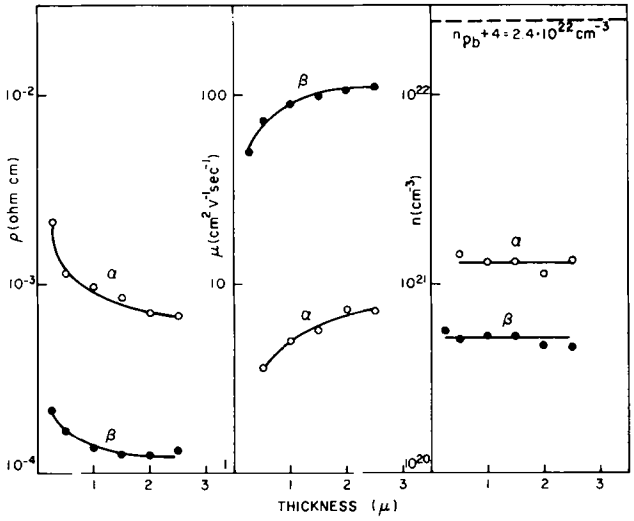

Fig. 3. Resistivity, mobility, and carrier density of α- and β-PbO_2 vs. film thickness.

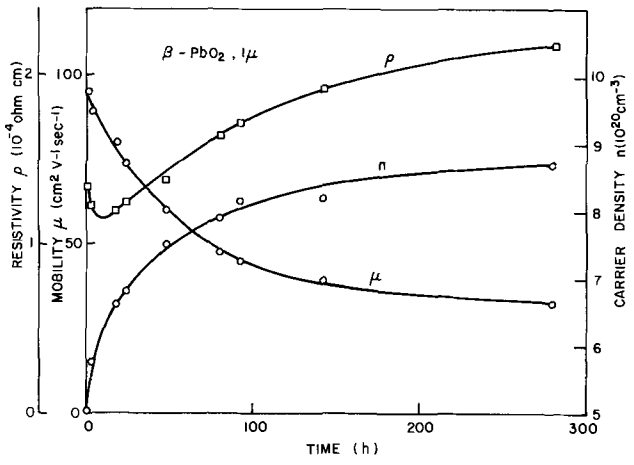

Fig. 4. Changes of resistivity, mobility, and carrier density of a 1μ thick β-PbO_2 film with time in air at room temperature.

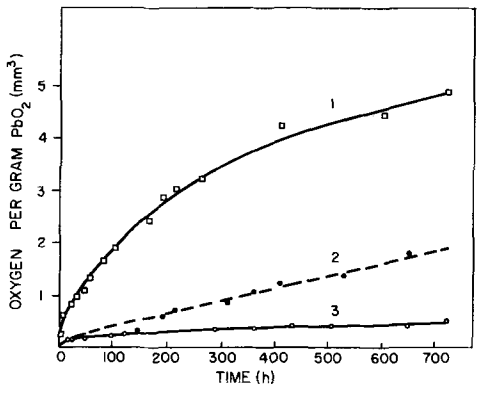

Fig. 5. Loss of oxygen from PbO_2 vs. time at room temperature. 1: β-PbO_2 in air saturated with water. 2: β-PbO_2 in dry air. 3: α-PbO_2 in air saturated with water.

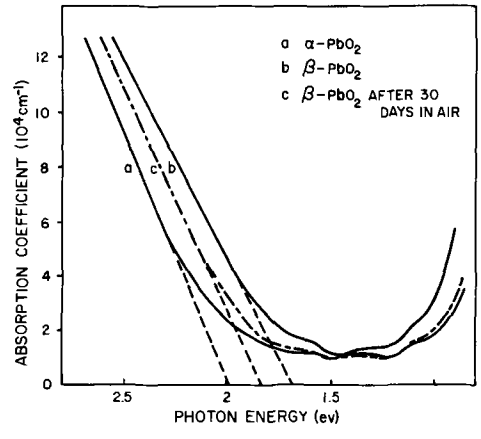

Fig. 6. Absorption coefficient of α- and β-PbO_2 vs. photon energy

of the lead perchlorate concentration between 20 mM/l and 2 M/l had only a small influence on the positions of these curves, no more than 20%. The influence of the anion in this pH range is of the same magnitude. Besides perchlorate, nitrate and acetate were also used. In acid solutions, the conditions under which a pure β-PbO_2 deposit is obtained are critical, as was described above. An increase in the lead ion concentration or a lowering of the pH caused the formation of some α-PbO_2 in the deposit. The resistivity of the mixed films was slightly higher than of the pure β-PbO_2 films.

The electrical measurements described to this point were carried out within an hour after deposition of the films. With longer storing at room temperature in air the properties, mainly of the β-PbO_2 films, change, as is shown in Fig. 4. The carrier concentration in a 1μ thick film increases from 5×10^{20} to 8.7×10^{20} cm^{-3} after 12 days. The mobility decreases by a factor of 3 in the same time. X-ray diffraction studies of the samples after this time showed no changes in the crystalline structure.

The increase in the carrier density suggests that a change in stoichiometry in the direction of a lower oxygen content or by the incorporation of hydrogen occurs under these conditions as will be discussed below. The amount of oxygen which corresponds to the observed increase in carrier density is large enough to be detected by simple manometric techniques if larger quantities of PbO_2 are taken. For this purpose, several grams of α- and β-PbO_2 were deposited under the conditions described above, powdered, and placed into a Summerson differential manometer. To study the effect of humidity, the experiments were carried out in dry air and in air saturated with H_2O. In the latter case the wells in the two reaction flasks of the manometer were filled with water. The results are shown in Fig. 5. Both modifications lose oxygen; however, α-PbO_2 far less than β-PbO_2. Humidity causes a considerable increase in the amount of liberated oxygen. Under humid conditions, 5 mm^3 O_2 per gram β-lead dioxide are obtained in 30 days. This amount is equivalent to a change in carrier concentration of $1.7 \times 10^{18} cm^{-3}$, if it is assumed that each liberated oxygen atom provides two free electrons. This increase in electron concentration is far less than that observed by Hall effect measurements on a β-PbO_2 film (Fig. 4). The reason for this difference is probably the larger size of the crystallites used for the manometric measurements, which results in a lower decomposition rate because of the smaller surface to volume ratio.

Optical measurements.—In Fig. 6, absorption coefficients of α- and β-PbO_2 films are plotted as a function of the photon energy. The absorption edges of α- and β-PbO_2 (curves a and b) differ by 0.2-0.3 eV. Extrapolation to zero absorption indicates values of the "optical" band gap, ΔE_0, of 2.0 and 1.7 eV for α- and β-PbO_2, respectively. At photon energies below 1 eV free electron absorption begins. This type of absorption is stronger in the α-modification which has the higher carrier density. Since free electron absorption also occurred in the SnO_2 substrate, the measurements could not be extended to lower photon energies. The waves in the curves in the region of low absorption are due to interference effects.

The values of ΔE_0 obtained here are not identical with the band gap, ΔE_g, of intrinsic PbO_2. As a result of the high electron concentration, the energy states in the bottom of the conduction band are occupied and electrons have to be excited to higher energy levels for absorption to occur. The shift in photon energy due to this effect is, for a degenerate semiconductor (17)

$$\Delta(h\nu) = \Delta E_0 - \Delta E_g \cong \left(1 + \frac{m_e^*}{m_h^*}\right) \cdot E_f \qquad [4]$$

where m_e^*, m_h^* are the effective masses of electrons and holes and E_f the Fermi energy. The Fermi energy of an ideal degenerate Fermi gas is

$$E_f = \left(\frac{3}{\pi}\right)^{2/3} \frac{h^2}{8m_e^*} \cdot n^{2/3} \qquad [5]$$

In β-PbO_2, a shift of the absorption edge could be observed when the sample was exposed to air for several days (curve c in Fig. 6). The experiment described previously showed that under these conditions an increase in carrier concentration occurs. With the two pairs of values of n and ΔE_0, a rough estimation of the effective electron mass, m_e^*, in β-PbO_2 is possible from Eq. [4] and [5]. Using values obtained shortly after deposition and 30 days later

$$n_1 = 5 \times 10^{20}\,cm^{-3}; \quad \Delta E_{0.1} = 1.7\,eV$$

$$n_2 = 9 \times 10^{20}\,cm^{-3}; \quad \Delta E_{0.2} = 1.84\,eV$$

and assuming that $m_e^* << m_h$,* an effective electron mass of 0.8 m_o is obtained. This leads, according to Eq. [4], to a band gap for intrinsic β-PbO_2 of $\Delta E_g = 1.4$ eV.

No change of the absorption curve with time could be detected on α-PbO_2. However, if the same effective mass is used as in β-PbO_2, a value of $\Delta E_g = 1.45$ eV is obtained.

These results are similar to the values of the band gap determined by Lappe (9) (1.5 eV) and Shapiro (18) (1.85 eV). A different value of 4.45 eV was obtained by Arai (19). The author described the method by which he prepared PbO_2 films as similar to the spraying technique commonly used for preparing conductive SnO_2 films. Since the substrate temperatures usually applied in this technique are between 500° and 800°C (20), these films may have contained lower lead oxides, because PbO_2 decomposes at temperatures above 270°C (21). This assumption is supported by the fact that the films were insulating.

Discussion

Lead dioxide belongs to a group of n-type metal oxides which show high electron mobilities. Other oxides of this type are ZnO, In_2O_3, and SnO_2. The electronic configurations of these compounds indicate that the conduction bands are formed from s-orbitals of the metallic species rather than from unfilled inner shells as, for example, in transition metal oxides. The mobilities in oxides of the latter type are, in general, several orders of magnitude smaller. The conduction band in PbO_2 arises, to a first approximation, from the 6s levels of Pb^{4+} and the valence band from the 2p levels of O^{2-}.

The presence of free electrons in PbO_2 can be due to the following effects: deviation from stoichiometry, incorporation of hydrogen, and presence of other impurities.

It is well established that lead dioxide exists in a wide range of nonstoichiometry, which was determined by Katz (22) as $PbO_{1.87\text{-}2.00}$. Other authors give different values for the lower limit of the composition which vary between $PbO_{1.95}$ (23, 24) and $PbO_{1.66}$ (25). It is not certain whether the nonstoichiometric composition is due to interstitial lead ions or to oxygen vacancies. The observations that the density of electrodeposited PbO_2 is lower than the x-ray value (1) and that oxygen appears to have a high mobility in PbO_2 (26) promote the assumption that oxygen vacancies are predominant.

Rüetschi and Cahan (4) suggested that free electrons in PbO_2 may be due in part to OH groups substituting for oxygen in the lattice. This is supported by the observation that an appreciable amount of bound hydrogen is found in electrodeposited PbO_2 (4, 5, 6, 15). A similar role of hydrogen is known in other oxide semiconductors, *e.g.*, in ZnO (27). The presence of hydrogen is, however, not necessary to explain high electron concentrations. This was shown by experiments with sputtered PbO_2 films by Lappe (9), which did not contain hydrogen and also had a carrier density of 10^{21} cm^{-3}.

The influence of impurities other than hydrogen is presumably small, since high concentrations are necessary to cause significant relative changes in the carrier concentration. For the same reason, doping of PbO_2 with 3- or 5-valent ions will not have a similar influence on the conductivity as, for example, in SnO_2.

It is in the frame of the present investigations not possible to decide whether electrons in electrodeposited PbO_2 are due mainly to nonstoichiometry or to incorporation of hydrogen. The carrier concentration of 1.4×10^{21} cm^{-3} found in the α-PbO_2 films corresponds to a composition of $PbO_{1.971}$ if electrons are due only to ionized oxygen vacancies, and to $PbO_{1.942}(OH)_{0.058}$ if they are due only to OH-groups substituting for oxygen. Chemical analytical methods are probably not sufficiently exact to distinguish between the two cases. In particular, the determination of hydrogen involves a large error (5), and it is difficult to distinguish between hydrogen bound in OH-groups in the lattice and hydrogen which is part of adsorbed water.

The decomposition of electrodeposited PbO_2 at room temperature can be interpreted in terms of the generation of oxygen vacancies or the incorporation of hydrogen due to oxidation of water. In both cases, oxygen is evolved and the electron concentration increased. The over-all reactions may be written as

$$(2\,O^{2-})_{latt} \rightarrow (2\,\square\,O + 4e^-)_{latt} + (O_2)_g \qquad [a]$$

$$(4\,O^{2-})_{latt} + 2H_2O \rightarrow (4\,OH^- + 4e^-)_{latt} + (O_2)_g \qquad [b]$$

The result that moisture in the air increases the decomposition rate makes reaction [b] more probable. However, a similar effect may result if adsorbed water increases the rate of one step of reaction [a].

The different electron mobilities in α- and β-PbO_2 are the result of several factors. The lower mobility in the α-PbO_2 films may be due in part to the smaller size of the crystallites in this modification. The average size of the α-PbO_2 crystallites was about 2000Å, compared to 5000Å for the β-modification. There is certainly also an influence of the higher carrier density in α-PbO_2, since this corresponds to a larger number of lattice defects at which electrons are scattered. Since the α-PbO_2 films have a high degree of orientation [the (100) axis is perpendicular to the substrate], an anisotropy of the mobility in α-PbO_2 could also influence the results.

There is, finally, the influence of the different crystalline structures of α- and β-PbO_2. α-PbO_2 has the structure of columbite, which is orthorhombic and has the space group Pbcn (V_h^{14}). β-PbO_2 has the tetragonal rutile structure, which belongs to the space group P4/mnm (D_{4h}^{14}). It was shown first by Pauling and Sturdivant (28) that a close relationship exists between the two lattices. In both cases, each metal ion is in the center of a distorted octahedron. The essential difference is in the way in which the octahedra are packed, as is illustrated in Fig. 7. In β-PbO_2, neighboring octahedra share opposite edges, which results in the formation of linear chains of octahedra. Each chain is connected with the next one by sharing corners. In α-PbO_2, neighboring octahedra share nonopposing edges in such a way that zig-zag chains are obtained. Each chain is connected with the next one also by sharing corners. The oxygen positions have actually been determined only in the case of β-PbO_2 (29), however, the Pb-O distances are thought to be the same in both modifications (30). Since the difference in the crystal structures results mainly from the

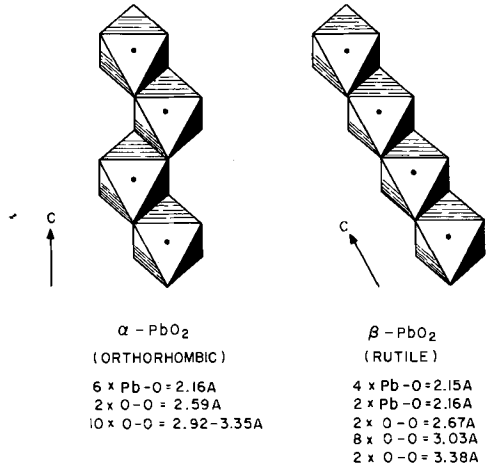

Fig. 7. Packing of oxygen octahedra in α- and β-PbO_2. Lead-oxygen and oxygen-oxygen distances as determined by (29) and (30).

different packing of octahedra of similar dimensions, large differences in the band structure and mobility are not expected.

Acknowledgments

The author wishes to thank U. B. Thomas and P. C. Milner for helpful discussions and interest in this work. He is also indebted to H. C. Montgomery and J. D. E. McIntyre for provision of facilities and to G. W. Kammlott for the careful accomplishment of all the x-ray, electron diffraction, and electron microscopic work involved in this study.

Manuscript received March 14, 1969. This was Paper 362 presented at the Montreal Meeting, Oct. 6-11, 1968.

Any discussion of this paper will appear in a Discussion Section to be published in the June 1970 JOURNAL.

REFERENCES

1. W. Palmaer, *Z. Elektrochem.*, **29**, 415 (1923).
2. A. Kittel, "Beiträge zum Mechanismus der elektrischen Leitung in PbO_2 und Se," Diss., Prag, Czech., 1944 [Some results of this work are described in ref. (4)].
3. U. B. Thomas, *This Journal*, **94**, 42 (1948).
4. P. Rüetschi and B. D. Cahan, *ibid.*, **105**, 369 (1958).
5. N. E. Bagshaw, R. L. Clarke, and B. Halliwell, *J. Appl. Chem.*, **16**, 180 (1966).
6. J. A. Duisman and W. F. Giauque, *J. Phys. Chem.*, **72**, 562 (1968).
7. W. B. White and R. Roy, *J. Am. Ceram. Soc.*, **47**, 242 (1964).
8. I. A. Aguf, A. I. Rusin, and M. A. Dasoyan, Zashitn. Metal. i Issled. v Obl. Elektrokhim., Akad. Nauk SSSR, Otd Obshch. i Tekhn. Khim., Sb. Statei 1965, pp. 328-333.
9. F. Lappe, *J. Phys. Chem. Solids*, **23**, 1563 (1962).
10. A. I. Zaslavskii, Yu. Kondrashev, and S. S. Tolkachev, *Dokl. Akad. Nauk*, **75**, 559 (1950).
11. M. Fleischmann and M. Liler, *Trans. Faraday Soc.*, **54**, 1370 (1958).
12. P. Rüetschi and B. D. Cahan, *This Journal*, **104**, 406 (1957).
13. H. Bode and E. Voss, *Z. Elektrochem., Ber. Bunsenges. Phys. Chem.*, **60**, 1053 (1956).
14. D. Spahrbier, "Zum elektrochemischen Verhalten der Bleidioxydelektroden," Diss., Stuttgart, 1960.
15. J. Giner, A. B. Gancy, and A. C. Makrides, "Preparation and Characterization of Lead Dioxide Electrodes for Reserve Batteries," Rep. No. 265, Harry Diamond Laboratories, 1967.
16. H. B. Mark and C. W. Vosburgh, *This Journal*, **108**, 615 (1961).
17. E. Burstein, *Phys. Rev.*, **93**, 632 (1954).
18. I. P. Shapiro, *Optika i Spectroskopiya*, **4**, 256 (1958).
19. T. Arai, *J. Phys. Soc. Japan*, **15**, 916 (1960).
20. R. W. Berry, P. M. Hall, and M. T. Harris, "Thin Film Technology," p. 339, D. van Nostrand Co., Inc., Princeton (1968).
21. E. M. Otto, *This Journal*, **113**, 525 (1966).
22. T. Katz, *Ann. Chim.*, **5**, 5 (1950).
23. G. Butler and J. L. Copp, *J. Chem. Soc.*, **145**, 725 (1956).
24. A. Byström, *Arkiv Kem. Min. Geol.*, **20A**, 1 (1945).
25. M. LeBlanc and E. Eberius, *Z. Phys. Chem.*, **A160**, 69 (1932).
26. B. N. Kabanov, E. S. Weisberg, I. L. Romanova, and E. V. Krivolapova, *Electrochim. Acta*, **9**, 1197 (1964).
27. D. G. Thomas in "Semiconductors," p. 304, N. B. Hannay, Editor, Reinhold Publishing Corp., New York (1960).
28. L. Pauling and J. H. Sturdivant, *Z. Krist.*, **68**, 239 (1928).
29. J. Leciejewics and I. Padlo, *Naturwissenschaften*, **49**, 373 (1962).
30. A. I. Zaslavskii and S. S. Tolkachev, *Z. Fiz. Khim. SSSR*, **26**, 743 (1952).
31. E. H. Putley, "The Hall Effect and Semiconductor Physics," Dover Publications, Inc., New York (1960).

Active and Passive Corrosion States in the High-Temperature Aqueous Corrosion of Mild Steel

John B. Moore, Jr.,[1] and Robert L. Jones*

Naval Research Laboratory, Washington, D. C.

ABSTRACT

In static high-temperature (300°C) corrosion tests of mild steel in dilute NaOH solutions, both the corrosion rate and morphology of the generated oxide film were observed to vary in a reproducible and presumably correlatable fashion as the NaOH concentration increased. A transitory corrosion rate minimum was found *circa* 2 g/l NaOH; there was at this same point a change in the structure of the oxide film, with a compact, randomly oriented, apparently continuous film giving way to a crystallographic surface oxide as the critical concentration was exceeded. The activation energy for corrosion differed depending on which oxide type prevailed, being 5-8 kcal/mol for the noncrystallographic oxide and 16 kcal/mol for the crystallographic. The transformation is thought to be basically a transition between passive and active corrosion states.

Although alkalization of the feed water is generally found to be beneficial in the operation of steam generating boilers (1), actually very little is known of the specific effects of this treatment on the corrosion processes occurring within the boiler. One discernible result of raising the feed water pH is the growth of larger crystallites in the oxide film on the boiler's interior, and it has been thought that these larger crystallites may provide increased corrosion protection because they are more resistant to erosion by the flowing streams present in a dynamic boiler system. Berl and Van Taack's research (2) suggests that alkalization has effects beyond just this, however, for they found that the corrosion suffered by mild steel in 310°C NaOH solution was relatively independent of alkali concentration up to about 0.7 g/l, at which point a rather sharp, localized reduction in corrosion was observed. The corrosion rate subsequently rose again, increasing smoothly with concentration for

* Electrochemical Society Active Member.
[1] Student summer employee. Present address: Department of Physiological Chemistry, Johns Hopkins School of Medicine, Baltimore, Maryland.

solutions up to 200 g/l NaOH. This region of minimum corrosion was later reinvestigated by Bloom and coworkers (3) who confirmed its existence. Their longer term studies revealed, however, that the minimum, while real, appeared to be only transitory, and that after 25 days the corrosion rate increased monotonically with pH from zero concentration NaOH onward.

Recent work at this laboratory (4) indicated that the corrosion rate of steel in high-temperature aqueous media may be related to the morphology of the oxide film concurrently produced, and that the rate data are at least partially understandable in terms of certain transitions which occur in the oxide film with time. To test this notion further, and perhaps to elucidate the pH dependency of the corrosion of mild steel in high-temperature alkaline waters, experiments were undertaken to determine both corrosion rates and oxide film morphologies for specimens at 300°C in NaOH solutions with concentrations spanning both sides of the corrosion minimum.

Experimental

The rates of oxide film formation were measured using a hydrogen effusion technique devised by Bloom and Krulfeld (5). With this method, the test specimen is a sealed capsule which is filled completely with the solution under study. The corrosion reaction takes place on the capsule interior, and its progress is monitored by measuring the hydrogen which diffuses through the hot capsule wall, that hydrogen having originated in a reaction which can be written over all as

$$3Fe + 4H_2O \rightarrow Fe_3O_4 + 4H_2$$

Our capsules were fabricated and filled as described previously (5). Simple vacuum vessels as shown in Fig. 1 were used to measure the rate of hydrogen evolution. The working volume of an individual vessel runs about 32 cm^3 and the interior area of a capsule about 12.5 cm^2 so that the growth of 100Å of oxide film corresponds to a pressure increase within the vessel of 0.85 Torr. The use of a cathetometer allows film growth of as little as 20Å to be readily detected. A constant voltage transformer was used as the power source for the block oven, and the oven temperature remained constant to ±1-2°C over a two-week run.

As the corrosion rate data were being accumulated, specimen capsules were withdrawn at appropriate times and the oxide films on their interiors detached and examined by electron microscopy, either directly by observation of the film itself or indirectly by observation of replicas of the upper oxide surface. The microscopy specimens were prepared as previously described (4).

The seamless mild steel tubing used here was 0.25 in. OD with 0.022 in. wall thickness and contained 0.15% C, 0.09% Si, 0.66% Mn, 0.22% Cr, 0.09% Ni, 0.026% S, 0.011% P, and 0.013% N. Pretreatment consisted of degreasing in trichloroethylene and then duPont Freon TF solvent, followed by vacuum annealing at 875°C and 10^{-5} Torr for 1 hr. The annealed specimens were stored in a closed container over anhydrous $CaSO_4$.

The NaOH solutions were prepared fresh in Pyrex glassware from A.R. NaOH and distilled water, with the less concentrated solutions being made up by dilution. The solution pH was measured before and after each run to determine any change in basicity.

Results

In Fig. 2, we have plotted curves showing total corrosion as a function of NaOH concentration from 0.006 to 10.24 g/l NaOH (approximately 9.5-13.3 pH at 25°C) for progressively increasing times at 300°C. A minimum corrosion region is found once again, although the minimum here appears to be slightly displaced, falling at 2-4 g/l rather than at 0.7 g/l as found by Berl and Van Taack. The points in Fig. 2 represent the arithmetic means of data from groups of 4-5 capsules, where individual capsules could vary by ±10% from the mean for a 312-hr run. Some uncertainty in the positioning of the corrosion minimum therefore exists; however in each of three separate runs, the minimum fell sufficiently closer to 2-4 than 0.7 g/l as to suggest that something more than experimental error may be involved.

With time, the corrosion rates for the individual NaOH solutions change and they become monotonic functions of concentration, *e.g.*, at 204 hr, the instantaneous rates are 0.58, 1.1, 1.2, 1.7, 1.9, 2.3, 2.8, and 3.3 $\mu g\ Fe_3O_4\ cm^{-2}\ hr^{-1}$ for the concentrations 0.006 through 10.24 g/l, respectively. This concentration-dependent progression of instantaneous corrosion rates is observed from about 200 hr onward, and it is evidently a persistent effect since Bloom has found the same trend in capsules heated 25 days. The inflections shown in Fig. 2 would therefore ultimately disappear

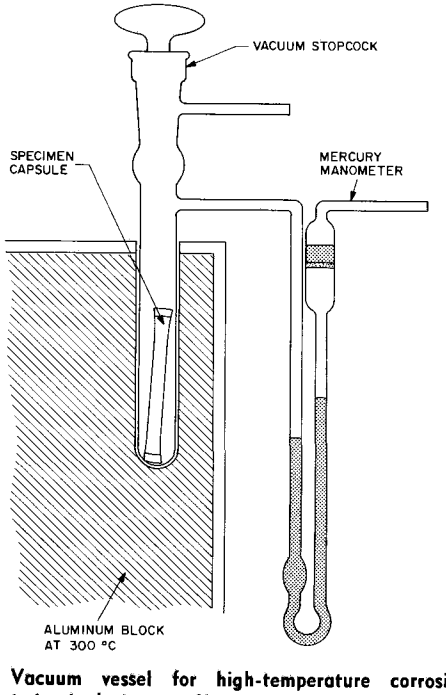

Fig. 1. Vacuum vessel for high-temperature corrosion rate measurements by the hydrogen effusion method.

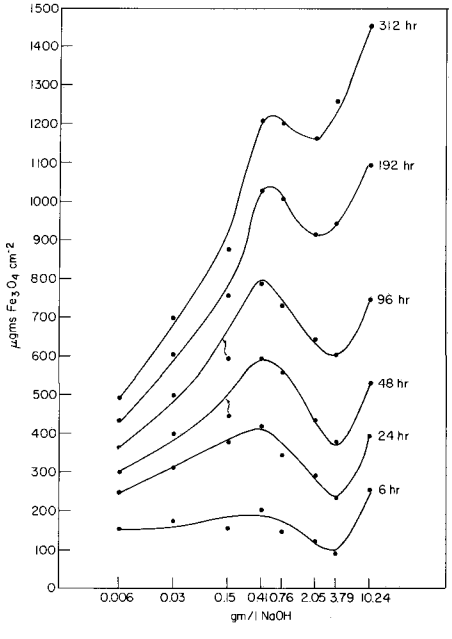

Fig. 2. Aqueous corrosion of mild steel as a function of NaOH concentration with increasing time at 300°C.

entirely and measurements taken at longer time intervals would fail to show the corrosion minimum either in terms of total corrosion or instantaneous corrosion rate.

Electron microscopy of oxide films grown during these runs shows that there is a distinct difference in the oxide morphology from one side of the minimum to the other. With 10.24 and 3.79 g/l NaOH solutions, the oxide film in its earlier stages of formation is strongly oriented and apparently in epitaxial relationship with the various substrate grains, *i.e.*, it is crystallographic (Fig. 3a). This tendency to orientation appears to persist, moreover, through the development of the film. Although crystals of considerable size come into being with time (Fig. 3b), the oxide film over the rest of the metal surface remains comparatively thin and can be seen to consist of small rectilinear crystallites. These crystallites continue to be well oriented with the orientation differing from point to point on the surface, an indication that the growth of the innermost oxide is still influenced by epitaxial forces from the substrate.

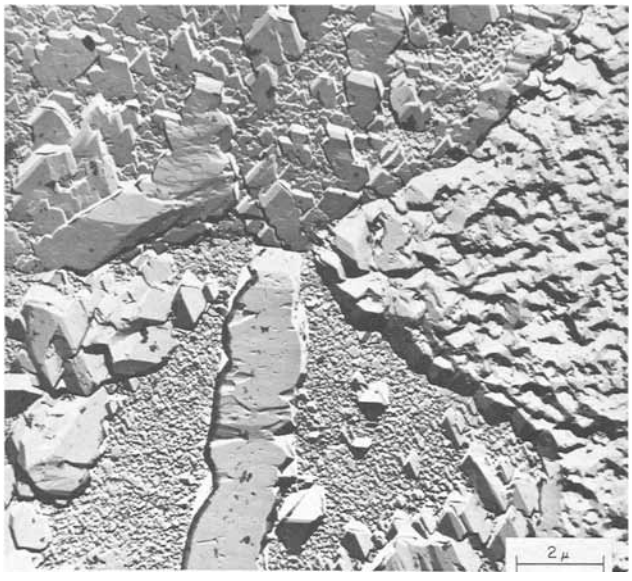

Fig. 3c. 0.76 g/l NaOH, 4 hr at 300°C

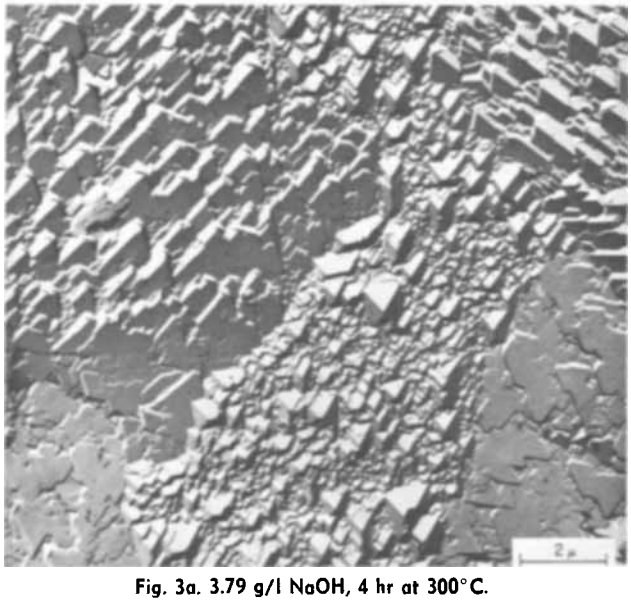

Fig. 3a. 3.79 g/l NaOH, 4 hr at 300°C.

On the other hand, while the oxide corrosion film also grows at first with epitaxial orientations in 0.76 g/l and lower solutions, it soon undergoes a degeneration, as described previously (4), to an apparently duplex film structure consisting of a thin, continuous innermost layer of very small, randomly oriented crystallites partially covered in turn by much larger, faceted crystals. The innermost film is noncrystallographic; it is not oriented to the substrate and its appearance is the same at every point at which it is visible on the metal surface. In Fig. 3c, three different orientations of the oxide film (as identified by the morphology of the residual oriented crystals) are shown at an intermediate state of degeneration. The orientation at the bottom of Fig. 3c is almost completely transformed, the orientation at the upper left partially transformed, while the oxide at the right remains virtually unchanged. This latter oxide is in the (001) orientation (4) which evidently represents one of the most stable epitaxial relationships under these conditions since it resists transformation longest. Eventually all of the oriented oxide is transformed, however, and the resultant oxide film has the structure shown in Fig. 3d. Note that the base oxide film has a distinctive pebblelike texture which is easily identified and quite different to that seen in

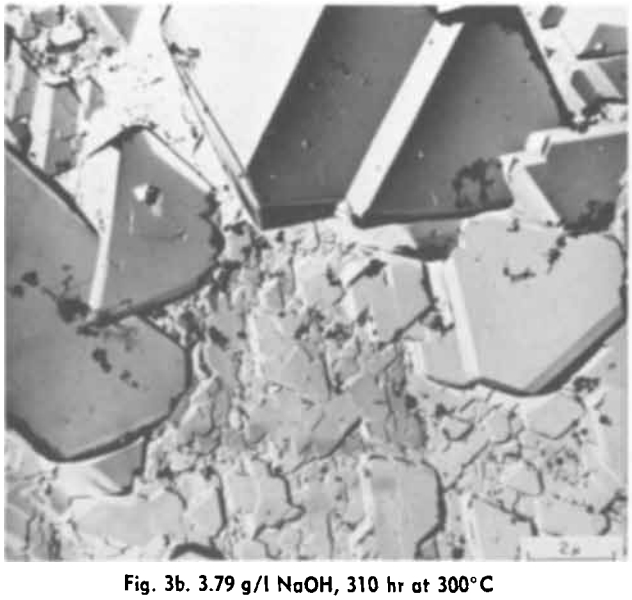

Fig. 3b. 3.79 g/l NaOH, 310 hr at 300°C

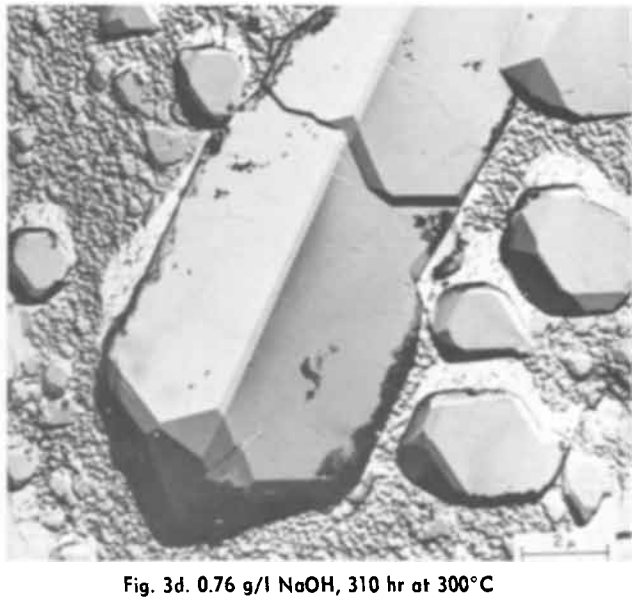

Fig. 3d. 0.76 g/l NaOH, 310 hr at 300°C

Fig. 3b. The NaOH concentration representing the point of transition between these two modes of film development lies evidently near 2.05 g/l NaOH, where degeneration of the epitaxial oxide occurs slowly. Oxide films at this concentration are still strongly oriented after 4 hr at 300°C, although they do eventually develop the duplex film structure, being completely transformed by 96 hr.

In very dilute NaOH, *e.g.*, 0.030 g/l NaOH, which gives approximately pH 11 at 25°C, degeneration to the duplex oxide structure does not proceed to any great extent, at least over our periods of investigation. [This is contrary to our earlier findings with pH 11 LiOH (4), where the transformation went freely.] Areas of randomly oriented base film are found, but much the greater part of the oxide remains oriented for both short (Fig. 3e) and long (Fig. 3f) heating intervals. The crystallographic nature of the oxide here is not as apparent from its morphology as it is with oxides produced in more concentrated solutions, but selected area diffraction, the final criterion, readily confirms that in both instances the oxide in question is strongly oriented. Oxide films grown in capsules containing just water are also crystallographic and virtually identical in appearance to Fig. 3e and 3f, except that evidences of the fine-grained base film are even more sparse.

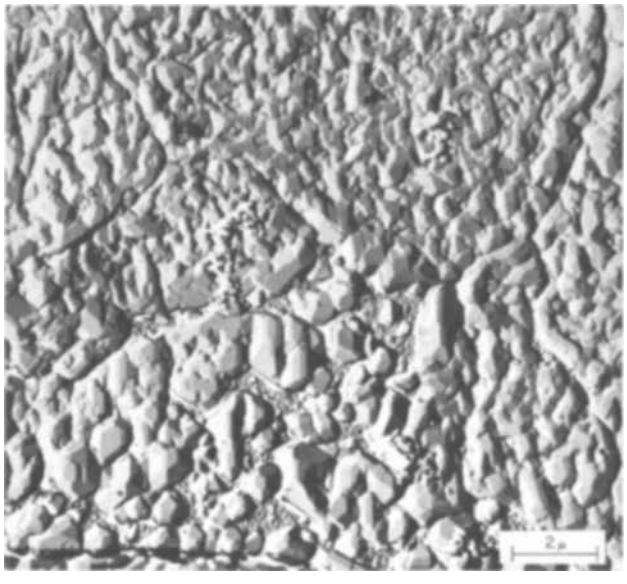

Fig. 3e. 0.03 g/l NaOH, 4 hr at 300°C

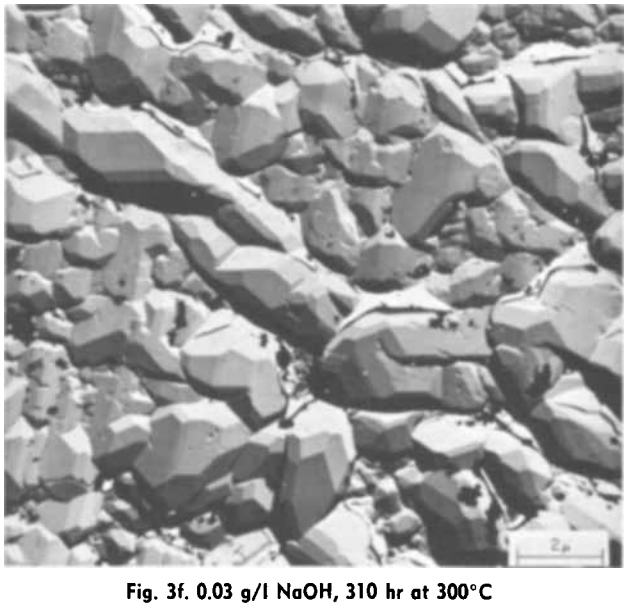

Fig. 3f. 0.03 g/l NaOH, 310 hr at 300°C

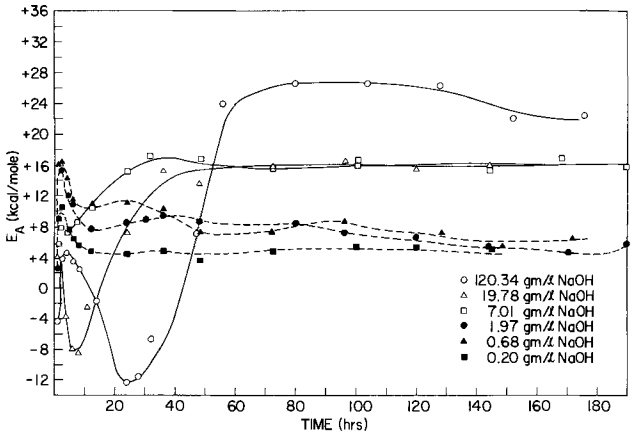

Fig. 4. Time dependence of activation energies (E_a) for corrosion in NaOH solutions above and below the corrosion rate minimum concentration.

On the assumption that the different oxide morphologies reflect a change in the oxide growth mechanism at the corrosion minimum point, we measured activation energies (E_a) of corrosion in NaOH solutions on both sides of the corrosion minimum to see if a simultaneous change in activation energy could be detected. The results are shown, plotted as a function of time, in Fig. 4. These are apparent activation energies only; they were calculated from a plot of the logarithm of the reaction rate at a given time *vs.* $1/T$ for three different temperatures (nominally 250°, 275°, and 300°C, in the main). The linearity of the points in the individual plottings was not particularly good, and the energy values obtained should probably be considered semiquantitative and suited mostly for purposes of comparison. Nonetheless, although there are early time fluctuations, a trend becomes discernible after about 72 hr in the activation energies in Fig. 4. As the NaOH concentration increases successively from 0.20 to 0.68 to 1.97 g/l, that is, as we cross the concentration range yielding the noncrystallographic duplex oxide film, the activation energies remain relatively constant at 5-8 kcal/mol. The next factor of 3 increase, however, brings us past the corrosion minimum point into the region where the crystallographic oxide predominates, and the activation energy jumps to 16 kcal/mol. A final concentration increase to 19.78 g/l yields an almost identical 16 kcal/mol value. Presumably then, the apparent activation energy for corrosion in NaOH solutions through this concentration range is not a first order function of the hydroxide concentration, but depends primarily on whether or not the point of transition for the oxide growth mechanism has been exceeded.

The activation energy with 120 g/l NaOH was measured so that comparison could be made with an energy value reported earlier by Potter and Mann (6) for 13% NaOH at 250°-355°C; their figure was derived from an Arrhenius plot of parabolic rate constants and was originally given as 15 ± 2 kcal, but subsequently corrected to 30 ± 2 kcal (7). If our rate data for 120 g/l NaOH after say 80 hr at temperature are recalculated, assuming parabolic kinetics, then an E_a of about 28 kcal is obtained (with the usual reservation that the linearity of the points is not good). However, the significance of this agreement is obscured by the fact that the corrosion behavior of our specimens was appreciably different here than with the less concentrated solutions (see Table I). The capsules containing 120 g/l NaOH corroded very rapidly and with nearly equal rates for all three temperatures up to about 24 hr, at which time the corrosion in the 275° and 300°C capsules dropped off sharply, and then settled down to rates showing an approximately appropriate temperature dependency. The 250°C capsules continued to corrode at a disproportion-

Table I. Corrosion rate data at 72 hr for activation energy calculation

Conc. NaOH, g/l	Temp, °C	Corr, $\mu g\text{-}Fe_3O_4/cm^2$	Corr rate, $\mu g\text{-}Fe_3O_4/cm^2\text{-}hr$	Temp, °C	Corr, $\mu g\text{-}Fe_3O_4/cm^2$	Corr rate, $\mu g\text{-}Fe_3O_4/cm^2\text{-}hr$	Temp, °C	Corr, $\mu g\text{-}Fe_3O_4/cm^2$	Corr rate, $\mu g\text{-}Fe_3O_4/cm^2\text{-}hr$	Temp, °C	Corr, $\mu g\text{-}Fe_3O_4/cm^2$	Corr rate, $\mu g\text{-}Fe_3O_4/cm^2\text{-}hr$
0.20	248	349	2.15	276	507	2.81	300	555	2.81	—	—	—
0.68	257	319	2.40	—	—	—	298	529	3.62	329	1090	6.15
1.97*	248	226	2.01	276	353	3.13	300	474	4.01	—	—	—
7.01	257	281	1.40	—	—	—	297	466	3.16	328	1100	8.66
19.78	248	429	1.03	276	434	2.58	300	594	4.13	—	—	—
120.34*	248	2360	0.39	276	2060	2.09	300	2320	3.99	—	—	—

* At 80 hr.

ately high rate for perhaps another 24 hr before dropping to what appears, in context of Table I, an abnormally low rate. The result of this is that at 80 hr, when the "steady state" has been reached, the total corrosion is actually greater at 250° than 300°C.

Discussion

We concluded earlier (4) that the thin, pebble-textured base film of the duplex oxide structure is a high-temperature passive oxide film which exists in an equilibrium state of formation and dissolution, and that the large, faceted crystals occurring on its upper surface are formed by precipitation of iron species put into solution by that process. Our present experiments support this theory by showing that the stability range of this particular oxide morphology (from 0.006 to 2 g/l NaOH, or about 9.5 to 12.5 *p*H at 25°C) agrees with that predicted by Pourbaix (8) for passive iron oxides in aqueous media. That this is so even though our experiments were at 300°C whereas Pourbaix's calculations are based on 25°C thermodynamic data may indicate that the relative stabilities of the pertinent species are not extensively affected in going from 25° to 300°C. Beyond these concentration limits, *i.e.*, when the specimen is in the active corrosion state, the morphology of the oxide film is changed, its distinguishing feature now being that it is crystallographic.

West (9) and Hoar (10) have offered mechanistic reasons as to why the physical structure of the surface oxide should differ depending on whether the corroding metal is in the active or passive state. According to Hoar, a metal may corrode, as determined by prevailing electrochemical conditions within the system, either by direct reaction of water molecules adsorbed at the metal surface to form the oxide essentially *in situ* or by dissolution with the formation of metal ionic species which subsequently deposit as the least soluble salt or hydroxide. (At the temperatures involved in our experiments, any iron hydroxide would be converted to magnetite by the Schikor reaction.) The first process yields the so-called passive oxide film and it is noncrystallographic since the generating reaction is as likely to occur at one point on the metal surface as another. The fundamental step in the alternative process, however, is the removal of an ion from the metal lattice, a feat most easily accomplished at certain specific crystal sites, and so the corrosive attack here will tend to be crystallographic in nature (and presumably the deposited oxide films also). West postulates, on the other hand, that a noncrystallographic oxide is produced on a metal undergoing passivation when the rate-determining factor comes to be diffusion through the passivating oxide film itself.

Morphological changes consistent with a passive-active corrosion state transition have not been reported previously for oxide films on mild steel, although there have been findings in studies of stainless steel corrosion in high-temperature water which appear in accord with this hypothesis. Maekawa *et al.* (11) observed that AISI 304 stainless steel corroded in high-temperature deaerated water (less than 0.1 ppm O_2) with the formation of a "crystalline" oxide corrosion film, but in undeaerated water (approximately 5 ppm O_2) with the formation of a noncrystalline film. Moreover, they found, just as we have, that the corrosion rates were effected differently by temperature in the two circumstances. In deaerated water, the corrosion rate increased strongly from 200° to 300°C but then decreased as the temperature was raised further to 350°C. With undeaerated water, the temperature effect was considerably less, and there was no corrosion maximum, the rate increasing smoothly from 200° to 350°C. They identified the films by infrared adsorption measurements as consisting of magnetite and chromite in deaerated water (with the chromite content increasing at higher temperatures) and γ-Fe_2O_3 in undeaerated water.

A transformation of the surface oxide, perhaps similar to the one observed here, has been found by Nakayama and Oshida (12) during the early stages of oxidation of an 18-8 stainless steel in 300°C water containing 8 ppm O_2. They showed by electron diffraction that a corundum type oxide film was generated on the stainless steel in the initial heating but that this converted with further heating (within 24 hr) to a spinel-structured surface film. The film was not identified as γ-Fe_2O_3 however, as in the works cited above and below, Nakayama and Oshida concluding rather that the film was probably $NiO\cdot(Cr, Fe)_2O_3$ and/or $NiFe_2O_4$ because electron probe microanalysis showed it to contain nickel and chromium as well as iron. (Since these authors were not able to show quantitative stoichiometries, it seems possible that the film could still in fact be γ-Fe_2O_3 with the foreign elements being present in occlusions or by ion substitution.)

A noncrystallographic-crystallographic transition in the mode of oxide growth can be induced not only by the presence of oxygen but also by increased *p*H. Francis and Whitlow (13) found differing oxide morphologies on AISI 304 stainless steel in 300°C aqueous corrosion tests depending whether the oxide is grown in neutral or alkaline (*p*H 12) waters, the *p*H 12 oxide being, from their description, essentially crystallographic and the oxide grown at *p*H 7 noncrystallographic. Their diffraction measurements (14) indicated the noncrystallographic *p*H 7 film to be γ-Fe_2O_3 and the crystallographic *p*H 12 film to be a Fe_3O_4-type spinel.

In terms of passivation phenomena, our interpretation of these observations would be that (*i*) 304 stainless steel is brought from an active to passive corrosion state (although it corrodes appreciably at these temperatures even while "passive") by 5 ppm O_2 in neutral water (Maekawa *et al.*); (*ii*) stainless steel may corrode in water by the "active state" mechanism for some time (perhaps depending on how the specimen was prepared) before converting to the passive growth mode even when O_2 is present (Nakayama and Oshida); and (*iii*) a passive-active transition can also be produced by raising the solution *p*H beyond a certain upper limit, as the Pourbaix diagram for the iron-water system would predict (Francis and Whitlow). There is an apparent contradiction here though, since Francis and Whitlow find a passive oxide morphology under nominally the same experimental conditions (300°C, O_2-free water) in which Maekawa *et al.* re-

port an active-type surface oxide. These conditions represent a point very near the boundary between active corrosion and passivation (in Pourbaix diagram reference) however, and only very slight increases of *p*H or minute traces of oxidizing impurities would be required to bring the passivation found in Francis and Whitlow's studies. The particular composition of the steels used may also be a factor here since Leckie (15) has shown that the *p*H at which a stainless steel spontaneously passivates is a function of its composition. In general, with consideration of all that is involved in high-temperature aqueous corrosion experiments, it would not be expected that the point of transition between active and passive corrosion would be precisely reproducible in every instance. And it is probably not noteworthy therefore that the minimum in the corrosion *vs.* NaOH concentration curve seems to fall in our experiments *circa* 2 g/l, whereas Berl and Van Taack, and later Bloom *et al.*, placed it at 0.7 g/l NaOH.

Iron oxide passive films in aqueous media are generally considered to consist of a nonstoichiometric oxide which is essentially Fe_3O_4 at the film's metal/oxide interface and γ-Fe_2O_3 at its oxide/solution interface (16). If this is so, then γ-Fe_2O_3 should be present in the high-temperature corrosion films which we have termed "passive" in this discussion. Of the three papers cited, one reports the detection of γ-Fe_2O_3 in such films by electron diffraction (14), the second finds γ-Fe_2O_3 identifiable by infrared adsorption, but not by electron diffraction (11), while the third describes the film's diffraction pattern as only spinellike and does not try to differentiate between the γ-Fe_2O_3 and Fe_3O_4 structures (12). Warzee *et al.* (17) have also tried to distinguish γ-Fe_2O_3 and Fe_3O_4 and failed because sufficiently good diffraction patterns could not be obtained. Selected area diffraction patterns from our "passive" films fail to show any rings beyond the Fe_3O_4 pattern to indicate the presence of γ-Fe_2O_3. However, Fe_3O_4 and γ-Fe_2O_3 have very similar diffraction patterns (18) and, if the proportion of γ-Fe_2O_3 is small, its pattern might well remain undetected. We believe therefore that more sensitive tests are required before concluding that γ-Fe_2O_3 is absent.

Only a limited analysis of the corrosion rate data can be made, but the corrosion minimum at 2-4 g/l NaOH would seem to have the following significance. If the only cathodic reaction is the reduction of hydrogen, then the rate of hydrogen effusion must be equivalent to the rate of anodic reaction and therefore proportional to the anodic current. Moreover, considering that passivation occurs here, and that the corrosion values given in Fig. 2 represent in a sense then passivating anodic currents, we can compare Fig. 2 with Pourbaix's (8) plot of minimum current densities for iron passivation as a function of solution *p*H. And we find that the minimum in the critical current density for passivation occurs at almost exactly the *p*H (12.5-13) at which the corrosion minimum occurs. This happens most likely not from coincidence, but because the point of emergence from the region of passive oxide stability has been reached in both instances; in our case, we can actually see the change from a passive to an active oxide morphology.

On the other hand, while Pourbaix's passivation current densities decrease linearly from *p*H 2 through *p*H 12.5-13 (although it appears that he made no current measurements in the 8-12 *p*H region), the corrosion values in Fig. 2 increase over *p*H 9 to 12 before dropping to their minimum *circa* *p*H 12.5. This is contrary to the corrosion behavior of iron in 25°C water where increasing *p*H beyond 9.5 brings decreasing corrosion rates up to *p*H 12 where the rate begins to rise once again (19), the *p*H-dependency here being essentially the same as shown by the passivation current densities. The early-time maximum near *p*H 12 in our 300°C corrosion data is evidently not spurious, however, for a similar maximum has been observed by Bloom *et al.* (3), and it is probably associated with the active to passive-type oxide transformation which occurs during the initial hours of capsule heating. Little can be said at present of the actual mechanism of transformation, but apparently competing effects are involved, for, as the *p*H is raised, the active state oxide which develops first grows thicker and persists longer until finally as the corrosion minimum concentration is exceeded, it becomes the stable surface oxide species and degeneration to the passive oxide morphology no longer takes place. The passivation experiments of Cartledge (20) with iron in molybdate solutions are interesting in this conjunction because they show that a prepassivation (active state) corrosion film is displaced by a second surface film as passivation occurs, and, moreover, that near this point of transition the surface film becomes highly oriented and gives single crystal diffraction patterns very similar to those found in our previous experiments (4).

Ultimately, however, our corrosion rates come to show a monotonic increase with alkali concentration from 0.006 to 10.24 g/l NaOH. This agrees with earlier findings by Bloom who also used the capsule system (3), but not those of Warzee *et al.* (17) who found that boilerplate steel corroded at 300°C, under dynamic flow conditions, at decidedly lower rates in *p*H 10 LiOH solutions than in *p*H 7 water. These authors also demonstrated that the outer layer of magnetite crystals in iron corrosion films grows by precipitation from solution by exposing strips of AISI 304 and 410 steels simultaneously in water in an autoclave at 250°C and showing that the 304 specimen which would ordinarily have only a very thin oxide coating at these temperatures now became covered with magnetite crystals similar to those on the 410 steel. And their conclusion was that raising the *p*H to 10 gave a more protective film because it induced the deposition of a thicker, more adherent outer crystal layer by decreasing the solubility of ferrous hydroxide. It may be therefore that, while the early corrosion rates in the capsules depend on the structure, *i.e.*, active or passive, of the innermost oxide film, the long-term rates are finally determined by how the precipitated secondary crystals germinate and grow, our having observed that the lower concentration solutions give more complete surface coverage than the high concentrations which yield larger crystals, but leave more areas of "base" film exposed.

In the time-plot of activation energies in Fig. 4, the solutions which give passive state corrosion show early activation energies up to 16 kcal before dropping to apparently stable 5-8 kcal values. These initial high energies most likely reflect the active state corrosion which the specimens experience before they become passive. Conversely, the solutions giving true active state corrosion exhibit negative activation energies during the first hours of heating. These "negative" energies really only indicate a maximum in the temperature-corrosion rate relationship, however, and may be related to similar maxima found with 304 and 410 stainless steels when these steels were also presumably corroding in the active state. Maekawa *et al.* (11) believe that the temperature-corrosion maximum occurs with 304 stainless because the corrosion film is transformed from magnetite to chromite with increasing temperature. On the other hand, according to Warzee and co-workers (17), 410 stainless steel dissolves giving ferrous hydroxide which subsequently decomposes to produce a magnetite surface film. The two reactions have different temperature dependencies, however, with the latter reaction being accelerated more rapidly at the higher temperatures, and there is therefore a temperature (about 250°C) at which maximum solubility and corrosion occurs. Unfortunately, although our x-ray diffraction measurements seem to indicate that there is no change in structure of the Fe_3O_4 outer layer here, it has not been possible yet to

show the cause of the E_a time dependence shown for active state corrosion in Fig. 4.

The change in activation energy from 16 to 8 kcal/mol may be characteristic of the active-passive transition for iron and perhaps certain other metals as well in neutral to alkaline pH regions. Leach and Nehru (21) have found, for instance, a sharp 7-16 kcal/mol rise in E_a during the cathodic polarization of uranium in pH 9.7 buffer solutions under circumstances where a passive-active transition might be possible, uranium being known to be passivatable (22) and to show a different oxide morphology in the passive and active states (23). It may ultimately be feasible to use this characteristic E_a change as a substitute criterion for passivation in cases where electrochemical measurements cannot be made.

Summary

Our experiments reconfirm the existence of a minimum in the corrosion rate/alkali concentration relationship for the high-temperature corrosion of iron (mild steel) in NaOH media.

The morphology of the oxide film produced in the corrosion reaction is a function of the NaOH concentration of the generating solution; concentrations below the corrosion minimum point (about 2 g/l) give a noncrystallographic oxide, those above, a crystallographic oxide.

That these morphological differences reflect two distinct growth mechanisms is shown by the fact that different activation energies are obtained with each, 5-8 kcal/mol for the noncrystallographic oxide and 16 kcal/mol for the crystallographic.

Drawing from these observations and the literature, we have concluded that the underlying phenomenon is a transition between passive and active corrosion states as described by Hoar (19), albeit at 300°C.

Acknowledgments

The authors are indebted to E. D. Osgood and R. W. Scott for their assistance in specimen preparation and to Dr. M. C. Bloom for a stimulating critique of the first draft of this paper.

Manuscript submitted Nov. 15, 1968; revised manuscript received *ca.* April 1, 1969.

Any discussion of this paper will appear in a Discussion Section to be published in the June 1970 JOURNAL.

REFERENCES

1. E. C. Potter, *J. Inst. Fuel*, **32**, 218 (1958).
2. E. Berl and F. Van Taack, *Forsch. Gebiete Ingenieurw.*, **330**, 1 (1930).
3. M. C. Bloom, G. N. Newport, and W. A. Fraser, *This Journal*, **111**, 1343 (1964).
4. J. B. Moore, Jr., and R. L. Jones, *ibid.*, **115**, 576 (1968).
5. M. C. Bloom and M. Krulfeld, *ibid.*, **104**, 264 (1957).
6. E. C. Potter and G. M. W. Mann, 1st Intl. Cong. Metal. Corr., p. 417, London (1961).
7. G. M. W. Mann, Private communication, August 1968.
8. M. Pourbaix, "Atlas of Electrochemical Equilibria in Aqueous Solutions," pp. 307-321, Pergamon, London (1966).
9. J. M. West, "Electrodeposition and Corrosion Processes," p. 104, Van Nostrand, London (1965).
10. T. P. Hoar, "Protection Against Corrosion by Metal Finishing," (Proc. Intl. Conf., Basel, 1966), p. 170, Forster Verlag, Zurich (1967).
11. T. Maekawa, M. Kagawa, and N. Nakajima, *Trans. Jap. Inst. Metals*, **9**, 130 (1968).
12. T. Nakayama and Y. Oshida, *Corrosion*, **24**, 336 (1968).
13. J. M. Francis and W. H. Whitlow, *Metallurgie Belg.*, **7**, 145 (1967).
14. J. M. Francis and W. H. Whitlow, *J. Nucl. Matl.*, **20**, 1 (1966).
15. H. P. Leckie, *Corrosion*, **24**, 70 (1968).
16. M. Nagayama and S. Kawamura, *Electrochim. Acta*, **12**, 1109 (1967).
17. M. Warzee, C. Sonnen, and Ph. Berge, "Corrosion of Carbon Steels and Stainless Steels in Pressurized Water at High Temperature," EURAEC 1896, S.E.R.A.I., Brussels (1967).
18. K. J. Gallagher, W. Feitknecht, and U. Mannweiler, *Nature*, **217**, 1118 (1968).
19. G. Butler and H. C. K. Ison, "Corrosion and its Prevention in Waters," p. 64, Leonard Hill, London (1966).
20. G. H. Cartledge, *Corrosion*, **24**, 223 (1968).
21. J. S. L. Leach and A. Y. Nehru, *J. Nucl. Matl.*, **13**, 270 (1964).
22. L. E. Kindlimann and N. D. Greene, *Corrosion*, **23**, 29 (1967).
23. J. W. Ward and J. T. Waber, *This Journal*, **109**, 76 (1962).

Electrochemical Reduction of 6-Substituted Purines Correlation with Structural and Energetic Characteristics

Borivoj Janik and Philip J. Elving

The University of Michigan, Ann Arbor, Michigan

ABSTRACT

The electrochemical reduction of 6-substituted purines has been examined over the available *p*H range by direct- and alternating-current polarography, and the effects of substitution evaluated in respect to significant electrochemical characteristics. Where the 1,6 and 3,2 N=C bonds are available in the pyrimidine moiety, a four-electron polarographic wave due to hydrogenation of these bonds is observed; purine itself and 6-methylpurine give two two-electron waves. The energy-controlling step involves reduction of the protonated 1,6 N=C bond. The current is essentially diffusion controlled at low *p*H where the wave is relatively constant in height and kinetically controlled at higher *p*H where it begins to disappear. Correlation of the ease of reduction, as measured by $E_{1/2}$, with total polar substituent constant (σ_p) and polar substituent constant (σ^*) indicates either an absence of mesomeric and steric effects due to the substituents or their transmittal by an inductive mechanism and, further, that none of the substituents exerts any specific effect different from those exerted by the other substituents. Substitution in the 6-position influences mostly the N(1)-C(6) bond order and the electronic charge distributions on N(1) and N(3), which, in turn, largely determine the reducibility; $E_{1/2}$ correlates linearly with the quantum mechanically calculated magnitudes of these quantities, but not with other bond orders and charges. $E_{1/2}$ also correlates linearly with electron-acceptor properties as represented by the calculated energy of the lowest empty molecular orbital (k_i coefficients) and with pK_a for proton acquisition (the protonation, which occurs prior to electron transfer, seems to have no significant role in the potential-determining step except in the region where the wave has nearly disappeared). Isoguanine generally deviates from the various correlations. Adsorption involving an uncharged site in the molecule is markedly greater with derivatives having bulky substituents.

The polarographic behavior of purine and some of its derivatives at the dropping mercury electrode, D.M.E., has been investigated (1-14). However, no systematic study of the electrochemical reduction of 6-substituted purines has been made in spite of their importance; the naturally occurring purines are, with few exceptions, substituted in that position, including major and minor purine constituents of nucleic acids.

Among the reasons for investigating the electrochemical behavior of biologically important compounds are the development of possible correlations based on the implicit or explicit postulation that the mechanistic paths involved and the characteristic potentials associated with them, *e.g.* half-wave potentials ($E_{1/2}$), are a function of electron density and other factors, which are also relatively simply related to some biological, clinical, physical, or chemical property and activity (15, 16). The resulting frequently linear relationship between $E_{1/2}$ for a series of more or less closely related compounds and a suitably selected mathematical function of the values of the given property for that series of compounds permits (*a*) prediction of the magnitude of the property of a compound from its readily measured $E_{1/2}$ and (*b*) the rapid comparative evaluation of a property based on comparison of $E_{1/2}$ values. Furthermore, correlation of $E_{1/2}$ with structural, reactivity, and other characteristics may provide a better understanding of the effect of structure on the redox behavior of purines and related heterocyclic compounds (17).

The present study covers purine and nine 6-substituted purines (*cf.* Fig. 1 for structure and numbering), largely involving amino functions, since only those 6-substituted purines were investigated whose substituent is unlikely to remove by tautomeric shift the 1,6 N=C bond, which is the more readily reduced of the two possible electrochemical reduction sites (1,6 N=C and 3,2 N=C) in purines (18). The objectives of the study were to gather sufficient information to define the essential features of the electrochemical behavior of the series and the effect of structure on such behavior, and to examine the validity of using potential data obtained under comparable conditions for correlation purposes in view of the somewhat complex set of factors involved in the electrochemistry of purines at mercury electrodes.

Experimental

Chemicals.—Purines from the sources indicated were used: adenine, 6-methylpurine and 6-methylaminopurine (A grade), and 6-n-hexylaminopurine and 6-methoxypurine (C grade) from Calbiochem; 6-benzylaminopurine, 6-phenylaminopurine, 6-dimethylaminopurine, and isoguanine sulfate monohydrate (the latter two in M.A. grade) from Mann Research Laboratories; the reported analytical data indicated sufficient purity for polarographic study. Stock solutions (0.5-5 mM in distilled water) were stored in a refrigerator; where ultraviolet absorptivities were available, the concentration was checked spectrophotometrically.

The following buffer systems, prepared from analytical grade chemicals (J. T. Baker), were used at an ionic strength of 0.5 (*p*H regions in parentheses): KCl + HCl (1-2); Na_2HPO_4 + citric acid + KCl, *i.e.* constant ionic strength McIlvaine buffers (19), (2.5-7.8); NaOAc + HOAc (3.9-5.9); NH_4Cl + NH_3 (8.5-9.1); K_2CO_3 + KOH (9.2-10).

Nitrogen used for deoxygenating was purified and equilibrated by bubbling it successively through vanadous chloride solution in dilute HCl containing heavily amalgamated mossy zinc (20), NaOH solution, and water.

Apparatus.—Polarograms were recorded on a Sargent Model XV Polarograph, using capillary A and a water-jacketed H-cell, maintained at 25.4° ± 0.1°C and containing in one leg a saturated calomel reference electrode (S.C.E.), which was separated from the test solution by a glass frit and agar plug. The height of mercury reservoir, *h*, was 64 cm, unless otherwise

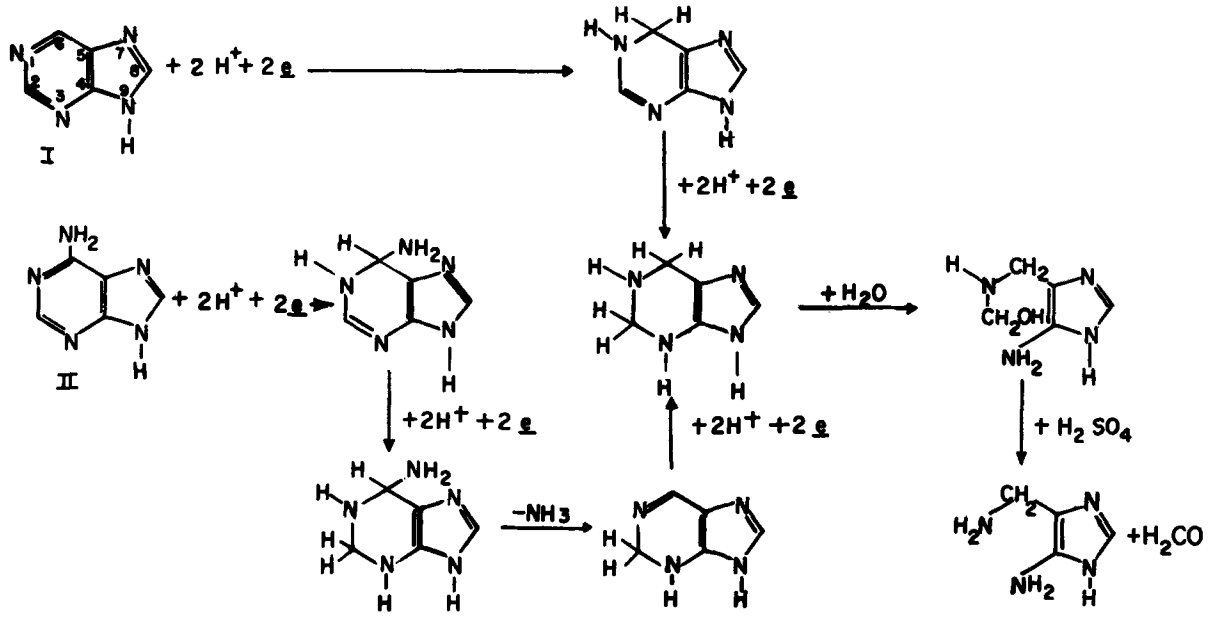

Fig. 1. Interpretation of the electrochemical and chemical behavior observed on polarographic reduction of purine (I) and adenine (II). Protonation, dissociation, and other acid-base and keto-enol equilibria, which may be involved, are not shown. Numbering is that of Chemical Abstracts.

stated. Capillaries (marine barometer tubing) had m values in distilled water (open circuit, 25°C) at 64 cm Hg of (A) 2.69 and (B) 2.22 mg/sec. Drop-times, measured at potentials of interest, were generally between 3 and 4 sec.

Current-time curves on a single drop, obtained with capillary B (h = 64 cm), were observed with a Tektronix Type 502 oscilloscope, whose traces were photographed on a Tektronix C-12 camera using 3000 speed Type 47 Polaroid film.

An operational amplifier-based polarograph (21) was used for alternating current polarography in conjunction with capillary B and an alternating voltage of 50 Hz and 4 mv rms amplitude.

pH was measured with a Beckman Model G pH meter.

Procedures.—Conventional procedures were used to obtain the experimental data; potentials are *vs.* S.C.E. The d-c polarographic measurements were made on 0.125 mM depolarizer solution except for isoguanine (0.25 mM) or as otherwise noted. Test solution pH was measured after diluting stock solutions to the desired depolarizer and buffer concentrations, and after polarographic measurement.

Polarographic data for purine were taken from Ref. (8) and (22).

A-C polarographic measurements were made on 0.25 mM purine solutions in pH 2.5 McIlvaine buffer. Current magnitudes given in Fig. 7 correspond to those measured at the end of the drop-life or before an abrupt current increase just previous to the fall of the drop. Current attenuation was 10%.

Observed Behavior

D-C polarography.—All 6-substituted purines examined show polarographic behavior comparable to those of the parental compounds, purine and adenine. Purines having substituted amino or methoxy groups at the 6-position exhibit a fairly well defined reduction wave similar to adenine (Table I); the diffusion current constants recorded under similar conditions are equal within ±8% and correspond to those of a four-electron (4e) faradaic process. 6-Methylpurine, similar to purine, shows two nearly equal waves, the sum of whose diffusion current constants equals that of the other 6-substituted purines. The diffusion current constant of isoguanine, whose behavior generally differs from that of the other 6-substituted purines, is about one-half of that of the latter.

Effect of pH and buffer components.—$E_{1/2}$ becomes more negative with increasing pH (Table I), while the wave height (sum if two waves appear) is relatively constant to about pH 5-6, when it sharply decreases, to vanish by pH 7-8 (Fig. 2-4), except for isoguanine, whose wave height remains practically constant up to

Table I. Diffusion current constants and variation with pH of $E_{1/2}$ for polarographic reduction of 6-substituted purines

Substituent (pK_a)	Potential variation[a]			
		pH	$E_{1/2}$, V	I^k
6-Hydrogen (purine; 2.30)	I	2-6	−0.697-0.083 pH	10.1[i]
	II	2-6	−0.902-0.080 pH	
6-Methyl (2.50)	I	1.0-3.9	−0.820-0.079 pH	8.5[i]
		3.9-6.0	−0.745-0.091 pH	
	II	2.5-6.0	−0.915-0.082 pH	
		3.9-5.9	−0.765-0.162 pH[b]	
	III	6.0-7.4	−0.785-0.095 pH	
		7.4-7.8	+0.080-0.209 pH	
6-Methoxy (2.17)		2.5-4.2	−0.825-0.105 pH	8.5
		4.2-5.5	−0.535-0.174 pH[c]	
6-Amino (adenine; 4.12)		1.0-6.5	−0.975-0.084 pH	9.8
6-Methylamino (4.15)		1.0-6.5	−0.995-0.081 pH	9.8
6-n-Hexylamino		1.0-2.5	−0.995-0.076 pH	8.3
		2.5-3.7	−1.105-0.047 pH[d]	
		3.7-6.5	−0.995-0.076 pH	
6-Benzylamino		2.0-4.8	−0.995-0.067 pH	9.8
		4.8-6.4	−0.805-0.106 pH	
6-Phenylamino		2.5-4.7	−0.915-0.072 pH[e]	8.3
		4.7-7.9	−0.640-0.131 pH	
6-Dimethylamino (3.82)		2.0-4.5	−1.025-0.068 pH[f]	8.9
		4.5-6.4	−0.930-0.089 pH	
2-Hydroxy-6-amino (isoguanine; 4.47)		1.0-4.6	−0.990-0.072 pH	4.6
		4.6-7.2	−0.820-0.109 pH	
		7.2-9.6	−1.210-0.055 pH	
		8.5-9.1	−0.705-0.104 pH[g]	

[a] Roman numbers indicate successive polarographic waves: potentials are *vs.* S.C.E. Data for purine taken from Ref. (8) and (9).
[b] Acetate buffer.
[c] Very ill-defined wave, which merges with background above pH 4.5.
[d] Since the normal and abnormal waves almost merge, only $E_{1/2}$ corresponding to their total height can be estimated.
[e] Maximum on the rising portion of the wave. $E_{1/2}$ is not changed after the maximum is suppressed by Triton X-100 addition.
[f] Maximum on the crest of the wave in pH range indicated. $E_{1/2}$ is not changed after the maximum is suppressed by Triton X-100 addition.
[g] Ammonia buffer.
[h] Diffusion current constant, $I = i_l/Cm^{2/3}t^{1/6}$, was calculated from average current data in that pH region, usually between pH 2.5 and 4.5 in McIlvaine buffer, where i_l varied least with pH.
[i] Calculated from the total current of the two reduction waves.

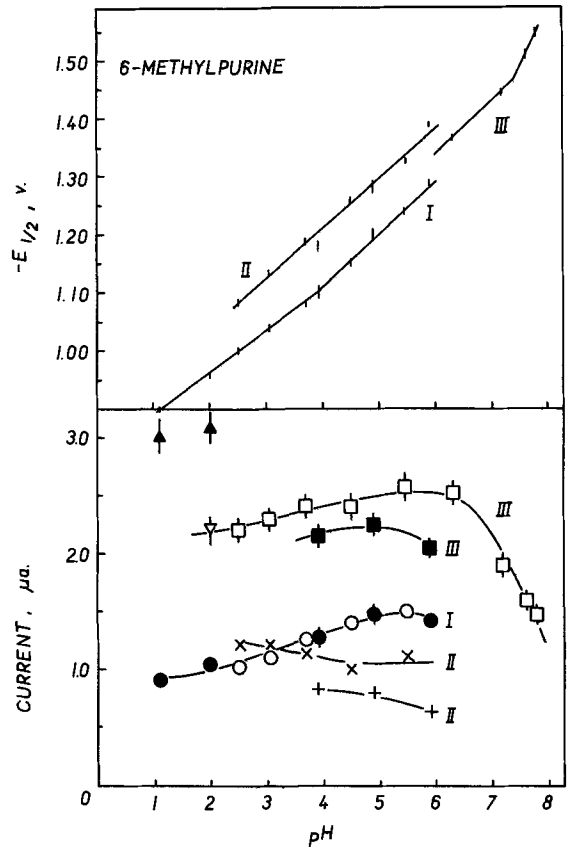

Fig. 2. Variation with pH of $E_{1/2}$ and limiting current of polarographic waves of 6-methylpurine (0.125 mM). (I) First reduction wave: circles, McIlvaine buffer; solid circles, chloride and acetate buffers. (II) Second reduction wave: crosses, McIlvaine buffer; pluses, acetate buffer. (III) Sum of I and II or third wave, which appears as a result of I and II merging: squares, McIlvaine buffer; solid squares, acetate buffer; solid triangles, II with a maximum on II; reversed triangles, III after suppression of maximum on II by Triton X-100 addition. Currents and potentials are plotted with a range of ± 5% and ± 5 mV, respectively, *i.e.* estimated average experimental errors.

pH 9, at which pH it suddenly drops (a small depression occurs in the *i*-pH plot at *ca.* pH 3.5) (Fig. 5). Plots of $E_{1/2}$ *vs.* pH for the normal reduction wave (two waves in case of 6-methylpurine) generally consist of two or three linear segments; 6-methylaminopurine gives a single line. The heights of the two 6-methylpurine waves are pH-dependent; wave I increases and wave II decreases with increasing pH; the waves merge at pH 6 to form wave III and their total height, which has been essentially constant, now decreases with increasing pH.

Buffer composition either has no influence on wave height, *e.g.* 6-methoxypurine and 6-methylpurine wave I, or shifts the descending part of the *i*-pH plot to lower pH in acetate than in McIlvaine buffer, *e.g.* 6-methylamino-, 6-n-hexylamino-, 6-phenylamino-, and 6-dimethylaminopurines.

$E_{1/2}$ values recorded in chloride and acetate buffers generally fall on the $E_{1/2}$-pH plot for McIlvaine buffer. In the alkaline region, $E_{1/2}$ values for isoguanine in McIlvaine and carbonate buffers fit the same line, while those in ammonia buffer are more positive.

Effects of concentration and drop-time.—The wave heights of 6-benzylamino-, 6-phenylamino-, and 6-n-hexylaminopurines are directly proportional to concentration (0.01-0.15 mM) in pH 4.9 acetate buffer, in which their $E_{1/2}$ values are independent of concentration while the diffusion current constants decrease by 10-20%; the ratio of $i_l/h^{1/2}$, where h is the mercury column height, increases slightly with increasing h. The $i_l/h^{1/2}$ ratio for 0.25 mM 6-methylaminopurine at pH 2.5 is roughly independent of h, and for isoguanine is independent of h at pH 2.5-3.7 and decreases slightly with increasing h at pH 1.1.

More extensive mercury height dependency studies were not made in view of the uncertainties in the case of waves close to background discharge, particularly in the presence of another more negative wave.

Maximum and its suppression.—All compounds examined, except 6-methylpurine, produce between pH 1 and 2 a maximum on the rising part of the wave, which more or less affects the wave plateau; the maximum decreases and finally disappears with increasing pH. 6-Dimethylamino- and 6-phenylaminopurines also produce maxima in McIlvaine but not in acetate buffer, below pH 4.3 and 4.7, respectively.

Triton X-100, even in concentration below 0.001%, completely suppresses the maxima and is more efficient at higher pH. $E_{1/2}$ of a wave with a just suppressed maximum is up to 10 mV more negative with the exception of 6-methoxypurine, whose $E_{1/2}$ shifts up to 20 mV more positive. The 6-phenylaminopurine wave height, which can be measured even in presence of the maximum above pH 2, is not altered on addition of just sufficient Triton to suppress the maximum; higher Triton concentrations, however, depress the wave height. In the absence of a maximum, Triton addition shifts $E_{1/2}$ 20-30 mV more negative and depresses the wave height by 0-20% per 0.001% Triton; these effects are less at higher pH.

Additional wave.—In addition to the normal reduction wave described, 6-methylamino-, 6-hexylamino-, and 6-benzylaminopurines exhibit, similar to adenine (22), a more negative wave in a limited pH region (the former two compounds below pH 3.7; the latter in pH 2.0 chloride buffer only), which is usually hard to define due to its merging either with background discharge, *e.g.* at pH 1.0, or with the normal wave at higher pH. Isoguanine forms a second more negative wave below pH 5, which is readily defined and decreases sharply with increasing pH.

The height of the normal reduction wave of 6-methylaminopurine, 6-n-hexylaminopurine, and isoguanine is depressed in the pH region where the second wave exists.

0.0006% Triton X-100 completely removes the second 6-benzylaminopurine wave without altering the normal wave, but decreases both 6-n-hexylaminopurine waves by 25 and 60% at pH 1.0, and 0 and 20% at pH 2.5. Triton is more effective at higher pH, *e.g.* 0.0012% completely eliminates the second 6-methylaminopurine wave in pH 3.7 buffer; in pH 2.5 and 3.0 buffer, it decreases the second wave by 20 and 50%, and the normal wave by 35 and 8%, respectively. $E_{1/2}$ of the first and second waves of 6-n-hexylamino- and 6-methylaminopurines are shifted *ca.* 10 mV and 0-5 mV more negative, respectively, per 0.0006% Triton, consequently, the waves first merge with each other and then with background discharge as the Triton concentration increases.

This additional wave is apparently due to streaming of the solution past the D.M.E. and reduction of a depolarizer, which is produced by the normal wave reduction product in a chemical step (23). This wave is, consequently, not specifically discussed except insofar as it affects the prior normal purine reduction wave. The second isoguanine wave, as indicated by its large current-concentration ratio and marked increase with decreasing pH (Fig. 5), is probably due to a catalytic hydrogen discharge.

Calculation of αn_a and p.—Values of αn_a (product of transfer coefficient and number of electrons involved per molecule of reactant in the rate-determining step of the electrode process) and of p (number of hydrogen ions involved per molecule of reactant in the rate-determining step) were calculated on the basis of Eq. [1] and [2] [*cf.* Chapter 4 of Ref. (20) for justification] and are summarized in Table II:

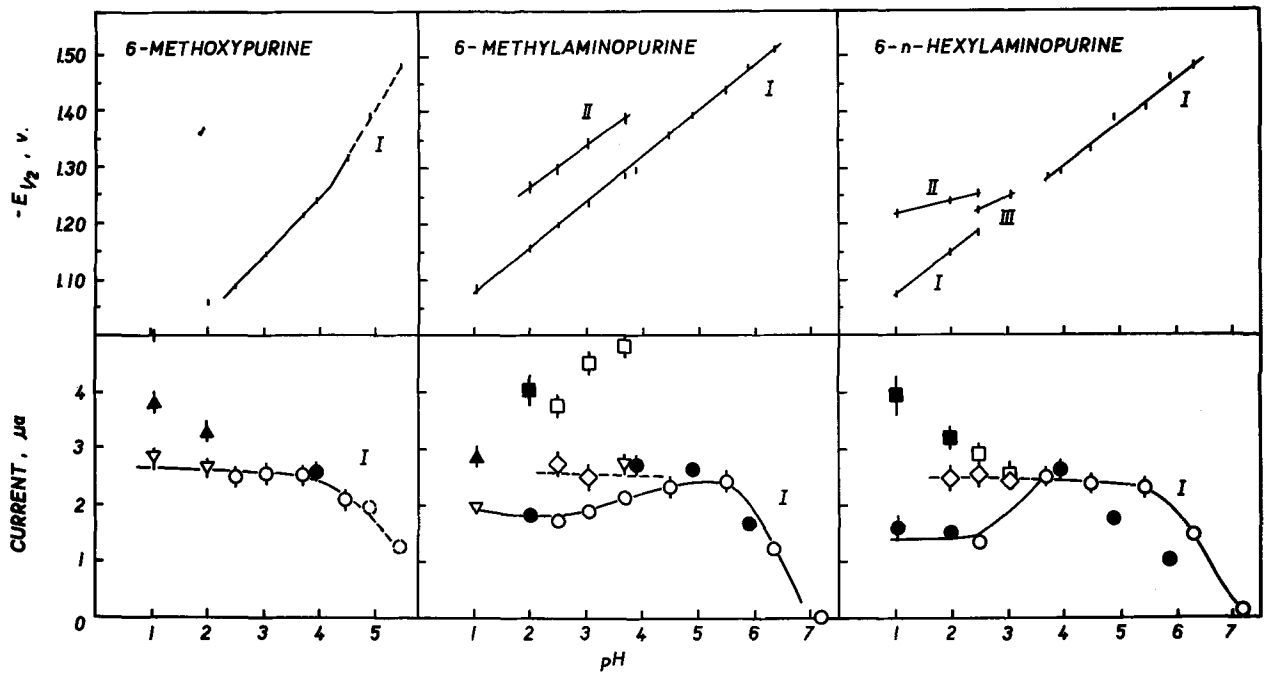

Fig. 3. Variation with pH of $E_{1/2}$ and limiting currents of polarographic waves of 6-methoxypurine, 6-methylaminopurine, and 6-n-hexylaminopurine (0.125 mM). (I) Normal reduction wave: circles, McIlvaine buffer; solid circles, chloride and acetate buffers; solid triangles, maximum in chloride buffer; reversed triangles, suppressed maximum or abnormal wave by Triton X-100 addition. (II) Abnormal reduction wave. (III) Sum of I and II: squares, McIlvaine buffer; solid squares, chloride buffer; diamonds, III suppressed to a constant height or III with I and II merging due to Triton X-100 addition (up to 0.002%). Currents are plotted with a range of ± 5% (I) and ±7% (III), and potentials with a range of ± 5 mV (I) and ± 10 mV (II), *i.e.* estimated average experimental errors, unless the deviation exceeds the average.

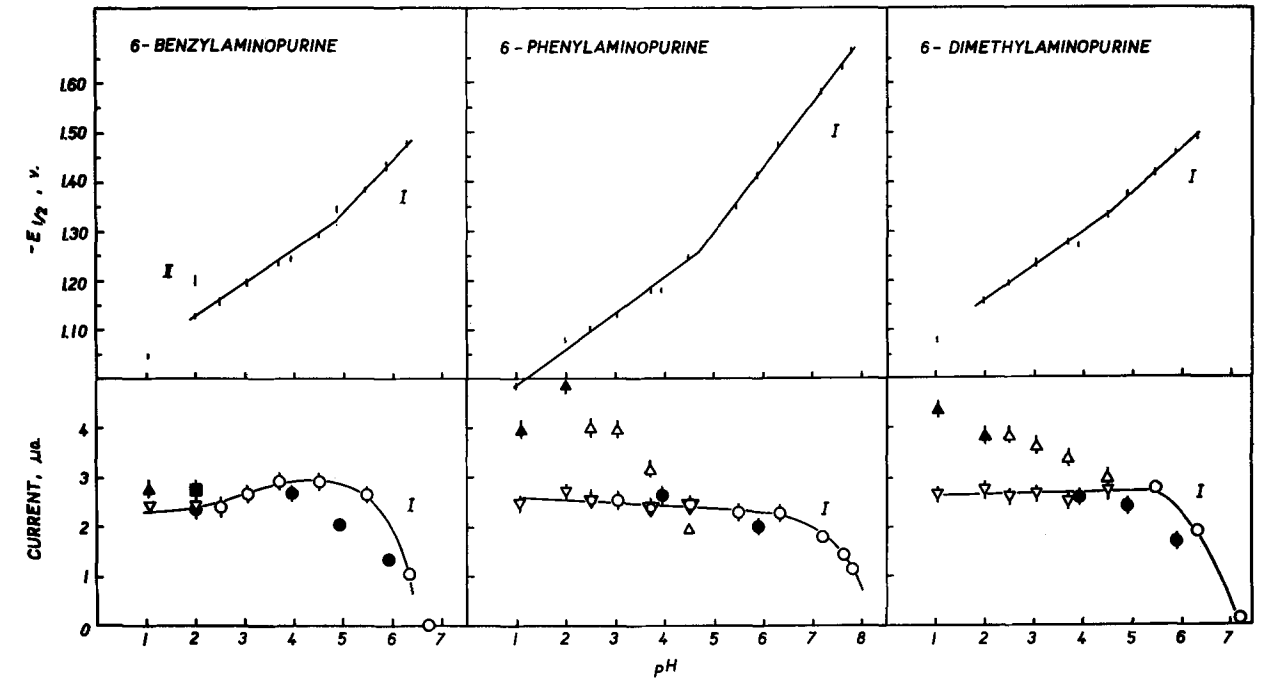

Fig. 4. Variation with pH of $E_{1/2}$ and limiting currents of polarographic waves of 6-benzylaminopurine, 6-phenylaminopurine, and 6-dimethylaminopurine (0.125 mM). (I) Normal reduction wave: circles: McIlvaine buffer; solid circles, chloride and acetate buffers; triangles, maximum in McIlvaine buffer; solid triangles, maximum in chloride buffer; reversed triangles, suppressed maximum or abnormal wave by Triton X-100 addition. (II) Abnormal wave. (III) Sum of I and II: solid squares, chloride buffer. Currents are plotted with a range of ± 5% (I) and ± 7% (III), and potentials with a range of ± 5 mV (I) and ± 10 mV (II), *i.e.* estimated average experimental errors, unless the deviation exceeds the average.

$$E_{1/4} - E_{3/4} = 0.0517/\alpha n_a \qquad [1]$$

$$d(E_{1/2})/d(\mathrm{pH}) = -0.05915\, p/\alpha n_a \qquad [2]$$

Values of αn_a, calculated for adenine and 6-methylaminopurine from the following equation, proposed by Oldham and Parry (24),

$$\frac{0.0592}{\alpha n_a} \log \left[\frac{2x(3-x)}{5(1-x)} \right] = E_{1/2} - E \qquad [3]$$

where x is the ratio of the current at potential E to the limiting current, are identical within experimental error with those obtained from Eq. [1].

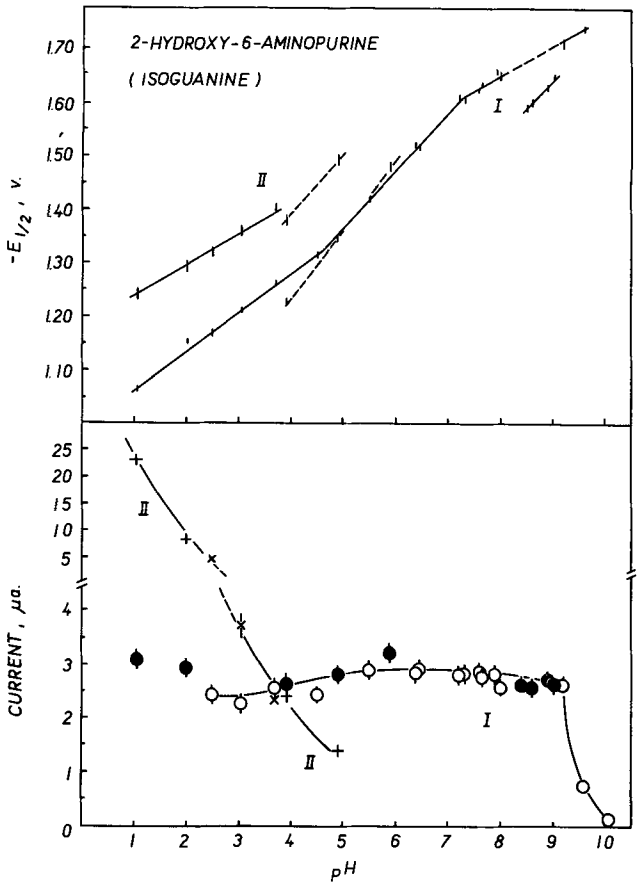

Fig. 5. Variation with pH of $E_{1/2}$ and limiting currents of polarographic waves of isoguanine (2-hydroxy-6-aminopurine) (0.25 mM). (I) Normal reduction wave: circles, McIlvaine and carbonate buffers; solid circles, chloride, acetate, and ammonia buffers. (II) Abnormal wave: crosses, McIlvaine buffer; pluses, chloride and acetate buffers. Currents are plotted with a range of ± 5% (I) and ± 7% (II), and potentials with a range of ± 5 mV (I) and ± 10 mV (II), *i.e.* estimated average experimental errors.

Values of αn_a and p cannot be meaningfully calculated for 6-benzylaminopurine below pH 2.5 and for 6-phenylaminopurine; in the former case αn_a sharply decreases with increasing pH up to *ca.* pH 2.5, probably due to the concomitant presence of an additional wave current in the normal reduction wave; in the latter case, maxima are present (up to pH 4.5), which cannot be suppressed by Triton X-100 addition without a change in wave slope. The high αn_a values for 6-methylpurine wave I may be due to the proximity of wave II ($E_{1/2}$ values are only 85 mV apart). Similarly, the normal and abnormal waves of 6-n-hexylaminopurine almost merge at pH 2.5-3.7.

Table II. Effect of pH on the rate-determining step in the polarographic reduction of 6-substituted purines

Substituent		pH	αn_a[a]	p[a]
6-Methyl	I	1.0-6.0	1.64 ± 0.08	2.33 ± 0.08
	II	2.0-6.0	0.99 ± 0.12	1.46 ± 0.10
		3.9-4.9[b]	1.11 ± 0.05	2.01 ± 0.09
	III	6.0-7.5	0.80 ± 0.02	1.20 ± 0.03
6-Methoxy		1.0-3.9	1.18 ± 0.16	2.10 ± 0.30
		3.9-4.5	0.77 ± 0.01	1.35 ± 0.01
6-Amino		2.0-2.5	1.36 ± 0.09	1.91 ± 0.14
		2.5-6.5	1.09 ± 0.07	1.54 ± 0.08
		3.9-4.9[b]	0.86 ± 0.08	1.22 ± 0.10
6-Methylamino		2.0-3.8	1.52 ± 0.08	2.07 ± 0.12
		3.8-6.5	1.00 ± 0.09	1.36 ± 0.12
6-n-Hexylamino		1.0-2.5	1.63 ± 0.06	2.10 ± 0.08
		3.7-6.5	1.10 ± 0.09	1.42 ± 0.12
6-Benzylamino		2.5-4.5	1.54 ± 0.12	1.75 ± 0.14
		4.5-6.4	1.07 ± 0.13	1.66 ± 0.26
6-Dimethylamino		1.0-6.4	1.25 ± 0.10	1.60 ± 0.16
2-Hydroxy-6-amino		1.0-4.2	1.05 ± 0.04	1.35 ± 0.06
		4.2-7.2	1.11 ± 0.16	1.96 ± 0.17
		7.2-9.6	1.22 ± 0.13	1.13 ± 0.13

[a] Data consist of mean and standard deviation. See text for method of calculation and discussion of experimental error.
[b] Acetate buffer only.

The data need to be interpreted with caution in view of the normal variation in measuring wave slopes; the standard deviations in Table II for αn_a, which also affect p, are of the order of 5-12%, due—at least in part—to the experimental error in estimating potential (*cf.* captions to Fig. 2-5). However, certain regularities are apparent, *e.g.* αn_a decreases with increasing pH, which may indicate decreasing reversibility and/or a decreasing number of electrons involved in the rate-determining step; however, since n_a is probably 1 or 2, the latter is unlikely. The apparent increase for wave II of 6-methylpurine is within experimental error; isoguanine, as usual, differs.

All 6-substituted purines examined, with the exception of isoguanine, seem to have two protons involved in the rate-determining step below *ca.* pH 4 with generally a lesser number at higher pH.

Current-time curves.—The variation of current with time during the life of a single drop (i-t curves) was recorded for sequential drops from a vertical capillary. Due to the depletion of the solution surrounding the drop (25), i-t curves obtained under such conditions produce log i *vs.* log t plots, which are convex to the time axis so that the choice of the slope is ambiguous. Such i-t curves cannot be used to estimate the extent of diffusion control; however, the instantaneous current would be expected to show a depression for an adsorption process (25, 26). Curves recorded at the limiting portion of the normal wave for 0.25 mM solutions of purine derivatives at pH 2.5 do not show any such depression.

Curves of i-t taken at the top of the maximum formed on the rising portion of the 6-phenylaminopurine reduction wave are very distorted (Fig. 6) and cannot be analyzed. Undistorted i-t curves are obtained on the limiting portion of the normal wave at potentials more negative than the foot of the maximum. The distorted shape of the i-t curve at a potential on the 6-phenylaminopurine maximum is usual for maxima of the second kind (25), while the position of the maximum on the rising portion of the polarographic wave corresponds to a maximum of the first kind (20); at present, this anomaly cannot be explained.

Distorted i-t curves, which are also obtained on the limiting portion of the second adenine and 6-methylaminopurine waves at drop times varying from 2 to 4.5

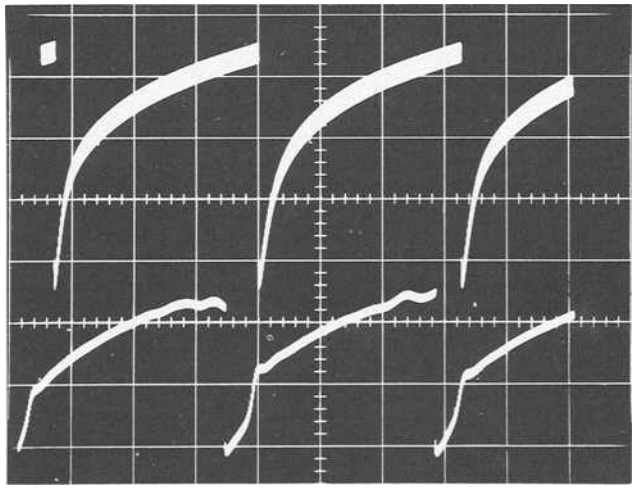

Fig. 6. Current-time curves for 0.25 mM 6-phenylaminopurine in pH 2.5 McIlvaine buffer. Upper curves taken at —1.25V (on limiting current portion of the normal reduction wave) with capillary B: x axis, 1 sec/(large) division; y axis, 2 μa/div. Lower curves taken at —1.17V (on maximum appearing on the normal reduction wave): x axis, 1 sec/div; y axis, 5 μa/div.

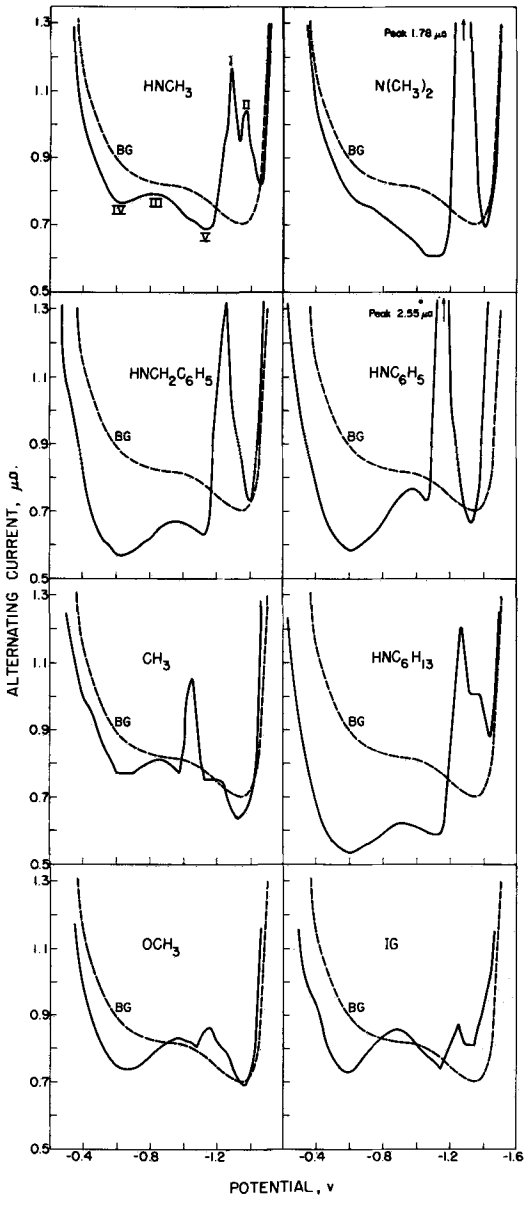

Fig. 7. Alternating current polarograms for 0.25 mM 6-substituted purines in pH 2.5 McIlvaine buffer; substituents are indicated. IG = isoguanine. Background electrolyte base current is marked BG.

sec (h = 36-81 cm), indicate that these waves are not diffusion controlled.

Alternating-current polarography.—A-C polarograms of all derivatives examined (Fig. 7) show a common pattern. A reduction peak (I) is seen in the potential region corresponding to that of the normal polarographic wave (Table III). In the case of 6-methylaminopurine, a new peak (II) appears at more negative potential than peak I with a height about 0.5 of that of peak I; 6-n-hexylaminopurine and 6-methylpurine exhibit a shoulder on the negative side of peak I. The base current is depressed below that of the supporting electrolyte at potentials more positive than that of peak I and usually forms two minima (IV and V) at about —0.6 and —1.1V, which are separated by a broad peak (III) at about —0.9V.

Depression of the base current below that of the background at potentials more negative than E_s of peak I was observed only with 6-phenylaminopurine and, more pronouncedly, with 6-methylpurine.

Peak III overlaps the background base current only in the cases of 6-methoxypurine and isoguanine. In the potential region where peak I appears and at more negative potentials, abnormal current increases are observed, when the mercury drop is about to fall, which could be due to hydrogen ion discharge catalyzed by the reduced form of the purine and/or streaming of the solution past the D.M.E. surface.

Reduction Mechanism and Structural Factors

The two *p*H-dependent polarographic waves of purine itself are due (8) to 2*e* reduction of the 1,6 N=C double bond to 1,6-dihydropurine, followed by a further 2*e* reduction, probably to 1,2,3,6-tetrahydropurine, which hydrolyzes to a 4-aminoimidazole (equations in Fig. 1). Under the conditions of macroscale electrolysis, the electrolytic reduction of adenine parallels that of purine for an over-all 6*e* reduction: 2*e* hydrogenation of the 1,6 N=C bond at a potential more negative than that of both purine waves is immediately followed by 2*e* reduction of the 2,3 C=N bond, slow deamination at the 6-position, further 2*e* reduction of the regenerated 1,6 N=C bond, and hydrolytic cleavage at the hydrogenated 2,3 position to give the same product as the over-all 4*e* purine reduction; however, at the D.M.E., the extent of deamination of the reduced adenine is negligible, resulting in a single *p*H-dependent 4*e* wave (8) (equations in Fig. 1).

The present results confirm the preceding; polarographic reduction of purines generally involves 4*e* hydrogenation of the 1,6 and 3,2 N=C bonds in the pyrimidine moiety, when such double bonds are not removed from the ring due to tautomeric shifts, which favor oxygen in a keto form and amino nitrogen in the amino form (27, 28). 6-Methylpurine resembles the parental purine in being reduced in two separate 2*e* waves, while 6-alkylamino-, 6-dialkylamino-, 6-phenylamino-, and 6-methoxypurines behave similarly to adenine (6-aminopurine).

Current control.—Diffusion as the principal factor controlling the reduction wave current is supported by the $i_l/h^{1/2}$ *vs.* h plots, which are generally independent of h, and by temperature coefficients, which range from 1.5 to 2.5%, *e.g.* for adenine and 6-methylaminopurine in *p*H 3.0 McIlvaine buffer. However, dif-

Table III. Comparison of a-c and d-c polarographic data for 6-substituted purines[a]

Substituent		Normal wave			Abnormal wave		Minimum[d]	
		i_s, μa	$-E_s$, V	$E_{1/2} - E_s$, mV	$-E_s$, V	$E_{1/2} - E_s$, mV	$-E_{min}$, V	i_{min}, μa
6-Methyl	I	0.30	1.05	50			0.67	0.12
	II	[b]	~1.17	85				
6-Methoxy		0.09	1.15	60			0.65	0.10
6-Amino		0.46	1.26	75			0.62	0.11
6-Methylamino		0.42	1.28	83	1.37	72	0.64	0.11
6-n-Hexylamino		0.48	1.27	85	~1.35[b]	~98	0.61	0.37
6-Benzylamino		0.65	1.25	90			0.63	0.31
6-Phenylamino		1.85	1.15	50			0.61	0.30
6-Dimethylamino		1.13	1.25	58			1.10	0.18
2-Hydroxy-6-amino		0.10	1.25	78	~1.30[c]	30	0.60	0.16

[a] Measured on 0.25 mM depolarizer solution in pH 2.5 McIlvaine buffer.
[b] Shoulder.
[c] A minimum, whose current is about 0.1 μa higher than the background base current.
[d] Minimum in the a-c curve indicated as IV in Fig. 7; current given is that below background electrolyte current.

fusion is not the only factor involved; a minor amount of kinetic control is present, *e.g.* the normal reduction wave is almost fully kinetically controlled in the *p*H region where the limiting current decreases and reaches about one tenth of the original value.

Effect of substituent nature.—$E_{1/2}$ of the 6-substituted purines becomes more negative in the following order (substituent in 6-position indicated; since $E_{1/2}$ is *p*H-dependent, data at *p*H 2.5 and 4.0 were chosen for reasons subsequently discussed): H, CH_3, CH_3O, C_6H_5NH, $C_6H_5CH_2NH$, (isoguanine), n-$C_6H_{13}NH$, $(CH_3)_2N$, NH_2, and CH_3NH at *p*H 2.5, and H, CH_3, C_6H_5NH, CH_3O, $C_6H_5CH_2NH$, (isoguanine), $(CH_3)_2N$, n-$C_6H_{13}NH$, CH_3NH, and NH_2 at *p*H 4.0.

Substitution in the 6-position with electron-repelling groups decreases the ease of reducibility of the parent purine with the magnitude of the effect increasing with increasing electron repellency (basicity) of the substituent; the effect of the amino group can be counterbalanced by electron-withdrawing substituents on that group. This is generally consistent with the order of electron-repellent groups, *e.g.* methyl < methoxy < arylamino < amino $\gtrless$ alkylamino (29), which increases the electron density at neighbor atoms due to the inductive effect (29), and with the order of increasing basicity of amines, *e.g.* $C_6H_5NH_2$ (pK_a for dissociation of the protonated amine = 4.6), NH_3 (9.24), $C_6H_5CH_2NH_2$ (10.33), $C_6H_{13}NH_2$ (10.56), CH_3NH_2 (10.66), and $(CH_3)_2NH$ (10.73) (30).

The presence of an amino or substituted amino group in the 6-position seems to be a necessary but not sufficient factor for the appearance of the abnormal polarographic wave mentioned, which may involve the adsorbed reduced form of the purine, *e.g.* Ref. (8) and (9); other factors involved are now under study (23).

Nature of reducible species.—The need for protonation prior to reduction, *i.e.* the presence of the conjugate acid of the purine as the polarographically reducible species, and the probability of the proton being intimately connected with N(1) of the pyrimidine moiety, are supported by the following:

(*A*) The reducibility, represented by $E_{1/2}$, is inversely proportional to pK_a for the addition of a proton to the purine (cf. below).

(*B*) Plots of limiting current *vs.* *p*H (Fig. 2-4) exhibit a sigmoidal decrease in current centering at a *p*H generally 2-3 units greater than the pK_a value of the purine. The current also shows kinetic control in this *p*H region. Such behavior is characteristic of the polarographic reduction of the acid form of a conjugate acid-base equilibrium as a result of the recombination of the nonprotonated form with protons. A depression, observed below *p*H 4 on the *i*-*p*H plot for 6-methylamino- and 6-n-hexylaminopurines, is due to the presence of the second (abnormal) wave, whose rising portion masks the limiting portion of the normal wave, so that its measured height is lower than the actual one.

(*C*) In a series of related compounds, reduction may be expected to be more difficult as the electron density at the reduction site increases. The fact that $E_{1/2}$ does become more negative as the net negative charge on N(1) and the pK_a value increase (cf. below) supports the association of the energy-controlling step of purine reduction with the 1,6 N=C bond (8) and with the site of protonation which is N(1); the latter is the most basic nitrogen in adenine (15, 16, 27) and presumably in other closely related 6-substituted purines. Correlations of reducibility with negative charge on N(1) and pK_a are also valid for the protonated species, since the net positive charge on N(1) is inversely proportional to the net negative charge of the nonprotonated form.

Adsorption of reactant and product.—All 6-substituted purines examined exhibit an a-c reduction wave at *p*H 2.5, whose summit potential, E_s, is 50-90 mV more negative than the corresponding $E_{1/2}$ (Table III; Fig. 7), which indicates that the oxidized and reduced forms of the depolarizer are not equally strongly adsorbed in the $E_{1/2}$ potential region (31). The similarity in d-c polarographic behavior of purine and 6-methylpurine, *e.g.* both give 2*e* waves, is also observed under a-c conditions; purine gives two a-c peaks (21, 32) with the smaller more negative peak corresponding in potential to a shoulder on the negative side of the main 6-methylpurine peak.

In general, the base current is deeply depressed at potentials positive to the a-c peak, indicating strong adsorption of the oxidized form, whereas at more negative potential, *i.e.* on the limiting current portion of the d-c wave, the depression of the a-c current is very small or zero; however, the lack of such depression need not mean that the reduced form is not appreciably adsorbed. Since the main a-c peak is located at moderately negative potential, the background discharge could begin before the main peak current drops below the background base current. The shift of background discharge to more positive potential in the presence of some 6-substituted purines (Fig. 7) and the second (abnormal) wave process of 6-amino-, 6-methylamino-, and 6-n-hexylaminopurines and isoguanine may contribute to the masking of the depression on the negative side of the main peak. Only 6-methylpurine, whose E_s is 0.1-0.2V more positive than those of the other purines, shows such depression on both sides of the main peak, which indicates that the oxidized and reduced forms are adsorbed to a comparable extent.

The base current for 6-substituted purine solutions in the potential range more positive than the a-c reduction peak forms two minima (Fig. 7), the more positive of which is near the potential of zero charge of the D.M.E., indicating that an uncharged species is predominantly adsorbed. Since pK_a for the 6-substituted purines fall in the range of 2.2-4.5, the protonated, *i.e.* positively charged, species is predominant at *p*H 2.5 and, consequently, an uncharged portion of the purine molecule is involved in the strong adsorption at —0.6V. The broad desorption peak and the consequent adsorption minimum, which indicate first decreasing effect due to adsorption and then increasing effect with increasing negative potential, are probably caused by the adsorbed molecule gradually rearranging its position on the surface so that the positively charged site of the molecule is now attached to the D.M.E. surface, rather than being due to an uncharged form of the molecule being desorbed and replaced by a protonated form.

Only in the cases of methoxypurine and isoguanine, whose desorption peaks exceed the base current of the supporting electrolyte itself, is the rearrangement apparently accompanied by complete desorption of an adsorbed species. Absence of the desorption peak and presence of the deep minimum at —1.1V in 6-dimethylaminopurine are likely due to the protonated form being relatively stronger adsorbed than the uncharged form.

The order of uncharged site-controlled adsorbability of 6-substituted purines [cf. depths of the more positive minima (Table III)] indicates that purines with more bulky substituents are more extensively adsorbed and/or cause greater changes in the double layer capacity, probably due to decreased aqueous solubility; the three derivatives, which exhibit by far the greatest adsorbability, are extremely insoluble in water, *i.e.* their saturated solutions are *ca.* 0.5 mM.

The abnormal d-c wave of 6-methylamino- and 6-n-hexylaminopurines has its a-c counterpart in a peak and in a shoulder, respectively, at potentials more negative than E_s of the main peak (Table III) at the same *p*H. The second, presumably catalytic, d-c wave of isoguanine has no a-c counterpart; however, the base current of isoguanine solutions at potentials

more negative than the main a-c peak is considerably elevated above the background base current and the latter is shifted to considerably more positive potential (Fig. 7), while the base current for solutions of other derivatives drops at least to the background base current; this may indicate a second faradaic process taking place at more negative potential than E_s of the main peak.

The derivatives, which exhibited a maximum on the d-c normal wave at pH 2.5 (6-dimethylamino- and 6-phenylaminopurines) also give an unusually high peak current (Table III).

Correlation of $E_{1/2}$ with Structural and Electronic Indexes

Half-wave potential data.—Since $E_{1/2}$ for 6-substituted purines is pH-dependent, data at pH 2.5 and 4.0 were compared for the following reasons: (*a*) Both pH values are available in the same buffer type (McIlvaine); (*b*) the purines are largely protonated at pH 2.5 and to a much lesser extent at pH 4, (even though the polarographic current is practically constant in the pH interval of 2.5-4); (*c*) values of $d(E_{1/2})/d(pH)$ are generally within the relatively narrow span of 0.067-0.084 V/pH in the pH range of 2-4; and (*d*) maxima do not appear above pH 2 except for 6-dimethylamino- and 6-phenylaminopurines, whose maxima at pH 2.5 are easily suppressed at only about 0.0007% Triton X-100.

In the case of purine and 6-methylpurine, which give two 2*e* waves, $E_{1/2}$ for the first wave was used on the basis that the initial energy-determining process both in the first 2*e* waves and in the 4*e* waves involves the identical reaction: attack on the 1,6 N=C double bond of the pyrimidine ring [*cf.* subsequent discussion and the initial 1*e* reduction observed for pyrimidine by d-c and a-c polarography (18, 33)].

The reliability of correlations of $E_{1/2}$ with experimental and calculated parameters, particularly the latter, depends on the calculations and measurements having been made on identical molecular species and for the proper reaction site. Theoretical calculations are generally based on an idealized gas-phase molecule and a reversible electron-transfer process. The assumption is made that, while solvation, irreversibility, and adsorption are complicated factors, they may be expected to operate uniformly in a closely related series; the usefulness of such correlations has been emphasized, *e.g.* Refs. (34) and (35). Thus, $E_{1/2}$ values for over-all irreversible polarographic reductions have frequently been correlated with MO and free energy indexes, *e.g.* Ref. (36) and (37).

In general, correlations of calculated MO and structure-reactivity indexes with experimental electron affinity values, *e.g.* $E_{1/2}$, and other properties, *e.g.* ultraviolet absorption maxima, must—for the time being —be considered as semiempirical, since there are no exact methods for calculation of MO and other parameters which involve all possible intra- and intermolecular effects. In any event, comparison of calculated values with $E_{1/2}$ for a series of related compounds may provide information on whether effects of the types mentioned operate with all individual derivatives to comparatively the same extent and on whether differences in $E_{1/2}$ due to structural changes have a counterpart in differences in MO and other indexes, and *vice versa.*

Linear free energy relations.—The physical basis for using $E_{1/2}$ values in linear free energy relations, *e.g.* the Hammett-Taft equations, is the fact that $E_{1/2}$ is a simple function of the logarithm of the heterogeneous rate constant for irreversible electrode processes or of the equilibrium constant for reversible electrode processes (17). Since the application of free energy relationships to the polarographic behavior of 6-substituted six-membered heterocyclic compounds analogous to the pyrimidine ring in which purine

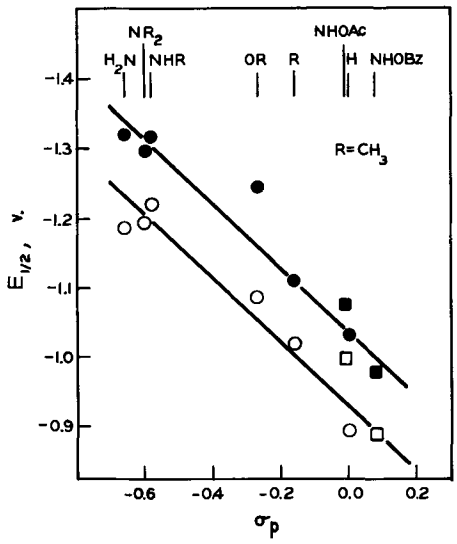

Fig. 8. Variation of $E_{1/2}$ of 6-substituted purines with the total polar substituent constant, σ_p (substituent indicated). $E_{1/2}$ determined in McIlvaine buffer (circles, pH 2.5; solid circles, pH 4.0); purine data from reference (8); 6-acetylamino- and 6-benzoylaminopurine data (squares, pH 2.5; solid squares, pH 4.0) from Ref. (14) (background not indicated). Slope, ρ, is 0.46V at pH both 2.5 and 4.0.

reductions occur has not been previously reported, a trial and error approach was used. Polar substituent constants were selected from the literature (38, 42); unfortunately, as was also true for the other parameters investigated, complete data are not available for all of the purines studied.

A fairly linear correlation is obtained in a plot (Fig. 8) of $E_{1/2}$ against total polar substituent constant, σ_p, which is dependent on the kind and position of the substituent, as well as to some extent on the nature of the aromatic ring, but is presumably independent of reaction and reaction conditions (17). Plots of $E_{1/2}$ against other constants, which are frequently used in modifications of the Hammett equation (17, 34, 42), do not result in reasonably linear correlations.

In the 6-substituted alkylaminopurines, the 1,6 N=C bond initially reduced polarographically is separated by an —NH— group from an alkyl or aryl group in a series of 6-alkylamino- or 6-arylaminopurines. As a rough approximation, the —NH— group may be considered analogous to the —CH_2— group in the sense of an additional atom being between the substituent and the reaction site, and $E_{1/2}$ may be plotted against polar substituent constant, σ^* (17, 39, 42); a linear relation is obtained (Fig. 9).

The positive ρ values (Fig. 8 and 9) indicate that the mechanism of the potential-determining step is a

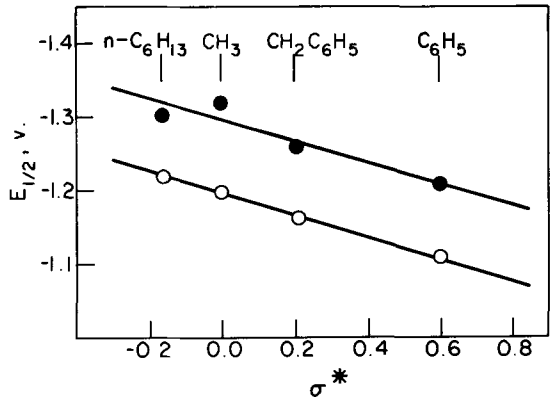

Fig. 9. Variation of $E_{1/2}$ of N'-substituted 6-aminopurines with the polar substituent constant, σ^* (substituent indicated). $E_{1/2}$ determined in McIlvaine buffer (circles, pH 2.5; solid circles, pH 4.0). Slope, ρ, is 0.14V for pH 4.0 and 0.15V for pH 2.5.

nucleophilic one (39), with an electron being the most probable nucleophilic agent. Thus, any primary electrophilic attack, *e.g.* protonation prior to electron-transfer, has no significant role in the potential-determining step (43). Since the protonated form is the species believed to undergo electroreduction, the protonation must be very rapid and, hence, not potential determining. The value of ρ depends on the charged state of the depolarizer and on the transfer coefficient (43). The similar values of ρ at pH 2.5 and 4.0 indicate that the same species is reduced at both pH values by the same mechanism.

In agreement with the polarographic behavior, the correlation of $E_{1/2}$ with σ_p (Fig. 8) places 6-methylpurine closer to purine than to the 6-amino derivatives. The small change in the polarographic reducibility of purine produced by introducing the 6-methyl group also corresponds to small differences in LEMO energies and other electronic indices (Fig. 10-12).

Support for the fact that the mechanisms for the polarographic reduction of the 6-substituted purines studied are essentially the same as those of the parental compounds, purine and adenine, is apparent from the data in Fig. 8 and 9; *i.e.*, the linear correlations of $E_{1/2}$ with the polar substituent constants for the series of 6-alkylamino purines and with the total

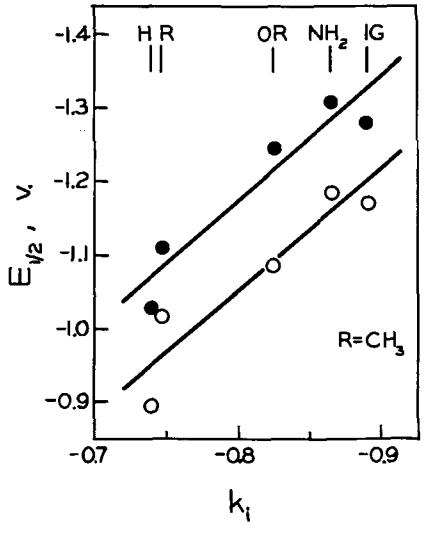

Fig. 10. Variation of $E_{1/2}$ of 6-substituted purines (substituent indicated) with LEMO energies (k_i). IG = isoguanine. $E_{1/2}$ determined in McIlvaine buffer (circles, pH 2.5; solid circles, pH 4.0).

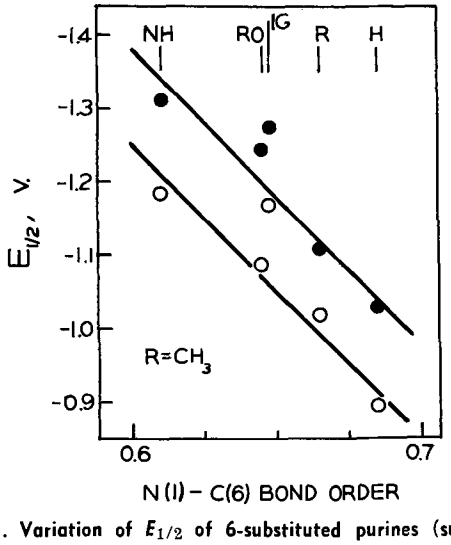

Fig. 11. Variation of $E_{1/2}$ of 6-substituted purines (substituent indicated) with calculated N(1)-C(6) bond order. IG = isoguanine. $E_{1/2}$ determined in McIlvaine buffer (circles, pH 2.5; solid circles, pH 4.0).

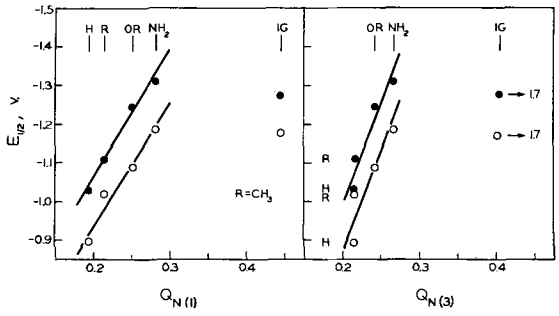

Fig. 12. Variation of $E_{1/2}$ of 6-substituted purines (substituent indicated) with net negative charges on N(1) and N(3). IG = isoguanine. $E_{1/2}$ determined in McIlvaine buffer (circles, pH 2.5; solid circles, pH 4.0).

polar substituent constants for 6-substituted purines indicate either that no mesomeric and steric effects due to the substituents are involved or that they are transmitted by an inductive mechanism (17, 39, 42); the correlation also indicates that none of the substituents exerts any specific effect different from those exerted by the other substituents (42).

Quantum mechanically calculated electronic indexes. —Correlations of MO calculations with $E_{1/2}$ data generally involve the energies for adding an electron to the lowest empty MO (LEMO) or removing one from the highest occupied MO (HOMO), based on calculation of the energies of the molecular orbitals of the mobile or π electrons, which are of the form

$$E_i = a + k_i\beta \qquad [4]$$

where a is the coulomb integral and β the resonance integral (15). For a homologous series, the smaller the absolute value of LEMO k_i, the greater the electronegativity and, consequently, the greater the electron acceptor properties of the molecule and, in turn, the easier should be the polarographic reduction.

In addition to correlation of $E_{1/2}$ with LEMO values, correlations were investigated between $E_{1/2}$ and bond orders for selected pairs of atoms, and between $E_{1/2}$ and net charges on certain atoms in order to see whether such correlations could be used to identify the electroactive sites in the molecules [*cf.* Refs. (15) and (44) for discussion of concepts of *bond order* and *net charge*]. Methods of calculation of the MO parameters used for the purines are described by Pullman and Pullman (15), from whose book the data were taken.

Fairly linear relationships (Fig. 10) are obtained between $E_{1/2}$ and the LEMO energy (k_i coefficient) for purine, 6-methylpurine, adenine, and 6-methoxypurine (data calculated for the hypoxanthine lactim form were used for the latter). The deviant behavior of isoguanine is subsequently discussed.

Correlation of $E_{1/2}$ data with LEMO and HOMO energies is of special interest. Since the latter have been correlated with chemical and biochemical activity for a variety of molecules, *e.g.* Ref. (15), a successful correlation with $E_{1/2}$ will facilitate correlation of such activity with polarographic data. It is clear, however, as previously mentioned, that the effects of adsorption, electron-transfer reversibility, and solvation must be considered, since these may alter the potentials associated with the redox processes and perhaps even the mechanistic route.

Substitution in the 6-position influences mostly the N(1)-C(6) bond order and the electronic charge distributions on N(1) and less on N(3), which, in turn, largely determine the reducibility; $E_{1/2}$ correlates with these (Fig. 11 and 12), but not with the C(2)-N(3) bond order and the charges on C(6) and C(2). These results are in accord with the association of the initial purine and adenine reduction steps with the 1,6 N=C bond, which bond, moreover, seems to be more acces-

sible for reduction than the 2,3 C=N bond; *e.g.*, isoguanine (2-hydroxy-6-aminopurine) produces a well-defined wave, while hypoxanthine (6-hydroxypurine) gives only an ill-defined inflection on the background discharge (8) and guanine (2-amino-6-hydroxypurine) is polarographically reducible only at potentials more negative than background discharge by a mechanism different than that for other purine derivatives (8, 11, 12, 45).

A least-square calculation for the $E_{1/2}$-bond order data at *p*H 2.5, omitting the isoguanine point, gives $E_{1/2} = -3.474 + 3.727$ (B.O.) with the standard error of estimate for $E_{1/2}$ being 0.018V.

Acid dissociation constants.—Since only the protonated 6-substituted purine is apparently polarographically reducible, correlation of $E_{1/2}$ with acidic dissociation constant (pK_a) for the protonated form might be expected on the basis that (*a*) the initial potential-determining reduction step is associated with N(1); (*b*) adenine—and presumably other 6-substituted purines—is protonated first at N(1), *i.e.* at the most basic nitrogen (15, 16, 27); and (*c*) the electron density at N(1) would affect both $E_{1/2}$ and pK_a; $E_{1/2}$ does become more negative as the net negative charge on N(1) increases. Although the electronic density on the ring nitrogen cannot be taken alone as a measure of its basicity (15), as a first approximation, the reducibility should be inversely proportional to the basicity represented by pK_a. Actually, six of the seven purines, for which pK_a data are available, do give a reasonably linear $E_{1/2}$-pK_a plot (Fig. 13). A least-square calculation for the data at *p*H 2.5, omitting the point for methoxypurine, gives $E_{1/2} = -0.653 - 0.128$ pK_a with the standard error of estimate for $E_{1/2}$ being 0.042V and $E_{1/2} = 0.562 - 0.916$ $pK_a + 0.118$ $(pK_a)^2$ with a standard error of 0.020V. Equilibrium constants (pK_a values) for the acid-base system involving the uncharged purine (P) and its conjugated acid,

$$HP^+ \rightleftharpoons H^+ + P \qquad [5]$$

were selected from the most reliable compilations available (30, 46).

$E_{1/2}$ for 6-methoxypurine, which is between those of 6-methyl- and 6-aminopurines as predicted by the order of electron-repelling groups, falls on the linear plot of $E_{1/2}$ *vs.* the net electronic charge at the reduction site; its deviation from the $E_{1/2}$-pK_a plot may be due to the pK_a value in the literature (30) being too low.

Anomalous behavior of isoguanine.—As previously mentioned, $E_{1/2}$ for the isoguanine reduction deviates markedly from the linear correlations of $E_{1/2}$ for other 6-substituted purines with net negative charge on N(1) and N(3), but only slightly from the linear plots of $E_{1/2}$ *vs.* LEMO energy and N(1)-C(6) bond order (Fig. 10-13). This behavior may be correlated—at least to some extent—with the reduction site and the effect of protonation on the latter.

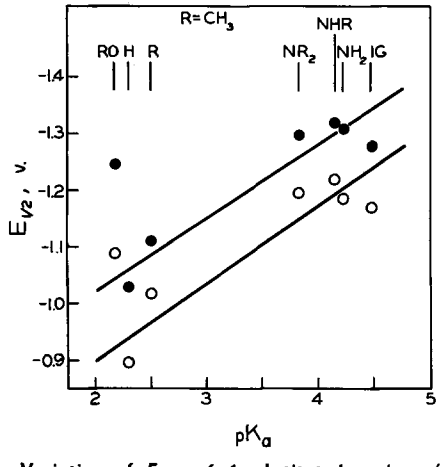

Fig. 13. Variation of $E_{1/2}$ of 6-substituted purines (substituent indicated) with acid dissociation constant (pK_a). IG = isoguanine. $E_{1/2}$ determined in McIlvaine buffer (circles, *p*H 2.5; solid circles, *p*H 4.0).

The diffusion current constant of isoguanine (Table I) is consistent with a 2*e* process based on only the 1,6 N=C bond being reducible since the 2,3 C=N bond is unavailable due to the stability of the keto form. Even though $E_{1/2}$ seems to fit the $E_{1/2}$-pK_a plot (Fig. 13), protonation of isoguanine at the reduction site does not seem to play a decisive role in its polarographic reduction; *i.e.*, the inflection point in the *i*-*p*H curve (Fig. 5) is at least 5 *p*H units higher than its pK_a compared to 2-3 units for other 6-substituted purines, and the most probable protonation site, based on comparison of N-charges (15), is N(7). The agreement of $E_{1/2}$ with LEMO energy and N(1)-C(6) bond order may then be ascribed to the connection of the latter with the reduction site.

Acknowledgments

The authors thank the U. S. National Science Foundation and the Office of Research Administration of The University of Michigan, which helped support the work reported.

Manuscript submitted Jan. 3, 1969; revised manuscript received *ca.* May 1, 1969.

Any discussion of this paper will appear in a Discussion Section to be published in the June 1970 JOURNAL.

REFERENCES

1. J. C. Heath, *Nature*, **158**, 23 (1946).
2. D. Hamer, D. M. Waldron, and D. L. Woodhouse, *Arch. Biochem. Biophys.*, **47**, 272 (1953).
3. N. G. Luthy and B. Lamb, *J. Pharm. Pharmacol.*, **8**, 410 (1956).
4. E. Palecek, *Naturwissenschaften*, **45**, 186 (1958).
5. E. Palecek, *Collection Czech. Chem. Commun.*, **25**, 2283 (1960).
6. F. A. McGinn and G. B. Brown, *J. Am. Chem. Soc.*, **82**, 3193 (1960).
7. E. Palecek and B. Janik, *Chem. Zvesti*, **16**, 406 (1962).
8. D. L. Smith and P. J. Elving, *J. Am. Chem. Soc.*, **84**, 1412 (1962).
9. D. L. Smith and P. J. Elving, *Anal. Chem.*, **34**, 930 (1962).
10. C. R. Warner and P. J. Elving, *Collection Czech. Chem. Commun.*, **30**, 4210 (1965).
11. B. Janik and E. Palecek, *Z. Naturforsch.*, **21b**, 1117 (1966).
12. B. Janik and E. Palecek, *Abhandl. Deut. Akad. Wiss. Berlin, Kl. Med.*, **1966**, 513.
13. P. J. Elving, *Abhandl. Deut. Akad. Wiss. Berlin, Kl. Med.*, **1966**, 485.
14. V. P. Skulachev and L. I. Denisovich, *Biokhim.*, **31**, 132 (1966).
15. B. Pullman and A. Pullman, "Quantum Biochemistry," John Wiley & Sons, New York (1963).
16. H. Berthod, C. Giessner-Prettre, and A. Pullman, *Theoret. Chim. Acta*, **5**, 53 (1966).
17. P. Zuman, "Substituent Effects in Organic Polarography," Plenum Press, New York (1967).
18. P. J. Elving, W. A. Struck, and D. L. Smith, *Mises Point Chim. Anal. Org. Pharm. Bromatol.*, **14**, 141 (1965).
19. P. J. Elving, J. M. Markowitz, and L. Rosenthal, *Anal. Chem.*, **28** 1179 (1956).
20. L. Meites, "Polarographic Techniques," John Wiley & Sons, New York (1965).
21. G. Dryhurst and P. J. Elving, *Talanta*, Accepted for publication.
22. D. L. Smith, Ph.D. Thesis, The University of Michigan (1962).
23. B. Janik and P. J. Elving, Work in progress.
24. K. B. Oldham and E. P. Parry, *Anal. Chem.*, **40**, 65 (1968).
25. J. Kuta and I. Smoler, in "Progress in Polarography," Vol. 1, pp. 43-63, P. Zuman and I. M. Kolthoff, Editors, Interscience Publishers, New York (1962).
26. J. Volke, *Talanta*, **12**, 1081 (1965).

27. C. A. Dekker, *Ann. Rev. Biochem.*, **29**, 463 (1960).
28. I. Tinoco and D. N. Holcomb, *Ann. Rev. Phys. Chem.*, **15**, 371 (1964).
29. L. F. Fieser and M. Fieser, "Organic Chemistry," Reinhold Publishing Corp., New York (1956).
30. D. D. Perrin, "Dissociation Constants of Organic Bases in Aqueous Solutions," Butterworths, London (1965).
31. B. Breyer, T. Biegler, and H. H. Bauer, in "Modern Aspects of Polarography," pp. 50-57, T. Kambara, Editor, Plenum Press, New York (1966).
32. G. Dryhurst, M. Rosen, and P. J. Elving, *Anal. Chim. Acta*, **42**, 143 (1968).
33. J. E. O'Reilly and P. J. Elving, *J. Electroanal. Chem.*, **21**, 169 (1969).
34. E. S. Pysh and N. C. Yang, *J. Am. Chem. Soc.*, **85**, 2124 (1963).
35. R. Zahradnik and C. Parkanyi, *Talanta*, **12**, 1289 (1965).
36. J. W. Sease, F. G. Burton, and S. L. Nickol, *J. Am. Chem. Soc.*, **90**, 2595 (1968).
37. W. W. Hussey and A. J. Diefenderfer, *J. Am. Chem. Soc.*, **89**, 5359 (1967).
38. H. H. Jaffe, *Chem. Rev.*, **53**, 191 (1953).
39. P. Zuman, *Ric. Sci., Suppl. Contrib. Teor. Sper. Polarogr.*, **5**, 229 (1960).
40. J. E. Leffler and E. Grunwald, "Rates and Equilibria of Organic Reactions," John Wiley & Sons, New York (1963).
41. C. D. Ritchie and W. F. Sager, in "Progress in Physical Organic Chemistry," Vol. II, pp. 323-400, S. G. Cohen *et al.*, Editors, John Wiley & Sons, New York (1964).
42. P. Zuman in "Modern Aspects in Polarography," pp. 102-116, T. Kambara, Editor, Plenum Press, New York (1966).
43. P. Zuman, *Collection Czech. Chem. Commun.*, **25**, 3225 (1960).
44. A. Streitwieser, "Molecular Orbital Theory for Organic Chemists," John Wiley & Sons, New York (1961).
45. B. Janik, *Z. Naturforsch.* (1969), *In press.*
46. A. Albert in "Physical Methods in Heterocyclic Chemistry," Vol. I, pp. 1-108, A. R. Katritzky, Editor, Academic Press, New York (1963).

Electrochemical Oxidation of 6-Thiopurine at the Pyrolytic Graphite Electrode

Glenn Dryhurst

Department of Chemistry, University of Oklahoma, Norman, Oklahoma

ABSTRACT

The electrochemical oxidation of 6-thiopurine (6-TP), which gives three well defined voltammetric waves at the pyrolytic graphite electrode (PGE), has been investigated by linear sweep and cyclic voltammetry, macroscale controlled electrode potential electrolysis at the PGE in aqueous 1*M* acetic acid (*p*H 2.3), ammonia buffer *p*H 9 and carbonate buffer *p*H 9, and by determination of reaction products and possible intermediates. The electrochemical oxidation of 6-TP appears to follow a pathway quite different from the major enzymatic oxidative route. The first *p*H dependent wave is an adsorption wave due to oxidation of 6-TP to give an adsorbed layer of product bis(6-purinyl) disulfide (PDS). The second *p*H-dependent wave is a 1*e* process to give PDS both at *p*H 2.3 and *p*H 9; however at *p*H 2.3 further slow chemical oxidation to a disulfone or disulfoxide occurs, while in ammonia *p*H 9 the PDS decomposes rapidly to 6-TP, purine-6-sulfinic acid (P-6-Si) and purine-6-sulfonamide (P-6-Sm), with possibly some purine-6-sulfonic acid (P-6-So), with the over-all result that somewhat in excess of 4*e* are transferred. The third *p*H dependent wave in carbonate *p*H 9 gives P-6-So as the final product; in ammonia *p*H 9 wave III gives rise to a mixture of P-6-Si, P-6-Sm and possibly some P-6-So; PDS appears to be an unstable intermediate in these oxidations at high *p*H capable of being chemically oxidized by dissolved atmospheric oxygen.

6-Thiopurine (6-TP) is widely employed for the treatment of acute leukemia. The action of 6-TP as an anticarcinogen is not understood, although it is known that it inhibits *de novo* synthesis of nucleic acids, probably by blocking the conversion of inosinic acid into other purine ribonucleotides (1). Studies have also indicated that 6-TP ribonucleotide inhibits the normal enzyme conversions of inosinic acid (2-4).

The mechanism of metabolic breakdown of 6-TP in man and other systems is also incompletely understood. However, various studies in man have revealed that 6-TP is at least partially biologically oxidized to 6-thiouric acid, although inorganic sulfate and other unidentified products are produced (5, 6). Xanthine oxidase catalyzes formation of 6-thiouric acid as a major urinary metabolite from 6-TP in bacteria, mice, and men (7).

Bergman and Ungar (8) have shown that 6-TP is attacked by xanthine oxidase first at C-8 and then at C-2. However, in the purine oxidizing system of *pseudomonas aeruginosa* 6-TP is apparently attacked first at C-2 and then at C-8 and subsequent further oxidation occurs (9). The biochemical effects of 6-TP have been summarized by Silberman and Wyngaarden (7) and Elion and Hitchings (10).

Relatively little work has been reported on the chemical oxidation of 6-TP. In sodium carbonate (11) solution or phosphate buffer *p*H 7.6 (12), it is oxidized by aqueous iodine-iodide to bis(6-purinyl)disulfide (PDS). Treatment of this disulfide with oxygen in alkaline solution or oxidation of 6-TP with excess iodine in alkaline solution yields purine-6-sulfinic acid (P-6-Si). Oxidation of 6-TP with alkaline permanganate gives purine-6-sulfonic acid (P-6-So) (12). Oxidation of 6-TP with chlorine in the presence of methanol, potassium fluoride, and hydrofluoric acid gives purine-6-sulfonyl fluoride which on further treatment with methanol and ammonia at 0°C yields purine-6-sulfonamide (P-6-Sm) (13).

Because of the importance of electron transfer processes in biological systems, and the close similarity between the conditions of enzymatic and biological

transformations and electrochemical reactions, it is likely that information obtained from the study of electrochemical processes regarding the potentials of the electron transfer step and associated electrode and subsequent chemical reaction mechanisms will prove helpful in understanding complete biological transformations. In view of the incomplete knowledge of the metabolism of 6-TP, the electrochemical oxidation of this compound was studied.

There are only two detailed studies of the electrochemical oxidation of the purines. Struck and Elving (14) found that uric acid (2,6,8-trioxypurine) is oxidized at controlled potential at a graphite electrode in 1*M* acetic acid in a process which was essentially identical to that observed for the enzymatic oxidation of uric acid. Dryhurst and Elving (15) showed that adenine (6-aminopurine) is electrochemically oxidized at a graphite electrode in 1*M* acetic acid by a pathway that was initially very similar to that observed for oxidation with xanthine oxidase, but further oxidation and fragmentation occurred and a complex over-all mechanism was obtained.

The work reported here of the electrochemical oxidation of 6-TP at controlled electrode potential over a wide *p*H range at the pyrolytic graphite electrode (PGE) indicates a mechanism whereby 6-TP is oxidized in three distinct steps; the first step is an adsorption process due to oxidation of 6-TP to give an adsorbed layer of product, PDS. The second step is a 1*e* process to give PDS both at *p*H 2.3 and *p*H 9; at *p*H 2.3 further slow chemical oxidation to a disulfone or disulfoxide occurs, while in ammonia background *p*H 9 the PDS decomposes rapidly to 6-TP, P-6-Si, P-6-Sm, and possibly some P-6-So, the over-all result being that slightly more than 4*e* are transferred.

The third process in carbonate buffer *p*H 9 is due to oxidation to P-6-So; in ammonia *p*H 9 the oxidation product is a mixture of P-6-Si, P-6-Sm, and possibly some P-6-So; PDS appears to be an unstable intermediate in these oxidations at high *p*H capable of being chemically oxidized by dissolved atmospheric oxygen.

Experimental

Chemicals.—6-Thiopurine was obtained from Calbiochem. Bis(6-purinyl) disulfide, purine-6-sulfinic acid (sodium salt), and purine-6-sulfonic acid (potassium salt) were prepared according to Doerr *et al.* (12), the latter compound being most conveniently prepared from 6-chloropurine (Calbiochem). Purine-6-sulfonamide was supplied as a gift from Dr. Roland K. Robins (University of Utah).

Buffer solutions were prepared from analytical reagent grade chemicals.

Argon (Linde) used for deoxygenating purposes was equilibrated with water; no other purification was necessary.

Apparatus.—Polarograms and voltammograms were recorded on a Sargent Model XV Polarograph, using a water-jacketed three-compartment cell maintained at 25° ± 0.1°C and containing a saturated calomel reference electrode (SCE), and a platinum counterelectrode in saturated potassium chloride solution. All potentials are referred to the SCE at 25°C.

The dropping mercury electrode had normal *m* and *t* values.

The preparation of the large PGE and the coulometric cell have been described earlier (15).

Cyclic voltammetry was performed with the apparatus described by Dryhurst, Elving, and Rosen (26); voltammograms were recorded on either a Moseley Model 7001A X-Y recorder or a Tektronix Model 502A Dual Beam Oscilloscope in the X-Y mode equipped with a C-27 polaroid camera.

Controlled potential electrolyses were carried out using a Wenking Model 66TA1 Potentiostat. Potentials of interest were measured with either a Sargent Laboratory Potentiometer or a Heathkit Model EUW-24 vacuum tube voltmeter. The *p*H was measured with a Beckman Zeromatic *p*H meter.

Current integration during coulometry utilized a titration coulometer as described by Lingane and Small (27) and Lingane (28).

Ultraviolet absorption spectra were obtained with a Beckman Model DB recording spectrophotometer using 1.00 cm stoppered quartz cells.

Lyophilization was accomplished using a Kinney Model KC-2 vacuum pump; cooling traps contained 2-propanol-dry ice; the lyophilization vessel was a round bottomed distillation flask of an appropriate size on whose walls the solutions were shell frozen.

Voltammetric procedure.—Test solutions were prepared by diluting appropriate quantities of stock solutions (0.8 m*M* in 6-TP in water was the maximum concentration attainable) with suitable background solution. The *p*H of the solution was measured. Solutions were deaerated for at least 10 min with water-saturated Argon. Once in position the PGE was allowed to stand for about 30 sec without applied potential; the starting potential was then applied for 5 sec (usually 0.00V) and the voltammetric scan commenced. The PGE was resurfaced before every run by polishing on a 600-grade silicon carbide paper disk mounted on a motor driven rotating disk. The electrode was then washed thoroughly with water and the surface wiped free of any loose or adhering graphite particles with a clean paper tissue.

Coulometry.—A measured volume of background solution was electrolyzed at the appropriate potential in the working electrode compartment until the coulometer gave a small constant titration rate. Then sufficient sample was introduced to give up to a 1 mM solution and the electrolysis continued until the current decayed to the background level or to a constant small value. In many studies 0.5 ml aliquots of the electrolysis solution were removed at appropriate time intervals and, after suitable dilution, the u.v. spectrum was immediately recorded. Completion of the electrolysis was always confirmed by the disappearance of the characteristic 6-TP absorption peak. The solutions were not normally deaerated during these electrolyses; in the cases where deoxygenation was performed appropriate reference is made in the text.

Determination of purine-6-sulfinic acid.—P-6-Si was determined at the completion of the electrolysis by transferring about 20 ml of the electrolysis solution to the polarographic cell, deaerating, running a polarogram between 0.0 and —2.0V, and comparing the height of the wave at —1.20V with a calibration curve prepared from authentic P-6-Si.

Determination of purine-6-sulfonamide.—P-6-Sm was determined in the same way as for P-6-Si except that since only a very small quantity of P-6-Sm was available a known volume of a standard solution of P-6-Sm was added to a known volume of the electrolysis solution and by measuring the increase in height of the polarographic wave at —1.03V the concentration of P-6-Sm could be computed utilizing the method of standard additions. A detailed account of the analytical procedures will appear elsewhere (25).

Results and Discussion

Voltammetry.—6-Thiopurine exhibits up to three distinct anodic waves at the stationary pyrolytic graphite electrode (PGE) (Fig. 1). The two more negative waves appear over the range *p*H 1-8, above which the first wave disappears; the most negative wave (wave I) only appears intermittently, and is never observed at some *p*H values. The most positive of the three waves (wave III) is often masked by background discharge and is only observed in 1*M* HOAc *p*H 2.3, acetate *p*H 5.4, ammonia *p*H 9.1, and hydroxide *p*H 10 buffer solutions. In 1*M* HOAc and occasionally at *p*H 3.7 a small postwave appears after

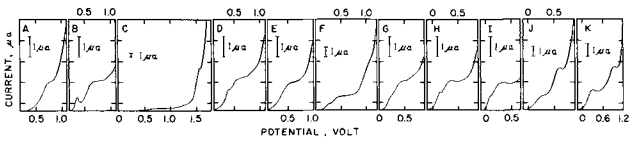

Fig. 1. Voltammograms of 0.4 mM 6-thiopurine at the PGE. A. 2M H_2SO_4 background; B and C. 1M acetic acid pH 2.3; D. pH 3.5 acetate buffer; E. pH 4.4 acetate buffer; F. pH 5.4 acetate buffer; G. pH 6.0 McIlvaine buffer; H. pH 6.9 McIlvaine buffer; I. pH 8.1 McIlvaine buffer; J. pH 9.1 ammonia buffer; and K. pH 9.9 chloride buffer.

wave II. This appears only at the highest concentration levels studied.

The peak potentials for all three waves become linearly more negative with increasing pH (Fig. 2): E_p = 0.51-0.047 pH for wave I, E_p = 0.805-0.052 pH for wave II, and E_p = 1.88-0.136 pH for wave III.

Waves I and II appear together most clearly in 1M HOAc, and waves II and III in ammonia or carbonate-bicarbonate background pH 9.0-9.2. Accordingly, the respective reactions were studied in detail at these pH values. Voltammetric studies were supplemented by coulometry and exhaustive electrolysis at large electrodes.

Examination of the changes in the composition of a 6-TP solution after the electrochemical oxidation at appropriately controlled anode potentials allowed qualitative identification and, at times, quantitative determination of the ultimate products as well as characterization of intermediate species.

Examination of the peak current for the three anodic waves of 6-TP at the 0.434 mM concentration level (Table I) indicates that for wave I the current density is 0.127 μA mM^{-1} mm^{-2}, for wave II 0.24 μA mM^{-1} mm^{-2}, and for wave III 0.65 μA mM^{-1} mm^{-2}. By comparison with previous data (15, 16) this indicates that wave I involves considerably less than 1e per 6-TP molecule. Wave II probably involves 1e, and wave III involves somewhat greater than 2e. In order to gain more insight into these ratios a concentration study was carried out in ammonia buffer pH 9.15 and 1M HOAc (Table II). At pH 2.3 wave I shows, an average, an almost constant current between 0.08 and 0.25 mM (Table II) although considerable variation was observed between replicate runs. At the 0.42 mM concentration level in this series of experiments wave I appeared as a very poorly defined inflection on the rising portion of wave II. Wave II showed a constant

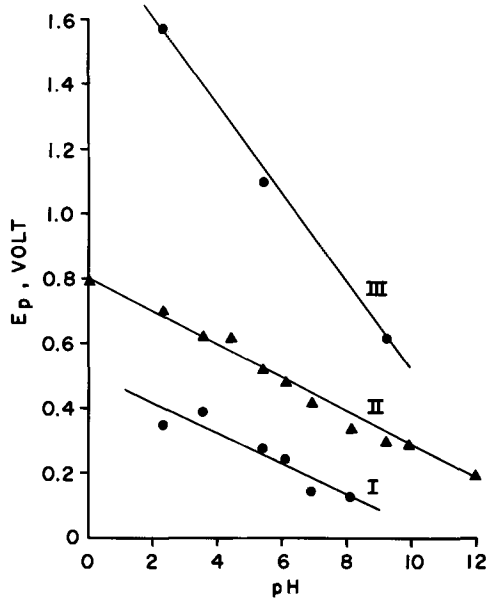

Fig. 2. Variation with pH of E_p of 6-thiopurine wave I, wave II, and wave III.

Table I. Oxidation of 6-thiopurine at a stationary pyrolytic graphite electrode[a]

	Wave I			Wave II			Wave III		
pH	i_p, μA	E_p, V	i_p/AC, μA/mM	i_p, μA	E_p, V	i_p/AC, μa/mM	i_p, μA	E_p, V	i_p/AC, μA/mM
0.00				1.10	0.79	0.202			
2.3	0.57	0.35	0.104	1.23	0.70	0.225		1.57[b]	
3.6	0.88	0.39	0.161	1.34	0.62	0.245			
4.4				1.05	0.62	0.192			
5.4	0.68[c]	0.28	0.125	1.32	0.52	0.241		1.10[b]	
6.1	0.56	0.25	0.102	1.21	0.48	0.221			
6.9	0.88[c]	0.15[c]	0.161	1.26	0.42	0.230			
8.1	0.58	0.13	0.106	1.25	0.34	0.229			
9.2				1.35	0.30	0.237	3.32	0.62	0.607
9.9				1.82	0.29	0.333	3.80	0.93	0.694
12.0				1.30	0.20	0.237			

[a] Concentration of 6-TP 0.43 mM; electrode area 12.6 mm^2.
[b] This peak appeared as a sharp point on the voltammogram. A current could not be measured because generally the background trace showed greater current than that in the presence of 6-TP.
[c] Often this peak did not appear.

Table II. Oxidation of 6-thiopurine at a stationary pyrolytic graphite electrode. Effect of concentration

6-TP	Current for Wave[a]					
	I			II		
Concen, mM	Range, μA	Mean, μA	i_p/C, μA/mM	Range, μA	Mean, μA	i_p/C, μA/mM
	Background 1M acetic acid					
0.08	0.14-0.38	0.24	3.0	0.26-0.28	0.27	3.4
0.17	0.21-0.37	0.31	1.82	0.54-0.59	0.57	3.4
0.25	0.15-0.27	0.21	0.84	0.78-0.95	0.86	3.4
0.42	[b]			1.33-1.48	1.39	3.3
	Background NH_3/NH_4Cl pH 9.15					
	II			III		
0.08	[c]			0.80-1.01	0.90	11.2
0.17	[c]			1.82-2.01	1.95	11.5
0.25	0.96-1.04	1.00	4.0	2.81-3.01	2.84	11.4
0.42	1.57-1.68	1.61	3.8	4.41-4.83	4.61	11.0

[a] At least three replicate runs were carried out at each concentration level.
[b] In this series of runs a well-defined peak was not obtained but a rather indistinct inflection on the rising portion of wave II.
[c] At these concentration levels wave II was too indistinct and drawn out to allow accurate measurement of the peak current.

i_p/C ratio over the range of concentration examined of 3.4 μA/mM.

Wave I does not appear at pH 9.1 although waves II and III do. At the concentration ranges where waves II and III are sufficiently well-defined to allow accurate measurements, both have constant i_p/C ratios; for wave II i_p/C is 3.9 and for wave III i_p/C is 11.3 μA/mM. This data suggests that about three times as many electrons are involved in wave III as are involved in wave II.

The concentration independence of wave I is characteristic of an adsorption wave. Because the adsorption wave appears prior to the diffusion controlled wave it is probable that the product of the wave II process is adsorbed since its activity would be lower in the adsorbed state than in solution, hence facilitating the oxidation of 6-TP (17). As a result of the very low current for wave I it was not possible to study its behavior at concentrations where 6-TP would be oxidized in a diffusion controlled process to the adsorbed product and where surface coverage was not complete.

Wave II must therefore be due to oxidation of 6-TP to the dissolved form of the oxidation product. The i_p/C ratio for the sum of wave I and wave II currents in 1M HOAc is the same as for the single wave II ratio at pH 9.1 where wave I does not appear which again indicates that wave I is a small adsorption wave.

Cyclic voltammetry.—Cyclic voltammetry supports the view that the wave I and wave II processes give

identical products since at a scan rate of 20 mV·sec^{-1} reversing the anodic voltage scan after scanning wave I or wave I and wave II gave essentially identical cathodic voltammograms (Fig. 3 and 4). Usually the cathodic wave produced from the anodic adsorption wave alone appears at slightly less negative potential than that obtained when both anodic processes were scanned (Table III). This was particularly so at polarographic scan rates (2 mV·sec^{-1}) when the cathodic peak observed after scanning only anodic wave I was about 0.2V more positive than when both wave I and wave II were scanned (Table III).

The peak potential of this cathodic wave shifted linearly more negative with increasing *p*H.

At a scan rate of 20 mV·sec^{-1}

$$E_p = -0.085\text{-}0.0386\ pH$$

Recently Wopschall and Shain (18) have presented an elegant theoretical treatment of adsorption effects in stationary electrode polarography. Attempts were made in the present study to apply the various diagnostic criteria outlined by these authors, although their calculations were based on model systems where the electrochemical reaction was perfectly reversible. Oxidation of 6-TP at the PGE is not electrochemically reversible as evidenced by the separation of the anodic and cathodic peaks obtained by cyclic voltammetry.

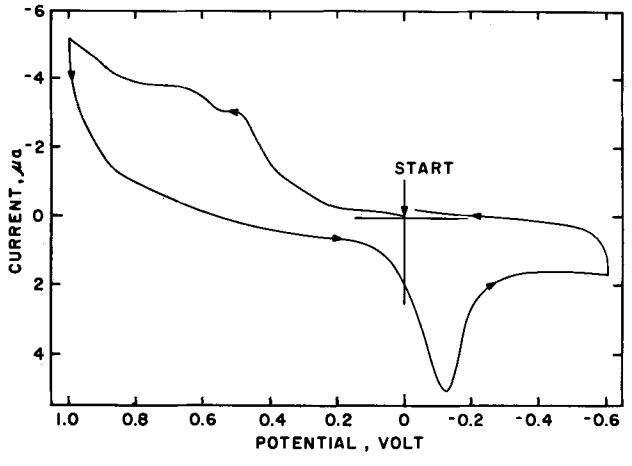

Fig. 3. Cyclic voltammogram at the PGE of 0.4 mM 6-thiopurine in 1M acetic acid background. Scan rate 20 mV.sec.$^{-1}$

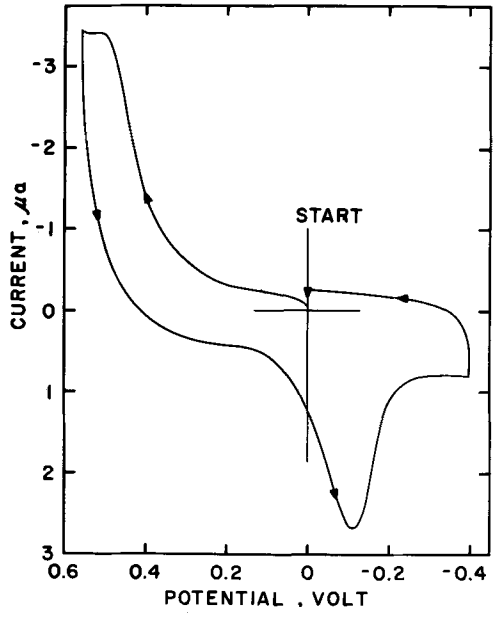

Fig. 4. Cyclic voltammogram at the PGE of 0.4 mM 6-thiopurine in 1M acetic acid background. Scan rate 20 mV.sec.$^{-1}$ Potential span limited to that of first wave.

Table III. Cyclic voltammetry of 6-thiopurine at a stationary pyrolytic graphite electrode in 1M acetic acid

Scan rate, mV·sec^{-1}	Peak potential for wave, V					
	Anodic				Cathodic	
	I	Mean	II	Mean	I	Mean
2	0.34[a]				0.18	0.21
	0.32	0.32			0.22	
	0.31				0.22	
	0.31[b]	0.32	0.63	0.63	−0.015	−0.012
	0.32		0.62		−0.01	
20	0.51[a]				−0.11	
	0.51	0.51			−0.12	−0.11
	0.50				−0.11	
	0.50[b]		0.69		−0.13	
	0.51	0.48	0.68	0.68	−0.13	−0.13
	0.38		0 68		−0.13	
200	0.61[c]	0.61			−0.24	−0.24
	0.60				−0.24	

[a] Only wave I was scanned.
[b] Both wave I and wave II were scanned.
[c] Only a single wave appeared; for discussion see text.

At *p*H 2.3 wave I shifts more anodic as the scan rate increases. At a scan rate of 2 mV·sec^{-1} wave I is almost always less than one half the height of wave II (Table II); at 20 mV·sec^{-1} scan rate wave I is of about the same height or slightly larger than wave II, whereas at 200 mV·sec^{-1} only wave I appears. Such effects are characteristic of an adsorption wave where the product of the electrochemical reaction is strongly adsorbed (18). It was rather difficult to obtain accurate data on the actual ratio of the peak current for waves I and II because of the somewhat variable height of wave I even on replicate scans. The cause of this irreproducibility was traced to variations in the electrode surface area under the conditions that were normally employed to prepare the PGE. Normally, the electrode was resurfaced before each voltammogram was run (see Experimental section) and, after washing the electrode with water, any loose graphite particles on the surface were removed by wiping the surface with a soft paper tissue. Experiment showed that if the surface were merely washed with water, but not wiped free of loose adhering graphite particles, the current for wave I was about three times larger than if the electrode were prepared in the usual fashion. Clearly the height of an adsorption wave such as wave I would be expected to increase as the surface roughness, hence surface area, increased. It is unlikely that either of these electrode preparation procedures would result in highly reproducible data for an adsorption process, although not apparently affecting a normal diffusion controlled process, hence the rather erratic behavior of wave I is not unusual.

At 200 mV·sec^{-1} scan rate in 1*M* HOAc the cathodic wave (E_p = −0.24V) has a greater slope on the rising portion of the wave than for the corresponding anodic wave, and the cathodic current is somewhat larger than the anodic current. Such behavior is characteristic of a process where the product of the initial electrochemical reaction is adsorbed (18-20).

The shift of the cathodic peak potential to more negative values with increasing scan rate is in accord with the expected shift for a process involving reduction of an adsorbed reactant (18). The fact that no post-peak is obtained may be associated with the rather irreversible nature of the over-all process.

Coupled with the very low current magnitude for wave 1 at polarographic scan rates (~2 mV·sec^{-1}), then wave I must be an adsorption wave due to adsorption of the product of the first electrochemical reaction.

Macroscale Electrolysis

Since wave I was shown to be due to an adsorption process, coulometry, and macroscale electrolysis were only carried out at potentials corresponding to waves II and III.

Coulometry at wave II in 1M acetic acid.—Electrolysis of 6-TP in 1*M* HOAc at a potential on the crest of anodic wave II gave an average coulometric n value of 0.98 (average of 0.94, 1.04, and 1.00). After the electrolysis had proceeded for some time a very pale yellow precipitate formed.

The ultraviolet absorption spectrum of the dissolved product differed considerably from that of 6-TP (1*M* HOAc λ_{max} = 324 mμ) having λ_{max} = 287-288 mμ.

The involvement of a single electron in the wave II process suggested that 6-TP was forming a dimer species similar to the disulfide species which are commonly encountered on mild oxidation of many alkyl and aryl thiols. Comparison of the ultraviolet absorption spectrum of the electrolysis product with that of authentic bis(6-purinyl)disulfide (PDS) showed them to be identical (12). The product of the electrolysis in 1*M* HOAc was isolated by lyophylizing the solution. The product was pale yellow and only very sparingly soluble in water. It gradually decomposed after turning orange at about 300°C [literature value 245(d) (12)]. Subsequent work indicated that this product was an impure sample of PDS and KCl (from the reference electrode and salt bridges) along with some disulfone and disulfoxide (*vide infra*). A suspension of this material in 1*M* acetic acid gave three distinct polarographic waves, $E_{1/2}$ = —0.03V, —0.26V, and —1.06V. Authentic PDS gave only two waves at $E_{1/2}$ = —0.05V and —1.05V. However, standing PDS in 1*M* HOAc for several hours (or warming the solution for a few minutes) resulted in the appearance of a new wave at $E_{1/2}$ = —0.30V with a decrease in the height of the most anodic wave. The wave at $E_{1/2}$ = —0.26V for the electrolysis product was only small when the electrolysis solution was polarographed immediately at the end of the electrolysis; it grew steadily in height over the course of several days or upon lyophylization of the solution. Hence the product giving rise to the wave at $E_{1/2}$ = —0.26V is due to chemical decomposition of PDS and is not due to a primary product of the electrochemical reaction.

Cyclic voltammetry of the electrolysis product solution at a scan rate of 20 mV·sec^{-1} showed that both anodic wave I and wave II had been eliminated and that a large cathodic wave, E_p = —0.15V had appeared along with a smaller wave at $E_{1/2}$ = —0.80V; the latter wave grew steadily over the period of several days. After scanning these cathodic peaks the original anodic waves I and II were observed on the subsequent anodic scan.

Once the nature and identity of the electrochemical oxidation reaction product had been ascertained (*i.e.*, PDS), a rate study of the oxidation was carried out by monitoring the rate of disappearance of 6-TP, the rate of appearance of PDS, and the rate of charge passage. The current and 6-TP concentration decreased exponentially with time and the PDS concentration increased exponentially at the same rate as predicted theoretically for a process which is diffusion controlled and free of long lived chemical or electrochemical intermediates (22).

Coulometry at wave II in ammonia background pH 9.1.—Electrolysis of 6-TP at a potential on the crest of anodic wave II gave an average coulometric n value of 4.08 (average of 4.00, 4.08, and 4.12).

As the electrolysis proceeded the ultraviolet absorption spectrum showed that the 6-TP peak (λ_{max} = 312 mμ) decreased in height and a new peak appeared at λ_{max} = 277-281 mμ. At completion of the electrolysis a peak λ_{max} = 277 mμ was observed.

The current did not decrease exponentially throughout the course of the electrolysis, but decreased fairly rapidly over the first hour or so and then decreased in a linear fashion until the completion of the electrolysis. Such behavior indicated the formation of an unstable intermediate, the breakdown of which to an electroactive species becomes the rate limiting step, although other kinetic explanations are possible.

On completion of the electrolysis, which was about three to four times as long as that in 1*M* HOAc, polarography of the solution showed five and, occasionally, six cathodic waves, $E_{1/2}$ = —0.41V, —1.02 to —1.05V, —1.18 to —1.20V, —1.39 to —1.43V, —1.50 to —1.55V and occasionally an even more negative wave of ill-defined potential at $E_{1/2}$ about —1.70V (Fig. 5). The wave at $E_{1/2}$ = —0.41V was always very small and on occasion was not even detected. The 6-TP wave II oxidation product solution showed a single well formed anodic wave at the PGE E_p = 0.87V and cathodic wave E_p = — 1.22V.

Since the height of voltammetric wave II at the PGE was approximately the same in both 1*M* HOAc and ammonia pH 9 (*i.e.*, same number of electrons involved) it seemed likely that PDS, the known product in 1*M* HOAc, was decomposing in alkaline solution to yield some further electro-oxidizable material. Accordingly, the stability of authentic PDS in ammonia pH 9.1 was examined. It was found, by ultraviolet spectrophotometric studies that 1 mole of PDS rapidly decomposed to give approximately 1.5 mole of 6-TP; no other easily observable spectrophotometric absorption peaks were observed. Polarograms of PDS in ammonia solution pH 9 after 6 hr at room temperature were qualitatively identical to those observed after complete electrolysis of 6-TP at wave II in the same background, except that the anodic wave of 6-TP was also observed, $E_{1/2}$ = —0.40V (23). Earlier workers have shown that PDS decomposes in alkaline solution to give 75% of 6-TP and 25% of the appropriate salt of purine-6-sulfinic acid (P-6-Si) (12). Authentic P-6-Si in ammonia pH 9.1 gave two polarographic waves $E_{1/2}$ = —1.20V and —1.70V (Fig. 6). Spectrophotometry of P-6-Si at pH 9.1 showed λ_{max} = 277 mμ and ϵ_{max} = 8.8 x 10^3 in agreement with earlier data (12). Voltammetry of P-6-Si at the PGE at pH 9.1 showed a well-formed anodic wave, E_p = 0.86V and a cathodic wave E_p = —1.21V.

Purine-6-sulfinic acid was found to be stable in ammonia pH 9.1 open to the atmosphere or with oxygen bubbling through the solution for at least 24 hr as evidenced by the almost constant height of its polarographic waves and absorption spectrum.

Doerr *et al.* (12) have reported that P-6-Si is converted to hypoxanthine in 95-100% yield in 0.1*M* hydrochloric acid. Treatment of the wave II electrolysis product solution (λ_{max} = 277 mμ) with hydrochloric acid resulted in the formation of two absorption peaks λ_{max} = 325 and 249 mμ, the latter being about three times as large as the former; in strongly acid solution λ_{max} 6-TP = 324 mμ, λ_{max} hypoxanthine = 248 mμ (24). This data therefore strongly supports the presence of P-6-Si in addition to other

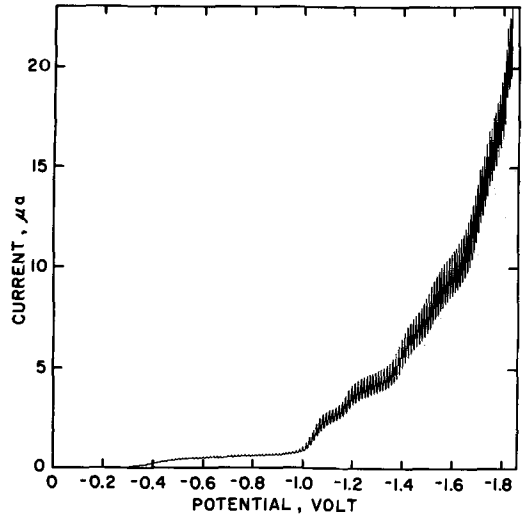

Fig. 5. Polarogram of 6-thiopurine wave II oxidation product in ammonia buffer pH 9.1. Solution originally 0.63 mM in 6-thiopurine.

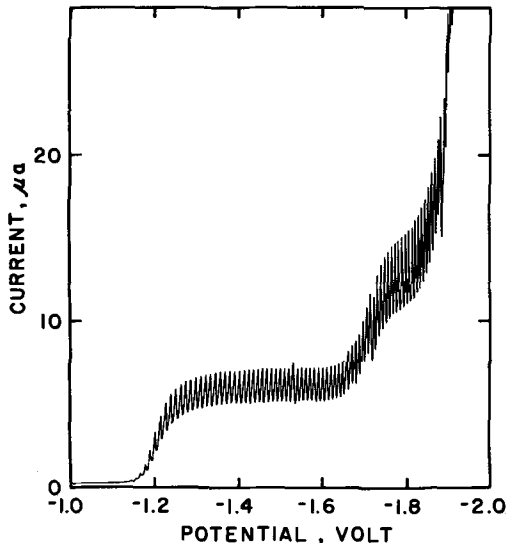

Fig. 6. Polarogram of approximately 1 mM purine-6-sulfinic acid (Na salt) in ammonia background pH 9.1.

products capable of regenerating 6-TP upon acidification.

It was thus fairly obvious at this stage that the primary electrochemical oxidation of 6-TP at potentials corresponding to wave II at pH 9.1 was a 1e process to give PDS, but that subsequent decomposition of this product leads to formation of 6-TP and P-6-Si along with other products. The nature of these other products became more obvious when the mechanism of the anodic wave III at pH 9.1 was studied. Further discussion will therefore be continued under Mechanism.

Coulometry at wave III in ammonia background pH 9.1.—Electrolysis of 6-TP at a potential on the peak of anodic wave III gave an average coulometric n value of 4.3 (average of 4.2, 4.4, 4.7, and 4.0).

The ultraviolet absorption spectrum of the electrolysis product differed quite considerably from that of 6-TP (λ_{max} = 313 mμ) having λ_{max} = 280 mμ. At no point in the electrolysis did the 313 and 280 mμ peaks appear together; rather there was merely a pronounced broadening of the peak in the intermediate stages of the electrolysis. The electrolysis was completed in less than one fourth the time required for complete electrolysis of 6-TP at wave II at pH 9.1.

Voltammetry of the product solution at the PGE showed a small rather poorly defined wave at E_p = 0.85V.

Polarography of the product solution showed five or possibly six waves cathodic $E_{1/2}$ = —0.49 to —0.50V, —1.03V, —1.20V, —1.43V, —1.55V, and possibly an ill-defined wave at —1.7 to —1.75V. The wave at $E_{1/2}$ = —0.49V was always extremely small and on occasion was not observed at all. The waves at —1.20 and —1.70V were also considerably smaller than observed in the electrolysis solution from wave II electrolysis in ammonia. The spectral data, voltammetry, and polarography indicated that P-6-Si was present in the electrolysis solution. However, the fact that the P-6-Si voltammetric anodic wave and polarographic cathodic waves ($E_{1/2}$ —1.20V and —1.70V) were lower than observed in the wave II electrolysis solution suggested that P-6-Si might itself be oxidized at wave III potentials (0.64V). A voltammogram of P-6-Si at pH 9.1 indicated that at 0.64V some oxidation would indeed occur. When a 1 mM solution of P-6-Si was electrolyzed at the PGE at 0.64V for 4 hr at pH 9.1, it was found that the original polarographic waves at $E_{1/2}$ —1.20V and —1.70V decreased in height and three new waves appeared at $E_{1/2}$ = —1.03V, —1.43V, and —1.54V and the polarogram had, qualitatively, the same form as that of the wave II and wave III electrolysis product solutions at pH 9.1. By altering the applied potential to 0.80V the polarographic waves at $E_{1/2}$ = 1.20V and —1.70V could be completely eliminated leaving only four waves at $E_{1/2}$ = 1.03V, —1.28V, —1.43V, and —1.56V; the wave at —1.28V was very small. Coulometry of P-6-Si at 0.8V in ammonia buffer pH 9.1 gave an average coulometric n value of 1.9. This at first suggested that the oxidation product was purine-6-sulfonic acid (P-6-So). However, polarography of authentic P-6-So at pH 9.1 gave waves at $E_{1/2}$ = —1.31V, —1.46V, and —1.56V indicating that the main product of the oxidation was not P-6-So. The only alternative therefore was that P-6-Si was being oxidized in a 2e process to purine-6-sulfonamide (P-6-Sm) (Eq. [1]).

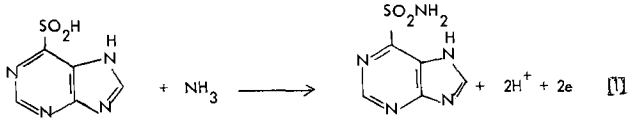

[1]

The spectra of P-6-Si, P-6-So, and P-6-Sm are so similar λ_{max} = 277 mμ, 279 mμ, 281 mμ, and ϵ_{max} = 1.09 x 10^4, 8.8 x 10^3, and 8.9 x 10^3, respectively, at pH 9, that it is impossible to determine or distinguish then in the presence of each other. However, polarography of P-6-Sm at pH 9.1 at about the same concentration as the product showed three distinct waves at $E_{1/2}$ = —1.03V, —1.43V, and —1.55V. P-6-Sm was stable in aerated ammonia pH 9 for several hours. Polarograms of P-6-Sm, P-6-So, and the solution of oxidized P-6-Si in ammonia buffer pH 9.1 are presented in Fig. 7. The mechanisms of the polarographic reduction of all these compounds have been elucidated (25). Clearly P-6-Si is oxidized in ammonia pH 9 predominately to P-6-Sm.

By preparation of suitable calibration curves for P-6-Si, and P-6-Sm it proved possible to determine quantitatively each of these electrolytic oxidation products of 6-TP wave III at pH 9. A 0.94 mM solution of 6-TP gave 0.35 mM P-6-Si and 0.50 mM P-6-Sm with possibly a very small quantity of P-6-So, *i.e.*, less than 0.1 mM. This represents better than 90% of the original 6-TP accounted for. It did not prove possible to identify the product which gave rise to the first small polarographic wave at $E_{1/2}$ = —0.40 to —0.50V.

Coulometry of 6-TP at wave III in carbonate buffer pH 9.—In carbonate-bicarbonate background pH 9, 6-TP shows two well-formed anodic waves at PGE at E_p = 0.3V and 0.82V. The average coulometric n value at an applied potential of 0.8V was 5.0 (average of 4.73 and 5.28). At completion of the electrolysis the ultraviolet absorption spectrum was quite different from that of 6-TP, having λ_{max} = 277-278 mμ. Polarography of the product solution showed that two waves were produced $E_{1/2}$ = —1.42V and —1.58V (6-TP showed no polarographic waves in this background). The involvement of 5e suggested that P-6-So might be an ex-

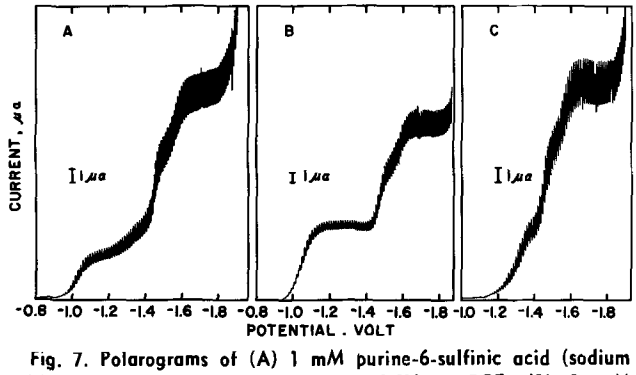

Fig. 7. Polarograms of (A) 1 mM purine-6-sulfinic acid (sodium salt) after exhaustive electrolysis at 0.8V at PGE, (B) 1 mM purine-6-sulfonamide, and (C) 1 mM purine-6-sulfonic acid (potassium salt) in ammonia buffer pH 9.1.

pected oxidation product, and indeed it was found that P-6-So gave an identical polarogram. Because of the involvement of only 5 electrons and the known instability of PDS in alkaline solution it was thought that the oxygen present in the electrolysis solution might chemically oxidize a small amount of some intermediately produced PDS. Coulometric electrolysis of 6-TP with argon bubbling through the solution gave an n value of 6.2. Analysis of a product solution after electrolysis of 1.02 m*M* 6-TP gave 1.10 m*M* P-6-So, which bearing in mind slight evaporation losses, accounts satisfactorily for the total 6-TP initially present.

Mechanism of Oxidation of 6-Thiopurine

The characteristic ultraviolet absorption spectrum of 6-TP is due mainly to the —C(4) = C(5) — C(6) = N(1) — chromophoric group, the fact that the u.v. absorption peak remains after oxidation, although λ_{max} is shifted slightly, indicates that the C(4) = C(5) — bond remains intact. Thus the electrochemical oxidation of 6-TP at the PGE must obviously involve attack at the exocyclic sulfur atom rather than attack on the purine nucleus unlike other purine electrochemical oxidations (14, 15). This at first sight is rather surprizing in view of these latter studies and the known partial biological oxidation of 6-TP to 6-thiouric acid.

Wave I of 6-TP is undoubtedly an adsorption wave due to adsorption of bis(6-purinyl)disulfide on the electrode as evidenced by the very low current observed for this wave, its dependence on surface roughness, and its behavior on both cyclic and linear sweep voltammetry.

Wave II of 6-TP is a true faradaic oxidation process involving 1*e* per mole of 6-TP to give bis(6-purinyl)-disulfide according to reaction

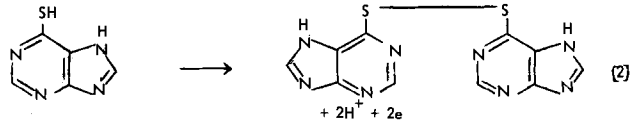

[2]

In 1*M* HOAc, PDS slowly decomposes to a product which is not 6-TP, P-6-Si, or P-6-So. The nature of this decomposition product is not definitely known but since its polarographic reducibility is somewhere intermediate between PDS and P-6-Si it is suggested that the decomposition product is either a disulfone [3a] or disulfoxide [3b].

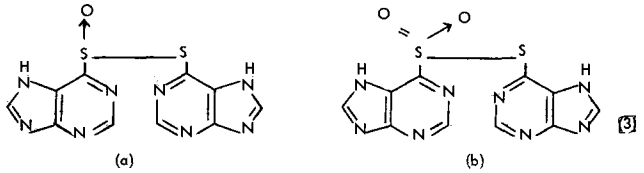

[3]

There is considerable evidence for the formation of these types of oxidized disulfides. For example oxidation of organic disulfides with cold nitric acid (31) or sulfuric acid (32) gives a disulfoxide as has oxidation with hydrogen peroxide (33-35). Disulfones have been formed by oxidation of the corresponding disulfide with perbenzoic acid (33, 34, 36). Many other references and data on these oxidized disulfide species are presented by Reid (37).

In ammonia buffer pH 9 PDS, the primary electrooxidation product, decomposes in a complex series of reactions to yield 6-TP, purine-6-sulfinic acid, purine-6-sulfonamide and possibly a small amount of purine-6-sulfonic acid according to a reaction of the type shown in Eq. [4].

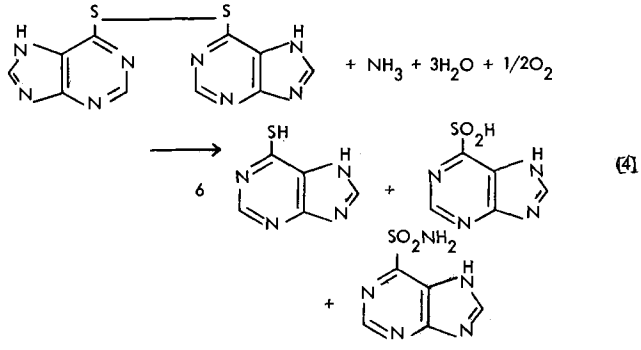

[4]

The involvement of this reaction in the over-all process is evidenced by the very slow nondiffusion controlled electrolysis and the fact that authentic PDS itself decomposes to the same products.

Wave III of 6-TP in ammonia background pH 9 is due to the oxidation of 6-TP to a mixture of P-6-Si and P-6-Sm and possibly a small amount of P-6-So according to reaction [5].

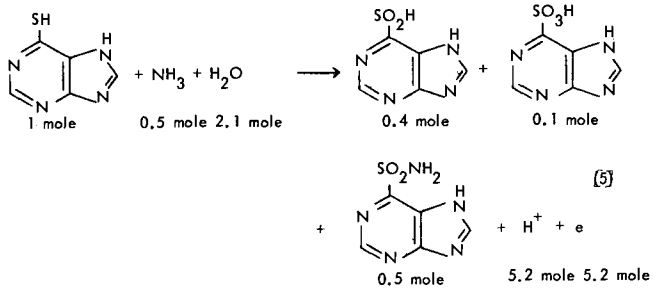

[5]

The fact that considerably less than 5.2*e* per mole of 6-TP are transferred may be interpreted as being due to intermediate formation of PDS which may either undergo further electrochemical oxidation, or may undergo chemical oxidation in the presence of dissolved oxygen to the same products via a route similar to reaction [4].

In the absence of ammonia and air in carbonate background pH 9 the wave III process involves 6*e* and 6-TP is quantitatively electrochemically oxidized to P-6-So according to Eq. [6].

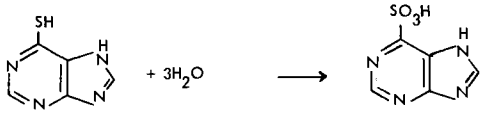

[6]

Since in the presence of atmospheric oxygen less than 6*e* are involved in the oxidation, it again seems reasonable to postulate that an intermediate species such as PDS may be partially chemically oxidized to P-6-Si or P-6-So.

Conclusions

Unlike the electrochemical oxidation of uric acid and adenine, which closely parallel enzymatic oxidations, 6-thiopurine is oxidized in a manner similar to chemical oxidation. These electrochemical mechanisms might however, aid in understanding the complete enzymatic mechanism, and not only suggest metabolites not previously suspected but provide the basis for selective analytical determinations of these compounds in complex mixtures.

The ease with which bis(6-purinyl)disulfide, purine-6-sulfinic, and sulfonic acids and particularly purine-6-sulfonamide are electrochemically prepared recommends further study of the utility of these findings in electrosynthetic chemistry, particularly in view of the difficulty with which P-6-Sm, for example, is prepared chemically (13).

Acknowledgment

The author would like to thank Professor Roland K. Robins of the University of Utah for a sample of purine-6-sulfonamide and Dr. Jack J. Fox of the Sloan-Kettering Institute for Cancer Research for samples of purine-6-sulfonic acid and purine-6-sulfinic acid. The author would also like to thank the National Science Foundation which supported the work described through grant number GP 8151.

Manuscript submitted Jan. 24, 1969; revised manuscript received *ca.* April 7, 1969.

Any discussion of this paper will appear in a Discussion Section to be published in the June 1970 JOURNAL.

REFERENCES

1. G. B. Elion, S. Singer, and G. H. Hitchings, *J. Biol. Chem.*, **204**, 35 (1953).
2. N. E. Balis, D. H. Levin, G. B. Brown, G. B. Elion, and G. H. Hitchings, *Arch. Biochem. Biophys.*, **71**, 358 (1957).
3. A. Hampton, *Federation Proc.*, **19**, 310 (1960).
4. J. S. Salser, D. J. Hutchinson, and E. M. Balis, *J. Biol. Chem.*, **235**, 429 (1960).
5. F. S. Philips, S. S. Sternberg, L. Hamilton, and D. A. Clarke, *Ann. N. Y. Acad. Sci.*, **60**, 283 (1954).
6. L. Hamilton and G. B. Elion, *ibid.*, **60**, 304 (1954).
7. H. R. Silberman and J. B. Wyngaarden, *Biochem. Biophys. Acta.*, **47**, 178 (1961).
8. F. Bergmann and H. Ungar, *J. Am. Chem. Soc.*, **82**, 3957 (1960).
9. F. Bergmann, H. Ungar, H. Govrin, H. Goldberg, and S. Leon, *Biochem. Biophys. Acta*, **55**, 512 (1962).
10. G. B. Elion and G. H. Hitchings, Ciba Foundation Symposium "Chemistry and Biology of Purines," 286 (1957).
11. G. H. Hitchings and G. B. Elion, U. S. Pat. 2,697,709 (1954).
12. I. L. Doerr, I. Wempen, D. A. Clarke, and Jack J. Fox, *J. Org. Chem.*, **26**, 3401 (1961).
13. A. G. Beaman and R. K. Robins, *J. Am. Chem. Soc.*, **83**, 4038 (1961).
14. W. A. Struck and P. J. Elving, *Biochemistry*, **4**, 1343 (1965).
15. G. Dryhurst and P. J. Elving, *This Journal*, **115**, 1014 (1968).
16. G. Dryhurst and P. J. Elving, *Anal. Chem.*, **39**, 606 (1967).
17. L. Meites, "Polarographic Techniques," second edition, p. 187, Interscience Publishers, New York (1966).
18. R. H. Wopschall and I. Shain, *Anal. Chem.*, **39**, 1514 (1967).
19. C. Olsen, H. Y. Lee, and R. N. Adams, *J. Electroanal. Chem.*, **2**, 396 (1961).
20. M. Brezina, *Collect. Czech. Chem. Communs.*, **24**, 4031 (1959).
21. L. F. Fieser and M. Fieser, "Organic Chemistry," third edition, pp. 139 and 594, Reinhold Publishers, New York (1956).
22. J. J. Lingane, *J. Am. Chem. Soc.*, **67**, 1916 (1945).
23. G. Horn and P. Zuman, *Collect. Czech. Chem. Communs.*, **25**, 3401 (1960).
24. S. F. Mason, *J. Chem. Soc.*, 2071 (1954).
25. G. Dryhurst, Work in preparation for publication.
26. G. Dryhurst, P. J. Elving, and M. Rosen, *Anal. Chim. Acta*, **42**, 143 (1968).
27. J. J. Lingane and L. A. Small, *Anal. Chem.*, **21**, 1119 (1949).
28. J. J. Lingane, "Electroanalytical Chemistry," Chap. XIX, pp. 457-458, Interscience Publishers, New York (1966).
29. N. Kharasch, S. J. Potempa, and H. L. Wehrmeister, *Chem. Revs.*, **39**, 269 (1946).
30. A. J. Parker and N. Kharasch, *ibid.*, **59**, 581 (1959).
31. W. F. Wolff and C. E. Johnson, U. S. Pat. 2,615,057 (1952) through *C. A.*, **46**, 3490.
32. H. T. Bennett and L. G. Story, *Oil Gas J.*, **27**, (8), 162 (1927) through *C.A.*, **21**, 2979.
33. H. J. Backer, *Rec. trav. chim.*, **67**, 894 (1948); *Bull. soc. chim. Belge*, **62**, 3 (1953).
34. H. Bretschneider and W. Klötzer, *Monatsh*, **81**, 589 (1950).
35. B. Weibull, *Arkiv Kemi*, **3**, 171 (1951).
36. C. J. Cavallito and L. V. D. Small, U. S. Pat., 2,508,745 (1950).
37. E. E. Reid, "Organic Chemistry of Bivalent Sulfur," Vol. III, Chap. 7, Chemical Publishing Co., New York (1960).

High Speed Non-Faradaic Resistance Compensation in Potentiostatic Techniques

A. A. Pilla,* R. B. Roe, and C. C. Herrmann*

Power Sources Division, Electronic Components Laboratory, USAECOM, Fort Monmouth, New Jersey

ABSTRACT

The general problem of the incorporation of IR compensation in a potentiostatic circuit is considered. The manner in which the number of time constants needed to describe the system affect the amount of stable positive feedback at short times or high frequencies is discussed and a theoretical model developed for present state of the art potentiostats and operational amplifiers. It is shown that the use of a model in which all series nonfaradaic resistance has been removed to establish a reference for complete IR compensation indicates that stable overcompensation cannot take place in any practical system. The use of positive feedback in pulse and a-c techniques is compared and it is concluded that great caution must be exercised in the latter with regard to the proper detection of optimum compensation. Interpretation of results using IR compensation is considered and it is shown that the use of frequency domain conversion to obtain the impedance of the system under, *e.g.*, pulse conditions allows potentiostat parameters to be eliminated such that meaningful results may be obtained at times of the order of 10 nsec.

The study of rapid or complex electrochemical reactions by means of the potentiostatic method is well known (1-5). One of the major limitations in the use of this technique is the presence of a nonfaradaic resistance across the potential control points in the potentiostat circuit. This may be caused by the presence of a relatively low conductivity electrolyte between the reference and working electrodes or to the resistivity of the particular working electrode configuration. The effect of the nonfaradaic resistance may be conveniently analyzed by considering the electrochemical system as linear. In this case the concept of impedance may be employed which allows the electrochemical system to be represented by an aperiodic equivalent electric circuit (6, 7). For most systems a circuit may be constructed such that the double layer capacitor, C_d, is shunted by a faradaic impedance, Z_F, the complexity of which depends on the actual reaction mechanism. The nonfaradaic resistance, R_e, is placed in series with the above elements. The total circuit is shown in Fig. 1. In order to provide a mathematical description of this circuit, Laplace transformation (8) will be used, as well as in the remainder of this study, since this allows simple algebraic expressions to be obtained which are sufficient to describe the frequency response of the system. Thus, the impedance, $Z(s)$, of this circuit is given by

$$Z(s) = R_e + \frac{1}{1/Z_F(s) + C_d s} \qquad [1]$$

where s is the Laplace transform variable. Note that s is a complex number given by $s = \sigma + j\omega$, where σ is the real part, and ω the angular frequency and $j = \sqrt{-1}$ define the imaginary part. The dimension of s is reciprocal time. Inspection of this equation indicates that evaluation of the faradaic portion of the impedance (*i.e.*, electrode kinetic constants) necessitates a knowledge of R_e and C_d, as well as Z_F. Of prime importance, then, is the establishment of experimental conditions such that R_e is not so large as to obscure the remaining electrode impedance during electrolysis times significant with respect to the faradaic time constant(s). In addition, the classical treatment of the potential step method (1) requires that constant potential conditions be achieved across C_d essentially at the beginning of electrolysis. Clearly a large R_e will not allow this. An elegant discussion of the effect of R_e on the time domain response of relatively simple systems to a variety of potential input signals has recently been presented (9). This study clearly shows that elimination of the effect of R_e would be highly desirable.

The potentiostatic technique lends itself readily to the use of the generally applicable positive feedback method for the reduction of the effect of R_e. Thus if a current-proportional voltage signal of the same sign as that of the input signal is appropriately fed back into the potentiostat input it is clear that the potential function desired across the interphase region of the working electrode will be more closely approximated. The positive feedback technique has long been employed by electrical engineers in amplifier design (10, 11), but has only recently been used in electrochemical studies. Several workers have given circuits devised to achieve compensation (*i.e.*, reduce the effect of R_e) in some cases (12-23), but frequency limitations and phase instabilities have been the major causes of the lack of generality of these techniques. Further, there appears to be a rather major misconception about what the oscillations (whether damped or undamped) caused by too much positive feedback mean in terms of the degree of compensation. For example, recent analyses (23-25) of the frequency behavior of some potentiostats with IR compensation appear to show that stability conditions can be such that what has been

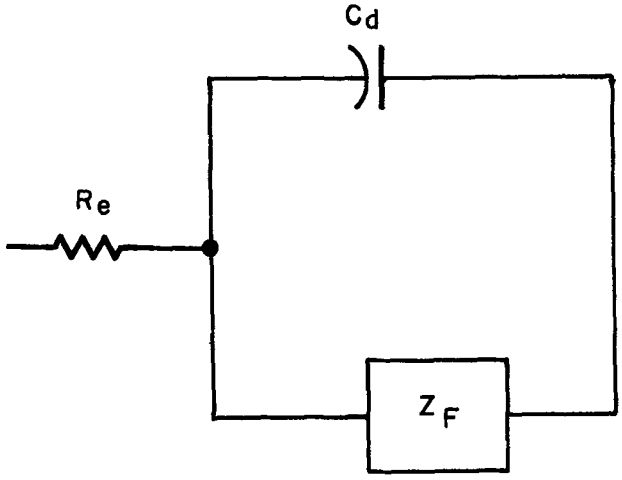

Fig. 1. General equivalent electric circuit for an active electrode. R_e is the nonfaradaic resistance, C_d the double layer capacitance, and Z_F the general faradaic impedance.

* Electrochemical Society Active Member.

called overcompensation can occur in some cases before the system becomes unstable. It will be shown below that if the reference point for complete compensation is correctly chosen then overcompensation cannot occur in any practical system.

The most versatile potentiostat-IR compensation system is that which can achieve the lowest effective R_eC_d time constant without the onset of severe ringing or oscillations which would render potential control impossible. The basic criteria for the realization of such a system are considered in detail and it is shown that a potentiostat and positive feedback amplifier are presently available which allow these criteria to be closely met.

Theoretical

In order to discuss the requirements for the proper design of a potentiostat which is able to operate effectively, and therefore with sufficient stability at short times (or high frequencies) with the incorporation of positive feedback IR compensation, it is appropriate to review the stability criteria for the transfer function of a feedback amplifier. The circuit description of a feedback amplifier is well known (26) and can be represented as shown in Fig. 2. The transfer function is defined as the ratio of the transform of the output voltage $O(s)$ to that of the input voltage $V(s)$. This ratio can be readily shown (26) to be given by

$$\frac{O(s)}{V(s)} = \frac{G(s)}{1 + G(s)\,H(s)} \qquad [2]$$

where $G(s)$ is the open loop gain function of the potentiostat and $H(s)$ is the function (often complex) representing the output voltage which is fed back to the input of the potentiostat.

Consideration of Eq. [2] will indicate in a straightforward fashion whether or not a given system can exhibit instabilities. For this the denominator of the r.h.s. of [2] need only be considered. It is clear that if

$$1 + G(s)\,H(s) = s + a \qquad [3]$$

where a is the inverse of the time constant, then the system, which can now be described as first order, will be inherently stable. This is so since its time domain behavior can only be a decreasing exponential function for real and positive a. Thus the voltage output of the potentiostat will be given in general by

$$O(t) = A \exp - at \qquad [4]$$

where A will depend on the explicit forms of $V(s)$, $G(s)$, and $H(s)$. However, if

$$1 + G(s)\,H(s) = s^2 + as + b \qquad [5]$$

then the system is now second order and may exhibit severe instabilities. This may be seen by considering the roots of the r.h.s. of [5]. If these roots are real, *i.e.*, $a^2 - 4b$ is real and positive, the time domain response will be of the form

$$O(t) \propto \frac{\exp(-at/2)\,\sinh(\sqrt{b - a^2/4}\,t}{\sqrt{b - a^2/4}} \qquad [6]$$

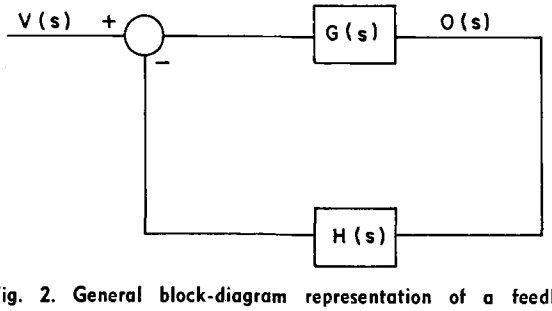

Fig. 2. General block-diagram representation of a feedback amplifier.

which is clearly a stable response function. However, for the case in which the roots are complex, *i.e.*, $4b - a^2$ real and positive, the system will exhibit damped oscillations (or ringing) since the response will be of the form

$$O(t) \propto \frac{\exp(-at/2)\,\sin(\sqrt{b - a^2/4}\,t}{\sqrt{b - a^2/4}} \qquad [7]$$

It is obvious from the above considerations that it is sufficient to consider the transfer function (which is therefore in the complex frequency domain) to obtain adequate information concerning the stability of the system. This is a simple matter in the second order case, but more complex for higher order systems. For these, the various stability criteria (*e.g.*, Routh-Hurwitz) have been adequately discussed elsewhere (27). It is to be noted, however, that the higher the system order the more difficult it will be in general to achieve smooth and stable response over a wide frequency range and to have sufficient gain at high frequencies for high speed applications. It is therefore of importance to have the minimum possible system order. That this is so can clearly be seen from the fact that a first order system will never oscillate, whereas second and higher order systems can and do indeed oscillate necessitating stabilizing networks which can increase the order of the system. It is to be noted that increasing the order of the system [*e.g.*, by the addition of zeros (28) to $G(s)\,H(s)$ in Eq. [2]] can increase the amount of positive feedback which can be tolerated before the onset of ringing. However, this is generally accomplished with a decrease in the power bandwidth of the system and therefore a decrease in maximum frequency at which a given degree of IR compensation can be obtained. Thus it may be advantageous when using a-c methods to increase the order of the system since this can allow a greater degree of compensation in the low frequency range of operation (23). In the case of pulse techniques, however, a maximum power bandwidth is desired since, *e.g.*, in the classical potential step method the object is to charge C_d in as short a time as possible (*i.e.*, minimum $R_e\,C_d$ time constant) under stable conditions.

The first step toward achieving minimum system order is therefore to employ a potentiostat which has the simplest possible gain function [$G(s)$]. The ideal potentiostat would be that for which $G(s) = K$, *i.e.*, a flat response in the frequency range of interest. Unfortunately this range is such that even the best practical potentiostats can rarely fulfill this condition simply because it has a finite rise time. A potentiostat frequently used for electroanalytical applications is constructed with three operational amplifiers (15), all of which are in the control loop and, at least two of which must be described by a minimum of a first order function for the respective $G(s)$, *i.e.*

$$G(s) = \frac{K}{s\tau + 1} \qquad [8]$$

where K is the open loop d-c gain and τ the open loop time constant of the potentiostat. A completely flat response [$G(s) = K$] is not attainable to the highest frequencies of interest in electrochemical applications. However, operational amplifiers which are adequately characterized by Eq. [8] are attainable and those having higher order gain functions should be avoided, if possible, for high speed applications.

An additional note should be made concerning the aspect of stabilizing a potentiostat both with and without IR compensation. If an operational amplifier is employed which has the desirable first order gain function (Eq. [8]) then every attempt should be made to assure that the process of stabilization does not increase the basic order of the system. Thus the incorporation of stabilizing networks in the control loop (23) normally increases the system order at high

frequencies. It is possible, however, to obtain stabilization through the use of operational amplifiers which have provision for external phase compensation. This is effectively an internal adjustment which does not change the essential gain function, merely its magnitude. Thus τ may be varied while Eq. [8] is still obeyed. This is a more desirable method of obtaining stabilization and it is recommended that all amplifiers employed in the potentiostat control loop be provided with external phase compensation when high speed applications are desired. It can now be seen that the use of two operational amplifiers in a standard potentiostatic circuit leads at least to an undesirable second order system even before the electrolytic cell characteristics are considered and also leads, as will be seen below, to a system of even higher order when IR compensation is employed. It is thus more advantageous to use a single operational amplifier for the potentiostat. This can be done through the use of a high impedance input differential amplifier. The basic circuit describing this approach is shown in Fig. 3 where R_o represents the output impedance of the amplifier to which eventually can be added a current sampling resistor. The necessary measurements of potential and current can easily be carried out by amplifiers which are not within the control loop and which therefore will not affect the stability of the control system. A possible arrangement is shown in Fig. 4 where R_C is the resistor across which a voltage proportional to the total current may be sampled, A_1 is the potentiostat, A_2 is a wideband differential amplifier, and A_3 is a high input impedance wideband voltage follower necessary only if reference electrode loading is unavoidable.

The incorporation of IR compensation in the single amplifier potentiostat described here can be achieved by voltage feedback of part of the signal appearing across a current sampling resistor to the noninverting input (+) of the potentiostat. This signal must be supplied by an additional amplifier which is now in a control loop and therefore must be considered when evaluating over-all system stability.

In order to evaluate the performance of the single amplifier potentiostat with IR compensation the circuit shown in Fig. 5 will be considered. Here A_1 and A_2

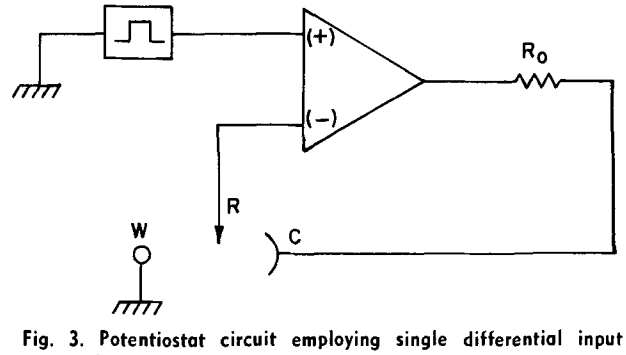

Fig. 3. Potentiostat circuit employing single differential input operational amplifier.

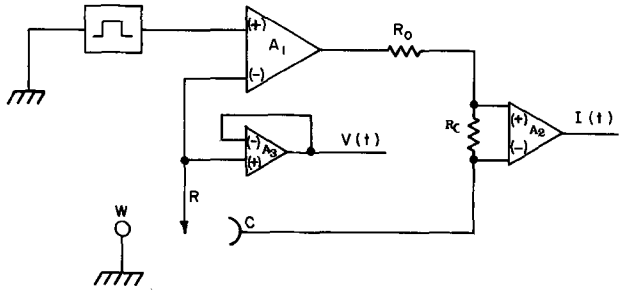

Fig. 4. Single amplifier potentiostat circuit with incorporation of potential and current measurement.

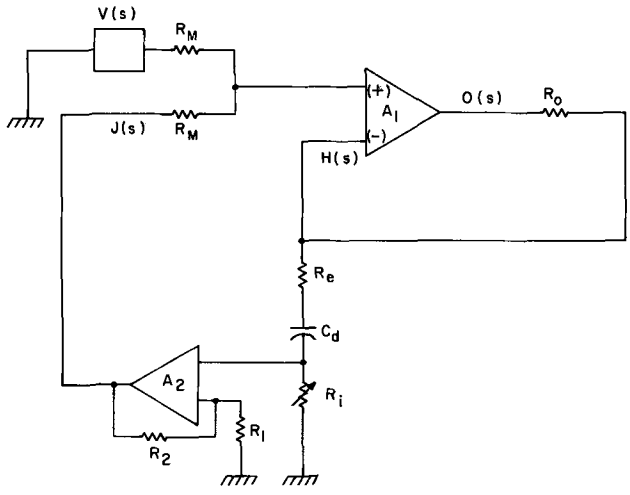

Fig. 5. Positive feedback potentiostat circuit with compensation outside the negative feedback loop.

are the potentiostat and IR feedback amplifiers respectively; R_e and C_d represent the electrochemical cell (a relatively accurate analog for high frequencies and low amplitude input signals); R_1 a resistor placed external to the cell for sampling the current-proportional IR voltage feedback signal, $J(s)$; $O(s)$ and $V(s)$ are defined in Eq. [2]; R_1 and R_2 fix the closed loop gain of the feedback amplifier; and R_M represents the mixing resistors for the addition of $V(s)$ and $J(s)$.

The over-all transfer function of this system may be written by considering Eq. [1] and taking into account $J(s)$. Thus

$$\frac{O(s)}{V(s)} = \frac{G_1(s)}{1 + (H(s) - J(s))\, G_1(s)} \qquad [9]$$

It will be considered here, that a potentiostat is available for which the gain function $G_1(s)$ is given by Eq. [8]. As indicated earlier it will be difficult to obtain a potentiostat which will have a zero order gain function for the variety of electrochemical cell conditions normally encountered. Since $H(s)$ is defined as the fraction of the output voltage which is fed back to the noninverting input of the potentiostat, it is given by

$$H(s) = \frac{(R_e + R_i)\, C_d s + 1}{(R_e + R_i + R_o)\, C_d s + 1} \qquad [10]$$

$J(s)$ is the voltage feedback ratio at the output of the IR feedback amplifier and is given by

$$J(s) = \frac{R_i\, C_d s\, G_2(s)}{(R_e + R_i + R_o)\, C_d s + 1} \qquad [11]$$

where $G_2(s)$ is the gain function of the IR feedback amplifier. Since the total order of the system is to be kept as low as possible, it is desirable that $G_2(s)$ be effectively given by K_2 which is simply the closed loop gain magnitude of the positive feedback amplifier. This can be accomplished if an operational amplifier, which is used merely as a voltage and not a current amplifier, can be obtained with a unity gain crossover point at least one order of magnitude above that which is possible with the potentiostat. If, in addition, the amplifier is employed at a relatively low ($\approx$10) closed loop gain, its closed loop time constant becomes small enough such that $G_2(s) = K_2$.

In order to use the above considerations to develop an expression which may be used to evaluate the stability of the system, it is convenient to define the quantity $E(s)/V(s)$ where $E(s)$ is the voltage function actually appearing across the potentiostat control points and $V(s)$ is the voltage function of the perturbation applied at the potentiostat input as defined earlier. $E(s)/V(s)$ can be regarded as an ideality ratio mea-

suring the degree to which the potentiostat can apply the input driving function across its control points. $E(s)$ is related to $O(s)$ by

$$E(s) = O(s) - i(s)\, R_o \qquad [12]$$

where $i(s)$ is the total output current. Using [9], [10], [11], and [12] the following expression for $E(s)/V(s)$ may be obtained

$$\frac{E(s)}{V(s)} = \frac{K}{K+1}\left[\frac{(R_e + R_i)\, C_d s + 1}{\left[\frac{(R_e + R_i + R_o)\, Cd\, \tau\, s^2}{K+1} + \left\{\frac{(R_e + R_i + R_o)\, C_d}{K+1} + \frac{K(R_e + R_i - R_i K_2)\, C_d}{K+1} + \frac{\tau}{K+1}\right\} s + 1\right]}\right] \qquad [13]$$

The system as chosen is thus second order and consideration of the expression between brackets in the denominator of the r.h.s. of [13] is, as indicated earlier, sufficient to evaluate the stability conditions for this particular electrochemical cell analog.

In order to analyze these conditions in terms of a real electrochemical system, it is convenient to define the following quantities

$$\tau_c = (R_e + R_i + R_o)\, C_d \qquad [14]$$

$$\tau_u = (R_e + R_i - R_i K_2)\, C_d \qquad [15]$$

$$\tau_e = \frac{\tau}{K+1} \qquad [16]$$

where τ_e is an experimentally obtainable quantity. Thus for any given potentiostat for which the open loop gain, K, is known (the manufacturers value may usually be relied upon), evaluation of the closed loop time constant, τ_e, under unity gain conditions on a purely resistive load allows relation [16] to be obeyed. This evaluation should be carried out at the power level of the particular experiment with IR compensation employed. The manufacturer's value of τ should not be used since this is usually obtained under essentially no-load conditions.

Using Eq. [14] to [16] the critically damped behavior allowable in terms of [13] is then

$$\tau_u + \frac{\tau_c}{K+1} + \tau_e = \sqrt{4\, \tau_c\, \tau_e} \qquad [17]$$

Equation [17] then allows the experimentally useful minimum time constant τ_{min} of the system at maximum stable positive feedback to be established

$$\tau_{min} = \sqrt{\tau_c \tau_e} \qquad [18]$$

Consideration of [18] indicates that the larger the cell time constant or the longer the closed loop potentiostat rise time, the larger the minimum time constant of the system. This means that, *e.g.*, for a given C_d, the larger R_e is, the larger τ_{min} will be at critical damping. The same reasoning holds true for every component of τ_c. Note that, in general the larger R_o is, (*i.e.*, the more resistance between counter and reference electrodes or the use of a large current sampling resistor), the larger τ_e will be since more power is thereby demanded of the potentiostat and τ_{min} is thus increased. It is therefore quite obvious that experimental conditions should be chosen to achieve minimum τ_e. This is of great importance in the choice of the manner in which IR compensation is carried out. Thus for maximum speed of compensation R_i should be placed in the working electrode circuit, *i.e.*, outside the negative feedback loop as opposed to being placed in this loop thereby effectively increasing R_o.

It is now appropriate to discuss what the minimum time constant, τ_{min}, signifies in terms of the degree of compensation of a given system. To do this it is necessary to establish what is actually meant by complete IR compensation. In the ideal case, for a perfect potentiostat, the current $i(s)$ required to charge C_d is given by

$$i(s) = V(s)\, C_d s \qquad [19]$$

where $V(s)$ is the input voltage function to the potentiostat. From a practical point of view this relation can of course never be satisfied for a voltage step or relatively high a-c frequencies, since it would require that the potentiostat be an infinite source of current. The charge of C_d will then always occur in some finite time and, for the model used in this study, the time for critically damped charging will be given by τ_{min}. In terms of Eq. [19], therefore, overcompensation can never take place due to the existence of the quantity τ_{min}. In fact, complete compensation can never take place even with a potentiostat which is several orders of magnitude better than the present state of the art models.

What then is meant by overcompensation? To understand the significance of this, it is sufficient to examine how τ_{min} is defined in terms of both the cell and potentiostat parameters. Using [17] and [18] τ_{min} may be defined as

$$\tau_{min} = \sqrt{\tau_c\, \tau_e} = \frac{\tau_u}{2} + \frac{\tau_c}{2(K+1)} + \frac{\tau_e}{2} \qquad [20]$$

Equation [20] shows that τ_{min} is a function of the amount of positive feedback τ_u as well as of both the cell and potentiostat time constants. Complete compensation in terms of previous definitions (23, 25) occurs when $\tau_u = 0$. It is quite clear that under these conditions τ_{min} still contains terms involving both the electrochemical system and the potentiostat. For the condition $\tau_u = 0$, Eq. [20] may be satisfied in a physically meaningful fashion only for the condition

$$\tau_c \geq 4\, \tau_e\, (K+1)^2 \qquad [21]$$

which means that the time constant of the cell has to be considerably larger than that of the closed loop potentiostat in which case the minimum time constant contains only electrochemical parameters.

Further examination of [20] indicates that, provided [21] is satisfied, it is possible for τ_u to become negative. This, however, does not mean that overcompensation has taken place since the system still has a finite time constant, but merely means that Eq. [20] is satisfied at the critical damping point of the system. The difficulty then essentially lies in the interpretation of the experimental results. If, as in the potential step method, it is desired merely to charge C_d as rapidly as possible in order to unmask faradaic current at the shortest possible times, then it is immaterial what constants τ_{min} is composed of. The only requirement is that the experimental conditions be arranged to achieve the smallest possible value for τ_{min}. However, it is often desirable to evaluate C_d using IR compensation. When this is so Eq. [20] clearly shows the conditions under which τ_{min} is appropriately determined by the electrochemical cell parameters, which then allow an unambiguous evaluation of C_d. Obviously there are cases in which this will not be possible.

In order to avoid the difficulty of determining C_d when employing compensation, it is possible to obtain results such that the quantity $Z(s)$ as defined by Eq. [1] may be evaluated. Equation [1] shows that $Z(s)$ is determined only by electrochemical cell parameters. For the model used in this study $Z(s)$ is given by

$$Z(s) = R_e + \frac{1}{C_d s} \quad [22]$$

Obtaining $Z(s)$ from experimental measurements necessitates a knowledge of the total current $i(s)$ flowing through the system. This quantity is related to $O(s)$ by the expression

$$O(s) = i(s)\,[R_o + R_i + R_e + 1/C_d s] \quad [23]$$

which states that the total output voltage of the potentiostat is the product of the current and the total impedance. Using [9], [10], [11], and [23] the following expression for $i(s)$ can be obtained

$$i(s) = \frac{K}{K+1} \frac{V(s)\,C_d s}{\tau_c \tau_e s^2 + (\tau_u + [\tau_c/K + 1] + \tau_e)s + 1} \quad [24]$$

where τ_c, τ_u, and τ_e are again defined in [14], [15], and [16], respectively.

The voltage appearing across the potentiostat control points (*i.e.*, between the reference and working electrodes) has been previously defined as $E(s)$ which is given in Eq. [13] for the case in which IR compensation is carried out in the working electrode circuit. The desired quantity $Z(s)$ is now obtained simply by dividing Eq. [13] by Eq. [24]. The result is

$$Z(s) = \frac{E(s)}{i(s)} = R_e + R_i + \frac{1}{C_d s} \quad [25]$$

This expression differs from Eq. [22] in the presence of the additional term R_i. This is to be expected since for this type of compensation R_i now appears between the potentiostat control points (see Fig. 5) and must be added to the electrochemical cell impedance. Inspection of [25] shows that the potentiostat characteristics, K and τ_e, as well as the time constant resulting from any degree of positive feedback, have been eliminated allowing only the desired electrochemical parameters to be obtained. Thus $Z(s)$ is a characteristic only of the quantities existing between the potentiostat control points and may be obtained no matter what the quality of the potentiostat is, or the type of perturbation, $V(s)$, applied to the system. $Z(s)$ is also obtained at any degree of compensation, however, the experimentally accessible information content at short times of both $E(s)$ and $i(s)$ becomes progressively better as the degree of positive feedback approaches critical damping, and for τ_{min} as small as possible. Thus, if R_e is large enough to effectively mask C_d at the short times of interest in this study ($s >> 1$), and if the system is such that the difference between τ_{min} and τ_c is only 10%, the evaluation of $Z(s)$ would still essentially allow only R_e to be evaluated at short times. This point is especially important when it is desired to determine C_d in the presence of a relatively fast faradaic reaction.

The impedance function $Z(s)$ may be obtained from either pulse or a-c measurements. For the former it is necessary to perform either real axis ($s = \sigma$) or imaginary axis ($s = j\omega$) Laplace transformation on both the total time domain (*i.e.*, experimentally measured) current, $i(t)$, and voltage $E(t)$ appearing across the potentiostat control points. This effectively converts the time domain results into the frequency domain as defined by the Laplace variable, s. The manner in which this may be performed has been discussed elsewhere (7, 29).

In the case of a-c measurements the results are obtained directly in the frequency domain since in this case, when steady-state is achieved, $s = j\omega$. The evaluation of the quantity $Z(s = j\omega)$ can then be carried out in a manner exactly analogous to that for pulse measurements. The experimental measurements, when a potentiostat is employed, are usually carried out either by direct measurement of the impedance magnitude and phase angle or by direct measurement of the real and imaginary parts of the impedance using phase sensitive detectors. Thus, in order to obtain $Z(s = j\omega)$ the a-c voltage across the potentiostat control points and the total a-c current must be employed. As in the pulse case, the information content at higher frequencies is increased when more positive feedback is employed and when τ_{min} is as small as possible. When measurements are performed in this way the phase angle will be the same at a given frequency independent of the amount of positive feedback employed (except of course when the stability conditions are exceeded). This is so since proper positive feedback merely changes the signal amplitude and not its phase relation provided that the voltage reference for phase is taken across the potentiostat control points as it must be in order to obtain $Z(s = j\omega)$.

The question of detection of optimum compensation conditions may now be examined. When a pulse or triangular voltage waveform is employed the onset of ringing is usually the most convenient manner to evaluate τ_{min}. In the a-c case phase angle measurements or phase sensitive detection cannot normally be used (this point will be discussed further below). However, the onset of nonlinearity caused, *e.g.*, by excitation of the ringing frequency may certainly be employed. This would probably necessitate the use of a distortion analyzer. As in the pulse or triangular waveform case complete IR compensation may not be achieved in a practical system. It is thus experimentally impossible to achieve either a phase angle of —90° or a zero in-phase component over the complete frequency range desired (*e.g.*, 1 Hz to 1 MHz) when the reference a-c voltage employed is that in the absence of compensation (*i.e.*, the total a-c voltage appearing across the potentiostat control points minus the compensation signal). The most convenient way to measure phase in this way would appear to be to use the voltage applied at the input of the potentiostat, $V(j\omega)$.

In order to determine what parameters have to be taken into account when the phase reference is taken as $V(j\omega)$, Eq. [24] may be employed. For the condition $s = j\omega$, and at critical damping, the following equation may be written

$$Z_A(j\omega) = \frac{V(j\omega)}{i(j\omega)} = \frac{1 + \omega^2 \tau_c \tau_e}{\omega C_d} e^{-j\pi/2}\, e^{j\theta} \quad [26]$$

where

$$\theta = \tan^{-1}\left[\frac{2\sqrt{\tau_c \tau_e}}{1 - \omega^2 \tau_e \tau_c}\right] \quad [27]$$

and $Z_A(j\omega)$ is the apparent complex electrochemical cell impedance.

Equation [26] may be compared to the expression for the ideal impedance $Z_I(j\omega)$ which would be obtained if the system behaved as though all series resistance ($R_e + R_i$) had been removed. This is given by

$$Z_I(j\omega) = \frac{1}{C_d} e^{-j\pi/2} \quad [28]$$

Comparison of [26] and [28] shows that in certain frequency ranges both the measured impedance magnitude and phase angle may differ substantially from that which would be obtained if all R_e and R_i were effectively removed. Thus, minimum magnitude error is obtained only for the condition $\omega << 1/\sqrt{\tau_c \tau_e}$, which means that only at frequencies much lower than the corresponding minimum time constant τ_{min} will the error be tolerable (two orders of magnitude lower for 1% error). Higher frequencies may of course be achieved as τ_{min} becomes lower and lower (*i.e.*, as the potentiostat employed for a given system becomes faster the higher is the minimum amplitude error frequency).

Evaluation of the minimum phase angle error may be carried out if the following equation, valid for small phase errors (≈1°) is employed

$$\theta = \frac{2\omega\sqrt{\tau_c \tau_e}}{1 - \omega^2 \tau_e \tau_c} \quad [29]$$

Using [29] the frequency ω_o at which the phase error is 1 degree is found to be

$$\omega_o = \frac{1.4 \times 10^{-3}}{\sqrt{\tau_c \tau_e}} \text{ Hz} \quad [30]$$

This again indicates that the minimum phase error frequency is substantially lower than τ_{min} and is one order of magnitude lower than the minimum amplitude error frequency. Conclusions identical to those for minimum amplitude error concerning the effect of a faster potentiostat prevail for minimum phase error.

The above considerations indicate that the evaluation of electrochemical parameters from a-c measurements must be carried out with extreme caution when IR compensation is employed particularly when phase angle measurements or phase sensitive detection are employed using $V(j\omega)$ rather than $E(j\omega)$ as phase reference.

Experimental and Results

In order to illustrate and test the model developed above for high speed ohmic drop compensation in the case of the potential step method, the basic circuit shown in Fig. 5 was employed. The potentiostat, A_1, is the ultrafast rise Tacussel Model PIT-20-2A provided with external phase compensation, the gain function for which is given by Eq. [8]. The IR feedback amplifier, A_2, is an Optical Electronics Inc. Model 9186 chosen for its unity gain cross-over point of 1 GHz and its provision for external phase compensation. This amplifier is the fastest known of the operational type having sufficient voltage and current range for the present application. Its low input impedance and limited current output (5 mA) prohibit its use as a potentiostat of the single amplifier type. For the present application the resistors in the loop of the OEI 9186 are chosen for appropriate closed loop gains to obtain sufficient positive feedback. For this $R_1 = 1$ k-ohm and R_2 is variable from 5 to 30 k-ohms in 5 k-ohm steps. Note that in general low value metal film resistors should be used for high speed operational amplifier applications (*e.g.*, R_1 and R_2 should not be tenfold larger, nor should they be wirewound). The step voltage source $V(s)$ is the Monsanto 300A pulse generator correctly mated to the potentiostat. The mixing resistors, R_M, are chosen in this case to be 1 k-ohm. Note that the best possible signal mixing should be carried out using a 50 ohm system. Unfortunately, however, an operational amplifier, having the characteristics of the OEI model, able to supply at least 5V into 50 ohms is not available at the present time. Thus in order to be able to obtain the required 5V from the OEI model, it is necessary that $R_M = 1$ k-ohm, which enables the time constant of the mixing network to be kept acceptably small.

Special attention must be given to the manner in which the amount of positive feedback voltage is adjusted. In the early applications of this technique R_i was simply a GR decade resistor box which enabled the feedback voltage to be increased to critical damping value by a stepwise augmentation of R_i. This approach has two inherent disadvantages if maximum compensation speed is desired. Thus as the critical damping point is approached τ_c becomes progressively larger because R_i is increased rendering τ_{min} larger than it need be. In addition, the residual inductance of these resistors is high enough ($\approx$1 μH) to cause considerable error at the frequencies attainable in this work. The use of, *e.g.*, a carbon potentiometer either in place of the decade resistor or at the output of A_2 is also not acceptable for high speed work since these are even more inductive and have high capacitance associated with them. The optimum manner found to attenuate the positive feedback signal with adequate resolution was to employ a fixed resistance for R_i and place a step-wise high frequency attenuator in series with the input to A_2. The attenuator chosen for this work is the Texscan Model RA-535 which allows 11 db of voltage attenuation in 0.1 db steps and is linear to 500 MHz. Use of this attenuator requires that it be terminated with 50 ohms which then restricts R_i to this value. In order to obtain sufficient positive feedback for values of R_c generally encountered in high speed kinetics studies (10-1000 ohms) the gain of A_2 was rendered adjustable in fixed steps from 6 to 30. The oscilloscope employed in this study was the Tektronix 556 equipped with two 1A5 preamplifiers. All voltage measurements were made using Tektronix P6045 probes at the input of the preamplifiers. These probes allow measurements to be made at nanosecond times with little or no perturbation on the system. In addition they can be matched to better than 0.5%.

In order to illustrate the affect of compensation on the observed current response to a potential step initial measurements were performed on an equivalent circuit with $R_e + R_i = 266$ ohms, $R_o = 0$, and $C_d = 0.15$ μF. Note that measurements performed on electrical analogs at the frequencies attainable in this work require that the components be suitable for high frequency work. Thus only metal film resistors and glass capacitors are used in this study. The photographs shown in Fig. 6 are oscilloscopic traces of the current-time curves experimentally obtained using the above components. The amplitude of the input voltage signal, $V(s)$, was chosen in each case so as to obtain 0.4 mA per major division on the vertical axis.

The validity of the model employed to evaluate the performance of the system employed in this study may readily be determined by evaluation of τ_{min}. This quantity is experimentally obtainable by determination of the time required for C_d to achieve 99% charge at critical damping. The results in Fig. 6b show that the experimental τ_{min} is 2.76 μsec. The closed loop potentiostat time constant τ_e for this circuit is 0.06 μsec and $\tau_c = 120$ μsec. Using these quantities τ_{min} is calculated from Eq. [18] to be 2.68 μsec. This is satisfactory agreement. In order to more fully test the theory a variety of equivalent circuits having τ_c from 15 to 350 μsec were examined. The results are shown in Table I. It may be seen that the average error between calculated and observed τ_{min} is approximately 5% which is sufficiently low to consider that the model considered in this study for IR compensation satisfactorily describes the actual experimental system.

An attempt was made to evaluate C_d from the time domain current response at critical damping for each of the circuits used above. The results in almost every case were ambiguous since a straight line plot of log i *vs.* t which would normally be valid for the series RC circuit used here was not obtainable over a sufficiently large time range. It is considered that a plot of this type over at least two orders of magnitude of t should be obtained for unambiguous results. In addition, this condition must be achieved at sufficiently short times if C_d is to be evaluated in the presence of a relatively fast faradaic reaction.

As was indicated earlier in the theoretical analysis, evaluation of the quantity $Z(s)$ from a knowledge of both $E(t)$ and $i(t)$ should alleviate the above difficulty. It will be remembered that $Z(s)$ is a characteristic only of the parameters existing between the potentiostat control points (in this case R_e, R_i, and C_d). Thus the actual shape of the current and voltage time curves is immaterial (*i.e.*, it does not matter whether or not the potential step has actually achieved its plateau value for meaningful results to be obtained). For this reason data points for both $E(t)$ and $i(t)$ as close to $t = 0$ as is experimentally possible may be utilized. In these experiments the first data point was normally obtained at 10 nsec to enable accurate real axis transformation to be accomplished for large σ values (29).

The evaluation of $Z(s)$ was carried out on a cell analog in which $R_e + R_i = 1050$ ohms and $C_d = 0.15$ μF.

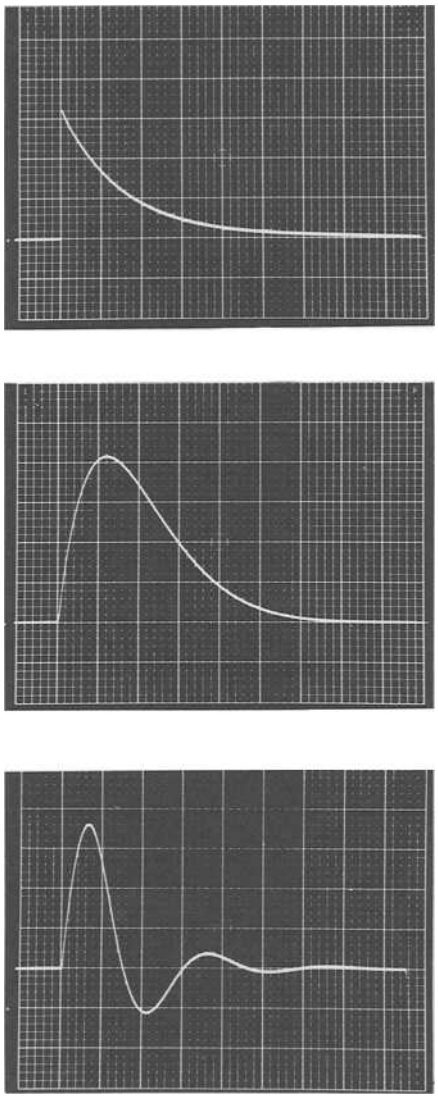

Fig. 6. Oscilloscope traces of current-time response curves to voltage step input. In each case the vertical axis (current) is 0.4 mA per major division and the horizontal axis is time as indicated below: (a) uncompensated system, 50 μsec per major division: (b) compensation at critical damping, 2 μsec per major division: (c) compensation exceeding critical damping, 10 μsec per major division.

Real axis ($s = \sigma$) Laplace transformation was performed with the aid of a digital computer (Burroughs 5500) on both $E(t)$ and $i(t)$. Results were obtained in the absence of compensation and at critical damping. In both cases $Z(s = \sigma)$ should be given by

$$Z(s = \sigma) = R_e + R_i + \frac{1}{C_d \sigma} \qquad [31]$$

Thus a plot of $Z(s = \sigma)$ *vs.* $1/\sigma$ should result in a straight line, the slope of which contains C_d while the intercept gives $R_e + R_i$. This plot is shown in Fig. 7 which shows the variation in $Z(s = \sigma)$ over two orders of magnitude in σ. This figure indicates that significant results are obtained in this time (frequency) range only when significant compensation is employed. Thus in the uncompensated case $R_e + R_i$ are overwhelmingly responsible for the current response and the experimental results reflect this condition enabling only the series resistance to be detected in the range $\sigma = 10^6 - 10^7$ and causing gross inaccuracies in the results down to $\sigma = 10^5$. It can then be seen that the use of compensation results in greatly increased experimentally accessible information content in the short time data enabling detection of, *e.g.*, double layer charging in the presence of a faradaic process. Particular attention should be paid to the fact that meaningful results have been obtained for σ values as large as 5 x 10^7 (see Fig. 7) which corresponds to a frequency of 50 x 10^6 rad/sec. This is a relatively high frequency necessitating certain experimental precautions. At these frequencies the major error is caused by the presence of inductance, *e.g.*, in the external electrical leads. For these experiments lead length could be kept to substantially less than 3 cm. However, in an actual electrolytic cell longer lead length is a necessity. In this laboratory cells requiring connecting leads of only 2-10 cm have been constructed which allow satisfactory results to be obtained at frequencies of up to 10^7 rad/sec. The description of this cell and results obtained with it will be reported elsewhere.

Table I. Comparison of theoretical and experimental τ_{min} values*

τ_c	τ_c	τ_{min} (calc.)	τ_{min} (obs.)
0.06	15	0.95	1.00
0.06	23	1.16	1.20
0.06	40	1.55	1.50
0.06	83	2.25	2.40
0.06	102	2.48	2.50
0.06	109	2.56	2.40
0.06	120	2.68	2.76
0.06	150	3.00	3.30
0.06	195	3.42	3.60
0.06	327	4.43	4.60

* All times are in microseconds.

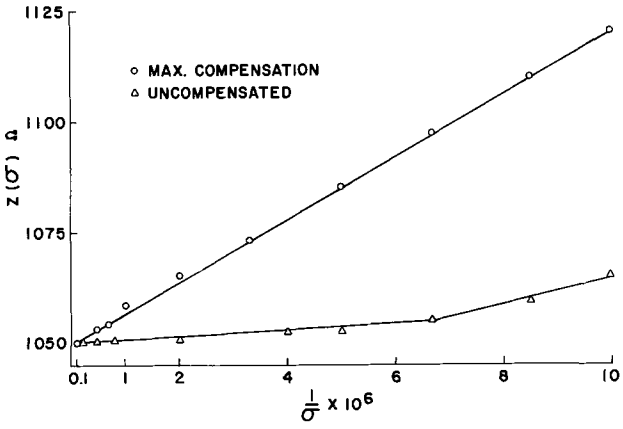

Fig. 7. Transient impedance obtained using frequency domain conversion for a potential step input.

Conclusion

The analysis presented in this study of the requirements for high speed IR compensation in potentiostatic techniques has enabled some basic criteria for the application of this technique to be established. The results indicate that the choice of a fast system should be predicated on achieving the lowest possible order for its transfer function which may be accomplished through the use of present state of the art potentiostats and operational amplifiers. However, the best that can presently be achieved is a second order system which by definition may exhibit instabilities if excessive positive feedback is employed. Examination of the stability criteria for this system allows the minimum time constant, τ_{min}, achievable at critical damping to be determined. The fact that τ_{min} is always a finite quantity implies that overcompensation in the absolute sense (*i.e.*, achieving the proper response to charge C_d in the absence of any series resistance) is a physical impossibility. Consideration of τ_{min} indicates that it is generally the sum of time constants involving both the electrochemical cell and the potentiostat, and it becomes difficult in some cases to evaluate unambiguously both the uncompensated resistance and the double layer capacitance. This problem may be overcome if the total cell impedance $Z(s)$ is determined

which effectively eliminates the potentiostat characteristics and τ_{min}. When compensation is employed, the experimentally accessible information content of the experimental data at critical damping is increased roughly by the percentage that τ_{min} differs from τ_e allowing more accurate results to be obtained at shorter times or higher frequencies thus allowing $Z(s)$ to be evaluated more precisely. This is of great importance when R_e is very large and it is desired to evaluate C_d in the presence of a relatively fast faradaic reaction. The detection of optimum compensation is straightforward for the case of the potential step technique, however, it becomes much less straightforward when a-c techniques are employed. For the latter, it is shown that the use of phase sensitive detection employing the potentiostat driving voltage, $V(j\omega)$, as phase reference can lead to severe errors in the interpretation of experimental data.

Manuscript submitted March 20, 1969; revised manuscript received April 17, 1969.

Any discussion of this paper will appear in a Discussion Section to be published in the June 1970 JOURNAL.

REFERENCES

1. H. Gerischer and W. Vielstich, *Z. Physik. Chem.*, **3**, 16 (1955).
2. W. Vielstich and H. Gerischer, *ibid.*, **4**, 10 (1955).
3. P. Delahay, in "Advances in Electrochemistry and Electrochemical Engineering," Vol. 1, p. 248, P. Delahay, Editor, Interscience Publishers, Inc., New York (1961).
4. A. A. Pilla, *Bull. Soc. Fr. Elec.*, **4**, 24 (1963).
5. R. S. Nicholson and I. Shain, *Anal. Chem.*, **36**, 706 (1964).
6. G. C. Barker, "Transactions of the Symposium on Electrode Processes," E. Yeager, Editor, John Wiley & Sons, New York (1961).
7. A. A. Pilla, D. Sc. Thesis, Paris, 1965; Proceedings of the Second International Fuel Cell Symposium, SERAI, Brussels, 1967.
7a. M. D. Wynen, *Rec. Trav. Chim.*, **79**, 1203 (1960).
7b. E. d'Orsay, *C. R. Acad. Sci. Paris*, **260**, 5266 (1965).
8. D. K. Cheng, "Analysis of Linear Systems," p. 351, Addison-Wesley, London (1959).
9. K. B. Oldham, *J. Electroanal. Chem.*, **11**, 171 (1966).
10. C. B. Aiken, *J. Opt. Soc. Am.*, **15**, 84 (1927).
11. J. E. Flood, *Wireless Engineer*, **27**, 201 (1950).
12. A. Hodgkin, A. Huxley, and B. Katz, *J. Physiology*, **116**, 424 (1952).
13. H. Gerischer and K. Staubach, *Z. Elektrochem.*, **61**, 789 (1957).
14. M. Bonnemay, E. Levart, A. A. Pilla, and E. Poirier d'Ange d'Orsay, *C. R. Acad. Sci. Paris*, **255**, 914 (1962).
15. G. L. Booman and W. B. Holbrook, *Anal. Chem.*, **35**, 1793 (1963); *ibid.*, **37**, 1322 (1965).
16. G. Lauer and R. A. Osteryoung, *ibid.*, **38**, 1106 (1966).
17. E. R. Brown, T. G. McCord, D. E. Smith, and D. D. DeFord, *ibid.*, **38**, 1119 (1966).
18. J. W. Hayes and H. H. Bauer, *J. Electroanal. Chem.*, **3**, 336 (1962).
19. M. E. Peover and J. S. Powell, *J. Palarog. Soc.*, **12**, 64 (1966).
20. P. Valenta and J. Vogel, *Chem. Listy*, **54**, 1279 (1960).
21. J. W. Hayes and C. N. Reilley, *Anal. Chem.*, **37**, 1322 (1965).
22. D. Pouli J. R. Huff, and J. C. Pearson, *ibid.*, **38**, 382 (1966).
23. E. R. Brown, D. E. Smith, and G. L. Booman, *ibid.*, **40**, 1411 (1968).
24. R. Koopman, *Ber. Bunsenges. Physik. Chem.*, **72**, 43 (1968).
25. A. Bewick, *Electrochim. Acta*, **13**, 825 (1968).
26. D. K. Cheng, "Analysis of Linear Systems," p. 262, Addison-Wesley, London (1959).
27. *Idem, ibid.*, p. 280.
28. A. Kuo, "Automatic Control Systems," 2nd ed., p. 313, Prentice Hall, Englewood Cliffs, N. J. (1967).
29. A. A. Pilla, R. B. Roe, and A. Anton, Communication presented at the Electrochemical Society Meeting, New York (1969).

Double Layer Capacitance on Platinum in 1M H_2SO_4 from the Reversible Hydrogen Potential to the Oxygen Formation Region

Murray Rosen,[1,*] David R. Flinn,[1,*] and Sigmund Schuldiner*

Electrochemistry Branch, Naval Research Laboratory, Washington, D. C.

ABSTRACT

Improved design and electronics which gave maximum oscilloscopic screen sensitivities of 5 mV and 5 nsec/div permitted measurements with single, relatively high intensity galvanostatic pulses of short duration so that the net perturbation of the system from equilibrium or steady state was small. This arrangement gave accurate separation of double layer, faradaic, and adsorption/desorption processes at times less than 200 nsec. The double layer capacitance at a clean, bright Pt electrode in 1M H_2SO_4 was measured from the reversible H_2/H^+ equilibrium potential to 1.2V *vs.* N.H.E. The double layer capacitance of the normal equilibrium hydrogen electrode on Pt was found to be 17 ± 1 μF/cm^2 (all measurements were on a true area basis). The double layer capacitance increases to 30 μF/cm^2 at 0.15V and uniformly decreases to 17 μF/cm^2 at 0.7V. Above 0.9V, the formation of highly polarized oxygen atoms on the Pt causes the capacitance to increase. The exchange current density for the $H \rightleftarrows H^+ + e$ reaction was found to be 0.44 A/cm^2. No "ideally" polarized potential region was found.

The measurement of the double layer capacitance on Pt has been complicated by impurities, fast faradaic reactions, and adsorption/desorption processes (1-3). At the reversible H_2/H^+ potential, double layer capacitance measurements have previously been masked by the pseudocapacitance which resulted from the fast hydrogen oxidation/reduction process occurring in parallel with the double layer charging. In the present work, the pseudocapacitance, adsorption/desorption, and impurity effects have been virtually eliminated, and the double layer capacitance *vs.* potential relation-

* Electrochemical Society Active Member.
[1] National Academy of Sciences–National Research Council Postdoctoral Research Associate at NRL.

ship has been determined from the equilibrium H_2/H^+ potential (N.H.E.) to 1.2V positive. The technique used examined the potential response of a Pt electrode/solution interface to a constant current pulse at very short times just after the perturbation time (4, 5). The latter phenomenon was shown to occur in 1M sulfuric acid solution in the first 38 nsec immediately after the application of a pulse.

Improvements in the cell design and electronic equipment used at this Laboratory to identify and to investigate the perturbation time have permitted a more precise separation of the faradaic, nonfaradaic, and double layer processes at times less than 200 nsec. A sensitivity of 5 mV/div on the oscilloscope potential axis and 5 nsec/div on the time axis of a single galvanostatic pulse has been achieved. As previously pointed out (6), high precision is required for double layer measurements on the non-ideally polarized Pt electrode.

Experimental

The electrochemical cell is shown in Fig. 1 and primarily varies from those used in past short pulse techniques (4, 5) by having a solution compartment above the coaxial arrangement of electrodes. The new cell permitted any arrangement of gas, a pre-electrolysis electrode, an α-Pd-H reference electrode, and a glass reference electrode to be introduced or removed at will.

In the circuitry shown in Fig. 2, the combination of resistor R_T and diode 1N914B are required to isolate the small d-c current which is always present at the output of the EH132A pulse generator. The value of resistor R_1 was such that the total pulse generator load exactly matched its output impedance, which was 50 ohms. The use of the Tektronix P6046 differential probe enabled potential measurement between the reference electrode and the grounded working electrode with *IR* compensation accomplished at the measurement point. This differential probe has a rise time of 3.5 nsec for all gain positions, with a maximum sensitivity of 1 mV/div. The Tektronix 454 oscilloscope also has a rise time of 3.5 nsec and has a maximum sweep rate of 5 nsec/div. A single sweep pulse was

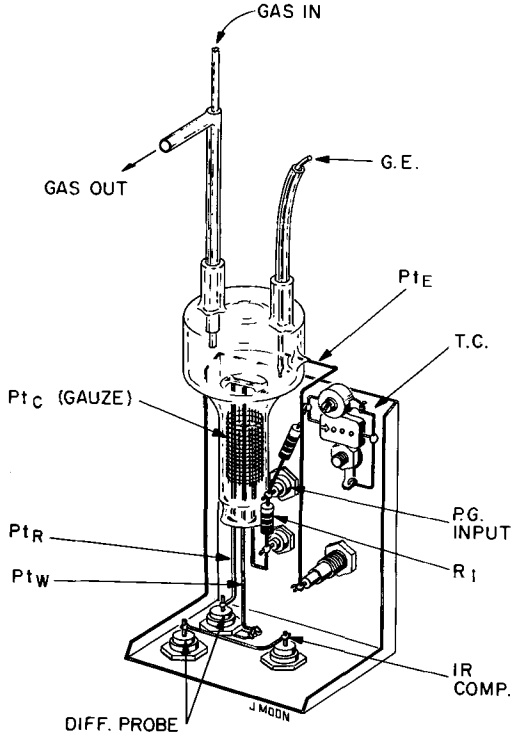

Fig. 1. Electrochemical cell: G. E.—glass electrode; Pt_E—electrolytic purification electrode; T. C.—trimming circuit; R_1—load resistor; Pt_W, Pt_R, Pt_C—working, reference, and counter electrodes, respectively.

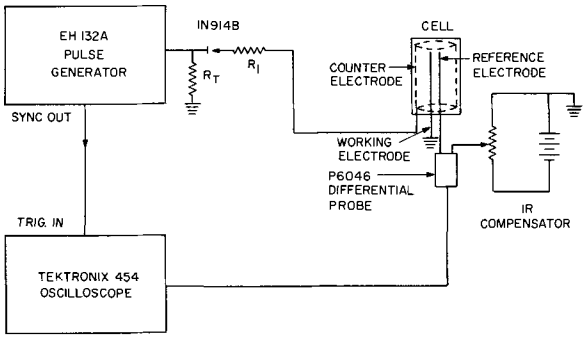

Fig. 2. Block diagram of short-pulse electrical circuit

recorded with a Tektronix C-31 Camera (f/1.2 lens) using Polaroid 10,000 ASA film. In order to maintain a useful relative perspective, most double layer capacitance measurements were made using a vertical sensitivity of 10 mV/div and a horizontal sweep rate of 20 nsec/div. The capacitance values at these sensitivities were the same as those determined at the maximum sensitivities of 5 mV/div and 5 nsec/div.

The working Pt electrode has a true area of 0.329 cm^2 as determined from measurements to be discussed later. All current density and area measurements reported in this paper are on the true area basis (2). The Pt reference electrode had slightly less area and was mounted parallel to the working electrode. These electrodes were surrounded by a large cylindrical Pt gauze counter electrode, approximately 0.5 cm in diameter and 2 cm in length. The circuit shown in Fig. 2 has been checked by substitution of the cell with several different equivalent circuits containing carefully calibrated components. Two differential probes were shown to have the same response and agree within experimental error when used with the equivalent circuits and the real cell.

The method of gas purification and distribution through a gastight, glass pipe system has been previously described (2). In addition to these pure gas sources, an electrolytic hydrogen-oxygen generator was placed directly in the He gas line. By the use of this generator, the partial pressure of hydrogen or oxygen passing through the cell could be varied from 0 to about 0.2 atm.

The method of cell cleaning has been previously described (5). In addition to this cleaning, the cell was later inverted while steam produced from triply distilled water was passed through the cell for at least 24 hr. The cell was then placed upright and allowed to fill with condensed water. The proper amount of ultrapure H_2SO_4 (E. Merck A. G., Darmstadt, containing impurities at generally less than the 10^{-7}% level) was then added to the cell.

Carefully cleaned shrinkable Teflon was used to couple short pieces of regular Teflon tubing to the cell. Concentric pieces of Teflon tubing were used for gas inlet and exit, giving the cell some flexibility when it was coupled into the regular glass pipe system. Gas entering the cell passed through the center Teflon tubing, while exit gases moved in the outer tube. This method effectively prevented appreciable oxygen leakage into the cell through the Teflon walls, as was shown by the fact that upon removing hydrogen from the cell and substituting helium the potential never rose above about 0.2V. Also, the seals made with the shrinkable Teflon tubing were gastight when checked with a leak detector sensitive to less than 0.1 ft^3/yr.

After the cell was cleaned and filled with solution, a pre-electrolysis treatment was performed. In this procedure, all of the Pt electrodes in the cell were made the anode with respect to a removable Pt cathode. A current of about 1 mA was passed through the cell for a 24-hr period in He-saturated solution. The removable cathode was then replaced by a clean glass

electrode, again coupled to the cell using several layers of clean, shrinkable Teflon tubing. Hydrogen was then introduced into the cell and the electrodes were left at open circuit for several hours to remove the last traces of oxygen.

A Pd wire was then introduced into the solution through the gas exit tube and was charged with hydrogen at 2 mA for ½ hr giving a stable reference electrode (7). This electrode was used for potentiostatic control of all further cell electrolytic purification and made it possible to control the electrolysis potential in the presence or absence of hydrogen. Electrolytic purification was repeatedly carried out between measurements using the working, reference, and counter electrodes as the anode and a small Pt wire mounted in the upper part of the cell as the cathode. It was necessary to remove the Pd wire from solution contact during capacitance measurements, since it was in effect an antenna which introduced sufficient noise in the reference electrode circuit making measurements impossible. The potential of the working electrode during electrolysis and during capacitance measurements was monitored by the use of the glass electrode, using a Keithley model 630 potentiometric electrometer. Cleanliness tests, which are discussed below, indicated that oxidation of organic impurities was more successful when done in the presence of a small amount of hydrogen mixed with helium than when done in pure helium. The hydrogen partial pressure during electrolytic purification was normally about 0.1 atm. The temperature was maintained at 25° ± 1°C.

Two tests were used for cleanliness. First is the shape of the anodic charging curve in H_2-saturated solution (2). In a clean system, the small breaks seen along the charging curve in the H atom ionization region are very distinct, as is the sharp transition from the H atom ionization to atomic oxygen formation region. Also, the O atom adsorption region is very linear in a clean system. The fact that an electrode remained at open circuit for many hours in a solution and still exhibited the same anodic charging curve was taken as good evidence of a clean system. The amount of charge required to move through the various regions had to remain invariant; that is, the charge required for hydrogen ionization and oxygen atom formation had to remain fixed.

The second check for cleanliness was less direct but was shown to parallel the first method. The capacitance at the N.H.E. potential was not strongly dependent on impurities. However, at potentials positive to 0.1V, the capacitance depended quite strongly on impurity adsorption at the electrode. This effect could be observed by first employing an anodic pulse to clean the electrode, followed by capacitance measurements made every few minutes for an hour or more. In an unclean solution the capacitance would slowly fall, while in a clean system the capacitance remained constant for times as long as 3 or 4 hr.

Results

The current density, i, is determined by measuring the time, t, required to generate one monolayer of O atoms, assuming that 456 $\mu C/cm^2$ is the charge required (2, 8). A pulse which represents a clean system and is used to determine current density is shown in Fig. 3a. The current density thus obtained is used to determine the double layer capacitance, C, from the potential response of the working electrode over a known period of time; hence,

$$C = i\frac{\Delta t}{\Delta E} \qquad [1]$$

The $\Delta t/\Delta E$ ratio at very short time and low polarization is considered to approach dt/dE, so that the true differential capacitance is virtually determined. For each measurement, a single, short, high current density galvanostatic pulse was applied to the working electrode which was at a steady-state potential prior to application of the pulse. The measured capacitance was independent of the galvanostatic pulse current density from 1 to 6 A/cm^2. Most of the data were taken using a 2.60 A/cm^2 pulse current.

A typical response of the working electrode to a single, constant current pulse is shown in Fig. 3b. This picture includes an approximately 0.4V solution IR drop and shows about 35 nsec of time from the initiation of the pulse to the point after which meaningful capacitance measurements may be taken. Because of experimental requirements, the cell used was not as compact as those previously used to determine perturbation time. The additional inductance and capacitance of the cell leads and components caused electrical disturbances which masked the perturbation region (4, 5).

The pulse current flow between counter and working electrode measured by use of a Tektronix P6020 probe placed around the working electrode lead wire is shown in Fig. 3c. The current is seen to be constant after about 30 nsec, and remained constant to 500 μsec.

In Fig. 3d, the response of the working electrode to a galvanostatic charging pulse of 2.60 A/cm^2 is shown on a more sensitive range of the differential probe with the solution IR drop fully compensated. The initial indeterminant electrode response has been shifted 40 nsec to the left on the oscilloscope screen. By measuring the initial linear potential response of 60 nsec, the capacitance may be calculated. The 40 nsec before capacitance measurements can be made does not appear to be as serious an experimental problem as might be thought, as was shown by the following experiment. By deliberately adding length to the connection between the cell and pulse generator, it was possible to produce an even longer indeterminate response, first up to 60 nsec and finally up to as long as 80 nsec, yet the initial capacitance determined after these longer times was the same, as was the over-all appearance of the curve. These results show that small electrical disturbances and inductive and capacitive time constant changes, which may delay the charging of the double layer up to 80 nsec, have no significant effect on double layer capacitance measurements.

The curvature present in the electrode response shown in Fig. 3d after the first 60 nsec does not appear to be due to a faradaic reaction. In the double layer capacitance *vs.* potential curve in Fig. 4, the capacitance is shown to increase with potential in the region from 0 to 0.15V, and it is possible to account for about 90% of the curvature observed in Fig. 3d by the changing capacitance. At more positive potentials, the response tends to become more linear as the capacitance becomes less potential dependent, but never becomes absolutely straight. This behavior seems to indicate rapid faradaic or adsorption/desorption processes at more positive potentials.

The potential of the working electrode as measured *vs.* the glass electrode was adjusted by four different procedures. In the first method, the amount of hydrogen in a helium gas stream was set to yield a given steady potential, after which the capacitance measurement was made. This procedure worked well in the region of 0 to 0.15V *vs.* N.H.E. In the second method, low concentrations of oxygen were introduced into the helium flow *via* the electrolytic generator. Potentials from equilibrium to about 1V *vs.* N.H.E. were set by this method. The rate of change of potential during oxygen addition could easily be controlled to less than 1 mV/min. In the third method, the working electrode was polarized by the use of repetitive short pulses, and the electrode was allowed to come to a steady potential for several minutes with continuous polarization. By this procedure, it was possible to collect capacitance data at any point over the entire potential range studied. Finally, in a few cases over the potential region between 0.3 and 1V, single, long pulses were employed to change the potential over a significant range, and the capacitance was determined as the electrode slowly

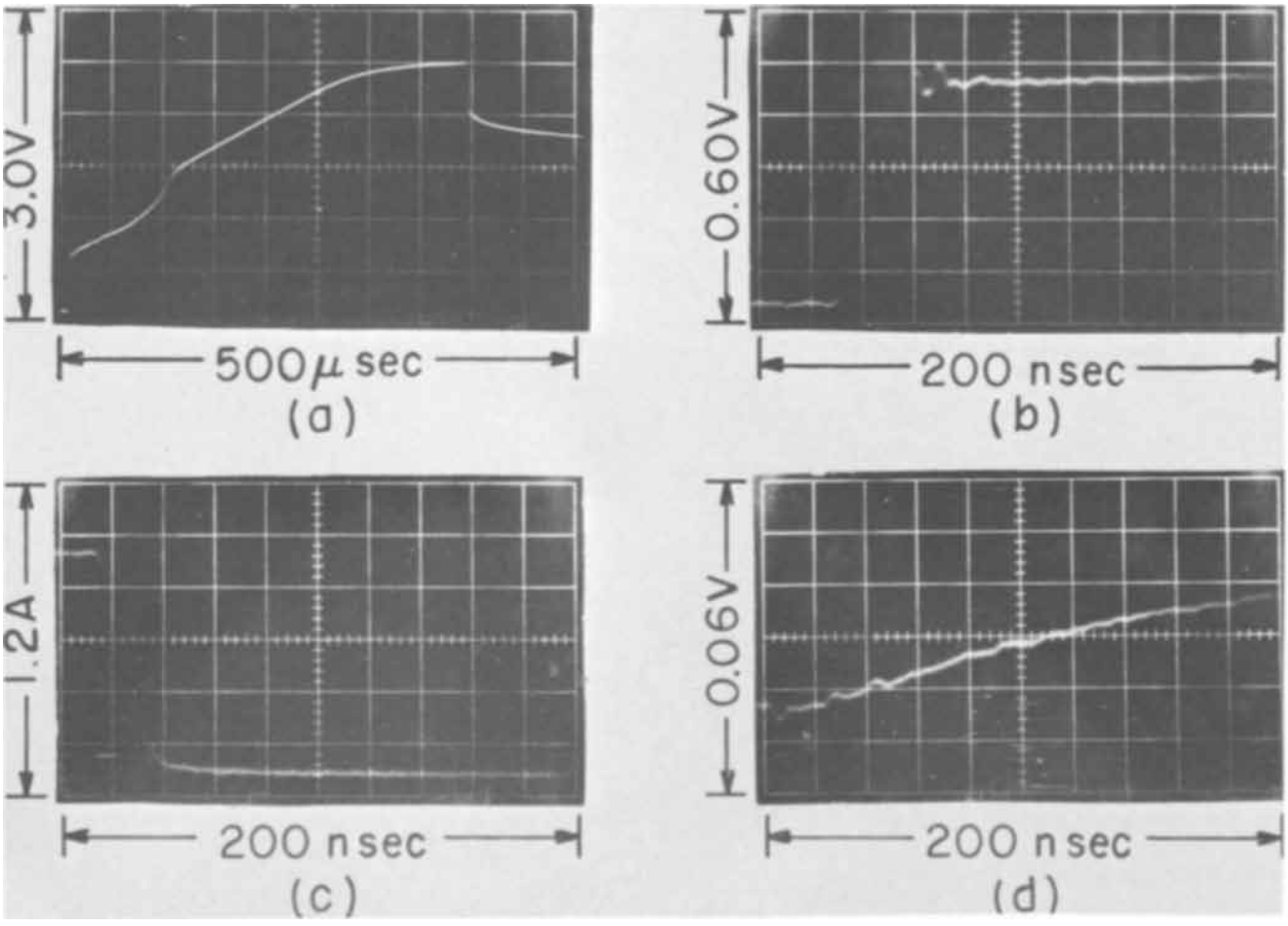

Fig. 3 (a) Typical anodic charging curve (i = 2.60 A/cm^2); (b) working electrode response at low sensitivity for 2.60 A/cm^2 constant current pulse without IR compensation; (c) pulse current flow between counter and working electrode measured with current probe; (d) working electrode response at high sensitivity for 2.60 A/cm^2 constant current pulse with IR compensation.

decayed through the desired potential. Within the ±5% experimental reproducibility, all of the above methods yielded the same result for the same measured potential from 0 to 0.95V *vs.* N.H.E. For the cases in which the electrode was made more positive than 1V for short times, and then allowed to decay to some less positive value, the measured capacitance would be too high for several minutes, indicating the presence of oxygen which is slowly removed from the electrode.

The double layer capacitance of Pt in 1M H_2SO_4 as a function of potential is shown in Fig. 4. The capacitance of 17 ± 1 μF/cm^2 measured at equilibrium appears to be the first accurately experimentally determined value of the double layer capacitance of an equilibrium hydrogen electrode. The capacitance is seen to pass through a maximum at about 0.15V *vs.* N.H.E. The scatter in the data was numerically largest in the region of the maximum, and this region was seen to be the most strongly influenced by organic impurities. In a clean system, the scatter of any point from the curve shown was about ± 5%. However, in the case of the presence of adsorbed impurities, an impurity level which reduced the capacitance at 0V by less than 1 μF/cm^2 reduced the capacitance by about 8 μF/cm^2 at 0.15V.

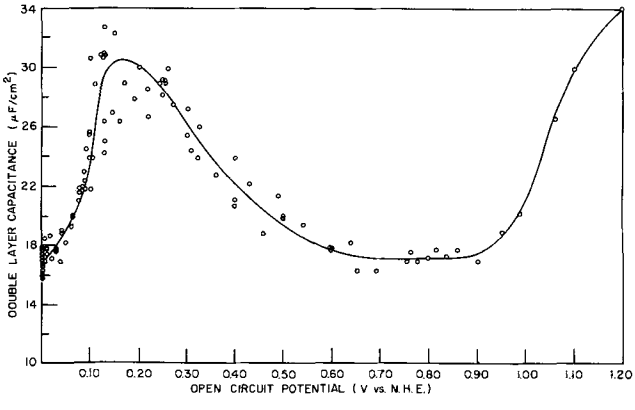

Fig. 4. Double layer capacitance *vs.* open-circuit potential

Discussion

The increase in capacitance noted above 0.9V has been cited and discussed (2, 9, 10) and is attributed to the presence in this region of a highly polarized chemisorbed oxygen-atom layer. The hysteresis noted here in capacitance measurements when the potential was reduced from above 1V down to some less positive potential has been observed by Laitinen and Enke in 0.01 and 1M $HClO_4$ solution (9). Near equilibrium, the potential response of the working electrode to the constant current pulse can be explained on the basis of the change in double layer capacitance with potential. This change means that the faradaic current component within the first 200 nsec is no more than about 5%, the average experimental error observed in these measurements. Consider the total applied anodic charging current density, i, to be divided between capacitive charging and a faradaic process, i_f(H = H$^+$ + e), then (11, 12)

$$i = C\frac{d\eta}{dt} + i_f \qquad [2]$$

$$i_f = \frac{i_o\,\mathbf{F}\eta}{RT} \qquad [3]$$

where η is the overvoltage, i_o is the equilibrium exchange current density, and R, T, and $\mathbf{F}$ are the gas constant, Kelvin temperature, and Faraday, respectively. Equation [3] assumes a linear current *vs.* overvoltage relationship over the low overvoltage region considered. Equations [2] and [3] may be integrated to yield

$$\eta = \frac{iRT}{i_o \mathbf{F}} \left\{ 1 - \exp \left[- \frac{i_o t \mathbf{F}}{CRT} \right] \right\} \qquad [4]$$

Equation [4] can be solved graphically to yield an i_o for the faradaic process, but care must be taken to assure that the experimental error does not override the faradaic contribution. For example, using a high current density pulse, we found $t = 100$ nsec, $\eta = 15.3$ mV, and $C = 17$ μF/cm^2. However, since the linear response found over the first 60-100 nsec shows that the contribution of the faradaic process to the measured capacitance is not detectable within the experimental limits of measurements, the above experimental results will not yield a solution for i_o. A necessary approach is to lower the amplitude of the applied current density pulse so that longer times are required to achieve comparable polarization, *i.e.* allow a significant faradaic component. To determine i_o, the amplitude of the galvanostatic pulse was reduced to 0.419 A/cm^2 causing a polarization of 13.6 mV in 800 nsec. Applying these values, along with $C = 17$ μF/cm^2, to the graphical analysis of Eq. [4] gave $i_o = 0.44$ A/cm^2.

An estimate of the experimental error involved in double layer capacitance determinations due to a faradaic component can now be made. If one assumes that the overvoltage in the typical high current density measurement given above ($t = 100$ nsec, $\eta = 15.3$ mV, and $C = 17$ μF/cm^2) is in error by 5% at the end of 100 nsec, η may be as small as 14.6 mV. Substituting into Eq. [4] gives $i_o = 0.1$ A/cm^2. If the error were 6%, i_o would be 0.4 A/cm^2. Therefore, even if i_o is of the order of 0.5 A/cm^2, the faradaic contribution to the calculated capacitance at times less than 100 nsec will be an insignificant portion (<5%) of the total capacitance. For longer times or higher polarizations, the faradaic component becomes a large portion of the total charging current.

In a paper by Schuldiner and Roe (2), the capacitance at Pt in 1M H_2SO_4 was determined using single 0.022 A/cm^2 current density pulses of 5 μsec duration. By this method, the measured capacitance near equilibrium was very erratic and varied from 100 to 300 μF/cm^2. These high capacitance values may now be explained on the basis of Eq. [4] and $i_o = 0.44$ A/cm^2. Schuldiner and Roe's measurement included pseudocapacitance, and they used Eq. [1] to calculate the net capacitance. For example, for a determined capacitance of 100 μF/cm^2, they observed an η of 1.1 mV. Using the correct capacitance value of 17 μF/cm^2, the 0.022 A/cm^2 current density and the 0.44 A/cm^2 i_o, Eq. [4] gives an η of 1.3 mV for a 5 μsec pulse. Thus, an $i_o = 0.44$ A/cm^2 satisfactorily predicts the observed overvoltage at the end of such a 5 μsec pulse. This observation means that an average of 80% of the applied current went into the faradaic reaction over this time. The possibility of the reaction of H_2 gas contributing to the total charge consumption at the low current density used should not be neglected. At higher current densities, contribution of H atoms from H_2 in solution is insignificant (8).

Schuldiner and Roe's (2) determination of double layer capacitance at potentials 0.1V positive to N.H.E. using 5-μsec pulses gives values about twice as high as those found in the present paper. These high capacitance values also have been found by others using similar techniques. The interesting feature of these measurements is that even those in the so-called double layer region (0.55-0.88V) require submicrosecond, high current density pulses to separate adequately double layer charging from faradaic and adsorption/desorption processes. In short, there is no "ideally" polarized potential region on Pt.

Measurement of the equilibrium capacitance also was made using the charge-step method. The current density was varied from 1 to 2.6 A/cm^2 and the time of charge input was varied from 60 to 140 nsec, so that q varied from 1 to 4 x 10^{-7} C. The decay responses, measured at 200 nsec/div, yield a linear log η against time curve. The initial overvoltage measured from these curves gave the same value as that measured directly from the oscilloscope pictures at pulse cut-off. The capacitance was found to be 17 $\pm$ 1 μF/cm^2 for all q values, so that decay and charging measurements result in the same capacitance value for the equilibrium case. Also, the slope of the log η *vs.* t curve yields a value of $i_o = 0.40$ A/cm^2 for the faradaic process, which is in good agreement with the low current-density pulse result.

The identical galvanostatic and charge-step results obtained at 0V indicates that adsorption-desorption processes are either of virtually infinite rate or that they are slow compared to the time periods of measurement used here. That the latter seems to be the case is supported by the high capacitance values found by Schuldiner and Roe (2) in the double layer region discussed earlier.

The agreement of the capacitance values determined by the use of both charging and decay techniques is, of course, important in itself. Moreover, the use of the charge-step technique is of interest for future work in dilute solutions in order to determine the potential of zero charge on a clean platinum electrode. Burshtein, Pshenichnikov, and Skevchenko (3) reported the presence of this capacitance minimum in 0.01N H_2SO_4 at 0.230V *vs.* N.H.E. and found its position to be pH independent.

Manuscript submitted March 24, 1969; revised manuscript received May 5, 1969. This was Paper 213 presented at the New York Meeting, May 4-9, 1969.

Any discussion of this paper will appear in a Discussion Section to be published in the June 1970 JOURNAL.

REFERENCES

1. M. C. Banta and N. Hackerman, *This Journal*, **111**, 114 (1964).
2. S. Schuldiner and R. M. Roe, *ibid.*, **110**, 332 (1963).
3. R. Burshtein, A. Pshenichnikov, and M. Shevchenko, *ibid.*, **113**, 1022 (1966).
4. S. Schuldiner and C. H. Presbrey, Jr., *ibid.*, **111**, 457 (1964).
5. B. J. Piersma, S. Schuldiner, and T. B. Warner, *ibid.*, **113**, 1319 (1966).
6. S. Schuldiner, D. R. Flinn, M. Rosen, and C. H. Presbrey, Jr., *J. Electroanal. Chem.*, Accepted for publication.
7. S. Schuldiner, G. W. Castellan, and J. P. Hoare, *J. Chem. Phys.*, **28**, 16 (1958).
8. S. Schuldiner and T. B. Warner, *This Journal*, **112**, 212 (1965).
9. H. A. Laitinen and C. G. Enke, *ibid.*, **107**, 773 (1960).
10. J. P. Hoare, *Nature*, **204**, 71 (1964).
11. C. H. Presbrey, Jr., and S. Schuldiner, *This Journal*, **108**, 985 (1961).
12. V. A. Roiter, V. A. Yuza, and E. S. Poluyan, *Zhur. Fiz. Khim.*, **13**, 605, 805 (1939).

The Rotating Split Ring-Disk Electrode and Applications to Alloy Corrosion

B. Miller*

Bell Telephone Laboratories, Incorporated, Murray Hill, New Jersey

ABSTRACT

The rotating ring-disk electrode technique has been extended to a split-ring design in which the half rings may be maintained at independent potentials. Availability of two detecting surfaces has facilitated studies in anodic dissolution of alloy or pure metal disks where two components or oxidation states can be simultaneously monitored. The construction of the split ring disk and operational amplifier circuitry for control of the three active electrodes (with disk potentiostatic or galvanostatic) are outlined. Applications to the anodic behavior of copper-zinc alloys in ammoniacal solution are discussed.

The utility of the rotating ring-disk system for observing both stable and unstable products of disk reactions has been well established since the original work of Levich, Frumkin, and Nekrasov (1-3). No studies of the dissolution under applied potential of metal disks appear to have been made to the time of Riddiford's review (4) but some such investigations (5-11) have been performed recently with ring-disks. Spontaneous reaction with disks (chemical corrosion or etching) has been studied [see (4)] where the solution is analyzed to determine the extent of reaction. The potential value of rotating disk studies for understanding metal and alloy corrosion processes is considerable, particularly with the addition of the ring to observe the products. To the measured corrosion behavior of the metal or alloy disk is added simultaneous information from the ring on the nature and amount of the species dissolving and, as the detectability of such ions varies with disk conditions, the results may be further interpretable in terms of film formation, change of mechanism, or chemical reaction in transit.

In many situations, *e.g.*, changing oxidation states in the anodic polarization of pure metals or multiple products in alloy dissolutions, the number of variables may make the combination of ring current and geometric collection efficiency (ratio of ring current to disk current for equal number of electrons transferred in the respective electrode reactions) insufficient to define the mass distribution adequately in a single experiment. In theory repetition of the experiment enough times or maintenance of a constant disk anodic reaction so that the ring can be adjusted to all necessary potentiostated conditions would give the total extractable information for that ring electrode. This requires that the experiment either be exactly duplicable or held in a constant state, conditions that may not be available when the surface of the disk or the composition of the solution is altered by the experiment. Particularly in the case of alloys where possible preferential dissolution of components may itself be the point of interest, repeated anodization experiments may well vary since the newly generated surface must necessarily be different from the original state when the effect is observed. In addition, holding all other experimental conditions constant may be difficult.

To extract more data from a single run and to measure reliably two oxidation states or components simultaneously, a split ring design has been constructed and investigated. This modification of the ring-disk system involves the use of a ring which is mechanically and electrically divided in half by two thin insulating regions 180° apart. Such a configuration extends the ring-disk method not simply through the more rapid accumulation of data numerically inherent in two simultaneous half-ring measurements, but more importantly for disk anodization, introduces the possibility of differentiating events in time (*e.g.*, selectivity in alloy dissolution and passivation) or distinguishing the details of simultaneous processes (*e.g.*, combined oxidation state changes and formation of solid phases for pure metals).

The construction of electrodes and the associated electronics based on operational amplifiers necessary to exploit the technique will be outlined. The degree of independence of the half rings and their alternate use when shorted as equivalent of a conventional ring are discussed. Applications to electrochemical problems and the various operating modes of the system will be illustrated in this paper by selected results from an investigation of the corrosion of copper-zinc alloys in ammoniacal media and its relation to stress cracking. The solutions employed were the NH_3-$(NH_4)_2SO_4$ mixtures one molar in total nitrogen of the type found by Mattson (12) to give very rapid cracking in the neutral pH range with 0.05M $CuSO_4$ present as oxidant. In our work initial Cu(II) concentration is replaced by anodic current. Potentiostatic and corrosion potential measurements in Mattson-type solutions on tensile-stressed 70/30 brass have been reported by Hoar and Booker (13). Ring-disk experiments addressed to the question of preferential dissolution of zinc in brass have been made in other media by Pickering and Wagner (5) and Feller (6) who found absence of selectivity beyond experimental error in the 70/30 alloy.

Experimental

Electrodes.—The fabrication of the split-ring design follows from a conventional ring-disk construction utilizing epoxy adhesive bonding and insulation of a concentric rod (disk) and tube (ring) similar to that of Albery and Bruckenstein (14). The working end of the completed split ring disk electrode is shown in Fig. 1 and the necessary steps in the procedure are schematically given in Fig. 2. For both rod and tube

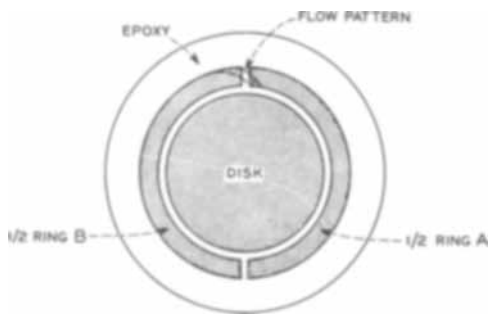

Fig. 1. Diagram of split-ring disk electrode surface showing insulating division of conventional ring. Flow pattern of electrolyte on rotation indicated over epoxy gap.

* Electrochemical Society Active Member.

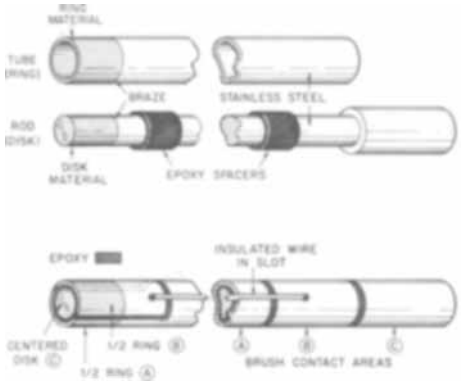

Fig. 2. Construction for split ring disk electrode (see text)

approximately ¼ in. length of the desired material is brazed or adhesively bonded with conductive silver-epoxy cement to one end. If the disk is not to be consumed in use, 50 mil thickness (*e.g.*, for platinum) suffices; for corrosion-oriented work ¼ in. provides a long period of use for disk electrodes that require polishing (to a final 0.3μ Linde A stage) intermittently to retain coplanarity of the surfaces in Fig. 1. Machining the attached materials to the rod diameter and inner and outer tube diameters (see Fig. 2) provides a standard method leading to nominal duplication of the geometry of all completed electrodes. Epoxy resin is applied and cured on two separate bands on the rod and then carefully machined to the ID of the tubes (epoxy spacers, Fig. 2).

Since the assembled electrode will rotate about the ring axis when the tube is eventually spindle-mounted for driving, errors in centering the disk affect both the ring geometry and the disk eccentricity. Bonding (and insulation) of the concentrically-aligned tube and rod is completed with fresh epoxy; particular care is taken with use of vacuum to fill the void at the working end of the electrode to avoid bubbles that would later appear as holes in the epoxy ring. The epoxy system (Union Carbide ERL 3794 resin and ERL 2807 curing agent, 5:1 by weight) has shown adequate chemical stability in both strongly acidic and basic aqueous environments and is essential to maintain the structural integrity of the electrode during subsequent division of the ring.

For a conventional ring-disk, the construction described to this point requires only an application of epoxy to the outside of the lower end of the electrode and machining to give an epoxy insulating region over the immersed portion with thickness about 50 mil. Normally heat-shrinkable polyethylene tubing is placed on the outer tube from about ¼ in. from the end to the point at which the electrode fits into its lower nylon collet on the driving spindle.

To obtain the split ring configuration, the adhesively bonded tube is appropriately sawed through both radially and axially along its length in the areas shown in Fig. 2 to expose the epoxy. These slots are then filled with epoxy for permanent insulation. A circular saw blade of 4 mil width is used for the ¼ in. ring material end to provide a minimal insulating gap division; for the further cutting areas 10 mil or wider blades may be employed for their greater rigidity and easier use. An approximately 15 x 15 mil slot is cut in the tube for the recessed insulated wire joining half ring B to its brush contact area. The slot and mounted wire are also back-filled with epoxy to the original diameter for further insulating protection (not shown in Fig. 2).

At the completion of these steps the half ring indicated as *B* is thus electrically isolated from the tube (half ring *A*) and the three active electrodes as specified in Fig. 1 have their appropriate brush contact areas at the top of the electrode. The body of the electrode sits in nylon collets in a side driven spindle and the projecting top of the electrode along with three pairs of silver-graphite electrode-radiused brushes in an acrylic mount are insulated from the mechanical rotating assembly. The final product corresponding to Fig. 1 has the nominal diameters of disk and inner and outer rings of 0.1875, 0.206, and 0.253 in., respectively, with the insulating epoxy gaps in the ring each less than 1% of the inner ring perimeter. Modification to provide different dimensions is readily performed. For example, to provide the thinner gap-thinner ring electrode of utility in various kinetic studies (15) the disk tip of the rod may be machined to diameters closer to the inner ring 0.206 in. diameter and then, when concentric bonding is complete, the ring tipped portion of the tube may be machined to the desired thinness.

The particular electrode employed for the experiments in this paper has a 70:30 Cu-Zn atom ratio α-brass disk and gold half rings. For runs with one mercury half ring, one of the gold surfaces was amalgamated with a drop of mercury with the excess carefully removed by either wiping off with twill cloth or by high speed rotation with the other gold surface-coated temporarily by an acetone soluble lacquer.

Circuitry.—The requirements for the operating circuitry of the split ring-disk system were chosen as the following:

1. Disk to be operable either under controlled potential or current with linear sweep of either variable if desired.
2. Half rings to be operable at controlled potentials independent of each other and the disk control scheme; with external short they provide the equivalent of a conventional ring using one of the two independent ring circuits. Linear potential sweeps of the rings for steady-state disk conditions are to be available.
3. One reference electrode and one counterelectrode should serve all three working electrodes.

Figure 3 is a schematic of the operational amplifier circuitry which, with addition of routine switching, satisfies the above; disk, reference, and auxiliary (counter) electrode configurations are shown for both potentiostatic and galvanostatic configurations. Only one half ring is shown connected; the other would have identical circuitry.

The operating configurations of the disk are conventional; inputs E_s from an integrator sweep generator provide the scanning modes. In both potential and current control schemes the disk is maintained at virtual ground by the control amplifier and thus the reference electrode follower output has the same relation to ground in both, whether it is controlled (potentiostat)

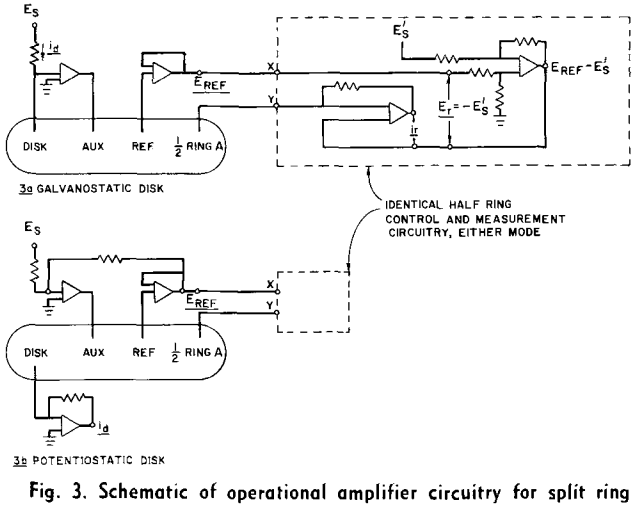

Fig. 3. Schematic of operational amplifier circuitry for split ring disk. (a) Disk galvanostatic control; (b) disk potentiostatic control (see text).

or measured (galvanostat). When a signal E_s', from a constant or linearly scanning source, is applied to the negative input of a unity gain difference amplifier whose positive input signal is the reference electrode potential, E_{REF}, the amplifier's output is $E_{REF} - E_s'$. The second amplifier serves to hold the half ring at this potential while converting the half ring current, i_r, into a corresponding voltage drop. The potential applied to the half-ring, E_r, is thus $-E_s'$ *vs.* the reference. The circuits are completed in each case by the disk control amplifier through the single counterelectrode. Switching from disk potentiostatic to galvanostatic modes is accomplished through a multipole wafer switch not involving the half ring control configuration. Capacitive damping is employed across the disk control and current follower amplifiers as required for stability; normally this involves capacitors of 10^{-3}-10^{-2} μf or less. The ring current followers need parallel capacitance across the load resistor to give RC time constants in the millisecond region.

All six variables of interest, E_d, i_d, E_{rA}, i_{rA}, E_{rB}, and i_{rB}, the potentials and currents at disk, half ring *A*, and half ring *B*, respectively, are available for recording from low impedance amplifier outputs as indicated in the schematic. Both E_r and i_r, the half-ring parameters, are measured differentially (all other outputs and signals are with respect to ground). In recent practice these differential outputs have been fed into a unity gain difference amplifier identical to that shown for subtracting E_s' from E_{REF} to produce a ground referenced output for convenience with conventional recorders which do not normally have true differential inputs. When any of the six quantities are held constant their values are obtained from calibrated controls. Booster amplifiers (Burr-Brown 1634A or 3069) provide a counterelectrode capability of 0.5A at $\pm$10V. The electrode potentials are all in some degree of error due to the uncompensated resistance between the electrode plane and the reference capillary tip. Most applications of a ring involve holding a constant potential at the limiting current of a disk product's reaction at the ring which normally allows for minor potential errors with minimal effects on the measured current of interest.

The first use of a current-measuring and voltage-controlling fourth electrode amplifier configuration was made by Anderson and Reilley (16) for thin layer studies. A ring-disk operational amplifier circuit involving the use of two balanced potentiostatic configurations of the type employed here for the disk circuit was recently described by Johnson, Napp, and Bruckenstein (17) and a circuit schematic offering disk current control was outlined by Tindall and Bruckenstein (18).

Data display for the split-ring system normally involves an *X* Y_1 Y_2 presentation which is obtained on a Honeywell 580 recorder or a Tektronix 564 Storage Oscilloscope equipped with a 3A3 dual differential vertical amplifier and either a 3B4 time base-amplifier or a 2A63 amplifier for horizontal axis. Choice of displayed variables depends on the experiment and will be illustrated in the results section.

Results

Interaction of half rings.—The typical flow pattern in the ring region of disk produced material, as derived, *e.g.*, from photographs of ring plated copper originating from a copper disk, is indicated in Fig. 1 for the insulating region between the half rings. As noted the two gaps produced by the construction technique outlined amount to 1-2% of the outside circumference. Interaction between the half rings is possible to the extent that a reaction at half ring *A* with a current i_A produces a change Δi_B in the current at half ring *B* if *B* is set at a limiting current region potential to detect the product of *A*. From the geometry of flow the maximum fraction of the area of *A* from which products could reach *B* is about 0.02 and this will be reduced by loss to the solution bulk. Experimental measurement of the quantity $\Delta i_B/i_A$ defining the interaction collection efficiency N_{INT} was made with the following pairs of reactions:

A	B	Solution
$Fe(CN)_6^{-4} \xrightarrow[ox]{} Fe(CN)_6^{-3}$	$Fe(CN)_6^{-3} \xrightarrow[red]{} Fe(CN)_6^{-4}$	0.1M $K_4Fe(CN)_6$, 1M NaOH
$Cu(II) \xrightarrow[red]{} Cu(I)$	$Cu(I) \xrightarrow[ox]{} Cu(II)$	Cu(II), pH 9 NH_3 buffer

In both cases a value of $N_{INT} = 0.004 \pm 0.001$, independent of rotation speed, was obtained. Measurement of N_{INT} where the *A* reaction is of a disk generated, rather than bulk solution transported, product is more difficult than the above but it does correspond to the true experimental situation of interest. For sequence 2 this corresponds to an initially copper-free NH_3 buffer and a copper disk polarized to Cu(II) generation. From such measurements and from results for Cu(I) generated at the disk with comparison of the equality of the 1 electron ring reactions I → II(ox) and I → O(red), where II can be cross-detected by the ring set for I → O, it is also seen that 0.004 is a reasonable measure of the interaction.

For the continuous ring form of our electrode the theoretical value of the defined collection efficiency, $N = i_r n_d/i_d n_r$ where n_d and n_r are the number of electrons transferred in disk and ring reactions, respectively, is 0.34 from the table of Albery and Bruckenstein (14). Typical values found for the quantities i_A/i_d and i_B/i_d are 0.165 for these electrodes in satisfactory agreement with the theory and the 1-2% loss due to the insulating gaps. With a half ring *N* of 0.165, the effect of interaction is to increase i_B to $0.165(1.004\ r)i_d$ where 1.004 is the contribution of N_{INT} and *r* is the ratio of electrons in the reaction producing Δi_b to that producing i_b in the particular case. The factor 0.004 implied by the computed interaction is negligible for practical purposes and means that each half ring may be treated independently of whether the other half ring is operating or off and further, that shorting the half rings at the cell gives conventional ring-disk operation with $N_A + N_B = N_{shorted}$, $N_{shorted}$ being the value 1-2% less than the continuous ring collection efficiency and which we shall henceforth abbreviate as *N* with that understanding.

Because of construction alignment and symmetry limitations, the values of N_A and N_B may not be exactly equal. The ratio of N_A and N_B is measured readily by looking at the same reaction simultaneously at both half-rings and measuring the ratio of i_A to i_B which becomes a permanent calibration factor. Alternatively the inequality may be cancelled in an experimental use of the ratio N_A/N_B by repeating a given split-ring experiment with half rings interchanged and averaging the two ratios (8). Assuming unchanged chemistry no requirement is placed on reproducing disk current exactly since the individual half-ring collection efficiencies should be independent of that value. For the brass disk-gold split-ring electrode the half-ring equality is shown experimentally in the oscilloscope picture of Fig. 4 in which both half rings are held at +0.5V *vs.* S.C.E. for the limiting current oxidation of Cu(I) generated at a linear current scan at the brass disk in pH 7.47 ammonia-ammonium sulfate. The slopes (collection efficiencies) of both are within os-

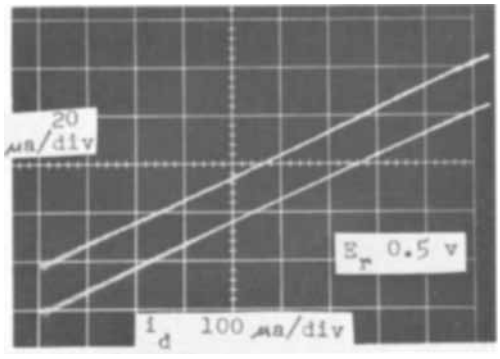

Fig. 4. Oscilloscope trace of split-ring currents *vs.* disk current with both half rings at +0.50V in pH 7.47 ammonia-ammonium sulfate. Current sensitivity; half rings 20 μA/major division, disk 100 μA/major division. Rotation speed 1580 rpm. Brass disk, gold half rings.

cilloscope accuracy of each other (0.089 ± 0.001). The linearity of the plots indicates no change in disk reaction in this region of current density.

Brass disk behavior.—The experimental data on brass will be presented in terms of the operating mode being used, for the purpose of demonstrating the information obtainable through the split-ring technique. Sufficient examples are included to cover most practical configurations. Inferences for brass anodization chemistry in neutral ammoniacal media will be collected in the discussion section.

Disk galvanostatic: ring potential sweep.—In this configuration a potential scan is applied to the ring(s) at constant disk current, suitable where E_d has acquired a steady value indicative of an unchanging composition of the flux reaching the rings. A special feature of the split-ring system in this mode is the ability to operate with two different electrode materials. Thus, with one gold and the other mercury, the anodic potential range of the former and the cathodic of the latter can be attained in single or successive scans. Figure 5 is a composite of a pair of scans with such an electrode; brass disk, gold and mercury half rings. The dissolving brass shows at gold the anodic wave due to Cu(I) → Cu(II) and the corresponding cathodic wave for Cu(I) → Cu(O). The absence of a Cu(II) → Cu(I) wave indicates essentially no Cu(II) is present. The anodic range is to +1V *vs.* S.C.E. (scan to +0.6V shown). For mercury positive potentials *vs.* S.C.E. yield electrode dissolution; for the negative potential scan from about —0.1V are seen Cu(I) → Cu(O) and Zn(II) → Zn(O) waves with effective range to —1.6V *vs.* S.C.E.

By offsetting one half-ring potential by 0.8V with respect to the other (*i.e.*, to the reference), the full 2.6V range can be scanned in a single run with simultaneous display from both electrodes. Corrosion studies, as commonly involved with solutions of H^+, OH^-, Cl^- and many complexing agents, are particularly amenable to observation over a wide potential range of the distribution of the anodized disk products, since interfering redox reactions from the electrolyte at the rings are minimized. Sweeps of the type shown in Fig. 5 indicate the feasibility of, and the proper ring potentials for, the potentiostatic monitoring of limiting currents due to individual components and states or the sum of two (or more) as a function of changing disk conditions. Where a steady-state condition obtains at the disk, a single ring scan can display the product distribution: a second surface might then be useful in extending the potential region available.

Disk potential sweep: ring(s) controlled potential.—This configuration serves the monitoring function discussed above for one or two potentials at the rings at limiting currents for selected reactions with an X Y_1 Y_2 display where X will be E_d or i_d as best suited to the experiment. Comparison of conventional and split-ring data for the distribution of the oxidation states of dissolved copper from the α-brass is shown in Fig. 6, 7, and 8. Ring oxidation current at +0.4V *vs.*

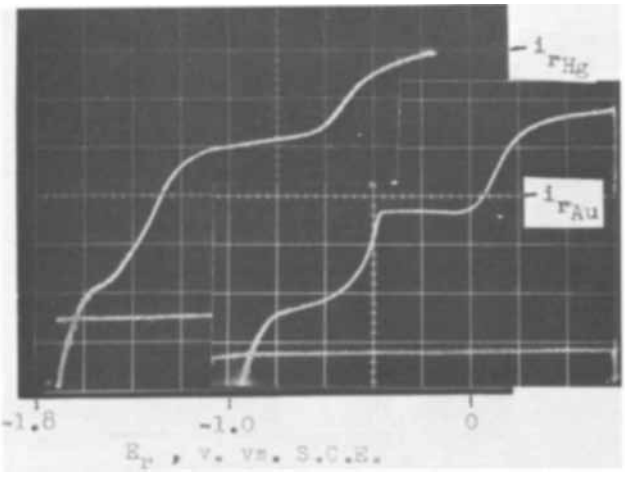

Fig. 5. Mercury half ring (upper trace) and gold half ring (lower trace) scanned at 20 mV/sec and plotted on common ring potential axis. Zero current indicated for each trace, sensitivities 50 μA/major division (Hg), 20 μA/major division (Au). Disk current 1 mA(Hg), 200 μA(Au) with brass disk at 2000 rpm. (Horizontal traces are disk potential monitored during ring scan.)

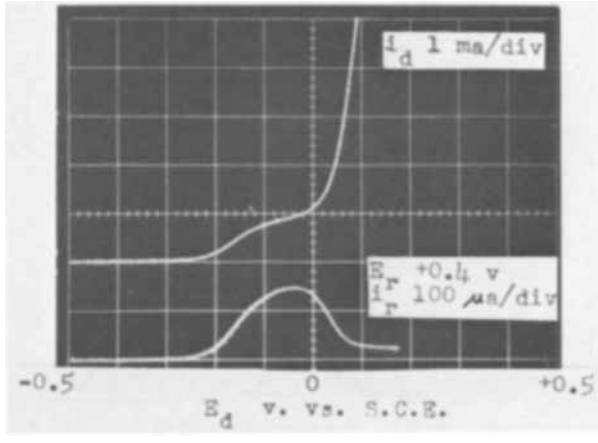

Fig. 6. Upper trace is i_d and lower trace is i_r, both *vs.* linear E_d scan of 20 mV/sec at 1000 rpm. Current sensitivities and anodic ring potential as indicated. Brass disk, gold half rings (shorted) in pH 7.45 ammonia-ammonium sulfate.

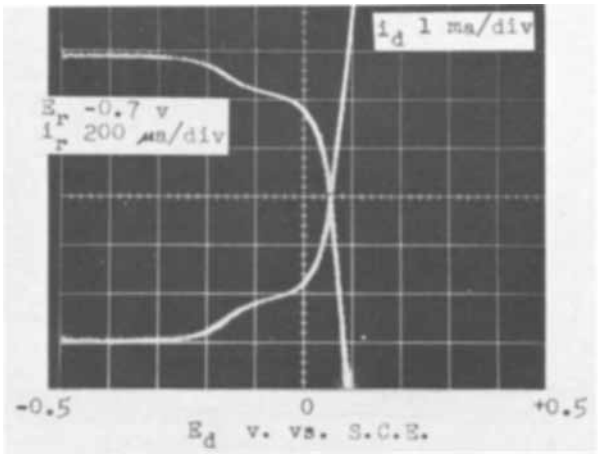

Fig. 7. Conditions of Fig. 6 except shorted half rings set for cathodic reaction at —0.7V and 200 μA/major division (ring trace beginning upper left).

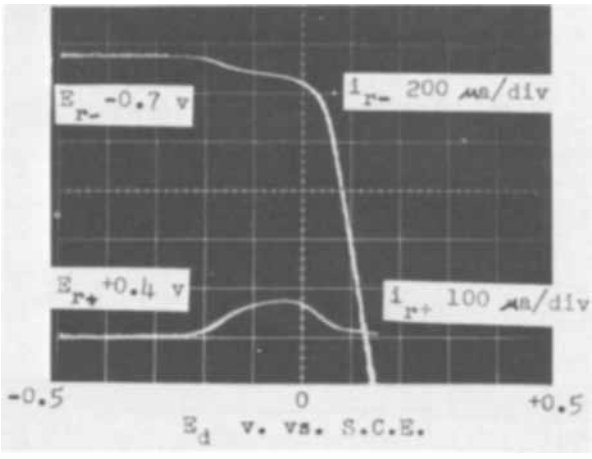

Fig. 8. Split-ring currents for solution-rotation conditions of Fig. 6 with cathodic (—0.7V., 200 μA/major division) and anodic (+0.4V., 100 μA/major division) half rings recorded against disk potential.

S.C.E. measures Cu(I) → Cu(II) while reduction at —0.7V is negative enough to measure limiting currents for both Cu(II) and Cu(I) reduced to Cu(O). Figures 6 and 7 show shorted rings operated at these potentials, respectively, and the corresponding disk current with its region of polarization and changing reaction. Figure 8 shows the split ring simultaneous measurement of both oxidation (i_r+) and reduction (i_r-) reactions from which it is then possible to calculate the ratio of copper product in (I) and (II) states at any time (or disk potential) from $(I)/(II) = i_r+/\left(\frac{i_r- - i_r+}{2}\right)$. Such a determination is independent of the assumption required in two conventional runs or a ring sweep of one that the value of i_d or E_d chosen for the measurement of the ring currents represents an exactly duplicable or steady-state experimental situation. The split-ring ratio thus determined is experimentally independent of both geometric collection efficiency and the fraction of disk current going to copper dissolution. This polarization of the anodic reactions of copper can then be referred to the disk potential; further, with the geometric collection efficiency and the corresponding value of the disk current, the selectivity of dissolution (ratio of zinc to copper dissolving compared to their atomic ratio in the alloy) can also be established. The zinc current is obtained by difference, $i_d - i_r-/N_-$, where i_r- is the cathodic current at one half ring for the copper species reduced to metal and N_- the geometric collection efficiency of that half ring. The utility of simultaneous monitoring of the two oxidation states or elements as described in this and the preceding section is even more clearly illustrated under circumstances where passivation (filming reactions) also occurs. Here the sequence of steps and transient selective dissolution (19) are of interest. Such processes, where transitions undergone by two components rather than steady states are under investigation, cannot be satisfactorily reconstructed by superposition of separate conventional single-ring scans.

The generation of Cu(I) at low currents and the polarization plateau region in the $i_d - E_d$ plots is evident for brass anodization under neutral Mattson buffer conditions in Fig. 6 and 7. No indication of filming reactions (no i_d peak, agreement of ring-determined copper with free nonselective disk dissolution) is seen, only a shift of soluble copper species from I to II as the surface concentration of the former becomes nearly comparable to the free ammonia available at pH 7.45. In the region of transition, the relative amounts of the products can be taken by current measurements as indicated; an experimentally more convenient technique with respect to data reduction is to use the split rings with controlled current sweep, as below.

Disk linear current sweep: ring(s) controlled potential.—This mode is that employed in Fig. 4 in testing the equality of the half rings. With the same solution conditions and half rings set for oxidation to Cu(II) [E_r+ + 0.5V *vs.* S.C.E.] and reduction to Cu(O) [E_r- — 0.7V *vs.* S.C.E.], the results are as in Fig. 9. The disk current is swept to 0.9 mA which is at the region of the peak of Cu(I) production (Fig. 6). The straight lines of the ring currents *vs.* disk current indicate a constant disk anodic chemistry up to about 0.5 mA (2.8 mA/cm²). The numerical values of the straight slopes are 0.089 for —0.7V reduction and 0.088 for +0.5V oxidation, equal within 1% of their average. This fact, independent of N and the concomitant zinc dissolution, within the single scan defines the oxidation state of the copper product as Cu(I), which gives equal current magnitudes for one electron oxidation to Cu(II) and one electron reduction to metal. The technique has been elsewhere applied to unstable intermediate states (8) and anodization complicated by film formation (10).

If the disk current scan is extended from the 100 μA/div of Fig. 9 to 1 mA/div (Fig. 10) the polarization of the Cu(I) reaction is seen as i_r+ changing from linear increase to decline as a function of disk current. The initial 100% current efficiency of Cu(I) generation indicated by the Ni_d relation decreases to 2% at 9 mA (50 mA/cm²). The split-ring scale sensitivities are different by a factor of 10 for reduction and oxidation in Fig. 10 (200 and 20 μA/div). The independence of the

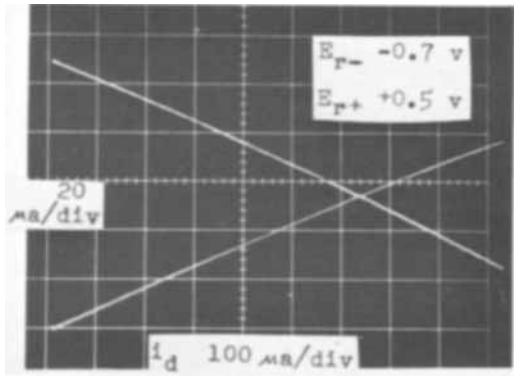

Fig. 9. Split-ring currents recorded *vs.* linearly scanned disk current; both half ring sensitivities 20 μA/major division. Cathodic trace (E_r- —0.7V) begins at upper left, anodic trace (E_r+ +0.5V) at lower left. Solution-rotation conditions of Fig. 4.

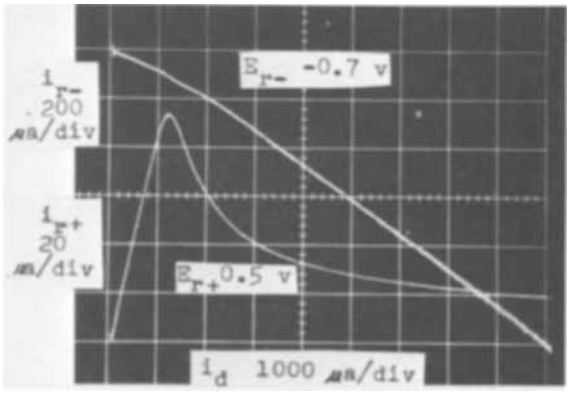

Fig. 10. Split-ring currents recorded *vs.* linearly scanned disk currents with half ring potentials and solution condition of Fig. 9 but with cathodic half ring current sensitivity changed to 200 μA/major division and disk current sensitivity changed to 1000 μA/major division. Rotation speed 2000 rpm.

half rings with the high absolute sensitivity and wide product ratios that are normally accessible make feasible the detection of low fractions of one state in the presence of large fluxes of a second state or identification of species in low concentrations at passivated surfaces.

Anodic dissolution of copper from the brass disk, as seen in Fig. 10, shows in the ring reduction trace two linear regions corresponding to the nearly quantitative appearance first of Cu(I), then of Cu(II), with an intermediate curved region of change. The first line at lower currents is amplified in Fig. 9 or with opposite sign in the linear oxidation region of either Fig. 9 or 10. The two linear regions offer either a means of analyzing the composition of binary alloys, or, knowing the composition, determining whether preferential dissolution is occurring independent of zinc measurements or of geometric collection efficiency. This feature, unique to ring-disk measurements, follows from considering collection efficiency for copper as a function of brass composition.

Copper may dissolve quantitatively under our neutral ammonia conditions with either 1 or 2 electrons, ignoring the mixed dissolution region. Thus we have, considering only a cathodic ring reaction at —0.7V *vs.* S.C.E.

Disk

$$Cu \rightarrow Cu^{+n} + ne \qquad n = 1 \text{ or } 2$$

$$Zn \rightarrow Zn^{+2} + 2e$$

Ring

$$Cu^{+n} + ne \rightarrow Cu$$

If no preferential dissolution occurs, as by the possible dezincification due to the more active metal, redeposition or filming reactions involving selective formation of an oxide, then the fraction of anodic disk current due to copper is proportional to na, where a is the atomic fraction of copper, and the fraction for zinc is proportional to $2(1 - a)$. Assuming further no complications in transit, the apparent (measured) collection efficiency for copper at the ring, N_n, will be related to the geometric collection efficiency by

$$N_1 = \frac{a}{2(1-a) + a} N = \frac{a}{2-a} N \qquad \text{when } n = 1$$

and

$$N_2 = \frac{2a}{2(1-a) + 2a} = aN \qquad \text{when } n = 2$$

Then the ratio N_2/N_1 is simply $2 - a$, the limiting cases being pure Cu, $a = 1$ and $N_2/N_1 = 1$ (no change in slope) and $a \rightarrow 0$ when $N_2/N_1 \rightarrow 2$. Chemical analysis of the disk material gave $a/1 - a = 2.34$ or $2 - a = 1.30$. The ring-disk determination of N_1 and N_2 individually requires knowledge of N. An experimental value of 0.320 for N (0.160 per half ring) was obtained by overplating the brass with pure copper from an acid sulfate bath, then, with linear anodic disk current scan and copper plating at the ring in fresh copper-free acidified sodium sulfate, determining the $i_r - i_d$ slope. From Fig. 9 anodic and cathodic measures of N_1 in pH 7.45 ammonia averaged 0.0885; predicted from $(a/2 - a)$ N is (0.70/1.30) (0.160) = 0.0862, less than 3% difference. This agreement is not reflected in the slope for N_2 from higher current measurements of the type shown in Fig. 10; the calculated aN is 0.112, whereas experimental values run 10-20% higher with reproducibility reduced partially by the fact that the i_r trace increases from linear to upward curvature. The source of the discrepancy may be involved in this latter effect. However, separately obtained values of N_1 and N_2 with the same electrode in media such that the 1 or 2 electron reactions were quantitative from "zero" current are within 4% of the theoretical nonselective dissolution ratio. The neutral ammonia value of N_1 was duplicated in a pH 5 acetate-buffered chloride solution and N_2 was determined in copper-free acidified sodium sulfate (technique comparable to that used to measure N).

Further work in this area is continuing to establish the reliability of the ratio method when applied to experimental situations like copper-ammonia where the reaction can be polarized. However, it is notable that the property of the ring-disk system of a fixed geometric collection efficiency that allows such ratio analysis to be made, either with or without knowledge of the N value, is not equivalently available for an anode alone, rotating disk or otherwise.

Disk open or zero external current: ring (s) controlled potential.—These configurations provide for the study of chemical corrosion by means of the ring current measurement of either the flux of corrosion product or the decrease in flux of corrodent. Operation of the disk at open circuit with ring potential controlled is simply done by using the regular disk potentiostat connection on the ring and leaving the disk open. More convenient and electrically equivalent is to use the ordinary galvanostatic configuration at zero applied current where the rings will operate as previously described.

Data in this type of study were obtained for copper etching in Mattson-type solutions, first as a function of added Cu(II) at pH 4-5, and then as a function of pH at constant Cu(II). Results are shown in Fig. 11, where ring potential of —0.6V *vs.* S. C. E. corresponds to the reduction of Cu^{+n} to metal, and +0.4V is limiting for oxidation of the etching product, Cu(I), to Cu(II). The etching reaction is Cu(II) + Cu(O) → 2Cu(I) with equilibrium shifted with pH mainly because of the concomitant alteration of the free NH_3 concentration. For example, the equilibrium constant of the reaction shifts approximately from 10^{-6} to 10^{3} from free ions to unit free NH_3 concentration. The constant in 0.2M H_2SO_4 was found to be 5.6×10^{-7} from a ring-disk electrode determination by Tindall and Bruckenstein (11). These authors also give a general treatment of heterogeneous equilibria involving oxidation of a metal by a soluble oxidant under mass transfer rate control.

For the present solutions, at the lower pH end, increments of Cu(II) are reflected in linear increase of ring reduction current at —0.6V but a negligible etching rate is found (very low +0.4V ring current, left side of Fig. 11). A sharp increase in the neutral region then occurs and the rate of etching becomes transport-limited above pH 8. Experiments with Matt-

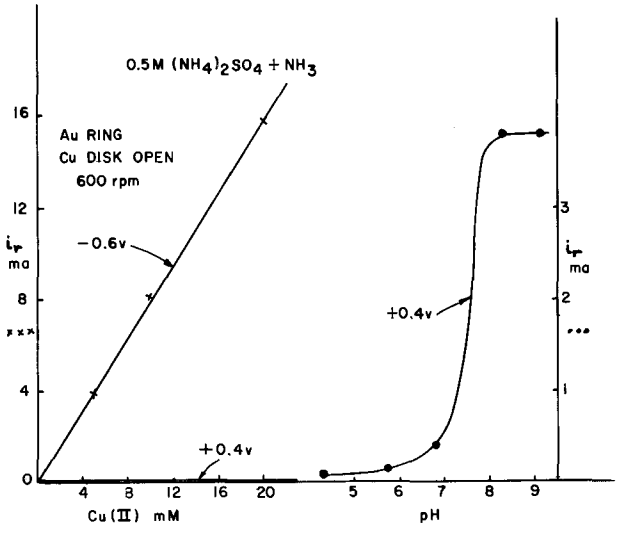

Fig. 11. Left side: initial solution of 0.5M $(NH_4)_2SO_4$, pH 5.4 with Cu(II) as sulfate added incrementally. Final pH 4.3 at 20 mM Cu(II). Ring currents for —0.6 and +0.4V plotted *vs.* [Cu(II)]. Right side: pH of 20 mM Cu(II) final solution at left raised incrementally with NH_3 with +0.4V ring current plotted *vs.* pH.

son's 0.05M Cu(II) solutions have indicated the 50% of maximum rate point to be about pH 7.6. These data complement well the above observations on brass dissolution under anodic current where the pH 7.45 reaction initially produces Cu(I) which shifts in favor of Cu(II) at higher currents (higher surface concentrations of dissolved copper and therefore equivalently reduced concentrations of free ammonia).

The other variation, when redox potentials and rates are suitable, of measuring the decrease of ring current resulting from a decrease in corrodent flux rather than a product reaction would be exemplified in the copper case by a discrete Cu(II) → Cu(I) wave at higher pH values in ammonia solution. Direct measurement of a product, as is available in the anodic determination of Cu(I), is preferable to the second, or difference, method.

Summary

The utility of the applications demonstrated for the split ring as an adjunct to conventional ring-disk observation in the study of anodic and corrosion reactions may be generalized in the following areas. In the dissolution of pure metals the split ring may be used to identify oxidation states (including relatively unstable intermediates), transition regions (reaction changes), and the determination of total material distribution even when such reactions are complicated by passive ⇌ active processes. In all these cases the ring and split-ring offer the distinct advantage of observing the solution products corresponding to what may be a thoroughly mixed system as viewed by disk current-potential curves alone. With a sufficiently versatile apparatus to take advantage of the optimum method of viewing a particular effect, the split-ring system in its power to identify oxidation states adds direct chemical information to supplement what can usually only be guessed at from the corresponding surface's current-potential behavior. For alloys direct simultaneous observation of more than one component is feasible as well as dual measurements made according to the techniques outlined on reactions of a single metal constituent whose dissolved state is in question. These techniques will also hold for film forming conditions where it may be possible, for example, to define the time dependency of the reactions of the components that contribute to passivity of the system or preferential dissolution.

Chemical corrosion of disks may be investigated as to rates and selectivity of constituent removal. Mixed anodic and cathodic reactions at the disk (*e.g.*, concurrent H^+ reduction) may in many cases be unscrambled if disk products are detectable. True corrosion rates may then be interpreted through ring currents which would be proportional to actual weight losses.

In the brass system the above techniques have shown the neutral ammonia-ammonium salt solutions to correspond to the pH region in which Cu(II)-ammonia complexes begin to etch copper (and zinc) with Cu(I)-ammonia complexes as product. The anodization of the brass produces the Cu(I) species at low current densities and Cu(II) at higher currents, the polarization being a function of free ammonia concentration and therefore of pH. Although precipitation of a Cu_2O film is not observed in these experiments it is not unlikely that accumulation of product would lead to such filming under anodic conditions with less vigorous mass transport (13). Split-ring experiments (10) with pure Cu in basic solution show Cu_2O films form in that medium without detectable supersaturation. More experiments in the ammonia system are in order to observe whether cracking reactions and media sensitivity correlate with film formation dependent mechanisms.

Manuscript submitted March 21, 1969; revised manuscript received May 5, 1969. This was Paper 53 presented at the Chicago Meeting, Oct. 15-19, 1967.

Any discussion of this paper will appear in a Discussion Section to be published in the June 1970 JOURNAL.

REFERENCES

1. A. N. Frumkin and L. N. Nekrasov, *Doklady Akad. Nauk. SSR*, **126**, 115 (1959).
2. A. N. Frumkin, L. N. Nekrasov, V. Levich, and Yu. Ivanov, *J. Electroanal, Chem.*, **1**, 84 (1959).
3. L. N. Nekrasov and N. P. Berezina, *Doklady Akad. Nauk. SSR*, **142**, 855 (1962).
4. A. C. Riddiford, in "Advances in Electrochemistry and Electrochemical Engineering," vol. 4, p. 47, P. Delahay, Editor, Interscience Publishers, Inc., New York (1966).
5. H. W. Pickering and C. Wagner, *This Journal*, **114**, 698 (1967).
6. H. G. Feller, *Z. Metallkunde*, **58**, 875 (1967).
7. A. I. Oshe, Ya. Ya. Kulyavik, T. I. Popova, and B. N. Kabanov, *Elektrokhimiya*, **2**, 1485 (1966).
8. B. Miller and R. E. Visco, *This Journal*, **115**, 251 (1968).
9. Y. Okinaka, Paper No. 48 presented at the Philadelphia Meeting of the Society, October 1966.
10. B. Miller, Paper No. 57 presented at the Chicago Meeting of the Society, October 1967.
11. G. W. Tindall and S. Bruckenstein, *Anal. Chem.*, **40**, 1402 (1968).
12. E. Mattson, *Electrochim. Acta*, **3**, 279 (1961).
13. T. P. Hoar and C. J. L. Booker, *Corros. Sci.*, **5**, 821 (1965).
14. W. J. Albery and S. Bruckenstein, *Trans. Faraday Soc.*, **62**, 1920 (1966).
15. W. J. Albery and S. Bruckenstein, *ibid.*, **62**, 1946 (1966).
16. L. B. Anderson and C. N. Reilley, *J. Electroanal. Chem.*, **10**, 295 (1965).
17. D. T. Napp, D. C. Johnson, and S. Bruckenstein, *Anal. Chem.*, **39**, 481 (1967).
18. G. W. Tindall and S. Bruckenstein, *ibid.*, **40**, 1637 (1968).
19. B. Miller, To be published.

The Mechanism of Operation of the Teflon-Bonded Gas Diffusion Electrode: A Mathematical Model

J. Giner*

Tyco Laboratories, Inc., Waltham, Massachusetts

and C. Hunter

Massachusetts Institute of Technology, Cambridge, Massachusetts

ABSTRACT

A mathematical analysis of the working mechanism of the Teflon-bonded gas diffusion electrode, based on the concept of "flooded agglomerates," is discussed. This model is used to predict the performance of the electrode as a function of such measurable physical characteristics as intrinsic activity of catalyst, agglomerate size, internal porosity, real surface area, etc. The alkaline oxygen electrode is taken as an example for the discussion.

The theory of porous electrodes has been the object of many publications. A general discussion of the behavior of fully flooded and gas diffusion porous electrodes, both for steady state and transient responses, can be found in a recent monograph by De Levie (1). The present paper is concerned only with the steady state behavior of gas diffusion electrodes which, although studied less than flooded electrodes, has also been the subject of attention in the last few years.

Four main models have been currently used to explain the behavior of the gas diffusion electrode: the simple pore model, the thin film model, the surface migration model, and the dual scale of porosity model.

Two comments should be made at this point. First, the applicability of a certain model will depend on electrode structure; thus it can be expected that a model which applies to a Teflon-bonded electrode will not apply to a Bacon sintered electrode and vice versa. Second, many of the models are microscopic models concerned with one element of the electrode producing the current (such as a thin film or a finite contact meniscus, etc.). While the relationship between theory and the results obtained with an experimental model system (such as half immersed wires, slit cells, etc.) is straightforward, the way in which the electrode is composed by the simple elements is usually not clear at all. Thus a comparison between theory and results obtained with an actual electrode is virtually impossible. A few models, on the other hand, are macroscopic and treated as continuum systems. The application of these models is limited by their abstract nature. From this point of view, the model to be discussed in this paper is a hybrid, with a microscopic division of the electrode in elements (flooded cylinders) and a macroscopic treatment of these elements.

The simple pore model.—This model as developed by Austin *et al.* (2), is a modification of the old theory (3) of the three-phase boundary and has been studied in some detail by Srinivasan, Hurwitz, and Bockris (4). It has also been proposed as the working mode of the Teflon-bonded electrode by Austin and Almaula (5), who state that only 2-5% of the electrode area is wetted. This is in contrast to our experiments (6) which show almost 100% wetting of the electrode surface area.

The thin film model.—The thin film model was introduced by Will who treated it mathematically (7) for the case of diffusion and ohmic control and has experimentally (8) confirmed his conclusions using a prewetted, half immersed Pt-wire in H_2SO_4 under H_2 atmosphere.

In a more recent publication (9) Will has made confirming measurements using horizontal electrodes with rather thick (1 mm) electrolyte films. He concludes that considerable stirring ought to exist to explain the lower than predicted concentration gradients along the film. It is questionable, however, whether the conclusions reached with these rather thick films can be scaled down to thin films. In addition, concentration gradients can be explained by a "distillation mechanism" [see ref. (15) and assumption No. 4 of this paper], which would cause, in its turn, only little convection.

The thin film model has been generalized by other authors (10-12) who have considered activation polarization in addition to concentration and ohmic polarization.

Lindstrom (13) and Lindholm *et al.* (14), have applied the thin film model to porous electrodes of the Bacon type. An important contribution of this work is the consideration of transport limitations in gas phase.

Bennion and Tobias (15) have studied the O_2-electrode according to the thin film model taking into consideration axial diffusion of electrolyte. These authors also considered the possibility that water transfer from one end of the film to the other may occur through the gas phase.

Variants to thin film model.—Models considering the shape of a meniscus can be considered as half-way between the thin film model and the simple pore model. An example is to be found in the work of Cahan (16) and Borucka and Agar (17).

The surface migration mechanism.—Migration of hydrogen on the surface of electrodes has been suggested by several authors (18-20).

Double scale of porosities model.—Burshtein and coworkers (21) have treated the Bacon type electrode, assuming that there is a spectrum of porosities, so that small pores are flooded, a model initiated by Markin (22, 23). Flooding of small pores increases the ionic conductivity across the electrode and results in a deeper utilization than with the thin film model. It should be noted that the experimental results of Brown and Rockett (20) with so-called "flooded electrodes" and the effect of pressure on activity observed by Lindstrom (13, 14) could be used to confirm the "double scale of porosity model," although these authors give a different interpretation.

A quantitative treatment for a somewhat related model has been given by Grens II (24). Grens considers gas filled macropores and electrolyte filled micropores. The electrode is represented by two one-dimensional continuum systems (a macro- and micropore system) which are joined by a series of "linking pores," the length of which is short compared with the length of the micropores. Some limitations of this treatment are as follows: (*a*) Diffusion is assumed to

* Electrochemical Society Active Member.

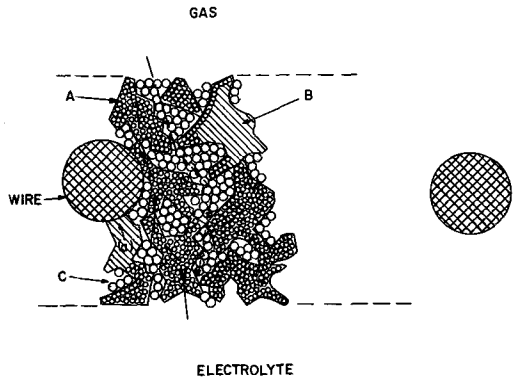

Fig. 1. Schematic representation of a hydrophobic, porous electrode made of Teflon-bonded platinum black. A, Catalyst particle; B, agglomerate; C, Teflon particle.

be linear. (b) It is implicitly assumed that concentration equalization in the micropore phase is not possible by evaporation and condensation; *i.e.* Q-term of ref. (15) is unity. (c) The diffusion of reactant gas and the ionic conductivity process in the micropore phase (*i.e.*, excluding linking pores) are considered along the same coordinate. (*d*) The thickness of flooded areas does not appear in the treatment. (*e*) Linking pores are assumed, the dimensions of which are arbitrarily selected.

The Flooded Agglomerate Model of the Teflon-Bonded Electrode

Qualitative Description

The Teflon-bonded electrode seems to us an ideal case of structure with a double scale of porosity. According to a qualitative description by Giner (25, 26) the working mechanism of this structure can be explained by assuming, as shown in Fig. 1, that the catalyst particles form porous (and electronically conductive) agglomerates which, under working conditions, are flooded with electrolyte. The catalyst agglomerates are kept together by the Teflon binder which creates hydrophobic gas channels. As current is drawn from the electrode, reactant gas diffuses through the channels, dissolves in the electrolyte contained in agglomerates and, after diffusing a certain distance, reacts on available sites of catalyst particles.

This qualitative explanation of the working mechanism based on the flooded agglomerate is confirmed by our own measurements which show (*i*) that the catalyst area in contact with electrolyte is the same when the Teflon-bonded electrode is working as a gas diffusion cell electrode as it is when it is completely flooded with electrolyte,[1] and (*ii*) that the microporosity of the agglomerates can be as large as 90%, *i.e.*, 10% catalyst and 90% electrolyte. [Microporosities of about 80% have also been measured by Horowitz (27), who also assumes the same qualitative model.]

Mathematical Treatment

One way of quantitatively treating this working mechanism is to substitute a column of flooded agglomerates perpendicular to the electrode surface by a porous cylinder of radius r_o and length h (as shown in Fig. 2), in which catalyst particles and electrolyte are homogeneously dispersed as a continuum. (Microporosity, θ, is defined as the volume of electrolyte per total volume of cylinder.) During operation, gas arrives at the lateral surface of the cylinder and diffuses radially to its center, with simultaneous reaction on catalyst particles in the diffusion path. Ionic current is conducted in the axial direction of the cylinder.

Assumptions.—For the mathematical treatment we assume that:

[1] This is conflict with the value of 2-5% reported by Austin and Almaula (5).

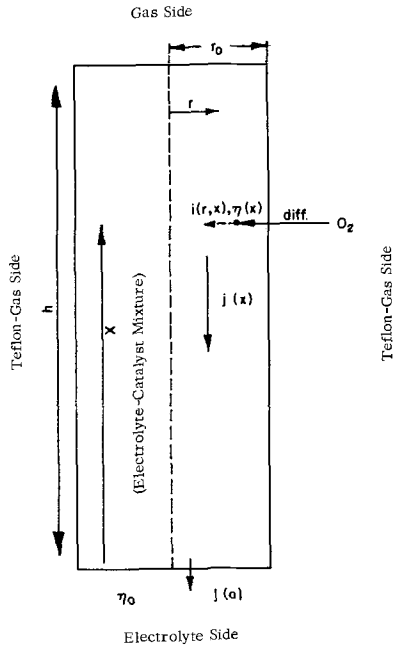

Fig. 2. Schematic representation of flooded cylinder

1. The electrode is made up of a number of porous cylinders of catalyst flooded with electrolyte. These cylinders are perpendicular to the external surface of the electrode.
2. Electrolyte and catalyst are homogeneously mixed as a continuum.
3. The intrinsic activity of the catalyst is constant throughout the cylinder.
4. Equilibration of electrolyte concentration in cylinders occurs efficiently via an evaporation-condensation process.
5. The local current density is directly proportional to the local concentration of reactant; *i.e.*, an expression such as Eq. [1] is pertinent.
6. The voltage in the cylinder changes only in the axial direction and diffusion of dissolved gas occurs only in the radial direction.
7. There are no transport limitations in the gas phase.
8. There are no kinetic limitations in the process of gas dissolution.
9. There is no electronic iR-drop in the cylinders.
10. Convection inside of the cylinders is low and has negligible effect on current.

In order to extend the theory of a single cylinder to the complete electrode we will further assume at this point that:

11. The radius of all porous cylinders has the same value. [Under these conditions the number of cylinders per square centimeter of electrode (N) is related to a measurable macroscopic factor, which we will call macroporosity (β), by the expression $\beta = 1 - N\pi r_o^2$].

General treatment.—The local current density $i(r, x)$, *i.e.*, current per unit of "real area," at a point (r, x) in the cylinder is assumed to be expressed by equation

$$i = i_o \left[\frac{C(x,r)}{C_o} \exp\left[\alpha z \eta(x)/\phi\right] - \exp\left[-(1-\alpha)\, z\, \eta(x)/\phi\right] \right] \quad [1]$$

The diffusion of the gas in the cylinder (with a simultaneous bulk consumption given by $i\gamma/n\mathbf{F}$, γ = surface to volume ratio) follows the second Fick's law for cylindric diffusion that for steady state can be written

$$\bar{D}\frac{\partial^2 C(x,r)}{\partial r^2} + \bar{D}\frac{1}{r}\frac{\partial C(x,r)}{\partial r} - \frac{i\gamma}{n\mathbf{F}} = 0 \quad [2]$$

and therefore

$$\bar{D}\left\{\frac{\partial^2 C}{\partial^2}+\frac{1}{r}\frac{\partial C}{\partial r}\right\} \quad [3]$$
$$=\frac{\gamma i_o}{n\mathbf{F}}\left\{\frac{C(x,r)}{C_o}\exp\frac{\alpha z\eta(x)}{\phi}-\exp\frac{(\alpha-1)z\eta(x)}{\phi}\right\}$$

Boundary conditions

$$\frac{\partial C}{\partial r}=0 \text{ at } r=0,\ C=C_o \text{ at } r=r_o$$

The solution of this equation for the r-variation of C under the boundary conditions is

$$C=C_o\exp\left(-\frac{z\eta}{\phi}\right)+C_o\left[1-\exp\left(-\frac{z\eta}{\phi}\right)\right]\frac{I_o\left(q\frac{r}{r_o}\right)}{I_o(q)} \quad [4]$$

where I_o is the modified Bessel function of zero order and

$$q=\left[\frac{\gamma i_o r_o^2}{n\mathbf{F}\bar{D}C_o}\exp\frac{\alpha z\eta}{\phi}\right]^{1/2} \quad [5]^2$$

Thus Eq. [4] gives the variation of C with the radius of the cylinder (agglomerate) at a given value of x. A similar equation relating i and r can be obtained from [1] and [4].

As assumed above, E (or η) is only a function of x (coordinate in the axis direction) according to Ohm's law

$$\frac{d\eta}{dx}=-\frac{j(x)}{\pi r_o^2\bar{\kappa}} \quad [6]$$

At the same time

$$-\frac{dj(x)}{dx}=2\pi\gamma\int_o^{r_o} irdr \quad [7]$$

while from Eq. [3], [6], and [7]

$$\frac{d^2\eta}{dx^2}=\frac{2n\mathbf{F}\bar{D}}{\bar{\kappa}r_o}\left(\frac{\partial C}{\partial r}\right)_{r=r_o} \quad [8]$$

or using solution [4]: The equation for η is

$$\frac{d^2\eta'}{dx'^2}=\frac{2n\mathbf{F}\bar{D}C_o h^2}{\eta_o\bar{\kappa}r_o^2}\left[1-\exp\left(-\frac{z\eta_o}{\phi}\eta'\right)\right]\frac{qI_1(q)}{I_o(q)} \quad [9]$$

Boundary conditions $\eta'=1_1$ at $x'=0$, $d\eta'/dx'=0$ at $x'=1$. (I_1 is the modified Bessel function of order 1, $\eta'=\eta/\eta_o$, $x'=x/h$ where η_o is the measurable overvoltage at the electrolyte side of the electrode.)

It can be seen that Eq. [9] expresses η' only as a function of x' and a series of measurable constants. This equation can be solved with a relatively simple computer program which will tell us the effect of parameters on the following: (*a*) The radial distribution of the local current at constant x. This is a measure of the depth utilization of the cylinder (or agglomerate), which is controlled mainly by diffusion. (*b*) The current production at different values of x'. This is a measure of the depth of utilization of the electrode, which is controlled mainly by ohmic drop. (*c*) The current density per unit area of electrode, *i.e.*, the measurable current density.

[2] The physical meaning of q can be understood by defining $I_{act}=\gamma i_o r_o\exp\frac{\alpha z\eta}{\phi}$ and $I_{diff}=\frac{n\mathbf{F}\bar{D}C_o}{r_o}$ so that $q=\left(\frac{I_{act}}{I_{diff}}\right)^{1/2}$

I_{act} is the current that would be obtained under exclusive activation control from a block with a 1 cm² surface and r_o thickness, made of the catalyst of bulk area γ, and I_{diff} is the diffusion limiting current density if the reactant were to be consumed at one of the surfaces of the same porous block after diffusing through it. Obviously q will be large when diffusion control is more important than activation control.

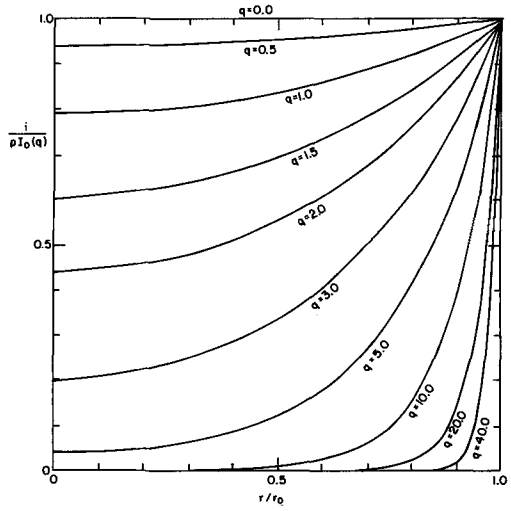

Fig. 3. Radial distribution of current in cylindric agglomerate as function of second distribution parameter of Eq. [5] and [10].

Depth utilization of cylinder.—The local current can be obtained from Eq. [1] since we know $C(x,r)$ and $\eta(r)$ from Eq. [4] and [9], respectively. Thus the equation relating i and r can be written as

$$i=pI_o\left(q\frac{r}{r_o}\right) \quad [10]$$

where p and q, which we will call distribution parameters, are suitably defined. From q the utilization of the catalyst as a function of r for a given x can be obtained, as shown in Fig. 3.

Depth utilization of electrode.—Other information of a pertinent nature is the current production for different cross sections of the cylinder. This current is, of course, $dj(x)/dx$. The total current per cylinder across the surface x = constant, is

$$j(x)=-\frac{\pi\bar{\kappa}r_o^2\eta_o}{h}\frac{d\eta'}{dx'} \quad [11]$$

Electrode current density.—The current density per unit area of electrode surface $I(o)$ can be obtained from the total current of a cylinder $j(o)$ by

$$I(o)=j(o)\frac{1-\beta}{\pi r_o^2} \quad [13]$$

or

$$I(o)=\frac{-\bar{\kappa}\eta_o(1-\beta)}{h}\left(\frac{d\eta'}{dx'}\right)_{x'=0} \quad [14]$$

Application of the model to oxygen electrode.—In the first application of the model we have used the computer program to calculate (*a*) radial distribution of current at constant x, (*b*) current generated at different planes perpendicular to cylinder axis, and (*c*) measurable electrode current density.

We have fixed the following data which we feel is realistic for a Teflon-bonded platinum electrode operating as oxygen electrode at 80°C in 30% KOH:

η_o = 0.3V
α = 0.5
n = 4 equiv/mol.
D = 2 x 10^{-5} cm²/sec[extrapolated from ref. (28)]
$\bar{\kappa}$ = 1.3 ohm^{-1}cm^{-1} (29)
S = 20 m²/g (6)
w = 20 x 10^{-3} g/cm² (6)
h = 0.02 cm (6)
C_o = 5.5 x 10^{-8} mol/cm³ (30)
z = 1
ϕ = 0.032
ρ = 20 g/cm³

The current derivative

$$\frac{dj}{dx} = -\frac{\pi\bar{\kappa}r_o^2\eta_o}{h^2}\frac{d^2\eta'}{dx'^2} \qquad [12]$$

Indirect structural parameters are

$$\gamma = S\rho(1-\theta) = 2 \times 10^5 \text{ cm}^2/\text{g} \times 20 \text{ g/cm}^2 (1-\theta) = 4 \times 10^6 (1-\theta) \text{ cm}^{-1}$$

$$\beta = 1 - \frac{w}{\rho h(1-\theta)}, \text{ macroporosity, and}$$

$\bar{D} = \theta D$ and $\bar{\kappa} = \theta\kappa$. (The tortuosity factor is taken as unity for the purpose of the present example.)

As variables we have taken microporosity θ, cylinder radius r_o, and exchange current i_o.

For a set of values of θ, i_o, and r_o computer tabulations have been obtained by varying x' from 0 to 1 at increments of 0.05. These tables were obtained for $\theta = 0.5$, 0.7, and 0.9, $r_o = 10^{-3}$, 10^{-4}, and 10^{-5} cm, and $i_o = 10^{-6}$, 10^{-7}, and 10^{-8} A/cm².[3] The columns of these tables showed (*a*) position $= x/h$; (*b*) relative potential $= \eta/\eta_o$; (*c*) current in amps flowing through a plane x of single cylinder; (*d*) current derivative, *i.e.*, current produced at the plane x of single cylinder; and (*e*) distribution parameter p, (see Eq. [10]), and distribution parameter q (see Eq. [5] and [10] and Fig. 3). At the end of each tabulation the measurable current density for the electrode (in A/cm²) was printed. Figure 4 shows a summary of effect of θ, r, and i_o on electrode current density. In all cases, decreasing the radius from 10^{-3} to 10^{-4} cm has a large effect on current, but a further decrease below 1μ has little effect on performance. This finding, of course, applies only under the diffusion conditions of this example.

According to Fig. 4 current densities higher than 150 mA/cm² are obtained for $i_o = 10^{-6}$ A/cm² and $r_o \leq 10^{-4}$ cm. For $r_o \leq 10^{-4}$ and $i_o < 10^{-7}$ the current density is proportional to i_o. These conditions correspond to high radial Pt utilization (small values of q).

When the Pt is well utilized, the current is also independent of microporosity (θ). This is due to the fact that in this range the current from the cylinder is directly proportional to $(1-\theta)$, and the number of cylinders is inversely proportional to $(1-\theta)$.

[3] Our own work with smooth platinum in KOH shows $i_o = 5 \times 10^{-7}$ A/cm² at 80°C (31, 32).

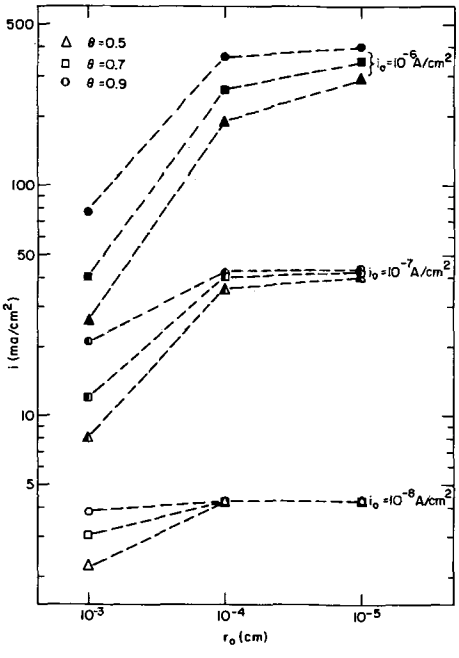

Fig. 4. Effect of r_o, i_o, and θ on measurable current density at 300 mV polarization.

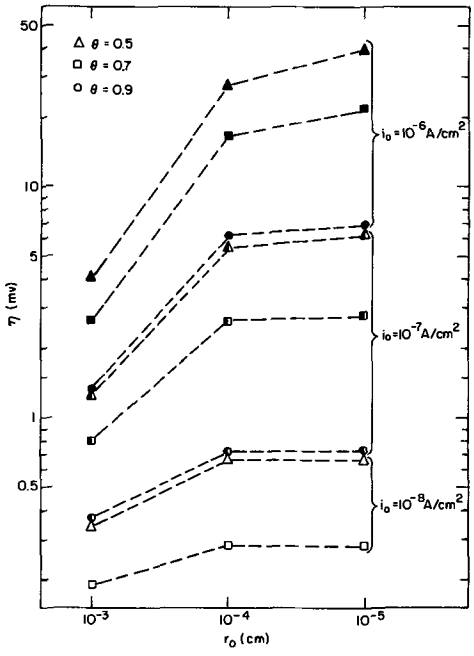

Fig. 5. Effect of r_o, i_o, and θ on internal drop (η) at 300 mV polarization.

A summary of the internal voltage drop as a function of θ, i_o, and r_o is given in Fig. 5 which shows that in all cases the internal voltage drop is small. For $\theta = 0.9$ $r_o = 10^{-5}$ and $i_o = 10^{-6}$ A/cm², a voltage drop of only 7 mv between front and back electrode is observed, even if the current density is 400 mA/cm². Correspondingly, the current produced at the plane $x' = 1$ is only 10% lower than the current at $x' = 0$. For $\theta = 0.5$, on the other hand, the internal voltage drop is 40 mV and the current produced at the plane $x' = 1$, 46% lower than at the plane $x' = 0$. This relatively poor transversal utilization of the electrode with $\theta = 0.5$ explains in part why, for instance, at $i_o = 10^{-6}$ and $r_o = 10^{-4}$ the current for this value of θ is only half of the current when $\theta = 0.9$. The obvious solution of using electrodes of a high degree of microporosity has to be re-examined after considering limitations of gas phase diffusion. Increase of microporosity (θ) at constant electrode loading (w) and thickness (h) results in a decrease of macroporosity (β) and therefore in a decrease of the residual volume. This volume includes volume of gas channels, of Teflon particles, and of wire screen, as shown in Table I. The fraction of gas volume in the residual volume is immaterial in the present treatment because we have assumed that diffusion in the gas phase is fast. But this assumption applies only under certain conditions of electrode structure, reactant gas concentration, and current drain.

Table II shows the value of the second distribution parameter (q) which is a measure of the radial utilization of the agglomerates. As shown in Fig. 3, the radial distribution is reasonably good for $q < 1$. Comparing the values of q in Table II with the curves of Fig. 3

Table I. Volume distribution in Teflon-bonded electrode ($w = 20$ mg/cm², $h = 0.02$ cm, $\theta = 0.9$, and 30% Teflon)

Component	Volume × 10^3 cm³/cm²
Total electrode	20
Platinum	1
Wetted agglomerate	10
Residual volume (gas, Teflon, screen)	10
Teflon (density ~ 2.3)	3
Screen	2
Gas	5

Table II. Effect of θ, r_o, and i_o on radial distribution parameter q of Eq. [5] and [10] for $x = 0.5$ at 300 mV polarization

		Cylinder radius, r_o (cm)		
	i_o (A/cm²)	10^{-3}	10^{-4}	10^{-5}
$\theta = 0.5$	10^{-6}	$3.12 \times 10^{+1}$	2.72	2.52×10^{-1}
	10^{-7}	1.00	9.79×10^{-1}	9.75×10^{-2}
	10^{-8}	3.19	3.19×10^{-1}	3.19×10^{-2}
$\theta = 0.7$	10^{-6}	$2.06 \times 10^{+1}$	1.90	1.84×10^{-1}
	10^{-7}	6.59	6.52×10^{-1}	6.51×10^{-2}
	10^{-8}	2.09	2.09×10^{-1}	2.09×10^{-2}
$\theta = 0.9$	10^{-6}	$1.06 \times 10^{+1}$	1.03	1.02×10^{-2}
	10^{-7}	3.36	3.36×10^{-1}	3.36×10^{-2}
	10^{-8}	1.07	1.07×10^{-1}	1.07×10^{-2}

we see that for $r_o \leq 10^{-4}$ and $i_o \leq 10^{-6}$ radial utilization of catalyst in agglomerate is reasonably good.

Discussion based on approximations.—When applying the model to the oxygen electrode, the potential changes very little along the cylinder in most cases (Table II). The current derivative is almost constant, a related result since this is a function of η'.

This result could have been anticipated from the fact that the right hand side of Eq. [9] is small for the range of values of i_o and r_o of interest to us.

Under these conditions the total current per unit area is

$$I(o) = \frac{2n\mathbf{F}\bar{D}C_o h(1-\beta)}{r_o^2}\left[\frac{qI_1(q)}{I_o(q)}\right] \quad [15]$$

(the exponential term is neglected)
where now

$$q \sim \left(\frac{10^{15}(1-\theta)i_o r_o^2}{\theta}\right)^{1/2} \quad [16]$$

Further analysis can be made in the two following extreme situations.

1. For q small, which is a good approximation when $r_o = 10^{-5}$, $i_o = 10^{-7}$ though not for $r_o = 10^{-3}$, $i_o = 10^{-6}$, we can use the approximation

$$\frac{qI_1(q)}{I_o(q)} \simeq \frac{q^2}{2}$$

Hence

$$I(o) \sim Swi_o \exp\left(\frac{\alpha z\eta_o}{\phi}\right) \quad [17]$$

The electrode current density is independent of r_o though it depends on C_o through i_o.

Total current increases linearly with i_o, S, and w, and is independent of θ.

The Tafel parameter b for the porous electrode is the same as for the smooth electrode.

The basic situation is one in which C is roughly uniform across the electrode, and the I_o Bessel function is roughly $=1$ everywhere.

2. For q large, as is the case when $r_o = 10^{-3}$, $i_o = 10^{-6}$ for instance, the Bessel function's arguments vary widely across the cylinder. C is then much larger near the outer surface than in the center, and the catalyst is not being so well utilized. Now we have

$$\frac{qI_1(q)}{I_o(q)} \simeq q$$

and hence

$$I(o) = \frac{2w}{\rho(1-\theta)r_o}(\gamma i_o n\mathbf{F}\bar{D}C_o)^{1/2}\exp\left(\frac{\alpha z\eta_o}{2\phi}\right) \quad [18]$$

$I(o)$ does depend on r_o, increasing when r_o decreases. It increases like $C_o^{1/2}$ and $i_o^{1/2}$, (over-all then current is proportional to C_o).

The Tafel parameter b for the porous electrode is twice that for the smooth electrode.

Also

$$I(o) \propto \frac{\theta^{1/2}}{(1-\theta)^{1/2}}$$

i.e., increasing θ increases current.

Analysis of Assumptions

The consideration of a Teflon-bonded electrode with flooded agglomerates as a bunch of parallel flooded cylinders consisting of a continuum mixture of catalyst and electrolyte is a very simplified treatment of a very complex structure. Therefore, the applicability of the assumptions used is restricted to relatively narrow limits. It is necessary to know these limits in order to use the model safely in the pertinent cases and/or to modify the assumptions when we want to extend the model to other cases. An exact discussion of the assumptions and an extension of the application of the model by using less restrictive assumptions should be the object of future work. A preliminary discussion however will be given in the following:

Cylindric configuration.—The difference between a cylindric surface and any other surface as gas/agglomerate interface is reflected mostly on the accessibility of the interior of the agglomerate to diffusion. For comparison let us consider a porous planar agglomerate of a thickness $2\,r_o$ perpendicular to the external surface of the electrode.

Now instead of Eq. [3]

$$\frac{\partial^2 C}{\partial r^2} = \frac{\gamma i_o}{n\mathbf{F}D}\left\{\frac{C(x,r)}{C_o}\exp\frac{\alpha z\eta}{\phi} - \exp\frac{(\alpha-1)\eta}{\phi}\right\} \quad [19]$$

Boundary conditions

$$\frac{\partial C}{\partial r} = 0 \text{ at } r = 0,\ C = C_o \text{ at } r = r_o$$

With Eq. [6] converted to

$$\frac{d\eta}{dx} = -\frac{j(x)}{2r_o\bar{\kappa}} \quad [20]$$

and Eq. [7] converted to

$$-\frac{dj(x)}{dx} = 2\gamma\int_o^{r_o} i\,dr \quad [21]$$

Under these conditions one obtains

$$\frac{d^2\eta'}{dx'^2} = \frac{n\mathbf{F}\bar{D}C_o h^2}{\eta_o\bar{\kappa}r_o^2}\left[1 - \exp\left(-\frac{z\eta_o\eta'}{\phi}\right)\right]\frac{q\sinh q}{\cosh q} \quad [22]$$

The only difference between this and the case of cylindric geometry is the absence of the factor 2 on the right hand side of the ratio of hyperbolic functions instead of Bessel functions.

The approximations are similar as before: (*i*) q small, the expression for the $I(o)$ *vs.* η_o relationship is identical with the previous result for the cylindrical geometry, which is a consequence of the full utilization of the electrode material. (*ii*) q large.

$$I(o) \sim \frac{h(1-\beta)}{r_o}(\gamma i_o n\mathbf{F}\bar{D}C_o)^{1/2}\exp\left(\frac{\alpha z\eta_o}{2\phi}\right) \quad [23]$$

There is a factor 2 difference between this result and the previous one for cylindric diffusion due to the geometry.

Continuum distribution of catalyst and electrolyte.—Such an assumption is acceptable if (*a*) the dimensions of the particles and pores making up the agglomerate are small compared with the radius of the agglomerate and (*b*) the dimension of the region where most of the current is produced is large compared with the dimensions of the catalyst particles and of the micropores. This second condition is, of course, more restrictive than the first and should suffice. For large values

of q (*i.e.*, for large values of i_o) the current is produced almost exclusively in the periphery of the cylinder; therefore, the continuum assumption cannot be used in the case of the hydrogen electrode.

As a consequence of the continuum distribution, a diffusion limiting current for an electrode of very high i_o, such as the hydrogen electrode, cannot be obtained mathematically with our model. This is easy to understand because assuming a continuum distribution of electrolyte and catalyst even on the external surface of the cylinder there are active catalyst sites which can be reached by the reactant gas without the hindrances of any diffusion path in the electrolyte.

Formally this problem can be solved by introducing a thin film of pure electrolyte around the cylinder. The model converts then for very high i_o to a thin film model with the reaction localized on the surface of the cylinder. Diffusion is through the thin film as in the thin film model, but with ionic current flowing mostly through the porous cylinder

If the thickness of the thin film is δ and we now call C_o' the concentration of the reactant on the interface cylinder thin film to differentiate from C_o solubility of gas, all the previous equations apply if C_o is substituted by C_o'. In addition we will have the following relation between C_o and C_o'.

$$-\frac{dj(x)}{dx} = \frac{n\mathbf{F}\bar{D}(C_o - C_o')2\pi r_o}{\delta} \qquad [24]$$

A computer program with an additional equation could, of course, be easily written. The merit of this approach is doubtful, however, since δ is not known. This correction will be necessary when $C_o' - C_o$ is large. $C_o' - C_o$ is large when δ/r_o and/or $dj(x)/dx$ are large.

For the oxygen electrode example treated with $C_o = 5.5 \times 10^{-8}$

$$\frac{C_o'}{C_o} = 1 - \frac{4 \times 10^5}{\theta} \cdot \left(\frac{\delta}{r_o}\right) \cdot \frac{dj(x)}{dx} \qquad [25]$$

Equation [25] can be used with $dj(x)/dx$ as printed out by computer to estimate for what values of δ/r_o there is a significant difference between C_o and C_o'.

Constant intrinsic activity of the catalyst throughout the cylinder.—This assumption seems reasonable, although it is possible that under certain conditions a larger amount of bulk area is located in the core of the agglomerate. This could be handled mathematically by an expression relating γ to r_o.

When large values of q exist (*i.e.*, high values of i_o, r_o, and η and/or low values of D and C_o), it may be advisable to form agglomerates with porous noncatalytic cores. This will result in significant savings of the catalyst.

Equilibration of electrolyte concentration in cylinder via gas phase.—Due to the small diameter of the cylinder compared with its length, this assumption seems more reasonable than the assumption [implicit in ref. (24)] that concentration equalization occurs only via ionic migration in the axial direction of the flooded micropore system.[4] As a consequence of evaporation and condensation, electrolyte transport to the gas side of the oxygen electrode should be expected. A compensating counterflow of electrolyte from the gas side to the electrolyte side can be expected also. Indeed, the often observed "weeping" of oxygen electrodes could be explained at least partially by this mechanism.

Absence of convection.—Convection caused by local heating has been found to occur at the meniscus of partially immersed electrodes (16). It seems unlikely that this type of convection occurs to an appreciable degree inside a highly porous and thermally conductive agglomerate. However, the evaporation-condensation process postulated in assumption 4 will cause convection. This convection should be negligible if the electrolyte, which tends to accumulate in the back side (gas side) of the electrode, returns to the front side (electrolyte side) through the very large pores always present as imperfections in a Teflon-bonded electrode.

All cylinders have the same radius.—This assumption is to some extent justified by the high degree of lateral interlocking of the agglomerates. The effect of having a spectrum of agglomerate radii on the calculation of total electrode current densities should be investigated in subsequent work.

With regard to the other assumptions, it seems that assumption 6 will apply in most cases since h is very large compared with r_o. Assumptions 5, 7, 8, and 9 can cease to apply under more severe conditions of operation of the porous electrode. When this happens or is expected to happen, the mathematical treatment can be suitably modified, without essential changes of the proposed model.

Conclusions

A working mechanism of the Teflon-bonded electrode is proposed in which the catalyst agglomerates are completely flooded and are surrounded by hydrophobic channels. The reacting gas diffuses through the hydrophobic channels, dissolves in the electrolyte in the agglomerate, and diffuses to the center of the agglomerate with simultaneous reaction along this diffusion path. For the mathematical treatment the model is further simplified by assuming cylindric flooded agglomerates with a continuous distribution of catalyst and electrolyte. The following conclusions have been obtained with this model:

1. The model allows one to predict not only the utilization of the catalyst across the thickness of the electrode (transversal utilization), but also the utilization of the catalyst along the radius of the flooded agglomerate. As a consequence, in addition to often studied variables such as porosity (macro- and micro-) bulk area, etc., the importance of agglomerate size is shown. A parameter (q) which determines the radial current distribution in agglomerate is introduced and quantitatively defined as a function of diffusion coefficient, microporosity, solubility of reactant gas, exchange current, bulk surface area, local potential, and agglomerate radius.

2. For the specific example of the oxygen reduction on Teflon-bonded Pt electrodes in 30% KOH at 80°C, a good radial distribution is obtained for agglomerate sizes below 1μ and polarizations up to 300 mV. Under similar conditions the transversal utilization of the electrode is very good (very low internal iR drops).

3. For the same example, both the radial utilization of agglomerates and the transversal utilization of the electrode become poor at higher current drains ($i >$ 300 mA/cm^2), and with poor structures (low microporosity and large agglomerate size).

4. For good transversal utilization of the electrode and good radial utilization of the agglomerate, the Tafel plot is obviously the same as that obtained with a smooth electrode. If, on the other hand, the transversal utilization of the electrode is good but the radial utilization of the agglomerate is very poor, a linear relationship is predicted with a Tafel slope twice that of the smooth electrode.

5. The present model and, more specifically, the parameter of radial distribution (q) introduced here can be used to design more efficient hydrophobic gas diffusion electrodes by predicting the maximum agglomerate size tolerable. When due to a high ratio of diffusion to activation control for a certain electrode reaction, high values of q are obtained for all reasonable agglomerate sizes, the model suggests the use of porous, conductive, but catalytically inactive agglomerates which have been activated with catalyst only on their periphery.

[4] This is independent of the fact that our assumptions greatly simplify the mathematical treatment.

6. The proposed model cannot be used without further modification to predict quantitatively the performance of electrodes with high exchange current as the hydrogen electrode in acid electrolyte, because the parameter q becomes too large and the assumption of a continuum distribution of catalyst and electrolyte does not apply.

Acknowledgment

This work was carried out under Contract No. NASW 1233. The authors would like to thank Mr. Ernst Cohn for his interest in this work.

Manuscript submitted Nov. 19, 1968; revised manuscript received May 6, 1969. This was Paper 327 presented at the Montreal Meeting, Oct. 6-11 1968.

Any discussion of this paper will appear in a Discussion Section to be published in the June 1970 JOURNAL.

LIST OF SYMBOLS

$C,C(r,x)$	Concentration of reactant gas at a point (r, x) (mol x cm^{-1})
C_o	Solubility of reactant gas (mol x cm^{-1})
D	Diffusion coefficient of reactant gas in liquid (cm^2 x cm^{-1})
$\overline{D}$	Effective diffusion coefficient of reactant gas in liquid; affected by microporosity and tortuosity
$\mathbf{F}$	Faraday constant
h	Thickness of electrode, cm
$i,i(r,x)$	Local real current density (A x cm^{-2})
i_o	"Real" exchange current density (A x cm^{-2})
I_o	Bessel function of order zero
I_1	Bessel function of order one
$I(o)$	Electrode current density (A x cm^{-2})
$j,j(x)$	Current flowing through plane x of cylinder (A)
$j(o)$	Total current produced by cylinder (A)
N	Number of cylinders in 1 cm^2 of electrode
n	Number of electrons involved in electrode reaction
p	First distribution parameter (see Eq. [15] and Fig. 3)
q	Second distribution parameter (see Eq. [15] and Fig. 3)
R	Gas constant
r	Radial coordinate in cylinder (cm)
r_o	Radius of cylinder (cm)
S	Surface area of catalyst (m^2 x g^{-1})
T	Absolute temperature (°K)
w	Catalyst load in electrode (g x cm^{-2})
x	Axial coordinate in cylinder (also in electrode) (cm)
x'	Scaled axial coordinate
z	Stoichiometric number
α	Transfer coefficient
β	Macroporosity
γ	Surface to volume ratio, (cm^{-1})
δ	Electrolyte outer layer, (cm)
$\eta, \eta(x)$	Overvoltage at plane (x), (V)
η_o	Measured overvoltage, at plane $x = 0$ (V)
η'	Scaled overvoltage ($\eta' = \eta/\eta_o$)
θ	Microporosity
κ	Ionic conductivity, ($ohm^{-1}cm^{-1}$)
$\overline{\kappa}$	Effective ionic conductivity, affected by microporosity and tortuosity, (ohm^{-1} cm^{-1})
ρ	Catalyst density (g x cm^{-3})
ϕ	$RT/\mathbf{F}$(V)

REFERENCES

1. R. DeLevie, "Electrochemical Response of Porous Electrodes," in "Advances in Electrochemistry and Electrochemical Engineering," Vol. 6, p. 329, P. Delahay, Editor, Interscience Publishers, Inc., New York (1967).
2. L. G. Austin, M. Ariet, R. D. Walker, G. B. Wood, and R. H. Comyn, *I&EC Fundamentals*, **4**, 321 (1965).
3. A. Schmid, *Helv. Chim. Acta*, **1**, 169 (1933).
4. S. Srinivasan, H. D. Hurwitz, and J. O'M. Bockris, *J. Chem. Phys.*, **46**, 3108 (1967).
5. L. G. Austin and S. Almaula, *This Journal*, **114**, 927 (1967).
6. J. Giner, J. M. Parry, and S. M. Smith, Paper No. 328 presented at the Society Meeting, Montreal, Oct. 6-11, 1968.
7. F. G. Will, *This Journal*, **110**, 152 (1963).
8. F. G. Will, *ibid.*, **110**, 145 (1963).
9. F. G. Will, Comptes Rendus des Deuxiemes Journees Internationales D'Etude des Piles a Combustible, Bruxels, p. 89 (1967).
10. R. P. Iczkowski, *This Journal*, **111**, 1078 (1964).
11. J. A. Rockett and R. Brown, *ibid.*, **113**, 207 (1966).
12. S. Srinivasan and H. D. Hurwitz, *Electrochim. Acta*, **12**, 495 (1967).
13. O. Lindström, Meeting Am. Chem. Soc., Div. Fuel Cell Chemistry, Sept. 1967.
14. I. Lindholm and I. Edwardsson, Reports by ASEA to National Aeronautics and Space Administration, Headquarters, Washington, on Contract No. NASW-1536.
15. D. N. Bennion and C. W. Tobias, *This Journal*, **113**, 593 (1966).
16. B. D. Cahan, The Mechanism of Electrode Reaction on Porous Surfaces, Doctor Thesis, University of Pennsylvania.
17. A. Borucka and J. N. Agar, *Electrochim. Acta*, **11**, 603 (1966).
18. E. Justi, M. Pilkuhn, W. Scheibe, and A. Winsel, "High Drain Hydrogen-Diffusion Electrodes Operating at Ambient Temperature and Low Pressure," Verl. Akad. Wissenschaft v. d. Lit, Wiesbaden (1959).
19. E. Justi and A. Winsel, Fuel Cells, Kalte Verbiennung, 245 Steiner, Wiesbaden (1962).
20. R. Brown and J. A. Rockett, *This Journal*, **113**, 865 (1966).
21. R. Chs. Burshtein, V. X. Markin, A. G. Pshenichnikov, V. A. Chismadgev, and Y. G. Chirkov, *Electrochim. Acta*, **9**, 773 (1964).
22. V. S. Markin, *Izv. ANSSR Otd. Khim. Nauk*, **9**, 1690 (1963).
23. V. S. Markin, *ibid.*, **11**, 1923 (1963).
24. E. A. Grens II, *I&EC Fundamentals*, **5**, 542 (1966).
25. J. Giner, Report to U.S. Army Engineer Research and Development Laboratories, Fort Belvoir, Va., on Contract No. DA 44-009-AMC-410(T) (Oct. 31, 1965).
26. J. Giner, Proceedings of 21st Annual Power Source Conference, p. 10 (1967).
27. H. H. Horowitz, *This Journal*, **114**, 650 (1967).
28. R. E. Davis, G. L. Horvatz, and C. W. Tobias, *Electrochim. Acta*, **12**, 287 (1967).
29. M. A. Klochko and M. M. Godneva, *Russian J. Inorganic Chem.*, **4**, 968 (1959).
30. R. D. Walker, Jr., 4th Semiannual Report on NASA Research Grant NGR 10-005-022, Aug. 31, 1967.
31. J. Giner, J. M. Parry, and L. Swette, Proceedings of the 5th Biennial Symposium on Fuel Cells, ACS; to be published in Advances in Chemistry Series No. 90, Washington, D. C. (1968).
32. Report Q-8 (June 1967) by Tyco Laboratories to National Aeronautics and Space Administration Headquarters on Contract No. NASW-1233.

An Electrochemical and Electron Microscopic Study of Activation and Roughening of Platinum Electrodes

T. Biegler

Division of Mineral Chemistry, CSIRO, Port Melbourne, Victoria, Australia

ABSTRACT

The factors which govern the behavior of platinum electrodes during anodic-cathodic cycling in 1M H_2SO_4 are examined. Cyclic voltammetry with linear potential sweep is found to be a sensitive criterion of the state of the electrode surface. With a new electrode, the shapes of these voltammograms change during the first few hundred cycles of any potential program in which a layer of adsorbed oxygen is periodically formed and reduced. These changes are considered to represent activation of the electrode and electron microscopy suggests that they are accompanied by surface structural changes in the form of shallow pitting. Further roughening occurs if the electrode is treated with a potential program fulfilling the conditions that (*a*) the amount of adsorbed oxygen after the anodic cycle exceeds the equivalent of one oxygen atom per platinum atom and (*b*) the reduction cycle is fast. The rate of roughening is proportional to the amount of adsorbed oxygen. Smoothing occurs when a program which does not fulfill conditions (*a*) and (*b*) is applied to an already roughened electrode. After extensive roughening, platinum can be detected in solution. The nature of the roughening process and also of the effects produced by flaming the electrode is examined by electron microscopy. It is suggested that activation and roughening occur through weakening of platinum interactions due to formation of the strong platinum-oxygen chemisorption bond. This allows rearrangement of platinum surface atoms and dissolution of a platinum-oxygen species. High energy platinum sites are probably lost in the initial activation process while a roughening program provides sufficient energy to dislodge atoms in more stable sites.

Electrochemical roughening of platinum surfaces subjected to anodic-cathodic treatments is now a well established phenomenon (1-6), although there is no general agreement as to the mechanism or the significant controlling factors. The main controversy concerns the roles played by successive formation and dissolution of adsorbed hydrogen- and oxygen-containing films at or in the electrode surface. Hoare (3, 7) based his mechanism on the concept of dermasorbed hydrogen, claiming that absorption and then removal of such hydrogen caused alternate lattice expansions and contractions and hence breaking up of the platinum surface. Gilman (4) disputed this explanation since he observed roughening under conditions where the presence of hydrogen would not be expected at any stage of the potential programs used. He considered (4) that the formation and reduction of surface oxide are the critical processes. On the basis of experiments in which sequences of sawtooth and rectangular potential pulses were applied to a platinum electrode in 85% phosphoric acid at 120°, Gilman also concluded (4) that fast reduction of surface oxide caused roughening, while slow reduction caused a decrease in the surface roughness. This seems to be the first report of such smoothing effects, although losses of area have been observed for platinized electrodes (8, 9) and are to be expected from the sintering behavior of high area unsupported catalysts.

There is a close connection between the questions of roughening and the well known activation of platinum electrodes by anodic-cathodic treatments. This connection arises, first, because one of the contending theories to explain electrochemical activation (10) invokes the idea that a kind of platinized layer is produced at the electrode surface and is responsible for the activity, and, second, because there are no adequate criteria for distinguishing between surface cleaning and true roughening as measured by the usual electrochemical methods of area determination (hydrogen adsorption, oxygen adsorption, double layer capacity). A convincing demonstration that activation produces surface changes which differ only in degree from the blackening found by Anson and King (2) and Hoare (3) is still lacking. As the following work will show, it is possible by means of cyclic voltammetry to make certain clear distinctions between activation and roughening but in several ways the processes are similar.

A second group of theories for the activation process (11-13) contains the notion of a structurally distinct active surface layer without necessarily implying that the electrode area increases at the same time. A third theory, that activation is essentially a cleaning process, has been gaining wide acceptance (14-16) and is based mainly on observations of deactivation as a function of factors such as solution purity and stirring rate. Interpretation of these experiments in terms of surface contamination seems indisputable, but it is doubtful whether their design could permit detection of any activation effects due to surface structural changes in view of the inadequate attention paid to electrode prehistory. The work presented here will show that both effects must be considered when explaining the activation of a platinum electrode by anodic-cathodic treatments.

Experimental

Glass cells (2 or 3 compartments) of conventional design were used. One compartment contained the reference electrode, mercury/mercurous sulfate in 1M H_2SO_4. Its potential was 0.68V with respect to a reversible hydrogen electrode in 1M H_2SO_4, to which all potentials are referred. In some experiments the platinum counter electrode was in the main compartment and in others it was placed in a third compartment separated from the working electrode by a fine sinter. No effects could be attributed to the placement of the counter electrode.

Platinum electrodes of 34 or 38 gauge wire were sealed into soft glass. Foil electrodes (~0.04 mm thick) of geometric areas around 1 cm^2 were spot welded to short lengths of 28 gauge platinum wire sealed into soft glass. Electrodes cut from one sheet of foil were found to contain a significant impurity, probably gold, and subsequent work was carried out with another sample of 99.99% purity. Apart from certain differences found during the initial activation process, which will be described below, the behavior of elec-

trodes from different sources was similar. None of the platinum used in this work had previously been employed in electrochemical experiments.

Two kinds of pretreatments were used before electrochemical runs were commenced. Those electrodes designated as "heat-treated" were subjected to the following sequence: (*i*) washed in cold chromic acid; (*ii*) rinsed in distilled water; (*iii*) held for several seconds at yellow heat in the oxidizing part of a coal gas/air flame; (*iv*) washed in cold chromic acid; (*v*) rinsed in distilled water; (*vi*) inserted in cell containing degassed electrolyte and held at open circuit during final degassing (5-10 min); (*vii*) connected into potentiostatic circuit during a cathodic sweep at the moment when the control potential reached the open circuit potential. The other pretreatment without heating the electrode started at step (*iv*).

All experiments were carried out using 1M H_2SO_4 as electrolyte. This solution was prepared from water redistilled from alkaline permanganate and reagent grade sulfuric acid purified by distillation under reduced pressure. Nitrogen for degassing the solution was first passed over heated copper turnings and then through a cold trap (liquid oxygen). Except where otherwise stated, experiments were carried out at 25°C.

Instrumentation was similar to that described earlier (17) except that in most experiments a Tacussel GSTP2 function generator was used to program the electrode potential. The main kinds of programs used are shown in Fig. 1.

Electrode area measurements were carried out by integrating the current due to deposition of adsorbed hydrogen atoms during the cathodic portion of a triangular cyclic voltammogram. Integration using the corrections for double layer charging and hydrogen evolution current shown in Fig. 2 was assumed to give the hydrogen monolayer charge, Q_H^S, and the real electrode area was calculated using $Q_H^S = 210$ μcoul/real cm². Area measurements were always carried out in carefully deoxygenated solutions.

A two stage replica technique was used in the electron microscope studies. The primary plastic replica (Bexfilm) was shadowed with platinum/carbon at an angle of 20° and the plastic dissolved in acetone. The platinum/carbon replica was examined in a Philips EM200 electron microscope at 100 kV.

Results

Activation of electrodes.—The initial changes in behavior of electrodes on anodic-cathodic cycling will be referred to as activation for reasons which will become apparent below. Figure 2 shows the shapes of triangular sweeps at various stages of the activation of an electrode by triangular cycling between 0.05 and 1.54V. Between the stages shown, cycling was speeded up by a factor of 10 faster than the sweeps in Fig. 2 so that the large number of cycles needed for activation could be completed in a reasonable time.

The most notable changes with activation are (*i*) development of the peaks in the hydrogen region, (*ii*) steepening of the current rise corresponding to the start of the "oxide region" at about 0.82V in the anodic sweep, (*iii*) development of two distinct peaks at 0.95

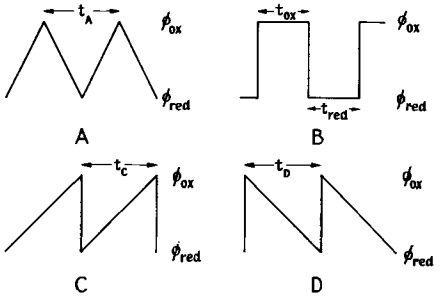

Fig. 1. Anodic-cathodic programs used in this work

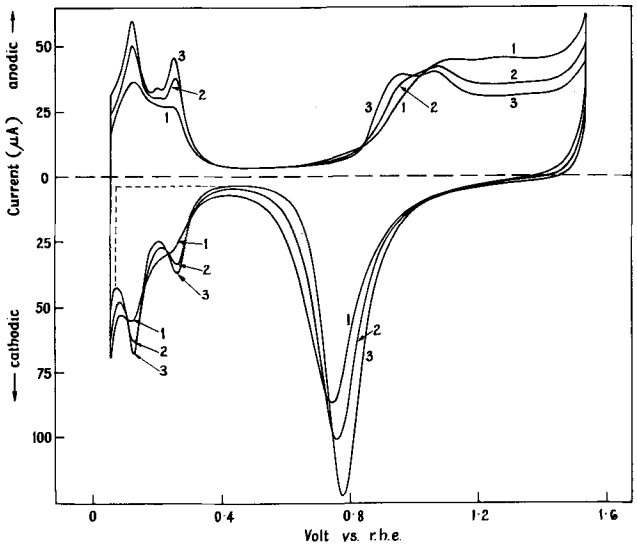

Fig. 2. Cyclic voltammograms during activation of Pt wire electrode by triangular cycling between 0.05 and 1.54V. 1, 2nd cycle; 2, 5th cycle; 3, 200th cycle. No significant changes between 200th and 500th cycle. Sweep rate 40 mV/sec. Boundaries for integrating Q_H^S are shown for curve 3.

and 1.07V, (*iv*) lowering of the current plateau in the region 1.1-1.5V, and (*v*) an increase in height and decrease in width of the oxide reduction peak in the cathodic sweep. Breiter (15) found similar changes in cyclic voltammograms during activation.

Detailed behavior depended somewhat on the source of the platinum and on the pretreatment. A series of electrodes made from one sample of foil consistently gave a steep anodic current rise between 1.3 and 1.5V and also a small peak at 1.16V on the cathodic sweep. These features gradually disappeared over about 300 cycles but returned after heat treatment. Comparison with curves given by Breiter (18) for platinum-gold alloy electrodes suggests a gold impurity in this sample of platinum foil and indicates further that this impurity accumulates preferentially at the platinum surface. Anodic-cathodic cycling removes the gold from the surface and after such activation the behavior is indistinguishable from that of purer electrodes.

The main effect of heat pretreatment is to produce an electrode which is initially more active than unheated platinum by the above criteria. Thus, hydrogen peaks are well developed in the early cycles, and the portions of the curves corresponding to "oxide" formation and reduction show smaller changes during the activation period than found with unheated electrodes.

Activation by triangular cycling takes some 200 to 500 cycles after which the rate of change in the shapes of voltammograms becomes negligible. It is this behavior which distinguishes activation from the electrode roughening to be described below. Activation is induced by any periodic program extending well into the "oxide" region, while, for example, triangular cycling between 0.08 and 0.88V (just at the start of the "oxide" region) does not produce the changes characteristic of activation. This is to be expected from the idea that alternate formation and reduction of the "oxide" film are responsible for activation.

The roughness factor reached on activation depends on the source of platinum and the pretreatment. Heat-treated electrodes from all sources had roughness factors in the range 1.10 to 1.20. Unheated foils varied between 1.22 and 1.45. An unheated wire had a roughness factor of 2.8 which fell to 1.13 after heating.

Deactivation by contamination.—Severe poisoning of the electrode occurs if it is left in the electrolyte for long periods (hours) at open circuit or held at potentials below about 0.9V. On the first cycle after such treatment, the peaks in the hydrogen region are low-

ered or disappear completely and large anodic currents are seen in the "oxide" region. The curves return to normal within about five triangular cycles, in agreement with the results of Breiter (15). Thus, the loss of activity through adsorption of impurities from 1M H_2SO_4 is easily reversed and seems to be quite different from the low activity of a new platinum electrode.

Activated electrodes held at potentials between about 1.1 and 1.6V retain their activity indefinitely, the first cycle showing full development of hydrogen peaks. An active electrode can be removed from the cell, washed in chromic acid, rinsed, and returned to the cell without change in activity or area. However, if the electrode is wiped with a paper tissue, some loss of activity occurs, and a considerable amount of cycling is needed to restore the hydrogen peaks to their former shape.

Roughening and smoothing of electrodes.—Once an electrode has been activated, its response to anodic-cathodic cycling depends on the kind of potential program used. Thus, as noted above, no further changes occur when a triangular sweep is employed. In agreement with the conclusions of Gilman (4), it is found that roughening occurs only with programs which cause fast reduction of surface "oxide." Rectangular pulse (B) and sawtooth (C) programs fall into this category, although such programs are roughening only under certain conditions which will be outlined below. The inherently nonroughening programs A and D leave an activated surface unaltered but will smooth a surface which has previously been roughened. These generalizations emerge from large numbers of experiments with 25 different electrodes, and their validity is independent of the prehistory of the electrode and of the order in which several programs are applied.

Prolonged application of a smoothing program brings the roughness factor down to about the value characteristic of an unroughened, activated electrode. The following example gives the history of an electrode which illustrates this effect. This electrode was roughened with program B from an initial roughness factor of 1.36 to a value of 4.90 and was then smoothed using program D, with ϕ_{ox} = 1.48V, ϕ_{red} = 0.48V, and t_D = 3.8 sec. After 2000 cycles the roughness factor had decreased to 1.97. ϕ_{ox} was then changed to 1.68V and further decreases in roughness factor to 1.63 (1000 cycles) and 1.44 (2500 cycles) occurred, after which there were no changes within 17,000 cycles. The final roughness factor was thus only 6% above the initial value. Similar smoothing effects are also found with programs A or D when ϕ_{red} is in the hydrogen region.

As observed previously (6), area changes are accompanied by changes in the shapes of the triangular cyclic voltammograms used to monitor the platinum surface properties. In the hydrogen region the more cathodic peak (0.12V) generally increases faster with roughening than the peak at 0.26V; at the same time the third peak, found only in anodic sweeps between the two main peaks (6, 19) increases in height and with extensively roughened surfaces (roughness factor >4) it becomes comparable to the peak at 0.26V. Roughening is also found to produce rather more subtle changes in the small peaks at the start of the "oxide" region (Fig. 2), the relative heights of which change in a manner roughly comparable with the two main hydrogen peaks. Thus, on roughening, the peak at 1.07V increases with respect to the peak at 0.95V. All these changes are reversed on smoothing.

Visible darkening of the surface is found to occur when the roughness factor exceeds about 7. Similar electrode blackening was also found by Anson and King (2) and Hoare (3), but roughness factors for their surfaces are not available. Gilman (4) observed only slight dulling of the electrode surface under conditions where the roughness factor did not exceed 4.

Roughening as a function of oxide coverage.—In the early stages of this work it was found that roughening with sawtooth program C occurred only when ϕ_{ox} was sufficiently anodic and then increased with increasing ϕ_{ox}. For example, with ϕ_{red} = 0.48V and t_c = 2.3 sec, the roughening rates (RR) for various ϕ_{ox} were: ϕ_{ox} = 1.54V, RR = 0; ϕ_{ox} = 1.67V, RR = 0.006% per cycle; ϕ_{ox} = 1.78V, RR = 0.012% per cycle. This observation led to the idea that the amount of "oxide" present on the surface just before rapid reduction occurred was important in determining the roughening rate.

The "oxide" coverage (the term will be used here to denote the total charge due to adsorbed oxygen-containing species) can be varied by changing the time and/or the potential of anodization. The dependence of roughening rate (measured over several hundred cycles) on both factors is shown in Fig. 3, all values being obtained with one electrode. Program B was used, ϕ_{ox} and t_{ox} were varied and ϕ_{red} and t_{red} kept constant at 0.48V and 3.7 sec, respectively. It can be seen that the roughening rate increased approximately linearly with ϕ_{ox} for each value of t_{ox} used.

In order to establish a quantitative relationship between roughening rate and "oxide" coverage, the charge needed to reduce the surface after a period of anodization was determined by the appropriate program of Fig. 4. For $\phi_{ox} \leq$ 1.28V program E was used. For higher ϕ_{ox} it was thought desirable to introduce the step down to 1.28V to ensure that no extra surface oxidation occurred during the first part of the cathodic sweep. In fact this precaution was later shown to be unnecessary, programs E and F giving identical results when ϕ_{ox} is in the range 1.28-1.7V. Program G, in which the solution was vigorously purged with nitrogen for about 10 sec while the electrode was held at 1.28V, was used whenever ϕ_{ox} was high enough to cause oxygen evolution. The limiting current due to dissolved oxygen was then undetectable in the double layer region. Slow cathodic stripping rates, around 40 mV/sec, were used with these pro-

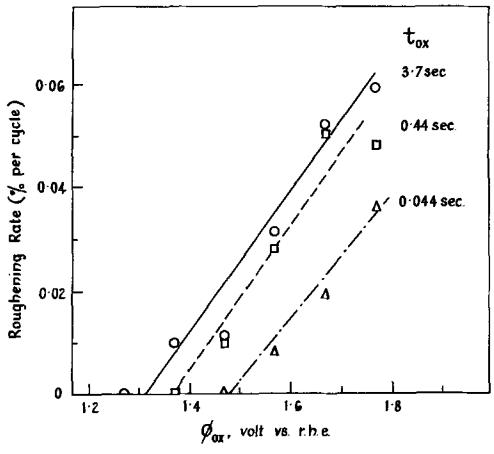

Fig. 3. Dependence of roughening rate of a Pt foil electrode on ϕ_{ox} and t_{ox} of program B. ϕ_{red} = 0.48V, t_{red} = 3.7 sec. —·△—· t_{ox} = 0.044 sec. - - □ - - t_{ox} = 0.44 sec. —○— t_{ox} = 3.7 sec.

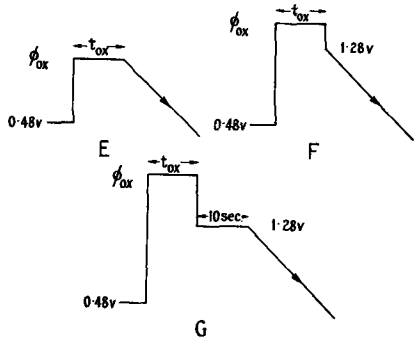

Fig. 4. Programs used to determine "oxide" coverage

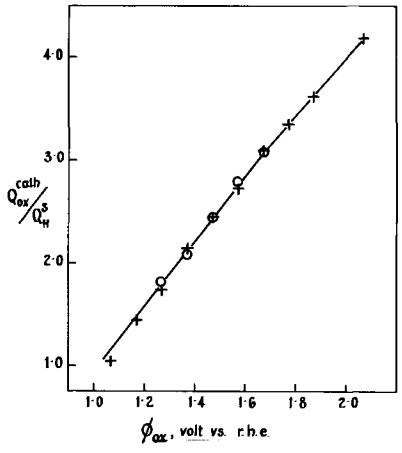

Fig. 5. Potential dependence of "oxide" coverage, expressed in terms of Q_H^S, for a constant oxidation time of 5 sec. Results for two different electrodes are shown.

grams. From the resulting curves, which resembled the cathodic sweep of Fig. 2, the amount of adsorbed oxygen, Q_{ox}^{cath}, was determined by integrating the cathodic "oxide" reduction peak. An arbitrary choice of base line is involved in this integration (here, the current at 0.48V was used as the double layer charging correction) but the error cannot amount to more than about 10%. The dependence of Q_{ox}^{cath} on potential for t_{ox} = 5 sec is shown in Fig. 5. The values are in reasonable agreement with the results of Becker and Breiter (20) and Gilman (21); discrepancies with other work on "oxide" coverage are discussed elsewhere (22).

Combination of results such as those shown in Fig. 3 and 5 gives Fig. 6 in which the roughening rate is plotted as a function of "oxide" coverage. Program B was used for roughening, t_{ox} and t_{red} kept constant at 5 sec, ϕ_{red} maintained at 0.48V and ϕ_{ox} varied. Results for two electrodes are given and the roughening rates for a variety of electrodes used in other aspects of this work are found to fit reasonably well onto this plot. The rather wide scatter reflects the generally poor reproducibility found in this study, not only for different electrodes but also for successive runs on a single electrode. However, Fig. 6 clearly shows that a minimum amount of "oxide" is required for roughening with a square wave potential program. This minimum value corresponds to one adsorbed oxygen atom per surface platinum atom and at higher coverages the roughening rate tends to increase linearly with oxygen coverage, although anomalies seem to be present at the highest potential examined (ϕ_{ox} = 2.08V).

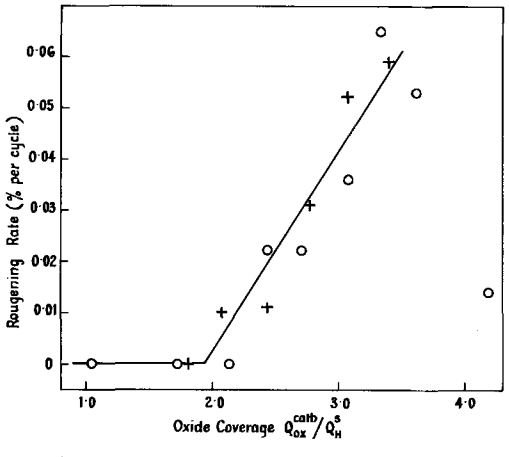

Fig. 6. Dependence of roughening rate on "oxide" coverage. Program B used for roughening, with t_{ox} = t_{red} = 5 sec, ϕ_{red} = 0.48V. Results for two electrodes shown.

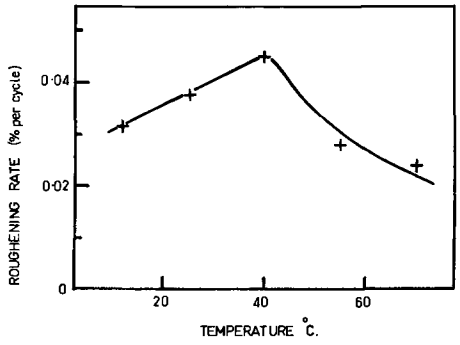

Fig. 7. Effect of temperature on measured roughening rate

Effect of temperature.—Roughening rate was measured over a range of temperatures using a constant roughening program (program B, t_{ox} = t_{red} = 5 sec, ϕ_{ox} = 1.68V, ϕ_{red} = 0.48V). Results are shown in Fig. 7. Contrary to Gilman's view (4) that roughening is appreciable only at the elevated temperatures used in hydrocarbon oxidation work, the roughening rate is seen to depend only slightly on temperature and shows a tendency to decrease at higher temperatures.

Effect of reduction potential.—The foregoing results with program B were all obtained using a reduction potential (ϕ_{red}) of 0.48V, *i.e.*, in the so-called double layer region. When ϕ_{red} was changed to 0.08V, all other factors being held constant, the roughening rate fell to about 20% of its former value. Thus, with the potentiostatic square wave program used here, the presence of hydrogen on the surface after reduction of the "oxide" layer inhibits the roughening process rather than initiating it as proposed by Hoare (3, 7).

Other factors.—Heat pretreatment produced no significant changes in the roughening rate although the scatter of results would not have allowed detection of an effect less than about 25%.

Stirring the solution with nitrogen appeared to produce a significant decrease in roughening rate compared with that in a quiescent solution. In a vigorously stirred solution the roughening rate was 50-75% of its value in unstirred solution, poor reproducibility once again making a more accurate assessment impossible. All of the previous results were obtained in quiescent solutions or with slow nitrogen bubbling, under which conditions the roughening rates are not significantly different.

In view of an earlier observation (6) that addition of methanol increased the roughening rate, a similar comparison was made under the somewhat different conditions of pretreatment and potential program used in the present study. Roughening with program B (ϕ_{ox} = 1.58 or 1.68V, ϕ_{red} = 0.48V, t_{ox} = t_{red} = 3 or 5 sec) was found to be 1.5-2 times faster in 1M H_2SO_4 containing 0.5M methanol than in 1M H_2SO_4 alone. Attempts to locate the source of the increased roughening by using programs C and D and by varying the ratio of t_{ox} to t_{red} in program B were inconclusive.

At several stages during this work, notably after extensive roughening or smoothing, cyclic voltammograms showed a small, stirring dependent cathodic current in the "double layer" region. The presence of dissolved platinum was suspected and confirmed using the stannous chloride test [*e.g.*, (23)]. The highest concentration found was about 1 ppm (5 x 10^{-6}M) which is close to the detection limit for this test. In the majority of runs, the absence of significant current indicates platinum concentrations less than about 2 x 10^{-6}M.

Electron microscopic observations.—Replicas of a number of foil electrodes at various stages of activation and roughness were examined in the electron microscope. Considerable variation from sample to sample, not directly attributable to the electrode treatment, was evident, especially in those electrodes sub-

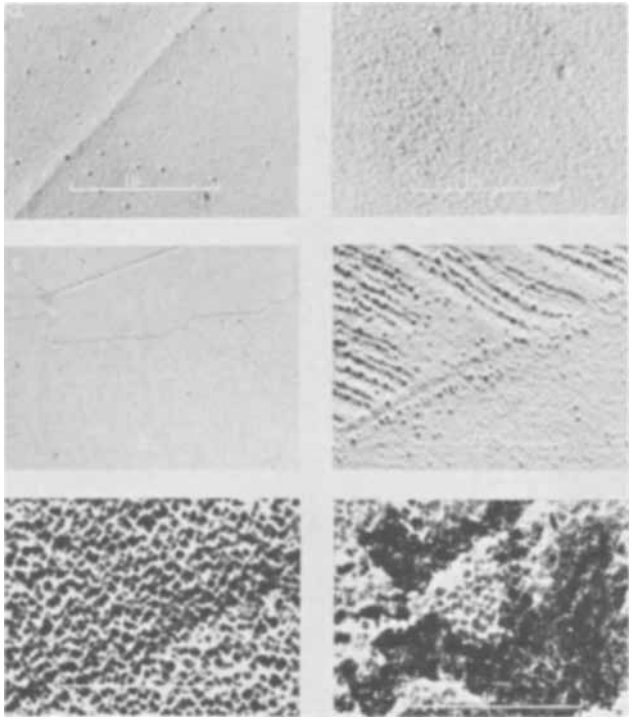

Fig. 8. Electron micrographs of shadowed replicas of platinum foil surfaces. (a) Heat pretreated electrode (no electrochemical treatment) showing grooved grain boundary and pitting. (b) Unheated electrode roughened with program B to roughness factor 1.62. (c) Heat pretreated electrode roughened with program B to roughness factor 2.55. Several grain boundaries and variable faceting are shown. (d) Detail near a grain boundary on same electrode as (c). (e) Unheated electrode roughened with program B to roughness factor 8.2. (f) Same electrode as (e) showing platinum particles stripped off with replica.

jected to heat pretreatment. The main observations are as follows and are illustrated by some representative micrographs in Fig. 8.

1. Electrodes which are subjected to no pretreatment except washing in cold chromic acid appear fairly smooth at high magnification.

2. The heat pretreatment used here produces three kinds of visible effects; grooving along grain boundaries (Fig. 8a and c), faceting (Fig. 8c and d), and development of pits uniformly distributed over the surface (Fig. 8a). Faceting, which gives a terraced appearance to the surface, is rather variable from sample to sample, a result probably due to the lack of close control of flaming conditions. On a given sample the extent of faceting depends strongly on grain orientation and at grain boundaries the change in direction and density of facets is clearly visible. The pits are of the order of 200Å in diameter.

3. Electrodes which have been subjected to an electrochemical treatment leading to an increase in the monolayer hydrogen coverage are also rough when examined by electron microscopy. In the roughening process the pits increase in diameter and depth; at high roughness the pit diameters reach about 800Å. Preferential enlargement of pits occurs at the edges of the facets. There are some indications that the pits assume an angular shape as the electrode roughens.

4. On surfaces which have darkened through roughening, some of the platinum is stripped from the surface with the plastic replica and its structure can be examined by electron diffraction. Distinct diffraction spots indicate that the particles originate from a single crystal. A number of such particles scattered over the surface of a grain all have the same orientation.

Considerable attention was paid to the question of whether or not activation by triangular anodic-cathodic cycling produced any surface structural changes. Unfortunately, any such changes were difficult to detect with certainty because of the limitations in resolution of the replica technique, the variability from sample to sample, and the problems in choosing truly representative fields under the microscope for purposes of comparison. There were however some indications that, on an unheated electrode, activation is accompanied by slight surface roughening and that on the pitted surface of a heat pretreated electrode some enlargement of the pits occurs on activation.

Discussion

Electrode activation.—The activation criteria adopted here are, to an extent, arbitrary in that a direct connection between the development of specific features on the cyclic voltammograms and the activity of the electrode to electrocatalytic processes in general has not yet been established. For the extreme cases, such as electrodes which have had no activation at all or are clearly contaminated in some way, there is general agreement that the corresponding voltammograms should be regarded as typifying lack of activity; in particular, the small activity toward hydrogen and oxygen electrosorption can be cited. However, with the more subtle changes which occur later during cycling, such as slight increases in the hydrogen peaks or steepening of the current rise at the start of the "oxide" region, the term activation will be used here as defining such changes rather than implying a relation to electrode activity in the practical sense.

Electron microscopy suggests that activation by anodic-cathodic cycling involves structural alteration of the surface. This is a slow process requiring several hundred cycles whereas cleaning of a contaminated surface occurs in fewer than ten cycles. The observation of a time-, stirring- and purity-dependent decay of electrode activity after anodic treatment is certainly good evidence for the role of contaminant adsorption in deactivation (14, 16) but does not exclude the possibility of structural changes being important in the initial activation. Several authors (10-13) have proposed that the time-dependence of electrode activity indicates the decay of an unstable layer of surface platinum atoms in a hypothetical active state. In fact, the activated structure is shown in the present work to possess long term stability and the deactivation found by these authors must be attributed to the inevitable contamination of the surface by dissolved impurities. The active structure can, however, be disrupted by mild mechanical means such as gentle wiping with a paper tissue as described above. Of course, more vigorous methods such as chemical attack or annealing will also disturb the active structure produced by anodic-cathodic cycling.

The mechanism of electrode activation (as distinct from cleaning) seems to involve some kind of redistribution of surface platinum atoms during anodic-cathodic cycling. The freedom of movement needed to bring about such a redistribution presumably arises from the periodic formation and breakage of platinum-oxygen bonds, since this work has shown that neither adsorbed nor absorbed hydrogen plays a part in the activation process. These observations suggest the following mechanism for electrode activation. After rolling or drawing during manufacture, a platinum surface probably contains a large proportion of high index crystal faces and many defects. There is a correspondingly large number of high energy surface platinum atoms with low co-ordination to the underlying lattice. Such a surface is essentially unstable to the formation of an electrochemically generated layer of adsorbed oxygen and when the strong Pt-O chemisorption bond forms [see (22) for discussion of the nature of the adsorbed oxygen layer], the further weakening of the co-ordination of the high energy platinum atoms allows rearrangement of the atoms or complete separation of the Pt-O entity from the surface. Repetition of this process using one of the nonroughen-

ing programs eventually removes most or all of the high energy platinum atoms and leaves a stable surface exposing predominantly low index, high co-ordination faces. It is presumably within the pits that such planes are exposed, an idea supported by the angular appearance which the pits assume on further roughening. From the electrochemical point of view, the featureless hydrogen adsorption curve which results from a large spread of energetically different kinds of sites gives way to well-defined peaks which, if the association of hydrogen peaks with crystal faces (19) is accepted, correspond to the smaller number of types of low index faces produced by cycling. Heat treatment in an oxidizing flame affects surface structure and activity in a manner similar to cycling because of the greater volatility of platinum oxide formed at high energy sites.

A clear analogy exists between this process and the recently proposed explanation (24, 25) for changes in surface properties of silver powder exposed to cyclic oxygen adsorption and reduction (*i.e.*, at gas/solid interface). Czanderna (24, 25) suggests that surface silver atoms rearrange by a small amount each time a layer of oxygen atoms is chemisorbed until finally a stable surface of minimum free energy, *i.e.*, low index planes, is generated; the driving force for the movement of the silver atoms is supplied by the bond energy between silver and oxygen. A similar mechanism was proposed earlier for the roughening of platinum electrodes (6). Note however that the possibility of complete removal of platinum atoms from the surface is now introduced.

Two arguments provide indirect support for a theory involving actual loss of surface platinum during activation. First, the tendency for platinum to dissolve under mild anodic conditions is becoming increasingly recognized (16, 26-29). Second, the assumption of such a dissolution process can provide a ready explanation for the difficulty in obtaining charge balance in the oxidation and reduction of a platinum surface [see ref. (30) for discussion of this problem]. Although impurity adsorption is undoubtedly an important factor, the loss of a species such as Pt-O to the solution at some stage during the cyclic process can help to explain some of these observations. For example, Breiter (15) measured the charges involved in oxidizing (Q_{ox}^{an}) and reducing (Q_{ox}^{cath}) a platinum surface during the first 110 cycles of an activation process (triangular cycling between 0.2 and 1.5V) similar to that used here. He found that the ratio of these charges decreased as the number of cycles increased and was still about 1.4 at the 110th cycle. The total difference between the two charges during the course of cycling was about 40 mcoulomb/cm^2 which is much greater than can reasonably be attributed to impurity adsorption but can be explained by assuming that, as cycling proceeds, a decreasing fraction of platinum atoms can leave the surface bound to an oxygen atom.

If the structural concept of platinum electrode activation is correct, then the various common pretreatments might differ in the way they alter either the platinum surface structure and/or its ability to respond to cathodic-anodic treatment. It is suggested that to obtain comparable electrode surface states it is necessary not only to use identical activation procedures but also to precede activation with an annealing step which will tend to produce similar types of surfaces on samples of different origin. However, the initial bulk platinum structure will also depend on the amount and nature of the cold working received during fabrication. Annealing is not expected to eliminate preferred grain orientations arising from different kinds of cold work so that unless a uniform and sufficiently vigorous cold work pretreatment is given to the platinum this factor will remain a variable of as yet unknown importance to activity. It should be mentioned that wire and foil electrodes used in this work gave slightly different ratios of the two main hydrogen peaks, supporting the idea (19) that grain orientation is important in determining the shape of the hydrogen adsorption curve.

Electrode roughening.—Roughening occurs when platinum atoms which are stable to triangular cycling (presumably those in low index planes) acquire sufficient energy to diffuse over or break away from the surface. The two conditions for roughening are:

(*a*) Surface oxygen : surface platinum atom ratio > 1. This suggests that sufficient weakening of Pt-Pt interactions occurs only when chemisorption bonds form between a Pt atom and more than one O atom. An explanation in terms of dissolution of a particular platinum oxide phase, *e.g.*, PtO_2, is less likely in view of the chemisorptive nature of the oxygen layer on Pt electrodes (22).

(*b*) Fast reduction of surface oxygen. This condition indicates that a concerted effect is needed to allow these Pt atoms to move to new positions or to leave the surface. The simultaneous reduction of a large amount of adsorbed oxygen provides the necessary activation energy for mobility of some of the surface Pt atoms. It is not clear in what form these atoms leave the surface but, as with activation, some kind of platinum-oxygen species is favored.

Adsorbed or dermasorbed hydrogen (3, 7) is not a causative factor in the roughening process which is actually inhibited in a program where the electrode is reduced at a potential in the hydrogen region. One can speculate that this is due to the rapid replacement of adsorbed oxygen with adsorbed hydrogen so that at no stage does the platinum surface energy rise to the same level as in the absence of chemisorbed species (in the double layer region).

The single crystal platinum particles present where an electrode is visibly darkened probably arise through undercutting of the metal surface due to lateral expansion of the pits. The alternative possibility that an epitaxed layer forms on redeposition of platinum which has entered solution is considered less likely in view of the fact that no platinum particles are stripped off with the replica until high roughness factors are reached.

As an electrode roughens, changes in shape of the cyclic voltammograms indicate changes in the state of the electrode surface. Thus, if the two main hydrogen peaks represent two major kinds of platinum surface sites, changes in relative peak heights indicate a greater stability of one type of site to the roughening program. The facts that parallel changes occur in the heights of the two small peaks near the start of the "oxide" region and that the separation of these peaks and the hydrogen peaks is similar suggest that the peaks in the "oxide" region correspond to adsorption of the OH radical and that adsorption of the species H and OH occurs with similar relative energies on the two main kinds of platinum sites. If this conclusion is correct, then one of the main effects of activation is to lower the potential at which adsorption of the more strongly bound OH radical commences, as indicated by the increase in steepness of the current rise at the start of the "oxide" region. In view of the role which adsorbed OH is supposed to play in the electro-oxidation of organic compounds [*e.g.*, (32, 33)], a correlation between the arbitrary activation criteria used here and the actual electrocatalytic activity can be expected.

Acknowledgment

The author is grateful to Dr. J. V. Sanders, CSIRO Division of Tribophysics, for obtaining and assisting with interpretation of the electron micrographs.

Manuscript submitted Jan. 9, 1969; revised manuscript received *ca.* April 10, 1969.

Any discussion of this paper will appear in a Discussion Section to be published in the June 1970 JOURNAL.

REFERENCES
1. S. Shibata, *J. Chem. Soc. Japan*, **79**, 239 (1958).
2. F. C. Anson and D. M. King, *Anal. Chem.*, **34**, 362 (1961).
3. J. P. Hoare, *Electrochim. Acta*, **9**, 599 (1964).
4. S. Gilman, *J. Electroanal. Chem.*, **9**, 276 (1965).
5. S. B. Brummer, J. I. Ford, and M. J. Turner, *J. Phys. Chem.*, **69**, 3424 (1965).
6. T. Biegler, *This Journal*, **114**, 1261 (1967).
7. J. P. Hoare, *J. Electroanal. Chem.*, **12**, 260 (1966).
8. R. Thacker, *Nature*, **212**, 182 (1966).
9. R. Woods, *Electrochim. Acta*, **13**, 1967 (1968).
10. F. C. Anson, *Anal. Chem.*, **33**, 934 (1961).
11. F. G. Will and C. A. Knorr, *Z. Elektrochem.*, **64**, 258 (1960).
12. S. Shibata, *Bull. Chem. Soc. Japan*, **36**, 525 (1963).
13. W. G. French and T. Kuwana, *J. Phys. Chem.*, **68**, 1279 (1964).
14. S. Gilman, *ibid.*, **67**, 78 (1963).
15. M. W. Breiter, *Electrochim. Acta*, **11**, 905 (1966).
16. S. D. James, *This Journal*, **114**, 1113 (1967).
17. T. Biegler, *J. Phys. Chem.*, **72**, 1571 (1968).
18. M. W. Breiter, *ibid.*, **69**, 901 (1965).
19. F. G. Will, *This Journal*, **112**, 451 (1965).
20. M. Becker and M. Breiter, *Z. Elektrochem.*, **60**, 1080 (1956).
21. S. Gilman, *Electrochim. Acta*, **9**, 1025 (1964).
22. T. Biegler and R. Woods, *J. Electroanal. Chem.*, **20** 73 (1969).
23. G. H. Ayres and A. S. Meyer, *Anal. Chem.*, **23**, 299 (1951).
24. A. W. Czanderna, *J. Phys. Chem.*, **70**, 2120 (1966).
25. A. W. Czanderna, *J. Colloid and Interface Sci.*, **24**, 500 (1967).
26. S. B. Brummer, *This Journal*, **112**, 633 (1965).
27. A. N. Chemodanov, Ya. M. Kolotyrkin, M. A. Dem'rovskii, and T. V. Kudryavina, *Doklady Akad. Nauk. SSSR*, **171**, 1384 (1966).
28. P. Malachesky, R. Jasinski, and B. Burrows, *This Journal*, **114**, 1104 (1967).
29. J. R. Aylward and S. W. Smith, Technical Report ECOM-02205-3, Contract No. DA-28-043-AMC-02205(E), May 1967.
30. S. Gilman in "Electroanalytical Chemistry," Vol. 2, pp. 111-192, A. J. Bard, Editor, Arnold, London (1967).
31. V. S. Bagotskii and Yu. B. Vasil'ev, *Electrochim. Acta*, **11**, 1439 (1966).
32. V. S. Bagotskii and Yu. B. Vasil'ev, *ibid.*, **9**, 869 (1964).
33. A. T. Kuhn, H. Wroblowa, and J. O'M. Bockris, *Trans. Faraday Soc.*, **63**, 1458 (1967).

Technical Note

The Oxygen Electrode in Molten Alkali Metal Nitrates

II. Standard Potentials as a Function of Na^+/K^+ Ratio

R. N. Kust*

Department of Chemistry, University of Utah, Salt Lake City, Utah

In the last several years an increased interest in the study of molten salt systems has occurred, not only in terms of the numerous applied industrial processes which utilize such solvents but also because of the increased need for fundamental knowledge of systems containing no protons.

Numerous workers have postulated the existence of the oxide ion in several such melts (1). Some of the investigations have involved the assay of small concentrations of oxide ion potentiometrically with an oxygen gas-oxide ion electrode in a sodium nitrate-potassium nitrate equimolar melt. The standard potentials of the oxygen electrode have been defined in this melt with a 1.0M silver nitrate reference electrode (2).

Several workers (3) have indicated that equilibrium constants and rate constants for some acid-base reactions in molten alkali metal nitrates are influenced to some degree by the ratio of cations present in the melt. Recent studies (4) suggest that solvation of anions by the alkali metal cation constitutes an important part of this influence. In order to investigate potentiometrically the changes in various acid-base equilibria when the cation ratio of the solvent is changed, the variation in the standard potential of the oxygen electrode with cation ratio must first be determined. This paper is a report of the evaluation of the standard potential of the oxygen-silver nitrate electrode system in sodium nitrate-potassium nitrate melts as a function of temperature and cation ratio.

Experimental Section

All chemicals used were of reagent grade. The sodium nitrate and potassium nitrate were dried for 24 hr at 140°C before being used to prepare the various solvents. Bulk quantities of solvent containing 22.9 m/o (mole per cent) sodium nitrate-77.1 m/o potassium nitrate and 82.6 m/o sodium nitrate-17.4 m/o potassium nitrate were made by fusing together the proper quantities of the salts, mixing well, filtering through a medium porosity fritted glass disk, molded into slugs of about 100g and stored over magnesium perchlorate. Melts of intermediate cation ratios were made by mixing suitable quantities of these two bulk solvents.

The reaction vessel and electrodes were similar to those previously described (2). An oxygen-platinum electrode was used as the indicator electrode and a silver-silver nitrate (1.0m $AgNO_3$ in equimolar $NaNO_3$-KNO_3) electrode enclosed in Pyrex glass was used as the reference electrode. Potential measurements were made with a high impedance potentiometric network as has been previously described (2).

The standard oxide ion solutions used were made by dissolving small quantities (*ca.* 10^{-4}m) of anhydrous sodium carbonate in equimolar sodium nitrate-potassium nitrate solvent. These solutions were held under a vacuum of less than 10μ for over 48 hr. The oxide in these solutions was then assayed by titration with hydrochloric acid. Titration of the oxide solutions with permanganate indicated that there were no oxidizable impurities and consequently that nitrites, peroxides, and superoxides were not present in significant quantities.

Results

The electrochemical cell used in this study can be described

$$\text{Pt, } O_2(g) \;\Big|\; \begin{matrix} x_{NaNO_3} \\ 1-x_{KNO_3} \end{matrix} \;\Big\|\; \underset{NaNO_3\text{-}KNO_3,}{\text{equimolar}} \; 1.0\text{m } AgNO_3 \;\Big|\; \text{Ag}$$

Pyrex

* Electrochemical Society Active Member.

where x is the mole fraction of sodium nitrate in the indicator electrode compartment, and where the vertical dotted lines indicate the Pyrex glass membrane, about 0.1 mm thick, which encloses the reference electrode compartment. The cell reaction can be written

$$2Ag^+ + O^{2-} \rightleftarrows 2Ag + \tfrac{1}{2} O_2 \qquad [1]$$

for which the Nernst equation is

$$E = E^\circ - \frac{2.3RT}{2F} \log \frac{P_{O_2}{}^{1/2}}{[O^{2-}][Ag^+]} \qquad [2]$$

The standard potential for this cell was determined in four different sodium nitrate-potassium nitrate solvents which had the following compositions expressed in mole per cent: 23% $NaNO_3$, 77% KNO_3; 44% $NaNO_3$, 56% KNO_3; 64% $NaNO_3$, 36% KNO_3; 83% $NaNO_3$, 17% KNO_3. The concentration of oxide ion in these solvents was varied from about 5 x 10^{-7}m to about 5 x 10^{-5}m. The temperature was varied from 290° to above 360°C. The reversible nature of the electrode system was checked in each of the different solvents at each temperature. The criteria used to determine whether or not the electrochemical cell was reversible were (*i*) adherence to the Nernst equation when the O^{2-} ion concentration and the oxygen pressure were independently varied, and (*ii*) lack of hysteresis in micropolarization plots of current *vs.* voltage when the voltage was scanned through ± 100 mV of the equilibrium potential. In all cases, the tests indicated the cell was reversible within experimental limits.

Standard potentials were calculated from the observed potentials with the aid of the Nernst equation [2]. Experimental data obtained in the various solvents at a temperature of 320° are indicated in Table I.

The variation of standard potential with temperature and composition is graphically represented in Fig. 1 and 2. The previously determined temperature dependence of the standard potential for the oxygen electrode in a melt of equimolar $NaNO_3$-KNO_3 is also shown in Fig. 2 for reference purposes.

Discussion

According to the data in Fig. 1 and 2, there is evidently a small but definite dependence of the standard potential of the oxygen gas-silver ion electrode system on the ratio of sodium nitrate to potassium nitrate in the solvent. The E°, in volts, can be calculated for any temperature between 290° and 360°C and for a sodium nitrate-potassium nitrate melt of any cation ratio from the equation

$$E^\circ(t, x_{Na}) = [0.6730 - 0.000130(t - 290^\circ)] - [0.0830 + 0.000275(t - 290^\circ)]x_{Na} \qquad [3]$$

Table I. Observed potentials and calculated standard potentials in millivolts for the oxygen electrode at 320°C in sodium nitrate-potassium nitrate melts of different cation ratios

Solvent, mole fraction $NaNO_3$	O^{2-} x 10^7m	P_{O_2}, atm	E, mV	E°, mV
0.23	5.12	0.851	281.9	649.1
	8.97	0.847	294.6	647.5
	16.7	0.847	310.9	647.9
	50.1	0.481	346.2	648.0
	79.1	0.480	357.3	647.5
			Average	648.0 ± 0.7
0.44	9.13	0.862	276.4	629.1
	24.1	0.862	301.9	629.8
	24.1	0.501	308.1	629.1
	53.6	0.461	328.7	628.3
	91.9	0.461	324.8	628.7
			Average	629.0 ± 0.6
0.64	8.30	0.851	255.5	610.4
	30.9	0.851	289.9	611.3
	69.2	0.850	310.4	611.2
	96.2	0.493	324.5	610.0
	187	0.493	341.6	610.1
			Average	610.6 ± 0.6
0.83	17.9	0.490	265.3	593.6
	38.7	0.490	284.9	593.5
	90.7	0.847	300.2	594.1
	231	0.847	324.1	594.1
			Average	593.8 ± 0.3

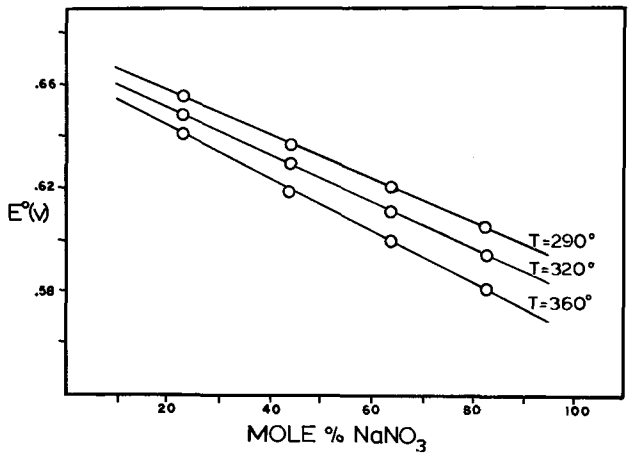

Fig. 1. Variation of standard potential of the oxygen electrode with mole per cent $NaNO_3$ in sodium nitrate-potassium nitrate melts at different temperatures.

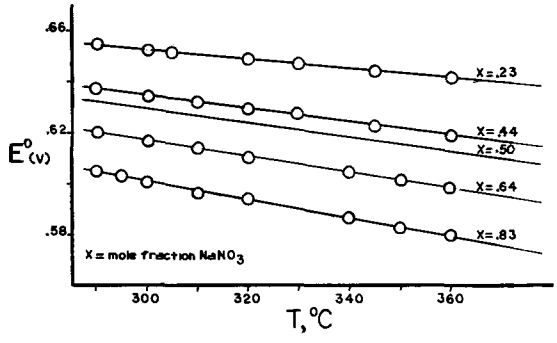

Fig. 2. Variation of standard potential of the oxygen electrode with temperature in sodium nitrate-potassium nitrate melts at different Na^+/K^+ cation ratios.

where t is the temperature in °C and x_{Na} is the mole fraction of sodium nitrate. The standard deviation is estimated to be ± 0.0009V.

The lower temperature limit of 290°C was dictated by the observation that melts containing 23 m/o $NaNO_3$ froze a few degrees below 290°C. However, for other salt mixtures melting at lower temperatures, a linear extrapolation of Eq. [3] would be reasonable, at least to temperatures down to 250°C since the above equation can be used to calculate standard potentials in equimolar sodium nitrate-potassium nitrate solvents which are within the error of experimentally determined values in melts of this composition (2).

The decrease in standard potential with increase in sodium nitrate concentration suggests that the activity of the oxide ion decreases as the sodium ion activity increases. An even more pronounced decrease in standard potential would be expected if lithium ion were substituted for the sodium ion. However, it cannot be claimed that this solvation process is the sole explanation for the variation in standard potential with cation ratio. The temperature dependence of the standard potential is negative in all of the melts studied, and, furthermore, becomes more negative as the sodium nitrate/potassium nitrate ratio increases. The negative temperature dependence indicates a negative entropy of reaction for the cell reaction. Since the oxide ion is a reactant in the cell reaction, more effective solvation of the oxide ion should cause the entropy change and hence the temperature coefficient of the standard potential to become less negative as the ratio of sodium nitrate to potassium nitrate is increased.

There are several features of this particular electrode system which are not well understood and which may contain the explanation for the temperature dependence of the standard potential. One such feature is the Pyrex glass membrane which is used to separate

the anode and cathode compartments of the cell. It has been shown (5) that in highly ionic nitrate melts, the behavior of the Pyrex glass membrane is most adequately described by an ion exchange model. Membrane potentials for Pyrex in sodium nitrate-silver nitrate systems have been approximately evaluated (5b) and generally are small, on the order of 8 to 10 mV. Similarly, membrane potentials in lithium nitrate-silver nitrate, sodium nitrate-silver nitrate, and potassium nitrate-silver nitrate systems have been evaluated (5c) and again are small. However, in both of these studies, potentials were measured when a finite activity of Ag^+ was present on both sides of the Pyrex membrane. In the electrode system presented in this article, the silver ion activity in the anode compartment is essentially zero. Hence the actual membrane potential of this system cannot be inferred from these other studies.

Another feature which is not completely understood and which may have bearing on the situation is the actual chemical process occurring at the platinum electrode. It has been shown (6) that in molten carbonate melts, platinum electrodes can function as electrodes reversible to the oxide ion, but that in so doing, platinum oxides are formed. Although these studies in nitrate melts have been carried out at much lower temperatures, formation of platinum oxides might still be possible and might lead to a complex relationship with the cations in solution.

More information regarding these systems is needed. An investigation of the cation and temperature dependence of the oxygen electrode when a reference electrode which substitutes an asbestos wick or glass frit for the glass membrane should contribute more information on what role the glass membrane plays. Also extension of the investigation to the lithium ion should prove interesting.

Acknowledgment

Acknowledgment is made to the donors of the Petroleum Research Fund, administered by the American Chemical Society, for support of this research.

Manuscript submitted Dec. 6, 1968; revised manuscript received April 30, 1969. This paper was presented in part at the American Chemical Society San Francisco Meeting, April 1968.

Any discussion of this paper will appear in a Discussion Section to be published in the June 1970 JOURNAL.

REFERENCES

1. (a) H. Flood and T. Forland, *Acta Chem. Scand.*, **1**, 92 (1947).
   (b) B. A. Rose, G. J. Davis, and H. J. T. Ellingham, *Disc. Faraday Soc.*, **4**, 154 (1948).
   (c) C. N. Bussom, S. Palous, and J. Millet, *C. R. Acad. Sci., Paris, Ser. C.*, **265** (20), 1076 (1967).
2. (a) R. N. Kust and F. R. Duke, *J. Am. Chem. Soc.*, **85**, 3338 (1963).
   (b) R. N. Kust, *J. Phys. Chem.*, **69**, 3662 (1965).
3. (a) F. R. Duke and J. M. Schlegel, *ibid.*, **67**, 2487 (1963).
   (b) F. R. Duke and E. A. Shute, *ibid.*, **66**, 2114 (1962).
   (c) A. M. Shams El Din, T. Gouda, and A. A. El Hosary, *J. Electroanal. Chem. Interfacial Electrochem.*, **17** (1/2), 137 (1968).
4. R. N. Kust, *Inorg. Chem.*, **6**, 2239 (1967).
5. (a) K. Notz and A. G. Keenan, *J. Phys. Chem.*, **70(3)**, 662 (1966).
   (b) R. H. Doremus, *This Journal*, **115**, 925 (1968).
   (c) A. G. Keenan, K. Notz, and F. L. Wilcox, *J. Phys. Chem.*, **72**, 1085 (1968).
6. G. Janz and F. Saegusa, *Electrochim. Acta*, **1**, 393 (1962).

Solid Solubility and Diffusion Coefficients of Boron in Silicon

G. L. Vick and K. M. Whittle

Instrument/Controls Division, Conrac Corporation, Duarte, California

ABSTRACT

The solid solubility and diffusion coefficients of boron in silicon have been determined as a function of temperature over the range of 700°-1151°C, by anodically sectioning diffused layers. The solid solubility was found to vary from 1.6×10^{19} atoms/cm^3 at 700°C to 2.4×10^{20} atoms/cm^3 at 1151°C. The diffusion coefficients for impurity levels below 10^{18} atoms/cm^3 may be represented by $D = 6.0 \times 10^{-7} \exp(-38600/RT)$. The diffusion coefficients above 10^{18} atoms/cm^3 were found to be dependent on the impurity level.

In view of the importance of boron as a dopant in the technology of silicon electronic devices, there is a remarkable paucity of information regarding the solid solubility of boron in silicon. In Trumbore's review of solid solubilities of elements in germanium and silicon (1), boron is represented by only two points, a eutectic point and a single point based on diffusion data.

This paper describes a series of experiments in which boron is diffused into silicon at a number of different temperatures between 700° and 1151°C from an effectively infinite source. The resulting diffusion profiles are anodically sectioned to determine the solid solubility of boron in silicon as a function of temperature. The diffusion coefficients of boron in silicon are also calculated as a function of temperature and boron concentration.

Experimental Procedure

A boron rich glass (B_2O_3) is pyrolytically deposited on the surface of 3.0 to 6.5 ohm-cm n-type wafers at relatively low temperature (688°C). The wafers are then diffused at higher temperatures in an nonoxidizing atmosphere (N_2). Under these conditions the boron glass is reduced by the silicon, making elemental boron available for diffusion into the silicon. The deposition and diffusion systems have previously been described by Whittle and Vick (2). The reduction of the B_2O_3 makes boron atoms available at a rate greater than the rate at which they are diffused away into the silicon. This results in a thin layer of a boron-rich phase such as that discussed by Busen *et al.* (3). This boron rich phase will act as an effectively infinite source of boron for diffusion into the silicon. Similar phases may be observed in phosphorus diffusion and have been used by Kooi (4) in determining solubility of phosphorus in silicon.

Experiments have been performed which show that the surface concentrations are independent of all deposition parameters over a wide range [ref. (2)] and are independent of diffusion time for all the different values of diffusion time reported in this paper and are dependent only on diffusion temperature. The work of Owen and Schmidt (5) could be interpreted as predicting a surface concentration independent of time under certain conditions. This work is not directly applicable here, however, because the rate of chemical decomposition of the B_2O_3 controls the rate at which boron is made available for diffusion. This is demonstrated by the fact that the doping will be inhibited by the presence of oxygen in the atmosphere. The presence of the boron-rich phase ensures an adequate supply of boron so that surface concentration will be determined by the solid solubility.

In view of the departures from complementary error function form of the profiles obtained at the higher temperature diffusions, experiments were performed to determine whether there was precipitation of the boron such as that found for phosphorus by Tannenbaum (6). Diffused wafers were cooled from 1150°C to room temperature in times ranging from 1 min to 1 hr without preceptible change in profile, leading to the conclusion that precipitation was not occurring to any measurable amount.

Sectioning of the diffused impurity profiles was accomplished by anodically growing and then removing layers of silicon dioxide. Anodic oxide growth was carried out in a solution consisting of 3 parts ethylene glycol and 1 part phosphoric acid at 100V. The oxide was removed with HF and the anodization repeated. After every fifth anodization-HF cycle a measurement was made of sheet resistivity and depth of silicon removal. Sheet resistivity was measured by a standard 4-point probe method. Silicon removal was measured by masking off a region of the wafer during anodization-HF cycles and measuring the height of the resulting plateau by means of interference fringes. Irwin's (7) plot of resistivity *vs.* impurity concentration was used to determine the impurity concentration of successively removed layers of boron concentration.

Accuracy

The diffusion temperatures were controlled to ±2°C and diffusion times were controlled to ±0.05 min.

The 4-point probe measurements on a given sample were consistent from reading to reading within 1%.

The depth of silicon removal was determined by calibrating the silicon removal per anodization cycle against depth measurements made by means of interference fringes. The calibration was made to a depth of 4μ with an accuracy of ±¼ fringe, giving a possible consistent error of about 7%. In addition, the random errors, represented as deviations of data points from the calibration curve amounted to about ±5% rms.

The plots of impurity concentration *vs.* depth shown in Fig. 1 and 2 involve the first derivative of the curve of conductivity *vs.* depth which was experimentally determined. The deviation of data points from complementary error functions in Fig. 1 and from the best smooth curves in Fig. 2 are ± 13% rms.

A significant source of inaccuracy in the values of diffusion coefficient at temperatures above 1000°C lay in graphical integration and differentiation of the impurity profiles. These procedures are somewhat subjective in nature and it was found that variations in diffusion coefficient as large as ±100% could be achieved by differing estimations of the slopes. The values reported in Fig. 4 represent the best judgment of the authors as to the interpretation of existing data. At temperatures less than 1000°C, the diffusions are too shallow to justify accuracy greater than ±100%.

Solid Solubility

In Fig. 1 and 2 are plotted the curves of impurity *vs.* depth. The curves for diffusions below 1018°C are

Key words: Solid solubility, diffusion coefficient, boron, silicon.

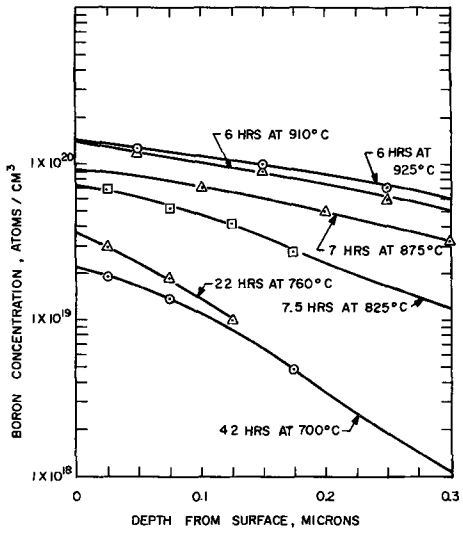

Fig. 1. Boron concentration vs. depth from surface

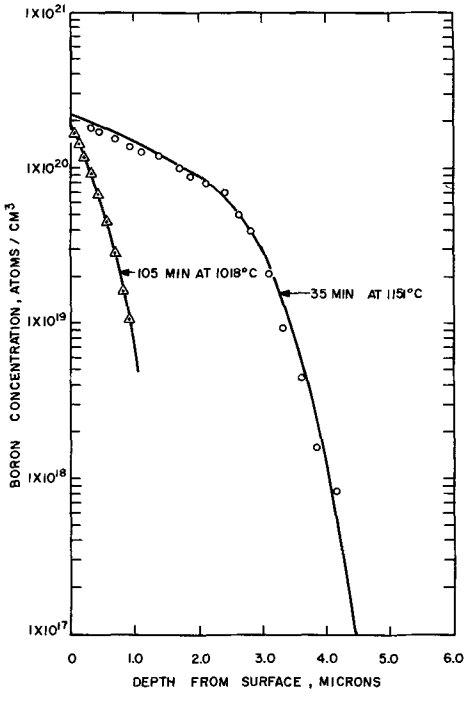

Fig. 2. Boron concentration vs. depth from surface

found to fit well the complementary error function. For diffusion at 1018°C and higher the curves are simply the smooth curve which best fits the data. Solid solubilities are obtained by extrapolating the diffusion profiles to zero depth and are plotted *vs.* temperature in Fig. 3.

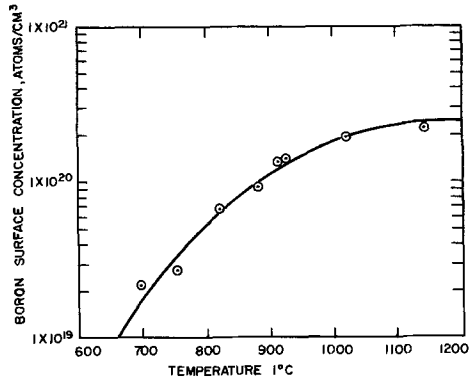

Fig. 3. Boron solid solubility vs. temperature

The solid solubility data indicate a lower solubility of boron in silicon than had previously been reported. There is, however, little actual data to support a higher value of solubility. Diffusion profiles having larger surface concentrations have been reported. These, however, have been calculated on the assumption of a complementary error function distribution which is shown to be false for temperatures above 1000°C.

Diffusion Coefficients

For those diffusion profiles which may be represented by the familiar complementary error function, $C_x = C_s\text{erfc}\ (x/2(Dt)^{1/2})$, calculation of diffusion coefficients is straightforward since C_x is the concentration of the diffusant at distance x after time t and C_s is the extrapolated surface concentration. All the necessary data can be obtained from the diffusion profiles in Fig. 1.

The profiles which do not fit a complementary error function must be dealt with differently. The possibilities of source depletion or of impurity precipitation as explanations for the shape of these curves have been ruled out as described earlier. It may be assumed, then, that the profiles result from a concentration dependent diffusion coefficient similar to that found by Tannenbaum (6) for phosphorus. The diffusion coefficients may be calculated as a function of impurity concentration by a method presented by Crank (8) using the equation

$$D_{c=c_1} = \frac{1}{2t}\frac{dx}{dc}\int_0^{c_1} x\,dC$$

where D is the diffusion coefficient at a concentration C, and x and t are depth and time, respectively.

Applying this equation to the curves in Fig. 2 results in the dependence of diffusion coefficient on impurity concentration shown in Fig. 4. The slope dx/dc and the area $\int_0^{c_1} x\,dc$ were determined graphically so that the curves in Fig. 4 should be considered to show a qualitative trend only. An accurate determination of diffusion coefficient as a function of impurity concentration could be made by subjecting the impurity profile data to computation by a computer. These curves in Fig. 4 are seen to approach a minimum value of the diffusion coefficient at each temperature at which the diffusion coefficient is independent of impurity concentration.

A plot of the logarithm of the diffusion coefficient *vs.* inverse temperature should yield a straight line since the temperature dependence of the diffusion coefficient follows the form

$$D = D_0 \exp\ (E_a/RT)$$

where E_a is the activation energy for diffusion, R is the gas constant, and T is the absolute temperature.

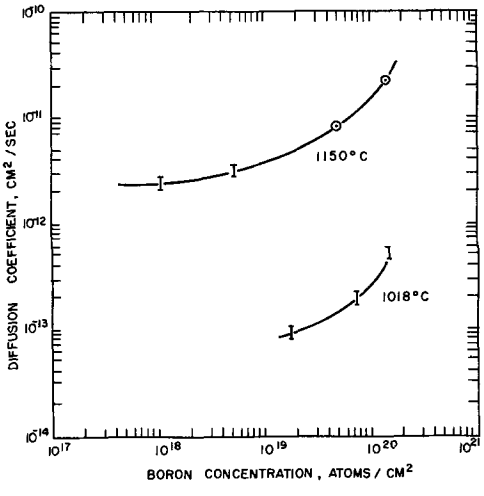

Fig. 4. Diffusion coefficient vs. boron concentration

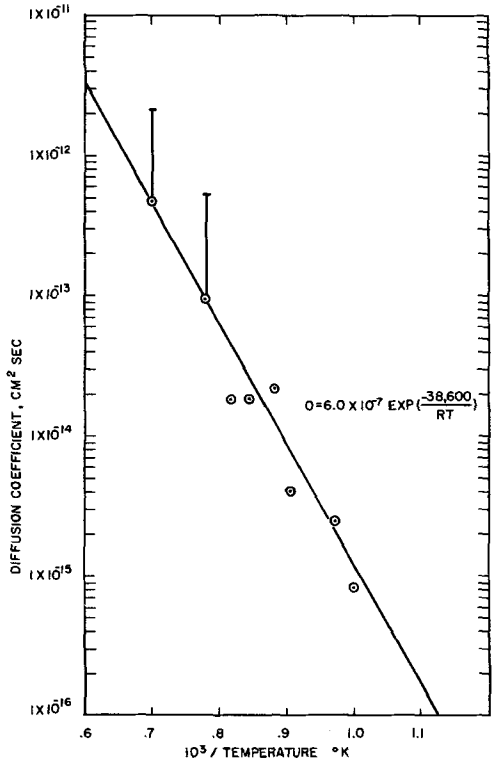

Fig. 5. Boron diffusion coefficient vs. temperature

The diffusion coefficients are plotted against the inverse of temperature in Fig. 5 and can be shown to follow the equation $D = 6.0 \times 10^{-7} \exp(-38600/RT)$.

Those diffusion coefficients (above 1000°C) for which the coefficients are dependent on impurity concentration are represented on Fig. 5 by a data point indicating the value of the concentration independent coefficient, together with a vertical line indicating the range of values which hold at higher concentrations.

Summary

Values for the solid solubility of boron as a function of temperature in silicon are presented in this paper for the first time.

Values of diffusion coefficients for boron in silicon are given over a range of temperature almost 300°C greater than was previously available (700°-1150°C) (9-11). Concentration dependent diffusion coefficients of boron in silicon are reported.

Manuscript submitted Oct. 7, 1968; revised manuscript received April 11, 1969.

Any discussion of this paper will appear in a Discussion Section to be published in the June 1970 JOURNAL.

REFERENCES

1. F. A. Trumbore, *Bell Systems Tech. J.*, **39**, 205 (1960).
2. K. M. Whittle and G. L. Vick, *This Journal*, **116**, 645 (1969).
3. K. M. Busen, W. A. Fitzgibbons, and W. K. Tsang, *ibid.*, **115**, 291 (1968).
4. E. Kooi, *ibid.*, **111**, 1383 (1964).
5. A. E. Owen and P. F. Schmidt, *ibid.*, **115**, 548 (1968).
6. E. Tannenbaum, Solid State Electronics, **2**, 123 (1961).
7. J. C. Irwin, *Bell Systems Tech. J.*, **41**, 387 (1962).
8. J. Crank, "The Mathematics of Diffusion," p. 232, Oxford University Press (1956).
9. E. C. Williams, *This Journal*, **108**, 795 (1962).
10. A. D. Kurtz and R. Yee, *J. Appl. Phys.*, **31**, 303 (1960).
11. C. S. Fuller and J. A. Ditzenberger, *ibid.*, **27**, 544 (1955).

Technical Notes

The Estimation of Bending Stresses from Flexure Measurements

R. E. Pawel*

Metals and Ceramics Division, Oak Ridge National Laboratory, Oak Ridge, Tennessee

The flexure technique, based on the physical deformation observed when a suitably prepared specimen is reacted on one side, has recently been employed in several investigations in which the characterization and measurement of stresses induced by surface or near-surface reactions were of interest. Originally the tool of the electroplater, this technique is now being used in other disciplines to collect special types of information which are otherwise difficult to obtain. Since the principal experimental measurements in flexure studies are ones of strain, the problem of transforming or assigning appropriate stress values must be faced. The general methods for doing this have existed in the literature for some time, but some uncertainty has arisen recently concerning the extent and importance of the Poisson (transverse) contributions during flexure experiments on various kinds of specimens. (This particular problem is, of course, entirely separate from the usually more tedious one of inferring the complete stress distribution from the bending stress values.) While it might be argued that this uncertainty is not a serious drawback because of the many other sources of error involved with the technique, such a possibility nevertheless warrants consideration, and it is the intent of the present note to express some thoughts and the results of an experiment which appear pertinent to the manner in which bending stresses are determined from bending strains.

Since the stress system imposed on the specimen may be considered to be uniform, it is helpful for purposes of this problem to think only in terms of bending stresses and to visualize the surface reaction that creates them, whatever it may be, as resulting in simple

* Electrochemical Society Active Member.

sets of bending moments rather than in the complex stress distribution which may actually exist. It is reasonable to do this, for uniform surface stresses, because the problem actually involves only the mutual transverse effects of the bending stresses.

The stress-strain relationship for a state of plane, biaxial elastic stress in a plate (which is an applicable approximation for most flexure experiments) is given by the following general equation

$$\sigma_x = \frac{E}{1-\nu^2}(\epsilon_x + \nu\epsilon_y) \qquad [1]$$

where σ and ϵ are the stress and strains in the indicated orthogonal directions, x is considered the "long" direction for strips, ν is Poisson's ratio, and E is Young's modulus. A similar expression can be written for the transverse, y, direction.

If a specimen is uniformly bent about a major axis, the maximum bending strain, located in the concave and convex surface layers of the plate, is given by the "flexure formula"

$$\epsilon_x = \pm\frac{t}{2\rho_x} \qquad [2]$$

where t is the plate thickness and ρ_x is the radius of curvature in the x direction.

In the analysis of the data obtained in a given flexure experiment, there are several possible configurations which need to be considered when relating the bending stresses to the measured flexure or strain by means of Eq. [1] and [2]. The relative applicability of each of these cases is dependent on the specimen geometry.

1. If equivalent surface forces result in the bending of a thin, rectangular specimen equally in the two directions, then $\epsilon_y \cong \epsilon_x$, and Eq. [1] yields $\sigma_x = (1/1-\nu)E\epsilon_x$. This is a "high-energy" situation for thin plates requiring that the specimen assume the shape of a part-surface of a sphere. Only comparatively "thick" specimens might be expected to exhibit this behavior for measurable curvatures.

2. Simple beam theory considers no stress to act in the y direction. Thus, if this condition exists, $\sigma_y \cong 0$, $\epsilon_y \cong -\nu\epsilon_x$, which leads to $\sigma_x = E\epsilon_x$, the relationship for uniaxial stress and strain. The specific assumption here is intuitively not an attractive one for bending in rectangular plates where bending is caused by a uniform surface reaction of some sort.

3. If, during bending, sufficient distortion occurs so that the bending strain is limited essentially to a single direction, then $\epsilon_y \cong 0$ and the pertinent equation becomes $\sigma_x = (1/1-\nu^2)E\epsilon_x$. Timoshenko (1) considered this to be the most likely condition for the bending of thin strips, although a correction for the specific geometry of the specimen was also included in his analysis. As indicated below, the corrections for specimen geometry typically employed in flexure experiments were in a direction and of such magnitude so as to make the "simple beam solution," condition 2, accurate within a few per cent.

While direct examination of thin strips which have undergone flexure as a result of either external forces or surface reactions seems to indicate that the geometric requirements for condition 3, above, are reasonably well met, a set of interesting experiments which more graphically supports the validity of Timoshenko's conclusion for bending due to surface reactions is as follows. Several 4- and 6-cm disk shaped specimens were cut from 0.015- and 0.010-in. tantalum sheet; they were annealed in vacuum at 1600°C and chemically polished. A thin layer of aluminum was vapor-deposited onto one side and the specimens then oxidized for various times at 500° and 550°C to yield a range in the observed degree of flexure.

The nature of the deformation exhibited by these specimens as a result of this reaction was informative. Although the disks were prepared carefully so that there would be no obvious mechanical axes, the deformation which occurred during oxidation at these temperatures was in all cases approximately uniaxial, cylindrical bending, resulting in the configuration shown in Fig. 1a. Please note that Fig. 1 is drawn with an exaggerated degree of bending to preserve clarity. While there are no long and short dimensions in disk-shaped specimens which would predetermine the axis of bending, the presence of any kind of flaw would be sufficient to influence the initial flexure of an otherwise perfect disk. Once started in a given direction, it is energetically favorable for elastic bending to continue in uniaxial fashion, and this shape will persist, even for a considerable degree of plastic deformation. Therefore, even for the case of biaxial stresses acting on one surface of a thin disk, flexure can result in bending about a single axis.

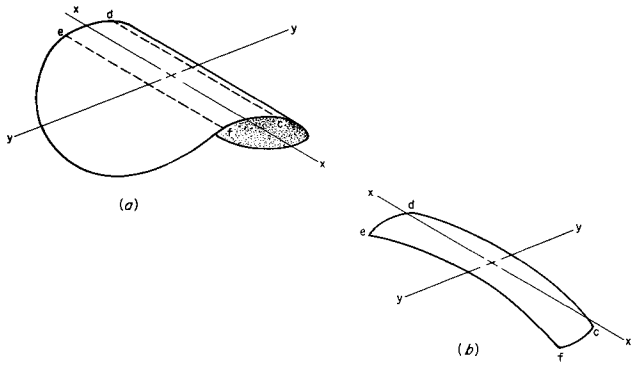

Fig. 1. Schematic drawing of the flexure behavior of a thin, disk-shaped specimen after oxidation of its upper side. The degree of bending shown here is exaggerated compared to that observed in most of our experiments concerning tantalum oxidation. (a) As-oxidized specimen; flexure has occurred predominantly in a single direction. (b) Section cdef, cut as indicated from original specimen after oxidation. The stresses, which also existed in (a), have now caused flexure in the x direction.

It should not be forgotten, however, that even though no bending takes place in the x direction in Fig. 1a, there should still be stresses present. The total stress existing in this direction would be composed of the same surface forces which caused bending in the y direction, plus the Poisson contribution from these associated bending stresses. For an elastic stress system, the stresses in the x direction might be allowed to exert themelves if a suitable change in specimen geometry were made after the initial bending was terminated. The results of such a change were determined for the deformed disks. Several of the bent oxidized specimens were cut parallel to the x direction to remove a rectangular strip of heretofore almost unstrained (in that direction) material. In all cases, the excised portion of the specimen then exhibited curvature in the x direction as illustrated in Fig. 1b. The geometry was then favorable for flexure in this direction and the stresses could manifest themselves accordingly.

While a strict quantitative analysis of these experiments was not attempted, it was observed that for experiments in which the total flexure was kept small (*i.e.*, the bending stresses were completely elastic), the subsequent bending of the cut strip was essentially the same as that observed originally for the disk in the transverse direction. On the other hand, several experiments obviously involved significant amounts of plastic strain and, in these cases, the flexure of the cut strip was only a fraction of that exhibited by the disk. Clearly, only the elastic components could contribute to the postoxidation distortion along the x direction. It was not practical to attempt to obtain the exact Poisson contribution or correction from these "excision" experiments. However, the behavior exhibited by these specimens establishes the deformation character-

istics and helps to ascertain the relevant stress-strain relationships during flexure.

A thin rectangular flexure specimen will generally bend along its long dimension and be constrained from similar bending along its short one. (One should be aware, however, that unless the specimen is carefully prepared, bending is likely to take place about a mechanical, rather than a geometric axis. For example, if a slight degree of curvature existed across the short dimension of a rectangular specimen prior to reaction, it very probably would continue to bend in this direction with virtually no curvature observed in the long dimension.) Although some distortion exists, the state of limited strain in the transverse direction does appear experimentally to be described best by the condition $\epsilon_y \cong 0$.

The above reasoning supports the use of the equation

$$\sigma_x = \pm \left[\frac{1}{1-\nu^2} \right] \frac{tE}{2\rho_x} \qquad [3]$$

to relate the maximum bending stress to the measured radius of curvature. However, Timoshenko, for only a slightly different set of conditions and a more sophisticated analysis, used a modified factor $(1-\nu^2 k)/(1-\nu^2)$, where k is a function of the strip dimensions and its radius of curvature. Typical dimensions for flexure specimens yield k-values only slightly less than unity. In other words, the simplest expression

$$\sigma_x = \pm \frac{tE}{2\rho_x} \qquad [4]$$

may also be the most appropriate. The best choice of the particular equation to represent the stress-strain relationships in a real system thus depends on the physical system itself, particularly the geometrical aspects. Recently, there have been several instances brought to our attention where an apparently arbitrary, or at least not fully justified, choice of the $1/(1-\nu)$ (case 1), correction was made. While there will be instances where this will be correct, it should be pointed out, as we have tried to do in this note, that this is not necessarily a straightforward choice, and a comparatively large absolute error in stress values may result if it is the incorrect one.

Acknowledgment

Thanks are extended to Drs. R. O. Williams, M. H. Yoo, H. E. McCoy, and J. V. Cathcart of the Metals and Ceramics Division, ORNL, for their helpful discussions. Research was sponsored by the United States Atomic Energy Commission under contract with Union Carbide Corporation.

Manuscript submitted March 27, 1969.

Any discussion of this paper will appear in a Discussion Section to be published in the June 1970 JOURNAL.

REFERENCE

1. For example, S. Timoshenko, *Mech. Engr.*, **45**, 259 (1923).

Reduction of Radiation Sensitivity in MOS Structures by Aluminum Doping of Silicon Dioxide

A. G. Revesz,[1] K. H. Zaininger, and R. J. Evans

RCA Laboratories, Princeton, New Jersey

The resistance of metal-insulator-semiconductor (MIS) devices against high energy electron bombardment or similar irradiation is important in several applications. Unfortunately, the metal-silicon-dioxide-silicon structures commonly used in many circuits are adversely affected by ionizing radiation and exhibit a shift of their device characteristics toward more negative voltage values. The extent of the shift and possible deformation of the surface capacitance *vs.* voltage (C-V) curve (compared with the ideal one) depend on the oxidation conditions and postoxidation treatments (1, 2). In the case of dry oxygen oxidation followed by high temperature helium-annealing, for example, it was found that irradiation by 1 MeV electrons under + 10V bias (fluence = 10^{14} e/cm^2) results in a shift of the C-V curve by 40-60V (for 1000Å thick oxide); this corresponds to the introduction into the oxide of positive surface electronic charges of the order of 10^{13}/cm^2. MIS structures using Al_2O_3 on Si, prepared either by plasma anodization of aluminum (3) or thermal decomposition of Al-alkoxide (4) show better radiation resistance than SiO_2 grown in dry O_2, especially under conditions of positive bias. However, because of the widespread use of SiO_2 and the emergence of Al_2O_3 as a possible insulator in MIS devices, it seemed that exploration of Al-doped SiO_2 was warranted.

We have found that by doping the SiO_2 film with aluminum the radiation resistance of MIS capacitors can be modified such that as the Al content in the oxide increases the radiation-introduced oxide charge under positive bias decreases.

[1] Present address: Comsat Laboratories, Washington, D. C.

Experimental

P-type Si wafers of (100) orientation were cleaned in H_2 at 1200°C, then oxidized in dry O_2 at 900° or 1250°C, and subsequently annealed in He at 1100°C in an r.f. heated, gas-cooled silica tube (5). These three processing steps were performed *in situ*. The only deviation from this fabrication method was that during oxidation Al was introduced into the oxidizing ambient by bubbling He through Al-acetylacetonate dissolved in acetylacetone. At both oxidation temperatures high (1.0 l/min) and low (0.1 l/min) flow rates of He were investigated. The oxygen flow was kept constant at 0.15 l/min. Several specimens were prepared in each group. Specimens oxidized at 900°C with the lower flow rate of He were very conducting and were not investigated further. The thickness and refractive index of the SiO_2 film at 5460Å wavelength were determined by ellipsometry. The Al content of the SiO_2 films was determined by mass-spectrometry using an ultra pure gold counterelectrode for sparking. The Al content of the Si substrate has also been determined before oxidation and after dissolution of the oxide film. Some specimens were also analyzed for other impurities. The structure of the oxide films was investigated with reflection electron diffraction.

The electric charge distribution at the Si-SiO_2 interface was determined by the MOS capacitance method at a frequency of 1 MHz (6). For these tests the speci-

Table I. Interface properties of Al-doped SiO_2 films*

Oxidation temperature, °C	He flow, 1 min^{-1}	Al/Si ratio	Before irradiation V_{FB}, V	Q_{FB}, e cm^{-2}	Q_{ss}, e cm^{-2} (eV)$^{-1}$	After irradiation under +10V bias V_{FB}, V	Q_{FB}, e cm^{-2}	Q_{ss}, e cm^{-2} (eV)$^{-1}$	ΔV_{FB}, V	ΔQ_{FB}, e cm^{-2}
1250	0.1	0.001	−5.7	1.5×10^{12}	$<2 \times 10^{10}$	−52.5	1.4×10^{13}	1.5×10^{12}	−46.8	1.3×10^{13}
1250	1.0	0.01	−3.3	7.4×10^{11}	$<2 \times 10^{10}$	−36.2	8.0×10^{12}	1.7×10^{12}	−32.9	7.3×10^{12}
900	1.0	0.1	−2.2	5.1×10^{11}	$<2 \times 10^{10}$	−23.0	5.4×10^{12}	3.3×10^{12}	−20.8	4.9×10^{12}
Al_2O_3		∞	+1.9 (+1.4)	-5.7×10^{11}	$<2 \times 10^{10}$	−13.6 (−9.8)	4.0×10^{12}	6.8×10^{11}	−15.2 (−11.2)	4.6×10^{12}

* The film thickness is about 1000Å except for the Al_2O_3 film which is 1400Å. In that case the values of V_{FB} corresponding to 1000Å oxide are given in parenthesis.
Legend: V_{FB} = voltage on the Al electrode at flat-band condition; Q_{FB} = charge in the oxide and/or at the interface at flat-band condition (includes charges originating from the work-function difference between Si and Al); Q_{ss} = charge in interface states within the Si forbidden band; e = absolute value of electronic charge.

mens were provided with 2000Å thick Al electrodes on the oxide and an Al back contact. This measurement, in combination with the thickness determination, also provided the dielectric constant of the oxide film. The specimens were irradiated with 1 MeV electrons while 0, −2, −5, −10, +2, +5, +8, and +10V bias was applied successively to the Al electrode. After each bombardment the MOS capacitance was determined. The fluence at each step was 10^{14} e/cm^2, amounting to a final fluence level of 1.4×10^{15} e/cm^2. Since the effect of irradiation under +2V bias is reasonably independent of an increase of fluence above 10^{14} e/cm^2, this sequence of irradiation and measurement is indicative mostly of the effect of applied bias rather than a combination of bias and fluence (1).

Results and Discussion

The mass-spectrometric analysis showed that aluminum was incorporated into the oxide film and that the concentration depended on the oxidizing conditions. In performing this analysis the oxide film and a portion of the silicon is removed. The major constituent in the vapor phase is silicon, but most of this comes from the substrate rather than the oxide film. The amount of Al is first determined in relation to the total amount of Si present in the vapor and expressed as an Al/Si ratio. This ratio varies from 40 to 2000 ppm (atomic). These values correspond to roughly 10^{19} to 10^{21} Al atoms/cm^3 in the oxide which are equivalent to 0.001 to 0.1 Al/Si ratio in the oxide.[2] The Al/Si ratio in the Si substrate, as determined before oxidation and after dissolution of the oxide, was 5 ppm. This clearly demonstrates that the measured Al is essentially in the oxide film. The impurity analysis (from B to Bi) before and after oxidation, as well as after dissolving the oxide, indicates that the oxide does not contain any impurity which is not present in the Si substrate, with the possible exception of chlorine.

Electron diffraction showed that the oxide films are noncrystalline. The thickness varies from 740 to 1000Å, the majority being about 1000Å. The refractive index (at 5460Å) varies from 1.49 to 1.53, with a modal value of 1.51. For thermally grown SiO_2 films the value is 1.48 (7), and for chemically deposited Al_2O_3 films about 1.60 (8). The relative dielectric constant at 1 MHz of the Al-doped SiO_2 films is 3.52. These observations demonstrate that despite their relatively high Al content the oxide films are essentially SiO_2.

The results of the MOS capacitance measurements are summarized in Fig. 1 and Table 1. Figure 1 shows that, as in the case of undoped SiO_2 (1), the effect of bias under irradiation is asymmetric and it saturates for both positive and negative voltages. The behavior of the specimen with the lowest Al content is essentially identical with that of an undoped SiO_2 film grown in dry oxygen. The shift of the flat-band voltage (determined from C-V measurements), ΔV_{FB}, as a result of irradiation under +10V bias, decreases with increasing Al content of the oxide film. Also, there is a tendency for saturation at lower voltage values under positive bias with increasing Al content.

The shift of the C-V curves alone is not the only indication of the irradiation effect, since these curves may deviate from the ideal C-V curve in their shape, indicating the presence of interface states. Furthermore, although the voltage shift is an important parameter from a device point of view, it is the charge at the interface and/or in the oxide which is relevant from the physical viewpoint.

The pertinent surface properties before and after irradiation under + 10V are given in Table I. We see that the amount of positive charge introduced by irradiation under +10V bias (measured at flat-band condition), ΔQ_{FB}, decreases with increasing Al content of the oxide. On the other hand, the density of interface states in the Si forbidden band, Q_{ss}, resulting from irradiation, increases with the Al content. This increase may be especially large in the accumulation regime. Thus, for the specimen with the highest doping level the average value of Q_{ss}, 3.3×10^{12} e/cm^2 (eV)$^{-2}$, can be divided into two components: 10^{13} e/cm^2 (eV) for $\psi < 0.05$V and 1.9×10^{12} e/cm^2 (eV) for $\psi > 0.05$V,[3] ψ being the surface potential and e the absolute value of the electronic charge.

A comparison of these results with undoped SiO_2 films and Si-Al_2O_3 structures reveals the following facts. The pre-irradiation values of the flat-band voltage, V_{FB}, for the Al-doped specimens are more negative than for dry O_2-grown and He-annealed SiO_2 (− 1 to − 2V) and deposited Al_2O_3 (+ 2 to + 4V) films of about 1000Å thickness. The effect of irradiation of V_{FB} for doped SiO_2 is much less than on dry

[3] These values were taken from a computer evaluation of C-V curves which supplied Q_{ss} as a function of ψ.

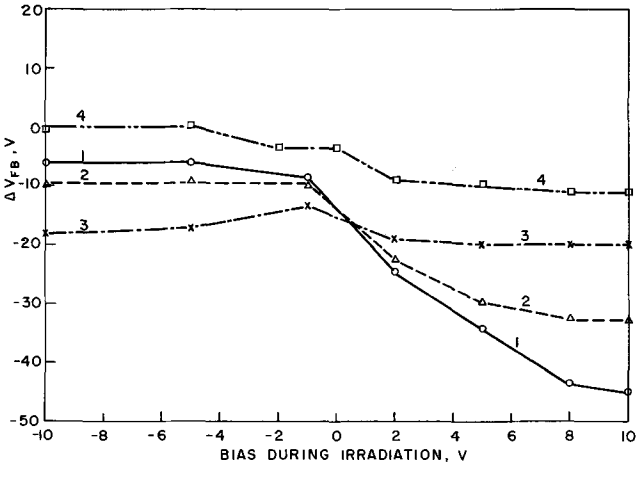

Fig. 1. Change in flat-band voltage, ΔV_{FB}, as a function of electrode bias during electron irradiation. For curves 1, 2, and 3 the values of the Al/Si ratio are ~0.001, ~0.01, and ~0.1, respectively. Curve 4 shows the behavior of a Si-Al_2O_3 structure.

[2] In the conversion of the measured Al/Si ratios to the Al content of the oxide the amount of Si removed from the substrate had to be taken into account. Because of uncertainties in the determination of this quantity, the Al-content of the oxide is given only as an order of magnitude. As a check the Al-content of a chemically deposited Al_2O_3 film was also determined. The value obtained was 6×10^{22} Al atoms/cm^3 oxide which is very close to the calculated one, 4.3×10^{22}, taking the density as 3.7 gcm^{-3}.

O_2-grown SiO_2 ($\Delta V_{FB} \cong 50V$) but is greater than on Al_2O_3 ($\Delta V_{FB} = 11.2V$ for one of the best specimens). (In the case of Al_2O_3 films even for the same value of ΔQ_{FB} and oxide thickness ΔV_{FB} is smaller because the dielectric constant of Al_2O_3 is about twice as large as that of SiO_2.) From the point of view of interface states introduced by irradiation, Al-doped SiO_2 is worse than either dry O_2-grown and annealed SiO_2 ($\Delta Q_{ss} \cong 0$) or properly prepared Al_2O_3 ($\Delta Q_{ss} \cong 7 \times 10^{11}$ e cm^{-2} $(eV)^{-1}$).

These observations can be tentatively explained by assuming that the defect structure of the aluminum oxide is significantly different from that of silicon dioxide. Recent investigations of Si-Al_2O_3 structures by MOS capacitance method showed indeed that, in contrast to SiO_2, substantial electron trapping occurs in Al_2O_3 (3, 4). This means that electrons and holes may be simultaneously trapped during electron bombardment, resulting in a build-up of two compensating space-charge layers. Another possibility is that the generated electrons and holes recombine before significant trapping took place. Thus, the insulator has essentially zero net charge after irradiation and no shifts in flat band voltage are observed. Apparently, introduction of Al into SiO_2 results in a similar behavior. Thermoluminescence glow curve studies also revealed a difference in the defect structures of Al_2O_3 and SiO_2 (9).

On the other hand, the presence of Al in SiO_2 apparently increases the radiation sensitivity of the interface. Thus, with increasing Al content the radiation induced disorder at the interface increases. In addition to interface states (as revealed by *C-V* measurements), a disordered interface generally shows slow trapping effects, *i.e.*, under negative gate bias electrons are injected into the silicon, shifting the flat-band voltage to more negative values (6). This is why V_{FB} shifts to more negative values under irradiation with negative bias.

Acknowledgments

R. Lenskold assisted in the fabrication and testing of samples. F. Kolondra cooperated in the irradiation experiments. The mass spectrometry analysis was provided by E. M. Botnick and W. L. Harrington. D. Dumin made valuable suggestions on the manuscript. The authors are indebted to all.

Manuscript submitted Feb. 5, 1969; revised manuscript received April 22, 1969. The research reported in this paper was supported by the Air Force Avionics Laboratory, Wright-Patterson Air Force Base, Ohio, under Contract No. F33615-67-C-1140.

Any discussion of this paper will appear in a Discussion Section to be published in the June 1970 JOURNAL.

REFERENCES

1. K. H. Zaininger and A. G. Holmes-Siedle, *RCA Rev.*, **28**, 208 (1967).
2. W. J. Dennehy, A. G. Holmes-Siedle, and K. H. Zaininger, *IEEE Trans. NS-14*, 276 (1967).
3. A. Waxman and K. H. Zaininger, *Appl. Phys. Letters*, **12**, 109 (1968).
4. M. Duffy and A. G. Revesz, To be published.
5. A. G. Revesz, *Phys. Stat. Sol.*, **19**, 193 (1967).
6. For a recent review of the Si-SiO_2 interface see, for instance, A. G. Revesz and K. H. Zaininger, *RCA Rev.*, **29**, 22 (1968).
7. R. J. Archer, *J. Opt. Soc. Am.*, **52**, 970 (1962).
8. J. A. Aboaf, *This Journal*, **114**, 948 (1967).
9. J. P. Mitchell, *IEEE Trans. NS-15*, No. 6, 154 (1968).

Correction

In the Brief Communication "Luminescence of Gallates" by W. L. Wanmaker and J. W. ter Vrugt, June 1969, Vol. 116, pp. 871-872, the following corrections should be made in Table I:

$ZnGa_2O_4$ λ_{max}	460-470 instead of 465
$ZnGa_2O_4$ T_{50}	460 instead of 560
$(Mg \cdot Zn)_{0.5}$ Ga_2O_4 T_{50}	400 instead of 500

Behavior of Hydrophilic Porous Oxygen Electrodes with Silver Electrocatalyst

I. Lindholm[1] and I. Jonsson

Chemistry Laboratory, Allmanna Svenska Elektriska Aktiebolaget (ASEA), Västeras, Sweden

ABSTRACT

An experimental study of the behavior of porous hydrophilic oxygen electrodes shows the important influence of the electrochemical reaction on the shape of the i-E curves at low current densities. A correlation between mass transport properties of the electrolyte, $\sqrt{SD\chi}$, and the slope of the polarization curve is found at medium current densities. Convection appears to be important at high current densities. The depth of the effective reaction zone has been calculated under varying conditions.

The importance of mass transport of gas molecules through a liquid film on the behavior of partially submerged electrodes was first demonstrated by Weber *et al.* (1) and Will (2) in model experiments with plane electrodes. Will limited himself in his theoretical treatment (3) to the consideration of the hydrogen transport in the film, which process was found to be rate determining. Grens *et al.* (4), as well as Bennion and Tobias (5), refined the model and took into account the activation polarization and the transport parameters. Attempts to analyze the results from experiments with partially immersed solid electrodes with the aid of the liquid film theory have thus been relatively successful.

The film theory was extended to porous gas-diffusion electrodes by Lindström (6, 7).

Practical porous gas electrodes possess two essential differences: larger electrocatalyst surface area and larger surface for mass transport of gas molecules through a liquid film. These differences make an analysis more difficult. Katan *et al.* (8), however, have carried out an experimental study on a more realistic model of the gas-diffusion electrode. They studied an oxygen cathode comprising a bed of spherical silver grains with a diameter of about 55×10^{-4} cm. The data agreed with a theoretical treatment based on the film hypothesis, if the film thickness was assumed to be 5×10^{-6} cm. A study of porous hydrogen electrodes was carried out by Lindholm (9, 10). He applied Austin's mathematical treatment of the thin-film model (11) and found qualitative agreement. He observed that Austin's mathematical treatment should be modified so as to take into account the varying effective zone depth, the film thinning-out effect at higher differential pressures, and a decreasing electrolyte content in the film for increasing current density. Many mathematical treatments of the kinetics in porous electrodes have been made (11-20). A feature common to many of these treatments is a limited experimental background. In order to obtain more information on the reaction mechanism and kinetics, we have made an experimental study of the behavior of porous oxygen electrodes. The mass transport properties of the electrolyte were varied by changing KOH content and temperature. The effect of the depth of the reaction zone on electrode behavior was investigated with the use of three-layer electrodes.

Experimental

The experimental arrangement is shown in Fig. 1. All components in contact with electrolyte in the test cell were made of nickel, Teflon, or Penton.

I-p and i-v curves were measured stepwise with an interval of 3 min. The potential was set manually for each step and then controlled with an ASEA potentiostat. Steady state was attained in less than 2 min. The differential pressure between the O_2 and the electrolyte was measured with a pressure sensor from Ateliers de Construction de Bagneux. The current density was measured in a half cell with a 35-mm diameter porous disk as oxygen electrode in a Penton holder. Each solution was titrated to ±0.05 mole/liter. The half cell was heated in a water bath. Potentials were measured with a Radiometer PHM 22 by means of a Luggin capillary with the tip placed at the center of the electrode, 1 mm from the surface. The reference electrode was a porous hydrogen electrode with nickel boride electrocatalyst in 7M KOH at 50°C with an absolute pressure of 2.6 atm. This pressure gives about equal volumes of hydrogen and electrolyte in the pore structure. The potential is stable within ±0.1 mV. The absolute pressure on the electrolyte was 1 atm.

The high current densities obtained result in a considerable measuring problem. Current and potential were measured with two separate silver wires, welded to the gas side of the electrode. The outlets at these wires from the holder were placed above the electrolyte surface. These outlets were tightened with epoxy resin. One of the measuring problems is an unavoidable voltage drop between the tip of the reference capillary and the electrode surface. This IR drop was measured through rapid interruption of the current with a mercury relay at the same time as the voltage process was recorded on a storage oscilloscope. This purely ohmic voltage drop decays in less than 1μsec and can be easily distinguished from the other polarization components. All measured values have been corrected for the IR drop in this way.

Although the electrode potentials were always measured against the hydrogen reference at 50°C, these primary data are of little value in comparing performances. The reversible oxygen potential in the same solution is a more suitable reference potential. Our porous electrodes are not reversible oxygen electrodes, and the reversible oxygen potential must be known from other information. This problem was solved by

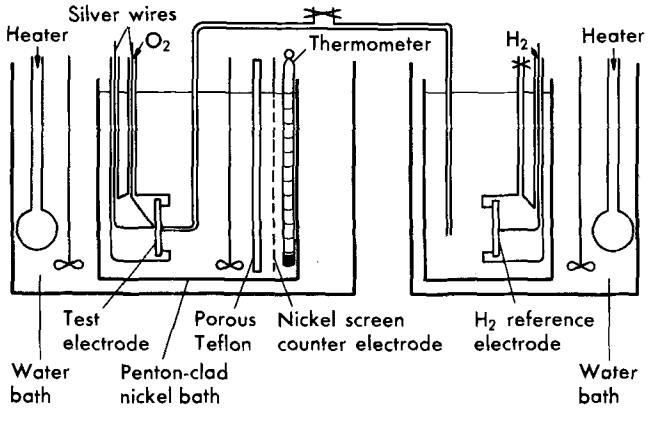

Fig. 1. Arrangement for electrode testing

[1] Present address: Swedish Delegation, OECD, 19, rue de Franqueville, Paris 8e, France.

first calculating the electromotive force for $H_2 - O_2$ in each combination of KOH concentration and temperature. This thermodynamic calculation includes the influence of temperature and KOH concentration using equations published by Salvi and de Bethune (21), Lee (22), and a correction for the gas pressures for equilibrium water pressure using data from Walker (23).

A nickel boride hydrogen electrode was then substituted for the O_2 test electrode in the arrangement of Fig. 1, and its potential against the hydrogen reference electrode of the same type in 7M KOH at 50°C was determined for each combination of temperature and KOH concentration used in the study. The reversible oxygen electrode potential was then calculated for the different electrolyte concentrations and temperatures.

An investigation of the potential distribution in three dimensions in the electrolyte, outside the electrode, showed a slightly uneven current distribution, with about 10% higher current density at the middle compared with the edge of the electrode disk. This test also showed that the distance of the capillary tip from the electrode is not important, since this is corrected for by measurement of the *IR* drop with the storage oscilloscope.

Hydrophilic oxygen electrodes were made with a diameter of 35 mm and a thickness of 1.8 mm. The electrodes for testing were provided with a fine porous layer on the electrolyte side. This layer did not contain any electrocatalyst. Three-layer electrodes were also manufactured. They consisted of an inactive coarse layer of nickel, an active layer of nickel with silver electrocatalyst, and a fine porous layer. The thicknesses of the layers were determined with an optical microscope. The silver content in the active layer was 5% by weight. The coarse, inactive layer had almost exactly the same pore structure as the coarse active layer. Figure 2 shows a model of a three-layer electrode with electrolyte films and gas phase.

The BET surface area of the active layer containing nickel and silver was 0.16 m^2/g and the surface area of the inactive coarse layer of nickel was 0.13 m^2/g.

The porosity of the active layer was 43.6% and that of the inactive layer 44.4%.

Results and Discussion

Effect of differential pressure.—The effect of the differential pressure between the oxygen and the electrolyte on the performance of electrodes with different active layer thicknesses is illustrated in Fig. 3, where current density at —350 mV from the reversible oxygen potential is plotted as a function of differential pressure. These curves were obtained in 7M KOH at 50°C. Curves with a similar shape are obtained in 1-10M KOH at 25°-85°C between —300 and —500 mV from the reversible oxygen potential. A change in these parameters will, of course, change maximum current density and the optimum differential pressure, but not the shape. In an electrode with a thick active layer, the current density increases with the differential pressure up to a maximum and then decreases. When the differential pressure is reduced, the maximum appears at a lower pressure. This hysteresis effect is consistent with a slow movement of the gas-electrolyte interface in smaller pores. It is possible to reduce the hysteresis effect somewhat by measuring with an interval of 60 min for each point.

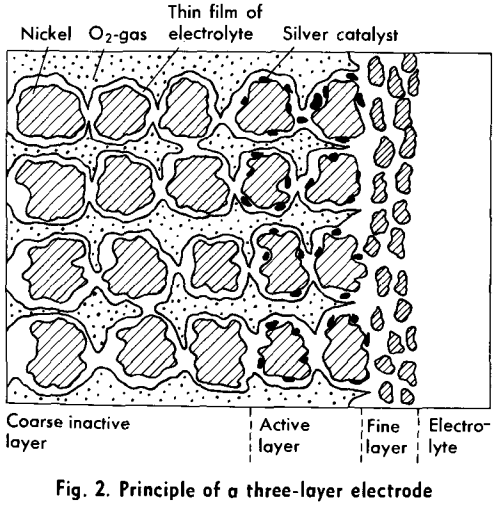

Fig. 2. Principle of a three-layer electrode

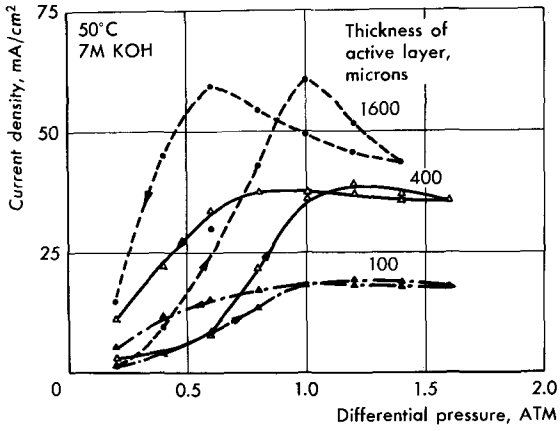

Fig. 3. Current density as a function of differential pressure at varying thickness of active layer.

There are three differences between a thick and a thin active layer:

(*A*) The maximum current density is higher for an electrode with a thick active layer.

(B) The optimum differential pressure is lower for an electrode with a thick active layer.

(*C*) Electrodes with a thick active layer show a considerable decrease in current density at a differential pressure above the optimum value, while electrodes with a thin active layer show an almost constant current at differential pressures above the optimum value.

The increase in the oxygen pressure leads to an increased solubility of O_2 in the electrolyte, which should increase the current density, if other conditions are equal. This occurs at first. The most probable physical explanation of the subsequent drop in the current density with increasing differential pressure for an electrode with thick active layer is that a thinning out of the electrolyte films in the pore system occurs (10), and this has two different effects. First, the speed of mass transport of gas through the liquid film is increased; second, the speed of mass transport of OH^- ions and water decreases. This decrease in mass transport of OH^- ions causes a lower current in electrodes with a thick active layer, *i.e.* long liquid films.

The current is generated in the active layer close to the fine layer. The results with three-layer electrodes show that the current is not proportional to the thickness of the active layer. An electrode with a thin active layer generates more current per micron thickness than an electrode with a thick active layer. It is thus possible to define a "reaction zone" in the active layer near the fine layer with a depth that gives 90% of the current compared to an electrode with a thick active layer operating under the same conditions. It is difficult to calculate the exact thickness of such a "reaction zone," but it is certainly possible to determine changes in "reaction zone" depth with changes in operating conditions.

Figure 3 indicates a decrease in the depth of the reaction zone with increasing differential pressure.

Effect of KOH *concentration.*—The dependence of electrolyte concentration has been studied at 50°C

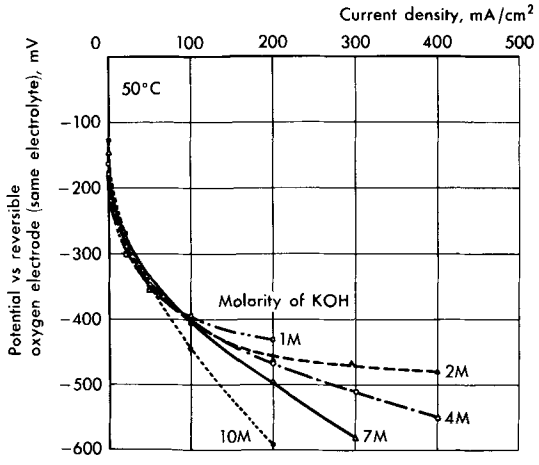

Fig. 4. Polarization curves for electrodes in varying KOH concentrations.

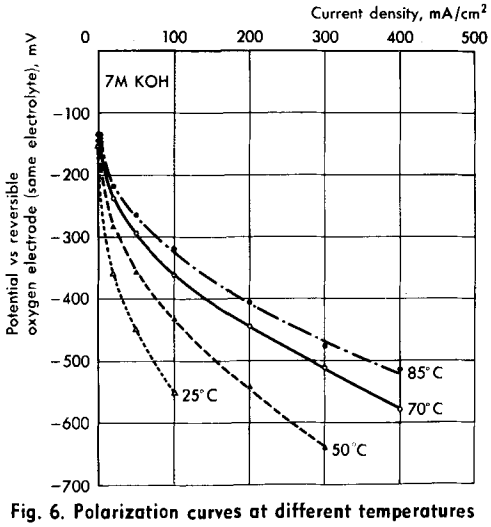

Fig. 6. Polarization curves at different temperatures

with potassium hydroxide varying from 1 to 10 moles/liter. Figure 4 shows polarization curves for an active layer depth of 1600μ. For a given low current density, the electrode shows the lowest polarization in 10M KOH. The rate-limiting step at low polarization is not associated with mass transport, but probably with the electrochemical reaction. At higher current densities, there is an increase in polarization for increasing KOH concentration and the highest polarization in 10M KOH. This behavior is in accord with rate-limiting mass transport at medium current density, as oxygen solubility and diffusivity are low in 10M KOH; compare Fig. 9.

Reaction zone depth at varying polarization.—In order to study the reaction zone depth, we have plotted in Fig. 5 the proportion of current density of an electrode with a thin active layer to the current density of an electrode with 1600μ active layer as a function of the electrode polarization in 2M KOH. The conclusion that can be drawn from Fig. 5 is that there is a relative increase in current density for thin active layer electrodes with increasing polarization, which implies that the depth of the reaction zone decreases with increasing polarization.

Effect of temperature.—Figure 6 shows polarization curves in 7M KOH for 25°, 50°, 70°, and 85°C at the optimum differential pressure for an electrode with an active layer of 1600μ. Electrodes with different active layer thickness give an approximately linear relationship between log current density at a given polarization and $1/T$, from which an activation energy can

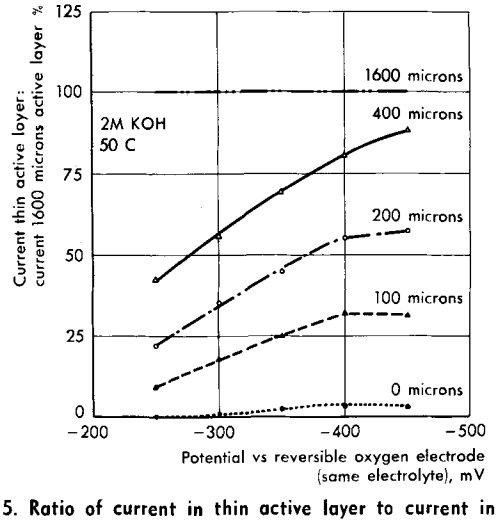

Fig. 5. Ratio of current in thin active layer to current in 1600μ active layer as a function of potential.

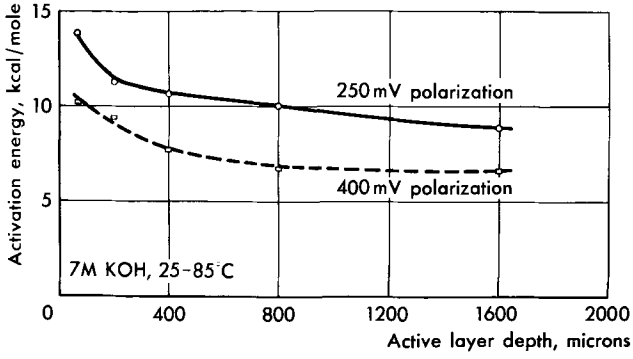

Fig. 7. Activation energies as a function of active layer thickness

be calculated which comprises the whole reaction cycle. Figure 7 shows activation energies for electrodes with varying active layer thickness at 250 and 400 mV polarization from reversible oxygen potential. The higher activation energy at −250 mV supports the conclusion that the electrochemical reaction is a rate-limiting factor at low current densities and that mass transport with a lower activation energy is the rate-limiting factor at medium current densities.

The activation energy is higher for electrodes with a thin active layer. This implies that the relation of current from a thin active layer to current from a thick active layer is increased with increased temperature, and indicates that the "reaction zone depth" decreases with increasing temperature.

Mass transport properties of the electrolyte.—The experimental results at medium polarization can be compared with data for mass transport of oxygen and hydroxyl ions in the liquid phase. Figure 8 shows oxygen solubility S, oxygen diffusivity D, and conductivity χ in 7M KOH as functions of temperature, and Fig. 9 the same variables as functions of KOH concentration at 50°C. These curves are calculated from literature data (24-26). D-values above 60°C are extrapolated.

Comparison with the thin-film theory.—The thin-film theory by Austin *et al.* (11) takes into account the diffusion of oxygen through a liquid film and the film resistivity. This theory predicts polarization curves of the form $i = k \cdot \eta^{1/2}$, if the activation polarization is small. Our experimentally measured curves do not obey this relationship, indicating an influence from the electrochemical reaction as well.

According to Austin's theory, the current-to-polarization ratio should be proportional to $\sqrt{SD\chi}$, when the film area and thickness are constant. This ratio should be valid at medium polarization, and we have

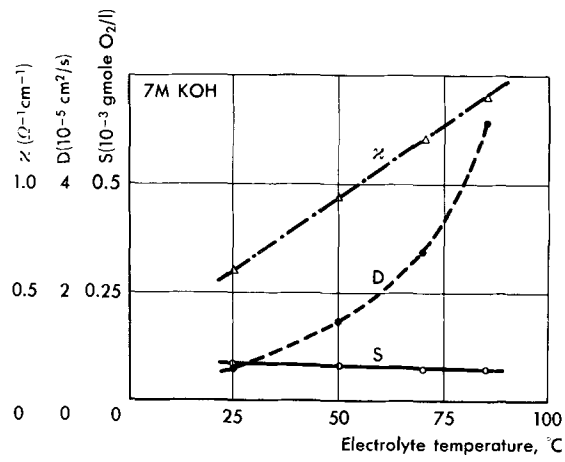

Fig. 8. Solubility and diffusivity of O_2 in KOH and conductivity of KOH as functions of temperature.

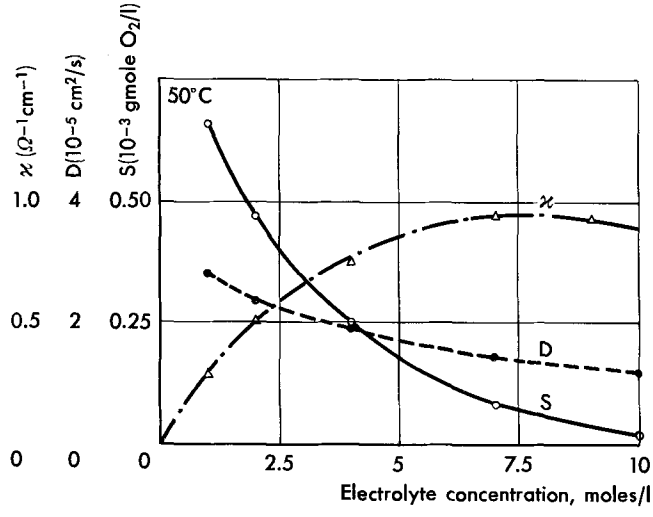

Fig. 9. Solubility and diffusivity of O_2 in KOH and conductivity of KOH as functions of KOH concentration.

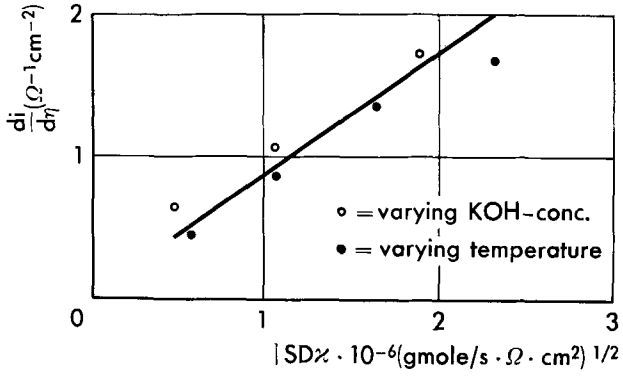

Fig. 10. Inverse slope of the polarization curve $di/d\eta$ at 450 mV polarization as a function of $\sqrt{SD\kappa}$.

tested it at —450 mV *vs.* reversible oxygen. Figure 10 shows experimentally measured $di/d\eta$-values at 450 mV polarization plotted as a function of $\sqrt{SD\kappa}$ for 4M KOH-10M KOH at 50°C and in 7M KOH at 25°-85°C for an electrode with 1600μ active layer. There is a linear relationship between $di/d\eta$ (—450 mV) and the mass transport parameter $\sqrt{SD\kappa}$. This relationship is not valid for lower concentrations than 4M KOH, because the half-cell reaction produces OH^- and gives a relatively large increase of OH^- in the films compared with bulk solution for low KOH concentration. The point with the highest temperature is below the line, which may be due to a thinner "reaction zone depth."

Austin's evaluation considers mass transport polarization through a liquid film and OH^- ion transport along the film, but not the polarization caused by the electrochemical reaction. A more detailed treatment has recently been carried out by Srinivasan and Hurwitz (27). Their treatment is also based on the thin-film model using cylindrical pores, but it considers mass transport of gas molecules through the liquid film, mass transport of ions along the film, and activation polarization on the inner electrode surface using i_o as reaction rate constant.

Figure 11 compares the numerical calculations according to Srinivasan and Hurwitz (27), with the rate constant for the electrochemical reaction $i_o = 10^{-9}$ A/cm² (28) and our experimental values for silver electrocatalyst in 4M KOH at 50°C.

This calculation requires a knowledge of the film geometry. This was obtained with an experimental technique using a gas porosimeter, which has recently been described in detail in a paper by Lindström (29). The relative amounts of gas and liquid in the pores are determined at varying differential pressure and the gas-electrolyte interface is calculated with a computer (GE 625).

The principal disadvantage of this method is that this physical measurement is carried out separately while there is no current flow. The mean thickness of the electrolyte film is 0.9μ and the gas-electrolyte interphase 360 cm²/cm² at optimum conditions.

The shape of the experimental curve is similar to the calculated curve. This indicates once more the strong influence of the electrochemical reaction on the polarization at low current densities. The agreement is good, considering the differences between the model and a real porous electrode, *i.e.* uneven liquid films introducing a tortuosity factor, and that the kinetics for the electrochemical reaction is probably more complex than indicated by one i_o-value.

Experiments up to high current densities.—Figure 12 shows a comparison of polarization curves up to high current densities for an electrode with an active layer thickness of only 100μ in 4M KOH, 7M KOH, and 10M KOH electrolyte. The optimum differential pressure oxygen-electrolyte was 1.4 atm at all KOH concentrations.

The local temperature at the electrode was measured during operation and is given in the figure at varying current densities. The increase of local temperature is about 20°C at 1500 mA/cm².

The polarization curves can be divided into three regions. In region I, low polarization (up to about —350 mV) *vs.* a reversible oxygen electrode, there is

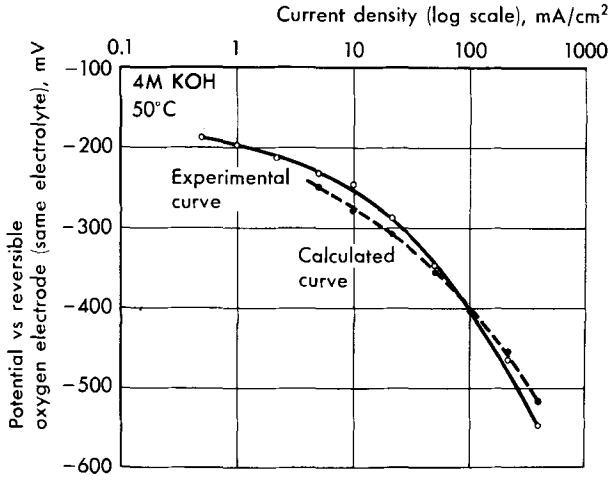

Fig. 11. Comparison of shapes of calculated and experimental polarization curves.

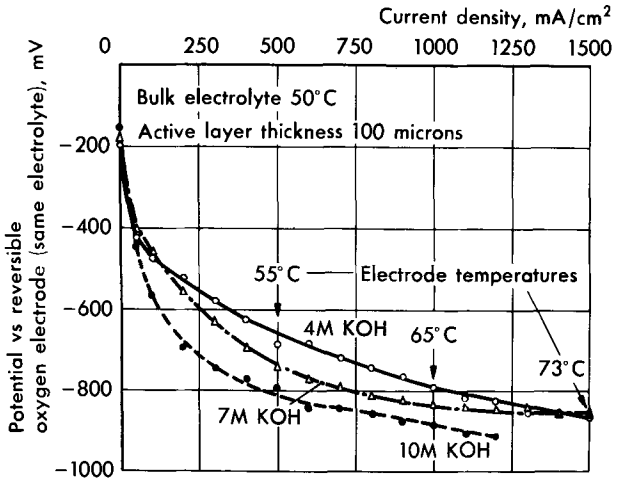

Fig. 12. Polarization curves up to 1500 mA/cm² with varying KOH concentration.

only a small difference among the curves. The polarization is slightly higher with 4M KOH. In region II, medium polarization from —350 to about —600 mV, there are approximately linear polarization curves. The slope is steepest with 10M KOH giving the highest polarization in the strongest KOH electrolyte. In region III, high polarization, more than —600 mV, there is a difference in the shape of the curves. The curves for 7M KOH and 10M KOH become less steep and the slopes of the three curves are almost the same at high current densities. There is a tendency for almost the same polarization to be obtained in 4M KOH and 7M KOH, in spite of the large difference in oxygen solubility and diffusivity, which are considerably lower in 7M KOH. The OH^- concentration in the liquid films is increased during the reaction owing to the formation of OH^- ions. A slow OH^- transport along the films would cause a further decrease in oxygen solubility and diffusivity at high current densities, and a *steeper* polarization curve at high current densities, while the experimental curves are almost horizontal at high current. This suggests that a new mechanism for mass transfer is operating. The positions of the regions depend on the active layer thickness, an electrode with 1600μ active layer, *i.e.*, larger electrocatalyst surface area, shows a shift from electrochemical reaction rate control to mass transport control at a lower polarization than 350 mV.

The limiting current densities for gas diffusion through a liquid film can be calculated from the formula:

$$i_l = \frac{n \cdot \mathbf{F} \cdot S \cdot D \cdot A}{W}$$

S = oxygen solubility in liquid
D = oxygen diffusivity in liquid
A = film surface area
W = film thickness.

The film thickness W was determined by the method previously described (29) to be 0.37μ and the film surface A was determined to be 35 cm²/cm² geometric by gas porosimeter experiments for an electrode with 100μ active layer at optimum differential pressure 1.4 atm. This electrode has a thin active layer. This means a high optimum differential pressure and a thinner film than the film in Fig. 11. The calculated value for limiting gas diffusion through an electrolyte film at a local temperature of 70°C is 410 mA/cm² in 10M KOH. The highest measured current density in 10M KOH is 1200 mA/cm², which is about three times higher than the calculated value and the limiting current is still higher.

The absence of limiting currents may reflect a new mass transport mechanism at high current densities.

The difference in mechanism at very high current densities is probably that convection occurs in the liquid film causing rapid transport of O_2 molecules through the film and OH^- and H_2O along the film. This can either be caused by the large amount of heat evolved in the solid-liquid interface or by a gradient in liquid tension, the Marangoni effect, as suggested by Will (30) and Ksenshek (31) for model electrodes.

Conclusions

A kinetic treatment of porous hydrophilic oxygen electrodes with three-layer electrodes indicates that the reaction zone decreases at higher differential pressure owing to a "thinning-out" effect of the liquid films. The reaction zone depth also decreases with increasing polarization.

The polarization curve can be divided into three regions. The reaction rate in region I (low polarization) is probably determined by the surface reaction with a low i_o-value.

In region II with medium polarization, the reaction rate is determined by a combination of mass transport of O_2 molecules by diffusion through a liquid film and mass transport of OH^- along the film. Region III with high polarization appears to have a convective mass transport of O_2 through the liquid film and the reaction rate is probably limited by transport of OH^- along the film.

Acknowledgment

This work was supported under contract NASW-1536 with the National Aeronautics and Space Administration, Washington, D.C., as part of an experimental study of mass transport polarization and activation polarization in porous electrodes.

Manuscript submitted Oct. 31, 1968; revised manuscript received May 10, 1969.

Any discussion of this paper will appear in a Discussion Section to be published in the June 1970 JOURNAL.

REFERENCES

1. H. C. Weber, H. P. Meissner, and D. A. Sama, *This Journal*, **109**, 884 (1962).
2. F. G. Will, *ibid.*, **110**, 145 (1963).
3. F. G. Will, *ibid.*, **110**, 152 (1963).
4. E. A. Grens II, R. M. Turner, and T. Katan, *Advanced Energy Conversion*, **4**, 109 (1964).
5. D. N. Bennion and C. W. Tobias, *This Journal*, **113**, 593 (1966).
6. O. Lindström, *Tekn. Tidskr.*, **93**, 593 (1963).
7. O. Lindström, *ASEA Journal*, **37**, 3 (1964).
8. T. Katan, S. Szpak, and E. A. Grens II, *This Journal*, **112**, 1166 (1965).
9. I. Lindholm, "Journées Internationales d'Étude des Piles à Combustible, Bruxelles" (1965). Proceedings, p. 26.
10. I. Lindholm, "Deuxièmes Journées Internationales d'Étude des Piles à Combustible, Bruxelles" (1967). Proceedings, p. 66.
11. L. G. Austin, M. Ariet, G. B. Wood, R. D. Walker, and R. H. Comyn, *Ind. Eng. Chem. Fundamentals*, **4**, 321 (1965).
12. A. W. Winsel, *Advanced Energy Conversion*, **3**, 677 (1963).
13. A. G. Psenicnikov in "Fuel Cells," by V. S. Bagotskii and Y. B. Vasilév, p. 11, Consultants Bureau, New York (1966).
14. R. Kh. Buhrstein, A. G. Psenicnikov, and N. A. Shumilova, *Dokl. Akad. Nauk. SSSR*, **143**, 168 (1962).
15. A. G. Psenicnikov, *Dokl. Akad. Nauk. SSSR*, **148**, 1121 (1963).
16. R. P. Iczkowski, *This Journal*, **111**, 605 (1964).
17. H. B. Urbach in "Fuel Cells," by G. J. Young, p. 72, Reinhold Publishing Corp., New York (1963).
18. O. S. Ksenzhek in "Fuel Cells," by V. S. Bagotskii and Y. B. Vasilev, p. 1, Consultants Bureau, New York (1966).
19. K. Micka, *Coll. Czech. Chem. Commun.*, **31**, 3623 (1966).
20. K. Micka, *ibid.*, **31**, 3653 (1966).

21. G. R. Salvi and A. J. de Bethune, *This Journal*, **108**, 672 (1961).
22. J. M. Lee, U. S. Army Signal R & D Lab. 2nd Semiannual Report (1960), Contract DA 36-039-SC-85259.
23. R. D. Walker, Research Grant NGR 10-005-022 Inst. Semiannual Report (1966).
24. M. B. Knaster and L. A. Apelbaum, *Zh. Fiz. Khim.*, **3**, 223 (1964).
25. K. E. Gubbins and R. D. Walker, *This Journal*, **112**, 46 (1965).
26. R. E. Davies, G. L. Horwath and C. W. Tobias, *Electrochim. Acta*, **12**, 287 (1967).
27. S. Srinivasan and H. D. Hurwitz, *ibid.*, **12**, 495 (1967).
28. S. Srinivasan and J. O'M. Bockris, Private communication.
29. O. Lindström, *Energy Conversion*, **8**, 33 (1968).
30. F. G. Will, "Deuxièmes Journées Internationales d'Etude des Piles à Combustible, Bruxelles" (1967). Proceedings, p. 161.
31. O. S. Ksenshek, *ibid.*, p. 217.

Cathodic Oxygen Reduction in the Sealed Lead-Acid Cell

S. Hills[1,*] and D. L. K. Chu[2]

Exide Power Systems Division, ESB, Incorporated, Philadelphia, Pennsylvania

ABSTRACT

The steady-state current observed during the cathodic reduction of O_2 at a partially exposed, electrochemically active electrode does not always represent its true recombination capability. This is usually the case when ohmic dissipation of the applied potential, resulting from inclusion of a highly resistive, thin electrolyte film in the current path, limits the passage of an externally supplied current to only a small distance above the free electrolyte level. Chemical reduction of O_2 can then occur over the area of substrate in contact with the thin film which is above the level of current penetration. O_2 reduction was studied at such electrodes in order to delineate the conditions under which both current penetration and O_2 access could be maximized, allowing a closer approximation of the true recombination capabilities of maintenance-free storage batteries. The magnitude of the difference between the rate of O_2 reduction and the steady-state current was determined by monitoring the current obtained after reimmersing the exposed electrode. The effect on this difference of variables, such as electrolyte concentration, O_2 partial pressure, applied potential, separator position, and degree of electrode exposure, are presented for the Pb-acid system.

Sealed and/or maintenance-free cells, which do not employ auxiliary electrodes, are at present designed to operate on an O_2 cycle during overcharge. Overcharge capability is obtained from the presence of a discharge reserve on the negative electrode so that H_2 evolution does not accompany the liberation of O_2 after charging of the active material on the positive is completed. The O_2 migrates *via* the gas space and is reduced at the negative electrode, maintaining the discharge reserve of the latter. A similar process occurs in fuel cells utilizing O_2 as one of the fuels, and therefore cathodic reduction of O_2 has been extensively studied in various systems. Most of the fundamental investigations employed smooth inert electrode substrates in order to circumvent the experimental and theoretical problems peculiar to the use of active porous electrodes. Both these and developmental studies of this phenomenon at porous battery electrodes generally involved determination of the relations between cathodic current at constant potential and either O_2 partial pressure (at constant degree of electrode exposure) or degree of electrode exposure (at constant O_2 pressure), and use of these relations as a measure of the effects of various cell parameters upon establishment of the steady state.

The majority of such studies concentrated on the area of the electrode in contact with the electrolyte meniscus, as the reaction rate beyond the limits of the meniscus was believed to be negligible. On one side, it was limited by extremely slow diffusion through the bulk electrolyte. Beyond the opposite limit, reaction between the dry electrode and the gas phase, at low temperatures, was insignificant if not nonexistent. O_2 reduction thus became meaningful only in the vicinity of the meniscus where, although the rate was still diffusion controlled, the electrolyte layer became sufficiently thin to allow appreciable transport of the electroactive species. The observed steady-state cathodic current was believed to be equivalent to the maximum rate of O_2 reduction under the given conditions.

Recent studies (1-10) have shown that a film of electrolyte exists beyond the intrinsic meniscus. Although O_2 transport should be even more rapid through such a thin barrier, the area of substrate in contact with the film usually did not contribute appreciably to the total O_2 reduction capability of the partially exposed electrode. Ohmic dissipation of the applied potential, resulting from inclusion of this highly resistive thin electrolyte film in the current path, can limit passage of an externally supplied current to only a small distance above the free electrolyte level. With an inert substrate, this merely limits the reaction zone. However, the supply of electrons on an electrochemically active substrate is not subject to this restriction, and chemical reduction of O_2 can occur on the portion of such an electrode in contact with the thin film. This has been found to be the case in both acid and alkaline systems, resulting, in all cases, in the formation of a layer of solid oxidation product.

The steady-state current observed, under potentiostatic conditions on a partially exposed active electrode, thus represents reduction of O_2 only over the area which can be reached by the externally supplied current. It is not equivalent to the total recombination capability of such an electrode. Further study of O_2 reduction on electrochemically active substrates was therefore initiated in order to delineate the conditions under which both current penetration and O_2 access could be maximized, and thereby obtain a closer approximation of the true recombination capabilities of maintenance-free storage batteries. The work re-

Key words: oxygen reduction, sealed cell, Pb-acid system.
[1] Present address: Power Transmission Division, General Electric Company, Philadelphia, Pennsylvania.
[2] Present address: Drexel Institute of Technology, Philadelphia, Pennsylvania.
* Electrochemical Society Active Member.

ported at this time details the investigation of O_2 reduction in the lead-acid system.

Experimental

Test electrodes (7.62 cm high x 3.81 cm wide x 0.25 cm thick) were prepared by halving dry-charged $Pb/PbSO_4$ electrodes selected from production stock.

Separators, where used, were cut to appropriate size from 1.3-mm thick, flat sheets of a commercially available grade of microporous rubber.

Various concentrations of electrolyte were prepared from reagent-grade H_2SO_4 to within ± 0.001 g/cm^3 of that desired.

A Plexiglas test cell, fabricated with replaceable inserts which divided the cell into three compartments, accommodated the test electrodes both in the presence and absence of separators. The configuration of the various components, for the three possible modes of electrode exposure, can be seen in Fig. 1. Both inserts were perforated to provide free electrolyte passage between the compartments. A screw-driven piston and appropriate shimming were employed to adjust the contact pressure between cell components whenever separators were present.

A controlled atmosphere was obtained by means of a Plexiglas pressure chamber capable of withstanding 50 psig. Provisions for evacuating the chamber and filling it with O_2, measuring the ambient pressure, thermostating the test cell, electrical connections, and variation of the degree of electrode exposure were made through the chamber walls. Electrolyte height was determined by visual sighting against a series of accurately ruled lines scribed on the optically clear test cell wall, and could be reproduced to within ± 0.4 mm.

Variation of electrolyte composition during a run was minimized by daily replacement of the relatively large volume held in the test cell and leveling bulb ($\sim$300 ml) and limiting electrochemical reactions to water decomposition by the use of charged test electrodes and sheet Pb counterelectrodes. Similarly, the large volume of the pressure chamber (1 ft^3) minimized variations in composition and total pressure of the ambient atmosphere resulting from the small amounts of gas evolved during the exposure studies. Except when it was the variable being investigated, O_2 pressure was maintained at 1 psig in order to prevent any leakage through faulty seals.

Electrode potential, cathodic current, and electrode temperature were continuously monitored with an L&N multipoint recorder-Keithley electrometer combination, capable after calibration of ± 5 mV accuracy over the 0-1V range. Signal currents were virtually eliminated by the 10^{14} ohm input impedance of the electrometer. A glass probe thermistor, encapsulated in epoxy to protect it from H_2SO_4, was fastened to the test electrode with its tip directly contacting the top grid member. Temperature could be determined to better than ± 0.5°C and was maintained at 25° $\pm$ 3°C without recourse to thermostatic control.

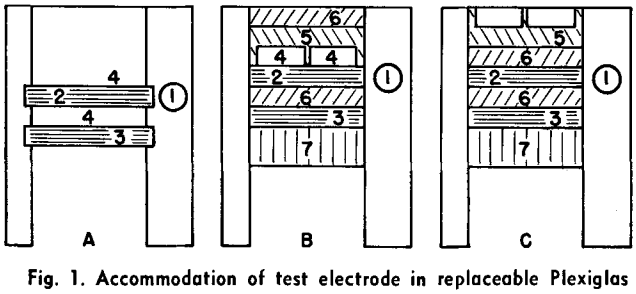

Fig. 1. Accommodation of test electrode in replaceable Plexiglas inserts: A—absence of separators, B—presence of separators on one side, C—presence of separators on both sides. 1—Reference electrode well (connected to test electrode chamber by salt bridge at bottom), 2—$Pb/PbSO_4$ test electrode, 3—sheet Pb counterelectrode, 4—gas space for test electrode, 5—Plexiglas spacer, 6—separators, 7—adjustable piston.

Potentiostatic conditions were obtained by means of an instrument designed and constructed by E.S.B. Incorporated. Before exposing an electrode to an O_2 atmosphere, it was charged overnight to assure that no utilizeable $PbSO_4$ remained.

O_2 reduction was first investigated in the absence of separators. The effect of each variable was studied on two electrodes to establish reproducibility of trends. Holding the cathodic overvoltage (η) constant at -50 mV, O_2 pressure at 1 psig, and H_2SO_4 s. g. at 1.300, the degree of exposure was varied from 1/16 to 7/8 of the full electrode height and I_{ss} determined for each exposure. After steady state was obtained, the electrode was reimmersed and the cathodic current monitored until it decreased to the value obtained prior to exposure. Graphical integration of the reimmersion current-time profile, taking the pre-exposure current into account, yielded the reimmersion capacity (Q_{im}). This represented the extent to which $PbSO_4$ was formed by chemical reduction of O_2. Division of Q_{im} by the time of exposure yielded an average current (I_{lag}), which represented the difference between I_{ss} and the current equivalent to the total rate of O_2 reduction. This was equivalent to the rate of formation of $PbSO_4$.

The effects of exposure time (10-60 min) and applied potential (-50 to -200 mV) were also investigated using the same technique. Cathodic η's larger than -200 mV were not investigated since in this region it was no longer possible to restrict the cathodic reaction to the reduction of O_2. Anodic overvoltage, equal to the difference in open-circuit voltage between the exposed and fully immersed electrode, was determined over the same exposure range mentioned previously.

Similar diagnostic experiments were run with varying thicknesses of microporous rubber separators on both sides of the test electrode. Under this condition, current penetrated the entire length of exposed electrode, removing this as a complicating variable, and enabling the effects of O_2 partial pressure and electrolyte concentration on diffusion control to be studied. A significant variation in open-circuit potential was observed over the range of concentrations investigated, 1.1 s.g. (1.68M) to 1.5 s.g. (9.15M). This was in agreement with data reported in the literature (11-13). The effect of the presence of other gases was spot-checked by determining I_{ss} in an air atmosphere.

Finally, O_2 reduction was studied with separator barriers of varying thicknesses sandwiched between the test electrode and the counterelectrode (inside face). Thus, when the free electrolyte level was dropped, the side of the test electrode facing away from the counterelectrode (back side) was exposed to the gas space by means of a spacer. This is a combination of the two cases discussed previously, and was studied more extensively since it proved to be the optimum combination of electrode and separator with regard to recombination.

Results and Discussion

In the absence of separators, establishment of the steady state always required times in excess of 10 min. Transient currents obtained prior to this always passed through a maximum. I_{ss} increased rapidly both with degree of exposure (Fig. 2) and η (Fig. 3), yielding reproducible limiting currents with regard to the former parameter. Reimmersion of the electrode after each exposure resulted in a rapid increase in cathodic current, sometimes as much as an order of magnitude over that obtained at steady state, followed by a slow decrease which often took hours to reach the value observed prior to exposure. I_{lag} and Q_{im} increased both with degree of exposure at a fixed time of exposure (Fig. 2) and with time at a fixed degree of exposure (Fig. 4). I_{lag} increased at a faster rate

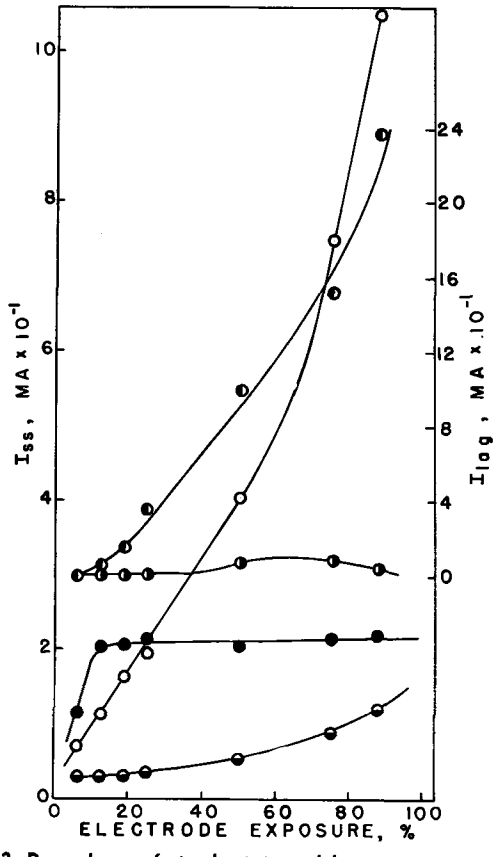

Fig. 2. Dependence of steady-state and lag currents on separator position and degree of test electrode exposure: 1 psig O_2, 1.3 sp gr H_2SO_4, —50 mV η. ●, Steady-state and ◐, lag current in absence of separators; ○, steady-state and ◑, lag current with separators on one side of test electrode; ◒, steady-state current with separators on both sides of test electrode.

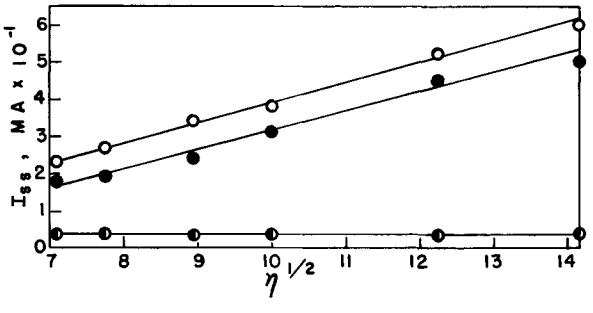

Fig. 3. Steady-state current *vs.* square root of electrode polarization: 1 psig O_2, 1.3 sp gr H_2SO_4. ○, No separators, 12.5% exposure; ●, 3 separators on one side of test electrode, 25% exposure; ◐, 3 separators on both sides of test electrode, 75% exposure.

than did the exposed area as can be seen in Fig. 2, indicating that the problem grew more severe with increased exposure. The existence of Q_{im} eliminated any possibility of the I_{ss} obtained at a given exposure being equivalent to the total recombination capacity of the electrode.

Similar behavior was reported in studies of various acidic and alkaline systems (1, 2, 4, 8, 9) in which it was concluded that, at a given applied potential, gas diffusion through the electrolyte was limiting. Most of the current was derived at a narrow zone in the vicinity of the upper boundary of the intrinsic meniscus, where the electrolyte layer was extremely thin and gas diffusion therefore extremely rapid. It was agreed that an even thinner film of electrolyte existed above the meniscus [except by Weber, Meissner, and Sama (1), who did not take this possibility into account] which could not contribute significantly to the electrochemical process, despite the fact that gas diffusion in this region should have been even more rapid, because of the inability of the current to penetrate the film. In agreement with the present study, Will (2) obtained transient currents on reimmersion of the electrode. However, in his case steady state was achieved within a few seconds after raising the electrode to a new position with I_{ss} always approached from below.

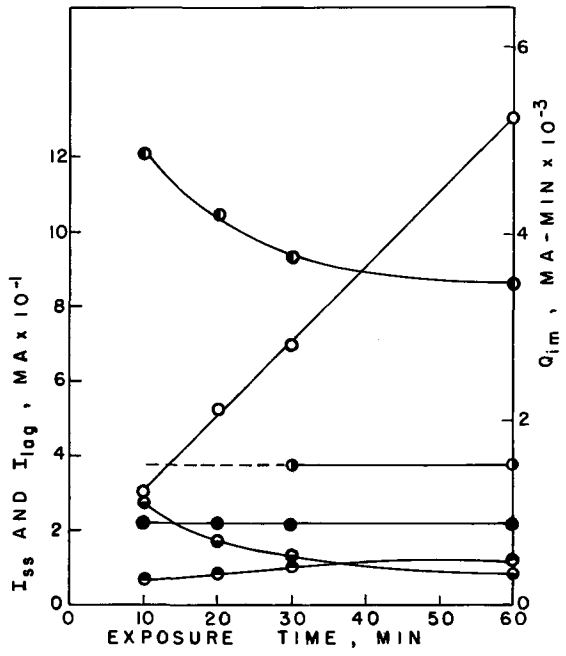

Fig. 4. Effect of exposure time on steady-state current, lag current, and reimmersion capacity in the absence of separators and with separators on one side of test electrode: 1.3 sp gr H_2SO_4, 1 psig O_2, 50% exposure, —50 mV η. ●, Steady-state current; ◐, lag current; ○, reimmersion capacity in the absence of separators; ◑, steady-state current; ◒, lag current; ◓, reimmersion capacity with separators on one side of test electrode.

These variations can be ascribed to a difference in the nature of the electrode substrates. Pt is essentially inert and H_2 oxidation can occur only by an electrochemical mechanism (no oxidized metal intermediates) at those sites at which electrons can be removed by an external source. The reaction product, H_3O^+, is soluble, eliminating the possibility of formation of a solid surface film. On the other hand, Pb was not inert under the experimental conditions employed. (This would also be the case for other metallic battery active materials.) Increased resistance in the electrolyte film, resulting from drainage, limited penetration of the externally supplied cathodic current to only a small distance above the intrinsic meniscus, and a film of $PbSO_4$ was formed (14). This provided an additional barrier to O_2 diffusion and possibly increased resistivity of the electrolyte film even further by removal of free acid. The net result was that the cathodic current passed through a maximum and I_{ss} was approached from above. I_{ss} was dependent on $\eta^{1/2}$ (Fig. 3) as predicted by Will (3) for a one-dimensional diffusional process which is further complicated by ohmic dissipation of the applied potential.

Upon reimmersion, the dissipation of the applied potential was eliminated and the $PbSO_4$ film became immediately available for reduction. Q_{im} was dependent on the amount of $PbSO_4$ formed, which in turn was a function of both the degree and time of electrode exposure, and thus the large reimmersion currents observed were not necessarily short lived. As the $PbSO_4$ film thickened, the access of O_2 was impeded further and the difference between the rate of O_2 reduction and I_{ss} decreased. However, this was a slow

process. I_{lag} for 50% exposure was still quadruple I_{ss} after 60 min exposure (Fig. 4), accounting for the relatively long time required for establishment of the steady state.

A penetration height of approximately 1.0 cm was observed with the 0.25-cm thick test electrodes which was similar to that obtained by Maget and Roethlein (10) for 100μ thick layers of sponge Pt and Teflon.

Anodic polarization of electrodes exposed to 1 psig O_2 in the absence of separators was slight because of the high exchange current for the conversion of Pb to $PbSO_4$ (15). It did not exceed 1 mV until the electrode was 50% exposed and reached a maximum of only 3 mV at 87.5% exposure. Smaller polarizations could be expected when one or both sides of the exposed electrode were shielded from the O_2 atmosphere by separator barriers wetted by H_2SO_4. Thus, it was likely that the externally supplied current was not significantly increased by the additional driving potential obtained from this source.

When both sides of the test electrode were masked from the gas space, Q_{im} was negligible for all exposures and applied potentials investigated and therefore I_{ss} was equivalent to the total rate of O_2 reduction. A true limiting current was obtained at each exposure as could be ascertained from the effect of applied potential upon I_{ss} at 75% exposure (Fig. 3). The slight decrease observed with increasing η was not unexpected, as eventually adsorbed, evolved H_2 occupied active sites and made them unavailable for O_2 reduction. The above resulted from a combination of hindered O_2 diffusion through and virtual elimination of ohmic dissipation of the applied potential in the highly conductive, thick electrolyte film retained in the separator barrier. Weber, Meissner, and Sama (1) found that even much thinner films would significantly reduce O_2 transport. In agreement with this, the magnitude and rate of increase of I_{ss} with degree of electrode exposure were greatly reduced below that obtained in the absence of separators (Fig. 2). Microporous rubber retains sufficient electrolyte that the *IR* drop through the separators for an 87.5% exposed electrode (as determined oscilloscopically by interruption of a known current) is the same as for a fully immersed electrode. This condition persisted for over an hour and there was no reason to suspect that it would change as long as the bottom of the separator was immersed in free electrolyte.

A linear relation was obtained between I_{ss} and O_2 pressure over the entire range investigated (Fig. 5), verifying that the limiting step under these conditions was the first-order diffusion of O_2 through the electrolyte retained in the separator barriers. Good agreement between the I_{ss}'s obtained at 0.2 atm of pure O_2 and those in an air atmosphere indicated that the rate of O_2 reduction, at a Pb electrode, was dependent on the partial pressure of O_2 regardless of the presence of other gases. However, other gases are to be avoided, if possible, since their presence will increase the total pressure in a sealed system.

Poor reproducibility could be ascribed to varying electrolyte retention in the test electrode separator combination (TESC) which depend on: (*a*) porosity of the test electrode, (*b*) porosity of the separator, (*c*) cell pack pressure, and (*d*) availability of free electrolyte. It was not believed feasible to control the first two factors in actual cell fabrication and so no attempt to do so had been made in this investigation. Cell pack pressure was adjusted by means of a movable piston and did not appear to be critical as long as reasonable contact with the test and counterelectrodes was maintained. The last factor is discussed later.

Maximum I_{ss} for a well-exposed electrode, at —50 mV η and 1 psig O_2 was obtained in the specific gravity range of 1.2-1.3. At the low η applied in the present study, electrolyte resistance was the most important factor controlling I_{ss}, outweighing both the solubility and diffusivity of O_2 in H_2SO_4. I_{ss} peaked strongly in

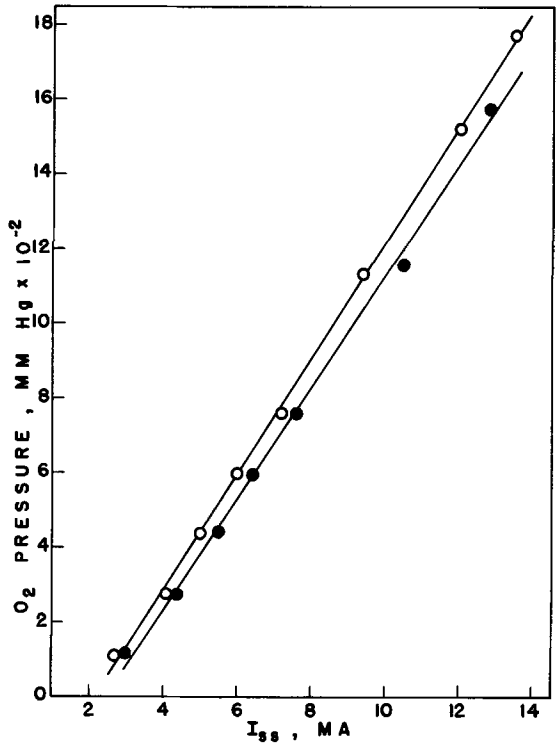

Fig. 5. Steady-state current with three separators on both sides of test electrodes as a function of O_2 pressure: —50 mV η, 1.3 sp gr H_2SO_4, 50% exposure. Data presented are for two similar electrodes.

the range of maximum electrolyte conductivity (16) at exposures of 50% and above. Below 1.2 sp gr, I_{ss} became controlled by ohmic dissipation of the applied potential, despite the presence of separators on both sides of the test electrode. This was manifested by the appearance of a significant Q_{im} at 1.1 sp gr. An increase in I_{ss} above 1.4 sp gr can probably be attributed to increased corrosion of Pb by H_2SO_4.

With only the back side of the test electrode exposed to the gas phase, the initial increase in I_{ss} with degree of exposure was not as rapid as in the absence of separators (Fig. 2). However, instead of becoming limited above 12.5% exposure, I_{ss} continued to increase. Above 50% exposure, the rate accelerated to the point where I_{ss} was increasing faster than was the area exposed. Despite a significant variation in I_{ss}'s between the TESC's the lowest values were much larger than the maximum current obtained in the absence of separators.

Use of separators on only the inside face of the test electrode decreased the severe O_2 diffusion limitation presented by separators on both sides, and increased the length of exposed electrode available for penetration of externally supplied cathodic current over that provided in the absence of separators. This physical setup allowed O_2 transport to take place relatively unhindered on the exposed back side of the $Pb/PbSO_4$ electrode, and at the same time provided a low resistance path for the externally supplied cathodic current through the well-wetted separators on the inside face of the test electrode.

The wide divergence of I_{ss} values observed with separators on only the inside face of the test electrode resulted from a change in the severity of diffusion limitation and extent of current penetration between electrodes. The lowest I_{ss}'s were found to be independent of potential and, in these instances, Q_{im} was negligible for all exposures and η's investigated. Apparently, sufficient electrolyte could be retained under certain conditions, as yet not completely understood, to provide a thick enough film of electrolyte on the exposed back side of the test electrode to greatly

inhibit O_2 diffusion. Under this condition, I_{ss}, for a given exposure, decreased with increasing thickness of separator barrier. This can be ascribed to the increased quantity of electrolyte retained and, consequently, the greater ability to "flood" the test electrode.

The highest cathodic currents were observed in those TESC's in which current penetration was incomplete even at very low exposures. Q_{im} and I_{lag} were significantly lower than in the absence of separators (Fig. 2 and 4) indicating that the improvement resulted from increasing penetration above the free electrolyte level. Apparently, ohmic dissipation of the applied potential was greatly decreased below that experienced in the absence of separators by the substantial amount of electrolyte retained in the separator barrier on the inside face of the test electrode. However, in these instances, the amount of electrolyte retained in the TESC was apparently reduced sufficiently to permit a significantly higher O_2 diffusion rate on the back side of the test electrode. A change from the "flooded" electrode condition to less-hindered O_2 access with increasing electrode exposure resulted in intermediate I_{ss} values. This accounted for the significant accelerations in the rate at which I_{ss} increased with degree of exposure usually observed above 50% exposure.

The relation between I_{ss} and O_2 pressure, when only the inside face of the test electrode was masked from the gas space, also varied depending on the extent of current penetration. A linear relation was obtained if ohmic dissipation of the applied potential was imposed over diffusion control over the whole range of pressures investigated. On the other hand, a relation which appeared to be parabolic but which in reality was probably two intersecting straight lines (Fig. 6) was obtained when inability to provide current equivalent to the total rate of O_2 reduction developed only at higher pressures. In the present case, this change occurred above 595 mm Hg. Good agreement between the I_{ss} obtained in air atmosphere and that at 0.2 atm of pure O_2 was again observed.

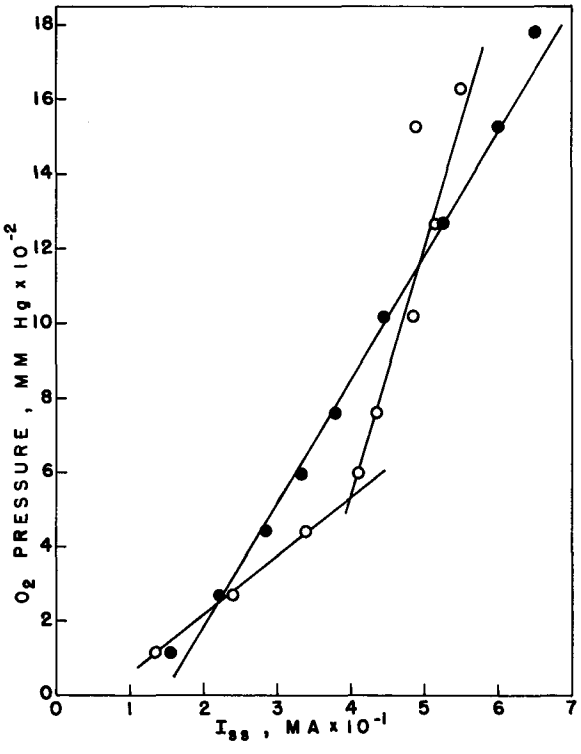

Fig. 6. Steady-state current with three separators on one side of the test electrode as a function of O_2 pressure: —50 mV η, 1.3 sp gr H_2SO_4, 50% exposure. ●, Ohmic dissipation imposed over diffusion control over entire pressure range; ○, pure diffusion control at low O_2 pressures with ohmic dissipation initiated at about 600 mm Hg.

Similar parabolic data were reported by Dehmelt and von Dohren (17) for the alkaline Cd electrode, and Maget and Roethlein (8) for the Pt electrode in H_2SO_4. The former believed that the relation between I_{ss} and O_2 pressure could best be described as parabolic below 1 kg/cm^2 (0.97 atm) but that it was linear from 1 to 6 kg/cm^2. The latter did not investigate O_2 pressures above 1 atm and concluded that a parabolic relation existed. It is likely that a gradual increase in the difference between I_{ss} and total recombination rate was responsible for the pseudoparabolic relation observed below 1 atm pressure in both cases. I_{ss}, in both studies, was dependent on applied potential, indicating the possibility of ohmic dissipation of the driving force as an additional complicating factor.

Maximum I_{ss} with separators on only one side of the test electrode was obtained at 1.3 sp gr (Fig. 7). The data are qualitatively similar to that obtained with separators on both sides of the test electrode. Q_{im} and I_{lag} data indicated that below 1.2 sp gr current penetration became severely limited by decreased electrolyte conductivity, while above 1.3 sp gr I_{ss} was essentially equivalent to the total rate of O_2 reduction. Several other studies (2, 4, 6-10) also indicated that the ability of cathodic current to penetrate the exposed section of the electrode was heavily dependent on the conductivity of the electrolyte film.

Conclusions

Optimum design for establishment of an O_2 cycle in a practical, maintenance-free Pb-acid cell has been demonstrated to require provisions for maximum access of O_2 gas to the negative electrode and a sufficiently conductive electrolyte path between the working electrodes. These requirements are necessary to prevent the imposition of severe limitations on I_{ss} by either diffusion control or ohmic dissipation of the applied potential. In general, both criteria can be satisfied by the use of negative electrodes with backs open to the gas space and well-wetted separators between the working electrodes.

It was also shown that, not only did limiting conditions vary between different TESC's, even when the type of separator was not changed, but that they could change on the same TESC because of varying electrolyte retention with increased electrode exposure.

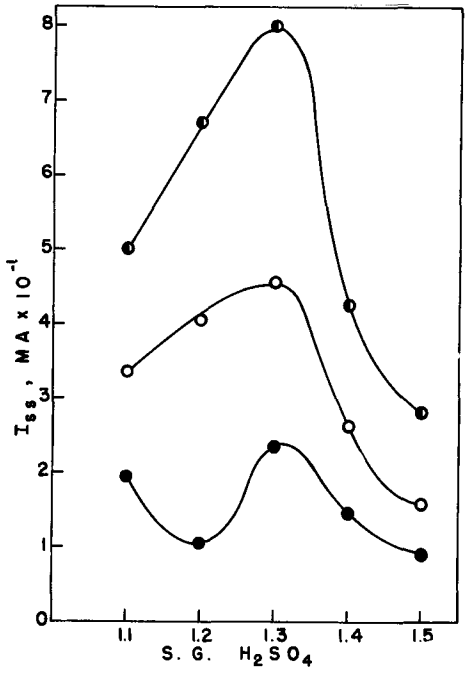

Fig. 7. Steady-state current with three separators on one side of the test electrode vs. specific gravity of H_2SO_4: 1 psig O_2, —50 mV η. Electrode exposure: ●, 25%; ○, 50%; ◐, 75%.

Apparently, electrolyte retention in the TESC was the most critical variable for reproducibility obtaining O_2 reduction at a rate sufficient to establish an O_2 cycle in a practical Pb-acid cell, without resorting to an auxiliary electrode. It is a complex function of the four variables mentioned previously. Since it was not feasible to optimize electrolyte retention through control of electrode and/or separator porosity or cell pack pressure, only elimination of the free electrolyte reservoir remained as a possible technique to achieve such control. This method was evaluated by raising the cell pack 0.5 in. above the bottom of the test cell. The electrolyte level could then be dropped below the bottom of the cell pack, eliminating all contact between them. Ionic contact to the reference electrode was maintained through a thin piece of separator on the back side of the test electrode which dipped into the electrolyte reservoir. Five such fully exposed electrodes, with three layers of microporous rubber on their inside faces, yielded I_{ss}'s of —110, —78, —114, —118, and —93 mA at —50 mV η and 1 psig O_2 in 1.3 sp gr H_2SO_4. These I_{ss}'s lie in a significantly narrower range toward the upper end of the values obtained previously.

Since both O_2 diffusion and the ability to send current through the system are heavily dependent on the amount of electrolyte retained in the TESC, over which there was no effective control, this data should not be considered to represent exactly the O_2 reduction capability of the $Pb/PbSO_4$ electrode. Satisfactory operation of maintenance-free Pb-acid cells will require close control of electrolyte metering. The optimum amount of electrolyte will have to be determined through a study of the initial distribution of electrolyte between electrodes and separators and its variation with cycling.

Manuscript submitted Jan. 16, 1969; revised manuscript received April 14, 1969.

Any discussion of this paper will appear in a Discussion Section to be published in the June 1970 JOURNAL.

REFERENCES

1. H. C. Weber, H. P. Meissner, and D. A. Sama, *This Journal*, **109**, 884 (1962).
2. F. G. Will, *ibid.*, **110**, 145 (1963).
3. F. G. Will, *ibid.*, **110**, 152 (1963).
4. D. N. Bennion and C. W. Tobias, *ibid.*, **113**, 589 (1966); **113**, 593 (1966).
5. F. G. Will, *ibid.*, **114**, 138 (1967).
6. A. G. Pshenichnikov, G. I. Shnaider, and R.Kh. Burshtein, *Elektrokhimiya*, **1**, 418 (1965).
7. Yu.V. Alekseev and Yu.A. Popov, *ibid.*, **1**, 422 (1965).
8. H. J. R. Maget and R. J. Roethlein, *This Journal*, **112**, 1034 (1965).
9. R. J. Roethlein and H. J. R. Maget, *ibid.*, **113**, 581 (1966); **114**, 1043 (1967).
10. H. J. R. Maget and R. J. Roethlein, *Electrochem. Technol.*, **6**, 150 (1968).
11. J. J. Lander, *This Journal*, **98**, 213 (1951).
12. P. Delahay, M. Pourbaix, and P. Van Rysselberghe, *ibid.*, **98**, 57 (1951).
13. S. C. Barnes and R. T. Mathieson, *Fourth International Battery Symposium, Brighton, England*, 41 (1964).
14. D. T. Sawyer and L. V. Interrante, *J. Electroanal. Chem.*, **2**, 310 (1961).
15. P. Ruetschi and B. D. Cahan, *This Journal*, **106**, 543 (1959).
16. G. W. Vinal, "Storage Batteries," 4th Ed., p. 110, John Wiley & Sons, Inc., New York (1955).
17. K. Dehmelt and H. von Dohren, *Proc. Ann. Power Sources Conf.*, **13**, 85 (1959).

Gas Depolarized Graphite Anodes for Aluminum Electrowinning

M. L. Kronenberg

Union Carbide Corporation, Consumer Products Division, Research Laboratory, Cleveland, Ohio

ABSTRACT

Anode potential sweep studies on electronic conducting refractories and several metals in a cryolite-alumina melt have shown copper, nickel, and graphite to be the most stable anode materials. However, even these materials were attacked in this electrolyte at anodic potentials normally attained in aluminum electrowinning. Uncatalyzed graphite electrodes could be depolarized by methane, but carbon monoxide would depolarize only catalyzed electrodes. There are significant fluoride losses from the electrolyte when hydrogen-containing fuel gases are used to depolarize the anode.

Carbon is an especially good anode choice for aluminum production for several reasons:

1. The products of anodic oxidation ($CO + CO_2$) are expelled from the electrolyte and do not contaminate the cathode product.
2. It is a good electronic conductor.
3. It is virtually insoluble in aluminum.
4. It is able to withstand the high operating temperature of Hall-Heroult cell (980°C).
5. It is a relatively inexpensive material.

Nevertheless, the use of 0.57 lb of carbon/lb of aluminum produced contributes about 8% to the cost of producing aluminum (1). This is not much less than the cost of the bauxite raw material.

Some work was initiated at Union Carbide to determine whether a gas depolarized anode using an inert, porous-refractory material might provide a reduction in anode costs if an inexpensive gas such as methane were used. This principle has been discussed elsewhere at various times, but to the author's knowledge no experimental data have been presented in support of it (2-5).

The plan of investigation was as follows:

1. Determine which anode materials exhibit the greatest resistance to attack by means of polarization and potential sweep studies of carbon, graphite, and other conductive materials (borides, carbides, and metals).
2. Conduct anode corrosion studies in the presence of depolarizing gases using the most stable materials as "inert" electrodes.
3. Improve anodic activity toward depolarizing gases by application of catalysts.

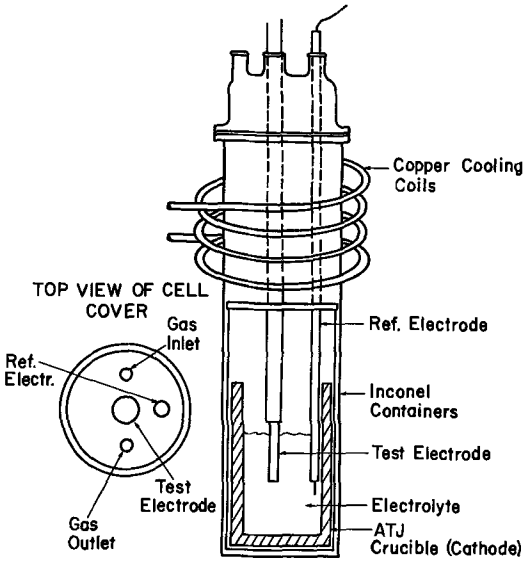

Fig. 1. Cell assembly used for Al electrowinning experiments

Experimental

A sketch of the cell evolved for polarization and sweep studies is shown in Fig. 1. The electrolyte commonly used was a melt containing 15 w/o (weight per cent) alumina, 78% cryolite, and 7% CaF_2 contained in the ATJ graphite crucible shown. The graphite crucible is contained in an Inconel crucible which in turn is contained in an Inconel sagger. A BN or alumina heat shield (not shown) was normally held just above the Inconel crucible. One final Inconel can (not shown) is used as an extra protection for the furnace walls and furnace thermocouple.

The cell cover had a ground glass flange which was held to the ground flange of the metal sagger by spring clips. A positive pressure flow of argon (Linde, 99.996%) was passed above the electrolyte except where noted.

A Lindberg model 59622 crucible furnace and 59344 controller were used to heat and control the cell temperature. An auxiliary thermocouple was not normally used, but the furnace controller was periodically rechecked against a shielded thermocouple in the melt.

A Pt-Al alloy reference electrode was chosen since it is solid at both operating temperatures, and the Pt component is inert. This alloy was prepared by cathodically diffusing aluminum from a saturated alumina, cryolite melt at 1000°C and 100 mA/cm² for 33 min. The reaction zone was 0.010 in. thick. Hardness tests gave a result of 100 kg/cm² for the Pt zone; 200 kg/cm² for the interface; and 320 kg/cm² for the reaction zone, suggesting that a Pt-Al alloy was formed. This reference electrode was checked against another Pt-Al electrode prepared in the same way. After an initial "settling down" period of about 30 min, the electrode potentials did not differ more than 20 mV over a period of several hours. A typical polarization or potential sweep run took about 20 min. While the reversible potential of this reference electrode is not known, it served our need for a simple, relatively stable electrode that would not contaminate our melt. The reference electrode was kept in an alumina sheath to prevent shorting to the anode or cathode.

The electrode construction used for testing nonporous anode materials is shown in Fig. 2. Only the test material was intentionally immersed in the electrolyte. The graphite crucible containing the electrolyte (Fig. 1) served as the cathode.

The potential correction for the position of the reference electrode was applied according to the following equation derived by Casper (6) for concentric cylinder electrodes:

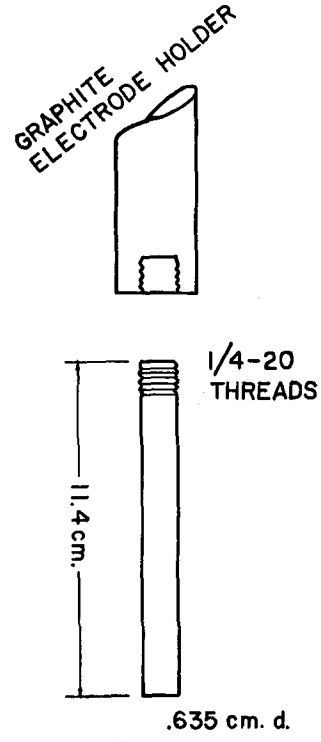

Fig. 2. Test electrode

$$R = \frac{2.3}{2\pi K} \log \frac{r_2}{r_1} \qquad [1]$$

where R is the total resistance per unit length, r_1 is the radius of the working electrode; r_2 the reference electrode distance from the center, and K the conductivity of the melt. The conductivity of the melt was taken as 2.09 ohm^{-1} cm^{-1}, averaging the values reported by Mashovets (7) and by Matrasovsky (8). The value r_1 was 0.634 cm and r_2 was 2.5 cm. The voltage correction as a function of current is $V = 0.107\,I$.

Polarization data were obtained with a Kordesch-Marko interrupter (9) which eliminated *IR* drop and activation polarization from the measurement. Calculations based on Eq. [1], direct resistance readings with an a-c bridge, and interrupter readings were used to help distinguish among solution resistance, interfacial resistance, and activation polarization.

An Anatrol 4100 potential controller, which was modified to provide slow linear sweeps, was used for potential sweep studies.

Experimental Results

Cell polarization data on nonporous materials.—Cell polarization data were obtained at 1000°C using the Kordesch-Marko interrupter. The electrolyte used for obtaining polarization data contained 87 w/o cryolite, 8% CaF_2 + 5% alumina. The cell resistance at 1000 cycles was 0.2-0.3 ohm for the cells discussed in this section of the report. The resistance-free polarization curves for AGKSP, pyrolytic graphite; L113 SP carbon; 50% TiB_2-50% BN; copper; and nickel are summarized in Fig. 3.

The data in Fig. 3 suggest that Cu and Ni have greater stability (less anodic current at corresponding potentials) than carbon and graphites.

Three copper-nickel alloy compositions ranging from 25 to 75% Cu were also tested. These had stabilities which were in between Cu (greatest stability) and nickel. Cu and Ni form solid solutions which range in melting temperatures from 1083° (pure Cu) to 1456°C (pure nickel). Carbon and graphite on the other hand were much more stable than pure TiB_2 or TiB_2-BN composites.

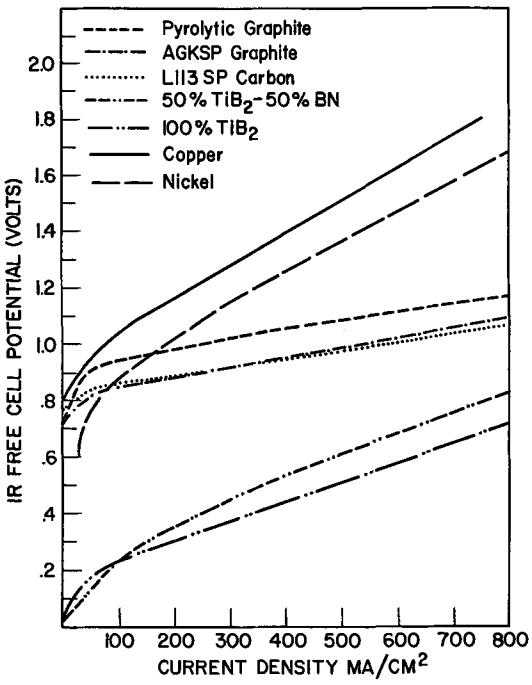

Fig. 3. Anodic polarization data for solid electrode materials

Tables I and II illustrate how polarization data were tabulated and results are given for AGKSP graphite and 50% TiB_2-50% BN, respectively. As seen in the tables, the difference between *IR*-free and *IR*-included cell voltage readings is used to determine the apparent cell resistance. This resistance always decreased with increasing currents until a steady value of about 0.2 ohm was obtained when carbon and graphite anodes were used.

The decrease in cell resistance with increasing cell voltage was not noted with materials other than carbon. This suggests that a resistive film is formed with carbon which tends to break up at high currents where significant gas evolution occurs. With materials other than carbon, either this film does not form or gas evolution occurs sooner (lower overvoltage).

Table I. Cell polarization data in ¼-in. AGKSP rod obtained with 60-cycle interrupter. Electrolyte temperature 1000°C. Electrode area 9.5 cm²

Current mA	Current potential (volts) *IR* free	*IR* incl.	ΔV *IR* incl.-*IR* free mV	Apparent resistance (ohms)
100	0.708	0.828	120	1.20
200	0.782	0.896	114	0.57
400	0.808	1.008	200	0.50
500	0.812	1.028	216	0.43
1000	0.834	1.161	327	0.33
2000	0.876	1.354	478	0 24
4000	0.928	1.820	992	0 25
6000	1.028	2.340	1212	0.20
10000	1.121	3.230	2109	0.21

Table II. Cell polarization data on ¼-in. rod of 50% TiB_2-50% BN. Electrode area = 9.5 cm²

Current mA	Current potential (volts) *IR* free	*IR* incl.	ΔV *IR* incl.-*IR* free mV	Apparent resistance (ohms)
100	0.045	0.066	21	0.21
200	0.073	0.112	39	0.20
300	0.096	0.156	60	0.20
500	0.152	0.251	99	0.20
750	0.188	0.350	162	0.22
1000	0.232	0.451	219	0.22
1500	0.278	0.566	288	0.19
2000	0.356	0.724	368	0.18
3000	0.460	1.040	580	0.19
5000	0.600	1.595	995	0.19
7000	0.760	2.20	1440	0.20
10000	0.890	2.98	2090	0.21

Cell resistance measured with an a-c bridge at 1000 cycles was 0.2 ohm which was about the same as the cell resistance calculated using the interrupter.

Sweep studies on nonporous materials.—All sweep experiments were run at potentials positive to the Pt-Al reference electrode already described. The potential of this reference was approximately 50 mV positive to the rest potential of the ATJ graphite cathode in an electrolyte containing 78 w/o cryolite, 7% CaF_2, and 15% alumina (saturated) (8). Reproductions of the sweep traces for Cu, Ni, AGKSP and pyrolytic graphite, L113-SP carbon, 50% TiB_2-50% BN, and silicon are summarized in Fig. 4. Except for a short range at low currents, the current-potential relationship was linear. It is this linear portion that is shown here extended to zero current. Only forward scans are shown, but in every case reverse scans were also run. These were virtually mirror images of the forward scans. The potentials were not corrected for resistance in Fig. 4, but the same geometric arrangement already described was used for each test. The scan rate was always 20 min for both the 0-1.0 and 0-2.0v scans. To verify that the system and refractory electrode were operating properly, a sweep on a new material was followed by a sweep on AGKSP graphite. The anode area immersed in electrolyte was close to 8 cm² for all the sweeps summarized in Fig. 4.

The potential sweep data show Cu as the most stable material, which is in agreement with the polarization studies. Intermediate in stability are Ni and graphite. Titanium diboride-BN and silicon were the least stable of the materials tested.

Data from potential sweep traces of six refractory borides and carbides are shown in Fig. 5. A potential sweep on AGKSP graphite was included for comparison. The anode area immersed in the electrolyte was

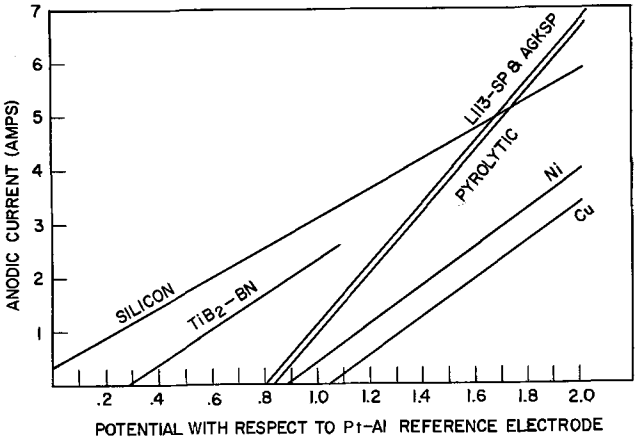

Fig. 4. Potential sweep data on various anode materials

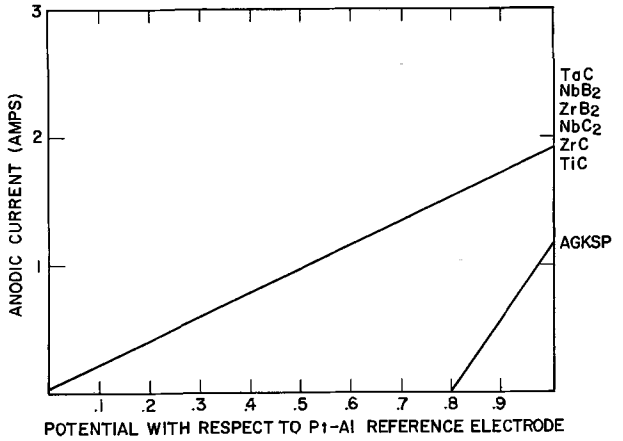

Fig. 5. Potential sweep data on refractory borides, carbides, and AGKSP graphite.

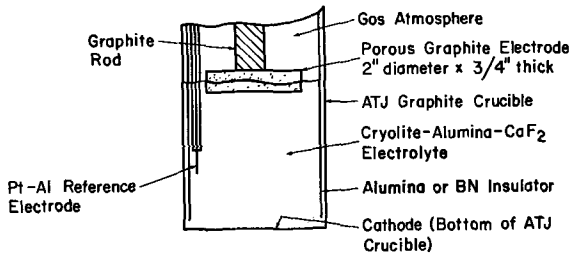

Fig. 6. Horizontal, porous gas depolarized anode

12-15 cm^2 for all six refractory materials tested. The refractory borides and carbides all had about the same resistance to anodic oxidation and this was far less than that of carbon and graphite.

Thus, the materials investigation to find something more stable than carbon as an anode material was only partially successful. While nickel and especially copper appear somewhat more stable, they are not immune from attack at the high current densities required. Porous electrodes for gas depolarization were, therefore, limited to carbon in this investigation to avoid possible contamination of aluminum product.

Results using porous, gas depolarized electrodes.— Two types of "flow-through" porous carbon electrodes were tried as gas depolarized electrodes. These were porous cylindrical electrodes and porous plug electrodes. No significant evidence of gas depolarization was observed for the four anodes run. The only porous electrodes that showed significant evidence of gas depolarization were the nonflow-through, horizontal ones.

These latter electrodes were operated as gas depolarized anodes in cryolite-CaF_2-alumina melts at 1000°C. The porous anode base materials used were PG-60 and PG-25 graphites which were impregnated with various salt solutions or run uncatalyzed. A sketch of the main cell components is shown in Fig. 6.

Table III summarizes the polarization data obtained when the gas atmosphere above the cell was changed as indicated. The electrode used was a PG-60 electrode catalyzed with 0.1% by weight of salts of platinum group metals. The reference electrode used was Pt-Al alloy, previously described.

Gases were alternated as shown in Table III and results were obtained on successive gasses within about 10 min. The higher currents at comparable polarizations in the presence of hydrogen and natural gas as compared with argon strongly suggest that the former gases depolarize the electrode. Similar depolarization experiments were conducted several times and verified both the gas depolarization of hydrogen and natural gas and the relative inactivity of the argon. Under the argon atmosphere, virtually all the anodic current is assumed to come from carbon utilization. A 254 A-hr experiment carried out under argon yielded an anode efficiency for carbon utilization of 98.4%.

To determine whether gas depolarization was possible without catalyst and to avoid possible catalysis by metal present as impurities, an anode was made of powders from AGKSP spectrographic graphite. The total metal content of the spectrographic rod was approximately 1 ppm. The *IR*-free cell voltage *vs.* time at a constant current of 2A while alternating the gas atmosphere between argon and natural gas is given in Table IV. The results suggest that gas depolarization has occurred, although the differences in cell voltage between argon and natural gas atmospheres settled down to only 20 mV.

Table III. Polarization data under various gas atmospheres using a catalyzed anode

Gas atmosphere above cell	Anode-reference potential (volts)	Current (mA)
Hydrogen	0.15	4000
Argon	0.17	500
Hydrogen	0.163	4000
Natural gas (92.7% methane)	0.19	2000
Hydrogen	0.15	2000
Argon	0.185	500

Table IV. Gas depolarization on an uncatalyzed electrode made of AGKSP graphite

Gas atmosphere	Cell potential (volts, *IR* free)	Time (minutes)
Argon	0.94	0
Natural gas	0.82	14
Natural gas	0.82	22
Argon	0.92	46
Argon	0.92	61
Natural gas	0.90	73
Natural gas	0.90	83
Argon	0.92	93

Table V. Gas depolarization on heavily catalyzed anode

Gas atmosphere	Cell potential (volts, *IR* free)	Time (minutes)
Argon	0.80	0
Carbon monoxide	0.74	10
Argon	0.80	20
Carbon monoxide	0.75	30
Argon	0.80	40

On heavily catalyzed electrodes with a highly developed gas-electrolyte interface, it is possible to observe gas depolarization by carbon monoxide. Table V summarizes the results obtained by alternating the gas atmosphere and comparing the cell potential at a constant current of 4A. The level of catalysis was 1% of salts from the platinum group metals. Carbon monoxide initially shows a very marked gas depolarization. However, the catalyst was not stable and was lost from the anode, even though the cell was left on open circuit in between measurements to slow down catalyst losses. After this happened carbon monoxide and argon gave the same polarization data.

Analytical results were obtained in two experiments which were run under a natural gas atmosphere using uncatalyzed graphite anodes for 167 and 533 A-hr, respectively. In these, and all other experiments under natural gas, a considerable quantity of a voluminous, white substance was condensed on the cell cover and cooler parts of the cell. The electrolyte analysis before and after a run and the condensate analysis for the 167 and 533 A-hr runs are given in Tables VI and VII.

It seems that the condensate has a high percentage of fluoride and contains a relatively low percentage of the principal metallic cations. It is probably a complex mixture of carbon-fluorine compounds, although this has not been verified by analytical results. The aluminum content of the electrolyte at the end of the

Table VI. Analytical results—167 A-hr run

	Weight per cent				
	Na	Al	Ca	F	O
Initial composition of electrolyte	26.9	14.7	6.49	50.0	3.68
Composition of condensed vapor	1.6	0.2	0.97	51.6	7.53
Final composition of electrolyte	15.7	20.85	5.50	37.6	9.41

Table VII. Analytical results—533 A-hr run

	Weight per cent				
	Na	Al	Ca	F	O
Initial composition of electrolyte	25.3	15.2	4.3	50.0	3.02
Composition of condensed vapors	4.0	5.8	0.4	58.6	1.12
Final composition of electrolyte	18.4	23.9	2.4	39.2	12.80

experiment is high because of Al_2O_3 additions and dispersions of Al product in the electrolyte.

Conclusion

The materials investigation did not result in a material that was significantly more resistant to attack than graphite at anodic potentials normally attained in aluminum electrowinning. Two metals, copper and nickel, however, exhibited stability comparable to graphite.

Through the use of porous graphite electrodes, this investigation has demonstrated that gas depolarization for aluminum electrowinning is possible with hydrogen or natural gas (~93% methane). Natural gas may be electrochemically equivalent to hydrogen since considerable thermal decomposition occurs at these temperatures. Carbon monoxide was far less reactive than hydrogen. While depolarization by hydrogen and methane occurred without added catalyst, carbon monoxide depolarization was accomplished only in the presence of active catalysts. Unfortunately, these catalysts were stripped from the anode even at moderate current densities.

There are serious fluoride losses from the electrolyte when hydrogen-containing fuels are used, due to reactions of the water product with the fluoride electrolyte. A quantitative determination of the rate of this deleterious reaction has not been made.

Manuscript submitted Dec. 23, 1968; revised manuscript received May 14, 1969.

Any discussion of this paper will appear in a Discussion Section to be published in the June 1970 JOURNAL.

REFERENCES

1. K. R. Nack, Ph.D. dissertation, "Productivity in the Production of Primary Aluminum Ingots," New York University (1965).
2. T. G. Pearson, "The Chemical Background of the Aluminum Industry," Royal Institute of Chemistry, Lectures, Monographs and Reports, 1955, p. 93, W. Heffer and Sons, Ltd., Cambridge, England.
3. Russian Pat. 161,125, March 9, 1964.
4. L. Ferrand, U.S. Pat. 2,593,741, April 22, 1952.
5. L. Ferrand, U.S. Pat. 2,900,319, Aug. 8, 1959.
6. C. Casper, *Trans. Electrochem. Soc.*, **77**, 353 (1940).
7. V. Mashovets and V. Petrov, *J. Appl. Chem. USSR*, **32**, 1561 (1959).
8. K. Matrosovsky and M. Malinovsky, *Electrochem. Acta.*, **11**, 1035 (1966).
9. K. Kordesch and A. Marko, *This Journal*, **107**, 480 (1960).

Technical Notes

Effects of Gamma Radiation on the Behavior of Nickel and Cadmium Electrodes[1]

G. R. Argue[2,*] and H. L. Recht*

Atomics International, A Division of North American Aviation, Incorporated, Canoga Park, California

and G. M. Arcand[3]

Jet Propulsion Laboratory, California Institute of Technology, Pasadena, California

A number of workers have reported studies in which alkaline batteries were exposed to gamma radiation (1-3) and have stated that doses as high as 10^8 rads produced no discernable effects. However, Ho's data (3) showed that nickel-cadmium batteries lost about 10% of their capacity when irradiated in a nuclear reactor. This loss fell within the requirements for his particular work. In no instance previous to the present work have alkaline battery electrodes been studied as entities in experimental cells. Many of the materials (separators, cases, *etc.*) in a complete battery are known to be degraded by nuclear radiation. The present work was undertaken to study the effects of radiation on the electrodes in alkaline solutions without the possible interferences of these other materials.

Experimental

Materials.—All electrodes were obtained from Gulton Industries, Incorporated, nickel-cadmium type VO-0.8 cells. Each cell contained three cadmium electrodes and two nickel electrodes. The electrodes were 4.2 x 3.8 cm with capacities of 0.4 amp-hr for nickel and 0.5 amp-hr for cadmium. Each electrode weighed about 5g. Before disassembly, the cells were fully charged according to the manufacturer's specifications.

Thirty weight per cent KOH solutions, used in all experiments reported here, were freshly prepared from reagent-grade pellets as required.

Equipment.—High-rate irradiation (1.4 x 10^6 rad/hr)[4] was provided by an Atomic Energy of Canada Gammacell Model GC 200 Co^{60} source, low rate irradiation (8 x 10^4 rad/hr) by a 3300-curie unit built by Atomic International (4). Harrison Lab Model 855 power supplies provided constant currents. Data were recorded on Minneapolis-Honeywell Universal 5 mV instruments. Timers were Kelelet Model K213 and Industrial Time Kit MCK. Self Organizing Systems Model SV100 solions indicated state of charge. Pressures were measured with CEC Model 316 transducers having ranges of ±12.5 psig or 0-15 psig. All other control and measuring equipment was constructed by Atomics International.

Cell design.—The cell consisted of a quartz cup mounted in a sealable, stainless-steel container. The

[1] This paper presents the results of one phase of research carried out at the Jet Propulsion Laboratory, California Institute of Technology, under Contract No. NAS7-100, sponsored by the National Aeronautics and Space Administration.

[2] Present address: General Telephone & Electronics Laboratories, Incorporated, Bayside, New York.

[3] Present address: Idaho State University, Pocatello, Idaho.

* Electrochemical Society Active Member.

[4] Radiation dosage is based on the absorption of gamma radiation by water.

cup was divided into two compartments by a partition containing a sintered-quartz disk to maintain electrolytic contact between electrodes. Tabs fused to the cup walls held the electrodes firmly against the disk. The cell was filled with 50 ml of electrolyte solution. Each pair of experimental cells was made with electrodes taken from a single commercial cell. A Hg/HgO reference electrode was installed inside the stainless-steel container.

Procedure.—A current of 0.2A permitted operation of experimental cells through many cycles within a reasonable time without damaging the electrodes. After assembly with formed electrodes, each cell was discharged until the voltage began an abrupt and rapid decrease. This point will be called the "knee" of the voltage-time curve. The cell was then charged to the equivalent of 25% overcharge, discharged to some arbitrary state of charge (*e.g.*, 75% of full charge), and cycled for 24 hr. Each cycle consisted of 6 min of discharge, 4 min of open circuit, 6 min of charge and 4 min of open circuit. Current was controlled at 0.2A. All cells were so treated before being placed in the radiation source or controlled-temperature bath.

Operation of a pair of matched cells constituted one experiment. The equilibrium temperature within the high-rate Co^{60} source was measured to be 45°C; therefore, the water-bath temperature was set at that value. In every experiment, the behavior of the irradiated cell was compared with that of the matching cell in the water bath. Irradiation was continued until the desired dose was obtained. Doses ranged from 10^5 to 2×10^8 rads at rates depending on the Co^{60} source used.

Changes in cadmium electrode capacity were determined in cells that were cadmium limited; *i.e.*, the capacity of the cadmium electrode was less than that of the nickel electrode. About one third of the commercial cadmium plate was cut off for this purpose. Each cell was fully charged and discharged to the knee of the voltage-time curve several times at room temperature before the experiment; the average discharge times were used to determine the initial capacity. This was repeated after the experiment. The difference was taken as the change in capacity.

Results and Discussion

Electrode material loss.—Electrodes lost weighable amounts of material (>0.2 mg) whenever the total radiation dose was 5.8×10^6 rads or more. Visual indication of disintegration, appearing as a turbidity in the electrolyte solution, began at 1.4×10^6 rads. Losses in comparison cells in the water bath were negligible.

Figure 1 shows the relationship between material loss and total irradiation dose when the cells were cycled around 75% of full charge. The weights shown are total amounts lost from both electrodes. Although the data are scattered, the increased loss with increased dose is evident. Data for both low- and high-dose rates are included; there was no indication of a rate effect. The results in Table I show that most of the loss occurs at the cadmium electrode. Both electrodes, particularly the nickel, lose considerably more material when cycled at 100% of full charge than at any other state.

It is not surprising that material is physically removed from the electrodes, although one might expect both the nickel and the cadmium electrodes to behave similarly. Gas is evolved during irradiation, much of which may be catalytically formed at the solid-solution interfaces of the electrodes. Bubbles may be produced within the pores of the electrodes loosening or dislodging material. The shedding process would be accelerated when the cell is cycled because the $Cd(OH)_2$ formed would adhere to the plate less strongly than the metal. The effect of the presence of the electrodes on the rate of gas formation is shown in Table II.

The losses would be aggravated when the cell is cycled around 100% of full charge because electrochemical formation of gas would occur during the short periods of overcharge. At lower states of charge, the major electrochemical reaction probably occurs within the body of the plate so that much of the dislodged material is retained.

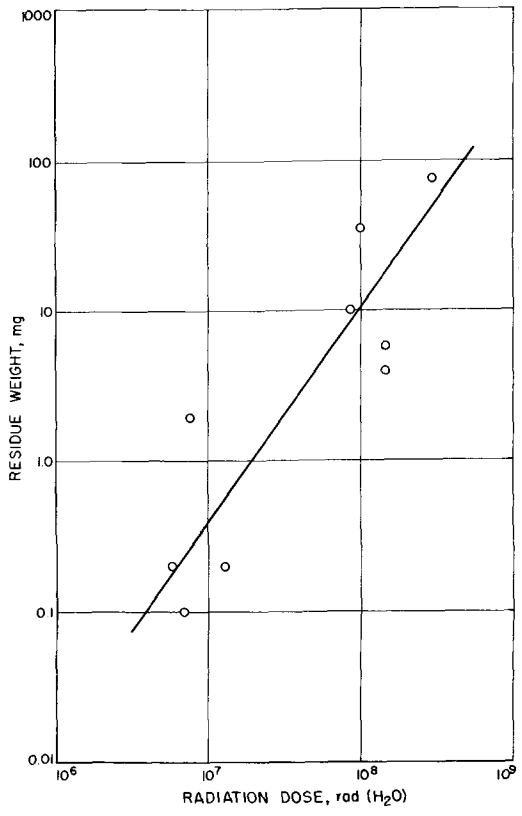

Fig. 1. Effect of radiation dose on electrode material loss

Capacity change.—Cadmium electrodes lost capacity when cycled during irradiations of 8×10^7 rads or more. Figure 2 represents the effects observed when the cells were cycled in the vicinity of preselected, initial state of charge. The solid line shows the difference in capacity between the irradiated and comparison cells and is considered the significant curve. The difference is quite constant except at 75% of full charge where the loss is greater. While data scatter is considerable, results of repeated experiments show the effects to be real.

Table I. Material loss from individual cycled electrodes during irradiation

No. of experiments	State of charge (%)	Cd electrode Weight loss (mg)	Cd electrode Standard deviation	Ni electrode Weight loss (mg)	Ni electrode Standard deviation
3	100	28.9	9.0	8.0	6.2
2	75	21.5	13.6	2.2	0.3
3	50	11.1	1.3	1.5	1.7
2	25	10.7	2.0	2.2	1.1

Total dose = 8×10^7 rads.

Table II. Gas formation in KOH solutions in presence of electrodes

Electrode	$G_{(H_2)}$	$G_{(O_2)}$
Ni	0.009	0.052
Cd	0.025	0

G = number of molecules of gas produced per 100 eV of gamma energy deposited in the sample.
Dose = 6.6×10^7 rads.
Cover gas is He.

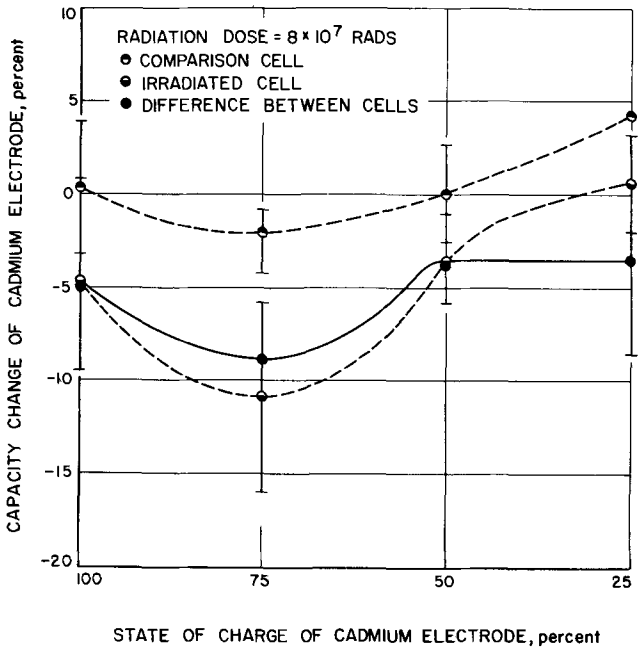

Fig. 2. Effect of radiation on capacity of cycled cadmium electrodes

Capacity losses were observed only when the cells were cycled; a few open-circuit experiments were performed at 75% of full charge with no loss observed. It is assumed that no open-circuit loss would be observed at other states of charge at the radiation doses used.

The effects of gas evolution may partly explain the permanent loss of cadmium electrode capacity. If the combination of gas formation and cycling causes a decrease in adhesion of active material, it may also result in poor electronic contact with the metallic collector so that some of the material is no longer available for electrochemical use. Certainly, the material loss cannot account for the capacity change. Whatever the mechanisms involved, they seem to occur whether or not the system is exposed to radiation; the radiation merely accentuates the effect.

Acknowledgments

The authors wish to thank W. A. McCollum who built and maintained most of the equipment used in this work and who collected most of the data, R. Shephard for the gas analyses, the Analytical Group of the Chemistry Department of Atomics International for all other analyses, and D. E. McKenzie and A. A. Uchiyama for many helpful discussions.

Manuscript submitted Oct. 4, 1965; revised manuscript received Feb. 17, 1969.

Any discussion of this paper will appear in a Discussion Section to be published in the June 1970 JOURNAL.

REFERENCES

1. Space Technology Laboratory Report No. STL-TR-2303-003-R4-000, April 1961.
2. E. B. Cupp, *Proc. Ann. Power Sources Conf.*, **17**, 82 (1963).
3. J. W. Ho, *ibid.*, **18**, 68 (1964).
4. E. L. Colichman, P. J. Mallon, and A. A. Jarrett, *Nucleonics*, **15**, No. 4, 115 (1957).

Correction Factors for a Two-Point Probe Resistivity Measurement of Cylindrical Crystals

Helen H. Gegenwarth

International Business Machines Corporation, Components Division, East Fishkill Facility, Hopewell Junction, New York

Consider a conducting cylinder of radius C and length $2a$ with electrodes placed at each end, through which a current, I, flows (*see* Fig. 1). Two probes may be placed on the cylindrical surface and the potential difference between them measured.

Measurement

The potential at any point in the cylinder ($r \neq 0$) is (1)

$$V(r,z) = \frac{I\rho}{\pi a}\sum_{1}^{\infty}{}' \sin\frac{n\pi}{2} \sin\frac{n\pi z}{2} \frac{K_1\left(\frac{n\pi C}{2a}\right)I_0\left(\frac{n\pi r}{2a}\right) + I_1\left(\frac{n\pi C}{2a}\right)K_0\left(\frac{n\pi r}{2a}\right)}{I_1\left(\frac{n\pi C}{2a}\right)}$$

where

I = current through cylinder
ρ = resistivity of cylinder
$2a$ = length of cylinder
C = radius of cylinder
I_n = modified Bessel function of the first kind
K_n = modified Bessel function of the second kind

The potential difference between the probes is then

$$\Delta V = V(C,D) - V(C,E)$$

Using the relation

$$K_{n+1}(x)I_n + K_n(x)I_{n+1}(x) = \frac{1}{x}$$

ΔV then simplifies to

$$\Delta V = \frac{I\rho}{\pi a}\sum_{1}^{\infty}{}' \sin\frac{n\pi}{2}\left(\sin\frac{n\pi D}{2a} - \sin\frac{n\pi E}{2a}\right)\left(\frac{2a}{n\pi C}\right)\left(\frac{1}{I_1\left(\frac{n\pi C}{2a}\right)}\right)$$

or

$$\Delta V = \frac{4I\rho}{\pi^2 C}\left[\sum_{1}^{\infty}{}' \sin\frac{n\pi}{2}\cos\frac{n\pi(D+E)}{4a} \sin\frac{n\pi(D-E)}{4a}\frac{1}{nI_1\left(\frac{n\pi C}{2a}\right)}\right]$$

Calling the expression in brackets F,

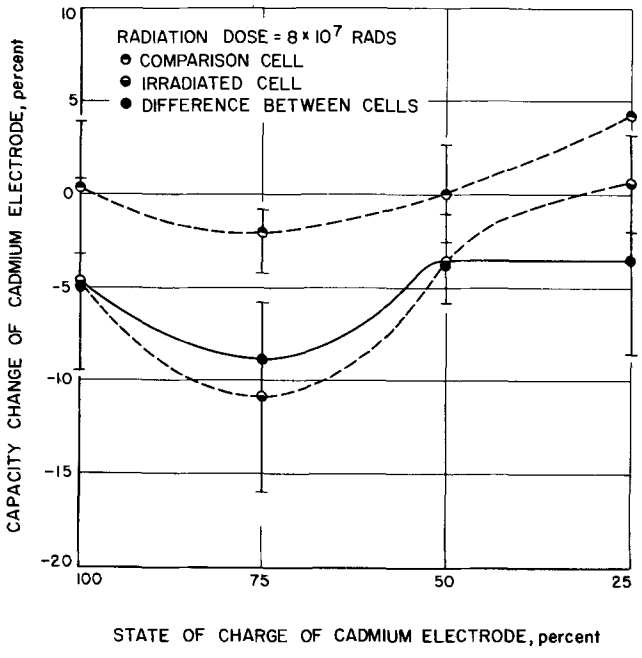

Fig. 2. Effect of radiation on capacity of cycled cadmium electrodes

Capacity losses were observed only when the cells were cycled; a few open-circuit experiments were performed at 75% of full charge with no loss observed. It is assumed that no open-circuit loss would be observed at other states of charge at the radiation doses used.

The effects of gas evolution may partly explain the permanent loss of cadmium electrode capacity. If the combination of gas formation and cycling causes a decrease in adhesion of active material, it may also result in poor electronic contact with the metallic collector so that some of the material is no longer available for electrochemical use. Certainly, the material loss cannot account for the capacity change. Whatever the mechanisms involved, they seem to occur whether or not the system is exposed to radiation; the radiation merely accentuates the effect.

Acknowledgments

The authors wish to thank W. A. McCollum who built and maintained most of the equipment used in this work and who collected most of the data, R. Shephard for the gas analyses, the Analytical Group of the Chemistry Department of Atomics International for all other analyses, and D. E. McKenzie and A. A. Uchiyama for many helpful discussions.

Manuscript submitted Oct. 4, 1965; revised manuscript received Feb. 17, 1969.

Any discussion of this paper will appear in a Discussion Section to be published in the June 1970 JOURNAL.

REFERENCES

1. Space Technology Laboratory Report No. STL-TR-2303-003-R4-000, April 1961.
2. E. B. Cupp, *Proc. Ann. Power Sources Conf.*, **17**, 82 (1963).
3. J. W. Ho, *ibid.*, **18**, 68 (1964).
4. E. L. Colichman, P. J. Mallon, and A. A. Jarrett, *Nucleonics*, **15**, No. 4, 115 (1957).

Correction Factors for a Two-Point Probe Resistivity Measurement of Cylindrical Crystals

Helen H. Gegenwarth

International Business Machines Corporation, Components Division, East Fishkill Facility, Hopewell Junction, New York

Consider a conducting cylinder of radius C and length $2a$ with electrodes placed at each end, through which a current, I, flows (*see* Fig. 1). Two probes may be placed on the cylindrical surface and the potential difference between them measured.

Measurement

The potential at any point in the cylinder ($r \neq 0$) is (1)

$$V(r,z) = \frac{I\rho}{\pi a}\sum_{1}^{\infty}{}' \sin\frac{n\pi}{2} \sin\frac{n\pi z}{2} \frac{K_1\left(\frac{n\pi C}{2a}\right)I_0\left(\frac{n\pi r}{2a}\right) + I_1\left(\frac{n\pi C}{2a}\right)K_0\left(\frac{n\pi r}{2a}\right)}{I_1\left(\frac{n\pi C}{2a}\right)}$$

where

I = current through cylinder
ρ = resistivity of cylinder
$2a$ = length of cylinder
C = radius of cylinder
I_n = modified Bessel function of the first kind
K_n = modified Bessel function of the second kind

The potential difference between the probes is then

$$\Delta V = V(C,D) - V(C,E)$$

Using the relation

$$K_{n+1}(x)I_n + K_n(x)I_{n+1}(x) = \frac{1}{x}$$

ΔV then simplifies to

$$\Delta V = \frac{I\rho}{\pi a}\sum_{1}^{\infty}{}' \sin\frac{n\pi}{2}\left(\sin\frac{n\pi D}{2a} - \sin\frac{n\pi E}{2a}\right)\left(\frac{2a}{n\pi C}\right)\left(\frac{1}{I_1\left(\frac{n\pi C}{2a}\right)}\right)$$

or

$$\Delta V = \frac{4I\rho}{\pi^2 C}\left[\sum_{1}^{\infty}{}' \sin\frac{n\pi}{2}\cos\frac{n\pi(D+E)}{4a} \sin\frac{n\pi(D-E)}{4a}\frac{1}{nI_1\left(\frac{n\pi C}{2a}\right)}\right]$$

Calling the expression in brackets F,

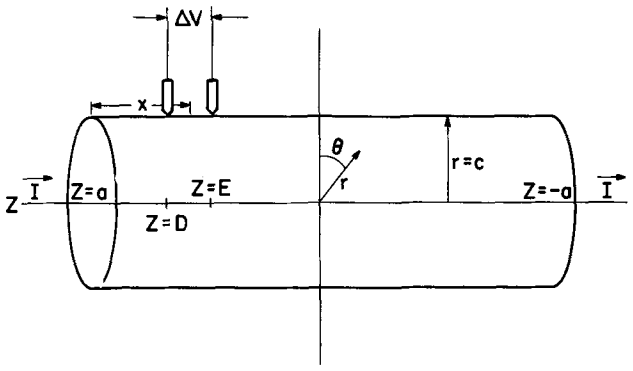

Fig. 1. Conducting cylinder through which a current flows

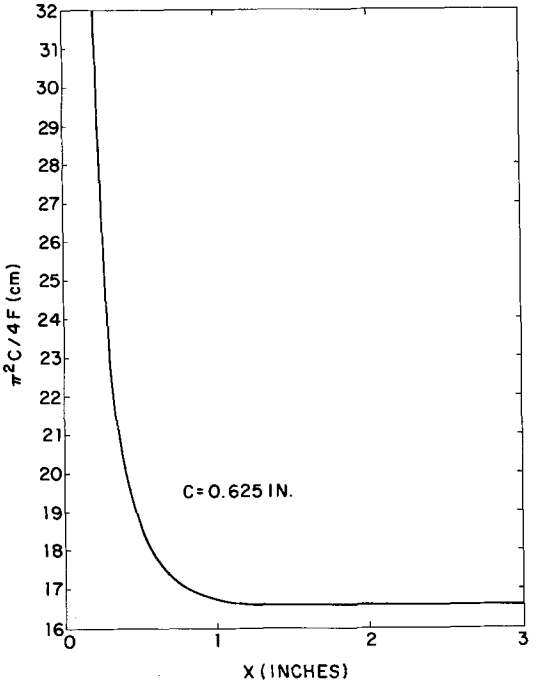

Fig. 2. Correction factor calculated for C = 0.625 in.

$$\Delta V = \frac{4I\rho F}{\pi^2 C}$$

or

$$\rho = \frac{\pi^2 C}{4F} \cdot \frac{\Delta V}{I}$$

Limiting Case

If the probes are placed symmetrically about the plane Z = 0,

$$\rho = \frac{\pi^2 C}{4F} \frac{\Delta V}{I}$$

should yield the same result as the case where the electrodes supplying the current I are disk contacts of the same diameter as the cylinder. In that case,

$$\rho = \frac{\pi C^2}{(D-E)} \frac{\Delta V}{I}$$

That is,

$$\lim_{(D+E)\to 0} \frac{\pi(D-E)}{4C} = F$$

Computer calculations of F verify that this is exactly true.

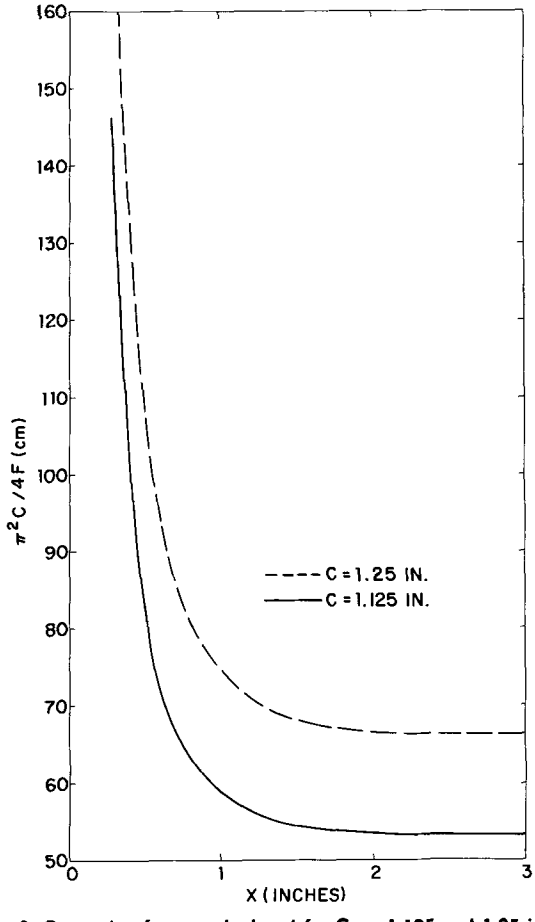

Fig. 3. Correction factor calculated for C = 1.125 and 1.25 in.

The correction factor, $\pi^2 C/4F$, has been calculated for several cases of particular interest. The results are given in Fig. 2 and 3. In each case, the quantity $(D-E)$, which is the probe spacing, is taken as 0.1878 in., and the correction factor is plotted against x, the average distance of the probes from the end of the cylinder (see Fig. 1).

Conclusions

The procedure for determining the resistivity along the length of a cylinder would be to place current probes at each end of the cylinder and measure ΔV between two travelling probes spaced a distance $(D-E)$ from each other. The resistivity at any given position is then calculated from

$$\rho = \frac{\pi^2 C}{4F} \cdot \frac{\Delta V}{I}$$

where the appropriate F is determined by X, the average distance of the probes from the end of the cylinder.

Acknowledgment

The author acknowledges the assistance of Mr. Everett Bruce, who wrote the program for the numerical evaluation of F.

Manuscript submitted May 27, 1968; revised manuscript received Oct. 22, 1968.

Any discussion of this paper will appear in a Discussion Section to be published in the June 1970 JOURNAL.

REFERENCE

1. A. Gray and T. M. MacRobert, "A Treatise on Bessel Functions and Their Applications to Physics," Dover Publications, New York (1966).

JOURNAL OF THE ELECTROCHEMICAL SOCIETY

REVIEWS AND NEWS

JUNE 1969

A Review of the Application of Stainless Steels in Desalination Equipment

E. H. Phelps,* R. T. Jones, and H. P. Leckie

Applied Research Laboratory, United States Steel Corporation, Monroeville, Pennsylvania

ABSTRACT

The corrosion performance of various types of stainless steels is discussed for the variety of environments associated with distillation-type sea-water desalination plants. Several factors related to the design and operation of desalination equipment can have important bearing on the corrosion performance of the stainless steels. The most important of these are flow rate, presence of crevices, deposit formation, temperature, and oxygen content. The performance of present-day steels has been evaluated by full-scale plant tests and also by specimen-exposure tests. For the future, electrochemical procedures will help to explain the corrosion behavior of stainless steels in high-temperature water and offer a means for evaluating new steel compositions with improved corrosion resistance.

It is the purpose of this paper to present a review of the performance of stainless steels in desalination plants, with particular emphasis on distillation-type equipment. Over the years, a large amount of data has been collected on the corrosion performance of the stainless steels in salt water and brackish water (1). These data show that stainless steels have good resistance to corrosion in these waters at temperatures near ambient, provided that crevices and deposits which might lead to oxygen concentration cells can be avoided. Experience has shown that good performance can be obtained in sea water by maintaining flow rates above about 5 fps (this minimizes build-up of marine organisms and other deposits) and by eliminating crevices in equipment design. Thus, on the basis of past experiences, the stainless steels should be considered as promising candidate materials for desalination equipment that operates at temperatures near ambient and in which moderate flow rates are maintained.

At elevated temperatures, however, such as those characteristic of distillation-type desalination plants, the availability of specific service data is much more limited and was practically nonexistent prior to the construction of the demonstration plants by the Office of Saline Water at Freeport, Texas, and San Diego, California. The environmental conditions in such plants, consisting of hot water with relatively high concentrations of chloride, would generally be considered detrimental to the stainless steels, particularly with reference to localized forms of attack such as pitting and stress-corrosion cracking. Contrary to these expectations, however, corrosion tests in the plants themselves have shown that certain stainless steels are capable of resisting attack if the oxygen content in the water is sufficiently low. This paper reviews the types of stainless steels that might be considered for desalination plants and the service data that have been obtained with some of the steels in the demonstration distillation plants. The electrochemical principles involved in hot sea-water corrosion are also discussed.

* Electrochemical Society Active Member Representative of a Sustaining Member Company.

Types of Stainless Steel

There are many specific types of stainless steel currently produced in this country. The American Iron and Steel Institute (AISI) lists 39 standard types, some of which are listed in Table I. In addition to these, there are many "nonstandard" grades. However, the standard grades and most of the nonstandard grades can be grouped into the following three main categories, on the basis of alloy content and crystallographic differences:

1. Martensitic, typified by AISI Type 410 (12% Cr). These steels are hardenable by heat treatment, and in the heat-treated condition have a body-centered tetragonal crystal structure (martensite).
2. Ferritic, typified by AISI Type 430 (17% Cr). These steels are not hardenable by heat treatment. The crystal structure is body-centered cubic (ferrite).
3. Austenitic, typified by AISI Type 304 (18% Cr, 8% Ni). These steels are also not hardenable by heat

Table I. Compositions of several standard grades of stainless steel

AISI Type	Nominal composition, per cent C	Mn, max	Si, max	Cr	Ni	Other
			Martensitic steels			
502	0.10 max	1.00	1.00	4.0-6.0	—	0.40-0.65 Mo
403	0.15 max	1.00	0.50	11.5-13.0	—	—
410	0.15 max	1.00	1.00	11.5-13.5	—	—
			Ferritic steels			
405	0.08 max	1.00	1.00	11.5-14.5	—	0.10-0.30 Al
430	0.12 max	1.00	1.00	14.0-18.0	—	—
446	0.20 max	1.50	1.00	23.0-27.0	—	0.25 N max
			Austenitic steels			
304	0.08 max	2.00	1.00	18.0-20.0	8.0-12.0	—
304L	0.03 max	2.00	1.00	18.0-20.0	8.0-12.0	—
310	0.25 max	2.00	1.50	24.0-26.0	19.0-22.0	—
316	0.08 max	2.00	1.00	16.0-18.0	10.0-14.0	2.0-3.0 Mo
316L	0.03 max	2.00	1.00	16.0-18.0	10.0-14.0	2.0-3.0 Mo
317	0.08 max	2.00	1.00	18.0-20.0	11.0-15.0	3.0-4.0 Mo
321	0.08 max	2.00	1.00	17.0-19.0	9.0-12.0	5xC min Ti
347	0.08 max	2.00	1.00	17.0-19.0	9.0-13.0	10xC min Cb-Ta

treatment. The crystal structure is face-centered cubic (austenite).

As a general rule, the inherent corrosion resistance of the stainless steels increases with increasing chromium content. Thus the steels with higher chromium content (18% and above) are generally of more interest for use in desalination equipment than steels with lower chromium content. The addition of 8% or more nickel to stainless results in the austenitic steels, which have very desirable fabricating characteristics. The addition of molybdenum in the Type 316 steels brings about a substantial improvement in resistance to pitting corrosion. The addition of titanium and columbium in the stabilized grades, Types 321 and 347, respectively, is intended to prevent grain boundary carbide precipitation and intergranular attack in environments causing this form of corrosion. Resistance to intergranular corrosion may also be obtained by restricting the carbon content of the steel to 0.03% maximum, as in Types 304L and 316L.

Field Corrosion Tests

Most of the field tests at the Freeport, Texas, and San Diego, California, demonstration plants have consisted of the installation of racks containing corrosion coupons in various process equipment of the two plants (2-4). Types 304 and 316 stainless steel tubes have also been tested in the first evaporator effect of the Freeport plant (4) to obtain corrosion data under actual service conditions. Although it is recognized that all of these tests were conducted under the inherently changeable process conditions associated with a production plant, the results obtained have aided in identifying the most important environmental factors governing the corrosion resistance of stainless steels in hot sea water. These are (a) dissolved oxygen concentration, (b) temperature, and (c) velocity of the sea water. The latter two factors are largely responsible for the extent to which solids are deposited from the sea water and, consequently, these factors govern the extent to which crevices are formed on the surface of stainless steels.

Dissolved oxygen concentration.—Data compiled from coupon tests conducted at the Freeport and San Diego desalination plants are presented in Tables II, III, and IV. These data indicate that localized penetration in stainless steels is substantially inhibited when the dissolved oxygen content is kept at a very low level. At Freeport, mechanical deaeration, which reduced the dissolved oxygen to 40-600 ppb (parts per billion), was not sufficiently complete to prevent pitting and/or crevice corrosion in the stainless steels tested (Table II). However, with essentially complete removal of the dissolved oxygen by evaporation (Table III), the depth of pitting and crevice corrosion was definitely less than that observed in the mechanically deaerated water (bottom portion of Table II). In this respect, it also is noteworthy that the amount of pitting and crevice corrosion was very low (or nonexistent) in deaerated brine at San Diego (Table IV), where efficient mechanical deaeration reduced the oxygen content to a low level of 5 ppb. The inhibiting effect of complete deaeration on pitting of stainless steels has also been obtained in pilot plant tests, Table V (3). It is apparent that localized corrosion of stainless steels was substantially prevented by complete removal of the dissolved oxygen in the sea water.

Temperature.—Increasing the temperature of sea water appears to increase somewhat the severity of pitting in stainless steels, as is shown from data in

Table II. Summary of corrosion coupon tests in raw and deaerated sea water—Freeport desalination plant

Average temperature, °F	Exposure period, days	Maximum penetration, mils: Surface Type 304	Surface Type 316	Crevice[a] Type 304	Crevice[a] Type 316
		Raw sea water[b]			
85[c]	90	7	6	14	9
85	156	8	None	19	4
98	156	Trace	None	14	Trace
114	156	Trace	None	10	1
117[c]	90	5	8	13	12
126	156	None	None	10	2
		Deaerated sea water[d]			
134	156	8	None	20	5
165	156	21	14	30	13
170[e]	90	10	16	5	15
186	156	18	30	>39*	27
212	156	21	27	>39*	23
230[e]	90	18	6	21	>39*

[a] Attack in crevice formed by Teflon washer on specimens.
[b] Environment—dissolved oxygen, saturated; concentration factor, about 1.0; turbulence moderate to high; pH, 7.5-7.8.
[c] Data from U.S. Steel coupon tests [Ref. (4)]; other data from Ref. (2).
[d] Environment—dissolved oxygen, 40-600 ppb; concentration factor, about 1.0; turbulence, moderate; pH, 6.2-7.8.
* Coupon perforated—initial thickness was 0.039 in.

Table III. Summary of corrosion coupon tests in completely deaerated sea water brine[a]—Freeport desalination plant

Average temperature, °F	Maximum penetration, mils: Surface Type 304	Surface Type 316	Crevice[c] Type 304	Crevice[c] Type 316
119	None	None	3	3
172[b]	8	5	14	5
198	4	5	4	5
235	None	None	None	None
242	4	None	11	8
250	13	6	12	10

[a] Except where noted, the environmental conditions were: dissolved oxygen, nil; turbulence, high; exposure period, 156 days; pH, 7.0. Data from Ref. (2).
[b] Data from U.S. Steel coupon tests [Ref. (4)]. Environmental conditions—dissolved oxygen, nil; turbulence, low; exposure period, 90 days.
[c] Attack in crevice formed by Teflon washer on specimens.

Table IV. Corrosion tests with Type 316 stainless steel coupons—San Diego desalination plant—Exposure period, 90 Days[a]

Temperature, °F	Brine concentration factor	Maximum penetration, mils: Surface	Crevice
	Raw sea water[b]		
65	1.0	None	1
85	1.0	Trace	2
	Deaerated brine[c]		
90	1.5-2.0	None	3
107	1.5-2.0	None	4
133	1.5-2.0	None	4
166	1.5-2.0	None	2
196	1.5-2.0	None	6
205	1.5-2.0	None	8
	Flashing brine[d]		
90	1.7-2.2	None	Trace
103	1.7-2.2	None	4
118	1.7-2.2	None	1
144	1.7-2.1	None	4
174	1.6-2.1	None	2
200[e]	1.5-2.0	None	8

[a] Data from Ref. (2).
[b] Environmental conditions—dissolved oxygen, 8 ppm (saturated); turbulence, high; pH, 7.5-7.8.
[c] Environmental conditions—dissolved oxygen, 5 ppb; turbulence, moderate; pH, 7.0-7.5.
[d] Environmental conditions—dissolved oxygen, nil; turbulence, moderate; pH, 7.0-7.5.
[e] Same environmental conditions as [d] except that dissolved oxygen was probably 5 ppb.

Table V. Sea water corrosion data from a pilot-plant operation—Ref. (3)

Temperature, °F	Environmental conditions[a] Dissolved oxygen content, ppm	pH	Indicated corrosion rate—mils penetration per year: Type 304	Type 316
180	Trace	6.7	9	0.7
290[b]	15.0	6.2	12*	13*
320[c]	0.0	7.0	<0.1	<0.1

[a] Sea water velocity—5 fps.
[b] Test pressure, 70 psi.
[c] Test pressure, 100 psi.
* Severe crevice attack beneath insulation washers.

Tables II, III, and IV. The effect of temperature, however, appears to be diminished if the sea water is raw or completely deaerated. This effect may, in the case of the plant coupon tests, be influenced by the amount of dissolved solids deposited from the sea water onto the coupon surfaces. An apparent interrelationship between dissolved oxygen, sea-water temperature, and dissolved solids deposited from the sea water is further indicated by the tests conducted with Type 304 stainless steel evaporator tubes at the Freeport plant (4). Data shown graphically in Fig. 1 represent the maximum pit depths measured on representative sections of the stainless-steel tubes after the tubes had been in service for various periods of time. The first effect of the long-tube-vertical evaporator system at Freeport receives hot sea water that has been deaerated to less than 100 ppb of dissolved oxygen. The sea water flows in a thin film down the tubes and heat passed through the tubes evaporates water from the film. As indicated in Fig. 1, during the first 12-15 months of service, the tubes were exposed to sea water at an average of 230°-235°F. However, the temperature was subsequently elevated to as high as 270°F during periods through the 25th month of service. As the graph shows, the depth of pitting in the top and middle tube sections increased when the evaporating temperature increased. However, the depth of pitting near the tube bottom appeared to be nearly independent of the temperature increase. It was noted during inspection that the inside surface of the top and middle sections of the tubes was consistently covered with scale deposit from the sea water, whereas the sections near the bottom of the tube remained nearly deposit-free. Furthermore, dissolved oxygen remaining in the deaerated sea water entering the first effect was being stripped from the sea water during initiation of boiling (evaporation) near the top of the tubes. Consequently, the sea water near the bottom of the tube was free of dissolved oxygen. It was postulated that the low rate of pitting and the independence of pitting rate with temperature change observed near the tube bottom were due to the deposit-free surface and low dissolved oxygen in the brine. The same type of pit inhibition has been observed by Russian investigators (5) in their studies utilizing experimental- and industrial-size long-tube-vertical evaporators.

Sea water velocity.—As mentioned previously, it is known that stainless steels are suitable for process equipment handling sea water at temperatures near ambient if the velocity is maintained above about 5 fps (6). At higher velocities, the deposition of solids onto stainless-steel surfaces is minimized, thereby reducing the number of crevice sites. The literature

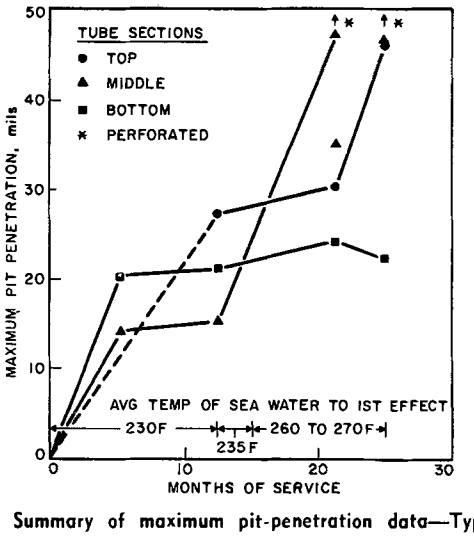

Fig. 1. Summary of maximum pit-penetration data—Type 304 stainless steel evaporator tubes.

Table VI. Data showing the effect of sea water velocity on pitting of stainless steels—Ref. (2)

Average temperature, °F[a]	Degree of turbulence	Maximum penetration, mils Surface Type 304	Surface Type 316	Crevice Type 304	Crevice Type 316
85	Low	—	—	39*	27
85	Moderate to high	8	None	19	Trace
126	Moderate to high	None	None	10	2
134	Low	Trace	None	22	10

* Coupon perforated, original thickness—0.039 in.
[a] Environmental conditions—raw sea water saturated with oxygen; brine concentration factor, 0.8-1.1; pH, 7.5-7.8.

indicates that stainless steels, particularly Type 316, are being successfully used for pump components (7,8) and for heat transfer tubes of steam condensers (9) in which sea water is the coolant. The results of tests on the effect of velocity in a desalination plant are shown in Table VI. Pitting and crevice attack were considerably less severe on stainless-steel coupons exposed at locations where turbulence was moderate to high (sea water impinged on the test coupons) than the attack on coupons exposed to low-velocity conditions.

Other environmental factors.—Other environmental factors of concern when stainless steel is used in hot sea water are sea water concentration (salinity or concentration factor) and hydrogen ion concentration (*p*H). With respect to salinity, the nature of the desalting processes at plants in which field tests have been conducted thus far has made it difficult to determine the single effect of salinity on the corrosion of stainless steels. Generally, other environmental factors, such as dissolved oxygen and/or temperature, have overshadowed the relatively small effects that might be expected with a change in salinity.

In regard to the effect of sea water *p*H, there are essentially no data available from the field tests in the demonstration desalination plants because the sea water in these plants is maintained nearly neutral except during the acidification operation which is utilized to remove carbonate-forming constituents. Plant operating experience has shown, however, that Type 316 stainless performs satisfactorily in deaeration equipment handling acidulated sea water at *p*H values as low as four.

Effect of steel composition on pit resistance in sea water.—Data from coupon tests at the Freeport Plant have shown that, regardless of the environmental conditions, the chromium stainless steels (Type 410 and 430) exhibit substantially less resistance to corrosion than the austenitic stainless steels (4). Corrosion of the chromium stainless steels was primarily the result of severe crevice corrosion initiated by solids that deposited from the sea water. The sensitivity of chromium stainless steels to crevice corrosion would probably eliminate them from consideration unless strict control of solids deposition could be assured.

A comparison of the effect of molybdenum on the pit resistance of austenitic stainless steels, Tables II through VI, shows that Type 316 is in general more pit-resistant than Type 304 in desalination environments. Type 316 stainless steel tubes exposed in the first evaporator effect at the Freeport plant have experienced, thus far, only slight pitting attack after about 20 months of service.

Effect of stress.—Erichsen-cup type, stress-corrosion specimens of Types 304 and 316 stainless steels were included in the field tests conducted at the Freeport plant. Examination of these specimens after exposure periods of several months' duration has not revealed any evidence of stress-corrosion cracking. Furthermore, stress-corrosion cracking has not been found to be a problem in the Type 304 and Type 316 stainless-steel test tubes exposed in the first evaporator effect at Freeport.

Electrochemical Principles Involved in Hot Sea Water Corrosion

Pitting of stainless steels is primarily associated with chloride environments, although a similar form of attack is also found in bromide solutions. This localized attack results from the breakdown of the passive film such that the local area of film breakdown becomes active, while the surrounding passive film serves to support the local cathodic reaction. Consequently, we find a condition of a very small anode supported by a large cathode, resulting in a very localized and rapid attack. The mechanism of breakdown of the passive film remains the subject of some controversy, but has been variously associated with the adsorption (10, 11) of chlorides or the inclusion (12) of chlorides at local sites in the passive film. After the initial breakdown, the process is autocatalytic in that the solution within the pit becomes increasingly acidic and corrosive because of the hydrolysis of ferrous ions resulting in an increased concentration of hydrogen ions. Pit geometry partially precludes the outward diffusion of these hydrogen ions into the bulk solution.

The pitting susceptibility of a passive steel is dependent on its alloy content and for a given steel also depends on such environmental variables as temperature, chloride concentration, pH, oxygen concentration, and the presence of inhibitors. The effect of many of these metallurgical and environmental variations has been described in the literature (10, 11, 13, 14).

The pitting susceptibility of a stainless steel in a given environment is characterized by a critical potential below which (more active) pitting does not occur. At potentials more noble than this value, pitting will occur at a rate primarily dependent on alloy composition.

The most noble corrosion potential that could be reached by a steel under natural corrosion conditions is governed by the equilibrium potential for the cathodic reduction reaction; under most conditions, this would correspond to the equilibrium oxygen reduction potential, which for the reaction:

$$O_2 + 4H^+ + 4\epsilon \rightarrow 2H_2O \qquad (E^\circ = 1.23v)$$

is given by the Nernst expression:

$$E = 1.23 + \frac{0.059}{4} \log [H^+]^4 pO_2$$

(at 1 atm) $E = 1.23 - 0.059$ pH (*vs.* hydrogen electrode).

Therefore, if no critical potential is observed during anodic polarization to the equilibrium potential for oxygen reduction, the alloy is immune to pitting because the natural corrosion potential could never be more noble than the critical pitting potential. This reasoning explains the immunity to pitting of titanium, which has an extremely noble critical potential in neutral chlorides (12-14v).

Most available data on electrochemical measurements of pitting susceptibility have been obtained in electrolytes at temperatures close to room temperature. The increased temperature used in desalination plants results in two opposing effects regarding localized corrosion of stainless steels. These are:

1. Increased propensity for pitting with an increase in temperature.

2. Reduction in oxygen concentration results in a more active corrosion potential. For a given set of environmental conditions, this decreases the tendency toward pitting.

Above approximately 100°F, there is only a very slight shifting of the critical pitting potential in the active direction with a further increase in temperature. Thus, for AISI Type 304 (see Fig. 2) in 0.1*N* sodium chloride solution, the critical potential shifts in the active direction by only approximately 0.1v as the temperature increases from 100° to 200°F. Increasing the temperature over this range only slightly

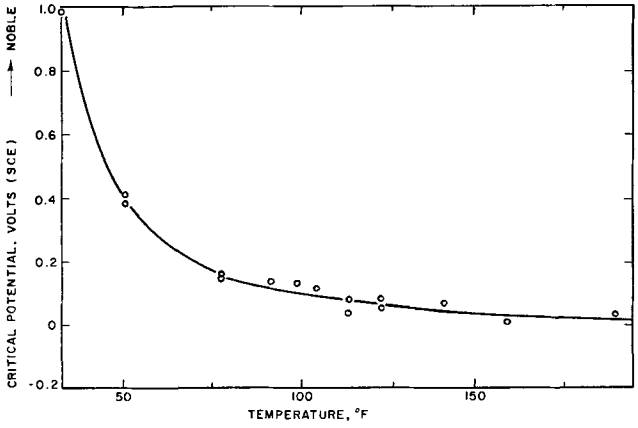

Fig. 2. Effect of temperature on critical potential for pitting of Type 304 stainless steel in 0.1*N* NaCl solution.

increases the aggressiveness of the environment for localized corrosion.

The removal of oxygen results in an increase in cathodic control in the system, with a corresponding shift of the corrosion potential in the active direction. This effect is demonstrated by Fig. 3, which shows potential-*vs*-time curves for AISI Type 304 stainless steel in air-saturated and deaerated 1M sodium chloride solution. In each case, the specimens were activated by holding at 1.2v for 5 min. The air saturated solution induced the formation of passivity in a relatively short time, as indicated by the noble potential attained after only 10 min. In deaerated solutions, however, the specimen potential remained approximately 0.5v more active than the air-saturated solutions. The decrease in oxygen content that occurs when water is heated and the resultant shift in corrosion potential in the active direction are more than sufficient to offset the slight active shift in critical potential, and result in the reduction in corrosion rate for stainless steels in chloride solutions that has been observed in open systems as the temperature approaches that for boiling (15). As mentioned, this pronounced effect of oxygen was observed in the plant tests at the Freeport plant.

Localized attack of stainless steels may be eliminated by the use of inhibitors. It has been shown that the mechanism of inhibition of pitting is one of competitive adsorption on the metal surface between the aggressive ions (chloride) and inhibitor (10). The concentration of inhibitor required depends primarily on the nature of the inhibitor and the concentration of chloride and follows an equation of the form:

$$\log [Cl] = A + B \log [\text{inhibitor}]$$

where chloride and inhibitor are expressed as activities.

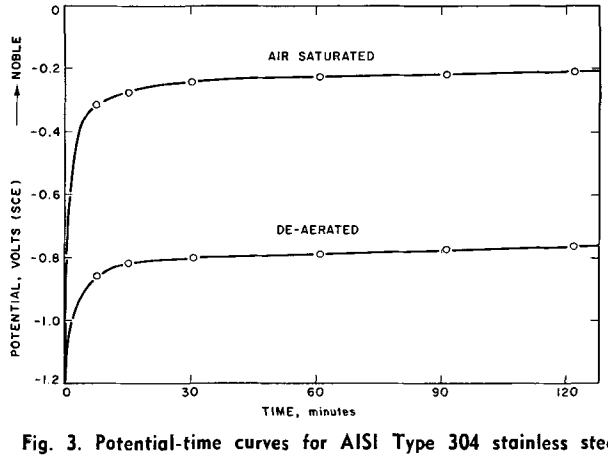

Fig. 3. Potential-time curves for AISI Type 304 stainless steel in aerated and deaerated 1M sodium chloride solution.

Electrochemical measurements have shown hydroxyl ions to be a very efficient inhibitor in preventing attack of stainless steels by chlorides. The amount of hydroxyl ion that may be added to sea water, however, is limited by scale formation which deposits under alkaline conditions and would hinder efficient heat transfer. Other anions (such as nitrates) are known to inhibit the pitting of stainless steels by chlorides and thus future studies might well include an evaluation of the effect of nitrate additions on stainless performance.

In addition to the reduction in efficiency of heat transfer produced by scale deposition, it may also be conducive to the occurrence of crevice corrosion. Crevice corrosion is normally initiated by a differential aeration cell having an anode located at a small area shielded from easy access of oxygen, and surrounded by a large cathode area where reduction of oxygen occurs. Once corrosion starts at anodic sites within the crevice, the outward diffusion of the corrosion product (predominantly hydrolyzed ferrous ions) is partially prevented by crevice geometry, resulting in a build-up in hydrogen ion concentration. The process is autocatalytic because the acid environment causes more rapid attack within the crevice. In this respect, pitting and crevice corrosion are very similar.

For the future, it is believed that electrochemical measurements should serve as the basis for the development of new stainless steels that are resistant to pitting attack and crevice corrosion in desalination environments. Elements should be added to the steel that will shift the critical potential as far as possible in the noble direction. It is believed to be particularly important that the critical potential measurements be made at temperatures encountered in desalination plants.

Summary

The field-test results reported herein indicate that under certain conditions the stainless steels exhibit excellent corrosion resistance in environments encountered in distillation-type desalination plants. The most important environmental factors are that the water or brine be substantially free of oxygen and that the operating conditions be adjusted so that deposits are not formed. Type 316 stainless offers the best resistance to attack; however, the test results indicate that Type 304 stainless may also have sufficient resistance to be a useful material of construction. Electrochemical measurements help to explain the effect of increased temperature on the corrosion of stainless steels and also offer a method for evaluating the performance of new steels.

Manuscript submitted Nov. 19, 1968; revised manuscript received Feb. 3, 1969. This paper was presented at the Montreal Meeting, Oct. 6-11, 1968, as Paper 399.

Any discussion of this paper will appear in a Discussion Section to be published in the December 1969 JOURNAL.

REFERENCES

1. "Corrosion Handbook," Edited by H. H. Uhlig, p. 413, John Wiley & Sons, New York (1948).
2. M. E. Mattson and R. M. Fuller, "A Study of Materials of Construction in Distillation Plants, 1962-1963," Office of Saline Water (OSW) Research and Development Progress Report No. 163 (Oct. 1965).
3. T. P. May, E. G. Holmberg, and J. Hinde, "Sea Water Corrosion at Atmospheric and Elevated Temperatures," Sonderdruck ans Dechema Monographien Band 47 (1962), available from the International Nickel Co., Inc.
4. R. T. Jones, *Metals Engineering Quarterly*, **7**, No. 3 (Aug. 1967).
5. E. V. Konstantinova, L. S. Semyonova, and A. A. Dyakov, USSR, *Proc. First Intern. Symp. Water Desalination*, **II**, 549-560 (1965).
6. F. W. Fink, "Corrosion of Metals in Sea Water," OSW Research and Development Progress Report No. 46 (Dec. 1960).
7. R. A. White, *Materials Protection*, **4**, No. 3, (Mar. 1965).
8. W. F. Dietrich, "Corrosion Test Program," OSW Research and Development Progress Report No. 244 (Feb. 1967).
9. R. B. Niederberger, *Trans. ASME, Ser. A., J. Eng. Power*, **8**, No. 4 (Oct. 1966).
10. H. P. Leckie and H. H. Uhlig, *This Journal*, **113**, 1202 (1966).
11. Y. Kolotyrkin, *Corrosion*, **19**, 261t (1963).
12. T. P. Hoar, D. Mears, and G. Rothwell, *Corrosion Science*, **5**, 279 (1965).
13. J. Defranoux, *ibid.*, **3**, 75 (1963).
14. H. H. Uhlig and J. Gilman, *Corrosion*, **20**, 289t (1964).
15. H. H. Uhlig and M. C. Morrill, *Ind. Eng. Chem.*, **33**, 875 (1941).

Electronic Conduction in Dielectric Films

A. K. Jonscher

University of London, Chelsea College of Science and Technology, London, England

ABSTRACT

This review starts with a brief discussion of the structure of technically important dielectric films and proceeds to outline the relevant theoretical and experimental aspects of amorphous semiconductors and dielectrics. This is followed by a discussion of d-c conductivity in dielectric films at low and high fields, including dependence on temperature. Alternating-current techniques represent one of the most important tools in the study of dielectrics, and an account is given of the experimental results over a wide range of frequencies. This is followed by a description of the application of the method of thermally stimulated currents to the study of dielectric films—a relatively little used technique capable of supplementing the more conventional d-c and a-c measurements. The review concludes with brief accounts of impurity-induced conduction, photoelectric phenomena, and the so-called switching in dielectric films.

Among the many studies of the properties of dielectric films, the subject of electronic conduction has attracted perhaps rather less interest than it may deserve. One reason for this may be found in the fact that most people wish their dielectric films to be insulating and accordingly consider conduction phenomena simply as an accidental nuisance to be eliminated. Another reason may be that conduction in these films has been frequently associated with the movement of ions and only relatively recently was attention seriously diverted to the study of specifically electronic processes. Nevertheless, it is possible to state that our

knowledge of film properties would be very incomplete without a good understanding of the electronic phenomena and that valuable insight into general film properties is obtained from this study. The present paper is intended as a review of some of the relevant experimental and theoretical topics and attempts to provide a unified picture of the present stage of the subject.

The approach adopted is based to a large extent on the familiar concepts of conduction mechanisms in electronic semiconductors, with the necessary allowance for the primarily amorphous and glassy nature of many of the dielectric films in use at present. In this respect, we are in the fortunate position that the science of heavily disordered and amorphous semiconductors has made great progress in recent years and it is possible at least to speculate on the probable extension of these concepts to dielectric films. For this reason, the present review goes beyond the strict limits of dielectric materials in one or two instances which are considered to be illustrative of the general principles involved.

A word of caution is indicated: the science of dielectric films is not an exact discipline, as many of its practitioners no doubt realize. Reproducibility leaves a great deal to be desired, mainly on account of the imperfect understanding of the technological factors involved in the preparation of films. All numerical data should therefore be treated with caution, especially where structure-sensitive parameters are concerned.

Electronic tunneling phenomena in very thin films are specifically excluded from the present treatment since they are adequately covered elsewhere (1, 2). Ionic transport processes are also mentioned only incidentally as they represent a specialist subject in their own right (3).

The following account is intended to some extent as a review of progress in the last two years and should be read as a follow-up to an earlier paper by the author (4) in which many of the basic concepts are discussed in detail and to which references are made in the text in order to avoid unnecessary repetition.

Influence of Structure on Film Conduction

The structure of thin films represents a large topic in its own right and is dealt with here only insofar as it is known to affect their electrical properties (5). Single-crystal films may be obtained by thermal oxidation of single-crystal substrates at elevated temperatures (6) or by the well-known processes of epitaxial growth from the vapor phase which are widely applied in the technology of semiconductor devices involving both elemental and compound semiconductors. A majority of dielectric films of technical significance, however, are deposited from the vapor phase on relatively cool substrates or are anodized in aqueous solutions and their structure is substantially amorphous in the sense that there is an absence of any long-range order in the atomic or ionic configuration. Between the extremes of amorphous and single-crystalline structures there is a whole range of micro- and polycrystalline materials which may be obtained from the former by the process of thermal annealing, sometimes under the influence of electron beam bombardment (7). The latter feature makes it rather difficult to carry out structural determinations using electron diffraction and electron microscopy, since the measuring technique itself may influence the properties being investigated.

The electrical behavior of crystalline dielectric films may be understood in terms of conventional semiconductor concepts (8, 9): they represent materials with relatively large forbidden energy gaps and relatively high carrier mobilities, say between 10 and 10^3 cm^2/vsec, but with very low thermal carrier densities. They normally contain high densities of localized trapping levels, usually distributed over a considerable part of the forbidden gap energy. The most prominent feature of their behavior is bulk space charge limited flow in the presence of injecting contacts (10) or Schottky thermionic emission over a field-lowered potential barrier in the case of blocking contacts (6, 4).

The electrical properties of amorphous and glassy materials are much less clearly understood, although considerable progress has been achieved in recent years (4, 11-13). Here the concepts of conduction, valence and forbidden bands, free electrons and holes, mobility of carriers, donor and acceptor levels, *etc.*, require considerable modifications.

With regard to the energy band structure, there is general agreement that this depends mainly on nearest-neighbor dispositions and, to the extent to which these are similar in amorphous and crystalline structures of the same chemical composition, it may be expected that the main features of the band structure remain similar. However, the sharp band edges of crystalline lattices become diffuse in amorphous materials and give rise to a gradual transition from conducting states in which carriers are free to move to deep trapping levels in which carriers are strictly localized, as shown in Fig. 1. Electronic conduction in such structures does not normally occur by free electrons or holes but rather by more or less localized carriers "hopping" between sites by tunneling with or without slight thermal activation. In the presence of thermal activation, which is the normal process at all but the lowest temperatures, there is frequently no clearly defined activation energy but, instead, the graph of resistance *vs.* reciprocal temperature shows a continuous curvature (14, 15). This is due to the fact that the hopping sites are randomly distributed both in space and in energy and the activation energy increases with increasing temperature as more and more carriers become excited into the conduction process. Figure 2 gives an example of this behavior in the case of amorphous films of silicon and germanium. Another significant feature is that the resistivity is apparently insensitive to the nature of the material, in this instance silicon or germanium, and is determined mainly by the type of disorder present. This is an example of structure sensitivity which may be representative of the behavior of other dielectric films.

The optical properties of amorphous films generally show reasonable correspondence with the crystalline forms since they also depend primarily on nearest-neighbor interactions which are similar in both. The detailed picture of the structure of amorphous layers such as silicon dioxide, the so-called "silicon monoxide," and silicon nitride is not at all clear and there is very little concrete evidence on it. Silicon dioxide is more covalent in nature than silicon oxide which

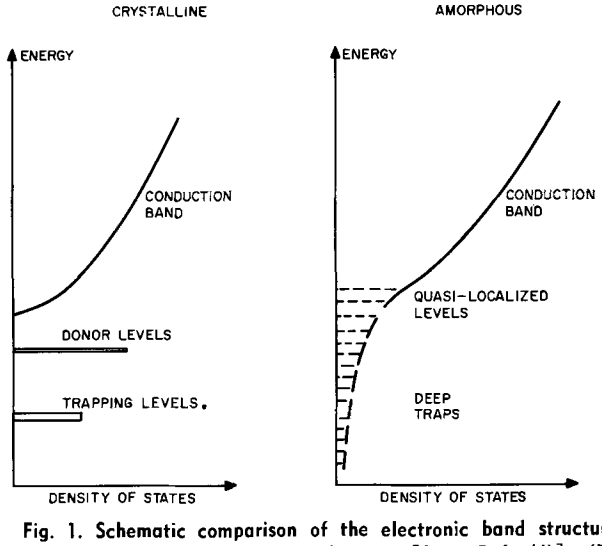

Fig. 1. Schematic comparison of the electronic band structures of crystalline and amorphous dielectrics [from Ref. (4)]. (Reprinted from *Thin Solid Films;* with the permission of Elsevier-Sequoia S.A., Lausanne, Switzerland.)

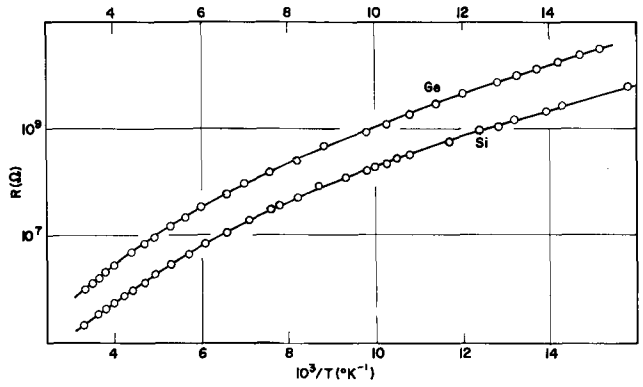

Fig. 2. Logarithm of resistance vs. reciprocal temperature for evaporated films of amorphous germanium and silicon [from Ref. (15)].

contains an appreciable ionic character in the bonding.

It may be said in general that the amorphous forms are less dense than the crystalline modification and they have a lower dielectric constant, at least in the absence of "doping" impurities (16-20).

Direct Current Conduction

In principle, any dielectric film should show an ohmic region of current-voltage characteristic at sufficiently low electric fields. In practice, most films other than those which are heavily "doped" or contaminated (*see* below) do not show this region because of very slow polarization phenomena at the contacts or in the bulk (29). Moreover, with the exception mentioned above, the ohmic region is normally characterized by high activation energies of the order of 1 ev (21) associated with ionic conduction and it is not discussed further in the present review.

At higher fields, the behavior depends to a large extent on temperature, and an example referring to evaporated silicon oxide is shown in Fig. 3, quoted from Servini and Jonscher (21). The dotted lines in the graph describe four regions. Region I is the ohmic region already mentioned. Region II gives linear graphs of log I *vs.* $V^{1/2}$, Fig. 3(b) corresponding to either Schottky or Poole-Frenkel emission (4) in which the current is given by

$$I = I_0 \exp\left[\frac{e}{kT}(\beta E^{1/2} - V_G)\right]$$

where E is the electric field, V_G is the ionization energy of the localized center (in P-F conduction) or the contact barrier height (in Schottky emission). The coefficient β is given by

$$\beta = (e/a\pi\epsilon_{0\epsilon})^{1/2}$$

where $\epsilon_{0\epsilon}$ is the high-frequency value of the dielectric permittivity and the coefficient $a = 1$ for Poole-Frenkel and $a = 4$ for Schottky mechanism.

Characteristics of this form have been obtained for a wide range of amorphous materials, frequently giving values of a between 1 and 4, and an extensive discussion of these mechanisms was given in Ref. (4). Some more recent results were reported for BN (22) and Si_3N_4 (19). It may be stated that, in the majority of known cases of amorphous materials, as distinct from thin crystalline films, the dominant mechanism in this range is some modification of bulk Poole-Frenkel electronic transport. It should be remembered that, in order to invoke the Schottky barrier emission mechanism, it is necessary to postulate that the bulk of the material offers negligible resistance so that the characteristic is barrier dominated up to the highest currents. This is seldom a plausible assumption in noncrystalline films of appreciable thickness, say in excess of 1000Å. The implication is, further, that the entire characteristic is electrode determined, down

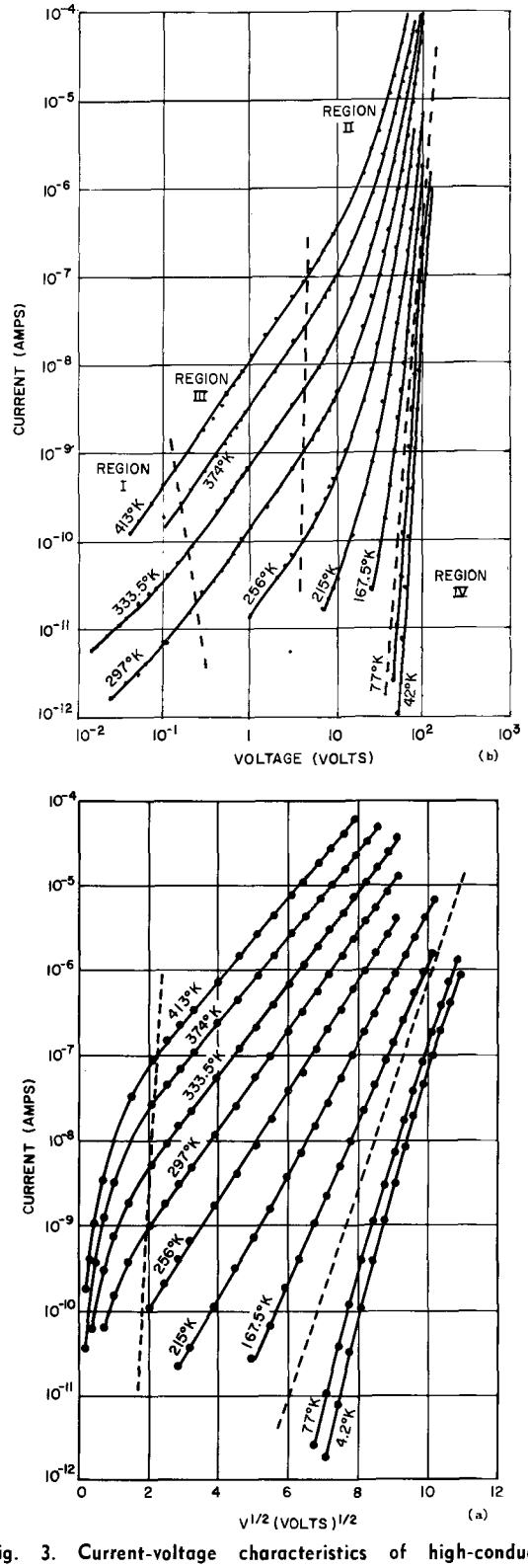

Fig. 3. Current-voltage characteristics of high-conductivity evaporated silicon "monoxide" at various temperatures, showing four regions of behavior. Film thickness 3800 Å/sec, pressure 1.5×10^{-5} Torr. Film area 0.4 mm². (a) log I — log V characteristics (b) log I — $V^{1/2}$ characteristics. [From Ref. (21).]

to the lowest currents. In this case, a useful check may be to try different metal electrodes with significantly different work functions.

The question of contacts to specimens showing bulk-limited Poole-Frenkel emission has been discussed in Ref. (4) and the point is merely repeated here that the available evidence suggests that no serious barrier limitation arises because electrons tunnel directly from the Fermi level of the metal into the localized

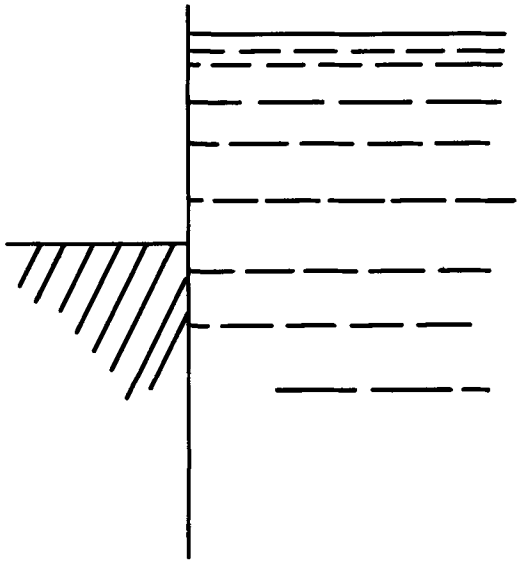

Fig. 4. Schematic diagram of a nonblocking contact between a metal and dielectric possessing a distribution of deep electronic levels [from Ref. (4)]. (Reprinted from *Thin Solid Films;* with the permission of Elsevier-Sequoia S.A., Lausanne, Switzerland.)

levels in the forbidden gap of the insulator and no activation over the contact barrier is involved, as shown in Fig. 4.

Region III of the characteristics shown in Fig. 3(a) is intermediate between regions I and II and is characterized by nonlinear V-I dependence, usually a power law $I \propto V^n$, with the exponent n in the range $1 < n < 2$. This region is strongly temperature dependent and may be due to some form of space charge limited flow. It should be pointed out, however, that it may be incorrect to apply directly to amorphous materials the concepts developed by Lampert (10) and others for crystalline insulators with traps.

An important aspect of d-c conduction which is not at present well understood is the mechanism dominating at low temperatures which has negligible temperature dependence and which is characterized by power-law dependence $I \propto V^n$, with large exponents n in excess of 5 and sometimes as high as 15. This power law corresponds to region IV in Fig. 3 and has already been discussed in Ref. (4). There are many examples of such characteristics in diverse amorphous films, for example SiO_x (21), Ge (23), TiO_2 (24). It may be stated that no other simple relation, exponential or otherwise, seems to fit the results quite so well as a high exponent power law. Figure 5 shows curves of current at constant voltage as a function of temperature for evaporated silicon oxide. It is seen that the current is independent of temperature up to approximately 20°K at lower voltages and up to 50°K at higher voltages. This mechanism, which is capable of passing currents as high as the Poole-Frenkel mechanism at much higher temperatures, is clearly related to some form of tunneling mechanism, and yet it differs from the familiar hopping mechanisms (4, 12, 25) which are thermally activated tunneling. It is suggested that the explanation may lie in tunneling between very closely spaced sites, for example nearest or next-nearest neighbor sites in the amorphous matrix. With their small separation, the energy difference due to either external or internal coulomb fields is sufficiently small to be accommodated by the inevitable "fuzziness" of the energy levels themselves so that no phonon collaboration need be involved, resulting in temperature-independent characteristics.

Mention may be made here of other power-law relations which are not necessarily temperature independent and may predominate at higher temperatures. Examples may be quoted of SiC (26), BN (22), and

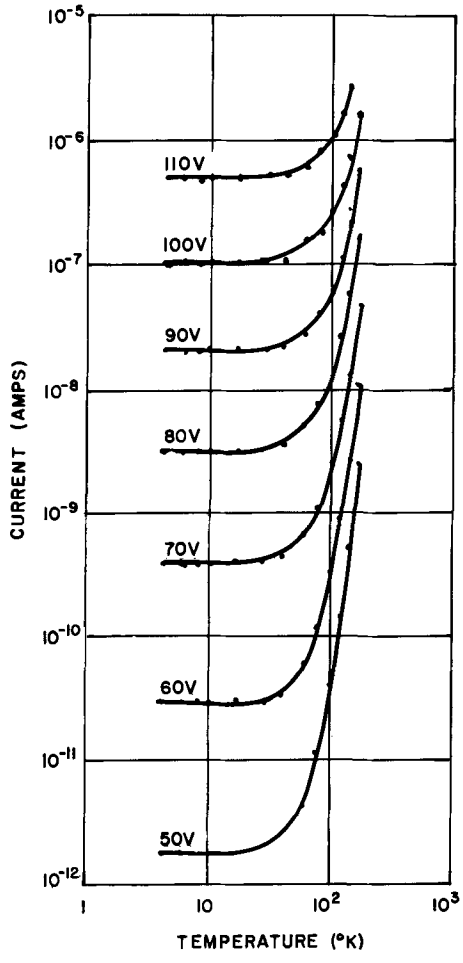

Fig. 5. The low-temperature part of the characteristics of Fig. 3, plotted as a function of temperature with voltage as a parameter and showing the constancy of current at low temperature [from Ref. (21)].

others, but it is not clear at this stage whether similar mechanisms apply there.

An interesting study of conduction in Nb-Nb_2O_5-Au structures produced by anodization of evaporated niobium was reported by Hickmott (27) who observed strong rectification and electroluminescence in the "forward" direction of current flow. His interpretation of the results is in terms of double injection into the insulator with space charge limited flow, with some conduction in impurity states. This is an example where concepts normally applicable to crystalline materials seem to fit the behavior of an amorphous film, although further results may be necessary before a firm judgment can be made of their validity.

The question may be asked to what extent is polaron transport responsible for conduction phenomena in dielectric films. Some speculation concerning the possibility of applying small polaron theory to conduction in glasses containing transition metal oxides was recently published by Schmid (28). Schmid points out the inadequacy of the present theory which deals mainly with ordered one-dimensional chains, while real glasses represent extremely disordered three-dimensional arrays. It is not proposed here to enter into detailed theoretical arguments, but it may be observed that the broad similarity of experimental results between amorphous polar and nonpolar (Ge,Si) materials suggests that polaron effects cannot dominate their behavior. The evidence in question relates in particular to voltage-current and conductivity-frequency dependence throughout the range of temperatures covered in the present paper.

In discussing the d-c conduction in dielectric films, it must be stressed that the essential criteria for the

predominance of electronic over ionic conduction must be the absence of long-term polarization and of mass transport effects.

Alternating-Current Conduction

Alternating-current measurements represent an important tool for probing the dynamic properties of a complex dielectric system with its relaxation times characteristic of the various processes of charge movement and dipole orientations. Available techniques cover a very wide frequency range, extending from below 10^{-3} Hz with the use of voltage step-function response methods, through a variety of a-c bridges, slotted line and microwave measurements up to 10^{11} Hz, with far infrared measurements becoming possible beyond that. The low frequency end of the spectrum gives information about slow, mainly ionic phenomena of both the bulk and interfacial type; they may also correspond to molecular rotations. Examples of such measurements on evaporated silicon oxide and anodized aluminum oxide were published recently by Argall and Jonscher (29) and they are discussed further here since they do not correspond to electronic phenomena. Characteristic features of this frequency region are the presence of pronounced peaks of loss tangent, a large dispersion of capacitance, and activation energies of the order of 1 ev typical of ionic phenomena.

A different behavior is found in evaporated silicon oxide and anodized aluminum oxide in the frequency range 10^2-10^6 Hz. Figure 6 shows the dependence of conductivity on frequency for a range of temperatures, while Fig. 7 shows the a-c conductivity plotted against reciprocal temperature for constant frequencies. The low-temperature activation energy is approximately 0.01 ev and is certainly of electronic origin. The high-frequency end shows a tendency to quadratic dependence of conductivity on frequency, a characteristic phenomenon observed in many other systems comprising highly disordered, amorphous, or glassy structures. Figure 8 gives the example of bulk polymeric CS_2 which is an "amorphous" substance lacking any long-range order (30). Resistivity and permittivity are plotted in the frequency range 10^2-5×10^{10} Hz. Conductivity shows three distinct regions: at frequencies below 10^6 Hz, conductivity increases rather less rapidly than proportionally to frequency and there is an activation energy of 0.15 ev. Beyond this frequency, there is a region of exact square-law dependence which appears to have a very small activation energy. The conductivity finally shows saturation at 10^9 Hz, which may be associated with a natural hopping frequency of the charge carriers. Somewhat similar frequency dependence has been found in some glasses (31) and also in transition metal oxides (32).

A common feature of all these mechanisms, showing a monotonic increase of conductivity with frequency with possible saturation at high frequencies, is their relatively weak temperature dependence. They have been interpreted (4, 29) in terms of electronic hopping motion, which corresponds to thermally assisted tunneling between discrete sites, as distinct from transport of effectively free carriers in the valence and conduction bands of conventional crystalline conductors, which shows a conductivity decreasing with frequency at sufficiently high frequencies.

It may be noted in this connection that the strong dependence of conductivity on frequency would normally be associated with electronic rather than ionic processes. This is so because the latter correspond to much lower natural hopping frequencies—of the order of 1 Hz or much less— and would therefore be saturated at radio and even audio-frequencies.

Thermally Stimulated Currents

The familiar voltage-current dependence at constant temperature, the $(I,V)_T$ characteristic, represents one means of characterizing the properties of a

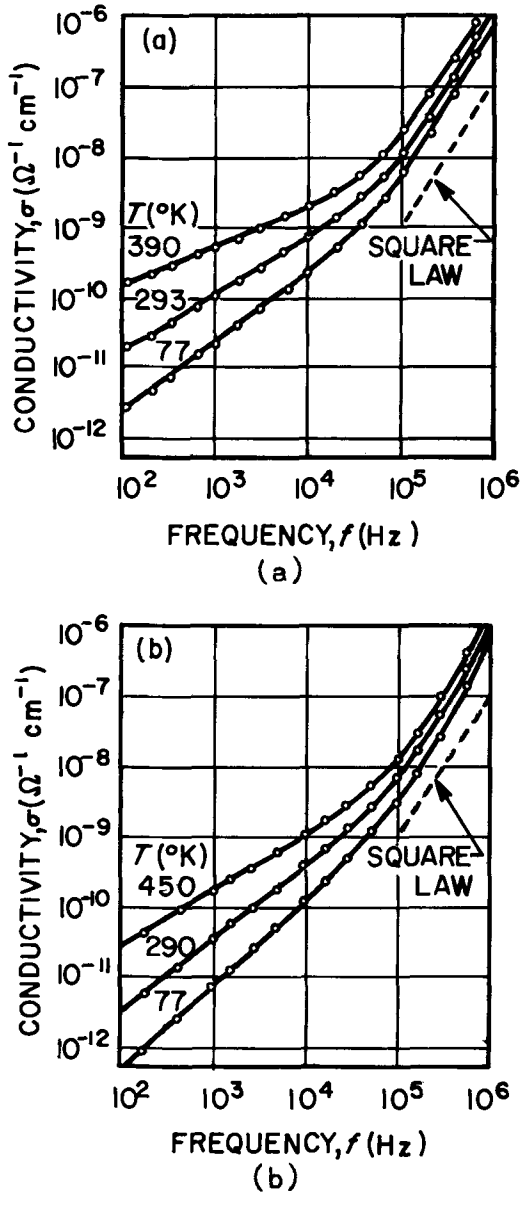

Fig. 6. Variation of a-c conductivity with frequency for (a) evaporated silicon oxide and (b) anodized aluminum oxide [from Ref. (29)]. (Reprinted from *Thin Solid Films;* with the permission of Elsevier-Sequoia S.A., Lausanne, Switzerland.)

conductor. A complementary characteristic which is particularly useful for dielectric and poorly conducting systems is the current-temperature characteristic at constant voltage, denoted as the $(I,T)_V$ characteristic. In nonconducting materials which have previously been excited from their thermal equilibrium condition by some external agency, this characteristic determines the thermal release of stored charge or polarization and is known as the method of thermally stimulated currents, in the case of photoconductors, and thermal glow curves in the case of phosphors (33-35). Prior excitation is an essential condition for obtaining thermally stimulated peaks, since without it one obtains the ordinary current-temperature characteristics at constant voltage, as for example in Fig. 5.

The application of this method to the thermally stimulated discharge of a capacitor previously charged by the application of a biasing voltage is not so well known, one account having come to our notice relating to thin layers of cadmium sulfide (36). One of the first experiments with silicon oxide and aluminum oxide films has been performed by Servini and Jonscher (21) and is described briefly here.

The method consists in applying a bias voltage V_b at some biasing temperature T_b and subsequently low-

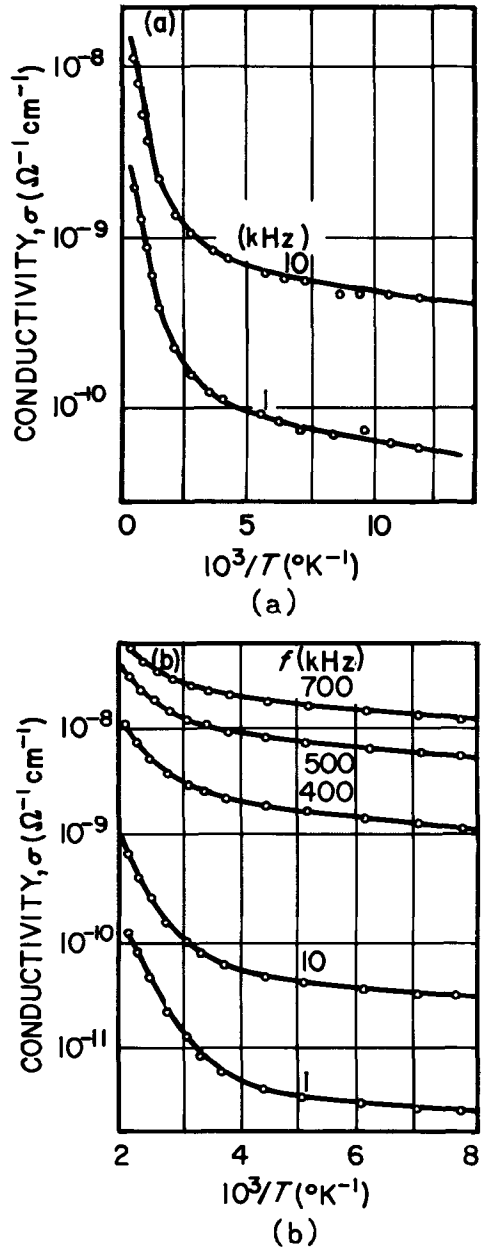

Fig. 7. Variation of a-c conductivity with reciprocal temperature for (a) silicon oxide and (b) aluminum oxide [from Ref. (29)]. (Reprinted from *Thin Solid Films;* with the permission of Elsevier-Sequoia S.A., Lausanne, Switzerland.)

ering the temperature, with the bias applied, to some suitable low temperature at which the current becomes negligibly small. A collecting voltage V_c, different from V_b, is then applied and the temperature is raised at a uniform rate $dT/dt = R$ and the current is recorded as a function of temperature. The response shows one or more peaks which correspond to the release of trapped charge or polarization. The relevant activation energies are related to the temperatures of the peak maxima and to the peak half-width. An example of the response with several peaks is shown in Fig. 9. Where two peaks are closely spaced on the temperature scale, the method of thermal quenching may be employed, as shown in Fig. 10, for peaks labeled H1 and H2. One of the characteristic features of thermally stimulated currents is the constant ratio of peak area A to heating rate R. The peaks reported here show a very good constancy of this ratio, confirming the correctness of the interpretation of their origin.

Altogether, five peaks have been identified in evaporated silicon oxide films. The one most easily ob-

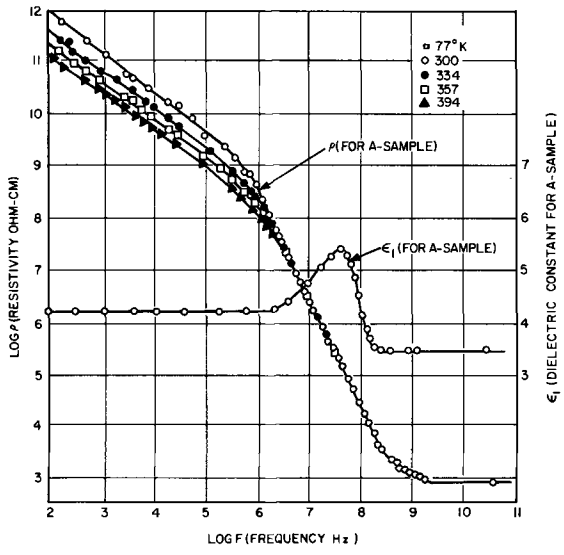

Fig. 8. Dielectric properties as a function of frequency of non-crystalline polymeric CS_2 showing resistivity and dielectric constant [from Ref. (30)].

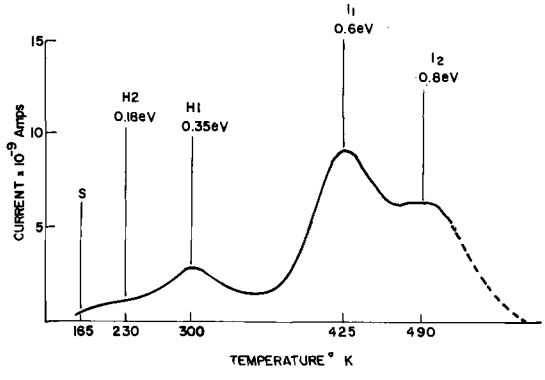

Fig. 9. Five thermally stimulated peaks observed in silicon oxide, showing their approximate positions in energy [from Ref. (21)].

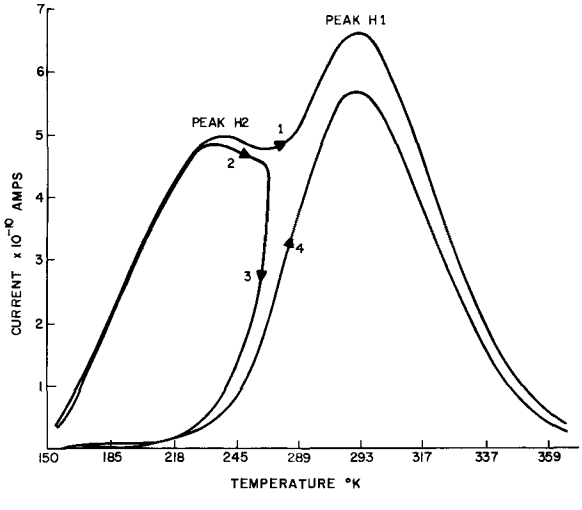

Fig. 10. Thermal quenching of two closely spaced peaks H1 and H2. Curve 1 gives a normal heating run. Curve 2 shows heating only up to the trough between the peaks, followed by cooling to low temperature (curve 3), and immediately reheating (curve 4) which produces peak H1 unencumbered by the tail of peak H2 [from Ref. (21)].

servable is labeled H1 and is obtained when films are cooled from room temperature or slightly lower with a moderate bias. Its area increases linearly with bias voltage and the charge involved is always much higher

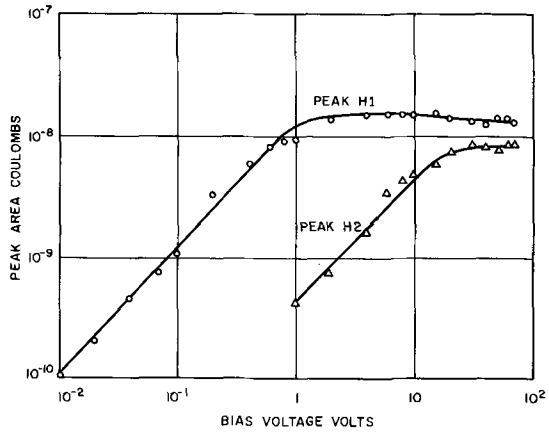

Fig. 11. The dependence of bias voltage of the area of peaks H1 and H2, expressed in coulombs, showing delayed onset of the lower energy peak H2 and eventual saturation of both peaks at high bias voltages [from Ref. (21)].

than that corresponding to the geometrical capacitance of the film. At sufficiently high bias voltages, corresponding to the onset of the Poole-Frenkel regime (region II), peak H1 saturates and a smaller peak H_2 appears. This peak has a lower activation energy than peak H1. The dependence of the areas of the two peaks on the biasing voltage is shown in Fig. 11.

At low biasing temperatures, of the order of 130°K, and high biasing voltages, a low-temperature, low-energy peak is observed, labeled S1. At high biasing temperatures, in excess of 330°K, two more peaks have been observed, labeled I1 and I2.

The interpretation of these results given by Servini and Jonscher is briefly as follows. Peak H1, the energy of which is 0.35 ev, corresponds to charge transfer between relatively widely spaced pairs of centers, *i.e.* a form of thermally assisted hopping. It is suggested that these are the same centers which are responsible for the d-c Poole-Frenkel process which shows an activation energy of 0.45-0.6 ev, when extrapolated to zero field. The lower value of the energy of peak H1 may be understood if one assumes that the peak arises from transitions between relatively closely spaced pairs of centers in which the barrier is lowered by Coulomb interaction, while the Poole-Frenkel emission occurs into relatively more distant centers against the full height of the barrier. Peak H2 is found to correspond to a spread of energies from 0.2 ev downward and is considered to be due to much more closely spaced centers than peak H1. It may be identified with the mechanism responsible for a-c conductivity reported by Argall and Jonscher (29).

Peak S1 is shown to be due to some form of injected space charge, its activation energy being distributed from probably 0.1 ev downward. All these peaks appear, thus, to be of electronic origin.

Peaks I1 and I2 have activation energies of 0.6 and 0.8 ev, respectively, and are clearly identified with bulk and interfacial ionic polarization mechanisms reported by Argall and Jonscher (29).

It is clear that further work on thermally stimulated peaks in a wider variety of dielectric films may lead to better elucidation of the mechanisms involved in the conduction processes.

Impurity-Induced Conductivity

In the case of crystalline semiconductors and insulators, impurity atoms and lattice defects of density N may act as relatively shallow donor and acceptor levels which at sufficiently low temperatures produce free electrons or holes in numbers n proportional to the square root of N

$$n \propto N^{1/2} \exp(-\epsilon_d/2kT)$$

where ϵ_d is the activation energy of the centers. At higher temperatures, such that $\epsilon_d < kT$, saturation may be reached with

$$n \approx N$$

A crystal lattice, however, has an upper limit to the solubility of defects, which is of the order of 10^{20} cm^{-3}, or 0.1 atomic per cent. Beyond this limit, the centers cease to be electrically active by forming a separate phase precipitating in the lattice.

The situation is rather different in an amorphous solid for two main reasons. First, the generally more loose structure of an amorphous material implies greater ability to accommodate impurities to the extent of several atomic per cent without necessarily losing the basic features of the host solid, for example the optical absorption spectrum. Second, however, the electrical effectiveness of defects is much reduced since, even if they did tend to produce free carriers, these are likely to be trapped in the deep levels present in the forbidden gap due to the disorder, Fig. 1. This point was made by Gubanov (11), among others, and is borne out by experimental evidence.

Given a sufficiently high density of impurities, however, the conductivity is found to increase, although as yet there is little quantitative information about this effect. Hu and Gregor (20) report an increase of the conductivity of amorphous silicon nitride films reactively sputtered in argon-nitrogen mixtures, with decreasing percentage of nitrogen in the gas. They attribute this to a dispersed silicon phase in the films. Walley (15) reported results with silicon and germanium films which may be interpreted in somewhat similar terms. Figure 12 shows his graph of the resistivity of silicon and germanium films *vs.* evaporation rate. At relatively fast deposition rates, the resistivity is independent of rate and hence, presumably, of the amount of oxygen included in the film. At sufficiently low rates, however, the resistivity increases rapidly until it reaches a value typical of silicon oxide. This end of the graph may be interpreted, therefore, as a contamination or "doping" of silicon oxide by silicon, with the resulting increase of conductivity. Germanium is less sensitive because of its lower oxygen affinity but the effect is qualitatively similar.

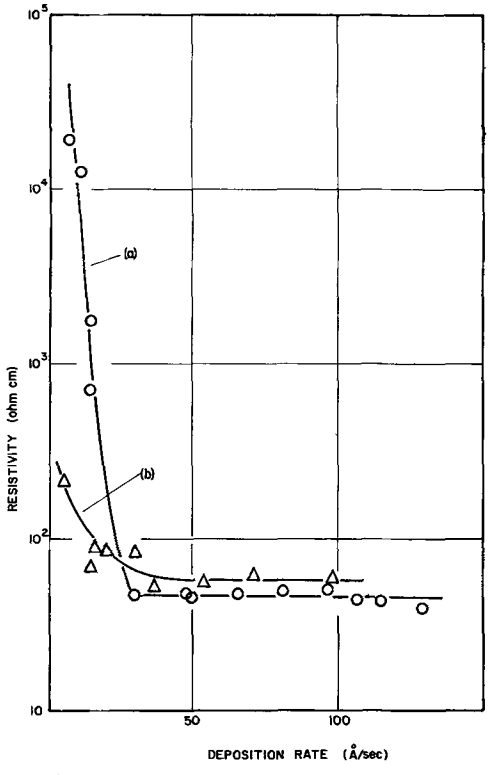

Fig. 12. The resistivity of evaporated amorphous films of silicon (a) and germanium (b) as a function of the deposition rate [from Ref. (15)].

The extreme case of highly impure dielectrics obtained by coevaporation of a metal such as chromium or gold and a dielectric such as silicon oxide are the so-called cermets which usually consist mostly of metal with up to, say, 40% of the dielectric. Relatively little quantitative information is available about the physical properties and mechanisms determining the conductivity in cermets (37), which is perhaps understandable in view of the very complex nature of these materials and also in view of the highly empirical and objective approach to their production (38-40).

Detailed work on the properties of silicon oxide coevaporated with copper and containing between 0 and 60% Cu shows not only an increase of conductivity by several orders of magnitude, but also the onset of ohmic electronic conduction at room temperature and a distinct lowering of the activation energy for Poole-Frenkel conduction (41).

Photoelectric Phenomena

In the case of crystalline conductors, especially those possessing relatively high resistivity, photoelectric phenomena offer valuable insight into the physical properties of the material, such as the mechanism of interaction with radiation and the kinetics of recombination processes. In addition, photoelectric effects at interfaces provide useful information about the barrier heights at contacts. Similar considerations apply to amorphous dielectric materials in the form of thin films, provided that due allowance is made for their structure. In particular, it is very unlikely that free electron-hole pairs should survive for anything like a sufficient length of time to give rise to ambipolar effects. Furthermore, transient measurements of rise and decay of photocurrent with rectangular light pulse excitation, which represent a most useful means of measuring the characteristic lifetimes in crystalline materials, may have limited application in view of the often long dielectric relaxation times.

The response of a dielectric film to illumination through a semitransparent top electrode may be due to one of three principal causes: photoinjection of carriers from one or both electrodes, photoconductivity due to excitation of carriers within the film itself, and spurious thermal effects due to heating by radiation. The last one represents a nontrivial problem and special experimental precautions are necessary to insure that it is negligible or properly allowed for.

Photoinjection from the electrodes was studied mainly in very thin films, of the order of 100Å, by Nelson and Anderson (42), Shepard (43), Schuermeyer (44), and Mead, Snow, and Deal (45), and in thicker SiO films by Hartman, Blair, and Bauer (46). These measurements give information about the height and shape of the potential barrier between the metal electrodes and the film. Photoconduction measurements by Ullman (47) on sputtered tantalum oxide films in the thickness range 700-7600Å were interpreted in terms of a single trap level of depth 0.25 ev. The presence in an amorphous film of such a clearly defined trapping level may be surprising, but it is confirmed in the case of silicon oxide by the results of Servini and Jonscher (21) already described above.

Switching in Dielectric Films

Many examples of so-called "switching" phenomena have been reported in the literature and many more are known by private contacts between individuals engaged in the study of this rather complex subject. Switching in this context is defined as a more or less controlled and reversible transition between two or more conducting states differing appreciably in resistance, with the proviso that one or both states may exhibit nonlinear voltage-current characteristics.

The whole subject has hardly yet reached a stage where detailed models may be put forward with any confidence and reproducibility leaves a good deal to be desired. The present discussion is therefore necessarily restricted to generalities and in the first place an attempt will be made to classify the rather diverse phenomena that are being referred to as switching.

It is felt that it may be helpful to distinguish between switching in definitely crystalline materials, on the one hand, and in amorphous and glassy materials, on the other. A variety of mechanisms have been proposed for the explanation of switching in the former (48), in particular double injection from end electrodes (10), avalanche injection (49), avalanche multiplication leading to a change in the scattering mechanism (50), more recently acousto-electric interaction in piezoelectric materials (51), and avalanche multiplication involving transit time effects (52). Some of these mechanisms are likewise being invoked in the case of glassy and amorphous materials, but the situation there is considerably more complex.

In general, in switching literature one distinguishes between current-controlled and voltage-controlled negative resistance, Fig. 13. This distinction is certainly helpful in those cases where the negative resistance itself is accessible and where no "memory" effects are involved. If memory is present, Fig. 14, then the distinction loses its significance since either branch may be traversed from the origin and it is not obvious which mechanism applies.

The presence of memory implies that some permanent changes take place in the material so that the last state of the device is preserved after the removal

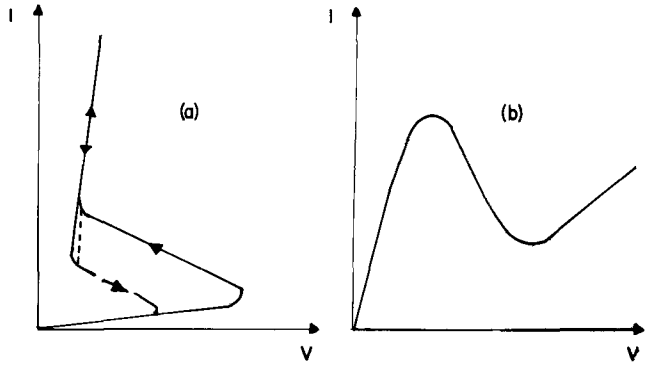

Fig. 13. Current-controlled negative resistance (a) and voltage-controlled negative resistance (b). A possible form of hysteresis is shown.

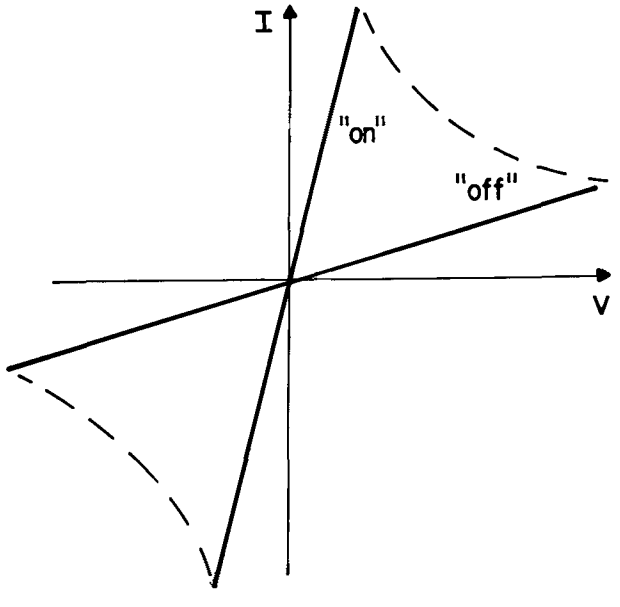

Fig. 14. Bistable switch with "memory"—the switch remains in either state when the current is reduced to zero and is subsequently increased again with the same or opposite polarity.

of bias. This normally means structural changes, although long-term trapping phenomena are sometimes mentioned as possible. Structural changes may mean, for example, localized crystallization in a noncrystalline matrix, transformation from one crystalline phase to another, or solid-state diffusion of atoms or ions. In the extreme case, it could mean localized melting of the material. The metal-insulator transition proposed by Mott (12) could fall in this category.

Switching was reported in semiconducting glasses by Pearson *et al.* (53) and Dewald *et al.* (54). In addition to fast reversible switching, these authors also describe the memory function which these devices could perform and which requires no holding voltage in either the "off" or "on" states. It was proposed that the effects could be explained in terms of a transformation of the glass to filaments of crystalline phases having high conductivity. This view was also expressed by Eaton (55). More recently, switching was also observed by Ovshinsky and led to the development of two devices, the Ovonic Threshold Switch and the Ovonic Memory Switch (56). The former is explained in terms of an increase of mobility, the latter by a transition to crystalline state in localized filaments.

Detailed studies of reversible memory switching in $CuO:P_2O_5$ glasses by Drake, Scanlan, and Engel (57) led to a model involving two valence states of the Cu ions which occupy differently coordinated sites in the glass. The high-resistance state is due to hopping between these sites, while the low-resistance state is the result of a structural transformation along a continuous path in the glass.

Argall (61) reported fast bistable switching in films of SiO_x and Al_2O_3. Chopra (62) postulated avalanche multiplication with space charge injection to explain current-controlled negative resistance which he found in films of anodized oxides of Nb, Ta, and Ti. A detailed account of switching in anodized TiO, showing three reproducible characteristics, is given by Argall (63), Fig. 15.

There is some discussion, mainly unpublished as yet, as to whether these and other switching phenomena observed in thin films are of a filamentary rather than distributed nature (64). It is suggested that crystalline filaments may grow in the glassy matrix under the influence of the intense electric field, particularly in the presence of some "nucleating" impurities. When once the filaments have bridged the film between the electrodes, enhanced current may flow, and memory persists, until a sufficiently high current causes thermal destruction of the filaments. It is rather early yet to pronounce definitely on the merits of this type of mechanism, although it is likely to account at least partially for some of the observed phenomena.

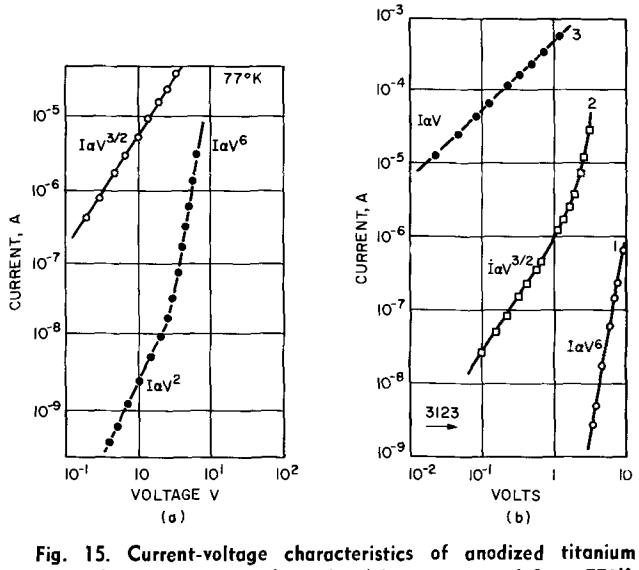

Fig. 15. Current-voltage characteristics of anodized titanium oxide with aluminum top electrode: (a) states 1 and 2 at 77°K, (b) states 1, 2, and 3 of a different sample at 300°K [from Ref. (61)]. (Reprinted from *Solid-State Electronics;* with the permission of Elsevier-Sequoia S.A., Lausanne, Switzerland.)

The principal shortcoming of all dielectric switches is their two-terminal nature which means the absence of a control or gate electrode. It may be that some mechanisms may be found possessing sufficient light sensitivity to be capable of being turned "on" by means of light. Purely two-terminal switches, especially those possessing memory, would be very useful if they could be made reliably in large numbers per unit area.

Conclusions

The experimental evidence and the theoretical considerations presented above lead to the conclusion that electronic conduction in dielectric films is responsible for a wide range of phenomena, even in materials which are traditionally considered to be ionic in nature. In particular, electronic conduction is likely to dominate the behavior at high electric fields, whether through Schottky or Poole-Frenkel mechanisms, at very low temperatures where the ionic motion is virtually "frozen out," and at frequencies in excess of the audio range, where the ions cannot move sufficiently rapidly. By contrast, low-frequency, low-field, and high-temperature transport is likely to be dominated by ionic motion with its higher activation energies and lower characteristic frequencies. Exceptions to this might be found in sufficiently heavily "doped" materials, so that electronic motion predominates even under these conditions. Combinations of ionic motion and electronic transport are possible, especially in phenomena such as switching, where the movement of ions may serve the purpose of modifying the electronic transport.

Our present-day knowledge of the detailed mechanisms of electronic conduction in dielectric films is rather scant. Experimental study of specific mechanisms, such as Poole-Frenkel transport, a-c conductivity, and thermally stimulated currents, may give information about the activation energies but not necessarily about the detailed nature of the centers which are responsible for conduction. More systematic study will be required of well-chosen specimens of dielectric films by a variety of complementary methods before a complete picture can be built up.

It is possible to state that d-c conduction is strongly structure sensitive and it may differ as much between samples of nominally the same material prepared by different methods, as between samples of different materials. Relatively large additions of foreign impurities or large departures from nominal composition are required to change significantly the level of d-c conduction. A-C conductivity may become high at sufficiently high frequencies. The dominant mechanism of a-c conduction is usually different from that responsible for d-c transport, as may be seen from different activation energies. Although both may well be interpreted as due to some form of hopping, little can be said at this stage about the nature of the hopping centers, and, in particular, about their correlation with structure.

Photoelectric studies appear to offer a rewarding field for further work and so does the effect of impurities. Switching is likely to remain a "happy hunting ground" for people with a strong device motivation and with confidence in their ability to conquer the forces of molecular chaos.

Acknowledgments

The author is indebted to his colleagues, especially A. Ansari, W. S. Chan, R. J. Jeacock, P. J. O'Sullivan, A. Servini, and P. A. Walley, for helpful discussions and permission to quote results. The work reported

was done partly under Research Contracts with the Science Research Council.

Manuscript submitted Nov. 15, 1968; revised manuscript received Jan. 13, 1969. This paper was presented at the Montreal Meeting, Oct. 6-11, 1968, as Paper 455.

Any discussion of this paper will appear in a Discussion Section to be published in the December 1969 JOURNAL.

REFERENCES

1. S. R. Pollack, Paper 457 presented at Electrochem. Soc. Meeting, Boston, Mass., May 5-9, 1968
2. R. M. Hill, *Thin Solid Films*, **1**, 39 (1967).
3. R. H. Doremus, *This Journal*, **115**, 181 (1968).
4. A. K. Jonscher, *Thin Solid Films*, **1**, 213 (1967).
5. A. G. Revesz, *Phys. Stat. Solidi*, **24**, 115 (1967).
6. C. A. Mead, *Proc. Intern. Symp. Clausthal-Goettingen 1965*. R. Niedermeyer and H. Meyer, Editors, "Basic Problems in Thin Film Physics," Vandenhoeck and Ruprecht, Goettingen (1966).
7. T. L. Chu, C. H. Lee, and G. A. Gruber, *This Journal*, **114**, 717 (1967).
8. R. A. Smith, "Semiconductors," Cambridge University Press (1961).
9. A. K. Jonscher, "Solid Semiconductors," Routledge and Kegan Paul, London (1965).
10. M. A. Lampert, *Rept. Progr. Phys.*, **27**, 329 (1964).
11. A. I. Gubanov, "Quantum Electron Theory of Amorphous Conductors," Consultants Bureau, New York (1965).
12. N. F. Mott, *Advan. Phys.*, **16**, 49 (1967).
13. M. I. Klinger, *Rept. Progr. Phys.*, **31**, Part 1, 225 (1968).
14. P. A. Walley and A. K. Jonscher, *Thin Solid Films*, **1**, 367 (1967/1968).
15. P. A. Walley, *ibid.*, **2**, 327 (1968).
16. V. Y. Doo, D. R. Kerr, and D. R. Nichols, *This Journal*, **115**, 61 (1968).
17. S. Yoshioka and S. Takayanagi, *ibid.*, **114**, 962 (1967).
18. J. Oroshnik and J. Kraitchman, *ibid.*, **115**, 649 (1968).
19. B. E. Deal, P. J. Fleming, and P. L. Castro, *ibid.*, **115**, 300 (1968).
20. S. M. Hu and L. V. Gregor, *ibid.*, **114**, 826 (1967).
21. A. Servini and A. K. Jonscher, *Thin Solid Films*, **3** (1969).
22. M. J. Rand and J. F. Roberts, *This Journal*, **115**, 423 (1968).
23. P. A. Walley, Private communication.
24. J. Maserjian and C. A. Mead, *J. Phys. Chem. Solids*, **28**, 1971 (1967).
25. M. Pollak and T. H. Geballe, *Phys. Rev.*, **122**, 1742 (1960).
26. T. E. Hartman, J. C. Blair, and C. A. Mead, *Thin Solid Films*, **2**, 79 (1968).
27. T. W. Hickmott, *J. Appl. Phys.*, **37**, 4380 (1966).
28. A. P. Schmid, *ibid.*, **39**, 3140 (1968).
29. F. Argall and A. K. Jonscher, *Thin Solid Films*, **2**, 185 (1968).
30. W. S. Chan and A. K. Jonscher, *Phys. Stat. Sol.*, **32**, (1969).
31. A. D. Yoffe and R. F. Shaw, To be published.
32. S. Kobashima and T. Kawakubo, *J. Phys. Sci. Japan*, **24**, 493 (1968).
33. K. H. Nicholas and J. Woods, *Brit. J. Appl. Phys.*, **15**, 783 (1964).
34. G. F. J. Garlick and A. F. Gibson, *Proc. Phys. Soc.*, **60**, 574 (1948).
35. J. T. Randall and M. H. F. Wilkins, *Proc. Roy. Soc. (London)*, **A184**, 390 (1945).
36. A. G. Zhdan, V. B. Sandomirskii, and A. D. Ozheredov, *Soviet Physics-Semiconductors*, **2**, 7 (1968).
37. D. E. Lood, *J. Appl. Phys.*, **38**, 5087 (1967).
38. R. Glang, R. Holmwood, and L. I. Maissel, *Thin Solid Films*, **1**, 151 (1967).
39. R. Glang and P. M. Schaible, *ibid.*, **1**, 309 (1967/1968).
40. K. E. G. Pitt, *ibid.*, **1**, 173 (1967).
41. P. J. O'Sullivan, Private communication.
42. O. L. Nelson and D. S. Anderson, *J. Appl. Phys.*, **37**, 77 (1966).
43. K. W. Shepard, *ibid.*, **36**, 796 (1965).
44. F. L. Schuermeyer, *ibid.*, **37**, 1998 (1966).
45. C. A. Mead, E. H. Snow, and B. E. Deal, *Appl. Phys. Letters*, **9**, 53 (1966).
46. T. E. Hartman, J. C. Blair, and R. Bauer, *J. Appl. Phys.*, **37**, 2468 (1966).
47. F. G. Ullman, *J. Phys. Chem. Solids*, **28**, 279 (1967).
48. A. K. Jonscher, *Progress in Semiconductors*, **6**, 143 (1962).
49. A. F. Gibson and J. R. Morgan, *Solid-State Electron.*, **1**, 59 (1960).
50. A. L. McWhorter, *Proc. Intern. Conf. Semicond. Phys., Prague*, **1960**, 134 (1961).
51. J. D. Maines and E. G. S. Paige, *Electronics Letters*, **4**, 450 (1968).
52. D. Rees, *ibid.*, **4**, 532 (1968).
53. A. D. Pearson, W. R. Northover, J. F. Dewald, and W. F. Peck, Jr., "Advances in Glass Technology," p. 357 (1962) and *ibid.*, Part 2, p. 144 (1963), Plenum Press, New York.
54. J. F. Dewald, A. D. Pearson, W. R. Northover, and W. F. Peck, Jr., *This Journal*, **109**, 2438 (1962).
55. D. L. Eaton, *J. Am. Ceram. Soc.*, **47**, 554 (1964).
56. S. R. Ovshinsky, *Phys. Rev. Letters*, **21**, 1450 (1968).
57. C. F. Drake, I. F. Scanlan, and A. Engel, To be published.
58. T. W. Hickmott, *J. Appl. Phys.*, **35**, 2118 (1964).
59. T. W. Hickmott, *ibid.*, **36**, 1885 (1965).
60. J. G. Simmons and R. Verderber, *Proc. Roy. Soc. (London)*, **301**, 77 (1967).
61. F. Argall, *Electronics Letters*, **2**, 282 (1966).
62. K. L. Chopra, *J. Appl. Phys.*, **36**, 184 (1965).
63. F. Argall, *Solid-State Electron.*, **11**, 535 (1968).
64. G. Dearnalay, *Phys. Letters*, **25A**, 760 (1967).

JOURNAL OF THE ELECTROCHEMICAL SOCIETY

REVIEWS AND NEWS

JULY 1969

The Role of the Scientific Community in the Scientific Age[1]

Ivor E. Campbell*

The present age has within recent years been called in succession, the Scientific Age, the Atomic Age, and the Space Age. It might well be called the Age of Unrest.

Within the past twelve months we have seen increasing demands in the ranks of our sister societies for society involvement in matters of social concern. A concerted effort has taken place and is continuing in one major scientific society to develop a division that would, in effect, become a political action division.

A major engineering school was the focal point for a "Research Strike" called in support of protest against involvement of universities in certain government programs.

A major chemical company—one of the patron members of this Society—was the victim of vandalism by a group protesting the company's involvement in preparation of materials for the Department of Defense.

Unfortunately these are but a few of many examples that could be cited as signs of the times.

Dissent and unrest are widespread. Institutions and what is commonly referred to as "The Establishment" are being challenged on all fronts. It may be an oversimplification but I submit that this is in large measure due to man's failure to learn to live with himself.

Mutual respect and understanding have always been moral and spiritual goals. Today, they become a necessity for continuation of society itself. The unrest of today is grounded largely in the realization that man may not be able to cope with his own knowledge.

In a recent article, Dean Marlow of Catholic University cautioned that technology is a two-edged sword and said "our society cannot exist without it", pointing out that the North American continent, "which now supports a sophisticated life for a quarter of a billion inhabitants, scarcely supported a million people at a subsistence level before the advent of Western technology." He went on to say, "Yet we do not yet know whether or not we can continue to exist with it."

Is it not paradoxical that science and technology which have made the "Good Life" possible must now face the challenge of those who would blame science and technology both for man's failure to distribute more broadly the fruits of science and technology and for man's tendency to exploit more fully the destructive potential in scientific discoveries than the constructive?

Science, like "The Establishment", is now being challenged from diverse directions with increasing vigor. Some would even equate knowledge and evil.

However, as Glenn Seaborg has pointed out, "Knowledge is born without moral properties. It is man who applies it according to his acquired patterns of behavior. Man, not knowledge, is the cause of violence."

Further, as Professor William Kiefer stated, "Another myth that needs exploding is that some kinds of knowledge are bad, and others are good. Even worse is the idea that the search for knowledge can be good or bad depending on the use to which knowledge is put."

James Bryant Conant provided a thought-provoking and positive approach to challenges of the ultimate value of the quest for knowledge when he said, "There never has been a discovery of physical science that has not strengthened the hand of the Good Samaritan."

Those of us concerned with science and technology might be inclined to regard the challenge as preposterous. But the fact that such eminent scientists and educators as Conant and Seaborg have felt constrained to address themselves to it is evidence of its seriousness.

It is well to recognize that a major share of our total scientific effort today is based on government support. James Shannon puts the matter in focus when he asserts, "The ultimate patron of science is the public" . . . and . . . "they have not been given an understanding of science that can serve as a base for its continued support and evolution."

He calls upon the scientific community to devise means of fostering a broader understanding of the revolutionary technological forces that can be unleashed by a vigorous science for the betterment of society.

Science has, in the past, been to a large degree isolated, or at least insulated from the real world. Public attitudes reflected an unquestioning faith in the ultimate good of science. This has now changed—"The Establishment" of science is being challenged by its patrons—The Public.

In analyzing this matter, Dr. Kenneth Pitzer focused attention on certain facts of life for those interested in factors surrounding support of research. The following excerpts are germane to our consideration here. "The period of increasing, and largely unquestioning, support has ended." "In leveling off appropriations for research, business leaders and congressmen are now evaluating science more critically than previously by the same criteria they use in making decisions about

* Electrochemical Society Active Member.

[1] The Electrochemical Society Presidential Address, delivered at the New York Meeting of the Society, May 6, 1969.

other matters." "Now we are faced with the collapse of the assumption that more science is unquestionably desirable."

He concluded "We must be more explicit about the contributions of scientific research to particular national goals. We must discuss recent research which has been valuable as well as the degree of relevance of various basic fields to practical problems."

He went on to caution that esoteric subjects should not be avoided but asserted that the desire of more and more people to work in a given field is no longer an adequate reason for indefinite expansion of Federal support and concluded that more convincing criteria must be developed to justify the magnitude of effort in each discipline.

Aside from the number of respected scientists and engineers who have expressed their concern as to the role of the scientific community in the scientific age—more concrete evidence that the hour is here for concern has developed. A bill was recently introduced in the United States Senate by Senator Muskie—to establish a Senate Select Committee on Technology and The Human Environment.

Those testifying at the preliminary hearings were uniformly in favor of the bill. And it is undoubtedly a step in the right direction. However, a comment by the Senator is interesting, to say the least. He said, "We don't know what our policies of controlling science and technology should be."

The Senator may not have meant quite what a literal interpretation would imply—but there are increasing numbers who would. This may well be a forecast of things to come, with science and technology being subject to more criticism and control from without.

This is not to deny that criticism and control are not only justifiable but even essential in certain areas.

Referring again to Dr. Pitzer's review, it was pointed out that most major new technologies are already influenced or regulated by the government in some way. Notable examples are drugs, pesticides, nuclear energy, television, air transportation, pollution control, and oil drilling. Quoting Dr. Pitzer, "Thus it would not necessarily extend the range of government control to ask that this influence on, or regulation of new technologies be more sensitive to humanistic factors."

However, the pendulum never stops at the happy medium in human affairs, and the probability of controls and directions that are other than optimum is very real.

It is the responsibility of the scientific community to see that control is from an enlightened base and to become involved as individuals in the political and social implications of science and technology.

Harvard's Harvey Brooks stated at the Senate hearings, "Our problem is to discipline our mastery of nature and society so that man can live in harmony both with nature and his own human nature." He went on to say, "This means not less, but more and more sophisticated, science and technology."

However, the matter of support for science and technology is not unilateral. Since even the federal government does not have unlimited resources, it becomes a matter of choice.

The demands of society clearly exceed its presently available resources. In the establishment of priorities it is to be hoped that the selection will be based on enlightened self interest of the public. Former President Kennedy pointed out, "Scientists alone can establish the objectives of their research, but society, in extending support to science, must take account of its own needs."

The basic question is as Frederick Lindvall put it, "How should resources be allocated between science and other activities and needs of society? And within science, pure and applied, how should resources be allocated?"

I do not propose to speak to this subject, let alone to offer answers. My purpose here is to point out some of the searching questions that are being asked by the public, by public officials, and by their advisers and to discuss the importance of establishing better communication between the scientific community of which we are a part and other elements of our society for our mutual benefit and, what is more to the point, for the benefit of society as a whole.

Technology today has "Bad Press" in certain areas. Former President Johnson cautioned, "An aggrieved public does not draw the fine line between good science and bad technology. In a democratic society, the public attitude toward science must always be a real concern of the scientific community. If that attitude is to be favorable, science must be prepared to play its part in correcting the flaw in our environment."

A famous scientist once said, "Just as middle ages man could not ignore the church, nor renaissance man the arts, nor eighteenth century man political thought, so modern man cannot ignore science." Today, modern man is not ignoring science, and now science cannot ignore modern man.

The majority of our college students today are non-science majors, and they as voters, business men, administrators, and legislators will have much to say as to the direction of science and technology. If they are to have an understanding and appreciation of the role science has in the modern culture, the scientific community must abandon its stand-off posture.

The scientific community, being best prepared to sense the impact of its advances, should become more deeply involved as individuals in community, national and international affairs, which are so dramatically affected by scientific advance.

Please note, I said as individuals. There are those who disagree, but I am personally convinced that there are valid and sufficient reasons for the scientific societies to address themselves to their stated objectives and to stay out political affairs.

As individuals, the contrary is true, and there are compelling reasons for involvement.

Having presented the case before the argument, let us go back and consider a few of those areas of scientific advance which have a profound and serious impact on our society.

The weapons area is well publicized and perhaps more widely understood, or at least of more general concern than other areas, and will be noted only in passing—nuclear weapons, guided missiles, and homing devices, particularly in combination, present awesome capabilities of self-destruction and have had a profound impact on our thinking and action in international areas.

The weapons arsenal makes massive research efforts geared to defense mandatory—thereby affecting in theory, at least, our efforts in other areas. I say in theory, because I am not personally convinced that we would be willing to divert equivalent efforts to domestic problems. We have not so far addressed ourselves to such problems as medical research, hospitals, schools, slum clearance, pollution control, highways, etc. with the same intensity and with the same high level of funding that we have granted, however reluctantly, to defense needs.

Let us pass on, nevertheless, to other areas perhaps less commonly recognized by the man on the street.

Medical science has not in reality succeeded, as yet, in affecting the life expectancy significantly of those who escape accident or major illnesses, i.e., the Biblical three score and ten is still not too far off. It has, however, sharply curtailed the death rate at birth and in infancy, particularly in underdeveloped lands, and thereby played a major role in the population explosion with its attendant problems. One expert in the area of population growth pointed out in 1957 that in 20 years the population of India alone could equal that of the entire world at that time if the death rate were reduced to that in the United States and the birth rate remained at its current level. Conceding that the birth rate has in the past declined as countries have become more prosperous, most recent projections of the world-wide population trend indicate that inherent compensation factors will not solve the problems resulting from the mushrooming population.

The population explosion presents major areas for scientific and engineering development—improved sources of food, both natural and synthetic, will be required, areas not currently suitable for habitation must be reclaimed, water supplies must be improved, improved means of waste disposal must be developed, and pollution problems must be attacked more

vigorously. It seems incredible to consider the necessity of going to great lengths to reclaim waste land, while continuing to render available areas less and less habitable.

In the past, man has abandoned areas which he has rendered desolate and moved on to more fertile fields. In the future, the point will be reached where this is no longer possible. Society will have to live with the environment it creates, it will no longer be able to abandon it.

Our water resources will be a major problem. In fact, in certain areas it is already the number one problem. Usable water is confined to a relatively small are of the globe, and human and industrial wastes area contaminating this limited supply at a steadily increasing rate. Further, industrial development in remote areas is frequently contingent upon development of economic sources of water.

Climate control, or at least climate modification, may well be on the horizon. This may present major international problems. We are all aware of the legal concepts of the right to receive and discharge surface waters. Consider how infinitely more complex are the legal ramifications inherent in climate control. We see a forerunner of these in controversies over cloud seeding experiments.

To develop resources for servicing the expanding population, it is not sufficient to provide a water supply. All of the requirements of a concentrated population must be met. These include availability of other material resources, availability of energy transportation, etc.

As raw materials become less abundant, or of lower quality, new materials, new sources, and new process technology must be developed.

Jet air travel affects not only the speed with which we arrive at our destination, but our mobility as well. Isolationism, which was never justifiable in many of our minds, becomes impossible.

Further, with world wide television, underprivileged nations will become increasingly aware of their lower standards of living and will no longer be satisfied with a disproportionate share of the "Good Life."

Our own consumption of internally available raw materials and increasing awareness of other nations of the leverage they possess in raw materials supplies will present domestic as well as international problems. We may find economic balances arbitrarily changed by political decree in more pedestrian areas than gold and diamonds.

We have all heard impressive statistics relative to today's scientific effort—it being said that 90% of the scientists and engineers who have ever lived are alive today. What is germane to our consideration is that the rate of technological change has accelerated, so that job obsolescence and its related problems are of major concern at both professional and non-professional levels. This creates needs for better programs of continuing education and of re-education. Changes in our thinking as a nation with respect to responsibility for such programs is in a state of transition and may well be reflected to an increasing degree in legislation as well as in contract negotiations. One attendant problem that has attracted the attention of some professional societies is that of securing industry-wide benefit programs, with pension plans the major concern.

Increased leisure time and increased percentages of people of retirement age will present both problems and opportunities to science and technology.

Quite aside from the impact of world-wide television, other advances may well convert the world to a giant goldfish bowl, with all of us living in glass houses. Privacy will become more and more difficult to attain, as miniature wireless electronic devices become more commercial.

Computerized banking, health records, etc. will have their impact and present peripheral problems to us as individuals and to legislative bodies at all levels.

Computerization, in general, presents challenges in such diverse fields as education, medicine, labor law, and banking.

Space exploration creates questions of air rights, satellite use, and espionage as well as medical and insurance problems.

Refuse generation problems are not confined to air and stream pollution but involve the less sensational but none the less critical problem of disposal space for solid refuse.

Jet aircraft are creating an air pollution problem in heavy traffic areas. This is to say nothing of the sound pollution problem.

We have all read of the controversies surrounding the use of pesticides. It is regrettable that here as in many other instances public attention has been focused almost entirely on the price we pay for the benefit—with little or nothing being said about the benefits derived from their use.

Without discussing at all the merits of this or any of the other areas of controversy spawned by scientific progress, can we not all at least agree that the public could be better alerted to and informed of the impact of technological advances, both with respect to their advantages and their disadvantages?

Now each of you could develop your own list of scientific and technological advances that will present both challenges and opportunities to society. I make no brief for those presented here, they are only illustrative, and I have drawn, where possible, on examples that have involved advances in areas of particular interest to one or more of our Divisions.

The matter that should concern us is that increasing awareness is required of the impact of present and potential advances on our society. While it may be true that scientists and engineers are not a priori best qualified to assess the total social impact of their own findings—they should, on balance, contribute significantly to any analysis of such impact.

Dr. Pitzer summarized our responsibility well when he said, "It will not be easy to foresee all of the possibly damaging effects of a new product or machine, but we should try to do so. Since scientists are peculiarly able to visualize possible applications of new scientific knowledge and their efforts, scientists must play a major role in this judgment process. But other citizens who are sensitive to individual and community attitudes should also participate and help apply the humanistic value tests.

Our federal government is apparently becoming increasingly aware of the complexity of these matters and scientific advisors are being used more extensively and utilized in more responsible positions.

This is all to the good. However, we should consider carefully a warning issued by Dr. Cairns in his recent Perkin Medal Award Address when he warned that industrial scientists were not bearing their proportionate share of this responsibility but leaving it for the most part to their academic counterparts.

Of perhaps greater importance, however, is the lack of concern of the individuals who comprise the scientific community. We should, as individuals, take increasing interest in both domestic and international affairs. We should become involved in the determinations of our political system at all levels—local, state and national.

Very recently, during a television interview, a legislator was expounding on the merits of a technological advance. He was clearly, to those aware of the technology, at least, out of his field. Yet his views were taken by his audience as authoritative because of the committee responsibility he held.

In areas of complex technology, with even more complex social ramifications, the need for significant representation by trained technical people in all bodies of government, the legislative as well as the administrative, is apparent.

The fault lies not with "The Establishment" but with us as individuals. Many of us have erred in not wanting to get involved, claiming that politics was, at best, a messy business. We should encourage those with scientific and engineering training and ability to concern themselves in increasing numbers and in greater depth with domestic and international politics which most assuredly are being, and will continue to be, in increasing degree affected by scientific progress.

Even as more and more businesses are looking for executive talent in the scientific and engineering ranks, even so government by virtue of the increasing impact of science and technology will benefit from greater utilization of technically trained talent. Please note, I do not make a case for a scientific or an engineering

degree as a requirement for political office. I am only making a case for the benefits to be derived from increasing first-hand involvement and suggest that participation in the political system in all branches and at all levels in increasing numbers will have a synergistic effect on both the scientific community and our political bodies.

This should be coupled with a concerted effort by scientists and engineers from all vantage points, academic and industrial, to see that the public is well informed on all matters of scientific concern. A high order of statesmanship is required to insure that the effort is not self-serving and promotional, but that it is instructive. It will then be constructive—not destructive.

In summary then, a major challenge to the scientific community lies in the direction of (1) fostering a broader, more realistic understanding of the role of science and technology and (2) personal involvement in the political and social consequences of technological progress. For this to be effective we must (1) develop greater concern for the broader ramifications of technological progress; (2) become better informed in this area; and (3) open better lines of communication with those responsible for legislation affecting subsidization, implementation, and control of our technological effort.

The scientific societies per se should, however, as corporate bodies maintain their dedication to their presently stated objectives. To do otherwise would seriously hamper their progress toward their stated objectives.

The need for a forum combining scientific, technological, and humanistic interests cannot and should not be denied. In all such deliberations primary emphasis must be placed on the public interest and the human dimension. I submit, however, that this will be more effective if established outside the framework of the scientific and technical societies.

Abstracts of "Recent News" Papers

Presented at the Electronics—Electrothermics and Metallurgy, Electronics-Luminescence, and Electronics-Semiconductors Sessions, New York, May 4-9, 1969

328RNP

The Luminescence Efficiency of YVO_4 and $Y(V, P)O_4$

Henry F. Ivey and T. J. Isaacs, Westinghouse Research Laboratories, Pittsburgh, Pa.

It has been reported in the literature that the quantum efficiency for the blue emission of unactivated YVO_4 at room temperature is very low (5%) and can be greatly improved by forming solid solutions with YPO_4. We find that with sufficient care to eliminate accidental impurities, the efficiency at room temperature can be at least as high as 42% and that at liquid nitrogen temperature the same as for $CaWO_4$. With reduced impurity level, and reduced room-temperature quenching, the improvement upon introduction of YPO_4 is small.

329RNP

Luminescence of Pr^{+3} in (Y, Gd, or La)$_2O_2S$

Lyuji Ozawa, Zenith Radio Corp., Chicago, Ill.

It has been found that the emission lines, in eV, of Pr^{+3} in (Y, Gd, or La)$_2O_2S$ linearly shifted to higher energy (shorter wavelengths) when the ionic radius of the rare earth cation increases. The hexagonal lattice constants, a and c, also increase with an increase in cation radius. The change of the emission lines can be correlated with the distortion of the Pr^{+3} center. It has also been found that there is energy transfer from host to Pr^{+3} and from gadolinium to Pr^{+3}.

330RNP

The Degradation of Aperture Lamps

George T. Bauer, Research Laboratories, Xerox Corp., Rochester, N. Y.

A relatively fast degradation of zinc silicate coated aperture lamps has been observed when compared with conventional fluorescent lamps. Measurements and calculations indicate that the main cause of the degradation is the effect of ultraviolet irradiation on the luminous efficiency and the reflectance of the lamps' coating. The time dependence of the formation of absorbing centers of x-rayed zinc silicate phosphor has been studied and related to the degradation process in the lamps.

331RNP

Scanning Electron Microscopy of Sulfide Phosphors

P. Lubin, R. Simon, and J. Varon, The Bayside Laboratory, Research Center of General Telephone and Electronics Laboratories, Inc., Bayside, N. Y.

The scanning electron microscope is an ideal instrument for the study of phosphor materials on a point by point basis. Besides topographical displays, information relating to cathodoluminescence can also be obtained. A cathodoluminescent attachment has been constructed for the JSM-1 scanning microscope. Scanning micrographs have been obtained in both the secondary electron mode and the cathodoluminescent mode. Resolution in the cathodoluminescent mode is a function of beam size, penetration distance, nonradiative surface layers, and the absorption distance. Illustrations of the effect of voltage are shown.

332RNP

X-Ray Excited Fluorescence in Rare Earth Fluorides for Trace Analysis

R. J. Jaworowski, J. R. Cosgrove, and D. J. Bracco, The Bayside Laboratory, Research Center of General Telephone and Electronics Laboratories, Inc., Bayside, N. Y.

The use of x-ray excited fluorescence to detect trace rare earth impurities in oxide matrices has been described[1,2,3]. This paper describes the extension of the method to metal fluoride matrices, particularly YF_3 and GdF_3. Relative to oxide matrices, these compounds exhibit lower intensity and more nonradiative resonance transfer among rare-earth ions to the extent that detection limits are two orders of magnitude higher than in Y_2O_3 and identification of individual species in mixtures is difficult.

[1] J. Makovsky, W. Low, and S. Yatsiv, Phys. Letters, **2**, 186 (1962).
[2] R. C. Linares, J. B. Schroeder, and L. A. Hurlbut, Spectrochimica Acta, **21**, 1915 (1965).
[3] R. J. Jaworowski, J. F. Cosgrove, D. J. Bracco, and R. M. Walters, Spectrochimica Acta, **23B**, 751 (1968).

333RNP

Measurement of Oxygen and Carbon Content of Semiconductor Grade Silicon

C. Cross,* G. Gaetano,* T. N. Tucker,† and J. A. Baker,† *Langley Research Center, Hampton, Va.; †Dow Corning Corp., Hemlock, Mich.

The oxygen and carbon content of several silicon single crystals have been measured using ^3He (15.4 MeV) activation techniques and are compared with values determined from infrared absorption measurements. The oxygen and carbon content of these crystals as determined from the activation analysis ranged from <0.05 to ~30 ppm and <0.05 to ~7 ppm, respectively. The infrared absorption measurements gave results that agreed favorably with these values.

334RNP

High-Field Effects and Ohm's Law in N-Type Silicon

R. Jaggi, IBM Zurich Research Laboratory, 8803 Rüschlikon, Switzerland

The nonohmic behavior of elemental semiconductors is well described by an effective conductivity

$$\sigma = \frac{J}{E} = \sigma_0 \cdot \left(1 - \frac{J^2}{J_c^2}\right)$$

where J = current density and E = electric field. σ_0 is the ohmic conductivity in the limit $J \to 0$, $E \to 0$ where Ohm's law is valid. J_c is the saturation value of the current density in the limit $E \to \infty$. It is of special importance for materials analysis that J_c depend not only on the carrier concentration, but also on the geometry of the specimen. This is shown by evaluation of literature data and by recent experiments.

335RNP

The Growth of Submicron Epitaxial Silicon Layers by Silane Pyrolysis

A. C. Adams and J. Simpson, Bell Telephone Laboratories, Murray Hill, N. J.

Epitaxial silicon layers, 0.3-1.0μ thick, have been grown on silicon substrates by the pyrolysis of silane between 950°-1150°C with

Cathode Materials and Performance in High-Temperature Zirconia Electrolyte Fuel Cells

C. S. Tedmon, Jr.,* H. S. Spacil,* and S. P. Mitoff

General Electric Research and Development Center, Schenectady, New York

ABSTRACT

The high-temperature zirconia electrolyte fuel cell is materials-limited in both its performance and its range of potential application. The most significant materials limitations and problems occur with the cathode. Cathode materials must satisfy four general criteria: (*i*) chemical, (*ii*) electrochemical, (*iii*) mechanical, and (*iv*) economical. In this paper, the interaction between cathode materials and cell performance is considered quantitatively for three general classes of cathodes, *viz.*, metals, oxides with embedded current collectors, and electronically conducting oxides.

Successful and economical operation of high-temperature, zirconia electrolyte fuel cells requires that the electric current generated by the electrochemical combustion of the fuel be conveniently and inexpensively extracted from the cell. The design and selection of materials for this purpose, *i.e.*, electrodes and electrode leads, is a challenging problem in view of the operational requirements and working environment of the cell. In terms of both its range of application as well as its performance capability, the high-temperature zirconia electrolyte fuel cell is a materials-limited device. The most significant materials limitations at this time are imposed by the cathode and the cathode leads. In this paper, operational criteria are identified and applied to the problem of selecting materials for the cathodes; in addition, the interactions between cathode materials and cell performance are considered quantitatively.

Criteria for Cathode Materials

A perspective of the materials problems associated with the cathode of a high-temperature zirconia fuel cell may be obtained from a brief consideration of the over-all device, including test leads and auxiliary electrodes, in a typical operating environment, such as shown schematically in Fig. 1. The environmental characteristic to be noted in particular is the exposure of the cathode to a highly oxidizing atmosphere (usually air) at very high temperatures, *ca.* 800°-1200°C. It is this combination of high temperature and oxidizing atmosphere that leads to severe materials limitations for the cathode.

There are four general types of criteria to be satisfied: chemical, electrochemical, mechanical, and economical. The first three define the degree of technical performance of the device, and the last establishes its range of application. These various requirements are considered separately.

Chemical requirements.—These requirements arise as a consequence of the physical environment in which the cathode operates, and may be summarized as follows:

1. Chemical stability in air (stable with respect to oxidation or nitrification reactions).
2. Phase stability over the temperature range of operation, *i.e.*, no allotropic transformations.
3. Low vapor pressure (minimize volatilization losses).
4. Inert with respect to chemical reactivity with the electrolyte and lead wires. It will be seen subsequently that most potential cathode materials fail to satisfy one or more of these criteria.

The reasons for these criteria are generally obvious. A practical fuel cell will almost certainly use air as the oxidant, hence nitrification as well as oxidation reactions must be considered. Furthermore, in the temperature range of cell operation, chemical inertness *per se* does not exist but rather must be considered in a kinetic context. For long term (several years) operation of fuel cells, the kinetics of the reaction "ZrO_2(Stab.) + cathode materials → reaction products" must be considered. Examples of this problem will be described.

Electrochemical requirements.—The most fundamental electrochemical requirement for the cathode is that it be a satisfactory oxygen electrode. Since a definitive model of a high-temperature solid-state oxygen electrode is lacking, this criterion is not especially informative from a materials viewpoint. The over-all cathode reaction is

$$O_2\ (\text{gas}) + 4e^- = 2\,\underline{O}^=$$

where $\underline{O}^=$ denotes an oxide ion, *i.e.*, an oxygen ion incorporated in the zirconia anion sublattice. Details of the various stepwise reactions comprising the net reaction, such as adsorption, dissociation, surface migration, and ionization, are not known. However, since fuel cells with good cathodes can be operated reversibly (1), these steps must be fast, which is not unexpected in view of the high temperatures involved.

In addition, there are mass transport effects which can arise leading to electrode polarization. Assuming the cathode reaction takes place at or near the cathode/electrolyte interface, it will be necessary to bring the species participating in the reaction, oxygen molecules, oxide ions, and electrons, to that site. Of particular interest is the transport of molecular oxygen to the reaction site. If the cathode is porous, then

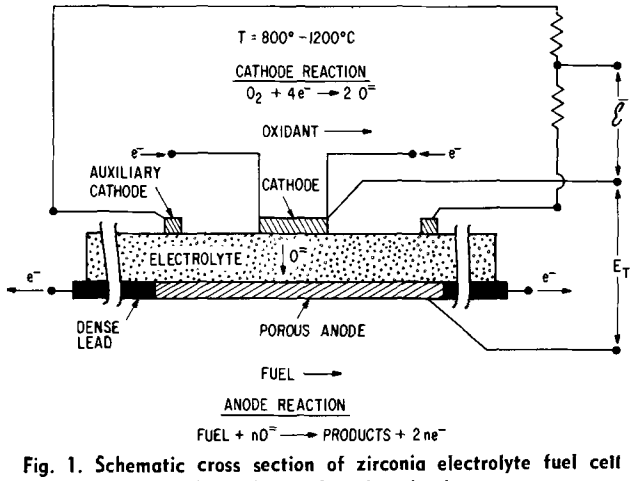

Fig. 1. Schematic cross section of zirconia electrolyte fuel cell with auxiliary electrodes and typical testing circuit.

* Electrochemical Society Active Member.

gas transport is involved, and a limiting current density may be defined based on the diffusion rate of oxygen gas from the air through the pores to the reaction site. As a consequence of nitrogen concentration (from oxygen depleted air) in the pores of the cathode, the amount of oxygen at the reaction sites is decreased. This phenomenon has been investigated using the experimental apparatus shown schematically in Fig. 1. The voltage E_T is the terminal voltage during cell operation and reflects changes in the oxygen partial pressure at each electrode as well as voltage drops across the electrolyte and at the electrodes. The voltage $\bar{\mathcal{E}}$ measures the difference between an average open-circuit voltage (obtained from two auxiliary electrodes which carry no current on the cathode side of the cell) and the terminal voltage. It then is a direct measurement of the total cell overvoltage including both ohmic and nonohmic voltage drops across the cell. Thus changes with different fuel and oxidant compositions in $\bar{\mathcal{E}}$ reflect changes in electrode characteristics. Results from a fuel cell tested using this apparatus are presented in Fig. 2. The cell employed in these experiments had a porous Ni anode, an yttria (10 m/o)-stabilized zirconia electrolyte, and a porous $PrCoO_3$ cathode about 0.13 mm thick. This particular cathode material is discussed in greater detail in a later section. The fuel was hydrogen containing initially 3% water vapor, and the oxidant was oxygen diluted with nitrogen to produce the compositions indicated. The effect of decreasing the initial oxygen content of the cathode gas from 50 to 5% is dramatic, leading to a large nonohmic overvoltage and a limiting current density of about 0.9 A/cm^2 for this cell. Although a practical fuel cell would not use an oxidant initially containing only 5% oxygen, it should be recognized that, if air is the oxidant, in cells operating with reasonably large fuel and oxidant conversion efficiencies, the oxidant composition at the downstream end of the cathode could very easily be reduced to 5% or less, resulting in significant gas phase polarizations. Since mass transport effects will be small at low current density, the fact that the slopes of the $\bar{\mathcal{E}}$ *vs.* current density curves are initially about the same indicates that any activation polarizations depending on oxygen pressure at the cathode are small compared to the resistive voltage drop.

A porous cathode operating on pure O_2 could show a mass transport polarization if pore sizes were sufficiently small, due to the viscous drag of the oxidant flowing through these pores. High-temperature fuel cell cathodes have pores exceeding the submicron size that would give rise to this effect, and the mass transport polarization of porous cathodes then results entirely from the interdiffusion of O_2 and N_2 in the pores. Under these conditions, since there is no net flow of N_2, the mass transport limiting current density can be obtained as

$$j_L = \frac{4\mathbf{F}cD_{O/N}p}{st} \ln \frac{1}{1 - x_{O_2}} \qquad [1]$$

where **F** is the Faraday constant, c is the molar density of the oxidant, $D_{O/N}$ is the interdiffusion coefficient for O_2 and N_2 mixtures. p, s, and t are the fractional porosity, tortuosity, and thickness, respectively, for the cathode, and x_{O_2} is the mole fractional O_2 content of the oxidant in the gas phase adjacent to the cathode. Taking $D_{O/N}$ at 900°C as 2.5 cm^2/sec, and assuming p and s have values of 0.25 and 1.5 for a cathode with a thickness of 0.15 mm (150μ), the value of j_L for air with 21% O_2 is 26.5 A/cm^2. This is not likely to be a problem as such, but Eq. [1] confirms that the value of j_L does depend on O_2 content, leading to the possibility of significant polarization at the cathode under some operating conditions as noted previously. Thus for 5% O_2, the same cathode parameters yield a value for j_L of 5.9 A/cm^2. The preceding analysis applies equally well to metallic or nonmetallic cathodes.

In addition to these features of a porous electrode, there is another factor that can introduce electrical losses, which arises from the fact that the cathode is generally not in continuous contact with the electrolyte, but rather is in contact in discrete areas separate from one another. Tannenberger and Siegert (2) have discussed this problem with zirconia cells having solid silver cathodes, and Gorin and Recht (3) have observed this effect in molten salt fuel cells. The result of this discrete contact is that ions and electrons will be restricted in their flow to points of cathode/ electrolyte/ oxidant contact, giving rise to regions of locally high current density. This introduces a resistive loss which is termed a "constriction" resistance and is added to the cell resistance that would be expected on the basis of bulk resistivities and geometry. Thus with porous cathodes, cathode voltage drop can arise from at least two sources: gas-phase polarization, and constriction resistances. The former can also show a mass transport limiting current density.

Nonporous cathodes have been tested. Because of its relatively high solubility for oxygen and its stability in an oxidizing environment, silver, both solid and molten, has been used in cells (4), but cell lifetimes are very short because of volatilization losses. Mixed conducting oxides, *i.e.*, oxides which conduct both oxygen ions and electrons, have also been tested. With a dense, nonporous cathode, constriction resistance is eliminated, but a limiting current density can again arise because of mass transport limitations in the electrode. For the case of a material, such as silver, which can dissolve oxygen and transport it to the electrolyte while simultaneously acting as an electronic conductor, the mass transport limiting current density is

$$j_L = \frac{2\mathbf{F}c_O D_O}{t} \qquad [2]$$

where c_O is the maximum solubility of oxygen in the material (expressed as a molar concentration) in equilibrium with the oxidant adjacent to the cathode, D_O is the diffusion coefficient for oxygen through the material, and t is the cathode thickness. For silver at 900°C, D_O is 3.5 x 10^{-5} while c_O is 1.8 x 10^{-5} when equilibrated with air. For a cathode with a thickness of 0.01 mm (10μ), the value of j_L is 0.125 A/cm^2. This is not high enough to allow satisfactory power densities. In addition, the value of j_L depends on c_O, which will decrease as the O_2 content of the oxidant decreases. Thus nonporous solid silver cathodes would have to be less than 10μ thick to allow sufficient oxygen transfer in operation.

Either the ionic or electronic conductivity in a mixed conduction oxide will be limiting, depending on which

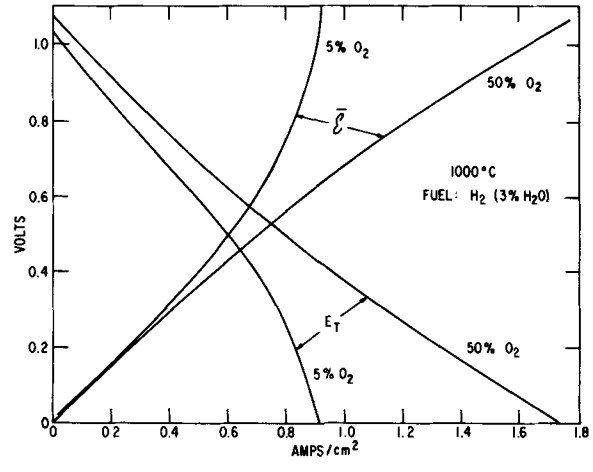

Fig. 2. Voltage-current characteristics for fuel cells operated with 50% O_2 and 5% O_2 initially in the oxidant, showing effect of oxidant composition on the terminal voltage (E_T) and the total cathode overvoltage ($\bar{\epsilon}$).

is smaller. In either case, the mass transport limiting current density in such a cathode is given approximately by the expression

$$j_L = \frac{\sigma_{i,e}\,\Delta E_c}{t} \quad [3]$$

where $\sigma_{i,e}$ is the conductivity of either ions or electrons, whichever is smaller, ΔEc is the maximum voltage drop across the cathode, and t is the cathode thickness. Equation [3] is employed by setting ΔE_c equal to 1V, the approximate value of the open-circuit voltage of most high-temperature cells. The relationship between Eq. [3] and the two preceding equations, both of which involved the product of a concentration and a diffusion coefficient, can be seen by substituting into Eq. [3] the value of $\sigma_{i,e}$ given by the Nernst-Einstein relation, namely

$$\sigma_{i,e} = \frac{z^2F^2c_{i,e}D_{i,e}}{RT} \quad [4]$$

where z is the number of electronic charges per charge carrier particle, $c_{i,e}$ is the molar concentration of ions or electrons, $D_{i,e}$ is the diffusion coefficient for ions or electrons through the oxide, R is the gas constant, and T is the absolute temperature. This relationship is actually used to determine the product $c_{i,e}D_{i,e}$ since neither of these quantities is normally experimentally accessible in conducting solids.

At 900°C, the value of $\sigma_{i,e}$ for either ions or electrons can be taken as 0.05 ohm-cm^{-1} for zirconia-based oxides that might be employed for cathodes. Then Eq. [3] gives the value of j_L of 3.3 A/cm^2 for a cathode 0.15 mm thick. From a mass transport standpoint only, this type of cathode should offer no problem.

In addition to these electrochemical criteria, there is an electrical resistance requirement, namely, that the cathode specific resistance, r_c (ohms-cm^2), cannot exceed a certain arbitrary upper limit, the magnitude of which will be dependent on the system configuration. For fuel cells which are electrolyte limited, that is, cells in which the electrolyte resistance dominates the total resistance of the cell, the specific resistance of the cell as viewed from the terminals is given by the relation

$$r_T = r_e + f(r_a + r_c) \quad [5]$$

where r_e, r_a, and r_c are the specific resistances of the electrolyte (including constriction resistances, if any), anode, and cathode, respectively, and f is a constant which takes into account the fact that the current distribution varies along the length of the electrodes ($f = 0.08 - 0.3$). This specific resistance, r_T, with dimensions of ohm-cm^2, is the resistance of a hypothetical cell 1 cm^2 in area which has the electrical properties of the actual cell under consideration. Equation [5] can be derived by a straightforward, although tedious, analysis of a one-dimensional distributed current network (5). The value of r_T must be 1 or less to achieve power densities above 0.25 w/cm^2, a realistic lower limit for feasible systems.

If r_a is small compared to r_e and r_c, as will generally be the case if metal anodes such as porous Ni are used, the following approximation results

$$r_T = r_e + f \cdot r_c \quad [6]$$

If L is the fractional voltage loss to be permitted at the cathode, then it follows directly that

$$r_c = \frac{r_e}{f}\,[L/(1-L)] \quad [7]$$

The application of this equation to specific systems will be demonstrated in a subsequent section.

The specific resistance of a cathode in the form of a thin layer is given by an expression of the form

$$r_c = \frac{\rho}{t}\,l^2 \approx \frac{1}{1-p}\,\frac{1}{\sigma t}\,l^2 \quad [8]$$

Table I. Summary of limiting current density and resistivity-thickness ratio data for thin cathodes

Cathode	t mm	σ ohm-cm^{-1}	j_L A/cm^2	ρ/t ohm/square	$j_L/(\rho/t)$
Porous oxide	0.15	5×10^2	26.5	0.178	149.0
Dense Ag	0.01	1.34×10^6	0.125	0.0075	16.7
Mixed σ oxide	0.15	5×10^{-2}	3.3	1340	0.0025

where ρ is the resistivity of the cathode material, σ the bulk conductivity, p the fractional porosity (if any), t the thickness, and l is the active length of the cell. Since a cathode should have a high value of j_L and a low value of ρ/t, a figure of merit for use without an embedded current collector grid is the ratio of these two quantities. This ratio, $j_L/(\rho/t)$, will be independent of thickness as can be seen by reference to Eq. [1]-[4] and [8], and is thus a measure of the ability of a cathode material to simultaneously deliver oxygen and electrons to the cathode/electrolyte interface. Table I summarizes the values of j_L, ρ/t, and their ratio for the three examples that have been considered so far. The conclusion is that porous oxides (with sufficiently high conductivity) and Ag (which is the most eligible material for a nonporous metallic cathode) have high figures of merit, but that a silver cathode would have to be very thin to be useful. Mixed conductivity oxides could not be used without embedded current collectors without a drastic increase in conductivity over that obtainable in zirconia-base oxides.

Mechanical requirements.—The mechanical criteria for the cathode are simply that the electrode must maintain any porosity required for O_2 transport and maintain physical and electrical contact with the electrolyte and lead wires throughout all phases of cell operation. This latter requirement applies especially to athermal conditions where differential thermal expansion can cause large interfacial stresses. If the cathode is largely metallic, stress-relief by plastic flow can occur without deleterious effects to the cell. However, if oxide electrodes are used, plastic deformation is unlikely and stress-relief may occur by means of cracking, spalling, or other mechanisms leading to loss of adherence at the interface. The mechanical integrity of an oxide cathode will depend on particular materials used. The strength of its bond to the electrolyte (which will probably depend in turn on the method of application) will also be a function of the thickness of the electrode, and the maximum temperature range traversed in a thermal cycle.

Economic requirements.—Technical and commercial success in high-temperature fuel cell technology essentially overlap in meaning since a fuel cell, as a power producing device, must compete economically with existent power producing systems. The use of noble metals in electrodes or leads, for example, may be acceptable from the viewpoint of their technical performance, but will generally place a significant, if not prohibitive, economic penalty on the system.

Electrode Materials

A wide variety of materials have been proposed for cathodes in high-temperature, zirconia electrolyte fuel cells. These materials may be categorized into three classes: (*a*) metals, (*b*) oxides with current collector grids, and (c) electronically conducting oxides without current collector grids. Each of these classes will be considered in turn.

Metals.—Because of the highly oxidizing environment at the cathode, only the noble metals, Pt, Pd, Au, and Ag, merit serious consideration. Since the oxygen solubility in the first three is relatively small, cathodes made from these metals will have to be porous in order to avoid a very low limiting current density arising from oxygen transport in the metal. The use of Au

as a cathode metal is limited by its melting point which would fix the maximum cell operating temperature. Furthermore, since typical cell operating temperatures are generally at least 90% of the absolute melting point of Au, excessive sintering of the porous electrode would occur. The same problem exists to an even greater degree with porous Ag cathodes. Because of their higher melting points, sintering of porous Pt or Pd electrodes is much less of a problem. Porous Pt electrodes are effective air electrodes and have been used by several investigators in zirconia fuel cells (6). Zirconia and Pt have very similar thermal expansion coefficients, and Pt electrodes can easily be applied from a resinate or paste, or by sputtering. Being a metal, Pt satisfies the electrical conductivity criterion. Porous Pd cathodes have also been tested and show satisfactory short-term performance. There are two disadvantages to using either Pt or Pd electrodes, however. The first is cost; their use imposes an economic penalty that is essentially intolerable for any practical application. The second disadvantage arises from the necessity of having a porous electrode, which means having a large surface to volume ratio in the metal. While this is desirable from the electrochemical viewpoint as previously discussed, it is deleterious with respect to surface reactions such as volatilization. Metal recession data are shown in Table II; these data were calculated from equilibrium vapor pressure data (7) assuming a vaporization coefficient of unity. Pd is obviously unacceptable because of volatilization.

Silver is an interesting material for fuel cell cathodes because of its high solubility and diffusivity of oxygen, particularly when it is molten, and because it is relatively oxidation resistant. It has been demonstrated (4) that molten silver is a satisfactory oxygen cathode in short term applications, and of course it has a high electronic conductivity. Unfortunately any long term use as a cathode is severely limited above its melting point (Table II). Below the melting point of Ag, its solubility for oxygen is greatly reduced, hence very thin electrodes must be employed to avoid significant limiting current densities (Table I). Even at temperatures as low as 800°C, volatilization rates are large, and the lifetimes of Ag electrodes at this temperature would be too short for practical consideration. It should be pointed out that the data shown in Table II were calculated assuming free evaporation into a vacuum with an evaporation coefficient of unit. In a fuel cell, the presence of the oxidant gas will substantially slow down volatilization. However, even if the evaporation coefficient for Ag, for example, were as small as 10^{-3}, substantial metal losses would still occur.

In summary, electrochemically effective oxygen cathodes can be made from Pt, Pd, or Ag, but their application in a practical fuel cell system is essentially nil because of economics in the cases of Pt and Pd, and volatilization in the cases of Pd and Ag.

Oxide-current collector cathodes.—Another type of oxygen electrode that has received attention is a composite system consisting of a matrix of an oxide which provides for oxygen transport either by being porous, or by being an anionic conductor, or both, and in which is embedded a grid of current collector wires which provide electronic conductivity. Porous stabilized zirconia, applied from a slip over a Pt grid, is an example of this type of electrode. Porous zirconia is a good cathode material, and obviously is compatible with the electrolyte. Its only shortcoming is its lack of electronic conductivity. This can be increased by doping with multivalent cations, but a current collector grid is still required as indicated by Table I. The use of nonnoble metals as current collectors is limited by their oxidation resistance and also by the fact that many of the oxidation resistant alloys commercially available form protective scales which are not electronic conductors and would thus insulate the current collector grid from the rest of the electrode. An approximate expression for the over-all specific resistance of this type of electrode is given by the relation

$$r_c = \frac{\rho}{12\,N\,t} \qquad [9]$$

where ρ is the resistivity of the oxide matrix (for electronic conduction), N is the number of square grids per unit area of cathode, and t is the cathode thickness. This expression is derived simply by considering the average distance that an electron must travel in a square grid to reach a current collector wire.

Fuel cells with this type of electrode have been built and tested, and satisfactory performance was obtained. However, cathodes of this type, using either Pt or Pd current collector grids, fail to satisfy economic criteria, as can be seen from the following discussion. In order to evaluate Eq. [9] for a typical case, consider an electrode with a porous zirconia matrix and Pt current collectors in a square grid. Assume the electrode is 0.25 mm thick, which is a typical value. Greater thicknesses will reduce the electrode resistance but increase the amount of gas-phase polarization. Further assume the oxide matrix of the cathode is yttria-doped zirconia, 50% dense, and heavily doped with iron to increase the electronic conductivity. At 1000°C, the resistivity for ionic conduction of zirconia, corrected for porosity, is about 20 ohm-cm (8). The electronic resistivity, due to the iron doping, is of the order of ten times the ionic resistivity, *i.e.*, about 200 ohm-cm. Let the maximum voltage loss to be tolerated be 10%, *i.e.*, $L = 0.1$. The specific resistance of the electrolyte, r_e, is the resistivity-thickness product, and for a fuel cell with an electrolyte of yttria-stabilized zirconia 0.50 mm thick, at 1000°C will be about 0.5 ohm-cm^2. Therefore, from Eq. [7] through [9], it is seen that $N = 950$, which means that the spacing of the wires is about 0.3 mm. Even using wire as small as 0.1 mm in diameter, the cost would be prohibitive for most applications. Substitution of Pd for Pt would not reduce the cost to an acceptable level for most applications. Consequently it is concluded that this type of cathode is not practical.

Electronically conducting oxide cathodes.—The third and most interesting class of cathodes is that in which the electrode is made from a porous oxide that has sufficiently high electronic conductivity that current collector grids are not required. The electrode must be porous because those oxides which possess high electronic conductivity do not exhibit high anionic conductivity. Therefore porosity is required to minimize gas-phase polarization.

Oxides of interest include Li-doped NiO, Sr-doped $LaCoO_3$, Sn-doped In_2O_3, doped ZnO, doped SnO_2, and $PrCoO_3$. Figure 3 presents electronic conductivity data as a function of temperature for these materials. The mechanisms by which these oxides obtain their high values of conductivity are not completely understood. Li-doped NiO has been most thoroughly investigated (9-11), and it is believed that when NiO, a p-type semiconductor is doped with Li_2O (up to 10 m/o), the Li^{+1} ions enter the Ni^{+2} cation sublattice, decreasing the cation vacancy concentration and increasing the number of electron holes, the latter being a consequence of the transition of Ni^{+2} to Ni^{+3} (10). Similarly in the case of the perovskite $Sr_{1-x}La_xCoO_3$ ($x \approx 0.9$), the replacement of the La^{+3} ions by Sr^{+2}

Table II. Metal recession due to volatilization in 10^4 hr

	800°C mm	1000°C mm	1200°C mm
Ag	25	2.3×10^3	—
Pd	—	0.067	0.25
Pt	—	0.001	0.005

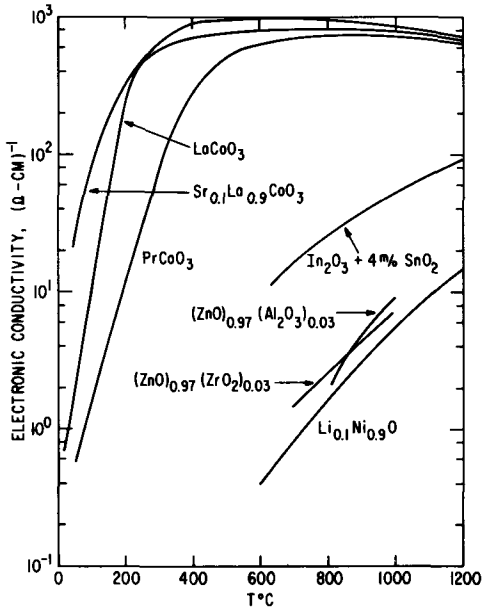

Fig. 3. Electrical conductivity as a function of temperature for various oxides proposed for use in cathodes. All data obtained at GE except for doped ZnO, which was taken from ref. (13).

ions forces the transition of an equivalent number of Co^{+2} ions to Co^{+3} ions (12). It is presumed that the interaction of Sn^{+4} ions with In^{+3} ions produces an analogous effect in the case of SnO_2-doped In_2O_3. The conduction mechanism for ZnO doped with small amounts of Zr or Al ions is believed to be due to substitution of the doping ion into the Zn^{+2} sublattice with the generation of electrons in the conduction band (13). The conduction mechanism for $PrCoO_3$ and undoped $LaCoO_3$ is not understood, although several models have been described for the latter (14, 15).

From the data shown in Fig. 3, it is apparent that several compositions possess adequate electronic conductivity to satisfy the resistivity criterion previously discussed. None of these materials is without its limitations, however. Li-doped NiO, which has only a marginal value of conductivity, is unsatisfactory because of rapid loss of Li due to the high vapor pressure of LiOH in moist air at typical cell operating temperatures. The effect of Li volatilization on the conductivity of Li-doped NiO as a function of time is shown in Fig. 4. These data were obtained from a cathode sample which consisted of two Pt current collector loops tied around a 1 cm diameter zirconia tube, over which a porous cathode of $Li_{0.1}Ni_{0.9}O$ was applied to a thickness of about 1 mm. Four-point resistance data were obtained as indicated. In this type

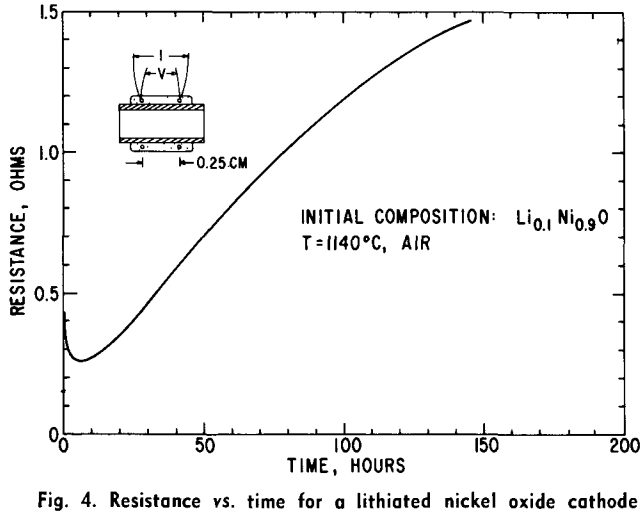

Fig. 4. Resistance vs. time for a lithiated nickel oxide cathode sample showing effect of Li loss on cathode resistance.

of test, the contact resistance between the current collectors and cathode is included in the total measurement. Also, the electrolyte substrate is in parallel electrically with the cathode; however, the resistance of the electrolyte is much larger than that of the cathode, at least initially. Many such tests of this type were conducted, and the results presented in Fig. 4 are typical. There is an initial decrease in resistance, probably due to sintering of the cathode. After several hours, the resistance begins to increase, and after several hundred hours, depending on the test temperature, will start to level out. Over a substantial interval the rate of increase is essentially linear with time, suggesting that Li volatilization is not diffusion limited. The slope dR/dt, for example, after 75 hr, is about 10^{-2} ohms/hr. The Li content for the sample shown in Fig. 4 after 150 hr was less than 10% of the original level, *i.e.*, the composition was less than $Li_{0.01}Ni_{0.99}O$.

Button and Archer (12) have examined in detail the performance of Sr-doped $LaCoO_3$ air electrodes and found a number of problems with them. Obtaining satisfactory adherence of the perovskite to the electrolyte was difficult. When the perovskite was applied to the electrolyte as a powder (in a slurry), and heated to a temperature high enough to produce a liquid phase, adherent coatings were produced, but subsequent electrical and structural studies indicated chemical interaction between the electrode and electrolyte. Vapor deposition from chlorides appeared to yield best results, but it is a rather complicated technique requiring close control.

During cell testing, other problems were reported, such as cracking of the cathodes due to thermal expansion mismatch with the electrolyte, and phase separation in the perovskite which had been melted. Also, overvoltages were frequently large, although this depended considerably on the fabrication technique for the cathode.

Fuel cells with $LaCoO_3$ air electrodes, with and without Sr-doping, were built and tested in this Laboratory. Like most of the cells tested, these cells were built with porous Ni anodes to which about 20 w/o zirconia had been added (to prevent grain growth and sintering), and yttria-stabilized zirconia electrolyte. The thicknesses of the anode and electrolyte were about 0.12 and 0.5 mm, respectively. The $LaCoO_3$ was applied from a slurry, forming a porous electrode about 0.3-0.4 mm thick. Initially, cell performance was quite good, with power densities in excess of 500 mw/cm^2 at 1100°C being obtained. However, this performance declined rapidly with time, and after 500 hr of operation, the power density was about one-half its initial value. Examination of the cells after operation disclosed that the $LaCoO_3$ electrode was chemically reacting with the electrolyte resulting in reaction products which were not electronically conducting. The reaction was complex and the reaction products were not completely identified. It was evident, however, that the electrolyte near the electrode was locally destabilized.

The adherence problem with $LaCoO_3$ electrodes arises from its large coefficient of thermal expansion. At 1000°C, the thermal expansion coefficient of $LaCoO_3$ is about 28 x 10^{-6} °C^{-1}, compared to a value for stabilized zirconia of about 10 x 10^{-6} °C^{-1}. Consequently, differential thermal expansion during athermal condition, particularly cooling cycles, leads to cracking and spalling of the electrodes.

Takahashi *et al.* (13) have reported on the use of ZnO cathodes doped with small amounts of Zr or Al. Conductivity data for these materials are presented in Fig. 3. They found that optimal conductivity was obtained with about 3% doping. Satisfactory results were obtained from fuel cells operated in the range of 800°-1000°C. Similar cells were tested in this Laboratory, and it was found that at temperatures above about 1000°C the ZnO attacked the zirconia electrolyte, leading to rapid failure of the cell. Below 1000°C, sat-

isfactory performance was obtained for tests of short duration.

Sverdrup *et al.* (16) have investigated the use of doped In_2O_3 and doped SnO_2 oxide films as air electrodes. Of these, Sn-doped In_2O_3 appeared the most promising as an air electrode for cells operating up to 1000°C. The electrodes were applied to the zirconia electrolyte by a vapor deposition process. Films of SnO_2 were applied in thicknesses between 10^{-3} and 10^{-2} mm; films of greater thickness than 3×10^{-2} mm led to cracking of the electrolyte during cooling of the cells. They concluded that satisfactory air electrodes could be built from doped SnO_2. In their tests with doped In_2O_3, they reported cracking of the electrode when its thickness exceeded 9×10^{-2} mm. Overvoltage measurements indicated that there was negligible electrode-electrolyte contact resistance. As-deposited electrodes exhibited high levels of gas-phase polarization, apparently due to the electrode being impervious to oxygen transport. However, a "reverse-current" treatment of the electrode, consisting of applying a voltage across the electrode/electrolyte interface with the electrode made positive compared to the electrolyte, resulted in a marked decrease in polarization. They postulated that this was due to oxygen paths opening up in the electrode during the reverse current cycle. This treatment did increase the contact resistance, however.

Another material of interest is the perovskite $PrCoO_3$. It is a good electronic conductor without doping; addition of Sr does not significantly change the over-all level of conductivity, but does result in a shift of the conductivity maximum from about 700° to 500°C (17). Like $LaCoO_3$, $PrCoO_3$ also reacts with zirconia in a complex manner. The result of this reaction in a fuel cell is an increase in resistance near the cathode/electrolyte interface, where the reaction is proceeding. However, the reaction kinetics of the $PrCoO_3$ are much slower than $LaCoO_3$ (18), and extrapolation from endurance tests on fuel cells with $PrCoO_3$ electrodes indicates that satisfactory performance should be possible for several years at cell operating temperatures of 1000°-1100°C.

Many tests have been carried out on cells with porous $PrCoO_3$ cathodes. The electrodes are applied by hand from a slurry, and are sintered *in situ* when the cell is heated to operating temperatures. Current-voltage characteristics have been obtained similar to those shown in Fig. 2. When air is used as the oxidant, the terminal voltage, and overvoltage curves fall between those shown for the 5 and 50% mixtures, as expected. Cathodes of this type typically have resistivity/thickness ratios of about 0.15 ohms/square. Using Eq. [7] this means that electrodes of 1-2 cm in length can be used without introducing significant losses. With hydrogen as the fuel and air as the oxidant, fuel cells of this construction have generated power densities of about 300 mw/cm² at 1000°C and 600 mw/cm² at 1100°C, for periods in excess of 5000 hr. Such cells, however, do not survive thermal cycling; the thermal expansion coefficient of $PrCoO_3$ is about 2.5-3 times larger than that of zirconia, which leads to interfacial stresses and spalling of the cathode during cooling. This problem does not arise on heating up a new cell, since the electrode is sintered *in situ*.

Table III. Summary of performance data on fuel cell cathodes made from electronically conducting oxides

Oxide	Investigator	Results
$Li_{0.1}Ni_{0.9}O$	GE	Li volatilizes leading to loss of conductivity.
Doped ZnO	Takahashi *et al.* (13)	Reported satisfactory at relatively low cell operating temperatures (800°C); marginal value of conductivity.
ZnO	GE	Reacted with zirconia.
Doped In_2O_3	Sverdrup *et al.* (16)	Satisfactory if applied in thin layers; some difficulty with cracking.
Doped SnO_2	Sverdrup *et al.* (16)	Satisfactory if applied in thin coatings.
$Sr_{0.1}La_{0.9}CoO_3$	Button and Archer (12)	Reacts with electrolyte; spalling and cracking during cooling cycles.
$LaCoO_3$	GE	Chemical reaction with zirconia prohibits long-term stable performance; thermal expansion mismatch.
$PrCoO_3$	GE	Satisfactory performance; capable of long-term performance; thermal expansion mismatch.

Summary

Of the three types of fuel cell cathodes considered, porous metals, oxides with current collectors, and electronically conducting oxides, the first two fail to satisfy economic criteria since they require the use of noble metals. Various types of electronically conducting oxides have been tested in fuel cells in this Laboratory and elsewhere. A summary of the results obtained with this type of electrode is presented in Table III.

It is apparent that a fully satisfactory air electrode for high temperature zirconia electrolyte fuel cells is still lacking.

Acknowledgments

The authors wish to acknowledge the assistance of T. F. Andrus, D. E. Broecker, C. W. Krystyniak, and W. A. Stoddard for their efforts in the fabrication of cells and the measurement of their properties.

Manuscript submitted Jan. 20, 1969; revised manuscript received May 2, 1969. This was Paper 355 presented at the Montreal Meeting, Oct. 6-11, 1968.

Any discussion of this paper will appear in a Discussion Section to be published in the June 1970 JOURNAL.

REFERENCES

1. H. S. Spacil, S. P. Mitoff, and C. S. Tedmon, Jr., "The Relationship of Performance and Material Properties in High Temperature Zirconia Electrolyte Fuel Cells," presented at Meeting of CITCE, Detroit, Sept. 1968.
2. H. Tannenberger and H. Siegert, "The Behavior of Silver Cathodes in Solid Electrolyte Fuel Cells," presented at the Chicago Meeting of the Amer. Chem. Soc., 1967.
3. E. Gorin and H. L. Recht, "High Temperature Fuel Cells," in "Fuel Cells," by W. Mitchell, Editor, Academic Press, p. 193 (1963).
4. H. H. Hirsch and D. W. White, Unpublished research at GE R & D Center.
5. See, for example, "Electronic Circuits and Tubes," Cruft Laboratory (Harvard University), McGraw-Hill Book Co., New York (1947), or "Electronics for Scientists," Malmstadt *et al.*, Benjamin, N.Y., 1962.
6. J. Weissbart and R. Ruka, *This Journal*, **109**, 723 (1962).
7. R. E. Honig, *RCA Rev.*, **23**, 567 (1962).
8. J. M. Dixon, L. D. LaGrange, U. Martin, C. F. Miller, and J. T. Porter, II, *This Journal*, **110**, 275 (1963).
9. E. J. W. Verwey, P. W. Haaijman, F. C. Romeijn, and G. W. van Oosterhout, *Philips Research Repts.*, **5**, 173 (1950).
10. R. R. Heikes and W. D. Johnston, *J. Chem. Phys.*, **26**, 582 (1957).
11. S. van Houten, *J. Phys. Chem. Solids*, **17**, 7 (1960).
12. D. D. Button and D. H. Archer, "Development of $La_{1-x}Sr_xCoO_3$ Air Electrodes for Solid Electrolyte Fuel Cells," presented at the Amer. Cer. Soc., Washington, D.C., Meeting, May, 1966.
13. T. Takahashi, Y. Suzuki, K. Ito, and H. Hasegawa, "The ZnO-Al_2O_3 and ZnO-ZrO_2 Systems as the Cathode Materials for Solid Electrolyte Fuel Cells," *ibid.*
14. R. R. Heikes, R. C. Miller, and R. Mazelsky, *Physica*, **30**, 1600 (1964).
15. J. B. Goodenough and P. M. Raccah, *J. App. Phys.*, **36**, 1031 (1963).
16. E. F. Sverdrup, D. H. Archer, and A. D. Glasser, "Stannic Oxide and Indium Oxide Films as Air Electrodes for High Temperature Coal Reacting Fuel Cells," presented at the Amer. Chem. Soc., Chicago Meeting 1967.
17. S. P. Mitoff, Private communication.
18. C. S. Tedmon, Jr., Unpublished research.

The Intrinsic Charging Rate Capability of the Cadmium Anode

P. Bro* and N. Marincic*

P. R. Mallory & Company, Inc., Laboratory for Physical Science, Burlington, Massachusetts

ABSTRACT

The intrinsic charging rate limitations of the cadmium anode used in a new series of Cd/AgCl cells were determined by depositing cadmium from cadmium chloride solutions on plane electrodes in half-cells under constant current conditions at current densities between 30 mA/cm^2 and 3.48 A/cm^2. The charging was terminated at the onset of hydrogen evolution. Very fast charging rates were obtained, but at the expense of the specific capacity of the electrodes. The maximum specific capacities were 0.54 mAhr/cm^2 at the 1000*C* rate, 1.6 mAhr/cm^2 at the 100*C* rate, and 5.4 mAhr/cm^2 at the 10*C* rate.

The search for battery electrodes capable of accepting very high charging rates with impunity led us to an examination of a variety of conventional and novel electrode systems. The cadmium electrode was of particular interest because of its favorable characteristics in regard to hydrogen evolution. It is used extensively in alkaline cells, but the alkaline electrolytes do not provide the conditions most favorable for the high rate charging of cadmium anodes, and conventional cells are capable of only low or moderate charging rates.

We have examined the rate capability of the cadmium electrode in solutions more likely to accept high charging rates than alkaline solutions, and we have developed a new series of rechargeable Cd/AgCl cells capable of very fast charging operations. Since the rate of charging of an anode would be limited by any concomitant evolution of hydrogen, we adopted the criterion that the maximum charging rate be defined by the onset of hydrogen evolution. Normally, hydrogen evolution occurs when the electrolyte or the discharged material adjacent to the electrode becomes depleted in reducible ions, cadmium ions in this case.

Two types of processes may be distinguished in the charging of electrodes, *viz.*, solid-solid and solid-solution reactions. Although an electrode may function in either mode, depending on the current density and the chemical properties of the system, one of these mechanisms generally dominates. We have found that the solid-solution type of operation has the higher intrinsic rate capability of the two, and we selected it for a more detailed analysis. Because of the hydrolysis of cadmium salts in neutral and alkaline solutions we chose to work with acid electrolytes in which appreciable concentrations of dissolved cadmium salts can be obtained. The rate capability of the cadmium anode would be given, therefore, by the rate of supply of cadmium ions to the electrode via a solution diffusion process.

If no other limiting factors intervene the useful charging of a battery will be terminated by the shorting of the cells due to the formation of dendrites. Although dendrites may appear before the depletion point is reached, they are most likely to appear when the depletion point is reached. Therefore, the depletion of cadmium ions at the electrode represents a reasonable definition for the end of efficient charging.

The depletion point can be determined by chronopotentiometric measurements (1). The electrode is charged at a constant rate, and the time is noted when the electrode potential shifts from that of the deposition of the active material to that of hydrogen evolution. This transition time signals the end of efficient charging, and it is a function of the current density, the compositon of the solution, and the geometry of the electrode.

* Electrochemical Society Active Member.

Experimental Techniques

The charging experiments were conducted at 25° ± 1°C in the cell shown in Fig. 1. The cell was designed to give a uniform current density at the electrode, and the cadmium was deposited on a platinum substrate with a 0.81 cm diameter. The diameter of the platinum disk was made equal to the inner diameter of the solution cavity to eliminate edge effects.

Conventional circuitry was used for the chronopotentiometric measurements with current pulses derived from a 240V stack of lead-acid batteries. An Ebert Electronics, Model HD-4, mercury switch gave fast and clean switching at all the currents used. The maximum change in the current during any one pulse was 2.3%, attributable to the changing resistance of the cell during the pulse. The currents were measured with an accuracy of ±0.5% with a Greibach Model 700 ammeter. A battery derived bias voltage was used with the cadmium reference electrode to position the pulse suitably on the Tektronix Model 550 CRO screen, and the traces were recorded photographically. The time scale of the CRO was calibrated with a Servomex waveform generator, Model LF141, and the transition times were taken at the point of inflection of the voltage-time curves.

The cadmium chloride solutions were prepared from analytical grade reagents and the cadmium concentration of the stock solutions was determined polarographically. The precipitates formed as a result of the hydrolysis of cadmium chloride were dissolved by the addition of just sufficient perchloric acid to clear the solutions. The resulting *p*H values are given in Table I.

The solutions were deaerated with nitrogen, and a nitrogen blanket was maintained over the solutions. The platinum electrode was restored after every pulse by the anodic dissolution of the cadmium to the point

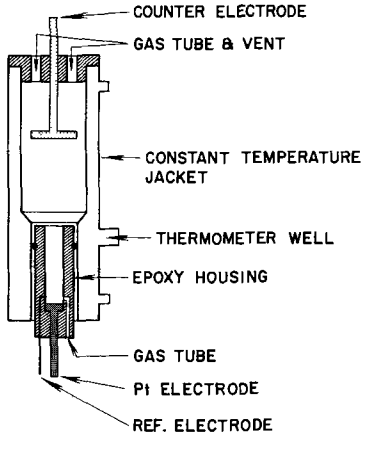

Fig. 1. Experimental cell

Table I. Transition time behavior of $CdCl_2$, 25° ± 1°C

$CdCl_2$, m/l	$NaClO_4$, m/l	pH	Current range mA/cm²	$(it^{1/2}/C)$* Asec$^{1/2}$ cm/mole
0.1	0	6.4	50-340	1030 ± 23
0.1	0.1	6.6	30-200	693 ± 26
0.1	0.3	6.6	30-200	650 ± 28
0.1	1.0	6.6	30-200	710 ± 22
0.1	1.5	6.3	30-200	660 ± 30
0.1	2.0	6.0	30-200	670 ± 33
0.3	0	6.4	190-970	940 ± 47
0.3	0.1	6.2	115-810	770 ± 23
0.3	0.3	6.4	115-700	720 ± 12
0.3	1.0	6.3	115-700	705 ± 21
0.3	1.5	6.1	115-580	730 ± 9
0.3	2.0	5.8	115-580	723 ± 49
1.0	0.1	5.3	390-1930	610 ± 38
1.0	0.3	5.5	390-2320	610 ± 14
1.0	1.0	5.3	390-1930	560 ± 16
1.0	1.5	5.0	390-1930	555 ± 24
1.0	2.0	5.0	390-1750	552 ± 18
1.5	0.1	4.9	580-2910	585 ± 12
1.5	0.3	5.0	580-2910	575 ± 13
1.5	1.0	4.8	580-2910	540 ± 13
1.5	1.5	4.6	580-2910	440 ± 44
1.5	2.0	4.5	580-2320	515 ± 24
2.0	0.3	4.7	780-3480	545 ± 18
2.0	1.0	4.5	580-3480	525 ± 31
2.0	1.5	4.2	580-3480	515 ± 7
2.0	2.0	4.2	580-3480	480 ± 10

* Extrapolated to a vanishing current density.
The precision is specified by the standard deviation about the linear plot of the chronopotentiometric constant *vs.* the current density.

of incipient oxygen or chlorine evolution when the solution was again degassed with nitrogen.

Experimental Results

The chronopotentiometric transition time for a simple reduction process is given by (2)

$$(it^{1/2}/C) = \tfrac{1}{2}\, n\mathbf{F}(\pi D)^{1/2} = \text{a constant for a fully supported electrolyte solution.}$$

It was found that $(it^{1/2}/C)$ increased with the current density, Fig. 2, but its rate of change with the current density, $\partial/\partial i(it^{1/2}/C)$, decreased as the concentration of the supporting electrolyte increased. The current dependency of $(it^{1/2}/C)$ was expected for neither a fully supported nor a partially supported solution, as may be seen from the equations of Morris and Lingane (3). The most probable cause was the increasingly significant resistive component of the overvoltage associated with a decreasing concentration of the supporting electrolyte. The greater the resistive component, the more the initial portion of the transition region would be occluded, and the transition time would appear to increase with the current density. The displacement of the transition time would be expected to decrease as the concentration of the supporting electrolyte increased, as observed, and it would be expected to vanish as the current density approached zero, as was found to be the case. All the data for each of the solution compositions were therefore extrapolated to a zero current density to obtain the $(it^{1/2}/C)$ values given in Table I. The anodic oxidation of the cadmium deposits showed that the deposition process occurred without any side reactions.

The transition time group, $(it^{1/2}/C)$, had an average value of 516 A · sec$^{1/2}$ · cm/mole in the 2M $CdCl_2$ solution, and it extrapolated to 730 Asec$^{1/2}$ cm/mole for a vanishing $CdCl_2$ concentration. At any one $CdCl_2$ concentration the value of the transition time group increased slightly as the concentration of the supporting electrolyte decreased, the change being appreciable only for supporting electrolyte concentrations below 0.1M $NaClO_4$.

The *p*H of the solutions did not affect $(it^{1/2}/C)$ above *p*H 3.0. In the unsupported solutions the acid acted as a supporting electrolyte below *p*H 3.0 and $(it^{1/2}/C)$ changed in the expected manner.

The charging rate capabilities of the cadmium anode calculated from the transition time data are presented in parametric form in Fig. 3. The data show that the rate capability and the attainable specific capacity increased markedly with the cadmium concentration of the solutions, the relative increase being more marked at the lower cadmium concentrations. A charging rate of *e.g.* 200C would appear to be feasible, but it would give a low specific capacity of about 1 mAhr/cm². High specific capacities could not be obtained at the high charging rates, a capacity of 5 mAhr/cm² being the maximum obtainable at the 10*C* rate.

Discussion of the Results

The most significant result of the investigation was the observation that the cadmium electrode could be charged at very high rates in the cadmium chloride solutions, but that low specific capacities resulted for the fast charging regime. The chronopotentiometric equations provided a convenient formalism for correlating the charging rate and the electrode capacity, and their applicability suggested that the charging process was diffusion controlled. In principle, the behavior of the electrode can therefore be described by the diffusion coefficient of Cd^{+2} or of $CdCl_2$ depending on whether or not a supporting electrolyte is used. However, no data are available in the literature for cadmium salt solutions more concentrated than 0.0127M Cd^{+2} (4), and extrapolations to the concentrations used in our studies cannot be made with a high degree of confidence. The results for the 2.0M $NaClO_4$ solutions could be correlated with a diffusion coefficient of the Cd^{+2} ion of 11.8 x 10^{-6} cm²/sec which may be compared with the most recent literature value of 7.2 x 10^{-6} cm² sec (5) for dilute solutions containing $Cd(NO_3)_2$ and KNO_3. The diffusion coefficient of the salt cannot be obtained from our data. It appears that whether the use of the diffusion equations can be justified on theoretical grounds or

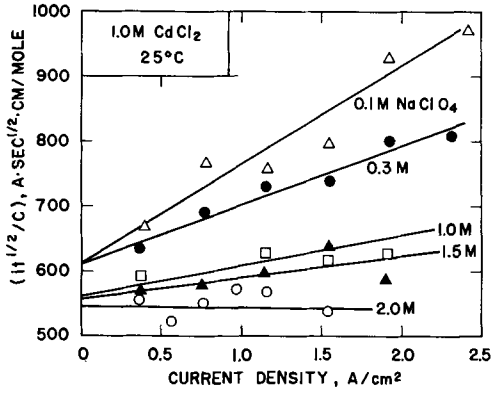

Fig. 2. Influence of the current density on the chronopotentiometric behavior.

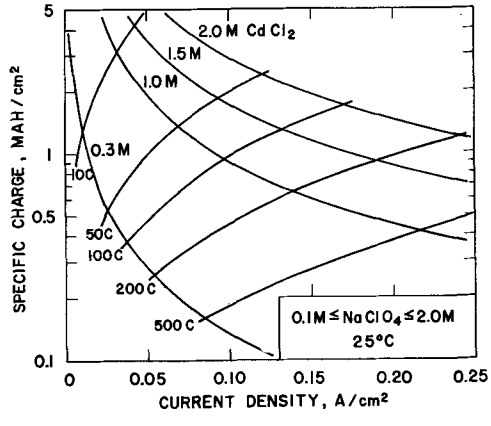

Fig. 3. Intrinsic performance curves for the charging of flat cadmium electrodes in acid solutions.

not they give a good estimate of the rate-capacity relationship of the electrode.

The changes of $(it^{1/2}/C)$ caused by the variations in the composition of the electrolyte are associated with the solution equilibria and the transference properties of the ions in a manner analogous to that discussed for zinc chloride solutions (6). However, they will not be discussed here since we are interested primarily in the charging rate of the electrode.

The experimental results indicated that highly concentrated cadmium chloride solutions were needed to achieve the ultra-fast charging rates. There was a practical upper limit to the attainable cadmium ion concentration because of the hydrolysis of the cadmium salts which led to the precipitation of $Cd(OH)_2$. The higher the concentration of the cadmium salt the lower must be the *p*H, and the more readily was hydrogen evolved during charging. A *p*H of about 6.6 could be maintained in the 0.1M $CdCl_2$ solutions without causing any $Cd(OH)_2$ precipitation, whereas the *p*H had to be maintained at about 4.2 in the 2.0M $CdCl_2$ solutions. The $(it^{1/2}/C)$ parameter decreased noticeably below about *p*H 3, *i.e.*, the specific capacity decreased.

Whereas the use of a completely unsupported cadmium salt solution would give a slightly higher rate capability than a supported solution, its use in a porous electrode would not be tolerable because of depletion polarization. In pure $CdCl_2$ solutions the deposition of Cd would deplete the reaction layer of charge carriers with a consequent resistive choking of the electrode. In porous electrodes, current penetration into the interior would be completely blocked in the absence of a supporting electrolyte. Furthermore, we observed that highly dendritic cadmium deposits were formed in the absence of a supporting electrolyte.

There was an upper limit to the amount of supporting electrolyte that could be used. The approximate rule appeared to hold that if the total salt concentration exceeded about 5 mols/liter, a solid phase would precipitate. Some of the solution conductivities are given in Table II. A high cadmium ion concentration was needed to achieve a high charging rate, yet a high supporting electrolyte concentration was also needed to achieve the same result. A 2M $CdCl_2$ concentration represented a reasonable compromise between the two conflicting requirements.

The experimental data are directly applicable to nonporous, flat cadmium electrodes, and the permissible operating regimes of such electrodes may be read directly from Fig. 3. More information would be needed for the application of the experimental data to porous electrodes, *e.g.*, the current distribution and the electrolyte thickness distribution in the electrode. Although the necessary calculations are possible in principle, adequate models remain to be developed to render the calculation practically meaningful. The more serious problem is the electrolyte thickness distribution in the electrode. In a porous electrode the local electrolyte layers are thinner and more complex in shape than the plane diffusion layer obtained in the chronopotentiometric experiments, and a lower rate capability would prevail in the interior of a porous electrode than at its front surface. It follows that for systems operating via a solution-solid charging process there is an optimum electrode thickness

Table II. Solution conductivities

$CdCl_2$ concentration, mols/l	Solution conductivity, ohm^{-1} cm^{-1} 10^3 $NaClO_4$ concentration, mols/l				
	0	0.5	1.0	1.5	2.0
1.0	26	52	70	84	101
1.5	26	48	64	75	91
2.0	25	44	57	68	80
2.5	22	38	50	63	72
3.0	19	34	43	55	61

for ultra-fast charging which is very small. The less soluble the salt from which the active material is obtained, the greater should be the effective participation of the interior of a porous electrode until the extreme case is reached of solid-solid transformation systems where very large interior surface areas are a pre-requisite for efficient charging. However, the intrinsic rate capability of solid-solid transformation systems is considerably less than that of solution-solid transformation systems.

Data on porous cadmium electrodes in alkaline electrolytes (7) indicate that they may possibly be charged at current densities of 200 mA/cm^2, based on the superficial electrode areas, to give a specific capacity of 5.1 $mAhr/cm^2$. This means that the porous cadmium electrode in an alkaline cell would have a higher capacity than a flat nonporous cadmium electrode in an acid cell at rates below about 150C. If the comparison is made on the basis of the actual surface areas rather than the superficial areas, the alkaline cadmium electrode can be operated at rates up to 0.005 mA/cm^2 to give a specific capacity of $1.3 \cdot 10^{-4}$ $mAhr/cm^2$, and the cadmium electrode operating in a cadmium chloride electrolyte would have the higher specific capacity at all rates of interest. The preceding remarks notwithstanding, it is believed that a realistic comparison must await data on comparable structures.

It is implicit in our studies that the conclusions are limited to constant current charging operations. No consideration was given to the optimization of the time profile of the charging current and the question remains open whether suitably shaped current profiles or pulse sequences may give greater net charging rates than those reported here.

The application of the cadmium charging rate data to rechargeable Cd/AgCl cells will be considered in a subsequent publication.

Manuscript submitted Nov. 6, 1968; revised manuscript received April 29, 1969.

Any discussion of this paper will appear in a Discussion Section to be published in the June 1970 JOURNAL.

REFERENCES

1. P. Delahay, "New Instrumental Methods in Electrochemistry," Interscience, New York (1954).
2. H. J. S. Sand, *Phil. Mag.*, **1**, 45 (1901).
3. M. D. Morris and J. J. Lingane, *J. Electroanal. Chem.*, **6**, 300 (1963).
4. M. Shinagawa and F. Nakashima, *J. Sci. Hiroshima Univ.*, Ser. A, **23**, 445 (1960).
5. Ya. V. Durdin and E. S. Svetashova, *Elektrokhimiya*, **4**, 1217 (1968).
6. P. Bro and N. Marincic, *This Journal*, **116**, 448 (1969).
7. J. C. Duddy and A. J. Salkind, *ibid.*, **108**, 717 (1961).

The Dissolution of MgO and $Mg(OH)_2$ in Aqueous Solutions

David A. Vermilyea*

Research and Development Center, General Electric Company, Schenectady, New York

ABSTRACT

This paper reports studies of the rates of dissolution of natural Brucite, optical grade MgO, and commercial $Mg(OH)_2$ in aqueous solutions. Natural Brucite dissolves by means of a surface reaction requiring protons, and while some protonated ions accelerate the dissolution no inhibitors were found. Dissolution of less perfect $Mg(OH)_2$ is normally diffusion limited; several substances which reduced the rate of dissolution of such $Mg(OH)_2$ were found. MgO first reacts with water to form an $Mg(OH)_2$ layer and the rate is controlled by dissolution of the $Mg(OH)_2$.

This paper is part of an effort aimed at relating the corrosion of metals with the dissolution rates of corrosion products formed on the metal surfaces. A recent study of aluminum corosion (1, 2) and inhibition has demonstrated that new understanding of corrosion phenomena as well as new ways of combating corrosion can be discovered by this approach.

In this report the dissolution behavior of MgO and $Mg(OH)_2$ in a variety of aqueous solutions is discussed. Perhaps the most interesting features of the dissolution are the following. Crystals of $Mg(OH)_2$ (natural Brucite) dissolve at rates limited either by a surface reaction or by proton arrival; the direct removal of Mg^{+2} and OH^- from the lattice into the solution seems to be slow. This behavior has the consequence that most proton donors such as carboxylic acids or inorganic oxyanions accelerate rather than inhibit the dissolution. Finely crystalline $Mg(OH)_2$ seems always to dissolve at a rate limited either by diffusion of protons to the surface or of dissolved species away. MgO behaves like Brucite at low *p*H and like finely crystalline $Mg(OH)_2$ at higher *p*H. It is probably always covered with a thin $Mg(OH)_2$ layer, and its rate of dissolution is controlled by dissolution of the $Mg(OH)_2$. The implications of these findings for corrosion of magnesium are discussed.

Experimental

The dissolution rates were determined by suspending 10-30μ diameter powders in the slowly stirred solution and computing the rate from the rate of change of *p*H. The *p*H was measured with a Corning model 12 *p*H meter and recorded on a Varian Model 14A-1 strip chart recorder. The initial *p*H of the 10^{-1}M KCl solution used in all experiments was about 3 and rose as the powder dissolved, so that a single experiment provided data for a wide *p*H range. Identical results were obtained using $KClO_4$ solutions. Most experiments were conducted at 25°C. Compared to methods based on titration, this method offers the advantages of speed and generation of data over a wide *p*H range from a single experiment.

Two major problems were encountered with this technique. The first was that the response of the glass electrode is very sluggish in unbuffered solutions between *p*H 6 and 8, so that only very low dissolution rates could be determined in that *p*H range. At *p*H 7 the time required to reach a stable reading following the addition of a small amount of acid or base to a 1M KCl solution was about 100 sec. A platinum-hydrogen electrode was somewhat faster but could not be used in all solutions and was subject to poisoning.

The second major problem was that the measured *p*H change following addition of acid or base to a solution containing no MgO or $Mg(OH)_2$ and having a *p*H in the range 5-9 was substantially less than that calculated from the known amounts added; Fig. 1 shows a typical result. It is believed that this effect results from traces of proton donors and acceptors in the solution, for in very carefully purified solutions made with water having a resistivity of 2×10^7 ohm-cm and dissolved spectroscopic KCl crystals for solute the effect was nearly absent. The use of such highly purified solutions did not change the results of dissolution rate studies, however, and as a practical expedient ordinary laboratory distilled water and reagent grade chemicals were used, and the calculated rates were corrected using data like that in Fig. 1. The same procedure was used for experiments in which a proton acceptor or donor was deliberately added, in which case the curve corresponding to Fig. 1 had a much more pronounced minimum.

The dissolution was conducted in a 1-l Pyrex vessel containing a Teflon covered magnetic stirrer, thermometer, and ports for inert gas inlet and outlet and for powder addition. Most of the results were obtained using an atmosphere of nitrogen purified by passing it over Ascarite to remove CO_2. Air or hydrogen gave indistinguishable results.

Powders of 10-30μ diameter were obtained by sieving and sedimentation in alcohol, followed by drying $Mg(OH)_2$ at 150°C and MgO at 400°C, and storage in a desiccator containing ascarite and anhydrous $CaSO_4$. Natural Brucite crystals were obtained from Ward's and ground in alumina mortars and ball mills. The natural Brucite contained 0.3% Ca, 0.05% Fe, 0.05% Mn, 0.02% Si, 0.02% Ba, 0.01% Al, and 0.001% Cu. The dissolution of 10^{-4} m/l (moles per liter) (a typical amount) of this material would introduce a maximum concentration of impurities of $5 \cdot 10^{-7}$ m/l, which is negligible. The MgO was ground from fused optical

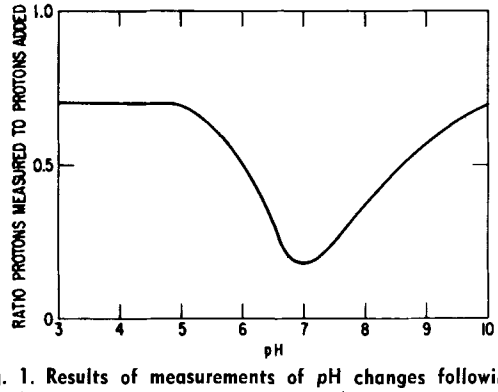

Fig. 1. Results of measurements of *p*H changes following additions of known amounts of HCl to a 10^{-1}M KCl solution.

* Electrochemical Society Active Member.

grade crystals obtained from Norton and from General Electric. Other $Mg(OH)_2$ powders were obtained by sedimentation fractionation of reagent chemicals and the "particles" were actually clumps of finely crystalline material. Examination of the various powders with a microscope confirmed that the particles were of reasonably uniform size and that the size was about that expected from a calculation based on Stoke's law.

The following method was used to calculate the dissolution rate from the pH change. Hydroxyl ions added from the dissolving crystals are utilized in two ways: to combine with protons and to increase the OH^- concentration of the solution. A mathematical description of this situation is

$$dN_{OH^-} = dC_{OH^-} - dC_{H^+} \quad [1]$$

in which N_{OH^-} is the number of hydroxyl ions (expressed as a concentration) dissolved from the crystal. Now using the following relationships

$$C_{H^+} = \exp(-2.3\,pH) \quad [2]$$

$$dC_{H^+} = -2.3 \exp(-2.3\,pH)\,d(pH)$$

$$= -2.3\,C_{H^+}\,d(pH) \quad [3]$$

$$C_{OH^-} = \frac{K_w}{C_{H^+}} \quad [4]$$

$$dC_{OH^-} = -\frac{K_w}{C_{H^+}^2}\,dC_{H^+} \quad [5]$$

$$= \frac{K_w}{C_{H^+}}\,2.3\,d(pH) \quad [6]$$

in which K_w is the dissociation constant of water, Eq. [1] reduces to

$$dN_{OH^-} = 2.3\,d(pH)\,(C_{OH^-} + C_{H^+}) \quad [7]$$

Using Eq. [7] the rate of addition of hydroxyl ions by dissolution is computed from the rate of change of pH and corrected by dividing by the ratio obtained at the appropriate pH from a curve like Fig. 1 for the solution used. The rates of dissolution were expressed as moles cm^{-2} sec^{-1}, the area being calculated from the particle size assuming the particle surfaces were smooth. The surface area was corrected for the amount of material dissolved.

Curves of rate *vs.* pH obtained for a particular sample of powder were reproducible to about 50%, and hence it is considered that the form of the curves is accurate, but because of uncertainties in the absolute area of the powders and because of effects of powder history the magnitudes of the rates should only be considered correct as to order of magnitude.

Results and Discussion

MCB $Mg(OH)_2$.—Figure 2 shows data for the dissolution of $Mg(OH)_2$ obtained from Matheson. Coleman, and Bell, and designated "MCB." The particles of this material are clumps of finer particles, and it is very reactive, probably because of a very high true surface area. When less than about 25% of the added powder has been consumed, the rate is quite simply diffusion limited as shown by the agreement between the calculated curve of Fig. 2 and the experimental points. The calculated curve was based on the assumption of spherical particles 2×10^{-3} cm in diameter. When about 50% of the powder has been dissolved away and then the solution acidified with HCl to make another run, the rate is considerably slower at pH > 4. At pH < 6 the rate is then controlled by arrival of protons at the surface, and from pH 6 to 9 the rate is approximately constant. Evidently there are two modes of dissolution for MCB material, one for highly active surfaces and one for surfaces produced by a considerable amount of dissolution. Probably the material which gave the lower curve of Fig. 2 still had some

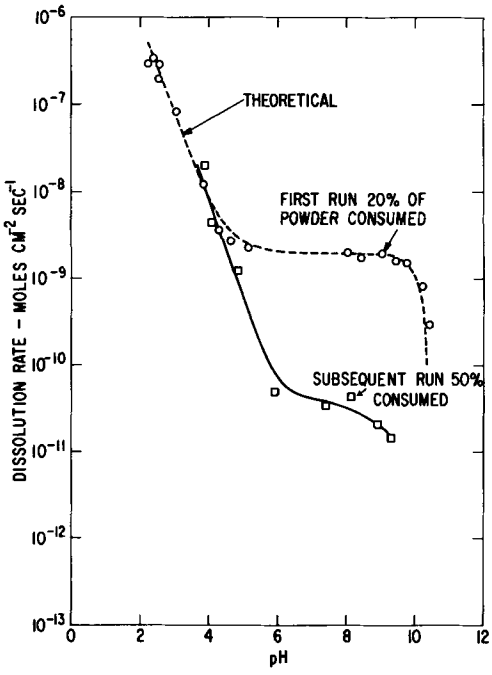

Fig. 2. Dissolution of MCB $Mg(OH)_2$ in 10^{-1}M KCl at 25°C. The dashed curve is calculated assuming control by diffusion of protons to the surface and of dissolved Mg^{+2} and OH^- away.

"active" surfaces and these were responsible for the approximately constant rate at pH 6-9.

Natural Brucite.—Natural Brucite behaves initially like MCB at pH > 5, except that the rates are lower than for MCB material. The first run (Fig. 3) already shows a rate which is nowhere diffusion limited, and after about 25% of the material has been dissolved, the rate finally reaches values which fall close to the theoretical line for control by proton arrival. Subsequent runs on the same sample give results indistinguishable from those for the third run. Such a low-rate sample will be referred to as "aged." It seems plausible that the initial, unaged surfaces contain

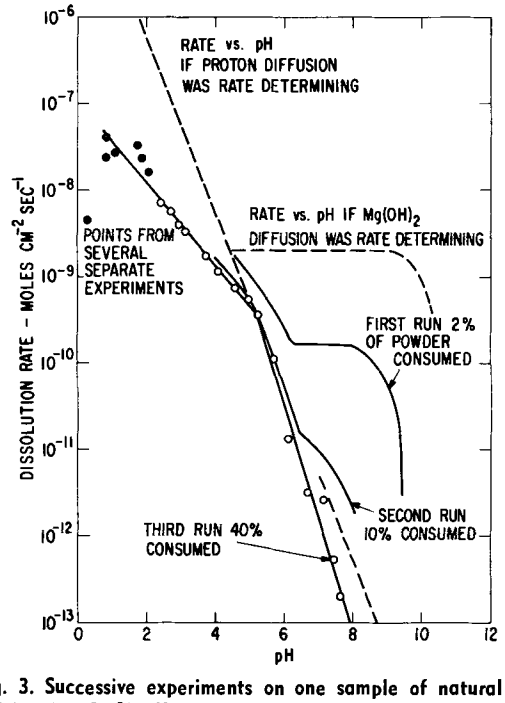

Fig. 3. Successive experiments on one sample of natural Brucite dissolving in 10^{-1}M KCl at 25°C. The open circles are from the third run only. Closed circles are from separate experiments, and indicate the greater uncertainty of the measurements at low pH.

"active" regions like those on the MCB material, and that these account for the higher rates of the first run.

The possibility that some impurity was dissolving into the solution from the natural Brucite and inhibiting the dissolution was investigated in two ways. First, some natural Brucite was dissolved completely to give a concentration more than ten times that normally reached, and then a fresh sample was introduced. No effect of the dissolved material could be detected. Second, a sample of natural Brucite was placed in the vessel at pH 10.55 with $2 \cdot 10^{-4}$ m/l $MgCl_2$ in the solution and left 50 hr. The initial run on that sample was very close to the second run in Fig. 3, although only 0.4% was consumed. Thus simply equilibrating the powder with the solution suffices to remove the highly active regions and the behavior is then like that of an aged sample.

At pH < 5 the curve deviates markedly from the proton diffusion line, and the dependence on proton concentration can be represented by the equation

$$\text{Rate} = \text{Const.}\ C_{H^+}{}^{0.47} \qquad [8]$$

Evidently the dissolution is controlled by a surface reaction in this pH range. A simple theory (3) of dissolution of oxides and hydroxides based on removal of hydroxyl ions by reaction with protons predicted that the dissolution rate of the hydroxide of a divalent metal would vary as $C_{H^+}{}^{2/3}$. According to the theory a dependence as in Fig. 3 could arise because of a low value of the transfer coefficient for cations. If, for example, the cation transfer coefficient was 0.35 and the anion transfer coefficient 0.7 the predicted exponent would be ½.

The fact that the curve for the third run at pH > 5 does not exactly follow the proton diffusion curve is probably the result of surface structure changes accompanying dissolution. Figure 4 shows some effects of such sample history. The sample was first dissolved between pH 4 and 8, then HCl was added to bring the pH to 5.2. There was a transient during which the rate increased with pH for a short time, followed by the usual decrease. Because of such history effects the absolute values of rates in this pH range are subject to a considerable uncertainty. The effect of adding Na_3PO_4 will be discussed in the section on accelerators and inhibitors.

Mechanism of $Mg(OH)_2$ *dissolution.*—The results for $Mg(OH)_2$ indicate the following. For single crystal particles (natural Brucite) the dissolution mechanism involves a surface reaction between hydroxyl ions and protons. At pH < 5 this surface reaction is rate determining and the rate increases roughly as the square root of the proton concentration. Above pH 5 proton arrival is the slow step, and there are some minor variations due to changes in surface activity. These surface activity changes may involve poisoning of portions of the surface or possibly changes in the number of surface steps and kinks.

A possible alternative mechanism, namely, direct removal of Mg^{+2} and OH^- ions at active sites and control by diffusion of such ions away from the crystal predicts a constant rate between pH 5 and 9 in conflict with experiment; the reasoning is as follows. The rate of removal of Mg^{+2} and OH^- together from such regions would be proportional to the product of the diffusion coefficient and concentration, $D_{Mg(OH)_2}\ C_{Mg(OH)_2}$. The rate of arrival of protons at such sites would be proportional to $D_{H^+}\ C_{H^+}$. In order for protons to influence the rate significantly it is necessary that

$$D_{H^+}\ C_{H^+} \gtrsim D_{Mg(OH)_2}\ C_{Mg(HO)_2} \qquad [9]$$

Using $D_{H^+} = 10^{-4}$, $D_{Mg(OH)_2} = 10^{-5}$, $C_{Mg(HO)_2} = 10^{-4}$ we obtain $C_{H^+} \gtrsim 10^{-5}$. Thus above pH 5 the proton concentration should not influence the rate, but at pH > 9 ($C_{OH^-} > 10^{-5}$) the rate would fall because of the common ion effect.

$Mg(OH)_2$ crystals normally have some (natural Brucite) or many (MCB) highly active regions from which direct removal of Mg^{+2} and OH^- is possible, and for such regions the rate is limited by arrival of protons or by diffusion away of dissolved $Mg(OH)_2$. These active regions give rise to a roughly constant rate from pH 5-9.

MgO.—The MgO powder comprised single crystal particles, and x-ray diffraction did not detect the presence of any $Mg(OH)_2$, although infrared absorption showed a small $Mg(OH)_2$ peak. Figure 5 shows that below pH 6 the dissolution behavior is similar to that for natural Brucite, while at pH 6-8 there is a nearly constant rate followed by a decreasing rate at pH 8-10.

It is proposed that the MgO first reacts to form $Mg(OH)_2$ and that dissolution of the latter is rate

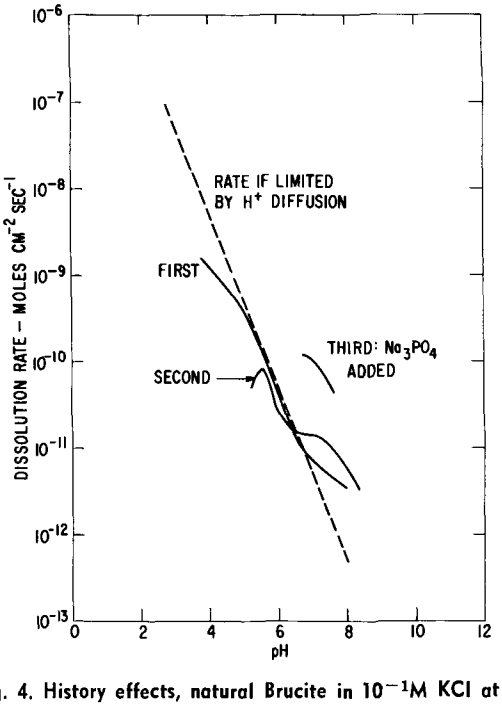

Fig. 4. History effects, natural Brucite in 10^{-1}M KCl at 25°C

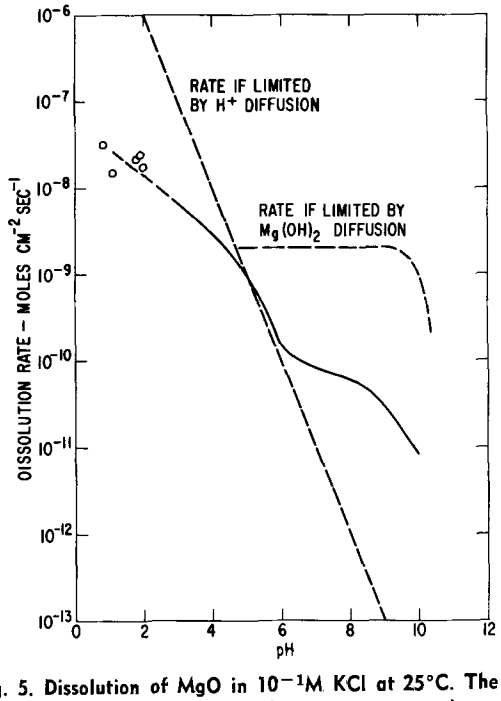

Fig. 5. Dissolution of MgO in 10^{-1}M KCl at 25°C. The individual points at low pH indicate the greater uncertainty of these measurements.

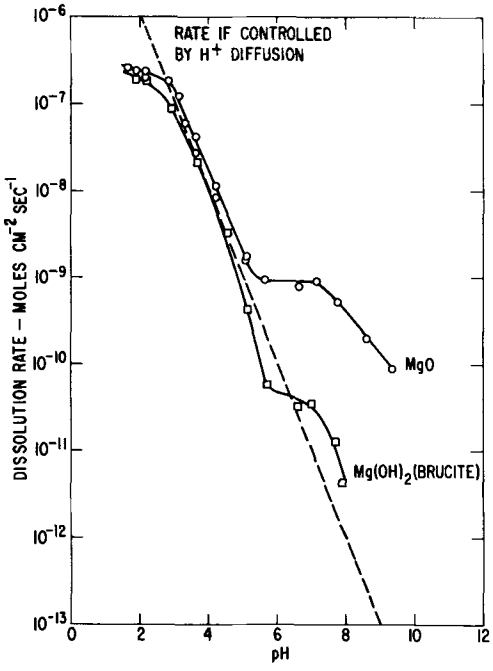

Fig. 6. Dissolution of MgO and natural Brucite in 10^{-1}M KCl at 75°C.

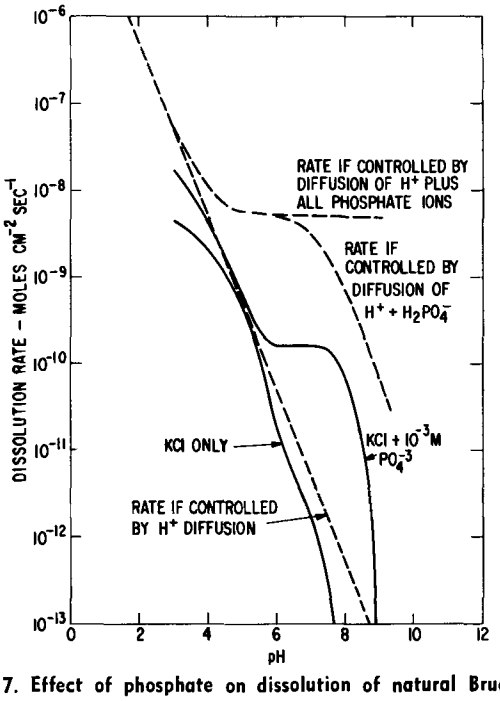

Fig. 7. Effect of phosphate on dissolution of natural Brucite at 25°C.

determining. The solubility of MgO is calculated to be about sixty times that of $Mg(OH)_2$, so it is reasonable that it should dissolve rapidly on initial exposure and become covered with a layer of $Mg(OH)_2$. The $Mg(OH)_2$ layer would probably in part be of the active type, hence the high rate (compared to Brucite) at pH > 6. Electron microscopic examination did not detect the proposed $Mg(OH)_2$ coating, which is probably very thin.

Effect of temperature.—Figure 6 shows results at 75°C for MgO and natural Brucite. At pH < 3 the rate appears to be limited by the surface reaction, which proceeds about ten times as fast as at 25°C. Such a change is consistent with an activation energy of about 10 kcal/mole. The dissolution of natural Brucite at pH > 3 is again controlled by proton arrival and the rate is only slightly higher than at 25°C. MgO dissolution is controlled by proton arrival at pH 3-5, while at higher pH direct dissolution of Mg^{+2} and OH^- plays a dominant role. At pH 5-7 the rate for MgO is nearly that expected if the surface were entirely covered with $Mg(OH)_2$ and if diffusion away of the latter controlled the rate.

Effects of solution composition.—Natural Brucite.—Many substances added to the solution were without effect on dissolution of natural Brucite. These included I^-, ClO_4^-, Na^+, Pb^{+2}, Ni^{+2}, Al^{+3}, Ca^{+2}, $Fe(CN)_6^{-4}$, and $(C_4H_9)_4N^+$. Several substances accelerated the dissolution in a limited pH range; the effect of phosphate is shown in Fig. 7. The accelerators, which include acetate, chromate, periodate, germanate, and tellurate are all substances which form protonated ions. However, not all protonated ions are accelerators. For instance, borate has no effect on the dissolution rate, and phosphate is not effective at higher pH. In fact, it seems that pK_a should be in the range of about 5 to 8 for a proton containing ion present at 10^{-3} m/l to accelerate dissolution of natural Brucite.

It seems likely that accelerators exert their influence by reacting directly with surface hydroxyl ions just as do protons. If pK_a is too small, then few protonated ions will be present except at low pH, where the more reactive protons are present in greater numbers. If pK_a is too large the proton is bound so tightly that it does not react readily with hydroxyl ions in the crystal.

One other possible effect of accelerators is that they might change the surface to one containing more highly active material. The third run of Fig. 4 shows that the addition of phosphate to an aged surface immediately increases the rate about an order of magnitude, and it therefore seems probable that a different type of surface is not the only factor involved in the acceleration.

No substances were found to inhibit the dissolution of natural Brucite.

MgO *and MCB* $Mg(OH)_2$.—A few moderately effective inhibitors of dissolution of these compounds were found, along with a large number of ineffective substances. Figure 8 shows the effects of periodate, one

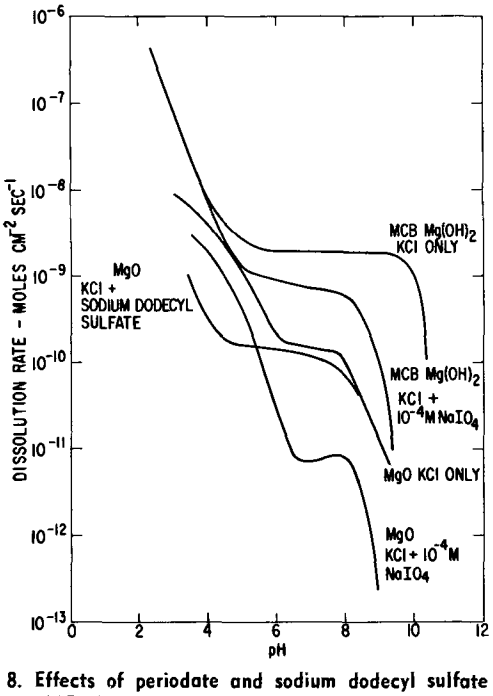

Fig. 8. Effects of periodate and sodium dodecyl sulfate on dissolution of MCB $Mg(OH)_2$ and MgO at 25°C.

of the strongest inhibitors, and sodium dodecyl sulfate. The greatest effect for periodate is found at pH > 8, while sodium dodecyl sulfate is only effective at pH < 6. The dodecyl sulfate ion is probably attached to the surface by the high positive charge of the particles at low pH, as well as by the repulsion between water and the aliphatic hydrocarbon portion of the ion.

Periodate, germanate, tellurate, vanadate, and tellurite are about equally strong inhibitors; arsenite, arsenate, and permanganate are very weakly effective. It is believed that these ions are effective because they are able to fit the structure of the $Mg(OH)_2$ and to make strong bonds with its surface. As with Al_2O_3 (2), the effective ions all fall in a small region of a plot of radius ratio against proton level (Fig. 9); the corresponding quantities for $Mg(OH)_2$ are also in the same region at pH 10. The radius ratio is believed to determine the structural fit of the ion and the surface, while the proper proton level is probably necessary in order that strong hydrogen bonds can be formed.

Some ineffective substances not shown in Fig. 9 are NH_4^+, dimethyl formamide, palmitic acid, and $Fe(CN)_6^{-4}$. The absence of an effect for $Fe(CN)_6^{-4}$, which should be strongly attracted to the positively charged particles, shows that electrostatic effects alone will not suffice to produce inhibition.

Implications for corrosion of magnesium.—The corrosion product formed on magnesium in aqueous solutions is usually $Mg(OH)_2$, and some protection is provided by this product. To the extent that the corrosion product resembles aged natural Brucite these results do not offer much hope that good inhibitors can be found. If the product resembles MCB $Mg(OH)_2$, however. then there are some possibilities for inhibition. It seems unlikely that the corrosion product would comprise $Mg(OH)_2$ crystals as perfect as those of natural Brucite, and more probable that some highly active surfaces would be present. It therefore seems likely that some of the inhibitors of MCB $Mg(OH)_2$ may also be effective for the metal. Studies to test this prediction are in progress.

Comparison with previous studies.—A reviewer has pointed out that Brunner (5) studied dissolution of $Mg(OH)_2$ in various organic acids and in HCl. Those studies were conducted for the purpose of verifying the Nernst diffusion layer theory of heterogeneous reactions. Rather concentrated solutions (compared to the present studies) were used (acid concentrations 0.02 to 0.05 equivalents/liter), and the rate of dissolution was shown to be always diffusion limited. There are no data showing surface reaction limited rates of dissolution with which the present experiments can be compared.

Conclusions

1. The mechanism of dissolution of natural Brucite involves a surface reaction between protons and hydroxyl ions. The activation energy for this process is about 10 kcal/mole.

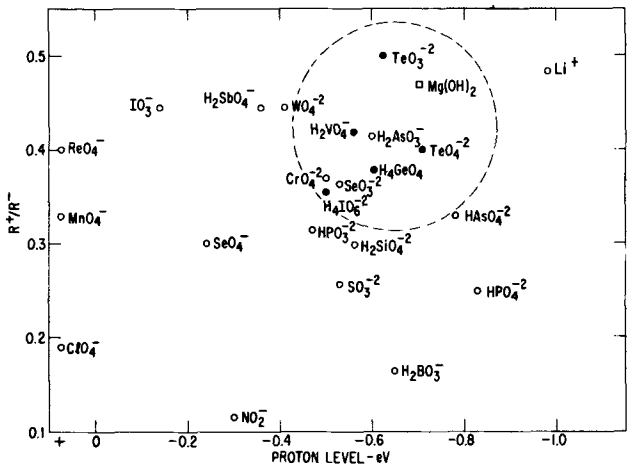

Fig. 9. Inhibitors of MCB $Mg(OH)_2$ dissolution. R^+ and R^- are the radii of the cation and oxygen ions in the oxyanion. The proton level is the free energy difference between the proton on the ion and a proton on a water molecule (H_3O^+) (4). The closed circles designate moderately effective substances, while ineffective substances are indicated by open circles.

2. Less well aged $Mg(OH)_2$ contains highly active surface regions from which dissolution is controlled either by proton arrival or by diffusion away of dissolved Mg^{+2} and OH^-.

3. MgO first reacts with water to form a $Mg(OH)_2$ layer on the surface and the rate is controlled by dissolution of the $Mg(OH)_2$.

4. No inhibitors were found for dissolution of natural Brucite. Protonated species with pK_a between 3 and 8 accelerate Brucite dissolution.

5. Inhibitors for dissolution of MCB $Mg(OH)_2$ and MgO are periodate, tellurate, tellurite, germanate, and vanadate.

Acknowledgment

Preparation of the powders from natural Brucite and MgO was accomplished by J. W. Szymaszek whose help is gratefully acknowledged. Very high purity water was kindly supplied by R. W. Powers. I am indebted to W. Vedder for many stimulating discussions of the experimental results.

Manuscript submitted Feb. 28, 1969; revised manuscript received *ca.* May 2, 1969.

Any discussion of this paper will appear in a Discussion Section to be published in the June 1970 JOURNAL.

REFERENCES

1. W. Vedder and D. A. Vermilyea, To be published in *Trans. Faraday Soc.* (1968).
2. D. A. Vermilyea and W. Vedder, To be submitted to *Trans. Faraday Soc.*
3. D. A. Vermilyea, *This Journal*, **113**, 1067 (1966).
4. R. W. Gurney, "Ionic Processes in Solution," McGraw-Hill, New York (1953).
5. E. Brunner, *Z. Physik. Chem.*, **47**, 56 (1904).

A Study of the Anodic Oxidation of Bismuth

D. J. De Smet* and M. A. Hopper*

Department of Physics, University of Alabama, University, Alabama

ABSTRACT

The galvanostatic oxidation of bismuth in sodium borate-boric acid and sodium carbonate solutions has been studied over a potential range of 90V by analysis of open-circuit transients. An anodic layer which shows bright interference colors is found to grow on the metal surface. Experimental results indicate that the dependence of the oxidation current density, i, on the overpotential, V, is expressable in the form $i = i_o \exp(V/V_o)$, where i_o and V_o are parameters determined from the data analysis. The parameter V_o is found to vary linearly with the overpotential during galvanostatic oxidation, while the parameter i_o depends on the applied current density. These results are related to a high field conduction model.

The anodic oxidation of the so-called "valve" metals has been the subject of many investigations (1). Nevertheless bismuth, although classified as a typical "valve" metal, has received little attention. Since the study of the anodic oxidation of bismuth by Guntherschulze and Betz in 1931 (2), there has been no published work on the anodic oxidation of bismuth in neutral or slightly alkaline solution, and little work in other electrolytes. This deficiency arises partly because bismuth does not find the application to capacitor manufacture that tantalum and some of the other "valve" metals do; and also because bismuth appears to have a somewhat more complex electrical behavior than, for example, tantalum does.

The open-circuit transient analysis technique has been used in the study of the anodic oxidation of several metals (3-8). Although bismuth and tantalum have been reported to show similar behavior, an examination of the literature shows that there are differences in the reported values of the electrical parameters of the oxide films formed on the two metals. The aims of this investigation were to determine whether the analysis of open-circuit transients would yield results when applied to the anodic oxidation of bismuth, and whether this technique would show the reported differences in the electrical behavior of the oxide films formed on bismuth and tantalum. In addition, a study of the anodic oxidation of bismuth and a comparison of these results with similar results found for other metals will aid in determining which properties of anodic oxidation are dependent on the particular system being investigated and which are more general properties of the process itself.

A study of the literature also reveals that there are differences in the reported values of certain electrical parameters of the anodic oxide film on bismuth, as determined by different methods. The present work thus helps to determine whether the differences were real or merely the result of some aspect of the experimental techniques used.

Experimental

The anodes used in this investigation were prepared from single crystals of bismuth (better than 99.99% pure) obtained from various sources. Hollow cylindrical samples 0.2 in. in diameter and 0.3 in. in length were machined from this material. The samples were then electropolished in a 2% hydrochloric acid, 98% saturated potassium iodide solution (9). After rinsing in distilled water and drying, the samples were mounted between Teflon washers in an electrode holder similar to that described by Feller and Osterwald (10). Each sample was then anodically oxidized to a potential of 100V using a constant current, and the oxide film thus formed was removed from the sample by dissolution in 0.1M sulfuric acid. This last procedure was repeated several times (usually 8 to 10) until the electrical behavior of the electrode became reproducible, thus ensuring that all experimental results reported here were obtained from identical surfaces.

The cell used was a jacketed four-necked flask fitted with standard taper joints through which the electrode assembly, a platinum wire cathode, a mercury-mercurous sulfate reference electrode, and a gas dispersion tube were fitted. All experiments reported here were carried out at room temperature.

Two electrolyte solutions were used in this study: a solution 0.0375M in sodium borate and 0.025M in boric acid (referred to as the borate buffer solution), and a 0.075M solution of sodium carbonate. Solutions were bubbled with argon for at least 12 hr prior to an experiment, the bubbling being continued throughout the course of the experiment.

A schematic diagram of the electrical circuitry used is shown in Fig. 1. High input impedance differential operational amplifiers (Philbrick SP102) were used for the galvanostat and follower. These amplifiers operate over a range of ± 100V. Potentials and open-circuit transients were recorded on a fast strip chart recorder (Sanborn 7700). All potentials were recorded relative to the mercury-mercurous sulfate reference electrode, and overpotentials were calculated from observed potentials by subtracting the value of the open-circuit potential. Current densities were calculated by dividing the applied current by the macroscopic surface area of the anode.

We have observed that the anodic layer on bismuth exhibits a fairly large optical effect when illuminated with visible light, therefore all results reported here were obtained in a darkened room unless otherwise noted. This eliminated the possibility that light falling on the electrode influenced the experimental results.

Results

If an oxide film on the surface of an electrode is considered to be equivalent to a capacitor with a dielectric medium between the capacitor plates which

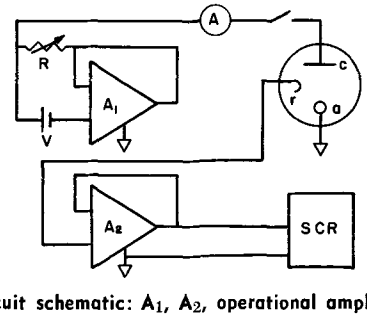

Fig. 1. Circuit schematic: A_1, A_2, operational amplifiers; R, variable resistor; V, battery; A, ammeter; SCR, strip chart recorder; a, anode; r, reference electrode; c, cathode.

* Electrochemical Society Active Member.

carries current in some manner, then the differential equation which relates the current density through the film, i, the overpotential, V, and the externally applied current density, i_e, is given by

$$C\ dV/dt + i = i_e \quad [1]$$

During an open-circuit transient $i_e = 0$, and the differential equation of the circuit becomes

$$i = -C\ dV/dt \quad [2]$$

so that if the rate of change of the potential is known, the current density through the layer may be determined (assuming that the behavior of the capacitance is known). If, for example, the voltage decay during such a transient were found to be an exponential function of time, then it could be deduced that the dielectric layer behaved as an ohmic resistance.

The experimental open-circuit transients found for bismuth fit an expression of the form

$$V = k - V_o \log(t + \theta) \quad [3]$$

extremely well. Here V_o, θ, and k are parameters which are determined by the particular transient and its initial conditions. Such transients may, for example, be analyzed by plotting the overpotential during the open-circuit decay against $(t + \theta)$ on semilogarithmic graph paper. For each transient θ is varied until a straight line is obtained for V against $\log(t + \theta)$ for the transient or some initial portion of the transient.

Differentiation of Eq. [3] with respect to time gives

$$dV/dt = -V_o/(t + \theta) \quad [4]$$

which may be written in the form

$$dV/dt = -V_o \exp(-k/V_o) \exp(V/V_o) \quad [5]$$

Comparison of Eq. [2] and [5] gives the current density in the layer as

$$i = CV_o \exp(-k/V_o) \exp(V/V_o)$$

which may be written as

$$i = i_o \exp(V/V_o) \quad [6]$$

where i_o and V_o are parameters which have the same dimensions as i and V, respectively, and whose values may be determined experimentally.

Certain assumptions have been made in the above derivation. First, it was assumed that the layer capacitance, C, does not change appreciably during the analyzed portion of the open-circuit transient. Because very little charge transfer occurs during an open-circuit transient no appreciable thickness changes take place, thus partially justifying this assumption. Second, open-circuit transients did not fit a relation of the form of Eq. [3] during the entire transient, but only over an initial portion of the transient. In terms of the results presented here, Eq. [6] may be considered to represent a high field conduction process. Since the electric field in the layer decays to zero as the overpotential decays to zero, this equation would not be expected to describe the relation between the overpotential and the current density after the circuit has been open a long time. Nevertheless, each transient analyzed was found to fit an expression of the form of Eq. [3] for at least 1½ decades of time, or a change in dV/dt of at least a factor of 30. An analysis of this type of transient was described by Grahame (11), and such transients have been employed in studies of the anodic films formed on passive iron (3-6) and of the anodic oxidation of tantalum (8).

A series of open-circuit transients were recorded during galvanostatic oxidation. In order to avoid confusion in the following discussion, we will use the term formation current density to designate the applied current density during galvanostatic oxidation and the term formation potential to designate the overpotential at which the circuit was opened. Figures 2 and 3 show the values of V_o, as determined from the open-circuit transient, as a function of the formation potential for bismuth in borate buffer (Fig. 2) and sodium carbonate (Fig. 3) at various formation current densities. For both electrolytes the plots of V_o against formation potential are linear for any particular formation current density, and all lines pass through the zero of overpotential. There is a noticeable difference in the slopes of the lines for different formation current densities.

A value for the parameter i_o can be determined from each open-circuit transient; but because the values of V_o are proportional to the formation potential (for any particular formation current density), i_o will have the same value for every open-circuit transient from the same formation current density. Thus i_o can be determined by using Eq. [6] and the slope of the graph of V_o *vs.* formation potential for each value of the formation current density. Figure 4 shows a plot of the logarithm of i_o (determined as above) against the logarithm of the formation current density, i_f, for formation current densities ranging from 5 to 175 μA/cm^2. From this figure, at least for formation current densities ranging from 5 to 50 μA/cm^2, the relation between i_f and i_o may be written in the form

$$i_o = \kappa(i_f)^\alpha \quad [7]$$

for both the borate buffer and the sodium carbonate solutions.

Assuming that all the charge passed during galvanostatic oxidation goes into the formation of a uniform layer, the change in overpotential with respect to charge passed (dV/dQ) can be used as a measure of the electric field in the layer. With this assumption it is possible to determine the dependence of the electric

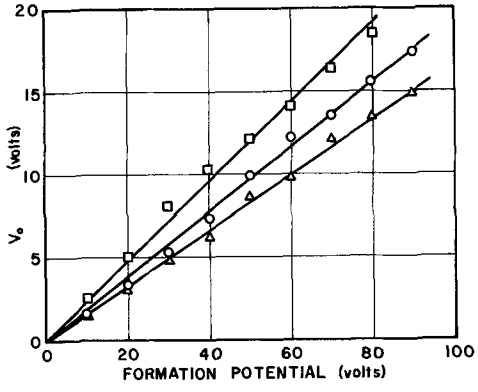

Fig. 2. Dependence of V_o on formation potential for bismuth in borate buffer. The formation current density was 5 μA/cm^2 for the data represented by the squares, 50 μA/cm^2 for the data represented by the circles, and 117 μA/cm^2 for the data represented by the triangles.

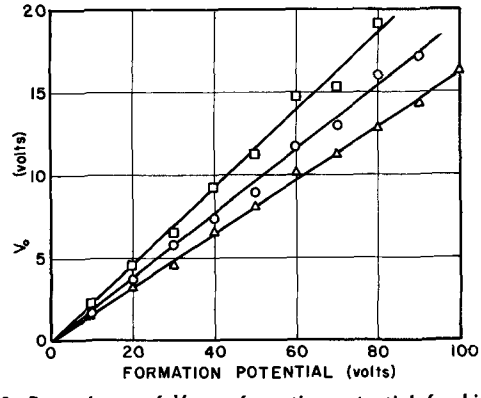

Fig. 3. Dependence of V_o on formation potential for bismuth in sodium carbonate. The formation current density was 10 μA/cm^2 for the data represented by the squares, 50 μA/cm^2 for the data represented by the circles, and 100 μA/cm^2 for the data represented by the triangles.

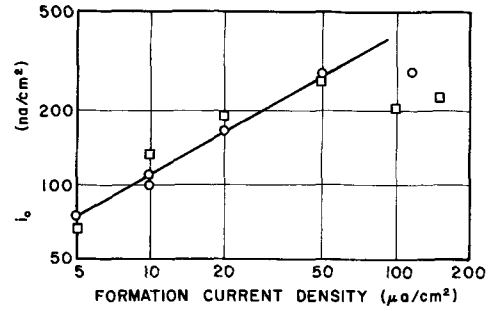

Fig. 4. Dependence of i_0 on the formation current density. The data represented by the squares are for the sodium carbonate electrolyte and the data represented by the circles are for the borate buffer electrolyte.

field in the layer on the formation current density by measuring dV/dQ as a function of the formation current density. Figure 5 shows dV/dQ as a function of the logarithm of the formation current density for bismuth in sodium carbonate solution.

Figure 6 shows a transient in which the formation current density was switched from 200 to 40 μA/cm^2 and then back to 200 μA/cm^2. In producing this figure the speed of the strip chart recorder was changed by a factor of five when the current density was switched from 200 to 40 μA/cm^2, and back to its original speed when the current density was returned to 200 μA/cm^2, producing a plot of potential against charge. This figure will be discussed further in the next section.

The effect of visible light on the overpotential of the electrode while undergoing galvanostatic oxidation is vividly shown in Fig. 7 for a bismuth anode in the borate buffer solution. The light was shone on the electrode when the formation potential reached a value of 43V, a formation current density of 10 μA/cm^2 being maintained. The light caused the overpotential to decrease suddenly, the electrode returning to its original overpotential when the light was removed.

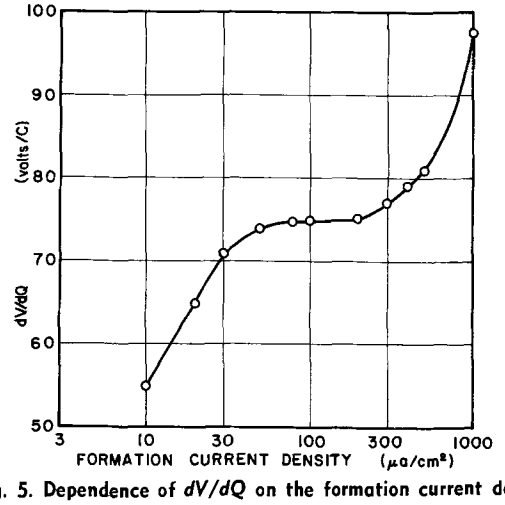

Fig. 5. Dependence of dV/dQ on the formation current density

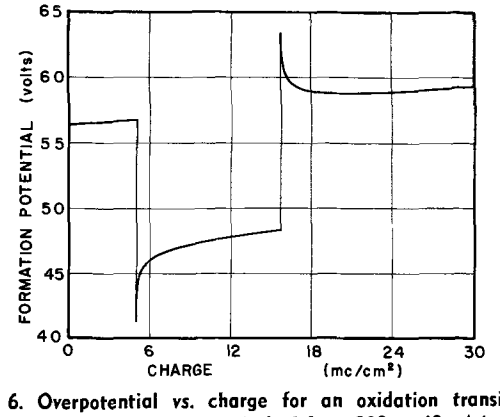

Fig. 6. Overpotential vs. charge for an oxidation transient in which the current density was switched from 200 to 40 μA/cm^2 and then back to 200 μA/cm^2. The electrolyte was borate buffer.

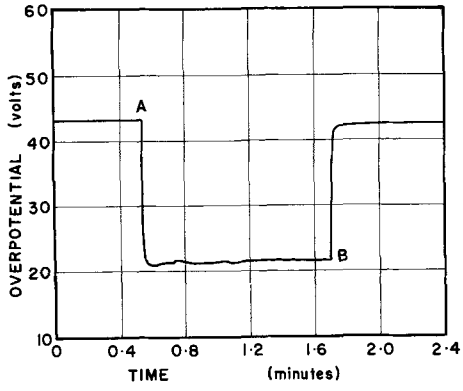

Fig. 7. Overpotential vs. time for a bismuth electrode in borate buffer under galvanostatic conditions with an applied current density of 10 μA/cm^2. At point A the electrode was illuminated with visible light and at point B the light was removed.

Preliminary experiments indicate that the magnitude of the photo effect (*i.e.*, the change in overpotential when light is allowed to reach the surface of the electrode) increases with increasing overpotential under galvanostatic conditions. The photo effect is thus related to the thickness of the oxide layer and perhaps to the electric field in the layer. The photo effect was found to decrease with increasing applied current density and could not be detected at all for applied current densities much above 100 μA/cm^2. It has also been determined that if only red light is used the effect diminishes considerably.

The above must be considered as only a qualitative discussion of the photo effect on bismuth; a more complete study is at present underway in this laboratory. Some of the preliminary results of this study are worthy of note here. One is that the oxide layer formed while under constant exposure to light proves far more difficult to remove than the layer formed in the dark. Another is that the film formed under strong illumination does not show uniform interference colors (certain crystal orientations showing distinctly different colors) which were always found on films grown in darkened conditions. These observations are true even when the formation current density is large enough to make the photo effect otherwise undetectable. These results suggest differences in the properties of the oxide formed in the two cases which may account for certain of the discrepancies in previously published results.

Discussion

An exponential dependence of the current density through the layer on the overpotential may be interpreted in terms of an activation energy controlled process (1) using a simple Mott-Cabrera model (12). The theoretical relation for such a process, in the high field case, is given in its simplest form by

$$i = 2a\nu n \exp(-U/kT) \exp(\lambda eaE/kT) \quad [8]$$

where a is the half-jump distance of the activation barrier, ν the frequency of oscillation of ions, n the density of charge carriers, U the activation energy for the process, λ the valence of the charge carriers, and E the electric field at the activation barrier. The other symbols have their usual meanings.

If the local electric field at the activation barrier may be presumed equal to the average electric field in the layer (*i.e.*, the overpotential across the layer divided by its thickness) then a comparison of Eq. [6] and [8] yields the relation

$$V_o = (kT/\lambda ea)\, D \quad [9]$$

Thus V_o is proportional to the thickness of the oxide layer, D.

The experimental data presented here strongly support a model of this type. Figures 2 and 3 show that the values of V_o are linearly proportional to the formation potential for a fixed formation current density over a wide range of values. This result indicates that a high field conduction process limits the current through the layer. Data taken for different formation current densities fall on lines of different slopes, indicating that the field in the layer depends on the formation current density, and also that i_o depends on the formation current density.

The dependence of i_o on the formation current density cannot be interpreted in terms of the model used, since the model assumes that all of the factors in Eq. [8] other than the exponential factor containing the electric field are constants. The variation of i_o could be made consistent with Eq. [8] by allowing at least one of the "field independent" factors in Eq. [8] to vary. We feel that we cannot deduce a meaningful model to account for the variation of i_o based solely on the present experimental data. It should be noted that i_o was plotted as a function of the formation current density in Fig. 4, but it could equally well be considered to be a function of the formation field.

The change in overpotential when the current density is suddenly switched from one constant value to another is shown in Fig. 6. This figure also shows the potential overshoot that occurs when the current density is changed in this manner. Such behavior has been reported for several other metals (1, 5). We have found that i_o depends on the formation current density; therefore, when the formation current density is changed i_o will change, at a rate less than the rate of change of the formation current density (or the rate of change of the electric field), until its value is correct for the new formation current density. Ord (5), in a study of the anodic oxidation of passive iron, suggested that it may be possible to account for the potential overshoot by consideration of the manner in which i_o changes. Similar arguments may be advanced here, since our experimental results clearly indicate that i_o is a function of the formation current density and changes when the formation current density is changed.

The results obtained for $d\nu/dQ$ (which may be considered to be directly proportional to the electric field in the layer) as a function of the formation current density (Fig. 5) suggest that the usual relation between the current density through the layer and the electric field, $i = A \exp(BE)$, is not valid for this system, at least over the range of applied current densities studied here. Even the modified form of this expression given by Young (13), $i = A \exp(BE + CE^2)$, cannot fit the experimental results of Fig. 5. The curvature of this plot at low applied current densities may be due to leakage; nevertheless, it proved possible to obtain a linear increase in overpotential with time for applied current densities as low as 0.1 μA/cm^2. Thus any leakage current present must be non-ohmic; that is, it must be a function of the applied current density but not an explicit function of the overpotential.

A comparison of the present work with earlier studies of the anodic oxidation of bismuth is difficult because dV/dQ was not found to be a linear function of the logarithm of the applied current density. In contrast, the relation $i = i_o \exp(V/V_o)$ has been shown to be applicable to this system. A high field conduction mechanism can be deduced from this relation without requiring dV/dQ to vary linearly with log i.

Guntherschulze and Betz (2) reported that the electric field strength in tantalum oxide was a factor of five greater than that in bismuth oxide. Young (1) found that at an applied current density of 100 μA/cm^2 and 25°C the electric field strength in tantalum oxide is about $7 \cdot 10^6$ V/cm, while Masing and Young (14) have determined that the electric field strength in bismuth oxide (formed in sodium hydroxide solution) was $8.5 \cdot 10^5$ V/cm. These latter results indicate that the electric field strength in tantalum oxide is about eight times that in bismuth oxide. To compare these determinations of the field strength with our results, Eq. [9] must be used to obtain the relation between V_o and thickness, *viz.*

$$V_o = D/(\lambda a A) \qquad [10]$$

where A is given by (e/kT). Dividing both sides of this equation into the formation potential, V, gives

$$V/V_o = \lambda a A E \qquad [11]$$

where E, the average electric field strength within the layer, is given by V/D. At an applied current density of 100 μA/cm^2 the value of V/V_o for tantalum oxide is approximately 12.0 (8), while for bismuth oxide it is approximately 6.0 (see Fig. 3). Thus, if the field strength in tantalum oxide is eight times that in bismuth oxide, the valence-jump distance product for bismuth oxide should be four times that for tantalum oxide. Masing and Young determined that the jump distance in bismuth oxide is four times as great as it is in tantalum oxide. The values of the electric field strength determined by Guntherschulze and Betz and by Masing and Young for bismuth oxide may be slightly low since they were apparently not aware of the photo effect of visible light. This effect, which we have found to cause large changes in the overpotential at low current densities, may produce a reduced field strength at higher current densities.

A comparison of the results presented here for bismuth with those found for iron (5) and tantalum (8), using the same experimental techniques and methods of data analysis, yields several striking similarities. The decay of the overpotential during an open-circuit transient has the same form for all three materials. The systems all show a linear dependence of V_o on the formation potential at fixed formation current density. The values of the slopes of these plots are comparable (0.09 for tantalum, 0.2 for iron, and 0.16 for bismuth). The slope of V_o against formation potential is dependent on the formation current density for all three systems, in all cases increasing with decreasing formation current density. The parameter i_o will therefore depend on the formation current density in much the same manner for each of these systems. (An equation of the form of Eq. [7] has been found for this dependence in tantalum, the exact form of the relation for iron is not presently known.) The values of i_o for these three systems at comparable formation current densities are $7 \cdot 10^{-5}$ μA/cm^2 for tantalum, $5 \cdot 10^{-3}$ μA/cm^2 for iron, and $3 \cdot 10^{-1}$ μA/cm^2 for bismuth. Finally, all three systems show a potential overshoot whenever the applied current density is changed abruptly from one value to another.

It is for these reasons that we feel that some of the features which these systems exhibit, as exemplified by this work, are general features of the anodic oxidation process which will be independent of the particular system under investigation. Further, it is our opinion that the analysis of open-circuit transients is a useful technique which yields valuable information as to the behavior of metals undergoing anodic oxidation.

Acknowledgment

The authors wish to acknowledge the support of the Office of Naval Research for this work carried out under Contract No. N00014-66-C0200.

Manuscript submitted Dec. 19, 1968; revised manuscript received April 2, 1969. This was Paper 409 presented at the Montreal Meeting, Oct. 6-11, 1968.

Any discussion of this paper will appear in a Discussion Section to be published in the June 1970 JOURNAL.

REFERENCES
1. L. Young, "Anodic Oxide Films," Academic Press, London and New York (1961).
2. A. Guntherschulze and H. Betz, *Z. Elektrochem.*, **37**, 726 (1931).
3. J. L. Ord and J. H. Bartlett, *This Journal*, **112**, 160 (1965).
4. J. L. Ord, *ibid.*, **112**, 46 (1965).
5. J. L. Ord, *ibid.*, **113**, 213 (1966).
6. J. L. Ord and D. J. De Smet, *ibid.*, **113**, 1258 (1966).
7. J. L. Ord, *ibid.*, **114**, 74C, Abstract 185 (1967).
8. J. L. Ord and D. J. De Smet, *ibid.*, **116**, 762 (1969).
9. W. J. McG. Tegart, "The Electrolytic and Chemical Polishing of Metals," Pergamon Press, London (1956).
10. H. G. Feller and J. Osterwald, *This Journal*, **111**, 119 (1964).
11. D. C. Grahame, *J. Phys. Chem.*, **57**, 257 (1953).
12. N. Cabrera and N. F. Mott, *Rept. Progr. Phys.*, **12**, 163 (1948-1949).
13. L. Young, *Proc. Roy. Soc.* (London), **A258**, 496 (1960).
14. L. Masing and L. Young, *Can. J. Chem.*, **40**, 903 (1961).

Cathode Overpotential and Electrosorption Effects of Straight-Chain Carboxylic Acids during Electrodeposition of Copper

Alan K. P. Chu[1] and A. J. Sukava*

Department of Chemistry, University of Western Ontario, London, Ontario, Canada

ABSTRACT

The effects of straight-chain carboxylic acids on cathode overpotential during electrodeposition of copper were studied by galvanostatic methods at current densities up to 0.020 A-cm^{-2}. No modification of the charge-transfer mechanism of copper deposition occurred. Overpotential increments caused by lengthening of the carbon chain can be correlated with the reduced concentrations of the carboxylic acids in accordance with Traube's rule. This can be rationalized in terms of the general relation between adsorbability and solubility of the additive. The general behavior is consistent with the blocking theory of additive function according to which overpotential increments are directly dependent on additive adsorbability. The fractional surface coverage calculated from overpotential increments appears to fit a Langmuir-type isotherm from which the free energies of adsorption of the carboxylic acids can be determined. The magnitudes of these free energies are consistent with physical adsorption forces. A relation was derived between the free energy of adsorption and the free energy contributions from the carboxyl group and the carbon chain. This shows that the longer the chain, the higher the adsorbability.

Overpotential and adsorbed additives.—The rate-determining step in electrodeposition varies with the overpotential region (1). The charge-transfer process is believed to be rate-determining at high overpotentials (2) and the accepted mechanism in the case of copper deposition is the two step charge transfer

$$Cu^{2+} + \epsilon \rightarrow Cu^{+} \qquad \text{slow}$$
$$Cu^{+} + \epsilon \rightarrow Cu \qquad \text{fast}$$

The charge-transfer overpotential η is related to the current density i by the Tafel equation (3)

$$\eta = a + b \ln i \qquad [1]$$

Under high overpotential conditions, the measured overpotential will represent the magnitude of η if other sources of overpotential can be eliminated or sufficiently minimized.

The presence in the solution of surface-active additives results in a considerable increase in cathode overpotential in many instances (4-7), due primarily to adsorption of the additive on the cathode surface (4-6, 8, 9). Since this adsorption undoubtedly modifies the surface conditions for electrodeposition, it is essential to try to correlate the resulting overpotential increment and the additive adsorbability.

In metal deposition, overpotential increments caused by additives are generally believed to arise from an increased true current density because of partial blocking of the electrode by adsorbed additive. If a fraction θ of the cathode surface is covered by additive molecules, and if electrodeposition occurs only on the uncovered fraction $1 - \theta$, then the true current density will be increased from i in the absence of aditive to i', in the presence of additive, such that

$$i' = \frac{i}{1 - \theta} \qquad [2]$$

If the charge-transfer process remains rate-determining, the increased charge-transfer overpotential η' in the presence of additive will be given by

$$\eta' = a + b \ln i'$$
$$= a + b \ln\left(\frac{i}{1 - \theta}\right) \qquad [3]$$

An expression relating the overpotential increment and the fractional surface coverage can then be obtained by subtracting Eq. [1] and [3] to give

$$\theta = 1 - \exp(-\Delta\eta/b) \qquad [4]$$

Equation [4], based on the simple blocking theory, has been used in the study of hydrogen overvoltage at solid electrodes (8, 10) and values of θ calculated in this way from overvoltage data have been found to agree satisfactorily with values obtained from double-layer capacity measurements (10). If it can be as-

* Electrochemical Society Active Member.
[1] Present address: ESB Inc., Research Center, Yardley, Pennsylvania.

sumed that this equation applies equally well to metal deposition, then the fractional surface coverage for additives which adsorb randomly on the electrolytically active sites is readily calculable from experimental measurements of $\Delta\eta$.

It should be pointed out that overpotential is not always increased by the presence of additive. Certain alkaloids have been found to lower the hydrogen overvoltage of mercury and lead, but presumably because the specifically adsorbed alkaloid acts as a low-stability source of electroactive hydrogen (11).

Electrosorption of additives.—Various aspects of electrosorption have been reviewed by Frumkin (12). Mercury electrodes have been used for much of this work because they allow the extent of adsorption to be determined from electrocapillary data. In the case of solid electrodes, radiotracer methods have been used with some success (13, 14), but useful information can also be derived from studies of ordinary adsorption (15, 16), particularly concerning the adsorbability of additive and the type of bonding with the electrode surface. It is known that adsorbability in ordinary adsorption depends on the solubility of the adsorbate (15). In general, the lower the solubility, the higher the adsorbability.

In electrosorption, as in ordinary adsorption, solvent adsorption occurs at the electrode, and adsorption of additive involves a displacement of solvent molecules (17-19). Competition between solvent and additives for the electrode surface therefore occurs. Generally, if the adsorbed molecules are polar, their orientation might be expected to depend on the sign of the electrode charge, and the competition for adsorption sites between water and an organic additive might be expected to be potential dependent (20, 21). Accordingly, water molecules should be least strongly attached to the electrode at the point of zero charge, with maximum adsorption of the organic additive the expected result, but this is not always the case (17, 20, 22). In chemisorption particularly, the orientation of an adsorbed molecule will depend on the functional group that determines the point of attachment (15), and so the potential dependence of such adsorption would be relatively unimportant.

The equilibrium between adsorbed additive on an electrode surface and additive in the solution phase can be described in the customary way by an adsorption isotherm. In general, since the major difference between gas-phase and liquid-phase adsorption is merely that the substrate surface is bare in the former and solvated in the latter, it follows that isotherms originally derived for gas-phase adsorption also find application in electrosorption studies. In these studies, the Langmuir isotherm has been found useful.

Langmuir adsorption isotherm.—The Langmuir isotherm, derivable from either a kinetic or statistical treatment (23, 24), can be written in the form

$$\frac{\theta}{1-\theta} = CK = C \cdot \exp\left(-\frac{\Delta G^\circ_a}{RT}\right) \qquad [5]$$

where θ and C are the fractional surface coverage and concentration of additive, respectively, K is the equilibrium constant (the adsorbability), and ΔG°_a is the standard free energy of adsorption. From the model and assumptions made in the derivation, this isotherm can be expected to apply to localized monolayer adsorption with no lateral interference (*i.e.*, free energy of adsorption is not coverage dependent) and to the condition where each adsorbed molecule occupies a single site on the surface. At low coverage, Eq. [5] describes many electrosorption systems to a good approximation (13, 25, 26).

Langmuir adsorption from solution.—Adsorption of an additive A on a solvated electrode surface can be written as a displacement reaction

$$A_{(soln.)} + nH_2O_{(ads.)} \rightleftarrows A_{(ads.)} + nH_2O_{(soln.)}$$

where n is the number of water molecules displaced by a molecule of additive. A Langmuir-type isotherm for this kind of displacement adsorption has been formulated as (17)

$$\frac{\theta}{(1-\theta)^n}\,\frac{\{\theta + n(1-\theta)\}^{n-1}}{n^n} = CK = \frac{C}{55.5}\exp\left(\frac{-\Delta G^\circ_a}{RT}\right) \qquad [6]$$

When n is unity, Eq. [6] reduces to the ordinary Langmuir isotherm

$$\frac{\theta}{1-\theta} = \frac{C}{55.5}\exp\left(\frac{-\Delta G^\circ_a}{RT}\right) \qquad [7]$$

This is essentially the same form as Eq. [5] except that it contains the factor 1/55.5 which arises from taking unit mole fraction of adsorbed species as standard state.

Experimental

Some of the overpotential measurements in this work were made with a Haring cell (5), while others were made with a Luggin probe in contact with the bottom end of a copper-wire cathode (about 2.0 mm diameter) in a specially constructed H-cell similar to one described by Turner and Johnson (7). The Haring cell was designed to contain 150 ml of solution with 10 cm^2 of electrode area immersed. The cathode compartment of the H-cell contained about 65 ml of solution with 1 cm^2 of cathode surface immersed. Cathode overpotentials were measured with a Sargent SR recorder in some cases and with a Leeds and Northrup Type K potentiometer in others. Overpotential increments were determined for several straight-chain carboxylic acids added to the standard reference solution of copper sulfate and sulfuric acid (4, 5). Effects of additive concentration and current density were determined.

Electrolyte containing 0.5M $CuSO_4$ and 1.0M H_2SO_4, both reagent grade, was used as the standard solution. The water was triply distilled in all-glass apparatus. Precautions were taken to remove possible organic contaminants from the copper sulfate pentahydrate solid before preparing the solutions. This was done by heating at 750°C for several days to cause complete decomposition to copper oxide, which was then dissolved in the required amount of sulfuric acid. All copper electrodes were heated to redness before use to remove any organic substances. Solutions containing the additives were always freshly prepared and only high-purity compounds were used.

Results

All overpotentials reported in this paper are steady-state total values reproducible to within ±5%. Minor variations in electrode surfaces appeared to be the main factor affecting the reproducibility. In the electrolysis of the standard solution at 25° ±0.1°C and 20 $mA\text{-}cm^{-2}$, the total cathode overpotential was 100 ±5 mV (4, 5). Some overpotential decay measurements indicate that under these conditions with natural free convection, the concentration overpotential, which is less than 5 mV, is not significantly affected by the additives employed in this work (27). It may therefore be assumed that the main effect of the additives is to increase the charge-transfer overpotential only. The overpotential increment in each case was obtained by subtracting 100 mV from the measured total value.

Steady-state overpotential.—The total steady-state cathode overpotential is shown in Fig. 1 as a function of additive concentration for several straight-chain carboxylic acids, methanoic, propanoic, pentanoic, heptanoic, and hexanedioic acids. These compounds were chosen to show the effect of carbon chain length on overpotential, the only variation in functional

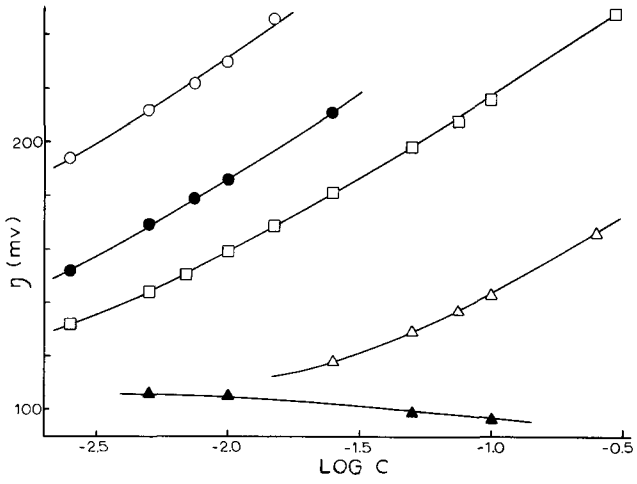

Fig. 1. Steady-state cathode overpotential and additive concentration. Temperature, 25° ± 0.1°C; current density, 20 mA-cm^{-2}. ○, Heptanoic acid; ●, hexanedioic acid; □, pentanoic acid; △, propanoic acid; ▲, methanoic acid.

group being in the dicarboxylic hexanedoic acid. Additives differing by two methylene groups were chosen to cover a wide range of chain length with a minimum of experimental data. The curves in Fig. 1 show that cathode overpotential generally increases with increasing concentration and with increasing chain length of these additives. No effect on overpotential was found with methanoic acid up to about 0.1M, apart from a tendency to decrease the overpotential slightly though not significantly.

In the measurement of cathode overpotential at constant current density and with different concentrations of additive, it was found that, apart from the overpotential increase, the carboxylic acids had no effect on the time variation of overpotential. Good steady states were obtained in most cases in about 1 hr, after which prolonged electrolysis for several hours produced no further change. An exception was observed with heptanoic acid at a concentration close to saturation (0.015M). In this case the time required for steady state was about 8 hr.

Overpotential-current density effects.—Overpotential measurements at different apparent current densities were made by reducing the current density in 2-mA steps from 20 mA-cm^{-2} down to 2 mA-cm^{-2} with no current interruption during the step. The time required for steady state at each new current density varied from about 5 to 10 min. Typical overpotential-current density data are shown as Tafel plots in Fig. 2. These show a linear behavior extending from about 8 mA-cm^{-2} to about 20 mA-cm^{-2}, with the additives having no marked effect on the Tafel slope. In accordance with Eq. [3] and the natural logarithm of current density, this slope was found to be 50 ± 1 mV, in agreement with the theoretical value calculated from the relation

$$b = RT/\alpha zF$$

with the transfer coefficient α taken as 0.5 and z taken as unity (2). Therefore, under conditions where charge transfer is rate-determining, carboxylic acids have no significant effect on the kinetics of copper deposition. Their primary effect is merely to increase the charge-transfer overpotential by increasing the true current density.

Discussion

Adsorption isotherm and surface coverage.—The fractional surface coverage θ due to additive adsorbed on the cathode was calculated from the overpotential increment $\Delta\eta$ by applying Eq. [4] to the data for propanoic, pentanoic, heptanoic, and hexanedioic acids. For these calculations, the Tafel slope b was taken as

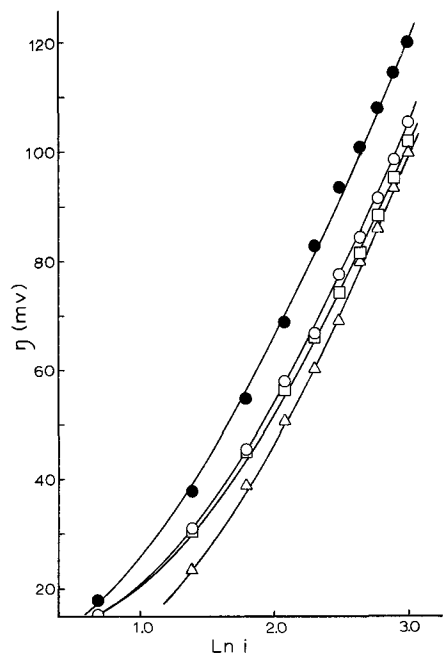

Fig. 2. Overpotential-current density relations. Temperature, 25° ± 0.1°C. △, Standard solution, □, 1.0 × 10^{-3} M methanoic acid; ○, 1.0 × 10^{-2} M methanoic acid; ●, 3.0 × 10^{-2} M propanoic acid.

the experimental 50 mV, with results as shown in Table I. A test was made for Langmuir adsorption by plotting the left hand side of Eq. [6] against additive concentration, and it was found that if n, the number of water molecules replaced by a molecule of adsorbed additive, is taken as 2, a straight line passing through the origin is obtained for each of the four additives. Typical results are shown in Fig .3.

Free energy of adsorption.—Since the behavior of carboxylic acids shown in Table I and Fig. 3 appears to be consistent with Langmuir adsorption, Eq. [6] may be used to evaluate the standard free energy of adsorption of these additives. The values of the adsorbability K and standard free energy $\Delta G°_a$, calculated from the slopes of the lines as illustrated in Fig. 3, are listed in Table II. The results show that, with other things being equal, the free energy of adsorption and the adsorbability increase with the length of the carbon chain. From the magnitude of the net standard free energy, it would appear that physical forces are primarily involved in the adsorption process.

Table I. Adsorption data

Temperature = 25° ± 0.1°C
Current density = 20 mA-cm^{-2}

$$f(\theta) = \frac{\theta}{(1-\theta)^2}\left[\frac{\theta + 2(1-\theta)}{4}\right]$$

(See Eq. [6])

Additive	C (moles l^{-1})	$\Delta\eta$ (mV)	θ	$f(\theta)$
Propanoic acid	2.5 × 10^{-2}	18.0	0.302	0.263
	5.0 × 10^{-2}	29.4	0.445	0.562
	7.5 × 10^{-2}	37.2	0.525	0.851
	1.0 × 10^{-1}	43.0	0.577	1.145
Pentanoic acid	2.5 × 10^{-3}	31.9	0.472	0.645
	5.0 × 10^{-3}	44.0	0.585	1.20
	6.9 × 10^{-3}	50.4	0.635	1.63
	1.0 × 10^{-2}	59.2	0.693	2.41
Heptanoic acid	2.5 × 10^{-3}	94	0.848	10.6
	5.0 × 10^{-3}	112	0.894	22.1
	7.5 × 10^{-3}	122	0.913	32.6
	1.0 × 10^{-2}	130	0.926	45.0
Hexanedioic acid	2.5 × 10^{-3}	52.0	0.647	1.75
	5.0 × 10^{-3}	69.5	0.751	3.78
	7.5 × 10^{-3}	79.0	0.794	5.65
	1.0 × 10^{-2}	86.0	0.821	7.56

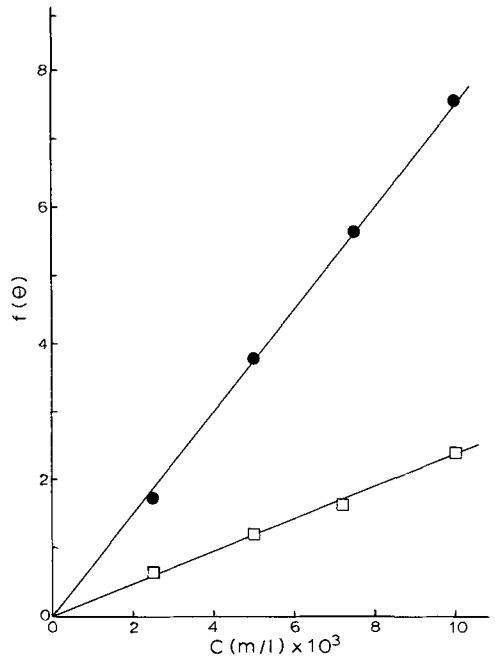

Fig. 3. Langmuir isotherm plots. ●, Hexanedioic acid; □, pentanoic acid.

Since the net free energy of adsorption shown in Table II is in every case significantly greater than the molal thermal energy *RT*, it may be argued that adsorption of carboxylic acids on a copper cathode is localized to a degree such that the effective blocking is the primary factor responsible for the overpotential increment. Delocalized (*i.e.*, mobile) adsorption of additive would presumably not contribute greatly to this increment.

With carboxylic acids as additives, the affinity of the carboxyl group for the copper surface is presumably sufficient to assure localized adsorption provided that the carbon chain is of sufficient size to have the necessary effect on the free energy of the process. Considerable surface coverages can be expected, as shown by the experimental results (Table I). The small or nearly zero overpotential effect of methanoic acid presumably arises from the hydrophilic nature of this compound, resulting in relatively ineffective competition with the solvent in the adsorption process, with a consequent low adsorbability. This view is supported by some studies of hydrogen evolution on a copper cathode with ethanoic acid as additive (10) which indicate that little or no adsorption occurs up to a concentration of 2.5M.

Components of adsorption free energy.—In the adsorption of carboxylic acids at the electrode surface, the polar functional group probably determines the energy required for appropriate bonding or physical attraction with the surface, while the hydrophobic carbon chain contributes part of the free energy to assist the adsorption process. The adsorption energy of the functional group presumably depends in part on the nature of the adsorbent (the electrode surface), while the adsorption energy of the carbon chain depends primarily on the solution. For the additives studied, the increase in adsorption free energy is found to be the same for each increase in chain length by two methylene groups, within experimental error. If the free energy of adsorption of the functional group, ΔG°_p, remains unchanged as the carbon chain is varied, the free energy due to each added methylene group, $\Delta G^\circ_{CH_2}$, may be calculated from the data for the monocarboxylic acids in Table II by applying the equation

$$\Delta G^\circ_a = \Delta G^\circ_P + n_{CH_2} \cdot \Delta G^\circ_{CH_2} \quad [8]$$

where n_{CH_2} is the number of methylene groups in the molecule (including the terminal methyl). The mean values of ΔG°_p and $\Delta G^\circ_{CH_2}$ were found to be 2047 and 885 cal-mole^{-1}, respectively. However, if these values are used for hexanedioic acid, taking into account the two carboxyl groups, the calculated ΔG°_a is found to be 7634 cal-mole^{-1}, significantly higher than the experimental 6309 cal-mole^{-1}. Steric effects and possible cyclization are probable factors in preventing adsorption of this compound to the extent predicted from the monocarboxylic behavior.

Calculation of ΔG°_a.—Since adsorption of additive from solution is a water-replacement process as stated previously, the net standard free energy of adsorption will be the difference between the free energies of adsorption of additive and water from solution

$$\Delta G^\circ_a = \Delta G^\circ_{A(soln)} - n\Delta G^\circ_{W(soln)} \quad [9]$$

But adsorption of additive at an electrode-solution interface can be regarded as the sum of two processes: (*i*) the transfer of additive from the solution bulk to the pre-electrode layer, and (*ii*) the attachment of additive, physically or chemically, to the electrode surface from the pre-electrode layer.

The first of these processes appears to be analogous to the adsorption of additive at a liquid-water interface (28, 29). In the adsorption of carboxylic acids on an electrode surface, the carboxyl group probably has a higher affinity for the metal than it does for the solvent, while the hydrophobic carbon chain is effectively rejected by the solvent. Due to this solvent rejection, the additive will transfer spontaneously to the pre-electrode layer and thus make further interaction with the electrode surface possible. The first term on the right in Eq. [9] is then given by

$$\Delta G^\circ_{A(soln.)} = \lambda + \Delta G^\circ_{A,M} \quad [10]$$

where λ is the free energy due to solvent rejection and $\Delta G^\circ_{A,M}$ is the free energy due to additive-metal interaction. The quantity λ may in turn be regarded as the sum of the energies required to bring both the polar and nonpolar portions of the additive molecule from the bulk to the pre-electrode layer

$$\lambda = \lambda_P + n_{CH_2}\lambda_{CH_2} \quad [11]$$

This equation, which has been generally accepted as valid for adsorption at the air-water and liquid-water interfaces (29, 30), can be used with adsorption data from such studies to provide useful information in the interpretation of additive adsorption on electrodes.

Combination of Eq. [9], [10], and [11] gives

$$\Delta G^\circ_a = \Delta G^\circ_{A,M} + \lambda_P - n\Delta G^\circ_{W(soln.)} + n_{CH_2}\lambda_{CH_2} \quad [12]$$

Accordingly, for a given functional group, the net standard free energy of adsorption ΔG°_a increases as the number of methylene groups increases, provided of course that the signs of ΔG°_a and λ_{CH_2} are the same. The magnitude of $\Delta G^\circ_{A,M}$ may be considered to depend primarily on the nature of the functional group as suggested earlier. Generally, the magnitude of λ_P is small relative to that of $n_{CH_2}\lambda_{CH_2}$. For an organic polar molecule with a long carbon chain, it may be expected that the greatest contribution to the free energy of adsorption from solution to the pre-electrode layer comes from the carbon chain. Thus, with other factors equal, the longer the carbon chain, the greater the adsorbability.

Table II. Net free energy of adsorption

Additive	Temperature = 25° ± 0.1°C *K* (l mole^{-1})	ΔG°_a (cal mole^{-1})
Propanoic acid	11.2	−3812
Pentanoic acid	243	−5597
Heptanoic acid	4400	−7351
Hexanedioic acid	758	−6309

To compare the quantities in Eq. [12] with the values calculated for $\Delta G°_{CH_2}$ and $\Delta G°_P$ (885 and 2047 cal-mole^{-1}), we may write, in view of Eq. [8]

$$\Delta G°_P = \Delta G°_{A,M} + \lambda_P - n\Delta G°_{W(soln.)} \quad [13]$$

and

$$\Delta G°_{CH_2} = \lambda_{CH_2} \quad [14]$$

The experimental value of $\Delta G°_{CH_2}$ for the carboxylic acids studied, 885 cal-mole^{-1}, may be compared with the value 820 cal-mole^{-1} for the oil-water interface (29) and 625 cal-mole^{-1} for the air-water interface (30). Hence, the value of $\Delta G°_{CH_2}$ for an electrode-solution interface may be approximately predicted from data for the liquid-water interface, which are readily available and known for many systems (15).

As a special case of Eq. [13], if the magnitude of $\Delta G°_{A,M}$ is comparable to that of $n\Delta G°_{W(soln.)}$, $\Delta G°_P$ is approximately equal to λ_P. For the carboxyl group, the values of λ_P for the oil-water interface, 1630 cal-mole^{-1} (29), and for the air-water interface, 437 cal-mole^{-1} (30), are relatively small compared to the value of $\Delta G°_{W(soln.)}$, 4800 cal-mole^{-1} (26, 31) calculated from data for adsorption of water vapor on mercury. Obviously, the magnitude of $\Delta G°_P$ depends largely on the number of water molecules replaced, *i.e.*, n. If other factors are equal, additives will tend to adsorb on an electrode surface in such a way that the least number of water molecules will be replaced.

For the carboxylic acids employed in this study, the number of water molecules replaced is taken as 2 (see Fig. 3). If the value of λ_P for the oil-water interface, 1630 cal-mole^{-1} (29), is applicable to the electrode-solution interface, and if the value of $\Delta G°_{W(soln.)}$ quoted above, 4800 cal-mol^{-1} (26, 31), is also applicable, the value of $\Delta G°_{A,M}$ may be found from Eq. [13], using the experimental value, 2047 cal-mole^{-1}, for $\Delta G°_P$. The value obtained is 10,020 cal-mole^{-1}.

Since $\Delta G°_{A,M}$ and $2\Delta G°_{W(soln.)}$ differ by only 420 cal-mole^{-1}, an approximate prediction may be made of the net standard free energy of adsorption of an additive on an electrode surface, using adsorption data from liquid-water interfacial studies. This is seen by writing Eq. [12] in the approximate form

$$\Delta G°_a \approx \lambda_P + n_{CH_2}\lambda_{CH_2} \quad [15]$$

Accordingly, with additives having a long carbon chain, the greatest contribution to the net free energy of adsorption comes from this chain.

Correlation between overpotential increment and additive solubility.—Since the adsorbability of a carboxylic acid depends to a considerable extent on the carbon chain length, for a given functional group, and since it is known that the solubility of a hydrocarbon compound is also carbon chain dependent, then it may be expected that a direct correlation can be derived between overpotential increment and additive solubility. If the simple blocking action arising from adsorption of additive is the primary cause of overpotential increase, then such a correlation should be possible between overpotential increment, a function of additive concentration, and the reduced concentration of additive, which accounts for the effect of solubility. The reduced concentration has been defined as (32, 33)

$$C_r = \frac{C}{C_s} \quad [16]$$

where C and C_s are the concentrations of bulk and saturated solution, respectively.

If overpotential increments are plotted against reduced concentration calculated from known solubilities (34, 35) of the additives used in this study, a generalized behavior results as shown in Fig. 4. It is seen that the overpotential increment for a given reduced concentration is approximately the same for all the carboxylic acids employed. These results may be compared with those obtained for the adsorption of carboxylic acids on graphite (33). The relation between overpotential increment and the chain length of the carboxylic acids can therefore be generalized if the solubilities are taken into account.

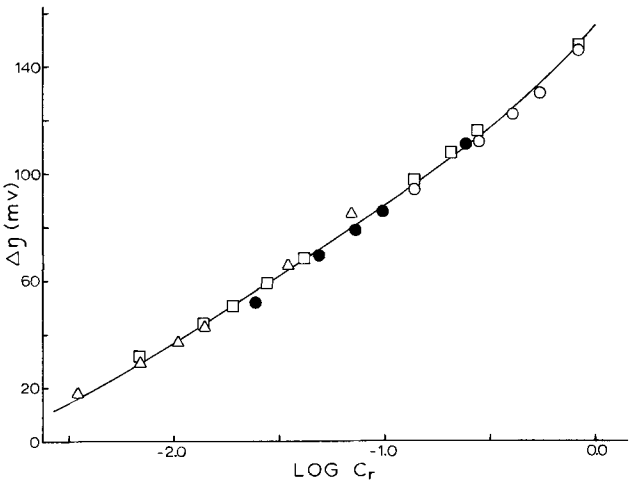

Fig. 4. Overpotential increment as a function of reduced concentration. Temperature, 25° ± 0.1°C. ○, Heptanoic acid; ●, hexanedioic acid; □, pentanoic acid; △, propanoic acid.

Since the effect of the carbon chain on the overpotential increment can be related to additive solubility, then Traube's rule which relates the effect of carbon chain on surface tension (36) might be applicable to overpotential data. This was verified for the monocarboxylic acids used in this study, and it was found that by adding one methylene group to the carbon chain, the additive concentration required to cause the same overpotential increment reduces to approximately 1/4.3. The value 4.3 can therefore be regarded as the approximate Traube coefficient in this instance. The relation can be generalized as

$$\Delta\eta_{(n_{CH_2},C)} = \Delta\eta_{(n_{CH_2}-s,(\omega)^sC)} \quad [17]$$

where $\Delta\eta_{(n_{CH_2},C)}$ is the overpotential increment due to additive containing n_{CH_2} methylene groups at concentration C, and $\Delta\eta_{(n_{CH_2}-s,(\omega)^sC)}$ is the overpotential increment due to additive containing $n_{CH_2}-s$ methylene groups at concentration $(\omega)^sC$, ω being the Traube coefficient 4.3. As an example, the overpotential increment caused by pentanoic acid can be predicted from data for propanoic acid by writing

$$\Delta\eta_{C(\text{pentanoic})} = \Delta\eta_{(4.3)^2C(\text{propanoic})}$$

since $s = 2$. This prediction can be generalized further in the form

$$C_1 = (4.3)^sC_2 \quad [18]$$

for straight-chain monocarboxylic acids 1 and 2 such that the chain length of 2 is longer than that of 1 by s methylene groups, and where C_1 and C_2 are concentrations that give the same overpotential increment. It is immediately apparent that Eq. [18] is consistent with the obvious parallelism of the overpotential *vs.* log C curves in Fig. 1. Since the difference between log C-values remains constant for any two of the monocarboxylic additives, then the ratio of the concentrations will also be constant.

Overpotential increments predicted in accordance with Eq. [17] and [18] are compared with experimentally measured values in Fig. 5. Satisfactory agreement is found. In a similar manner, a theoretical prediction can be made concerning the concentration of methanoic acid that would be required to cause a given overpotential increment. As an example, for an increment of 50 mV (total overpotential 150 mV), the methanoic acid concentration would have to be about 2.5M, high enough to have a significant effect on the solvent activity.

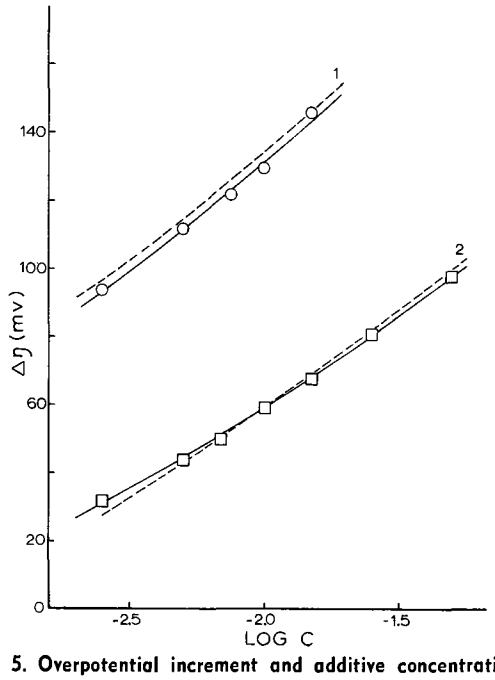

Fig. 5. Overpotential increment and additive concentration. ○, Heptanoic acid. Curve 1, calculated for heptanoic acid from pentanoic data. □, Pentanoic acid. Curve 2, calculated for pentanoic acid from propanoic data.

Another observation concerns the overpotential effects of hexanedioic acid shown in Fig. 1. According to Eq. [17] and [18], the η *vs.* log C curve for hexanoic acid should lie halfway between the curves for heptanoic and pentanoic acids, meaning that the overpotential effect of hexanedioic acid is less than that expected for hexanoic acid. This difference might be rationalized on the basis of partial cyclization of the hexanedioic acid in the aqueous solution. Studies are in progress to compare overpotential effects of a series of straight-chain dicarboxylic acids with their monocarboxylic counterparts.

Acknowledgments

Financial support for this work came from the National Research Council, Ottawa, and from the Department of University Affairs of Ontario, the latter as a graduate fellowship award to A.K.P.C.

Manuscript submitted Nov. 21, 1968; revised manuscript received *ca.* May 19, 1969.

Any discussion of this paper will appear in a Discussion Section to be published in the June 1970 JOURNAL.

REFERENCES

1. J. O'M. Bockris and A. Damzanovic, "Modern Aspects of Electrochemistry," Vol. 3, pp. 224-346, (J. O'M. Bockris and B. E. Conway, Editors, Butterworths, London (1964).
2. E. Mattson and J. O'M. Bockris, *Trans. Faraday Soc.*, **55**, 1586 (1959).
3. J. Tafel, *Z. Physik. Chem.*, **50**, 641 (1905).
4. A. J. Sukava *et al.*, *This Journal*, **112**, 571 (1965).
5. H. Schneider *et al.*, *ibid.*, **112**, 568 (1965).
6. O. Volk and H. Fischer, *Electrochim. Acta*, **5**, 112 (1961).
7. D. R. Turner and G. R. Johnson, *This Journal*, **109**, 798 (1962).
8. E. J. Duwell, *ibid.*, **109**, 1013 (1962).
9. S. S. Kruglikov *et al.*, *Electrochim. Acta*, **12**, 1129 (1967).
10. R. S. Hansen and B. H. Clampitt, *J. Phys. Chem.*, **58**, 908 (1954).
11. B. E. Conway, J. O'M. Bockris, and B. Lovrecek, Proc. 6th Meeting Intern. Comm. Electrochem. Thermodynamics and Kinetics, pp. 207-230, Butterworths, London (1955).
12. A. N. Frumkin and B. B. Damaskin, "Modern Aspects of Electrochemistry," Vol. 3, pp. 149-223, J. O'M. Bockris and B. E. Conway, Editors, Butterworths, London (1964).
13. E. Gileadi *et al.*, *J. Phys. Chem.*, **69**, 3335 (1965).
14. E. Gileadi, *J. Electroanal. Chem.*, **11**, 137 (1966).
15. J. J. Kipling, "Adsorption from Solutions of Non-Electrolytes," Academic Press, New York (1965).
16. A. W. Adamson, "The Physical Chemistry of Surfaces," 2nd edition, Interscience, New York (1967).
17. J. O'M. Bockris and D. A. J. Swinkels, *This Journal*, **111**, 736 (1964).
18. K. J. Mysels, "Introduction to Colloid Chemistry," p. 179, Interscience, New York (1959).
19. E. Gileadi, Editor, "Electrosorption," Chap. 1 and 2, Plenum Press, New York (1967).
20. J. O'M. Bockris *et al.*, *Proc. Roy. Soc. London*, **A274**, 55 (1963).
21. J. O'M. Bockris and G. A. Razumney, "Fundamental Aspects of Electrocrystallization," p. 113, Plenum Press, New York (1967).
22. J. O'M. Bockris *et al.*, *This Journal*, **111**, 743 (1964).
23. D. M. Young and A. D. Crowell, "Physical Adsorption of Gases," p. 106, Butterworths, London (1962).
24. T. L. Hill, "An Introduction to Statistical Thermodynamics," Chap. 7, Addison-Wesley, Reading (1960).
25. W. Heiland *et al.*, *J. Phys. Chem.*, **70**, 1207 (1966).
26. E. Blomgren *et al.*, *ibid.*, **65**, 2000 (1961).
27. W. J. Newby, Ph.D. Thesis, University of Western Ontario, London (1966).
28. W. D. Harkins and E. C. Humphrey, *J. Am. Chem. Soc.*, **38**, 242 (1916).
29. D. A. Haydon and F. H. Taylor, "Proceedings of the Third International Congress of Surface Activity," Vol. 1, 157, Verlag der Universitatsdruckerei, Mainz (1960).
30. I. Langmuir, *J. Am. Chem. Soc.*, **39**, 1848 (1917).
31. C. Kemball, *Proc Roy. Soc.*, **A190**, 117 (1947).
32. O. M. Dzhigit *et al.*, *Doklady Akad. Nauk S.S.S.R.*, **58**, 413 (1947).
33. R. S. Hansen and R. P. Craig, *J. Phys. Chem.*, **58**, 211 (1954).
34. K. S. Markley, "Fatty Acids," p. 177, Interscience, New York (1947).
35. "Handbook of Chemistry and Physics," Chemical Rubber Publishing Co., Cleveland (1963).
36. J. Traube, *Lieb. Annalen*, **265**, 27 (1891).

Epitaxial Chromium Deposition

David W. Hardesty*

Electrochemistry Department, Research Laboratories, General Motors Corporation, Warren, Michigan

ABSTRACT

On nickel, copper, iron, and steel substrates, chromium has been deposited epitaxially from a fluoride catalyzed chromic acid electrolyte at temperatures above 80°C. Prominent planar facets on the deposit surfaces are parallel to chromium {110} crystallographic planes and have structural details indicative of growth by "bunching." Reflections from these facets differ in intensity, according to orientations of substrate grains, and suggest applications in metallography for study of preferred orientations and contrast improvement of "flat etching" metals.

In the course of work reported previously (1), it was observed that appearance and porosity of 0.5 μm (micrometer) thick chromium deposits depended on the crystallographic orientation of electropolished nickel substrates. It was inferred that the topography and deposit structure of the chromium were significantly affected by interfacial epitaxy. Epitaxy of chromium has previously been observed only in thin (<0.1 μm) deposits on nickel (2-4) and on copper (5). Anticipating discernible effects on deposit structure, 15-30 μm deposits from sulfate and sulfate plus silicofluoride catalyzed baths were examined microscopically and by x-ray diffraction. Only the structures and preferred orientations described by Kaiser and Wiegand (6) were found (7). Together with information previously available (8, 9), these results indicate that the characteristic structural elements of chromium deposits are submicroscopic crystallites (10^{-7} to 10^{-4} cm), and further investigation of the influence of epitaxy would require that electron microscopy and diffraction be used. No further work was done as it was obvious that epitaxial effects on deposit structure were limited to a very thin zone at the interface.

The work was resumed when it was noted that surfaces of chromium deposited from a fluoride catalyzed bath at 85°C consisted of well-formed, apparently crystalline, facets. Strongly epitaxed deposits, it was found, can be plated on a number of different metals. This report describes the procedures employed in an exploration of the characteristics of such epitaxial chromium deposits, using metallographic and x-ray diffraction methods. The results obtained are discussed with reference to the deposition process.

Experimental

The chromium plating bath, prepared from reagent grade materials and distilled water, contained 250 g/l (2.5M) chromium trioxide and 5 g/l (0.25M) fluoride ion (from hydrofluoric acid or sodium fluoride). The bath, in a Teflon beaker, was maintained at temperatures of 75°-95°C by immersion in a controlled temperature water bath. Anodes were cut from sheet lead and had areas of 120 cm^2. A polyethylene propeller-type stirrer was used to provide mild agitation to minimize temperature and concentration gradients. Cathodic current density was varied from 300 to 1500 mA/cm^2, but was usually 500-700 mA/cm^2. Power was obtained from a laboratory rectifier (filtered, single-phase full wave) or an electronically regulated constant voltage/current power supply.

The cathodes used were nickel (single crystal disks and annealed polycrystalline sheet), copper (blocks cut from large-grained castings), high purity iron, stainless steel (Type 434), and low carbon sheet steels. Grain sizes ranged from 0.01 mm (steels) to 15 mm (nickel single crystals). Cathodes (1.2-1.5 cm wide by 2.5-3.0 cm long) cut from sheet materials were plated in half-boxes (10) to assure uniform current density. Cathodes cut from bar stock or castings were mounted in cold setting epoxy resin and prepared by metallographic polishing. To ensure that surfaces were free of distortion, all specimens were subjected to suitable chemical or electrolytic polishing treatment.

Nickel was electropolished in the phosphoric-sulfuric-chromic acid mixture used before (1), or chemically polished in a mixture of 70 parts (by volume) glacial acetic acid, 30 parts concentrated nitric acid, and 0.5 parts concentrated hydrochloric acid (11). Although the steels could be electrolytically polished to a smooth, dull surface in the same electrolyte used for nickel, a fully bright polish was obtained in a modification of a solution used by Takeiuchi (12) containing 5 parts concentrated hydrofluoric acid, 40 parts 30% hydrogen peroxide, and 55 parts water. Copper was electropolished in conventional orthophosphoric acid solution (11). After chemical or electrolytic polishing, the specimens were rinsed thoroughly with running water to remove viscous polishing solution. To permit the cathode to come to bath temperature before beginning deposition, electrical connections were made after immersion in the chromium bath.

It was shown, by dissolving representative samples of substrates in 25-50% (by volume) nitric acid and examining the substrate side of the chromium deposit, that there was no appreciable etching of the polished surface. Cross-sections and surfaces of deposits were examined metallographically. Cross-section structure of chromium was revealed by etching at room temperature with Fry's alkaline ferricyanide reagent (13). It was found necessary to etch the substrate prior to the chromium deposit. For nickel, electrolytic etching in acidulated potassium bromide (1) was employed. Copper was etched to high contrast in ammonia-peroxide reagent (14) and the steels in 2-4% nital. All etching times were determined by inspection and were, typically, 30 min for chromium, 1 to 2 min for nickel, and approximately 5 sec for copper or steel.

The angles of facets, with respect to the substrate surface, were determined with a microgoniometer. Back-reflection Laué photographs of large (at least 2 mm) substrate grains and of deposits on these grains were made in a 3-cm camera using unfiltered copper x-rays Intensity of "white" radiation from copper is low and intensities of diffraction spots, except for those from sets of lattice planes so oriented as to satisfy diffraction conditions for the higher intensity K_α emissions, were also low. Contrast between diffraction spots and background darkening therefore tended to be poor. Attempts to improve contrast, so that diffraction patterns could be completely indexed and to provide illustrative examples, were unsuccessful. However, symmetry of patterns from favorably oriented grains (those with surfaces near low index planes) was qualitatively obvious, and identification of orientation could be made.

Results and Discussion

At bath temperatures below 80°C, structures are not substantially different from the usual deposits, while

* Electrochemical Society Active Member.

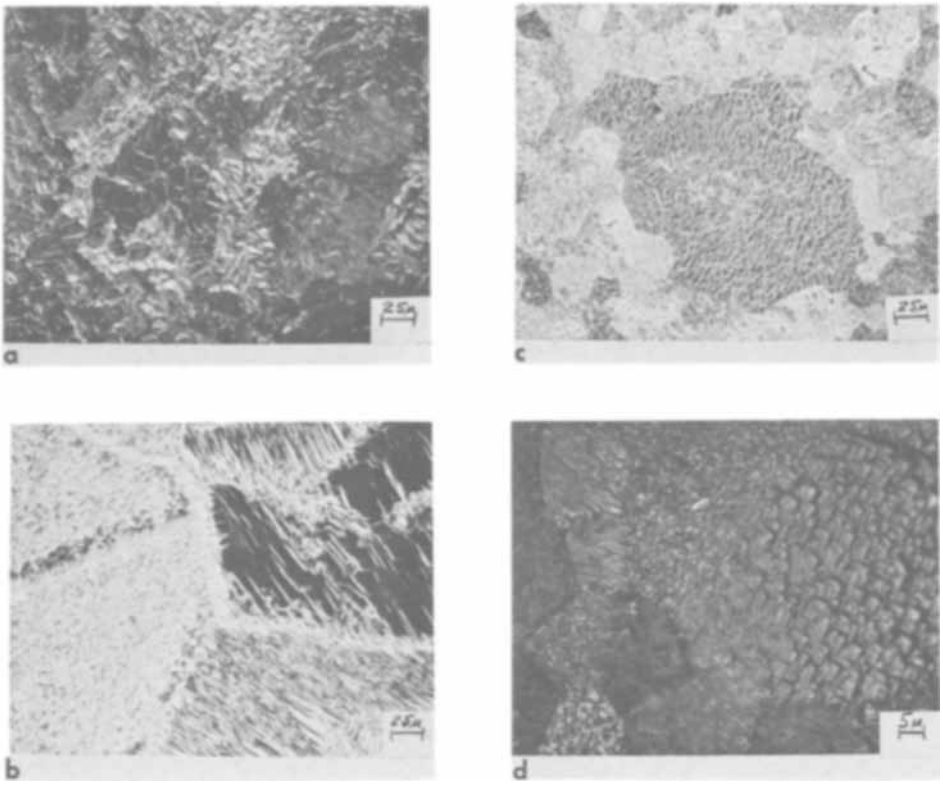

Fig. 1. Typical faceted surfaces of chromium deposited from fluoride catalyzed bath at high temperatures on polycrystalline substrates. Current density: 500 mA/cm^2. (a) On electropolished copper, 10 μm thick, (dark field, 300X); (b) on electropolished nickel, 10 μm thick, (dark field, 300X); (c) on chemically polished low-carbon steel, 2 μm thick, (dark field, 300X); and (d) detail of deposit "c", (bright field, 1000X).

faceted deposits are obtained, at all current densities, at temperatures above 80°C. Typical examples are illustrated in Fig. 1. On these polycrystalline substrates, it was found that size and distinctness of facets depend complexly on the substrate material, grain size, and grain surface orientation. The facets tend to become smaller, more uniform, and less differentiated as deposit thickness is increased. The effect of substrate structure on deposit structure is indicated by the cross-section shown in Fig. 2. Most clearly shown here is the continuation of substrate grain boundaries through the deposit. Differences in the fine structure of deposit above substrate grains can be observed visually, but are not so readily apparent in the photograph.

Relationships between substrate and deposit orientations were demonstrated using large-grained substrates, an example of which is illustrated in Fig. 3. This sample of high-purity iron was etched before plating, and the crystallographic orientation of three large grains was determined by x-ray diffraction. In these grains (indicated by the markings), the iron {110} planes were tilted 2°, 8°, and 15° (± ½°) with respect to the surface. After plating with 20 μm of chromium, orientations of the deposits on these grains was again determined and found to be identical to that of the iron substrates. Clearly, the chromium deposit continued, or copied, the structure of the iron substrate as expected, since the lattice parameters of these isomorphic (body-centered cubic) metals differ by less than 1%. On face-centered cubic (nickel, copper) substrates, the orientations of the deposit were as found by Reddy and Wilman (5) in very thin deposits on copper.

The angles of facets to the surface were found to be those of deposit {110} planes. Where these planes were near to being parallel to the surface (angle <20°), only one distinct reflection, the direction of which could be determined to within ± 1°, could be detected with the microgoniometer. Where the facet angles were greater, the reflecting direction could be determined with less precision (± 2°-3°), but several reflections at approximately 90° angles were observed. Interference microscopy of low-angle facets showed them to be non-planar surfaces with curvatures similar to those on the surfaces of facets on copper deposits noted by Howes (15) who, in his detailed discussion, attributed the apparent curvature to submicroscopic morphology engendered by lateral advance of layers as the deposit

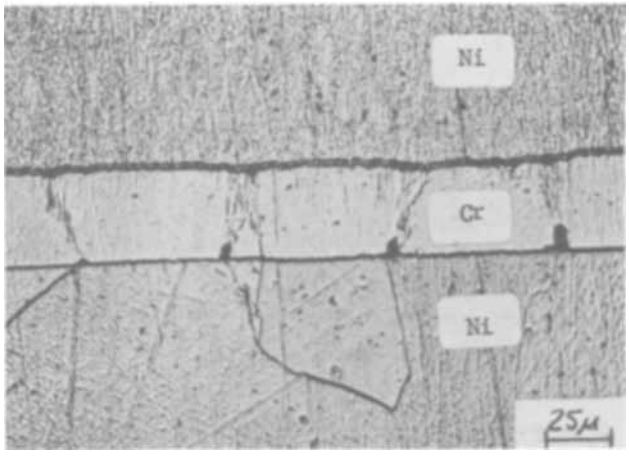

Fig. 2. Cross-section of thick chromium deposit from fluoride catalyzed bath on electropolished nickel (400X).

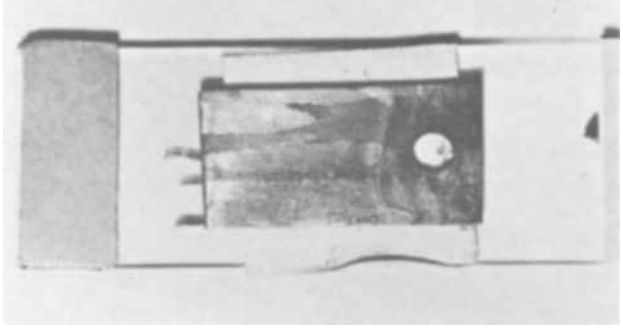

Fig. 3. Macrograph of chromium deposit on large-grained iron cathode used in determination of orientations. Plated area: 1.5 × 2 cm (coupon size 1.5 × 3 cm); chromium thickness, 25 μm.

grew. By a "bunching" process, these layers cease to grow, and the microscopic (and even macroscopic) morphology is developed.

Further evidence that the topography of these epitaxed chromium deposits is a manifestation of the crystallinity of the deposits is provided by the effect of using polarized light. When deposit surfaces are examined, each grain appears to reflect in a shade of gray as shown in Fig. 4a. When the plated sample is rotated through 360°, the gray shade from each grain will change, passing through four diffuse maxima and four distinct minima of reflected light intensity. If the "sensitive tint" technique is employed, each grain has a distinctive color which varies systematically, as the sample is rotated, from magenta through blue to green to gold. The effects are striking in color and photograph in black-and-white as finely graded shades of gray as shown in Fig. 4b. Such responsiveness to illumination by polarized light depends, as shown by Jones (16) and confirmed by electron microscopy (17), on the surface being composed of parallel, right-angle grooves. In the present instance, these grooves are formed by {110} plane facets on the chromium deposit surface.

A somewhat similar, but less distinct, effect is observed if dark-field illumination is used, as shown in Fig. 5. Here, the shading variations depend solely on the angular inclinations of facets of the deposit on each substrate grain. This was the first nonstandard

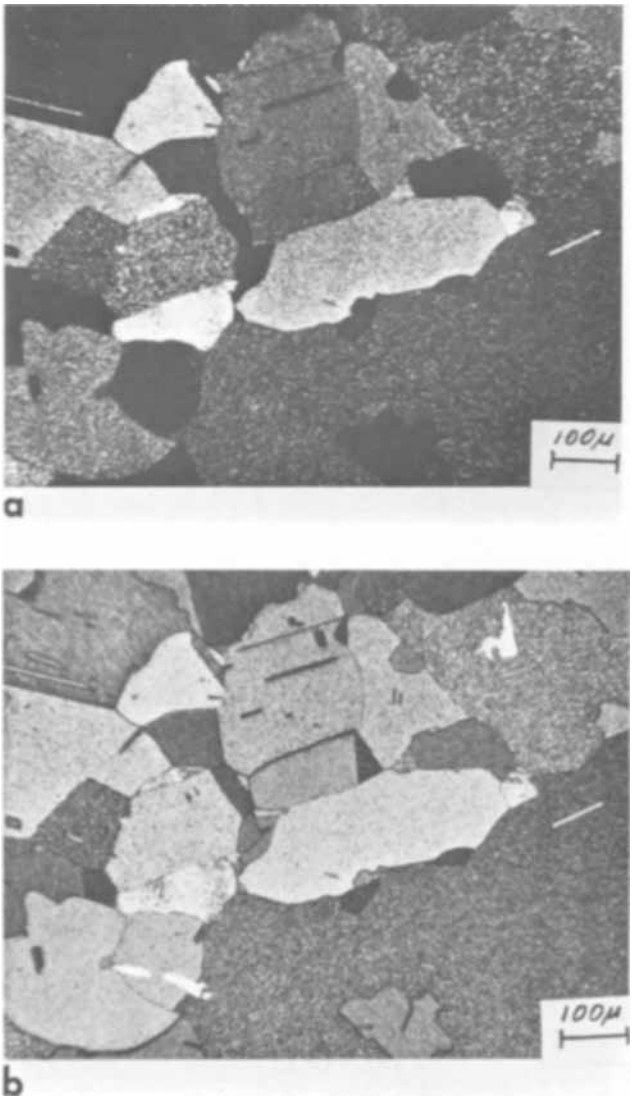

Fig. 4. Orientation-sensitive effects of chromium deposit revealed by using polarized light: (a) crossed polarizers only and (b) "sensitive tint" plate added. Chromium thickness, 5 μm (100X).

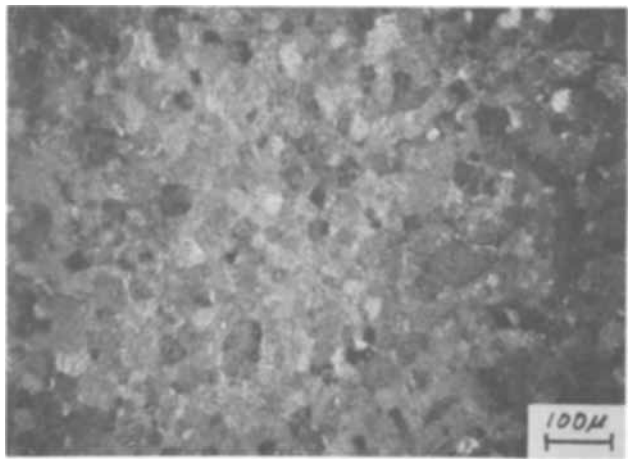

Fig. 5. Epitaxial chromium deposit surface. Substrate: low carbon steel (fully annealed) (dark field, 100X).

illumination technique employed, and it was found that bands of similarly reflecting grains were readily detected visually in deposits on Type 434 stainless steel which displayed "roping" when drawn. An example is illustrated in Fig. 6, which shows one such band. Steel with satisfactory drawing properties contained no such bands. It was concluded that the banding was evidence of preferred orientation or rolling texture made visible by nearly uniform intensity of light reflected from {110} facets on bands of similarly oriented grain surfaces resulting from rolling and annealing treatments of the steel. With dark-field illumination, such texture can easily be detected visually and could perhaps be used as an inspection method. Such a method would, unfortunately, be only qualitative in nature. The polarized light effects probably can be used quantitatively since such use has been reported (18) for etched metals.

It seems clearly established that chromium can be deposited epitaxially on a variety of isomorphous (iron, steel, ferritic Type 434 stainless steel) and nonisomorphous (copper, nickel) substrate metals. From the similarities of morphologies of the deposits, it appears that chromium is deposited from this fluoride catalyzed bath at high temperatures (above 80°C) under conditions whereby growth occurs by a "bunching" mechanism. Keen and Farr suggest that this may be a widely applicable concept, and evidence is available which so indicates (15, 19, 20) for copper, zinc, and other metals. Such growth was demonstrable in nickel and

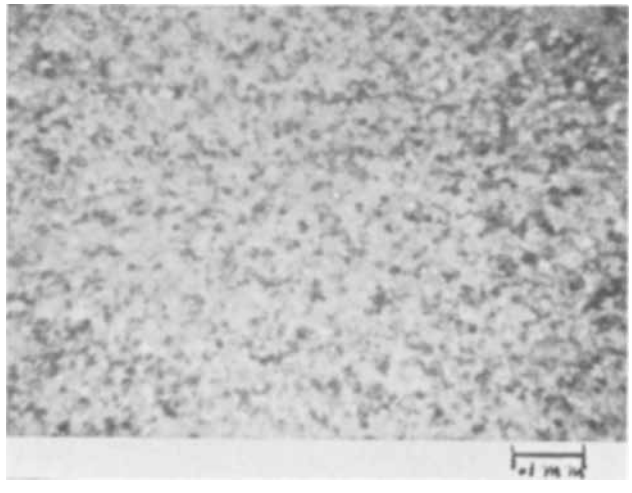

Fig. 6. Possible zone of differential orientation in Type 434 stainless steel from lot which displays "roping" when drawn. Chromium thickness, 1.2 μm (dark field, 100X).

cobalt deposits (20) only at high electrolyte temperatures, confirming Keen and Farr's caution that the applicability of the bunching hypothesis is probably limited to specific conditions of deposition (19). In the present instance, it is obviously the combination of high bath temperature and the fluoride catalyst which permits deposition of clearly crystalline, epitaxed chromium with morphology indicating that the deposit grew by "bunching."

It may be postulated that the deposition of chromium under the conditions employed in this work is not actually different from those more usually employed. With conventional conditions (sulfate catalyst and lower bath temperatures), the deposits tend to develop preferred orientations and consist of extremely small crystallites (8). This may be due to the disruptive influence of chromium depleted complexes at the cathode surface (21). When the chromium cation is removed from such a complex and added to the deposit, the residuum may, by adsorption on the cathode or merely by being slow to diffuse away, effectively insulate the cathode and inhibit further deposition so that crystallites reach only a limited size as the available supply of chromium ion is exhausted. When a new supply of ions becomes available, growth evidently resumes on the previously deposited crystallite, but under such conditions that appreciable enlargement of the crystallite does not occur. Such a process could account for the periodic activity observed at chromium cathodes (22, 23) and the small, rodlike bodies discernible in cross-sections at high magnifications (24). When the temperature of a sulfate catalyzed bath is raised, the deposit structure gradually changes from apparently laminar to markedly columnar (6, 7), possibly due to enhanced mobility or more rapid desorption of the depleted complex. In the case of the fluoride catalyst, the change in deposit structure is more radical in that epitaxy occurs and the deposit grain size duplicates that of the substrate. This indicates either that growth is continuous or, if interrupted, the "new" growth adopts the "old" orientation. If as theorized, deposition of chromium does involve complexes, the complex formed in the fluoride bath has properties vastly different from the complexes formed in a sulfate or sulfate-silicofluoride bath. The parallelism of effect of temperature on chromium deposit structure and the structure of nickel plated from a bath containing organic additives (25) suggests that the adsorption hypothesis is the more tenable.

Conclusions

1. It has been found that substantial thicknesses of chromium can be deposited epitaxially on a number of metals.

2. Structural details of surface facets on these deposits indicate that growth takes place by a "bunching" mechanism similar to that governing the growth of other metals deposited from simpler electrolytes.

3. The specific effects of catalysts and bath temperature on deposit structure indicate that adsorption of some species, possibly a chromium depleted complex, is the cause of the small crystallite size of the ordinary chromium deposit.

4. The differences of reflected light intensity from {110} facets of these epitaxial deposits, due to varying orientation of each substrate grain, may prove useful in metallography of "flat etching" meals by improving contrast.

Acknowledgments

Thanks are due to personnel of the General Motors Research Laboratories: Miss F. A. Forster, who did the x-ray diffraction work; Mr. E. R. Cprek, who called the writer's attention to the preferred orientation problem; and Dr. J. V. Laukonis, who provided the large-grained iron substrate material.

Manuscript submitted March 3, 1969; revised manuscript received May 12, 1969.

Any discussion of this paper will appear in a Discussion Section to be published in the June 1970 JOURNAL.

REFERENCES

1. D. W. Hardesty, *This Journal*, **111**, 912 (1964).
2. R. Weil and H. K. Tsourmas, *Plating*, **49**, 624 (1962).
3. W. H. Cleghorn and J. M. West, *Trans. Inst. Metal Finishing*, **44**, 105 (1966).
4. W. H. Cleghorn, D. H. Warrington, and J. M. West, *Electrochim. Acta*, **13**, 331 (1968).
5. A. K. N. Reddy and H. Wilman, *Trans. Inst. Metal Finishing*, **36**, 97 (1958-1959).
6. H. Wiegand and H.-R. Kaiser, *Metalloberflaeche*, **19**, 161 (1965).
7. D. W. Hardesty, Unpublished results.
8. P. Morisset, "Chromage dur et decoratif," pp. 397-411, Centre d'Information du Chrome Dur, Paris (1961).
9. G. Dubpernell, "Chromium," Chap. 5 in "Modern Electroplating," 2nd Ed., pp. 111-116, F. A. Lowenheim, Editor, John Wiley & Sons, Inc., New York (1963).
10. J. B. Mohler and R. A. Schaefer, *Monthly Rev. AES*, **34**, 1361 (1947).
11. P. A. Jacquet, *Metal Rev.*, **1**, 157 (1956).
12. T. Takeiuchi, *J. Phys. Soc. Japan*, **20**, 942 (1965).
13. H. Fry, *Trans. Inst. Metal Finishing*, **32**, 107 (1955).
14. "Metals Handbook," p. 901, American Society for Metals, Cleveland, Ohio (1948).
15. V. R. Howes, *Proc. Phys. Soc.*, **74**, 616 (1959).
16. O. Jones, *Phil. Mag.*, **48**, 207 (1924).
17. R. E. Read-Hill, C. R. Smeal, and L. Lee, *Trans. Met. Soc. AIME*, **230**, 1019 (1964).
18. R. C. Hendrickson and B. N. Iannone, "Applications of Metallurgical Microscopy," pp. 14 and 18, Bausch and Lamb, Inc., Rochester, N. Y. (undated).
19. J. M. Keen and J. P. G. Farr, *This Journal*, **109**, 668 (1962).
20. D. R. Cliffe and J. P. G. Farr, *ibid.*, **111**, 299 (1964).
21. P. Morisset, *op. cit.*, pp. 17-27.
22. M. H. Jones and J. Saiddington, *Proc. Amer. Electroplaters' Soc.*, **48**, 32 (1961).
23. C. P. Brittain and G. C. Smith, *Trans. Inst. Metal Finishing*, **33**, 289 (1956).
24. P. A. Jacquet, *Compt. Rend.*, **256**, 4209 (1963).
25. R. J. Clauss, *Proc. Amer. Electroplaters' Soc.*, **47**, 105 (1960).

Film Formation at Anodes in Nominally Anhydrous Acetic Acid Solutions

H. W. Salzberg,* Allan Barnett, and Stephen Kandler

City College, City University of New York, New York, New York

ABSTRACT

Steady-state measurements over prolonged time periods were made on platinum, gold, and palladium anodes in unstirred, nominally anhydrous potassium acetate-acetic acid solutions, at current densities as low as 10^{-8} A/cm^2. Between 10^{-8} and 10^{-4}-10^{-5} A/cm^2, the results were reproducible and the Tafel lines had a slope of 0.06-0.07. Within experimental error, the points for platinum and gold both fell on the same straight line. The results are interpreted to mean that below about 10^{-4} A/cm^2, acetate ions were oxidized in a reversible 1-electron reaction. At about 10^{-4}-10^{-5} A/cm^2, a film of adsorbed acetic acid molecules was formed and molecular acetic acid became the source of anodic electrons.

In previous work (1) steady-state current-potential measurements were made at platinum anodes in "nominally anhydrous" (2) potassium acetate-acetic acid systems. The curves were roughly sigmoid with a large hysteresis loop, as shown in Fig. 1. We suggested that the lower plateau corresponded to the oxidation of acetate ion

$$CH_3COO^- - e \rightleftharpoons CH_3COO \qquad [1]$$

and that the upper plateau corresponded to the oxidation of molecular acetic acid. The rise from the potentials of the lower plateau to those of the upper plateau we felt, at the time, was due to the depletion of acetate ion from the surface when the current exceeded the limiting diffusion current of acetate ions in the unstirred solution. The oxidation of the molecular acetic acid could take place by either of the following reaction mechanisms. The first is an electron transfer followed by a proton transfer, Eq. [2], and the second is a simultaneous electron and proton transfer, Eq. [3].

$$(a)\quad CH_3COOH - e \rightleftharpoons CH_3COOH^+$$

$$(b)\quad CH_3COOH^+ + CH_3COO^- \rightarrow CH_3COOH + CH_3COO\cdot \qquad [2]$$

$$CH_3COOH - e \xrightarrow{CH_3COO^-} CH_3COOH + CH_3COO\cdot \qquad [3]$$

In the present work we have extended the investigation of this system to gold and palladium anodes and to current densities as low as 10^{-8} A/cm^2.

Experimental

The solutions were not rigorously anhydrous. The solvent was glacial acetic acid. For some runs the solvent was purified by freezing and discarding any unfrozen liquid. For most runs, a sample of solvent was boiled down to about half of its volume. The solution was saturated with potassium acetate, concentration being 7 moles/kg of solvent. The potassium acetate was dried by melting and heating at temperatures in excess of 300°C. The cell was kept in a dessicator during runs and the only contact between solution and laboratory air was during the short periods when the heated reagents were transferred to the dessicator and when the cell was filled. Undoubtedly, some moisture entered the system during those time periods but we estimate the quantity to be rather small, based on a rough calculation of the moisture present in the air in the empty cell.

The cell was a Teflon cylinder with a fitted Teflon top and Teflon tubes extending through the top into the cell. The electrode wires were passed through these tubes into the cell. The cell volume was about 24 ml. Some runs were made with one anode in the solution, others were made with two or three anodes, so that comparisons could be made using several different electrodes in the same batch of solution. There was no detectable difference in results due to the number of electrodes present.

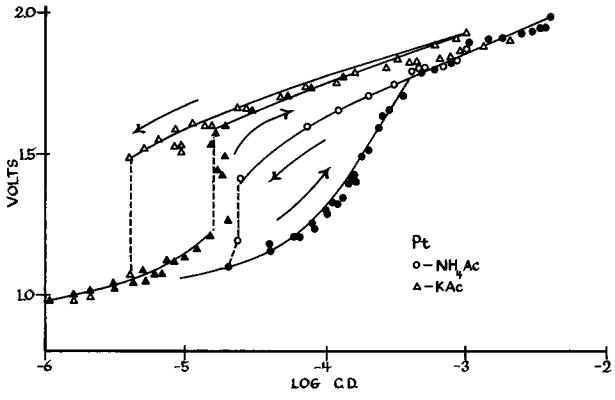

Fig. 1. Voltage-current density measurement on platinum anodes in anhydrous acetic acid. Ordinate is potential *vs.* a silver-silver chloride reference.

Measurement techniques were varied. In runs at high current densities, the interrupter method was used. Both working potential and ohmic drop were measured at each point in the curve. In other runs we obtained a complete curve of working potential *vs.* current density, by direct measurement, and then used the interrupter method to determine the ohmic drop. The electrode potential was then obtained by difference. The results of this procedure showed that at current densities below 10^{-5} A/cm^2, the ohmic drop was within the experimental error of the potential measurement. In further work, therefore, no correction was made for ohmic drop below 10^{-5} A/cm^2 and potentials were obtained by direct measurements.

Constant potential runs were made with a Heath operational amplifier system, equipped with a polarography module and with a Beckman Electroscan 30. Constant current runs were made with the Electroscan. The results did not depend, perceptibly, on the choice of apparatus. When the steady state was reached, results were the same for both constant current and constant voltage runs. Differences between constant current and constant voltage runs occurred only during the approach to the steady state.

The cathode was a silver-silver chloride electrode about 4 cm^2 on a face. The reference electrode was a silver-silver chloride wire. The platinum and palladium anodes and one of the gold anodes were of the flag type, about 1 cm^2 on a face. Both faces of the flag electrodes were exposed and no attempt was made to

* Electrochemical Society Active Member.

determine the potentials of each face separately. The gold flag was 24 karat, the other gold electrode was an 18 karat wire whose tip was melted to a hemisphere of 0.2 cm^2 surface area. The gold wire was inserted in a Teflon tube so that only the hemispherical surface was exposed to the solution. The platinum and palladium electrodes were repeatedly flamed and dipped into nitric acid and then soaked in acetic acid. The gold electrodes were soaked in nitric acid for prolonged periods and then in acetic acid. The solution was saturated with KCl to supply the Ag/AgCl electrodes. The solution contained about 3×10^{-2} moles of KCl/kg of solvent. The temperature range of the experiment was 25° ± 2°C, *i.e.*, room temperature.

Some runs were galvanostatic, others potentiostatic. At the start of a run it took many hours for the first few points. Sometimes overnight runs were made. However, after the first few points had been obtained, steady-state values could be determined within an hour or so, for each point. Our arbitrary criterion of steady state was a voltage change of less than 5 mv (about 1%) in a half hour.

Other authors (2, 3) have made measurements at fixed time intervals, for example, 60-sec intervals, 1-hr intervals, etc., to avoid "long-time variations in the potential which commonly occur in anodic processes" (4). Almost certainly, most data obtained in time intervals of less than one hour per point are not steady-state data. To check our experimental method, we took trial points at fixed time intervals and found the data relatively irreproducible, while our steady-state measurements, as defined above, were quite reproducible, as shown below.

Results and Discussion

Figure 2 shows a typical current-voltage curve at a gold anode. Note that the hysteresis loop is much wider than in the case of platinum and extends down to current densities at least as low as 5×10^{-5} A/cm^2. At points 1 and 2 both current and potential are stable for 18 hr or more. If the difference in potential between the upper and lower plateaus resulted from depletion of ions from the surface at 10^{-4} A/cm^2 (the rising portion of the curve) then, after 18 hr at point 1, enough acetate ions should have diffused in to lower the potential to that of the lower plateau. No such change takes place. If, however, the current is interrupted for a few seconds, the potential drops immediately down to that corresponding to the lower plateau. Obviously, the potential at point 1 is not maintained by slowness of ion transport to the surface. If diffusion to the surface were slow enough so that at 10^{-5} A/cm^2 the surface should be depleted of acetate ions, then after 18 hr the potential should rise from that at point 2 to the values of the upper plateau. This rise also does not occur. The wide hysteresis loop

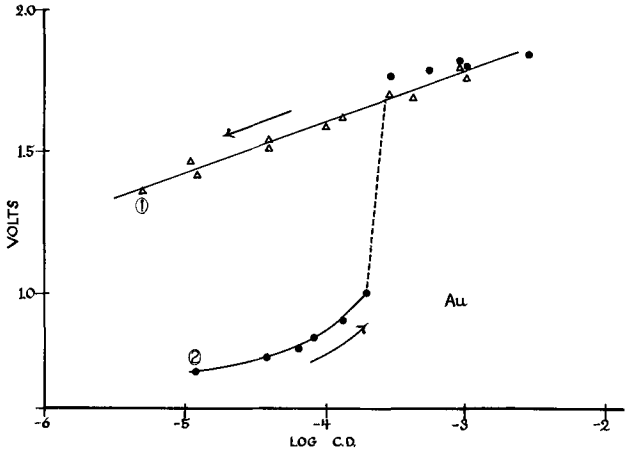

Fig. 2. Voltage-current density measurements on a gold anode in KAc-HAc.

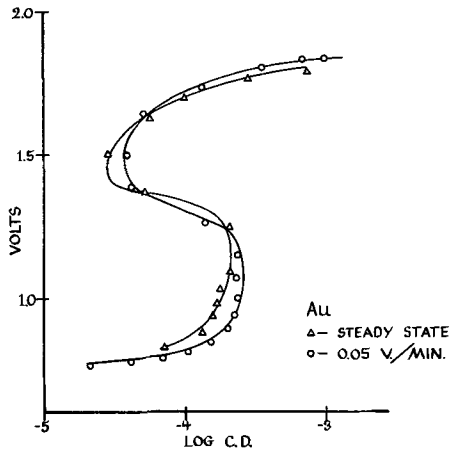

Fig. 3. Potentiostatic voltage-current density measurements on a gold anode in KAc-HAc.

at 10^{-5} A/cm^2 and below is therefore not due simply to a mass-transport phenomenon.

Some potential-step measurements were made on platinum. At currents below 10^{-4}-10^{-5} A/cm^2, when the potential was stepped up, there was the expected initial sharp increase in current followed by a slow decrease. At current densities above 10^{-4}, there was no decay in the current after the initial sharp rise. We interpret this as indicating that at these higher current densities, the solvent (molecular acetic acid) is oxidized, and that at lower currents acetate ions are being oxidized.

Figure 3 shows potentiostatic voltamograms on gold anodes. Qualitatively similar results were observed on platinum. The circular points were obtained with a linear sweep, the triangular points were the result of steady-state measurements. Both curves show a decrease in current at constant potential at currents corresponding to the rise in potential from the low plateau to the high values. Curves such as these are characteristic of film formation and are often associated with passivation (5).

Figure 4 shows the results of measurements of the lower plateaus over prolonged periods (up to two weeks per solution) with several different anodes in several different batches of solution. The currents were kept (for the most part) below values at which the potential rise commenced. In some cases, the potentials rose to the upper plateau. However, opening the circuit for a few seconds was sufficient for the potential values to drop back down to those shown on the graph. Some runs were deliberately continued to the upper plateau, where the observed values were in agreement with previously published data (1, 6). The results at the low currents were sufficiently reproducible for one straight line to be drawn through several sets of

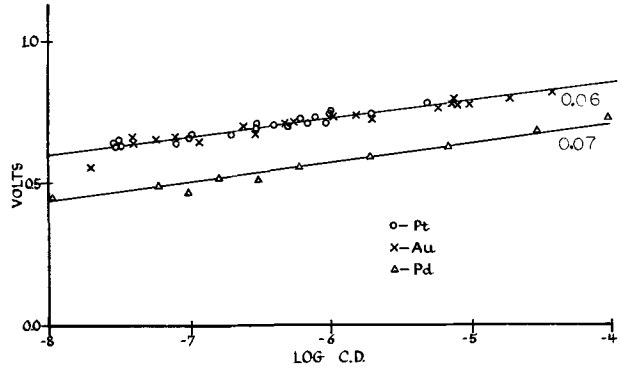

Fig. 4. Steady-state measurements at low current densities in KAc-HAc.

measurements with each of two gold and two platinum electrodes in several batches of solution. This is in marked contrast to the previously published data, at high current densities, on the upper portion of the curve, where at the same electrode in the same solution results differed by as much as 60 mV from day to day (6).

Figures 2 and 3 taken together indicate that the hysteresis loop shown in Fig. 1 is the result of formation of a film. Figure 4 shows that at current densities below that necessary for film formation, *i.e.*, below 10^{-4} A/cm^2, the slope of the voltage-log current density curve is 0.06, which is consistent with a reversible 1-electron transfer, such as that in Eq. [1]. The voltage-log current curves in the region of the upper plateau, *i.e.*, at 10^{-3} A/cm^2 and above, have slopes of 0.10-0.15 (1) which correspond to irreversible 1-electron oxidations, such as in Eq. [2] and [3].

The Tafel slopes and the close agreement between results on platinum, gold, and palladium electrodes indicate that the process taking place is probably thermodynamically controlled and reversible, rather than irreversible and kinetically controlled. The small difference (0.1V) between the values on Pd and those on the other two electrodes could be explained either on the basis of a roughness factor or on the basis of a small heat of adsorption. If the radical formed in Eq. [1] were adsorbed on the electrode surface, a difference in heats of adsorption of only 2-3 kcal/equivalent would be enough to account for the potential difference.

At this point it is necessary to discuss the effects of the undoubted presence of trace amounts of water in our solutions. This water could: (*a*) be the substance oxidized at low currents and potentials (*i.e.*, at current densities below 10^{-4} A/cm^2); (*b*) be the substance which is oxidized to produce a film.

Any water present would be in the form of either hydronium ions, which would not diffuse to the anode, or water molecules. (Since the ionization constant of acetic acid is 10^9 that of water, the OH^- resulting from the self-ionization of water in acetic acid solution should be negligible.) The water molecules oxidizing at the anode would form either molecular oxygen with a Tafel slope of 0.12 (7, 8) or a metallic oxide.

In the low-potential low-current density region, the Tafel slopes are 0.06 and there is no evidence of either film formation or of any change in either mechanism or identity of reacting substance until the current density has reached the 10^{-4} A/cm^2 region. In addition, since the potential current density curves on gold and platinum are identical, any oxides forming would have to form at the same potential, which would be within 0.1V of the potential at which the palladium oxide would form. This would be unlikely. Finally, for the lower slope to be due to the oxidation of water up to 10^{-4} A/cm^2, the water concentration would have to be about 10^{-3} moles/liter. While our solutions were not rigorously anhydrous, this figure is probably several orders of magnitude above our water concentration. By the same argument, for water to be the source of the current at 10^{-4} A/cm^2 and above, the water concentration would have to be hundredth or even tenth molar, which is out of the question. To arrive at the figure of 10^{-3} moles/liter as being necessary to support a current density of 10^{-4} A/cm^2, we assume only that the diffusion constant for water molecules in acetic acid is 10^{-5}, which is the same order of magnitude as that of most salts in aqueous or methanolic solution. To support a current of 10^{-4} A/cm^2 = 10^{-9} moles/sec-cm^2, if the diffusion constant is 10^{-5} cm^2/sec, the concentration gradient, $dC/dx = 10^{-4}$ mole/cm^4. In a stirred solution, the diffusion zone is 10^{-2}-10^{-3} cm (9), so taking the larger figure for our work in unstirred solutions, the difference in concentration across the Nernst diffusion layer is 10^{-6} moles/cm^3 or 10^{-3} moles/liter. Even if the surface concentration were zero, the bulk water concentration to support a 10^{-4} A/cm^2 current density would have to be millimolar.

We therefore conclude that under our steady-state conditions, the effect of water is not significant. Under conditions where rapid potential measurements were made, the presence of water would most probably have significant effects.

Conclusions

We consider that these results can best be explained in terms of the reversible 1-electron oxidation of acetate ions at current densities up to about 10^{-4} A/cm^2, in unstirred solution, and the irreversible oxidation of molecular acetic acid at current densities above 10^{-4} A/cm^2. At about 10^{-4} A/cm^2, the diffusion layer is depleted of acetate ions and the potential rises, by about 0.8V, to the level at which acetic acid molecules are oxidized. At these high potentials, the field across the adsorbed double layer is strong enough to both polarize and adsorb the un-ionized acetic acid molecules, forming a film. Once the film has formed, the potential across the double layer maintains it, even when the current is lowered. The persistence of the film would explain the hysteresis loop, and the stability of point 1 on Fig. 2. At current densities below 10^{-4} A/cm^2 when the circuit is interrupted, the field relaxes and the film desorbs. The potential then drops immediately down to the level at which acetate ions are oxidized.

The film most probably consists of a monolayer of acetic acid molecules oriented with the carboxy groups at the surface of the metal and the hydrocarbon tails in the diffuse double layer. [This is essentially the type of barrier film proposed by Conway *et al.* (10-12).] Since most preparative runs utilizing the Kolbe reaction take place at current densities in the 0.1-1 A/cm^2 region, probably most of the reactions reported in the organic chemistry literature have taken place at a surface of adsorbed acid molecules.

Acknowledgment

We wish to thank the National Research Foundation for assistance to Mr. Barnett under the National Science Foundation Student Participation Program.

Manuscript submitted Jan. 2, 1969; revised manuscript received May 30, 1969. This was Paper 209 presented at the Boston Meeting, May 5-9, 1969.

Any discussion of this paper will appear in a Discussion Section to be published in the June 1970 JOURNAL.

REFERENCES

1. M. Leung, J. Herz, and H. W. Salzberg, *J. Org. Chem.*, **30**, 310 (1965).
2. (a) B. E. Conway, E. Beatty, and P. A. D. De Maine, *Electrochim. Acta*, **7**, 39 (1962).
   (b) B. E. Conway and A. K. Vijh, *J. Phys. Chem.*, **71**, 3637 (1967).
3. T. Dickenson and W. F. K. Wynne-Jones, *Trans. Faraday Soc.*, **58**, 382, 388, 400 (1962).
4. A. K. Vijh and B. E. Conway, *Chem. Rev.*, **67**, 663 (1966).
5. K. S. Vetter, "Electrochemical Kinetics: Theoretical and Practical Aspects," chap. 6, Academic Press, New York (1967).
6. H. W. Salzberg and M. Leung, *J. Org. Chem.*, **30**, 2873 (1965).
7. Ref. (5) above, pp. 624 *et seq.*
8. M. Breiter, "Advances in Electrochemistry and Electrochemical Engineering," VII, chap. 3, Interscience Publishers, New York (1961).
9. J. Heyrovsky, "Principles of Polarography," p. 111, Academic Press, New York (1966).
10. B. E. Conway and M. Dzieciuch, *Can. J. Chem.*, **41**, 21, 38, 55 (1963).
11. A. K. Vijh and B. E. Conway, *J. Phys. Chem.*, **71**, 3655 (1967).
12. A. K. Vijh and B. E. Conway, *Z. Anal. Chem.*, **230**, 81 (1967).

Polarographic Reduction of Alkyl Halides at a Stationary Lead Electrode

Harris E. Ulery

Jackson Laboratory, Organic Chemicals Department,
E. I. du Pont de Nemours and Company, Wilmington, Delaware

ABSTRACT

The polarographic reduction of some simple alkyl halides at a stationary lead electrode was investigated. Both the iodides and bromides undergo an irreversible one electron reduction with sacrifice of the electrode metal in acetonitrile. The bromide results are compatible with a "backside attack" by the electrode, while the iodides, in keeping with the reverse polarization of the C-I bond, have a substantially different orientation. In both series the reductions were strongly dependent on the nature of the supporting electrolyte cation. The process of metal alkylation and removal are discussed in light of supplementary data from large scale electrosyntheses of organoleads.

The electroreduction of organic halides has drawn much attention in recent years (1), but principally in the context of the dropping mercury electrode (dme), and generally under conditions which give hydrocarbon as the major product (Eq. [1])

$$RX + H^+ + 2e^- \rightarrow RH + X^- \qquad [1]$$

In solvents of low proton activity such as anhydrous DMF and acetonitrile, however, many soft metal electrodes (2, 3) are consumed on reduction of the organic halide. The sacrificial cathode reaction can conform to Eq. [2] (M = cathode metal)

$$nRX + M + ne^- \rightarrow R_nM + nX^- \qquad [2]$$

In view of the economic importance of lead alkyls, a study was undertaken of the polarographic behavior of some simple alkyl halides at a stationary lead electrode.

Experimental

Materials.—The tetralkylammonium halides were Eastman white label grade. These will be referred to by their acronyms (*e.g.*, TEAB for tetraethylammonium bromide). Commercial acetonitrile was dried by the usual P_2O_5 method (4), although improved procedures have appeared since this work (5). Excepting the t-butyl halides which were distilled and stored under argon prior to use, the alkyl halides (also white label or equivalent grade) were used without additional purification. Lead metal obtained as shot analyzed as 99.97%.

Equipment.—The three electrode system used has been described previously (6). The reference electrode was aqueous saturated calomel (SCE). Transfer of water across the bridge during the course of a run was found to be negligible by Karl-Fischer titration.

The stationary working electrode was the 4 mm disk end of a melt-cast lead rod with a heat shrunk outer sheath of polyethylene. The assembly was thermostated at 25.0° ± 0.5°C.

Method.—The use of relatively high alkyl halide (RX) concentrations (1-20 mM) was dictated by two considerations: (*i*) the interference by background electrolyte activity which was appreciably greater than observed with a quiet mercury electrode, and (*ii*) the sloughing of metallic lead which occurs, depending on the supporting electrolyte, when the RX concentration is too low. Convection, pronounced at the sacrificial electrode due to the high densities of the organometallic products, was further aggravated by the passage of high currents. A 3-10% increase in the $it^{1/2}$ values over a 30 sec interval was common.

Key words: alkyl halides, lead cathode, polarography, reduction, sacrificial electrode, tetraalkyllead.

To avoid volatilization of RX (7), these and the solvent were thoroughly deoxygenated by sparging with argon prior to volumetric preparation of the test solutions.

Typically, the electrode was lightly polished on filter paper and the blank electrolyte was scanned from −1.0V one or more times to provide a suitable reference and to insure the reduction of all surface halide. The calculated amount of a 1.0M RX solution was added and the mixture scanned cathodically several times. Half-wave potentials and not peak potentials are reported in view of the greater uncertainty associated with the latter. Values given are the averages of four or more runs. Unless otherwise specified the scan rate was 0.22 V/min.

Results and Discussion

Limiting potentials.—The potential ranges accessible to the lead electrode with tetraalkylammonium bromide are illustrated by the limiting cathodic values given in Table I. In anhydrous acetonitrile, the organic cation is reduced to the trialkyl amine, which was identified for R = Et, n-Pr, and n-Bu; some soluble lead product is also formed. In aqueous media reduction of hydrogen ion may be the limiting reaction, although this does not seem to be the case on mercury (8) which has the greater hydrogen overvoltage. For aqueous acetonitrile mixtures the limiting potentials varied linearly between these extremes with log $[H_2O]$.

Reaction products for bromide system.—The reduction of MeBr at a lead electrode in TEAB/MeCN/H_2O mixtures gives TML in yields approaching 100% based on metal consumption and current use (9, 10). The observed stoichiometry is (RX=MeBr)

$$Pb + 4RX + 4e^- \rightarrow PbR_4 + 4X^- \qquad [3]$$

Table I. Limiting potentials on lead for aqueous and acetonitrile solutions of the tetraalkylammonium bromides at 25°C[a]

R	0.2 F $NR_4^+Br^-/H_2O$	0.2 F $NR_4^+Br^-/CH_3CN$
H	−1.80	[b]
Me	−1.84	[c]
Et	−1.85	−2.75
n-Pr	−1.87	−2.85
n-Bu	−1.90	−2.90
n-Pe	—	−2.92

[a] *vs.* SCE. Current density was 3 mA/cm².
[b] Insoluble.
[c] Solubility of tetramethylammonium bromide is only ~7.8 mM at 25°C.

Table II. Polarographic parameters of alkyl bromides at a Pb electrode[a]

RBr	TEAB $E_{P/2}^{Pb}$	TEAB $E_{3/4} - E_{1/4}$	TEAB $(i_p\eta^{1/2})_{Rel}$[b]	TPAB $E_{P/2}^{Pb}$	TPAB $E_{3/4} - E_{1/4}$	TPAB $(i_p\eta^{1/2})_{Rel}$[b]	TBAB $E_{P/2}^{Pb}$	TBAB $E_{3/4} - E_{1/4}$	TBAB $(i_p\eta^{1/2})_{Rel}$[b]	$E_{1/2}^{Hg}$	log (K_1)[c]
MeBr[g]	−1.56 ± 0.04	−0.09 ± 0.04	1.00	−1.59 ± 0.03	−0.09 ± 0.04	0.95	−1.68 ± 0.03	−0.08 ± 0.03	0.79	−1.63[d]	−1.67
EtBr[g]	−1.92 ± 0.05	−0.19 ± 0.04	0.95	−1.96 ± 0.04	−0.21 ± 0.06	0.85	−2.04 ± 0.03	−0.20 ± 0.04	0.69	−2.13[e]	−2.77
i-PrBr	−2.00 ± 0.11	−0.21 ± 0.04	0.91	−2.05 ± 0.11	−0.20 ± 0.04	0.78	−2.30 ± 0.10	−0.21 ± 0.04	0.64	−2.26[e]	−4.31
t-BuBr[f]	−1.80 ± 0.04	−0.20 ± 0.04	0.89	−1.80 ± 0.04	−0.20 ± 0.02	0.75	−1.84 ± 0.05	−0.20 ± 0.04	0.64	−2.19[e]	−2.00

[a] Medium was 0.2 F electrolyte/MeCN at 25°C; all potentials *vs.* SCE.
[b] Corrected currents relative to MeBr/0.2 TEAB system. $i_p/C = 14.7$.
[c] Data taken from ref (12). Solvolysis medium was EtOH:H_2O 80:20 (V/V).
[d] Ref. (27).
[e] Ref. (13).
[f] Small prewave near −1.3V.
[g] Small secondary wave 0.1-0.3V cathodic to primary.

The reduction of EtBr produces both TEL and hexaethylbilead. Schuler (9) has estimated that only about 40% of the current is consumed by way of Eq. [3], while the remainder is used according to Eq. [4] (RX = EtBr).

$$2Pb + 6RX + 6e^- \rightarrow Pb_2R_6 + 6X^- \qquad [4]$$

With i-PrBr less than 30% of the current is utilized in the formation of organolead products, and only traces of organoleads are found among the reduction products of t-BuBr. Respectively, isopropylene and isobutylene are also produced. The formation of metal fines is greatest for the reduction of i-PrBr.

Peak currents (bromide system).—The polarograms of the alkyl bromides are strongly influenced by the nature and concentration of the supporting electrolyte, as well as the concentration of RBr itself. MeBr and EtBr produced principal peaks whose heights were proportional to concentration up to 5-6 mM, after which low but increasing values were observed to 15 mM. A second, more cathodic peak, ¼ to ½ the height of the primary was evident for RBr concentrations > 3-4 mM. The total current was proportional to concentration in all cases. In TEAB especially, a decrease in the residual current occurred on addition of RBr, and a small capacity wave near −1.5V preceded their reductions.

The relative, viscosity corrected currents (Table II) decrease with the increasing size (lower mobility) of RBr and with increasing supporting cation size. The latter may reflect cation adsorption leading to a decrease in the active electrode area (11).

Half-wave potentials (bromide system).—The ease of reduction as evidenced by the half-wave potentials of the principal peaks (Table II) decreases in the order Me>t-Bu>Et>i-Pr. Also listed are the pseudo first-order rate constants for the decomposition of the alkyl bromides in aqueous ethanol (12). The nearly linear relationship between $E_{P/2}$ and log (K_1) suggests a possible mechanistic similarity between the two reactions; *i.e.*, the factors which dominate in controlling the rate of RBr reduction at the lead electrode and the rate of RBr solvolysis may be the same. This result is accommodated by Elving's postulate (1) of a general nucleophilic substitution process in which the electrode, functioning as the nucleophile, performs a backside displacement on the halogen bearing carbon. The transfer step may be written as follows:

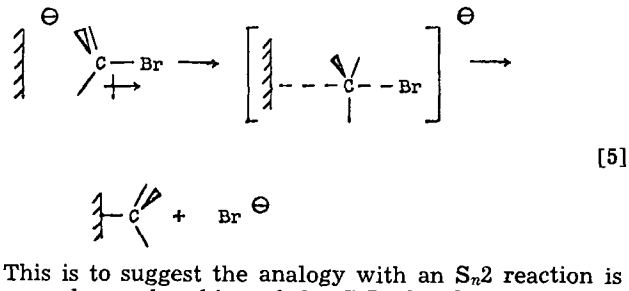

[5]

This is to suggest the analogy with an S_n2 reaction is a good one: breaking of the C-Br bond is concurrent with and to some extent compensated by the formation of the new C-M bond. An alternative would be bond rupture without new bond formation [6]:

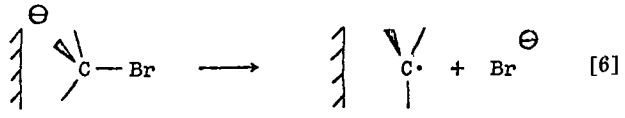

[6]

Such a scheme would be expected when C-M bond formation is opposed by the nature of the metal, high R· stability, steric hindrance, or possibly precluded by the interposition of sorbed species. In such cases, a separate chemical step is required to produce the C-M bond, one perhaps analogous to Paneth's classic metal scavenging reaction (14).

Although several examples of cathodic dimerization are known (15) which establish the intermediacy of radicals (Eq. [6]), the efficiency of the electrosynthesis of Me_4Pb and Et_4Pb argues for direct formation of the Pb-C bond. Only at high current densities does dimerization become significant. We believe the principal polarographic wave for MeBr and EtBr is due to the reduction mode of Eq. [5], while the more energetic process of Eq. [6] could account for the smaller, more cathodic secondary wave (bond breaking only).

An increase from 5 to 10 mM in the MeBr or EtBr concentration results in an anodic E_p shift of 20-30 mV. This behavior is consistent with (*i*) deposition of the reduction product (29), *e.g.*, Eq. [5], or (*ii*) a rate determining step greater than 1st-order in depolarizer concentration (25) such as the metal removal step (*vide infra*).

The similarity of the reduction potentials of the alkyl bromides on lead and mercury invites further consideration in view of the *ca.* 0.35V difference in the zero-charge potentials (ψ_o) of these metals (16). For comparison, the reductions of the alkyl bromides at a stationary cast tin electrode were examined briefly. Only methyl bromide gives a distinct wave in 0.2 F TBAB. The product is Me_4Sn. The reduction data for MeBr on these three metals and estimates of the corresponding rational half-wave potentials ($E_{p/2} - \psi_o$) are included in Table III. The importance of rational potentials for comparing reductions on different metals has been stressed (17).

Both measures of the reaction potential point to metal participation in determining the over-all reaction rate. Some pertinent characteristics of these metals are also collected in Table III. The only obvious correlations are with the atomic numbers and the related average electron densities. As in a familiar chemical S_n2 reaction, the rate should be enhanced as the nucleophilicity of the electrode is improved, *i.e.*, as the availability of electrons is improved by increased density and/or polarizability. Accordingly we might expect the larger directed 6p orbitals on lead[1] to be much more available to participate in the transition state of Eq. [5] than would the 5p orbitals on tin and slightly more so than the smaller symmetric 6s orbitals on mercury.

[1] Strictly speaking one must consider the orbitals of the metal crystal and not atomic orbitals.

Table III. Comparison of metal electrode characteristics

Metal	$E_{1/3}$ (MeBr)[a]	$E_{1/2} - \psi_o$[b]	At. No.	Electron density (E/A³)	$D_{m\,m}$[c]	ϕ_{M/M^+}[d]	E_F[e]	ψ[f]
Pb (s)	−1.68	−0.75	82	5.6	23	7.38	100	3.94
Hg (liq.)	−1.77	−1.23	80	5.5	3.2	10.39	9	4.50
Sn (s)	−2.45	−1.93	50	3.5	46	7.30	31	4.09

[a] 0.2 F TBAB/MeCN at 25°C.
[b] ψ_o measured in the absence of specific adsorption.
[c] Metal-metal bond dissociation energy in kcal/mole.
[d] First atomic ionization potential in eV.
[e] Fermi energy in ergs $\times 10^{14}$.
[f] Work function from contact potential method in eV. Recent work has shown that this function cannot affect the electrode kinetics (28).

The negative shift in $E_{P/2}$ with increasing cation size is consistent with cation adsorption (18). Alternatively, extensive ion pairing in acetonitrile (19) could facilitate the transfer step as indicated below

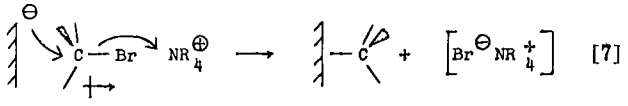

[7]

The rate enhancement would be greatest for the smallest member of the cation series and be revealed as the largest positive shift. A very similar rationalization has been proposed to account for some observed salt effects in the reduction of quinones in DMF (20) and nitroaromatics in DMF and MeCN (19b).

Reduction products (iodide system).—Both MeI and EtI are reduced to the corresponding lead alkyls. Although the iodide reaction has not been explored in as great detail as in the case of the bromides, it is clear that very high current efficiencies are obtainable. It appears that more hexaethyl dilead is produced from ethyl iodide than from the bromide, and that the amount of this product depends on the supporting electrolyte.

Peak currents (iodide system).—The polarograms of RI in tetraalkylammonium iodide media were more sharply spiked than those of the analogous bromide system. MeI and EtI displayed the smaller more cathodic peak in the concentration range 8-10 mM. The polarograms of i-PrI and t-BuI were more complicated displaying a small prewave which was most prominent with the latter halide. These might be associated with alkyl iodide desorption (7) or the reduction of HI derived through elimination (21). In all cases the sums of the wave heights were proportional to concentration. Erratic results were obtained with TPAI.

The relative over-all currents are shown in Table IV. The order with respect to alkyl group is the same as for the bromides. In the presence of the corresponding tetrabutylammonium halide (0.2 F) the ratios of the viscosity corrected currents, *i.e.*, $(i_p\eta^{1/2})_{RBr}/(i_p\eta^{1/2})_{RI}$, were 1.28 (Me), 1.31 (Et), 1.10 (i-Pr), and 1.02 (t-Bu). The bromides would be expected to have larger diffusion coefficients, differences being least for the largest alkyl group.

Reduction potentials (iodide system).—The pattern of RI reduction potentials contrasts significantly with that of the bromides. In TPAI and TBAI the half-wave potential of the principal wave becomes more negative as the alkyl size increases. In TEAI, the reductions are nearly reversible and virtually independent of R. Since the slopes differ widely within a series, a potential near the foot of the wave, *e.g.*, $E_{1/4}$, better reflects the relative ease of reduction. The indicated order is

$$Et > Me \gtrsim i-Pr > t-Bu$$

The range of potentials is only 20-200 mV depending on the supporting electrolyte *vs. ca.* 550 mV for RBr.

The general positive shift and narrower spread in the RI potentials is consonant with C-I bond rupture during the potential determining step. The observed order, however, cannot be understood in terms of an S_n2 process analogous to that of Eq. [5]. A consideration of the polarization properties of C-I and C-Br bonds suggests a plausible basis for a difference in reduction mechanism. Although some discrepancies exist in the literature, it is likely that the C-I bond differs from the other carbon-halogen bonds in the direction of polarization. The recent Allred-Rochow (22) electronegativities which most strongly bear out this conclusion are considered the most reliable since the values are strictly empirical (23). Accordingly, under the influence of the electrode field, the RI orientation would favor a proximal location of the iodine atom; two reasonable orientations are shown in [8a] and [9a].

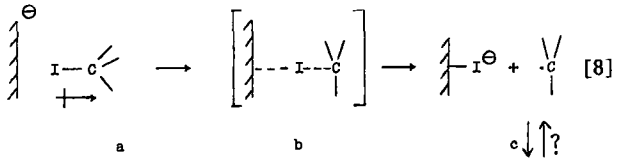

[8]

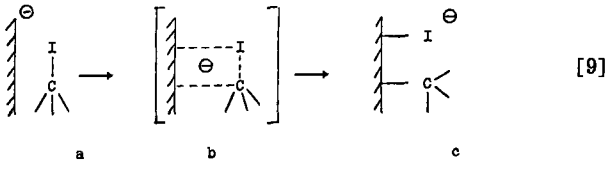

[9]

If iodine is presented directly to the surface, a displacement process, *e.g.*, Eq. [8], should be relatively insensitive to the bulk attached to carbon and the potential should be controlled essentially by the R-I bond strength. If C-M bond formation is concurrent with electron transfer, a compromised orientation such as [9a] may be required; a greater potential dependence on the alkyl identity follows. The transition state could resemble that for S_ni type displacements as has been suggested for the reduction of certain bridgehead bromides (24) or the 4-centered configuration, [9b].[2] The greater chemisorption of iodide at relatively negative potentials could also favor its proximal orientation. Molecular models show [9a] to be plausible for MeI and EtI. Additional α-alkyl substitution, however, forces the orientation in the direction of [8a].

The potentials for MeI and EtI in the various electrolytes parallel the expected shifts in the E.C.M. Just

[2] Note that the transfer [9a] → [9b] is very similar to the model proposed by Lambert (1f). The principal distinction is that the product [9b] is chemisorbed, *i.e.*, some carbon-metal bond formation occurs. In other words, the radical anion RX· exists not as a diffusible species but only as a component in the resonating transition state structure, so long as alkylation is strongly favored.

Table IV. Polarographic properties of alkyl iodides at a Pb electrode[a]

	CA 0.15 F TEAI[b]			0.1 F TPAI			0.2 F TBAI			
RI	$E_{P/2}^{Pb}$	$E_{3/4} - E_{1/4}$	$(i_p)_{Rel}$	$E_{P/2}^{Pb}$	$E_{3/4} - E_{1/4}$	$(i_p)_{Rel}$	$E_{P/2}^{Pb}$	$E_{3/4} - E_{1/4}$	$(i_p)_{Rel}$	$E_{1/2}^{Hg}$
Me I	-1.37 ± 0.03	-0.02 ± 0.01	1.00	-1.34 ± 0.03	-0.03 ± 0.01	1.00	-1.17 ± 0.04	-0.13 ± 0.02	1.00	1.63[f]
Et I	-1.36 ± 0.03	-0.03 ± 0.01	0.93	-1.33 ± 0.03	-0.09 ± 0.01	0.94	-1.22 ± 0.04	-0.31 ± 0.02	0.99	1.67[f]
i-Pr I	-1.38[d] ± 0.03	-0.03 ± 0.01	0.90	-1.40 ± 0.06[c]	-0.20 ± 0.02	0.85	-1.25 ± 0.04[d]	-0.19 ± 0.02	0.88	—
t-Bu I	-1.36[e] ± 0.04	-0.04 ± 0.01	0.79	-1.50 ± 0.06[e]	-0.21 ± 0.02	0.76	-1.35 ± 0.06[e]	-0.27 ± 0.02	0.74	—

[a] 25°C; [RI] = 5 mM.
[b] Saturated solution.
[c] Small prewave near −1.2V, possibly due to HI.
[d] Small prewave near −0.95V, possibly due to HI.
[e] Prewave near −0.9V, possibly due to HI.
[f] Data from ref. (27).

the opposite was observed for the bromide system; apparently another reflection of a change to a mechanism in which steric factors are less important. Compared to bromide, displacement of the larger iodide ion should not be much facilitated by ion-pairing, nor is there any evidence that it is.

Metal removal.—The very high current efficiencies with respect to organometallics formation noted for the methyl and ethyl halides suggests that the alkyl group resulting from the reduction is either unable to diffuse into solution and react in the manner of a simple free radical, or that alkylation is faster than diffusion. The first step in the metal removal sequence will be alkylation of the surface; for convenience the unit species may be written as $(Pb)_xPbR$. There is no evidence that the monomer Pb-R is formed. Such a species is known at the present time only among the mass spectral products of organoleads. The dialkyl metal, PbR_2 may be free to quit the electrode surface depending on the nature of R. Thus some organolead halide is formed when R = i-propyl or phenyl and the solutions are darkly colored. These observations correlate directly with known properties of isolable PbR_2 compounds (26).

With MeBr and EtBr alkylation probably proceeds at the interface at least until a trialkyllead species is formed. The trialkyllead radical is believed to have an appreciable lifetime in solution and has been implicated as an intermediate in numerous conversions of organolead compounds (26). Hexaethylbilead could result either from the trialkylation of adjacent lead atoms or the combination of two diffusing trialkyllead radicals. About 40% of the triethyl lead, however, is further ethylated before the above "hexa" reaction can occur. With MeBr tetralkylation is sufficiently favored to preclude "hexa" formation altogether.

To summarize the processes leading to metal removal, we write the following equations

$$(Pb)_xPb + RX + e^- \rightarrow (Pb)_xPbR + X^- \quad [10i]$$

$$(Pb)_xPbR + RX + e^- \rightarrow (Pb)_xPbR_2 + X^- \quad [10ii]$$

$$(Pb)_xPbR_2 + RX + e^- \rightarrow (Pb)_xPbR_3 + X^- \quad [10iii]$$

$$(Pb)_xPbR_3 + RX + e^- \rightarrow (Pb)_x + PbR_4 + X^- \quad [10iv]$$

$$2(Pb)_xPbR_3 \rightleftarrows 2(Pb)_x + 2 \cdot PbR_3 \quad [10v]$$

$$\downarrow\uparrow$$

$$2(Pb)_xPbR_3 \leftrightarrows 2(Pb)_x + Pb_2R_6 \quad [10vi]$$

When R = Me alkylation proceeds rapidly through [10iv]. For R = Et, however, reaction [10iv] is slowed appreciably by the increased steric requirements of this larger alkyl. At the same time, increased crowding at the trialkylated surface would facilitate expulsion of either $R_3Pb\cdot$ [10v] or Pb_2R_6 [10vi]. For larger R groups the degree of alkylation which the surface can sustain diminishes accordingly.

Acknowledgments

The author is indebted to C. W. Urion for extensive laboratory assistance and to J. D. Sterling for his helpful discussions of the resulting manuscript.

Manuscript submitted March 24, 1969; revised manuscript received June 2, 1969.

Any discussion of this paper will appear in a Discussion Section to be published in the June 1970 JOURNAL.

REFERENCES

1. (a) P. J. Elving, *Record Chem. Prog.*, **14**, 99 (1953).
   (b) G. Rigatti, *Adv. Polarog.*, **3**, 904 (1960).
   (c) P. J. Elving and B. Pullman, *Adv. Chem. Phys.*, **3**, 1 (1961).
   (d) P. Zuman, *Chem. Listy*, **56**, 219 (1962).
   (e) H. Lund, *Talanta*, **12**, 1065 (1965).
   (f) F. L. Lambert, *J. Org. Chem.*, **31**, 4184 (1966).
2. E. F. Silversmith and W. J. Sloan (to E. I. du Pont de Nemours and Co.), U. S. Pat. 3,197,392, July 1965.
3. S. Wawzonek, R. C. Duty, and J. H. Wagenknecht, *This Journal*, **111**, 74 (1964).
4. S. Wawzonek and M. E. Runner, *ibid.*, **99**, 457 (1952).
5. G. A. Forcier and J. W. Olver, *Anal. Chem.*, **37**, 1447 (1965).
6. H. E. Ulery, *This Journal*, **113**, 479 (1966).
7. A. Cisak, *Roczniki Chem.*, **37**, 1025 (1963).
8. F. Cappellina, *Ann. chim. (Rome)*, **50**, 744 (1960).
9. M. Schuler, Unpublished results.
10. M. Kegelman, Unpublished results.
11. (a) M. Bonnemay, E. Levart, and E. P. d'A. d' Orsay, *Compt. Rend.*, **260**, 2493 (1965).
    (b) J. Koryta and S. Vavricka, *J. Electroanal. Chem.*, **10**, 451 (1965).
12. L. C. Bateman *et al.*, *J. Chem. Soc.*, **1940**, 925.
13. F. L. Lambert and K. Kobayshi, *J. Am. Chem. Soc.*, **82**, 5324 (1960).
14. F. Paneth and W. Hofeditz, *Ber.*, **62**, 1335 (1929).
15. L. G. Feoktistov and S. I. Zhdanov, *Electrochim. Acta*, **10**, 657 (1965), and references cited therein.
16. (a) R. Parsons, "Modern Aspects of Electrochemistry," Vol. 1, p. 140, J. O'M. Bockris and B. E. Conway, Editors, Academic Press, Inc., New York (1954).
    (b) S. V. Karpachev, *Trudy Inst. Met. Akad. Nauk SSSR, Uralsk. Fili.*, **1951**, No. 4, 3; *C. A.*, **50**, 3123g. (1956).
    (c) B. Jakuszewski and Z. Kozlowski, *Roczniki Chem.*, **38**, 93 (1964).
17. (a) J. O'M. Bockris and E. C. Potter, *This Journal*, **99**, 169 (1952).
    (b) A. N. Frumkin, *J. Electroanal. Chem.*, **9**, 173 (1965).
18. (a) M. A. Loshkarev and A. A. Kryukovo, *Zhur Fiz. Khim.*, **31**, 452 (1957).
    (b) L. E. I. Hummelstedt and L. B. Rogers, *This Journal*, **106**, 248 (1959).
    (c) S. R. Missan, E. I. Becker, and L. Meites, *J. Am. Chem. Soc.*, **83**, 58 (1961).
    (d) K. M. Joshi, W. Mehl, and R. Parsons, "Transactions of the Symposium on Electrode Processes," p. 249, E. Yeager, Editor, John Wiley & Sons, New York (1961).
19. (a) C. Treiner and R. M. Fuoss, *Z. phys. Chem.*, **228**, 343 (1965).
    (b) L. Holleckand and D. Becker, *J. Electroanal. Chem.*, **4**, 321 (1962).
    (c) P. G. Sears, E. D. Wilhoit, and L. R. Dawson, *J. Phys. Chem.*, **59**, 373 (1955).
    (d) D. F. Evans, C. Zawoyski, and R. L. Kay, *J. Phys. Chem.*, **69**, 3878 (1965).

20. M. E. Peover and J. D. Davies, *J. Electroanal. Chem.*, **6**, 46 (1963).
21. S. Winstein, S. Smith, and D. Darwish, *Tetrahedran Letters*, No. 16, 24 (1959).
22. (a) A. L. Allred and E. G. Rochow, *J. Am. Chem. Soc.*, **79**, 5361 (1957).
(b) *Ibid, J. Inorg. and Nuclear Chem.*, **20**, 167 (1961).
23. F. A. Cotton and G. Wilkinson, "Advanced Inorganic Chemistry," pp. 90ff., Interscience Publishers, New York, (1962).
24. J. W. Sease, P. Chang, and J. L. Groth, *J. Am. Chem. Soc.*, **86**, 3154 (1964); *cf.* F. L. Lambert, A. H. Albert, and J. P. Hardy, *ibid.*, 3156 (1964).
25. N. L. Meites, "Polarographic Techniques," 2nd. ed., pp. 288-289, Interscience Publishers, New York (1965).
26. (a) L. C. Willemsens, "Organolead Chemistry," a publication of the International Lead Zinc Research Organization (ILZRO), Semper Avanti N. V. The Hague, Netherlands, February, 1964, pp. 44-45.
(b) L. C. Willemsens and G. J. M. Van der Kerk, "Investigations in the Field of Organolead Chemistry," an ILZRO publication Schotanns and Jens Utrecht N. V., Utrecht, Netherlands, 1965, p. 17.
27. M. von Stackelberg and W. Stracke, *Z. Elektrochem.*, **53**, 118 (1949).
28. A. M. Kuznetnov, *Electrochim. Acta*, **13**, 1293 (1968).
29. P. Delahay, "New Instrumental Methods in Electrochemistry," pp. 57-59, Interscience Publishers, New York (1954).

Preparation of Thick Crystalline Films of Tin Oxide and Porous Glass Partially Filled with Tin Oxide

R. F. Bartholomew and H. M. Garfinkel

Research and Development Laboratories, Corning Glass Works, Corning, New York

ABSTRACT

A method is described for producing films of SnO_2 on a 96% silica glass substrate by oxidation of stannous chloride. Surface x-ray patterns of such films showed the preferred orientation of the films depended on temperature and time of growth. The pores of porous glass were partially filled with SnO_2 by the same technique used for the growth of the films. The measured resistivities of the porous glass-tin oxide material are discussed in terms of a model of cylindrical noninterconnecting pores going from one side of the sample to the other.

In recent years considerable effort has been made in the area of producing metal oxide films. Tin oxide, in particular, has been studied in detail. Methods of preparing tin oxide films include hydrolyzing a volatile tin compound on a hot surface (1, 2) and reactive sputtering (3-5). Films of this oxide exhibit a small temperature coefficient of resistance and are chemically stable, making them ideal resistor materials. New methods for the growth of such oxides, in films and other forms, are of interest, therefore, for possible applications in the electronics field.

This paper will describe a new method for growing films of SnO_2 and for partially filling porous glass with SnO_2. The characterization of the products was carried out by x-ray diffraction methods. Some of the electrical properties of the materials obtained are reported.

Experimental

Materials.—Anhydrous $SnCl_2$ (Technical Grade) was supplied by Fisher Scientific. No attempt was made to purify this material.

Corning Code 7900 96% silica glass was used as a substrate for growth of the films. The porous glass was Corning Code 7930 with a nominal pore diameter of 60Å.

Procedure for preparing films of SnO_2.—The anhydrous $SnCl_2$ (mp 246°C) was fused in a 100-ml VYCOR® brand glass crucible contained in a 500-ml VYCOR® brand glass beaker placed in a furnace. The initial experiments were carried out open to the atmosphere, except for flushing continuously with predried argon. The tin chloride is oxidized to SnO_2 by reaction with oxygen in the air. This is discussed further in the Results and Discussion section. To verify the required conditions for growth, a completely closed system was used in later experiments in which a Corning Code 7900 96% silica glass tube was used instead of the beaker. The tube was sealed at one end and had a silicone oil trap at the other end. Dry argon was flushed continuously through the system. Plates of the 96% silica glass (approximately 5 x 1.8 x 0.65 cm) were placed in the melt, such that part of the glass was in the melt and part in the vapor above the melt. Treatment temperatures varied from 400° to 525°C, with times ranging from 1 to 72 hr.

Impregnation of the porous glass.—Samples of porous glass of dimensions 5 x 1.8 x 0.5 cm (approximately) were cut from sheets of the material. These plates were pretreated by evacuating at temperature (>400°C) in order to remove moisture; in some cases the plates were reacted further with O_2, then reevacuated in order to remove organic materials absorbed in the glass. The pores were filled either by direct immersion in a melt, or by suspension in the vapor above the melt. A closed system was used throughout the filling of the glass by the halide. The resulting material was then transferred to a closed container in a furnace and treated by heating in an oxygen atmosphere to convert the halide to the oxide. For treatment times and temperatures see Table IV.

After converting the tin chloride to the oxide, the samples were ground and polished. The initial polishing was done with diamond paste; the final polishing was performed by using 0.05μ Al_2O_3 paste, until no scratch marks could be detected with a low power magnifying glass. The sample was then washed in water several times to remove the polishing paste. Some of the samples cracked during the oxidation reactions. However, if the pretreatment was carried out at about 500°C, this did not occur.

Electrical measurements.—The d-c electrical resistance of the tin oxide films was measured at room temperature with a Model 260 Simpson meter. Point

Table I. Summary of experimental data on the growth of SnO_2 film from stannous chloride

Sample	Substrate	Temp, °C	Atmosphere	Time of treatment, hr	Comments
1	Code 7900 Plate	525	Argon, system open to air	1	Black coating, SnO_2
2	Code 7900 Plate	525	Argon, system open to air	4	Black coating, of SnO_2. Thick at melt-atmosphere interface becoming thinner as distance from interface decreases
3	Code 7900 Plate	400	Argon, system open to air	16	Thin black coating, SnO_2
4	Code 7900 beaker	Used in previous three runs	Argon, system open to atmosphere	48	Thick black coating, SnO_2
5	Code 7900 crucible	Used in previous three runs		48	Black coating above level of melt
6	Code 7900 Plate	525	Completely sealed system, Argon blanket	72	No SnO_2
7	Alumina plate	525	Completely sealed system, Argon blanket	72	No SnO_2

contact probes were used to connect the sample to the meter. The resistivity of the films quoted in this paper are only meant to be estimates.

Silver electrodes with a guard ring were applied to ground and polished plates of the porous glass-tin oxide material as du Pont Silver Preparation 4817-Electrical Grade and air dried. A Model 311 Simpson VTVM was used to measure resistance. Contact to the meter was made through heavy stainless steel gold plated electrodes placed on the silver electrodes. Dielectric properties of the porous glass-tin oxide material were investigated with a General Radio capacitance bridge.

X-ray measurements.—A General Electric XRD-5 diffractometer was used. The radiation was nickel-filtered Cu K_α.

Results and Discussion

Films of tin oxide.—Table I summarizes the effect of temperature and time on the growth of SnO_2 films on the 96% silica glass substrate. After a 1-hr treatment at 525°C, a black coating of SnO_2 was observed on the glass. The black color of the films indicates an oxygen deficient material. Longer treatment times led to a thicker coating; the thickness of this coating became less the further the distance from the melt-air interface. After this series of runs, the crucible containing the melt and the VYCOR® brand glass beaker holding the crucible were covered with a black coating. The thickness of these coatings was never determined precisely, but was of the order of 1 mm at the most.

A spectrographic technique was used to examine the coating on the beaker for impurities. These data are given in Table II. Silica, the major impurity, in all probability results from a reaction between the oxide and glass at their mutual interface. Bond formation of the type -Si-O-Sn- has been postulated by Kuznetsov to occur at SnO_2-silica surfaces (1). The spectrographic analysis of the melt is given in Table II for comparison.

The experiment in which a closed system was used showed that after 72 hr 96% silica glass plates as well as alumina plates gave no evidence of film formation. This result rules out the possibility of a reaction taking place at the halide-glass interface.

Surface x-ray diffraction patterns were determined on some of the samples listed in Table I. The pattern given by sample 4 is shown in Fig. 1. As indicated in Table III, the side of the film that was in contact with the vapor phase has a slightly different x-ray diffraction pattern from that side in contact with the glass.

Table II. Spectrographic analysis of SnO_2 film and quenched sample of $SnCl_2$ melt

Melt	Film	% Range
SnO_2	SnO_2	>10
	SiO_2	0.05-0.5
	Al_2O_3	0.01-0.1
Fe_2O_3, CaO	CdO	0.005-0.05
SiO_2, NiO	B_2O_3, MgO, Fe_2O_3, PbO	0.001-0.01
PbO, Al_2O_3	TiO_2	0.0005-0.005
MgO, MnO_2, CuO	CuO	0.0001-0.001

Table III. Preferred orientation of SnO_2 film on 96% silica glass substrate as determined by surface x-ray (nickel-filtered Cu K_α radiation)

Sample No. (Table I)	Temp, °C	Time, hr	Preferred orientation
2	525	4	Random (211)
3	400	18	002 (101)
4	525	48	Film-vapor interface: 301* Glass-film interface: 301 (211)

Values in parenthesis indicate minor orientation.
* See Fig. 1.

Presumably, the film was grown initially by nucleation on the glass surface followed by growth on the oxide film. However, it appears that temperature as well as time has an effect on the orientation of the SnO_2 film. By going to a lower temperature, the film is no longer oriented in the 301 plane, but rather in the 002 plane with some growth along the 101 plane. With Corning Code 7740 borosilicate glass substrates, the deposited film was determined by x-ray techniques to be polycrystalline. There was no x-ray evidence to indicate the presence of metallic tin within the limits of detection of this technique. Previous work in these laboratories has shown that it is not possible to predict beforehand the orientation of a film of SnO_2 (6).

The room-temperature value for the surface resistivity of the film was of the order of 1 ohm/square. Several identical heat treatments on the same samples gave similar results. In some instances the measurements were made on films bonded to the glass substrate. With some samples, the film remained strongly

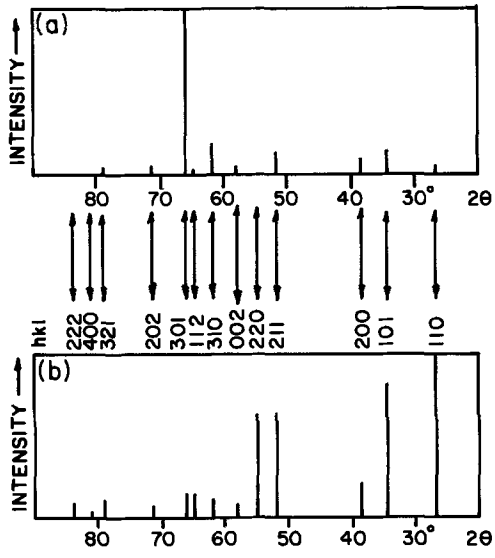

Fig. 1. Comparative x-ray scattering of oriented and nonoriented tin oxide (nickel-filtered Cu K_α radiation). (a) Surface x-ray of film; (b) powder x-ray of polycrystalline material.

Table IV. Summary of experimental data on the methods used for filling porous glass with SnO_2

Sample No.	Pretreatment	Method of filling with $SnCl_2$	Treatment in O_2 Temp, °C	Time, hr	Comments
8	Filled with water	Vapor	540	48	Black coating on outside, gray inside
9	Evacuated at 500°C, then cooled in O_2	Vapor	540	48	Black coating outside, white center
10	Evacuated at 200°C for 3 days	Vapor	540	4	2 hr in O_2 at 550°C. Sample black clear through
11	Evacuated at 200°C for 3 days	Vapor	540	4	550°C in O_2 for 3 days. Sample brown throughout
12	Evacuated at 500°C for 3 days, then exposed to O_2 at 500°C, and evacuated	Vapor	525	24	16 hr at 500°C in oxygen. Black outside, white inside
13	Evacuated at 500°C for 2 days, oxygen at 500°C for 1 day. Evacuated	Dipped in melt	500	16	24 hr in oxygen. Black clear through
14	Evacuated 125°C for 2 days	Melt (+4 wt % $SbCl_3$)	390	16	24 hr at 500°C in oxygen. Only surface was black
15	Same as 13	Same as 14	390	16	24 hr at 500°C in oxygen. Gray outside and black inside

bonded to the glass surface, while spalling resulted after two or more cycles with other samples.

Tin oxide in porous glass.—The results of different schedules for the growth of SnO_2 in porous glass are given in Table IV. It appears from these data that the optimum treatment requires evacuation of the porous glass sample at 200°-500°C for several days, followed by treatment in an oxygen atmosphere to remove any absorbed organic compounds. The sample is treated in the melt at 500°C for nearly a day. The resulting sample is oxidized then in an oxygen atmosphere at 500°-550°C for a day. Sample 3 had the shortest treatment schedule that resulted in a sample of uniform black color. Powder x-ray diffraction patterns indicated the presence of SnO_2 in all samples. No attempt was made to determine accurately the percentage of free volume in the pores occupied by the SnO_2 as a function of experimental conditions. However, one weight change measurement showed that the SnO_2 occupied approximately 20% of the pore volume.

The fact that SnO_2 was produced in porous glass by reaction between $SnCl_2$ and oxygen to the exclusion of everything else, means that the over-all reaction can be written as

$$SnCl_2 + O_2 \rightarrow SnO_2 + Cl_2 \qquad [1]$$

This reaction would also explain the formation of the films on the 96% silica glass substrate.

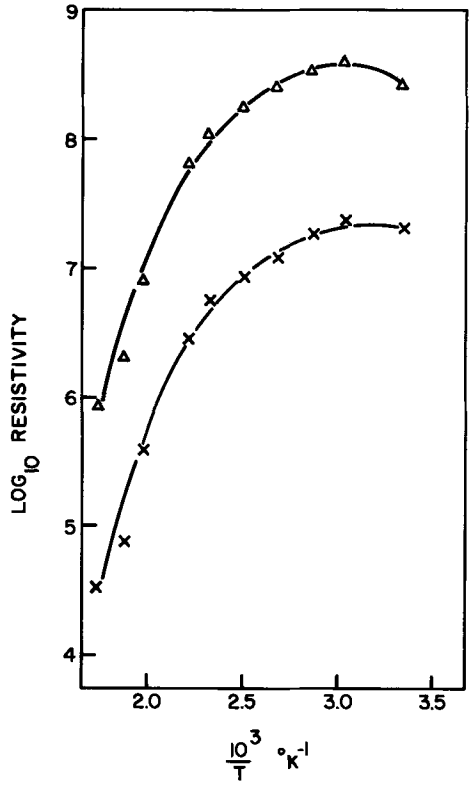

Fig. 2. Resistivity of porous glass partially filled with tin oxide. x, Volume resistivity (ohm-cm); Δ, surface resistivity (ohm/square).

Thermodynamic calculations were carried out to determine the feasibility of reaction [1] occurring at 700°K. The value of ΔG_{700} for $SnCl_2$ was obtained from emf data (7), while data for the other compounds involved in the reactions were obtained from thermodynamic tabulations (8). The free-energy change for reaction [1] was calculated to be −88 kcal mole^{-1}. This calculation predicts that the reaction lies far to the right-hand side, as the case was found to be experimentally.

The electrical resistivity is given in Fig. 2 for sample 13 (Table IV) as a function of temperature. X-ray diffraction patterns of this sample showed only SnO_2 present. There was no evidence for unreacted $SnCl_2$. The surface and volume resistivities were obtained by measuring the surface and volume resistances from 25° to 200°C, then cooling to 25°C and measuring the resistances again to 200°C. The surface and volume resistances shifted to slightly higher values with reheating; the results shown in Fig. 2 were obtained after one heating cycle. Unfortunately, these data are not reproducible from sample to sample, but the same dependence on temperature was evident with different samples. Moreover, several things should be noted. First, "volume" represented the total volume of the sample, not just the pores filled with oxide. Second, the surface and volume resistivities roughly parallel each other, with the value for the former being approximately an order of magnitude higher than the latter. Finally, the temperature coefficients of the surface and volume resistivities of the sample are approximately zero from around room temperature to 100°C, then increase with increasing temperature above 125°C. A value of approximately 1 eV was obtained for the temperature coefficient as the plots in Fig. 2 approached linearity at temperatures above 150°C for the d-c-resistivity data. Attempts were made to increase the electrical conductivity by doping the melt with $SbCl_3$ (Table IV, samples 14, 15). The volume resistivity of sample 15, ground and polished to remove the gray coating, was about 1.5 x 10^7 ohm-cm at 25°C. This is about the same as that given in Fig. 2 for sample 13 with no antimony (III) chloride. No attempt was made to determine whether any antimony had actually been incorporated in the tin oxide.

The values of the specific resistivity obtained for the SnO_2-porous glass sample are surprisingly high. Calculations based on a model of cylindrical noninterconnecting pores going from one side of the sample to the other suggest that the specific resistivity should be approximately 10^{-3} ohm-cm. This value was determined using a radius of 30Å for each pore, and 10^{12} pores per unit cross sectional area. Several explanations for this high resistivity can be given. First, the pores are incompletely filled and not interconnecting from one side to the other. Second, using the bulk resistivity of SnO_2 may be incorrect when considering bundles of SnO_2 of radius 30Å. Electrical conductivity measurements on SnO_2 films as a function of thickness showed that above several hundred angstroms thickness the specific resistivity was independent of thickness. However, below this thickness the specific resistivity increased as the film thickness decreased (1).

Unfortunately, it is not possible to use the data to extrapolate back to the thickness of "films" present in porous glass. Another factor which might influence the reproducibility of data is the problem of contact resistance between the porous glass and the measuring device.

The dielectric constant of sample 13 was found to be 15.1 at room temperature and 21.7 at 75°C. Above this temperature the dielectric constant increased rapidly to a value of 132 at 176°C. A plot of log of the loss tangent against room temperature was linear between room temperature and 176°C. The room-temperature value of the loss tangent was 0.38, rising to 1.5 at 176°C.

Acknowledgments

The authors wish to thank S. S. Lewek for preparation of the samples, Dr. H. J. Holland for the x-ray data, Mrs. M. T. Mizzoni and Dr. M. P. Teter for the electrical measurements, and Dr. J. A. Murphy and Dr. M. E. Nordberg for helpful discussions.

Manuscript submitted Feb. 6, 1969; revised manuscript received May 20, 1969.

Any discussion of this paper will appear in a Discussion Section to be published in the June 1970 JOURNAL.

REFERENCES

1. A. Ya. Kuznetsov, *Soviet Phys.-Solid State*, **2**, 30 (1960).
2. R. E. Aitchison, *Australian J. Appl. Sci.*, **5**, 10 (1954).
3. L. Holland and G. Siddall, *Vacuum*, **3**, 375 (1953).
4. W. R. Sinclair and F. G. Peters, *J. Am. Ceram. Soc.*, **46**, 20 (1963).
5. W. R. Sinclair, F. G. Peters, D. W. Stillinger, and S. E. Koonce, *This Journal*, **112**, 1096 (1965).
6. J. A. Murphy and H. J. Holland, Private communication.
7. Iu. K. Delimarskii and B. F. Markov, "Electrochemistry of Fused Salts, p. 102, Sigma Press, Washington, D. C. (1961).
8. K. K. Kelley, "Contributions to the Data on Theoretical Metallurgy," Part XIII, Bureau of Mines Bulletin 584, U. S. Government Printing Office, Washington, D. C., 1960.

Adsorption of Cadmium(II) and Zinc(II) on Mercury Induced by Azide Anions

Zygmunt Kowalski[1] and Fred C. Anson*

Gates and Crellin Laboratories of Chemistry, California Institute of Technology, Pasadena, California

ABSTRACT

The adsorption of cadmium(II) and zinc(II) on mercury electrodes from solutions containing azide ion has been measured. The effects of electrode potential, electrode charge, and azide concentration were determined. The data support the conclusion that the neutral complexes, $Cd(N_3)_2$ and $Zn(N_3)_2$, are the species that are preferentially adsorbed.

The ability of anions which are specifically adsorbed on mercury electrodes to induce the adsorption of white metal cations which can form complexes with the anion has been studied recently in some detail (1-3). The data for the induced adsorption of cadmium(II) in iodide, bromide, and thiosulfate solutions have led to the conclusion that the primary adsorbing species is the neutral complex, *i.e.*, CdI_2 or CdS_2O_3, which becomes attached to the electrode by means of the specifically adsorbed anions (2, 3). It has been suggested that this adsorption scheme is general and will account for the anion induced adsorption of many of the white metallic cations such as lead(II), zinc(II), cadmium (II), and indium(III). In this paper we report studies in which the azide anion is examined as an adsorption inducer. Azide, like thiocyanate but in contrast with the halides, forms strong complexes with zinc(II) as well as cadmium(II) so that a comparison could be made of the relative effectiveness of azide to induce the adsorption of both metals.

Experimental

The experimental technique employed was double potential-step chronocoulometry. The procedure and apparatus were identical to that used in previous studies (2, 3) and made use of the computer-based data acquisition and analysis system which has been described in detail (4).

Sodium azide solutions were prepared freshly each day from twice recrystallized salt. The zinc, cadmium, and sodium nitrate employed were reagent grade salts. Solutions were prepared from triply distilled water and were deoxygenated with prepurified nitrogen. The ionic strength of all solutions was maintained at 1.0 with sodium nitrate. The temperature was 25° ± 2°C. All potentials are referred to the saturated calomel electrode.

Results

Adsorption of cadmium (II).—The dependence of cadmium(II) adsorption on potential, azide concentration, and Cd(II) concentration was measured. The reproducibility of the individual values of $2F\Gamma_{Cd}$ was about ± 0.5 $\mu C/cm^2$. Figures 1, 2, and 3 summarize the data. Because the charge on the electrode or, better, the amount of adsorbed anion appear to be more characteristic independent parameters for anion induced adsorption (2) the values of $2F\Gamma_{Cd}$ were also plotted against q_m and $\Gamma_{N_3^-}$, Fig. 4 and 5. In the chronocoulometric experiments the electrode potential was stepped from the initial potential, E_i, to —1.0V in every case. The charge on the electrode at —1.0V was assumed equal to the value given by Russell (5) for 1M NaF because the data of Parsons (6) shows that N_3^- adsorption at —1.0V is negligibly small. The values of q_m at the initial potentials, E_i, needed to prepare Fig. 4, were obtained in the presence of adsorbed cadmium by subtraction of the charge at —1.0V (—10 $\mu C/cm^2$) from $\Delta Q_{d.l.}$ (the difference in q_m between E_i and —1.0V), a parameter that results from the analysis of the double potential step charge time data (1, 7).

The values of $\Gamma_{N_3^-}$ needed for Fig. 5 were taken directly from the data of Parsons (6) or by linear extrapolation of plots of $\Gamma_{N_3^-}$ *vs.* q_m to values of q_m outside the range covered by Parsons' data.

Adsorption of zinc.—Data for zinc adsorption were obtained by the same procedure that was employed

* Electrochemical Society Active Member.
[1] Present address: Department of Silicate Chemistry, Academy of Mining and Metallurgy, Cracow, Poland.

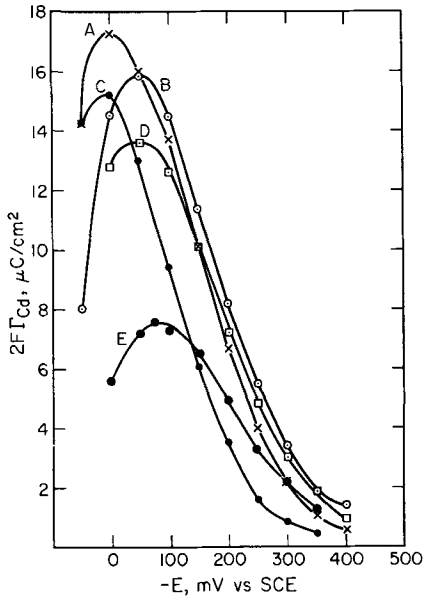

Fig. 1. Potential-dependence of Cd(II) adsorption in azide solutions. All solutions were 0.5 mM in $Cd(NO_3)_2$. A, 0.2M NaN_3-0.8M $NaNO_3$; B, 0.3M NaN_3-0.7M $NaNO_3$; C, 0.1M NaN_3-0.9M $NaNO_3$; D, 0.5M NaN_3-0.5M $NaNO_3$; E, 1.0M NaN_3.

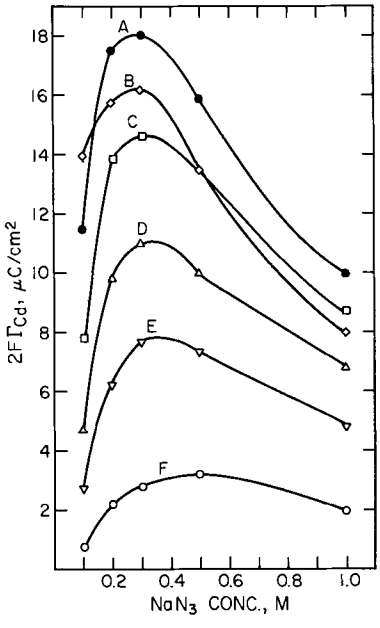

Fig. 2. Dependence of Cd(II) adsorption on the concentration of azide. All solutions were 0.5 mM in $Cd(NO_3)_2$. A, E_i = —100 mV; B, E_i = —50 mV; C, E_i = —150 mV; D, E_i = —200 mV; E, E_i = —250 mV; F, E_i = —350 mV.

with cadmium except that the potential was stepped to —1.4V to attain diffusion limited zinc reduction. The value of q_m at —1.4V was taken to be —17.8 μC/cm² (5). The data are summarized in Fig. 6-9. In contrast with solutions of cadmium(II), the pH of the zinc azide solutions appeared to be a critical parameter. Unless the pH was carefully controlled to lie between *ca.* pH 7-8 anomalous results were often obtained in the form of larger and irreproducible slopes in the chronocoulometric charge—(time)½ plots and erratic values of 2 $F\Gamma$. This difficulty is apparently associated with hydrazoic acid catalyzed hydrogen evolution at —1.4 V if the initial pH is too low or incipient formation of zinc hydroxide if the pH is too high.

Discussion

The general features of the azide induced adsorption of both cadmium(II) and zinc(II) are similar to those for halide induced adsorption of cadmium(II) (2). It seems reasonable therefore to interpret the adsorption

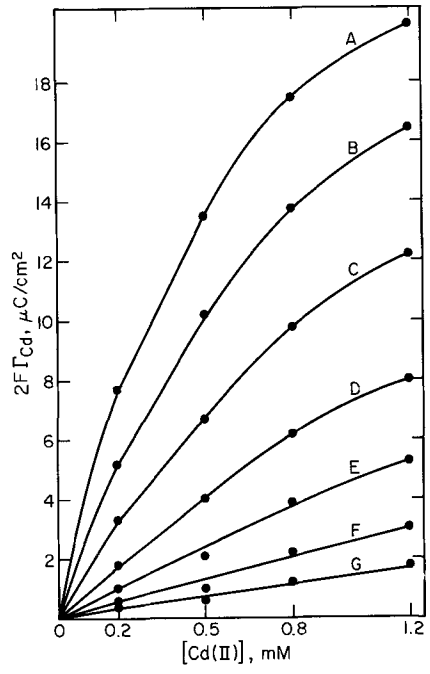

Fig. 3. Dependence of Cd(II) adsorption on the concentration of Cd(II). Electrolyte was 0.2M NaN_3-0.8M $NaNO_3$. A, E_i = —100 mV; B, E_i = —150 mV; C, E_i = —200 mV; D, E_i = —250 mV; E, E_i = —300 mV; F, E_i = —350 mV; G, E_i = —400 mV.

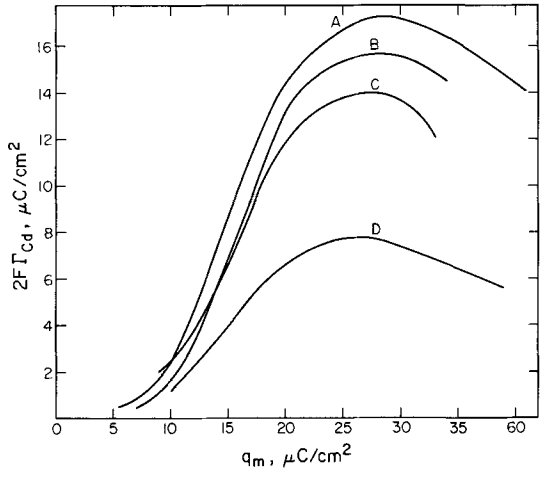

Fig. 4. Adsorption of Cd(II) plotted *vs.* the charge on the electrode. All solutions were 0.5 mM in $Cd(NO_3)_2$. A, 0.2M NaN_3-0.8M $NaNO_3$; B, 0.1M NaN_3-0.9M $NaNO_3$; C, 0.5M NaN_3-0.5M $NaNO_3$; D, 1.0M NaN_3.

patterns with the same kind of rationale as was previously employed (2): (*i*) The adsorbed species is the neutral, bisazido complex. Evidence in support of this is the correspondence of the maximum cadmium(II) adsorption with the solution composition corresponding to the maximum concentration of $Cd(N_3)_2$ when 2 $F\Gamma_{Cd}$ is evaluated at constant values of $\Gamma_{N_3^-}$, Fig. 10. The reason for preferring to construct figures such as Fig. 10 at constant values of specifically adsorbed anions has been given. It represents an attempt to hold constant one factor involved in the adsorption while systematically varying the other. Comparison of Fig. 10 with Fig. 2 shows that if 2 $F\Gamma_{Cd}$ is not evaluated at a constant value of $\Gamma_{N_3^-}$ the maximum in the adsorption occurs at a somewhat higher concentration of azide than corresponds to the maximum concentration of $Cd(N_3)_2$. (Insufficient complex formation constants are available for the zinc-azide system to permit a similar comparison.) (*ii*) The charge on the electrode changes very little when Cd(II) or Zn(II) are adsorbed, Table I.

Points (*i*) and (*ii*) taken together imply that only very small changes in the potential at the outer Helmholtz plane, ϕ_2, should result from the adsorption of

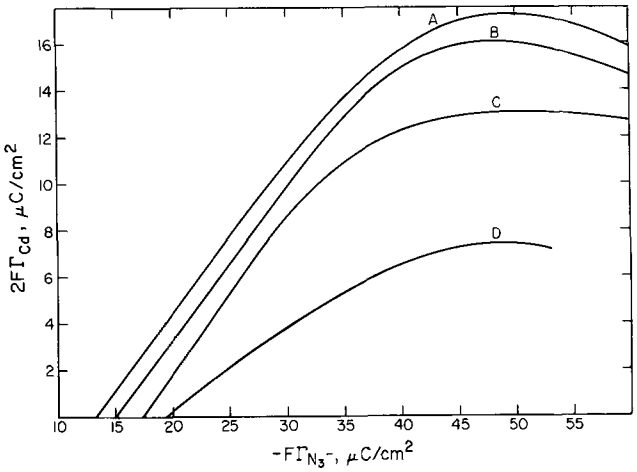

Fig. 5. Adsorption of Cd(II) plotted vs. the amount of adsorbed azide anions. All solutions were 0.5 mM in $Cd(NO_3)_2$. A, 0.2M NaN_3-0.8M $NaNO_3$; B, 0.1M NaN_3-0.9M $NaNO_3$; C, 0.5M NaN_3-0.5M $NaNO_3$; D, 1.0M NaN_3.

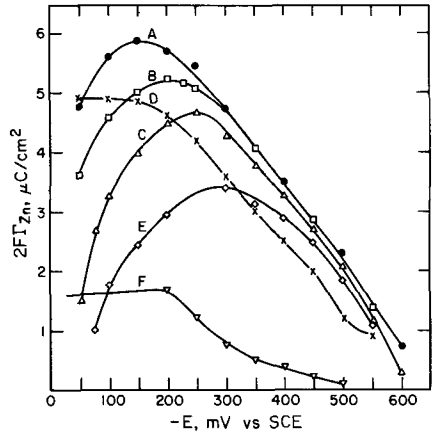

Fig. 6. Potential dependence of Zn(II) adsorption in azide solutions. All solutions were 0.5 mM in $Zn(NO_3)_2$. A, 0.3M NaN_3-0.7M $NaNO_3$; B, 0.4M NaN_3-0.6M $NaNO_3$; C, 0.5M NaN_3-0.5M $NaNO_3$; D, 0.2M NaN_3-0.8M $NaNO_3$; E, 0.6M NaN_3-0.4M $NaNO_3$; F, 0.1M NaN_3-0.9M $NaNO_3$.

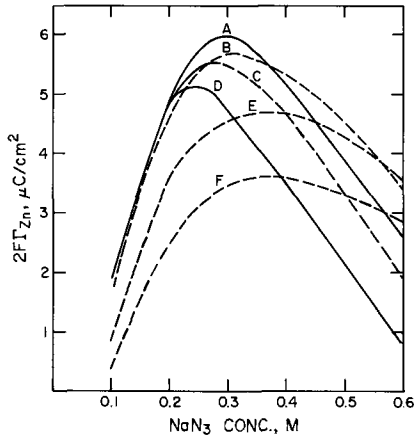

Fig. 7. Dependence of Zn(II) adsorption on the concentration of azide. All solutions were 0.5 mM in $Zn(NO_3)_2$. A, E_i = —150 mV; B, E_i = —200 mV; C, E_i = —100 mV; D, E_i = —50 mV; E, E_i = —300 mV; F, E_i = —400 mV.

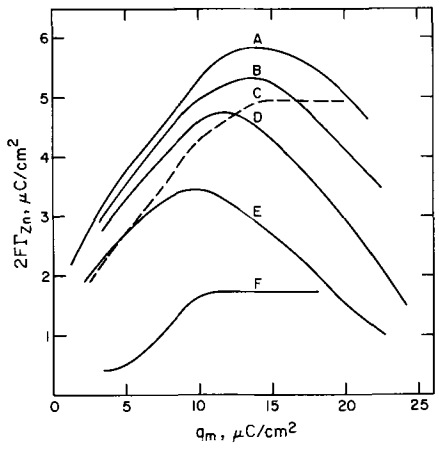

Fig. 8. Adsorption of Zn(II) plotted vs. the charge on the electrode. All solutions were 0.5 mM in $Zn(NO_3)_2$. A, 0.3M NaN_3-0.7M $NaNO_3$; B, 0.4M NaN_3-0.6M $NaNO_3$; C, 0.2M NaN_3-0.8M $NaNO_3$; D, 0.5M NaN_3-0.5M $NaNO_3$; E, 0.6M NaN_3-0.4M $NaNO_3$; F, 1.0M NaN_3.

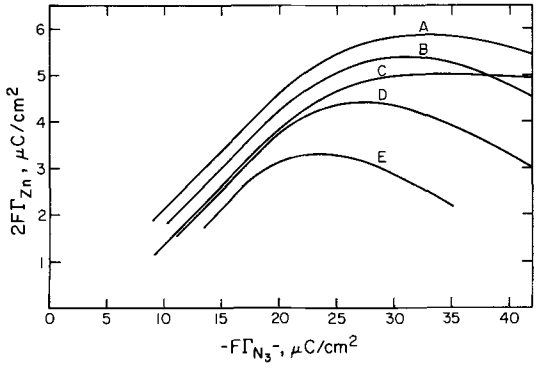

Fig. 9. Adsorption of Zn(II) plotted vs. the amount of adsorbed azide anions. All solutions were 0.5 mM in $Zn(NO_3)_2$. A, 0.3M NaN_3-0.7M $NaNO_3$; B, 0.4M NaN_3-0.6M $NaNO_3$; C, 0.2M NaN_3-0.8M $NaNO_3$; D, 0.5M NaN_3-0.5M $NaNO_3$; E, 0.6M NaN_3-0.4M $NaNO_3$.

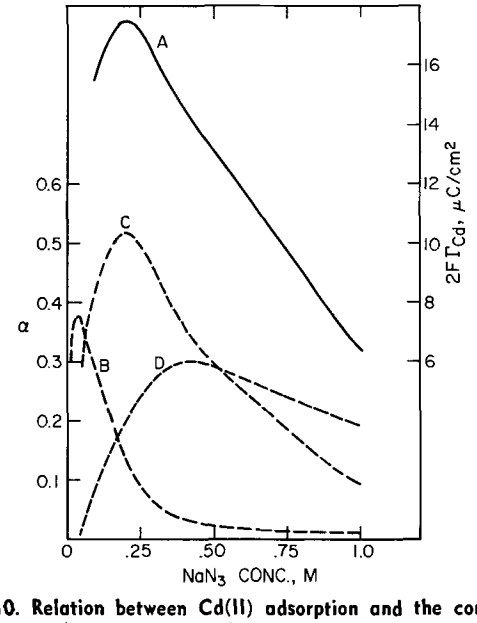

Fig. 10. Relation between Cd(II) adsorption and the concentrations of CdN_3^+, $Cd(N_3)_2$, and $Cd(N_3)_3^-$. A, 2 $F\Gamma_{Cd}$ evaluated at $F\Gamma_{N3-}$ = —40 $\mu C/cm^2$, which corresponds to near the maximum adsorption of Cd(II) at all azide concentrations; B, $\alpha_1 \equiv [CdN_3^+]/[Cd(II)]$; C, $\alpha_2 \equiv [Cd(N_3)_2]/[Cd(II)]$; D, $\alpha_3 \equiv [Cd(N_3)_3^-]/[Cd(II)]$. The α-values were calculated from the complex formation constants given in ref. (8).

Table I. Changes in q_m resulting from adsorption of Cd(II) and Zn(II) in 0.2M NaN_3-0.8M $NaNO_3$. Cd(II) or Zn(II) = 0.5 mM

$-E_i$, mV	50	100	200	300	400
$2F\Gamma_{Cd}$ $\mu C/cm^2$	15.9	13.5	6.7	2.1	0.6
Δq_m(Cd) $\mu C/cm^2$	2	1	0.5	0.5	−0.3
$2F\Gamma_{Zn}$ $\mu C/cm^2$	4.9	4.9	4.5	3.6	2.5
Δq_m(Zn) $\mu C/cm^2$	0	0	0.2	0	0.2

Cd(II) or Zn(II), because the adsorbing species is neutral and the electronic charge on the electrode is little affected by its adsorption. Hence, the rate of a suitable irreversible electrode reaction should remain relatively unchanged when Cd(II) or Zn(II) is added to an azide supporting electrolyte. [This line of reasoning has been expounded in detail in a previous study (2).] The reduction of $Co(NH_3)_6^{+3}$ in 0.2M NaN_3 at *p*H 6 proved to be a suitable irreversible reaction. At −0.05V, the rate of this reaction was increased by factors of 1.5 and 2.3 on addition of 1.2 mM/l of Zn(II) and Cd(II), respectively. Under these conditions, $2F\Gamma_{Zn}$ is 7.9 $\mu C/cm^2$ and $2F\Gamma_{Cd}$ is 24 $\mu C/cm^2$ and both of these adsorptions change q_m by less than 1 $\mu C/cm^2$. If the adsorbing species bore a positive charge the reduction of $Co(NH_3)_6^{+3}$ should have decreased sharply. If a singly charged anion were the adsorbing species, the rate of reduction of $Co(NH_3)_6^{+3}$ can be calculated[2] to increase by a factor of 3.2 in the case of Zn(II) and 74 in the case of Cd(II) adsorption. The observed rate enhancements are smaller than the calculated values which supports the contention that the adsorbing species is uncharged. The small rate enhancements that are observed could arise in a number of ways [partial anionic complex adsorption, changes in the electric field in the compact layer resulting from the adsorption, specific chemical interactions between $Co(NH_3)_6^{+3}$ and the adsorbing complexes which lead to catalysis of the reduction, etc.] which were not further examined.

(*iii*) The adsorbed metal-azide complex is bound to the electrode by means of one or two additional, specifically adsorbed azide anions. Evidence for this assertion is the shape of the plots of the amount of adsorbed metal *vs.* potential, electrode charge, and specifically adsorbed azide (Fig. 1, 4, 5, 6, 8, and 9). At every azide concentration, the metal adsorption increases in parallel with increasing azide anion adsorption as the electrode is made more positive. This reflects strong participation of adsorbed azide in the metal adsorption. The decrease in adsorption at the highest azide coverages may reflect a steric limitation that arises when the adsorbed azide anions are packed too closely to accommodate their bonding to the adsorbing metal azide complex. Thus, when the coverage of the electrode with adsorbed azide ions is very large, the distance between adjacent azide ions can become smaller than their equilibrium distance of separation in the metal-azide complex. Similar behavior is observed with the cadmium(II)-halide systems (2). In the case of Cd(II) in azide, the decrease in adsorption at the most positive charges comes quite close to the anodic limit of accessible potentials and may arise, in part, from the incipient oxidation of the electrode to form a precipitate of mercurous azide on the electrode surface.

The fact that the Cd(II) adsorption increases rapidly only after the adsorbed azide exceeds *ca.* 10 $\mu C/cm^2$ suggests that more than one adsorbed azide ion participates in the attachment of each $Cd(N_3)_2$ complex to the electrode. On the other hand, the slope of the rising portion of the Γ_{Cd} *vs.* $\Gamma_{N_3^-}$ plots varies from 0.35 mole Cd(II)/mole N_3^- with 0.2 mM Cd(II) up to 0.82 mole Cd(II)/mole N_3^- with 1.2 mM Cd(II), so that at high Cd(II) concentrations a single additional adsorbed azide anion may be sufficient to induce the adsorption of a $Cd(N_3)_2$ molecule.

The importance of specifically adsorbed azide in inducing the adsorption of Zn(II) can be demonstrated in another way: zinc(II), unlike cadmium(II), forms only very weak complexes with iodide ion and is not adsorbed to a measurable extent in sodium iodide supporting electrolytes. Iodide anion is adsorbed more strongly on mercury than azide so that addition of iodide to an azide solution would be expected to lead to a gradual replacement of the specifically adsorbed azide ions by iodide ions as the iodide concentration is increased. Figure 11 shows how the adsorption of Zn(II) is diminished as the iodide concentration is increased in a 0.5M NaN_3 – 0.5M $NaNO_3$ solution. The added iodide should have no effect on the zinc-azide complex species present in the bulk of the solution because there is so little tendency for Zn(II) to form iodide complexes (10). The lowering of Γ_{Zn} by iodide addition must therefore result from the competitive desorption of the N_3^- anions from which it follows that adsorbed anions which also form complexes with Zn(II) are essential for the induced adsorption to occur.

The adsorption of zinc(II) is not as great as that of cadmium(II) and it increases much less rapidly as more azide anions are adsorbed on the electrode (Fig. 9). Both of these features reflect the fact that zinc(II) forms weaker complexes with azide than does cadmium(II). The lower dependence of Γ_{Zn} on the amount of adsorbed azide results, under some conditions, in a crossing of the Γ_{Cd} and Γ_{Zn} *vs.* $\Gamma_{N_3^-}$ curves at low values of $\Gamma_{N_3^-}$ so that the adsorption of Zn(II) exceeds the Cd(II) adsorption. Thus, with 0.5 mM Cd(II) or Zn(II) in 0.3M azide at −450 mv, $2F\Gamma_{Cd} = 0.6$ $\mu C/cm^2$ while $2F\Gamma_{Zn} = 2.9$ $\mu C/cm^2$.

A puzzling feature of the data is the fact that the maxima in the plots of Γ_{Cd} *vs.* $\Gamma_{N_3^-}$ occur at higher values of $\Gamma_{N_3^-}$ for Cd(II) than for Zn(II) (Fig. 5, 9). On the basis of crystal radii, $Cd(N_3)_2$ is expected to be slightly more voluminous than $Zn(N_3)_2$ so that one might have expected the maxima for Zn(II) to come at even higher values of $\Gamma_{N_3^-}$ than that for Cd(II). A possible explanation for the observed behavior is the fact that zinc-halide complexes tend to retain coordinated water more strongly than the corresponding cadmium complexes (11). If the adsorbing zinc species carried one or two water molecules with it, the steric interactions of the adsorbed zinc-azide complexes with each other and with adsorbed azide anions could become large enough to result in a decrease in Γ_{Zn} at smaller values of $\Gamma_{N_3^-}$ for Zn(II) than for Cd(II).

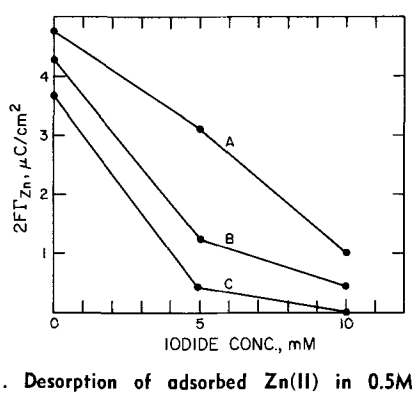

Fig. 11. Desorption of adsorbed Zn(II) in 0.5M NaN_3-0.5M $NaNO_3$ electrolyte by addition of sodium iodide. A, $E_i = -200$ mV; B, $E_i = -300$ mV; C, $E_i = -350$ mV.

[2] The relative rate (with and without added metal ion) is equal to $\exp\left[\frac{\Delta\phi_2 F}{RT}(\alpha n - Z)\right]$, where $\Delta\phi_2$ is the change in the potential at the outer Helmholtz plane produced by the addition of Zn(II) or Cd(II), $\alpha n = 0.5$, and Z is the average charge of the reactant in the bulk of the solution. Ion-pairing occurs between N_3^- and $Co(NH_3)_6^{+3}$ (9) to the extent that $Z = 2.2$ in 0.2M NaN_3. The expression for the relative rate therefore reduces to: $10^{-1.7(\Delta\phi_2/59.6)}$, where $\Delta\phi_2$ is in millivolts.

Conclusions

This study permits azide ion to be added to the list of specifically adsorbed anions that induce the adsorption on mercury of white metal cations with which they form complexes. The consistency in behavior from system to system suggests that the same chemical factors are involved in all the systems studied. Recent faradaic impedance measurements with Pb(II) in chloride solutions by Timmer *et al.* (12) lead them to conclude that chloride-induced adsorption of Pb(II) occurs. The precision of the adsorption data available from these experiments is not as high as that obtained from chronocoulometric measurements but Timmer *et al.* found that their data could be interpreted best if the uncharged complex, $PbCl_2$, were the adsorbed species. Unpublished data obtained in this laboratory (13) support the same conclusion in the case of thiocyanate induced adsorption of Pb(II). It was suggested earlier (2) that an explanation for the preferential adsorption of the uncharged complexes in every case is the importance of solvation energy and entropy in determining the resistance toward adsorption of individual species. This explanation continues to be attractive. For example, the entropy of reaction in aqueous solution for the reaction $MCl_2 + Cl^- \rightarrow MCl_3^-$ is over 30 eu greater for M = Zn(II) than for M = Cd(II) (10). This presumably reflects a considerably stronger hydration of $ZnCl_2$ than of $CdCl_2$ and the same trend would be expected with the azide complexes. A recent report that the uncharged complex, $PbBr_2$, appears to be preferentially adsorbed from molten nitrate electrolytes (14) suggests that similar factors may also be important in molten salt solvents.

Acknowledgments

This work was supported in part by the U.S. Army Research Office (Durham). Z. K. was the holder of a Ford Foundation grant under the auspices of the Institute of International Education. Dr. Roger Parsons kindly supplied his unpublished double layer data for azide. We are also indebted to Dr. Donald Barclay for thoughtful suggestions and Roger Abel for much assistance with the computerized data acquisition system.

Manuscript submitted April 8, 1969; revised manuscript received May 26, 1969. This is Contribution No. 3838, Gates and Crellin Laboratories of Chemistry.

Any discussion of this paper will appear in a Discussion Section to be published in the June 1970 JOURNAL.

REFERENCES

1. F. C. Anson, J. H. Christie, and R. A. Osteryoung, *J. Electroanal. Chem.*, **13**, 343 (1967).
2. F. C. Anson and D. J. Barclay, *Anal. Chem.*, **40**, 1791 (1968).
3. D. J. Barclay and F. C. Anson, *This Journal*, **116**, 438 (1969).
4. G. Lauer, R. Abel, and F. C. Anson, *Anal. Chem.*, **39**, 765 (1967).
5. C. D. Russell, *J. Electroanal. Chem.*, **6**, 486 (1963).
6. R. Parsons, Unpublished data.
7. J. H. Christie, R. A. Osteryoung, and F. C. Anson, *J. Electroanal. Chem.*, **13**, 236 (1967).
8. P. Senise and E. F. d'A. Neves, *J. Am. Chem. Soc.*, **83**, 4146 (1961).
9. M. G. Evans and G. H. Nancollas, *Trans. Faraday Soc.*, **49**, 363 (1953).
10. A. Martell and L. G. Sillen, "Stability Constants," 2nd ed., The Chemical Society, London (1964).
11. D. E. Irish, B. McCarroll, and T. F. Young, *J. Chem. Phys.*, **39**, 3436 (1963).
12. B. Timmer, M. Sluyters-Rehbach, and J. H. Sluyters, *J. Electroanal. Chem.*, **18**, 93 (1968).
13. J. Christie and F. C. Anson, Unpublished experiments, California Institute of Technology, 1965.
14. D. Inman, D. G. Lovering, and R. Narayan, *Trans. Faraday Soc.*, **64**, 2487 (1968).

Oxygen Dissolution and Evolution on Platinum in 85% Orthophosphoric Acid at Elevated Temperatures

A. J. Appleby* and Alina Borucka*

Institute of Gas Technology, Chicago, Illinois

ABSTRACT

Kinetics and mechanisms of oxygen electrode reactions on bright platinum have been studied in 85% orthophosphoric acid at elevated temperatures. Oxidized, oxide-free, and active platinum surfaces are kinetically different. Results obtained on oxidized and oxide-free platinum show that two different reaction mechanisms are followed. We consider that these mechanisms are common to all stable acid electrolytes in which platinum and its oxides remain unattacked, irrespective of concentration and temperature. For the oxidized surface we suggest that the mechanism may be more complex than has hitherto been supposed, although the predominant rate-determining step is water discharge. For oxide-free and active platinum the rate-determining step is the primary charge transfer involving activated oxygen adsorption, which takes place under Temkin and Langmuir conditions, respectively. The nature of the three platinum surfaces is discussed and explanations for their kinetic, adsorption, and mechanistic differences are offered. Fuel cell implications are also briefly discussed.

The kinetics and mechanism of the oxygen electrode reaction on platinum have been extensively studied in dilute acid electrolytes at room temperature (1-5) and have been recently reviewed by Hoare (6).

However, in concentrated orthophosphoric acid the studies published so far deal only with diffusion-controlled phenomena (7, 8) and rest potentials (9). This acid is of special importance as a fuel cell electrolyte. It has a particularly wide range of thermal stability and is neither reduced nor oxidized at the potentials of fuel cell electrodes. On the other hand, it is sufficiently different in physical and chemical character from the dilute strong acids previously studied (2-4)

* Electrochemical Society Active Member.

to discourage any *a priori* conclusions concerning its effect on the oxygen electrode mechanism or kinetics.

The present paper is intended as a general summary of the kinetic and mechanistic features of the oxygen electrode in 85% orthophosphoric acid, with some emphasis on aspects which are of interest in fuel cell development. The conclusions presented concerning oxygen reaction mechanisms and kinetics are based on results covering the temperature range 25°-136°C, but the typical kinetic data presented here are predominantly those obtained at 95.9°C.

Experimental

The apparatus for this work was constructed so that only fused silica was in direct contact with the electrolyte. To eliminate oxidizable impurities, the 85% orthophosphoric acid was refluxed with 20% of its volume of 30% hydrogen peroxide for 40 min before use. The remaining water was then distilled out until the acid returned to its original concentration with no detectable hydrogen peroxide content. Specially purified oxygen and nitrogen were mixed accurately using capillary flowmeters and a mixing chamber.

Platinum foil or disk electrodes of 99.999% purity were washed with HCl, conductivity water, and the electrolyte itself before use. The rotating disk-ring electrode used in this work will be described elsewhere. Steady-state measurements were obtained galvanostatically, although for the disk-ring electrode a potentiostat was used. Potential-scan techniques were used in the study of platinum oxidation kinetics. All potentials were measured directly against the hydrogen reference electrode (HRE) in the same solution at the working temperature. Cathodic currents are treated as negative.

Oxidized, oxide-free, and "active" platinum surfaces. —It is now well established that the kinetics and mechanism of the oxygen electrode on platinum differ according to the nature of the metal surface, which depends on electrode pretreatment (3). For this reason, the present study was conducted on three types of carefully prepared electrode surfaces:

1. A fully oxidized surface, covered by a separate oxide phase produced by anodizing at high potential
2. An oxide-free surface, considered to have oxygen atoms or —OH radicals adsorbed is less than monolayer quantity (3, 10). This surface is produced by reduction of an oxidized surface at about +300 mV HRE for 10-12 hr or, alternatively, it is a surface which has had no history of oxidation.
3. A surface in an "active" state, consisting of a partially reduced oxide film, considered by Schuldiner and Warner (11) to contain oxygen atoms absorbed in the first few layers of the lattice and by Feldberg *et al.* (12) as an oxide layer half-reduced to PtOH.

As illustrated by the results of Fig. 1, the three surfaces studied display very different kinetics; for this reason, they are discussed separately.

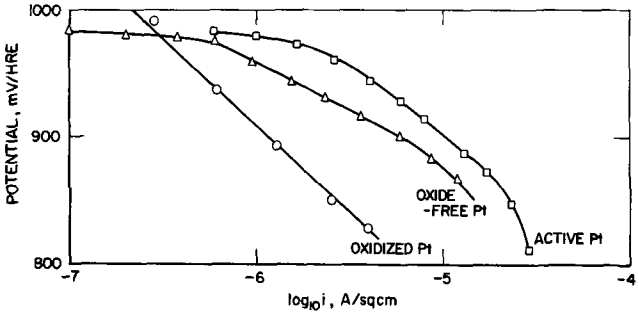

Fig. 1. Comparison of Tafel plots for reduction of oxygen on platinum in 85% orthophosphoric acid at 95.9°C.

Oxidized Electrodes

Above about 1000 mV/HRE platinum is covered by a phase oxide (13). For accurate kinetic study the thickness of the oxide film must be made reproducible by anodizing the platinum surface, as was first noted by Hoar (1).

In the work reported here, anodic treatment of platinum electrodes at 2000 mV/HRE for 15 min led to very reproducible anodic galvanostatic Tafel plots which could be traced backwards and forwards with very little hysteresis. For these experiments the electrolyte was saturated with oxygen at atmospheric pressure. At current densities below about 10^{-7} A/cm^2, a depolarizing effect was noted where the potential of the electrode fell rapidly with decreasing current density. In all probability, this current density represents the diffusion current for the oxidation of traces of impurities present in the solution (10), probably mainly hydrogen peroxide produced at the counter-electrode during anodizing.

Cathodic Tafel lines on the oxidized surface were obtained by reversing an anodic current until the potential of the electrode fell to 1100-1050 mV/HRE on a preanodized electrode, and then the current was adjusted to the appropriate value. An initial plateau was observed for each applied current density, after which a decay occurred due to gradual reduction of the oxide. To overcome this difficulty, a reproducible oxidized surface was obtained by anodizing the electrode at 2000 mV for 2 min before each reading was taken.

Typical examples of anodic and cathodic Tafel slopes obtained on oxidized platinum are shown in Fig. 2. The intersection of these slopes occurs at about 1200 mV/HRE.

For the over-all reaction

$$O_2 + 4H^+ + 4e^- = 2H_2O$$

at 95.9°C, E° (calculated from data for the free energy of formation of liquid water) (14) is 1169 mV. However, corrected for the presence of water vapor above 85% orthophosphoric acid at 95.9°C (15), the theoretical emf of the cell

$$Pt/H_2, \quad 85\% \text{ orthophosphoric acid}, \quad O_2/Pt$$

is 1199 mV/HRE, which agrees very closely with the intersection point in Fig. 2.

A typical exchange current is about 5 x 10^{-9} A/cm^2, but this value was observed to depend to a small ex-

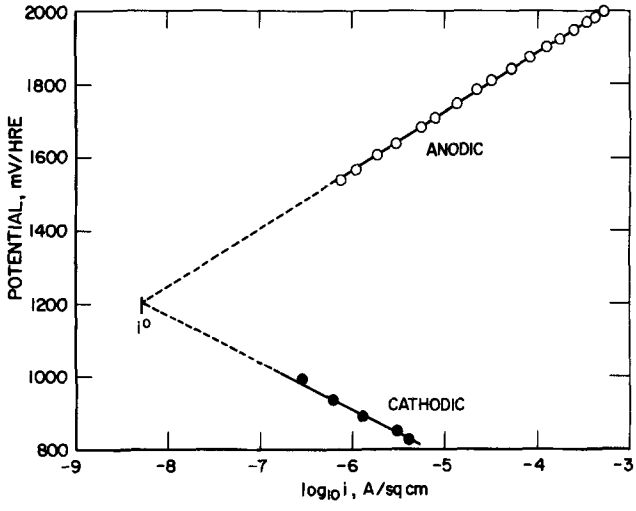

Fig. 2. Oxygen electrode on oxidized platinum in 85% orthophosphoric acid at 95.9°C.

Table I. Reaction paths on oxidized platinum electrodes

		ν	$\left(\frac{\partial \log i}{\partial \log p_{O_2}}\right)_V$
A. Oxide path			
1. Rate-determining	$S + H_2O \rightarrow SOH + H^+ + e^-$	4	0.25
2.	$2SOH \rightarrow SO + SH_2O$		
3.	$2SO \rightarrow O_2 + 2S$		
B. Hydrogen peroxide path			
4. Rate-determining	$S + H_2O \rightarrow SOH + H^+ + e^-$	4	0.25
5.	$2SOH \rightarrow SH_2O_2 + S$		
6.	$SH_2O_2 + SOH \rightarrow SOH_2 + SO_2H$		
7.	$SO_2H + SOH \rightarrow SH_2O + S + O_2$		
C. Metal peroxide path			
8. Rate-determining	$S + H_2O \rightarrow SOH + H^+ + e^-$	4	0.25
9.	$2SOH \rightarrow SO + SH_2O$		
10.	$SO + SOH \rightarrow S + SHO_2$		
11.	$SHO_2 + SOH \rightarrow O_2 + S + SH_2O$		
D. Electrochemical oxide path			
12.	$S + H_2O \rightarrow SOH + H^+ + e^-$	2	0.5
13.	$SOH \rightarrow SO + H^+ + e^-$	2	0.5
14.	$2SO \rightarrow 2S + O_2$		

Note: "S" represents an undefined surface site on platinum oxide, which must remain unaffected during the reaction sequence.

tent on the time allowed for the anodic treatment of the electrode surface. Anodic Tafel slopes were 159 mV/decade (or 2.17 x 2.3 $RT/\mathbf{F}$), and cathodic slopes were —131 mV/decade (or —1.78 x 2.3 $RT/\mathbf{F}$).

The order of reaction for oxygen was measured at 25.1°C because at this temperature oxide films were observed to be more stable and results were therefore more reproducible.

The oxygen concentration in dilute oxygen-nitrogen mixtures was determined by the magnitude of the diffusion-limiting current, compared with that for 1 atm oxygen. The difficulty of obtaining reproducible Tafel slopes made the determination of the reaction order somewhat unreliable, but a value of 0.29 was obtained at constant potential. For the same temperature but at constant overpotential in N $HClO_4$, Damjanovic *et al.* (4) obtained the value of 0.30, which is equivalent to 0.34 at constant potential, as $(\partial E/\partial \log i)_{P_{O_2}} = 2 \times 2.3\ RT/\mathbf{F}$ and $(\partial E/\partial \log p_{O_2})_i = 2.3\ RT/4\mathbf{F}$. Considering the general difficulty of obtaining good cathodic Tafel slopes, this agreement is reasonably good.

To clarify the mechanism further, H^+ reaction order data would be desirable. Unfortunately, it is not possible to vary H^+ at constant ionic strength in concentrated acids.

Since the anodic Tafel line extends over a very wide range of potentials, we may assume that we are dealing with Langmuir, rather than Temkin, adsorption of reaction intermediates. Furthermore, the intersection of the anodic and cathodic Tafel slopes at the reversible potential (1200 mV/HRE) suggests that the rate-determining steps for the cathodic and for the anodic reactions are the same and that their rates at the reversible potential must be approximately equal.

If these assumptions are valid and if we express the experimental Tafel slope as $b = 2.3\ RT/\alpha\mathbf{F}$, then we may use the equation of Parsons (16) for the determination of the stoichiometric number ν

$$\frac{n}{\nu} = (\alpha_a - \alpha_c) \qquad [1]$$

where n is the number of electrons involved in the over-all process, ν is the stoichiometric number of the rate-determining step, and α_a, α_c refer to the anodic and cathodic processes, respectively.

Using the observed values of $1/\alpha_a = 2.17$ $1/\alpha_c = -1.78$, we have $\nu = 3.9$ (effectively 4) for $n = 4$. At room temperature Hoar (17) obtained the value of 3.1 in $N/10$ H_2SO_4 on bright platinum, Bockris and Huq (2) obtained 3.5 in N H_2SO_4, and Damjanovic, Dey, and Bockris (4) also obtained the value of 3.5 in N $HClO_4$.

Assuming the simplest case of a sequence of simple consecutive steps and Langmuir adsorption, we may apply the equations[1]

$$\alpha_a = \beta n_k + \frac{n_a}{\nu} \qquad [2]$$

and

$$\alpha_c = (1-\beta) n_k + \frac{n_c}{\nu} \qquad [3]$$

where β is the anodic symmetry factor, n_k is the number of electrons involved in the (unique) rate-determining step, and n_a, n_c are the total number of electrons transferred before the rate-determining step in the anodic and cathodic directions, respectively.

According to Eq. [2] and [3] we see that: for $\nu = 4$, assuming $\beta \sim \frac{1}{2}$, and $\alpha_a \sim -\alpha_c \sim \frac{1}{2}$

$$n_k + \tfrac{1}{2} n_c = 1 = n_k + \tfrac{1}{2} n_a$$

The only consistent solutions for this equation are either $n_k = 1$, with $n_c = n_a = 0$; or $n_k = 0$, with $n_c = n_a = 2$. Assuming, therefore, that the rate-determining step is a charge transfer, $n_k = 1$ and $n_c = n_a = 0$ for $\nu = 4$.

This requires that no electrons are transferred before the rate-determining step in either the anodic or cathodic directions. The rate-determining step itself occurs four times in the over-all sequence and results in the total transfer of four electrons.

The only reactions schemes proposed so far (20) which satisfy these conditions are A, B, and C in Table I. Another interesting proposition for the mechanism of this reaction was offered by Riddiford (18). He supposes that steps 12 and 13 in path D (Table I) have similar exchange currents and suggests that step 12 will control anodically and step 13 cathodically; in each case the reaction with the higher slope controls the over-all process. The simple stoichiometric number equation (Eq. [1]) is, of course, not applicable to such reactions.

It is interesting to note that in another connection, Böld and Breiter (21) have postulated that the reactions

$$Pt + H_2O \rightarrow PtOH + H^+ + e^-$$

and

$$PtOH \rightarrow PtO + H^+ + e^-$$

which resemble steps 12 and 13, have about the same rate constants.

The oxygen reaction order data in the current work (about 0.3) suggest that Riddiford's proposition cannot

[1] These equations have been quoted without derivation in ref. (17) and derived in ref. (18) and (4) from the equations of Mauser (19).

fully explain either our experimental results or those obtained by Damjanovic *et al.* (4). It is possible, however, that, apart from the dual rate-determining steps that Riddiford (18) suggests, more than one reaction path may occur simultaneously on the electrode. In particular,[2] of the paths quoted in Table I, D and A may occur in parallel on different parts of the electrode surface. Both of these paths involve initial dissociative adsorption of oxygen. The occurrence of steps 2 or 13 followed by the controlling steps 1 or 12 could depend on local variations in oxide structure. This would explain the inexact values of the stoichiometric numbers and oxygen reaction orders observed here and by other workers (2, 3).

The anodic Tafel slopes in the present work are higher than those observed at room temperature in dilute acids (1, 2, 4). However, increase of these slopes with acid strength as observed by Kaganovich *et al.* (22) may be due to changes in the symmetry factor caused by alteration of the double-layer structure in highly concentrated acid electrolytes.

In conclusion, our results suggest that oxygen reduction and evolution mechanisms on anodized platinum in 14.6M (85%) orthophosphoric acid at a relatively high temperature are essentially similar to those in dilute acids such as sulfuric (1, 2) and perchloric (4) at room temperature and involve the same rate-determining step, namely, the water-discharge mechanism proposed by Bockris and Huq (2) for dilute sulfuric acid at room temperature. However, this step may not necessarily be rate-controlling cathodically, and more than one mechanism may operate simultaneously. The data obtained suggest that the water-discharge rate-determining step for oxygen evolution may generally apply in all acid electrolytes in which platinum oxides are stable, irrespective of the anion, concentration, and temperature. The nature of the anion appears to influence only the rate constant of the reaction and, to some extent, the symmetry factor.

Oxide-Free Electrodes

The surface of these electrodes was prepared as already described. Particular experimental precautions are necessary for these surfaces to ensure reproducibility because of their sensitivity to capillary-active impurities which always persist in the electrolyte.

After being subjected to a procedure for desorbing capillary-active impurities (23) (consisting of an anodic pulse to 1.2 V/HRE for 1 sec followed by a number of cathodic pulses to +0.50 V/HRE, for a few seconds each), they reached steady rest potentials of 985-999 mV in a few minutes. The initial rest potential usually rose to over 1000 mv after a few hours, reaching potentials of about 1010 mV. A slow decay followed; a final potential of about 990-1000 mV was generally noted after 24 hr, which then remained steady for some days. A typical galvanostatic Tafel plot for this surface is shown in Fig. 1. To ensure a reproducible surface, a cathodic pulse was used between each point, as it was noted that a slow decay of potential at constant current took place after initial stability. This is caused by the deactivation of the electrode by nonoxidizable impurities and is more apparent at lower potentials, leading to steeper Tafel slopes than those initially observed. The adsorption of capillary-active impurities is evidently potential-dependent, as has been noted by other workers (24, 25). Such nonoxidizable impurities, which may be of organic origin (or, in this case, possibly polyphosphates), are eliminated from the electrolytic solution only by extreme purification procedures (25).

With the precautions described above, very reproducible Tafel plots with slopes close to 2.3 RT/F were obtained. The i° value (corrected to 1 atm oxygen) was 4×10^{-10} A/cm^2 (Fig. 1).

The reaction order for oxygen was measured at 52.1°C. Galvanostatic results for four different oxygen partial pressures are shown in Fig. 3. In contrast to the oxidized platinum results in this case oxygen reduction at constant potential is approximately first order.

Ring-disk electrode studies.—Studies with a rotating ring-disk electrode, were carried out at 76.1°C to examine the possibility of hydrogen peroxide formation. Figure 4 shows a plot of the ring (maintained at 1.3V) and disk currents at 3140 rpm. The apparent double-wave effect is due to impurity adsorption. In the region of the plot between +700 to +400 mV/HRE, the disk was reactivated (pulsed to +50 mV/HRE) before each point. Points shown in Fig. 4 are the highest stable values of current that could be attained. The limiting current for oxygen (not reached in Fig. 4) can be calculated from Levich's equation (26) using published data for the oxygen solubility (27), its diffusion coefficient (27), and the kinematic viscosity of the acid (15). The expected value lies between 50 and 100 mV/HRE. As observed by other workers (24, 25), currents shown in Fig. 4 in the potential range of 600-400 mV/HRE slowly decayed to lower values with time.

No hydrogen peroxide was detected in the Tafel region, but, in the region where impurities are adsorbed, small amounts of hydrogen peroxide were present (25), as may be seen in Fig. 4. The maximum detected at the ring amounted to 16% of the total oxygen consumed at the disk, as the ring collects about 35% of the hydrogen peroxide produced. If impurity adsorption causes a reduction in bond energy of adsorbed peroxy-radical reaction interme-

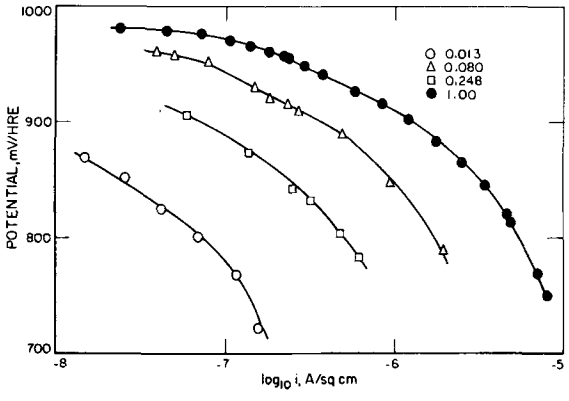

Fig. 3. Effect of oxygen partial pressure reduction of oxygen on oxide-free platinum in 85% orthophosphoric acid at 52.1°C.

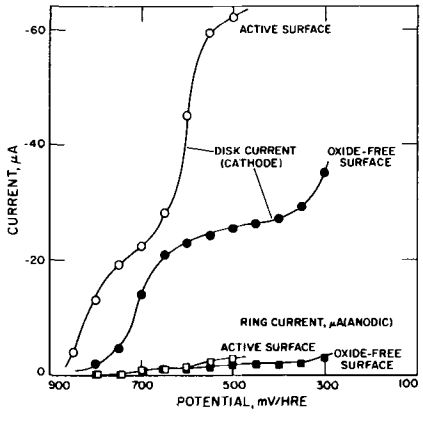

Fig. 4. Oxygen reduction on platinum ring-disk electrode at 3140 rpm and 76.1°C.

[2] The rotating ring-disk electrode detected less than 2.10^{-7} A/cm^2 at the ring at 76.1°C and 3140 rpm when the disk was anodized and held at a potential of 850 mV/HRE in oxygen-saturated solution. We may therefore conclude that hydrogen peroxide is not appreciably involved in the mechanism.

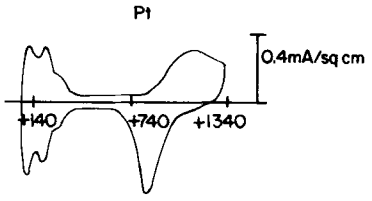

Fig. 5. Cyclic voltammetric scan on platinum at 260 mV/sec at 95.9°C (horizontal scale = mV/HRE).

diates,[3] the latter may tend to desorb rather than undergo O-O bond dissociation on the platinum surface.

Nature of the oxide-free surface.—Before considering the reaction mechanism for this surface, it is necessary to decide which adsorption isotherm is likely to apply on this surface. Böld and Breiter (21) have shown that a platinum electrode which is oxidized and reduced by a continuously cycling potential in *N* $HClO_4$ and other dilute acid solutions has a coverage of adsorbed oxygen radicals which reaches one monolayer at a potential of about 1.5 V/HRE. In the range of 900-1500 mV, an approximately linear variation of coverage with potential exists, which they interpreted in terms of the Temkin adsorption isotherm.

An integrated curve, showing the variation of coverage with potential, based on this work, is quoted by Damjanovic and Brusic (3). It must be emphasized that results obtained by this rapid-scanning technique do not allow equilibrium to be attained, especially at lower potentials. The steady-state coverage-potential plot given by Damjanovic and Brusic (3) shows that, in fact, the linear variation of coverage extends to potentials about 130 mV lower than those shown in cyclic voltammetric plots taken at a scan rate of 1 V/sec.

A cyclic scan plot on 85% orthophosphoric acid at 260 mV/sec at 95.9°C is shown in Fig. 5. Compared with results in 0.1*N* perchloric acid at room temperature (21), Fig. 5 shows a considerable anodic displacement of the oxygen region. This may be attributed to adsorption of phosphate ion in the double layer, which would tend to reduce the bond strength of adsorbed oxygen radicals on the platinum surface, leading to less favorable kinetics. It seems reasonable that Temkin conditions will also apply for 85% orthophosphoric acid, but will exist in a somewhat higher range of potential than that noted by Damjanovic and Brusic (3) in *N* perchloric acid at room temperature.

Mechanism.—Damjanovic and Brusic (3) showed that their results were accounted for by the rate-determining step

$$S + O_2 + H^+ + e^- \rightarrow S\text{-}O_2H$$

where the adsorption of the O_2H radical (the reaction product of the rate-determining step) is presumed to follow the same Temkin isotherm as that experimentally obtained for the O radical adsorbed on the electrode above 700 mV (21). The equation then accounts for the observed first-order dependence of current on oxygen partial pressure, Damjanovic and Brusic's experimental order of reaction for $[H^+]$ (3), and has a Tafel slope of 2.3 $RT/\mathbf{F}$ in the case where the heat of adsorption of O_2H is potential dependent. Under Langmuir conditions without previous charge transfer the same reaction would be expected to have a Tafel slope of $1/\beta \times 2.3\ RT/\mathbf{F}$, where β is the symmetry factor ($2 \times 2.3\ RT/\mathbf{F}$ if $\beta = \frac{1}{2}$).

It is concluded that the same rate-determining step is applicable in 85% orthophosphoric acid. It is also interesting to note that the i° in the present electrolyte at 95.9°C (4×10^{-10} A/cm²) is of the same order of magnitude as that noted by Damjanovic and Brusic (3) in *N* perchloric acid at 25°C. It seems therefore that, as in the case of the oxidized surface, the rate-determining step on the oxide-free platinum is common to all acid electrolytes, independently of the nature of the anion, the temperature, and the concentration. Normally it takes place under Temkin conditions of adsorption; however, in the presence of a strongly adsorbing anion (*e.g.*, Cl^-), it apears that low rate constants (weakening of the $S\text{-}O_2H$ bond) and higher slopes do occur. This effect is probably indicative of Langmuir adsorption (high coverages of strongly adsorbed material, in this case Cl^-) and of the progressive deactivation of the electrode with increasing overpotential. This is apparent from results obtained by Bianchi and Mussini in dilute halo-acids at room temperature where Tafel slopes greater than 2 x 2.3 $RT/\mathbf{F}$ were observed (5). Apart from this case, Tafel slopes of 2.3 $RT/\mathbf{F}$ appear to be typical if capillary-active material is absent.

[3] This may be equivalent to saying that impurity adsorption blocks the high energy sites where O-O bond dissociation can take place.

Active Platinum

Active platinum electrodes were prepared by anodizing at 2000 mV/HRE for a period of about 5 min. They were then reduced galvanostatically, but were not allowed to reach potentials below +500 mV/HRE. On switching off the galvanostatic cathodic current, these electrodes immediately took up an open-circuit potential of about 1000 mV/HRE.

Very reproducible galvanostatic Tafel plots, which could be retraced forwards and backwards several times, were obtained. They had a slope of about 1.69 x 2.3 $RT/\mathbf{F}$ (124 mV/decade), with an i° of about 4×10^{-8} A/cm². A typical Tafel plot for this surface is shown in Fig. 1 for 95.9°C.

The active surface is clearly a better electrocatalyst than oxidized or oxide-free surfaces. The reaction order for oxygen on active platinum was determined at 52.1°C. The Tafel plots shown in Fig. 6 were obtained after preparing a fresh surface for each partial pressure. Because of oxygen evolution during anodizing, a short time elapsed before steady readings were obtained in each case. Again, an approximately first-order dependence of current on oxygen partial pressure is observed.

Hydrogen peroxide formation was studied using the rotating ring-disk electrode. Potential current plots of ring and disk currents at 76.1°C are shown in Fig. 4. It can be seen that the active surface suffers less than the oxide-free surface from the effect of impurities in the range of potential below 700 mV; in proportion, much smaller amounts of hydrogen peroxide were detected.

Nature of the active surface and discussion of reaction.—Feldberg *et al.* (12) have explained the well-known observation, [reviewed by Vetter (28) and Hoare (6)] that about twice as many coulombs are required to produce a platinum-phase oxide than to reduce it by supposing that the reactions

$$Pt + H_2O \rightarrow PtOH + H^+ + e^-$$

$$PtOH \rightarrow PtO + H^+ + e^-$$

are, respectively, slow and very fast. These authors have noted that a platinum electrode which has been strongly oxidized and then reduced is in an "active" form which remains stable for some hours. They consider this electrode to be covered by a layer of PtOH. This would imply that the surface of a platinum electrode undergoing cyclic potential scanning as described by Böld and Breiter (21) is covered by a layer of PtOH during the reduced part of the cycle.

On the other hand, Schuldiner and Warner (11) have suggested that, after anodizing and reduction, a disordered lattice of metal atoms is formed which contains dissolved atoms. This they termed "dermasorbed" oxygen.

In the discussion of the oxide-free electrode above, we have assumed that the coverage data, obtained by

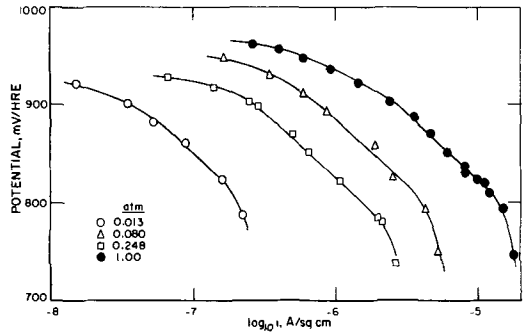

Fig. 6. Effect of oxygen partial pressure on reduction of oxygen on active platinum in 85% orthophosphoric acid at 52.1°C.

Damjanovic and Brusic (3), included all strongly bound oxygen-containing species, including —OH. Breiter (29) and Lukyanycheva *et al.* (30) have shown that the first cycle of a cyclic voltammetric scan behaves differently from subsequent cycles. There is evidence that the first anodic cycle is of a considerably larger area than subsequent cycles, so that the number of coulombs involved is greater than in the reduction part of the cycle, as in charging curves. This could be explained equally well either in terms of the proposition of Feldberg *et al.* (12) or in terms of oxygen radicals being "dermasorbed" during the first cycle (11).

However, from the present results and from those of Damjanovic and Brusic (3), it appears that an electrode which has been taken momentarily to 1.2-1.5V followed by reduction is not "active," but behaves as a normal oxide-free surface. According to Feldberg *et al.* (12), such an electrode should have an adsorbed monolayer of PtOH. If such were the case, adsorption of OH and other oxy-intermediates would not obey the Temkin isotherm, which only applies in the region $0.1 < \theta < 0.9$. Hence, we consider that the coulombs unaccounted for in the reduction of platinum oxide correspond to "dermasorbed" oxygen rather than to a layer of PtOH.

Undoubtedly, the surface produced by momentarily oxidizing at 1.5V, followed by reduction, must involve some "dermasorbed" oxygen. It is, however, important to note that the true active surfaces are only produced by prolonged anodizing or treatment with powerful oxidizing agents (31). It seems reasonable to suppose that the reduced oxide lattice contains a good deal of trapped oxygen (oxide ions or oxygen radicals), and perhaps also OH radicals, as proton diffusion through the lattice is likely to be easy. The outermost layers of the platinum surface must therefore be disordered and contain numerous vacancies. The surface is not particularly stable, but is more stable than would be expected if it were only lightly platinized as was suggested by Anson (32).

The high lattice energy created by the presence of oxygen radicals prevents easy diffusion and restoration of a regular crystalline array. With increased metal lattice energy, it is reasonable to suppose that the bond strength of adsorbed reaction intermediates in the oxygen reduction reaction will increase substantially, hence accounting for the higher reaction rates observed on this surface.

Because of the permanent presence of relatively large amounts of dissolved oxygen radicals in the few monolayers of the lattice, we may expect that oxygen radicals additionally adsorbed on the outer surface as potential increases will have a much smaller effect on the heat of adsorption of reaction intermediates than is the case on oxide-free platinum. In this situation adsorption should more nearly approach Langmuir rather than Temkin conditions.

We therefore suggest that the same rate-determining step applies as on bare platinum, that is

$$S + O_2 + H^+ + e^- \rightarrow SO_2H$$

but under more nearly Langmuir conditions. This explanation agrees with our Tafel slopes and the results of oxygen partial-pressure dependence.

Another interesting implication of the above concept concerns the reaction

$$S - OH + H^+ + e^- \rightarrow S + H_2O$$

which is rate-determining on oxidized platinum but apparently much faster on the oxide and active surfaces. In all cases it is likely to be the last step in the over-all cathodic process (3). The slow rate of this reaction on oxidized platinum can be explained by considering that oxidized surfaces are highly negative in character, as shown by their ability to absorb cations, even at high anodic potentials (33). We may conclude therefore, that, on such a substrate, adsorption of —OH would be weak, making the free energy of activation for this step correspondingly high.

Fuel Cell Implications

Neither oxidized nor active surfaces are stable with time at about 800 mV/HRE on massive platinum substrates; both ultimately degrade to bare platinum.

At fuel cell operating temperatures oxide-free platinum has a relatively poor i° value compared with the oxidized surface, but its more favorable Tafel slope makes it a more effective reducing surface in the relevant range of potential. Active surfaces, in spite of their high Tafel slopes, are still more effective.

It is possible that, owing to the highly fragmented nature of platinum black, kinetics on such electrodes may resemble those on active massive platinum, although the two differ drastically in their stability characteristics.

Acknowledgments

We wish to thank the sponsors of the TARGET Fuel Cell Program, Pratt & Whitney Aircraft Division of United Aircraft Corporation, for permission to publish this work. We also thank the members of IGT who helped to prepare this publication.

Manuscript submitted Feb. 17, 1969; revised manuscript received *ca.* May 17, 1969. This was Paper 338 presented at the Montreal Meeting, Oct. 6-11, 1968.

Any discussion of this paper will appear in a Discussion Section to be published in the June 1970 JOURNAL.

REFERENCES

1. T. P. Hoar, *Proc. Roy. Soc. (London)*, **A142,** 628 (1933).
2. J. O'M. Bockris and A. K. M. S. Huq, *Proc. Roy. Soc. London*, **A237,** 277 (1956).
3. A. Damjanovic and V. Brusic, *Electrochim. Acta*, **12,** 615 (1967).
4. A. Damjanovic, A. Dey, and J. O'M. Bockris, *ibid.*, **11,** 791 (1966).
5. G. Bianchi and T. Mussini, *ibid.*, **10,** 445 (1965).
6. J. P. Hoare, "Advances in Electrochemistry and Electrochemical Engineering," Vol. 6, P. Delahay, Editor, Interscience Publishers, New York (1967).
7. L. A. Mazitov, N. A. Fedotov, and Yu. A. Mazitov, *Elektrokhimiya*, **2,** 1021 (1966).
8. L. A. Mazitov, N. A. Fedotov, and Yu. A. Mazitov, *ibid.*, **2,** 1189 (1966).
9. R. Thacker and J. P. Hoare, *This Journal*, **113,** 862 (1966).
10. H. Wroblowa, M. L. B. Rao, A. Damjanovic, and J. O'M. Bockris, *J. Electroanal. Chem.*, **15,** 139 (1967).
11. S. Schuldiner and T. B. Warner, *This Journal*, **112,** 212 (1966).
12. S. W. Feldberg, C. G. Enke, and C. E. Bricker, *ibid.*, **110,** 826 (1963).
13. A. K. N. Reddy, M. Genshaw, and J. O'M. Bockris, *J. Electroanal. Chem.*, **8,** 406 (1964).
14. G. Lewis and M. Randall, "Thermodynamics and Free Energy of Chemical Substances," McGraw-Hill Publishing Co., New York (1923).
15. Monsanto Corp., Technical Bulletin *1-239*.

16. R. Parsons, *Trans. Faraday Soc.*, **47**, 1332 (1951).
17. T. P. Hoar, "Proc. 8th Meeting CITCE, Madrid 1956," p. 439, Butterworth, London (1958).
18. A. C. Riddiford, *Electrochim. Acta*, **4**, 170 (1961).
19. H. Mauser, *Z. Elektrochem.*, **62**, 419 (1958).
20. J. O'M. Bockris, *J. Chem. Phys.*, **25**, 817 (1956).
21. W. Bold and M. Breiter, *Electrochim. Acta*, **5**, 145 (1961).
22. R. Kaganovich, M. Gerovich, and E. Enikeev, *Doklady Akad. Nauk S.S.S.R.*, **108**, 107 (1956).
23. S. D. James, *This Journal*, **114**, 1113 (1967).
24. L. Myuller and L. N. Nekrasov, *Doklady Akad Nauk S.S.S.R.*, **154**, 437 (1964).
25. A. Damjanovic, M. A. Genshaw, and J. O'M. Bockris, *ibid.*, **114**, 466 (1967).
26. V. G. Levich, "Physicochemical Hydrodynamics," p. 297, Prentice-Hall New York (1962) (English translation).
27. K. E. Gubbins, University of Florida Engineering and Industry Experiment Station, Gainesville, U. S. Army Report DA-49-186-AMC-45(x), AD620205 (June 30, 1965).
28. K. J. Vetter, "Electrochemische Kinetik," Springer, Berlin (1961).
29. M. W. Breiter, *J. Electroanal. Chem.*, **8**, 230 (1964).
30. V. I. Lukyanycheva, V. I. Tikhomirova, and V. S. Bagotskii, *Elektrokim.*, **1**, 262 (1965).
31. J. P. Hoare, *J. Electroanal. Chem.*, **12**, 260 (1966).
32. F. C. Anson, *Anal. Chem.*, **33**, 934 (1961).
33. A. Frumkin, *Electrochim. Acta*, **5**, 265 (1961).

Specific Conductance of Molten Potassium Nitrate

G. D. Robbins* and J. Braunstein

Reactor Chemistry Division, Oak Ridge National Laboratory, Oak Ridge, Tennessee

ABSTRACT

A careful determination of specific conductance of molten potassium nitrate over the temperature range 345°-541°C has demonstrated its suitability as a molten salt standard in electrical conductance work. The data are well represented ($\sigma = 0.0008$) by the computer-fitted, least squares equation

$$\kappa = -0.7098 + 4.6203 \times 10^{-3}\, t(°C) - 2.0221 \times 10^{-6}\, t^2$$

The estimated accuracy is better than ±0.5%. Of the previous investigations on this system, the limited temperature equation of Smith and Van Artsdalen agrees best with the results reported here.

Investigations of electrical conductivity in molten salts are essential to the understanding of transport processes in these materials. In particular, the testing of theories, such as the zero mobility concept of Angell (1, 2) requires accurate and precise determination of the temperature variation of specific conductance. In addition, the advent of molten salt nuclear reactors employing fused salts as fuel salt solvent and coolant salts (3) necessitates accurate measurement and better understanding of electrical transport.

As is well known, specific conductances, κ, are obtained from measured resistances, R, by employing the relation

$$\kappa = \frac{1}{R}\,(l/a) \qquad [1]$$

where (l/a) is the cell constant. The value of (l/a) usually is obtained by measuring the resistance of a material of known specific conductance, preferably one having similar properties to the system to be investigated. There are, at present, no accepted molten salt secondary standards for the determination of cell constants for conductivity measurements. Based on ease of handling, availability, stability to atmospheric conditions, and compatibility with container materials (especially silica), molten potassium nitrate would seem the most reasonable choice among molten salts for such a reference material. However, as Fig. 1 demonstrates, the results of several reported investigations in this system at temperatures up to 100°C above the melting point differ by amounts considerably larger than the claimed experimental uncertainty. In the work of Bloom and co-workers (4) and Smith and Van Artsdalen (5) specific conductance data are not given, only an equation. Although in the early work of Jaeger and Kapma (6) considerable attention was devoted to experimental detail, the scatter in the data is large. The recent results of De Nooijer (7) appear uncommonly low in the low temperature region, where one would expect nitrite formation to be least and results to agree best.

In a recent review of electrical conductance measurements in molten fluorides (8) errors arising from the indiscriminate use of a Wheatstone type (or Jones) conductance bridge were discussed. Some possible origins of frequency variation of the measured resistance were also presented. Two subsequent discussions (9, 10) of the relation of measured resistance to measuring frequency have also appeared. Kröger and Weisgerber (11) have addressed themselves to these questions, and as Fig. 1 demonstrates, their data show some divergence from those of the others, although they do not result in a smooth curve. In addition, resistance measurements were performed only over the frequency range 1-4 kHz, and the resultant extrapolation to infinite frequency was 2-3%.

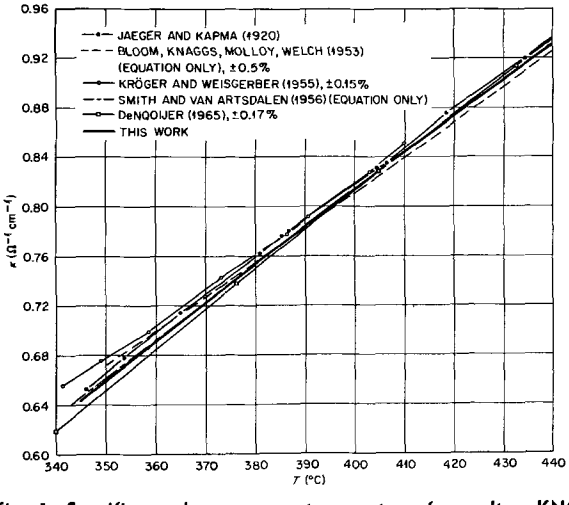

Fig. 1. Specific conductance *vs.* temperature for molten KNO_3. Comparison of this and previous work.

* Electrochemical Society Active Member.

No attempt has been made in Fig. 1 to include all references to work on molten potassium nitrate due to the limited number of curves which can be distinctly represented. Investigations in this system date back to 1874 (12), and no work previous to 1920 is cited. Several investigations not referenced in Fig. 1 should be mentioned: Direct current measurements at four temperatures have been reported by King and Duke (13). Over the larger part of their temperature range the data lie above those of Kröger and Weisgerber. Angell (14) has measured specific conductances employing an a-c technique over a 75° temperature interval. Agreement of ±0.1% with the data of King and Duke is claimed, although one of the seven data reported differs by 2.8% probably the result of a typographical error. For additional references, the recent compilation by Janz *et al.* (15) is useful.

In this paper we present new measurements on the conductance of KNO_3 over an extended range of temperature with a bridge designed for use with molten salts. We consider the possible effects of impurities and demonstrate the suitability of KNO_3 as a secondary standard for molten salt conductance measurements.

Because of the frequent use of potassium nitrate as a reference point in studies of transport properties of molten salts (1, 2, 7, 16), accurate values of its specific conductance and temperature dependence are important quantities in their own right to the physical chemistry of molten salts.

Experimental and Results

Since the importance of this work lies in the credibility of the data, careful attention will be given to the experimental details of the measurements.

Figure 2 shows the type of silica conductance cell employed in these determinations. The interior dip cell consists of two silica tubes, the lower portions of which are 3 mm ID tubing, attached to a silica rod. Platinized platinum electrodes (20 gauge) are held immobile relative to the dip cell assembly by silica hooks and glass tape. The 12-cm conducting path resulted in measured resistances of 120-225 ohms, and the L-shaped electrode design rendered measured resistance independent of depth of immersion (3-7 mm below salt surface). The electrolyte is contained in a 3.3-cm ID silica cell which stands on a silica foot. A Teflon cap (not shown) holds the dip cell in place and admits the electrodes and a thermocouple through close fitting holes. The entire cell assembly is immersed in a stirred, temperature controlled, molten potassium nitrate bath contained in a silica and lavite furnace (17) which permits visual observation of the melt (9). A calibrated chromel-alumel thermocouple contained in the silica thermocouple well and a type K-4 potentiometer measured temperature with an estimated uncertainty of ±0.5°C.

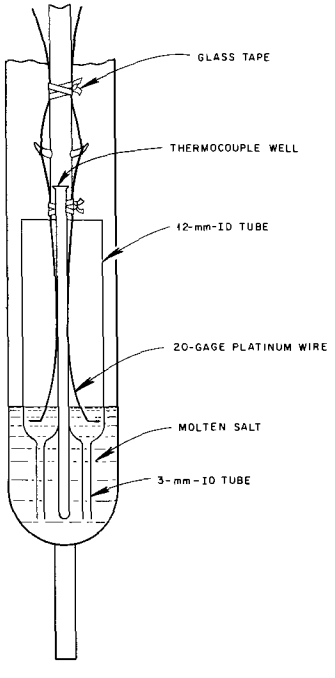

Fig. 2. Silica conductance cell

As discussed previously (8, 9), errors can arise in determining molten salt conductivities from the use of measuring bridges with a balancing arm having a parallel resistance and capacitance. Accordingly, a specially constructed bridge (9) with series components in the balancing arm was employed in measuring resistances in the molten nitrate. A test of the bridge employing a dummy cell consisting of a standardized resistance and capacitance connected in series revealed that the accuracy was better than ±0.2% for resistance of the order of 100 ohms (with a capacitance of 21 μf) in the frequency range 1-50 kHz. Measurements with the dummy cell included leads employed with the real cell, thus insuring no error from lead resistance. The accuracy in determining capacitance was much less and depended on the magnitude of the resistance and on the frequency (for 100 ohms ±1% at 2.5 kHz and ±10% at 7.5 kHz). However, even though the value of capacitance required for bridge balance was not an accurate measure of the dummy capacitance at higher frequencies, at balance the accuracy of the resistance measurement was maintained.

Similar tests on a Jones bridge available in our laboratory (Leeds and Northrup) (18), which has a parallel-component balancing arm, revealed that while this bridge is extremely accurate for measuring high resistance, the accuracy at 100 ohms was only ±1% in the frequency range 1-50 kHz. Consequently, the Jones bridge was employed in determining cell constants in dilute aqueous solution where the resistances were large and the bridge accuracy high, while the much lower resistances of the molten salt were determined with our specially constructed bridge, its accuracy being high in this resistance range.

For the determination of the cell constant a 0.1 demal aqueous potassium chloride solution (prepared from single crystal KCl) was used for which the specific conductance is well established (19, 20). The resistance of the aqueous electrolyte was determined in a controlled temperature bath at 25°C employing the Jones bridge because of the large resistances involved. A test of the bridge with dummy components of magnitude comparable to this solution showed an accuracy of ±0.05% in the frequency range 0.5-5 kHz. The cell constant (145.9 cm^{-1}), determined on two consecutive days and at three depths of immersion, was independent of frequency in this range and of the depth of immersion (3-7 mm) to ±0.3 cm^{-1}.

"Baker Analyzed," reagent grade, potassium nitrate was dried at 100°C for several days, and a molten portion showed no clouding on addition of silver nitrate crystals. The maximum peak-to-peak voltage applied to the series-component bridge was 30-110 mV, and the measured resistance did not vary with frequency (±0.2 ohm < 0.2%, random) from 1-20 kHz. Table I shows specific conductance *vs.* temperature data for molten potassium nitrate as determined with the series-component bridge.

To check for errors in conductance due to nitrite formation, the following procedure was adopted. Between each resistance determination at successively higher temperatures, the resistance was remeasured near the melting point (see Fig. 3). It was planned to discard the last datum at the elevated temperature when a value failed to duplicate the previously determined values. However, no discrepancy appeared up to 541°C, the temperature limit of the furnace. From this one might conclude either that sufficiently little nitrite had formed to be detected, or that the specific conductances of KNO_3 and KNO_2 were identical

Table I. Specific conductance of KNO_3 vs. temperature

T(°C)	κ(ohm^{-1} cm^{-1})
345.4	0.645_0
349.9	0.659_0
351.6	0.664_7
353.5	0.670_5
353.5	0.669_6
354.9	0.675_8
355.4	0.676_4
357.5	0.683_4
358.5	0.686_7
360.6	0.692_1
360.8	0.693_4
363.7	0.704_2
376.6	0.744_4
380.0	0.753_0
386.6	0.774_0
392.0	0.790_8
419.9	0.873_1
445.2	0.946_2
464.4	1.001_4
485.2	1.056_5
485.7	1.055_7
499.5	1.093_7
520.5	1.147_0
541.3	1.198_8

within the limits of measurement, in which case the results remained valid. However, the possibility exists for identical conductivities near 350°C with divergent values appearing at increased temperatures. Accordingly, an addition of 5 m/o (mole per cent) KNO_2 resulted in the triangular datum (see Fig. 3) at 359°C, a change of 1.8%, well outside the data scatter. This is consistent with the data of Bartholomew (21), who studied the equilibrium $KNO_3 \rightleftharpoons KNO_2 + \frac{1}{2}O_2$ from 550° to 750°C and found an equilibrium nitrite concentration of only 0.009 mole fraction at 550°C. The effect of 1 m/o nitrite on the specific conductance of KNO_3 may be estimated from specific conductance data for $NaNO_3$ and $NaNO_2$ (22). Assuming additivity of conductances, the increase in specific conductance due to 1 m/o nitrite would be 0.3% at 550°C.

The curve shown in Fig. 3 represents the computer-fitted, least squares equation ($\sigma = 0.0008$)

$$\kappa = -0.7098 + 4.6203 \times 10^{-3}\, t(°C) - 2.0221 \times 10^{-6}\, t^2 \quad [2]$$

based on the 24 data of Table I.

To recheck the KNO_3 specific conductance results, a completely new dip cell was constructed and its cell constant (141.4 cm^{-1}) determined in 0.1 demal KCl as before. A newly calibrated Pt vs. Pt-Rh (10%) thermocouple measured temperature. The open circle data points at 370° and 422°C show these results, which agreed with the previous results within 0.2% A comparison of these data with previous investigations is shown in Fig. 1, where it is evident that only the limited temperature range equation of Smith and Van Artsdalen (5) agrees well with the results reported here (maximum deviation = 0.4%). If all errors are assumed to be random and independent with uncertainties assigned to κ of 0.2% from cell constant determination, 0.1% from resistance measurement, 0.2% from possible nitrite impurity, and 0.2% from temperature measurement, the probable error is 0.3%. We consider these results to have an accuracy of better than ±0.5%.

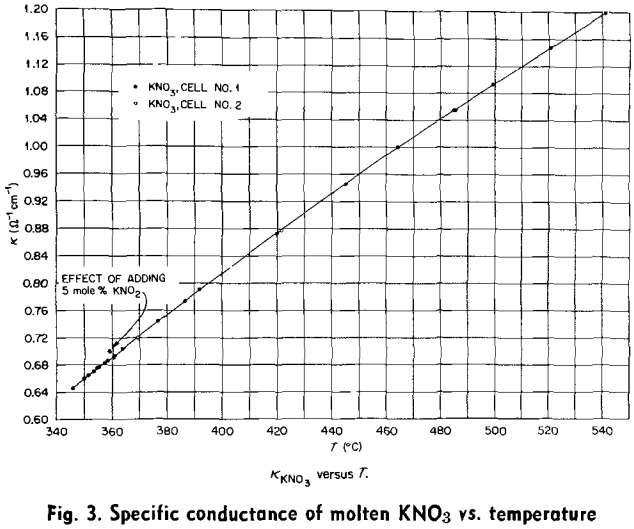

Fig. 3. Specific conductance of molten KNO_3 vs. temperature

Discussion

The density-temperature equation of Smith and Petersen (23) was employed in calculating equivalent conductances, Λ, the natural logarithms of which were examined for curvature when plotted vs. $1/T$(°K). These density data were employed because of the wide temperature range which they encompass. Still, the two conductance points of highest temperature are beyond their range of measurement, and densities at these two temperatures were estimated from the same equation. Similar calculations with the density data of Smith and Van Artsdalen (5) in the limited temperature range 344°-398°C resulted in slightly lower values of ln Λ, which paralleled the previous plot.

The slight curvature observed in the graph of specific conductance vs. temperature (Fig. 3) persisted in the ln Λ vs. $1/T$(°K) plot. Thus, the three parameter, Vogel-Tammann-Fulcher (VTF) equation successfully employed by Angell (1, 2, 24, 25) for glass-forming melts in the KNO_3-$Ca(NO_3)_2$ system has been fitted to the data with the aid of a computer. The least squares representation of the data ($\sigma = 0.0012$) is

$$\ln \Lambda = 9.590\ (\pm 0.029) - \tfrac{1}{2} \ln T - \frac{1308.9\ (\pm 31.4)}{T - 153.93\ (\pm 6.43)} \quad [3]$$

where T is in degrees Kelvin and the values in parentheses are standard errors of the parameters. It is not surprising that Angell's values for k and T_0 (the zero mobility temperature) in the VTF equation

$$\ln \Lambda = A - \tfrac{1}{2} \ln T - \frac{k}{T - T_0} \quad [4]$$

of 690°K (±5%) and 237°K (extrapolated from a plot of T_0 vs. composition from the glass-forming region) do not agree with the constants in Eq. [3]. Equation [4] was strictly applicable only for temperatures $\leq 1.7\ T_0$, while the data presented here are in the range $2.6\ T_0 \leq T \leq 3.4\ T_0$ based on Angell's suggested value of $T_0 = 237$°K. In addition, Angell's data for pure KNO_3 do not lie exactly on his linear plot [see ref. (24), Fig. 2], but on a line corresponding to a k of 580°K. Constraining a two-parameter least squares fit of our data to the equations

$$\ln \Lambda = A - \tfrac{1}{2} \ln T - \frac{690}{T - T_0} \quad [5]$$

or

$$\ln \Lambda = A - \tfrac{1}{2} \ln T - \frac{k}{T - 237} \quad [6]$$

resulted in fitted values of $T_0 = 300$°K (±1) ($\sigma = 0.0078$) or $k = 935$°K (±3) ($\sigma = 0.0039$). [The corresponding values of A were 8.932 (±0.006) and 9.220 (±0.007), respectively.] Thus, we must conclude that the temperature range of our data is sufficiently outside the "low temperature" region ($\leq 2\ T_0$) as not to warrant a precise evaluation of T_0 based on data in this range.

From the derivative of the analytic representation of our data (Eq. [3]) the Arrhenius coefficient for equivalent conductance, E_Λ can be evaluated

$$E_\Lambda = -R \frac{\partial \ln \Lambda}{\partial\,(1/T)} = -\tfrac{1}{2} RT + 1308.9R \left(\frac{T}{T - 153.93}\right)^2 \quad [7]$$

The variation of E_Λ with temperature is shown in Fig. 4, together with that obtained from data by other in-

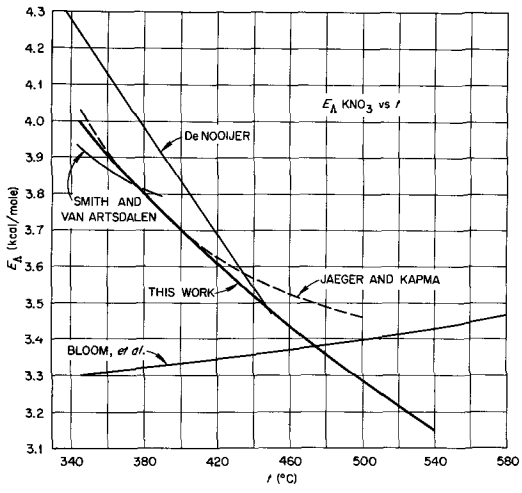

Fig. 4. Arrhenius coefficient for equivalent conductance vs. temperature for molten KNO_3.

vestigators. While agreement among our work, that of Smith and Van Artsdalen (5), and that of Jaeger and Kapma (6) (at lower temperatures) is good, the sign of the variation of E_A with t from the data of Bloom and co-workers (4) is opposite to that of all others.

Conclusion

While no set of specific conductance data should be considered as an unequivocal standard until such measurements are directly compared with an absolute standard, the authors feel the results reported herein demonstrate the suitability of molten potassium nitrate for use as a reference standard in molten salt conductivity work. Of the previous investigations of electrical conductivity in this system the limited temperature range equation of Smith and Van Artsdalen (5) agrees best with these data.

The temperature dependence of the energy of activation for equivalent conductance, while significant over the temperature range investigated, does not result in a value of the zero mobility temperature in agreement with that predicted by extrapolation from the glass-forming region of a binary system.

Acknowledgment

The authors wish to thank W. L. Marshall and A. S. Quist for the aqueous KCl solution. The research was sponsored by the U.S. Atomic Energy Commission under contract with Union Carbide Corporation.

Manuscript submitted Feb. 17, 1969; revised manuscript received *ca.* May 19, 1969. This was Paper 197 presented at the New York Meeting, May 4-9, 1969.

Any discussion of this paper will appear in a Discussion Section to be published in the June 1970 JOURNAL.

REFERENCES

1. C. A. Angell, *J. Phys. Chem.*, **68,** 1917 (1964).
2. *Ibid.*, **70,** 2793 (1966).
3. W. R. Grimes, in "Materials and Fuels for High Temperature Nuclear Energy Applications," M. T. Simnad and L. R. Zumwalt, Editors, The M.I.T. Press, Massachusetts (1964).
4. H. Bloom, I. W. Knaggs, J. J. Molloy, and D. Welch, *Trans. Faraday Soc.*, **49,** 1458 (1953).
5. D. F. Smith and E. R. Van Artsdalen, AEC Report ORNL—2159, p. 80, Oak Ridge National Laboratory, Oak Ridge, Tennessee, June 1956.
6. F. M. Jaeger and B. Kapma, *Z. Anorg. Chem.*, **113,** 27 (1920).
7. B. De Nooijer, "The Electrical Conductivity of Molten Nitrates and Binary Nitrates," Thesis, University of Amsterdam, The Netherlands, 1965.
8. G. D. Robbins, *This Journal*, **116,** 813 (1969).
9. G. D. Robbins and J. Braunstein, in "Molten Salts: Characterization and Analysis," G. Mamantov, Editor, Marcel Dekker, New York (1969).
10. G. J. Hills and S. Djordjevic, *Electrochim. Acta*, **13,** 1721 (1968).
11. K. Kröger and P. Weisgerber, *Z. Phys. Chem. (Frankfurt)*, **5,** 192 (1955).
12. F. Braun, *Chem. Ber.*, **7,** 958 (1874).
13. L. A. King and F. R. Duke, *This Journal*, **111,** 712 (1964).
14. C. A. Angell, *ibid.*, **112,** 956 (1965).
15. G. J. Janz, F. W. Dampier, G. R. Lakshminarayanan, P. K. Lorenz, and R. P. T. Tomkins, "Molten Salts," Vol. 1, "Electrical Conductance, Density, and Viscosity Data," p. 26, NSRDS NBS 15 (October 1968).
16. J. C. T. Kwak, "Diffusional and Electrical Mobilities of Tracer Ions in Ionic Liquids," Thesis, University of Amsterdam, The Netherlands, 1967.
17. K. A. Romberger, AEC Report ORNL-4254, p. 149, Oak Ridge National Laboratory, Oak Ridge, Tennessee, Feb. 1968.
18. P. H. Dike, *Rev. Sci. Instr.*, **2,** 379 (1931).
19. R. A. Robinson and R. H. Stokes, "Electrolyte Solutions," 2nd ed., p. 462, Butterworths, London (1959).
20. G. Jones and B. C. Bradshaw, *J. Am. Chem. Soc.*, **55,** 1780 (1933).
21. R. F. Bartholomew, *J. Phys. Chem.*, **70,** 3442 (1966).
22. G. J. Janz, "Molten Salts Handbook," pp. 295, 297, Academic Press, New York, (1967).
23. G. P. Smith and G. F. Petersen, *J. Chem. Eng. Data*, **6,** 493 (1961).
24. C. A. Angell, *J. Phys. Chem.*, **68,** 218 (1964).
25. C. A. Angell and C. T. Moynihan, in "Molten Salts: Characterization and Analysis," G. Mamantov, Editor, Marcel Dekker, New York (1969).

Polarization of Partly Wetted Porous Electrodes

P. Ruetschi*[1] and J. B. Ockerman[2]

ESB Incorporated, C. F. Norberg Research Center, Yardley, Pennsylvania

ABSTRACT

The polarization behavior of partly wetted electrodes, on which the electrode reaction proceeds beneath thin electrolyte films in the large, nonflooded pores, is described for the two cases where either diffusion through the liquid films, or the charge transfer process at the solid-liquid interface beneath the film, are rate limiting, and whereby consideration is given to the ohmic drop in the electrolyte films and the flooding of the small pores. The treatment is verified experimentally with waterproofed porous graphite electrodes.

During the past decade, porous electrodes which are only partly wetted by electrolyte have been the subject of many studies. Such electrodes are generally used when the reactant is a gas with relatively small solubility in the electrolyte, as for instance in continuous-feed galvanic cells (1), air-depolarized cells (2), and hermetically sealed cells (3). As realized some time ago for the case of electrodes in which pores are completely filled or flooded, electrolyte resistance effects in the pores and wetting films are of major importance in determining polarization characteristics (4-17). Progress in the understanding of partly wetted electrodes has been achieved in studies on partly immersed, nonporous electrodes. Oxygen reduction was investigated in this manner by Hersch (18), Weber, Meissner, and Sama (19), and more recently by Maget and Roethlein (20), Fedotov *et al.* (21), and Bennion and Tobias (22). Hersch was the first to point out that gases could diffuse rapidly through thin electrolyte films existing above the wetting meniscus, thus allowing fast transport rates.

Experiments relating to the electrochemical oxidation of hydrogen on partly immersed solid electrodes were first carried out by Will (23), who also has given the first thepretical treatment for the polarization behavior of such electrodes. His treatment was restricted to the particular case when diffusion of the gas through the electrolyte meniscus or film was current-limiting. However, under certain conditions the wetting films may be extremely thin, and diffusion therefore very fast, such that the ionization rate could become limiting.

Theoretical and experimental studies with partly wetted porous electrodes were carried out by Winsel (24), Iczkowski (25), Grens *et al.* (26), Austin *et al.* (27), Rockett and Brown (28), Lightfoot (29), and Grens (30), as well as by others.

Recent work in the USSR (31-36) stresses the importance of electrocapillary equilibrium and relative distribution of gas and electrolyte in the pores. Small pores are completely flooded with electrolyte, while large pores remain gas-filled. Assuming certain pore-size distributions, the relative gas to electrolyte volume ratio in porous electrodes may be calculated. The small electrolyte-filled pores are thought to intersect randomly with large gas-filled pores, and with this model certain characteristic features, in particular relating to the effect of applied pressure differential across the electrode, may be derived. However, one is not allowed to neglect the consequences originating from the extremely small wetting angles of strong electrolytes with most solid surfaces. Thus, even the walls of the large, nonflooded pores are therefore covered with very thin electrolyte films, resulting from electrolyte "creep" along the metallic surface.

The model used here is that of the Russian workers, with special emphasis on the influence of wetting films in the nonflooded pores. As illustrated in Fig. 1, the electrolyte is depicted to wet the solid internal surface of the nonflooded pores, forming long and thin films. Hydrophobic particles, *e.g.*, of Teflon, prevent flooding of the large pores, but do not restrict the spreading of thin films. In the flooded portion, at $x < 0$, gas diffusion is slow, and the current generated there thus is negligible.

A high concentration of H^+ or OH^- ions is provided to minimize concentration effects. Although such effects may in certain cases be important, they are neglected in the present treatment. The conductivity of the solid electrode is presumed high, such that no noticeable ohmic voltage drops occur within the solid parts of the electrode. Diffusion limitations in the gas phase, that is in the gas-filled portions of the porous electrode, are not considered here.

The present analysis lies largely with the mathematical framework of the listed references but relates specially to a comparison of the behavior for limiting diffusion of the reacting gas through the electrolyte films on one hand, and limiting ionization beneath the films on the other hand, whereby proper consideration is given in both cases to the ohmic drop in the electrolyte films.

According to the model of Fig. 1, the electrode is characterized by the presence of a specific volume of electrolyte per cubic centimeter contained in the films of the nonflooded pores, v_f. The electrode is further characterized by the total specific electrolyte volume v_e/cm^3. The surface area of the pores whose walls are covered with thin electrolyte films (that is the electrochemically active surface) is designated s_f (cm^2/cm^3). The average effective film thickness of the nonflooded pores is thus v_f/s_f.

Theoretical Framework

A thin sectional layer, positioned across the electrode at depth x, and normal to the x axis, contributes

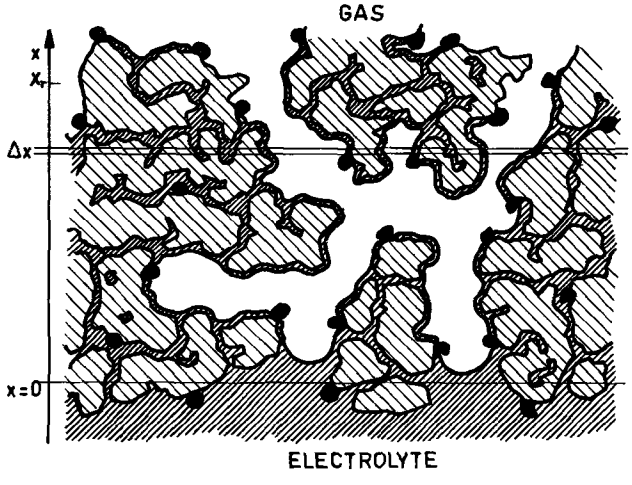

Fig. 1. Model of partly wetted electrode. Dark hatched area, electrolyte; light hatched area, solid particles with catalyzed surface; white area, gas filled pores; black dots, Teflon waterproofing particles.

* Electrochemical Society Active Member.
[1] Present address: Leclanché S.A., Yverdon/Switzerland.
[2] Present address: Gould National Batteries Inc., Research and Development Laboratories, Minneapolis, Minnesota.

to the total electrode current density in the direction of x, the infinitesimal fraction

$$dI(x) = -s_f\ i(x)\ dx \qquad [1]$$

where $i(x)$ is the true average local current density across the solid-liquid interface at depth x.

The decrease in local polarization $\eta(x)$ due to the ohmic drop caused by the current flowing in the electrolyte in the direction of x is given by[3]

$$\mp d\eta(x) = I(x)\ d\ R_e \qquad [2]$$

where $d\ R_e$ is the electrolyte resistance of a thin cross-sectional layer, parallel to the geometric electrode surface, and normal to the direction x, placed at a given depth x

$$d\ R_e = (\rho/v_e)\ dx \qquad [3]$$

Diffusion is rate limiting.—If the local current density i is determined by the diffusion rate at which dissolved gas can be transported across the electrolyte film, one obtains from Ficks law for the one-dimensional case (valid for v_f very much smaller than the porosity, that is, for very thin films) and the Nernst equation

$$i(x) = (s_f/v_f)\ C_o n_m\ \mathbf{F} D\ \{1 - \exp\ [\mp\ \eta(x)\ n\mathbf{F}/RT]\} \qquad [4]$$

where C_o is the solubility of the gas in the electrolyte (moles/cm^3) at the partial pressure and temperature in question, n_m the number of electrons required to ionize one gas molecule ($n_m = 2$ for H_2, and $n_m = 4$ for O_2), n the number of electrons in the potential determining Nernst equation, $\mathbf{F}$ the Faraday number, D the diffusion coefficient (cm^2/sec), and $\eta(x) = E(x) - E_r$ the local polarization. E_r is the reversible open circuit potential of the electrode approached at x_r; η is positive for hydrogen oxidation, negative for oxygen reduction.

The current $I(x)$ flowing through the cross section at any particular depth x must be a continuous, single valued function of the independent variable x. The same must be true for $\eta(x)$. One can therefore eliminate the differential dx between Eq. [1], [2], and [3], and substituting [4] for $i(x)$ one derives a differential equation which is readily integrated to give with the boundary conditions

$$x = 0; \quad \eta = \eta_a; \quad I = I_a$$

$$x = x_r; \quad |\eta|\ (x_r) << |\eta_a|; \quad I\ (x_r) << I_a$$

the following result

$$I_a^2 = 2n_m \mathbf{F} D C_o\ s_f^2\ v_e/v_f\rho\ \{\pm\ \eta_a - (RT/n\mathbf{F}) + (RT/n\mathbf{F})\ \exp\ [\mp\ n\mathbf{F}\eta_a/RT]\} \qquad [5]$$

where I_a is the projected current density relating to the geometric electrode surface in contact with the electrolyte, and where $\eta_a = E_a - E_r$, with E_a being the external potential applied to the porous electrode. According to [5] the current depends at constant η_a on the square root of the pressure of the reacting gas, since, in accordince with Henri's law

$$C_o = k_h\ p \qquad [6]$$

where k_h is the solubility constant. It must be pointed out that pressure here means the absolute partial pressure of the reacting gas in the gas-filled pores of the system, but not some sort of pressure differential across the porous electrode.

If the potential E_a of the porous electrode is expressed *vs.* the potential E_{r0} of a reference gas electrode in the same electrolyte held at $p_0 = 760$ mm, then

$$\eta_a = E_a - E_{r0} \pm (RT/n\mathbf{F})\ \ln\ (p/p_0) \qquad [7]$$

[3] Here, and in the following, the upper sign for η is valid for H_2 oxidation, the lower sign for O_2 reduction.

With [5], [6], and [7] one derives the pressure-dependence of the current under conditions where the potential is held constant with respect to a reference electrode which is independent of the partial pressure of the reacting gas. For absolute values of η_a larger than about 0.05V one obtains from [5] the relation

$$\log\ I_a = \text{const} + (1/2)\ \log\ p + (1/2)\ \log\ (\pm\ \eta_a - RT/n\mathbf{F}) \qquad [8]$$

The result [5] is equivalent to an equation already derived by Will (31) in a less general and more complicated manner for the case of limiting hydrogen diffusion to a partly wetted platinum electrode. The present derivation brings out the importance of the ratio v_e/v_f, a fact neglected in previous treatments, and is extended to show for the first time the proper pressure-dependence of current at fixed potentials.

Ionization is rate-limiting.—If the electrode process is rate-limiting then the local true current density $i(x)$ across the solid-liquid interface may, in the absence of H^+ and OH^- concentration effects, be described by the equation

$$i(x) = i_0\ \{\exp\ [\pm\ \alpha n_i \mathbf{F}\eta(x)/RT] - \exp\ [\mp\ (1-\alpha)\ n_i\mathbf{F}\eta(x)/RT]\} \qquad [9]$$

with i_0 being the exchange current, α the transfer coefficient and n_i the valence change in the ionization step.

Again eliminating dx between Eq. [1], [2], and [3], and inserting [9] for $i(x)$, one derives a differential equation between $I(x)$ and $\eta(x)$, which is easily solved in closed form for the case where v_f and v_e are constant throughout the limits involved.

With the boundary conditions stated earlier,[4] one obtains the following result

$$I_a^2 = (2i_0\ RT\ s_f\ v_e/\rho\alpha n_i\mathbf{F})\ \{\exp\ [\pm\ \alpha n_i\mathbf{F}\eta_a/RT] - 1\} - (2i_0\ RT\ s_f\ v_e/\rho(1-\alpha)\ n_i\mathbf{F})\ \{1 - \exp\ [\mp\ (1-\alpha)\ n_i\mathbf{F}\eta_a/RT]\} \qquad [10]$$

which reduces for absolute values of η_a larger than 0.1V to

$$I_a = (2i_0\ RT\ s_f\ v_e/\rho\alpha n_i\mathbf{F})^{1/2}\ \exp\ [\pm\ \alpha n_i\mathbf{F}\eta_a/2\ RT] \qquad [11]$$

If one writes for the hydrogen oxidation process

$$H_2(g) \rightarrow 2\ H^+\ (aq) + 2e^-$$

one derives from [11] with $\alpha = 1/2$ and $n_i = 2$ a theoretical Tafel slope of $b = 0.118$V.

For oxygen reduction, written in the form

$$2e^- + 2\ H^+\ (aq) + O_2 \rightarrow H_2O_2\ (aq)$$

one would calculate with $\alpha = 1/2$ and $n_i = 2$ the same value, namely, $b = 0.118$V.

However, these calculated Tafel slopes are not to be used as "diagnostic criteria" because of the uncertainty relating to values of α and n_i for these ionization processes involving uncharged reacting molecules. Nevertheless, the logarithmic dependence of potential on current remains a valid criterion for indicating limiting ionization rate.

Although equations similar to [10] and [11] have been derived previously (6, 7, 24) the influence of gas pressure on the current I_a for limiting ionization has not yet been discussed. The exchange currents for hydrogen oxidation and oxygen reduction, as written above, depend on concentration of the reacting species as follows

$$i_0\ (H_2) = k_f \cdot 2\mathbf{F} \cdot p_{H_2}{}^{(1-\alpha)} \cdot a_{H^+}{}^{2\alpha}$$

$$i_0\ (O_2) = k_f \cdot 2\mathbf{F} \cdot p_{O_2}{}^{(1-\alpha)} \cdot a_{H^+}{}^{2(1-\alpha)} \cdot a_{H_2O_2}{}^{\alpha} \qquad [12]$$

[4] (x) approaches zero in fact only for infinite values of x_r, that is, for infinite film length.

where the k_f's are the formal rate constants at $E = E_r$. With [7], [11], and [12] one deduces for values of $|\eta_a|$ larger than 0.1V the following dependence of current on pressure at constant applied potential E_a

$$\log I_a = \text{const} + (1/2) \log p \qquad [13]$$

A comparison of [8] and [13] shows that under the stated conditions and for constant E_a the response of current on pressure is nearly identical for rate-limiting diffusion and rate-limiting ionization.

Electrochemical Reduction of O_2

The cell used for the experimental tests is shown in Fig. 2. The electric arrangement schematically is indicated in Fig. 2a. The partly wetted electrode F consisted of a porous graphite rod (National Carbon, grade 60), 25 mm long and 12 mm in diameter. This electrode was mounted vertically into the cell, such that it was half-way immersed in the electrolyte. In order to impose a fixed potential to this porous graphite electrode it was short-circuited to a large $Pb/PbSO_4$ electrode, immersed below the porous graphite rod. The $Pb/PbSO_4$ electrode consisted of a section of a lead-acid storage battery plate, measuring 17 x 30 x 1.5 mm and containing an antimony-free grid alloy (99.95% Pb + 0.05% Ca).

The porous graphite was pretreated in the following manner (37). It was first repeatedly heated to a bright red heat with an oxygen-gas torch. After cooling, the graphite cylinder was dipped for 30 sec into a solution of 2g of $AgNO_3$ in 100 cm^3 H_2O to which was added 0.1 cm^3 of the non-ionic wetting agent Triton X-100. The $AgNO_3$ absorbed in the graphite was then decomposed to metallic silver by heating over a Bunsen flame until a faint red glow appeared. The porous graphite cylinder was then rendered water repellent by saturating it with a dilute aqueous emulsion of Teflon particles, and subsequently baking it in an oven at 360°C for 30 min. At this temperature, the individual Teflon particles are sintered firmly to the silver-impregnated porous graphite matrix. The dilute Teflon emulsion was prepared by stirring 5 cm^3 of 60% commercial du Pont Teflon emulsion into 100 cm^3 of distilled water. The Teflon particles do not prevent the spreading of electrolyte films, but do avoid complete flooding of the pores (Fig. 1). Reference (37) appears to be the first disclosure concerning the use of Teflon for waterproofing electrodes.

With this treatment, the porous graphite electrode was able to reduce oxygen at a rate of up to 70 mA/cm^2 of submerged geometric electrode surface at 760 mm pressure and at 25°C. Molten lead was poured into a central hole of the graphite electrode to establish a soldered joint to the lead-acid storage battery plate below.

The positive electrode was a pure lead wire. Oxygen gas or oxygen-containing gas mixtures could be introduced at the stopcock C. Gases leaving the exit trap were passed through a mercury manostat and collected in a gas burette. The cell pressure could be varied between 25 and 1150 mm Hg by means of the manostat. The electrolyte, 1.225 sp. gr. sulfuric acid, was prepared from cp H_2SO_4 and triple distilled water. All experiments described here were performed at 25°C.

A first series of experiments was carried out by evacuating the cell to 25 mm Hg and filling it with pure O_2 at a given pressure. Then stopcock C was rapidly closed and a constant current applied between the two cell terminals. The current was adjusted to a value that no O_2 was leaving the exit trap, the pressure remaining constant. In this manner, oxygen gas was anodically generated at the positive electrode and cathodically reduced at the graphite electrode at equal rates, thus simulating the steady state condition during overcharge of a sealed lead-acid cell (3). The steady-state current was investigated as a function of partial oxygen pressure. Also studied was the influence of inert foreign gases, N_2 and He, on the steady state current.

In the current range between 1 and 500 mA, the potential of the combined graphite-lead electrode remained at the reversible $Pb/PbSO_4$ potential, that is at — 0.368V *vs.* H_2, corresponding to a polarization of the O_2/H_2O_2 couple in the order of one volt. At steady state currents below 300 mA, the logarithm of the current was found to depend linearly on the logarithm of O_2 pressure (Fig. 3), the slope being close to that predicted by [13]. At higher currents, there is a pronounced deviation from the predicted behavior, due probably at least in part to lagging gas flow in the pores of the electrode. Local heating might create relatively high water vapor pressures in the interior of the electrode, hindering the diffusion of O_2. Local heating might also be the reason for the somewhat higher than theoretical slope.

In the presence of foreign gases, the steady-state currents were strongly decreased. For instance at a constant partial O_2 pressure of 100 mm Hg, the current decreased from 170 mA in pure O_2 to 105 mA in 80% He/20% O_2 and even to 45 mA in 80% N_2/20% O_2.

This drastic reduction of the steady state current in the presence of foreign gas is due to the accumulation of inert gas in the pores and a concurrent depletion of oxygen therein. As oxygen is being electrochemically removed, the inert gases are left behind, effectively decreasing the partial oxygen pressure in the pores. This depletion effect has been treated theoretically by Winsel (38).

In order to study the influence of electrode potential on the rate of O_2 reduction, the lead electrode was disconnected from the porous graphite electrode, and various constant currents applied between the positive lead wire and the porous graphite electrode. The potential of the latter now became a function of the applied current, and was followed with a Hg/Hg_2SO_4

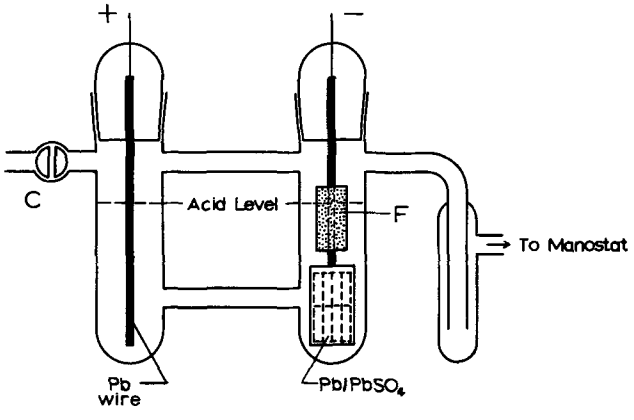

Fig. 2. Experimental cell for the study of electrochemical reduction of oxygen on partly immersed electrodes.

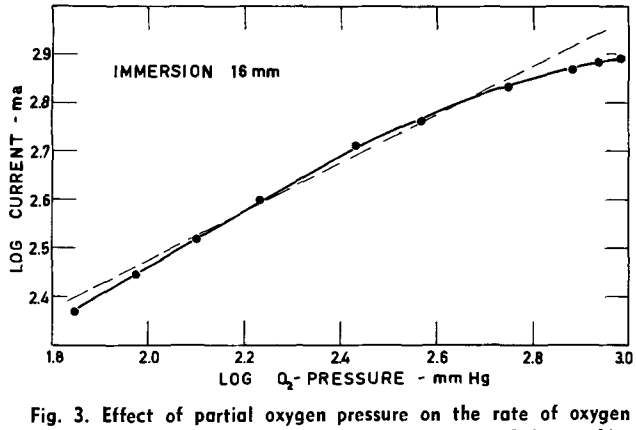

Fig. 3. Effect of partial oxygen pressure on the rate of oxygen reduction on a silver-activated, porous waterproofed graphite electrode in sulfuric acid at —0.368V vs. H_2.

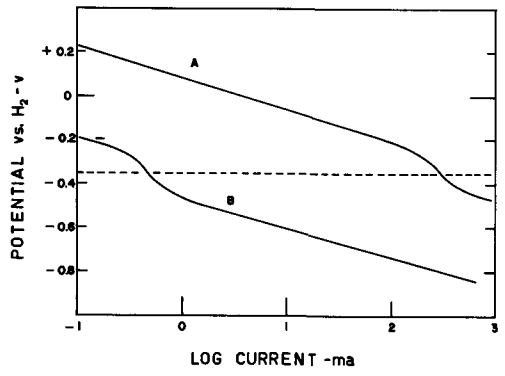

Fig. 4. Rate of oxygen reduction as a function of electrode potential at 760 mm Hg oxygen pressure. Curve A, oxygen reduction; curve B, hydrogen evolution.

reference electrode, not shown in Fig. 2. The results of these experiments are shown in Fig. 4. Curve A represents measurements in pure oxygen at 760 mm Hg, maintained by steady external gas flow through the manostat. The semilogarithmic plot is linear up to currents of 200 mA, with a Tafel slope of 0.130. At higher currents, the curve shows a deviation toward negative potentials, indicating a less rapid increase of the O_2 ionization in the potential range between —0.2 and —0.4V. It is possible that increased water vapor pressure due to local heating, as indicated earlier, as well as concentration effects in the film might enter into the picture. At the most negative potentials H_2 evolution sets in, while simultaneously O_2 reduction proceeds at a high rate.

The linear relation between potential and logarithm of current over three decades, between 0.2 and 200 mA, suggests, in accordance with Eq. [11], that the process is limited by the ionization rate.

Curve B of Fig. 4 was obtained with the graphite electrode completely submerged in the electrolyte. Under these conditions, hydrogen begins to evolve at the graphite electrode even at small currents, since hardly any oxygen reaches the electrode. The Tafel slope for hydrogen evolution was found to be 0.13 which is a conventional value. Of interest is the relatively high absolute value for the hydrogen overvoltage on the silver-Teflon-treated porous graphite electrodes used here. At the potential of the $Pb/PbSO_4$ electrode, indicated in Fig. 4 by a dotted line, extrapolation of the Tafel line yields a current of 10^{-4}A.

The deviation of the curve B toward more positive potentials at low currents is probably due to the effect of dissolved oxygen, diffusing toward the submerged graphite electrode, and causing a depolarizing effect on hydrogen overvoltage.

In sulfuric acid, the silver-activated porous graphite electrodes cannot be held at potentials higher than about + 0.4V *vs.* H_2, otherwise Ag starts to dissolve anodically. The Ag/Ag_2SO_4 electrode has a potential of about + 0.6V, and Ag_2SO_4 is appreciably soluble in H_2SO_4. For practical O_2-consuming electrodes in sealed lead-acid cells, where a long life is required, the potential should be kept below about 0.1V since the partly wetted structure encounters locally much higher potentials than those applied externally. Oxygen consuming electrodes catalyzed with platinum may be held at potentials much more positive, *e.g.*, up to +0.9V *vs.* H_2.

Experiments on Electrochemical Oxidation of H_2

The experimental set-up used for hydrogen oxidation is schematically shown in Fig. 5. The cell again contained three electrodes: (*i*) A positive electrode consisting of a section of a lead-acid battery positive plate, 7 x 2 x 0.6 cm, with calcium alloy grid; (*ii*) a negative electrode of a pure lead wire (99.99% Pb), and (*iii*) a partly wetted porous graphite electrode. This simulates conditions for sealed lead-acid cell operation on the H_2

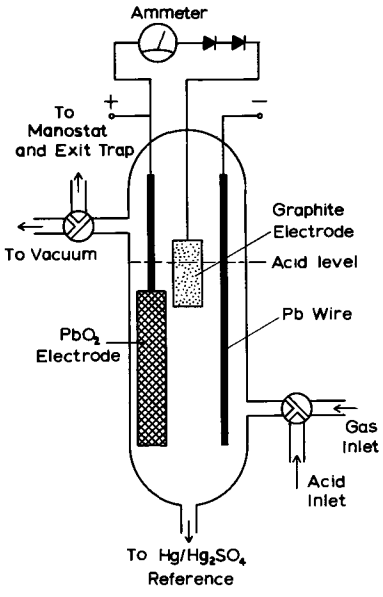

Fig. 5. Experimental cell for the study of hydrogen oxidation on partly immersed electrodes.

cycle (3). The graphite electrode was a cylinder machined from National Carbon grade 60 porous graphite, 25 mm long and 12 mm in diameter. After repeated heating of the graphite cylinder to a bright red glow at about 800°C with an oxygen-gas torch, it was cooled and impregnated with a solution of 2g, of $PdCl_2$ in 100 cc of 10% HCl. After drying under infrared light, the graphite cylinder was heated over a Bunsen flame to dull red heat or about 550°C to decompose the palladium salt. The graphite was then waterproofed by immersion in a dilute Teflon emulsion, prepared by mixing 10 cm^3 of du Pont Teflon 30 emulsion with 100 cm^3 of water, containing 0.1 cm^3 of a non-ionic wetting agent (Triton X-100). After drying by infrared light at 100°C, the graphite cylinder was then baked at 400°C for 30 min, a procedure which destroyed the wetting agent and firmly sintered the Teflon particles to the palladium-impregnated graphite matrix (39). The graphite cylinder was tapped centrically to a depth of 12 mm at the upper end to receive a threaded nonporous graphite rod to which electrical contact was made by a platinum wire.

To start the experiment, the cell was filled with H_2, and the PbO_2 electrode connected to the graphite electrode through a low-resistance ampere-meter and voltage regulating means, *e.g.*, diodes or a variable voltage supply. The purpose of these means was to keep the potential of the graphite electrode at a less positive potential than that of the PbO_2 electrode (39). As constant currents were applied between the terminals, hydrogen generated at the negative lead electrode was electrochemically oxidized at the positive graphite electrode.

Steady state currents were determined for various H_2 pressures in the cell. At 760 mm Hg hydrogen pressure, electrodes activated in the described manner were able to oxidize hydrogen at rates up to 100 mA/cm^2 of geometric submerged electrode area. For a submerged area of 4.6 cm^2, currents up to 460 mA were therefore obtained. At the highest currents, the voltage drop across the two silicon diodes in series shown in Fig. 5 was about 1.32V. Since the open circuit potential of the PbO_2 electrode in sulfuric acid of 1.225 sp. gr. is 1.72V, the graphite electrode was forced to a potential of about 0.40V *vs.* H_2 at this current, and slightly more positive at smaller currents.

The influence of H_2 partial pressure on the steady state current at constant polarization of about 0.4V is illustrated in Fig. 6. It is clearly apparent that the current is approximately proportional to the square root of pressure, in agreement with Eq. [8]. The somewhat

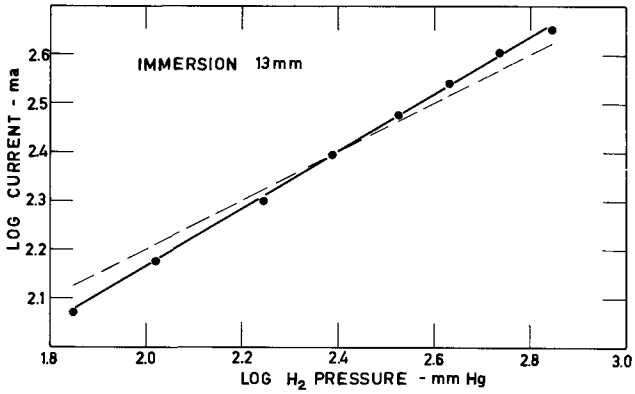

Fig. 6. Dependence of hydrogen oxidation current on hydrogen pressure at 0.4V polarization.

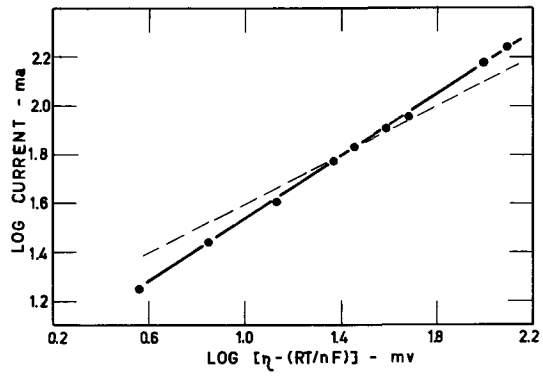

Fig. 8. Logarithm of current as a function of log $[\eta - (RT/nF)]$

higher than theoretical slope is probably due to heating effects in the wetting films.

The presence of foreign gases decreased the current. At 650 mm Hg of partial nitrogen pressure, *e.g.*, a partial hydrogen pressure of 130 mm Hg was required to produce 100 mA. In the presence of 430 mm Hg of carbon dioxide, the partial hydrogen pressure had to be 150 mm Hg to achieve the same steady state current of 100 mA. In the absence of foreign gases, the same current was obtained already at 65 mm Hg hydrogen pressure. Hydrogen diffuses considerably faster than oxygen. The accumulation of foreign gas in the pores produced therefore a smaller effect in the case of H_2 oxidation than of O_2 reduction.

Steady state currents were also investigated as a function of electrode potential at constant H_2 pressure of 760 mm Hg. A typical result is shown in Fig. 7. The electrode potential is here given with respect to a reversible H_2 electrode in the same solution. With the particular electrode immersion depth used in this experiment, the current reached a maximum of 190 mA when the hydrogen electrode potential was +1.5 to +1.7V, then passed through a minimum at +1.9V, and increased rapidly at more positive potentials. At the point of minimum current, visible oxygen evolution began on the graphite electrode. Above 1.9V, the relation between potential and logarithm of current became linear, representing a Tafel line for oxygen evolution. The result of Fig. 7 is very similar to a curve obtained by Will (23) for the oxidation of hydrogen on a partly immersed Pt rod. In Fig. 8, the logarithm of current has been plotted against

$$\log\left[\eta_a - \frac{RT}{n\mathbf{F}}\right]$$

The straight line up to potentials where adsorption inhibition sets in [3], that is at 1.5V, indicates, in accordance with Eq. [8], that H_2 diffusion through the wetting film is rate limiting. Solubility and diffusion coefficient of H_2 in sulfuric acid (40, 41) are smaller than the corresponding values for O_2. Again, the higher than theoretical slope is probably caused by local heating in the electrolyte films.

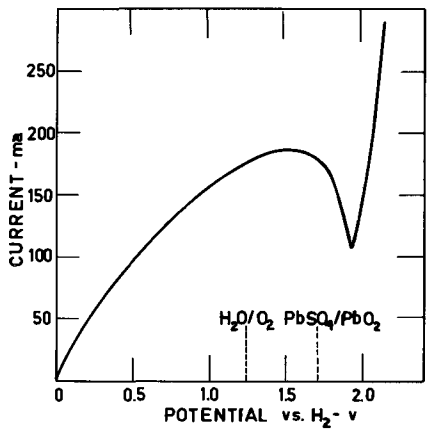

Fig. 7. Hydrogen oxidation rate as a function of electrode potential.

Conclusions

From the result of the present study, it may be concluded that for oxygen reduction on silver-activated, waterproofed porous graphite electrodes in sulfuric acid, the rate of ionization is the current limiting factor, except at the very highest currents investigated, where concentration effects started to interfere. For hydrogen oxidation on palladium-activated, waterproofed porous graphite electrodes in sulfuric acid, the rate of H_2 diffusion through the wetting films was limiting, except at the highest anodic potentials, where the rate of ionization became inhibited by adsorbed oxygen.

The technically important result is, that both hydrogen and oxygen may be consumed at high rates in sealed lead-acid cells on partly immersed porous, waterproofed electrodes, held at suitable potentials for the corresponding reactions.

Acknowledgment

The authors are indebted to the management of the Electric Storage Battery Company, in particular to Dr. R. A. Schaefer, for permission to publish this investigation.

Manuscript submitted Aug. 17, 1964; revised manuscript received May 22, 1969.

Any discussion of this paper will appear in a Discussion Section to be published in the June 1970 JOURNAL.

REFERENCES

1. E. Justi and A. Winsel, "Fuel Cells," Franz Steiner Verlag GmbH, Weisbaden (1962); W. Vielstich, "Brennstoffelemente," Verlag Chemie GmbH, Weinheim (Bergstrasse), (1965); R. F. Gould, "Fuel Cell System," Advances in Chemistry Series, Am. Chem. Soc., Washington, D. C. (1965).
2. G. Heise, *This Journal*, **75**, 147 (1939); E. Berl, *ibid.*, **76**, 281 (1939); E. A. Schumacher and G. W. Heise, *ibid.*, **99**, 191C (1952).
3. P. Ruetschi and J. B. Ockerman, *Electrochem. Technol.*, **4**, 383 (1966).
4. J. J. Coleman, *This Journal*, **90**, 545 (1946); **98**, 29 (1951).
5. V. S. Daniel-Beck, *Zhur. Fiz. Khim.*, **22**, 697 (1948).
6. A. N. Frumkin, *ibid.*, **23**, 1477 (1949).
7. O. S. Ksenzhek and V. V. Stender, *Dokl. Akad. Nauk. SSSR*, **106**, 487 (1956); **107**, 280 (1956).
8. O. S. Ksenzhek and V. V. Stender, *Zhur. Fiz. Khim.*, **31**, 117 (1957).
9. O. S. Ksenzhek, and V. V. Stender, *Zhur. Priklad Khim.*, **32**, 110 (1959).
10. O. S. Ksenzhek, *Zhur. Fiz. Khim.*, **36**, 243, 633 (1962).

11. J. Euler, *Z. Elektrochem.*, **63**, 1008 (1959).
12. J. Euler and L. Horn, *ibid.*, **64**, 1114 (1960).
13. J. Euler and W. Nonnenmacher, *Electrochim. Acta*, **2**, 268 (1960).
14. J. Euler and K. N. Muller, *ibid.*, **8**, 949 (1963).
15. J. Euler, *ibid.*, **7**, 205 (1962); **8**, 409 (1963).
16. R. Buvet, M. Guillon, and B. Warszawski, *ibid.*, **6**, 113 (1962).
17. J. S. Newman and C. W. Tobias, *This Journal*, **109**, 1183 (1962).
18. P. Hersch, *Nature*, **180**, 1407 (1957); *Corrosion Technol.*, **6**, 293 (1959).
19. H. C. Weber, H. P. Meissner, and D. A. Sama, *This Journal*, **109**, 884 (1962).
20. H. J. R. Maget and R. Roethlein, *ibid.*, **112**, 1034 (1965); **113**, 581 (1966).
21. N. A. Fedotov, V. I. Veselovsky, K. I. Rosenthal, and Y. A. Mazitov, "Batteries," p. 283, Collins, Editor, Pergamon Press, Symposium Publications Division (1965).
22. D. N. Bennion and Ch. W. Tobias, *This Journal*, **113**, 589 (1966).
23. F. G. Will, *ibid.*, **110**, 145, 152 (1963).
24. A. Winsel, *Z. Elektrochem.*, **66**, 287 (1962); *Advanc. Energy Conversion*, **3**, 427, 677 (1963).
25. R. P. Iczkowski, *This Journal*, **111**, 605, 1078 (1964).
26. E. A. Grens, R. M. Turner, and T. Katan, *Advanc. Energy Conversion*, **4**, 109 (1964).
27. L. G. Austin, M. Ariet, R. D. Walker, G. B. Wood, and R. H. Comyn, *J. and EC. Fundamentals*, **4**, 321 (1965).
28. J. A. Rockett and R. Brown, *This Journal*, **113**, 207, 865 (1966).
29. E. N. Lightfoot, *ibid.*, **113**, 614 (1966).
30. E. A. Grens, *J. and EC. Fundamentals*, **5**, 542 (1966).
31. R. C. Burshtein, V. S. Markin, A. G. Pshenichnikov, V. A. Chismadgev, and Y. G. Chirkov, *Electrochim. Acta*, **9**, 773 (1964).
32. O. S. Ksenzhek, *Zhur. Fiz. Chem.*, **37**, 1298 (1963).
33. O. S. Ksenzhek, E. A. Kalinovskii, and E. L. Baskin, *Zhur. Priklad. Khim.*, **37**, 1045, 2619 (1964).
34. O. S. Ksenzhek, *Electrochim. Acta*, **9**, 629 (1964).
35. O. S. Ksenzhek, "Fuel Cells," p. 1, Bagotskii and Vasilev, Editors, Consultants Bureau, New York (1966).
36. Y. A. Chizmadzhev, *ibid.*, p. 111.
37. P. Ruetschi, U. S. Pat. 2,951,106 (filed Feb. 19, 1957, issued Aug. 30, 1960).
38. W. Baucke and A. Winsel, *Advanc. Energy Conversion*, **3**, 613 (1963).
39. P. Ruetschi and B. D. Cahan, U.S. Pat. 3,080,440 (filed Dec. 31, 1959, issued March 3, 1963).
40. P. Ruetschi and R. F. Amlie, *J. Phys. Chem.*, **70**, 718 (1966).
41. P. Ruetschi, *This Journal*, **114**, 301 (1967).

Brief Communications

Electrodeposition of Titanium Diboride Coatings

David Schlain,* Frank X. McCawley,* and Charlie Wyche

College Park Metallurgy Research Center, Bureau of Mines, U. S. Department of the Interior, College Park, Maryland

Adherent, smooth coatings of titanium diboride, metallic in appearance and 3 to 6 mils in thickness, were electrodeposited on Inconel[1] from a molten salt electrolyte at 900°C (Fig. 1). The electrolyte consisted chiefly of $NaBO_2$ and $LiBO_2$ with smaller amounts of Na_2TiO_3, Li_2TiO_3, and TiO_2. The electrolytic cell was operated under an argon atmosphere at cathode and anode current densities of approximately 0.4 A/in.^{2} (6.2 A/dm^2). The coating was formed at the rate of about 1 mil/hr. The soluble titanium anode was stationary and the cathode was rotated at 250 rpm. The cell voltage was approximately 0.3V.

The deposits were identified as TiB_2 by x-ray diffraction. Titanium and boron were the only elements detected in the deposits by optical spectrographic analyses. However, it should be noted that both of the sampling techniques used, the laser microprobe and electrode transfer, may reduce the sensitivity of detection to the point where many trace elements would not be detected. Hardness measurements were made on surfaces and cross sections of the titanium diboride deposits using a Tukon Microhardness Tester with a Knoop indentor, a X50 objective, and a 100g load. Variations in hardness on the cross sections were random with respect to distance from the substrate; there was no indication of diffusion. The data in Table I show that the cross-section hardness of the electrodeposits is approximately the same as the hardness value Lynch and his co-workers obtained for annealed single crystals of TiB_2 (1), but that it is higher than those for unannealed single crystals of TiB_2 (1) or for hot-pressed material (2). However, the surface hardness of the electrodeposits was higher than any known value for TiB_2. Figure 2 is a cross section of a 2.3 mil thick deposit showing columnar structure and good bonding to the substrate.

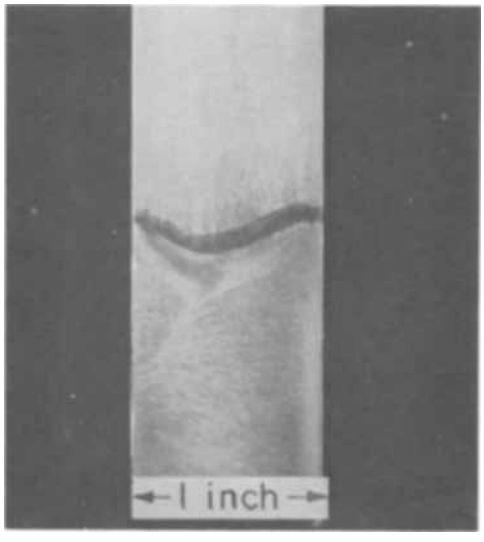

Fig. 1. Titanium diboride coating on Inconel

* Electrochemical Society Active Member.

[1] Reference to trade names or company names is made for identification only and does not imply endorsement by the Bureau of Mines.

Table I. Average Knoop hardness numbers

	KHN_{100}	Average deviation
Surfaces of TiB_2 electrodeposits	5000	300
Cross sections of TiB_2 electrodeposits	3200	200
Cross section Inconel substrate	232	5
Tungsten carbide[a]	1760	90
Hot-pressed TiB_2[b]	2710	
Single crystals TiB_2,[c] as grown	2800 ± 250	
Single crystals TiB_2,[c] annealed	3370 ± 375	

[a] Hardness measured in order to evaluate technique. Literature value for tungsten carbide is 1880 (3).
[b] Value given by Powell, p. 367 (2).
[c] Values given by Lynch and co-workers (1).

Initially, the electrolyte contained 39.08% $NaBO_2$ (33.08 m/o), 58.62% $LiBO_2$ (65.79 m/o), 0.99% Na_2TiO_3 (0.39 m/o), 0.76% Li_2TiO_3 (0.39 m/o), and 0.55% TiO_2 (0.38 m/o). Residual moisture was carefully removed from each component before preparing the mixture. Prior to the preparation of the coatings the electrolyte was conditioned by 12 hr of electrolysis with a titanium anode and a cathode of molybdenum or Inconel. During the conditioning step, the titanium content of the bath increased from 1 to 2.3%. Deposits made during this period consisted of dark, fine, nonadherent powder over a bright, consolidated, adherent coating. The quantity of material which was in the form of powder became progressively less with successive deposits. The powder was identified by x-ray diffraction as chiefly TiB_2 with a minor amount of TiO. At the end of the series of experiments the platinum crucible was found to have been attacked; the corrosion product contained platinum and titanium.

Andrieux (4) and Powell (2) have described the electrodeposition of TiB_2 from molten baths such as MgO, MgF_2, $2B_2O_3$ and ½ TiO_2 or 2CaO, CaF_2, $2B_2O_3$, and ¼ TiO_2, but the material was deposited only in the form of fine crystals or powders. The use of powder metallurgy techniques is required to form such powders into massive articles. Mellors and Senderoff described the electroforming and the electrodeposition of coherent coatings of ZrB_2 from a molten bath of LiF-KF-K_2ZrF_6 containing 12 w/o KBF_4 at 800°C (5, 6).

Fig. 2. Cross section of titanium diboride coating on molybdenum. Deposit is 2.3 mils thick and has columnar structure. Magnification approx. 430X.

Satisfactory coatings of TiB_2 will find many applications. The material is extremely hard and has high electrical conductivity, low volatility, and a high melting point (*ca.* 2600°C). It is stable up to the melting point. Titanium diboride is resistant to oxidation up to 1400° to 1500°C, superior in this respect to most other borides.

Manuscript received May 5, 1969.

Any discussion of this paper will appear in a Discussion Section to be published in the June 1970 JOURNAL.

REFERENCES

1. C. T. Lynch, S. A. Mersol, and F. W. Vahldiek, *Trans. Metallurgical Society AIME*, **233**, 631 (1965).
2. C. F. Powell, "Borides," in "High-Temperature Materials and Technology" by I. E. Campbell and E. M. Sherwood, p. 349, John Wiley & Sons, Inc., New York (1967).
3. Handbook of Physics and Chemistry, p. F-15, Chemical Rubber Publishing Co., 47th ed., 1966-67.
4. J. L. Andrieux, *Rev. Met.*, **XLV**, Nos. 1 & 2 (1948).
5. G. W. Mellors and S. Senderoff, Canadian Pat. 688,546, June 9, 1964.
6. G. W. Mellors and S. Senderoff, *This Journal*, **113**, 60 (1966).

Electrochemical Reduction of the Benzene Ring by Electrogenerative Hydrogenation

Stanley H. Langer and Sergei Yurchak

Chemical Engineering Department, University of Wisconsin, Madison, Wisconsin

Benzene is notoriously difficult to hydrogenate by conventional cathodic electrochemical means, often requiring complex solvent mixtures and high potentials while reaction does not proceed stoichiometrically (1-5). This prompted us to attempt the electrochemical reduction of benzene with the electrogenerative hydrogenation technique (6) whereby the favorable thermodynamic driving force of the reduction is brought to bear on the reaction; a positive potential is generated and no external power source is necessary. Hydrogen (at the anode) and benzene (at the cathode) were reacted at catalytic porous electrodes separated by strong acidic electrolyte for hydrogen ion transport with generated current being conducted through an external circuit. Benzene reacted to give cyclohexane at a porous platinum black electrode (7, 8) in a conventional filter paper matrix cell (6-8) as well as in a horizontal liquid cell in which a platinized platinum screen electrode was placed at the liquid aromatic-liquid electrolyte interface.

Over-all reaction may be represented as

$$\text{Anode:}\quad 3H_2 \rightarrow 6H^+ + 6e \qquad [1]$$

$$H^+ \text{ transported through electrolyte} \qquad [2]$$

$$\text{Cathode:}\quad 6H^+ + 6e + C_6H_6 \rightarrow C_6H_{12} \qquad [3]$$

Some data from our ensuing study of electrogenerative hydrogenation of benzene, toluene, and fluorobenzene vapors on several American Cyanamid porous noble metal-Teflon electrodes (7, 8) are reported in Table I.

Nitrogen saturated with the aromatic compound at room temperature was passed through the cathode compartment at an excess rate so as not to affect current. The platinum black hydrogen anodes exhibit

Table I. Electrogenerative hydrogenation
Room temperature; 3N perchloric acid electrolyte

Compound	Cathode[a]	Open-circuit voltage	Calculated open-circuit voltage[b]	Current density V vs. H_2 ref. 0.10	0.07
Benzene*	Pt	0.14[c]	0.17	1.4 mA/cm²	6.0
Benzene	Ru	>0.2[d]	0.17	0.2	0.5
Toluene[1]	Pt	0.13[c]	0.16	0.35	2.5
Toluene	Pd	>0.17[d]	0.16	0.2	0.9
Fluorobenzene†	Pt	>0.20	0.16[e]	2	7.0
Fluorobenzene	Pd	0.46	0.16[e]	0.3	0.8
Cyclohexene*	Pt	0.16	0.39	19	37

[a] Catalyst loading is 9 mg/cm² on tantalum screen.
[b] Estimated from standard free energies of formation assuming complete hydrogenation. Values obtained for reactants and products as follows:
* Latest values R. C. Wilhoit, private communication.
[1] F. D. Rossini, *et al.*, American Petroleum Institute Project 44.
† Estimated from group contributions, O. A. Hougen, K. M. Watson, R. A. Ragatz, "Chemical Process Principles," Vol. 2, 2nd ed., J. Wiley & Sons, New York, 1959, Chap. 25.
[c] Cathode gas flow interrupted.
[d] Unstable.
[e] $E° = 0.45V$ for $C_6H_5F_{(g)} + H_{2(g)} \rightarrow C_6H_{6(g)} + HF_{(g)}$.

negligible polarization at the current densities of this study (7, 8). The electrolyte matrix consisted of 4 sheets of filter paper saturated with 3*N* perchloric acid. All experiments were performed at room temperature. The system was designed so that coulometric data could be obtained (6). The current generated by the hydrogenation cell was equivalent to hydrogen consumed as measured by gas volume changes. The effluent cathodic product gas mixture was collected in gas bulbs and analyzed by gas-liquid chromatography.

Under favorable reaction conditions, the open-circuit potentials of Table I were surprisingly close to the calculated ones as had been observed for olefins (6). Hexafluorobenzene also gives an open-circuit potential (~ 0.19V); this and consideration of our earlier results for olefin-hydrogen cells (6) would indicate that the characteristic open-circuit potentials of these cells does not result from dissociative carbon-hydrogen adsorption (9, 10) although this process probably takes place under some conditions on the electrode surface. However, with cyclohexene on platinum, the open-circuit potential could be a consequence of disproportionation and bezene (11, 12) formation at the cathode. Indeed benzene was found in the effluent stream at all current densities studied.

On platinum, while benzene was hydrogenated quantitatively to cyclohexane (cyclohexene was less than 0.1% if present at all), electrochemical hydrogenation of toluene to methylcyclohexane accounted for only about 80% of the observed current; the remainder was due to simple electrochemical hydrogen transport (13, 14) to the reducing electrode gas stream from whence it was analyzed in the exit stream. The electrochemical reduction of fluorobenzene gave an approximately equal mixture of cyclohexane and benzene, probably a result of relatively strongly adsorbed fluorobenzene displacing benzene. The hydrogenolysis of the carbon-fluorine bond to give benzene is of interest since a similar hydrogen treatment in a chemical system gave only cyclohexane (15). With the other metals and substrates of Table I, electrochemical hydrogen transfer accounted for at least 75% of the generated current. It would appear that electrochemical discharge of hydrogen ions to form atoms and a subsequent addition to the substrate (16), where kinetically favored, is the initiating sequence of events in aromatic electrogenerative hydrogenation.

The currents of Table I at given voltages are an approximate measure of over-all reaction rates especially when product analyses are taken into account. On this basis, the order for electrochemical hydrogenation of aromatics is Pt >> Pd ~ Ru—approximately the same as that observed for chemical hydrogenation (17). However, the low electrochemical activity of palladium relative to platinum is in contrast to the earlier results of Langer and Landi (6) for electrogenerative ethylene hydrogenation where the metal activities were quite comparable. A similar diminution in activity has been observed for chemical hydrogenation of benzene (18,19). In a nitrogen-hydrogen concentration cell (13, 14) the activity sequence was Pt ≈ Pd > Ru with platinum being more active than ruthenium by less than a factor of two. Thus differences in reduction rate would seem to be an indication of catalytic effectiveness for reaction of aromatic substrate with hydrogen atoms (under these conditions) rather than a measure of rate of hydrogen ion discharge. Improving catalytic activity through alloying of platinum as reported for ruthenium-platinum (20) catalysts would seem to be a strong possibility. Because of its advantages and the similarity between electrogenerative catalytic activity and conventional catalytic hydrogenation, we hope to continue our investigation of electrogenerative aromatic systems.

Acknowledgment

We gratefully acknowledge the support of this work by the Wisconsin Alumni Research Foundation and the Union Carbide Corporation as well as the gift of some commercial electrodes from the American Cyanamid Company.

Manuscript received April 1, 1969.

Any discussion of this paper will appear in a Discussion Section to be published in the June 1970 JOURNAL.

REFERENCES

1. A. Misono, T. Osa, T. Yamagishi, and T. Koduma, *This Journal*, **115**, 266 (1968).
2. R. A. Benkeser, E. M. Kaiser, and R. F. Lambert, *J. Am. Chem. Soc.*, **86**, 5272 (1964).
3. H. W. Sternberg, R. E. Markby, I. Wender, and D. M. Mohilner, *ibid.*, **89**, 186 (1967).
4. G. A. Bogdanovskii, L. G. Feoktistov, and A. I. Shlygin, *Nauch. Doklady Vysshei Shkoly, Khim. i Khim. Tekhnol.*, 443 (1958); *C. A.*, **53**, 920e (1959).
5. P. S. Farrington, and D. T. Sawyer, *J. Am. Chem. Soc.*, **78**, 5536 (1956); and references therein.
6. S. H. Langer and H. P. Landi, *ibid.*, **85**, 3043 (1963); **86**, 4694 (1964).
7. S. H. Langer and H. P. Landi, U.S. Pat. 3,248,267, April 26, 1966.
8. R. G. Haldeman, W. P. Colman, S. H. Langer, and W. A. Barber, in "Fuel Cell Systems," R. F. Gould, Editor, Advances in Chemistry Series 47, American Chemical Society, Washington, D.C., 1965, p. 106.
9. O. A. Petrii, B. I. Podlovchenko, A. N. Frumkin, and H. Lal, *J. Electroanal. Chem.*, **10**, 253 (1965).
10. R. L. Burwell, Jr., *Chem. and Eng. News*, **44**, pp. 56-67, Aug. 22, 1966.
11. S. Carrá and V. Ragaini, *Tetrahedron Letters*, 1079 (1967).
12. S. Carrá, P. Beltrame, and V. Ragaini, *J. Catal.*, **3**, 353 (1964).
13. S. H. Langer and R. G. Haldeman, *Science*, **142**, 225 (1963).
14. G. M. Barrow, "Physical Chemistry," p. 605, McGraw Hill Book Co., Inc., New York (1961).
15. F. Swarts, *Acad. roy. Belg. Classe sci.*, **6**, 399 (1920).
16. F. Hartog, J. H. Tebben, and C. A. M. Weterings, "Proc. 3rd International Congress on Catalysis," W. M. H. Sachter, G. C. A. Shuit and P. Zwietering, Editors, Vol. II, North-Holland Publ. Co., Amsterdam, 1965, pp. 1210-1214.
17. G. C. Bond, "Catalysis by Metals", pp. 311-320, Academic Press, Inc., New York, 1962.
18. J. R. Anderson and C. Kemball, *Adv. Catalysis*, **9**, 51 (1957).
19. A. Amano and G. Parravano, *ibid.*, **9**, 716 (1957).
20. D. V. Sokol'skii, K. K. Dzhardamalieva, A. G. Sarmurzina, and T. Tonamov, *Dokl. Akad. Nauk. SSSR*, **176**, 1093 (1967).

Mechanical Properties of Metal Oxide Films

J. C. Grosskreutz

Center for Applied Research on Materials, Midwest Research Institute, Kansas City, Missouri

ABSTRACT

A brief review is given of mechanical property measurements on oxide films. This review is followed by a detailed discussion of the mechanical and fracture properties of anodic aluminum oxide films as observed in the author's laboratory. Extensive measurement of Young's modulus, E_c, and fracture strain, ϵ_f, for separated films 3000Å thick is reported as a function of environmental water vapor pressure. The fracture of these unsupported films is shown to occur by a brittle mechanism. Mechanical properties of adhering aluminum oxide films are given as a function of their thickness. These oxides were observed to fracture either at slip steps, or at right angles to the tensile axis in a regularly spaced fashion. A theory of adhering oxide fracture is discussed which accounts well for the observations. An equation which describes the spacing d of regular oxide fracture cracks as a function of substrate strain ϵ is given in the form $\ln(\epsilon/\epsilon_o) = k\sqrt{t}(1/d - 1/d_o)$, where (ϵ_o, d_o) are the initial conditions for regular fracture, t is the oxide thickness, and k is a constant.

The effect of oxide coatings on the mechanical properties of the metal substrate was first observed nearly 35 years ago (1). In general the effect of the coating is to increase the critical resolved shear stress for plastic yielding in the substrate. The thickness of the oxide and the thickness of the substrate both have an important bearing on the magnitude of the effect. Not only oxide layers, but other surface films as well can significantly affect the macroscopic stress-strain behavior (2). More importantly, surface oxide layers can often have a direct effect on the fracture of the substrate, particularly in the cases of fatigue and stress corrosion cracking.

The above macroscopic effects are the result of certain microscopic, surface events which depend sensitively on both the presence and the properties of the oxide film. For example, dislocations can either be attracted or repelled by the surface, depending on whether the elastic modulus of the oxide, E_c, is less than, or greater than, the modulus of the substrate E_s (3). For a certain range of the ratio E_c/E_s, dislocations become trapped at the oxide-metal interface (4). The way slip steps develop at a surface will be quite different depending on whether or not the oxide fractures. For example, the formation of slip band intrusions and extrusions, which act as fatigue crack nuclei, can occur only after rupture of the original oxide film. Finally, microfractures in the protective oxide coating on metals like stainless steel and titanium may provide the initiation site for stress corrosion cracking.

Any quantitative treatment of these microscopic events requires a knowledge of the mechanical and fracture properties of the oxide film as well as the substrate metal. For this reason, there has recently developed an intense interest in the measurement of these oxide properties. It is not enough to assume that the properties of bulk alumina, for example, can be used to describe a natural aluminum oxide layer which is amorphous and only 50Å thick. Rather, it is necessary that measurements be performed on very thin oxide films which have been separated from their substrate, or that measurements on the oxide-metal system be made in such a way that the mechanical and fracture properties of the oxide can be inferred.

Except for some early measurements of the tensile strength of completely oxdized wire ($\sim$ 0.010 in. — 0.030 in. diameter) (5), the first comprehensive study of thin oxide films was made by Bradhurst and Leach on adhering and separated Al_2O_3 films (6). The fracture strain of adhering films was measured by a variety of techniques, and stress-strain curves of separated films 1500Å thick were obtained from which Young's modulus and the fracture stress and strain could be obtained. The thin films were about five times stronger than bulk alumina and could be strained about ten times more prior to fracture. In the five years since these results were published, several other workers have attacked the problem with various modifications in technique (4, 7-9).

Reliable measurement of the mechanical properties of thin oxide films, whether adhering or separated, is difficult. Nearly always the natural oxide must be enhanced in thickness by anodization or thermal treatment in order to make any measurement at all. Thus, the question remains open as to whether the results are indeed representative of the natural oxide layer. There is also a large scatter in the measured values of moduli and fracture stresses which is most likely due to variations in the films or to problems in experimental technique. These difficulties notwithstanding, the results thus far reported have been quite useful.

In the paper which follows, the mechanical and fracture properties of both separated and adhering aluminum oxide films are reported. Part of the paper is an extension of earlier work which demonstrated the effects of water vapor on the properties of separated films (4). In addition, some new measurements are given for the fracture strain of adhering films as a function of their thickness. Finally, an extensive analysis of the fracture of adhering coatings is given, and the results are compared with both existing and new data. An important feature of this work is the ability to deal quantitatively with the fracture of adhering films.

Mechanical Properties of Separated Al_2O_3 Films

The oxide films used in these measurements were grown to 3000Å thick on 99.99% Al in tartaric acid electrolyte.[1] These anodic films are coherent and amorphous and resemble closely the natural oxide film (10). Thin film specimens 2 x 6 mm were prepared by (*a*) coating the anodized sheets of aluminum with Kodak KMER photoetch resist; (*b*) placing a mask over the sheet so as to expose a large number of rectangular areas 2 x 6 mm to ultraviolet light; (*c*) removing the unexposed photoresist and dissolving the unprotected anodic film in 2% hydrofluoric acid solution; and (*d*) removal of the exposed photoresist which still covered the "islands" of aluminum oxide. The sheet of anodized aluminum was then cut into individual rectangles, each containing an Al_3O_2 sample. The thin films were removed from these substrates by amalgamation in mercuric chloride.

[1] Thickness was measured by (*i*) using the growth relation of 13.5 Å/V in this electrolyte, and (*ii*) by direct measurement in the electron microscope. The figure 3000Å is accurate to ±5%.

Stress-strain curves for these separated anodic films were obtained by means of a specially constructed microtensile tester. The ends of the separated film were carefully glued with Eastman 910 cement to a fixed and to a movable grip. The driving force for the movable grip was supplied by thermal expansion of a silicone oil which is contained in the space between concentric fixed and movable cylinders. Expansion of the oil drives the movable cylinder to which the movable grip is attached. Displacement of the movable grip was measured by a photopotentiometer, and the load applied to the specimen was measured by semiconductor strain gauges mounted on a proof ring. The electrical output of the photo pot and the strain gauge bridge was fed to an XY recorder so that load-displacement curves were plotted directly. The displacement sensitivity of the apparatus is 0.2 μ/cm of chart and the load sensitivity is 0.7 g/cm of chart. The apparatus is mounted in an enclosed chamber which allows control of the surrounding atmosphere.

These films behave elastically to the point of fracture. Values of Young's modulus, E_c, the fracture stress σ_f, and the fracture strain, ϵ_f, were obtained from each stress-strain curve. Results are shown in Fig. 1, where E_c is plotted as a function of the absolute humidity. The remarkable increase of E_c with decreasing water vapor content, which was previously reported (4), is seen to occur monotonically with decreasing water vapor content. The decade between 10^{-4}-10^{-5} g/m^3 of water vapor was not explored. It represents the gap between the driest air we could obtain and a vacuum of 1 x 10^{-5} Torr. As the oxide films were exposed to lower vacua, the modulus increased toward the value for bulk, crystalline γ-Al_2O_3 (marked on the ordinate of Fig. 1). Values for ϵ_f (and hence σ_f) were subject to considerable scatter, due principally to defects in the films and occasional fracture at the grips. Nevertheless, a trend was clearly observable as water vapor concentration decreased. In the range 10^{-2}-20 g/m^3, ϵ_f was fairly constant and $\approx$ 3 x 10^{-3}. At lower values of the humidity, ϵ_f decreased, reaching a value $\approx$ 1.5 x 10^{-3} in the range 10^{-5}-10^{-6} g/m^3.

While it is intriguing to speculate on the mechanism by which the removal of water vapor increases the modulus of these films, it is more useful at this point to analyze the data in terms of fracture mechanisms. Examination of the fracture of adhering oxide films (see section on Fracture of Elastic Oxide Coating on Aluminum) has shown that all fractures begin at defects in the oxide. This observation, coupled with the purely elastic behavior of these films, suggests that fracture may be occurring by a brittle (Griffith) mechanism. If such be the case, the nominal fracture stress will be given by

$$\sigma_f = (\gamma E_c/2c)^{1/2}$$

where γ is the average surface energy, and c is the size of the flaw at which the crack begins.

The ratio of the fracture stress in vacuum to that at nominal air pressures is then given by (assuming crack growth is too rapid for γ to be affected by environment)

$$\frac{\sigma_f(\text{vacuum})}{\sigma_f(\text{air})} = \left(\frac{E_c(V)}{E_c(A)}\right)^{1/2} = \frac{\epsilon_f(A)}{\epsilon_f(V)}$$

This equality can be checked by substituting our experimental values for ϵ_f and E_c measured in vacuum and in moist air. For the ratio of fracture strains, we find the value 1.96; for the square root of the ratios of Young's moduli, we find 2.0. This rather good agreemen is consistent with the hypothesis that the fracture proceeds by a brittle mechanism.

If one assumes that the average surface energy for Al_2O_3 is approximately 10^3 ergs/cm^2, then the average length c of the microcracks which cause failure is c $\cong$ 300Å.

The advantage of measuring the mechanical properties of separated oxide films is that it is direct and unambiguous. On the other hand, experimental techniques are extremely tedious and time-consuming, and only about one-fifth of the test attempts are successful. Thus, the greater amount of effort and time required to obtain statistically significant measurements is only justified if there are not other means for obtaining the same, or related data. Although ϵ_f can be obtained by simpler methods (see next section), E_c has not yet been measured by methods other than the one described in this section.

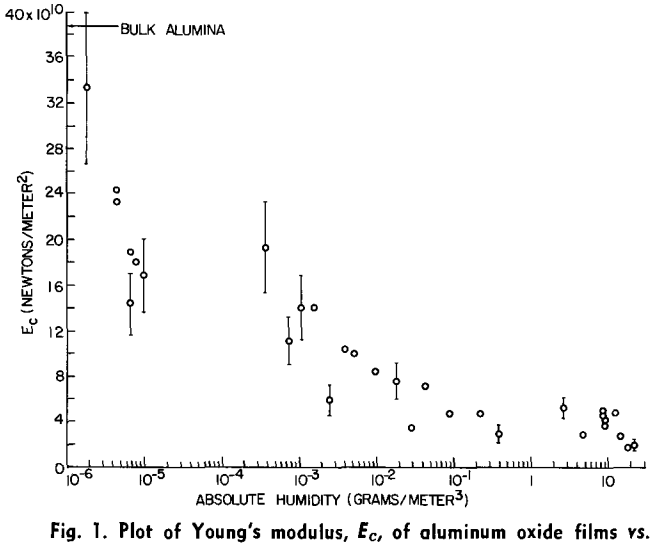

Fig. 1. Plot of Young's modulus, E_c, of aluminum oxide films vs. water vapor concentration. Each point represents one test. Error of $\sim$ 20% is shown for selected points.

Mechanical Properties of Adhering Al_2O_3 Films

Although Young's modulus for an adhering oxide film has not yet been measured, the environmental effect which was reported in the previous section does indeed hold for adhering, natural oxide films on aluminum. This conclusion was reached in an earlier paper (4) in which the behavior of dislocations near the surface was observed by means of transmission electron microscopy. The fact that dislocations were trapped near the oxide metal interface under vacuum, but did not accumulate there under normal atmospheric conditions could only be interpreted in terms of a change in the elastic modulus of the oxide under these two different conditions.

Direct measurement of fracture strains for adhering oxides are, however, easily obtained. The technique we have used involves pulling an anodized aluminum sample in an Instron testing machine until the oxide fractures. A water-tight cell of molded silicon rubber was built to surround a portion of the gauge length. The cell was filled with the anodizing solution and a 5V potential applied between the sample and a platinum electrode. Any microcrack which occurs in the oxide film will then produce a current flow in the cell. The fracture strain ϵ_f is then taken as the macroscopic strain at which measurable current begins to flow.

Values of ϵ_f for various thicknesses of anodic films on 1100-0 aluminum are given in Table I. A few results are also included for films on some of the more common alloys of aluminum.

The lower fracture strains recorded for the thinner oxide films on high-purity and commercially pure aluminum can be accounted for in terms of the observed fracture modes. The thinner films are observed to crack along slip bands whereas the thicker films fracture at right angles to the applied tensile load without regard for crystallographic orientation. (A detailed analysis of these two fracture modes is given in the next section.) Inasmuch as the measured frac-

Table I. Fracture strain, ϵ_f, of anodic layers on various aluminum substrates

Substrate	Film thickness (Å)	ϵ_f
99.99%	500	$(6.7 \pm 1.6) \times 10^{-4}$
	1500	$(2.3 \pm 1.3) \times 10^{-3}$
(separated film; moist air)	3000	$(3.0 \pm 1.0) \times 10^{-3}$
1100-0	100	$(1.3 \pm 0.2) \times 10^{-3}$
	200	$(1.3 \pm 0.1) \times 10^{-3}$
	500	$(4.5 \pm 0.5) \times 10^{-3}$
	1000	$(4.0 \pm 1.8) \times 10^{-3}$
	1500	$(5.5 \pm 0.7) \times 10^{-3}$
2024-T4	1500	$(3.1 \pm 0.4) \times 10^{-3}$
7075-T6	500	$(1.7 \pm 0.4) \times 10^{-3}$
	1000	$(2.5 \pm 0.3) \times 10^{-3}$
	1500	$(2.0 \pm 0.2) \times 10^{-3}$

ture strain, ϵ_f, is actually the macroscopic strain in the substrate-oxide system at which oxide failure begins, we conclude that (*i*) the values quoted for the thicker coatings are characteristic of the strains in the oxide at fracture, and (*ii*) that strain concentrations of the order of 3 occur at the slip steps where fracture occurs for the thinner coatings.

The correlation of these fracture strains with those observed for separated anodic films must be made with caution. Values quoted in Table I are strictly applicable only for films fractured in a tartaric acid electrolyte. These differences in environment notwithstanding, the agreement between the fracture strain of adhering films on high-purity aluminum and separated films fractured in a high-humidity atmosphere is quite good.

Fracture of Elastic Oxide Coatings on Aluminum

Mechanisms of fracture.—In the previous section, the observation was introduced that the mode of oxide fracture depended on the thickness of the coating. In general, films 500Å thick or less on high-purity aluminum will fracture at slip steps when the substrate is strained. The frequency and spacing of these cracks appears to be determined entirely by the plastic deformation of the substrate. On commercially pure aluminum (1100-0) somewhat thinner films are necessary for the slip step cracking mode to occur (Table I). For thicker films on these substrates and for all of the films we have observed on high-strength aluminum alloys, regularly spaced cracks occur at right angles to the tensile axis, *e.g.*, Fig. 2.

The development of these regularly spaced cracks is interesting. Cracks initially appear at the defects in the oxide (Fig. 2) and are randomly spaced at rather wide intervals. Although the fracture strains recorded by the potentiometric method (Table I) are

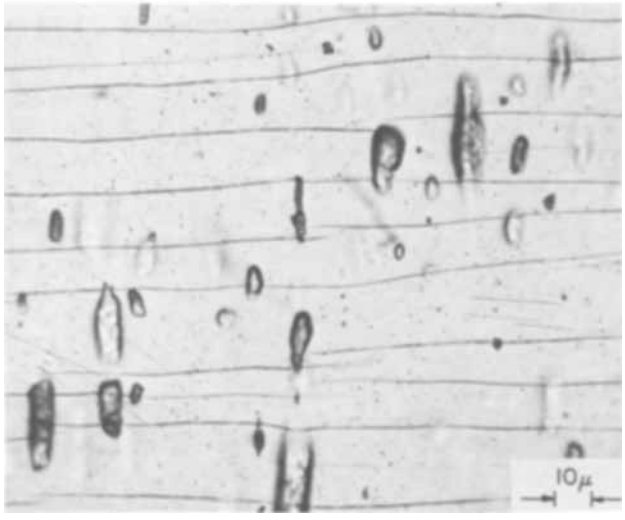

Fig. 2. Regular fracture of 1500Å anodic film on 1100-0 Al. Tensile axis at right angles to cracks (optical micrograph).

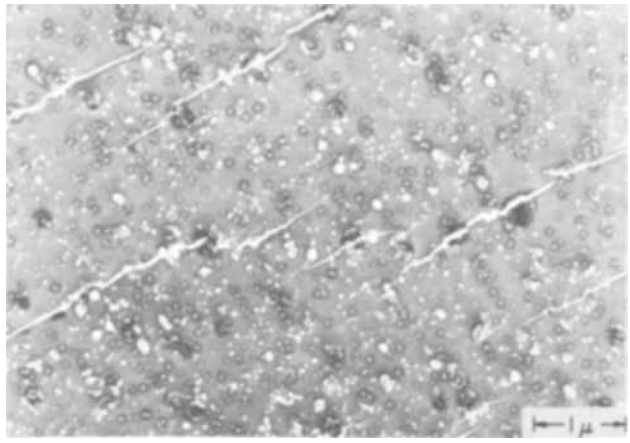

Fig. 3. Regular fracture cracks in 1500Å anodic film grown on 7075-T6 Al showing initiation at defects (electron micrograph).

of the order of 3×10^{-3}, cracks are not observed at optical magnification (1000X) until strains of about 0.01 are reached. As the substrate is further strained, additional random cracks appear and existing cracks continue to grow in length. A point is reached where interaction between adjacent cracks apparently reduces the probability of further crack formation between them. Eventually this "minimum random crack spacing" exists between all cracks and the sample is rather uniformly filled with cracks. Additional straining now begins to produce cracks at the midpoints between existing cracks, and this mechanism continues (with the crack spacing being approximately halved with the formation of each new generation of cracks) until the crack density reaches some saturation value. Further straining of the substrate then produces only a widening of the existing cracks. Similar observations were reported by Edeleanu and Law (11).

Regular fracture cracks initiate almost entirely at defects in the oxide film. (And for this reason the crack spacings are statistically scattered about mean values.) Unusually good micrographs have been obtained by transmission electron microscopy of anodic films strained to fracture on a 7075-T6 substrate. Portions of the substrate were electropolished away leaving the oxide film intact across the perforation. Figure 3 illustrates some of these cracks.

Two experiments were performed to determine whether plastic deformation in the substrate had any significant effect on the mechanism of regular fracture of the oxide coating. In the first experiment three aluminum alloys with different yield stresses were anodized to 1500Å thickness and pulled well into the plastic region ($\epsilon = 0.045$). The average spacing of the cracks in the oxide was then measured. Results are shown in Table II. The obvious conclusion is that the density of cracks is not influenced by differences in the plasticity of the substrate.

The second experiment was designed to look directly for evidences of plastic deformation in the regions just below cracks in the oxide layer. Specimens of 7075-T6 which had been anodized to 1500Å and pulled to a strain of 0.045 were thinned to electron transmission thickness by electropolishing from

Table II. Regular fracture spacings on substrates having different yield stresses

Substrate	(Spacings measured at $\epsilon = 0.045$) Yield stress (psi)	Average fracture spacing (microns)
7075-T6	61,950	3.3
7075-W	36,500	3.3
2024-T4	47,000	3.1

the side opposite the oxide coating. Dislocation structures which were characteristic of the alloy were observed, and there were no variations in dislocation density in the vicinity of oxide cracks. From this and the preceding experiment, it was concluded that the mechanism of regular fracture depends only on the total strain in the substrate.

Theory of oxide fracture.—In a recent paper (12) Grosskreutz and McNeil considered the theory of oxide fracture on a strained substrate. For those substrates which deform by slip we showed that fracture at a slip step occurs only if the oxide coatings are unable to sustain the tensile stresses necessary to separate and peel the oxide from the substrate in the vicinity of the slip step, Fig. 4(a). Fracture is more likely to occur for thinner films and lower fracture strains. Because the adhesion stresses between oxide and substrate are not known with any degree of certainty, it was impossible to predict accurately the conditions under which fracture at slip steps occurs. However, assuming the shear adhesion stress to be the maximum shear strength exhibited by whiskers, and inserting the fracture strain of adhering oxides into the formulas, we found that an oxide thickness of approximately 500Å forms the dividing line between the fracture and nonfracture at a slip step, in agreement with the results of the section on Mechanical Properties of Adhering Al_2O_3 Films.

In the case of thick (> 500Å) anodic coatings, or if substrate slip does not occur before the oxide fracture strain is reached, regular fracture will occur in the manner described in the preceding section. Quantitative treatment of the development of these fractures is possible in the following way. Suppose that a crack has occurred at a randomly located defect in the oxide. In the immediate vicinity of this crack the stress in the oxide layer will be relaxed and will not build back up to the fracture stress until some distance removed from the initial crack. This situation is shown schematically in Fig. 5(a). We represent the stress in the coating, σ_c, as

$$\sigma_c(x) = \sigma_f - \Delta\sigma; \quad x > w/2$$

where $\Delta\sigma$ is the stress relaxation. In ref. (12) we took $\Delta\sigma$ to be equal to $g\sigma/x$ where σ is the nominal stress level in the coating and g is a parameter with dimensions of length. Under these conditions the stress in the coating builds asymptotically back toward σ_f as x approaches infinity. Theoretically, the next crack will occur at $x = \infty$ where $\sigma_c = \sigma_f$. Actually, because the fracture stresses in the oxide will be distributed around a mean value, the next fracture will occur wherever σ_c exceeds the local fracture stress at some given defect.

Random cracking will continue until two cracks appear closely enough together that their stress fields interact to give a significant reduction in the coating stress at all points between the two cracks. This situation is illustrated in Fig. 5(b). The stress in the coating between the two cracks can now be represented as

$$\sigma_c(x) = \sigma_f \left[1 - g\left(\frac{1}{x} + \frac{1}{d_o - x}\right)\right]; \quad w/2 < x < (d_o - w/2) \quad [1]$$

At the midpoint, $x = d_o/2$

$$\sigma_c(d_o/2) = \sigma_f\,[1 - 4g/d_o] \quad [2]$$

As a boundary condition on Eq. [1] we have that at $x = w/2$ and $d_o - w/2$, $\sigma_c = 0$. For this condition to hold

$$g = w/2 - w^2/4d_o$$

In general, $w << 4d_o$ and we can write $g = w/2$.

In this treatment w is the crack width, illustrated in Fig. 5. Actually, the crack will look more nearly like the schematic drawing shown in Fig. 6 because of the relaxation of the shear stress in the film as the free surface is approached. If the appropriate value of w is taken to be the crack width at the top surface of the oxide film, then w can be expressed in terms of the thickness, t. The free surface of the cracked film can be approximated either as linear (dashed line, Fig. 6) or as parabolic. In these two approximations, g would be given as

$$g = w/2 = k't \text{ --- (linear approximation)} \quad [3a]$$

or

$$g = w/2 = k\sqrt{t} \text{ --- (parabolic approximation)} \quad [3b]$$

Once the configuration shown in Fig. 5(b) obtains over the entire surface of the strained oxide, regular cracking can proceed if the stress in the oxide film is raised until the stress at $x = d_o/2$ reaches σ_f. Additional cracks will occur at $x = d_o/4$, $d_o/8$, etc., as the stress is increased continuously.

Given this model for the multiplication of cracks, it can be shown that (12)

$$\ln \epsilon/\epsilon_o = (4g/d)\,[1 - d/d_o] \quad [4]$$

where ϵ_o and d_o are the substrate strain and oxide fracture spacing for which the coating begins the process of regular fracture. Given the initial conditions (ϵ_o, d_o),

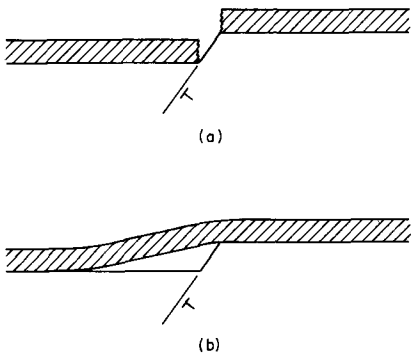

Fig. 4. Schematic drawing of oxide behavior at a slip step. Fracture occurs in (a) and separation without fracture in (b).

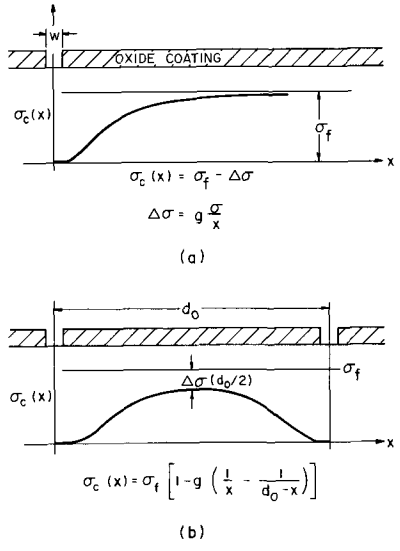

Fig. 5. Stress distribution in oxide coating near cracks: (a) single, random crack, and (b) interacting cracks.

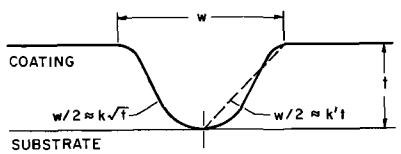

Fig. 6. Schematic drawing of possible crack-face configuration. Solid line is approximately parabolic; dashed line is linear.

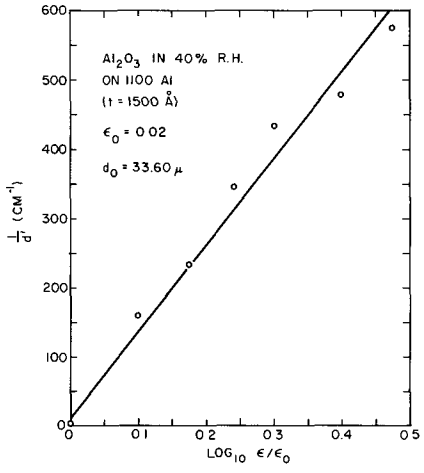

Fig. 7. Plot of crack density $1/d' = \left(\frac{1}{d} - \frac{1}{d_o}\right)$ vs. $\log_{10} \epsilon/\epsilon_o$ for anodic film on 1100-0 Al pulled in laboratory air.

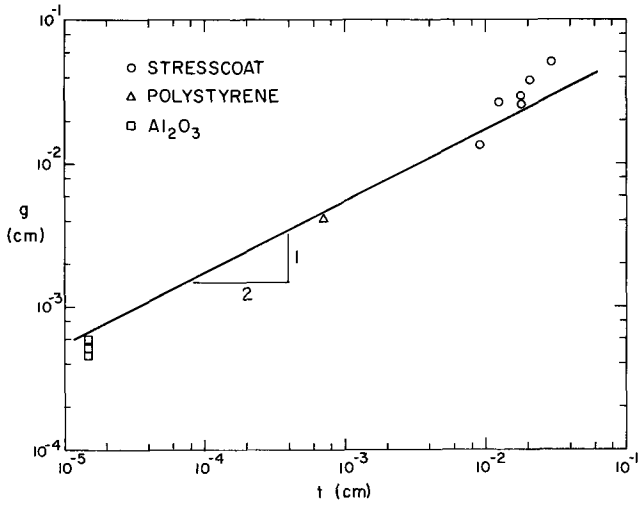

Fig. 8. Plot of g (Eq. [4]) vs. film thickness, t. Solid line has slope of 1/2.

Eq. [4] allows us to predict the spacing, d, at any subsequent strain, ϵ. The constant, g, depends on the thickness of the film (Eq. [3]) with a constant of proportionality, k, to be determined by experiment.

An interesting consequence of our model of regular fracture is that when d is of the order of $2g = w$, further cracking should not occur. Thus, the saturation crack spacing, d_s, should be larger, the thicker the oxide film.

Experiments on regular fracture.—Equation [4] has already been checked (12) against published crack density *vs.* strain data for both Al_2O_3 and "stresscoat," a brittle surface coating used to determine surface stress distributions. In both cases, the fit of the data with the theoretical equation was excellent. Further verification is shown in Fig. 7 where recent measurements of crack density in an adhering, anodic coating are fitted to Eq. [4]. Data on regular fracture of anodic layers strained under distilled water and in dry air have also been compared with Eq. [4] with equally good agreement. The fracture spacings in a thin polystyrene film on a cellulose acetate substrate have correlated well. There is a wealth of experimental data on "stresscoat" of various thicknesses and fracture strains with which Eq. [4] can be compared (13). All of these different data have been analyzed to yield values of the parameter, g. Table III lists the important results.

The first item of interest is the dependence of g on the thickness of the oxide coating. A log g *vs.* log t plot is shown in Fig. 8, and it is evident that the parabolic dependence assumed in Eq. [3b] most nearly fits the experimental results. The parameter k in the expression $g = k\sqrt{t}$ has the dimensions of (length)$^{1/2}$ and varies between 0.1 and 0.25 for the data recorded in Table III.

A second item of interest in Table III is that the parameter, g, is independent of ϵ_o for a given thickness of coating. Finally, we note that the saturation crack spacing, d_s, is very nearly equal to $2g$, as predicted, for the majority of cases cited.

The predictive value of Eq. [4] remains limited because the initial conditions (ϵ_o, d_o) cannot be expressed in terms of measurable, mechanical properties of the oxide film. ϵ_o is certainly related to ϵ_f, the fracture strain, but is, in fact, somewhat larger by an indeterminant amount depending on the distribution of fracture strengths about the mean. The parameter d_o is surely a function of the physical properties of the film, but as yet no quantitative relationship has been derived without introducing yet another parameter, equally difficult to estimate.

Table III. Analysis of fracture spacing data in terms of the parameters in Eq. [4]

Coating	Thickness, t (cm.)	ϵ_o	d_o (cm.)	g (cm.)	$d_{sat}/2g$
Al_2O_3[a]	1.5×10^{-5}	0.02	3.4×10^{-3}	4.6×10^{-4}	1.24
Al_2O_3[b]	1.5×10^{-5}	0.02	3.6×10^{-3}	5.2×10^{-4}	1.16
Al_2O_3[c]	1.5×10^{-5}	0.025	3.8×10^{-3}	5.9×10^{-4}	1.34
Polystyrene	7×10^{-4}	0.015	4.7×10^{-3}	4.1×10^{-3}	0.432
Stresscoat[d]	1.78×10^{-2}	0.0007	11.3×10^{-2}	2.61×10^{-2}	1.09
Stresscoat[d]	1.78×10^{-2}	0.0006	8.9×10^{-2}	2.93×10^{-2}	0.87
Stresscoat[d]	1.78×10^{-2}	0.0008	9.6×10^{-2}	2.93×10^{-2}	1.02
Stresscoat[d]	1.78×10^{-2}	0.0012	8.2×10^{-2}	2.93×10^{-2}	1.07
Stresscoat[d]	0.91×10^{-2}	0.0008	6.0×10^{-2}	1.35×10^{-2}	1.20
Stresscoat[d]	1.27×10^{-2}	0.0007	7.5×10^{-2}	2.71×10^{-2}	0.95
Stresscoat[d]	2.11×10^{-2}	0.0006	11.5×10^{-2}	3.84×10^{-2}	0.89
Stresscoat[d]	2.95×10^{-2}	0.0009	9.3×10^{-2}	5.34×10^{-2}	0.73

[a] Pulled in laboratory air with 40% relative humidity.
[b] Pulled under distilled water.
[c] Pulled in dry air, dew point −60°C.
[d] All data on stresscoat taken from Ref. 13.

Effects of Environment on Fracture of Adhering Films

Because water vapor was observed to have such a marked effect on the mechanical behavior of separated oxide films of aluminum (Fig. 1), an experiment was performed to determine whether similar effects could be observed for adhering films. Two sets of anodized, 1100-aluminum samples were pulled in tension, the one immersed in distilled water and the other contained in an atmosphere of dry air whose dew point was −60°C. Results are plotted in terms of d *vs.* ϵ in Fig. 9. That an effect exists is clear from the data. It was not

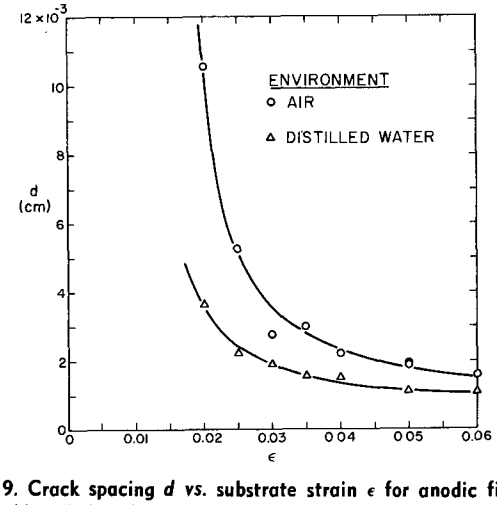

Fig. 9. Crack spacing d vs. substrate strain ϵ for anodic films on 1100-0 Al pulled under distilled water and in a dry air (dew point −60°C) environment.

possible to measure the onset of fracture of these films in a manner consistent with that reported in the section on Mechanical Properties of Separated Al_2O_3 Films. However, optical examination of the films showed that detectable cracks occurred at a lower strain for the sample immersed in distilled water than for the dry oxide. This observation is contrary to the results obtained on separated films where the fracture strain was higher for films in an atmosphere of saturated water vapor.

Analysis of the curves in Fig. 9 in terms of Eq. [4] reveals that both sets of data give the same value of g. Hence, we can conclude that g is independent of E_c. On the other hand, we must account somehow for the fact that smaller crack spacings occur in the wet film for a given total strain. The best explanation for this behavior is in terms of the relative magnitude of ϵ_o for the two cases. The fact that the wet film started to crack earlier allowed uniform coverage with cracks at a lower strain than for the dry sample. Hence, the progress of regular fracture is more advanced at a given strain in the case of the wet film.

The difference in the influence of moisture on the strain at which cracks grow in adhering and separated films must be attributed to the effect of the substrate. The details of this interaction are not yet clear and will require further experimentation.

Conclusions

From this survey of the mechanical properties and fracture behavior of separated and adhering aluminum oxide films several important conclusions can be drawn.

1. Separated aluminum oxide films fail by a brittle mechanism. Increasing water vapor concentration decreases both E_c and σ_f and raises ϵ_f, consistent with such a mechanism.

2. The fracture strains measured on separated and adhering Al_2O_3 films are of the same order of magnitude, *i.e.*, 1-3 x 10^{-3}; however, the effect of environment on the strain at which cracks grow appears to be different for separated and adhering films.

3. Fracture of adhering oxide films may occur at slip steps or regularly spaced at right angles to the tensile axis. The choice of mode depends on the oxide thickness, on ϵ_f, and on the adhesion stresses between the oxide and substrate.

4. Initiation of regular fracture is dominated by defects in the oxide.

5. The mechanism of regular fracture is mainly elastic; plasticity in the substrate does not play a major role.

6. The dependence of regular fracture spacing on ϵ is well accounted for by the expression $\ln \epsilon/\epsilon_o = [kt^{1/2}](1/d - 1/d_o)$. The saturation (minimum) spacing $d_s \cong 2kt^{1/2}$.

Acknowledgments

The author would like to acknowledge the Metallurgy Branch of the Office of Naval Research for their continued support, and to thank Dr. W. G. Rauch and Dr. R. C. Carlston for their encouragement. Mr. C. Q. Bowles performed the difficult experiments on separated oxide films, and Dr. Michael McNeil and Mr. David K. Benson provided stimulating discussion concerning the interpretation of regular fracture mechanisms. This work was supported by the Office of Naval Research, Contract No. Nonr-3908(00).

Manuscript submitted March 3, 1969; revised manuscript received *ca.* May 28, 1969. This was Paper 81 presented at the Chicago Meeting, Oct. 15-19, 1967.

Any discussion of this paper will appear in a Discussion Section to be published in the June 1970 JOURNAL.

REFERENCES

1. R. Roscoe, *Nature*, **133**, 912 (1934).
2. I. Kramer and L. J. Demer, *Progr. Mater. Sci.*, **9** [3], 131 (1961).
3. A. K. Head, *Australian J. Phys.*, **13**, 278 (1960); *Phil. Mag.*, **44**, 92 (1953).
4. J. C. Grosskreutz, *Surface Sci.*, **8**, 173 (1967).
5. R. F. Tylecote, *J. Iron Steel Inst.*, **196**, 135 (1960); **78**, 301 (1950).
6. D. H. Bradhurst and J. S. Llewelyn Leach, *Trans. Brit. Ceram. Soc.*, **62**, 793 (1963).
7. S. F. Bubar and D. A. Vermilyea, *This Journal*, **113**, 892 (1966); *ibid.*, **114**, 882 (1967).
8. I. A. Menzies and K. N. Strafford, *J. Mater. Sci.*, **2**, 358 (1967).
9. D. H. Bradhurst and J. S. Llewelyn Leach, *This Journal*, **113**, 1245 (1966).
10. J. C. Grosskreutz and G. G. Shaw, *J. Appl. Phys.*, **35**, 2195 (1964).
11. C. Edeleanu and T. J. Law, *Phil. Mag.*, **7**, 573 (1962).
12. J. C. Grosskreutz and M. B. McNeil, *J. Appl. Phys.*, **40**, 355 (1969).
13. A. J. Durelli and S. Okubo, *Proc. Soc. Exp'l. Stress Anal.*, **11**, [2], 153 (1954).

An Imaging Technique for Studying Localized Electronic Conduction in Valve Metal-Oxide Systems

N. Ramasubramanian

Chalk River Nuclear Laboratories, Atomic Energy of Canada Limited, Chalk River, Ontario, Canada

ABSTRACT

The light sensitive and semiconducting properties of cuprous iodide are used in a new technique for studying the electronic conduction behavior of oxide films on valve metals. Information about the distribution and nature of the conduction sites can be obtained. The chief advantage of this method over existing methods is that specimens biased to positive or negative potentials can be tested. The resolution (size of the copper deposits in the image) is better than or equal to that of the other methods. Specimens can also be studied directly by optical and/or electron optical means at different stages during the testing, because the process is a solid-state one. Oxide films on zirconium and its alloys were studied.

The color change associated with redox indicators in going from one state to another has been used to detect easy paths of electronic conduction in valve metal-oxide systems (1, 2).

In our research program on the corrosion behavior of zirconium and its alloys, electron transport through zirconia films is one of the important factors (3). The presence of localized conduction sites was indicated by

preferential reduction of Ag^+, Cu^{++}, Au^{+++}, or MnO_4^- from suitable electrolytic baths at these areas and by the iodide printing technique (1). We were interested in developing a technique that was nondestructive and could be used to study these conduction sites during both anodic and cathodic polarization of the metal or alloy. In the imaging technique described here, use is made of the photosensitive properties of cuprous iodide. The iodide is reduced to the metal at sites of electronic current flow and the deposits may be examined by optical and/or electron optical means. Current-voltage measurements, which were complementary to the observations by the imaging process, were obtained using aqueous electrolyte or evaporated metal counterelectrodes.

Experimental

Materials.—Oxide films on zirconium and Zircaloy-2 grown by anodic and thermal means were tested. Paddle shaped samples (the blade portion measuring 2x2x 0.1 cm) were cut from material supplied by Wah Chang Corporation and Foote Mineral Company. The surface preparation employed was the standard procedure of abrasion followed by pickling in a hydrofluoric-nitric acid bath. Anodic films were grown in a variety of electrolytes and thermal films in flowing oxygen at 300°C.

Imaging technique.—The method consisted of two parts, *viz.*, evaporation onto the oxide surface of a thin film of cuprous iodide followed by either the image recording step or current-voltage measurements with a suitable counterelectrode.

The system was pumped to 10^{-6} Torr and cuprous iodide was evaporated onto the oxide surface from a platinum boat at a rate of ~25 Å/sec. The specimen to source distance could be varied and was maintained at ~5 cm. Cuprous iodide showed a sequence of color changes with increasing temperature and the heater current was adjusted to maintain the orange-red color during evaporation.

A control strip of pickled zirconium foil of known area was attached to the specimen during the iodide evaporation and covered part of the specimen surface. The iodide from the control strip was dissolved and the copper determined by the dithiozone complexing method (4). The thicknesses of the evaporated films were calculated assuming a density of 5.62 for the cuprous iodide.

The images were produced by polarizing a small area of the specimen with its evaporated cuprous iodide film to a cathodic or anodic potential in a 1M NH_4NO_3 solution 0.0005M in $Na_2S_2O_3$ under irradiation from a u.v. lamp (100w, Type H-4 mercury vapor with peak emission at ~3660Å) for about a minute. A silicone rubber gasket carrying a platinum wire electrode was pressed down firmly onto the surface and contact made by a few drops of the solution. The area of contact was only 0.16 cm^2 and therefore different areas of the specimen could be tested with a positive or negative potential applied. The applied potentials ranged from 1% of the formation voltage to 0.4 V/1000Å for the anodic and thermal films, respectively.

The iodide film with the copper deposits was then washed, dried, and stripped off the oxide surface. The initial method was to dip the specimen in a collodion solution and allow to drain and dry, when a slight pressure along the edges would release the iodide film with the collodion backing. A procedure similar to the replica technique used in electron microscopy was found to be better, however. A thin coating of Formvar overlaid by one of polyvinyl acetate was applied to the specimen and this combination with iodide film was peeled off using an adhesive tape. Then the routine of coating with platinum-carbon and dissolving the PVA and Formvar was followed. The platinum-carbon film was collected on copper grids. The stripped films were examined on the optical and electron microscopes. The specimen was subsequently rinsed with dilute ammonia, washed and dried, when it was ready for another experiment.

Current-voltage measurements were made using gold or 1M NH_4NO_3 solution contacts.

Results

The evaporated film showed bright interference colors and the control strip was used to monitor the thickness during evaporation. The thickness of the evaporated iodide film was usually in the range 900-1100Å. Electron optical examination showed that the iodide film was for the most part a continuous sheet of crystals, oriented randomly and varying in size and thickness.

Imaging.—Anodic oxide films to ~4000Å and thermal films up to 1 μm thick were studied. To illustrate the usefulness of the technique a few typical sets of data on anodic films are presented here.

The current flow during imaging was usually in the μA/cm^2 range. An increase in the voltage or the time of recording led to a slight increase in the size of the copper deposits; the use of dilute thiosulphate solution for dissolving the unreacted iodide had no effect. In the absence of either the u.v. irradiation or the bias during the imaging the area tested showed only a few large deposits, similar to the untested parts of the surface.

The use of the collodion for stripping the iodide film with the image had the advantage of retaining the replicated grain structure of the specimen. In Fig. 1a are shown transmission micrographs of a collodion film carying the recorded image of copper deposits. It was stripped from a 500Å anodic film on zirconium following the imaging step and was washed in dilute thiosulfate solution. The light beam was incident obliquely and the copper particles scattering the light appear bright on a dark background. The collodion film had a wavy topography which led to difficulty in focusing the whole field of view. Nevertheless, this stripping procedure was helpful in identifying the locations of the copper deposits.

Using the two stage replica method of stripping the iodide film, a larger portion of the area under study could be brought into focus on the optical microscope. An added advantage was that the iodide film could be examined in the electron microscope also. A set of transmission micrographs of the same area of an iodide film stripped off a 1800Å anodic film on zirconium with varying incident light is shown in Fig. 1b. It is seen that a number of deposits remain un-

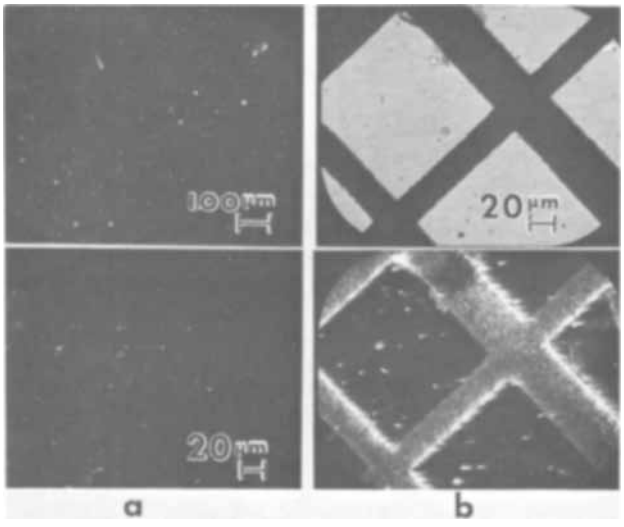

Fig. 1. Transmission optical micrographs of (a) collodion film carrying copper deposits and (b) cuprous iodide film supported on platinum-carbon with the incident light normal and oblique to the film.

focused and appear as circular interference fringes in this technique of supporting the iodide film also. However, a comparison with Fig. 1a shows a definite improvement in focusing conditions and therefore a higher visible density of deposits.

There was good reproducibility of the position of the deposits but not their size when a cathodic or anodic test was repeated on the same area. The irreproducibility of the deposit size may be due to variations of crystal size and thickness in the evaporated films. In successive anodic or cathodic testings on the same area nearly half the number of deposits matched precisely as to their location. It is believed that the difficulty in focusing is partly responsible for the lack of a complete one to one correlation.

In Fig. 2 transmission electron micrographs and diffraction patterns of the film referred to in Fig. 1b are shown. The copper deposits (a) are several times the size of the cuprous iodide crystallites (b), and range in size from ~0.5 to 2 μm. Electron diffraction patterns of the deposits show additional reflections arising from copper and cuprous oxide.

Current-voltage relationships.—The curves obtained in testing a specimen carrying gold contacts of different areas (varying from 0.1 to 0.6 cm^2) were identical in shape and the current density was constant to within ±5%. The results of these measurements and of other experiments in which an evaporated guard ring of gold was used and the area of the iodide film was varied confirmed the fact that no surface conduction was involved.

The current density was found to decrease with increasing iodide film thickness. Therefore, variations in the conductivity of the oxide with thickness were inferred from results on individual specimens carrying anodic films of several thicknesses. By such a procedure the only variations in iodide film thickness were those inherently present and were the same on the different anodized areas of the specimen. Any effects due to variations in the properties of the cuprous iodide and in the conductivity of different specimens from the same batch were also avoided. In the case of thermal films comparison was made among specimens oxidized to different extents with the iodide evaporated onto them simultaneously.

In Fig. 3a and b curves obtained with anodic oxide films of two different thicknesses grown on the same specimen are compared. It should be noted that the current density at a given voltage decreases with but not proportionately to the increase in oxide thickness. The curves shown in Fig. 3c and d were obtained with 1M NH_4NO_3 contacts. Cuprous iodide was evaporated onto part of the oxide surface. The anodic blocking behavior of such oxide films is readily seen from curve d obtained with direct contact to the oxide. With cuprous iodide present, curve c, an anodic current flow was observed. This current was time dependent and the current density at a fixed anodic voltage decreased only slightly with increase in oxide thickness and was not proportional to the oxide thickness. The anodic current at zero volt is due to the emf developed by the metal when the iodide is contacted by the electrolyte.

Observations using the SEM.—Because the imaging technique involves a solid-state process, an added advantage is that specimens can be examined by optical and/or electron optical means immediately following one or other of the various steps, *viz.*, evaporation of the iodide, the gold counterelectrode, and polarization. For such studies the scanning electron microscope (SEM) offers a wide range of possibilities. Specimens were examined in the JSM-2 before and after evaporation of cuprous iodide, with and without gold counterelectrodes and in the biased and unbiased conditions. In Fig. 4 the images of the specimen surface obtained in the secondary electron mode of operation of the SEM are shown. The presence of the iodide layer did not produce detectable changes in the image characteristics but gold did. At a few selected spots (Fig. 4a and b) deposits, varying in size from 1 to 10 μm, were thicker. When polarized, circular regions several mi-

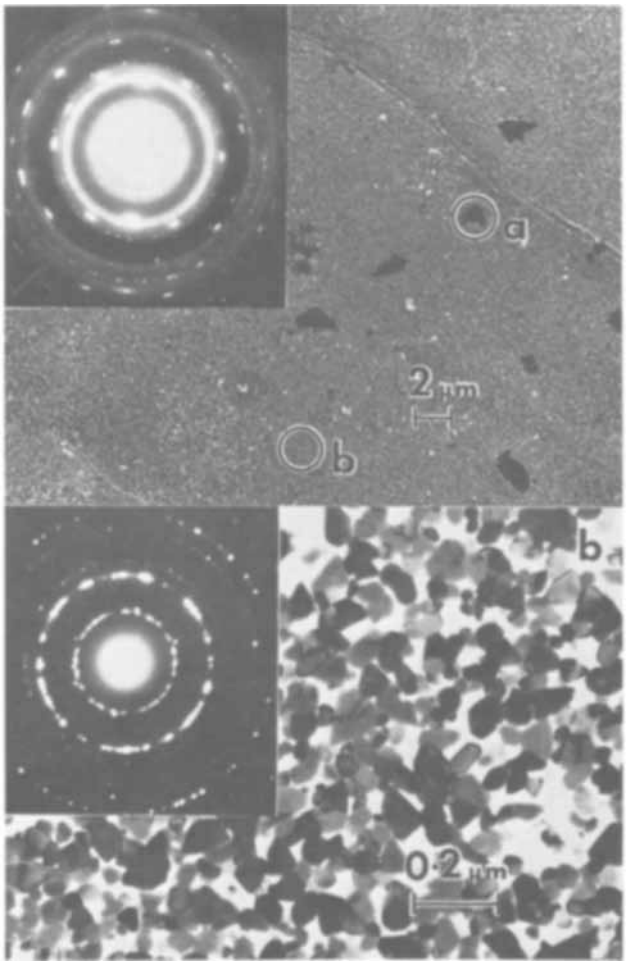

Fig. 2. Transmission electron micrographs and diffraction patterns of the film referred to in Fig. 1b; (a) regions of imaging (b) undeveloped cuprous iodide.

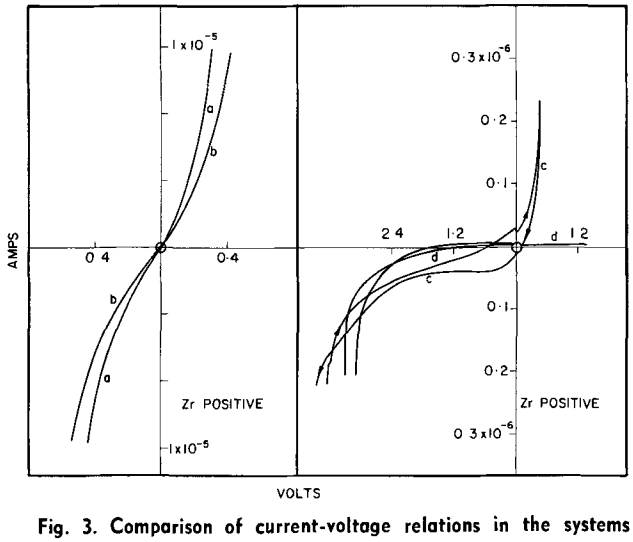

Fig. 3. Comparison of current-voltage relations in the systems:

$$Zr\left|\frac{\text{oxide 1}}{\text{oxide 2}}\right|CuI\left|\frac{Au}{Au}\right. \text{ and } Zr\left|\frac{\text{oxide}}{\text{oxide}}\right|CuI\left|\frac{NH_4NO_3, Pt}{NH_4NO_3, Pt}\right.$$

(a and b) anodic oxide films (1) 400 and (2) 2500Å thick, respectively with 0.27 cm^2 gold contacts and (c and d) anodic oxide film 2000Å thick with 0.16 cm^2 NH_4NO_3 (1M) contacts on oxide with and without an iodide film, respectively.

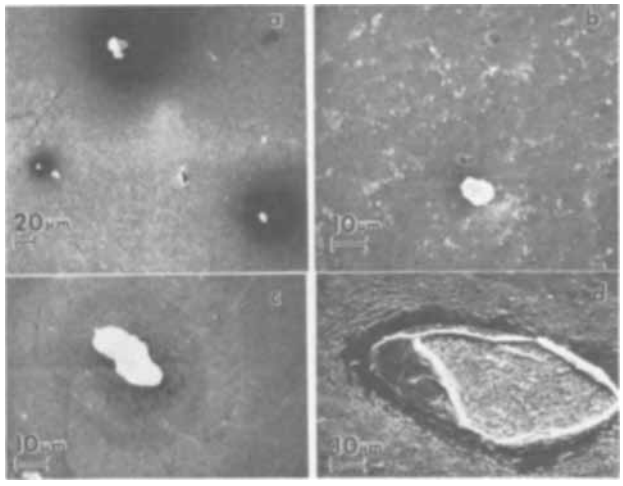

Fig. 4. SEM micrographs of anodic-oxide films on zirconium and Zircaloy-2 following cuprous iodide evaporation and one of the various steps; (a) 1000Å anodic oxide film on zirconium; the gold contact on cuprous iodide is biased to +0.2V wrt specimen; (b) 500Å anodic oxide film on Zircaloy-2 after evaporation of gold contacts; (c and d) breakdown areas; 1500 and 1000Å anodic oxide films on zirconium and Zircaloy-2 with gold and 1M NH_4NO_3 contacts, respectively, taken to breakdown voltages.

crons in diameter around these deposits showed different image characteristics from the rest of the surface (dark areas in Fig. 4a). A negative bias on the specimen was associated with large sporadic current increases (0.5 to 10 $\mu A/cm^2$ at $\sim$0.2V) as the electron beam scanned the surface and the subsequent observation of breakdown regions similar to that in Fig. 4c. Specimens were examined after polarization studies using 1M NH_4NO_3 solution contacts. A few sites of the type shown in Fig. 4d were observed.

Discussion

A number of semiconducting halides, sulfides, etc. have been shown to possess image forming characteristics (5, 6). Cuprous iodide was chosen because of its low solubility in water, a high vapor pressure at moderate temperatures, and its usefulness as a solid ohmic contact (7).

The conducting sites in the metal-insulating oxide system might form an ohmic or blocking contact with the evaporated cuprous iodide film. In the present study imaging was carried out on dielectric substrates at room temperature with low applied fields and therefore the mechanism proposed by Tubbs *et al.* is to be preferred (5). The various processes that lead ultimately to the formation of copper deposits during the imaging step are the production of excitons on u.v. absorption (8), reaction between a pair of excitons at a suitable site, and formation of copper nuclei. The centers for the initiation of reaction between a pair of excitons are likely to be Cu^{++} sites and are provided by the forward hole current. Growth of the nuclei would then follow by pairs of excitons reacting at a site adjacent to a copper nucleus.

Both n and p-type (homogeneous) conductivity have been reported for zirconia films on zirconium and Zircaloy-2 (9, 10). The alloy has intermetallic precipitates (major constituents are Zr, Fe, Cr, and Ni) distributed fairly uniformly through the material, and the metal a number of impurity centers. When imaging the metal or alloy-oxide structures the copper deposits are located at these sites of intermetallic and impurity precipitates. The purity of the materials used in the present study compares favorably with those used by the other workers and the reported homogeneous conductivity might very well be that of similar localized conduction sites.

The complex nature of these sites is revealed by the results obtained in the imaging step and the current-voltage characteristics. From the data reported here it is seen that cuprous iodide forms an ohmic contact with some of these sites. More than half the number of sites were imaged by both anodic and cathodic polarization. The inference would then be that a doped oxide film is formed on these conduction sites during the oxidation. A small fraction behaves as either an n or p-type semiconductor and is imaged during cathodic or anodic bias on the specimen; whereas the majority is of the compensated intrinsic type and under the testing conditions allows current to flow in either direction. The results obtained in experiments using the SEM and imaging in the absence of u.v. irradiation or bias indicate a wide range of conductivity among these sites; a large percentage of current flowing at a few excessively active sites.

Conclusions

The imaging technique reported here has several advantages for studying the sites of easy electronic conduction in valve metal-oxide systems. The photosensitivity and carrier injection capacity of cuprous iodide permit the use of low testing voltages, a favorable requirement in studying low dielectric strength materials. The technique is nondestructive and provides information about the distribution and electrical properties of the conducting sites. The resolution is good and sites active during both anodic and cathodic polarization can be studied. Because the process is a solid state one samples can also be studied directly by electron optical means.

In zirconia films on zirconium and its alloys, localized conduction sites are present and assigning a homogeneous conductivity for oxide films up to $\sim$1 μm thick is questionable. The electrical characteristics of these sites are of a complex nature.

Acknowledgments

The author wishes to thank Mr. T. Trottier for his assistance in the experimental part of this work and Dr. B. Cox for his encouragement and helpful discussions.

Manuscript submitted Feb. 19, 1969; revised manuscript received May 20, 1969. This was Paper 543 presented at the Montreal Meeting, Oct. 6-11, 1968.

Any discussion of this paper will appear in a Discussion Section to be published in the June 1970 JOURNAL.

REFERENCES

1. G. P. Klein, *This Journal*, **113**, 345 (1966).
2. J. P. McCloskey, *ibid.*, **114**, 643 (1967).
3. B. Cox, AECL-2777, October 1967.
4. I. M. Kolthoff and E. B. Sandell, "Textbook of Quantitative Inorganic Analysis," MacMillan Co., New York (1963).
5. M. R. Tubbs, *Proc. Roy. Soc.*, **A280**, 566 (1964); R. I. Dawood, A. J. Forty, and M. R. Tubbs, *ibid.*, **A284**, 272 (1965).
6. M. T. Kostyshin, E. V. Mikhailovskaya, and P. F. Romanenko, *Soviet Phys. Solid State, (English Transl.)*, **8**, 451 (1966).
7. I. Granacher, *Solid State Commun.*, **2**, 365 (1964).
8. S. Nikitine, L. Wenger-Wursteisen, and J. P. Eberhart, *C. A.*, **65**, 14583d (1966); W. F. Krolikowski, Tech. Report No. 5218-1, SU-SEL-67-039, May 1967.
9. P. J. Harrop and J. N. Wanklyn, *Brit. J. Appl. Phys.*, **16**, 155 (1965).
10. M. W. Mallett and W. M. Albrecht, *This Journal*, **102**, 407 (1955).

Exposure of Photoresists: Electron Beam Exposure of Negative Photoresists

Barret Broyde

Engineering Research Center, Western Electric Company, Inc., Princeton, New Jersey

ABSTRACT

A threshold flux is required to form an image in negative photoresists when they are exposed to kilovolt electron beams. This threshold is related to the gel point of the photoresist. Using the known number of crosslinks per molecule at the gel point, the G values for the crosslinking of KPR and KTFR, were calculated from the absorbed energy of 2.5 ± 0.2 x 10^{20} ev/cm^3 at the threshold, to be 0.65 and 1.20, respectively. An energy transfer model based on Bethe's penetration range for an electron and on the distribution of energy with depth of penetration found by Charlesby describes the change in threshold flux with changes in accelerating potential. Electron fluxes above the threshold value fully insolubilize the resist. The efficiency of absorbed energy for total insolubilization is a function of the energy of the incident electrons. 5 keV electrons are 3.3 times more efficient than uv light, but 15 keV electrons are only as efficient as photons.

During the manufacture of semiconductor devices, parts of the semiconductor substrate have to be protected against etchants. This is accomplished by exposing photosensitive etch-resistant polymers called photoresists to light through a mask. The desired pattern of etch resistant polymeric material is obtained after a development process, which removes the unexposed portions of negative resists and removes the exposed portions of positive resists (1). The use of light in patterning the photoresist through a mask, limits the narrowest line and the edge resolution that can be routinely made in the photoresist to be wider than 2 μm and 0.3 μm, respectively.

On the other hand, lines only 0.25 μm wide (2) with edge resolutions of 0.05 μm (3) have been prepared by using an electron beam to expose photoresist. Thornley and Sun (4) showed that both 14 and 20 keV electron beams could expose negative resists so that the resists were able to protect SiO_2 against etchants. They found that a threshold existed in the exposing electron flux, below which no protection was provided. Above the threshold the amount of protection increased with increasing flux until full protection resulted. Kanaya, Yamazaki, and Tanaka (3) also found a threshold when they studied the thickness of a developed negative resist as a function of electron flux, for electrons accelerated between 20 and 100 keV. Matta (5) showed that the flux required for optimum exposure depends on the energy of the electrons. He feels that backscattered electrons play a part in the exposure process, but Kanya *et al.* (3) indicate that backscattering should be negligibly small for energies below 20 keV.

The electron beam exposure of two negative photoresists has been investigated here. The first resist, Kodak Photosensitive Resist (KPR), contains a polyvinyl cinnamate polymer, while the second Kodak Thin Film Resist (KTFR), contains a polymerized isoprene dimer.

This work assumes that the threshold flux found in the exposure of these resists is related to the gel point of the resist. If this is the case, then the threshold flux should change when the accelerating potential of the electron beam is varied, but the amount of energy absorbed at the threshold should be constant. It is shown here, using Bethe's model for penetration range and Charleby's data on energy transfer, that the calculated threshold energies are constant, although the experimentally determined values of the threshold flux are a function of the energy of the electron beam. The shape of the exposure curve and the efficiency of energy usage in totally exposing the photoresist is also discussed.

Experimental

The exposure characteristics of photoresists were determined by irradiating thin films of the resists with varying electron fluxes. Typically, resist solution was spun onto a flat glass plate covered by 700Å of chromium to the required thickness. The resist-covered-plate was then baked at 150°C for 10 min to remove solvents, put into a specially designed vacuum system and pumped down to 2 x 10^{-5} Torr. At this point, the electron gun was turned on, allowed to stabilize at the desired accelerating potential, focused to give a spot about 2.5 cm^2, and the beam current measured using a Faraday cup. The resist-coated plate was then moved into the beam and left there until the desired electron flux was reached. After exposure, the plate was moved out of the beam, and the beam current was measured again to make sure that it did not change during the irradiation of the resist. Typical exposure times were 100 sec. Fluxes measured in this way were accurate to ± 5%. The resist-coated-plate was spray developed and baked at 150°C before its thickness was measured with either a Model 3 Taylor-Hobson Talysurf Profilimeter or with an interferometer. The thickness measurements on the Talysurf were reproducible to ± 300Å.

Identical results were obtained when either a glass plate or an oxidized silicon wafer was used instead of a chromium coated plate. Applying the resist by spray methods and dip developing after exposure also yielded the same data, as long as the application and development were carefully done.

Results

The thickness of exposed and developed resist layers was determined as a function of electron flux for different accelerating potentials and for different initial thicknesses of resist. Results for the exposure of KTFR are shown in Fig. 1 and 2, while Fig. 3 contains the data on KPR.

Both KPR and KTFR always show a threshold in exposure; that is, below a specific flux no insolubilized resist is formed. Above the threshold, an increase in flux gives an increase in resist thickness until the maximum resist thickness is reached. Both Thornley and Sun (4) and Kanaya *et al.* (3) have shown that resists must be exposed to their full thickness in order to afford full protection to SiO_2 layers. For this reason the lowest flux required to achieve maximum thickness will be designated as the lowest usable flux.

The lowest usable flux is a function of both the incident electron energy and the initial thickness of the resist, but the threshold flux principally depends

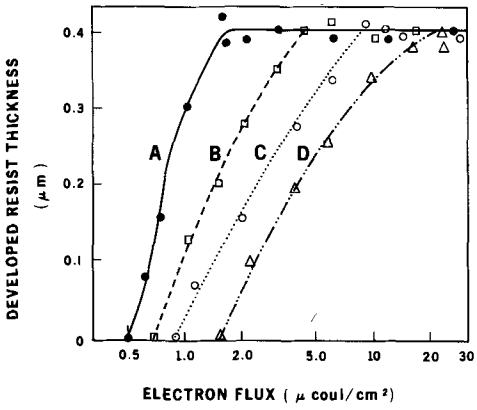

Fig. 1. Exposure of KTFR films (initial thickness 6000Å) to kilovolt electrons. Curve A, exposure to 5 keV electrons; curve B, to 10 keV electrons; curve C to 15 keV electrons; curve D to 20 keV electrons.

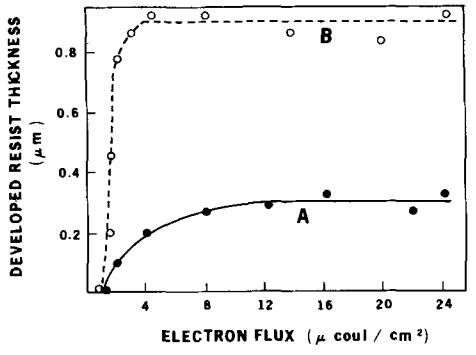

Fig. 2. Exposure of KTFR films to 15 keV electrons. Initial film thickness curve A, 12000Å, curve B, 3600Å.

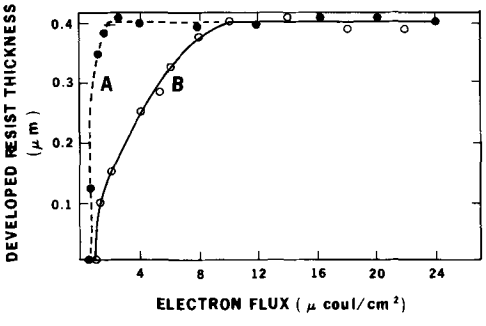

Fig. 3. Exposure of KPR films (initial thickness 6000Å) to kilovolt electrons. Curve A, exposure to 5 keV electrons, curve B to 15 keV electrons.

on the incident energy of the beam and is only somewhat dependent on the initial resist thickness (Fig. 1-3). The data that have been obtained are summarized in Table I. Also included in this table is the value of the contrast function of the resist, Γ, which is defined here as

$$\Gamma = \frac{\text{threshold flux}}{\text{lowest usable flux}}$$

Γ is a function of both the beam energy and resist thickness. It increases with the initial thickness of the resist, but decreases as the potential energy of the beam is increased, in the regions examined here.

It will be shown in the next section that one of the factors that determine the threshold flux is the range that the electron can penetrate into the photoresist. This range has been taken to be the maximum thickness of resist that can be exposed by a given incident electron energy. The range for 5 keV electrons has been determined to be 6500 ± 200Å, while 10 Kev electrons can penetrate between 2.0 and 2.5 μm. If

Table I. Exposure and contrast values for KTFR and KPR

Incident electron energy, keV	Resist	Initial thickness of resist, Å	Threshold flux, μcoul/cm²	Minimum useful flux, μcoul/cm²	Contrast function, Γ
5	KTFR	6000	0.5	1.5	0.33
10	KTFR	6000	0.7	3.5	0.20
15	KTFR	3600	1.1	12.0	0.09
		6000	0.9	8.0	0.11
		12000	0.9	4.0	0.22
20	KTFR	6000	1.6	16.0	0.10
5	KPR	6000	0.5	1.8	0.28
15	KPR	6000	0.9	10.0	0.09

layers thicker than these are exposed and developed, the exposed spot floats off the substrate. The maximum thickness of resist that can be exposed by 15 and 20 keV electrons was too great (> 3 μm) to be determined accurately by the Talysurf.

Discussion

Solubility of crosslinking systems.—Polymer molecules may react together forming intermolecular bonds, which eventually result in an "infinite" three-dimensional network of molecules. If the molecules are initially in solution, then a gelled or insoluble product is obtained when this occurs, and the reaction is said to have reached the gel point (6). This terminology has been carried over to describe the point at which solid crosslinking polymers, such as negative photoresists, become insoluble.

The solubility of irradiated crosslinking systems after radiation has been described by Charlesby (7, 8). He showed that polymers in which an initiated reaction does not propagate and therefore can lead to no more than one set of crosslinked units, will become insoluble, when the number of crosslinked units per weight average molecular weight molecule, designated δ, equals one. At this point, the weight average molecular weight of the polymer approaches infinity (7). This model should predict the behavior shown by KPR, since it becomes insoluble after being exposed to light, as the result of the formation of 4-membered rings having a substituted truxillic acid structure (9). The formation of 4-membered rings (10), indicates that in the insolubilization of KPR, the initiated reaction does not propagate. The lack of dependence of the photosensitivity of KPR on the presence of oxygen indicates that free radical reactions are improbable (10, 11).

On the other hand the exposure of KTFR is oxygen dependent, and its polymerized isoprene dimers (12) probably crosslink via a chain propagating free radical reaction. Its solubility characteristics would therefore be different from those of KPR. Charlesby has determined that, when a single crosslink can propagate and if the initiation sites are far enough apart so that chain termination arises from an inherent property of the polymer such as resonance stabilization, then the weight average molecular weight of the polymer approaches infinity when $\delta = [V/(V-1)][i/2(1-i)]$ (8). V is number of sites on the entire polymer molecule that are available for crosslinking and $(1-i)/i$ is the number of links in the crosslinking chain. Chain termination by disproportionation or by the combination of two chains is excluded in this discussion. $[V/(V-1)]$ is unity for photoresists since KTFR has a number average molecular weight of 6.5×10^4 and a weight average molecular weight of about 100,000 (13) and each isoprene dimer (molecular weight = 130) in the molecule has a site available for crosslinking, so that $V > 700$.

Gel point requires a threshold flux.—As long as the weight average molecular weight does not approach infinity, *i.e.*, $\delta < 1$ for KPR and $\delta < i/2(1-i)$ for KTFR, then the photoresists can be dissolved. The value of δ which is initially zero is determined by the amount of energy absorbed per molecule and the number of crosslinks formed by a molecule per unit of

absorbed energy. When crosslinking systems such as negative photoresists are exposed to an electron beam, then the average number of crosslinks per molecule is related to the dose by

$$\delta = 1.04 \times 10^{-6} rGW \qquad [1]$$

where r is the absorbed dose in megarads (10^8 ergs absorbed/g), G is the number of crosslinks formed per 100 eV absorbed, and W is the weight average molecular weight of the polymer being irradiated.

A value for W of about 3.2×10^5 has been reported for KPR (13) so that unless $r \geq 3/G$ megarads for this resist or $r \geq 4.8\, i/(1 - i)G$ megarads when KTFR is irradiated, none of the resist will be insolubilized. The value of r required to reach the gel point is called the gel dose and is designated as r_{gel}. The exposure threshold is the flux of electrons needed to transfer the amount of energy equivalent to r_{gel} from the beam to the resist. The thresholds that are reported with light exposures (10, 11, 14) are also brought about by the existence of a gel point and gel dose in crosslinking systems.

A method for calculating r_{gel} is presented in the next sections.

Energy transfer to photoresists.—It is expected that the amount of ionization and excitation produced by electrons changes as the electrons penetrate the absorber, since the probability of inelastic collisions increases as the energy of the electron decreases, but the amount of energy transferred at each collision decreases. Studies of energy loss as a function of penetration in polymers (15), water (16), and luminescent materials (17) show that the amount of energy transfer varies in essentially the same way in all media.

Charlesby determined (15) the density of ionization in polymers as a function of

$$\frac{\text{penetration into the polymer}}{\text{penetration range in the polymer}}$$

The density of ionization is related to the fraction of energy transferred, and his data are replotted in Fig. 4. Hatzakis (18) has reported that electron radiation of a positive resist yielded a pear shaped hole. His observation is consistent with Charlesby's measurements.

If it is assumed that the fraction of energy transferred from the beam to the photoresist layer also follows Charlesby's function and is related to

$$\frac{\text{thickness of the photoresist layer}}{\text{penetration range in the photoresist}}$$

then the amount of energy transferred from the beam to the resist can be calculated if the penetration range of electrons into photoresist is known. This calculation assumes negligible backscatter from the substrate and is valid since changing the substrate from chromium to oxided silicon did not affect the results.

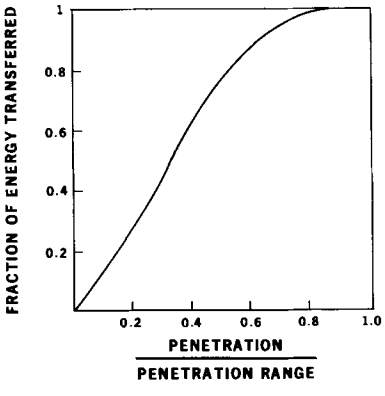

Fig. 4. Charlesby's relation of energy transfer as a function of (penetration/penetration range).

Since the penetration range of electrons into resists could not be precisely measured over the full range of exposure energies used here, a theoretical model for penetration range was chosen.

Penetration range of electrons.—Bethe has advanced a model for the transfer of energy from nonrelativistic electrons by inelastic collisions, in which the electrons follow a straight path into the absorbing medium up to a point, after which they randomly diffuse (19). The energy loss per cm is

$$\frac{dE}{dx} = \frac{2\pi e^4 NZ}{E} \ln \frac{2E}{J} \qquad [2]$$

which, when integrated using the limits proposed by Worthington and Tomlin (20), gives the range

$$R = \frac{J^2}{8\pi e^4 NZ}\left[Ei\left(2 \ln \frac{2E}{J} \right)\right] \qquad [3]$$

In these equations R is the range of the electron, and E, e, and x are its energy, charge and its distance into the absorber, respectively. NZ is the number of electrons/cc in the absorber and is equal to 3×10^{23} for both KPR and KTFR. $J = \frac{8}{\epsilon} I$ is the energy needed to form an ion pair in the absorber (ionization potential) and ϵ is the base of natural logarithms. I has been measured to be 26.4 eV when gaseous ethylene is irradiated with electrons (21). Since photoresists contain ethylenic groups, and since it is usually presumed that I is the same in solids and liquids (22), I has been taken to be 26.4 eV for photoresists. Any error arising from the use of this value should be small since other hydrocarbon vapors have values between 24.8 and 27.1 eV (21). $[Ei\ 2 \ln(2E/J)]$ is the exponential integral (23) which can be evaluated as

$$\left[\frac{\epsilon^{2 \ln(2E/J)}}{2 \ln(2E/J)}\right]\left(1 + \frac{1}{2 \ln(2E/J)} + \frac{2}{[2 \ln(2E/J]^2} \right)$$

to give the ranges shown in Table II.

The range of 5 and 10 keV electrons predicted by this model is in good agreement with the maximum thickness of photoresist that can be exposed at these accelerating potentials. On the other hand, the Thomson-Whiddington law (24) predicts ranges that are 5 times lower than the thickness of photoresist that can be exposed.

The ranges from Eq. [3] can now be used to calculate the total amount of energy transferred to the photoresists by the threshold fluxes at various incident electron energies. The gel doses obtained for the energies used here (Table III) show that layers of KPR and KTFR require the threshold flux to transfer $2.5 \pm 0.2 \times 10^{20}$ eV/cm^3 just to make an image visible in the photoresist. The uncertainty is within experimental error. Charlesby's experimentally obtained function was used for these calculations since Eq. [2] does not predict correctly energy transfer as a function of penetration in materials (15-17). The constant value of the threshold dose supports the assumption of a gel point.

G value.—The G value for KPR can be calculated from Eq. [1] since the threshold flux is 0.5 μcoul/cm^2

Table II. Penetration range in KPR and KTFR

Incident electron energy, keV	Range, μm Experimental	Calc.
5	0.65	0.66
10	2-2.5	2.3
15	—	4.8
20	—	8.3

Table III. Energy transfer in KTFR and KPR

Incident electron energy, keV	Resist thickness, Å	Resist thickness / Penetration range	Fraction of energy transferred, from Charlesby	Energy transferred (keV) per electron	Threshold flux, μcoul/cm²	Gel dose (eV/cm² × 10⁻¹⁶)	Gel dose (eV/cm³ × 10⁻²⁰)
5	6000	0.90	1.0	5.0	0.5	1.6	2.7
10	6000	0.26	0.36	3.6	0.7	1.6	2.7
15	3600	0.075	0.082	1.2	1.1	0.83	2.3
	6000	0.125	0.16	2.4	0.9	1.4	2.3
	12000	0.245	0.34	5.1	0.9	2.9	2.4
20	6000	0.072	0.078	1.6	1.6	1.6	2.7

at 5 keV, and it was established in the last section that the energy of the beam is totally transferred to the resist layer so that r_{gel} is 4.65 megarads and $G = 0.65$. The G value of KTFR cannot be as readily calculated since the number of links in the free radical chain is not known.

If it is presumed, however, that the number of intermolecular reactions initiated per hundred eV absorbed is the same for KPR and KTFR, i can be estimated. With this assumption, the G value for intermolecular reactions initiated in KTFR is equal to G_{KPR} since there are 2 bonds between each pair of KPR molecules and

$$G_{KTFR} = G_{initiated}\left(1 + \frac{1-i}{i}\right) = \frac{G_{KPR}}{i}$$

$$\text{At the gel point } G_{KTFR} = \frac{i}{2(1-i)} \quad (0.48)$$

so that $i = 0.54$ and $G_{KTFR} = 1.20$

This value of i implies that there is about 1 link in a crosslinking KTFR chain. A G value of 1.05 has been reported for smoked-oriented isoprene rubber (25) indicating that the result obtained here is reasonable.

These calculations presume that chain scission does not occur to an appreciable extent at low fluxes. Thornley and Sun (4) showed that scission is a minor process in the radiation of negative resists, since they were able to irradiate resists with up to 6 x 10^{-4} coul/cm² without increasing the solubility of the resists. Fluxes greater than 10^{-3} coul/cm² caused changes in solubility which may arise from scission.

Characteristic curves.—The curves in Fig. 1-3 can be considered to be the characteristic curves of the photoresists. They are analogous to the curves reported for silver halide emulsions except that thickness rather than optical density is measured as a function of exposure. Contract functions can be used to describe the properties of a photoresist and to predict the relative edge accuities expected in photoresist systems. Consider the contrast function, Γ, defined in the Results Section. Γ has been related to the end points of the thickness *vs.* exposure curve, rather than the slope of the curve, since each of the end points has special significance. As defined, $0 < \Gamma \leq 1$.

Γ appears to depend on the properties of the resist, its thickness, and the incident energy of the beam, but in a manner different from the threshold flux. The different functional dependence probably arises because the lowest usable flux is not reached when a certain number of crosslinks is achieved (as is the threshold flux) but rather is reached when all the photoresist molecules have reacted. Thus, the distribution of energy to uncrosslinked molecules becomes important and determines the efficiency of energy usage for total insolubilization.

The efficiency of energy usage for total insolubilization can be measured by comparing the minimum number of crosslinking reactions theoretically required for total insolubilization to the number of crosslinking reactions that actually occur during irradiation. The minimum number of crosslinks required is equal to the number of molecules, for if each molecule reacts with its neighbor then all the molecules could be linked together. The number of crosslinks that actually occur is equal to the number of electrons multiplied by the number of reactions that each electron can cause. This latter quantity is the product of the G value and the energy each electron transfers to the photoresist divided by 100. The number of molecules in a photoresist layer can be calculated from the molecular weight and the density of 0.9. Table IV contains the information required to calculate efficiency. It can be seen by comparing Tables I and IV that KTFR has an efficiency of about 1.7Γ, while for KPR it is 1.1Γ, but this quantitative relation has not yet been explained.

While no quantitative relation has been established between Γ and the most probable amount of energy transferred during an inelastic collision, they both vary in the same way when the energy of the beam is decreased or when the thickness of the resist is increased. The most probable amount of energy transferred in a collision is (26)

$$\Delta E_p = \frac{2\pi e^4 NZT}{2E}\left(\ln\frac{2\pi e^4 NZT}{I^2(1-\beta^2)} - \beta^2 - 0.34\right) \quad [4]$$

where the symbols are the same as in Eq. [2] while T is the thickness of the resist layer and β is the velocity of the incident electron divided by the velocity of light. Values of ΔE_p are given in the last column of Table IV.

Exposure energy: light vs. electrons.—Htoo has reported that 6000Å layers of KTFR can be fully exposed by 2.75 x 10^5 erg/cm² of 3650Å light (11). It

Table IV. Efficiency and probable energy transfer

Incident electron energy, keV	Resist	Initial thickness of resist, Å	Number of molecules in resist layer/cm², × 10⁻¹⁴	Number of electrons required for total exposures/cm², × 10⁻¹²	Number of molecules an electron can react with	Total number of reactions that actually occur/cm² (× 10⁻¹⁴)	Efficiency	Most probable amount of energy transferred ΔE_p (eV)
5	KTFR	6000	3.24	9.38	60	5.62	0.58	1780
10	KTFR	6000	3.24	21.9	43.2	9.46	0.34	887
15	KTFR	3600	1.94	75.0	14.4	10.8	0.18	344
		6000	3.24	50.0	28.8	14.4	0.23	582
		12000	6.48	25.0	61.2	15.3	0.42	1330
20	KTFR	6000	3.24	100	19.2	19.2	0.17	467
5	KPR	6000	1.08	11.3	32.6	3.68	0.30	1780
15	KPR	6000	1.08	62.5	15.6	9.75	0.11	582

was found here that when 5 keV electrons are used to expose this thickness of KTFR, 1.5 μcoul/cm^2 are required for full exposure. Since complete energy transfer occurs under these conditions, this flux is equivalent to 7.4 x 10^4 erg/cm^2 and 5 keV electron energy is 3.3 times more efficient than light energy in exposing KTFR. As the energy of the incident beam is increased, its efficiency in exposing the resist is decreased (lower Γ) and 15 keV electrons are only about as efficient in exposing KTFR as 3650Å light.

Conclusions

It has been shown here that:

1. The range of electrons in photoresist can be predicted from Bethe's integrated energy loss equation.
2. The amount of energy transferred at the threshold can be calculated from Charlesby's energy transfer relation and the range.
3. The amount of energy transferred/cm^3 at the threshold is constant for a given photoresist and is equal to 2.5 $\pm$ 0.2 x 10^{20} eV/cm^3 for KPR and KTFR. This is strong evidence that supports the assumption that the threshold is due to the gel point of the photoresist.
4. G values for KPR and KTFR were calculated to be 0.65 and 1.20, respectively. On the average, an excited KTFR molecule reacts only with one nearest neighbor.
5. The efficiency of insolubilization changes with both the thickness of the photoresist layer and the energy of the incident electrons. The efficiency may be related to the contrast function of the resist and to the most probable amount of energy transferred by an electron during an inelastic collision.

Acknowledgment

Both Dr. M. W. Sagal and Dr. W. R. Samaroo of the Engineering Research Center have provided the author with many helpful discussions. The author is also indebted to Mr. C. A. Adams for his proficient technical assistance.

Manuscript submitted April 17, 1969; revised manuscript received *ca.* June 2, 1969. This was Paper 551 presented at the Montreal Meeting, Oct. 6-11, 1968.

Any discussion of this paper will appear in a Discussion Section to be published in the June 1970 JOURNAL.

REFERENCES

1. W. C. Hittinger and M. Sparks, *Scientific American*, November, 1965, Page 57 provides an introductory discussion of microelectronics.
2. A. N. Broers, *Microelectronics and Reliability*, **4**, 103 (1965).
3. K. Kanaya, H. Yamazaki, and K. Tanaka, *Optik*, **25**, 471 (1967).
4. R. F. M. Thornley and T. Sun, *This Journal*, **112**, 1151, (1965).
5. R. K. Matta, *Electrochem. Technol.*, **5**, 382 (1967).
6. P. J. Flory, *J. Am. Chem. Soc.*, **63**, 3083 (1941).
7. A. Charlesby, *Proc. Roy. Soc.*, **A222**, 542 (1954).
8. A. Charlesby, *ibid.*, **A241**, 495 (1957).
9. F. I. Sonntag and R. Srinivasan, Postprint of papers presented at the Society of Plastics Engineers Regional Conference (November, 1967).
10. J. H. Altman, *ibid.*
11. M. S. Htoo, *Photographic Science and Engineering*, **12**, 169 (1968).
12. DDC AD-484, 487
13. H. A. Levine, L. G. Lesoine, and J. A. Offenbach presented at the Kodak Photoresist Seminar, June (1967).
14. T. Yoshinaga, Y. V. Chien, and S. Kikuchi, *Kogo Kagaku Zasshi*, **66**, 665 (1963).
15. A. Charlesby, "Atomic Radiation and Polymers," p. 32, Pergamon Press, New York (1960).
16. J. G. Trump and R. J. Van de Graaff, *J. Appl. Phys.*, **19**, 599 (1948).
17. W. Ehrenberg and D. E. N. King, *Proc. Phys. Soc.*, **81**, 751 (1963).
18. M. Hatzakis, Paper 164 presented at the Montreal Meeting of the Society, May 6-11, 1968.
19. H. A. Bethe and J. Ashkin in "Experimental Nuclear Physics," Vol. II, Eq. 51, p. 253, E. Segrè, Editor, J. Wiley & Sons, Inc., New York (1953).
20. C. R. Worthington and S. G. Tomlin, *Proc. Phys. Soc.*, **69A**, 401 (1956).
21. A. J. Swallow, "Radiation Chemistry of Organic Compounds," pp. 13-16, Pergamon Press, New York (1960).
22. A. Chapiro, "Radiation Chemistry of Polymeric Systems," pp. 39-49, Interscience Publishers, New York (1962).
23. E. Jahnke and F. Emde, "Tables of Functions," Dover Publications, New York (1945).
24. G. D. Archard, *J. Appl. Phys.*, **32**, 1505 (1961).
25. A. Charlesby and E. von Arnim, *J. Poly. Sci.*, **25**, 151 (1957).
26. H. A. Bethe and J. Ashkin, *loc. cit.* Eq. 54B, p. 256.

Electronic Structure of the Vanadate and Tungstate Complexes

Wolfgang Walter and Keith H. Butler*

Sylvania Electric Products Incorporated, Danvers, Massachusetts

ABSTRACT

The excitation and emission spectra of unactivated yttrium vanadate and calcium tungstate have been measured. Relative absorption spectra were derived from the excitation spectra. In order to aid in the interpretation of the absorption and emission, a series of semiempirical LCAO-MO calculations were carried out on the vanadate and tungstate complexes. These calculations indicate that the transitions primarily responsible for absorption are the charge transfer transitions $t_1 \rightarrow 2e$ and $t_1 \rightarrow 4t_2$. The vanadate emission peak is accounted for by an increase of 0.15Å in the vanadium-oxygen distance for the excited state. Electrostatic splitting and the effects of lowering of symmetry from T_d to D_{2d} are discussed.

Calcium and magnesium tungstates (1) are important phosphors, frequently used for color correction in fluorescent lamps. Yttrium vanadate is an important host material in the red emitting phosphor obtained by activating it with trivalent europium. Various unactivated vanadates (2) are also known to fluoresce with moderate efficiency when excited by a low pressure mercury discharge. It has also been shown that the anions WO_4^{-2} and VO_4^{-3} can serve as activators in sulfates and silicates (3).

* Electrochemical Society Active Member.

In general, the excitation and emission spectra of phosphors activated by cations, such as Sb^{+3}, Sn^{+2}, Pb^{+2}, can be explained as being due to the promotion of an electron of the activator to an excited state, followed by lattice relaxation to a new equilibrium position and then by a transition to the ground state with emission of radiation. The energy levels of the ion are modified by the influence of the surrounding ions so that the energy required to excite the ion in the crystal is approximately half that needed to excite the free ion.

If the ion responsible for fluorescence is considered to be W^{+6} or V^{+5}, it is found that the energy needed for excitation would fall deep in the vacuum ultraviolet, if the crystal field effect were the same as that on a cation activator. Hence it was recognized very early (4) that the luminescence must be ascribed to the whole complex rather than to the central ion and that the energy levels of the complex must be quite different from those of the central ion.

In spite of this recognition of the unique nature of the activation, no attempt has been made to apply modern molecular orbital calculations to the problem of interpreting the excitation and emission spectra of crystals containing these complex ions.

For these reasons we have made a study of the electronic structure of the VO_4^{-3} and WO_4^{-2} complexes in YVO_4 and $CaWO_4$, respectively. These two complexes can be studied together because of their identical symmetry and coordination and because they are isoelectronic in their valence electrons.

Phosphors were made with high-purity components using methods described in the section on Preparation of Materials. The excitation and emission spectra of YVO_4 and $CaWO_4$ were measured and the excitation spectra were converted into relative absorption spectra, as described in the section on Excitation and Derived Absorption Spectra. Semiempirical LCAO-MO (linear combination of atomic orbitals-molecular orbital) calculations were carried out on the complexes assuming them to have tetrahedral symmetry. The methods of calculation are described and the results are given. The effects of electrostatic splitting and the reduction to D_{2d} symmetry are discussed and an interpretation of the derived absorption spectra is given.

Preparation of Materials

The yttrium vanadate sample was prepared from a mixture of American Potash and Chemical Company Y_2O_3 of 99.9999% purity and Baker V_2O_5, 99.8% pure. The mixture was fired for 1 hr at 1300°C.

The calcium tungstate sample was prepared by mixing hot solutions of highly purified Na_2WO_4 and $CaCl_2$, followed by washing until free of sodium chloride and firing for 16 hr at 1040°C.

Excitation and Derived Absorption Spectra

The excitation spectra of unactivated YVO_4 and $CaWO_4$ were measured with a vacuum spectroradiometer that automatically corrects for the spectral variation of the lamp output. These are shown in Fig. 1 and 2. In order to get a more appropriate experimental basis for our theoretical studies, we converted the excitation curves into relative absorption spectra. This was done by applying some results of the theory of the optical properties of powder layers (5). For powder layers thick enough for no transmission of exciting radiation, the absorption coefficient μ is related to the reflectance R by

$$\mu/\beta = (1-R)^2/2R \qquad [1]$$

where β is the scattering coefficient. If the reflectance spectrum is known, Eq. [1] can be used to derive a relative absorption curve since β remains nearly constant with wavelength. Reflectance spectra of YVO_4 and $CaWO_4$ were measured with a Beckman DK spectrophotometer. However, the resolution was not great enough to show any appreciable structure. In the excitation spectrum the emitted light intensity I of the phosphor layer is proportional to the absorbance A or, for a thick layer, proportional to $1 - R$

$$I = KA = K(1-R) \qquad [2]$$

The constant K was determined by estimating the value of R at the wavelength of the highest excitation peak. The relative absorption spectrum was calculated from the excitation data by application of Eq. [1] and [2]. The derived relative absorption spectra, which are shown in Fig. 1 and 2, were resolved into Gaussian functions by a computerized trial and error method. The resolutions are shown in Fig. 3 and 4, and Table I

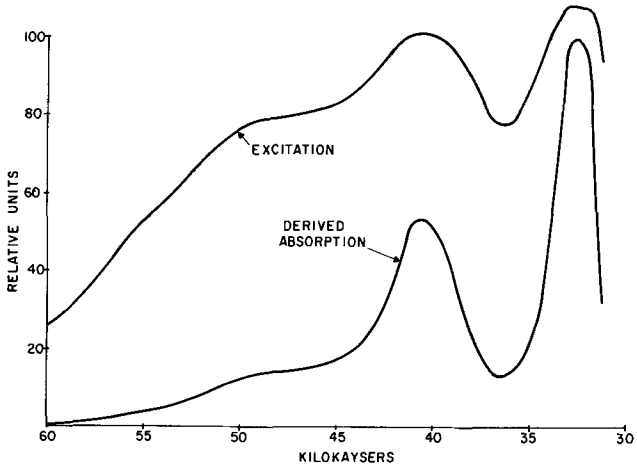

Fig. 1. Excitation and derived relative absorption curve of YVO_4

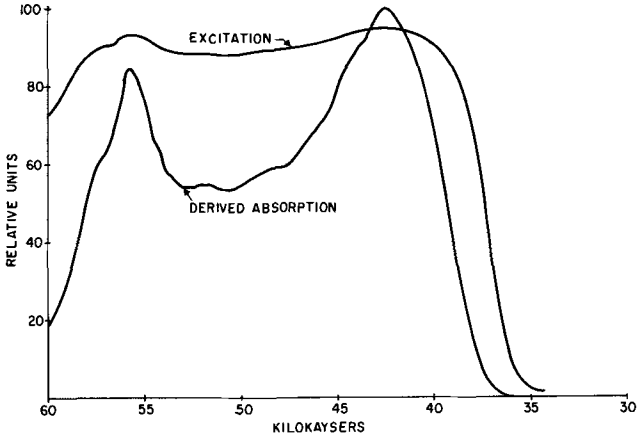

Fig. 2. Excitation and derived relative absorption curve of $CaWO_4$

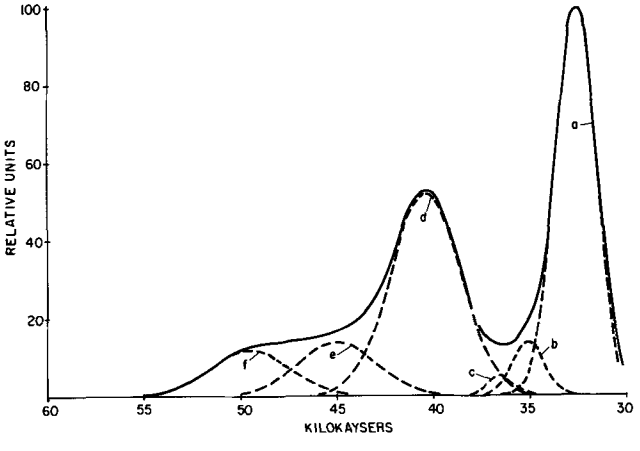

Fig. 3. Derived absorption spectrum of YVO_4 resolved into Gaussian functions. The solid curve shown is the sum of the Gaussians. Compare this to the actual absorption curve in Fig. 1. States are assigned to the peaks; see text for details.

Table I. Gaussian function parameters used in fitting absorption curves and transition assignments. The functions have the form: A exp- $(\nu - \nu_0)^2/\sigma^2$. The transitions are all from the ground state, $^1A_1$.

	ν_0 (kK)	A	σ (kK)	Assignment
		YVO_4		
a	32.6	100	1.05	$^1T_1$ ($t_1 \rightarrow 2e$)
b	35.1	14	0.80	$^3T_2$ ($t_1 \rightarrow 2e$)
c	36.6	5	0.60	$^1T_1$ ($3t_2 \rightarrow 2e$)
d	40.4	52	1.80	$^1T_2$ ($t_1 \rightarrow 2e$)
e	45.0	14	2.00	$^1T_1$ ($t_1 \rightarrow 4t_2$)
f	49.5	12	2.00	$^1T_2$ ($t_1 \rightarrow 4t_2$)
		$CaWO_4$		
a	40.0	47	1.00	$^3T_1$ ($t_1 \rightarrow 2e$)
b	42.4	94	1.40	$^1T_1$ ($t_1 \rightarrow 2e$)
c	44.8	54	1.00	$^3T_2$ ($t_1 \rightarrow 2e$)
d	46.5	24	0.80	$^1T_1$ ($3t_2 \rightarrow 2e$)
e	48.4	53	1.70	$^1T_2$ ($t_1 \rightarrow 2e$)
f	52.3	49	1.75	$^1T_1$ ($t_1 \rightarrow 4t_2$)
g	55.8	77	1.24	$^1T_2$ ($t_1 \rightarrow 4t_2$)
h	58.0	37	0.70	$^1T_1$ ($3t_2 \rightarrow 4t_2$)

lists the Gaussian parameters. We have used the minimum number of Gaussians that result in a good fit to the absorption curves. The emission spectra of YVO_4 and $CaWO_4$ are shown in Fig. 5. Each curve consists of a single almost perfect Gaussian with maxima at 22.5 kK and 24.0 kK, respectively (kK = kilokayser, 1 kK = 10^3 cm^{-1}).

Semiempirical Molecular Orbital Calculations

In order to facilitate the interpretation of the absorption spectra, semiempirical molecular orbital calculations were carried out on the VO_4^{-3} and WO_4^{-2} complexes. The method is described below.

LCAO-MO theory.—As usual in molecular orbital theory (6), the molecular orbitals ϕ_i are assumed to be linear combinations of the atomic orbitals u_j

$$\phi_i = \Sigma_j C_{ij} u_j \quad [3]$$

The atomic orbitals considered in the calculations were the 3d, 4s, and 4p orbitals of the vanadium or the 5d, 6s, and 6p of tungsten, together with 2s and 2p orbitals of the four oxygen ligands. The inner orbitals were regarded as part of the core. By application of the variational principle, the assumption of Eq. [3] leads to a set of linear homogeneous equations for the coefficients C_{ij}

$$\Sigma_k C_{ki} (H_{jk} - E_i S_{jk}) = 0 \quad [4]$$

H_{jk} is the matrix element of the one-electron Hamiltonian between orbitals u_j and u_k, S_{jk} is the overlap integral between the two orbitals, and E_i is the energy. The set of Eq. [4] can only have nontrivial solutions for the C_{ki} if the determinant of their coefficients is zero. This leads to the secular equation

$$|H_{jk} - ES_{jk}| = 0 \quad [5]$$

Equations [3] to [5] can be solved for the molecular energies and orbitals.

Considerable simplification in the calculation results from the application of group theory. Instead of using the ligand orbitals directly in the expansion of Eq. [3], one first finds linear combinations of them that are basis functions for the irreducible representations of the tetrahedral group T_d, and then combines these with the central atom orbitals (7). The orbital combinations used are the same as those given by Viste and Gray (8). The simplification comes about because the matrix elements between orbitals belonging to different irreducible representations and to different rows of the same representation are zero. This reduces the determinant of Eq. [3] to a product of smaller determinants. In our case, there are twenty-five atomic orbitals, so that Eq. [5] contains a 25 x 25 determinant. This determinant reduces to a 3 x 3 determinant of A_1 symmetry, two identical 2 x 2 determinants of E symmetry, three identical 5 x 5 T_2 determinants, and three identical 1 x 1 T_1 determinants.

Matrix elements.—The overlap integrals were calculated by means of a computer program from published analytic atomic orbitals of neutral vanadium (9) and oxygen (10) atoms. The tungsten orbitals were computed by the Herman-Skillman (11) program and then converted to analytic form.

The metal-oxygen internuclear distances were taken to be 1.706Å for vanadate (12) and 1.79Å for tungstate (13). Ligand-ligand overlaps were neglected.

The diagonal elements of the Hamiltonian matrix were approximated in different ways in two separate calculations. In the first method, we followed the procedure of Basch, Viste, and Gray (14). Namely, the diagonal elements were set equal to their respective VOIP's (valence orbital ionization potentials). That is, H_{ii} was set equal to the energy the i'th electron would have if its ion were free. This, of course, is a function of the charge on the ion. Following Basch *et al.*, we varied the vanadium VOIP's as a function of effective charge and fixed the oxygen VOIP's to the values given in their paper. We did not, however, consider the variation of VOIP with configuration, but only used the VOIP's for the lowest configuration. We felt that the change of VOIP with configuration was relatively small and the roughness of the approximation involved in this type of calculation did not warrant the additional refinement.

The second method of approximation of the diagonal Hamiltonian elements consists essentially, of adding a term to each VOIP. The VOIP only takes into account the effect on the electron of its own ion and neglects the effects of the other ions. To compensate for this, we have added the Madelung potential; that is the electrostatic energy due to the other ions in the complex and in the rest of the solid, assuming them to be point

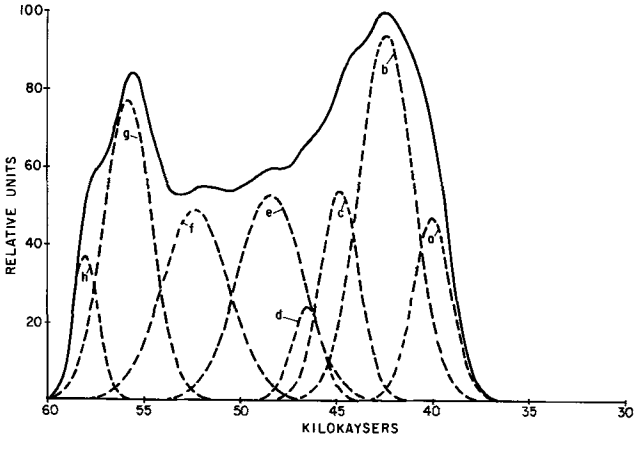

Fig. 4. Derived absorption spectrum of $CaWO_4$ resolved into Gaussian functions. The solid curve shown is the sum of the Gaussians. Compare this to the actual absorption curve in Fig. 2. States are assigned to the peaks; see text for details.

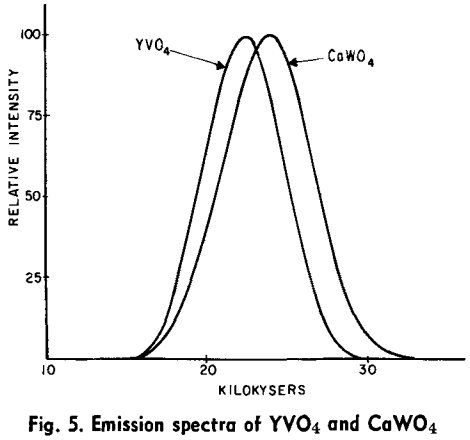

Fig. 5. Emission spectra of YVO_4 and $CaWO_4$

charges (15). With this method, we did not fix the oxygen VOIP's but allowed them to vary with charge as with the vanadium VOIP's. Basch *et al.* (14) fixed the oxygen VOIP's to correspond to the experimental values found in oxygen containing molecules. This partially compensated for the neglect of the effect of the other ions. In our method, there is no need to fix the VOIP's. The addition of a point charge energy was also suggested by Fenske *et al.* (16), and more recently by Brown *et al.* (17).

The off-diagonal matrix elements of the Hamiltonian were approximated by using the Wolfsberg-Helmholtz approximation (18)

$$H_{ij} = \frac{1}{2} F(H_{ii} + H_{jj}) G_{ij} \qquad [6]$$

where G_{ij} is the group overlap integral and F is an adjustable parameter. This relationship was used for both methods of approximating the diagonal elements. In order to minimize the number of parameters, the same value of F was used for both σ and π overlaps.

The calculations were performed on an I.B.M. 1130 computer. The input effective charge was varied to make it self-consistent with the charge calculated from the resulting wave functions by a Mulliken populations analysis (19).

Results of Calculations

Figure 6 shows the energy level diagrams for the vanadate and tungstate complexes obtained from these calculations using the first method of approximation. A value of F, the Wolfsberg-Helmholtz parameter, of 1.87 was used for both complexes. The self-consistent effective charge on the vanadium was 0.98 and therefore —0.995 on each of the oxygens. The tungsten effective charge was 0.63 with —0.66 on its ligands. Vanadate and tungstate are isoelectronic in their valence electrons. In their ground states the t_1 level is the highest occupied level and is completely filled. We believe that the transitions primarily involved in absorption are transitions from the filled t_1 level to the first two unoccupied levels: $2e$ and $4t_2$ (see next section). The orbital of the t_1 level is based solely on the ligands. On the other hand, the $2e$ and $4t_2$ levels have orbitals that are shared between the metal and its ligands. The calculated molecular orbitals in vanadate indicate that an electron on the $2e$ level spends 65% of its time in a vanadium orbital and the rest in ligand orbitals, while if it is on the $4t_2$ level the percentage increases to 75%. The corresponding figures for tungstate are 52% and 53%. This shows that the tungsten bonds are more covalent than those of vanadate.

The order of the levels resulting from the second method of calculation, in which the Madelung potential is added to H_{ii}, is substantially the same. However, there are notable differences in some of the results. Smaller values of F are required to give reasonable results. The dependence of the position of the $2e$ and $4t_2$ levels on F for both methods are shown in Fig. 7. F values of 1.65 for vanadate and 1.54 for tungstate leave the positions of the two levels at about the same positions as in the previous calculations. The self-consistent effective charges were quite different than previously. In vanadate, they were 3.0 and —1.5 for vanadium and oxygen, respectively, and in tungstate 3.9 and —1.5. These values are closer to the ones expected in a purely ionic model, indicating the approximation has been improved.

The emission peak can be accounted for by a $2e \rightarrow t_1$ transition after the excited state has come to equilibrium with a larger metal-ligand distance. A series of calculations on vanadate were made to study the effect of the metal-ligand distance R on the energy levels. The results are summarized in Fig. 8 for the $2e$ and $4t_2$ levels. It can be seen that in order to get the observed emission at 22.5 kK, the value of R for the excited state must be 1.85Å. This requires an increase in R of 0.15Å, which is quite reasonable.

Additional Splitting of Energy Levels

The calculations described in the previous section neglected to take into account the complete effects of the electrostatic repulsion of electrons. These interactions will further split the energy levels. The ground state configuration of both complexes is $(t_1)^6$, which results in a singlet term, $^1A_1$. The configuration of the first excited state is $(t_1)^5$ $(2e)$. This configuration splits up into the multiplets $^1T_1$, $^1T_2$, $^3T_1$, and $^3T_2$. Ballhausen (20) gives the order of the levels as $^1T_1 > {}^1T_2 > {}^3T_2 \approx {}^3T_1$. The other excited state of interest has the configuration $(t_1)^5$ $(4t_2)$ and splits into singlets and triplets of T_2, T_1, E, and A_1 in that order of decreasing energy, according to Wolfsberg and Helmholtz (18).

The order of the levels taken from the above two

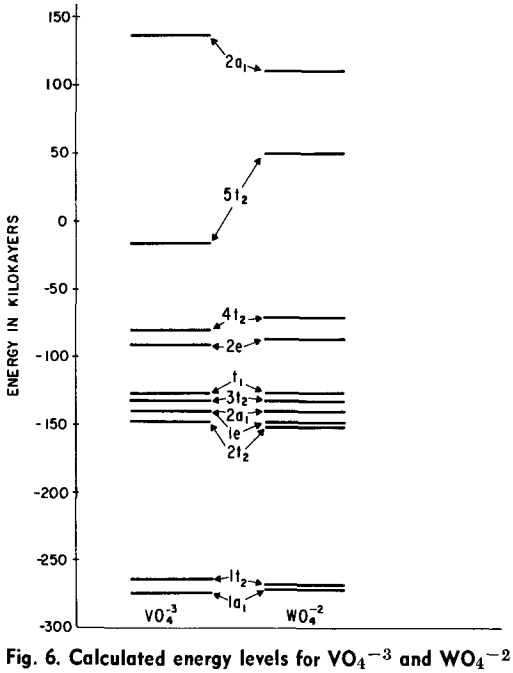

Fig. 6. Calculated energy levels for VO_4^{-3} and WO_4^{-2}

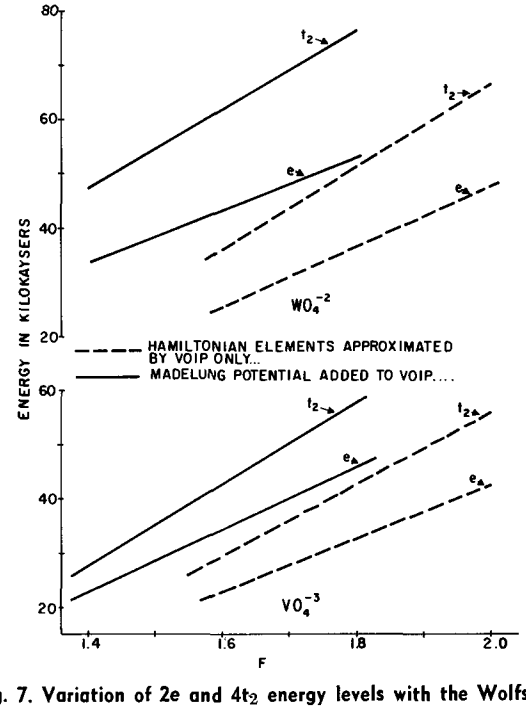

Fig. 7. Variation of 2e and $4t_2$ energy levels with the Wolfsberg-Helmholtz parameter F for the vanadate and tungstate complexes. Energy is measured from the t_1 level.

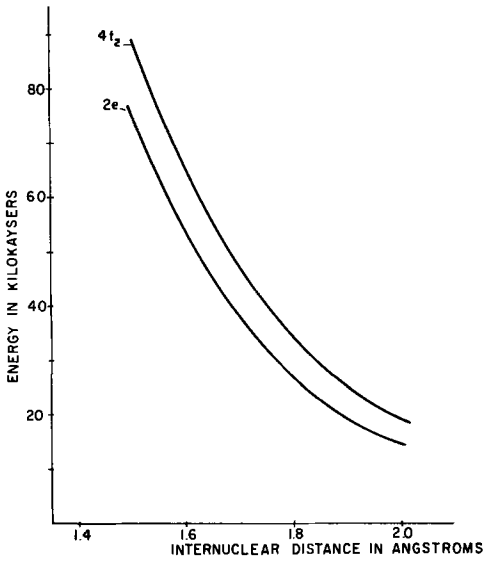

Fig. 8. Variation of 2e and $4t_2$ energy levels with internuclear distance *R* in vanadate. The base line represents the t_1 level.

references were based on simplified calculations that neglected overlap integrals. Since some of the overlaps are large, the order given need not necessarily be the actual order. From symmetry considerations, the only allowed electric dipole transitions from the $^1A_1$ ground state are to T_2 states. Each of the two excited configurations has one triplet $^3T_2$ and one singlet $^1T_2$. Since the ground state is a singlet, transitions to triplet states are allowed only to the extent that there is spin-orbit coupling. The magnitude of spin-orbit coupling is greater in tungsten than in vanadium so that the transition intensities to the triplet states should be relatively larger.

The analysis thus far does not account for all the peaks in the absorption spectrum. The magnitude of the spin-orbit splitting is too small to be observed in such a curve. This indicates that "forbidden" transitions are present. These can become allowed because of vibronic interactions or a reduction of symmetry. The vanadate and tungstate complexes in YVO_4 and $CaWO_4$ are actually slightly distorted tetrahedra having D_{2d} symmetry. The vanadate is elongated along the z axis, while the tungstate is contracted. The lowering in symmetry splits each of the tetrahedral levels, except the A_1 levels, into two separate levels. Because of the smallness of this perturbation, it is not expected that this splitting is observed in our derived absorption curves. However, the new selection rules now allow a greater number of transitions. The T_1 states split into E and A_2 states in D_{2d} symmetry. With tetrahedral symmetry transitions to T_1 states were forbidden. However, in D_{2d} symmetry transitions to E states are allowed.

Assignment of the various Gaussian components of the calculated absorption spectra to specific transitions is necessarily highly speculative. Using Ballhausen's ordering, it is probable that the two major absorptions in the vanadate at 32.6 kK and 40.4 kK are the $^1T_1$ and $^1T_2$ levels of the transition $t_1 \rightarrow 2e$. The two absorptions at 45.0 kK and 49.5 kK are then assigned to $^1T_1$ and $^1T_2$ of $t_1 \rightarrow 4t_2$.

The weaker absorption at 35.0 kK may be $^3T_2$ of $t_1 \rightarrow 2e$ with the $^3T_1$ being buried in the major absorption peak. The weak peak at 36.4 kK may be a $^1T_1$ level for the transition $3t_2$ to 2e. The assignments give an experimental gap of 11 kK between 2e and $4t_2$ and 4.0 kK between $3t_2$ and t_1. The triplet level is 5.5 kK below the singlet.

In the more complex tungstate spectrum, the 42.4 kK and 48.4 kK peaks are assigned to $^1T_1$ and $^1T_2$ of $t_1 \rightarrow 2e$ with the triplets $^3T_1$ and $^3T_2$ giving 40.0 kK and 44.8 kK peaks. The greater intensities of the triplets is in agreement with the greatly increased spin-orbit coupling in tungsten which will mix singlet and triplet states.

The singlets $^1T_1$ and $^1T_2$ for the $t_1 \rightarrow 4t_2$ transitions are placed at 52.2 kK and 55.8 kK. The remaining absorptions at 46.0 kK and 58.0 kK can be tentatively ascribed to $^1T_1$ for $3t_2 \rightarrow 2e$ and $3t_2 \rightarrow 4t_2$.

These assignments give an experimental gap of 9.0 kK between 2e and $4t_2$ with an average value of 4.6 kK between $3t_2$ and t_1. The triplet levels are about 3.0 kK below the singlets. These assignments are summarized in Table I.

Conclusions

This paper is a first attempt to apply semiempirical molecular orbital theory to problems of oxygen-dominated phosphors. The excitation spectra, assumed to be due to absorption by a complex ion with appreciable covalent bonding, allows derivation of an absorption spectrum with much more detail than can be obtained by a reflectance measurement. Analysis into Gaussian components reveals that a rather complex array of separate energy levels must be present in the ions.

The approximations made in the molecular orbital calculations were introduced in order to simplify the rather formidable mathematical problem involved in computing the electronic structure of such complex systems. These approximations limit us to determining the average energies of configurations only.

Recently, molecular orbital calculations were performed by Dahl and Johansen (21) on a series of tetrahedral complexes, including VO_4^{3-} but not WO_4^{2-}. Their calculations involved the actual computation of diatomic coulomb and exchange integrals and thus contained less severe approximations than in our work. However, their extensive computations on the permanganate complex have shown that the results are quite sensitive to the choice of atomic orbitals. It therefore might be questionable as to whether more exact calculations are warranted until more is known on how the atomic functions change when the ion is brought into the complex. The order of the levels obtained by Dahl and Johansen for vanadate is different from ours. Their results show the $4t_2$ level to be lower in energy than 2e. From a simple crystal field theory point of view, it is more plausible for the 2e state to be lower in tetrahedral symmetry (22). Furthermore, this would make the results consistent with the level ordering in permanganate.

Even with these limitations, the present calculation gives useful results. Selection of a value of the parameter *F* to fit the lowest major peak by a t_1 to 2e transition places the t_1 to $4t_2$ transition at energy very close to the second major peak of the absorption spectrum.

The existence of other energy levels is predicted by group theory for the distorted tetrahedral shape of the complex ion in its crystal site. For the vanadate ion, tentative assignments can be made and the observed splitting of the average energy of the configuration into singlet A, E, T_1, and T_2 terms is of the anticipated order of magnitude.

The more complex spectrum of the tungstate can be ascribed to transitions to triplet terms. The probability of such transitions would be low for vanadate and considerably higher for tungstate.

Assuming a relaxation of the lattice after excitation is responsible for the Stokes shift giving visible blue emission from the ultraviolet absorption, the change in interionic spacing was found to be 0.15Å, which appears reasonable.

Further refinement of the calculation to fix more definitely the order and position of the separate terms of the various configurations would add to its value. Work on such a refinement is in progress.

Acknowledgments

We wish to thank Costas Lagos for synthesizing the YVO_4 sample and Robert F. Craig, Stanley Reczek, and Robert Maleszyk for taking measurements of the spectra.

Manuscript submitted March 24, 1969; revised manuscript received May 23, 1969. This was Paper 29 presented at the Boston Meeting, May 5-9, 1968.

Any discussion of this paper will appear in a Discussion Section to be published in the June 1970 JOURNAL.

REFERENCES

1. J. L. Ouweltjes in "Modern Materials," Vol. 5, Academic Press, New York (1965).
2. M. A. Aia, *This Journal*, **114**, 367 (1967).
3. Y. Kotera *et al.*, *ibid.*, **108**, 540 (1961).
4. F. A. Kroger, "Some Aspects of the Luminescence of Solids," Elsevier, 1948 (Reprint University Microfilms 1965).
5. J. W. ter Vrugt, *Philips Res. Rept.*, **20**, 23 (1965); K. H. Butler, Extended Abstracts of Electrochem. Soc. Meeting, Boston, May 1968.
6. J. C. Slater, "Quantum Theory of Molecules and Solids," Vol. 1, McGraw-Hill Publishing Co., New York (1963).
7. C. J. Ballhausen, "Introduction to Ligand Field Theory," McGraw-Hill Publishing Co., New York (1962).
8. A. Viste and H. B. Gray, *Inorg. Chem.*, **3**, 1113 (1964).
9. R. E. Watson, *Phys. Rev.*, **119**, 1934 (1960); J. W. Richardson, R. R. Powell, and W. C. Nieuwpoort, *J. Chem. Phys.*, **38**, 796 (1963).
10. E. Clementi, C. C. J. Roothaan, and M. Yoshimine, *Phys. Rev.*, **127**, 1618 (1962).
11. F. Herman and S. Skillman, "Atomic Structure Calculations," Prentice-Hall, (1963).
12. J. A. Baglio and G. Gashurov, *Acta Cryst.*, **B24**, 292 (1968).
13. A. Zalkin and D. H. Templeton, *J. Chem. Phys.*, **40**, 501 (1964).
14. H. Basch, A. Viste, and H. B. Gray, *ibid.*, **44**, 10 (1966)
15. W. Walter and J. L. Birman, *Bull, Am. Phys. Soc.*, **10**, 598 (1965); W. Walter, Thesis, New York University, 1966, unpublished; W. Walter and J. L. Birman in "II-VI Semiconducting Compounds," D. G. Thomas, Editor, W. A. Benjamin Inc. (1967).
16. R. F. Fenske *et al.*, *Inorg. Chem.*, **5**, 951 (1966).
17. R. D. Brown, M. F. O'Dwyer, and K. R. Roby, *Theoret. Chim. Acta*, **11**, 1 (1968).
18. M. Wolfsberg and L. Helmholtz, *J. Chem. Phys.*, **20**, 837 (1952).
19. R. S. Mulliken, *ibid.*, **23**, 1833, 1841, 2338 (1955).
20. C. J. Ballhausen, *Theoret. Chim. Acta*, **1**, 285 (1963).
21. J. P. Dahl and H. Johansen, *ibid.*, **11**, 8, 26 (1968).
22. D. S. McClure, "Solid State Physics," Vol. 9, F. Seitz and D. Turnbull, Editors, Academic Press (1959).

Luminescence Properties of Rare Earth Tellurates

S. Natansohn

The Bayside Research Center of General Telephone & Electronics Laboratories Incorporated, Bayside, New York

ABSTRACT

The fluorescent properties of a new class of inorganic phosphor materials based on rare-earth tellurates R_2TeO_6 as host materials are discussed. Yttrium, lanthanum, gadolinium, and lutetium tellurates, activated by trivalent rare-earth or by uranyl ions, show significant luminescence under ultraviolet or cathode ray excitation. The cathodoluminescent response of the uranyl-activated rare-earth tellurates is comparable to that of the most efficient uranyl phosphors known. The effect of structural variations on the spectral energy distribution of the UO_2^{2+} and Eu^{3+} emission is considered.

The chemical literature contains few references to the rare-earth tellurates. Mellor (1) reports the synthesis of yttrium tellurate by Berzelius but gives no formula for the compound. Kent and Eick (2) mention parenthetically the formation of compounds of the form R_2TeO_6 under certain conditions in their synthesis of rare-earth (III) monoxotellurides without providing identifying information about these materials. Furthermore, available literature sources contain no reference to fluorescent materials based on metal tellurates as the host matrix. This paper describes the luminescence phenomena observed on activation of the optically inert Y, La, Gd, and Lu tellurates. The green-emitting uranyl ion, UO_2^{2+}, and the red-emitting trivalent Eu ion were the principal activators used in this study, although other activators were also examined.

Experimental

The compounds were prepared by mixing equimolar amounts of the appropriate reagent-grade rare-earth sesquioxides and orthotelluric acid, $Te(OH)_6$, and then heating the mixture in silica crucibles in a series of steps up to a temperature of 1200°C. For best luminescent results, the heat treatment was done in an oxygen atmosphere, although the compounds can be readily formed in air. Typically, the samples were fired at 800°, 1000°, and 1100°C for 4 hr each, and the charge was mortared between the heating steps. The rare-earth activators were added substitutionally in the form of oxides, while the uranyl activator was conveniently added as the nitrate or acetate. The activator concentration was generally between 0.005 and 0.10 mole/mole of R_2TeO_6.

The procedure for establishing the composition of the rare earth tellurates was given elsewhere (3) and the presence of the desired phases was checked after each firing step by x-ray diffractometry. Unless otherwise indicated, the excitation and emission spectra are given in terms of relative energy *vs.* wavelength and were obtained by the procedure described by Amster and Wiggins (4). Diffuse reflectance spectra were obtained on the Cary 14 spectrophotometer.

Results and Discussion

The Y, La, Gd, and Lu tellurates are white crystalline substances whose x-ray powder diffraction patterns were indexed on the basis of a hexagonal unit cell (3) (Table I). They are structurally different from the rare-earth tungstates and molybdates with analogous formulas which have been the subject of extensive investigations as phosphor materials (5-7). The nature of the diffractograms and analysis of the observed systematic extinctions indicate that Y, La, and Gd tellurates are isomorphous, but Lu_2TeO_6, although hexagonal, is of a different crystalline system. The x-ray powder diffraction data are insufficient to determine the space

Table I. Crystallographic data of rare earth tellurates

Formula Structure	Y_2TeO_6 Hexag.	Le_2TeO_6 Hexag.	Gd_2TeO_6 Hexag.	Lu_2TeO_6 Hexag.
a_o [Å]	10.46	10.95	10.60	8.94
c_o [Å]	9.95	10.35	10.05	5.08
Z	8	8	8	3
$d_{theor.}$ [g/cm³]	5.67	6.22	7.27	8.12
$d_{meas.}$ [g/cm³]	5.60	6.10	7.17	8.19

group of these compounds; however in the case of Y, La, and Gd tellurates it is possible to narrow down the choice to three space groups $P6_3$, $P6_{3/m}$, and $P6_322$.

Spectroscopic Properties of Eu^{3+}*-Activated* R_2TeO_6

Activation of the rare-earth tellurates by lanthanide luminogens results in phosphors with emission characteristics typical of the particular activator. The photoluminescent spectra of Eu^{3+}-activated lutetium and yttrium tellurates are depicted in Fig. 1. The dominant emissions in the fluorescence spectra of the rare-earth tellurates are observed in the 600-620 nm spectral region corresponding to the $^5D_0$-$^7F_2$ transition. Significant emission is also observed around 700 nm, corresponding to the $^5D_0$-$^7F_4$ transitions. The intensity of these electric dipole transitions implies that the Eu^{3+} site is not a center of symmetry. Emissions corresponding to transitions from the $^5D_0$ to the other levels of the ^7F multiplet, namely $^7F_0$, $^7F_1$, and $^7F_3$, are also present. Blasse and Bril (8) postulate the occurrence of the $^5D_0$-$^7F_0$ transition only for point symmetries of C_s, C_n, and C_{nv}. These site symmetries are found in each of the three possible space groups formulated for the Y, La, and Gd tellurates on the basis of x-ray powder diffraction data.

The luminescence spectrum of Eu^{3+}-activated yttrium tellurate is quite complex, and the multiplicity of emission lines suggests strongly that the Eu is located in more than one site. This is supported by the fact that there are two distinct emission lines present in the spectral region of 575 to 578 nm, where the $^5D_0$-$^7F_0$ transition is generally found. Since this $J = 0 \rightarrow J = 0$ transition is not split by the crystal field, the occurrence of two components of this assignment would indicate that the Eu in Y_2TeO_6 occupies sites of different symmetry. This is not the case for the structurally different lutetium tellurate, where only one emission line is observed for the $^5D_0$-$^7F_0$ transition at 576 nm and where the total number of spectral lines is significantly lower. These facts imply a single Eu site in this compound. The emission spectra of Eu-activated lanthanum and gadolinium tellurates (Fig. 2) are similar in their gross features to the spectrum of Y_2TeO_6 with which they are isostructural but are different in detail. The two components of the $^5D_0$-$^7F_0$ transition can be distinguished in both phosphors. The relative intensity of the various emission lines of the $^5D_0$-$^7F_2$ transition, however, varies in the isostructural rare-earth tellurate phosphors. It is possible to distinguish two groupings

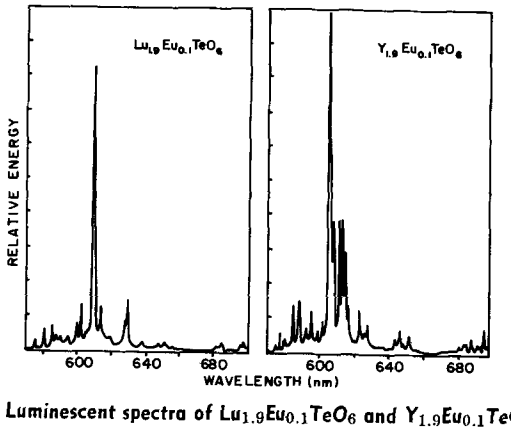

Fig. 1. Luminescent spectra of $Lu_{1.9}Eu_{0.1}TeO_6$ and $Y_{1.9}Eu_{0.1}TeO_6$

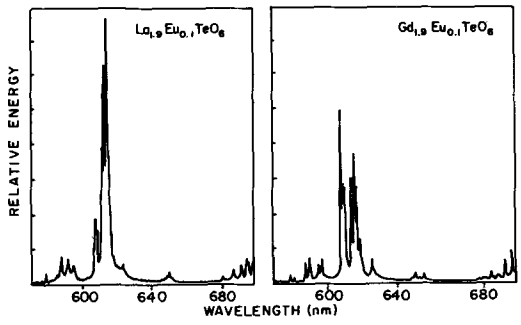

Fig. 2. Luminescent spectra of $La_{1.9}Eu_{0.1}TeO_6$ and $Gd_{1.9}Eu_{0.1}TeO_6$

in the emission lines of the $^5D_0$-$^7F_2$ transition. The relative fluorescence intensity of the group at longer wavelength increases with increasing ionic radius of the host cation, *i.e.*, from Y → Gd → La. A detailed analysis of the luminescence spectrum of Eu^{3+} in rare-earth tellurates is in progress.

The excitation spectra for the Eu^{3+} emission in these four phosphors are given in Fig. 3. They all have broad excitation bands in the short ultraviolet range which have been ascribed by Blasse and Bril (9) to a europium-oxygen charge-transfer band. The positions of the band maxima are 240 nm for Lu_2TeO_6, 255 nm for Y_2TeO_6, 260 nm for Gd_2TeO_6, and 272 nm for La_2TeO_6. The excitation spectra also contain narrow bands of varying intensity in the near ultraviolet corresponding to the f-f absorptions of the Eu^{3+} ion. The diffuse reflectance spectra (Fig. 4) show an absorption band at 300 nm which does not appear in the excitation spectrum of the phosphors. This absorption is most clearly defined in the Lu_2TeO_6 phosphor but is present in all the investigated compounds, and apparently results in a nonradiative dissipation of the absorbed energy.

The Eu-activated rare-earth tellurates are moderately efficient phosphors. They respond to ultraviolet or cathode ray excitation with a luminous efficiency up to 40% that of the YVO_4:Eu^{3+} (10). The energy trans-

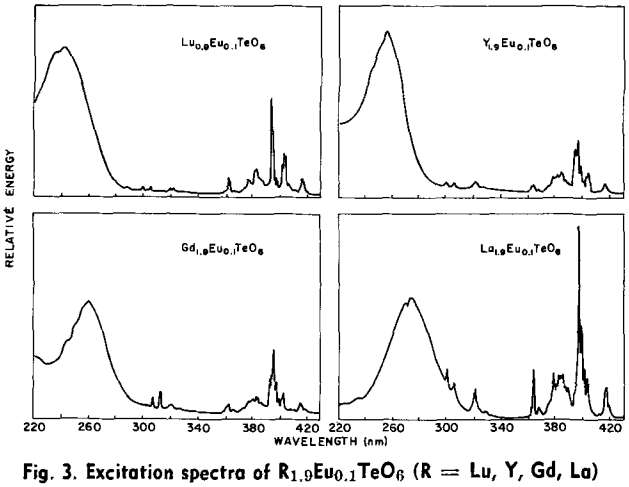

Fig. 3. Excitation spectra of $R_{1.9}Eu_{0.1}TeO_6$ (R = Lu, Y, Gd, La)

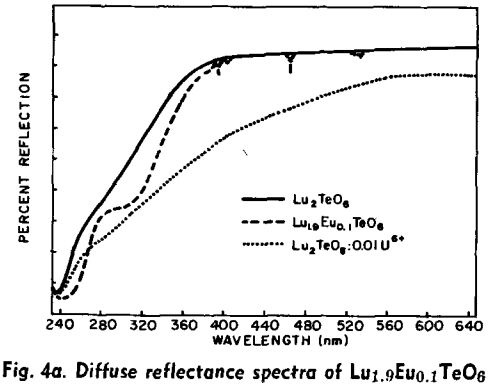

Fig. 4a. Diffuse reflectance spectra of $Lu_{1.9}Eu_{0.1}TeO_6$

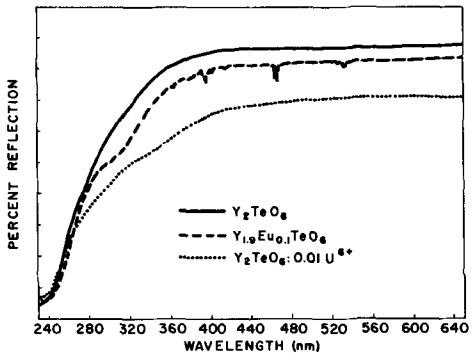

Fig. 4b. Diffuse reflectance spectra of $Y_{1.9}Eu_{0.1}TeO_6$

fer from the tellurate lattice to the rare-earth activators appears to be inefficient. This is indicated by the uncorrected fluorescence spectra of the Dy, Ho, and Er-activated lanthanum tellurates (Fig. 5) which show the dominant excitations occurring directly into the 4f levels of the particular trivalent lanthanide ion and no apparent excitation of the host matrix.

Spectroscopic Properties of U^{6+}*-Activated* R_2TeO_6

The fluorescence spectra of the uranium-activated Y, La, and Gd tellurates are virtually identical. A typical example is given in Fig. 6 which depicts the cathodoluminescence spectrum of La_2TeO_6:$0.01U^{6+}$. The peak emission is at 515 nm and the halfwidth is 35 nm. The emission curve is asymmetrical and skewed toward the longer wavelength. The position of the emission band is at a shorter wavelength than that observed in other uranium-activated phosphors such as $Mg_5Li_6Sb_2O_{13}$:U^{6+} (10) and Li_4WO_5:U^{6+} (12). The cathodoluminescence spectrum of uranium-activated lutetium tellurate is shown in Fig. 7. The different crystalline structure of this compound results in a significant change in the spectral energy distribution. The emission is characterized by two distinct peaks, a

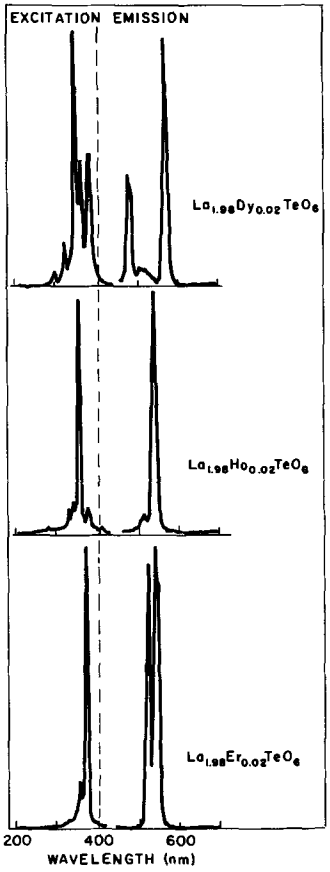

Fig. 5. Emission spectra of $La_{1.98}R_{0.02}TeO_6$ (R = Dy, Ho, Er)

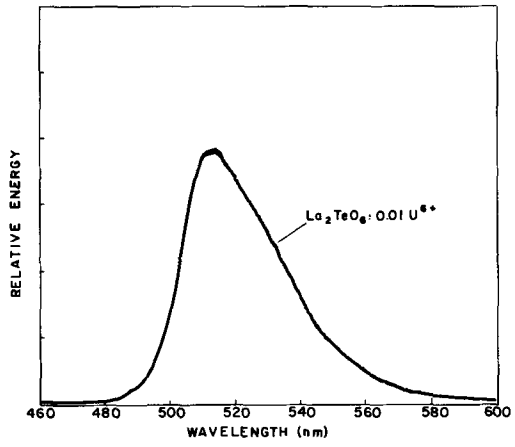

Fig. 6. Cathodoluminescent spectrum of La_2TeO_6:$0.01U^{6+}$

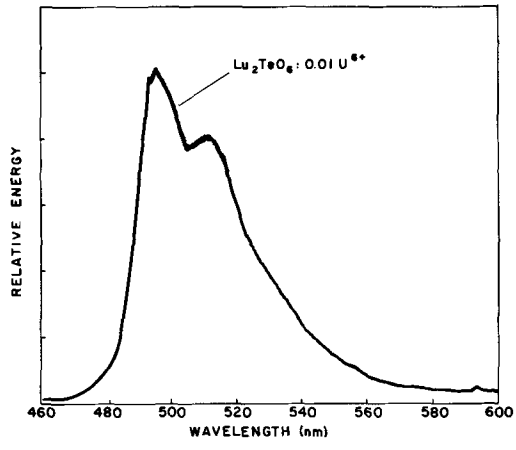

Fig. 7. Cathodoluminescent spectrum of Lu_2TeO_6:$0.01U^{6+}$

principal one at 495 nm and a secondary band with a maximum at 510 nm. These results demonstrate that the spectrum of the hexavalent uranium center is strongly affected by the nature of the crystalline host matrix.

The exact nature of the emission center in uranium-activated phosphors is not known. The emission is generally ascribed to the molecular uranyl ion, UO_2^{2+}, which when solvated or in loosely coordinated compounds such as uranyl salts or glass, exhibits a series of equispaced narrow fluorescence bands in the blue and green regions of the visible spectrum. In Fig. 8, which depicts the spectrum of uranyl nitrate, it is possible to

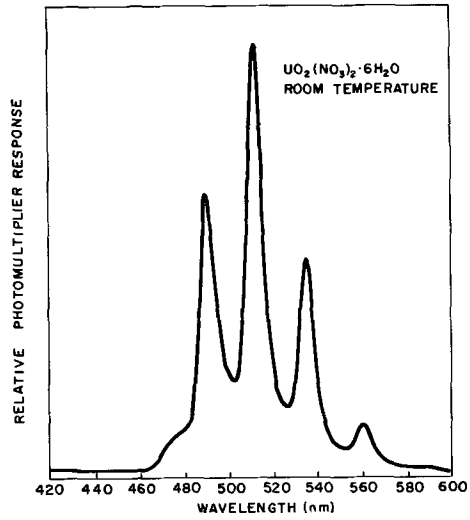

Fig. 8. Emission spectrum of $UO_2(NO_3)_2 \cdot 6H_2O$

distinguish six of these bands which are ascribed (13) to electronic transitions from the lowest excited level to the vibrational levels of the ground state. Recently, Bell and Biggers (14), in a study of aqueous uranyl ion in perchlorate medium, reported the existence of two radiation-emitting levels. They found that five emission bands separated by the ground state vibrational frequency came from the lowest absorption level of the uranyl ion, while the emission band at the shortest wavelength (whose separation is smaller than that of the others) came from the next higher absorption level; the higher level is not noticeably affected by the ground state vibrations and accounts for only a small fraction (some 4-5%) of the emitted energy.

In the case of solids such as uranyl-activated phosphor materials, it is assumed that the molecular UO_2^{2+} species is preserved in the oxygen-dominated crystalline matrix by having the uranium coordinated by two oxygen ions at a distance which is of the order of that found in the uranyl linkages (the length of the U-O bond in solids varies considerably and is given as 1.6-2.3Å), while the additional oxygen ligands required by the crystal symmetry are located at distinctly greater distances (15). In such systems the interaction of the host lattice with the uranyl ion is sufficiently strong to alter significantly the nature of the radiative transition so that the uranyl emission in such compounds is characterized by a relatively broad fluorescence band which may have some additional structure. The fact that the identity of the uranyl ion is preserved to some extent in the rare-earth tellurates is demonstrated by Fig. 9 which depicts the photoluminescent spectrum of uranyl-activated Gd_2TeO_6 taken at room and liquid N_2 temperatures. In the low-temperature spectra it is possible to discern the presence of at least three emission peaks which were undistinguishable at room temperature. There seems to be no radiation at liquid N_2 temperatures in the blue-green region where Bell and Biggers (14) observed the transition from the second, higher absorption level, although it is present at room temperature. Similar resolution at liquid nitrogen temperature of the SED curve into more distinct bands is observed in Y, La, and Lu tellurates.

The positions of the clearly discernible uranyl emission peaks in the rare-earth tellurates at liquid N_2 temperatures and the separation between them is given in Table II. Data for uranyl nitrate at room temperature measured here are included for comparison; these agree quite well with the values cited in the literature (16). The vibrational spacings obtained in the rare-earth tellurates are significantly smaller than those of the uranyl nitrate. This fact implies the crowding of the vibrational levels which is indicative of the weakening of the internal bonding of the uranyl ion. There is a significant difference between the spacing observed in lanthanum tellurate and the other three compounds. It may be due to an increase in length of the uranyl axial bond in the larger La-compound which could lead to a decrease in vibrational frequency (17).

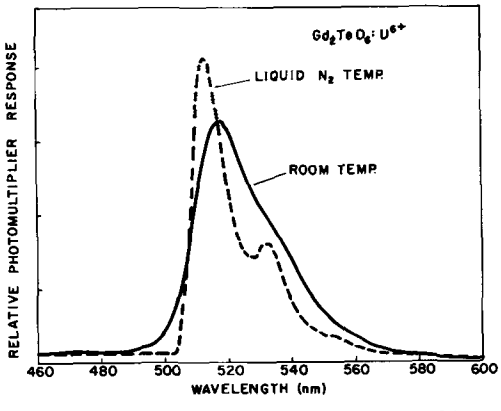

Fig. 9. Emission spectrum of $Gd_2TeO_6:0.01U^{6+}$

Table II. Vibrational spacing of uranyl emission peaks

Compounds	Emission peaks λ (nm)	ν (cm⁻¹)	Δν (cm⁻¹)
$UO_2(NO_3)_2 \cdot 6H_2O$	489	20,450	880
	512	19,570	840
	534	18,730	870
	560	17,860	
$La_2TeO_6:0.01U^{6+}$	508	19,680	600
	524	19,080	630
	542	18,450	
$Gd_2TeO_6:0.01U^{6+}$	513	19,490	690
	532	18,800	680
	552	18,120	
$Y_2TeO_6:0.01U^{6+}$	513	19,490	690
	532	18,800	680
	552	18,120	
$Lu_2TeO_6:0.01U^{6+}$	491	20,370	690
	508	19,680	700
	527	18,980	

The band spacing and the relative intensity of the discernible bands is the same in the Y, Gd, and Lu tellurates regardless of the position of the principal emission peak (in liquid N_2, 491 nm for Lu_2TeO_6 or 513 nm for Y_2TeO_6 and Gd_2TeO_6). This implies that the transitions involved are the same in all compounds but that the energy gap between the ground state and first excited level is different.

Bell and Biggers (14) distinguish seven major absorption bands in the spectrum of solvated uranyl ion. The oscillator strength of these bands increases with increasing band energy. A somewhat analogous situation exists in the uranium-activated rare-earth tellurates. In the excitation spectra of these materials, shown in Fig. 10, several bands can be distinguished whose intensity increases with increasing band energy. The location of the bands corresponds approximately to the positions resolved by Bell and Biggers (14). This analogy leads to the assumption that the excitation occurs directly into the uranium center which in this case, where the uranium most likely occupies a tellurium site in the lattice, is coordinated by oxygen in such a manner so as to preserve the identity of the uranyl species. This hypothesis is supported by the fact that the diffuse reflectance spectra of these compounds (Fig. 4) do not show corresponding host absorption bands which would indicate an absorption of the energy into the lattice and subsequent transfer to the activator.

As indicated by their excitation spectra, the uranium-activated rare-earth tellurates respond to both short- and long-wave u.v. radiation. They are comparable in luminous efficiency to $Zn_2SiO_4:Mn^{2+}$ under excitation by a low-pressure mercury vapor lamp (dominant λ:2537Å) and to ZnS:Cu under medium-pressure Hg lamp (dominant λ:3650Å). The luminosity under cathode-ray excitation compares favorably with that of the best cathodoluminescent uranium-activated phosphors known, but it is only 20-25% that of Zn_2SiO_4:Mn.

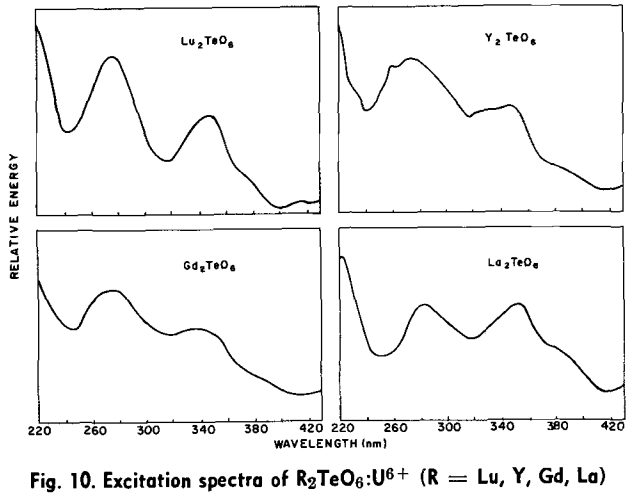

Fig. 10. Excitation spectra of $R_2TeO_6:U^{6+}$ (R = Lu, Y, Gd, La)

The rare-earth tellurates are a new class of inorganic phosphors with interesting luminescent properties. When activated by trivalent europium, they exhibit characteristics which are consistent with the observations made by numerous researchers in the field. The exact assignment of transitions is not possible pending the clarification and resolution of the crystal structure. The significant conclusion of the research with uranium activated tellurates is the indication that the identity of the molecular ion uranyl species is preserved in a solid crystalline matrix as demonstrated by its fluorescent properties. Further analysis is required to define more closely the luminescence mechanisms in uranium activated compounds.

Acknowledgment

The author gratefully appreciates the assistance of R. Francis in much of the experimental work, the spectroscopic measurements of C. Wiggins, and the helpful discussions with F. Avella, G. Gashurov, F. Palilla, and O. Sovers. The diffuse reflectance spectra were kindly provided by E. Lanning.

Manuscript submitted March 20, 1969; revised manuscript received May 21, 1969. This was Paper 36 presented at the Boston Meeting, May 5-9, 1968.

Any discussion of this paper will appear in a Discussion Section to be published in the June 1970 JOURNAL.

REFERENCES

1. J. W. Mellor, "A Comprehensive Treatise on Inorganic and Theoretical Chemistry," Vol. XI, p. 96, Longmans, Green, London (1931).
2. R. A. Kent and H. A. Eick, *Inorg. Chem.*, **1**, 956 (1962).
3. S. Natansohn, J. Inorg. *Nucl. Chem.*, **30**, 741 (1968).
4. R. L. Amster and C. S. Wiggins, *This Journal*, **116**, 68 (1969).
5. H. J. Borchardt, *J. Chem. Phys.*, **39**, 504 (1963).
6. G. Blasse and A. Bril, *ibid.*, **45**, 2350 (1966).
7. G. Blasse, *ibid.*, **45**, 2356 (1966).
8. G. Blasse and A. Bril, *Philips Res. Rept.*, **21**, 368 (1966).
9. G. Blasse and A. Bril, *Solid State Commun.*, **4**, 373 (1966).
10. A. K. Levine and F. C. Palilla, *Appl. Phys. Letters*, **5**, 118 (1964).
11. R. W. Mooney, *This Journal*, **108**, 1110 (1961).
12. Yu. S. Leonov, *Opt. Spectry. (USSR) (Engl. Transl.)*, **9**, 145 (1960).
13. G. H. Dieke and A. B. F. Duncan, "Spectroscopic Properties of Uranium Compounds," pp. 41-43, McGraw-Hill Co., New York (1949).
14. J. T. Bell and R. E. Biggers, *J. Mol. Spectry.*, **25**, 312 (1968).
15. E. Rabinowitch and R. L. Belford, "Spectroscopy and Photochemistry of Uranyl Compounds," pp. 2-5, Macmillan Co., New York (1964).
16. J. T. Bell and R. E. Biggers, *J. Mol. Spectry.*, **18**, 247 (1965).
17. G. P. McGlynn and J. K. Smith, *ibid.*, **6**, 164 (1961).

Glow Curves with General Order Kinetics

Reuven Chen

Physics Department, Polytechnic Institute of Brooklyn, Brooklyn, New York

ABSTRACT

Thermoluminescence and thermally stimulated current curves obeying general order kinetics laws are being investigated. For these cases, whose order is not necessarily first or second but rather may have some noninteger value, an effective method of calculating the activation energy is given. This method is based on measuring the temperature at the maximum of the glow peak and the half intensity temperatures. Numerical calculations for orders between 0.7 and 2.5, activation energies between 0.1 and 1.6 eV and frequency factors between 10^5 and 10^{13} sec^{-1} have been done using an I.B.M. 360 computer. The results reveal the general characteristics of these peaks and their dependence on the parameters. The new method for calculating the activation energy is also checked numerically.

The measuring of glow curves was found to be one of the most convenient ways to determine the activation energies of trapping levels in crystals. This includes the phenomena of thermoluminescence (TL) (1), thermally stimulated current (TSC) (2), thermally stimulated electron emission (TSEE) (3), and thermally stimulated capacitor discharge (TSCD) (4). The glow curves were analyzed usually by assuming first or second order kinetics. The first order case was investigated first by Randall and Wilkins (5) who assumed that the glow intensity I may be given by

$$I = -dn/dt = sn \exp(-E/kT) \quad [1]$$

where n is the concentration of trapped carriers (cm^{-3}), t the time, s the frequency factor (sec^{-1}), sometimes referred to as "the preexponential factor," E is the activation energy (ev), k is Boltzmann's constant, and T the absolute temperature. By solving this differential equation and assuming a linear heating rate of β °K/sec, one has for the intensity

$$I = sn_o \exp(-E/kT) \exp\left[-(s/\beta)\int_{T_o}^{T} \exp(-E/kT')\,dT'\right] \quad [2]$$

Key words: glow curves, thermoluminescence, thermally stimulated current, activation energy, kinetics order, frequency factor.

where n_o is the initial concentration of carriers and T_o the initial temperature. The condition for the maximum of the peak is found by differentiating Eq. [2] and equating the derivative to zero. Thus

$$\beta E/(kT_m^2) = s \exp(-E/kT_m) \quad [3]$$

where T_m is the temperature at the maximum. Garlick and Gibson (6) introduced the possibility of second order glow peaks, obeying the equation

$$I = -dn/dt = s'n^2 \exp(-E/kT) \quad [4]$$

where s' is a "preexponential constant" (cm^3 sec^{-1}). The solution of the equation gives

$$I = s'n_o^2 \exp(-E/kT) \left[1 + (s'n_o/\beta)\int_{T_o}^{T} \exp(-E/kT')\,dT'\right]^{-2} \quad [5]$$

and the condition for the maximum is

$$1 + (s'n_o/\beta)\int_{T_o}^{T_m} \exp(-E/kT)\,dT = \frac{2kT_m^2\, s'n_o}{\beta E} \exp(-E/kT_m) \quad [6]$$

Many methods for calculating the activation energies of glow curves have been given (2). Only one of these, the "initial rise" method (6) is expected to be useful for all the possible orders of the process. However, in many cases, the use of this method is limited because of experimental (7) and theoretical (8, 9) reasons.

A useful method of calculating the activation energy by using the temperature maximum T_m and the falloff half of the peak $\delta = T_2 - T_m$ where T_2 is the higher of the two half intensity temperatures, was given by Lushchik (10) for first and second order kinetics. Another method using the low temperature half width $\tau = T_m - T_1$ was developed by Halperin and Braner (11). These two methods were slightly modified by Chen (12) and are now more accurate and more easily usable. Chen also gave another method in which the total width $w = T_2 - T_1$ is used, and showed that in certain cases this method is preferable. The three methods were summed up (12) as

$$E_\alpha = c_\alpha (kT_m^2/\alpha) - b_\alpha (2kT_m) \qquad [7]$$

where α is δ, τ, or w. The values of c_α and b_α for the three methods and for first and second order processes are given in Table I. The equations [7] are slightly changed in cases where the preexponential factor depends on temperature as a power function $s = s''\ T^a$ where usually $-2 \leq a \leq 2$ (11-13) (see below).

Halperin and Braner (11) showed that an easy way to determine the order of a peak is by checking the values of $\mu_g = n_m/n_o$ where n_m is the concentration of carriers at the maximum. Values of μ_g of about $(1 + \Delta)/e$ where $\Delta = 2kT_m/E$, should indicate first order kinetics, whereas values around $(1 + \Delta)/2$ indicate second order. As an aproximation to μ_g the value of $\mu_g' = \delta/w$ was taken. Chen (12) found that a characteristic value of μ_g' for first order peaks is 0.42 and for second order 0.52.

Although the conventional way for analyzing glow curves is assuming either first or second order kinetics, this by no means covers the general case even if only a single activation energy is involved. Halperin and Braner (11) wrote three simultaneous differential equations relating the variables n = the concentration of trapped electrons, m = the concentration of holes in centers, and n_c = the concentration of free electrons. However, Halperin and Braner solved the problem only for those conditions leading to reduction of the three equations to the first or second order cases.

A better approximation for the general case may be given by the equation given by May and Partridge (14)

$$I = -dn/dt = s'n^l \exp(-E/kT) \qquad [8]$$

where l is not necessarily 1 or 2. The general case of $l \neq 1$ is essentially limited to samples in which the concentration of trapped carriers involved in the glow peak is equal to that of the empty centers. May and Partridge (14) proved that for simultaneous activation of two electrons, the value of l should be 1.5. This same value was found by them experimentally for TL peaks in KCL samples. Partridge and May (15) report the same order of 1.5 for NaCl samples after a certain heat treatment, whereas other peaks in NaCl yield values of 0.7 ± 0.1.

In the present paper, this problem of general order kinetics is further investigated. Some of the properties of the peaks are found by numerical calculations of the peaks' parameters by the use of an I.B.M. 360 computer. Several interpolation methods for calculating the activation energies based on the methods of Lushchik, Halperin and Braner, and Chen for first and second order are introduced and checked. The method based on the measurement of τ is found to be the most accurate.

Table I. Coefficients appearing in Eq. [7] for the various methods of calculating activation energies

	First order			Second order		
	τ	δ	w	τ	δ	w
c_α	1.51	0.976	2.52	1.81	1.71	3.54
b_α	1.58	0	1	2	0	1

Theoretical Approach and Numerical Calculation

The solution of Eq. [8] gives for $l \neq 1$

$$I = s'n_o^l \exp(-E/kT) \left[\frac{(l-1)s'n_o^{(l-1)}}{\beta} \int_{T_o}^{T} \exp(-E/kT')\,dT' + 1 \right]^{-l/(l-1)} \qquad [9]$$

A special case of this equation for $l = 2$ is Eq. [5]. $s'n_o^{l-1}$ has the units of sec^{-1} and in this sense it is similar to s in the first order case. If one writes s instead of $s'n_o^{l-1}$, one has

$$I = sn_o \exp(-E/kT) \left[\frac{(l-1)s}{\beta} \int_{T_o}^{T} \exp(-E/kT')\,dT' + 1 \right]^{-l/(l-1)} \qquad [10]$$

Although Eq. [10] is not valid for the case $l = 1$, it can easily be shown that it reduces to Eq. [2] in the limit when $l \to 1$. It is in this sense that Eq. [10] is a general formula applicable for all possible values of l.

The condition for maximum is found by equating the derivative of [10] to zero

$$[(l-1)\ s/\beta] \int_{T_o}^{T_m} \exp(-E/kT)\,dT + 1 = \frac{slkT_m^2}{\beta E} \exp(-E/kT_m) \qquad [11]$$

Again, a special case for $l = 2$ would be Eq. [6]. It should also be noted that Eq. [11] reduces to Eq. [3] for $l = 1$ which might be expected from the fact that Eq. [9] and [10] are valid for the first order case in the sense of the limit for $l \to 1$.

In a way similar to what has been done previously (12) for first and second order peaks, Eq. [11] can be solved numerically for given values of l, s, E, and β (and assuming that T_m is sufficiently larger than T_o) to give the value of T_m. This is done by approximating the integral of the left hand side of Eq. [11] by a certain number of terms of the asymptotic series (7)

$$\int_{T_o}^{T} \exp(-E/kT')\,dT' \cong T \exp(-E/kT) \sum_{n=1} \left(\frac{kT}{E}\right)^n (-1)^{n-1}\, n! \qquad [12]$$

and solving the equation by the iterative Newton-Raphson method (12).

This has been done for values of l between 0.7 and 2.5, values of s between 10^5 sec^{-1} and 10^{13} sec^{-1} and values of E between 0.1 and 1.6 eV. These ranges seem to cover practically all the parameters' values found experimentally. β was taken to be 0.5°K/sec and this parameter has not been varied since we can consider s/β as one parameter in Eq. [11] and s was varied by several orders of magnitude. As a first approximation for the iterative process, it was found useful to take $T_m = 500 \times E$. These calculated values of T_m are seen in column 4 of Table I for given values of E, s, and l shown in columns 1, 2, and 3, respectively. Only the cases with $1 < l < 2$ are given in some detail, whereas only examples for $l = 2.5$ and $l = 0.7$ are shown. The calculations were done, however, for the whole mentioned range and the conclusions are based on all of these results. It is to be noted that the computed values of T_m for fixed values of E and s depend

very slightly on the value of l. This can be understood by examining Eq. [11]. By taking only the first two terms in the series [12] which is a good approximation for most of the cases (11), Eq. [11] yields

$$\beta E/(kT_m^2) = s\exp(-E/kT_m)[1 + (l-1)\Delta] \quad [13]$$

where $\Delta = 2kT_m/E$. This again, reduces to the simple equation [3] for the first order case ($l = 1$). Since Δ is usually of the order of magnitude of 0.1, the term in brackets changes by 20% at most for extreme l values, which may cause changes of only around 1% in T_m because of the appearance of T_m in the exponential. Thus we may expect T_m to depend only very slightly on l for the same values of E and s, which is clearly seen in column 4.

Once the value of T_m is found, the intensity at the maximum I_m can be found by inserting T_m into Eq. [9] and using again the asymptotic series as a good approximation for the integral.

Now the values of T_1 and T_2, the low and high temperatures of half intensity, can be calculated by solving numerically the equation $I(T) = I_m/2$, when $I(T)$ is given by Eq. [9]. Again, the series approximating the integral is used throughout the iteration process. As a convenient first approximation we take 0.95 T_m for T_1 and 1.05 T_m for T_2. A similar process with somewhat more details was given previously by Chen (12) for the case of $l = 1$ and $l = 2$. By using the T_1, T_m, and T_2 values, the parameters $\delta = T_2 - T_m$ (the high temperature half width), $\tau = T_m - T_1$ (the low temperature half width and $w = T_2 - T_1$ (the total half width) are easily found, and shown in columns 5, 6, and 7 of Table I, respectively. The geometrical factor $\mu_g' = \delta/w$ is found and shown in column 8. Figure 1 gives calculated values of μ_g' as a function of the given l values. The upper and lower curves give the limits of variations of μ_g' values when E and s are varied, whereas the center curve shows the average values. This curve may be used for estimating the value of l by the measured μ_g's. The possible error is seen not to exceed ±7%. The curve gives more information than column 8 in Table II since the given average values and possible deviations (for various E and s values) are based on many sets of calculations not included in the table. Another factor characterizing the geometrical shape of a peak, namely, $\gamma = \delta/\tau$ (13) can be directly found, this is shown in column 12.

Methods for Calculating E and s

In order to find the activation energies by one of the half width methods, it is suggested to interpolate (and to some extent extrapolate) the constants appearing in the first and second order equations [7]. The interpolation could be done according to the values of l. However, this magnitude is not found directly by the experimental results. A much more convenient interpolation parameter seems to be μ_g' which is found directly and easily from the geometrical shape of the peak. μ_g' depends almost only on l, with only minor dependence on E and s (Fig. 1). Thus, interpolation with respect to the argument μ_g' is in a way interpolation with respect to l. We tried first, naturally, the simplest way of interpolation, namely, the linear interpolation. We have to write the general equations so that they would give the first order case for $\mu_g' = 0.42$ and the second order one for $\mu_g' = 0.52$ (12). With the coefficients given in Table I, the factors in Eq. [7] for the interpolated-extrapolated τ method would be

$$c_\tau = 1.51 + 3.0\,(\mu_g' - 0.42);\quad b_\tau = 1.58 + 4.2\,(\mu_g' - 0.42) \quad [14]$$

For the equation using the δ value one has

$$c_\delta = 0.976 + 7.3\,(\mu_g' - 0.42);\quad b_\delta = 0 \quad [15]$$

and for the w method we find

$$c_w = 2.52 + 10.2\,(\mu_g' - 0.42);\quad b_w = 1 \quad [16]$$

Table II. Calculated parameters for given energies, frequency factors, and orders of kinetics

1 E	2 s	3 l	4 T_m	5 δ	6 τ	7 w	8 μ_g'	9 E_δ	10 E_τ	11 E_w	12 γ
1.6	10^{13}	2.5	554.1	33.9	28.1	62.0	0.548	1.486	1.583	1.535	1.210
0.1	10^{5}	2.5	82.1	11.4	8.8	20.2	0.566	0.104	0.098	0.101	1.302
1.6	10^{13}	1.9	554.6	27.4	26.4	53.8	0.509	1.575	1.599	1.595	1.038
0.4	10^{13}	1.9	144.3	7.4	7.1	14.5	0.510	0.395	0.400	0.399	1.041
0.1	10^{13}	1.9	37.6	2.0	1.9	3.9	0.511	0.099	0.100	0.100	1.043
1.6	10^{9}	1.9	746.3	49.2	46.5	95.7	0.514	1.623	1.597	1.618	1.060
0.4	10^{9}	1.9	196.7	13.7	12.8	26.5	0.516	0.408	0.399	0.408	1.064
0.1	10^{9}	1.9	52.0	3.8	3.6	7.4	0.517	0.103	0.100	0.102	1.069
1.6	10^{5}	1.9	1124.3	110.3	100.2	210.5	0.524	1.713	1.589	1.659	1.100
0.4	10^{5}	1.9	303.6	32.1	28.9	61.0	0.526	0.434	0.397	0.417	1.110
0.1	10^{5}	1.9	82.5	9.4	8.4	17.8	0.529	0.110	0.099	0.105	1.121
1.6	10^{13}	1.5	554.9	22.7	25.0	47.7	0.476	1.616	1.606	1.623	0.907
0.4	10^{13}	1.5	144.4	6.1	6.7	12.9	0.476	0.406	0.402	0.406	0.910
0.1	10^{13}	1.5	37.6	1.7	1.8	3.5	0.477	0.102	0.100	0.102	0.912
1.6	10^{9}	1.5	747.1	40.9	44.2	85.1	0.481	1.668	1.605	1.645	0.926
0.4	10^{9}	1.5	196.9	11.4	12.2	23.6	0.482	0.420	0.401	0.412	0.930
0.1	10^{9}	1.5	52.0	3.2	3.4	6.6	0.483	0.106	0.100	0.103	0.934
1.6	10^{5}	1.5	1126.6	92.3	95.9	188.2	0.490	1.765	1.598	1.687	0.962
0.4	10^{5}	1.5	304.3	26.9	27.7	54.6	0.492	0.447	0.399	0.424	0.970
0.1	10^{5}	1.5	82.7	7.9	8.1	16.0	0.495	0.113	0.100	0.107	0.980
1.6	10^{13}	1.1	555.2	16.7	23.3	40.9	0.431	1.591	1.605	1.613	0.757
0.4	10^{13}	1.1	144.5	4.8	6.3	11.1	0.431	0.399	0.401	0.404	0.759
0.1	10^{13}	1.1	37.6	1.3	1.7	3.0	0.432	0.100	0.100	0.101	0.761
1.6	10^{9}	1.1	747.8	31.9	41.3	73.2	0.436	1.647	1.604	1.635	0.772
0.4	10^{9}	1.1	197.1	8.7	11.4	20.3	0.437	0.414	0.400	0.409	0.775
0.1	10^{9}	1.1	52.1	2.5	3.2	5.7	0.438	0.104	0.100	0.103	0.778
1.6	10^{5}	1.1	1129.1	72.4	90.4	162.7	0.445	1.755	1.598	1.676	0.801
0.4	10^{5}	1.1	305.1	21.1	26.1	47.3	0.447	0.445	0.399	0.421	0.808
0.1	10^{5}	1.1	82.9	6.2	7.6	13.9	0.449	0.113	0.100	0.106	0.816
1.6	10^{5}	0.7	1131.6	49.7	82.6	132.2	0.376	1.449	1.568	1.530	0.602
0.1	10^{8}	0.7	57.6	2.1	3.5	5.6	0.372	0.086	0.098	0.094	0.591

The results found by [14], [15], and [16] calculated by the computed μ_g' values are given in columns 9, 10, and 11 of Table II, respectively. These results may be compared to the known energies in order to evaluate the accuracy of each method separately. It is seen very clearly that the methods using the values of δ or w give poor evaluations for the activation energy, whereas Eq. [14] gives results which are always within 2% or better of the correct E value. This is true not only for the examples given in Table II but also for all the checked possibilities (see the ranges of the parameters above). Thus we cover most of the experimentally possible cases.

Once the activation energy is known, an estimate on the frequency factors can be found by the use of Eq. [13]. A reasonable value of s is found even when the factor $(l - 1)\Delta$ is neglected. A better evaluation can be calculated by estimating the value of l according to the measured μ_g' and using Fig. 1. It is self evident

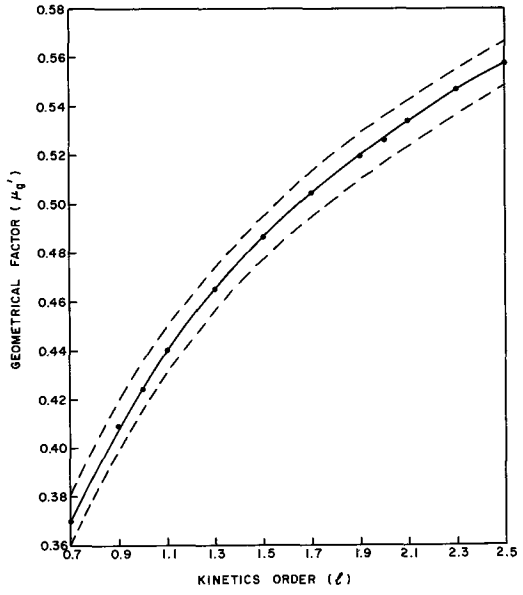

Fig 1. Calculated geometrical factor (μ_g') as a function of the given kinetics order (l). Central line gives the average values, upper and lower lines give the largest possible variations (for various E's and s's) for the given l's.

that the better the approximation in finding E, the better the corresponding calculated factor s. In order to find the constant $s'(s = s'n_o^{l-1})$, we have to have some additional information about n_o.

Discussion

Glow curves obeying a general kinetic law of the form given by Eq. [8] have been investigated. A method for calculating activation energies by the use of the maximum temperature and the low temperature half width was found by linear interpolation between the known formulas of first and second order kinetics. Similar methods using the high temperature half width and the total half width have failed. It is possible that by the use of nonlinear interpolation, better formulas could be found for the energy. However, this would make the equations more complicated. The results found by Eq. [14] are accurate to about 2%, which is comparable to the precision of the original first and second order formulas. This seems to be satisfactory for practically all the cases, especially since the possible experimental errors may contribute higher inaccuracies. Moreover, it has been shown (11, 12) that methods using the low temperatures half width are better in the sense that this portion of the peak can be "cleaned" by thermal bleaching in order to get rid of possible satellites, which would result in better calculated energy values.

It should be mentioned that the success of interpolating the equations using the low temperatures half width seems to be due to the fact that the value of τ does not depend strongly on l. The error done by using the first order τ equation for a second order peak, for example, would not exceed usually 20%. The reduction of the possible error to less than 2% by interpolation seems, however, to be essential.

Interpolation with respect to the other geometrical factor γ (7) in the same way yielded results about as good as the mentioned ones when the τ method was used, and about as bad for the δ and w methods. Another method employing the value of τ for finding the activation energy was given by Grosswiener (16) as follows

$$E_G = a_\tau kT_1T_m/\tau \qquad [17]$$

where $a_\tau = 1.41$ for first order and $a_\tau = 1.68$ for second order (12). By interpolation between these two coefficients according to the μ_g' values, results good to about 2% were found again.

The present method for estimating the value of l by the use of Fig. 1 seems to be quite reliable and appreciably simpler than the method mentioned by May and Partridge (14). An important point to be emphasized is that the present investigation gives a better insight to the relation between the various order kinetics. Equations [8], [9], [10], [11], and [13] are applicable for all values of l including 1 and 2 (Eq. [9] and [10] in the sense of the limit for $l \to 1$). Although the present treatment does not cover the problem of general glow peak associated with one activation energy, this approach seems to give much more reliable results for the calculated parameters than just using first or second order assumptions, which is the conventional approach.

Finally, it has to be noted that we dealt here only with the case of frequency factors independent of temperature. It has been mentioned above that in some cases s depends on temperature as some power function, $s = s'' T^a$ where s'' is a constant and $-2 \leq a \leq 2$. For this case, it has been shown (12) for first and second order kinetics that a better approximation can be found by subtracting akT_m from the value calculated by any of the usable methods. It can be shown that this correction is applicable for the presently discussed more general case, and thus, when "a" is known by some other measurements, it may be used. This correction seems to be significant, since in some cases it may change the calculated energy value by up to 10%.

Symbols

E	activation energy, eV
s	frequency factor, sec^{-1}
s'	preexponential factor, sec^{-1} $cm^{3(l-1)}$
l	kinetics order
T, T'	temperatures, °K
T_o	initial temperatures, °K
T_m	temperature at the maximum, °K
T_1, T_2	half intensity temperatures, °K
β	heating rate, °K/sec
t	time, sec
k	Boltzmann constant, eV/°K
I	glow intensity
I_m	maximal glow intensity
n	concentration of trapped electrons, cm^{-3}
n_o	initial concentration of trapped electrons, cm^{-3}
n_m	concentration of trapped electrons at the maximum, cm^{-3}
m	concentration of holes in centers, cm^{-3}
n_c	concentration of free electrons, cm^{-3}
τ	low temperature half width, ° K
δ	high temperature half width, ° K
w	total half width, °K
$E_\alpha, E_\tau, E_\delta, E_w$	activation energies calculated by various methods, eV
$c_\alpha, b_\alpha, c_\tau, b_\tau, c_\delta, b_\delta, c_w, b_w, a_\tau$	constants appearing in various equations for finding activation energies
Δ	correction factor $(=2kT_m/E)$
μ_g	characteristic factor $(=n_m/n_o)$
μ_g'	geometrical factor $(=\delta/w)$
λ	geometrical factor $(=\delta/\tau)$

Manuscript submitted March 4, 1969; revised manuscript received May 21, 1969. The research was supported by the National Science Foundation Grant SDP-GU-1557.

Any discussion of this paper will appear in a Discussion Section to be published in the June 1970 JOURNAL.

REFERENCES

1. For example see: G. F. J. Garlick, "Encyclopaedia of Physics," Vol. XXVI, pp. 1-128, Springer-Verlag, Berlin (1958).
2. For a review article see: K. H. Nicholas and J. Woods, *Brit. J. Appl. Phys.*, **15**, 783 (1964).
3. P. A. Pipins and N. P. Grigas, *Opt. Spectry. (USSR), (English transl.)*, **18**, 43 (1965).
4. A. G. Zhdan, V. B. Sandomirskii, and A. D. Ozheredov, *Soviet Phys. Semicond. (English transl.)*, **2**, 7 (1968).
5. J. T. Randall and M. H. F. Wilkins, *Proc. Roy. Soc.*, **A184**, 347, 365, 390 (1945).
6. G. F. J. Garlick and A. F. Gibson, *Proc. Phys. Soc.*, **60**, 574 (1948).
7. C. Haake, *J. Opt. Soc. Am.*, **47**, 649 (1957).
8. P. Braunlich, *J. Appl. Phys.*, **38**, 2516 (1967).
9. F. Aramu, P. Brovetto, and A. Rucci, *Phys. Letters*, **23**, 308 (1966).
10. C. B. Lushchik, *Dok. Akad. Nauk. SSSR*, **101**, 641 (1955).
11. A. Halperin and A. A. Braner, *Phys. Rev.*, **117**, 451 (1960).
12. R. Chen, *J. Appl. Phys.*, **40**, 570 (1969).
13. P. N. Keating, *Proc. Phys. Soc.*, **78**, 1408 (1961).
14. C. E. May and J. A. Partridge, *J. Chem. Phys.*, **40**, 1401 (1964).
15. J. A. Partridge and C. E. May, *ibid.*, **42**, 797 (1965).
16. L. I. Grossweiner, *J. Appl. Phys.*, **24**, 1306 (1953).

Growth of Calcite Crystals in Gels

H. J. Nickl and H. K. Henisch[1]

Materials Research Laboratory, The Pennsylvania State University, University Park, Pennsylvania

ABSTRACT

Procedures for the growth and doping of calcite crystals in gel systems are described. Crystals surrounded by gel tend to incorporate the silica network with its structure intact. Hybrid methods avoid this contamination. Crystals then grow in small volumes of solution, the solution being replenished by diffusion through gel filtering media. The solution cavities can be seeded with calcite crystals which then serve as substrates for epitaxial growth. Weight increases by factors up to 10 are easily achieved.

Calcite crystals have well-known applications in optical instrumentation and laser technology (1), and since the sources of natural specimens appear to be diminishing, a special interest attaches to all methods of growing the material artificially. Control over the nature and concentration of dopants should be achieved at the same time. Previous growth attempts of calcium carbonate by a hydrothermal method have been described by Ikornikova and co-workers (2), experiments on growth in solution by Gruzensky (3) and by Kaspar (4), and in electrochemical systems by Barta and Zemlicka (5). Morse and Donnay (6) and McCauley (7) have dealt with growth in gels, the last with emphasis on reaction mechanism and phase aspects. In the present paper some new procedures for gel growth are described and the factors which control crystal perfection are discussed, with special reference to the inclusion of silica. Experiments with rare earth and transition metal dopants are also reported.

Growth Methods

The formation of calcite is accomplished by the reaction between carbonates and calcium salts in sodium metasilicate gels. Two methods have been developed for this purpose. In the first the gel itself contains the carbonate. An aqueous mixture of sodium metasilicate and a carbonate is prepared and the *p*H adjusted to between 7 and 8, usually by means of acetic acid. After the gel has set, calcium salt solution is put on top and allowed to diffuse. Test tubes (25 x 200 mm) are used in the ordinary way (Fig. 1), but bottles up to ½ gallon volume were employed for some of the large scale experiments. Attempts to mix the calcium salt with the gel in the same way fail because calcium silicate precipitates at and above a *p*H of 7. At lower *p*H values this precipitation is avoided, but any subsequent diffusion of carbonate leads to CO_2 production which destroys the gel.

In the second method the neutral gel is initially free of calcium and carbonate ions. The reagents diffuse into it from two sides and form calcite where they meet. This is conveniently done in U-tubes (25 x 200 mm) or in tubes (45 x 130 mm) with fritted inserts (Fig. 2).

There appears to be no significant difference between the merits of the two methods; both produce well-shaped calcite rhombohedra of up to 6 mm size, within 6 to 10 weeks. A few spherulites of aragonite and vaterite also appear. The three modifications have been verified by comparison of the d-values derived from x-ray diffraction measurements with those compiled by Swanson and Fuyat (8, 9) and by McConnel (10). Room temperature (25°C) proved to be optimum for growth. High temperatures, *e.g.*, 70°C or so, favor the formation of aragonite (11-13) and cause bubbles to appear which disrupt the medium.

In all cases the gels were made from analytic grade $Na_2SiO_3 \cdot 9H_2O$, with final densities between 1.02 and 1.03, corresponding to between 0.17 and 0.23M Na_2SiO_3 in the gelling solutions. As a source of carbonate ions, solutions of Na_2CO_3 (*p*H 11.6), $(NH_4)_2CO_3$ (*p*H 9), $NaHCO_3$ (*p*H 8.6), and NH_4HCO_3 (*p*H 8.4) were used, and the calcium was derived from $CaCl_2$ or $CaAc_2$. The combination which yielded the best results was found to be $(NH_4)_2CO_3$ + $CaCl_2$ in equal concentrations (0.16M). Na_2CO_3 is less suitable on account of its high *p*H which, on neutralization, leads to high sodium acetate concentrations. These have been found to affect the quality of the resulting crystals adversely whereas ammonium acetate appears to have no such effect.

Growth Products

Crystals grown in the normal way as described, although well-formed rhombohedra (Fig. 3), are almost invariably turbid, obviously due to inclusions. As far as metals are concerned, the crystals contain

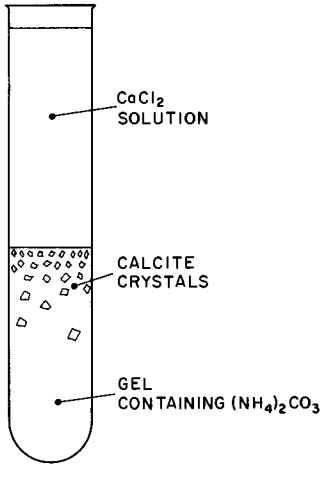

Fig. 1. Test-tube method for growing calcite crystals in gel

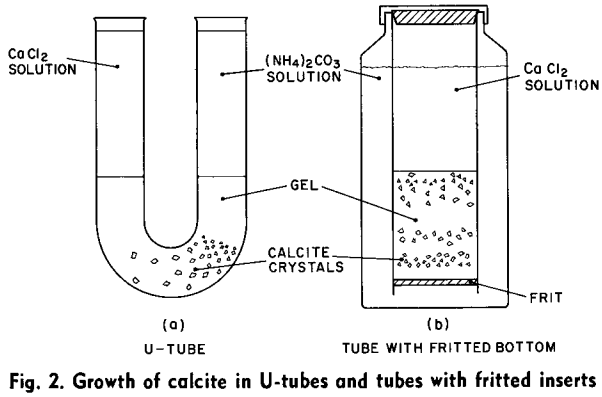

Fig. 2. Growth of calcite in U-tubes and tubes with fritted inserts

[1] Also Department of Physics.

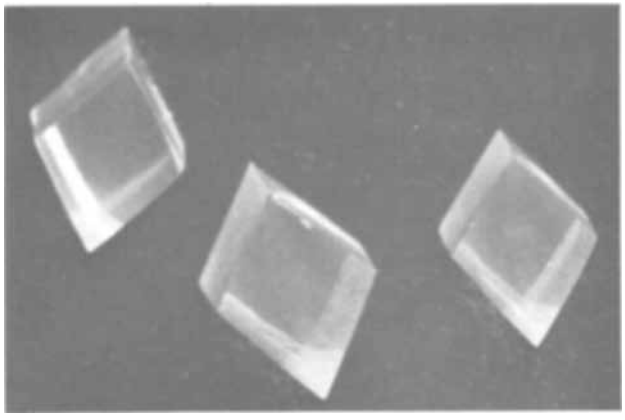

Fig. 3. Rhombohedra of gel-grown calcite. Edge lengths: 2.5 mm

about 80 ppm of Sr and smaller amounts of Ba, Mg, and Cu, as determined by emission spectroscopy. However, they also contain relatively large amounts of Na and Si (as SiO_2), both nonuniformly distributed, but not in coinciding patterns, as shown by electron microprobe tests. Quantitative analysis showed that the amount of SiO_2 varies between 0.47 and 1.7% when prepared in gels of varying density between 1.02 and 1.03 g/cc. Despite this gross contamination, the specimens have well-developed and smooth crystal faces. Dissolution of a turbid crystal in acid leaves a residue which maintains the shape of the original specimen. Figure 4 shows this after partial solution; the dense inner core is part of the original calcite crystal. The surrounding residue turns out to be silica gel which can be examined by the freeze-drying technique already described (14) and shown to have the same structure as the original growth medium (Fig. 5). It is clear from the results that the silica network which constitutes the gel is incorporated into the growing crystals more or less intact. In this way, calcite differs greatly from other gel-grown crystals, *e.g.*, calcium tartrate, which are surprisingly free from silica contamination. In these cases, the gel is bodily displaced by the advancing growth surface, whereas calcite permeates the silica network while maintaining a high level of short-range order. In this respect, the gel-grown specimens resemble certain natural calcite structures, *e.g.*, the spikes of sea urchins.

A few of the crystals are found to grow in fissures, and thus at the boundaries between gel and solution. These are turbid to the extent to which they overlap the gel and clear to the extent to which they grow in solution. The two regions can be clearly seen in Fig. 6. The same observations were made on crystals

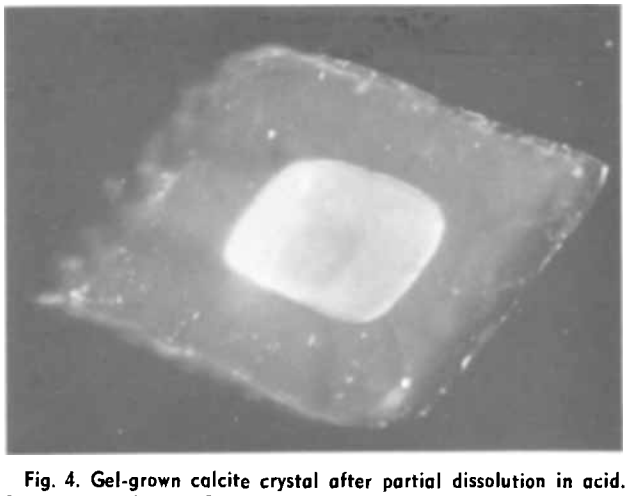

Fig. 4. Gel-grown calcite crystal after partial dissolution in acid. Original edge length: 2.5 mm.

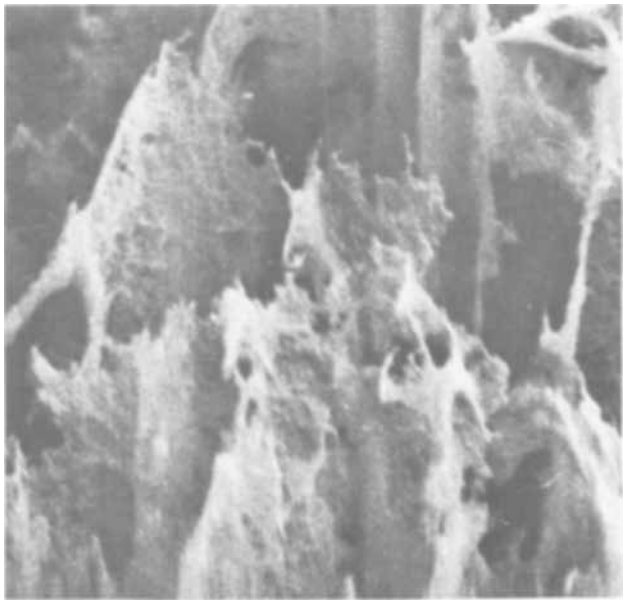

Fig. 5. Gel structures revealed by an electron scanning microscope after vacuum freeze drying: (a) gel residue after crystal dissolution.

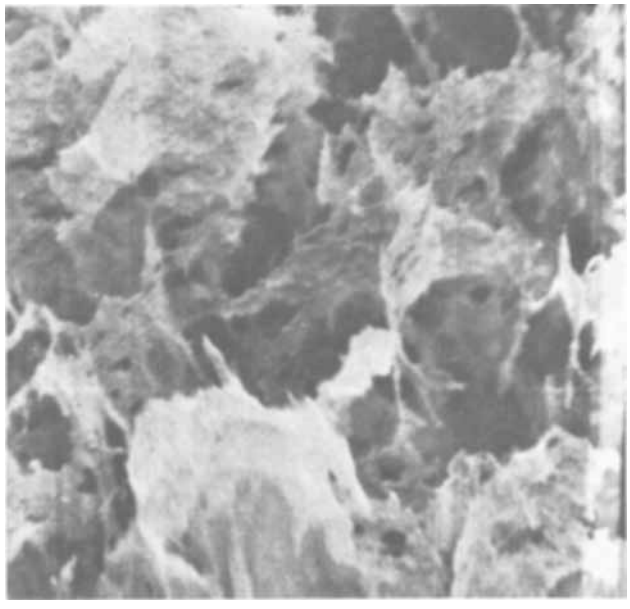

Fig. 5 (b). Normal growth medium. x3000

of aragonite and vaterite grown by the same procedures.

Doping

The methods described above can also be used for the preparation of doped crystals. Dopants in the form of chlorides or nitrates can be incorporated in the sodium metasilicate solution before gelling or else in the supernatant solution. Small amounts did not affect the growth habit of the calcite crystals, but high dopant concentrations were found to prevent the growth of regular rhombohedra. The maximum permissible concentrations for regular growth differed for the various metal ions examined. For Co^{+2}, Ni^{+2}, Cu^{+2}, Mn^{+2}, Mg^{+2}, and Zn^{+2}, they were of the order of 10^{-3}M in the gel and 5 to 20 times higher in the supernatant solution. For Cr^{+3} the maximum is about 0.1M (in the gel). All these metals form hydroxides which are insoluble in pure water but somewhat soluble in the presence of NH_4OH and ammonium salts. For Nd^{+3}, Ho^{+3}, Er^{+3} and Fe^{+3}, the maximum permissible concentrations in the gel were of the order

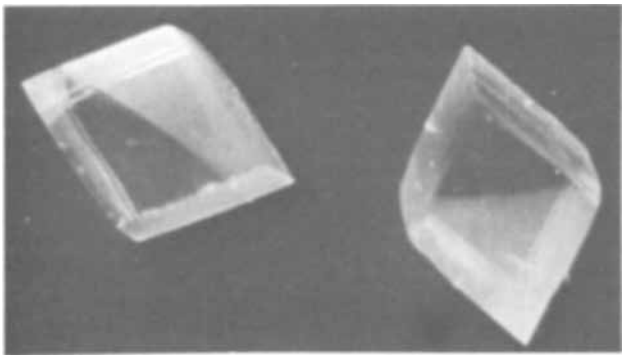

Fig. 6. Boundaries between calcite regions grown in gel and those grown in solution. Edge lengths: 2.5 mm.

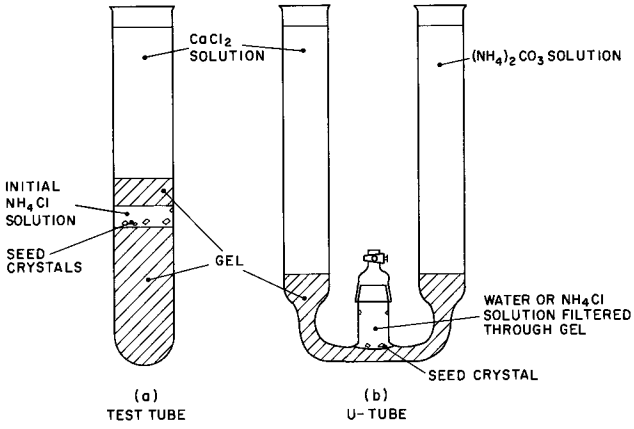

Fig. 7. Systems for calcite growth by hybrid gel method

of 10^{-4}M or, as in the last case, too small to be readily determined. These metals form hydroxides and carbonates which are even more insoluble than those listed above under the growth conditions employed. It is therefore reasonable to assume that they precipitate earlier in microcrystalline form. Subsequent calcium carbonate growth would then occur by epitaxy, as suggested by Johnston and co-workers (12, 15), and discussed by McCauley (7) who list many other references. Epitaxy would lead to growth without any particular relation to the rhombohedra found at lower concentrations. For the metals which form more soluble hydroxides and carbonates, the same effect would occur at higher concentrations. This interpretation is in harmony with the fact that dopant concentrations which are high enough to destroy regular growth also lead to greatly increased nucleation. Valency consideration must, of course, enter into this picture, but the high permissible concentrations of Cr^{+3} discount their dominating importance. For reasons which are not yet clear, there is an enrichment of dopants in the crystals by a factor of about 100, as compared with the average dopant concentrations in the gel.

It was shown by means of the electron-microprobe that the dopants are uniformly distributed within the crystals, whether clouded by silica networks or not. Of the crystals doped with the above elements, only those containing Mn were found to be (slightly) photoluminescent in the orange region of the spectrum, and also cathodoluminescent in the red.

Hybrid Procedures

The success of the gel method is believed to depend, in the ordinary way, on two principal features: (*a*) crystals are grown by diffusion, which means that the solute concentration at the growth boundary is self-regulating in accordance with the needs of the growth process itself, and (*b*) nucleation is suppressed by the gel, partly because it acts as an efficient filtering medium and serves also to isolate a good deal of solute in cavities which are too small to permit homogeneous nucleation to be effective. As shown above, the method has, at any rate for calcite, the disadvantage of leading to substantial inclusions of silicate gel network into the growing crystals. This suggested that hybrid methods should be more successful. In these, crystals are grown in solution without, in principle, losing the general benefits of the gel method. To achieve this, the volume of the solution should always be comparable with that of the growing crystals, a condition not easily achieved, and especially not during the initial stages of growth. In practice, a compromise must therefore be made, the solution volume being kept as small as is technically feasible. The solute must be replenished by diffusion in order to approach the self-regulating boundary concentration mentioned above, and the diffusion medium must be a gel. These requirements distinguish the optimum arrangement from the systems, otherwise similar, proposed by Torgesen and Peiser (16). Figure 7 gives two examples. In the test-tube system on the left, sodium metasilicate solution is floated on a concentrated solution of NH_4Cl and allowed to gel before adding the supernatant $CaCl_2$ solution. Crystals then grow primarily in the solution belt. Unwanted nucleation on the wall of the tube can be diminished by giving it an initial gel coating. The system on the right involves diffusion of the reagents through separate gel columns, and the entire growth medium is filtered in this way. The solution can be seeded with a small calcite crystallite derived from a pure gel system or from other sources. Epitaxial growth occurs, and the new layers are clear, no matter whether the seed contains a silica network or not. When clear seeds are used, no boundary between substrate and new growth can be optically detected. Weight increases by factors up to 10 are easily achieved.

Manuscript submitted March 20, 1969; revised manuscript received May 24, 1969.

Any discussion of this paper will appear in a Discussion Section to be published in the June 1970 JOURNAL.

REFERENCES

1. J. Wakabayashi, *J. Chem. Phys.*, **38,** 1910 (1963).
2. N. Yu. Ikornikova and V. P. Butuzov, *Doklady Akad. Nauk SSSR,* **111,** 105 (1956).
3. P. M. Gruzensky, *J. Phys. Chem. Solids, Supp. No. 1,* 365 (1967).
4. J. Kaspar, "Growth of Crystals," Vol. 2. Interim reports between the first (1956) and second Conference on Crystal Growth, Institute of Crystallography, Academy of Sciences USSR. Consultants Bureau, Inc., New York (1959).
5. C. Barta, Institute of Solid State Physics, Prague, Personal communication (1967).
6. H. Morse and D. H. Donnay, *Bull. Soc. Franc. Mineral.,* **54,** 19 (1931).
7. J. W. McCauley, M. S. Thesis in Geochemistry and Mineralogy, Pennsylvania State University (June 1965).
8. H. E. Swanson and R. K. Fuyat, *NBS Circular 539,* Vol. II, 51 (1953).
9. H. E. Swanson and R. K. Fuyat, *ibid.,* Vol. III, 54 (1953).
10. J. D. C. McConnell, *Mineral. Mag.,* **32,** 535 (1960).
11. Y. Kitano, *Bull. Chem. Soc. Japan.,* **35,** 1980 (1962).
12. J. Johnston, H. E. Merwin, and E. D. Williamson, *Am. J. Sci.,* **41,** 473 (1916).
13. W. L. DeKeyser and L. Degueldre, *Bull. Soc. Chem. Belg.,* **59,** 40 (1950).
14. E. S. Halberstadt, H. K. Henisch, J. Nickl, and E. W. White, *J. Colloid and Interface Sci.,* **29,** 469 (1969).
15. J. Johnston and E. D. Williamson, *J. Geol.,* **24,** 729 (1916).
16. J. L. Torgesen and H. S. Peiser, U. S. Pat. 3,371,038, Feb. 27, 1968.

The Etching of Germanium with Water Vapor and Hydrogen Sulfide

T. L. Chu* and R. W. Kelm

Electronic Sciences Center, Southern Methodist University, Dallas, Texas

ABSTRACT

The reaction of single crystal germanium with water vapor and hydrogen sulfide at low partial pressures in hydrogen was studied in a gas flow system in the temperature range 650°-900°C. At linear gas velocities of 30 cm/sec or higher and water partial pressures of 26 Torr or lower, the reaction of germanium with water vapor is surface limited with an activation energy of 46 ± 2 kcal/mole. Clean and structureless surfaces were produced, independent of the dislocation density in germanium, at 900°C and a water partial pressure of 26 Torr. At low partial pressures of hydrogen sulfide in hydrogen, the etching of germanium is diffusion limited at temperatures above 800°C and is surface limited at lower temperatures with an activation energy of 20 ± 1 kcal/mole. The hydrogen-hydrogen sulfide mixture is a less effective nonpreferential etchant than the hydrogen-water vapor mixture.

Chemical etching is the most common technique for the surface preparation of semiconductor crystals. Room temperature aqueous etchants, such as CP_4 (1) and iodine etch A (2), and high-temperature gaseous etchants, such as hydrogen chloride (3) and hydrogen iodide (4), are used for germanium. The behavior of germanium toward these etchants depends strongly on the mechanical preparation of its surface prior to etching. Smooth and damage-free surfaces are readily obtained from a mechanically polished specimen. The etching of mechanically lapped surfaces always induces preferential attack along dislocations in the bulk leading to the formation of pits. This is highly undesirable. For example, an epitaxial layer grown on a pitted substrate retains its surface appearance, and any junctions formed in the epitaxial layer would not be planar.

The etching of silicon by gaseous reagents has been studied more extensively. Water vapor and hydrogen sulfide at low partial pressures in a hydrogen atmosphere are superior to hydrogen halides in several respects (5, 6). The reaction between silicon and water vapor is chemically irreversible, thus facilitating the control of electrical resistivity of epitaxial layers. The use of hydrogen sulfide as an etchant provides clean and structureless surfaces at temperatures considerably below those required by hydrogen halides. However, water vapor and hydrogen sulfide have not been used as etchants for germanium.

Germanium reacts with water vapor or oxygen at high temperatures to produce volatile germanium monoxide (7, 8). The chemical reactions may be written as

$$Ge(s) + H_2O(g) = GeO(g) + H_2(g)$$

$$2Ge(s) + O_2(g) = 2\ GeO(g)$$

The vapor pressure of germanium monoxide over germanium and germanium dioxide corresponding to the reaction

$$Ge(s) + GeO_2(s) = 2GeO(g)$$

is at least 10^{-3} Torr at temperatures above 550°C (9). The equilibrium constant of the reaction between germanium and water vapor has been approximated as $\log K = 6.45 - 10{,}270/T$ (10). Since the equilibrium is shifted to the formation of germanium as the temperature is decreased, germanium monoxide produced in the high-temperature region will be reduced by hydrogen in the lower temperature region. This reversibility has been utilized in the chemical transport of germanium.

The reaction of germanium with hydrogen-hydrogen sulfide mixtures at 850°-870°C yields volatile germanium monosulfide (11). Germanium monosulfide is the most stable divalent germanium compound and may be melted and vaporized without decomposition.

* Electrochemical Society Active Member.

In the present work, the reaction of a germanium single crystal with hydrogen-water vapor and hydrogen-hydrogen sulfide mixtures was studied in the temperature range 650°-900°C. Clean and structureless surfaces have been obtained by using hydrogen-water vapor mixtures over a limited range of concentration and temperature conditions.

Experimental

The etching of germanium crystals with hydrogen-water vapor and hydrogen-hydrogen sulfide mixtures was carried out in a gas-flow system. Hydrogen was purified by diffusion through a palladium-silver alloy. Hydrogen-water vapor mixtures containing up to 26 Torr of water were obtained by saturating all or part of the hydrogen with distilled water at 26.5°C. To insure saturation, hydrogen was first bubbled through water at 45°C and excess water was condensed in a second reservoir maintained at 26.5°C. A hydrogen-hydrogen sulfide mixture containing 2.8% hydrogen sulfide, purchased from the Matheson Company, East Rutherford, New Jersey, was further diluted with hydrogen to the desired concentration.

Germanium crystals were in the form of wafers, 1.7 x 1.7 x 0.05 cm in size, with main faces of {111}, {110}, and {100} orientations. The {111}-oriented wafers, 3 ohm-cm p-type with an average dislocation density of 4×10^3 cm^{-2} and 0.03 ohm-cm p-type with an average dislocation density of 2×10^4 cm^{-2}, were used in most experiments. The {110} and {100}-oriented wafers were 1 ohm-cm p-type and 0.02 ohm-cm n-type, respectively. These wafers were mechanically lapped with 15μ alumina or polished with 0.3μ alumina followed by chemical etching with iodine etch A (2) for 1 to 2 min. The lapped and etched specimens always exhibited pitted surfaces with the degree of pitting related to the dislocation density.

Both resistance heating and rf heating of germanium wafers were used. In the former, the wafers were supported on a fused silica plate in a silica tube of 2.5 cm ID, heated by a tube furnace. In rf heating, the wafers were supported on a silicon carbide coated-graphite susceptor in a fused-silica tube of 5.5 cm ID, and the susceptor was heated externally by an rf generator. Results obtained by both heating techniques were qualitatively the same. Resistance heating was used in obtaining the data reported here because of the ease of temperature control. The specimen temperature usually fluctuated no more than ± 1°C during the etching experiments.

The etch rate of germanium was determined by the weight change of the sample, its surface area, and the reaction time. The reaction time, 30-120 min, was adjusted so that weight differences were more than 20 mg. The weights were measured to ± 0.1 mg. The etch rates were usually reproducible within 5% or better.

The surface conditions of germanium wafers were also examined before and after etching with an optical microscope.

Results and Discussion

The reaction of germanium with hydrogen-water vapor mixtures in a gas flow system involves five consecutive steps: (*a*) transport of water molecules to the germanium surface, (*b*) chemisorption of water molecules, (*c*) chemical reaction at the surface to yield hydrogen and germanium monoxide, (*d*) desorption of germanium monoxide, and (*e*) the transport of germanium monoxide away from surface. The rate-controlling step in this type of gas-solid reaction can be distinguished by measuring the etch rate as a function of etchant composition, etchant flux, and temperature. In transport-controlled processes, the etch rate depends strongly on etchant flux and is essentially independent of temperature. On the other hand, the surface processes have high activation energies, and, if these processes were rate controlling, the etch rate would depend appreciably on temperature.

The effect of etchant flux on the etch rate of germanium by hydrogen-water vapor mixtures was first determined under conditions of fixed temperature and etchant composition. The etchant flux over the germanium surface was varied by a large factor using hydrogen flow rates in the range of 1-12 l/min. The etching temperature and the partial pressure of water vapor in the etchant were 900°C and 26 Torr, respectively, the upper limits of experimental conditions used in this work. If the etching process is surface controlled under these conditions, it will remain surface controlled at lower temperatures and pressures. The etch rates of p-type germanium of {111} orientation and 3 ohm-cm resistivity are shown in Fig. 1. N-type germanium of 20 ohm-cm resistivity showed the same etch rates. At hydrogen flow rates lower than approximately 2 l/min, corresponding to a linear gas velocity of 30 cm/sec, the etch rate decreases rapidly with decreasing etchant flow rate. The etching process is thus limited by the transport processes. At higher flow rates, the etch rate is essentially independent of the etchant flow rate, and the etching process becomes surface limited. Under this condition, the observed rate represents the difference between the etching and its reverse reaction and is approximately 0.5 μ/min. The presence of large excess of hydrogen greatly impedes the etching process. The use of argon as a diluent under similar conditions increases the etch rate by more than a factor of five.

The etch rate of germanium in the surface-controlled region was determined as a function of temperature and etchant composition. The hydrogen flow rate was 4 l/min, the partial pressures of water vapor in the etchant were 26, 13, and 6.5 Torr, and the etching temperature was in the range of 800°-900°C. The etch rates become too low at lower temperatures. Results obtained from p-type germanium of {111} orientation and 0.03 ohm-cm resistivity are shown in Fig. 2. The 3 ohm-cm p-type germanium exhibited the same etch rates. In the concentration range under study, the etch rate at a given temperature is essentially a linear function of concentration. Furthermore, the logarithm of etch rate is linear with respect to reciprocal temperature, and the lines obtained at various etchant concentrations are parallel. The activation energy of the over-all reaction calculated from the slope of the lines is 46 ± 2 kcal/mole. At a water partial pressure of 26 Torr, the etch rates of {110} and {100}-oriented germanium were also determined in the same temperature range (Fig. 2). The etch rate was found to vary with the crystallographic orientation of germanium, increasing in the order {111}, {100} and {110}. However, the slope of the Arrhenius plots remains the same, indicating that the rate-controlling step is independent of the crystallographic orientation. The variation of etch rate with orientation may be attributed to the difference in atomic arrangements on the {111}, {110}, and {100} faces. On a {110} face, each surface atom is bonded to two neighboring surface atoms and one atom in the layer below, while each surface atom on the {111} and {100} faces is bonded to three and two atoms in the next layer, respectively. It is thus reasonable that reactivity of atoms increases with orientation in the order {111}, {100}, and {110}.

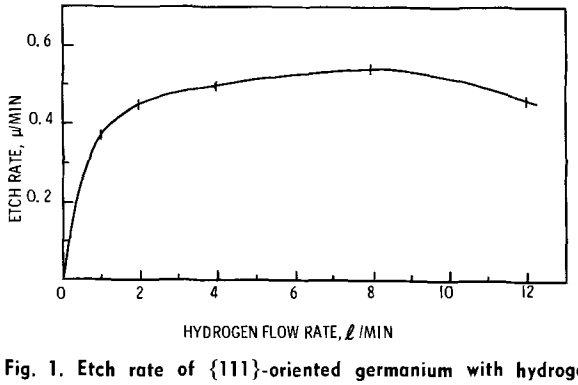

Fig. 1. Etch rate of {111}-oriented germanium with hydrogen-water vapor mixture as a function of hydrogen flow rate. Temperature, 900°C, partial pressure of water vapor, 26 Torr.

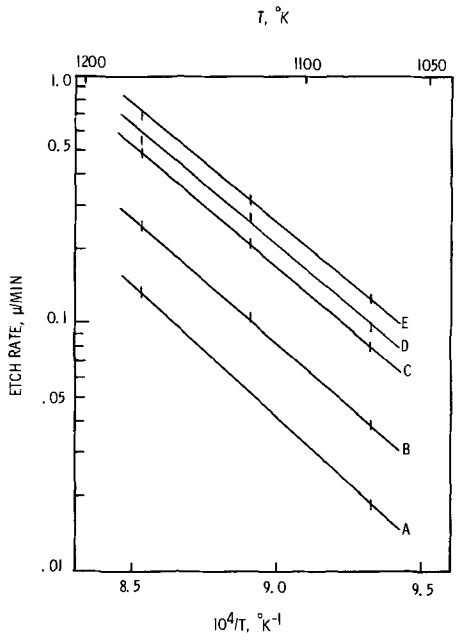

Fig. 2. Etch rate of germanium with hydrogen-water vapor mixture as a function of temperature. Hydrogen flow rate: 4 l/min. A, {111} orientation, partial pressure of water, 6.5 Torr; B, {111} orientation, partial pressure of water, 13 Torr; C, {111} orientation, partial pressure of water, 26 Torr; D, {100} orientation, partial pressure of water, 26 Torr; E, {110} orientation, partial pressure of water, 26 Torr.

The appearance of germanium surfaces after etching with hydrogen-water vapor mixtures varies with temperature and etchant composition. Clean and structureless surfaces were obtained at high temperatures and high water partial pressures. For example, the treatment of lapped and etched germanium surfaces at 900°C with a hydrogen-water vapor mixture containing 26 Torr water vapor at a flow rate of 4 l/min for 30 min is sufficient to yield pitless surfaces. The appearance of the germanium surface is essentially independent of the linear gas velocity in the surface-controlled region. However, as the etching temperature and water partial pressure gradually decreased, the pitted germanium surface from lapping and polishing showed correspondingly less improvement.

The reaction of germanium with hydrogen-hydrogen sulfide mixtures was also studied at a hydrogen flow

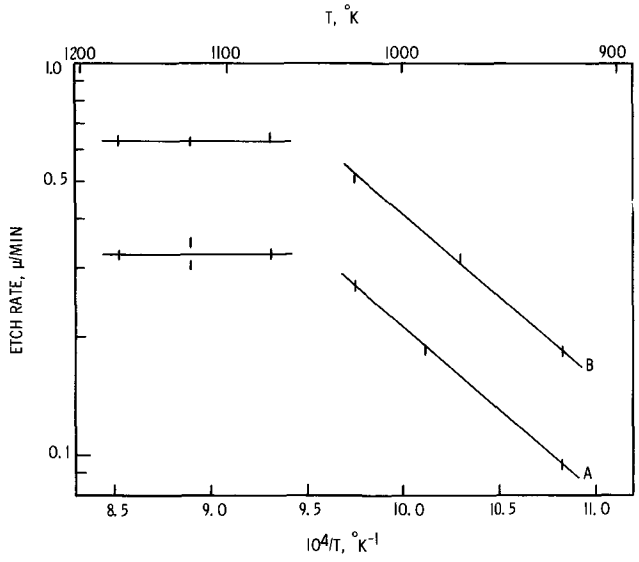

Fig. 3. Etch rate of {111}-oriented germanium with hydrogen-hydrogen sulfide mixture as a function of temperature. Hydrogen flow rate: 4 l/min. A, Partial pressure of hydrogen sulfide, 0.19 Torr; B, Partial pressure of hydrogen sulfide, 0.38 Torr.

rate of 4 l/min. Appreciable etch rates were obtained at relatively low partial pressures of hydrogen sulfide. Figure 3 shows the etch rates of {111}-oriented 0.03 ohm-cm p-type germanium using hydrogen sulfide partial pressures of 0.38 and 0.19 Torr in the temperature range 650°-900°C. In the higher temperature region, the etch rate is essentially independent of temperature, indicating that the etching process is limited by the transport processes. At temperatures below 800°C, the logarithm of etch rate becomes linear with respect to reciprocal temperature with an activation energy of 20 ± 1 kcal/mole. In this region, the etching of germanium is limited by the surface processes. A comparison of Fig. 2 and 3 indicates that, to achieve the same etch rate at a given temperature, the concentration of hydrogen sulfide required in the etchant is considerably lower than that of water vapor. This difference may be related to the difference in bond energies. The H-S bond energy is approximately 81 kcal/mole as compared with 110 kcal/mole for the H-O bond (12); the lower bond energy in hydrogen sulfide would facilitate its reaction with germanium. However, the etching of germanium by hydrogen-hydrogen sulfide mixtures is more selective than that by hydrogen-water vapor mixtures, particularly at high temperatures. At 800°-900°C, the germanium surface is usually quite pitted after etching. Marked improvements are observed at lower temperatures; lapped germanium surfaces etched with hydrogen-hydrogen sulfide mixtures at 650°C are less pitted than those etched with iodine etch A.

Summary and Conclusions

Germanium surfaces are readily etched with hydrogen-water vapor mixtures in the temperature range 800°-900°C. Using a water partial pressure of 26 Torr, a clear demarcation between surface-limited and transport-limited regions exists. The etching process is transport-limited at linear gas velocities lower than about 30 cm/sec and becomes surface limited at higher gas velocities. In the surface-limited region, the rate is approximately proportional to the partial pressure of water vapor, and the activation energy is 46 ± 2 kcal/mole. Clean and structureless germanium surfaces can be produced at 900°C by using hydrogen-water vapor mixture as an etchant.

Germanium surfaces can also be etched by using hydrogen-hydrogen sulfide mixtures in the temperature range 650°-900°C. Using a linear gas velocity of 60 cm/sec and hydrogen sulfide partial pressures of 0.38 and 0.19 Torr, the etching process is transport limited at 800°C and above, and is surface limited at lower temperatures with an activation energy of 20 ± 1 kcal/mole. Hydrogen-hydrogen sulfide mixtures are less effective polishing etchants than hydrogen-water vapor mixtures.

Manuscript submitted April 21, 1969; revised manuscript received May 16, 1969. This work was supported by SMU Foundation for Science and Engineering and NASA Grant NGR 44-007-006 administered through SMU Space Research Awards Committee.

Any discussion of this paper will appear in a Discussion Section to be published in the June 1970 JOURNAL.

REFERENCES

1. F. L. Vogel, W. G. Pfann, H. E. Corey, and E. E. Thomas, *Phys. Rev.*, **90**, 489 (1953).
2. P. Wang, *Sylvania Tech.*, **11**, 50 (1958).
3. J. A. Amick, E. A. Roth, and H. Gossenberger, *RCA Rev.*, **24**, 473 (1963).
4. A. Reisman and M. Berkenblit, *This Journal*, **112**, 812 (1965).
5. T. L. Chu and R. L. Tallman, *ibid.*, **111**, 1306 (1964).
6. T. L. Chu, *ibid.*, **115**, 1207 (1968).
7. J. T. Law and P. S. Meigs, *ibid.*, **104**, 154 (1957).
8. M. J. Sparnaay, *Ann. N. Y. Acad. Sci.*, **101**, 973 (1963).
9. W. L. Jolly and W. M. Latimer, *J. Am. Chem. Soc.*, **74**, 5757 (1952).
10. R. F. Lever and F. Jona, *J. Appl. Phys.*, **34**, 3139 (1963).
11. G. N. Sosnovskii and M. I. Abdeeva, *Tr. Atlaisk. Gorno-Met. Nauchu-Issled. Inst., Akad. Kuz., SSR*, **14**, 114 (1963). *C. A.*, **59**, 10963 (1963).
12. L. Pauling, "The Nature of The Chemical Bond," p. 85, Cornell University Press, Ithaca, N. Y. (1960).

Calculation of the Minimum Pressure, *p*-T Diagrams, and Solidus of ZnTe

A. S. Jordan and R. R. Zupp[1]

Bell Telephone Laboratories, Incorporated, Murray Hill, New Jersey

ABSTRACT

The partial pressures of the components, p_{Zn} and p_{Te_2}, for the Zn-Te system were evaluated along the liquidus curve on the basis of previously derived activities for a regular associated solution. Results are in good agreement with available experimental data. The minimum pressure of ZnTe was calculated from ΔH°_{vap} (298°K) and the free energy function, $(G^\circ_T - H^\circ_{298°K})/T$, of ZnTe and the component gases. The thermodynamic data for ZnTe needed for these calculations have also been critically reassessed or evaluated. By a combination of the measurements of Thomas and Sadowski with the values of p_{Zn} along the liquidus, a retrograde solidus for ZnTe was calculated. The calculated maximum solid solubility of Te in ZnTe is approximately 4.6 x 10^{-3} a/o (atom per cent) at 1200°C.

ZnTe is a group II-VI semiconducting compound which has been investigated extensively in the last decade for its potentially promising electrical and optical properties. The physical properties of ZnTe are governed to a great extent by its defect chemistry which in turn depends on the thermodynamic properties of the Zn-Te system at the high temperatures prevailing during the growth or annealing of the crystalline compound. The equilibrium thermodynamic properties of the Zn-Te system can be best described in terms of its pressure-temperature-composition (p-T-x) diagram. The primary object of this communication is to calculate some sections of this diagram.

First, the thermodynamic properties of solid ZnTe required for further calculations are reassessed or evaluated. Then, by the third law method the heat of vaporization of ZnTe and the minimum pressure of congruently subliming ZnTe are calculated. In addition, the partial pressures of the components in the Zn-Te system are evaluated as a function of temperature along the liquidus curve (p-T diagrams) by the use of a theory of regular associated solutions (1). Finally, by a combination of the results of Thomas and Sadowski (2) for the concentration of Zn vacancies as a function of p_{Zn} with the values of p_{Zn} along the liquidus, the solidus for ZnTe is calculated.

Thermodynamic Properties of ZnTe

Specific heat.—Kelemen *et al.* (3) have measured the specific heat, C_p, of ZnTe between 273° and 773°K. From their graphically presented data one can derive the following equation for C_p

$$C_p = 11.03 + 3.84 \times 10^{-3}T \qquad [1]$$

where T is the temperature in °K and the unit of C_p is cal/g mole deg. At 298°K the experimental value of C_p is 12.17 cal/g mole deg, in excellent agreement with the value of 12.22 cal/g mole deg, calculated from standard tabulated values and the Neumann-Kopp rule.

Debye temperature.—One can calculate the Debye temperature, θ_D, of ZnTe from the room temperature elastic constants measured by Berlincourt *et al.* (4). θ_D is evaluated at 0°K by the semianalytic method of deLaunay (5). Unfortunately no measurements of the elastic constants have been made near absolute zero. However, Berlincourt *et al.* (4) have measured the elastic constants of ZnS at 298° and also at 77°K. Assuming that the temperature coefficients of the elastic constants of ZnS and ZnTe are not too different, one can adjust the elastic constants of ZnTe to 0°K and obtain $C_{11} = 7.35 \times 10^{11}$ dynes/cm^2, $C_{12} = 4.17 \times 10^{11}$ dynes/cm^2, and $C_{44} = 3.16 \times 10^{11}$ dynes/cm^2. Substituting these values into deLaunay's expression yields $\theta_D = 223$°K for ZnTe.

Standard entropy at 298°K.—Two methods have been used to evaluate the standard entropy of ZnTe at 298°K, $S^\circ_{298°K}$. Assuming that ZnTe behaves like a Debye solid, one can compute $S^\circ_{298°K}$ using standard tables (6) of Debye entropy functions. Using the calculated value of $\theta_D = 223$°K, one obtains $S^\circ_{298°K} = 9.80$ eu/g atom = 19.6 eu/g mole.

From the electrochemical cell data of McAteer and Seltz (7), one can derive $\Delta S^\circ_{660°K} = 2.85$ eu for the reaction

$$ZnTe(s) = Zn(s) + Te(s), \quad \Delta S^\circ_{660°K} \qquad [2]$$

Then, $S^\circ_{298°K}(ZnTe)$ is given by

$$S^\circ_{298°K}(ZnTe) = S^\circ_{298°K}(Zn) + S^\circ_{298°K}(Te) - \Delta S^\circ_{298°K} \qquad [3]$$

where

$$\Delta S^\circ_{298°K} = \Delta S^\circ_{660°K} - \int_{298°K}^{660°K} \frac{\Delta C_p}{T}\, dT$$

Values of $S^\circ_{298°K}$ for the pure solid elements were obtained from Stull and Sinke (8). The heat capacities of the pure solid elements in Eq. [5] were taken from the tables of Kelley (9) and that of ZnTe from Eq. [1]. Finally one gets $S^\circ_{298°K} = 19.5$ eu, in excellent agreement with the entropy derived from the Debye temperature. The estimated error in $S^\circ_{298°K}$ is ±0.3 eu.

Free energy function.—The function $(G^\circ_T - H^\circ_{298°K})/T$ is defined as the free-energy function (FEF) (6). For solids the FEF is calculated from a combination of related thermodynamic data, if the third law of thermodynamics is applicable ($S^\circ_{0°K} = 0$). The following identity is used to calculate the FEF of ZnTe

$$\text{FEF} = \frac{G^\circ_T - H^\circ_{298}}{T} = \frac{H^\circ_T - H^\circ_{298}}{T} - S^\circ_T \qquad [4]$$

where

$$\frac{H^\circ_T - H^\circ_{298}}{T} = \left(\int_{298}^{T} C_p\, dT\right) \Big/ T$$

and

$$-S^\circ_T = -\left[S^\circ_{298°K} + \int_{298}^{T} \frac{C_p\, dT}{T}\right]$$

Substituting C_p from Eq. [1] and $S^\circ_{298°K} = 19.5$ eu into Eq. [4], the FEF of ZnTe was evaluated. Numerical values are presented in 50°K intervals in Table I. The probable error in these values is approximately ±2%.

[1] Present address: University of Washington, Seattle, Washington.

Heat of Vaporization and Minimum Pressure of ZnTe(s)

Sublimation of ZnTe(s).—In an exhaustive study of nine II-VI compounds, Goldfinger and Jeunehomme (10) have demonstrated by the use of mass spectrometry that ZnTe decomposes at high temperature into the component gases according to

$$ZnTe(s) = Zn(g) + \tfrac{1}{2}Te_2(g), \quad K = p_{Zn}\sqrt{p_{Te_2}} \quad [5]$$

where p_{Zn} and p_{Te_2} are the partial pressures of Zn and Te_2 and K is the equilibrium constant.

It can be shown that, if an evaporating solid compound is in equilibrium with its vapor phase and both have the same composition, at a constant temperature, then the total pressure is at a minimum (or maximum) (11) and one speaks of congruent sublimation (12). The vapor is stoichiometric if $p_{Te_2} = \tfrac{1}{2}p_{Zn}$. It can be readily demonstrated that, if the composition of the solid deviates only slightly from stoichiometry, then the composition of the congruently subliming vapor equals that of the stoichiometric vapor and the total pressure is at a minimum. Moreover, if the total pressure is at a minimum, mass transfer from solid to vapor of the same composition occurs without diffusional limitation at a maximum rate, as if molecules of ZnTe were transported.

The concept of minimum pressure is analogous to that of the azeotropic pressure in binary liquid-vapor systems. The composition of the congruent vapor corresponds to the azeotropic point (13).

In order to calculate the minimum pressure of ZnTe at high temperatures the ΔG° for reaction [5] is required. Unfortunately measurements of ΔG° have been restricted to temperatures below 1100°K, which is approximately 470°K below the melting point of the compound. However, a thermodynamically consistent extrapolation of the low-temperature data can be performed by the third law method.

Heat of vaporization of ZnTe(s).—Goldfinger and Jeunehomme (10) have measured the pressures over ZnTe(s) between 862° and 1100°K by Knudsen's method. They calculated K for Eq. [5] and derived ΔH° and ΔS°, the standard heat and entropy of reaction, by the use of the Gibbs-Helmholtz equation, assuming $\Delta H^\circ/T - \Delta S^\circ = \Delta G^\circ/T = -R \ln K$ is a linear function of temperature (the second law method).

Likewise, Reynolds *et al.* (14) have used a Knudsen cell to measure pressures over subliming ZnTe(s) between 923° and 1003°K. They have given K for Eq. [5] and also calculated ΔH° and ΔS° by the second law method.

Korneeva *et al.* (15) have utilized a modified Langmuir technique between 793° and 993°K and a Knudsen cell between 938° and 983°K. They presented the observed total pressure, p_{obs}, as a function of temperature, assuming, wrongly, that ZnTe(g) was the major volatile species. However, it is possible to reinterpret their tabular data of p_{obs} for the correct mode of vaporization in terms of p_{Zn} and p_{Te_2} and to calculate K for Eq. [5] based on an analysis given by Goldfinger and Jeunehomme (10). Accordingly, one has

$$p_{obs} = p_{Zn}\left(\frac{M_{ZnTe}}{M_{Zn}}\right)^{1/2} = (p_{Te} + \sqrt{2}p_{Te_2})\left(\frac{M_{ZnTe}}{M_{Te}}\right)^{1/2} \quad [6]$$

where p_{Te} is the pressure of monatomic Te_1 related to p_{Te_2} by the equilibrium constant $k = p_{Te}/\sqrt{p_{Te_2}}$ for the reaction $\tfrac{1}{2}Te_2(g) = Te(g)$, and M_i is the molecular weight of the designated species. Solving Eq. [6] for the partial pressures at selected temperatures, obtaining k from the tables of Stull and Sinke (8), one finds that in the temperature range of interest p_{Te} is negligible. Hence Eq. [6] and the condition of congruent vaporization yield the following simple proportionality between the minimum total pressure, p_{tot} (min), and p_{obs}

$$1.09\ p_{obs} = p_{tot}\ (min) = 1.5 \times 2^{1/3} K^{2/3} \quad [7]$$

Using the tabular data of Korneeva *et al.* (15) for p_{obs}, values of K for Eq. [5] were readily evaluated by solving Eq. [7].

In order to facilitate the comparison of all these experimental data obtained by different techniques at various temperatures in a thermodynamically consistent manner, the third law method was utilized (16), (17). The heat of vaporization at 298°K, ΔH°_v (298°K), was calculated, for every experimental determination reported above, according to the identity

$$\Delta H^\circ_v(298°K) = -T\Delta(FEF) - RT \ln K \quad [8]$$

where for Eq. [5]

$$\Delta(FEF) = FEF[Zn(g)] + \tfrac{1}{2}FEF[Te_2(g)] - FEF[ZnTe(s)]$$

The FEF of ZnTe(s) is given in Table I. The FEF's of Zn(g) and Te_2(g) were taken from the tables of Stull and Sinke (8) and values of K were obtained from the previously discussed experimental sources. The results of these calculations are summarized in Table II.

Two values of ΔH°_v(298°K) derived from low-temperature measurements for the reaction represented by Eq. [2] are also listed in Table II. Pool has used (18) a liquid tin solution calorimeter to measure the enthalpy change, ΔH°_1, associated with Eq. [2] at 273°K. Since the difference between ΔH°_1 at 273° and 298°K is very small, one can readily calculate ΔH°_v (298°K) by adding the enthalpy changes for the reactions Zn(s) = Zn(g), ΔH°_2(298°K), and Te(s) = $\tfrac{1}{2}Te_2$(g), ΔH°_3(298°K), as given by Stull and Sinke (8), to ΔH°_1 which yields

$$\Delta H^\circ_v(298°K) = \Delta H^\circ_1 + \Delta H^\circ_2 + \Delta H^\circ_3 \quad [9]$$

McAteer and Seltz (7) have utilized a reversible galvanic cell to measure the electromotive force, E, between 628° and 691°K for the reaction represented by Eq. [2]. Using the third law method for that reaction, one obtains ΔH°_1(298°K) according to

$$\Delta H^\circ_1(298°K) = -T\Delta(FEF) - RT \ln K_1 \quad [10]$$

Table I. Free energy function and minimum pressure of ZnTe

T, °K	$-FEF = -(G^\circ - H^\circ_{298})/T$ (cal/g mole deg)	p_{tot} (min) (atm)
298	19.50	
300	19.50	
350	19.63	
400	19.96	
450	20.40	
500	20.89	
550	21.40	
600	21.94	
650	22.47	
700	23.00	
750	23.53	
800	24.05	
850	24.56	
900	25.06	
950	25.56	
1000	26.03	8.45×10^{-5}
1050	26.50	2.85×10^{-4}
1100	26.96	8.56×10^{-4}
1150	27.41	2.33×10^{-3}
1200	27.85	5.81×10^{-3}
1250	28.28	1.35×10^{-2}
1300	28.70	2.91×10^{-2}
1350	29.11	5.91×10^{-2}
1400	29.52	1.14×10^{-1}
1450	29.92	2.09×10^{-1}
1500	30.31	3.67×10^{-1}
1550	30.69	6.19×10^{-1}

Table II. Heat of vaporization of ZnTe

ΔH°_v (298°K) in kcal	Author	Exptl. technique
78.4 ± 0.6	Korneeva *et al.* (15)	Knudsen Modif. Langmuir
79.5 ± 0.5	Pool (18)	Calorimetry
79.0 ± 0.5	McAteer and Seltz (7)	Electrolytic cell
79.5 ± 0.6	Goldfinger and Jeunehomme (10)	Knudsen
82.8 ± 0.7	Reynolds *et al.* (14)	Knudsen

where $-RT \ln K_1 = -nFE$ and $\Delta(\text{FEF}) = \text{FEF}[\text{Zn(s)}] + \text{FEF}[\text{Te(s)}] - \text{FEF}[\text{ZnTe(s)}]$. Finally, $\Delta H^\circ_v(298^\circ\text{K})$ can be immediately calculated from Eq. [9].

The errors listed in Table II were obtained by a combination of the standard deviation in the measurements of any one of the authors with the estimated error in the free energy functions. It is apparent that the value of ΔH°_v derived from the results of Reynolds *et al.* (14) is outside the error limits of all the other measurements. The reason for this disagreement is not at all obvious. It is possible that the results are too low due to calibration error. However, the estimated calibration error (25%) (19) could not account for the observed difference among the listed values of ΔH°_v.

Since four of the calculated ΔH°_v values are in good agreement within their respective errors, we recommend their average of 79.1 ± 1.0 kcal/mol as the best value for the heat of vaporization of ZnTe(s) into Zn(g) and ½Te_2(g) at 298°K.

Minimum pressure over ZnTe(s).—p_{tot}(min) was extrapolated to higher temperatures by the third law method. Using Eq. [7], one can obtain ln p_{tot} (min) in terms of ln K in the form

$$\ln p_{tot}(\text{min}) = 2/3 \ln K + 0.637 \qquad [11]$$

ln K was readily evaluated by rewriting Eq. [8] to yield

$$\ln K = -\frac{\Delta H^\circ_v(298^\circ\text{K})}{RT} - \frac{\Delta(\text{FEF})}{R} \qquad [12]$$

Calculated values of p_{tot}(min) above 1000°K are given in Table I in 50°K intervals.

A plot of p_{tot}(min) as a function of $1/T$ above 1300°K is presented in Fig. 1. $p_{Zn}(\text{min}) = 2/3p_{tot}(\text{min})$ and $p_{Te_2}(\text{min}) = 1/3p_{tot}(\text{min})$ are also given. In Fig. 2 and 3, p_{Zn}(min) and p_{Te_2}(min) are extended to temperatures below 1300°K. The minimum pressure-temperature curves are terminated at their intersection with the partial pressure-temperature curves of the three phase solid-liquid-gas equilibria, constructed in the following section.

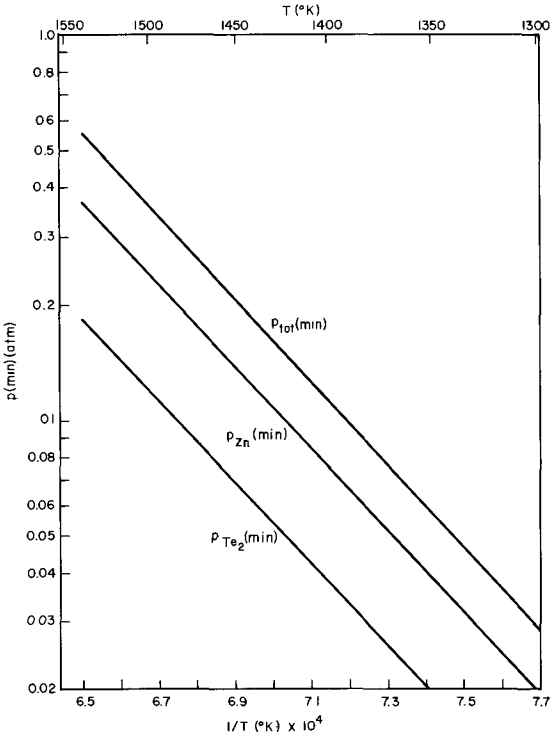

Fig. 1. Calculated dependence of minimum pressure on reciprocal temperature over congruently subliming ZnTe(s).

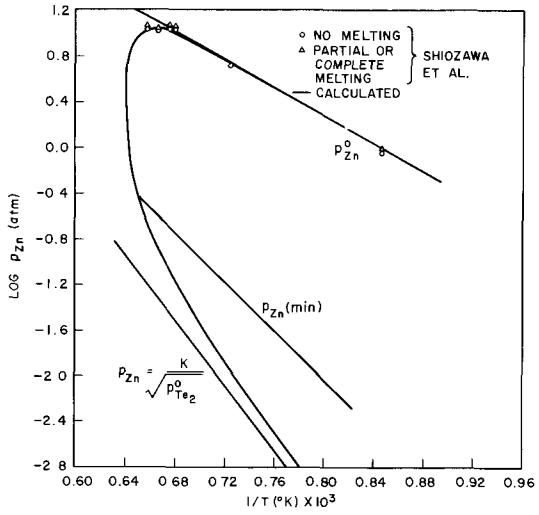

Fig. 2. Log Zn pressure vs. reciprocal temperature for the Zn-Te system.

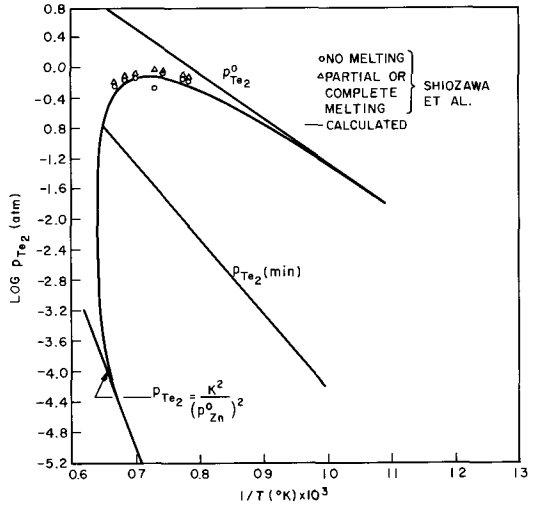

Fig. 3. Log Te_2 pressure vs. reciprocal temperature for the Zn-Te system.

Calculation of the p-T Diagrams

Theory.—It has already been pointed out that at the temperatures of interest ZnTe dissociates into the component gases according to Eq. [5]. In order to calculate the variation of the partial pressures of these gases with temperature in a binary system with three coexisting phases, *i.e.*, ZnTe in simultaneous equilibrium with a liquid and a gas phase, it is necessary to know the activities along the liquidus curve. By definition in the Zn-Te system

$$p_{Zn} = p^\circ_{Zn} a_{Zn} \qquad [13]$$

and

$$p_{Te_2} = p^\circ_{Te_2} a^2_{Te} \qquad [14]$$

where a_i and p°_i are the activity and pressure of pure liquid component i (Zn or Te), respectively, at the temperature of the solution.

The partial pressures of the group V components along the liquidus in some III-V compounds have been calculated assuming regular solution behavior in the liquid by Vieland (20). Kroger (21) and Reynolds *et al.* (14) have evaluated some segments of the p-T diagrams in the Zn-Te system assuming that the liquid was ideal. However, it has been demonstrated by one of us (1) that the Zn-Te and also the Cd-Te liquidus curves could not be described by assuming regular or ideal behavior in the liquid. In fact, the liquidus curves for the Cd-Te and Zn-Te systems, in which the observed shapes of the liquidus strongly

suggest association in the liquid, have been calculated in good agreement with experimental results by the use of activities derived from a regular associated solution model. Assuming the presence of ZnTe complexes as well as Zn and Te atoms in chemical equilibrium in the liquid and identifying the activity coefficients of these species with those of a regular ternary solution, the approximate gross activities for the components in a regular associated solution have been derived in the following form

$$\frac{p_{Zn}}{p^{o}_{Zn}} = a_{Zn} = \gamma_{Zn}x_{Zn} = \frac{x_{Zn} - x_{Te} + P}{1 + P} e^{\alpha x^2_{Te}/RT} \quad [15]$$

$$\sqrt{\frac{p_{Te_2}}{p^{o}_{Te_2}}} = a_{Te} = \gamma_{Te}x_{Te} = \frac{x_{Te} - x_{Zn} + P}{1 + P} e^{\alpha x^2_{Zn}/RT} \quad [16]$$

where

$$P = \sqrt{1 - 4x_{Zn}x_{Te}(1 - \beta^2)}$$

and x_i and γ_i are the atom fraction and activity coefficient for component i (Zn or Te). α and β are constants incorporating the equilibrium constant for association and the interaction coefficients among the species.

Using Eq. [15] and [16] the equation of the liquidus boundary for the Zn-Te and Cd-Te was derived and given by (1)

$$T = \frac{\alpha(x_{Te} - 0.5)^2 + \Delta H_f}{R/2 \ln s(x_{Te}) + \Delta H_f/T_f} \quad [17]$$

where

$$s(x_{Te}) = \frac{[1 + \sqrt{4(x_{Te} - 0.5)^2 + \beta^2[1 - 4(x_{Te} - 0.5)^2]}]^2}{(1 + \beta)^2[1 - 4(x_{Te} - 0.5)^2]}$$

ΔH_f and T_f are the heat of fusion/gram atom and melting point of the compound, respectively. Approximate values of ΔH_f and T_f for both systems can be obtained from the work of Kulwicki (22). Values of α and β were evaluated (1) for the Zn-ZnTe, Te-ZnTe, Cd-CdTe, and Te-CdTe subsystems by the application of an approximate form of Eq. [17], valid for small values of β and if $2(x_{Te} - 0.5) > \beta$, to the liquidus data of Kulwicki (22) which, as discussed in ref. (1), appears to be the most reliable source of data.

The p-T diagrams in the Zn-Te system can be readily calculated by the use of Eq. [13] through [17].

Computational procedure.—The calculation of p_{Zn} and p_{Te_2} as a function of temperature along the liquidus curve was performed on a computer. First, x_{Zn} was decreased from 1.0 to 0.0 in intervals of 0.02, and the liquidus temperature corresponding to each of these compositions was computed by the use of Eq. [17]. Then, pairs of values of x_{Zn} and T were substituted into Eq. [15] and [16] to obtain the pressures. Equation [15] was used to calculate p_{Zn} in the Zn-ZnTe subsystem and Eq. [16] to calculate p_{Te_2} in the Te-ZnTe subsystem. Having obtained p_{Zn}, p_{Te_2} in the Zn-ZnTe subsystem was evaluated from the equilibrium constant for Eq. [5] by $p_{Te_2} = K^2/p^2_{Zn}$.

Similarly, p_{Zn} in the Te-ZnTe subsystem was calculated from Eq. [5] as $p_{Zn} = K/\sqrt{p_{Te_2}}$.

K was evaluated by the third law method according to Eq. [12]. The pressures of the pure superheated liquids, p^{o}_{Zn} and $p^{o}_{Te_2}$, were obtained from the recent high-pressure measurements of Baker (23, 24). $p^{o}_{Te_2}$ was computed from the total pressure data of Baker by subtracting from it a small pressure ($\approx$1%) due to monatomic Te. The dissociation constant to perform this calculation was taken from Stull and Sinke (8).

Comparison with experiment.—Figures 2 and 3 illustrate the calculated dependence of log p_{Zn} and log p_{Te_2} on $1/T$, respectively, and the measurements of Shiozawa *et al.* (25) along the liquidus curve of the Zn-Te system. These p-T diagrams also show the limiting straight lines at $x_{Zn} = 1$ and 0. For example, in Fig. 2 the limiting lines log p^{o}_{Zn} and log p_{Zn} = log $K/\sqrt{p^{o}_{Te_2}}$ *vs.* $1/T$ were drawn. In addition, as mentioned earlier, values of log p_{Zn} and log p_{Te_2} *vs.* $1/T$ at p_{tot}(min) were also plotted.

The p-T diagrams in the Zn-Te system have been recently studied by Shiozawa *et al.* (25). An evacuated ampoule containing a ZnTe crystal and Zn or Te at opposite ends was placed in a two-zone furnace. At a constant temperature ZnTe was exposed to increasing Zn or Te_2 pressures by raising the reservoir temperature, in steps, until partial or complete melting of the crystal was achieved. At each step the ampoule was removed from the furnace for observation. Figures 2 and 3 illustrate the experimental maximum values p_{Zn} and p_{Te_2}, taken from the report of Shiozawa *et al.* (25), at which no melting took place and the minimum values of p_{Zn} and p_{Te_2}, at which partial or complete melting was observed. Noting that the actual experimental points must lie between the upper and lower pressure limits, the agreement with the theoretical p-T diagrams is excellent.

Solidus Curve of ZnTe

De Nobel (26) has calculated the deviation from stoichiometry of solid CdTe in equilibrium with the liquid from a knowledge of p_{Cd} and the defect structure. Similarly, Kroger (21) and Reynolds (27), utilizing the defect study of Thomas and Sadowski and assuming ideal solution behavior in the liquid, have estimated the solidus of ZnTe. In this section the solidus curve of ZnTe will be determined on the basis of the previously calculated p_{Zn}, plotted in Fig. 2.

Thomas and Sadowski (2) have measured the p-type conductivity of ZnTe crystals between 973° and 1223°K and for p_{Zn} between 10 and 400 Torr. By assuming the presence of doubly ionized Zn vacancies on the Zn sublattice, V''_{Zn}, in excess of any other acceptor, they could explain their experimental results. They showed that the concentration of the vacant Zn sites, $[V''_{Zn}]$, can be related to the hole concentration, $[h\cdot]$, and to p_{Zn} by the equilibrium constant for the reaction

$$Zn_{Zn} = V''_{Zn} + 2h\cdot + Zn(g)$$

Consequently, observing that $[V''_{Zn}] = [h\cdot]/2$, they fitted their data by the following equation

$$[h\cdot] = 3.73 \times 10^{23}\, p_{Zn}^{-1/3} \exp - \left(\frac{1.31 \text{ ev}}{kT}\right) \quad [18]$$

where p_{Zn} is given in Torrs, the unit of $[h\cdot]$ is holes/cc, and k is Boltzmann's constant. By simple conversion of units, one can readily rewrite Eq. [18] in terms of the site fraction of Zn vacancies on the Zn sublattice, v, as

$$v \equiv \frac{[V''_{Zn}]}{[Zn_{Zn}] + [V''_{Zn}]} = \frac{1.17}{p_{Zn}^{1/3}} \exp - \left(\frac{30.2 \text{ kcal}}{RT}\right) \quad [19]$$

where p_{Zn} is in atmospheres.

If one assumes that the major defect in the crystal is V''_{Zn}, then utilizing the relations $[Te_{Te}]/[Zn_{Zn}] + [V''_{Zn}] + [Te_{Te}] = 0.5$, $[Zn_{Zn}] + [V''_{Zn}]/[Zn_{Zn}] + [V''_{Zn}] + [Te_{Te}] = 0.5$ and Eq. [19], one can express the atom fractions of Zn and Te in the solid, x^{s}_{Zn} and x^{s}_{Te}, in the form

$$x^{s}_{Zn} = \frac{[Zn_{Zn}]}{[Zn_{Zn}] + [Te_{Te}]} = \frac{1 - v}{2 - v}$$

and

$$x^{s}_{Te} = \frac{[Te_{Te}]}{[Zn_{Zn}] + [Te_{Te}]} = \frac{1}{2 - v} \quad [20]$$

where $[Zn_{Zn}]$ and $[Te_{Te}]$ denote the concentrations of Zn atoms on the Zn sublattice and Te atom on the Te sublattice, respectively.

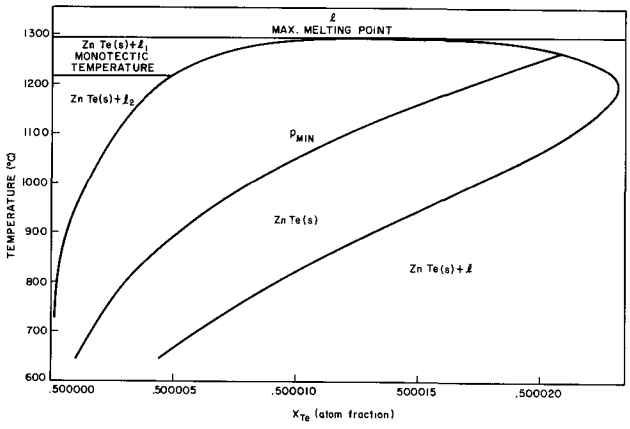

Fig. 4. Calculated solidus curve of ZnTe(s)

At any temperature along the p-T curve (Fig. 2) p_{Zn} over the liquid equals p_{Zn} over the coexisting solid. Therefore, if these values of p_{Zn} are substituted into Eq. [19], v as a function of temperature is obtained. Furthermore, a knowledge of v makes it possible by the use of Eq. [20] to evalaute x^s_{Te} and x^s_{Zn} as a function of temperature, thus giving the solidus curve.

The values of x^s_{Te} and x^s_{Zn} along the solidus curve were computed, and they are plotted in Fig. 4. If in the calculation p_{Zn} along the three phase equilibria is replaced by $p_{Zn} = 2/3p_{tot}(min)$ on the minimum pressure line, the composition of solid ZnTe corresponding to congruently subliming ZnTe is obtained. The curve labeled p_{min} in Fig. 4 shows the dependence of this specific solid composition on temperature. The monotectic temperature at 1213°C is a consequence of the theory of regular associated solutions and it is consistent with the flat experimental liquidus curve in the Zn-ZnTe subsystem (1).

Qualitatively, the shape of the calculated solidus agrees with the previously reported curves of Kroger (21) and Reynolds (27). This is a consequence of utilizing in all of these calculations the study of Thomas and Sadowsky (2) for the defect structure of ZnTe. At low temperatures the boundary in Fig. 4 essentially coincides with the previously estimated curves, but at high temperatures the curves differ. This is not surprising since at low temperatures ZnTe is in equilibrium with almost pure Zn (or Te) liquid and the p_{Zn} calculated from the theory of regular associated solutions reduces to that of an ideal solution. However, at high temperatures ZnTe is in equilibrium with concentrated solutions of Zn and Te in which departures from ideality become significant.

The solidus curve of ZnTe delineates a region with an excess of Te. This is consistent with the p-type behavior of ZnTe. It can also be seen in Fig. 4 that the solidus of ZnTe is retrograde with a maximum at 1200°C. At this temperature the solid solubility of Te in ZnTe is approximately 4.6×10^{-3} a/o or 8.1×10^{17} at./cc. The retrograde nature of the ZnTe solidus has already been suggested by Reynolds *et al.* (14). Moreover, according to de Nobel (26), the solidus of CdTe is also retrograde. It is interesting to note that below 600°C the ZnTe crystal becomes nearly stoichiometric.

Acknowledgments

The authors are grateful to Dr. C. D. Thurmond and Dr. F. A. Trumbore for helpful discussions, to Professor Goldfinger for providing some unpublished data, and to Mr. J. Jost, of Clevite Corporation, for bringing the work of Shiozawa *et al.* to our attention.

Manuscript submitted Jan. 10, 1969; revised manuscript received June 11, 1969. This was Paper 527 presented at the Montreal Meeting, Oct. 6-11, 1968.

Any discussion of this paper will appear in a Discussion Section to be published in the June 1970 JOURNAL.

REFERENCES

1. A. S. Jordan, Paper presented at the TMS-AIME Annual Meeting, February 17-20, 1969, Washington, D.C.
2. D. G. Thomas and E. A. Sadowski, *J. Phys. Chem. Solids*, **25**, 395 (1964).
3. F. Kelemen, E. Cruceanu, and D. Niculescu, *Phys. Stat. Sol.*, **11**, 865 (1965).
4. D. Berlincourt, H. Jaffee, and L. R. Shiozawa, *Phys. Rev.*, **129**, 1009 (1963).
5. J. deLaunay, "The Theory of Specific Heats and Lattice Vibrations" in "Solid State Physics," Vol. 2, F. Seitz and D. Turnbull, Editors, Academic Press Inc., New York (1956).
6. G. N. Lewis and M. Randall, "Thermodynamics," Revised by K. S. Pitzer and L. Brewer, 2nd ed., McGraw-Hill Book Co., Inc., New York (1961).
7. J. H. McAteer and H. Seltz, *J. Am. Chem. Soc.*, **58**, 2081 (1936).
8. D. R. Stull and G. C. Sinke, "Thermodynamic Properties of the Elements," Advances in Chemistry Series, No. 18, A.C.S.
9. K. K. Kelley, U.S. Bureau of Mines Bull. 584, U.S. Government Printing Office, Washington, D.C. (1960).
10. P. Goldfinger and M. Jeunehomme, *Trans. Faraday Soc.*, **59**, 2851 (1963).
11. E. A. Guggenheim, "Thermodynamics," North-Holland Publishing Co., Amsterdam (1959).
12. R. F. Brebrick, "Nonstoichiometry in Binary Semiconductor Compounds $M(\frac{1}{2}-\delta)N(\frac{1}{2}+\delta)$ (c)," in "Progress in Solid State Chemistry," Vol. 3, Pergamon Press, Oxford and New York (1966).
13. I. Prigogine and R. Defay, "Chemical Thermodynamics," Longmans Green and Co., London (1954).
14. R. A. Reynolds, D. G. Stroud, and D. A. Stevenson, *This Journal*, **114**, 1281 (1967).
15. I. V. Korneeva, A. V. Belyaev, and A. V. Novoselova, *Russ. J. Inorgan. Chem.*, **5**, 1 (1960).
16. J. L. Margrave, "Thermodynamic Calculations on High Temperature Systems," in "Physiochemical Measurements at High Temperatures," J. O'M. Bockris, J. L. White, and J. D. Mackenzie, Editors Butterworths Scientific Publications, London (1959).
17. R. Hultgren. R. L. Orr, P. D. Anderson, and K. K. Kelley, "Selected Values of Thermodynamic Properties of Metals and Alloys," John Wiley & Sons, Inc., New York (1963).
18. M. J. Pool, *Trans. Met. Soc. AIME*, **233**, 1771 (1965).
19. D. A. Stevenson, Private communication.
20. L. J. Vieland, *Acta Met.*, **11**, 137 (1963).
21. F. A. Kroger, *J. Phys. Chem.*, **69**, 3367 (1965).
22. B. M. Kulwicki, Ph.D. Thesis, University of Michigan, School of Engineering, July 1963.
23. E. H. Baker, *J. Chem. Soc.*, (A), **1967**, 1558.
24. E. H. Baker, *J. Appl. Chem.*, **16**, 321 (1966).
25. L. R. Shiozawa, J. M. Jost, and G. A. Sullivan, 1965-1968, "Research on Improved II-VI Compounds," Final Report, Contract AF 33(615)-2708 for the Aerospace Research Laboratories, U.S.A.F., Wright-Patterson Air Force Base, Ohio.
26. D. de Nobel, *Philips Res. Repts.*, **14**, 361 (1959).
27. R. A. Reynolds, Thesis Progress Rept. No. 3, June 1964, Dept. of Materials Science, Stanford University.

Vapor Phase Growth of Stannic Oxide Single Crystals

C. G. Fonstad, A. Linz, and R. H. Rediker

Department of Electrical Engineering and Center for Materials Science and Engineering, Massachusetts Institute of Technology, Cambridge, Massachusetts

ABSTRACT

Single crystals of stannic oxide, SnO_2, of higher purity and with higher Hall mobility than any previously reported have been grown from the vapor using the reaction

$$SnCl_4 + 2H_2 + O_2 \overset{\Delta}{\rightleftarrows} SnO_2 + 4HCl$$

at 1250°C and 10 Torr. The stannic chloride is obtained from the reaction

$$Sn + 2Cl_2 \rightleftarrows SnCl_4 + \Delta$$

which is performed in an external reactor and electrical doping is achieved by adding the desired dopant materials to tin charges in parallel doping reactors. The growth rate of the SnO_2 is controlled by adding additional Cl_2 to the $SnCl_4$ flow before it is introduced into the furnace; with sufficient Cl_2 the crystals can also be etched. Important to the furnace design is a gas injection nozzle which eliminates growth immediately where the gases enter the furnace. Undoped crystals of 6 x 10^5 ohm-cm resistivity at 300°K, and antimony-doped n-type crystals with resistivity, carrier concentration, and mobility of 0.1 ohm-cm, 4 x 10^{17} cm^{-3}, and 160 cm^2/V-sec at 300°K and of 0.1 ohm-cm, 6 x 10^{16} cm^{-3}, and 1200 cm^2/V-sec at 77°K have been grown, as have n-i junctions.

As part of a program to evaluate stannic oxide, SnO_2, as a material for semiconductor devices that will operate in excess of 400°C, single crystals of SnO_2 have been grown from the vapor phase. Single crystals of stannic oxide have previously been obtained from the reaction of tin vapor and oxygen at 1450°C (1), by growth from a Cu_2O flux at 1250°C (2), and by the high-temperature decomposition of SnO_2 to produce SnO vapor which in turn reoxidizes at lower temperatures to form SnO_2 crystals (3-5). Of the published SnO_2 growth methods ours is closest to that of Nagasawa *et al.* (6), who grew these crystals using the vapor reaction of $SnCl_4$ with H_2O at 1100°-1300°C. The growth technique reported in this paper, however, is more comparable to that used by Schaffer (7) to grow Al_2O_3 in that no carrier gases are used and all reactions and growth occur at low pressure. The process to be described has produced SnO_2 with higher Hall mobilities and of higher purity than previously reported and is compatible with introducing dopants during the growing process. High resistivity ($> 10^5$ ohm-cm) crystals as well as lower resistivity (0.1 ohm-cm) n-type crystals produced by Sb doping have been grown and crystals containing $n-i$ junctions have also been grown.

Preparation of Single Crystals

The growing system is based on reacting oxygen, hydrogen, and stannic chloride in a quartz tube at 1250°C at reduced pressure of 10 Torr to produce stannic oxide

$$SnCl_4 + 2H_2 + O_2 \overset{\Delta}{\rightleftarrows} SnO_2 + 4HCl \qquad [1]$$

The $SnCl_4$ is produced by flowing chlorine through 30-mesh tin metal at 100°C also at 10 Torr pressure

$$Sn + 2Cl_2 \rightleftarrows SnCl_4 + \Delta \qquad [2]$$

Figure 1 shows the furnace system. The starting materials for the growth of SnO_2 crystals are the gases Cl_2, O_2, and H_2 and metallic Sn; in the results reported here reagent grade Sn and Cl_2, and prepurified H_2 were used. The flows of the gases are controlled by a system of gas cylinder regulators, shut-off valves, and flowmeters (not shown in Fig. 1) before they enter the furnace system through needle valves as indicated in the lower left of the figure. The total gas flow is typically 100 cm^3/min as measured at 900 Torr and 300°K by the flowmeters which are on the upstream side of the needle valves; this total flow is made up of individual Cl_2, H_2, and O_2 flows in the proportions of 2:10:5, respectively. On the downstream side of the needle valves and in the entire system shown in the figure the pressure is maintained at 10 Torr through the use of a vacuum pump with a throttling valve.

As shown in Fig. 1, the reaction of Sn and Cl_2, Eq. [2], occurs in a Pyrex Buchner type funnel with a coarse fritted disk on which a 30 mesh tin charge rests. This "$SnCl_4$ reactor" is wrapped with heater tape and heated to 100°C which is sufficient at 10 Torr to give a uniform and complete reaction. Electrically active dopants are introduced into the crystals by using, in parallel with the "pure" $SnCl_4$ reactor, other $SnCl_4$ reactors in which the tin charges contain small proportions of the desired dopants (Sb for example).

The furnace tube is a 5-cm diameter mullite tube horizontally mounted in a Globar furnace and sealed with Inconel endcaps. As shown in Fig. 1, the O_2 inlet, and the H_2 and Cl_2-$SnCl_4$ injector tubes are on the input endcap; the output endcap provides a mount for a diaphragm pressure gauge, a quartz viewing window, and a connection to the cold traps and vacuum pump. A quartz tube closely fitting inside the mullite tube is used as the growing substrate. It is made long enough to cover the entire high-temperature region of the furnace to protect against contamination from the mul-

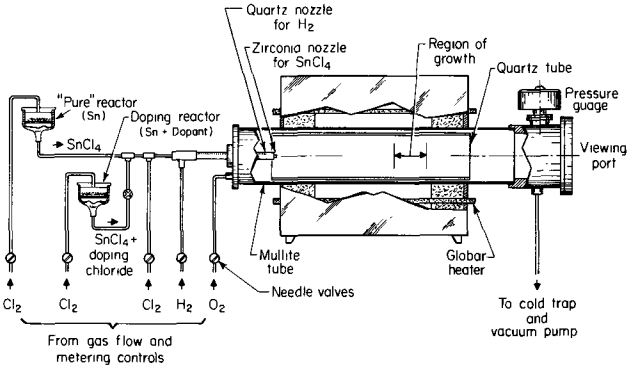

Fig. 1. Stannic oxide crystal growing system. The drawing is not to scale; the actual mullite tube is 90 cm long, 5 cm ID.

lite and to preserve the mullite tube. A spiral of 20-mil Pt wire wrapped around the quartz liner keeps it from touching and possibly sticking to the mullite.

In the SnO_2 growth, chlorine gas flows into the $SnCl_4$ reactor and reacts with the tin to form stannic chloride, $SnCl_4$, which at 10 Torr is also a gas. When doped material is desired, the chlorine flow to the doping reactor is turned on, and the appropriate dopant chloride is also formed and travels with the $SnCl_4$ gas. The total chlorine flow to all the reactors is kept constant and the desired doping concentration and/or doping profile is obtained by adjusting the fraction of this flow which goes to the doping reactor. As shown in Fig. 1, additional chlorine (< 1 cm^3/min) is added to the combined $SnCl_4$ gas from the reactors, and these gases are injected into the furnace tube through a 0.32-cm OD, 0.16-cm ID zirconia nozzle coaxial with the furnace tube. Hydrogen gas is introduced into the furnace through a 0.9-cm ID quartz tube concentric with the nozzle and acts as a sheath about the zirconia nozzle shielding it from the oxygen which enters the furnace near the periphery of the input endcap and is flowing in the region about the injection nozzles. Using this H_2 shield prevents the immediate occurrence of the reaction, Eq. [1], and eliminates the growth of SnO_2 on the injector tubes which has plagued several groups (3, 5). The concentric tubes must, of course, be properly constructed to minimize turbulence at their ends or the purpose of the H_2 shield is defeated. As the gases flow further into the furnace tube they mix and react producing tin oxide. The additional Cl_2 which was added to the $SnCl_4$ flow slows the reaction, Eq. [1], and is used to control the growth rate and can even be used to reverse the reaction if it is desired to back-etch seeds or remove unwanted nucleation. Nucleation occurs on the walls of the quartz liner and the largest, best-formed crystals grow in the region downstream from the center of the furnace where the temperature is decreasing at 10°C/cm from 1250° to 1175°C. The "exhaust" gases are passed through liquid nitrogen cold traps and are then pumped into the exhaust of a chemical hood. Helium gas is used to purge the lines before and after a growth run.

The procedure for a growth run is as follows. Initially, He gas is flowing in all of the system with the furnace hot and the pressure adjusted to approximately 10 Torr. To start the run the He flow is turned off and the other gas flows are started, H_2 and O_2 first,[1] then Cl_2. The progress of the growth is observed through the viewing window and the flow of additional Cl_2 is varied to give slow initial growth which has been found to be advantageous. This additional Cl_2 flow, approximately 1 cm^3/min initially, is slowly reduced to zero as the crystals grow larger and expose more surface area. If and when it is desired doping can be started. After growth has proceeded as far as desired the gas flows are stopped, He gas is again turned on, the pressure is increased to 760 Torr, and the crystals are removed, usually as soon as possible. Such a growth run typically results in over 10 large crystals, such as shown in Fig. 2, and many smaller ones.

Properties of Crystals Grown

The stannic oxide crystals grow as rods with diamond cross section, anchored at their base to the quartz liner and sticking out into the gas stream. Figure 2 illustrates the most common habit (note the twinning). Typical dimensions are $A = 2.5$ mm, $B = 5$ mm, and $C = 5$ mm for crystals grown 40 hr. Undoped crystals are clear and colorless showing no optical distortion in untwinned portions. Antimony-doped crystals are slightly bluish in color. No change in growth habit is observed when small concentrations of antimony are introduced, and we have successfully grown antimony-doped layers

[1] Because of the small gas flows (<100 cm^3/min at STP), the exothermic reaction of H_2 and O_2 produces approximately 10w of power and does not significantly affect the furnace temperature.

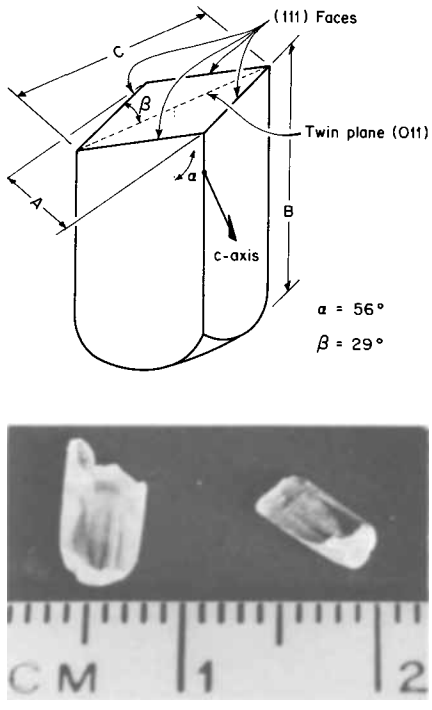

Fig. 2. Stannic oxide crystals: (top) artist's sketch of a crystal illustrating growth habit, and (bottom) photograph of two typical crystals.

on undoped crystals by turning on the chlorine flow to the doping reactor during the run as described above.

In order to characterize the crystals, x-ray and spectrochemical analyses and electrical measurements have been made. Laue x-ray photographs, taken mainly for purposes of orienting crystals, show a large number of sharp spots indicating good crystal quality. Spectrochemical analysis of crystals indicates less than 10 ppm Si (except at the base where the crystals anchor to the liner and where over 0.1% Si is found in the crystals) and less than 1 ppm of Ca, Cu, and Fe. No other elements were found except for the dopants in doped crystals, but the analysis technique used cannot detect the presence of chlorine so its existence cannot be discounted.

Hall effect and resistivity measurements of two antimony-doped crystals indicate n-type Hall mobilities, resistivities, and carrier concentrations of 160 cm^2/V-sec, 0.1 ohm-cm, and 4×10^{17} cm^{-3}, respectively, at 300°K, and of 1200 cm^2/V-sec, 0.1 ohm-cm, and 6×10^{16} cm^{-3} at 77°K. The resistivity of an undoped crystal has been measured as 6×10^5 ohm-cm at 300°K. In determining the carrier concentrations above, the Hall and drift mobilities have been assumed to be the same, which is not *a priori* obvious for this wide band-gap semiconductor.

Discussion

The spectrochemical analysis of the crystals grown indicates that they contain fewer impurities than those grown by other techniques (1-6). The fact that the Hall mobility at 77°K is 1200 cm^2/V-sec as compared to the highest previously reported value of 1000 cm^2/V-sec (8) is a further indication that the crystals are very pure. The high purity results from the method's inherent requirement that the elements in the crystals either be inside the furnace initially or be transported into the furnace in a gaseous form, most probably as a compound with chlorine. The dry chlorine used reacts slowly, if at all, with many elements below 100°C, and few of the compounds formed when it does react have sufficient vapor pressure at room temperature to readily enter the gas stream (9). This fact, of course, must also be taken into account when choosing dopants to insure that they will be transported into the furnace as

desired. Another interesting and very useful feature of the described method is the use of additional chlorine to control the reaction rate. Its main utility comes at the start of a run where it can be used to obtain slow initial growth and can be used by increasing the flow enough to reverse the reaction to back-etch seeds or to remove unwanted nucleation. Finally, the method of growing SnO_2 presented here, in addition to producing crystals having high mobility, is well suited for growing crystals for various electrical studies. Since dopants are introduced as the crystals grow and can be switched on and off without interrupting growth, the production of doped, conducting layers on higher resistance bases is straightforward as is the production of numerous other layered geometries.

Acknowledgments

This research was sponsored by the Air Force Office of Scientific Research, Office of Aerospace Research, United States Air Force, under AFOSR Grant Nr. 68-1571, and the Advanced Research Projects Agency under Contract number SD-90. The authors are grateful for helpful discussions with R. C. Folweiler, T. B. Reed, and J. A. Marley.

Manuscript submitted March 27, 1969; revised manuscript received *ca.* May 15, 1969.

Any discussion of this paper will appear in a Discussion Section to be published in the June 1970 JOURNAL.

REFERENCES

1. D. F. Morgan and D. A. Wright, *Brit. J. Appl. Phys.*, **17**, 337 (1966).
2. H. F. Kunkle and E. E. Kohnke, *J. Appl. Phys.*, **36**, 1489 (1965).
3. J. A. Marley and T. C. MacAvoy, *ibid.*, **32**, 2504 (1961).
4. T. B. Reed, J. T. Roddy, and A. N. Mariano, *ibid.*, **33**, 1014 (1962).
5. H. J. vanDaal, *Solid State Commun.*, **6**, 5 (1968).
6. M. Nagasawa, S. Shionoya, and S. Makishima, *Japan. J. Appl. Phys.*, **4**, 195 (1965).
7. P. S. Schaffer, *J. Am. Ceram. Soc.*, **48**, 508 (1965).
8. M. Nagasawa and S. Shionoya, *J. Phys. Chem. Solids*, **29**, 1959 (1968).
9. "Supplement to Mellors Comprehensive Treatise on Inorganic and Theoretical Chemistry," Suppl. II, Part I, pp. 379-387, Longmans, Green & Co., New York (1956); and "Handbook of Chemistry and Physics," 43rd ed., Chemical Rubber Publishing Co., Cleveland, Ohio (1962).

Phosphorus and Arsenic Doping of Epitaxial Silicon Films in the 1000° to 1200°C Temperature Range

Terry B. Swanson*[1] and Ross N. Tucker*

Research and Development Laboratory, Fairchild Semiconductor, Palo Alto, California

ABSTRACT

The doping of silane grown epitaxial films has been studied in the 1000°-1200°C temperature range. Dopant sources were PH_3 and AsH_3. It is found that a gas phase equilibrium between the dimer (P_2 or As_2) and monomer (P or As) species occurs. The monomer is responsible for doping the silicon and does so in accordance with Henry's law. Reasonable agreement between the calculated and experimental doping concentration has been obtained.

Although a great deal of effort has been expended on studies concerning the doping of epitaxial silicon films, very little is known about the physicochemical processes involved. However, Shepherd (1) recently proposed a model to explain the doping of silicon epitaxial films grown in horizontal, gas flow reactors. Although Shepherd (1) tested his model for films deposited by the hydrogen reduction of $SiCl_4$ (temperature range 1100°-1350°C) and doped with n-type dopants introduced as the chloride species, many of the ideas are thought to be of general applicability. In the present work, we have studied the doping of SiH_4 grown epitaxial films using PH_3 and AsH_3 as the dopant gases. Several ideas are extracted from the Shepherd (1) model and are found to apply quite well to the temperature range suitable for epitaxial growth with SiH_4 ($\sim$ 1000°-1200°).

Theory

Both PH_3 and AsH_3 are thermodynamically unstable molecules at high temperatures. When introduced into a high temperature gas stream these molecules undergo almost complete decomposition and various other atomic and molecular species are formed. In the 1000°-1200° temperature range the two important gas phase species formed from the PH_3 molecule are the phosphorus monomer and the phosphorus dimer. This has been found from thermodynamic calculations (2). A similar situation exists in the case of AsH_3 in that the arsenic monomer and dimer are the predominant species between 1000° and 1200°C (3). In each case an equilibrium exists between the monomeric and the dimeric species in the gas phase. Only minute quantities of PH_3 or AsH_3 remain in the high temperature gas stream.

$$2PH_3(g) \xrightarrow{\Delta} P_2(g) \rightleftharpoons 2P(g) \quad [1]$$

$$2AsH_3(g) \xrightarrow{\Delta} As_2(g) \rightleftharpoons 2As(g) \quad [2]$$

Following the approach of Shepherd (1), we propose that the monomer in the gas phase is in equilibrium with the monomer in the solid phase. The solid phase in the present case is predominantly single crystal silicon formed by the thermal decomposition of SiH_4. The equilibrium can be expressed as

$$P(g) \rightleftharpoons P\ (ss) \rightarrow P^+\ (ss) + e^- \quad [3]$$

$$As(g) \rightleftharpoons As(ss) \rightarrow As^+\ (ss) + e^- \quad [4]$$

In Eq. [3] and [4], P (ss) and As (ss) refer to phosphorus and arsenic in solid solution at the silicon surface.

* Electrochemical Society Active Member.
[1] Present address: Applied Materials Technology, Santa Clara, California.

Both the phosphorus and arsenic monomers in the solid phase ionize to give an ionized donor (P^+ or As^+) and an electron. This nearly complete ionization of the donor species occurs at the actual doping temperature and persists at room temperature. In no case in the present work is the doping level sufficiently high such that both the ionized and un-ionized species need be considered.

We now assume that Henry's law may be applied to the above equilibria allowing us to write the following relationships. These relationships are correct as long as the intrinsic electron concentrations are large compared to the concentrations of ionized donors.

$$p_P = k_P [N_{P+}/N_{Si}]_s \quad [5]$$

$$p_{As} = k_{As} [N_{As+}/N_{Si}]_s \quad [6])$$

In the above equations p_P and p_{As} refer to the partial pressures of the phosphorus monomer and the arsenic monomer, respectively. The Henry's law constants are k_P and k_{As} for the two monomers while the bracketed terms refer to the ratio of the number of ionized donors to the number of silicon atoms in the solid phase, s. In order to calculate the expected doping level under various experimental conditions we need to know the partial pressures of the monomer species in the gas phase and the Henry's law constants. The partial pressure of the monomer can be obtained if one knows the partial pressure of the hydride originally introduced into the gas stream along with the appropriate equilibrium constant for either Eq. [1] or [2].

Using phosphorus as an example, the equilibrium constant for Eq. [1] is given by

$$K_p = [p_P]^2/[p_{P_2}] \quad [7]$$

and an analogous relationship exists for the arsenic equilibrium, Eq. [2]. Solving for the partial pressure of the phosphorus monomer we see that

$$p_P = [\{K_p(8p_{PH_3} + K_p)\}^{1/2} - K_p]/4 \quad [8]$$

Again, a similar relationship holds for the arsenic case. Combining Eq. [5] and [8] allows calculation of the expected doping level as a function of the equilibrium constant for the dimer-monomer equilibrium, the partial pressure of the dopant hydride introduced into the gas stream, the Henry's law constant for the monomer, and the density of silicon. For phosphorus

$$[N_{P+}]_s = [N_{Si}]_s [\{K_p(8p_{PH_3} + K_p)\}^{1/2} - K_p]/4k_P \quad [9]$$

It should be noted that Eq. [9] contains two strongly temperature dependent terms; namely, the equilibrium constant and the Henry's law constant. Both depend in an exponential manner on the temperature. The relative temperature variation of these terms will determine the nature of the calculated temperature dependence of the doping level. An expression analogous to Eq. [9] holds for arsenic doping.

Experimental Details

The experiments in the present investigation were carried out in a horizontal, RF heated, gas flow reactor operating at atmospheric pressure. A reaction chamber containing a silicon carbide coated-graphite susceptor and having a length of 29 in. and a rectangular cross section 2 in. x 4 in. was used. Highly doped substrates ($\sim$ 0.005 ohm-cm) of (111) orientation and approximately 1 in. diameter were placed along the length of the susceptor.

A typical run consisted of three substrates of opposite type to that of the grown epitaxial films. Prior to introduction of the substrates into the reactor, the susceptor was coated with high resistivity silicon ($\sim$ 60 ohm-cm). After introduction of the substrates into the reactor but prior to growth, the substrates were etched for about 5 min with HBr at 1250°C. This procedure removed surface damage from the substrates. The source of silicon in the present work was 5% SiH_4 in ultrahigh purity hydrogen obtained from The Matheson Company, Inc. The silane-hydrogen mixture was combined with additional hydrogen obtained from a liquid hydrogen source. In all experiments the total gas flow was maintained at 68 liters/min. The silane concentration was approximately 0.15 m/o (mole per cent). Doping sources for the present work were 10 ppm PH_3 in hydrogen and 46 ppm AsH_3 in hydrogen, both obtained from The Matheson Company, Inc. Gas flows were monitored through Fischer & Porter Tri-Flat Variable-Area Flowmeters.

Deposit thicknesses were normally about 15μ and were determined by the IR interference technique. In all cases in the present work, a growth rate of 0.5 μ/min was maintained. Four point probe V/I measurements and IR thicknesses were used to obtain the film resistivity. Dopant concentrations were then obtained from the relationship between dopant concentration and resistivity (4). All temperature measurements quoted in the present study are actual temperatures which were obtained by correcting optical pyrometer readings. Temperatures are believed accurate to $\pm$5°C. Concentrations are estimated to have a $\pm$10% uncertainty.

Results and Discussion

Phosphorus doping experiments were carried out at four temperatures between 1000° and 1200°C: 1010°, 1050°, 1100°, and 1175°C. Table I shows the equilibrium constants for the phosphorus dimer-monomer equilibrium and the Henry's law constant for the phosphorus monomer at the above four temperatures. The equilibrium constants were calculated from free energy functions and heats of formation taken from the literature (2). Henry's law constants were taken from the work of Shepherd (1) and Coupland (5). Since these workers performed their experiments at temperatures generally higher than those used in the present work, a simple linear extrapolation of the k *vs.* $1/T$ curves was necessary to obtain some of the k-values in Table I.

Arsenic doping experiments were carried out at 1000°, 1050°, 1100°, and 1150°C. Calculated equilibrium constants (3) for the arsenic dimer-monomer equilibrium and Henry's law constants (1) for the arsenic monomer are shown in Table II.

Figure 1 shows the calculated per cent monomer obtained at various temperatures for both phosphorus and arsenic. The two curves refer to one particular initial dopant hydride pressure, namely, the lowest pressure used in each set of doping experiments. At any chosen temperature the per cent monomer decreases as the initial hydride pressure increases. Note that the phosphorus composition ranges from $\sim$ 0.25% monomer at 1000°C to $\sim$ 5% monomer at 1175°C, whereas the arsenic composition ranges from $\sim$ 20%

Table I. Equilibrium constants for the phosphorus dimer-monomer equilibrium and Henry's law constants for the phosphorus monomer at various temperatures.

T, °C	$P_2(g) \rightleftharpoons 2P(g)$ K_p	k_P
1010°	9.1×10^{-15}	6.8×10^{-6}
1050°	4.0×10^{-14}	2.0×10^{-5}
1100°	1.9×10^{-13}	6.2×10^{-5}
1175°	2.1×10^{-12}	3.6×10^{-4}

Table II. Equilibrium constants for the arsenic dimer-monomer equilibrium and Henry's law constants for the arsenic monomer at various temperatures.

T, °C	$As_2(g) \rightleftharpoons 2As(g)$ K_p	k_{As}
1000°	2.9×10^{-10}	1.1×10^{-4}
1050°	1.1×10^{-9}	2.9×10^{-4}
1100°	3.9×10^{-9}	7.3×10^{-4}
1150°	1.2×10^{-8}	1.7×10^{-3}

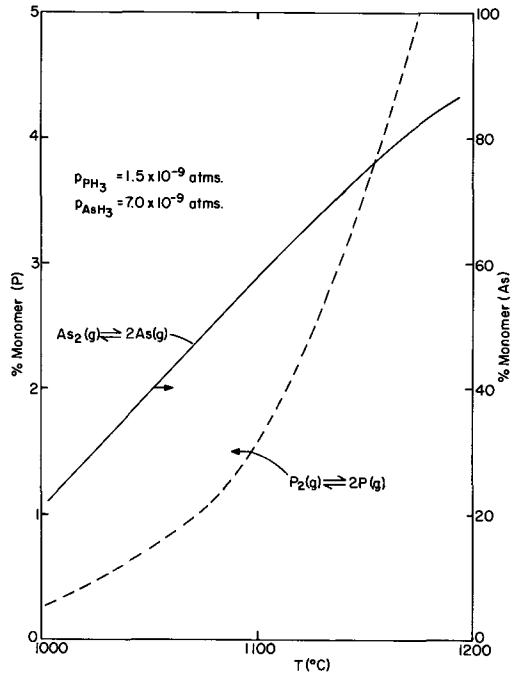

Fig. 1. Calculated per cent monomer as a function of temperature. Obtained from the equilibrium constants for the dimer-monomer equilibria of phosphorus and arsenic.

monomer to ~ 80% monomer over the same range of temperature.

Through the use of Eq. [9] and Table I, we are able to find the expected effect of increasing temperature on phosphorus doping level for a given phosphine partial pressure. As the temperature increases the dimer-monomer equilibrium constant increases; *i.e.*, the monomer partial pressure increases. In addition the Henry's law constant increases with increasing temperature. Since in Eq. [9] one term (K_p) occurs in the numerator and the other (k_p) occurs in the denominator, the effect of a temperature increase on the doping level ($[N_{P+}]_s$) will depend on which of the two terms is dominant. Calculations show that for phosphorus the doping level is expected to decrease with increasing temperature since the k_P term dominates. In the case of arsenic a similar situation occurs in that the calculated doping level decreases as the temperature increases.

Figure 2 shows a comparison between the calculated and observed doping level for phosphorus doping. The dotted lines represent the calculated doping level, as a function of phosphine pressure, obtained using Eq. [9] along with the data of Table I. A value of $[N_{Si}]_s = 5.00 \times 10^{22}$ atoms/cm³ taken from the literature (4) was used in the calculations. The phosphine partial pressure was that determined experimentally from the gas flow rates. For the calculated doping level note that doping decreases as the temperature increases for a given phosphine partial pressure. The agreement between calculated and experimental values of the dopant concentration, as shown in Fig. 2, is reasonably good in view of the complexity of the situation. Better agreement is obtained at the low end of the phosphine partial pressure range and although the dopant concentration increases with phosphine partial pressure for a given temperature the agreement becomes less satisfactory as the partial pressure increases. Probably the most significant point regarding Fig. 2 is the experimental observation that dopant concentration at constant pressure falls off as the temperature increases. This is what is predicted by the theory. In connection with Fig. 2 it should be pointed out that the background doping level (*i.e.*, the dopant concentration obtained in a nominally intrinsic deposition) is approximately 2 x 10¹⁴ atoms/cm³.

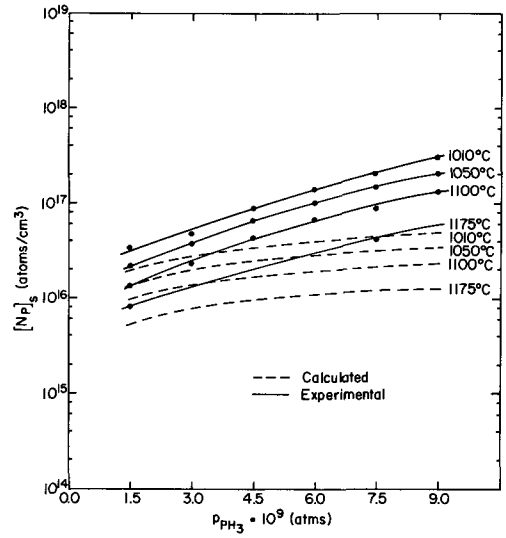

Fig. 2. Doping concentration vs. partial pressure of phosphine at various temperatures. Comparison of calculated and experimental values.

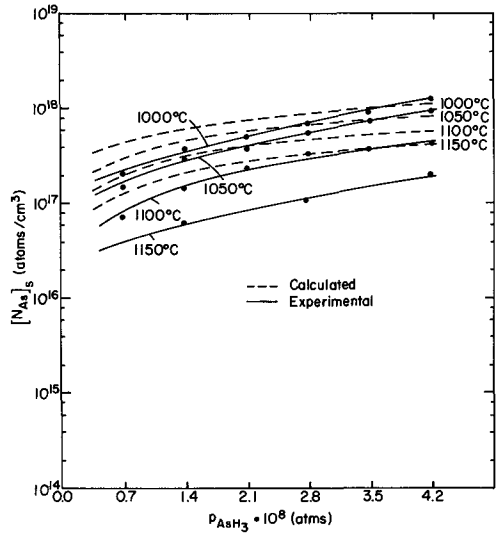

Fig. 3. Doping concentration vs. partial pressure of arsine at various temperatures. Comparison of calculated and experimental values.

Figure 3 shows a comparison between experimental and calculated doping concentrations for arsenic. The effects are qualitatively similar in all respects to those noted for phosphorus doping. We find, however, that the agreement between calculated and experimentally determined concentrations is better in the case of arsenic than it is in the case of phosphorus. We also note that for arsenic the agreement becomes less satisfactory at the higher end of the temperature range.

For the case of phosphorus doping and under the experimental conditions used in the present work, Eq. [9] can be simplified as follows. Rewriting this equation in a slightly different form gives

$$[N_{P+}] = [N_{Si}]_s K_p [(8p_{PH_3}/K_p + 1)^{1/2} - 1]/4k_P \quad [10]$$

Since $(8p_{PH_3}/K_p + 1) \approx 8p_{PH_3}/K_p$ for our experimental conditions and also since $[(8p_{PH_3}/K_p)^{1/2} - 1] \approx (8p_{PH_3}/K_p)^{1/2}$ we find that

$$[N_{P+}]_s = \frac{[N_{Si}]_s (2K_p)^{1/2}}{2k_p} (p_{PH_3})^{1/2} \quad [11]$$

Clearly the theory predicts a phosphorus doping level proportional to the square root of the phosphine partial

pressure. Experimentally we find that the doping level increases somewhat more rapidly with phosphine pressure than predicted by Eq. [11].

In the case of arsenic doping a simplification similar to Eq. [11] cannot be made since the relationship $(8p_{AsH_3}/K_p + 1) \approx 8p_{AsH_3}/K_p$ is not always valid and indeed the term $8p_{AsH_3}/K_p$ can be as small as approximately 4.7.

We can offer no explanation for the deviation of the experimental and calculated doping levels. It is possible that some refinement of the theory is needed. However, it is felt that the theory is essentially correct in that the trends in the experimental results closely approximate calculated values.

Acknowledgment

The authors thank F. Nicholson for obtaining the experimental results.

Manuscript submitted Nov. 25, 1968; revised manuscript received *ca.* May 4, 1969. This was Paper 518 presented at the Montreal Meeting, Oct. 6-11, 1968.

Any discussion of this paper will appear in a Discussion Section to be published in the June 1970 JOURNAL.

REFERENCES

1. W. H. Shepherd, *This Journal*, **115**, 541 (1968).
2. JANAF Thermochemical Data Tables, Compiled by Dow Chemical Co.
3. Thermodynamic Properties of the Elements, Stull and Sinke, Advances in Chemistry Series No. 8 (1956).
4. A. S. Grove, "Physics and Technology of Semiconductor Devices," John Wiley and Sons, Inc., New York (1967).
5. M. J. Coupland, *Proc. Phys. Soc.*, **73**, 577 (1959).

Partial Pressures of Zn and Te_2 over ZnTe up to 917°C

R. F. Brebrick

Lincoln Laboratory, Massachusetts Institute of Technology, Lexington, Massachusetts

ABSTRACT

The partial pressures of Zn, P_{Zn}, and of Te_2, P_2, for ZnTe(c) of different compositions have been determined up to 917°C by measuring the optical density of the coexisting vapor as a function of wavelength in the uv and visible. Over the whole temperature range the value of P_{Zn} over Zn-saturated ZnTe is the same as that over pure Zn to within the experimental error of ±2%. The values of P_2 for Te-saturated ZnTe indicate a solubility of Zn in Te(c) at 450°C of the order of 1 a/o (atomic per cent). For compositions within the homogeneity range both P_{Zn} and P_2 were measured. Evidence is presented for a slow reaction with silica near 900° by which Zn is lost from the ZnTe but which can be inhibited by a carbon coating on the silica tube. Between 688° and 917°C

$$\log P_{Zn}P_2^{1/2}\ (atm^{3/2}) = -(16{,}350 \pm 68)/T + (9.680 \pm 0.062)$$

with a standard deviation of 0.016 in the logarithm. The result is compared with published values, which spread over a factor of 10 in $P_{Zn}P_2^{1/2}$.

In this paper we report the determination of, (*a*) the partial pressures of Zn, P_{Zn}, over Zn-saturated ZnTe(c), (*b*) the partial pressure of Te_2, P_2, over Te-saturated ZnTe(c), and (c) both P_{Zn} and P_2 over ZnTe with compositions within the homogeneity range. Such data are useful in investigations of the correlation between the electrical and optical properties of ZnTe and the concentrations of native, atomic, point-defects present in the compound. The defect concentrations are determined by deviations from the stoichiometric composition, which are most readily controlled, when small, by fixing the temperature and either P_{Zn} or P_2. No previous detailed measurements have been reported for cases (*a*) and (*b*). Three investigations (1-3) have determined the product, $P_{Zn}P_2^{1/2}$, by using Knudsen-cell, weight-loss measurements. Lee and Munir (4) determined this product by using the angular displacement (but not weight-loss) of a torsion-effusion cell. Although all four determinations give nearly the same temperature dependence of $P_{Zn}P_2^{1/2}$, the magnitudes of the product at a given temperature vary by a factor of ten. The values reported here, which are about 40% below the highest values obtained by the dynamic methods, were obtained by a static method in which the optical density of the vapor coexisting with ZnTe(c) in a closed system was measured as a function of wavelength.

Experimental

In a number of synthesis steps it was necessary to heat samples. This was always done in a fused silica tube which had been rinsed in HF, followed by distilled water, dried, and outgassed 16 hr at 1060°C and pressures of 10^{-7} Torr or below. After the sample was loaded into the tube, it was outgassed again for 3-5 hr at 200° and 10^{-7} Torr and finally sealed off.

Samples containing Te-saturated or Zn-saturated ZnTe(c) were synthesized by weighing the individual high-purity elements to the nearest 0.1 mg to make a total of 15g. The over-all compositions were respectively 55.0 and 40.0 a/o (atomic per cent) Te. The elements were loaded into a silica tube which was evacuated and sealed off. A vigorous, exothermic reaction was initiated with a hand torch, and heating was continued until it appeared that all the Zn had been attacked. The tube was then heated for 16 hr at 560° for the 55.0% sample and for 168 hr at 596° for the 40.0% sample. The material was ground with an agate mortar and pestle to pass a 1 mm opening, stainless steel, standard sieve. For each composition about 2g of material was loaded into the sidearm of an optical cell which was then evacuated, outgassed, and sealed off.

Experiments with samples inside the homogeneity range used ZnTe crystals which were either vapor-grown by using ZnTe at 1080°C as a vapor source and He as a carrier gas (5) or were grown from a 70 a/o Te melt by a traveling-zone technique (6). In the latter case, the crystals to be used were annealed in liquid Zn for 24 hr at 1050°, then 24 hr at 700°, then furnace cooled. This served to significantly reduce, if not completely eliminate the amount of Te present as

an internal precipitate and visible as black occlusions under magnification with transmitted light. The crystals were ground to a maximum particle size of 1 mm and loaded into the sidearm of a silica optical-cell, which was then evacuated, outgassed, and sealed off. The weight of the samples used ranged from 0.5 to 300 mg. There were no significant differences in the values of $P_{Zn}P_2^{1/2}$ obtained that could be attributed to sample origin or size. In one case the sidearm of the optical cell was coated with carbon by the pyrolytic decomposition of acetone vapor before the cell was outgassed at 1060° in the cleaning step. A small, carbon-coated silica tube outgassed with the optical cell was used to transfer the 2.1 mg, 0.125 mm maximum particle size, sample into the sidearm of the optical cell.

The 22 mm OD, cylindrical, silica, optical cells were generally about 103 mm long. A 22 cm long sidearm bisected this length at right angles. The sample was spread over the last 2 cm of the sidearm. The optical cell proper was held at a fixed temperature of 1000°C by a 32 cm long, 3.8 cm ID, 3-zone split furnace. The opening through the wall of this furnace, through which the sidearm of the optical cell passed, also contained a 5 cm long, 1.3 cm ID auxiliary furnace. The auxiliary furnace extended about 1 cm into a 30 cm long, 3 cm ID sidearm furnace. The power through the auxiliary furnace could be set so that no minimum in temperature developed between the main furnaces. A 10 cm long, 6 mm wall thickness, Pt-coated, Ag liner surrounded the end 5 cm of the sidearm and served to reduce the temperature variation over the sample to less than 2° for all the measurements. Only a slight surface reaction could be observed between the liner and the surface of a silica tube after about 100 hr at 900°C. The sample temperature was taken as that measured by a calibrated Pt; Pt, 13% Rh thermocouple protected by a two hole alundum tube and located in the Ag liner at a position corresponding to the middle of the sample. Calibrations taken over a period of months showed no change in the thermocouple. The sample temperature was measured to the nearest 0.1°C and varied by less than 0.3° during the 5-10 min required to make the optical density measurements.

The procedure used to make optical density measurements with a Cary 14H double-beam spectrophotometer has been described in detail (7). To obtain the lowest values of P_{Zn} and P_2 the spectrum was scanned between 2200 and 1990Å at 5/8 Å/s using the hydrogen light source of the Cary, a chart speed giving a display of 3.4 Å/cm, and a recorder-pen period of 1s. For the highest values of P_2 the spectral measurements were made in the visible portion of the spectrum as previously described (8). According to the manufacturer's dispersion curves, the spectral band-pass was 1.12Å at 2138Å and 1.84Å at 1995Å. Special care was taken to reproduce the slitwidths in each scan, especially in the uv. Optical densities, $D = \log I_0/I$, were measured between about 0.01 and 2.0. The noise near zero optical density was ± 0.005. Using optical density measurements, we have determined the partial pressures for a number of tellurides and selenides as well as for Te and Se themselves. These references are given in ref. (7) and (8).

Results

Pure tellurium.—For a pure Te sample the spectrum is that of $Te_2(g)$. The dependence of the optical density on the temperature of the liquid Te sample has been described for a number of wavelengths in the visible and for a 1000°C optical cell (8). The behavior of a number of band maxima in the uv has been described for an optical cell temperature of 755°C (7). These uv band maxima behave similarly when a 1000° optical cell is used. The results for a 1000°C optical cell can be summarized by the equations

$$P_2(\text{atm}) = 0.0433\, D_{1995}/L(\text{mm}) \quad [1]$$

$$D_{1995}:D_{2025}:D_{2056}:D_{2138}:D_{4357}:D_{5000} = 100:43.5:37.3:4.70:11.2:2.57 \quad [2]$$

where D_λ is the optical density at a wavelength λ, and L is the optical path length. These equations are accurate to within ± 2% for path lengths between 22 and 100 mm and for values of D_λ between about 0.01 and 2 provided: (*i*) one corrects for instrumental stray-light errors at values of D_λ greater than about 1, and (*ii*) one uses D_λ/L values greater than 0.007 for λ = 4357 or 5000Å. Band maxima occur at the wavelengths cited above except at 2138 and 5000Å, where the spectrum is apparently continuous.

Pure zinc.—The strongest Zn(g) absorption line is centered at 2138Å. This line has a calculated Doppler half-width of about 0.03Å at 1000°C, some 40 times smaller than the narrowest spectral band-pass which we used. As a result D_{2138} is sensitive to slit-width. The slope of log D_{2138} *vs.* $10^3/T$ for a 1000° optical cell varies with temperature and is somewhat smaller than the slope of log P_{Zn} *vs.* $10^3/T$. Calibration runs with a pure Zn sample were made with 49.3 and 98.8 mm path-lengths and with slit-widths of 0.08 and 0.158 mm (1.12 and 2.2Å band-pass, respectively). Measurements were taken at about 5° intervals in the Zn-sample temperature and covered optical densities between 0.02 and 2.0. For a given path length the values of D_{2138} obtained with the two slit-widths fall on parallel lines, that for the smaller slit-width being higher by a factor of 1.60, somewhat less than the factor of 2 expected. At a given Zn-sample temperature and slit-width, the values of D_{2138} obtained with the 98.8 mm cell are 1.31 times as large as those obtained with a 49.3 mm cell. This is consistent with D_{2138} depending on the 0.39 power of the path-length rather than the first power. These anomalies in path length and slit width dependence can be attributed to the fact that the spectral band-pass used is so much larger than the half-width of the 2138Å adsorption line.

With increasing Zn-sample temperature the 2138Å line broadens extensively toward the visible (9), a subsidiary line develops at 2066Å, and the well-known line at 3070 develops. Between 2150 and 2800Å, in the long wavelength tail of the 2138 line, the slope of log D_λ *vs.* $10^3/T$ is twice that shown by log P_{Zn} for p_{Zn} between 0.01 and 1 atm. Thus the absorption grows as the square of the number of atoms in the light path, consistent with the statistical theory of pressure broadening (10) and similar to the behavior of the 2540 Hg (9, 11, 12) and 2287 Cd (9) absorption lines. For D_{2138} as high as 1.6 the optical density at 1995Å is below 0.01. Thus in those cases where we see absorption due to both Zn and Te_2, the absorption at 1995 is essentially all due to Te_2.

The vapor pressure of Zn was taken from the table in the critical compilation of Hultgren *et al.* (13). To within better than 1% in P_{Zn} the data can be represented by the equations

$$\log_{10}P_{Zn}(\text{atm}) = -6{,}714.7/T + 5.9839 \quad (600 < T°K < 692.7) \quad [3]$$

$$\log_{10}P_{Zn}(\text{atm}) = -6{,}281.3/T + 5.3586 \quad (692 < T°K < 900) \quad [4]$$

Zn-*saturated* ZnTe(*c*).—From 500° to 910°C, the maximum temperature measured, the value of P_{Zn} over Zn-saturated ZnTe(c) is the same as that over pure Zn(l) within the experimental error of ±2%. This is 1.17 atm at 1200°K and 0.114 atm at 1000°K (13). This is to be expected in view of the fact that the compositions along the Zn-rich liquidus fall below 0.1 a/o Te up to 910°C. The values of P_{Zn} were obtained from D_{2138} below 540° and from D_{2150} and D_{2200} at higher temperatures. The value of P_2 was below our

experimentally detectable limit of about 10^{-5} atm at all temperatures.

Te-saturated ZnTe(c).—The partial pressure of Te_2, P_2 over Te-saturated ZnTe(c) between 398° and 913°C was determined using two different optical cells at 1000°C. For sample temperatures above 520° the values of D_λ for the uv maxima were greater than 2.0 so that P_2 was obtained from D_λ at 4357 and 5000Å. Between 398° and 438°C the measurements were repeated with a 755° optical cell temperature to check on the magnitude of possible thermal effects arising because of the difference in temperature between the sample and the optical cell proper. No such effects were seen. The values of P_{Zn} were below the detection limit of 8×10^{-6} atm. The values of P_2 from the two optical cells and the two optical cell temperatures all fall within ±3% of a smooth curve. For this reason and because we have 63 experimental points, values interpolated from this curve are listed in Table I. (The proportionality constants between D_λ and P_2 for the 755° optical cell were taken from an earlier study (7).) Near 900°C the observed values of P_2 are close to those calculated from the liquidus (14) assuming the liquid is ideal. This is not true at the lower temperatures, however, the P_2 curve running parallel to that for pure Te (l) and about 15% lower between about 540° and 450°C. The P_2 curve shows a break at 450°, similar to that for pure Te, and continues to run parallel to the pure Te(c) curve down to the lowest temperature measured, 398°C. It would seem that this result is most likely, though not necessarily, inconsistent with the results of thermal analysis. The ZnTe-Te eutectic temperature has been reported (14) as 449° ± 2°C, agreeing with the melting point of pure Te. The eutectic composition appears to be not less than 98 a/o Te, indicating a solubility of Zn in Te(c) at 450° of less than 2 a/o. On the other hand, according to our results, the solubility of Zn in Te(c) must be large enough to depress the Te_2-partial pressure by 15%. One would think this requires a solubility of the order of 1 a/o.

ZnTe(c) *within the homogeneity range.*—The spectra obtained with ZnTe(c) samples within the homogeneity range were a superposition of those obtained with pure Zn and pure Te. Thus Zn(g) and Te_2(g) were the major vapor species, in agreement with mass spectrographic results (2). It is characteristic of the II-VI compounds that the gaseous MX molecule is a minor constituent of the vapor phase (2, 12, 15, 16).

The Te_2 contribution to the absorption at 2138Å, which is $0.047D_{1995}$ according to Eq. [2], was about 10% of the observed value of D_{2138} and was subtracted from the latter to get the Zn contribution. The value of $10^3/T$ of a pure Zn sample that would give the same value of D_{2138} for the same path length was then read from the calibration graphs. (The cells used had path lengths matching one of the two used in the measurements on pure Zn.) The corresponding value of P_{Zn} was calculated using Eq. [3] or [4]. For the various samples, P_{Zn} and P_2 could both be measured from about 688° to 917°C. At the lowest measurable pressures, P_{Zn} was as much as 5 times larger than P_2. The ratio $P_{Zn}/P_2 = R$ decreased to values between 1 and 2 as the ZnTe sample was heated, due to the preferential loss of Zn to the vapor phase and the dependence of the partial pressures on solid composition. Although the D_λ values apparently became steady simultaneously with the sample temperature, they changed slightly on standing 16 hr at temperature in the 850°-917°C range, in such a way as to yield a reduction in the ratio R. Values as low as 1.3 were observed. However, the product $P_{Zn}P_2^{1/2}$ obtained after such changes was within 3% of that obtained before.

Table I. Partial pressure of Te_2(g), P_2, over Te-saturated ZnTe(c)

$10^3/T$	$10^4 \times P_2$ (atm)	$10^3/T$	$10^4 \times P_2$ (atm)
0.85	3460	1.25	16.3
0.90	1880	1.30	8.15
0.95	1000	1.35	4.07
1.00	515	1.38	2.69
1.05	265	1.39	2.23
1.10	135	1.40	1.83
1.15	65.5	1.45	0.667
1.20	32.5	1.49	0.300

The measurements obtained with the carbon-coated cell gave values of $P_{Zn}P_2^{1/2}$ in good agreement with those obtained with the uncoated cells. However, there were no significant changes in either P_{Zn} or P_2 on standing 16 hr at 855°C. Presumably the carbon barrier inhibited a reaction between ZnTe(c) and silica which caused a relative loss of Zn from the ZnTe(c). The data from the carbon-coated cell are listed in Table II. It is seen that with increasing temperature the ratio R decreases from 4.58 and between 827° and 919°C holds at an average value of 1.8 ± 0.1. Now if the homogeneity range of ZnTe were between 49.5 and 50.5 a/o Te, congruent sublimation with Zn and Te_2 as the only vapor species would give a value of R between 2.05 and 1.95. The reason we obtain a value that appears to be significantly different is not clear. Perhaps the experimental conditions of sample weight and gas phase volume were not right to obtain congruent sublimation although comparable conditions gave (15) congruent sublimation with CdTe(c). Perhaps our values of P_{Zn} and P_2 suffer a systematic error when both pressures are comparable. Our estimated error of 3% in each pressure leads to a 4.2% error in R. However, an error of 10% in either pressure for any cause, including errors in the published vapor pressures, would account for an observed value of 1.8 for R when the true value is 2.0. Or least likely, we believe, perhaps the homogeneity for ZnTe(c) is more Te-rich than 50.5 a/o Te.

The behavior seen in the last four sets of measurements shown in Table II is consistent with the above hypothesis concerning the loss of Zn in an uncoated silica tube. The ZnTe(c) temperature was dropped from 919° to about 855°C and a measurement made. Over the next 40 hr three additional measurements were made with the temperature between 851° and 885°C. As can be seen, the ratio, R, decreases with time and is significantly below 2.0. The initial cooling resulted in the deposition of some ZnTe(c) at the extreme end of the sidearm, where there was no carbon coating. The subsequent slow loss of Zn from the ZnTe(c) led to a continuing decrease in R.

Table II. Partial pressure of Zn(g), P_{Zn}, and of Te_2(g), P_2, for compositions within the ZnTe(c) homogeneity range (carbon-coated cell)

$10^3/T$°K	$10^5 \times P_{Zn}$ (atm)	$10^5 \times P_2$ (atm)	$P_{Zn}/P_2 \equiv R$	$10^7 \times P_{Zn}P_2^{1/2}$ ($atm^{3/2}$)
1.017	4.88	1.065	4.58	1.59
0.9967	8.07	2.17	3.72	3.76
0.9770	11.8	4.60	2.56	8.00
0.9593	17.1	7.30	2.34	14.6
0.9504	21.6	9.14	2.36	20.6
0.9411	29.0	12.3	2.36	32.1
0.9331	33.3	15.2	2.19	41.0
0.9251	38.9	19.2	2.02	53.9
0.9170	47.5	24.2	1.96	73.9
0.9093	55.7	29.9	1.86	96.3
0.9017	68.4	36.5	1.87	130
0.8939	80.1	44.4	1.80	168
0.8870	95.1	53.0	1.79	219
0.8864*	94.6	57.0	1.66	225
0.8795	117	68.0	1.72	305
0.8724	139	77.7	1.79	387
0.8653	170	94.2	1.80	521
0.8594	199	111	1.79	663
0.8565	213	119.6	1.78	736
0.8514	249	135	1.84	915
0.8450	286	154	1.86	1,120
0.8390	325	174	1.87	1,350
0.8868	98.1	61.4	1.60	243
0.8888	90.3	58.1	1.55	217
0.8889	87.1	58.3	1.49	210
0.8891	81.4	59.5	1.37	198

* 16 hr at temperature before making measurements.

A least squares fit of all 26 points in Table II gives

$$\log P_{Zn}P_2^{1/2} = -(16{,}350 \pm 68)/T + (9.860 \pm 0.062) \quad (961°\text{-}1190°K) \quad [5]$$

where the pressures are in atmospheres and the quoted errors are the standard deviations in the slope and intercept. The standard deviation in the logarithm of the pressure product is 0.016. Equation [5] fits 17 of the points to within 3% in $P_{Zn}P_2^{1/2}$ and all 26 are fit to within 7.5%.

A least squares fit to the 107 points from 4 uncoated optical cells gives

$$\log P_{Zn}P_2^{1/2} = -(16{,}328 \pm 74)/T + (9.835 \pm 0.068) \quad (961°\text{-}1190°K) \quad [6]$$

The standard deviation in the logarithm of the pressure product is 0.038. Equation [6] fits 38 points to within 3% in $P_{Zn}P_2^{1/2}$, 67 to within 6%, 94 to within 20%, and all 107 to within 30%. It is seen that within the statistical error, Eq. [5] and [6] are the same. We emphasize for future reference, that Eq. [5] and [6] hold for values of R between 5 and 1.3 and therefore for $R = 2$.

Lattice parameters.—The Te-saturated and Zn-saturated ZnTe samples used in this study were further characterized by determining their lattice parameters at 25°C. The x-ray patterns were taken with 40 kV, 40 mA, CuKα radiation and a Philips diffractometer using a 1° divergence slit and a LiF monochromator in the diffracted beam. A scanning speed of ¼°/min in 2θ and a chart speed of 30 in./hr allowed the value of 2θ to be read with a precision of ±0.005°. Si(a_0 = 5.4301Å) and 99.99%W (a_0 = 3.1650Å) powders were used as external standards. Zn-lines were seen in the pattern for the 40 a/o Te samples and Te lines in the 55 a/o Te sample patterns. Since the 2θ-values for the various peaks of ZnTe between 25° and 151° were measured with about the same precision, the cubic parameter was obtained by using a computer technique (17) to minimize the residual function, $\sigma(\Delta 2\theta) = \{\sum_{i=1}^{M} (2\theta_{i,obs} - 2\theta_{i,calc})^2/M\}^{1/2}$. The results are shown in Table III for four samples. It is seen that the parameters are close to the literature value (18) and in three cases agree with it within the standard deviations shown. Assuming equilibrium had been attained in annealing the powders and that no large changes in the composition of the ZnTe phase occurred on quenching, the homogeneity range of ZnTe(c) must lie within the 40-55 a/o Te interval near 1000°C. In contrast, Godau and Ormont (19) find the lattice parameter of ZnTe decreases linearly with decreasing Te content, attaining a minimum value of 6.092Å at 40 a/o Te. The inference of course is that the ZnTe homogeneity range extends between 40 and 50 a/o Te at some high but ill-defined temperature. These authors synthesized samples near 1200°C, then lowered the temperature to 1000°C over 2 hr, then furnace-cooled the samples. It seems unlikely to the author that these results are correct.

Table III. Lattice parameters for ZnTe(c) at 25°C using λ = 1.5405Å for CuKα_1 radiation

Sample	$\sigma(\Delta 2\theta)$, °2θ	$a_0 \pm \sigma(a_0)$ Å
40 a/o Te Zn-Te, 20 hr 345°C[a]	0.012	6.1026 ± 0.0001
40 a/o Te Zn-Te, 2 hr 1000°C[b]	0.014	6.1028 ± 0.0002
55 a/o Te Zn-Te, 20 hr 345°C[c]	0.014	6.1024 ± 0.0001
55 a/o Te ZnTe, 120 hr 1050°C[d]	0.017	6.1023 ± 0.0002
ZnTe[e]	0.010	6.1026 ± 0.0001

[a] Synthesized as described in the text, ground to pass a 44μ standard sieve, heated in evacuated, sealed-off silica tube 20 hr 345°C, then quenched in water.
[b] As in (*a*) except that anneal at 345°C replaced by anneal at 1000°C.
[c] Similar to (*a*).
[d] After synthesis as described in text, sample heated 120 hr 1050°C, quenched in water, sintered sample then ground to pass 44μ standard sieve.
[e] Ref. (18). Data analyzed using our program. Parameter agrees with that given in ref. (18).

Discussion

The use of absorption measurements at a few wavelengths to determine partial pressures is subject to possible error due to the distortion of the absorption spectra of one vapor species by another. In a number of previous investigations [listed in ref (8)] we have found that this type of error is in fact negligible for molecular species, and for Te_2 in particular, for pressures as high as 10^{-2} atm. However, when as is done here for P_{Zn}, the peak value of a narrow absorption line is used to obtain a partial pressure, the possibility of error is greater. To an unknown extent the error is compensated by the use of a spectral bandpass much wider than the true half-width of the absorption line. The magnitude of this error was checked in one run on a ZnTe crystal. The values of P_{Zn} were determined between 800° and 900°C (where the values of P_2 observed for ZnTe crystals were the highest and the magnitude of the error should be the largest) from measurements using a 0.158 mm slit width at 2138Å as well as the 0.086 mm slit width used for the measurements given in the last section. (In both cases the same Te_2 contribution was subtracted from the total optical density at 2138Å.) It was found that the values of P_{Zn} obtained using the two slit widths agreed to within 5%. Since the spectral bandpass was varied by almost a factor of 2 in the alternate determination, we conclude our values of P_{Zn} are in error by 5% or less due to broadening of the Zn absorption line by Te_2.

For the measurements given in Table II, as well as for those obtained with the other four ZnTe crystals investigated, the value of P_{Zn} at any temperature is intermediate between that observed for the 40 a/o Te sample and that for the 55 a/o Te sample, which was below our experimental limit of 8 x 10^{-6} atm. Moreover, the value of P_2 is similarly between the value observed for the 55 a/o Te sample as given in Table I and that for the 40 a/o Te sample, which was below our experimental limit of 10^{-5} atm. Therefore, what we have called ZnTe crystals were indeed within the homogeneity range of the ZnTe(c) phase over the temperature range of the measurements. Second, the values of $P_{Zn}P_2^{1/2}$ obtained from these crystals all fall within a few per cent of the same straight line on a log-1/T plot for all values of R between about 5 and 1.3. By the Gibbs phase rule, all intensive variables of the ZnTe(c)-vapor system are fixed when any two are given. In particular they are fixed when T and R are given. Thus for a given T and for $R = 2$, the composition of ZnTe(c) is unambiguously defined in a thermodynamic sense regardless of the lack of any analytical data specifying this composition in terms of atomic per cent and independent of the width or the position of the ZnTe(c) homogeneity range. For brevity we shall call this particular composition, whose coexisting vapor is stoichiometric, the s-composition. It is recognized that if the homogeneity range is narrow, say within 0.5 a/o of 50.0 a/o, that the partial pressures must then depend very strongly on composition and the s-composition at any temperature will be very close to the congruently subliming composition for which R must be between 2.05 and 1.95.

At any temperature, the standard Gibbs free energy of formation of 2 g-atoms of the s-composition from pure Zn and Te is given in terms of the atomic fraction of Te for this composition, ½ + δ, by

$$\Delta G^\circ_f = (\tfrac{1}{2} + \delta)RT \ln (P_2/P^\circ_2) + 2(\tfrac{1}{2} - \delta)RT \ln (P_{Zn}/P^\circ_{Zn}) \quad [7]$$

Here P_2 and P_{Zn} are the partial pressures for the s-composition and P°_2 and P°_{Zn} are those for the pure elements. Using Eq. [5], $P_{Zn} = 2P_2$, and published data

for the vapor pressures of Te and Zn, Eq. [7] becomes

$$\Delta G^{\circ}_f = -(34{,}360 \pm 310) + (11.49 \pm 0.28)T + C;$$
(cal/2 g-atoms, 960°-1190°K) [8]

where C is a correction term that goes to zero if δ does and is given by

$$C = 3.974\,\delta\{T \ln (P^{\circ}_{Zn}/P^{\circ}_{2}{}^{1/2}) + 12{,}501 - 8.031T\}$$
(cal/2 g-atoms) [9]

Thus a free energy of formation cannot be obtained from our data unless δ is known. However, even for $|\delta| < 0.02$, corresponding to the composition falling between 48 and 52 a/o Te, the correction term given by Eq. [9] is only 300 cal/2 g-atoms or less between 900° and 1200°K and the error in ΔG°_f committed by neglecting C in Eq. [8] is only 1.2%.

For those measurements in which there appeared to be no loss of Zn to the silica, *e.g.*, all those in Table II except the last four, the change in composition of the sample due to preferential sublimation of one component can be obtained in terms of the unknown initial composition. For the 40 cm³ gas phase volume and the initial sample weight of 2.5 mg, the calculated change is about the same for all assumed values of the initial composition between 45 and 55 a/o Te. For each of the first eight measurements in Table II (through $10^3/T = 0.9251$), the Te content of the sample is greater than initially by an amount between 0.01 and 0.05 a/o. The estimated error in the calculated change is comparable to the change itself. For the measurements with $R < 2$, the Te-content of the sample is less than initially. The decrease is largest at $10^3/T = 0.8864$, where it is 0.2 a/o. However, for this particular measurement, as well as for the others with $R < 2$, an error of 3% in either partial pressure introduces an error in the calculated composition change comparable to the change itself. Thus over the range of the measurements the composition of the sample, known to be in the ZnTe homogeneity range from the values of the partial pressures, changes by no more than 0.2 ± 0.2 a/o. The measurements therefore are consistent with the assumption that the homogeneity range of ZnTe is less than 1 a/o wide, although they do not prove this assumption.

We have shown that our results are meaningful independent of any assumption concerning the homogeneity range of ZnTe(c). In the remaining discussion, in which we compare our results with other studies, we shall assume, as indeed the previous workers have implicitly or explicitly assumed, that the homogeneity range of ZnTe(c) is narrow and close enough to 50 a/o that $P_{Zn}P_2{}^{1/2}$ and ΔG°_f can be taken as independent of composition without incurring any significant errors in these quantities.

Our values of $P_{Zn}P_2{}^{1/2}$ as given by Eq. [5] are plotted on a log scale against $10^3/T$ in Fig. 1. Results from other measurements are summarized in Table IV and shown in Fig. 1 for comparison. Korneeva *et al.* (1) made Knudsen-cell, weight-loss measurements. Langmuir measurements gave identical results within

Table IV. Literature values for the constants A and B in the equation, $\log_{10}P_{Zn}P_2{}^{1/2}$ (atm$^{3/2}$) $= -A/T + B$

Authors	Experimental temperature range, °K	A	B
Korneeva *et al.*[a]	628-691	15,940	9.632
Goldfinger and Jeunehomme[b]	826-1110	16,084	9.419
Reynolds *et al.*[c]	923-1103	17,270	9.840
Lee and Munir[d]	800-1150	15,975	8.819
Present results	961-1190	16,350	9.860

[a] Ref. (1).
[b] Ref. (2).
[c] Ref. (3).
[d] Ref. (4).

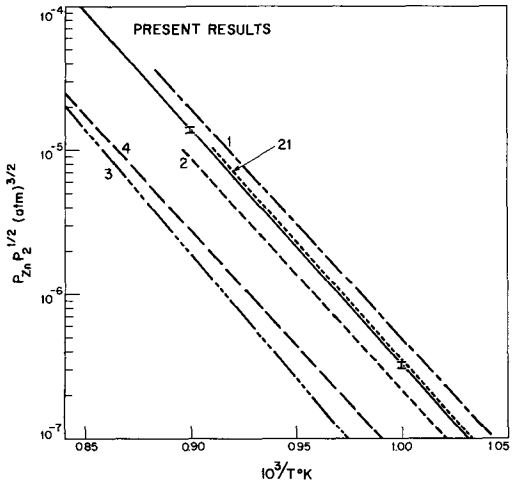

Fig. 1. Partial pressure of Zn times the square root of the partial pressure of Te_2, $P_{Zn}P_2{}^{1/2}$ (atm$^{3/2}$) $= K$, for ZnTe(c) plotted on a log scale against $10^3/T$. The solid line shows the present results as given by Eq. [5]. The total width of the brackets at $10^3/T = 1.00$ and 0.90 is twice the standard deviation in log K. The numbers on the other lines are the appropriate reference numbers.

experimental error. Their analysis erroneously assumed ZnTe(g) was the only vapor species. Assuming a steady state effusion with Zn(g) and Te_2(g) as the vapor species, we have converted their values for the apparent ZnTe pressure, P^*, to the corresponding partial pressures of Zn and Te_2 using the equations: $P_{Zn} = 0.582\,P^*$, $P^*_2 = 0.575\,P^*$, and calculated the product (*i.e.*, we have assumed a steady state in which the composition of the material emanating from the effusion cell and that in the cell are both 50.0 a/o Te). The values so obtained are shown as line 1 in Fig. 1, which is nearly parallel to ours but about 40% higher. Goldfinger and Jeunehomme (2) made Knudsen-cell, weight-loss measurements. Their results are represented by line 2, which is nearly parallel to ours but is about 55% lower. By using radioactive Zn, Reynolds *et al.* (3) confirmed that the composition of the effusion produce from their Knudsen-cell was ZnTe. Their results (line 3 in Fig. 1) are the lowest obtained, about eight times smaller than ours, but in fair agreement with those of Lee and Munir (4) shown as line 4. The latter authors used a torsion-cell but made only angular displacement measurements, assuming the same steady state we assumed above in the recalculation of the data of Korneeva *et al.*

The large discrepancies in Fig. 1 could be attributed to a lack of solid-vapor equilibrium in those studies yielding the lowest values of $P_{Zn}P_2{}^{1/2}$. However, the ratio of the cell orifice area to the sample area is apparently about the same for all the dynamic determinations. Moreover, as mentioned above, Korneeva *et al.* (1) obtained the same results in both Knudsen-cell and Langmuir measurements. Thus a low sticking coefficient and consequent difficulty in attaining solid-vapor equilibrium does not seem to be a plausible explanation. It has been observed (20) that between 1000° and 1200°C the vapor transport of ZnTe is effectively stopped when ZnO is formed and presumably coats the ZnTe. Perhaps the low results are due to such an accidental oxide coating.

McAteer and Seltz (21) measured the emf of a cell whose reaction was the formation of ZnTe(c) from the solid elements. They obtained $\epsilon = 0.5703$V at 387°C and $-d\epsilon/dT = 6.17(10^{-5})$V/°C between 355° and 418°C. From these results and tabulated (22) melting points and heats of fusion for Zn and Te, the Gibbs' energy of formation for the reaction

$$Zn(l) + Te(l) \rightarrow ZnTe(c)$$

is given by

$$\Delta G^{\circ}_f = -34{,}128 + 11.4302T \quad \text{cal/mol}, T > 723°K \quad [10]$$

assuming $\Delta C_p = 0$. Using Eq. [10] and published data (22) for Zn and Te, the product $P_{Zn}P_2^{1/2}$ was calculated. The results are shown as line 21 in Fig. 1, which is slightly higher than ours but just within the brackets set by our standard deviation in log $P_{Zn}P_2^{1/2}$. It is seen that Eq. [10] agrees with our result given by Eq. [8] if the correction term C in Eq. [8] is zero.

Acknowledgments

The author wishes to thank T. B. Reed, J. Steininger, and G. Iseler for several ZnTe crystals. He also wishes to acknowledge the capable experimental assistance of R. N. Capes. This work was sponsored by the U.S. Air Force.

Manuscript submitted Dec. 16, 1968; revised manuscript received May 30, 1969.

Any discussion of this paper will appear in a Discussion Section to be published in the June 1970 JOURNAL.

REFERENCES

1. I. V. Korneeva, A. V. Belyaev, and A. V. Novoselova, *Russ. J. Inorg. Chem.*, **5**, 1 (1960).
2. P. Goldfinger and M. Jeunehomme, *Trans. Faraday Soc.*, **59**, 2851 (1963).
3. R. A. Reynolds, D. G. Stroud, and D. G. Stevenson, *This Journal*, **114**, 1281 (1967).
4. W. T. Lee and Z. A. Munir, *ibid.*, **114**, 1236 (1967).
5. T. B. Reed, Personal communication.
6. J. Steininger and R. E. England, *Trans. AIME*, **242**, 444 (1968).
7. R. F. Brebrick, *J. Phys. Chem.*, **72**, 1032 (1968).
8. R. F. Brebrick, *J. Chem. Phys.*, **49**, 2584 (1968).
9. F. L. Mohler and H. R. Moore, *J. Opt. Soc. Am.*, **15**, 74 (1927).
10. H. Kuhn, "Atomic Spectra," p. 395, Academic Press, New York (1962).
11. H. Kuhn, *Proc. Roy. Soc. (London)*, **158**, 230 (1967).
12. R. F. Brebrick and A. J. Strauss, *J. Phys. Chem. Solids*, **26**, 989 (1965).
13. R. Hultgren, R. L. Orr, P. O. Anderson, and K. K. Kelley, "Selected Values of Thermodynamic Properties of Metals and Alloys," John Wiley and Sons, Inc., New York (1963).
14. B. M. Kulwicki, The Phase Equilibria of Some Compound Semiconductors by DTA Calorimetry, Doctoral Dissertation, Univ. of Michigan (1963), p. 73.
15. R. F. Brebrick and A. J. Strauss, *J. Phys. Chem. Solids*, **25**, 1441 (1964).
16. R. F. Brebrick, *J. Chem. Phys.*, **43**, 3846 (1965).
17. R. F. Brebrick, *J. Appl. Crystallography*, **1**, 241 (1968).
18. H. E. Swanson, M. C. Morris, E. H. Evans, and L. Ulmer, Standard X-ray Diffraction Powder Patterns, National Bureau of Standards Mono. 25, Section 3, p. 38, July 1964.
19. I. Godau and B. F. Ormont, *Izv. AN SSSR, Neorgan. materialy*, **4**, 182 (1968).
20. G. Iseler, Personal communication.
21. J. H. McAteer and H. Seltz, *J. Am. Chem. Soc.*, **58**, 2081 (1936).
22. D. R. Stull and G. C. Sinke, "Thermodynamic Properties of the Elements," American Chemical Society, Washington, D. C. (1956).

The Purification of Cesium and Rubidium Metals by Chloride Reduction under High Vacuum Conditions

P. H. Schmidt

Bell Telephone Laboratories, Incorporated, Murray Hill, New Jersey

ABSTRACT

High-purity Cs and Rb metal has been obtained for the first time for electronic structure studies. High-purity results were obtained by the reduction of a purified chloride using Ca metal. Apparatus design, low operating temperature (<400°C), high-purity salts, improved collection practices, and high vacuum operation were essential for successful results. Electrical resistivity ratios of purified Cs and Rb metals are $R_{300°K}/R_{1.5°K}$ 4400 and 3500, respectively.

The purification of cesium and rubidium metals by chloride reduction has been discussed by Schmidt, Studer, and Sottysiak (1), Hackspill (2), Hampel (3), Ephraim (4), Perel'man (5), and Mellor (6). Electronic structure studies of cesium and rubidium require metal of very high purity that has not been obtained using the techniques described by the above. Investigations were therefore initiated to satisfy our requirements and obtain the highest possible purity cesium and rubidium metals. Salt reduction (7) was selected as the method for purification. Although purity improvements could be made by distillation of these metals, removal of cesium or rubidium impurities from the desired alkali was marginal as a result of their similar vapor pressures. Alkali metal purity was found to be affected by apparatus design, salt purity, reduction temperatures, and collection practices. For the first time, very high-purity cesium and rubidium metals were obtained that were useful for electronic structure studies (8-10). Modification of previous salt reduction techniques combined with distillation was determined to be most successful.

Highly purified chlorides of both Cs and Rb [1] Table I, and fractionally redistilled Ca [2] metal granules were used for the reduction process. The reduction typically proceeds according to the following reaction

$$2MCl + Ca \xrightarrow{\text{Heat}} CaCl_2 + 2M \qquad [1]$$

where M is the alkali Cs or Rb. High vapor pressure impurities in both the chloride and reducing metal change the above reaction to

$$2MCl + \text{excess Ca} + \text{metal impurities} \xrightarrow{\text{Heat}} CaCl_2 + 2M + (\text{Ca} + \text{metal impurities}) \qquad [2]$$

The primary objective was therefore separation of the alkali metal from its respective contaminants and prevention of any reaction of the purified alkali with its container material.

[1] RbCl and CsCl purchased from Johnson Matthey & Company, Limited, London (99.999+% purity).
[2] Ca metal purchased from NELCO Metals, Inc., Canaan, Connecticut (redistilled grade).

Table I. Emission spectrographic analysis in ppm

	Ca	RbCl	CsCl
K		1-5	3
Fe	1-3	1	
Ca		<1-3	2
Mg	500	<1	1
Na	3-5	<1-5	1
Ba	10		
Cu	5		
Mn	5		
Sr	8000		

Apparatus

Three purification and reaction devices were constructed for this purpose and they are shown in Fig. 1 A, B, and C.

Device A.—This is an all metal system previously described for the purification of Li (11) Na and K (12). The charge is contained in a 100 cc capacity molybdenum cup, 1*,[3] which rests on the bottom of a closed end 321 stainless steel tube 16½ in. long and 2½ in. diameter, 4*. A molybdenum sheet liner protects the inner stainless surfaces and extends from the top to the bottom of the column. Ten molybdenum sieve-type baffle plates, 2*, are placed directly above the cup. Each plate is separated with molybdenum tube spacers 0.292 in. long. The top of the column is water cooled. A closed end stainless steel tube projects downward from the top of the column and is terminated with a detachable inverted molybdenum cup collector, 3*. The column is heated externally with an electric resistance furnace 6*. A large temperature gradient is imposed across the baffle section. Purified metal is collected in the molybdenum cup collector after by-passing a gettering fraction to the top of the column by controlling the temperature of the collector. Removal of the alkali metal could be effected by either back-filling the column with degassed and prereacted mineral oil or unloading in an argon filled dry box.

Device B.—This unit is similar to system A, having a molybdenum reducing chamber or cup containing a mixture of the alkali metal chloride and Ca metal granules, 1*, and a set of three molybdenum sieve plates, 2*. The plates were completely enclosed with ring spacers. An inverted molybdenum cup 7 in. long covered the reducing chamber and plates for reverse take-off of the alkali metal vapor. This unit was enclosed within a fused silica tube, 8*, and attached to a vacuum system. The chloride was reduced by heating the inner molybdenum container with an electric heater, 6*, placed around the outside of the fused silica tubing. Alkali chloride was reduced, distilled, deflected downward through the plates below the reducing chamber and then collected in a fused silica ampoule. The ampoule could be torched off at any time for material measurement and storage.

Device C.—Fused silica and molybdenum construction made this system very much like B, Fig. 1. The molybdenum reducing chamber, 1*, and baffle section, 2*, however, were located separately from an all fused silica collecting area, 3*, and ampoule section, 8*. The two sections were connected with a silica tube, 5, 7*. The alkali chloride was reduced and distilled in the first section. The alkali metal was redistilled in the connecting tubing at a much lower temperature. The purified metal was then condensed as a solid on a water-cooled silica collector after bypassing a getter envelope on the walls surrounding the collector tube. The alkali metal on the collector was protected from reaction with residual gasses in the system by this getter envelope. Fractions could be collected for storage and measurement in silica ampoules located directly below the collector tip. Ampoules were filled by heating the collector tip with an electric cartridge heater and melting off the desired material into an ampoule. The getter envelope was always left in place to protect the condensed metal on the collector.

[3] The numbers with asterisks used in the following paragraphs refer to Fig. 1.

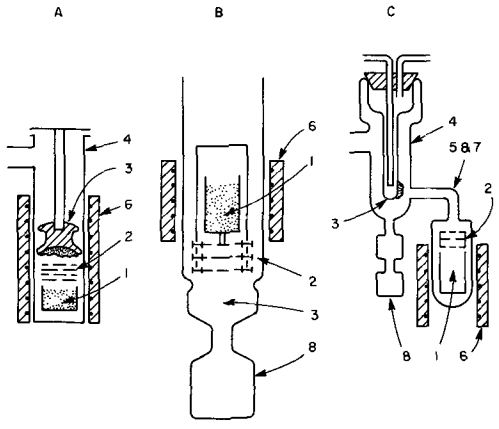

Fig. 1. Schematic drawing of three reduction and purification systems. System A is an all metal device. Systems B and C are constructed from fused silica and molybdenum. The reduction chamber 1; baffles 2; collector 3; getter shield 4; connecting tubing 5; heater 6; heater tapes 7; and ampoules 8 are indicated.

Each device was theoretically capable of producing ~ 40 cc of either Cs or Rb metal. Typical yields of high-purity metal, however, were ~ 35% of the theoretical value as predicted from reaction [1]. High vacuum conditions, with pressures of $< 1 \times 10^{-8}$ Torr, were maintained for all reduction operations using a 15 l/sec diode-type getter ion pumping system, stainless steel plumbing, and copper o-ring seals. A molecular sieve-type roughing pump was used to start the ion system and eliminated any possibility of oil contamination.

Each of the systems incorporated both reduction and distillation operations. Construction geometry however, drastically affected the purity of metal produced in both systems A and B. In system A it was difficult to prevent vapor channeling of impurities such as Ca, Mg, K, and Na through the baffle plates. It was also difficult to maintain a large enough temperature gradient between the reducing chamber and baffles necessary for optimum purification. Reduction of the chloride was carried out at the lowest possible temperature to minimize the vapor pressure of the reducing metal. This led to incomplete fill of the baffle plates in system A resulting in vapor channeling of impurities to the collector and incomplete distillation. Unloading the apparatus was awkward (oil backfill) and could be associated with possible contamination from the reduced chloride and calcium metal. Alkali metal that condensed in the collector cup deteriorated due to moisture and gas pick-up from the oil in which the alkali was stored. The primary disadvantage of system B was that the alkali metal vapor was forced to pass downward back through the high-temperature reducing zone where it could then impinge on the fused silica wall. High-purity results were never obtained from either of these systems.

System C was designed to overcome the difficulties and disadvantages associated with the above systems. Reduction and collection areas were separated, thereby permitting more precision in controlling the operating temperature of each section. The reduction chamber, baffles, and collector could therefore be set at any desirable temperature independently of each other. Alkali metal vapor was directed upward through the baffle plates. The fused silica connecting tube acted as another distillation stage. It was preset to a very low temperature so that only Cs or Rb could be transported to the collector. The getter envelope helped to reduce contamination of the condensed alkali metal

on the collector with any residual gasses in the vacuum system.

Experimental Procedure

Assembly and operation of system C is outlined below. Prior to any run all components of the system were thoroughly cleaned. Molybdenum cups and baffle plates were cleaned in an acid mixture of 80p HNO_3, 20p H_2SO_4, and 1p HCl followed by several rinses in water and a final rinse in methanol. Just prior to loading of the reactants, the molybdenum cup was induction heated to ~1100°C in dry hydrogen. The fused silica tubing was cleaned for 30 sec in 1p HF and 1p H_2O followed by several rinses in water and a final methanol rinse. The inside of all stainless steel vacuum fittings were electropolished and given a final rinse in methanol. The ion pump was also acid cleaned and given several rinses in methanol. The fused silica components, stainless steel vacuum fittings and ion pump were subsequently heated to 200°C for 2 hr following acid cleaning. The apparatus was now completely assembled and the system baked for several days at 250°C. The system was then cooled and back-filled with dry nitrogen gas.

The crucible was loaded with a mixture of the purified chloride and Ca metal granules. Weighing and mixing of the reactants was carried out in a polyethylene bag in air. Four to five times the theoretical weight of Ca metal required was added to the charge. The system was resealed and then baked as above.

The system was now slowly brought to operating temperature (~4 days). The vacuum system, collector, and all fused silica components were maintained at 160°C and continuously monitored at several points with thermocouples. At the first sign of alkali metal, usually a bluish film, the vacuum system and silica tubing were cooled to room temperature. The getter envelope was deposited on the walls of the silica tubing surrounding the collector. The collector was then cooled to ~10°C with cold water. A desired fraction was then deposited on the collector and later melted into an ampoule. The collection rate was ~1 cc/day of either Cs or Rb. The getter envelope always remained in place. Ampoules were removed by sealing the silica tubing with a hand torch. The alkali metal was maintained as a solid during the seal-off procedure.

Critical details of operation for obtaining high-purity metal were as follows:

1. Highest purities were obtained with reduction temperatures of 395°-405°C for Rb and 382°-400°C for Cs. Higher reduction temperatures resulted in less pure alkali metal.
2. The fused silica connecting tubing should not be heated above 160°-170°C. Contamination was observed to occur at 200°C.
3. The getter envelope should always remain in place to protect the alkali on the collector.
4. High vacuum operation ($<1\times10^{-8}$ Torr) and system cleanliness are essential for high-purity results.
5. The alkali metal was maintained as a solid during the removal of an ampoule from the system. This procedure prevented contamination of the bulk alkali from any contaminants subliming from the hot fused silica.

Discussion

Analysis for residual metallic impurities was attempted by both atomic absorption and emission spectroscopy. Principal contaminants of commercial purity Cs and Rb are other alkalies (with the exception of Li), Al and Ca. No detectable impurities were observed in either purified Cs or Rb samples. Primary purity evaluation was therefore based on electrical resistivity ratio measurements. The eddy current decay method (13) for measuring resistivity ratios was used since electrical connections to the samples were not required. Bulk alkali metal was used for these measurements and was typically contained in fused silica collecting ampoules. A summary of these measurements is shown below.

		Cs	Rb
Highest purity (this study)	$R_{295°K}/R_{4.2°K}$	680	1230
	$R_{295°K}/R_{1.5°K}$	4.4×10^3	3.5×10^3
	$R_{295°K}/R_{1.0°K}$	4.7×10^3	$3.5\text{-}3.6\times10^3$
Highest purity of commercially available alkalies Cs and Rb[4]	$R_{295°K}/R_{4.2°K}$	460	400
	$R_{295°K}/R_{1.5°K}$	1375	600
Highest purity obtained by distillation	$R_{295°K}/R_{4.2°K}$	475	550

A detailed study of annealing effects has not been made; however, improvement of resistivity ratios were observed to occur after annealing Cs and Rb at 77°K for 24 hr. Ratio improvement may be due to stain relief, solid-state precipitation of impurity elements, or vacancy migration. Crystallite size was not believed to affect ratio measurements since ampoules typically contained from 2 to 4 large grains.

Electron spin resonance line width measurements made on bulk Cs and Rb samples taken at 12 GHz frequency at 1.5°K yielded line widths of 30 gauss and and 0.4 gauss, respectively. This is the narrowest line width ever reported for bulk Rb. Line width measurements on Cs metal were believed to be broadened by strain.

Since resistivity ratio measurements are not specific for any one impurity a residual gas partial pressure analyzer was used to determine the predominant gas species in both systems A and C, as shown in Fig. 2. Both traces were taken under similar source temperatures and pressures during collection of Rb metal. Higher residual gas levels of H_2, OH, O_2, N_2, and H_2O are seen to occur in system A. No chlorine was detectable in either system A or system C. Since Rb and Cs oxidize and nitride very easily, contamination was therefore thought more likely to occur in system A. System C was therefore believed to be constructed of superior materials.

Pure Cs is golden in color and Rb a silver color. The first Cs or Rb deposited as the getter envelope however is a blue color. A blue colored film was also observed after melting of either alkali off the collector. Pink or purple colorations were always observed when using impure starting salts. The blue color of the getter envelope was therefore always thought to be associated with high-purity metal.

Growth of single crystals was markedly affected by purity. Commercial purity Cs or Rb always displayed a characteristic "burlap-like" surface appearance. It was very difficult to grow single crystals of impure Cs or Rb. Pure Cs or Rb however could be easily grown into large single crystals having near "mirror-like" surfaces.

High-purity results were never obtained from those runs using impure salts, high reduction temperatures, or where alkali metal was allowed to react with fused silica at temperatures >200°C. The effect of reduction temperatures on resistivity ratios of Rb is shown below.

Reduction temp, °C	$R_{295°K}/R_{1.5°K}$
500	710
420	2.8×10^3
395-400	3.5×10^3

Similar results were obtained for cesium. The lowest reduction temperatures were always associated with the highest purity results. Reduction temperatures of 382°-400°C for Cs and 395°-405°C for Rb are the

[4] Special high-purity Cs and Rb samples from the Kawecki Chemical Company, Royertown, Pennsylvania, and MSA Research Corporation, Callery, Pennsylvania.

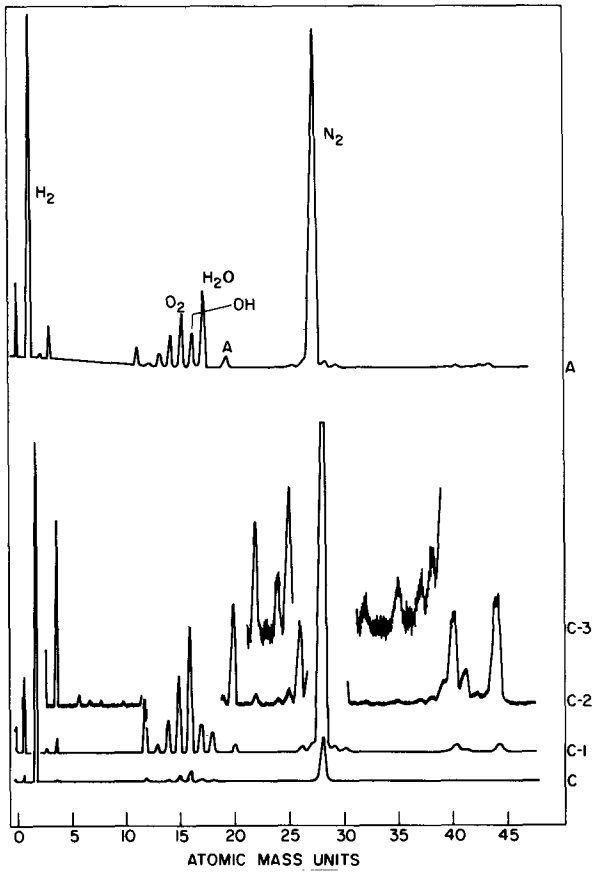

Fig. 2. Partial pressure analyzer traces from 0 to 50 atomic mass units taken of system A (top) and C (bottom) during collection of rubidium at 400°C. The y sensitivity has been increased 10X, 100X, and 1000X, respectively, in traces c-1 to c-3. Only a very slight trace of Cl_2 is observable with maximum sensitivity (c-3).

lowest reduction temperatures yet observed for salt reduction systems.

Conclusion

For the first time high-purity Cs and Rb has been obtained that is useful for electronic structure studies. High-purity results are critically dependent on low operating temperature (<400°C), high vacuum operation, and use of a high-purity salt and reducing metal. A getter envelope was used to protect the collected alkali from contamination by residual gases. Maximum electrical resistivity ratios obtained between 295° and 1.5°K for Cs and Rb are 4.4×10^3 and 3.5×10^3, respectively. The eddy current decay method of measuring resistivity ratios was found to be a simple and rapid means for material evaluation.

Acknowledgments

The author would like to thank W. M. Walsh, Jr., and C. C. Grimes for their encouragement and many helpful discussions. He would also like to acknowledge G. Adams for many resistivity ratio measurements and L. W. Rupp, Jr. for ESPR line width measurements. Special thanks should also be given to Mrs. L. M. Steuber for her capable assistance.

Manuscript submitted April 21, 1969; revised manuscript received June 4, 1969.

Any discussion of this paper will appear in a Discussion Section to be published in the June 1970 JOURNAL.

REFERENCES

1. F. C. Schmidt, F. J. Studer, and J. Sottysiak, *J. Amer. Chem. Soc.*, **60**, 2780 (1938).
2. L. Hackspill, *Bull. Soc. Chim. France*, **9**, 446 (1911).
3. C. A. Hampel, "Rare Metals Handbook," p. 434, Reinhold Publishing Corp., New York (1961).
4. F. Ephraim, P. L. Thorne, and E. R. Roberts, "Inorganic Chemistry," p. 204, Oliver and Boyd, London (1954).
5. F. M. Perel'man, "Rubidium and Caesium," p. 116, Pergamon Press, The MacMillan Co., New York (1965).
6. J. W. Mellor, "A Comprehensive Treatise on Inorganic and Theoretical Chemistry," Longmans, Green and Co., **2**, 450 (1922).
7. L. Hackspill and R. Grandadan, *Compt. rend.*, **180**, 67 (1925).
8. W. M. Walsh, Jr., L. W. Rupp. Jr., and P. H. Schmidt, *Phys. Rev. Letters*, **16**, 181 (1966).
9. C. C. Grimes, G. Adams, and P. H. Schmidt, *Bull. Am. Phys. Soc.*, **12**, 414 (1967).
10. P. S. Peercy and W. M. Walsh, Jr., *Phys. Rev. Letters*, **17**, 741 (1966).
11. P. H. Schmidt, *This Journal*, **113**, 201 (1966).
12. P. H. Schmidt, Purification of Potassium and Sodium Metals by High Vacuum Distillation, To be published.
13. C. P. Bean, R. W. DeBlois, and L. B. Nesbitt, *J. Appl. Phys.*, **30**, 1976 (1959).

Technical Note

A Method for Reducing the Mobile Electric Charge in MNOS Structures

C. T. Naber*

The National Cash Register Company, Dayton, Ohio

The adverse effect of alkali ions, particularly sodium, on the electrical charge stability of metal-oxide-semiconductor (MOS) structures is well known (1-3). Silicon dioxide, which is the most widely used passivating layer over semiconductor devices has a distinct deficiency in that it offers a low resistance to the electric field migration of sodium ions (1). Yarash and Deal have recently shown that sodium ions can readily be incorporated in device structures during fabrication (4). Silicon nitride is impervious to sodium ions (5, 6); however, the charge distribution of metal-nitride-silicon (MNS) structures is unstable under

* Electrochemical Society Active Member.

large voltage bias at room temperature (7, 8). The charge instability is suppressed if a layer of silicon dioxide is imposed between the silicon nitride and silicon. In order to realize the advantages of silicon nitride in metal-silicon nitride-silicon dioxide-silicon (MNOS) structures, it is essential that sodium ions be absent from the silicon dioxide portion of the structure.

In this work, the mobile charge of MNOS structures is determined by analyzing the capacitance-voltage (C-V) characteristics before and after bias-temperature treatments. A method for reducing the mobile charge in silicon dioxide prior to silicon nitride deposition is described.

Structure Fabrication

N-type silicon wafers of (100) orientation with resistivities between 10 and 14 ohm-cm were used. Thermal oxides were grown in a resistance-heated tube furnace by two standard techniques (9): (*i*) in dry oxygen at 1100°C, and (*ii*) in steam at 1100°C. No special precautions were taken to eliminate the sodium content in the furnace or in the laboratory glassware used in growing the silicon dioxide layers. The thermal oxide coated wafers were then placed in a vertical epitaxial reactor with a silicon-coated graphite susceptor and silicon nitride was deposited by the nitration of silane with ammonia in an excess of hydrogen (10, 11). The silicon nitride films were deposited at 900°C with a hydrogen flow of 30 l/min, a silane flow of 30 ml/min, and an ammonia flow of 380 ml/min. The thicknesses of the silicon nitride films were between 1000 and 1500Å. Aluminum electrodes of 1 mm diameter were deposited by vacuum evaporation from a tungsten filament and the thermal oxides were etched off the reverse sides of the wafers. C-V measurements were then made on the MNOS structures at a frequency of 130 kHz.

Sodium in Thermal Silicon Dioxide

Figure 1 shows C-V plots, before and after bias-temperature treatments of (*a*) 20 min at 200°C and +18V and (*b*) 20 min at 200°C and −18V, of a MNOS structure which has approximately 1000Å of silicon nitride on top of approximately 1200Å of silicon dioxide grown in steam at 1100°C. As can be seen, the flat-band voltage shifts approximately 12V after the positive and negative bias-temperature treatments. Figure 2 shows C-V plots before and after bias-temperature treatments of a MNOS structure which has approximately 1000Å of silicon nitride on top of approximately 1200Å of silicon dioxide grown in dry oxygen at 1100°C. As can be seen, a flatband voltage drift of only 0.2V occurs due to the bias-temperature treatment. This indicates, in agreement with Yurash and Deal, that silicon dioxide layers grown in dry oxygen have less sodium ions than silicon dioxide layers grown in steam (4).

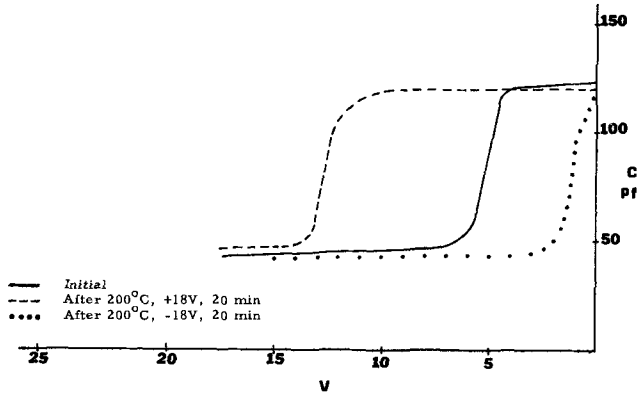

Fig. 1. C-V plots for MNOS structure with 1200Å of oxide grown in steam at 1100°C.

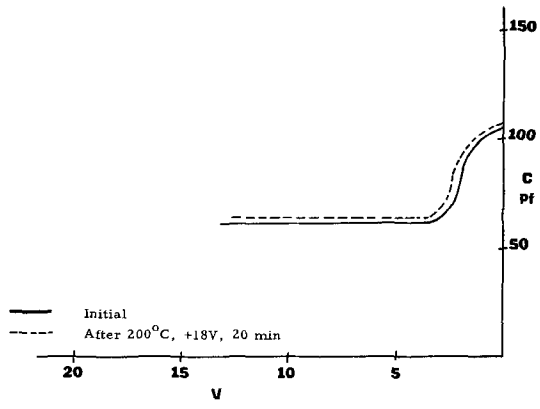

Fig. 2. C-V plots for MNOS structure with 1200Å of oxide grown in dry oxygen at 1100°C.

Reduction of Mobile Charge in Silicon Dioxide

Figure 3(a) shows C-V plots, before and after a bias-temperature treatment of 20 min at 200°C and +18V, of a MNOS structure which has approximately 1200Å of silicon nitride on top of approximately 5500Å of silicon dioxide grown in steam at 1100°C. Figure 3(b) shows similar C-V plots for a similar structure, but in this case the silicon dioxide-coated silicon wafer was heated *in situ* in the epitaxial reactor at 1200°C for 2 min with hydrogen flowing at a rate of 30 l/min prior to the nitride deposition at 900°C. As can be seen, a flatband voltage drift of approximately 90V occurs in the MNOS structure that was not heated in hydrogen, while a drift of only 2V occurs in the structure that was heated in hydrogen prior to nitride deposition. This indicates the high-temperature hyrogen treatment reduces the effects of mobile charge in the silicon dioxide layer.

It has previously been shown that the surface-state density of MOS structures can be reduced by either a low-temperature (400°-700°C) or a high-temperature (1000°-1200°C) hydrogen heat-treatment (12-14). In order to determine the effect of temperature and time

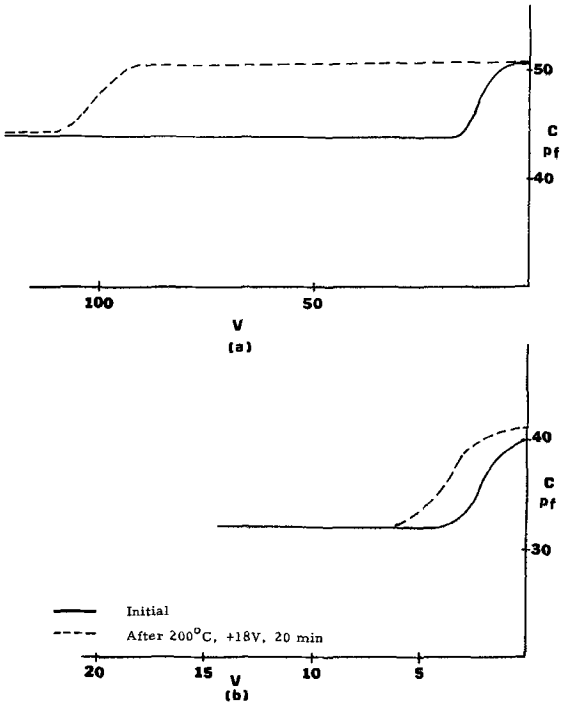

Fig. 3. C-V plots for MNOS structures with 5500Å of oxide grown in steam: (a) oxide not heated in hydrogen prior to nitride deposition; (b) oxide heated in hydrogen at 1200°C for 2 min prior to nitride deposition.

on the reduction of the mobile charge in silicon dioxide by the high-temperature hydrogen treatment described here, a number of samples which had 5000Å of oxide grown in steam were heated in hydrogen at temperatures between 1000° and 1200°C for durations between 1 and 4 min prior to nitride deposition. The flat-band voltage shifts were measured after bias-temperature treatments of 20 min at 200°C and +18V. The results of this investigation are listed in Table I. It should be pointed out that no attempt was made to reproducibly control the amount of sodium incorporated in the silicon dioxide during growth. It can be seen from Table I that a high-temperature (1100°-1200°C) hydrogen treatment is required to reduce the mobile-charge content in silicon dioxide effectively. The mechanism by which the quantity of mobile charges is reduced by the high-temperature hydrogen treatment is not fully understood.

Table I. Flat-band voltage shifts of hydrogen processed MNOS structures

Temp, °C	Time, min	ΔV_{FB}, V
1000	1	48
	2	109
	2	100
	4	17
	4	86
1100	1	46
	2	44
	4	8
1150	2	5.0
	2	2.0
1200	1	10
	2	2.0
	4	2.0

Manuscript submitted March 4, 1969; revised manuscript received May 23, 1969.

Any discussion of this paper will appear in a Discussion Section to be published in the June 1970 JOURNAL.

REFERENCES

1. E. H. Snow, A. G. Grove, B. E. Deal, and C. T. Sah, *J. Appl. Phys.*, **36**, 1664 (1965).
2. A. S. Grove, B. E. Deal, E. H. Snow, and C. T. Sah, *Solid-State Electronics*, **8**, 145 (1965).
3. E. H. Snow and B. E. Deal, *Trans. Met. Soc. AIME*, **242**, 512 (1968).
4. Bernard Yurash and B. E. Deal, *This Journal*, **115**, 1191 (1968).
5. J. V. Dalton and J. Drobek, *ibid.*, **115**, 865 (1968).
6. T. E. Burgess, J. C. Baum, F. M. Fawkes, R. Holmstrom, and G. A. Shirn, Paper presented at the Boston Meeting of the Society, May 5-9, 1968, Electronics Semiconductor Abstract 82.
7. T. L. Chu, J. R. Szedon, and C. H. Lee, *Solid-State Electronics*, **10**, 897 (1967).
8. B. E. Deal, P. J. Fleming, and P. L. Castro, *This Journal*, **115**, 300 (1968).
9. "Integrated Silicon Device Technology, Volume VII Oxidation," Technical Report No. ASD-TDR-63-316, Research Triangle Institute, June (1965).
10. V. Y. Doo, D. R. Nichols, and G. A. Silvey, *This Journal*, **113**, 1279 (1966).
11. K. E. Bean, P. S. Gleim, R. L. Yeakley, and W. R. Runyan, *This Journal*, **114**, 733 (1967).
12. E. Kooi, *IEEE Trans. Electron Devices*, ED-**13**, 238 (1966).
13. S. R. Hofstein, *ibid.*, ED-**13**, 222 (1966).
14. S. R. Hofstein, *Solid-State Electronics*, **10**, 657 (1967).

Brief Communications

Solubility of Gold in p-Type Silicon

R. C. Dorward[1] and J. S. Kirkaldy

Department of Metallurgy & Materials Science, McMaster University, Hamilton, Ontario, Canada

In recent years considerable attention has been given to the properties of gold in silicon because of its use in controlling minority carrier lifetime. At room temperature this element introduces a donor level 0.35 eV above the valence band and an acceptor level 0.54 eV below the conduction band (1). Both of these levels are believed to be due to substitutional gold. Wilcox and LaChapelle (2), for example, have shown by diffusion measurements that the ratio of substitutional to interstitial gold is about 10 at 1000°C and increases with decreasing temperature.

Numerous investigations have dealt with the enhanced solubility of gold in n-type silicon (3-6). This was originally attributed to an electronic effect arising from a change in the Fermi energy. Assuming that the acceptor level population is predominant at elevated temperatures, an increase in the Fermi energy should cause an increase in solubility (7). The most recent study (6), however, has shown that ion pairing also plays an important (and perhaps dominant) role, at least when phosphorus and arsenic are used as the n-type dopants. These ionic and electronic effects often interfere in experiments of this kind and make data analysis difficult and uncertain.

If the electronic interaction contributes to the increased solubility of gold in n-type silicon, there should also be a solubility decrease in p-type material, provided of course that the acceptor concentration used is not large enough to increase greatly the number of gold donor states. In this case ion pairing should not influence the results since both dopants have the same charge state, *i.e.*, a repulsive interaction.

Recent exploratory work on the solubility of gold in boron-doped silicon helps to clarify this question. Wafers of intrinsic (2000 ohm-cm) and boron-doped (1×10^{19} at./cm^3)[2] silicon were displacement plated from a radioactive gold chloride solution containing a small amount of hydrofluoric acid. They were then diffused to saturation at 1000°C, and the gold solubilities were determined by standard radiochemical techniques. The details of the equilibration and analysis procedures are given elsewhere (8). The solubility of gold in intrinsic silicon was found to be (11.1 ± 0.6)

[1] Permanent mailing address: Box 248, Viking, Alberta, Canada.

[2] Purposely chosen low to eliminate possible effects due to degeneracy and band gap shrinkage.

x 10^{15} at./cm^3 (8) compared to (7.0 ± 0.4) x 10^{15} at./cm^3 for the boron-doped material. We note a reduction in solubility of about 40%. As shown below, this is in good agreement with what may be expected on the basis of the electronic interaction.

According to the Shockley-Moll theory (7), the solubility, N, of gold in p-type silicon is given by

$$N = N_o \exp(-\Delta E_f/kT)$$

where N_o is the intrinsic solubility and ΔE_f is the absolute difference between the Fermi energy of intrinsic and extrinsic material. ΔE_f may be determined from the relation

$$p/n_i = \exp(\Delta E_f/kT)$$

where p, the hole concentration, is given by

$$p = \tfrac{1}{2}[N_B + (N_B^2 + 4n_i^2)^{\tfrac{1}{2}}]$$

n_i is the intrinsic carrier concentration, and N_B is the boron concentration. Setting n_i = 7 x 10^{18}/cm^3 at 1000°C (9) gives $N \simeq 0.5N_o$.

The gold solubilities found by Cagnina (6) in n-type silicon must therefore be due to joint contributions of an electronic effect as predicted by the Shockley-Moll theory and ion pairing. This result is also additional proof that the concentration of gold in the negatively charged state is predominant at elevated temperatures as well as at room temperature.

Acknowledgment

This research was supported by the National Research Council of Canada through a research grant and a fellowship.

Manuscript received May 16, 1969.

Any discussion of this paper will appear in a Discussion Section to be published in the June 1970 JOURNAL.

REFERENCES

1. C. B. Collins, R. O. Carlson, and C. J. Gallagher, *Phys. Rev.*, **105**, 1168 (1956).
2. W. R. Wilcox and T. J. LaChapelle, *J. Appl. Phys.*, **35**, 240 (1964).
3. W. R. Wilcox, T. J. LaChapelle, and D. H. Forbes, *This Journal*, **111**, 1377 (1964).
4. G. J. Sprokel and J. M. Fairfield, *ibid.*, **112**, 200 (1965).
5. M. L. Joshi and S. Dash, *J. Appl. Phys.*, **47**, 2453 (1966).
6. S. F. Cagnina, *This Journal*, **116**, 498 (1969).
7. W. Shockley and J. L. Moll, *Phys. Rev.*, **119**, 1480 (1960).
8. R. C. Dorward and J. S. Kirkaldy, *Trans. Met. Soc. AIME*, **242**, 2055 (1968); R. C. Dorward, Ph.D. Thesis, McMaster University (1967).
9. R. N. Hall and J. H. Racette, *J. Appl. Phys.*, **35**, 379 (1964).

Calculation of the p-T Diagrams of CdTe

A. S. Jordan and R. R. Zupp[1]

Bell Telephone Laboratories, Incorporated, Murray Hill, New Jersey

In this communication we present the calculated p-T diagrams for the Cd-Te system and compare them with the available experimental data. The partial pressures of components (p_{Cd} and p_{Te_2}) were evaluated along the liquidus curve of the Cd-Te system based on approximate activity functions in two semi-empirical parameters, α and β, derived for a regular associated solution (RAS) (1).

The theory of RAS has been discussed elsewhere (1). It is sufficient to note for the purposes of this comunication that the theory was necessitated by the inability of regular solution theory to describe the liquidus curves of the Zn-Te and Cd-Te systems. The appearance of the liquidus curves in these systems suggests association in the liquid phase. Therefore, Jordan (1) assumed the presence of ZnTe (or CdTe) complexes in addition to Zn (or Cd) and Te atoms in the liquid, all three species forming a regular ternary solution. The analysis of a RAS resulted in explicit expressions for the approximate activities of the components. These were substituted into the thermodynamic equation of the liquidus boundary to yield a liquidus equation in the constants α and β. Having evaluated α and β from the liquidus data of Kulwicki (2), Jordan (1) calculated the full liquidus curves in the Zn-Te and Cd-Te systems, in very good agreement with the available experimental determinations.

Recently, we reported (3) the calculated p-T diagrams for the Zn-Te system. The calculated partial pressures p_{Zn} and p_{Te_2} along the liquidus curve of this system, evaluated from the approximate activity functions for a RAS and the previously derived values of α and β (1), are in excellent agreement with the experimental results of Shiozawa *et al.* (4).

The calculation of p_{Cd} and p_{Te_2} along the liquidus curve of the Cd-Te system followed the procedure adopted in calculating the p-T diagrams in the Zn-Te system (3). Thermodynamic data required to perform the calculations were obtained from several sources. The constants α and β were previously derived (1) for the Cd-Te system from the liquidus data of Kulwicki (2). The equilibrium constant, K, for the dissociation reaction

$$CdTe(s) = Cd(g) + \tfrac{1}{2}Te_2(g) \qquad [1]$$

was evaluated from the free energy equation of Brebrick and Strauss (5) for Eq. [1]. The pressures of pure superheated liquid Cd and Te, p^o_{Cd} and $p^o_{Te_2}$, were taken from the recent high pressure measurements of Baker (6, 7). It should be noted that $p^o_{Te_2}$ was computed from the total pressure data of Baker by subtracting from it approximately 1%, due to the presence of monatomic Te (8).

The calculated dependence of log p_{Cd} and log p_{Te_2} on reciprocal temperature for the Cd-Te system is shown in Fig. 1 and 2, respectively. In addition, the experimental pressure data of Lorenz (9) and de Nobel (10) are presented. The p-T diagrams also illustrate the limiting straight lines at x_{Cd} = 1 and 0, where x_{Cd} is the atom fraction of Cd in the liquid. For example, in Fig. 1, log p^o_{Cd} and log p_{Cd} = log $K/\sqrt{p^o_{Te_2}}$ *vs.* $1/T$ were drawn. Finally, values of log p_{Cd} (min) and log p_{Te_2} (min) as a function of $1/T$ at the minimum total pressure, p_{tot} (min), were plotted. These pressures are interrelated by p_{Cd} (min) = 2/3 p_{tot} (min) and p_{Te_2} (min) = 1/3 p_{tot} (min). p_{tot} (min) was calculated from the equilibrium constant for Eq. [1] according to p_{tot} (min) = $3(K/2)^{2/3}$.

The calculated p-T diagrams for the Cd-Te system are generally in good agreement with the experimental data of Lorenz (9) and de Nobel (10). Both of these authors have directly observed the freezing points of solid CdTe, corresponding to various fixed Cd or Te_2 pressures. In particular, it can be seen in Fig. 1 that there is indeed a very good agreement

[1] Present address: University of Washington, Seattle, Washington.

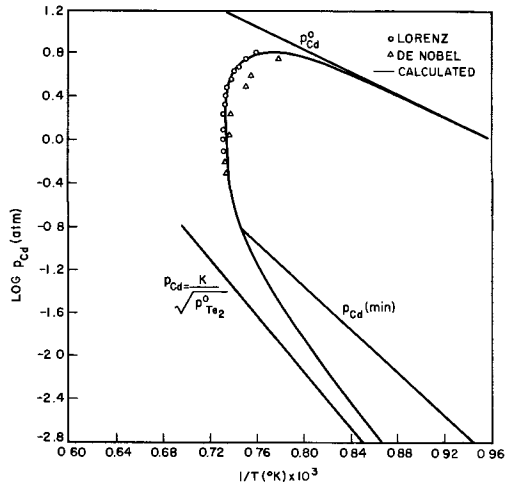

Fig. 1. Log Cd pressure vs. reciprocal temperature for the Cd-Te system.

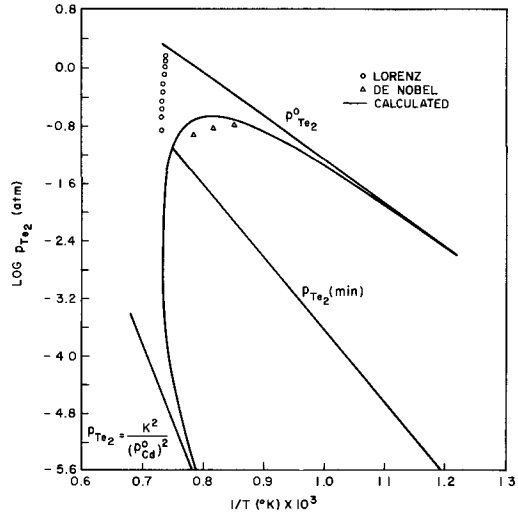

Fig. 2. Log Te_2 pressure vs. reciprocal temperature for the Cd-Te system.

between Lorenz's (9) experimental values of p_{Cd} and the theoretical curve. However, the calculated p_{Te_2} curve, shown in Fig. 2, lies between the somewhat discrepant experimental points of Lorenz and de Nobel.

In Fig. 2, one can observe that, according to the data of Lorenz, near the melting point of the compound the maximum p_{Te_2} along the liquidus is only slightly lower than $p^o_{Te_2}$. This pressure would correspond to $a_{Te} \approx 0.9$ for x_{Te} extending almost to 0.5, which would seem unlikely unless the liquidus were as flat as in the Zn-ZnTe subsystem (1, 2). However, the liquidus curve in the Te-CdTe subsystem (2) changes gradually without any flat regions. It is very difficult to explain the seemingly high results of Lorenz. In fact, in the Hg-Te system, a similar system where thorough measurements have been made, Brebrick and Strauss (11) found the maximum value of p_{Te_2} to be much lower than $p^o_{Te_2}$, corresponding to $a_{Te} \approx 0.4$. Similarly, in the Zn-Te system it is estimated from the work of Shiozawa *et al.* (4) that $a_{Te} \approx 0.5$ at the maximum pressure of Te_2.

Manuscript submitted Jan. 10, 1969; revised manuscript received June 11, 1969. This was part of Paper 527 presented at the Montreal Meeting, Oct. 6-11, 1968.

Any discussion of this paper will appear in a Discussion Section to be published in the June 1970 JOURNAL.

REFERENCES

1. A. S. Jordan, Paper presented at the TMS-AIME Annual Meeting, February 17-20, 1969, Washington, D.C.
2. B. M. Kulwicki, Ph.D. Thesis, University of Michigan, School of Engineering, July 1963.
3. A. S. Jordan and R. R. Zupp, *This Journal*, **116**, 1264 (1969).
4. L. R. Shiozawa, J. M. Jost, and G. A. Sullivan, 1965-1968, "Research on Improved II-VI Compounds," Final Report, Contract AF33(615)-2708 for the Aerospace Research Laboratories, U.S.A.F., Wright-Patterson Air Force Base, Ohio.
5. R. F. Brebrick and A. J. Strauss, *J. Phys. Chem. Solids*, **25**, 1441 (1964).
6. E. H. Baker, *J. Chem. Soc.*, (A), **1967** 1558.
7. E. H. Baker, *J. Appl. Chem.*, **16**, 321 (1966).
8. D. R. Stull and G. C. Sinke, "Thermodynamic Properties of the Elements," Advances in Chemistry Series, No. 18, A.C.S.
9. M. R. Lorenz, *J. Phys. Chem. Solids*, **23**, 939 (1962).
10. D. de Nobel, *Philips Res. Repts.*, **14**, 361 (1959).
11. R. F. Brebrick and A. J. Strauss, *J. Phys. Chem. Solids*, **26**, 989 (1965).

Metal Transport in Voids at Metal-Oxide Interfaces

V. R. Howes[1]

Materials Division, Central Electricity Research Laboratories, Leatherhead, Surrey, England

It has been shown recently (1, 2) that, during high-temperature oxidation of an Fe-28% Cr alloy, the metal surface became extremely corrugated due to the formation of voids at the metal-oxide interface. The detection of a fine line structure on the smooth metal surfaces in the voids was associated with chromium transport within the voids.

Further observations have shown that for alloys of lower chromium content (16 and 19%) the fine structure takes the form of regular terracing or faceting as can be seen in the scanning electron micrograph in Fig. 1. The surface of the Fe-19% Cr alloy specimen has been revealed by the spalling away of the oxide during cooling after 6-hr oxidation at 950° in pure oxygen. The high peaks are where the metal and oxide were in contact, and the hollows are where voids had formed during oxidation.

[1] Present address: Wolfson Institute of Interfacial Technology, University of Nottingham, Nottingham, NGY 2 Rd., England.

Benard *et al.* (3, 4) have shown that specular surfaces of Fe-Cr alloys are obtained at extremely low oxygen pressures, but that at higher pressures (still lower than the dissociation pressure of chromium oxide) adsorbed oxygen produces surface energy anisotropies so that energy minimization leads to the formation of facets. Morris and Smeltzer (5) have measured the evaporation rates for Fe-Cr alloys and have pointed out that the low oxygen pressures necessary for the prevention of faceting may be obtained in the vicinity of the surface by the gettering action of evaporating metal. They obtained facets on Fe-5% Cr alloy surfaces, but specular surfaces were found on an Fe-25% Cr alloy after evaporation at 950°C in a nominal vacuum of 10^{-6} Torr. This difference was explained by the observed increased evaporation rate for the second alloy, which reduced the effective oxygen pressure at the surface so that adsorption became negligible.

Fig. 1. Metal surface, observed at a tilt of 30°, showing terracing, beneath an oxide layer where this has spalled away from a specimen of an Fe-19% Cr alloy during cooling after oxidation at 950°C for 6 hr in pure oxygen.

These results suggest that the terracing observed in the interfacial voids in the present 16 and 19% Cr alloys was a consequence of adsorbed oxygen on the metal and that the rate of metal evaporation into the voids was likely to have been less than 3.3×10^{-3} mg cm^{-2} hr^{-1} (the value for the Fe-25% Cr alloy at 950°C found by Morris and Smeltzer). In the presence of evaporation and an adsorbed oxygen layer that has led to faceting by surface energy minimization, long distance surface diffusion of metal around the voids seems unlikely. The oxygen that was adsorbed on the metal most probably came from the voids, supplied either by dissociation of the Cr_2O_3 on the other side or by an anion component of diffusion through the oxide during oxidation. The rate of Cr evaporation across the voids is certainly less than the metal consumption rate after 6-hr oxidation at 950°C ($\sim 9 \times 10^{-2}$ mg cm^{-2} hr^{-1}) calculated from the measurements of Mortimer and Sharp (6). The consequent reduction in the supply of chromium to the oxide is most probably a main reason for the slight but definite negative deviation from the initial parabolic oxidation rate that has been observed previously (6) and discussed in relation to interfacial void formation (7).

Acknowledgment

This communication is published by permission of the General Electricity Generating Board.

Manuscript received May 8, 1969.

Any discussion of this paper will appear in a Discussion Section to be published in the June 1970 JOURNAL.

REFERENCES

1. V. R. Howes, *Nature*, **216**, 362 (1967).
2. V. R. Howes, *Corrosion Sci.*, **8**, 221 (1968).
3. J. Benard, J. Moreau, and J. Plateau, *Z. Elektrochem.*, **61**, 59 (1957).
4. J. Moreau and J. Benard, *J. Chim. Phys.*, **53**, 787 (1956).
5. L. A. Morris and W. W. Smeltzer, *This Journal*, **110**, 997 (1963).
6. D. Mortimer and W. B. A. Sharp, *British Corrosion J.*, **3**, 61 (1968).
7. V. R. Howes, *Corrosion Sci.*, **8**, 729 (1968).

Voltage Oscillations of the H_2-CO System

Max C. Deibert*

Department of Chemical Engineering, Massachusetts Institute of Technology, Cambridge, Massachusetts

and David L. Williams*,[1]

Monsanto Company, Everett, Massachusetts

ABSTRACT

A Pt catalyst in a porous fuel cell anode is poisoned by adsorption of CO from a H_2-CO fuel mixture. Under constant current conditions, this forces the electrode to high potentials. The electrode may reach potentials sufficiently high to oxidize the adsorbed CO and initiate a period of efficient electro-oxidation of the H_2 in the fuel mixture. Natural oscillations of potential are caused by repeated poisoning and reactivation of the electrode. More efficient activation of the electrode at high currents can result in a lower time-averaged anode potential at high current than at lower currents. The frequency of natural oscillations of the H_2-CO system is relatively independent of the current density, but is dependent on the partial pressure of CO. The oscillatory behavior is explained on the basis of poisoning of an electrode system having a passivation-type polarization curve. The maximum rate of potential increase is correlated with the charging of the double layer by the imposed constant current. The maximum rate of potential recovery is explained by the charging, or collapsing, of the double layer by the electrode reaction current.

Naturally occurring oscillations have been observed in many fuel cell systems, and in fundamental studies at smooth electrodes even for simple fuels such as H_2 (1, 2). Analyses of the interrelationships between the operating characteristics of auto-oscillating electrochemical systems and their surface chemical, electrical, and kinetic properties have been presented by Chizmadzhev (3) and Hunger (4). The first paper concludes that the slow reaction of oxygen-containing species on the electrode compared to hydrogen is the cause of oscillations. The second paper attributes the oscillations of a formaldehyde anode to a diffusion-adsorption step coupled to surface reaction steps in the reaction sequence. A discussion of fuel cell battery operating characteristics in cells containing naturally oscillating anodes has also been presented by Hunger (5). This paper indicates the operating conditions under which natural oscillations can be expected and the types of oscillations that can be obtained depending on cell operating constraints, *i.e.* constant cell current, potential, or load.

The importance of this area to fuel cell technology is that electrocatalysts are often susceptible to periodic activation processes which improve the performance of electrodes. The improvement of fuel cell power production by the imposition of electrical pulses under operating conditions in which natural oscillations do not occur has been extensively reported (6-9). Diller (10) describes a technique of decreasing the power requirements in cells for the Hall process for electrowinning aluminum by periodically imposing short, high-power electrical pulses to the cell, indicating the applicability of similar activation procedures to process electrochemistry.

This study demonstrates the cyclic operating characteristics of an anode consuming a simple fuel, H_2, in the presence of dilute CO. The dependency of the amplitude and frequency of the oscillations on the anode current and fuel composition were investigated in an attempt to determine conditions of electrode design and operation in which CO might be efficiently electro-oxidized, or otherwise removed, by the aid of the natural activation process at the anode. This type of fuel mixture is important in fuel cell technology, since it may result from incompletely purified hydrogen, produced from the reaction of steam with carbon or hydrocarbons. The system is also a model fuel-poison couple in which the poison concentration can be varied at will by changing the CO partial pressure.

Key words: fuel cell, oscillations.

* Electrochemical Society Active Member.

[1] Present address: American Hospital Supply Corp., Everett, Massachusetts.

Experimental

The electrochemical system utilized a platinized porous carbon anode with 1.3 cm^2 apparent area, a platinum foil auxiliary cathode, and a saturated calomel reference electrode. The electrolyte was 2M H_2SO_4 maintained at 95°C. Current was supplied by a Harrison Laboratory Model 6200A power supply. In initial tests, time average potentials were measured with a damped voltmeter. In later tests, voltage-time traces were measured with a Tektronix 545-A Oscilloscope with Polaroid camera attachment. The fuel gas was continuously passed behind the electrode, the excess being vented.

The electrode was prepared from Shawinigan acetylene black, Teflon powder, and a platinum mesh screen support, by the method described by Deibert (11). The carbon loading was about 8 mg/cm^2. The electrode was platinized by the method of Brown and Brown (12). The final microporous electrode contained about 10 w/o (weight per cent) platinum, based on the carbon content. The Shawinigan acetylene black had a BET surface area of about 65 m^2/g. This was probably not greatly affected by the addition of 10% platinum. The total surface area of conductive solid was therefore about 5000 cm^2/cm^2 of electrode. Since the Pt rendered the entire structure hydrophilic, nearly all this surface was wetted by the electrolyte.

Results

Three fuel streams were tested for their polarization behavior. These were pure H_2, 1% CO in H_2, and 5% CO in H_2. The recorded, time-averaged potentials relative to the open-circuit potential of the pure hydrogen electrode are shown in Fig. 1 as a function of apparent current density. The polarization curve for pure H_2 demonstrates that hydrogen is readily oxidized on the platinum electrode, sustaining a current density of 200 mA/cm^2 with a polarization of less than 0.05V. The reversible character of the H_2-Pt electrode makes this open-circuit potential a valid reference for this system. Addition of 5% CO to the H_2 severely poisons the electrode, increasing the open-circuit potential by 0.77V and polarizing the electrode to oxygen evolution potentials below a current density of 200 mA/cm^2.

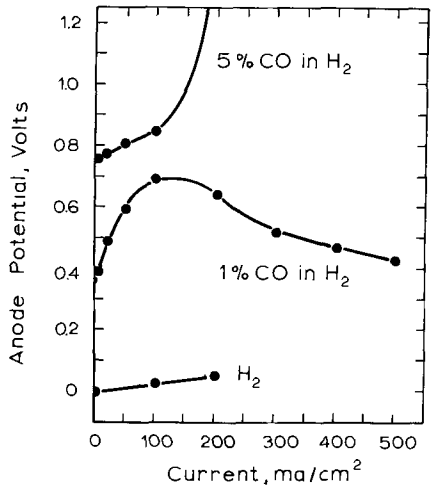

Fig. 1. Time-averaged polarization of H_2-CO system using current control.

The electro-oxidation of 1% CO in H_2 mixture poisons the electrode, but less than 5% CO in H_2. Above a current density of 100 mA/cm², the polarization of the electrode decreases with increasing currents up to 500 mA/cm². This is a demonstration of an unusual phenomenon of an increase in reaction rate being accompanied by a decreasing time-average thermodynamic driving force for the reaction. That this is most probably the result of a natural periodic activation of the platinum electrocatalyst is revealed by the time-dependent potential measurements.

The oscillatory behavior of the potential of the 1% CO in H_2 fuel electrode is shown by potential-time traces in Fig. 2 for six current densities between 50 and 500 mA/cm². The effect of CO content of the fuel on potential oscillation frequency is shown by replacing the flow of 1% CO in H_2 with pure H_2 while maintaining the current at 100 mA/cm². A potential-time trace taken a short time after this replacement is shown by the broken line in Fig. 2(c).

Low-amplitude (0.2V) potential oscillations are observed at 75 mA/cm² in Fig. 2. The amplitude of these oscillations increases with increasing current density, to about 1.3V at 500 mA/cm². The frequency decreases slightly with increasing current between 75 and 200 mA/cm², and then remains relatively constant at approximately 1.7 Hz at higher current densities up to 500 mA/cm². At 100 mA/cm², the frequency of the potential oscillations decreased gradually to zero after introducing pure hydrogen. However, the oscillation amplitude remained approximately constant as the CO content decreased.

Discussion

One possible explanation for the observed voltage oscillations can be based on the assumption that the electrode reaction has a passivation-type polarization curve. Figure 3 shows a schematic of such a curve. This curve could be obtained by voltage control of the electrode, as for example by use of a potential sweep. In a passivation-type curve on an anode, there is a region in which an increasing potential lowers the current. This effect may be caused by anion adsorption or oxide formation, which would commence at the potential near *D* in Fig. 3. These effects can poison a platinum electrode for hydrogen oxidation. Passivation-type curves have been reported by Schuldiner for H_2 oxidation which he attributes to anion adsorption on the Pt catalyst (13). At very high potentials, other anodic reactions will occur, *e.g.* water oxidation, which may not be passivated, section *E, F*, Fig. 3. A deactivation phenomenon which is relatively independent of potential can also occur on the anode. This can result from CO adsorption in the present case. In other instances, deactivation can be attributed to adsorption of impurities from solution (14), or to catalyst recrystallization as suggested by Sawyer and Seo (2) for H_2 anode deactivation. Thus, both deactivation and passivation may be expected even for H_2 oxidation under normal fuel cell conditions.

The importance of the passivation and deactivation effect is that together they can give rise to potential oscillations of the type observed in this investigation. If the current is adjusted to the level indicated by the straight line *ABC*, the voltage will initially be at point *A*. However, as deactivation occurs, the voltage shifts toward *B*. At this time, the voltage shifts quickly to *C*. It is possible that at *C* the poison is oxidized or electrodesorbed. It is known that CO oxidation occurs on this PtO surface at high potentials (15). When this occurs, the electrode is reactivated and the potential shifts to *A*. At this point, deactivation again occurs and the oscillations repeat.

These phenomena are demonstrated by the experimental data shown above. The high potential attained at 500 mA/cm² is believed to cause a more efficient cleaning of the electrode surface (*i.e.*, more complete oxidation of CO), than the potential achieved in the 100 mA/cm² oscillation. This effect is believed to be the cause of decreasing time average overpotential with increasing current at 1% CO (Fig. 1). That is, the oscillating effect with high current is more effective in oxidizing the CO poison, thus giving a longer period of efficient oxidation of H_2. In the data of Fig. 1, no

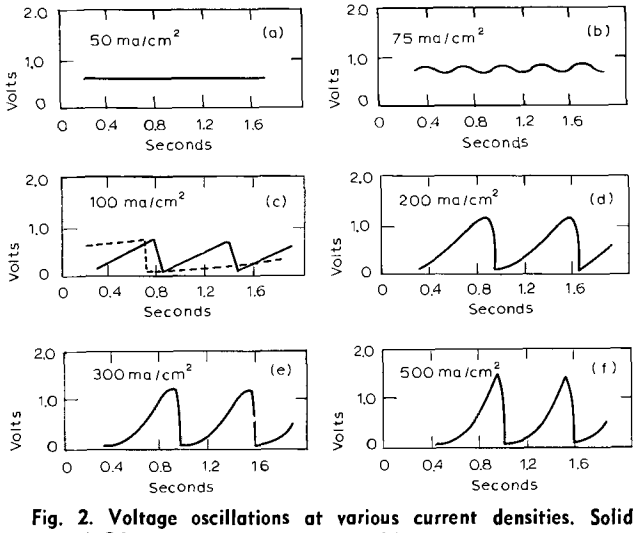

Fig. 2. Voltage oscillations at various current densities. Solid lines, 1% CO in H_2. Dashed line, <1% CO in H_2.

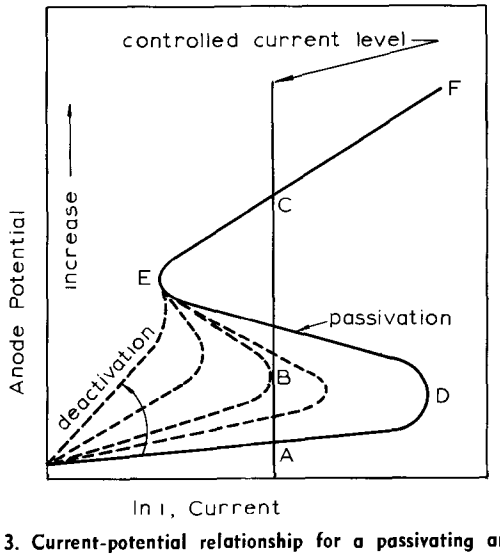

Fig. 3. Current-potential relationship for a passivating and deactivating anode.

attempt was made to read the damped meter needle to observe oscillations.

Figure 2(c) shows the effect of decreasing the partial pressure of CO. The curve shape is similar but the period of oscillation increases as less CO is available to cause deactivation. Thus, the rate of deactivation is slower. With 5% CO, there is no oscillation and the electrode is permanently poisoned. Thus, the oxidation of CO is not sufficiently rapid at the high potential to generate a clean surface for a period of H_2 oxidation at low overpotential.

An analysis of this oscillatory behavior will be made based on an equivalent circuit for the anode involving a resistor and capacitor in parallel. The capacitor C denotes the double layer capacitance of the electrode, and R is the resistance to current flow due to electrode polarization. The analysis assumes that the current passing through the electrode is held at a constant value i_c which goes either into the charge or discharge of the capacitor or into the electrode reaction process. Experimentally, the voltmeter reads the anode potential *vs.* a reference voltage (saturated calomel electrode). This potential is adjusted to the H_2/H^+ potential of the solution for further analysis.

The reaction current is denoted, for illustrative purposes, in terms of the exchange current, i_o, and the overvoltage. Such a behavior might be expected at low potentials even for the complex electrode system used in this study. The capacitance current is $C\ dV/dt$ giving a total current of:

$$i_c = C\frac{dV}{dt} + i_o \exp aV \qquad [1]$$

It was noted earlier that, when the electrode became deactivated to B of Fig. 3, due to decreased i_o values, the potential shifted to C. The rate of this voltage change will depend primarily on the double-layer capacitance. If the reaction current is assumed to be small compared to i_c during deactivation, then a limiting rate of voltage change is:

$$\frac{dV}{dt} = \frac{i_c}{C} \qquad [2]$$

Based on this model and assumption, the experimental data shown in Fig. 2 can be used to calculate an electrode capacitance. Taking the limiting, steepest slopes of the voltage increase lines as a measure of this limiting case, this method yields values of 0.08, 0.07, 0.07, and 0.10 farads/cm^2 for currents 100, 200, 300, and 500 mA/cm^2, respectively. This constancy of the calculated capacitances gives credence to the model and assumptions. The platinized carbon electrode used had an actual (BET) surface area of about 5000 (cm^2/cm^2). The capacitances calculated above indicate that the specific capacitance of this surface was about 15 to 20 μf/cm^2, which is the correct magnitude for a double-layer capacitance of this system.

The speed of potential recovery, from C to A, can also be explained in terms of the above equivalent circuit. In this case, the current applied is assumed to be much smaller than the "regenerated" reaction current. The limiting rate of reactivation is therefore denoted by:

$$\frac{dV}{dt} = \frac{i_o}{C} \exp aV \qquad [3]$$

Thus, the rate of potential decrease will be the rate of the reaction current charging or discharging the double-layer capacitance. This is shown as an exponential function of overvoltage, but is directly dependent on the reaction exchange current and inversely dependent on the double-layer capacitance. Although no calculations are presently warranted, based on this model, it should be noted that the voltage decrease is much faster than the voltage increase which was dependent on the applied current charging the double layer capacitance.

Conclusion

The oscillatory behavior of an electrode is explained on the basis of poisoning of an electrode having a passivation-type polarization curve. The maximum rate of potential increase has been correlated with the charging of the electrode double layer by the applied current, and the maximum rate of potential recovery is explained by the charging or discharging of the double layer by the reaction current, after electrode reactivation.

Many other observations of oscillatory behavior of anodes operating at constant current have revealed much more rapid potential recovery than potential decay (1, 2, 13). The observation by Schuldiner (13) of oscillations in the electro-oxidation of formaldehyde on platinized platinum shows breaks in the slope of the potential decay line. Using the average actual surface area of the electrode given in that paper, the specific capacitances of his electrode are 40-60 μf/cm^2 in the low potential region, and 10-22 μf/cm^2 in the high potential region. The latter values are probably closer to the real capacitance values, since more complete passivation, in this case by anion adsorption, would be expected at high potentials. In any case, both the present study and Schuldiner's data indicate that poisoning of an oscillating electrode is essentially complete at the initiation of potential decay, rather than progressively effecting the entire decay process.

Acknowledgments

This work was supported partly by the U. S. Army Materiel Command, Harry Diamond Laboratories, Contract DA-49-186-AMC-166 (X), and partly by NASA Grant NsG-496.

REFERENCES

1. G. Armstrong and J. A. Butler, *Disc. Faraday Soc.*, **1**, 122 (1947).
2. D. T. Sawyer and E. T. Seo, *J. Electroanal. Chem.*, **5**, 23 (1963).
3. Yu A. Chizmadzhev, *Doklady Akad. Nauk. S.S.S.R.*, **113**, 1136 (1960).
4. H. F. Hunger, *This Journal*, **115**, 492 (1968).
5. H. F. Hunger, J. E. Wynn, and N. J. San Filippo, *Proc. 19th Ann. Power Sources Conf.* **19**, 8, (1965).
6. J. O'M. Bockris, B. J. Piersma, E. Gileadi, and B. D. Cohen, *J. Electroanal. Chem.*, **7**, 487 (1964).
7. M. L. Kronenberg and C. Kordesch, *Electrochem. Technol.*, **4**, 460 (1966).
8. T. J. Gray, A. A. Schneider, R. B. Rozelle, and M. S. Suder, "Fuel Cell Research: An Investigation of Non-Steady-State Operation," N.A.S.A., Grant NsG-384, Final Report, p. 9 (1965).
9. P. J. Chludzinski and J. Lennon, "Hydrocarbon-Air Fuel Cells," Contract Nos. DA-44-009-ENG-4909 and DA-44-009-ENG-479 (T) Report No. 5, p. 4-216 (Jan.-June 1964).
10. I. M. Diller, U.S. Pat. 3,244,604 (April 5, 1966).
11. M. C. Deibert, "Fuel Cell Membrane Electrode Configuration," Technical Report MRB 4020T (DDC No. AD-606-289), U. S. Army Materials Command, Aug. (1964); and U.S. Pat. 3,385,736 (1968).
12. H. C. Brown and C. A. Brown, *J. Am. Chem. Soc.*, **84**, 2827 (1962).
13. S. Schuldiner, *This Journal*, **115**, 362 (1968).
14. H. Binder, A. Kuhlina, H. Krupp, K. Richter, and G. Sandstede, *ibid.*, **112**, 355 (1965).
15. S. Gilman, *J. Phys. Chem.*, **68**, 70 (1964).

The Electrochemical Behavior of Decorative Nickel-Chromium Coatings in 3% NaCl under Potentiostatic Conditions

S. R. Maloof*, [1]

Exploratory Development Laboratory, United-Carr, Incorporated, Watertown, Massachusetts

ABSTRACT

Electrochemical measurement of the corrosion currents of commercially prepared decorative nickel-chromium coatings indicates that the addition of a chromium topcoat to duplex nickel reduces the dissolution rate of nickel by only a factor of 2, while at the same time increasing the susceptibility of the coating system to pitting corrosion. Indications are that a "critical" potential for macro pitting may exist for these coating systems that could explain the frequent disagreement of results obtained on the pitting behavior of decorative nickel-chromium coatings at different tests sites. Preliminary results obtained with a silver undercoat indicate that the corrosion current may be reduced by a factor of 10 compared to that for duplex nickel with a similar topcoat of microcracked chromium. Moreover, there is little or no corrosion penetration of the silver layer. A possible explanation for these findings is advanced and a model developed to explain the corrosion behavior of decorative nickel-chromium coatings.

Introduction in the early 1950's of decorative duplex nickel-chromium coatings for protection against corrosion of car bumpers and exterior automotive trim was a major step forward, since the partial replacement of the semibright nickel by an outer layer of bright nickel served a dual purpose. It eliminated the need for buffing of the nickel prior to chromium plating and, more important, it caused the corrosion pits to spread sideways instead of directly downward to the basis metal. These facts are generally well known and well documented in static and mobile tests carried out by earlier investigators (1-5).

Wesley and Knapp (1) were probably the first to identify the mechanism of failure as due to pitting corrosion in the nickel undercoat. Pitting is initiated at flaws or cracks in the chromium topcoat serving as the cathode for the reduction of oxygen, while the dissolution of the nickel underneath occurs at the anode of the galvanic cell. Furthermore, Flint and Melbourne (3) showed that the process is under cathodic control and increasing the degree of cathodic polarization should lead to increased corrosion protection. This is undoubtedly the explanation for the apparent, improved corrosion resistance of coating systems with a topcoat of microcracked or microporous chromium instead of ordinary chromium. In more recent years, further improvements have resulted from the use of multilayered nickel coatings of different electrochemical properties (6, 7).

The purpose of this research was threefold: (*a*) to measure electrochemically the corrosion currents of nickel-chromium type protective systems, (*b*) to determine if pitting is initiated at a fairly well-defined potential as is known for stainless steel and aluminum anodically polarized in 3% NaCl (8); this point was not investigated in any great detail; and (c) to determine if another undercoat metal might provide improved corrosion resistance by virtue of its electrode potential being more nearly equal to that of chromium after atmospheric exposure or by its forming a protective reaction film *in situ* in the aqueous environment after anodic polarization. One metal investigated was silver, since a solid film of silver chloride is formed at small positive overpotentials (20-40 mV) in 3% NaCl.

* Electrochemical Society Active Member.

[1] Present address: Block Engineering, Incorporated, 19 Blackstone St., Cambridge, Massachusetts 02139.

Experimental

The decorative nickel-chromium coatings were furnished by the Harshaw Chemical Company on an annealed low-carbon steel substrate in the form of panels approximately 4 in. by 6 in. by 1/16 in. thick. They were cut with a jeweler's saw into specimens ½ in. wide by 2 in. long. One end of each specimen was carefuly bent to a ½-in. radius and a hole drilled and tapped at the apex of the bend to accommodate an 0-80 threaded rod for electrical connection. The method of attachment and the electrolytic cell used were similar to that described by Leckie and Uhlig (9).

The decorative coatings were of duplex nickel ¾ mil thick, duplex nickel 1 mil thick with a topcoat of 0.10 mil of ordinary chromium, and duplex nickel 1.25 mils thick with a topcoat of 0.050 mil of microcracked chromium. In all these coatings, the outer bright nickel was about 1/3 the thickness of the semibright nickel.

Two other coating systems were prepared: one consisted of 1.3 mils of silver electrodeposited directly onto a cold-rolled steel substrate, followed by a layer 0.060 mil thick of electroless nickel and an outer layer 0.120 mil thick of microcracked chromium; the other consisted of a layer of 0.050 mil of silver interleaved between duplex nickel and ordinary chromium.

Anodic and cathodic polarization curves were developed for each of the coating systems investigated. The electrolyte in all cases was 3% NaCl (pH = 5.5) deaerated with bubbling argon and stirred at 200 rpm. The exposed area to the electrolyte was 1 cm^2—the remainder of the surface was covered with a commercial stop-off lacquer. No special attempt was made to control the temperature but, in general, the temperature did not deviate more than ±1° from a temperature of 23°C. All potentials were measured relative to a SCE with a Luggin capillary located within 2-3 mm of the sample surface. The potentials were set with a potentiostat constructed from commercially available parts. The potential could be set to within 1 mV of the desired potential and the current read in the range of 0.05 μA to 1.5A.

The specimens were cathodically polarized first. Current readings were taken at each preset value of the potential after a period of 5 min. The solution was then changed and the anodic polarization curve developed in a similar manner.

Anodic polarization was not continued beyond a potential of +500 mV (*vs.* H_2), since in some cases the corrosion had already penetrated to the basis metal.

The corrosion currents were determined from the polarization data as described earlier (10). Current densities given on the abscissa are to be read as apparent current densities.

Results

Any study of pitting corrosion is usually concerned not only with the mechanism of pitting, but also with the location of the pitting sites. It is evident in Fig. 1 that pitting occurs mainly at the microcracked boundaries. The metallographic evidence shown in Fig. 2 shows that the pits formed in the bright nickel directly below the cracks in the chromium topcoat are hemispherical in shape. Since there is little or no apparent attack of the chromium, pitting is the apparent result of the anodic dissolution of the nickel below as postulated earlier (3, 5). It is also of interest to note that, as the pits grow in size and merge together, there is undermining of the chromium topcoat.

The potentiostatic anodic and cathodic polarization curves of duplex nickel over an annealed low-carbon steel substrate are shown in Fig. 3. The apparent corrosion rate as determined by extrapolation of the linear portions of the polarization curves to the open-circuit potential is 0.18 $\mu A/cm^2$. The anodic polarization curve which is of special interest shows a linear Tafel slope (40 mV per decade) between a potential of —0.10V and 0V on the hydrogen scale. In this potential range, the bright nickel surface turned black. At higher positive potentials, the initially formed black film began to disintegrate and, at a potential of +0.13V where a reversal in current occurs, it was completely free of the surface, revealing a matte surface below. Beyond a potential of +0.14V there is a further increase in the current, but at a slower rate, indicative of the dissolution of the more noble semibright nickel. Semibright nickel is known to be more noble than bright nickel (3, 11).

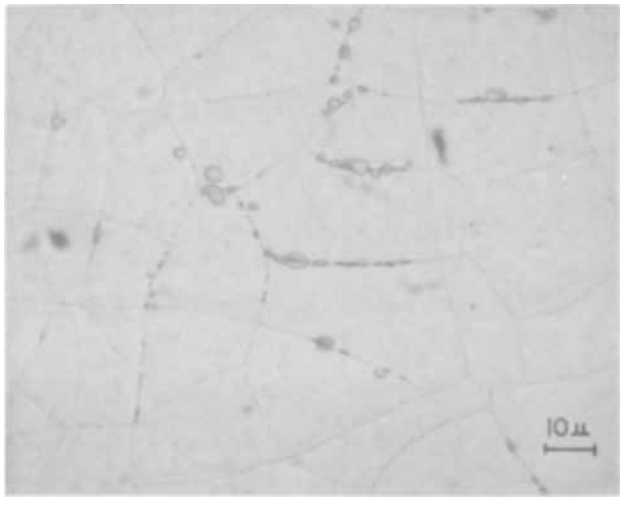

Fig. 1. Duplex nickel plus microcracked chromium over low-carbon steel corroded under static conditions for 6 days in 3% NaCl. Note that pitting is initiated mainly at the boundaries of the microcracked regions.

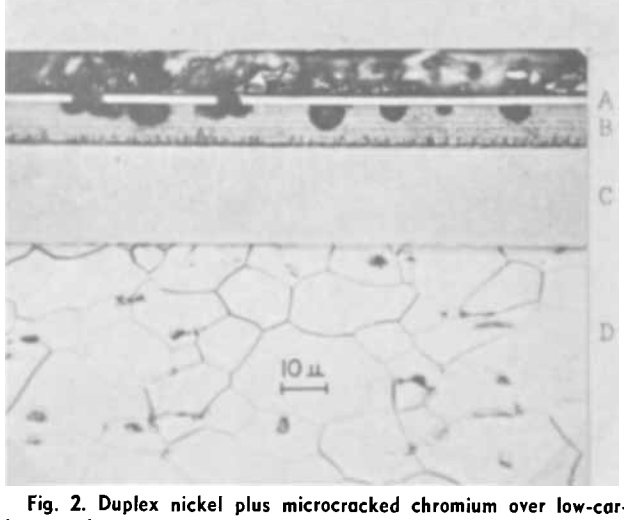

Fig. 2. Duplex nickel plus microcracked chromium over low-carbon steel corroded under static conditions for 30 days in 3% NaCl: A—chromium, B—bright nickel, C—semibright nickel, D—steel. Etched in 50:50 glacial acetic-nitric acid.

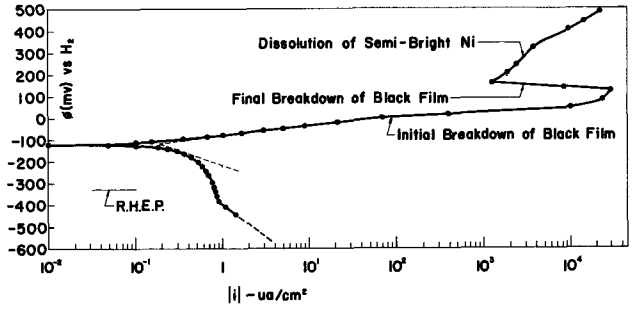

Fig. 3. Anodic and cathodic polarization curves of duplex nickel over low-carbon steel in 3% NaCl (pH = 5.5). Rotation @ 200 rpm and bubbling argon.

The anodic and cathodic polarization curves of duplex nickel and ordinary chromium over steel under the same test conditions are shown in Fig. 4. The open-circuit potential of this coating sytem is —0.30V on the hydrogen scale, and its apparent corrosion rate is 0.10 $\mu A/cm^2$. This particular sample was not anodically polarized beyond a potential of +0.060V. However, an identical sample gave a similar anodic polarization curve and the onset of pitting was observed at a potential of about +0.20V. This is indicated by the dotted portion of the curve. Anodic polarization to as high as +0.50V showed that the corrosion pits had penetrated to the steel basis metal (Fig. 8). Similar polarization curves obtained for duplex nickel and microcracked chromium over steel are shown in Fig. 5. This sample was initially polarized only to a potential of —0.10V and showed no evidence of macropitting. At a later date, it was anodically polarized further to a potential of +0.30V and the current flowing was 90 mA. Visible pitting, however, occurred at a potential of about +0.10V and at +0.30V the surface was heavily pitted. Attempts to polarize this coating system anodically to a potential of +0.50V on other identical samples resulted in a complete separation of the chromium topcoat.

The polarization curves shown in Fig. 6 are of special interest. In this coating system, a thick layer of electroplated silver (1.3 mils) was used in place of

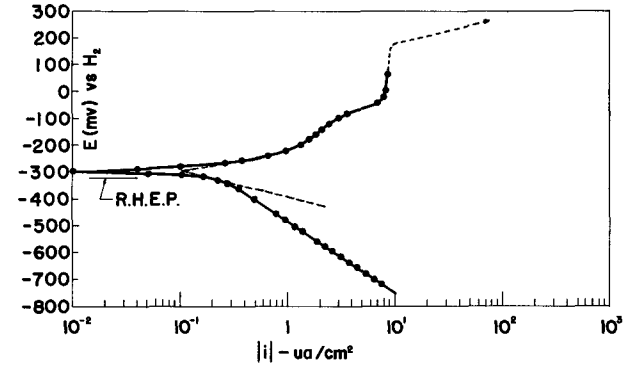

Fig. 4. Anodic and cathodic polarization curves of duplex nickel and ordinary chromium over low-carbon steel in 3% NaCl (pH = 5.5). Rotation @ 200 rpm and bubbling argon.

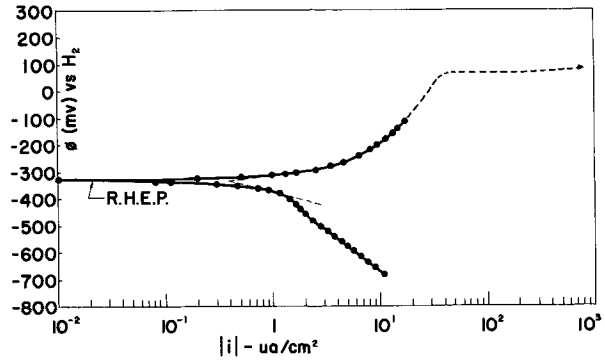

Fig. 5. Anodic and cathodic polarization curves of duplex nickel and microcracked chromium over low-carbon steel in 3% NaCl (pH = 5.5). Rotation @ 200 rpm and bubbling argon.

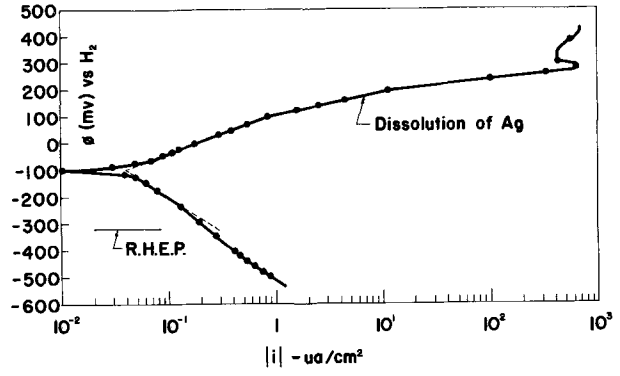

Fig. 6. Anodic and cathodic polarization curves of electroplated silver and electroless nickel and microcracked chromium over low-carbon steel in 3% NaCl (pH = 5.5). Rotation @ 200 rpm and bubbling argon.

duplex nickel. Although the open-circuit potential is comparable to that for duplex nickel (Fig. 3), the apparent corrosion rate is lower, namely 0.04 μA/cm^2 compared to 0.18 μA/cm^2. This is attributed to the greater degree of anodic and cathodic polarization. Above a potential of about +0.20V, there is a sudden increase in the anodic dissolution rate. This is due to the anodic dissolution of silver as was shown by anodic polarization of pure solid silver in the same electrolyte. The limiting current density occurring at about 1 mA/cm^2 is the result of the formation of silver chloride as was demonstrated by x-ray diffraction studies. As will be shown presently, this coating system appeared to be the most resistant to pitting corrosion.

The results of the metallographic studies conducted on these coating systems after anodic polarization to a maximum potential of +0.50V are shown in Fig. 7-10. Figure 7 shows the appearance of duplex nickel before and after anodic polarization. It is evident that complete anodic dissolution of the bright nickel has occurred with little dissolution of the semibright nickel. This result is in good agreement with that expected from the appearance of the anodic polarization curve for this coating system shown in Fig. 3. Furthermore, and more important, there is no evidence of pitting either in the semibright nickel layer or the steel basis metal. Evidently, the dissolution of bright nickel under the test conditions used occurs quite uniformly over the entire exposed surface.[2] On the other hand, the coating systems shown in Fig. 8 and 9 are apparently very susceptible to pitting corrosion. In the case of duplex nickel plus ordinary chromium anodically polarized to +0.50V (Fig. 8), corrosion due to the anodic dissolution of the duplex nickel has penetrated to the basis metal with the formation of a large hemispherical-shaped pit in the steel (far right) and a well-defined taper in the semibright nickel layer. Anodic polarization of several additional samples of this coating system to the same potential indicated that only a few (3-4) large pits are formed. Also, in the system duplex nickel plus microcracked chromium anodically polarized to the +0.30V pitting is quite evident down to the semibright nickel layer as shown in Fig. 9. As mentioned earlier, anodic polarization to +0.5V resulted in a complete separation of the chromium topcoat and corrosion penetrated to the basis metal. The pits developed electrochemically are quite similar in appearance to those developed under static conditons of corrosion (Fig. 2) and this is further confirmation of the fact that pitting corrosion in these systems is electrochemical in nature. Consequently, it appears that the addition of a chromium topcoat to duplex nickel increases the susceptibility of the coating system to pitting corrosion.

The result shown in Fig. 10 is quite striking. Corrosion appears to be restricted mainly to attack of the electroless nickel and there is some blistering or lifting of the chromium topcoat, but there is no evidence of pitting. Electroless nickel is known to be less noble than pure silver in 3% NaCl; in other words, it serves as a sacrificial coating. The anodic polarization curve for this coating system (Fig. 6) indicated that dissolution of silver also occurs, but at a small overpotential the dissolution rate is controlled by the dissolution rate of the protective film of silver chloride. Thus, the metallographic findings are in good general agreement with the electrochemical data. The results obtained with the thin layer of silver interleaved between duplex nickel and ordinary chromium were not encouraging. Nevertheless, the idea of obtaining corrosion protection through the formation of a reaction film *in situ* embodies a new principle and hitherto has received no attention in these coating systems. Additional work with an undercoat of silver is planned.

The measured corrosion currents expressed as ap-

[2] In static corrosion tests, however, indications are that duplex nickel is slightly susceptible to pitting corrosion.

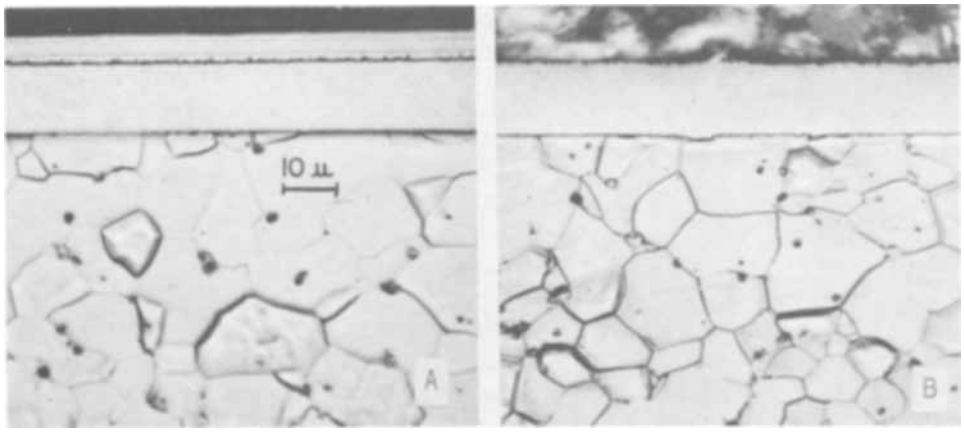

Fig. 7. Duplex nickel over low-carbon steel, (a) before, and (b) after, anodic polarization to +0.50V (vs. H_2) in 3% NaCl (pH = 5.5). Etched in 50:50 glacial acetic-nitric acid. Note the complete dissolution of the bright nickel layer and the absence of pitting.

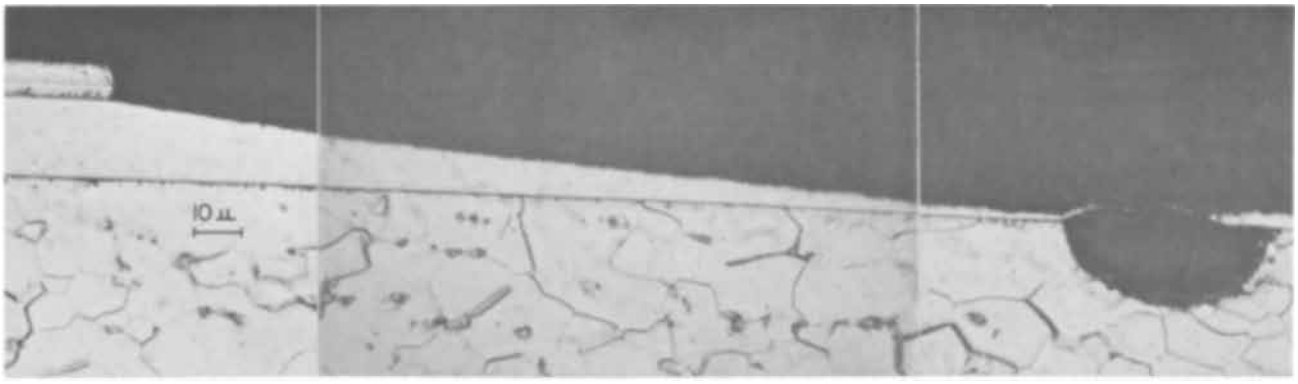

Fig. 8. Duplex nickel and ordinary chromium over low-carbon steel anodically polarized to +0.50V (vs. H_2) in 3% NaCl (pH = 5.5). Etched in 50:50 glacial acetic-nitric acid. Note the hemispherical-shaped pit at the right in the steel and the taper in the semibright nickel layer.

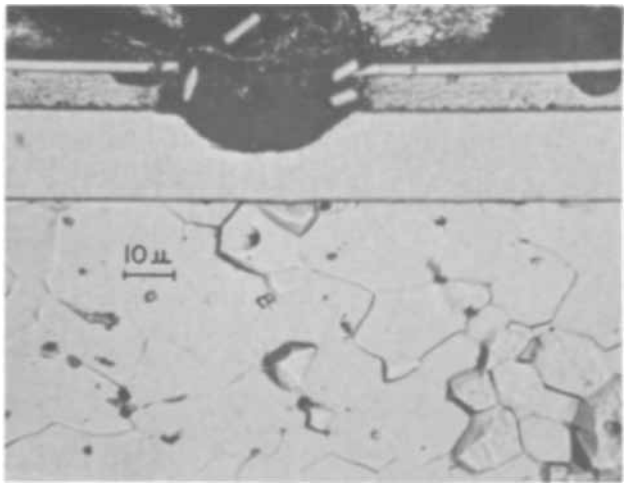

Fig. 9. Duplex nickel and microcracked chromium over low-carbon steel anodically polarized to +0.30V (vs. H_2) in 3% NaCl (pH = 5.5). Etched in 50:50 glacial acetic-nitric acid. Note the undermining of the chromium topcoat by the coalescence of pits in the bright nickel and the absence of corrosion in the chromium layer.

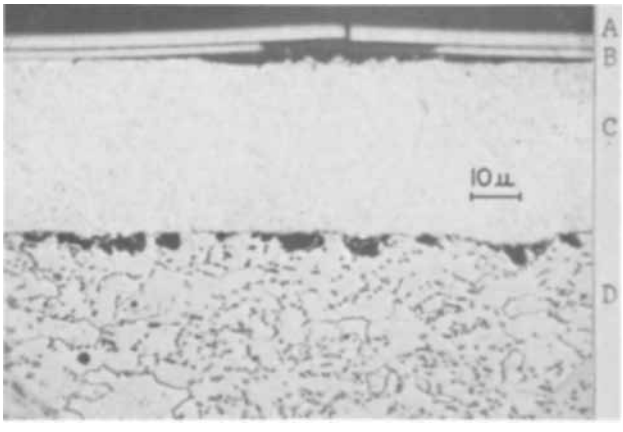

Fig. 10. Electroplated silver and electroless nickel and microcracked chromium over low-carbon steel anodically polarized to +0.50V (vs. H_2) in 3% NaCl (pH = 5.5). A—chromium, B—electroless nickel, C—silver, D—steel. Etched in 1% Nital. Note the very shallow corrosion penetration of the silver layer and the sideways attack of the electroless nickel.

parent corrosion rates in $\mu A/cm^2$ for the various coating systems investigated are summarized in Table I.

Discussion

For many years, it has been assumed that the only purpose of the chromium topcoat is to prevent tarnishing of the nickel. Chromium is known to possess good tarnish resistance as well as good resistance to "fogging" by H_2S. As shown in this study and in an earlier study (12), the addition of a topcoat of ordinary chromium reduces the dissolution rate of nickel by only a factor of about 2. The data of Saur (12) also show that, while the initial dissolution rate of nickel is linear with the area of exposed nickel, it becomes constant above an exposed nickel area of about 10%. This indicates that as the concentration of chromium defects is increased, exposing more underlying nickel, the time to basis metal corrosion should increase. Since no one has advanced an explanation as to why increasing the number of defects in the chromium layer leads to a saturation of the dissolution rate of nickel, we propose the following model to explain this behavior.

The chromium layer is considered to have a uniform surface density N of round pits of radius r, one of which is shown in Fig. 11. The dissolution of nickel occurs at the bottom of the circular hole as the result of a "local" current developed between the chromium, the nickel, and the electrolyte centered about the reentrant corner o. The electrical resistive path length (l) for both the nickel and chromium is taken to be of the same order of magnitude as the distance oo', although most of the potential drop will occur at the metal-solution interface. As corrosion proceeds as the result of nickel dissolution, the corrosion product formed (assumed to be nickelous hydroxide) is imagined to fill each circular well and even to spill over, covering a certain area a of the chromium top surface. Consequently, in order for the dissolution of nickel to continue at a steady rate, the reduced species (assumed to be oxygen) must be now supplied to the chromium cathodic surface in the vicinity of the bottom of the well by diffusion from the bulk electrolyte (surface SAS') through the "mushroom-shaped" cap. Since only mild agitation of the electrolyte is assumed, the rate-controlling step for nickel dissolution must therefore be considered to be the diffusion of oxygen.

Table I. Electrochemical corrosion currents of various protective coating systems over low-carbon steel in 3% NaCl (pH = 5.5). Rotation @ 200 rpm plus bubbling argon

Material	Apparent corrosion rate ($\mu A/cm^2$) *
Low-carbon steel	2.50
Duplex nickel over steel	0.18
Duplex nickel plus ordinary chromium over steel	0.11
Duplex nickel plus microcracked chromium over steel	0.40
Electroplated silver plus electroless nickel plus microcracked chromium over steel	0.04
Duplex nickel plus electroplated silver plus ordinary chromium over steel	0.10

* Geometrical area = 1 cm^2.

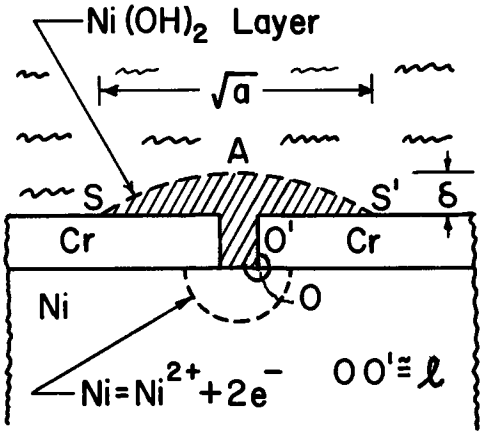

Fig. 11. Schematic representation of the corrosion of nickel in the vicinity of a circular pit in the chromium layer. As corrosion proceeds, a hemispherical pit is formed in the nickel undercoat as indicated by the dotted line.

The diffusion path length for oxygen is of the same order of magnitude as the distance δ shown in Fig. 11.

The mass rate of nickel dissolution per unit area may be written as

$$\frac{dm}{dt} = kI_p \cdot N \qquad [1]$$

where k is a constant relating the electrical current to the material current, I_p the equivalent electrical current passing through the well, and N the surface density of pits. If ρ_a, ρ_c, and ρ_e represent the resistivities of the nickel, chromium, and electrolyte, and assuming that Ohm's law is valid for small currents, the pit current, I_p, can be written as

$$I_p = \frac{E}{\frac{l}{2\pi rl} \cdot (\rho_a + \rho_c) + \rho_e \left(\frac{\delta}{a}\right)} \qquad [2]$$

where E is the potential difference between the nickel and chromium, and all other geometrical symbols are as defined in Fig. 11. The resistivity of the electrolyte ρ_e is considered here to be an equivalent electrical resistivity in our electrical analog model; in reality, it represents the diffusional resistivity of the mushroom-cap to oxygen.

When the surface area a of the mushroom-cap is less than the surface area $A = 1/N$ allocated to a pit, there is no interference between pits and the dissolution rate of nickel will increase linearly with increasing numbers of pits according to Eq. [1]. When the pit density increases to such an extent that the area a is equal to A, then the pits will begin to interfere and the resistance per pit will rise as a decreases with decreasing A. This is tantamount to saying that the current flowing from each pit (I_p) will decrease as the number of pits is increased. We represent this phenomenon by writing the area a as

$$a = \alpha\pi r^2 \qquad [3]$$

where α is a constant and equal to α_o in the noninterference region and decreases with the reciprocal of the fraction $c (c = \pi r^2/A)$ of the nickel area exposed in the interference region as shown in Fig. 12. Substitution of Eq. [2] and [3] in [1] leads to the final form for the dissolution rate equation, namely

$$\frac{dm}{dt} = \begin{cases} \dfrac{K\dfrac{c}{c_o}}{1+R} & \text{for } c/c_o \leq 1 \qquad [4a] \\ \dfrac{K\dfrac{c}{c_o}}{1+R\dfrac{c}{c_o}} & \text{for } c/c_o \geq 1 \qquad [4b] \end{cases}$$

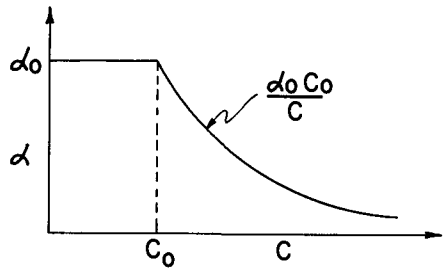

Fig. 12. Influence coefficient α as a function of fraction c of the area of nickel exposed.

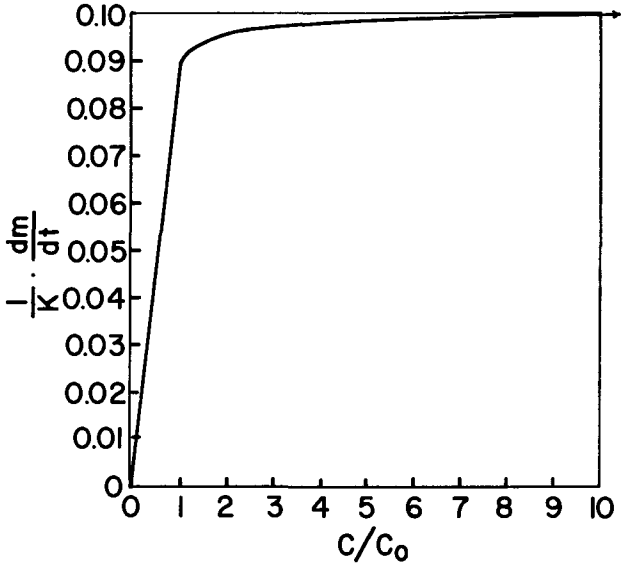

Fig. 13. Dissolution rate of nickel plotted as a function of the ratio c/c_o. Note that for c/c_o values > 1, the rate approaches the saturation value of 0.10.

where

$$K = \frac{2kEc_o}{r(\rho_a + \rho_c)}$$

$$R = \left(\frac{\rho_e}{\rho_a + \rho_c}\right) \cdot \frac{\beta}{\alpha_o}$$

and

$$\beta = \frac{\delta}{r}$$

It is assumed that the ratio $\rho_e/(\rho_a + \rho_c)$ is of order larger than 10^2, while β and α_o are of order unity and 10, respectively, making R of order larger than 10.

The dissolution rate $1/K \cdot dm/dt$ is shown plotted in Fig. 13 as a function of the ratio c/c_o[3] where R was taken equal to 10. It is seen that the rate is initially linear and rises very steeply in the range $c/c_o \leq 1$; thereafter, the rate increases much more slowly, tending to approach a steady-state value. The result appears to be in excellent agreement with the experimental data of Saur (12). Saturation of the dissolution rate is, therefore, a result of pit interference with increasing pit density N. For large N and dm/dt = constant, the product $kI_p \cdot N$ is also a constant as dictated by Eq. [1]. In other words, the pit current I_p decreases with increasing N so as to maintain essentially a constant value for their product.

An examination of Eq. [4a] and [4b] indicates the dissolution rate for a given value of the ratio c/c_o may be reduced further by minimizing the value of K and maximizing the value of R. For large c/c_o, it is easily shown that $dm/dt = K/R$. Since $K \sim 1/r$ and $R \sim 1/r$,

[3] This ratio is the ratio of the fraction of the area of nickel exposed to the fraction at the initial interference of the surface area a of each mushroom-cap shown in Fig. 11. At this instant, $c = c_o$, or $c/c_o = 1$.

the dissolution rate of nickel is independent of r and should not be affected by changes in pit size. Also, increased agitation should increase c_o because a is decreased with agitation, resulting in an increase in the value of K. This agrees with the general observation that increased agitation results in an increase in the dissolution rate of a corroding surface.

On the basis of the foregoing model, it now appears possible to explain the experimental observations. Where only a few corrosion sites are active, the "true" current density per pit (corrosion rate) is obviously much higher than in a uniformly corroding surface. Consequently, the rate of corrosion penetration of nickel should be most rapid in the former case, slowest in the latter case, and intermediate in cases where a greater number of defects exist in the chromium layer (microcracked or microporous chromium). These predictions are in reasonably good agreement with the results shown in Fig. 7 and 8, but the result obtained with the topcoat of microcracked chromium over duplex nickel (Fig. 9) was not very convincing. As mentioned earlier, anodic polarization of this coating system to +0.50V resulted in a complete separation of the chromium layer and corrosion did extend to the steel basis metal (not shown).

The addition of a topcoat of chromium to duplex nickel is also shown to increase the susceptibility of the coating system to pitting corrosion. Furthermore, the results, although limited, suggest that a "critical" potential for macro pitting may exist for these coating systems. Since the critical potential for pitting of stainless steel is known to be affected by temperature, chloride ion concentration, and the presence of other anions (9), it is no wonder that the results obtained at different test sites (Birmingham, Detroit, Kure Beach, *etc.*) are frequently in disagreement. Furthermore, the results obtained on the pitting behavior of these materials can be influenced also by the test conditions. As a case in point, no pitting was observed when duplex nickel was anodically polarized to +0.50V. Earlier investigators (11, 13), however, did observe pitting in both bright and semibright nickel. The former investigators carried out their pitting studies at a constant current density of only 2 $\mu A/cm^2$ and, as indicated in Fig. 3, the bright nickel is coated with a black film in this current density range. However, at higher current densities, the film is completely exfoliated and no pitting is observed in the semibright nickel layer (Fig. 7).

Finally, the result shown in Fig. 10 is considered remarkable in comparison to the results shown in Fig. 8 and 9 for the more conventional decorative nickel-chromium coatings. The corrosion as seen in Fig. 10 has been confined essentially to the electroless nickel layer and there has been little or no penetration of the silver layer. The low value for the corrosion current of this coating system (Table I) appears to result from the increased anodic polarization as suggested in Fig. 6. The remarkable resistance of the silver layer to penetration by corrosion may in part be attributed to the sacrificial nature of the electroless nickel layer. It is believed, however, that the main reason for the improved resistance to corrosion results from the slower dissolution rate of the protective film of silver chloride compared to that of duplex nickel. A further benefit to be accrued from the use of a silver undercoat is that the enhanced ductility of the silver would permit larger strains to be imposed on the coating system. One of the beneficial effects of the semibright nickel layer in duplex nickel is that cracks induced in the more brittle bright nickel layer by bending are arrested at the semibright/bright nickel interface (14).

Conclusions

1. The corrosion currents determined electrochemically for duplex nickel, duplex nickel plus ordinary chromium, and duplex nickel plus microcracked chromium do not differ by more than a factor of 2-4.
2. A coating system with a silver undercoat and a microcracked chromium topcoat possesses superior corrosion resistance to any of the commercial decorative nickel-chromium coatings tested under the same conditions.
3. The addition of a chromium topcoat to duplex nickel increases the susceptibility of the coating system to pitting corrosion.
4. A high density of pores of uniform size and distribution in the chromium layer should lead to increased corrosion protection of steel by nickel-chromium coatings due to a reduction in the current density per pit as the number of pores is increased.

Acknowledgments

The author would like to acknowledge the stimulating discussions with Professor A. S. Argon of the Materials Division in the Mechanical Engineering Department at Massachusetts Institute of Technology and Dr. M. S. Osman of the Exploratory Development Laboratory, United-Carr, Incorporated, concerning the formulation of a model for the pitting process. The support and kind permission of W. R. J. Brown, Director and Vice President of the Exploratory Development Laboratory, to publish this work, is greatly appreciated. The Harshaw Chemical Company kindly furnished the decorative nickel-chromium coated panels used in the present study.

Manuscript received Nov. 26, 1968. This was Paper 429 presented at the Montreal Meeting, Oct. 6-11, 1968.

Any discussion of this paper will appear in a Discussion Section to be published in the June 1970 JOURNAL.

REFERENCES

1. W. A. Wesley and B. B. Knapp, *Trans. Inst. Metal Finishing*, **31**, 267 (1954).
2. G. N. Flint and H. Melbourne, *ibid.*, **38**, 35 (1961).
3. G. N. Flint and S. H. Melbourne, in "Electrochemistry," Edited by J. A. Friend and F. Gutman, p. 399 (1963).
4. F. L. LaQue, *Trans. Inst. Metal Finishing*, **41**, 127 (1964).
5. O. Jones, *Metal Finishing J.*, **11**, 223 (1965).
6. R. H. Eshelman, *Metals Progr.*, **93**, 85 (1968).
7. H. Brown, Paper 428 presented at Electrochem. Soc. Meeting, Montreal, Oct. 6-11, 1968.
8. Ja. M. Kolotyrkin, *Corrosion*, **19** (8), 261t (1963).
9. H. P. Leckie and H. H. Uhlig, *This Journal*, **113**, 1262 (1966).
10. S. R. Maloof, "Determination of Corrosion Rates from Electrochemical Data," AFML Symposium on Corrosion, Denver, Colo., May 23, 1967.
11. V. Haspadaruk and J. V. Petrocelli, *Plating*, **48**, 479 (1961).
12. J. Saur, *ibid.*, **48**, 1310 (1961).
13. S. H. Melbourne and G. N. Flint, *Trans. Inst. Metal Finishing*, **39**, 85 (1962).
14. G. N. Flint, *ibid.*, **40**, 98 (1963).

Surface and Corrosion Characteristics of Tin-Free Steel—Chromium Type for Beverage Containers

G. G. Kamm,* A. R. Willey, and N. J. Linde

American Can Company, Research and Development, Barrington, Illinois

ABSTRACT

The new tin-free steel-chromium type (TFS-CT) materials are described which constitute a new generation of tin-free materials for can making. The steel is electroplated with a very thin film of metallic chromium approximately 0.3 x 10^{-6} in. thick which is covered by a thin layer of chromium oxide. Processes for producing TFS-CT are reviewed and the relative amounts of metallic chromium and chromium oxide are indicated for the products now available commercially. Performance requirements, bench tests for rapid evaluation of performance, and analytical techniques for measuring the amounts of chromium in the metallic and oxide layers are described. Results of electrochemical and corrosion tests are reported which indicate the relative importance of the metallic chromium and chromium oxide layers as they affect corrosion resistance.

TFS (tin-free steel) was first introduced in August 1965 for use in cemented side seam cans for beer and carbonated beverages. This required good rust resistance both before and after enameling, exceptional enamel adhesion, resistance to undercutting corrosion of enameled plate exposed to beverages, and a lustrous surface resistant to discoloration during enamel baking. These requirements, along with corrosion resistance of the base steel needed for use in cans for carbonated beverages, dictated that the TFS be a steel of the type normally used for tin plate but with a surface treatment applied instead of tin plating.

The first TFS available commercially in the United States was an electrolytic chromate-phosphate treated steel which showed promise initially for use in beer cans but was recognized as being inadequate for carbonated beverages which are more corrosive. This led to a search for improved materials.

Work in our own laboratories during 1957-1958 had shown that steel plated with a thin film of metallic chromium performed better than chromate chemically treated steel available at that time; it was also observed that chromium films 1 μin. or less in thickness were superior to heavier chromium deposits. That experience, augmented by evaluation and analyses of two commercial materials, one a chromium-plated steel with a chromate chemical post treatment (1) and another purported to be steel covered by an electrolytically deposited chromium oxide film (2), suggested that the desired performance could be obtained from steel covered by a duplex film consisting of less than 1 μin. of electroplated chromium with a thin layer of chromium oxide over the metallic chromium. This information was obtained through use of analytical and performance test techniques developed in our earlier work on chromium plating and in more recent studies of TFS materials.

The presently produced TFS-CT (tin-free steel—chromium type) is the result of those observations and subsequent cooperative work with steel producers which established that adequate performance can be obtained with metallic chromium in the range of 0.3-0.5 μin. and chromium oxide films containing 0.5-4.0 mg/ft^2 of chromium. The TFS-CT designation is applied to a number of chromium-chromium oxide treated steels, all of which meet the performance requirements outlined earlier.

Review of TFS-CT Processes and Products

Processes.—A number of papers and patents have been published (1-11) pertaining to processes for producing the chromium-chromium oxide films characteristic of TFS-CT. No attempt is made here to describe the various processes in detail; instead, they are divided into two categories, one-step and two-step, and the general differences between the two types are reviewed.

In the one-step processes (2, 5, 11), the chromium is plated from a relatively dilute solution containing less than 100g/liter of chromic acid. Plating takes place through a layer of chromium oxide which forms before chromium starts to plate (6). Reduction to metallic chromium takes place at the oxide-metal interface, forming a layer of chromium metal on the steel surface under the oxide layer. Final thickness of the oxide is controlled by regulation of solution concentration, bath temperature, and current density, particularly in the last tank of the treatment section. Plating efficiencies of around 20%, very close to those obtained with conventional chromium plating baths, are claimed for the two one-step processes being used commercially in Japan and by at least two companies in Europe.

Two-step processes are being operated by three companies in the United States (3, 4, 8). These processes differ markedly from the process originally patented (1) and used commercially in Japan as late as 1966. The early material was plated with approximately 2 μin. of metallic chromium from a conventional plating bath containing approximately 250g/liter of chromic acid. The chromium plating was followed by a dilute chromic acid rinse as a post treatment. The resultant chromium oxide layer over the relatively thick chromium deposit did not provide the same high degree of corrosion resistance achieved by the oxides on present TFS-CT materials with thinner metallic chromium films. A cathodic post treatment which produces a heavier, more corrosion resistant oxide has since been developed (9) and has been found satisfactory for TFS-CT production.

The two-step processes operated in the United States employ a chromium-plating step followed by one of several cathodic post treatments which add a stable and resistant chromium oxide over the chromium metal, in most cases considerably thicker than the natural oxide formed during plating (0.35 mg/ft^2 of Cr in the oxide). The chromium layer is only 0.3-0.5 μin. thick, but in combination with the oxide layer provides exceptional corrosion performance.

A fourth company in the United States is also producing a TFS-CT product, consisting of a 0.3-0.5 μin. layer of metallic chromium covered by a relatively thin layer of chromium oxide. The exact nature of the process, whether one-step or two-step, has not been disclosed.

Products.—The various TFS-CT materials being produced commercially are all considered equivalent on

* Electrochemical Society Active Member.

Table I. TFS-CT materials. Typical chromium and oxide weights

	Metallic chromium mg/ft²	μin.	Chromium in oxide, mg/ft²
One-step			
Product R (2)	13.4	0.8	3.5
Product S (5)	13.4	0.8	2.0
Two-step			
Product T (3)	5.0	0.3	0.8
Product U (4)	5.0	0.3	1.8
Product V (8)	5.0	0.3	1.5
Unclassified			
Product W	5.0	0.3	0.5

the basis of performance for beer and carbonated beverage cans, even though they differ somewhat with regard to metallic chromium and chromium oxide weights. Typical chromium and oxide weights for the various materials are shown in Table I.

Experience indicates that metallic chromium in the range of 0.3-0.5 μin. is desirable, with no areas less than 0.2 μin. Below 0.2 μin., the chromium layer is less continuous and results in reduced corrosion resistance. The one-step materials with 0.8 μin. show acceptable performance but, for the applications under consideration in the United States, have shown no increase in performance to justify the additional cost of the thicker chromium layer.

The chromium oxide layer is an essential part of the TFS-CT material, being equally as important as the layer of metallic chromium for providing corrosion resistance. The amount of oxide present varies from one material to another, as seen in Table I, but all seem to be equivalent in performance. Appearance may differ somewhat, with the heavier oxides giving blue or brown interference colors; however, when the plate is enameled the colors disappear, giving a lustrous gray appearance closely related to the surface finish of the steel base.

Performance Characteristics

The TFS-CT materials described in Table I were developed to meet the specific needs for use in cemented side seam beer and carbonated beverage cans. This usage required that they possess certain performance characteristics. Bench tests were established for screening of developmental materials, and some of the tests are now used for checking quality of commercial production.

Enamel adhesion.—Extremely good lap shear and peel adhesion is obtained with organic coatings applied to the TFS-CT materials. This is important in cemented side seam cans where the enamel-to-plate bond is a part of the adhesive bonding system. A peel adhesion test was devised whereby two ¾ in. wide strips of TFS-CT, enameled with epoxy-phenolic enamel and bonded in a heated press by means of a polyamide cement, are pulled in peel around a special fixture of the type shown in Fig. 1. Maximum load is recorded as the peel strength. The TFS-CT materials average over 60 lb/¾ in. width (after subtracting a 5 lb blank, *i.e.* the force required to pull unbonded 0.006 in. 2CR type L steel strips through the test fixture). In lap shear, a ¼ in. overlap bond is stronger than the 0.006 in. steel which has a tensile strength around 90,000 psi.

In addition to having excellent enamel adhesion initially, the chromium-chromium oxide surface resists undercutting attack at the enamel-plate interface when the edge of a bond is exposed to corrosive acid media. Untreated steels or steels treated with chromate, phosphate, or combinations of chromate and phosphate are attacked by media such as carbonated beverages; corrosion at the enamel-plate interface can ultimately result in complete failure of the adhesively bonded joint. The metallic chromium prevents this undercutting attack completely.

Corrosion resistance.—Rust resistance unenameled.—Resistance to rusting during shipment and storage is necessary to provide a rust-free surface for enameling.

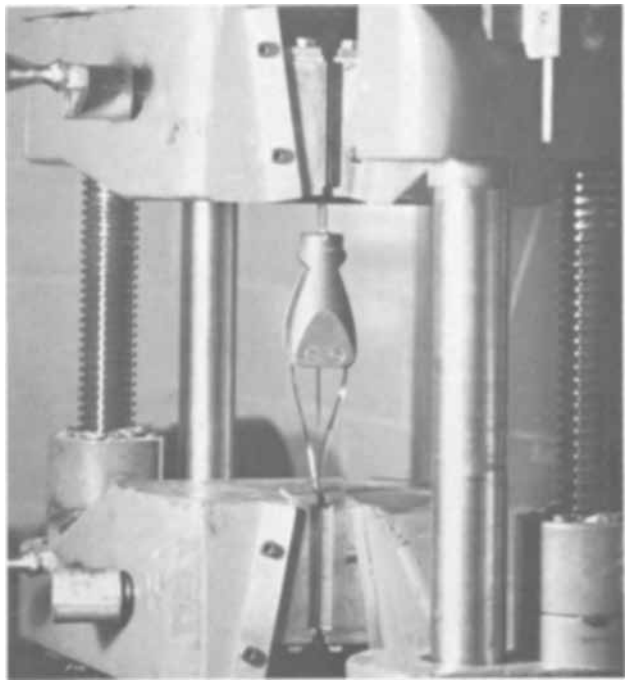

Fig. 1. Peel adhesion test fixture

A pack rust test is used to check this characteristic. It consists of stacking approximately 25 unenameled panels 6 in. x 6 in. between two pieces of ½ in. plywood and strapping the stack tightly before placing in storage at 85°F and 85% relative humidity. The pack of panels is shown in Fig. 2. One month without rusting is considered satisfactory; this is roughly equivalent to 12 months' storage in a warm, humid climate such as Houston or New Orleans. Most treated steels will meet this requirement. TFS-CT materials have passed the pack rust tests and have also undergone more than 1 yr of storage at Houston with good results.

Underfilm rusting.—Rusting after enameling is also a problem with untinned steel. Without a surface treatment on the steel, rusting may start from edges, scratches, or imperfections in the enamel, or even at areas which show no defects. This type of rust spreads under the enamel, resulting in unsightly appearance. This property can be checked by putting scribed enameled samples of the type shown in Fig. 3 in a cabinet at 85°F and 85% R.H. for 2 months. There should be no underfilm rusting at the end of 2 months under those conditions. The TFS-CT performs well in this respect, as indicated in Fig. 4. Chromate-phosphate TFS, which has no metallic chromium in the treatment layer, is far superior to the cleaned and oiled steel but is not as good as the TFS-CT. Both the

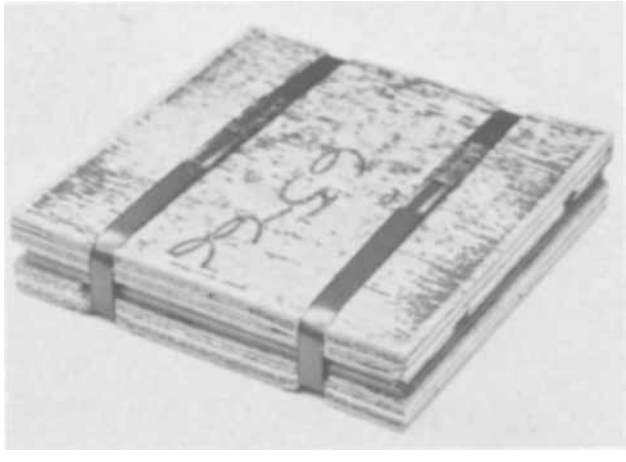

Fig. 2. Pack rust test—strapped panels

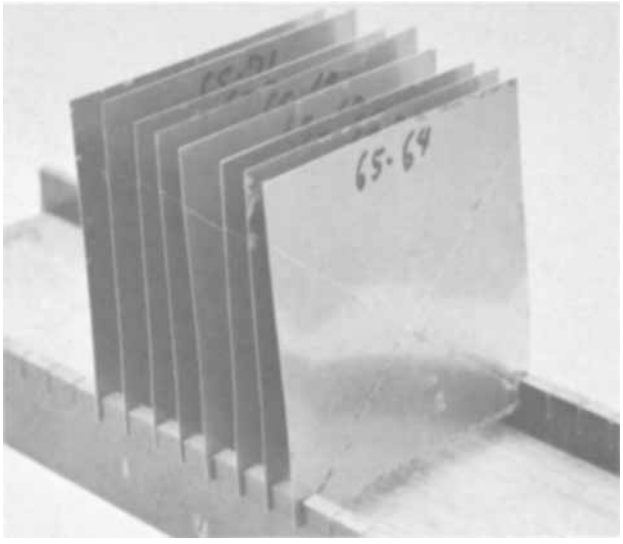

Fig. 3. Underfilm rust test panels

metallic chromium and chromium oxide of the TFS-CT are important to good performance.

Ability to resist underfilm rusting is important for the outside of can parts where possible scratches or fractures in enamel at end seams may be exposed to humid conditions during storage or chilling. A number of tests are employed for measuring rust resistance of can end seams, all of which are quite severe and not very reproducible. However, from many tests comparing TFS-CT, No. 25 electrolytic tin plate, and other TFS materials, the TFS-CT consistently ranks better than the other TFS materials and is equivalent to the No. 25 tin plate.

Undercutting resistance.—Resistance to undercutting corrosion at edges or imperfections in enameled plate is one of the most difficult requirements for a tin-free material. To test this property, scribed enameled samples are placed in a lemon-lime beverage under a CO_2 atmosphere for 2 weeks at 80°F; samples are then removed, rinsed, and dried, and then "Scotch taped" prior to examining for evidence of undercutting corrosion and enamel lifting adjacent to the scribe marks. Examples of materials after the undercutting test are seen in Fig. 5. It is apparent that the TFS-CT is far superior to cleaned and oiled steel and electrolytic chromate-phosphate treated steel, and is even slightly better than No. 25 electrolytic tin plate. Immersion for 4 days in a 1.5% sodium chloride-1.5% citric acid solution provides the same evaluation in a shorter time (3). Only TFS materials with metallic chromium on the steel surface show excellent resistance to this type of attack, a characteristic required for good performance in beer and carbonated beverage cans where undercutting could result in high iron pickup or, in some carbonated beverages, failure of cemented side seams as mentioned earlier. The chromium appears to be more important than the chromium oxide in this particular type of corrosion.

Sulfide stain resistance.—The TFS-CT materials offer exceptional resistance to staining by products containing high levels of sulfides. This is not a direct requirement for use in beer and carbonated beverage cans but results from the same combination of chromium and chromium oxide that provides good resistance to rusting before and after enameling. This stain resistance would be more important if TFS-CT were to be used in containers for meat, fish, and sulfide-containing vegetables. Figure 6 shows a comparison of No. 25 tin plate, electrolytic chromate-phosphate treated TFS, and TFS-CT, all of which were coated with the same enamel and processed as ends on cans packed with a synthetic medium known to cause severe sulfide staining. The TFS-CT is far superior to the chromate-phosphate material and is even substantially better than the electrolytic tin plate. The one completely blackened end is TFS-CT with the chromium oxide removed prior to enameling. Without the protective oxide film, a black chromium sulfide forms over the entire surface, emphasizing the need for a resistant chromium oxide layer.

Appearance.—The appearance of TFS is important to the external appearance of the finished containers. In many cases, the outside lithographed can labels utilize clear inks or varnishes to take advantage of the bright appearance of the metal underneath. Although TFS-CT is not as bright as tin plate, it does present a consistent lustrous gray appearance which has been used successfully with transparent labels. Other TFS materials present a less attractive appearance initially and some show variable tendency to turn brown during baking of enamels before can manufacture. The inconsistent and relatively unattractive surface is a problem, both under labels and in can ends, because of the effect on appearance under clear or tinted varnishes and even under solid colors unless extremely heavy coatings are applied. Some variations are seen in TFS-CT before enameling because of interference colors at certain oxide thicknesses; however, these disappear when a coating or varnish is applied to the surface.

Surface mobility.—Most TFS materials, and TFS-CT in particular, have a higher coefficient of friction than tin plate, thus requiring slightly greater surface lubrication for ease of handling before enameling. For TFS-CT, a DOS (dioctyl sebacate) level of approximately 0.27 g/BB[1] has been found adequate to allow shearing on coil lines and handling in enameling operations, without interfering with enamel wetting or integrity. This is higher than the 0.17 g/BB of DOS normally specified for tin plate but is in the range commonly found on aluminum stock for beer and carbonated beverage ends.

Even with the higher level of lubrication, the coefficient of friction of the TFS-CT surface is too high

[1] BB stands for base box, equivalent to 62,720 in.^{2} of plate surface (includes both top and bottom surfaces of 31,360 in.^{2} of plate).

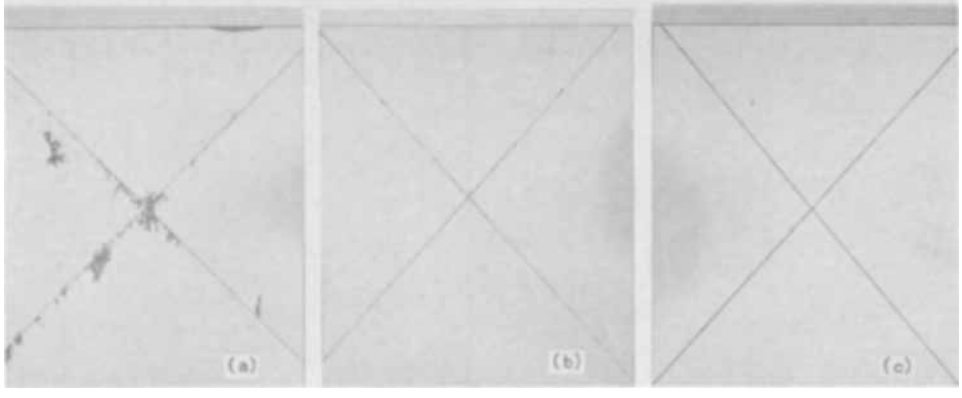

Fig. 4. Examples of underfilm rusting: (a) cleaned and oiled steel, (b) chromate-phosphate TFS, (c) TFS-CT.

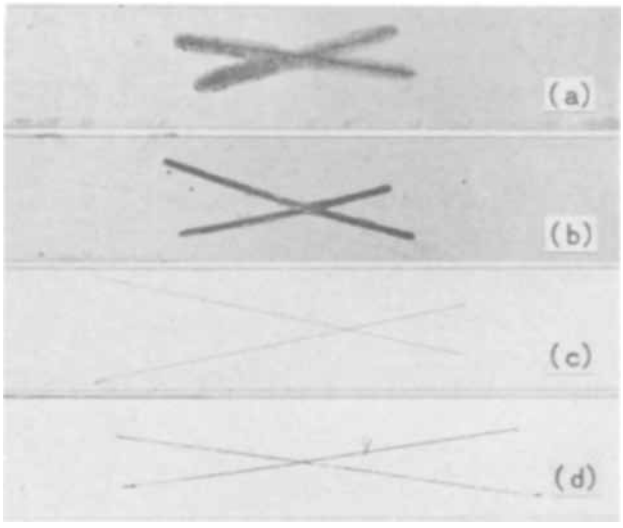

Fig. 5. Examples of undercutting corrosion: (a) cleaned and oiled steel, (b) chromate-phosphate TFS, (c) TFS-CT, (d) No. 25 tin plate.

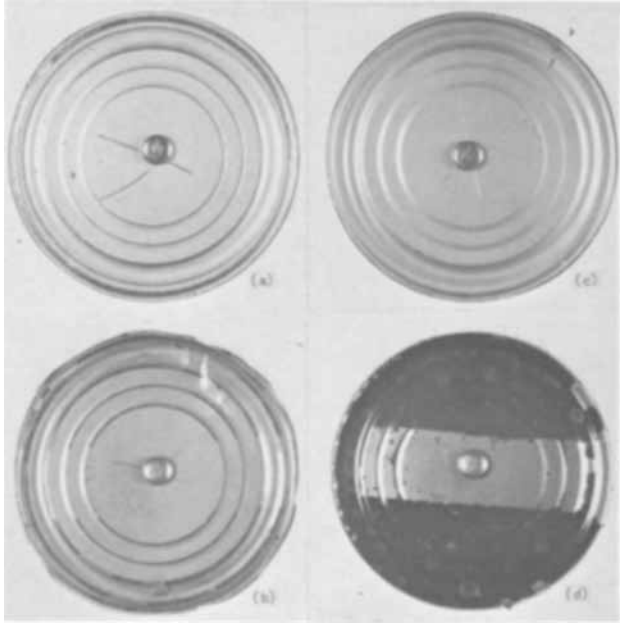

Fig. 6. Sulfide stain resistance: (a) No. 25 tin plate, (b) chromate-phosphate TFS, (c) TFS-CT, (d) TFS-CT (oxide removed).

to permit efficient fabrication of container parts from unenameled stock. Work to date indicates that both sides of the TFS-CT must be coated prior to fabrication for practical operation.

Chromium and Chromium Oxide Films

Analysis of the duplex treatment.—Considerable effort was expended in establishing suitable methods for determining chromium and oxide weights. The results are a coulometric method for determining metallic chromium and a chemical colorimetric procedure for measuring chromium in the oxide.

The oxide determination consists of stripping the entire oxide film from the plate surface by immersing for 3 min in 7.5*N* KOH at 195°F. This removes essentially all of the oxide without removing a significant amount of metallic chromium. The chromium in the stripping solution is then measured colorimetrically by the diphenylcarbazide method. The procedure is described in detail in Appendix A. Measurement of chromium in the stripping solution can also be achieved by atomic absorption techniques if desired.

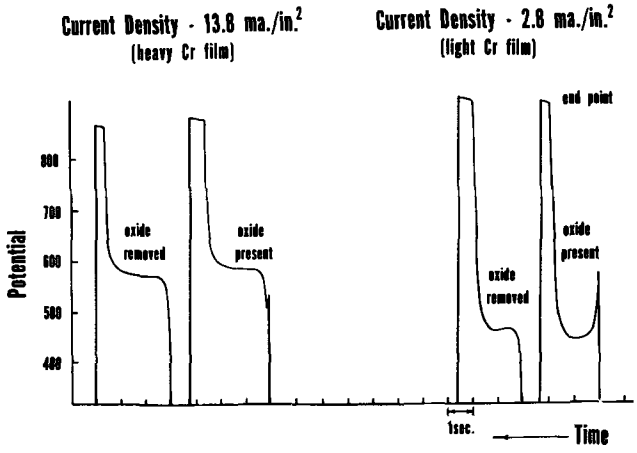

Fig. 7. Potential-time curves for coulometric determination of metallic chromium.

Metallic chromium is determined coulometrically by anodic stripping at constant current in 1*N* NaOH, using a platinum cathode and a stainless steel reference electrode. Current densities ranging from 2.8 to 13.8 ma/in.² have been used with equivalent results. The end point is determined by the potential break measured on a recording potentiometer.

For all practical purposes, the order in which chromium and oxide are measured is not important, since either can be measured first without affecting appreciably the subsequent measurement of the other. The shape of the time-potential curve in the metallic chromium determination will differ somewhat depending on whether the oxide has been removed or is still present. Typical curves are shown in Fig. 7. With the oxide present, there is a peak in the curve at the start which drops off rapidly to the dissolution potential of metallic chromium. If the oxide is removed first, there is no initial peak in the potential curve but the total coulombs measured are the same as when the oxide was not removed. Apparently the anodic treatment oxidizes only the metallic chromium and has no effect on the oxide film. The oxide remains on the steel surface and can then be removed by the hot KOH method; the amount of chromium in the oxide so determined is the same as when the oxide is removed for analysis before anodic stripping of the metallic chromium.

Peroxide should *not* be used in hot alkaline solutions for stripping the oxide film. The presence of peroxide causes attack of the metallic chromium layer which results in erroneously high values for chromium in the oxide and low values in subsequent coulometric measurement of metallic chromium.

The composition of the oxide layer appears to be somewhat variable, even for a given process. The data in Table II show the total oxide weight, weight of chromium in the oxide, and the ratio of the two. For the two-step material the ratio varied from 1.2 to 3.9, and for the one-step material from 2.9 to 6.8. Some of this variability is probably the result of inaccuracies in measuring the total weight of these very thin films by weight loss technique. However, a substantial part is believed to be real and may represent differences

Table II. Total oxide weight *vs.* weight of Cr in oxide

Material	Total oxide wt, mg/ft²	Cr in oxide, mg/ft²	Ratio Total wt/Cr wt
Two-step Lot A	2.2	1.9	1.2
Two-step Lot B	3.6	1.6	2.3
Two-step Lot C	5.4	1.7	3.2
Two-step Lot D	4.1	1.4	3.0
Two-step Lot E	9.0	2.3	3.9
One-step Lot F	16.2	3.5	4.6
One-step Lot G	10.5	3.6	2.9
One-step Lot H	14.4	2.9	5.0
One-step Lot I	11.5	1.7	6.8
One-step Lot J	12.6	3.4	3.7

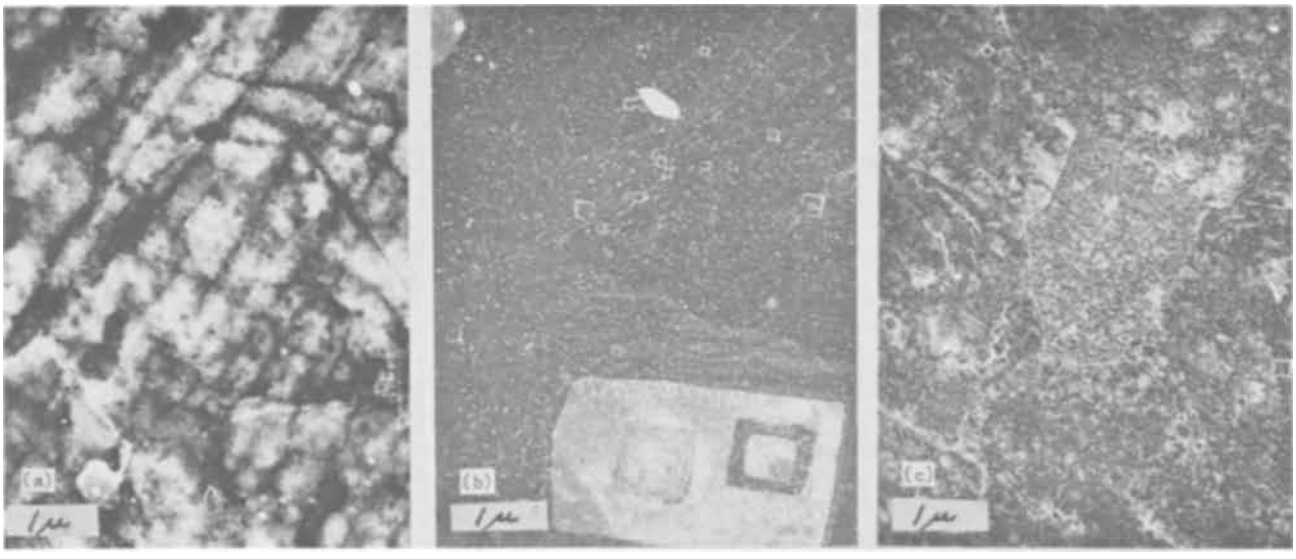

Fig. 8. Transmission electron micrographs of chromium and chromium oxide films from TFS-CT: (a) chromium and oxide, (b) chromium only, (c) oxide.

in degree of hydration of the oxide film. These variations over the range indicated have not been found to affect performance, either corrosion-wise or with regard to enamel adhesion.

The true nature of the chromium and chromium oxide films is not firmly established. Schneider *et al.* (8) have indicated that the layer of metallic chromium is relatively continuous but does require the oxide layer to provide essentially complete coverage. Carter and Lee (7) have shown optical photomicrographs of duplex chromium-chromium oxide films indicating relatively large voids in the chromium layer which are filled in by the chromium oxide layer to give continuous coverage. Our own experience with transmission electron microscopy supports the concept of a surprisingly continuous film of metallic chromium covered by a continuous layer of amorphous chromium oxide. Typical electron micrographs (transmission) are shown in Fig. 8. All transmission samples were obtained by evaporating carbon onto the surface prior to scribing in ⅛ in. squares and separation from the base steel in an alcoholic bromine solution. Figure 8a is the duplex chromium-chromium oxide film which appears to be continuous but variable in thickness or density. There is evidence of what appear to be grain boundaries suggesting epitaxial growth on the grains of the steel substrate. Figure 8b shows the metallic chromium layer with the oxide removed. Again, the layer appears continuous but with what appear to be small nodules of heavier chromium scattered over the surface. The square area and square loops have been related to etch pits in the steel base (8); the chromium appears more dense but this may only be an orientation effect. Evidence of grain boundaries of the base steel is less pronounced. Figure 8c shows the oxide film after the metallic chromium was stripped anodically from under the oxide in 1*N* NaOH. There appear to be definite differences in texture which follow the grain structure of the steel base, but the oxide appears quite continuous.

Electrochemical and corrosion studies.—Electrochemical measurements indicate that the metallic chromium layer is not completely continuous. Corrosion studies in two carbonated beverages and a fruit juice also support the idea that the chromium oxide layer plays an important role by providing protection to both the chromium layer and the areas of steel not covered by the chromium.

Potential measurements with steel, pure chromium, and steel plated with various thicknesses of metallic chromium (no post treatment) indicate that the chromium electroplate does not cover the steel base completely, leaving some active sites exposed through voids in the chromium layer. The data shown in Fig. 9 were obtained by immersing samples, masked with microcrystalline wax to expose the desired area, in cola and lemon-lime beverages (CO_2 atmosphere) and grapefruit juice (N_2 atmosphere) at 80°F and measuring potentials after 1 day against a saturated calomel electrode as a reference. The pure chromium samples included: (*a*) reagent grade electrolytic chromium, (*b*) a 100 μin. layer of electroplated chromium separated from the base steel by controlled anodic dissolution of the steel base in 1*N* H_2SO_4, and (*c*) a 10,000 μin. layer of chromium electroplated on a steel base. Although the chromium samples were activated in dilute HCl prior to immersion in the test media, they appeared to passivate after 1 day in test to give corrosion potentials considerably less negative than plain steel, the difference ranging from 100 mv in cola to 175 mv in grapefruit juice. Therefore, if the chromium layer on plated samples were continuous the potential would be that of pure chromium, and if not continuous the potential of plated samples would be expected to fall between the potentials measured for pure chromium and unplated steel. Instead, plated samples with more than 0.1 μin. of metallic chromium show potentials significantly more negative than either chromium or steel. The shape of the curves suggests that maximum coverage of the steel is attained with 0.2 μin. or more of chromium.

A possible explanation for the negative potentials of plated steel is that, during the chromium electroplating process, the chromium plates preferentially

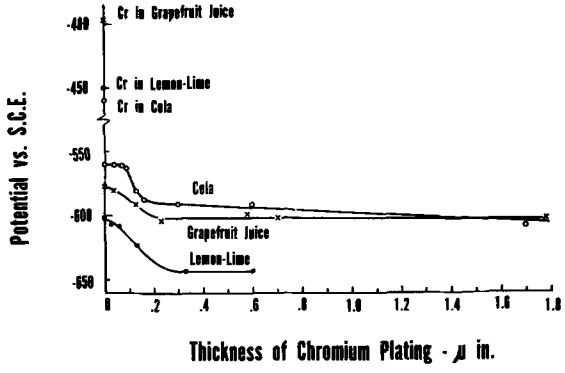

Fig. 9. Potentials of steel, chromium, and steel plated with various thicknesses of chromium, measured against a saturated calomel electrode in three acid media.

on the less negative (cathodic) areas of the steel surface, leaving the most negative (anodic) areas exposed through voids in the chromium layer. The corrosion potential of the plated steel then becomes the couple potential of the plated chromium and the steel anodes exposed through it. Because the chromium is a less efficient cathode than the original steel cathodes and polarizes more easily, the corrosion potential of the plated steel is more negative than the original steel corrosion potential as illustrated schematically in Fig. 10. This should result in either a reduction in steel corrosion rate (Fig. 10A) or essentially no change (Fig. 10B), depending on the polarization characteristics at the steel anode areas.

Corrosion studies were also conducted in cola and lemon-lime beverages to determine the effect of the chromium and oxide layers on rate of corrosion of the steel base. TFS-CT samples were tested as received, after removal of the chromium oxide layer in hot 7.5*N* KOH, and after removal of both the oxide in hot 7.5*N* KOH and the metallic chromium by anodic stripping in 1*N* NaOH. Samples masked with microcrystalline wax to cover all edges and expose an 8 cm^2 area of surface were corroded in the beverages (CO_2 atmosphere) for 96 hr at 80°F. Two samples, not in electrical contact, were immersed in each flask containing 500 ml of beverage. At the end of the test, the samples were removed, rinsed, and dried with acetone. Metallic chromium remaining on the test surfaces was measured electrolytically in 1*N* NaOH. Steel corrosion rate was determined after removal of the wax masking by comparing final weight to the weight of the samples before masking and testing. The extremely small weight loss from stripping of the metallic chromium did not affect the steel weight loss significantly. Typical data are shown in Table III.

The oxide layer contributes significantly to corrosion resistance in both cola and lemon-lime beverages by providing protection to both the metallic chromium and steel base. With the oxide present, the chromium showed no corrosion during the 96 hr test and the rate measured for the base steel was held to a low level.

With the oxide removed, the metallic chromium provides little, if any, protection to steel in cola, except in the case of the heavy 1.77 μin. plating. However, not all heavy chromium coatings showed this beneficial effect. The chromium layer also shows corrosion by the cola. On the other hand, in lemon-lime beverage the chromium is not attacked, even with the oxide removed, and the chromium alone provides appreciable protection to the base steel.

The significance of the potential and corrosion data from the unenameled samples has not been fully determined. Results indicate that the chromium is not completely continuous in the thickness applied to TFS-CT materials, but the coverage is approximately the same for thickness from 0.2 μin. on up to levels far heavier than are practical for these materials. Less than 0.2 μin. provides less coverage to the steel which should result in lower corrosion resistance. The oxide definitely adds to the corrosion resistance by reducing corrosion of both the metallic chromium and the base steel. This undoubtedly is important to good rust resistance before enameling and probably after enameling, also. It is clear that the TFS-CT would not be suitable for use in acid products without a protective coating of enamel, but the exact significance to corrosion of enameled TFS-CT in acid foods or beverages cannot be ascertained from the work reported.

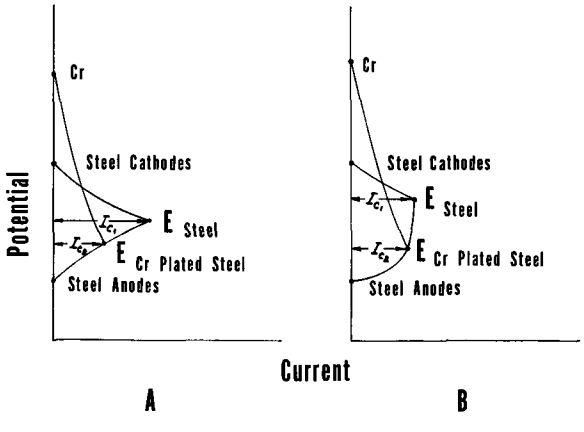

Fig. 10. Schematic potential-current diagrams illustrating (A) potential shift with reduced steel corrosion, and (B) potential shift with little or no reduction in steel corrosion, as a result of chromium plating.

Table III. Corrosion in carbonated beverages

Code	Material Condition	As received: Cr in oxide, mg/ft²	As received: Met. Cr, μin.	After test: In cola: Met. Cr, μin.	In cola: Steel corr, μA/cm²	In lemon-lime: Met. Cr, μin.	In lemon-lime: Steel corr., μA/cm²
R	As received	0.5	0.24	0.23	4.4	0.23	2.3
	Oxide removed			0.11	15.0	0.23	3.8
	Cr & oxide removed				13.7	0	7.6
S	As received	1.8	0.38	0.38	4.8	0.35	1.7
	Oxide removed			0.15	21.3	0.36	2.5
	Cr & oxide removed			0	15.2	0	6.7
T	As received	0.6	1.77	1.78	4.2	1.80	1.9
	Oxide removed			1.64	16.2	1.70	5.5
	Cr & oxide removed			0	45.6	0	10.1
U	As received	4.0	0.51	0.52	5.1	0.50	1.3
	Oxide removed			0.40	20.1	0.50	3.2
	Cr & oxide removed			0	22.8	0	10.5

The superiority of TFS-CT over other tin-free materials for beer cans was discussed by Kidder *et al.* (12). It has also been found satisfactory for use in carbonated beverage cans. Limited experience with test packs of other products indicates that, for moderate to highly corrosive acid foods, enameled TFS-CT ends combined with unenameled tin plate bodies perform very well; the tin surface apparently provides cathodic protection to any of the TFS-CT exposed. With the same products packed in fully enameled tin plate bodies, enameled TFS-CT ends are subject to rapid pitting corrosion at any enamel fractures.

Summary

TFS-CT materials are now produced by at least eight companies throughout the world. All are characterized by a layer of metallic chromium in the range of 0.2-0.8 μin. in thickness, covered by a layer of chromium oxide containing from 0.5 to 3.5 mg of Cr/ft^2. Some are produced by one-step processes and others by two-step processes, but corrosion resistance, enamel adhesion, and appearance of all are essentially equivalent.

Performance tests and analytical procedures are described which were used in cooperative work with the steel companies in establishing optimum levels of chromium and chromium oxide for performance in beer and carbonated beverage cans. The TFS-CT materials show performance superior to that of other tin-free materials in those applications and also show promise of providing excellent performance in certain food can applications where other chemically or electrochemically treated steels have been only borderline or unacceptable.

Electrochemical and corrosion studies are reported which indicate that the metallic chromium layer is not continuous, but suggest that a 0.2-0.5 μin. thickness is the most practical range for this material. It is also shown that the chromium oxide layer plays an important part in the over-all corrosion performance of TFS-CT materials.

Manuscript submitted Dec. 23, 1968; revised manuscript received May 2, 1969. This was Paper 433 presented at the Montreal Meeting, Oct. 6-11, 1968.

Any discussion of this paper will appear in a Discussion Section to be published in the June 1970 JOURNAL.

REFERENCES

1. H. Uchida and O. Yanabu, U.S. Pat. 3,113,845, Dec. 10, 1963.
2. Y. Kitamura, U.S. Pat. 2,998,361, Aug. 29, 1961.
3. E. J. Smith, *Iron Steel Engr.*, **44**, 125 (1967).
4. G. W. Ward and S. E. Rauch, Jr., "Bethlehem's Chromium-Coated Tin Mill Product," Philadelphia Regional Technical Meeting of the American Iron & Steel Institute, Nov. 1, 1967.
5. S. Yonezaki, H. Nitto, and H. Asano, U.S. Pat. 3,296,100, Jan. 3, 1967.
6. H. Okada and K. Yamamoto, Paper 207 presented at Electrochem. Soc. Meeting, Chicago, Oct. 15-19, 1967.
7. W. H. Carter and H. H. Lee, Paper 210 presented at Electrochem. Soc. Meeting, Chicago, Oct. 15-19, 1967.
8. E. J. Schneider, R. L. Martin, V. Kupsis, and S. M. Purdy, "Structure and Properties of Thin Chemically Treated Chromium Electrodeposits," 97th AIME Annual Meeting, Feb. 1968.
9. H. Uchida, O. Yanabu, T. Hada, and H. Sato, "On the Development of Chromium-Plated Steel as a Unique Variety of Tin Free Steel," Fall Meeting of the AISE, 1967.
10. S. Yonezaki, H. Nitto, M. Kamada, and H. Asano, Paper 208 presented at Electrochem. Soc. Meeting, Chicago, Oct. 15-19, 1967.
11. Y. Kitamura, T. Inui, H. Yamaguchi, and E. Shuto, U.S. Pat. 3,337,431, Aug. 22, 1967.
12. D. R. Kidder, G. G. Kamm, and A. A. Kopetz, *Proc. Am. Soc. Brewing Chemists*, p. 138 (1967).

APPENDIX A

Determination of Chromium Oxides on TFS-CT

Alkaline Stripping—Permanganate Oxidation

Reagents

A. 56g KOH dissolved in 90 ml H_2O (approx. 7.5*N*).
B. (1 + 5) H_2SO_4 (1 part conc H_2SO_4 + 5 parts H_2O).
C. Saturated $KMnO_4$.
D. Diphenylcarbazide reagent: add 0.2g diphenylcarbazide to 10 ml acetone. Next, add 10 ml 95% ethanol and 20 ml of dilute H_3PO_4 (85% H_3PO_4 diluted with an equal part of water). For the diphenylcarbazide reagent, we are currently using Eastman-Kodak No. 618 1,5-Diphenylcarbohydrazide.

Procedure

Place 20 ml of the KOH reagent in a 250 ml beaker. Immerse a 4 in.^{2} disk (dimpled) or, if only one side is to be determined, place the disk on a "vacuum-rubber stopper" and immerse in the solution. Heat near boiling for 3 min. Remove the sample and rinse, collecting the rinsings in the beaker. Dilute and add 50 ml of the H_2SO_4 reagent (B). Heat to boiling and add 2 drops of saturated $KMnO_4$. Boil for 2-3 min and add 5 drops conc HCl to decompose the permanganate. Boil for several minutes until the pink color has been replaced by a brown suspension. Cool, dilute, and transfer to a 100 ml volumetric flask. Add 3.0 ml of diphenylcarbazide reagent. Dilute to the mark and allow to stand for 15 min. Read at 540μ. The color is stable for 15 min after color is read.

Prepare standards by placing a solution of 0, 10, 20 μg, *etc.*, Cr as $K_2Cr_2O_7$ in beakers. Add the KOH, H_2SO_4, and $KMnO_4$, *etc.*, just as above. It is not necessary to include a precleaned steel disk inasmuch as the plot of absorbance *vs.* concentration will be the same whether or not the disk has been present, according to our findings.

Intergranular Corrosion of Ferritic Stainless Steels

A. P. Bond* and E. A. Lizlovs*

Research Laboratory, Climax Molybdenum Company of Michigan, Ann Arbor, Michigan

ABSTRACT

The susceptibility of both commercial and experimental ferritic stainless steels to intergranular corrosion was investigated. It was found that heating to 1700°F or higher and cooling rapidly sensitized a wide variety of ferritic steels to intergranular corrosion. The effects of Mo, Ni, Cb, and Ti additions to the steels were studied. It was found that Cb and Ti were effective in preventing intergranular corrosion in the Strauss test after high-temperature heat treatment. However, in highly oxidizing media such as boiling 65% nitric acid, titanium-containing steels could be sensitized to intergranular corrosion, while the columbium steels resisted intergranular attack even in boiling 65% nitric acid. Controlled potential polarization experiments gave results that agreed with the exposure results.

It is well known that some ferritic stainless steels are subject to intergranular corrosion after welding or improper heat treatment (1, 2). There is also evidence, although it is somewhat contradictory, that additions of titanium or columbium reduce or eliminate this problem in a manner analogous to that for austenitic stainless steels (1, 3, 4). The influence of other alloy additions on the susceptibility of ferritic stainless steels to intergranular corrosion has not been extensively investigated.

The influence of molybdenum on the intergranular corrosion of this class of steels is of particular interest since it has been shown that molybdenum has a very strong favorable effect on the resistance to general and pitting corrosion (5, 6). Nickel additions were also studied since it has been suggested that the presence of austenite at high temperature alleviates the sensitivity of nominally ferritic steels to intergranular corrosion (7); however, nickel additions to ferritic stainless steels can cause susceptibility to stress corrosion cracking in chlorides (8). Thus, nickel additions to steels of this type would probably be limited to special applications.

The present work was undertaken to investigate the effects on intergranular corrosion of additions of Mo, Ni, Ti, and Cb to ferritic stainless steels containing about 18% chromium. In addition, some information was obtained on the interaction of these alloying elements.

Experimental Procedures

Materials

This work was performed with commercially produced steels and with experimental alloys. The experi-

* Electrochemical Society Active Member.

Table I. Chemical compositions of stainless steels studied

Alloy	Chemical composition, % Cr	Mo	Ni	Cu	Si	Mn	Cb	Ti	C	N
					Experimental alloys					
1a	NA[a]	NA	0.11	—	—	—	—	—	NA	—
1b	NA	NA	0.62	—	—	—	—	—	NA	—
1c	18.53	1.95	1.08	—	—	—	—	—	0.031	—
1d	NA	NA	2.05	—	—	—	—	—	NA	—
2a	18.45	1.97	0.11	—	0.13	—	—	0.47	0.034	0.045
2b	NA	NA	NA	—	—	—	—	0.81	NA	NA
2c	NA	NA	NA	—	—	—	—	1.27	NA	NA
2d	NA	NA	NA	—	—	—	—	1.86	0.035	0.023
3a	18.79	1.97	0.57	—	—	—	—	0.91	0.032	—
3b	NA	NA	1.10	—	—	—	—	0.80	NA	—
3c	NA	NA	2.08	—	—	—	—	0.66	NA	—
3d	NA	NA	2.08	—	—	—	—	1.75	NA	—
4a	17.75	2.07	—	—	0.22	0.41	0.02	—	0.036	0.031
4b	NA	NA	—	—	NA	NA	0.13	—	NA	NA
4c	NA	NA	—	—	NA	NA	0.32	—	NA	NA
4d	NA	NA	—	—	NA	NA	0.61	—	NA	NA
4e	17.59	1.85	—	—	NA	NA	0.93	—	0.030	0.033
					Commercially prepared alloys					
5	16.30	—	0.33	0.10	0.60	0.70	—	—	0.046	—
6	16.52	0.99	0.30	0.11	0.54	0.42	—	—	0.069	—
7	17.45	1.00	0.21	—	0.47	0.49	0.47	—	0.092	0.064

[a] NA = Not analyzed, but in the range of the series.

mental alloys were produced by induction melting in an argon atmosphere. Each series was prepared using the split heat technique. In this technique, the base composition is melted and part of the melt is poured off to produce an ingot. To the balance of the melt, the required titanium or nickel additions are made and the next ingot cast. This process is repeated until the desired compositions are cast. By this procedure, the impurity levels are held nearly constant within each series. The compositions of the steels produced are shown in Table I. The steel of the base composition contained 0.11% nickel as a residual element. This level of nickel is thought to be somewhat lower than would be encountered in similar steels produced commercially.

The resulting ingots were hot forged and hot rolled to 0.76-cm-thick strips, and then cold rolled to a 0.38-cm thickness. All strips were given a 1-hr anneal at 1500°F before test specimens were prepared.

Heat treatment.—The sensitizing heat treatments at 1700°, 1900°, and 2100°F were performed in air, followed by water quenching. The simulated welds were made on specimens annealed at 1500°F, except the specimens from the 1.27% titanium steel and the 2.08% nickel-1.75% titanium steel which were annealed at 1700°F, and those from the 1.86% titanium steel which were annealed at 1900°F. Welds in the corrosion specimens were simulated by forming a molten puddle across one surface of each specimen using the TIG welding technique.

Specimen preparation.—Specimens measuring 1 by 2 in. for the 65% nitric acid test and ⅜ by 3 in. for the modified Strauss test were wet-surface ground to remove surface irregularities and polished through 3/0 dry metallographic paper. Specimen thickness was about 0.14 in. Immediately prior to testing, the specimens were washed in acetone and then in a solution of detergent in hot water, rinsed in distilled water, dipped in methanol, dried, and weighed.

Nitric acid tests.—Tests in 65% nitric acid (HNO_3) were performed according to ASTM Designation A262-64. The corrosion cells consisted of 1-liter Erlenmeyer flasks fitted with cold-finger condensers. The test specimens were immersed in 700 ml of boiling 65% HNO_3 solution for 48 hr. They were then removed, washed in distilled water, rinsed in methanol, dried, and weighed. The specimens were then exposed in fresh solution for another 48-hr period. This procedure was repeated for a total of five 48-hr periods.

Modified Strauss tests.—Modified Strauss tests (9, 10) were performed in 1-liter Erlenmeyer flasks fitted with cold-finger condensers. The specimens were suspended in vented glass cradles made from 30-ml beakers. A total of 50g of heavy copper turnings was packed around the sample in the cradle. Care was taken to ensure good electrical contact between turnings and test piece. The baskets containing the copper and the specimen were immersed in 700 ml of solution containing 16% sulfuric acid and 6% copper sulfate by weight. The test was conducted in the boiling solution for 24 hr. After exposure, the specimens were bent through 180 deg or until failure. In the case of welded specimens, the weld was at the apex of the bend. If no cracks could be detected at a magnification of 20 diam, the steel was considered to have passed the test.

Some bend tests were supplemented by measuring the electrical resistance of the specimens before and after testing. This was done by passing a constant current of about 1A through the specimen and through a standard specimen of similar material and dimensions in series with it. A potentiometer was used to measure the *IR* drop across the test specimen and across the standard specimen. Since measurements on the standard and test specimens were completed in less than 1 min, the effects of variations in current or temperature were largely eliminated by normalizing the test specimen resistance against the standard specimens.

Polarization measurements.—The polarization measurements were made with the aid of a potentiostat. Standard procedures were followed. The electrolyte was 1*N* sulfuric acid saturated with argon. The temperature was 24° ± 1°C.

Results

Effects of molybdenum.—The results of applying the modified Strauss test to the alloys containing molybdenum alloying additions are shown in Table II. Annealing at 1500°F led to a satisfactory resistance. This was true regardless of the rate of cooling from the annealing temperature. Heat treatment at 1700°F sensitized all the alloys to intergranular corrosion in the test environment.

These same alloys and heat treatments were examined using the boiling nitric acid test, as shown in Fig. 1. This test also shows that heat treatment at 1700°F sensitized all the alloys to intergranular corrosion. However, these results do show that the behavior of the steels containing 1 or 2% molybdenum is sensitive to the rate of cooling after annealing, but the steel containing no molybdenum was only slightly affected by changes in cooling rate. To ascertain whether or not the higher corrosion rates of the molybdenum steels after a slow cool represented intergranular attack, the corroded specimens were examined metallographically. Figure 2 shows a definite intergranular attack by boiling nitric acid on the furnace-cooled specimen containing 1% molybdenum. There was less preferential grain boundary attack on the air-cooled specimens, but there was enough to be clearly evident. Although the water-quenched specimen showed some nonuniformity of attack, there was no evidence of intergranular corrosion.

Table II. Results obtained from the modified Strauss test on ferritic stainless steel containing 0-2% molybdenum

Final heat treatment	Strauss test results[a] on indicated alloy: Alloy 5 (0% Mo)	Alloy 6 (1% Mo)	Alloy 1a (2% Mo)
1 hr at 1550°F, furnace cooled at 50°F/hr to 1100°F, air cooled	P	P	P
1 hr at 1500°F, air cooled			P
1 hr at 1500°F, water quenched	P	P	P
1 hr at 1700°F, water quenched	F	F	F

[a] P = No cracks visible at a magnification of 20 diam on bending the specimen through 180 deg after 24 hr of Strauss testing; F = Cracks visible at a magnification of 20 diam on bending the specimen through 180 deg after 24 hr of Strauss testing.

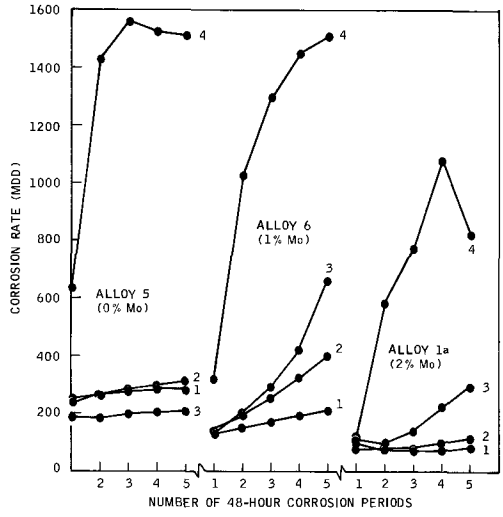

Fig. 1. Effect of heat treatment on the intergranular corrosion susceptibility in boiling 65% nitric acid 18% chromium steels containing 0-2% molybdenum: 1 = 1 hr at 1500°F, water quench; 2 = 1 hr at 1500°F, air cool; 3 = 1 hr at 1550°F, furnace cool at 50 F/hr to 1100°F, air cool; 4 = 1 hr at 1700°F, water quench.

These results suggest that the behavior of molybdenum-containing ferritic steels is analogous to that of austenitic stainless steels containing molybdenum. Under some conditions, the steels may be susceptible to intergranular corrosion only in highly oxidizing media such as boiling nitric acid, but not in less oxidizing media.

Effects of nickel.—The effect of nickel additions on the behavior of these steels in the Strauss test is shown in Table III. Nickel additions did raise the heat treatment temperature that could be tolerated without producing susceptibility to intergranular attack. However, the 2% nickel addition was insufficient to avoid sensitization by welding.

Metallographic examination of these alloys revealed that the 2% nickel alloy contained a large amount of martensite after quenching from 1900°F. The 1% nickel alloy contained only a small amount of martensite. Thus, increased resistance to intergranular corrosion was associated with the presence of austenite in the alloy at the sensitizing temperature.

Tests on a few of these combinations of alloys and heat treatments were also run in boiling nitric acid (Table IV). These results are in complete agreement with the results of the Strauss tests.

To learn how the effects of a prior sensitization could be removed, heat treatment of sensitized specimens was studied. Welding was chosen as the sensitizing treatment because it is believed to lead to the most severe susceptibility to intergranular corrosion. The results of postweld heat treatment of the nickel-containing steels are shown in Table V. In the presence of 1 or 2% nickel, a 1-hr postweld treatment at 1500°F is sufficient to alleviate the susceptibility to intergranular corrosion. The lower nickel steels required 4 hr, indicating that they were more severely sensitized by welding, but in all cases intergranular corrosion could be prevented by appropriate postweld heat treatment.

Effects of titanium.—The effect of titanium additions on the behavior of the 18% Cr-2% Mo alloys in the Strauss test was examined (Table VI). Titanium additions as small as 0.47% completely prevented intergranular corrosion in the Strauss test after all sensitizing treatments. This amount of titanium is about 14

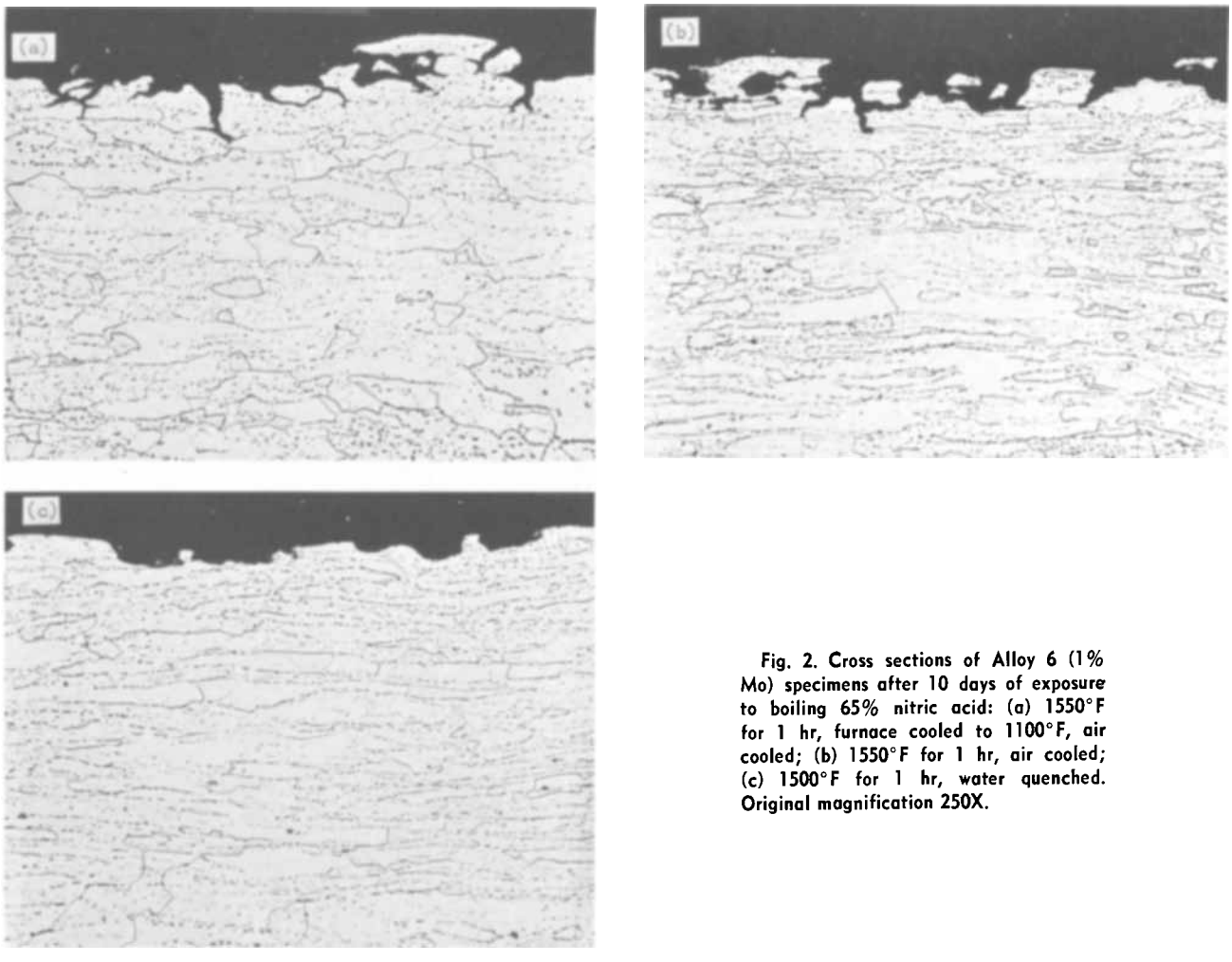

Fig. 2. Cross sections of Alloy 6 (1% Mo) specimens after 10 days of exposure to boiling 65% nitric acid: (a) 1550°F for 1 hr, furnace cooled to 1100°F, air cooled; (b) 1550°F for 1 hr, air cooled; (c) 1500°F for 1 hr, water quenched. Original magnification 250X.

Table III. Results obtained from the modified Strauss test on the 18% chromium-2% molybdenum ferritic stainless steels containing nickel

Final heat treatment	Modified Strauss test results[a] on indicated alloy: Alloy 1a (0.11% Ni)	Alloy 1b (0.62% Ni)	Alloy 1c (1.08% Ni)	Alloy 1d (2.05% Ni)
1 hr, 1500°F, water quenched	P	P	P	P
1 hr, 1700°F, water quenched	F	F	P	P
1 hr, 1900°F, water quenched		F	F	P
welded				F

[a] P = No cracks visible at a magnification of 20 diam on bending the specimen through 180 deg after 24 hr of Strauss testing; F = Cracks visible at a magnification of 20 diam on bending the specimen through 180 deg after 24 hr of Strauss testing.

Table IV. Results obtained from the boiling 65% nitric acid test on the 18% chromium-2% molybdenum ferritic stainless steels containing nickel

Alloy	Nickel content, %	Corrosion rate, mdd, of specimens in successive 48-hr periods after indicated initial treatment: 1 hr at 1500°F, water quenched	1 hr at 1700°F, water quenched	1 hr at 1900°F, water quenched
1a	0.11	98	126	
		71	588	
		74	774	
		77	1080	
		84	824	
1c	1.08			130
				349
				547
				927
				759
1d	2.05		105	102
			148	128
			178	154
			209	189
			218	204

Table V. Effect of postweld heat treatment on intergranular corrosion during the modified Strauss test of welded specimens of 18% chromium-2% molybdenum stainless steels containing nickel

Post weld treatment: Temperature, °F	Time, hr	Condition of specimen[a]: 0.11% Ni	0.62% Ni	1.08% Ni	2.05% Ni
	0				F
1500	1	F	F	P	P
1500	4	P	P		

[a] P = No cracks visible at a magnification of 20 diam on bending the specimen through 180 deg after 24 hr of Strauss testing; F = Cracks visible at a magnification of 20 diam on bending the specimen through 180 deg after 24 hr of Strauss testing.

times the weight per cent carbon or about six times the combined carbon and nitrogen content. The addition of up to 2% nickel along with the titanium had no pronounced effect on the behavior of these alloys.

It should be noted that the three alloys containing more than 1.2% titanium were brittle after the 1500°F annealing treatment, probably because titanium promoted the formation of sigma or some similar brittle second phase (11). This brittle phase could be avoided by solution treating at 1900°F and quenching in water.

Some of these alloys were also subjected to the boiling nitric acid test and quite different results were obtained after the higher-temperature heat treatments (Table VII). All the titanium-containing alloys suffered severe intergranular attack after heat treatment at 1900°F or welding. This was true whether or not nickel was also present in amounts up to 2%. Thus, titanium additions prevent intergranular corrosion in media with oxidizing potentials typified by the Cu-$CuSO_4$ couple (Strauss test) but not under the highly oxidizing conditions represented by boiling 65% nitric

Table VI. Results obtained from the modified Strauss test on the 18% chromium-2% molybdenum ferritic stainless steels containing titanium or titanium and nickel

Alloy	Titanium content, %	Nickel content, %	Condition of specimen[a] after indicated treatment: 1 hr at 1500°F, water quenched	1 hr at 1700°F, water quenched	1 hr at 1900°F, water quenched	As-welded
2a	0.47	0.11	P	P	P	P
2b	0.81	0.11	P	P	P	P
2c	1.27	0.11	C	P	P	P
2d	1.86	0.11	C	C	P	P
3a	0.91	0.57	P	P	P	P
3b	0.80	1.10	P	P	P	P
3c	0.66	2.08	P	P	P	P
3d	1.75	2.08	C	P	P	P

[a] P = No cracks visible at a magnification of 20 diam on bending the specimen through 180 deg after 24 hr of Strauss testing; C = The specimens cracked on bending prior to corrosion testing.

Table VII. Results obtained from the boiling 65% nitric acid test on the 18% chromium-2% molybdenum ferritic stainless steels containing titanium or titanium and nickel

Alloy	Titanium content, %	Nickel content, %	Corrosion rate, mdd, of specimens in successive 48-hr periods after indicated initial treatment: 1 hr at 1500°F, water quenched	1 hr at 1900°F, water quenched	As-welded
2a	0.47	0.11	72	2070	
			87	8500	
			108		
			139		
			164		
2d	1.86	0.11	112	1350	2590
			189	4000	
			245		
			265		
			320		
3a	0.91	0.57			320
					1020
3d	1.75	2.08			1670

acid. This is in accord with the observations of others (1, 12).

Effects of columbium.—Columbium, as well as titanium, is commonly used to stabilize austenitic stainless steels against intergranular corrosion. In austenitic steels, columbium is generally considered to be more effective than titanium under highly oxidizing conditions. The results obtained in the Strauss test on the series of alloys containing columbium additions are shown in Table VIII. Columbium additions of 0.61 and 0.93% were sufficient to prevent intergranular corrosion in the Strauss test even for the welded specimens. An addition of 0.32% columbium was sufficient to prevent sensitization at 1700°F but was borderline at 1900°F and ineffective at 2100°F. The alloy with 0.61% columbium has a Cb to C ratio of 17 or a Cb to (C+N) ratio of 8. Electrical resistance measurements on these specimens were less responsive to intergranular corrosion than was the bend test. This is similar to the observation of Streicher on austenitic steels (10).

Representative combinations of alloys and heat treatments were also tested in boiling nitric acid (Table IX). In marked contrast to the titanium-stabilized steels, the columbium-containing steels that passed the Strauss test also showed good resistance to intergranular corrosion in the Huey test. Even the as-welded samples containing 0.61% or more columbium were highly resistant to corrosion in this test. However, the as-welded 0.93% columbium specimen showed some preferential corrosion at the edges of the fusion zone.

Controlled potential experiments.—In addition to the standard tests for intergranular corrosion, controlled potential measurements were made on several alloys. Figure 3 shows typical results of potentiodynamic scans on a sensitized (1900°F anneal) and a nonsen-

Table VIII. Results obtained from the modified Strauss test on the 18% chromium-2% molybdenum alloys containing columbium

Alloy	Columbium content, %	Modified Strauss test results after indicated temperature of final heat treatment[a] 1700°F Bend test[b]	1700°F R_a/R_b[c]	1900°F Bend test[b]	1900°F R_a/R_b[c]	2100°F Bend test[b]	2100°F R_a/R_b[c]	As-welded Bend test[b]	As-welded R_a/R_b[c]
4a	0.02	P	1.012	F	2.08	F			
		P	1.003						
		F	1.156						
4b	0.13	F	1.018	F		F			
		P	0.994						
		F	1.162						
4c	0.32	P	0.997	F	1.002	F	1.22		
		P	0.995	P	0.985	F	1.04		
4d	0.61			P	0.998	P	0.997	P	0.976
				P	0.98	P	1.002		
4e	0.93			P	0.992			P	1.012

[a] Heat treated for 1 hr and water quenched.
[b] P = No cracks visible at a magnification of 20 diam on bending the specimen through 180 deg after 24 hr of Straus testing; F = cracks visible at a magnification of 20 diam on bending the specimen through 180 deg after 24 hr of Strauss testing.
[c] Ratio of resistance after test to resistance before test.

Table IX. Results obtained from the boiling 65% nitric acid test on 18% chromium-2% molybdenum ferritic stainless steels containing columbium

Alloy	Columbium content, %	Corrosion rate, mdd, of specimens in successive 48-hr periods after indicated initial treatment: 1 hr at 1500°F, water quenched	1 hr at 1700°F, water quenched	1 hr at 1900°F, water quenched	1 hr at 2100°F, water quenched	As-welded
4a	0.02		41			
			58			
			93			
			100			
			131			
4b	0.13		66			
			203			
			194			
			673			
			587			
4c	0.32		68	125	81	
			75	112	147	
			104	130	260	
			118	148	287	
			114	261	670	
4d	0.61	60		126	82	138
		83		116	140	130
		155		158	192	175
		155		163	236	187
		159		242	283	255
4e	0.93			105	129	139
				37	29	99
				142	150	151
				180	118	140
				306	166	192

sitized alloy (1500°F anneal). All alloys that had been sensitized to intergranular corrosion as indicated by the Strauss test results had higher currents throughout the passive region than did the corresponding alloys annealed at 1500°F. This was most pronounced at potentials of — 0.1 to 0.0V *vs.* SCE. In the active region and in the transpassive region, no difference could be detected in polarization behavior between sensitized and nonsensitized specimens.

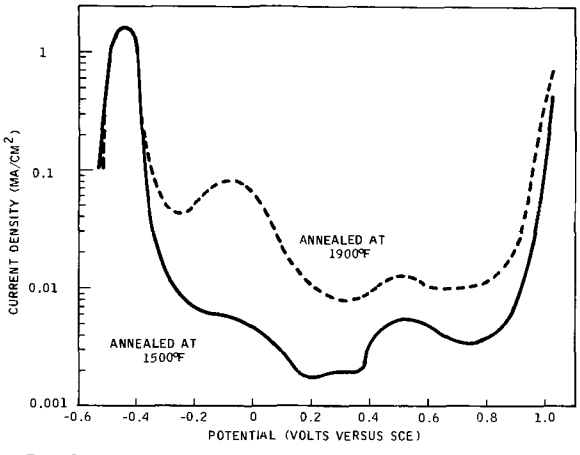

Fig. 3. Potentiodynamic polarization curves obtained at a scanning rate of 600 mV/hr in 5% sulfuric acid at 24°C on the 18% chromium-2% molybdenum alloy water quenched after a 1500° or 1900°F heat treatment.

The alloys that were stabilized by titanium additions showed identical polarization curves whether heat-treated at 1500° or 1900°F. Thus, for all alloys, the results of the Strauss test and of potentiodynamic polarization scans in 1*N* sulfuric acid were consistent. However, these polarization scans would not be used to predict the results of the boiling nitric acid test since all titanium-stabilized steels heat treated at 1900°F or higher were severely attacked by nitric acid, but showed polarization behavior identical to the unsensitized similar steels.

Some of these alloys, including Alloys 1a, 2a, 5, and 6, were subjected to potentiostatic polarization at 1.1V for 2 hr in 1*N* sulfuric acid at 24°C. These alloys were tested after annealing at 1500°F and after sensitizing at 1700° or 1900°F. In all tests, the current density was nearly the same with no correlation between heat treatment and current density. However, microscopic examination after these tests showed very clear intergranular attack on all the specimens that had been given a sensitizing heat treatment and no intergranular attack on any of the steels annealed at 1500°F and water quenched (Fig. 4). Thus, the appearance of electrodes held at 1.1V for 2 hr was in complete accord with the results of the Huey tests.

Discussion

These results show that ferritic stainless steels such as Type 430 become sensitized to intergranular corrosion when heated to 1700°F or higher. This behavior is in marked contrast to that of austenitic stainless steels, since they become sensitized only in a considerably lower temperature range. Nevertheless, there is considerable evidence that chromium depletion adjacent to chromium-rich precipitates is an important factor in causing intergranular corrosion in both classes of stainless steel (2, 13).

The differences in heat treatments leading to sensitization are a result of the differences in solubilities of carbides in ferrite and in austenite. Since the solubility of carbon in ferrite at temperatures as high as 1500°F is very low, no normal heat treatment can avoid the precipitation of carbides in ordinary ferritic stainless steels. Thus, at 1700°F, the solubility of carbides in the matrix is high enough to put a considerable amount of carbon into solution. On cooling from this temperature, the decrease in solubility results in precipitation of carbides containing a high proportion of chromium. If the cooling is moderately rapid, this causes the matrix adjacent to the carbides to be depleted of chromium and therefore susceptible to corrosion.

Most of the effects of alloying elements observed in this work are consistent with the chromium depletion mechanism. Thus, molybdenum is not a very strong carbide former and is a ferrite stabilizer, so it would not be expected to have much effect on the tendency

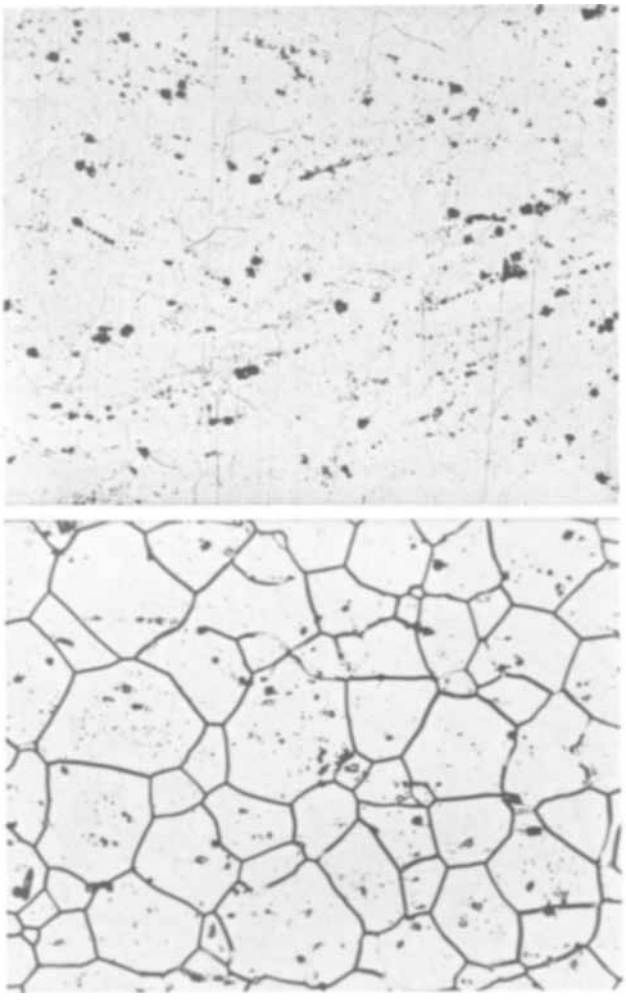

Fig. 4. Appearance of electrodes of 18% Cr-2% Mo-0.47% Ti alloy after heat treatment at 1500° or 1900°F for 2 hr and potentiostatic polarization in sulfuric acid at 1.1V *vs.* SCE: *top*—heated at 1500°F, *bottom*—heated at 1900°F. Original magnification 250X.

of a fully ferritic stainless steel to become sensitized to intergranular corrosion when heated above 1700°F.

The sensitivity to intergranular corrosion produced in molybdenum-containing steels on cooling slowly from temperatures of 1500°F or less is probably not caused by carbide precipitation. Rather, it is most probably a result of the same phenomenon as that which produces the so-called 885°F embrittlement. It has been shown that this embrittlement is the result of formation of a chromium-iron phase containing about 80% chromium (14), which either leads to local chromium depletion that causes susceptibility to preferential attack in nitric acid, or the chromium-rich phase itself is attacked by the highly oxidizing nitric acid. Evidently the function of molybdenum is to accelerate the precipitation reaction sufficiently so that it occurs when the ferritic alloys are cooled slowly through temperatures in the range of 900°F. As can be seen from Fig. 1, this form of sensitization can be eliminated by quenching from 1500°F.

The effects of nickel additions on intergranular corrosion are evidently a consequence of the tendency of nickel to promote the formation of austenite at the sensitizing temperature. This austenite will contain much of the carbon present, leaving the ferrite depleted. Consequently, a continuous chromium carbide precipitate is less likely to form at the grain boundaries. As a result, a continuous chromium-depleted region is not present for intergranular corrosion to follow. Since austenite does not form at the very high temperatures encountered in welding, the partitioning of carbon does not occur to an extent sufficient to prevent formation of continuous chromium-depleted zones. Baerlecken *et al.* (7) also found that austenite-forming alloy additions were ineffective in preventing intergranular corrosion after very high-temperature heat treatment.

On the other hand, titanium additions do prevent sensitization to intergranular corrosion even by welding, at least with respect to conditions represented by the Strauss test. Titanium carbides and possibly nitrides are formed in preference to chromium-rich precipitates so that no chromium-depleted zone is present. However, a grain boundary network of titanium carbides does form after heat treatment at 1900°F or welding. The network was severely attacked in the boiling 65% nitric acid test. The results of Bäumel (15) showed that bulk titanium carbide is attacked at oxidizing potentials corresponding to the oxidation potential of boiling nitric acid.[1] Evidently, the presence of up to 2% nickel or molybdenum has no effect on the tendency for formation of a grain boundary precipitate of titanium carbonitride that is attacked by boiling nitric acid.

The performance of columbium as a stabilizing addition was very similar to that of titanium with respect to the Strauss test results. Presumably, the mechanism leading to stabilization against intergranular attack is the same for titanium and columbium. However, columbium is also effective in reducing intergranular attack even in boiling nitric acid, which is also consistent with the work of Bäumel (15), who found that bulk columbium carbide was not attacked at oxidizing potentials up to and considerably beyond the oxidation potential of concentrated nitric acid.

Conclusion

Ferritic stainless steels containing molybdenum attain maximum resistance to intergranular corrosion in highly oxidizing media when cooled from 1500°F as rapidly as possible.

Titanium additions of about six times the combined carbon and nitrogen content, all in weight per cent, prevent intergranular corrosion as long as the corrodent medium is not strongly oxidizing.

Columbium additions of about eight times the combined carbon and nitrogen content minimize intergranular corrosion even under highly oxidizing conditions.

Nickel additions of up to 2% raised the temperature required to sensitize these steels, but provided as-welded steel with no protection against intergranular corrosion.

Manuscript submitted Jan. 20, 1969; revised manuscript received May 1, 1969. This was Paper 422 presented at the Montreal Meeting, Oct. 6-11, 1968.

Any discussion of this paper will appear in a Discussion Section to be published in the June 1970 JOURNAL.

REFERENCES

1. R. A. Lula, A. J. Lena, and G. C. Kiefer, *ASM Trans.*, **46,** 197 (1954).
2. A. Bäumel, *Arch. Eisenhüttenw.*, **34,** 135 (1963).
3. A. Bäumel, *Stahl Eisen,* **85,** 1462 (1965).
4. E. Houdremont and W. Tofaute, *ibid.*, **72,** 539 (1952).
5. E. A. Lizlovs, *Corrosion,* **22,** 297t (1966).
6. E. A. Lizlovs and A. P. Bond, *This Journal,* **116,** 574 (1969).
7. E. Baerlecken, W. A. Fischer, and K. Lorenz, *Stahl Eisen,* **81,** 768 (1961).
8. A. P. Bond and H. J. Dundas, *Corrosion,* **24,** 344 (1968).
9. L. R. Scharfstein and C. M. Eisenbrown, "Advances in the Technology of Stainless Steel and Related Alloys," Special Technical Publication 369, pp.

[1] Streicher found the potential of a platinized platinum electrode to be 1.07V against SCE in boiling 65% nitric acid. This value increased to 1.2V with time at boiling temperature (10).

235-239, American Society for Testing Materials, Philadelphia (1965).
10. M. A. Streicher, *This Journal*, **106**, 161 (1959).
11. L. Smith and K. W. S. Bowen, *J. Iron Steel Inst. (London)*, **158**, 295 (1948).
12. G. Herbsleb, *Werkstoffe Korrosion*, **19**, 406 (1968).
13. A. P. Bond, *AIME Trans.*, To be published.
14. R. M. Fisher, E. J. Dulis, and K. G. Carroll, *AIME Trans.*, **197**, 690 (1953).
15. A. Bäumel, *Stahl Eisen*, **84**, 798 (1964).

Minimizing Aluminum-to-Silicon Contact Resistance

G. McNeil

Fairchild Semiconductor, Research and Development Laboratory, Palo Alto, California

ABSTRACT

The effects of various alloy temperatures and times on aluminum-to-silicon contact resistance were determined using a special test vehicle that simulated integrated circuit processing. Contact resistance was measured to both p- and n-type doped silicon. The electrical data are summarized to show at what alloy conditions minimum contact resistance occurs.

Aluminum-to-silicon contacts have been used in integrated circuits for several years. Various alloy[1] conditions have been tried in processing, but until now no one has proved that a particular alloy cycle gives the lowest contact resistance.

In order to study the effects of various alloy conditions on contact resistance, a special test vehicle was designed. The test vehicle minimized the aluminum and silicon sheet resistances while maximizing the aluminum-to-silicon contact resistance. Figure 1 shows a cross section of the test vehicle. The test vehicle used polished silicon wafers that were subjected to typical integrated circuit diffusion and oxidation processes. An n^+-type layer simulating an emitter was diffused into p-type wafers, and a p-type diffusion representing a base was diffused into n-type wafers. After oxidation, the surface concentrations were 3 x 10^{20} cm^{-3} and 7 x 10^{18} cm^{-3}, respectively. Ten equal-sized contact holes were then etched in the oxide. The wafers received a 10-sec 10:1 HF dip before 1μ of aluminum was evaporated. The aluminum was etched so that alternate pairs of contact holes were connected by either 0.2-mil long metal or 0.6-mil long silicon, resulting in ten aluminum-silicon contacts in series. After alloying in nitrogen, the vehicle was tested with a 4-point probe (shown in Fig. 1) to avoid the problem of variable contact resistance between the probe and the wafer. A constant current of 10 mA was passed through the two outer probes and the voltage drop was measured between the two inner probes, with a Kintel high-impedance input microvoltmeter, model 202B. The shallow diffusions (0.9μ n^+ and 1.5μ p) kept the current near the surface and since, the silicon sheet resistance was much greater than that of the metal, most of the current would pass through the ten contacts.

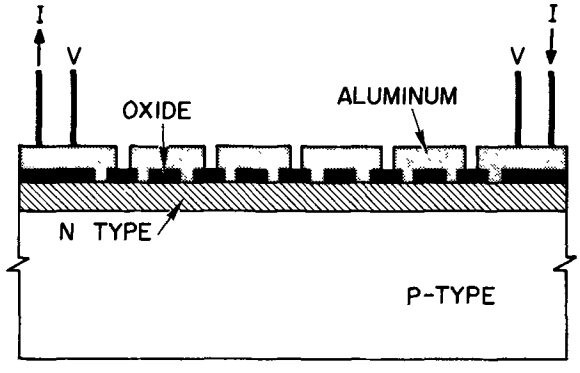

Fig. 1. Contact resistance test vehicle

Results

For each alloy condition at least 20 dice on each of three wafers were measured for each data point. The tests were repeated on a separate lot of wafers with similar results. Table I shows the effects of alloying at 500°, 550°, and 565°C on contact resistance. The numbers listed in the columns below the surface concentrations are measured resistances. The surface concentrations were measured with a 4-point probe. The measured resistance contains the silicon sheet resistance caused by the 0.6 mil between contacts, the small resistance from the aluminum, and the contact resistance of ten equal-size contacts. This is based on the assumption that all the current flows through the contacts. If this is not the case, then the actual contact resistance will be greater than indicated in this paper, but the condition of minimum contact resistance will not change. Each test pattern had three sets of contact holes. The hole size in each set was 0.2 x 0.2 mil, 0.2 x 0.8 mil, and 0.4 x 0.4 mil. Since the wafers were processed together, except for alloying, the only variable involved in the measured resistance was the contact resistance due to alloying. Therefore, any change in measured resistance corresponds to an equal change in contact resistance.

From Table I, it is obvious that two trends are present. For silicon with 7 x 10^{18} cm^{-3} p-type surface concentration, there is very little change in contact resistance when alloyed in the 500°-565°C range. However, for n^+ silicon, there is a great change in contact

[1] The term "alloy" is used in this paper as it is used in the semiconductor industry. Even though the temperature is below the silicon-aluminum eutectic, the heat treatment step to achieve a low aluminum-silicon contact resistance is referred to as an alloy.

Table I. Resistance after alloy

Alloy temperature (°C)	and time (min)	Contact size (mils)	Measured resistance (ohms) 7 x 10^{18} cm^{-3} p-type	3 x 10^{20} cm^{-3} n-type
500	5	0.2 x 0.2	105	6.2
		0.2 x 0.8	80	4.4
		0.4 x 0.4	91	5.0
500	10	0.2 x 0.2	102	7.3
		0.2 x 0.8	80	5.3
		0.4 x 0.4	90	5.9
550	5	0.2 x 0.2	104	7.4
		0.2 x 0.8	82	5.2
		0.4 x 0.4	91	5.9
550	10	0.2 x 0.2	101	7.8
		0.2 x 0.8	82	5.9
		0.4 x 0.4	93	6.7
565	5	0.2 x 0.2	105	8.3
		0.2 x 0.8	81	6.1
		0.4 x 0.4	90	7.3
565	10	0.2 x 0.2	106	10.6
		0.2 x 0.8	82	9.0
		0.4 x 0.4	93	9.9

235-239, American Society for Testing Materials, Philadelphia (1965).
10. M. A. Streicher, *This Journal*, **106**, 161 (1959).
11. L. Smith and K. W. S. Bowen, *J. Iron Steel Inst. (London)*, **158**, 295 (1948).
12. G. Herbsleb, *Werkstoffe Korrosion*, **19**, 406 (1968).
13. A. P. Bond, *AIME Trans.*, To be published.
14. R. M. Fisher, E. J. Dulis, and K. G. Carroll, *AIME Trans.*, **197**, 690 (1953).
15. A. Bäumel, *Stahl Eisen*, **84**, 798 (1964).

Minimizing Aluminum-to-Silicon Contact Resistance

G. McNeil

Fairchild Semiconductor, Research and Development Laboratory, Palo Alto, California

ABSTRACT

The effects of various alloy temperatures and times on aluminum-to-silicon contact resistance were determined using a special test vehicle that simulated integrated circuit processing. Contact resistance was measured to both p- and n-type doped silicon. The electrical data are summarized to show at what alloy conditions minimum contact resistance occurs.

Aluminum-to-silicon contacts have been used in integrated circuits for several years. Various alloy[1] conditions have been tried in processing, but until now no one has proved that a particular alloy cycle gives the lowest contact resistance.

In order to study the effects of various alloy conditions on contact resistance, a special test vehicle was designed. The test vehicle minimized the aluminum and silicon sheet resistances while maximizing the aluminum-to-silicon contact resistance. Figure 1 shows a cross section of the test vehicle. The test vehicle used polished silicon wafers that were subjected to typical integrated circuit diffusion and oxidation processes. An n^+-type layer simulating an emitter was diffused into p-type wafers, and a p-type diffusion representing a base was diffused into n-type wafers. After oxidation, the surface concentrations were 3 x 10^{20} cm^{-3} and 7 x 10^{18} cm^{-3}, respectively. Ten equal-sized contact holes were then etched in the oxide. The wafers received a 10-sec 10:1 HF dip before 1μ of aluminum was evaporated. The aluminum was etched so that alternate pairs of contact holes were connected by either 0.2-mil long metal or 0.6-mil long silicon, resulting in ten aluminum-silicon contacts in series. After alloying in nitrogen, the vehicle was tested with a 4-point probe (shown in Fig. 1) to avoid the problem of variable contact resistance between the probe and the wafer. A constant current of 10 mA was passed through the two outer probes and the voltage drop was measured between the two inner probes, with a Kintel high-impedance input microvoltmeter, model 202B. The shallow diffusions (0.9μ n^+ and 1.5μ p) kept the current near the surface and since, the silicon sheet resistance was much greater than that of the metal, most of the current would pass through the ten contacts.

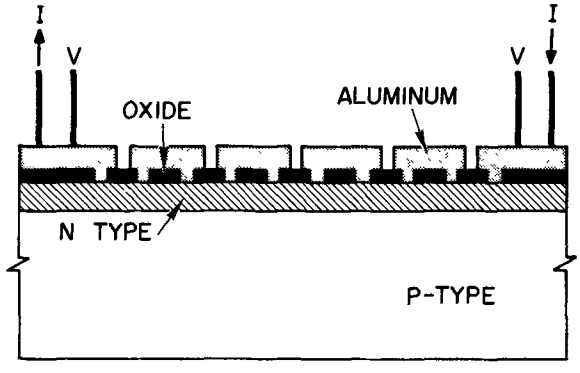

Fig. 1. Contact resistance test vehicle

Results

For each alloy condition at least 20 dice on each of three wafers were measured for each data point. The tests were repeated on a separate lot of wafers with similar results. Table I shows the effects of alloying at 500°, 550°, and 565°C on contact resistance. The numbers listed in the columns below the surface concentrations are measured resistances. The surface concentrations were measured with a 4-point probe. The measured resistance contains the silicon sheet resistance caused by the 0.6 mil between contacts, the small resistance from the aluminum, and the contact resistance of ten equal-size contacts. This is based on the assumption that all the current flows through the contacts. If this is not the case, then the actual contact resistance will be greater than indicated in this paper, but the condition of minimum contact resistance will not change. Each test pattern had three sets of contact holes. The hole size in each set was 0.2 x 0.2 mil, 0.2 x 0.8 mil, and 0.4 x 0.4 mil. Since the wafers were processed together, except for alloying, the only variable involved in the measured resistance was the contact resistance due to alloying. Therefore, any change in measured resistance corresponds to an equal change in contact resistance.

From Table I, it is obvious that two trends are present. For silicon with 7 x 10^{18} cm^{-3} p-type surface concentration, there is very little change in contact resistance when alloyed in the 500°-565°C range. However, for n^+ silicon, there is a great change in contact

[1] The term "alloy" is used in this paper as it is used in the semiconductor industry. Even though the temperature is below the silicon-aluminum eutectic, the heat treatment step to achieve a low aluminum-silicon contact resistance is referred to as an alloy.

Table I. Resistance after alloy

Alloy temperature (°C)	and time (min)	Contact size (mils)	Measured resistance (ohms) 7 x 10^{18} cm^{-3} p-type	3 x 10^{20} cm^{-3} n-type
500	5	0.2 x 0.2	105	6.2
		0.2 x 0.8	80	4.4
		0.4 x 0.4	91	5.0
500	10	0.2 x 0.2	102	7.3
		0.2 x 0.8	80	5.3
		0.4 x 0.4	90	5.9
550	5	0.2 x 0.2	104	7.4
		0.2 x 0.8	82	5.2
		0.4 x 0.4	91	5.9
550	10	0.2 x 0.2	101	7.8
		0.2 x 0.8	82	5.9
		0.4 x 0.4	93	6.7
565	5	0.2 x 0.2	105	8.3
		0.2 x 0.8	81	6.1
		0.4 x 0.4	90	7.3
565	10	0.2 x 0.2	106	10.6
		0.2 x 0.8	82	9.0
		0.4 x 0.4	93	9.9

Table II. Resistance after alloy

Alloy temperature (°C)	Alloy time* (min)	Contact size (mils)	Measured resistance (ohms) 7×10^{18} cm^{-3} p-type	Measured resistance (ohms) 3×10^{20} cm^{-3} n-type
500	5	0.2 × 0.2	105	7.2
		0.2 × 0.8	80	5.1
		0.4 × 0.4	91	5.8
480	10	0.2 × 0.2	107	6.8
		0.2 × 0.8	84	5.0
		0.4 × 0.4	95	5.8
460	10	0.2 × 0.2	110	6.5
		0.2 × 0.8	82	4.9
		0.4 × 0.4	95	5.6
440	10	0.2 × 0.2	115	6.6
		0.2 × 0.8	86	5.0
		0.4 × 0.4	97	5.8

* Furnace recovery time ≈ 4 min as measured with a thermocouple in the wafer boat.

resistance when alloyed in this temperature range. It is evident that the more severe the alloy, the greater the contact resistance. The measured resistance increases by 5 ohms going from the least severe to the most severe alloy listed in Table I. This 5-ohm increase for ten contacts corresponds to a 0.5-ohm increase in contact resistance per contact.

This sharp increase in the measured resistance might be caused by the fact that the n^+ diffusion was relatively shallow and highly conductive. At the higher alloy temperatures, the silicon-aluminum interface moves rapidly down into the silicon. Since the n^+ diffused silicon increases quickly in sheet resistance as one goes deeper into the wafer, the increased measured resistance could be due to the increased silicon sheet resistance at the metal-silicon interface. Whatever the cause, this increase in resistance means more resistance within the circuit.

Since a 5-min, 500°C alloy gave the best results in Table I, alloy temperatures below 500°C were investigated as shown in Table II. Different trends were evident below 500°C. For the 7×10^{18} cm^{-3} p-type silicon, there was an increase in contact resistance when alloyed below 500°C. But the n^+ silicon, which had such a great change in contact resistance with alloy temperature above 500°C, showed very little change in contact resistance when alloyed in the 440°-500°C range. Wafers which had not been alloyed gave considerably higher and more erratic resistances than alloyed wafers. The typical spread across three alloyed wafers for a data point was ± 4%.

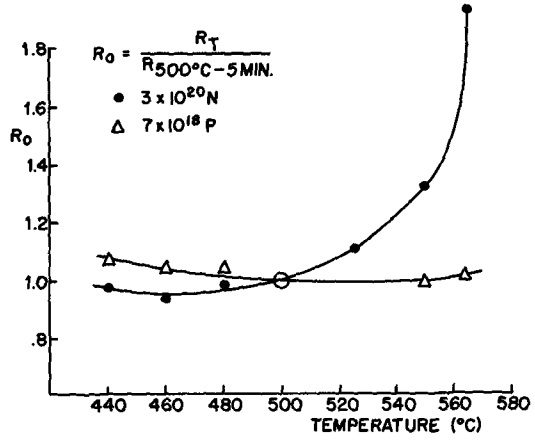

Fig. 2. Contact resistance vs. alloy temperature (10-min alloys)

Figure 2 is a plot of the data presented in Tables I and II. The basis of the normalized resistance, R_o, is the measured resistance after a 5-min, 500°C alloy, which was also the condition that gave the lowest contact resistance. The normalized resistance, R_o, equals the measured resistance after a given alloy divided by the measured resistance after a 5-min, 500°C alloy.

Conclusions

A 5-min, 500°C alloy gives the lowest contact resistance of aluminum to 7×10^{18} cm^{-3} p-type and 3×10^{20} cm^{-3} n-type silicon. Alloy conditions above 500°C greatly increase the contact resistance to n^+ diffused silicon. After punching through the film in the contact holes, overalloying will be quite damaging because it actually increases contact resistance.

Manuscript submitted Oct. 24, 1968; revised manuscript received April 3, 1969.

Any discussion of this paper will appear in a Discussion Section to be published in the June 1970 JOURNAL.

Determination of Sodium in Furnace Atmospheres by Atomic Absorption Spectroscopy

T. E. Burgess and H. M. Donega

Sprague Electric Company, North Adams, Massachusetts

ABSTRACT

The extremely low sodium vapor pressures which are present in hot quartz furnace tube atmospheres have been measured by atomic absorption spectroscopy. In the system described, sodium vapor pressures are measured between 10^{-6} and 10^{-9} Torr; however, this range can be extended by simple changes in optics and/or absorption cell length. The data show that the sodium vapor pressure in a new quartz tube changes slowly during heating until the rate of sodium in-diffusing from the hot ceramic liner is balanced by the rate of sodium out-diffusing to the cooler portions of the system. If the design of the furnace tube system is such that the source of the sodium, the furnace liner, is separated by an air space from the inner quartz tube, then the equilibrium sodium vapor pressure inside this tube may be decreased at least tenfold. Foreign gas composition has little effect on the sodium vapor pressure, providing no chemical reactions occur in the system. However, the reaction of hydrogen with the quartz surface results in a marked increase in the sodium vapor pressure. The system described may be easily adapted for determination of other contaminant vapors which could be present in hot quartz furnace tube atmospheres.

The detection of trace amounts of impurities in semiconductors which adversely affect their electrical characteristics continues to be a source of problems which tax the limits of most analytical methods. Analyses for these micro amounts of contaminants require more sophisticated approaches and specialized equipment than are usually used in routine problems.

The effect of sodium contamination on the electrical properties of silicon oxide and silicon nitride films has been the subject of many investigations (1-6). The distribution of this contaminant in these films and on cleaned silicon surfaces has been studied by flame emission, radiotracer, and neutron activation analytical methods (7-11). The main source of this impurity has been suggested to be the furnace tube and liner in which oxidation and diffusion reactions occur (4).

Analysis of furnace atmospheres for contaminants such as sodium ideally should be carried out under conditions which at least approach those used during actual operation when these contaminants become a problem. This report concerns the development of an atomic absorption method whereby the vapor pressure of sodium and that of many other trace elements can be measured at high temperatures over materials such as firebrick, mullite, quartz, and other ceramics or contaminated surfaces employed in furnace tube construction or subjected to high temperatures in production processes.

Theory

Atomic absorption spectroscopy is the study of absorption of resonance lines by free atoms in the vapor phase. In the process, radiant energy is absorbed by ground state atoms, and the outer valance electrons are excited. Measurement of the absorption of radiant energy and its relation to the number of absorbing atoms is the basis for this analytical procedure.

The relationship of the concentration of free atoms in the vapor phase to the absorption of radiant energy can be represented by equations and has been thoroughly discussed by several authors (12-17). These equations, which account for the various line-broadening phenomena occurring in the absorption process, are used to arrive at the results reported here.

If a parallel light beam of intensity, I_o, and frequency, ν, is allowed to pass through an absorbing media, x centimeters long, then the transmitted light I_ν, will be given by:

$$I_\nu = I_o e^{-K_\nu x} \qquad [1]$$

where K_ν is the absorption coefficient of the gas at frequency, ν.

This basic equation is modified to correct for certain line-broadening phenomena which tend to decrease absorption and reduce sensitivity. The most important of these are Doppler and Lorentz broadening. Doppler broadening is due to the random motion of the absorbing atoms and requires that the absorption coefficient, K, be modified to include the partial pressure of the absorbing atoms. Lorentz broadening is due to the presence of the foreign gas and introduces terms depending on its composition and partial pressure.

Equation [2] is derived from Eq. [1] by incorporating corrections for Doppler and Lorentz broadening, the sodium spectrum hyperfine structure and sodium oscillator strength.

$$\frac{I}{I_o} = \tfrac{3}{8} \exp\left(-A\frac{Px}{T^{3/2}}\right) + \tfrac{5}{8} \exp\left(-B\frac{Px}{T^{3/2}}\right) \qquad [2]$$

In Eq. [2], the experimentally measured quantity, I/I_o, is related to the partial pressure of the absorbing species. This equation in addition to P, the partial pressure of the sodium atoms, includes two constants, A and B, whose values depend on temperature, molecular weight, and pressure of the foreign gas. The reader is directed to the work of Vidali (16) for the complete review of this derivation.

Figure 1 shows a series of curves obtained by solving Eq. [2] with the aid of an IBM 1130 computer for selected values of I/I_o and certain experimental parameters. This particular set of curves shows the relationship between sodium vapor pressure and transmittance at three different partial pressures of argon. Between transmittance values of 0.1 and 0.9, this relationship is nearly linear and has a reasonably small slope. Beyond these values, the sensitivity of the method drops rapidly as the slopes approach infinity. By comparing the three curves, it can be seen that the effect of a foreign gas pressure of < 200 Torr on the relationship represented by the curves is small and, in fact, below 20 Torr the effect is insignificant. Foreign gas pressures used in these experiments were easily controlled to within a few Torr.

The influence of temperature on the relationship is somewhat less than that of foreign gas pressure. In the vicinity of 1300°K where most of these measurements were made, a 200° change in temperature has about the same effect as a 200-Torr change in pressure at the 100-Torr level.

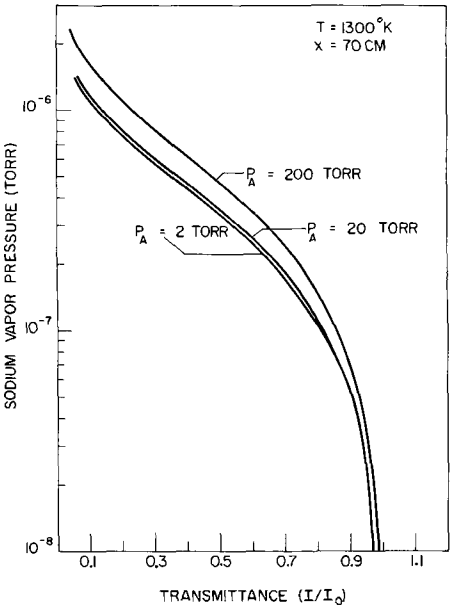

Fig. 1. Effect of foreign gas pressure on transmittance.

Since the transmittance, I/I_0, is a function of the product of the sodium vapor pressure, P, and the absorption path length, x, then any increase in this path length will increase the sensitivity of the method. For example, a change of path length from 10 to 70 cm increases the sensitivity 7 times. The curves shown in Fig. 1 were calculated for an absorption path length of 70 cm.

It is apparent from Eq. [2] that the substitution of appropriate values for the molecular weight of any foreign gas will produce curves very similar to those shown in Fig. 1. However, if the foreign gas has an influence on the ground state atom population of the absorbing element, then a corresponding influence will be observed in the transmittance. For example, oxygen would be expected to react with sodium at the temperatures used in this experiment and would reduce the ground state atom population by formation of the oxide. Although the amount of sodium in the atmosphere could remain unchanged, the sodium ground state atom population would be reduced and a corresponding decrease in absorption would be observed. Similar reactions could be expected such as reactions between foreign gases and quartz tube walls which would result in an increase in sodium vapor pressure.

If the conditions of temperature, foreign gas pressure, composition, and cell length described in Fig. 1 are met, then these curves may be used to determine the actual sodium vapor pressure existing in a tube furnace. These or similar curves calculated for the specific conditions of the experiment were used in this work.

Equipment

Measurements were made with an atomic absorption spectrophotometer which consisted of a hollow cathode light source and power supply, tube furnace, quartz furnace tube with quartz end windows, monochromator, strip chart recorder, lenses, chopper, and optical bar. A diagram of the optical system is shown in Fig. 2. Each element in the system was firmly mounted on a two-meter optical bar and a heat shield was placed between the furnace and the monochromator to reduce the effect of temperature changes on the monochromator optical system.

The light source was a Jarrell-Ash model #45-585 neon-filled hollow cathode sodium lamp which was operated from a Jarrell-Ash hollow cathode power supply. During operation, the lamp required about 30 min of warm-up before a stable source was obtained. The output from a Zeiss model M4Q III monochromator

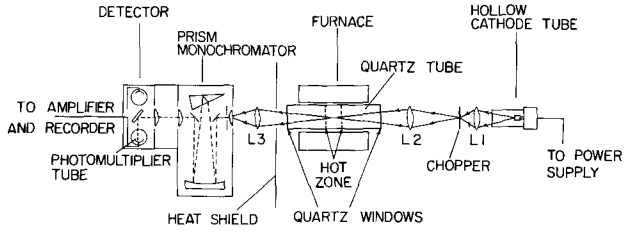

Fig. 2. Optical path diagram

and a model PMQ II indicator unit was monitored with a Sargent model SR strip chart recorder. The regular chopper in the Zeiss monochromator was disconnected for this application, and an external chopper of the same design, phase-locked to the photomultiplier a-c amplifier, was placed in the light beam between the lamp and the furnace. Only the modulated light from the hollow cathode lamp was amplified with this arrangement, and interference from stray radiation was avoided.

A 23-cm-long tube furnace with Kanthal windings on a 52-mm ID Norton Alundum-98 winding core was used as the means of producing the atomic vapor. This furnace was capable of reaching 1378°K and had a flat zone of about 5 cm at 1323° ± 5°K. The furnace temperature was controlled by a platinum-platinum 10% rhodium thermocouple connected to a Honeywell Regulator in the power supply. The temperature was regulated to within a few degrees of the setting at the upper end of the heating range. The furnace was mounted on a hinged platform which allowed it to be easily removed from the light path to permit calibration of the spectrophotometer during the heating cycle.

Two types of quartz furnace tubes fabricated from G.E. #204 quartz were used in this study. The tube shown in Fig. 2 which extended well beyond the hot zone had an outside diameter of 42 mm and an overall length of 70 cm. It was fitted with standard taper joints, fused quartz windows at each end, and an inlet for control of the foreign gas atmosphere within the furnace tube. The second tube which was designed to fit completely within the hot zone was only 5 cm long with an outside diameter of 38 mm. This tube was used to observe absorption where diffusion of the sodium vapor to cooler portions of the tube could not occur.

Results and Discussion

The system described in the preceding section allowed the sodium vapor level to be monitored in quartz furnace tubes under a variety of operating conditions.

Figure 3 shows the decrease in sodium vapor pressure in the furnace atmosphere which occurred upon extended heating of a new quartz 70 cm tube at 1323°K using a foreign gas mixture of 80% N_2 and 20% H_2 (forming gas) at 200 Torr. All the measurements were not made during one continuous heating period, but for various practical reasons three or four cooling and heating cycles were involved and actual measurements were made on three different days. Only the actual time at the selected temperature is plotted here.

The rapid decrease of the sodium vapor pressure from 16.5×10^{-8} to 7.0×10^{-8} Torr during the first 2 hr of heating is due to superficial cleaning of the quartz surface. The gradual decline in sodium vapor pressure after 2 hr of heating is caused by the approach of an equilibrium between the sodium in-diffusing from the furnace liner through the quartz tube at the hot zone and the sodium out-diffusing from the hottest area to the cooler parts of the tube. These results indicate that the preheating of new furnace tubes for several hours before their use for oxidation or other production procedures will result in a less contaminated operation.

Existence of this equilibrium is demonstrated by the fact that changes in the system, especially those

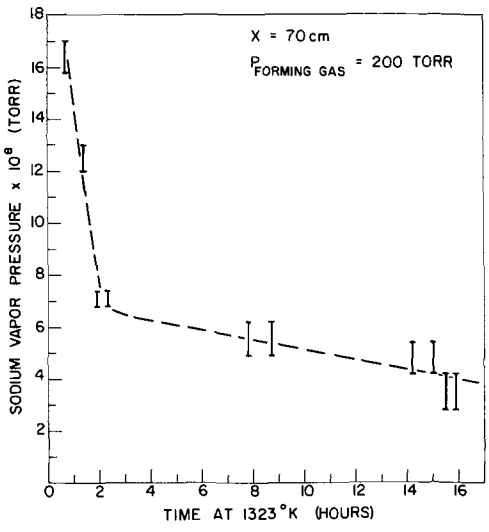

Fig. 3. Approach of equilibrium sodium vapor pressure in new quartz furnace tube.

which result in a shift of the "hot zone," are immediately reflected in the sodium vapor pressure level. For example, when the position of the quartz tube was shifted laterally 2.5 cm, the sodium vapor pressure reached after 16 hr of heating at 1323°K immediately increased from 3.5 x 10^{-8} to 5.0 x 10^{-8} Torr. Large instantaneous increases in the sodium vapor pressure occurred when rapid changes were made in the foreign gas pressure. Sodium vapor pressures as high as 10^{-6} Torr were observed at these times with a few minutes required for the sodium level to return to its equilibrium value of 10^{-8} Torr. These high sodium vapor pressures are caused by the disturbance of the equilibrium flow of sodium in the furnace atmosphere. Such temporarily high sodium levels in the furnace atmosphere could easily result in sodium contamination of products which are being treated in an otherwise "clean" system.

The influence of various furnace tube arrangements on the sodium vapor pressure within the tube is shown in Table I. These measurements were all made at 1323°K in a 200-Torr H_2 atmosphere. The equilibrium sodium vapor pressure in the 5-cm tube, fitting entirely within the hot zone with its walls touching the ceramic liner, was 7.2 x 10^{-7} Torr. The equilibrium sodium vapor pressure in this tube under the same conditions except with the quartz tube walls separated from the ceramic liner by an air space was below the detection limit of 5.2 x 10^{-8} Torr. In this case, sodium coming from the ceramic diffused from the hot portion of the furnace through the space between the ceramic and the quartz to the cooler parts of the system without penetrating the quartz walls.

The equilibrium sodium vapor pressure level in the 5-cm tube, 7.2 x 10^{-7} Torr, is much higher than that measured in the 70-cm tube, 6.4 x 10^{-8} Torr. This is contrary to what might be expected since the 70-cm tube with a larger diameter and a greater surface area in the hot zone should have favored the release of sodium into the furnace atmosphere. The results observed can be explained by the ease with which sodium inside the 70-cm tube can diffuse from the hot area to the cooler zones of the tube. In the case of the 5-cm tube, this can only occur by diffusion through the quartz end windows.

The effectiveness of a simple multiwalled tube system in lowering the sodium contamination level within the furnace was measured. The sodium vapor pressure in a 70-cm quartz furnace tube, previously contaminated with a small amount of sodium oxide, was lowered from 9.4 x 10^{-7} to 7.6 x 10^{-8} Torr by placing a second quartz tube inside the original tube, leaving a 1-mm space between the walls of the concentric tubes. This space allowed the sodium vapor to diffuse to the cooler portions of the system without penetrating into the inner furnace atmosphere.

Theoretically, for a given partial pressure of sodium, the I/I_0 observed will differ with the composition and pressure of the foreign gas. However, these effects are accounted for in Eq. [2]. If the proper values are used in its solution, the same partial pressure of sodium is obtained for each set of parameters.

Some experimentally measured equilibrium sodium vapor pressures obtained for the same 70-cm tube at 1357°K with different foreign gas compositions and pressures are shown in Table II. The same sodium vapor pressure within the precision of the measurement was observed for each of three inert gases at 2 and 200 Torr; however, in the presence of H_2, the sodium vapor pressures measured were considerably higher. These results reflect the reaction of H_2 at the quartz surface releasing sodium into the furnace atmosphere. The reaction of H_2 with a quartz surface has been previously proposed by Fewer and Gill (4).

Summary

Atomic absorption spectroscopy has been used to measure low sodium vapor concentrations present in hot quartz furnace tubes. Sodium vapor pressure measurements show that an equilibrium level is reached when the rate of sodium in-diffusing from the furnace liners through the quartz walls is equal to the rate of sodium deposition on the cooler portions of the system. In the case of a new quartz furnace tube, several hours of heating may be required before this equilibrium is established. Inert foreign gases present in the quartz tube have no effect, but chemical reactions of other gases with components in the system are possible which will change the measured sodium vapor concentration. The sodium contamination level of the furnace atmosphere may be decreased as much as tenfold by a simple multiwalled tube system.

Manuscript submitted Jan. 2, 1969; revised manuscript received May 7, 1969. This was Paper 522 presented at the Montreal Meeting, Oct. 6-11, 1968.

Any discussion of this paper will appear in a Discussion Section to be published in the June 1970 JOURNAL.

REFERENCES

1. J. Lindmayer, *Solid State Electron.*, **8**, 523 (1965).
2. E. H. Snow, A. S. Grove, B. E. Deal, and C. T. Sah, *J. Appl. Phys.*, **36**, 1664 (1965).

Table I. Effect of furnace tube arrangement on equilibrium sodium vapor pressure (1323°K, 200 Torr H_2)

Tube		P_{Na} (Torr)
Quartz, 5 cm	Tube adjacent to ceramic liner	7.2 x 10^{-7}
Quartz, 5 cm	Space between tube and ceramic liner	<5.2 x 10^{-8}
Quartz, 70 cm (uncontaminated)	Tube adjacent to ceramic liner	6.4 x 10^{-8}
Quartz, 70 cm (contaminated)	Tube adjacent to ceramic liner	9.4 x 10^{-7}
Quartz, 70 cm (contaminated)	1 mm concentric space between tube and inner quartz liner	7.6 x 10^{-8}

Table II. Sodium vapor pressures observed in the presence of inert gases and a chemically reactive gas

(1357°K, x = 70 cm)

Foreign gas	Pressure (Torr)	Transmittance (I/I_0)	P_{Na} x 10^8 (Torr)
A	2	0.959	1.7 ± 1.0
He	2	0.967	1.5 ± 1.0
N_2	2	0.947	2.5 ± 1.0
A	200	0.985	0.7 ± 1.0
He	200	0.984	0.7 ± 1.0
N_2	200	0.984	0.7 ± 1.0
H_2	2	0.579	26.0 ± 0.4
H_2	200	0.255	93.0 ± 0.1

3. F. Kooi, *Philips Res. Repts.*, **21**, 477 (1966).
4. D. R. Fewer and W. L. Gill, Texas Instrument, Inc., Technical Report No. RADC-TR-345 (1966).
5. T. E. Burgess, J. C. Baum, F. M. Fowkes, G. A. Shirn, and R. A. Holmstrom, Paper 87 presented at Electrochem. Soc. Meeting, Boston, May 5-9, 1968.
6. J. R. Mathews, W. A. Griffin, and K. H. Olson, *This Journal*, **112**, 899 (1965).
7. E. Yon, W. H. Ko, and A. B. Kuper, *IEEE Trans.*, **ED-13**, 276 (1966).
8. T. M. Buck, F. G. Allan, J. V. Dalton, and J. D. Struthers, *This Journal*, **114**, 862 (1967).
9. J. F. Osborne, G. B. Larrabee, and V. Harrap, *Anal. Chem.*, **35**, 1144 (1967).
10. J. E. Barry, H. M. Donega, and T. E. Burgess, *This Journal*, **116**, 257 (1969).
11. B. Yurash and B. E. Deal, *ibid.*, **115**, 1191 (1968).
12. A. Walsh, *Spectrochim. Acta*, **7**, 108 (1955).
13. A. C. G. Mitchell and M. W. Zermansky, "Resonance Radiation and Excited Atoms," The MacMillan Co., New York (1935).
14. E. U. Condon and G. H. Shortley, "The Theory of Atomic Spectra," Cambridge University Press, London (1951).
15. B. V. L'Vov, *Spectrochim. Acta*, **17**, 761 (1961).
16. G. L. Vidale, General Electric Co., TIS Report R60SD330.
17. J. W. Robinson, "Atomic Absorption Spectroscopy," Marcel Dekker, Inc., New York (1966).

Studies on Chlorate Cell Process

V. Theory and Practice of a Modified Technology for Electrolytic Chlorate Production

M. M. Jaksić,* A. R. Despić, I. M. Csonka,[1] and B. Z. Nikolić

Electrochemistry Department, Institute of Chemistry, Technology and Metallurgy, Beograd, Yugoslavia

ABSTRACT

A modified technology for electrolytic chlorate production has been developed. The cell is considered as a hypochlorite generator and the holding volume as a reactor for the conversion of available chlorine to chlorate. The holding volume is operated at an elevated temperature. The process as a whole then leads to higher current efficiencies. For such a closed-loop system, theoretical relationships were established between the current efficiency and other determining factors. These relationships were confirmed experimentally. Foerster's theory of electrolytic chlorate formation has also been confirmed by the present results.

Maximum current efficiency in chlorate production, according to Foerster (1, 2) is obtained when the conversion of hypochlorous acid and hypochlorite, *i.e.* the total available chlorine[2]

$$C_s = [HClO] + [ClO^-] \quad [1]$$

into chlorate occurs only by the chemical reaction

$$2HClO + ClO^- + 2H_2O \rightarrow ClO_3^- + 2Cl^- + 2H_3O^+ \quad [2]$$

However, almost unavoidably a simultaneous anodic oxidation of available chlorine to chlorate takes place, accompanied by oxygen evolution, *i.e.*

$$6ClO^- + 9H_2O \xrightarrow{6e} 2ClO_3^- + 6H_3O^+ + 4Cl^- + 3/2\,O_2 \quad [3]$$

and this represents an unnecessary loss of current.

The cathodic reduction of hypochlorite ions is also possible, but is usually eliminated by adding small amounts of dichromate to the electrolyte (3).

Let the anodic evolution of chlorine with successive hydrolysis and conversion into chlorate by reactions [2] and [3] be considered as the useful process, resulting in the current efficiency, t_1. In a closed-loop system in which the electrolyte is circulated between the cell and a holding volume (Fig. 1), the quasi steady state attained in respect to the available chlorine is characterized by the balance in the cell (*see* Appendix I):

$$V_c\left(\frac{dC_{sc}}{d\tau}\right) = \frac{(3t_1 - 2)\cdot I}{2F} - 3f_c^2 \cdot k_{r,c} \cdot V_c \cdot [HClO]_c^2 \cdot [ClO^-]_c - q(C_{sc} - C_{sh}) = 0 \quad [4]$$

where I represents the total current; f_c is the activity coefficient of hypochlorous acid; $k_{r,c}$ is the rate con-

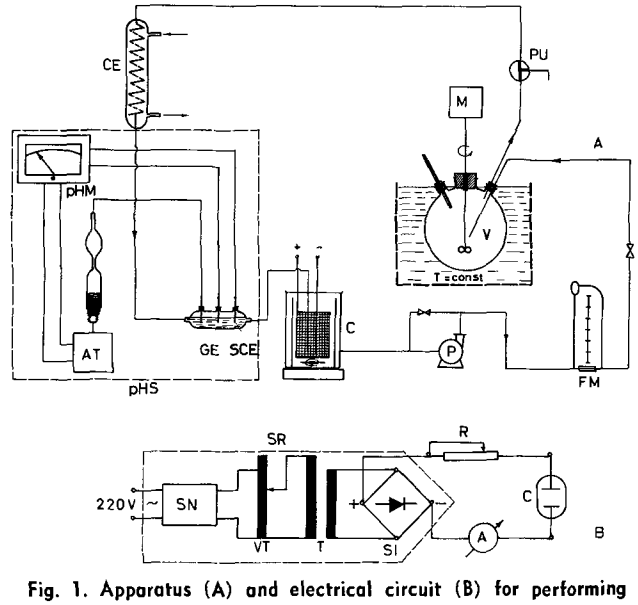

Fig. 1. Apparatus (A) and electrical circuit (B) for performing the modified process. C—the cell; V—holding volume; P—pump; CE—cooling coil; pHS—pH·Stat; FM—flow meter; SR—silicon rectifier; R—rheostat; A—ammeter.

* Electrochemical Society Active Member.
[1] Present address: "Jugovinil," Kastel Sucurac, Split, Yugoslavia.
[2] The term "available chlorine" comprises the sum of concentrations of the hypochlorite ions, hypochlorous acid, and of the molecular chlorine in solution. Under operating conditions of chlorate cells and in all our experiments, the concentration of the molecular chlorine was negligible.

stant for reaction [2]; V_c is the volume of the electrolyte in the cell; and q is the flow rate. Subscripts h and c shall refer, throughout, to the quantities relating to the holding volume and the cell, respectively.

The first term of Eq. [4] takes care of the generation of available chlorine by the current, the second term represents the chemical conversion to chlorate in the cell, while the third term represents the difference in the amount of available chlorine leaving the cell and entering the cell from the holding volume. Equation [4] assumes that the cell works as a back-mix flow reactor.

One should note that losses due to evaporation of chlorine and hypochlorous acid in the stream of the evolving hydrogen, as well as that due to cathodic reduction of available chlorine and its catalytic decomposition, are neglected.

Hence, for the usual conditions of chlorate production, the current efficiency can be obtained from Eq. [4] as

$$t_1 = \frac{2}{3} + \frac{2f_c^2 \cdot k_{r,c} \cdot V_c \cdot \mathbf{F}}{I} [HClO]_c^2 \cdot [ClO^-]_c + \frac{2}{3}\mathbf{F}\left(\frac{q}{I}\right) \cdot (C_{sc} - C_{sh}) \quad [5]$$

The concentrations of hypochlorous acid and hypochlorite ions in Eq. [4] and [5] are difficult to assess analytically. However, they can be replaced by the concentration of available chlorine. Thus, the thermodynamic dissociation constant of hypochlorous acid is

$$K_a = \frac{a_{H3O+} \cdot f_{ClO-} \cdot [ClO^-]}{f \cdot [HClO] \cdot a_{H2O}} \quad [6]$$

or, rearranging (*cf.* [7])

$$K^* = \frac{a_{H3O+} \cdot [ClO^-]}{[HClO]} = K_a \cdot \frac{f \cdot a_{H2O}}{f_{ClO^-}} \quad [7]$$

Using Eq. [7] with [1], one can find the concentrations of hypochlorous acid and introduce them into Eq. [5]. One obtains

$$t_1 = \frac{2}{3} + \frac{2f_c^2 \cdot k_{r,c} \cdot V_c \cdot \mathbf{F}}{I} \cdot \frac{K_c^* \cdot (a_{H3O+})_c^2 \cdot C_{sc}^3}{[K_c^* + (a_{H3O+})_c]^3} + \frac{2}{3}\mathbf{F} \cdot \left(\frac{q}{I}\right) \cdot (C_{sc} - C_{sh}) \quad [8]$$

Separately, and if the holding volume is considered as a back-mix flow reactor, the material balance in it renders as follows

$$q(C_{cs} - C_{sh}) = 3 \cdot f_h^2 \cdot k_{r,h} \cdot V_h \cdot [HClO]_h^2 \cdot [ClO^-]_h \quad [9]$$

From Eq. [1], [7], and [9], it follows

$$q(C_{sc} - C_{sh}) = 3f_h^2 \cdot k_{r,h} \cdot V_h \cdot \frac{K_h^* \cdot (a_{H3O+})_h^2 \cdot C_{sh}^3}{[K_h^* + (a_{H3O+})_h]^3} \quad [10]$$

Replacing this into Eq. [8], one obtains

$$t_1 = \frac{2}{3} + \frac{2f_c^2 \cdot k_{r,c} \cdot V_c \cdot \mathbf{F}}{I} \cdot \frac{K_a^* (a_{H3O+})_c^2 \cdot C_{sc}^3}{[K_c^* + (a_{H3O+})_c]^3} + \frac{2f_h^2 \cdot k_{r,h} \cdot V_h \cdot \mathbf{F}}{I} \cdot \frac{K_h^* (a_{H3O+})_h^2 \cdot C_{sh}^3}{[K_h^* + (a_{H3O+})_h]^3} \quad [11]$$

Equation [11] shows that current efficiency can be treated as dependent on the operation of two parts of the chlorate production system, *i.e.* electrolytic cell and the holding volume. So far the two parts were considered isothermal, and the temperature in industrial electrolysis was limited by the graphite corrosion wear, which increases with the latter. This has placed limits to the value of the rate constant for the chemical conversion of hypochlorite to chlorate and hence to the increase of t_1. Actual t_1 values in usual production practice are known to be about 80% (16).

In the present treatment, it is seen that an increase in t_1 can be obtained if the holding volume, as a separate unit, is heated to higher temperatures than the cell, for the usual exponential dependence of the rate constant may make the third term in Eq. [11] significantly larger.

Since this possibility of increasing the current efficiency may be of considerable practical importance, the validity of Eq. [11] and its consequences are investigated in the present work.

Experimental

The apparatus used for the experiments is shown in Fig. 1. The cell was made of hard PVC (Fig. 2). A continuous flow of the electrolyte and a magnetic stirrer provided conditions of operation of a back-mix flow reactor. The overflow mantle allowed the separation of gas bubbles from the electrolyte prior to leaving the cell. Temperature in the cell was maintained constant by circulating the thermostat liquid through a cooling coil. The majority of experiments were carried out at a cell temperature of 25°C. The *p*H value of the outflow was controlled and maintained constant to ±0.1 *p*H unit by adding acid or base from an automatic titrator. Cell volume was 600 cm³.

The flow of electrolyte was provided by means of a membrane pump made of PVC, and was controlled by a differential manometer as a flow meter.

The flow rate could be varied from 1 to 4 liters/hr.

Two different holding volumes were used, 1.0 and 2.0 liters. A stirrer was used to provide the conditions of a back-mix flow reactor. The holding volume was thermostated to temperatures of 15.0°, 25.0°, 40.0°, 60.0°, and 80.0°C.

The electrolyte was 300 gpl of NaCl and 2.4 and 8 gpl of sodium dichromate. Electrolysis was carried out to 30 gpl of sodium chlorate, whereupon the electrolyte was renewed.

*p*H values in the cell were varied between 6.0 and 8.0 and currents of 2.0, 4.5, 9.0, and 12.0A, or current densities of 2.96-17.8 A/dm^{-2} were used.

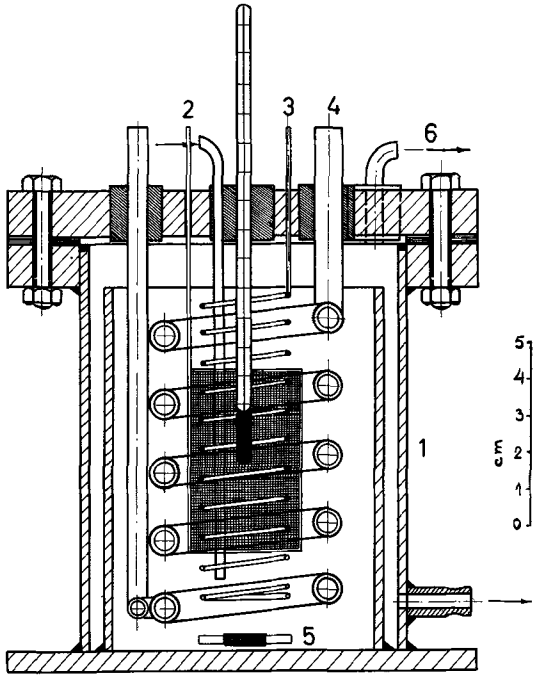

Fig. 2. Details of the electrolytic cell: 1—cell body; 2—platinum gauze anode; 3—platinum wire cathode; 4—glass cooling coil; 5—magnetic stirrer; 6—gas outflow.

Table I. Typical quasi steady-state data for electrolytic chlorate production in the closed-loop system of Fig. 1

(t_c = 25.0°C, V_c = 0.6 liter, V_h = 2.2 liter, A = 67.5 cm²)

No.	t_h, °C	pH_c	pH_h	$C_{sc} \cdot 10^2$, moles/liter	$C_{sh} \cdot 10^3$, moles/liter	t_1	$q \cdot 10^4$, liters/sec	I, amp
1	25	8.04	8.29	9.73	94.20	0.699	8.20	4.5
2	25	8.16	8.21	9.80	96.10	0.690	8.20	4.5
3	40	7.68	7.56	4.14	35.70	0.836	8.33	2.0
4	40	8.37	8.51	13.55	124.9	0.766	8.33	6.0
5	40	7.91	7.77	15.00	132.4	0.843	10.2	6.0
6	40	8.34	8.30	17.58	156.9	0.738	5.34	10.0
7	40	8.05	7.80	6.47	53.4	0.788	8.20	4.5
8	50	6.34	5.83	2.66	14.35	0.936	6.22	2.0
9	60	6.07	5.70	2.00	9.86	0.958	8.33	2.0
10	60	6.10	5.78	1.76	9.48	0.949	10.2	2.0
11	60	6.45	5.80	3.00	12.48	0.967	10.2	4.05
12	60	7.45	7.15	2.23	14.30	0.908	8.33	2.0
13	60	6.46	5.56	4.95	19.60	0.966	8.33	6.0
14	60	8.16	7.80	10.68	81.60	0.823	8.33	6.0
15	60	6.80	5.60	7.98	31.90	0.948	10.2	10.0
16	60	5.74	5.15	4.56	19.90	0.939	4.30	2.0
17	60	7.36	6.83	3.77	20.10	0.881	8.20	4.5
18	80	6.52	5.98	3.14	8.06	0.960	8.20	4.5

Platinum gauze electrode used as the anode was of 67.5 cm² of active surface area.

Several quantities were measured simultaneously: the pH, the total available chlorine of inflowing and outflowing electrolyte (C_{sc}) and (C_{sh}), respectively, and the chlorine and oxygen content in the evolving gas. The total amount of the latter was measured with time using a soap bubble flow meter [17] and the amount of hydrogen was obtained by subtracting the amounts of oxygen and chlorine. The results of such a gas analysis were used to determine the current efficiency (*see* Appendix II).

Results and Discussion

A typical set of experimental data is given in Table I.

Under conditions where the chemical conversion inside the cell can be neglected (small cell volume and low temperature relative to those of the holding volume), Eq. [8] reduces to

$$t_1 - 2/3 = 2/3 \cdot \mathbf{F} \cdot (q/I) \cdot (C_{sc} - C_{sh}) \qquad [12]$$

The left-hand side gives a measure of the chemical conversion in the holding volume. If this is plotted as a function of $(q/I) \cdot (C_{sc} - C_{sh})$, a straight line should be obtained with a slope of 2/3 · **F**. Figure 3 represents the plot of the obtained experimental data.

The points are seen to follow fairly well the expected relation over the whole range of different q and I values, as well as over the range of holding volume temperatures whose effect is implicitly contained in $(C_{sc} - C_{sh})$.

This represents an experimental confirmation of the validity of the derived Eq. [12], and essentially also an additional confirmation of the validity of the Foerster equations (1, 2). Deviations should be due mostly to the fact that in some circumstances of relatively close temperatures in the two parts of the system the chemical conversion inside the cell was not negligible. The points near to the origin correspond to high pH values and low temperatures rendering relatively low current efficiencies (*see* Table I). Conversely, upper points reflect higher temperatures and lower pH values of the holding volume.

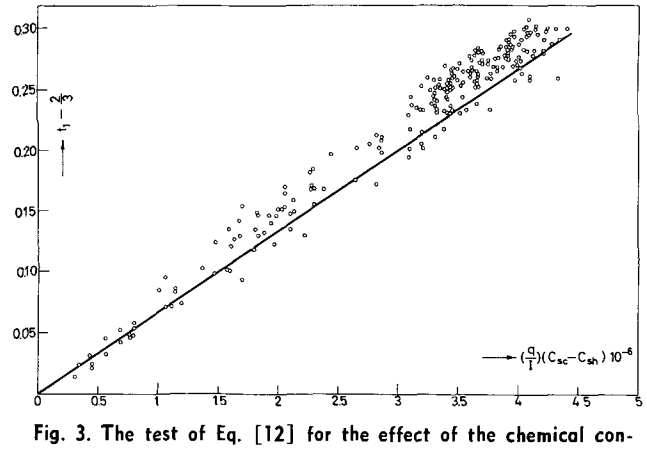

Fig. 3. The test of Eq. [12] for the effect of the chemical conversion in the holding volume. The solid line represents the theoretical slope.

The dependence of t_1 on holding volume temperature is not a straightforward one. One should have in mind that in addition to $k_{r,h}$, the effect of C_{sh} in Eq. [11] is also temperature dependent in a complex manner. This can be understood as follows. Equation [5], to which all others are related, merely reflects the Faradaic stoichiometry which determines that, the larger t_1, the higher should be the accumulation of available chlorine in the cell $(C_{sc} - C_{sh})$. However, there is an intrinsic reason, arising from the hydrodynamics of the problem (8), that the converse is true. An increasing C_{sc} decreases t_1, because of increased direct anodic oxidation of available chlorine. For this reason, although one should attempt to have $(C_{sc} - C_{sh})$ as large as possible, one should at the same time try to keep the C_{sc} as low as possible.

The C_{sc} can be lowered and yet $C_{sc} - C_{sh}$ increased if the removal of available chlorine from the cell is speeded up and at the same time the rate of conversion of available chlorine in the holding volume is increased by increasing the temperature. However, this possibility is obviously limited by two factors: (*a*) The increase in the rate of conversion with temperature must show an asymptotic tendency to some maximum value, in spite of the fact that the rate constant is increasing, because the concentration factor in the rate expression decreases with the third power; (*b*) the increase in the difference $C_{sc} - C_{sh}$ can be achieved only as long as C_{sh} is significant compared to C_{sc}.

The effect of temperature on t_1 at a constant pH in the holding volume is show in Fig. 4. It is seen to exhibit the expected asymptotic tendency toward a t_1 value determined by the hydrodynamic conditions in the cell at inflowing available chlorine concentration, C_{sh}, considerably smaller than the one generated by the cell process, C_{sc}. At large enough flow rates to make C_{sc} relatively as low as the one used in the given experiment, this value of t_1 is seen to approach unity.

When controlling the pH in the holding volume, it was found that the rates of conversion increased when pH was changed from the region of 7.0-7.5 [believed in literature to be optimal (4, 5, 6)] to the region of 6.0-6.5. This matter was discussed in detail elsewhere (7).

One should note also that our measurements show that, if a pH of 8.0 is maintained in the cell, the lowest efficiency of 66.7% is not obtained at temperatures of the holding volume other than 25°C or lower. At any higher temperatures the efficiencies are higher, since chemical conversion makes the expected contributions.

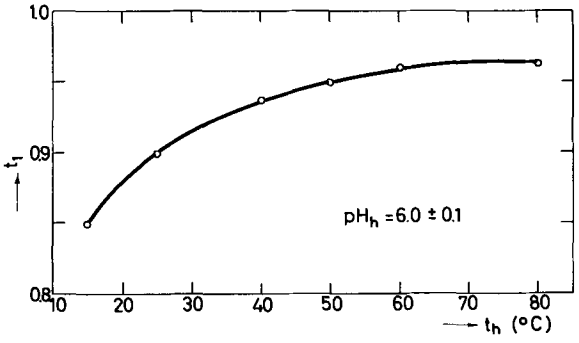

Fig. 4. The dependence of current efficiency on temperature of the holding volume at constant $pH_h = 6.0$, $I = 4.5A$, $q = 2.95$ liters/hr, $V_h = 2.2$ liters.

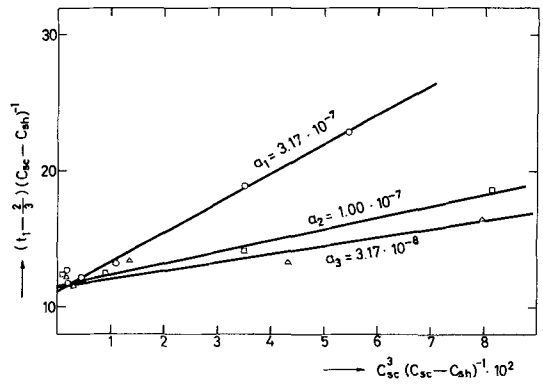

Fig. 5. y vs. x graph (Eq. [13] and [14]) for different pH of the cell electrolyte.

The effect of increasing flow rate, q, was also confirmed. This is not to be taken, however, as evidence of the effect of the linear velocity of flow past the electrodes [cf. Despić, Jaksić, and Nikolić (8)], but rather reflects a decreasing apparent current density per unit volume with increase in flow rate, and consequently smaller C_{sc} values.

Another way of testing Eq. [8] and its consequences was found in the following rearrangement

$$\frac{t_1 - \frac{2}{3}}{C_{sc} - C_{sh}} = \frac{2}{3} \cdot \frac{\mathbf{F} \cdot q}{I} + \frac{2f_c^2 \cdot k_{r,c} \cdot V_c \cdot \mathbf{F}}{I} \cdot \frac{K_c^* \cdot (a_{H_3O^+})_c^2}{[K_c^* + (a_{H_3O^+})_c]^3} \cdot \frac{C_{sc}^3}{C_{sc} - C_{sh}} \quad [13]$$

which is of the type

$$y = m + px \quad [14]$$

It is seen that if y is plotted *vs.* x for each constant pH value of the cell and constant q/I ratio, a straight line should be obtained. A set of results to be interpreted in this way is given in Table II. The resulting dependence [13] is seen in Fig. 5.

The slopes are seen to be functions of pH. By a digital computer analysis of pairs of slopes, the average value of the two unknown constants contained in them, $k_{r,c}$ and K_c^*, could be found since other parameters were known. The result was

$$k_{r,c} = 0.0304 \text{ liters}^2/\text{mole}^2 \cdot \text{sec}$$

$$K_c^* = 1.6 \cdot 10^{-7}$$

The rate constant, $k_{r,c}$, is in agreement with the value obtained by Foerster (1, 2). The dissociation constant is an order of magnitude higher (*cf.* [12]) than the known thermodynamic value in dilute solutions (*cf.* [9], [10]). This is in accordance with the fact discussed elsewhere (7), that the activity coefficient of hydrogen ions in the concentrated electrolyte is about 10.

The approach used seems to offer an interesting possibility for kinetic analysis of other similar systems consisting of back-mix flow reactors in a loop.

Figure 3 shows that, using appropriate conditions of electrolysis and chemical conversion in the described system, it is possible to obtain current efficiencies as high as 96% which are not reached in the usual practice of isothermal circulation in the chlorate cell process with graphite anodes.

Our measurements with graphite anodes in the same apparatus (Fig. 1) show that, other conditions being equal, graphite electrodes yield about the same current efficiency as platinum, although a systematic difference of about 2% seems to exist. Shliapnikov and Filippov (13, 14), however, showed that the maximum difference between the current efficiency obtained by electrolyte analysis and that calculated from gas analysis data is about 1%. Hence, the systematic difference in current efficiency on graphite and platinum is probably due to a direct chemical oxidation of graphite sludge during the process, by hypochlorous acid (15).

To implement the modification of the process based on the concept investigated above in chlorate production practice, two techniques are available:

1. Modern mercury cells in chlor-alkali electrolysis are operated at very high current densities (up to 10 kA/m^2) and there is a need to remove considerable quantities of heat (11). Since chlorate electrolyzers are usually built in the immediate vicinity of chlorine plants, it is possible to cool the mercury cell brine to a desired temperature in a heat exchanger by counterflowing the chlorate electrolyte. The latter can thus be heated up to 60°-80°C. The water used so far to cool the brine can be used to cool the chlorate electrolyte instead, in an additional heat exchanger.

2. It should also be possible to use the recuperation principle for the chlorate electrolyte itself, by flowing

Table II. Typical quasi steady-state data for testing of Eq. [13]

(q = 2.95 liters/hr, I = 4.5A, t_c = 25.0°C, V_c = 0.6 liter)

t_1	C_{sc}, moles/liter ×10^2	C_{sh}, moles/liter ×10^2	$pH_c \simeq$ const (±0.1 pH)	pH_h	$\frac{t_1 - 2/3}{C_{sc} - C_{sh}}$	$\frac{C_{sc}^3}{C_{sc} - C_{sh}}$ ×10^2	t_h, °C
0.872	7.60	6.79	6.54	6.47	22.8	5.43	15.0
0.881	7.35	6.22	6.43	6.24	18.9	3.52	25.0
0.900	5.78	4.02	6.47	6.11	13.2	1.10	40.0
0.925	4.15	1.76	6.47	6.00	10.8	0.299	60.0
0.935	3.14	1.006	6.52	5.98	12.6	0.145	80.0
0.797	8.30	7.60	7.02	7.04	18.6	8.16	15.0
0.838	7.35	6.22	6.95	6.88	15.1	3.52	25.0
0.925	5.72	3.64	7.04	6.62	12.4	0.90	40.0
0.905	3.83	1.82	6.99	6.45	11.8	0.280	60.0
0.919	2.95	0.942	7.10	6.37	12.5	0.128	80.0
0.791	8.41	7.66	7.47	7.53	16.5	7.93	15.0
0.826	8.04	6.84	7.40	7.45	13.3	4.32	25.0
0.835	5.52	4.27	7.56	7.41	13.4	1.34	40.0
0.877	3.83	2.01	7.44	6.90	11.5	0.309	60.0
0.897	3.14	1.26	7.60	6.94	12.2	0.165	80.0

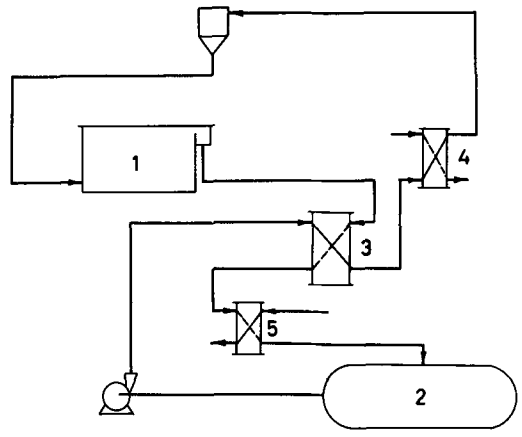

Fig. 6. Schematic representation of the industrial application of the modified process: 1—the cell; 2—holding volume; 3—heat exchanger; 4—additional cooler; 5—additional heater.

the inflow and outflow of the cell through a heat exchanger. Additional heat should be supplied in this case to compensate the losses (Fig. 6).

The first technique seems to be more favorable. It adds to the cost of the chlorate plant only the cost of a suitable titanium-plate type heat exchanger. Yet it should be able to increase the current efficiency by about 10%, reducing by that amount the cost of electrical energy. For a 10,000-tons/yr plant unit a total increase in capital cost should not be larger than U.S. $30,000. The modified technology should save about 6.0 x 10^6 kwhr of electrical energy per annum (about $42,000 at the price of 7 mills/kwhr).

Manuscript submitted Nov. 14, 1968; revised manuscript received April 25, 1969. This paper was presented in part as Paper 257 at the Boston Meeting, May 5-9, 1968.

Any discussion of this paper will appear in a Discussion Section to be published in the June 1970 JOURNAL.

REFERENCES

1. F. Foerster and E. Müller, *Z. Elektrochem.*, **9**, 171, 195 (1903).
2. F. Foerster, *Trans. Am. Electrochem. Soc.*, **46**, 23 (1924).
3. E. Müller, *Z. Elektrochem.*, **5**, 469 (1899); **7**, 398 (1900); **8**, 909 (1902); and **32**, 399 (1926).
4. V. de Valera, *Trans. Faraday Soc.*, **49**, 1338 (1953).
5. N. V. S. Knibbs and H. Palfreeman, *ibid.*, **16**, 402 (1920).
6. L. Hammar and G. Wranglén, *Electrochim. Acta*, **9**, 1 (1964).
7. M. M. Jaksić, B. Z. Nikolić, I. M. Csonka, and A. B. Djordjević, *This Journal*, **116**, 684 (1969).
8. A. R. Despić, M. M. Jaksić, and B. Z. Nikolić, "The Effect of Mass-Transfer on Current Efficiency in the Chlorate Cell Process," Paper to be presented at 20th C.I.T.C.E. Meeting, Strasbourg, Sept. 1969.
9. R. Caramazza, *Gazz. Chim. Ital.*, **87**, 1507 (1957).
10. J. C. Morris, *J. Phys. Chem.*, **70**, 3798 (1966).
11. E. C. Krebs, Paper 109 presented at Electrochem. Soc. Meeting, Cleveland, May 1-6, 1966.
12. M. Gallart, *Anales. Soc. Espan. Fis. Quim.*, **31**, 422 (1933).
13. V. A. Shlyapnikov and T. S. Filippov, *Elektrokhimia*, **2**, 1273 (1966).
14. V. A. Shliapnikov and T. S. Filippov, *ibid.*, **4**, 20 (1968).
15. O. S. Ksenzhek and Z. V. Solovei, *Zhur. Prikl. Khim.*, **33**, 279 (1960).
16. Krebs & Co., Zürich, Know-How for Chlorate Cell Process, 1966.
17. A. Levy, *J. Sci. Instr.*, **41**, 449 (1964).
18. J. D. Ans and H. E. Freund, *Z. Elektrochem.*, **61**, 10, (1957).
19. H. Imagawa, *Denki Kagaku*, **18**, 382 (1950); **19**, 271 (1951); **20**, 25, 571 (1952); **21**, 520 (1953); **25**, 607 (1957).

NOMENCLATURE

(Subscripts c and h refer to the quantities relating to the cell and the holding volume, respectively.)

C_s	the total available chlorine concentration (moles/liter) (C_{sc}, C_{sh})
[HClO], [ClO$^-$]	concentrations (moles/liter) of hypochlorous acid and hypochlorite ions, respectively ([HClO]$_c$, [HClO]$_h$, [ClO$^-$]$_c$, [ClO$^-$]$_h$)
t_1	the fraction of current (dimensionless unit) used for generation of chlorine by anodic oxidation of chloride ions with subsequent hydrolysis of elemental chlorine and chemical conversion or further anodic oxidation of available chlorine to chlorate.
I	cell load (amp)
A	active surface area of anode (cm^2)
$\mathbf{F}$	Faraday's constant ($\mathbf{F}$ = 96.500 coulombs/mole)
τ	time (sec)
k_r	rate constant (liters^2/mole^2 · sec) for reaction [2] ($k_{r,c}$; $k_{r,h}$)
V	volume of electrolyte (liters) in the cell (V_c) and in the holding volume (V_h)
q	electrolyte flow rate (liters/sec)
f, f_{ClO-}	activity coefficients of hypochlorous acid and hypochlorite ions, respectively (f_c, f_h)
a_{H3O+}, a_{H2O}	activities (moles/liter) of hydronium ions and water, respectively [$(a_{H3O+})_c$, $(a_{H3O+})_h$]
K_a, K^*	thermodynamic dissociation constant and rearranged dissociation constant of hypochlorous acid (K_c^*, K_h^*)
t_c, t_h	temperature of the cell and the holding volume respectively (°C)

The meaning of other symbols used is described in Appendix I and II.

APPENDIX I

One can arrive at Eq. [5] both in the given and an extended form, which takes into account all kinds of losses in the electrolytic production of chlorate for a closed-loop system, by considering the material balance of available chlorine with respect to the cell at quasi steady-state condition, which is defined by (*cf.* [4])

$$V_c \cdot \left(\frac{dC_{sc}}{d\tau} \right) = 0 \qquad [15]$$

The partial contributions of individual components of production, consumption, and loss of available chlorine during the process would be as follows:

(*a*) Anodic generation of available chlorine, which is converted to chlorate by two possible parallel paths (Eq. [2] and [3])

$$V_c \cdot \left(\frac{dC_{sc}}{d\tau} \right)_{G1} = \frac{t_1 \cdot I}{2\mathbf{F}} \qquad [16]$$

where t_1 is the fraction of current used for generation of chlorine by anodic oxidation of chloride

$$2\,Cl^- \rightarrow Cl_2 + 2e \qquad [17]$$

with subsequent hydrolysis

$$Cl_2 + 2H_2O \rightleftarrows HClO + H_3O^+ + Cl^- \qquad [18]$$

and conversion (Eq. [2]), or further *anodic oxidation* (Eq. [3]) to chlorate.

(*b*) Anodic generation of available chlorine, which is subsequently lost in the electrolytic production process by cathodic reduction

$$ClO^- + H_2O + 2e \rightarrow Cl^- + 2OH^- \qquad [19]$$

is described as

$$V_c \cdot \left(\frac{dC_{sc}}{d\tau} \right)_{G2} = \frac{t_2 \cdot I}{2\mathbf{F}} \qquad [20]$$

where t_2 is the fraction of the current used for generation of that part of available chlorine.

(c) Anodic generation of available chlorine, which is subsequently lost by evaporation in the hydrogen stream

$$V_c \cdot \left(\frac{dC_{sc}}{d\tau} \right)_{G3} = \frac{t_3 \cdot I}{2F} \quad [21]$$

where t_3 is the fraction of the current used for unhydrolyzed chlorine.

(d) Further anodic oxidation of available chlorine to chlorate (Eq. [3]).

$$V_c \cdot \left(\frac{dC_{sc}}{d\tau} \right)_{OX} = \frac{t_4 \cdot I}{2F} \quad [22]$$

where t_4 is the fraction of the current for the anodic chlorate formation.

(e) Available chlorine consumption by cathodic reduction

$$V_c \cdot \left(\frac{dC_{sc}}{d\tau} \right)_{RED} = -\frac{t_2 \cdot I}{2F} \quad [23]$$

which corresponds to Eq. [20]

(f) Current losses by chlorine evaporation in the hydrogen stream

$$V_c \cdot \left(\frac{dC_{sc}}{d\tau} \right)_{E} = -\frac{t_3 \cdot I}{2F} \quad [24]$$

(g) Conversion of available chlorine to chlorate (Eq. [2]) inside the cell (18, 19), which operates as back-mix flow reactor

$$V_c \cdot \left(\frac{dC_{sc}}{d\tau} \right)_{CH} = -3f_c^2 \cdot k_{r,c} \cdot V_c \cdot [HClO]_c^2 \cdot [ClO^-]_c \quad [25]$$

(h) The difference in quantities of available chlorine leaving the cell and entering the cell from the holding volume in the considered time interval (which is equal to the conversion of available chlorine to chlorate inside the holding volume)

$$V_c \cdot \left(\frac{dC_{sc}}{d\tau} \right)_{H} = -q\,(C_{sc} - C_{sh}) \quad [26]$$

The material balance (Eq. [15]) thus is given by the following relation

$$\frac{t_1 \cdot I}{2F} + \frac{t_2 \cdot I}{2F} + \frac{t_3 \cdot I}{2F} - \frac{t_4 \cdot I}{F} - \frac{t_2 \cdot I}{2F} - \frac{t_3 \cdot I}{2F} - 3f_c^2 \cdot k_{r,c} \cdot V_c \cdot [HClO]_c^2 \cdot [ClO^-]_c - q\,(C_{sc} - C_{sh}) = 0 \quad [27]$$

Individual fractions of the anodic current are, in that case, connected by the relation

$$t_1 + t_2 + t_3 + t_4 = 1 \quad [28]$$

By combining Eq. [27] and [28], one obtains the explicit expression for the current efficiency on chlorate

$$t_1 = \frac{2}{3} + \frac{2f_c^2 \cdot k_{r,c} \cdot V_c \cdot F}{I} \cdot [HClO_c^2] \cdot [ClO^-]_c + \frac{2}{3}F\left(\frac{q}{I}\right) \cdot (C_{sc} - C_{sh}) - \frac{2}{3}(t_2 + t_3) \quad [29]$$

in which further transformations of the second and third terms are possible, as given in the main part of the paper. By dividing all terms of Eq. [27] by three, one can relate the generation and consumption of available chlorine with chlorate production, which means that t_1 also defines the current efficiency in the process of electrolytic chlorate production.

The current losses due to the catalytic decomposition of available chlorine and chlorate, or the anodic oxidation to perchlorate, are practically avoided under normal conditions of production, and thus need not be taken into consideration in the presented analysis.

The fraction of the current loss due to cathodic reduction is given as a ratio of the difference between the theoretical amount of hydrogen (V_o) and that actually produced amount (V_1), to the theoretically given amount (V_o) for a certain duration of electrolysis, namely

$$t_2 = \frac{V_o - V_1}{V_o} \quad [30]$$

The fraction of the current loss due to chlorine evaporation can also be determined by gas analysis as the ratio of percentage fractions of chlorine (Q) and hydrogen (H)

$$t_3 = \frac{Q}{H} \quad [31]$$

under the conditions of negligible cathodic reduction of available chlorine. If it is not negligible, this relation gives the ratio of evaporated chlorine to the theoretical amount of hydrogen developed for the same time interval.

In the presence of dichromate ions, with sufficiently high current densities and in a suitably defined pH region, both kinds of loss tend to zero, and Eq. [29] reduces to Eq. [5]

APPENDIX II

The equation for calculating the current efficiency from the gas analysis, which takes into account all kinds of losses, listed in Appendix I, can be derived using Faradaic stoichiometry, *i.e.* coulometric balance.

Consider the passage of N faradays through the cell during a definite time interval under quasi steady-state conditions of electrolytic chlorate production. This should be distributed as follows:

(a) Let x be the fraction of the charge, N, at the anode which is used to oxidize those chloride ions (Eq. [17]), which on discharge give molecular chlorine subsequently lost by evaporation (unhydrolyzed chlorine). Then $x \cdot F$ produce $x \cdot F/2$ moles of evaporated chlorine at the anode, and $x \cdot F/2$ moles of hydrogen at the cathode.

(b) Let y be the fraction used to oxidize chloride ions which produce available chlorine to replace that which is consumed by chemical conversion to chlorate (Eq. [2]). Then $y \cdot F$ produce $y \cdot F/2$ moles of available chlorine at the anode and $y \cdot F/2$ moles of hydrogen at the cathode.

(c) Let z be the fraction used to oxidize further the available chlorine into chlorate (Eq. [3]). Then $z \cdot F/4$ moles of oxygen are produced at the anode and $z \cdot F/2$ moles of hydrogen at the cathode.

(d) Let w be the fraction which produces hypochlorite ions to replace those reduced at the cathode (Eq. [19]). Then $w \cdot F$ produce $w \cdot F/2$ moles of available chlorine at the anode and reduce the same amount at the cathode.

All the fractions must sum up to give the total amount of charge as

$$x + y + z + w = N \quad [32]$$

The fraction of oxygen (S) in the gas mixture should then be

$$S = \frac{O_2}{H_2 + O_2 + Cl_2} = \frac{\frac{z \cdot F}{4}}{\left(\frac{x}{2} + \frac{y}{2} + \frac{z}{2} + \frac{z}{y} + \frac{x}{2}\right) \cdot F} \quad [33]$$

while the content of unhydrolyzed (evaporated) chlorine (Q), obtained by gas analysis, is given by the equation

$$Q = \frac{Cl_2}{H_2 + O_2 + Cl_2} = \frac{\frac{x \cdot F}{2}}{\left(\frac{x}{2} + \frac{y}{2} + \frac{z}{2} + \frac{z}{y} + \frac{x}{2}\right) \cdot F} \quad [34]$$

The current fraction lost by cathodic hypochlorite reduction ($P = t_2$) is expressed by the following relation

$$P = \frac{\frac{w \cdot F}{2}}{\left(\frac{x}{2} + \frac{y}{2} + \frac{z}{2} + \frac{w}{2}\right) \cdot F} \quad [35]$$

The current efficiency of chlorate formation (t_1), which has to be equal to the theoretical amount of electricity required for the yield divided by the actual amount used, is then given, expressed as a fraction of unity, by

$$t_1 = \frac{\frac{y \cdot F}{2}}{\left(\frac{x}{2} + \frac{y}{2} + \frac{z}{2} + \frac{w}{2}\right) \cdot F} \qquad [36]$$

Equations [33-36] represent a system of four homogenous linear equations, which can be solved for t_1 by eliminating the unknown quantities x, y, z, and w

$$t_1 = \frac{(1 - 2Q - 3S)(1 - P)}{1 - Q - S} \qquad [37]$$

The partial fractions of oxygen (S) and chlorine (Q) are determined by the gas analysis, while the determination of the current fraction losses by hypochlorite reduction at the cathode ($P = t_2$) is discussed in Appendix I. Carbon dioxide is added to the oxygen content in the present calculations.

Technical Notes

A High-Voltage, Solid-State Battery System

I. Design Considerations

Charles C. Liang* and P. Bro*

P. R. Mallory & Company, Incorporated, Laboratory for Physical Science, Burlington, Massachusetts

The solid electrolyte battery systems developed during the 1950's (1) had low voltages and high impedances which limited their usefulness drastically. The recent discovery (2-6) of high-conductivity ionic conductors of the $RbAg_4I_5$ type has stimulated the development of solid-state batteries with a high current carrying capability (7). Although these solid electrolytes have high conductivities, their composition limits their use to low-voltage systems with low energy densities.

We have investigated solid electrolytes compatible with high-voltage systems, and we report results below to demonstrate that thin-film, solid-state batteries can be made with energy densities approaching those of the best aqueous systems available.

Experimental Results

The Li/LiI/AgI system was chosen for investigation because of its high voltage and the low equivalent weight of lithium. The use of lithium restricted the choice of electrolyte to LiI which is a pure cationic conductor. Because of the high resistivity of LiI, 10^7 ohm-cm at 25°C (8), it was necessary to construct thin-film cells.

We found that thin films of the active materials and the electrolyte could be formed by carefully controlled vacuum evaporations, and cells were constructed by this means using purified analytical grade reagents. The thicknesses of the components of the cells were, typically: silver current collector, 13μ; AgI cathode, 30μ; LiI electrolyte, 15μ; and lithium anode, 5μ. The details of the experimental procedures and the cell structures will be given in subsequent publications.

The thin-film cell had an open-circuit voltage of 2.1V, and it exhibited the polarization curve shown in Fig. 1. The cell voltage decreased linearly with an increase in the current density and reached zero volts at about 120 $\mu A/cm^2$. This behavior demonstrated the ohmic nature of the cell impedance. A resistivity of 1.17×10^7 ohm-cm was calculated for LiI from the polarization curve, which agreed well with the published value. The resistivity of the AgI, 10^4 ohm cm (9), was neglected as being insignificant in comparison with that of LiI.

Discussion

The open-circuit voltage of the cells of 2.1V agreed well with the value of 2.09V calculated from the Gibbs free energy change (10) for the reaction:

$$Li + AgI = LiI + Ag$$

and it confirmed this to be the reaction of the cell.

The formation of LiI as a reaction product implied that the impedance of the cell would increase markedly during discharge. For example, the resistance of a single unit cell with a capacity of 100 mah/cm^2 would increase linearly from 12 kohms at the start of discharge to 1230 kohms at the end of discharge. Such a high impedance would render the cell useless for most practical applications, and it is evident that multilayer, parallel connected cell structures must be developed if practically interesting current carrying capabilities are to be achieved.

The impedances of hypothetical multilayer parallel plate cells were calculated to give the results shown in

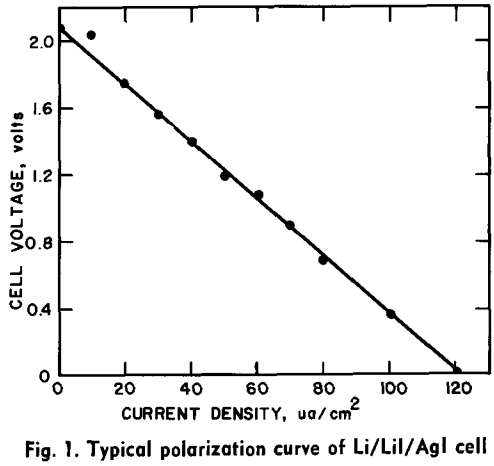

Fig. 1. Typical polarization curve of Li/LiI/AgI cell

* Electrochemical Society Active Member.

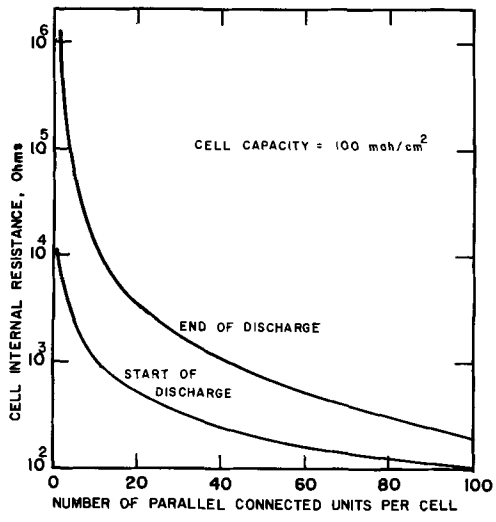

Fig. 2. The internal resistance of multilayer cell structures

Fig. 2. A capacity of 100 mah/cm² and a 100% depth of discharge were assumed. It may be seen that substantial improvements may be expected by the use of multilayer structures. The experimental unit cell had a stoichiometric anode limited capacity of 1 mah/cm² which indicated the technical feasibility of constructing from it a 100 mah/cm² consisting of 100 parallel connected units. Such a cell would have a short-circuit current density of 10 mA/cm² at the end of discharge. Practical cells have been made which delivered approximately 0.5 mah/cm² in a single unit cell to a 1V cutoff voltage at 20 μA/cm².

The stoichiometric energy densities of the multilayer cells would be less than that of single unit cells with the same capacity because of the added volume of the current collectors and substrates. Calculations showed that stoichiometric volumetric energy densities between 2 and 9 whr/in.³ may be realizable, depending on the number of units per cell, when the volumes of all the components except the outer cans were included in the calculations. The operating energy density of the single-layer, thin-film cell under a current drain of 10 μA/cm² was found to be 2.2 whr/in.³ (50% efficiency to a cutoff voltage of 1.0V at an average cell voltage of 1.7V).

It is concluded that the development of the high-voltage Li/LiI/AgI system is feasible and that multilayer, thin-film structures are required for cells capable of delivering currents in the low milliampere range. The volumetric energy densities of the cells may be expected to vary between 1 and 5 whr/in.³ for the various designs.

Manuscript submitted Jan. 13, 1969; revised manuscript received May 23, 1969.

Any discussion of this paper will appear in a Discussion Section to be published in the June 1970 JOURNAL.

REFERENCES

1. J. N. Mrgudich, "Solid Electrolyte Batteries," in "Encyclopedia of Electrochemistry," C. A. Hampel, Editor, pp. 84-88, Reinhold Publishing Corp., New York (1964).
2. J. N. Bradley and P. D. Greene, *Trans. Faraday Soc.*, **62**, 2069 (1966).
3. *Ibid.*, **63**, 427 (1967).
4. *Ibid.*, **63**, 1023 (1967).
5. *Ibid.*, **63**, 2516 (1967).
6. B. B. Owens and G. R. Argue, *Science*, **157**, 308 (1967).
7. G. R. Argue and B. Owens, Paper 281 presented at Electrochem. Soc. Meeting, Boston, May 5-9, (1968).
8. Landolt-Bornstein, "Zahlenwerte und Funktionen," Vol. 2, Part 6, Section I, p. 226, Springer, Berlin (1959).
9. J. N. Mrgudich, *This Journal*, **107**, 475 (1960).
10. W. M. Latimer, "Oxidation Potentials," 2nd Ed., pp. 190 and 329, Prentice-Hall, Inc., Englewood Cliffs, N. J. (1961).

Some Electrochemical Studies on Ceramic Barium Titanate

Ashok K. Vijh*,[1]

Research & Development Laboratories, Sprague Electric Company, North Adams, Massachusetts

In the present investigations, an attempt has been made to oxidize anodically semiconducting ceramic barium titanate (BT) disk electrodes. The object of this study was to obtain a thin insulating layer of oxidized BT, possibly with good dielectric properties, onto the body of the parent disk of reduced, semiconducting BT.

Experimental Procedures

Thermally reduced ceramic barium titanate, either pure or Nb-doped (*ca.* 0.1%) and of *ca.* 2-20 ohm-cm resistivity, was used in the form of pressed disks as the working electrode. The disks were masked either by a resin or were accommodated in a suitable glass-Teflon assembly. The nature of the electrolytic solutions, where relevant, will be mentioned in the section on Results and Discussion.

Ohmic contact to the ceramic was made by means of a Ga-In alloy.

Counterelectrodes were bright platinum wires.

Electronic circuits consisted of routine constant voltage and galvanostatic configurations similar to those described previously (1).

For metallographic studies, the anodized disks were angle lapped at the desired angle and subsequently polished to expose the enlarged (due to angle lapping, of course) anodized layer. This layer was then metallographically examined and photographic record was thus obtained of the thickness and appearance of the layer.

The final cleaning of the working electrodes was carried out in boiling trichloroethylene.

Results and Discussion

Anodization and cathodization.—Anodizations and reduction attempts were carried out in a variety of solutions in open beakers. The sole purpose of these studies was to obtain an insulating layer which might act as a good dielectric. Since kinetic-mechanistic aspects were *not* of interest in these particular runs, anodizations and cathodizations under crude experimental conditions of open beakers were regarded as quite satisfactory.

It was observed, rather empirically, that neutral (buffered phosphate) or mildly alkaline (0.1*N* Na_2CO_3 in water) solutions tend to give anodized layers which show better gross coherence than the ones obtained in highly acidic ($HClO_4$ or H_2SO_4) or highly alkaline (NaOH) or some other (NH_4NO_3) electrolyte compositions. Solutions only partially aqueous (*e.g.*, glycol-borate electrolyte + 20% H_2O) or nonaqueous

* Electrochemical Society Active Member.
[1] Present address: Institute of Research, Hydro-Quebec, 75 Blvd. Dorchester West, Montreal, P. Q., Canada.

(formate in formic acid) make it possible to anodize a BT disk to higher voltages than aqueous solutions. However, the anodized layers obtained in the partially or totally nonaqueous solutions are very uneven and show a spectrum of patches of anodically oxidized (white) and reduced (*i.e.*, the parent bluish-black disk) BT. In all cases of anodization in aqueous media, gas (presumably oxygen) evolution could be observed as a process parallel to the anodic "growth," from the very commencement of anodization. Attempts to reduce the anodic layer by cathodization were unsuccessful (*cf.*, cathodization of valve metal oxides).

Chemical composition of the layer.—The chemical characterization of the layer was carried out by electron probe microanalysis and by x-ray diffraction. The electron-probe microanalysis was carried out by employing a defocused beam of approximately 50μ diameter. It was observed that none of the films showed Ba:Ti ratio which would be expected for pure BT. For example, films formed in neutral phosphate solutions were rich in Ti, whereas those in carbonate solution were very low in Ti. The departures from stoichiometry in every case were very significant and varied randomly over a very wide range. Further, in the anodized layers formed in neutral phosphate solutions, presence of some phosphorus was also detected.

In the x-ray diffraction studies, several peaks *not* corresponding to pure BT were detected; this would indicate presence of compounds other than BT in the anodized layer. Only one of these extraneous compounds, however, could be identified and it was $BaCO_3$. It may be mentioned that the anodized layer that showed $BaCO_3$ was obtained by electrochemical oxidation of Nb-doped BT in 0.1*N* Na_2CO_3. Both electron probe microanalysis and x-ray diffraction studies thus indicate rather strongly that, during anodization, the components of the electrolyte solution get incorporated in the anodized layer. This observation is quite consistent with similar incorporation of the electrolyte components in the anodic films formed during oxidation of valve metals (2).

General appearance, porosity and mechanical strength of the anodic layer.—The layer was quite flaky and brittle. It was white and opaque as contrasted to the translucence of pure BT layer of perovskite structure. It did not, however, show any gross porosity as determined, *e.g.* by dye test at 30 psi.

Metallographic studies and the thickness of the layer.—Angle-lapping and subsequent metallographic examination of the anodized disks showed that a rather sharp boundary exists between the anodized layer and the parent reduced disk in the great majority of cases (Fig. 1). At least in one instance, it was observed that this boundary can sometimes be quite diffuse. The behavior represented in Fig. 1, however, is more representative of the general thickness and appearance of the anodized layer.

By controlling the voltage (in constant-voltage experiments) or current density (in galvanostatic experiments) and time of anodization, one can obtain anodized layers with the thickness range of 1-5 x 10^{-3} cm. The most suitable conditions for obtaining a layer of this thickness were a constant voltage (~50-70V) "pulse" lasting 5-10 sec in an aqueous (0.1*N* Na_2CO_3) solution. Longer times of anodization combined with higher anodization voltage (or current densities) gave much thicker deposits. These thicker deposits, however, were mechanically damaged since pieces of the "chipped" anodized layer could be seen falling into the solution. Again, applying a high-voltage pulse (~100V) in aqueous solutions at the very commencement of the anodization would result in the dielectric breakdown of the disk; the breakdown in some cases would be severe enough to blow the electrode to smithereens and cause sparking near the electrode surface. When the anodization voltage was increased gradually, *i.e.* in a manner which follows the anodic growth, much higher voltages (~300V) could be built across the disk.

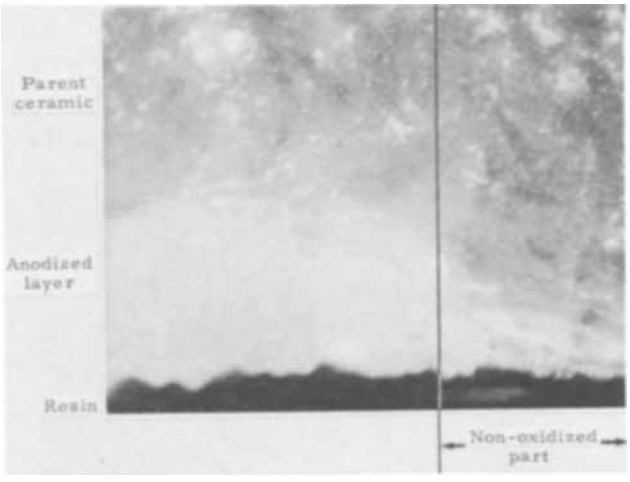

Fig. 1. A photographic record of the appearance of a typical angle-lapped anodized layer under metallographic examination. Boundary between the layer and the parent ceramic is reasonably sharp. The BT is Nb doped and was anodized in 0.1*N* Na_2CO_3 aqueous solution by a constant voltage (~60V) "pulse" (~2 sec); X1750 approximately; thickness ca. 2.1 μm.

Electrical resistivity of the film.—The d-c resistivity of the layer as "seen" by a low-signal, d-c voltage was in the range of 1 x 10^8-1 x 10^9 ohm-cm. This was measured both by the electrolyte contact to the anodized layer, as well as by electrodepositing a metallic copper electrode on this layer. This resistivity, it may be remarked, is appreciably lower than that of a thermally oxidized BT layer (~10^{12} ohm-cm) or a typical valve metal oxide, *e.g.* Ta_2O_5 (~10^{15} ohm-cm).

Dielectric properties.—Attempts were made to measure the a-c capacitance (C) and RC of a few assorted anodized disks. Non-zero values (in the range 0.01-1 μ**F** cm^{-2}, approximately) of C were obtained on some disks. However, the values of RC were usually in the range of 8-12 x 10^3 ohm-μ**F**/disk (area *ca.* 0.5 cm^2) thus showing high resistance in series. These values were *quite erratic*, and were strongly dependent on a-c frequency, d-c bias, time of subjection to d-c bias, and the area of the anodized disk on which the contact is made, thus showing that the layer is a very poor dielectric. Several types of "electrodes" were explored for dielectric measurements; none of these contacts, however, gave satisfactory values for C and RC.

Some theoretical considerations.—Here an attempt is made to speculate on some theoretical aspects of these studies, *e.g.* the comparison and contrast between thermal and anodic oxidation of semiconducting BT.

The only requirements in thermal oxidation are high melting point (so that the ceramic does not fuse during thermal oxidation) and high ionicity because otherwise the activation energy for the migration of oxygen vacancies would be too high. These two requirements are easily met for the case of perovskite oxides since the Madelung constants and lattice energies for these structures are very high (3); hence, probably the satisfactory dielectric layers obtained on *thermal* oxidation of semiconducting BT, *e.g.* in capacitor industry. During electrochemical oxidation, however, not only high lattice energies are required but the bond energies also need to be fairly high to sustain high fields (4). As pointed out elsewhere (4), high ionicity alone would give oxides on anodization, which have rather poor mechanical and electrical characteristics, *e.g.* oxides of alkaline earth metals. Since $BaTiO_3$ [1] contains both Ba-O and Ti-O bonds, weak

[1] In a complex structure (*i.e.*, perovskite) like that of BT, however, strength of Ba-O and Ti-O bonds would be expected to be somewhat different than that in BaO and TiO_2, respectively.

BaO bond energy (5) would, on electrochemical oxidation, give rise to a rather poor dielectric, as indeed is actually observed. Low bond energies and high ionicity would, further, result in a relatively easy dissolution, either "chemical" or anodic, of the growing oxide. This dissolution may very well be uneven, depending on the electrochemical factors (including surface heterogeneity, plane defects, *etc.*) that obtain in a given experiment; hence, perhaps, the departures from stoichiometry. The argument that relatively low Ba-O bond energy (5) would not result in a good anodized layer on reduced BT is also consistent with some other empirical evidence. It has been empirically observed that (2) for anodic oxides, high dielectric constant tends to be associated with low bond energies (4) and with *lower* ability of the oxide to sustain high fields for ionic growth. Since BT, even when not ferroelectric, has a fairly high dielectric constant, its ability to sustain fields would be quite low. It is indeed observed that "dielectric strength" [*i.e.*, ability to sustain field, without breakdown, during anodization, *e.g.* Ref. (2)] of the anodically grown BT in aqueous solutions is in the range *ca.* 1-3 x 10^5V cm^{-1}. This value is lower than that for any valve metal oxide (6).

Acknowledgments

Contributions made by N. Eror and M. Kahn to the metallographic and other studies, and helpful discussions with R. S. Alwitt and D. M. Smyth are gratefully acknowledged.

Manuscript submitted Dec. 17, 1968; revised manuscript received *ca.* May 22, 1969.

Any discussion of this paper will appear in a Discussion Section to be published in the June 1970 JOURNAL.

REFERENCES

1. A. K. Vijh and B. E. Conway, *Chem. Rev.*, **67**, 623 (1967).
2. J. J. Randall, Jr., W. J. Bernard, and R. R. Wilkinson, *Electrochim. Acta*, **10**, 183 (1965).
3. T. C. Waddington in "Advances in Inorganic and Radio Chemistry," Vol. 1, H. J. Emeleus and A. G. Sharpe, Editors, Academic Press, New York (1959).
4. A. K. Vijh, *Electrochim. Acta*, Accepted for publication; *idem*, *This Journal*, **116**, 972 (1969); *idem*, *ibid.*, **116**, 353 (1969).
5. R. T. Sanderson, "Chemical Periodicity," Reinhold Publishing Corp., New York (1960).
6. L. Young, "Anodic Oxide Films," Academic Press, New York (1961).

Brief Communication

Ethylene Diamine-Catechol-Water Mixture Shows Preferential Etching of p-n Junction

J. C. Greenwood

Standard Telecommunication Laboratories, Harlow, Essex, England

We have found that the ethylene diamine-catechol-water etch described recently by Finne and Klein (1) will etch only n-type silicon in samples containing p-n junctions. The etching of the p-type part of the sample appeared to be completely inhibited, not just slowed down, until the n-type part of the sample had been removed.

This effect is demonstrated clearly in one particular experiment described here in more detail.

A slice of <100> n-type silicon was polished and diffused to give a p-type layer about 5 μm thick on the underside. The top side was chemically polished to give a thickness of about 200 μm and coated with silicon dioxide. Square windows were etched in the silicon dioxide. A diagrammatic cross section of the slice at this stage is shown in Fig. 1(a). The slice was etched in a mixture, described by Finne and Klein, of ethylene diamine, 17 ml; water, 8 ml; catechol, 3g, for a total of 6¾ hr at 110°C in a flask fitted with a reflux condenser. Nitrogen was bubbled through the mixture.

Square pits with sloping sides and flat bottoms were formed in the windows as shown diagrammatically in Fig. 1(b). At the bottoms of the pits, the etching stopped at the p-n junction, leaving a thin even layer

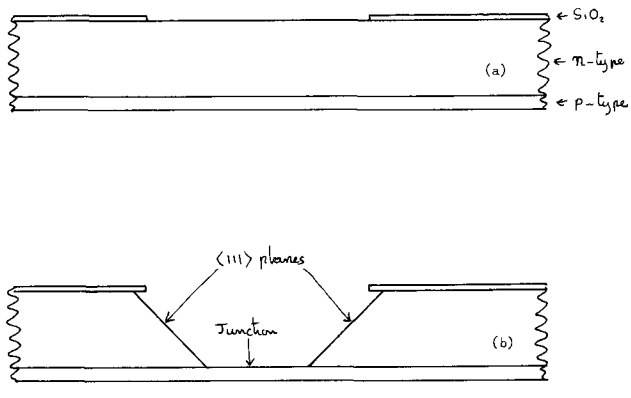

Fig. 1. Cross section of the slice: (a) before etching, (b) after etching.

of unattacked p-type silicon. The evenness of this layer is shown in Fig. 2 in which the slice is illuminated from underneath. The uniform thickness is main-

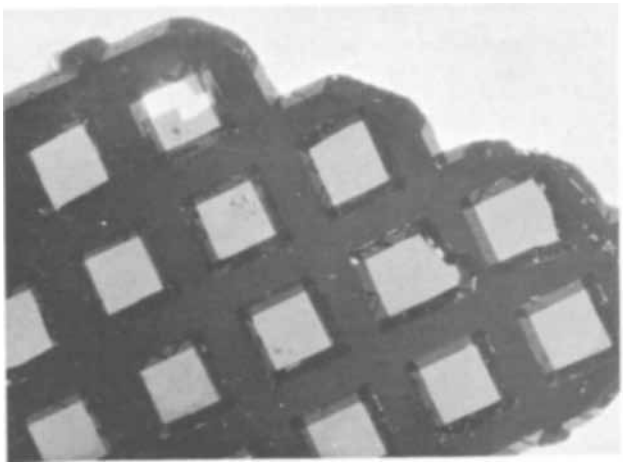

Fig. 2. Looking down on the slice after etching. It is illuminated from underneath to show light being transmitted through the silicon at the bottoms of the pits. The spacing of the squares is 0.050 in.

tained right to the edge of the slice where the junction was revealed early in the period of etching.

The sides of the pits corresponded to <111> planes; this is a result of the much slower rate of attack on <111> planes as is described by Finne and Klein.

The bottoms of the pits had a fabriclike texture, in contrast with the sloping sides which were smooth. It is believed that this is the actual shape of the junction and that the departure from flatness is due to irregularities in the crystal structure.

The inhibition effect described here could be useful in preparing thin samples of silicon, examining defects in junctions, and in making devices such as strain gauges in which the shape is critical.

Manuscript submitted Jan. 27, 1969; revised manuscript received May 29, 1969.

Any discussion of this paper will appear in a Discussion Section to be published in the June 1970 JOURNAL.

REFERENCE

1. R. M. Finne and D. L. Klein, *This Journal*, **114**, 965 (1967).

A Theory for Porous Electrodes Undergoing Structural Change by Anodic Dissolution

Richard C. Alkire, Edward A. Grens II,* and Charles W. Tobias*

Inorganic Materials Research Division, Lawrence Radiation Laboratory, and Department of Chemical Engineering, University of California, Berkeley, California

ABSTRACT

A theoretical model is proposed for the description of flooded porous metal electrodes which undergo anodic dissolution by electrochemical reaction. Equations are developed to represent the pseudosteady state which prevails during dissolution after the concentration gradients have become fully established within the pores. The analysis leads to an understanding of how mass transfer, kinetic and geometric parameters of the system determine the electrode overpotential and its change during dissolution. The most uniform current distributions are predicted to occur not at vanishingly small currents but at finite anodic currents because of mass transfer limitations to the cathodic back reaction. Thus, for a range of anodic currents, an increase of applied current will result in a more uniform distribution of the electrochemical reaction throughout the porous electrode. Calculations illustrating the behavior are presented for the acid-copper system.

Electrodes which are porous have come into widespread use in electrochemical energy conversion devices because, in these, the electrochemical reaction takes place with a higher rate per unit volume and is accompanied by a lower polarization than would be possible with nonporous electrodes. Accordingly almost all batteries and fuel cells employ porous electrodes. In batteries the electrode pores are flooded with liquid electrolytic solution, and reactants and/or products are incorporated in the solid electrode matrix. Thus, during operation, the composition and configuration of the solid material changes, leading to departures from behavior that might be expected for electrodes with invariant matrices. The nature of such changes, which are dependent on the electrode system involved, can be very complicated indeed. In this work an analysis has been conducted of a simple class of electrodes experiencing structural change during operation: porous metal anodes undergoing electrochemical dissolution. The investigation of this type of electrode can illuminate some of the salient effects of structural changes in battery electrodes and can serve as a basis for extension of model studies of systems encountered in batteries.

The dissolving metal anode, of course, involves a relatively simple type of structural change. No changes in solid composition are involved. The behavior of most battery electrodes is far more complicated, but the state of description of such systems has not yet advanced sufficiently far to embrace these more complicated events. Theoretical analyses to date have proceeded by one of two routes. In the first, an idealized geometrical structure of the porous body is assumed and is taken into consideration when equations are derived for the current and potential distributions (1-3). This "microscopic" approach has been found to lead to severe mathematical difficulties and has been restricted to extremely simple geometries. The second method ignores the detailed structure of the porous electrode and, rather, treats the porous electrode as a pseudohomogeneous region in which there is transfer of current between electronic and ionic modes of conduction according to basic laws of transport phenomena and electrode kinetics. This "macroscopic" approach has been applied to electrode behavior in the initial state without concentration gradients (4-10), during the mass transfer transients (11), and in the steady state where concentration gradients are fully established (11-13). As more sophisticated models were examined, the solution of the equations was found to be more conveniently carried out by numerical methods implemented by high-speed digital computers (11).

To date, no theoretical analysis has been reported which takes into consideration the variation of electrode structure with extent of reaction. The macroscopic theory presented here examines the behavior of porous metal electrodes that are undergoing dissolution of anodic reaction and predicts the external electrode polarization and the electrode porosity distribution as a function of the extent of reaction.

The operation of battery systems involves other effects beyond those considered in the theoretical model used in this work. Typically, sparingly soluble salts take part in the reactions during cycling. These salts may be insulators or semiconductors and hence may greatly affect the potential distribution within the electrode. There may be composition gradients in the solid phase (for instance $Ag/Ag_2O/AgO$) and, furthermore, electronic transport in the solid phase may be important. Also, reactions may be locally nonuniform, and geometrical effects of crystal growth may be involved. Nevertheless, the theoretical model presented below represents an advance relative to existing treatments in the literature and should be useful in leading to some insight into more complex systems.

Model Formulation

The mathematical model for a dissolving porous anode is based on consideration of a porous metal plate whose accessible void spaces are completely filled with an aqueous electrolyte. On one side of the porous plate the pores are blocked (or a center of symmetry exists), and the other side (the face) is in contact with the electrolytic solution, which also fills the pores. There is no forced flow of solution through the pores. A second (counter) electrode is also in the solution but is of no concern in this model and serves only to complete the electrochemical circuit. With passage of anodic current through the porous electrode, the metal dissolves with formation of a soluble salt. The local rate of anodic dissolution varies from place to place within the porous electrode because the various positions are not equally accessible to the current and the reacting species transported in the electrolyte. The distribution of the reaction depends on the mass transfer, kinetic and geometric characteristics of the particular system.

When anodic current is switched on, two major changes begin to take place.[1] Because the removal of

* Electrochemical Society Active Member.

[1] During the first few milliseconds the electrical double layer becomes established. We shall not be concerned with the electrode behavior during this brief period of double layer charging.

dissolved product species from the pore is transport controlled, as is also the passage of current and movement of nonreacting ions in the electrolyte, the potential and concentrations of species in the solution within the pores change from the initially uniform values and become more or less unevenly distributed throughout the pores. Typically this mass transfer transient process is completed within a period of 10 sec to 1 hr, depending on the system (11). Second, and simultaneously, the geometry of the porous metal matrix changes owing to its dissolution by anodic reaction. As the nature of the electrode structure thus changes, the potential and concentration distributions also change, and these changes continue to take place as long as current is passed.

When anodic current thus passes through the porous metal electrode, the current in the metal is carried by electrons and the current in the solution is carried by the ions. The conversion from the electronically to the ionically conducting "phase" takes place throughout the porous electrode by virtue of the electrochemical reaction. If the local concentrations and potentials are known in both phases, the local reaction rate may be calculated, in principle, by a relation which suitably describes the kinetics of the electrode process. In turn, the local concentrations and potentials may be obtained by solving the equations of transport in each phase. Thus the local reaction rate may be determined throughout the electrode.

During the first moments of operation, the reaction distribution changes principally because of the production of ionic reaction products whose removal in the solution phase from the porous electrode is transport restricted. Along with this mass transfer transient process, the reaction distribution changes at some other rate owing mainly to the changes in structure caused by dissolution. The characteristic times of these two effects are usually different, the former being much faster. Consequently, after the mass transfer transient has been essentially completed, the reaction distribution continues to change, and it becomes a very good approximation to determine the rate of change solely from the effects of the structural dissolution. This is the pseudosteady state approximation that will be invoked in the present theory.

The equations describing electrode behavior arise from transport relations and electrode kinetic expressions. In definition of the model it is necessary to introduce a number of simplifying assumptions to facilitate the required calculations:

1. The one-dimensional macroscopic approach is applicable; pore dimensions are assumed to be small with respect to distances over which significant changes take place within the electrode.
2. The electrode operation under consideration takes place in the pseudosteady state. Behavior during the mass-transfer transient is ignored.
3. The electrical double layer can be disregarded. The pore dimensions are large compared to those of the double layer, and the time variations are slow compared to the rate of establishment of the double layer.
4. The motion of solute species in the electrolytic solution is adequately described by the equations of dilute solution theory. The transport parameters are constant, and hydrodynamic flow in the pores is due only to the net change of electrode and electrolyte volume with the extent of reaction. The density of the electrolytic solution is essentially constant throughout the pores, and the metallic electrode structure is isopotential.
5. The only electrochemical reaction is the anodic dissolution of the metal electrode to form ions having a single charge number, and the kinetic behavior of the reaction is adequately characterized by an expression of the Volmer form (14).
6. There are no insoluble substances within the pores.
7. The pores are circular cylinders which all have the same size at the onset of dissolution.
8. Mass transfer resistances external to the porous electrode can be disregarded.
9. The system is isothermal.

The analysis of electrochemical systems by the equations of transport as delineated, for instance, by Levich (15) and by Newman (16), has been applied to the formulation of a macroscopic porous electrode model by Grens and Tobias (11). It is here extended to account for the changes in matrix properties accompanying anodic dissolution of the matrix. Under the conditions described above, the conservation of solute species in the pseudosteady state is described by[2]

$$c_i \frac{\partial a}{\partial t} = -\frac{\partial}{\partial y}(N_i a) + S_i \qquad [1]$$

In this equation the left hand side represents the amount of species i associated with changes in pore volume while the terms on the right hand side are the divergence of the species flow (flux times local pore cross section) and the reaction source, respectively. For nonreacting species, the only net movement is that which must take place in order to fill the void volume created by the dissolving metallic phase. The time rate of change of the pore cross-sectional area may be related to the convective velocity by use of the relation for conservation of mass in the pores which, in the pseudosteady state, is

$$\rho_s \frac{\partial a}{\partial t} = -\frac{\partial}{\partial y}(\rho_s v a) + S_m \qquad [2]$$

The spatial coordinate, y, is taken to be zero at the back of the porous electrode and has the value of $+d$ at the mouth of the pores (face of the porous layer). The flux of solute species in the one dimensional electrolytic solution is given by the dilute solution expression

$$N_i = -D_i \frac{\partial c_i}{\partial y} - z_i D_i \frac{\mathbf{F}}{RT} c_i \frac{\partial \phi}{\partial y} + v c_i \qquad [3]$$

Here ϕ is the potential in the solution referred to the isopotential electrode matrix. For the electrode reaction which occurs in the pores, with the dissolved metal ion being designated species 1

$$\nu_0 M \rightarrow -\nu_1 M_1^{z_1} + ne^- \qquad [4]$$

the pseudohomogeneous species source term is

$$S_1 = -\frac{l\nu_1}{n\mathbf{F}} j \qquad [5]$$

where j is the local reaction (transfer) current density. Other source terms are absent. The transfer current density is in turn related to local concentrations and potential by the kinetic expression associated with the dissolution reaction, here the Volmer form

$$j = i_o \left[e^{-\frac{\alpha_a n\mathbf{F}}{RT}(\phi - \phi_e)} - \frac{c_1}{c_1^\infty} e^{\frac{\alpha_c n\mathbf{F}}{RT}(\phi - \phi_e)} \right] \qquad [6]$$

The pseudohomogeneous mass source term for the pore space is

$$S_m = \frac{m_1 l}{n\mathbf{F}} j \qquad [7]$$

Substitution of Eq. [2], [3], [5], [6], and [7] into Eq. [1] eliminates the time derivative term for pore area and incorporates the definitions of fluxes and sources in the species conservation equations. With neglect of the pseudohomogeneous mass source term, and with assumption of constant solution density, these equa-

[2] The meaning of symbols used in equations is given in the Notation section at the end of this article.

tions are

$$D_i \frac{d}{dy}\left(a\frac{dc_i}{dy}\right)+\frac{z_iD_i\mathbf{F}}{RT}\frac{d}{dy}\left(c_ia\frac{d\phi}{dy}\right)-\frac{d}{dy}(c_ivа)$$
$$=\frac{\nu_i l}{n\mathbf{F}}i_o\left[e^{-\frac{\alpha_a n\mathbf{F}}{RT}(\phi-\phi_e)}-\frac{c_1}{c_1{}^\infty}e^{\frac{\alpha_c n\mathbf{F}}{RT}(\phi-\phi_e)}\right]$$
$$-c_i\frac{d}{dy}(va) \qquad \nu_i=0 \text{ for } i\neq 1 \quad [8]$$

A conservation equation is written for each of the solute species i. These equations, along with the electroneutrality approximation

$$\sum_i z_ic_i=0 \qquad [9]$$

are sufficient in number for the calculation of the concentrations and the potential, provided that the pore area, pore perimeter, and convective velocity have been specified. For the system considered here, these are determined by the effect of local reaction on the solid matrix.

With the assumption that pores are circular cylinders, the radius will change at a rate proportional to the local reaction rate according to

$$\frac{d}{dt}(r^2)=\frac{2\bar{V}}{n\mathbf{F}}jr \qquad [10]$$

By integration of Eq. [10], the area and perimeter of the pores may be obtained at any one time during dissolution. The average local velocity past a point within the electrode is derived from a mass balance and is

$$v(y)=\frac{m_1}{n\mathbf{F}\rho_s a}\int_o^y l\left(1-\frac{\rho_s}{\rho_m}\right)j\,dy \qquad [11]$$

when the density of the electrolytic solution is constant. This equation indicates that the induced velocity arises from the difference between the densities of the solution and the metal, and that the velocity at position y depends on reaction in the portion of the electrode between that point and the back of the electrode.

The model is completely described when the appropriate boundary and initial conditions are specified. Prior to dissolution the pores are assumed to be of identical size and shape

$$a=a_o \text{ at } t=0 \qquad [12]$$

At the rear of the pores, the flux of each species is zero

$$N_i=0 \text{ at } y=0 \qquad [13]$$

At the entrance of the pores, the concentration of each solute species is equal to its value in the external electrolytic solution

$$c_i=c_i{}^\infty \text{ at } y=d,\ i\neq 1 \qquad [14]$$

The current density in the electrolyte at the mouth of the pores is defined as the sum of the individual ionic fluxes according to

$$i=\mathbf{F}\sum_i z_iN_i \qquad [15]$$

If the metal electrodes were not dissolving, then the current entering the pores could be solely attributed to the flux of the reacting ion. However, since the liquid volume within the pores is increasing by dissolution, that portion of the flux of the reacting ion passing into the electrode only to fill the void spaces is accompanied by equivalent counter ions and thus will not contribute to the current. The appropriate boundary condition in this case, derived by integration of the conservation equation over the entire electrode, is

$$i=-z_1\mathbf{F}D_1\frac{dc_1}{dy}-\frac{z_1{}^2\mathbf{F}D_1}{RT}c_1\frac{d\phi}{dy}+\frac{1}{a_f}\int_o^d va\,dc_1$$
$$\text{at } y=d \quad [16]$$

In many instances, the integral term will be negligibly small with respect to the sum of the other two terms and thus may be deleted from consideration. This was the case in the system for which numerical results were obtained for this paper.

The treatment of the equations is more convenient if the variables are made dimensionless. The following dimensionless variables are conveniently defined

$$Y=\frac{y}{d}, \qquad C_i=\frac{c_i}{c_{\text{ref}}}, \qquad \Phi=\frac{\mathbf{F}}{RT}(\phi-\phi_e),$$
$$V=\frac{vn\mathbf{F}}{i^*\bar{V}}, \qquad A=\frac{a}{a_o}, \qquad L=\frac{l}{l_o},$$
$$I=\frac{i}{i^*}, \qquad J=\frac{ld}{i^*a_f}j, \qquad \tau=\frac{\bar{V}i^*a_f}{n\mathbf{F}d}t$$

When these are introduced in Eq. [8] and [16], the following dimensionless groupings of the system parameters arise

$$\beta=\frac{i^*a_fd}{n\mathbf{F}c_{\text{ref}}D_{\text{ref}}a_o}, \qquad \xi=\frac{i_od^2l_o}{n\mathbf{F}c_{\text{ref}}D_{\text{ref}}a_o},$$
$$\zeta=\frac{i^*a_f\bar{V}d}{n\mathbf{F}D_{\text{ref}}a_o}, \qquad \gamma_i=\frac{c_i{}^\infty}{c_{\text{ref}}}, \qquad \pi_i=\frac{D_i}{D_{\text{ref}}}$$

With use of the notation prime (′) to denote differentiation with respect to the spatial variable Y, the dimensionless equations which describe the pseudo-steady state model become

$$(C_i'A)'+z_i(C_iA\Phi')'-\frac{\zeta}{\pi_iA_f}(C_i'AV)$$
$$=\frac{\nu_i\xi L}{\pi_i}\left[\exp(-\alpha_an\Phi)-\frac{C_1}{\gamma_1}\exp(\alpha_cn\Phi)\right] \qquad [17]$$

$$\sum_i z_iC_i=0 \qquad [18]$$

$$A=1+\int_o^\tau J\,d\tau \qquad [19]$$

$$V=\left(\frac{\rho_m}{\rho_s}-1\right)\frac{A_f}{A}\int_o^Y J\,dY \qquad [20]$$

Since the pores are circular cylinders, $L=\sqrt{A}$. The boundary conditions become

$$C_i'+z_iC_i\Phi'=0 \qquad \text{at } Y=0 \qquad [21]$$

and

$$\left.\begin{aligned} C_i&=\gamma_i\ (i\neq 1)\\ -\frac{n\beta}{z_1\pi_1A_f}&=C_1'+z_1C_1\Phi'\end{aligned}\right\}\ \text{at } Y=1 \qquad [22]$$

The calculations in this study were made with neglect of the integral term in Eq. [16], resulting in a boundary condition of the form of Eq. [22].

The mathematical model described above has extended previous treatments by accounting for two phenomena which take place during electrolytic dissolution: the change in specific surface area, and the convective motion arising from volumetric changes.

Solution of Equations

The solution of the set of equations and boundary conditions which describe the porous electrode model was carried out by a computer-implemented numerical technique. In principle, the calculation was accomplished in a stepwise manner, with use of finite difference methods for solution of the differential equations at each step. First, the conservation and electroneutrality equations, [17] and [18], were solved without the convection term and with constant porosity. The first approximation to the local convective velocity was then calculated by Eq. [20]. Conserva-

Table I. Parameters for porous copper anode system

$\rho_m = 8.94$ g/cm³		$n = 2$
$\rho_s = 1.00$ g/cm³		$\alpha_a = 0.5$
$m_m = 63.54$ g/gmol		$\alpha_c = 0.5$
$a_o = 1.964 \times 10^{-5}$ cm²		$c_{ref} = 10^{-3}$ gmol/cm³
$l_o = 2.22 \times 10^{-2}$ cm		$D_{ref} = 10^{-5}$ cm²/s
$d = 0.5$ cm		
$P_o = 0.035$		
$\nu_1 = -1$	$\nu_2 = 0$	$\nu_3 = 0$
$z_1 = +2$	$z_2 = -1$	$z_3 = +1$
$\gamma_1 = 0.145$	$\gamma_2 = 2.33$	$\gamma_3 = 2.04$
$\pi_1 = 0.7188$	$\pi_2 = 1.331$	$\pi_3 = 9.312$

tion and electroneutrality equations were again solved with use of the velocity distribution now at hand; these results corresponded to the conditions prevailing within the electrode at the end of the mass transfer transient but before appreciable dissolution had taken place. Then the calculations were made for specified time intervals during the pseudosteady state dissolution. With use of Eq. [19] and [20], the pore area (*i.e.*, porosity) distribution and the convective velocity distribution were calculated. With use of these new distributions, the conservation and electroneutrality equations were again solved, and the sequence repeated for as many time intervals as required.

The central problem of these calculations was the simultaneous solution of the species conservation expressions along with the electroneutrality condition. These coupled nonlinear ordinary differential equations were first linearized about an approximate solution and then put into finite difference form. The resulting set of tridiagonal matrices was solved by use of a computer-implemented technique described by Newman (17). The solution of the nonlinear problem was obtained by iteration with successive correction of the approximate solution.

Results and Discussion

The theoretical model developed above was used for generating predictions regarding the behavior of one porous electrode system. Ultimately it is intended that these model predictions be compared with the results of dissolution experiments that have been undertaken in a related project (18). Consequently the dissolution of porous copper anodes in acidified copper sulfate has been examined. For this system there are two alternate models for the electrolyte composition (and thus for electrolyte transport): the sulfate model (Cu^{+2}, H^+, SO_4^{-2}) and the bisulfate model (Cu^{+2}, H^+, HSO_4^-). For solutions having a larger concentration of sulfuric acid than copper sulfate the bisulfate model gives a more accurate prediction of the solution conductivity than does the sulfate model, and thus was chosen for these calculations. The system parameters are given in Table I.

For the moment, consider the state which exists after the mass transfer transient has decayed but before significant dissolution has taken place. Figure 1 shows the corresponding distribution of reaction rate

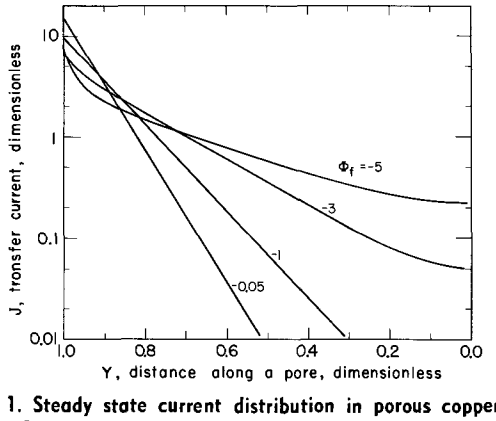

Fig. 1. Steady state current distribution in porous copper anode for $\xi = 25$ at several electrode overpotentials (Φ_f).

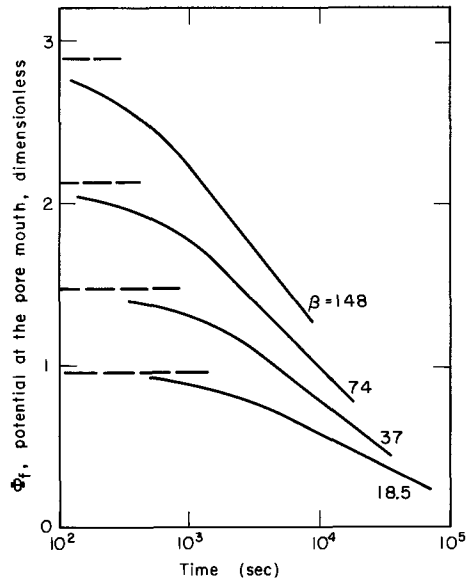

Fig. 2. Potential variation during dissolution of porous copper anode for $\xi = 400$ at several applied current densities (β).

throughout the porous electrode for various anodic values of applied potential, Φ_f. From this figure it may be seen that this initial steady state current distribution varies with applied potential, and that as the anodic potential is increased the reaction distribution generally becomes more uniform. For the case at hand, increasing $-\Phi_f$ above 3.0 renders the distribution still more uniform in the depth of the electrode while, nearer the pore entrance, the distribution begins to become more nonuniform.[3] This interesting situation may be understood by the following reasoning. Since the electrode consists of copper metal, the anodic reactant (the copper atom) is available in unlimited quantity whereas the cathodic reactant (the copper ion in solution) is not. Therefore the cathodic (back) reaction suffers from mass transfer limitations which do not hinder the anodic reaction. Consequently, at the same value of absolute potential, the cathodic reaction will be less uniformly distributed through the electrode. This tendency for the cathodic reaction to be less uniformly distributed carries over into the region of low anodic current where the cathodic back-reaction still occurs to an appreciable extent. Thus the most uniform reaction distribution is shifted into the anodic range of potentials. If both cathodic and anodic reactants had been available in unlimited quantity, the reaction distribution would have been most uniform at vanishingly small currents. This behavior is not predicted by simpler models which assume either constant concentration (thus neglecting concentration polarization of the back reaction) or a Tafel kinetic expression (neglecting the back reaction altogether).

The variation of electrode overpotential on dissolution is shown in Fig. 2. Results are shown for several values of the applied current density, β. The total overpotential of the electrode (the potential in the electrolytic solution at the pore entrance) increases with applied current density.[4] It can be seen that the polarization decreases below the "steady state" value (dashed lines in Fig. 2) and that the decrease in potential sets in earlier for the higher currents.

For the system at hand the theoretical model predicts that the uniformity of the reaction distribution near the pore entrance passes through a maximum at

[3] Hence for applied potentials more anodic than 3.0 it is not easy to designate which reaction distribution is most uniform, and arbitrary criteria must be used.

[4] Although the figure does not illustrate it, one may realize that for the same applied current density, the more rapid reactions, having higher values of ξ, suffer lesser polarization. For the slow reactions, charge transfer overpotential near the pore entrance forces the current deeper into the pore so that the reaction is more uniformly distributed at the expense of higher overpotential.

anodic potentials because of the mass transfer limitation of the back reaction as discussed above. Since the porosity distribution is equivalent to the time average current distribution, the "most uniform" final porosity distribution will correspond to a particular anodic current. Currents different from this particular one should lead to porosity distributions which are more nonuniform near the pore entrance. Final porosity distributions are given in Fig. 3 for several applied current densities. The total amount of charge passed is the same for all curves, and thus it may be seen that the model predicts the most nonuniform reaction distribution at the lowest applied current density ($\beta = 18.5$). As the applied current density is increased and the duration of electrolysis is decreased, the predicted final porosity distribution becomes more uniform. As the applied current density is increased still further, above $\beta = 148$, the porosity distribution near the entrance again begins to become nonuniform.

As dissolution proceeds, the current distribution becomes more uniform since the increased porosity facilitates penetration of current into the pores. Therefore the effect of porosity variation is to render the time average current distribution more uniform than the steady state distribution at uniform (initial) porosity. Also, for the system under study, the induced convection due to volumetric changes on dissolution tends to make the current distribution more uniform although, for this system, the current distribution is affected by less than 1% over the range of parameters presented here. It is possible that the pseudosteady state approximation would not be valid for cases where the induced convection was really significant. Although the current distribution thus changes as dissolution proceeds, if the change is only slight, the final porosity distribution may be estimated from the current distribution prevailing at the initial steady state conditions. When the final porosity distributions calculated by the pseudosteady state model (Fig. 3) were compared with similar results obtained with use of the initial steady state current distribution, the two methods gave results which agreed within 2% for the lower current densities. For β values of 148 and 296, the steady state model predicted porosities near the pore entrance which were up to 10% higher than the pseudosteady state model.

Conclusions

The performance of dissolving porous electrodes predicted in this work is, of course, subject to the limitations associated with the pseudosteady state macroscopic model used. The calculated results of the changing electrode structure are all entirely consistent in pattern with what should be expected on the basis of qualitative reasoning.

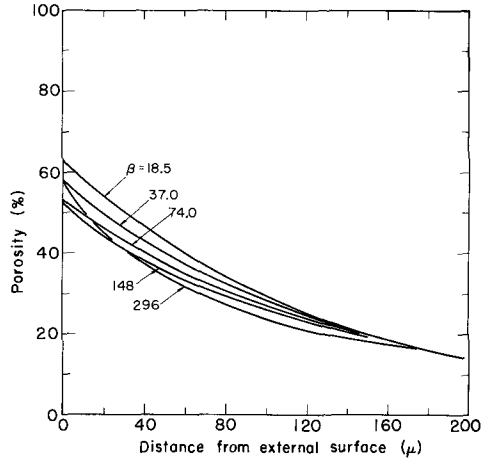

Fig. 3. Porosity distribution for porous copper anode after dissolution for 0.05 A-hr at several current densities ($\xi = 400$).

An interesting aspect of the behavior of anodically dissolving porous systems, although one not directly connected with matrix changes, is also evident in these results. That is the occurrence of the most uniform current distribution within the flooded porous electrode at a particular, nonvanishing applied current density as the result of mass transport limitations on the local cathodic (back) reaction.

In most practical flooded electrodes local variations in overpotential behavior due to inhomogeneities in the solid state, changes in microscopic configuration in the course of electrode reaction, and effects from reaction at the external electrode surface may cause significant deviations from the behavior patterns predicted by this theory. Also, in many systems, products, as well as reactants, appear in the solid state. However, consideration of these more complex cases will require better knowledge of mechanisms of electrode reactions and of the composition and distribution of solid materials in such electrodes before any meaningful quantitative analysis can be undertaken. In the meantime, useful insight into several performance characteristics for flooded porous electrodes can be gained from the present simplified theory. The pseudosteady state approach can be extended to more realistic cases as necessary information becomes available.

Acknowledgment

This work was supported by the United States Atomic Energy Commission.

NOTATION

A	a/a_o, cross sectional area of electrolyte, dimensionless.
a	Cross-sectional area of electrolyte, cm^2.
C_i	c_i/c_{ref}, concentration of species i, dimensionless.
c_i	Concentration of species i, gmol/cm^3.
c_{ref}	Reference concentration, gmol/cm^3.
D_i	Diffusion coefficient of species i, cm^2/s.
D_{ref}	Reference diffusion coefficient, cm^2/s.
d	Thickness of electrode, cm.
e	Symbol for electronic charge.
$\mathbf{F}$	Faraday's constant, 96,500 coul/g-equiv.
I	i/i^*, current density in the electrolyte, dimensionless.
i	Current density in the electrolyte, A/cm^2.
i^*	Current density in the electrolyte at the pore mouth, A/cm^2.
i_o	Exchange current density of the reaction rate expression, A/cm^2.
J	ldj/i^*a_f, transfer current density, dimensionless.
j	Transfer current density, A/cm^2.
L	l/l_o, perimeter of pore, dimensionless.
l	Perimeter of pore, cm.
M_i	Symbol for species i taking part in electrode reaction.
m_i	Molecular weight of species i.
N_i	Flux of species i, gmol/cm^{2}s.
n	Number of electrons taking part in reaction according to Eq. [5].
P	Porosity of electrode.
R	gas constant, joules/gmol °K.
r	Equivalent pore radius, cm.
S_i	Source term for species i, gmol/cm^{3}s.
T	Temperature, °K.
t	Time, s.
$\overline{V}$	Specific volume of electrode metal, cm^3/gmol.
v	Mass average fluid velocity, cm/s.
Y	y/l spatial variable in one-dimensional model, dimensionless.
y	Spatial variable in one-dimensional model, cm.
z_i	Charge number of ionic species i.

Greek Letters

α_a	Anodic transfer coefficient in reaction rate expression.
α_c	Cathodic transfer coefficient is reaction rate expression.
β	$i^*a_f d/n\mathbf{F}c_{ref}D_{ref}a_o$, dimensionless applied current density parameter.
γ_i	c_i/c_{ref}, bulk concentration of species i, dimensionless.

ρ_m Density of metal, g/cm³.
ρ_s Density of electrolytic, solution, g/cm³.
ζ $i^*a_f\bar{V}_m d/n\mathbf{F}D_{ref}a_o$, dimensionless velocity parameter.
ν_i Stoichiometric coefficient of species i according to Eq. [5].
ξ $i_o d^2 l_o/n\mathbf{F}c_{ref}D_{ref}a_o$, dimensionless kinetic parameter.
π_i D_i/D_{ref}, diffusion coefficient of species i, dimensionless.
Φ $\mathbf{F}(\phi-\phi_e)/RT$, polarization, dimensionless.
ϕ Electrode potential, V.
ϕ_e Equilibrium electrode potential, V.
τ $\bar{V}i^*a_f t/n\mathbf{F}d$, time, dimensionless.

Subscripts

f Value at entrance of pore, $y = d$.
i Species i.
o Initial value at onset of dissolution.

Superscripts

' Derivative with respect to spatial variable y.
∞ Value of variable in bulk electrolyte solution external to the porous electrode.

Manuscript submitted Feb. 24, 1969; revised manuscript received June 17, 1969.

Any discussion of this paper will appear in a Discussion Section to be published in the June 1970 JOURNAL.

REFERENCES

1. A. Frumkin, *Zh. Fiz. Khim.*, **23**, 1477 (1949).
2. C. Wagner, *Plating*, **43**, 997 (1961).
3. A. Winsel, *Z. Elektrochem.*, **66**, 287 (1962).
4. V. S. Daniel-Bekh, *Zh. Fiz. Khim.*, **22**, 697 (1948).
5. J. Euler and W. Nonnenmacher, *Electrochim. Acta.*, **2**, 268 (1960).
6. O. S. Ksenzhek, *Ukr. Khim. Zh.*, **23**, 443 (1957).
7. O. S. Ksenzhek and V. V. Stender, *Dokl. Akad. Nauk SSSR*, **106**, 487 (1956).
8. J. S. Newman and C. W. Tobias, *This Journal*, **109**, 1183 (1962).
9. F. A. Posey, *ibid.*, **111**, 1173 (1964).
10. I. A. Zaideman and R. M. Perskaya, *Zh. Fiz. Khim.*, **33**, 50 (1959).
11. E. A. Grens and C. W. Tobias, *Ber. Buns. f. Physik. Chem.*, **68**, 236 (1964).
12. L. G. Austin, in "Fuel Cells," Vol. 2, G. J. Young, Editor, Reinhold Publishing Co., New York (1963).
13. I. J. Gurevich and V. S. Bagotzky, *Electrochim. Acta*, **12**, 593 (1967).
14. M. Volmer and T. Erdey-Gruz, *Z. Physik. Chem.*, **150**, 205 (1930).
15. V. G. Levich, "Physicochemical Hydrodynamics," Prentice-Hall, Englewood Cliffs, N. J. (1962).
16. J. S. Newman, "Advances in Electrochemistry and Electrochemical Engineering," Vol. 5, C. W Tobias and P. Delahay, Editors, Interscience Publishers, New York (1967).
17. J. S. Newman, Report UCRL-17739, Lawrence Radiation Laboratory, University of California, Berkeley, August 1967.
18. R. C. Alkire, Report UCRL-18425, Lawrence Radiation Laboratory, University of California, Berkeley, September, 1968.

Cyclic Voltammetry of Mixed Metal Electrodes

Jaspal S. Mayell* and William A. Barber*

Central Research Division, American Cyanamid Company, Stamford, Connecticut

ABSTRACT

Repetitive potentiostatic triangular voltage sweeps cause a significant change in the surface structure and catalytic activity of mixed metal fuel cell electrodes. For the particular case of a platinum-rhodium black electrode, each successive cycle causes a decrease in the platinum oxidation and reduction peaks with a proportionate increase in the rhodium oxidation and reduction peaks. The complete elimination of the platinum peaks is related to the resistance of an electrode to CO poisoning. A possible mechanism of the above behavior along with data on other mixed metal electrodes is presented.

The electrochemical study of the surface characteristics of mixed metals can give new insight into their catalytic activity. Cyclic voltammetry of smooth platinum-gold alloys (1), has shown that the areas under the current-potential curves are proportional to the concentration of the metal present in the alloy. Using smooth platinum-chromium alloys, Breiter (2) attributed the change in the shape of the current-potential curves during the first 20 cycles to the gradual removal of impurities from the surface of the alloys. However, in our study repetitive triangular voltage sweeps caused a significant change in the surface structure and catalytic activity of mixed metals or alloy type electrodes. This behavior has not been reported previously.

The ultimate objective of this investigation is the development of fuel cell catalysts and electrodes which give enhanced performance on a hydrogen fuel containing up to 10% carbon monoxide. The most promising carbon monoxide resistant fuel cell electrodes reported are catalyzed by platinum-rhodium (3), platinum-ruthenium (4, 5), and platinum covered with sulfur (6-9). Repetitive cycling is shown in this study to improve the resistance of some mixed metal catalysts to carbon monoxide poisoning.

* Electrochemical Society Active Member.

Experimental

The working and the auxiliary electrodes were accommodated in a conventional H-type Pyrex glass electrolysis cell. Each compartment had a sintered glass disk through which nitrogen was continuously bubbled. Both compartments were covered by polytetrafluoroethylene (PTFE) stoppers with holes for the electrode holders, reference probe, and other equipment. The cell was maintained at constant temperature by means of an oil bath. The auxiliary electrode was an 80-mesh platinum gauze. The use of a sintered glass disk as well as continuous bubbling of nitrogen prevented the gases evolved at the cathode from reaching the anode.

All porous test electrodes were made according to the procedure described previously (10). They were acid washed before use. They were made liquid impermeable by application of a 15 mil thick porous polyfluorocarbon backing material (Cyanamid L-3 backing). The backing was applied at 150°C, by pressing at 150 psi for 5 min. The electrodes were held in the anode halfcell by a PTFE screw cap (11). Electrical connection to the fluorocarbon-backed anode (test electrode) was made by a platinum wire spot-welded to the tantalum screen. The advantages of this electrode assembly include ease of changing the elec-

trodes and of keeping any desired gas atmosphere at the back of the electrode.

The hydrogen reference electrode was constructed from PTFE-bonded platinum black on platinum screen. Hydrogen was bubbled over the electrode in 85% phosphoric acid. The reference electrode assembly was separated from the main body of the solution by a porous Vycor bulb. Connection to the test cell was made through an electrolyte bridge and Luggin capillary. All potentials mentioned in this study are with respect to the above hydrogen reference electrode, kept at room temperature. However, since the work was performed at 100°C (where the phosphoric acid concentration is more nearly 95-97%), a correction of 30 mV[1] due to temperature and concentration gradients has been subtracted from the observed potentials. The electrolytes phosphoric acid and sulfuric acid were of reagent grade quality and no special precautions were taken to purify the electrolytes. Some experiments were performed with hydrogen peroxide treated phosphoric acid (excess H_2O_2 removed by heating) but the results were similar to those of untreated phosphoric acid.

Platinum black used alone or in physical mixtures was commercial material (Engelhard Industries) with a BET surface area of 25-30 m^2/g. Rhodium black used alone or in physical mixtures was prepared by diphenylsilane reduction of rhodium chloride in ethanol at 70°C. It had a BET surface area of 40 m^2/g. Codeposited mixed blacks were prepared by coreduction from mixed solutions of the corresponding noble metal halides using diphenylsilane under the conditions mentioned above. All ratios and percentages reported are by weight.

For cyclic voltammetry, a Hewlett-Packard Model 202A low frequency generator was used to drive the Wenking potentiostat, Model 61TRS. The potentiostat was connected to the appropriate electrodes and the resulting current-potential curves were followed on a Moseley Model 135 X-Y recorder. Cycling the electrodes at different scan rates, from 3 mV/sec to 100 mV/sec, made no difference in the over-all behavior. In this study most of the cycling was performed at 30 mV/sec. While cycling, a nitrogen atmosphere was maintained at the back of the porous electrodes.

Polarization curves were obtained by applying a constant potential between the working and the reference electrodes for 2-3 min (which time was enough to reach a steady state) and recording the currents at a set of predetermined potentials.

Results and Discussion

Cyclic voltammetry of porous electrodes.—Electrodes of physically mixed platinum black and rhodium black (at 15 mg noble metal/cm^2 and later at 5 mg/cm^2) were cycled by repetitive triangular voltage sweeps between 0.05V and 1.50V. During the first cycle of mixed electrodes the size of the peaks corresponding to each metal was roughly proportional to the concentration of platinum and rhodium, as would be expected. Each successive cycle caused an increase in the rhodium oxidation and reduction peaks with a proportionate decrease in the platinum oxidation and reduction peaks (Fig. 1). With continued cycling, complete disappearance of the platinum peaks was observed (curve 2, Fig. 2). Further cycling beyond the disappearance of the platinum peaks caused a further increase in rhodium oxidation and reduction peaks (to 700 cycles) as shown in curve 3 of Fig. 2. Finally, with prolonged cycling, a gradual decrease of the rhodium peaks occurred followed by reappearance of the platinum peaks, as shown by curve 4 of Fig. 2 (2500 cycles).

A similar over-all behavior was observed in 6*N* H_2SO_4 at room temperature. However, the platinum peaks reappeared much earlier in sulfuric acid, after

[1] The corrective value of 30 mV was observed when the reference hydrogen electrode was at room temperature and the electrolysis cell (with hydrogen atmosphere over the working electrode) was at 100°C.

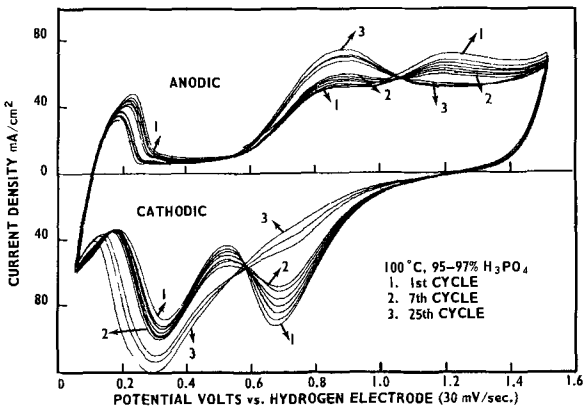

Fig. 1. Repetitive cycling of a porous mixed Pt-Rh electrode, 15 mg/cm^2 (2:1).

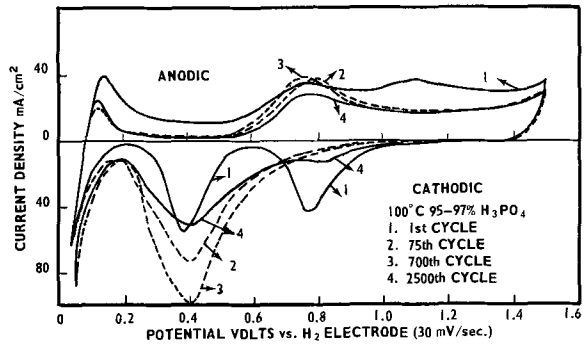

Fig. 2. Repetitive cycling of a porous mixed Pt-Rh electrode, 5 mg/cm^2 (1:1).

about 750 cycles, and they were approximately equal to the platinum peaks of the first cycle. The elimination and the reappearance of the platinum peaks with cycling is very characteristic, and its importance will be explained as the discussion proceeds. It should, however, be mentioned that the reproducibility of the peak heights (and consequently active electrochemical area) among different electrodes was not very good because of some apparently inherent nonuniformity in making the porous test electrodes.

Cyclic voltammetry of smooth electrodes.—To compare with high area electrodes, some work with smooth electrodes was performed. Cyclic voltammetric curves of smooth platinum, smooth rhodium and a smooth alloy of platinum-rhodium [50 w/o (weight per cent), 66 a/o (atom per cent) rhodium] are shown in Fig. 3. X-ray diffraction pattern of the platinum rhodium alloy (supplied by Engelhard Industries) showed the presence of a single phase. The first sweep of the alloy (curve 3) showed no platinum peaks. From the similarities of the curves 2 and 3, Fig. 3, the electrochemical surface characteristics of the alloy in the

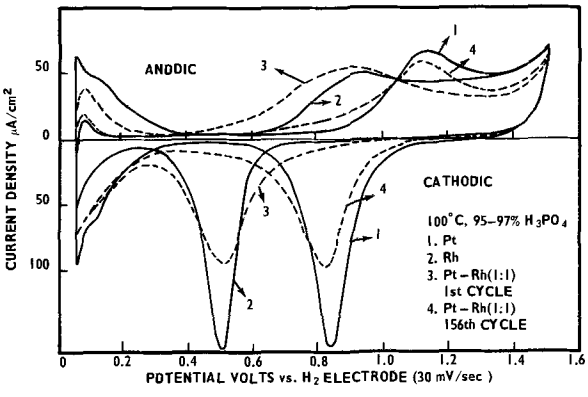

Fig. 3. Repetitive cycling of smooth electrodes

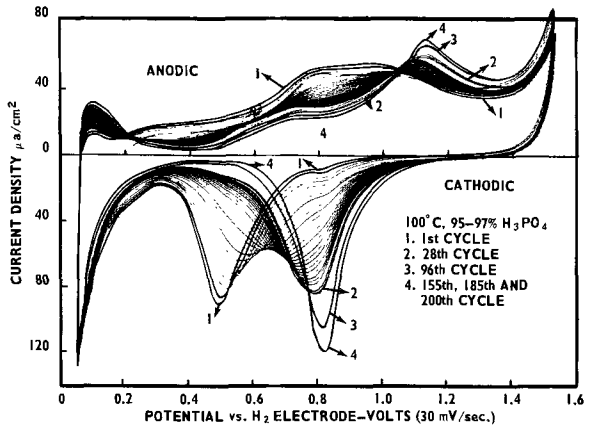

Fig. 4. Repetitive cycling of smooth Pt-Rh alloy (1:1)

beginning are similar to those of pure rhodium. However, a typical continuous cycling of the smooth alloy, Fig. 4, showed a gradual decrease in rhodium peaks and a proportionate increase in the platinum peaks with each successive cycle. Finally, only platinum peaks were visible as seen by curves 2 to 4, Fig. 4. Thus, cycling changed the surface characteristics of the smooth platinum-rhodium alloy from those of rhodium to those of platinum in about 150 cycles.

On first glance, the results obtained with a smooth alloy seem to contradict those reported earlier with porous mixed metals. However, we can reasonably well explain the above behavior if we assume that the rhodium oxides formed during the anodic cycle are at least partly soluble in the acid medium. In the case of smooth alloys, the rhodium oxides have a chance to diffuse away from the electrode surface and are not redeposited in the reduction half of the cycle, so that each succeeding cycle exposes more and more of the underlying immobile platinum sites and finally the surface behaves more like a pure platinum surface. In a porous electrode, however, the rhodium oxides are formed within the porous structure and do not have a chance to diffuse away completely but are redeposited during the cathodic half of the cycle covering some of the platinum in the process. Such a repetitive process of selective dissolution and random deposition would convert a physically mixed platinum-rhodium black surface to one with characteristics of rhodium alone. Not all of the rhodium oxides formed during each cycle were redeposited, as after very long cycling (2000 times or more) the rhodium peaks decreased and the platinum peaks reappeared. Qualitative analysis by atomic emission spectroscopy of the phosphoric acid electrolyte in which the porous platinum-rhodium electrode had been cycled showed the presence of rhodium and absence of platinum, indicating the validity of our assumption of the dissolution of rhodium oxides.

During cycling at 30 mV/sec two "iso-electronic" points, one at about 1.04V on the anodic sweep and the other at about 0.65V on the cathodic sweep, were observed both with porous as well as smooth platinum-rhodium electrodes. By analogy with "iso-sebestic" points of spectroscopy, it is likely that, during cycling, formation and reduction of oxides of rhodium and platinum occurred with the exclusion of other side reactions.

Polarization.—It is quite evident from the polarization curves of a series of electrodes (Fig. 5) made from physical mixtures of platinum black and rhodium black with from 0 to 100% rhodium, that the cycled electrodes (3 mV/sec) polarized less severely than the original uncycled electrodes. The over-all level of performance of the anode improved as the proportion of rhodium in the mixtures was increased both in the cycled as well as the original electrodes. Platinum black alone at 100°C performed very poorly while rhodium black showed the least polarization (Fig. 5).

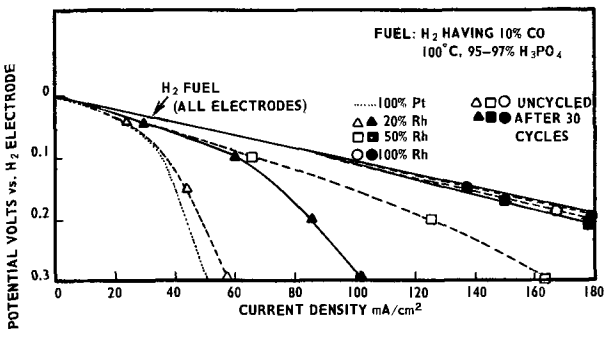

Fig. 5. Polarization curves of porous mixed Pt-Rh electrodes (15 mg/cm²).

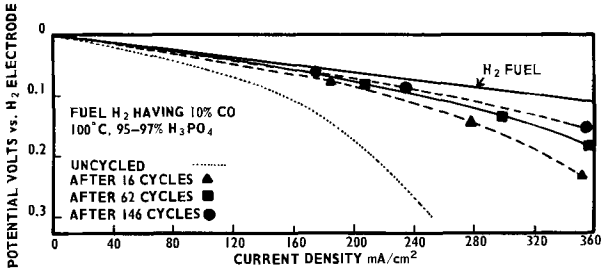

Fig. 6. Polarization curves of a porous mixed Pt-Rh electrode, 15 mg/cm² (1:1).

However, the cycled electrode having 50% or more of rhodium was almost as good as pure rhodium. Cycling (30 mV/sec) beyond the disappearance of the platinum peaks (about 30 cycles) caused a further decrease in polarization as seen in Fig. 6.

With the object of extending the performance improvements observed to lower catalyst levels, the concentration of the noble metals was decreased from 15 to 5 mg/cm². It was hoped that the catalyst could be spread to more advantageous sites by cyclic voltammetry. The polarization of such a physically mixed electrode decreased with cycling, as seen in Fig. 7 (during these cycles the rhodium peaks increased as at higher loadings but more gradually). However, after extremely long cycling (2350 times), the polarization increased considerably and was a little more than that of the original uncycled electrode (during these latter cycles, rhodium peaks decreased with reappearance of the platinum peaks). Attempts to increase the performance of 5 mg/cm² of a physically mixed platinum-rhodium with the addition of 5 mg/cm² of graphite as a conductive support were not successful. A new very small reduction peak at 0.85V was observed when the electrode containing graphite was oxidized to 1.50V. The identity of this peak was not established, but it may be due to reduction of oxides of carbon. In all cases of physically mixed platinum-rhodium black, a severe loss in performance was observed in going from 15 to 5 mg/cm².

No significant improvement in performance was observed when physically mixed platinum-rhodium

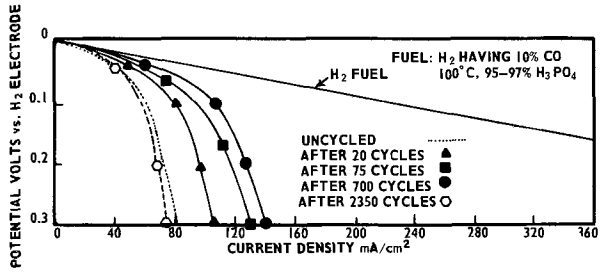

Fig. 7. Polarization curves of a porous mixed Pt-Rh electrode, 5 mg/cm² (1:1).

electrodes were cycled over the narrower region of 0.2-0.9V. Also, controlled potential oxidations at 0.9V (where rhodium oxide formation occurs) and at 1.5V (where both rhodium and platinum oxides are formed) caused no noticeable decrease in polarization. In one experiment the tantalum screen was replaced by a platinum screen to ascertain whether the disappearance of platinum peaks and the enhancement of rhodium peaks while cycling was in any way related to the presence of tantalum in the electrode. Cyclic voltammetric curves were similar with electrodes having either type of screen. However, the polarization obtained with a platinum screen electrode was less than that for a similar electrode using tantalum screen. This may be due to the better conductivity of the platinum screen.

Codeposit vs. physical mixture.—A codeposit of platinum and rhodium blacks was made by reduction of their chlorides with sodium borohydride and this catalyst was made into an electrode at 15 mg noble metal/cm^2. The results were then compared with a similar physically mixed electrode. On cycling, both electrodes showed improvement in resistance to carbon monoxide poisoning. However, the physically mixed electrode performed better at high current densities than the codeposited electrode. On the first cycle of a codeposited electrode, only one reduction peak (at 0.49V) was observed, and this shifted gradually to 0.45V after 150 cycles. This peak was between the platinum (0.77V) and rhodium (0.38V) reduction peaks of a physically mixed electrode. Prolonged cycling (1000 to 2000 times) of a codeposited electrode caused the appearance of a platinum reduction peak with a proportionate decrease in the initial peak. Qualitatively, this behavior was similar to a smooth alloy of platinum-rhodium, although only about 100 cycles were required to remove all the rhodium from the surface of the smooth alloy. The gradual appearance of the platinum peak with cycling on smooth alloy and codeposited platinum-rhodium electrodes is another indication of the dissolution of rhodium.

X-ray diffraction patterns using Cu-K radiation having a Ni filter (effective wavelength of 1.54050Å) of the physically mixed platinum and rhodium electrodes show two distinct phases, one platinum peak at 40° and the other rhodium peak at 41°, curve 1 of Fig. 8. After about 150 cycles, the two phases become better defined (curve 2, Fig. 8). The peaks were identified by comparing with the known samples of platinum and rhodium and also by checking with the literature data.

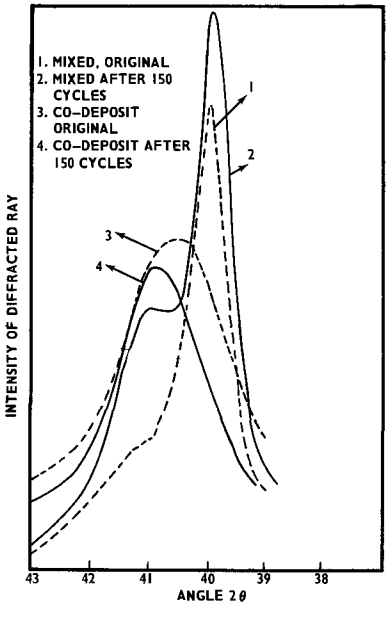

Fig. 8. X-ray diffraction patterns of mixed and codeposited Pt-Rh electrode, 15 mg/cm^2 (1:1).

The codeposited platinum-rhodium electrode on the other hand showed only a single (alloy) phase. After about 150 cycles, the peak shifted from about 40.5° to 40.8° (curves 3 and 4, Fig. 8) suggesting rhodium enrichment of the alloy phase near the electrode surface. This probably occurs by dissolution of the rhodium oxide during the anodic cycle and redeposition of rhodium on the platinum sites when the cycling is reversed. Cycling seems to result in crystallite size growth of the particles.

Electron microscopic data reveal that the metal phase in both codeposited and physically mixed platinum-rhodium electrodes is very fine and well-dispersed. Cycling caused an increase in the size of the particles and, in the case of the codeposited electrode, the formation of spheroidal metal particles (0.1 to 0.5μ).

It can be inferred from the results of cyclic voltammetry and x-ray diffraction data that a codeposited electrode is an "alloy," while the physically mixed electrode behaves as a simple mixture of platinum and rhodium even after cycling.

Palladium-rhodium electrode.—The results obtained with a physically mixed palladium black and rhodium black electrode were qualitatively similar to those obtained with the mixed platinum-rhodium electrode as discussed previously. As shown in Fig. 9, the initial twin peaks for palladium and rhodium were present, but with cycling the palladium reduction peak (at 0.63V) decreased leaving two small well-defined peaks (at 0.75 and 0.63V). The new peak at 0.75V may be due to platinum which is exposed at the surface because cycling caused dissolution of most of the palladium. Qualitative analysis by atomic emission spectroscopy of the electrode showed the presence of platinum (approximately 600 ppm) as an impurity. The performance of the uncycled electrode on H_2 having 10% CO at 100°C in phosphoric acid was good and improved with cycling (to 25 cycles). However, after longer cycling (to 214 times), the polarization increased while the rhodium peaks decreased. Also, during cycling a black precipitate, presumably due to the dissolution of palladium oxides, came out of the electrode. The black color became more intense during the anodic cycle at potentials > 1.20V. No significant change in polarization was observed when the mixed palladium-rhodium electrode was cycled between 0.2-0.9V instead of the usual 0.05-1.50V.

Platinum-ruthenium electrode.—Attempts to make electrodes of physically mixed platinum black and ruthenium black were not successful, since ruthenium dissolves in the acid wash given to all electrodes before use. A codeposit of platinum-ruthenium formed into an electrode was more stable and showed behavior qualitatively similar to a codeposited platinum-rhodium electrode. However, the ruthenium peaks disappeared almost completely in about 100 cycles, curve

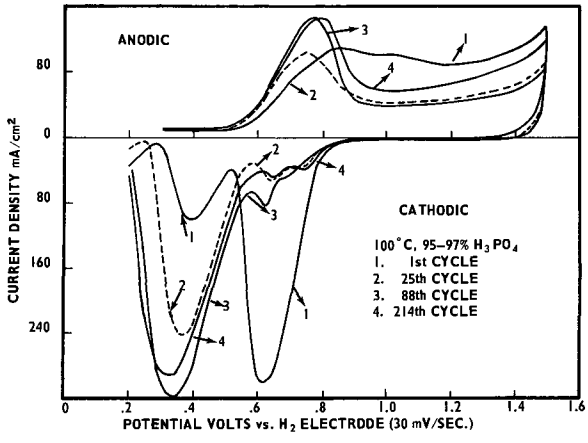

Fig. 9. Repetitive cycling of a porous mixed Pd-Rh electrode, 15 mg/cm^2 (1:1).

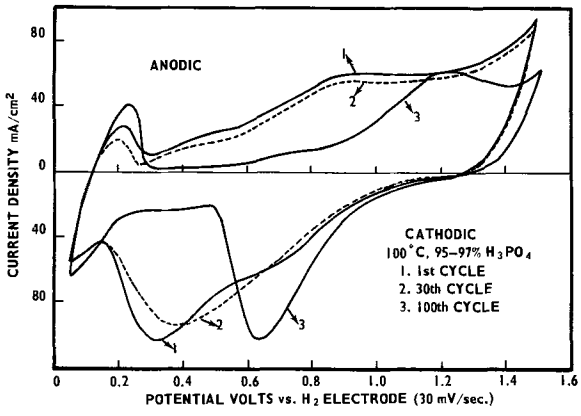

Fig. 10. Repetitive cycling of a porous codeposit of Pt-Ru, 10 mg/cm² (8:2).

3 of Fig. 10, and well-defined platinum peaks reappeared. This coincided with a sharp increase in polarization after 100 cycles. The disappearance of the ruthenium peaks and the formation of a brown precipitate during cycling suggests the dissolution or dispersion of ruthenium oxides into the acid electrolyte.

Gold-rhodium electrode.—Gold black (8 m²/g surface area) and rhodium black (30-40 m²/g surface area) were mixed in equal weight proportion to give an electrode with a total loading of 15 mg/cm². Cyclic voltammetry showed the oxidation and reduction peaks of rhodium (at 0.8 and 0.38V, respectively) and of gold (at 1.36 and 1.27V). Repetitive cycling decreased the gold peaks gradually. After about 20 cycles, no gold peaks were observed while a proportionate increase in rhodium peaks occurred. The original as well as the cycled electrode performed poorly on 10% CO in hydrogen.

RA (platinum-rhodium-WO_x) electrodes.—The RA catalyst is a special type found by empirical study to be unusually resistant to carbon monoxide poisoning. It is made (12) by codeposition of platinum-rhodium black in the presence of tungsten oxide (WO_x) with an oxidation state of the tungsten between 4 and 6. Cycling of this type of electrode showed only very large and well-defined rhodium peaks and no platinum peaks at all (curve 3, Fig. 11). Repetitive cycling decreased the rhodium peaks, evolved a yellow precipitate (more intense at potentials > 1.30V) presumably due to dissolution of higher oxides of tungsten, and caused an increase in polarization. Exceptionally good performance of such an electrode was obtained (Fig. 12) even at a total loading of noble metals of 5 mg/cm².

In another experiment platinum black and rhodium black were made separately in the presence of tungsten oxide. Although the two catalysts were made in a similar manner, on analysis it was found that the

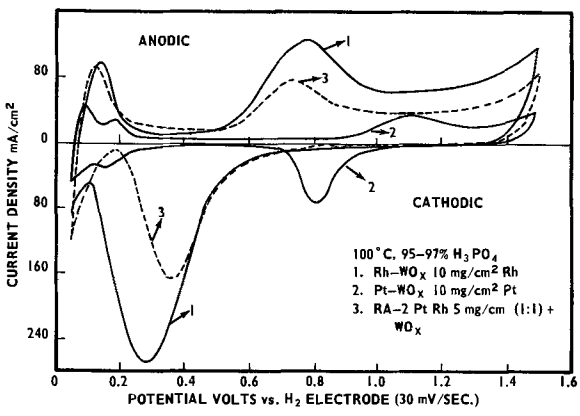

Fig. 11. Cyclic curves of various porous electrodes (first cycle)

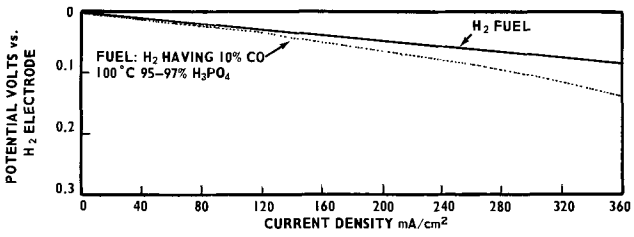

Fig. 12. Polarization curves of a porous RA2 electrode 5 mg/cm² Pt-Rh (1:1) 4 mg/cm² graphite + WO_x.

concentration of tungsten in the platinum black was about 3% while only about 0.3% in the rhodium black. Cyclic voltammetry of the rhodium-tungsten electrode shows a very large rhodium peak, curve 1 of Fig. 11, indicating that in the presence of tungsten oxide rhodium sites are readily exposed at the electrode surface. On the other hand, a platinum-tungsten electrode shows a very small platinum peak, curve 2 of Fig. 11, thereby indicating relatively few platinum electroactive sites.

Conclusions

Repetitive triangular voltage sweeps markedly changed the apparent surface structure of both porous mixed platinum-rhodium black electrodes and smooth alloy electrodes containing the same metals. In the case of mixed black electrodes, cycling changed the dual surface characteristics of platinum and rhodium to those of rhodium alone. However, very prolonged cycling caused the reemergence of platinum surface characteristics and diminution of rhodium characteristics. For a smooth platinum-rhodium alloy electrode, cycling changed the initial surface characteristics from those of rhodium alone to those typical of platinum.

The explanation of these observations appears to be the oxidation and selective partial dissolution of rhodium from the electrode surface. For the smooth alloy electrode it appears that rhodium oxide is selectively dissolved and diffuses into bulk solution before reduction can occur. For the mixed black electrode there appears to be selective solution and redeposition of rhodium on platinum within the porous electrode structure. Loss to bulk electrolyte is relatively slow, although when cycling is continued exhaustively, transfer to the bulk electrolyte becomes significant and platinum surface reappears with diminution of rhodium surface characteristics.

Studies of electrode polarization on hydrogen containing 10% CO indicate that maximum electrochemical performance (minimum polarization due to CO poisoning) occurs under conditions of maximum surface coverage of rhodium. Thus a cycled 1:1 platinum-rhodium black electrode which exhibited total replacement of platinum surface with rhodium was equivalent in performance to an electrode made of rhodium black alone.

In summary, the observed variations in electrocatalytic performance can be largely explained in terms of rhodium oxide dissolution and redistribution on cycling and the concept that maximum rhodium surface is required for minimum polarization due to CO poisoning.

The palladium-rhodium, platinum-ruthenium, and gold-rhodium systems all showed qualitative similarities to platinum-rhodium with respect to migration and redistribution of rhodium or ruthenium. The gold-rhodium system, however, was poor from an electrocatalytic standpoint, perhaps indicating that substrate composition can have an important influence on the activity of the rhodium surface. The general phenomena observed are thought to have broad application in the study of electrocatalysis.

Acknowledgments

The authors wish to thank Dr. L. A. Siegel for x-ray diffraction work and U. S. Army Mobility Equipment

Research and Development Center for their financial support under Contract No. DA-44-009-AMC-897(T).

Manuscript submitted June 3, 1969; revised manuscript received June 26, 1969. This was Paper 329 presented at the Montreal Meeting, Oct. 6-11, 1968.

Any discussion of this paper will appear in a Discussion Section to be published in the June 1970 JOURNAL.

REFERENCES

1. M. W. Breiter, *J. Phys. Chem.*, **69**, 901 (1965).
2. M. W. Breiter, *J. Electroanal. Chem.*, **10**, 191 (1965).
3. W. A. Barber, U.S. Pat. 3,364,072 (1968).
4. D. W. McKee, L. W. Niedrach, J. Paynter, and I. F. Danzig, *Electrochem. Technol.*, **5**, 419 (1967).
5. D. W. McKee and A. J. Scarpellino, Jr., *ibid.*, **6**, 101 (1968).
6. H. Binder, A. Köhling, and G. Sandstede, *Advan. Energy Conversion*, **7**, 77 (1967).
7. H. Binder, A. Köhling, and G. Sandstede, *ibid.*, **7**, 121 (1967).
8. H. Binder, A. Köhling, and G. Sandstede, *Biennial Fuel Cell Symposium*, Am. Chem. Soc., Chicago, **11**, 106 (1967).
9. H. Binder, A. Köhling, and G. Sandstede, *Nature*, **214**, 268 (1967).
10. R. G. Haldeman, W. P. Colman, S. H. Langer, and W. A. Barber, *Advan. Chem. Ser.*, **47**, 106 (1965).
11. J. D. Voorhies, J. S. Mayell, and H. P. Landi, "Hydrocarbon Fuel Cell Technology," p. 455, Academic Press, New York (1965).
12. L. K. Ziering, U. S. Pat. 3,357,863 (1967).

The High Rate Oxidation of Silver Electrodes in Chloride Solutions

P. Bro* and N. Marincic*

P. R. Mallory & Company, Inc., Laboratory for Physical Science, Burlington, Massachusetts

ABSTRACT

The anodic oxidation of silver in zinc chloride solutions demonstrated the feasibility of operating rechargeable silver/silver chloride battery electrodes at charging rates up to 150C without any gas evolution. Specific capacities of about 2 mA-hr/cm^2 were obtained at current densities between 60 and 300 mA/cm^2. The greatest charge acceptance was obtained with thin silver electrodes and with zinc chloride solutions containing sodium perchlorate. The charging process was generally terminated by the boiling of the electrolyte in the diffusion layer at the electrode.

Conventional storage batteries have low intrinsic charging rate capabilities, and attempts to charge them quickly invariably lead to unwanted parasitic reactions. We have searched for a system with a high intrinsic charging rate capability, and we have reached the conclusion that the highest rates can be obtained, most probably, with electrodes formed by deposition from concentrated solutions of their salts. The rate capabilities have already been discussed of anodes which are formed by deposition from chloride solutions of the anode metals (1, 2), and the results indicated that very high charging rates could be employed. It would be expected, likewise, that cathodes might be charged rapidly when formed by the oxidation of suitable metals in concentrated solutions of salts containing the cathode anion.

We found that silver electrodes could be oxidized electrochemically at very high rates in chloride solutions without gassing, particularly in the case of thin silver electrodes, to give useful silver/silver chloride battery cathodes. The studies reported here were undertaken to obtain an understanding of the fast charging process and to establish the rate limiting factors. We also report the rate and charge acceptance capabilities of the silver/silver chloride cathode in an electrolyte suitable for the operation of rechargeable zinc/silver chloride cells.

Experimental Techniques

Flat silver electrodes were charged in zinc chloride solutions under constant current conditions in cells shown schematically in Fig. 1. Conventional chronopotentiometric circuitry was used. The constant current was derived from a 240V stack of lead acid storage batteries in series with a variable resistor or from a Harrison power supply, Model 6443B. The electrode potentials were measured with respect to a Ag/AgCl reference electrode in the same solution located about 0.5 cm in front of the working electrode. The chronopotentiograms were recorded with a Sargent recorder, Model DSRG. It is estimated that the currents remained constant within 2% during the charging process. The currents were measured with a Greibach ammeter, Model 560 or 700, with an accuracy of $\pm$ 0.5%.

The circular silver electrodes were made from 99.9% pure silver and had a diameter of 1.85 cm, almost equal to that of the inner diameter of the cylindrical cell, 1.90 cm, to provide a uniform current density on the electrode. Copper-constantan thermocouples made of 1 mil wires were cemented to the rear of the electrodes with silver amalgam, and the mounted thermocouples were calibrated in a constant temperature bath. The potential of the thermocouples was recorded directly on the Sargent DSRG duo-channel recorder concurrently with the potential of the working electrode. The response time of the electrode-thermocouple system was limited by that of the recorder, about 1 sec for full scale deflection. The finite thickness of the electrodes introduced a short but noticeable delay in the thermal response of the thermocouple to a change

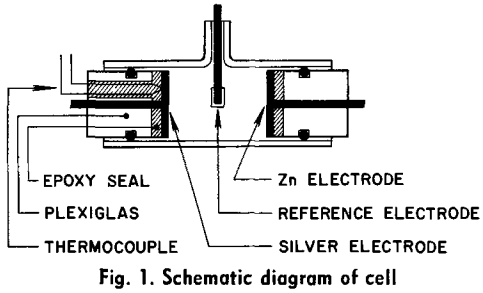

Fig. 1. Schematic diagram of cell

* Electrochemical Society Active Member.

in the temperature of the front surface of the electrodes.

The electrodes were reconditioned after each charge by the removal of the silver chloride and the repolishing of the electrode with a grade 500 emery cloth. The oxidation occurred uniformly over the silver surface, with occasional pitting, which allowed the change in the thickness of the electrodes to be calculated from the total charge per pulse. Measurements of the electrode thickness after several runs confirmed the validity of these calculations.

Zinc was used as a counterelectrode to avoid gas formation at the negative electrode during charging. All the solutions were prepared from reagent grade chemicals, and the zinc salt concentrations of the stock solutions were determined polarographically.

Experimental Results

A typical thermal response curve of a thin silver electrode is shown in Fig. 2. After an initial delay in the thermocouple response caused by the finite thickness of the electrode the temperature of the silver electrode rose rapidly with a positive curvature. Then, the rate of rise decreased, and strong thermal fluctuations developed. The voltage across the electrode followed a similar pattern. At the point where the thermal and potential fluctuations began, the silver chloride film began to deteriorate. Generally, microvolcanic eruptions occurred in the film accompanied by incipient boiling noises and an intense agitation of the electrolyte in the crater regions. Strong convective currents were generally observed within 5-20 sec of the start of the charging pulse, depending on the electrolyte composition and the current density. Occasionally, boiling occurred before film failure. The onset of film failure or boiling signalled the end of efficient charging and was used to define the charge acceptance of the electrode.

The charge acceptance of the electrodes did not vary much with the current density. The greatest change was observed in the 2.0M $ZnCl_2$, 0.5M $NaClO_4$ solution, Fig. 3, where it increased from about 1.5 mA-hr/cm^2 at current densities above 200 ma/cm^2 to values greater than 2.0 mA-hr/cm^2 at current densities below 60 ma/cm^2. Smaller changes were observed for the less concentrated supporting electrolytes. The smallest charge acceptance of about 0.8 mA-hr/cm^2 was found for electrodes charged in 2.0M $ZnCl_2$ containing no supporting electrolytes. At current densities below the values reported here the silver chloride films were either poorly attached to the electrode or the silver chloride was present as a loosely adhering powder. Although the low current densities gave high specific capacities on charge the poor quality of the silver chloride rendered the charge nonrecoverable.

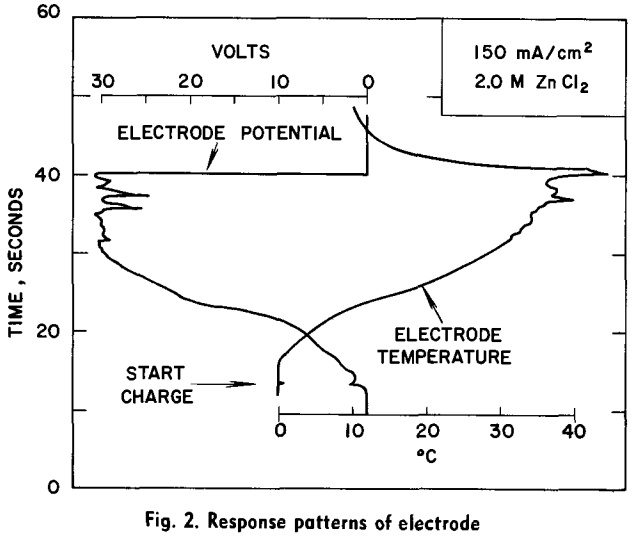

Fig. 2. Response patterns of electrode

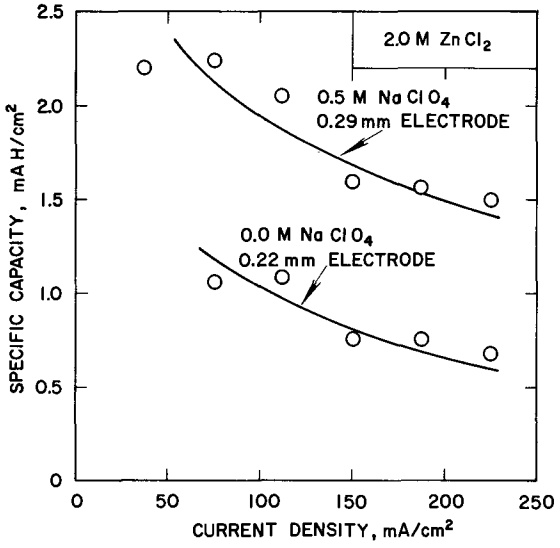

Fig. 3. Influence of the current density on the charge acceptance

The reported charge acceptance pertains to the charge rather than the discharge of the silver/silver chloride electrode. Separate experiments established that discharge efficiencies above 95% were obtained whenever visually sound films of silver chloride were formed. The discharges were performed at 0.4-4.4 mA/cm^2. Repeated cycling of Zn/AgCl cells under various conditions confirmed the high coulombic efficiency of the sytsem.

The zinc chloride concentration of the electrolyte exerted a strong influence on the behavior of the Ag/AgCl electrode. In saturated zinc chloride solutions the silver chloride films dissolved rapidly, 70 μA/cm^2, presumably due to the formation of soluble $AgCl_2^-$. The self-discharge rate was reduced to less than 1 μA/cm^2 at room temperature for zinc chloride concentrations below 2M. This was considered an acceptable self-discharge rate for the Zn/AgCl cells. Since it was desirable to use high zinc ion and high chloride ion concentrations to enhance the mass transfer rates at the electrodes, the 2.0M zinc chloride electrolyte represented a satisfactory compromise, and most of the studies were limited to this electrolyte.

The exploratory experiments had indicated that the high rate charging process gave higher capacities on thin electrodes than on thick ones. This led to the conjecture that a successful high rate charging depended on the heating of the silver chloride film. At elevated temperatures film defects would heal during the charging process and the film would also be more conductive. Because of its large heat capacity the temperatures of the silver chloride film on a thick silver electrode would remain low, the film would not heal, and the charge acceptance would be low. A series of experiments with a thick electrode containing 35g silver/cm^2 showed that it had only about one third the charge acceptance of the thin electrodes reported on here; the latter contained less than 0.7g silver/cm^2.

An examination of the charging curves indicated that the half-cell voltages at the film failure points varied little with the current density, which allowed the use of a mean failure voltage for each solution, Fig. 4. In the absence of a supporting electrolyte, the end of useful charging occurred at about 27V. It rose to about 31V in the 2.0M $ZnCl_2$, 0.5M $NaClO_4$ solution, and it decreased to about 21V in the 2.0M $ZnCl_2$, 1.0M $NaClO_4$ solution. The thickness of the electrodes did not influence the failure point voltages noticeably for the thin electrodes.

The initial thermal response of the electrodes would be expected to reflect the influence of the system variables more clearly than would their temperature at the failure points because of the strong convective disturbances in the electrolyte toward the end of the

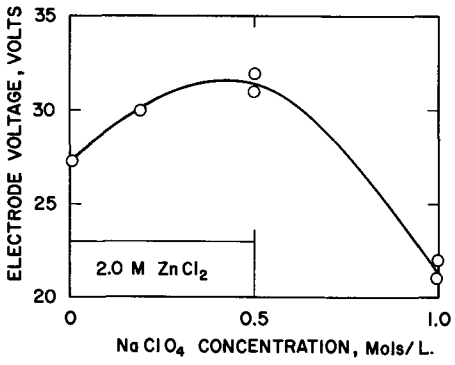

Fig. 4. End of charge voltage of the Ag/AgCl electrode

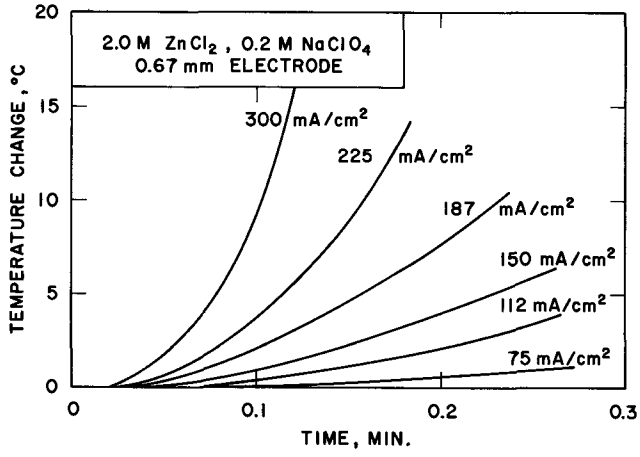

Fig. 5. Heating rate of the electrode

charging process. The rate of heating of the electrodes increased rapidly with the current density, Fig. 5. Rates were reached of 5°C/min at 75 mA/cm² and 250°C/min at 300 mA/cm² after 6 sec of charging in the 2.0M $ZnCl_2$, 0.2M $NaClO_4$ solution for a 0.067 cm thick electrode. The thickness of the thin silver substrates did not affect the rate of heating noticeably, Fig. 6. However, the composition of the electrolyte exerted a strong influence on the heating rate, Fig. 7. The lower the concentration of the supporting electrolyte, the greater the heating rate under otherwise identical conditions. In 2.0M $ZnCl_2$, 1.0M $NaClO_4$ it reached a value of 21°C/min after 12 sec at 150 mA/cm²; the corresponding value in 2.0M $ZnCl_2$ was 280°C/min.

The thermal histories beyond the initial charging period increased in variability, and the influence of the various parameters could not be discerned unambiguously.

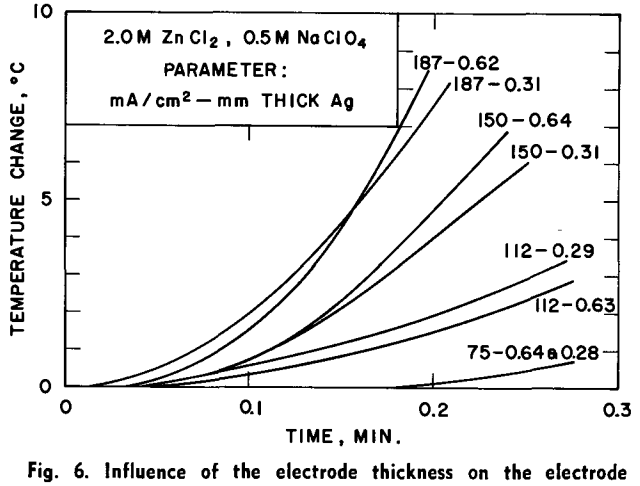

Fig. 6. Influence of the electrode thickness on the electrode temperature.

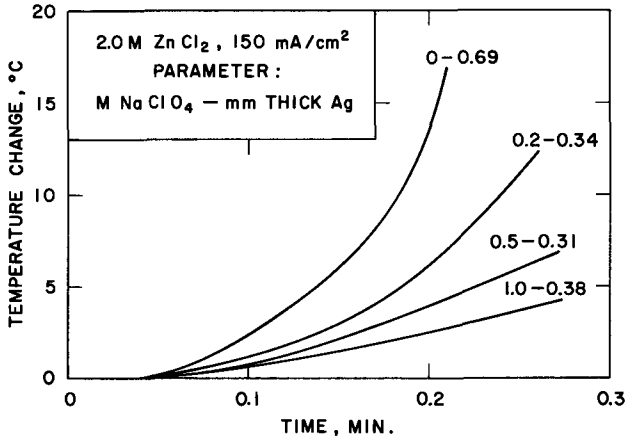

Fig. 7. Influence of the supporting electrolyte on the electrode temperature.

Discussion

The experimental work demonstrated that flat silver electrodes could be charged efficiently at very high current densities, at rates as high as 150C in battery terminology, to give recoverable specific capacities of about 2 mA-hr/cm². The charging process was strongly dependent on the quality of the silver chloride film formed on oxidation. At current densities below about 40 mA/cm² inferior films were formed on the flat electrodes and they gave low discharge efficiencies. Above about 60 mA/cm² good films were formed which gave high coulombic efficiencies on discharge. These observations are in general agreement with the results reported in the literature. Jaenicke *et al.* (3) found that patchy films were obtained at low current densities which adhered poorly to the substrates. Above 30 mA/cm² silver chloride films were obtained which adhered well to their substrates.

Once a uniform silver chloride layer is present on a silver electrode no gas evolution would be expected at the AgCl/electrolyte interface since silver chloride is a purely ionic conductor. Exceptions were noted at the lower current densities where a transitory, thin, dark film appeared on the electrodes at the onset of charging. Very light gassing could then be seen which may be attributed to the electronic conductivity of the dark film which was, presumably, silver chloride with a high defect concentration. At the higher current densities the dark film persisted for a very short time only and no gas evolution could be seen.

In principle, it should be possible to oxidize a silver electrode at a very high rate since the process consists of the simple abstraction of electrons from the metal. Any rate limiting factors, if present, would be associated with the transport processes in the system. The evolution of chlorine at the silver/silver chloride interface might be a limiting process, but no observations indicated its occurrence. Two processes may be considered. Once a uniform silver chloride film is present on the electrode the rate of transport of silver ions through the film would be limited only by the voltage across the film. High potentials were used to operate the electrodes at the high rates and constant rates of transport could be maintained, but only by the use of a rapidly increasing voltage across the electrode to match the increasing resistance of the electrodes. Adequate rates of transport were maintained until the films failed. The failures appeared as localized fusion of the silver chloride film, and local boiling ensued which terminated the efficient charging process. It is probable that the failures began in the micropores thought to be present in silver chloride films (3). The other rate limiting process to be considered may be attributed to the removal of chloride ions by the precipitation of silver chloride and the attendant depletion of charge carriers in the electrolyte. The efficient deposition of silver chloride on the electrode indicated

that an adequate supply of chloride ions was available at the electrode. However, the heating and eventual boiling of the solution indicated that an appreciable carrier depletion had occurred which gave rise to an excessive resistive heating of the electrolyte adjacent to the electrode. The design of the cell and the experimental procedures did not allow a discrimination between the potential differences across the silver chloride film and across the diffusion layer. The discussion will be based, therefore, on inferences drawn from the effects of the electrolyte composition on the electrode performance.

The constant current charging process was accompanied by strong convective currents at the electrode which invalidated a conventional chronopotentiometric analysis of the charge acceptance. Nevertheless, it is instructive to consider this simple mass transfer limitation. Using the transition time data for concentrated zinc chloride solutions (1) it was estimated that specific capacities of 3 mA-hr/cm^2 should be obtained at 300 mA/cm^2 in the absence of a supporting electrolyte and about 1.5 mA-hr/cm^2 in the presence of a supporting electrolyte for 2.0M $ZnCl_2$ solutions. A contrary behavior was observed. The charge acceptance increased with an increase in the concentration of the supporting electrolyte. However, the charge acceptance increased with a decrease in the current density in conformity with the expectations based on the chronopotentiometric equations. These observations suggested that the charging process was transport limited in the supporting electrolyte. The observed and expected capacities were both 1.5 mA-hr/cm^2 at 300 mA/cm^2, and at 100 mA/cm^2 they were about 2 mA-hr/cm^2 and 4 mA-hr/cm^2, respectively. This is a reasonably good agreement, but not adequate for any quantitative deductions.

The smaller capacity in the absence of a supporting electrolyte suggested that a limiting process other than mass transport intervened, and, as noted earlier, the charging process was terminated by the excessive heating of the electrolyte. The thermal response of the electrodes showed that the heating rate of the system increased markedly with a decrease in the concentration of the supporting electrolyte. If the silver chloride film had been the principal source of ohmic heat, the rate of heating would have been the same at the same current density for the various solutions. Since they were markedly different, the principal voltage drop and heat generation must have occurred in the electrolyte; the more so the lower the concentration of the supporting electrolyte, and the electrode capacities would be less than those expected for a mass transport limited system, as observed.

The potential difference across the Ag/AgCl half-cell at the failure points reached a maximum value of about 32V for a 0.5M $NaClO_4$, 2.0M $ZnCl_2$ solution, and it decreased for both lower and higher concentrations of the supporting electrolyte. The smaller failure point voltages in the more concentrated supporting electrolytes may be attributed to the greater conductivity of the electrolytes. The smaller failure point voltages in the less concentrated supporting electrolytes may be explained with reference to the thickness of the silver chloride films. The charge acceptance data showed that the film thickness decreased for concentrations of the supporting electrolyte below about 0.5M $NaClO_4$; it remained essentially constant for more concentrated solutions. Therefore, for the given rate of energy deposition in the electrolyte needed to cause boiling, the total potential drop across the half-cell at the failure point would be less for the less concentrated solutions, as observed.

Conclusions

The search for a rechargeable battery cathode capable of accepting a high charging rate with a high efficiency showed that flat silver/silver chloride electrodes could be charged under constant current conditions at rates as high as 150C (300 mA/cm^2) to specific capacities of about 2 mA-hr/cm^2 in zinc chloride solutions. The high rate of charge was accompanied by a considerable evolution of heat at the electrode, and the charging process was generally terminated by the boiling of the electrolyte. The ohmic heating of the electrolyte in the diffusion layer was the principal cause of heat generation. Some heat was also generated by the ohmic heating of the silver chloride film. Low rates of charge in the same system, below 60 mA/cm^2, led to the formation of silver chloride films which could not be discharged efficiently.

The addition of sodium perchlorate as a supporting electrolyte in the zinc chloride solution decreased the rate of heat generation in the system and increased the charge acceptance by delaying the onset of boiling. When the termination of efficient charging was thus delayed the charge acceptance reached values close to those predicted from the chronopotentiometric equations for the depletion of chloride ions at the electrode.

The application of these results to a rechargeable cell will be considered in a subsequent report.

Manuscript submitted Feb. 24, 1969; revised manuscript received June 20, 1969.

Any discussion of this paper will appear in a Discussion Section to be published in the June 1970 JOURNAL.

REFERENCES

1. P. Bro and N. Marincic, *This Journal*, **116**, 448 (1969).
2. P. Bro and N. Marincic, *ibid.*, To be published.
3. W. Jaenicke, R. P. Tischer, and H. Gerischer, Z. *Elektrochem.*, **59**, 448 (1955).

Erratum

In the paper "Study of the Lithium Oxide-Nickel Oxide System, I. Thermodynamics of Dilute Solid Solutions" by S. Pizzini, R. Morlotti, and V. Wagner which was published on pp. 915-920 of the July 1969 issue of the JOURNAL, Vol. 116, No. 7, there is a small error in Eq. [8] and [8a]. These should be written as follows:

$$\mathbf{F}E = -[\bar{G}_{LiNiO_2(x_1)} - \bar{G}_{LiNiO_2(x_2)}] \equiv RT \ln \frac{a^*_{2(LiNiO_2)}}{a^*_{1(LiNiO_2)}} \quad [8]$$

$$E = \frac{RT}{\mathbf{F}} \ln \frac{x_2}{x_1} \quad [8a]$$

The Effect of High Pressure on the Voltage and Current Output of Silver Oxide-Zinc and Mercury Oxide-Zinc Miniature Batteries

T. N. Andersen, B. A. Miner,[1] M. H. Ghandehari, R. J. Brodd,*[2] and H. Eyring

Departments of Chemistry and Metallurgy, University of Utah, Salt Lake City, Utah

ABSTRACT

The open circuit voltage (emf) and the voltage under load of alkaline silver oxide-zinc and mercuric oxide-zinc miniature batteries have been measured at pressures up to 20 kbars. The emf of these batteries varies with pressure in the manner expected based on the thermodynamics of the cell reactions. Pressure affects the voltage of the discharging silver oxide batteries only through its effect on the emf. The voltage of the discharging mercuric oxide battery is lowered with increasing pressure by approximately 5 mV/kbar. This decrease in voltage is due both to an increase in the overvoltage at the HgO electrode and also to the ohmic resistance. These pressure effects are discussed in terms of the postulated diffusion of hydroxyl ions through water channels in the reduced oxide and the influence of these channels on the number of oxide sites at which reduction may occur.

From thermodynamics it is possible to theoretically calculate the effect of pressure on the reversible emf, $E°$, of a voltaic cell or battery. The emf is related to the standard Gibbs free energy for the battery reaction according to the well-known relationship

$$\Delta G = n\mathbf{F}E° \qquad [1]$$

The standard free energy of the reaction is related to the standard change in entropy and volume for the battery reaction according to the expression

$$\Delta G = -\Delta S dT + \Delta V dP \qquad [2]$$

From Eq. [1] and [2] the pressure coefficient of the emf is given (at constant temperature) as follows

$$\left(\frac{dE°}{dP}\right)_T = \frac{\Delta V}{n\mathbf{F}} \qquad [3a]$$

or

$$\left(\frac{dE°}{dP}\right)_T \text{(in mV/kbar)}^3 = 1.036\,\frac{\Delta V}{n} \text{ (in cm}^3\text{/mole)} \qquad [3b]$$

Here n is the number of moles of electrons transferred during the consumption of one mole of reactants. For a particular reaction ΔV can be calculated by subtracting the molar volumes of the reactants from those of the products. At atmospheric pressure the molar volumes of the substances of concern to us here are readily found from density data (1). At high pressures one would need pressure *vs.* volume data in order to obtain ΔV and hence $(dE°/dP)_T$.

The circuit of a battery under load is shown schematically in Fig. 1. The voltage output, E_{AB}, of such a cell is given by

$$\left.\begin{aligned} E_{AB} &= iR_l = E_1 - E_2 - iR_{\text{int}} \\ &= E°_1 - E°_2 - |\eta_1| - |\eta_2| - iR_{\text{int}} \\ &= E° - |\eta_1| - |\eta_2| - iR_{\text{int}} \\ &= E° - |\eta_1| - |\eta_2| - (E_1 - E_2)\,\frac{R_{\text{int}}}{R_{\text{int}} + R_l} \end{aligned}\right\} \qquad [4]$$

Here R_{int} is the ohmic resistance of the electrolyte (including the matrix in which it is embedded, see Fig. 3) in the battery, E_1 and E_2 are the potentials of the electrodes 1 and 2 with respect to a fixed reference electrode, $E°_1$ and $E°_2$ are the open circuit potentials of electrodes 1 and 2 (such that $E°_1 - E°_2 = E°$, the emf of the battery), and η_1 and η_2 are the overvoltages of the electrodes at the given current output of the battery. The overvoltage terms both act to diminish the potential difference between the two electrodes and are due to free energy barriers to charge-transfer at the metal-metal oxide and metal oxide-electrolyte interphases as well as to concentration polarization of the reactants at these interphases due to the slow diffusion of ions or to slow crystallization. The effect of pressure on E_{AB} (Eq. [4]) cannot be predicted from thermodynamics alone, since only $E°$ is a thermodynamic quantity while η_1, η_2 and iR_{int} depend on the chemical kinetics and the transport properties of the system.

In this study we have measured the emf of Ag_2O-zinc and HgO-zinc batteries as a function of pressure. We have also compared the pressure effects on the voltage of these batteries while under load to the pressure effects on $E°$, relevant to studying the relative changes with P of the various terms in Eq. [4].

Experimental Setup

The batteries were squeezed in a piston-cylinder press as shown in Fig. 2. The pistons, of diameters 0.5 or 1.0 in., were driven by a hydraulic ram which was operated with a manual pump. Each battery under study was placed in a talc pressure medium within the cylinder such that the positive pole contacted the sintered tungsten carbide piston (*cf.* Fig. 2). A lead from the piston to the potentiometer thus contacted the latter with the battery. A wire lead was connected to the negative pole of the battery by means of a conductive-epoxy cement, and this lead was run out of the pressure cell between insulating sheets (as shown in Fig. 2) to the negative jack of the potentiometer. The flow properties of the talc under pressure made for a quite uniform pressure around the battery (semihydrostatic), and also prevented the battery

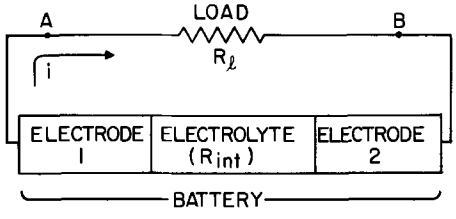

Fig. 1. Schematic diagram of a battery under load

* Electrochemical Society Active Member.

[1] Present address: Department of Chemistry, Weber State College, Ogden, Utah.

[2] Present address: Union Carbide Corporation, Consumer Products Division, Parma, Ohio.

[3] In this work the pressure is expressed in kilobars (kbar) where 1 atm = 1.01325 bar.

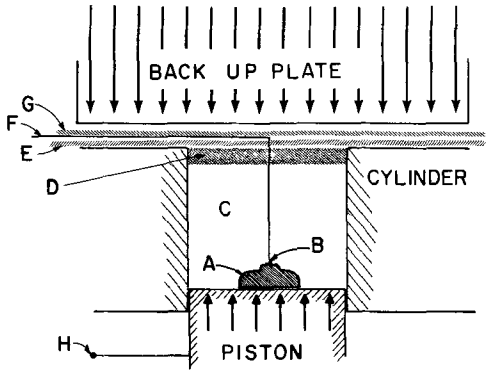

Fig. 2. Cross-sectional view of the essential components of the sample cell in the piston-cylinder press. A, battery; B, conductive epoxy connection between battery and wire lead; C, talc pressure medium; D, pyrophyllite disk; E, Teflon sheet; F, metal lead connecting negative battery terminal and potentiometer; G, mica sheet; H, wire lead to positive pole of potentiometer.

from deforming significantly during a run. Before measurements were made the pressure was increased to its maximum value in order to crush the talc around the battery, after which the pressure was decreased to 1 atm and then slowly increased to the desired pressure and the measurement made. From the above arrangement the pressure on the battery was considered to be equal to the average pressure on the face of the piston, which in turn was calculated from the oil pressure in the hydraulic line and the ratio of the areas of the faces of the ram and piston. Calibration studies (2) have shown the loss of pressure due to friction between the piston and cylinder wall to be small enough so as not to seriously alter these results. Emf measurements as a function of pressure were made by progressively and slowly increasing the pressure by small increments and then measuring the emf as the battery relaxed at the new pressure. When the voltage value did not change significantly with time, this value was recorded as the equilibrium value at the existent pressure. In practice 10 min was usually a sufficient relaxation time to allow between emf readings. Emf measurements were also made as the pressure was decreased, and typical results for such measurements are recorded in Fig. 4 and 9. Small differences in voltage between various batteries were found to be as great as the voltage changes produced by the pressure. Therefore, the effect of pressure on the dynamic battery voltages (under load or during recovery) was studied by taking continuous voltage readings of a battery as a function of time while simultaneously (slowly) varying the pressure as step functions of time. Through such a procedure, an effective voltage *vs.* time plot could be made at different pressures as is done in Fig. 5 and 7, and as could be done in Fig. 10 and 11.

The potential readings were made with a potentiometer to a precision of ±0.1 mV.

Experimental miniature batteries of Zn-Ag_2O and Zn-HgO varieties similar to types S-312 and E-312 (3) were studied. A schematic cutaway of these cells is shown in Fig. 3. The diameter of these batteries is approximately 0.31 in. and the thickness or height is approximately 0.14 in. The silver oxide battery consists of a depolarizing silver oxide cathode mixed with a small amount of graphite, a porous zinc anode of high surface area, and an electrolyte of potassium hydroxide solution absorbed into an inert material to produce a "solid" electrolyte. In addition, a cellophane type separator was used in the silver cell to prevent silver diffusion to the anode. The mercury battery has the depolarizing mercuric oxide cathode mixed with a small amount of graphite, a porous zinc anode, and an electrolyte of potassium hydroxide absorbed into an inert material.

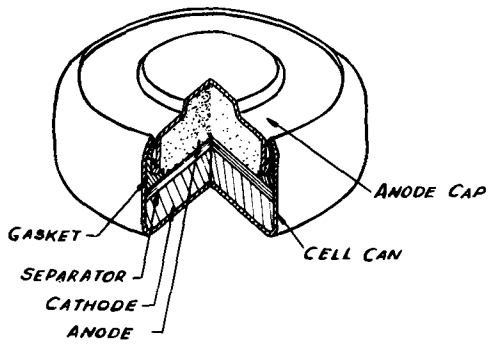

Fig. 3. Schematic cutaway of the batteries studied [from ref. (3)].

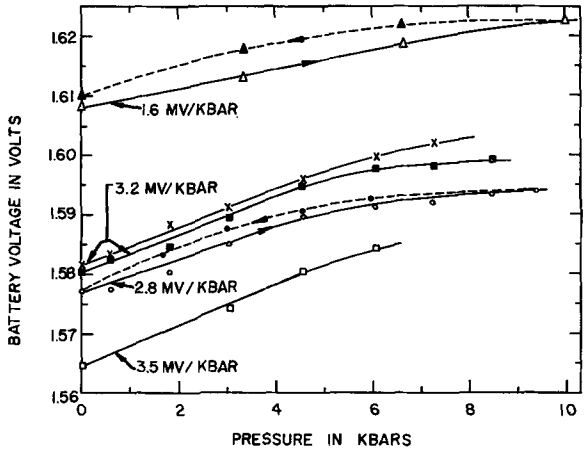

Fig. 4. Electromotive force vs. pressure for silver oxide batteries. Solid lines correspond to increasing pressure and dashed lines to decreasing pressure. $T = 25°C$.

Experimental Results

Silver oxide batteries.—The emf (open-circuit potential) as a function of pressure is shown in Fig. 4 for five different silver oxide batteries along with the measured value of $(dE°/dP)_T$ at atmospheric pressure. It is seen that the emf increases regularly with an increase in pressure, the slope $dE°/dP$ decreasing at higher pressures. The solid lines show $E°$ *vs.* P for increasing pressure while the dashed lines connect the points obtained while decreasing the pressure. The resulting hysteresis loop is due to friction at various places in the cylinder as well as within the sample as the materials relax to the newly applied pressures. Relaxation of the sample and pressure medium seemed to be more complete on the increasing branch (as evidenced by potential drift with time) and we accordingly have used the $dE°/dP$ values for increasing pressure in our discussion.

The effect of pressure on a battery under load can be seen from the voltage discharge curves at 1 atm and 6.1 kbars which are shown in Fig. 5. The voltage difference at the two pressures is seen to be independent of time and also is equal to the differences of emf at the two pressures (*cf.* Fig. 4). The manner in which this difference depends on the current through the battery is shown in Fig. 6. In this figure the i *vs.* E relationship is only shown for such low currents that the voltage is essentially a steady-state value 1 min after the current is allowed to flow.

The effect of pressure on the recovery of a silver oxide battery after current flow is stopped is shown in Fig. 7 and 8. In Fig. 7 the decay curves were constructed by measuring different segments of the decay curve at different pressures and by then joining the segments of equal pressures. In Fig. 8 the initial part of the decay curve was repetitively measured at different pressures in order to detect differences in the ini-

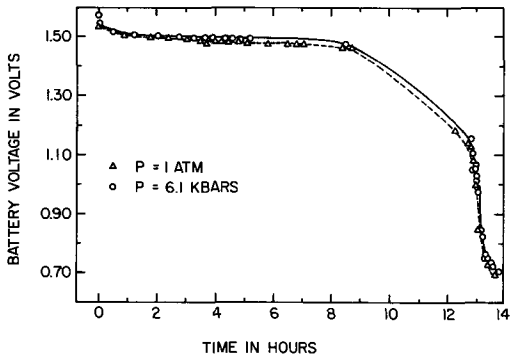

Fig. 5. Battery voltage *vs.* time at 1 atm and 6.1 kbars for silver oxide battery discharging through a load of 1065 ohms. The points at the two pressures were obtained with one battery by alternately increasing and decreasing the pressure.

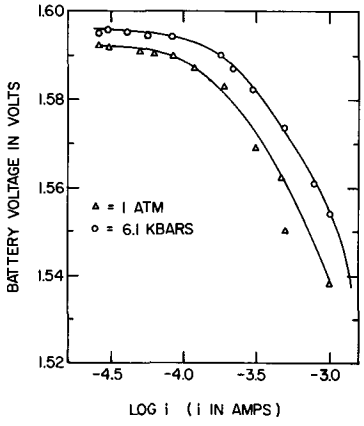

Fig. 6. Steady-state current *vs.* voltage for silver oxide battery. Voltage was measured within 1 min after circuit was closed.

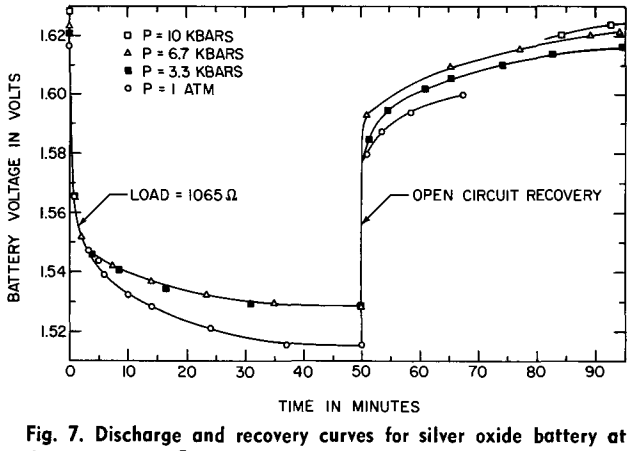

Fig. 7. Discharge and recovery curves for silver oxide battery at various pressures. Curves drawn from points read consecutively as pressure was raised or lowered.

tial rate of decay with changing pressure. Again only the difference in the emf at different pressures is noted in the charging and recovery curves.

Mercuric oxide batteries.—Open circuit voltage measurements (the emf) *vs.* pressure are shown for two mercuric oxide batteries in Fig. 9. Also listed are the experimental limiting slopes at atmospheric pressure.

The pressure effect on the voltage of the HgO battery under a load of 1065 ohms is shown in Fig. 10 and 11 in which cases the pressure on a given battery was successively raised or lowered while the current was passing. Two important differences are observed between the results of Fig. 10 and 11 for HgO batteries and those of Fig. 5 and 7 for Ag_2O batteries. (*i*) For working HgO batteries the differences between the voltages at different pressures are much greater (approximately 10 times) than the differences between

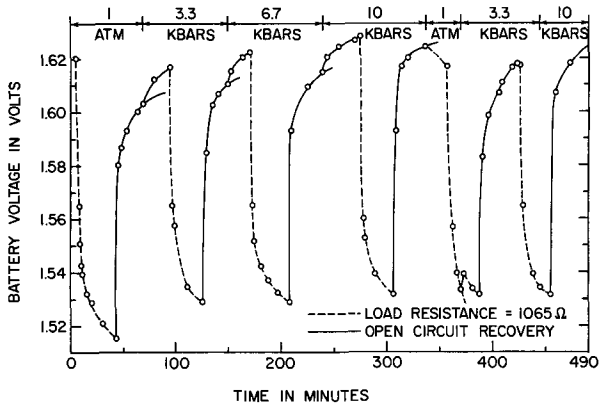

Fig. 8. Discharge and recovery curves for silver oxide battery at various pressures. The pressure or load was successively changed as indicated.

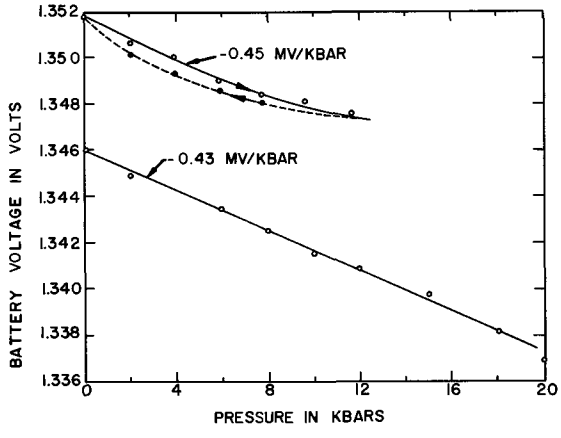

Fig. 9. Electromotive force *vs.* pressure for mercury oxide battery. Solid lines correspond to increasing pressure and dashed line to decreasing pressure. $T = 25°C$.

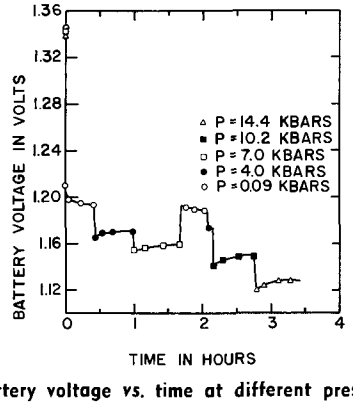

Fig. 10. Battery voltage *vs.* time at different pressures for mercury oxide battery discharging through a load of 1065 ohms. The voltage at zero time is equal to the emf. The pressure was intermittently changed without interrupting the flow of current. $T = 25°C$.

the emf's at these pressures. In the case of Ag_2O batteries these voltages differ by approximately the same amount whether or not current is passed. (*ii*) When the pressure is increased, the voltage of a working HgO battery does not immediately shift to a new value and "level out" but rather overshoots and then drifts back to the steady-state values. This overshooting of potential when the pressure is increased no doubt occurs at 20 kbars but is not observed in Fig. 11 due to the long waits between increasing the pressure and measuring the voltage. In Fig. 11 it is observed that the voltage at 20 kbars tends to decrease after the battery has operated for several hours, as if the battery were about to fail. Runs at 9.3 and 5.4 kbars with-

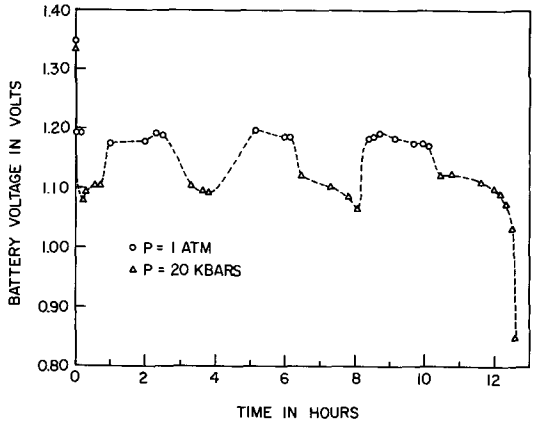

Fig. 11. Battery voltage *vs.* time for mercury oxide battery discharging through a load of 1065 ohms. The pressure was alternated between 1 atm and 20 kbars. $T = 25°C$.

out intermittently decreasing the pressure on the batteries, however, failed to show any decrease in voltage up to 8 hr.

After discharging an HgO battery through a load of 1065 ohms for several minutes at various pressures, the current was cut off and the voltage decay of the battery on open circuit was measured with an oscilloscope. This was done in order to determine what part of the polarization potential ($E - E°$) of the battery was due to ohmic resistance and how this resistance varied with pressure. Part of the polarization potential which is due to the ohmic resistance within the electrolyte and within the oxide (*i.e.*, those resistances which are in "series" with the potential-determining "capacitances") decays much more rapidly than the other overvoltage contributions, and may thus be readily separated out. From this determination we found that the fast potential decay corresponds to only a small fraction (~10%) of the total polarization [in agreement with the finding of others (4, 5)] and also that the change in this contribution with pressure was less than half the total change in polarization with pressure. Although part of the slow decay may be due to ohmic resistance (those resistances shunted by capacitances) as well as overvoltage, one may conclude that pressure must still cause a substantial increase in $\eta_1 + \eta_2$ in Eq. [4] as well as some increase in iR_{int}.

Discussion of Results

Silver-oxide batteries.—The probable reactions (6-8) which may occur at a silver-oxide-alkaline-zinc battery are listed in Eq. [5a], [5b], and [5c] along with the standard emf (8) and ΔV at 1 atm for each reaction. ΔV was calculated from the molecular weights and densities found in ref. (1).

$$\left.\begin{array}{l} Zn + Ag_2O + H_2O \rightarrow Zn(OH)_2 + 2Ag \\ E° = -1.587V\ (6);\ \Delta V = -6.5\ cm^3/mole \end{array}\right\} \quad [5a][4]$$

$$Zn + 2AgO + H_2O \rightarrow Zn(OH)_2 + Ag_2O$$
$$E° = -1.849V\ (6);\ \Delta V = +4.5\ cm^3/mole \quad [5b]$$

$$Zn + AgO + H_2O \rightarrow Zn(OH)_2 + Ag$$
$$E° = -1.718V;\ \Delta V = -0.99\ cm^3/mole \quad [5c]$$

$Zn(OH)_2$ rather than $HZnO_2^-$ ions is considered to be the product of the oxidation of zinc since the electrolyte is saturated with zincate ions. $Zn(OH)_2$ should thus be the thermodynamic product of the reaction even though some other species may kinetically form first.

From Eq. [3b] and the above ΔV values, the values for $(dE°/dP)_{1\ atm}$ calculated for reactions [5a] to [5c] are ($n = 2$) 3.37, −2.33, and +0.51 mV/kbar, respectively. In comparing the above values of $E°$ and $(dE°/dP)_{calc'd}$ with the $E°$ values and the $dE°/dP$ values of Fig. 4 it is apparent that the predominant reaction in the silver oxide batteries is that of reaction [5a]. One particular battery is seen to give $E°$ values several millivolts higher than those of the other batteries and also the value of $dE°/dP$ is significantly lower. Both of these tendencies indicate that reaction [5b] or [5c], as well as [5a], is important in establishing the behavior of the battery in question. Freshly prepared silver oxide electrodes yield potentials indicative of the AgO/Ag_2O couple (the corresponding battery equilibrium would be Eq. [5b]), but the spontaneous occurrence of the reaction

$$AgO + Ag \rightarrow Ag_2O \quad [6]$$

causes the decomposition of AgO (7, 5) such that electrodes which are not freshly prepared exhibit the potential of the Ag_2O/Ag couple (7).

From Fig. 5 it is observed that the battery voltage is increased approximately 15 mV by the application of 6.1 kbars of pressure. Since this voltage increase corresponds closely to the increase in emf with the same pressure increase (*cf.* Fig. 4), one may conclude that the change in emf is the dominant effect of pressure on the voltage at low overvoltages. Therefore the effect of pressure on the overvoltage (concentration polarization would appear to be the dominant overpotential contribution in this work based on the slow recovery shown in Fig. 7) is small compared to that on $E°$. Figure 6 shows that the effect of P on E is similar at all currents less than and equal to the value shown in Fig. 4. The precision of the points is not good in Fig. 6 because the voltage drifts somewhat at 1 min after the circuit is closed (see the steepness of the V *vs.* time curve in Fig. 7 and 8 at voltages from 1.54 to 1.60V). The insensitivity of the ionic diffusion to the pressure (compared to sensitivity of the emf to P) is also reflected in the recovery curves of the battery shown in Fig. 7 and 8.

Mercuric oxide batteries.—The over-all battery process is given by (6)

$$Zn + HgO + H_2O \rightarrow Zn(OH)_2 + Hg \quad [7]$$

for which $E° = 1.345V$ (6) and $\Delta V(1\ atm) = +0.747\ cm^3/mole$. Therefore the theoretical value for $(dE°/dP)_{1\ atm}$ is −0.39 mV/kbar which compares favorably with those obtained experimentally (see Fig. 9).

The contrasting effects of pressure on the discharge curves of the Ag_2O and HgO batteries help to distinguish the mechanism of reduction of these oxides, since the electrolyte and anode for both types of batteries are the same. We should first emphasize that the results of pressure in no way appear to be due to impairment or destruction of the batteries due to deformation, intermixing of phases, shorting, etc. Inspection of batteries which were bisected after pressing showed the same well-defined boundaries to be present between phases as were present before pressing (*cf.* Fig. 3). Pressing compacted the layers and hence diminished the size of the batteries by a few per cent, but the shape of a cell and the order within a cell were retained since the pressure medium (talc) distributed the pressure quite uniformly around the cell. Electrical measurements likewise indicated that the pressure did not destroy the boundaries between cell parts. Under pressure the HgO batteries as well as the silver oxide batteries readily recovered when the current was shut off. The emf and subsequent behavior of a battery after squeezing depended primarily on the total amount of discharge which a battery had undergone, in a way quite analogous to that of batteries discharged at atmospheric pressure.

In the case of the HgO electrode to which a small amount of graphite has been added, the mercury formed during reduction is found at the oxide-solution

[4] In order for the ΔV and $E°$ to correspond to the forward reactions as written in Eq. [5], the value of $E°$ must be taken as $E_{Zn} - E_{Ag}$ which is negative.

interface (9). Thus the electrons are conducted through the graphite from the metallic terminal to the oxide-solution surface where the Hg^{+2} ions are reduced and the $O^{=}$ ions react with the water. As the oxide surface is completely reduced the water must diffuse through pores and capillaries in the mercury and graphite matrix (the spent portion of the electrode) to the unreduced oxide in order for $O^{=}$ ions to be removed and thus for the cell process to continue. It is easy to envision the deleterious effect of pressure on this process. Since water is much more compressible than Hg (10), pressure would tend to diminish the size of these channels. In addition to the above effect one would expect the mercury formed to agglomerate into globules and shut off some of the channels. From these effects one would expect an increase in ohmic resistance as the migration and diffusion of OH^{-} ions in the capillaries is made more difficult. One would also expect an increase in overvoltage (*i*) due to concentration polarization of OH^{-} ions in the shrunken capillaries and (*ii*) due to the increased current density at the head (the HgO end) of the remaining channels as others are eliminated and thus as the effective HgO reaction area is diminished. Both an increase in ohmic resistance and in overvoltage with increased pressure are observed as discussed earlier. The above description is in accord with the studies of Mendzheritskii and Bagotskii (9) at atmospheric pressure. These investigators found that the concentration of KOH in the pores of the spent portion of the electrode is higher than that in the bulk of the solution, and also that a high porosity of the HgO leads to a more complete utilization of the HgO present in the electrode. Although studies were not made in this work of the effect of pressure on the output capacity of the HgO battery, Fig. 11 suggests that high pressures may cut short the life of the battery. When the size of and changes in the overvoltage with increasing pressure are considered (*cf.* Fig. 10 and the results of the resistance changes) one concludes that cause (*ii*) above for increasing overvoltage is more important than the concentration overvoltage [cause (*i*)] since the KOH is already concentrated enough that large increases in concentration (a 10 fold increase would be required for each 59 mV increase in η) cannot occur. The existence of and changes in the overvoltage due to the decrease in the number of reaction sites is directly seen from the voltage overshooting and then decaying back to the steady-state value on the application of pressure. Thus as OH^{-}-carrying channels are eliminated by the sudden increase in pressure which results in the current stoppage at some HgO sites, the overvoltage must increase until the discharge of Hg can occur at new sites in order to maintain constant current. After discharge has occurred at new sites at a higher overvoltage, nucleation of Hg occurs and the overvoltage decreases (corresponding to the positive decay in voltage) since the discharge of Hg against the metal occurs more easily than discharge without the presence of Hg. Micrographs of a partially reduced HgO surface (9) verify that Hg accumulates as droplets. An overshoot in voltage also occurs with a sudden decrease in pressure (*cf.* Fig. 10) due to first the expansion of some channels allowing new sites to be reactive (the decrease in η) followed by the plugging of some of these sites with Hg droplets (the increase in η as the battery voltage decays to its steady value). The plateaus in the voltage *vs.* time plot (see Fig. 10) are indicative of the effective number of HgO sites to which OH^{-}-carrying H_2O channels are available. Of course this number decreases with the discharge time. Other factors may influence the shape or "flatness" of the discharge curve also, such as the local *p*H and the formation of other solid substances during reduction [the effects of each of these factors have been determined for the Leclanché cell in ref. (4)].

Mercury freezes at approximately 12 kbars at 21.9°C (10) and water freezes at approximately 9 kbars at the same temperature (11). Thus freezing of the electrolyte and mercury would be expected to influence the operating characteristics of these batteries at high enough pressures. The present study did not deal with high enough pressures, for the most part, to directly see these freezing effects. However, one difference is noted between the discharge curve of the HgO battery at 20 kbars (see Fig. 11) and the discharge curves at pressures below the freezing point of the liquids. At 20 kbars the voltage of the discharging battery drifts to smaller values much more rapidly than at lower pressure. Figure 11 shows such a rapid loss of voltage whereas similar curves at 5 and 9 kbars showed no apparent decrease in voltage in an 8 hr run. This result indicates that ion movement is impeded progressively with time at 20 kbars as if the source of current-carrying ions was initially available but then depleted. Such a phenomena may arise from partial freezing of the liquid resulting in slush formation. The ion movement in the solid would be much slower than that in the liquid; then when the ions in the liquid are depleted the voltage is severely lowered.

Pressure does not influence the overvoltage or resistance of the Ag_2O cell to the same extent that it influences the HgO cell as is seen from the data. It has also been noted that the Ag formed during the reduction of an Ag_2O or AgO electrode forms at the cathode grid-oxide interface rather than at the oxide-solution interface (7). This implies that silver ions migrate from the oxide-solution interface to the metal grid or that the large $O^{=}$ ions migrate outward. If $O^{=}$ ions moved it would be difficult to explain the difference in the behavior of Ag_2O and HgO batteries, so we believe that Ag^{+} ions are the species which migrate. The resistivity of Ag_2O (5) is so high that the large current densities observed in battery operation would seem to require that the above ionic movement does not occur through the dry oxide but rather electrolytically through water-filled capillaries or channels. Since the divalent Hg^{+2} ion carries more primary hydration and hence has a larger effective size in diffusion or migration than Ag^{+}, it is not possible for Hg^{+2} ions to be transported to the metal grid at the cathode and hence Hg must be deposited from the solution side of the oxide (with additional needed overvoltage compared to that of the Ag_2O reduction, based on the differences in overvoltage we observe for HgO and Ag_2O batteries of equal size). That the overvoltage of the Ag_2O battery is not increased by pressure indicates that pressure is not effective in destroying the passageways through the irregular solid as it is with passageways in metallic mercury.

Conclusions

Studies dealing with pressure effects on the reduction of other oxides would be enlightening in terms of enlarging on the present model. Also this work suggests the need for, and perhaps the means of studying, the porosity of various materials and conduction through these pores.

On the practical side, this study shows that silver oxide batteries may be efficiently used as a power source under high pressures (such as at the bottom of the ocean or in other geophysical applications) whereas mercury oxide batteries suffer from diffusion and overvoltage effects in similar circumstances. Additionally, both types of batteries studied might be utilized as pressure sensors since the emf's are regular and predictable at elevated pressures. The small size of the miniature batteries studied would lend to the convenience of placing them in high pressure laboratory apparatus.

Since studies of smelting (12) and of corrosion indicate that the formation and the disappearance of metals is by electrolytic processes and since mercury, silver, copper, antimony, and bismuth as well as the

more noble metals occur in native form these studies of pressure effects on diffusion and reduction are relevant to an understanding of such ore bodies. Any conductor such as graphite or the metal itself can act as a floating electrode to collect electrons from reducing agents which in turn reduce the metal as in the developing of the latent image of photography.

Acknowledgment

The authors from the University of Utah gratefully acknowledge the financial support of their portion of this work from the U.S. Army Research Office (Durham) (Contract No. DA-31-124-ARO-D-408 Mod. No. 1) and the National Science Foundation (Grant No. Gp 6496).

Manuscript submitted April 14, 1969; revised manuscript received July 9, 1969.

Any discussion of this paper will appear in a Discussion Section to be published in the June 1970 JOURNAL.

REFERENCES

1. "Handbook of Chemistry and Physics," 49th Ed., Chemical Rubber Co., Cleveland, Ohio (1968).
2. M. Tamayama and H. Eyring, *J. Sci. Instr.*, **38**, 1009 (1967).
3. Eveready Battery Applications and Engineering Data, Union Carbide Corporation (1968).
4. R. Glicksman and C. K. Morehouse, *This Journal*, **102**, 273 (1955).
5. B. D. Cahan, J. B. Ockerman, R. F. Amlie, and P. Ruetschi, *ibid.*, **107**, 725 (1960).
6. E. C. Potter, "Electrochemistry," pp. 375-377, Cleaver-Hume Press, Ltd., London, (1956).
7. T. P. Dirkse, *This Journal*, **107**, 859 (1960).
8. S. Barnartt and D. A. Forejt, *ibid.*, **111**, 1201 (1964).
9. E. A. Mendzheritskii and V. S. Bagotskii, *Elektrokhim.*, **2**, 1312 (1966).
10. P. W. Bridgman, "The Physics of High Pressure," G. Bell and Sons, Ltd., London (1958).
11. P. W. Bridgman, *J. Franklin Inst.*, **117**, 315 (1914).
12. X. De Hemptinne, H. Eyring, and T. Ree, "Physical Chemistry of Process Metallurgy," Part 1, Vol. VII, pp. 69-93, G. R. St. Pierre, Editor, Interscience Publishers, New York (1961).

A Study of the Formation and Dissolution of Porous Anodic Oxide Films on Aluminum: Behavior of the Porous Layer

J. W. Diggle,*[1] T. C. Downie,[2] and C. W. Goulding[3]

Physical Chemistry Laboratories, Rutherford College of Technology, Newcastle-upon-Tyne, England

ABSTRACT

The formation and dissolution of porous alumina films in sulfuric acid was studied by the incorporation of the radiotracer $^{35}SO_4^=$ into the film during preparation. The results have shown that (*a*) the formation site of the porous oxide is the barrier layer-porous layer interface, (*b*) the dissolution time for porous films is independent of thickness. Comparison with former work, on "duplex" barrier films, suggests a method of identifying barrier and porous type films. By the use of "duplex" films, dissolution studies have shown that a simple pore widening mechanism of dissolution is incompatible with the results. A pore widening-concurrent pore shortening dissolution mechanism based on a truncated pore model is proposed, and has been found to be experimentally valid.

In a previous paper (1), these authors reported the results of a study of the "open circuit" dissolution of the barrier layer underlying the porous layer in anodically produced alumina films. Since this study involved the use of a low signal frequency capacitance technique, no information as to the behavior of the porous layer during this dissolution was obtained.

Although much work (2-4) has suggested that some dissolution process occurs during porous film formation at the outer porous surface/electrolyte interface, only recently has any mechanism for such dissolution been proposed (5). It is the purpose of this study to investigate the behavior of the porous layer during "open circuit" dissolution in an attempt to add to the information previously published (5, 6).

It is well known (7-9) that anodic films produced in sulfuric acid contain some degree of incorporated electrolyte anions. Throughout this paper the incorporated sulfur will be assumed to be in the form of the anion [following Lan Tran *et al.* (10)]. Although it is realized that some doubt exists as to whether this is true (11, 12), the essential arguments presented here would be unaffected. If the distribution of this electrolyte anion was uniform throughout the porous layer, and if the anion was in a radioactive form of reasonable half-life, then the amount of radiation emitted after some dissolution time t could be used as an indicator as to the amount of porous layer remaining. Evidence that the distribution of incorporated anions is uniform has been reported by Wood, Marron, and Lambert (13) for an aluminum-magnesium alloy anodized in 15% sulfuric acid, and, therefore, considering that the nature of the porous film formed on an Al/Mg alloy is similar (13) to that formed on pure Al, the assumption on which the work is based is considered established.

Experimental

Preparation of the super-purity wire aluminum electrodes and their pretreatment and other preliminary work was identical to that reported in a previous paper (14).

The anodizing electrolytes used throughout this work were 15% w/w sulfuric acid with and without the addition of ^{35}S. When radioactive electrolyte was required, 2.5 mC $^{35}SO_4^=$ were added as neutral sulfate solution—this addition had a negligible effect on the

* Electrochemical Society Active Member.
[1] Present address: The Electrochemistry Laboratory, University of Pennsylvania, Philadelphia, Pennsylvania 19104.
[2] Present address: Rutherford College of Technology, Newcastle-upon Tyne Polytechnic, England.
[3] Present address: Sunderland Polytechnic, Sunderland, Co. Durham, England.

electrolyte pH. Anodizing conditions were constant throughout at 25° ± 0.1°C, 10V applied voltage with a current density of 7.1 mA cm^{-2}. As in previous work, the aluminum wire electrodes of 1.5 cm^2 area were allowed to attain the steady value of 10 μF cm^{-2} before anodizing was commenced.

Two types of experiments were done, (*i*) a study of the build-up of radioactivity during formation and (*ii*) the loss of radioactivity during dissolution. In both types of experiments, so-called "duplex" films were prepared by anodizing first in radioactive H_2SO_4, and then in nonradioactive H_2SO_4 and vice-versa; the thickness of each porous layer formed was controlled by varying anodizing times.

Following preparation in the appropriate electrolyte, the electrode was washed in running distilled water for 1 min (this time being chosen from the impedance work of Hoar and Wood (15) where it was shown that all adhering electrolyte was removed in this time), rinsed with acetone and air-blown dry, and a radioactivity count taken. The number of disintegrations was determined using a thin window Geiger-Muller tube with Dekatron Tube scaler. The electrode was rotated through four 90° turns, and an average of the four readings was taken.

In the dissolution experiments, the electrode was then immersed in the dissolution media 1.0*N* sulfuric acid at 25°C, previously deaerated with hydrogen. Purified hydrogen was continually passed over the solution to reduce oxygen diffusion inward. After a known dissolution time the electrode was withdrawn, the washing procedure outlined earlier was performed, and then the average activity was redetermined. The decrease in activity was then related to the progress of porous layer dissolution.

The average count rates were not corrected for natural decay since the half life of S^{35} is 87 days and the experimental times were such that the error incurred was < 0.1%. No subtraction of background level (15 c.p.m.) was performed, since the interest lies not in the amount of activity but in the change of activity with time during either formation or dissolution.

Results

Porous film formation.—Figure 1 shows the average radioactivity content of a "duplex" film prepared for 30 min in radioactive H_2SO_4 and then subjected to prolonged anodization in nonradioactive H_2SO_4. The c.p.m. is seen to decrease to near-background level after 2 hr anodizing in nonradioactive H_2SO_4.

Figure 2, curve i shows that the c.p.m. increases linearly for the reverse procedure, *i.e.*, 30 min film prepared in nonradioactive H_2SO_4 followed by anodization in radioactive H_2SO_4. Immediately following this experiment, curve ii in Fig. 2 was determined,

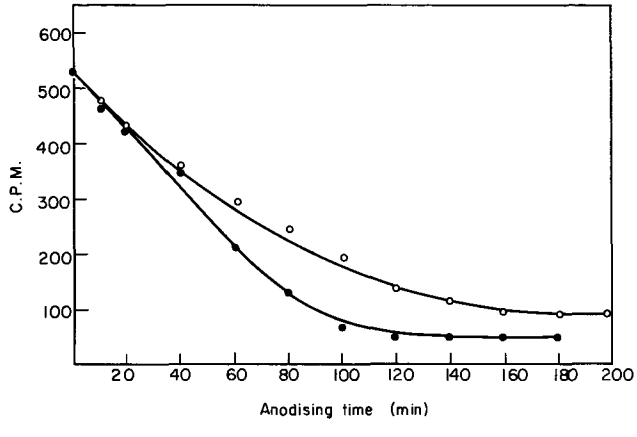

Fig. 1. ●, Experimental radioactivity (c.p.m.) as a function of anodizing for the second stage formation of a "duplex" film, R followed by NR; ○, theoretical curve based on NR being the outermost layer, and the c.p.m. decrease being due to absorption of weak β-radiation.

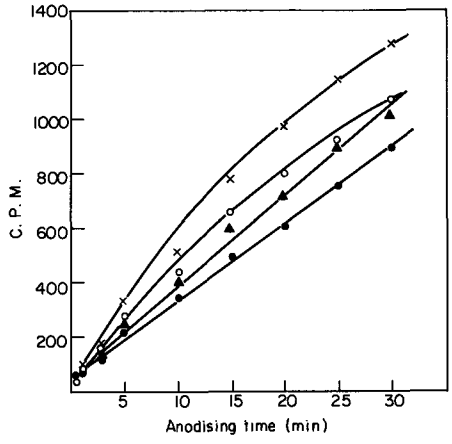

Fig. 2. ●, C.p.m. as a function of anodizing time for second stage formation of a "duplex" film NR followed by R (designated curve i); ○, similar curve for radioactive anodizing only (designated curve ii); x, c.p.m. for radioactive anodizing only corrected for a 20% thickness loss; ▲, theoretical curve resulting from absorption of β-radiation from a 30 min radioactive film by an outer film of NR material whose thickness is increasing with time.

which shows the increase in the c.p.m. against anodizing time for a film prepared only in radioactive H_2SO_4. It can be seen that, except during the initial stages, curve i, *i.e.*, the "duplex" film, is below curve ii.

Porous film dissolution.—Dissolution as a function of porous layer thickness.—Figure 3 shows how the radioactivity decreases as dissolution proceeds for three films, anodized for 30, 60, and 90 min, respectively. It is evident that the time required for the dissolution of the ^{35}S species is independent of the anodizing time in the active electrolyte. Since the pore separation is the only constant factor in these three films (16), this would suggest that the dissolution proceeds via a pore wall attack increasing the pore diameter to the oxide cell size (5, 6).

Dissolution of "duplex" films.—The results for a series of films prepared as previously outlined are shown in Fig. 4 and 5.

The dissolution time, which had been indicated to be independent of the porous film thickness, is seen to be appreciably constant (Fig. 4) for the preparation nonradioactive NR followed by radioactive R, while for the preparation R followed by NR, the dissolution time decreases as the ratio of the anodizing times NR to R increases (Fig. 5).

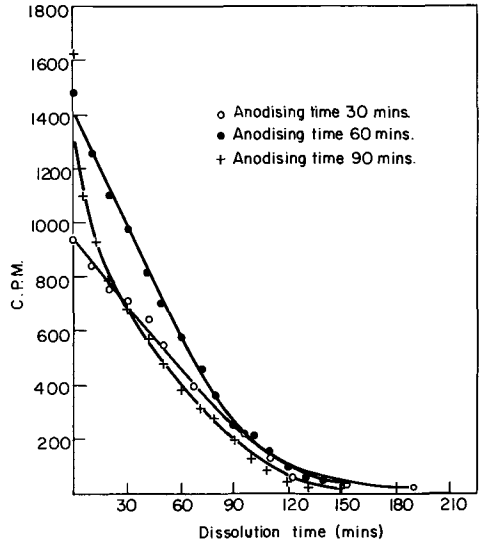

Fig. 3. Dissolution of porous alumina films prepared in 15% w/v H_2SO_4 + 1 mc $S^{35}O_4^{2-}$. Dissolution medium—deaerated N H_2SO_4.

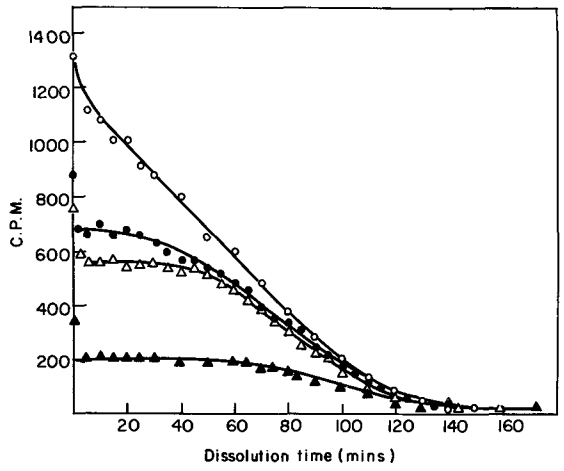

Fig. 4. Dissolution of porous "duplex" films, formed by NR followed by R, in deaerated N H_2SO_4. ○, NR 30 min, R 60 min; △, NR 60 min, R 30 min; ●, NR 30 min, R 30 min; ▲ NR 60 min, R 10 min.

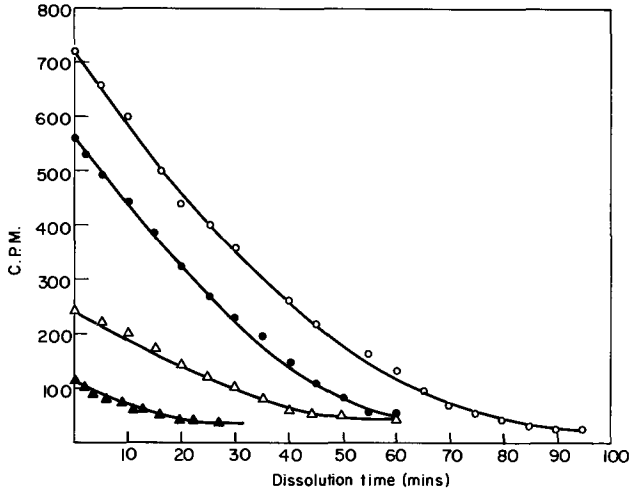

Fig. 5. Dissolution of porous "duplex" films, formed by R followed by NR, in deaerated N H_2SO_4. ○, NR 30 min, R 60 min; △, NR 60 min, R 30 min; ●, NR 30 min, R 30 min; ▲, NR 90 min, R 15 min.

Discussion

Radioactive marker $^{35}SO_4^=$ mobility.—The essence of any investigation involving the use of radioactive markers (17-19) is that an assumption has to be made concerning its immobility. This assumption is often dubious, particularly when the marker is charged (17) and high electric fields are present under whose influence marker mobility can occur.

In the present experiments, the radioactive marker used exists in an area of the film where high field strengths are absent, *i.e.*, the porous layer. If mobility of $^{35}SO_4^=$ were to occur, the concentration at the inner sections of the porous layer, *i.e.*, nearest the metal, would be expected to possess higher sulfate concentrations than the outer sections of the film. The results in the literature (13) show that this is not so, but that sulfate distribution is uniform throughout the porous layer depth. The present authors propose that the results in this paper also suggest that the sulfate in alumina porous layers is immobile (Fig. 6).

For the anodizing sequence NR followed by R, the structure represented by Fig. 6(c) would be consistent with the results of Fig. 4. This structure can result from two causes, (*i*) that R forms below NR, (a) Fig. 6, or (*ii*) R forms above NR and that $^{35}SO_4^=$ migrates toward metal, (b) Fig. 6. For the reverse sequence, R followed by NR, Fig. 6(f) would be the structure suggested by Fig. 5, and this would result from either Fig. 6(d) or (e).

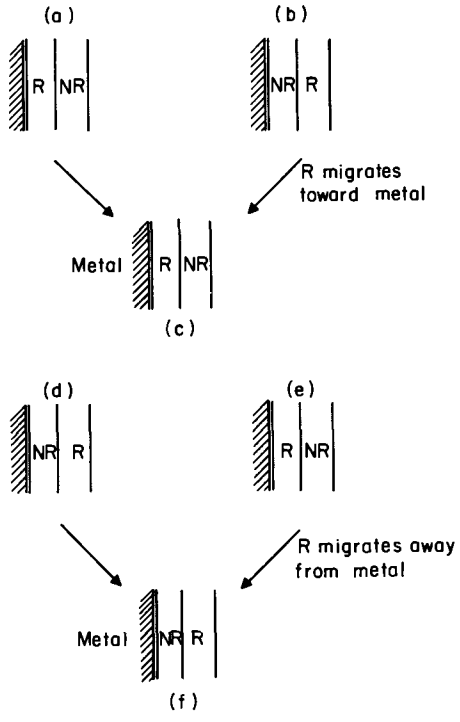

Fig. 6. Schematic representation of the formation of porous alumina "duplex" films. (a), (b), and (c) correspond to NR followed by R preparation, and (d), (e), and (f) correspond to R followed by NR preparation.

Since the migration of $^{35}SO_4^=$ away from an anode, Fig. 6(e), to produce Fig. 6(f) is clearly untenable, Fig. 6(d) then represents the porous film "duplex structure" for the R followed by NR preparation. However, to accept Fig. 6(d) requires that $^{35}SO_4^=$ be immobile, and, therefore, to be consistent, Fig. 6(b) is rejected as the model for the NR followed by R preparation.

The conclusion is that the $^{35}SO_4^=$ marker, in the present experiments, is immobile, and that the electrolyte used last characterizes the porous layer lying nearest the metal.

Porous film formation.—Figure 1 shows that the second stage anodizing in nonradioactive H_2SO_4 of a first formed radioactive film produces an essentially linear decrease in the count rate with increasing anodizing time. This may be accounted for in three possible ways: (*a*) exchange between $^{35}SO_4^=$ in the film and $SO_4^=$ in solution, (*b*) the growth of the second nonradioactive porous layer on top of the first radioactive porous layer with subsequent loss in radiation due to adsorption, and (c) by assuming the growth area of the porous layer to be at the barrier layer-porous layer interface, and postulating an outer surface dissolution process resulting in the loss of radioactivity to the solution.

Possibility (*b*) can be rejected on the grounds of (*i*) ionic transport, since for the growth area of the nonradioactive porous layer to be the oxide-solution interface, ionic transport of Al^{3+} ions through several microns of oxide would be necessary, a process which is clearly untenable, when one considers the electric field required for such a process, (*ii*) if a "duplex" film were produced in which the outermost section of the film were nonradioactive, then dissolution of such a film would not be expected to proceed according to Fig. 5, where the preparation mode was identical to that in Fig. 1, and (*iii*) the upper curve in Fig. 1, based on absorption of weak β-emission from the $^{35}SO_4^=$ decay due to a nonradioactive outer layer, is inconsistent with the experimental curve (lower curve, Fig. 1).

Possibility (c) in which the growth area is taken as the barrier layer-porous layer interface is much more probable, the oxygen-bearing species reaching the

reaction interface by mass transport down the previously formed pores in the radioactive film. The conclusion is that the electrolyte used first characterizes the outermost layer of a "duplex" porous film, a conclusion reached in some previously reported work (17). It is proposed here that the outer radioactive layer of porous oxide is dissolved by the nonradioactive H_2SO_4 during concurrent porous oxide formation near the metal-oxide interface.

From Sacchi's formula (20), the thickness of the radioactive porous layer prior to further anodizing is approximately 6 μm. After a further 2 hr anodizing, the total theoretical porous layer thickness should be 30 μm. If it is assumed that the outer 6 μm of radioactive layer has been completely dissolved, then the experimental thickness is 20% less than the theoretical thickness. Wood *et al.* (13) have shown that, for an Al/Mg alloy anodized in sulfuric acid, the films formed are of the theoretical thickness at 15°C, but are 33% less than theoretical at 30°C. Thus, the estimate of 20% less at 25°C is in good agreement with these results of Wood (13).

The possibility (*a*) of $SO_4^=$ ion exchange between the radioactive film and solution could perhaps give the result shown in Fig. 1. Since the thickness of the films formed in this work were not measured, the possibility of exchange cannot be overlooked, although the authors do consider the possibility of outer porous layer dissolution as more probable.

The reverse procedure for "duplex" film formation, *i.e.*, NR followed by R, is shown Fig. 2. If, as has been proposed, the formation of the innermost layer is characteristic of the second electrolyte, then the c.p.m. at any one dissolution time should be lower for NR followed by R (curve i) than for R alone (curve (ii) due to the absorption of the β-emission in the former case. Experimentally this is found to be the case. Calculations, represented in Fig. 2, demonstrate how, after correcting the radioactive film for a 20% thickness loss, the experimental curve (ii) produces a c.p.m.-anodizing curve in reasonable agreement with experimental curve (i) when it is assumed that the NR outer layer absorbs the weak β-emissions from $^{35}SO_4^=$ decay. Some deviation is observed as the anodizing time increases, this being due possibly to some electrolyte-dissolution penetration into the radioactive section as the film thickness increases.

Thus, the conclusion made earlier that the outermost section of a "duplex" porous film is characterized by the first electrolyte is confirmed. In this sense it produces "duplex" structures similar to those of barrier "duplex" layers formed by anion motion only. Comparison with the work of Lewis and Plumb (17), who reported that the outermost layer of "duplex" barrier films is that characteristic of the last electrolyte used, shows that, providing some cation motion is involved in barrier layer formation, the correlation of the outermost layer of any "twin duplex" film to either the first or second electrolyte can identify the film as either of a barrier or porous type.

Porous film dissolution.—Figure 3 shows that the time required for dissolution of the ^{35}S species in the porous layer is independent of the anodizing time in the active electrolyte, *i.e.*, the porous layer thickness, the dissolution time being seen as constant at approximately 120-140 min. It is of interest to note that this time is approximately equal to the time required for barrier layer dissolution of a film prepared at 10V(1).

For the "duplex" films NR followed by R, since the radioactive layer would be nearest to the metal the dissolution time would be expected to be constant, independent of the NR to R anodizing time ratio, and equal to the dissolution time of Fig. 3. From Fig. 4 this is seen to be the case.

Figure 5 shows that, for "duplex" films formed R followed by NR, the dissolution time decreases as the R to NR anodizing time ratio decreases from 2:1 to 1:6. This gives the first indication that the dissolution mechanism is not purely pore widening (5), for if it were, then the dissolution time should again be independent of R to NR ratio and equal to that in Fig. 3 and 4. A concurrent pore widening-pore shortening dissolution mechanism is proposed in which the pore diameter increases and approaches the oxide cell size, as the pore height decreases and approaches zero. Thus, the effect of the ratio R to NR should only be of importance in defining the dissolution time when the radioactive section of the "duplex" film is outermost (Fig. 5). Table I shows the experimental (taken as the time at which the c.p.m. became constant) and theoretical values (based on a pore shortening or a concurrent pore shortening-pore widening mechanism) for the dissolution time of the films in Fig. 5 (assuming that the time for complete dissolution is 140 min). Although some doubt exists as to where to define the experimental time, the agreement is seen to be reasonable.

Table I. Theoretical and experimental dissolution times required for the loss of porous alumina film activity for "duplex" films formed by radioactive followed by nonradioactive anodizing.

Minutes of radioactive anodizing	Minutes of nonradioactive anodizing	Theoretical dissolution time radioactive layer (min)	Experimental dissolution time (min)
60	30	93	90
30	30	70	60
30	60	47	50
15	90	23	20

Referring again to Fig. 4, it is clear that if a simple pore shortening mechanism for dissolution were operative, the count rate would be expected to increase during initial dissolution due to reduced absorption thickness of overlying nonradioactive oxide. Furthermore, if a simple pore widening mechanism were operative, the count rate would be expected to decrease initially and continue to decrease linearly (assuming dissolution to be uniform and constant). It is proposed that there are two possible ways in which the curves in Fig. 4 can be satisfactorily accounted for, both being based on the concurrent pore widening-pore shortening mechanism: (*a*) the time during which the count rate is appreciably constant can be considered to be due to a balance between the tendency for the count rate to increase due to pore shortening, and a tendency for the count rate to decrease due to pore widening—this model assumes uniform pore widening from pore mouth to pore base, (*b*) the time during which the count rate is appreciably constant is due to the reduced dissolution of the radioactive section in the lower reaches of the pore.[4] As dissolution proceeds, *i.e.*, the pore height decreases, the dissolution of the radioactive section increases due to a more free access of electrolyte to these areas—this second model is then based on nonuniform dissolution down the pore length, with the dissolution rate being greatest at the pore mouth.

Irrespective as to whether model (*a*) or (*b*) is correct, it can be seen that the rest period of the count rate should increase as the ratio of R to NR anodizing times decreases.

A paradox can be seen to exist in this data since Fig. 3 shows the dissolution time to be independent of radioactive porous film thickness, hence the pore widening concept, while Fig. 5 shows the dissolution time of the radioactive layer in a NR:R "duplex" film increasing with increasing radioactive layer thickness, hence the pore shortening concept. It is considered that this paradox can be resolved in terms of a pore shortening-pore widening mechanism based on the truncated pore model of Paolini, Masaero, Sacchi, and Paganelli (22).

[4] Some dissolution of the radioactive section of the pore must occur because in the complete absence of such dissolution the count rate must increase due to reduced absorption of β-radiation by the NR layer. Calculations show that after 50 min dissolution for the 60 min NR followed by 30 min R (Δ symbol, Fig. 4) the activity should have risen by 170 c.p.m.

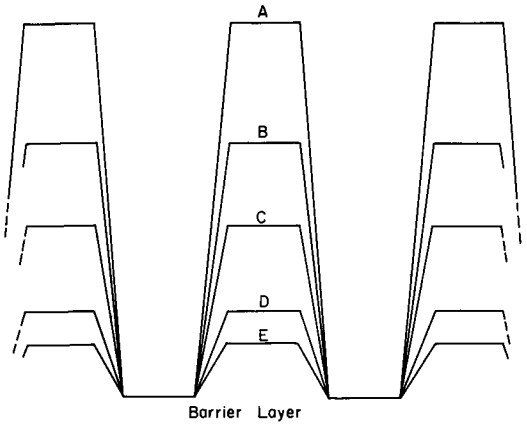

Fig. 7. Schematic representation of an idealized dissolution model based on a truncated pore and concurrent pore widening-pore shortening model. A is the original pore; B, C, D, and E are successive stages during dissolution.

Figure 7 shows how such a model, taken in conjunction with a greater dissolution rate at the pore mouth (due to the ease with which reaction products can diffuse away from the reaction site), leads naturally to a pore widening-pore shortening dissolution mechanism. It can be seen that a pore widening dissolution process, *i.e.*, dissolution of alumina from the pore walls, can, if the walls themselves are slanted, produce pore shortening. Thus, the major dissolution site in porous film dissolution is the internal surface of the pore; this is as expected since the internal surface presents the highest surface area for attack. Details of this dissolution model are to be published.

Acknowledgments

The work reported here was carried out in the Physical Chemistry Laboratories at the Rutherford College of Technology, Newcastle-upon-Tyne, England. The authors wish to acknowledge the facilities extended to them by the Principal of the College and the Head of the Chemistry Department. One of the authors (J. W. D.) wishes to acknowledge the award of a Research Studentship from the Newcastle-upon-Tyne Education Committee. Finally, the authors are indebted to the referees of this paper for their many helpful suggestions during the reviewing stage.

Manuscript submitted Dec. 10, 1968; revised manuscript received May 21, 1969.

Any discussion of this paper will appear in a Discussion Section to be published in the June 1970 JOURNAL.

REFERENCES

1. J. W. Diggle, T. C. Downie, and C. W. Goulding, *Electrochim. Acta*, To be published.
2. R. B. Mason and P. E. Fowle, *This Journal*, **101**, 53 (1954).
3. A. Brace and H. Baker, *Trans. Inst. Met. Finishing*, **40**, 31 (1963).
4. R. C. Spooner, *This Journal*, **102**, 156 (1955).
5. M. Nagayama and K. Tamura, *Electrochim. Acta*, **12**, 1097 (1967).
6. M. Nagayama and K. Tamura, *ibid.*, **13**, 1773 (1968).
7. N. D. Pullen, *J. Electrodepos. Tech. Soc.*, **15**, 69 (1939).
8. R. B. Mason, *This Journal*, **102**, 671 (1955).
9. H. Ginsberg and K. Wefers, *Metall.*, **17**, 202 (1963).
10. Thach Lan Tran, F. Naudin, and P. Robbe-Bourget, *J. Phys.* (*Paris*), **25**, 11 (1964).
11. F. Liechti and W. D. Treadwell, *Helv. Chim. Acta*, **30**, 1204 (1947).
12. G. A. Dorsey, Jr., *This Journal*, **113**, 169 (1966).
13. G. C. Wood, V. J. J. Marron, and B. W. Lambert, *Nature*, **199**, 239 (1963).
14. J. W. Diggle, T. C. Downie, and C. W. Goulding, *Corrosion Sci.*, **8**, 907 (1968).
15. T. P. Hoar and G. C. Wood, *Electrochim. Acta*, **7**, 333 (1962).
16. F. Keller, M. S. Hunter, and D. L. Robinson, *This Journal*, **100**, 411 (1953).
17. J. E. Lewis and R. C. Plumb, *ibid.*, **105**, 496 (1958).
18. J. A. Davies, B. Domeij, J. P. S. Pringle, and F. Brown, *ibid.*, **112**, 675 (1965).
19. G. Amsel and D. Samuel, *J. Phys. Chem. Solids*, **23**, 1707 (1965).
20. F. Sacchi, *Galvanotechnica*, **13**, 1 (1962).
21. G. D. Chase and J. L. Rabinowitz, "Principles of Radioisotope Methodology," Chap. 5 and 7, Burgess Publishing Co., Minneapolis (1967).
22. G. Paolini, M. Masaero, F. Sacchi, and M. Paganelli, *This Journal*, **112**, 32 (1965).

Electron-Optical Examination of Sealed Anodic Alumina Films: Surface and Interior Effects

G. C. Wood and J. P. O'Sullivan†

Corrosion Science Division, Department of Chemical Engineering, University of Manchester Institute of Science and Technology, Manchester, England

ABSTRACT

Sealing of porous anodic films, formed on aluminum in an oxalic acid electrolyte, has been studied by direct replica electron microscopy and electron diffraction. Pore plugging and changes in pore-wall material occur throughout the film but most rapidly at its exterior, while crystalline material forms on the outer film surfaces. Sealing appears to occur in three distinct but overlapping steps, the first being precipitation of material in the pores, especially near the outer film surface, the second formation of crystalline material at the surface which is a minor process, and finally further changes in the film depths involving aggregation of the oxide microcrystallites and a redistribution of porosity.

Many early theories for the sealing of porous anodic oxide films on aluminum involved a reaction which only occurred close to the outer film surface, producing there a pore "plug" of crystalline hydrated oxide from the initially denser amorphous oxide. More recently, Hoar and Wood (1, 2), Wood and Marron (3, 4), and Spooner and Forsyth (5) all postulated that long-term sealing occurs throughout the film depth but to a greater extent at the outer surface. The theories of Hoar and Wood (1, 2) and Wood and Marron (3, 4)

† Deceased.

were both suggested after impedance studies of film sealing. The former theory involved an initial outer boehmite plug with some inward movement of the pore walls, while the latter featured an initial gel-like precipitate which increased in depth and solid content during further sealing. Spooner and Forsyth (5) postulated a sealing mechanism involving pore wall dissolution in the depth of the film and its reprecipitation closer to the outer film surface. In contrast, Murphy proposed that the sole function of the sealing treatment is to plug the entrances to the intercrystallite surfaces, leaving only major pores unaltered (6).

Much of the previous work has suffered from the lack of direct visual evidence concerning the physical changes occurring during the sealing reaction. The objects of the present work were to clarify by electron microscopy the nature of these changes, particularly the extent of pore closure and other morphological changes, occurring throughout the depths of the anodic films, to correlate these changes with any crystallographic changes identifiable by electron diffraction and to consider the results together with detailed chemical and structural data obtained by infrared spectroscopy (7). The ability to observe the barrier layer and porous structure of high-voltage films directly (8) made this possible.

Experimental

Spade electrodes, 2 x 1 x 0.1 cm, of 99.99% aluminium (Cu 0.002%, Fe 0.004%, Si 0.003%) were individually electropolished in a perchloric acid/ethanol bath, washed, and dried. A porous anodic oxide film, about 40 μm thick, was then formed by anodizing each individual specimen for 1 hr at 25 mA/cm^2 in stirred 2% w/v oxalic acid (Analar grade) at 25°C. After the initial voltage fluctuations, a value of 50V was attained and this slowly rose to 100V by the end of the run. Each specimen was immediately removed from the electrolyte and washed in running distilled water to remove residual acid.

Electrodes which were not to be sealed were washed in ethanol and dried in a cold air stream. Specimens to be sealed were transferred immediately to the sealing solution without any prior drying, the sealing solution boiling under reflux. Sealing was carried out on individual specimens for varying times up to 24 hr, followed by removal, washing in running distilled water then ethanol, and finally drying in a cold air stream. The following sealants were used: (*a*) doubly-distilled water (pH 5.7, conductivity 10^{-5} to 10^{-6} ohm^{-1} cm^{-1} before boiling); (*b*) 6 g/l nickel acetate (as quadrahydrate) + 8 g/l boric acid, (pH 5.7); (*c*) 37 g/l potassium dichromate (0.25M Cr, pH 2.0); and (*d*) 79 g/l potassium chromate (0.25M Cr, pH 7.7).

The unsealed and sealed films were examined by both electron microscopy and electron diffraction. For the former technique a freshly anodized specimen was bent into a V-shape, thus producing cracks in the oxide parallel to the sides of the specimen which had not been bent. Excess debris was removed by an ultrasonic cleaner and by washing in distilled water. Direct carbon replicas of the film surfaces and sections were prepared by depositing a thin layer of carbon onto the film surfaces and exposed cleavage planes. These were then shadowed with a Pt/C mixture, deposited at an angle of incidence of 60°, but in the same vertical plane as the direction of the cracks in order to give maximum contrast to the replica of the porous structure. The replicas were stripped from the specimen surface by immersing the specimen in a 0.5% w/v HF solution, (made up with a 50:50 mixture of water and ethanol), which dissolved the oxide film, allowing the replicas to float free. The carbon was then transferred to a 10% w/v HCl solution to remove excess oxide before being given a final wash in distilled water. The replicas were removed, dried, and stored, prior to examination in an A.E.I. EM6 electron microscope (8, 9).

Several methods were attempted to obtain successful electron diffraction patterns from film surfaces and sections. These involved one-stage carbon and two-stage plastic/carbon extraction replicas, extraction replicas of the debris made by scratching metallographic sections of films with a microhardness tester (10) and diffraction through thin separated films. The only successful technique was that of reflection diffraction from film surfaces. In this technique, the specimen was grazed at a glancing angle in the diffraction stage of the electron microscope by the electron beam. Pure aluminum was used as a calibrating standard. The apparent *d* values of the crystalline materials produced on sealing were then compared with reference tables giving the known lattice parameters of likely products of the reaction between anodic alumina and boiling water (11).

Results

Electron microscopy.—Unsealed film.—The over-all morphology of unsealed anodic films formed in oxalic acid was similar to that of films formed in sulfuric and phosphoric acids (8, 9) (Fig. 1), corresponding generally to the model of Keller, Hunter, and Robinson (12). Some "texture" is visible in the micrographs but it is uncertain whether this is characteristic of the oxide itself or of its fracture. Both surface and section could be seen in situations similar to Fig. 1b because the replica relaxed into a planar configuration during stripping and washing. Since the cell voltage rose slowly during the anodization the oxide cell and pore sizes increased correspondingly, so that the last-formed film (Fig. 1c) contained larger cells and pores than that near to the outer film surface (Fig. 1b). Mean values of the cell diameter measured directly from electron micrographs of film sections were 1240Å close to the outer surface and 2300Å near the barrier layer. The pores showed a corresponding increase in diameter, the dependence being linear with voltage (9). The barrier layer thickness of 100V films was *ca.* 900Å, giving an Å/V ratio of 9.0. The barrier layer structure was again relatively uniform, whereas the pores visible on the outer surface (Fig. 1a) showed a range of diameters and were not always regular, in accordance with recent theory (9).

Water-sealed films.—Micrographs of outer surfaces of water-sealed films (Fig. 2) were not generally of a good quality due to a film of material covering them. Pores were still visible after 1 min sealing (Fig. 2a) and even after 10 min (Fig. 2b). After 30 min treatment (Fig. 2c), the porous structure was completely obliterated, to be replaced by a crystal-like arrangement. After 24 hr, a needle-like structure was observed above this (Fig. 2d).

Micrographs were taken from all regions across sections of films sealed for various times, but especially from locations close to the oxide/air and metal/oxide interfaces. After 1 min, little effect could be seen in any region of the film. After 5 min, some slight effect could be detected close to the outer interface (Fig. 3a), while close to the barrier layer, there was no significant change (Fig. 3b). Treatment for 10 min gave a more pronounced result, the porous structure being difficult to detect in the outer region of the film (Fig. 3c), although the pores were still visible on the corresponding outer surface (Fig. 2b).

Close to the barrier layer, however, (Fig. 3d), although the porous morphology was still clearly visible, the pores were now partly filled with apparently solid particles, *ca.* 100-400Å in size. Comparison of Fig. 3c and d indicates that the sealing reaction had affected both the pores and the cell walls near to the outer interface, while close to the barrier layer the cell walls remained apparently unaffected. Little further morphological change occurred in the film structure close to the outer interface on more prolonged sealing, except that the porous structure became virtually undetectable (Fig. 3e).

Nevertheless, changes were still occurring close to the metal; the regions corresponding to the pores in the unsealed film could still be detected there clearly for sealing times up to 30 min-1 hr (Fig. 3f), although

these were possibly more difficult to define after treatment for 24 hr (Fig. 3g). These "filled pores" had a rougher, more open structure than the apparently unreacted parts of the cell walls, which seemed to consist of a more compact oxide, even after treatment for 24 hr. The longer the sealing time, at least up to 30 min-1 hr, the more the fibrous regions extended laterally into the more compact cell walls, producing an effective increase in the "filled pore" diameter (Table I). This was quite clear despite the limitations of direct measurements of pore diameters from film sections (9, 13).

Any corresponding decrease in the thickness of the unreacted part of the barrier layer was not readily detected due to the tendency for the film to break away from the metal through the barrier layer rather than at the film/metal interface. However, such a reac-

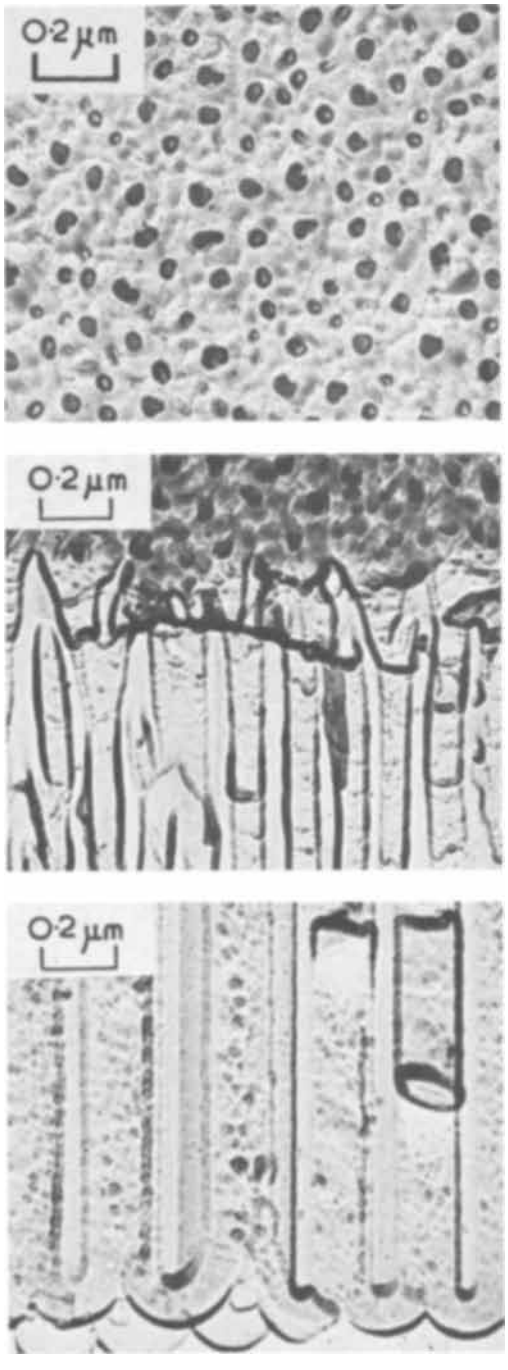

Fig. 1. Electron micrographs of films grown for 1 hr at 25 mA/cm^2 in 2% w/v oxalic acid at 25°C (voltage rising from 50 to 100V), (a, top) outer surface, (b, center) section near outer interface, (c, bottom) section near barrier layer.

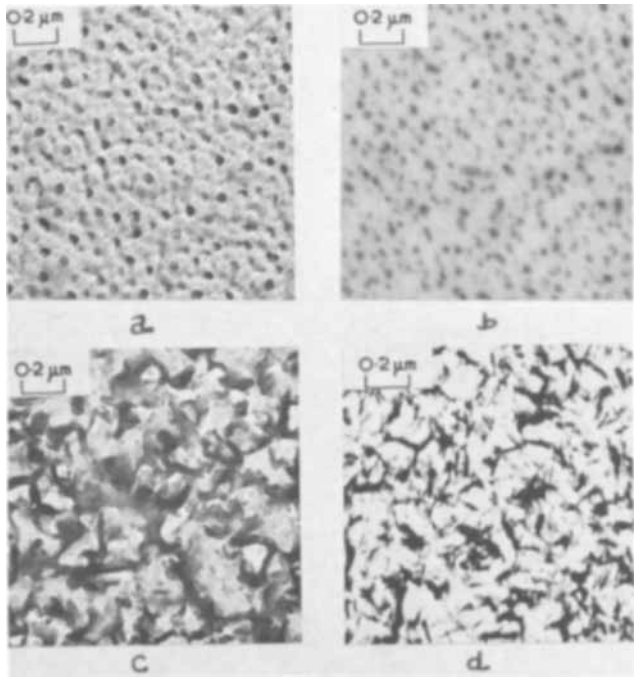

Fig. 2. Electron micrographs of surfaces of films sealed for various times in boiling water, (a) 1 min, (b) 10 min, (c) 30 min, (d) 24 hr.

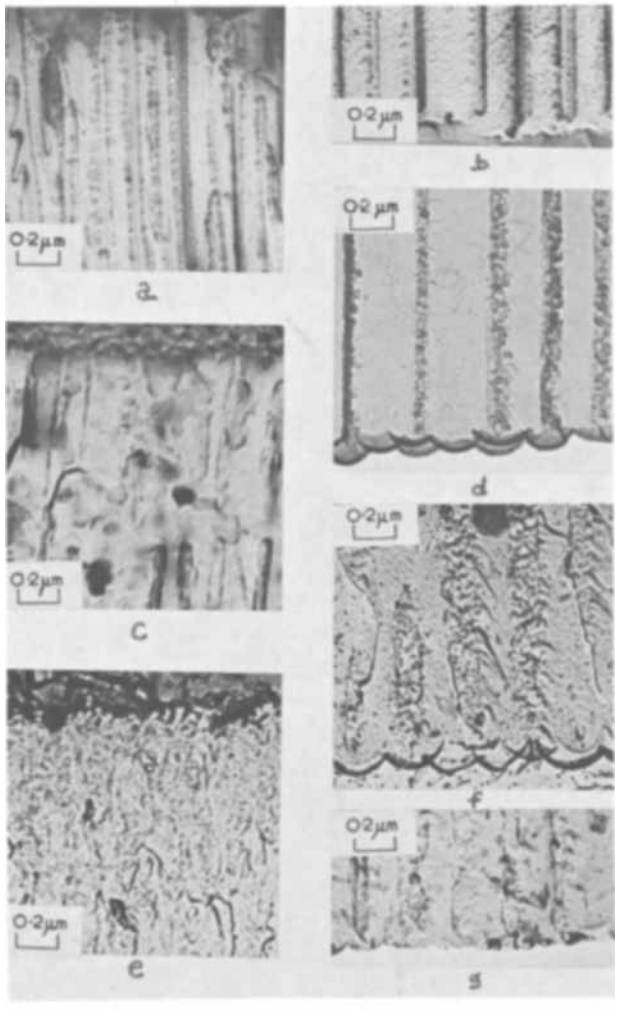

Fig. 3. Electron micrographs of sections of films sealed for various times in boiling water, (a) and (b) 5 min, (c) and (d) 10 min, (e) and (f) 30 min, (g) 24 hr. Micrographs on the left depict the outer interface and on the right the region near the barrier layer.

Table I. Variation of "filled pore" diameter next to the barrier layer, measured directly from film section micrographs, with sealing time

Sealing time (min)	"Filled pore" diameter (Å)
0	760
10	900
30	1500
60	1600
1440	1400

tion would probably occur, and there is some evidence for it with the 24 hr specimen (Fig. 3g).

Examination of micrographs from entire sections showed the extent of sealing to decrease gradually as the metal was approached, rather than there being a distinct "plug" near the outer interface (Fig. 4). Figures 3c and d show the extreme interfaces of the film depicted in Fig. 4, but at a higher magnification. To some extent, the gradual change in the extent of sealing may have been due to the progressively smaller pore diameter toward the outer surface, this being the result of the steadily rising voltage during anodizing. However, it is unlikely that such large variations in film morphology with depth were due simply to a variation in pore diameter.

Salt-sealed films.—The salt type had a profound effect on the extent of film sealing. After 30 min in potassium dichromate at pH 2.0, the film surface was virtually unaltered (Fig. 5a) although some slight sealing was evident in section near the barrier layer (Fig. 5b). In nickel acetate/boric acid solution (pH 5.7) sealing was more obvious, the morphology having changed to a similar extent as after treatment in boiling water for the same time (Fig. 3e and f). However, in potassium chromate (pH 7.7) the porous structure was completely obliterated on the surface (Fig. 5c) and at the pore bases the extent of filled pore encroachment on the cells and probably the barrier layer was much greater than in the previous solutions (Fig. 5d).

Electron diffraction.—Only reflection diffraction from the outer film surfaces gave any evidence of crystallinity. The unsealed films revealed no diffraction patterns but charged up in the electron beam, probably due to their low conductivity. Films sealed for 5 min (Fig. 6a) and 24 hr (Fig. 6b) showed definite diffraction patterns, certain lines becoming more intense after the longer time. Comparison of the calculated d values with those of the known aluminas and their hydrates (11) gave no indication of any specific modification. The failure to identify the crystalline material may have been due to insufficient accuracy in the line measuring techniques and the unavailability of any data giving the intensities of individual lines in the electron diffraction patterns. Furthermore, more than one crystalline modification may have been formed during sealing, which would complicate any interpretation.

Thus, during sealing in water, crystalline material of an unknown composition was formed on the outer surfaces of the anodic oxide films and this corresponded with the crystallites seen in the micrographs.

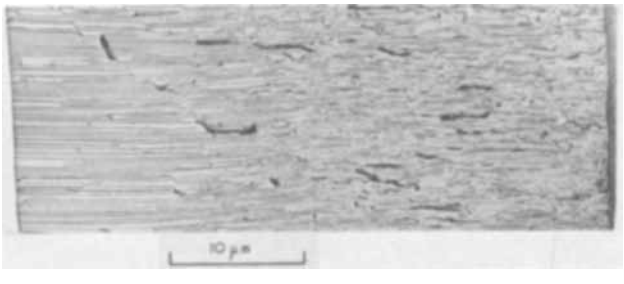

Fig. 4. Electron micrographs of section of film sealed for 10 min, showing the variation of film morphology with thickness. The outer film surface is on the right.

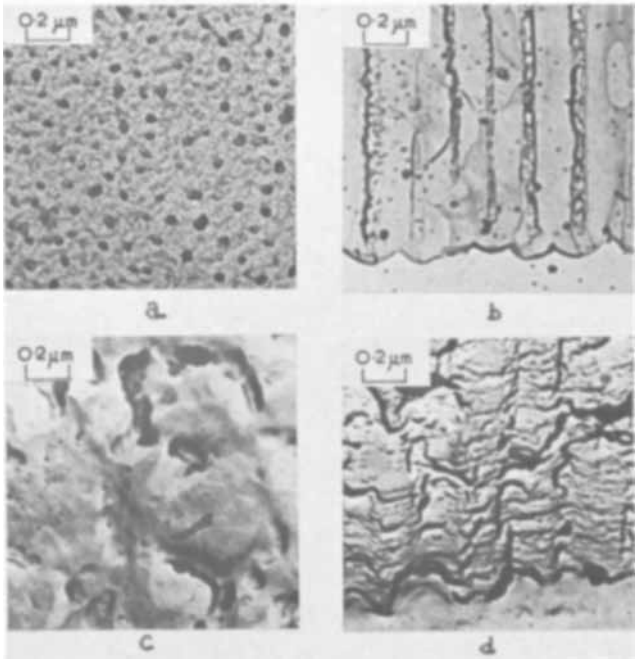

Fig. 5. Electron micrographs of films sealed for 30 min at 100°C (a) surface, and (b) section near barrier layer, for potassium dichromate (pH 2.0), (c) surface, and (d) section near barrier layer, for potassium chromate (pH 7.7).

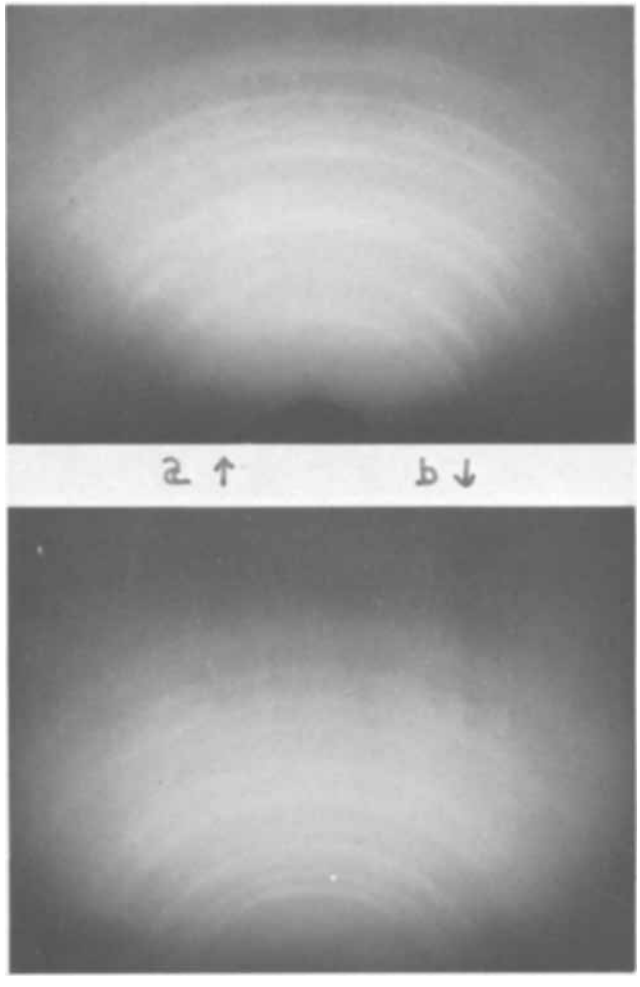

Fig. 6. Reflection electron diffraction patterns from film surfaces after sealing at 100°C for (a) 5 min, (b) 24 hr.

This material was not detected in the film depths and probably did not exist there.

Discussion

Preliminary considerations.—It is appropriate to mention briefly here other new data and theories on the mechanism of formation of unsealed and sealed films (7-9). Electron microscopy shows that the pore and cell geometry is broadly similar to Keller, Hunter, and Robinson's model but the detail and the mechanism of formation are different. The steady-state barrier layer thickness, the cell diameter and the pore diameter are all measured to be directly proportional to the anodizing voltage. Furthermore, the barrier layer thickness, decided largely by the equilibrium established between oxide formation in the barrier layer and field-assisted dissolution at the pore base, determines the cell and pore sizes by a simple geometrical mechanism. The dissolving power of the electrolyte in the presence of the field is far more important than the anion type in determining the pore structure. A natural consequence is that nonaggressive electrolytes produce thicker barrier layers, larger cells, and larger pores next to the barrier layer, although subsequent pore widening toward the outside of the film by simple chemical dissolution is more severe in aggressive electrolytes.

This model explains why the voltage, and therefore the barrier layer, cell, and pore dimensions next to the barrier layer, rise with time during anodizing at constant current density in oxalic acid. Depletion of the relatively weak solution in the depth of the pores, by anion incorporation into the film and pH changes, would lead to a reduction in the dissolving power of the electrolyte under the field. Such effects are not found in relatively concentrated solutions of the stronger sulfuric and phosphoric acids.

In contrast, the structure and composition of the interpore material profoundly influence the sealing reactions. Infrared spectroscopy (7), supported by electron diffraction data, suggests that the cells of unsealed films formed in sulfuric acid, are a relatively open array of amorphous, largely anhydrous crystallites, invisible to the electron microscope, permeated by molecular water, the surfaces of the crystallites carrying hydroxyl groups or ions, and the system being hydrogen bonded. Thus, the intercrystallite surfaces (14, 15) which carry the water and the acid anion are partially accessible to the anodizing solution and sealant. In more aggressive electrolytes too, the outer intercrystalline regions are opened up by acid action. Boiling water produces little change in the bulk oxide composition to specific alumina hydrates but causes major pore blockage, closure of the intercrystallite regions and possibly an increase in the hydroxyl and entrapped water content of the film, as judged by the evacuation and deuterium exchange properties (7). An agglomeration process causing rearrangement of the material to a form of lower surface area and energy was briefly proposed as a major contributor to the sealing process.

The sealing of films formed in oxalic acid are morphologically and structurally largely complete after 10-30 min near the surface, although more subtle changes occur near the barrier layer and on the film surface for 24 hr. At least three different, but to some extent concomitant processes appear necessary to explain the entire phenomenon: (*a*) an initial precipitation occurring in the pores, largely close to the outer surface except in high pH sealants; (*b*) crystalline material forms on the exterior film surface only, this being a minor process; and (c) the oxide, and any hydroxide, redistributes itself during prolonged sealing by the agglomeration process.

Precipitation reaction.—Pore closure is most efficient near the outer film surface, its efficiency gradually falling off as the metal is approached. The bulk solution pH of salt solutions also considerably affects the extent of sealing. Thus, the local conditions within the pores, such as pH and residual anion and Al^{3+} content, must influence the extent of sealing greatly. On introducing the film into the sealant, a gradient of these properties exists down the pore, with high pH sealing solution predominating at the top and residual acid concentration and Al^{3+} ion concentration near the bottom. A precipitation reaction, as proposed by Wood and Marron (3) and Spooner and Forsyth (5), occurs where the solubility product of hydroxide or hydrated oxide is exceeded. The precipitation is more extensive in the more open outer film regions affected by electrolyte and where the pH is highest, gradually declining toward the metal. Electron probe microanalysis (3) indicates that for most sealing solutions the precipitate plug is completed very quickly near the outer surface, severely limiting further entry of sealant into the pore and therefore further precipitation, although with dichromate solution, where the precipitation is slow, it may enter for long periods.

Initial precipitation is more extensive in higher pH sealants, the rapidity and depth of precipitation decreasing in the order potassium chromate (pH 7.7) > nickel acetate (pH 5.7) > potassium dichromate (pH 2.0), confirming the results of Wood and Marron (3) and Hoar and Wood (1, 2). Differences in pore closure rates for anodic films formed in various acids (the rates being sulphuric > oxalic > phosphoric) are partly due to pore size differences but are undoubtedly related to anion adsorption affecting the initial precipitation reaction.

The material precipitated in the pores is insufficiently well crystallized to produce a sharp diffraction pattern. Furthermore, the sealing weight gains of Spooner and Forsyth (5) indicate that only a relatively small fraction of the pore volume can be blocked by precipitate, produced by uptake of liquid from outside the film. The same argument applies to the crystalline material on the outer surface now to be described.

Formation of the outer crystallites.—There is little or no evidence from the present or previous (5, 16) diffraction studies to suggest that this well-known outer crystalline material extends any significant depth into films sealed in water. The reaction cannot therefore be considered a major sealing process, with the proviso that it is this outer crust which contacts any corroding environment.

It is quite likely that the discrete crystals of alumina hydrate are formed by a process allied to the initial reaction within the pores, namely a dissolution and reprecipitation reaction. However, conditions on the surface are quite different from those in the pores, boiling sealant being rapidly replenished and any acid anions which might inhibit crystallization being rapidly dispersed or kept to a low level. Even on the surface, crystals visible in the electron microscope were only produced after 30 min although they were detectable by electron diffraction after 5 min.

Agglomeration process.—The above considerations require that the major, long-term, visible, pore-filling process in the film depths involves an extensive rearrangement of the oxide/hydroxide system, left after the first rapid precipitation reaction. A simple mass transfer reaction from the cell walls to the major pores must occur without physical collapse or deformation of the main film structure. Although possibly some increase of material volume occurs, the absence of extensive new phases such as crystalline hydrates (7, 9) suggests this is not predominant and that a redistribution of porosity is involved. The large initial regular pores are generally filled, the initial crystallites agglomerate into larger ones, and the intercrystallite regions, although occupying a lesser area, are in places larger in size. The outer crystallites, the precipitate, and the blocked pores prevent rapid entry of corrodants or dyestuffs; however, if the barrier layer is etched off, the underside of the film takes up some dye. This mechanism is supported by the fibrous appearance of the wide filled pore regions.

The cell wall structure after the initial precipitation is as described earlier except where the intercrystallite regions have been partly blocked by precipitate, especially near the outer surface. The incompletely filled pores contain some of the molecular water entrapped in the film (7). The most obvious mechanism for a mass transfer reaction in such a situation again involves slow dissolution of oxide from the cell microcrystallites and its reprecipitation some distance away in the pores. Thomas and Whitehead (17) have characterized the various steps in the formation of aluminum oxide from aqueous solutions, thus

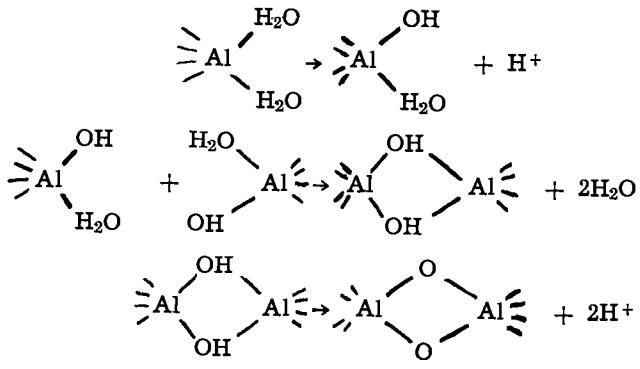

Oxide production from a solvated aluminum ion basically requires replacement of water molecules by O^{2-} ions. The first two steps occur during the formation of an intermediate hydroxide precipitate, while the third step represents the final conversion of this hydroxide to oxide in a place other than where the original oxide molecule became hydrated. The precipitation probably occurs on the particles of oxide in the pores or on the cell walls. The initial step in the above scheme is favored by high *p*H, but clearly subsequent oxide formation results in a reduction in *p*H, slowing the precipitation reaction, and providing elsewhere dissolution and the consequent solvated Al^{3+} ions necessary for the continuation of the process. In places where the final conversion of hydroxide to oxide is incomplete, hydroxylic material is left attached to the growing crystallites, explaining the minor increase in OH^- ion content detected by infrared analysis (7).

Evidently such a reaction scheme, in which both the reactants and products are the same, *i.e.*, oxide, must have some driving force other than the change in chemical free energy between reactants and products. It is proposed that the over-all driving force is the decrease in the large surface area, and hence surface energies, of the relatively inaccessible microcrystallites, the net result being an increase in the average crystallite size. If the aggregation process occurred throughout the cell wall then a reduction in the bulk film thickness would be expected due to the compaction occurring in the film. Thickness measurements, however, gave no indication of any reduction in the bulk film thickness, which would seem to indicate that unreacted "pillars" of oxide remain between the pores, except perhaps at the very outer surface where the film was initially more open and aggregated quicker. These columns "support" the remainder of the unreacted film. Thus, there is no net reduction in film porosity after the initial precipitation reaction, but only a redistribution of the remaining porosity. After the sealing process there are less "intercrystallite" pores, but these are bigger than those in the unsealed film. Hence the filled pores spread laterally and eventually much of the film, other than the pillars, appears to consist of relatively larger but irregular oxide crystallites.

Kingery has suggested a mechanism for the aggregation of solid particles having only a limited solubility in a surrounding liquid phase (18, 19). This theory has been mainly applied to the phenomenon of liquid phase sintering, which occurs at much higher temperatures than used for sealing. Kingery considers the point of contact between two solid particles, where there is a sharply negative radius of curvature. In a gas/liquid system, the vapor pressure over such a localized surface is much reduced. In a solid/liquid system, such a pressure difference appears as a decrease in solubility. Thus, in a restricted region the oxide is less soluble than elsewhere, resulting in a deposition of solid material there by any possible mechanism, such as the proposed dissolution/reprecipitation reaction.

Other factors.—The current results and theories agree with earlier studies of the effects of sealing solution and type, and of film thickness, using impedance methods and electron probe microanalysis (1-3), although some modification of the theory has proved necessary, particularly with regard to the extent of boehmite formation and the final sealing stages. Aging effects could be due to long-term aggregation processes.

The variation in extent of sealing with different sealants may be due to the differing adsorbabilities of the various anions, as well as the *p*H effects. Thomas and Whitehead (17) found that aluminum hydroxide precipitates can be peptized by stabilization of the large ionic micelles, due to repulsion of the charges of strongly adsorbed anions, and thus precipitation could be prevented. Ginsberg and Wefers (20) have suggested a similar theory for the stabilization of internal surfaces in unsealed films. Murphy has proposed that such anions can greatly affect the sealing reaction, claiming that is consists largely of the replacement of such adsorbed anions, or even a proton space charge, by OH^- ions, thereby preventing the entry of further ions onto the cell walls (6). This theory, although it may be one factor, cannot explain the major deposition of material in the large pores, observed directly in the present work. Preferential adsorption of PO_4^{3-} ions must interfere with the initial precipitation reaction as well as with any subsequent aggregation process, presumably by preventing initial dissolution within the pores or deposition of precipitate. The induction period observed with dichromate sealing (1-3) must be related to the *p*H rise eventually achieved in the pores due to the adsorption of the anion on the film and its subsequent entry between the microcrystallites.

Acknowledgments

The authors are indebted to Professor T. K. Ross for the provision of facilities and to Mr. B. Vaszko for his collaboration with the electron microscopy.

Manuscript submitted April 7, 1969; revised manuscript received June 7, 1969.

Any discussion of this paper will appear in a Discussion Section to be published in the June 1970 JOURNAL.

REFERENCES

1. T. P. Hoar and G. C. Wood, *Proc. Conf. on Anodising Aluminium*, p. 186, Aluminium Development Assoc., Nottingham, 1961.
2. T. P. Hoar and G. C. Wood, *Electrochim. Acta*, **7**, 333 (1962).
3. G. C. Wood and V. J. J. Marron, *Trans. Inst. Metal Finishing*, **45**, 17, 107 (1967).
4. V. J. J. Marron, Ph.D. Thesis, University of Manchester, 1965.
5. R. C. Spooner and W. J. Forsyth, *Plating*, **55**, 336, 341, 345 (1968).
6. J. M. Murphy, *Proc. Symposium on Anodising Aluminium*, p. 3, The Aluminium Federation, Birmingham, 1967.
7. J. P. O'Sullivan, J. A. Hockey, and G. C. Wood, *Trans. Faraday Soc.*, **65**, 535 (1969).
8. G. C. Wood, J. P. O'Sullivan, and B. Vaszko. *This Journal*, **115**, 618 (1968).
9. J. P. O'Sullivan, Ph.D. Thesis, University of Manchester, 1968.
10. A. Adams, M. A. Silva, and V. M. Spiers, *Nature*, **186**, 147 (1960).

11. X-Ray Powder Data File, A.S.T.M., Philadelphia, 1957.
12. F. Keller, M. S. Hunter, and D. L. Robinson, *This Journal*, **100**, 411 (1953).
13. C. J. L. Booker, J. L. Wood, and A. Walsh. *Brit. J. Appl. Phys.*, **8**, 347 (1957).
14. J. F. Murphy and C. E. Michelson, *Proc. Conf. on Anodising Aluminium*, p. 83, Aluminium Development Assoc., Nottingham, 1961.
15. M. J. Dignam, *This Journal*, **112**, 722 (1965).
16. H. Akahori and T. Fukushima, *J. Electronmicroscopy of Japan*, **13**, 162 (1964).
17. A. W. Thomas and T. H. Whitehead, *J. Phys. Chem.*, **35**, 27 (1931).
18. W. D. Kingery, "Ceramic Fabrication Processes," p. 131, M.I.T. Technology Press and John Wiley & Sons Inc., New York (1960).
19. W. D. Kingery, "Introduction to Ceramics," p. 386 ff, John Wiley & Sons Inc., New York (1960).
20. H. Ginsberg and K. Wefers, *Metall.*, **16**, 173 (1962); **17**, 202 (1963).

Electrochemical Reduction of 6-Thiopurine and Related Compounds: Polarography, Voltammetry and Macroscale Electrolysis

Glenn Dryhurst

Department of Chemistry, University of Oklahoma, Norman, Oklahoma

ABSTRACT

The electrochemical reduction of 6-thiopurine, purine-6-sulfinic acid, and purine-6-sulfonic acid has been investigated polarographically, coulometrically and by macroscale electrolysis. The reduction products have been investigated spectrophotometrically and chemically as well as by electrochemical methods. Between *p*H 1 and 3,6-thiopurine is reduced in two distinct steps; the first a 4*e* process to 1,6-dihydropurine; the second a 2*e* process to 1,2,3,6-tetrahydropurine which is subsequently hydrolyzed to a 4-aminoimidazole. At higher *p*H these two processes merge so that only a single 6*e* polarographic wave is observed. The *p*H dependence and slopes of the polarographic waves have been utilized to determine the rate controlling steps in these reductions. Purine-6-sulfinic acid is polarographically reduced in three separate processes; the first is the two electron reduction of the sulfinate monoanion to the 1,6-dihydro sulfinate which, between *p*H 2 and 6, decomposes to the purine-6-sulfenate which is immediately further reduced, in a 2*e* process, to 6-thiopurine. Between *p*H 7 and 9 the 1,6-dihydrosulfinate anion loses sulfoxylic acid to give purine. The second wave involves reduction of the purine-6-sulfinate dianion to the corresponding 1,6-dihydro derivative, which breaks down to yield purine and the sulfoxylate anion. The third wave involves, over-all, 4*e* and is due to further reduction of the 1,6-dihydrosulfinate to the corresponding 1,2,3,6-tetrahydro derivative which then loses sulfoxylic acid to give 2,3-dihydropurine; this is immediately further reduced to 1,2,3,6-tetrahydropurine which hydrolyzes to a 4-aminoimidazole. Purine-6-sulfonic acid is also polarographically reduced in three steps; the first wave involves a 2*e* reduction of the monoanionic species to the 1,6-dihydrosulfonate which decomposes to purine and, at low *p*H, purine-6-sulfinic acid; the latter is immediately reduced to 6-thiopurine. The second wave is the 2*e* reduction of the dianionic sulfonate to the 1,6-dihydro derivative which decomposes to purine. The third process is, over-all, a 4*e* reduction of the 1,6-dihydrosulfonate to a 4-aminoimidazole.

In some recent studies of the electrochemical oxidation of 6-thiopurine it became necessary to be able to both detect and quantitatively determine both the 6-thiopurine and two of its oxidation products, purine-6-sulfinic acid and purine-6-sulfonic acid (1). The analytical determinations of these and other electrooxidation products will be described elsewhere (2). This paper describes in detail the electrochemical reduction mechanisms for these reactions. 6-Thiopurine is used extensively as an antileukemia agent; it is also possible that both purine-6-sulfinic and purine-6-sulfonic acids or their salts may be minor, although important products of metabolism of 6-thiopurine in man and other species. Recent work (1, 3, 4) has suggested a possible parallelism between modes of electrochemical oxidation and biological oxidative transformations (*e.g.*, enzymatic oxidation). It is also important however, to fully understand the reduction behavior of biologically important molecules especially regarding those factors that influence the electron transfer processes, such as, for example *p*H.

There have been only a few reports of the electrochemical reduction of 6-thiopurine. Humlova has reported the oscillographic polarography of 6-thiopurine (5). Vacek (6) developed a method for the determination of 6-thiopurine by utilizing the height of the polarographic wave in McIlvaine buffer *p*H 7.1. There have been no reports of the polarographic behavior of purine-6-sulfonic or sulfinic acids. Consequently, it was decided to study systematically the polarography and voltammetry of 6-thiopurine, purine-6-sulfinic acid, and purine-6-sulfonic acid in order to define the nature and mechanisms of the electrochemical reduction.

Experimental

Chemicals.—6-Thiopurine was obtained from Calbiochem. Purine-6-sulfinic acid (sodium salt) and purine-6-sulfonic acid (potassium salt) were prepared accord-

ing to Doerr *et al.* (7). Hypoxanthine and purine were obtained from Nutritional Biochemicals.

Buffer solutions were prepared from analytical reagent grade chemicals.

Argon (Linde) used for deoxygenating purposes was equilibrated with water; no other purification was necessary.

Apparatus.—Polarograms and voltammograms were recorded on either a Sargent Model XV or Model XVI polarograph equipped with Sargent IR correctors. Water jacketed three compartment cells maintained at 25° ± 0.1°C and containing a saturated calomel electrode (SCE), and a platinum counterelectrode in saturated potassium chloride solution were employed. All potentials are referred to the SCE at 25°C.

The dropping mercury electrodes had normal m and t values. Triple distilled mercury was used for all coulometric and polarographic studies.

Cyclic voltammetry was performed with the apparatus described by Dryhurst *et al.* (8).

Controlled potential electrolyses were carried out using a Wenking Model 66TAl potentiostat. Potentials of interest were measured with a Sargent laboratory potentiometer. The pH was measured with a Beckman Zeromatic pH meter.

Current integration during coulometry utilized a titration coulometer described by Lingane (9).

Ultraviolet absorption spectra were obtained with a Beckman Model DB recording spectrophotometer, using 1.00 cm glass stoppered quartz cells.

The preparation of the PGE has been described earlier (4). A conventional two compartment macroscale electrolysis cell was employed using a mercury pool cathode and a platinum gauze counterelectrode. A Beckman pH type calomel reference electrode dipped directly into the working electrode compartment. The solution in the working electrode compartment was stirred with a magnetically rotated Teflon coated iron bar. A stream of argon gas was always bubbled through the test solution.

Polarographic procedure.—The test solution was prepared by diluting appropriate quantities of stock solutions with suitable background electrolyte; (on occasion when the compound was unstable at a particular pH, material was weighed directly into the deaerated buffer solution), the solutions were then deaerated for 10 min and then the polarogram run. The residual current was subtracted arithmetically from the total current; $E_{1/2}$ and i_l were determined graphically utilizing the average of the recorder trace.

Coulometric procedure.—One hundred and fifty milliliters of buffer solution was introduced into the electrolysis cell and deoxygenated for at least 20 min; the mercury was then introduced and the solution electrolyzed at the electrolysis potential until the titration coulometer showed a constant small titration rate. Then after turning off the potentiostat a weighed amount of the electroactive species was added. After dissolution, the desired potential was again applied; argon was bubbled continuously through these solutions.

At appropriate intervals 0.5 or 1.0 ml samples of the electrolysis solution were withdrawn and after dilution with water spectrophotometric measurements were taken.

Often polarographic or voltammetric runs were made directly in the test solution.

6-Thiopurine

Polarography.—Below pH 2.3 6-thiopurine exhibits two very close polarographic waves (waves I and II, respectively). The half-wave potential for both waves shifts linearly more negative with increasing pH; $E_{1/2} = -0.79\text{-}0.116$ pH for wave I, and $-1.00\text{-}0.0483$ pH for wave II. The two waves merge at about pH 3, the composite wave, up to pH 5, having the same pH dependence as that for wave I. Above pH 5 a further wave appears (wave III) whose $E_{1/2}$ also shifts linearly more negative with pH, $E_{1/2} = -1.29\text{-}0.027$ pH. Above pH 8 wave III disappears; one further wave is observed in ammonia buffer pH 9.1 (wave IV), which appears only at this pH, $E_{1/2} = -1.74$V.

At low pH the very large values of the diffusion current constant ($I = i_l/Cm^{2/3}t^{1/6}$) for both waves I and II are indicative of the involvement of catalytic hydrogen discharge (Table I). In 1*M* HOAc the I value indicates a 4*e* process as does the value for wave II; the involvement of catalytic hydrogen discharge however undoubtedly enhances these values, particularly that of wave II. Between pH 3 and 5.5 the sum of the diffusion current coefficients for wave I and wave II is indicative of six or more electrons. For wave III the diffusion coefficient decreases very rapidly with pH between pH 6 and 8; for wave IV the value is again indicative of at least a 6*e* process.

At pH 3.5 (acetate) the dependence of the limiting current on drop time supports the view that waves I and II are under over-all effective diffusion control (*i.e.*, linear dependence on $h^{1/2}$). However, at pH 8.1 (McIlvaine) the limiting current increased with h but less so than predicted by the square root relationship, hence it was concluded that wave III was partly under kinetic control at this pH (10). A concentration study at pH 3.5 showed a marked decrease in the i_l/C ratio with increasing concentration from 41.4 μA mM^{-1} at 0.028 m*M* to 30.9 μA mM^{-1} at 0.42 m*M*. The systematic decrease of the i_l/C ratio with increasing concentration is probably associated with the lowering of the hydrogen overpotential by 6-thiopurine. As the 6-thiopurine concentration increases hydrogen becomes more readily reduced so that there is a much poorer separation between the 6-thiopurine and hydrogen discharge waves.

At pH 3.5 the half wave potential becomes slightly more negative with increasing concentration. The temperature dependence of the wave at pH 3.5 was 1.0% per degree.

Electrolysis at wave I and wave II.—Attempts to determine a coulometric n value for wave I plus wave II between pH 3.5 and 5.5 gave extremely high values. Over the period of many hours electrolysis in these pH regions it was not possible to eliminate the 6-thiopurine polarographic wave; the electrolysis current remained at a high value throughout the course of the electrolysis and the solution pH increased. Such behavior indicates that a major part of the current controlling process under such conditions is the catalytic reduction of hydrogen ion. At the beginning of such electrolyses hydrogen sulfide was liberated. As the electrolysis proceeded a red color developed in the solution which intensified in the presence of air, and after a few days exposure to the atmosphere a fine black precipitate developed.

Electrolysis at wave III.—Macroscale electrolysis of 6-thiopurine on the crest of wave III (McIlvaine pH 7) also gave extremely high coulometric n values, H_2S was evolved, the pH increased and a red color devel-

Table I. Variation of 6-thiopurine diffusion current constant with pH

pH	Background[a]	Diffusion current constant Wave I	Wave II	Wave III	Wave IV
0.0	1*M* H_2SO_4	24.4	30.7		
1.0	Chloride	24.5	34.7		
2.3	1*M* HOAc	8.3	9.1		
3.4	Acetate	14.3			
4.4	Acetate	14.8			
5.7	Acetate	14.2			
6.0	McIlvaine			12.7	
7.0	McIlvaine			5.4	
8.0	McIlvaine			1.8	
9.1	Ammonia				14.8

[a] Except in the case of the 1*M* H_2SO_4 and 1*M* HOAc backgrounds, all buffers were 0.5*M* in ionic strength.

oped in the solution which behaved in an identical manner to the product obtained from waves I and II. However, after standing such a solution in air for only a few hours, a black precipitate formed.

Purine-6-Sulfinic Acid

Purine-6-sulfinic acid (P-6-Si) shows several polarographic waves over the normal *p*H range. In order that the origins of these waves could be completely understood it was necessary to ascertain the stability of P-6-Si in each of the backgrounds and to identify the breakdown products.

Stability studies.—Spectrophotometric and polarographic studies showed that between *p*H 1 and 5, P-6-Si decomposes to hypoxanthine (major product) along with sulfur dioxide and 6-thiopurine. The rate of decomposition decreased with increasing *p*H. At around *p*H 2 there were also indications, on occasion, that traces of purine were produced. Between *p*H 5 and 8.0, P-6-Si decomposed very slowly over the course of several days to P-6-So and hypoxanthine. P-6-Si was stable for several days in ammonia buffer *p*H 9.1.

Polarography.—Because of the number of electroactive decomposition products from P-6-Si the observed polarographic behavior of solutions of P-6-Si is extremely complex.

P-6-Si itself gives rise directly to three polarographic waves; all shift linearly more negative with increasing *p*H; $E_{1/2}$ = —0.37-0.094 *p*H for wave I, —0.79-0.075 *p*H for wave II and —0.99-0.080 *p*H for wave III.

The effect of *p*H on the diffusion current constant, I, reflects the instability of P-6-Si at low *p*H (Table II). Between about *p*H 3 and 7 the magnitude of I indicates that two 2*e* waves are involved (waves I and III). At *p*H 8 wave III disappears, wave I becomes much smaller and a new small wave (wave II) appears. At *p*H 9.1 again two 2*e* waves (waves I and III) appear. At higher *p*H only the single wave II appears having an I value intermediate between that expected for a one or two electron process.

At *p*H 9 (ammonia) the i_l/C ratios for waves I and III are 5.9 ± 0.1 and 6.4 ± 0.7 μA mM^{-1}, respectively; in carbonate buffer at the same *p*H the i_l/C ratio for wave II decreased slightly with increasing concentration from 6.7 μA mM^{-1} at 0.25 m*M* to 5.1 μA m*M* at 1.26 m*M*. At *p*H 4.4 (acetate) and 9.1 (ammonia) both waves I and III were entirely under diffusion control ($i_l/h^{1/2}$ constant). However, at *p*H 8 (McIlvaine) the droptime dependence of the limiting current for wave I was characteristic of a process partly under kinetic control although this effect was small.

Electrolysis of wave I.—Because of the instability of P-6-Si, coulometry and macroscale electrolyses were not performed below *p*H 3.

Table II. Variation of diffusion current constant with *p*H for polarographic waves of purine-6-sulfinic acid[a]

Background[b]	*p*H	Diffusion current constant[c] Wave I	Wave II	Wave III
1*M* HOAc	2.3	0.24		
Acetate	3.6	4.57		4.32
Acetate	5.4	4.23		4.45
McIlvaine	7.0	2.91		3.77
McIlvaine	8.0	1.62	1.35	
Ammonia	9.1	3.41		3.02
Carbonate	9.0		3.28	[d]
Hydroxide	11.6		2.79	
Hydroxide	12.3		2.32	

[a] Concentration 0.914 m*M*.
[b] With the exception of 1*M* HOAc all backgrounds had an ionic strength of 0.5*M*.
[c] $I = i_d/Cm^{2/3}t^{1/6}$.
[d] A wave was observed but was so indistinct that a meaningful I value could not be computed.

At *p*H 3.6 and 5.4, P-6-Si decomposes slowly primarily to hypoxanthine which is not electrochemically reducible, the observed *n* values of 2.4 and 3.6, respectively, were therefore expected to be low; the major electrolysis product was 6-thiopurine (along with some purine). At *p*H 7 and above 2*e* were transferred; the major product was purine; at *p*H 9.1 (ammonia) however purine is slowly further reduced in a 2*e* process to 1,6-dihydropurine. Product identification in these studies was based chiefly on polarography and ultraviolet spectra.

Electrolysis at wave II.—Attempts to obtain any meaningful coulometric data at the first wave in carbonate background *p*H 9 (wave II) were unsuccessful since a high current was observed throughout the electrolysis leading to extremely high *n* values. The solution turned pink as the electrolysis proceeded, particularly when air was allowed to come in contact with the solution.

Coulometry at wave II at *p*H 11.6 (λ_{max} for P-6-Si = 278 mμ) indicated that about 2*e* were transferred fairly rapidly with the formation of purine (λ_{max} = 271 mμ) followed by very slow transfer of a further 2*e* to form 1,6-dihydropurine (λ_{max} = 305 and 230 mμ).

Electrolysis at wave III.—After elimination of P-6-Si wave I in acetate *p*H 3.6 the potential was adjusted to coincide with the rising portion of the second wave (wave III). Immediately H_2S was evolved and the current increased to a large value; extremely high *n* values were obtained. After several hours electrolysis polarography showed no reducible products and the *p*H had increased by several units. As soon as the solution was exposed to the atmosphere it turned bright red-pink. Two u-v absorption peaks were observed (λ_{max} = 320 and 240 mμ corresponding to 6-thiopurine and the purine wave II electrolysis product.) Treatment of this solution with sodium nitrite then alkaline β-naphthol gave an orange pink dye (λ_{max} = 500 mμ). The wave III process at this *p*H thus involved reduction of 6-thiopurine in part to the wave II product of purine which is known to be a diazotizable primary amine (11). Because of the effect of 6-thiopurine and the purine wave II electrolysis product on the overpotential for hydrogen discharge the large *n* values were not unexpected.

Attempted coulometry directly on wave III at *p*H 6.9 (McIlvaine) gave very high *n* values, the *p*H increased, and the solution turned pink on exposure to air. The u-v spectrum showed a single broad absorption peak at $\lambda_{max} \cong$ 308 mμ, although the product solution did not give a good test with sodium nitrite-β-naphthol.

Purine-6-Sulfonic Acid

Polarography.—Purine-6-sulfonic acid (P-6-So) shows four polarographic waves over the normal *p*H range. At very low *p*H (*p*H 1.0 and below) P-6-So decomposes to hypoxanthine and sulfur dioxide although the decomposition is much slower than for P-6-Si.

Three of the waves shift linearly more negative with increasing *p*H. Wave I appears between *p*H 1 and 7, $E_{1/2}$ = —0.45-0.0782 *p*H. Between *p*H 3.6 and 12.5 wave II appears, $E_{1/2}$ = —0.675-0.0789 *p*H. Wave III appears between *p*H 1 and 9, $E_{1/2}$ = —0.98-0.0635 *p*H. A fourth wave, wave IV, is observed at *p*H 9.1, $E_{1/2}$ = —1.450V.

The temperature and droptime dependence of the current indicates that the waves are under diffusion control except at *p*H 6.9 (McIlvaine) when wave I was partly under kinetic control. The magnitude of the diffusion current constants (Table III) indicated that the polarographic *n* values for waves I and II reach a limiting value of 2; the magnitude of the constant for waves III and IV seems to indicate similar values, although at certain *p*H values (*e.g.*, wave III at *p*H 2 and 6.9) the involvement of more than 2*e* is suggested.

Table III. Variation of diffusion current constant with pH for polarographic waves of purine-6-sulfonic acid[a]

Background[b]	pH	Diffusion current constant[c] Wave I	Wave II	Wave III	Wave IV
Chloride	1.05	2.74		[d]	
Chloride	2.0	3.43		10.00	
1M HOAc	2.3	3.36		5.23	
Acetate	3.6	4.52	1.60	3.04	
Acetate	5.4	4.68	2.72	4.84	
McIlvaine	6.9	1.36	4.39	7.86	
McIlvaine	8.0		3.82	6.80	
Carbonate	8.9		5.3	3.82	
Ammonia	9.1		3.25	3.32	3.58
Hydroxide	11.6		2.86		
Hydroxide	12.3		3.38		

[a] Concentration of P-6-So, 0.81 mM.
[b] With the exception of 1M HOAc all backgrounds had an ionic strength of 0.5M.
[c] $I = i_d/Cm^{2/3}t^{1/6}$.
[d] A very large maxima appeared.

In ammonia and carbonate backgrounds pH 9 waves I, II, and III all give linear i_l-C plots.

Electrolysis at wave I.—The instability of P-6-So below pH 2 precluded coulometry in these regions. The data indicates that below pH 3 between 3 and 4e are consumed and electrolysis produces a mixture of 6-thiopurine and purine; above this pH purine is the sole product and 2e are consumed.

Electrolysis at wave II.—Coulometry on the plateau of wave II in acetate pH 3.6 and 5.4 after first eliminating wave I by electrolysis showed that 2e were involved in each case giving 1,6-dihydropurine as the product. The same product was obtained up to pH 8.0 by direct reduction of P-6-So at wave II although 4e were transferred. Above this pH the sole product was purine again with the involvement of 2e.

Confirmation of the nature of the product of wave II was obtained by cyclic voltammetry at the pyrolytic graphite electrode (PGE). If the initial sweep was toward negative potential (starting at 0.0V) no cathodic peaks were observed in the electrolysis solution; on sweeping toward positive potential a well-formed anodic peak was always observed. If the scan was run toward negative potential after having scanned this anodic peak a well-formed cathodic peak was observed. Purine, itself, on the initial scans showed only a cathodic peak, but having once scanned this peak a well-formed anodic peak was produced on sweeping toward positive potential. The potentials of these anodic and cathodic peaks observed for both purine and the P-6-So wave II product solutions always agreed exactly. Dryhurst and Elving (12) have discussed the mechanism of these processes.

Electrolysis at wave III.—Attempts to electrolyze at potentials corresponding to wave III and determine an n value were never successful. Very large n values were obtained and the pH increased several units after electrolysis; the solution turned red-pink especially when exposed to the atmosphere. The u-v absorption spectra of an electrolyzed solution was different to the wave II product, although no well-defined peaks were observed, rather plateaux at $\lambda_{max} \cong 330$, 300, and 270 mμ with end absorption occurring somewhat earlier than for background solution alone.

Electrochemical Reduction Mechanisms

6-Thiopurine.—Between about pH 2.3 and 5 the magnitude of the diffusion current constant for waves I and II suggests the involvement of six or more electrons. However, the evidence from concentration and coulometric studies and the more positive potentials for background discharge in the presence of 6-thiopurine suggests that catalytic hydrogen discharge enhances the magnitude of the constant. At low pH, wave I probably involves about 4e and wave II 2e, although catalytic hydrogen discharge obscures the values. The fact that H_2S is immediately evolved upon commencement of the electrolysis suggests that the initial point of attack is at 1,6-double bond to give purine. At low pH purine would be rapidly further reduced in a 2e process to 1,6-dihydropurine (11). The formation and reduction of purine in the over-all wave I process is evidenced by the magnitude of I at pH 2.3 indicating 4e and the fact that between pH 0 and 3 a second wave appears. Calculation from earlier data (11) indicates that the second purine reduction wave should occur at $E_{1/2} = -0.90$V at pH 0, −0.98V at pH 1.0, and −1.18V at pH 2.3; wave II for 6-thiopurine appears at −0.97V, −1.05V, and −1.12V, respectively, at the same pH. Because of the closeness of the two 6-thiopurine waves and hence the error involved in measurement of $E_{1/2}$ for wave II, these values are in good agreement. Beyond pH 3 the expected half-wave potentials for the second wave of purine occur at more positive potentials than those required for the initial reduction of 6-thiopurine and accordingly only a single 6e wave is observed. The red electrolysis product of 6-thiopurine produced between pH 3 and 5 which deepened in color on exposure to air and finally gave a black precipitate, agrees exactly with the behavior reported for the product of electrolysis at the second wave of purine, the black material being of a polymeric nature (11).

More detail regarding the electrode mechanism and rate controlling steps was obtained by computing αn_a values utilizing the wave slope $(E_{1/4} - E_{3/4})$ (13). Below pH 3, αn_a data was calculated for wave I, between pH 3 and 5 for wave I plus wave II and above pH 5 for wave III (Table IV). There appeared to be three distinct regions of constant αn_a values which correspond to these latter three pH regions. The rate of change of $E_{1/2}$ with pH along with αn_a data was used to calculate p, the number of hydrogen ions involved in the rate determining step (13).

For each of the pH regions examined there were only minor changes in droptime at the half-wave potentials so that $E_{1/2}$ was employed uncorrected (13). Values of p and αn_a are reported in Table IV. On the basis of α being *ca.* 0.5 the data suggests that wave I below pH 3 involves a two electron two proton rate controlling process; the diffusion current constant at pH 2.3 indicates a polarographic n value of 4. Accordingly, the mechanism can be represented as an initial rate determining attack at the 1,6-double bond to give the 1,6-dihydro derivative of 6-thiopurine (Fig. 1A, II) which rapidly loses H_2S to give purine which is further reduced in a two electron, two proton process to 1,6-dihydropurine (Fig. 1A, I → IV).

Wave II, which probably involves two electrons, is therefore identical to the second reduction wave of purine (11) namely reduction of IV, Fig. 1, to 1,2,3,6-tetrahydropurine (VI, Fig. 1) which is hydrolyzed by water to a 4-aminoimidazole (Fig. 1C).

Above pH 3 and below pH 5 the wave I and wave II processes occur simultaneously; the rate controlling step involves a one electron and one proton reduction

Table IV. Effect of pH and background composition on the rate determining step in polarographic reduction of 6-thiopurine

Background[a]	pH	$(E_{1/4} - E_{3/4})$[b]	αn_a[c]	p
Chloride	1.0	0.048	1.18	2.3
1M HOAc	2.3	0.055	1.02	2.0
McIlvaine	3.0	0.085	0.66	1.3
Acetate	3.7	0.116	0.49	0.96
Acetate	4.7	0.121	0.47	0.92
Acetate	5.0	0.077	0.73	1.4
Acetate	5.4	0.047	1.20	0.54
Acetate	5.7	0.044	1.30	0.58
McIlvaine	7.0	0.051	1.10	0.50
McIlvaine	8.0	0.070	0.81	0.37

[a] With the exception of 1M HOAc all backgrounds 0.5M in ionic strength.
[b] Average of three replicate determinations.
[c] See ref. (13) for method of calculation.
[d] A large maxima was produced at this pH.

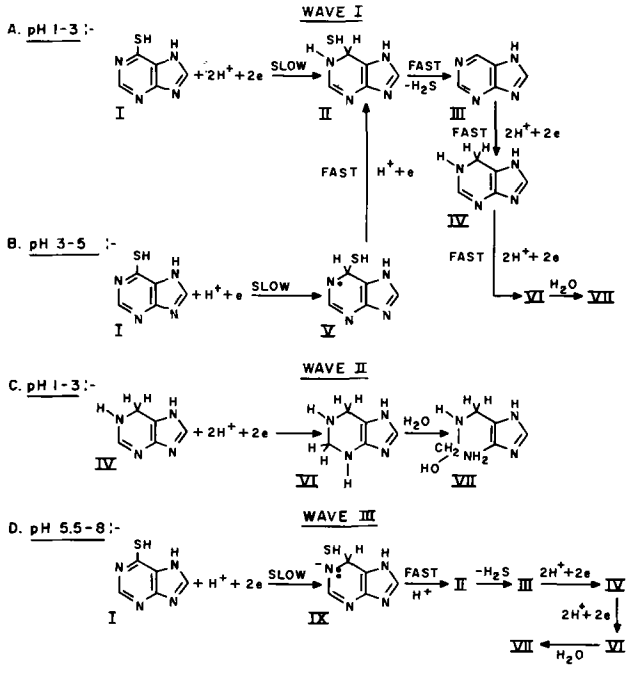

Fig. 1. Interpretation of electrochemical and chemical behavior observed for polarographic reduction of 6-thiopurine.

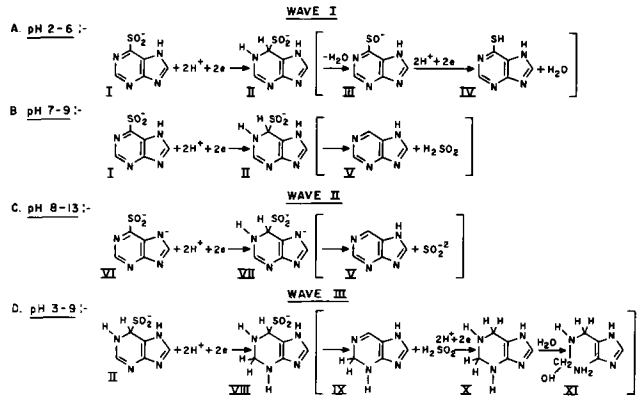

Fig. 2. Interpretation of electrochemical and chemical behavior for three polarographic waves observed for purine-6-sulfonic acid. Compounds and reactions enclosed in brackets are those which occur after the initial polarographic reactions (e.g., under coulometric conditions).

to give a free radical species (V, Fig. 1) which is rapidly further reduced to the 1,6-dihydro derivative of 6-thiopurine the further breakdown of which would be the same as for wave I and wave II so that the ultimate product is a 4-aminoimidazole, and a total of 6e are transferred (Fig. 1B).

Above pH 5.5 the rate controlling process again appears to involve two electrons and probably a single proton. Since the value of the diffusion current constant decreases with increasing pH and the wave is partly kinetically controlled, then the mechanism can be represented by an initial reduction to anionic species (IX, Fig. 1) which is rapidly protonated to give again the 1,6-dihydro derivative of 6-thiopurine which then undergoes the same reactions as outlined for waves I and II (Fig. 1D) so that again six electrons are finally consumed. Intermediate or mixed mechanisms apparently occur at pH 3 and 5.

Purine-6-sulfinic acid.—Due account being taken of the stability of P-6-Si particularly at low pH, the value of the diffusion current constant for wave I up to about pH 7 is in accord with a two electron reduction process. At pH 8 wave I appears to split into two waves (waves I and II) since the sum of the diffusion current coefficients are the same as for wave I alone at lower pH. At pH 9 and above, with the exception of ammonia background pH 9.1, wave I disappears and wave II becomes of about the same size as that for wave I at lower pH. Wave III has a diffusion current constant indicative of a 2e reduction except that it does not appear at pH 8 and it disappears behind background discharge above pH 9.

Between pH 3.6 and 5.7 coulometry indicates that more than two electrons are transferred at potentials corresponding to wave I and, bearing in mind the instability of P-6-Si at these pH regions, n probably approaches 4. Since the ultimate product is 6-thiopurine it is likely that the initial electrochemical reduction product decomposes, at low pH, to a species capable of further reduction with consumption of a further two electrons. That the ultimate product is 6-thiopurine at low pH indicates that electrochemical attack involves carbon atom 6; by analogy with earlier data for purine (11), the initial product is probably the 1,6-dihydroderivative of P-6-Si (II, Fig. 2) which subsequently loses water to give purine-6-sulfenic acid (III, Fig. 2) which is immediately reduced to 6-thiopurine (IV, Fig. 2). Purine-6-sulfenic acid has never been isolated; however, being an intermediate oxidation state between bis(6-purinyl)disulfide and P-6-Si it is probably reduced at some intermediate value between these two latter compounds. Bis(6-purinyl) disulfide is polarographically reduced at potentials close to 0.00V (1).

At pH 6.9 the pH dependence of wave I, and the diffusion current constant indicate that the polarographic reduction mechanism is unchanged (*i.e.*, steps I → II Fig. 2A). Coulometry, however, gives an n value of 2 and the main product is purine along with 6-thiopurine as the minor product. Accordingly, it is likely that the dehydration step (II → III, Fig. 2A) becomes less important and the chief breakdown route of the 1,6-dihydropurine-6-sulfinic acid involves liberation of sulfoxylic acid, H_2SO_2, and purine (V, Fig. 2B). Sulfoxylic acid has been shown to be the major product of reduction of sulfur dioxide at the DME (14).

At pH 8 (McIlvaine) wave I decreases in height and wave II appears, the sum of both waves being the same as wave I at lower pH. Wave I becomes partly kinetic controlled. Coulometry at wave I, however, involves two electrons and purine is the final product; wave II disappears and the product shows only the waves and spectra of purine. Doerr *et al.* (17) have calculated the pK_a for the imidazole dissociation of P-6-Si as 9.3. The evidence here seems to indicate a slightly lower pK_a such that at pH 8 the P-6-Si is predominantly in the dianionic form, the height of wave I, due to reduction of the monoanionic form, therefore being at least partially kinetically dependent on the rate of protonation of the former species. Wave II must, therefore, be due to reduction of the dianionic form of P-6-Si to the same product as for wave I. That this is so is indicated by the fact that coulometry of P-6-Si at wave II potentials at pH 11.6 gives an initial two electron reduction to purine, which at the potentials employed (—1.70V) is slowly further reduced to 1,6-dihydropurine (*i.e.*, this potential corresponds to one slightly more positive than $E_{1/2}$ for the first wave of purine at this pH) (12). Calculation shows that the potentials applied in carbonate buffer pH 9 (—1.60V) for electrolysis of P-6-Si wave II are sufficiently negative to completely electrolyze the expected product purine, hence giving rise to the large catalytic hydrogen discharge and hence very large n values. However, the evidence suggests that the product is identical to that obtained on complete electrochemical reduction of purine or 6-thiopurine.

The behavior of P-6-Si in ammonia buffer pH 9 is not readily explained. Since polarography in carbonate buffer pH 9 is quite different it must be assumed that ammonium ion (or ammonia) influences the ionization of the acid, since coulometry and polarography of the product solutions indicate that the over-all products are the same in ammonia buffer as in other compar-

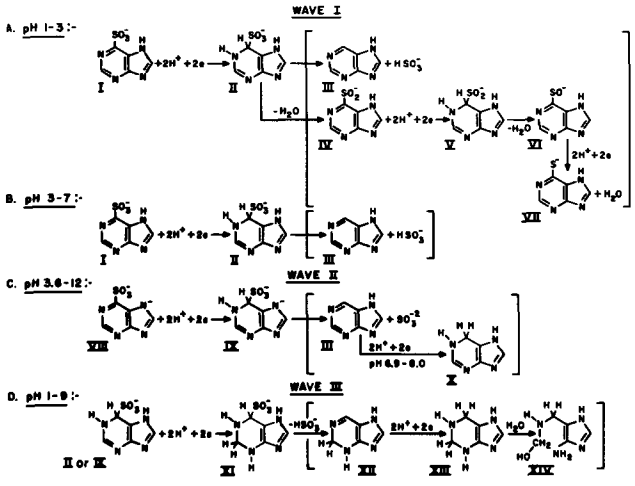

Fig. 3. Interpretation of electrochemical and chemical behavior observed for polarographic reduction of purine-6-sulfonic acid. Compounds and reactions enclosed in brackets are those which occur after the initial polarographic reactions (e.g., under coulometric conditions).

able backgrounds. The formation of amide or imide species may be important in interpreting the behavior in ammonia background.

Purine-6-sulfonic acid.—Between pH 1 and 5.5 the wave I diffusion current constant indicates that the polarographic reaction involves 2*e*. Coulometry at pH 2.3, however, indicates that more than 3*e* are involved and that the ultimate products are purine and 6-thiopurine. This immediately suggests that the initial attack is at C-6 but that the initial product is rather unstable at low pH. Accordingly, the probable initial product is 1,6-dihydropurine-6-sulfonate. The nonintegral number of electrons transferred and the fact that two products are produced suggests that this compound slowly decomposes by two routes; one by loss of sulfurous acid to purine, the other by loss of water to P-6-Si which is then further reduced by the mechanism developed earlier (Fig. 2A) to 6-thiopurine (Fig. 3A). Between pH 2.3 and 5.7 the only product is purine; the I value and coulometry indicate a two electron reduction.

At pH 3.6 wave II appears, and with increasing pH this wave grows until the diffusion current constant indicates a two electron process. At pH 6.9 wave I is very small and is under kinetic control. Doerr *et al.* (7), have calculated the pK_a for the second dissociation of P-6-So (imidazole dissociation) as 8.56. This would indicate that above pH 7 some dianionic species should be in solution. The kinetic nature of wave I at pH 6.9 suggests that this wave is due in part to the rate of protonation of the dianionic species to the monoanionic species. The fact that wave II is observed at pH values as low as 3.6 suggests that the literature pK_a value (7) is high. Accordingly, wave I is due to a two electron reduction of the monoanionic P-6-So to the 1,6-dihydro compound which a low pH, under coulometric conditions, decomposes to purine and purine-6-sulfinate, the latter undergoing further reduction. Between pH 3 and 6.9 the 1,6-dihydro derivative decomposes solely to purine (Fig. 3B).

Wave II is due to reduction of the dianionic form of P-6-So. The value of the diffusion current constant indicates that the polarographic process involves two electrons. Above pH 9 coulometry also indicates that two electrons are transferred and that the ultimate product is purine (Fig. 3C). However, coulometry at pH 6.9 and pH 8 indicated the transfer of 4*e* and that the product was identical to that obtained upon electrolysis of purine at its first wave. Calculations from earlier data (12) show that the potentials employed at pH 6.9 and 8.0 for electrolysis of P-6-So (—1.30V and —1.40V, respectively) were sufficiently negative to allow electrolysis of purine which is a breakdown product of the initial electrochemical product 1,6-dihydropurine-6-sulfonate (dianionic species) (Fig. 3C). For coulometry at pH 9.1 and 10.6 the applied potential (—1.30 and —1.58V, respectively) was not sufficiently negative to allow appreciable reduction of the ultimate product, purine.

The exact nature of the wave III process is difficult to assign. The I value indicates that at many pH values more than 2*e* are involved. Coulometry suggests that the product of wave III aids the catalytic reduction of hydrogen ion and the nature of the final product is very similar to that obtained on electrolysis of purine at its second wave (11, 12). The pH dependence of the wave III process is also very similar to that observed for the second wave of purine; hence, it is likely that wave III involves reduction of the wave I or wave II product (1,6-dihydro derivative) at the 2,3-position to give the 1,2,3,6-tetrahydro derivative. Presumably subsequent breakdown of this product to yield sulfurous acid followed by further reduction would be analogous to the mechanism developed for adenine (11) (Fig. 3D) resulting in the formation of a 4-aminoimidazole.

The exact nature of the electrode mechanisms in ammonia buffer pH 9.1 cannot at this time be explained, however, since the behavior in a carbonate buffer at the same pH agrees with the postulated mechanism suggests that the change in mechanism is associated specifically with ammonia.

Acknowledgments

The author would like to thank the National Science Foundation which supported the work described through Grant No. GP 8151.

Manuscript submitted March 10, 1969; revised manuscript received June 12, 1969.

Any discussion of this paper will appear in a Discussion Section to be published in the June 1970 JOURNAL.

REFERENCES

1. G. Dryhurst, *This Journal*, **116**, 1097 (1969).
2. G. Dryhurst, *Anal. Chim. Acta*, In press (1969).
3. W. A. Struck and P. J. Elving, *Biochem.*, **4**, 1343 (1965).
4. G. Dryhurst and P. J. Elving, *This Journal*, **115**, 1014 (1968).
5. A. Humlova, *Collect. Czech. Chem. Communs.*, **29**, 182 (1964).
6. J. Vacek, *Ceskoslov. farm.*, **9**, 126 (1960).
7. I. L. Doerr, I. Wempen, D. A. Clarke, and J. J. Fox, *J. Org. Chem.*, **26**, 3401 (1961).
8. G. Dryhurst, M. Rosen, and P. J. Elving, *Anal. Chim. Acta.*, **42**, 143 (1968).
9. J. J. Lingane, "Electroanalytical Chemistry," Chap. XIX, pp. 457-58, Interscience Publishers, New York (1966).
10. L. Meites, "Polarographic Techniques," 2nd Ed., Chap. 3, Interscience Publishers, New York (1965).
11. D. L. Smith and P. J. Elving, *J. Am. Chem. Soc.*, **84**, 1412 (1962).
12. G. Dryhurst and P. J. Elving, *Talanta*, **16**, 855 (1969).
13. Ref. 10, Chap. 4.
14. I. M. Kolthoff and C. S. Miller, *J. Am. Chem. Soc.*, **63**, 2818 (1941).

Stirred H-Cell Measurements on Liquid Alloys of Cadmium with a Small Amount of Gold

Barton L. Houseman[1]

Department of Chemistry, Goucher College, Baltimore, Maryland

and Guy R. B. Elliott*

University of California, Los Alamos Scientific Laboratory, Los Alamos, New Mexico

ABSTRACT

Stirred H-cell emf measurements on solvent concentration cells of the type

$$W\text{-}Cd, Au_{(liq\ soln)}/CdI_{2(l)}/Cd_{(l)}\text{-}W$$

were made with high precision using compositions from 0.001 to 0.021 mole fraction gold at 673°, 742°, and 773°K. Solubility and anodic current efficiency measurements are reported. Plotting techniques are discussed.

Olander (1) has shown that, for solid gold-cadmium alloys, electrochemical cells of the type

$$W\text{-}Cd_{(l)}/CdCl_2 \text{ in } K(Rb)Cl\text{-}LiCl_{(liq\ soln)}/Cd, Au_{(solid\ soln)}$$

can be used for measurements with a precision of about ± 0.1 mV. Other measurements by Elliott and Chipman (2) have shown that the precision can be pushed to about ± 0.02 mV using solvent concentration cells of the type $W\text{-}Cd,X_{(liq\ soln)}/CdCl_2$ in $LiCl\text{-}KCl_{(liq\ soln)}/Cd_{(l)}\text{-}W$. It is advisable to avoid lithium halide solutions if possible. however, because these halides are not easy to purify (3, 4).

The present measurements were obtained by an extension of the stirred H-cell technique (5-7) to the use of molten cadmium iodide as the electrolyte with cadmium and cadmium alloy electrodes.

Experimental Technique

The cells and furnace.—Stirred H-cells as in Fig. 1 were modified from an earlier design (5-7) and used for runs IV to VI. For runs I to III the cross arm was a simple horizontal section, constricted by each H-cell leg. Uniform temperatures were again established by regulating the temperature outside nesting copper cylinders (5, 6). Gold solute pieces could be added at will by tilting the cell and tapping the side arm.

Chemical purity.—Molten cadmium (99.999% pure by manufacturer's analysis) was freed of oxide and electrochemically important impurities by washing with boiling CdI_2 under vacuum.[2] Reagent CdI_2 was vaporized under vacuum (run I) or merely fused twice under vacuum (all other runs) then melted into the H-cell legs. Gold (99.98% pure by manufacturer's analysis) was cut up with clean cutters, washed with petroleum ether and acetone, and vacuum dried. Argon was purified by distillation. Tungsten was cleaned electrolytically using a-c current in concentrated NaOH with water wash.

EMF.—Temperatures were measured by the emf of Pt/Pt-10% Rh thermocouples read on a Leeds and Northrup K-2 potentiometer with an electronic null detector. This same potentiometer was used to measure the cell voltages and was checked against a calibrated potentiometer to assure that it was indicating proper emf values. No short-term fluctuations in the cell could be detected at the galvanometer, *i.e.*, these values were steady in the 0.0001 mV range. Except for one point (36B) which appears to be in error by 0.0057 mV, the similarities in the emf/T°K values indicate a long-term variation of < 0.001 mV in the emf for a particular alloy composition.

Cell operation.—Compared with the tin solutions (5-7), the cadmium solutions required considerably more stirring before equilibrium was reached. Presumably this was because the solubility of cadmium in its iodide (8-11) is greater than that of tin in its chloride (12, 13) near the halide melting points. (There is considerable contradiction in the literature regarding these values, but there is agreement that the iodide dissolves less cadmium than do the other cadmium halides.) For the gold additions, after about 1½ hr the equilibrium was achieved, and further stirring or long standing did not alter the emf except as discussed above.

Solubility measurements.—Cursory solubility measurements were undertaken to convince ourselves that the cadmium solubility in CdI_2 was not greater than the largest reported solubility (11) among the measurements mentioned above. First, the cadmium which had dissolved into the electrolyte in run I was deter-

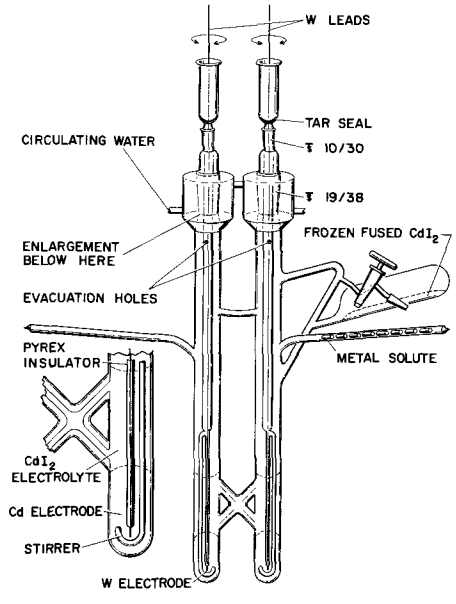

Fig. 1. Stirred emf concentration cell used in runs IV to VI. (Main tubes drawn oversize below standard taper joint for clarity in reproduction. The evacuation holes are in the stirrers.)

* Electrochemical Society Active Member.
[1] Visiting Staff Member, Los Alamos Scientific Laboratory.
[2] "Under vacuum" refers to a pressure of 10^{-5} or 10^{-6} Torr beyond the cold trap. $CdI_{2(g)}$ and $Cd_{(g)}$ would, of course, be present in this case.

mined by breaking open the cell, washing away the electrolyte, and establishing the weight loss from the cadmium reference electrode. Second, weighed cadmium and CdI_2 sealed in an evacuated quartz capsule were heated at ~ 765°K for a day, then the temperature was dropped to 756°K and held for a week. A handle on the capsule allowed the capsule to be spun in the furnace to stir it; this was done occasionally. The capsule was finally taken from the furnace, laid on its side to cool, then broken open. The washed cadmium button was weighed and the weight loss was assumed to measure the cadmium solubility.

Measurements of n in $\Delta G = -nF\epsilon$.—At the end of run VI the voltage was followed for two days to be sure it was not drifting. Current was then supplied from a lead-acid battery (of the stable voltage type used to operate potentiometers) to the cell and to a 10.01 ohms calibrated resistance in series. Current was monitored by occasionally measuring the voltage drop across the resistance. After passing current for four days, the cell was allowed to return to equilibrium by stirring and standing for four days; the cell voltage did not change during the last 2½ days. The process was then repeated twice, but using smaller current passage. Cadmium transfer was determined from the known emf-composition relationships as established from the solute addition experiments. (Again these were considered to be cursory measurements since the cell design was not right for highest accuracy for these particular measurements.)

Results

The voltages corresponding to different gold additions are presented in Table I. The activities are calcu-

Table I. Concentration cell emf data at ~674°K, ~742°K, or ~773°K
W-Cd, $Au_{(soln)}/CdI_{2(l)}/Cd_{(l)}$-W

Point No.	Cadmium added (−solubility),[a] g	Gold added, g	Cadmium mole fraction[b] Added	Solubility corrected	Temperature, °K	Emf reading,[c] mV	Cadmium activity,[d] a_{Cd}	Deviations from Eq. [3] and [4]
Run I								
1	40.6542	0.21579	0.996980	0.996958	675.7	0.0934	0.99679	+0.00004
2	(−0.3031)	0.14835	0.994915	0.994877	672.8	0.1591	0.99453	0.00000
3		0.19614	0.992197	0.992139	673.5	0.2463	0.99154	−0.00006
4		0.15270	0.990091	0.990018	674.2	0.3153	0.98920	—
Run II								
5	60.7681	0.46866	0.995618	0.995602	681.2	0.1376	0.99530	0.00000
6	(−0.2204)	0.52505	0.990755	0.990721	681.8	0.2932	0.99007	—
7		0.18934	0.989012	0.988973	672.4	0.3465	0.98811	0.00000
8		0.05200	0.988535	0.988494	672.2	0.3631	0.98754	−0.00005
9		0.04244	0.988146	0.988103	672.6	0.3764	0.98709	−0.00007
10		0.05798	0.987614	0.987570	673.0	0.3918	0.98658	0.00000
11		0.04715	0.987183	0.987137	673.5	0.4056	0.98612	+0.00002
12		0.09466	0.986317	0.986268	673.6	0.4339	0.98515	0.00000
13		0.43523	0.982357	0.982294	673.8	0.5630	0.98079	0.00000
Run III								
14	49.0357	1.35795	0.984443	0.984248	743.9	0.5684	0.98241	+0.00001
15	(−0.6154)	0.15902	0.982652	0.982436	744.9	0.6465	0.98006	−0.00028
Run IV								
16	49.7733	0.21540	0.997536	0.997513	736.8	0.0864	0.99729	−0.00001
17	(−0.4704)	0.15670	0.995752	0.995712	739.3	0.1500	0.99530	−0.00005
18		0.14892	0.994062	0.994006	740.3	0.2063	0.99355	+0.00004
19		0.16430	0.992204	0.992130	740.7	0.2774	0.99135	−0.00004
20		0.12254	0.990823	0.990736	740.5	0.3302	0.98971	−0.00009
21		0.12371	0.989432	0.989333	740.3	0.3754	0.98830	+0.00010
22		0.08878	0.988437	0.988328	740.2	0.4152	0.98706	+0.00001
23		0.08791	0.987453	0.987335	740.2	0.4463	0.98611	+0.00019
24		0.08584	0.986495	0.986368	740.1	0.4818	0.98500	+0.00018
25		0.08281	0.985571	0.985436	740.0	0.5207	0.98380	+0.00004
26		0.11524	0.984290	0.984143	740.0	0.5774	0.98205	−0.00023
27		0.19897	0.982085	0.981917	739.9	0.6554	0.97964	−0.00011
27A[e]					737.8	0.6515	0.97963	—
Run V								
28	40.2869	0.11569	0.998364	0.998342	771.8	0.0625	0.99812	−0.00007
29	(−0.5347)	0.09632	0.997006	0.996966	771.9	0.1122	0.99663	−0.00006
30		0.11912	0.995331	0.995269	772.3	0.1724	0.99483	0.00000
31		0.13241	0.993477	0.993390	771.6	0.2424	0.99273	−0.00005
32		0.13079	0.991652	0.991540	770.6	0.3115	0.99066	—
33		0.14853	0.989587	0.989449	770.8	0.3935	0.98822	+0.00005
34		0.16108	0.987358	0.987187	771.2	0.4843	0.98553	−0.00001
35		0.17260	0.984980	0.984781	772.9	0.5813	0.98269	−0.00005
36		0.19774	0.982270	0.982036	773.9	0.6875	0.97959	+0.00003
36A					774.1	0.6877	0.97959	—
36B[f]					771.3	0.6795	0.97976	—
37		0.23284	0.979098	0.978823	774.4	0.8138	0.97590	+0.00008
37A[g]					773.5	0.8132	0.97589	—
Run VI								
38	62.8520	0.14384	0.998696	0.998678	773.6	0.0502	0.99849	−0.00007
39	(−0.8432)	0.15613	0.997284	0.997247	774.4	0.1006	0.99699	0.00000
40		0.17617	0.995696	0.995637	775.4	0.1597	0.99523	−0.00001
41		0.45618	0.991606	0.991493	774.2	0.3057	0.99087	—
42		0.29196	0.989007	0.988859	772.0	0.4239	0.98733	−0.00015
43		0.30601	0.986296	0.986113	773.5	0.5240	0.98440	+0.00010
44		0.34215	0.983284	0.983060	774.3	0.6384	0.98104	+0.00028
44A[h]					775.2	0.6400	0.98102	—

[a] Assumed solubility from Topol and Landis (8): 773°K, $N_{Cd} = 0.067$; 743°K, $N_{Cd} = 0.053$; 673°K, $N_{Cd} = 0.028$. These values lead to almost the maximum solubility correction. If these solubility values are superseded by other data, a new correction can be calculated by multiplying the value in parentheses by the ratio of the new value over Topol's value. The correction is subject to uncertainty of ~5% of the value listed for the correction even if Topol's value is exact. This is because the electrolyte will not saturate itself by taking exactly half of its cadmium from each cell leg.

[b] Although the absolute compositions are not known this well, the extra figures are justified as relative values and to show the magnitude of the solubility correction for Cd into CdI_2.

[c] Corrections have been added to the observed emf to give the listed reading. These corrections were measured when no solute had been added to either cell leg. Values: run I, +0.0060 mV; run II, −0.0006 mV; run III, −0.0010 mV, run IV, +0.0020 mV; run v, −0.0155 mV; run VI, −0.0286 mV.

[d] Calculated as $\log a = 10082.11 \times \epsilon/T$ (10082.11 times emf in volts divided by temperature in degrees Kelvin). It is here assumed that $n = 2$ for the electrons involved per cadmium atom transferred.

[e] After 26 hr wait to test for cadmium diffusion through cadmium iodide electrolyte.

[f] After 18 hr wait.

[g] After 23 hr wait.

[h] After 48 hr wait.

lated using $n = 2$ in $\Delta G = -n\mathbf{F}\epsilon$, corresponding to a reaction in which Cd II species carry the current. The cadmium mole fractions are based on either zero solubility of cadmium in CdI_2 or on Topol and Landis' (8) large reported solubility to show the effect of this solubility uncertainty. The mole fractions plotted on Fig. 2 to 4 include the solubility corrections.

The value of n is given in Table II. It should be emphasized that the cell resistance during current passage from an external source (70.3 ohms) was not the same as the internal resistance (48.7 ohms) as evaluated by comparing the open circuit voltage with the voltage during drain through a 52 ohms shorting resistance. This difference suggests that the same reaction is not involved in both cases.

The solubility measurement results were: $N_{Cd\ in\ CdI_2} = 0.0148$ at 673°K and 0.0269 at 756°K. (Since two different methods of determination were used, these data should not be used to calculate a temperature coefficient of solubility.)

Discussion

Problems in establishing absolute activities.—The purpose of the present work was to determine the activity of cadmium in cadmium-gold solutions from precise emf and other corollary measurements. The determination of activity from emf is surprisingly difficult, both with the present system and with other types of electrolytes. Harned and Owen (14) have emphasized that the electrochemical cell reactions must always be treated as hypothetical until the corollary thermodynamic properties are checked by other techniques. In addition for active metals such as cadmium, the electrolyte solvent often is not sufficiently stable chemically (*e.g.*, for most metals, water is thermodynamically unstable and can only be safely used if it can be shown that the kinetics of attack are slow enough to let equilibrium be approximated by the electrochemical mechanism).

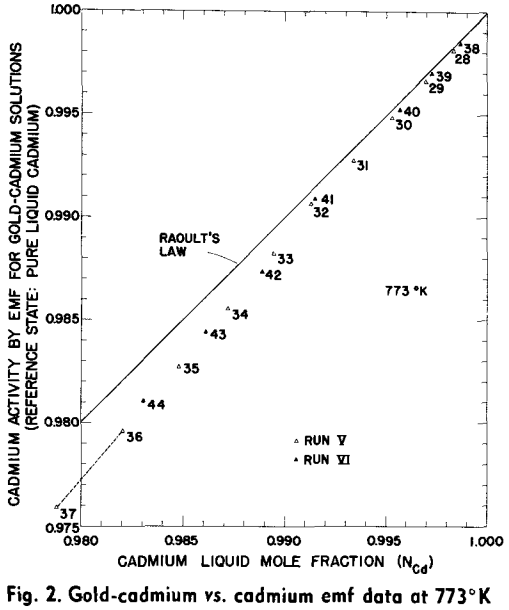

Fig. 2. Gold-cadmium *vs.* cadmium emf data at 773°K

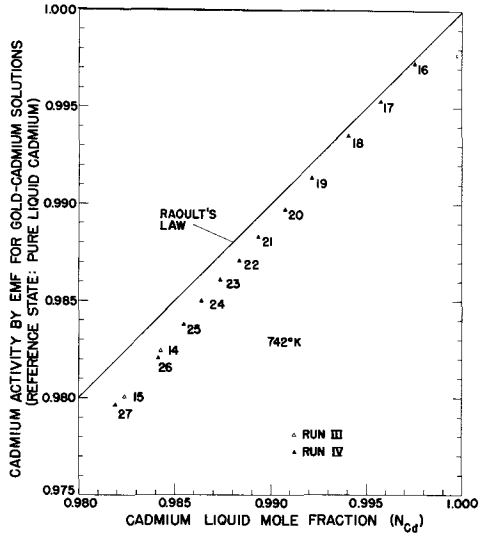

Fig. 3. Gold-cadmium *vs.* cadmium emf data at 742°K

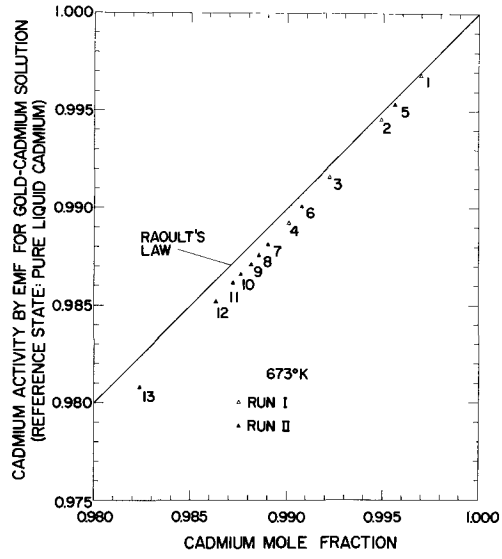

Fig. 4. Gold-cadmium *vs.* cadmium emf data at 673°K

With reference to molten salt electrolytes, one can often (*a*) fairly readily establish equilibrium concentrations, (*b*) effectively eliminate continuing side reactions, and (c) apparently achieve electrode reversibility. However, molten salts often dissolve significant quantities of metals, particularly their parent metals. The effects of the dissolved metals on the electrolyte activity and on n in $\Delta G = -n\mathbf{F}\epsilon$ are not easy to establish. If mixed molten electrolytes are used to reduce the metal solubility, the metal solubility problem is not eliminated, and the very difficult problem is created of achieving identical electrolyte compositions in both legs of the electrochemical cell.

In a corollary report [LA-4031, ref. (15)] there is given a rather extensive discussion of problems in evaluating the effects of these and other difficulties. Because the following discussion is less complete, we urge that the interested reader obtain this report either from us or from the Office of Technical Services, Washington, D. C. 20025.

The value of n.—Of all the uncertainties discussed in LA-4031, the most important for the present work is the effect of the cadmium dissolved in the electrolyte on the value of n in $\Delta G = -n\mathbf{F}\epsilon$. Table II in-

Table II. Electrons per atom from current-composition relationships following run VI

	Initial	After 1st current	After 2nd current	After 3rd current
Cadmium present:				
n_{Cd}[a]	0.55168	0.60755	0.64229	0.68393
N_{Cd}	0.98306	0.98459	0.98542	0.98629
(mV) $(10^3)/T°K$[b]	0.8259 ±0.0020	0.7503 ±0.0016	0.7109 ±0.0028	0.6739 ±0.0025
Current passed:				
amps		0.02635	0.02626	0.02649
hours		90.0	49.1	46.0
coulombs		8604	4643	4382
Apparent n for total change:		1.6 ± 0.1	1.5 ± 0.1	1.4 ± 0.1

[a] Topol and Landis (8) solubility assumed for Cd in CdI_2. Composition evaluated by interpolation from the data of run VI.
[b] Uncertainty evaluated from the scatter in the readings over two or three days. Ratio corresponds to cell open circuit voltage divided by the absolute temperature after composition changes.

dicates the results of an attempt to evaluate n directly from the cadmium transfer in the cell when current is passed through it.

The measured values for n range from about 1.6 to 1.4, *i.e.*, a third more ampere-seconds (coulombs) would have been required to move the material if n had equalled 2 as expected for pure CdI_2. Prior to interpreting these results, some aqueous results should be discussed.

An apparent efficiency of over 100% is not unusual in aqueous anodic corrosion measurements (16). Although in many cases the possibility of reaction with water has existed, this would seem to be absent in the copper(II) solutions studied by Royer *et al.* (17). Their value of n corresponds with over 100% efficiency, and this efficiency varied with temperature, current density, and concentration. Royer suggested that the primary reaction is the formation of copper(I) and that this species often gives up a second electron to form copper(II), thus leading to nonwhole-number values for n.

Regarding the present electrolyte, the conduction results may be interpreted as confirming the existence of a lower valence cadmium species which can carry current. The extra cadmium movement through the electrolyte far exceeds the proportion of cadmium dissolved in the electrolyte. The movement might result from kinetic processes under electrolysis which do not form the thermodynamically stable ratio of cadmium species, or it might be because the lower valence cadmium species simply have high mobility and high conductivity. These alternatives cannot be resolved from the present measurements. Certainly, however, the large apparent n value and the difference in the cell resistance under electrolysis or under drain both warn that the measured n is probably not applicable to the equilibrium situation. Therefore, in the absence of better information, we have assumed $n = 2$ for the activity calculations.

(It should be pointed out that approximate evaluations of n are made by checking emf results against other measurements such as phase diagrams. However, precise evaluations of n are seldom reported for molten salt equilibrium measurements.)

To pursue the implications if Cd_2^{++} forms when cadmium dissolves in CdI_2, as an approximation the value of n may be expected to drop about the same percentage as the percentage solubility of cadmium in the electrolyte. However, as discussed by Conant (18), the thermodynamically exact calculation is complex and requires an exact knowledge of the cadmium solubility, the species formed, and the species mobilities. This information is not available, and there are anomalies even when one tries to establish from published experiments whether the mobilities of Cd^{++} and the lower cadmium species are similar or are rather different.[3]

Reversibility and nonelectrochemical side reactions.—With these present emf measurements, after the solubility reactions are satisfied, the emf values are almost certainly close to equilibrium for the conditions reported. The long-term stability of emf is very good.

If there were a metallic conductivity character to the electrical conductivity of the CdI_2-Cd solutions, then this would lead to an internal drain of the cells and their emf would not be stable. Furthermore, runs III and IV used radically different shapes of H-cell cross arms which would change the resistance to internal drain and the measured emf values. Finally Aten's work (19) showed that the conductivity of $CdCl_2$ decreases smoothly as the amount of dissolved cadmium is increased: this is hardly in line with significant metallic conductivity in the salt.

As to the cell reversibility, the high precision of the data whether the equilibrium emf is approached from too high or too low a potentiometer emf, the smooth variations of emf with composition, and the stability of the cell all argue for reversibility. Actually an irreversible cell would tend to destroy part of the cell emf and would not cause deviations from Raoult's law in the direction shown on the plots to follow.

The zero voltage (bias) correction for unalloyed cadmium.—After the present measurements were carried out, Conant (18) studied the voltage bias when only cadmium was present in the legs of a stirred H-cell of this type. He established that the position of the cell in the furnace was the primary factor affecting the bias. If both legs touched the inner copper cylinder (see Experimental Technique), the bias was essentially zero (*i.e.*, ~0.0001 mV). If the H-cell was centered in the copper cylinder the bias rose as high as 0.05 mV.

The bias seems clearly to be a thermocell effect resulting from a slight difference in temperature between the two legs due to heat conduction up the H-cell tube legs and outside the furnace. However, the H-cell design essentially uncouples the two legs (or three legs, if that design is being used) as far as large heat transfer is concerned, and each leg achieves a very uniform temperature in the furnace. To avoid shifts in the bias due to slight movements of the cell during stirring, Conant concluded that the center position was to be preferred even if the starting bias was larger.

One may presume that the higher precision achieved by Conant as compared to the present work was primarily the result of his better H-cell positioning.

The temperature variations associated with these emf values have been discussed elsewhere (6, 7, 15, 18). To summarize: thermocell values of 0.3 to 0.8 mV per degree are customary. A bias of 0.0286 mV (this was the largest observed in the present group of measurements) would correspond with about 0.03° to 0.1°K temperature difference between the cell legs. However, the effects of stirring within a cell leg ($<$0.002 mV) indicate that temperature gradients within a leg and in the region of the metal-salt interface (where the reaction takes place) were not over 0.001°K.

Activity coefficient relationships.—Because activity coefficients are now so widely used to describe activity measurements, and because we normally prefer not to use them to present our data, this matter should be discussed.

Empirically excellent descriptions of the solvent activity derived from emf or vapor pressure measurements (5, 18, 20-24) have been developed using equations with the constant temperature forms

$$a_1 = c_1 - k_1 N_2 \quad [1]$$

or

$$a = c_1 - k_1 N_2 + b_1 N_2^2 \quad [2]$$

where c_1 is a reference activity applicable over a region of composition ($c_1 = 1$ in the case of very dilute solutions), k_1 adequately (Eq. [1]) or partially (Eq. [2]) describes the changes of solvent activity per mole fraction unit of solute added and b_1 describes the changes in solvent activity associated (perhaps) with solute-solute interactions. Again in the present case an empirically excellent description of the measurements at all three temperatures can be obtained by the use of two temperature dependent equations applying in different regions of composition: in the region 0.001 to 0.008 mole fraction of gold

$$a_{Cd} = 1 - 1.068\, N_{Au} - (T - 673)\,(0.00024) N_{Au} \quad [3]$$

and in the region 0.01 to 0.02 mole fraction of gold

$$a_{Cd} = 1.00020 + (T - 673)\,(0.00036) - 1.096\, N_{Au} - (T - 673)\,(0.00067) N_{Au} \quad [4]$$

[3] Conant cites an argument that the mobilities are similar. On the other hand Aten's work (19) which is discussed in the next section indicates a lower conductivity when cadmium dissolves in $CdCl_2$; this suggests a comparatively low mobility for Cd_2^{++}. One interpretation of the high transfer of cadmium discussed in the previous section would require a high mobility for the lower valence cadmium species.

The deviations are indicated in Table I, col. 9, with dashes to indicate the transition region points for which the relationships do not hold.

A mathematical analysis using a computer and fitting equations of the form

$$a_{Cd} = 1 - k_1 N_{Au} + b_1 N_{Au}^2 + d_1 N_{Au}^3 \quad [5]$$

by least squares rejects the Raoult's law based form, $k_1 = 1$, in favor of $k_1 \neq 1$. The mathematical analysis also favors the use of Eq. [3] and [4] at all temperatures instead of three independent equations, one for each temperature, of Eq. [5] form. This latter conclusion is less clear, however. This mathematical analysis is presented in LA-4031 (15).

A more customary presentation of the data would plot $(\log \gamma_{Cd})/N_{Au}^2$ *vs.* N_{Au} or N_{Cd}. This plot is closely related to Eq. [5] with $k_1 = 1$. Often in such a plot, one must try to extrapolate a curve to its supposedly finite interception with the axis at pure solvent. [For example, see the curvature in the mercury solvent region for the solutions in Fig. 10-22 of Darken and Gurry (25).] When a linear extrapolation is used, it is tacitly assumed that $(\log \gamma_1)/N_2^2 = \alpha + \beta N_2$ where α and β are constants in that region. If the assumption is valid, then it is a mathematical corollary that $(\log \gamma_1)/N_2 = \alpha N_2 + \beta N_2^2$, and $(\log \gamma_1)/N_2$ approaches zero at pure solvent.

A plot of this type is presented in Fig. 5 for the present data. As will be noted, there is little reason to be confident that these activity data as evaluated do approach a zero-zero intercept. Whether this deviation from apparent approach to Raoult's law would be removed by a more accurate calculation of the activity (*e.g.*, by using a more realistic value for n) is not clear. However, for the present, and consistent with our experience with the other precise vapor pressure and emf measurements (5, 20-24) we find an empirically better fit by assuming a nonzero intercept. This is equivalent to assuming that regular solution theory (as well as bN_2^2 deviations from Raoult's law) are not being followed by these activities, as calculated, within the region of measurement.

The plots in Fig. 5 magnify the absolute errors at low concentrations and are probably not as good as the mathematical analysis discussed three paragraphs back in choosing between the two-equation (Eq. [3] and [4]) or the three-equation (Eq. [5] with three sets of constants) fit to the data. The minimum deviation of the mean is achieved using the two-equation fit.

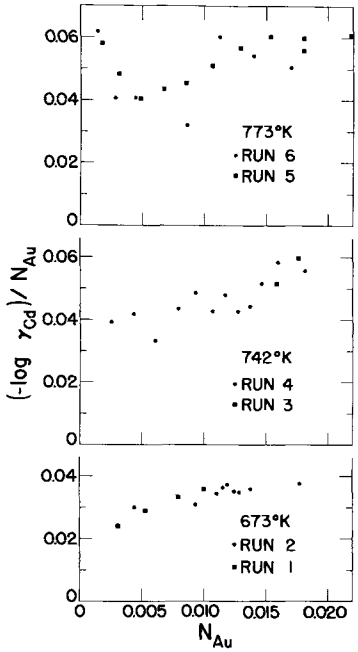

Fig. 5. Activity coefficient plots for these data. (Note that the abscissa is not of the usual form. See text.)

Conclusions

As evaluated by customary methods of calculation, the present emf data do not lead to activities in agreement with Raoult's law. We believe that these data are accurate, in the senses that the techniques used were proper and that anyone repeating these experiments would repeat these results.

Since we have not measured below 0.001 mole fraction of gold in cadmium, we cannot assert that we know what happens to the composition-activity measurements at lower concentrations. By making assumptions regarding the various species in solution and their mobilities, we could surmise values for the "effective" n for $\Delta G = -n\mathbf{F}\epsilon$ which would bring the cadmium activities for compositions below 0.008 mole fraction gold into good agreement with Raoult's law at the different temperatures. However, for both theoretical and experimental reasons, many of which have been discussed elsewhere (in order, 20, 26-28, 23, 29-31. 7, 32-34), we are not willing to accept the customary "thermodynamic" derivation of Raoult's law for dilute solutions.

Epilogue

One of our reviewers has proposed an equation to describe the 742°K data. The equation is equivalent (by our mathematical manipulations) to

$$\log a_{Cd} = \log N_{Cd} - 0.0001000 - 2.9\ (1 - N_{Cd})^2 \quad [6]$$

The equation is consistent with customary theory where our equation form is not generally accepted. Equation [6] can be reached by assuming 7 μV error in all 742°K measurements and then finding a curve to pass through the data and to the now different origin. Other postulated errors and other equation forms could also be proposed which would be appropriate for $n = 2$ and a Raoult's law-based equation.

Several questions are brought up. "Is a 7 μV error in all measurements a viable postulate?" Perhaps. Certainly any experimental data are subject to question. However, there were direct measurements of emf values between the cadmium samples in both legs of the cells before any gold was added. It was presumed that this should correct for any problems of this type such as thermocell effects. For the runs at 742°K these corrections were respectively -1.0 μV and $+2.0$ μV. That these direct measurements gave answers which actually were each in 7 μV error seems most unlikely to us.

"Can one properly assert that $n = 2$?" If n is not 2, then there is no theoretical basis to expect that activities calculated assuming $n = 2$ should approach Raoult's law. This n value question was not settled by our measurements, and we know of no experiments which have settled it for Cd-CdI_2 electrolytes or other electrolytes which dissolve their parent metal. Regarding this question there is another paper (35) which we found recently which gives an evaluation of n for mixed-valence working-electrolytes. There are important differences between that approach and the one used by Conant (18). The practical result of both approaches, and also of our own earlier approximation (15), is to reduce n from 2 to a value lower by the per cent solubility of cadmium in CdI_2. All the authors recognize that theirs is not a complete calculation when applied in this way, but a better approximation is not obviously available in the absence of more data no matter which method of calculation is used.

"Even if $n = 2$, can one really be sure that Raoult's law will be approached in this range of measurement?" The references in the Conclusions indicate why we question this.

Manuscript submitted Aug. 9, 1968; revised manuscript received May. 23, 1969.

Any discussion of this paper will appear in a Discussion Section to be published in the June 1970 JOURNAL.

REFERENCES
1. H. Olander, *J. Am. Chem. Soc.*, **54**, 3819 (1932).
2. J. F. Elliott and J. Chipman, *Trans. Faraday Soc.*, **47**, 138 (1951).
3. H. A. Laitinen, W. S. Ferguson, and R. A. Osteryoung, *This Journal*, **104**, 516 (1957).
4. J. L. Clark and G. R. B. Elliott, Diamond Ordnance Fuze Laboratories classified reports (1954).
5. G. R. B. Elliott and J. F. Lemons, *This Journal*, **114**, 935 (1967).
6. G. R. B. Elliott and J. F. Lemons, Los Alamos Sci. Lab. Report LA-3733 (March 1967).
7. G. R. B. Elliott, *This Journal*, **115**, 1143 (1968).
8. L. E. Topol and A. L. Landis, *J. Am. Chem. Soc.*, **82**, 6291 (1960).
9. J. D. Corbett, S. von Winbush, and F. C. Albers, *ibid.*, **79**, 3020 (1959).
10. G. von Hevesy and E. Löwenstein, *Z. anorg. allgem. Chem.*, **187**, 266 (1930).
11. V. P. Mashovets and V. P. Poddymov, *Zh. Prikl. Khim (Engl. Ed.)*, **37**, 1268 (1964).
12. J. D. Corbett and S. von Winbush, *J. Am. Chem. Soc.*, **77**, 3964 (1955).
13. A. A. Kolotii, *Sb. Tr. Tsentr. Nauchn.-Issled. Inst. Chernoi Met.*, No. **34**, 34 (1963) as reported in *C. A.*, **60**, 8704e (1964).
14. H. S. Harned and B. O. Owen, "The Physical Chemistry of Electrolytic Solutions," p. 302-303, Reinhold Publishing Corporation, New York (1950).
15. B. L. Houseman and G. R. B. Elliott, Los Alamos Scientific Laboratory Report LA-4031 (Oct. 1967).
16. E. A. Ukshe and N. G. Bukun, *Russ. Chem. Rev.*, **30**, 90 (1961).
17. D. J. Royer, J. Kleinberg, and A. W. Davidson, *J. Inorg. Nucl. Chem.*, **4**, 115 (1957).
18. D. R. Conant, Los Alamos Scientific Laboratory Report, LA-4102, 1969.
19. A. H. Aten, *Z. Physik. Chem.*, **73**, 579 (1910).
20. G. R. B. Elliott, J. F. Lemons, and H. S. Swofford, Jr., *J. Phys. Chem.*, **69**, 933 (1965).
21. G. R. B. Elliott, and H. S. Swofford, Jr., *Inorg. Chem.*, **7**, 666 (1968).
22. D. R. Conant and G. R. B. Elliott, *J. Chem. Eng. Data*, **13**, 354 (1968).
23. G. R. B. Elliott, D. R. Conant, H. S. Swofford, Jr., and B. L. Houseman, Third International Symposium on High Temperature Technology, Asilomar, California, September 1968, D. D. Cubicciotti, Editor, IUPAC, In press.
24. G. R. B. Elliott, C. C. Herrick, J. F. Lemons, and P. C. Nordine, Los Alamos Scientific Laboratory Report, LA-3526 (1966), *High Temp. Sci.*, **1**, 58 (1969).
25. L. S. Darken and R. W. Gurry, "Physical Chemistry of Metals," p. 272, McGraw-Hill Book Co., Inc., New York (1953).
26. S. D. Christian and N. Fogel, *J. Phys. Chem.*, **69**, 2135 (1965).
27. G. R. B. Elliott and J. F. Lemons, *ibid.*, **69**, 2135 (1965).
28. N. A. Gokcen, *ibid.*, **69**, 3222 (1965).
29. M. O'Keeffe, *ibid.*, **70**, 596 (1966).
30. G. R. B. Elliott, H. S. Swofford, Jr., and D. R. Conant, Appendix to Los Alamos Scientific Laboratory Report, LA-3657, (1967).
31. M. O'Keeffe, *J. Phys. Chem.*, **70**, 2065 (1966).
32. D. R. Conant, *J. Chem. Eng. Data*, **14**, 9 (1969).
33. G. R. B. Elliott and D. R. Conant, Los Alamos Scientific Laboratory Report, LA-4083 (1968).
34. G. R. B. Elliott, Los Alamos Scientific Laboratory Report, LA-3891 (1968).
35. N. G. Ilyushchenko, N. I. Kornilov, and A. I. Anfinogenov, "Electrochemistry of Molten and Solid Electrolytes," Vol. 5, A. N. Baraboshkin, Editor, *Trans.* No. 8 of the Institute of Electrochemistry, Urals Academy of Sciences, Engl. Ed., Consultants Bureau, New York, 1967.

A Brief Review of the State of the Art and Some Recent Results on Electromigration in Integrated Circuit Aluminum Metallization

Stuart M. Spitzer and Seymour Schwartz*

National Aeronautics and Space Administration, Electronics Research Center, Cambridge, Massachusetts

ABSTRACT

This paper presents a report of the state of the art with respect to the electromigration phenomenon in integrated circuit (IC) metallization. Reported here are some of the latest research efforts, including the authors' research, on the effects of dielectric overcoatings on electromigration in aluminum interconnections. This research has shown that dielectric overcoating of the aluminum stripes yields interconnections with greater mean time between failures than found in many conventional integrated circuits.

Aluminum metallization is used almost exclusively in today's microelectronic circuitry. All industrial trends indicate that no other single-component metallization will replace aluminum, while the use of multicomponent metallization will be restricted to specialized applications for some time in the future (1).

In spite of the seemingly simple technology of a single-component metallization method, there are still many unanswered questions with regard to the characterization and utilization of aluminum in integrated circuits (IC's). For example, the interface involved in thermal-compression bonding (2) of gold wires to aluminum pads has produced intermetallic compounds leading to high resistivity and structural brittleness. The use of ultrasonic bonding (2) of aluminum to aluminum eliminates intermetallic compounds, but structural weakness results because lack of understanding of this process makes it difficult to establish controls in this system. Further problems arise with interactions at the Si-SiO_2-Al interface. When aluminum traverses oxide steps or oxide windows to contact the silicon, aluminum thickness varies, penetrating cracks and voids appear in the interconnection, and dissolution of silicon into aluminum occurs during thermal processing.

These problems become increasingly important in the light of the requirements for newer microelectronic devices. In large scale integrated circuits, multilevel integrated circuitry, and high speed switching devices, all dimensions must be reduced to accommodate the increased number of components, and to reduce inter-

* Electrochemical Society Active Member.

electrode interaction (capacitance, leakage, etc.). This reduction in dimensions causes increased current density at the original power level. For this reason, major emphasis has been concentrated on this new failure mode, the high current density problem.

The loss of aluminum from IC conductors at high current densities, once thought to be a result of evaporation due to internal heating, or of chemical reaction with other integrated circuit materials, is now known to be caused primarily by electromigration (3). Electromigration in the migration of atoms by momentum transferred from impinging electrons under d-c bias.[1] A result of this phenomenon is void formation near the electron source (cathode) and solute accumulation near the electron sink (anode). If, after the application of a d-c bias for sufficient time and temperature to produce electromigration and voids, the d-c bias potential is reversed, aluminum conductors will sometimes heal, and new voids will be formed at the other electrode. Blech and Sello (4) have qualitatively shown the dynamics of electromigration in a time lapse film.

It is important to note that in certain cases the problem of electromigration can be eliminated by proper device design and processing. In such instances, aluminum thickness is designed to maintain current densities below a predetermined threshold value. There are many times, however, where the need for small dimensions will not allow thicker conductors. For these cases research on the problem of electromigration in aluminum interconnections is needed and ways must be found to extend the operating limits of aluminum. The degrading effects of electromigration on integrated circuit interconnections are further aggravated by any metallization defects and these become increasingly significant as film thickness decreases.

Electromigration is a self-diffusion effect, and has an associated activation energy. Although the activation energy for bulk self-diffusion in aluminum is 1.48 eV, experimentally measured energies for electromigration in integrated circuit films range approximately from 0.5 to 1.2 eV. The lower observed energy may be or has been ascribed by investigators to structural imperfections in and on the surface of the aluminum film. It is to this problem that the following investigations have been addressed.

Review

Experimental relations predicting mean time between failure of aluminum interconnections with respect to electromigration have been determined. Black (5) has found

$$MTBF = \exp(\phi/kT) AJ^2 \qquad [1]$$

where $MTBF$ = mean time to failure in hours, ϕ = an effective activation energy of the film, k = Boltzmann constant, T = absolute temperature, A = constant for a given film and inversely proportional to the cross sectional area, and J = current density in A/cm^2.

Chhabra *et al.* (6) found $MTBF$ proportional to $1/J^3$ for constant temperature (between 100°-200°C) and for J 10^6 A/cm^2.

The importance of obtaining films of higher quality, *i.e.*, higher activation energy, can be seen by considering [1]. At a fixed current density, the ratio of the equations appropriate for two different films yields

$$\frac{MTBF_1}{MTBF_2} = \frac{A_2}{A_1} \exp(\phi - \phi_2)/kT \qquad [2]$$

At room temperature kT = 0.025 eV, and if $\phi_1 - \phi_2$ = 0.1 eV, then the exponential term gives a factor of 55.

We can further see, that at an elevated temperature, say 125°C, kT = 0.033 eV, and for the same increase in ϕ, the exponential of [2] gives a factor of only 20. Thus, at higher temperatures, increases in the activation energy ϕ, become less significant in increasing $MTBF$.

There are three basic factors contributing to the activation energy for the electromigration failure of the aluminum metallization; surface, grain boundary, and bulk diffusion components. It is clear that deposition and post-deposition heat treatment techniques can affect only the latter two components. Inasmuch as the activation energies for bulk diffusion, grain boundary diffusion, and surface diffusion decrease in that order, it would be expected that the relative advantage of well ordered metallization covered by a dielectric would be higher at low temperatures, and that at high temperatures the advantage of the higher effective activation energy would be relatively small in light of the exponential dependence on the activation energy.

Evaporation experimentation (5) has shown that for films less than 5000Å thick, deposition on a hot substrate is necessary to obtain large crystallite size. In this case, substrates heated to 200°C yield measured energies around 0.50 eV. For films thicker than 5000Å or for those deposited at high rates, the substrate heating becomes unimportant. Apparently these thicker films lose "memory" of the lower layers and grow with high crystalline order, attaining measured energies of 1.20 eV.

The two most common aluminum deposition techniques are filament evaporation and electron beam bombardment. Filament evaporation is more often used because of simplicity, however the electron beam method gives a higher degree of aluminum purity. High quality (1.20 eV), low resistivity aluminum films may be produced by evaporating from high purity tungsten or tantalum filaments at pressures in the 10^{-8} Torr range. The improvement obtained at high vacuum may be due to less oxide at grain boundaries, with less tendency for lattice vacancies to agglomerate, causing voids.

The surface is a discontinuity or defect in crystalline order, and diffusion along the surface will have a lower activation energy than in the bulk. The relative importance of the surface may be evaluated by finding the ratio of surface atoms to bulk atoms. For long thin conductors, this ratio is inversely proportional to thickness, t.

It should be noted here that aluminum atoms at the Al-SiO_2 interface are not equivalent to atoms at the exposed Al surfaces. Furthermore, the true surface to bulk ratio is one or more orders of magnitude greater than this apparent ratio due to surface irregularities or film porosity. The intent of this discussion is only to point out the $1/t$ dependence of the surface to bulk ratio. For films wherein bulk and grain boundary components of the activation energy have been maximized through good deposition and heat treatment techniques, the thickness of the film will determine the influence of the surface component.

By coating the surface of the test circuit with a dielectric, broken electron bond at the aluminum surface may be presumed to be filled, electromigration at the surface will be reduced (5, 7), and a higher activation energy should be realized. In light of the above discussion, such a surface treatment would be expected to have the greatest effects on thinner films.

Recent Results

At the Seventh Annual Reliability Physics Symposium, Washington D.C., December 1968, a complete session was devoted to electromigration (selected papers published in "Transactions on Electron Devices," April 1969). Summarized here are some of the results from I.B.M. (8, 9), Motorola (3), and NASA/ERC (10). It is important to note that many of the reported findings have resulted from examination by scanning electron microscopy [the uses of which were also reported at this symposium (11)].

Attardo *et al.* (8) have reported that the activation energy associated with electromigration corresponds

[1] Electromigration is observed under a-c stress, but much more slowly, because the oscillating electron motion tends to cancel any migration effects.

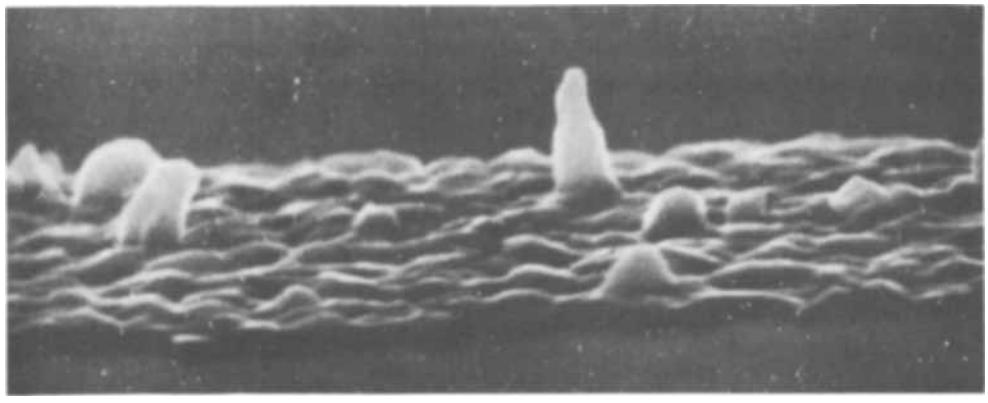

Fig. 1. Scanning electron micrograph of electromigration of aluminum perpendicular to the interconnection. (2145X and 80° from normal).

to the activation energy of grain boundary diffusion. An empirical relationship between *MTBF* and the critical parameters of electromigration in the same form as [1] has been found, but with a different interpretation of the effective activation energy. The activation energy is assumed independent of grain size (as long as grain size is smaller than the stripe width), whereas in Black's (3, 5) formulation the activation energy is a function of grain size. Thus the pre-exponential factors of Eq. [1] necessarily take on different values in Attardo's formulation. A further difference in measurements by Black and Attardo can be seen in the effects of stripe width. Where Black had determined *MTBF* to be directly proportional to cross section area, Attardo reports a greater than linear dependence on conductor width. These results have been interpreted as the grain boundary acting as a diffusion barrier in the narrow stripes and causing a divergence in the vacancy flux at that point. In the wider stripes this effect does not occur because grain size is less than stripe width.

Berenbaum and Rosenberg (9), and Black (3), have given some interesting examples of aluminum whisker growth perpendicular to the conductor stripe. The I.B.M. group reported on aluminum stripes deposited on thermally oxidized silicon, while Black at Motorola also examined the case where the aluminum was was coated with SiO_2.

Figure 1 (from Berenbaum and Rosenberg) illustrates a scanning electron micrograph of whisker growth at 2145X. In coated conductors, the whisker growth cracked the silicon dioxide in a "trap-door" type of effect. Both authors present extensive scanning electron micrographs in their papers, which give a good pictorial understanding of electromigration phenomena.

Research at NASA/ERC

Spitzer and Schwartz (10) of NASA/ERC, have made studies of electromigration in aluminum conductors passivated with dielectric overcoating. These studies suggest that improved *MTBF* is observed in dielectric coated conductors; a brief summary of this work follows.

In order to make comparisons between coated and uncoated conductors, test circuits were prepared using filament and electron beam aluminum evaporation. The aluminum thicknesses used were 1500 through 6000Å. The thinner stripes were used in accelerated tests to observe whether any trends would develop, and to emphasize the effects of the aluminum surface in the high surface to volume atom ratio. The thicker stripes were used to simulate more closely actual integrated circuit geometries.

The dielectric overcoat materials utilized were those found to be compatible in both integrated circuit and multilevel large scale integration (LSI) fabrication. These dielectrics are an amorphous mixture of SiO_2 and Al_2O_3, and an amorphous mixture of SiO_2 and P_2O_5.[2] To apply these coatings we used a relatively simple, chemically clean process wherein the dielectric is condensed from gases reacting on a heated silicon wafer. For example, wafers to be coated with SiO_2-P_2O_5 are heated on a hot plate to 375°C, then a mixture of oxygen, nitrogen, silane, and phosphine is introduced for approximately ½ min. The entire cycle takes 10 min. Control wafers, not to be coated, are placed on a hot plate and heated to the same temperature, in a dry nitrogen atmosphere, for the same time. By this means, the metallizations will be compatible for both coated and control wafers.

Tests were run to determine the mean time between failure of the aluminum interconnects as a function of current and temperature. We had special interest in the temperature range of 25°-200°C, and current density range of 10^5 to 2 x 10^6 A/cm^2, because this represents the area of maximum practical application. In order to learn the effect of dielectric overcoating (10), the *MTBF* was measured for coated and uncoated aluminum strips, which had undergone exactly the same thermal processing. The effective activation energy of the strips was found from [1], using the *MTBF*. In Fig. 2, we show the effect of dielectric overcoating (Al_2O_3-SiO_2). Significant improvements in the activation energy were observed for aluminum films less than 5000Å thick. Thus, the greatest contribution of surface passivation was made in cases where the surface to bulk atom ratio is appreciable.

Figure 3 shows the *MTBF* plotted against film thickness, with temperature as an independent parameter. Here we see that the effect of dielectric overcoating (or any treatment which helps to increase the effective activation energy) is minimized at elevated temperature.

In order to understand modes of failure and verify effects of electromigration, metallurgical analyses were made on most test devices.

Figure 4 shows a time sequence of electromigration failure. Figure 4A shows the unstressed device, while Fig. 4B and 4C show the development of voids. Figure 4D shows the final open circuit failure.

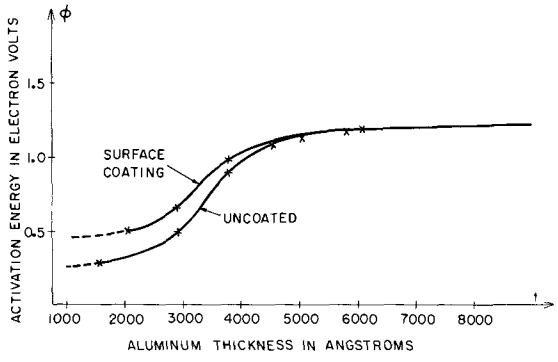

Fig. 2. Self diffusion activation energy as a function of aluminum thickness and surface passivation.

[2] It is interesting to note that glass passivation techniques have been used to protect the entire semiconductor chip. The intent in this earlier industrial application was to hermetically seal the silicon surface. Glass passivation has further application in multilevel isolation and metal protection.

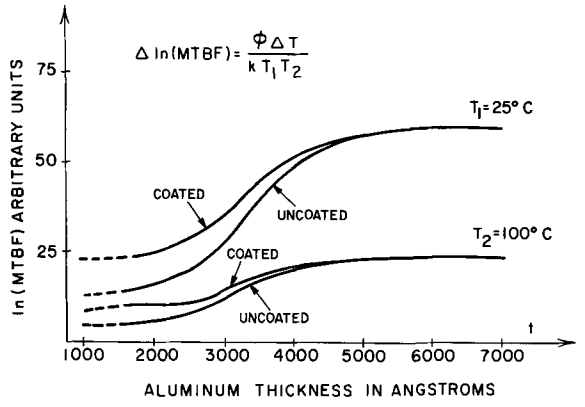

Fig. 3. Dependence of *MTBF* on temperature and surface passivation.

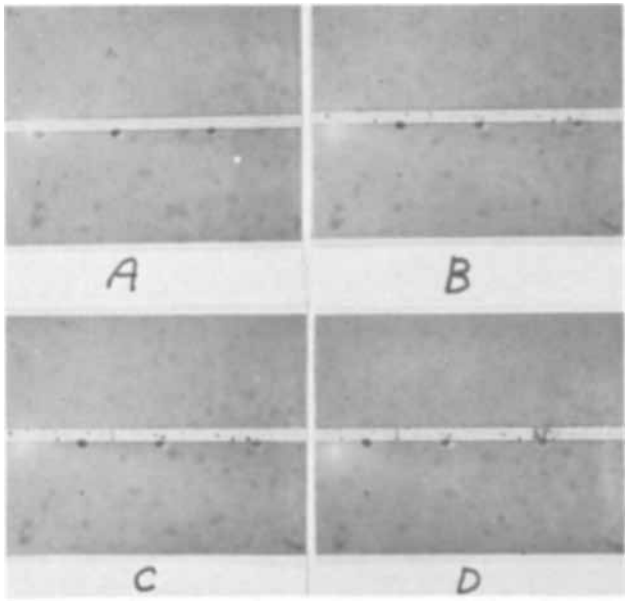

Fig. 4. Time sequence progression of electromigration. A. Unstressed 5000Å aluminum conductor. B. Same as A after 350 mA for 10 min and 500 mA for 5 min. Note development of spotted areas. C. Same device after 5 min more at 500 mA. The spots, electromigration areas, have grown. D. Same device which after 1 min more at 500 mA has open circuited.

It is important to point out that in many analyses of failed circuits electromigration is not easily identifiable as the failure mode (Fig. 5). When a conducting strip opens up due to electromigration, arcing masked the failure mode. Figure 6 is an electron microprobe x-y scan showing aluminum K-alpha counts of the device after electrical stress. We can clearly see the depletion of aluminum at the right (negative) side and the build up of aluminum just to the left of the void. Figure 7 shows the microprobe line scan used for thickness determination of the same device.

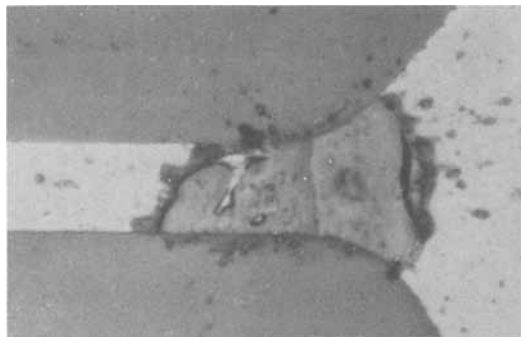

Fig. 5. Electromigration failure, 5000Å aluminum test strip (Al_2O_3-SiO_2 overcoat).

Figure 8, using the scanning electron microscope, shows by detection of secondary electrons, details of an area thinned by electromigration (2000X). The strip had not as yet failed, and is undamaged from electrical arcing.

Discussion

The ultimate goal of this electromigration study is to provide guidelines for reliable device design. The following areas of investigation are suggested for intensive activity.

First, confidence in the predicted *MTBF* is vague. Researchers (5, 6) have determined empirical relations, but variables such as crystallite size and aluminum impurities are not yet quantitatively included in these relations.

Next, the notion that electromigration can always be designed out of the circuit should be dispelled. Not only is this untrue in many cases, particularly in LSI, multilevel integrated circuitry, and high-speed switching circuits, but there is also the problem of processing errors which may increase current densities an order of magnitude above the designed circuit value.

Third, there is a need for better integrated circuit simulation in electromigration test devices. Most work has been done with aluminum on top of silicon dioxide, except at windows. In many cases aluminum is alloyed in, and the effects of this "dilute" metallization must be characterized.

Finally, electromigration life testing is generally carried out at currents exceeding normal maxima. For this reason, many circuits which fail due to electromigration under these accelerated conditions, would not do so under normal use. Tests should be devised which would provide an awareness of other possible failure mechanisms.

Acknowledgment

We wish to thank Dr. Ralph R. Nash, Chief, and Dr. Irving Weinberg of Materials Science Branch, NASA/HQ for their encouragement and support of this pro-

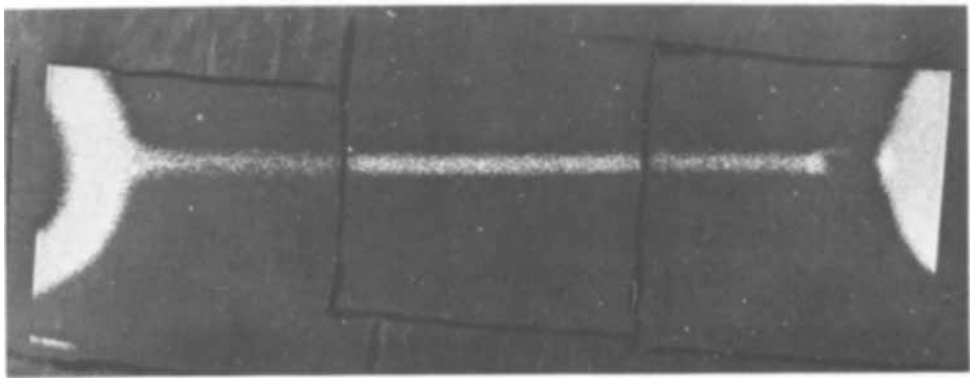

Fig. 6. Electron microprobe x-ray scan of failed test device.

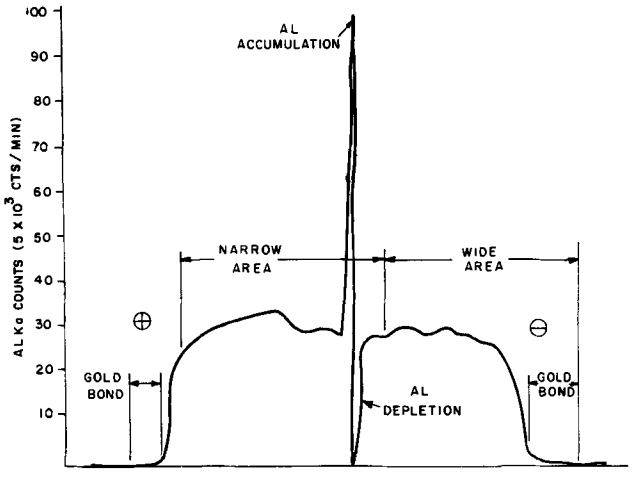

Fig. 7. Electron microprobe x-ray scan after failure

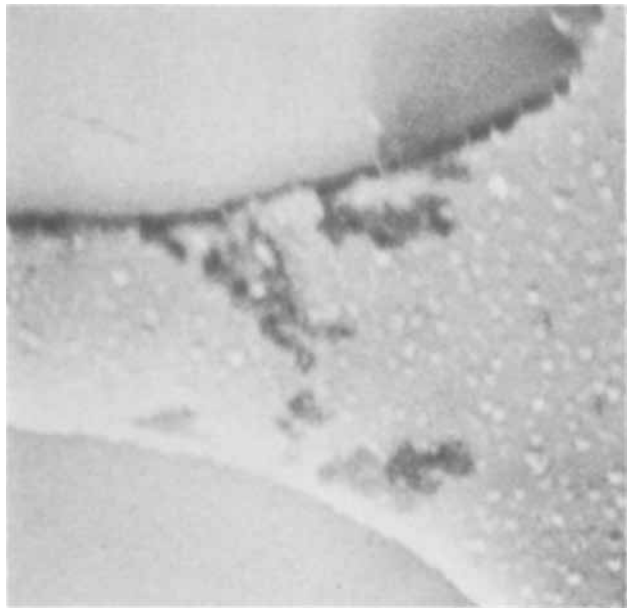

Fig. 8. Scanning electron micrograph of region depleted by electromigration (5000Å aluminum).

ject. We also wish to thank Mr. Dennis Gosselin, Failure Mechanisms Branch, NASA/ERC, for his valuable technical contributions to this report. This work was done under NASA Program Area Code 129-03-15-23.

Manuscript submitted March 26, 1969; revised manuscript received *ca.* July 5, 1969.

Any discussion of this paper will appear in a Discussion Section to be published in the June 1970 JOURNAL.

REFERENCES

1. G. Schnable and R. Keen, "Aluminum Metallization—Advantages and Limitations for Integrated Circuit Application," *Proc. I.E.E.E.*, October 1969.
2. S. Schwartz, "Integrated Circuit Technology," McGraw-Hill Book Co., New York (1967).
3. J. R. Black, "Electromigration—A Brief Survey and Some Recent Results," *Trans. on Electron Dev.*, **ED-16**, No. 4, April 1969.
4. I. A. Blech and H. Sello, "Physics of Failure in Electronics," Vol. 5, pp. 496-505, T. S. Shilliday and J. Vaccaro, Editors, RADC, USAF, June, 1967. Presented at Physics of Failure Symposium, Columbus, Nov. 1966.
5. J. R. Black, "Metallization Failures in Integrated Circuits," Technical Report No. RADC-TR-67-477, prepared by Motorola, Inc. for Rome Air Development Center under contract No. F30603-67-C-0166, September 1967.
6. D. Chhabra, N. Ainslie and D. Jepren, Recent News Paper, Dallas Meeting of The Society, May 7-12, 1967.
7. D. Whitcomb, "Advanced Technology of Interconnections in Microelectronics," Reports prepared by Motorola, Inc. for NASA/ERC under Contract NAS 12-132, January 1968.
8. M. J. Attardo, A. H. Landzberg, W. E. Reese, and G. T. Weening, "Aluminum Electromigration in Long Stripes," presented at the Seventh Annual Reliability Physics Symposium, Washington, D.C. December 1968, I.E.E.E. presentation abstracts.
9. L. Berenbaum and R. Rosenberg, "Electromigration Effects in Aluminum Thin Films," Presented at the Seventh Annual Reliability Physics Symposium, Washington, D. C., December 1968, and Personal communication, January 1969.
10. S. Spitzer and S. Schwartz, "The Effects of Dielectric Overcoating on Electromigration in Aluminum Interconnections," *Trans. on Electron Dev.*, **ED-16**, No. 4, April 1969.
11. J. E. Cline, S. Schwartz, and J. M. Morris, "Applications of Scanning Electron Mirror Microscopy for Integrated Circuit Analysis," *ibid.*, **ED-16**, No. 4, April 1969.

Bi-ionic Potentials with Sulfonic and Phosphonic Acid Cation-Exchange Membranes

D. K. Hale[1] and K. P. Govindan[2]

Ministry of Technology, National Physical Laboratory, Teddington, Middlesex, England

ABSTRACT

The use of bi-ionic potential measurements for the study of the selective behavior of synthetic sulfonic and phosphonic acid membranes toward sodium and potassium ions is described, and the effects of membrane thickness and solution flow rate on the results are discussed. A procedure for obtaining the thickness of the diffusion layer in the solution at the membrane surface from experiments on the interdiffusion of sodium and hydrogen ions is described. The bi-ionic potentials obtained with the Na^+-K^+ system and the sulfonic and phosphonic acid membranes (over the *p*H range 2.0-13.0) are correlated with the relative mobilities of the ions in the membranes and their selectivity coefficients and the significance of the results discussed.

If an ion-exchange membrane separates two electrolyte solutions which differ in concentration or composition, then, in general, an electrical potential difference will exist between the two solutions. This potential difference is termed the membrane potential. If the two solutions contain the same electrolyte at different concentrations, the membrane potential is known as a concentration potential. With an ideal ion-exchange membrane which is impermeable to co-ions and through which water transport is zero, an equilibrium will be set up in which there is a continuous interdiffusion of counter ions between the two solutions but no change in their concentrations. The membrane potential will be given by the Nernst equation

$$E_m = -\frac{RT}{z\mathbf{F}} \ln \frac{a''}{a'} \qquad [1]$$

where a' and a'' are the activities of the counter ion in the two solutions and z is its electrochemical valency (negative for anions).

When the membrane separates a solution of the electrolyte, AY, from one of the electrolyte, BY, at the same equivalent concentration, where A and B are membrane counter ions, then a rapid interdiffusion of counter ions will take place between the two solutions and, at equilibrium, the two solutions will have the same composition. If, however, the solutions of AY and BY flow continuously past the membrane surface or if the solution volumes are sufficiently large, then a stationary or quasi-stationary state can be set up in which the composition of the two solutions does not change appreciably with time and the effect of cross contamination is negligible. Under these conditions, with negligible co-ion transport and with the electrolytes AY and BY at the same equivalent concentration, the membrane potential is known as the bi-ionic potential (BIP). This term was introduced by Sollner (1, 2) who proposed the equation

$$E_{BIP} = \pm \frac{RT}{\mathbf{F}} \ln \frac{t_A^{\pm}}{t_B^{\pm}} \qquad [2]$$

in which $t_A^{\pm}$ and $t_B^{\pm}$ represent the transference numbers of the counter ions (either cations or anions) in the membrane.

If, for the case of a pair of uni-univalent electrolytes, the ratio of the transference numbers is replaced by the ratio of the products of the mobilities and concentrations, then the above equation may be written in the form

$$E_{BIP} = \pm \frac{RT}{\mathbf{F}} \ln \frac{\bar{u}_A}{\bar{u}_B} \frac{\bar{C}_A}{\bar{C}_B} \qquad [3]$$

where $\bar{u}_A$ and $\bar{u}_B$ are the mobilities of the ions in the membrane and $\bar{C}_A$ and $\bar{C}_B$ are the corresponding molar concentrations. The molar selectivity coefficient (K'^A_B) is given by

$$K'^A_B = \frac{\bar{C}_A}{\bar{C}_B} \frac{C_B}{C_A}$$

where C_A and C_B are the ion concentrations in solution so that when $C_A = C_B$

$$E_{BIP} = \pm \frac{RT}{\mathbf{F}} \ln \frac{\bar{u}_A}{\bar{u}_B} K'^A_B \qquad [4]$$

In this derivation of an equation for the BIP, the existence of concentration gradients in the membrane and Donnan potentials at the interfaces is, in effect, disregarded and it is implicitly assumed that the ion with the higher affinity is present to the greater extent in the membrane. Wyllie (3), extending an earlier treatment by Marshall (4), derived equations for the membrane potentials in bi-ionic and multi-ionic systems by using the Henderson equation to obtain the diffusion potential in the membrane, adding the Donnan potentials at the interfaces and making allowance for the effect of the preferential absorption which was assumed to take place in the membrane.

In his general treatment, using the Nernst-Planck flux equations, of transport processes in membranes, Teorell (5) discussed the bi-ionic potential as a special case. For simplicity, it was assumed that the distribution ratio was the same for all univalent ions at the solution-membrane interfaces. Teorell stated, however, that there was nothing to prevent the choice of other theoretical or empirical relations between the concentrations at the interfaces. Using this approach, Helfferich and Ocker (6) obtained an expression for the membrane potential in bi-ionic systems which, if the mobility ratio, the selectivity coefficient, and the total counter ion concentration in the membrane are constant, can be integrated (7) to give the equation

$$E_m = \frac{RT}{\mathbf{F}} \left[\frac{\bar{u}_B - \bar{u}_A}{\bar{u}_A z_A - \bar{u}_B z_B} \ln \frac{\bar{u}_B z_B}{\bar{u}_A z_A} + \frac{1}{z_A z_B} \ln K'_a{}^A_B + \frac{z_A - z_B}{z_A z_B} \ln \frac{\bar{C}}{C'} + \frac{1}{z_B} \ln \frac{C'}{C''} + \ln \frac{f'_A{}^{1/z_A}}{f''_B{}^{1/z_B}} \right] \qquad [5]$$

[1] Present address: Division of Inorganic and Metallic Structure, National Physical Laboratory, Teddington, Middlesex, England.
[2] Present address: Central Salt and Marine Chemicals Research Institute, Bhavnagar-2, India.

where $K'_{a}{}^{A}{}_{B}$ is the molar selectivity coefficient corrected for activity coefficients in solution, f'_A and f''_B are the molar activity coefficients for the ions A and B in the two solutions, C' and C'' are the total solution concentrations, and $\overline{C}$ is the total counter ion concentration in the membrane. For two univalent cations, this equation reduces to

$$E_m = \frac{RT}{\mathbf{F}} \ln \frac{\overline{u}_A}{\overline{u}_B} \frac{a'_A}{a''_B} \frac{\overline{f}_B}{\overline{f}_A} \quad [6]$$

$$= \frac{RT}{\mathbf{F}} \ln \frac{\overline{u}_A}{\overline{u}_B} \frac{a'_A}{a''_B} K'_{a}{}^{A}{}_{B} \quad [7]$$

It follows from Eq. [7] that the membrane potential in bi-ionic systems with univalent ions is given approximately by

$$E_m = \frac{RT}{\mathbf{F}} \ln \frac{\overline{u}_A}{\overline{u}_B} \frac{C'_A}{C''_B} K'^{A}{}_{B} \quad [8]$$

where C'_A and C''_B are the molar concentrations of the ions in the two solutions and $K'^{A}{}_{B}$ is the molar selectivity coefficient (assumed to be constant).

It is important to note that, in this derivation of the membrane potential equation, a selectivity factor is introduced as a consequence of the inclusion of the Donnan potentials. The selectivity has no effect on the concentration profiles; in fact, the slower ion tends to accumulate in the membrane (8). A more detailed treatment of systems with concentrated solutions, in which the effects of simultaneous co-ion and water transport are considered, has been given by Mackay and Meares (9).

In systems of the type under consideration, the rate of ionic interdiffusion between the two solutions will depend not only on the rate of diffusion of ions within the membrane but also on the rate of diffusion of ions up to and away from the membrane surfaces. However vigorously the solutions are agitated, it is often impossible, especially with dilute solutions, to maintain the solution composition uniform right up to the membrane surface, and concentration gradients develop in a layer of solution adjacent to the membrane. The theoretical treatment of the diffusion processes in the solutions can be greatly simplified by making use of the Nernst concept of a hypothetical "diffusion layer," the thickness of which depends on the degree of agitation in the solution. In effect, the bulk solution is assumed to be of uniform composition and to be separated from the membrane surface by a layer of completely unstirred solution. This approximation has been used successfully both in the theoretical treatment of the kinetics of ion exchange with particulate resins (10-12) and of transport processes in membranes (13, 14).

Two limiting conditions may be distinguished: (*a*) complete *membrane diffusion control*, in which case the composition of the solution is the same at the membrane surface as in the bulk solution, and (*b*) complete *film diffusion control* when there are no concentration gradients within the membrane.

In the interdiffusion of counter ions, the system is often subject to partial or almost complete film diffusion control especially when the solutions are dilute and the ionic mobilities and concentrations in the membrane are high. The equations previously given for the membrane potentials are applicable only to systems subject to membrane control. In other cases, corrections for the effect of unstirred diffusion layers have to be applied. In this paper, the term "bi-ionic potential" is taken to be the potential obtained with complete membrane control.

The effect of unstirred diffusion layers on the measurement of bi-ionic potentials has been discussed by Helfferich (7, 8) who used the Nernst-Planck equations for the calculation of the concentrations at the membrane-solution interfaces. Equations for the potentials in bi-ionic cells with unstirred diffusion layers have also been derived by Mackay and Meares (15). In their treatment, the effect of bulk flow, and of variations in the ionic mobilities and activity coefficients with membrane composition, were also considered. Good agreement was obtained in most cases between the experimental and calculated potential differences. For many purposes, however, where a high order of accuracy is not required, it would appear that the relatively simple relationships based on the Nernst-Planck treatment with films (but without solvent transfer and variations of mobilities and selectivity coefficient) are usually adequate. In previous work by Helfferich and Ocker (6), reasonably good agreement was obtained between experimental values for the membrane potential and theoretical values calculated using Eq. [5] not only with Na^+/K^+ and Na^+/H^+ systems but also with the Na^+/Sr^{++} system.

Since, for a given membrane and a given pair of counter ions of equal valency, the BIP is practically independent of concentrations and the nature of the co-ion (provided the activity ratio of the two counter ions is kept constant), it can be regarded as a measure of the ability of the membrane to discriminate in its permeability behavior between two counter ions, A and B. It should be noted, however, that if the counter ions are not of equal valency then it follows from Eq. [5] that the BIP will vary approximately linearly with the logarithm of the solution concentration (7). The relative mobilities of the two ions in the membrane can be calculated from the BIP if the ratio of the activity coefficients is known, or the latter may be calculated knowing the relative mobilities (16).

In the present work, the conditions for membrane control have been established and bi-ionic potentials have been measured for the sodium-potassium ion system with both sulfonic and phosphonic acid membranes. These have then been correlated with the relative affinity coefficients and mobility ratios. With the phosphonic acid membrane, the effect of *p*H on the BIP has been investigated and, with both membranes, the effect of film diffusion on the membrane potentials has been examined. The BIP of the phosphonic acid membrane is of special interest since, like the phosphonic acid ion-exchange resins (17-19), the membrane would be expected under neutral and alkaline conditions to have a higher affinity for sodium than potassium.

Previous work on the effect of membrane structure on bi-ionic potentials has been discussed by Malherbe and Mandersloot (20). It appears that little work has been published on the effect of the nature of the functional group on the BIP. Sollner and his co-workers (21) found significant differences in the behavior of different anion-permselective membranes toward, for example, chloride and acetate ions and in the behavior of polystyrene sulfonic acid and polyacrylic acid collodion matrix membranes toward potassium and lithium ions. Gregor and co-workers (22, 23) also found higher absolute values for the BIP with the Li^+/K^+ system and a carboxylic acid membrane than with a sulfonic acid membrane. Bergsma and Staverman (24) measured the BIP for four different pairs of ions and five different cation-exchange membranes, including a cellophane-type membrane with phosphonic acid groups. Rather surprisingly, they found that all the membranes behaved in more or less the same way toward Na^+ and K^+ ions and that there was no significant difference between the phosphonic and sulfonic acid membranes. They concluded that bi-ionic potentials had not been sufficiently investigated, either theoretically or experimentally, and that various phenomena could not be satisfactorily explained.

It appears that further work on the effect of the nature of the membrane on the BIP is desirable. The consequences of ion-exchange selectivity on transport processes in membranes are clearly of great biological interest and, in addition, may be of considerable importance in the utilization of membranes in separation processes.

Experimental

Preparation of sulfonic acid membranes.—The method used was essentially the same as that described by Hazenberg and Knoll (25). A weighed sheet of polyethylene film (10 cm × 10 cm) of thickness $\simeq 13 \times 10^{-3}$ cm was immersed for 5 min in a mixture of 90 parts of styrene and 10 parts of 50% divinylbenzene solution with 0.5 parts of benzoyl peroxide as catalyst, at 65°C. The impregnated film was blotted between filter papers and then heated in a bath of saturated sodium chloride solution at 65°C for 24 hr to effect the polymerization of the monomers. The film containing the cross-linked polystyrene was then washed with deionized water, wiped with filter paper, and dried in a vacuum desiccator over phosphorus pentoxide for 3 hr. From the weights of the film before and after impregnation, the percentage of the copolymer in the film was calculated. For the sulfonation, a glass tube containing the impregnated film and a mixture of 200 ml of 98% sulfuric acid with 50 ml of nitrobenzene was heated over a steam bath for 2 hr. The sulfonated film was washed with carbon tetrachloride and then with distilled water. After conditioning the membrane to the appropriate form, the characteristics were determined and are given in Table I.

Preparation of phosphonic acid membranes.—A cross-linked polystyrene matrix was incorporated in a polyethylene film (thickness: 25×10^{-3} cm) by the procedure described above. Phosphonic acid groups were introduced by a procedure similar to that described by Kressman and Tye (26) for the preparation of phosphonic acid resins. The film (10 cm × 10 cm) was refluxed with a mixture of ethylene dichloride (150 ml), phosphorous trichloride (65 ml), and anhydrous aluminum chloride (32.5g) in a glass tube over a steam bath for 6 hr. The film was removed, washed with ethylene dichloride, and then heated with a 10% solution of sodium hydroxide on a steam bath for 3 hr. The membrane characteristics are given in Table I. There was some variation in the total exchange capacity between different samples and the average value (2.5 mg equiv./g) was slightly less than that calculated from the phosphorus content (2.8 mg equiv./g).

Titration curve of phosphonic acid membrane.—Membrane strips were converted into the hydrogen form and, after washing with distilled water, their wet weights were determined. These strips were allowed to attain equilibrium with suitable mixtures of 0.1*N* solutions of hydrochloric acid, sodium chloride, and sodium hydroxide to cover the *p*H range from 1 to 13. After equilibration (about 1 week), the strips were removed from the solutions and rinsed quickly with distilled water after blotting them between filter paper. The strips were then leached with 5% hydrochloric acid and the sodium eluted was determined using a Unicam flame spectrophotometer. The equilibrium *p*H of the solutions was measured and the quantity of Na^+ ion exchanged, expressed as mg equiv./g dry membrane (H^+ form), was plotted against *p*H (Fig. 1).

Table I. Characteristics of sulfonic and phosphonic acid membranes

	Sulfonic acid membrane	Phosphonic acid membrane
Thickness (cm)	16×10^{-3}	28×10^{-3}
Total exchange capacity (mg equiv./g dry H^+ form membrane)	2.24	2.5
Swelling (g water/g dry H^+ form membrane)	0.78	0.19
Specific resistance (ohm-cm)		
in 0.1*N* NaOH	—	430
in 0.1*N* KOH	—	220
in 0.1*N* NaCl	110	1800
in 0.1*N* KCl	72.5	1055
in 0.1*N* HCl	15	—
Selectivity coefficient, $K'_{Na}{}^{K}$		
at *p*H 5	1.4	0.88
at *p*H 13	1.3	0.63
Selectivity coefficient $K'_{H}{}^{Na}$	1.40	—

Determination of relative affinity coefficient (sulfonic and phosphonic acid membranes).—The relative affinity coefficients were determined by equilibrating the membranes with a solution consisting of a mixture of equal volumes of decinormal sodium chloride and potassium chloride, sodium hydroxide and potassium hydroxide, or sodium chloride and hydrochloric acid solutions. For the determination of K^{K}_{Na}, the sodium and potassium contents of the equilibrated membrane were obtained by elution with hydrochloric acid and analysis with the flame spectrophotometer. The values obtained for the two membranes are included in Table I. The relative affinity coefficient is given as the ratio of potassium to sodium or sodium to hydrogen in the membrane when the concentrations of the two ions in the external solution are equal.

Measurement of membrane resistance (sulfonic and phosphonic acid membranes).—The membrane was conditioned with a suitable electrolyte solution and mounted in a "Perspex" conductivity cell similar to that described by Lorimer, Boterenbrood, and Hermans (27). The solution flowed through the cell in such a way that the two faces of the membrane, each 1 cm in diameter, were flushed with a slow stream of the electrolyte solution at 25°C. The resistance was measured by means of a Wayne Kerr Universal Bridge B221. A low-impedance adaptor unit was employed when the resistance measured was below 10 ohms. The resistance of the cell without the membrane was also measured in the same way and, from the difference between the two values, the membrane resistance was obtained.

Cell for measurement of fluxes and potentials.—The cell consisted of two symmetrical halves provided with suitable inlets and outlets (Fig. 2a). The membrane was clamped between the two halves in such a way that the inflowing solutions, after passing through distributors, impinged directly on the membrane surfaces. The outflowing solutions passed through electrode cells fitted with thermometers (Fig. 3). The outflow from the electrode cells passed into two receivers from which the solutions were pumped into two upper reservoirs. From the upper reservoirs,

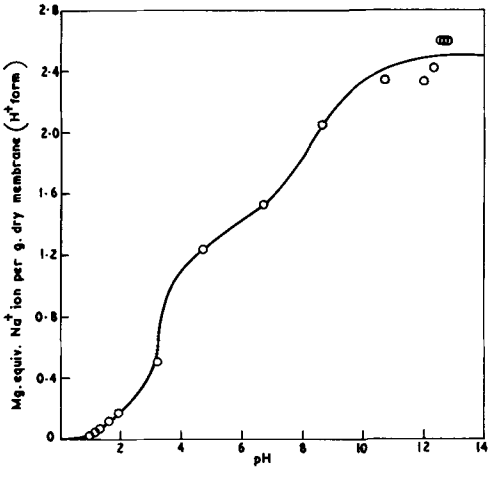

Fig. 1. Titration curve for phosphonic acid membrane

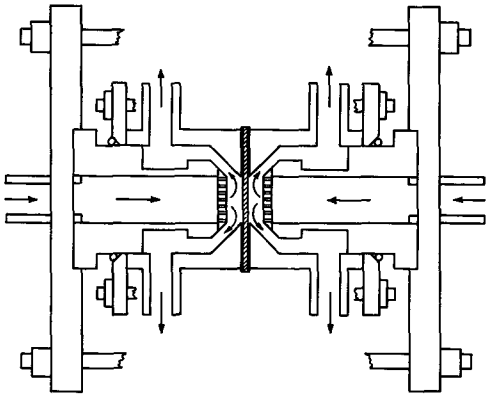

Fig. 2a. Cell for measurement of membrane potentials

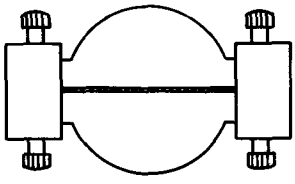

Fig. 2b. Membrane clamp

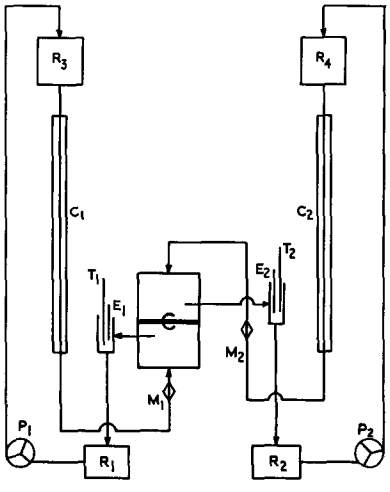

Fig. 3. Apparatus for measurement of membrane potentials: R_1, R_2—bottom reservoirs; R_3, R_4—top reservoirs; P_1, P_2—pumps; M_1, M_2—flow meters; E_1, E_2—electrodes; T_1, T_2—thermometers; C—Perspex cell; C_1, C_2—condensers.

the solutions (2 liters) flowed down through two condensers and through the flowmeters into the cell. By circulating water at a controlled temperature through the condenser jackets, the temperature of the solutions was maintained at 25°C. For the investigation of the effect of membrane thickness, narrow membrane strips were mounted in "Perspex" clamps so that only the outer edges of the strips were exposed to the solution. In this way, the effective membrane thickness was determined by the thickness of the membrane clamp. These clamps consisted of two parallel-faced "Perspex" sheets which were held in position on either side of the membrane strip by metal clips (Fig. 2b).

Flux measurements.—Flux measurements were carried out using the sulfonic acid membrane with the system, sodium chloride-hydrochloric acid. Equinormal solutions (2 liters of sodium chloride and 2 liters of hydrochloric acid solution) were circulated at 1500 ml/min past the membrane surfaces at 25°C. The hydrogen ion which had diffused through the membrane was determined by titrating a small aliquot of the sodium chloride solution at known intervals. From the membrane area and the quantity of H^+ ion which had diffused through the membrane in a given time, the flux values (g equiv. cm^{-2} sec^{-1}) were calculated (Table II).

Table II. Effect of concentration of bulk solution on interdiffusion of Na^+ and H^+ ions, and solution concentrations at the membrane surface

Concentration of bulk solution	Flux (g ion cm^{-2} sec^{-1})	C^b	C^o	δ (cm)
1.00*N*	3.10×10^{-7}	0.98*N*	1.02*N*	1.8×10^{-3}
0.10*N*	2.15×10^{-7}	0.084*N*	0.116*N*	2.3×10^{-3}
0.01*N*	0.645×10^{-7}	0.0063*N*	0.0137*N*	1.8×10^{-3}

Potential measurements.—Potential measurements were carried out using a Pye Cambridge Universal Precision potentiometer with a high-impedance amplifier unit between the cell and the potentiometer. Silver-silver chloride electrodes were used except in the experiments with alkaline solutions where calomel electrodes with saturated potassium chloride bridges were employed. Concentration potential measurements with sulfonic and phosphonic acid membrane strips were carried out using sodium chloride solutions. All potential measurements were made with the solutions at a temperature of 25.0°C.

Effect of flow rate on membrane potentials.—Membrane potentials were determined with the sulfonic acid membrane ($\simeq 16 \times 10^{-3}$ cm and 132×10^{-3} cm thickness) and decinormal solutions of sodium chloride and potassium chloride (2 liters each) using flow rates ranging from 200 to 1500 ml/min.

Measurement of BIP.—Potentials were measured using flow rates of 1500 cc/min with a fixed concentration of sodium chloride and varying concentrations of potassium chloride and *vice versa*. A positive value for the potential indicates that the electrode in the sodium chloride solution was positive with respect to the other electrode. The potential values were plotted as a function of concentration of one solution when the concentration of the other was fixed and *vice versa*. The point of intersection of the two lines obtained was taken as the BIP value at that particular concentration.

Measurement of BIP of phosphonic acid membrane as a function of pH.—The BIP measurements were carried out using 0.1*N* solutions adjusted to different pH values. Calomel electrodes and KCl bridges were employed for potential measurements with alkaline solutions.

Results and Discussion

Although the importance of eliminating the effects of diffusion layers in measurements of bi-ionic potential has been recognized by several authors (2, 28-31), it would appear that these effects have frequently been overlooked probably because, in many of the systems investigated, the membrane potential observed with partial film diffusion control differs little from that with complete membrane control. With some systems, however, and especially with those containing two ions of different valency, the magnitude and even the sign of the potential under the two conditions may be completely different (32). Helfferich (8) has shown that, for the interdiffusion of two isotopes of the same counter ion, deviations from ideal membrane control are to be expected when

$$\frac{DCd}{\overline{D}\overline{C}\delta} < 50$$

where D and $\overline{D}$ are the diffusion coefficients of the counter ion in solution and in the membrane, C is the solution concentration, $\overline{C}$ is the total counter ion concentration in the membrane, d its thickness, and δ the thickness of each of the diffusion layers. Complete film control will be attained when $DCd/\overline{D}\overline{C}\delta < 0.1$. With

a typical ion-exchange membrane, $\bar{C} \approx 1N$, $D/\bar{D} \approx 5$ and $d \approx 0.1$ cm so that, with $0.1N$ solutions, a film thickness of less than 10^{-3} cm is necessary for the attainment of complete membrane control. With $0.001N$ solutions, the film thickness has to be reduced to 10^{-5} cm.

In the measurement of bi-ionic potentials, it is therefore clearly necessary to make sure that complete membrane diffusion control has been established. In previous work on the measurement of membrane potentials, the absence of any significant change in the potential on increasing the rate of stirring or the flow rate of the solutions has frequently been taken to indicate the establishment of membrane control. In the present work, however, in addition to investigating the effect of flow rate on the membrane potential, the thickness of the diffusion layers has been measured and the effect of varying the membrane thickness has been investigated.

Estimation of diffusion-layer thickness.—For the estimation of film thickness, the results obtained in the study of the rate of interdiffusion of sodium and hydrogen ions across the sulfonic acid membrane were used. Similar procedures have previously been employed by Mackay and Meares (13) and by Peterson and Gregor (33). Equations relating the cation flux in bi-ionic exchange systems to the thickness of the diffusion layers were derived by Mackay and Meares. These equations are, however, restricted in their application to systems in which the difference between the compositions of the two solutions, expressed as the equivalent fraction of either cation, is not too large. Peterson and Gregor, using the potassium-ammonium system, were able to assume that these two ions resembled one another sufficiently closely to serve as "tracers" for each other, and they could therefore obtain values for the film thickness by making use of the relatively simple relationships applicable to such systems. With the sodium-hydrogen system where the diffusion potential in the unstirred films is associated with an appreciable anion concentration gradient, we no longer have simple relationships for the interfacial boundary conditions. The interfacial concentrations and the film thickness can, however, be obtained by a graphical method. In this method, it has been assumed that the cation-exchange membrane separates solutions of the uni-univalent electrolytes AY and BY at the same equivalent concentration and that a steady state has been achieved in which there is negligible cross contamination of the two solutions. The boundaries of the membrane and the diffusion layers are represented by planes a, b, c, and d (*see* Fig. 4). It has also been assumed that the membrane is impermeable to anions, that water transport can be neglected, that the mobility ratios are independent of mole fraction, that equilibrium is attained at the membrane-solution interfaces, and that this equilibrium can be represented by the relationship

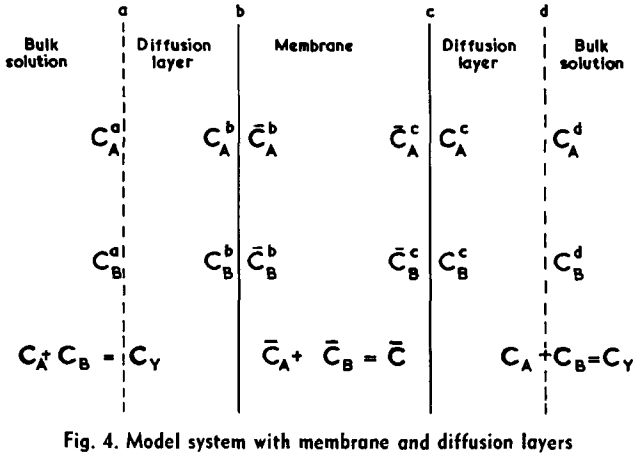

Fig. 4. Model system with membrane and diffusion layers

$$\frac{\bar{C}_A}{\bar{C}_B} = K'^{A}_{B}\frac{C_A}{C_B}$$

where C_A and C_B are the concentrations of the ions in solution and $\bar{C}_A$ and $\bar{C}_B$ are the concentrations in the membrane.

For the diffusion of the cations and anions in the unstirred films, we have the following flux equations

$$J_A = -u_A C_A\left(RT\frac{d\ln C_A}{dx} + \mathbf{F}\frac{d\phi}{dx}\right) \quad [9]$$

$$J_B = -u_B C_B\left(RT\frac{d\ln C_B}{dx} + \mathbf{F}\frac{d\phi}{dx}\right) \quad [10]$$

$$J_Y = -u_Y C_Y\left(RT\frac{d\ln C_Y}{dx} - \mathbf{F}\frac{d\phi}{dx}\right) \quad [11]$$

where J_A, J_B, and J_Y are the fluxes of the cations A and B and the anion Y; u_A, u_B, and u_Y, and C_A, C_B, and C_Y are the corresponding mobilities and concentrations; and ϕ is the potential at the plane x in the diffusion layer.

We also have the following relationships

$$J_A = -J_B = J \quad [12]$$

$$J_Y = 0 \quad [13]$$

$$C_Y = C_A + C_B \quad [14]$$

If $C_Y{}^a = C_Y{}^d = C$, it can be shown that

$$\frac{C_Y{}^b}{C} = 1 + \frac{a_A\delta}{2C}\left(\frac{u_B - u_A}{u_B}\right) \quad [15]$$

and

$$\frac{C_Y{}^c}{C} = 1 - \frac{a_A\delta}{2C}\left(\frac{u_B - u_A}{u_B}\right) \quad [16]$$

where

$$a_A = -\frac{J}{u_A RT}$$

and δ is the thickness of the diffusion layer. If $C_A{}^a = C_B{}^d = C$ and

$$\frac{\bar{C}_A{}^b C_B{}^b}{\bar{C}_B{}^b C_A{}^b} = \frac{\bar{C}_A{}^c C_B{}^c}{\bar{C}_B{}^c C_A{}^c} = K'^{A}_{B}$$

where barred symbols denote concentrations in the membrane, then it can also be shown that

$$\frac{\bar{C}_A{}^b}{\bar{C}} = \frac{1}{1+S} \quad [17]$$

and

$$\frac{\bar{C}_A{}^c}{\bar{C}} = \frac{1}{1+T} \quad [18]$$

where

$$S = \frac{-\frac{u_A}{u_B}\frac{a_A\delta}{2C}\left(\frac{C_Y{}^b}{C}+1\right)}{K'^{A}_{B}\left\{\left(\frac{C_Y{}^b}{C}\right)^2 + \frac{u_A}{u_B}\frac{a_A\delta}{2C}\left(\frac{C_Y{}^b}{C}+1\right)\right\}}$$

$$T = \frac{\left(\frac{C_Y{}^c}{C}\right)^2 + \frac{a_A\delta}{2C}\left(\frac{C_Y{}^c}{C}+1\right)}{-\frac{a_A\delta}{2C}\left(\frac{C_Y{}^c}{C}+1\right)K'^{A}_{B}}$$

and $\bar{C}$ is the total concentration of counter ions in the membrane.

By applying the Nernst-Planck flux equations to the diffusion processes in the membrane, it can be shown (*cf.* Eq. [3. 11b] in the paper by Helfferich (8)) that

$$bd = \ln \frac{\frac{\bar{C}_A{}^b}{\bar{C}} - \frac{\bar{u}_B}{\bar{u}_B - \bar{u}_A}}{\frac{\bar{C}_A{}^c}{\bar{C}} - \frac{\bar{u}_B}{\bar{u}_B - \bar{u}_A}} \quad [19]$$

where

$$b = -\frac{J}{RT\bar{C}}\left(\frac{\bar{u}_B - \bar{u}_A}{\bar{u}_A \bar{u}_B}\right)$$

$\bar{u}_A$ and $\bar{u}_B$ are the mobilities of the counter ions in the membrane and d is the membrane thickness.

If the value of $a_A\delta/C$ is known, then bd can be calculated using Eq. [15]-[19]. The relationship between bd and $a_{Na}\delta/C$ for the sodium-hydrogen ion system and the membrane used in these experiments is shown in Fig. 5. (In these calculations, the sodium ion was taken as ion B with a negative flux. Since J is then positive, Eq. [12], it follows that $-a_{Na}\delta/C$ is also positive). Values of bd were calculated from assumed values of $a_{Na}\delta/C$ by also assuming that $u_{Na}/u_H = 1.43$, $K'_H{}^{Na} = 1.40$, and $\bar{u}_{Na}/\bar{u}_H = 0.125$. Complete membrane control is attained when $a_{Na}\delta/C = 0$ and $bd = \ln \bar{u}_{Na}/\bar{u}_H$; and, under these conditions, the flux will be independent of the solution concentrations. Complete film control is attained when

$$bd = 0 \text{ and } -\frac{a_{Na}\delta}{C} = \frac{2}{\left(\sqrt{\frac{u_{Na}}{u_H}} + 1\right)^2} \quad [20]$$

and the flux will then be proportional to the solution concentration. [A more general solution for the case of complete film diffusion control has been given by Helfferich (15).]

It was found that, over a period of 4 hr, the rate of interdiffusion was approximately constant. With the 0.01N solutions, the amount of H^+ ion diffusing through the membrane in this time was approximately 2 mg equiv. Since the total volume of each solution is 2 liters, an interdiffusion flux of this magnitude could have led to appreciable cross contamination if the solutions had not been renewed at frequent intervals during the subsequent potential measurements.

The thickness of the diffusion layer was obtained from the results of the flux experiments by first calculating the value of bd corresponding to the interdiffusion flux at each of the three solution concentrations and then calculating the film thickness from the corresponding values of $a_{Na}\delta/C$ obtained from the curve shown in Fig. 5.

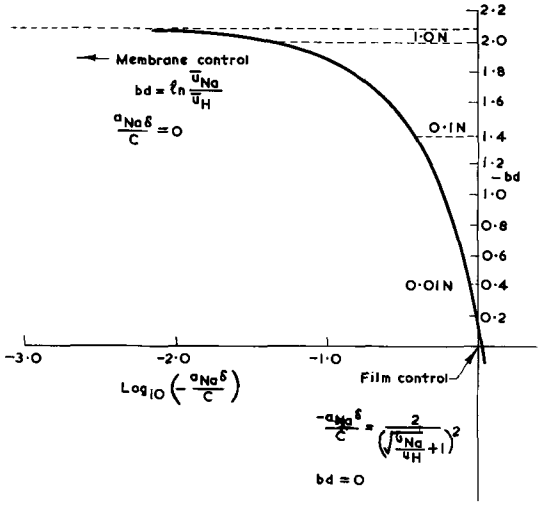

Fig. 5. Relationship between bd and

$$\log_{10}\left(-\frac{a_{Na}\delta}{C}\right) \text{ for } K_H{}^{Na} = 1.40$$

Calculated values for the film thickness and the solution concentrations at the membrane surface are given in Table II. It will be noted that with the 1.0N solutions there is little difference between the concentrations of the bulk solutions and the concentrations at the membrane surfaces. With the 0.1N and 0.01N solutions, however, the difference in the mobilities of the two cations leads to the development of marked concentration gradients in the diffusion layers. It will also be seen from Fig. 5 that complete membrane control is approached with the 1.0N solutions and that with the 0.01N solutions complete film control is approached but not achieved. With the 0.1N solutions, the system is in an intermediate condition. In these circumstances, the agreement between the values calculated for the film thickness is surprisingly good and may be partly due to the fortuitous cancellation of errors and approximations. The value of 2 x 10^{-3} cm for the film thickness is less than that of 4.5 x 10^{-3} cm obtained by Mackay and Meares (13) for a cell provided with mechanical stirring. Peterson and Gregor (33), who also used a cell fitted with stirrers, obtained values for the film thickness which ranged from 0.1 x 10^{-3} to 3.0 x 10^{-3} cm, depending on the rate of stirring. Cooke and van der Walt (34), using a cell in which NaCl solution flowed through a narrow compartment bounded on one face by the membrane, obtained values for the Nernst layer thickness ranging from approximately 3 to 7 x 10^{-3} cm, depending on the velocity of the solution. By using a spacer to promote eddy formation, the thickness was reduced to approximately 1 x 10^{-3} cm.

The effects of membrane and diffusion-layer thickness on membrane potentials.—If we consider the interdiffusion of two isotope counter-ions through the sulfonic acid membrane, we can calculate the value of $DCd/\bar{D}\bar{C}\delta$ assuming the film thickness is 2 x 10^{-3} cm. For this membrane, we may assume $D/\bar{D} \simeq 8$, $\bar{C} \simeq 1.4$ x 10^{-3}g ion cm^{-3}, and we obtain the following approximate values for $DCd/\bar{D}\bar{C}\delta$

Solution concentration	$DCd/\bar{D}\bar{C}\delta$		
	d = 0.016 cm	0.132 cm	0.320 cm
1.0N	45	400	900
0.1N	4.5	40	90
0.01N	0.45	4	9

With a membrane thickness of 16 x 10^{-3} cm, membrane control will therefore be closely approached with 1.0N solutions; complete film control will be approached but not attained with 0.01N solutions. Satisfactory measurements of bi-ionic potentials cannot therefore be made with 0.1N or 0.01N solutions, a membrane of this thickness, and a film thickness of 2 x 10^{-3} cm.

The effect of solution flow rate and membrane thickness on the potential with 0.1N solutions of KCl and NaCl is shown in Fig. 6 which clearly illustrates the difficulties which can arise in the measurement of bi-ionic potentials with ion-exchange resin membranes. With a membrane thickness of 16 x 10^{-3} cm, and above a flow rate of 500 cm^3/min, there is very little change in the potential with increase in flow rate. This clearly cannot be taken to indicate the absence of film control since, with a membrane thickness of 132 x 10^{-3} cm, the potential is considerably greater and, as shown above, complete membrane control would not be expected with a membrane thickness of 16 x 10^{-3} cm. The absence of a change in potential with change in flow rate cannot, in this case, be taken to indicate the establishment of membrane control; instead, it probably indicates the attainment of a limiting film thickness.

In these experiments, Ag, AgCl electrodes were used; and the emf of the cell therefore involves the

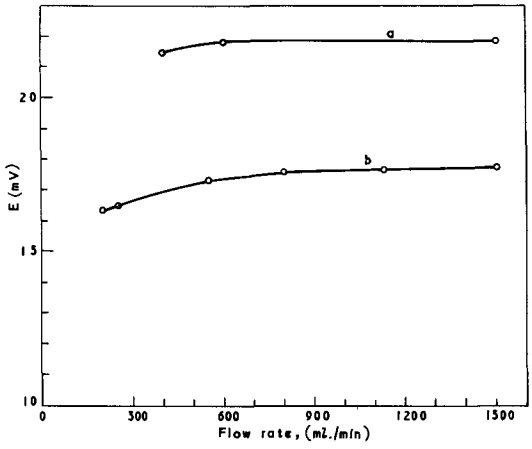

Fig. 6. Effect of flow rate on membrane potentials with a sulfonic acid membrane, 0.1*N* NaCl and 0.1*N* KCl solutions and Ag, AgCl electrodes: (a) membrane thickness, 132 x 10^{-3} cm; (b) membrane thickness, 16 x 10^{-3} cm.

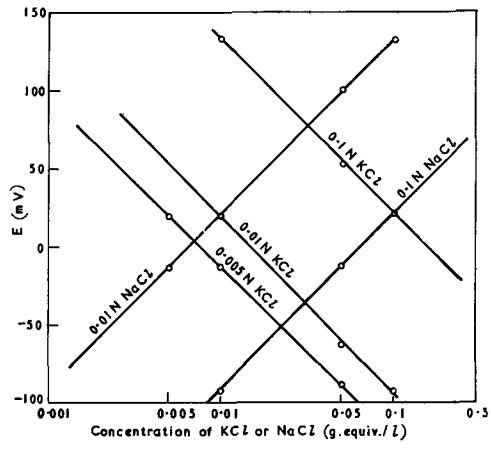

Fig. 7. Effect of solution concentration on potentials with a sulfonic acid membrane (thickness, 132 x 10^{-3} cm), NaCl and KCl solutions, and Ag, AgCl electrodes.

difference between the two electrode potentials as well as the membrane potential which is inaccessible to direct measurement. The emf of the cell is given by the equation

$$E = \frac{RT}{\mathbf{F}} \ln \frac{a_Y'}{a_Y''} + \frac{RT}{\mathbf{F}} \ln \frac{\bar{u}_A a_A'}{\bar{u}_B a_B''} K'_{a}{}^{A}{}_{B}$$

$$= \frac{RT}{\mathbf{F}} \ln \frac{\bar{u}_A}{\bar{u}_B} K'_{a}{}^{A}{}_{B} + \frac{2RT}{\mathbf{F}} \ln \frac{a_{\pm AY}}{a_{\pm BY}}$$

where $a_{\pm AY}$ and $a_{\pm BY}$ are the mean activities of the electrolytes AY and BY in the two solutions.

The potential corresponding to the system in which the mean activities $a_{\pm AY}$ and $a_{\pm BY}$ are equal can be found by the procedure described by Wyllie and Kanaan (16). If the mean activity of electrolyte BY is kept constant and the potential is measured with solutions of AY of differing mean activities, then, on plotting the potential against ln $a_{\pm AY}$, a straight line should be obtained with a gradient equal to $2RT/\mathbf{F}$. If the mean activity of AY is kept constant and the concentration of BY is varied, then, on plotting the results in a similar way, a straight line with slope $-2RT/\mathbf{F}$ is obtained. The intercept will correspond to the condition in which $a_{\pm AY} = a_{\pm BY}$. Since at these concentrations the mean activity coefficients for the two electrolytes differ by less than 1.1%, the emf obtained from the intercept will be very close to that obtained with solutions of equal concentration.

The effect of varying the concentration of one solution on the emf with a sulfonic acid membrane (thickness: 132 x 10^{-3} cm) is shown in Fig. 7. In all cases, linear relationships between the emf and the logarithm of the solution concentration were obtained. The gradients were slightly less than the theoretical but this was largely due to the use of concentrations instead of mean activities.

The effect of solution concentration and membrane thickness on the membrane potential when the solutions are equal in concentration is shown by the results given in Table III. With a membrane thickness of 16 x 10^{-3} cm, the membrane potential decreases slightly with decrease in solution concentration reaching a value of 16.4 mV at a solution concentration of 0.01*N*. With complete film control, there will be no concentration gradients in the membrane and the membrane potential should be the sum of the difference between the two Donnan potentials at the interfaces and the two diffusion potentials in the films. The total concentrations in solution at the interfaces can be obtained from Eq. [15], [16], and [20]. From the ratio of these concentrations, the difference between the two Donnan potentials is found to be $RT/\mathbf{F}$ ln $\sqrt{\bar{u}_A/\bar{u}_B}$. From the total concentrations in solution at the membrane surfaces and Eq. [9], [10], [11], and [13], it can be shown that the sum of the two diffusion potentials is also $RT/\mathbf{F}$ ln $\sqrt{\bar{u}_A/\bar{u}_B}$ so that the membrane potential is given by

$$E = \frac{RT}{\mathbf{F}} \ln \frac{u_A}{u_B} \quad [cf. \text{ Helfferich (8)}]$$

With KCl and NaCl solutions, the theoretical value for the membrane potential in 0.01*N* solutions is 10.2 mV (if the mobility ratio is estimated from transport number and conductivity data). This value is much lower than the experimental value quoted above and we may therefore conclude that complete film control has not been attained with the 0.01*N* solutions.

Comparison of results obtained with sulfonic and phosphonic acid membranes.—With the sulfonic acid membranes, the potentials obtained with membrane thicknesses of 132 x 10^{-3} cm and 320 x 10^{-3} cm are significantly higher than those obtained with a membrane thickness of 16 x 10^{-3} cm and, from the values of $DCd/\bar{D}\bar{C}\delta$ given above, complete membrane control would be expected to be closely approached with 0.1*N* solutions. The value of 21.5 mV obtained for the membrane potential with a membrane thickness of 132 x 10^{-3} cm can therefore be taken to be the bi-ionic potential. The results of measurements of concentration potentials showed that the slightly lower value obtained with 0.1*N* solutions and a membrane thickness of 320 x 10^{-3} cm was undoubtedly due to a slight leakage of chloride ion presumably between the membrane and the membrane clamp.

In the experiments with the phosphonic acid membranes, the membrane potential was measured over the *p*H range 2.0-13.0 using 0.1*N* solutions and membrane thicknesses 27 x 10^{-3} cm, 132 x 10^{-3} cm, and 320 x 10^{-3} cm. Silver-silver chloride electrodes were used for the experiments with solutions of *p*H < 9.6; calomel electrodes and KCl bridges were used when the *p*H was greater than 5. With the calomel electrodes, it was assumed that the emf of the cell was equal to the membrane potential and that the difference between the diffusion potentials at the KCl

Table III. Effect of solution concentration on membrane potentials with sulfonic acid membranes

Solution concentration *N*	Membrane thickness (cm) 16 x 10^{-3}	132 x 10^{-3}	320 x 10^{-3}
0.10	17.42	21.50	18.64
0.05	16.58	—	20.22
0.01	16.44	20.22	20.72
0.005	—	19.43	—

Table IV. Membrane potentials with phosphonic acid membranes

	Membrane thickness				
	27×10^{-3} cm	132×10^{-3} cm		320×10^{-3} cm	
pH	E (a) (mV)	E (a) (mV)	E (b) (mV)	E (a) (mV)	E (b) (mV)
2.0	—	4.28	—	3.34	—
≃6	18.2	5.17	—	5.01	5.23
≃10	—	5.76	5.81	—	6.30
13.0	—	—	6.68	—	6.04

(a) Silver/silver chloride electrodes.
(b) Calomel electrodes.

bridges could be neglected. It will be seen from Table IV that good agreement is obtained under conditions where both Ag, AgCl, and calomel electrodes could be used.

The results obtained with the two thicker membranes are in reasonably good agreement. In both cases, there is a slight decrease in the BIP with decrease in pH. Under all conditions, the value for the BIP with the thicker membranes is very much less than that obtained with a membrane thickness of 27 x 10^{-3} cm and considerably less than the value of 21.5 mV obtained for the BIP with the sulfonic acid membrane. This result is in contrast to that of Bergsma and Staverman (24) who found little difference in the behavior of membranes containing sulfonic and phosphonic acid groups toward sodium and potassium ions. It would, however, appear likely that, in these experiments, because of the low flow rate, the bi-ionic systems were subject to partial film control (35). This view is supported by the approximate agreement between the values obtained for the potentials with the thin sulfonic and phosphonic acid membranes.

The values obtained for the relative affinity coefficient K_{Na}^{K} with the two membranes are given in Table V. The value for the sulfonic acid membrane is approximately equal to that which would be expected for a sulfonated polystyrene resin with a 5% divinylbenzene content. With the phosphonic acid membrane, the value of K_{Na}^{K} in alkaline solution is less than unity and Na^+ is absorbed more strongly than K^+. At pH 5, there is a decrease in the affinity for sodium ion and the value of K_{Na}^{K} approaches unity. The affinity order Na > K, which obtains in alkaline solutions, is the same as that previously observed by Bregman and Murata (17, 18) with a phosphonic acid resin, and by Kennedy, Marriot, and Wheeler with a methylene phosphonic acid resin (19). It is, however, the reverse of that usually observed with sulfonic acid resins of normal capacity and cross linking. Bregman (18) suggested an explanation for this reversal of selectivity, which was based on the work of Teunissen and Bungenberg de Jong (36, 37) on the concentration of alkali chlorides necessary to bring about reversal of charge on organic colloids. This explanation assumed the following order of polarizability for the functional groups and for water: phosphonic acid group > water > sulfonic acid group. The greatest interaction through polarization would be expected with the Li^+ ion (with the highest field strength) and the phosphonic acid group, and with the phosphonic acid resins the affinity sequency would be expected to be $Li^+ > Na^+ > K^+$. With the sulfonic acid resins, the interaction between the cations and water would be of greater importance: the Li^+ ion would be the most strongly hydrated and this would lead to the affinity sequence $K^+ > Na^+ > Li^+$.

Table V. Correlation of bi-ionic potentials with relative affinity coefficients and mobility ratios

Membrane	pH	K^{K}_{Na}	$\frac{\bar{u}_K}{\bar{u}_{Na}}$	BIP calc. (mV)	BIP observed (mV)
Sulfonic acid	≃5	1.4	1.55	19.9	21.5
Phosphonic acid	≃5	0.88	1.62	9.1	5.0
	≃13	0.63	1.82	3.5	6.5

In Eisenman's approach to the problem of ion selectivity (38), the emphasis is placed on the "field strength" of the anionic group. He showed that a variation in the field strength of the anionic group could lead to the development of 11 different affinity sequences for alkali metal cations. If we assume that the pK_a values for the phosphonic acid groups in the membrane are 3 and 8, then from the relation between pK_a, r^-, and the affinity sequence given by Eisenman, we would expect the affinity order Na > K in alkaline solutions, and a sequence with K > Na in acid solutions.

Values for the relative mobilities of the Na and K ions in the membranes were obtained from the results of the conductance measurements and are given in Table V. No correction was applied for convection conductivity and the ratios can therefore be regarded only as approximate. The table also includes the observed bi-ionic potentials, and the bi-ionic potentials calculated from Eq. [15]. It will be seen that, taking into account the errors and approximations, fairly good agreement is obtained between observed and calculated values. The low value for the BIP obtained with a phosphonic acid membrane is clearly due mainly to the preferential absorption of sodium ion by this membrane, and it is noteworthy that at pH 5 there is relatively little difference in the relative mobilities of the sodium and potassium ions in the two membranes. In the experiments of Woermann described by Bonhoeffer (39), it was found that with a membrane prepared from a potassium selective ion-exchange resin the self-diffusion coefficient of K^+ was smaller than that of Na^+ and the activation energy for diffusion of K^+ was greater than that of Na^+. Similarly, with the phosphonic acid membrane, it appears that the higher relative affinity for the Na^+ ion under alkaline conditions is associated with a somewhat lower relative mobility in the membrane compared with that observed with a sulfonic acid membrane.

The above work was carried out as part of the research program of the former National Chemical Laboratory.

Manuscript submitted Feb. 13, 1969; revised manuscript received *ca.* May 30, 1969. This was Paper 235 presented at the Boston Meeting, May 5-9, 1968.

Any discussion of this paper will appear in a Discussion Section to be published in the June 1970 JOURNAL.

REFERENCES

1. K. Sollner, *Disc. Faraday Soc.*, **21**, 123 (1956).
2. K. Sollner, *J. Phys. Chem.*, **53**, 1211, 1226 (1949).
3. M. R. J. Wyllie, *ibid.*, **58**, 67 (1954).
4. C. E. Marshall, *ibid.*, **52**, 1284 (1948).
5. T. Teorell, "Progress in Biophysics and Biophysical Chemistry," Vol. 3, p. 305, Pergamon Press Ltd., London.
6. F. Helfferich and H. D. Ocker, *Z. Phys. Chem., N.F.*, **10**, 213 (1957).
7. F. Helfferich, "Ion Exchange," p. 378, McGraw-Hill, New York (1962).
8. F. Helfferich, *Disc. Faraday Soc.*, **21**, 83 (1956).
9. D. Mackay and P. Meares, *Koll.-Zeit.*, **176**, 23 (1961).
10. G. E. Boyd, A. W. Adamson, and L. S. Myers, Jr., *J. Am. Chem. Soc.*, **69**, 2836 (1947).
11. D. Reichenberg, *ibid.*, **75**, 589 (1953).
12. R. Schlögl and F. Helfferich, *J. Chem. Phys.*, **26**, 5 (1957).
13. D. Mackay and P. Meares, *Koll.-Zeit.*, **167**, 31 (1959).
14. F. Helfferich, "Ion Exchange," p. 346, McGraw-Hill, New York (1962).
15. D. Mackay and P. Meares, *Koll.-Zeit.*, **171**, 139 (1960).
16. M. R. J. Wyllie and S. L. Kanaan, *J. Phys. Chem.*, **58**, 73 (1954).
17. J. I. Bregman and Y. Murata, *J. Am. Chem. Soc.*, **74**, 1867 (1952).

18. J. I. Bregman, *Ann. N.Y. Acad. Sci.*, **57**, 125 (1953).
19. J. Kennedy, J. Marriot, and V. J. Wheeler, *J. Inorg. Nucl. Chem.*, **22**, 269 (1961).
20. P. le R. Malherbe and W. G. B. Mandersloot, in "Demineralization by Electrodialysis," Edited by J. R. Wilson, p. 48, Butterworths Scientific Publications, London (1960).
21. R. McClintock, R. Neihof, and K. Sollner, *This Journal*, **107**, 315 (1960).
22. H. P. Gregor, H. Jacobson, R. C. Shair, and D. M. Wetstone, *J. Phys. Chem.*, **61**, 141 (1957).
23. H. P. Gregor and D. M. Wetstone, *ibid.*, **61**, 147 (1957).
24. F. Bergsma and A. J. Staverman, *Disc. Faraday Soc.*, **21**, 61 (1956).
25. J. F. A. Hazenberg and B. P. Knol, S. A. Pat. Appln. 1754/58 (*see* also Brit. Pat. 896,739-740).
26. T. R. E. Kressman and F. L. Tye, Brit. Pat. 726,918.
27. J. W. Lorimer, E. I. Boterenbrood, and J. J. Hermans, *Disc. Faraday Soc.*, **21**, 141 (1956).
28. K. Sollner, S. Dray, E. Grim, and R. Neihof, in "Ion Transport Across Membranes," Edited by H. T. Clarke, p. 144, Academic Press, Inc., New York (1954).
29. S. Dray and K. Sollner, *Biochem. Biophys. Acta*, **18**, 341 (1955).
30. G. Manecke, *Z. Elektrochem.*, **55**, 672 (1951).
31. D. Oppen and H. Staude, *ibid.*, **64**, 834 (1960).
32. G. Scatchard and F. Helfferich, *Disc. Faraday Soc.*, **21**, 70 (1956).
33. M. A. Peterson and H. P. Gregor, *This Journal*, **106**, 1051 (1959).
34. B. A. Cooke and S. J. van der Walt, *Electrochim. Acta.*, **5**, 216 (1961).
35. F. Helfferich, *Disc. Faraday Soc.*, **21**, 122 (1956).
36. P. H. Teunissen and H. G. Bungenberg de Jong, *Kolloid-Beihefte*, **48**, 33 (1949).
37. H. G. Bungenberg de Jong, in "Colloid Science, II," Edited by H. R. Kruyt, p. 289, Elsevier Publishing Corp. (1949).
38. G. Eisenman, in "Symposium on Membrane Transport and Metabolism, Prague 1961," p. 163, Academic Press (1962).
39. K. F. Bonhoeffer, *Disc. Faraday Soc.*, **21**, 217 (1956).

Effect of LiF and Li_3AlF_6 on the Electrical Conductivity of Cryolite-Alumina Melts

K. Matiasovsky, V. Danek, and M. Malinovsky

Institute of Inorganic Chemistry, Slovak Academy of Sciences, Bratislava, Czechoslovakia

ABSTRACT

Electrical conductivities of molten LiF, Li_3AlF_6, of two-component systems Na_3AlF_6-LiF, Na_3AlF_6-Li_3AlF_6 and of three-component systems Na_3AlF_6-Al_2O_3-LiF and Na_3AlF_6-Al_2O_3-Li_3AlF_6 were measured. It has been found that by the addition of both LiF and Li_3AlF_6, the electrical conductivity of cryolite-alumina melts is increased, the effect of LiF being much more pronounced. The effect of Li_3AlF_6 is relatively higher at high concentrations of lithium cryolite, which, on the other hand, is less attractive with regard to the technology of aluminum production.

Measurement of the electrical conductivity of molten fluorides and of their mixtures is interesting both from the theoretical as well as the practical point of view. In the field of fundamental research the investigation of electrical conductivity can, together with the investigation of other physicochemical properties, give us valuable information concerning the structure of fused salts. From the practical point of view the electrical conductivity is important especially with regard to the use of fluoride mixtures as electrolytes in electrometallurgy; namely, in the case of cryolite-alumina melts for aluminum production.

There is a close relationship between the electrical conductivity and the energy efficiency of Al electrolysis, which, at present, is approximately 30% (1-3). This relatively low energy efficiency is due mainly to the following factors: anodic overvoltage; anode effect; ohmic voltage drop in the electrolyte; and secondary reactions, *i.e.*, reactions which are not directly connected with the primary anodic or cathodic processes and hence do not influence the cell potential and which, nevertheless, lower the current efficiency (4, 5). These are especially the solution of deposited metallic aluminum in the electrolyte and reactions between the products of electrolysis.

It can be shown that the electrical conductivity of the electrolyte will influence not only the ohmic voltage drop in the cell but also, indirectly, the secondary reactions and thus the current efficiency of the electrolysis (6).

During the last years a series of papers was published dealing with the influence of different additions on certain, from the technical point of view interesting, physicochemical properties of aluminum electrolytes; the pertinent results were reported (1-7). As additives, fluorides and chlorides of alkali metals, of alkaline earth metals, and AlF_3 were used. As it follows from the above papers, from among different additives only LiF, Li_3AlF_6, and NaCl affect favorably most of the important physicochemical properties of electrolytes, including electrical conductivity. Influence of NaCl on the specific conductivity of cryolite-alumina melts was presented by Matiasovsky *et al.* (8, 9).

Measurement of the electrical conductivity of fused fluorides and of their mixtures is experimentally rather difficult owing to the reactive properties of these melts and with regard to the conditions of the experiment, especially the relatively high temperature at which the measurements must be performed. Experimental problems, together with some methodological aspects of measurement of the electrical conductivity of fused fluorides were discussed by Abramov *et al.* (1), Winterhager and Werner (10), and recently by Danek *et al.* (11).

With regard to the experimental difficulties of measurements it is not surprising that the values of electrical conductivity of individual fluorides and of their mixtures, as reported by different authors, vary considerably. Thus, *e.g.*, for specific conductivity of LiF at 950°C the values of 20.3 $ohm^{-1} \cdot cm^{-1}$ (12) and 8.8 $ohm^{-1} \cdot cm^{-1}$ (13) are reported. The reported values of specific conductivity of Li_3AlF_6 at 1000°C lie in the range of 3.93-4.71 $ohm^{-1} \cdot cm^{-1}$ (13-16). There are similar differences in case of the melts of the two-component systems Na_3AlF_6-Al_2O_3 (1, 9, 13, 17-20), Na_3AlF_6-LiF (2, 21) and Na_3AlF_6-Li_3AlF_6 (11, 15, 22). Concerning the three-component systems Na_3AlF_6-

Al_2O_3-LiF and Na_3AlF_6-Al_2O_3-Li_3AlF_6, the data reported by Belyaev (2) and by Mashovets and Petrov (15), respectively, are somewhat controversial regarding the electrical conductivity of pure cryolite and of the binary Na_3AlF_6-Al_2O_3 mixtures.

Experimental

A detailed description of the equipment used is reported by Danek *et al.* (11). A Pt crucible containing 15g of fused salt was used as conductivity cell. Disk electrodes of bright platinum, 5 mm in diameter, were used. Each electrode was provided with a current and a voltage connection (Pt30Ir, d = 0.5 mm). The interpolar distance was 12 mm. The electrodes were immersed 7 mm into the melt with the aid of a micrometric screw with an accuracy of ±0.01 mm. A Thompson double bridge was used for measuring the resistance of the melt (23).

Measurements were carried out with 10 mA current at a frequency of 18 kHz. At this frequency, only the ohmic resistance of the melt was measured (6, 11). The cell constant was determined by calibration with fused Na_3AlF_6. For the conductivity of cryolite at 1000°C the value of 2.80 $ohm^{-1} \cdot cm^{-1}$, determined by Edwards *et al.* (24) and later confirmed by Yim and Feinleib (13) and Bajcsy *et al.* (23) was accepted. (The above value is extrapolated, since the melting point of pure cryolite is 1010° ± 2°C). The reproducibility of the measurement was better than ±2%.

For preparation of samples the following substances were taken: Al_2O_3, reagent grade; LiF, reagent grade; AlF_3 prepared by sublimation of technical fluoride by procedure reported by Matiasovsky *et al.* (25); and Greenland hand-picked cryolite with melting point at 1006° ± 2°C, in which 54.7% of fluorine were determined by the pyrohydrolytic method (26), which corresponds to the composition of pure Na_3AlF_6.

Temperature was measured with Pt/Pt10Rh thermocouples. The hot junction of the thermocouple was placed in the melt between the electrodes. The alternating voltage induced from the furnace into the thermocouple was eliminated by the use of a frequency filter.

Results and Discussion

The influence of temperature on the electrical conductivity of LiF and Li_3AlF_6 was determined. Using the measured values the equations $\sigma = f(t)$ were calculated by the least squares method and the polytherms of electrical conductivity of LiF and Li_3AlF_6 were constructed. The dependence of conductivity on temperature can be expressed by quadratic equations

$$\sigma_{LiF} = -2.4871 + 17.2245 \cdot 10^{-3}t - 5.5475 \cdot 10^{-6}t^2 \quad [1]$$

$$\sigma_{Li_3AlF_6} = -0.7844 + 8.4400 \cdot 10^{-3}t - 3.4658 \cdot 10^{-6}t^2 \quad [2]$$

The values of conductivity of LiF calculated from Eq. [1] are in very good agreement with data reported by Yim and Feinleib (13). The value of specific conductivity of Li_3AlF_6 calculated from Eq. [2] is also in very good agreement with values reported in the aforementioned paper.

In Fig. 1 isotherms of conductivity of melts in the system Na_3AlF_6-LiF are presented. The effect of LiF on the increase of conductivity of cryolite, as it was found in the present work, is less pronounced than the effect at low concentrations of LiF reported by Belyaev (2) and Vakhobov and Belyaev (21). We may assume that this difference is caused by inaccurate calibration of the conductivity cell and by low frequency of the measuring current used by the above authors.

Isotherms of conductivity of melts in the system Na_3AlF_6-Li_3AlF_6 are shown in Fig. 2. The measured values of conductivity are somewhat higher than the values reported in papers (11, 14), but the general character of the dependence $\sigma = f$ (conc) is in all cases the same. The relatively lower values reported in the above works are evidently due to the low frequency of the measuring current. Basically different are the data reported by Mashovets and Petrov (15), both with as regard to the measured values and to the general character of the isotherm of conductivity of melts in the system Na_3AlF_6-Li_3AlF_6, which are probably due to deficiencies of their experimental technique.

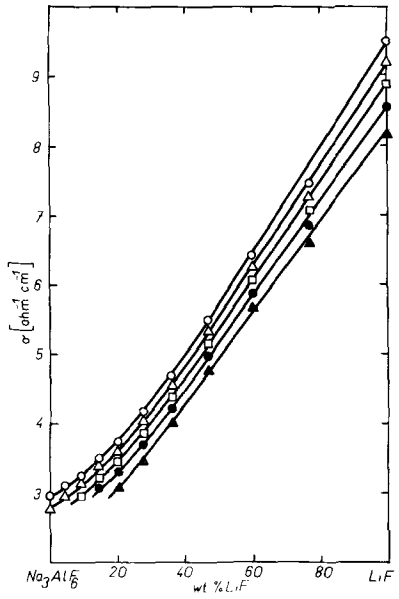

Fig. 1. Isotherms of the conductivity of molten Na_3AlF_6-LiF mixtures. ○, 1050°C; △, 1000°C; □, 950°C; ●, 900°C; ▲, 850°C.

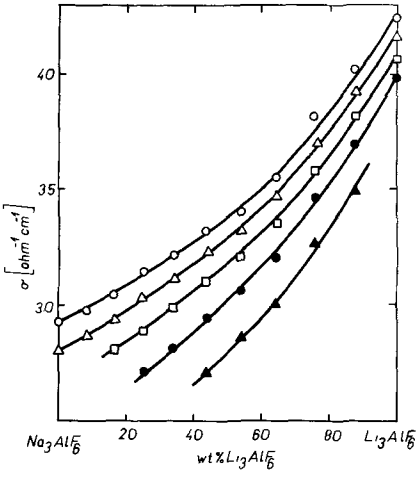

Fig. 2. Isotherms of the conductivity of molten Na_3AlF_6-Li_3AlF_6 mixtures. ○, 1050°C; △, 1000°C; □, 950°C; ●, 900°C; ▲, 850°C.

Data on conductivity of melts in the system Na_3AlF_6-Al_2O_3 were presented in our previous papers (8, 9).

Figure 3 shows the isotherm of the conductivity of the melts in the system Na_3AlF_6-Al_2O_3-LiF and Fig. 4

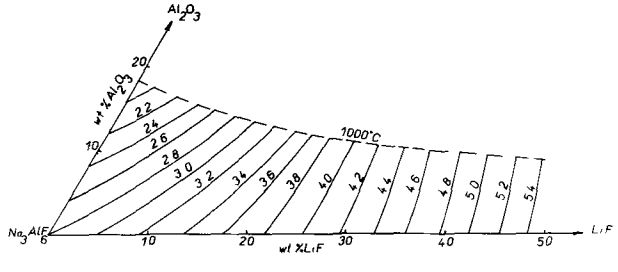

Fig. 3. Isotherm of the conductivity of molten Na_3AlF_6-Al_2O_3-LiF mixtures at 1000°C.

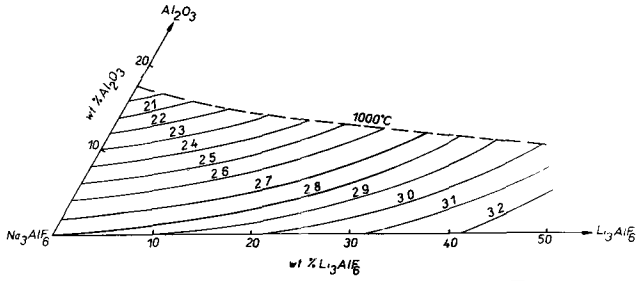

Fig. 4. Isotherm of the conductivity of molten Na_3AlF_6-Al_2O_3-Li_3AlF_6 mixtures at 1000°C.

the isotherm of conductivity of the ternary Na_3AlF_6-Al_2O_3-Li_3AlF_6 mixtures at 1000°C.

On comparison of the influence of additives on the electrical conductivity of cryolite-alumina melts it is evident that the gradient of conductivity increase caused by the addition of Li_3AlF_6 is relatively low, being but about 15% of the gradient for LiF and is even lower than the corresponding values for the addition of NaCl (8, 9). From the diagrams in Fig. 2 and 4 it may be seen that the gradient of electrical conductivity increase shows an increase in the area of higher concentration of Li_3AlF_6, which, however, is not suitable for technical application. It is very probable that the reason for this behavior lies somewhere in the structure of the melt similar to the negative deviation from the additive line of the melts in the systems Na_3AlF_6-LiF and Na_3AlF_6-Al_2O_3-LiF (Fig. 1, 3). In case of LiF we may assume that the negative deviation from the additivity is caused by the suppression of the dissociation of the complex ion AlF_6^{3-}, which, according to (27), dissociates partly in the fused cryolite according to the scheme $AlF_6^{3-} \rightleftarrows AlF_4^- + 2F^-$. By the admixture of LiF, the F^- ions are introduced into the melt and the dissociation equilibrium is shifted toward the left so that we may assume that the relative increase of the concentration of free F^- ions, which, apart from cations Li^+ and Na^+ contribute to the current transport, is smaller than the additive.

In spite of the fact that in the case of LiF the conductivity increase is also somewhat smaller than it should be according to the additivity line, the addition of LiF increases substantially the conductivity of the fundamental electrolyte. Thus, *e.g.*, at the concentration of 5% of LiF the conductivity of the electrolyte increases by 10%, which, as we pointed out in the introduction, is of great importance for the technical application. From the abovesaid it also follows that, with regard to the relatively poor effect of Li_3AlF_6 on the electrical conductivity of cryolite-alumina melts, it would be advisable to use the addition of LiF only in electrolytes that do not contain free AlF_3.

Manuscript submitted March 24, 1969; revised manuscript received May 26, 1969.

Any discussion of this paper will appear in a Discussion Section to be published in the June 1970 JOURNAL.

REFERENCES

1. G. A. Abramov, M. M. Vetyukov, I. P. Gupalo, A. A. Kostyukov, and L. N. Lozhkin, "Teoreticheskie osnovy elektrometallurgii alyuminia," Metallurgizdat, Moscow (1953).
2. A. I. Belyaev, "Elektrolit alyuminievykh vann," Metallurgizdat, Moscow (1961).
3. K. Grjotheim and K. Matiasovsky, *Tidsskr. Kjemi, Bergvesen Met.*, **26**, 226 (1966).
4. K. Grjotheim, J. L. Holm, C. Krohn, and J. Thonstad, in "Selected Topics in High Temperature Chemistry," p. 151, T. Førland, K. Grjotheim, K. Motzfeld and S. Urnes, Editors, Universitetsforlaget, Oslo (1966).
5. K. Grjotheim, J. L. Holm, C. Krohn, and K. Matiasovsky, *Svensk Kem. Tidskr.*, **78**, 547 (1966).
6. K. Grjotheim, M. Malinovsky, and K. Matiasovsky, *J. Metals*, **21**, 28 (1969).
7. A. V. Vakhobov and A. I. Belyaev, in "Fizicheskaya khimia rasplavlennykh solei," Edited by The Institute of General and Inorganic Chemistry of the Soviet Academy of Sciences, p. 99, Metallurgizdat, Moscow (1965).
8. K. Matiasovsky, S. Ordzovensky, and M. Malinovsky, *Chem. Zvesti*, **17**, 839 (1963)
9. K. Matiasovsky, M. Malinovsky and S. Ordzovensky, *This Journal*, **111**, 973 (1964).
10. H. Winterhager and L. Werner, "Präzisions-Messverfahren zur Bestimmung des elektrischen Leitvermögens geschmolzener Salze," Westdeutscher Verlag, Köln (1956).
11. V. Danek, M. Malinovsky, and K. Matiasovsky, *Chem. Zvesti*, **22**, 707 (1968).
12. E. Ryschkewitsch, *Z. Elektrochem.*, **39**, 531 (1933).
13. E. W. Yim and M. Feinleib, *This Journal*, **104**, 622, 626 (1957).
14. G. A. Abramov and P. A. Kozunov, *Tr. Leningr. Politekhn. Inst., Razdel Metallurgia*, **1**, 60 (1939).
15. V. P. Mashovets and V. I. Petrov, *Zh. Prikl. Khim.*, **32**, 1528 (1959).
16. V. Danek, J. Novák, and M. Malinovsky, *Chem. Zvesti*, **21**, 832 (1967).
17. K. Arndt and W. Kalass, *Z. Elektrochem.*, **30**, 12 (1924).
18. K. P. Batashev, *Legkie Metally*, **10**, 48 (1936).
19. A. I. Belyaev, "Fiziko-khimicheskie protsessy pri elektrolize alyuminia," Metallurgizdat, Moscow (1947).
20. A. Vajna, *Alluminio*, **19**, 215 (1950).
21. A. V. Vakhobov and A. I. Belyaev, *Izv. Akad. Nauk. SSSR, Met. i Gorn. Delo*, **4**, 80 (1964).
22. G. A. Abramov, A. A. Kostyukov, and L. V. Nordvik, *Tr. Leningr. Politekhn. Inst.*, **188**, 40 (1957).
23. J. Bajcsy, M. Malinovsky, and K. Matiasovsky, *Electrochim. Acta*, **7**, 543 (1962).
24. J. D. Edwards, C. S. Taylor, A. A. Russel, and L. F. Maranville, *This Journal*, **99**, 527 (1952).
25. K. Matiasovsky, M. Malinovsky, E. Plsko, and C. Kubík, *Chem. Zvesti*, **14**, 487 (1960).
26. K. Matiasovsky and C. Kubík, *Chem. Zvesti*, **16**, 808 (1962).
27. K. Grjotheim, "Contribution to the Theory of the Aluminium Electrolysis," Det Kgl. Norske Videnskabers Skrifter Nr. 5, F. Bruns Bokhandel, Trondheim, Norway (1956).

High Rate Anodic Dissolution of Copper

Dieter Landolt,*[1] Rolf H. Muller,* and Charles W. Tobias*

Inorganic Materials Research Division, Lawrence Radiation Laboratory and Department of Chemical Engineering, University of California, Berkeley, California

ABSTRACT

The anodic dissolution of copper at current densities of 10-150 A/cm^2 has been studied in neutral KNO_3 and K_2SO_4 solutions. An experimental flow system has been built which allows electrochemical measurements of the dissolution process to be performed under defined hydrodynamic conditions typical for the technical electrochemical machining operation. Design criteria for such a system have been analyzed. Copper dissolution proceeds in an active or a transpassive mode which differ in overvoltage by 10-20V. The onset of passivation seems to be due to the limiting mass transfer of dissolved metal from the electrode surface. The still higher dissolution rates in the passive state appear to be made possible by the removal of solid dissolution products. Etched, dull surfaces have resulted from active dissolution; pitted, bright surfaces from passive dissolution.

Electrochemical machining (ECM) has found widespread use in recent years for the shaping of metals. In this process, the workpiece is dissolved anodically at current densities in the order of 100 A/cm^2, characteristically with electrolyte flow rates of 0.5-70 m/sec and electrode spacings of 0.1-0.5 mm. As an electrochemical process, ECM is of particular interest because the current densities employed are about three orders of magnitude higher than those applied in conventional electrolysis. Most of the published literature on ECM deals with the correlation of practical process variables such as cathode feed rate, applied voltage, and electrolyte pressure, but little is known about the electrochemical factors involved.

A more detailed understanding of ECM may not only lead to further development and wider practical adoption of this highly interesting process, but it may also yield information relevant to the operation of other electrochemical processes at much higher rates than employed in current industrial practice. With this purpose in mind, the anodic dissolution of a metal with reasonably well understood electrochemical and metallurgical properties was subjected to study under conditions similar to those employed in ECM. The principal goal of the study was to develop an experimental method for estimating the anode potential values prevailing at high current density and for investigating the role of hydrodynamics in the anodic dissolution process. In addition, optical observations of the interelectrode gap were to be carried out in order to determine the influence of flow rate and current density on cathodic hydrogen evolution. The design of the experimental system and results obtained on the dissolution of copper in neutral KNO_3 and K_2SO_4 solutions in the current density range of 10-150 A/cm^2 are reported here.

Design Considerations

Cell voltage.—In order to keep the cell voltage in manageable limits electrodes have to be spaced closely. For example, assuming a current density of 100 A/cm^2, a specific electrolyte resistance of $\rho = 10$ ohm-cm, and an inter-electrode gap of 0.5 mm, the ohmic drop is as large as 50V. Geometrical arrangements like rotating disks or cylinders are not well suited since the cell resistance is dependent on the diameter which determines the surface area. The characteristic length (diameter) therefore can not be varied independent[2] of the resistance.

Temperature increase in solution.—The temperature rise is primarily due to ohmic heating which is determined by the power density. By neglecting heat losses, the rate of temperature rise can be expressed by

$$\frac{\Delta T}{\Delta t} \simeq \frac{i^2 \rho}{d\, c_p} \ (^\circ/\text{sec}) \qquad [1]$$

As an example, setting $i = 100$ A/cm^2, $\rho = 10$ ohm-cm, $d = 1$ g/cm^3, $c_p = 4.18$ joule/°g, one obtains

$$\frac{\Delta T}{\Delta t} \simeq 2.4 \times 10^4 \ (^\circ/\text{sec})$$

In order to limit the temperature rise, extremely short experimental times would be required, or the residence time of the solution has to be kept short by high flow rates.

In the latter case, the use of parallel plate electrodes is more suitable than, *e.g.*, rotating disk or cylinder electrodes, but high linear velocities of the electrolyte are to be employed, and the length of the electrode in flow direction is to be kept short. A rough estimate of the temperature increase in the flow direction is obtained from [1] by setting $\Delta t = L/u$ with L = electrode length and u = linear velocity. For example, using the current density and electrolyte properties given above, one obtains for $u = 1000$ cm/sec, and $L = 1$ cm, $\Delta T = 25°$.

Pressure drop.—The pressure drop in a flow system is proportional to the square of the flow velocity and proportional to the length of the system. In a flow channel cell, it is desirable to have a hydrodynamic entrance length of 70 to 100 hydraulic diameters[3] upstream of the electrodes. The entrance length serves to establish a fully developed velocity profile (2, 3), which is necessary in order to have well reproducible and analytically amenable mass transfer conditions. The requirement of a hydrodynamic entrance length increases the value of the inlet pressure necessary to maintain a given linear velocity at the electrode manifold. A decision therefore has to be made as to whether close control of mass transfer conditions justifies a substantial increase in pressure requirements. Data of a channel cell containing a hydrodynamic entrance length are given in the next section.

Mass transfer conditions.—Numerical estimations indictate that a rectangular flow channel cell under turbulent flow conditions is the most suitable experimental arrangement for realizing extremely high mass transfer rates. This arrangement has the drawback

* Electrochemical Society Active Member.

[1] Present address: University of California, Department of Engineering, Los Angeles, California 90024.

[2] Using the values above, one obtains for a rotating disk electrode of $R = 2$ mm radius [primary current distribution (1)] $U \simeq \pi/4\, i\rho R \simeq 160$V. For two concentric cylinder electrodes of 2 and 10 mm radius $U \simeq i\rho R_1 \ln(R_2/R_1) \simeq 320$V.

[3] The hydraulic diameter is defined as $D_h = \dfrac{4 \text{ cross section}}{\text{perimeter}}$.

that the thickness of the diffusion layer increases in the flow direction (4). However, under turbulent flow conditions, if the electrode is sufficiently long the variation of the diffusion layer thickness can be neglected (6), since a constant value is reached at a short distance from the leading edge of the electrode. Mass transfer rates for turbulent flow in pipes have been reported by Van Shaw, Reiss, and Hanratty (6). If the pipe diameter is replaced by the hydraulic diameter D_h, their results should be applicable to predict mass transfer in rectangular flow channels. In the mass transfer entry region, *i.e.*, at short distances from the leading edge of the electrode, experimental mass transfer rates under conditions corresponding to fully developed velocity profiles were described by Van Shaw, Reiss, and Hanratty (6) by the relation

$$Nu = 0.28\, Re^{0.58}\, Sc^{1/3} \left(\frac{D_h}{L}\right)^{1/3} \qquad [3]$$

where Nu represents the average Nusselt number defined by $Nu = \dfrac{i_l D_h}{z\mathbf{F}c_o D}$ with i_l = limiting current density, D_h = hydraulic diameter, z = number of electrons transferred per mole, $\mathbf{F}$ = Faraday constant, c_o = bulk concentration of reacting species, D = diffusion coefficient. The Reynolds number Re is defined by $Re = \dfrac{u\, D_h}{\nu}$ with u = linear flow velocity, ν = kinematic viscosity. Sc represents the Schmidt number defined by $Sc = \nu/D$. L is the distance from the leading edge of the electrode. Relation [3] applies if the condition

$$\frac{0.2\, L\, Re^{7/8}}{D_h} < 10^3 \qquad (4)$$

is satisfied.[4] Such was the case in the metal dissolution experiments described below.

In the region of laminar flow ($Re < 2000$) average mass transfer rates at fully developed velocity profile are given by (5)

$$Nu = 1.85 \left(Re\, Sc \frac{D_h}{L}\right)^{1/3} \qquad [7]$$

The hydrodynamic entrance length here is $S = 0.035\, D_h\, Re$ (3).

Current distribution.—Uniform current distribution can be realized with cylindrical or spherical electrodes. Nonuniform current distribution on the rotating disk electrode has been treated by Newman (1, 8). Wagner (9) gave an analytic solution of the Laplace equation for two parallel plate electrodes for linear current-voltage relationships. Uniform current distribution is approximated if the parameter $\dfrac{1}{\rho}\dfrac{d\epsilon}{di}$ (conductivity of solution times slope of current voltage curve) is large compared to a characteristic dimension, either the distance between two plane electrodes or the length of a small electrode, positioned far from the counterelectrode. In high-rate electrolysis studies, both a small length of the electrode and a small distance from the counterelectrode (see above) are desirable. This is in conflict with the requirement of uniform current distribution.[5]

Potential measurement.—Under the assumptions of the present study, potential gradients in the solution are in the order of 1000 V/cm. Consequently a separation of electrode surface and reference electrode junction (capillary tip) of only 0.1 mm leads to an error of 10V. If a backside capillary arrangement is used, high potential gradients parallel to the electrode surface near the electrode-insulator boundary still lead to errors. Furthermore, due to fast dissolution of the anode, the wall of the capillary may soon protrude from the surface. It has to be concluded that direct steady state potential measurements under high current density conditions are not possible. Certain electrode geometries such as cylindrical or spherical arrangements allow reasonable estimates of ohmic contributions, but, in view of their large value, such a procedure does not recommend itself at very high current densities, particularly since the conductance may vary considerably near the electrode. A similar comment applies to a procedure where several reference electrodes are placed at various distances from the working electrode and the ohmic part of the measured potential values is eliminated by extrapolation to zero distance (11). When using a fast transient method, the geometrical position of the reference tip is less critical, but due to the high rate of charging and discharging processes, subtraction of ohmic contributions from the measured potential value becomes difficult.

Anode positioning.—Due to rapid dissolution, the anode has to be readjusted continuously during a measurement or the amount of dissolved material has to be kept small. Continuous electrode adjustment is used in commercial ECM machines. In the present study only small amounts of material were dissolved, thereby maintaining the plane parallel electrode configuration. The use of this method is possible because at high flow rates steady state mass transfer conditions are reached in a short time, as shown theoretically by Siver (12). Assuming a stagnant diffusion layer the thickness of which is determined by convection, the author finds that for an applied constant current density smaller than the limiting current a steady state is approached when

$$\frac{Dt}{\delta^2} \geq 2 \qquad [8]$$

where D = diffusion coefficient, δ = diffusion layer thickness, t = time. Condition [8] corresponds well to results reported by Hale (13) who numerically solved the unsteady state mass transfer equation, including convection terms for a rotating disk electrode. The average value of the thickness δ of the diffusion layer is related to the average Nusselt number Nu by

$$Nu = \frac{D_h}{\delta} \qquad [9]$$

The value of δ to be used in Eq. [8] can therefore be estimated from known mass transfer relations, such as Eq. [6] and [7].

If the applied current density is larger than the theoretical limiting current density,[6] zero concentration of the reacting species at the electrode surface is reached after a transition time τ which is always smaller than the time t satisfying condition [8]. In the extreme case where the applied current density exceeds the limiting current density by at least a factor of 10, the transition time t may be predicted by the well known Sand equation (12).

The foregoing discussion demonstrates the impossibility of designing an experimental system satisfying all requirements. A compromise has to be made in each case, depending on the type of information desired. The use of fast transient measurements may be advisable in many instances, but not the same type

[4] For fully developed mass transfer profiles, *i.e.*, if

$$\frac{0.2\, L\, Re^{7/8}}{D_h} >> 10^3 \qquad [5]$$

mass transfer rates are described by the Deissler relation

$$Nu = 0.079 \sqrt{f^*}\, Re\, Sc^{1/4} \qquad [6]$$

where f^* represents the friction coefficient which is often given by the Blasius relation (7)

$$f^* = \frac{0.079}{Re^{1/4}}$$

[5] In this paragraph current distribution due to mass transfer is not considered. Near the limiting current, current distribution is no longer described by Laplace's equation alone, but local mass transfer values become determining (5).

[6] In a dissolution process a limiting maximum concentration of reaction products might be reached at the electrode surface. Passivation might then set in after a transition time τ.

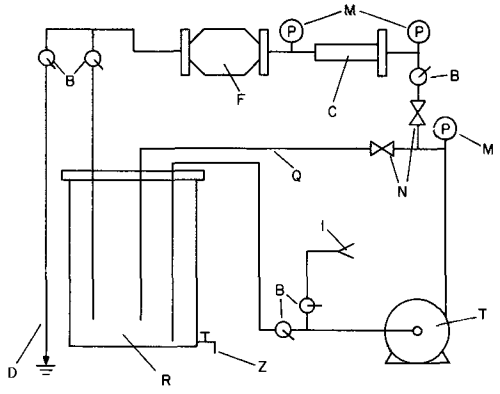

Fig. 1. Flow apparatus for high current density metal dissolution studies. C, flow channel cell; T, regenerative turbine pump; R, storage tank; F, magnetic flow meter; M, pressure gauge; Q, bypass for flow regulation through cell; N, needle valve; B, ball valve; I, deionized water for cleaning; Z, D, drain.

of information is obtained as in steady state experiments. In the present study, an experimental arrangement was designed for steady state measurements in experiments of short duration.

Experimental Flow System

An apparatus has been built which allows electrochemical measurements to be performed under defined hydrodynamic conditions at linear flow rates along the electrodes of 1-25 m/sec. Figure 1 shows a diagram of the flow system. The electrolyte is pumped continuously through the electrochemical cell (C) by means of a regenerative turbine pump (T) made of "Hastelloy C."[7] The maximum pressure at the cell inlet is approximately 150 psi, which results in a volume flow of 1.65 gpm through the cell. The flow rate through the cell (C) is measured by means of a magnetic flow meter (F)[8] and regulated with two needle valves in connection with a bypass (Q). Stainless steel pipes are used throughout the system. An electrolyte reservoir (R) made of polyethylene typically contains 10-20 gal of solution. The electrochemical cell is made of epoxy resin. It is shown in Fig. 2 and 3. The electrolyte flows in a rectangular channel (d) of 0.5 x 8 mm cross section and 120 mm length. Two glass windows (e) serve as side wall and allow optical observation of the interelectrode gap. They are held in place by two stainless steel plates (f). The cell is sealed by O-rings (c) embedded in the cell body. The flow channel contains a hydrodynamic entrance length of 77 hydraulic diameters, which serves to establish a fully developed velocity profile at the electrodes (2). Capillaries (b) are drilled into the cell wall near the two electrodes. They provide for potential measurements against a reference electrode. Calomel reference electrodes[9] used in the present study were placed in a small glass container and connected to the capillaries by means of a short Tygon tubing. The electrochemical cell is connected to the stainless steel piping system by means of an O-ring sealed flange at the entrance and a short piece of tubing at the exit. The electrodes are of rectangular shape, 0.53 by 3.17 mm (area = 1.67 mm^2). They are cast into a cylindrical epoxy insert (a). The arrangement allows suppression of edge effects which might arise if there is a finite gap between metal and epoxy. The epoxy insert contains a flat shoulder, which allows the electrode surface to be easily positioned flush with the channel wall. The critical distance between shoulder and surface plane is obtained by mechanical grinding and polishing of the epoxy insert in a stainless steel holder of the desired dimensions. The electrode inserts are attached to the cell by means of three set screws, and sealed by

[7] Model 5SC2129 HC, Roy E. Roth Company, Rock Island, Illinois.
[8] Model 346 921516 with signal converter Model 460-1, Brooks Instrument Division, Hatfield, Pennsylvania.
[9] Fiber Junction Reference Electrodes, Beckman, Inc., Fullerton, California 92634.

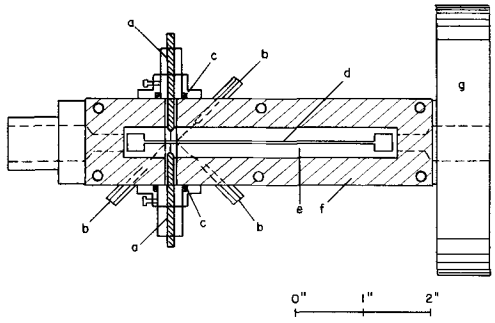

Fig. 2. Experimental cell for metal dissolution studies at high current densities. a, copper electrodes cast into epoxy resin; b, backside capillary for potential measurements; c, O-ring seal; d, flow channel; e, glass side wall; f, stainless steel plate; b, flange for connection to stainless steel piping system; h, bolts; k, Teflon insert.

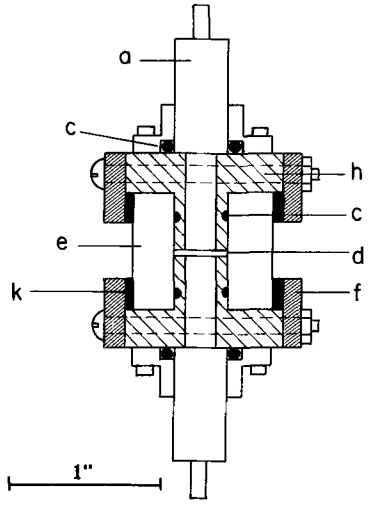

Fig. 3. Cross section of experimental cell. Legend same as Fig. 2.

means of an O-ring (c). The described arrangement allows easy and reproducible exchange of electrodes between experiments. During the metal dissolution experiments described here, the short dimension of the electrodes was oriented parallel to the flow direction. This way, temperature differences along the electrodes and the influence of cathodically generated gas bubbles on the anode were kept to a minimum.

Mass transfer conditions corresponding to the described arrangement were estimated from the relations given in the previous paragraph. Estimated values of the average diffusion layer thickness (mass transfer entry region) ranged from 4 x 10^{-4} cm at a flow rate of 100 cm/sec to 8 x 10^{-5} cm at a flow rate of 2500 cm/sec.[10]

The electrical current was drawn from a constant current power supply[11] having a maximum output of 3A. At the start of an experiment the constant current was switched from a dummy circuit having negligible impedance to the cell circuit by means of a mercury wetted contact relay switch.[12] The relay was actuated by means of a pulse generator. It was switched back automatically after a presct time period by means of a flip flop circuit. The relay could be actuated manually if experimental times longer than 2 sec were desired. Experiments usually lasted between 160 msec and a few seconds, depending on current density. A charge of 25 coulomb/cm^2 was passed which corresponds to an average dissolution of copper in the order of 10μ. It was assumed that dissolution of such a small amount would not change the hydrodynamic conditions signi-

[10] It was assumed here that $D = 10^{-5}$ cm^2/sec, $\nu = 10^{-2}$ cm^2/sec.
[11] Type C 618 Electronics Measurements Company, Inc., Eatontown, New Jersey.
[12] Type HG 1003, C. P. Clare and Company, Chicago, Illinois.

ficantly. The experimental times were long enough, on the other hand, that a steady state could be reached during each run.

Anode and cathode potentials were measured against saturated calomel electrodes. The measured values which included large ohmic contributions were recorded simultaneously with over-all cell voltage and current by means of a light beam oscillograph.[13] The oscillograph had a frequency response of 1000 Hz. The input impedance of the preamplifiers was 100 k-ohms. This value is low for precise potential measurements against reference electrodes. It was sufficient, however, for the present study where gross effects were measured only. Each experimental run was started with a freshly prepared anode. Anode preparation consisted of grinding the surface on 0000 emery paper and then polishing it mechanically on 1μ diamond powder, using conventional metallographic equipment. Residual scratches in the copper surface after the polishing operation were less than 0.3μ deep as determined from interference micrographs and from electromicrographs of carbon replicas. The electrodes were cleaned with acetone and detergent. They were pre-electrolyzed cathodically at 100 mA/cm^2 for approximately 3 min in a solution of 1N NaOH. After an experimental run, the anode was removed from the cell immediately. It was rinsed with distilled water and dried with acetone. The surface texture was then examined microsopically.

Results

Current voltage relationships.—Typical voltage transients observed in constant current dissolution experiments are shown in Fig. 4 and 5. Under conditions corresponding to the experiment given in Fig. 4, constant values of all measured voltages were reached within the time resolution limit of the oscillograph (2-5 msec, depending on amplitude). The transient illustrated by Fig. 5 showed a step at the voltage value comparable to the steady state value of the experiment of Fig. 4, which was performed at the same current density of 50 A/cm^2 but at a higher flow rate. A second voltage rise occurred after a few milliseconds. After reaching a peak value both anode potential and cell voltage decayed slowly to a constant value lying in between the initial step value and the peak value. Irregular fluctuations were observed in this region. Experiments performed at different current densities and flow rates showed the decay time of the overshoot of the peak value to decrease with increasing flow rate and with increasing current density. Measured decay time in KNO_3 solutions varied from approximately 180 msec at a current density of 50 A/cm^2 and a flow rate of 100 cm/sec, to approximately 13 msec at 150 A/cm^2 and 2500 cm/sec. No systematic study of the phenomenon has been undertaken, however. After switching off the current, the measured voltage values decayed to zero within the time resolution of the oscillograph.

In all KNO_3 solutions studied, anode potential and cell voltage transients of the types shown in Fig. 4 and 5 were observed. Transients observed in sulfate solutions also showed the general behavior of Fig. 3 and 4, but the second voltage rise was about twice as high. In addition, they exhibited slow periodic fluctuations of many volts under certain conditions of current density and flow rate. Periodic fluctuations associated with passivation phenomena have been reported in the literature for experiments performed in stagnant solutions (10). No attempt has been made here to investigate the observed phenomena further.

The cathode potential trace in Fig. 5 shows a slight increase during the first few milliseconds, but a steady state is reached soon. Fast oscillations were observed at low flow rates and high currents. The relation of these oscillations to characteristics of the cathodic gas evolution is currently being studied by stop motion photography.

[13] Series 2300, Brush Instrument Division, Cleveland, Ohio.

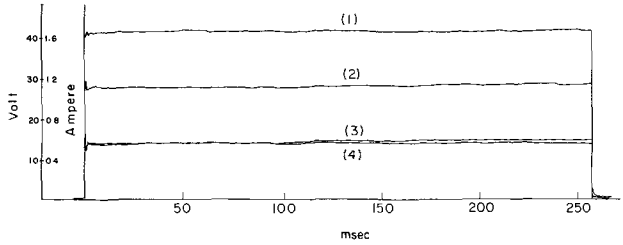

Fig. 4. Oscillograph trace typical for active dissolution region. 1, current; 2, cell voltage; 3, anode potential; 4, cathode potential.

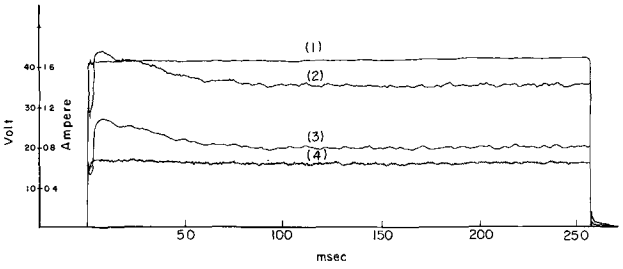

Fig. 5. Oscillograph trace typical for transpassive dissolution region. 1, current; 2, cell voltage; 3, anode potential; 4, cathode potential.

Measured values of anode and cathode potential under different flow conditions during copper dissolution in 2M KNO_3 are plotted *vs.* current density in Fig. 6. The given values represent steady state values in the case of transients of the type shown in Fig. 4, or peak values in the case of transients of the type of Fig. 5. Because the measurements contain large ohmic contributions, the absolute potential values of Fig. 6 have no significance. Figure 6 illustrates, however, the fact that the occurrence of the steep rise in the anode potential depends strongly on both current density and electrolyte flow rate. Variations in the cathode potential are less pronounced. Most of the observed deviation from linearity is probably due to partial coverage of the cathode with gas bubbles and to changes in over-all current distribution coincident with the drastic rise of the anode potential. It has been mentioned above that anode potential and cell voltage transients behave analogously. In Fig. 7 cell voltage measurements in different solutions are compared. All three solutions studied, namely 2M KNO_3, 0.4M KNO_3, and 0.2M K_2SO_4, exhibited a similar current-voltage behavior. The voltage jump was larger in the sulfate solution and for given flow conditions it occurred at lower current densities.

Surface textures.—Surface textures resulting from anodic dissolution were strongly dependent on the relative value of the applied current density, with respect to the current density corresponding to the

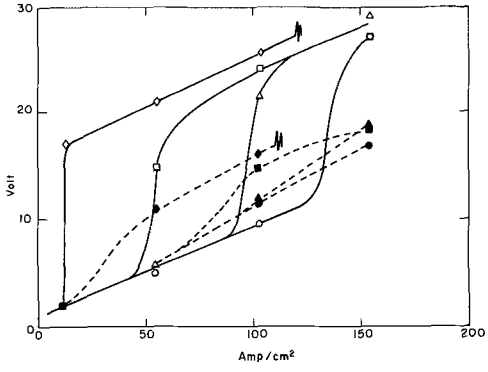

Fig. 6. Measured potential values during copper dissolution in 2N KNO_3 at various flow rates. ———, anode potential; - - - - -, cathode potential; electrolyte flow rates: ◇ ◆, 100 cm/sec; □ ■, 400 cm/sec; △ ▲, 1000 cm/sec; ○ ●, 2500 cm/sec.

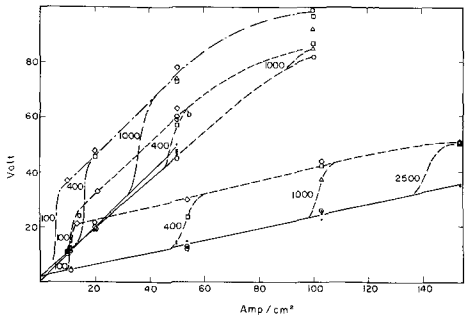

Fig. 7. Current cell voltage relationships during copper dissolution in nitrate and sulfate solution. ————, least square fit of values for active dissolution and initial step values for transpassive dissolution for all flow rates; — — —, 2M KNO_3 passive; - - - -, 0.4M KNO_3 passive; —— · ——, 0.2M K_2SO_4 passive; passivation: electrolyte flow rate: ◇, 100/sec; □, 400 cm/sec, △, 1000 cm/sec; ○, 2500 cm/sec.

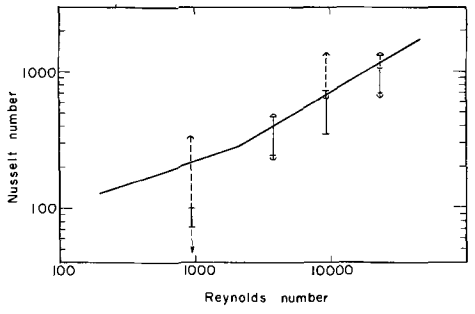

Fig. 8. Semiquantitative tests of theory predicting onset of passivation by salt precipitation. Curve, theoretical prediction of limiting mass transfer rate by Eq. [3] and [7]. Vertical ranges onset of passivity as determined from experiments illustrated in Fig. 7. Solid lines, KNO_3 solution; broken lines, K_2SO_4 solution.

voltage jump discussed above. Etching was observed in connection with voltage transients of the type of Fig. 4, pitting and brightening in connection with transients of the type of Fig. 5. Photomicrographs of representative samples obtained in 2M KNO_3 solution at a current density of 50 A/cm² at flow rates of 2500 and 400 cm/sec are given in Fig. 9 and 10, respectively. At the high flow rate, the local dissolution rate seemed to depend on crystallographic parameters and the grain structure of the anode was clearly visible after dissolution.[14] The surface appeared dull, and steps and etch pits could be observed within each grain. Reduction of the electrolyte flow rate to 1000 cm/sec resulted in a similar surface structure with less microroughness. Figure 10 shows a surface obtained at 400 cm/sec (voltage transient of the type shown in Fig. 5). This surface appeared bright and contained round pits which were located preferentially, although not exclusively, along grain boundaries. Further decrease of flow rate to 100 cm/sec resulted in a strongly pitted surface of considerable microroughness between pits. Surfaces obtained under identical conditions in 0.4M KNO_3 solutions showed the same characteristics as those discussed. The appearance of the surfaces after dissolution in potassium sulfate solutions was less clear cut, although the same general pattern, *i.e.*, etching and pitting was observed. It may be added that in all cases the transition from the dull to the bright surface finish could be accomplished by changing current density or flow rate. The study of surface textures under different experimental conditions suggested that the best surface appearance was obtained in the immediate vicinity of the voltage jump.

Discussion of Results

Current cell voltage relationships.—The behavior of measured anode potentials illustrated by Fig. 4 and

[14] The large grains visible on Fig. 9 appear highly distorted. This is due to the fact that the electrodes (99999 copper) were made from extruded wire. Chemical etching confirmed the distorted structure.

Fig. 9. Etched surface texture after dissolution of 99999 copper in the active mode (2M KNO_3, 50 A/cm², 2500 cm/sec).

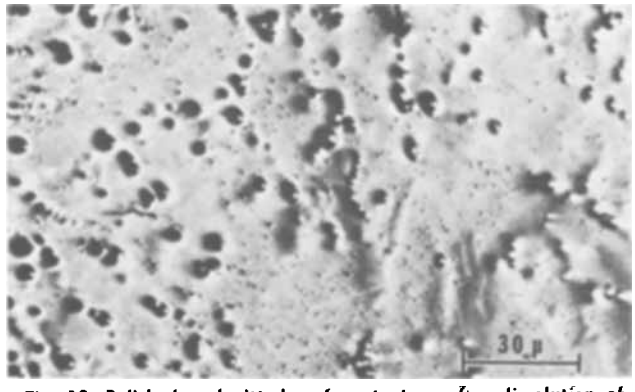

Fig. 10. Polished and pitted surface texture after dissolution of 99999 copper in the transpassive mode (2M KNO_3, 50 A/cm², 400 cm/sec).

5 suggests that passivation phenomena occurred under certain conditions. Visual evidence obtained both in experiments performed in stagnant solution and under forced convection conditions indicated that passivation coincided with the formation on the anode of a thick layer consisting of loosely attached powdery material. During dissolution in nitrate solution under forced convection, the anodic layer seemed to disappear in a few milliseconds after current was shut off. This was evidenced by studying potential transients by means of an oscilloscope, while two consecutive current pulses at various time intervals were applied to the cell. The anodes, after being taken out of the solution at the end of dissolution experiment in nitrate solution, appeared bright and no solids were adhering to the metal.[15] Electrodes examined after dissolution in sulfate solutions often were partly covered by anode films. No correlation between the pattern of film coverage and flow direction was observed. The composition of anodic films and the apparent valence of the dissolution process are being studied by Kinoshita (14). Distinct changes which coincide with the transition from active to transpassive dissolution have been observed.

It was mentioned above that exact values of the electrode potentials could not be measured with the present arrangement. There is evidence, however, born out by the results shown in Fig. 7, that the prevailing values of anode and cathode potentials were relatively low, compared to the voltage difference due to the ohmic resistance of the solution, as long as the experiment was performed at a current density smaller than the passivation current density, *i.e.*, for experiments performed in the active dissolution region.

Cell voltages corresponding to steady state values during active dissolution yielded straight lines when plotted against current density, up to current density

[15] Some solid material adhering to the epoxy downstream from the anode was found occasionally.

values of 50 to 150 A/cm^2 depending on the composition of the solution. Equivalent specific resistances ρ_i*[16] were calculated by dividing the least square fit slopes of the straight lines by the electrode separation. The ratios of the values obtained for different solutions were then compared to the ratios of the specific resistances of these solutions. A close correspondence between experimental and theoretical ratios has been observed: Experimental values obtained were ρ_1* = 4.37 ohm-cm, (2M KNO_3), ρ_2* = 17.7 ohm-cm (0.4M KNO_3), ρ_3* = 19.5 ohm-cm (0.2M K_2SO_4). Literature values for the specific resistance at 25°C are ρ_1 = 6.31 ohm-cm (2M KNO_3) (27), ρ_2 = 24.14 ohm-cm (0.4M KNO_3) (28), ρ_3 = 24.70 ohm-cm (0.2M K_2SO_4) (28). Corresponding ratios then become ρ_2*/ρ_1* = 4.05, ρ_2/ρ_1 = 3.83, ρ_3*/ρ_1* = 4.46, ρ_3/ρ_1 = 3.91.

Linear current-voltage relationships dominated entirely by the ohmic resistance of the solution have been reported in the literature for conditions corresponding to ECM (21, 22). Cole and Hopenfield (26) explained observed deviations from linear current voltage behavior by a model which considered the influence of cathodically generated gas bubbles on the ohmic resistance of the solution. Attempts aimed at measuring actual anode potentials during anodic dissolution under ECM conditions have been reported (21, 22), but no reliable results were obtained. A study aimed at separating ohmic contributions from measured potentials by using current interruptor techniques is in progress at this laboratory.[17]

The current-voltage curves given above demonstrate that passivation may lead to an increase in the anode potential of many volts. In this case, the ohmic resistance of the bulk solution can no longer be considered the only important resistance of the system. Local current distribution may, therefore, change significantly at the transition point between active and transpassive dissolution.

Passivation has been mentioned (25) as playing a role in improving dimensional accuracy during ECM, but the statement was based mainly on observations made at low current densities. The present investigations confirms that passivation phenomena play a decisive role in determining local metal dissolution rates under ECM conditions.

The results given in Fig. 6 and 7 demonstrate that the onset of passivation is determined by flow rate and current density. The results strongly indicate that, in the systems investigated here, the onset of passivation is controlled by mass transfer. The fact that in both nitrate solutions studied (Fig. 7) passivation occurred in the same range of current density suggests that the transport of anions was not a controlling factor. An anion limited dissolution mechanism is expected if a net consumption of anions at the anode occurs, *e.g.*, by complex formation of dissolved metal ions. Such a mechanism has been reported for the dissolution of gold in chloride solutions (33) and a similar but more complex case is represented by the dissolution of copper in chloride solution, where under some conditions formation of stable cuprous chloride complexes is possible (30, 33). If noncomplexed metal ions are produced during the dissolution process, accumulation of anions in the vicinity of the anode is necessary in order to maintain electroneutrality.

At a high dissolution rate, the product of the metal ion concentration and anion concentration may exceed the solubility product. This may lead to precipitation of salt crystals. Initiation of passivity by salt precipitation has been described by Muller (31). A critical review of more recent literature dealing with the phenomena has been given by Hoar (32). The fact that, in our experiments, the onset of passivity was independent of concentration in nitrate solutions, but occurred at lower current densities in the sulfate solution, is qualitatively consistent with the above mechanism, since copper sulfate has a lower solubility than copper nitrate.

A semiquantitative test of the theory is illustrated by the results of Fig. 8, in which Nusselt numbers derived from the experimentally observed passivation current densities were compared with those predicted from the known mass transfer relations [3] and [9]. A band of possible values of the passivation current density i_p was estimated from Fig. 7. Nusselt numbers corresponding to these values were calculated by assuming a concentration driving force corresponding to the saturation concentration c_s of copper nitrate and copper sulfate, respectively. The experimental Nusselt number is then given by

$$Nu_p = \frac{i_p D_h}{2\mathbf{F} c_s D} \qquad [10]$$

The value of D was assumed to be 10^{-5} cm^2/sec. It has to be regarded as an order of magnitude estimate of an effective diffusion coefficient of copper ion including the influence of migration and of possible changes in physical properties in the vicinity of the anode. Values for the saturation concentration c_s were estimated from solubility data given in (15) and (16) to be 7 mole/liter for copper nitrate and 1.5 mole/liter for copper sulfate (25°C). The influence of the presence of potassium ions on the value of c_s was neglected, since due to migration, their concentration at the interface is much smaller than that of copper ions. A reasonable order of magnitude agreement between experimental and predicted passivation current densities was obtained (Fig. 8). The observed agreement indicates that in the systems studied here, the application of a model which considers maximum possible mass transfer rates of dissolution products leads to valid predictions of the conditions, which correspond to the onset of passivation.

Surface textures.—The results reported in the previous section indicated that the surface texture resulting from anodic dissolution depended strongly on whether dissolution occurred in the active or transpassive mode. As to which dissolution mode prevailed at a given current density depended on mass transfer conditions. The findings of the present investigation are thus comparable to results reported in recent studies about the conditions leading to electropolishing (17-20). While the detailed mechanism leading to polishing is disputed, it is well established now that passivation phenomena play a dominant role. The current density leading to passivation (sometimes referred to as limiting current density in the literature) is determined by mass transfer. Obtaining polished surfaces during ECM has been reported by various authors (21-23). The fact that, under appropriate operating conditions, a very low surface roughness can be obtained allows the application of ECM to technical surface finishing operations (24). No current potential curves indicating passivation have been reported so far for conditions corresponding to ECM. In view of the results obtained in the present study and of some findings reported in the literature (25,29), it seems very probable that passivation phenomena play an important role in practical ECM, not only with respect to dimensional accuracy (see above) but also with respect to obtainable surface finish. The present study confirms and extends a general observation (20) valid for metal dissolution at conventional current densities, that active dissolution leads to etched surfaces while transpassive dissolution often results in anodic brightening, pitting, or polishing.

Many questions remain unanswered by the present study such as, *e.g.*, why pitting is observed at all under the present experimental conditions which would seem highly unfavorable for dissolution within pits, not only from a point of view of local current distribution, but also from a point of view of mass transfer. The role of the metallurgical factors in determining

[16] The effective specific resistance ρ_i* is always smaller than ρ_i because the actual cross section of the current flux in the solution is larger than the electrode area.

[17] Such measurements are complicated by the extremely fast discharge of the double layer under the conditions employed.

how etching and pitting proceed or the influence of the chemical composition of the electrolyte on the nature of anodic films formed are other areas which need more research. A study of the dissolution of copper single crystals under conditions comparable to those of the present study has been initiated recently at this laboratory.

Conclusions

The present work demonstrates the feasibility of studying an electrochemical process proceeding at a current density of many amperes per square centimeter under controlled hydrodynamic conditions. A rectangular flow channel cell operated under fully developed turbulent flow conditions has been found to be well suited for this investigation. Steady state mass transfer rates corresponding to an equivalent diffusion layer thickness of the order of 10^{-4} cm have been realized.

A study of copper dissolution in KNO_3 and K_2SO_4 solutions has shown two distinct dissolution modes. Active dissolution resulting in etched surfaces occurred at relatively low overpotentials. Observed dissolution rates were well within the limits estimated from known mass transfer relations for the transport of cupric ions away from the surface. Transpassive dissolution proceeded at higher anode potentials, leading to pitting and brightening. Current densities applied during transpassive dissolution were up to ten times higher than the minimum current density leading to passivation; the latter is believed to correspond to the highest rate at which cupric ions may be removed from the anode by convective diffusion. It appears, therefore, that a large part of the oxidized copper was transported away from the anode in the form of solid dissolution products formed at or near the anode. It is probable that a similar transport mechanism is involved in many practical ECM operations.

Acknowledgment

This work was conducted under the auspices of the U.S. Atomic Energy Commission.

Manuscript submitted Feb. 24, 1969; revised manuscript received June 2, 1969.

Any discussion of this paper will appear in a Discussion Section to be published in the June 1970 JOURNAL.

REFERENCES

1. J. Newman, *This Journal*, **113**, 501 (1966).
2. F. S. Bromfield, The Hydrodynamic Entry Length in Rectangular Channels, p. 30, Ph.D. Thesis, University of Washington (1964).
3. R. Bird, W. E. Stewart, and E. N. Lightfoot, "Transport Phenomena," p. 47, John Wiley & Sons, Inc., New York (1960).
4. N. Ibl, *Chem. Ingr.-Tech.*, **35**, 353 (1963).
5. J. Newman, *Ind. Eng. Chem.*, **60**, (4), 12 (1968).
6. P. Van Shaw, L. P. Reiss, and T. J. Hanratty, *Am. Inst. Chem. Engrs. J.*, **9**, 362 (1963).
7. R. Bird, W. E. Stewart, and E. N. Lightfoot, *op. cit.*, p. 187.
8. J. Newman, *This Journal*, **113**, 1235 (1966).
9. C. Wagner, *ibid.*, **98**, 116 (1951).
10. K. Vetter, "Electrochemical Kinetics," Springer Verlag, Berlin (1961).
11. J. O'M. Bockris and A. M. Azzam, *Trans. Faraday Soc.*, **48**, 145 (1952).
12. Yu. G. Siver, *Russ. J. Phys. Chem. (Engl. Transl.)*, **34**, 273 (1960).
13. J. M. Hale, *J. Electroanal. Chem.*, **6**, 187 (1963).
14. K. Kinoshita, Ph.D. Thesis, University of California, To be issued in 1969.
15. Gmelin, "Handbuch der Anorg. Chemie," 8, Aufl. System Nr. 60, Teil B, p. 530 (1958).
16. Landolt-Bornstein, "Zahlenwerte und Funtionen," 6 Aufl. 2 Teil, 3-166 (1962).
17. J. Epelboin and M. Keddam, *Compt. rend.*, **258**, 137 (1964).
18. M. Daguenet and M. Froment, *ibid.*, **260**, (21), 5534 (1965).
19. J. Epelboin, "Proc. International Conference of Protection Against Corrosion by Metal Finishing," pp. 161-169, N. Ibl *et al.*, Editors, Foster Verlag AG Zurich (1967).
20. T. P. Hoar, *Corr. Sci.*, **7**, 341 (1967).
21. J. Bayer, M. A. Cummings, and H. U. Jollis, Tech. Doc. Rept. No. ML TDR 64 313, General Electric Co. (1964).
22. R. Cole and J. Hopenfeld, *Trans. ASME (B) J. Eng. Ind.*, **85**, 395 (1963).
23. M. A. LaBoda and M. L. McMillan, *Electrochem. Technol.*, **5**, 340 (1967).
24. J. A. Gurklis, Battelle Memorial Institute, Defense Information Center, DMIC Rept., January 1965.
25. M. L. McMillan and M. A. LaBoda, *Electrochem. Technol.*, **5**, 346 (1967).
26. J. Hopenfeld and R. Cole, *Trans. ASME (B) J. Eng. Ind.*, **88**, 455 (1966).
27. Landolt-Bornstein, "Zahlenwerte und Funktionen," 6. Aufl. 7. Teil 2. Band (1960).
28. "International Critical Tables," **6**, 238 (1929).
29. D. Ponteves, *Ann. of CIRP*, **XV**, 274 (1967).
30. T. Hurlen, *Acta Chem. Scand.*, **15**, 1231 (1961).
31. W. J. Muller, "Die Bedeckungstheorie der Passivitat der Metalle und ihre experimentelle Begrrundung," Verlag Chemie, Berlin (1933).
32. T. P. Hoar, "Modern Aspects of Electrochemistry," p. 286 ff., J. O'M. Bockris, Editor, Butterworths, London (1959).
33. G. Just and R. Landsberg, *Electrochim. Acta*, **9**, 817 (1964).

Diffusion of Oxygen through a Platinum Diaphragm

James P. Hoare*

Electrochemistry Department, Research Laboratories, General Motors Corporation, Warren, Michigan

ABSTRACT

A thin Pt foil was mounted in a cell between two compartments filled with 2*N* sulfuric acid solution. On the polarization side, the foil was anodized, and oxygen was detected on the diffusion side by observing the increase in potential *vs.* an α-Pd reference electrode in the N_2-stirred acid solution. When the foil was made a cathode, the potential on the diffusion side shifted toward less noble values. The diffusion coefficient was determined with Fick's First Law from the cathodized foil data to be 1.8×10^{-11} cm^2 sec^{-1} at 24°C and by the time lag method from the anodized foil data to be 4.4×10^{-11} cm^2 sec^{-1} at 24°C.

In a recent report (1), it was demonstrated that oxygen can penetrate Pt foil bielectrodes by migrating from the anodized side through the metal to the cathodized side. The presence of oxygen was detected on the cathodic side of the bielectrode by its effect on the hydrogen overvoltage. It was suggested (2) that additional evidence in favor of the conclusions drawn from the bielectrode studies may be obtained by anodizing the Pt foil connected as a diaphragm (1) and

* Electrochemical Society Active Member.

observing the potential on the unpolarized or diffusion side of the Pt diaphragm. The results of such an experiment are described in the following paragraphs.

Preparation of the electrodes, solutions, and Teflon cell is the same as described for the bielectrode studies (1) except that an α-Pd reference electrode (3) was placed in the cell compartment on the diffusion side of the Pt diaphragm. After preelectrolyzing all the electrodes and both sides of the foil against removable Pt wire cathodes for 24 hr, purified hydrogen was bubbled through the $2N$ H_2SO_4 solution contained in both compartments of the cell until the potential between any two Pt electrodes was zero volts and until the Pd bead electrode was converted to an α-Pd reference electrode. Then H_2-stirring was replaced with N_2-stirring at a flow rate of about 250 cc/min. All potentials are recorded against the normal hydrogen electrode (NHE).

A Pt foil (0.00127 cm thick with an apparent exposed area of 0.7 cm^2) was anodized (potential $\sim$ 2600 mV) at 24.6 mA/cm^2 against a large Pt gauze counter electrode in the polarization compartment of the cell, and the potential of the diffusion side of the foil was recorded against the α-Pd reference electrode in the N_2-stirred acid solution as a function of the time of polarization. Potentials were recorded with a Model 1230A General Radio Electrometer with an input impedance of 10^{14} ohms. The results are presented in Fig. 1 by the circles.

After an induction period of about 1.75 hr where the potential remained in the vicinity of the hydrogen potential, the potential rose relatively rapidly to a fairly steady value (increase in potential of 2 to 3 mV in 30 min) between 1050 and 1060 mV. Duplicate runs yielded similar results.

A possible explanation is as follows: The driving force of anodic polarization enables oxygen to penetrate the Pt lattice beyond the dermasorbed regions (4). This dissolved oxygen can migrate through the Pt lattice to the diffusion side of the Pt where it can react with any dermasorbed or surface adsorbed hydrogen to form water. Once the hydrogen is removed, oxygen can saturate the dermasorbed layers and migrate to the surface of the diffusion side of the Pt foil diaphragm. At this point, the potential rises rapidly to more noble potentials. Finally, a point is reached where a steady-state concentration of oxygen is maintained on the Pt surface as indicated by the steady value of 1060 mV.

It is interesting to note that in one run in which a tiny leak developed between the polarization and diffusion compartments of the cell, any polarization applied to the polarization side of the diaphragm appeared immediately on the diffusion side.

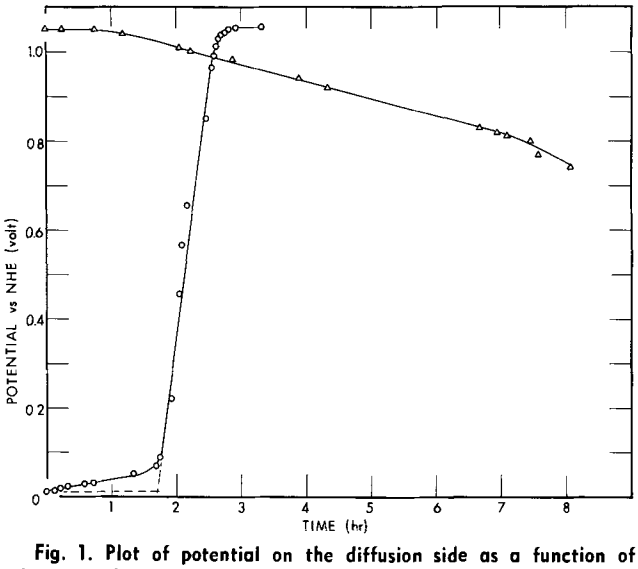

Fig. 1. Plot of potential on the diffusion side as a function of the time the Pt foil was anodized (circles) and cathodized (triangles) on the polarization side. The dotted lines indicate how the time lag was determined.

When the potential of the diffusion side of the Pt foil diaphragm had reached the steady value of 1060 mV, the polarization side of the foil was cathodized. Nitrogen-stirring was maintained. A plot of the potential of the diffusion side as a function of the length of time of cathodization at — 24.6 mA/cm^2 on the polarization side is shown in Fig. 1 by the triangles. The potential does fall with time but at an extremely slow rate.

This result is in agreement with the findings that hydrogen does not penetrate Pt foils with clean surfaces (5, 6). When H_2 is evolved on the polarization side of the Pt foil, atomic hydrogen can penetrate the Pt lattice no further than the dermasorbed region (first 2 or 3 atom layers), but oxygen can diffuse from the interior of the Pt to react with hydrogen on the polarization side of the foil setting up an oxygen concentration gradient across the Pt diaphragm. As oxygen diffuses from the diffusion side to the polarization side of the diaphragm to react with hydrogen, the surface concentration of oxygen on the diffusion side of the Pt foil decreases with time, producing a shift of the potential to less noble values. It seems, then, that the rate of diffusion of oxygen through the Pt diaphragm under the driving force of the oxygen concentration gradient set up under open-circuit conditions is much slower than the migration of dissolved oxygen through the foil under the driving force of the concentration gradient set up by anodization.

If one can assume for the case where the foil is cathodic that a steady-state removal of oxygen takes place during the second to the sixth hour of a run (triangles in Fig. 1), and that Fick's First Law applies, an estimate of the diffusion coefficient of oxygen through Pt can be made. It is likely that Fick's law holds because a thickness effect was observed in the bielectrode studies (1). It must also be assumed (*a*) that the dermasorbed layers on the polarization side of the foil are saturated with dissolved hydrogen, (*b*) that the dermasorbed layers on the diffusion side are saturated with dissolved oxygen, and (c) that an oxygen atom reaching the polarization side will be removed by the reaction with dermasorbed hydrogen atoms to form water.

The layers saturated with oxygen are kept saturated as long as surface adsorbed oxygen is present to diffuse into the dermasorbed layers. From cathodic stripping curves, it has been shown (7) that the potential of an oxygen electrode depends directly on the amount of oxygen adsorbed on the Pt surface. The rate of change of potential with surface coverage, θ, is 2.28 mV μC^{-1} cm^{-2}. In Fig. 1 (triangles), the decrease in potential is directly related to the decrease in coverage or the disappearance of oxygen.

Fick's First Law may be written as

$$P = D\, dc/dx$$

where D is the diffusion constant (cm^2 sec^{-1}), dc/dx the concentration gradient (atoms cm^{-1}), and P the permeation rate (atoms cm sec^{-1}). If the dissolved oxygen atom resides in the octahedral holes of the face centered cubic Pt lattice, there is associated ideally with each surface Pt site a dermasorbed oxygen (in the surface layer the four nearest neighbor Pt atoms are shared with four other unit cells). Since the quantity of charge associated with a monolayer of adsorbed oxygen atoms is 420 μC cm^{-2} (7, 8) and with an oxygen atom, 3.2 x 10^{-19} C, the saturated dermasorbed layer contains 1.31 x 10^{15} oxygen atoms cm^{-2}. The thickness of the foil is 1.27 x 10^{-3} cm and the concentration of oxygen atoms on the polarization side is zero. Then, dc/dx is 1.03 x 10^{18} atoms cm^{-1}.

The slope of the curve (triangles) in Fig. 1 is 38 mV hr^{-1}, and using 2.28 mV μC^{-1} cm^{-2} as the rate of change of potential with coverage along with the foil

thickness, 1.27 x 10^{-3} cm, a value of 1.85 x 10^{7} atoms cm sec^{-1} is obtained for P. From these calculated values of P and dc/dx, a value of 1.8 x 10^{-11} cm^2 sec^{-1} is obtained for D at 24°C. This value is about three orders of magnitude smaller than the D for hydrogen through iron (1.16 x 10^{-8} at 85°C) and about two orders smaller for hydrogen through nickel (2.59 x 10^{-9} at 20°C) (9). Such values for D for oxygen through Pt seem reasonable in consideration of the larger size of the oxygen atom.

The diffusion constant can also be determined from the time lag method (ref. 9, p. 217) by the equation

$$D = d^2/6t_{lag}$$

where d is the thickness of the diaphragm and t_{lag} is the time required to set up the steady state of flow after starting the run. In the case where the foil was anodized (circles in Fig. 1), an induction period was observed. From this curve, t_{lag} is 101 min, and D has a value of 4.4 x 10^{-11} cm^2 sec^{-1}, in good agreement with 1.8 x 10^{-11} cm^2 sec^{-1} calculated from the triangles in Fig. 1.

Acknowledgment

The author is indebted to Dr. R. Thacker of the Research Laboratories, General Motors Corporation, for his invaluable advice and suggestions.

Manuscript submitted April 11, 1969; revised manuscript received May 14, 1969.

Any discussion of this paper will appear in a Discussion Section to be published in the June 1970 JOURNAL.

REFERENCES

1. J. P. Hoare, *This Journal*, **116**, 612 (1969).
2. B. E. Conway, Private communication.
3. D. J. G. Ives and G. J. Janz, "Reference Electrodes," p. 112, Academic Press, New York (1961); J. P. Hoare, *G. M. Eng. J.*, **9**, No. 1, 14 (1962).
4. S. Schuldiner and T. B. Warner, *This Journal*, **112**, 212, 853 (1965).
5. J. P. Hoare and S. Schuldiner, *ibid.*, **103**, 237 (1956).
6. S. Schuldiner and J. P. Hoare, *Can. J. Chem.*, **37**, 228 (1959).
7. R. Thacker and J. P. Hoare, *This Journal*, Submitted for publication.
8. S. Trasatti, *Electrochim. Metall.*, **2**, 12 (1967).
9. R. M. Barrer, "Diffusion in and Through Solids," p. 222, Cambridge University Press (1951).

Thermodynamics of LiBr in Anhydrous Dimethyl Sulfoxide

Mark Salomon

NASA, Electronics Research Center, Cambridge, Massachusetts

ABSTRACT

The activity coefficients of LiBr in anhydrous dimethyl sulfoxide have been determined at several temperatures by the emf method. The results differ considerably from the analogous LiCl-DMSO system and it is concluded that anion solvation effects are mainly responsible for this behavior.

The properties of dipolar aprotic solvents such as dimethyl sulfoxide differ so widely from those of the protic solvents that interest in them has grown both in kinetic (1-5) and thermodynamic studies (5-9). In the present paper, the thermodynamics of LiBr in dimethyl sulfoxide (DMSO) is reported. The activity coefficients were determined at several temperatures by emf measurements on the cell

$$Li \mid LiBr - DMSO \mid TlBr, Tl\ (Hg) \qquad [1]$$

The observed emf's of cell [1] can be converted to the emf's of cell [2] for solid thallium by the relation

$$\mathcal{E}_2 = \mathcal{E}_1 - \mathcal{E}_3$$

where $\mathcal{E}_2$ and $\mathcal{E}_3$ are, respectively, the emf's of the following cells

$$Li \mid LiBr - DMSO \mid TlBr, Tl \qquad [2]$$

$$Tl \mid Tl^+ \mid Tl\ (Hg) \qquad [3]$$

The Nernst relation for cell [2] is

$$\mathcal{E}_2 = \mathcal{E}^\circ_2 - \frac{2RT}{\mathbf{F}}\{\ln m_\pm + \ln \gamma_\pm\} \qquad [4]$$

where R is the gas constant, T the absolute temperature, $\mathbf{F}$ the Faraday constant, and $m_\pm$ and $\gamma_\pm$ are, respectively, the mean molality and activity coefficient. To evaluate the standard potential $\mathcal{E}^\circ_2$ the Guggenheim approximation (10) for $\gamma_\pm$ was used; *i.e.*

$$\ln \gamma_\pm = -\frac{Am^{1/2}}{1 + m^{1/2}} + 2\beta m \qquad [5]$$

where A is the Debye-Huckel constant and β is an empirical constant. The constant β has been associated with ion-pairing effects (6, 11, 12) but can also be associated with specific hydration effects (see below) as suggested by Stokes and Robinson (13).

It is also of interest to determine the solubility product for TlBr from the relation

$$\ln Ksp\ (TlBr) = (\mathcal{E}^\circ_2 - \mathcal{E}^\circ_7)\ \mathbf{F}/RT \qquad [6]$$

where $\mathcal{E}^\circ_7$ is the standard emf of cell [7] below.

$$Li \mid Li^+ \mid Tl^+ \mid Tl \qquad [7]$$

In DMSO, $\mathcal{E}^\circ_7$ = 2.641V at 25°C (5).

Experimental

The cells, solutions, and thallium amalgams were prepared in a manner similar to that described earlier (12, 14). The solutions were prepared by weight in a dry-box from a stock LiBr-DMSO solution whose molality was determined by a potentiometric titration with standard (aqueous) 0.1*M* $AgNO_3$. The solvent (Matheson, Coleman and Bell, "Spectroquality") was dried with Linde 4A molecular sieves. Typical solvent purity as determined by gas chromatography is less than 25 ppm water and less than 25 ppm organic impurities (15).

The amalgam was prepared entirely in the dry box and one batch of 3.147% Tl (by weight) in mercury was used for all of the experiments.

The cells, which were used in earlier studies (6, 12, 14), were assembled in the dry-box and then removed and placed in a water bath regulated to ±0.02°C. Potentials were read from a Fluke model 881A differential voltmeter to ±5 μV.

Results

Emf measurements were begun almost immediately after placing the cell in solution. The initial values at 25°C became constant to within ±0.1 mV after some 3 to 5 hr. The temperature was then changed to 15°C and raised to 35° and 45°C. The experiment was usually initiated in the morning and a complete set of emf's were recorded by evening (*i.e.*, about 8-10 hr). The emf at 25°C after 8-10 hr was reproducible to within ±0.1 mV in most cases and to within ±0.3 mV in several other cases. After 48 hr at 25°C, the emf of cell [1] usually decreased by almost 1 mV. Continual decrease in emf was observed over longer times presumably due to the solubility of TlBr (see *K*sp below). After three days in the temperature bath, the Li electrodes had become discolored due to the reaction (6)

$$Li_{(s)} + TlBr\ (soln) \rightarrow Tl_{(s)} + LiBr\ (soln)$$

Similar behavior over shorter time periods were observed in the LiCl-DMSO system (6).

The physiochemical properties of DMSO used to evaluate $\mathcal{E}^\circ_2$ are listed in Table I. $\mathcal{E}_3$ values used to obtain $\mathcal{E}_2$ were taken from the work of Richards and Daniels (16). From Eq. [4] and [5] it is seen that a plot of $\mathcal{E}'$ *vs.* m should be linear with a slope proportional to β and an intercept of $\mathcal{E}^\circ_2$. Here $\mathcal{E}'$ is defined as

$$\mathcal{E}' = \mathcal{E}_2 + \frac{2RT}{F}\left\{\ln m_\pm - \frac{Am^{1/2}}{1 + m^{1/2}}\right\} \qquad [8]$$

Figure 1 shows a typical plot for 25°C. A least squares was then fitted to the data and the results are shown in Table II. In this table $\mathcal{E}^\circ_2$ values are given in terms of molarity units ($\mathcal{E}^\circ_{2,c}$) molality units ($\mathcal{E}^\circ_{2,m}$), and mole fraction units ($\mathcal{E}^\circ_{2,N}$). Also given in Table II are the standard enthalpies and entropies for cell [2] based on molal units along with the values for β (*c.f.*, Eq. [5]). The thermodynamic quantities were calculated from a least squares fit to a second order polynomial, *i.e.*

$$\Delta G^\circ_{2,c} = -60.657 + 0.02876 \cdot T - 4.9719 \cdot 10^{-6} T^2$$

$$\Delta G^\circ_{2,m} = -60.592 + 0.02970 \cdot T - 7.6290 \cdot 10^{-6} T^2$$

$$\Delta G^\circ_{2,N} = -61.286 + 0.04442 \cdot T - 1.5190 \cdot 10^{-5} T^2$$

Here ΔG°_2 is in kcal/mole and ΔH°_2 and ΔS°_2 are easily obtained by differentiating with respect to temperature.

The activity coefficients were calculated from Eq. [4] and the results are shown in Table III. A plot of $\ln\gamma_\pm$ *vs.* $m^{1/2}$ is shown in Fig. 2. In Fig. 2, the $\ln\gamma - m^{1/2}$ relation for LiBr in H_2O (13) is also shown.

Table I. Properties of DMSO*

°C	$\mathcal{E}$	d_o†	A
15	47.4	1.1050	2.7688
25	46.6	1.0960	2.6822
35	45.9	1.0867	2.6056
45	45.1	1.0770	2.5345

* The Debye-Hückel constant (A) values are based on ln (e) units and conversion to log (10) units is accomplished by dividing by 2.3026.
† The density of pure DMSO, d_o, is given in g/cc.

Table II. Free energies, enthalpies, and entropies of cell [2]*

°C	$\mathcal{E}^\circ_{2,c}$	$\mathcal{E}^\circ_{2,m}$	$\mathcal{E}^\circ_{2,N}$	β	$\Delta H^\circ_{2,m}$	$\Delta S^\circ_{2,m}$
15	2.28877	2.28381	2.15721	0.514	−59.96	−25.30
25	2.27767	2.27301	2.14201	0.485	−59.91	−25.15
35	2.26655	2.26214	2.12675	0.460	−59.87	−25.00
45	2.25526	2.25120	2.11141	0.439	−59.82	−24.84

* $\mathcal{E}^\circ$ values are in volts; ΔH° is in kcal/mole; ΔS° is in e.u.; β units are kg/mole.

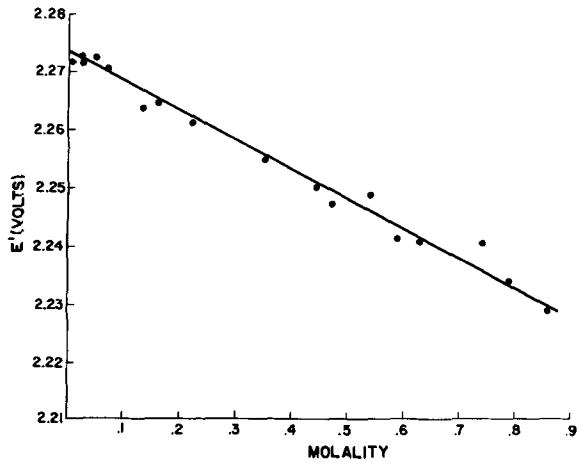

Fig. 1. Plot of E' (see Eq. [8]) vs. molality

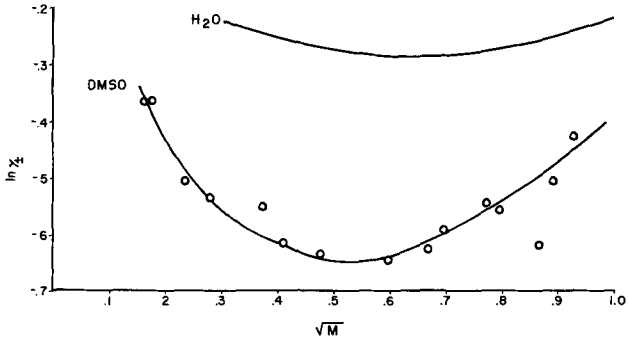

Fig. 2. Plot of $\ln\gamma_\pm$ *vs.* the square root of the molality

Finally the solubility product for TlBr at 25°C can be calculated from Eq. [6]; with $\mathcal{E}^\circ_7 = 2.641$V (5),[1] a value of $10^{-6.23}$ is obtained for *K*sp (TlBr).

Discussion

Parker (17) in a review on dipolar aprotic solvents concluded, on the basis of solubilities, conductivities, and half-wave potentials, that not only are anions poorly solvated in solvents such as DSMSO, but also that the extent of solvation by solvent molecules increases in the order

$$Cl^- < Br^- < I^-$$

Considering the emf results for LiCl in DMSO (6, 9) and LiBr in DMSO (present results), more proof of this conclusion is found. From Fig. 2, the plot of $\ln\gamma_\pm$ *vs.* $m^{1/2}$ for LiBr in DMSO shows that at about $m = 0.4$, the activity coefficient begins to increase. A similar treatment for LiCl in DMSO [using the data in ref. (6)] shows no indication of any curvature up to concentrations of 0.9M. In terms of the theory of Stokes

[1] $\mathcal{E}^\circ_7 = 2.641 \pm 0.003$V and this uncertainty is carried over to the value of *K*sp (TlBr).

Table III. Mean molal activity coefficients of LiBr in DMSO

m	15°C	$\gamma_\pm$ 25°C	35°C	45°C
0.02673	0.6815	0.6950	0.7024	0.7120
0.02965	0.6810	0.6930	0.7050	0.7155
0.05606	0.5922	0.6025	0.6121	0.6195
0.07024	0.5797	0.5872	0.5959	0.6039
0.13458	0.5698	0.5779	0.5867	0.5937
0.16782	0.5373	0.5426	0.5479	0.5542
0.22445	0.5318	0.5333	0.5344	0.5369
0.35390	0.5219	0.5269	0.5323	0.5363
0.44634	0.5315	0.5360	0.5411	0.5454
0.47745	0.5521	0.5549	0.5583	0.5608
0.54635	0.5125	0.5145	0.5173	0.5188
0.59054	0.5805	0.5814	0.5833	0.5844
0.63292	0.5694	0.5736	0.5674	0.5808
0.74850	0.5422	0.5401	0.5416	0.5421
0.79123	0.6035	0.6044	0.6071	0.6076
0.86155	0.6608	0.6560	0.6536	0.6501

Table IV. Energetics of transfer of Li salts from H_2O to DMSO at 25°C

Salt	$\Delta G°_t$	$\Delta H°_t$	$\Delta S°_t$	$\delta\Delta H°_t$	Reference
LiCl	4.865	−3.12	−26.77		6
LiBr	2.515	−2.05		3.38	1
		−5.67	−27.46		Present work
		−5.43		0.0	1
Li I		−9.07		−3.64	1

Units refer to molal scale: $\Delta H°_t$, $\Delta G°_t$ are in kcal/mole, $\Delta S°_t$ in e.u.

and Robinson (13), the curvature in plots such as Fig. 2 can be accounted for by the decreasing solvent activity. In this context then, one concludes that the chloride ion is practically unsolvated in DMSO whereas the bromide ion is solvated to a fairly large extent.

This behavior is also reflected in the energetics of solvation. Table IV lists, on the basis of molal units, the standard free energy, enthalpy, and entropy of transfer of various lithium salts from water to DMSO.

The quantity $\delta\Delta H°_t$ is a relative enthalpy of transfer defined as

$$\delta\Delta H°_t = \Delta H°_t\,(X^-) - \Delta H°_t\,(Br^-)$$

which shows that $\Delta H°_t\,(X^-)$, for halides, becomes larger (more negative) as the anion size increases. Similar behavior was found for lithium halides in propylene carbonate (18, 12, 14). The heats of solution, ΔH_{soln}, become more negative as anion size increases whereas heats of solvation, ΔH_{solv}, become less negative (1). This is analogous to aqueous solutions of lithium halides [*e.g.*, see ref. (19)]. This behavior has led Fuchs *et al.* (1) to conclude that while anions may be less solvated in the dipolar aprotic solvent, the order of increasing solvation is

$$I^- < Br^- < Cl^-$$

This conclusion is opposite to that resulting from the present work based on the activity coefficients of LiCl and LiBr and from other work discussed above (2, 3, 5, 12, 14, 17). The danger in comparing ΔH_{solv} values in this manner rather than $\delta\Delta H°_t$ or activity coefficients can be demonstrated as follows: Let us consider the Born equation

$$\Delta H_{solv}(X^-) = -\frac{e^2}{2(r+\delta)}\left\{1 - \frac{1}{\epsilon} - \frac{T}{\epsilon^2}\cdot\frac{d\epsilon}{dT}\right\} \quad [9]$$

where e is the electronic charge, ϵ is the dielectric constant, T the absolute temperature, r the Pauling anion radius, and δ is an empirical constant assumed to be independent of temperature (20). Equation [9] predicts that for transfer from the gas to solution phase, ΔH_{solv} should decrease (become less negative) as r increases which is in fact the case. The δ corrections are quite complex as it was found that in order to "predict" the correct $\Delta H°_{solv}$ for Cl^-, Br^-, I^-, from the gas phase to propylene carbonate, δ values had to be adjusted such that $\delta\,(Cl^-) = \delta\,(Br^-) = 0.67$ and $\delta\,(I^-) = 0.72$ (14). In aqueous solutions δ takes on a constant value of 0.10 for all anions (20). The δ values then take on more (complex) significance rather than simply being an empirical parameter associated with a solvent molecule radii (14). Additional support of the present conclusion can be drawn from the similarity in the solubility of TlBr ($Ksp = 10^{-6.23}$) as compared to Butler's (5) determination of the solubility of TlCl ($Ksp = 10^{-6.26}$).

Manuscript submitted April 29, 1969; revised manuscript received June 17, 1969.

Any discussion of this paper will appear in a Discussion Section to be published in the June 1970 JOURNAL.

REFERENCES

1. R. F. Rodewald, K. Mahendran, J. L. Bear, and R. Fuchs, *J. Am. Chem. Soc.*, **90**, 6698 (1968).
2. J. Miller and A. J. Parker, *ibid.*, **83**, 117 (1961).
3. I. M. Kolthoff, M. K. Chantooni, and S. Bhowmik, *ibid*, **90**, 23 (1968).
4. M. E. Peover and B. S. White, *Electrochim. Acta*, **11**, 1061 (1966).
5. D. R. Cogley and J. N. Butler, *This Journal*, **113**, 1074 (1966).
6. W. H. Smyrl and C. W. Tobias, *ibid.*, **115**, 33 (1968).
7. G. Holleck, D. R. Cogley, and J. N. Butler, *ibid.*, In press.
8. E. M. Arnett and D. R. McKelvey, *J. Am. Chem. Soc.*, **88**, 2599 (1966).
9. J. C. Synnott and J. N. Butler, *J. Phys. Chem.*, In press.
10. E. A. Guggenheim, *Phil. Mag.*, **19**, 588 (1935).
11. E. A. Guggenheim, "Thermodynamics," North-Holland, Amsterdam (1959).
12. M. Salomon, *J. Phys. Chem.*, In press.
13. R. A. Robinson and R. H. Stokes, "Electrolyte Solutions," Second Revised Edition, Butterworths, London (1968).
14. M. Salomon, *J. Phys. Chem.*, In course of preparation.
15. R. J. Jasinski and S. Kirkland, *Anal. Chem.*, **39**, 1963 (1967).
16. T. W. Richards and F. Daniels, *J. Am. Chem. Soc.*, **41**, 1732 (1919).
17. A. J. Parker, *Quart. Rev., London*, **16**, 163 (1962).
18. Y. Wu and H. L. Friedman, *J. Phys. Chem.*, **70**, 501 (1966).
19. B. E. Conway and J. O'M. Bockris, "Ionic Solvation," in "Modern Aspects of Electrochemistry", Vol. 1, Butterworths, London (1954).
20. W. M. Latimer, K. S. Pitzer, and C. M. Slansky, *J. Chem. Phys.*, **7**, 108 (1939).

The Thermal Temperature Coefficient of the Calomel Electrode Potential Between 0° and 70°C

II. Thermodynamic Results—The Moving and Transport Entropies and Heat Capacities of Aqueous Chloride Salines and Their Ions

Andre J. de Bethune*

Department of Chemistry, Boston College, Chestnut Hill, Massachusetts

and Henry O. Daley, Jr.*

Department of Chemistry, Bridgewater State College, Bridgewater, Massachusetts

ABSTRACT

The initial thermal temperature coefficient of the calomel electrode reported in Part I is combined with the results of thermal diffusion studies elsewhere to yield information about: the entropy of transport S^* of the aqueous electrolytes KCl, NaCl, LiCl, HCl, and $CaCl_2$; the experimentally determinable moving (transported)entropy $\overline{\overline{S}}$ of the ion constituents Cl^-, K^+, Na^+, Li^+, H^+, and Ca^{++}. A four-constant equation analogous to the Fuoss-Onsager conductance equation is developed for the concentration dependence of the entropy of transport S^* and is applied to the salts KCl and NaCl. The division of the moving entropy $\overline{\overline{S}}$ into its nonmeasurable ionic component terms: the ionic transport entropy S^* and the stationary entropy $\overline{S}$, is attempted via two postulates: the Agar postulate and the KCl-bridge postulate which give results mutually consistent within about 0.8 eu (35 μVF/deg), *e.g.*, $\overline{S}^\circ(H^+) = -5.22$ eu from our data under the Agar postulate, and −4.42 eu under the KCl-bridge postulate. These values are in good agreement with previously reported values of −4.48, −5.5, and −5.7 based on a number of alternative postulates. Values are also obtained for the transport heat capacity C^* of the electrolytes and for the measurable moving heat capacity $\overline{\overline{C}}$ of the ion constituents at 30°. A division of $\overline{\overline{C}}$ into its nonmeasurable ionic components: C^* and $\overline{C}$ is also carried out on the basis of Fales and Mudge's hydrogen thermal emf data via the KCl-bridge postulate, and yields, *e.g.*, $C^*_0 = 30$ eu (Cl^-), 5 (H^+); $\overline{C}^\circ = -24$ (Cl^-), −5 (H^+); $\overline{\overline{C}}^\circ = 6$ (Cl^-), 0 (H^+).

In Part I(1), the initial thermal emf of the calomel electrode in several aqueous chloride salines was represented between 0° and 70°C by the quadratic

$$V_t - V_{25} = A_{25}(t-25) + B(t-25)^2 \qquad [1]$$

where the A's range between +294 and +1024 μV/deg and the B's between −1.9 and −0.1 μV/deg^2. The A's measure the initial thermal temperature coefficient (thermoelectric power) $\epsilon_0 = (dV/dT)_{\text{th,initial}}$ of the corresponding calomel electrode at 25°. At constant chloride ion concentration, the difference between ϵ_0 in two different salts (2) is given by

$$\mathbf{F}[\epsilon_0(MCl) - \epsilon_0(KCl)] = t_K S^*(KCl) - t_M S^*(MCl)/z_M \qquad [2]$$

where S^* is the entropy of transport (Eastman's entropy of transfer) of the salt. S^* is related to the Soret (thermal diffusion) coefficient σ by

$$\sigma = d\ln m/dT = -S^*/[\nu RT(1 + (d\ln\gamma/d\ln m)_T)] \qquad [3]$$

S^* is the entropy transported reversibly from the hot to the cold heat reservoir by the reversible transfer of one mol of solute from the hot to the cold region of the solution, in the limit $\Delta T \to 0$.

Another quantity of interest is the final thermoelectric coefficient $\epsilon_\infty = (dV/dT)_{\text{th,final}}$ of a thermal cell after thermal diffusion has come to a steady state. Theory (2) shows that the final thermal emf is given by the initial thermal emf plus the isothermal emf of the concentration cell created by thermal diffusion. In general

$$\epsilon_\infty = \epsilon_0 \mp t_g S^*/\nu\mathbf{F} \quad (\text{if } z_r = \pm) \qquad [4]$$

where z_r is the charge of the ion to which the electrodes are reversible, t_g the transference number of the gegenion, and ν the valence of the salt. For calomel thermal cells

$$\epsilon_\infty = \epsilon_0 + t_+ S^*/z_+\mathbf{F} \qquad [5]$$

In the present work, S^* values for KCl, and occasionally for other salts, as obtained from thermal diffusion studies elsewhere, have been used in the calculation of ϵ_∞.

Temkin and Khoroshin (3) first proved that the final thermal emf is independent of the nature of the gegenion. For a calomel thermal cell

$$\mathbf{F}(dV/dT)_{\text{th,final}} = \mathbf{F}\epsilon_\infty = \Delta\overline{\overline{S}} = S^\circ(Hg, l) - \tfrac{1}{2}S^\circ(Hg_2Cl_2, c) + \overline{\overline{S}}(Cl^-, aq) - \overline{\overline{S}}(e^-, Cu) \qquad [6]$$

where $\overline{\overline{S}}$ denotes the moving entropy [Agar's "transported" entropy (4), Temkin and Khoroshin's "Entropiya dvizhushchiksya Iona," entropy of the moving ion (3)] of a solute species, which is

$$\overline{\overline{S}} = \overline{S} + S^* \qquad [7]$$

i.e., the sum of the stationary partial molal entropy $\overline{S}$ [also known, for an ion constituent, as the absolute ionic entropy (4) or the entropy of electrochemical

* Electrochemical Society Active Member.

Key words: calomel electrode, electrolytes, entropy of transport, heat capacity of transport, ionic entropy, ionic heat capacity, ions, thermodynamic properties of salines, thermoelectric power, transported entropy, transported heat capacity.

transport (6)] plus the transport entropy S^* [also known as the Eastman entropy of transfer (5) or the entropy of migration transport]. For ionic species, $\overline{\overline{S}}_i$ is the partial molal entropy of an ion including the ΔS of building up of that part of the solvation sheath which travels with the ion (known as Eastman's second region, the first region is the ion itself). On the other hand, S^*_i as originally defined by Eastman (5), is the ΔS of disintegration of that portion of the ionic solvation sheath which is left behind when the ion goes away. Therefore, $-S^*_i$ is the ΔS of building up of this outer solvation sheath (known as Eastman's third region). The more positive S^*_i, the more the ion is a structure maker in the third region. The sum $\overline{S}_i = \overline{\overline{S}}_i + (-S^*_i)$ is therefore the partial molal entropy of the stationary ion including the ΔS of building up of its complete solvation sheath. This sum is therefore the entropy transported across a thermal cell when an ion is transferred from one half-cell to the other by the agency of the two equal and opposite electrode reactions, a mechanism in which the ion sheds its complete hydration sheath in one half-cell (at one temperature) and forms a complete hydration sheath in the other half-cell (at a different temperature). $\overline{S}_i$ can therefore appropriately be called the ionic entropy of electrochemical transport (6, 8).

In view of Eq. [6], the moving entropy $\overline{\overline{S}}$ is experimentally measurable for a single ionic species from final thermal emf's, or from initial thermal emf's and thermal diffusion data, as was originally shown by Temkin and Khoroshin (3). On the other hand, neither the stationary entropy $\overline{S}$, nor the transport entropy S^*, are separately measurable for a single ionic species. Estimates of these quantities can be made on the basis of certain postulates, which include (*i*) the KCl-bridge postulate, (*ii*) the Agar postulate, and (*iii*) the Gurney postulate. The KCl-bridge postulate was utilized by de Bethune, Licht, and Swendeman (6) to interpret Fales and Mudge's (9) thermal emf data for the 0.1 molal HCl hydrogen electrode with a saturated KCl bridge. By assuming that the bridge potential was zero, they obtained for the standard stationary entropy of hydrogen ion

$$\overline{S}^\circ(H^+) = -4.48 \pm 0.5 \text{ eu} \qquad [8]$$

at 25°. This result can be compared with Gurney's −5.5 eu (10) from his assignment of equal viscosity *B*-coefficients to K^+ and Cl^-, also with Lin and Breck's −5.7 eu (11) based on their postulate that trichelated redox ion pairs are approximately isentropic because the large organic structures tend to shield the solvent water from the charge on the central ion. The Agar postulate selects the arbitrary value

$$S^*(Cl^-, 0.01 \text{ molal}) = 0 \qquad [9]$$

as a basis for deducing conventional ionic transport entropies so that $S^*(K^+, 0.01 \text{ molal}) = S^*(KCl, 0.01 \text{ molal}) = 1.65$ eu at 25°. The thermal diffusion potential of 0.01 molal KCl, computed from $[t_{Cl}S^*_{Cl} - t_K S^*_K]\mathbf{F}^{-1}$, is −35.1 μV/deg on the basis of the Agar postulate, as compared with the value zero assigned under the KCl-bridge postulate. The two postulates thus yield results mutually consistent within better than 1 entropy unit (43.36 microvolt-faradays per degree).

The moving entropy $\overline{\overline{S}}_i$ has a twofold concentration dependence, (*i*) that of $\overline{S}_i$ given by the ordinary mass action expression

$$\overline{S}_i = \overline{S}^\circ_i - R \ln m_i\gamma_i - RT\, d \ln \gamma_i/dT \qquad [10]$$

and (*ii*) the further concentration dependence of S^*_i which is akin to that of the activity coefficient or of the ionic conductance. In dilute solutions, the concentration dependence of S^*_i can be approximated by the Debye-Hückel theory (4, 12), and in more concentrated solutions, by equations of the Fuoss-Onsager form (12). These relationships show that, at infinite dilution, S^*_i tends to a finite limiting value S^*_{oi} which can be calculated in principle from the Eastman electrostatic model (5) quantitated by taking a temperature derivative of the Born free energy of hydration expression to yield (2)

$$S^*_{oi} = (z_i^2e^2/2D_0r_i)\, d(1/D)/dT \qquad [11]$$

where r_i is the ionic radius at the "boundary" between the Eastman second and third regions. In water, $d(1/D)/dT = 5.83 \times 10^{-5}$ deg^{-1} at 25° (2). Equation [11] takes the form $S^*_{oi} = +9.68\, z_i^2/r_i(\text{Å})$ eu, which shows that conventional ionic transport entropies, generally between 0 and 3 eu, are reasonable for r_i values of a few angstroms.

The moving entropy $\overline{\overline{S}}_i(m)$ at molality m is transformed, by addition of the mass action terms $R \ln m_{i,\gamma} + RT\, d \ln \gamma/dT$, to the quantity

$$\overline{\overline{S}}^{\circ\prime}(m) = \overline{S}^\circ_i + S^*_i(m) \qquad [12]$$

which is a first approximation to the limiting standard value $\overline{\overline{S}}^\circ = \overline{S}^\circ + S^*_{oi}$. Here the measurable mean ion activity coefficient γ of the salt is substituted for the unmeasurable single ion activity coefficient γ_i in 1,1 salts (in binary salts of multiply charged ions, an extension of the Debye-Hückel theory (2) suggests taking the single ion activity coefficient as $\gamma_i = \gamma^{-z_i/z_j}$).

Reference Values for Salt Transport Entropies

Potassium and sodium chlorides at 25°.—The transport entropies of potassium and sodium chlorides have been investigated experimentally up to 0.05 molal by Agar and Turner (15) and Snowdon and Turner (16, 17) by a conductimetric method based on unbalancing a Wheatstone bridge by applying a thermal gradient to a conductance cell, and, between 0.5 and 4 molal by Longsworth (18) and Chanu and Lenoble (19) by optical methods based on the tilting of interference fringes in a thermal field. From their reported Soret coefficient data, S^* values for aqueous KCl and NaCl at 25° were computed. de Bethune (12) showed that these S^*'s can be well fitted from 0 to 4 molal by a four-constant equation analogous to the Fuoss-Onsager (20) conductance equation

$$S^* = A + Bm^{1/2} + Cm + Dm \log m \qquad [13]$$

The least squares values for the constants are listed in Table I and fit the data almost everywhere within better than ±0.1 eu. The four constant equation can therefore be used to calculate S^* at infinite dilution and at 0.1 molal where no direct experimental data are available. The results of this calculation are given in Table II.

Other reference values.—Other experimental values of the salt transport entropy as based on measured Soret coefficients have been adopted as listed in Table III.

Salt Transport Entropies and Final Thermoelectric Coefficients of Calomel Electrodes

The results at 25° are given in Table IV. The second column gives ϵ_0 from Part I (1). The third column

Table I. Least squares constants used to fit the four constant Eq. [13] to the transport entropies of potassium and sodium chlorides at 25°C

	S^* in calories · degree^{-1} · mol^{-1} Range: 0 to 4 molal	
Constant	KCl	NaCl
A	2.2400	2.9698
B	−7.0393	−7.3126
C	5.1724	5.6201
D	−2.9822	−3.3379

Table II. Transport entropies of potassium and sodium chlorides in water at 25° calculated from the four constant equation

Molality	S^* (KCl)	S^* (NaCl)
	calories · degree^{-1} · mol^{-1}	
0	2.240	2.970
0.01	1.647	2.362
0.1	0.829	1.553
1.0	0.373	1.277

lists the cation transference numbers utilized [Daley (25)]. The fourth column gives the salt transport entropies S^*/z_M in eu·eq^{-1}. Reference values from Tables II and III are given in parentheses. Other values are calculated from the thermoelectric data as described below. The fifth column gives ϵ_x calculated from ϵ_0 and the reference values of S^* via Eq. [5]. The last column gives values of S^* taken from the literature and based on either thermal diffusion or thermoelectric studies.

The salt transport entropies listed in the fourth column were calculated from the observed ϵ_0 and the mean final $\langle\epsilon_x\rangle_{avg}$ via Eq. [5]. The results of Table IV are extended to 35° for KCl, the only salt for which reference S^*'s were available (Table III) or could be estimated.

Table III. Salt transport entropies from measured Soret coefficients adopted for this study

Salt	S^*	Source
	calories · degree^{-1} · mol^{-1}	
0.01m LiCl	−0.010 at 25°	Agar (4), based on Snowdon and Turner (16)
0.01m HCl	10.19 at 25°	Agar (4), based on Snowdon and Turner (16)
0.01m KCl	−0.708 at 9.3°	Butler and Turner (21)
0.01m KCl	3.151 at 34.7°	Agar and Turner (15)
1.0m KCl	1.197 at 35°	Longsworth (18)
1.0m KCl	2.018 at 45°	Longsworth (18)
2.0m KCl	0.087 at 15°	Longsworth (18)
2.0m KCl	1.632 at 35°	Longsworth (18)
2.0m KCl	2.311 at 45°	Longsworth (18)

Moving Entropy of Chloride Ion and Related Quantities at 25°

The final thermoelectric coefficient ϵ_∞ from Table IV can be used in Eq. [6] to compute the moving entropy $\overline{\overline{S}}$ of chloride ion in 0.01, 0.1, and 1.0 molal solutions. Standard entropy data used are $S^\circ(Hg,l) = 18.5$ eu, $S^\circ(Hg_2Cl_2, c) = 46.8$ eu, Latimer (29), $\overline{\overline{S}}(e^-, Cu) = -0.045$ eu, Khoroshin and Temkin (3), Agar (4). The results of the computation are given in Table V, line 1. The mass action correction $R \ln m_{Cl}\gamma_{Cl} + RT\, d \ln \gamma_{Cl}/dT$, with γ_{Cl} set equal to γ_{KCl}, is introduced

Table IV. Salt transport entropies and final thermoelectric coefficients of calomel electrodes at 25°

Reference values of S* are given in parentheses
S^* in calories · degree^{-1} · equivalent^{-1}

Salt	ϵ_0[a], μV/deg	t_M[d]	S^* (salt)$/z_M$, This study eu/eq.	ϵ_∞, μV/deg	S^* (salt)$/z_M$, Lit. values, eu/eq.
			0.01 molal chloride ion		
KCl	921.23	0.4902	(1.647)[b]	956.25	1.66[f], 1.68[g], 1.72[h]
NaCl	915.98	0.3912	(2.362)[b]	956.04	2.60[h], 2.58[g], 2.32[i] 2.56[j], 1.88[k]
LiCl	1023.69	0.329	(−0.01)[c]	1023.55	−0.067[g], −0.242[l] 2.73[k]
HCl	678.24	0.825	(10.19)[c]	1042.78	10.5[k], 10.1[m]
½ $CaCl_2$	988.8[r]	0.4264	0.32[e]	—	2.54[n]
				Avg. 994.7 ± 22.6	
KCl (35°)	891.39	0.4886	(3.198)[cu]	959.14	3.15[cg] at 34.7[o]
			0.1 molal chloride ion		
KCl	776.44	0.4900	(0.829)[b]	794.06	—
NaCl	767.27	0.3853	(1.553)[b]	793.22	—
LiCl	815.47	0.317	−1.588[e]	—	—
HCl	464.61	0.832	9.12[e]	—	11.0[m]
½ $CaCl_2$	775.24	0.407	1.044[e]	—	—
				Avg. 793.6 ± 0.4	
KCl (35°)	757.78	0.4888	(2.0)[e]	800.17	—
			1.0 molal chloride ion		
KCl	581.44	0.488	(0.373)[b]	589.33	0.372[p], 0.446[q]
NaCl	549.04	0.372	(1.277)[b]	569.84	1.34[q], 2.54[k]
LiCl	639.22	0.287	−4.80[e]	—	−1.96[k], −3.0[j]
HCl	294.23	0.841	7.82[e]	—	9.7[k], 16.1[m]
½ $CaCl_2$	546.1	0.386*	1.99[e]	—	2.9[j]
				Avg. 579.5 ± 9.8	
KCl (35°)	566.14	0.487*	(1.197)[c]	591.42	1.197[cp] at 35[o] 1.05[t] at 31[o]

[a] From Part I (1).
[b] Reference value, Table II.
[c] Reference value, Table III.
[d] Daley (25), * values interpolated from other concentrations.
[e] From average ϵ_∞ and ϵ_0 via Eq. [5].
[f] Snowdon and Turner (16).
[g] Agar and Turner (15).
[h] Agar (14).
[i] Snowdon and Turner (17).
[j] de Bethune (2), Richards (33).
[k] Bernhardt and Crockford (27).
[l] Temkin and Khoroshin (3).
[m] Breck, Cadenhead, and Hammerli (26).
[n] Payton and Turner (28).
[p] Longsworth (18).
[q] Chanu (19).
[r] Based on a logarithmic extrapolation from data in ref. (1) for 0.01 and 0.05 molal $CaCl_2$, in which the shift in thermoelectric coefficient with concentration is taken proportional to log $m_-\gamma_-$, and γ_- is taken equal to the square root of γ (see text). Activity coefficient data from Latimer (29).
[s] By graphical interpolation of data in Table III.
[t] Tyrrell (31).
[u] Adjusted to 35°.

Table V. Moving entropy of chloride ion and related quantities at 25°

All entropy terms are given in calories · degree^{-1} · equivalent^{-1}

Quantity	Hypothetical standard state (°) or infinite dilution (∞)	0.01*m* Cl⁻	0.1*m* Cl⁻	1.0*m* Cl⁻
1. $\bar{\bar{S}}$(Cl⁻)	—	27.79	23.16	18.23
2. γ^a	1.000	0.901	0.770	0.607
3. *p*Cl^a	0.000	2.042	1.111	0.203
4. d ln γ/dT^a (deg^{-1})	—	−0.0001	0.0000	0.0008
5. $\bar{\bar{S}}^{o\prime}$(Cl⁻)	18.69	18.39	18.07	17.76
6. $\bar{\bar{S}}^{o\prime}$(KCl)	39.94	39.35	38.53	38.07
7. $\bar{\bar{S}}^{o\prime}$(K⁺)	21.25	20.96	20.46	20.31
8. $\bar{\bar{S}}^{o\prime}$(NaCl)	30.57	29.96	29.15	28.88
9. $\bar{\bar{S}}^{o\prime}$(Na⁺)	11.88	11.57	11.08	11.12
10. $\bar{\bar{S}}^{o\prime}$(LiCl)	17.2	16.6	15.0	11.8
11. $\bar{\bar{S}}^{o\prime}$(Li⁺)	−1.5	−1.8	−3.1	−6.0
12. $\bar{\bar{S}}^{o\prime}$(HCl)	23.96	23.36	22.29	20.99
13. $\bar{\bar{S}}^{o\prime}$(H⁺)	5.27	4.97	4.22	3.23
14. $\bar{\bar{S}}^{o\prime}$(½ $CaCl_2$)	8.0	6.9	7.6	8.6
15. $\bar{\bar{S}}^{o\prime}$(½ Ca^{++})	10.7	−11.5	−10.4	−9.2
The following numbers depend on the Agar postulate S^*(Cl⁻, 0.01 molal) = 0				
16. S^*(Cl⁻)	0.30	(0.00)	−0.32	−0.63
17. S^*(K⁺)	1.94	1.65	1.15	1.00
18. S^*(Na⁺)	2.67	2.36	1.87	1.91
19. S^*(Li⁺)	0.29	−0.01	−1.27	−4.17
20. S^*(H⁺)	10.49	10.19	9.44	8.45
21. S^*(½ Ca^{++})	1.1	0.3	1.4	2.6
The following numbers depend on the KCl-bridge postulate, *i.e.*, *tdp*(KCl) = 0 at all concentrations				
22. S^*(Cl⁻)	1.10	0.81	0.41	0.18
23. S^*(K⁺)	1.14	0.84	0.42	0.19
24. S^*(Na⁺)	1.87	1.55	1.14	1.10
25. S^*(Li⁺)	−0.51	−0.82	−2.00	−4.98
26. S^*(H⁺)	9.69	9.38	8.71	7.64
27. S^*(½ Ca^{++})	0.3	−0.5	0.6	1.8
The following *tdp*'s, relative to KCl = 0, are given in microvolts degree^{-1}. The algebraic sign coincides with the sign of the double-layer charge at the hot end of the thermal diffusion dipole				
28. *tdp*(NaCl)	−3.4	−4.96	−8.3	−12.8
29. *tdp*(LiCl)	+39.0	+35.2	+39.5	+67.6
30. *tdp*(HCl)	−336.5	−329.5	−311.4	−277.4
31. *tdp*($CaCl_2$)	+20.6	+29.2	−0.8	−25.4

[a] KCl values, de Bethune, Licht, and Swendeman (6).

next to convert $\bar{\bar{S}}$(Cl⁻) to $\bar{\bar{S}}^{o\prime}$(Cl⁻), the preliminary standard value (line 5). By introduction of $\bar{S}^o$ from Latimer (29) or NBS Circular 500 (30): KCl 37.7, NaCl 27.6, LiCl 16.6, HCl 13.17, ½$CaCl_2$ 6.6 eu·eq^{-1}, and S^* from Tables II, III, and IV, $\bar{\bar{S}}^{o\prime}$ is calculated next for these salts including the limiting value $\bar{\bar{S}}^o$ at infinite dilution (lines 6, 8, 10, 12, 14). From these it is possible to compute $\bar{\bar{S}}^{o\prime}$ for the cations (lines 7, 9, 11, 13, 15).

To obtain the standard values $\bar{\bar{S}}^o$ for the individual ions, it is necessary to split the experimental difference $S^*_o - S^*_{0.01m} = 0.60$ eu (Table II) for KCl and NaCl between their respective ions. Electrostatic theory (4, 12) suggests that this difference should be equally divided between the two ions of a 1,1 salt, *i.e.*, $S^*_o - S^*_{0.01m} = 0.30$ eu for a univalent ion. The same differences are also applied to LiCl and HCl and to their ions (lines 10-13).

For $CaCl_2$, the above differences of S^* values must be adjusted to the valence pattern of a 1,2 salt. Electrostatic theory suggests a limiting law of the form $dS^*_i/d\mu^{1/2} \sim -z_i^2$. This yields $S^*_o - S^*_{0.01m\ Cl^-} = 2.20$ eu·mol^{-1} or 1.10 eu·eq^{-1} for a divalent chloride. Values of $\bar{\bar{S}}^{o\prime}$ including $\bar{\bar{S}}^o$ are calculated in this manner for ½$CaCl_2$ (line 14) and for ½Ca^{++} (line 15).

Lines 16-21 in Table V give the single-ion transport entropies S^*_i based on the data of Table II-IV, calculated from Eq. [12] from the Agar postulate. These values are consistent with a standard stationary entropy of hydrogen ion $\bar{S}^o(H^+) = -5.22$ eu, a value which compares well with the set of alternative values of −4.48, −5.5, and −5.7 discussed above.

Lines 22-27 give single-ion transport entropies S^*_i based on the KCl-bridge postulate. These values lead to $\bar{S}^o(H^+) = -4.42$ eu, showing excellent agreement with de Bethune, Licht, and Swendeman's (6) −4.48 eu and with the large volume of thermal emf data satisfactorily correlated therewith (6). The thermal diffusion potentials (*tdp*) of the various salts, relative to KCl = 0, are given in lines 28-31. The *tdp*'s according to the two postulates would differ by an amount proportional to the shift of S^*(Cl⁻) under the two postulates

$$tdp'' - tdp' = [S^*(Cl^-)'' - S^*(Cl^-)']\mathbf{F}^{-1} \quad [14]$$

The KCl-bridge postulate gives values of S^*(Cl⁻) about 0.7 to 0.8 eu (30 to 35 μV**F**/deg) higher than the Agar postulate, and its *tdp*'s would be consistently higher algebraically by the same amount. For single ionic values of S^*_i and $\bar{S}^o_i$, the following conversion rules hold among the several postulates

to convert	*from*	*to*	*add*
$S^*_\mp$ and $\bar{S}^o_\pm$	Agar postulate	Gurney postulate	$\mp$0.3 eu · eq^{-1}
$S^*_\mp$ and $S^o_\pm$	Gurney postulate	KCl-bridge postulate	±1.0/±1.1 eu · eq^{-1}
$S^*_\mp$ and $S^o_\pm$	Agar postulate	KCl-bridge postulate	±0.7/±0.8 eu · eq^{-1}

The mutual consistency of these three postulates, within about 1 eu, is interesting but does not *per se* justify adopting any one of them as an "absolute" basis for ionic entropies (34). The Gurney (10) postulate is based on his division of the viscosity *B*-coefficient of KCl at 25° into equal ionic terms: $B(K^+) = B(Cl^-) = -0.0070$, both coefficients being small as compared with other ionic terms (on this basis) ranging from $B(Li^+) = +0.147$ to $B(I^-) = -0.080$. If the KCl-bridge value $\bar{S}^o(H^+) = -4.5$ eu were adopted instead of the Gurney value of −5.5, a satisfactory Gurney plot could be prepared on the basis of ionic viscosity *B*-values shifted by only $\mp$0.007 (for ± ions). The entries of Table V, usually given to the nearest 0.01 eu·eq^{-1}, are generally valid to within a few tenths of an entropy unit.

Salt Transport Heat Capacities

The transport heat capacity of a salt has been defined by Agar (14) as $C^* = T(dS^*/dT)_p$. Temperature differentiation of Eq. [2], neglecting any temperature dependence of t_i, yields

$$\mathbf{F}T[d\epsilon_0(MCl)/dT - d\epsilon_0(KCl)/dT] = 2\mathbf{F}T[B(MCl) - B(KCl)] = t_K C^*(KCl) - t_M C^*(MCl)/z_M \quad [15]$$

where the *B*'s are the quadratic coefficients of Eq. [1]. The reference values of C^*(KCl) in Table VI are based, at 0.01 and 1.0 molal, on direct thermal diffusion observations of S^* at 25° and 35° as summarized in Table II and III. For 0.1 molal, use was made of a graphically interpolated value of S^* at 35° which may be uncertain by ± 0.1/0.2 eu, the corresponding uncertainty in C^* would amount to ± 3/6 eu. An uncertainty in *B* of ± 0.1 μV/deg^2 would correspond to a little more than ± 4 eu in C^*/z_M for LiCl to a little less than ± 2 eu for HCl.

The data are summarized in Table VI. The first three columns give the salt, concentration, and quadratic *B*-coefficients from Part I (1). The fourth column gives C^*/z_M in eu·eq^{-1} as calculated from the KCl reference values at 30° via Eq. [15]. The uncertainty of these values amounts to several calories per degree·equivalent. They can be compared with in-

Table VI. Salt transport heat capacities at 30° and related quantities

All heat capacity terms are given in calories · degree^{-1} · equivalent^{-1}
Reference values of C^* are given in parentheses

Salt	m (Cl$^-$)	B^a, μV · deg^{-2}	C^*/z_M, This study	$\overline{C}_p/z_M{}^b$	$\overline{\overline{C}}/z_M$, This study	C^*/z_M, Lit. values
KCl	Std. st.	—	50.^{b}	−29.0	21.2^b	—
KCl	0.01	−1.492	(47.0)^a	−27.32	19.7	46.6^c, 45.8^d, 44.0^e at 17°
KCl	0.1	−0.933	(35.5)^a	−23.69	11.8	29.6^j in 0.05m
KCl	1.0	−0.765	(25.0)^a	−12.20	12.8	25.0^f
NaCl	Std. st.	—	51.^{b}	−23.8	27.1^b	—
NaCl	0.01	−1.211	48.4^i	−21.64	26.8	44.9^a, 38.1^d, 28.0^e at 17°
NaCl	0.1	−0.837	41.4^i	−16.97	24.4	32.3^j in 0.05m
NaCl	1.0	−0.490	22.3^i	−2.20	20.1	—
LiCl	Std. st.	—	—	−15.63	—	—
LiCl	0.01	−1.910	86.8^i?	−14.84	72.0?	—
LiCl	0.1	−0.582	39.3^i	−13.14	26.2	23.4^j in 0.05m
LiCl	1.0	−0.264	18.0^i	−7.75	10.3	—
HCl	Std. st.	—	35.6^b	−29.20	6.4^b	—
HCl	0.01	−1.865	34.4^i	−28.45	5.9	32.4^e at 17°
HCl	0.1	−1.498	30.5^i	−26.83	3.7	—
HCl	1.0	−0.885	16.6^i	−21.70	−5.1	—
½ $CaCl_2$	Std. st.	—	—	−34.3	—	—
½ $CaCl_2$	0.01	−2.353^r	80.2^i?	−32.55	47.6?	23.8^{e,k} in 0.02m Cl$^-$ at 17°
½ $CaCl_2$	0.1	−0.819	38.5^i	−29.55	9.0	—
½ $CaCl_2$	1.0	−0.104	7.6^i	−20.8	−13.2	—

^{a} Based on S^* at 35° and 25° (Tables II-IV).
^{b} From a $\sqrt{m}$-extrapolation.
^{c} Agar (14); ^{d}Agar and Turner (15); ^{e}Butler and Turner (21); ^{f} Longsworth (18).
^{g} From Part I (1); ^{h}Harned and Owen (22, p. 354), Pitzer and Brewer (35, p. 653), values for 25°.
^{i} From KCl-reference value and Eq. [15].
^{j} Agar (4); ^{k}value for ½ $BaCl_2$.
^{r} See Table IV, note r.

dependent determinations from other observers, sometimes at other concentrations and temperatures, as listed in the last column. The values for 0.01 molal LiCl and ½$CaCl_2$ appear to be high. The fifth column lists the partial molal heat capacity of the salt $\overline{C}_p$ at 25° as calculated from constants given by Harned and Owen (22) from their equation

$$\overline{C}_p(m) = \overline{C}_p{}^o + \overline{J}(m) = \overline{C}_p{}^o + Sm^{1/2} \qquad [16]$$

where the slope S is valid up to 3 molal. Values for calcium chloride were calculated from Pitzer and Brewer (35, p. 653). The sixth column gives the moving heat capacities of the salts defined by

$$\overline{\overline{C}}(m) = \overline{C}_p(m) + C^*(m) \qquad [17]$$

The partial molal heat capacity of these electrolytes is large and negative, becoming less negative at increasing concentrations, according to Eq. [16]. This expresses the influence of the addition of ions to water in ordering the surrounding water structure in the Eastman second and third regions both, and in thus depriving the water structure of some of its ability of absorbing energy as its temperature is raised. C^* on the other hand measures the increase in the heat capacity of the water structure in the third region when the ions are removed. This quantity is large and positive, becoming less positive as the concentration increases. Their sum, the moving (transported) heat capacity $\overline{\overline{C}}$ of the salt is then given by a much smaller quantity, usually positive, which decreases slowly with increasing concentration. Agar (14) suggested that $\overline{\overline{C}}_i$ should equal the Dulong and Petit value of 6 eu for the vibration of the center of mass of each monatomic ion. This would make $\overline{\overline{C}}$ = 12 eu for 1,1 salts and 18 eu·mol^{-1} or 9 eu·eq^{-1} for 1,2 salts, an expectation which is only roughly verified by the $\overline{\overline{C}}$ values listed in the sixth column.

The Eastman-Born electrostatic model, given in Eq. [11], permits an evaluation of the ionic transport heat capacity as

$$C^*{}_{oi} = TdS^*{}_{oi}/dT = (z_i{}^2e^2/2D_or_i)\,d^2(1/D)/dT^2 \qquad [18]$$

if r_i is not a function of temperature. In water, Gurney (10) has suggested the empirical formula $D(T)$ = 305.7 exp(−T/219) which leads to

$$C^*{}_{oi} = (T/219)S^*{}_{oi} = 13.4\,z_i{}^2/r_i(\text{Å})\ \text{eu} \qquad [19]$$

at 303°K. If ionic crystal radii (10) are substituted into Eq. [19], theoretical ionic transport heat capacities are obtained as follows: Cl^- 7.4, K^+ 10.1, Na^+ 13.7, Li^+ 17.2, ½Ca^{++} 25.3 eu. These theoretical transport heat capacities are of the right order, but yield salt values smaller than the experimental ones (Table VI, col. 4). As in the case of the transport entropy $S^*{}_o$, the correlation between the electrostatic model and observations is only approximate and does not lead to any useful results regarding the radius r_i at the boundary between the Eastman second and third regions.

Moving Heat Capacity of Chloride Ion and Related Quantities at 30°

The final thermoelectric coefficients ϵ_∞ at 25° and 35° permit calculation of the second derivative of the final thermal emf (Table VII, line 1) for which the thermodynamic equation is

$$\mathbf{F}T(d^2V/dT^2)_{\text{th,final}} = \mathbf{F}T(d\epsilon_\infty/dT) = Td\Delta\overline{\overline{S}}/dT = \Delta\overline{\overline{C}}$$
$$= C_p{}^o(\text{Hg, l}) - \tfrac{1}{2}C_p{}^o(Hg_2Cl_2, \text{c})$$
$$+ \overline{\overline{C}}(Cl^-, \text{aq}) - \overline{\overline{C}}(e^-, \text{Cu}) \qquad [20]$$

Standard heat capacity data are $C_p{}^o$(Hg, l) = 6.65 eu, $C_p{}^o$ (Hg_2Cl_2, c) = 24.3 eu, NBS(30), and $\overline{\overline{C}}(e^-$, Cu) = −1.5 μVF/deg = −0.034 eu, Temkin and Khoroshin (3).

The moving heat capacity $\overline{\overline{C}}(Cl^-)$ at 0.01, 0.1, and 1.0 molal is given in Table VII, line 2, and is close to the Dulong and Petit value of 6 eu. From the data of Table VI, $\overline{\overline{C}}_i$ is then calculated for the cations at the three concentrations (lines 3 to 7), the values for 0.01 molal Li^+ and ½Ca^{++} appear to be high. The other values are probably reliable within several eu·eq^{-1}. Values at infinite dilution, where given, are obtained from a $\sqrt{m}$-extrapolation.

The attempt to split $\overline{\overline{C}}_i$ into its constituent terms $C^*{}_i$ and $\overline{C}_i$ was made, via the KCl-bridge postulate, by assuming that the saturated KCl-bridge in Fales and Mudge's 0.1 molal HCl-H_2 thermal cell (9) did not contribute to the second derivative of their observed thermal emf's, for which deBethune, Licht, and Swen-

Table VII. Moving heat capacity of chloride ion at 30° and related quantities

All heat capacity terms are given in calories · degree^{-1} · equivalent^{-1}

	Quantity	Infinite dilution ($_0$)	0.01m Cl$^-$	0.1m Cl$^-$	1.0m Cl$^-$
1.	$d\epsilon^\infty/dT$[a] (μV/deg^2)	—	0.289	0.611	0.208
2.	$\overline{\overline{C}}$(Cl$^-$)	6.4[b]	7.5	9.7	6.9
3.	$\overline{\overline{C}}$(K$^+$)	14.8[b]	12.2	2.1	5.9
4.	$\overline{\overline{C}}$(Na$^+$)	20.7[b]	19.3	14.6	13.2
5.	$\overline{\overline{C}}$(Li$^+$)	—	64.5?	16.4	3.3
6.	$\overline{\overline{C}}$(H$^+$)	0.0[b]	−1.6	−6.0	−12.1
7.	$\overline{\overline{C}}$(½ Ca^{++})	—	40.1?	−0.8	−20.2
	The following numbers depend on the saturated KCl-bridge postulate (see text)				
8.	$\overline{C}$(H$^+$)	−5.1[b]	−5.2	−5.4	−6.0
9.	C^*(H$^+$)	+5.1[b]	+3.6	−0.6	−6.1
10.	$\overline{C}$(Cl$^-$)	−24.1[b]	−23.2	−21.5	−15.7
11.	C^*(Cl$^-$)	30.5[b]	30.8	31.2	22.6
12.	$\overline{C}$(K$^+$)	−4.9[b]	−4.0	−2.2	+3.5
13.	C^*(K$^+$)	19.7[b]	16.2	4.3	2.4
14.	$\overline{C}$(Na$^+$)	+0.3[b]	1.6	4.5	13.5
15.	C^*(Na$^+$)	20.4[b]	17.7	10.2	−0.3
16.	$\overline{C}$(Li$^+$)	8.5[b]	8.4	8.3	7.9
17.	C^*(Li$^+$)	—	56.1?	8.1	−4.6
18.	$\overline{C}$(½ Ca^{++})	−10.1[b]	−9.3	−8.1	−5.1
19.	C^*(½ Ca^{++})	—	49.4?	7.3	−15.1
	The following numbers result from the addition of C_p(H$_2$O) to $\overline{\overline{C}}$ and $\overline{C}$ for H$^+$				
20.	$\overline{\overline{C}}$(H$_3$O$^+$)	18.0[b]	16.4	12.0	6.0
21.	$\overline{C}$(H$_3$O$^+$)	12.9[b]	12.8	12.6	12.0
22.	C^*(H$_3$O$^+$)	See line 9 above			

[a] Based on KCl values at 25° and 35° (Table IV).
[b] From a $\sqrt{m}$-extrapolation.

deman (6) calculated +1.286 μV/deg^2, after correction to unit activity of hydrogen gas. By setting $FT(d^2V/dT^2) = 384\ \mu VF/\text{deg} = 8.8$ eu $= \frac{1}{2}C_p^\circ(H_2, g) - \overline{C}(H^+, 0.1m) - \overline{\overline{C}}(e^-, Cu)$, with $C_p^\circ(H_2, g) = 6.892$ eu (30), one gets

$$\overline{C}(H^+, 0.1 \text{ molal}) = -5.4 \text{ eu} \qquad [21]$$

(line 8). This value can be used, in conjunction with $\overline{\overline{C}}$ values above and $\overline{C}_p$(HCl, 0.1 molal) (Table VI) to obtain $\overline{C}$ and C^* for 0.1 molal H$^+$ and Cl$^-$ (lines 9-11). To extend these values to other concentrations, use was made of the postulate that $\overline{J}(Cl^-) = \overline{J}(K^+) = \frac{1}{2}\overline{J}(KCl)$. Values of $\overline{C}$ and C^* for H$^+$, Cl$^-$, K$^+$, Na$^+$, Li$^+$, and ½Ca^{++} based on these postulates are given in lines 8-19. In lines 20 and 21, the heat capacity of water, 18 eu, is added to the H$^+$ values for $\overline{\overline{C}}$ and $\overline{C}$ to convert them to the H$_3$O$^+$ basis. C^* is the same for H$^+$ and H$_3$O$^+$ since this represents the heat capacity loss of the solvent in the third region resulting from the presence of the hydrated ion.

The single ion values generally present the following picture: $\overline{C}$ for Cl$^-$, K$^+$, and ½Ca^{++} is negative at infinite dilution, and increases (algebraically) with increasing concentration, becoming positive for K$^+$ by 1.0 molal. $\overline{C}$ for Na$^+$ is close to zero at infinite dilution and increases with increasing concentration. $\overline{C}$ for H$^+$ is negative, for Li$^+$ positive, both approximately independent of concentration. A negative value for $\overline{C}$ suggests that the ion becomes a more pronounced structure maker with increasing temperature in the combined second and third Eastman regions.

The transport heat capacity C^* is large and positive for Cl$^-$ and decreases with increasing concentration. C^* is smaller but still positive for the cations, in the order (at 0.1 molal) Na$^+$ > Li$^+$ > ½Ca^{++} > K$^+$ > H$^+$, and comes close to zero or even negative at 1.0 molal in the order K$^+$ > Na$^+$ > Li$^+$ > H$^+$ > ½Ca^{++}. A positive value of C^* is associated with an increase in structure making tendency with increasing temperature in the Eastman third region. Thus all ions appear to become more pronounced structure makers in the third region with increasing temperature in dilute solutions, but the tendency reverses for Na$^+$, Li$^+$, H$^+$, and Ca^{++} in concentrated solutions.

The role played by the ion in the second region appears to be twofold. A negative value of $\overline{\overline{C}}$ (H$^+$, Ca^{++} except for its high value) suggests a marked increase in structure making tendency with increasing temperature in the Eastman second region. On the other hand, a value of $\overline{\overline{C}}$ in excess of the Dulong and Petit value of 6 eu/g-ion (Na$^+$, Li$^+$, K$^+$) suggests an inverse effect in which the ion contributes an increase in the ability of its entourage of tightly bound waters to absorb energy.

Conclusion

An interpretation of the results presented above will be developed in Part III to follow, and will be based on modern theories of the water structure, and on a simplified form of the partition function of water which will be extended to hydronium ion (36, 37)

Manuscript submitted Dec. 2, 1968; revised manuscript received *ca.* June 19, 1969. This paper is based in part on the Ph.D. dissertation of Henry O. Daley, Jr., at Boston College. Grateful acknowledgement is made to the Office of Saline Water, U.S. Department of the Interior, for support of this investigation under Grants No. 14-01-0001-389 and -1466 at Boston College. All symbols will be found listed after Part III p. 1406.

Any discussion of this paper will appear in a Discussion Section to be published in the June 1970 JOURNAL.

REFERENCES

1. A. J. de Bethune, H. O. Daley, N. A. Swendeman Loud, and G. R. Salvi, *This Journal*, **114**, 578 (1967).
2. A. J. de Bethune, *ibid.*, **107**, 829 (1960).
3. M. I. Temkin and A. V. Khoroshin, *Zh. Fiz. Khim.*, **26**, 500, 773 (1952).
4. J. N. Agar, "Thermogalvanic Cells," in "Advances in Electrochemistry and Electrochemical Engineering," Vol. 3, P. Delahay, Editor, Interscience Publishers, New York (1963).
5. E. D. Eastman, *J. Am. Chem. Soc.*, **48**, 1482 (1926); **50**, 283, 292 (1928).
6. A. J. de Bethune, T. S. Licht, and N. A. Swendeman, *This Journal*, **106**, 616 (1959).
7. W. G. Breck and J. L. Lin, *Trans. Faraday Soc.*, **61**, 2223 (1965).
8. P. D. Miller, A. B. Tripler, and J. J. Ward, *This Journal*, **113**, 746 (1966).
9. H. A. Fales and W. A. Mudge, *J. Am. Chem. Soc.*, **42**, 2434 (1920).
10. R. W. Gurney, "Ionic Processes in Solution," McGraw-Hill Book Co., New York (1953).
11. J. L. Lin and W. G. Breck, *Can. J. Chem.*, **43**, 766 (1965).
12. A. J. de Bethune, "The Concentration Dependence of the Soret Transport Entropy," In preparation.
13. A. J. de Bethune and J. J. Perez, *Am. J. Phys.*, **24**, 584 (1956).
14. J. N. Agar, "Thermal Diffusion in Electrolyte Solutions," pp. 200-223 in "Structure of Electrolytic Solutions," W. J. Hamer, Editor, John Wiley and Sons, New York (1959).
15. J. N. Agar and J. C. N. Turner, *Proc. Royal Soc.*, **A255**, 307 (1960).
16. P. N. Snowdon and J. C. R. Turner, *Trans. Faraday Soc.*, **56**, 1409 (1960).
17. P. N. Snowdon and J. C. R. Turner, *ibid.*, **56**, 1812 (1960).
18. L. G. Longsworth, "Soret Coefficients of Electrolytes," pp. 183-199 in "Structure of Electrolytic Solutions," W. J. Hamer, Editor, John Wiley and Sons, New York (1959).
19. J. Chanu and J. Lenoble, *J. Chim. Phys.*, **53**, 309 (1956); **55**, 733, 738, 743 (1958).
20. L. Onsager and R. M. Fuoss, *J. Phys. Chem.*, **36**, 2689 (1932); R. M. Fuoss and F. Accascina, "Electrolytic Conductance," Interscience Publishers, New York (1959).

21. B. D. Butler and J. C. R. Turner, *J. Phys. Chem.*, **69**, 3598 (1965).
22. H. S. Harned and B. B. Owen, "Physical Chemistry of Electrolytic Solutions," 3d ed., Reinhold Publishing Co., New York (1958).
23. G. M. Barrow, "Physical Chemistry," McGraw-Hill Book Co., New York (1961).
24. G. Kortüm and J. O'M. Bockris, "Textbook of Electrochemistry," Vol. II, Elsevier, New York (1951).
25. H. O. Daley, Jr., Ph.D. Dissertation, Boston College (1963).
26. W. Breck, G. Cadenhead, and M. Hammerli, *Trans. Faraday Soc.*, **61**, 37 (1965).
27. H. A. Bernhardt and H. D. Crockford, *J. Phys. Chem.*, **46**, 473 (1942); H. D. Crockford and J. L. Hall, *ibid.*, **54**, 731 (1950).
28. A. D. Payton and J. C. R. Turner, *Trans. Faraday Soc.*, **58**, 55 (1962).
29. W. M. Latimer, "Oxidation Potentials," 2d ed., Prentice Hall, New York (1952).
30. National Bureau of Standards, Selected Values of Chemical Thermodynamic Properties, Circular 500 (1952).
31. H. J. V. Tyrrell, "Diffusion and Heat Flow in Liquids," Butterworth, London (1961).
32. R. Haase, K. Hoch, and H. Schönert, *Z. physik. Chem.*, **27**, 421 (1961).
33. T. W. Richards, *Z. physik. Chem.*, **24**, 39 (1897).
34. A. J. de Bethune, S. A. Carrano, T. P. O'Connor, and M. Y. C. Fu, Paper No. 180 presented to the Boston Meeting, May 5-9, 1968.
35. K. S. Pitzer and L. Brewer, "Lewis and Randall's Thermodynamics," 2nd ed., McGraw-Hill Book Co., New York (1961).
36. A. J. de Bethune, Office of Saline Water, R.&D. Progress Report No. 412, January, 1969.
37. A. J. de Bethune and H. O. Daley, Jr., *This Journal*, **116**, 1401 (1969).

The Thermal Temperature Coefficient of the Calomel Electrode Potential Between 0° and 70°C

III. Discussion: Moving, Transport and Stationary Entropies and Heat Capacities of Aqueous Chloride Salines and Their Ions. The Approximate Partition Function of Water and Hydronium Ion

Andre J. de Bethune*
Department of Chemistry, Boston College, Chestnut Hill, Massachusetts

and Henry O. Daley, Jr.*
Department of Chemistry, Bridgewater State College, Bridgewater, Massachusetts

ABSTRACT

The moving (transported) ionic properties $\overline{\overline{S}}$ and $\overline{\overline{C}}$ are partial molal properties of the ion itself and include the effect of its electrical charge on that portion of the solvation layer which travels with the ion (Eastman first and second regions). The negatives of the ionic transport properties $-S^*$ and $-C^*$ measure the influence of the ion (plus its tightly bound waters if any) on the remainder of the solvent (Eastman third region). A positive value of S^* identifies the ion as a structure maker in the third region. The sums $\overline{X} = \overline{\overline{X}} + (-X^*)$, where $X = S$ or C, measure the partial molal properties of the stationary ion, including the effect of the ionic charge on both Eastman second and third regions of the solvent. Observed values of $\overline{C}$ suggest a twofold effect of the ionic charge on its entourage of water molecules: a loosening of the O-H covalent bonds coupled with a stiffening of the O . . . H hydrogen bonds. The moving entropy and heat capacity of hydronium ion can be understood in terms of the hydrogen-bonded model of water structure, in which every H_2O or H_3O^+ can be 4-, 3-, 2-, 1-bonded to its neighbors or unbonded. By ascribing both bond and vibrational energy levels on this model, an approximate partition function is constructed for H_2O and H_3O^+, which can be made to fit our data for the unitary entropy and heat capacity of H_3O^+ at 25° and standard data for the entropy and heat capacity of H_2O between 0° and 100°. This model predicts the following fraction of hydrogen bonds broken in liquid H_2O at 0°, 25°, and 100°: 0.183, 0.218, and 0.310; in H_3O^+ at 25°, 0.094. The addition of H^+ to H_2O thus introduces a distinct amount of structure to the $H_3O^+ \ldots (H_2O)_4$ complex since it reduces the number of hydrogen bonds broken at 25° to a level, 9.4%, equal to half the number of hydrogen bonds broken in the liquid $H_2O \ldots (H_2O)_4$ complex at the melting point. The need to break about 12% more hydrogen bonds when the proton moves away at 25° is consistent with a calculated heat of transport of 3530 cal/mol, which compares favorably with the observed heat of transport of around 3000 cal/mole (on the Agar postulate). The single-ion stationary heat capacities $\overline{C}$ for K^+, Na^+, Li^+, and Cl^- obtained experimentally in the present study via the KCl-bridge postulate compare very favorably with theoretically calculated values of $\overline{C}_v$ for these ions based on the statistical model of Scheraga-Griffith.

A summary of the results of Part II (1a) is provided in Table I where the standard moving (transported) entropy $\overline{\overline{S}}^o$ of chloride ion, and related quantities, at 25°, are compared with data from previous observers (lines 1 to 5). For all the ions, our values of $\overline{\overline{S}}^o_i$ agree within 0.5 eu with Agar's (1), ours being smaller for chloride and larger for the cations. The values of Breck and Lin (2), and Haase, Hoch, and Schönert (3) are also given, as are also the earlier values of Khoroshin and Temkin (4) which are to-

* Electrochemical Society Active Member.
Key words: electrolytes, entropy of transport, heat capacity of transport, ionic entropy, ionic heat capacity, ions, partition function of water, partition function of hydronium ion, statistical mechanics, thermodynamic properties of salines, transported entropy, transported heat capacity.

Table I. Standard moving entropy of chloride ion and related quantities at 25°C from various sources

			calories · degree^{-1} · equivalent^{-1}					
			Cl^-	K^+	Na^+	Li^+	H^+	$\frac{1}{2}Ca^{++}$
1.	$\overline{\overline{S}}^o$	This study	18.69	21.25	11.88	−1.5	5.27	−10.7
2.	$\overline{\overline{S}}^o$	Breck and Lin (2)	19.4	20.5	11.1	—	4.7	—
3.	$\overline{\overline{S}}^o$	Agar (1)	19.16	20.7	11.4	−2.0	4.82	—
4.	$\overline{\overline{S}}^o$	Haase, Hoch, & Schönert (3)	19.3	21.0	11.6	−0.6	5.6	−7.9
5.	$\overline{\overline{S}}^o$	Khoroshin & Temkin (4)	19.5	20.0	10.8	−1.4	5.2	−7.75
		Ionic entropies based on the Agar postulate: $S^*(Cl^-, 0.01m) = 0$						
6.	S^*_o	This study	0.30	1.94	2.67	0.29	10.49	1.1
7.	$\overline{S}^o$	This study	18.39	19.3	9.2	−1.8	−5.22	−11.8
		Ionic entropies based on the KCl-bridge postulate: $tdp(KCl) = 0$						
8.	S^*_o	This study	1.10	1.14	1.87	−0.51	9.69	0.3
9.	S^*_o	Khoroshin & Temkin (4), de Bethune (6)	1.8	0.0	3.1	−0.3	9.7	3.35
10.	$\overline{S}^o$	This study	17.59	20.1	10.0	−1.0	−4.42	−11.0
11.	$\overline{S}^o$	Khoroshin & Temkin (4), de Bethune (6)	17.7	20.0	7.7	−1.1	−4.48	−11.1
		Ionic entropies based on Gurney's viscosity standard: $\overline{S}^o(H^+) = -5.5$ eu						
12.	S^*_o	Breck and Lin (2)	0.7	1.5	2.2	—	10.2	—
13.	S^*_o	Agar (1)	0.49	1.7	2.5	0.1	10.3	—
14.	$\overline{S}^o$	Breck and Lin (2)	18.7	19.0	8.9	−2.1	−5.5	−12.1
15.	$\overline{S}^o$	Agar (1)	18.67	19.0	8.9	−2.1	−5.5	−12.1

day largely of historical interest. The bottom three sections of Table I represent three different divisions of $\overline{\overline{S}}^o_i$ into its constituent terms $\overline{S}^o_i$ and S^*_{oi} according to the Agar, KCl-bridge, and Gurney viscosity postulates, which yield, for $S^o(H^+)$, values of −5.2, −4.4, and −5.5 eu, respectively. Mention must also be made of Lin and Breck's −5.7 eu (5) based on the isentropicity of trichelated redox ion pairs.

Interest focuses on the values of $S^*_o(Cl^-)$ as deduced by the different methods. The present study gives 0.30 eu under the Agar postulate and 1.10 eu under the KCl-bridge postulate. Agar (1) had previously obtained 0.49 eu and Breck and Lin (2) 0.7 eu, both under the Gurney postulate. This concordance of values leads one to believe that the absolute value of this quantity, which still remains to be unambiguously determined (8), will probably not be significantly different from any of them. An examination of the S^*_o values of all the ions, under all postulates, identifies them as structure makers in the Eastman third region of the solvent in the order $H^+ > Na^+ > K^+ > Ca^{++}$ (?) $> Cl^- > Li^+$, lithium ion being either a very weak structure maker ($S^*_o = 0.29$, Agar postulate) or a structure breaker ($S^*_o = -0.51$, KCl-bridge postulate). At higher concentrations, Li^+ becomes a structure breaker in the third region (S^* negative, Part II, Table V, lines 19 and 25) under both postulates.

The standard moving entropy $\overline{\overline{S}}^o$, *i.e.*, the partial molal entropy of the central ion plus its tightly bound waters, of the ions K^+, Cl^-, and Na^+ ranges from 21 to 11 eu. By subtraction of the cratic entropy (7) for a standard aqueous saline, R ln 55.51 or 8.0 eu for each ion, the unitary part of the moving entropy of these ions is found to range from 13 to 3 eu, values comparable to but smaller than the molal entropy of simple liquid molecules such as H_2O, 16.7; D_2O, 18.2; HDO, 19.0; Hg 18.5 eu. This somewhat lower entropy is consistent with a degree of organization imposed by the presence of the electrostatic charge. The entropy of transports S^*_o of K^+, Cl^-, and Na^+ appears, on both Agar and KCl-bridge postulates, to be small and positive, in the range 0-3 eu. The transport entropy is the entropy loss of the solvent in the third region due to the ordering influence of the ion and its tightly bound waters. A partial freezing of vibration in the hydrogen bonds between the Eastman second and third regions would be sufficient to account for an entropy loss of this magnitude. The fundamental frequency of hydrogen-bond stretching vibrations is 175 cm^{-1} (9), about 1/20th of the frequency of the covalent O-H bond [3600 cm^{-1}, (10)]. A partial freeze-out of one such hydrogen-bond vibration by a stiffening of the bond would be sufficient to account for a loss of a significant portion of the Einstein vibrational entropy

$$S_{vib} = R[u(e^u - 1)^{-1} - \ln(1 - e^{-u})] \qquad [1]$$

equal to 1.2 R or 2.4 eu at 300°K, where $u = hc\tilde{\nu}/kT$. This is an entropy loss of the right magnitude. The standard partial molal entropy $\overline{S}^o_i$ of the stationary ion is thus positive for Cl^-, K^+, and Na^+ and slightly smaller than the moving entropy $\overline{\overline{S}}^o_i$.

For Li^+ and Ca^{++}, the moving entropy $\overline{\overline{S}}^o_i$ is negative, which suggests a highly ordered structure in the Eastman first and second regions, *i.e.*, in the ion itself and its tightly bound waters. The entropy of transport S^*_{oi} is close to zero or slightly negative for Li^+, and small and positive for Ca^{++}. The partial molal entropy $\overline{S}^o_i$ of the stationary Li^+ and Ca^{++} ions thus emerges in both cases as negative, due principally to the ordering influence of these small ions in the Eastman second region. The role of Li^+ is thus contrasted: a structure maker in the second region, and a slight structure breaker in the third region.

Hydrogen plays a unique role in this regard. Take the round numbers: $\overline{\overline{S}}^o = +5$, $S^*_o = +10$, $\overline{S}^o = -5$ eu for H^+. The addition of one water entropy, 16.7 eu, yields $\overline{\overline{S}}^o = 21.7$ eu as the partial molal moving entropy of H_3O^+. Subtraction of the cratic entropy gives the unitary part of the moving entropy of hydronium ion as $\overline{\overline{S}}^u(H_3O^+) = 13.7$ eu. This is 3.0 eu smaller than the water entropy. Thus the hydronium ion structure appears to be sufficiently stiffened by its electrostatic charge to make its unitary entropy less than the entropy of water, despite the presence of one extra atom with its three additional degrees of freedom. The entropy of transport S^* of hydrogen ion is large and positive, around +10 eu, the same value holds for H_3O^+ as for H^+, since this is an interaction negentropy between the ion (plus its tightly bound waters if any) and the surrounding solvent in the third region [negentropy (11) because it measures the amount of order created by the presence of the ion]. This large positive value indicates the particular influence of H^+ as a structure maker in the solvent through enhanced hydrogen bonding. The energy of the hydrogen bond has been estimated between 3.1 and 7 kcal/mol (9, 12). Thus an entropy of transport as high as 10 eu could be contributed by the need to break hy-

drogen bonds when the proton moves away (2) and the structure shifts from the more highly hydrogen bonded $H_3O^+ \cdot (H_2O)_x$ structure to the less hydrogen bonded $H_2O \cdot (H_2O)_x$ structure.

If one looks at hydroxyl ion, whose conventional standard entropy is $\bar{S}^o(OH^-, \text{conv.}) = -2.52$ eu (13) and entropy of transport S^* (under the Agar postulate) 13.5 eu (1, 6), one obtains $\bar{S}^o(OH^-) = +2.5$ eu, and $\bar{\bar{S}}^o(OH^-) = 16$ eu. The unitary part of the latter is $\bar{\bar{S}}^u(OH^-) = 8$ eu, *i.e.*, about half of the water entropy. The contribution of OH^- to the ordering of the solvent through enhanced hydrogen bonding is even more marked than for H^+, as measured by the comparative S^*'s for the two ions. Consider the reaction

$$H_2O + H_2O = H_3O^+ + OH^- \qquad [2]$$

for which $\Delta S^o = -19.2$ eu (13). This large negative entropy change can be visualized as the summation

$$\Delta S^o = [\bar{\bar{S}}^u(H_3O^+) + \bar{\bar{S}}^u(OH^-)] + [-S^*_o(H^*) - S^*_o(OH^-)] + 2R \ln 55.51 - 2\,S^o(H_2O) = [13.7 + 8] + [(-10) + (-13.5)] + 2(8.0) - 2(16.7) = -19.2 \qquad [3]$$

in which the unitary entropies of the ions themselves contribute 21.7 eu, a loss of 11.7 eu over the two parent waters, and the interaction negentropy of the ions with the solvent contributes a further entropy loss of 23.5 eu, while the cratic (dilution) term contributes an entropy gain of 16.0 eu.

The data on heat capacities can be visualized in terms of the expression $\bar{C}_i = \bar{\bar{C}}_i + (-C^*_i)$. The moving heat capacities of ions such as Cl^-, K^+, Na^+, Li^+ (excluding its high value) which range from 2 to 20 eu (Part II, Table VII, lines 2-5) are comparable to C_p values of simple monatomic, diatomic, or triatomic liquids such as Hg(l), 6.6; Zn(l), 7.5; Cu(l), 7.5; Xe(l), 10.7; CO(l), 14.5; Cl_2(l), 16.0; H_2O(l), 18.0; SO_2(l), 20.7 [ref. (14), pp. 63-66]. The central ion, together with its tightly bound waters if any, manifests a partial molal heat capacity $\bar{\bar{C}}_i$ comparable to the C_p of small neutral molecules. The moving hydrogen ion has a slightly negative $\bar{\bar{C}}$, *i.e.*, it transports a reduction of heat capacity wherever it goes, and this also appears to be true for Ca^{++} (excluding its high value) (lines 6, 7).

As pointed out in Part II (1a), the role of the ion on its immediate entourage of tightly bound waters appears to be twofold, according as $\bar{\bar{C}}_i$ is greater or less than the Dulong and Petit value of 6 eu for the vibrations of a monatomic ion. $\bar{\bar{C}}_i$ is the partial molal heat capacity of the ion in motion, *i.e.*, it is the change in heat capacity of the solvent system that moves with the ion on addition of the ion to this system. Any excess of $\bar{\bar{C}}_i$ above 6 eu suggests that the ion is contributing an increase in the heat capacity of its tightly bound waters, perhaps by loosening the covalent O-H bonds, and permitting a heat capacity contribution to develop from the three internal vibrations of the tightly bound H_2O's whose frequencies are normally so high that quantum restrictions ordinarily prevent them from contributing to $C_p(H_2O)$. Where $\bar{\bar{C}}$ is less than 6 eu, or even negative, the ion brings in a reduction in heat capacity in its immediate entourage. This suggests that the ordering influence of the ion, which enhances the degree of hydrogen bonding of the surrounding water structure, affects the water system that moves with the ion (second region), and causes it to lose heat capacity.

The ionic transport heat capacity C^*_i represents the gain in heat capacity of the solvent in the third region when the ion moves away, it is positive for all ions (Part II, Table VII, lines 9, 11, 13, 15, 17, 19) except Li^+, Na^+, H^+, and $\frac{1}{2}Ca^{++}$ at 1.0 molal. Therefore C^*_i measures the heat capacity squeezed out of the solvent in the third region by the introduction of the ion plus its tightly bound waters if any. This loss of heat capacity, which results from an electrostatic enhancement of the degree of hydrogen bonding in the third region, is often larger than the heat capacity $\bar{\bar{C}}_i$ of the central ion itself plus any possible effect it may have in loosening up the covalent structure of its tightly bound waters. The resultant is then a negative value for $\bar{C}_i$, the partial molal heat capacity of the stationary ion, *i.e.*, the heat capacity change of the entire solvent system (second and third regions both) on introduction of the ion.

It is interesting to note that, for Cl^-, $\bar{\bar{C}}$ is very close to the Dulong and Petit value, and that C^* is large and positive (30 eu). This suggests that Cl^- either has no tightly bound waters and the ordering effect of its charge occurs entirely in the third region or else that the two effects of the charge: loosening of the covalent O-H bonds, and enhancement of the O ... H hydrogen bond structure exactly offset each other in the second region, probably the former.

With hydrogen ion, C^* is small (Part II, Table VII, line 9). Since hydrogen ion is a pronounced structure maker in the third region, its small C^* indicates that its structure making tendency shows little variation with temperature. An extrapolation according to a $\sqrt{m}$-law gives $C^*_o = 5.1$ eu. Coupled with our KCl-bridge value of $\bar{C}^o(H^+) = -5.1$ eu (line 8), this gives $\bar{\bar{C}}^o(H^+) = 0.0$ eu. The corresponding values for hydronium ion are then $\bar{C}^o(H_3O^+) = 12.9$ eu and $\bar{\bar{C}}^o(H_3O^+) = 18.0$ eu, *i.e.*, the hydronium ion has a moving heat capacity which is the same as $C_p(H_2O)$.

The molal heat capacity of liquid water, 18.0 eu, is three Dulong and Petit values, while C_v for water vapor is only a little over 6 eu (for three translations and three rotations), and C_p for ice is a little over 9 eu. Thus the liquid water structure picks up, through intermolecular interaction (hydrogen bonding) an increment of heat capacity of close to 12 eu over that of the vapor. A crude model of the water structure could be visualized as consisting of its three atoms loosely bound in a hydrogen-bonded quasi-lattice, possessing nine fully excited vibrational degrees of freedom. Such a model would have a heat capacity of $9 \times (2/2)R = 17.9$ eu. This model is an oversimplification, however, because the internal modes of vibration of H_2O retain frequencies high enough in the liquid state [bond stretching vibrations $\nu_1 = \nu_3 = 3440$ cm^{-1}, bond bending $\nu_2 = 1645$ cm^{-1} (9) as compared with 3652, 3756, and 1595 cm^{-1} in the vapor (15)] to make as negligible a contribution to the heat capacity of the liquid as they do to that of the vapor. Recently, Scheraga and Griffith (16) proposed a model of water structure in which the three internal modes of vibration are disregarded, and are replaced by a series of five energy levels for 4-bonded (ground state) and for 3-, 2-, 1-, and unbonded water molecules (excited states) within the hydrogen bonded quasi-lattice. The remaining six vibrations are assigned as translational modes (3) and librational modes (3) of the H_2O molecule as a whole within the lattice. Griffith (16) adjusted the energy levels and frequencies to give a best fit to the experimental thermodynamic data as follows

Type of H_2O molecule	Energy level (cal/mol)	Translational vibrations (cm^{-1})	Librational vibrations (cm^{-1})
unbonded	6670	26	197
1-bonded	4970	86	374
2-bonded	3870	61	500
3-bonded	2030	57	750
4-bonded	0	210	750

For liquid water at 0°, 25°, and 100°, this model predicts the following mol-fractions: 4-bonded H_2O: 0.368, 0.278, and 0.129; 3-bonded: 0.600, 0.671, and 0.740; 2-bonded: 0.030, 0.046, and 0.105; 1-bonded: 0.0014, 0.0026, and 0.0091; unbonded: 0.0008, 0.0023, and 0.0176. The fraction of hydrogen bonds broken at these temperatures is 0.167, 0.192, and 0.266, respectively. The calculated energy of fusion is 1347 cal/mol (compared with the experimental $\Delta H_{fus}(H_2O) = 1436$ cal/mol).

The Scheraga-Griffith partition function for H_2O provides for different sets of vibrational states for each energy level. It is therefore not separable according to the two types of molecular energy: bond and vibrational, and becomes quite cumbersome for analysis. It will here be replaced by a separable approximation. This approximate partition function for H_2O and H_3O^+ takes the form (21)

$$Q = \frac{(1 + ge^{-\epsilon/kT})^4}{(1 - e^{-h\nu^T/kT})^3(1 - e^{-h\nu^L/kT})^3} \quad [4]$$

in which the five energy levels are assigned an equal spacing ϵ. These levels have the geometrical multiplicities 1, 4, 6, 4, 1 corresponding to the number of ways a given H_2O or H_3O^+ can be 4-, 3-, 2-, 1- or unbonded in the quasi-lattice. In addition to these geometrical multiplicities which naturally appear in the fourth power expansion of the binomial, the multiplicity factor g is introduced as a correction needed to compensate for the fact that the higher energy levels, with their lower vibrational frequencies, have a higher density of vibrational states in the Griffith partition function than they would have in the approximate partition function if the factor g were to be omitted. Values of g calculable from the Griffith frequency assignments range between 2 and 18. The value 3 has been determined empirically for g as described below. Unique frequencies ν^T and ν^L are assigned to the three translational and three librational modes of vibration in all energy levels for both H_2O and H_3O^+. The approximate partition function thus has four adjustable parameters for H_2O, and one more for H_3O^+, as compared with 14 parameters in the Griffith partition function for H_2O.

To determine the frequencies ν^T and ν^L, the approximate partition function Q was also applied to the ice structure at 273°K, with the numerator set equal to unity, *i.e.*, ice is assumed to be 4-bonded throughout. The experimental values for the entropy S^o (ice, 273°K) = 9.88 eu, less the residual entropy of ice: R ln 3/2 = 0.81 eu (17), and for the heat capacity C_p^o (ice, 273°K) = 9.11 eu, neglecting the small difference between C_p and C_v, were equated to the vibrational contributions from Q. A fit was found at $\nu^L = 498.1$ and $\nu^T = 153.6$ cm^{-1}, values not inconsistent with the set of Griffith frequencies and in a ratio not far from 4:1, *i.e.*, $(m_O/m_H)^{1/2}$, a result which is not surprising since the translational vibrations involve largely motions of the oxygen atom, and the librational vibrations involve largely motions of the hydrogen atoms (22).

To evaluate the hydrogen bond energies in the numerator of Q, use was made of the experimental differences at 298°K

$$S^o(H_2O) - \bar{\bar{S}}^u(H_3O^+) = 3.0 \text{ eu} \quad [5]$$

$$C_p^o(H_2O) - \bar{\bar{C}}^o(H_3O^+) = 0 \quad [6]$$

as obtained above. The residual moving entropy of H_3O^+ was evaluated by a method to be described below as R ln 4/3 = 0.57 eu. Correction for the residual entropies of H_2O and H_3O^+, together with the assumption of equal vibrational contributions for both, gives the difference in bond entropies and heat capacities as

$$S_{bond}(H_2O) - \bar{\bar{S}}_{bond}(H_3O^+) = 2.78 \text{ eu} \quad [7]$$

$$C_{bond}(H_2O) - \bar{\bar{C}}_{bond}(H_3O^+) = 0 \quad [8]$$

Values of $\epsilon(H_2O)$ and $\epsilon(H_3O^+)$ were sought that would satisfy these differences. These were found to be $\epsilon(H_2O) = 1409$ and 1540; $\epsilon(H_3O^+) = 1996$ and 2060 cal/mol, for $g = 3$ and 4, respectively. Then complete bond and vibrational entropies and heat capacities for H_2O were computed from the full partition function Q, yielding, after inclusion of the residual entropy, at 298°K: $S^o = 16.74$ and 17.53 eu, and $C_v^o = 17.11$ and 18.91 eu, for $g = 3$ and 4, respectively. Since the experimental values are $S^o = 16.716$ eu and $C_v^o = 17.81$ eu for H_2O, the choice $g = 3$ gives a closer fit and was adopted empirically together with the parameters: $\nu^T = 153.6$, $\nu^L = 498.1$ cm^{-1}, $\epsilon(H_2O) = 1408.7$, $\epsilon(H_3O^+) = 1996.4$ cal/mol. Calculated entropies and heat capacities from Q are listed in Table II together with the experimental values for comparison. The partition function does correctly give the entropy of water from 0° to 100° as well as the entropy of fusion of ice. It does follow the decreasing trend of $C_v(H_2O)$ with increasing temperature, but not so abruptly as the experimental values. This is also a characteristic of the full Griffith-Scheraga partition function which predicts, however, a steeper drop than that observed (Table II).

The residual entropy of hydrogen ion can be calculated by a method analogous to Pauling's computation for ice (17). For a tetrahedral lattice of N oxygen atoms with $2N$ hydrogen atoms distributed among the $2N$ O ... O bonds and two sites available to each hydrogen atom (at 0.99 and at 1.77Å away from any particular oxygen atom), the number of configurations is 2^{2N}. These configurations include the following arrangements of H around O: 1 H_4O^{++}, 4 H_3O^+, 6 H_2O, 4 OH^- and 1 $O^=$. Thus for each O atom, only 6/16 of all possible configurations are H_2O's, and for the entire system, $W = 2^{2N}(6/16)^N$. The residual entropy is k ln $W = R$ ln $2^2 \cdot 6/16 = R$ ln 3/2 (17).

The residual contribution to the unitary partial molal entropy of hydrogen ion is the change in residual entropy of a large mass of H_2O per H^+ added to it. Take a central H_2O molecule and add H^+ to it. The number of distributions of 3H's among two sites each is 2^3, and the fraction of possible configurations that correspond to H_3O^+ is 4/16, making $W = 2^3$ (4/16) for the central O atom. The three vicinal O's, bonded by the three H's of the central H_3O^+, have each two further H's to be distributed among two sites per bond in three bonds. The fraction of possible configurations allowed here is only 3/16, instead of 6/16, since only three, instead of four, bonds are available. This makes $W = [2^2(3/16)]^3$ for these three O's. The fourth vicinal O whose own H bonds it to the central H_3O^+, has only one further H to be distributed among two sites per bond in three bonds. Again, the fraction of allowed configurations is only 3/16, instead of 6/16, making $W = 2(3/16)$ for this fourth O. For the remaining O's further away from the central

Table II. Comparison of calculated and experimental entropies and heat capacities of water and hydronium ion

All values in calories · degree^{-1} · mol^{-1}
Calculated values from the approximate partition function Q, Eq. [4], except where noted

Residual entropies: $S_{resid}(H_2O) = R$ ln 3/2; $\bar{\bar{S}}^u{}_{resid}(H_3O^+) = R$ ln 4/3

H_2O	S^o (calc)	S^o (exp)	C_v^o (calc)	C_v^o (exp)	C_p^o (exp)	C_v^o (calc)[a]
0° (Ice)	(9.86)	9.88	(9.11)	—	9.11	—
0° (Water)	15.24	15.14	17.11	18.15	18.16	19.67
25° (Water)	16.74	16.716	17.11	17.81	18.00	18.01
50° (Water)	18.11	18.13	16.94	17.33	18.00	16.95
75° (Water)	19.37	19.51	16.67	16.72	18.05	16.55
100° (Water)	20.51	20.76	16.35	16.03	18.15	16.64

H_3O^+	$\bar{\bar{S}}^u$ (calc)	$\bar{\bar{S}}^u$ (exp)	$\bar{\bar{C}}^o$ (calc)	$\bar{\bar{C}}^o$ (exp)
25°	13.73	13.7	17.11	18.0

[a] Calculated from the Griffith-Scheraga (16) partition function.

H_3O^+, W appproaches the Pauling value of $2^2(6/16)$ for pure water. The change in residual entropy resulting from the addition of one H^+ to an ice-like lattice of N H_2O's is then

$$k \ln \frac{2^3(4/16)[2^2(3/16)]^3\, 2(3/16)\, [2^2(6/16)]^{N-5}}{2^{2N}(6/16)^N} \quad [9]$$

and this is $\bar{S}^u_{resid}(H^+)$ which becomes $-R$ ln 24 = −6.32 eu on a molar basis. Now, $\bar{S}^u_{resid} = \bar{\bar{S}}^u_{resid} + (-S^*_{resid})$. The moving entropy term is the increment in residual entropy of the central H_2O itself on its transformation to H_3O^+, this is k ln $[2^3(4/16)]/[2^2(6/16)]$ which gives $\bar{S}^u_{resid}(H_3O^+) = R$ ln 4/3 = 0.57 eu. The residual entropy of transport of H^+ is then $S^*_{resid}(H^+) = R$ ln 32 = 6.89 eu. Since experimentally $S^*_o(H^+)$ is around 10 eu (Table I), this result suggests that the electrostatic part of the entropy of transport of H^+ amounts to a little over 3 eu, a value which would be consistent with the Eastman-Born equation at r_i = 2.8Å, *i.e.*, close to the O . . . O distance in the ice lattice.

The experimental values for H_2O in Table II are based on the NBS value for the entropy at 25° (18) and the NBS values for the specific heat as recorded in the "Handbook of Chemistry and Physics." C_v was computed from the observed C_p by the usual formula involving the compressibility and thermal expansion of water. Observed values for H_3O^+ are based on research reported above in the present paper.

The approximate partition function predicts the following mol fractions at 0°, 25°, and 100°: 4-bonded H_2O: 0.446, 0.375, and 0.227; 3-bonded: 0.399, 0.417, and 0.408; 2-bonded: 0.134, 0.174, and 0.274; 1-bonded: 0.020, 0.032, and 0.082; unbonded: 0.0011, 0.0022, and 0.0095, so that the fraction of hydrogen bonds broken becomes 0.183, 0.218, and 0.310 at these temperatures, i.e., about 10-16% larger than in the Griffith-Scheraga model. For H_3O^+ at 25°, Q predicts the mol fractions: 4-bonded: 0.675; 3-bonded: 0.279; 2-bonded: 0.043; 1-bonded: 0.0030; unbonded: 0.000077, for a fraction of hydrogen bonds broken of only 0.094. Thus the approximate partition function Q confirms that H_3O^+ is a strong structure maker in the solvent. The addition of H^+ to H_2O introduces a distinct amount of structure to the $H_3O^+ \ldots (H_2O)_4$ complex since it reduces the number of hydrogen bonds broken at 25°: 9.4%, to a level of half the number of hydrogen bonds broken, 18.3%, in the liquid $H_2O \ldots (H_2O)_4$ complex at the melting point. The need to break 12.4% more bonds, *i.e.*, from 9.4 to 21.8%, when the proton moves away at 25° is consistent with a heat of transport of $0.124 \times 4[\epsilon_{(H_3O^+)} + \epsilon_{(H_2O)}] + 0.782 \times 4\,[\epsilon_{(H_3O^+)} - \epsilon_{(H_2O)}]$ = 1689 + 1838 cal/mol = 3527 cal/mol, a value which is higher than but of the right order as compared with the observed heat of transport TS^* of H^+ of around 3000 cal/mol (on the Agar postulate). Lin (19, 20) has recently shown that S^* for hydrogen ion is strongly lowered by the addition of ethanol to water, where the ethanol effectively tends to hinder the proton transfer mechanism of H^+ mobility. Thus the heat of transport for proton transfer, calculated above to be 3527 cal/mol, from our present model of the H_2O and H_3O^+ structures, should be larger than the observed heat of transport, which contains a contribution from the much smaller heat of transport of the H_3O^+ migration. As the numbers quoted above show, this expectation is indeed found to be the case.

Further validation of the model is provided from the surface energy of water which is $\gamma - Td\gamma/dT$ (γ is surface tension), and is equal to 117.8 erg/cm² at 25°. Taking the surface population of water as $(\rho N_0/M)^{2/3} = 1.038 \times 10^{15}$ molecules/cm², the molar surface energy is 1634 cal, a value which compares favorably with our $\epsilon_{(H_2O)}$ of 1409 cal/mol, the energy increment when one H_2O molecule goes from a 4-bonded to a 3-bonded state, as it must when it moves into a position in the surface.

Despite its success (Table II), the approximate partition function Q has a number of defects. It overestimates the heat capacity of ice in the interval −50° to −200° by about 10-18%, but yields a satisfactory 1392 cal for the energy E-E_o of ice at 0° as compared with the experimental value of around 1310 cal. It underestimates the energy of fusion as 1031 cal as compared with the experimental 1436 cal. The calculated free energies are rather poor. The predicted ΔA(fusion) is negative at all temperatures so that the melting point of ice should then be 0°K. On the other hand, the calculated ΔA(fusion) remains small (−439 cal at 273°K) up to several hundred degrees, and then bends over sharply and drops linearly with increasing T. When this high temperature limit for ΔA(fusion) is extrapolated back to zero, it predicts a melting point of 383°K, *i.e.*, about 110° too high.

With OH^- ion, there are three translational vibrations and two librational vibrations. If the same frequencies and bond contributions are utilized as for H_3O^+, $\bar{\bar{S}}^u$ is calculated to be 13.2 eu, a value much higher than the observed 8 eu. The hydroxyl ion should be more tightly bound to the hydrogen bonded water lattice than H_3O^+, as evidenced by its higher entropy of transport. This factor alone would tend to raise the frequencies and the bond energies for OH^- and would significantly lower $\bar{\bar{S}}^u$. If the observed unitary part of the moving entropy of hydroxyl ion $\bar{\bar{S}}^u(OH^-)$ = 8 eu is arbitrarily divided into a vibrational contribution of 7 eu plus a bond contribution of 1 eu, the observed value can be fitted with the assignments: ν^T = 196, ν^L = 784 cm^{-1}, ϵ = 3000 cal/mol, all of which are about 50% higher than the corresponding values for H_3O^+, *i.e.*, the hydrogen bond $OH^- \ldots H_2O$ would seem to have about 50% greater stiffness than $H_3O^+ \ldots H_2O$. The corresponding moving heat capacity would then be, for the five vibrations: 6.9 eu, for the bonds: 3.8 eu, giving a calculated total $\bar{\bar{C}}^o(OH^-)$ of about 11 eu.

Since the conventional partial molal heat capacity is $\bar{C}_p^o(OH^-, conv.) = -32$ eu (18), it is possible from our KCl-bridge value $\bar{C}^o(H^+) = -5.1$ eu to obtain $\bar{C}^o(OH^-) = -27$ eu, and, in view of the moving heat capacity calculated above, $C^*(OH^-) \approx 38$ eu is the heat capacity loss of the third region surrounding the OH^- ion, a value comparable to and even larger than C^* for the chloride ion (Part II, Table VII, line 11).

Griffith (16) extended his statistical theory of the water structure to infinitely dilute solutions of alkali halide salts. Adjusting his statistical parameters to the experimental properties of the salts and to Breck and Lin's (2) choice of absolute partial molal ionic entropies (Table I, line 14), his theory yields values of the single ion partial molal heat capacities which can be compared with our experimental results based on the KCl-bridge postulate (Part II, Table VII). The comparison is as follows with our values given in parentheses: Li^+, 11.94 (8.5); Na^+, 0.16 (0.3); K^+, −4.37 (−4.9); Cl^-, −30.71 (−24.1). There is an interesting and close parallel between Griffith's statistical values and our experimental results in this case.

Acknowledgment

Grateful acknowledgment is made to the Office of Saline Water, U.S. Department of the Interior, for support of this investigation under Grants No. 14-01-0001-389 and −1466 at Boston College.

Manuscript submitted Dec. 2, 1968; revised manuscript received *ca.* June 19, 1969.

Any discussion of this paper will appear in a Discussion Section to be published in the June 1970 JOURNAL.

LIST OF PRINCIPAL SYMBOLS

A Linear coefficient in thermoelectric equation, μV/deg.
A Helmholtz free energy, cal/mol.
B Quadratic coefficient in thermoelectric equation, μV/deg^2.
B Gurney's relative viscosity coefficient.
C_p, C_v Molal heat capacity at constant pressure, or constant volume, cal/deg·mol (eu/mol); cal/deg·eq (eu/eq).
$\overline{C}_p^o$ Partial molal heat capacity at infinite dilution.
C^* Transport heat capacity of a salt or an ion constituent.
C^*_o Transport heat capacity of a salt or an ion constituent at infinite dilution.
$\overline{\overline{C}}$ Partial molal moving (transported) heat capacity of a salt or an ion constituent.
$\overline{\overline{C}}^o$ Partial molal moving (transported) heat capacity of a salt or an ion constituent at infinite dilution.
$\overline{C}$ Partial molal stationary heat capacity of an ion constituent.
$\overline{C}^o$ Partial molal stationary heat capacity of an ion constituent at infinite dilution.
c Velocity of light, 2.998 x 10^{10} cm.s^{-1}
D Dielectric constant, dimensionless.
D_o Coulomb's law constant: (10^{-9}/9) a.s.v^{-1}·m^{-1}, or 1 statampere. second·statvolt^{-1}. cm^{-1}, see ref. (13), Part II.
E Molal energy, cal/mol.
E_o Molal entropy, at 0°K.
e Elemental charge, 1.602 x 10^{-19} a.s.
F The Faraday, 96487 a.s.
g Empirical multiplicity factor in approximate partition function Q.
H Molal enthalpy, cal/mol.
h Planck's constant, 6.62 x 10^{-27} erg.s.
i, j Ionic indexes.
$\overline{J}$ Relative partial molal heat capacity.
k Boltzmann constant, 1.38 x 10^{-16} erg/deg, 86.17 microvolt-electrons/deg.
m Molality: mols of solute per kilogram of solvent.
m Mass, grams.
M Molecular weight, molar mass, grams/mol.
N Number of molecules; N_o: Avogadro's number
n Number of mols.
p Pressure, dyne·cm^{-2}, atm.
Q Partition function for water and hydronium ion (dimensionless).
r Ionic radius, cm, Å.
R Gas constant, 1.98717 eu/mol, 86.17 microvolt-faradays/deg-mol.
S molal entropy, cal/deg-mol (eu/mol), cal/deg·eq (eu/eq).
$\overline{S}$ Partial molal entropy of a salt, partial molal stationary entropy of an ion constituent.
$\overline{S}^o$ Partial molal entropy of a salt in the hypothetical standard state with $m = 1$, but all other properties at infinite dilution.
S^* Transport entropy of a salt or an ion constituent.
S^*_o Transport entropy of a salt or an ion constituent at infinite dilution.
$\overline{\overline{S}}$ Partial molal moving (transported) entropy of an ion constituent.
$\overline{\overline{S}}^o$ Partial molal moving (transported) entropy of an ion constituent in the hypothetical standard state.
$\overline{\overline{S}}^{o\prime}$ $\overline{S}^o + S^*(m)$, preliminary standard value of the moving entropy for an ion constituent.
$\overline{\overline{S}}^u$ Unitary part of $\overline{\overline{S}}^o$ for an ion constituent.
T Temperature, °K; t temperature, °C.
t_+, t_-, t_i, t_r, t_g Hittorf transference numbers of + ions, − ions, ions of species i, ions of species r to which electrode is reversible, ions of species g gegenions of r.
V Electrical potential of copper electrode terminal, volts.
v Valence of a salt.
$z, z_+, z_-, z_i, z_r, z_g$ Ionic valence (with sign). See t_+ . . . for explanation of subscripts.
γ Mean ion activity coefficient of a salt; γ_i: ionic activity coefficient.
ϵ Energy level in hydrogen-bonded structure of H_2O and H_3O^+.
ϵ_o $= (dV/dT)_{th,initial}$ Initial thermoelectric coefficient, μV/deg.
ϵ_∞ $(dV/dT)_{th,final}$ Final thermoelectric coefficient, μV/deg.
μ Ionic strength; ν: number of ions per molecule of salt.
$\tilde{\nu}, \nu$ Frequency, wave number, s^{-1}, cm^{-1}.
ρ Density, g·cm^{-3}.

REFERENCES

1. J. N. Agar, "Thermogalvanic Cells," in "Advances in Electrochemistry and Electrochemical Engineering," P. Delahay, Editor, Vol. 3, Interscience, New York (1963).
1a. A. J. de Bethune and H. O. Daley, Jr., *This Journal*, **116**, 1395 (1969).
2. W. G. Breck and J. L. Lin, *Trans. Faraday Soc.*, **61**, 2223 (1965).
3. R. Haase, K. Hoch and H. Schönert, *Z. physik. Chem.*, **27**, 421 (1961).
4. M. I. Temkin and A. V. Khoroshin, *Zh. Fiz. Khim.*, **26**, 500, 773 (1952).
5. J. L. Lin and W. G. Breck, *Can. J. Chem.*, **43**, 766 (1965).
6. A. J. de Bethune, *This Journal*, **107**, 829 (1960).
7. R. W. Gurney, "Ionic Processes in Solution," McGraw-Hill Book Co., New York (1953).
8. A. J. de Bethune, S. A. Carrano, T. P. O'Connor, and M. Y. C. Fu, Paper No. 180 presented at Boston Meeting, May 5-9, 1968.
9. B. E. Conway, "Proton Solvation and Proton Transfer Processes in Solution," pp. 43-148, in "Modern Aspects of Electrochemistry," No. 3, J. O'M. Bockris and B. E. Conway, Editors, Butterworths, Washington (1964); B. E. Conway, *Ann. Rev. Phys. Chem.*, **17**, 481 (1966).
10. J. C. Davis, "Advanced Physical Chemistry," Ronald Press, New York (1965).
11. L. Brillouin, "Science and Information Theory," Academic Press, New York (1956).
12. B. H. Mahan, "University Chemistry," Addison Wesley, Reading, Mass. (1965).
13. W. M. Latimer, "Oxidation Potentials," 2nd ed., Prentice Hall, New York (1952).
14. K. S. Pitzer and L. Brewer, "Lewis and Randall's Thermodynamics," 2nd ed., McGraw-Hill Book Co., New York (1961).
15. G. Herzberg, "Molecular Spectra and Molecular Structure, Polyatomic Molecules," Van Nostrand, New York (1950).
16. J. H. Griffith, Ph.D. Dissertation, Cornell University (1967).
17. L. Pauling, "Nature of the Chemical Bond," 2nd ed., Cornell University Press, Ithaca, N. Y. (1942).
18. National Bureau of Standards, Circular 500 (1952).
19. J. Lin and J. J. De Haven, *This Journal*, **116**, 805 (1969).
20. J. Lin, *ibid.*, Paper submitted for publication.
21. A. J. de Bethune, Office of Saline Water, R.&D. Progress Report No. 412, January, 1969.
22. G. Nemethy and H. A. Scheraga, *J. Chem. Phys.*, **36**, 3382 (1962) catalogued the spectral bands of ice and water as: 800, 650, 500 cm^{-1} (assigned to librational modes); 210, 160 cm^{-1} (assigned to translational modes); plus 175 and 145 cm^{-1} in water only. Our calculated frequencies of 498.1 and 153.6 cm^{-1} very nearly coincide with the low frequency limits of these observed sets of bands.

Technical Notes

Electron Microprobe Study of the Active Materials in the Lead-Acid Storage Battery

Takewo Chiku and Koichi Nakajima

Toyota Central Research & Development Laboratories, Inc., Nagoya, Japan

The electrochemical processes of forming the active materials in a lead-acid storage battery have been thoroughly examined. However, the mechanism of formation is not clear as yet. Based on observations of the electrochemical polarization in a cylindrical mass of litharge, one of the present authors (1) clearly showed that the polarization was largely dependent on the potential gradient produced in the mass. Thus, it was shown that negative polarization began to develop from a region near the positive end of the cylindrical mass, while positive polarization began to develop from the interior of the mass. Simon and Jones (2, 3) have studied the structural changes occurring during the electrochemical formation of positive active material, and they showed that the microstructure depended on the condition under which the active materials were formed.

Tudor *et al.* (4) proposed the autoradiographic technique to apply to battery research, and by using this technique they have shown (5) the electrochemical behavior, especially of the Pb-Ca grid battery with the addition of phosphoric acid. However, their technique is not suitable for microanalysis of the structural change of electrode plates during the process of charge and discharge.

The present study was undertaken to elucidate with the aid of an electron probe x-ray microanalyzer the concentration changes of lead sulfate and its distribution on charge and discharge in the electrode plate.

Experimental Procedure

The samples examined were taken from automobile batteries, each cell consisting of 5 positive and 6 negative plates. Specifications of this battery are as follows: 12V, 40 Ahr at the 20-hr rate, terminal voltage 9.5-9.7V after discharge with 150A at −15°C for 5 sec, and the specific gravity of the electrolyte solution 1.260 at 20°C.

The batteries were discharged under various conditions after having been charged at 3A for 13 hr. A negative and a positive plate were taken from each stage shown in Table I. These stages are designated as A, B, C, D, E, and F. Three blocks of active material surrounded by the unit grid section were then cut out carefully from the upper, middle and lower portions of each electrode plate as shown in Fig. 1, the size of the unit section being 17 x 4 x 1.4 mm³. These blocks were then completely cleansed with distilled water until no sulfate ion was detected and finally dried at room temperature under reduced pressure.

Table I. Time of discharge or charge and terminal voltage in each stage of the electrode plate

Stage	Charge at 0.0022 A/cm² Time of charge, hr	Charge at 0.0022 A/cm² Terminal voltage, volt	Discharge at 0.003 A/cm² Time of discharge, hr	Discharge at 0.003 A/cm² Terminal voltage, volt	Discharge at 0.011 A/cm² Time of discharge, min	Discharge at 0.011 A/cm² Terminal voltage, volt
A	0.1	2.07	0.5	2.05	0.5	1.70
B	0.5	2.07	1	2.04	1	1.72
C	2	2.11	2	2.03	2	1.71
D	5	2.20	3	2.01	3.5	1.62
E	8	2.37	6	2.00	5.7	1.50
F	13	2.87	8	1.00	6.2	0.80

The intensity of Pb-Lα and S-Kα radiation was measured on these block samples along the surface or in the direction of depth from the surface by using a Shimadzu ARL electron probe x-ray microanalyzer operated at 30 kV. The area of the irradiated specimen surface was 2μ or 10μ in diameter for making a line analysis and 360 x 360 μ^2 for measuring the electron beam scanning pattern (EBS). The intensity of the characteristic radiation of each element in the sample was determined as the average value of at least twenty different measurements.

Experimental Results and Discussion

Figure 2 shows the EBS pattern of S-Kα radiation obtained from the defined portions on the surface of the discharged positive plate in which the effective depth of penetration of the electron beam into the sample was estimated to be about 2μ. Line analyses were also carried out on samples taken from each stage shown in Table I. A typical example of the analysis is shown in Fig. 3. This result shows that the electrochemical reaction which occurs on the electrode plates does not proceed homogeneously over the entire plate, but that the content of $PbSO_4$ produced during discharging varies from area to area in the samples. It is clearly seen from these figures that for a given position the slopes of the intensity curves of Pb-Lα and S-Kα radiation are opposite to each other. Thus, an increase (or decrease) of the intensity of Pb-Lα corresponds to a decrease (or increase) of that of S-Kα. This can be explained in terms of the nucleation and growth (or decomposition) of $PbSO_4$ (6), if the sources of S-Kα radiation emitted from the electrode plate are related completely to the presence of $PbSO_4$ in the region observed. The concentration of $PbSO_4$ and its distribution in the samples can be estimated on this assumption. Figure 4 shows the per cent change of

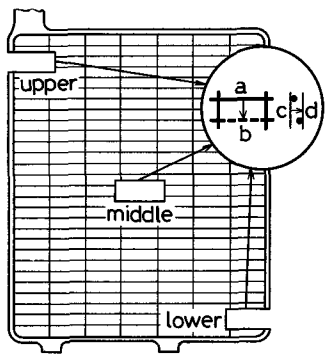

Fig. 1. Upper, middle, and lower positions of electrode plate from which specimens were prepared.

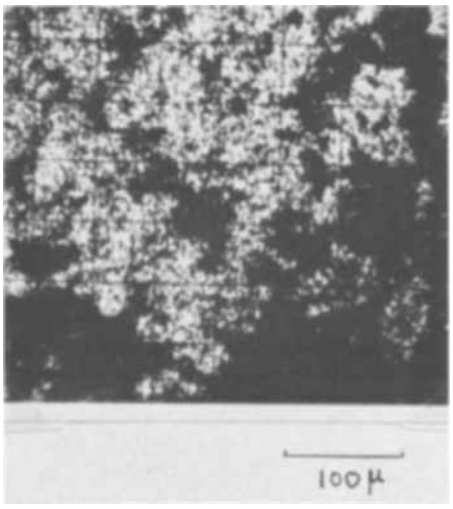

Fig. 2. EBS pattern of S-Kα radiation obtained from discharged positive plate.

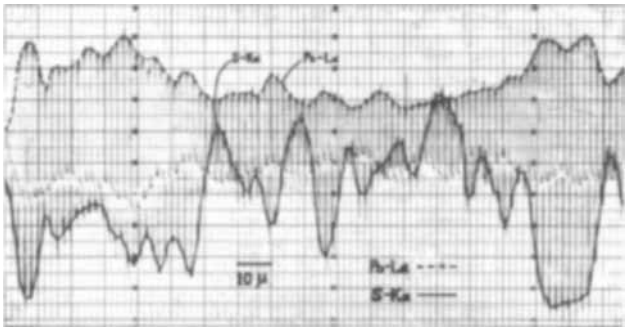

Fig. 3. Example of line analysis of S-Kα and Pb-Lα radiation across the surface of the negative plate (see Fig. 1) taken from stage D.

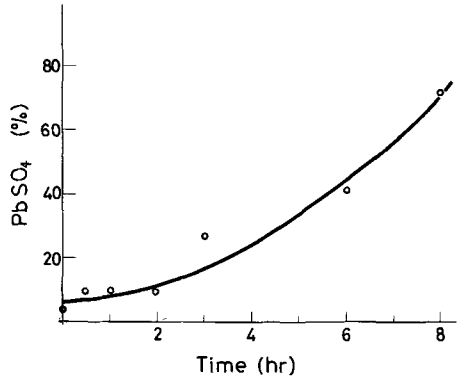

Fig. 4. Dependence of the content of $PbSO_4$ in the negative plate on the time of discharge (at 0.003 A/cm²).

the content of $PbSO_4$ in the surface of a negative plate with time of discharge: the content of $PbSO_4$ increases gradually with the time, and after 8 hr the increase attains to about 75%, which agrees with the result (6) obtained by x-ray.

It is very interesting to note that the surfaces of the electrode plates are not covered entirely with the substance containing sulfur even in the latter stage of discharge. This result enables us to suggest that some Pb crystallites must remain randomly to the final stage of discharge, and they will make nuclei for changing $PbSO_4$ into Pb during charging.

The concentration gradient of $PbSO_4$ sampled from the surface to the inner part was measured on samples which corresponded to the stages in the process of charge or discharge shown in Table I. The content of $PbSO_4$ in the positive plate had a tendency to decrease with depth from the surface for any stage of the discharge and charge, confirming the previous results (1) and also that of Tudor *et al.* (5).

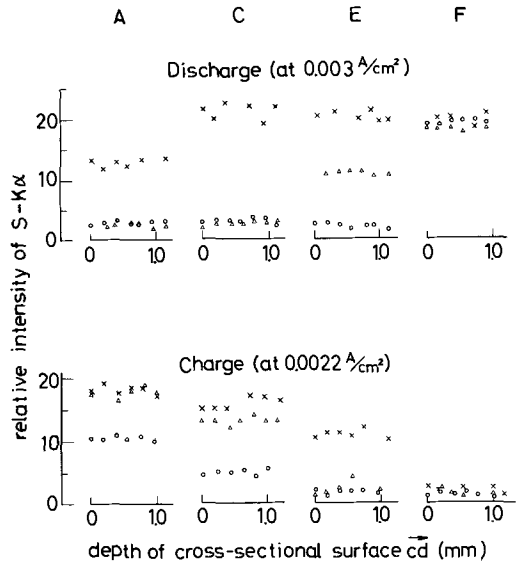

Fig. 5. Relative intensity of S-Kα radiation vs. depth from the surface of negative plate. —x— lower, —△— middle, —○— upper.

Figure 5 is the intensity change of S-Kα radiation with depth of the negative plate, showing somewhat different behavior from that of the positive plate, that is, the concentration gradient of $PbSO_4$ is almost zero for any stage of charge and discharge. The result of electron microprobe analysis shown in Fig. 4 indicates the existence of S-Kα radiation corresponding to a few per cent of $PbSO_4$ in the charged state. It will be understood by this fact that $PbSO_4$ in the electrode plate is not entirely changed into lead even in the fully charged state, and its amount increases with time of battery usage (6). It should be noted here that the total amount of $PbSO_4$ estimated from the x-ray analysis corresponds to that of crystallites a few hundred angstroms or more in size.

One of the authors (Chiku) has expected from his previous experiments (1) performed in a large quantity of the electrolyte solution without using a separator and glass mat that the electrochemical reaction occurring in the negative plate should develop from the interior to the surface for the stage of discharge, and *vice versa* for the stage of charge. The present results, however, do not coincide absolutely with the above description, suggesting that the concentration change of $PbSO_4$ and its distribution depend on the effective quantity of electrolyte solution next to the electrode plate.

It will be noted that the intensity of S-Kα radiation in both negative and positive plates becomes a maximum in the lower part of plate for any stage of the discharge and charge, showing that the electrochemical reaction proceeds first in the lower part for the stage of discharge and in the upper for the stage of charge. This may be explained as being caused by the formation of a concentration gradient of electrolyte solution along the surface of the plate (and also a temperature gradient) during the progressive reaction. An experimental confirmation of this will be given by electron microscopic observations of the morphological change of $PbSO_4$ crystallites in the lower and upper parts of the plate.

Summary

The dependence of the concentration of $PbSO_4$ and its distribution on charge and discharge in the electrode plate were examined in commercial lead-acid storage batteries by using an electron probe x-ray microanalyzer.

The concentration change of $PbSO_4$ in the negative plate during discharge was found to be stationary with

the depth from the surface. Similar distribution curves of $PbSO_4$ were also obtained for the electrode plates during charging.

Acknowledgment

The authors wish to give hearty thanks to Dr. Ninomiya for his informative discussion. Thanks are also given to Messrs. H. Haba, A. Isogai, and K. Satta for their diligent aid throughout the course of the work.

Manuscript submitted Jan. 15, 1969; revised manuscript received June 13, 1969.

Any discussion of this paper will appear in a Discussion Section to be published in the June 1970 JOURNAL.

REFERENCES

1. T. Chiku, *Bull. Chem. Soc. Japan*, **13**, 110 (1938); T. Chiku, *Toyoda-Kenkyû-Ihô*, **2**, 83 (1934) (in Japanese); T. Chiku, *ibid.*, **5**, 29 (1938) (in Japanese); T. Chiku, *Proc. Physico-Math. Soc. Japan*, **17**, 248 (1943) (in Japanese).
2. A. C. Simon and E. L. Jones, *This Journal*, **102**, 279 (1955).
3. A. C. Simon and E. L. Jones, *ibid.*, **109**, 760 (1962).
4. S. Tudor, A. Weisstuch, and S. H. Davang, *Electrochem. Technol.*, **3**, 90 (1965).
5. S. Tudor, A. Weisstuch, and S. H. Davang, *ibid.*, **5**, 21 (1967).
6. T. Chiku, *This Journal*, **115**, 982 (1968).

The Dissociation Pressure of Hematite

P. E. C. Bryant and W. W. Smeltzer*

Department of Metallurgy and Materials Science, McMaster University, Hamilton, Ontario, Canada

Several determinations of the dissociation pressure for hematite to magnetite have been made during the past several years. Greig *et al.* (1) determined the temperatures at which these oxides exist in equilibrium with air and pure oxygen. Darken and Gurry (2) confirmed and expanded these results by an extensive investigation on the equilibration of these oxides in atmospheres of known oxygen potentials at several temperatures in the range 1100°-1500°C. More recently, Norton (3) and Salmon (4) measured the equilibrium pressures directly at temperatures from as low as 780° to 1362°C and, most recently, Blumenthal and Whitmore (5) and Charette and Flengas (6) have determined the dissociation pressure and standard free energy of formation at temperatures in the range 690°-1100°C using a solid state electrochemical method.

The difference is significant between the results obtained from the two electrochemical investigations. Charette and Flengas (6) used a closed cell with a nickel oxide reference electrode, the zirconia-calcia electrolyte in the form of a closed tube separating the electrode compartments. On the other hand, Blumenthal and Whitmore (5) used the open cell stacked tablet technique, the cell operating with a zirconia-calcia electrolyte tablet and iron, wustite as the reference electrode. Hematite exhibits a relatively high dissociation pressure in comparison to wustite; consequently a low mixed potential rather than an equilibrium potential may have been generated by this latter cell due to transfer of oxygen from one electrode compartment to the other through the inert gas atmosphere surrounding the stacked tablets. In this work, a different cell has been used containing copper-cuprous oxide as the reference electrode. Since the electromotive force generated by this cell is small, it should be possible to obtain equilibrium values of the potentials by the open cell stacked tablet technique.

The galvanic cell may be represented as

$$\begin{matrix} & \text{Cu} & & & \text{Pt} \\ & | & & & | \\ Cu_2O, & Cu & | \; Zr_{0.85}Ca_{0.15}O_{1.85} \; | & Fe_3O_4, & Fe_2O_3 \end{matrix} \qquad [1]$$

where Cu and Pt represent the metal leads embedded between the solid tablets in the electrode compartments. The tablets of the zirconia-calcia electrolyte containing 15 w/o (weight per cent) calcia and the metal-oxide components were prepared from Fisher C. P. reagent powders, the Cu_2O, Cu and Fe_3O_4, Fe_2O_3 electrodes containing metal and oxygen in the ratios 2.10 and 8.75, respectively. Cell construction, preparation of the electrode and electrolyte tablets, and the apparatus for potential measurements have been reported (7).

The temperature of a cell was controlled within ± 1°C and potentials were determined to a precision of 10^{-3} mV. To insure potential stability, the inert gas atmosphere flowing around the cell contained trace amounts of oxygen resulting from dissociation of cuprous oxide contained in a small silica combustion boat outside each electrode compartment and in a copper tray below the cell supporting tube. Oxygen was provided by this means to the argon atmosphere at a partial pressure below the hematite-magnetite equilibrium oxygen pressure but sufficient to prevent appreciable dissociation of hematite.

In Fig. 1, the electromotive force values produced are shown for several temperatures in the range 1060°-1323°K. The results were obtained from cycles of ascending and descending temperatures on three cells. Potential stability was excellent being steady at a specific test temperature for a period of 20 hr. Investigation of each cell at completion of the experiment showed that the reaction electrodes had plastically flowed about the copper and platinum leads, virtually encasing them in the metal-oxide mixtures, and that the electrode-electrolyte tablets were sintered together.

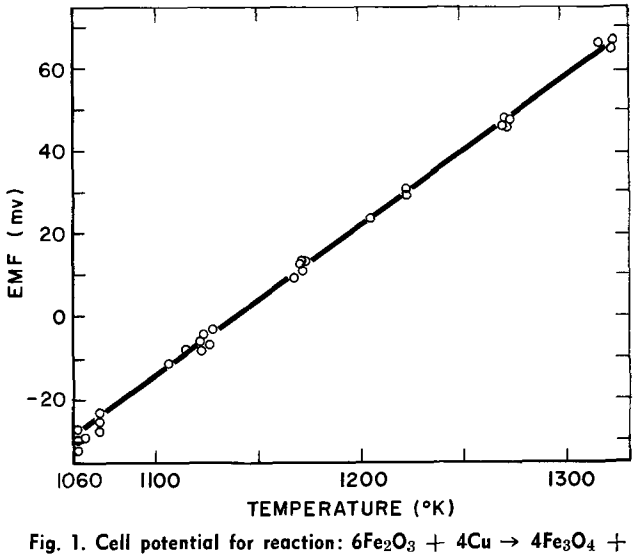

Fig. 1. Cell potential for reaction: $6Fe_2O_3 + 4Cu \rightarrow 4Fe_3O_4 + 2Cu_2O$.

* Electrochemical Society Active Member.

Table I.

Cell potential: E (mV) = A + BT (°K)
Cell Reaction: $6Fe_2O_3 + 4Cu \rightarrow 4Fe_3O_4 + 2Cu_2$

Reference	Temperature range (°K)	A	B	Standard deviation (mV)
This work	1060-1323	−413.7	0.363	±1.6
(6)	967-1373	−416.12	0.36471	±1.14

Kiukkola and Wagner (8) have expressed the thermodynamic parameter to be obtained from this type of galvanic cell involving only oxygen migration through the electrolyte. In the case of cell [1], the potential is

$$E = \frac{RT}{4F} \ln PO_2(Fe_2O_3, Fe_3O_4)/PO_2(Cu_2O, Cu) \quad [2]$$

where R is the gas constant, $\mathbf{F}$ is the Faraday, and the oxygen pressures are the dissociation pressures for the designated oxides. In turn, these dissociation pressures may be related to the standard free energies of formation of the oxide per mole of oxygen. For example, this free energy change for hematite formation from magnetite is

$$\Delta G°_T = -RT \ln PO_2\ (Fe_2O_3, Fe_3O_4) \quad [3]$$

assuming that the activities of the pure solid oxides are unity. Consequently the values of the dissociation pressure for hematite at the investigated temperatures, which may be calculated from the potential determinations and the values reported for the standard free energy of formation of cuprous oxide, may then be represented by the Van't Hoff isochore.

Since the cell potentials were linearly related to temperature, the constants of the line illustrated in Fig. 1 were evaluated by the least-squares method. These values, as illustrated in Table I, show close agreement with those calculated from the electrochemical results previously presented for the same temperature range by Charette and Flengas (6). Accordingly both the closed tube cell and the stacked tablet open cell with a suitable reference electrode have yielded values for the equilibrium potentials of the hematite-magnetite system within an accuracy better than ±2 mV.

The dissociation pressures of hematite calculated from the results of this investigation may be represented by the equation

$$\log PO_2\ (Fe_2O_3, Fe_3O_4) = \frac{-26{,}196 \pm 69}{T} + 15.124 \pm 0.003 \quad [4]$$

where T is °K and pressure is an atm. In this calculation, the expression used for the standard free energy of formation of cuprous oxide per mole oxygen is that given from two previous investigations (6, 9)

$$\Delta G°_T = -79{,}780 + 34.120T \pm 345 \text{ cal} \quad [5]$$

The above results and those reported in the literature for the temperature range 690°-1500°C are plotted in Fig. 2. It is apparent that Eq. [4] when extrapolated gives a good estimate to the higher temperature results. The least-squares line for all reported values at temperatures in the range 690°-1470°C is

$$\log PO_2\ (Fe_2O_3, Fe_3O_4) = \frac{-25{,}908 \pm 215}{T} + 14.862 \pm 0.007 \quad [6]$$

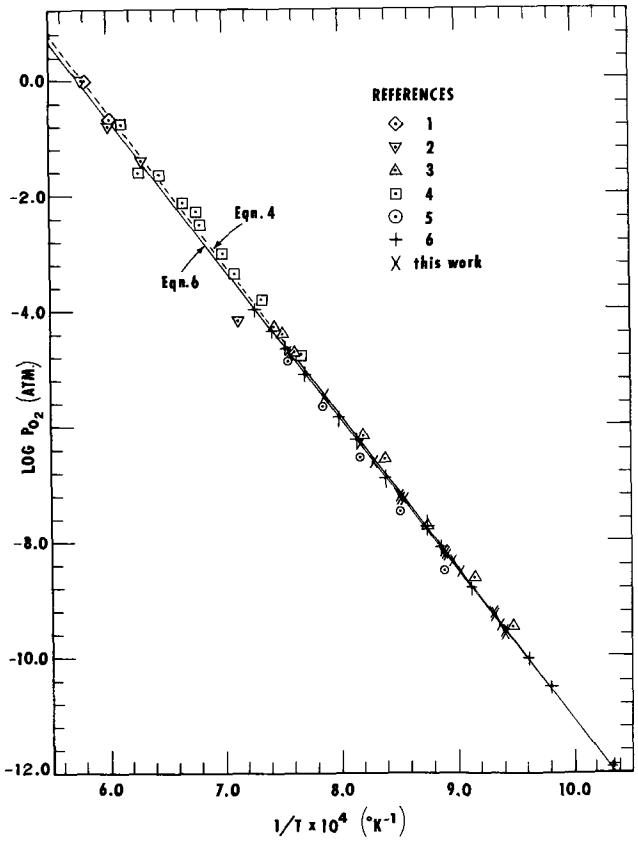

Fig. 2. Van't Hoff isochore, log p_{O_2} vs. $1/T$, for the dissociation pressure of hematite to magnetite.

This latter equation would thus appear to be the best estimate presently available for determining the dissociation pressure of hematite at temperatures where the oxides exist as solids.

Acknowledgments

The authors were indebted to T. Homma for assistance with the computer calculations. This work was sponsored by the American Iron and Steel Institute and the Defence Research Board, Ottawa, Canada.

Manuscript submitted April 14, 1969; revised manuscript received June 19, 1969.

Any discussion of this paper will appear in a Discussion Section to be published in the June 1970 JOURNAL.

REFERENCES

1. J. W. Greig, E. Posnjak, H. E. Merwin, and R. B. Sosman, *Am. J. Sci.*, **30**, 239 (1935).
2. L. S. Darken and R. W. Gurry, *J. Am. Chem. Soc.*, **68**, 798 (1946).
3. F. J. Norton, General Electric Res. Lab. Report No. 55-RL-1248, March 1955, Schenectady, N. Y.
4. O. N. Salmon, *J. Phys. Chem.*, **65**, 550 (1961).
5. R. N. Blumenthal and D. H. Whitmore, *J. Am. Ceram. Soc.*, **44**, 508 (1961).
6. G. G. Charette and S. N. Flengas, *This Journal*, **115**, 796 (1968).
7. G. A. Roeder and W. W. Smeltzer, *ibid.*, **111**, 1074 (1964).
8. K. Kiukkola and C. Wagner, *ibid.*, **104**, 379 (1957).
9. B. C. H. Steele, "Electromotive Force Measurements in High Temperature Systems," p. 3, American Elsevier Publishing Co. Inc. (1968).

Brief Communication

Dicarbonium Ions as Products of Electrochemical Oxidation of Biologically Important Purines at the Pyrolytic Graphite Electrode

Glenn Dryhurst

Department of Chemistry, University of Oklahoma, Norman Oklahoma

Recent studies have indicated that the primary electrochemical oxidation product of uric acid (1) (2,6,8-trioxypurine) and adenine (6-aminopurine) (2) in aqueous solution at the pyrolytic graphite electrode is a dicarbonium ion; this results from removal of two electrons from the 4,5-carbon-carbon double bond of the purine ring. Uric acid is oxidized in a single rapid 2*e* process (Eq. [1]), while adenine first undergoes two 2*e* oxidations at the 2 and 8 positions to the oxy- and then dioxyadenine, the latter compound then being further oxidized to a dicarbonium ion (Eq. [2]).

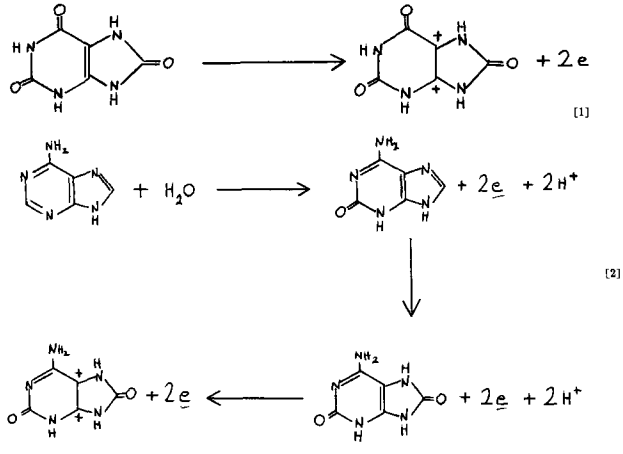

Subsequent work (3) suggests that many other biologically important purines may give a similar primary electrooxidation product. Such a dicarbonium ion could not have a long lifetime and indeed many ultimate breakdown products have been observed (1-3). The oxidation waves for all purines shift positive with increasing *p*H which suggests that the primary electrochemical product results from a concerted removal of two electrons and attack by water to give a 4,5-dihydroxy species with the liberation of two protons. Nevertheless, for the purpose of this report the primary electrochemical product will be referred to as a dicarbonium ion. Purines containing exocyclic sulfur atoms do not appear to be oxidized in the purine ring, but rather at the sulfur moiety (4).

It appeared reasonable to suppose that carbonium ions of the type shown in Eq. [1] and [2] would be very readily electrochemically reducible. Accordingly a number of purine derivatives were studied by fast sweep cyclic voltammetry in the hope of detecting a short lived electrochemically reducible oxidation product. Initially pyridine was employed as solvent but the very low solubility of all the purines precluded its extensive use. Accordingly an aqueous acetate buffer solution *p*H 4.7 was utilized in which all the important purines are reasonably soluble.

Experimental

Chemicals.—Uric acid, xanthine, hypoxanthine, adenine, guanine, guanosine, adenosine were obtained from Nutritional Biochemicals, 2,8-dioxyadenine from Aldrich and isoguanine sulfate from K and K.

The *p*H 4.7 acetate buffer had an ionic strength of 0.5. Deaeration was accomplished with water saturated Linde Argon without further purification.

Apparatus.—Cyclic voltammetry was accomplished with the apparatus described by Dryhurst *et al.* (5) with the triangular voltage sweeps supplied by an Exact Electronics Model 502 function generator. Current-voltage curves were recorded on a Tektronix Model 502A dual beam oscilloscope equipped with a Model C-27 polaroid camera. A water jacketed three compartment electrochemical cell was used maintained at 25° ± 0.1°C containing a saturated calomel reference electrode (SCE) to which all potentials are referred; a platinum gauze counterelectrode in saturated KCl was employed.

The preparation of the pyrolytic graphite electrode has been described earlier (2, 4).

Results and Discussion

Uric acid was studied in the first instance because the 2*e* electrooxidation of this compound should result directly in formation of a dicarbonium ion. At scan rates below about 300 mV sec^{-1} a saturated solution of uric acid showed a well-formed oxidation peak at about 0.47V but no corresponding cathodic behavior except for a peak at around —0.8V due to parabanic acid, one of the ultimate products (1). At faster scan rates, however, a well formed cathodic peak appears at about 0.42V and with increasing scan rate, it grows in height relative to the anodic peak (Fig. 1). The separation of the anodic and cathodic peak potentials is indicative of an almost totally reversible couple; the peaks do separate somewhat with increasing scan rate.

Oxidation of xanthine appears to involve about 4*e* (3) which may indicate a two step oxidation to uric acid and then a dicarbonium ion. That this is essentially true seems to be proven by the fact that, using fast scan rates, as soon as the oxidation peak of xanthine has been scanned (E_p = 0.81V), on the reverse sweep a reduction peak is observed (E_p = 0.42V), and on the subsequent anodic sweep a new oxidation peak (E_p = 0.45V) appears before the original xanthine peak (Fig. 2). These new peaks form an almost reversible couple and, within experimental accuracy are identical to those observed for uric acid (Table I).

Similar studies on hypoxanthine, 2,8-dioxyadenine, isoguanine, adenine, and guanine (Fig. 3) reveal a similar behavior, *i.e.*, after scanning the original oxidation peak a reduction peak is observed on the reverse scan which forms a reversible couple with a new

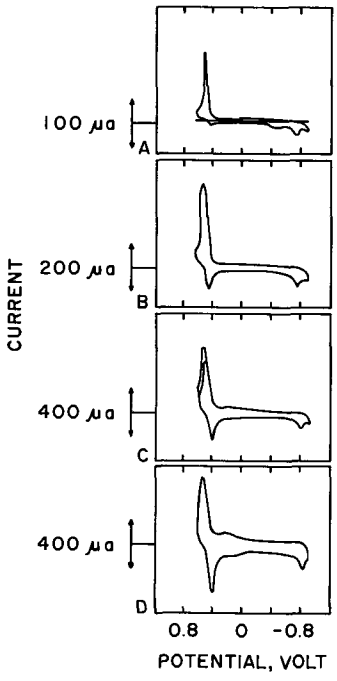

Fig. 1. Cyclic voltammograms of saturated uric acid in acetate buffer pH 4.7 at the PGE. Scan rates: A, 0.32V·sec^{-1}; B, 1.6V·sec^{-1}; C, 3.2V·sec^{-1}; D, 6.4V·sec^{-1}.

oxidation peak on the second and subsequent anodic sweeps. The very close agreement between the anodic and cathodic peak potentials for all the compounds studied (Table 1) no doubt reflects the very similar structure and nature of the intermediate species. It is noticeable (Fig. 3) that as the extent of oxygenation of the compounds decreases so the magnitude of the reversible dicarbonium ion peaks decreases. This is presumably due to the fact that at fast scan rates only a minor portion of the electroactive material at the electrode surface is completely oxidized, *i.e.*, adenine requires 6e for the complete primary oxidation reaction (2).

Complete interpretation of all the additional peaks observed for some compounds is not possible at this time but will be reported later, however, the reduction peak generally observed at about —0.8V is no doubt due to parabanic acid or its derivatives (1, 2).

Two nucleosides, adenosine and guanosine, were studied; significantly the reversible intermediate redox couple was not observed although a new oxidation peak was noted at 0.50V on all scans following the first. Final interpretation of this phenomenon will be reported soon.

Table I. Potentials for oxidation and reduction peaks observed on cyclic voltammetry of purines at the PGE

Compound	Scan rate, V · sec^{-1}	Peak potentials of intermediate species Anodic, volt	Cathodic, volt
Uric acid	3.84	0.47[a]	0.42
Xanthine	3.84	0.45	0.42
Hypoxanthine	3.84	0.44	0.40
2,8-Dioxyadenine[b]	3.88	0.45[a]	0.43
2-Oxyadenine	4.6	0.51	0.45
Adenine	3.84	0.44	0.41
Guanine	3.84	0.47	0.42
Adenosine	6.2	0.50	None
Guanosine	5.8	0.51	None

[a] These compounds are fully oxygenated and further electrooxidation probably involves direct attack at the 4,5-double bond.
[b] The numbering system is that employed in chemical abstracts and ref. (1) and (2).

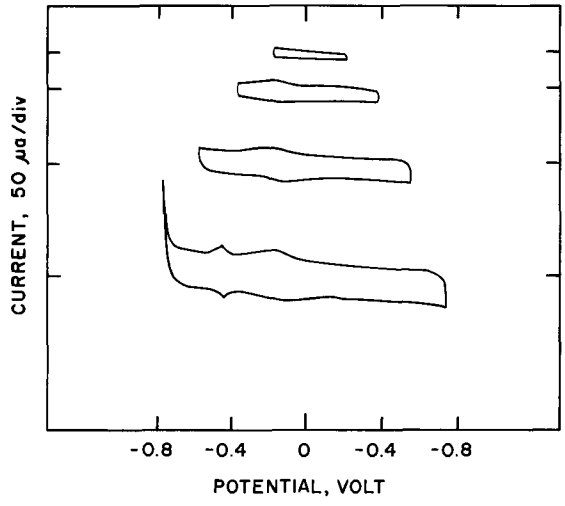

Fig. 2. Cyclic voltammograms of saturated xanthine solution in acetate buffer 4.7 at the PGE with gradually increasing voltage span. Calibration marks on current axis indicate the position of zero current for each voltammogram. Scan rate in all cases 1 Hz.

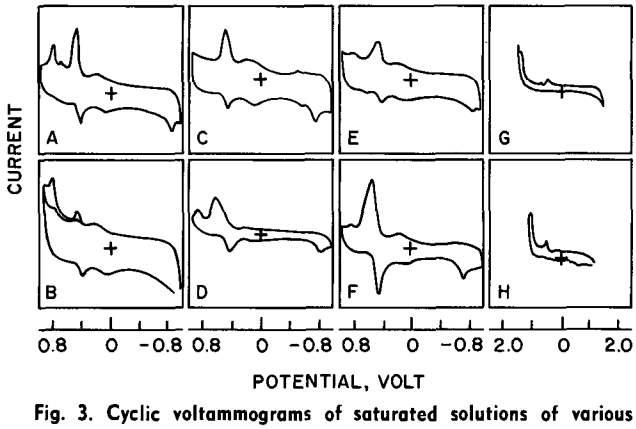

Fig. 3. Cyclic voltammograms of saturated solutions of various purine derivatives in acetate background pH 4.7 at the PGE; all curves were photographed after about 3-4 repeated cycles had been run at a clean electrode. A, xanthine; B, hypoxanthine; C, 2,8-dioxyadenine; D, isoguanine; E, adenine; F, guanine; G, adenosine; H, guanosine. Current sensitivity: A, 100 μa·div^{-1}; B, 50 μa·div^{-1}; C, 50 μa·div^{-1}; D, 500 μa·div^{-1}; E, 100 μa·div^{-1}; F, 100 μa·div^{-1}; G, 500 μa·div^{-1}; H, 200 μa·div^{-1}. Scan rate in all cases 1 Hz.

Acknowledgment

The author would like to thank the National Science Foundation which supported the work described through Grant No. GP 8151.

Manuscript received June 4, 1969.

Any discussion of this paper will appear in a Discussion Section to be published in the June 1970 JOURNAL.

REFERENCES

1. W. A. Struck and P. J. Elving, *Biochem.*, **4**, 1343 (1965).
2. G. Dryhurst and P. J. Elving, *This Journal*, **115**, 1014 (1968).
3. G. Dryhurst, B. J. Hansen, and G. Pace, Work in progress.
4. G. Dryhurst, *This Journal*, **116**, 1097 (1969).
5. G. Dryhurst, M. Rosen, and P. J. Elving, *Anal. Chim. Acta*, **42**, 143 (1968).

Scanning Electron Microscopy and the Growth and Mechanical Properties of Cu_2O Scales

I. A. Menzies and P. Aldred

Corrosion Laboratories, Department of Chemical Engineering, University of Manchester Institute of Science and Technology, Manchester, England

ABSTRACT

The morphology of growth of Cu_2O on Cu has been studied using scanning electron microscopy. The mechanical properties of columnar Cu_2O specimens prepared by total oxidation of metallic copper have been studied as a function of bend rate and temperature. The modulus of elasticity of cuprous oxide was constant ($\sim 4 \times 10^6$ psi) from room temperature to 500°C and thereafter decreased linearly with increasing temperature to $\sim 2 \times 10^6$ psi at 800°C. The oxide exhibited a pseudo brittle-ductile transformation at 360°C and 400°-500°C when slow and fast bending rates, respectively, were used. There was also a maximum strength peak at a critical temperature related to the onset of plastic deformation. Load-deflection functions indicated large amounts of plastic deformation and in the light of fracture surface observations this can be interpreted in terms of a slow cleavage mechanism.

Although a knowledge of the mechanical properties of oxide scales is important with respect to understanding completely the mechanisms of environmental degradation and breakdown of metals and alloys, few measurements of the mechanical properties of scales formed by thermal oxidation of the metal have been made. Tylecote (1) first attempted to measure the properties of copper oxide films on copper by a hot torsion method and more recently Harrison (2) has measured the fracture strain of Fe_3O_4 films formed on steel at 316°C in 2.5M NaOH at ambient temperature by an electrochemical method. Douglass (3) also presented evidence for the plasticity of ZrO_2 films on Zr at 500°C. None of the experimental techniques were completely satisfactory and most of the available information concerning properties has been obtained for oxide specimens produced by complete oxidation of the metal. The strength (4, 5) and creep (6) of iron oxides, the strength, elasticity, and creep of NiO (4, 7, 8) and the strength of Cu_2O (1) have all been measured. In the earlier investigations little attention was given to the effects of scale structure on properties and more recent studies of NiO (8, 9) indicated that the temperature of oxide growth and hydrogen annealing of nickel prior to oxidation had a significant effect on oxide structure and hence on properties. Strafford and Gartside (10) succeeded in establishing that the mechanical behavior of CoO is markedly affected by oxide stoichiometry and in particular that plastic deformation decreased as stoichiometry was approached and the number of cation vacancies decreased.

The present study of Cu_2O has been carried out to provide detailed structural and mechanical information for totally oxidized material to provide a suitable background for future studies of the properties of films attached to the metal. Oxide growth and fracture morphology have been investigated using scanning electron microscopy and the modulus of elasticity and the yield and fracture stress and strain studied as a function of loading rate and temperature. It was of particular interest to examine the onset and mechanism of plasticity in Cu_2O. It is anticipated that in the long term, this knowledge, with additional information concerning the properties of cupric oxide will permit a better understanding of certain aspects of the oxidation of copper to be achieved.

Experimental

Copper of 99.999% purity, in the form of 0.006 in. thick sheet by Metals Research Ltd., Cambridge, was used. No metallic impurities were detected by spectrographic methods. Standard specimens 0.3 cm broad and 3 cm long were oxidized in purified air at 1030°C for the required period of time to effect partial or complete oxidation of copper to Cu_2O.

The mechanical properties of the oxide specimens were measured using a three point loading bend technique (7, 9, 11). The apparatus used in the present work (11) was fully automatic and capable of measuring the properties up to 1200°C and under controlled atmosphere conditions. The load applied to the specimen and its central deflection were measured by a load cell and displacement transducer, respectively. The electrical outputs from the load cell and displacement transducer were fed into an X-Y autoplotter from which a load-deflection function was obtained. Bending rates of 0.011 and 0.508 cm/min were used throughout the work. The load-deflection functions were carefully analyzed to determine the modulus of elasticity, yield stress and strain, or fracture stress and strain as appropriate.

The modulus of elasticity (E) was calculated from the relationship $E = PL^3/4bd^3h$ where P is the load, L is the coupon length between its supports, b and d are the specimen width and thickness, respectively, and h is the measured deflection. Individually measured values of d must be used in order to maintain accuracy of the value of E. The fracture stress (Su) of specimens exhibiting only elastic deformation is given by $Su = 3PuL/2bd^2$ where Pu is the fracture load and the other terms have the same significance as above. The fracture strain (ϵ) of coupons exhibiting only elastic deformation is given by Su/E. If however the oxide coupons exhibit elastic and plastic deformation the methods outlined above for the calculation of stress and strain cannot be used. It can, however, be shown (11) that under these conditions the fracture strain is given by $\epsilon = 8hy/L^2 red$ where y is $d/2$ and $L red \approx \sqrt{8hR}$ where R is the radius of curvature of the bent specimen. Furthermore it can be shown (12) that the stress (S) of a plastically bent rectangular section is given by

$$S = \frac{2}{bd^2}(2M + \phi\, dM/d\phi)$$

where M is the bending moment of the coupon and ϕ is half the angle subtended by two plane sections after bending. This relationship can be used to obtain the fracture stress when the coupons exhibit both elastic and plastic behavior (11).

Specimens for scanning electron microscopy were fractured either in the bend test apparatus or by hand while immersed in liquid nitrogen. The fractured samples of oxide or composite coupons were cemented to small Duralumin stubs by means of Durofix cement. The fracture surface was mounted normally to the stub and set at ~ 45° to the stub surface. In order to prevent surface charging of the specimen in the microscope the Durofix cement was coated with a thin layer of carbon black. A conducting path from the oxide sample to the Duralumin stub was also obtained using carbon black, great care being taken to avoid contamination of the fractured surface. The specimens thus prepared were examined in a Cambridge Instrument Company, Stereoscan Mk IIa. The theory of the instrument has been discussed by Oatley *et al.* (13) and will not be discussed here. The specimen detail resolution was always better than 500Å and as good as 150Å in some cases with a depth of focus at least 300 times greater than that of a normal light microscope.

Results

Morphology of oxide formation on copper.—An SCEM study was made of the nature of growth of Cu_2O. The structure of the Cu_2O film formed after 2 min at 1030°C is shown in Fig. 1a. It can be seen that a portion of the Cu_2O film has lifted straight off the Cu substrate during the fracture process. The Cu_2O film is compact and the metal-oxide interface is relatively smooth. After oxidation for 10 min at 1030°C the oxide was again compact although in one special area numerous voids were present (Fig. 1b). The pronounced markings in the Cu_2O film are cleavage steps produced by the fracture process and the points marked x in Fig. 1b are cleavage facets. The structure of a completely oxidized coupon is shown in Fig. 1c and a number of voids can be seen at the core of the coupon.

The structure of the oxide film formed at the corners of copper coupons was unusual and consisted of an outer columnar-grained layer and an inner fine-grained layer which exhibited numerous pores. The formation of this structure is shown clearly in the scanning electron micrographs in Fig. 2. The Cu-Cu_2O interface after only 2 min oxidation at 1030°C is shown in Fig. 2a. It is immediately apparent that Cu_2O crystallites (B) have grown at the interface beneath a compact columnar layer of Cu_2O and pores are associated with the crystallites. This area was found to have developed into a fine-grained porous structure after oxidation for 10 min at 1030°C (Fig. 2b). The remaining metal core is indicated in Fig. 2b and the finger-like crystallites of Cu_2O, observed in Fig. 2a, can be seen growing from this region near the corner of the Cu-Cu_2O interface. An extremely porous and confused mass of small crystals is shown in Fig. 2c. Detailed examinations of specimens after total oxidation indicated the presence of large holes and small grains of Cu_2O in the specimen center between the outer compact columnar-grained layers of Cu_2O (*cf.* Fig. 1c). It was now of interest to measure the mechanical properties of such totally oxidized coupons and to examine the fracture surfaces in some detail.

Effect of measurement temperature, atmosphere, and bending rate on the mechanical behavior of Cu_2O coupons.—The properties of the coupons were measured at temperatures ranging from ambient to 800°C in both Ar and O_2 atmospheres. Over-all the load-deflection functions and mechanical properties were found to be the same for both Ar and O_2 atmospheres. For the slow bending rate, the Cu_2O coupons exhibited elastic behavior prior to fracture at 325°C whereas at 360°C some plastic deformation was also observed (Fig. 3). The amount of plastic deformation observed at 360°C was such that some coupons were unbroken at the maximum deformation limit of the apparatus and hence the properties were not investigated at higher temperatures. For the fast bending rate elastic behavior to fracture was observed at 325°, 360°, and 400°C and plastic deformation was only observed

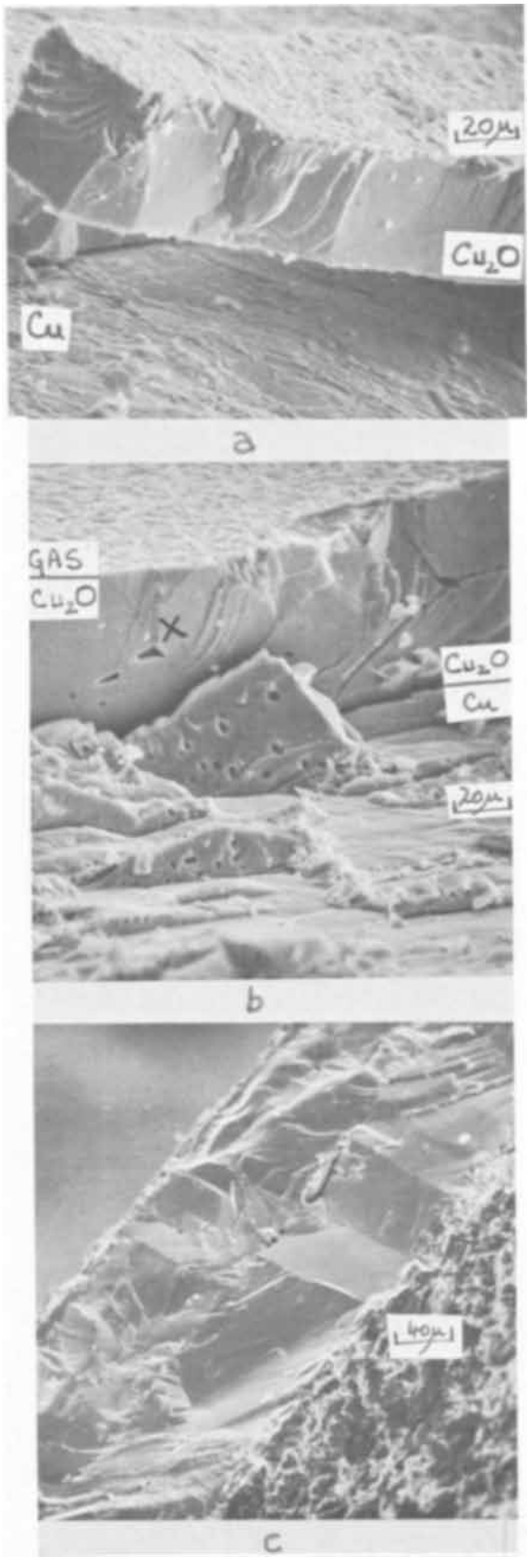

Fig. 1. Fracture surfaces of Cu or Cu_2O specimens. (a) Cu specimen after partial oxidation for 2 min in air at 1030°C. (b) Cu specimen after partial oxidation for 10 min in air at 1030°C; isolated area near edge showing marked porosity in Cu_2O film. (c) Cu_2O specimen produced by total oxidation of Cu in air at 1030°C after bending at the slow rate at 360°C in argon.

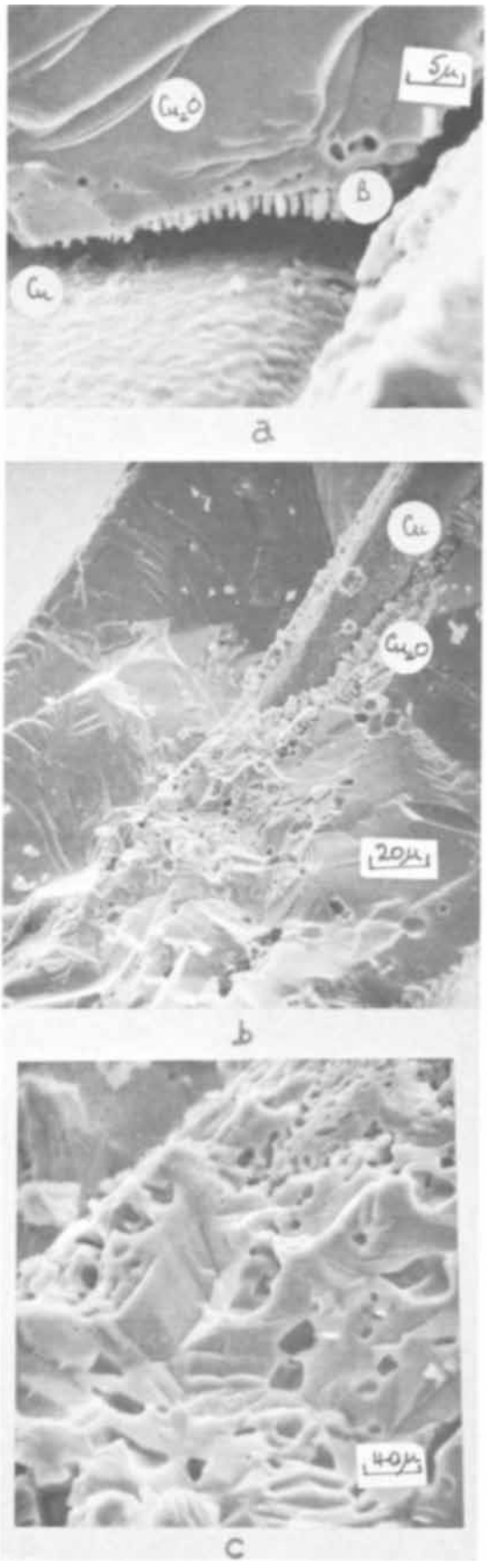

Fig. 2. Details of Cu-Cu_2O interface and of porosity in Cu_2O films. (a) Metal-oxide interface at specimen corner after 2 min oxidation in air at 1030°C. (b) General view of metal-oxide interface; exposure as in (a). (c) Details of porous region in specimen (b).

at temperatures > 500°C. The load-deflection functions obtained at both bending rates exhibited marked

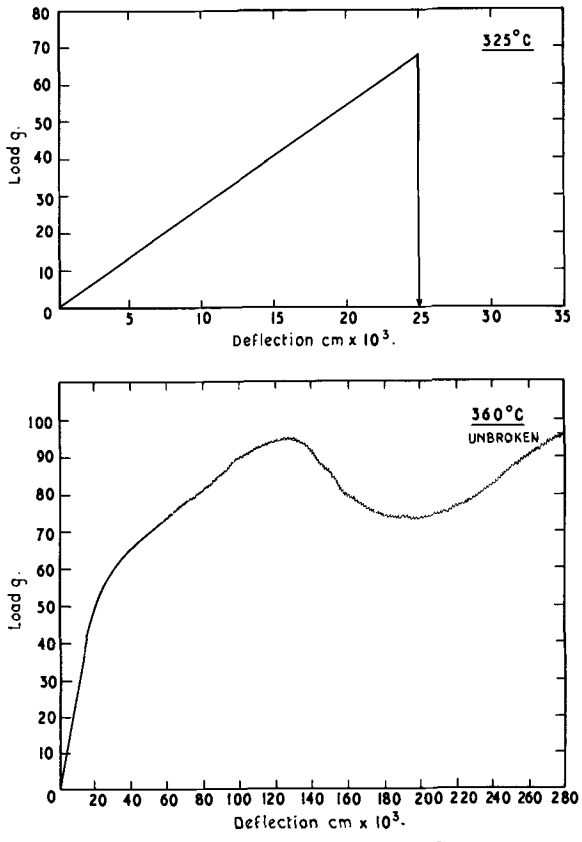

Fig. 3. Load-deflection functions obtained for Cu_2O specimens at the slow bending rate (0.011 cm/min) in O_2 or argon at 325° and 360°C.

serrations when the Cu_2O coupons were plastically deformed to an amount > 65 x 10^{-3} cm (Fig. 3).

The mechanical properties of the Cu_2O coupons were calculated from the load-deflection functions and the results are given as a function of temperature in Tables I and II for the slow and fast bending rates, respectively. The modulus of elasticity was independent of the bending rate and was constant at ~4 × 10^6 psi when the temperature was increased from ambient

Table I. Mechanical properties of Cu_2O coupons bent at 0.011 cm/min as a function of temperature

Temperature, °C	Oxide yield strain, %	Oxide fracture strain, %	Oxide modulus of elasticity, psi × 10^{-6}	Oxide yield stress, tsi	Oxide fracture stress, tsi
Ambient	—	0.15 (0.01)	4.0 (0.5)	—	2.7 (0.5)
325	—	0.22 (0.01)	3.8 (0.5)	—	3.7 (0.5)
360	0.11 (0.02)	0.56/7.8	4.2 (0.5)	2.1 (0.3)	—

Standard deviation values are given in parentheses.

Table II. Mechanical properties of Cu_2O coupons bent at 0.508 cm/min as a function of temperature

Temperature, °C	Oxide yield strain, %	Oxide fracture strain, %	Oxide modulus of elasticity, psi × 10^{-6}	Oxide yield stress, tsi	Oxide fracture stress, tsi
Ambient	—	0.17 (0.01)	4.0 (0.5)	—	3.1 (0.5)
325	—	0.19 (0.01)	4.0 (0.5)	—	3.4 (0.5)
360	—	0.23 (0.02)	4.2 (0.5)	—	4.2 (0.5)
400	—	0.23 (0.02)	4.2 (0.4)	—	4.2 (0.5)
500	0.065 (0.005)	—	4.2 (0.5)	1.2 (0.2)	—
600	0.032 (0.003)	—	3.5 (0.5)	0.5 (0.1)	—
700	0.027 (0.002)	—	2.5 (0.5)	0.3 (0.05)	—
800	0.014 (0.002)	—	2.0 (0.3)	0.1 (0.02)	—

Standard deviation values are given in parentheses.

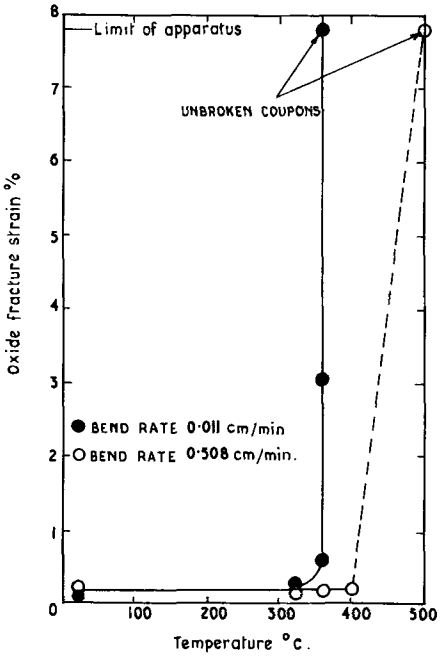

Fig. 4. Fracture strain of Cu_2O coupons as a function of the measurement temperature and bending rate.

to 500°C. Above 500°C a rapid decrease in the modulus of elasticity from $\sim 4 \times 10^6$ psi to 2×10^6 psi was observed when the temperature was increased to 800°C. The Cu_2O coupon fracture strain is shown as a function of the bending rate and temperature in Fig. 4 in order to bring out clearly the presence of a pseudo brittle-ductile transformation which was dependent on the bending rate. For the slow bending rate the transformation occurred at ~360°C, whereas for the fast bending rate the transformation was delayed to some temperature between 400° and 500°C. At temperatures above the transformation temperature Cu_2O specimens remained unbroken after 7.8% strain (apparatus limit) for both bending rates. The fracture strain of the oxide specimens at temperatures below the transformation temperature increased from 0.16 to 0.23% when the temperature was increased from ambient to just below the transformation temperature for each bending rate. In this temperature range the fracture stress remained constant at ~3-4 tsi. Finally, it is clear that the yield strain and yield stress of the Cu_2O coupons bent at the fast rate decreased from 0.065 to 0.014% and from 1.2 to 0.1 tsi, respectively, when the temperature was increased from 500° to 800°C.

Microscopic examination of mechanically deformed Cu_2O *specimens.*—A Cu_2O specimen after bending at 360°C in an argon atmosphere is shown in Fig. 5. Examination of the surface topography of such specimens indicated by the presence of numerous slip lines and few deformation bands that plastic deformation had occurred during bending. Other specimens bent to fracture at the slow rate were examined with the SCEM. A typical area of the fracture surface is shown in Fig. 6a and in more detail in Fig. 6b. A comparison of these figures shows that the nature of the crack front, commencing at point x (Fig. 6a) was complex. A separate area of the fracture surface is shown in Fig. 6c, and this provides evidence that fracture occurred at 360°C both by transgranular and intergranular crack propagation. The crack front propagated in the direction shown by the arrows. Originally the crack progressed in a transgranular manner then in the vicinity of the arrows it changed partially to an intergranular front (indicated by the solid arrows) while the remainder continued in a transgranular manner across another grain (dotted arrows).

Discussion

The SCEM study of the growth of Cu_2O on copper confirms the columnar nature of the grains and the smooth nature of the oxide-metal interface in general (Fig. 1a). The formation of isolated crystallites and oxide bridges at the corners of specimens (Fig. 2a, b) was of especial interest. This has most probably arisen due to the severe mechanical constraint at the corners which has prevented plastic flow of the oxide.

It is also clear from the present work that there was no significant difference in the properties of Cu_2O as a function of atmosphere (Tables I and II). Thus under these conditions the same results were obtained whether the measurements were made in argon or oxygen at atmospheric pressure. There was thus no indication of changes in properties of the specimens with possible changes in vacancy distribution across the scales.

There are few absolute values of elastic modulus for Cu_2O in the literature. Dankov and Churaev (14), however, suggested that a value $\sim 3 \times 10^6$ psi was typical for Cu_2O at ambient temperature. They obtained this value indirectly from internal stress measurements and the agreement with the measured value of 4×10^6 psi in the present work is satisfactory. The rapid decrease in the modulus of elasticity at a critical temperature is a common occurrence in metals and oxides, *e.g.*, in polycrystalline MgO at ~ 1000°C (15, 16), and it has been suggested (17) that this rapid decrease may be caused by grain boundary sliding. Since this can be an important deformation mechanism at temperatures > 0.5 Tm (Tm for Cu_2O ~ 460°C) the decrease in modulus of elasticity at 500°C would be in reasonable agreement with a grain boundary sliding mechanism. This will be discussed more fully later with respect to fracture.

The yield strain and stress of Cu_2O specimens decreased with increasing temperature from 500° to 800° (Table II). This is in agreement with the fact that an increase in temperature increases dislocation mobility thus facilitating plastic flow at lower stresses. The values obtained are in excellent agreement with those obtained (18) from compression experiments at similar temperatures at a crosshead speed of 0.13 cm/min, *i.e.*, between the two values used in the present work. However, Vagnard and Washburn found that yielding occurred at 200°C and not at 400°-500°C as observed for the fast bending rate in the present work. Compressional experiments are better suited for observing plastic deformation in oxide materials because the tensile stresses which develop in bending accentuate brittleness and therefore higher temperatures will be required to initiate yielding in bending.

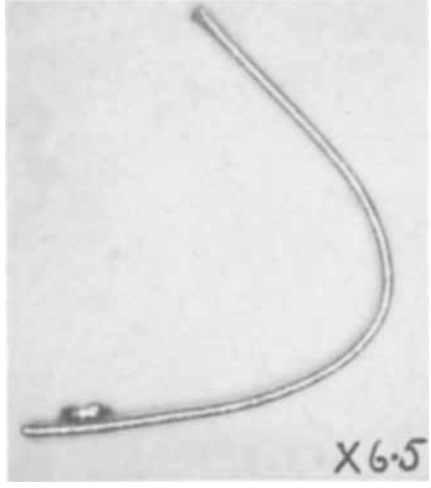

Fig. 5. Cu_2O specimen after bending at the slow rate (0.011 cm/min) at 360°C. X6.5.

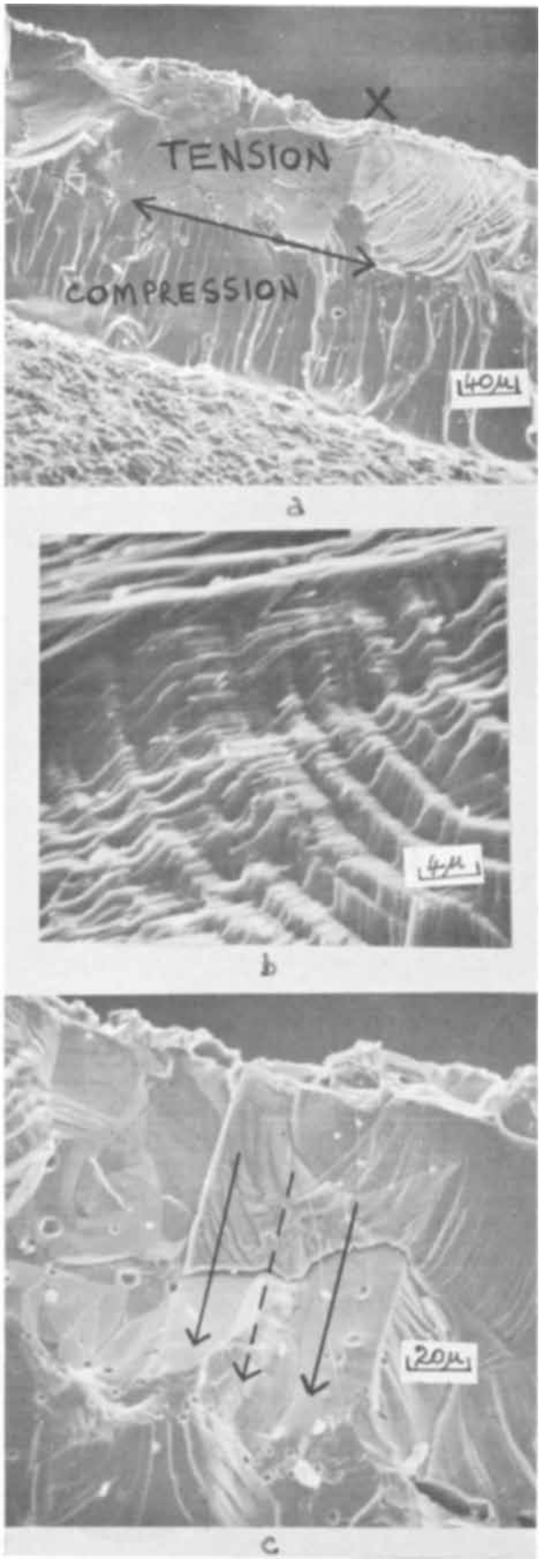

Fig. 6. Fracture surfaces of Cu_2O coupon after 3.6% strain at 360°C in argon at the slow bend rate (0.011 cm/min). (a) General view. (b) Detail of cleavage facets on tensile side of neutral axis. (c) Additional aspects of tensile side of neutral axis.

The fracture strains of Cu_2O at temperatures below the pseudo brittle-ductile transformation temperature are in agreement with the fracture strains observed in brittle materials (19). At temperatures greater than the transition temperature the observed strains of $\geq$7.8% before fracture can be compared with previous work (1) in which Cu_2O elongations of ~12% and ~25% were observed at 500°-600°C and 700°-900°C, respectively. The observation that plastic deformation is observed at lower temperatures (~360°C) with a slow bend rate is in general agreement with observations in metals where the flow stress is increased by an increased strain rate (20). Over-all the yield stress corresponding to the onset of plastic deformation was lower at higher temperatures (*cf.* Table II), in further agreement with the mechanical behavior of metals. Since the flow stress is the stress required to initiate plastic deformation it will depend on such material factors as purity, grain size, and crystal structure. In the case of Cu_2O here this is of high purity and of large columnar grain structure. The relatively easy deformation of Cu_2O is reflected in the relatively low yield stress at all temperatures and the relatively high fracture strains. Cuprous oxide has an unusual structure (18) in that oxygen atoms are ordered on a b.c.c. lattice and the copper atoms occupy the sites of an f.c.c. lattice. The structure consists of two interpenetrating and identical networks which are not cross-connected by any primary Cu-O bonds. Slip lines have been observed on the tensile surfaces of Cu_2O but examination of specimens after fracture at 360°C (Fig. 6a) did not show any dimple formations which are characteristic of ductile fractures (21). In contrast the fracture surfaces exhibited cleavage with some isolated areas showing intergranular fracture. These observations are in contrast to the shape of the load-deflection functions (Fig. 3) which suggest extensive plastic deformation. Observations on the Cu_2O specimens strongly suggest that slow cleavage is responsible for the shape of the load-deflection functions of the type shown in Fig. 3. Surface cracks were also found in the Cu_2O specimens. This was also observed in Cu_2O by Vagnard and Washburn (18) during compressional experiments at <400°C. They found that cracks nucleated at local stress concentrations where slip bands crossed and also where they met grain boundaries. A similar type of crack nucleation has been observed in MgO (22, 23) and analyzed by Stroh (24, 25). It seems likely that cracks observed in the present work nucleated in the manner described by Vagnard and Washburn, since large local deformations were observed at slip band intersections (Fig. 7a) and also where slip lines piled up at a grain boundary (Fig. 7b). This inhomogeneity of slip observed in this system could offer a possible explanation for the complicated shape of the load-deflection function in Fig. 3. The peaks in the plastic region of the curve were observed continuously up to deformations of ~800 x 10^{-3} cm and it seems possible that these peaks are associated with the initiation of slip in grains which, up to that point, were undeformed. The increase in work hardening observed after the initial yield point will be due to grain boundary and crystallographic blockages which oppose slip. At some critical strain these blockages will be overcome and slip will be initiated in neighboring grains. When this occurs there will be an initial decrease in the work hardening rate followed by an increase as further slip becomes blocked. This process will repeat itself giving rise to the observed peaks in the load-deflection functions.

Once surface cracks have formed their rate of propagation will depend on the bending rate, temperature, and degree of plastic relaxation at the crack tip. This plastic relaxation absorbs energy and prevents rapid crack propagation (26). In fact it has been observed that cracks have propagated through Cu_2O grains which do not exhibit slip deformation and that crack propagation has been halted at the grain exhibiting extensive slip deformation. The cracks prop-

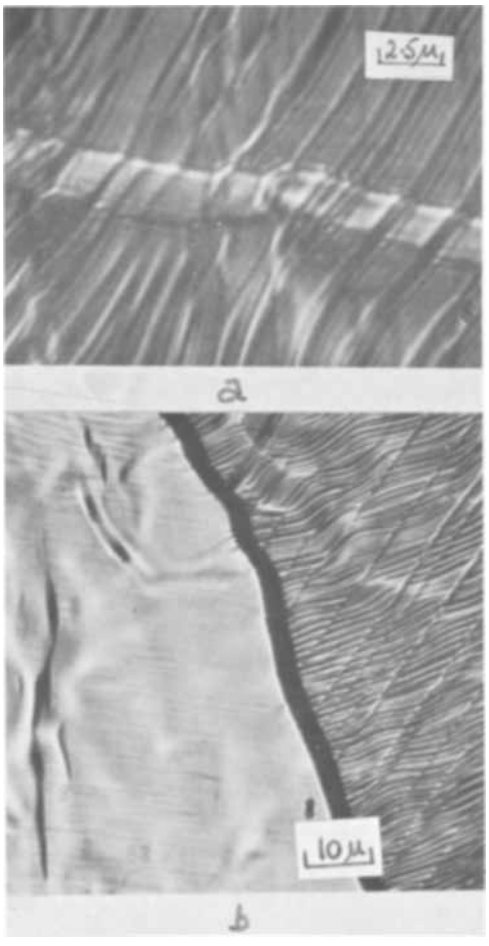

Fig. 7. Surface topography of Cu_2O specimen, formed in air at 1030°C, after bending at 360°C in argon. (a) Intersection of slip bands. (b) Intersection of slip lines with a grain boundary.

agate by repeated breaking of crystal bonds at the crack tip. In Cu_2O the {111} planes have weak bonds and cleavage occurs along them (18). During bending therefore, slow cleavage on {111} planes would be expected if most of the surface energy, created by crack formation, was absorbed by plastic deformation. Such plastic deformation during cleavage of ionic crystals has been observed even at ambient temperatures (27) and hence at the higher temperatures in the present work plastic relaxation is even more favored. The fracture surface of a Cu_2O specimen (Fig. 6a) indicates that a crack was initiated at a grain boundary marked x on the tensile side of the neutral axis. To the left of the boundary, cleavage occurred mainly on one crystal plane within the large grain, whereas to the right of the boundary a complicated crack front was observed (Fig. 6b). It would appear that this crack front could be described by two main vectors situated at 90° to each other. At the same time as the crack front was moving directly perpendicular to the neutral axis it was also moving parallel with this axis. The resultant crack front was therefore most likely situated at ~45° to the point marked x in Fig. 6a. It can be visualized that this duplex direction of crack propagation would produce a "tearing" effect resulting in a confused structure (cf. Fig. 6b). It can be seen in Fig. 6b that numerous small cleavage steps are associated with larger cleavage steps which are situated at ~90° to each other and could therefore represent cleavage on the {111} planes. It is suggested therefore that during bending cracks are nucleated on the tensile surface. These cracks are prevented from drastic propagation by plastic relaxation at the crack tip. Bending continues and the stress at the crack tip builds up until it is sufficient to cause further propagation of the crack which in turn is halted by plastic relaxation. This process will be continuous and the crack propagates slowly along the {111} planes. This intermittent crack propagation is probably responsible for the serrations in the load-deflection function. Gilman *et al.* (28) have shown that the increases in surface energy that accompany cleavage step formation in ionic crystals may cause the cracks to move more slowly than they would normally do under the same driving force. Thus the suggested crack propagation mechanism would account for the shape of the load-deflection functions and the lack of evidence in the oxide fracture surfaces for extensive ductility.

Finally the strength peak observed at a temperature immediately below that for which plastic deformation was observed (Tables I and II) requires comment. A similar phenomenon has been reported previously for Cu_2O wires (1) and for NiO wires and sheet specimens (4, 8). Silicon and germanium also exhibit such strength peaks with increasing temperatures (29). The strength will tend to rise as the heat-induced ability to deform plastically increases with temperature. Plastic deformation relieves stress concentrations and thereby promotes the full strength properties of the material. Above the temperature of maximum strength, the strength decreases with further increase in temperature, as in the case of ductile metals.

Acknowledgments

We wish to thank Professor T. K. Ross for the provision of research facilities and one of us (P.A.) wishes to thank the Science Research Council for the award of a research studentship. We also wish to thank Mrs. P. Cross of the Department of Textile Technology for her valued advice and assistance with the SCEM study.

Manuscript submitted Jan. 24, 1969; revised manuscript received June 12, 1969.

Any discussion of this paper will appear in a Discussion Section to be published in the June 1970 JOURNAL.

REFERENCES

1. R. F. Tylecote, *J. Inst. Metals*, **78**, 301 (1950).
2. P. L. Harrison, *Corrosion Sci.*, **7**, 789 (1967).
3. D. L. Douglass, *ibid.*, **5**, 255 (1965).
4. R. F. Tylecote, *J. Iron Steel Inst.*, **196**, 135 (1960).
5. J. Vagnard and J. Manenc, *Mem. Sci. Rev. Met.*, **62**, 251 (1965).
6. J. D. Mackenzie and C. E. Birchenall, *Corrosion*, **13**, 783 (1957).
7. I. A. Menzies and K. N. Strafford, *J. Mater. Sci.*, **2**, 358 (1967).
8. P. Aldred, M. Sc. Thesis, Manchester, England 1966.
9. I. A. Menzies and P. Aldred, *Corrosion Sci.*, **8**, 525 (1968).
10. K. N. Strafford and H. Gartside, *Nature*, **220**, 158 (1968).
11. I. A. Menzies and P. Aldred, In press.
12. A. Nadai, "Theory of Flow and Fracture in Solids," Vol. 1, p. 359, McGraw Hill, London (1950).
13. C. W. Oatley, W. C. Nixon, and R. F. W. Pease, "Advances in Electronics and Electron Physics," Vol. 21, p. 181, Academic Press, New York (1965).
14. P. D. Dankov and P. V. Churaev, *Dokl. Akad. Nauk. SSSR.*, **73**, 1221 (1950).
15. B. Schwartz, *J. Am. Ceram. Soc.*, **35** (12), 325 (1952).
16. R. M. Spriggs, T. Vasilos, and J. B. Mitchell, *ibid.*, **47** (12), 606 (1964).
17. R. L. Coble and W. D. Kingery, *ibid.*, **39** (11), 377 (1956).
18. G. Vagnard and J. Washburn, *ibid.*, **51** (2), 88 (1968).
19. N. F. Astbury, Brit. Ceram. Res. Assn., Research paper No. 504 (1961).
20. A. G. Guy, "Elements of Physical Metallurgy," 2nd Ed., Addison-Wesley Publishing Co. (1960).
21. R. M. N. Pillaux, *Metals Eng. Quart.*, **5** (4), 26 (1965).
22. R. J. Stokes, T. L. Johnston, and C. H. Li, *Phil. Mag.*, **4**, 920 (1959).

23. W. G. Johnston, *ibid.*, **5**, 407 (1960).
24. A. N. Stroh, *Proc. Roy. Soc.* (*Lond*), **A 223**, 404, (1954); **232**, 548 (1955).
25. A. N. Stroh, *Advances in Phys.*, **6**, 418 (1957).
26. A. R. C. Westwood and M. H. Kamdar, *Phil. Mag.*, **8**, 878 (1963).
27. C. T. Forwood and B. R. Lawn, *ibid.*, **13**, 595 (1966).
28. J. J. Gilman, C. Knudsen, and W. Walsh, *J. App. Phys.*, **29**, 601 (1958).
29. E. M. Savitsky, "The Influence of Temperature on the Mechanical Properties of Metals and Alloys," Oxford Univ. Press, London (1962).

The Free Energy of Formation of Tantalum Silicides Using Solid Oxide Electrolytes

S. R. Levine and M. Kolodney*

The City College of The City University of New York, New York, New York

ABSTRACT

A method is described for determining the standard free energies of formation of the tantalum silicides from emf measurements on cells with solid thoria-yttria electrolytes. Measurements were conducted over the temperature range 900°-1100°C in a purified argon atmosphere. Corrections for electronic conduction were established with Ta, Ta_2O_5 electrodes. Difficulties were encountered because the hard, refractory nature of the compounds prevented fabrication of dense electrodes and because silica films interfered with the measurements. At 1300°K, the measured standard free energies of formation in kcal per gram atom of silicon are: $TaSi_2$, —8.1 (+1.8/—3.7); Ta_5Si_3, —24.0 ±3; Ta_2Si, —27.2 ±3.1; $Ta_{4.5}Si$, —37.3 ±7.2.

Silicides are of interest as protective coatings for tantalum and other refractory metal alloys exposed to oxidizing conditions. Since the formation of a silica glass is essential for protection, a desirable reaction is one that produces silica and a lower silicide, as for example

$$5TaSi_2 + 7\,O_2 = 7SiO_2 + Ta_5Si_3 \qquad [1]$$

On the other hand, since the formation of the oxide of the substrate may interfere with the integrity of the silica film, the following reaction is undesirable

$$4TaSi_2 + 13\,O_2 = 2Ta_2O_5 + 8SiO_2 \qquad [2]$$

However, the refractory metal oxide may be tolerable where SiO_2 and the metal oxide form a glass or where the metallic oxide is volatile (1, 2).

In order to predict and understand the oxidation behavior of refractory metal silicides accurate free energy of formation data are required for the silicides and their oxidation products. Data for silica and for the refractory metal oxides are available (3), but data for silicides are scanty. Free energies of formation are known only for some of the rhenium silicides (4). For most other refractory metal silicides only enthalpies of formation are available. Thermodynamic information on the tantalum-silicon system, which is the subject of this study, has been collected by three classical techniques: Brewer and Krikorian (5) determined limits for the stability of refractory silicides by direct reaction of the compounds with carbides and nitrides. Robins and Jenkins (6) measured the heats of formation of some transition metal silicides from the heat evolved during formation of the compounds from their elements. In the third technique, employed by Searcy and co-workers (7-9), the dissociation pressure of silicon over the silicide of interest was measured by the Knudsen effusion method. The vapor pressure data were analyzed by a Second or Third Law approach to obtain enthalpies of formation for the silicides. Data for the tantalum silicides, obtained by these three techniques are presented in Table I. The values listed in column IV are based on an average of the Second and Third Law techniques using a value of —112 kcal for the heat of sublimation of silicon at 298°K. The values in column V are based on the same vapor pressure data as column IV but an improved value of the heat of sublimation of silicon (—108.4 kcal at 298°K) was used and the calculations were made using only the Third Law method (10, 11).

In the present work a fourth method was for the first time applied to the determination of the thermodynamic properties of the tantalum silicides. This technique employs a solid oxide electrolyte between a silicide electrode and a reference electrode. Solid electrolytes for the measurement of thermodynamic properties were brought into prominence by Kiukkola and Wagner (12), Schmalzried (13), and others. Oxide electrolytes are binary oxides which conduct almost entirely by transport of oxygen ions over a given temperature-oxygen partial pressure domain. A simple cell employing an oxide electrolyte and an iron-iron oxide (Fe_xO) reference electrode may be formulated as

$$Pt/Fe,Fe_xO//\text{oxide electrolyte}//M,MO/Pt \qquad [3]$$

where the cell reaction is

$$M + Fe_xO = MO + xFe \qquad [4]$$

If the cell is reversible, the free energy of the reaction

Table I. Enthalpy of formation data for the tantalum silicides (kcal/g-atom of silicon)

I Compound	II Brewer and Krikorian (5), $\Delta H°_{298}$	III Robins and Jenkins (6), $\Delta H°_T$	IV Myers and Searcy (7), $\Delta H°_{298}$	V Searcy and Finney (10), $\Delta H°_{298}$
1/2 $TaSi_2$	−12.8 to −32.3	−13.9 ± 1	−11.6 ± 5	−12 ± 3
1/3 Ta_5Si_3	−20 to −77.2	−25.3 ± 1	−26.7 ± 5	−24 ± 4
Ta_2Si	−20 to −90.1	—	−29.3 ± 5	−30.2 ± 4
$Ta_{4.5}Si$	−20	—	−34.4 ± 5	−35.8 ± 4

* Electrochemical Society Active Member.

Keywords: silicides, tantalum silicides, solid electrolytes, free energies of formation, emf measurements, electronic conduction.

ΔG_R is related to the cell voltage E and to the oxygen partial pressure by

$$\Delta G_R = -nFE = RT \ln \frac{P_{O_2}\ (\text{for M,MO})}{P_{O_2}\ (\text{for Fe,Fe}_x\text{O})} \quad [5]$$

where T is the temperature (°K) and P_{O_2} refers to the oxygen partial pressures over the respective metal-metal oxide electrodes. From Eq. [4] and [5], the standard free energy of formation of MO may be obtained provided that all solid phases are pure (unit activity) and the free energy of formation of the reference oxide Fe_xO is known.

$$\Delta G^\circ_{MO} = \Delta G^\circ_{Fe_xO} - nFE \quad [6]$$

For the more complex reaction of Eq. [1] a cell using an iron-iron oxide reference electrode would be formulated as follows.

$$\text{Pt/Fe,Fe}_x\text{O//oxide electrolyte//SiO}_2, \text{TaSi}_2, \text{Ta}_5\text{Si}_3\text{/Pt} \quad [7]$$

The over-all cell reaction is

$$5TaSi_2 + 14Fe_xO = 7SiO_2 + Ta_5Si_3 + 14xFe \quad [8]$$

and the free energy of formation of the highest silicide $TaSi_2$ may be obtained from

$$5\Delta G^\circ_{TaSi_2} = 7\Delta G^\circ_{SiO_2} + \Delta G^\circ_{Ta_5Si_3} - 14\Delta G^\circ_{Fe_xO} + nFE \quad [9]$$

Obviously, success of the measurement depends on an accurate knowledge of the free energies of formation of not only SiO_2 and Fe_xO, but also of the lower silicide, Ta_5Si_3. Since the latter is unknown, it becomes necessary to establish free energies for all four of the silicides in the system. Furthermore, oxidation of a silicide to silica and the lower silicide is not the sole possibility. Instead, oxidation may yield Ta_2O_5 and a higher silicide or it may produce both SiO_2 and Ta_2O_5 as in Eq. [2]. All of the possible half-cell reactions for the four silicides of the Ta-Si system ($TaSi_2$, Ta_5Si_3, Ta_2Si, and $Ta_{4.5}Si$) are shown in Table II where they are arranged in terms of their reaction products. In addition, this table lists expected emf values *vs.* an iron-iron oxide (Fe,Fe_xO) reference electrode calculated using the enthalpy data of Searcy and Finnie (10) in lieu of free energies of the silicides. Other thermodynamic data are from Wicks and Block (3).

Examination of the estimated cell voltages of Table II indicates that the silicide pair $TaSi_2$-Ta_5Si_3 should be oxidized only to SiO_2 (compare reactions I and IV). Similarly, from the expected values for reactions II and V for the Ta_5Si_3-Ta_2Si pair, silica appears to be the preferred oxidation product. For the Ta_2Si-$Ta_{4.5}Si$ pair, tantala formation clearly gives the desired free energy minimum as indicated by the expected values for reactions III and VI of Table II.

In order to confirm these expectations, an experimental stability study was conducted. This study was performed at about 1600°C in vacuum using x-ray diffraction to follow changes in the relative amounts of phases. It confirmed the stability of silica in the presence of $TaSi_2$ and Ta_5Si_3 and the stability of tantala in the presence of Ta_2Si and $Ta_{4.5}Si$. However, for the Ta_5Si_3-Ta_2Si pair, the thermal stability study indicated that tantala rather than silica is the stable oxide.

Since each of the reactions I, V, and VI involves a pair of silicides, emf measurements for these cannot provide individual free energies of formation. However, data for a reaction from group C of Table II would yield the free energy of a single silicide and would thereby permit calculation of all. It may be shown from phase rule considerations that only one reaction in group C is permissible. Since the preferred reaction I yields Ta_5Si_3 and SiO_2, while the preferred reaction V yields Ta_5Si_3 and Ta_2O_5, it appears that reaction VIII is a possible one in group C. In any case, emf data for four cell reactions are needed to evaluate the individual free energies of formation of all four silicides in the system.

Experimental

The tantalum silicides were prepared by direct reaction of the elements. The tantalum used in the synthesis was —120 mesh powder obtained from Fansteel Metallurgical Corporation. The minimum purity was 99.9%. The silicon was —325 mesh powder of 99.99% purity obtained from United Mineral and Chemical Corporation. The tantalum and silicon were weighed out in the desired proportions and mixed in plastic vials in a high speed mixer for a minimum of 20 min. They were pressed into ½ in. diameter pellets weighing approximately 3g under a pressure of 20 tsi and were reacted in a covered alumina crucible. The crucible, containing a tantalum susceptor, was placed in an induction heated vertical tube furnace connected to a vacuum system. The pellets ignited at about 1125°C with visible evolution of heat. The reaction lasted less than 1 min and the rapid evolution of the heat of reaction brought the temperature up to about 1400°C. During the reaction period the pressure rose above 10^{-2} Torr because of silicon sublimation, but less than 0.01% of the silicon was lost. The reacted pellets were crushed and mixed with tantalum oxide and/or silica and with less than 1 w/o (weight per cent) nickel sintering aid. The tantalum oxide was a purified grade obtained from Fisher Scientific Company. Silica was also obtained from Fisher. The mixed powders were pressed into 2.5g pellets in a ½ in. diameter die under a pressure of 20 tsi. Because the silicides are extremely hard and brittle, a binder was necessary to provide strength for handling the green pellets. A 1% solution of polymethyl-methacrylate in methyl ethyl ketone was used to yield a dry pellet containing approximately 0.2% binder by weight. The pellets were presintered at about 550°C in vacuum to remove the binder and were then sintered on alumina trays in vacuum at about 1625°C for 10 min. The

Table II. Possible half-cell reactions and expected emf values with respect to Fe-Fe_xO at 1000° and 1300°K

Half-cell reactions		Expected voltages, mV	
A. SiO_2(a)* is the oxidation product:		1000°K	1300°K
I. $5TaSi_2 + 14\ O^=$	$= 7SiO_2(a) + Ta_5Si_3 + 28e^-$	634 ± 65	613 ± 65
II. $2Ta_5Si_3 + 2\ O^=$	$= SiO_2(a) + 5Ta_2Si + 4e^-$	895 ± 477	870 ± 477
III. $9Ta_2Si + 10\ O^=$	$= 5SiO_2(a) + 4Ta_{4.5}Si + 20e^-$	433 ± 113	409 ± 113
B. β-Ta_2O_5 is the oxidation product:			
IV. $4Ta_5Si_3 + 35\ O^=$	$= 7Ta_2O_5 + 6TaSi_2 + 70e^-$	548 ± 52	528 ± 52
V. $6Ta_2Si + 5\ O^=$	$= Ta_2O_5 + 2Ta_5Si_3 + 10e^-$	475 ± 208	457 ± 208
VI. $4Ta_{4.5}Si + 25\ O^=$	$= 5Ta_2O_5 + 4Ta_2Si + 50e^-$	617 ± 28	598 ± 28
C. Complete oxidation to SiO_2(a) and β-Ta_2O_5:			
VII. $2TaSi_2 + 13\ O^=$	$= Ta_2O_5 + 4SiO_2(a) + 26e^-$	603 ± 20	580 ± 20
VIII. $2Ta_5Si_3 + 37\ O^=$	$= 5Ta_2O_5 + 6SiO_2(a) + 74e^-$	577 ± 14	556 ± 14
IX. $Ta_2Si + 7\ O^=$	$= Ta_2O_5 + SiO_2(a) + 14e^-$	565 ± 13	543 ± 13
X. $4Ta_{4.5}Si + 53\ O^=$	$= 9Ta_2O_5 + 4SiO_2 + 106e^-$	590 ± 7	570 ± 7

* SiO_2(a) silica is amorphous as grown on silicide electrodes.

system pressure was maintained below 10^{-5} Torr. The temperature was measured with an optical pyrometer. With the exception of ($TaSi_2$-Ta_5Si_3-SiO_2) electrodes containing little silica, the electrodes sintered poorly. Those electrodes that sintered well were ground and polished to a bright metallic finish. However, the lower silicide electrodes crumbled when ground, so in order to present a dense surface to the electrolyte, these electrodes had to be used in the as-sintered condition. However, because of silicon losses their surfaces within a particular batch showed considerable variation in composition. Therefore, electrodes suitable for use in the cells were selected by x-ray diffraction analysis of the surfaces. This permitted a determination of the relative amounts of the lower silicides present.

Reference electrodes for the emf measurements were prepared from the appropriate metal and metal oxide powders by cold pressing followed by sintering in vacuum. Iron-ferrous oxide electrodes were prepared from 97.1% pure iron powder obtained from the J. T. Baker Chemical Company. The iron was oxidized in air at about 500°C until about one-third of the oxygen required to oxidize all of the iron to FeO had been gained. The powder was then pressed into 2g pellets in a ½ in. diameter die at 15 tsi and sintered in vacuo at 1250°C for 15 min. Tantalum, ditantalum pentoxide electrodes were fabricated from 99.9% pure tantalum powder and purified grade Ta_2O_5 in the ratio 4:1 by weight. The ½ in. diameter pellets weighing 2.5g were sintered in vacuum at 1650°-1700°C for 15 min. All reference electrodes were ground flat on emery papers and polished on a napless nylon cloth with 5μ levigated alumina.

Thoria-yttria electrolytes were fabricated from 99.9% pure thoria powder and 99.9% pure yttria powder obtained from A. D. Mackay, Inc. The powders were weighed out in the desired proportions and mixed for either 20 min in a high speed mixer or for 60 hr in a conventional ball mill. The mixed powder was pressed into ½ in. diameter pellets weighing from 3-6g and were sintered in vacuum for 3-36 hr at temperatures from 1900° to 2200°C. The sintered pellets were cut on a diamond wheel to remove the surface layer and any fractured areas. Opposite faces were maintained parallel to within 0.002 in. The electrolytes were also polished on a napless nylon cloth with 5μ levigated alumina abrasive. The density, as measured by water displacement, ranged from 87 to 100% of theoretical depending on sintering time, temperature, and the manner in which the thoria and yttria were mixed. The electrolytes were dark green in the as-sintered condition probably because of the trapping of electrons in defects. Heating in air at temperatures as low as 300°C caused the electrolytes to turn white in 30 min or less. They also turned white during their use in the electrochemical cells where the oxygen partial pressure was low.

The emf apparatus employed in this work was similar to the apparatus used by Kiukkola and Wagner (12). The cell, consisting of three pellets, was assembled between fused quartz rods. The platinum lead wires were brought through the end flanges of the apparatus with Teflon lead-throughs. A chromel-alumel thermocouple was used to measure the cell temperature. The cell emf was measured with a Keithley Model 610B electrometer with 10^{14} ohm input impedance on the volt scale. Part or all of the cell voltage was biased by a potentiometer in series with the electrometer. The electrometer output was recorded on a potentiometric strip chart recorder. The cell was enclosed in a Vycor tube which was closed off by brass flanges with O-ring seals. The cell was heated by a silicon carbide tube furnace and the temperature was controlled to ± 5°C. The cell was operated under argon that was purified by passing in succession over anhydrous magnesium perchlorate, zirconium-12.5 a/o (atom per cent) titanium chips at 425°C, anhydrous magnesium perchlorate, Zr-12.5 a/o Ti chips at 375°C and tantalum at 600°C. EMF measurements were made over the range of 700°-1100°C, but most satisfactory measurements were made in the 900°-1100°C region.

Results and Discussion

Test of apparatus and electrolyte.—The apparatus was tested by performing emf measurements on the cell

$$Pt/Ni,NiO//0.925ThO_2\text{-}0.075Y_2O_3//Fe,Fe_xO/Pt \quad [XI]$$

over the temperature range of 700°-1000°C. The data obtained were in good agreement with the results of other investigators (12, 14, 15).

Tests of low pressure electrodes were carried out with

$$Pt/Fe,Fe_xO//ThO_2\text{-}Y_2O_3//Ta,Ta_2O_5/Pt \quad [XII]$$

Results obtained with these cells employing dense Ta, Ta_2O_5 electrodes are summarized in Table III. Electrolyte compositions of 1 m/o (mole per cent) Y_2O_3 and 7.5 m/o Y_2O_3 in thoria were used. Electrolyte thickness was varied from 0.19 to 0.46 cm, while the argon flow rate was varied over the range of 1-3 CFH. The electrolyte composition, electrolyte thickness, and argon flow rate were found to have no effect on the results for cells employing dense Ta,Ta_2O_5 electrodes. Therefore, it was concluded that the deviations of the observed emf's from the expected values computed from the data for Fe_xO (14) and Ta_2O_5 (3) were caused by electronic conduction in the thoria-yttria electrolytes. That is, conduction in the electrolyte was not 100% ionic as assumed for Eq. [5]. However, the temperature coefficients of these cells were in excellent agreement with the expected coefficients. Such behavior should be expected if the electrodes are not appreciably polarized by the electronic exchange current. Therefore, emf data obtained under these conditions are useful if a correction for electronic conduction is made.

This correction may be made by applying an equation derived by Schmalzried (13). Since the oxygen partial pressures over silicide electrodes are not very different from those over Ta,Ta_2O_5 electrodes, the corrections will be closely applicable. The average transport number for ionic conduction, $\bar{t}_i$ is defined simply in terms of the measured and true cell voltages $E_{meas.}$ and E, by

$$\bar{t}_i = \frac{E_{meas.}}{E} \quad [10]$$

Now for the present case where the Fe,Fe_xO reference electrode possesses a high oxygen pressure relative to its Ta,Ta_2O_5 mate, $E_{meas.}$ may be expressed by

$$E_{meas.} = -\frac{mRT}{4\mathbf{F}}\left[\ln\frac{P_e^{1/m} + P_{Ta}^{1/m}}{P_{Fe}^{1/m}}\right] \quad [11]$$

Table III. Corrected emf measurements (mV)

Temperature, °C	700	750	800	850	900	950	1000	1050	1100
Cell I							658 ± 40	648 ± 40	
Cell II			537 ± 4	565 ± 4	578 ± 8	583 ± 4	589 ± 9	585 ± 4	
Cell V						494 ± 3	523 ± 3	521 ± 1	519 ± 3
Cell VI					563 ± 4	562 ± 4	561 ± 4	560 ± 4	559 ± 4
Cell XII	618 ± 2		610 ± 2		604 ± 2		598 ± 2		

where P_e is an oxygen partial pressure characteristic of the electrolyte, P_{Ta} and P_{Fe} are the oxygen partial pressures over the Ta, Ta_2O_5 and the Fe,Fe_xO electrodes, and m has a theoretical value of 4.

The value of P_e may be calculated from Eq. [11] using experimental values of $E_{meas.}$ and calculated pressures for P_{Ta} and P_{Fe}. At 1300°K, the result is

$$P_e = 2.59 \times 10^{-29} \text{ atm}$$

It then becomes possible to derive $E_{meas.}$ as a function of P_{Ta} referred to a fixed P_{Fe}. The true voltage, E, is calculated for the same pressures using Eq. [5] and appropriate data (3, 14). As a matter of interest, a local ion transport number, t_i, may be calculated for the electrolyte at its interface with the low pressure electrode (13)

$$t_i = \exp\left[4\mathbf{F}(E_{meas.} - E)/mRT\right] \qquad [12]$$

The results of the calculations are presented in Table IV. This table may also be used to evaluate corrections for the silicide electrodes where electronic conduction is significant.

Examination of Table IV discloses that the thoria-yttria electrolytes were found essentially free of electronic conduction ($\bar{t}_i \geqq 0.99$) down to oxygen partial pressures of about 10^{-24} atm at 1300°K. This confirms the work of Steele and Alcock (15) and Vecher and Vecher (16), but is in substantial disagreement with the results described by Rapp (17).

Silicide electrodes.—A very large number of electrodes was prepared from pairs of silicides in each of the three phase fields. These were mixed with silica and/or tantala to correspond to the reactions of Table II and were tested in cells. Two major kinds of difficulties were encountered. First, many of the mixtures of refractory silicides and oxides did not sinter well even when activated with small amounts of nickel. Consequently, the interior structure was often porous so that the very low partial pressures of oxygen could not be maintained and cell voltages were too low. This was especially true at the lower test temperatures where the electrode-electrolyte reaction was sluggish. As previously explained, this problem was partially overcome by utilizing a dense pressed and sintered surface whose composition was determined by x-ray diffraction. A second difficulty occurred when oxidation of the silicide yielded a silica glass whose high resistivity resulted in ultimate decrease of voltage. Because of these problems, emf readings were considered reliable only when they were stable, insensitive to the flow rate of the surrounding argon, and displayed the expected small negative temperature coefficient. In all cases, corrections for electronic conduction were made using Table IV. The corrected measurements are summarized in Table III where the cell numbers correspond to the reactions given in Table II.

$TaSi_2$-Ta_5Si_3 *phase field.*—Fifteen electrodes were prepared and tested, but only two points, representing six observations were satisfactory. These are listed under cell I.

Ta_5Si_3-Ta_2Si *phase field.*—Nineteen electrodes were prepared and tested. The ratio of the two silicides was varied while the content of Ta_2O_5 was in the range of 0-25% and that of SiO_2 varied between 0-7% by weight. X-ray and microscopic examinations of the electrodes before and after use led to the conclusion that the anticipated oxidation of Ta_2Si_3 to Ta_2O_5 and SiO_2 (VIII) did not occur. Instead, electrodes that were primarily Ta_5Si_3 were oxidized to SiO_2 and the lower silicide (II). On the other hand, Ta_2Si was oxidized to Ta_2O_5 and the higher silicide, Ta_5Si_3 (V). The corrected potentials measured for these electrodes are given in Table III under the appropriate cell numbers.

Ta_2Si-$Ta_{4.5}Si$ *phase field.*—The expected reaction is VI of Table II. Four electrodes were examined and two performed satisfactorily. The average values are listed in Table III. In this case, correction was made not only for electronic conduction, but also to normalize all measurements to the slightly higher values measured at maximum argon flow rates. Hence, although the variability of the measurements was ±4 mV, the results were considered reliable to only ±10 mV.

Evaluation of free energies of formation.—The measured emf values were combined with free energy of formation data for Fe_xO (14) and for Ta_2O_5 and SiO_2 (3) to produce four linear equations which could be solved for the free energies of formation of the individual silicides. An upper bound for cell I was set by the limitation that its potential may not exceed that of Si,SiO_2 *vs.* the same reference electrode. The results of the calculations are presented in Table V.

Although the free energies are given at three temperatures because measurements were made in the vicinity of these temperatures, it is obvious that the estimated errors are too large to permit calculation of entropy changes. It is worth noting that nearly one-half of the uncertainty in the data for the silicides is attributable to uncertainties in the free energy data for the oxides of iron, tantalum, and silicon. This sets a limit on the accuracy that may be achieved.

The free energies of formation may be compared with little error to the enthalpies of formation given in Table I. Since by the Neumann-Kopp rule the formation of a compound from its elements involves no change in heat capacity, then

$$\Delta G^\circ_T \cong \Delta H^\circ_{298} - T\Delta S^\circ_{298} \qquad [13]$$

Furthermore, for the formation of ordered solids from the solid elements, ΔS°_{298} is very close to zero (4). Hence

$$\Delta G^\circ_T \cong \Delta H^\circ_{298} \qquad [14]$$

Comparison of the values in Tables I and V shows that for the three lower silicides the results obtained by the emf method are in substantial agreement with those obtained by effusion. Some improvement in the confidence interval for Ta_5Si_3 and Ta_2Si has been achieved in this work. Furthermore, the results obtained in this investigation are thermodynamically consistent in that the activity of silicon must increase monotonically from the lower to the higher silicides, while the activity of tantalum must decrease. Therefore, emf's of electrodes where SiO_2 is the oxidation product must increase from the lower to higher silicides, while those where Ta_2O_5 is the oxidation product must fall. This requirement is obeyed by the present results but not by results inferred from earlier data.

Table IV. Transport properties for thoria-yttria electrolytes at 1300°K with an Fe, Fe_xO reference electrode

P_{O_2}	E	$E_{meas.}$	$\bar{t}_i$	t_i
10^{-20}	361	361	1	1
10^{-21}	426	425	0.998	0.990
10^{-22}	490	488	0.997	0.982
10^{-23}	555	550	0.992	0.956
10^{-24}	619	612	0.989	0.939
10^{-25}	685	670	0.979	0.875
10^{-26}	750	726	0.968	0.807
10^{-27}	813	775	0.953	0.712
10^{-28}	878	817	0.931	0.580
10^{-29}	943	850	0.902	0.435
10^{-30}	1007	875	0.869	0.307

Table V. Free energies of formation of the tantalum silicides (kcal/g atom silicon)

Temp, °K	1/2 $TaSi_2$	1/3 Ta_5Si_3	Ta_2Si	$Ta_{4.5}Si$
1200		−24.8 ± 3	−28.1 ± 3.1	−39.2 ± 7.2
1300	−8.1 +1.8 −3.7	−24.0 ± 3	−27.2 ± 3.1	−37.3 ± 7.2
1400		−23.1 ± 3	−26.1 ± 3.1	−35.3 ± 7.2

Summary

It has been demonstrated that solid oxide electrolytes may be successfully employed for the measurement of the free energies of formation of refractory silicides. Problems were encountered because the electrode pellets consisted of mixtures of high melting hard compounds that could not be readily fabricated with low porosities. Consequently, it was difficult to maintain low oxygen partial pressures at the electrode-electrolyte interface. This drawback was overcome by using as-sintered surfaces, but may be overcome by hot-pressing of electrodes or by improved sealing techniques. Another difficulty caused by the formation of silica films of low conductivity may be solved by performing measurements at much higher temperatures.

A fundamental limitation of the method is the uncertainty in the free energies of formation of the oxides employed as reference electrodes and the oxide products of reaction. In the present study this represented nearly one-half of the total uncertainty of the measurements.

Acknowledgments

The authors thank the Lewis Research Center of the National Aeronautics and Space Administration for its support under grant No. NGR 33-013-017 and Mr. R. Oldrieve who monitored the grant. They are especially grateful to Professor R. A. Graff for numerous discussions and to J. Bodnaruk and D. Marden for assistance with the equipment.

Manuscript submitted June 18, 1969; revised manuscript received March 14, 1969.

Any discussion of this paper will appear in a Discussion Section to be published in the June 1970 JOURNAL.

REFERENCES

1. J. Huminik, "High Temperature Inorganic Coatings," Reinhold Publishing Corp., New York (1963).
2. A. W. Searcy, *J. Am. Ceram. Soc.*, **40**, 431 (1957).
3. C. E. Wicks and F. E. Block, *U.S. Bur. Mines Bull.* **605**, (1963).
4. O. Kubaschewski and E. LL. Evans, "Metallurgical Thermochemistry," 3rd edition, Pergamon Press (1958).
5. L. Brewer and O. Krikorian, *This Journal*, **103**, 38, 701 (1956).
6. D. A. Robins and I. Jenkins, *Acta Met.*, **3**, 598 (1955).
7. C. E. Myers and A. W. Searcy, *J. Am. Chem. Soc.*, **79**, 526 (1957).
8. A. W. Searcy, and R. A. McNees, *ibid.*, **75**, 1578 (1953).
9. A. W. Searcy and A. G. Thorp, *J. Phys. Chem.*, **64**, 1539 (1960).
10. A. W. Searcy and L. N. Finnie, *J. Am. Ceram. Soc.*, **45**, 268 (1962).
11. S. G. Davis, D. F. Anthrop, and A. W. Searcy, *J. Chem. Phys.*, **34**, 659 (1961).
12. K. Kiukkola and C. Wagner, *This Journal*, **104**, 308, 379 (1957).
13. H. Schmalzried, *Z. Electrochem.*, **66**, 572 (1962).
14. G. G. Charette and S. N. Flengas, *This Journal*, **115**, 795 (1968).
15. B. C. H. Steele and C. B. Alcock, *Trans. Met. Soc. AIME*, **233**, 1359 (1965).
16. A. A. Vecher and D. V. Vecher, *Russian J. Phys. Chem. (Engl. Transl.)*, **42**, (3), 418 (1968). Also, *ibid.*, **41**, (6), 685 (1967).
17. R. A. Rapp, "Thermodynamics of Nuclear Materials, 1967," IAEA, Vienna (1968).

Vapor Growth of High Resistivity ZnTe

A. S. Jordan and L. Derick

Bell Telephone Laboratories, Incorporated, Murray Hill, New Jersey

ABSTRACT

High resistivity crystals of ZnTe, essentially free of the usual Te precipitates, have been vapor grown from a powdered ZnTe charge, containing a small amount (8×10^{-3} a/o) of In, by a modification of the Piper and Polich technique. Attempts to incorporate larger amounts of In in the charge resulted in negligible vapor transport rates which are qualitatively related by means of the transport theory of Lever and Jona to the p-T and the solidus diagrams of ZnTe. The observed Te precipitation is consistent with the retrograde solidus of ZnTe and with the diffusion coefficient of Te in the crystal.

ZnTe, a group II-VI wide band-gap semiconductor, has been considered a potentially useful electroluminescent and electrooptic material for some time (1, 2). There are several feasible methods for the growth of pure and doped ZnTe crystals. Fischer *et al.* (3) have successfully grown n-type ZnTe in an autoclave from Zn-rich melts, containing 20 m/o (mole per cent) excess Zn, under 30-50 atm of argon pressure. Solution growth of ZnTe crystals from Te-rich melts has been reported by Title *et al.* (4).

It is a well-established fact that ZnTe crystals doped with group III impurities are generally high resistivity p-type due to self-compensation (4). Usually the impurities, such as Al, are introduced by diffusion into the II-VI compounds (5, 6). However, Title *et al.* (4) have prepared Al-doped solution grown ZnTe by the addition of Al to the Te-rich liquid. Tubota (7) and Nahory and Fan (8) have grown In-doped ZnTe crystals in graphite reinforced quartz capsules according to a modified Bridgman technique originated by Fischer (9).

In the present study we report on the vapor growth of pure and In-doped ZnTe utilizing a vertical modification of the Piper and Polich (10) technique.

Experimental

Piper and Polich (10) have grown single crystals of undoped CdS by condensing Cd(g) and S_2(g) escaping from a dissociating source of powdered CdS. According to Piper and Polich, Aven has utilized their method to grow ZnTe crystals by the reversible reaction

$$ZnTe(s) \rightleftarrows Zn(g) + \tfrac{1}{2} Te_2(g) \qquad [1]$$

In the present study their method was modified to permit the use of evacuated sealed tubes. Figure 1 illustrates the vertical vapor transport furnace and its temperature profile. The heating element was a platinum-20% rhodium resistance wire wound on a 12 in. long high purity alumina core. The furnace temperature was controlled to better than ± 0.5°C by the use of a saturable core reactor in conjunction with a Leeds and Northrup Speedomax H controller, providing an ap-

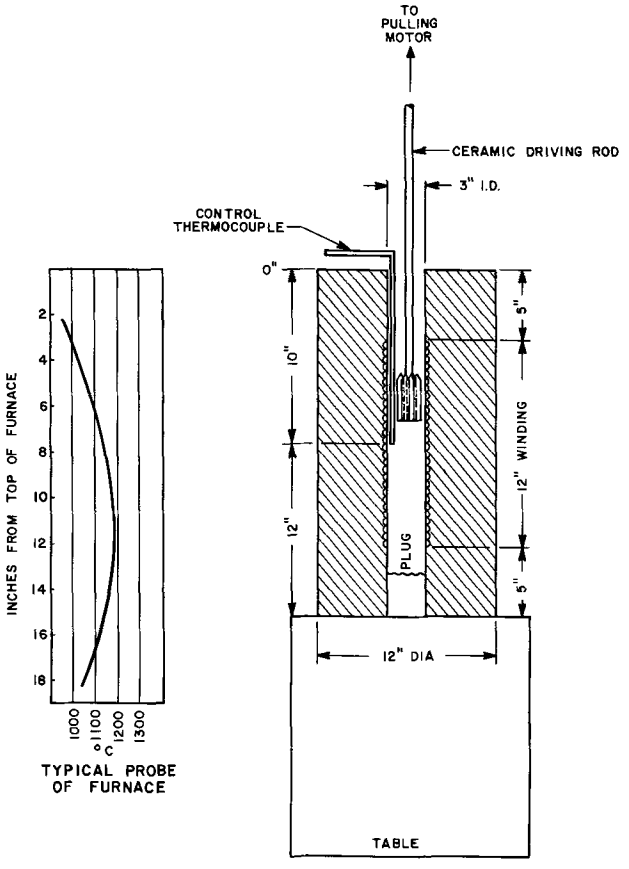

Fig. 1. ZnTe vapor transport furnace and temperature profile

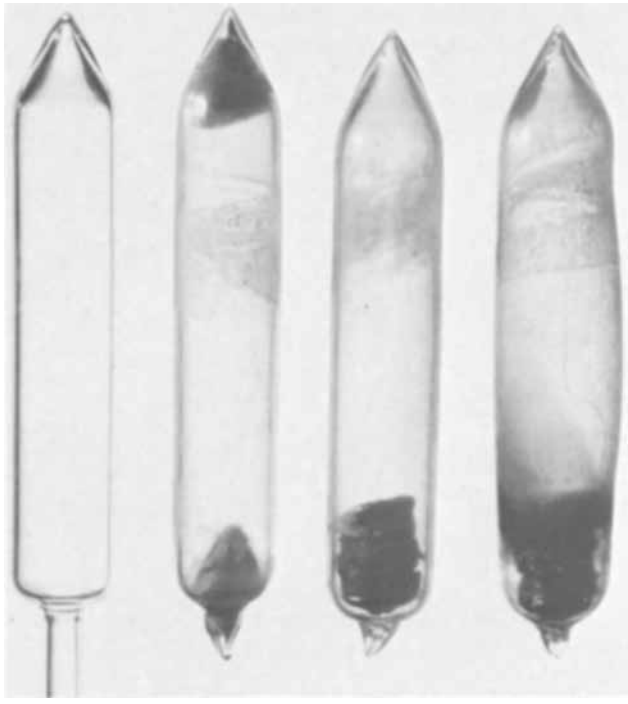

Fig. 2. Expansion of ampoules after vapor growth. A clean ampoule, 105 mm long by 18 mm OD, is shown on the left of the photograph. Three other ampoules after the completion of a simultaneous run are shown on the right. The following amounts of In were added to the charge in these ampoules (left to right): 1, 8×10^{-3} a/o; 2, 8×10^{-2} a/o; 3, 9×10^{-1} a/o. Note the expansion of ampoules 2 and 3.

proximately 2 in. long uniform temperature zone. Outside this zone the temperature gradient was found to be $\approx$ 15°C/in.

It was possible to load up to four ampoules containing powdered ZnTe into the furnace. Figure 1 indicates a cluster of four ampoules, held together by platinum straps, suspended from a Pt wire to a ceramic driving rod which was connected by a chain to a variable speed motor. A clean ampoule is shown in Fig. 2.

Usually three thermocouples were attached by wire to the cluster. One was near the tip, another approximately 1 in. away from the tip, and the third was in the vicinity of the charge. The temperatures corresponding to these locations were continuously monitored on a multipoint recorder.

In a typical experimental run between 12-20g ZnTe powder, supplied by Harshaw Chemical Corporation, was charged into the conical part of the ampoule for subsequent evacuation and sealing at approximately 10^{-7} Torr pressure. The furnace, loaded with the cluster of ampoules, was slowly heated in about 2 hr to approximately 1160°C. Initially, the tip of the ampoule was positioned approximately 11 in. from the top of the furnace (Fig. 1). This facilitated the cleaning of the tip by sublimation of some adhering ZnTe powder. After a few hours the ampoule was raised to a position where the tip and the charge were at the same temperature. This took place, as seen in Fig. 1, when the tip was 9 in. from the top of the furnace. Then, the variable speed motor drive was connected and the ampoules were pulled upwards at approximately 0.2 mm/hr. Usually, at the completion of a run the tip was at 1140°C and the source at 1160°C, corresponding to a minimum total pressure of 98 Torr and 125 Torr (11), respectively. A typical run lasted from five to eight days and yielded an ingot about 20-30 mm long and 8-13 mm in diameter. The ampoules were slowly withdrawn from the cooling furnace to avoid cracking. In many runs a pyrolytic BN liner with a conical tip was placed inside the quartz ampoule.

Results and Discussion

Perfection of crystals.—All the crystals grown by vapor transport were p-type, as indicated by a thermoelectric probe. A typical boule is illustrated in Fig. 3. From this boule it was possible to obtain cubes of single crystals with sides as large as 0.6 cm. When the growth was interrupted after a short time, say 1 hr, one could see that two or three triangular shaped nuclei had already formed near the tip of the cone. Recently, Lind (12) was able to eliminate spurious nucleation in some II-VI compounds by a periodic reversal of the temperature gradient during growth, resulting in the re-evaporation of the unstable nuclei. Often the monocrystalline regions were twinned which we could minimize by the use of BN inserts in the ampoules.

Suppression of vapor transport.—In the present study, in order to prepare high resistivity ZnTe, In, a relatively volatile impurity, was added to the ZnTe charge in the ampoule. It was anticipated that In would vaporize and codeposit with ZnTe since at 1150°C, the usual growth temperature, the vapor pressure of In is approximately 0.5 Torr.

Fig. 3. Boule of vapor grown ZnTe crystal

Initially, 0.9 a/o (atom per cent) In was added to the charge. However, after a five day run no vapor transport was observed and the ampoule diameter had increased. In a subsequent experiment a cluster of three ampoules was placed in the furnace with 0.9, 8×10^{-2}, and 8×10^{-3} a/o In added to the source material. By simultaneously growing in several ampoules, uncertainties which might be inherent in consecutive runs could be eliminated. Figure 2 illustrates the three ampoules together with an unused ampoule after the completion of this run. A sizable (6g) crystal grew in the ampoule with 8×10^{-3} a/o In addition. In the two other ampoules vapor transport was negligible except for several minute crystallites which had an approximate total weight of 10 mg. In addition, considerable expansion of the ampoules was observed when the amount of In was over 8×10^{-3} a/o.

Further experiments have shown that the expansion of the ampoules and the suppression of the vapor transport was neither due to the excessive pressure of some volatile species of In and Te nor particularly to the specific presence of In. On the one hand, heating InTe in an ampoule for a day at 1150°C did not cause any change in the geometry of the ampoule. On the other hand, an addition of Sn or Ga to the charge also led to negligible vapor transport rates. Moreover, the effect of excess Zn in the charge was similar to that of 0.9 a/o In. However, when InTe, In_2Te_3, or SnTe were added to the ZnTe source, significant vapor transport was observed. In Fig. 4 all the starting compositions containing ZnTe and Sn, Ga, SnTe, InTe, In_2Te_3, In + Te, excess Te, or excess Zn expressed in a/o are plotted using triangular coordinates. The reported solid solubility of In_2Te_3 in ZnTe (13) is also included.

It was possible to separate the region of compositions where vapor transport was observed from the region where vapor transport was negligible. It is noticeable in Fig. 4 that starting compositions in the direction of the Zn-rich side of the diagram were not favorable to vapor transport.

Interpretation.—A qualitative interpretation of the suppression of vapor transport rates is possible in terms of thermodynamic and kinetic arguments. When a pure solid compound such as ZnTe evaporates in a closed container at a constant temperature, the composition of the solid changes due to the preferential volatilization of one or the other of the components. However, by continuously removing the vapor phase from the vicinity of the subliming solid, eventually an equilibrium state is reached in which the solid and the vapor have the same composition (congruent vaporization). In this state the total pressure is at a minimum and the congruent vapor composition for solids with a narrow range of departures from stoichiometry is nearly that of the stoichiometric vapor ($p_{Zn} = 2p_{Te_2}$). It is expected that the eventual vapor composition resulting from the high purity ZnTe source is not too different from the composition of congruently subliming ZnTe. However, when impurities such as In, Sn, or Ga are added to the ZnTe charge the vapor compositions and pressures change from their values corresponding to congruent vaporization, *i.e.*, $p_{Zn} \neq 2p_{Te_2}$.

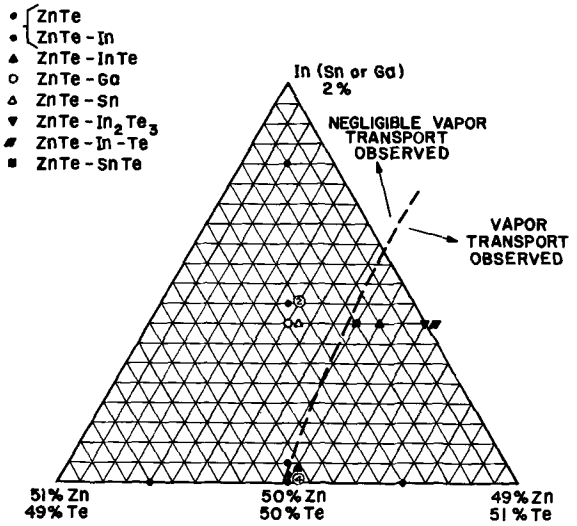

Fig. 4. Dependence of vapor transport on charge composition. The initial charge compositions, expressed in a/o, are plotted on an expanded triangular composition diagram. The ○ shown outside the diagram at 47.7 a/o Zn and 50.5 a/o Te represents the solid solubility of In_2Te_3 in ZnTe at 1150°C.

The equilibrium constant, $K = p_{Zn}\sqrt{p_{Te_2}}$, for reaction [1] is thought to remain essentially constant when small amounts of impurities are present in the charge. At the same time the pressure ratio p_{Zn}/p_{Te_2} may significantly change by the addition of an impurity because at the run temperature ($\approx$ 1150°C) the charge composition moves from a point in the binary solidus phase field (11), characterized by $p_{Zn}/p_{Te_2} \approx 2$, into a ternary solidus (*i.e.*, solid solutions of ZnTe + In or ZnTe + Ga) or solid and liquid phase field. There seems to be no thermodynamic or diffusional limitation to ternary solid solution formation in the systems under consideration.[1] Since the solidus isotherms in these ternary systems are not presently available, it is necessary to make some qualitative remarks about their probable shapes.

It has been previously reported (11) that the solidus curve of pure ZnTe is retrograde and lies entirely in the Te-rich region of the phase diagram. This suggests, if one assumes that excess Zn is insoluble for example in the ZnTe + In solid solution, and if the relatively large solid solubility of In_2Te_3 in ZnTe (13) is taken into account,[2] that the ternary Zn-Te-In solidus isotherm is offset toward Te and In rich concentrations ($x_{Zn}/x_{Te} < 1$). Accepting this tentative model for the ternary solidus isotherm, one concludes that at a constant initial impurity concentration, say 0.8-0.9 a/o in Fig. 4, the range of compositions where vapor transport was observed most probably corresponds to compositions within the ternary solidus isotherm at the run temperature. This view is strongly supported by the chemical analysis of some crystals which indicates that the In concentration in the vapor grown ZnTe crystals is nearly that of the respective initial charges. It has been found by atomic absorption spectroscopy that the addition to the charge of 8×10^{-3} a/o In and 0.8 a/o In (in the form of In_2Te_3) resulted in crystals containing 6.9×10^{-3} a/o and 0.66 a/o In, respectively.

One can readily show that in the ternary solid solution which consists of ZnTe and an impurity, say In, p_{Zn} is related to the atom fraction of In in the solid, x_{In}. The work of Thomas and Sadowski (16) has established that the major defect in ZnTe is a doubly ionized Zn vacancy. Furthermore, it is known that group III impurities are donors, substituting on Zn sites. Based on this information, taking into account the charge neutrality condition for p-type ZnTe and the simultaneous equilibria for the creation of Zn vacancies and the incorporation of In donors, one obtains for the relation of p_{Zn} to x_{In} the following equation

$$k_1 x_{In} + p_{Zn} = k_2/[\dot{h}] \qquad [2]$$

where $[\dot{h}]$ is the hole concentration and k_1 and k_2 are proportional to the two equilibrium constants.

[1] The relatively large solid solubilities of In and Ga in ZnTe have been well-established (13, 14). Lacking the appropriate diffusion coefficients for ZnTe, one can estimate the diffusion coefficient of In at 1150°C from the measurements of Kato and Takanayagi (15) for CdTe. A relatively large coefficient (10^{-7} cm^2/sec) is obtained, consistent with solid solution formation within the time available for crystal growth.

[2] According to Mason and O'Kane (13), 2 m/o In_2Te_3 can be dissolved in ZnTe at 1150°C.

In general, ZnTe changes from a low resistivity p-type ($[\dot{h}]$ large) to a high resistivity p-type ($[\dot{h}]$ small) semiconductor when doped with a group III element. Therefore, p_{Zn} changes with the addition of In. As the relationship $K = p_{Zn}\sqrt{p_{Te_2}}$ is still expected to hold, the ratio $p_{Zn}/p_{Te_2} = 2$ is necessarily upset.

One would intuitively expect the rate of transport to be proportional to the lowest partial pressure in the system. Indeed it is demonstrated in the Appendix by an application of the vapor transport theory of Lever and Jona (17) that the transport rate is at a maximum when $p_{Zn}/p_{Te_2} = 2$, hence, any change in this ratio would result in a decrease in the transport rate. Moreover, as p_{Zn} or p_{Te_2} approaches zero, the rate also approaches zero. The experimental transport rates were not uniform in the solid solution region, the region in Fig. 4 where vapor transport was observed. For example, in a simultaneous run the ratio between the yields for an ampoule with 8×10^{-3} a/o In added to ZnTe and for one with pure ZnTe was 0.58, indicating a decrease in the transport rate by approximately a factor of 2.

It is thought that the addition of 1.6 a/o In, 0.9 a/o In, 8×10^{-2} a/o In, 0.8 a/o Sn, or 0.8 a/o Ga similar to the addition of 0.5 a/o excess Zn moved the over-all charge composition into the two phase liquid and solid solution region. As seen in Fig. 4, the vapor transport rate was negligible for all of the above compositions. Moreover, in all these cases an expansion of the ampoules was observed.

The effect of Zn addition can be completely explained in terms of the p-T diagrams for the Zn-Te system proposed by Jordan and Zupp (11). According to their results, $p_{Zn} = 7.9$ atm, $p_{Te_2} = 10^{-5}$ atm, and $p_{Zn}/p_{Te_2} = 7.9\times10^{5}$ in the Zn-rich binary two phase region and also on the solidus boundary at 1150°C. Consequently, in view of the high values of p_{Zn} in the vicinity of the Zn-rich side of the solidus isotherm, the expansion of the quartz ampoules is not surprising. Furthermore, as the values of p_{Zn}/p_{Te_2} are large, the vapor transport rates, as observed, become negligible. The ratio p_{Zn}/p_{Te_2} is expected to change along the ternary solidus isotherm.[3]

Moderate suppression of vapor transport rates is also expected near the Te-rich solidus boundary. In fact, an approximate calculation given in the Appendix indicates that the ratio of transport rates on the Zn-rich side to the Te-rich side is of the order of 10^{-4}. Although only few crystals have been grown near the Te-rich boundary due to the large density of Te precipitates resulting from growth in this region, in all cases diminished vapor transport rates have been observed.[4]

Te *precipitates*.—Tellurium precipitates have been previously observed in solution and vapor grown ZnTe crystals (18). Figures 5 and 6 are photomicrographs of precipitates, viewed in transmitted light, in undoped crystals grown from a Te-rich solution and from the vapor phase, respectively. The precipitates are tetrahedral in shape, separated by 30-70μ, having 2-6μ long edges. Sometimes, as illustrated in Fig. 7 and 8, a dislocation network or a grain boundary is decorated by the precipitates.

According to Reynolds (18), the relative x-ray and electron back-scatter intensities from the matrix and the precipitates indicated that the precipitates were rich in Te. However, Reynolds was unable to determine the Te content of the precipitates more quantitatively by electron microprobe or by x-ray diffraction analysis.

[3] On the Te-rich side of the binary solidus $p_{Zn}/p_{Te_2} = 4\times10^{-2}$ at 1150°C (11). The partial pressures are the following: $p_{Zn} = 2.8\times10^{-2}$ atm and $p_{Te_2} = 7.1\times10^{-1}$ atm.

[4] For instance, when 0.5 a/o excess Te was added to the charge, the resulting small crystal weighed only 0.5g, corresponding to an approximately twenty-fold rate reduction, compared to the crystal grown from a pure ZnTe charge.

A consideration of the liquidus and solidus curves (11) in the Zn-Te system clearly demonstrates that Te precipitation in the solid is possible. The solidus of ZnTe is retrograde with an excess of Te. At approximately 1200°C, the maximum solubility of Te in the crystal is

$$\frac{4.6\times10^{-5}\text{ mole excess Te}}{\text{mole ZnTe}}\left(\text{or}\ \frac{1.48\times10^{-4}\text{g Te}}{\text{cc ZnTe}}\right)$$

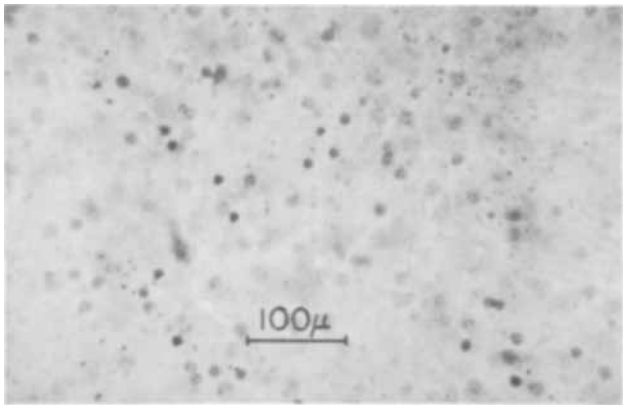

Fig. 5. Transmission photomicrograph of Te precipitates in undoped solution grown ZnTe.

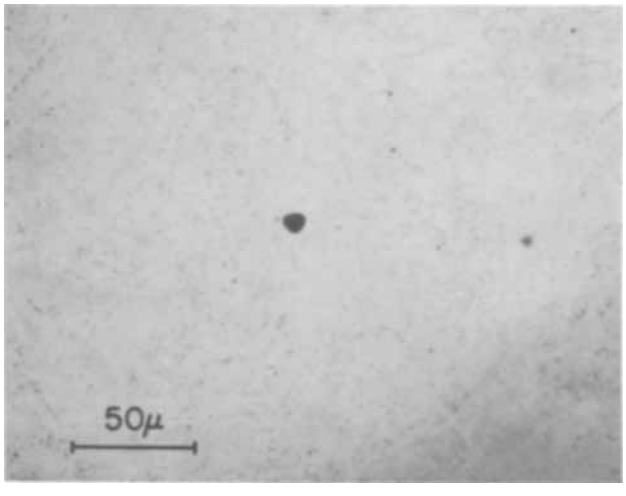

Fig. 6. Transmission photomicrograph of Te precipitates in undoped vapor grown ZnTe. Some precipitates are not in focus.

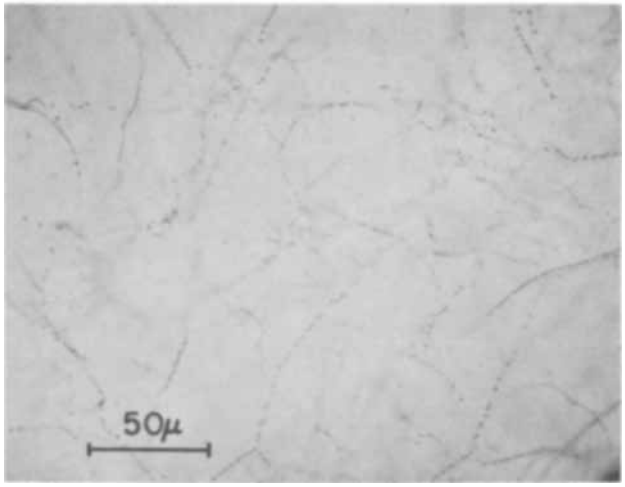

Fig. 7. Transmission photomicrograph of a dislocation network in undoped vapor grown ZnTe.

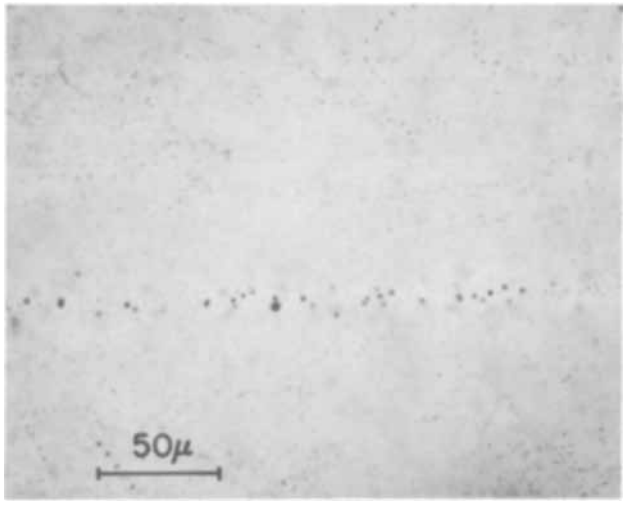

Fig. 8. Transmission photomicrograph of a decorated grain boundary in undoped vapor grown ZnTe.

If a crystal grown from either a Te-rich solution of the vapor phase is cooled to room temperature, the phase diagram requires separation into a nearly stoichiometric compound and a solid Te phase.

One can readily estimate the mean separation of the precipitates by an order of magnitude calculation[5] and obtain $\approx 67\mu$. This is in good agreement with the experimentally observed separation of 30-70μ.

Moreover, it can also be shown that there is no kinetic limitation to precipitation. The average distance, $\overline{X}$, the Te atoms move during the cooling of a crystal in t minutes can be estimated by the graphical integration of the function

$$\overline{X} = \int \sqrt{6D}\, d\sqrt{t} \qquad [3]$$

where the integrand is the three dimensional random walk formula of Shewmon (19) and D is the temperature dependent self-diffusion coefficient of Te in ZnTe obtained from the data of Reynolds (18). Integrating Eq. [3] between room temperature and 1150°C and using an estimated cooling rate of 50°C/min, one has $\overline{X} = 18\mu$.[6] Accordingly, during cooling each precipitate can be formed from the surrounding crystal volume which, if assumed to be spherical, has an 18μ radius. The resulting mean separation of precipitates is 36μ, in reasonable agreement with the experimental and thermodynamic estimates, thus demonstrating that precipitation is consistent with the known diffusional and thermodynamic behavior of Te in ZnTe.

Precipitation has also been observed in vapor grown In-doped crystals. Figures 9 and 10 are photomicrographs of ZnTe crystals grown from a charge with an addition of In_2Te_3, resulting in an over-all composition with 0.8 a/o In and 0.2 a/o excess Te. The high density of Te precipitates, shown in Fig. 9, is due to the relatively large amount of Te present in the charge. Figure 10 illustrates a grain boundary decorated with precipitates and a parallel depletion region.

Usually, Te precipitates have been removed from ZnTe by annealing after growth in a Zn atmosphere (18, 20, 21). However, Fig. 11 shows the microstructure of a crystal, vapor grown from a charge containing 8×10^{-3} a/o In, which is essentially free of precipitates, virtually featureless, with a lightly decorated dislocation network in view. The starting composition of this charge was near the region in Fig. 4 where vapor transport was suppressed. This composition is in the solid solution region, probably in the vicinity of the solidus line separating the two condensed phases Zn-rich liquid and ZnTe from ZnTe. A consideration of the solidus (11) of ZnTe indicates that precipitation of Te should not be expected in a crystal which was vapor grown from a charge composition near the Zn-rich boundary.

Electrical and optical properties.—The electrical and optical properties of vapor grown ZnTe were strongly effected by In-doping. The room temperature resistivity of the crystals was measured by the four point probe method. A Ga-In amalgam served as a contact for the crystals. The resistivity of undoped ZnTe was 2 ohm-cm. The addition of 8×10^{-3} a/o In to the charge increased the resistivity to 740,000 ohm-cm, due to self-compensation via the incorporation of 1.2×10^{18} In atoms/cc in the crystal. To the best of our knowledge, this was the first successful attempt to grow high resistivity In-doped ZnTe crystals by a static vapor transport technique. The resistivity is in good agreement with the previously reported value of Tubota (7) which was about 300,000 ohm-cm for an In-doped sample grown by Bridgman's method.

Figure 12 illustrates the dependence of the absorption coefficient, α, on energy for ZnTe. The curves were derived from spectrometric data taken at 30°K. According to the measurements of Nahory and Fan (8),

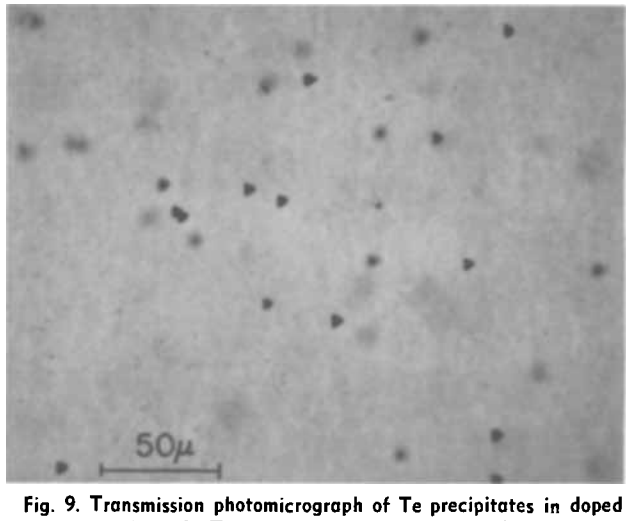

Fig. 9. Transmission photomicrograph of Te precipitates in doped vapor grown ZnTe. In_2Te_3 was added to the charge. Over-all composition of the charge: 0.8 a/o In, 50.2 a/o Te, 49 a/o Zn. In content of crystal: 1.15×10^{20} atoms/cc.

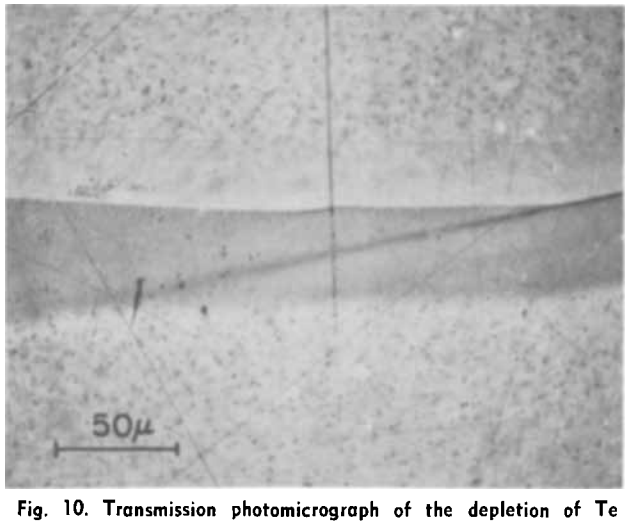

Fig. 10. Transmission photomicrograph of the depletion of Te precipitates near a grain boundary in the crystal shown in Fig. 9.

[5] The approximate volume of a tetrahedral precipitate, using an average edge length of 4μ, is 7.5×10^{-12} cc, weighing 4.5×10^{-11}g Te/precipitate. Assuming that an amount corresponding to the retrograde maximum of Te precipitates out during cooling, the density of precipitates, ρ, is 3.3×10^{6}/cc ZnTe. The mean separation of precipitates is given by $3\sqrt{1/\rho}$.

[6] The integrand in Eq. [3] can be readily transformed into a function of T if the cooling rate, r, is given by $r = (T_{\text{initial}} - T)/t$. Then, $d\sqrt{t} = dt/2\sqrt{t} = -dT/2\sqrt{r(T_{\text{in}} - T)}$.

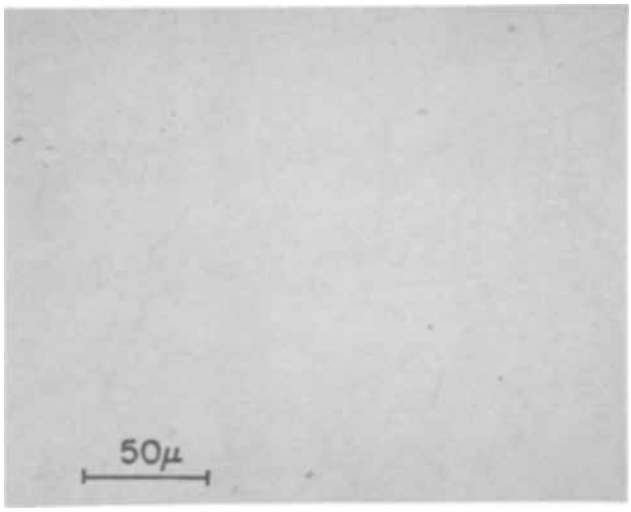

Fig. 11. Transmission photomicrograph of doped vapor grown ZnTe. 8×10^{-3} a/o In was added to the charge. In content of crystal: 1.2×10^{18} atoms/cc. This crystal is essentially free of precipitates.

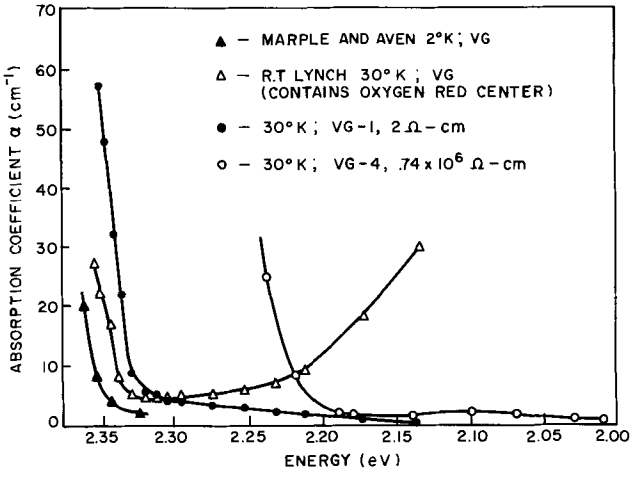

Fig. 12. Absorption coefficient vs. energy for doped and undoped ZnTe crystals.

the energy gap of ZnTe is at 2.385 eV. It can be seen in Fig. 12 that the 2°K results of Marple and Aven (20) extrapolate to this value. However, the absorption edge between 2.33-2.35 eV observed in the undoped vapor grown crystal does not correspond to the true energy gap of this material. In fact, Nahory and Fan have suggested that the edge located below $\alpha = 100$ cm^{-1} near 2.33 eV at 1.7°K was due to electron transitions to the conduction band from a level 0.05 eV above the valence band. This level is probably produced by Zn vacancies.

It can be observed in Fig. 12 that the incorporation of In in the lattice causes the absorption edge to rise at a lower energy, at about 2.2 eV. Nahory and Fan (8) found the position of the In donor level at 0.2 eV from the conduction band. Therefore, the edge observed in the doped crystal is associated with the In donor level.

Usually the color of undoped ZnTe is orange. Crystals containing In or O centers are red. The change in color caused by the addition of impurities can be readily understood on the basis of the absorption curves in Fig. 12.

Conclusions and Summary

High resistivity p-type crystals of ZnTe were grown by transporting powdered ZnTe with In added in a closed, evacuated ampoule. Only certain special charge compositions yielded appreciable vapor transport rates. It was possible to grow 740,000 ohm-cm ZnTe, free of Te precipitates, by the addition of 8×10^{-3} a/o In to the charge.

Acknowledgments

The authors are grateful to Dr. F. A. Trumbore and Dr. C. D. Thurmond for stimulating discussions, Dr. J. Merz for the absorption data, Dr. S. Wemple for the electrical measurements, Dr. R. Saul for taking some of the photomicrographs, and to Dr. R. Buckley and Dr. R. Curran for their help in the initial phases of the work. Mr. T. Y. Kometani performed the chemical analysis of the crystals. Thanks are also due to Dr. A. Strauss of M.I.T. Lincoln Laboratories for supplying InTe.

Manuscript submitted Feb. 4, 1969; revised manuscript received June 25, 1969. This was Paper 528 presented at the Montreal Meeting, Oct. 6-11, 1968.

Any discussion of this paper will appear in a Discussion Section to be published in the June 1970 JOURNAL.

APPENDIX

According to the theory of Lever and Jona (17) for chemical transport in nonconvective systems, the deposition rate, J, can be written as

$$J = \frac{\Delta \ln K - \delta}{\xi \Delta z} \qquad [A\text{-}1]$$

where Δz is the separation between source and seed, δ is the supersaturation over the solid surface not in equilibrium with the vapor, and $\Delta \ln K$ is the difference in equilibrium constant between source and seed temperatures for the volatilization reaction; *i.e.*, $ZnTe(s) = Zn(g) + \frac{1}{2}Te_2(g)$. One can evaluate ξ for the present system by a combination of Eq. [28] and [29] of ref. (17) to yield

$$\xi = \frac{(p_{Te_2} - \frac{1}{2}p_{Zn})^2}{p_{Zn}p_{Te_2}ND_{Zn\text{-}Te_2}} + \xi_i \qquad [A\text{-}2a]$$

where

$$\xi_i = \frac{p_A}{p_{Zn}ND_{Zn\text{-}A}} + \frac{p_A}{4p_{Te_2}ND_{Te_2\text{-}A}} \qquad [A\text{-}2b]$$

p_A is the partial pressure of a residual inert gas A (present in the container), N is the total gas density in moles/cc, $D_{Zn\text{-}Te_2}$, $D_{Zn\text{-}A}$, and $D_{Te_2\text{-}A}$ represent the gaseous interdiffusion coefficients.

It is possible to evaluate $\xi - \xi_i$ in terms of $\alpha = p_{Zn}/p_{Te_2}$ and obtain

$$\xi - \xi_i = \frac{\left(\frac{\alpha}{2} - 1\right)^2}{\alpha ND_{Zn\text{-}Te_2}} \qquad [A\text{-}3]$$

A combination of Eq. [A-3] and [A-1] shows that for $\alpha = 2$, *i.e.*, for congruent vaporization, ξ is at its minimum and J is at its maximum value. Furthermore, $\xi - \xi_i$ is proportional to $\alpha/4$ when $\alpha >> 2$; hence, J is at a minimum for very large α. Similarly, $\xi - \xi_i$ approaches $1/\alpha$ as $\alpha << 2$ and J again reaches a minimum at $\alpha = 0$. In the Zn-rich two phase region $\alpha = 7.9 \times 10^5$ and in the Te-rich two phase region $\alpha = 4 \times 10^{-2}$ at 1150°C. Therefore, J is small in both instances. The transport rate near the Te-rich side is approximately 10^4 higher than in the vicinity of the Zn-rich side. This estimate is based on the ratio of Eq. [A-3] for the two sides using the known values of α.

REFERENCES

1. B. L. Crowder, F. F. Morehead, and P. R. Wagner, *Appl. Phys. Letters*, **8**, 148 (1966).
2. S. K. Kurtz, *Bell System Tech. J.*, **45**, 1209 (1966).
3. A. G. Fischer, J. N. Carides, and J. Dresner, *Solid State Comm.*, **2**, 157 (1964).
4. R. S. Title, G. Mandel, and F. F. Morehead, *Phys. Rev.*, **136**, A300 (1964).
5. M. Aven and B. Segall, *ibid.*, **130**, 81 (1963).
6. M. Aven and R. E. Halsted, *ibid.*, **137**, A228 (1965).
7. H. Tubota, *Japan J. Appl. Phys.*, **2**, 259 (1963).
8. R. E. Nahory and H. Y. Fan, *Phys. Rev.*, **156**, 825 (1967).
9. A. G. Fischer, *This Journal*, **106**, 838 (1959).
10. W. W. Piper and S. J. Polich, *J. Appl. Phys.*, **32**, 1278 (1961).

11. A. S. Jordan and R. R. Zupp, *This Journal*, **116**, 1264 (1969).
12. M. Lorenz, in "II-VI Semiconducting Compounds," D. G. Thomas, Editor, W. A. Benjamin, Inc., New York-Amsterdam (1967).
13. D. F. O'Kane and D. R. Mason, *Trans. Met. Soc. AIME*, **233**, 1189 (1965).
14. N. A. Gorjunova, V. A. Kotavich, and V. A. Frank-Kamenetsky, *Dokl. Akad. Nauk. SSSR*, **103**, 659 (1955).
15. H. Kato and S. Takanayagi, *Japan J. Appl. Phys.*, **2**, 250 (1963).
16. D. G. Thomas and E. A. Sadowski, *J. Phys. Chem. Solids*, **29**, 395 (1964).
17. R. F. Lever and F. P. Jona, *A.I.Ch.E. Journal*, **12**, 1158 (1966).
18. R. A. Reynolds, Thesis, Department of Materials Science, Stanford University (1965).
19. P. G. Shewmon, "Diffusion in Solids," McGraw-Hill Book Co., New York (1963).
20. D. T. F. Marple and M. Aven in "II-VI Semiconducting Compounds," D. G. Thomas, Editor, W. A. Benjamin, Inc., New York-Amsterdam (1967).
21. W. Albers and A. C. Aten, *Philips Res. Repts.*, **20**, 556 (1965).

The Effect of Oxygen Pressure on the Oxidation of Iron at 350° and 400°C

M. J. Graham and M. Cohen*

Division of Applied Chemistry, National Research Council, Ottawa, Ontario, Canada

ABSTRACT

A kinetic study has been made of the effect of oxygen pressure (10^{-6} to 60 Torr) on the oxidation of Ferrovac E iron at 350° and 400°C. The initial rate of oxidation is found to increase with increasing oxygen pressure, while after 180 min the weight gain is independent of pressure (for pressures greater than 10^{-5} Torr). Initially Fe_3O_4 forms on the surface, and once this is covered by a continuous layer of αFe_2O_3 the oxidation rate is markedly reduced. The lower the oxygen pressure, the longer the time before αFe_2O_3 starts to nucleate, and no αFe_2O_3 is observed after oxidation at very low pressures (5×10^{-6} and 1×10^{-6} Torr). An induction period is observed for the oxidation at 5×10^{-6} Torr.

The literature contains a great number of papers on the oxidation of iron [*e.g.*,(1)], but few studies have considered the effect of oxygen pressure on the oxidation kinetics. Recently Boggs and co-workers (2) have reported a study of the oxidation of zone-refined iron in the temperature range 220°-450°C, using pressures of 10^{-2} to 100 Torr. These authors find that for oxidation up to 350°C the oxide film thickness, after a given oxidation time, increases as the oxygen pressure is lowered. At 450°C, the oxidation appears to be independent of oxygen pressure. The present work examines more closely the low pressure oxidation of iron at 350° and 400°C, also extending the pressure range down to 10^{-6} Torr. The weight gains were measured using a vacuum microbalance (except for the very low pressure oxidation). The oxide phases present were identified by reflection electron diffraction and some oxide surfaces were replicated for examination by electron microscopy.

Experimental

Apparatus.—The oxidation apparatus is shown schematically in Fig. 1. A Cahn R. G. Electrobalance was mounted in a stainless steel chamber of an all metal U.H.V. system. After an overnight bake at 100°C (the maximum permissible temperature for the balance), pressures of less than 5×10^{-8} Torr were obtained, the outgassing rate of molecules from the walls, balance, etc. being $\sim 8 \times 10^{-8}$ Torr·l·sec^{-1}. The background gas as determined by a partial pressure analyzer (an A.E.I., M.S. 10 spectrometer) was mainly water vapor. To improve the vacuum capabilities of the system, all the original soldered connections in the balance were replaced by spot-welded platinum joints.

The electrobalance was used either on the 0.4 mg or 1.0 mg Recorder Range (weight change corresponding to recorder full scale deflection), with a total noise level of about 3 μg.

Low oxygen pressures were measured using Varian ionization gauges; a U.H.V. gauge for pressures below 10^{-5} Torr and a milli-Torr gauge in the range 10^{-5} to 10^{-1} Torr. These pressures were controlled by a Granville-Phillips Automatic Pressure Controller, using the ion gauges as transducers. Higher oxygen pressures were measured using an Edwards capsule dial gauge, which was installed in the gas-handling section of the apparatus.

Materials purity.—Ferrovac E[1] iron, analyzed to contain the following impurity concentrations (in ppm); Mn, 24; Si, 10; Cr, 5; O_2, 200; Ni, 11; Al, 26; Cu, 10; Co, 5; and C, 70 was used. In some of the experiments 99.997% iron (zone-refined material from the Battelle Memorial Institute[2]) was also used.

[1] Ferrovac E is the trade name of a high purity iron produced by Vacuum Metals Corporation, Division of Crucible Steel Company of America.

[2] This material was supplied through the American Iron and Steel Institute.

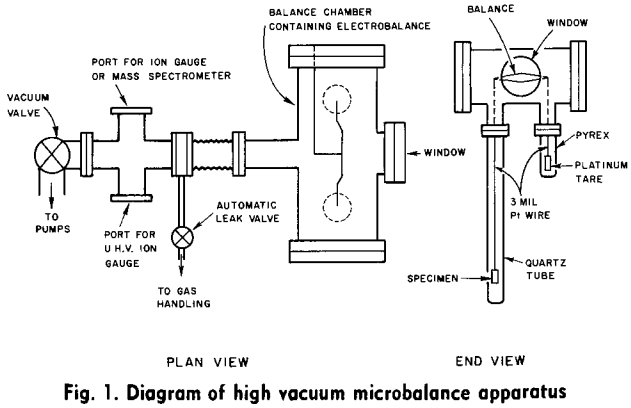

Fig. 1. Diagram of high vacuum microbalance apparatus

* Electrochemical Society Active Member.

Spectroscopically standardized oxygen and hydrogen, supplied by Baker Chemical Company were used. The oxygen contained <70 ppm total impurity and the hydrogen < 14 ppm.

Specimen preparation.—Iron coupons, 5 × 1 cm, were cut from a 9 mil thick cold-rolled sheet. They were degreased, abraded with 600 grit silicon carbide, and electropolished for 1 min in a 95% glacial acetic acid-5% perchloric acid (70%) solution (3). The specimens were then annealed in vacuum at 700°C for 2 hr and finally re-electropolished for a further minute. This method of preparation resulted in a flat surface with about 20-30Å of oxide.

Oxidation procedure.—Specimens prepared as above were first weighed on a Mettler analytical microbalance before loading into the oxidation apparatus. (The weighing of specimens on the Mettler balance before and after oxidation provided a check on the weight gain measured by the Cahn electrobalance and a small drift usually encountered with the electrobalance could be compensated for by adjusting the Cahn weight change to that given by the Mettler balance). After the system had cooled following an overnight bake, and when the pressure was $<10^{-7}$ Torr, the specimen was reduced at 600°C in about 10 Torr of hydrogen for 1 hr. After this time the hydrogen was pumped out of the system and fresh hydrogen admitted. After a few minutes this hydrogen was removed and a further dose of fresh hydrogen admitted. The system was finally evacuated and the temperature was adjusted to the value at which the oxidation experiment was to be performed. Originally, hydrogen reductions were performed at 400°C, but oxidations following reductions at this temperature gave nonreproducible results. The problem was resolved by raising the reduction temperature to 600°C.

Following the removal of hydrogen from the system, oxygen was admitted when the pressure was $<8 \times 10^{-8}$ Torr. Extra pumping time was used to reduce the background to $\sim 3 \times 10^{-8}$ Torr before oxidations were performed at the very low pressures (10^{-6}-10^{-5} Torr). At the end of an oxidation, the system was again evacuated and the weight gain was found from the difference between the initial and final weights of the specimen at the temperature of the experiment and in high vacuum. This procedure corrected for the so-called thermomolecular effect (4) which is pressure and temperature dependent and gives rise to the largest spurious mass changes encountered with the vacuum microbalance. The exact magnitude of this pressure effect was determined at the end of an oxidation experiment by re-admitting oxygen a number of times and noting the apparent mass change from the reading in vacuum. Knowing the variation of the pressure effect with time, it is then possible to accurately define the initial portion of the oxidation curve.

Oxide examination.—Reflection electron diffraction was carried out in a G. E. Diffraction Apparatus, using an accelerating voltage of 45 kV and a camera length of 50 cm. Two-stage formvar platinum-carbon replicas of the oxide surfaces were examined in the electron microscope.

Results

Kinetic data.—A comparison was first made of the oxidation of Ferrovac E iron with zone-refined iron, and the weight gain-time curves for the two materials, oxidized at 350°C and 10^{-3} Torr oxygen pressure, are shown in Fig. 2. It is observed that both materials oxidize in a similar manner for the first 10 min, after which time the rate of oxidation of Ferrovac E slows markedly while the zone-refined material continues to oxidize at a fairly rapid rate. After 2 hr, the oxide is nearly twice as thick on the zone-refined iron as on the Ferrovac E. This difference in oxidation behavior may possibly be accounted for in terms of different grain size and different crystal orientations present in

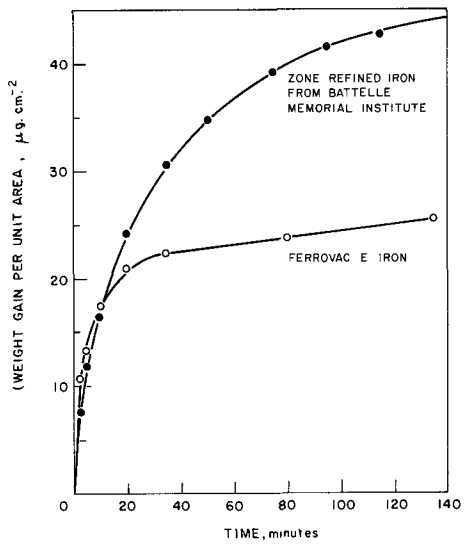

Fig. 2. Comparison of the oxidation of iron supplied by the Battelle Memorial Institute with Ferrovac E iron; 10^{-3} Torr oxygen at 350°C.

the two materials. Following the 700°C vacuum anneal, the grain size of the Battelle iron is about 2-3 mm in diameter, compared with a few microns for the Ferrovac E, and as the oxidation rate is strongly dependent on crystallographic orientation (5-7), larger grains present in the zone-refined material exposing planes with high oxidation rates may be responsible for the observed enhanced oxidation over Ferrovac E iron. Also, the time to formation of αFe_2O_3 varies with crystal plane (5), and the continued rapid oxidation observed with the zone-refined material may be taking place on large grains of such orientation that αFe_2O_3 has not yet formed a continuous film over the magnetite. The statement that a continuous outer layer of αFe_2O_3 slows the reaction rate will be discussed later. The reproducibility of oxidation runs on zone-refined iron was found to be not as good as with Ferrovac E. A series of oxidations, performed at 350°C and 10^{-3} Torr oxygen pressure on seven zone-refined iron specimens, annealed under similar conditions but some of them at different times, were reproducible to within about 10%. Specimens annealed together yielded results in closer agreement, presumably due to a more similar grain growth and grain size. Oxidations of Ferrovac E iron, under similar conditions, were reproducible to about 5%, irrespective of whether specimens were annealed at the same time or not. Because of this better reproducibility it was decided to use the Ferrovac E iron in the study of the effect of pressure on the oxidation kinetics, despite its inferior purity as compared to the zone-refined material. Also, the smaller grain sized Ferrovac E is more typical of the polycrystalline material.

The weight gain-time curves obtained for the oxidation of Ferrovac E at 350° and 400°C and oxygen pressures of 10^{-6} to 10^{-2} Torr are shown in Fig. 3 and 4, and oxidation curves for the higher pressure oxidation (10^{-2}, 35, and 60 Torr), are given in Fig. 5. In Fig. 6, a comparison is made of the very low pressure oxidation (10^{-6}, 5 x 10^{-6}, and 10^{-5} Torr), at 350° and 400°C.

Considering Fig. 3 to 6, the effect of oxygen pressure on the kinetics is clearly evident, particularly in the pressure range 10^{-6}-10^{-2} Torr. As the oxygen pressure is increased from 10^{-6} through to 35 or 60 Torr, the initial rate of oxidation is increased. The position and extent of turnover of the curves to a reduced oxidation rate is also pressure dependent. At 10^{-5} Torr and below only a small, if any, reduction in the oxidation rate is observed (with the exception of the oxidation at 10^{-5} Torr and 350°C) after 3 hr of oxidation. Although the initial rate of oxidation in-

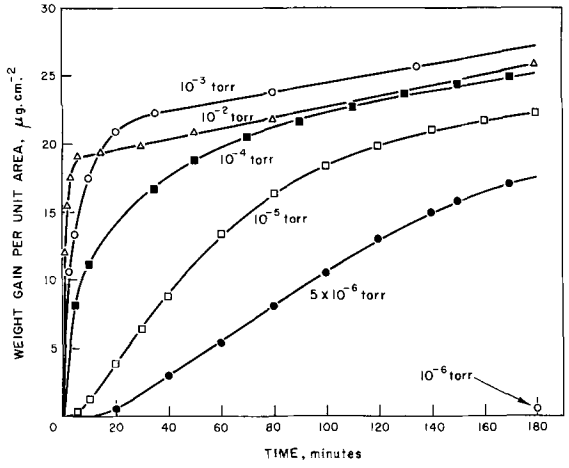

Fig. 3. Effect of oxygen pressure on the oxidation of Ferrovac E iron at 350°C.

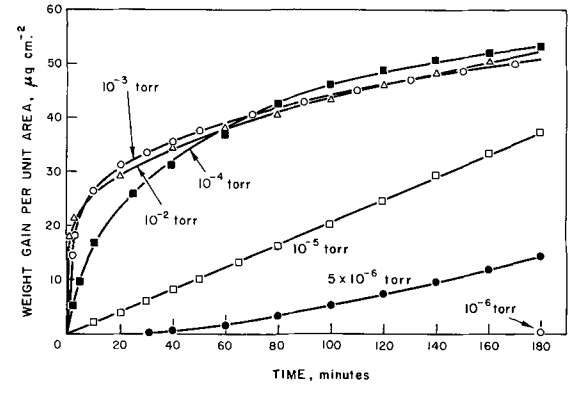

Fig. 4. Effect of oxygen pressure on the oxidation of Ferrovac E iron at 400°C.

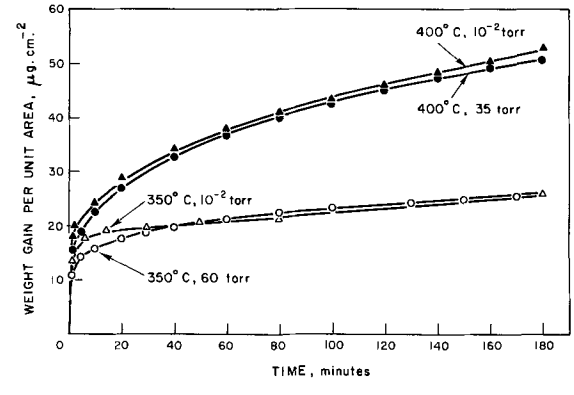

Fig. 5. High pressure oxidation of Ferrovac E iron at 350° and 400°C.

creases with increasing oxygen pressure in the range 10^{-4} to 35 or 60 Torr of oxygen, the weight gain after 3 hr is essentially pressure independent, as summarized in Table I. After 3 hr oxidation at 350°C, the average weight gain for this pressure range is about 26 μg

Table I. Weight gain per unit area after 3 hr oxidation

Pressure, Torr	Weight gain (μg cm⁻²) after 3 hr (a) 350°C	(b) 400°C
10^{-6}	~0.5	~0.1
5 x 10^{-6}	17.0	14.2
10^{-5}	22.6	37.0
10^{-4}	24.8	53.2
10^{-3}	27.3	51.0
10^{-2}	25.8	53.0
35	—	50.9
60	25.1, 25.0, 25.8	—

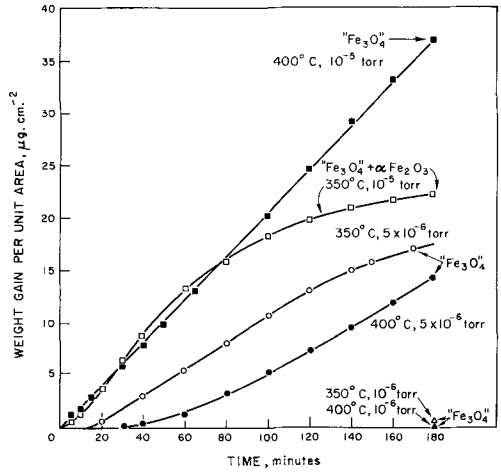

Fig. 6. Comparison of the low pressure oxidation of Ferrovac E iron at 350° and 400°C.

cm^{-2}, compared with a value of about 52 μg cm^{-2} at 400°C. An induction period is observed for oxidations at 5 x 10^{-6} Torr at both 350° and 400°C.

The weight gains after 3 hr of oxidation at 10^{-6} Torr were obtained by difference from the weight of the specimen before and after oxidation, as determined by the Mettler analytical microbalance, (taking into account the removal of the oxide film resulting from the electropolishing), the Cahn electrobalance being not sufficiently stable to identify this small weight change.

The kinetic data from oxidations at 10^{-4}, 10^{-3}, and 10^{-2} Torr oxygen at 350° and 400°C is plotted in a parabolic manner in Fig. 7 and 8, respectively. Another parabolic plot of the data from the oxidation at 35

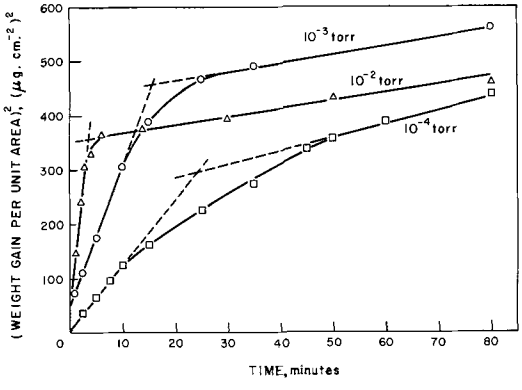

Fig. 7. Parabolic plot of data from the oxidation at 350°C; 10^{-4}, 10^{-3}, and 10^{-2} Torr oxygen pressure.

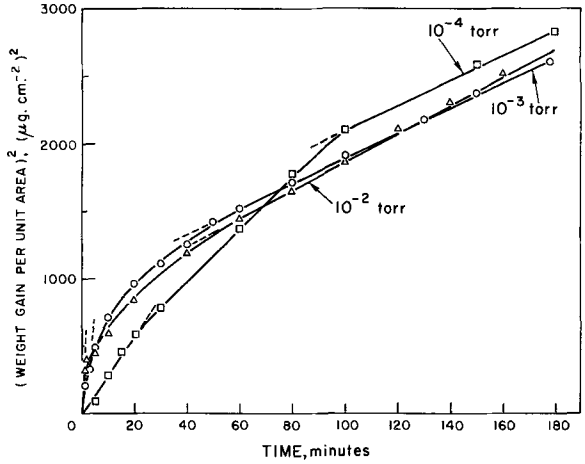

Fig. 8. Parabolic plot of data from the oxidation at 400°C; 10^{-4}, 10^{-3}, and 10^{-2} Torr oxygen pressure.

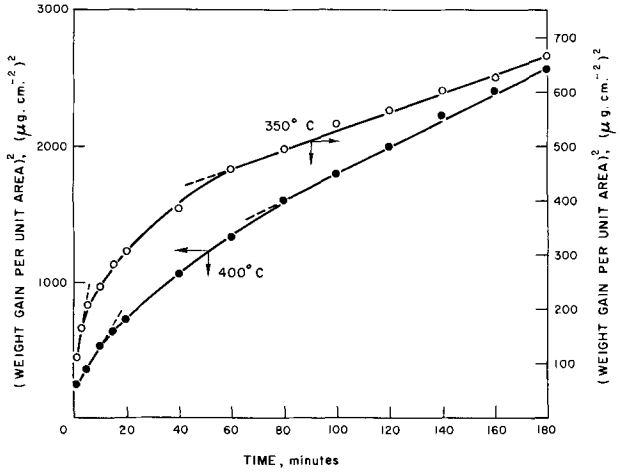

Fig. 9. Parabolic plot of data from the high pressure oxidation at 350° and 400°C.

Torr and 400°C; 60 Torr and 350°C, is shown in Fig. 9. In all cases, the initial oxidation conforms to a parabolic rate law, the duration of this period becoming shorter as the pressure is increased. The slower oxidation rate at 350°C makes the initial data for this temperature more reliable than the data at 400°C, and the time scale is expanded in Fig. 7 to show more clearly the first parabolic agreement. At the end of the first stage, the oxidation proceeds through an intermediate range before entering a second parabolic region of lower rate. It was found that the data did not fit a single logarithmic plot.

Electron diffraction.—The oxides present after oxidation, at various pressures and times at both 350° and 400°C, were identified by reflection electron diffraction and the results are summarized in Table II. "Fe_3O_4" in the table represents a cubic oxide, either Fe_3O_4 or γFe_2O_3, or both. Where αFe_2O_3 was detected (with the exception of the oxidation at 10^{-5} Torr and 350°C), this layer was too thick to permit reflections from the underlying Fe_3O_4 layer.

It can be seen from Table II that only a cubic oxide is formed at oxygen pressures below 10^{-5} Torr for both 350° and 400°C, while after 3 hr of oxidation at 10^{-4} and above, an outer layer of αFe_2O_3 is formed at both temperatures. For short time oxidations at 10^{-3} Torr and 350° and 400°C, only a cubic oxide is found to be present. An interesting finding is that αFe_2O_3 (in addition to cubic oxide), is detected after 3 hr of oxidation at 350°C and 10^{-5} Torr oxygen, while no αFe_2O_3 is found after the corresponding oxidation at 400°C.

Electron microscopy.—Electron photomicrographs of replicas of metal and different oxide surfaces are shown in Fig. 10 (a to i); the average thickness of the oxide is given in parenthesis.

Figures 10 (a) and (b) show the nature of the metal surface immediately prior to oxidation, *i.e.*, after the specimen had been hydrogen reduced at 600°C, and then held at 400°C for a few hours while the background pressure was reduced to $\sim 3 \times 10^{-8}$ Torr, it was quenched to room temperature. A smooth area of the surface is illustrated in Fig. 10 (a), compared with one of the roughest areas in Fig. 10 (b). The observed thermal facetting is similar to that found by Sewell *et al.* (8) on iron surfaces hydrogen annealed at 800°C.

Table II. Summary of electron diffraction analysis

Pressure and time of oxidation	Phases observed 350°C	400°C
10^{-6} Torr, 3 hr	"Fe_3O_4"	"Fe_3O_4"
5×10^{-6} Torr, 31 min	"Fe_3O_4"	"Fe_3O_4"
5×10^{-6} Torr, 3 hr	"Fe_3O_4"	"Fe_3O_4"
10^{-6} Torr, 3 hr	αFe_2O_3 + "Fe_3O_4"	"Fe_3O_4"
10^{-4} Torr, 3 hr	αFe_2O_3	αFe_2O_3
10^{-3} Torr, 2¼ min	—	"Fe_3O_4"
10^{-3} Torr, 5 min	"Fe_3O_4"	—
10^{-2} Torr, 3 hr	αFe_2O_3	αFe_2O_3
35 Torr, 3 hr	—	αFe_2O_3
60 Torr, 3 hr	αFe_2O_3	—

Oxide nuclei present after the oxidation at 10^{-6} Torr for 3 hr at 400°C are observed in Fig. 10 (c), and the growth of these nuclei appears to be completely random. Replicas of specimens oxidized for 31 min at 5×10^{-6} Torr at both 400° and 350°C are shown in Fig. 10 (d) and (e); this was after the induction period when a noticeable weight increase could be observed with the Cahn microbalance (see Fig. 6). The influence of substrate structure on the oxidation is shown in Fig. 10 (e) where the outer texture of the oxide on the two grains is different. Large oxide nuclei are seen in Fig. 10 (d), and triangular shaped nuclei ~200Å in height are present near the grain boundary.

Surfaces of thicker oxides are shown in Fig. 10 (f to i). Figures 10 (f) and (g) show the variation of the degree of roughness of the oxide outer surface with the underlying crystal plane of the metal. The height of oxide facets on the upper left grain in Fig. 10 (f) range up to 300-400Å. The ridged structure of the αFe_2O_3 surface, found after oxidation for 3 hr at 10^{-3} Torr and 400°C [Fig. 10 (h) and (i)], is similar to that observed by Boggs *et al.* (2, 5) for oxidations under similar conditions.

Discussion

The marked effect of oxygen pressure on the oxidation of iron at 350° and 400°C is clearly shown in Fig. 3, 4, and 5. As the pressure is increased from 10^{-6} to 60 Torr the initial rate of oxidation is increased. This period of high oxidation rate is, in general, followed by one of much lower oxidation rate.

The proposed mechanism to explain the different initial rates is as follows; initially Fe_3O_4 forms on the surface and the oxide layer grows as iron ions diffuse outward through cation vacancies in the oxide. The cation vacancies are formed at the outer surface of the oxide when oxygen is incorporated into the lattice. The concentration of vacancies and hence the concentration of iron ions diffusing to the O_2/Fe_3O_4 interface depends on the availability of oxygen at the outer surface. Thus, as the oxygen pressure is increased, the concentration of vacancies is increased and so the flux of iron ions is increased leading to an increased oxidation rate. This assumes that in the low pressure region the incorporation of oxygen into the lattice to form oxygen ions is pressure dependent.

The lowering of the oxidation rate may be due to either the formation of a continuous layer of αFe_2O_3, over the Fe_3O_4, or loss of contact between the oxide and the metal. Taper sections of these thin oxides did not yield conclusive evidence of oxide separation from the metal. Moreover, the electron diffraction data, summarized in Table II, supports the argument that the formation of a continuous hexagonal oxide layer reduces the oxidation rate. At pressures below 10^{-5} Torr, where no marked reduction in oxidation rate was observed, only cubic oxide was found to be present after 3 hr of oxidation (Table II). Also specimens which were removed before the decrease in rapid rate observed at higher pressures showed only "Fe_3O_4" by electron diffraction. In all cases where a marked decrease in oxidation rate had already occurred, electron diffraction showed only an outer layer of αFe_2O_3. These observations would indicate that in the rapid rate region, diffusion, probably of cations, through magnetite is the rate controlling process, while in the low rate region, diffusion, probably of oxygen ions, through αFe_2O_3 is the controlling process. This was partially confirmed by an experiment in which iron had been oxidized into the αFe_2O_3 region and then annealed, in vacuo, to convert all the oxide to Fe_3O_4 (9). On readmitting oxygen a rapid "magnetite-type" rate was initially observed, with again a later falling off in rate characteristic of control by αFe_2O_3.

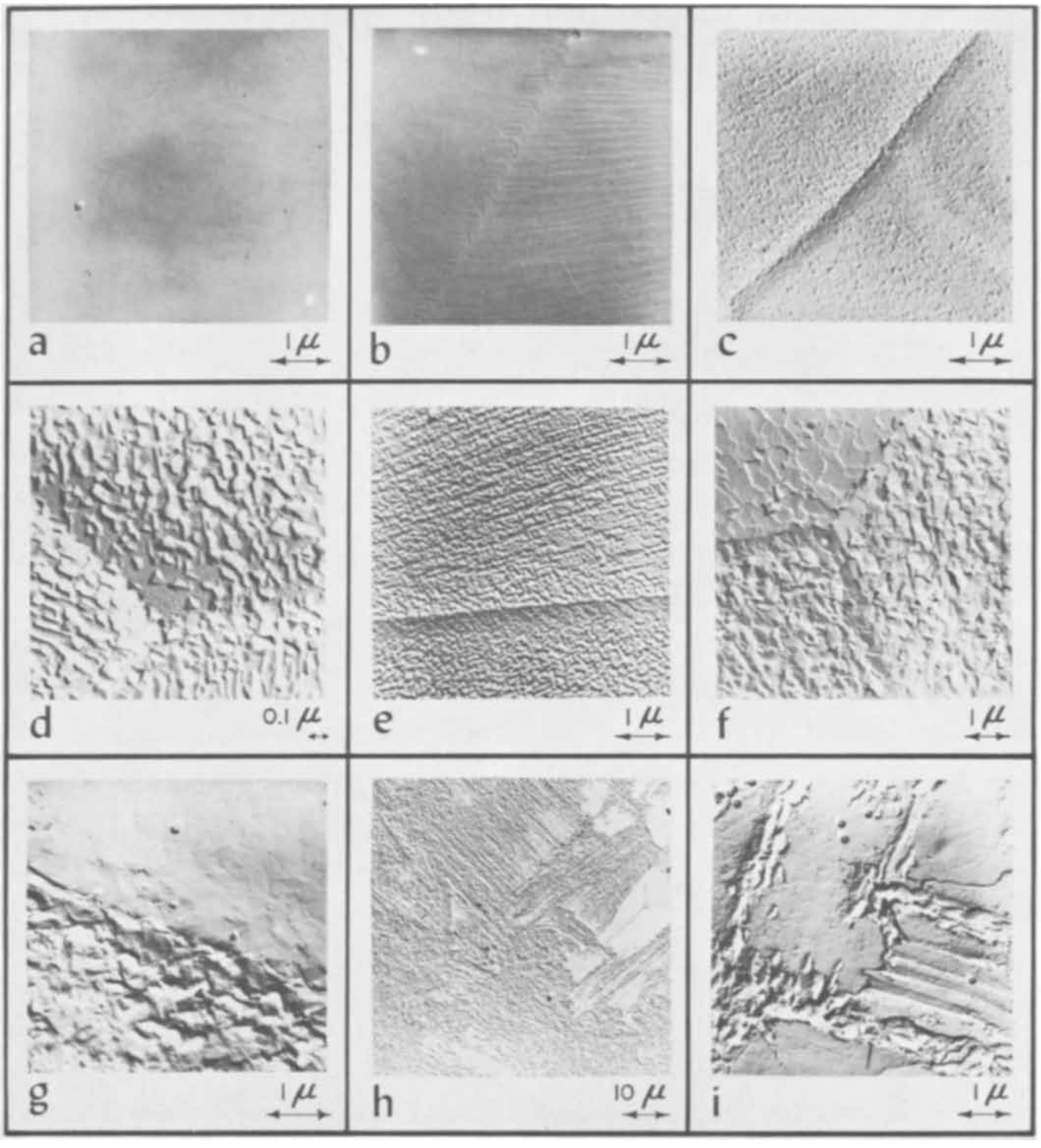

Fig. 10 (a) to (i). Electron photomicrographs of replicas of metal and different oxide surfaces; the oxide thicknesses are given in parenthesis. (a) and (b) metal immediately prior to oxidation; (c) oxidized at 10^{-6} Torr, 400°C for 3 hr (~70Å); (d) oxidized at 5 x 10^{-6} Torr, 400°C for 31 min (~50Å); (e) oxidized at 5 x 10^{-6} Torr, 350°C for 31 min (~60Å); (f) oxidized at 5 x 10^{-6} Torr, 400°C for 3 hr (900Å); (g) oxidized at 10^{-5} Torr, 400°C for 3 hr (2200Å); (h) and (i) oxidized at 10^{-3} Torr, 400°C for 3 hr (3100Å).

The time to formation of αFe_2O_3 will depend on the temperature, oxygen pressure, and crystallographic orientation of the underlying metal. The kinetic stability of an αFe_2O_3 film depends on a balance between its reduction to Fe_3O_4 by diffusing iron and the oxidation of Fe_3O_4 to αFe_2O_3 by oxygen. Thus, at 10^{-5} Torr, the higher diffusion of iron through Fe_3O_4 at 400°C leads to continuous reduction of any αFe_2O_3 to Fe_3O_4, while at 350°C a presumably slower flux of iron allows, after some time, the formation of a continuous layer of αFe_2O_3 (Fig. 6). At lower oxygen pressures only Fe_3O_4 is observed. As the pressure is increased between 10^{-5} and 10^{-2} Torr the time to formation of αFe_2O_3 is decreased. At above 10^{-2} Torr the oxidation rates are essentially pressure independent, but, of course, temperature dependent. At these high pressures αFe_2O_3 nucleates after a short time, accounting for the early turnover of the oxidation curves.

The similarity between the oxidation at 10^{-2} Torr and 35 or 60 Torr is in disagreement with the results of Boggs *et al.* (2) who report that at 350°C the oxidation rate is strongly pressure dependent over this pressure range. Although Boggs finds the initial rate of oxidation to increase as the pressure is increased,

and the present results confirm this finding over a very wide pressure range, after 150 min of oxidation he reports the weight gain with 100 Torr oxygen pressure to be about only one quarter of the weight gain found at 10^{-2} Torr. It is difficult to explain the discrepancy between the two sets of data. Part of the discrepancy may be due to the different compositions of iron used and different methods of preparation.

The reason for the induction period observed at 5×10^{-6} Torr for both 350° and 400°C is probably either to a slow nucleation process (10) taking place or the removal of oxidizable impurities, most likely carbon from the specimen. Micrographs of replicas of oxide surfaces at the end of the induction period are shown in Fig. 10 (d) and (e), where the growth of nuclei into a continuous film is taking place. As seen in Fig. 6, the induction period appears to be longer at 400°C than at 350°C, but the times involved are not sufficiently reproducible to unequivocably make such a distinction. Sewell (11) using an x-ray technique to study the kinetics of oxidation has also observed an induction period for the oxidation of (100) iron at 400°C and 3×10^{-6} Torr oxygen. It is also noteworthy that the oxide thickness determined using this new technique correlates well with the present microbalance data.

The parabolic plots shown in Fig. 7, 8, and 9 indicate two distinct regions of conformity; an initial good parabolic fit of the data, the oxidation rate increasing with increasing pressure and the duration of the agreement becoming shorter as the pressure is increased from 10^{-4} to 60 Torr. The initial parabolic behavior is followed by an intermediate stage before a second parabolic region is reached where the plots are approximately parallel, signifying that this second region is essentially independent of pressure. The two distinct parabolic rates are most clearly observed in Fig. 7, and the values of the rate constants derived from the data in this figure are the most accurate obtained; the actual values of the initial rate constants at 10^{-4}, 10^{-3}, and 10^{-2} Torr oxygen pressure and 350°C are 1.9×10^{-13}, 4.3×10^{-13}, and 1.35×10^{-12} g^2cm^{-4} sec^{-1}, respectively. In this parabolic region at 350°C and during the initial parabolic region at 400°C (Fig. 8), we are probably dealing solely with the growth of Fe_3O_4. The electron diffraction analysis of oxides formed after short times of oxidation at 10^{-3} Torr shows only Fe_3O_4 to be present (Table II), supporting this view. Thus, if initially we are only concerned with the growth of magnetite, then the rate of oxidation as given by the parabolic rate constant should be proportional to the concentration of cation vacancies at the oxide-oxygen interface, which in turn is proportional to the (oxygen pressure)$^{1/2}$. As the pressure is increased more oxygen is incorporated into the oxide and so more cation vacancies are formed, leading to enhanced diffusion of iron through these cation vacancies giving rise to an increased oxidation rate. It may be seen in Fig. 11 that for the oxidation at 10^{-4}, 10^{-3}, and 10^{-2} Torr and 350°C, the parabolic rate constant, taken from the initial slopes of the curves in Fig. 7, is proportional to the (pressure)$^{1/2}$.

Linear behavior is observed for part of 5×10^{-6} Torr at 350°C and at 10^{-5} Torr at 400°C (Fig. 3 and 4). If it is assumed that under these conditions the oxidation rate is controlled by a combination of the rate of impingement of oxygen on the surface and the sticking factor of oxygen on the oxide, a sticking factor of 0.03 at 350°C and 0.025 at 400°C can be calculated.

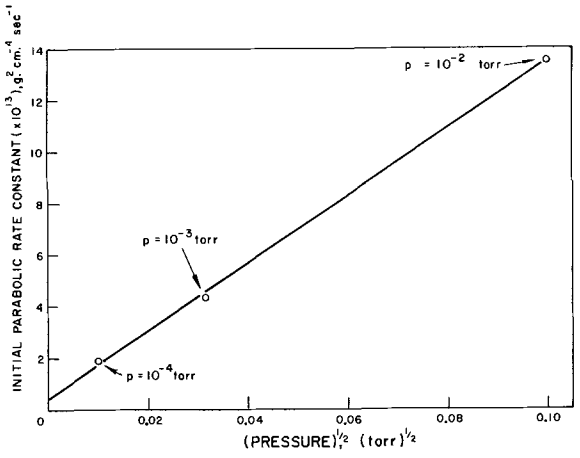

Fig. 11. Initial parabolic rate constant for the oxidation at 350°C and oxygen pressures of 10^{-4}, 10^{-3}, and 10^{-2} Torr plotted against the square root of the pressure.

Activation energies derived from the initial K_p values at 350° and 400°C, and 10^{-4}, 10^{-3}, 10^{-2} Torr are 15, 17, and 22 kcal · $mole^{-1}$, respectively. The values are obviously not too reliable as oxidation rates were only measured at two temperatures, but they are of some significance. No comparable data for oxidations under similar conditions exists in the literature but higher values of 33 kcal · $mole^{-1}$ (12), for composite oxide formation in the temperature range, 500°-900°C and 45 kcal · $mole^{-1}$ (13) for the growth of magnetite in the range 400°-570°C, are quoted for higher temperature oxidations.

Acknowledgment

The authors wish to thank Mr. G. I. Sproule for the electron microscopy.

Manuscript submitted Dec. 14, 1967; revised manuscript received July 1, 1969.

Any discussion of this paper will appear in a Discussion Section to be published in the June 1970 JOURNAL.

REFERENCES

1. O. Kubashchewski and B. E. Hopkins, "Oxidation of Metals and Alloys," Second Edition, p. 108, Academic Press, Inc., New York (1962).
2. W. E. Boggs, R. H. Kachik, and G. E. Pellissier, *This Journal*, **112**, 539 (1965).
3. P. B. Sewell, C. D. Stockbridge, and M. Cohen, *Can. J. Chem.*, **37**, 1813 (1959).
4. "Vacuum Microbalance Techniques," Vol. 1, M. T. Katz, Editor, pp. 111-150, Plenum Press, Inc., New York (1961).
5. W. E. Boggs, R. H. Kachik, and G. E. Pellissier, *This Journal*, **114**, 32 (1967).
6. M. Ramasubramanian, P. B. Sewell, and M. Cohen, *ibid.*, **115**, 12 (1968).
7. S. I. Ali and M. Cohen, Unpublished results.
8. P. B. Sewell, E. G. Brewer, and M. Cohen, *J. Phys. Chem.*, **67**, 2008 (1963).
9. E. J. Caule and M. Cohen, *This Journal*, **108**, 834 (1961).
10. J. Bénard, *Acta Met.*, **8**, 272 (1960).
11. P. B. Sewell, Unpublished work.
12. J. K. Stanley, J. von Hoene, and R. T. Huntoon, *Trans. A.S.M.*, **43**, 426 (1951).
13. M. H. Davies, M. T. Simnad, and C. E. Birchenall, *Trans. AIME*, **191**, 889 (1951); *J. Metals* (October 1951).

The Chalcogenide Semiconductor System: As_2Se_3-Sb_2Se_3

N. S. Platakis, V. Sadagopan,* and H. C. Gatos*

Department of Metallurgy and Materials Science, Massachusetts Institute of Technology, Cambridge, Massachusetts

ABSTRACT

The glass formation region of the system As_2Se_3-Sb_2Se_3 and the vitreous-crystalline transformation were investigated. Electrical and optical properties in the vitreous and in the polycrystalline state were studied as a function of composition on homogeneous and geometrically well defined samples prepared by a new method. Activation energies obtained from electrical and optical measurements were in excellent agreement and were found to decrease with increasing content of Sb_2Se_3. For a given composition, the activation energy in the vitreous state was greater than in the crystalline state by 0.2-0.4 eV. Excepting the absorption edge, no absorption or reflection bands were observed in all of the compositions studied in the ranges of 0.7-1.7 and of 2.5-50μ.

Chalcogenide glasses have been extensively investigated in recent years. As photoconductors they have found applications in vidicon type camera tubes (1-4). Since their properties are relatively unaffected by the presence and variation of impurities (5-9) these materials are of interest for this type of application or electronic applications in general. Infrared optics and xerography are further areas of research and development where the role of vitreous semiconductors is very important.

The over-all behavior of vitreous semiconductors is not nearly as well understood as that of the crystalline semiconductors. For example, electrical conduction in the vitreous materials is still a poorly understood process (5, 9-18).

The present study examines the pattern of property changes as a function of composition in the pseudobinary system As_2Se_3-Sb_2Se_3. It is also concerned with the extension of the glass formation region and the corresponding effects on the electrical and optical properties. The stability of the vitreous state and the parameters affecting it are of considerable interest particularly in view of the encouraging results reported (4) on the pseudobinary Sb_2Se_3-Bi_2S_3.

Experimental

The compounds As_2Se_3 and Sb_2Se_3 were prepared individually from their elements which were of high purity (semiconductor grade, 99.999+%). For each compound nominally stoichiometric amounts were placed in a quartz ampule which was repeatedly evacuated, flushed with argon and finally evacuated to 10^{-6} Torr before sealing off. Each sealed ampule was heated for about 5 hr at 350°C, whereupon the temperature was raised to 750°C and maintained for about 5 hr.

The resulting As_2Se_3 and Sb_2Se_3 were placed, in the desired proportions, in a quartz ampule which, in turn, was flushed, evacuated, and sealed off. The ampule was fitted to a horizontal shaft of a motor and positioned in a horizontal furnace. While under rotation (about 25 rpm) the ampule was held for about 1 hr at 750°C. It was then withdrawn from the furnace and quenched in air while still under rotation. This technique, described in more detail elsewhere (18), allowed the preparation of hollow cylinders of uniform wall thickness and uniform composition. Typical dimensions of the cylinders employed were: length 3 cm, thickness 0.07 cm, and ID 1 cm.

Appropriate lengths of the samples were cut with ordinary cutting wheels while still in the quartz ampule from which they were separated by simply immersing in acetone. The hollow-cylinder samples exhibited no porosity or other macroscopic defects. Electron probe analysis along the cylinders and across their thickness revealed no detectable variation in chemical composition. Visual examination and x-ray diffraction techniques were employed for confirming the vitreous state of the alloys.

Electrodes for electrical measurements were attached to the inner and outer surface of each sample after immersing it first in silver paste. The silver paste shorting the inner and outer electrodes was removed by grinding the two ends of the cylinders. The ohmic behavior of the contacts was tested over a wide range of current and temperature (0-600V, 293°-520°K). The possibility of current leakage through the edges of the samples was examined by an electrode arrangement recommended by the American Society for Testing Materials (ASTM Designation, D257-1961): During the silver paste coating of the cylinders two bands one near each edge of the outer surface of the sample were masked and left uncoated. Thus, one electrode could be attached to the main outer silver-paste covered portions of the outer surface and another (common) electrode to the outer areas near the edges of the cylinder. In this way the resistance of the sample could be measured between the inner electrode and the main outer electrode, while the third electrode was grounded or was kept at the same potential with the main outer electrode. No difference in resistance between the inner and the main outer electrode was found in these cases. This result indicates that no fringing effect nor leakage were present.

Resistivity measurements as a function of temperature were carried out in a vertical furnace under argon atmosphere. The temperature was controlled to within ±0.5°C. Before each measurement the samples were allowed to equilibrate for 15 to 40 min. Unless the vitreous samples underwent crystallization during heating, the resistivity measurements were reproducible on temperature recycling (within 5%) and exhibited no hysteresis (9). The d-c potential employed was less than 100V.

For the optical measurements (absorption and reflection) the samples were cut from the same cylinders as the samples for the electrical measurements. They were mechanically polished down to 20-800μ. A copper cold-finger cryostat was used for the low temperature measurements. Standard commercial instruments were employed to study the optical properties in the ranges of 0.7-1.7 and 2.5-50μ.

Results and Discussion

General characteristics.—In the vitreous system $(1-x)As_2Se_3 \cdot xSb_2Se_3$ the compositions with $x = 0, 0.1,$

* Electrochemical Society Active Member.

[1] Present address: IBM, Thomas J. Waston Research Center, Yorktown Heights, New York.

0.2, 0.3, 0.4, 0.45, and 0.5 were investigated. They exhibited a relatively high mechanical strength and no inclusions or other macroscopic heterogeneities. These characteristics are attributable to the method of preparation employed (18). All compositions were found to be chemically stable in air at room temperature and were hardly reactive in water or dilute acids. However, chemical attack was clearly observed in alkaline solutions even at room temperature. This chemical reactivity decreased with increasing Sb_2Se_3 content. At room temperature no transformation to the crystalline state was observed even after extended periods of time. At higher temperatures crystallization was observed for some compositions and is discussed below.

Region of glass formation.—A value of $x \cong 0.5$ has been reported (19) as the limit of glass formation in the system $(1\text{-}x)As_2Se_3 \cdot xSb_2Se_3$. In the present study this value was found to be reasonable. However, the values of $x = 0.45$ and 0.50 could be reached only by quenching in horizontal quartz tube under rotation as described above; the commonly used quenching techniques lead invariably to a two phase structure with the crystalline areas readily visible. It was not possible to extend usefully (in the form of single phase) the region of glass formation to higher Sb_2Se_3 content by employing higher quenching rates; the material could not sustain the thermal shock and invariably shattered so that no samples suitable for examination could be obtained.

Electrical characteristics.—The hollow cylinder samples employed had thin walls (<1 mm), were about 1 cm in diameter and 3 cm long; thus, their outer area was essentially the same as the inner area so that within experimental error the electrical resistivity ρ could be taken as

$$\rho = R\frac{A}{l}$$

where R is the total resistance, A is the outer (or inner) area of the cylinder, and l its thickness.

The resistivity was measured as a function of temperature (296°-520°K) for all of the vitreous compositions indicated above. Those with $x = 0.3$, 0.4, 0.45, and 0.5 were also studied in the crystalline state. The results are plotted in Fig. 1. It is seen that the resistivity is significantly greater in the vitreous state, consistent with the expected decreased mobility and carrier concentration as compared with the crystalline state (19). As in typical semiconductors, the resistivity is exponentially decreasing with temperature in both the vitreous and in the crystalline state. The corresponding activation energies are tabulated in Table I. A decrease in the activation energy with increasing Sb_2Se_3 content is apparent. In the compositions with $Sb_2Se_3 > 0.3$, the activation energy appears relatively insensitive to the Sb_2Se_3 content; in fact, in the crystalline state the activation energy of the compositions studied is essentially the same as that reported for crystalline Sb_2Se_3. This result is surprising and not understood. It should be noted that the resistivity in the vitreous state decreases with increasing Sb_2Se_3 content, but it increases in the crystalline state. Similar reversals in resistivity trends have been reported for other vitreous systems (20); however, the reasons for this behavior are not clear as yet.

Table I. Resistivity activation energies (E_ρ)

Material	E_ρ, eV		log ρ_0*	
	Vitreous	Crystalline	Vitreous	Crystalline
As_2Se_3	1.85		4.30	
0.9 As_2Se_3 · 0.1 Sb_2Se_3	1.76		4.20	
0.8 As_2Se_3 · 0.2 Sb_2Se_3	1.72		4.00	
0.7 As_2Se_3 · 0.3 Sb_2Se_3	1.56	1.18	3.50	1.95
0.6 As_2Se_3 · 0.4 Sb_2Se_3	1.55	1.20	3.70	1.85
0.55As_2Se_3 · 0.45Sb_2Se_3	1.47	1.25	3.55	2.00
0.5 As_2Se_3 · 0.5 Sb_2Se_3	1.44	1.11	3.90	1.60
Sb_2Se_3		1.15 (27)		

* ρ_0 values were obtained from $\rho = \rho_0 e^{E_\rho/2KT}$.

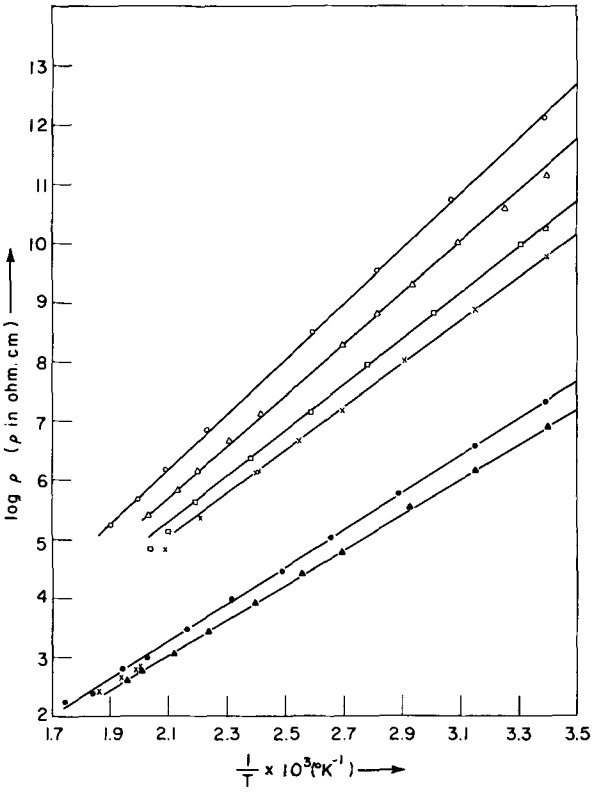

Fig. 1. Dependence of the electrical resistivity on temperature in the system $(1-x)As_2Se_3 \cdot xSb_2Se_3$. ○, $x = 0$ (vitreous); △, $x = 0.2$ (vitreous); □, $x = 0.4$ (vitreous); x, $x = 0.45$ (vitreous); ●, $x = 0.45$ (crystalline); ▲, $x = 0.4$ (crystalline). For clarity the plots for the compositions $x = 0.1$, 0.3, and 0.5 were omitted.

The deviations from the exponential dependence of the resistivity on temperature (see Fig. 1) in the vitreous compositions with $x = 0.3$, 0.4, 0.45, and 0.5 were associated with transformations to the crystalline state as confirmed by x-ray diffraction patterns; on temperature recycling, the samples exhibited the resistivity values of the crystalline state. In contrast the compositions with $x = 0$, 0.1, and 0.2 exhibited the same resistivity values on recycling and even after heating at 220°C for two days. No impurity effects (no change in slope in the activation energy curves) were observed in the present materials consistent with previous results (19) and theoretical considerations (21, 22). It is also of interest to note that in As_2Se_3 no change in the slope of the resistivity *vs.* temperature curve was observed in going through the softening point (187°C). This behavior certainly reflects the direct dependence of the electrical properties on short range order.

The difference in activation energy between the vitreous and the crystalline state is still theoretically unresolved. The presently determined higher values for the vitreous states are consistent with Banyai's views (10) that in going from the ordered to the disordered state electronic states near the band edges are strongly perturbed. They enter the forbidden energy gap and most of them become localized. The nonlocalized electronic states retreat into the energy bands. Assuming that the nonlocalized states are responsible for electrical conduction then the activation energy for conduction should be greater in the vitreous state. However, in the case of As_2Se_3 (19, 23) the activation energy in the crystalline state is greater by 0.1-0.2 eV than in the vitreous state. Although attempts have been made to account theoretically for this behavior of

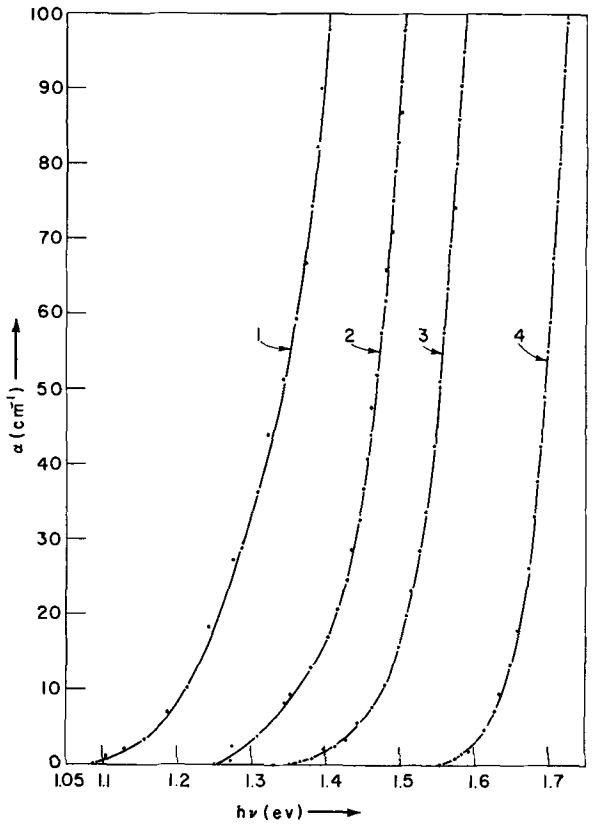

Fig. 2. Typical data on the dependence of the absorption coefficient on photon energy for the system $(1-x)As_2Se_3 \cdot xSb_2Se_3$. Curve 1, $x = 0.4$ at $T = 296°K$ (vitreous); curve 2, $x = 0.2$ at $T = 296°K$ (vitreous); curve 3, $x = 0.1$ at $T = 296°K$ (vitreous); curve 4, $x = 0.1$ at $T = 77°K$ (vitreous).

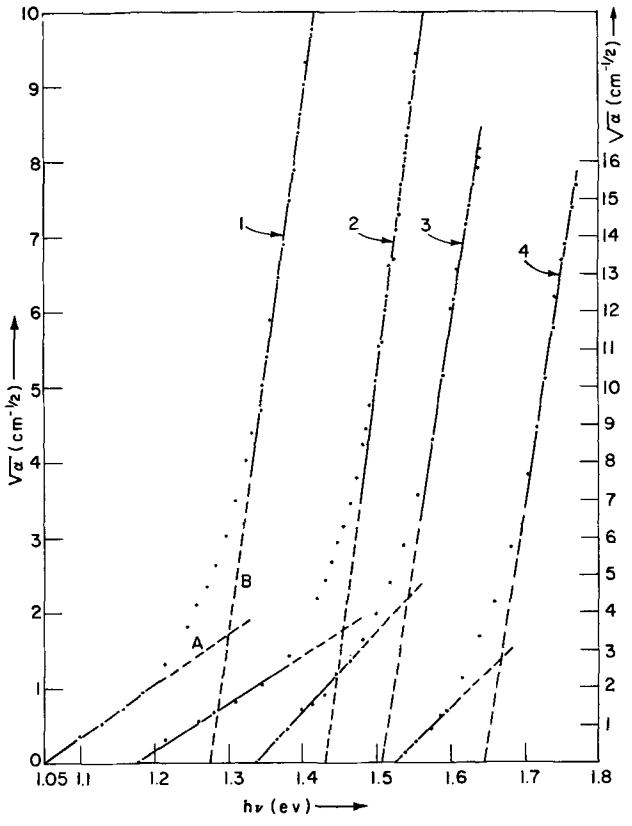

Fig. 3. Dependence of $\sqrt{\alpha}$ (absorption coefficient) on the photon energy for the system $(1-x)As_2Se_3 \cdot xSb_2Se_3$. Curve 1, $x = 0.45$ at $T = 296°K$ (vitreous); curve 2, $x = 0.45$ at $T = 77°K$ (vitreous); curve 3, $x = 0.1$ at $T = 296°K$ (vitreous); curve 4, $x = 0.1$ at $T = 77°K$ (vitreous). Curves 1 and 2 correspond to the left hand side ordinate and curves 3 and 4 correspond to the right hand side ordinate.

As_2Se_3 and the similar behavior of other materials, no definitive stage of understanding has been achieved as yet.

Optical measurements.—The optical absorption characteristics of the compositions discussed above were examined at 296° and 77°K. Typical results for some compositions and two temperatures are shown in Fig. 2 and 3 where the absorption coefficient α and $\sqrt{\alpha}$ are plotted against the energy of the radiation. It is seen that the absorption edge shifts to shorter wavelengths with decreasing Sb_2Se_3 content and with decreasing temperature. The absorption edges were determined from plots of the $\sqrt{\alpha}$ *vs.* the photon energy as shown for some representative cases in Fig. 3. For each absorption curve the edge is taken as the mean of the intersects with the abscissa of the two component straight lines, A and B (24, 25).

The numerical results are summarized in Tables II and III. Here also, the activation energies follow the same trends observed in the values obtained by electrical resistivity measurements. In the vitreous state the absorption edges of the compositions with $x = 0.1$, 0.45, and 0.5 were determined both at 296° and 77°K.

Table II. Optical activation energies (E_λ) in the vitreous state

Material	E_λ (exp), eV, 296°K	E_λ, eV, 77°K	$\frac{\Delta E}{\Delta T}$, $\frac{eV}{°K}$	E_λ (calc), eV, 0°K	$(E_\rho^* - E_\lambda)$, eV, 0°K	$E_a = \frac{1}{2}(E_\rho - E_\lambda)$, eV, 0°K
As_2Se_3	1.50 (19)	1.66 (calc) †	-7.3×10^{-4} (26)	1.72	0.13	0.065
0.9 As_2Se_3 · 0.1 Sb_2Se_3	1.43	1.58 (exp)	-6.8×10^{-4}	1.63	0.13	0.065
0.8 As_2Se_3 · 0.2 Sb_2Se_3	1.38	1.53 (calc) †	-6.6×10^{-4} ‡	1.58	0.14	0.07
0.7 As_2Se_3 · 0.3 Sb_2Se_3	1.20	1.35 (calc) †	-6.6×10^{-4} ‡	1.40	0.16	0.08
0.6 As_2Se_3 · 0.4 Sb_2Se_3	1.15	1.30 (calc) †	-6.6×10^{-4} ‡	1.35	0.2	0.1
0.55As_2Se_3 · 0.45Sb_2Se_3	1.16	1.30 (exp)	-6.4×10^{-4}	1.35	0.12	0.06
0.5 As_2Se_3 · 0.5 Sb_2Se_3	1.13	1.26 (exp)	-5.9×10^{-4}	1.30	0.14	0.07

* E_ρ values from Table I.
† Calculated using the corresponding thermal coefficient of the next column in the table.
‡ These values represent the average of -6.8×10^{-4} and -6.4×10^{-4}.

Table III. Optical activation energies (E_λ) in the crystalline state

Material	E_λ (exp), eV, 296°K	E_λ (exp), eV, 77°K	$\frac{\Delta E}{\Delta T}$, $\frac{eV}{°K}$	E_λ (calc), eV, 0°K	$(E_\rho^* - E_\lambda)$, eV, 0°K	$E_a = \frac{1}{2}(E_\rho - E_\lambda)$, eV, 0°K
0.7 As_2Se_3 · 0.3 Sb_2Se_3	1.02	1.13	-5×10^{-4}	1.17	0.01	0.005
0.6 As_2Se_3 · 0.4 Sb_2Se_3	0.98	1.13	-6.8×10^{-4}	1.18	0.02	0.01
0.55As_2Se_3 · 0.45Sb_2Se_3	1.00	1.11	-5×10^{-4}	1.15	0.10	0.05
0.5 As_2Se_3 · 0.5 Sb_2Se_3	0.95	1.08	-5.9×10^{-4}	1.12	−0.01	—

* E_ρ values from Table I.

Assuming that the absorption edge depends linearly on temperature in this temperature range [such a linearity has been found (26) for As_2Se_3 in the range 353°-77°K] the thermal coefficients of the absorption edge of those compositions were determined (Table II). In view of the fact that in these extreme compositions the absorption edge changed by about the same amount (0.13 to 0.15 eV) for the 220°K interval it was assumed that the temperature coefficient for the vitreous compositions with $x = 0.2$, 0.3, and 0.4 is the average of the temperature coefficients of the compositions with $x = 0.1$ and 0.45. These values are consistent with those determined in earlier investigations. Thus for vitreous As_2Se_3 and $As_2Se_3 \cdot Tl_2Te$ the values -7.3×10^{-4} eV/°K and -6.7×10^{-4} eV/°K have been found (26). In the crystalline state the absorption edges of all four compositions investigated were determined at 296° and 77°K. Making the same assumption as before the thermal coefficients of the absorption edge were calculated (Table III). It is of interest to note that the thermal coefficients are eventually the same for the vitreous and the crystalline state consistent with the results on As_2Se_3 (19). Employing the presently determined coefficients and assuming the linear dependence of the absorption edge to extend down to 0°K [such a linearity has been assumed (26) for As_2Se_3] the optical activation energies were adjusted to 0°K for comparison with the resistivity activation energies of Table I which, as determined, correspond to 0°K. The agreement between the two sets of values is very good, the maximum difference ($E_\rho - E_\lambda$) being 0.2 eV (Tables II and III).

The difference between the resistivity activation energy, E_ρ, and the optical activation energy, E_λ, is a measure of the degree of localization of the carriers; accordingly the value $E_\alpha = \frac{1}{2}(E_\rho - E_\lambda)$ is taken as the activation energy for the translational motion of the electrons (5). As seen in Tables II and III, E_α in the present case is relatively small indicating that nonlocalized electronic states are predominant in the conduction process.

In the infrared region of 2.5 to 50μ no absorption nor reflection bands were observed in any of the compositions. Both absorption and reflection remained constant throughout the range and increased somewhat as the content of Sb_2Se_3 increased.

Regarding the transformation from the vitreous to the crystalline state it was found by electrical and optical techniques that its temperature decreases and its rate increases with increasing Sb_2Se_3 content. A discussion of the transformation energetics and kinetics will be reported in a future communication.

Acknowledgment

This work was supported by the National Aeronautics and Space Administration under Grant NGL 22-009-019.

Manuscript submitted May 15, 1969; revised manuscript received *ca.* July 5, 1969.

Any discussion of this paper will appear in a Discussion Section to be published in the June 1970 JOURNAL.

REFERENCES

1. B. T. Kolomiets and B. V. Pavlov, *Sov. Phys.-Solid State (Engl. Transl.)*, **2**, 592 (1960).
2. B. T. Kolomiets and V. M. Lyubin, *ibid.*, **4**, 291 (1962).
3. B. T. Kolomiets and V. M. Lyubin, *ibid.*, **1**, 819 (1959).
4. B. T. Kolomiets and V. M. Lyubin, *ibid.*, **1**, 674 (1959).
5. R. L. Myuller, *J. Appl. Chem. USSR (Engl. Transl.)*, **35**, 519 (1962).
6. M. P. Coutts and E. R. Levin, *J. Appl. Phys.*, **38**, 10, 4030 (1967).
7. I. Z. Fischer, *Sov. Phys.-Solid State (Engl. Transl.)*, **1**, 171 (1959).
8. B. T. Kolomiets and T. F. Nazarova, *ibid.*, **2**, 159 (1960).
9. L. A. Baidakov, Z. U. Borisova, and R. L. Myuller, *J. Appl. Chem. USSR (Engl. Transl.)*, **34**, 2316 (1961).
10. L. Banyai, *Proc. 7th Int. Conf. on Physics of Semiconductors, Paris*, p. 417, Dunod, Paris (1964).
11. A. I. Gubanov, "Quantum Electron Theory of Amorphous Semiconductors," p. 49, Consultants Bureau, New York.
12. R. E. B. Makinson and A. P. Roberts, *Proc. Phys. Soc.*, **79**, 222, 630 (1962).
13. J. L. Hartke, *Phys. Rev.*, **125**, 1177 (1962).
14. A. F. Ioffe, *Sov. Phys.-Solid State (Engl. Transl.)*, **1**, 139 (1959).
15. I. I. Boiko, *ibid.*, **1**, 518 (1959).
16. H. P. D. Lanyon, *Phys. Rev.*, **130**, 134 (1963).
17. A. I. Gubanov, *Sov. Phys.-Solid State (Engl. Transl.)*, **3**, 1564 (1961-1962).
18. N. S. Platakis, H. C. Gatos, and A. F. Witt, *This Journal*, **116**, 510 (1969).
19. B. T. Kolomiets, *Phys. Status Solidi.*, **7**, 359, 713 (1964).
20. T. N. Vengel and B. T. Kolomiets, *Sov. Phys.-Tech. Phys. (Engl. Transl.)*, **2**, 2314 (1957).
21. A. I. Gubanov, *Sov. Phys.-Solid State (Engl. Transl.)*, **3**, 1694 (1961-1962).
22. I. Z. Fischer, *ibid.*, **1**, 330 (1959).
23. E. V. Shkol'nikov, "Solid State Chemistry," p. 132, Z. U. Borizova, Editor, Consultants Bureau Translation, New York (1966).
24. R. A. Smith "Semiconductors," p. 201, Cambridge University Press (1961).
25. G. G. Macfarlane and V. Roberts, *Phys. Rev.*, **97**, 1714 (1955); *ibid.*, **98**, 1865 (1955).
26. J. T. Edmond, *Brit. J. Appl. Phys.*, **17**, 979 (1966).
27. N. I. Butsko and A. P. Oksenyuk, *Sov. Phys.-Solid State (Engl. Transl.)*, **10**, 1759 (1969).

β-Silicon Carbide Films

P. Rai-Choudhury* and N. P. Formigoni

Westinghouse Research Laboratories, Pittsburgh, Pennsylvania

ABSTRACT

β-SiC films were grown in a horizontal reactor using a flow system in either H_2 or argon carrier gas. Substrates used were silicon single crystals, hexagonal SiC platelets, and sapphire. Films were grown by three essentially different methods; namely, (*i*) reaction of pyrocarbon (from CH_4 or C_2H_2) with substrate silicon atoms, (*ii*) reaction of $SiCl_4$ and CH_4, and (*iii*) pyrolysis of $(CH_3)_2SiCl_2$. The quality and the growth mechanisms of films grown under different reaction conditions are discussed. It is inferred from the results of the pyrocarbon reaction that silicon diffuses through the initially formed SiC film and reacts with surface carbon atoms. Infrared absorption spectra indicate that the growth rate of thin films of β-SiC depends on the orientation of the silicon substrates. Electron diffraction patterns indicate ordered films of β-SiC.

The cubic form of silicon carbide (β-SiC) has a forbidden energy gap of 2.3 eV (1) and behaves as an intrinsic semiconductor up to temperatures near 1000°C. It is, therefore, an interesting material for electron devices at high operating temperatures. Films of β-SiC have been grown by several investigators either by chemical vapor deposition (2) or by reacting hydrocarbons with the surface silicon atoms (3-5). Rohan and Sampson (6) have pointed out that because of relatively large differences in both the thermal expansion coefficients and tensile strengths of β-SiC and silicon, it is not possible to grow single crystal films thicker than a few microns. They chose sapphire as a substrate and listed different planes of sapphire and the matching planes of β-SiC. The films of β-SiC grown by them from a $SiCl_4 + C_3H_8$ system were, however, neither epitaxial nor single crystal. The available literature on this subject generally points out the difficulty in obtaining good heteroepitaxy of especially refractory (high melting) materials. For many potential device applications, considerable improvement is desirable in purity as well as crystalline perfection (*e.g.*, large area single crystal films). A better understanding of the various chemical reactions involved and of the growth mechanism might aid in improving the quality of the films. In this paper we have examined: (*i*) the preparation of thin films of β-SiC using different vapor deposition reactions, (*ii*) infrared transmission spectra and electron diffraction patterns, and (*iii*) film growth mechanisms under different reaction conditions.

Experimental

The reaction chamber used was a horizontal quartz tube having a SiC-coated graphite susceptor heated externally by an rf coil. Reactions were carried out using a flow system in either H_2 or Ar ambient. The substrates used were chemically polished single crystal silicon slices, and in different experiments, hexagonal platelets of SiC and sapphire of (0001) orientation. All silicon used was boron doped. The silicon substrates were 10 ohm-cm of (100) orientation as well as 0.1 ohm-cm of (110) and (111) orientations. Predeposit etching of the silicon substrates with water vapor (7) was done in situ. A 500 to 1000 ohm-cm n-type silicon layer was grown epitaxially on the differently oriented silicon substrates prior to the growth of the SiC film. Thus, a freshly generated epitaxial silicon provided clean and comparable initial surfaces on different silicon substrates for heteroepitaxial films. In cases where α-SiC and α-Al_2O_3 substrates were used along with silicon substrates they were prepared separately and epitaxial silicon layers were not grown on the silicon wafers prior to film deposition. Four methods were used for the growth of SiC films, *viz.*, (*a*) reaction of methane with Si surface, (*b*) reaction of acetylene with Si surface, (c) reaction of methane and silicon tetrachloride, and (*d*) pyrolysis of dimethyldichlorosilane. X-ray topography, electron microscopy, and infrared spectroscopy were used to study and characterize various phases of film growth.

* Electrochemical Society Active Member.

Results

The various methods of SiC preparation, the structural perfection of the films, and the infrared absorption data are presented in this section. In the preparation of SiC films by different techniques silicon substrates of (100), (110), and (111) orientations were always used except when films were prepared above the melting point of silicon using α-Al_2O_3 and α-SiC substrates.

Preparation of the films.—Methane pyrolysis.—In the present investigation, depending on the experimental conditions, films ranging from oriented single crystals to near amorphous structure were grown. For example, it was possible to reduce the rate of nucleation to the point where growth occurred only at the dislocations as shown in Fig. 1. The layer in Fig. 1 was grown at 1200°C on a (100) substrate by pyrolysis of CH_4 ($p_{CH_4} \simeq 1.5 \times 10^{-3}$ atm). X-ray topographs indicated the presence of at least one dislocation under-

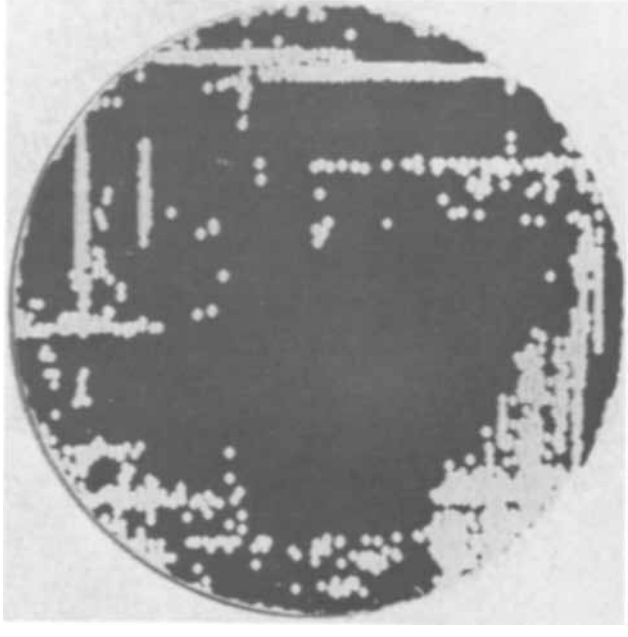

Fig. 1. Photomicrograph of β-SiC layer grown on (100) Si substrate by pyrolysis of CH_4. Magnification: 5 times.

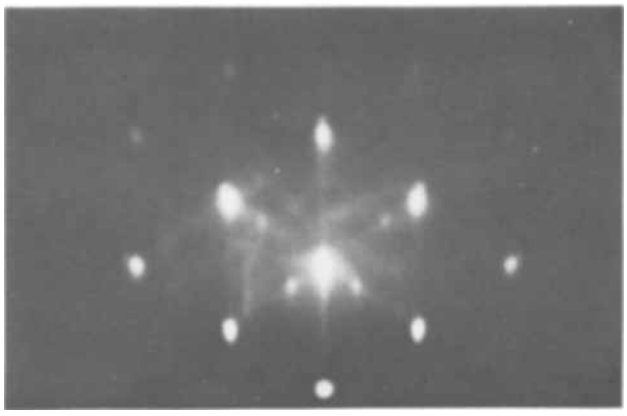

Fig. 2. Electron microprobe X-ray scan of failed test device

neath every SiC crystallite. Examination of a number of these substrates prior to film growth indicated that these dislocations were most likely present in the starting material. Figure 2 shows an electron diffraction pattern of these discontinuous films. A strong (100) orientation is represented, superimposed on the streaked Si (100) pattern of the substrate. Additional diffraction spots, two-thirds along the diagonals which connect the permitted reciprocal lattice points, are evident and indicate twinning in the β-SiC film on {111} planes. The CH_4 partial pressure was then increased in order to obtain a continuous film. Transmission electron microscopic (TEM) examination of the latter films indicated that a complete surface coverage was obtained by increasing the CH_4 partial pressure to about 1.3×10^{-2} atm. However, higher CH_4 partial pressure and consequent increased growth rate resulted in films which sometimes indicated the presence of a ring component in the diffraction pattern. In all films grown by CH_4 pyrolysis, presence of any excess carbon at the film surface could not be detected by electron microscopy. In general, β-SiC films were obtained and consisted of grains of the order of 2000Å.

Acetylene pyrolysis.—SiC films were then grown by pyrolysis of C_2H_2 ($p_{C_2H_2} \simeq 3.7 \times 10^{-3}$ atm) in the temperature range of 1100°-1200°C. No deposit was observed at temperatures of 1050°C and below. All SiC films deposited from C_2H_2 were found to be coated by a film of pyrolytic carbon which had to be removed by oxidation before a characteristic diffraction pattern could be obtained. Films grown by this method always gave diffraction patterns which consisted primarily of rings, and therefore were considerably less crystalline than those from CH_4 pyrolysis.

Silicon tetrachloride and methane reaction.—Obviously SiC films by pyrolysis of methane and acetylene can be grown only on silicon substrates. In order to deposit on substrates other than silicon, SiC films were deposited by reacting $SiCl_4$ ($p_{SiCl_4} \simeq 2.8 \times 10^{-4}$ atm) with CH_4 ($p_{CH_4} \simeq 1.3 \times 10^{-2}$ atm) at 1200°C. When silicon substrates of three different orientations were used, a continuous film was deposited indicating random nucleation, and the deposits exhibited considerable preferred orientation. It was anticipated that hexagonal SiC and α-Al_2O_3 might be suitable substrates because they permit higher deposition temperatures and provide better lattice matching (*e.g.*, for β-SiC $a = 4.36$Å; for α-Al_2O_3 $a = 4.76$Å, $c = 12.99$Å). Films of SiC were deposited on these substrates under conditions similar to those for deposition on Si except at a temperature of about 1500°C. The deposits on α-SiC substrate were of β-form having two orientations with crystallite size larger than on Si. It was not possible to obtain any deposits on α-Al_2O_3 substrates because Si deposited from the hydrogen reduction of $SiCl_4$ reacted with Al_2O_3 to form volatile aluminum suboxides, leaving an etched Al_2O_3 surface (8). Thus Si was not available to react with the carbon from the pyrolysis of CH_4.

Dimethyldichlorosilane pyrolysis.—With the hope of producing SiC directly rather than via Si and C formation, films were deposited on silicon, α-SiC as well as α-Al_2O_3 substrates by the pyrolysis of $(CH_3)_2SiCl_2$. When H_2 was used as a carrier gas the deposited film at temperatures of 1100°-1200°C always indicated presence of unreacted Si in the SiC films, whereas in an inert carrier gas, such as Ar, Si was not present. Although β-SiC films were formed on α-Al_2O_3 substrates by this method they were polycrystalline and of poor quality. Unfortunately, it was not possible to deposit at high temperatures using this organo-silane, due to the formation of excess carbon in the films. Although the SiC formation from $(CH_3)_2SiCl_2$ was much more efficient than from $SiCl_4$ and CH_4, the films on silicon and α-SiC substrates were less ordered in the former case.

In closing this section it should be mentioned that when SiC was grown and/or deposited from CH_4, $SiCl_4$, and CH_4, and from $(CH_3)_2SiCl_2$, the films on (100) silicon substrates showed a single preferred orientation. However, the films on (110) and (111) silicon displayed multiple oriented growth. As was pointed out earlier, the films from pyrolysis of C_2H_2 was of random orientation.

Infrared absorption.—The IR transmission spectra of SiC films grown onto single crystal silicon substrates of different crystal orientation were examined in the spectral range 2500 to 700 cm^{-1}. The instrument employed was a Perkin-Elmer 13 single pass double beam spectrophotometer equipped with NaCl optics. Operations in the ratio mode was chosen so that the atmospheric absorption bands were compensated within about 2%.

Figure 3 shows the spectra of the continuous films grown on (111), (110) and (100) oriented silicon substrates by the pyrolysis of CH_4 at 1200°C and a CH_4 partial pressure of 1.3×10^{-2} atm. The predominant feature of this spectrum is the band centered at 789

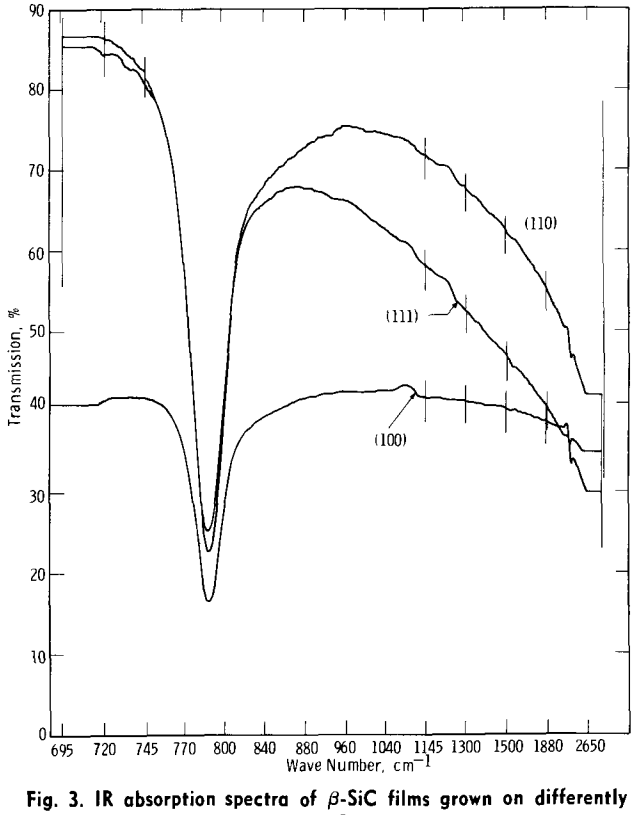

Fig. 3. IR absorption spectra of β-SiC films grown on differently oriented Si substrates by pyrolysis of CH_4.

cm^{-1}, a wave number which coincides within the experimental accuracy with the one attributed by Spitzer to the fundamental vibration of the SiC oscillator (9). The half-band width of about 30 cm^{-1} measured on this spectrum coincides very closely with the corresponding data published by Spitzer and co-workers (9). Because of the very small thickness of the SiC films examined, free carrier absorption in the grown film is not appreciable. However, two of the three spectra recorded in Fig. 3 exhibit a sloping background transmission line. This is due to unbalance between the free carrier absorption in the silicon wafer used as substrate for the film *vs.* the silicon wafer placed in the reference beam. The (100) oriented substrate shows instead excellent compensation of the free carrier absorption because the concentration of electrically active impurity in the substrate and the reference wafer were nearly identical. However, the inverted peak centered around 1070 cm^{-1} (residual-ray wavelength of the SiO_2) indicates that the reference wafer contained a larger amount of bonded oxygen than the sample wafer.

Because of the very thin films grown and the important conclusions to be drawn from these results it is necessary to examine the uniformity of these films. The β-SiC films appeared continuous and free from any pin-holes when viewed in reflection and transmission through an optical microscope after removal of various portions of the substrate by chemical etching. Optical absorption measurements of these films, after removal of the Si substrate, in the u.v. down to 2000Å leave little doubt (negligible transmission) that the films are free from any pin-holes. The coincidence of the present value of the half-band width with that of Spitzer and co-workers can be considered as another evidence in support of a continuous film. If, for example, 10% of the area examined was not covered by the film, then the half-band width would be larger because of the transmission by the uncovered portion of the Si wafer. In general the spectrometer beam covered about 50% of the wafer surface and therefore films of average thickness were examined. By deliberately changing the sampling area the optical density of the film did not change significantly. It can therefore be concluded that the films examined here were free from pin-holes and of uniform thickness.

On the basis of Spitzer and co-worker's results an estimate of film thickness was obtained from Fig. 3. The results are listed in Table I. Such extremely small thicknesses are measurable with a good degree of confidence only because the absorption of the resonance band for SiC is very intense, having an extinction coefficient roughly equal to 2.5×10^5 cm^{-1}. The film thickness measurements indicate that the growth rate is orientation dependent. Similar effects are also observed in the case when films are deposited from the reaction of $SiCl_4$ and CH_4, as well as from pyrolysis of dimethyldichlorosilane on silicon substrates. The IR spectrum is very similar to those shown in Fig. 3.

Discussion

In this study SiC has been prepared by three essentially different methods; namely, (*i*) pyrolysis of hydrocarbons (CH_4 and C_2H_2), (*ii*) reaction of $SiCl_4$ and CH_4, and (*iii*) pyroylsis of $(CH_3)_2SiCl_2$. The first method proceeds with the formation of pyrocarbon at the surface of the initially formed SiC film followed by the diffusion of either carbon or silicon through the SiC film. The reaction zone is either the C-SiC or SiC-Si interface. The second method consists of the reduction of $SiCl_4$ to elemental silicon and decomposition of CH_4 to carbon in H_2 followed by the reaction between silicon and carbon to SiC on the substrate surface (10). SiC formation by this reaction does not proceed in the absence of H_2, at least up to a temperature of 1200°C. SiC films prepared by the third method, *viz.*, by the pyrolysis of $(CH_3)_2SiCl_2$, always indicated presence of unreacted silicon when deposited in hydrogen ambient. The films deposited in an inert carrier gas such as argon did not show the presence of any excess silicon. These results can be explained by examining the over-all $(CH_3)_2SiCl_2$ reaction which can be written as follows

$$(CH_3)_2SiCl_2(g) = SiC(s) + CH_4(g) + 2HCl(g) \quad [i]$$

$$\Delta F_{1500°K} = -32.8 \text{ kcal/mole}$$

$$(CH_3)_2SiCl_2(g) + 2H_2(g) = Si(s) + 2CH_4(g) + 2HCl(g) \quad [ii]$$

$$\Delta F_{1500°K} = -14.9 \text{ kcal/mole}$$

$$CH_4(g) = C(s) + 2H_2(g) \quad [iii]$$

$$\Delta F_{1500°K} = -17.9 \text{ kcal/mole}$$

$$Si(s) + C(s) = SiC(s) \quad [iv]$$

$$\Delta F_{1500°K} = -17.9 \text{ kcal/mole}$$

In the absence of H_2, reaction [*ii*] does not proceed, and therefore elemental Si is not formed. When H_2 is present, excess Si is produced, which can form SiC according to reaction [*iv*], provided reaction [*iii*] takes place. The partial pressure of CH_4 formed by reactions [*i*] and [*ii*] is expected to be considerably less than the equilibrium CH_4 partial pressure ($p^e_{CH_4} \sim 2.6 \times 10^{-3}$ atm) required by reaction [*iii*]. Also the presence of excess H_2 (used as carrier gas) will derive reaction [*iii*] to the left. Therefore reaction [*iii*] is unlikely to proceed in spite of its negative standard free energy because of low CH_4 and high H_2 partial pressures. This probably explains why only SiC is formed directly from $(CH_3)_2SiCl_2$ in an inert ambient, whereas a mixture of SiC and silicon is formed in H_2 carrier gas.

Considering now the growth of SiC by pyrolysis of CH_4 or C_2H_2, let us assume that the growth occurs at the Si-SiC interface via diffusion of carbon through the initially formed thin SiC film as was postulated by Nakashima *et al.* (4). Using a diffusion controlled model, together with the assumption of infinite source, constant diffusivity and a capturing boundary at the SiC-Si interface, the time dependent thickness, x, of the SiC film is given by (11)

$$x = 2\alpha(Dt)^{1/2} \quad [1]$$

where α is a constant. For the present purpose it is assumed that $\alpha = 1$. In the above expressions, D is the diffusivity of C in SiC and t is the diffusion time. For a measured film thickness of 350Å grown in 1 min at 1200°C, the value of diffusivity obtained from Eq. [1] is 5×10^{-14} cm^2/sec. On the other hand, the upper limit for the diffusivity of carbon in SiC, extrapolated from the work of Ghoshtagore and Coble (12), is of the order of 10^{-18} cm^2/sec at 1200°C. Such extrapolation over large temperature (from 1850°C) is reasonable for the present purpose since there is no compositional phase change in the limits of temperatures involved and the effect of crystallographic forms on diffusivity is small. Further, the value of the diffusivity calculated from the film thickness is only intended as a guide for the determination of a possible growth mechanism. Thus, a difference of four orders of magnitude between the minimum diffusivity calculated from the film thickness and the maximum diffusivity obtained from the literature rules out the

Table I. Evaluation of film thickness using the absorption band at 790 cm^{-1} (9)

Crystal orientation of substrate	Thickness of SiC grown in 1 min deposition, Å
(111)	350
(110)	320
(100)	410

mechanism that C diffuses through SiC film. To further substantiate this view films grown by CH_4 pyrolysis were examined for the presence of excess carbon at the surface by a spark source mass spectrometer. A complete stoichiometry of the films (*i.e.*, C/Si ratio of unity) indicate absence of any surface carbon which could act as a diffusion source. Also, as was mentioned earlier, carbon could not be detected by transmission electron microscopy on the surface of films grown by CH_4 pyrolysis.

In the alternative growth mechanism silicon diffuses through SiC to react with the pyrocarbon at the film surface. This model is supported by the fact that the diffusivity of silicon is expected to be considerably higher than that of carbon in SiC (12, 13). However, in this case extrapolation of the diffusivity of silicon in SiC to temperatures of our interest is not possible due to inadequate data (*i.e.*, the activation energy of the process is not reported). The fact that the growth of the SiC films involves outward diffusion of Si is also supported in a recent communication by Haq *et al.* (14). The question now is whether the film growth is diffusion-limited or not.

In cubic systems such as Si and β-SiC diffusivity is independent of the direction of the flux relative to the crystallographic axes (15), and therefore in a diffusion-limiting case the film growth rate should be independent of crystal orientation. However, contrary to this, the film growth rate (experienced with all four deposition methods) was found to be orientation dependent. Therefore, although silicon diffuses through SiC film it is not the controlling step. The only rate controlling step to explain the orientation dependence of the growth rate is adsorption, desorption, and/or surface reaction.

Conclusion

Under the growth conditions used in this investigation, epitaxy of β-SiC on (100) Si has been achieved, together with multiple-oriented growth on (110) and (111) Si. The results using β-SiC substrates indicate that in order to grow β-SiC single crystal over the entire substrate area, it may be necessary to exceed the deposition temperature of 1500°C adopted in these experiments. Because of the high reactivity of silicon with Al_2O_3 films of β-SiC could not be grown on sapphire substrates by reacting CH_4 and $SiCl_4$. When pyrolysis of $(CH_3)_2SiCl_2$ was used as a deposition technique films were formed on sapphire, but, were of poor quality. It has been deduced from film thickness data that the reaction of pyrocarbon with substrate silicon atoms is preceded by the diffusion of Si through the initially formed SiC film. Orientation dependence of the growth rate appears to indicate a process controlled by surface reaction, rather than diffusion of silicon through the grown SiC film. Of course, as the film grows thicker diffusion will eventually become the controlling factor. In the pyrolytic decomposition of $(CH_3)_2SiCl_2$, SiC is formed directly when inert carrier gas is used, while excess Si is formed in H_2 carrier gas.

Acknowledgments

The authors wish to thank Dr. A. J. Noreika for the electron diffraction analysis and Mr. W. Cifone for assistance with the experimental work. The comments of Dr. W. J. Choyke and Dr. J. E. Johnson were greatly appreciated.

Manuscript submitted Sept. 5, 1968; revised manuscript received July 11, 1969.

Any discussion of this paper will appear in a Discussion Section to be published in the June 1970 JOURNAL.

REFERENCES

1. W. J. Choyke, D. R. Hamilton, and L. Patrick, *Phys. Rev.*, **133**, A1163 (1964).
2. D. M. Jackson, Jr., and R. W. Howard, *Trans. AIME*, **233**, 468 (1965).
3. N. C. Tombs, J. J. Comer, and J. F. Fitzgerald, *Solid State Electron*, **8**, 839 (1965).
4. H. Nakashima, T. Sugano, and H. Yanai, *Jap. J. Appl. Phys.*, **5**, 874 (1966).
5. I. H. Khan and R. N. Summergrand, *Appl. Phys. Letters*, **11**, 12 (1967).
6. J. J. Rohan and J. L. Sampson, *J. Phys. Chem. Solids*, Supplement No. 1, 523 (1967).
7. T. L. Chu and R. L. Tallman, *This Journal*, **111**, 1306 (1964).
8. P. Rai-Choudhury and R. R. Fergusson, *ibid.*, **114**, 65C (1967).
9. J. R. O'Connor and J. Smiltens, Editors, "Silicon Carbide: A High Temperature Semiconductor," p. 357, Pergamon Press, Oxford (1960).
10. M. L. Pearce and R. W. Marek, *J. Am. Ceram. Soc.*, **15**, 84 (1968).
11. J. Crank, "Mathematics of Diffusion," p. 117, Clarendon Press (1956).
12. R. N. Ghoshtagore and R. L. Coble, *Phys. Rev.*, **143**, 623 (1966).
13. R. N. Goshtagore, Sc. D. Thesis, M.I.T. (1965).
14. K. E. Haq and A. J. Learn, *J. Appl. Phys.*, **40**, 431 (1969).
15. P. G. Shewmon, "Diffusion in Solids," Ch. 1, McGraw-Hill Book Co., Inc., New York (1963).

Epitaxial Growth and Properties of Silicon on Alumina-Rich Single-Crystal Spinel

G. W. Cullen,* G. E. Gottlieb,* C. C. Wang,* and K. H. Zaininger

RCA Laboratories, Princeton, New Jersey

ABSTRACT

Mobilities similar in magnitude to bulk silicon mobilities may be realized in 1.4 to 1.6μ thick films on flame fusion magnesium aluminate spinel, for carrier concentrations greater than $\approx 2 \times 10^{16}$ cm^{-3} (p-type). The electrical properties of these films are not significantly altered by thermal oxidation at 1200°C for 1 hr. In this carrier concentration range the electrical characteristics are not highly dependent on the deposition rate within the limits investigated. For carrier concentrations between 5×10^{15} and 2×10^{16} cm^{-3} (p-type) the "as deposited" film mobilities are near bulk values, but the mobilities are degraded by the thermal oxidation. In this doping range the electrical properties of the oxidized films are critically dependent on the deposition rate. The films deposited at the higher rates are altered less on oxidation than films deposited at the lower rates. Using a growth rate of 2 μ/min, a mobility of 300 cm^2/V-sec (~80% of bulk) at $N_a = 4 \times 10^{15}$ cm^{-3} may be realized in a film oxidized 1 hr at 1100°C. Below this carrier concentration the mobility of the oxidized films decreases sharply with decreasing carrier concentrations. Minority carrier lifetimes as high as 40 nsec have been realized in 4μ thick films of silicon on spinel. The carrier concentration as a function of temperature and mobility as a function of thickness of silicon on spinel have been measured.

The semiconducting properties of silicon thin films epitaxially grown on sapphire (1-4) appear to be limited by the crystalline quality of the cubic silicon deposited on the rhombohedral sapphire (5-7), and by contamination of the silicon by aluminum from the substrate (6, 8, 9). As a result of the aluminum contamination (autodoping), the electrical properties of silicon films on sapphire change considerably during the thermal formation of oxide films for device fabrication (10). Magnesium aluminate spinel has been investigated as a substrate material for epitaxial growth of silicon because the lattice match of the cubic silicon to cubic spinel is better than the match between silicon on sapphire. Single crystal silicon has been successfully grown on spinel (11, 12), and the crystallographic nature of the silicon has been examined in detail (13). It has been demonstrated that epitaxial silicon on spinel is less contaminated by substrate constituents than silicon on sapphire (14). There has been, however, a serious drawback to the use of the spinel as a substrate material. The commercially available $MgO \cdot 3.3Al_2O_3$ single crystals are unstable at the temperatures commonly employed for device processing. The thermal stability of the single crystal spinel increases with decreasing alumina content in the range between $MgO \cdot 3.3Al_2O_3$ and $MgO \cdot 1Al_2O_3$ (14, 15), but unfortunately the difficulty of preparing good quality crystals also increases with the decreasing alumina content (15). In order to pursue further the possibility of using spinel as a substrate material, it has been necessary to prepare single crystals with alumina content less than the commercially available $MgO \cdot 3.3Al_2O_3$. In the compositional range from $MgO \cdot 1.0Al_2O_3$ to $MgO \cdot 2.5Al_2O_3$ the crystals are sufficiently stable during the device processing thermal treatments for use as substrate material (15).

Other investigators have reported on the characteristics of 20μ thick silicon on low alumina rich spinel (19). However, for many of the device geometries of interest at this time, silicon films less than 2μ in thickness are required. In the case of silicon on sapphire, the electrical properties are a strong function of the film thickness, and the properties of the thinner films ($< 2\mu$) are considerably more sensitive than the thick films ($> 7\mu$) to deposition and substrate variables (4, 10, 14).

It has previously been demonstrated that the mobilities of 2.0μ thick silicon deposited on flux grown stoichiometric spinel are higher than the mobilities of silicon on sapphire (17). In this paper we report on the properties of 1.4-1.6μ thick silicon on flame fusion spinel in the composition range $MgO \cdot 1.5Al_2O_3$ to $MgO \cdot 2.2Al_2O_3$. The hole mobility and the stability of the mobility during thermal oxidation were studied as a function of the deposition rate and carrier concentration. The carrier concentration as a function of temperature and the minority carrier lifetime of the thin films were also measured.

Deposition Methods and Apparatus

Silicon is epitaxially grown on the single crystal spinel surface by pyrolysis of silane (SiH_4) in a hydrogen atmosphere at 1100°C. The substrate is heated by direct contact with an inductively heated susceptor which is positioned in a water-cooled quartz ampoule. Since the reaction chamber walls are held at room temperature by the water-cooling, deposition occurs only on the susceptor and substrate wafer, and contamination from the quartz is minimized. The rf susceptor is a pyrolytic-carbon coated pure carbon block. The dense pyrolytic coating prevents outgassing of the pressed carbon block. This type of susceptor has been found to be more free of impurities than the silicon carbide coated carbon blocks commonly used as rf susceptors.

The gas-metering and -mixing apparatus is schematically presented in Fig. 1. The system is He leak-tight. The gases are mixed in glass bulbs before they are passed into the growth chamber. The doping gas is diluted twice in the system so that the flow meters can be used with sufficiently high gas flows to provide good accuracy. Accurate metering is necessary because, depending on the doping level desired, the dopant source gas of 10 ppm dopant in H_2 is diluted by as much as 500 to 1 before it passes into the growth chamber.

Provision has been made in the gas control system to stabilize the flows and metering valve settings before the reactants are exposed to the substrate. The

* Electrochemical Society Active Member.

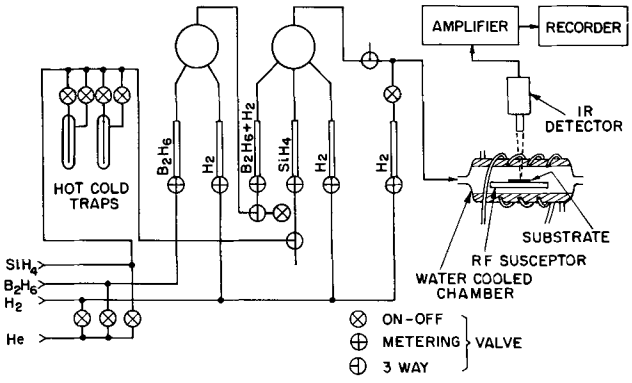

Fig. 1. Apparatus employed for the deposition of silicon on spinel

deposition chamber is flushed with H_2 while the desired flows are established in the control system. During stabilization, the SiH_4-B_2H_6-H_2 mixture is exhausted through a three-way valve immediately prior to the deposition chamber. The mixture is then suddenly switched into the growth chamber. This method is used because the total deposition time is often as brief as 45 sec, and thus the time needed to set up and to stabilize the system may be a significant portion of the deposition time.

The H_2 used as the carrier gas and diluent is purified by passing through a hot Pd-Ag membrane (Engelhard Industries, Newark, New Jersey). The silane-H_2, diborane-H_2, and arsine-H_2 gas mixtures are commercially prepared (Scientific Gas Products Company, Edison, New Jersey).

Since the deposition rate is one of the most critical parameters, the thickness of the growing film is continuously monitored by an IR detector (20) (Beckman Instruments Model 924-1230). The system is schematically shown in Fig. 1. The hot substrate acts as the IR source, and interference in the IR intensity is observed as the thickness of the silicon film increases. The growth chamber of the horizontal growth system was originally constructed to provide a sight path through the water jacket; however, it has been found that if the filter provided with the radiation pyrometer is removed, the detector is sufficiently sensitive to the radiation that passes through the water jacket to be used with the conventional horizontal growth ampoule. Since the thickness measurement is a function of the wavelength used, the method must be recalibrated when the filter is removed. Unexpected changes in the deposition conditions can be immediately observed with the IR detector. An interference pattern is shown in Fig. 2 taken during a growth run in which an accidental surge in the source gas occurred. It is also seen that the film growth started within a second of the introduction of the silane-hydrogen mixture, the growth rate was constant prior to the gas surge,

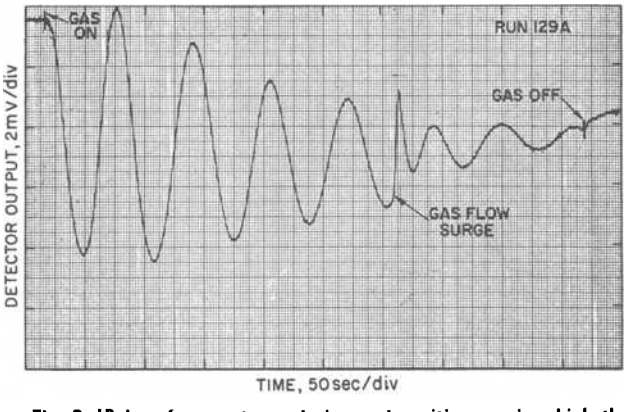

Fig. 2. IR interference trace during a deposition run in which the gas flow conditions momentarily changed.

and the growth stopped within a second of the termination of the source gas. The properties of the deposited films are remarkably sensitive to these variables in the gas flow.

Electrical Properties of Silicon on Spinel

Mobility and stability of electrical properties to thermal oxidation.—The deposition conditions for the epitaxial growth of silicon on spinel were evaluated by preparing a series of samples at various doping levels to measure the mobility as a function of the carrier concentration. Since the mobility is highly dependent on both the crystallographic structure and the impurity content of the films, this is an appropriate property for the comparison of the quality of the silicon on spinel films with silicon on sapphire and bulk silicon. The mobility is also a strong function of the film thickness and the post-deposition treatment, and thus these factors are explicitly stated when comparisons are made. The oxide of the MOS transistor structure is commonly prepared by exposure of the silicon to dry oxygen for 1 hr at temperatures between 1100° and 1200°C, and therefore it was important to examine the change in the electrical properties during this treatment. The mobility of 1.4-1.6μ thick silicon films, before and after thermal oxidation, was measured as a function of the carrier concentration at three different growth rates.

The substrates used are within the compositional range $MgO \cdot 1.5Al_2O_3$ to $MgO \cdot 2.2Al_2O_3$. All depositions were carried out on the (111) surface. The 20 mil thick substrate wafers were lapped with 30μ boron carbide and polished with alumina. The final mechanical polishing was carried out with 0.3μ alumina. The substrates then were degreased thoroughly. Immediately prior to the deposition of the silicon film, the substrates were annealed in H_2 at 1150°C for 20 min. All the depositions were carried out at 1100°C, and the rates were adjusted by control of the silane concentration. The mobilities of the as-deposited films were measured, the films were oxidized in dry oxygen for 1 hr, and the mobility measurement was repeated. Initially, the films were oxidized at 1200°C, but during the course of this study device processing procedures were developed which required a maximum oxidation temperature of 1100°C; therefore, the films deposited at 2μ/min were oxidized at 1100°C.

The mobilities as a function of carrier concentration and oxidation for films deposited at a rate of 0.4 μ/min are presented in Table IA. This rate has been commonly employed in the past for the deposition of silicon on sapphire. It is seen that for carrier concentrations greater than 2 x 10^{16} cm^{-3} (p-type) the as-deposited mobilities of the 1.4-1.6μ films are similar to the bulk mobilities. The electrical properties in this doping range are not significantly altered by thermal oxidation. These mobilities, both before and after oxidation, are at least double the mobilities of oxidized silicon on sapphire for equivalent doping levels (10). Below a doping level of 2 x 10^{16} cm^{-3} the as-deposited mobilities are nearly bulk to N_a as low as 5 x 10^{15} cm^{-3}, but the change in the mobility on thermal oxidation increases with decreasing carrier concentration below $N_a \approx 2 \times 10^{16}$ cm^{-3}. For sample 49, the μ = 350 cm^2/V-sec, which is 95% of bulk at N_a = 4.5 x 10^{15} cm^{-3}, decreased to μ = 55 cm^2/V-sec and N_a = 1.5 x 10^{15} cm^{-3} after thermal oxidation.

Doubling the deposition rate to 0.8 μ/min yields an improvement in the stability to oxidation at the low carrier concentrations (Table IB). The as-deposited μ = 335 cm^2/V-sec at N_a = 5.6 x 10^{15} cm^{-3} of sample 73 changed after oxidation to μ = 225 cm^2/V-sec at N_a = 4.2 x 10^{15} cm^{-3}. Although this represents a 33% decrease in mobility, it is appreciably more stable to oxidation than the sample 49 cited above.

Further improvement in thermal stability is realized by depositing the films at a growth rate of 2 μ/min

Table I. Silicon on spinel mobility and stability of mobility to thermal oxidation

Sample No.	Thermal treatment	N_a, cm^{-3}	Mobility cm^2/V-sec	% Decrease in μ on oxidation	% of Bulk (18), μ
	A. Deposition rate 0.4 μ/min				
65	As-deposited	3.3×10^{17}	260		>100
	Oxidized	2.9×10^{17}	270	0	>100
47	As-deposited	9.5×10^{16}	320		>100
	Oxidized	8.3×10^{16}	315	~0	>100
45	As-deposited	3.4×10^{16}	270		85
	Oxidized	2.7×10^{16}	290	0	90
61	As-deposited	1.9×10^{16}	300		90
	Oxidized	6.7×10^{15}	270	10	75
69	As-deposited	1.4×10^{16}	340		100
	Oxidized	1.4×10^{16}	280	18	80
49	As-deposited	4.5×10^{15}	350		95
	Oxidized	1.5×10^{15}	55	85	13
48	As-deposited	1.8×10^{16}	240		65
	Oxidized	Sample ρ too high for measurement		—	—
	B. Deposition rate 0.8 μ/min				
78	As-deposited	1.8×10^{16}	330		100
	Oxidized	1.1×10^{16}	320	3	92
72	As-deposited	1.5×10^{16}	330		97
	Oxidized	9.1×10^{15}	300	9	85
73	As-deposited	5.6×10^{15}	335		92
	Oxidized	4.2×10^{15}	225	33	60
	C. Deposition rate 2.0 μ/min				
184	As-deposited	2.9×10^{16}	360		>100
166	As-deposited	8.9×10^{15}	340		97
	Oxidized	6.4×10^{15}	315	7	88
170	As-deposited	4.9×10^{15}	330		91
	Oxidized	4.0×10^{15}	300	9	82
179	As-deposited	4.0×10^{15}	275		74
	Oxidized	1.4×10^{15}	140	49	37
177	As-deposited	3.1×10^{15}	270		72
	Oxidized	1.7×10^{15}	215	20	55
176	As-deposited	1.8×10^{15}	235		63
		1.3×10^{15}	155	34	41
165	As-deposited	1.0×10^{16}	265		76
	Oxidized	6.6×10^{15}	310	+17	87
168	As-deposited	4.1×10^{15}	195		54
	Oxidized	4.0×10^{15}	255	+31	69

Conditions for data in Table I:
Rates: ±10%
Substrate orientation: (111)
Substrate composition: x of $MgO \cdot x\ Al_2O_3$
A, 1.5 to 2.0
B, 1.7 to 2.0
C, 2.2
Thickness of deposits: 1.4 to 1.6μ
Thermal oxidation: A and B, 1 hr at 1200°C
C, 1 hr at 1100°C
Temperature of deposition: 1100°C

(Table IC). The as-deposited μ = 330 cm^2/V-sec at N_a = 4.9 x 10^{15} cm^{-3} of sample 170 changed after oxidation to μ = 300 cm^2/V-sec and N_a = 4.0 x 10^{15} cm^{-3}. This represents a decrease in mobility of less than 10%. The three samples cited, at the three growth rates, have very similar as-deposited characteristics, and therefore the effect of deposition rate on stability to thermal oxidation is clearly demonstrated. The similar as-deposited electrical characteristics also indicate that the substrate crystal quality is uniform from boule to boule. The electrical characteristics of the films have been a stronger function of the substrate surface crystallinity than the substrate composition within the compositional range employed. The effect of lowering the oxidation temperature by 100°C was checked by further oxidation of films at 1200°C. The change in mobilities after a second oxidation at the higher temperature were about equal in magnitude to the initial change, as has previously been observed for two oxidations at 1200°C. Even considering the total changes after two oxidations, the mobility degradation of the 2.0 μ/min rate samples is about half of the degradation of the 0.8 μ/min rate samples.

At carrier concentrations below 5 x 10^{15} cm^{-3}, and at a growth rate of 2 μ/min, the as-deposited mobility decreases, and the change in mobility on oxidation increases, with decreasing carrier concentration. It is interesting to note that the after-oxidation properties of two anomalous samples, 165 and 168, fall very nearly on the curve described by the other after-

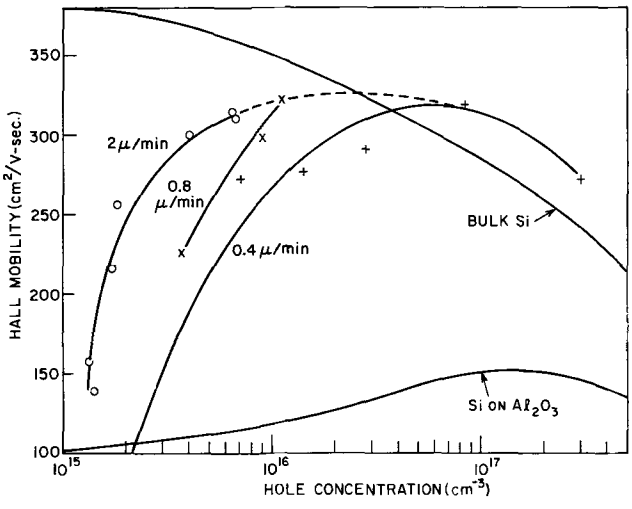

Fig. 3. Mobility as a function of hole concentration for oxidized 1.4-1.6μ thick (111) silicon on spinel, oxidized 2.0μ thick (100) silicon on sapphire, and bulk silicon.

oxidation samples deposited at the same rate (Fig. 3), even though the as-deposited mobilities are unusually low. This behavior is not understood at this time. All of the samples of Table IC were prepared from the same tank of silane-H_2, the same tank of diborane-H_2, and on substrates cut from the same spinel crystal. There is appreciable scatter in the properties of films with N_a< 5 x 10^{15} cm^{-3} because, for these doping levels, the magnitude of unintentionally added impurities is similar to that of the dopant, and therefore the quality of the deposits is critically dependent on the deposition parameters and nature of the substrate surface. Real but nonreproducible high mobilities have been obtained in a number of samples. At the lowest deposition rate an as-deposited mobility greater than 400 cm^2/V-sec was realized at a carrier concentration of 5.2 x 10^{15} cm^{-3}. This deposit was not oxidized. A mobility of 395 cm^2/V-sec was realized at N_a = 4.2 x 10^{16} cm^{-3}. The latter sample did not change significantly on oxidation.

In Fig. 3 a comparison is made between the mobility *vs.* hole concentration relationships of silicon on spinel, silicon on sapphire (10), and bulk silicon (21). The silicon films on the insulating substrates have been oxidized for 1 hr at 1200°C, with the exception of the 2.0 μ/min samples which were oxidized for 1 hr at 1100°C. The silicon on spinel films are 1.4-1.6μ in thickness, while the silicon on sapphire films are 2.0μ in thickness. The mobility *vs.* carrier concentration relationship of 2μ thick (111) silicon on (0001) sapphire has not been reported, presumably due to the difficulties involved in depositing silicon on (0001) sapphire. Therefore, it has been necessary to compare the (111) silicon on spinel with (100) silicon on sapphire. It has been shown, however, that for 2μ thick silicon on sapphire, the hole mobilities in (100) silicon are higher than in (111) silicon (22). Therefore, the data compared in Fig. 3 represent the optimum results that have been obtained to date on each of the insulating substrate materials. The bulk silicon curve included in Fig. 3 represents an average of experimental values collected from a number of sources (21). This curve has been used as a reference to calculate the per cent of bulk mobility values, for the silicon on spinel films, presented in Tables I and III.

In comparing the properties of silicon on spinel with silicon on sapphire it should also be pointed out that the hole concentrations of the silicon films on sapphire typically decrease by an order of magnitude on thermal oxidation (10) for films with as-deposited hole concentrations less than ~1 x 10^{17} cm^{-3}. The changes have been attributed to electrical deactivation during oxidation of aluminum contamination

from the substrate (22). Due to the "autodoping" effects from both spinel and sapphire, it is impractical to use as a standard of reference the electrical properties of silicon films with no dopant intentionally added.

Effect of hydrogen firing on the mobility of silicon on spinel.—The low mobilities which result from thermal oxidation of low carrier concentration films deposited at 0.4 μ/min may be driven back to at least the as-deposited value by exposure to a hydrogen atmosphere for 1 hr at 1100°C (see Table II). In both cases cited the carrier concentration increased during the hydrogen treatment. Similar characteristics have been observed in silicon films on sapphire (22).

Mobility as a function of silicon film thickness.—The mobility as a function of the Si film thickness, holding other variables as constant as possible, is presented in Table III. The carrier concentration was held in the mid 10^{16} cm^{-3} (p-type) because in this carrier concentration range the electrical properties are not so critically dependent on the deposition conditions. The deposits were grown at 1.1 μ/min. The thickness was monitored during growth by observing interference bands with an IR pyrometer, and the total deposit thickness was checked on the Cary spectrometer. The films were grown on 20 mil thick wafers cut from one $MgO \cdot 2.0Al_2O_3$ single crystal boule.

The mobility increases sharply with thickness between thicknesses of 0.6 and 3.1μ. At 3.1μ the mobility is 129% of the reference bulk silicon mobility (21) for an equivalent carrier concentration. Between 3.1 and 8.8μ the mobility does not appear to be a strong function of film thickness. The highest mobility of 430 cm^2/V-sec was obtained at a thickness of 10.5μ. The study was not carried beyond the 10.5μ thickness because silicon deposits above this value are of little interest for device applications and because the composite is fragile due to thermally induced stresses. In order to study thicker films, thicker substrates must be employed, but the values obtained using the thicker substrates are not directly comparable with values obtained using the thinner substrate because the compressive stresses (18, 19) are a function of the substrate thickness. At present the film thickness requirement for most device configurations is 1.5μ. At this thickness the mobility is approximately equal to the reference bulk mobility for the carrier concentration studied.

Table II. Effect of thermal treatment in oxidizing and reducing atmospheres on the electrical properties of low carrier concentration Si on spinel

Sample	N_a, cm^{-3}	Mobility, cm^2/V-sec	Thermal treatment
49	4.5×10^{15}	350	As-deposited
	1.5×10^{15}	50	O_2, 1200°C, 1 hr
	6.7×10^{15}	400	H_2, 1100°C, 1 hr
48	1.8×10^{15}	240	As-deposited
	ρ too high for Hall measurement		O_2, 1200°C, 1 hr
	7.7×10^{15}	280	H_2, 1100°C, 1 hr

Table III. Si on spinel mobility as a function of Si thickness

Thickness, μ	N_a, cm^{-3}	Mobility, cm^2/V-sec	% of bulk, μ
0.6	1.9×10^{16}	110	34
1.1	3.4×10^{16}	260	83
1.5	3.4×10^{16}	330	104
1.9	6.6×10^{16}	310	104
3.1	5.0×10^{16}	395	129
4.8	5.0×10^{16}	360	117
6.4	2.7×10^{16}	395	122
6.8	1.4×10^{16}	350	102
8.8	4.1×10^{16}	365	117
10.5	4.8×10^{16}	430	140

Rate of deposition: approx. 1.1 μ/min.
Substrate (111) $MgO \cdot 2.0Al_2O_3$.

The observed increase in mobility with increasing thickness between 0.6 and 3.1μ can be attributed in part to decreasing local concentrations of impurities from the substrate and increasing crystalline perfection, as the film grows away from the substrate. Charges at the surfaces, particularly at the substrate-film interface, undoubtedly exert a significant influence on the mobility. These factors are difficult to examine experimentally. If one neglects the effect of the surface charge, with a Debye length of 200Å (for a carrier concentration of 2×10^{16} cm^{-3}) and a carrier mean free path of 100Å (22), the surface scattering is confined to a maximum of $\sim$ 20% of the thinnest (0.6μ thick) film measured.

Carrier concentration as a function of temperature.—Hall measurements were made at temperatures between 77° and 300°K in a nitrogen gas ambient. The sample measured was a 1.5μ thick silicon film on (111) $MgO \cdot 1.7Al_2O_3$ spinel. The film was oxidized at 1200°C for 1 hr. The hole concentration *vs.* temperature for this film, and for comparably boron doped bulk silicon (23), is presented in Fig. 4. It is seen that the characteristics of the silicon on spinel film are in good agreement with bulk silicon. This demonstrates the absence of unknown deep level acceptors or compensating donors.

MOS capacitance vs. voltage characteristics of silicon on spinel.—Metal-oxide-semiconductor (MOS) capacitor units have been constructed and studied in silicon on spinel. The characteristics of the MOS units provide an assessment of the silicon-spinel system for various device applications.

Prior to oxidation, the sample was cleaned by a standard procedure (24) for removing organic contamination and metal ions from the surfaces. The silicon was oxidized (25) at about 1200°C to form a SiO_2 layer $\sim$ 1000Å thick, and then exposed to hydrogen at 500°C to reduce the interface states (26). Evaporated aluminum gate dots or mercury probes were used as the metal contacts of the silicon-on-spinel MOS system. The back contact was provided by etching off a part of the oxide and establishing a silver paste contact to the exposed silicon.

The capacitance (C) *vs.* bias voltage (V) characteristics (Fig. 5) of a typical sample were measured using an automatic C-V display system (27). The epitaxial silicon is 4μ thick with a carrier concentration of 3×10^{15} cm^{-3} (n-type) and an electron mobility of 1065 cm^2/V-sec. From Fig. 5 it is seen that the flatband voltage shift is less than 2V, and very little positive charge ($\sim 10^{11}$ cm^{-2}) is present in the oxide layer. The breakdown strength of the oxide film is greater than 10^6 V/cm.

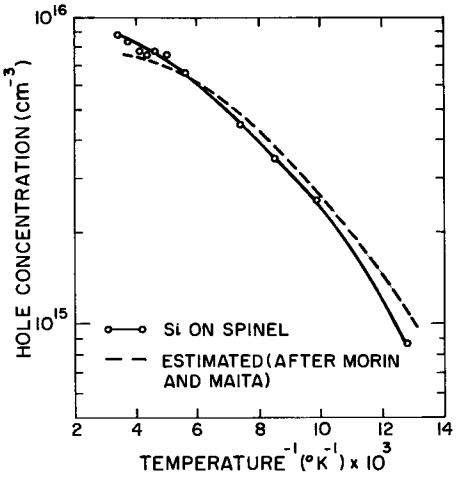

Fig. 4. Carrier concentration as a function of temperature for p-type silicon on spinel.

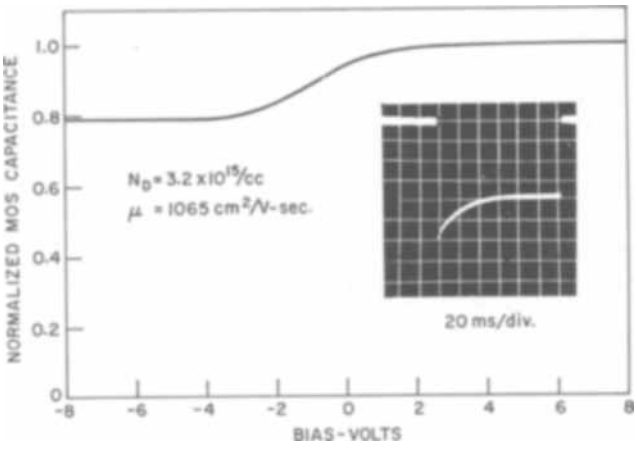

Fig. 5. Capacitance *vs.* bias characteristic and transient response of the inversion layer capacitance for an MOS capacitor in silicon on spinel.

The minority-carrier lifetime in the silicon was determined by the MOS transient response method (28). A step voltage is applied to the gate of an MOS capacitor of correct polarity to deplete the majority carriers from the semiconductor surface, and the rate at which the inversion layer forms is measured. A time constant T can be derived from measurements of the initial slope of the transient response curve, and the minority-carrier lifetime τ is related to T by

$$\tau = 1/2(Tn_i/N_A)$$

where N_A is the doping density and n_i is the intrinsic carrier density of the semiconductor. The transient response of the inversion layer capacitance is shown in the insert in Fig. 5. The time constant is $\sim$ 10 msec, giving a lifetime of over 40 nsec.

Minority carrier lifetimes of $\sim$ 0.1 nsec have been commonly measured in silicon on spinel MOS units prepared using the commercial alumina rich $MgO \cdot 3.3Al_2O_3$ spinel substrates. These low lifetimes are believed to be due to the poor crystallinity of the substrate and to heavy metal contamination (29, 30) from the substrate. The heavy metals are added to the commercial flame fusion spinel to improve the crystallinity. By using the pure low alumina rich spinel as a substrate material the minority carrier lifetime has been improved by more than a factor of 100. This also represents a considerable improvement over the 4.5 nsec lifetime (28) reported for 5μ thick 3 x 10^{16} cm^{-3} (boron doped) silicon on sapphire MOS structures.

Discussion

The mobility *vs.* hole concentration relationship in as-deposited 1.5-1.6μ thick (111) silicon films on spinel is similar to that of bulk silicon for carrier concentrations as low as 5 x 10^{15} cm^{-3}. The mobilities are considerably higher than have been obtained in 2μ thick (111) or (100) silicon on sapphire (10, 22). It is reasonable to assume that the closer silicon-substrate crystallographic match (11, 12), and the lower autodoping (14) of the silicon on spinel as compared to silicon on sapphire, are factors which contribute to the increase in the mobilities observed.

For hole concentrations greater than $\sim$ 2 x 10^{16} cm^{-3} the as-deposited mobilities are relatively insensitive to the deposition rate between rates of 0.4-2.0 μ/min, and the mobilities change insignificantly on thermal oxidation of 1 hr at 1100°C. However, below hole concentrations of $\sim$ 2 x 10^{16} cm^{-3}, the mobilities of the oxidized films decrease with decreasing carrier concentration, the magnitude of the degradation of mobility on thermal oxidation increases with decreasing carrier concentration, and after-oxidation mobilities are highly sensitive to the deposition rate. The near-bulk as-deposited mobilities and degradation induced by thermal oxidation suggest that the after-oxidation low carrier concentration mobilities are more limited by the influence of unintentionally added impurities than by the crystalline imperfections in the film. The electrical properties of the silicon deposited at the highest rate used (2.0 μ/min) are the least sensitive to thermal oxidation. This is consistent with observations that rapid coverage (31) of the substrate suppresses contamination of the growing silicon film by gaseous reaction products (32) from the substrate material.

The sharp decrease observed in the after-oxidation mobility with decreasing carrier concentration below $N_a \sim 5 \times 10^{15}$ cm^{-3} is difficult to explain since the concentration of the unintentionally added impurities is not a function of the doping level. A possible explanation is an increase in the space charge region around inhomogeneously distributed defects as the doping level is decreased for carrier concentrations less than 2 x 10^{16} cm^{-3}. Weisberg (33) has proposed this model to explain a similar decrease in mobility with decreasing carrier concentration observed in the III-V compounds. As the carrier concentration is decreased, due to an increasing space charge region, the effective radius of a heterogeneity may increase to an order of magnitude higher than the physical size of the heterogeneity. Under these circumstances, the mobility decreases with decreasing carrier concentration. In the III-V compounds the inhomogeneously distributed defects have been identified with compositional variations. In the silicon on spinel films, the heterogeneities may be impurities concentrated in lattice defects. Because of the critical dependence of the mobility on the deposition rate the effects observed are assigned to impurities from the substrate, such as aluminum, rather than impurities in the deposition gases. The decrease in mobility on thermal oxidation may then be associated with a change in oxidation state of the aluminum with a corresponding change in the space charge region around the aluminum.

It has recently been demonstrated that compressive stresses introduced into the silicon film during cooling of the silicon-spinel composite from the deposition temperature can result in significant enhancement of the hole mobility in the (111) plane (19). Thus, in addition to the good silicon-spinel lattice match and the decrease in autodoping, the stress in the film may contribute to the relatively high hole mobilities observed in the (111) silicon on spinel.

Acknowledgment

The authors wish to acknowledge F. C. Dougherty and J. F. Corboy for the deposition of the silicon films, R. Bates and H. Temple for the growth of the spinel crystals, and E. Ross and R. Lenskold for the carrier concentration and lifetime measurements. The research reported in the paper was supported in part by the Naval Electronic Systems Command, Contract No. N00039-68-C-2512 and in part by the Air Force Materials Laboratory, Contract No. F33615-68-C-1025.

Manuscript submitted Feb. 24, 1969; revised manuscript received July 11, 1969. This was Paper 282 presented at the New York Meeting, May 4-9, 1969.

Any discussion of this paper will appear in a Discussion Section to be published in the June 1970 JOURNAL.

REFERENCES

1. R. W. Bicknell, J. M. Charig, B. A. Joyce, and D. J. Stirland, *Phil. Mag.*, **9**, 965 (1964).
2. H. M. Manasevit and W. I. Simpson, *J. Appl. Phys.*, **35**, 1349 (1964).
3. C. W. Mueller and P. H. Robinson, *Proc. IEEE*, **52**, 1487 (1964).
4. A review of the many contributions in this field is: J. D. Filby and S. Nielson, *Brit. J. Appl. Phys.*, **18**, 1357 (1967).
5. R. L. Nolder, D. J. Klein, and D. H. Forbes, *J. Appl. Phys.*, **36**, 3444 (1965).

6. R. W. Bicknell, B. A. Joyce, J. H. Neave, and G. V. Smith, *Phil Mag.*, **14**, 31 (1966).
7. P. H. Robinson and C. W. Mueller, *Trans. Met. Soc. AIME*, **236**, 268 (1966).
8. D. J. Dumin and P. H. Robinson, *This Journal*, **113**, 469 (1966).
9. P. B. Hart, P. J. Etter, B. W. Jervis, and J. M. Flanders, *Brit. J. Appl. Phys.*, **18**, 1389 (1967).
10. D. J. Dumin and P. H. Robinson, *J.Appl.Phys.*, **39**, 2759 (1968).
11. H. Seiter and C. Zaminer, *Z. Angew. Phys.*, **20**, 158 (1965).
12. H. M. Manasevit and D. H. Forbes, *J. Appl. Phys.* **37**, 134 (1966).
13. H. Schlotterer and C. Zaminer, *Phys. Status Solidi.*, **15**, 399 (1966).
14. P. H. Robinson and D. J. Dumin, *This Journal*, **115**, 75 (1968).
15. C. C. Wang. To be published.
16. C. C. Wang, *J. Cryst. Growth*, **3, 4**, 485 (1968).
17. C. C. Wang, G. E. Gottlieb, G. W. Cullen, S. H. McFarlane III, and K. H. Zaininger, *Trans. Met. Soc. AIME*, **245**, 441 (1969).
18. W. Heywang, *Mat. Res. Bull.*, **3**, 315 (1968).
19. H. Schlotterer, *Solid State Electron*, **11**, 947 (1968).
20. D. J. Dumin, *Rev. Sci. Instr.*, **38**, 1107 (1967).
21. W. R. Runyan, "Silicon Semiconductor Technology," p. 179, McGraw Hill Book Co., New York (1965).
22. D. J. Dumin, *J. Appl. Phys.*, **38**, 1909 (1967).
23. F. J. Morin and J. P. Maita, *Phys. Rev.*, **96**, 28 (1968).
24. R. Stickler and J. W. Faust, Jr., *Electrochem. Technol.*, **2**, 298 (1964).
25. B. E. Deal, *This Journal*, **110**, 527 (1963).
26. E. Kooi, *Philip Res. Rept.*, **20**, 578 (1965).
27. K. H. Zaininger, *RCA Rev.*, **27**, 341 (1966).
28. F. P. Heiman, *IEEE Trans.*, **ED-14**, 781 (1967).
29. G. Bemski, *Phys. Rev.*, **111**, 1515 (1958).
30. S. J. Silverman and J. B. Singleton, *This Journal*, **106**, 591 (1958).
31. R. W. Bicknell, B. A. Joyce, J. H. Neave, and G. V. Smith, *Phil. Mag.*, **14**, 31 (1966).
32. G. von Grube, A. Schneider, V. Esch, and M. Flad, *Z. Anorg. Chem.*, **260** 120 (1949).
33. L. R. Weisberg, *J. Appl. Phys.*, **33**, 1817 (1962).
34. H. Schlotterer and C. Zaminer, *Phys. Status Solidi.*, **15**, 399 (1966).

Brief Communication

Growth of Single Crystal GaP from Organometallic Sources

Robert W. Thomas

Department of Electrical Engineering, Syracuse University, Syracuse, New York

Single crystal growth of GaP on the (111) face of a silicon substrate has been achieved at atmospheric pressure by the thermal decomposition of a gas phase mixture of gallium triethyl and phosphorous triethyl at 485°C.

The system used for this experiment was designed for epitaxial growth of silicon on silicon by the pyrolysis of silicon tetrachloride. No substantial changes were made in the system with the exception that a nonchlorinated fluorocarbon grease was used throughout and extreme attention was paid to the elimination of atmospheric leaks. The system consists of a vertical flow reaction chamber, a single crystal silicon susceptor heated by rf induction, palladium purified hydrogen carrier gas, and liquid source flasks in a temperature controlled bath.

The growth was preceded by a high temperature bake-out (1260°C) in hydrogen. The proper growth mixture was obtained by electron microprobe analysis of the resulting growth layer.

Kα lines of Ga and P at 20 kV were used for the electron microprobe analysis. Sample growth was compared with a single crystalline standard under the same measurement conditions. Gallium to phosphorous ratios corrected for background only, were 3.85 to 1. This was well within the margin of error of the GaP standard crystal measurements.

The growth was transparent and showed the characteristically brilliant interference fringes commonly observed for SiO_2. Growth thickness was measured by angle lapping and shown to vary from 2700 to 4500Å over the surface area. The deposition time for this thickness was 2 hr.

Reflection electron diffraction measurements were made on the films (see Fig. 1). The results of this analysis substantiated the single crystalline nature of the film. The film was shown to be (111) in orientation and single crystalline over the entire 1 in. silicon substrate. The satellite spots occurring at approximately 1/3 the major lattice spacing are thought to be either due to some twinning or a super lattice at the surface. The exact nature of the GaP surface super lattice has not been confirmed as yet. Electrical measurements of the film showed it to be conducting with a conductivity somewhat lower than the 1 ohm-cm substrate. Although the measurements were made with a mercury probe the surface effects made an exact measurement very difficult. Mesa heterodiodes were made by selective etching using an apiezon mask. These diodes exhibited rectification with reverse breakdown knees between 15 and 50V. The absence of gallium or phosphorous diffusion into the silicon was verified by V-I measurements on the stripped silicon surface and by angle lapping and staining techniques. Electrical characterization of the film and heterojunction will be

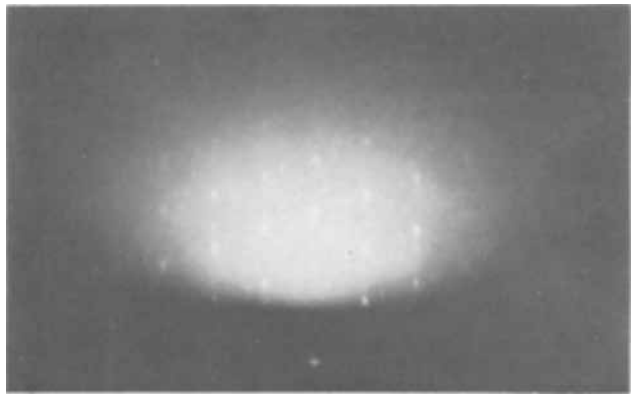

Fig. 1. Reflection electron diffraction pattern of gallium phosphide on silicon.

carried out when suitable ohmic contacts on the film are made.

A word of caution is included on the reactivity and toxicity of these organometallic compounds. Phosphorous triethyl was demonstrated to be stable in air and water but has been reported previously to react violently under certain oxygen pressures. This compound is closely related to several nerve gases and should be considered highly toxic. Gallium triethyl was demonstrated to be highly unstable in air and reacted with explosive violence. Its toxicity is not known. However, both of these compounds are highly aromatic and will give an appropriate warning to the user when inhaled in very low concentrations.

Present work on the growth of thicker films and the electrical characterization of the resulting heterojunctions are to be reported at a later date.

Acknowledgment

The author wishes to acknowledge support from Rome Air Development Center, USAF in the form of a full-time fellowship for graduate study.

Manuscript received June 24, 1969.

Any discussion of this paper will appear in a Discussion Section to be published in the June 1970 JOURNAL.

A High-Voltage, Solid-State Battery System

II. Fabrication of Thin-Film Cells

Charles C. Liang,* James Epstein,* and Gerard H. Boyle*

Laboratory for Physical Science, P. R. Mallory & Company Incorporated, Burlington, Massachusetts

ABSTRACT

The cell fabrication processes were studied of a high-voltage, solid-state battery system, Li/LiI/AgI. Thin-film cells were made by the following procedures: (*a*) AgI was sprayed on a Ag foil and run through a three-zone furnace to melt the AgI film on the foil; (*b*) LiI electrolyte was vacuum deposited on the AgI film; (c) Li was vacuum deposited on the electrolyte. In order to obtain a pinhole-free electrolyte layer, the thickness of the LiI film must be in excess of 5μ The yield of the thin-film cells with the expected open-circuit voltage of 2.1V was affected by the substrate temperature during Li deposition. It was found that, when the temperature of the substrate was properly controlled and the thickness of the LiI film exceeded 15μ, the yield could be as high as 95%.

The cell structure of a high-voltage, solid-state battery system Li/LiI/AgI was considered in a previous publication (1). It was concluded that, due to the high resistivity of the electrolyte and discharge product LiI, a thin-film multilayer parallel-connected cell structure must be developed if practical, interesting current-carrying capabilities are to be achieved.

One of the major tasks in the construction of a thin-film multilayer parallel-connected cell is the fabrication of the thin-film cell units. The present investigation was undertaken to study the fabrication processes for such thin-film cell units.

Experimental

Formation of the cathode.—Mallinckrodt silver iodide powder was used as the cathode material. It was blended with water in a Virtis blender to form a AgI-H_2O slurry. The slurry was sprayed on a heated (150°±10°C) 25μ thick silver foil. The silver iodide and silver foil were then passed through a 30-in. long three-zone furnace (Fig. 1) to fuse the silver iodide film onto the silver foil. Three thermocouples were mounted at points 5 in., 15 in., and 25 in. from the entrance of the furnace and the temperatures at these points were controlled by means of West model JL controllers at 200°, 600°, and 200°C, respectively. The silver iodide coated silver foil was sent through the furnace by means of a conveyor belt driven by a Bodine variable speed motor.

The silver iodide film formed by this process was tightly bonded to the silver foil and the surface of the film was reasonably smooth.

Cathodes of various sizes were stamped from the coated foil and mounted in the substrate holder (Fig. 2) for the vacuum depositions of electrolytes and anodes.

Deposition of the electrolyte.—Foote Mineral LiI · $3H_2O$ was melted at 100°C and the molten LiI · $3H_2O$ was filtered through glass wool maintained at 100°C. The filtrate was then dried in a vacuum oven at 250°C for at least 16 hr. The dried LiI was vacuum deposited on the silver iodide cathode as the electrolyte.

A Consolidated Vacuum Corporation Economy Coater type CVE-19 vacuum system was used for the deposition process. A Vacuum Atmosphere Corporation model Vac-Lab HE-233-46 vacuum box served as the vacuum chamber during the vacuum deposition process and as the inert atmosphere chamber before and after the deposition.

The deposition setup shown in Fig. 3 contained a lithium iodide deposition and a lithium deposition compartment separated by a steel shield. The evaporation sources, a tantalum boat containing lithium iodide and a cylindrical titanium crucible containing lithium, were mounted approximately 1 in. above the base plate. Lithium iodide was evaporated by passing current through the tantalum boat directly, whereas lithium was evaporated by passing current through a heating coil which in turn heated the titanium crucible. The substrate holder with the cathodes in position was installed in the slots of a cooling plate positioned 10-12 in. above the evaporation sources. At the center of the cooling plate in each compartment, a sensor head of a Sloan model OMNI-II deposit control master was installed facing the evaporation source for the purpose of controlling the deposition rate and measuring the film thickness. In the lithium deposition compartment, a mask was mounted on the cooling plate and extended below the substrate holder so that the diameter of the lithium deposit would be slightly smaller than that of the electrolyte to avoid any possibility of shorting between the two electrodes. The substrate holder could be moved from one compartment to the other by a gear controlled from the outside of the vacuum chamber.

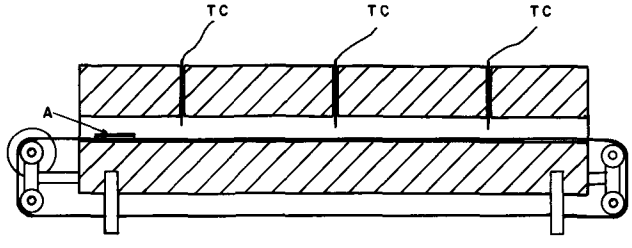

Fig. 1. Three-zone furnace: TC = thermocouple; A = Ag/AgI foil.

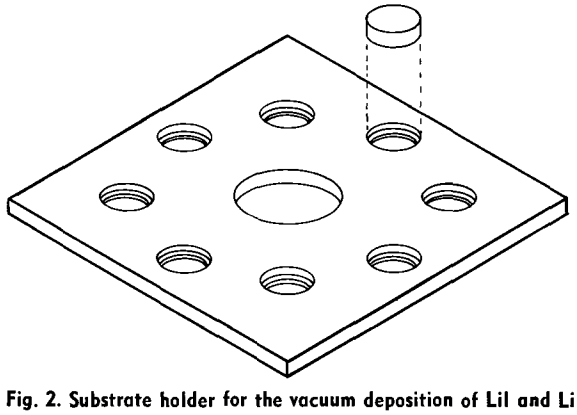

Fig. 2. Substrate holder for the vacuum deposition of LiI and Li

* Electrochemical Society Active Member.

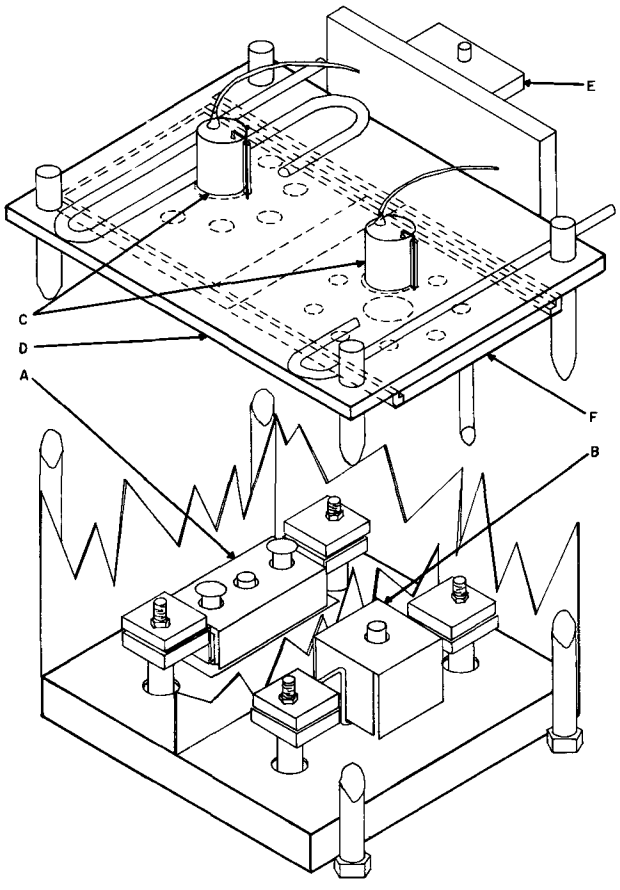

Fig. 3. Deposition setup: A—LiI source, B—Li source, C—Sloan OMNI-II Sensor Head, D—cooling plate, E—substrate position control, F—Li deposition mask.

The deposition of lithium iodide on the silver iodide cathode was carried out under a pressure of 2 to 8 x 10^{-6} mm Hg and the deposition rate was controlled at 0.03-0.08 μ/sec by means of the Sloan model OMNI-II deposit control master.

Deposition of the anode.—Foote Mineral reactor-grade lithium rods (99.983% pure) were used as the raw material for the deposition of the anodes.

After the lithium iodide deposition, the substrate holder was moved to the lithium deposition compartment and the lithium anodes were deposited at a rate of 3 ± 1 mμ/sec under a pressure of 2-5 x 10^{-6} mm Hg.

Polarization studies.—The thin-film cells were tested in the vacuum box under an argon atmosphere. Cell voltages were measured by means of a Keithly Model 610B electrometer and recorded by a Varian G14A strip chart recorder. An Electronic Measurements model C631 constant current power supply was used for the polarization of the test cells under constant current conditions. For the construction of the polarization curve, the cell voltage readings were taken after the constant current had been applied for at least 10 min to reach a steady-state condition. All the tests were carried out at temperatures of 25° ± 2°C.

Results and Discussion

The spray-melting process produced satisfactory cathode films. The adherence of the cathode film was tested by attempting to separate the silver iodide film from the silver foil by rubbing the silver iodide surface with a silver foil. In addition, the resistance of the silver iodide film was measured between the silver substrate and an amalgamated silver electrode with known surface area. It was found that the measured resistance of the cathode film agreed reasonably well (± 10%) with the expected value calculated from the conductivity of silver iodide (5). The uniformity of the film depended on the speed at which the sprayed film was passed through the three-zone furnace. At a speed of 15 in./min, the melted cathode film was very smooth and the variations in the film thickness were less than 20% of the film thickness.

The dehydration process for lithium iodide was carefully controlled to avoid hydrolysis. It was found that the upper limit of the drying temperature for the dehydration process in the vacuum oven was 250°C. At temperatures above 250°C, extensive hydrolysis would occur. In fact, even under the present experimental conditions, hydrolysis occurred to some extent as shown by the fact that a 1M LiI solution prepared from the evaporated lithium iodide exhibited a *p*H of 9 at 25°C. However, no apparent effect on the cell operation was observed by the presence of the small amount of LiOH in the electrolyte. This was shown by the fact that the discharge characteristics of the cell containing the 250°C vacuum oven dried lithium iodide was similar to that of the cell containing the 60°C vacuum oven dried lithium iodide.

One of the most critical operations in the fabrication of the thin film Li/LiI/AgI cells was the vacuum deposition of the lithium iodide electrolyte film on the cathode. The electrolyte film must be pinhole free to prevent internal shorting between the two electrodes. It was found that, in order to obtain a smooth and coherent lithium iodide film on the silver iodide cathode, the substrate should be maintained at a low temperature by circulating a refrigerant through the cooling plate, preferably below —20°C. However, more importantly, the thickness of the deposited lithium iodide film determined the effectiveness of the film as a separator between the two electrodes. It was found that, in order to obtain a pinhole-free lithium iodide film on the cathode, the thickness of the film must be greater than 5μ. This was evident as the results showed that practically all of the thin-film Li/LiI/AgI cells were short-circuited and exhibited 0V as their open-circuit voltages when the deposited lithium iodide film was less than 5μ thick.

Table I shows the effect of the electrolyte film thickness on the yield of the thin-film cells with the expected 2.1V open-circuit voltage. It was noted that an acceptable yield of 95% was obtained as the film thickness reached 15μ.

The temperature of the substrate during the lithium deposition on the electrolyte film had a distinct effect on the characteristics of the thin-film cell. Lithium was deposited on lithium iodide under the following conditions:

(*a*) No heat shield was installed between the substrate and the evaporation source. The radiative heat from the evaporation source reached the substrate and caused a temperature rise.

(*b*) A heat shield was applied to block most of the radiative heat from reaching the substrate.

(c) In addition to the heat shield, the substrate was cooled by circulating tap water through the cooling plate.

(*d*) In addition to the heat shield, the substrate was cooled by circulating a refrigerant at —20°C through the cooling plate.

Table I. The effectiveness of the LiI film as a separator as a function of film thickness*

LiI film thickness, μ	Total No. of cells fabricated	No. of cells exhibiting open-circuit voltage of 2.1V	Yield, %
1	48	0	0
2	48	0	0
5	48	2	3.6
10	48	30	62
15	56	53	95

* Temperature of the substrate was controlled as —20°C during the deposition of LiI and Li.

Table II. The effect of substrate temperature during the Li deposition on the yield of thin-film cells*

Li deposition condition	Total No. of cells fabricated	No. of cells exhibiting open-circuit voltage of 2.1V	Yield, %
No heat shield	56	0	0
With heat shield	56	0	0
Substrate was cooled by tap water	56	15	27
Substrate was cooled by refrigerant at −20°C	56	53	95

* The thickness of electrolyte = 15μ.

Table II summarizes the results from these studies. It was evident that the temperature of the substrate during the lithium deposition had a pronounced effect on the yield of the process.

The effect of the substrate temperature on the yield of the process was to be expected. It is well known (2) that, when an alkali-halide crystal is heated in the vapor of the corresponding alkali metal, it acquires a nonstoichiometric excess of alkali metal to form "color centers" which increase its electronic conductivity. If the temperature of the substrate was not properly controlled during the deposition of lithium on lithium iodide, conditions favoring the formation of color centers in lithium iodide were indeed present. Lithium iodide was heated by the radiative heat from the evaporation source and the lithium vapor was in direct contact with the heated lithium iodide. In addition, the high temperature of the substrate could also cause diffusion of lithium atoms through the electrolyte, resulting in electronic conductivity. Therefore, it was imperative to cool the substrate properly during the deposition of lithium so that the lithium iodide electrolyte would not acquire an excess of lithium to become an electronic conductor.

The geometrical area of the anode of all the test cells was 2.36 cm^2 and the thicknesses of the components of the cell were typically: silver current collector, 25μ; silver iodide cathode, 30μ; lithium iodide electrolyte, 15μ; and lithium anode, 4μ.

The thin-film cell had an open-circuit of 2.1V which agreed well with the value of 2.09V calculated from the Gibbs free energy change (3) for the reaction:

$$Li + AgI \rightarrow LiI + Ag$$

and it confirmed this to be the discharge reaction of the cell. From the linearity of the polarization curve of the Li/LiI/AgI thin film cell (Fig. 4), it was concluded that the cell impedance was ohmic in nature and the resistivity of lithium iodide was calculated to be 1.17 x 10^7 ohm-cm (4). The resistivity of silver iodide, 10^4 ohm-cm (5), was negligible in comparison with that of lithium iodide.

The discharge curves of the thin-film cells under various constant loads are shown in Fig. 5. The discharge efficiencies were approximately 50% and the current capabilities of the cells demonstrated the usefulness of the system for low rate applications especially in view of the fact that the current capability can be increased by parallel connecting such thin-film cells.

The initial voltage decay of the thin-film cell during discharge agreed well with the expected increase in cell resistance due to the production of lithium iodide. However, a more severe decrease in cell voltage occurred when the cell reached about 20% depth of discharge. The polarization characteristics of the system are sufficiently complex to deserve a separate discussion in a subsequent publication.

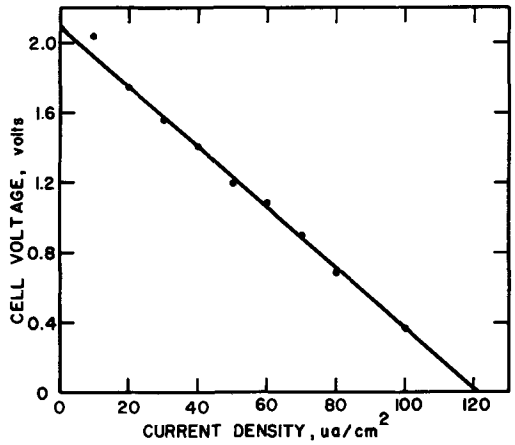

Fig. 4. Typical polarization curve of Li/LiI/AgI thin-film cell. Temperature: 25° ± 2°C. Cell dimensions: geometrical area = 2.36 cm^2, anode thickness = 0.4 x 10^{-3} cm, electrolyte thickness = 1.5 x 10^{-3} cm, cathode thickness = 3.0 x 10^{-3} cm.

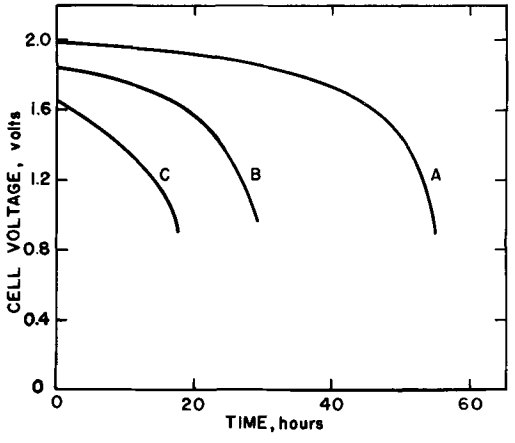

Fig. 5. Constant load discharge curves of thin-film Li/LiI/AgI cells. Temperature: 25°±2°C. Cell dimensions: geometrical area = 2.36 cm^2, anode thickness = 0.4 x 10^{-3} cm, electrolyte thickness = 1.5 x 10^{-3} cm, cathode thickness = 3.0 x 10^{-3} cm. Stoichiometric capacity = 1.9 mah. Load: A = 100 kohm, B = 47 kohm, C = 25 kohm. Efficiency: A = 50%, B = 51%, C = 50%.

Acknowledgments

The authors wish to thank Dr. P. Bro for his comments on the paper and Mr. J. Omasta for his assistance in part of the experimental work. The Li-AgI solid cell patent was issued to Dr. M. L. B. Rao in this laboratory.

Manuscript submitted April 9, 1969; revised manuscript received ca. June 28, 1969.

Any discussion of this paper will appear in a Discussion Section to be published in the June 1970 JOURNAL.

REFERENCES

1. C. C. Liang and P. Bro, *This Journal*, **116**, 1322 (1969).
2. N. F. Mott and R. W. Gurney, "Electronic Processes in Ionic Crystals," 2nd Ed., pp. 109-113, Oxford University Press, Oxford (1957).
3. W. M. Latimer, "Oxidation Potentials," 2nd Ed., pp. 190 and 329, Prentice Hall, Inc., Englewood Cliffs (1961).
4. Landolt Bornstein, "Zahlenwerte und Funktionen," Vol. 2, Part 6, Section I, p. 226, Springer, Berlin (1959).
5. J. N. Mrgudich, *This Journal*, **107**, 475 (1960).

Mechanism of Bonding Electroless Metal to Organic Substrates

G. V. Elmore* and K. C. Davis

International Business Machines Corporation, CD-Manufacturing Research Laboratory, Endicott, New York

ABSTRACT

The use of electroless metal bonded organic substrates has many possible applications. The present state-of-the-art is limited to a few organic substrates. Initial studies included the mechanism of bonding electroless copper to acrylonitrile-butadiene-styrene and to polysulfone. This was investigated by using a scanning electron microscope to view the interfacial surfaces of substrates subsequent to chemical processing and electroless and electrolytic plating. The examination revealed that interlocking surfaces were present which permitted mechanical interaction at the copper-organic interface. When these surfaces were replicated on epoxy, bonding between this surface and electroless copper was obtained.

This investigation was performed to examine the mechanism of bonding electroless copper to organic substrates. Previous investigators of this bonding mechanism have been divided essentially into two groups. There are those who feel the mechanism is mainly a mechanical interlocking type bond (1, 2, 5, 6, 9, 10), while others are of the opinion that the etchant chemically alters the surface of the substrate so that chemical bonding of the substrate and electroless metal takes place (3, 7). A review of the theoretical studies has been given by Saubestre (8).

Examination of Treated Surfaces

As an initial step in this investigation, a study was made of interfacial surfaces of electroless copper and treated acrylonitrile-butadiene-styrene (ABS) utilizing the scanning electron microscope (SEM). The SEM is particularly suitable for this study because replication is not required, the depth of focus is excellent, and the high magnification is very desirable. Electron microscope photographs of conditioned ABS have been previously published (1, 4, 9, 10). Also, scanning electron microscope photographs of conditioned polysulfone have been published by Ryan *et al.* (6). Zahn and Wiebusch (10) postulate that the conditioning of the surface results in a loss of butadiene that was present as dispersed spheroids in the acrylonitrile-styrene matrix. The conditioner attacks the butadiene at a faster rate than the acrylonitrile-styrene, thus leaving spheroidal voids in the surface. In this study, SEM photographs of the treated ABS were made; and, in addition, SEM photographs of the copper interface were taken.

Plating-grade ABS (obtained from Marbon Chemical Division of Borg-Warner Corporation) 0.090 in. thick, was treated for 15 min in chromic-sulfuric etchant at 65°C. The prepared sheet was subsequently plated with electroless copper and then electroplated to 0.001 in. of copper with copper pyrophosphate electrolyte. The peel strength was 5 lb/in. peel (Jacquet 90° peel test). The SEM was used to take photographs of the plastic and copper. Figure 1 illustrates the surface of the untreated ABS at 10000 magnification. Figure 2 illustrates, at 7000 magnification, the ABS surface after a conditioning treatment. Figure 2 shows, in the same manner as previously illustrated by other investigators (1, 4, 9, 10), that the treatment has preferentially etched cavities in the surface. Figure 3 illustrates, at 5000 magnification, the ABS surface after peeling of the copper. The surface of the plastic has been torn by the peeling action, indicating the fracture occurred in the ABS substrate. Figure 4 similarly illustrates, at 7000 magnification, the copper surface after peeling; the particles of ABS torn away during peeling partially cover the copper spheroids. Figure 5 illustrates, at 10000 magnification, the copper surface after the ABS particles have been removed with acetone. The spheres of copper which are clearly visible had filled the holes in the ABS left by the etchant. Thus, the interlocking mechanical bond

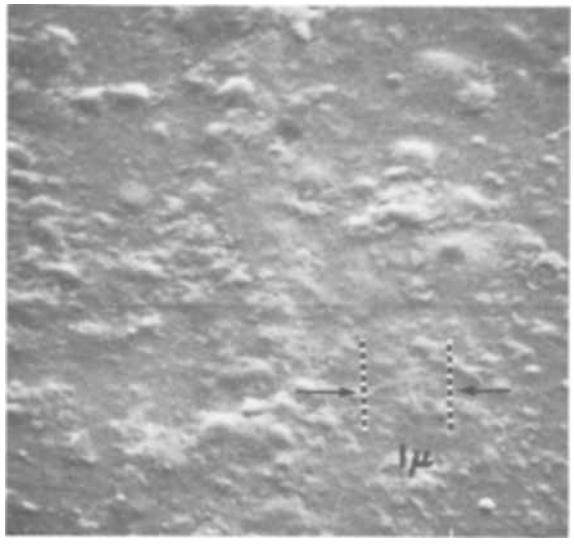

Fig. 1. Untreated ABS surface

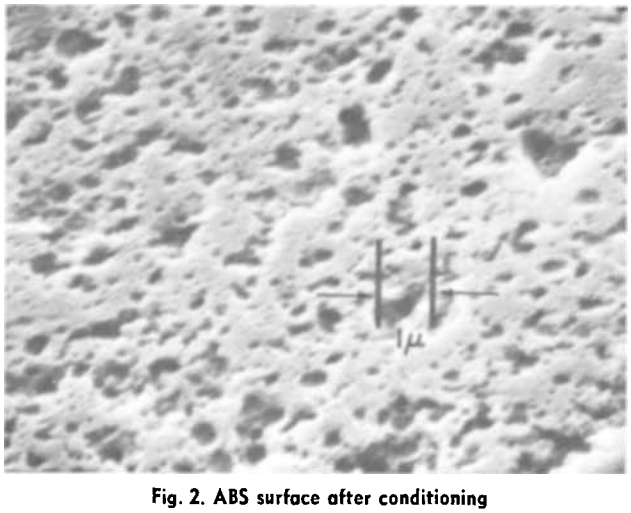

Fig. 2. ABS surface after conditioning

* Electrochemical Society Active Member.

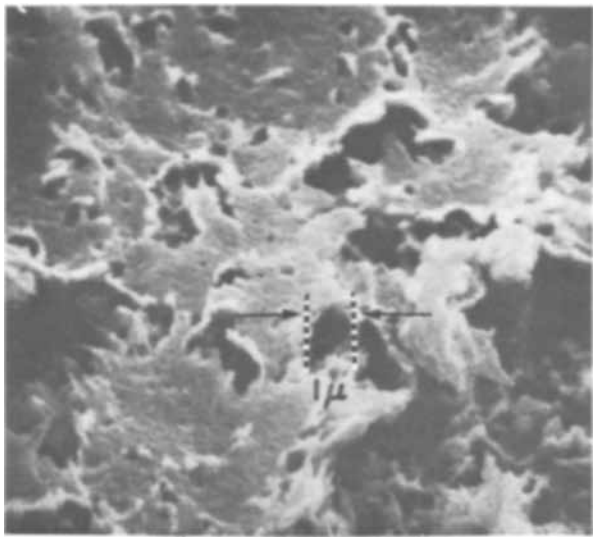

Fig. 3. Treated and plated ABS after copper has been peeled

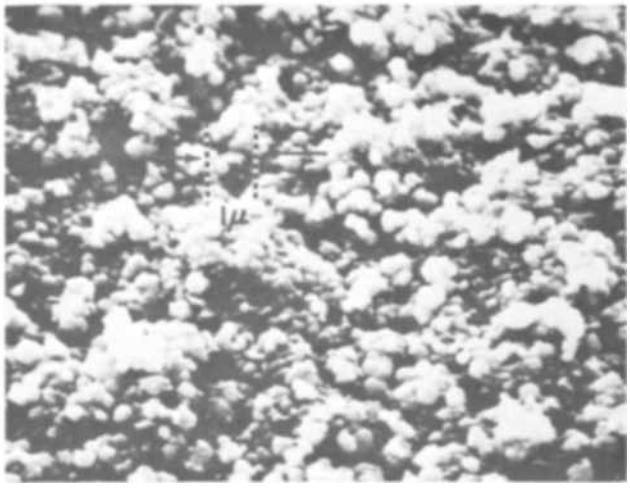

Fig. 4. Copper surface after peeling from treated ABS

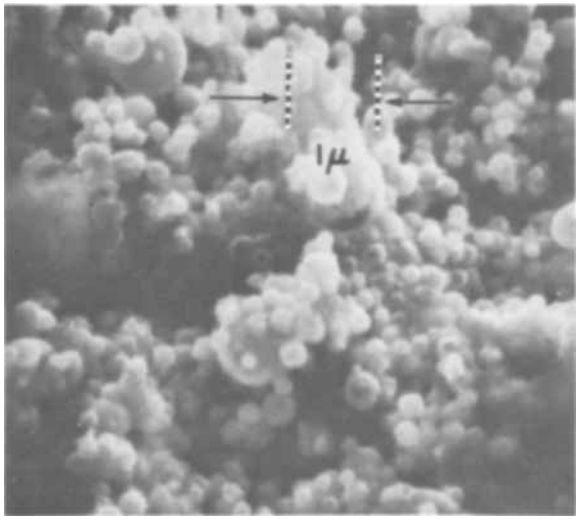

Fig. 5. Cleaned copper surface after peeling from treated ABS

formed between the copper and the treated ABS is clearly demonstrated.

Enthone and Union Carbide, in conjunction, have developed a method of treating polysulfone that yields a good bond between electroless copper and the polysulfone. Samples of copper-plated polysulfone

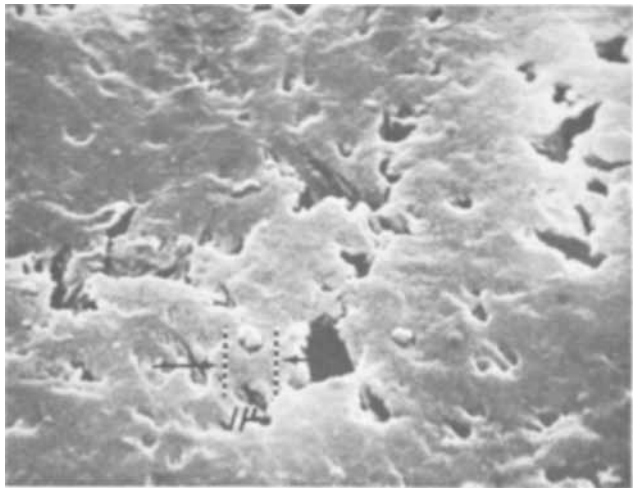

Fig. 6. Treated polysulfone surface

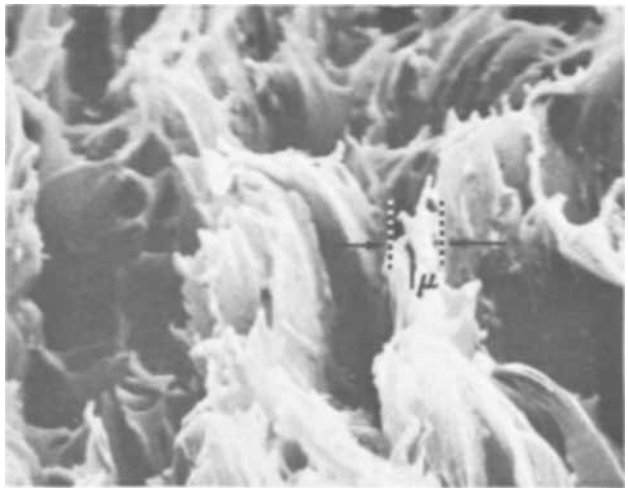

Fig. 7. Treated polysulfone after copper has been peeled

were obtained from Enthone. An additional electroplating with pyrophosphate copper was added to the samples increasing the copper thickness to 0.001 in. The resulting peel strength was 11 lb/in.

A set of SEM photographs was taken similar to those of the ABS samples. Figure 6 illustrates the treated polysulfone surfaces at 7000 magnification. Similar SEM photographs have been published by Ryan (6). Figure 7 illustrates, at 7000 magnification, the polysulfone surface after the copper has been peeled. The polysulfone has been stretched by the peeling action as the copper was removed from the crevices. Figure 8 illustrates, at 7000 magnification, the peeled copper surface with an intermingling of copper and polysulfone. Figure 9 illustrates the copper surface after cleaning with methylene chloride; the interlocking nature of the copper and polysulfone is again quite evident.

Replication of Treated Surfaces

To determine whether the nature of the substrate had an effect on the bond, assuming the same surface roughness, a copper surface treated for bonding by the Clevite Company was replicated on various substrates. A sheet of fluorinated ethylene propylene copolymer (FEP) was molded to this treated copper surface at 500 psi and 280°C. A sheet of polysulfone was molded at 500 psi and 280°C to the surface of treated Clevite copper. Lastly, an epoxy-glass laminate was molded to the surface of treated Clevite copper at 500 psi and 170°C. Then the Clevite copper was removed with ammonium persulfate copper etchant.

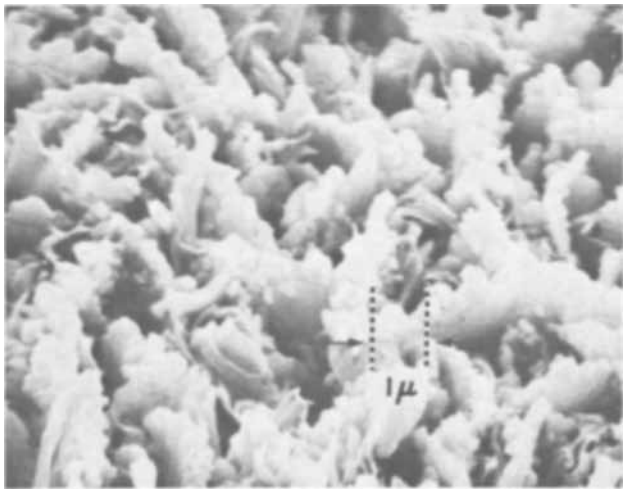

Fig. 8. Copper surface after peeling from treated polysulfone

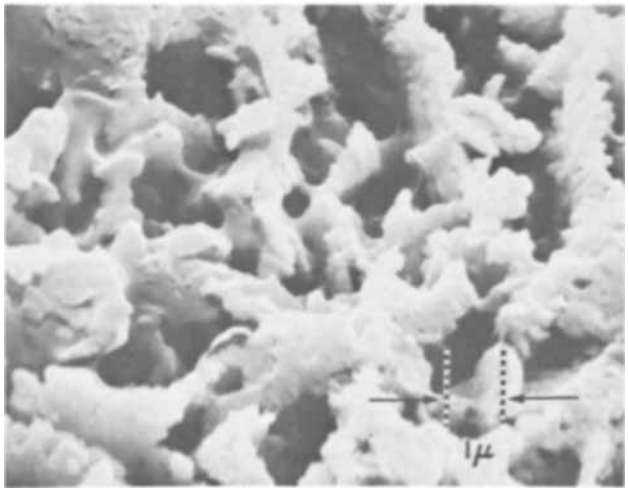

Fig. 9. Cleaned copper surface after peeling from treated polysulfone.

Figure 10 illustrates, at 2800 magnification, the surface of the epoxy after this treatment. The surface of the FEP and of the polysulfone was the same. After rinsing, the three different substrates—with a matte finish that is wetted by water—were plated with electroless and electrolytic copper to 0.001 in. in thickness. The resulting bonds after heating at 170°C for 15 min were all in the same range from ½ to ¾ lb/in. in peel strength. The copper, upon peeling, had the appearance of the original Clevite copper and did not change color in HCl, which is a characteristic of treated Clevite copper.

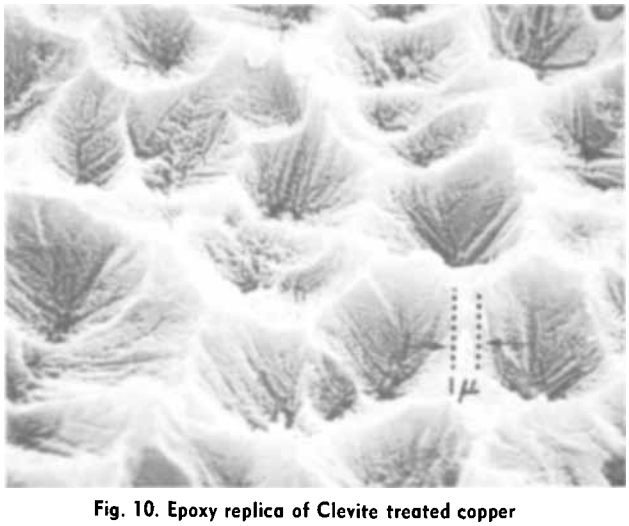

Fig. 10. Epoxy replica of Clevite treated copper

This type of roughness is sufficient for bonding molten substrate to copper but is insufficient to obtain good bonding of organic substrate to electroless copper. Logie (3) has found that a copper surface taken from conditioned ABS can be molded to ABS to yield a bond of 15 lb/in. As can be seen from Fig. 10, the microroughness of the Clevite surface is much less than either treated ABS or polysulfone. However, if the substrate is melted and processed onto the Clevite copper, different mechanisms of bonding are a factor. Not only is much more intimate contact and exact matching obtained than when electroless copper is formed on the surface but, also, when the substrate is liquid, possibilities of chemical interaction between substrate and copper are much enhanced. Thus, Clevite copper bonded to epoxy-glass by lamination produced bonds with peel strength of approximately 10 lb/in. Even when the possibility of chemical reaction is low, if a liquid substrate is contacted with the Clevite replicated surface, an excellent bond is obtained. Thus, when uncured epoxy in solvent is poured on the replicated Clevite-FEP surface, dried, and cured at 170°C, the materials could not be separated without badly tearing the FEP.

To determine if epoxy with a surface texture of treated ABS or treated polysulfone could have a good bond to electroless copper, the surfaces were replicated in epoxy. The replications were made in every case without the use of pressure because it had been found that application of pressure, while the organic substrate was liquid, flattened and distorted the copper surface that was being replicated. Logie and Rantell (3) have previously done studies with ABS replicated surfaces. For the polysulfone, the replication was accomplished by beginning with Enthone copper-clad polysulfone. The treated polysulfone was removed from the deposited copper by dissolving the polysulfone in methylene chloride. After hot alkaline-anodic-cleaning, a brominated epoxy in solvent (25% solids) was poured on the surface, dried, and cured at 170°C. This was then backed with a thick layer of 100% solid epoxy and cured. The copper was then removed with ammonium persulfate copper etchant, the board was rinsed, and electroless and electrolytic copper were applied. After aging for 1 day, the peel strength was 3 lb/in. After 5 days of aging at room temperature, the peel strength increased from 3 to 5 lb/in. The original polysulfone-copper bond of 10-12 lb/in. was not duplicated because of differences in elasticity between the polysulfone and epoxy. Higher bonds are always obtained when the substrate is flexible than when it is brittle. When smooth epoxy is treated with ammonium persulfate copper etchant and electroless and electrolytic copper is applied, there is essentially no bond.

The experiment was repeated with plating-grade ABS. In this test, the original bond of ABS copper was 10-12 lb/in. The ABS was removed with acetone; however, because of pigmentation and a nonhomogeneous nature, the last traces of ABS were much more difficult to remove than the polysulfone. After vapor degreasing and a hot alkaline anodic-cleaning, the copper was treated with concentrated H_2SO_4 for 5 min, rinsed, and dried. The brominated epoxy was applied as previously described and the same procedures were followed. Initially, the peel strength was ¾ lb/in. After heating for 15 min at 170°C, the peel strength was 4 lb/in. The ABS and polysulfone also indicated similar increased bond strength with aging either at room temperature or at elevated temperatures.

Investigation of Aging

The increase of bond with aging is caused by changes occurring in the surface of the substrate. This is indicated by the appearance of the copper when

it is peeled away. On freshly plated samples of ABS, the copper, when peeled, has no ABS on the surface of the copper. As the sample ages, more and more ABS is pulled off with the copper, indicating a gradual strengthening of the cohesive strength of the surface layers of ABS. Undoubtedly, the conditioning agent affects the acrylonitrile-styrene, weakening and altering the surface of the ABS. In this investigation, it has been found that the rate of improvement in copper-ABS bond during aging is greatly accelerated if the ABS is clad only on one side with copper compared to ABS clad on both sides with copper. It would appear that a diffusion-controlled reaction occurs which affects improvement of bond with aging. Perhaps the conditioning makes the ABS surface more susceptible to water adsorption from the solutions, thus weakening the strength. As the adsorbed water diffuses away from the surface layers, the strength of the surface layers increases. Even in substrates which have had no conditioning, a film of water solution or hydrated compounds, such as $Sn(OH)_2$, may be initially present between the copper and organic substrate, since the copper is formed from solution, thus weakening the bond until diffusion of this layer from the surface occurs. Vacuum aging of ABS samples increased rate of improvement of bond; aging in water or 100% humid air impeded the improvement of bond with aging.

From this work, it is concluded that good bonding of epoxy to electroless copper can be obtained if the epoxy has the surface roughness characteristics of ABS or polysulfone.

Conclusions

On the basis of the replication experiments and the scanning electron microscope photographs of treated samples, it may be concluded that a major factor contributing to good bonding between organic substrate and electroless copper is a mechanical interlock of the bonding surfaces. The results do not disprove that chemical bonding does not also take place; however, no significant bond has been obtained on samples that were seen to be smooth by SEM photographs.

Acknowledgments

The authors wish to acknowledge the invaluable assistance of J. B. Kurzweil and W. R. Merwarth, MRL Electron and Ion Beam Development, in obtaining the SEM photographs.

Manuscript submitted Nov. 25, 1968; revised manuscript received June 8, 1969. This was Paper 490 presented at the Montreal Meeting, Oct. 6-11, 1968.

Any discussion of this paper will appear in a Discussion Section to be published in the June 1970 JOURNAL.

REFERENCES

1. H. Ebneth and W. Klimaschewski, *Galvanotechnik*, **58**, 308 (1967).
2. K. Heymann, W. Riedel, and B. Woldt, "Metallische Ueberzuege auf Kunstoffen," pp. 48-63, Carl Harser Verlag, Muenchen (1966).
3. G. R. Logie and A. Rantell, *Trans. Inst. Metal Finishing*, **46**, 91 (1968).
4. M. Matsunaga, Y. Haguida, and K. Ito, *Metal Finishing*, **66**, No. 11, 80 (1968).
5. W. Riedel, *Galvanotechnik*, **57**, 579 (1966).
6. R. J. Ryan, T. E. McCurdy, and N. E. Wolff, *RCA Rev.*, **29**, 582 (1968).
7. E. B. Saubestre, L. J. Durney, J. Hajdu, and E. Bastenbeck, *Plating*, **52**, 982 (1965).
8. E. B. Saubestre, Society of Automotive Engineers, "Theory and Practice of Plating on Plastic," No. 690090, Jan. 1969.
9. R. R. Smith, *Coating*, Jan. 1967, p. 65.
10. E. Zahn and K. Wiebusch, *Kunstoffe*, **56**, 773 (1966).

Measurement of the Throwing Power of Electrolytes Used in Electrochemical Machining

P. A. Brook and Q. Iqbal[1]

Department of Metallurgy, University of Nottingham, Nottingham, England

ABSTRACT

A method of measuring the throwing power of solutions under conditions pertinent to electrochemical machining has been developed, based on the Haring-Blum cell. Results on solutions of sodium chloride and sodium chlorate show that the latter has a lower throwing power under the present conditions in agreement with previously reported data. Additions of 0.12% potassium dichromate and of 1% benztriazole to sodium chloride solutions reduced the throwing power to values comparable to those of the chlorate solutions. The results are discussed in terms of passivation effects.

Recent advances in the technology of electrochemical machining (ECM) make increasingly stringent demands on the electrolytes used. Increased productivity calls for higher currents (and current densities) which in turn require electrolytes with greater electrical conductivities. To use the current at the optimum efficiency, the "stray cutting," *i.e.* the anodic dissolution from areas not directly opposite the cathode, must be reduced to a minimum and, for ease of tool design, a very close correspondence between the tool and the final machined anode is required. For many years, electroplaters have been concerned with a related problem and have measured the ability of a solution to give a deposit over a complex cathode by its "throwing power." Normally a uniform deposit is required, corresponding to a throwing power of 100%. In the case of ECM a low, or even negative, throwing power is required to reduce stray cutting, which could be eliminated when the throwing power approaches $-\infty$.

Thus if we want to machine a simple re-entrant (Fig. 1) using a tool EFGHJK and an anode ABDC, the current density, and hence dissolution, should be large across BD opposite GH but should be zero across

[1] On study leave from West Pakistan University of Engineering and Technology, Lahore.

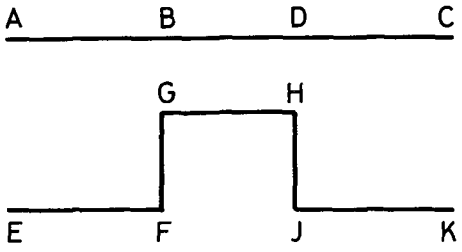

Fig. 1. Arrangement of nonuniform electrodes

AB and DC. The reverse problem of deposition onto EFGHJK requires a uniform current density over the whole surface.

The throwing power of a plating bath is normally measured in a Haring-Blum cell (1) and calculated by means of one of the following formulas (1-4):

$$TP = ((P - M)/P)\ 100 \quad [1]$$

$$TP = ((P - M)/(P - 1))\ 100 \quad [2]$$

$$TP = ((P - M)/(P + M - 2))\ 100 \quad [3]$$

where P is the linear ratio, *i.e.* the ratio of the distances of the equipotential plane parallel cathodes from the anode, and M is the metal distribution ratio, *i.e.* ratio of the weights of the metal deposited on the cathodes. The advantages and disadvantages of these formulas have been discussed frequently and it is sufficient to say that [3] is in general use in the U.K.

The arguments (4) used to support formula [3] for throwing power in electrodeposition have an equal validity when anodic processes are being discussed, and in this paper all throwing powers have been calculated on this formula with the minor alteration that the metal distribution ratio is now the ratio of weight of metal dissolved from the nearer anode/weight of metal dissolved from the farther anode.

The Haring-Blum cell itself has a number of disadvantages but it does enable throwing power to be described in a quantitative fashion.

The use of a similar cell for measuring the throwing power of ECM electrolytes seems desirable but the normal Haring-Blum cell is not immediately useful for ECM measurements because (*a*) the anode-cathode separations are of the order of inches and (*b*) it is essential to be able to measure the electrolyte flow rate in the interelectrode gap.

This paper describes a modified Haring-Blum cell suitable for ECM electrolytes and some results are reported.

Experimental

A rectangular two-compartment cell was designed and built from Perspex to take the above factors into account. A cross section (not to scale) is shown in Fig. 2 and the associated flow system in Fig. 3. This arrangement allows the flow rates in the two compartments to be controlled and measured independently. The bulk flow rate, 0.7 liter/min, was kept constant through both compartments as it was thought that this situation corresponded most closely with that obtaining during practical machining.

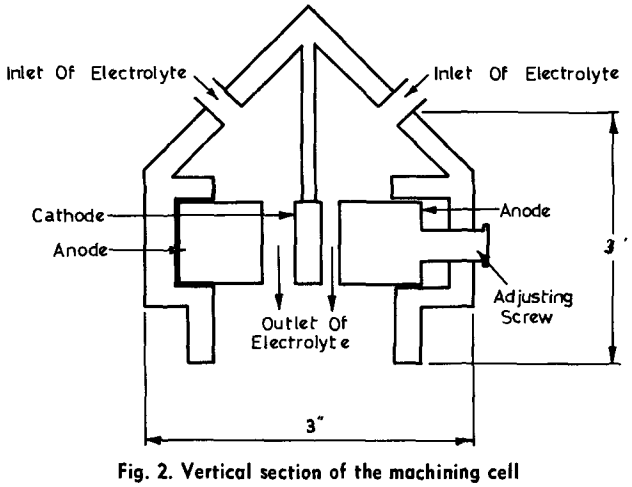

Fig. 2. Vertical section of the machining cell

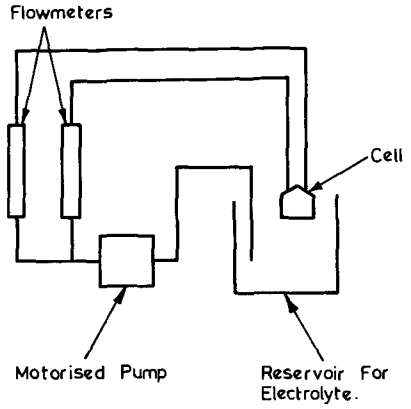

Fig. 3. Layout of the apparatus

The cell voltage required to maintain the working current density of 15 A/in.^{2} varied between 2 and 10V.

The linear ratio (the ratio of the two anode-cathode separations) was usually kept at 5:1 but, where necessary, variations from this were made by the use of insulated packing. The smaller anode-cathode separation was either 0.005 or 0.010 in. and the gap depth 0.5 in.

The cathodes, made from copper, and the anodes, from 18/8 stainless steel,[2] were ½ x ½ x 2 in. The electrodes were masked on the sides and on the working faces so that the exposed area was 1 in.^{2}. The metal distribution ratio was calculated from the weight losses of the two anodes after 2 min machining.

The electrolytes were made of A. R. material to a total volume of 8 liters and were discarded after 5 runs. Conductivities of the electrolyte were measured by means of a standard conductivity bridge.

Results and Discussion

The results are shown in Tables I and II. There is some degree of scatter but, with one or two exceptions, the results are reproducible within ~5%. A correlation was sought between throwing power and specific conductivity and, while some evidence of a positive correlation was obtained, it was not strong enough to warrant further discussion at this stage.

The results from Table I indicate that sodium chlorate has a lower throwing power than sodium chloride,

[2] Complete analysis of the steel is: C, 0.08%; Si, 0.58%; Mn, 0.88%; S, 0.174%; P, 0.029%; Ni, 8.78%; Cr, 17.81%; and Ti, 0.46%.

Table I. Throwing power results

	Temp, °C \ Smaller gap	Concentrations: 5% 0.005 in.	5% 0.010 in.	20% 0.005 in.	20% 0.010 in.	Saturated 0.005 in.	Saturated 0.010 in.
$NaClO_3$	25	−13	7	21	−14	4	10
		−21	6	23	−25	4	16
			3				14
	40	21	10	31	23	−3	−9
		18	18	29	19	−7	−13
		22			21	−11	
					11		
NaCl	25	26	19	63	56	45	43
		11	12	67	48	56	45
	40	63	39	67	60	63	41
		61	41	66	56	61	43
NaCl + 0.12% K_2CrO_7	25	−25					
		−22					
NaCl + 1% BTZ	25	−17					
		−15					

Table II. Linear ratios and metal ratios for 20% NaCl and 20% $NaClO_3$ at 25°C

Linear ratio	Solution: NaCl (Metal ratio)	Solution: $NaClO_3$ (Metal ratio)
5	1.8	3.6
7	2.6	7.8
9	3.2	10.0
12	4.2	20.0
Throwing index	3.67	0.48

confirming the results of Laboda and McMillan (5). At the lower concentrations temperature increases have the effect of increasing throwing power, but at higher concentrations temperature increases produce only small changes in the case of chloride solutions or a decrease in the chlorate solutions. The effects of concentration changes are variable. The result of increasing the absolute gap width while retaining the initial linear ratio is generally to decrease the throwing power. This effect is not linearly dependent on the absolute gap width, since results reported by Cuthbertson and Turner (6) indicate that with gap width in the region of 0.05-0.15 in. the throwing power increases with increasing gap width.

The finish of all the machined anodes was that of a lightly etched surface with no marked grain boundary attack, with the exception of the nearer anodes machined in the saturated solutions of sodium chlorate which showed some regions of polishing. This would suggest that the dissolution, in the majority of the reported cases, takes place according to the prepolishing regime obtained on a typical Jacquet curve.

A few results, obtained for nitrate solutions under the same conditions, generally confirm these trends. The throwing power of nitrate solutions is intermediate between chloride and chlorate solutions, but one or two values are lower than the values for the corresponding chlorate solutions. This is not in entire agreement with Laboda and McMillan but this apparent contradiction may be a result of the different measuring techniques.

The effects of chlorate ions have been discussed in terms of passivation of the anode in the regions of low current density (7). If this is the case then the deliberate addition of suitable passivators to, for example, sodium chloride solutions should have the result of reducing the throwing power. Two such additions were made, benztriazole (BTZ), which is an efficient passivator for copper (8), and potassium dichromate. In both cases these additions, at the concentrations shown in Table I, markedly decrease the throwing power of chloride solutions; the effect in the case of potassium dichromate is very large. The additions of BTZ and sodium dichromate had no visual effect on the surface finish which were again lightly etched. The amounts of metal dissolved from the nearer anodes were not significantly altered by the presence of the two additions, but the metal dissolved from the farther anodes was reduced by a factor of ~2. Hence the metal removal rates of the nearer anodes remain virtually unchanged, while those of the farther anodes are reduced. These observations seem to confirm the hypothesis that the reduction in throwing power is associated with passivation in the low current regions. The probable consumption of BTZ at the electrodes makes it unlikely that this observation will be of practical use. A further consequence to the effect of chromate ions on the throwing power is that the throwing power of a machining electrolyte would be expected to change during its life due to a progressive build-up of chromate ions derived from the chromium present in suitable anode materials, while the presence in solution of other machining products would have related effects. Aged chloride solutions used elsewhere in our laboratory were examined for the presence, or otherwise, of chromate ions and tests indicated that chromate was present in these solutions at the same order of concentration as that used for the throwing power measurements previously. This change of throwing power could be responsible in part for the "aging" of electrolytes which occurs in practice when the machining properties change with increasing time of use.

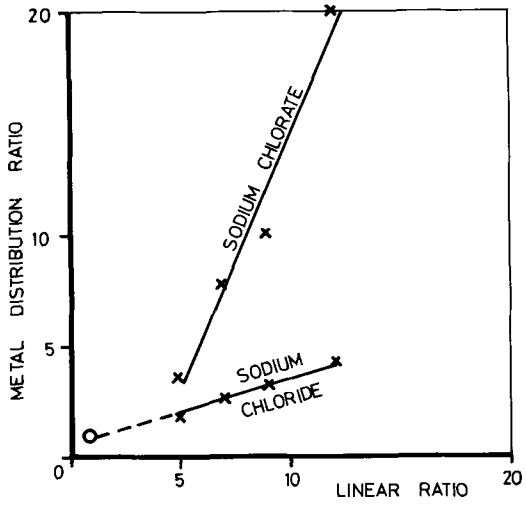

Fig. 4. Throwing index plot

The work of Jellinek and David (9) shows that some of the ambiguities associated with the use of the concept of "throwing power" can be resolved by use of the throwing index which is obtained by plotting the metal ratios against a range of linear ratios. The reciprocal of the gradient of the line is described as the "throwing index," the major advantages of which are that (a) a single number is obtained which is characteristic of a range of linear ratios, and (b) the throwing index is obtained from the number of experimental points thus reducing the effects of experimental error. The solution with a good throwing power gives a line which is nearly horizontal and one with a poor throwing characteristic will give a steeper gradient. The present work was extended to include this concept by measuring the metal ratios for linear ratios between 5 and 12 for 20% NaCl and $NaClO_3$ at 25°C. The results, shown in Table II and Fig. 4, give reasonably linear plots. All the curves should go through the point represented by the linear ratio equal to 1 and the metal distribution ratio equal to 1 and a linear extrapolation of the data for the sodium chloride solutions does indeed do so, but this is not the case for the chlorate solutions. The value for 20% sodium chloride is well in the range ~1 to 10 reported by Jellinek and David for electroplating solutions, but the result for the chlorate solution, while confirming the earlier throwing power work, is outside the range quoted. Again this confirms the results of Laboda and McMillan.

Conclusions

It has been shown that throwing power of machining electrolytes can be measured with a fair degree of reproducibility. The improvements obtained by using the $NaClO_3$ electrolyte reported elsewhere have been confirmed for the anodic material used in the present work. The mechanism of the chlorate improvement is probably due to passivation effects, in agreement with the effects of additions of other passivators such as BTZ and chromate ions.

The use of the throwing index has been investigated and shown to give reasonable results.

Acknowledgments

We would like to thank the Ministry of Technology and the University of Engineering and Technology, Lahore, West Pakistan, for financial support to Q.I. and Dr. P. J. Boden for many helpful discussions.

Manuscript submitted Dec. 19, 1968; revised manuscript received June 8, 1969.

Any discussion of this paper will appear in a Discussion Section to be published in the June 1970 JOURNAL.

REFERENCES

1. H. E. Haring and W. Blum, *Trans. Electrochem. Soc.*, **44**, 313 (1923).
2. A. H. Heatley, *ibid.*, **44**, 283 (1923).
3. L. C. Pan, *ibid.*, **58**, 423 (1930).
4. S. Field, *J. Electrodep. Tech. Soc.*, **9**, 144 (1934).
5. M. A. Laboda and M. L. McMillan, *Electrochem. Technol.*, **5**, 340 (1967).
6. J. W. Cuthbertson and T. S. Turner, *The Prod. Eng.*, **5**, 346 (1967).
7. M. L. McMillan and M. A. Laboda, *Electrochem. Technol.*, **5**, 346 (1967).
8. J. Dugdale and J. B. Cathe, *Corrosion Sci.*, **3**, 69 (1963).
9. R. V. Jellinek and H. F. David, *This Journal*, **104**, 279 (1957).

Multilayer Theory of Correction Factors for Spreading-Resistance Measurements

T. H. Yeh* and K. H. Khokhani

IBM Components Division, East Fishkill Facility, Hopewell Junction, New York

ABSTRACT

The spreading-resistance technique has shown the versatility of determining either the thickness of diffused or epitaxial layers or establishing the impurity profiles for various multilayered silicon structures. However, correction factors must be applied to the measured spreading-resistance values in order to get the corrected resistivities. The calculation for the correction factors based on the unilayer step-junction theory has been reported previously by the authors. In this paper, the calculation of the correction factors based on the multilayer step-junction theory and the utilization of a computer for such calculations are presented.

The calculation of the correction factors based on the assumption of the unilayer step-junction theory, for the resistance values measured on silicon layers by the spreading-resistance technique, was presented in an earlier report (1, 2). The unilayer step-junction theory assumes that the resistivity is homogeneous throughout the thickness of each structure below the point of measurement, and that the resistivity changes at an interface are abrupt (1, 4). This assumption was used extensively to establish the impurity profile for the measurements made on N(epitaxial)/N+ (substrate) silicon structure (1, 2).

For such a structure, the measured spreading-resistance values are converted to resistivity values from the calibration curve (1, 2), and plotted against distance as shown in Fig. 1. The calculation of correction factors is based on a two-layer problem as shown in Fig. 2, according to the following equation:

$$R_{S.R.} = \frac{\Delta V}{I} = \frac{\rho_1}{4r_0}\left\{\frac{4}{\pi}\int_0^\infty \left[\frac{1 + K_1 e^{-2H_1X}}{1 - K_1 e^{-2H_1X}}\right] \sin(X) \left[\frac{J_1(X)}{X^2} - \frac{J_0\left(\frac{S}{2}X\right)}{X} + \frac{J_0(SX)}{2X}\right] dX\right\} \quad [1]$$

where

$R_{S.R.}$ = Spreading resistance

$K_1 = \dfrac{\rho_2 - \rho_1}{\rho_2 + \rho_1}$

$S = 2s/r_0$

$H_1 = h_1/r_0$

s = Probe spacing

r_0 = The effective radius of contact of the probe

X = Integration parameter

J_1, J_0 = Bessel function

The terms within the curl bracket of Eq. [1] are generally labeled as a correction factor, C.F. The corrected resistivity value is then given by the following expression:

$$\rho_{1\ \text{corrected}} = \frac{\rho_1}{\text{C.F.}} \quad [2]$$

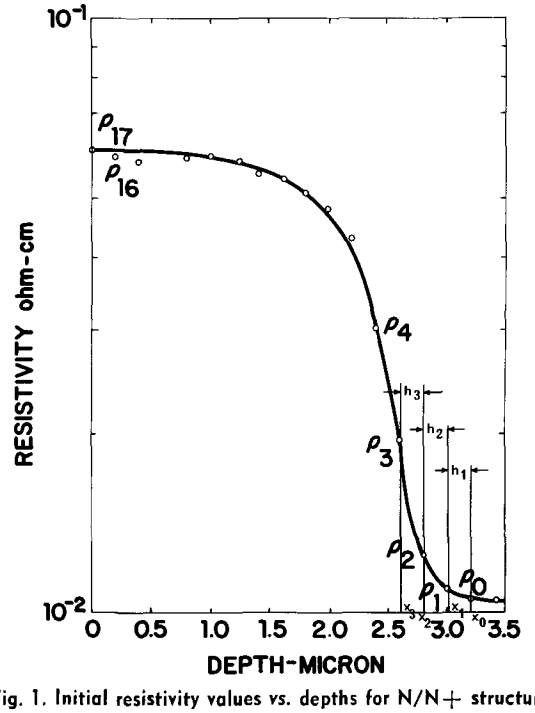

Fig. 1. Initial resistivity values vs. depths for N/N+ structure

* Electrochemical Society Active Member.

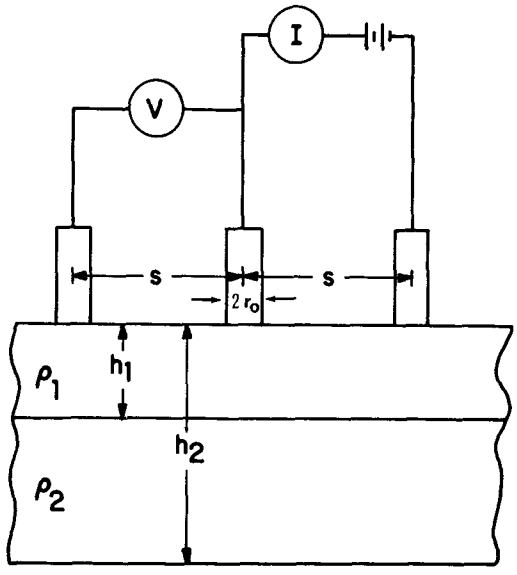

Fig. 2. Spreading resistance technique on a two-layered structure

The first measured resistivity to be corrected is labeled ρ_1, which actually is the last measurement in the N/N+ structure, and this resistivity is assumed to be uniform throughout the layer thickness of $x_0 - x_1 (= h_1)$. The resistivity change at the interface is abrupt, and the resistivity of the substrate can be assumed for ρ_0. The K_1 value in Eq. [1] for this problem is equal to $\rho_0 - \rho_1/\rho_0 + \rho_1$. Upon determining the correction factor, the resistivity is corrected using Eq. [2]. This corrected resistivity value $\rho_{1\ \text{corrected}}$ may then be used to find a new effective radius of contact, r_0, from the calibration curve (1, 2), a new correction factor, and a new corrected resistivity. This procedure is repeated to get an exact value of resistivity (*e.g.*, until either the r_0 value or the correction factor does not change), because the r_0 value initially obtained from the calibration curve for the first correction factor calculation is not necessarily exact.

Because of the unilayer step-junction assumption, neither this corrected resistivity, $\rho_{1\ \text{corrected}}$, nor its initial resistivity, ρ_1, are utilized when the second measured resistivity, ρ_2, is corrected. For correcting ρ_2, it is assumed that the resistivity, ρ_2, is homogeneous throughout its thickness $x_0 - x_2 (= h_1)$, even though we know that within its thickness one of the layers has a different resistivity value, $\rho_{1\ \text{corrected}}$. The calculation of the correction factor for ρ_2 is again evaluated by Eq. [1] using the K_1 value of $\rho_0 - \rho_2/\rho_0 + \rho_2$.

Undoubtedly, certain accuracy of the correction factor is sacrificed for each of the subsequent resistivity values, such as $\rho_3, \rho_4 \ldots \rho_{17}$ for the structure because of the unilayer step-junction assumption. This is especially true for the corrected value of ρ_{17}, because in the calculation of its correction factor this resistivity, ρ_{17}, is assumed to be uniform throughout the total thickness, even though there are 16 layers of corrected resistivity values, $\rho_{1\ \text{corrected}} \ldots \rho_{16\ \text{corrected}}$ below ρ_{17}.

Obviously, if one uses the corrected resistivity values to obtain a correction factor for any one of the measured values, *e.g.* utilizing $\rho_{1\ \text{corrected}}$ and $\rho_{2\ \text{corrected}}$ to correct ρ_3, then the value $\rho_{3\ \text{corrected}}$ should be more accurate than the one without the consideration of the values of $\rho_{1\ \text{corrected}}$ and $\rho_{2\ \text{corrected}}$.

Multilayer Theory

However, if one wants to use the preceding corrected resistivities for the calculation of the correction factor for the subsequent initial resistivity, one must use the multilayer step-junction theory to solve the problem. The geometry is shown in Fig. 3. The solution to LaPlace's equation in cylindrical coordinate

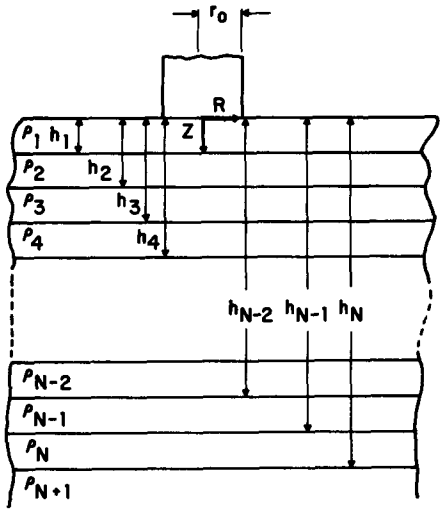

Fig. 3. Geometry for the multilayered problem

for this problem is:

$$R_n = \frac{V_n(R,Z)}{I} = \frac{\rho_n}{2\pi r_0} \left\{ \int_0^\infty \frac{e^{-XZ} \sin X\, J_0(RX)}{X}\, dX + \int_0^\infty \frac{{}_N\theta_n\,(X/r_0)\, e^{-XZ} \sin X\, J_0(RX)}{X}\, dX + \int_0^\infty \frac{{}_N\psi_n\,(X/r_0)\, e^{XZ} \sin X\, J_0(RX)}{X}\, dX \right\}$$

$$n = 1, 2, 3 \ldots N \quad [3]$$

The boundary conditions for this type of problem are relatively standard with the exception of the current distribution under the contact. These boundary conditions are:

Surface:

$$\frac{\partial V_1(R,Z)}{\partial Z} = 0 \text{ for } R > r_0,\ Z = 0 \quad [4]$$

$$\frac{\partial V_1(R,Z)}{\partial Z} = -\frac{I\rho_1}{2\pi r_0 (r_0^2 - R^2)^{1/2}} \text{ for } R \leq r_0,\ Z = 0 \quad [5]$$

These first two conditions relate to the field at the surface. Equation [4] states that there is no current flow out of the surface away from the contact. Equation [5] is developed from considerations of the current flow under a flat circular contact on an infinite geometry (5).

Region 1:

$$\lim_{R \to \infty} V_1(R,Z) = 0 \quad [6]$$

First interface:

$$\frac{1}{\rho_1}\frac{\partial V_1(R,Z)}{\partial Z} = \frac{1}{\rho_2}\frac{\partial V_2(R,Z)}{\partial Z} \quad [7]$$

$$V_1(R,Z) = V_2(R,Z) \text{ for } Z = h_1 \quad [8]$$

The equations at the interfaces state that the current density must be the same across the boundary and that the potential is continuous.

Region 2:

$$\lim_{R \to \infty} V_2(R,Z) = 0 \quad [9]$$

Second interface:

$$\frac{1}{\rho_2}\frac{\partial V_2(R,Z)}{Z} = \frac{1}{\rho_3}\frac{\partial V_3(R,Z)}{\partial Z} \quad [10]$$

$$V_2(R,Z) = V_3(R,Z) \text{ for } Z = h_2 \quad [11]$$

and similarly for Region 3, 4 . . . N.

Region N:

$$\lim_{R\to\infty} V_N(R,Z) = 0 \quad [12]$$

$$\lim_{Z\to\infty} V_N(R,Z) = 0 \quad [13]$$

These boundary conditions are then imposed on the solutions given in Eq. [3] to specify

$${}_N\theta_n\left(\frac{X}{r_0}\right) \text{ and } {}_N\psi_n\left(\frac{X}{r_0}\right)$$

The application of the boundary conditions results in a series of linear equations:

$${}_N\theta_1\left(\frac{X}{r_0}\right) - {}_N\psi_1\left(\frac{X}{r_0}\right) = 0 \quad [14]$$

$$e^{-2H_nX} \cdot {}_N\theta_n\left(\frac{X}{r_0}\right) + {}_N\psi_n\left(\frac{X}{r_0}\right) - e^{-2H_nX} \cdot {}_N\theta_{n+1}\left(\frac{X}{r_0}\right) - {}_N\psi_{n+1}\left(\frac{X}{r_0}\right) = 0 \quad [15]$$

$$-e^{-2H_nX} \cdot {}_N\theta_n\left(\frac{X}{r_0}\right) + {}_N\psi_n\left(\frac{X}{r_0}\right) + \beta_n \cdot e^{-2H_nX}\, {}_N\theta_{n+1}\left(\frac{X}{r_0}\right) - \beta_n \cdot {}_N\psi_{n+1}\left(\frac{X}{r_0}\right) = (1-\beta_n)\, e^{-2H_nX} \quad [16]$$

$${}_N\psi_{n+1}\left(\frac{X}{r_0}\right) = 0 \quad [17]$$

where N = Number of layers of different resistivity and finite thickness

n = Index, from 1 to N

$$\beta_n = \frac{\rho_n}{\rho_{n+1}}$$

$$H_n = \frac{h_n}{r_0}$$

and Region $N + 1$ is infinitely thick.

Using the simplified notation

$${}_N\theta_n\left(\frac{X}{r_0}\right) = {}_N\theta_n \quad [18]$$

$$e^{-2H_nX} = E_n \quad [19]$$

The above equations become:

$${}_N\theta_1 - {}_N\psi_1 = 0 \quad [20]$$

$$E_n \cdot {}_N\theta_n + {}_N\psi_n - E_n \cdot {}_N\theta_{n+1} - {}_N\psi_{n+1} = 0 \quad [21]$$

$$-E_n \cdot {}_N\theta_n + {}_N\psi_n + \beta_n E_n \cdot {}_N\theta_{n+1} - \beta_n \cdot {}_N\psi_{n+1} = (1-\beta_n)E_n \quad [22]$$

$${}_N\psi_{n+1} = 0 \quad [23]$$

For example, if $N = 2$, the set of linear equations becomes:

$${}_2\theta_1 - {}_2\psi_1 = 0 \quad [24]$$

$$E_1 \cdot {}_2\theta_1 + {}_2\psi_1 - E_1 \cdot {}_2\theta_2 - {}_2\psi_2 = 0 \quad [25]$$

$$-E_1 \cdot {}_2\theta_1 + {}_2\psi_1 + \beta_1 E_1 \cdot {}_2\theta_2 - \beta_1 \cdot {}_2\psi_2 = (1-\beta_1)E_1 \quad [26]$$

$$E_2 \cdot {}_2\theta_2 + {}_2\psi_2 - E_2 \cdot {}_2\theta_3 - {}_2\psi_3 = 0 \quad [27]$$

$$-E \cdot {}_2\theta_2 + {}_2\psi_2 + \beta_2 E_2 \cdot {}_2\theta_3 - \beta_2 \cdot {}_2\psi_3 = (1-\beta_2)E_2 \quad [28]$$

$${}_2\psi_3 = 0 \quad [29]$$

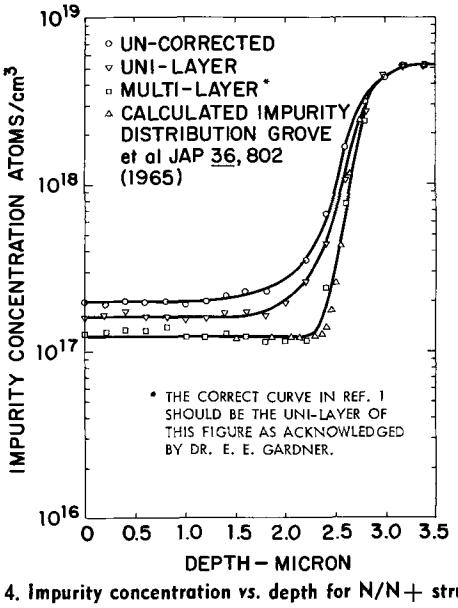

Fig. 4. Impurity concentration vs. depth for N/N+ structure

There are six equations and six unknowns. The matrix is, with the columns given by:

${}_2\theta_1$	${}_2\psi_1$	${}_2\theta_2$	${}_2\psi_2$	${}_2\theta_3$	${}_2\psi_3$	Constant
1	−1	0	0	0	0	0
E_1	1	$-E_1$	−1	0	0	0
$-E_1$	1	$\beta_1 E_1$	$-\beta_1$	0	0	$(1-\beta_1)E_1$
0	0	E_2	1	$-E_2$	−1	0
0	0	$-E_2$	1	$\beta_2 E_2$	$-\beta_2$	$(1-\beta_2)E_2$
0	0	0	0	0	1	0

Determinants may then be formed to solve for any of the θ's and ψ's. In general, the matrix will be $2N + 3$ by $2N + 2$. The determinants will be $2N + 2$ by $2N + 2$.

Prior to this paper, the multilayer theory has never been tested because, for a sample having 17 layers (as shown in Fig. 1) to be considered, one must solve an ever-increasing number of determinants by hand, starting with a 4 by 4 matrix then steadily expanding to a 37 by 36 matrix. It is almost an unthinkable task. However, with the aid of a computer, this multilayer approach is feasible. For a 17-layer problem it took an IBM 7090 computer about 10 min to obtain 17 corrected resistivities. These values were then converted to net impurity concentration according to Irvin's curve (6), and plotted against the depth as shown in Fig. 4. In the same figure, the uncorrected impurity profile and the corrected profile obtained by the unilayer step-junction approach plus the calculated impurity profile according to the method of Grove *et al.* (7) are also included for comparison. The agreement between the multilayer corrected profile and the one calculated according to Grove *et al.* is remarkably good.

A computer program for obtaining 17 corrected resistivities on a typical N(epitaxial)/N+ (substrate) structure is written in Fortran language.[1] The computer output for the sample shown in Fig. 4 is given in Table I.

Conclusion

The calculation of the correction factors for spreading-resistance probe measurements based on the multilayer step-junction theory and the utilization of a computer for such calculations are presented. A detailed computer program, written in Fortran language, for obtaining 17 corrected resistivities on a N/N+ silicon structure is also given. The advantage and the importance of using multilayer theory instead of unilayered theory for the calculation of the correction factors are discussed.

Acknowledgment

The authors gratefully acknowledge the helpful suggestions provided by P. A. Schumann, Jr., and C. M. Sakkas.

[1] This computer program is available by request to the authors.

Table I. Evaluations based on multilayer theory iterative approach

Sample AR 1458-5 N/N+ 0.20 μ/step N(111) type
Probe spacing = 0.6350E-01 cm
Step size = 0.2000E-04 cm
Material type is N111

Number of layer	Depth from surface	Spreading resistance	Resistivity	Corrected Resistivity	Impurity concentration
1	0.00000E-38	0.19000E 03	0.60933E-01	0.68391E-01	0.14851E 18
2	0.20000E-04	0.18500E 03	0.59567E-01	0.66682E-01	0.15560E 18
3	0.40000E-04	0.18000E 03	0.58200E-01	0.62681E-01	0.17438E 18
4	0.60000E-04	0.18500E 03	0.59567E-01	0.71522E-01	0.13676E 18
5	0.80000E-04	0.17000E 03	0.55467E-01	0.57057E-01	0.20734E 18
6	0.10000E-03	0.18500E 03	0.59567E-01	0.70420E-01	0.14073E 18
7	0.12000E-03	0.18000E 03	0.58200E-01	0.71321E-01	0.13747E 18
8	0.14000E-03	0.17000E 03	0.55467E-01	0.67213E-01	0.15334E 18
9	0.16000E-03	0.16500E 03	0.54100E-01	0.66521E-01	0.15629E 18
10	0.18000E-03	0.16500E 03	0.54100E-01	0.77548E-01	0.11783E 18
11	0.20000E-03	0.14000E 03	0.47473E-01	0.70083E-01	0.14198E 18
12	0.22000E-03	0.12000E 03	0.42287E-01	0.77457E-01	0.11809E 18
13	0.24000E-03	0.75000E 02	0.29500E-01	0.58035E-01	0.20095E 18
14	0.26000E-03	0.40000E 02	0.18687E-01	0.36169E-01	0.48003E 18
15	0.28000E-03	0.24000E 02	0.12632E-01	0.19504E-01	0.14970E 19
16	0.30000E-03	0.19000E 02	0.10439E-01	0.11846E-01	0.37501E 19
17	0.32000E-03	0.18000E 02	0.99707E-02	0.99944E-02	0.51282E 19
18	0.34000E-03	0.18000E 02	0.99707E-02		

Manuscript submitted Sept. 30, 1968; revised manuscript received June 7, 1969.

Any discussion of this paper will appear in a Discussion Section to be published in the June 1970 JOURNAL.

REFERENCES

1. E. E. Gardner, P. A. Schumann, Jr., asd E. F. Gorey, IBM Tech. Report 22.394, May 24 ,1967, Electrochem. Soc. Symposia Proceedings "Measurement Techniques for Thin Films," April 1967.
2. T. H. Yeh and K. H. Khokhani, to be published.
3. P. A. Schumann, Jr., and E. E. Gardner, Paper 165 presented at Electrochem. Soc. Meeting, Philadelphia, Oct. 9-14, 1966.
4. P. A. Schumann, Jr., and E. E. Gardner, To be published in *Solid State Electronics*.
5. P. A. Schumann, Jr., and E. E. Gardner, *This Journal*, **116**, 87 (1969).
6. J. C. Irvin, *Bell System Tech. J.*, **41**, 387 (1962).
7. A. S. Grove, A. Roder, and C. T. Sah, *J. Appl. Phys.*, **36**, 802 (1965).

Photochromic Spiropyran Resists

M. Orlovic, E. Stone,* and I. M. Pearson*,[1]

Electronics Division, The National Cash Register Company, Hawthorne, California

ABSTRACT

Many photochromic spiropyrans form amorphous continuous films which are colored intensely by u.v. radiation. The colored and uncolored forms display marked differences in solubility in common nonpolar solvents. These properties enable the photochromic spiropyrans to be used advantageously as resists in chemical etching and RF sputter etching processes and in a novel differential adhesion process. Experimental procedures and results are given for applications of these spiropyran resist processes to thin-film pattern preparation in metals, semiconductors, and SiO.

Photochromic (PC) spiropyrans are generally colorless or lightly colored under visible or infrared light, but become intensely colored because of breaking of the bond between the spirocarbon and the pyran-oxygen, when exposed either in liquid (1, 2) or solid (3-5) solution or in amorphous solid form (6) to ultraviolet (u.v.) radiation (no polymerization occurs). The spiropyrans are soluble in polar organic solvents but the colored form is less soluble than the uncolored form in nonpolar solvents such as petroleum ether, methyl cyclohexane, and other saturated hydrocarbons. Moreover, many of these PC substances, *e.g.* the Fischer's base-salicylaldehyde condensation compounds (6) shown in Fig. 1, form continuous amorphous films when deposited either singly or in mixtures from solutions in volatile aromatic hydrocarbons such as benzene or toluene. The amorphous deposits develop persistent and uniform coloration on appropriate u.v. irradiation at ambient temperatures. Figure 2 shows the absorption spectra of the unexposed and u.v.-exposed forms of a typical spiropyran (PCI) deposit at room temperature. Both forms absorb strongly in the u.v.; however, only the colored form does so in the visible.

These film-forming, PC, and solubility properties enable numerous spiropyrans to be utilized advantageously as resists in chemical etching and RF sputter etching processes, and in a novel differential adhesion process, for making thin film patterns in metals, semiconductors, and the insulator, SiO.

Experimental Procedures and Results

Chemical etching.—The procedure for using PC spiropyran resists, similar in many respects to that employed for common photoresists, consists of the following:

1. A thin pattern-material film, approximately 0.1-0.3 μm thick, is laid down on glass (some other rigid, nonporous substrate may be used), generally by evaporation or sputtering in a vacuum system.
2. An amorphous[1] PC film is spin-coated onto the pattern material from a filtered solution in A.R.-grade

* Electrochemical Society Active Member.
*[1] Correspondence should be addressed to this author.
Key words: amorphous films, photochromic spiropyrans, resists, thin films, chemical etching, RF sputter etching, differential adhesion, metals, semiconductors, SiO.

[1] Crystalline films of spiropyrans tend to remain uncolored when exposed to u.v. However, the films of the PC already cited, and many others, can remain amorphous for many days. Some spiropyrans may crystallize unless mixed with a closely related derivative (6) such as PCI.

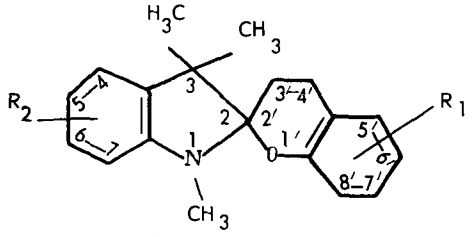

where I. R_1 = 6′-NO_2, 8′-OCH_3
II. R_1 = 5′-Br, 6′-NO_2, 8′-OCH_3
III. R_1 = 6′-NO_2; R_2 = 5-CH_2CH_2OH
IV. R_1 = 6′-NO_2, 8′-OCH_3; R_2 = 5-CH_2CH_2OH
V. R_1 = 5′-Br, 6′-NO_2, 8′-OCH_3; R_2 = 7-C_6H_5
or R_1 and R_2 are hydrogens if not substituted.

Fig. 1. Examples of photochromic spiropyrans which form amorphous films.

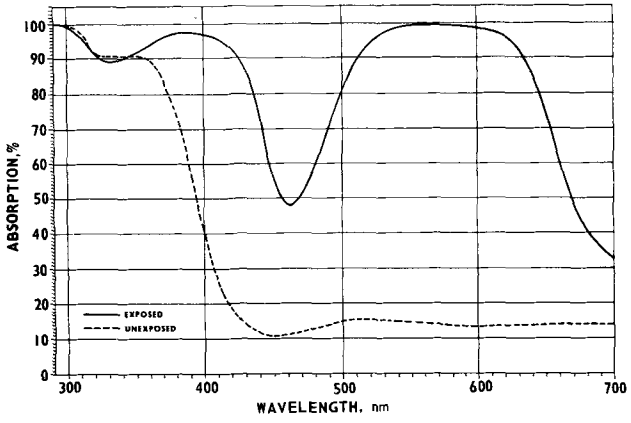

Fig. 2. Absorption spectra at 24°C of 0.6-μm-thick amorphous 1, 3, 3-trimethylindolino-5′-bromo, 6′-nitro, 8′-methoxy-benzospiropyran (PCI).

benzene, preferably in a clean atmosphere, under yellow lighting (u.v. filtered out). The PC film thickness is approximately 0.6 μm when deposited from a 10 w/o (weight per cent) solution in benzene which is spin-coated at 1000 rpm.

3. A mask on a u.v.-transmissive substrate, preferably glass, is laid down on the PC film and a contact print is made using u.v. illumination (< 400 nm). Uncollimated light from a Spectroline Model B-100 BLE (Spectronics Corporation, Westbury, L.I., N.Y.) or Blak-Ray Model X-4 (Ultra-Violet Products, San Gabriel, Calif.) lamp is often satisfactory. Oxygen need not be excluded. Suitable optical densities of 1 or more are achieved with a u.v. energy of 0.5 w-sec. The exposure time can be varied considerably without appreciable effect.

Laser recording instead of contact printing with u.v. may be carried out on the PC material. A u.v. laser, such as the Kr (ion) laser which emits in the 330-360 nm region, seems suitable. Argon and He-Ne lasers which have outputs in the visible are satisfactory if the PC is colored with u.v. before recording, since the maximum absorptions in the visible of the colored forms of most PC spiropyrans of interest lie in the 470-650 nm region.

4. The pattern is washed with petroleum ether (*e.g.*, the 30°-60°C bp fraction)[2] to remove unexposed PC if a negative pattern[3] is desired.

[2] In the case of PCI, the solubility of the unexposed material is ≈0.9 mg/g of this solvent at 24°C. The exposed PCI solubility is ≈0.3 mg/g of solvent.

[3] The capability of making positive images also exists (6). For this purpose, the unexposed PC pattern is treated with conc HCl acid vapor. Both the unexposed and exposed portions of the image form a yellow complex with HCl. However, the exposed PC complex is preferentially soluble in aqueous dil. HCl and can be removed with this reagent.

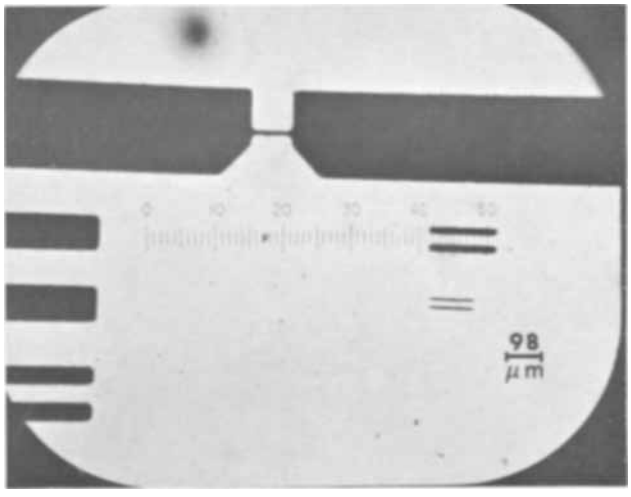

Fig. 3. Pattern etched in 1000Å-thick Cu with 42 w/o $FeCl_3$ for 20 sec. Each micrometer scale division is 19.6 μm.

5. The pattern is etched by dipping or gentle spraying with mild agents to remove the material unprotected by PC. As examples, aqueous solutions of $FeCl_3$ are used to etch Cu, Sn, and permalloy and aqueous $PdCl_2$ to etch Al; HCl vapors convert CdSe to $CdCl_2$ which is then washed off with water.

6. Exposed PC is removed by gentle spraying with acetone, leaving the pattern in the underlying material.

An application of the chemical etching process to the preparation of a Cu pole and rectangle pattern is shown in Fig. 3. The pole gap width is 18.7 μm. The smallest rectangle widths are 5-7.5 μm. The resist material was an equal-weight mixture of 1, 3, 3-trimethylindolino-5′-bromo, 6′-nitro, 8′-methoxy-benzospiropyran (PCI) and 7-phenyl, 1, 3, 3-trimethylindolino-5′-bromo, 6′-nitro, 8′-methoxy-benzospiropyran (PCII). (In general, the PC spiropyrans specific-

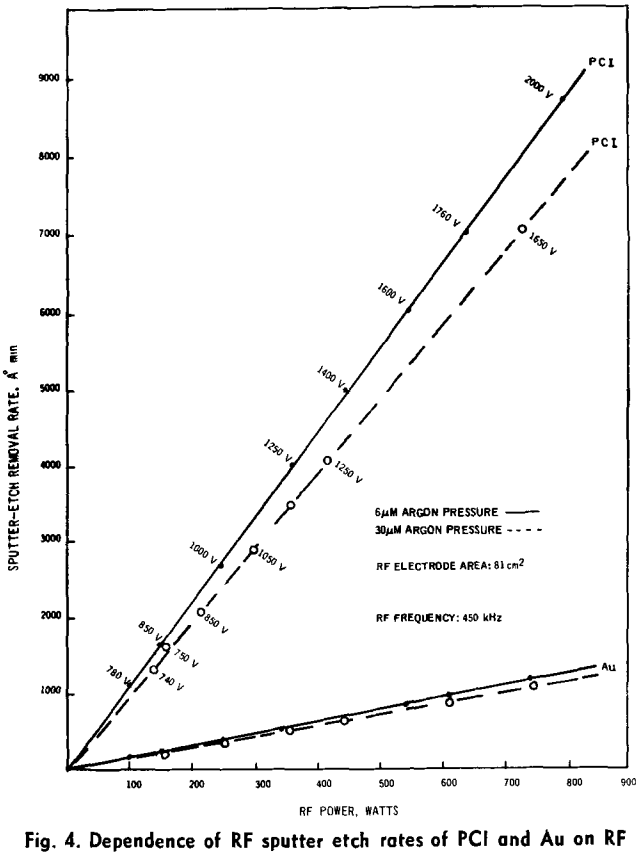

Fig. 4. Dependence of RF sputter etch rates of PCI and Au on RF power at 6 and 30 μm argon pressure.

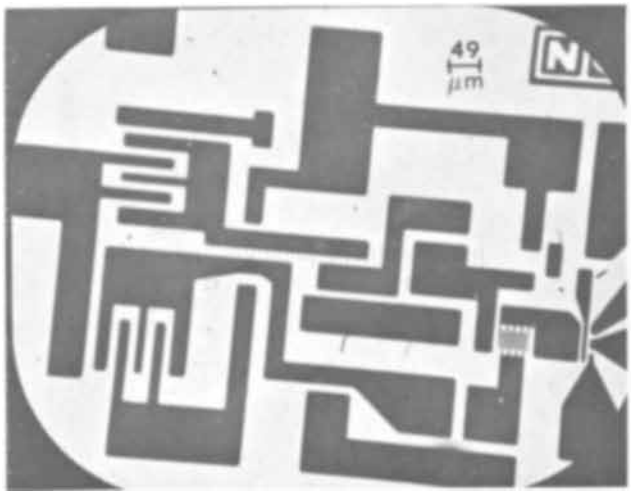

Fig. 5. RF sputter etched TTL circuit in 850Å-thick Au. Each scale division is 9.8 μm.

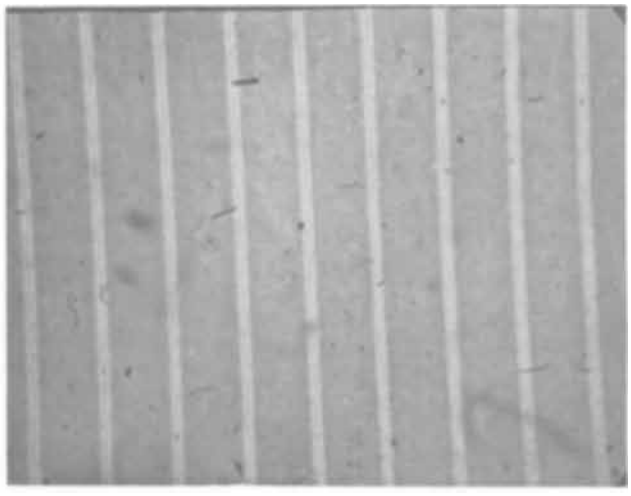

Fig. 6. RF sputter etched He-Ne laser raster in 200Å-thick Au (2.2-μm line widths).

ally referred to in this paper are interchangeable in all the applications described.)

As is true for other chemical etch resist processes, undercutting and pinholing, which impair film continuity, edge acuity, and resolution capability, often occur. However, line widths of ≈8 μm are obtained readily with good feature characteristics, using PC resists.

RF sputter etching.—This PC resist process is similar to chemical etching except that the pattern material from which the unexposed PC has been washed away is not removed by chemical agents, but rather by RF sputtering (7, 8) with argon ions. Unlike chemical etching, RF sputter etching produces straight lines with sharp edges and avoids undercutting.

Plots are shown in Fig. 4 of the dependence on the RF power of the sputter etch rate for u.v.-exposed PCI and for Au films, at two suitable argon pressures (Linde high-purity dry argon, 99.99 +%, was used without further purification). The specific voltages

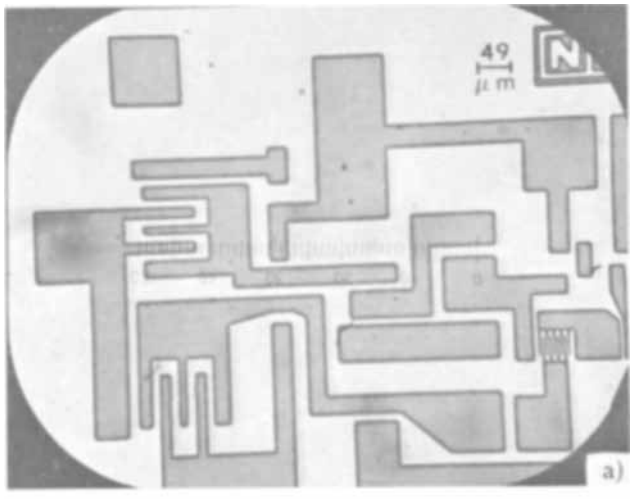

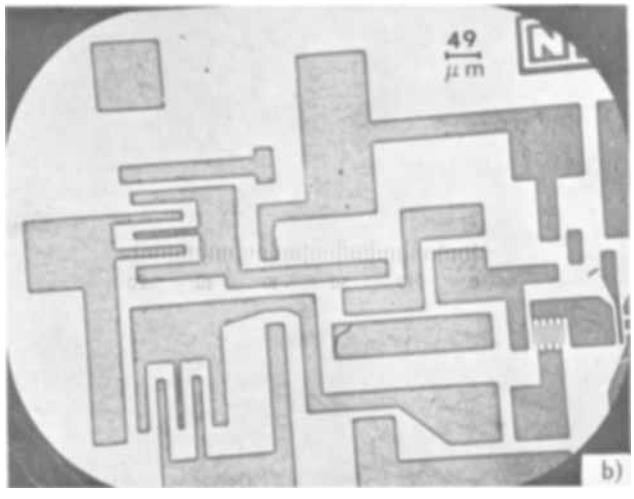

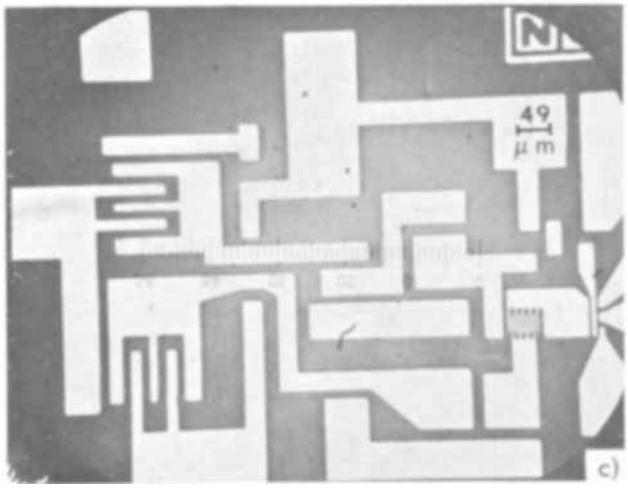

Fig. 7. Differential adhesion TTL pattern in 450Å-thick Al made using RF sputter cleaning of washed PCI image: (a) washed PC image; (b) RF sputter cleaned PC image; (c) Al pattern. Each scale division is 9.8 μm.

are indicated for each data point and other operating conditions are given, including the area of the 10.2-cm-diameter RF electrode. The RF vacuum apparatus employed is otherwise essentially similar to that described previously (7).

The rates for PCI and Au are as much as 10% higher at the lower argon pressure, and are linear functions of the RF power under our conditions. PCI etches at a considerably higher rate than Au. Consequently, the PC film used must be thicker than Au (or other basis materials). In most cases, the PC process is used to make thin-film patterns which are <0.1 μm thick. An initial PCI film thickness of ≈ 0.6 μm is employed at an RF power of 100-200w (power density of 1.2-2.5 w/cm^2).

Comparative tests indicate that, under our conditions, the rate of RF sputter etching of the well-known photoresist, KTFR, is $\approx 20\%$ higher than is the case for Au, and consequently also etches more slowly than PCI.

An application of RF sputter etching using PCI resist and contact printing is shown in Fig. 5. The interconnection pattern of a transistor-transistor logic (TTL) circuit with source and sink was made with 850Å-thick Au for the purpose of demonstration. The small interconnection fingers are 5 μm in width. A pattern in 200Å-thick Au is shown in Fig. 6. This raster was sputter etched after recording with a He-Ne laser on a u.v.-exposed PC coating of 1, 3, 3-trimethylindolino-6'-nitro, 7'-methoxy-benzospiropyran (PCIII) overlying the Au basis film on glass.

Differential adhesion.—Unlike the chemical or RF sputter etching processes, the pattern material in the differential adhesion (DA) process is deposited over the developed, *i.e.* exposed and washed, PC image pattern. Pressure-sensitive adhesive tape, *e.g.* ordinary Scotch tape, is applied to the overlying pattern material and is then pulled away. The material overlying the (exposed) PC is removed in this manner, while the material in contact with the substrate continues to adhere to the latter and delineates the pattern. Careful cleaning of the developed PC image by glow discharge or by RF sputter bombardment prior to overlaying is desirable, to remove traces of unexposed PC and thus ensure good adhesion of the overlay material to the substrate. Unlike chemical or RF sputter etching, the final pattern step in the differential adhesion method can be carried out under relatively simple conditions, well suited for automation.

The DA process works well with materials which adhere sufficiently to the substrate. Substances which are known to readily form oxygen bonds with the substrate seem particularly utilizable.

This process has been tried with both baked and unbaked films, of various thicknesses, of the negative-acting KTFR (Eastman Kodak) and the positive-acting Azoplate AZ-111 (Shipley) photoresists. In all cases, the overlay deposited over the developed photoresist patterns tended to adhere to both the resist and to the glass substrate. Consequently, the PC spiropyrans have a unique advantage over these photoresists in the DA process.

The application of the DA process to the formation of the TTL circuit in 450Å-thick Al is shown in Fig. 7. The beneficial effect of RF sputter cleaning on the PCI image of (a) is shown in (b). Note how the gaps between the interconnection fingers have been cleared. Photograph (c) shows the final evaporated Al over-

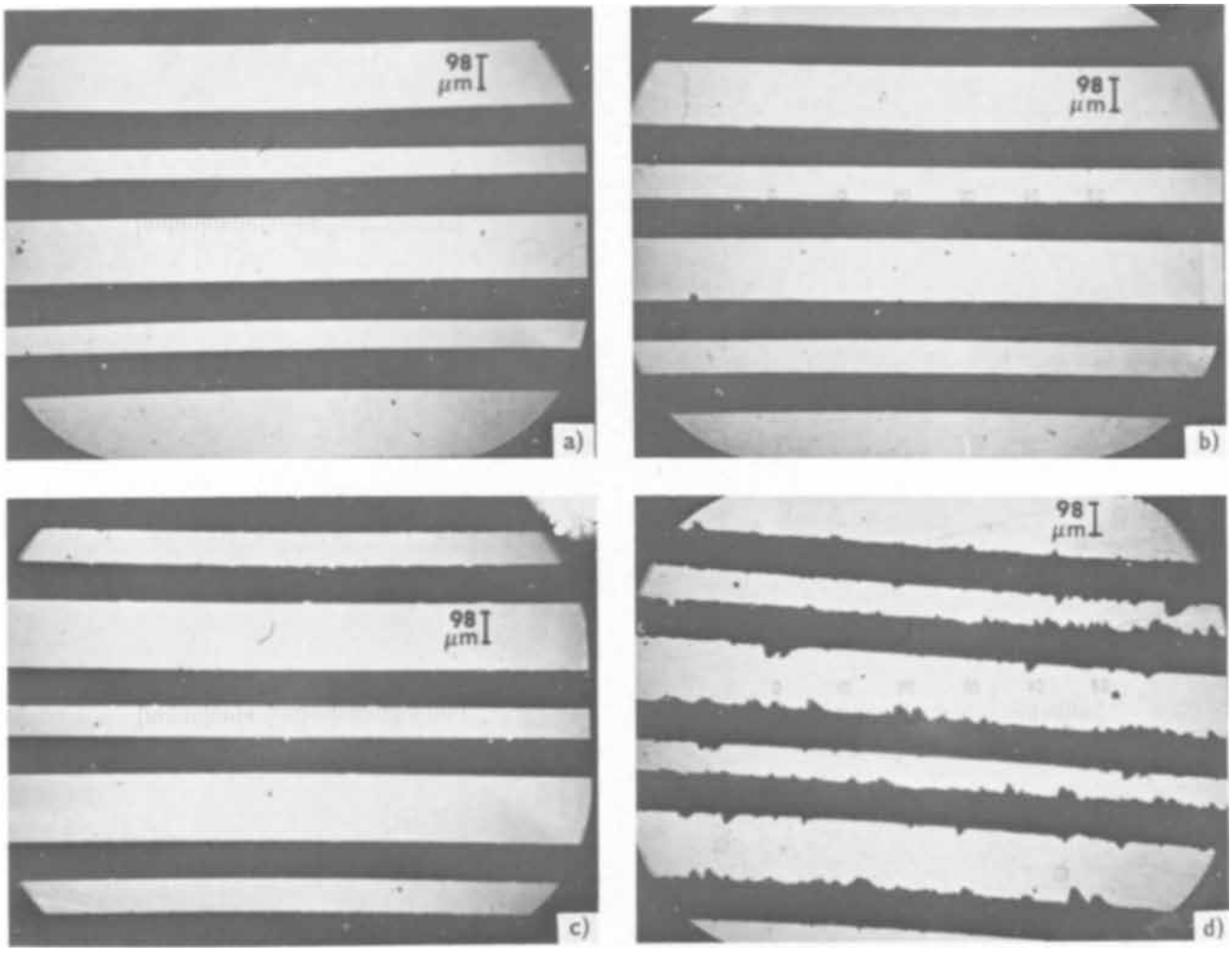

Fig. 8. Dependence of edge acuity of a differential adhesion line pattern on Al overlay thickness: (a) 600Å Al; (b) 1150Å Al; (c) 1650Å Al; (d) 3000Å Al. Each scale division is 19.6 μm.

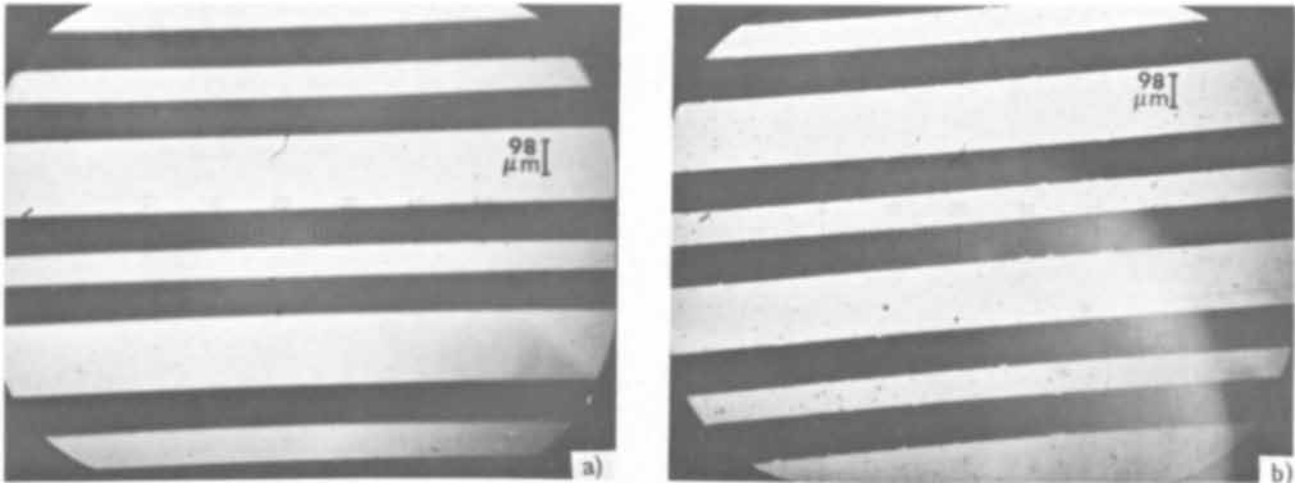

Fig. 9. Dependence of the edge acuity of a differential adhesion line pattern on Al-Ag overlay thickness: (a) 1500Å Al-1500Å Ag; (b) 1750Å Al-1750Å Ag. Each scale division is 19.6 μm.

lay pattern after pressure tape was applied and removed.

The results of a series of eight tests of the preparation by the DA process of thin-film Ta dual pole patterns (using PCIII), which are another version of the pattern shown in Fig. 3, are described in Table I. Measurements of two different pole gap widths are given for the eight samples and for the photo mask employed. Test averages and the standard deviation of a single test are also shown to illustrate the precision of the process in this application.

The dependence of the edge acuity of a DA line pattern (using PCI) on the Al overlay thickness is shown in Fig. 8. The photos were taken with reflected light. The white Al lines are 85 and 185 μm wide, respectively, and the dark spaces are 120 μm wide. The patterns in which the Al is 600 and 1150Å thick, (a) and (b), have good edge acuity. The 1650Å pattern in (c) begins to exhibit some general raggedness. The 3000Å pattern, (d), is very ragged. It thus appears that the maximum thickness of the Al overlay should be <1650Å if optimum line edge acuity is to be obtained. The maximum overlay thickness at which satisfactory edge acuity is obtained can be increased by, *e.g.*, using an Al-Ag bilayer overlay. This is illustrated in Fig. 9. The 1500Å Al-1500Å Ag bilayer (total thickness of 3000Å) shown in (a) has good edge acuity although this thickness is unsatisfactory for Al alone as previously shown. However, the 3500Å Al-Ag bilayer in (b) has some edge raggedness.

A 450Å-thick Al resolution test pattern made by the DA process using PCI is presented in Fig. 10. The photo mask which was employed is a 40:1 reduction of an NBS Microscopy Resolution Test Chart. The No. 10 group has 400 lines/mm; the actual line width in the photograph is 2.45 μm.

Discussion

In all the resist applications described, the PC spiropyrans have the following important advantages over some, or all, commercial photoresists:

Table I. Pole gap widths (in μm) of differential adhesion Ta patterns

Test No.	Pole gap I	Pole gap II
Photo mask	32.3	22.5
1	30.0	23.0
2	29.2	25.0
3	30.2	25.4
4	32.4	23.8
5	34.0	28.0
6	34.8	25.2
7	32.2	25.2
8	32.2	23.8
Test mean	32.0	24.9
Std. dev. of a single test	1.99	1.41

1. The PC exposure time to u.v. light is not critical (because the monomolecular colored material is obtained easily) and is consequently not a troublesome process parameter. Suitable coloration occurs quickly and reproducibly.
2. The PC image pattern is delineated clearly by the intensely colored exposed PC. Contrast is high.
3. Both the unexposed and exposed PC are washed away readily with volatile solvents under normal operating conditions. No mechanical aids or severe stripping procedures are ordinarily required for exposed PC removal.
4. Both the unexposed and exposed PC are recoverable from solutions in the solvents by distillation or evaporation. The exposed form can be decolored by visible or infrared light or mild heating, and may subsequently, be reusable for a number of cycles.
5. The PC solids and their solutions are stable indefinitely when protected from light and heat.

PC spiropyran resists are not as mechanically strong or as chemically inert as, *e.g.*, Kodak photoresists. Reasonable care must be taken to avoid excessive abrasion or shear of the PC films.

The chemical etching resist application is limited mostly to pattern preparation in metals such as those cited previously and bilayers thereof, which can be etched with mild agents such as aqueous $FeCl_3$, dil. HCl and HF acids.

Table II lists the materials which we have thus far utilized satisfactorily in making thin film patterns by

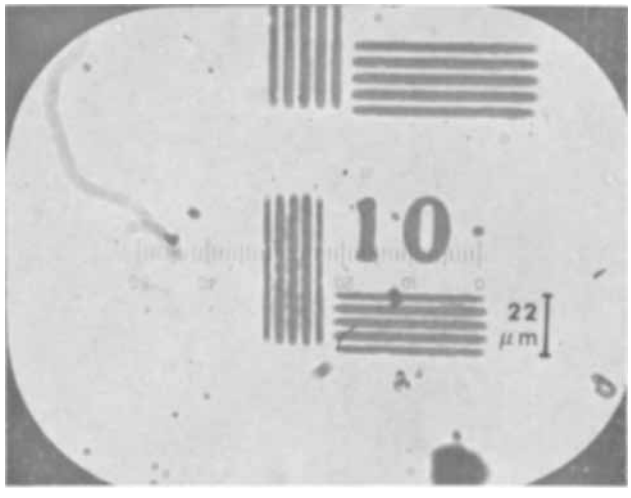

Fig. 10. Al (450Å thick) resolution test pattern made by differential adhesion process (No. 10 group has line width of 2.45 μm). Each scale division is 2.45 μm.

Table II. Materials utilized in PC resist processes

PC resist process	Metals	Semiconductors	Insulator
1. Differential adhesion	Sputtered: Ta, Cr, Cr-permalloy, Cr-Au Evaporated: Al, Ti, Sn, Al-Ag	Evaporated: Ge, CdSe	Evaporated: SiO
2. RF sputter etching	Evaporated: Au, Pb, Zn, Sn, Bi	Evaporated: Ge, CdSe	

the PC spiropyran resist RF sputter etching and DA processes. The list includes a number of substances widely used in microcircuits. Other single and composite materials seem utilizable but have not yet been studied in sufficient detail.

Acknowledgments

The authors wish to thank Dr. H. Schwab and coworkers at NCR-Dayton for providing the PC spiropyrans. We are also indebted to various NCR colleagues for the photo masks employed in this work.

Manuscript submitted March 26, 1969; revised manuscript received June 23, 1969. This was Paper 23 presented at the Boston Meeting, May 5-9, 1968.

Any discussion of this paper will appear in a Discussion Section to be published in the June 1970 JOURNAL.

REFERENCES

1. R. Heiligman-Rim, Y. Hirshberg, and E. Fischer, *J. Phys. Chem.*, **66**, 2465 (1962).
2. J. Kolc and R. S. Becker, *ibid.*, **71**, 4045 (1967).
3. Z. G. Gardlund, *Polymer Letters (J. Polymer Sci., Part B)*, **6**, 57 (1968).
4. G. I. Lashkov, A. V. Shablya, and D. N. Glebovskii, *Opt. Spectry. (USSR) (English Transl.)*, **20**, 95 (1966).
5. A. V. Shablya, K. B. Demidov, and Yu. N. Polyakov, *ibid.*, **20**, 412 (1966).
6. P. L. Foris, U.S. Pat. 3,346, 385, Oct. 10, 1967.
7. P. D. Davidse, *This Journal*, **116**, 100 (1968).
8. R. T. C. Tsui, *SCP and Solid State Tech.*, **10**, 33 (1967).

Technical Note

Electron Probe Microanalysis of Discharged MnO_2 Particles in Relation to Leclanche Battery Performance

K. Miyazaki

Mitsui Mining and Smelting Company, Central Research Laboratories, Mitaka-shi, Tokyo, Japan

Many previous works (1-5) have dealt with the x-ray examination, chemical analysis, and other studies of the discharge products of MnO_2 in simplified Leclanché electrodes as well as alkaline cell systems. There are, however, only a limited number of works that focus attention on the changes in the states of MnO_2 as it functions as depolarizer in actual dry battery service. Among them are the elaborate works of pioneering authors, including Matsuno (6) reporting the existence of Mn_3O_4 in exhausted dry cells, McMurdie (7) finding $Mn_2O_3 \cdot ZnO$ and $ZnCl_2 \cdot 4Zn(OH)_2$, and Copeland and Griffith (8) also describing the formation of $Mn_2O_3 \cdot ZnO$ with the use of actually worked dry cells or the like.

No attempts have been made to examine the interiors of individual MnO_2 particles that have served in the Leclanché cathode mix during actual battery discharge. It was therefore desired to study the micro state of the interior of a very small volume of MnO_2 during discharge. In previous works of the present author (9, 10), the behavior of oxygen in MnO_2 electrodes was followed with an electron probe microanalyzer using Leclanché, as well as alkaline, type wet cells. It was shown that the oxygen atoms of the MnO_2 electrodes were actually released during discharge reactions through the solid phase. The relative concentration of oxygen after discharge was found to be markedly reduced from its initial value. This indicated that the use of microanalytical examination may possibly be a powerful tool in revealing changes in the MnO_2 phase during discharge and especially in determining how and where the discharge reaction proceeds at a thin zone to which application of other analytical means is inconvenient.

In the present paper, the behaviors of MnO_2 particles which were incorporated into Leclanché dry cells were investigated with this tool. Particular attention was given to the battery quality of the MnO_2 ores employed. Three MnO_2 ores were chosen to represent a poorly performing, a fairly well performing, and an excellently performing material, respectively. A series of D-size, pasted-type dry cells with each of these materials as the depolarizer was constructed and the change in the intrastate of the MnO_2 particles due to the discharge was examined on the basis of line profiles of manganese, oxygen, and zinc elements across the depolarizer particles. The purpose here is to observe whether a relationship exists between the discharge quality of MnO_2 and the behaviors of the elements at the inner part of the MnO_2 particle during discharge.

Experimental

Manganese dioxide materials.—Three typical battery grade manganese dioxide ores from commercial sources were available with approximate fineness of −150 mesh; one was a naturally occurring ore and the other two were electrolytically synthesized products. All were of γ-type MnO_2. The physical and chemical characteristics of these materials are listed is Table I, in which the materials are denoted as samples I, II, and III, repectively.

Table I. Characteristics of MnO_2 materials used

Sample	Origin	Physical			Chemical						
		Apparent density	True density	BET surface area, m^2/g	Mn	MnO_2	SiO_2	Fe	Ca	SO_4	Water cont., %
I	Natural	1.21	4.43	32	56.8	88.5	0.9	0.4	0.10	—	1.5
II	Electrolytic	1.39	4.25	67	59.6	91.9	—	0.03	0.13	1.15	5.1
III	Electrolytic	1.27	4.28	83	58.5	89.7	—	0.01	0.02	0.91	2.8

The failure of the analyses in Table I to add up to 100% may be due primarily to the presence of lower oxides and bound water. From the Mn and MnO_2 percentages in Table I, the n value of MnO_n for each sample is calculated as 1.97, 1.95, and 1.94, respectively, if a nonstoichiometric expression (11, 12) for γ-type MnO_2 is employed. The water content listed in Table I is the loss in weight obtained by heating any of the samples at 100°-110°C according to the definition in many practical standards including The Japanese Industrial Standards (JIS) (13).

A number of previous works have dealt with the problem of lower oxides and bound water in MnO_2, and it is interesting to note for instance that Gattow (14) defined manganese dioxide as $MnO_{1.7\text{-}2.0}$, independent of the content of H_2O and foreign ions. Sasaki and Kozawa (15) described two types of water in MnO_2; one escapes at a lower temperature and is resorptive, and the other is released at higher temperature and is not resorptive. Actually, the amount of the latter type of water, *i.e.* the bound water, was found to be about 4-5% for samples I and III, and about 1% for sample I with the standard Karl Fischer method by heating the samples from 110° up to 600°C.

Cell construction.—Each one of the ores was mixed with the cathode components and was constructed into D-size, pasted-type dry cells containing 22g of manganese dioxide per cell with the standard formulation shown in Table II.

Discharge of the cells.—Two types of discharge, relatively heavy and light, were performed with these cells to a cut-off voltage of 0.75V. Intermittent discharges were employed considering the fact that the daily usage of dry batteries is mostly intermittent. The heavy discharge was performed through 4 ohms for 30 min/day and 5 days a week, while the light discharge was performed through 40 ohms for 4 hr/day and 5 days a week, according to the test methods in JIS (16). The discharge temperature was controlled at 20° ± 1°C.

The discharged dry batteries were disassembled and the cathode mixes containing the discharged MnO_2 were washed with water and dried at 105°C in preparation for parallel examination by means of electron probe microanalysis and x-ray diffraction.

Electron probe microanalysis.—Each discharged sample was mixed with an epoxy resin and set into a shape having a well-polished surface. The mounted samples were scanned with an accelerating voltage of 25 kV, an average electron intensity of 0.15 μA, a scanning electron beam diameter of 1μ, and a magnification of 300X, to obtain the line profiles of manganese, oxygen, and zinc across transverse sections of typical discharged MnO_2 particles representing the three MnO_2 species used.

Several precautions were taken to obtain good EPMA images of the three elements under examina-

Table II. Standard formulation used for D-size cells

Constituents	Dry mix	Electrolyte	Paste	Total	Weight, %
MnO_2	69.9	—	—	69.9	47.5
Acetylene black	9.1	—	—	9.1	6.2
Graphite	3.5	—	—	3.5	2.4
NH_4Cl	17.6	3.6	4.0	25.1	17.0
$ZnCl_2$	—	4.5	4.6	8.9	6.0
$HgCl_2$	—	—	0.03	0.03	0.02
Corn starch	—	—	4.0	4.0	2.7
Wheat flour	—	—	1.3	1.3	0.9
Water	—	12.2	13.2	25.4	17.3
Total	100	20.1	27.13	147.23	100

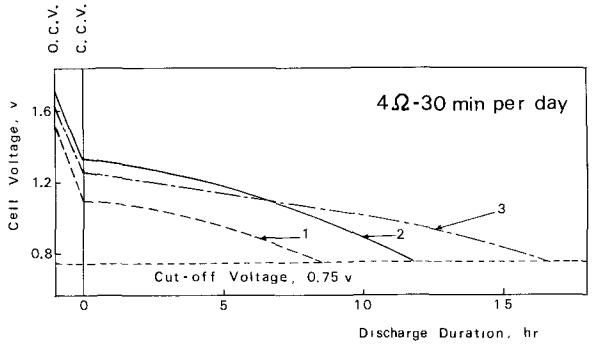

Fig. 1. Discharge curves of three representative MnO_2 materials: 1—sample I, 2—sample II, and 3—sample III, on 4 ohms-30 min/day and five days/wk basis.

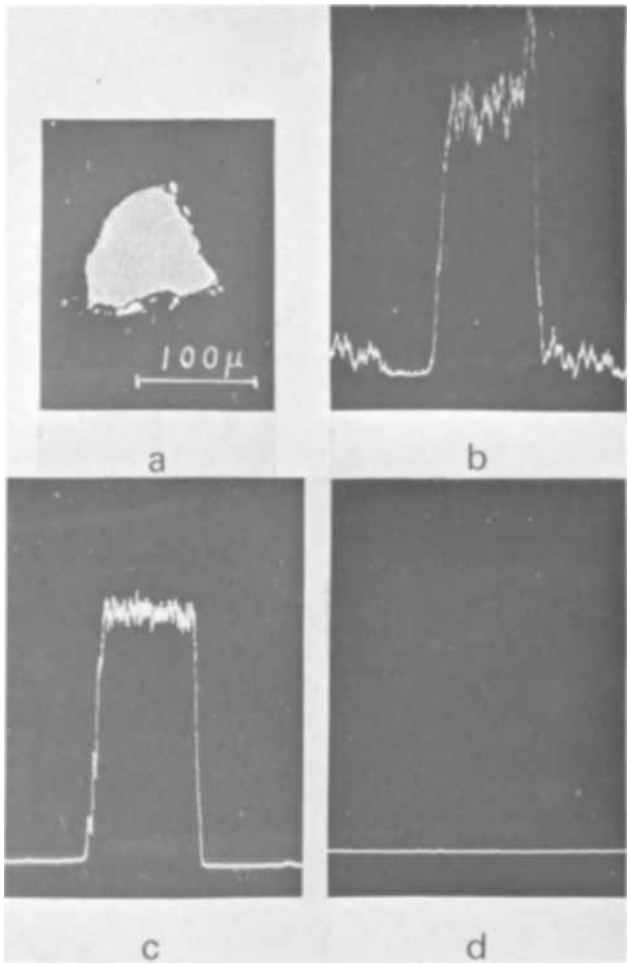

Fig. 2. Typical MnO_2 particle before discharge: (a) cross-sectional view, (b) and (c) oxygen and manganese distributions in the diametrical direction of the same cross section, and (d) zinc not present before discharge.

Table III. Discharge products of MnO_2 materials found by x-ray diffraction technique

Types of MnO_2	Discharge	
	Heavy	Light
Sample I	MnO_2 + Mn_3O_4 + very small amount of $ZnCl \cdot 4Zn(OH)_2$	MnO_2 + Mn_3O_4 + very small amount of $ZnCl_2 \cdot 4Zn(OH)_2$
Sample II	Mn_3O_4 + residual MnO_2 + $ZnCl_2 \cdot 4Zn(OH)_2$ intense at (003) peak	$ZnCl_2 \cdot 4Zn(OH)_2$ intense at (003) peak + a minor amount of $Mn_2O_3 \cdot ZnO$
Sample III	$Mn_2O_3 \cdot ZnO$	Well-developed $Mn_2O_3 \cdot ZnO$

tion. A thin film of carbon (100-200Å in thickness) was vacuum sputtered on surfaces of all the specimens. The carbon sputtering was run simultaneously for all the specimens in a multisample sputtering device to secure a uniform carbon thickness. When mounting each specimen thus prepared to the metallic holder of the microanalyzer, a small amount of an electrically conducting paint was applied to fill the gap between the specimen and the holder to electrically earth the specimen. This procedure provided very stable images by eliminating static charge from the specimen during operation. It also aided in the removal of heat. Care was also exercised to take the oxygen line profile first, while possible contamination, if any, from the epoxy remained minimal; the profiles of manganese and zinc then followed. The scanning operation above provided a sufficient reproducibility of line analysis to compare the relative concentrations of the three elements before and after discharge of MnO_2.

X-ray diffraction.—Each discharged sample was also examined with an x-ray diffractometer using nickel filtered FeK_α radiation.

Results

Discharge curve and x-ray diffraction.—Figure 1 shows the heavy discharge performances of the three MnO_2 materials. It is seen that sample I is a rather poorly performing MnO_2, while sample II is a fairly well-performing one. The latter is actually a most average electrolytic MnO_2, while sample III is an excellent material. The light discharge has also shown the same order of performances for the three types of MnO_2, with hours of discharge being approximately 130, 170, and 250, respectively.

In Table III are summarized the discharge products of each type of MnO_2 found by the conventional x-ray diffraction technique.

Electron probe microanalysis.—Microprobe profiles of MnO_2 particles before and after discharge are shown in Fig. 2-7. These figures illustrate how the MnO_2 particles undergo changes in their microstructures due to transport of the reacting elements during discharge.

Discussion

It would be difficult to generalize completely all of the intraparticle phenomena in conjunction with dis-

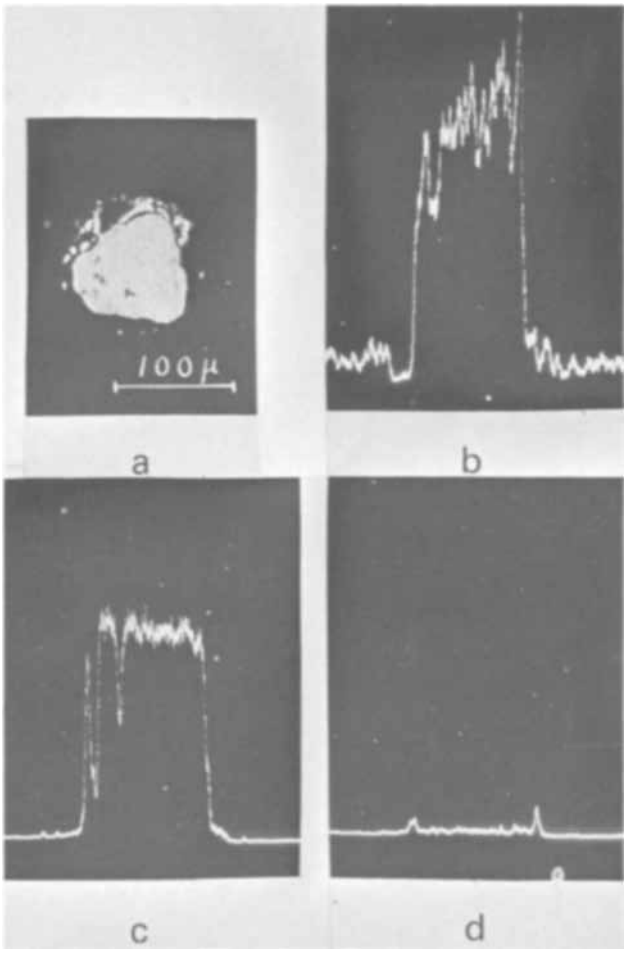

Fig. 3. Typical MnO_2 particle of sample I after heavy and light discharges: (a) cross section without generation of microcracks, (b) and (c) oxygen and manganese distributions showing minor decreases from before discharge, and (d) zinc reaching only the outermost surface but essentially not entering the inside of the particle.

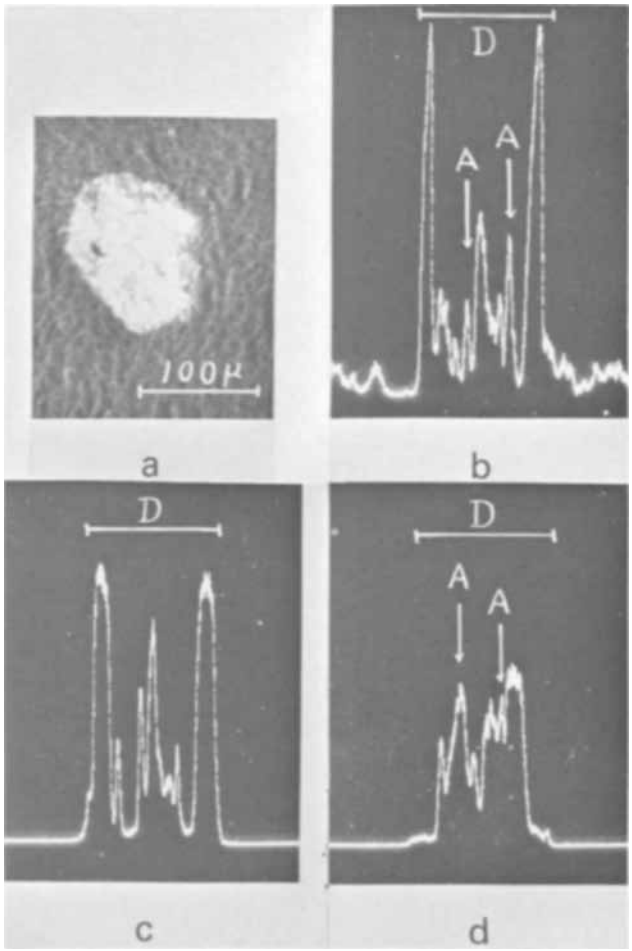

Fig. 4. Sample II particle after heavy discharge, representative of about one half in number: (a) a network of microcracks generated across the particle: (b) and (c) oxygen and manganese, having a maximum concentration at a region slightly inside of the diameter "D"; and (d) zinc replacing most of the inner sites of manganese and oxygen. Zinc coexists with a minor amount of oxygen at such points as "A" corresponding to $ZnCl_2 \cdot 4Zn(OH)_2$.

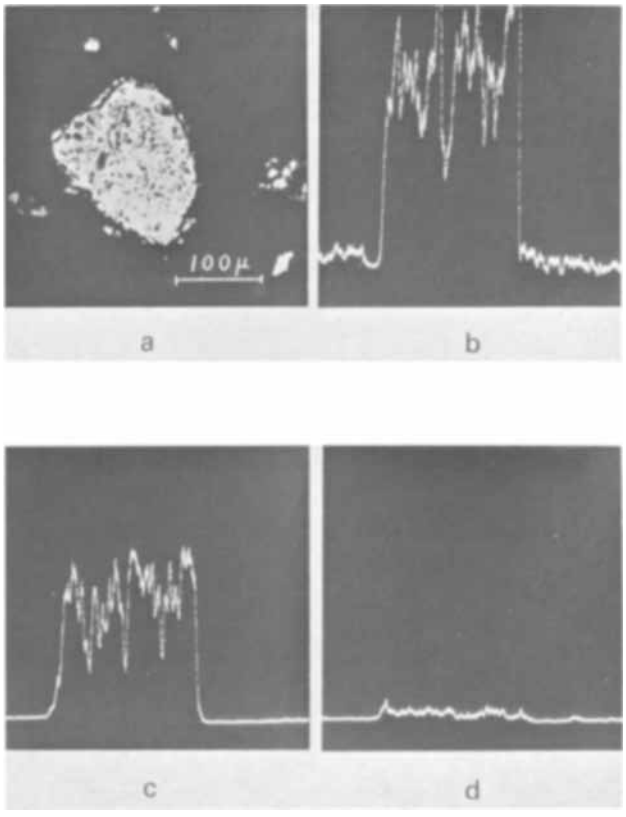

Fig. 5. Sample II particle after heavy discharge, representing the other half in number: (a) microcracks beginning to form across the particle; (b) and (c) a zigzag pattern of decreasing oxygen and manganese concentrations, yet not deeper than in Fig. 4; and (d) zinc beginning to penetrate into the particle.

charge mechanisms for MnO_2. However, it is believed that sufficient examples are presented to give an appreciation of the discharge process of MnO_2 in dry cells in terms of the behaviors of the constituent elements of the MnO_2 including the external zinc ion.

In considering how and where the discharge proceeds at individual MnO_2 particles in the dry cells, it is helpful to postulate two regions; first, the outer region near the surface, *X*, in Fig. 8, and second the inner region including the central part, *Y*, in Fig. 8. The role of the region *X* on the discharge can be taken for granted, as previous workers pointed out the importance of the surface characteristics of MnO_2 involving the surface area (5, 17) and the pore distribution (18, 19). The role of the region *Y*, the inside of the particle, must be added here, and it is apparent from the foregoing microanalytical photographs that the discharge proceeds in a competitive manner between the two regions.

In Fig. 8, which is a schematic illustration of a discharging MnO_2 particle, a proposed relationship is given between the microanalytical patterns of line profiles and the difference in the magnitudes of v_x and v_y where v_x denotes the discharge rate at *X* and v_y the one at Y in arbitrary units.

When v_x and v_y are equally small or v_y is significantly smaller than v_x in spite of a normal rate of v_x, the line profiles of manganese and oxygen may show the pattern of Fig. 8(B), which is exactly the case of Fig. 3 with sample I. In case that v_x is smaller than v_y, the pattern of distributions of manganese and oxygen may become something like Fig. 8(C), which corresponds to the line profiles in Fig. 4 with sample II. Lastly, if v_x and v_y are equally and sufficiently large, a pattern such as Fig. 8(D) may be obtained for the elements, which is equivalent to Fig. 7 with sample III. Intermediate states can be produced in between these clear-cut patterns due to various conditions including the depth of discharge even with the same samples of MnO_2 shown in Fig. 5 and 6.

The reason it is possible for v_y to become larger than v_x is attributed to an intrinsic ability of the MnO_2 material to develop a network of micropores connecting the regions *X* and *Y* as soon as the discharge reaction has initiated at the particle. It is interesting to note that sample I showed no sign of microcracks on the cross-sectional view of the particle after discharge, while samples II and III produced microcracks linking together the inner and the outer regions of the particles. The initial pore openings were not detected before discharge as in Fig. 2(a) because the magnitude of a pore diameter is too small, previously calculated to be less than 400Å by Cahoon *et al.* (19) and predominantly 180Å by Kozawa (18). However, as a result of discharge at the inner regions, *Y*, along these pores, transfer of manganese and oxygen toward the outside occurred and the invaded regions became detectable in the cross-sectional views (a) in Fig. 4, 6, and 7. Furthermore, the developed networks may be a possible path for the external zinc ions to approach into the inner part of the MnO_2 particle.

As a matter of fact, in Fig. 9 are illustrated the x-ray distribution pictures of the three elements for another typical particle of sample II which underwent the Fig. 4 type of discharge. It is seen in the pictures of Fig. 9 that a network of pores developed between the central part and the surface of the particle and the oxygen and manganese in the central region was much reduced, and that, inversely, the zinc concentrated in this region. It is to be noted here again in Fig. 9 that the residual "islets" of the oxygen and manganese are lined up at the region a little inside of

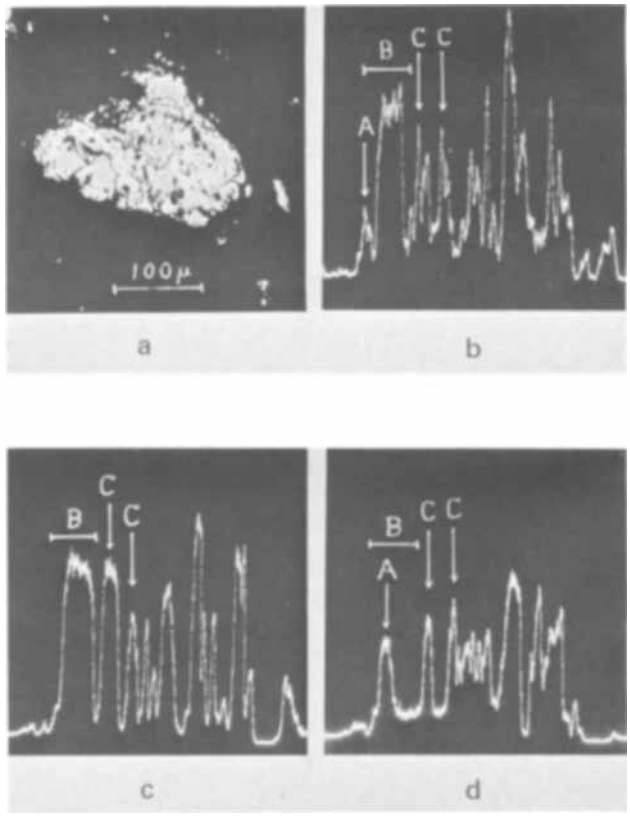

Fig. 6. Sample II particle after light discharge: (a) microcracks covering the cross section; (b), (c), and (d) oxygen, manganese, and zinc distributions, respectively, indicating that zinc replaces manganese in the region "B" on the one hand and coalesces with manganese at the region "C" on the other. At such a point as "A" even in region "B," zinc is accompanied by oxygen as in Fig. 4, showing a microstate of $ZnCl_2 \cdot 4Zn(OH)_2$ plus $Mn_2O_3 \cdot ZnO$ in the particle.

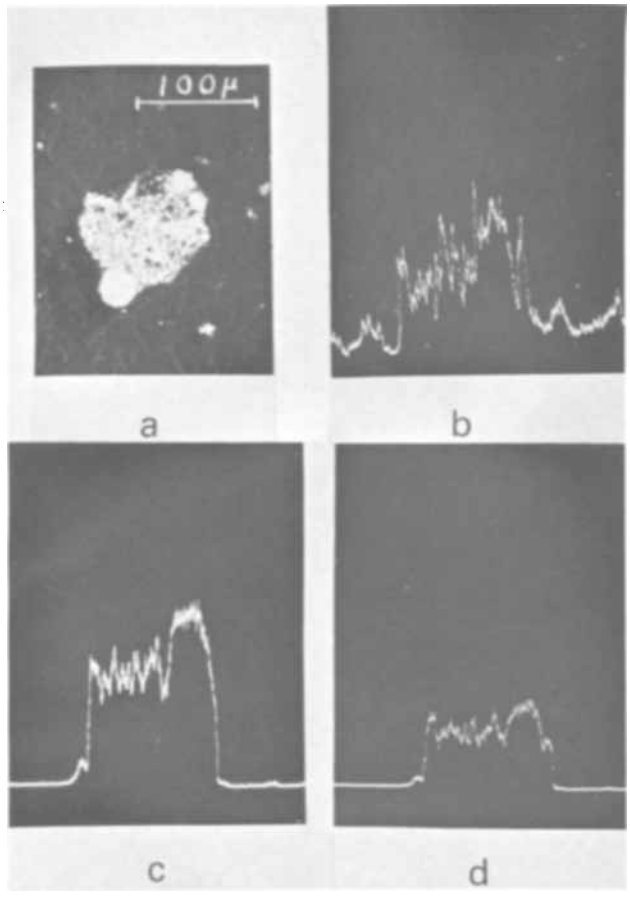

Fig. 7. Typical sample III particle after heavy and light discharges: (a) microcracks generated across the particle, (b) and (c) a noticeable reduction in oxygen and manganese distributions in a rather uniform fashion, and (d) zinc having a distribution pattern almost identical with those of oxygen and manganese, indicating that the three elements have combined into one form of compound, $Mn_2O_3 \cdot ZnO$.

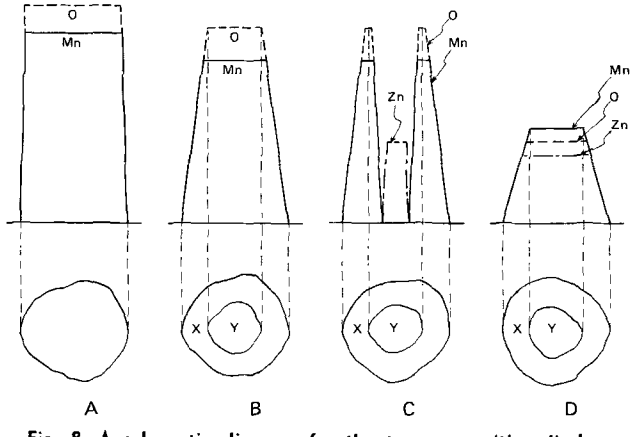

Fig. 8. A schematic diagram for the two competitive discharge reactions, one from the surface and the other from the inside of the MnO_2 particle: (A) before discharge; (B) v_x and v_y are equally small, corresponding to a poor quality MnO_2; (C) v_y is larger than v_z, corresponding to a medium-quality MnO_2; and (D) v_x and v_y are large, corresponding to a superior-quality MnO_2.

the surface of the particle. Therefore, the low concentration region at the outermost surfaces of both in Fig. 4 and 9 will invariably be attributed to the actual decrease in the existing elements. A more quantitative treatment will need to take into consideration a possible topographic effect of the specimen surface on line intensities. However, a full discussion in terms of detailed microanalytical factors is not within the scope of this paper.

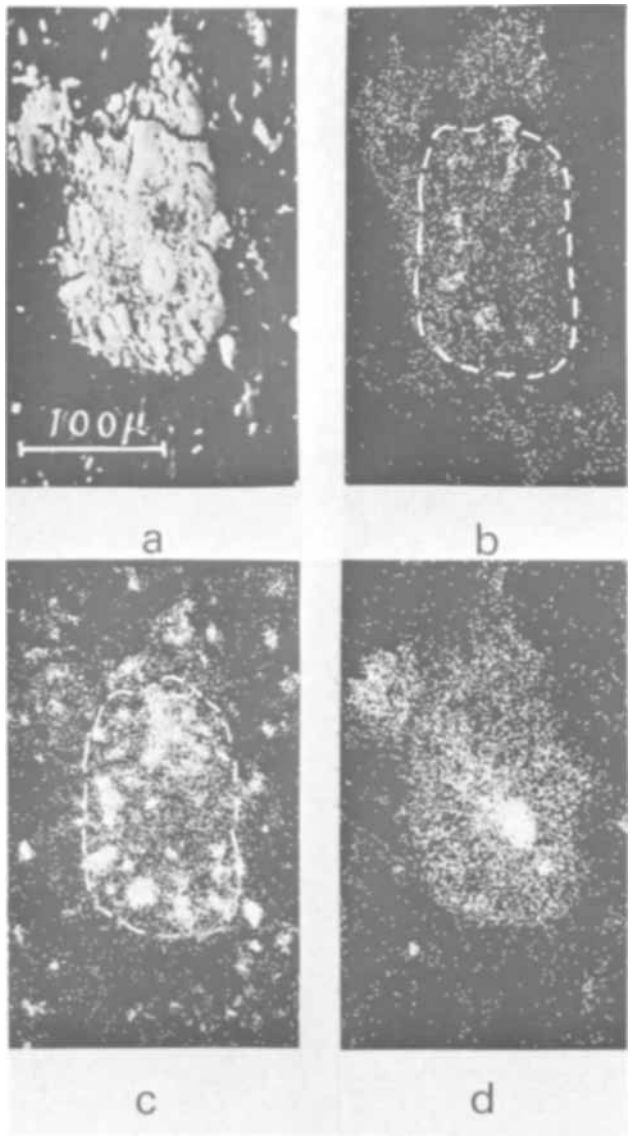

Fig. 9. A plane view of the distribution of oxygen, manganese, and zinc elements in MnO_2: (a) electron optical image of microcracks generated across the particle; (b) and (c) x-ray distribution pictures of oxygen and manganese, showing "islets" of the elements remaining along the network of the microcracks; and (d) zinc x-ray distribution profile showing this element has occupied the central sites which were occupied by manganese and oxygen before discharge.

A limitation of the geometrical model of Fig. 8 in interpreting the discharge mechanism is the fact that it will not account for the chemical affinity of elements. The entry of external zinc into the MnO_2 particles in Fig. 8(C) and (D) can be explained by the large rates of v_y in both cases to form enough geometrical room to receive the zinc ion which is migrating in along the micropores. However, it may not be straightforward as to the reason why the entering zinc remained independent of manganese in the former case, while the zinc coalesced with manganese in the latter. In this respect, the reaction velocities v_x and v_y will not directly relate to the mode of existence of zinc in the lattice, which may be governed by the intrinsic quality of the MnO_2 species itself.

However, the geometrical interpretation in terms of the competitive reaction rates v_x and v_y in Fig. 8 will lead to a clearer understanding as to how and where the discharge proceeds at a thin zone of the MnO_2 on the particle-wide basis, on which not much information was obtained by means of the conventional x-ray diffraction examination of Table III.

It is also interesting to note that the manganese has decreased in intensity in all the line profiles of Fig. 3-7, although the extent is generally smaller than that for oxygen. Dissolution of MnO_2 into Mn^{+2} ions from a discharging MnO_2 electrode was described by Brenet *et al.* (20) and Cahoon *et al.* (21-23) as being one of the possible discharge products of MnO_2, and Vosburgh *et al.* (24) identified two discharge products, an oxide with a composition of about $MnO_{1.6}$ and Mn^{+2} ions, using MnO_2 electrodes deposited on graphite rods and discharging them in NH_4Cl electrolyte. The results obtained here with the reduced oxygen and manganese line profiles after discharge may provide visual evidence for the escape of a portion of the manganese as well as the oxygen through the solid phase of MnO_2 particles during discharge of the dry cells.

Summary and Conclusions

The electron probe microanalytical techniques used in this study are useful in revealing the changes in the inside of MnO_2 particles during the cathodic reactions in the dry cell, and in supplementing the discussions of previous workers on the discharge of MnO_2.

The discharge quality of MnO_2 materials used are interpreted on the basis of manganese, oxygen, and zinc line profiles. The amounts of manganese and oxygen in MnO_2 decrease during discharge, and the release of oxygen is large in the case of MnO_2 ores with better discharge performances.

The pattern of decrease of manganese and oxygen in combination with the entrance of zinc is tentatively classified into three types according to the discharge quality of the MnO_2 ores employed. With a poor grade ore, the entrance of external zinc into the MnO_2 particles is not noticeable. However, with a fair-grade MnO_2, the zinc is observed to occupy the inner portions of the particle, where the manganese was situated before discharge. With a high-grade ore, the zinc is distributed in a rather uniform fashion in the diametrical direction of the particle together with the residual manganese and oxygen.

An intermediate between these three typical patterns for the distribution of the elements may be explained as a special case of combinations of the three cases. This implies that the discharge proceeds through two processes in a competitive manner, one from the surface and the other along the micropores or cleavages inside of the particles, the balance of which may govern the discharge quality of the MnO_2 materials.

Acknowledgments

The author wishes to thank his colleagues, N. Sasaki for the x-ray diffraction, H. Nakamura and T. Kobayashi for the electron probe microanalysis, and M. Yamamoto for helpful discussions during the course of this investigation.

Manuscript submitted Jan. 20, 1969; revised manuscript received *ca.* July 10, 1969.

Any discussion of this paper will appear in a Discussion Section to be published in the June 1970 JOURNAL.

REFERENCES

1. J. J. Coleman, *Trans. Electrochem. Soc.*, **90**, 545 (1946).
2. R. S. Johnson and W. C. Vosburgh, *This Journal*, **100**, 471 (1953).
3. A. B. Scott, *ibid.*, **107**, 941 (1960).
4. H. Bode, A. Schmier, and D. Berndt, *Z. Elektrochem.*, **66**, 586 (1962).
5. A. Kozawa and R. A. Powers, *Electrochem. Technol.*, **5**, 535 (1967).
6. S. Matsuno, *Denki Kagaku*, **12**, 2 (1944).
7. H. F. McMurdie, *Trans. Electrochem. Soc.*, **86**, 313 (1944).
8. L. C. Copeland and F. S. Griffith, *ibid.*, **89**, 495 (1946).
9. K. Miyazaki, *Bull. Chem. Soc. Japan*, **41**, 2785 (1968).
10. K. Miyazaki, *J. Electroanal. Chem.*, In press.
11. W. Feitknecht and W. Marti, *Helv. Chim. Acta*, **28**, 129 (1945).
12. J. Brenet, J. P. Gabano, and M. Seigneurin, *Congr. Intern. Chem. Pure et Appl., 16e Paris, 1957, Mém. Sect. Chim. Minerale*, 69 (Pub. 1958).
13. JIS (Japanese Industrial Standards) K1467-1965.
14. G. Gattow, *Batterien*, **15**, 201 (1961).
15. K. Sasaki and A. Kozawa, *Denki Kagaku*, **25**, 115 (1957).
16. JIS (Japanese Industrial Standards) C8501-1963.
17. M. Fukuda, T. Hirai, and H. Manabe, *Denki Kagaku*, **27**, 204 (1959).
18. A. Kozawa, *This Journal*, **106**, 552 (1959).
19. N. C. Cahoon and M. P. Korver, *ibid.*, **109**, 1 (1962).
20. S. Gosh and J. Brenet, *Ber. Bunsenges. Physik. Chem.*, **67**, 723 (1963).
21. N. C. Cahoon and G. W. Heise, *Trans. Electrochem. Soc.*, **94**, 214 (1948).
22. N. C. Cahoon, R. S. Johnson, and M. P. Korver, *This Journal*, **105**, 296 (1958).
23. M. P. Korver, R. S. Johnson, and N. C. Cahoon, *ibid.*, **107**, 587 (1960).
24. W. C. Vosburgh, R. S. Johnson, J. S. Reiser, and D. R. Allenson, *ibid.*, **102**, 151 (1955).

The Cathodic Reduction of Oxygen on Platinum in Alkaline Solutions

K. F. Blurton[1]* and E. McMullin[2]

Leesona Moos Laboratories, Great Neck, New York

ABSTRACT

Measurements with rotating disk and ring/disk electrodes have been used to elucidate the reaction paths for oxygen reduction on platinum in concentrated alkaline electrolyte. It is concluded that oxygen is reduced to hydrogen peroxide at potentials between the open circuit voltage and 0.4V *vs.* a reversible hydrogen electrode. Between 0.4 and 0.0V *vs.* a reversible hydrogen electrode, oxygen is reduced to OH^- with peroxide as an intermediate product. The effect of hydrogen peroxide decomposition on the limiting current density for oxygen reduction at a rotating disk electrode and on the value of the ring current of a rotating ring/disk electrode is discussed.

Studies on the electrochemical reduction of oxygen have been stimulated in the last few years by the interest in fuel cells and metal/air batteries. It has been previously demonstrated that hydrogen peroxide is the product of oxygen reduction on carbon electrodes in alkaline solution (1, 2). However the role played by this species during oxygen reduction on platinum electrodes in the same electrolyte is open to more controversy and probably depends on the electrode potential and surface pretreatment. Thus it has been postulated that during oxygen reduction on platinum in alkaline electrolyte hydrogen peroxide is either an intermediate in a single reaction path (3-7) or the sole product of the reaction (8-10) or an intermediate in a path parallel to a second reaction path involving oxygen reduction directly to OH^- (11, 12). It has also been suggested (13) that oxygen is reduced directly to OH^- without peroxide being involved.

The aims of the present study were to elucidate the role of hydrogen peroxide in the reduction of oxygen on platinum, to measure the effect of the peroxide decomposition on the limiting current at a rotating disk electrode, and to analyze the effect of the peroxide decomposition on the current measured at the ring of a rotating ring/disk electrode. It was decided to perform these studies in concentrated alkaline electrolyte at elevated temperatures, *i.e.*, under conditions similar to those for the operation of fuel cells.

Experimental

The reaction cell was a one liter, glass cylindrical vessel fitted with a lucite lid. Gas inlets were positioned above and below the surface of the electrolyte and were placed as far as possible from the rotating electrode to prevent interference with the fluid flow. The counterelectrode was a platinum gauze (geometric area 23 cm^2) which was placed on the bottom of the glass vessel. The reference electrode was a reversible hydrogen electrode immersed in the test electrolyte and located in a second compartment. This compartment was connected to the main one by a Luggin capillary. The tip of the Luggin capillary was located slightly above the surface of the disk electrode again to prevent interference with the electrolyte flow and the ohmic drop was found to be less than 1 mV in the test solution at all the experimental currents.

The construction of the disk electrode was similar to that described by Blurton and Riddiford (14). The construction of the ring/disk electrode is shown in Fig. 1. The insulating material was 7/16 in. diameter Kel F. The internal and external radii of the ring electrode were 0.260 cm and 0.375 cm, respectively, and the radius of the disk electrode was 0.245 cm. Electrical contact was made by platinum wire welded onto the inner ends of the disk and ring electrodes. There was no electrolyte creep between the platinum and the shielding and these were found to be inert to the caustic potash solutions at 70°C. Both the rotating disk and ring/disk electrodes were stored in distilled water between runs.

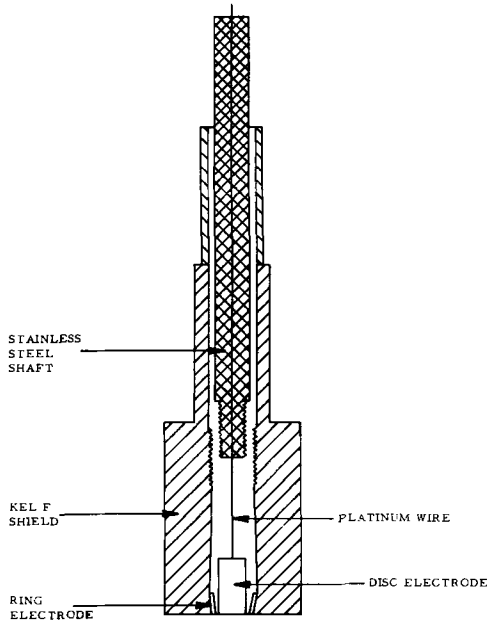

Fig. 1. Construction of rotating ring/disk electrode

Before making measurements with the ring/disk electrode a light coating of platinum was electrodeposited onto the working surface of the ring. The polarization curve on the disk was then measured by changing the disk potential in steps of 50 mV in the potential range of open circuit to 0V with a low impedance potential divider. At each disk potential, the ring current was measured at a potential of 1.3V.[3] At this potential the current due to oxygen evolution is insignificant and all the hydrogen peroxide produced at the disk, which reaches the ring, is oxidized, *i.e.*, the ring is operated in the hydrogen peroxide limiting current region.

* Electrochemical Society Active Member.
[1] Present address: Energetics Science, Inc., New York, New York.
[2] Present address: Quantachrome Corporation, Greenvale, New York.

[3] All potentials refer to the reversible hydrogen electrode in the same solution.

A solution of 6.9M KOH was prepared from Baker Analyzed Reagent grade chemical and triple distilled water. Oxygen and hydrogen were obtained from cylinders and were used without further purification. Potentials were measured with a differental voltmeter (J Fluke Model 801H) and the current was measured from the potential drop across a standard resistor. No rigorous purification schemes were used for the electrolyte for a previous study (12) showed that electrolyte impurities in alkaline electrolyte did not influence peroxide formation.

Results

The polarization curve for oxygen reduction on a rotating platinum disk electrode in 6.9M KOH solution at 70°C is given in Fig. 2. The steady state current was attained in 5-10 min. The shape of this curve was similar at all electrode rotation speeds and showed three distinct regions. At potentials between open circuit and 0.7V the current increased with increasing polarization, between 0.7 and 0.6V a limited current region was observed and between 0.6 and 0V the current again increased with increasing polarization. In agreement with the work of Tikhomirova, Luk'yanycheva, and Bagotskii (8) but in contrast to that of Müller and Nekrasov (3) no peak was observed in the current/voltage curves. Figure 2 also shows the current/voltage curve obtained by decreasing the polarization from 0V to open circuit. The currents during the reverse sweep were similar to those obtained by increasing the polarization in the potential range 0-0.5V but differed from those obtained by increasing the polarization in the potential range 0.5V to open circuit. The experimental open circuit voltage at the end of the hysteresis measurement was more cathodic than that determined initially, but it increased steadily to the original value on standing.

The value of the limiting current was found to depend markedly on electrode history and reproducible plots of i_L *vs.* (electrode rotation speed)$^{1/2}$ were only obtained when all the limiting currents were determined within a period of a few hours (Fig. 3). This was achieved by potentiostating the electrode at 0.70V and measuring the limiting current at a fixed electrode rotation speed. The electrode was then allowed to stand on open circuit until the original open circuit voltage was obtained and the limiting current at another electrode rotation speed was measured by repotentiostating at 0.70V. This procedure was repeated by potentiostating the electrode at 0.65V to check that the measured current was indeed the limiting current. Similar current/voltage curves for oxygen reduction were obtained on a lightly platinized as on the bright platinum disk electrode but the limiting currents were greater on the former electrode (Fig. 3). The platinum electrodeposit on these electrodes was sufficiently smooth so that the hydrodynamic flow was not disturbed.

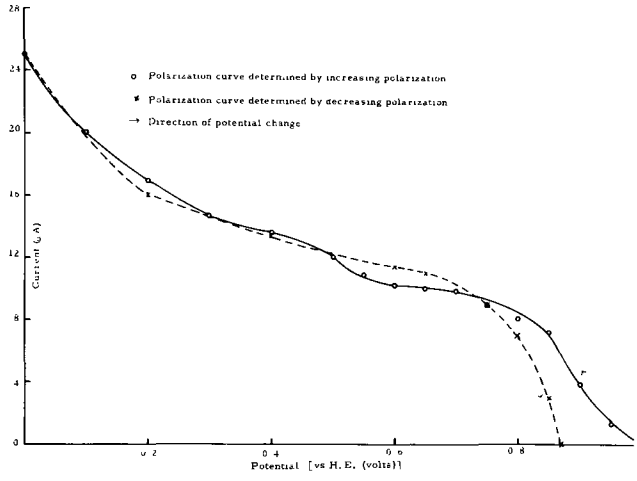

Fig. 2. Polarization curve for oxygen reduction on a rotating platinum disk electrode in 6.9M KOH solution at 70°C; electrode rotation speed 500 rpm.

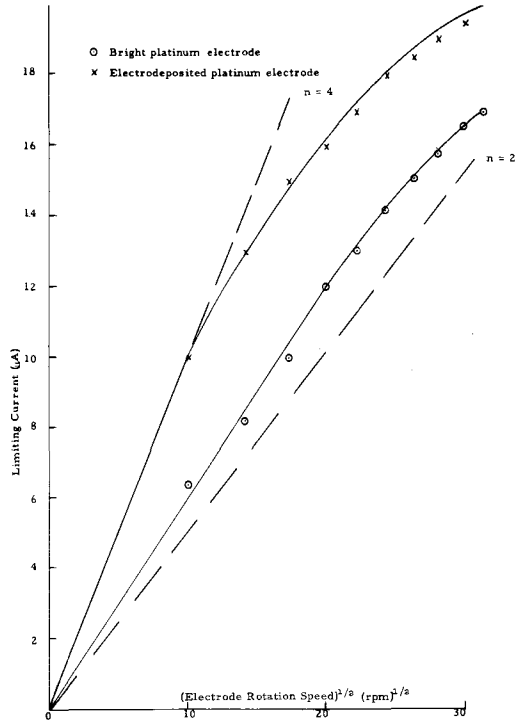

Fig. 3. Limiting current vs. (rpm)$^{1/2}$ for oxygen reduction at the rotating disk electrode. The theoretical plots for the 2 and 4 electron processes were calculated using the values of D_{O_2}, ν_{KOH}, and C_{O_2} given in the text.

The plot of the limiting current *vs.* (electrode rotation speed)$^{1/2}$ was nonlinear (Fig. 3). Now the values of the bulk concentration of oxygen (C_{O_2}), the oxygen diffusion coefficient (D_{O_2}), and the KOH solution viscosity (ν_{KOH}) have not been determined under the present experimental conditions, but extrapolation of the available data (15-17) gives $C_{O_2} = 6.1 \times 10^{-5}$ mole l^{-1}, $D_{O_2} = 1 \times 10^{-5}$ cm^2 sec^{-1}, and $\nu_{KOH} = 8.3 \times 10^{-3}$ cm^2 sec^{-1} (18). From this data it was found that the values of the experimental limiting currents were intermediate between those calculated (19, 20) for a 2 and 4 electron process (Fig. 3).

The current/voltage curve for oxygen reduction at the disk electrode in 6.9M KOH solution at 70°C with the corresponding ring current at 1.3V is given in Fig. 4 at an electrode rotating speed of 1000 rpm. The ring current reaches a maximum value at disk potentials between 0.75 and 0.45V and, in the same potential range, there is a limiting current on the disk electrode. At potentials more cathodic than 0.5V the disk current increases and the ring current decreases, *i.e.*, the hydrogen peroxide produced at the disk is further reduced to water. Similar results have been obtained at other electrode rotating speeds and Fig. 5 gives the values of the ratio of the disk current to the ring current (I_D/I_R) at these rotation speeds. The accuracy of these ratios is limited by the small values of the ring and disk currents which, in turn, are limited by the low oxygen solubility in the concentrated alkaline solution. The ratios were generally reproducible to ± 1 although larger deviations were recorded particularly at low electrode rotation speeds when the disk and ring currents are at their minimum values.

At disk potentials more cathodic than 0.4V the variation of I_D/I_R with electrode rotating speed was less reproducible due to the very small values of the ring current. However, the values of I_D/I_R were clearly dependent on the electrode rotation speed and, in gen-

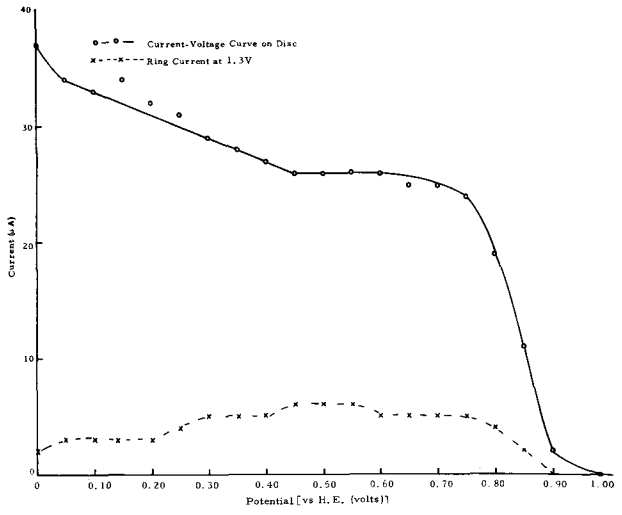

Fig. 4. Current/voltage plot for oxygen reduction at the disk of the rotating ring/disk electrode in 6.9M KOH solution at 70°C with the corresponding ring current at 1.3V; electrode rotation speed 1000 rpm.

eral, decreased as the electrode rotation speed increased.

Discussion

Comparison of the current/voltage relationship for oxygen reduction on a dropping mercury (21) with the corresponding plot obtained on a rotating platinum disk electrode (Fig. 2) suggests that, on the rotating disk electrode, oxygen is reduced to hydrogen peroxide in the potential range of open circuit to 0.6V whereas at more cathodic potentials oxygen is reduced to water probably with hydrogen peroxide as an intermediate. The low value of the open circuit voltage at the end of the potential scan also indicates that peroxide is formed by the reduction of oxygen for, in the presence of peroxide, the oxygen electrode attains the potential of $O_2 + H_2O + 2e \rightarrow HO_2^- + OH^-$ rather than that of $O_2 + 2\,H_2O + 4e \rightarrow 4\,OH^-$ (1, 22). The hysteresis observed in the polarization curves (Fig. 2) is probably due to the influence of the hydrogen peroxide. This phenomenon has been discussed by Bowen and Urbach (10) and was attributed by them to the influence of the peroxide on the platinum surface oxides.

The experimental limiting currents for the reduction of the tri-iodide ion in 0.1M potassium iodide were equal to the theoretical values for electrode rotation speeds of 100-1000 rpm inclusive. Thus the nonlinearity of the limiting current *vs.* (electrode rotation speed)$^{1/2}$ plots (Fig. 3) is due to the nature of the electrode reaction and not to an experimental deviation from the theoretical requirements. The dependence of the limiting current on the electrode surface treatment indicates that the hydrogen peroxide is decomposing by a surface chemical reaction.

McIntyre (23) has shown that plots of i_L *vs.* (electrode rotation speed)$^{1/2}$ similar to that in Fig. 3 indicate that the product formed by the electrochemical reaction decomposes by a second order surface catalyzed chemical reaction to form the reactant, *i.e.*, in the present study the reaction is represented by the equations

$$O_2 + H_2O + 2e \rightarrow HO_2^- + OH^- \qquad [1]$$

$$2\,HO_2^- \rightarrow O_2 + 2\,OH^- \qquad [2]$$

For this reaction scheme the limiting current density is given by (23)

$$\frac{i_L}{2F} = 2L_{O_2}\,\omega^{1/2}C_{O_2} - \frac{L^2_{H_2O_2}\omega}{2k_h}\left[\left(1 + \frac{4k_hL_{O_2}C_{O_2}}{L^2_{H_2O_2}\omega^{1/2}}\right)^{1/2} - 1\right] \qquad [3]$$

where ω(rad. sec^{-1}) is the angular velocity of the disk, k_h is the second order heterogeneous chemical rate constant of the regenerative reaction (*i.e.*, Eq. [2]), and L_i is given by (23, 24)

$$L_i = \frac{0.62048\,D_i^{2/3}\,\nu^{-1/6}}{1 + 0.2980\,(D_i/\nu)^{1/3} + 0.14514\,(D_i/\nu)^{2/3}} \qquad (i = O_2, H_2O_2) \qquad [4]$$

By assuming that $D_{O_2} = D_{H_2O_2}$ the values of k_h have been calculated from Eq. [3] and data given in Fig. 3 and they are reported in Table I.

The values of k_h given in Table I are based on the geometric area of the electrode and the difference between the values on bright and electrodeposited platinum is due to the difference in the true surface area of the electrode. The constancy of the values of k_h suggests that Eq. [1] and [2] do indeed represent the over-all process for the reduction of oxygen in alkaline solution and that the peroxide decomposition is occurring by a 2nd order surface catalyzed reaction. A similar reaction scheme has also been proposed by Tikhomirova, Luk'yanycheva, and Bagotskii (8) for oxygen reduction on platinum in 1*N* KOH solution.

Damjanovic, Genshaw, and Bockris (11, 12) suggested, from an analysis of plots of I_D/I_R *vs.* $\omega^{-1/2}$, that oxygen reduction on platinum in alkaline solution proceeds along two parallel reaction paths (*i.e.*, Eq. [5] and [6]) and that these reactions occur at similar rates.

$$O_2 + 2H_2O + 4e \rightarrow 4\,OH^- \qquad [5]$$

$$O_2 + H_2O + 2e \rightarrow HO_2^- + OH^- \qquad [6]$$

The relationship between I_D/I_R and $\omega^{-1/2}$ was shown to be (25)

$$\frac{I_D}{I_R} = \frac{x+1}{N} + \frac{(x+2)}{N}\,\frac{1.61 \cdot k \cdot \nu^{1/6}}{D^{2/3} \cdot \omega^{1/2}} \qquad [7]$$

where k is the rate constant for the electrochemical reduction of hydrogen peroxide to water, N is a factor dependent on the geometry of the rotating ring/disk electrode, and x is the ratio of the current for the reaction represented by Eq. [5] to that represented by Eq. [6].

For the electrode assembly used in the present study the calculated (26) value of N and the experimental value (for the redox reaction $2Br^- \rightarrow Br_2 + 2e$) were equal to 0.495 (*i.e.*, $1/N = 2.021$). The experimental value of I_D/I_R for oxygen reduction in 6.9M KOH solution was greater than $1/N$ and it was independent of electrode rotation speed and of potential between 0.8 and 0.4V (Fig. 5). Thus the treatment of Damjanovic, Genshaw, and Bockris (25) indicates that two parallel reactions are occurring during oxygen reduction (Eq. [5] and [6]) in the potential range 0.8-0.4V. Also, since the peroxide is not further reduced electrochemically (*i.e.*, $k = 0$) Eq. [7] simplifies to

$$\text{Intercept in Fig. 5} = \frac{x+1}{N} \qquad [8]$$

which gives x equal to 1.5. Thus the two parallel

Table I. Values of the rate constant for the second order heterogeneous decomposition of H_2O_2

m (rpm)	k_h cm^4 mole^{-1} sec^{-1}	
	Bright Pt	Electrodeposited Pt
100	1.3×10^4	3.8×10^5
200	1.7×10^4	3.7×10^5
300	3.5×10^4	6.3×10^5
400	2.5×10^4	3.9×10^5
500	2.4×10^4	2.1×10^5
600	2.2×10^4	1.7×10^5
700	2.0×10^4	1.4×10^5
800	1.7×10^4	1.1×10^5
900	1.9×10^4	0.9×10^5
1000	0.9×10^4	0.7×10^5

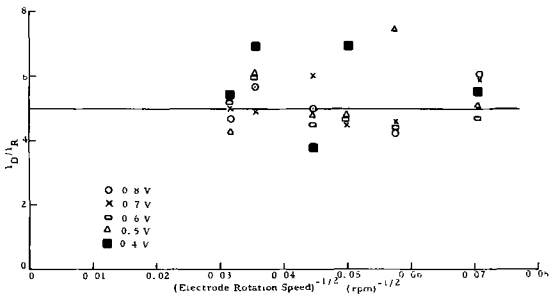

Fig. 5. Plot of I_D/I_R vs. (electrode rotation speed)$^{-1/2}$ at selected potentials.

processes are occurring with comparable rates and, since the value of I_D/I_R is independent of potential in the range 0.8-0.4V, the relative rates of the two reactions are independent of potential.

The inconsistency as to whether the over-all reaction is represented by Eq. [1] and [2] or by Eq. [5] and [6] may be resolved by a closer inspection of the derivation of Eq. [7]. This derivation (25) utilizes the equation

$$I_R = \frac{I_D \cdot N}{1 + k\delta/D} \qquad [9]$$

where δ is the diffusion layer thickness of the intermediate and it is applicable (19) to the electrochemical reaction at the disk electrode of a reactant to an intermediate with partial electrochemical conversion of the intermediate to a final product. Thus it is necessary to determine whether Eq. [9], and hence Eq. [7], requires modification to apply to the reactions represented by Eq. [1] and [2]. Another approach, which we propose, is to assume that Eq. [9] is correct and modify Eq. [7]. This has been achieved by determining the effect of the hydrogen peroxide concentration (and hence decomposition rate) on the disk and ring currents.

When oxygen is electrochemically reduced to hydrogen peroxide which then decomposes by a second order heterogeneous chemical reaction (*i.e.*, Eq. [1] and [2]), McIntyre (23) has shown that the disk limiting current ($I_{L,D}$) is given by

$$\frac{I_{L,D}}{2F} = J_{H_2O_2} + 2\, k_h\, [\bar{C}_{H_2O_2}]^2 \qquad [10]$$

where $J_{H_2O_2}$ is the flux of the peroxide to the uniformly accessible surface of the disk and $\bar{C}_{H_2O_2}$ is the surface concentration of hydrogen peroxide. The flux of peroxide when the oxygen surface concentration is zero is related to the peroxide surface concentration by (23)

$$J_{H_2O_2} = L_{H_2O_2}\, \omega^{1/2}\, [\bar{C}_{H_2O_2}] \qquad [11]$$

and $\bar{C}_{H_2O_2}$ is given by (23)

$$\bar{C}_{H_2O} = \frac{L_{H_2O_2}\omega^{1/2}}{2k_h}\left[\left(1 + \frac{4k_h L_{O_2} C_{O_2}}{L^2_{H_2O_2}\omega^{1/2}}\right)^{1/2} - 1\right] \qquad [12]$$

The thickness of the H_2O_2 diffusion layer, $\delta_{H_2O_2}$, at the rotating disk electrode, is given by (20)

$$\delta_{H_2O_2} = \frac{D_{H_2O_2} \cdot \omega^{-1/2}}{L_{H_2O_2}} \qquad [13]$$

and the current at the ring electrode is related to the hydrogen peroxide surface concentration (27) by

$$I_R = 2\,NF\,\frac{\bar{C}_{H_2O_2} \cdot D_{H_2O_2}}{\delta_{H_2O_2}} \qquad [14]$$

By substituting Eq. [11], [12], and [13] into the equation obtained by dividing Eq. [10] by [14]

$$\frac{I_{L,D}}{I_R} = \frac{1}{N}\left(1 + \frac{4k_h L_{O_2} C_{O_2}}{L^2_{H_2O_2}\omega^{1/2}}\right)^{1/2} \qquad [15]$$

Thus for the reaction scheme represented by Eq. [1] and [2], the rate of change of $I_{L,D}/I_R$ depends to a much lesser extent on $\omega^{-1/2}$ than that predicted by Damjanovic, Genshaw, and Bockris (25). Equation [15] may be simplified by assuming that $D_{O_2} = D_{H_2O_2}$, by assuming that $C_{O_2} = 6.1 \times 10^{-5}$ mole l^{-1} and by using the average value of k_h for the smooth electrode from Table I. Then

$$\frac{I_{L,D}}{I_R} = \frac{1}{N}\left(1 + \frac{7.7}{\omega^{1/2}}\right)^{1/2} \qquad [16]$$

In the present study $20 < \omega < 100$, so that

$$3.3 > I_{L,D}/I_R > 2.7 \qquad [17]$$

It was not possible to detect the small variation of $I_{L,D}/I_R$ with $\omega^{-1/2}$ predicted by Eq. [17] due to the small values of the ring current. However, the apparent independence of $I_{L,D}/I_R$ on ω (Fig. 5) does indicate that oxygen is electroreduced by a reaction scheme represented by Eq. [1] and [2]. Also, the values of k_h were determined on a different electrode from that used for the ring/disk electrode and this causes the discrepancy between the calculated (Eq. [17]) and experimental (Fig. 5) values of I_D/I_R since k_h depends on the electrode roughness.

Thus we suggest that the measurements with the rotating ring/disk electrode coupled with those of the limiting currents on the rotating disk electrode confirm that the reduction of oxygen on platinum in alkaline solution in the given potential range proceeds via reactions represented by Eq. [1] and [2] and that the parallel reactions do not occur. The treatment given here does show that caution must be exercised in the interpretation of I_D/I_R *vs.* $\omega^{-1/2}$ plots and that, in contrast to Nekrasov's statement (6), the catalytic decomposition of peroxide does modify the ring current. It should be stressed that the derivation of Eq. [15] is applicable only under limiting current conditions and depends on the validity of Eq. [9].

The results obtained with the rotating disk electrode (Fig. 2) suggest that peroxide electroreduction occurs at potentials more cathodic than 0.6V whereas measurements with the ring/disk electrode (Fig. 5) indicate that peroxide reduction occurs at potentials more cathodic than 0.4V. This difference is probably due to the different condition of the electrode surfaces and indicates the importance of the nature of the surface on peroxide reduction. The difference in the plots of I_D/I_R *vs.* (electrode rotation speed)$^{-1/2}$ between Fig. 5 and those of Damjanovic, Genshaw, and Bockris (11, 12) may also be due to a variation in the state of the electrode surface.

The results reported in this paper demonstrate that the catalytic decomposition of peroxide formed at a disk electrode during the reduction of oxygen influences both the value of the disk limiting current and the value of the ratio of the disk to ring current. In the limiting case, *i.e.*, $k_h \to \infty$, the disk limiting current equals the value calculated for a four electron process but for other values of k_h the disk limiting current is intermediate between that for a 2 and 4 electron process. Clearly the peroxide decomposition reaction will also affect the shape of the galvanostatic chronopotentiometric curve and the apparent number of electrons calculated from the transition time (13, 21, 28, 29).

Acknowledgment

The authors wish to thank Dr. H. G. Oswin for many helpful discussions and Mr. D. Rutt for technical assistance.

Manuscript submitted March 17, 1969; revised manuscript received June 20, 1969.

Any discussion of this paper will appear in a Discussion Section to be published in the June 1970 JOURNAL.

REFERENCES

1. W.G. Berl, *Trans. Electrochem. Soc.*, **83**, 253 (1943).
2. M. O. Davies, M. Clark, E. Yeager, and F. Hovorka, *This Journal*, **106**, 56 (1959).
3. L. Müller and L. N. Nekrasov, *Electrochim. Acta*, **9**, 1015 (1964).
4. E. I. Khrushcheva, N. A. Shumilova, and M. R. Tarasevich, *Elektrokhimiya*, **1**, 649 (1965).
5. L. Müller and L. N. Nekrasov, *J. Electroanal. Chem.*, **9**, 282 (1965).
6. L. N. Nekrasov, *Elektrokhimiya*, **2**, 438 (1966).
7. V. S. Bagotskii, L. N. Nekrasov, and N. A. Shumilova, *Usp. Khim.*, **34**, 1697 (1965).
8. V. I. Tikhomirova, V. I. Luk'yanycheva, and V. S. Bagotskii, *Electrokhimiya*, **3**, 762 (1967).
9. A. Kozawa, *J. Electroanal. Chem.*, **8**, 20 (1964).
10. R. J. Bowen and H. B. Urbach, *J. Chem. Phys.*, **49**, 1206 (1968).
11. A. Damjanovic, M. A. Genshaw, and J. O'M. Bockris, *J. Phys. Chem.*, **70**, 3761 (1966).
12. A. Damjanovic, M. A. Genshaw, and J. O'M. Bockris, *This Journal*, **114** 1107 (1967).
13. J. J. Lingane, *J. Electroanal. Chem.*, **2**, 296 (1961).
14. K. F. Blurton and A. C. Riddiford, *J. Electroanal. Chem.*, **10**, 457 (1965).
15. R. E. Davis, G. L. Horvath, and C. W. Tobias, *Electrochim. Acta*, **12**, 287 (1967).
16. K. E. Gubbins and R. D. Walker, *This Journal*, **112**, 469 (1965).
17. K. E. Gubbins and R. D. Walker, Report to U.S. Army Engineer Research and Development Laboratory, Fort Belvoir, Virginia, Contract No. DA-49-186-AMC-45(X), 1965.
18. "Caustic Potash," Solvay Technical and Engineering Bulletin No. 15, 1959.
19. V. G. Levich, "Physicochemical Hydrodynamics," Prentice-Hall Inc., Englewood Cliffs, N. J. (1962).
20. A. C. Riddiford, "Advances in Electrochemistry and Electrochemical Engineering," Vol. 4, P. Delahay, Editor, Interscience Publishers Inc., New York (1966).
21. I. M. Kolthoff and C. S. Miller, *J. Am. Chem. Soc.*, **63**, 1013 (1941).
22. R. J. Bowen, H. B. Urbach, and J. H. Harrison, *Nature*, **213**, 592 (1967).
23. J. D. E. McIntyre, *J. Phys. Chem.*, **71**, 1196 (1967).
24. J. Newman, *ibid.*, **70**, 1327 (1966).
25. A. Damjanovic, M. A. Genshaw, and J. O'M. Bockris, *J. Chem. Phys.*, **45**, 4057 (1966).
26. W. J. Albery and S. Bruckenstein, *Trans. Faraday Soc.*, **62**, 1920 (1966).
27. A. Frumkin, L. Nekrasov, V. Levich, and Ju. Ivanov, *J. Electroanal. Chem.*, **1**, 84 (1959/60).
28. D. T. Sawyer and L. V. Interrante, *J. Electroanal. Chem.*, **2**, 310 (1961).
29. D. T. Sawyer and R. J. Day, *Electrochim. Acta*, **8**, 589 (1963).

Redox Coulometers

Joseph L. Weininger*

General Electric Research and Development Center, Schenectady, New York

ABSTRACT

A coulometer is described which cumulatively measures periods of time, up to a preset limit, during which a repetitive event occurs. The redox couple ferrocyanide-ferricyanide is reversibly reduced and oxidized at pyrolytic graphite electrodes. An ion exchange membrane prevents the mixing of the electrolytic solutions surrounding the electrodes, thereby setting up a concentration cell with transference. The cell potential follows the Nernst relation, but depending on cell geometry and operating parameters, partial diffusion control of electrode reactions is also observed. At a given potential limit the process is reversed. This cycling is repeated for a cell life in excess of 2000 cycles with less than 1% error when interrupted for as long as 24 hr.

A coulometer measures the quantity of electricity passed through a circuit by means of the electrolysis of an electrochemical couple. The principle of its operation is based on Faraday's law. In this report a coulometer is discussed which, integrating a constant current signal, will measure the duration of time, up to a preset limit, during which a repetitive event occurs. Such timing operations are important in process controls where a fixed time limit may be divided into different time segments.

Henderson (1) has designed a variety of coulometers with battery plates as electrodes. These devices are based on and are used in battery technology. For example, two identical cadmium-cadmium hydroxide plates are operated against each other. Their predetermined states of charge and discharge, indicated by the cell voltage, time a process which in Henderson's case is the charging of a battery at high constant current density. For applications requiring extremely long life and reliability such a device may be unsuitable, because the repeated cycling of most battery plates is accompanied by noticeable evolution of gases due to the electrolysis of solvent water. Also, the mechanism of the battery operation involves the chemical transformation of solid phases of the electroactive material, for example, the interconversion of cadmium and cadmium hydroxide. Such electrodes, known as "electrodes of the second kind," experience structural changes as a result of the electrode reaction which during repeated cycling tend to reduce the capacity of the plates.

To overcome these difficulties a redox couple is used in the present coulometer, which is soluble in both its oxidized form (concentration C_O) and its reduced form (concentration C_R). The couple is chemically stable and has a potential far removed from that required for evolution of either hydrogen or oxygen from water.

Mechanism of the Coulometer

In the schematic drawing of Fig. 1 the coulometer is connected to a constant current switching circuit.[1] The direction of the current (polarity) is controlled by the cell which reverses the current at preset upper and lower voltage limits. The limits at which this switching occurs can be adjusted arbitrarily.

The cell consists of two chambers, each containing an inert electrode and each filled with a solution of composition C_O and C_R. In effect, the cell is a "concentra-

* Electrochemical Society Active Member.

Key words: timing devices, coulometers, electrochemical cells, concentration cells, redox systems.

[1] Details of this circuit will be published elsewhere by F. G. Will, who designed the circuit.

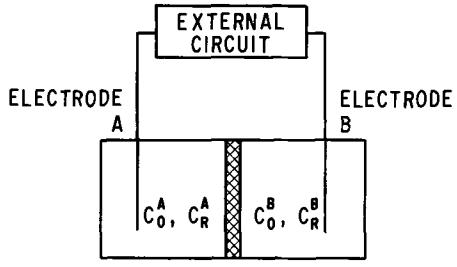

CELL $C/C_O^A+C_R^A/$I.E.M.$/C_O^B+C_R^B/C$

rig. 1. Schematic of redox coulometer

tion cell with transference," which implies that there is electrolytic continuity between the two half-cells. Diffusion of the redox species from one compartment to the other must be prevented. This is accomplished with an ion exchange membrane. A cation exchange membrane is used when the changing concentrations involve anions; conversely, an anion exchange membrane is required for electroactive cations.

The mechanism of the coulometer operation is illustrated by the data of Table I. The emf of the cell is given by the Nernst relation

$$E = \frac{RT}{n\mathbf{F}} \cdot \ln \frac{C_O{}^A \cdot C_R{}^B}{C_R{}^A \cdot C_O{}^B}$$

where the superscripts indicate the respective cell compartments. Either the reduced or oxidized species may be in limited supply. As the ratios C_O/C_R vary, so will the potential difference exhibited by the cell. It is this cell voltage which will reverse the current flow in the external circuit. In this manner the capacity of the coulometer, *i.e.*, the duration of time which the cell adds cumulatively and linearly, is predetermined by the concentration of the redox couple.

The time measurement occurs in the first half-cycle, also called the "timing period." The second half-cycle, the "reset period," has only the function of bringing the cell back to the original starting point so that repetitive timing can be accomplished during the first half-cycles under identical conditions.

In the examples of Table I both compartments A and B are filled with the same solution, having concentration ratio C_O/C_R of 4/1. The reduced species is oxidized at the positive electrode until a negligible amount of C_R is present in A at the start of the first half-cycle (timing or discharge). A corresponding amount of the reduced species, but one still in limiting supply, is produced at cathode B. In the following half-cycle (reset or charging) the polarity is reversed, hence cathodic and anodic processes are reversed, and so on. In Table I the ratio of 4/1 was chosen for purpose of illustration. Other values could be chosen and, similarly, the oxidized species with concentration C_O could be limiting.

Cell Design and Components

A detailed sketch of the cell is shown in Fig. 2. Each half-cell consists of a poly(methylmethacrylate) housing with a cavity 1-in. in diameter and 0.1-in. deep, in which graphite electrodes (with Pt contacts) are located. The two half-cells are separated by a cation

Table I. Concentration of redox species (Arbitrary units)

	Initial (on filling) Compartments		First half-cycle Reset (Start of timing) Compartments		Second half-cycle Timing (Completion of timing) Compartments	
	A	B	A	B	A	B
C_O	4	4	5	3	3	5
C_R	1	1	0	2	2	0

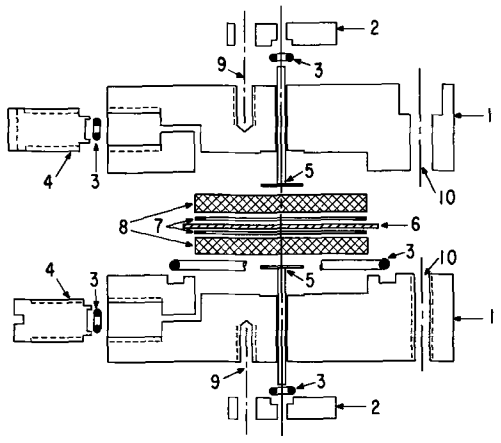

Fig. 2. Details of redox coulometer; 1, polymethyl methacrylate (PMM) body; 2, PMM end caps; 3, Viton O-rings; 4, PMM sealing plugs; 5, Pt electrode contacts; 6, ion exchange membrane; 7, Teflon spacers; 8, space for carbon electrodes and electrolytic solution; and 9 and 10, Nylon screws.

exchange membrane, are fastened together with Nylon bolts, and are sealed with Viton O-rings. The redox solution is introduced after partially evacuating the cell.

Pyrolytic graphite is used as an indicator electrode because it is cheaper than platinum and chemically as stable. Electrodes are heated in vacuum before use in order to expel reducing gases trapped in the pyrolytic graphite during its preparation.

The couple used in this coulometer is the ferrocyanide-ferricyanide couple, for which the electrode reaction is

$$Fe(CN)_6{}^{-4} \rightleftarrows Fe(CN)_6{}^{-3} + e$$

Its oxidized and reduced components are both soluble, it has a potential far removed from that required for evolution of either hydrogen or oxygen from water, it reaches a reversible equilibrium with high exchange current density, it is chemically stable above pH 3.5, provided it is stored in the absence of oxygen so as to prevent oxidation of ferrocyanide, and it is easily prepared and purified in the form of the potassium salts.

The "parent"-metal ion couple is

$$Fe^{++} \rightleftarrows Fe^{+++} + e \quad E^o = 0.771\text{V (}vs.\text{ NHE)}$$

Even in this one metal ion system, with ions of iron, there is a wide choice of couples available by complexing ferrous and ferric ions with different ions, of which the cyanide is only one example. It has a higher equilibrium potential ideally suited for the coulometer operation in a cell voltage range of +0.3 to —0.3V. In the ferrocyanide-ferricyanide case, this corresponds to a potential range of +0.16 to +0.76V (*vs.* NHE), precisely the "safe" range, in which there is no interference from either hydrogen ion reduction at the lower potential limit or oxidation of water at the upper limit.

The large size of the hydrated anions of the ferrocyanide-ferricyanide couple practically eliminates co-ion (anion) diffusion through the ion-exchange membrane charged with the same polarity. Furthermore, because this couple consists of large negative ions, it is compatible with the use of cation exchange membranes, which are commercially better developed than anion exchange membranes.

Different commercially available cation exchange membrane materials, mostly sulfonated polystyrene membranes, were satisfactory. The final choice was an oxidatively stable fluorocarbon polymer with ion exchange based on sulfonated trifluorostyrene. The ion exchange membranes, supplied in the hydrogen ion form, were stored in the coulometer redox solution. This assured exchange with potassium and sodium ions and equilibrated the ion exchange membrane with the coulometer solution before use.

Because of the small coulombic charge required for operation of the coulometer through a single half-cycle, it is necessary that the redox couple be present in dilute concentration, of the order of 1-10 mM/liter in small volumes of less than 1 ml. This requires a supporting electrolyte. Since chemical stability of the couple also requires a *p*H above 3.5, preferably near 7, the function of the buffer and supporting electrolyte is combined by the use of Sorenson's phosphate electrolyte (2) which gives a *p*H 6.67 for the mixture 0.5M KH_2PO_4 + 0.5M Na_2HPO_4. Latimer gives a rest potential of 0.48V (*vs.* NHE) for the couple with equal concentrations of negative ions (3). Our determination in a buffered solution at *p*H 6.67 is E^o = 0.475V (*vs.* NHE).

Results

The symmetrical cell had pyrolytic graphite electrodes with 5.07 cm^2 surface area. The spacing between the electrode and the ion exchange membrane was 0.0254 cm and defined a volume of 0.129 ml for each of the half-cells. Thus, a total of only 0.258 ml of the redox solution was required. Slightly more is available because of the presence of channels for filling the cell.

Figures 3 and 4 show the performance of this cell at constant current flow of 67 μA. The cell contained a solution of 0.016M $K_3Fe(CN)_6$ + 0.004M $K_4Fe(CN)_6$ + 0.5M Na_2HPO_4 + 0.5M KH_2PO_4. Figure 3 traces the voltage as a function of time for cycles 138-142 with current reversal at ± 0.3V. During cycles 168 and 169 the current was interrupted for 17 and 20 min, respectively, as shown in Fig. 4. No increase in the timing or reset periods of the cycles occurred as a result of the interruptions. The second period at open circuit, at —100 mV, when there was a difference of almost two orders of magnitude in the concentrations C_R of the two half-cells, gave the following small voltage changes

Time (min)	0	0.25	0.50	1.00	4.00	12.0	18.0	20.0
E (mV)	100	88	86	85	79	76	74	75
ΔE (mV)	0	12	14	15	21	24	26	26

Considering the S-shaped discharge curve, 100 mV is near the time limit of a half-cycle. The change of ΔE = 26 mV represents elimination of concentration polarization in the absence of current flow. When it is resumed, all or most of the voltage drop is made up as the previous partial diffusion control is reestablished.

Concentration polarization is also illustrated in an experiment with a similar cell, containing a more concentrated solution, 0.088M $K_3Fe(CN)_6$ + 0.022M $K_4Fe(CN)_6$ + 0.5M Na_2HPO_4 + 0.5M KH_2PO_4. Figure 5 shows a typical half-cycle of this cell, at a constant current of 100 μA. The curve is the experimental voltage trace; points are calculated values based on the Nernst relation with concentrations varying according to Faraday's law. Since the concentrations of the redox couple are small and that of the supporting electrolyte is large, concentrations rather than activities were used in the calculation.

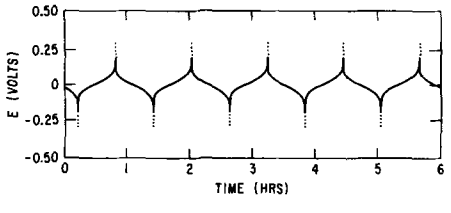

Fig. 3. Cycling of coulometer with pyrolytic graphite electrodes between +0.3 and —0.3V; constant current at 67 μA.

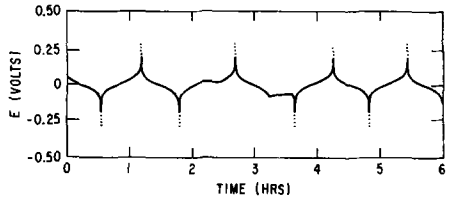

Fig. 4. Cycling of coulometer of Fig. 3. Current interruptions with cell on open circuit.

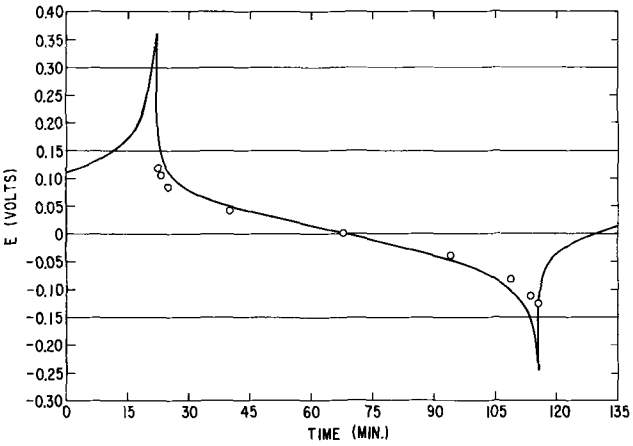

Fig. 5. Comparison of experimental (solid line) and calculated (points) values of potential as a function of time for cell and conditions described in text.

Discussion

As constant current is applied to the cell, reversible electrode reactions involve two soluble species in a layer of electrolyte, in which the concentrations of reactant and product are alternately depleted and enriched. The mechanism of the coulometer can be understood as the change in Nernst potential arising from changes in concentrations. For example, starting at zero voltage, electrode reactions depend only on the redox couple. However, as reactions proceed, the limiting concentration C_R decreases in one half cell and transport phenomena alter the voltage-time relation. Depending on the magnitude of the constant current and the extent of mixing due to convection in the thin electrolyte layer, concentration polarization sets in and will result in greater than calculated voltage changes.

Figure 5 shows that diffusion limitation becomes effective and more pronounced near the end of a half-cycle, which is characterized by greater concentration changes and consequently more rapid changes in cell voltage. The nonlinear and sharp increase in the voltage response of the cell is an advantage in applications for simple binary logic circuits which require an end-of-cycle signal.

The accuracy of the coulometer's measurements can be estimated from the errors introduced by keeping the cell on open circuit for different periods of time. The errors are less than 0.1% for consecutive cycles involving at least 5 min open circuit stands, and less than 1% for 24 hr on open circuit. This stability reflects the exclusion of co-ions from the ion exchange membrane. Ion exclusion depends on the charge and size of the diffusing ion, the degree of crosslinking of the membrane, the external ionic strength (supporting electrolyte), and the electrolyte concentration. At a co-ion concentration of 0.01M, the dynamic transport number of the counter-ion (the cation in the present case), t_+, is 0.97-1.00. The diffusion of anions through the cation exchange membrane will be negligible except in the most stringent application of the redox coulometer, when extended open circuit stands near the voltage limit (large concentration differences) are involved.

Although some time may be required to charge the double layer at very low current density, this does not introduce an appreciable error. In the experiments of Fig. 3, 4, and 5, the current densities are 13.2 and 19.7 x 10^{-6} A/cm^2; hence assuming a double layer capacitance of 10 μF/cm^2 and a cell voltage of 0.6V (start of half-cycle), the charging of the double layer at the pyrolytic graphite electrode would require 0.45 and 0.30 sec.

The only long-term systematic source of error was the evaporation of water. The first cell described here was operated for more than 2000 cycles, but required addition of 0.1 ml of distilled water after about 1500 cycles in order to replenish the solution for evaporated water.

The question of accuracy and possible changes in cell capacity also arises. Although solutions can be prepared accurately, it is simpler to adjust the constant current level and so obtain the desired cycling regime. In this work the solution concentration ratio C_O/C_R was arbitrarily chosen to be 4:1. Any other ratio is suitable if it conforms to the cell mechanism. Likewise, ratios of 4:1, in one half cell, and another ratio, such as 8:2 in the other, would be feasible but would not offer any advantage in timing applications.

Conclusions

1. The redox coulometer is suitable for measuring periods of time continuously or cumulatively.
2. The cell performance is reliable and reversible over a very long lifetime provided only that the cell is hermetically sealed to prevent evaporation of solvent water.
3. The voltage limits of operation are determined by the concentration of the redox couple according to the Nernst relation. Deviation (increased voltage at constant current) occurs near the end of a half cycle due to transport phenomena.
4. Within the voltage limits, the redox couple is chosen for the most stable voltage region with regard to solvent decomposition.
5. The nature of the ion in limiting supply determines the choice of the ion exchange membrane to be used.

Acknowledgment

The author greatly appreciates discussions with F. G. Will and the use of his switching circuit. He is particularly indebted to W. L. Mowrey for his ingenious and efficient design of the coulometer cells.

Manuscript submitted Aug. 14, 1968; revised manuscript received June 24, 1969. This was Paper 376 presented at the Montreal Meeting, Oct. 6-11, 1968.

Any discussion of this paper will appear in a Discussion Section to be published in the June 1970 JOURNAL.

REFERENCES

1. I. H. S. Henderson, Can. Pat. 715,196, issued August 1965.
2. B. E. Conway, "Electrochemical Data," p. 209, Elsevier Publishing Co., New York (1952).
3. W. M. Latimer, "Oxidation Potentials," p. 212, 1st ed., Prentice Hall Inc., New York (1938).

Lithium Anode Properties in a Nonaqueous Cell

G. W. Jackson* and G. E. Blomgren

Union Carbide Corporation, Consumer Products Division, Research Laboratory, Cleveland, Ohio

ABSTRACT

The anode discharge characteristics for the cell system Li/1.0M $AlCl_3$ in propylene carbonate/AgCl have been studied by use of an interrupter and a constant load pulse technique called potential profile analysis. The potential profile results show a severe polarization of the concentration type. A speculation concerning the mechanism responsible for the polarization is advanced, which postulates a nonsteady-state diffusional process through an insoluble layer of LiCl reaction product. A large volume of electrolyte which dissolves the product or sufficient stirring to remove the product eliminates the severe concentration polarization of the anode.

The use of alkali and alkaline earth metals as anodic materials in combination with nonaqueous electrolytes has been of increasing interest because of the high theoretical value of the energy per unit of weight. However, most attempts to construct cells which use these materials have resulted in numerous difficulties in overcoming the considerable losses due to polarization of the electrodes. Because of this, studies were undertaken to attempt to understand the nature of these polarization problems. This paper reports on studies of anode polarization for the cell system

Li/1.0M $AlCl_3$ in propylene carbonate/AgCl

Experimental

Inert atmosphere.—All experiments were run in a Forma dry box which contained several trays of phosphorus pentoxide for scavenging moisture. To obtain a dry argon atmosphere, cylinders of 99.995%, high purity, Linde argon were used.

Measuring apparatus.—The polarization measurements were obtained at ambient temperature by the use of two current pulse techniques. The first method employed the use of the Kordesch-Marko interrupter (1). The results obtained through the use of such a technique were IR free. The second method was a current interrupted pulse technique which required an oscilloscope to measure the voltage. The cells were operated on closed circuit under a 1 mA drain and were pulsed on 1 sec open circuit and 5 sec closed circuit. From the voltage-time profiles, information about the nature of the polarization could be obtained. Figure 1 shows a block diagram of the apparatus used in the second technique.

Cells.—Information was desired under two types of cell conditions, one in which a large volume of electrolyte was present in order to better define the electrode properties and one in which a limited amount of electrolyte was present in order to simulate the conditions of a finished cell. Therefore, two types of test holders were used. For the limited electrolyte experiments, a Teflon plastic test holder was used. This test cell holder was equipped with a threaded cap to place

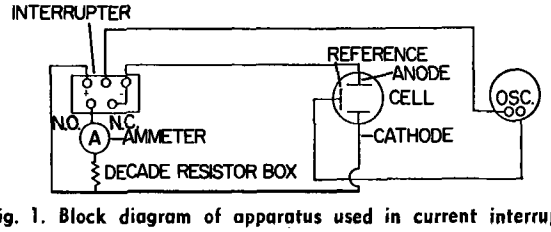

Fig. 1. Block diagram of apparatus used in current interrupted pulse technique.

* Electrochemical Society Active Member.

the electrodes under pressure to ensure contact. Two sizes of this test holder were used. One had an electrode area of 1 cm^2 and the other 6.41-cm^2 area. Figure 2A shows the cell holder.

For the experiments under electrolyte-rich environments, both a rectangular Teflon plastic test cell and a threaded cap cell were used. Figure 2B shows the rectangular cell. For the threaded cap cell the electrolyte volume was approximately 1 cm^3/cm^2 of electrode area.

Electrolyte and separators.—In every case where electrode separation was required, two pieces of nonwoven Viskon were used. This material was obtained from the Chicobee Manufacturing Company, North Little Rock, Arkansas.

The reagent grade solvent, propylene carbonate, was obtained from Fisher Scientific Company. The water content was determined to be 0.8% by Karl Fisher titration. The solvent as received from the vendor was stored over molecular seive, type 4A, and then distilled using a Podbielniak Semi-Cal distillation unit under 10 mm Hg. Only the middle third fraction was used in the experiments. The final water content according to Karl Fisher was below the lowest detectable level by this method of 0.002%.

The aluminum chloride used was anhydrous reagent grade material from Fisher Scientific Company. The lithium was 2 x 0.015 in. lithium metal ribbon obtained from Foote Mineral Company, Exton, Pennsylvania.

Reference electrode.—The reference electrode was an Ag, AgCl electrode made by anodizing a piece of silver wire. This electrode remained quite stable over the time in which the experiment was carried out. The stability was verified by checking against a calomel reference electrode every 2 hr. The Ag/AgCl reference was found to be stable ± 2 mV over the time of the experiment.

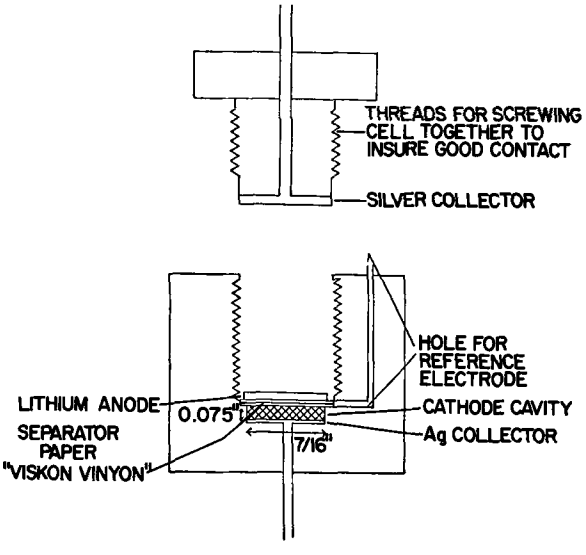

Fig. 2A. Threaded cap Teflon test cell

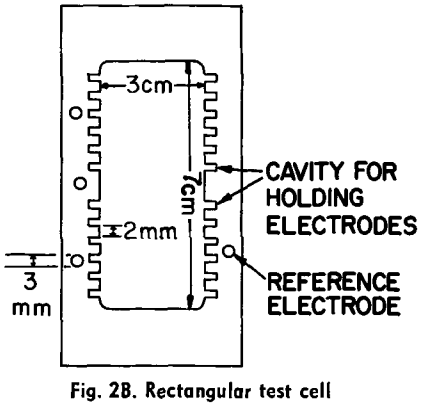

Fig. 2B. Rectangular test cell

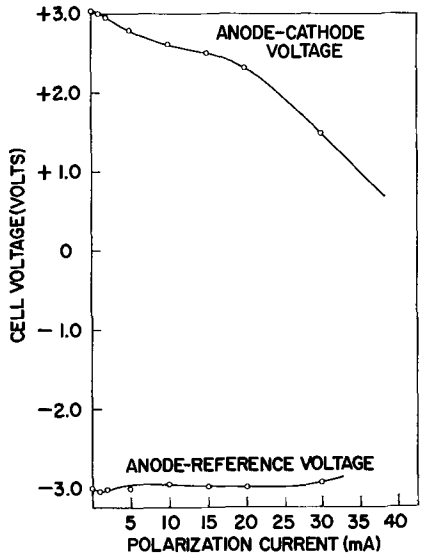

Fig. 3. IR-free polarization curves in electrolyte-rich cell (1 cm^3 electrolyte/cm^2 electrode).

Results and Discussion

Figure 3 shows an electrolyte-rich polarization curve using the Teflon plastic test holder and a Kordesch-Marko interrupter (1). The anode, which was 2.86 cm in diameter, had an apparent surface area of 6.41 cm^2. The electrolyte concentration was a 1.0M solution of $AlCl_3$ in propylene carbonate. A word might be said at this point about making electrolytes of aluminum chloride. It was found that extreme care had to be taken in order to avoid the breakdown of the solvent when aluminum chloride was added. Even when aluminum chloride was added at a very slow rate and the solution was vigorously stirred, heat was generated and the resultant solution turned straw-brown. When the solute was added more rapidly the reaction was more violent, gave off excess heat, evolved white pungent vapors, and turned dark brown to almost black in color. The IR-free readings in Fig. 3 indicated that the anode polarized very little, while the cathode showed a large polarization.

To observe time effects on the polarization occurring at the anode, a continuing 1 mA, 5 sec on-time, 1 sec off-time current pulse was applied to the cell. Figure 4 shows a series of tracings obtained using the threaded cap Teflon plastic cell having an anode of 1 cm^2 apparent surface area and containing approximately 1 cm^3 electrolyte.

Figure $4A_1$ shows that the OCV was 2.88V; Fig. $4A_2$ shows anodic and cathodic polarizations of 400 and 500 mV, respectively. The anodic polarization appeared to be equivalent to an ohmic resistance as shown in Fig. $4A_3$ by the rapid recovery to a higher voltage the instant the circuit is broken. Because the sweep time is 1 cm/sec, the ohmic and activation polarizations are not distinguishable. In Fig. $4B_1$, both anodic and cathodic tracings are shown, while Fig. $4B_2$ shows an enlarged view of the anodic polarization. In Fig. 4C, it was noted that the open-circuit voltage had begun to drop, but the anodic polarization remained about the same, although it appeared to take on some diffusional characteristics. This is indicated by the portion of the curve which slowly sweeps upward. On further discharge, the drop in open-circuit voltage continued as shown in Fig. 4D and 4E. If the circuit was opened long enough, the cell returned to an open-circuit voltage of 2.88V and remained there. Figure 4F shows an example of a slow recovery of the anode. As can be

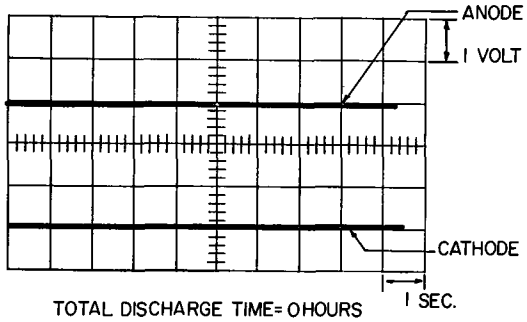

TOTAL DISCHARGE TIME= 0 HOURS

4A1

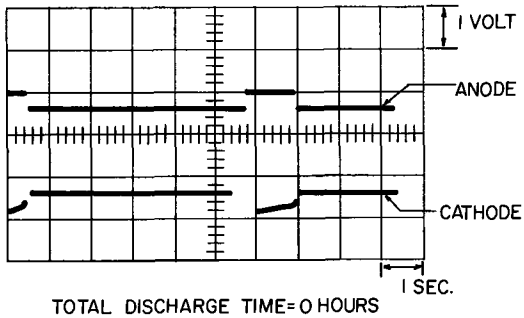

TOTAL DISCHARGE TIME= 0 HOURS

4A2

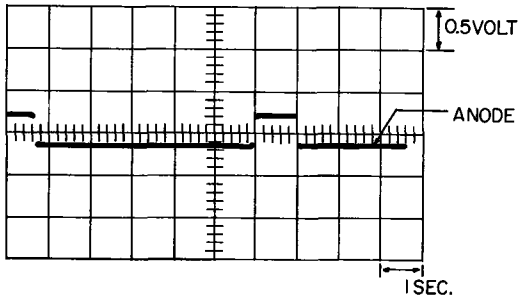

TOTAL DISCHARGE TIME= 0 HOURS

4A3

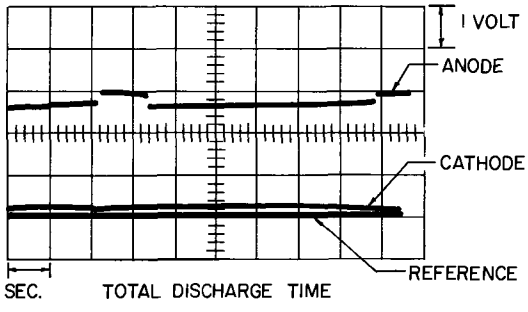

TOTAL DISCHARGE TIME
15 MINUTES

4B1

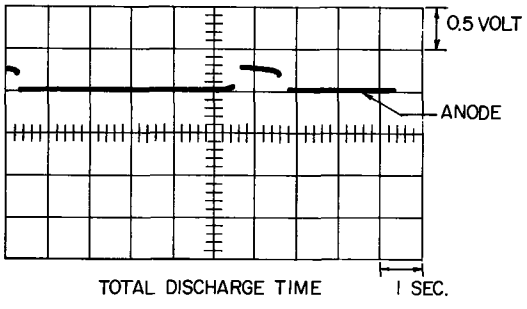

TOTAL DISCHARGE TIME
15 MINUTES

4B2

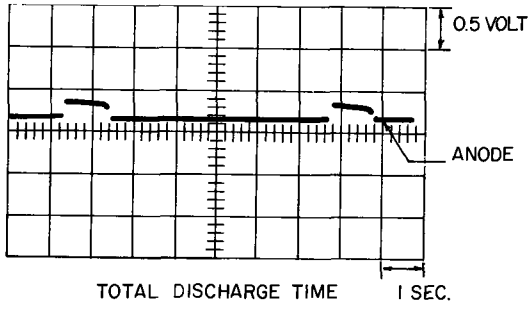

TOTAL DISCHARGE TIME
1 HOUR 20 MINUTES

4C1

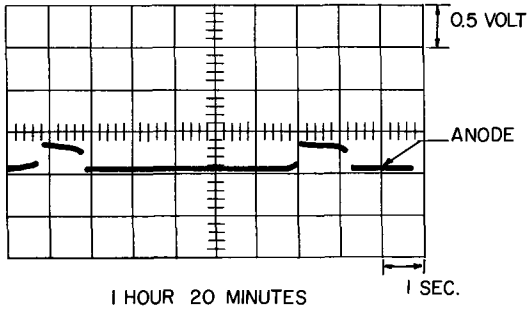

1 HOUR 20 MINUTES
TOTAL DISCHARGE TIME

4C2

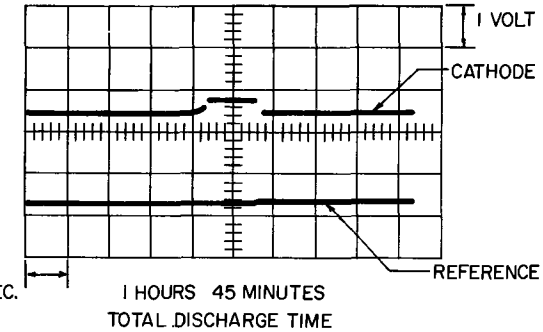

1 HOURS 45 MINUTES
TOTAL DISCHARGE TIME

4D

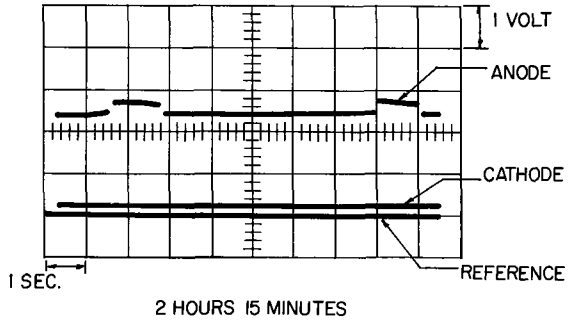

2 HOURS 15 MINUTES
TOTAL DISCHARGE TIME

4E

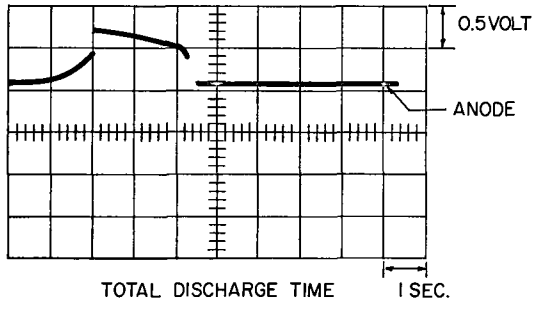

TOTAL DISCHARGE TIME
3 HOURS

4F

Fig. 4. Oscilloscopic tracings of current interrupted discharge characteristics of electrolyte-rich threaded-cap Teflon test cell at 1 mA/cm^2.

seen, no steady state was reached in 2 sec. It could be surmised then, that the open-circuit voltages shown were not true equilibrium potentials but represented a potential which was dependent on the diffusional characteristics of the cell. A porous product was observed to build on the surface of the anode. X-ray analysis of scrapings of the surface showed that the product on the surface was LiCl. In the rectangular Teflon plastic cell where there is an abundance of electrolyte, the discharge continues much longer before concentration polarization becomes a large factor.

While the precise mechanism responsible for the polarization is undoubtedly complex, a speculation concerning the nature of the observed concentration effects can be made with the aid of a simplified model. Since the anode reaction product is observed to be LiCl, a half-cell reaction scheme can be written for the anode alternatively as

$$Li + Cl^- \rightarrow LiCl\downarrow + e \qquad [1]$$

or

$$4\ Li + AlCl_4^- \rightarrow 4\ LiCl\downarrow + Al^{3+} + 4\ e \qquad [2]$$

while the cathode reaction may proceed via the reaction

$$AgCl + e \rightarrow Ag + Cl^- \qquad [3]$$

or

$$4\ AgCl + Al^{3+} \rightarrow 4\ Ag + AlCl_4^- \qquad [4]$$

Reactions [2] and [4] would be consistent with the ionic species observed by Hon (2) in an NMR study of solutions of $AlCl_3$ in acetonitrile, which could be expected to behave similarly to propylene carbonate. Reactions [1] and [3] would require the presence of some free chloride ion, probably in equilibrium with the complex aluminum species. In the case of reactions [1] and [3] chloride ion must be transported from the cathode to the anode and for [2] and [4], $AlCl_4^-$ must be transported.

If one assumes that all of the insoluble LiCl product remains at the anode surface in the form of a somewhat porous layer, then diffusion of chloride ion or the complex aluminum chloride ion through the LiCl barrier will occur, but at a drastically reduced rate compared to diffusion through the bulk solution. The effect of this will be to define a diffusion layer which is equivalent to the thickness of the product LiCl layer and which is set up due to the passage of current. When the current is switched off, as in the transient profile technique, the ions in the solution will diffuse into the diffusion layer in such a way as to dissipate the concentration gradient, and this is observed as a gradual return of the open-circuit voltage to the equilibrium value. We can test this model of the lithium anode polarization by a solution of the linear diffusion equation for the nonsteady state

$$D\frac{\partial^2 c}{\partial x^2} = \frac{\partial c}{\partial t} \qquad [5]$$

where D is regarded as an effective diffusion coefficient for diffusion through the porous layer and c the concentration of the diffusing species. The general solution of Eq. [5] for an arbitrary concentration profile at time zero, $C_0(x)$; is given by (3)

$$C(x,t) = \frac{1}{\sqrt{\pi\ Dt}}\int_0^\infty C_0(x')\ e^{-(x-x')^2/4\ Dt}\,dx' \qquad [6]$$

We can test the model with a step concentration gradient as an initial condition where δ is the thickness of the diffusion layer, C_e is the concentration at the anode surface and C_0 the bulk concentration, *i.e.*

$$\begin{aligned} x > \delta,\ C_0(x) &= C_0 \\ 0 \leq x < \delta,\ C_0(x) &= C_e \end{aligned} \qquad [7]$$

The solution for the concentration at the electrode surface is

$$\frac{C_0 - C(0,t)}{C_0 - C_e} = \phi\left(\frac{\delta}{2\sqrt{Dt}}\right) \qquad [8]$$

where $\phi\left(\frac{\delta}{2\sqrt{Dt}}\right)$ is the error function defined by

$$\phi(y) = \frac{2}{\sqrt{\pi}}\int_0^y e^{-\zeta^2}\,d\zeta \qquad [9]$$

The problem was also solved for a linear gradient initial condition, but within the range of times studied here, no distinction could be made between the two cases. Now, using the Nernst equation to express the diffusion overpotential we have

$$\begin{aligned} \eta_d &= \frac{RT}{z_i F}\ln\frac{C(0,t)}{C_0} \\ \eta_d{}^0 &= \frac{RT}{z_i F}\ln\frac{C_e}{C_0} \end{aligned} \qquad [10]$$

where $\eta_d{}^0$ is the overpotential at the instant the current is switched off and η_d is the overpotential at any time t, which is taken in the calculations at 1 sec. Finally, the diffusion equation in terms of overpotentials is given by

$$\frac{1 - \exp(\eta_d\ z_i F/RT)}{1 - \exp(\eta_d{}^0\ z_i F/RT)} = \phi\left(\frac{\delta}{2\sqrt{Dt}}\right)_{t=1} \qquad [11]$$

The method of calculation is to measure the overpotentials at time zero and at 1 sec from the potential profiles of Fig. 4, evaluate the left hand side of Eq. [11] and find the value of the argument from error function tables. The thickness δ is then calculated from the total "on" time of the discharge and the bulk density of LiCl and thus the effective diffusion coefficient is obtained. The results are given in Table I. The order of magnitude of the diffusion coefficient obtained is about what might be expected for diffusion through a porous body, *i.e.*, at $\sim 10^{-8}$ it is between the value of solid state diffusion $\sim 10^{-12}$ or less and of solution diffusion $\sim 10^{-5}$. The lack of constancy of the effective diffusion coefficient with increasing time could be due to a number of factors which could change the value of the calculated diffusion coefficient in the direction observed. Among these factors are loss of product as a function of discharge time, increasing porosity of product with increasing discharge time or a finite, but diminishing effect of a concentration gradient in the bulk electrolyte as the porous product layer thickens. The first two factors could be reflected in a nonlinear growth rate of the porous layer with discharge time. (It should be recalled that one of the assumptions of the model is a strictly linear rate of growth of the product layer.) In fact, if the layer is assumed to grow at an arbitrary rate, *i.e.*, $\delta(T) = \delta' T^n$, where T is the

Table I

Time (min)	η_0 (V)	$\eta_d{}^0$ (V)	η_d (1 sec) (V)	$\left(\frac{\delta}{2\sqrt{Dt}}\right)_{t=1}$	$\delta \times 10^4$ (cm)	$D \times 10^8$ (cm²/sec)	$\left(\frac{\delta}{2\sqrt{Dt}}\right)^{T-0.43}_{t=1}$
0	0.31	0.04	0	—	—	—	—
15	0.25	0.14	0.08	1.44	1.59	0.30	0.49
80	0.22	0.36	0.28	3.03	8.39	1.9	0.51
105	0.25	0.40	0.33	3.33	11.1	2.8	0.49
135	0.25	0.47	0.38	3.59	14.3	4.0	0.47

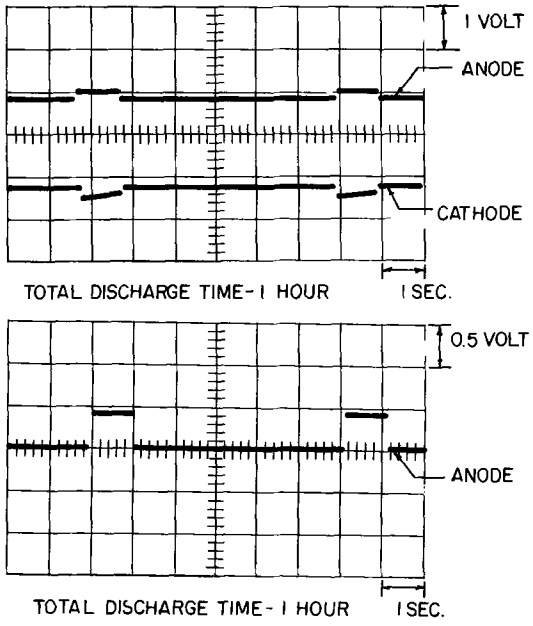

Fig. 5. Oscilloscopic tracings of current interrupted discharge characteristics in test cell with an excess of electrolyte; saturated = LiCl.

total time of current flow, the value of n can be determined from a plot of $\log(\delta/2\sqrt{Dt})_{t=1}$ *vs.* $\log T$. The log-log plot is linear within experimental error and the value of n determined in this way is $n = 0.43$. The constancy of $(\delta/2\sqrt{Dt})_{t=1}\ T^{-0.43}$ is shown in the last column of Table I where the values obtained in this way are constant to within the experimental error. In the absence of more definite information about the nature of the porous film it does not seem advisable to try to extract any further significance from these results.

The column in the table labeled η_0 is the measured combined ohmic and activation overpotential. Its constancy indicates that the electrolyte remains invariant and that there are no unusual ohmic or activation effects which further substantiates the porous layer diffusion model. Further experiments with a large volume of electrolyte containing only $AlCl_3$, in which all of the product LiCl is soluble, show no such concentration polarization but only show the effect of ohmic and activation polarizations. Also, the concentration effect is not observable in solutions which are presaturated with LiCl and stirred during the discharge (see Fig. 5). In the stirred solutions, no layer is observed on the surface of the lithium, but LiCl product does appear on the bottom of the test cell after stirring is ceased. This shows that the product is not very adherent and can be removed with even gentle stirring and its removal eliminates the severe concentration polarization.

In summary, while there are troubling questions about some of the quantitative aspects of the porous product layer diffusion model, it is believed that the qualitative description of this system is accurate and semiquantitative agreement of the theory with the observed results is obtained. Furthermore, it is believed that the technique of observation of open-circuit voltage recovery can offer a valuable diagnostic criterion for cases in which an insoluble product is formed at an electrode.

Conclusions

This study indicates that the discharge of a lithium anode in an $AlCl_3$-propylene carbonate electrolyte can be severely affected by a build-up of product LiCl at the anode surface. Sufficient electrolyte to dissolve the product or stirring of the electrolyte which mechanically removes the product from the surface, eliminates the severe polarization effect. A simplified model of diffusion through a porous product layer has been advanced to attempt to describe the observed polarization effects.

Manuscript submitted Sept. 12, 1968; revised manuscript received July 2, 1969.

Any discussion of this paper will appear in a Discussion Section to be published in the June 1970 JOURNAL.

REFERENCES

1. K. Kordesch and A. Marko, *This Journal*, **107**, 480 (1960).
2. J. F. Hon, *Mol. Phys.*, **15**, 57 (1968).
3. H. Margenau and G. M. Murphy, "The Mathematics of Physics and Chemistry," p. 233, D. Van Nostrand & Co., New York (1943).

Studies of Inhibition of Magnesium Corrosion

David A. Vermilyea* and Carol F. Kirk

Research and Development Center, General Electric Company, Schenectady, New York

ABSTRACT

The corrosion of pure magnesium in aqueous solutions of various pH has been studied. The reaction product is a porous layer consisting mainly of $Mg(OH)_2$ in the absence of inhibitors, but films formed in solutions containing $NaIO_4$ are composed of substances which could not be identified. The reaction in inhibitor-free solutions proceeds by the formation and dissolution of a primary film, possibly an oxide, followed by precipitation of a film of $Mg(OH)_2$. In $NaIO_4$ solutions the reaction product is thicker and probably denser because the periodate decreases its dissolution rate, and the over-all metal removal rate is less by a factor of 10 at pH 9-10.

Recent studies (1) of the dissolution of MgO and $Mg(OH)_2$ revealed that periodate, germanate, vanadate, and tellurate ions retarded dissolution in alkaline solutions, while sodium dodecyl sulfonate was an inhibitor in acid solutions. This paper presents the results of a study of inhibition of corrosion of metallic magnesium by those substances.

* Electrochemical Society Active Member.

Experimental

The metal specimens, cut from ingots of 99.99% Mg obtained from United Mineral and Chemical Corporation, were about 3 cm x 1 cm x 0.05 cm. We do not know what impurities were present in the magnesium. Etching for 30 sec in 10% HNO_3 followed by 10 sec in 2% HCl produced a surface which was fairly smooth on a microscopic scale. The grain size was about 0.2

cm. Surfaces prepared with other chemical etching pretreatments gave similar results.

Weight measurements made using a Cahn RG Electrobalance were repeatable to about 10^{-6} g/cm^2. Specimens were weighed before and after exposure and after a 60 sec immersion in 10% CrO_3. The latter treatment removed the reaction product with little attack on the metal; freshly prepared specimens lost 5×10^{-6} g/cm^2 after the chromic acid treatment.

The specimens were exposed at 25°C in 500 cc of solution in vessels with ground glass covers to prevent absorption of CO_2 in the alkaline solutions. It is known (2) that the corrosion rate of magnesium in water is not greatly affected by the presence of oxygen. We actually found little difference in a period of a week whether the vessel was open or closed. The solutions were not agitated.

The reaction product was examined using standard diffraction and electron microscopic techniques and also by reflection infrared spectroscopy. For the latter examination a Beckmann IR-12 spectrometer was used with a specimen holder which gave three reflections from polished magnesium sheets which were cut from the ingots, metallographically polished, and chemically etched by the procedure described above.

Results

Nature of the reaction product.—Specimens were usually exposed to solutions containing 10^{-4} M $MgSO_4$ plus the inhibitor to be studied plus KOH to pH 10.0 ± 0.2. We added the $MgSO_4$ in order that the total Mg^{+2} concentration would not change greatly during an experiment, but actually we could not detect any difference when it was absent.

Electron diffraction from samples exposed to solutions with no inhibitor revealed that $Mg(OH)_2$ and Mg were present, with no other substances giving diffraction. The lines were somewhat diffuse. Samples exposed to $NaIO_4$ solutions, on the other hand, yielded diffuse electron diffraction lines which could not be associated with any known compound.

Electron microscope studies showed that films produced in inhibitor-free solutions were composed of platelets the outer portions of which were about 300 by 3000Å. Figure 1 shows a typical example, but does not reveal the three-dimensional structure visible with stereo photomicrographs. The structure appears very similar to that observed on $Al(OH)_3$ films formed by reaction of aluminum with water (3). At least the outer portion of the layer is evidently quite porous. Presumably the platelets are $Mg(OH)_2$. Longer exposures gave similar films with slightly smaller platelets.

The platelets shown in Fig. 1 appear to have random orientations. A specimen exposed in plain water developed the film shown in Fig. 2. In that film it appears that there are some platelets oriented nearly perpendicular to the surface while a majority have their major faces parallel to the surface. Probably the platelets dissolve faster at the edges, so that platelets which nucleate with an orientation perpendicular to the surface are dissolved preferentially, leaving those oriented parallel to the surface. The somewhat higher dissolution rate in plain water as compared with the pH 10 solution is responsible for the different film morphology.

By contrast, with the above results, the outer surface of a specimen exposed in a $NaIO_4$ solution had the appearance of a mud flat, Fig. 3. In Fig. 3 the white areas are probably cracks in the replica. Evidently the periodate has caused a profound change in the character of the layer. It is not certain that this layer is porous. Shorter exposures to $NaIO_4$ solutions gave products with some platelets and some "mud flat" areas. It therefore appears that as the film grows the spaces between platelets are filled in.

Infrared spectroscopic studies over the region 800-4000 cm^{-1} of films grown in inhibitor-free solutions showed only a single intense absorption at 3700 cm^{-1} with a width of 20 cm^{-1} at half maximum intensity. Using the same spectrometer we found that this absorption, which is the OH stretching vibration, occurred at 3698 cm^{-1} in natural Brucite and at 3702 cm^{-1} in $Mg(OH)_2$ precipitated from $MgSO_4$ solution with KOH. In the latter two spectra the width at half maximum intensity was only 12 cm^{-1}. In the spectrum from the reaction product there were no bands, even weak broad ones, corresponding to liquid water or to hydroxyl ions in other crystallographic positions. It is concluded that these films are mostly reasonably well crystallized $Mg(OH)_2$.

Infrared spectra from specimens exposed in $NaIO_4$ solutions, by contrast, showed the rather more complicated structure. In addition to the band at 3700

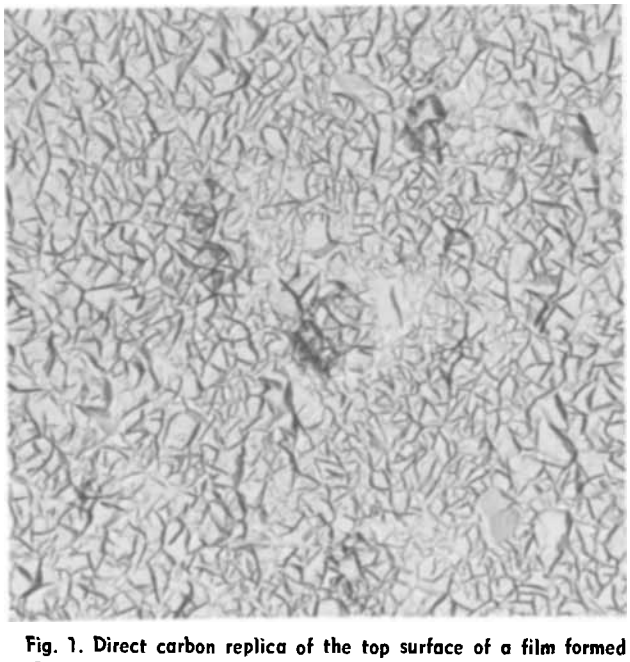

Fig. 1. Direct carbon replica of the top surface of a film formed in 294 min on magnesium in $MgSO_4$ + KOH solution, pH 10.1 Magnification 15,000X.

Fig. 2. Top surface of a film formed on magnesium in 100 min in pure water. Magnification 15,000X.

Fig. 3. Top surface of a film formed in 68 hr in a 10^{-3}M $NaIO_4$ solution, pH 10. Magnification 15,000X.

cm^{-1} there was a broad, intense absorption between 2600 and 3800 cm^{-1}, other weaker ones at 1450 cm^{-1} and 1650 cm^{-1}, and finally a broad absorption at 720 cm^{-1}. While the broad absorption at 2600-3800 cm^{-1} suggests hydroxyl ions in various binding states the interpretation of the details of this spectrum is not obvious, since the remaining bands did not correspond exactly to those for likely substances like periodate or iodate. However, the complexity of this result reinforces the conclusion from diffraction and microscopy that the product formed in periodate solutions differs substantially from that formed in inhibitor-free solutions. $Mg(OH)_2$ precipitated with KOH from a $MgSO_4$ solution containing $NaIO_4$ gave a spectrum with the same features as that from the film, except that the band at lower energy was at 680 cm^{-1}.

Corrosion rate, inhibitor-free solutions.—Figure 4 shows the weight loss after removal of the reaction product in CrO_3 for exposures in 10^{-4}M $MgSO_4$ plus KOH to *p*H 10. The unexposed specimens would lose about 5×10^{-6} g/cm^2 in CrO_3 because of the dissolution of the initial film, and extrapolation of data from longer times indicates that the initial film would be produced in about 12 min. Hence each exposure time was increased by 12 min to take account of the film initially present.

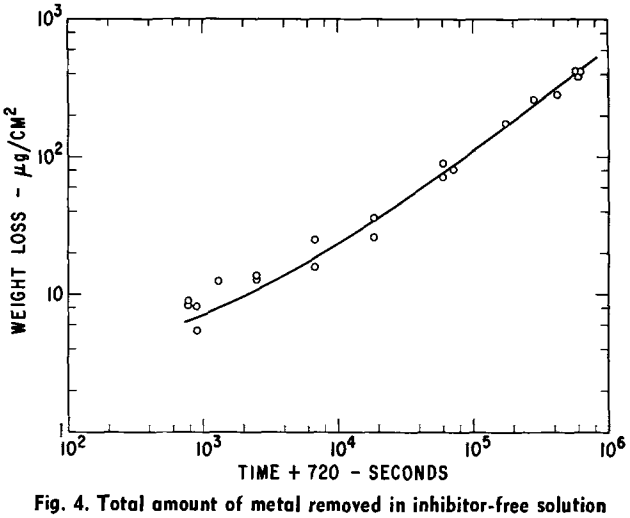

Fig. 4. Total amount of metal removed in inhibitor-free solution

Table I. Rates of various processes

Process	Time, sec	Rate, moles/cm^2-sec
Corrosion of Mg in inhibitor-free solution	6×10^3	6.6×10^{-11}
	6×10^4	3.7
	6×10^5	2.1
Formation of Mg^{+2} in inhibitor-free solution	6×10^5	1.6×10^{-11}
Corrosion of Mg in $NaIO_4$ solution	6×10^3	4.8×10^{-11}
	6×10^4	1.2
	6×10^5	0.29
Dissolution of MgO		10^{-11}
Natural brucite ($Mg(OH)_2$)		10^{-13}
High energy Mg $(OH)_2$		10^{-10}

The average slope of the log-log plot of Fig. 4 is about 2/3, so that the rate decreases with time but not as fast as if controlled by a diffusion process. The slope appears to increase somewhat at long times, suggesting an approach toward a constant rate, probably ultimately controlled by dissolution of the product. Table I gives corrosion rates calculated from the data of Fig. 4. Blanchet *et al.* (3) found a steady corrosion rate of about 11.7 mdd or 5.6 10^{-11} moles/cm^2-sec for pure magnesium in refreshed pure water at 22°C, in reasonable agreement with the results of this study. Corrosion rates in 3% NaCl are from two to ten times higher (2, 4); we have found that a solution of 10^{-4}M $MgCl_2$ plus KOH to *p*H 10 causes pitting attack and increased weight loss.

Table I also gives rates from the previous study (1) for dissolution of MgO; highly reactive, fine particle $Mg(OH)_2$ obtained from Mathieson, Coleman, and Bell and designated "high energy $Mg(OH)_2$"; and for natural Brucite, all at *p*H 10. If diffusion of dissolved $Mg(OH)_2$ away from the specimens was the controlling process the rate would be about 10^{-10} moles/cm^2-sec for a diffusion layer thickness of 10^{-2} cm. A comparison of the observed corrosion rate with these values shows the following. The rates are always less than the diffusion limited rate, especially at longer times. The rates are less than that for high energy $Mg(OH)_2$, which suggests the presence of a reasonably well crystallized product. The electron micrographs of Fig. 1 and 2 support this conclusion. The rates are much greater than the rate for natural Brucite, however.

Figure 5 shows that before the CrO_3 treatment the specimens exposed in the inhibitor-free solution showed a small weight gain at short times but a large weight loss at long times. From the data in Fig. 4 and 5 it is possible to determine the rate of dissolution to form Mg^{+2} and the rate of formation of $Mg(OH)_2$. Assuming that the reaction produces only Mg^{+2} and $Mg(OH)_2$, the following relationships are valid

$$\Delta W_I = \Delta W_1 \times 2 \times \frac{\text{mol.wt OH}}{\text{mol.wt Mg(OH)}_2} - \Delta W_2 \quad [1]$$

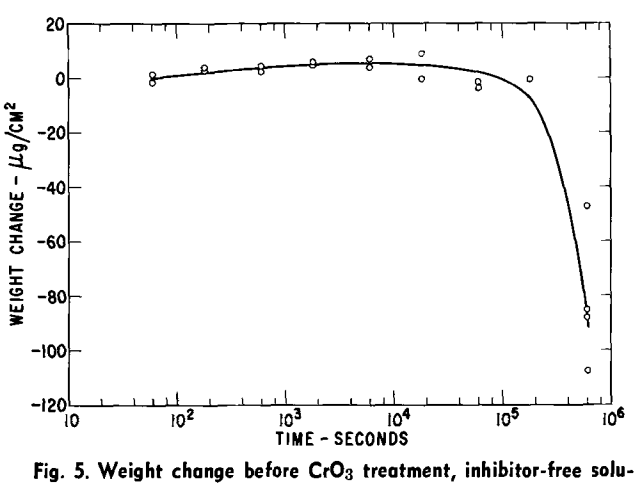

Fig. 5. Weight change before CrO_3 treatment, inhibitor-free solution.

$$\Delta W_{II} = -\Delta W_1 \times \frac{\text{mol.wt Mg}}{\text{mol.wt Mg(OH)}_2} - \Delta W_2 \quad [2]$$

In Eq. [1] and [2], ΔW_I and ΔW_{II} are the weight changes after exposure and after the removal of the product in CrO_3 respectively, and ΔW_1 and ΔW_2 are the weight of $Mg(OH)_2$ formed and the weight of Mg^{+2} dissolved. Solving for ΔW_1 and ΔW_2 gives

$$\Delta W_1 = \Delta W_I - \Delta W_{II} \quad [3]$$

$$\Delta W_2 = -0.583\,\Delta W_{II} - 0.417\,\Delta W_I \quad [4]$$

Figures 6 and 7 show log-log plots of ΔW_1 and ΔW_2; the average slopes are about 0.58 and 0.84, respectively, so that both weight change rates decrease with time. The slope of the curve for growth of $Mg(OH)_2$ suggests diffusion control while the rate of dissolution of Mg^{+2} is nearly constant. At 10^6 sec the dissolution rate is $1.6 \cdot 10^{-11}$ moles/cm^2-sec which is only slightly less than the total corrosion rate of $2.1 \cdot 10^{-11}$ moles/cm^2-sec; evidently dissolution is the most important process at long times.

Corrosion rates in $NaIO_4$ solutions.—Figure 8 presents data for specimens exposed in 10^{-3}M $NaIO_4$ plus 10^{-4}M $MgSO_4$ plus KOH to *p*H 10. The scatter of these results is very large for reasons which are not apparent. There was some pitting and also crevice corrosion where the specimen rested against a glass support; perhaps the scatter is associated with variations in the amount of local attack.

The slope of the log-log plot is only 0.38, so the rate falls off faster than for a process under diffusion control. Corrosion rates calculated from the curve and listed in Table I are initially about the same as in the absence of inhibitors but at long times are less by a factor of 10. Apparently the modifications of the corrosion product which were revealed by diffraction, microscopy, and infrared spectroscopy result in a reduced corrosion rate.

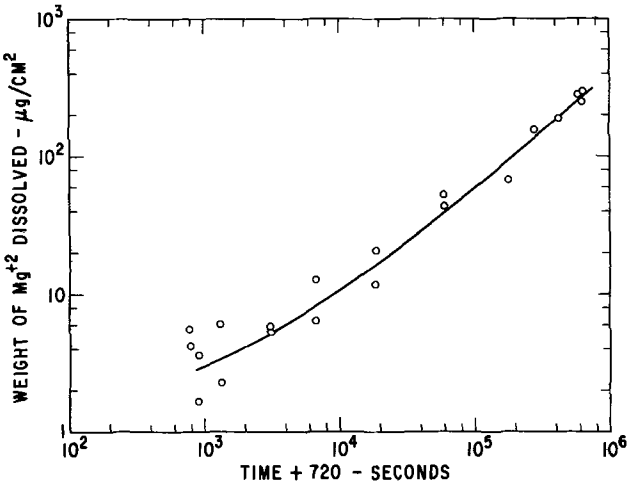

Fig. 6. Mg^{+2} dissolved in inhibitor-free solutions, calculated from Eq. [4].

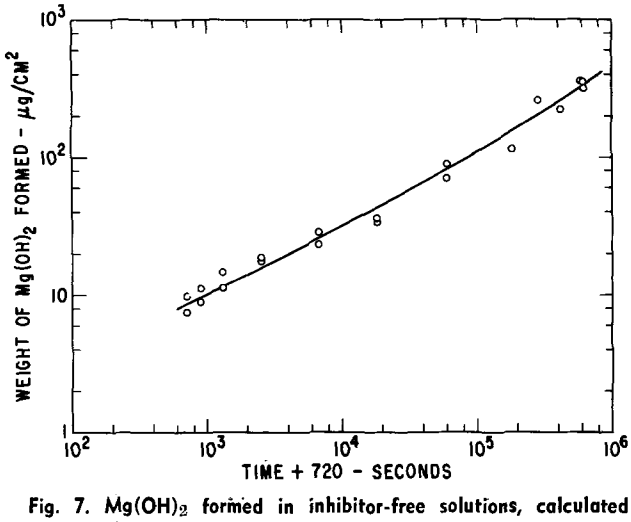

Fig. 7. $Mg(OH)_2$ formed in inhibitor-free solutions, calculated from Eq. [3].

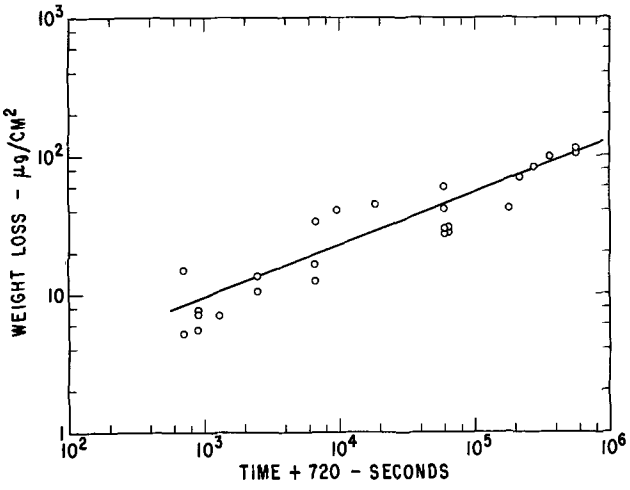

Fig. 8. Total amount of metal removed in $NaIO_4$ solutions

Figure 9 shows that the specimens gained weight when measured before the CrO_3 treatment, in contrast to the results in inhibitor-free solutions. If the assumption is again made that only $Mg(OH)_2$ and Mg^{+2} are formed as corrosion products and the results analyzed with Eq. [3] and [4], it is found that the amount of Mg^{+2} formed is less than zero for many specimens. Evidently the assumption that only $Mg(OH)_2$ and Mg^{+2} form is incorrect, a result which reinforces the conclusions from infrared spectroscopic studies.

Increasing the $NaIO_4$ concentration to 10^{-2}M did not decrease the corrosion rate much below that for 10^{-3}M, but at 10^{-4}M the specimen was pitted and the total corrosion rate was about twice as great as in inhibitor-free solutions.

Role of pH.—In inhibitor-free solutions with an initial *p*H of 10 the *p*H increased during exposure, and at 10^6 sec reached 10.5. In $NaIO_4$ solutions, on the other hand, the *p*H fell and reached 9.3 at 10^6 sec. Table II gives results of studies of the effect of *p*H on the rate of attack. In inhibitor-free solutions the total corrosion rate, the amount of $Mg(OH)_2$ formed and the amount of Mg^{+2} dissolved all decreased with increasing *p*H. In $NaIO_4$ solutions the total corrosion was least at *p*H 9, although the weight gain before CrO_3 increased continuously with increasing *p*H. The interpretation of these results will be given in the discussion.

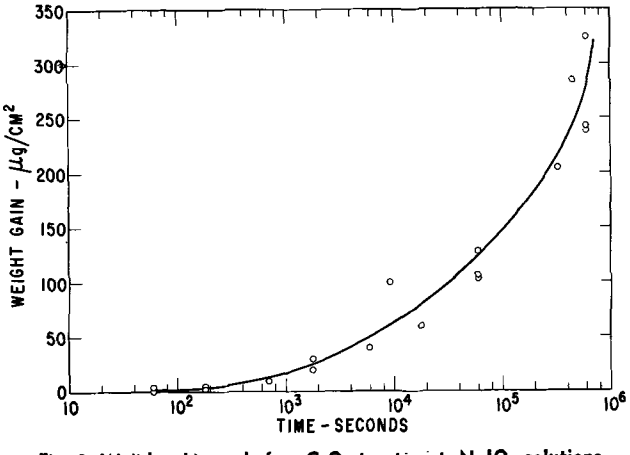

Fig. 9. Weight change before CrO_3 treatment, $NaIO_4$ solutions

Table II. Effect of pH on rates

A. Inhibitor-free solutions

Weight change at 1.8 x 10^5 sec (interpolated)

pH	Total corrosion, $\mu g/cm^2$	Before CrO_3, $\mu g/cm^2$	$Mg(OH)_2$ formed, $\mu g/cm^2$	Mg^{+2} dissolved, $\mu g/cm^2$
8	−250	−70	165	160
9	−210	−55	155	150
10	−118	−3	115	70
11	−57	+13	70	38

B. $NaIO_4$ solutions

Weight change at 3 x 10^5 sec (interpolated)

pH	Total corrosion, $\mu g/cm^2$	Before CrO_3, $\mu g/cm^2$
8	−130	+40
9	−63	+112
10	−84	+204
11	−100	+350

Other inhibitors for alkaline solutions.—Much less work was done with other inhibitors than periodate, which was found to have greatest influence on the dissolution of $Mg(OH)_2$. In other studies it was found that tellurate was reduced, evidently to tellurium, and a black deposit covered the specimen; tellurium was detected in the deposit by x-ray fluorescence. Germanates and vanadates did reduce the corrosion rate somewhat, but not by as large a factor as did periodate. Germanium and vanadium were not detected on the specimens after exposure. All inhibitors were present at 10^{-3}M.

Corrosion at low pH.—In pH 1 H_2SO_4 magnesium was found to corrode at a rate equal to that calculated on the basis of control by proton diffusion to the surface. In pH 3 H_2SO_4 and $HClO_4$ however, the rate was found to be constant at about 3.4 x 10^{-10} moles/cm^2-sec, while the rate calculated on the basis of control by proton diffusion and a stationary layer thickness of 10^{-2} cm is about 5 x 10^{-9} moles/cm^2-sec. X-ray diffraction and infrared spectroscopy disclosed the presence of $Mg(OH)_2$ on the samples, while electron microscopy revealed a structure similar to that of Fig. 1.

The reduced rates and presence of $Mg(OH)_2$ in pH 3 solutions can be understood if the effect of the diffuse double layer near the surface is considered. The point of zero change of $Mg(OH)_2$ is about pH 12 (5). At pH 3 the potential difference between the surface of $Mg(OH)_2$ and the solution could be as large as about 0.5V. In a 10^{-3}M solution the concentration of positively charged ions at the plane of closest approach is then calculated to be about 10^{-6}, so the pH in the vicinity of $Mg(OH)_2$ particles is about 6 instead of 3. The dissolution rate of the natural Brucite at pH 6 is about 10^{-10} moles/cm^2-sec. Using Eq. [3] and [4] with the observed values of $\Delta W_I = -118$ $\mu g/cm^2$ and $\Delta W_{II} = -413$ $\mu g/cm$ for a specimen exposed in pH 3 H_2SO_4 for 6 x 10^4 sec gives $\Delta W_1 = 295$ $\mu g/cm^2$ and $\Delta W_2 = 290$ $\mu g/cm^2$. Converting ΔW_2 to a rate gives 2 x 10^{-10} moles/cm^2-sec for formation of Mg^{+2}, in reasonable agreement with the calculated rate.

Confirmation of the role of the diffuse double layer was obtained by adding M Na_2SO_4 and M $NaClO_4$ to the pH 3 solutions. In M Na_2SO_4 (pH 3.0) the total corrosion rate was 3.1 x 10^{-9} moles/cm^2-sec, while in M $NaClO_4$ (pH 3.1) it was 5.2 x 10^{-10}. Using the analysis of Eq. [3] and [4] the dissolution rates were 2.1 x 10^{-9} and 3.9 x 10^{-10} for sulfate and perchlorate solutions, respectively; the expected rate for Brucite at pH 3 is 4 x 10^{-9} moles/cm^2-sec. For the perchlorate solution there is still an appreciable double layer correction which makes the surface pH 3.6 and the expected rate 2 x 10^{-9} moles/cm^2-sec. The agreement is within a factor of 2 for Na_2SO_4 and a factor of 5 for the $NaClO_4$, which is fair. It is concluded that the double layer effect is plausible.

Corrosion accelerators.—Buffer solutions at around neutral pH act as accelerators of magnesium corrosion. In carbonate solutions for example, rates of 1.6 x 10^{-7} moles cm^2-sec and 1.4 x 10^{-10} moles/cm^2-sec were measured in M $NaHCO_3$ and 10^{-3}M $NaHCO_3$, respectively; solution pH's were 7.95 and 8.35. Assuming that the process was controlled by diffusion of HCO_3^- to the surface the theoretical rates are 5 x 10^{-7} and 5 x 10^{-10} moles/cm^2-sec, in reasonable agreement with the measured values.

Corrosion in gases.—Specimens exposed in the laboratory atmosphere gained only 1 $\mu g/cm^2$ in 7 days, while at 240°C the weight gain in 18 hr was about 1.4 $\mu g/cm^2$. Other samples were exposed at 25°C in a closed vessel containing a M NaCl solution to produce an atmosphere with a humidity of about 98%. After 2.3 x 10^5 and 3.4 x 10^5 sec the weight gains were 2.4 and 9.6 $\mu g/cm^2$. After CrO_3 treatment total weight losses were 7.1 and 10.1, respectively. (It should be remembered that an unexposed specimen would lose 5 $\mu g/cm^2$.) Corrosion in gaseous environments at moderate temperatures is evidently very slow, even when the gas is nearly saturated with water vapor. For rapid corrosion liquid water is necessary.

Discussion

These studies have shown that the corrosion of pure magnesium in water has characteristics very similar to those of the aluminum-water reaction (3). For instance, the reaction does not proceed in the absence of a liquid phase; a porous product of similar appearance is produced; there is little effect of temperature (4); and the kinetics suggest control by diffusion through the porous reaction product. These similarities suggest that for magnesium as for aluminum the reaction proceeds by the formation and dissolution of a primary film, with the rate controlled by the disposition of the soluble species. The magnitude of the corrosion rate observed in these studies for inhibitor-free solutions is similar to the rate of dissolution of MgO, which suggests that the primary film may be an oxide.

A possible corrosion mechanism is then the formation of a magnesium oxide, dissolution of the oxide to form soluble species, and precipitation of an $Mg(OH)_2$ film which gradually impedes the process. At long times, when the corrosion rate is sufficiently reduced, there would be a balance of the formation and dissolution of the $Mg(OH)_2$, which would finally have a constant thickness. The corrosion rate would then be constant. The role of pH is then easy to understand, for as the pH increases the rates of dissolution of the oxide and the hydroxide decrease sharply, so that all the rates decrease.

The role of periodate is to decrease the rate of dissolution of $Mg(OH)_2$ so that more reaction product accumulates and stifles the reaction. The nature of the reaction product is substantially altered in the presence of periodate. The role of pH is slightly different in periodate solutions. As the pH increases from 8 there is first a decrease in rate because of the slower rate of dissolution of the reaction products. However, at higher pH as the point of zero charge is approached the potential of the $Mg(OH)_2$ or MgO relative to the solution decreases and the attraction of IO_4^- to the surface is less. The inhibition is then decreased and at pH 11 the rates in inhibitor-free and inhibitor-containing solutions are about the same.

Conclusions

1. Periodate ion decreases the rate of the corrosion of magnesium in the pH range 8-10 after a week's exposure by about a factor of 10.

2. The effect of periodate is to change the nature of the reaction product and retard its dissolution.

3. A mechanism comprising formation of magnesium oxide, its dissolution to form Mg^{+2}, followed by precipitation of some of the Mg^{+2} as $Mg(OH)_2$ is consistent with the observations.

Acknowledgment

We are indebted for electron microscopy to E. Koch, for infrared spectroscopy to R. Chrenko, for diffraction studies to A. Davis and W. Dorfeld, and for preliminary experimental work to D. Ochar.

Manuscript submitted April 8, 1969; revised manuscript received ca. June 30, 1969.

Any discussion of this paper will appear in a Discussion Section to be published in the June 1970 JOURNAL.

REFERENCES

1. D. A. Vermilyea, To be published.
2. H. H. Uhlig, "Corrosion and Corrosion Control," pp. 307-309, John Wiley & Sons, Inc., New York (1963).
3. W. Vedder and D. A. Vermilyea, *Trans. Faraday Soc.* (1969).
4. J. Blanchet, H. Coriou, L. Grall, M. Pelras, G. Plante, and M. Salesse, *J. Nuclear Materials*, **7**, 311 (1962).
5. G. A. Parks, *Chem. Rev.*, **65**, 177 (1965).

Partial Currents During Anodic Dissolution of Cu-Zn Alloys at Constant Potential

H. W. Pickering* and P. J. Byrne

E. C. Bain Laboratory for Fundamental Research, United States Steel Corporation, Monroeville, Pennsylvania

ABSTRACT

The partial currents, i_{Zn} and i_{Cu}, for anodic dissolution of single phase Cu-Zn alloys in a sulfate solution are shown for the potential range $-1000 < E < 500$ mV. The results show the conditions for preferential dissolution of the less noble component and in which potential range transition to simultaneous anodic dissolution takes place. The polarization curve for Zn exhibits a potential region of low, relatively constant current and another region above a certain potential, E_c, where the current increases sharply with potential. E_c increases with increasing Cu content. Copper dissolution is observed only at the higher potentials in accord with its more noble standard potential. These results are in qualitative agreement with the dissolution behavior of Cu from Cu-Au alloy found by Gerischer and Rickert.

Over a decade ago Gerischer and Rickert (1) presented probably the first polarization curve for the less noble component of an alloy in a study of the dissolution of various Cu-Au alloys as a function of applied potential. Since Au did not dissolve for their experimental conditions the measured current was due mainly to Cu dissolution. The curves contain complex features not before observed for metals or alloys. They include a potential region where Cu dissolves at a low, potential-independent rate. Above a certain potential, referred to as the critical potential, E_c, the current increases sharply with potential. Also E_c is a function of alloy composition, increasing with increase in gold content. Gerischer and Rickert further showed that long times were required in arriving at a quasi-stationary current. The current starts out high but decreases at an ever decreasing rate; after an hour there is very little further decrease. For the potential range investigated Cu was found to dissolve at an appreciable rate only from the Cu-rich Cu-Au alloys. These results have been confirmed in our own investigations where all the above-mentioned features were observed (2).

More recently Feller (3) has shown, with the help of a rotating disk-ring electrode, that preferential dissolution of Zn from Cu-Zn alloys occurs more predominantly with the Zn-rich than with the Cu-rich alloys. Similar results have been obtained by Sugawara and Ebiko (4), as shown by metallographic examination of dissolved specimens, and by others (5). For the same rates of dissolution a higher potential was required the higher the copper content of Cu-Zn alloys. This is similar to the aforementioned behavior of Cu-Au alloys and also to the behavior of Ag-Au alloys (6) and the ternary Fe-Cr-Ni alloys (7, 8). In none of these investigations, however, was a potential region of low, constant current observed, similar to that found with Cu-Au alloys by Gerischer and Rickert. Also Graydon and co-workers (9) obtained kinetic data on the dissolution of copper from α brass during immersion in an oxygen-saturated sulfuric acid solution. Periodic polarographic measurements indicated that the rate of copper dissolution increased with time for many hours prior to the attainment of a steady value.

In order to determine the conditions for preferential and simultaneous dissolution, the partial currents for various binary alloys are being currently determined as a function of potential. These are alloys for which both components dissolve over part or all of the potential range of interest, so that one obtains for each alloy two polarization curves, one for each component. In this paper are presented the partial currents of Cu (i_{Cu}) and of Zn (i_{Zn}) as a function of potential for dissolution of three single-phase Cu-Zn alloys, which range from Cu-rich to Zn-rich.

Experimental

In order to obtain i_{Zn} and i_{Cu} during potentiostatic dissolution of Cu-Zn alloy at 23°C, the amounts of Cu and of Zn in the electrolyte were periodically determined by chemical analysis. Data were obtained for dissolution of single-phase alloys of α, γ, and ϵ brass in the buffered electrolyte (pH $\cong$ 5), 1*N* Na_2SO_4 — 0.05*N* $NaC_2H_3O_2$ — 0.05*N* $HC_2H_3O_2$.

Specimens, ~0.1 cm thick and 1.25 cm in diameter, of single-phase γ and ϵ brass were prepared as described elsewhere (10). Chemical and x-ray analysis indicated their compositions to be Cu 65 a/o (atomic per cent) Zn (Cu65Zn) and Cu 86 a/o Zn (Cu86Zn), respectively. The α brass designated as 70/30 brass was provided by American Smelting and Refining Company. It was homogenized for 2½ days at 600°C in an

* Electrochemical Society Active Member.

evacuated capsule, rolled to a thickness of 0.015 cm and then annealed at 600°C for 16 hr in an evacuated capsule. X-ray diffraction analysis indicated the composition to be approximately Cu 30 a/o Zn (Cu30Zn). Specimens of α brass were prepared with an area of ~6 cm^2. γ brass is complex bcc, ϵ brass is hcp, and α brass is fcc.

The cell of Pyrex construction is shown in Fig. 1. The Pyrex tube prevents Cu and Zn ions, formed by dissolution of the specimen, from coming in contact with the counter electrode where they may be deposited. Contact of the electrolyte between the two chambers occurs via three small (3 mm diameter) fine frits located approximately 120° apart. The electrolyte was made from reagent-grade chemicals and doubly distilled water. Prepurified helium was passed through the cell before and during dissolution in order to remove oxygen. The reference cell was a mercury-mercurous sulfate electrode. The potentials, which were maintained with a Wenking potentiostat, are all reported relative to the standard hydrogen electrode (SHE). Electrical contact to the specimen was made with a Teflon-coated copper rod which has one end slotted and fitted with a tightening screw. The small contact area between the sample and rod was sealed from the environment with polyethylene. Immediately prior to insertion at a particular potential the specimen surfaces were ground with 600 emery paper, cleaned with methanol and rinsed in water.

Quantitative chemical analysis of the electrolyte from the anode (inner) compartment of the cell provided the amounts of Cu and Zn dissolved. In an auxiliary experiment using a pure Cu specimen it was determined that negligible amounts of Cu^{2+} ion were lost from the inner compartment by transport through the frits. In the runs at high potentials (currents), however, the Pyrex tube was removed in order to be within the output of the potentiostat; Cu and Zn which deposited on the Pt counter electrode were then dissolved chemically prior to quantitative chemical analysis. For low concentrations of both copper and zinc ions, colorimetric analysis was used. Positive identification of the presence of copper and zinc ion in the electrolyte could be made for concentrations as low as 0.05 μg/cc Cu and 0.02 μg/cc Zn. Usually the concentrations of Cu and Zn ions in the electrolyte, if detectable at all, were considerably higher than this. For example, oxidation of Cu or Zn to the divalent ion at a current density of 1 x 10^{-6} A/cm^2 corresponds to a concentration in the electrolyte after 20 hr of 0.5 μg/cm^3 in the case of the γ and ϵ specimens; in the case of the α brass specimens, with their larger surface area, the same current density corresponds to a concentration of Cu or Zn ions of 1.4 μg/cm^3 after 20 hr. For high concentrations of the ions coulometric and titrimetric methods were used for copper and zinc, respectively. In order to obtain data on the partial currents as a function of time of dissolution, fresh electrolyte was placed in the cell after the initial dissolution period and dissolution was continued. This electrolyte was then drained and analyzed, and again the cell was replenished with fresh electrolyte, etc.

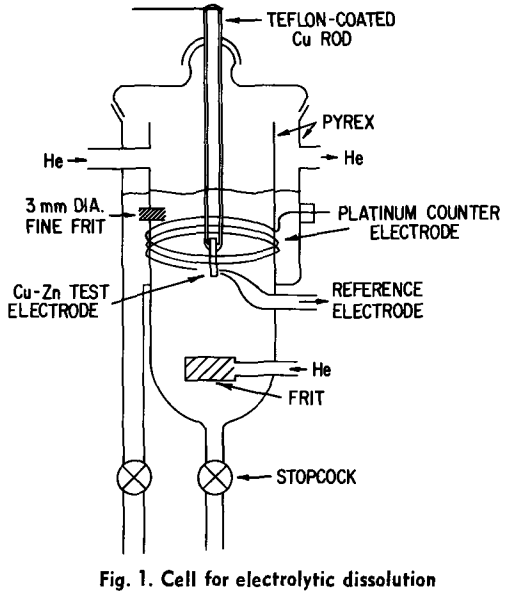

Fig. 1. Cell for electrolytic dissolution

Specimens were usually dissolved in two dissolution periods; the data obtained during the second period were used to arrive at a polarization curve. The lengths of the first and second periods were set at 1 and 20 hr, except when the quasi-stationary currents were large ($\gtrsim$10 mA/cm^2), when shorter times were used. The average current densities calculated on the basis of the geometrical area from data obtained in the second period were then plotted as a function of potential to give the polarization curves for the individual components. IR corrections were negligible since for all but the most positive potentials the net current, anodic or cathodic (measured off the meter), did not exceed 10 mA/cm^2 corresponding to an IR value of ~10 mV.

Results

Current-time behavior.—i_{Zn} for dissolution of Zn from all three alloys in 1*N* Na_2SO_4 — 0.05*N* $NaC_2H_3O_2$ — 0.05*N* $HC_2H_3O_2$ starts out high but falls at an ever decreasing rate. Most of the relatively large amount of dissolution associated with the approach to the quasi-stationary current occurs during the first hour and after many hours the rate of decrease is quite low; at the higher potentials, especially for α brass, the approach to a quasi-stationary current is much faster. Typical i_{Zn}-time behavior for Zn dissolution is shown in Fig. 2. After the 1-hr initial period, consecutive periods of 16-24 hr duration were used. In plotting the points allowance was made for the passage of a larger amount of charge during the earlier part of each dissolution period. The points accordingly lie at shorter times than the mid-times of the dissolution periods.

i_{Cu}-time behavior for dissolution of Cu is similar to that for Zn. The rate of decrease of i_{Cu} is usually less than that of i_{Zn} so that the ratio of the copper and zinc currents, i_{Cu}/i_{Zn}, increases with time; for some potentials this ratio becomes the same as the Cu/Zn atom ratio in the alloys (simultaneous dissolution). Exceptional i_{Cu}-time behavior in these investigations, but similar to that reported by Graydon and co-workers (9) for immersion of α brass in oxygen-saturated sulfuric acid, is an increase in i_{Cu} with time at the highest potentials rather than a decrease.

Current-time behavior at higher potentials than in Fig. 2 is shown in Fig. 3 where the total current due to metal dissolution ($i_{Zn} + i_{Cu}$) is plotted as a function of time of dissolution of a γ and an α brass specimen.

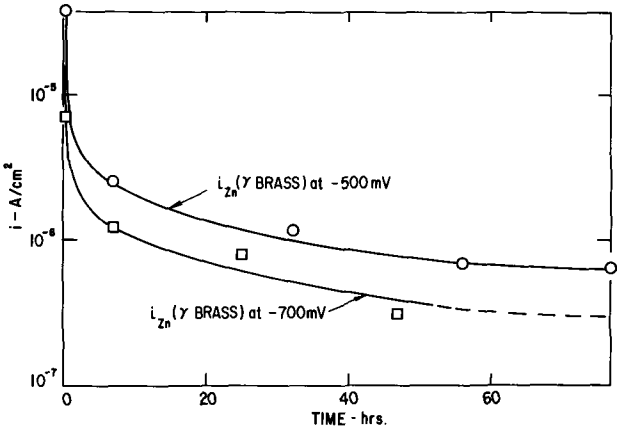

Fig. 2. i_{Zn}-time behavior for dissolution (preferential) of Zn from γ brass in 1*N* Na_2SO_4-0.05*N* $NaC_2H_3O_2$-0.05*N* $HC_2H_3O_2$.

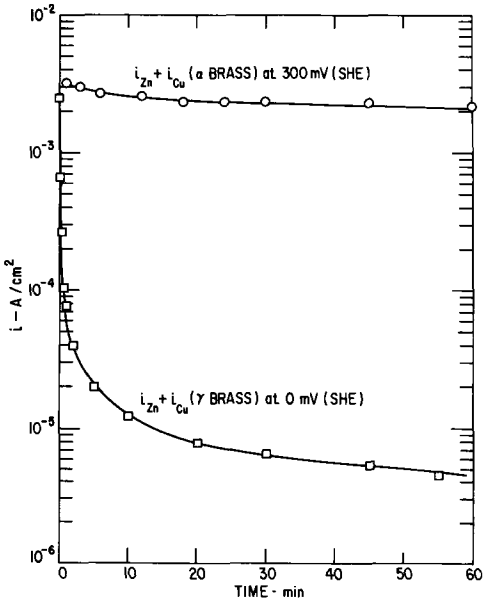

Fig. 3. ($i_{Zn} + i_{Cu}$)-time behavior for dissolution of Zn and Cu from α and γ brass.

The above-mentioned faster approach to a quasi-stationary current at high potentials is seen in the top curve for α brass. The data points are not from chemical analysis data; rather they are the directly measured currents (from the microammeter) which may be taken as the $i_{Zn} + i_{Cu}$ values since hydrogen evolution was negligible.

Partial polarization curves.—Curves of $i_{Zn} - E$ and $i_{Cu} - E$ for dissolution of Zn and Cu from single-phase Cu-Zn alloys in 1*N* Na_2SO_4 — 0.05*N* $NaC_2H_3O_2$ — 0.05*N* $HC_2H_3O_2$ are shown in Fig. 4. The polarization curves for the less noble component, Zn, exhibit complex behavior. There is a critical potential, E_c, where the rate of dissolution and its dependency on potential changes sharply. Below E_c there is a potential region of low, relatively constant current, whereas above E_c there is a potential region of rapidly increasing current, the rate of increase falling off at the higher potentials. E_c is a function of alloy composition, increasing with increasing content of the more noble component, Cu. E_c has values of roughly −950, 0, and +100 mV (SHE) for ε, γ, and α brass, respectively, although for ε brass the potential range of the low-current region is small or nonexistent in view of the proximity of the reversible potential of Zn in the electrolyte. Good agreement was observed between the Zn current calculated from the chemical analysis data and the directly measured value when conditions were such that the latter was due mainly to Zn dissolution. For example the data points in Fig. 4, ▽ at −470 mV and ◇ at 125 mV, for the i_{Zn} (ε brass) and i_{Zn} (γ brass) curves, respectively, are the directly measured currents.

Polarization curves for dissolution of Cu are shown (Fig. 4) only for γ and α brass. With ε brass no copper dissolution was detected for the potentials investigated. Cu dissolves from γ brass at $E \gtrsim 50$ mV with i_{Cu} rising rapidly to a value of ~0.1 mA/cm² at ~250 mV. Even at this potential, however, i_{Cu} is less than i_{Zn} by two orders of magnitude. The partial currents for Cu dissolution from γ brass at $E > 150$ mV are for shorter dissolution periods than the normal 1- and 20-hr periods (since i_{Zn} was so high); hence these currents are larger than they would have otherwise been and the scatter is greater.

Cu dissolves from α brass at about 50 mV with i_{Cu} rising rapidly to a value of ~16 mA/cm² at 400 mV. Above ~200 mV $i_{Cu} \cong 2i_{Zn}$.

Metallographic examination.—Cross-section metallographic examination of the specimens is revealing in the case of the higher current densities ($E > E_c$). For both ε and γ brass specimens a porous (poorly reflecting) layer is observed after appreciable dissolution. Pronounced, localized (cracklike) dissolution was also evident with γ brass, especially at the higher potentials. These features are illustrated in Fig. 5. Also at the higher potentials a (outer) scale sometimes is observed although not in Fig. 5. Cross-section metallographic examination of the dissolved α brass specimens for $E > E_c$, on the other hand, indicates that the porous-type alloy layer usually does not form; a scale, which was identified by x-ray diffraction analysis as Cu_2O, was observed at the higher potentials ($\lesssim 300$ mV). Figure 4, therefore, gives apparent current densities at $E > E_c$ for dissolution of ε and γ brass; the true current densities can be expected to be lower and to vary over the surface, being greatest at the advancing front of the porous structure. On the other hand the current densities for α brass in Fig. 3 and 4 may vary little over the surface and be close to the true value.

Discussion

The data in Fig. 4 show that two modes of dissolution may occur depending on the potential: preferential and simultaneous. Preferential dissolution changes gradually with potential from virtually no dissolution of the more noble metal to simultaneous dissolution of both components. Comparison of the Cu and Zn polarization curves for dissolution of α brass shows that preferential dissolution occurs for $E < 200$ mV, and that simultaneous dissolution occurs usually for $E \lesssim 200$ mV. Below ~50 mV virtually only Zn dissolves, and between 50 and 200 mV a gradual transi-

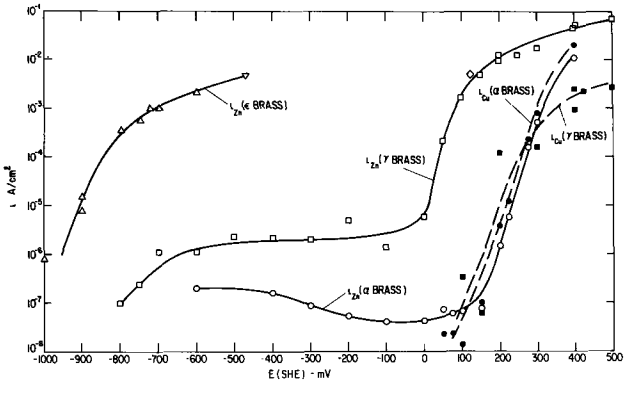

Fig. 4. i_{Zn}-E and i_{Cu}-E curves for dissolution of Zn and Cu from single-phase Cu-Zn alloys in the buffered (pH = 5) Na_2SO_4 electrolyte. Solid and dashed lines are the Zn and Cu currents, respectively.

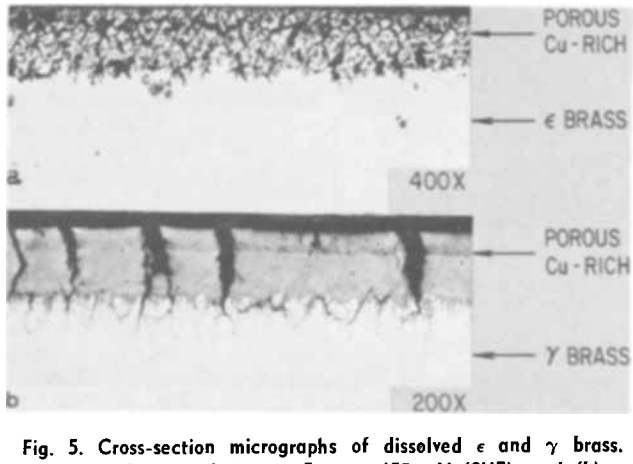

Fig. 5. Cross-section micrographs of dissolved ε and γ brass. (a) ε brass after dissolution at $E = -455$ mV (SHE), and (b) γ brass after dissolution at $E = 500$ mV (SHE).

tion occurs from Zn dissolution alone to simultaneous dissolution.

Comparison of the Cu and Zn polarization curves for dissolution of γ brass shows that preferential dissolution of Zn occurs at all potentials investigated; only Zn dissolves for potentials up to ~50 mV. Above ~50 mV Cu also dissolves, with $i_{Zn}/i_{Cu} > 10:1$. Since this ratio is much larger than the Zn/Cu ratio in γ brass, preferential dissolution of Zn occurs as well at these higher potentials; however, the degree of preferential dissolution of Zn clearly decreases with increasing potential in this region. Since it also decreases with time, it may be supposed, therefore, that at some higher potential and/or longer time, simultaneous dissolution of Zn and Cu would occur.

With ϵ brass only Zn dissolves in the potential range investigated. Since the potential was always well below the standard potential of Cu ($E_{Cu}^{\circ} = 337$ mV), the absence of significant Cu dissolution during dissolution of ϵ brass specimens is not surprising.

The potential at which Cu begins to dissolve from γ and from α brass is approximately the same as with pure Cu according to an auxiliary experiment in which pure Cu was used as the specimen. Similarly Zn dissolution commences at potentials near the reversible potential for pure Zn in the electrolyte, but the rate of Zn dissolution is suppressed by the accumulation of Cu on the surface and only becomes appreciable when a higher potential (E_c) is reached.

Pickering and Wagner (11) theorize that preferential dissolution of the less noble component may be expected when the difference between the single-electrode potentials of the two constituent metals in the electrolyte is sufficiently large, *i.e.*, several times RT/F, and when the potential of the dissolving alloy is higher than that of the less noble metal and lower than that of the more noble metal. The results presented herein for Cu-Zn alloys are in agreement with these concepts. In addition there is also the occurrence of preferential dissolution in a potential region where the free energy change for dissolution of both Cu and Zn is negative (with α and γ brass at $E \gtrsim +50$ mV). This is especially noticeable with γ brass (Fig. 4) and may be accounted for by the difference in the overpotentials (driving force) for dissolution of the components, the overpotential being far greater for Zn than for Cu.

The curves for Zn dissolution from the Zn-rich Cu-Zn alloys are qualitatively the same as those for dissolution of the less noble component, Cu, from Cu-rich Cu-Au alloys (1, 2). The similarity of the curves for the less noble metal in the two alloy systems probably extends to the alloys rich in the more noble metal, but a comparison is not possible due to the absence of data for the Cu-Au system at potentials noble of the oxygen evolution reaction. Dissolution of Cu from Au-rich alloys at higher potentials would be analogous to the dissolution of Zn from (Cu-rich) α brass (Fig. 4). For the same reason no comparison is possible of the polarization curves of the more noble components for the two alloy systems.

The formation of porous layers on ϵ and γ brass specimens during anodic dissolution is similar to the formation of porous layers during preferential anodic dissolution of Cu from Cu-Au alloys under similar conditions (11, 12) and during corrosion of Cu-Zn and Cu-Au alloys (13). The porosity is understood to be due to surface roughening. With diffusion of Zn to the surface as the controlling step in the over-all dissolution process of Cu-Zn alloy (10), a plane surface is unstable according to Harrison and Wagner (14), so that surface roughening and subsequent porosity may be expected.

The absence of porous layers on the α brass specimens is in agreement with the usual occurrence for α brass of simultaneous dissolution for $E \gtrsim 200$ mV. In its simplest form simultaneous dissolution may involve only consecutive removal of atom layers, as in the case of a pure metal. Even so one may expect that the surface atomic layer is enriched in Cu, in accord with ionization of Cu as the controlling step as suggested by others (9, 15). The situation becomes complex when appreciable preferential dissolution occurs prior to the onset of simultaneous dissolution; in this case simultaneous dissolution may occur in the presence of a Zn-depleted layer of finite depth.

Concluding Remarks

The results clearly show under which conditions preferential dissolution of the less noble component and in which potential range transition to simultaneous anodic dissolution take place. The anodic polarization behavior of Cu-Zn alloys appears to be similar to that of Cu-Au alloys. This behavior is not well understood. In particular, as Uhlig (16) has pointed out, a satisfactory understanding requires an explanation for the occurrence of a rather well-defined critical potential and insight concerning the low current region is almost totally lacking. At potentials above E_c some understanding exists. According to recent x-ray and electron diffraction investigations on Cu-Au (11, 12) and Cu-Zn (10) alloys, preferential dissolution at $E > E_c$ occurs via interdiffusion in the alloy next to the surface, accompanied by exceedingly fast surface roughening (17, 18).

A cursory examination of polarization data on alloys available in the literature gives some indication that other alloys exhibit similar polarization behavior. For example, in the practically important system, 18-8 stainless steel in hot $MgCl_2$ solution, an appreciable anodic current is observed at potentials more noble than —150 mV (SHE) according to Hoar and Hines (7) and others (8, 19, 20). Yet anodic dissolution of Fe and Cr at $E < -150$ mV may occur since the reversible potentials of Fe and Cr in the electrolyte are much lower. Further indication of a marked similarity with the Fe-Cr-Ni alloys is found in the recent data of Condit, Beauchamp, and Staehle (21). These authors show that as the Ni content is increased from 0 to 20 w/o (weight per cent) in a base alloy of fixed Cr content (20 w/o) the potential required to sustain a given rate of dissolution of the alloy becomes more noble. Ni, therefore, influences the dissolution of stainless steel in the same way as does Cu in the Cu-Zn alloys and Au in the Cu-Au alloys. For further insight it is desirable to determine the partial currents of the components, Fe, Cr, and Ni. Such data would also give information on whether or not passivation occurs for this alloy-electrolyte system at 150°C. A marked increase in metal dissolution in a potential region negative of —150 mV would indicate that passivation occurs; whereas an anodic current which is essentially independent of potential at $E < -150$ mV would indicate preferential dissolution (of Fe and/or Cr) in the absence of passivation. This is particularly important in connection with understanding stress corrosion in the austenitic stainless steels.

Acknowledgment

The authors want to record their indebtedness to Professor C. Wagner of the Max Planck Institut für physikalische Chemie for pointing out the need for data of the kind presented herein, and for his comments as well as those of Drs. R. A. Oriani, L. S. Darken, and R. P. Frankenthal on reading the manuscript. They want also to acknowledge the skillful assistance of Messrs. G. W. Momeyer and W. L. Doyle, who made the numerous chemical analyses, and of Mr. R. M. Lytle who did the metallography. All except Professor Wagner are staff members of the E. C. Bain Laboratory for Fundamental Research of the United States Steel Corporation.

Manuscript submitted April 18, 1969.

Any discussion of this paper will appear in a Discussion Section to be published in the June 1970 JOURNAL.

REFERENCES
1. H. Gerischer and H. Rickert, *Z. Metallkunde*, **46**, 681 (1955).
2. H. W. Pickering and P. J. Byrne, To be published.
3. H. G. Feller, *Habilitationsarbeit*, T. U., Berlin (1965), *Corr. Sci.*, **8**, 259 (1968).
4. H. Sugawara and H. Ebiko, *Corr. Sci.*, **7**, 513 (1967).
5. I. K. Marshakov and V. P. Bogadanov, *Russian J. Phys. Chem.*, **38**, 1041, 1043 (1964).
6. R. P. Tischer and H. Gerischer, *Z. Elektrochem.*, **62**, 50 (1958).
7. T. P. Hoar and J. G. Hines, *J. Iron Steel Inst.*, **177**, 248 (1954); *ibid.*, **182**, 124 (1956); CITCE, VIII, Butterworths, London (1956), p. 273.
8. S. Barnartt and D. van Rooyen, *This Journal*, **108**, 222 (1961).
9. J. Bumbulis and W. F. Graydon, *ibid.*, **109**, 1130 (1962); T. J. Kagetsu and W. F. Graydon, *ibid.*, **110**, 709 (1963).
10. H. W. Pickering, *ibid.*, To be published.
11. H. W. Pickering and C. Wagner, *ibid.*, **114**, 698 (1967).
12. H. W. Pickering, *ibid.*, **115**, 143 (1968).
13. A list of references is found in ref. (11).
14. J. B. Harrison and C. Wagner, *Acta Met.*, **7**, 722 (1959).
15. B. E. Wilde and G. A. Teterin, *Br. Corros. J.*, **2**, 125 (1967).
16. H. H. Uhlig, Unpublished discussion (1966).
17. H. W. Pickering, *This Journal*, **115**, 690 (1968).
18. C. Wagner, *ibid.*, **116**, 343 (1969).
19. H. H. Uhlig and E. W. Cook, Jr., *ibid.*, **116**, 173 (1969).
20. L. Graf and G. Springe, Proceedings of the Conference on the Fundamental Aspects of Stress Corrosion Cracking, Columbus, Ohio (1967), N.A.C.E., R. W. Staehle, Editor, p. 335 (1969).
21. R. M. Latanision and R. W. Staehle, *ibid.*, p. 223.

Electrodeposition of Lead Dioxide from Alkaline Solution

A. B. Gancy*

Tyco Laboratories, Inc., Waltham, Massachusetts

ABSTRACT

An investigation has been made of the properties of lead dioxide electrodeposited from dilute $Pb(NO_3)_2$ solutions made alkaline with NaOH, *i.e.*, under conditions which were expected to produce α-PbO_2. The apparent coulombic efficiency, measured gravimetrically, is strongly dependent on both the *p*H and the lead (biplumbite) ion concentration. Efficiency values encountered in this study ranged as high as 115%. A detailed composition analysis has been made on a material deposited from 5×10^{-2}M $Pb(NO_3)_2$-0.9M NaOH solution at an apparent coulombic efficiency of 112%. Analyses for water, lead, and active oxygen lead to the empirical composition

$$PbO_{1.868} \cdot 0.136\,H_2O, \text{ or its equivalent, } PbO_{1.732}(OH)_{0.272}$$

Si is the major trace contaminant, as measured by emission spectrography, but it is not present to the extent that silicate need be considered as an integral part of the electrodeposited compound. Quantitative analysis shows that nitrate is not an inclusion. Electron photomicrographs reveal a uniform fine-grained structure in which the crystal faces and boundaries are slightly curved. X-ray diffraction analysis gives an α-PbO_2 pattern. This is the same pattern reported in the literature for $PbO_{1.87}$, prepared by chemical methods. The real coulombic efficiency of plating, recalculated on the basis of the analysis for composition, is 98%. The rapid drop in the apparent coulombic efficiency as the *p*H is increased is suggested to be the result of an approach in the net lead oxidation state to 4.00.

A study has been initiated in this laboratory to investigate a report in the literature (1) that O_2 evolution on α-PbO_2 in strong acid solutions is distinctly different from that on β-PbO_2. In order to eliminate as much as possible effects arising from the known morphological differences between electrodeposited α- and β-PbO_2, an attempt was made to match the well-defined polycrystalline β-PbO_2 with a similar α modification. Inasmuch as electrodeposition from more alkaline solutions seemed to favor the α form (2), initial efforts were directed toward $Pb(NO_3)_2$-NaOH solutions. The *p*H was maintained above 9 to avoid precipitation of PbO and/or $Pb(OH)_2$ at the lead solubility minimum.

It was soon discovered that higher lead oxides could be produced from dilute, alkaline $Pb(NO_3)_2$ solutions with coulombic efficiencies far in excess of 100%, assuming the transfer of two electrons per mole of lead oxidized. Efficiencies below 100% can always be attributed to competitive anodic processes or other factors. But apparent efficiencies consistently and reproducibly far in excess of 100% require explanation. Some of the possibilities were inclusion of carbonates (absorption of atmospheric CO_2), inclusion of water, coprecipitation of PbO or $Pb(OH)_2$, and a net valence of lead in the electrodeposit appreciably lower than 4.0. The matter becomes especially interesting in light of references in the literature to the compound $PbO_{1.87}$ and to a continuous solid solution region between $PbO_{1.87}$ and PbO_2 (3).

The present paper describes the apparent plating efficiency as a function of NaOH concentration. A single electrodeposit is then studied in detail by x-ray diffraction, emission spectrography, electron microscopy, and wet chemical analysis. A knowledge of detailed composition and structure then allows a determination of the true anodic electrodeposition efficiency.

Experimental

Electrodeposition methods.—Two distinct groups of samples were prepared, one in which the deposit weighed ~ 150 mg, and the other, 1-1.5g. The former were large enough for a carbon, hydrogen microcombustion analysis, as well as for x-ray diffraction, elec-

* Electrochemical Society Active Member.

REFERENCES
1. H. Gerischer and H. Rickert, *Z. Metallkunde*, **46**, 681 (1955).
2. H. W. Pickering and P. J. Byrne, To be published.
3. H. G. Feller, *Habilitationsarbeit*, T. U., Berlin (1965), *Corr. Sci.*, **8**, 259 (1968).
4. H. Sugawara and H. Ebiko, *Corr. Sci.*, **7**, 513 (1967).
5. I. K. Marshakov and V. P. Bogadanov, *Russian J. Phys. Chem.*, **38**, 1041, 1043 (1964).
6. R. P. Tischer and H. Gerischer, *Z. Elektrochem.*, **62**, 50 (1958).
7. T. P. Hoar and J. G. Hines, *J. Iron Steel Inst.*, **177**, 248 (1954); *ibid.*, **182**, 124 (1956); CITCE, VIII, Butterworths, London (1956), p. 273.
8. S. Barnartt and D. van Rooyen, *This Journal*, **108**, 222 (1961).
9. J. Bumbulis and W. F. Graydon, *ibid.*, **109**, 1130 (1962); T. J. Kagetsu and W. F. Graydon, *ibid.*, **110**, 709 (1963).
10. H. W. Pickering, *ibid.*, To be published.
11. H. W. Pickering and C. Wagner, *ibid.*, **114**, 698 (1967).
12. H. W. Pickering, *ibid.*, **115**, 143 (1968).
13. A list of references is found in ref. (11).
14. J. B. Harrison and C. Wagner, *Acta Met.*, **7**, 722 (1959).
15. B. E. Wilde and G. A. Teterin, *Br. Corros. J.*, **2**, 125 (1967).
16. H. H. Uhlig, Unpublished discussion (1966).
17. H. W. Pickering, *This Journal*, **115**, 690 (1968).
18. C. Wagner, *ibid.*, **116**, 343 (1969).
19. H. H. Uhlig and E. W. Cook, Jr., *ibid.*, **116**, 173 (1969).
20. L. Graf and G. Springe, Proceedings of the Conference on the Fundamental Aspects of Stress Corrosion Cracking, Columbus, Ohio (1967), N.A.C.E., R. W. Staehle, Editor, p. 335 (1969).
21. R. M. Latanision and R. W. Staehle, *ibid.*, p. 223.

Electrodeposition of Lead Dioxide from Alkaline Solution

A. B. Gancy*

Tyco Laboratories, Inc., Waltham, Massachusetts

ABSTRACT

An investigation has been made of the properties of lead dioxide electrodeposited from dilute $Pb(NO_3)_2$ solutions made alkaline with NaOH, *i.e.*, under conditions which were expected to produce α-PbO_2. The apparent coulombic efficiency, measured gravimetrically, is strongly dependent on both the *p*H and the lead (biplumbite) ion concentration. Efficiency values encountered in this study ranged as high as 115%. A detailed composition analysis has been made on a material deposited from 5×10^{-2}M $Pb(NO_3)_2$-0.9M NaOH solution at an apparent coulombic efficiency of 112%. Analyses for water, lead, and active oxygen lead to the empirical composition

$$PbO_{1.868} \cdot 0.136\,H_2O, \text{ or its equivalent, } PbO_{1.732}(OH)_{0.272}$$

Si is the major trace contaminant, as measured by emission spectrography, but it is not present to the extent that silicate need be considered as an integral part of the electrodeposited compound. Quantitative analysis shows that nitrate is not an inclusion. Electron photomicrographs reveal a uniform fine-grained structure in which the crystal faces and boundaries are slightly curved. X-ray diffraction analysis gives an α-PbO_2 pattern. This is the same pattern reported in the literature for $PbO_{1.87}$, prepared by chemical methods. The real coulombic efficiency of plating, recalculated on the basis of the analysis for composition, is 98%. The rapid drop in the apparent coulombic efficiency as the *p*H is increased is suggested to be the result of an approach in the net lead oxidation state to 4.00.

A study has been initiated in this laboratory to investigate a report in the literature (1) that O_2 evolution on α-PbO_2 in strong acid solutions is distinctly different from that on β-PbO_2. In order to eliminate as much as possible effects arising from the known morphological differences between electrodeposited α- and β-PbO_2, an attempt was made to match the well-defined polycrystalline β-PbO_2 with a similar α modification. Inasmuch as electrodeposition from more alkaline solutions seemed to favor the α form (2), initial efforts were directed toward $Pb(NO_3)_2$-NaOH solutions. The *p*H was maintained above 9 to avoid precipitation of PbO and/or $Pb(OH)_2$ at the lead solubility minimum.

It was soon discovered that higher lead oxides could be produced from dilute, alkaline $Pb(NO_3)_2$ solutions with coulombic efficiencies far in excess of 100%, assuming the transfer of two electrons per mole of lead oxidized. Efficiencies below 100% can always be attributed to competitive anodic processes or other factors. But apparent efficiencies consistently and reproducibly far in excess of 100% require explanation. Some of the possibilities were inclusion of carbonates (absorption of atmospheric CO_2), inclusion of water, coprecipitation of PbO or $Pb(OH)_2$, and a net valence of lead in the electrodeposit appreciably lower than 4.0. The matter becomes especially interesting in light of references in the literature to the compound $PbO_{1.87}$ and to a continuous solid solution region between $PbO_{1.87}$ and PbO_2 (3).

The present paper describes the apparent plating efficiency as a function of NaOH concentration. A single electrodeposit is then studied in detail by x-ray diffraction, emission spectrography, electron microscopy, and wet chemical analysis. A knowledge of detailed composition and structure then allows a determination of the true anodic electrodeposition efficiency.

Experimental

Electrodeposition methods.—Two distinct groups of samples were prepared, one in which the deposit weighed ~ 150 mg, and the other, 1-1.5g. The former were large enough for a carbon, hydrogen microcombustion analysis, as well as for x-ray diffraction, elec-

* Electrochemical Society Active Member.

tron microscopy, emission spectrography, and nitrate analysis. Such samples were too small, however, for a precise analysis for lead by $PbSO_4$, and 1-1.5g deposits were obtained using larger scale apparatus. This same apparatus was used to prepare the 0.5g samples for As_2O_3 titration (active oxygen analysis).

The 150 mg samples were plated onto rectangular electrodes cut from 0.030 in. platinum sheet. Platinum support wires were spot welded to the electrodes. The ~ 5 cm^2 geometric area electrode was made long and narrow so that the entire piece, including the support wire, could be inserted into microcombustion tubes. Prior to deposition the electrodes were degreased, etched to a dull finish in aqua regia, and finally heat-treated for 3 hr at 600°C, the approximate temperature used in the combustion analysis. They were then weighed to the nearest 0.1 mg. Electrodeposition was from $Pb(NO_3)_2$, NaOH solutions, prepared two liters at a time and stored in tightly sealed polyethylene bottles. A Pt mesh cylinder surrounded the anode and functioned as cathode. 500 ml of rapidly stirred solution were used per plating. The temperature was maintained at 50°-55°C. A constant current source device was used in conjunction with an electric timer. Current was read from a sensitive milliameter (Sensitive Research Instrument Corporation, 05-100 mA). Prior to weighing, the samples were washed with distilled water and air-dried.

In order to examine the reproducibility of electrodeposition, 15.00 mA (~ 3 mA/cm^2) were passed for 7200 sec in a 5 x 10^{-2}M $Pb(NO_3)_2$, 0.9M NaOH solution. The average deposit weight for eight determinations was 150 ± 0.3 mg (theoretical, 133.8 mg). This falls well within the readability of the milliameter (3 parts/1000) and is close to the indeterminate error of a deposit weight determination which requires four individual weighings. The apparent coulombic efficiency is 112.2 ± 0.2%.

The larger samples, ranging from 0.5 to 1.5g, were plated onto a 0.030 in. Pt sheet electrode having a ~ 25 cm^2 geometric area. The cathode was made of thin Pt stock and fashioned so as to produce a uniform current density on both sides of the anode plate. Five liters of vigorously stirred $Pb(NO_3)_2$-NaOH solution were used per plating. Temperature was maintained at 50°-53°C. As with the smaller samples, the electrodeposit was washed with distilled water and air dried prior to weighing.

Analytical methods.—Analysis for water.—To analyze for H_2O, samples were decomposed in a microcombustion apparatus customarily used for carbon, hydrogen analysis of organic compounds. Carbon analysis was routinely made along with the hydrogen analysis, but carbon contents were found to be negligibly low. This is evidence that the inordinately high plating efficiencies found were not not caused by CO_2 absorption.

Analysis for lead.—The method was to plate at least a gram using the 5l apparatus, to dissolve the deposit in acidic H_2O_2, and then to precipitate and weigh $PbSO_4$. A negative blank correction and a positive correction for the solubility of $PbSO_4$ in H_2SO_4 were made.

Analysis for nitrate.—According to Raub (4) metal and metal alloy electrodeposits can codeposit with certain anions present in the electrolyte such as citrate, tartrate, and nitrate. The α-naphthylamine-sulfanilic acid spot test for nitrate (5) indicated about 0.01% nitrate in the sample.

Using a colorimetric method employing brucine in perchloric acid, the nitrate content of the PbO_2 was found to be less than 0.001%. Nitrate was therefore not considered further in the composition study.

Active oxygen determination.—The postulate of the simple compound $Pb(OH)_xO_y$ requires only two knowns for the determination of x and y; these are provided by the lead and the water analyses. However, a third analysis is required as a check on the first two and also functions to reveal any possible third unknown in the form of anion inclusion or inert contaminant. This third analysis is for active oxygen or a measure of the lead oxidation state. A standard As_2O_3 titration method was used (6).

The reaction proceeds as follows

$$2PbO_a \cdot bH_2O + (a-1)\,As_2O_3 + 4H^+ = 2Pb^{++} + (a-1)As_2O_5 + 2(1+b)H_2O$$

The As_2O_3 equivalent is expressed

$$As_2O_3 \text{ equivalent} = \frac{2(a-1)\,(\text{wt sample})}{(207.2 + 16.00\,a + 18.02\,b)}$$

This result can be expressed as "oxide ion" by multiplying by $(8a/a - 1)$.

Solubility of lead dioxide.—The solubility of lead dioxide at 25°C is given by the expression (7) $\log (PbO_3^=) = 2\,pH - 31.32$. At pH = 14, the solubility of lead dioxide is predicted to be an appreciable 10^{-3} mols/l.

Weight loss measurements were made in 0.97M NaOH solutions at 50°C using the electrodeposited PbO_2 of interest in the over-all analysis. Even in the absence of $Pb(NO_3)_2$ and at a higher NaOH concentration (0.97 *vs.* 0.90M NaOH), the solubilization rate was observed to be so low as to produce a negligible effect on the gravimetric analysis.

Results and Discussion

Coulombic efficiency of lead dioxide electrodeposition.—In Fig. 1 the apparent coulometric efficiency is plotted against the NaOH concentration for three levels of $Pb(NO_3)_2$ concentration. The position of the rising portion of the curve is very much dependent on the lead concentration. The point at which the curves cross the "100%" axis has no special significance, as will become apparent from the ensuing discussion of real electrodeposition efficiencies. The rather steep drop in the 5 x 10^{-3}M $Pb(NO_3)_2$ curve at NaOH concentrations greater than 1*N* is of interest only in regards to competing processes and the effect of stirring on the electrodeposit.

The region of high apparent coulombic efficiency was considered most intriguing and was therefore chosen for closer study. Thus conditions corresponding with the highest efficiencies were examined, consistent with the avoidance of PbO or $Pb(OH)_2$ precipitation at lower *p*H's. Finally, as a matter of convenience in scaling up the electrodeposition for more precise analysis, all of the composition studies were made on a deposit plated from a 5 x 10^{-2}M $Pb(NO_3)_2$-0.9M NaOH solution. It can be seen from Fig. 1 that the apparent coulombic efficiency for this material is about 112%. The deposits were intense black, with a smooth lustrous metallic surface.

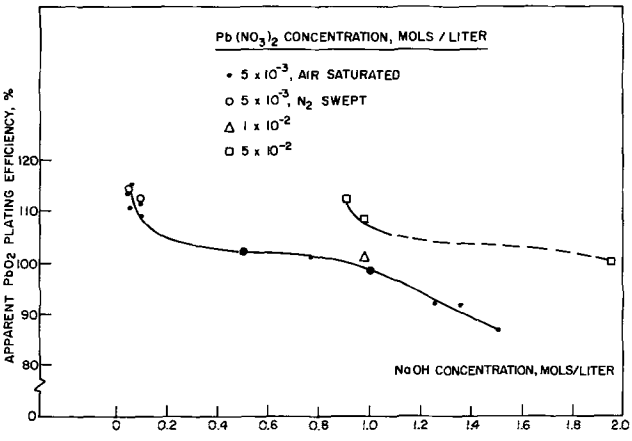

Fig. 1. Electrodeposition of lead dioxide from alkaline $Pb(NO_3)_2$ solution. T = 50°C; C.D. = 3 mA/cm^2.

Figure 1 also shows that there is no alteration in the results due to bubbling N_2 through the closed electrodeposition apparatus so as to avoid absorption of CO_2 from the atmosphere. The electrodeposition or inclusion of basic lead carbonates in the solid can therefore be ruled out as an explanation of the inordinately high efficiencies.

Water content.—Table I gives the water analyses of four separate preparations of the material picked for the composition analyses, that plated from 5 x 10^{-2}M $Pb(NO_3)_2$ to 0.9M NaOH solution at 50°C. Three were 150 mg samples, while the fourth was a 1.1g deposit. The latter was analyzed in order to check on the scaleup of the deposition procedure. All samples were plated at 3 mA/cm² geometric area.

The agreement between small and large sample analyses is good. The value 1.04% H_2O will subsequently be used in the over-all composition determination. Note that this water content is considerably higher than that of the various commercial PbO_2 powders (8).

Lead analysis.—Table II gives the Pb analyses for the electrodeposited PbO_2 under study. The overlap between small and large sample results is satisfactory. The precision of the former, however, is considered insufficient for a satisfactory composition analysis. The value 86.50% Pb is used in the composition analysis. (The theoretical amount of Pb in $PbO_{2.00}$ containing no water would be 86.62%.)

Active oxygen analysis.—The lead dioxide under study was, again, plated from a 5 x 10^{-2}M $Pb(NO_3)_2$-0.9M NaOH solution at 3 mA/cm² and 50°C. The As_2O_3 titrations gave 0.725 ± 0.004% As_2O_3 equivalents on a 0.5g sample. The error is the indeterminate error in reading the buret. (The theoretical % As_2O_3 equivalents for $PbO_{2.00}$ containing no water would be 0.836.)

A 0.5g sample of reagent grade PbO_2 was similarly analyzed to give 97.7 ± 0.5% as lead dioxide. This compared well with the manufacturer's assay of 97.5%. This analysis in itself suggests a net lead valence less than four in addition to the presence of water and other foreign constituents.

Spectrographic analysis for trace metals.—The PbO_2 electrodeposit under study was analyzed by the emission spectrograph. Silicon is the major trace constituent at a 0.03-0.3% level.

Lead dioxide composition.—Since the minimum total trace metal concentration is low enough to be ignored, there are only two unknowns to solve for in the formulation $PbO_a \cdot bH_2O$. Three independent relationships are available in the form of a water, lead, and active oxygen analysis. The approach will be to use the information in pairs, and then to examine each of the three results critically. In this analysis the following expressions are used and referred to by number:

$$\% H_2O = \frac{18.02b}{207.2 + 16.00a + 18.02b} \times 100 = 1.04 \quad [1]$$

$$\% Pb = \frac{207.2}{207.2 + 16.00a + 18.02b} \times 100 = 86.50 \quad [2]$$

Table I. Water content of electrodeposited lead dioxide

Sample wt	Apparent coulombic efficiency, %	% H_2O	
150.3 mg	112.1	1.098	average
150.0	112.0	0.96	1.04 ± 0.05
149.6	111.8	1.056	
1.1278 g	112.5	1.04 ± 0.04	(duplicate analysis)

Table II. Analysis for lead in electrodeposited PbO_2

Sample wt, g	% Pb
~0.15	86.7 ± 0.6 (average of 3 determinations)
~1.5	86.50 ± 0.04 (average of 2 determinations)

Table III. Determination of the constants in $PbO_a \cdot bH_2O$

Combination of equations	a	b	Derived quantities % O	% Pb	% H_2O	Total assay, %
[1] and [2]	1.86₅	0.138	12.50	—	—	100.04
[1] and [3]	1.85₉	0.137	—	86.55	—	100.14
[2] and [3]	1.86₈	0.136	—	—	1.02	100.00

$$\% As_2O_3 \text{ equiv} = \frac{2(a-1)}{207.2 + 16.00a + 18.02b} \times 100 = 0.725 \quad [3]$$

"Oxide ion" cannot be expressed independently since it is related to the As_2O_3 equivalent through the parameter a

$$\% O = \frac{8a}{(a-1)} \% As_2O_3 \text{ equiv}$$

Table III gives the three solutions for a and b. Also listed are the total assays obtained by adding to the two measured quantities the third component computed using the derived values of a and b. The agreement between measured and calculated quantities is very satisfactory. Relatively speaking the agreement in % H_2O is much poorer than that in % Pb. But in absolute terms, the % H_2O error is the smaller. An examination of the analytical methods and results shows that the precision of the data decreases in the order % Pb, % As_2O_3 equiv., % H_2O. Thus combination [2] and [3] would appear to be the best choice. It also happens to give the total assay closest to 100% although this is only a reflection of error accumulation in the calculations.

The lead dioxide composition is then $PbO_{1.868} \cdot 0.136$ H_2O with a net lead valence of 3.74. The good agreement between calculated and measured quantities leads to the conclusion that the formulation $PbO_a \cdot bH_2O$ is the correct one, and that silicate impurity need not be taken into account. The indicated formula is possibly incorrect only insofar as ~0.1% trace metal silicates have not been worked into the analysis.

X-ray diffraction analysis.—The x-ray diffraction pattern for the electrodeposit under discussion is that of α-PbO_2 (9) whose composition was reported as $PbO_{1.94-2.02}$. The pattern is essentially the same as that obtained for $PbO_{1.87}$, a composition prepared from PbO_2 by Katz (3).

Structure.—It must be concluded that all three compositions (*i.e.*, α-PbO_2, $PbO_{1.87}$, and $PbO_{1.868} \cdot 0.136$ H_2O) have the same basic structure. Evidently a large deficiency of oxygen atoms can occur in α-PbO_2 without changing the basic structure of the molecule, if indeed the formula $PbO_{1.87}$ is a correct one. The formula for the compound prepared in the present work can be rewritten to give

$$PbO_{1.732}(OH)_{0.272}$$

The numerical coefficients add to give 2.004, which is equal to 2.00 within the experimental error. This suggests very strongly that OH^- ions replace some of the $O^=$ ions in the α-PbO_2 lattice.

Within experimental error, the compound under discussion can be represented by the expression

$$19PbO_2 \cdot 3Pb(OH)_2$$

(expressed in terms of fractional coefficients, $PbO_{1.862} \cdot$

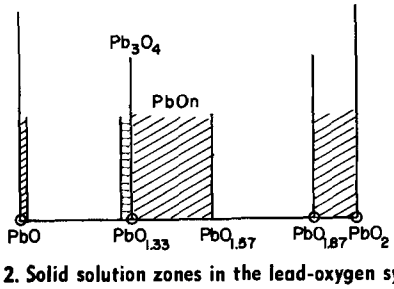

Fig. 2. Solid solution zones in the lead-oxygen system

0.136 H_2O). This can be considered to be a solid solution of lower and higher valent lead oxides. As such, it falls within the solid solution zone reported by Katz (Fig. 2). The only difference is that Katz defines the anhydrous case, while here some oxide ions are replaced by hydroxyl ions. Structurally, they are both equivalent. While it cannot be disproved, the $Pb(OH)_2$ is not believed to be present as a colloidal dispersion.

Real plating efficiency.—The compound $PbO_{1.86_8}$ · 0.136 H_2O was plated from 5 x 10^{-2}M $Pb(NO_3)_2$-0.9M NaOH solution at 50°C. The passage of 1078.6 coulombs produced 1.5030g. From this it can be determined that the real plating current efficiency was 98%. This is to be compared with the apparent coulombic efficiency of 112%. The importance of knowing the exact composition of the deposit when determining coulombic efficiency is clear.

Summary

1. PbO_2 plated from $Pb(NO_3)_2$ solutions between pH 9 and 10 has the structure of α-PbO_2 but contains, probably in solid solution, some $Pb(OH)_2$. One such deposit has the composition: $PbO_{1.73}(OH)_{0.27}$ or 19 PbO_2 · 3 $Pb(OH)_2$ and was obtained with current efficiency of 98% based on the real mean lead valence of 3.74.

2. Except for very low concentrations of lead and high concentrations of NaOH, the current efficiency from solutions with pH greater than 10 is close to 100% based on tetravalent lead.

Acknowledgment

The author is indebted to Dr. A. C. Makrides for advice and suggestions in the course of the investigation, and to Dr. S. B. Brummer and Dr. J. Giner for assistance in preparing the manuscript. Valuable discussions were also held with Dr. J. N. Butler and Dr. G. A. Wolff.

This work was made possible by the Department of the Army, Harry Diamond Laboratories, Washington, D.C., under Contract No. DA-49-186-AMC-136(D).

Manuscript received Feb. 7, 1969; revised manuscript received June 30, 1969.

Any discussion of this paper will appear in a Discussion Section to be published in the June 1970 JOURNAL.

REFERENCES

1. P. Ruetschi, R. T. Angstadt, and B. D. Cahan, *This Journal*, **106**, 547 (1959).
2. R. A. Baker, *ibid.*, **109**, 337 (1962).
3. T. Katz, *Ann. Chim.*, **5**, 5 (1950).
4. E. Raub, *Z. Metalik*, **39**, 33 (1948).
5. F. Feigl, "Spot Tests in Inorganic Analysis," p. 330, Elsevier Publishing Co., New York (1958).
6. I. M. Kolthoff and E. B. Sandell, "Textbook of Quantitative Inorganic Analysis," 3rd ed, p. 575, MacMillan Co., New York (1952).
7. M. Pourbaix, "Atlas D'equilibres Electrochimiques," p. 485, Gauthier-Villars, Paris (1963).
8. R. G. Myers, *Anal. Chem.*, **20**, 654 (1948).
9. A. L. Zaslavskii *et al.*, *Doklady Akad. Nauk SSSR*, **75**, 559 (1950).

Electrochemical Oxidation of Aliphatic Sulfides under Nonaqueous Conditions

Peter T. Cottrell and Charles K. Mann*
Department of Chemistry, Florida State University, Tallahassee, Florida

ABSTRACT

The anodic oxidation of aliphatic sulfides has been investigated, using cyclic voltammetry and controlled potential electrolysis. Reactions of dimethyl sulfide in acetonitrile have been studied in detail, considering the effects of variation of water content and of type of supporting electrolyte. With as much as 1% water in MeCN, dimethyl sulfide is completely oxidized to dimethyl sulfone. In anhydrous $NaClO_4$-MeCN, the products are CH_3SO_3Na and CO. It is suggested that the electrochemical reaction involves formation of protons and $CH_3SCH_2^+$, which condenses with CH_3SCH_3 to form $CH_3SCH_2^+S(CH_3)_2$. When perchlorate is present as supporting electrolyte, it is involved in a slow chemical reaction which produces Cl^-, CO, and CH_3SO_3Na. The reaction of benzyl methyl sulfide is very similar, leading to benzaldehyde and CH_3SO_3Na.

Previous investigation has shown that organic sulfides are oxidized in aqueous systems at platinum anodes to sulfones and sulfonium salts (1). Many aromatic and olefinic sulfides form cation radicals which exhibit appreciable lifetimes when they are oxidized in nonaqueous systems. Examples are tetramethylthio-, tetraethylthio-, and tetraphenylthioethylene (2); 1,2,4,5-tetramethylthiobenzene, dithiohydroquinone dimethyl ether, 1,6-bis(methylthio)pyrene and 1,4-bis(methylthio)naphthalene (3, 4). Similarly, heterocyclic sulfur compounds such as thianthrene undergo reversible one-electron reactions leading to cation radicals (5, 6). There have apparently been no studies of the anodic reactions of aliphatic sulfides in nonaqueous media. This report describes the anodic oxidation of dimethyl sulfide and benzyl methyl sulfide in acetonitrile. Special attention is paid to the influence of small amounts of water and to effects caused by variations in supporting electrolyte.

Experimental

Reagents.—Acetonitrile was purified as previously described (7); anhydrous sodium perchlorate was recrystallized from 95% ethanol and dried in a vacuum oven. Reagent grade tetramethylammonium tetrafluoborate was recrystallized from water-ethanol and similarly dried. Sulfides were purified by careful distillation of commercially available samples. Dimethyl sulfide boiled at 37°; lit. bp_{760}, 38° (8). Benzyl methyl sulfide boiled at 87° under 11 mm; lit. bp_{11}, 87°-88° (9).

Acetonitrile was dried by stirring with calcium hydride at room temperature for several hours and degassed by repeated freezing and pumping. Solutions were prepared by transferring dried solvent, protected from atmospheric contact, to a flask containing supporting electrolyte which had previously been dried by heating under a vacuum. Chlorine dioxide was prepared by the method of Atkins *et al.* (10). Dimethylmercaptomethyl sulfonium chloride was prepared from dimethyl sulfide and methylchloromethyl sulfide (11).

Procedures.—Controlled potential electrolyses were performed in closed, three-electrode, three-compartment cells, using an electronic potentiostat with platinum anodes and mercury cathodes. Details have been described (12). Cyclic voltammetry results were ob-

* Electrochemical Society Active Member.

tained using the apparatus previously described (13). Throughout the work, a silver-0.10*M* silver nitrate-acetonitrile reference electrode was used. All potentials are cited relative to this electrode, which is itself +0.30V *vs.* aqueous SCE.

Anhydrous perchloric acid was prepared by oxidizing hydrogen gas at a platinum anode at +0.8V in 0.1*M* $NaClO_4$ (14). The following columns were used for gas chromatography: dimethyl sulfide on SE 30, on Chromosorb P; dimethyl sulfide, benzyl methyl sulfide, and benzaldehyde on Dowfax 9N9-NaOH on Chromosorb W; methanesulfonyl chloride on Dow-Corning silicone grease on Chromosorb P; acetamide, dimethyl sulfoxide, dimethyl sulfone and water on Porapak Q; carbon monoxide and oxygen on 13X molecular sieves; benzaldehyde and benzyl methyl sulfide on potassium oleate on Chromosorb W. Gas chromatography was used, as will be described, for qualitative and quantitative examination. In all cases, unknown peaks were compared with those produced by valid samples, chromatographed at the same time. When GLC was used for identification of components in a mixture, this identification was supported by other types of evidence, *e.g.*, spectroscopy, and by chromatographing at more than one temperature or on more than one type of column.

Results

Cyclic voltammetry.—Cyclic voltammetry curves for a series of commercially available organic sulfides and mercaptans were obtained at a platinum wire microelectrode. Results are collected in Table I. The sulfides and mercaptans examined all showed irreversible oxidation reactions at potentials more positive than would have been true for the corresponding amines. For example, dimethyl sulfide is oxidized at a more positive potential than is trimethylamine. Some of the compounds showed two or more oxidation steps; two of them also showed reduction peaks at potentials positive relative to the reference electrode. However, none of them gave any indication of reversible oxidation. No trends or simple correlations between substituent effects and peak potentials were observed.

Controlled potential electrolysis.—Oxidation of 30 m*M* dimethyl sulfide in dry 0.4*M* $NaClO_4$-MeCN was carried out at +1.40V. After a preelectrolysis at +1.7V, during which current dropped quickly from about 10 mA to 50 μA, the potential was lowered to 1.4V, dimethyl sulfide was added and the current increased to as much as 100 mA and then dropped to approximately 50 μA within about 90 min. The current-time variation was not exponential, as would have been the case with a simple first order reaction in the apparatus used, but was instead nearly linear. Coulometric measurement, typically made with 0.3 to 3 mM of reactant, showed 0.84 ± 0.02 electrons per molecule of sulfide taken. Charge involved in the preelectrolysis amounted typically to 1% of that in the subsequent reaction.

Table I. Cyclic voltammetry for sulfides and mercaptans

Compounds[a]	Peak potential,[b] volts		
dimethyl sulfide	1.41		
diethyl sulfide	1.50		
diallyl sulfide	1.74		
dibenzyl sulfide	1.48		
di-*i*-propyl sulfide	1.47		
di-*n*-butyl sulfide	1.45		
di-*s*-butyl sulfide	1.43		
di-*t*-butyl sulfide	1.06	1.7	
n-butyl mercaptan	1.49		
t-butyl mercaptan	1.59		
s-butyl mercaptan	1.33	1.99	
dibenzylthiophene	1.35	1.64	
ethylene sulfide	1.51		
diphenyl sulfide	1.26	1.51	1.81
propylene sulfide	1.69		
pentamethylene sulfide	0.55	1.42	0.12[c]
sym-trithiane	1.30	1.47	
tetrahydrothiophene	1.45		
ethylenetrithiocarbonate	1.53	0.17[c]	
p-dithiane	1.46	1.91	
thiophene	1.84		

[a] Voltammetry at a platinum wire electrode at 10 V/sec sweep rate, reactant 5-10 m*M* in 0.10*M* $NaClO_4$-acetonitrile.
[b] Potentials measured at ambient temperature of about 22°, Ag-0.10*M* $AgNO_3$-MeCN reference electrode.
[c] Reduction peak, all those unmarked are oxidation peaks.

The reaction of dimethyl sulfide was carried out with 0.1*M* tetramethylammonium tetrafluoborate as supporting electrolyte, but with other conditions as described above. The reaction was considerably slower than with $NaClO_4$; initial current was typically 40 mA, dropping steadily to 90 μA after 3 to 4 hr. This reaction involved 0.85 electrons per molecule of sulfide.

In order to investigate the influence of water on the reaction, an elctrolysis of 35 m*M* dimethyl sulfide was performed in 0.4*M* $NaClO_4$-MeCN with 1% of water added. This experiment was run at +1.20V, rather than at +1.40V, because of the very large currents observed. Preelectrolysis at 1.6V resulted in currents ranging from 5 to 0.09 mA. On addition of dimethyl sulfide, current increased to, typically 110 mA and dropped exponentially to about 0.110 mA. Current integration showed 4.0 ± 0.1 electrons per molecule of sulfide taken.

Benzyl methyl sulfide was oxidized in anhydrous 0.4*M* $NaClO_4$-MeCN at 1.40V. Reaction currents varied from 90 to 0.15 mA in an approximately linear fashion, similar to the dimethyl sulfide reaction. The coulometric measurement amounted to 0.82 ± 0.02 electrons per molecule of sulfide.

Product analysis—Me_2S *electrolysis.*—Immediately on conclusion of the reaction of Me_2S in dry $NaClO_4$-MeCN, starting material in an amount corresponding to approximately 25% of that originally present could be determined by GLC on the reaction mixture. Small amounts (approximately 3 m/o (mole per cent) of original sulfide) of dimethyl sulfone and dimethyl sulfoxide and a trace of acetamide could also be detected. A reaction was run during which samples were taken at intervals for dimethyl sulfide assay by GLC. A plot of Me_2S concentration *vs.* time shows an approximately linear decrease, while current is decreasing, but with little change after the current had become constant.

When the reaction mixture was allowed to stand under a nitrogen atmosphere at room temperature for 5 to 10 days, a white precipitate formed. This was identified as sodium methanesulfonate by comparison of its infrared, ultraviolet, and NMR spectra with those of a valid sample. For quantitative determination of the yield of $MeSO_3Na$, the volatile fraction of a reaction product was removed under vacuum. The residue was treated with thionyl chloride and N,N-dimethylformamide to convert any sulfonic acid or sulfonate present into methanesulfonyl chloride (15) which was determined by GLC. The indicated recovery of $MeSO_3Na$ amounted to 95 ± 5 m/o of dimethyl sulfide originally taken.

In addition to the products mentioned, the reaction mixture contained strong acid, corresponding to 58 m/o of starting sulfide. As $MeSO_3Na$ precipitated on standing, carbon monoxide was shown, by GLC identification, to be evolved. During the period after completion of the electrolysis, the reaction mixture developed a green-yellow color. Although reaction solutions did not exhibit any ESR spectra during or immediately after electrolysis, the green solutions did show a single broad band centered at $g = 2.0$.

During the precipitation of $MeSO_3Na$, uv spectra were recorded. A broad intense absorption band was found which was thought to be due to chlorine-oxygen compounds produced during the decomposition of Cl_2O_7. Chlorate, chlorite, hypochlorite, and other oxides of chlorine are known to absorb strongly in the uv (16). When the volatile fraction of the reaction mixture was removed, it exhibited a much weaker absorption which was qualitatively identical with that of ClO_2 in acetonitrile. This fraction was acidic and gave a substantial silver chloride precipitate. After separation from the volatile components, an acetoni-

trile solution of the residue showed the intense uv absorption described above.

When Me_2S was oxidized in the presence of 1% water, it was apparently converted quantitatively to dimethyl sulfone. There was no evidence of participation of perchlorate or other chlorine compound. When the recation was carried out in a dry 0.1*M* tetramethylammonium tetrafluoborate-MeCN solution, approximately 30% of starting material was detectable by GLC after the electrolysis had come to a stop. However, there was no indication of any continuing chemical reaction and no evidence of oxygen-containing products. The reaction mixture showed only a very weak uv absorption at 255 mμ, in contrast to the very strong absorption observed when perchlorate was present.

Discussion

Dimethyl sulfide oxidation.—On the basis of the results which have been described, the reaction scheme outlined in Chart I is suggested for the reaction of Me_2S in dry $NaClO_4$-MeCN. It consists of a sequence of electrochemical and chemical steps, reactions 1, 2, and 3, which occur during the electrolysis to produce dimethylmethylthiomethyl sulfonium ion 3, which is thought to be the immediate major product. On standing, it is suggested that the sequences of chemical reactions 5,6,7,8 and 1b,2b,3,4,5,6,7,8 occur slowly, resulting in ultimate conversion of all of the original starting material to the sodium salt of methane sulfonic acid.

The process is initiated by electrochemical step 1 which involves removal of one electron from the substrate to produce the cation radical 1 which rapidly undergoes loss of a proton and of a second electron to form the sulfonium derivative 2. Some aromatic sulfides undergo reversible one-electron oxidations analogous to reaction 1 to produce cation radicals that are stabilized by delocalization of charge in the aromatic pi-system; since this stabilization of aliphatic cation radicals is impossible they would be expected to react too rapidly to permit step 1 to appear reversible. The sulfonium ion 2, however, would be expected to be resonance stabilized as indicated (17, 18). The hexachloroantimonate salt of 2 has been shown to react with Me_2S as indicated in step 3 to form the sulfonium derivative 3 (17).

CHART I

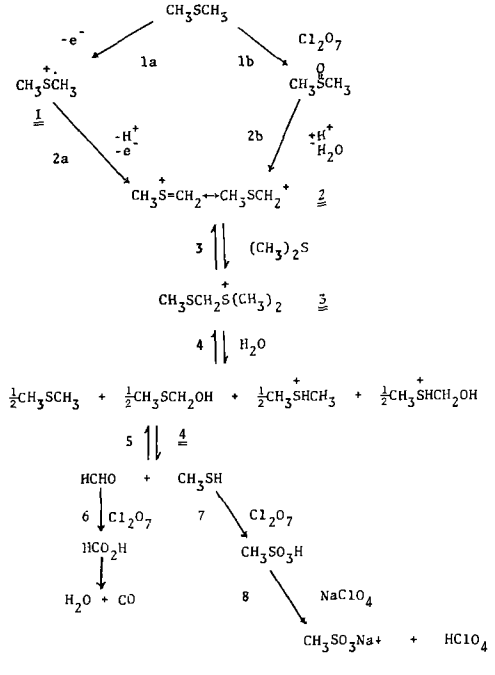

One observation that must be accounted for is the chromatographic detectability of Me_2S at the conclusion of the electrolysis. Presumably a compound is present which is electrochemically unreactive but which decomposes in the chromatograph to yield Me_2S. One possibility would be protonated sulfide. The reaction mixture is strongly acidic and such a salt could dissociate in the chromatograph injection port. However, a sample of $Me_2S \cdot HClO_4$ in MeCN was prepared as described above and was found not to produce a Me_2S peak.

A sample of 3 was prepared as described above and was found to show a peak for Me_2S. This corresponded to approximately 50 m/o of the sulfonium salt taken. It is suggested, therefore, that the presence of 3 at the end of the electrolysis would account for the chromatographic observations. Hydrolytic cleavage of 3 in step 4 is suggested to account for the scission of the carbon-sulfur bond. Pocker and Parker (19) reported that while trimethyl sulfonium iodide in ethanol decomposes to dimethyl sulfide and methyl iodide, the perchlorate salt yields the sulfide and methylethyl ether, as indicated in Eq. [9]. It is suggested that a similar reaction is

$$(CH_3)_3S^+ClO_4^- \xrightarrow{EtOH} (CH_3)_2S + CH_3OC_2H_5 + HClO_4 \quad [9]$$

involved in decomposition of 3, but with traces of water, rather than ethanol, as the reactant.

Step 5 is the decomposition of a hemithioacetal of formaldehyde (8, p. 330). If this occurs in the presence of a strong oxidizing agent, the formation of methane sulfonic acid, shown in step 7, would be expected. Under the conditions of these experiments, the sodium salt would precipitate because it is insoluble in MeCN. Decomposition of formic acid to give carbon monoxide would also be expected.

It is known that dimethyl sulfoxide undergoes the acid catalyzed dehydration indicated in Eq. [10] and that 2 will react with Me_2S

$$CH_3S(O)CH_3 \xrightarrow{+H^+} CH_3S(OH^+)CH_3 \rightleftarrows CH_3S^+=CH_2 + H_2O \quad (2)$$

$$2 + Me_2S \rightarrow CH_3SCH_2S^+(CH_3)_2 \quad (3) \quad [10]$$

to produce 3 (20). It should therefore be possible to produce chemically a solution very similar to that thought to exist at the end of the electrolysis by allowing stoichiometric amounts of dimethyl sulfoxide and protonated dimethyl sulfide to react in $NaClO_4$-MeCN solution. It was indeed found that, when equimolar amounts of Me_2SO and Me_2SH^+ were allowed to react, Me_2S corresponding to one half of that originally taken could be detected by GLC. Before mixing, neither the dimethyl sulfoxide nor the protonated dimethyl sulfide produced a peak. This recovery is in agreement with the stoichiometry implied in step 4 in which each mole of 3 is cleaved to produce one half mole of unprotonated Me_2S. It is also in agreement with the observed recovery of 25 m/o of the original Me_2S after electrolysis, since two moles of Me_2S are required to produce one mole of 3 electrochemically. Furthermore, on standing or after being warmed, the sodium salt of methanesulfonic acid was precipitated, carbon monoxide was generated, chloride could be detected and the uv spectrum showed the very intense end absorption described.

One significant difference was noted between the chemical and electrochemical reaction mixtures; acet-

amide was a major product in the former, but was present only in small concentrations in the latter. It is thought to be produced by acid catalyzed hydrolysis of MeCN (21). This would be possible in formation of the chemical reaction mixture because dehydration of dimethyl sulfoxide, Eq. [10], represents a major source of water. By contrast, in the electrochemical process, the major source of compound 2 is Me_2S through steps 1a and 2a which do not involve water. It was found that, on mixing anhydrous samples of dimethyl sulfoxide and protonated dimethyl sulfide, water would then be detected. After a period of time, the water content decreased and acetamide appeared.

Participation by perchlorate.—When significant yields of oxygen-containing products are formed as a result of an anodic oxidation, it is of interest to identify the oxygen source. Three reasonable possibilities exist here, elemental oxygen, water, and the perchlorate anion of the supporting electrolyte. Molecular oxygen can be eliminated from consideration because of the care taken in degassing the solutions and in protecting them from atmospheric contamination.

The results of the experiment with 1% water present show that it most certainly does enter into the reaction scheme if it is present, since an entirely different product, dimethyl sulfone, is produced. We believe that when water is present in concentrations larger than that of the sulfide, the reaction leads to formation of sulfone; however, when the water concentration is sufficiently low, this reaction path is unavailable and steps 7 and 8 occur to produce the sulfonic acid, providing perchlorate is available. In these experiments, care was taken to exclude water, including drying solvent with CaH_2, baking all glassware and supporting electrolyte in a vacuum, making all transfers out of contact with the atmosphere, and operating under a blanket of purified nitrogen or helium. Water concentrations in the electrolysis vessel typically amounted to 0.5 m*M*, compared with 30 m*M* for initial Me_2S concentration. We think that much of the water detected was introduced by the syringe used to inject samples into the chromatograph; that reaction mixtures were actually drier than our assays indicate.

We suggest, therefore, that the major source of oxygen in these experiments was perchlorate. Some was introduced from water formed by equilibration of perchloric acid, itself produced by reaction of the supporting electrolyte with electrochemically generated protons, with its anhydride. This is indicated in Eq. [11]

$$2\ HClO_4 \rightleftarrows H_2O + Cl_2O_7 \qquad [11]$$

which would be shifted to the right by uptake of water in step 4. This same reaction makes Cl_2O_7 available to react, both with methyl mercaptan in step 7 and possibly with starting material in steps 1b and 2b. We do not know the actual sequence of steps involved in Cl_2O_7 (7) reduction; however, observation of the uv spectrum of ClO_2 and recovery of chloride shows that this is occurring.

Tetrafluoborate supporting electrolyte.—If this reaction scheme is correct, elimination of perchlorate should substantially prevent the formation of oxygen-containing products. Reaction with Me_4NBF_4 supporting electrolyte, rather than perchlorate, did have this effect. No sulfonate was formed, and the product mixture showed very little uv absorption. We suggest that the reaction may have gone through steps 1a, 2a, and 3 only. Fluoborate salts similar to 3 are known to be stable (17); however, the products of the fluoborate reaction were not investigated. The similarity in coulometric results for the perchlorate and fluoborate reactions supports this suggestion, since steps 5 through 8 do not involve electrode reactions. The difference in shape of the current-time curves is not in accord with this suggestion, since perchlorate participation should not affect the rate of the anodic steps. It does not necessarily follow, however, that this rate difference indicates a different reaction mechanism, for variation in supporting electrolyte may cause appreciable changes in reaction conditions. The actual reaction potential is subject to variations with change in electrolyte because of alteration of the liquid junction potential involved in the reference probe. In addition, variation in supporting electrolyte may alter the double layer at the electrode-solution interface enough to cause significant variation in reaction rate.

Benzyl methyl sulfide oxidation.—The reaction of benzyl methyl sulfide in anhydrous $NaClO_4$-MeCN has been carried out under conditions similar to those described for Me_2S. The results were in substantial agreement. $PhCH_2SMe$ could be detected by GLC at the end of the electrolysis. On standing, $MeSO_3Na$ precipitated from solution and benzaldehyde could be detected by GLC. We suggest that this reaction may be a general one for aliphatic sulfides.

Implications for study of anodic oxidations.—It is fairly general practice to use perchlorate salts as supporting electrolytes for anodic oxidations. It has been observed by a number of workers that, at very anodic potentials in MeCN, it is possible to encounter direct reaction of perchlorate to form, among other products, ClO_2. In the present example, although considerable care has been taken to avoid the direct anodic oxidation of perchlorate, we have nevertheless produced ClO_2 as well as chlorine in other oxidation states. A possibly similar case has been reported in connection with hydrocarbon oxidation (22). An additional similar example has been observed by one of the present writers in studying the anodic oxidation of nitrate (23). It may be true that this complication should be considered whenever anodic reactions are performed in a very anhydrous medium.

Acknowledgment

Support from the Department of the Army through contract DA18-035-AMC-741(A) and from the National Institutes of Health through grant GM-10064 is acknowledged.

Manuscript submitted May 15, 1969; revised manuscript received July 19, 1969.

Any discussion of this paper will appear in a Discussion Section to be published in the June 1970 JOURNAL.

REFERENCES

1. F. Fichter and W. Wenk, *Ber.*, **45**, 1373 (1912).
2. D. H. Geske and M. W. Merritt, Paper No. 171, 155th A.C.S. Meeting, San Francisco, Calif., April 1968.
3. A. Zweig and W. G. Hodgson, *Proc. Chem. Soc.*, **1964**, 417.
4. A. Zweig, A. H. Maurer, and B. G. Roberts, *J. Org. Chem.*, **32**, 1322 (1967).
5. H. J. Shine, C. F. Dais, and R. J. Small, *ibid.*, **29**, 21 (1964).
6. J. P. Billon, *Bull. Soc. Chim. France*, **1960**, 1754.
7. J. F. O'Donnell, J. T. Ayres, and C. K. Mann, *Anal. Chem.*, **37**, 1161 (1965).
8. E. E. Reid, "Organic Chemistry of Bivalent Sulfur," Vol. II, p. 105, Chemical Publishing Co., Inc., New York (1960).
9. *Ibid.*, p. 114.
10. P. W. Atkins, A. Horsefield, and M. C. R. Symons, *J. Chem. Soc.*, **1964**, 5220.
11. H. Bohme, R. Frank, and W. Krause, *Ber.*, **82**, 433 (1949).
12. P. J. Smith and C. K. Mann, *J. Org. Chem.*, **34**, 1821 (1969).
13. C. K. Mann, *Anal. Chem.*, **36**, 2424 (1964).
14. J. Vedel and B. Tremillon, *J. Electroanal. Chem.*, **1**, 241 (1959/60).
15. J. J. Kirkland, *Anal. Chem.*, **11**, 1388 (1960).
16. T. Chen, *ibid.*, **39**, 804 (1967).
17. H. Meerwein, K. F. Zenner, and R. Gipp, *Ann. Chem.*, **688**, 71 (1965).
18. M. C. Caserio, R. E. Pratt, and R. J. Holland, *J. Am. Chem. Soc.*, **88**, 5747 (1966).

19. Y. Pocker and A. J. Parker, *J. Org. Chem.*, **31**, 1526 (1966).
20. H. H. Szmant in "Organic Sulfur Compounds," Vol. I, p. 162, N. Kharasch, Editor, Pergamon Press, New York (1961).
21. J. D. Roberts and M. C. Caserio, "Basic Principles of Organic Chemistry," p. 564, Benjamin, New York (1965).
22. K. Koyama, T. Susuki, and S. Tsutsumi, *Tetrahedron*, **23**, 2665 (1967).
23. R. R. Rao, S. B. Milliken and C. K. Mann, Unpublished data.

The Mechanism of the Dendritic Electrocrystallization of Zinc

J. W. Diggle,*,[1] A. R. Despic,[2,]* and J. O'M. Bockris*

The Electrochemistry Laboratory, The University of Pennsylvania, Philadelphia, Pennsylvania

ABSTRACT

Measurements have been made of the growth rate of zinc dendrites in alkaline zincate solutions as a function of overpotential (η), concentration (c), and temperature (T). The tip radii have been measured by electron microscopy. At constant potential, an initiation time of between 5 and 100 min is observed, depending on η, c, and T. The dendrite grows linearly with time, at a rate depending on η, c, and T. The total current to base and dendrite was independent of time until a time τ_i, where $\tau_i > \tau_d$ (the time for initiation obtained from the growth rate *vs.* time relation). Thereafter, $i \propto t^2$. A critical overpotential was determined, -75 mV $> \eta_{crit} > -85$ mV. Below this η_{crit}, sponge was formed. Dendrites were observed up to $\eta = -160$ mV; above this the deposition was heavy sponge. At a given c, the growth rate of a given dendrite increased with η according to an exponential law. The growing tip is parabolic, where $10^{-5} < r_{tip} < 10^{-4}$ cm. No twinning was observed.

The basic model used depended on the increase in c.d. possible for an electrodic reaction when the diffusion current depends on a radius of curvature of the substrate, rather than the linear diffusion layer thickness, δ_0. When the tip of a dendrite-precursor attains this condition, its growth is released from the diffusion control characteristic of it in the predendrite situation, and it grows further under predominantly activation control at a rate far greater than that possible in any other direction, where the radii of curvature are much greater. The Gibbs radius-dependent overpotential term is also present, although it has a minimized influence. The initiation of the dendrite is treated in terms of growing pyramids on the substrate surface. At first the growth is linear-diffusion controlled, but it is shown that the rotation of the spiral, within the linear diffusion boundary surrounding the sphere, gives rise to a decrease of the effective radius of curvature of the dendrite tip until the value $r < 0.1\ \delta_0$ is attained, which is effectively the condition for the dendrite initiation. The theory of the propagation in terms of the activation, diffusion and Gibbs overpotential is consistent, in terms of τ_d, with experiment. A derived growth-time line is also numerically consistent with experiment. The dendrite growth rate as a function of c and η are numerically calculated with reasonable consistency. The tip radius can also be approximately calculated in terms of the present model.

Dendrite formation in electrodeposition and in the spontaneous crystallization of metals from their melts is related, respectively, to overpotential, for the former phenomenon, and to the degree of undercooling. Thus, the theory of rate determination of the growing dendrite in electrodeposition depends partly on mass transfer, while that for thermal crystallization depends on heat transfer. Correspondingly, there is an analogous response to variables, *e.g.*, if the overpotential exceeds a limit, dendritic deposition ceases (1), and if the degree of undercooling is sufficiently high, dendritic crystallization of metals does not occur (2).

Studies with silver dendrites deposited from molten salts (3) indicated that a critical overpotential η_{crit} is a necessity for dendrite initiation, and related this overpotential to a sharp increase at η_{crit}, of the dendrite radius for maximal growth. Reddy (4) has suggested that the critical overpotential may be related to the stacking fault energy of the crystal lattice (5, 6) necessary for the formation of a twin plane, through which it was proposed that the dendrite propagated. The existence of twin planes in dendrites has been reported on numerous occasions (7-9), whereas evidence for the single crystal nature of dendrites (10) has also been reported. It has yet to be shown that twin planes play a necessary part in dendrite initiation and propagation (11, 12).

The Barton and Bockris theory (3) involves a model of spherical diffusion to the dendrite tip. However, to allow for the fact that the rate of growth should then increase continuously toward zero tip radius, it was necessary to include the change of the reversible electrode potential with radius. In this way a maximum dendrite growth rate would be achieved at some optimum rip radius (3)

$$r_{opt} \frac{1 \pm [1 + DC_bF^2\eta/2\gamma Vi_0]^{1/2}}{F\eta/2\gamma V}$$

where D is the diffusion coefficient of the silver ion, C_b is the bulk concentration of the silver ion, V is the molar volume of silver, and i_0 is its exchange current density, and γ is the surface tension between metal and electrolyte.

Hamilton (13), assuming that the dendrite tip was a moving paraboloid, has shown that, to correlate his

* Electrochemical Society Active Member.
[1] Present address: Allied Chemical Corporation, Corporate Research, Morristown, New Jersey.
[2] Present address: The Faculty of Technology, University of Belgrade, Yugoslavia.
Key words: zinc, dendrites, electrocrystallization, electrodeposition, mechanistic study.

19. Y. Pocker and A. J. Parker, *J. Org. Chem.*, **31**, 1526 (1966).
20. H. H. Szmant in "Organic Sulfur Compounds," Vol. I, p. 162, N. Kharasch, Editor, Pergamon Press, New York (1961).
21. J. D. Roberts and M. C. Caserio, "Basic Principles of Organic Chemistry," p. 564, Benjamin, New York (1965).
22. K. Koyama, T. Susuki, and S. Tsutsumi, *Tetrahedron*, **23**, 2665 (1967).
23. R. R. Rao, S. B. Milliken and C. K. Mann, Unpublished data.

The Mechanism of the Dendritic Electrocrystallization of Zinc

J. W. Diggle,*,[1] A. R. Despic,[2,]* and J. O'M. Bockris*

The Electrochemistry Laboratory, The University of Pennsylvania, Philadelphia, Pennsylvania

ABSTRACT

Measurements have been made of the growth rate of zinc dendrites in alkaline zincate solutions as a function of overpotential (η), concentration (c), and temperature (T). The tip radii have been measured by electron microscopy. At constant potential, an initiation time of between 5 and 100 min is observed, depending on η, c, and T. The dendrite grows linearly with time, at a rate depending on η, c, and T. The total current to base and dendrite was independent of time until a time τ_i, where $\tau_i > \tau_d$ (the time for initiation obtained from the growth rate *vs.* time relation). Thereafter, $i \propto t^2$. A critical overpotential was determined, -75 mV $> \eta_{crit} > -85$ mV. Below this η_{crit}, sponge was formed. Dendrites were observed up to $\eta = -160$ mV; above this the deposition was heavy sponge. At a given c, the growth rate of a given dendrite increased with η according to an exponential law. The growing tip is parabolic, where $10^{-5} < r_{tip} < 10^{-4}$ cm. No twinning was observed.

The basic model used depended on the increase in c.d. possible for an electrodic reaction when the diffusion current depends on a radius of curvature of the substrate, rather than the linear diffusion layer thickness, δ_0. When the tip of a dendrite-precursor attains this condition, its growth is released from the diffusion control characteristic of it in the predendrite situation, and it grows further under predominantly activation control at a rate far greater than that possible in any other direction, where the radii of curvature are much greater. The Gibbs radius-dependent overpotential term is also present, although it has a minimized influence. The initiation of the dendrite is treated in terms of growing pyramids on the substrate surface. At first the growth is linear-diffusion controlled, but it is shown that the rotation of the spiral, within the linear diffusion boundary surrounding the sphere, gives rise to a decrease of the effective radius of curvature of the dendrite tip until the value $r < 0.1\ \delta_0$ is attained, which is effectively the condition for the dendrite initiation. The theory of the propagation in terms of the activation, diffusion and Gibbs overpotential is consistent, in terms of τ_d, with experiment. A derived growth-time line is also numerically consistent with experiment. The dendrite growth rate as a function of c and η are numerically calculated with reasonable consistency. The tip radius can also be approximately calculated in terms of the present model.

Dendrite formation in electrodeposition and in the spontaneous crystallization of metals from their melts is related, respectively, to overpotential, for the former phenomenon, and to the degree of undercooling. Thus, the theory of rate determination of the growing dendrite in electrodeposition depends partly on mass transfer, while that for thermal crystallization depends on heat transfer. Correspondingly, there is an analogous response to variables, *e.g.*, if the overpotential exceeds a limit, dendritic deposition ceases (1), and if the degree of undercooling is sufficiently high, dendritic crystallization of metals does not occur (2).

Studies with silver dendrites deposited from molten salts (3) indicated that a critical overpotential η_{crit} is a necessity for dendrite initiation, and related this overpotential to a sharp increase at η_{crit}, of the dendrite radius for maximal growth. Reddy (4) has suggested that the critical overpotential may be related to the stacking fault energy of the crystal lattice (5, 6) necessary for the formation of a twin plane, through which it was proposed that the dendrite propagated. The existence of twin planes in dendrites has been reported on numerous occasions (7-9), whereas evidence for the single crystal nature of dendrites (10) has also been reported. It has yet to be shown that twin planes play a necessary part in dendrite initiation and propagation (11, 12).

The Barton and Bockris theory (3) involves a model of spherical diffusion to the dendrite tip. However, to allow for the fact that the rate of growth should then increase continuously toward zero tip radius, it was necessary to include the change of the reversible electrode potential with radius. In this way a maximum dendrite growth rate would be achieved at some optimum rip radius (3)

$$r_{opt} \frac{1 \pm [1 + DC_bF^2\eta/2\gamma Vi_0]^{1/2}}{F\eta/2\gamma V}$$

where D is the diffusion coefficient of the silver ion, C_b is the bulk concentration of the silver ion, V is the molar volume of silver, and i_0 is its exchange current density, and γ is the surface tension between metal and electrolyte.

Hamilton (13), assuming that the dendrite tip was a moving paraboloid, has shown that, to correlate his

* Electrochemical Society Active Member.
[1] Present address: Allied Chemical Corporation, Corporate Research, Morristown, New Jersey.
[2] Present address: The Faculty of Technology, University of Belgrade, Yugoslavia.
Key words: zinc, dendrites, electrocrystallization, electrodeposition, mechanistic study.

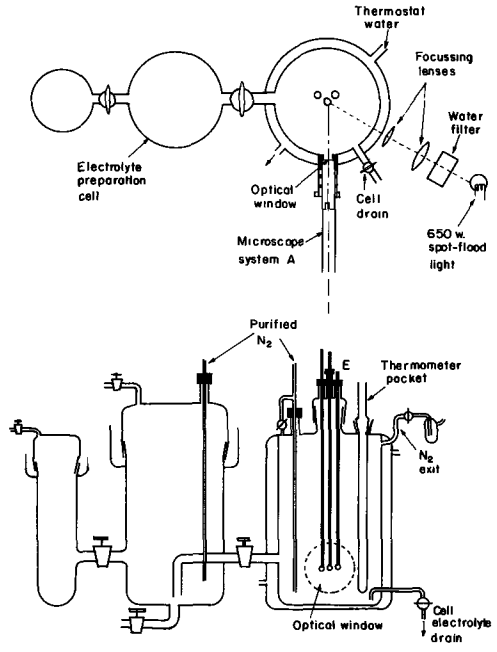

Fig. 1. Experimental cell, plan and side elevation

equations to the results of Barton and Bockris (3), it was necessary to assume that γ and i_0 were a magnitude lower and higher, respectively, than that assumed by Barton and Bockris. The computed values of the tip radius and the growth velocity with respect to overpotential were then in good agreement with experimental observations (3). Hamilton concluded that the dendrite growth was diffusion controlled and occurred at the maximum velocity, the process having a high i_0 value due to a twin plane growth mechanism [*cf.* also Reddy (4)].

In summary, some agreement exists as to the importance of diffusive transfer in dendritic deposition; however, the details of initiation and the concept of the critical overpotential are hardly understood. This study attempts to answer the following questions: (*i*) why do silver and zinc dendrites have such widely differing apparent η_{crit} values, 3 mv and 80 mv, respectively; (*ii*) why can the initiation of single dendrites be observed for silver, yet not for zinc; (*iii*) what significance can be attached to the so-called initiation time (3), and (*iv*) what electrodic parameters control the value of the critical overpotential η_{crit}?

Experimental

Electrolyte.—The electrolye used throughout this work was a 10% w/w solution of potassium hydroxide (Baker reagent grade) in conductivity water to which was added sufficient reagent grade ZnO to produce zincate concentrations between 0.01 and 0.2 moles liter^{-1}. All electrolytes were de-aerated with purified nitrogen for 4 hr in the subsidiary cell (Fig. 1), prior to introduction into the observation cell.[3]

Electrodes.—Spherical electrodes (0.5 mm radii) were used and prepared as follows: A short length of 0.2 mm diameter platinum wire was sealed into 3 mm bore glass tubing. This platinum wire was slowly melted in a gas jet until a sphere was formed in contact with the tip of the glass tubing. The Pt sphere was cleansed in a mixture of sulfuric and nitric acids (5 min), then washed with conductivity water. The Pt surface was highly reflective and void of imperfection on 60X microscopic inspection.

The Pt sphere was immersed in a strongly agitated solution containing 1 mole liter^{-1} $ZnSO_4 \cdot 7H_2O$ dissolved in 0.01*N* H_2SO_4 and a low (< 50 mV) cathodic overpotential applied. Under such conditions, ($i_L \sim 0.5$ A-cm^{-2}), smooth compact zinc deposits were observed. The deposition was continued for 10 min, after which, assuming 100% coulombic zinc deposition efficiency, the deposit was 10^{-3} cm thick. The electrode was withdrawn from the preparation cell, washed in conductivity water, and introduced into the observation cell.

The anode and reference electrodes were prepared in a similar manner, but to a 50μ zinc thickness. Electrode reproducibility was good. Freshly prepared cathode and reference electrodes were used in each experiment, and freshly prepared anode in every other experiment.

Apparatus.—(*i*) *Cell.*—The cell (Fig. 1) allows observation of the zinc deposition process and the dendrite growth rate. The electrode assembly, E, consisted of the three electrodes in glass guide tubes clamped in position with gas-tight Teflon seals. Temperature control was maintained ±0.05°C by circulating thermostatted water through the outer jacket of the cell.

(*ii*) *Optical system.*—The optical tube (A in Fig. 1) is similar to that of Barton and Bockris (3). A real image of the spherical electrode is projected on the objective lens of a telescope-microscope system mounted horizontally. This system, which has only one optical window between the lenses and the electrode, avoids the problem of image distortion found with externally mounted optical arrangements. Therefore, the resolution and possible magnification range are extended; the magnification was up to 800 (300X was used).

(*iii*) Potentiostatic control was used (Wenking potentiostat).

Procedure.—Following the insertion of the electrodes into the observation cell, the electrolyte from the subsidiary cell was introduced and the overpotential applied immediately electrolyte contact between the electrodes occurred.

Observation of the cathode electrode was maintained until dendrites were initiated. In the dendrite growth rate experiments, the electrode assembly E was slowly rotated until the required dendrite was normal to the observation axis. Polaroid photographs were taken at intervals (minutes); alternatively, visual rate measurements were made.

The dendrite growth rate and the current changes were determined as a function of overpotential in the range −85 to −140 mV, zincate ion concentration 0.01 to 0.20 moles liter^{-1}, and temperature in the range 25°-50°C.

Results

Dendrite initiation time and morphology of the deposited zinc.—Two initiation times are distinguished. First, the time observed experimentally was found to correlate with the initiation time, τ_i, from current-time phenomenon (see Fig. 5, 7, and 8); since at this time, dendrites were clearly visible, τ_i is in excess of the true initiation time. Second, the initiation time obtained by extrapolating the dendrite length-time plot to zero dendrite length, τ_d. This is regarded as the more significant initiation time. Experimentally, $\tau_d < \tau_i$.

Dendrites were observed to be initiated at overpotentials between −85 and −140 mV. Below −85 mV the zinc morphology was spongy. Above −140 mV the zinc morphology was sponge mixed with dendrites (1) (Fig. 2). Within the range of overpotential required to initiate dendrites, the character of the deposits was dendritic, but not of the 'ideal" shape (10), and appeared dependent on the conditions of growth (Fig. 3a and 3b). In the majority of experiments the dendrite main axis and primary branches were of a swordlike nature, and the area at the tip was flat and stepped (Fig. 4). Secondary branching was rare, as

[3] No rigorous electrolyte purification was performed since it has been shown (14) that in highly purified systems the results, in terms of dendrite initiation and propagation, are essentially identical.

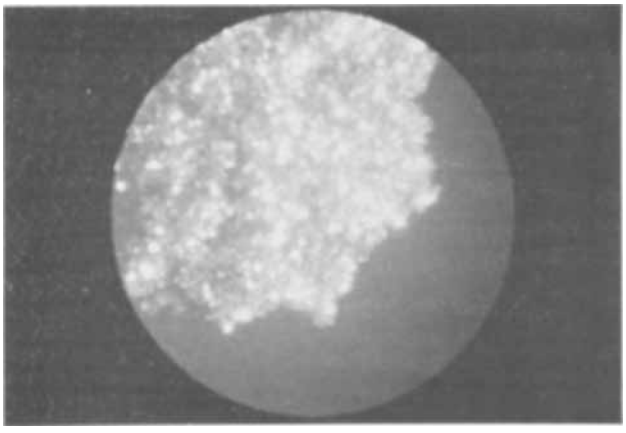

Fig. 2. Example of the zinc deposition obtained at $\eta = -200$ mV; $c_0 = 0.1$ moles liter^{-1} and $T = 35°C$. Magnification 25X.

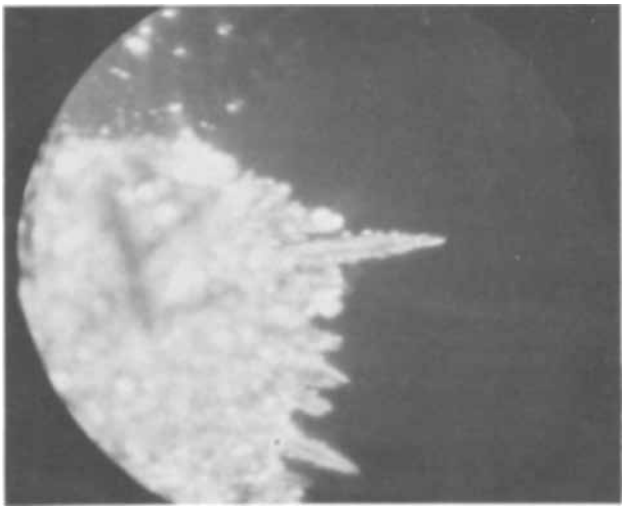

Fig. 3a. Typical dendritic growth resulting from a low propagation rate experiment. $c_0 = 0.01$ moles liter^{-1}, $\eta = -100$ mV, $T = 35°C$, where $v = 0.04$ μsec^{-1}. Magnification 100X.

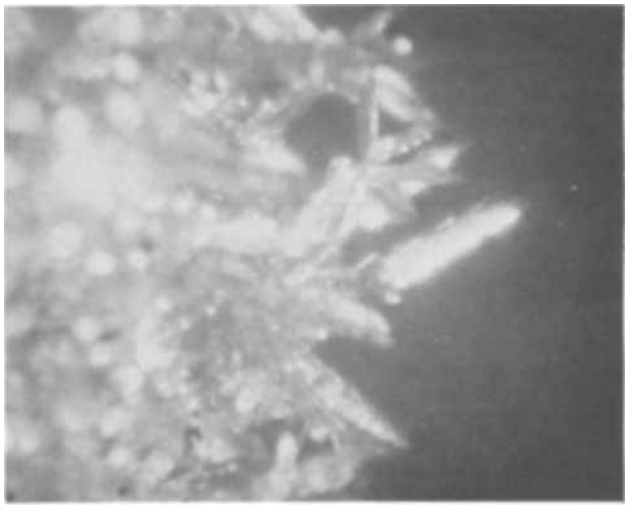

Fig. 3b. Typical dendritic growth resulting from a high propagation rate experiment. $c_0 = 0.1$ moles liter^{-1}, $\eta = -100$ mV, $T = 35°C$, where $v = 0.4$ μsec^{-1}. Magnification 75X.

has been previously reported by Powers (15) at —100 mV overpotential [Fig. 28, ref. (15)].

Examination in polarized light and by electron diffraction indicated that the dendrites were single crystals; no evidence of twinning was found.

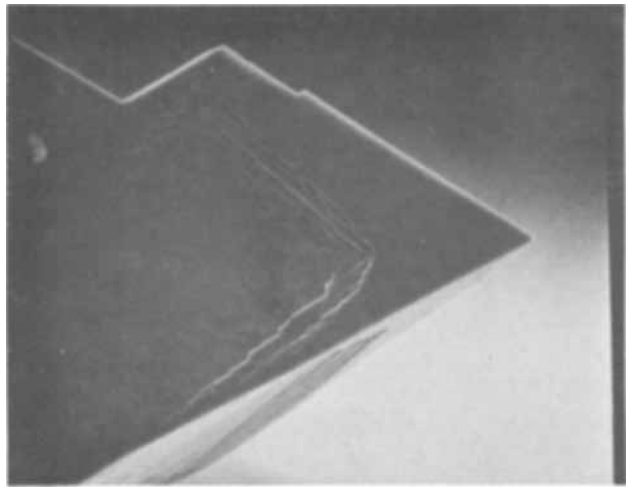

Fig. 4. Dendrite tip geometry. $c_0 = 0.1$ moles liter^{-1}, $\eta = -85$ mV, $T = 35°C$. Magnification 850X.

Change in the total current with respect to time.—The total current (Fig. 5, 7, and 8) increases according to an approximate t^2 relationship (Fig. 9). The region of sharp current change appeared to coincide with the visual appearance, under 300X magnification, of dendrites.

Total current against time as a function of zincate concentration.—Figure 5 shows the total current plotted against time as a function of zincate concentration. The time required for the appearance of dendrites, as determined from the inflection point, decreases as the zincate concentration increases. For 0.01 mole liter^{-1}

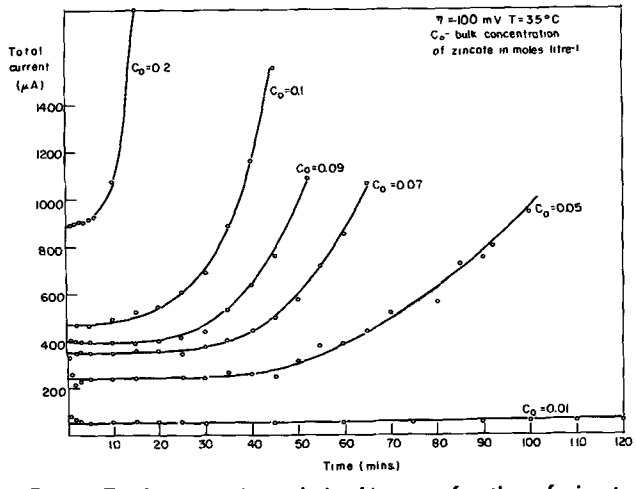

Fig. 5. Total current-time relationship as a function of zincate concentration. $\eta = -100$ mV, $T = 35°C$.

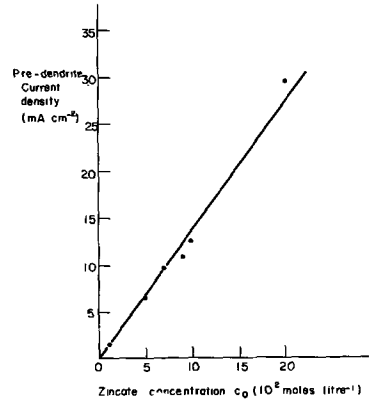

Fig. 6. Predendrite current density as a function of zincate concentration from which D/δ_0 is evaluated.

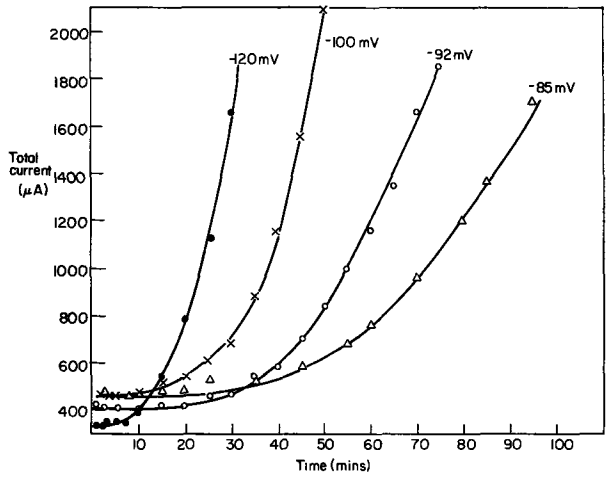

Fig. 7. Total current-time as function of overpotential. $c_0 = 0.1$ moles liter^{-1}, $T = 35°C$.

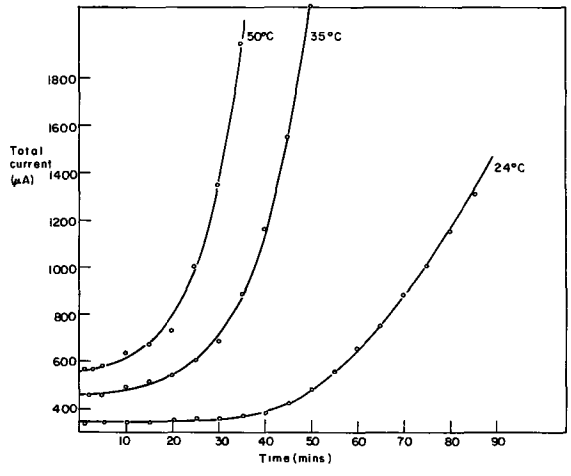

Fig. 8. Total current-time as a function of electrolyte temperature. $c_0 = 0.1$ moles liter^{-1}, $\eta = -100$ mV.

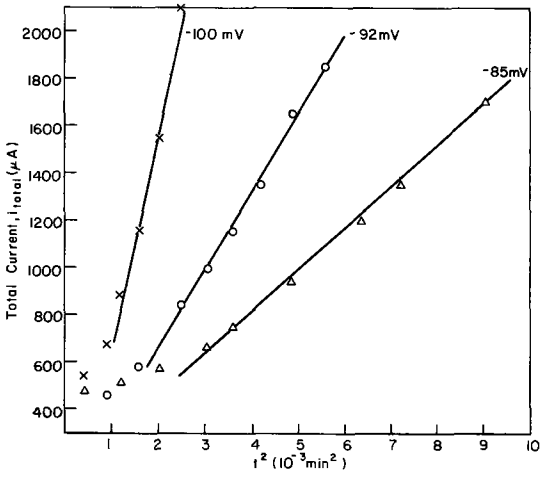

Fig. 9. Power law dependence of total current on time as a function of overpotential. $c_0 = 0.1$ moles liter^{-1}, $T = 35°C$.

zincate, the experimental initiation time τ_i was > 120 min.

The relationship between the initial predendrite current density, calculated on the geometric area, and the zincate concentration c_0 is shown in Fig. 6. From the linear slope, assuming the applicability of $i_L = (nFDc_0)/\delta_0$, the value of the term D/δ_0 was found to be 6.8×10^{-4} cm sec^{-1}. Taking the value of δ_0 as 10^{-2} cm produces $D = 6.8 \times 10^{-6}$ cm^2 sec^{-1}, a value

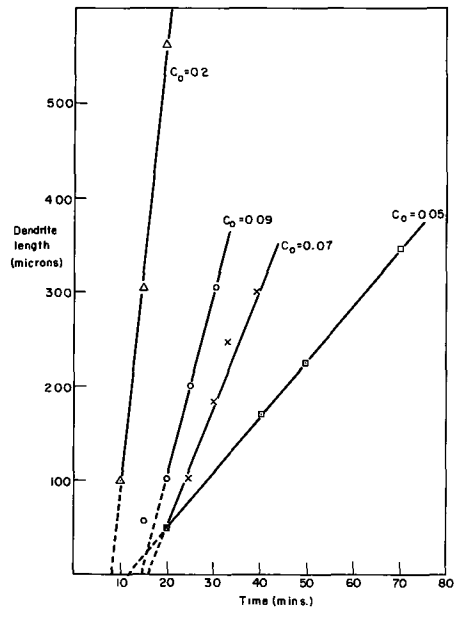

Fig. 10. Dendrite length, y, with respect to time as a function of zincate concentration. $\eta = -100$ mV, $T = 35°C$.

in excellent agreement with that reported by McBreen (16).

Total current against time as a function of overpotential.—Figure 7 shows that the value of τ_i decreases with increase of η.

Total current against time as a function of temperature.—The time required for the appearance of the first dendrites τ_i decreases as the temperature increases (Fig. 8).

Rate of dendrite propagation.—As a function of zincate concentration.—Figure 10 shows the change in observed dendrite length with respect to time (time measured from the moment of overpotential application) as a function of zincate concentration. The extrapolations from the linear regions to zero dendrite length gives the initiation times, τ_d, as defined by Barton and Bockris (3). From Table I, where the dendrite propagation rates (v) are tabulated, the rate of propagation increases as the zincate concentration increases. The value of the term dv/dc_0 is obtained as 0.43 cm^4 mole^{-1} sec^{-1}, where v is expressed in cm sec^{-1} and c_0 in moles cm^{-3}. In Table I is tabulated the dendrite tip current density (i) calculated from the propagation rate (v) assuming that no thickening occurs. Then

$$i_{tip} = v\frac{nF}{V} \qquad [1]$$

where V is the molar volume of zinc.

Figure 11 shows the relationship between log i and log c_0—the best statistical straight line is shown, the slope of which is 1.00 ± 0.14; the dotted line represents a slope of 0.75.

As a function of overpotential.—The extrapolated initiation time τ_d decreases with increasing overpotential (Fig. 12), as do the observed times, τ_i.

Table I. Experimental propagation rate (v) and dendrite tip current density (i_{tip}) as a function of zincate concentration

η, mV	T, °C	c_0, moles liter^{-1}	v, μsec^{-1}	i_{tip}, A cm^{-2}
−100	35	0.01	0.04	0.084
		0.05	0.10	0.20
		0.07	0.20	0.43
		0.09	0.31	0.66
		0.10	0.40	0.84
		0.20	0.75	1.60

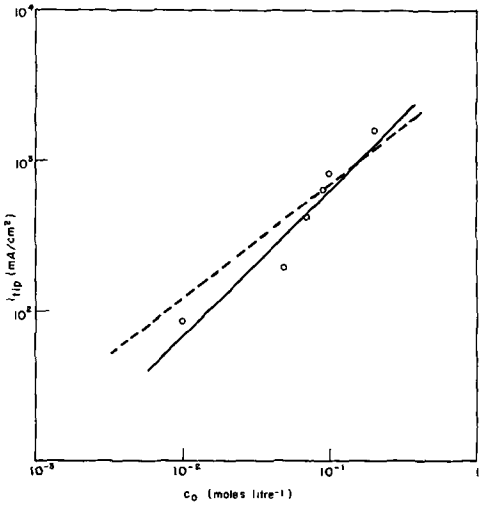

Fig. 11. Log i_{tip} as a function of log c_0. The dotted line has a theoretically significant slope of 0.75; solid line is the best statistical line through experimental points.

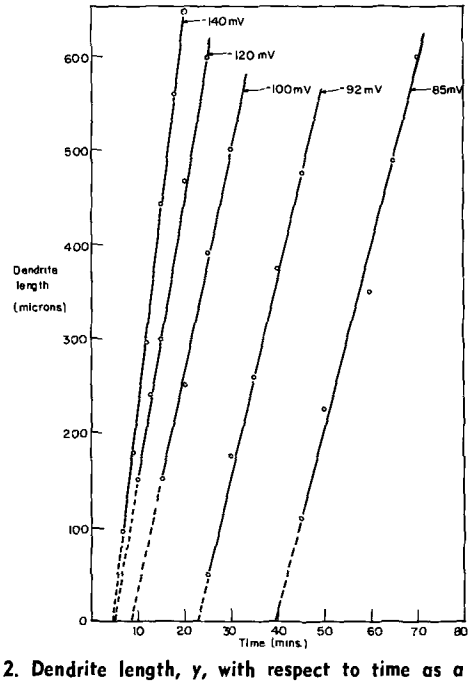

Fig. 12. Dendrite length, y, with respect to time as a function of overpotential. $c_0 = 0.1$ moles liter^{-1}, $T = 35°C$.

The dendrite propagation rate, v, increases with increasing overpotential (Table II); the $v - \eta$ slope increases with increasing η (Fig. 13). The logarithm of the tip current density when plotted against η was found to be linear (Fig. 14) where $d\eta/d \log i_{tip} = 0.17v$.

As a function of temperature.—The extrapolated times, τ_d, were observed to decrease with increasing temperature (Fig. 15).

Table III shows the propagation rate, v, and the calculated dendrite tip current density (i) as a function of temperature: the value of dv/dT being 1.3×10^{-6} cm sec^{-1} deg^{-1}.

Table II. Experimental propagation rate (v) and dendrite tip current density (i_{tip}) as a function of overpotential

c_0, moles liter^{-1}	T, °C	η, mV	v, μsec^{-1}	i_{tip}, A cm^{-2}
0.10	35	−140	0.7	1.46
		−120	0.5	1.05
		−100	0.4	0.84
		−92	0.36	0.75
		−85	0.33	0.70

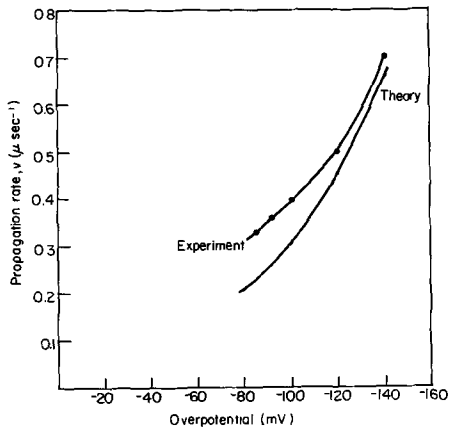

Fig. 13. Propagation rate, v, as a function of overpotential. $c_0 = 0.1$ moles liter^{-1}, $T = 35°C$. Theory line is based on a propagation theory developed in the section on Propagation under Discussion.

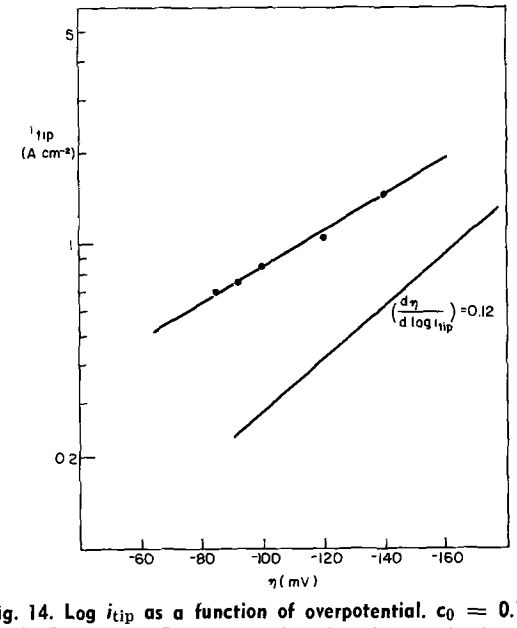

Fig. 14. Log i_{tip} as a function of overpotential. $c_0 = 0.1$ moles liter^{-1}, $T = 35°C$. Theoretical slope based on activation control, with $\alpha_c = 0.5$, is included for comparison.

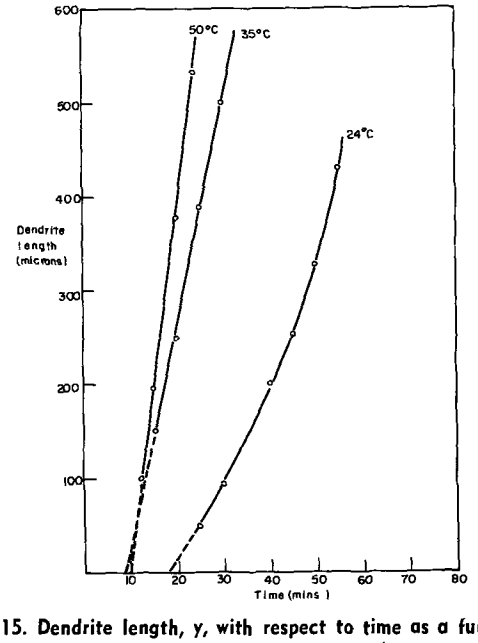

Fig. 15. Dendrite length, y, with respect to time as a function of electrolyte temperature. $c_0 = 0.1$ moles liter^{-1}, $\eta = -100$ mV.

Table III. Experimental propagation rate (v) and dendrite tip current density (i_{tip}) as a function of temperature

η, mV	c_0, moles liter^{-1}	T, °C	v, μsec^{-1}	i_{tip}, A cm^{-2}
−100	0.1	24	0.25	0.53
		35	0.40	0.84
		50	0.60	1.26

The log i_{tip} — $1/T$ plot (Fig. 16) shows a linear relationship of slope -1.25×10^3 deg. From this the electrochemical activation energy ΔH^o, at the overpotential of — 100 mV, can be calculated at 6 kcal mole^{-1}.

Initiation overpotential, η_{crit}, and initiation time, τ.— Experimentally, $-75 > \eta_{crit} > -85$ mV; below —75 mV dendrites were not observed. Extrapolation of Fig. 13 to zero propagation rate suggests that the value of η_{crit} lies below —10 mV. Dendrites were not observed at potentials more anodic than —75 mV because the initiation time is so long (Fig. 17); only black spongy zinc was observed.

Influence of dendrite propagation current on measured total current.—To relate the changes in total current flowing to a dendrite initiation process, it is necessary to show that the dendrite propagation current is negligible when compared to the current at the substrate surface. From Table I, the propagation rate of dendrites in a zincate concentration of 0.1 moles liter^{-1} at 35°C and an overpotential of —100 mV is equivalent to a dendrite tip current density of 840 mA cm^{-2}. The dendrites were *ca.* 10μ in width; assuming that the dendrite tip is a hemisphere, the current through the dendrite can be calculated as 1.2 μA. Figure 5 shows that this level of dendrite propagation current is negligible compared to the total current observed, even allowing for the simultaneous growth of 30 dendrites on an electrode area of *ca.* 3×10^{-2} cm^2. This conclusion is also valid for other zincate concentrations. This conclusion can be confirmed experimentally by initiating dendrites at, say, —100 mV and then lowering the overpotential to —50 mV. The growth rate of the dendrites eventually decreases to zero; the total current remains at a value only slightly less than that at —100 mV.

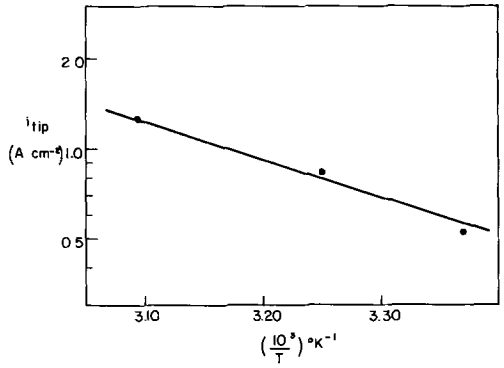

Fig. 16. Log i_{tip} as a function of reciprocal temperature. From the slope an electrochemical activation energy is evaluated.

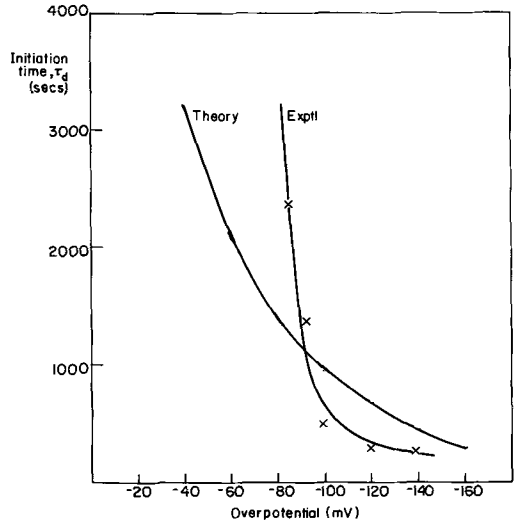

Fig. 17. Initiation time, τ_d, as a function of overpotential. $c_0 = 0.1$ moles liter^{-1}, $T = 35$°C. Theory line is calculated from an initiation theory developed in the section on Model of dendrite initiation.

Discussion

Summary of the phenomenology.—Facts are: (*i*) an initiation overpotential ($\sim$ —80 mV) is required to produce dendrites; (*ii*) two initiation times have been observed, one for dendrites, τ_d, and the other for current, τ_i, *e.g.*, Fig. 7 and 12, $\tau_d < \tau_i$. The times required for the dendrites to approach the boundary of the linear diffusion layer are in agreement with the times, τ_i; (*iii*) the growth of dendrites, beyond the initiation time, is linear with time; (*iv*) the total current increases with time such that $i \propto t^2$ (Fig. 9).

Basic model. The model is that of Barton and Bockris (3) extended to the Tafel region of overpotential. Then

$$\eta = \frac{RT}{\alpha_c \mathbf{F}} \ln \frac{i}{i_0} + \frac{RT}{z\mathbf{F}} \ln \left(\frac{i_L - i}{i_L} \right) + \frac{2\gamma V}{n\mathbf{F}r} \quad [2]$$

where

$$i_L = \frac{n\mathbf{F}D}{r} c_{tip} = i_{L(s)}$$

where subscript (*s*) indicates spherical diffusion, V is the molar volume of zinc, r is the radius of the dendrite tip at which the zincate concentration is c_{tip}, γ is the surface energy of the zinc/electrolyte interface, other parameters have their usual significance.

An optimum tip radius will exist where the growth rate is maximal and constant.

Propagation.—Equation [1] which relates the propagation rate v to the dendrite tip current density i can be rewritten as

$$\frac{dy}{dt} = \frac{M}{\rho n \mathbf{F}} i_{tip} \quad [3]$$

where y is the dendrite length. Expressing i_{tip} in terms of an irreversible activation-diffusion current density, an equation relating propagation rate to overpotential, zincate concentration and temperature can be obtained. The current density i_{tip} can be set equal to

$$i_{tip} = i_0 \left\{ \left(\frac{a_i^0}{a_e^0} \right)_c \exp \left(\frac{-\alpha_c \mathbf{F} \eta}{RT} \right) - \left(\frac{a_i^R}{a_e^R} \right)_a \exp \left(\frac{\alpha_a \mathbf{F} \eta}{RT} \right) \right\} \quad [4]$$

for the general reaction $0 + e^- \rightleftarrows R$. a_i is the activity of the oxidized (o) or reduced (R) state at the current density i_{tip}, and a_e are the activities in the equilibrium state.

Neglecting double layer effects (valid at the high ionic strength used in this work), the ratio of the activities for the cathodic reaction may be written as

$$\left(\frac{a_i^0}{a_e^0} \right) = \left(1 - \frac{i}{i_L} \right) \quad [5]$$

The ratio of the activities for the reverse anodic reaction must take into account the Kelvin term which becomes appreciable at low values of dendrite tip radii. The change in the free energy accompanying the anodic reaction at equilibrium (ΔG_e) and that accompanying the reaction at current density i_{tip} (ΔG_i) will

differ appreciably when the Kelvin term is high, *i.e.*, at low dendrite tip radii. Thus

$$\Delta G_i - \Delta G_e = RT \ln \left(\frac{a_i^R}{a_e^R} \right)_a \quad [6]$$

ΔG_i and ΔG_e differ by the Kelvin term $\frac{2\gamma V}{r}$

$$\therefore \Delta G_i - \Delta G_e = \frac{2\gamma v}{r} \quad [7]$$

Thus

$$\frac{2\gamma V}{RT \cdot r} = \ln \left(\frac{a_i^R}{a_e^R} \right)_a \quad [8]$$

or

$$\exp \left(\frac{2\gamma V}{RT \cdot r} \right) = \left(\frac{a_i^R}{a_e^R} \right)_a \quad [9]$$

From [9], [5], and [4]

$$i_{tip} = i_0 \left\{ \left(1 - \frac{i}{i_L} \right) \exp \left(\frac{-\alpha_c F \eta}{RT} \right) - \exp \left(\frac{2\gamma V}{RT \cdot r} \right) \exp \left(\frac{\alpha_a F \eta}{RT} \right) \right\} \quad [10]$$

The concentration of zincate at the tip is the bulk zincate concentration when the tip is close to or outside the outer boundary of the linear diffusion layer. The value of c_{tip} at a dendrite whose length is y, where $y < \delta$, can be obtained by linearization of the concentration profile in the diffusion layer (Fig. 18). Then

$$c_{tip} = c_0 y / \delta_0 \quad [11]$$

Therefore, substituting Eq. [11] and [10] with the equation for the spherical diffusion limiting current density, $i_{L(s)}$, into Eq. [3] one obtains ($i_{L(tip)} = i_{L(l)} y/r$ where subscript l indicates linear diffusion)

$$\frac{dy}{dt} = \frac{M}{\rho n F} \frac{n F D c_0 y / \delta_0 \, i_0 \left\{ \exp \left(\frac{-\alpha_c F \eta}{RT} \right) - \exp \left(\frac{2\gamma V}{RT \cdot r} \right) \exp \left(\frac{\alpha_a F \eta}{RT} \right) \right\}}{n F D c_0 y / \delta_0 + i_0 r \exp \left(\frac{-\alpha_0 F \eta}{RT} \right)} \quad [12]$$

which produces, when $i_{L(l)} = nFDc_0/\delta_0$

$$\frac{dy}{dt} = \frac{M}{\rho n F} \frac{i_{L(l)} y \, i_0 \left\{ \exp \left(\frac{-\alpha_c F \eta}{RT} \right) - \exp \left(\frac{2\gamma V}{RT \cdot r} \right) \exp \left(\frac{\alpha_a F \eta}{RT} \right) \right\}}{i_{L(l)} y + i_0 r \exp \left(\frac{\alpha_c F \eta}{RT} \right)} \quad [13]$$

Rearranging Eq. [13] produces

$$\frac{dy}{i_0 \left\{ \exp \left(\frac{-\alpha_c F \eta}{RT} \right) - \exp \left(\frac{2\gamma V}{RT \cdot r} \right) \exp \left(\frac{\alpha_a F \eta}{RT} \right) \right\} + \frac{r \exp \left(\frac{\alpha_a F \eta}{RT} \right)}{i_{L(l)} y}} \Bigg/ \frac{dy}{\left\{ \exp \left(\frac{-\alpha_c F \eta}{RT} \right) - \exp \left(\frac{2\gamma V}{RT \cdot r} \right) \exp \left(\frac{\alpha_a F \eta}{RT} \right) \right\}} = \frac{M}{\rho n F} dt \quad [14]$$

Taking r as a constant, and placing

$$\left\{ \exp \left(\frac{-\alpha_c F \eta}{RT} \right) - \exp \left(\frac{2\gamma V}{RT \cdot r} \right) \exp \left(\frac{\alpha_a F \eta}{RT} \right) \right\} = u \quad [15]$$

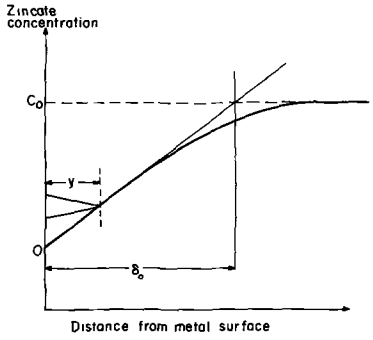

Fig. 18. Schematic representation of the calculation of the concentration at the dendrite tip.

Eq. [14] integrates to the general expression between y and y_0, where y_0 is the limit when $t = 0$

$$\frac{y}{i_0 u} + r \ln y \frac{\exp \left(\frac{\alpha_a F \eta}{RT} \right)}{i_{L(l)} u} = \frac{M}{\rho n F} t + \frac{y_0}{i_0 u} + r \ln y_0 \frac{\exp \left(\frac{\alpha_a F \eta}{RT} \right)}{i_{L(l)} u} \quad [16]$$

Two limiting cases arise: (*i*) when $\frac{y}{i_0 u} >> \frac{r \ln y}{i_{L(l)} u} \exp \left(\frac{\alpha_a F \eta}{RT} \right)$, a linear relation will exist between y and t; (*ii*) in the reverse situation, where $\frac{y}{i_0 u} << \frac{r \ln y}{i_{L(l)} u} \exp \left(\frac{\alpha_a F \eta}{RT} \right)$, an exponential relationship exists between y and t. For the present experiments, when $r/y > 10^{-3}$ at $\eta = -100$ mV, the exponential form is valid, *i.e.*

$$\frac{r \log y}{i_{L(l)} u} \exp \left(\frac{\alpha_a F \eta}{RT} \right) = \frac{M}{2 \cdot 3 \rho n F} t + \frac{r \log y_0}{i_{L(l)} u} \exp \left(\frac{\alpha_a F \eta}{RT} \right) \quad [17]$$

and when $r/y < 10^{-3}$, the linear form will be valid, *i.e.*

$$y = i_0 u \frac{M}{\rho n F} t + y_0 \quad [18]$$

Thus, the linear form will be valid ($r = 10^{-5}$ cm) from dendrite length > 100μ. This prediction is confirmed in Fig. 10, 12, 15. Below 100μ the exponential form of y and t applies.

In the linear region, the propagation rate, v, can be written from Eq. [3] and [18] as

$$v = i_0 u \frac{M}{\rho n F} \quad [19]$$

or, in terms of dendrite tip current density, as

$$i_{tip} = i_0 \left\{ \exp\left(\frac{-\alpha_c \mathbf{F}\eta}{RT}\right) - \exp\left(\frac{2\gamma V}{RT \cdot r}\right) \exp\left(\frac{\alpha_a \mathbf{F}\eta}{RT}\right) \right\} \quad [20]$$

Similarly for the exponential $y - t$ region

$$v = y_0 \frac{M}{2 \cdot 3\rho n\mathbf{F}} \frac{u}{r} i_{L(l)} \exp - \left(\frac{\alpha_a \mathbf{F}\eta}{RT}\right) \exp\left[\frac{M}{2 \cdot 3\rho n\mathbf{F}} \frac{u}{r} i_{L(l)} \exp - \left(\frac{\alpha_a \mathbf{F}\eta}{RT}\right) t\right] \quad [21]$$

and

$$i_{tip} = i_{L(l)}\, y_0 \frac{u}{r} \exp - \left(\frac{\alpha_a \mathbf{F}\eta}{RT}\right) \exp\left[\frac{M}{2 \cdot 3\rho n\mathbf{F}} \frac{u}{r} i_{L(l)} \exp - \left(\frac{\alpha_a \mathbf{F}\eta}{RT}\right) t\right] \quad [22]$$

Since the $y - t$ linear region is that for which data are available (Fig. 10, 12, and 15), differential relations for comparison with experiment will be worked out in terms of the linear condition. From Eq. [19], at high η

$$\left(\frac{dv}{d\eta}\right)_{c_0,T} = - i_0 \frac{\alpha_c \mathbf{F}}{RT} \frac{M}{\rho n\mathbf{F}} \exp\left(\frac{-\alpha_c \mathbf{F}\eta}{RT}\right) \quad [23]$$

The dependence of the propagation rate on the zincate concentration (c_0) arises so: if it can be assumed that the discharge of zinc is a 2-step, one electron per step, reaction, where the first electron transfer is reported (17-19) as rate determining, then for the cathodic direction of the rate-determining step[4]

$$Zn(OH)_4^{=} + e \overset{\vec{k}}{\rightarrow} Zn(OH)_2^{-} + 2\,OH^{-}$$

the exchange current density can be written as

$$i_0 = 2\mathbf{F}\vec{k}\, c_0 \exp\left(\frac{-\alpha_c \mathbf{F}}{RT} V_{rev}\right) \quad [24]$$

where V_{rev} is the reversible equilibrium potential for $Zn(OH)_4^{=}$ to Zn reduction.

Introducing Eq. [24] into [19]

$$v = 2\mathbf{F}\vec{k} c_0 u \frac{M}{\rho n\mathbf{F}} \exp\left(\frac{-\alpha_c \mathbf{F}}{RT} V_{rev}\right) \quad [25]$$

Differentiating with respect to c_0 at constant η and T

$$\left(\frac{dv}{dc_0}\right)_{\eta,T} = 2\mathbf{F}\vec{k} u \frac{M}{\rho n\mathbf{F}} \exp\left(\frac{-\alpha_c \mathbf{F}}{RT} V_{rev}\right) - 2\mathbf{F}\vec{k} c_0 u \frac{M}{\rho n\mathbf{F}} \frac{\alpha_c \mathbf{F}}{RT} \left(\frac{dV_{rev}}{dc_0}\right) \exp\left(\frac{-\alpha_c \mathbf{F}}{RT} V_{rev}\right) \quad [26]$$

Substituting the dependence of V_{rev} on c_0 into Eq. [26] and simplifying produces

$$\left(\frac{dv}{dc_0}\right)_{\eta,T} = \frac{v}{c_0}\left(1 - \frac{\alpha_c}{2}\right) \quad [27]$$

Since, for the mechanism assumed, $\alpha_c = \beta = 0.5$

[4] The authors recognize the possibility of the following reaction as being rate determining

$$Zn^{++} + e \rightarrow Zn^{+}$$

this step being superseded by the equilibrium chemical step

$$Zn(OH)_4^{=} \rightleftarrows Zn^{++} + 4\,OH^{-}$$

The kinetic expressions derived in either case are identical. In the absence of firm evidence as to whether the oxidized state is Zn^{++} or $Zn(OH)_4^{=}$, the anion form is assumed here.

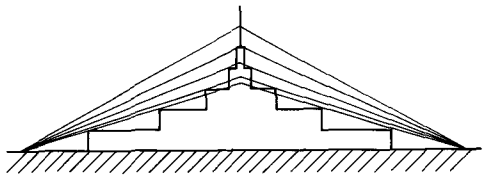

Fig. 19. Successive stages involved in the growth of a pyramid under linear diffusion control. Approximating pyramid to a cone shows how the effective radius of curvature decreases as the height increases.

$$\left(\frac{dv}{dc_0}\right)_{\eta,T} = \frac{v}{c_0} 0.75 \quad [28]$$

Expressing Eq. [19] as a dendrite tip current density

$$i_{tip} = i_0 \exp\left(\frac{-\alpha_c \mathbf{F}}{RT}\eta\right) \quad [29]$$

produces, assuming that the anodic current is negligible, the dependence of an activation current density upon overpotential and concentration of zincate.

Model of dendrite initiation.—The model proposed is that the dendrites originate from the tips of pyramids arising as the result of the rotation of a screw dislocation.

Experimentally, for all potentials above the critical initiation overpotential of about —80 mV, the current density measured during the initiation period, with respect to geometric substrates area, approaches the limiting current density for linear diffusion. Under such conditions any surface irregularity will tend to amplify according to the present, and to an earlier model (20), in an exponential manner with time, *e.g.*, Eq. [1] of ref. (20) or Eq. [17] of the present paper. There is, however, an additional effect when screw dislocation pyramids are increasing in height under linear diffusion control: since the distance between two successive steps on a spiral is given (21) by $4\pi r$, as the dendrite precursor height increases the step length distance decreases. Thus, the pyramid grows according to the model in Fig. 19, *i.e.*, the radius of curvature of the tip decreases as the pyramid height increases.

Since the radius of curvature is related to the curvature overpotential η_r by[5]

$$\eta_r = \frac{2A\gamma}{n\mathbf{F}\rho r} \quad [30]$$

where A is the atomic weight of zinc, γ is the surface energy at the spiral tip/electrolyte interface, and ρ is the density (g cm^{-3}) (for example, if η_r were 5 mV, r would be 4×10^{-6} cm).

As the spiral rotates, the concentration at the spiral apex increases since the apex is moving up the concentration gradient (Fig. 18); thus $i_{L(l)}$ at the apex increases, and therefore η_d at the apex decreases. Since the total overpotential is constant (potentiostatic control), η_d and/or η_r at the apex must increase.

As the spiral tip radius of curvature continues to decrease at some value of r, the tip becomes a point for spherical, rather than linear, diffusion. The condition for the onset of spherical diffusion at the spiral tip (see Appendix) is $r/\delta_0 << 1$. Taking $\delta_0 = 0.02$ cm and $r/\delta_0 = 0.01$, then r required for spherical diffusion is 2×10^{-4} cm. The term η_d must now be expressed in terms of the limiting current density for spherical diffusion, *i.e.*, $i_{L(s)}$.

As the dendrite precursor height increases further, η_d continues to decrease and η_r continues to increase. At some optimum value of r, where η_d is minimal and η_r is sufficient to stabilize the low radius of curvature, the

[5] Here η_r takes the place of Δe_r [Barton and Bockris (3)], the change in the reversible potential due to curvature, r. Both η_r and Δe_r are based on the same thermodynamic arguments which produce Eq. [30].

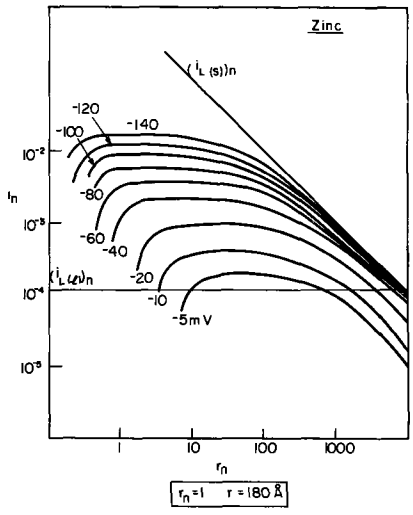

Fig. 20. i_n — r_n relationship for the zinc system from the present work.

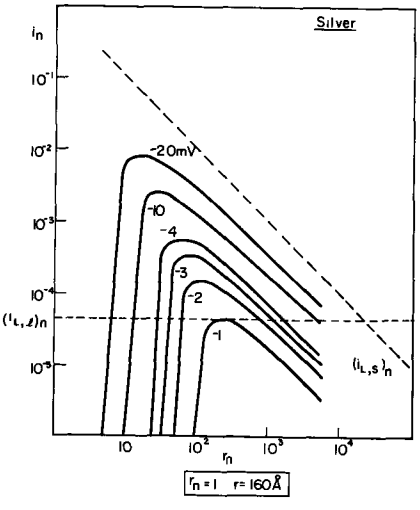

Fig. 21. i_n — r_n relationship for the silver system [Barton and Bockris (3)].

tip will have achieved a maximum growth rate under predominant activation control (this optimum value of r is clearly seen in Fig. 20 and 21 for zinc and silver, respectively).

It is our contention that this is the essence of the initiation of dendritic growth, the initiation time being that time required to attain the necessary stable radius of curvature, for spherical diffusion, due to an increase in η_r.

If the growing pyramid can be regarded as a growing paraboloid whose tip can be taken as hemispherical, then the radius of curvature at the tip is given by (22)

$$r_c = \frac{r_0^2}{2y} \qquad [31]$$

where r_0 is the radius of the pyramid base and y is the pyramid height.[6] Considering $r_0 = 2 \times 10^{-4}$ cm, which is equivalent to an original step length of 2×10^{-4} cm, which would require $\eta_r = 0.05$ mV to cause rotation, and taking y as 20μ, the radius of curvature is equal to 10^{-5} cm. Therefore, the radius of curvature at the tip has decreased from 10^{-3} to 10^{-5} cm as the pyramid height increases from 0.2 to 20μ, thereby producing an increase in η_r from 0.05 to 1 mV.

If it can be assumed that the rate control during propagation of the dendrite is entirely activation,

[6] In this derivation it is assumed that the parabola is symmetrical around the a-axis, and can be represented by the general form, $a = bx^2$.

Table IV. Initial and final conditions at the growing pyramid during the initiation period τ with respect to overpotential terms, pyramid height, and radius of curvature

Total overpotential = −100 mV, c_0 = 10^{-4} moles cm^{-3}, T = 35°C	Initial	Final
η_d	97	1
η_a	3	98
η_r	<0.1	1
Pyramid height	0.2μ	20μ
Tip radius of curvature	10μ	0.1μ

The initial overpotential terms are those terms for the initial substrate calculated at the point the potentiostatic control is applied. For example, $\eta_a = RT/n\mathbf{F} \cdot i/i_0$, where i is the initial substrate c.d., i_0 is taken as 100 mA cm^{-2}. η_r is taken as <0.1 mV (see text), then η_d is taken to be the difference between the applied overpotential and $(\eta_a + \eta_r)$. The final overpotential terms are those terms calculated from the propagation rate of the dendrite (see text).

utilizing i_0 from the literature (23) and placing i equal to the dendrite propagation rates (Fig. 10, 12, and 15), agreement is found between η_a thus calculated and the total applied overpotential. Thus, η_d and η_r are small during dendrite propagation, a result consistent with the above model. Table IV summarizes these changes which occur during initiation at the growing pyramid.

How will the attainment of the critical radius of curvature depend on exchange current density and η_{total}? Since η_a approximately equals η_{total} at time τ, then for a constant dendrite growth rate the value of this η_{total} at time τ will decrease as i_0 increases. Therefore, those metals for which i_0 is relatively low will have a larger η_{crit} than those metals for which i_0 is high, *e.g.*, zinc ($i_0 = 10^{-1}$ A cm^{-2}), $\eta_{crit} = -80$ mV, whereas silver ($i_0 = 1 - 10$ A cm^{-2}) $\eta_{crit} = -3$ mV.

Theoretical calculation of extrapolated initiation time, τ_d.—From Eq. [18] at $y = 0$, the extrapolated initiation τ_d can be expressed as

$$\tau_d = -y_0 \frac{\rho n \mathbf{F}}{i_0 u M} \qquad [32]$$

The term y_0 is the extrapolated dendrite length at zero time (a negative quantity). Values for y_0 were obtained by extraploation to $t = 0$ of Fig. 10, 12, and 15, respectively. Figure 17 and Tables V and VI show the theoretical and experimental τ_d values as a function of overpotential, zincate concentration and temperature, respectively. From Eq. [18] it can be seen mathematically that y_0 should be a constant, thus the values of τ_d were calculated from an average extrapo-

Table V. Theoretical and experimental τ_d values (from Eq. [32]) as a function of zincate concentration. η = −100 mV, T = 35°C, y_0 = −310 μ, standard exchange current density i_0^0 = 0.6 A cm^{-2} mole$^{-3/4}$ liter$^{3/4}$

Zincate concentration c_0, moles liter^{-1}	Experimental τ_d, sec	Theoretical τ_d, sec
0.2	480	470
0.1	540	800
0.09	900	870
0.07	960	1050
0.05	620	1440

Table VI. Theoretical and experimental τ_d values (from Eq. [32]) as a function of temperature. $c_0 = 10^{-1}$ moles liter^{-1}, η = −100 mV, $i_0 = 10^{-1}$ A cm^{-2}, and $(\Delta H^0)_{rev}$ = 10 kcal mole^{-1}

Temperature, °C	Experimental τ_d, sec	Theoretical τ_d, sec
24	1080	910
35	540	620
50	600	380

lated value of y_0. The agreement between experiment and theory is seen to be qualitative in the case of Fig. 17, and three results in Tables V and VI differ due to the fact that the extrapolations do not terminate at the same value of y_0. However, the agreement reported for the propagation rates (section below on Experimental test of theoretical propagation equations) indicates that Eq. [18] is valid.

Total current-time phenomenon.—The increase in the total current with time can be said to be due to one (or both) of two possible causes: (*i*) processes which occur during the initiation of a dendrite, or (*ii*) processes which occur during the propagation of a dendrite.

The former model was the subject of an earlier publication (20) which, at that time, appeared valid. Further examination of this model has, however, revealed two seemingly basic discrepancies. These are (*a*) the theoretical τ is greater than the experimental τ to the extent of 1-2 orders of magnitude (agreement being obtained only when $\delta = 10^{-3}$ cm for unstirred solutions), and (*b*) zinc deposition during the initiation time τ has been shown (24) to produce roughening of the electrode surface without any increase in the total current; such microsurface roughening, according to the former model (20) above, should have led to an exponential $i - t$ relationship.[7]

Thus, it would appear that these discrepancies, along with the observation that the total current does not increase appreciably until the dendrite length approaches the value of δ (section above on Summary of the phenonemology), indicate that the $i - t$ phenomenon is due to processes following initiation.

The dependence of total current on time has been shown to be $i = kt^2$ (Fig. 9) when $t > \tau_i$. The increase in the total current is proposed to be due to an increase in the electrode area due to the formation of the dendrites. Under such conditons, the total current is

$$i_{\text{total}} = i_{\text{subslrate}} + i_{\text{dendrites}} = i_s + A_t N_t i_d \quad [33]$$

where A_t and N_t are the area of one dendrite and the number of dendrites at time t, respectively, and i_d is the dendrite side current density. The identity of i_d is taken to the limiting current density under linear diffusion, since the sides appear essentially planar (Fig. 4).

The value of A_t can be expressed by assuming that the dendrite has a rectangular cross section with width w, thickness d, and length y at time t. Thus

$$i_d A_t = 2wyi_d + 2dyi_d + wdi_{\text{tip}} \quad [34]$$

The last term in Eq. [34] is the dendrite propagation current which is negligible (section above on Influence of dendrite propagation current on measured total current). Therefore

$$i_d A_t = 2(wy + dy)i_d \quad [35]$$

Since w and d change under a linear current flux while y changes under a spherical current flux, w and d remain constant when compared to y. Expressing the time dependence of y with respect to τ, the initiation time produces, in the linear form of $y - t$, the equation (cf. Eq. [18])

$$y = i_0 u \frac{M}{\rho n \mathbf{F}} (t - \tau) + y_\tau \quad [36]$$

Substituting Eq. [36] into [35] produces

$$i_d A_t = 2(w + d)\left\{ y_\tau + i_0 u \frac{M}{\rho n \mathbf{F}} (t - \tau) \right\} i_d \quad [37]$$

This is an expression for the side current of one dendrite as a function of time, providing that the dendrite length changes linearly with time.

How will N_t behave as a function of time (Eq. [33])? If the dendrite initiation process were instantaneous (25), N_t would be constant. Thus, i_{total} would be linear with time, contrary to the experimental results. Under galvanostatic conditions Naybour (25) found that dendrite initiation was instantaneous; however, since overpotential will decrease as initiation proceeds, the condition required for initiation outlined earlier may be lost. Under potentiostatic conditions, dendrite initiation may be continuous, as is reported by Powers (15) for so-called protrusions.

The nucleation or initiation law is assumed (26) to be first order with a low initiation constant K; thus the total number of dendrites at time t is given by

$$N_t = N_0 K t \quad [38]$$

where N_0 is the number of initiation sites on the substrate taken.

Since initiation is taken to be progressive, τ can have values between time t and $\tau_{\min}$ ($\tau_{\min}$ is the experimentally reported τ since this is the initiation time of the first dendrites). The total current due to dendrites will be the sum of all the individual currents from the dendrites initiated at a range of τ values; thus

$$i_{\text{dendrites}} = \int_{\tau_{\min}}^{t} 2(w + d)\left\{ y_\tau + i_0 u \frac{M}{\rho n \mathbf{F}} (t - \tau) \right\} i_d N_0 K d\tau \quad [39]$$

Simplifying Eq. [39] by considering $y_\tau = 0$, and integrating, produces

$$i_{\text{dendrites}} = (w + d) i_0 u \frac{M}{\rho n \mathbf{F}} i_d N_0 K (t - \tau_{\min})^2 \quad [40]$$

If, at sufficiently large t, $\tau_{\min} << t$, then Eq. [40] approximates to

$$i_{\text{dendrites}} = (w + d) i_0 u \frac{M}{\rho n \mathbf{F}} i_d N_0 K t^2 \quad [41]$$

According to Eq. [40], i_{total} against time should show a parabolic relationship. Further, when $t >> \tau_{\min}$, Eq. [41] shows i_{total} should show a t^2 dependence (Fig. 9).

The general validity of Eq. [40] can be seen by considering Fig. 7 where $\eta = -100$ mV, $c_0 = 0.1$ moles liter^{-1}, and $T = 35°$C and the total current is 850 μA after 35 min, *i.e.*, $i_{\text{dendrites}} = 400$ μA, where $i_s = 450$ μA. Assuming $i_0 = 10^{-1}$ A cm^{-2}, $u = 6.65$ (Eq. [15]) when $\eta = -100$ mV and $i_d = 10^{-2}$ A cm^{-2} (Fig. 6), a value of N_0K can be calculated providing an estimate can be made of $(w + d)$. In the section on Influence of dendrite propagation current on the measured total current, the width w of the dendrite main axis was taken as 10^{-3} cm; however, the present $(w + d)$ must include contributions due to side branches. An effective w (main axis + side branches) can be obtained from Fig. 3a where the effective width is seen to be approximately one-fifth of the dendrite length, y. In the present calculation $y = 6 \times 10^{-2}$ cm; thus w can be approximated as 1.2×10^{-2} cm. From Fig. 3b, which corresponds to the conditions of this calculation, w can be seen to be approximately 10^{-2} cm. Since it is observed experimentally that d is small compared to w, $(w + d)$ can be approximated as w. Using these experimental estimates, N_0K is calculated as 1.3 cm^{-2} sec^{-1} from [40]. Thus, on the electrode area under examination, the initiation rate of dendrites will be such that every 25 sec, beyond $\tau_{\min}$, a dendrite will be formed from the precursor pyramid.

Experimentally, it is observed that $\approx$30 dendrites are formed in 35 min under conditions of the above calculation ($\tau_{\min} = 10$ min), *i.e.*, the experimental initiation rate is 0.7 cm^{-2} sec^{-1}. This degree of agreement supports Eq. [40].

Experimental test of theoretical propagation equations.—Table VII shows the theoretical and experimental values of the terms $(dv/d\eta)_{c_0,T}$ and $(dv/dc_0)_{\eta,T}$ according to Eq. [23] and [28], respectively, for the

[7] The theory developed here is for $t >> \tau$ where $i \propto t^2$; when τ is appreciable compared to t the exponential $i - t$ relationship is probably essentially valid, where the 10^{-3} cm corresponds to the value of τ at that time.

Table VII. Experimental test of Eq. [23] and [28]

Assumed parameters	Parameter		Theory	Experiment
$i_0 = 100$ mA cm^{-2} $\eta = -100$ mV	$\left(\frac{dv}{d\eta}\right)_{c_0, T}$	cm sec^{-1} volt^{-1}	7.3×10^{-4}	5.0×10^{-4}
$c_0 = 10^{-4}$ moles cm^{-3} $\alpha_c = 0.5$	$\left(\frac{dv}{dc_0}\right)_{\eta, T}$	cm sec^{-1} mole^{-1} cm^3	0.3	0.43

conditions shown. The agreement can be seen to be consistent with the assumed model involving monoelectronic transfer steps with the redox step rate determining (section above on Propagation), *i.e.*

$$Zn(OH)_4^{=} + e \rightarrow Zn(OH)_2^{-} + 2\,OH^- \quad [42]$$

$$Zn(OH)_2^{-} + e \rightleftarrows Zn + 2\,OH^- \quad [43]$$

Figure 14 produces $(d\eta/d \log i_{tip})_{c_0,T} = 0.17$V, whereas the Tafel slope for the above mechanism where $\alpha_c = 0.5$ produces 0.12V at 35°C.

Figure 11, whose slope $(d \log i_{tip}/d \log c_0)_{\eta,T} = 1.00 \pm 0.14$, can be compared with the theoretical slope, from the above mechanism, of 0.75.

The electrode kinetic parameters obtained here from the dendrite propagation under activation control are in much closer agreement with the above mechanism than with either (*a*) a simultaneous transfer of two electrons, as proposed for zinc amalgam studies (27-29), or (*b*) a monoelectronic two-step transfer with the second step rate determining.

From Eq. [10] the current density at the dendrite tip for the condition $y > \delta_0$ is

$$i_{tip} = \frac{n\mathbf{F}Dc_0 i_0 \left\{ \exp\left(\frac{-\alpha_c \mathbf{F}\eta}{RT}\right) - \exp\left(\frac{\alpha_a \mathbf{F}\eta}{RT}\right) \exp\left(\frac{2\gamma V}{RTr}\right) \right\}}{n\mathbf{F}Dc_0 + r\, i_0 \exp\left(\frac{-\alpha_c \mathbf{F}\eta}{RT}\right)} \quad [44]$$

which, when simplified, produces

$$\frac{i_{tip}}{K} = i_n = \frac{\exp\left(\frac{-\alpha_c \mathbf{F}\eta}{RT}\right) - \exp\left(\frac{\alpha_a \mathbf{F}\eta}{RT}\right) \exp\left(\frac{1}{r_n}\right)}{\frac{K}{i_0} + r_n \exp\left(\frac{-\alpha_c \mathbf{F}\eta}{RT}\right)} \quad [45]$$

where $K = \frac{RTn\mathbf{F}Dc_0}{2\gamma V}$ and $r_n = \frac{RT}{2\gamma V} r$.

Figure 20 shows a plot of $i_n - r_n$ for the zinc system as a function of overpotential, assuming the mechanism outlined earlier. Theoretically, it may be said that dendrites should appear when $i_n > (i_{L(l)})_n$ where $i_{L(l)}$ is the limiting linear current density to the substrate surface. However, from Fig. 17 it is experimentally observed that the initiation time below —80 mV is long and hence dendrites do not appear until the overpotential lies in the region of —80 mV.

Figure 13 shows the theoretical propagation rate, as a function of overpotential, calculated from Fig. 20; the agreement with experiment is reasonable.

Figure 21 shows a theoretical $i_n - r_n$ plot for the silver system assuming the parameters of Barton and Bockris (3). Figures 20 and 21 differ considerably, in that zinc exhibits a wide range of dendrite radii which can grow at the maximum rate, whereas silver shows a small range. Such a difference can be used to account for the fact that it is easier to initiate single dendrites of silver than of zinc.

The theoretical values, or range of values, of dendrite tip radii, r, at which the propagation rate is a maximum, obtained from Fig. 20 and 21, are shown in Table VIII. The agreement with experiment for silver is satisfactory; that for the present study on zinc is somewhat less so.

Table VIII. Theoretical and experimental values of optimum dendrite tip radius required for maximum propagation rate

Metal	Overpotential, mV	Theoretical, cm	Experimental, cm
Zinc	−85	5×10^{-6} to 10^{-4}	10^{-4} to 10^{-5}
	−100	5×10^{-6} to 10^{-4}	4×10^{-4} to 10^{-4}
Silver	−5.2	5.6×10^{-5}	11.0×10^{-5}
	−8.8	4.8×10^{-5}	4.3×10^{-5}
	−16.7	3.2×10^{-5}	2.1×10^{-5}

Conclusions

(*A*) Dendrite initiation is the result of pyramidal growth under bulk diffusion control until the required radius of curvature, to give spherical flux to the propagating tip, is attained.

(*B*) Two critical overpotentials are established, the first being that required to rotate a screw dislocation, the second being that required to produce bulk-diffusion controlled deposition at a rate necessary to produce the change in tip radius required to alter diffusion from linear to spherical. It is the latter which has been identified as the critical overpotential.

(*C*) The initiation time (τ) is the time from the moment of current flow to the attainment of spherical diffusion at a stable propagating tip; this condition is established within the linear diffusion boundary layer, δ_0. τ is not identifiable with either τ_d (that from dendrite length-time extrapolation) or τ_i (that from total current-time graph), but $\tau_d < \tau < \tau_i$.

(*D*) The growth of the zinc dendrite, once initiated, is linear with time and under activation control. Therefore, the dendrite tip current density shows the usual activation current density dependences.

(*E*) The predominance of single dendrites for silver, as compared to that of zinc, is due to a much narrower range, for Ag, of tip radii which can grow at the optimum, maximum rate (Fig. 20 and 21).

(*F*) The total current increase with time, according to a second power law, is due to the increase in electrode area during dendrite growth. This law is consistent with a linear dendrite growth rate (experimentally observed) and a continuous (rather than instantaneous) initiation of dendrites while current passes.

Acknowledgments

Financial assistance from the National Aeronautics and Space Administration (Contract number NsG-325) and the National Science Foundation (Grant number GK-1724) is gratefully acknowledged. Useful discussions with Mr. Ernst Cohn, Mr. G. Razumney, Mr. Z. Nagy, Professor B. Lovrecek, and Dr. A. Damjanovic are also acknowledged.

The authors are also indebted to IBM Corporation and particularly to Mr. W. J. Sutkowski for their assistance in a scanning electron-microscopic study, and to Mr. R. White, of the University of Pennsylvania, for his assistance during a transmission electron-microscopic study.

Manuscript submitted April 1, 1969; revised manuscript received July 22, 1969. This was Paper 375 presented at the Montreal Meeting, Oct. 6-11, 1968.

Any discussion of this paper will appear in a Discussion Section to be published in the June 1970 JOURNAL.

APPENDIX

*Condition for the Establishment of Spherical Diffusion**

The steady-state equation for diffusion states that

$$\nabla^2 c = 0 \qquad [A1]$$

which, when related to spherical coordinates and spherical symmetry, becomes

$$\nabla^2 c = \frac{1}{r^2}\frac{\partial}{\partial r}(r^2\,\partial c/\partial r) = 0 \qquad [A2]$$

General integration of [A2] produces

$$r^2\frac{dc}{dr} = \text{constant } (k) \qquad [A3]$$

Integration of Eq. [A3] between the limits r_0 and $(r_0 + \delta_0)$ gives

$$c(r_0 + \delta_0) - c(r_0) = \int_{r_0}^{r_0+\delta} \frac{k}{r^2}\,dr = \frac{k}{r_0} - \frac{k}{(r_0 + \delta_0)} \qquad [A4]$$

The constant, k, can now be written as

$$k = \frac{c(r_0 + \delta_0) - c(r_0)}{\dfrac{1}{r_0} - \dfrac{1}{(r_0 + \delta_0)}} \qquad [A5]$$

The flux at the electrode surface is given by

$$J(r_0) = -D\left(\frac{dc}{dr}\right)_{r=r_0} \qquad [A6]$$

Substituting for (dc/dr) from Eq. [A3] and then for k (Eq. [A5]) produces

$$J(r_0) = \frac{D}{r_0^2}\,\frac{c(r_0 + \delta_0) - c(r_0)}{\dfrac{1}{r_0} - \dfrac{1}{(r_0 + \delta_0)}} \qquad [A7]$$

The current density at the electrode surface is given by

$$i = \frac{2FD}{r_0^2}\,\frac{c(r_0 + \delta_0) - c(r_0)}{\dfrac{1}{r_0} - \dfrac{1}{(r_0 + \delta_0)}} \qquad [A8]$$

which, when $\delta_0 >> r_0$ reduces to

$$i = \frac{2FD[c(r_0 + \delta_0) - c(r_0)]}{r_0} \qquad [A9]$$

which is the spherical diffusion equation. Thus, the condition for spherical diffusion is $\delta_0 >> r_0$, where r_0 is the radius of curvature of the tip to which diffusion is proceeding.

* The authors are indebted to Mr. G. Razumney for this derivation.

REFERENCES

1. Z. Stachurski, Investigation and Improvement of Zinc Electrodes for Electrochemical Cells, Final Rept. (1965), Yardney Electric Corp., New York.
2. T. Z. Kattamis and M. C. Flemings, *Trans. Met. Soc. AIME*, **236**, 1523 (1966).
3. J. Barton and J. O'M. Bockris, *Proc. Roy. Soc. (London)*, **A268**, 485 (1962).
4. T. B. Reddy, *This Journal*, **113**, 117 (1966).
5. I. L. Dillamore, R. E. Smallman, and W. T. Roberts, *Phil. Mag.*, **9**, 517 (1964).
6. P. S. Dobson and R. E. Smallman, *Proc. Roy. Soc. (London)*, **A293**, 423 (1966).
7. I. Giron and F. Ogburn, *This Journal*, **108**, 842 (1961).
8. F. Ogburn, B. Paretzkin, and H. S. Peiser, *Acta Cryst.*, **17**, 774 (1964).
9. F. Ogburn, C. Bechtoldt, J. B. Morris, and A. de Koranyi, *This Journal*, **112**, 574 (1965).
10. G. Wranglen, *Electrochim. Acta*, **2**, 130 (1960).
11. N. A. Pangarov, *Phys. Stat. Sol.*, **20**, 371 (1967).
12. N. A. Pangarov, *Electrochim. Acta*, **13**, 1641 (1968).
13. D. R. Hamilton, *ibid.*, **2**, 130 (1960).
14. J. W. Diggle and A. Damjanovic, Submitted for publication.
15. R. W. Powers, *Electrochem. Technol.*, **5**, 429 (1967).
16. J. McBreen, Study to Investigate and Improve the Zinc Electrode for Spacecraft Electrochemical Cells. Yardney Electric Corp., Contract NAS 5-10231 (June 1967).
17. B. Lovrecek and I. Mekjavic, *Electrochim. Acta*, **14**, 301 (1969).
18. V. V. Gorodetskii and V. V. Losev, *Electrokhimiya*, **3**, 1192 (1967).
19. D. A. Payne, H. Tachikawa, and A. J. Bard, Adsorption of Organic Materials on Zinc Electrodes, Final Rept. Contract AF 33(615)3487 (October 1968).
20. A. R. Despic, J. W. Diggle, and J. O'M. Bockris, *This Journal*, **115**, 507 (1968).
21. J. O'M. Bockris and A. Damjanovic, "Modern Aspects of Electrochemistry," Vol. 3, Chap. 4, p. 224. J. O'M. Bockris and B. E. Conway, Editors, Butterworths (1964).
22. G. Horvay and J. W. Cahn, *Acta Met.*, **9**, 695 (1961).
23. J. P. G. Farr and N. A. Hampson, *J. Electroanalyt. Chem.*, **13**, 433 (1967).
24. J. W. Diggle and B. Lovrecek, Submitted for publication.
25. R. D. Naybour, *Electrochim. Acta*, **13**, 763 (1968).
26. M. Fleischmann and H. R. Thirsk, "Advances in Electrochemistry Electrochemical Engineering," Vol. 3, Chap. 3, p. 123. P. Delahay and C. W. Tobias, Editors, Interscience Publishers Inc., New York (1963).
27. H. Gerischer, *Z. Physik. Chem. (Leipzig)*, **202**, 302 (1953).
28. J. P. G. Farr and N. A. Hampson, *J. Electroanalyt. Chem.*, **18**, 407 (1968).
29. B. Timmer, M. Sluyters-Rehbach, and J. H. Sluyters, *ibid.*, **14**, 181 (1967).

Stress Induced Binary Diffusion in a Solid

R. J. Charles

General Electric Research and Development Center, Schenectady, New York

ABSTRACT

Operational methods are used to describe the migration transients of two ions which respond to concentration gradients and ion space charge when a nonuniform stress is applied to a solid. The results indicate two characteristic time constants for the approach to equilibrium. The shorter time constant is related to the establishment of space charge and thus to electrical properties. The long time constant is related to an ion interchange process which depends on the sample geometry.

The application of nonuniform mechanical pressure to a bounded solid containing diffusible ions may result in ion transport and accumulation similar to that obtained by the application of an electric field. For the case where more than one ion type responds to applied stress the electric field from displaced ions is common to all diffusing species. The effects of concentration and stress gradients, however, are specific to the type

of diffusing ion. Because of electric field coupling in multiple ion diffusion, the ion flows occurring after stress application may interact with one another such that the transient leading to steady state is highly complex.

The main object of this work is to present a model which examines the transient conditions by which a steady state is achieved when a stress gradient is applied to a solid containing two diffusible ions. The problem has particular application to delayed elastic effects and internal friction in glasses containing mixed alkali ions (1) but is relevant to ion substituted crystals (2) and to some physiological materials (3).

Statement of the Problem

Single ion case.—Weber and Goldstein (4) propose an equation of the following form for the flux, J, of a single ion of concentration, C, and diffusion coefficient, D, in a solid subjected to a stress gradient, η

$$J = -D[dC/dx + CeE/(kT) + C\overline{V}\eta/(kT)] \quad [1]$$

In this equation x is the flux direction, e is unit charge, E is the electric field, $\overline{V}$ is the partial molar volume of the diffusing ion, and kT has its usual significance.

In the present work it is desirable to utilize Eq. [1] by defining diffusion coefficients and concentrations with respect to a particular diffusional process. The case treated here consists of a solid in which ions diffuse by an interstitialcy mechanism. Thus, in the following, the symbols D and C refer to the interstitial diffusion coefficient and interstitial concentration of a mobile ion. These values are related to the ion self-diffusion coefficient D_o, and total ion concentration C_o, by the relation $D\,C = D_oC_o$. If a Frenkel defect model is adopted, then C may be estimated by an equation of the form $C/C_o = \exp(-W/(2kT))$ where W is the energy of formation of such a defect.

Interstitials are produced by dissociating neutral pairs of anions and cations and locally must obey the mass action principle for such a reaction. Let us consider the sample initially under no stress or electric field and write n^o for the vacancy concentration, p^o for the interstitial concentration, and $C_o - p^o$ for the bound pair concentration. The equilibrium constant for bound pair dissociation then equals $n^op^o/(C_o - p^o)$ and generally since $p^o << C_o$ and there is no space charge

$$K \approx (p^o)^2 \quad [2]$$

where K is another constant.

If, by application of a stress, ρ cations/cm^3 accumulate in a local region of the specimen then the space charge density will be ρ but the interstitial and vacancy concentrations must adjust to maintain equilibrium. The vacancy concentration changes from n^o to n and the interstitial concentration changes from p^o (equal to n^o) to $(\rho + n)$ and, conforming to local equilibrium

$$(\rho + n)\, n \approx K \approx (p^o)^2 \quad [3]$$

Thus, by choosing the positive root, one obtains

$$n \approx ((1 + 4(p^o/\rho)^2)^{1/2} - 1)\, \rho/2 \quad [4]$$

If the space charge density, ρ, is small compared to the zero stress state interstitial concentration then

$$n \approx p^o - \rho/2 \quad [5]$$

and the interstitial concentration is given by

$$(\rho + n) \approx p^o + \rho/2 = C \quad [6]$$

The above assumption can only be proved valid by proceeding with actual calculations to see if the space charge density, for reasonable stress gradients, may always be considered small compared to interstitial concentrations. Equation [4] shows that Eq. [6] is still reasonably valid when $(p^o/\rho)^2 = 25$ or when ρ is approximately 10% of p^o. In summary, one may view Eq. [6] as stating that local equilibrium is preserved if half the ions that enter a region to produce space charge drop into the bound state and the other half remain as interstitials.

Using the previous assumptions (*i.e.* $\rho << n$ and thus $n \approx n^o \approx p^o$) Eq. [1] may be written for the interstitial case as

$$J = -D[d(\rho + n)/dx + ep^oE/(kT) + p^oV\eta/(kT)] \quad [7]$$

Differential forms of Eq. [6] and [7] may be combined with Poisson's equation (*i.e.*, $dE/dx = -e\rho/\epsilon\epsilon_0$) to give

$$J(x,t)_x = \rho(x,t)_t = D[2e^2p^o(\epsilon\epsilon_0kT)^{-1}\rho - \rho_{xx}] \quad [8]$$

where ϵ is the dielectric constant of the solid, ϵ_0 is the permittivity of free space (8.854×10^{-12} A sec volts^{-1} meters^{-1}) and the subscripted letter method is used to denote differentiation. The equation is linear, and the factor 2 results from the approximation concerning equilibrium between bound and interstitial ions.

For the single ion case Eq. [8] is to be solved subject to the conditions that the stress gradient is constant, all ions are conserved (*i.e.*, the integral excess ion density from surface to surface of the sample is zero) and that ions will not be discharged at the sample surfaces [*i.e.*, J(surface) = 0]. The solution is symmetrical and may be obtained by the method of separation of variables which yields the familiar type of diffusion equation involving an infinite sum of trigonometric and exponential terms. For sample edges at $\pm\, a/2$ and a stress gradient η along the sample length

$$\rho(x,t) = \frac{\beta \sinh(\gamma a)}{\gamma \cosh(\gamma a/2)}\left[\frac{\sinh(\gamma x)}{\sinh(\gamma a)} - \frac{2}{\pi}\sum_{n=1}^{\infty}\frac{n(-1)^n}{n^2 + (\gamma a/\pi)^2}\sin(n\pi x/a)\exp[\gamma^2 + n^2\pi^2/a^2)Dt]\right] \quad [9]$$

where $\beta = p^oV\eta/(kT)$ and $\gamma = [2p^oe^2/(\epsilon\epsilon_0kT)]^{1/2} = L^{-1}$.

The term L is a Debye length and for a material, such as a glass, of dielectric constant 4.0 containing 10^{21} mobile ions per cm^3 with an energy of defect formation of 1 eV (giving, from Eq. [2], a zero stress defect concentration of about 2×10^{12} ions per cm^3) this length calculates to be 1.2μ. Since the Debye length is small compared to normal sample dimensions it may be interpreted as that distance from the sample surface at which the excess ion concentration falls to e^{-1} times its surface value.

For usual sample dimensions ($a >> L$) the time constant to establish steady state in Eq. [9] is essentially the factor L^2/D. Since the conductivity, σ, equals $D\,p^o\,e^2/(kT)$ this time constant equals $\epsilon\epsilon_0/(2\sigma)$ or one-half of the electrical time constant for the material. On the other hand if the sample is multiphase, such that the diffusion occurs in an isolated phase having characteristic dimensions of the order of the Debye length, then a number of relaxation times, all smaller than the electrical time constant, are involved.

For a typical partial molar volume of 6Å^3 per ion (4 cm^3/mole), a stress gradient of 3×10^8 dynes/cm^3 (approximately equal to 10^4 psi/in.) and p^o equal to 2×10^{12} ions per cm^3 the stress coefficient β, for the glass at room temperature, calculates to be about 10^{11} ions cm^{-4}. Thus, from Eq. [9], the steady-state excess ion concentration at the sample surfaces calculates to be $\rho(\pm a/2, \infty) = \pm 10^{11}\ (1.2 \times 10^{-4}) = \pm 1.2 \times 10^7$ ions cm^{-3} or approximately five orders of magnitude smaller than the zero stress interstitial concentration, p^o. Thus the approximation concerning local equilibrium between bound and interstitial ion states (*i.e.*,

$\rho << p^0$) appears justified for usual applications.

For steady state the field, E, is given by

$$E(x, \infty) = \beta e(\gamma^2 \epsilon\epsilon_0)^{-1}\left[\frac{\cosh(\gamma x)}{\cosh(\gamma a/2)} - 1\right] \quad [10]$$

and the potential from end to end is

$$V = \int_{-a/2}^{a/2} E(x, \infty)\, dx = \beta e a(\gamma^2 \epsilon\epsilon_0)^{-1}\left[\frac{2\tanh(\gamma a/2)}{\gamma a} - 1\right] \quad [11]$$

A sample with the above characteristics and stress state and of a length greater than a few Debye lengths would thus develop a maximum field of about 1 mV/cm and, correspondingly, a 1 cm sample would develop about 1 mV potential.

Two ion case.—Two ions, each with a different mobility and a different response to stress, are now considered. While the solutions of the flux equations will encompass virtually all combinations of diffusion coefficients, stress response factors and concentrations, application to real cases will generally demand that the ion with the largest diffusion coefficient will exhibit the lowest partial molar volume. This results from the fact that small ions are expected to move more easily through a given lattice or structure than big ions whereas a given deformation of the structure would affect a large ion more than a small one.

Denoting the two ions by subscripts 1 and 2, two parallel flux equations may be written following Eq. [7]. We assume that the ions exhibit separate partial molar volumes, interstitial diffusion coefficients and energies of defect formation and that the conditions for local equilibrium discussed previously hold independently for each ion. Thus, following the single ion procedure (Eq. [8]) two simultaneous divergence equations may be obtained for the two ion types.

$$\left.\begin{aligned} J_1(x, t)_x = \rho_1(x, t)_t = D_1[\gamma_1^2(\rho_1 + \rho_2) - (\rho_1)_{xx}] \\ J_2(x, t)_x = \rho_2(x, t)_t = D_2[\gamma_2^2(\rho_1 + \rho_2) - (\rho_2)_{xx}] \end{aligned}\right\} \quad [12]$$

where, if i takes a value of either 1 or 2, $\gamma_i = [2\rho_i{}^0 e^2/(\epsilon\epsilon_0 kT)]^{1/2} = L_i^{-1}$.

The boundary conditions for these equations are

$$\left.\begin{aligned} \rho_i(x, o) &= 0 \\ \rho_i(\pm a/2, t)_x &= \beta_i \\ \int_{-a/2}^{a/2} \rho_i(x, t)\, dx &= 0 \end{aligned}\right\} \quad [13]$$

The equations in [12] are first reduced to ordinary differential equations by Laplace transforms of the time variable, t, in terms of the variable s. Thus, denoting a tranfsormed variable by a circumflex, one obtains for ion 1 an equation of the form

$$\hat{\rho}_1(x, s)_{xx} = (s/D_1 + \gamma_1^2)\hat{\rho}_1(x, s) + \gamma_1^2\hat{\rho}_2(x, s) \quad [14]$$

Interchanging the subscripts 1 and 2 will yield the parallel equation for ion 2.

Rearranging the above, differentiating twice with respect to x and substituting one obtains fourth order equations

$$(\hat{\rho}_i)_{4x} - A(\hat{\rho}_i)_{xx} + B\hat{\rho}_i = 0 \quad [15]$$

where i is again either 1 or 2. The constants in these equations are $A = s/D_1 + s/D_2 + \gamma_1^2 + \gamma_2^2$ and $B = s(s/(D_1D_2) + \gamma_2^2/D_1 + \gamma_1^2/D_2 + (\gamma_1\gamma_2)^2)$. Solutions of the form $\rho = \Sigma\, a_n \exp(\lambda_n x)$ are assumed yielding identical auxilliary equations for the four roots λ_n.

$$\lambda_{1-4} = \pm\,(A/2 \pm (A^2/4 - B)^{1/2})^{1/2} \quad [16]$$

and thus λ_1 equals $-\lambda_3$ and λ_2 equals $-\lambda_4$. For i equal to either one or two the boundary conditions transform to

$$\left.\begin{aligned} \hat{\rho}_i(o, s) &= 0 \\ \hat{\rho}_i(\pm a/2, s)_x &= \beta_i/s \\ \int_{-a/2}^{a/2} \hat{\rho}_i(x, s)\, dx &= 0 \end{aligned}\right\} \quad [17]$$

Applying these boundary conditions to the assumed solutions one obtains for ion one

$$\hat{\rho}_1(x, s) = \frac{[\beta_2 - \beta_1(\lambda_2^2\gamma_1^{-2}) - s(D_1\gamma_1^2)^{-1} - 1]\gamma_1^2}{s(\lambda_1^2 - \lambda_2^2)} \frac{\sinh(\lambda_1 x)}{\lambda_1 \cosh(\lambda_1 a/2)} - \frac{[\beta_2 - \beta_1(\lambda_1^2\gamma_1^{-2}) - s(D_1\gamma_1^2)^{-1} - 1]\gamma_2^2}{s(\lambda_1^2 - \lambda_2^2)} \frac{\sinh(\lambda_2 x)}{\lambda_2 \cosh(\lambda_2 a/2)} \quad [18]$$

Interchanging subscripts 1 and 2 in Eq. [18] yields the appropriate solution for ion two.

Equations of the form given in Eq. [18] may be integrated in the complex plane to yield inverse transforms by the theory of residues. Each term of these equations may be expressed in the form $q(x, s)/r(s)$, consequently by the above, the inverse transform is

$$\mathbf{L}^{-1}[q(x, s)/r(s)] = \sum_{n=1}^{\infty} q(x, s_n)/r'(s_n)\exp(s_n t) \quad [19]$$

where the prime denotes differentiation with respect to s. Examination of Eq. [18] shows that singularities or poles occur only when $s = 0$ or when $r = \cosh(\lambda_i a/2) = 0$ (there are no real values of s and thus no real singularities for $\lambda_1^2 - \lambda_2^2 = 0$). Steady-state solutions result from the pole at $s = 0$ and are obtained from

$$\rho(x, \infty) = \underset{\text{Lim. } s \to 0}{s\hat{\rho}(x, s)} \quad [20]$$

Thus

$$\rho_1(x, \infty) = \gamma_1^2(\beta_1 + \beta_2)(\bar{\gamma})^{-3}\frac{\sinh(\bar{\gamma}x)}{\cosh(\bar{\gamma}a/2)} - \frac{(\beta_2\gamma_1^2 - \beta_1\gamma_2^2)x}{(\bar{\gamma})^2} \quad [21]$$

where $\bar{\gamma} = (\gamma_1^2 + \gamma_2^2)^{1/2}$.

Interchanging subscripts yields a parallel steady-state solution for ion two.

Values of s for the remaining poles are obtained from $\gamma_i^2 = -(\pi/a)^2(2n - 1)^2$. We now write z for $(\pi/a)(2n - 1)$ and thus from Eq. [16] and the above

$$s_n^{\pm} = 1/2[-(z^2(D_1 + D_2) + D_2\gamma_2^2 + D_1\gamma_1^2) \pm [(z^2(D_1 + D_2) + D_2\gamma_2^2 + D_1\gamma_1^2)^2 - 4D_1D_2z^2(z^2 + \gamma_1^2 + \gamma_2^2)]^{1/2}] \quad [22]$$

Because of the multiplicity of signs in the quadratic expressions for λ_i^2 and s_n, care must be exercised so that sign errors and duplicate terms are avoided in the summations of Eq. [19]. As shown in Eq. [22], each value of n results in two values of s_n (*i.e.*, s_n^+ or s_n^-). Considering s_n^+, two λ^2 values are possible only one of which equals $-z^2$. The same is true for s_n^-. Let us designate the unequal root for s_n^+ as λ^+ and that for s_n^- as λ^-. The derivative of r(*i.e.*, r') is first evaluated at those values of s_n for which $\lambda^2 = -z^2$. Thus

$$r'|_{s_n} = (a/2)\sinh(z\alpha/2)\left|\frac{dz}{ds_n}\right|_{s_n} = (a(-1)^n/2)\left|\frac{dz}{ds_n}\right|_{s_n} \quad [23]$$

Differentiation of λ^2 (from Eq. [16]) yields

$$\left|\frac{dz}{ds_n}\right|_{s_n} = \frac{1}{4z}\left[\frac{1}{v} \pm \frac{(s_n/v^2 - 4s_n/(D_1D_2) + (\bar{\gamma})^2(D_2 - D_1)/(D_1D_2)}{[(s_n/v + (\bar{\gamma})^2)^2 - 4s_n(s_n + D_2\gamma_2^2 + D_1\gamma_1^2)/(D_1D_2)]^{1/2}}\right] \quad [24]$$

where the plus sign is associated with s_n^+ and the minus sign with s_n^- and $v = D_1D_2/(D_1 + D_2)$. Thus, using trigonometric expressions for hyperbolic functions of complex arguments, one obtains

$$\rho_1(x,t) = \rho_1(x,\infty) + \frac{8}{a}\sum_{n=1}^{\infty}\frac{[\beta_2 - \beta_1((\lambda^+/\gamma_1)^2 - s_n^+/(D_1\gamma_1^2) - 1)]\gamma_1^2}{s_n^+(z^2 + (\lambda^+)^2)z\left|\frac{dz}{ds_n^+}\right|_{s_n^+}}\cos(z\alpha)\exp(s_n^+t) + \frac{8}{a}\sum_{n=1}^{\infty}\frac{[\beta_2 - \beta_1((\lambda^-/\gamma_1)^2 - s_n^-/(D_1\gamma_1^2) - 1]\gamma_1^2}{s_n^-(z^2 + (\lambda^-)^2)z\left|\frac{dz}{ds_n}\right|_{s_n^-}}\cos(z\alpha)\exp(s_n^-t) \quad [25]$$

where x varies over $\pm a/2$ and $\alpha = (a/2 - n)$. Once again the interchange of subscripts 1 and 2 yields the corresponding excess ion density equation for the second ion.

Examination of Eq. [22] and [25] shows that in the binary case there exist two sets of time constants which control the stress induced diffusion processes. If we consider a sample long compared to the Debye length of either of the ions ($a >> L_1 >> L_2$) and diffusion coefficients of these ions which are appreciably different (eq. $D_2 << D_1$) then the largest and dominant time constants of each of these sets may be obtained from Eq. [22] by considering small z (*i.e.*, for $n = 1$, $z = \pi/a$ and $z^2(D_1 + D_2) << D_1\gamma_1^2 << D_2\gamma_2^2$). The first time constant is then

$$\tau_{first} \approx (D_1\gamma_1^2)^{-1} \approx L_1^2/D_1 \approx \epsilon\epsilon_0/(2\sigma_1) \quad [26]$$

which is, as in the single ion case, simply one-half of the electrical time constant for the fast diffusing species. The second time constant, which is considerably larger than the first, is approximately

$$\tau_{second} \approx \frac{a^2}{\pi^2 D_2}(\gamma_1/\bar{\gamma})^2 \approx \frac{L_2^2}{\pi^2 D_2}\left(\frac{a^2}{L_1^2 + L_2^2}\right) \approx \frac{\epsilon\epsilon_0}{2\pi^2\sigma_2}\left(\frac{a^2}{L_1^2 + L_2^2}\right) \quad [27]$$

This latter time constant is dependent not only on the electrical time constant of the slower moving species but also on the diffusion path length relative to the Debye lengths of both ions. As with the single ion this diffusion path is to be considered the sample length for a homogeneous material or the diffusion path length of conductive regions if the sample is inhomogeneous. If this latter path length is of the order of the Debye lengths, then simple reduced expressions for either time constant are not possible.

Steady-state space charge densities (or excess ion concentration) are given by Eq. [21] where, for diffusion paths long compared to the Debye lengths, an exponential form may be substituted for the hyperbolic functions. In general, for the case of differing partial molar volumes of the two ions, the solutions indicate excesses or deficiencies in ion concentrations which are linear with distance except within a few Debye lengths of the sample surfaces where the distance-concentration relationship becomes exponential.

The total space charge density at steady state is obtained from Eq. [21] and is given by

$$(\rho_1 + \rho_2) = (\beta_1 + \beta_2)(\bar{\gamma})^{-1}\frac{\sinh(\bar{\gamma}x)}{\cosh(\bar{\gamma}a/2)} \quad [28]$$

Thus the field is

$$E = \frac{(\beta_1 + \beta_2)e}{(\bar{\gamma})^2\epsilon\epsilon_0}\left[\frac{\cosh(\bar{\gamma}x)}{\cosh(\gamma a/2)} - 1\right] \quad [29]$$

and the end to end potential is

$$V = \frac{(\beta_1 + \beta_2)ea}{(\bar{\gamma})^2\epsilon\epsilon_0}\left[\frac{2\tanh(\bar{\gamma}a/2)}{\bar{\gamma}a} - 1\right] \quad [30]$$

These equations are of similar form to those for the one ion case.

Interpretation

The general behavior of the stress induced diffusion of a single ion, as given by Eq. [9], is straightforward and requires little comment. After stress application a steady state is approached continuously by a unidirectional net flow of ions. Net ion flow halts when sufficient space charge is developed at a surface to produce a flux which is opposed and balanced by the flux due to the stress gradient. Two ion behavior is considerably more complex but the general ion motions, as given by forms of Eq. [25], do have a relatively simple interpretation. On application of a stress gradient the fast diffusing species move to regions of lower compressive stress, and the space charge that is initially developed hinders the motion of the slower moving species to these regions. If the activation volume $\bar{V}$ is greatest for the fast moving species (the unlikely case), then the space charge due to these ions overcomes the stress effect on the slower moving ions and these latter ions are forced to accumulate in the higher compressive stress regions until a steady state is achieved. On the other hand if the slow moving ions exhibit the greatest response to stress (the likely case), then these ions slowly accumulate in the low compressive stress regions and displace the fast moving ions which had previously migrated to these regions. Thus, the fast moving ions, which initially moved in the direction of lower compressive stress, reverse direction and flow back through the sample to regions of higher compressive stress.

At steady state a stable space charge situation arises since the excess of large ions (high stress response factor) exceeds the deficiency of small ions at the low stress end of the specimen while the deficiency of large ions exceeds the excess of small ions at the opposite end. At intermediate positions in the sample a continuous interchange of large and small ions takes place and since this interchange occurs over virtually the whole length of the sample the time to reach steady state is extremely long. If the diffusion coefficients of the two ions differ greatly, then a pseudo-steady state is first obtained when the fast moving ions accumulate sufficiently at the low stress end of the sample. The time to reach this state is relatively short since diffusion of the fast moving ions over distances of the order of only a few Debye lengths is involved.

Figure 1 shows the results of a typical calculation for a thin plate (0.1 mm) containing two mobile ions

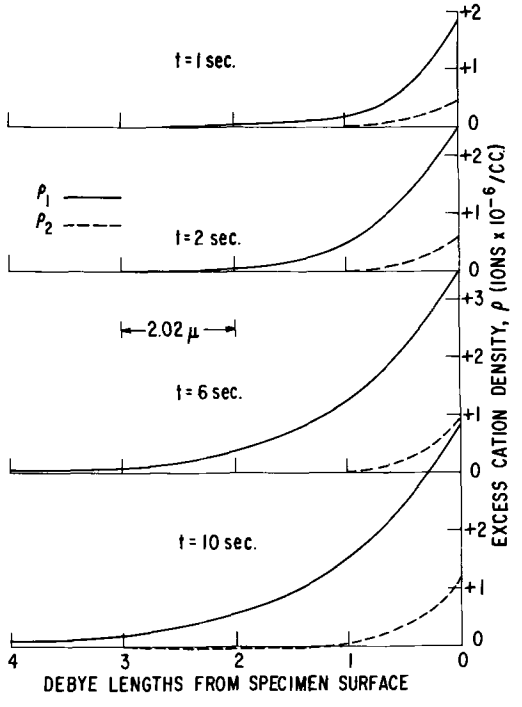

1A

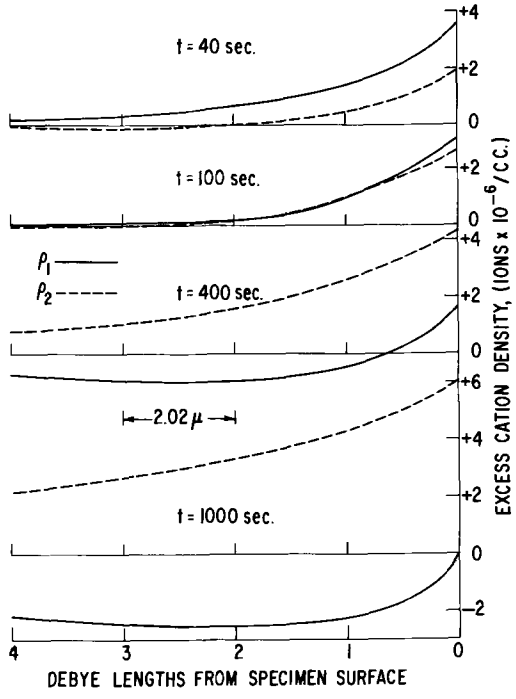

1B

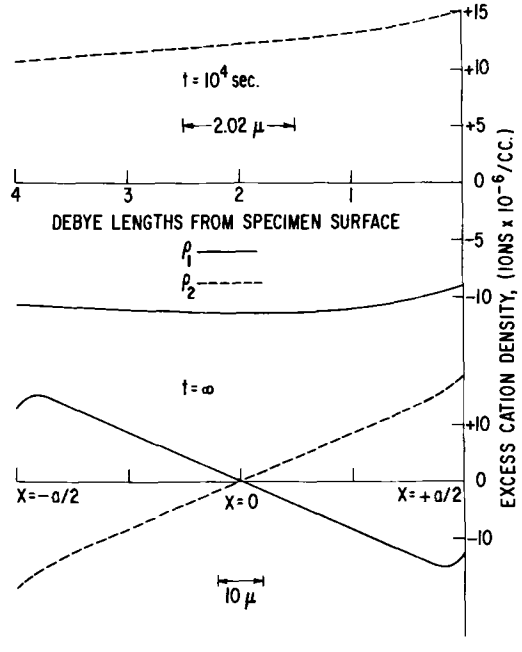

1C

Fig. 1. Excess ion distributions as a function of time after stress application for a bent plate having the characteristics listed in Table I.

which is bent to produce a uniform stress gradient through the plate. The characteristics of this particular problem are given in Table I and roughly correspond to those that would pertain to a mixed alkali silicate glass at room temperature.

Figure 2 compares the total space charge distribution ($\rho_1 + \rho_2$) with the steady-state distribution for times equal to one, two, and three times the time constant for the fast moving species. It is evident that appreciable space charge only occurs within a few Debye lengths of the sample surfaces for any stage of the migration process. It is also evident that equilibrium space charge is essentially established within a few multiples of the time constant of the fast moving species. We conclude that the preliminary migration of the fast moving species develops the major portion of the space charge distribution in the sample and that the subsequent long term ion interchange proceeds under virtually constant electrical field conditions.

Table I. Example data

η = 300 kg/cm³	a = 0.01 cm	T = 300°K
p^o_1 = 5 × 10¹¹ ions/cc	interstitial	
p^o_2 = 2 × 10¹¹ ions/cc		
L_1 = 2.40 × 10⁻⁴ cm	L_2 = 3.78 × 10⁻⁴ cm	
$\overline{V}_1$ = 3cc/mole	$\overline{V}_2$ = 5cc/mole	
β_1 = 1.8 × 10¹⁰ ions/cm³	β_2 = 1.2 × 10¹⁰ ions/cm³	
D_1 = 10⁻⁸ cm²/sec	D_2 = 10⁻⁹ cm²/sec	
τ_1 = 5.75 sec	τ_2 = 7100 sec	

Little experimental data exists to which the above transient theory for binary diffusion may be applied. Weber and Goldstein (4) show that for the case of nonblocking electrodes the application of a stress field to a sodium ion conducting glass produces a measurable electrical current. Comparison of this current, under short-circuit conditions, with the current obtained by a known electrical field allowed a calculation

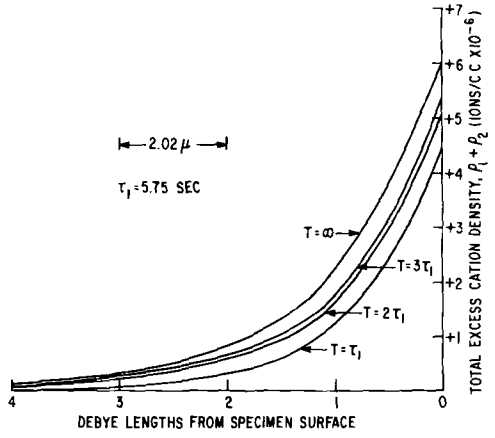

Fig. 2. Total space charge distribution for the plate in Fig. 1 at times equal to one, two, and three times the time constant for the fast moving ion.

of the volume term in Eq. [1]. This volume, having a value of 1.3 cc/mole, was interpreted as the partial molar volume of sodium ions in the glass and is of the same order of magnitude as activation volumes for sodium ion conduction under hydrostatic pressure for similar glasses (5). It would appear reasonable, therefore, that activation volumes determined from hydrostatic pressure measurements would be satisfactory data for calculating the stress response (β) factors in the present work.

Steinkamp, Shelby, and Day (1) progressively substituted K_2O for Li_2O in silicate glasses and, by the fiber technique, observed the reduction of an internal friction peak attributed to lithium ions and the growth of another peak at a very much higher temperature. The first peak was associated with the migration of lithium ions which exhibited relatively short relaxation times at room temperature. The second peak would be attributed therefore to a process involving very long relaxation times at room temperature. These observations are consistent with the present theory for the interaction and diffusion of two types of ions in a stress gradient but further confirmation would require correlation of the long relaxation times to either the macroscopic dimensions of the pendulum fiber or diffusion path lengths within the fiber as well as to the diffusional properties of K^+ ions. The above authors state that the first internal friction peak, due to Li^+ ions migration, is well correlated with the electrical behavior of Li^+ ions in the material (*i.e.*, dielectric loss and electrical conductivity) whereas no association of the second, long time constant peak with electrical properties was possible. From the present theory this result seems reasonable for the time constants for the development of an internal friction peak or a dielectric loss peak by migration of a fast moving species (*e.g.*, Li^+) involve the same parameter, namely the electrical conductivity due to the fast moving ion. On the other hand the long term ion interchange, with which would be associated a mechanical loss, would not occur in electrical measurements since the stress gradient responsible for this interchange would be absent.

Acknowledgments

The author wishes to express his gratitude for the assistance and encouragement afforded him by G. M. Roe, W. B. Hillig, and S. P. Mitoff.

Manuscript submitted Dec. 16, 1968; revised manuscript received July 18, 1969.

Any discussion of this paper will appear in a Discussion Section to be published in the June 1970 JOURNAL.

REFERENCES

1. W. E. Steinkamp, J. E. Shelby, and D. E. Day, Jr., *Am. Ceram. Soc.*, **50**, 271 (1967).
2. Yung-Fang Yu Yao and J. T. Kummer, *J. Inorg. Nucl. Chem.*, **29**, 2453 (1967).
3. G. V. B. Cochran, R. J. Pawluk, and C. A. L. Bassett, Clinical Orthopaedics and Related Research, No. 58, May-June, 1968.
4. N. Weber and M. Goldstein, Jr., *Chem. Phys.*, **41**, 2898 (1964).
5. R. J. Charles, Jr., *Am. Ceram. Soc.*, **45**, 105 (1962).

Participation of Oxygen Species in Periodic Anodic Processes

Herbert F. Hunger*

Institute for Exploratory Research, United States Army Electronics Command, Fort Monmouth, New Jersey

ABSTRACT

Galvanostatic periodic potential transients of the half element Pt/1M CH_2O, 3.75M H_2SO_4 were measured. A combination of coulometric analysis of the transients and of estimates of surface coverages of the electrodes with organic and oxygen species provided a useful method to study the mechanism of the periodic anodic process over the whole oscillation domain. Three regions with marked differences in mechanism were found experimentally: (*i*) the region of the "valve" mechanism, from 0.15 to 0.92V *vs.* SHE, where anodic oxidation of formaldehyde with readsorption of the latter as the coupling step occurs; (*ii*) the region of a mixed mechanism, from 0.18 to 1.1V *vs.* SHE, where anodic oxidation of the platinum surface occurs in addition to the anodic oxidation of the organic species; chemical reduction of the surface oxide leads to readsorption of formaldehyde at the oxide free surface; and (*iii*) the region of the oxide formation-reduction mechanism, from 0.6 to 1.15V *vs.* SHE where solely anodic oxidation of the platinum surface occurs, followed by chemical reduction with formaldehyde, the coupling step. Based on mechanistic considerations the nonlinear relationship between process frequency and the process variables was established over the whole frequency domain.

The occurrence of oscillatory behavior during the anodic oxidation of organic compounds (formic acid) at noble metal electrodes in aqueous electrolytes at room temperature was observed as early as 1927 and a mechanism was postulated (1, 2). Further early observations of periodic behavior were reported by Thalinger and Volmer and by Butler and Armstrong (3, 4). Early theoretical work on conditions for periodic behavior, such as the concept of simultaneous re-

* Electrochemical Society Active Member.

actions and of coupling, was reported by Bonhoeffer (5). This was followed by work of Franck on the general theory of instable electrical states and the oscillatory behavior of the iron electrode during anodic polarization (6, 7). Franck's work resulted in an explanation of the specific phenomena and a mathematical model (8). In 1954 pertinent work on organic compounds was resumed by Pavela (9). Numerous papers on oxidation of organic compounds have appeared in the 1960's; on the subject of periodic phenomena, a recent publication by Conway and co-workers reports on oscillatory kinetics during the electrochemical oxidation of formate (10). In this work the theory of general conditions for appearance of oscillatory kinetics formulated by Higgins (11) was applied to potentiostatic oscillation data. In this specific case, the general necessity for an autocatalytic type of effect (chemical reduction of a surface oxide by organic species) was found.

In a recent paper we reported on a mechanism of oscillatory behavior during the anodic oxidation of formaldehyde at platinized platinum electrodes in sulfuric acid at room temperature (12). The mechanism could account mainly for the experimental observations in the electrode potential region below +0.8V *vs.* SHE where platinum surface oxidation was suppressed. In this paper we are extending our considerations into the potential region above +0.8V *vs.* SHE thus covering the whole oscillation region. The involvement of oxygen species in the periodic process will be discussed.

Experimental

The cell used to study the oscillation phenomena can be presented by the scheme (−)Pt/1M CH_2O, 3.75M H_2SO_4/1M CH_2O, 3.75M H_2SO_4/Pt(+). It contained a platinized platinum electrode in an anolyte consisting of 1M formaldehyde in 3.75M sulfuric acid. The electrode was placed in the center tube of a modified glass-H-cell (E. H. Sargent & Company). A dynamic hydrogen reference electrode of the type described by Giner (−26 mV *vs.* SHE) was arranged in the second leg of the cell and connected with a properly arranged Luggin capillary to the anode. The platinized platinum electrodes were made from platinum-foil (0.076 cm thickness with a geometrical cross section area of 1 cm^2). Both anode and reference electrode were platinized in a controlled manner. The third leg of the glass vessel which was separated by a fritted glass disk from the anode compartment contained a platinum counter electrode. The chemicals used to prepare the electrodes and the electrolytes were of highest purity grade commercially available. Preelectrolyzed 3.75M sulfuric acid was used as the electrolyte. All necessary connections were made with standard glass joints and purified argon gas was bubbled through the anode chamber. The temperature during experimentation was controlled with a constant temperature bath.

A precision current source (Model CS-12, North Hills, Electronics, Inc.) was used to control the current (1 μA-999 mA) between the working anode and the counterelectrode. A potentiometric recorder (Model FW 5A-3332 from Texas Instruments, Inc.) was used for measuring the stationary anode potentials and the potential transients *vs.* the reference electrode.

Different experimentation was used to study the mechanism:

(*a*) *Galvanostatic anodic stripping of adsorbed organic species with variation of the anodic stripping current.*—In the first publication we discussed adsorption-desorption experiments whereby the anodic stripping current was kept constant at 50 mA, close to the threshold current density of the oscillations to avoid anodic oxidation of the platinum surface (12). In these adsorption experiments we varied the stripping current in order to measure the pulse charge Q and the process frequency ν of periodic transients over a wider range of current densities. The following previously established procedure was followed (12). Adsorption of organic species at platinized platinum electrodes took place from 1M formaldehyde in 3.75M sulfuric acid. After adsorption the electrodes were dipped in 3.75M sulfuric acid to remove the adherent liquid and transferred immediately into the anode chamber of the cell described previously which contained in this case only 3.75M sulfuric acid as the electrolyte. A preset circuit permitted the oxidation of the absorbed organic species immediately at a preselected constant current. A defined adsorption time and defined dipping conditions, which lead to partial or complete removal of the liquid film without substantial desorption of adsorbed organic species, resulted in defined amounts of organic species at the electrode. From the potential transients observed, the amount of organics could be determined. Depending on the amount of organic species, two types of transients were found: Linear and periodic ones.

(*b*) *Galvanostatic measurements of periodic, anodic potential transients under conditions where the bulk concentration of formaldehyde in the electrolyte was controlled.*—This permitted the measurement of the potential-current density relationship over the total oscillation region, yielding data of Q, the pulse charge expressed in $\mu C/cm^2$, and the process frequency ν as a function of I, the current density, as well as of ΔV, the potential transient response.

(*c*) *Determination of the rate of the chemical reduction of platinum-oxygen species with formaldehyde.*—For that purpose platinized platinum anodes in 1M formaldehyde-3.75M sulfuric acid mixtures were treated galvanostatically. The constant current which was varied between 100 and 999 mA was interrupted when the desired upper oxidation potential was reached (0.9-1.18V *vs.* SHE). The potential transient at zero current was followed with the potentiometric recorder to the rest potential (0.1-0.2V *vs.* SHE) and compared with the corresponding transient under current. In Fig. 1 the periodic potential transients at a constant current of 400 mA are shown. τ_B is the time required for the transient under current (ΔV = 1.06 to 0.33V). The chemical reduction transient can be seen in the $i = 0$

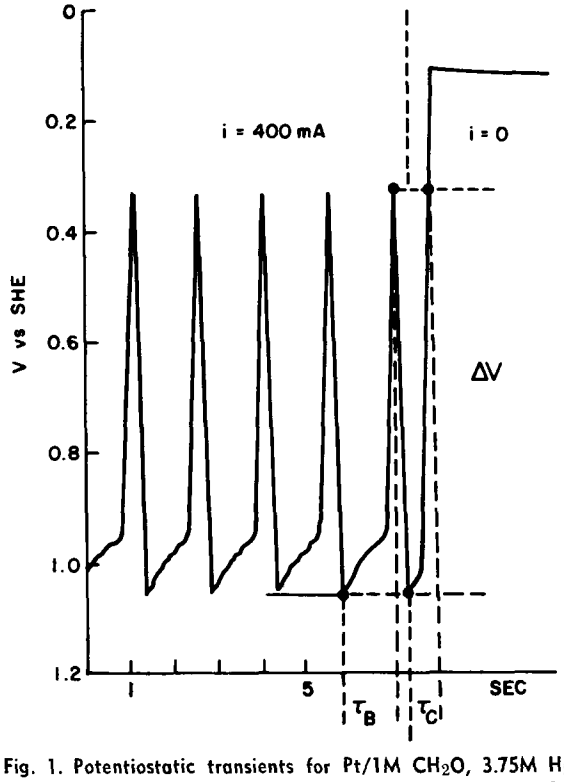

Fig. 1. Potentiostatic transients for Pt/1M CH_2O, 3.75M H_2SO_4 at 25°C. Potential measured *vs.* SHE. i =400 mA and i = 0.

region. τ_C corresponds to ΔV. The rest potential lies at about 0.12V.

(*d*) *Estimation of the real surface area of the platinum anodes.*—Before any measurements under (*a*), (*b*), or (*c*) were taken, the real surface area of the platinized platinum electrodes was determined from the anodic charging curve in sulfuric acid in accordance with established procedures (12). These procedures were based on the method used by Butler and coworkers, measuring the number of oxygen atoms deposited on the surface (13, 14). The galvanostatic anodic transients showed three regions marked by different slopes: one for the anodic oxidation of adsorbed hydrogen (0.0-0.33V *vs.* SHE), the region where charging of the double layer occurs (0.33-0.92 *vs.* SHE), and the region for build up of an oxygen monolayer (0.92-1.6V *vs.* SHE). A charge of about 420 μC/cm^2 was associated with the deposition of the oxygen monolayer (12). The length of the transient which is due to deposition of the oxygen monolayer was used to compute the area. Electrodes with real surface areas above 1000 cm^2 were used in the experimentation.

In addition, the region where charging of the double layer occurred was closely examined. From twenty transients at a constant current of 50 mA (transition time 0.95-1.6 sec), the corresponding μC/cm^2 of real surface area were computed. The double layer charging transients showed a linear relationship between potential and time. The charge Q_D between 0.33 and 0.92V *vs.* SHE was about 30 μC/cm^2. The corresponding capacitance, $C = Q_D/\Delta V$, can be computed to 51 μF/cm^2. This comes close to the double layer capacitance value reported by Schuldiner (15).

Results and Discussion

The results of (*a*) adsorption experiments with variation of the anodic stripping current are given in Table I. An adsorption time of 300 sec and a stripping current between 50 and 250 mA resulted in periodic transients. Above 250 mA linear transients were observed. The pulse charges constitute the average value over all pulsations. It is apparent from Table I that both Q and ν increase with I.

The results of (*b*) galvanostatic measurements of potential transients at constant bulk concentration of formaldehyde in the electrolyte are given in Table II.

We have found previously from adsorption-desorption experiments that the pulse charge Q close to the threshold of the oscillations is on the average 85 μC/cm^2 (range 76-94 μC/cm^2) (12). Considering the frequency dampening effect, the value observed for the very first oscillation was 46-59 μC/cm^2. This is in good agreement with the data of the first region in Table II (57-116 μC/cm^2).

Mechanisms of periodic anodic processes.—Table II can be subdivided into three regions corresponding to three different mechanisms in the periodic anodic process, discussed in more detail below.

1. *"Valve" mechanism.*—If the upper value of the potential transient remains below +0.92V *vs.* SHE no noticeable oxide formation occurs and the anodic oxidation of formaldehyde follows the "valve" mechanism path which is identical with reaction path II of the previous paper (12).

$$CH_2(OH)_{2sol} \rightarrow CH_2(OH)_{2ads} \quad (a)$$
$$CH_2(OH)_{2ads} \rightarrow A + H^+ + e^- \quad (b)$$
$$A \rightarrow B + H^+ + e^- \quad (c)$$
$$B \rightarrow C + H^+ + e^- \quad (d)$$
$$C \rightarrow CO_2 + H^+ + e^- \quad (e)$$

This mechanism postulates the stepwise anodic oxidation of formaldehyde. Step (a) is a diffusion-absorption step and steps (b) through (e) are charge transfer steps leading to anodic oxidation of organic species adsorbed during one cycle. No attempt was made in this work to determine the actual organic species which were adsorbed or oxidized. Step (e) is followed by readsorption (a), the coupling step, which is required to continue the periodic electrode process. The valve mechanism is based on the observation that adsorption of organic species becomes small at about +0.6V *vs.* SHE and above (16, 17).

It is of interest to note that there is apparently a numerical relationship between the pulse charge Q and the double layer charge Q_D of the electrode in pure sulfuric acid electrolyte. Q_D was practically zero at 0.33V *vs.* SHE and reached linearly with potential a value of 29.5 μC/cm^2 at 0.92V *vs.* SHE. Comparing Q and Q_D for any upper potential value in the region of the "valve" mechanism (0.69-0.86V *vs.* SHE) it was found that $Q_D \sim 1/4Q$ (Table III).

2. *Mixed mechanism* (valve mechanism plus anodic oxidation of platinum followed by chemical reduction of the oxide).—At current densities above 100 μA/cm^2, potential transients beyond +0.9V *vs.* SHE are observed. A second reaction path in addition to the valve mechanism accounting for the anodic oxidation of the platinum surface explains the observed increase in pulse charge Q above 100 μC/cm^2. These platinum oxygen species are formed by adsorption of water and through further anodic discharge of adsorbed OH groups (f), (g) (18, 10).

$$Pt + HOH \rightleftharpoons Pt/OH + H^+ + e^- \quad (f)$$
$$Pt/OH \rightarrow Pt/O + H^+ + e^- \quad (g)$$

Pt/O is the surface oxide formed (stoichiometric representation is purposely avoided).

Table I. Variation of the anodic stripping current

IM CH_2O, 3.5M H_2SO_4, platinized platinum; 25°C; adsorption time 300 sec

Stripping current i, mA	Stripping c.d. I, μA/cm^2*	Pulsecharge Q, μC/cm^2*	Frequency ν, Hz	Number of pulses
50	24	85	0.16	10
100	41	105	0.39	5
150	62	140	0.44	3
200	82	163	0.51	2
250	103	196	0.53	1
300				0

* Data refer to real surface areas of electrodes $2.43 \cdot 10^3$ and $3.63 \cdot 10^3$ cm^2.

Table II. V-I Relationship

IM CH_2O, 3.75M H_2SO_4, platinized platinum; 25°C

I, μA/cm^2*	Q, μC/cm^2*	ν, Hz	ΔV (V *vs.* SHE)	$Q_{org}/(Q_{org} + Q_{ox})$
11.2	116	0.1	0.53-0.69	
12.68	68	0.19	0.44-0.75	
15.2	57	0.28	0.24-0.8	
25.4**	73	0.35	0.18-0.82	
35.5	102	0.4	0.16-0.84	
50.7	109	0.47	0.15-0.86	
102	173	0.59	0.18-0.94	0.49
152	228	0.67	0.23-0.99	0.37
203	285	0.71	0.28-1.02	0.30
254	329	0.77	0.33-1.04	0.26
304	365	0.83	0.4-1.05	0.23
406	387	1.05	0.51-1.10	0.21
438	330	1.33	0.52-1.12	
482	291	1.66	0.59-1.13	
501	302	1.66	0.62-1.15	

* Data refer to real surface areas of electrodes $1.97 \cdot 10^3$ cm^2.
** Corresponds to about 50 mA/cm^2 geometrical cross section.

This comes close to the double layer capacitance value reported by Schuldiner (15).

It is of interest to note that there is apparently a numerical relationship between the pulse charge Q and the double layer charge Q_D of the electrode in pure sulfuric acid electrolyte. Q_D was practically zero at 0.33V *vs.* SHE and reached linearly with potential a value of 29.5 μC/cm^2 at 0.92V *vs.* SHE. Comparing Q and Q_D for any upper potential value in the region of the "valve" mechanism (0.69-0.86V *vs.* SHE) it was found that $Q_D \sim 1/4Q$ (Table III).

Table III. Comparison of pulse charge Q with Q_D

Q, μC/cm^2	Upper value of ΔV	Q_D, μC/cm^2
116	0.69	18
68	0.75	21
57	0.80	24
63	0.81	24
73	0.82	25
102	0.84	26
109	0.86	27

This is followed by chemical reduction of the platinum oxygen species by formaldehyde which explains the reverse of the anodic transient to less positive potentials (h) (10, 19).

$$Pt/O + 1/2CH_2O \rightarrow 1/2CO_2 + 1/2H_2O + Pt \quad (h)$$

The chemical reduction prepares the electrode for the coupling step, the readsorption of formaldehyde at the oxide free platinum surface at less positive potentials through step (a).

In order to find some proof for oxide reduction reaction (h), the rate of the chemical reduction of the platinum-oxygen species with formaldehyde was measured and compared with that of the anodic back transient. The results are shown in Table IV.

It can be seen that the time τ_C required to reach the same end potential from a defined starting potential by the chemical reduction reaction is always smaller than the time required for the back transient at current under otherwise equivalent constant current conditions. Thus it appears possible that chemical reduction of platinum oxide can occur with a sufficiently fast rate during the anodic back transient. The pulse charge Q at 600 $\mu A/cm^2$ is 300 $\mu C/cm^2$. Thus the anodic and cathodic short circuit current densities during the chemical reaction amount to 2000 $\mu A/cm^2$.

If we relate the Q values of Table II to surface coverages we come up with the following picture. Surface coverage estimates for formaldehyde and oxygen yield both about 420 $\mu C/cm^2$ for a 4 $e^-/2$ site attachment ratio at full coverage (12). In the following we use Pt as the symbol of a platinum site (surface atom) and $\Sigma \circledcirc$ to characterize the coverage. The chemisorption of formaldehyde is probably dissociative (i).

$$2Pt + CH_2O \rightarrow Pt \cdot CHO + Pt \cdot H \qquad \Sigma \circledcirc \sim 0.2 \quad (i)$$

Dissociative chemisorption is a well-established fact in the case of saturated hydrocarbons on transition metals (20). A saturated ad-layer of 180 $\mu C/cm^2$ found experimentally would mean a 43% organic coverage of the platinum surface. The average pulse charge of 85 $\mu C/cm^2$ indicates an initial coverage of about 20%, a half depleted ad-layer (12). The rest of the surface is available for other species. In accordance with the stoichiometry of the valve mechanism we can consider another adsorption step, the dissociative chemisorption of water in the presence of adsorbed organic species (j).

$$Pt \cdot CHO + 2Pt + HOH \rightarrow Pt \cdot CHO + Pt \cdot OH + Pt \cdot H \qquad \Sigma \circledcirc \sim 0.3 \quad (j)$$

With respect to adsorbed OH groups it was found in water adsorption experiments on platinum that about $6.8 \cdot 10^{14}$ water molecules are strongly adsorbed per square centimeter of real surface area (21, 22). This suggests that one water molecule attaches to two platinum sites. This chemisorption mechanism of water has been discussed by Bond (23). Equation (j) gives the maximum coverage of the electrode with reactants during one oscillation cycle as required by the stoichiometry of the valve mechanism. Thus we can see that there will always be available a minimum of 70% of the platinum surface for other occupants. Expressed in $\mu C/cm^2$ corresponding to oxide formation, this 70% rest amounts to 294 $\mu C/cm^2$. From Table II it can be noted that a maximum value of the pulse charge of 387 $\mu C/cm^2$ was measured which accounts at the given upper potential (1.1V *vs.* SHE) for both oxidation of organics and oxide formation. Considering the average value of Q for oxidation of organics (85 $\mu C/cm^2$), oxide coverage build up over one cycle at 1.1V *vs.* SHE reaches about 302 $\mu C/cm^2$. This is in good agreement with the theoretical value above for oxide formation (294 $\mu C/cm^2$), assuming a mixed mechanism.

Table IV. Comparison of time required for chemical reduction of platinum-oxygen species τ_C and anodic back transient τ_B for a given ΔV

IM CH_2O, 3.5M H_2SO_4, platinized platinum; 25°C			
I, $\mu A/cm^2$*	ΔV (V *vs.* SHE)	τ_B, sec	τ_C, sec
60	0.90-0.18	1.32	0.4
120	0.99-0.23	0.98	0.3
240	1.06-0.33	0.9	0.38
300	1.08-0.38	0.85	0.3
600	1.18-0.72	0.2	0.15

* Data refer to real surface areas of electrodes.

3. *Oxide formation-reduction mechanism* (anodic platinum oxide formation followed by chemical reduction with formaldehyde).—In Fig. 2 the pulse charges expressed in $\mu C/cm^2$ are shown as a function of the current density. Data are from adsorption experiments, from experiments with constant bulk concentration, and from chemical reduction experiments.

The decrease in pulse charge Q (Fig. 2) above 400 $\mu A/cm^2$ can be explained by strongly diminished adsorption of organic species above +0.6V *vs.* SHE. The average value of $\overline{Q}_{org}$ of 85 $\mu C/cm^2$ agrees well with the experimentally observed drop of 96 $\mu C/cm^2$. Transients above 400 $\mu A/cm^2$ are therefore probably due purely to the formation of an oxide layer followed by chemical reduction with formaldehyde in accordance with reactions (f) through (h). Using the previous coverage data the surface oxide build-up during one cycle corresponds approximately to the composition $Pt_2O_{1.5}$.

Frequency-current density relationship.—The frequency-current density relationship was derived from experimental data such as in Table I and Table II. The relationship is nonlinear. Equation [1], which was found at first empirically, but could be derived later on basis of the mechanism, describes the relationship

$$\nu = k \cdot I \cdot \frac{Q_{org}}{Q_{org} + Q_{ox}} \quad [1]$$

The frequency ν is proportional to the anodic current density I. The deviation from initial linearity is given through the ratio $Q_{org}/Q_{org} + Q_{ox}$ (last column in Table II). Q_{org} is the pulse charge due to oxidation of the formaldehyde in accordance with the value mechanism and Q_{ox} that due to anodic oxidation of the platinum surface.

In Fig. 3 the frequency-current density relationship is shown. Data are from the experiments described previously. The frequency data from the adsorption experiments are slightly lower since they constitute averaged values and consider the frequency dampening effect observed for the pulses with higher order (12).

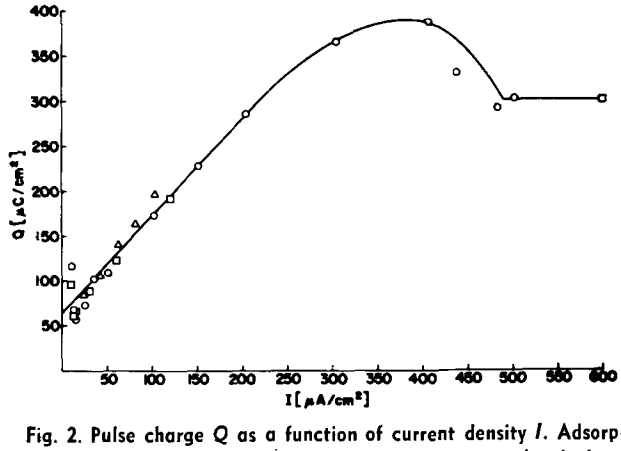

Fig. 2. Pulse charge Q as a function of current density I. Adsorption experiments △; constant bulk concentration ⊙; chemical reduction experiments ⊡.

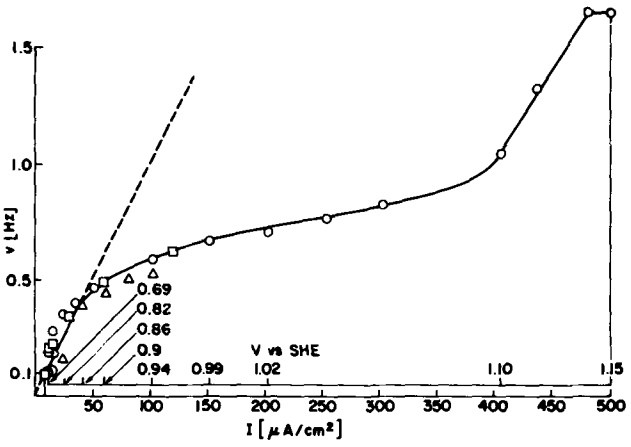

Fig. 3. Frequency-current density relationship. Adsorption experiments △; constant bulk concentration ⊙; chemical reduction experiments ⊡.

It has been observed previously that an initial linear region can be found up to about 0.5 Hz (24). This is followed by a region of deviations from the initial slope. Finally there is again a linear rise up to the limiting frequency of 1.66 Hz for the given anolyte composition and temperature.

In the initial linear region the valve mechanism prevails. There the frequency is directly proportional to the current density [2].

$$\nu = k \cdot I = k \cdot I_{org} \qquad [2]$$

Above +0.92V the formation of surface oxides in an additional reaction path to the valve mechanism has to be taken into account in the frequency computation. Since the time period τ_a for one cycle exceeding 0.92V accounts for both, the anodic oxidation of the adsorbed organic species plus the formation of the oxide, we can write [3]

$$\tau_a = \tau_{org} + \tau_{ox} \qquad [3]$$

If we compare the oxide build up at various current densities, a value of $\overline{Q}_{org} = 85\ \mu C/cm^2$ can be taken as the point of practical zero oxide coverage. If no oxides were formed, the same amount of formaldehyde adsorbed at the electrode should become oxidized twice as fast if the current density were doubled. Thus if no increase in τ is caused by an additional reaction, the frequency would be directly proportional to the current density [2]. It would be identical in this case with I_{org}, the anodic organic oxidation current density. By expanding the equation with $(I_{org} + I_{ox})$ thus taking an additional path in account we obtain [4].

$$\nu = k\ (I_{org} + I_{ox})\ \frac{I_{org}}{(I_{org} + I_{ox})} \qquad [4]$$

Multiplying Eq. [4] with the anodic transient time for one cycle we obtain [5].

$$\nu = k\ (I_{org} + I_{ox})\ \frac{\tau_a I_{org}}{\tau_a I_{org} + \tau_a I_{ox}} \qquad [5]$$

There are two ways open to relate the coulombs Q_x for anodic oxidation of a specie x to the current density and transient time [6] [7]

$$Q_x = I_a \tau_x \qquad [6]$$

$$Q_x = I_x \tau_a \qquad [7]$$

Combining Eq. [5] with Eq. [7] leads to [8]

$$\nu = k\ (I_{org} + I_{ox})\ \frac{Q_{org}}{Q_{org} + Q_{ox}} \qquad [8]$$

Since $(I_{org} + I_{ox})$ is the total anodic current density we obtain our original Eq. [1] which describes the second part of the $\nu - I$ curve with its deviation from the original slope up to about 1 Hz. Deviation from linearity is found if $Q_{org}/Q_{org} + Q_{ox} < 1$ and $\neq$ const with I, which is the experimental case.

The third region of the $\nu - I$ curve is again linear. It appears that this region falls together with that of oxide formation and chemical reduction of the oxides with formaldehyde. The oscillations are caused by the counterplay between oxide formation and reduction and are mass transport controlled. Turbulence in the electrolyte layer next to the electrode is created through the vigorous evolution of carbon dioxide. This leads to periodic changes in the thickness of the mass transport boundary layer. The frequency of such oscillations can be estimated by forming the ratio of the transport coefficient D of the specie which is controlling to the square of the thickness of the mass transport boundary layer ζ [9] (25).

$$\nu = 2D/\zeta^2 \qquad [9]$$

For a mass transport coefficient of 10^{-5} for CH_2O and a boundary layer thickness of $3.46 \cdot 10^{-3}$, a limiting frequency of 1.66 Hz can be computed. A further increase in frequency can be expected if mass transport is enhanced. This can be done by raising the temperature. At 90°C the frequency was about 10 Hz with full stability of the oscillations (ΔV = 0.74-0.77V). The frequency limitation of the half element lies around 15 Hz, due to diminishing amplitude ($\Delta V \rightarrow 0$).

Acknowledgment

The author gratefully acknowledges the continued interest and support of Dr. E. A. Gerber, Director, Electronics Components Laboratory, U.S. Army Electronics Command, Fort Monmouth, New Jersey.

Manuscript submitted Oct. 28, 1968; revised manuscript received June 28, 1969. This was Paper 332 presented at the Montreal Meeting, Oct. 6-11, 1968.

Any discussion of this paper will appear in a Discussion Section to be published in the June 1970 JOURNAL.

REFERENCES

1. E. Mueller and G. Hindemith, *Z. Elektrochem.*, **33**, 562 (1927).
2. E. Mueller and S. Tanaka, *ibid.*, **34**, 256 (1928).
3. M. Thalinger and M. Volmer, *Z. Phys. Chem.*, **1950**, 401 (1930).
4. J. A. V. Butler and G. Armstrong, *Nature*, **129**, 613 (1932).
5. K. F. Bonhoeffer, *Z. Elektrochem.*, **51**, 24 (1948).
6. U. F. Franck, *Z. Naturforsch.*, **4a**, 378 (1949).
7. U. F. Franck, *Z. Phys. Chem., N. F.*, 3, 183 (1955).
8. U. F. Franck and R. Fitzhugh, *Z. Elektrochem.*, **65**, 2, 156 (1961).
9. T. O. Pavela, *Ann. Acad. Sci. Fennica*, **59**, 1 (1954).
10. J. Wojtowicz, N. Marincic, and B. E. Conway, *J. Chem. Phys.*, **48**, 4333 (1968).
11. J. J. Higgins, *Ind. Eng. Chem.*, **59**, 18 (1967).
12. H. F. Hunger, *This Journal*, **115**, 492 (1968)
13. J. A. V. Butler, "Electrical Phenomena at Interfaces," p. 204, MacMillian Co., New York (1951).
14. J. D. Pearson and J. A. V. Butler, *Trans. Faraday Soc.*, **34**, 1163 (1938).
15. S. Schuldiner and R. M. Roe, *This Journal*, **110**, 332 (1963).
16. W. M. Breiter and S. Gilman, *ibid.*, **109**, 622 (1962).
17. S. B. Brummer and A. C. Makrides, *J. Phys. Chem.*, **68**, 1448 (1964).
18. B. E. Conway, N. Marincic, D. Gilroy, and E. Rudd, *This Journal*, **113**, 1144 (1966).
19. J. E. Oxley, G. K. Johnson, and B. T. Buzalski, *Electrochim. Acta*, **9**, 897 (1964).
20. S. J. Gregg and K. J. W. Sing, "Adsorption, Surface Area, and Porosity," p. 75 ff, Academic Press, London, New York (1967).
21. Final Technical Report, Contract Number DA-91-591-ECU-4035, Sept. 1967.
22. G. Sandstede, G. Walter, and G. Wuzbacher, *Nature*, **216**, 476 (1967).
23. G. C. Bond, "Catalysis by Metals," p. 217 ff, Academic Press, London, New York, (1962).
24. H. F. Hunger, in Proc. Journees Int. D'Etude des Piles Combustible, Brussels (1965).
25. K. Vetter, "Elektrochemische Kinetik," p. 308, Springer Verlag, (1961).

The Reaction of Titanium(IV) with Hydrogen at Palladium Membranes

Thomas C. Franklin* and J. Albert McDaniel[1]**

Chemistry Department, Baylor University, Waco, Texas

ABSTRACT

A colorimetric study was made of the kinetics of the reduction of acidic titanium(IV) chloride solutions by hydrogen diffusing through a palladium membrane. The rate of this reaction was found to be first order with respect to the concentration of the titanium and was inhibited by the addition of organic poisons. The inhibition followed an adsorption isotherm leading to the conclusion that the rate of the reaction was controlled either by adsorption of titanium(IV) or by a reaction involving an adsorbed titanium(IV) species.

A number of studies have been made of the migration of electrolytically generated hydrogen through palladium membranes (1-3) and the reaction of previously hydrided palladium (4-8) with oxidizing agents. Castellan (9) has studied the reaction of cerium(IV) with hydrogen diffusing through palladium membranes. In most of the studies with oxidizing agents, it was concluded that the rate-determining step was the diffusion of the oxidizing agent to the hydrided surface (6, 9). If this is the rate-determining step, the addition of poisons should have no effect on the rate of the reaction; therefore, a study was initiated to determine whether poisons did affect the rate of reduction of titanium(IV) by hydrogen diffusing through a palladium membrane.

Experimental Methods and Procedures

Figure 1 shows the cell used. Hydrogen was electrolytically generated from the 2*N* sulfuric acid on the interior wall of the palladium tube and then diffused through the palladium to the exterior wall. The exposed palladium tube was 11 cm long and approximately 5 mm in diameter. In the exterior chamber the hydrogen diffusing out reacted with titanium(IV) reducing it to colored titanium(III). The rate of the chemical reduction was followed by pulling samples of the solution and analyzing them spectrophotometrically for titanium(III).

At the same time the potential of the exterior of the palladium was measured against a reference calomel electrode using a Luggin capillary.

The exterior solution was a 30% sulfuric acid solution which in different experiments contained different amounts of titanium(IV). The solution was stirred by bubbling with nitrogen. The exterior of the palladium tube was palladized lightly between each series of runs.

Hydrogen was generated on the interior at 67.39 mA until the potential measured between the exterior of the assembly and the saturated calomel electrode became constant. A measured quantity of a titanium(IV) stock solution, prepared by adding titanium(IV) chloride to 30% sulfuric acid, was added to the reaction vessel. Then at 1 or 2 min intervals the potential of the outside of the palladium electrode was measured, and a sample was removed and analyzed spectrophotometrically for titanium(III). After each analysis, the sample was returned to the cell. At no time did the volume of added solutions or removed samples exceed 2% of the total volume. Thus, the addition or removal of solution did not appreciably alter the rate of reaction. After about 14 min a measured amount of an organic additive was rapidly injected into the solution, and the progress of the reaction was followed for another period of time; at regular time intervals additional amounts of additive were introduced into the solution. The additives studied were sodium 2-propene-1-sulfonate, thiourea, 1, 3-diethyl-2-thiourea, 1-ethylquinolinium iodide, and sodium 2-propanesulfonate. All experiments were performed at 25°C using the purest grade of chemicals commercially available.

Results and Discussion of Results

Figure 2 shows typical data for the initial rate of reaction with two different concentrations of titanium (IV), one twice that of the other. As can be seen, the initial rate of reduction at the higher concentration is approximately double that of the lower concentration, showing that the reaction is first order with respect to titanium(IV). The average first order rate constant obtained for 29 different runs was 2.02 x 10^{-3} min^{-1} with a standard deviation of ± 0.30 x 10^{-3}. As seen in Fig. 2, the deviation was small when the only change was a change in the concentration of titanium(IV). The observed deviations were attributed primarily to a lack of reproducibility of the palladized surface.

The fact that the reaction is first order with respect to the titanium(IV) is in agreement with other studies on different oxidizing agents (5, 6, 9). In these studies the first order kinetics was attributed to a diffusion limited process. However, in this study changing the rate of stirring by changing the nitrogen bubbling rate did not appreciably alter the rate of the reac-

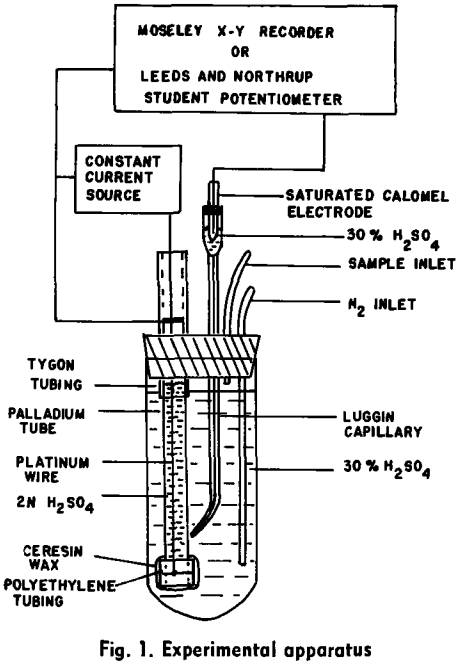

Fig. 1. Experimental apparatus

* Electrochemical Society Active Member.
** Electrochemical Society Student Associate.
[1] Present address: Chemistry Department, University of Illinois, Urbana, Illinois.

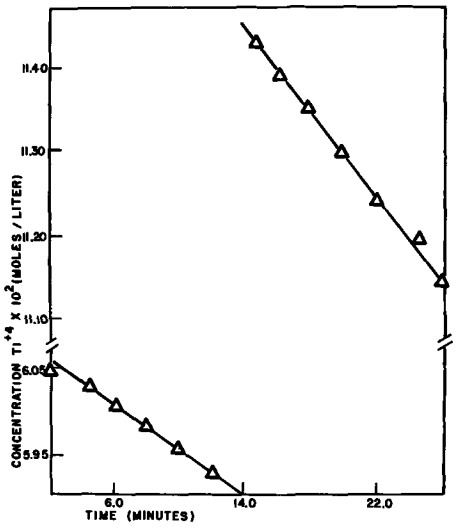

Fig. 2. Order determination plot for the reaction of titanium(IV) with hydrogen.

Initial concentration of Ti(IV)	Slope (rate)
6.07	—0.0125
11.65	—0.0246

tion which was contrary to what was expected if the rate was controlled by the rate of diffusion of the titanium(IV).

Much more damaging to the concept of a diffusion controlled process was the effect of poisons on the rate of the reaction. Figure 3 shows the effect of 1, 3 diethyl-2-thiourea on the rate of reduction. Each organic additive tried gave similar results in that the addition of the organic compound decreased the rate of the reaction. This shows that the rate-determining step involves neither the diffusion of hydrogen through the metal nor diffusion of titanium(IV) to the surface. Diffusion processes depend on the geometrical surface area and not the real surface area (10).

From the poisoning data, it was concluded that the rate of the reaction was a function of the real area and that the poison blocked the surface area. That the poison is being adsorbed on the electrode is indicated by examining the effect of different concentrations of additive on the rate of reduction. Unfortunately, one can introduce only two concentrations of an additive such as thiourea before the electrodes become almost completely poisoned, but it can be seen in Fig. 4 that the effect looks very much like an adsorption isotherm. In the case of the propenesulfonate, a number of different concentrations can be used, and it can be seen in Fig. 5 that one can fit the data to a Freundlich-type adsorption isotherm.

It is possible that the poison could act by decreasing the amount of adsorbed hydrogen. The potential of the electrode should be a measure of the amount of hydrogen (11, 12) in the neighborhood of the electrode surface. Figure 6 shows definitely that the potential decreases sharply after the introduction of the titanium(IV) indicating that the rate of diffusion

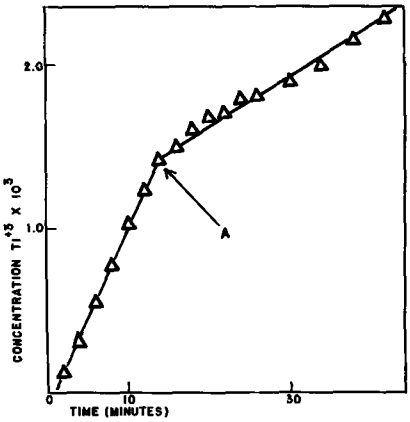

Fig. 3. Effect of 1, 3 diethyl-2-thiourea on the rate of reduction of titanium(IV) with hydrogen: A, time of introduction of additive.

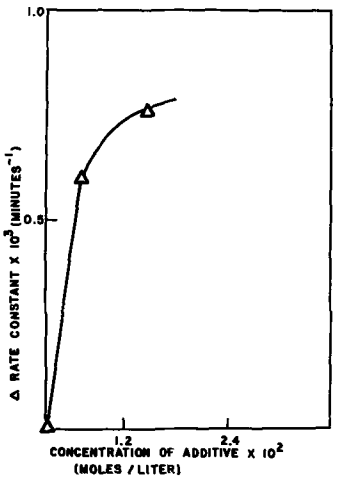

Fig. 4. Apparent adsorption isotherm from rate data for the additive thiourea.

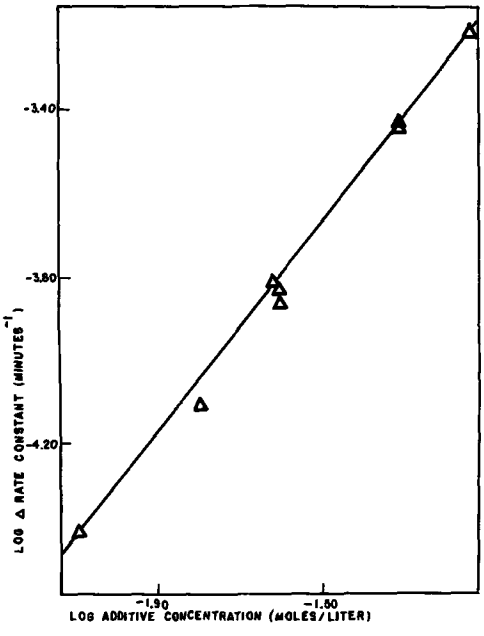

Fig. 5. Freundlich isotherm for the additive sodium 2-propenesulfonate.

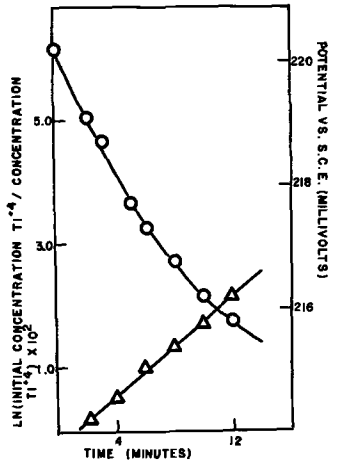

Fig. 6. Potential-time (○) and first order rate constant plots (△) for the reduction of titanium(IV) with hydrogen.

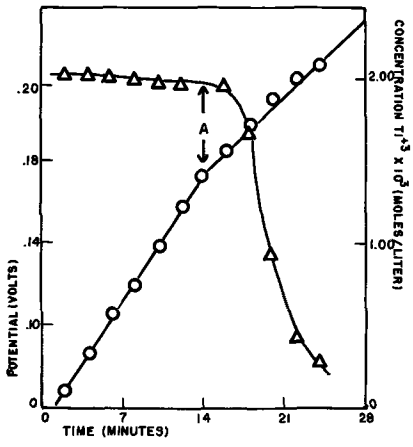

Fig. 7. Effect of 1-ethylquinolinium on the rate of reaction and potential change. A, Time of addition of ethyl quinolinium iodide; △, potential; ⊙ concentration of titanium(III).

of hydrogen is not as rapid as the rate of reaction of the hydrogen with titanium. Eventually, the potential approaches a limiting value indicating a new steady-state condition for the adsorbed hydrogen. During this entire process, however, the rate of reaction is constant. This effect is much more pronounced in the presence of additives (Fig. 7). In the presence of thiourea, 1-ethylquinolinium iodide and 1, 3 diethyl-2-thiourea the rate of reaction stayed constant while the potential changed approximately 0.1V. This indicates first of all that under the conditions of these experiments the rate of the reaction is independent of the electrode potential and, second, that it is independent of the amount of hydrogen at the surface.

A generalized mechanism for this process could be written as follows:

$$H_{\text{evolution side}} \rightarrow H_{\text{metal}} \rightarrow H_{\text{reaction side}} \quad \text{(A)}$$

$$Ti(IV)_{\text{soln}} \rightarrow Ti(IV)_{\text{electrode}} \quad \text{Diffusion} \quad \text{(B)}$$

$$Ti(IV)_{\text{electrode}} \rightarrow Ti(IV)_{\text{adsorbed}} \quad \text{Adsorption} \quad \text{(C)}$$

$$Ti(IV)_{\text{adsorbed}} \rightarrow Ti^*(IV)_{\text{adsorbed}} \quad \text{Rearrangement} \quad \text{(D)}$$

$$Ti(IV) \text{ or } Ti^*(IV) + H_{\text{reaction side}} \rightarrow \text{Products} \quad \text{(E)}$$

It would appear from the poisoning data that neither reactions (A) or (B) can be rate determining. Since the rate of reaction was independent of the potential, no electron transfer step was included in the mechanism. Also, since the potential depends on the amount of hydrogen at the surface, reaction (E) was regarded as being nonrate determining. Reaction (E), of course, since it is beyond the rate-determining step, could easily be made up of a series of electron transfer steps.

It was thus concluded that either reaction (C), the adsorption of the Ti(IV) complex, or (D), the rearrangement of the complex to some more reactive form, was thus concluded to be the rate-determining step.

Acknowledgment

Grateful acknowledgment is given to The Robert A. Welch Foundation for the support given to the research reported in this paper.

Manuscript submitted June 4, 1969. This was Paper 211 presented at the New York Meeting, May 5-9, 1969.

Any discussion of this paper will appear in a Discussion Section to be published in the June 1970 JOURNAL.

REFERENCES

1. F. A. Lewis, "The Palladium Hydrogen System," Academic Press, London, New York (1967).
2. M. A. V. Devanthan and Z. Stachurski, *Proc. Roy. Soc.*, **270A**, 90 (1962).
3. S. Schuldiner and J. P. Hoare, *This Journal*, **103**, 178 (1956).
4. C. A. Knorr, *Z. Phys. Chem.*, **157A**, 143 (1931).
5. F. A. Lewis and A. R. Ubbelohde, *J. Chem. Soc.*, **1954**, 1710.
6. J. C. Barton, W. F. N. Leitch, and F. A. Lewis, *Trans. Faraday Soc.*, **59**, 1208 (1963).
7. L. D. Burke, C. Kemball, and F. A. Lewis, *ibid.*, **60**, 913 (1964).
8. L. D. Burke, F. A. Lewis, and C. Kemball, *ibid.*, **60**, 919 (1964).
9. R. A. La Pietra and G. W. Castellan, *This Journal*, **111**, 1276 (1964).
10. H. A. Laitinen and I. M. Kolthoff, *J. Phys. Chem.*, **45**, 1061 (1941).
11. M. J. Vasile and C. G. Enke, *This Journal*, **112**, 865 (1965).
12. R. V. Bucur, *J. Electroanal. Chem.*, **17**, 427 (1968).

The Mechanism of Oxygen Evolution on Nickel, Platinum, and Other Metals and Alloys

Robert F. Scarr*

Union Carbide Corporation, Consumer Products Division, Research Laboratory, Cleveland, Ohio

ABSTRACT

The oxygen evolution reaction in 1M KOH has been studied by low speed linear sweep voltammetry of several metals including: Ni, Pt, Co, Fe, NiFe, NiPt, and Ni_3Pt. The Tafel slope for all these metals at early stages of the oxygen evolution wave was found to be about 46 mV/dec. For nickel and its alloys, dual Tafel regions were observed wherein, at even lower current densities, the slope was 34 mV/dec. A recently proposed theory for interpreting Tafel slopes is applied to these results, and a mechanism involving a three-step formation of adsorbed hydrogen peroxide is given. The exchange current density for several of these steps is evaluated, and the results are found to be consistent with the properties of the metals.

The process of oxygen evolution has been studied extensively over the years to the point where there seems to be general agreement on certain aspects of the reaction (1). For example, the rate-determining step (rds) is usually accepted as being the electrochemical adsorption of hydroxide radical, while the substrate is suspected of playing more than just a passive role. There is enough disparity in the results, however, to forestall general acceptance of a more detailed understanding of oxygen evolution.

In order to study this reaction, investigators have used, for the most part, steady-state galvanostatic or potentiostatic techniques to measure kinetic param-

* Electrochemical Society Active Member.

Key words: oxygen evolution mechanism; oxygen evolution on nickel, platinum, and alloys; potential sweep of oxygen evolution.

eters, and high-speed linear sweep voltammetry to characterize the electrode surface. Each of these techniques is applicable to only a limited aspect of the entire problem. In order to obtain further information, one must study the reaction under somewhat different experimental conditions, either at very short times or at very low currents where ultimate conditions do not yet prevail.

One technique which may offer some advantages is linear sweep voltammetry (LSV) at low sweep rates. At scan speeds between 0.2 and 100 mV/sec, the electrode can be investigated both at low currents and at stages early in the chronology of electrode surface change. At these sweep rates, nonfaradaic double layer charging currents are negligible, although care must be taken to ascertain the influence of convective forces.

This paper describes a study of oxygen evolution in alkaline electrolyte using LSV on several metals including nickel, platinum, cobalt, iron, and three alloys of nickel corresponding to NiFe, NiPt, and Ni_3Pt.

Experimental

Apparatus and materials.—The cell for this investigation was a three-compartment cell, about 100 ml in total volume, made from Lucite plastic which had been leached with caustic for several years prior to use. Nickel foil counterelectrodes were placed in each of the two outer compartments. The test electrode and reference electrodes were contained in the center section. The reference electrode was situated aside and in the plane of the test electrode, and about 1 mm away at its closest point. The center compartment was isolated from the counterelectrode compartments by separators of fine mesh Teflon gauze whose purpose was to minimize convective transfer of counterelectrode reaction products. The chamber above the electrolyte surface was continually flushed with deoxygenated nitrogen. Although the cell materials may normally be regarded as a source of contaminants, their influence on the electrode reaction was diminished by frequent changes of electrolyte. Due to the nature of the experimental procedure and in view of the reproducibility of results, the effect of impurities is considered to be negligible in this work.

Test electrodes were made from spectrographically pure metal obtained from Johnson and Matthey, Ltd. Single metal electrodes were used in the form of wire, foil, or rods. Parts of these electrodes which were not intended to contact the electrolyte were coated with several protective layers of Miccrotex masking lacquer from Michigan Chemical Corporation. Alloy samples, which were produced in the form of large beads, were made into electrodes by trimming the bead to the desired shape, attaching a current collector wire with silver epoxy, and then potting the bead in epoxy resin. The final finish was achieved by polishing with 600 grit silicon carbide paper. Apparent area of all electrodes was controlled and known. The surfaces of the foil electrodes were mounted vertically in the cell while those of the alloy beads were horizontal.

The reference electrode for all measurements was mercury-mercuric oxide. All potentials given in this paper are reported with respect to this electrode. The electrolyte was 1M KOH which had been preelectrolyzed under nitrogen between a nickel anode and a mercury pool cathode of about 3 cm^2. Preelectrolysis was conducted at controlled current while the solution was agitated by the nitrogen stream. As the potential of the cathode became increasingly negative, the magnitude of the current was progressively reduced from 2 mA/cm^2 toward the final stage, an overnight run at 2 $\mu A/cm^2$. The potential of the mercury pool during this period approached —1.2V *vs.* mercury-mercuric oxide. Teflon vessels were used for preparation and storage of the electrolyte.

The potential of the test electrode in the linear sweep experiments was controlled with a Wenking potentiostat. The sweep signal was electronically synthesized using conventional operational amplifier circuitry. Current-voltage curves were recorded on an Electro Instruments Model 520 X-Y recorder.

Alloys were made from mixtures of spectrographic grade wire or metal powder which were fused in magnesia crucibles under argon in an induction furnace. The stoichiometric composition of the alloys corresponded to NiPt, Ni_3Pt, and NiFe. Nickel is continuously soluble in platinum or iron, with no compound formation. Some "ordering" in the solid structure is believed to occur in the nickel-platinum alloys at the particular atomic ratios used (2). As a consequence of using induction heating, sample beads were quite homogeneous due to agitation by eddy currents. At the conclusion of the heating period, such rapid cooling occurred as to essentially quench the melt, thus preserving uniformity. Metallographic examination of the specimens revealed quite homogeneous surface composition with rather large grain size.

Procedure.—At the beginning of the experimental investigation of each metal, the electrode was scrubbed with Alconox detergent, rinsed thoroughly with distilled water, and placed in the cell. After the potential had become reasonably stable on open circuit, an anodic linear sweep voltamogram was obtained at 1 mV/sec beginning at the open-circuit potential and sweeping (forward) toward more positive potentials. At this slow sweep rate, the characteristic peaks, if any, for the oxidation of the metal would appear followed by the onset of oxygen evolution. Thereafter, during forward and reverse sweep cycling, the potential was never carried more negative than the foot of the anodic oxygen wave, that is, about 0.4V. An exception to this procedure occurred with the nickel electrode where the negative extreme was 0.2V. It was expected that this measure would render the surface of the electrode fairly stable and reproducible with respect to the formation of metal oxides themselves.

At the termination of each forward half-cycle, the potential was held only a few seconds in the oxygen evolution region before reversing the sweep. At the conclusion of the reverse sweep, the potential was held at the foot of the oxygen wave for longer periods of time, *i. e.*, at least 10 min. Additional sweeps were made at other scan rates between 0.2 and 100 mV/sec. Consecutive runs at each sweep speed showed the current-voltage curves to be reproducible.

Results and Discussion

A typical linear sweep voltamogram for nickel metal is given in Fig. 1. This plot was obtained at 1 mV/sec, and it shows both the forward and reverse sweeps. The peak for the oxidation of the substrate is quite prominent and is limited to a narrow range of potential preceding oxygen evolution. The evolution of oxygen was visually confirmed at potentials positive to 0.55V. The featureless increase in current at potentials positive to 0.55V and the near coincidence of forward and reverse sweeps in the oxygen evolution region indicate that (*a*) the nature of the surface has remained unchanged during gassing, and (*b*) the oxygen evolution reaction is at least momentarily at steady state.

The area of the electrode did increase from cycle to cycle, however, due to oxidation of the metal in the region of the peak. This effect was evaluated at fixed sweep rate in two ways which yielded roughly the same results. First, the area under the nickel oxidation peak was measured graphically and found to increase about 5% per cycle. Second, the current at a given potential in the oxygen evolution region also increased at nearly 5% per cycle.

Typical sweeps at each sweep rate in the positive direction are plotted on a semilogarithmic scale in Fig. 2. The combined ohmic resistance of the electrode and the solution was of the order of 1 ohm; measured

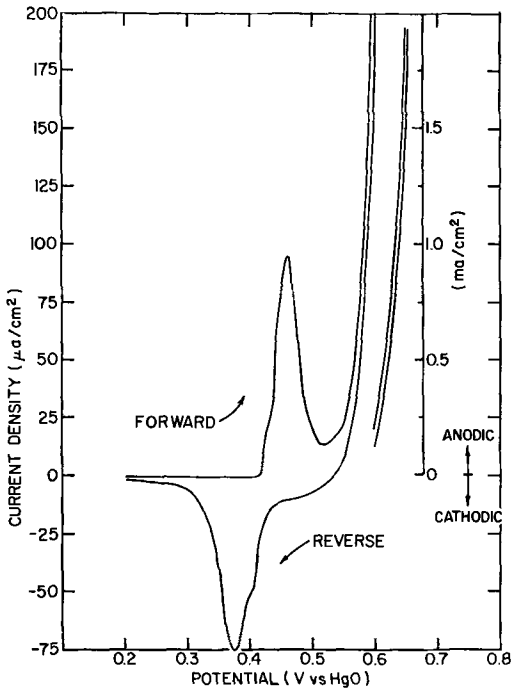

Fig. 1. Typical linear sweep voltamogram of nickel metal in 1M KOH taken at 1 mV/sec scan rate.

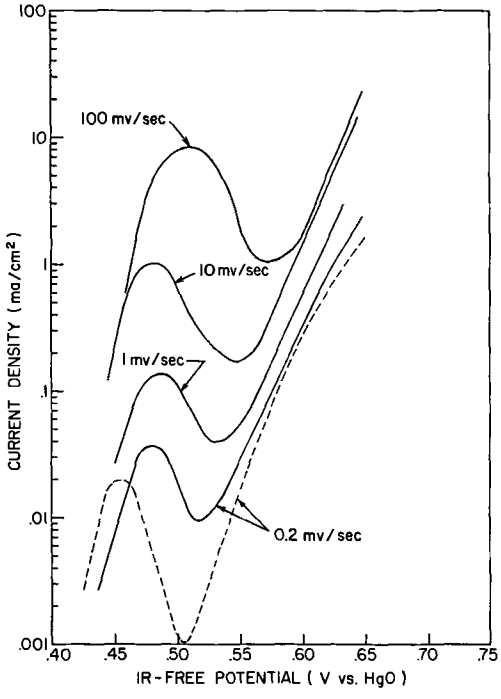

Fig. 2. Linear sweep voltamograms of nickel metal at various scan rates. Slope of the Tafel region for solid curves is 45 ± 2 mV/dec; that for the dashed curve is 34 mV/dec. In ascending order, the solid curves represent the 17th, 16th, 10th, and 11th cycles, respectively. The dashed curve is for the 7th cycle of another electrode.

potentials were corrected graphically for ohmic drop. In the oxygen evolution region, the log plots for all sweep rates exhibit a linear section whose slope ($d\eta/d \log i$) is 45 ± 2 mV/dec. The effect of stirring was investigated by bubbling nitrogen through the cell. In the region of the linear log plot, stirring had a noticeable effect on the magnitude of the current, indicating some dependence on mass transport, but the slopes of the current-voltage curves were unaffected. The existence of a linear section indicates that the electron transfer process is rate controlling.

At potentials higher than those shown, the current is no longer linear with potential due to the onset of some other limiting process, possibly mass transport, increasing ohmic polarization, or attainment of limiting coverage by the particular rate-determining intermediate. Of the several nickel electrodes used in this study, there was one for which the nickel oxidation peak was small enough and sufficiently separated from oxygen evolution so that very small currents could be detected in the interjacent region. In this one case, a second linear section was found. This region, as is shown by the dashed line in Fig. 2, had a slope of 34 mV/dec. With repeated cycling, as the surface gradually changed, the voltamograms of this electrode became more like the other electrodes.

In the linear region, the differences in current at a given potential are not wholly accounted for by area changes, but are to a great extent dependent on sweep rate below 10 mV/sec. The dependence of current as a function of potential and sweep rate has been discussed by Srinivasan and Gileadi (3) for both reversible and irreversible first order processes where an insoluble product is formed. Their findings are applicable in the present case as the reaction step under consideration will be shown later to be pseudo-first order. According to their analysis, when current at a given potential is dependent on sweep rate, the rate-controlling process may be considered to have some kinetic reversibility. By the same token, at sweep rates above 10 mV/sec, the reaction is found to be irreversible since the current becomes dependent on potential alone. Under these conditions, the exchange current for the rds may be evaluated by extrapolation of the customary log plot to the equilibrium potential.

The same experimental procedure was repeated with platinum metal. Except for the first sweep which began at the initial open-circuit potential of −0.03V, the platinum electrode was never carried more negative than 0.4V. At low sweep rates, a shoulder often appeared at about 0.75V in both forward and reverse sweeps such as those shown in Fig. 3. This voltamogram was obtained at 0.2 mV/sec and constitutes the fourth cycle for that electrode. This shoulder might be considered an indication of further platinum oxide formation. At these potentials and at this point in treatment, however, the electrode should be fully covered with PtO_2. There is some evidence in the literature for even higher oxides of platinum (1),

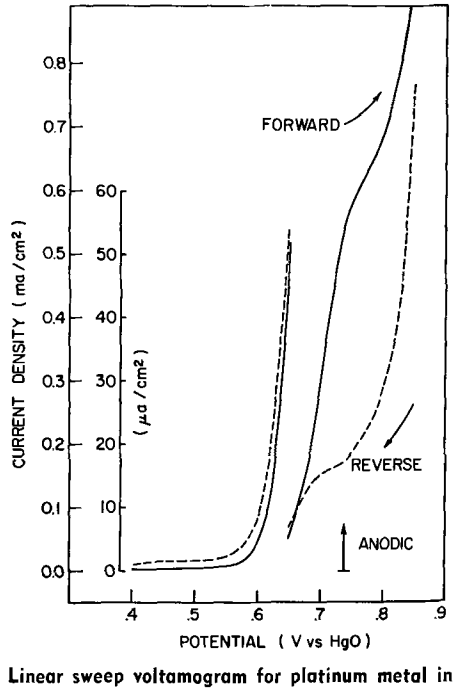

Fig. 3. Linear sweep voltamogram for platinum metal in 1M KOH taken at 0.2 mV/sec scan rate.

but these species are unstable with respect to oxygen evolution in aqueous systems. If platinum is indeed oxidized beyond PtO_2, such species might well be regarded as metastable intermediates in the process of oxygen evolution. In any case, it would be difficult to make even a conceptual distinction between higher oxide formation and oxygen evolution intermediates.

An even more pertinent argument against the oxide theory may lie in quantitative considerations. The quantity of charge represented by the shoulder, over and above an imaginary base line for oxygen evolution, is at least an order of magnitude greater than that expected for oxide formation. Such behavior can only be explained by continual removal of the reaction product as in the case of an intermediate in the oxygen evolution process.

In view of the foregoing, the shoulder is regarded as the attainment of its limiting rate by an oxygen evolution reaction step whose linear region immediately precedes the shoulder. This hypothesis is substantiated by the marked change, in contrast to nickel, in the current between forward and reverse sweeps. Growth of the electrode area, as estimated by changes in current from cycle to cycle under otherwise identical conditions, amounted to about 5% per cycle.

Typical voltamograms at several sweep rates are given on a semilogarithmic scale in Fig. 4. With the exception of the sweep at 100 mV/sec, the slope of the linear region is 48 ± 2 mV/dec, a value very close to that for nickel. The slope for the 100 mV/sec sweeps is 68 mV/dec, but a small peak due to oxidation of the substrate appears to overlap this region. The voltamograms shown are not corrected for the change in area but represent the 4th, 15th, 18th, and 19th cycles in order of increasing sweep rate. Again, the differences in the linear regions are not wholly accounted for by area change.

Several other metals also showed Tafel slopes of approximately 46 mV including cobalt, iron, and all three nickel alloys. In addition, at slow sweep rates, both of the nickel-platinum alloys exhibited at low currents a second Tafel region with a slope of 35 ± 2 mV/dec. This dual linear region is illustrated in Fig. 5 for NiPt at 0.2 mV/sec. Such behavior is in agreement with that observed in the earlier instance with nickel metal.

In accordance with the treatment of Damjanovic *et al.* (4), the existence of a dual linear log plot may be interpreted to indicate a change in the rate-determining step within a single reaction path. Dual linear regions have been reported by other investigators using galvanostatic techniques for platinum as well as other noble metals. In the case of platinum, the usually reported values of $d\eta/d \log i$ are about 60 mV/dec (5) or both 60 and 115 mV/dec (4). Values in the vicinity of 45 mV/dec such as those found in the present investigation have not been previously reported for platinum but were obtained for rhodium, iridium, and a Pt-Rh alloy by Damjanovic *et al.* (6). Similar values for nickel have been reported by Lukovtsev and Malandin (7), and by Sato and Okamoto (8) in sulfate electrolyte at high *p*H.

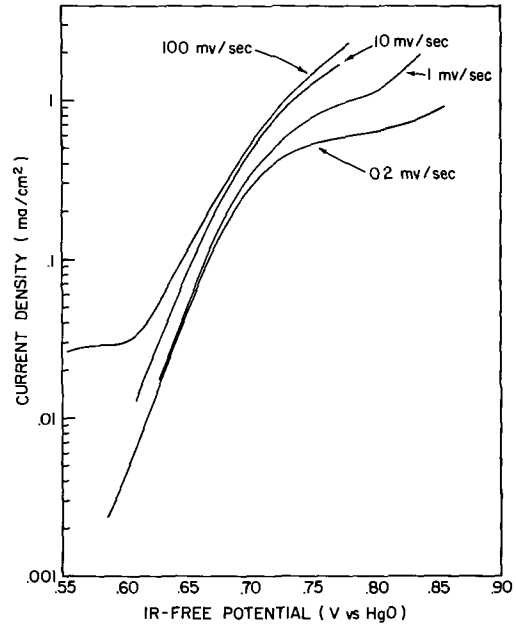

Fig. 4. Linear sweep voltamograms of platinum metal at various scan rates. Slope of the Tafel region for all but the 100 mV/sec curve is 48 ± + mV/dec.

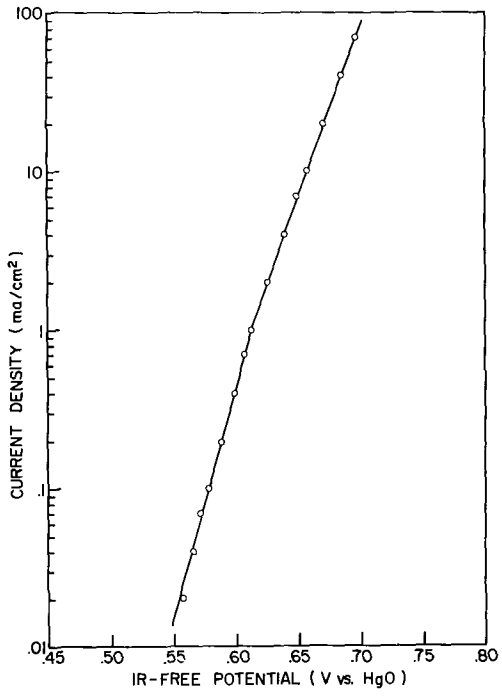

Fig. 5. Linear sweep voltamogram for NiPt alloy in 1M KOH taken at 0.2 mV/sec scan rate.

Current voltage curves obtained at constant current represent the steady state; consequently, the electrode surface has achieved the ultimate coverage of adsorbed intermediates. Linear sweep voltammetry, on the other hand, is essentially a relaxation technique, and it reflects the electrode behavior before the reaction intermediates have achieved their final distribution. The rate-determining steps under these circumstances are associated with the formation of a set of intermediates earlier in the reaction sequence than for the steady-state case. Thus, present and literature values of $d\eta/d \log i$ for platinum can be expected to be different. Had the sweep continued without encountering limiting conditions or at higher sweep rates (hence higher initial currents), a slope of 120 mV/dec would be expected. The difference between the sweeps at 10 and 100 mV/dec for platinum indicate the initial stages of the case where a different rds becomes effective.

Taking into account the value $2.3RT/\mathbf{F} = \rho$ for the present experimental conditions (58.7 mV), $d\eta/d \log i$ for the two linear log current regions may be expressed as $4\rho/7$ and $4\rho/5$ for the lower and upper overvoltage regions, respectively. The equation customarily used to predict Tafel slopes has been given by several authors (4, 5, 9) as

$$b_a = \frac{\nu}{n_p + (1 - \alpha) \cdot n_r} \cdot \rho \qquad [1]$$

where b_a is the anodic Tafel slope,
ν, the stoichiometric number,

α, the cathodic transfer coefficient,
n_p, the number of electrons transferred prior to the rds and,
n_r, the number of electrons transferred during the rds.

It can be shown that, if α is assigned the usual value of 0.5, it is impossible to obtain values of $4\rho/5$ or $4\rho/7$ using this expression. For example, if $\nu = 2$, then n_r must be an even number; therefore, the term $(1 - \alpha) \cdot n_r$ cannot be fractional. Thus the observed Tafel slope cannot be explained by Eq. [1].

McDonald and Conway (10), who obtained a value of $4\rho/5$ for gold electrodes in KOH electrolyte, have interpreted their findings on the basis of a twin barrier model. Here, the formation of an ohmic film alters the potential distribution at the electrode surface so that only a part (one-half) of the applied potential is effective in charge transfer. This theory cannot be applied to platinum since ohmic films are not known to form on this metal.

Gnanamuthu and Petrocelli (9) have recently proposed a similar theory which considers the effect of the potential gradient on reaction intermediates as a consequence of their position in the interfacial region. The potential between the metal and the bulk of the solution is considered to be divided into two regions at the inner Helmholtz plane where reside adsorbed reaction intermediates. In cases where these adsorbed intermediates are involved in charge transfer with either the electrode or the bulk alone, they are acted upon only by that portion of the potential associated with the respective region. As a first approximation it is assumed that the inner Helmholtz plane marks the halfway point in the potential gradient, hence the fraction of the total potential applicable to either region is one-half.

The following expression has been given for this theory

$$b_a = \frac{\nu}{\Sigma_i Z_i f_i + (1 - \alpha) Z_r f_r} \cdot \rho \qquad [2]$$

where Z_i is the number of charges transferred in a given step prior to rds,
f_i, the fraction of the total potential difference which is effective in the ith charge transfer.
Z_r and f_r, which refer to the rds, have meanings similar to their counterparts above.

Tafel slopes calculated using this equation will be referred to as "corrected" values.

Consider the generalized electrode process (M = metal electrode)

$$1.\ M + A^- \rightarrow MA + e^-$$

$$2.\ MA + A^- \rightarrow MB^-$$

in which an electrochemical adsorption step is followed by a chemical reaction to form an adsorbed ion. If step 1 were the rds, the predicted Tafel slope using Eq. [2] would be 2ρ, the same as that obtained with the conventional Eq. [1]. Step 2, on the other hand, involves charge transfer only between species in the solution and the adsorbed state; hence a part, and only a part of the applied potential is effective in this exchange. Applying Eq. [2] to this step with $\nu = 1$, $Z_1 = 1$, $f_1 = 1.0$, $Z_r = 1$, $f_r = 0.5$, we find a corrected Tafel slope of $4\rho/5$, whereas the conventional method gives ρ.

While there is no direct evidence to support the assumption that $f_r = 0.5$, it would appear that the experimentally observed Tafel slope, $4\rho/5$, is adequately predicted by an electrode process of the above form in conjunction with the theory of Gnanamuthu and Petrocelli. Several mechanisms have appeared in the literature which conform to the generalized scheme given above. Three of these suggested reaction paths are listed in Table I along with the expected Tafel slope for each step rate-determining as calculated both by Eq. [1] and [2].

Table I. Previously suggested reaction paths for oxygen evolution

		Tafel slope	
		Corrected	Conventional
I.	"Alkaline" path of Hoar (9)		
	$M + OH^- \rightarrow MOH + e^-$	2ρ	2ρ
	$MOH + OH^- \rightarrow MH_2O_2^-$	$4\rho/5$	ρ
	$2MH_2O_2^- \rightarrow M + MO_2^{=} + 2H_2O$	$\rho/3$	$\rho/2$
	$MO_2^{=} \rightarrow M + O_2 + 2e^-$	$2\rho/7$	$\rho/3$
II.	Krasil'shchikov path (11)		
	$M + OH^- \rightarrow MOH + e^-$	2ρ	2ρ
	$MOH + OH^- \rightarrow MO^- + H_2O$	$4\rho/5$	ρ
	$MO^- \rightarrow MO + e^-$	$2\rho/7$	$2\rho/3$
	$2MO \rightarrow O_2 + 2M$	$\rho/4$	$\rho/4$
III.	Damjanovic, Dey, and Bockris path (4)		
	$M + OH^- \rightarrow MOH + e^-$	2ρ	2ρ
	$MOH + OH^- \rightarrow MO\text{-}H\text{-}OH^-$	$4\rho/5$	ρ
	$MO\text{-}H\text{-}OH^- \rightarrow MO\text{-}H\text{-}OH + e^-$	$4\rho/7$	$2\rho/3$
	$MO\text{-}H\text{-}OH \rightarrow MO + H_2O$	$\rho/2$	$\rho/2$
	$MO + OH^- \rightarrow MO_2H + e^-$	$2\rho/5$	$2\rho/5$
	$MO_2H + OH^- \rightarrow M + O_2 + H_2O + e^-$	$2\rho/7$	$2\rho/7$
	or,		
	$2MO \rightarrow O_2 + 2M$	$\rho/4$	$\rho/4$

These various mechanisms may be further differentiated by considering the rate-determining step next in order, that is the one likely to prevail at lower current densities. Experimentally, at least for nickel metal and its platinum alloys, this step was found to have a Tafel slope of $4\rho/7$. Of the mechanisms given, a slope of this value occurs in only one, path III, which has been proposed by Damjanovic *et al.* (4). Two alternative routes have been given involving the adsorbed atomic oxygen species, MO. The first represents the electrochemical discharge of MO, and the second, atomic recombination to give O_2. Verification of this mechanism cannot be carried past the third step without further experimental information.

In view of Rozental's and Veselovskii's results with O^{18} tracers (12), the involvement of the MO species in this reaction may not be likely. These investigators, using platinum which had been preanodized in acid solution at potentials cathodic to oxygen evolution, found that the layer of adsorbed oxygen did not participate in the gassing reaction. Oxygen adsorbed at these potentials is known to have the stoichiometry PtO (1), and if it is not in fact identical to the species MO, then the two should be equivalent through an exchange process. Since none of this oxygen is found in the product gas, it is doubtful that MO is a reaction intermediate.

A reaction sequence which does not incorporate the species MO, yet whose Tafel slopes predicted with Eq. [2] conform to experimental observations is given as follows:

		Corrected Tafel slope
1. $M + OH^-$	$\rightarrow MOH + e^-$	2ρ
2. $MOH + OH^-$	$\rightarrow MO_2H_2^-$	$4\rho/5$
3. $MO_2H_2^-$	$\rightarrow MO_2H_2 + e^-$	$4\rho/7$
4. $MO_2H_2 + OH^-$	$\rightarrow MO_2H^- + H_2O$	$4\rho/9$
5. MO_2H^-	$\rightarrow MO_2H + e^-$	$4\rho/11$
6. $MO_2H + OH^-$	$\rightarrow M + O_2 + H_2O + e^-$	$2\rho/7$

This mechanism differs from those proposed by most other investigators in that the oxygen-oxygen bond is formed very early in the reaction sequence, no later than step 3. Although step 2 is shown as the formation of an adsorbed hydrogen peroxide radical ion, a species such as that proposed by Damjanovic *et al.* (4), MO-H-OH$^-$, is not ruled out. In this case the species then rearranges to give an adsorbed hydrogen peroxide molecule upon extraction of an electron in step 3.

Because of the relatively high concentration of electrolyte in these experiments, step 2 acts as a pseudo-first order process. The slight dependence on stirring can be expected, however, due to the involvement of the soluble OH^-. The remaining steps

which consist of the consecutive removal of hydrogen atoms from this species are purely speculative. Steps 4 and 5 which differentiate the processes of hydrogen removal and charge transfer might very reasonably be combined to give a single step whose Tafel slope would then be $2\rho/5$.

According to this mechanism, that oxygen which is destined to be evolved as gas remains completely unique from the oxide film oxygen; that is, it is quickly bound to another oxygen atom which serves to distinguish it from the oxide type. Hence the substrate M in this discussion may be interpreted to include both bare and oxide covered metal. Furthermore, the formation of adsorbed hydrogen peroxide itself, as opposed to peroxide free radical or other related species less stable in solution, seems reasonable since hydrogen peroxide is found (13) on reduction of oxygen. If it is true that the forward and reverse reaction paths are identical, formation of H_2O_2 would precede the slow step in the cathodic direction. Hence its presence in solution would be expected.

Approximately the same value of the Tafel slope has now been obtained for a number of metals in alkaline electrolyte: for gold by MacDonald and Conway (10), for rhodium and iridium by Damjanovic *et al.* (6), and for nickel, platinum, cobalt, and iron in the present work. Therefore, it is suggested that the rds, and probably the mechanism, is identical for all these metals.

It might be postulated that differences in over-all behavior of various metals, as well as slow variation of single electrodes over their lifetime, can be attributed to the presence of impurities. In the absence of impurities, however, such behavior may be due to the influence of the state of the surface, as determined by the history of the electrode, on the relative rates of specific steps.

The results of Damjanovic *et al* (6) who obtained a value of 40 mV/dec for the Tafel slope on both iridium and a Pt-Rh alloy, may therefore be interpreted in terms of the presently given mechanism. If the state of the electrode surface in their experiments were such that the rates of steps 2 and 3 were nearly equivalent, then a mixed rate-determining process would result. Application of Eq. [2] to the combined steps gives an expected Tafel slope of 40 mV/dec in agreement with the results obtained. In a similar fashion, the Tafel slope of 60 mV/dec found for platinum by several workers (4, 5) may be attributed to a combination of steps 1 and 2.

Referring to the totally irreversible current-voltage curves at 100 mV/sec for nickel and platinum in Fig. 6, it may be seen that the rate of step 2 on platinum is considerably below that for nickel. As a result, rate-determining step 3 is not observed on platinum. The experimentally determined apparent exchange current for step 2, evaluated at the standard potential for the over-all process, is given in Table II for these and other metals.

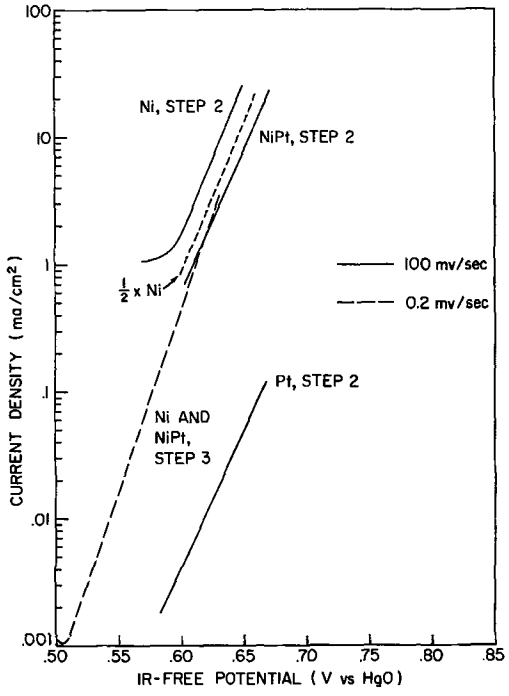

Fig. 6. Comparison of current voltage curves obtained by LSV for various reaction steps for nickel, platinum, and NiPt.

Step 2 may be expected to be faster on nickel than on platinum because the bonding energy of hydroxide ion is much greater on nickel metal. This is known to be true because nickel forms lower valent hydroxides at quite cathodic potentials. Cobalt, another metal which easily forms surface hydroxides, also has a moderately high exchange current for step 2.

Since step 2 is faster on nickel than on platinum, it is to be expected, for alloys of the two metals, that the rate for step 2 might be diminished in proportion to the platinum content. Indeed, this is found to be the case by comparing the position of the current-voltage curve for NiPt in Fig. 6 with the plot for pure nickel diminished by a factor of one-half. The two curves agree within experimental error. Correspondingly, if the rate for step 3 is likewise significantly different on the two metals, the alloy curve for step 3 will be shifted from that of pure metal. Experimentally, no such shift was found since, as shown in Fig. 6, the current voltage plots for the two metals are exactly colinear. Therefore, although the current-voltage curve for rate-determining step 3 on platinum could not be obtained experimentally, it may be inferred that it is kinetically identical with that for nickel.

Table II. Kinetic parameters for oxygen evolution on several metals in alkaline solution

Metal	Step 1 i_o*	Step 1 b_a†	Step 1 & 2 i_o*	Step 1 & 2 b_a†	Step 2 i_o*	Step 2 b_a†	Step 2 & 3 i_o*	Step 2 & 3 b_a†	Step 3 i_o*	Step 3 b_a†	Reference
Ni					2×10^{-10}	45			1×10^{-12}	34	
					4×10^{-10}**	40-50					(7)
					5×10^{-12}	48					(8)
Ni_3Pt					6×10^{-11}	45			4×10^{-13}	34	
Pt					4×10^{-12}	47					
	1×10^{-9}	115	3×10^{-12}	60							(4)
Co					8×10^{-11}	47					
Rh	1×10^{-6}	115					6×10^{-12}	42			(6)
Ir	1×10^{-6}	120					1×10^{-11}	40			(6)
Pt-Rh	1×10^{-6}	120					1×10^{-12}	40			(6)
Pd	1×10^{-10}	113									(10)
Au					4×10^{-24}	45					(10)
NiPt					2×10^{-10}	46			8×10^{-12}	34	
NiFe					1×10^{-9}	48					
Fe					2×10^{-12}	48					

† Anodic Tafel slope, mV/decade.
* Apparent exchange current evaluated at E_o for O_2, A/cm².
** Evaluated by present investigator from data given.

Summary

It has been shown that linear sweep voltammetry at slow scan rates is a useful tool for studying kinetically complex electrochemical processes. Similar Tafel slopes have been found for several metals indicating that the same rate-determining step is involved. An additional rate-determining step which is effective at lower current levels has been observed for nickel and nickel-platinum alloys.

A mechanism based on these findings has been proposed which suggests that following the electrochemical adsorption of hydroxide ion, the formation of adsorbed hydrogen peroxide radical ion, $MO_2H_2^-$, occurs. This species is then discharged and successively dehydrogenated to give the product oxygen. The formation of $MO_2H_2^-$ is faster on nickel than on platinum, but the discharge of this species to an adsorbed hydrogen peroxide molecule seems to occur at the same rate on the two metals.

Acknowledgment

The author gratefully acknowledges the assistance in the laboratory of Mr. Peter Briedis, and the technical discussions of Prof. Ernest B. Yeager and his group at Case Western Reserve University.

Manuscript submitted March 6, 1969; revised manuscript received *ca.* June 30, 1969.

Any discussion of this paper will appear in a Discussion Section to be published in the June 1970 JOURNAL.

REFERENCES

1. J. P. Hoare, in "Advances in Electrochemistry and Electrochemical Engineering," Vol. 6, p. 207, P. Delahay, Editor, Interscience Publishers, New York (1967).
2. Max Hansen, "Constitution of Binary Alloys," McGraw-Hill Publishing Co., New York, 1958.
3. S. Srinivasan and E. Gileadi, *Electrochim. Acta*, **11**, 321 (1966).
4. A. Damjanovic, A. Dey, and J. O'M. Bockris, *ibid.*, **11**, 791 (1966).
5. T. P. Hoar, *Proc. CITCE*, **8**, 439 (1958).
6. A. Damjanovic, A. Dey, and J. O'M. Bockris, *This Journal*, **113**, 739 (1966).
7. P. D. Lukovtsev and O. G. Malandin, Proc. of 6th Intl. Power Source Symposium, Brighton, 1968 (in press).
8. N. Sato and G. Okamoto, *Electrochim. Acta*, **10**, 495 (1965).
9. D. S. Gnanamuthu and J. V. Petrocelli, *This Journal*, **114**, 1036 (1967).
10. J. J. MacDonald and B. E. Conway, *Proc. Roy. Soc. (London) Ser. A*, **269**, 419 (1962).
11. A. I. Krasil'shchikov, *Zhur. Fiz. Khim.*, **37**, 531 (1963).
12. K. I. Rozental' and V. F. Veselovskii, *Doklady Akad. Nauk, SSSR*, **111**, 637 (1956).
13. W. G. Berl, *Trans. Electrochem. Soc.*, **84**, 253 (1943).

Technical Notes

Electrocapillary Measurements at the Interface Insulator-Electrolytic Solution

H. Dahms[1]

IBM Thomas J. Watson Research Center, Yorktown Heights, New York

Our present knowledge of the electrical double layer is almost exclusively based on investigations of the conductor-solution interface, with the bulk of the information being derived from studies of mercury-solution systems (1). There are no equivalent investigations of the insulator-solution interface, due mainly to the lack of experimental methods.

Here, an apparatus for obtaining electrocapillary data at an insulator surface is described. Results for the systems polyethylene/0.1M KCl + n-butanol and polyethylene/0.1M NaI are reported.

Figure 1 shows a schematic diagram of the apparatus. A tube of the insulator material, A, containing the solution to be investigated is inserted into vessel B. Vessel B is filled with an electrolytic solution. A d-c voltage is applied across the insulator by means of electrodes C and D. The difference, h, of the liquid levels in the tubing and the communicating vessel, E, is recorded with a cathetometer. The surface tension, γ, is then derived from the capillary depression, h. At contact angles approaching 0° or 180° the surface tension is given by the well-known equation

$$\gamma = \frac{r \cdot h \cdot \Delta\rho \cdot g}{2} \qquad [1]$$

where γ is the surface tension in dynes cm^{-1}, r the radius of capillary in cm, h the capillary depression (or rise) in cm, $\Delta\rho$ the difference in density between liquid and gas phase in g cm^{-3}, g the acceleration due to gravity (980 cm sec^{-2}). It should be noted that for

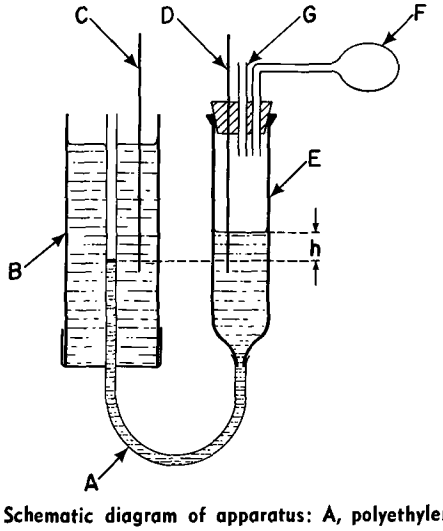

Fig. 1. Schematic diagram of apparatus: A, polyethylene tubing; B, E, glass tubing; C, D, silver wire; F, rubber bulb; G, outlet.

[1] Present address: 22 Lakeview Road, Ossining, New York 10562.

small values of capillary depression correction terms have to be applied to Eq. [1] (2).

The surface tension is related to parameters of the electrical double layer by Gibb's equation (3) which can be written for our purposes as

$$d\gamma = q\,dE - \Gamma_{Cl^-}\,d\mu_{KCl} - \Gamma_A\,d\mu_A \qquad [2]$$

where γ is surface tension, q the total charge of the interface, Γ_{Cl^-} the surface excess of Cl^- ions, μ_{KCl} the chemical potential of KCl in the solution, Γ_A the surface excess of neutral species, and μ_A the chemical potential of neutral species in the solution.

Charge and surface excesses are derived on the basis of Gibb's equation

$$q = \left(\frac{d\gamma}{dE}\right)_{\mu_{KCl},\,\mu_A} \qquad [3]$$

$$\Gamma_{Cl^-} = \left(\frac{d\gamma}{d\mu_{KCl}}\right)_{E,\,\mu_A} \qquad [4]$$

$$\Gamma_A = \left(\frac{d\gamma}{d\mu_A}\right)_{E,\,\mu_{KCl}} \qquad [5]$$

Experimental

A polyethylene tubing of 0.039 in. ID and 0.059 in. OD was used (Medical Grade Polyethylene Tubing PX 039, Becton, Dickinson and Company, Rutherford, New Jersey). Teflon tubing was also used in some experiments, giving less reproducible results probably because the diameter appeared to vary slightly along the tubing, while that of the polyethylene tubing seemed to be more constant. The ID of both glass vessels B and E was 0.75 in. Tubing A was inserted into vessel B through a rubber serum cap. It should be noted that the solution to be investigated is contacting only glass surfaces. Electrodes C and D were silver wires. F is a small rubber bulb which is briefly compressed to vary the liquid level in order to prevent sticking of the meniscus, as recommended for capillary measurements (4). Tubing G is open to the atmosphere. The meniscus height was measured with a cathetometer with an accuracy of ± 0.01 mm. At voltages higher than 600V the meniscus had a tendency to "stick," *i.e.*, to remain at a constant level regardless of the voltage applied.

Results and Discussion

Figure 2 shows the experimental data for the system polyethylene/0.1M KCl + xM n-butanol; $x = 0, 3\cdot10^{-3}, 10^{-2}, 3\cdot10^{-2}, 10^{-1}$. The adsorption isotherms for n-butanol resulting from the data are shown in Fig. 3. The potential dependence of adsorption is shown in Fig. 4. The maximal adsorption for n-butanol can be calculated from molecular models (5). The values are $4.6\cdot10^{-10}$ moles/cm² for a planar position and 7.9 for a perpendicular position. On mercury the maximum butanol adsorption is at least $6.5\cdot10^{-10}$ moles/cm², indicating a perpendicular orientation (5). The fact that the experimental data on polyethylene point to a saturation value in the range of $4\text{-}5\cdot10^{-10}$ mole/cm² is noteworthy. However, definite conclusions can be drawn only after investigations of a homologous series of alcohols or other hydrocarbons. If the polyethylene surface had a considerable roughness factor the actual coverage would be even lower.

Another interesting problem which can be approached by the present technique is the controversy over the causes of "specific adsorption" on metal surfaces (1). Graham and co-workers (6, 7) suggested that this involves a certain covalent bond between the adsorbed ion and the metal surface. More recently, however, it has been proposed that electrical image energy (8), or the degree of solvation (9), are the main factors. Figure 5 shows an electrocapillary curve

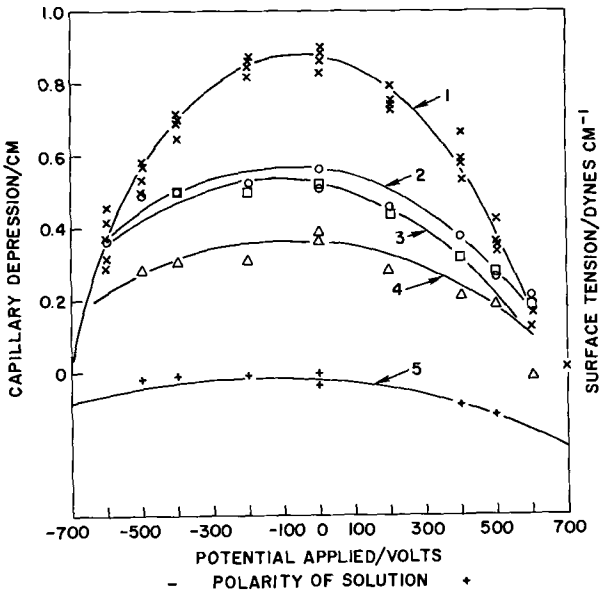

Fig. 2. Electrocapillary curves in polyethylene tubing of aqueous solutions containing 0.1M KCl and xM n-butanol. Curve 1, $x = 0$; curve 2, $x = 3\cdot10^{-3}$; curve 3, $x = 10^{-2}$; curve 4, $x = 3\cdot10^{-2}$; curve 5, $x = 10^{-1}$.

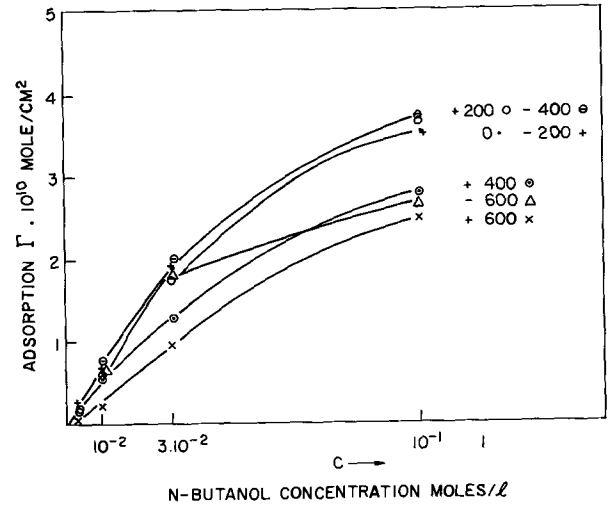

Fig. 3. Adsorption isotherms of the system polyethylene/0.1M KCl + n-butanol. Numbers in plot indicate voltage applied. For example, + 200 is 200V applied with polarity of solution being positive.

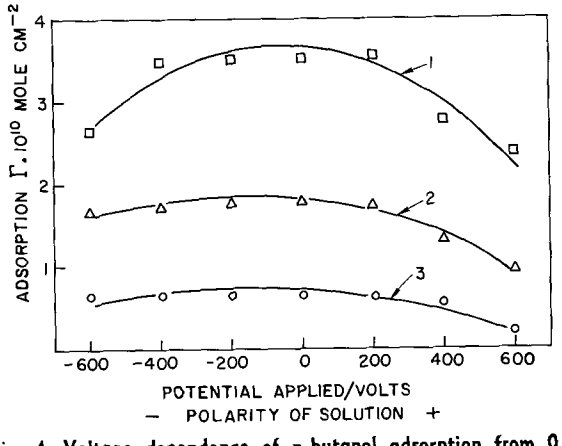

Fig. 4. Voltage dependence of n-butanol adsorption from 0.1M KCl solution. Curve 1, 10^{-1} M n-butanol; curve 2, $3\cdot10^{-2}$ M n-butanol; curve 3, 10^{-2} M n-butanol.

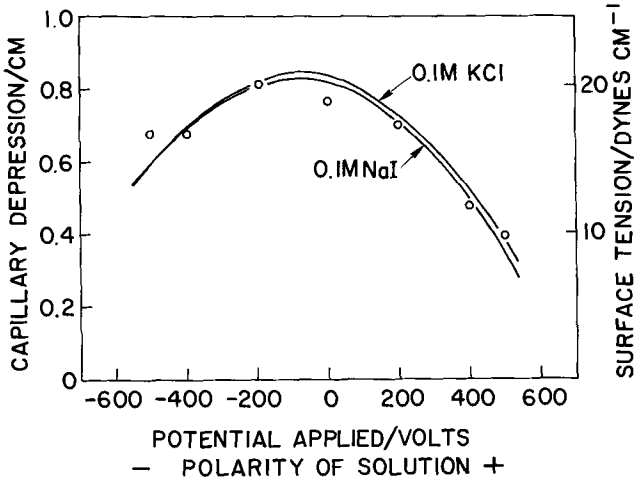

Fig. 5. Electrocapillary curves of polyethylene 10.1M NaI and polyethylene 10.1M KCl.

taken at the interface polyethylene/0.1M NaI. For comparison, the electrocapillary curve in 0.1M KCl is also plotted. Although there is admittedly a considerable scatter of the data, it can be seen that the curves coincide rather well. Similar electrocapillary curves on mercury (10, 11) show a strong decrease of surface tension in the case of iodide when the iodide ions are attracted to the surface, *i.e.*, on the left side of our plot (polarity of solution negative). It should be noted that such a rapid decrease cannot be seen in Fig. 5. This preliminary result seems to indicate that the main cause of strong specific adsorption, such as found in the case of iodide on mercury (10, 11), is due to covalent metal-ion bonding since the specific adsorption is absent at the polyethylene surface. However, more systematic measurements are needed.

Data obtained with the present method do not presently have the same high precision achieved in mercury-solution studies which have been refined for nearly a century. Many experimental aspects such as the application of adjustable hydrostatic pressure to keep the position of the solution meniscus in the capillary constant, can be directly applied to the present apparatus.

Acknowledgments

This investigation was sparked by the idea of J. N. Cole who suggested to move droplets on an insulating surface by applying an electrostatic field. Z. Kovac gave experimental advice.

Manuscript received June 9, 1969.

Any discussion of this paper will appear in a Discussion Section to be published in the June 1970 JOURNAL.

REFERENCES

1. For a recent review see D. M. Mohilner, "The Electrical Double Layer," A. J. Bard, Editor, Electroanalytical Chemistry, Vol. I, Marcel Dekker, New York (1966).
2. A. W. Adamson, "Physical Chemistry of Surfaces," Interscience Publishers, New York (1960).
3. J. W. Gibbs, "Collected Works of J. W. Gibbs," Vol. I, p. 336, Longmans, Green & Co., New York (1928).
4. M. A. V. Devanathan, Thesis, London, 1951.
5. J. O'M. Bockris, E. Blomgren, and C. Jesch, *J. Phys. Chem.*, **65**, 2000 (1961).
6. D. C. Grahame, *Chem. Rev.*, **41**, 441 (1947).
7. D. C. Grahame, M. A. Poth, and J. I. Cummings, *J. Am. Chem. Soc.*, **74**, 4422 (1952).
8. S. Levine, G. M. Bell, and D. Calvert, *Can. J. Chem.*, **40**, 518 (1962).
9. T. N. Anderson and J. O'M. Bockris, *Electrochim. Acta*, **9**, 347 (1964).
10. M. Gouy, *Ann. Chim. phys*, **29**, 145 (1903); **8**, 291 (1906); **9**, 75 (1906).
11. S. Jofa, B. Kabanow, E. Kuchinsky, and F. Chistyakow, *Acta physiochim. USSR*, **10**, 317 (1939).

Electroosmotic Transport in Mixed Solvents, the γ-Butyrolactone-Water System

P. Bro* and A. N. Dey*

P. R. Mallory & Company, Inc., Laboratory for Physical Science, Burlington, Massachusetts

Investigations have shown that the trace amounts of water contained in organic electrolyte solutions are bound to the cation, *e.g.*, the lithium ion (1), and that the transference number of the lithium ion through suitable cation exchange membranes is close to unity (2). These observations suggested that the residual water would be transferred selectively during electroosmosis, and experiments confirmed our conjecture (3). A description of the electroosmotic process is given here, and we present a set of equations for electroosmotic transfer in mixed solvents.

Experimental Techniques

The cell used for the electroosmotic measurements was similar to the one described earlier (3), except that each electrode compartment was provided with calibrated capillaries for the measurement of the volume changes. No corrections were introduced for the volume changes associated with the electrode reactions. They were estimated to be less than 10% of the reported values, but there is a basic uncertainty in this value because of the unknown partial molar volume of lithium chloride in butyrolactone-water solutions. All the experiments were performed with a cation exchange membrane (AMF No. C-60) in the lithium form. The voltage drops between the electrodes at 3% water level were 0.25V at 0.05 mA/cm^2 and 2.70V at 0.50 mA/cm^2.

The γ-butyrolactone (BL, Eastman Organic Chemicals) was purified by vacuum distillation at 61°-65°C and 1.0 mm Hg in a 90 cm long vacuum jacketed column using a reflux ratio of 2 to 1. The 2.5 cm ID column was packed with 0.4 cm Berl saddles. The water concentration in the purified solvent was less than 10^{-3}M as determined by gas chromatographic analysis (Perkin-Elmer chromatograph, Model 801). The 6-ft long stainless steel column had a diameter of ⅛ in. and it was packed with 50-80 mesh Porapack Type Q. We used a hot wire detector with automatic integration of

* Electrochemical Society Active Member.

the output. Calibrations with known BL/H_2O mixtures indicated an accuracy of ± 2% for the analyses.

In order to determine the H_2O/BL ratio in the membranes, they were equilibrated with known volumes of 0.10M LiCl solutions in specified mixtures of water and butyrolactone. The membranes were weighed, after superficial drying, before and after equilibration and the solution compositions were determined gas chromatographically. The membranes were finally vacuum dried at 60°C to remove water and butyrolactone and were weighed again. The amounts of water and butyrolactone sorbed by the membranes were calculated by making a material balance over the system.

Experimental Results

The passage of current through the cell resulted in the enrichment of water in the catholyte, Table I. The associated volume changes given in Table II showed that the catholyte volume increased as well. Although the specific solution transport decreased with an increase in the concentration of water, Fig. 1, the specific water transport increased. At water concentrations above 5% (vol.) the water transport became nearly constant. The composition of the membrane solutions was calculated from the data in Tables III and IV and the results are shown in Fig. 2. A molar enrichment factor of about ten was obtained for the enrichment of water in the membrane.

Discussion

The enrichment of water in the cathodic exudate may be examined from an equilibrium and a transport point of view.

Table I. Electroosmotic concentration changes*

Water concentration, vol % (v/o) Initial	Final Anolyte	Final Catholyte	Charge Coulombs
1.015	0.98	1.05	16.2
0.93	0.66	1.20	32.4
0.98	0.70	1.26	52.0
3.85	3.60	4.10	18.7
3.85	3.40	4.30	39.7
3.30	2.80	3.80	48.5
4.62	4.39	4.84	18.3
4.60	3.80	5.40	58.5
7.30	7.10	7.50	7.2
7.45	7.00	7.90	25.2
7.15	6.70	7.60	40.6
10.05	9.80	10.29	6.1
10.35	10.10	10.60	17.2
9.80	9.49	10.10	24.4
10.05	8.70	10.40	43.5

* 0.05 mA/cm² series at 25° ± 1°C in 0.10M LiCl solutions. 3.00 cm³ solution in each cell compartment.

Table II. Electroosmotic volume changes*

Solution v/o H_2O	Charge coulombs	Volume change, cm³ Anolyte (decrease)	Catholyte (increase)
0	0	—	0
0	1.89	—	0.007
0	5.06	—	0.019
0	5.80	—	0.020
0	6.66	—	0.023
0	7.80	—	0.026
0	9.10	—	0.030
1.00	0	0	0
1.00	0.778	0.0025	0.0020
1.00	1.47	0.0041	0.0040
1.00	1.77	0.0050	0.0048
1.00	2.39	0.0065	0.0062
1.00	5.00	0.0132	0.0136
1.00	6.18	0.0165	0.0170
1.00	7.63	0.0205	0.0215
5.00	0	0	0
5.00	2.57	0.0025	0.0023
5.00	3.78	0.0040	0.0038
5.00	5.52	0.0060	0.0060
5.00	6.96	0.0075	0.0070
10.0	0	0	0
10.0	1.8	0.0010	0.0015
10.0	3.6	0.0025	0.0020
10.0	7.2	0.0050	0.0040

* 0.05 mA/cm² series at 25° ± 0.1°C in 0.10M LiCl solutions.

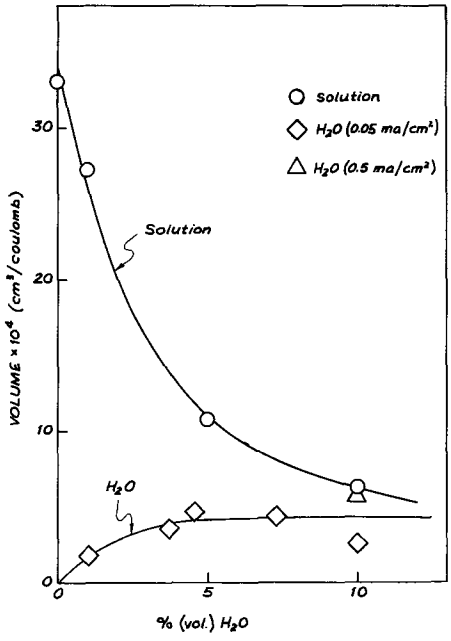

Fig. 1. Electroosmotic water and solution transport in 0.10M LiCl, BL, H_2O solutions.

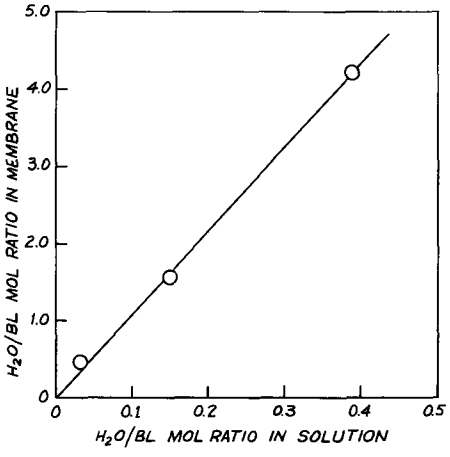

Fig. 2. Equilibrium composition of the solution retained by the membrane.

The equilibrium state of the system corresponded to the preferential sorption of water by the membrane, Fig. 3, and an attempt was made to describe the equilibrium in terms of the osmotic pressure formalism (4).

Table III. Specific gravity of 0.10M LiCl butyrolactone solutions*

Water concentration, v/o	Specific gravity
0	1.125
1.00	1.126
5.00	1.122
10.0	1.118
20.0	1.109
40.0	1.089
60.0	1.064
80.0	1.035

* At 25° ± 0.1°C.

Table IV. Membrane equilibrium data in 0.10M LiCl solutions*

Initial water concentration, v/o	0.95	5.25	9.50
Volume of solution, cm³	10.0	15.0	10.0
Weight of BL soaked membrane, g	0.8024	3.4329	0.8397
Final water concentration, v/o	0.79	3.40	8.40
Weight of equilibrated membrane, g	0.8121	3.3628	0.8990
Weight of dry membrane, g	0.6300	2.2370	0.6530

* At 25° ± 1°C.

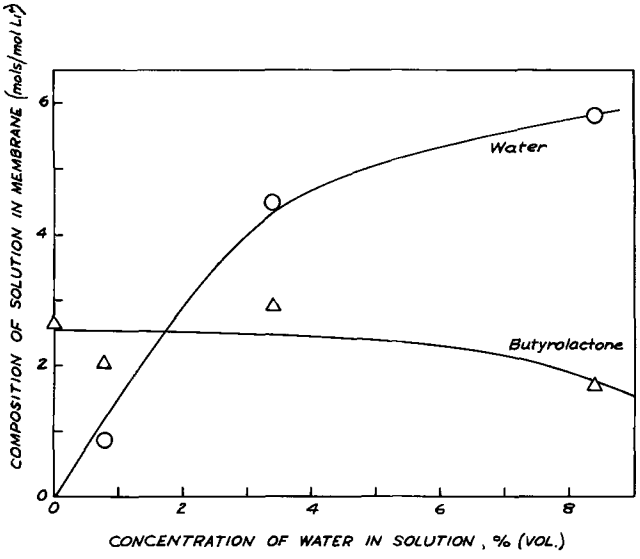

Fig. 3. Membrane/solution equilibrium

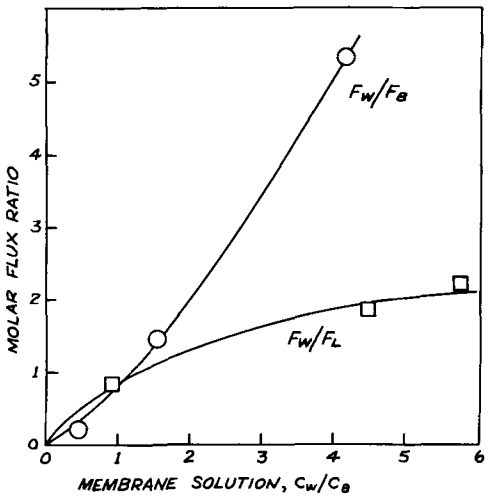

Fig. 4. Electroosmotic flux ratios

However, the calculated osmotic pressures were far in excess of the values reported for ion exchange membranes (4), and this approach was rejected.

An analysis in terms of a Langmuir sorption process gave a more credible result. The Langmuir isotherm is based on localized sorption with a constant binding energy and no interactions between the sorbed species (5). The experimental data agreed with the Langmuir model and gave a binding energy of 0.5 kcal/mole (1 mole/liter was used as a reference state for water) and a saturation value of 33 moles/liter for the water in the membrane. The absence of any noticeable swelling of the membrane suggested the reasonableness of the low binding energy. However, we do not attach any significance to the precise values reported because of the paucity of our data.

In regard to the transfer process we note that the rates of transfer were independent of the current density (3) which indicated that the membrane maintained its equilibrium composition during the process.

No mathematical description is available in the literature of the preferential electroosmotic transfer of a solvent component in a mixed solvent system, and we developed a set of equations for this process based on the friction coefficient formalism. Our equations represent an extension of Spiegler's treatment (6), and they reduce to his equations as a limiting case.

A force balance over a unit volume of the membrane leads to the basic equations

$$C_L G_L = C_A K_{LA}(u_L - u_A) + C_W K_{LW}(u_L - u_W) + C_B K_{LB}(u_L - u_B) + C_L K_{LM} u_L \quad [1]$$

$$C_A G_A = C_L K_{AL}(u_A - u_L) + C_W K_{AW}(u_A - u_W) + C_B K_{AB}(u_A - u_B) + C_A K_{AM} u_A \quad [2]$$

$$C_W G_W = C_L K_{WL}(u_W - u_L) + C_A K_{WA}(u_W - u_A) + C_B K_{WB}(u_W - u_B) + C_W K_{WM} u_W \quad [3]$$

$$C_B G_B = C_L K_{BL}(u_B - u_L) + C_A K_{BA}(u_B - u_A) + C_W K_{BW}(u_B - u_W) + C_B K_{BM} u_B \quad [4]$$

from which we obtain

$$\frac{F_W}{F_B} = \frac{C_W}{C_B} \frac{C_L K_{WL} K_{BL} + C_W K_{WL} K_{BW} + C_B K_{BL} K_{WB} + C_B K_{WL} K_{BM}}{C_L K_{WL} K_{BL} + C_W K_{WL} K_{BW} + C_B K_{BL} K_{WB} + C_W K_{BL} K_{WM}} \quad [5]$$

for the molar electroosmotic flux ratios.

- G_i = generalized force on one mole of i
- F_i = molar flux of i = $u_i C_i = \Sigma L_{ij} G_j$ (this defines L_{ij})
- C_i = molar concentration of i in the membrane solution
- K_{ij} = frictional force on i due to one mole of j in a unit velocity gradient of i and j
- W, B, L, A, M designate water, butyrolactone, lithium ions, chloride ions, and membrane, respectively.

The experimental flux ratios have been plotted in Fig. 4 and it may be seen that the flux ratio F_W/F_B was approximately equal to the concentration ratio C_W/C_B, which with Eq. [5] leads to

$$C_W K_{WM}/K_{WL} = C_B K_{BM}/K_{BL} \quad [7]$$

This equality would hold identically if $K_{WM} = 0$ and $K_{BM} = 0$, *i.e.*, if the frictional interactions between the solvent components and the membrane matrix vanish. Such an hypothesis is not unreasonable since the interaction energy for water sorption was found to be small and the membrane did not swell in any of the solutions.

If the frictional interactions between water and butyrolactone are negligible, *i.e.*, $K_{WB} = 0$, we find from [6] that

$$\frac{F_W}{F_L} = \frac{C_W}{C_L} \frac{1}{1 + \frac{C_W}{C_L}\frac{K_{WM}}{K_{WL}}} \quad [8]$$

and the flux ratio of water and lithium should be increasingly less than their concentration ratio as the water concentration increases. The experimental results did exhibit this behavior, Fig. 4, and we find that $K_{WM}/K_{WL} = 0.3$ under the stated assumption. This result in conjunction with [7] shows that K_{BM}/K_{BL} increased from 0 to 1.2 as the water/butyrolactone concentration ratio increased from 0 to 4. Since there are no reasons for believing that the interactions between the butyrolactone and the membrane should change with the water concentration, the increase of K_{BM}/K_{BL} is probably due to a decrease of K_{BL} with an increase in the water concentration, *i.e.*, the friction between the butyrolactone and the lithium ions decreases as the water concentration increases. Since the lithium ions and the water interact strongly, this means

$$\frac{F_W}{F_L} = \frac{C_W K_{WL}(C_L K_{BL} + C_W K_{BW} + C_B K_{BM}) + C_W C_B K_{BL} K_{WB}}{(C_L K_{BL} + C_W K_{BW} + C_B K_{BM})(C_L K_{WL} + C_W K_{WM} + C_B K_{WB}) - C_W C_B K_{WB} K_{BW}} \quad [6]$$

that as the water concentration increases and the lithium ions become increasingly shielded by the water, the interactions between the lithium ions and butyrolactone should decrease, *i.e.*, K_{BL} should decrease, as would be expected if $K_{WB} = 0$, and the electroosmotic equations appear to provide a consistent description of this effect.

Conclusions

The electroosmotic transfer of water-butyrolactone-lithium chloride solutions in a cation exchange membrane led to an appreciable enrichment of water in the cathodic exudate. Equilibrium studies showed that the water was sorbed preferentially by the membrane, and a molar enrichment factor of about ten was obtained for the transfer of the water.

The electroosmotic transfer was analyzed in terms of a new set of equations derived for mixed solvent systems, and the equations indicated that the electroosmotic process was dominated by the water-lithium ion interactions.

Manuscript submitted March 26, 1969; revised manuscript received July 2, 1969. This was Paper 166 presented at the New York Meeting, May 4-9, 1969.

Any discussion of this paper will appear in a Discussion Section to be published in the June 1970 JOURNAL.

REFERENCES

1. A. N. Dey, *This Journal*, **114**, 823 (1967).
2. A. N. Dey, *ibid.*, **115**, 160 (1968).
3. P. Bro and A. N. Dey, *J. Am. Inst. Ch. Eng.*, **15**, 293 (1969).
4. H. P. Gregor, *J. Am. Chem. Soc.*, **73**, 642 (1951).
5. P. H. Hermans in: H. R. Kruyt, "Colloid Science," Vol. 2, p. 517, Elsevier Publishing Co., New York (1949).
6. K. S. Spiegler, *Trans. Faraday Soc.*, **54**, 1408 (1958).

A Theoretical Equation for the Mobility of an Ion in an Electromagnetic Field

David S. Newman,* Carl Schober, and Cyrus Lawyer

Department of Chemistry, Bowling Green State University, Bowling Green, Ohio

The total current density in an ionic conductor can be described by Eq. [1]

$$\vec{J} = \sum_{k=1}^{n} \rho_k Z_k \vec{v}_k \qquad [1]$$

where ρ_k is the charge density, Z_k the charge, and $\vec{v}_k$ the average drift velocity of the k'th ion. Limiting the discussion to 1:1 electrolyte systems for the sake of simplicity, Eq. [1] can be rewritten

$$\vec{J} = \rho^+ Z^+ \vec{v}^+ + \rho^- Z^- \vec{v}^- \qquad [2]$$

From Eq. [2] it is obvious that an experimental measurement of $\vec{J}$ gives the difference between the average drift velocities of the positive and negative ions. A second measurement, to be combined with the first, must be made in order to evaluate the velocities of the positive or negative ions separately. In practice a conductance measurement, combined with a transference number measurement, is usually employed to arrive at average drift velocities, or average mobilities. An alternative and more general method, however, is available for calculating mobilities which makes use of the ionic Hall effect (2, 3) in conjunction with conductivity data.

The force acting on a charged particle in a combined electric and magnetic field is given in MKS units by the equation

$$\vec{F} = Z_k (\vec{E} + \vec{v} \times \vec{B}) \qquad [3]$$

where $\vec{F}$ is the Lorentz force, $\vec{E}$ is the electric field, $\vec{v}$ is the average drift velocity of the particle, and $\vec{B}$ is the magnetic field. If the direction of the magnetic field is perpendicular to the direction of the electric field, as is the case in a conventional Hall effect experiment, Eq. [3] shows that the magnetic field does not change the magnitude of the average drift velocity of ions that are moving in the direction of the electric field. This concept makes it possible to calculate the average drift velocity of an ion in an ionic conductor.

* Electrochemical Society Active Member.

The equations

$$\vec{F}^+ = Z^+ \rho^+ (\vec{E} + \vec{v}^+ \times \vec{B}) \qquad [4a]$$

$$\vec{F}^- = Z^- \rho^- (\vec{E} + \vec{v}^- \times \vec{B}) \qquad [4b]$$

are next introduced where $\vec{F}^+$ and $\vec{F}^-$ are the Lorentz forces experienced by the plus and minus ions, respectively, in the combined electromagnetic field. The positive and negative ions will react to this force in an opposite sense, but since they are already moving on the average in opposite directions the two kinds of ions will move in the same direction at right angles to both the electric and magnetic fields.

If $\vec{v}^+$ were equal to $\vec{v}^-$, there would be no observable macroscopic effect due to the Lorentz force acting on the ions, but since in general $\vec{v}^+$ is not equal to $\vec{v}^-$, a Hall voltage will develop. This Hall voltage will reflect the difference between the average drift velocities (or mobilities) since it can be considered to be the electric field necessary to reduce the transverse ionic current to zero.

Under these conditions, for a current density $\vec{J}$, Eq. [4] becomes

$$0 = \rho^+ Z^+ \vec{E} + \rho^+ Z^+ (\vec{v}^+ \times \vec{B}) \qquad [5a]$$

$$0 = \rho^- Z^- \vec{E} + \rho^- Z^- (\vec{v}^- \times \vec{B}) \qquad [5b]$$

and the Hall voltage is written as

$$\vec{V} = \rho^+ Z^+ \vec{E} - \rho^- Z^- \vec{E} \qquad [6a]$$

$$= (\rho^+ Z^+ |\vec{v}^+| - \rho^- Z^- |\vec{v}^-|) |\vec{B}| \qquad [6b]$$

Dividing both sides of Eq. [6] by unit field gives

$$\vec{V}_H = (\rho^+ Z^+ u^+ - \rho^- Z^- u^-) |\vec{B}| \qquad [7]$$

where u^+ and u^- are the usual symbols for the mobilities of the plus and minus ions, respectively, and $\vec{V}_H$

is the Hall voltage for unit field. Equation [7] should be compared with a similar equation derived by Wendhausen (4) which does not indicate that the measured Hall voltage is, in fact, current dependent.

The usual scalar form of the conductance equation

$$\sigma = Z^+\rho^+u^+ + Z^-\rho^-u^- \qquad [8]$$

is then combined with Eq. [7] and u^+ and u^- are solved for.

This leads to the equations

$$u^+ = \sigma/2\rho^+Z^+ + [V_H/2(\rho^+Z^+ \mid \vec{B} \mid)] \qquad [9a]$$

$$u^- = \sigma/2\rho^-Z^- - [V_H/2(\rho^-Z^- \mid \vec{B} \mid)] \qquad [9b]$$

It can be seen that all quantities on the right hand side of Eq. [9] are measurable, in principle. Assuming the proton to be more mobile than say, Cl^- in HCl solution, Eq. [9] qualitatively is seen to have the correct sign in front of the term containing the Hall voltage.

As a test of the validity of Eq. [9], the mobilities of the carriers in a 0.01M HCl solution were calculated using Friedman's value of 3 x 10^{-7}V (2) for the Hall voltage. The specific conductivity for the HCl was taken as 4.2 x 10^{-3} ohm^{-1} cm^{-1} and a field of 10 kilogauss was assumed present (the units for magnetic field used in the calculation are volt sec/cm^2). Using these numbers a value of 4 x 10^{-3} cm^2/volt sec was calculated for the proton mobility and a value of 7 x 10^{-4} cm^2/V-sec was calculated for the chloride mobility. These numbers compare quite favorably with literature values (5) considering the nature of the approximations involved.

Alternatively, this calculation is an excellent check on Friedman's estimated value for the Hall voltage based on a "Brownon" model.

Discussion

Experimental problems.—The major experimental difficulty is measuring the very low Hall voltage, approximately 0.2 μV, in the presence of a low signal to noise ratio. Several methods for improving the signal to noise ratio have been used to study metal-liquid ammonia systems (6) and liquid mercury systems (7), and are applicable to ionic systems. The best results should be obtained from an a-c, a-c technique (6, 8) in which the Hall voltage is measured at the sum and difference frequencies.

Temperature gradients and magnetohydrodynamic effects must be minimized. Magnetoresistance has to be accounted for and the external magnetic field should be homogeneous and on the order of 10 kilogauss. It is estimated that with present instrumentation and considerable effort Hall voltages can be measured to $\pm$ 10%.

Justification for the use of the scalar form of the conductance equation in the presence of an external magnetic field.— For a system in an external magnetic field at constant temperature and pressure, Ohm's law can be generalized in the form [9]

$$\vec{J} = \sigma_E \vec{E} + \sigma_B \vec{B} \times \vec{E} \qquad [10]$$

where σ_E and σ_B are the electric and magnetic components of the conductance tensor. σ_E and σ_B are related to each other by the equation

$$\text{Tan}\,\Phi = \vec{B}\,\sigma_B/\sigma_E \qquad [11]$$

where Φ is the Hall angle. From Eq. [10] it is obvious that $\vec{J}$ is affected by the magnetic field. However, the effect is very small and can either be neglected or, in principle, measured. The change in $\vec{J}$ due to the magnetic field changing the distribution of ionic velocities in directions not parallel to the electric field, approaches zero. This is the same result predicted for the free electron model of a metal. In this model both the transverse and longitudinal components of the magnetoresistance vanish.

The change in $\vec{J}$ due to a Hall current, while not being zero, will be on the order of 1 x 10^{-6} times the electric current for magnetic fields of 10 kilogauss and will also be negligible. Therefore, the total decrease in the conductance due to the magnetic field (the second term on the right-hand side of Eq. [10]) is usually very small and the scalar form of the conductance equation is applicable.

For very large magnetic fields, on the order of 300 kilogauss, the "magnetoresistance" will probably no longer be negligible, and a more general form of the conductance tensor will have to be used.

Generality of the method.—The Hall effect-conductance technique for measuring mobilities is closer to being completely general than any other technique now in use. Any ionic system, including fused salts and solids, is accessible to Hall effect experiments because the limitations, while formidable, are all experimental. This is not the case with transference number experiments. For example, there are at least two theoretical limitations on the Hittorf technique. One of the electrode reactions must be reversible, and it is not always possible to correct for differences in solvation between anion and cation. Similar kinds of problems limit the number of systems accessible to either moving boundary or emf measurements.

Conclusion

The equations derived form the basis of a potentially useful method for studying transport properties of ionic solutions. Extension of the method to incorporate fused salts represents a fertile area for future investigation. In fused salt systems the problem of reference frames would be virtually eliminated.

Manuscript submitted March 12, 1969; revised manuscript received *ca.* July 18, 1969.

Any discussion of this paper will appear in a Discussion Section to be published in the June 1970 JOURNAL.

REFERENCES

1. S. R. Degroot and P. Mazure, "Non-Equilibrium Thermodynamics," Chap. XIII, North Holland Publishing Co., Amsterdam (1962).
2. H. L. Friedman, *J. Phys. Chem.*, **69**, 2616 (1965).
3. P. L. Read and E. Katz, *Phys. Rev. Letters*, **5**, 446 (1960).
4. H. Wendhausen, *Z. Phys. Chem. N. F.*, **58**, 325 (1968).
5. S. Glasstone, "Textbook of Physical Chemistry," 2nd Ed., p. 909, D. Van Nostrand Co., New York (1946).
6. R. D. Nasby and J. C. Thompson, *J. Chem. Phys.*, **49**, 969 (1968).
7. N. E. Cusack, J. E. Enderby, P. W. Kendall, and Y. Tieche, *J. Sci. Instrum.*, **42**, 256 (1965).
8. D. S. Kyser and J. C. Thompson, *J. Chem. Phys.*, **42**, 3910 (1965).
9. J. M. Ziman, "Electrons and Phonons," p. 487, Oxford University Press (1960).

On the Breakdown of Passivity on Stainless Steels in Halide Media

B. E. Wilde* and E. Williams

Applied Research Laboratory, U. S. Steel Corporation, Monroeville, Pennsylvania

This note presents some observations made in a program to develop an alloy resistant to pitting by studying passivity breakdown during potentiodynamic anodic polarization. The concept of "critical breakdown potential for passivity," E_c, as a means of screening alloys for pitting resistance has been described by Brennert (1), Mahla and Nielsen (2), Pourbaix *et al.* (3), and many others. Further, a large number of experimental and environmental factors that influence E_c have also been presented by Leckie and Uhlig (4), and Horvath and Uhlig (5). Recent findings at U. S. Steel's Applied Research Laboratory, however, have indicated another environmental variable not previously reported, which in the opinion of the writers, lends strong support to the concept of competitive adsorption in passivity breakdown proposed by Tamman (6), Uhlig and Wulff (7), Kolotyrkin (8), and Brauns and Schwenk (9).

Experiments were conducted on two steels having the chemical composition shown in Table I. Cylindrical electrodes were machined from solution-annealed stock and were polarized from the steady-state corrosion potential, E_{corr}, in the noble direction. An electronic potentiostat[1] was used along with auxiliary equipment and preparation procedures described elsewhere (10, 11). The corrosive was 1M reagent-grade sodium chloride, dissolved in distilled water (6.3 meg ohm cm^{-1}), with a final *p*H of 6.3 at 25°C. The atmosphere inside the cell was maintained by bubbling any one of four gases through the solution at a rate of 1 to 1.5 l/min. The four gases used were hydrogen, nitrogen, argon, and oxygen, drawn from high-pressure gas cylinders. The residual oxygen levels in the corrodent, after it was purged with the above gases for 24 hr, were measured with a Beckman polarographic oxygen analyzer.[2]

Results of polarization experiments are shown in Fig. 1 and 2. Clear breakdown potentials were observed on both alloys, which increased in nobility in the order $H_2 < N_2 < A < O_2$, as shown in Table II. Each value of E_c was found to be reproducible to ± 10 mV on triplicate runs. These data clearly indicate that the stability of the "passive film" to localized breakdown (pitting), as measured by the relative nobility of E_c, is related to the presence of nonionic, nonelectroactive constituents in the corrodent. It is possible, however, that H_2 may be electroactive in that it could be involved in electrochemical oxidation on the electrode surface, and similarly, oxygen may be reduced at local cathode sites, but to our knowledge, no electrochemical reactions, involving N_2 and argon can occur. The possible influence of dissolved oxygen on E_c was discounted, from inspection of Table III, where it is clear that argon with the lowest oxygen content gave next to the most noble E_c on both steels. Because of the above data, we must

* Electrochemical Society Active Member.
[1] Anatrol Model 4700, Sweep unit Model 4510.
[2] Beckman Process Analyzer, Model 778.

Table I. Chemical composition of steels used in this study

Steel	Chemical composition, w/o						
	C	Cr	Ni	Mn	Si	S	P
AISI Type 304 stainless steel	0.06	18.1	9.1	1.2	0.51	0.01	0.02
AISI Type 430 stainless steel	0.058	17.0	0.025	0.33	0.47	0.006	NA

NA—Not analyzed.

Table II. Influence of dissolved gases on the magnitude of the critical breakdown potential

Gas	E_c (V_{SCE})	
	Type 304	Type 430
Hydrogen	−0.050	−0.185
Nitrogen	−0.020	−0.130
Argon	0.050	−0.100
Oxygen	0.065	−0.035

Table III. Dissolved oxygen content of the 1M NaCl as a function of the controlled atmosphere at 25°C

Gas	Oxygen content in solution, ppm
Hydrogen	0.076
Nitrogen	0.46
Argon	0.057
Oxygen	30.1

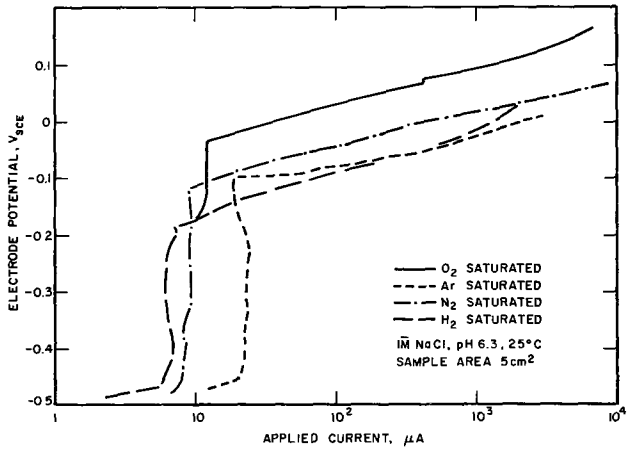

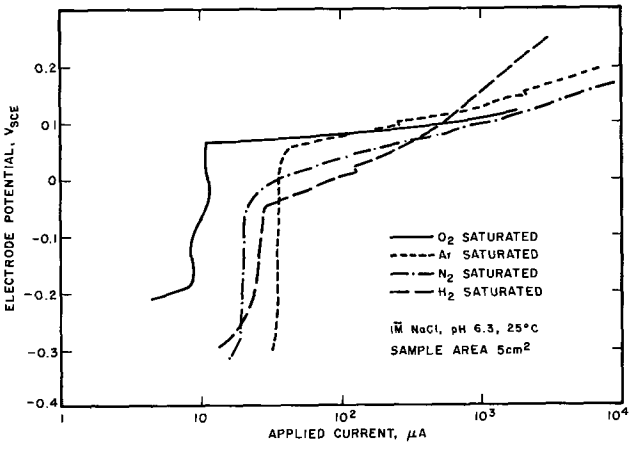

turn to physical adsorption processes to explain the dependence of E_c on nonionic species in solution.

Without specifying the primary passivation mechanism (other than some type of film formation either adsorbed O_2 or nonstoichiometric phase oxides), one may view the localized breakdown of the passive state as the displacement of any adsorbed or bound species on the surface by Cl^- ions at a specific electrode potential, leading to accelerated anodic dissolution (12) and autocatalysis (13). The resistance to displacement from the film presumably must depend, in the case of N_2 and argon, on the relative polarizability of the molecule. The above data form the basis for a future publication explaining the reasons for the reported lack of agreement between electrochemical and chemical pitting tests (14).

Acknowledgment

The authors acknowledge helpful discussion with Dr. M. Pourbaix, Director of CEBELCOR, Brussels, Belgium.

Manuscript received July 17, 1969.

Any discussion of this paper will appear in a Discussion Section to be published in the June 1970 JOURNAL.

REFERENCES

1. S. Brennert, *J. Iron Steel Inst.*, **135,** 101 (1937).
2. E. M. Mahla and N. A. Nielsen, *Trans. Electrochem. Soc.*, **89,** 167 (1946).
3. M. Pourbaix and L. Klimzack—Mathieu, Ch. Mertens, J. Meunier, Cl. Vanleugenhaghe, L. de-Munk, L. Laureys, L. Neelemans, M. Warzee, *Corrosion Sci.*, **3,** 239 (1963).
4. H. P. Leckie and H. H. Uhlig, *This Journal,* **113,** 1262 (1966).
5. J. Horvath and H. H. Uhlig, *ibid.*, **115,** 791 (1968).
6. G. Tamman, *Z. Anorg. Chem.*, **107,** 104, 236 (1919).
7. H. H. Uhlig and J. Wulff, *Trans. AIME,* **135,** 494 (1939).
8. Ya. Kolotyrkin, *Corrosion,* **19,** 261t, (1963).
9. E. Brauns and W. Schwenk, *Archiv. Eisenhuttenw.*, **32,** 387 (1961).
10. B. E. Wilde and N. D. Greene, Scientific Report No. 3, Air Force Cambridge Research Lab., AFCRL 64-518, June 15, 1964.
11. W. D. Henry, C. D. Kim, and B. E. Wilde, U. S. Steel ARL Report, to be published.
12. T. P. Hoar, *Discussions Faraday Soc.*, No. 1, 299, (1947).
13. N. D. Greene and M. G. Fontana, *Corrosion,* **15,** 25t, (1959).
14. W. D. France, Jr., and N. D. Greene, Paper presented before the annual Conference of the National Association of Corrosion Engineers, Houston, Texas, March 1969.

Oxidation of Co-25 w/o Cr at High Temperatures

P. K. Kofstad[1] and A. Z. Hed

Metal Science Group, Battelle Memorial Institute, Columbus Laboratories, Columbus, Ohio

ABSTRACT

Studies of the oxidation behavior of Co-25 w/o Cr at temperatures between 900° and 1300°C and oxygen pressures in the range 0.2-760 Torr are reported and analyzed. The oxidation behavior of this alloy is complex and does not follow a single mechanism. The parabolic rate constant at high oxygen pressures ($p_{O_2} > 100$ Torr) in the temperature range of 900°-1300°C is about two orders of magnitude larger than that at low oxygen pressures ($p_{O_2} < 10$ Torr). The scales formed at high oxygen pressures have a duplex structure, the outer layer being virtually pure CoO as in Co-10 w/o Cr (1, 2), and the inner layer being mainly the spinel $CoCr_2O_4$ with small amounts of CoO and Cr_2O_3 (Cr_2O_3 is concentrated near the alloy-scale interface). At low oxygen pressures, the morphology of the scale is dependent on the radius of curvature of the specimen; at the edges where this radius is small, the structure is similar to the structure developed at high oxygen pressures; on the large surfaces, Cr_2O_3 is the dominant oxide.

The mechanism of parabolic oxidation of Co-25 w/o Cr at high oxygen pressures involves cobalt-ion diffusion through a CoO network in the inner layer. Initial oxidation under these conditions is nonparabolic and this is due to selective oxidation of chromium to Cr_2O_3 which takes place when the specimens are exposed to the "vacuum" of the reaction furnace prior to the start of the actual oxidation run. The transition from the high- to low-pressure oxidation is due to a transition to selective oxidation of chromium. The oxidation is then governed by diffusion of the reacting ions (probably chromium) through the Cr_2O_3 scales.

This paper is part of an extended study of the high-temperature behavior of binary Co-Cr alloys. Previous papers have covered oxidation kinetics and microstructures of oxide scales in high-temperature oxidation of Co-10 w/o Cr (1,2). A literature survey pertaining to the oxidation behavior of Co-Cr alloys has been given in ref. (1).

Materials and Methods

An alloy with the nominal composition Co-25 w/o (weight per cent) Cr was prepared in a vacuum furnace and cast in a tapered zirconite sand mold. The dimensions of the mold were: top, 6.3 x 6.3 cm; bottom, 3.0 x 3.8 cm; length, 24.5 cm. Subsequent chemical analysis showed that the alloy composition was Co-24.6 w/o Cr.

After sandblasting, the ingots were heat treated at 1125°C for 2 hr and then forged at high temperatures to the size 2.2 x 6.3 x 43.1 cm. The optimum forging temperatures for this alloy appeared to be 1150°-1200°C.

The forged plates were then hot rolled to a 0.22-cm thickness and subsequently cold rolled to a thickness of about 0.18 cm. After rolling, the sheets were again sandblasted. The sheets were than cut into specimens measuring 2.5 x 1.9 cm; these specimens were subsequently ground on emery paper and diamond polished. The polishing procedure removed some 50-100μ of the alloy. The final thickness of the specimens varied between 0.15 and 0.165 cm. The specimens were then measured and washed in water and trichlorethylene. A metallographic inspection of these specimens revealed a small amount of Cr_2O_3 inclusions in the alloy; these are probably due to oxygen contamination during casting, forging, and hot rolling.

Oxidation rates in controlled oxygen atmospheres were measured with an automatic Cahn R-H electrobalance enclosed in a high-vacuum system. The balance had a sensitivity of 100 μg and the weight gain was continuously recorded on an AZAR Leeds and Northrup recorder. Temperature in the mullite tube reaction chamber was controlled by an on-off Barber-Coleman controller to within 3°C, and was measured with a Pt/Pt-10 Rh thermocouple placed 10-15 mm from the specimen. The system was pumped down with a 450-liter CVC diffusion pump and an Edwards mechanical pump. Pressures down to 10^{-5} Torr were achieved, as measured on the CVC ionization and thermocouple gauges.

The specimens were connected to the balance with an annealed Pt-10 Rh wire and placed in a cold sidetube of the apparatus, and then the system was evacuated. After the furnace was temperature equilibrated and while the furnace was still under the high vacuum (10^{-4}-10^{-5} Torr), specimens were lowered into the hot zone by a magnetic device. Oxygen was then admitted to the system through a Granville-Phillips metering needle valve. One to two minutes generally elapsed from the time the specimens were loaded into the hot zone until the desired oxygen pressure in the system was reached. Zero time for the oxidation was taken as the instant when the desired oxygen pressure was attained. At the lower oxygen pressures ($\leq$ 10 Torr), oxygen was continuously pumped through the system during the oxidation.

After the specimens had been oxidized to the desired extent, they were raised out of the hot zone. The system was backfilled with oxygen, and the specimens were taken out and immersed in a molten lead bismuth alloy, which in turn was rapidly cooled and solidified. In this manner, retention of the oxide scales was accomplished.

A limited number of oxidized specimens were chosen for further examination and characterization by means of metallographic techniques, x-ray diffraction, and electron-microprobe analysis.

Results

Thermogravimetric studies.—The rate of oxidation of diamond-polished Co-25 w/o Cr alloy was studied in the temperature range 900°-1300°C. The oxidation was carried out in pure oxygen in the pressure range 0.2-760 Torr.

In Fig. 1 through 3, the weight gain of Co-25 w/o Cr alloy during oxidation is plotted *vs.* time at different oxygen partial pressures at temperatures of 1000°, 1100°, and 1300°C, respectively. Parabolic plots of the oxidation at 900°, 1100°, and 1300°C are given in Fig. 4 to 7.

[1] Present address: Central Institute for Industrial Research, Blindern, Oslo 3, Norway.

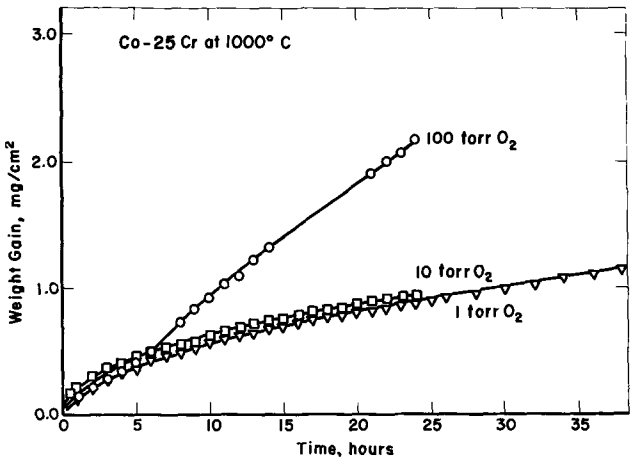

Fig. 1. Oxidation of Co-25Cr alloy at 1000°C in oxygen at pressures from 1 to 100 Torr oxygen.

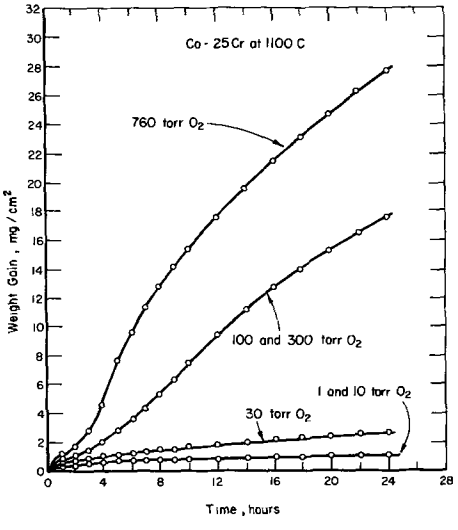

Fig. 2. Oxidation of Co-25Cr alloy at 1100°C in oxygen at pressures from 1 to 760 Torr oxygen. The experimental points of 100 and 1 Torr are not given since they fell very close to those of 300 and 10 Torr, respectively.

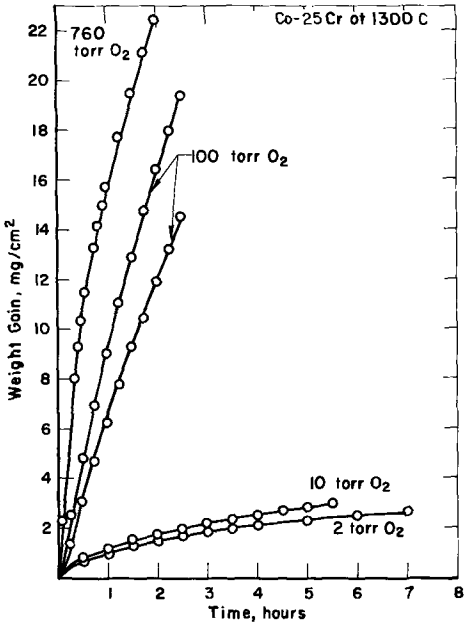

Fig. 3. Oxidation of Co-25Cr alloy at 1300°C in oxygen at pressures from 2 to 760 Torr oxygen.

A significant feature of the results is a marked decrease in the rate of oxidation when the ambient partial pressure is decreased below approximately 100 Torr. This feature is particularly evident from the results at 1100° and 1300°C (Fig. 2, 3, 5-7).

The oxidation kinetics at and above 100 Torr may be divided into two main parts: (*i*) an initial stage during which the oxidation is difficult to characterize in terms of simple rate equations, and (*ii*) a parabolic oxidation after more extended reaction. These features may particularly be noted from Fig. 5 and 7.

At low oxygen pressures the oxidation tends to a more parabolic behavior during the whole reaction period. However, at both 900° and 1100°C (Fig. 4 and 6), the results also indicate small changes in the kinetics after an initial period of oxidation.

Parabolic rate constants, k_p, evaluated from the later oxidation stages are plotted in Fig. 8 as a function of p_{O_2} at different temperatures. The sharp decrease in the oxidation at an oxygen pressure of about 50-100 Torr may be noted. At low oxygen pressures

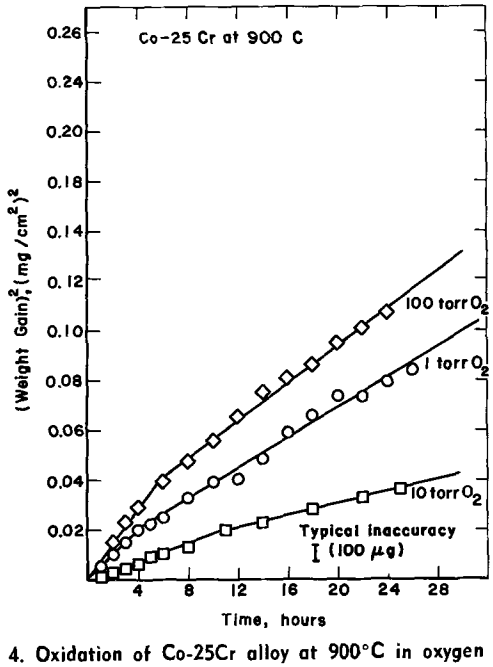

Fig. 4. Oxidation of Co-25Cr alloy at 900°C in oxygen at pressures from 1 to 100 Torr oxygen (parabolic plot).

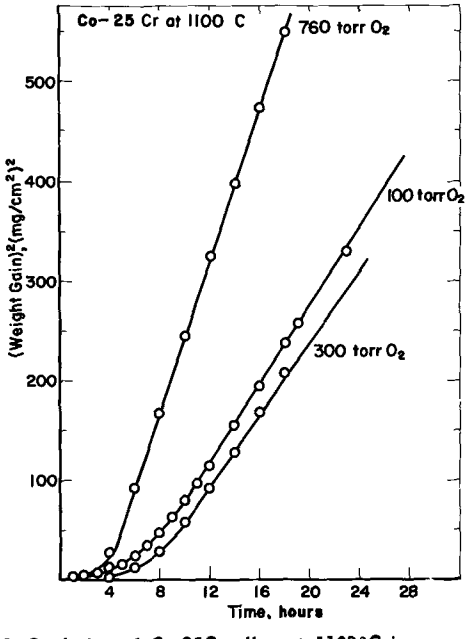

Fig. 5. Oxidation of Co-25Cr alloy at 1100°C in oxygen at pressures from 100 to 760 Torr oxygen (parabolic plot).

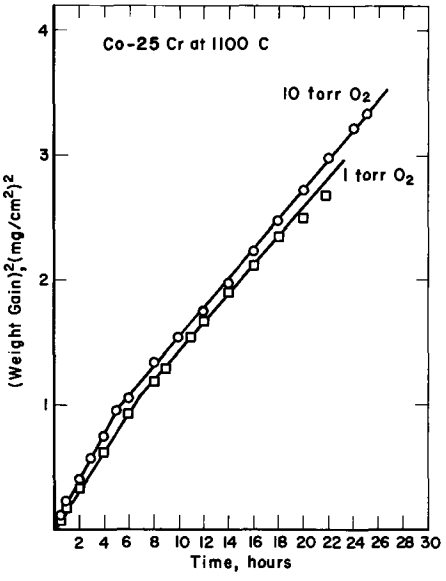

Fig. 6. Oxidation of Co-25Cr alloy at 1100°C in oxygen at pressures of 1 and 10 Torr (parabolic plot).

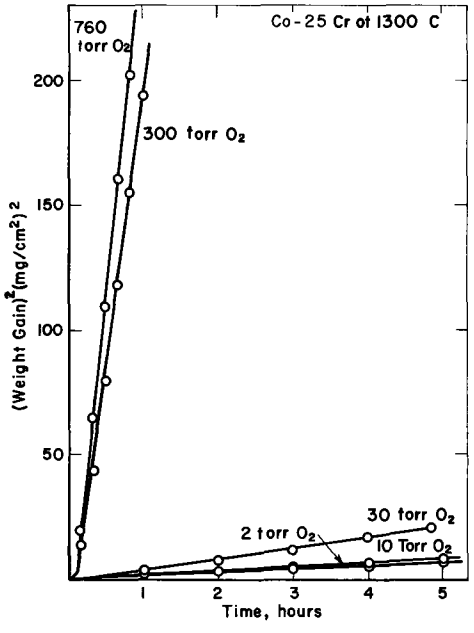

Fig. 7. Oxidation of Co-25Cr alloy at 1300°C in oxygen at pressures from 2 to 760 Torr oxygen (parabolic plots).

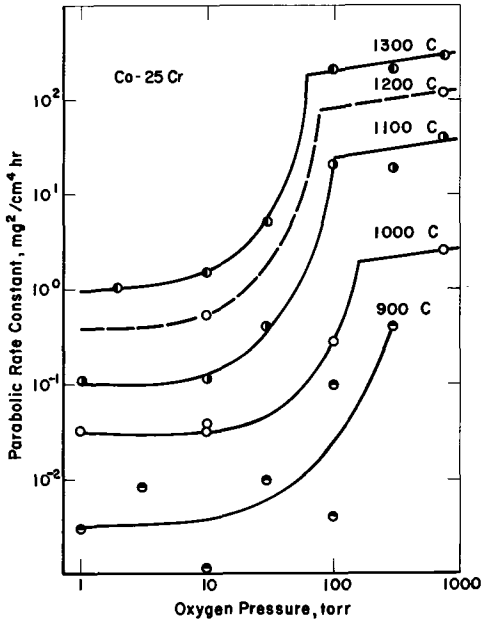

Fig. 8. Parabolic rate constant for oxidation of Co-25Cr as a function of oxygen pressure at temperatures from 900° to 1300°C.

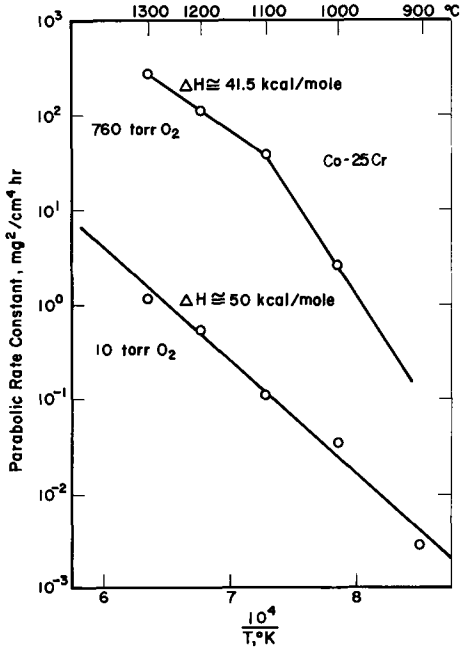

Fig. 9. Arrhenius plot of the parabolic rate constant for oxidation of Co-25Cr alloy at 10 and 760 Torr oxygen.

(below 10 Torr), k_p is approximately independent of oxygen pressure. The scatter at 900°C in Fig. 8 is partially due to experimental error and partially due to a real effect that will be mentioned later. At high oxygen pressures it is difficult to evaluate an accurate oxygen-pressure dependence of k_p, but the results suggest a small increase of k_p with oxygen pressure, which is not incompatible with a relation $k_p \propto p_{O_2}^{1/3}$ or $p_{O_2}^{1/4}$, as found for the oxidation of pure cobalt and Co-10 w/o Cr (1, 2).

In Fig. 9 the parabolic rate constant at 760 and 10 Torr is plotted as a function of $1/T$. The activation energy at 10 Torr is approximately 50 kcal/mole, while at 760 Torr it changes with temperature.

During at least part of the oxidation, evaporation of oxide occurred. This was evidenced by deposits of Cr_2O_3 on the hangdown wire, and in the upper cool part of the reaction chamber. The oxide evaporation was more pronounced at high oxygen pressures, which is expected if the evaporating oxide is CrO_3. It was not possible to estimate the amount of oxide evaporation during any single run. However, the presence of an outer CoO layer on the Co-25 w/o Cr alloy at high oxygen pressures leads us to assume that this evaporation occurs only during the initial stages of oxidation under these conditions.

Metallographic studies.—The scales on oxidized Co-25 w/o Cr alloys almost invariably spalled off during cooling to room temperature. When the specimens were oxidized at high oxygen pressures, the scales would just disjoint from the substrate and could be collected as relatively large chips of oxide. When the specimens were oxidized at low oxygen pressures, the spalling was violent and collection of scale chips was very difficult. In an attempt to retain the scales with their correct orientation relative to the substrate, oxidized specimens were quenched into a liquid lead-bismuth alloy which expands under cooling. The alloy is softer than the specimen, and this results in rounded edges of the metallographically polished specimens.

In Fig. 10 a cross section of a Co-25 w/o specimen oxidized at 1100°C in 300 Torr O_2 for 14 hr is given.

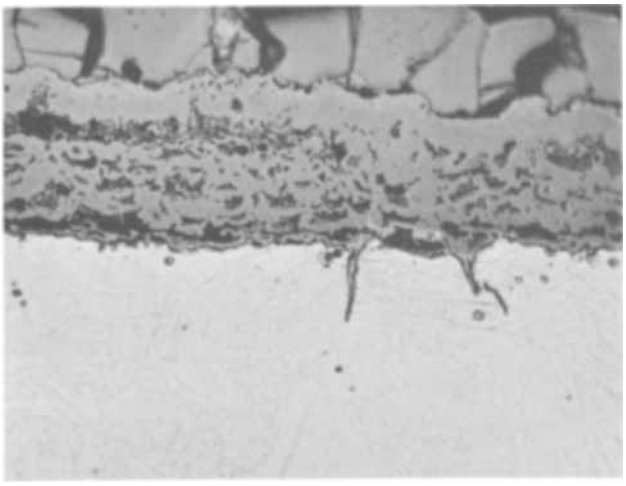

Fig. 10. Metallographic cross section of Co-25Cr alloy oxidized for 14 hr at 1100°C and 300 Torr oxygen. 350X.

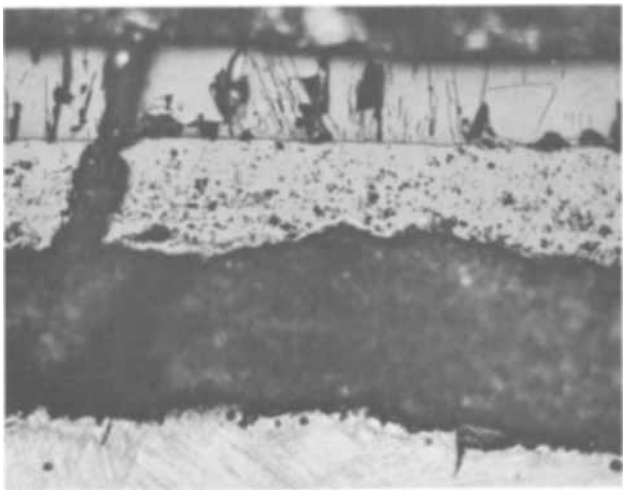

Fig. 11. Metallographic cross section of Co-25Cr alloy oxidized for 2 hr at 1300°C and 760 Torr oxygen. 200X.

Figure 11 shows the cross section of a sample oxidized at 1300°C in 760 Torr O_2 for 2 hr. The scales produced on other specimens oxidized in the region of high oxidation rates (see Fig. 8 where the k_p's are given) are similar to the ones shown in Fig. 10 and 11.

In all these cases, the scales have a duplex structure similar to that found on Co-10 w/o Cr (1) alloys. The outer layer consists of columnar CoO and the inner layer is porous. A major difference is that the inner layer consists mainly of the spinel $CoCr_2O_4$, while on Co-10 w/o Cr alloys, spinel occurred in the inner layer as a dispersion within a predominantly CoO matrix.

To provide better insight into the structure of the scale formed during oxidation at high pressures, a taper of a spalled scale has been prepared. In Fig. 12, a low magnification of the scale is shown, and in Fig. 13(a) through 13(d), different portions of Fig. 12 have been magnified. The curvature of the inner-outer layer interface is due to the bending of the scale after spalling. In Fig. 13(a), a portion of the outer layer is shown. The appearance is very similar to the appearance of the outer layers of scales found in Co-10 w/o Cr alloys (see ref. (1), Fig. 14). This part of the scale is virtually pure CoO. The cracks probably occurred during cooling, and the small precipitates are Co_3O_4.

Figure 13(b) shows the inner-outer layer interface, and Fig. 13(c) and (d) show sections of the inner

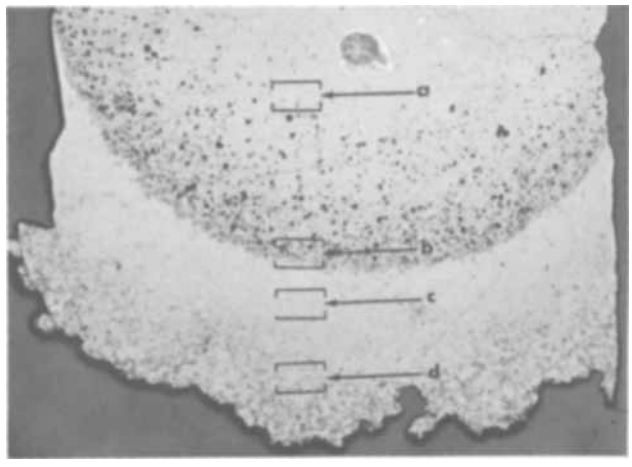

Fig. 12. Metallographic tapered cross section of scale of Co-25Cr alloy oxidized for 3 hr at 1300°C and 300 Torr oxygen. 15X.

layer. Electron-microprobe analysis (described below) shows that the inner layer is mainly spinel with CoO and Cr_2O_3 inclusions. From Fig. 13(c) and (d), one can see that the amount of these inclusions increases as the alloy/oxide interface is approached.

The microstructure of the oxidized specimen at low oxygen pressures (below 10 Torr) differs greatly from the behavior observed at high pressure.

X-ray analysis of the spalled scales reveals the presence of CoO, Cr_2O_3, and $CoCr_2O_4$. However, metallographic examination of the quenched specimen shows that CoO and $CoCr_2O_4$ are present only at the edges of the specimen. In Fig. 14, a specimen oxidized at 1300°C in 30 Torr O_2 for 7 hr is given. One can easily observe the duplex structure of the edge, and its similarity to the scales developed at high oxygen pressures. The thin layer on the large surface was identified by its optical activity and by microprobe analysis as Cr_2O_3; however, it is not known whether or not an additional outer layer spalled off. We were not able to find remnants of such a layer in the quenching alloy, and we therefore conclude that the CoO and $CoCr_2O_4$, identified by x-ray diffraction, originated from the edges of the specimens only.

Electron-microprobe analyses.—Electron-microprobe analyses have been made on some of the specimens to determine the composition of the different constituents of the scale. A scale from the specimen represented in Fig. 12 and 13 has been used for the high-pressure range.

In Fig. 15(a) through (c), some traces of the chromium content in the scale are shown, together with a micrograph of the actual trace on the scale. Trace "a" begins near the alloy oxide interface. The first 50μ of the trace show a large concentration of chromium in an erratic manner. This is due to the fact that the Cr_2O_3 at the alloy-scale interface is very powdery and is partially lost during polishing. The specimen shown in this figure has been slightly repolished and etched to remove the carbon layer deposited for the tracing, and to accentuate the scale features. This treatment caused further deterioration of the high chromium part of the scale as seen in the micrograph. At the points marked A, B, and C, the trace passes through relatively large CoO inclusions, and accordingly the chromium concentration is decreased. The bright area marked D has been probed separately and contained less than 10% chromium, which indicates CoO. The brightness and the 10% chromium observed are due to the fact that in this area the CoO inclusion is very thin and reflection from below is observed optically, as well as with the electron beam. The points marked E are typical CoO inclusions, while the points marked F are voids partially filled with Cr_2O_3. The dashed line on the trace is at about 46% chromium which corresponds to a spinel with the stoichiometric composition

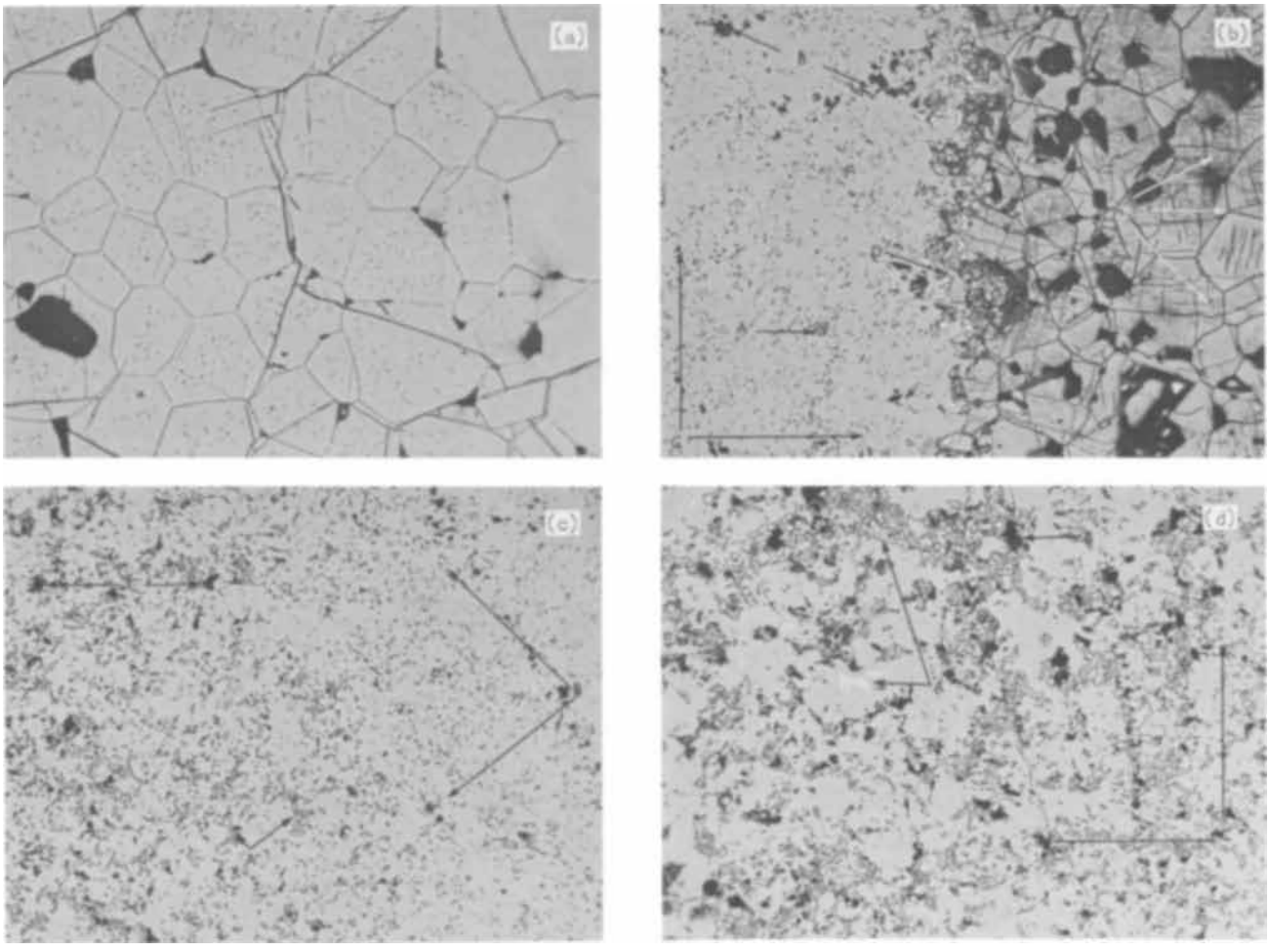

Fig. 13. Portions of Fig. 12. 200X. (a) Outer CoO layer. (b) Inner layer/outer layer interface. A, CoO inclusion; B, Cr_2O_3 and pores; C, $CoCr_2O_4$ layer; D, $CoCr_2O_4$ enclosed by CoO; E, CoO outer layer. (c) Inner layer. A, CoO inclusion; B, Cr_2O_3 and pores; C, $CoCr_2O_4$ body. (d) Inner layer close to the alloy scale interface. A, CoO channels; B, Cr_2O_3; C, $CoCr_2O_4$.

$CoCr_2O_4$. Trace "b" shows the chromium content somewhere in the middle of the inner layer and three well-marked decreases in chromium corresponding exactly to three small inclusions of CoO. One can note that the general size of the CoO inclusions has been markedly decreased relative to trace "a." Trace "c" has been taken at the inner layer-outer layer interface. The shallowness of the decrease in the chromium content at the interface, point B, is due to the tapering of the specimen, where the probe is "seeing" part of the inner layer below the outer layer. Point A corresponds to a very small CoO inclusion. The mean value of chromium content in the inner layer here is about 40%, corresponding to a spinel with the composition $Co_{1.3}Cr_{1.8}O_4$. The sudden increase of chromium in the outer layer, point C, corresponds to a void in the outer layer where the underlying inner layer is exposed to the probe beam.

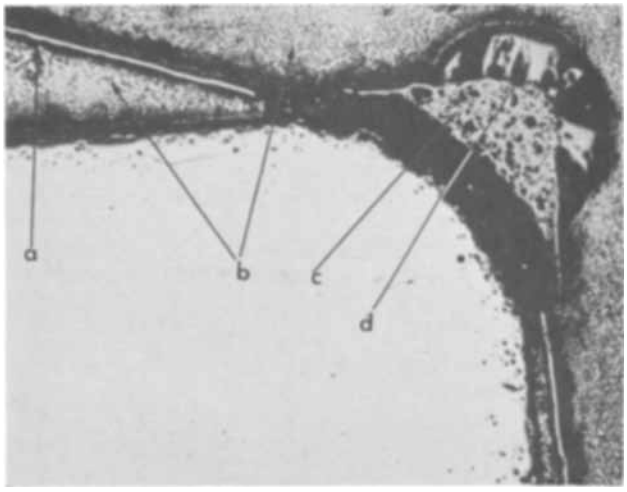

Fig. 14. Metallographic cross section of Co-25 w/o Cr alloy oxidized for 7 hr at 1300°C and 30 Torr oxygen. 70X. a, Cr_2O_3 scale; b, quenching alloy; c, spinel; d, CoO.

An analysis of a similar perpendicular cross section supported the conclusions that the outer layer is virtually pure cobalt oxide.

An electron-microprobe analysis was also made on a specimen oxidized at low oxygen pressures. Since it was impossible to retain a spalled section for shallow taper mounting, samples were prepared in two different ways. One of the samples was quenched in a liquid lead bismuth alloy and a perpendicular trace was made; another sample was left to spall, and a shallow taper of 4 degrees was prepared.

In Fig. 16, a trace through a quenched specimen oxidized at 1300°C in 2 Torr O_2 for 19 hr is shown. The area B in the micrograph is the quenching alloy and has been deleted from the trace. A and C are the traces through the alloy and scale, respectively. The sudden decrease in chromium content in the scale corresponds to a void. A trace through an adherent part of the scale on the large surface (after spalling) and a trace through the edge of the same specimen (oxidized at 1300°C in 10 Torr O_2 for 149.5 hr) are given in Fig. 17(a) and (b), respectively. In Fig. 17(a), which is a very shallow taper (4 degrees) only Cr_2O_3 is pres-

ent in the scale. The alloy is strongly depleted in chromium; however the size of the depleted region is not determined here due to the tapering. From both specimens it appears that the scale developed on the flat surfaces consists of pure Cr_2O_3. (This is in accordance with the optical observation, namely, green color and optical activity.) Owing to the violent spalling of these scales, one may question whether additional oxide was present in the scale. However, no remnants of an outer spalled layer could be found in the surrounding quenching alloy, and this leads us to conclude that the large surfaces of these specimens consist of single-layered Cr_2O_3.

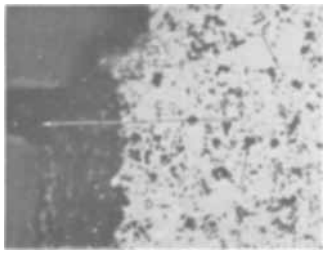

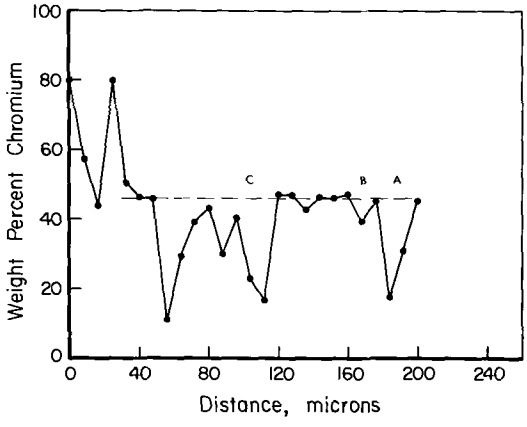

Fig. 15(a). Chromium concentration in part of the inner layer of the scale shown in Fig. 12 and 13, and corresponding micrograph. Trace near the alloy/scale interface. A, B, and C are CoO inclusions on the trace. D and F are other CoO inclusions. E are voids containing Cr_2O_3. 155X.

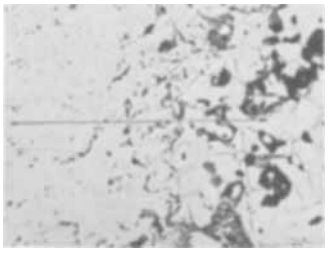

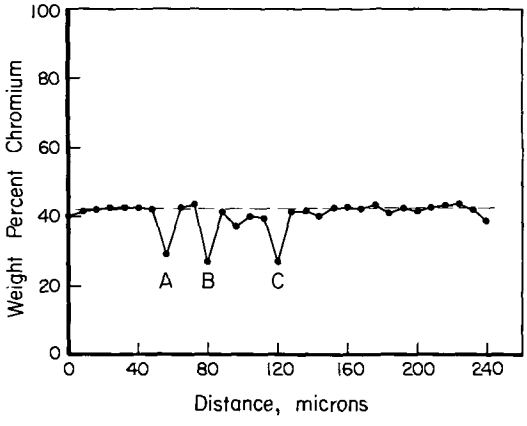

Fig. 15(b). Chromium concentration in part of the inner layer of the scale shown in Fig. 12 and 13, and corresponding micrograph. A trace in the middle of the inner layer. A, B, and C are small CoO inclusions on the trace. 155X.

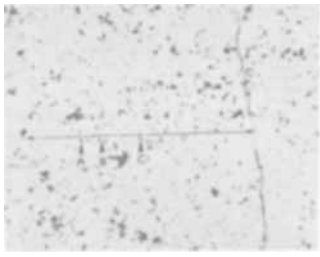

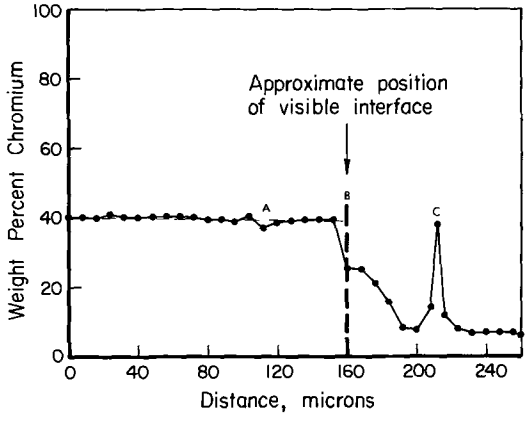

Fig. 15(c). Chromium concentration in part of the inner layer of the scale shown in Fig. 12 and 13, and corresponding micrograph. A trace near the inner/outer layer interface. A, a small CoO inclusion; B, the inner/outer layer interface; C, a void in the outer layer through which the inner spinel layer is seen. 155X.

From Fig. 17(b) we see that a structure is present at the edges which is similar to that found on the specimen oxidized at high oxygen pressure. In the alloy phase of the trace, the probe passed through two large internal Cr_2O_3 particles, A and B, and immediately at the alloy's edge a semicontinuous Cr_2O_3 layer is present. A small separation or void line is crossed at C. Then we penetrate the inner spinel layer marked D (some CoO inclusions are present in this part of the scale) until we reach the outer CoO layer (marked E), which in this case is sometimes mixed with spinel (like at F). From the metallographic cross-sections one can see that at some places the base of the scale contains metallic inclusions.

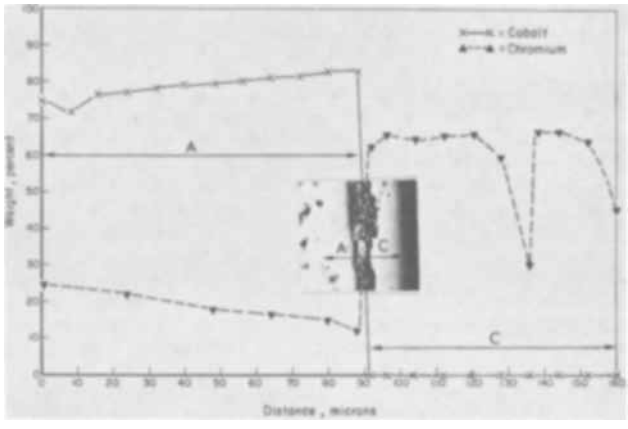

Fig. 16. A trace through the scale of a Co-25 w/o Cr alloy oxidized for 19 hr at 1300°C and 2 Torr oxygen, and a corresponding micrograph. 230X. A and C are correspondingly the alloy and the scale, B is a separation gap filled with the quenching alloy and is deleted from the trace.

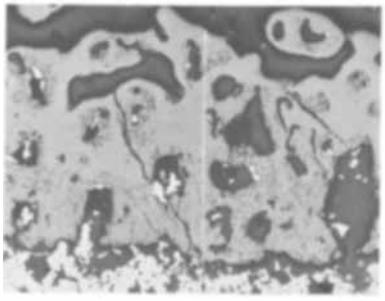

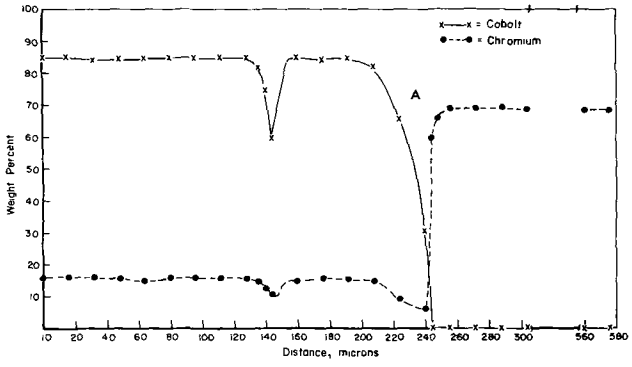

Fig. 17(a). Metallographic cross-section and electron microprobe trace of a tapered Co-25Cr alloy oxidized for 149.5 hr at 1200°C and 10 Torr oxygen. Flat surface taper (taper angle ~ 4 deg). The scale starts at A. 40X.

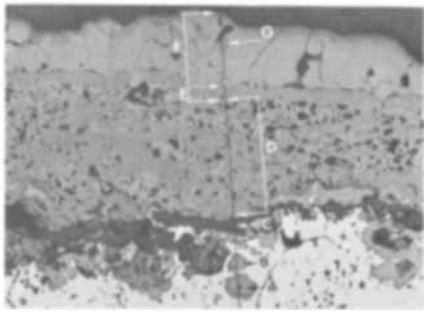

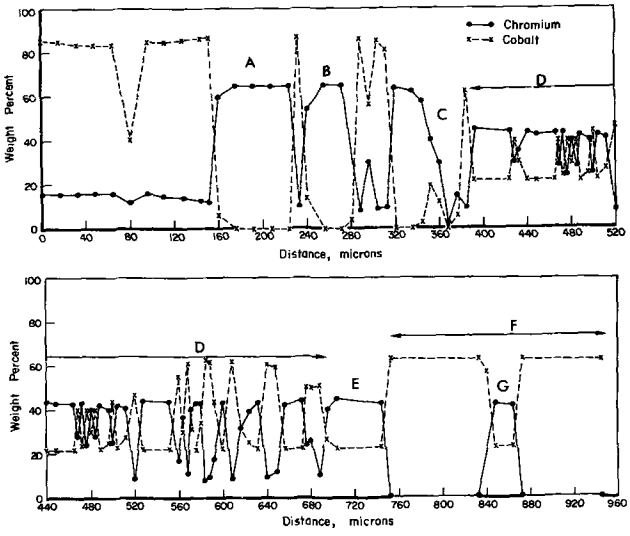

Fig. 17(b). Metallographic cross section and electron microprobe trace of a tapered Co-25Cr alloy oxidized for 149.5 hr at 1200°C and 10 Torr oxygen. Edge taper (taper angle ~ 86 deg). A and B are internal Cr_2O_3 particles, C is a separation of the scale and alloy. D is the spinel layer with CoO inclusions. F is the outer CoO layer, and G is a spinel inclusion in the outer CoO layer. E is a fairly continuous spinel layer without CoO inclusions. 50X.

This oxide structure at the edges is probably responsible for the CoO and $CoCr_2O_4$ x-ray line found in the powder collected from spalled specimens.

In Fig. 16, one can see the extent of the chromium-depleted region in the alloys; this supports the observation that at these pressures chromium oxidizes preferentially. (This is not well demonstrated in Fig. 17(a) because of the tapering.)

Discussion

The experimental evidence suggests that oxidation of Co-25 w/o Cr is governed by two oxidation mechanisms depending on the partial pressure of oxygen. At and above about 100 Torr O_2, the oxide scale has a duplex structure with an outer layer of CoO and an inner layer consisting predominantly of the Co-Cr spinel and with minor amounts of CoO. The scale has qualitatively the same microstructure as that found on Co-10 w/o Cr, but the spinel content is correspondingly higher in the inner layer of the scale on the Co 25 w/o Cr alloy. When the oxygen pressure is reduced below 100 Torr a drastic change in the composition and morphology takes place. Except at the edges of the specimens, the surface oxide consists of Cr_2O_3, and the oxidation thus involves a selective oxidation of chromium. The transition from the "high"- to "low"-pressure-oxidation regions is accompanied by a large, almost abrupt decrease in the oxidation rate.

Oxidation at high partial pressures.—Table I lists values of the thickness of the inner and outer layers on specimens oxidized in air at 1100°C for different periods of time. The ratio of layer thicknesses remains essentially constant during oxidation. This means that the mechanism must account for a continuous transport of cobalt through the inner layer and a resultant growth of the outer CoO layer.

Table I. Thickness of layers of specimens

	Oxidation period, hr		
	1	6.5	19
Thicknesses of inner layer, mm	0.01	0.034	0.1
Thicknesses of outer layer, mm	0.006	0.02	0.06
Ratio of layer thicknesses, inner/outer	1.67	1.7	1.67

This cobalt transport could conceivably take place by a diffusion through the spinel phase. However, the measured diffusion rate through the spinel is much too low (3) to account for the oxidation rates. Furthermore, the electron-microprobe analysis indicates that the spinel composition changes from approximately $CoCr_2O_4$ next to the alloy/oxide interface to $Co_{1.3}Cr_{1.8}O_4$ at the interface between the inner and outer layers [Fig. 15(a), (b), and (c)]. On this basis, a cobalt transport through the spinel phase is also highly improbable, as it would involve diffusion against the concentration gradient.

The inner layer also contains the CoO phase, and by analogy with the oxidation behavior of Co-10 w/o Cr (1, 2), we conclude that the CoO phase in the inner layer is present as a network which provides a continuous path for the outward migration of cobalt. As the diffusion coefficient of cobalt ions in CoO is 10^3 times higher than in the spinel, the fractional cross section of these channels need be only of the order of 0.001 of the total cross section to allow faster transport of Co cations than in the surrounding spinel.

In addition to the outward cobalt-diffusion, the over-all oxidation involves a continuous formation of Cr_2O_3 in the alloy phase (internal oxidation) or at the alloy/oxide interface. This leads to an enrichment of cobalt in the very outer layer of the metal phase; the cobalt is oxidized to CoO, which in turn reacts to form the spinel. As a result of the outward diffusion of cobalt and the growth of the outer CoO layer, appreciable porosity is formed in the inner layer. As described elsewhere (1, 2), oxygen is probably transported across the pores in the gaseous state, and the

porosity serves to partially short circuit the solid-state diffusion through the scale. The spinel phase, on the other hand, inhibits the oxidation by decreasing the effective CoO diffusion area in the inner scale.

In the previous considerations of the oxidation mechanism of Co-10 w/o Cr, the short-circuiting effect of the pores and the blocking effect of the spinel have been incorporated in the ideal expression for the parabolic growth of compact scales (1, 2). The resultant expression for the oxidation rate is given by (2)

$$\frac{dx}{dt} = k_p \frac{\left(1 - \frac{S_o}{A}\exp\frac{Q}{RT}\right)}{x(1-\gamma)} = \frac{k_p''}{x} \qquad [1]$$

k_p is the parabolic rate constant for growth of a compact scale, S_o/A is a parameter related to the relative blocking cross section of the spinel, Q is the activation energy associated with the increase in the radius of the spinel particles with temperature, and γ is a constant which expresses the fractional reduction in the total diffusion length, x.

Equation [1] gives an approximate phenomenological description of parabolic oxidation of Co-10 w/o Cr (1, 2). At high partial pressures of oxygen, Co-25 w/o Cr yields oxide scales with the same type of microstructure, but with a higher spinel content in the inner layer. It is believed that Eq. [1] similarly applies to the parabolic oxidation of Co-25 w/o Cr after extended oxidation. However, the spinel is, in this case, the major oxide, in contrast to the situation in Co-10 w/o Cr, and the expression $(S_o/A)\exp(Q/RT)$ should be replaced by a single parameter A describing the fractional cross section of the CoO phase. The pressure and temperature dependence of A are not easily predicted, and the activation energy at high oxygen pressures in Fig. 9, cannot be simply interpreted.

In accordance with this interpretation, the parabolic rate constant for the oxidation at the high oxygen pressures suggests a pressure dependence $k_p \propto p_{O_2}^{1/n}$, where n has the value of approximately 3. This is the same as that observed for unalloyed cobalt and Co-10 w/o Cr.

In contrast to cobalt and Co-10 w/o Cr, the oxidation of Co-25 w/o Cr exhibits a marked deviation from parabolic behavior during the initial oxidation stages. As a clue to the origin of this behavior, it was noted that exposure of specimens to the "vacuum" of the reaction furnace before introduction of oxygen resulted in thin films of Cr_2O_3. Thus the short vacuum treatment ($\sim 10^{-5}$ Torr) before the actual oxidation runs resulted in selective oxidation of chromium. In order to further study this aspect, specimens were exposed to the "vacuum" for different lengths of time before introducing the oxygen. The results at 1300°C are shown in Fig. 18. An increasing "vacuum" exposure drastically decreased the initial oxidation rate. We conclude that this is due to the formation of increasingly thicker films of Cr_2O_3.

If these Cr_2O_3 films are compact and assuming an unlimited supply of chromium from the alloy, one would expect the Cr_2O_3 films to continue their growth and the formation of the duplex scale would in this case not take place. However, the initial protective film of Cr_2O_3 will probably be broken down for two main reasons: (*i*) the alloy phase next to the oxide phase will be depleted in chromium; the rate of Cr_2O_3 growth will correspondingly be reduced and, eventually, formation of CoO and spinel will begin to take place beneath the outer Cr_2O_3 layer; (*ii*) the outer Cr_2O_3 layer will continuously evaporate, probably as CrO_3. These combined effects plus a change in the effective diffusional area through the solid-state reaction of CoO + Cr_2O_3 to the spinel will yield an initial nonparabolic behavior. After evaporation of the initial Cr_2O_3 film, the characteristic duplex scales will eventually be formed and the oxidation will then follow an approximately parabolic rate. The thicker the initial Cr_2O_3 film (Fig. 18) is, the longer the duration of the initial stage will be. This critical dependence of the pretreatment of the specimens will also significantly affect the reproducibility of parallel runs unless the experimental procedure is exactly the same from run to run. Such differences in vacuum exposure are partially responsible for the large scatter observed in k_p at 900°C in Fig. 8. The actual values of A and their pressure and temperature dependence will also be affected by the initial conditions. The deviation from parabolic behavior during the initial oxidation period may be rationalized on the basis of a time-dependent A. A more detailed model for the initial oxidation period will be published soon (4).

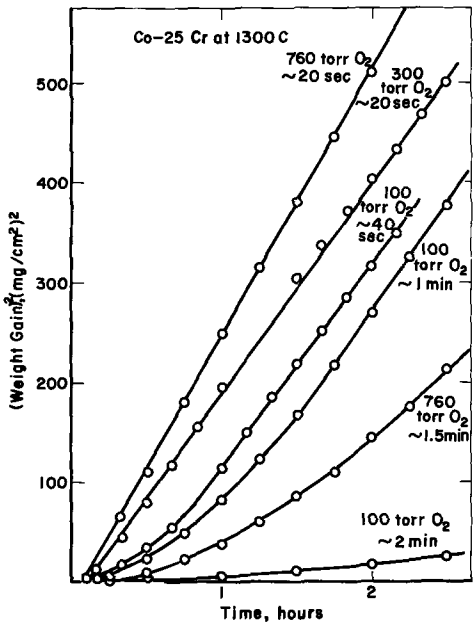

Fig. 18. Oxidation of Co-25Cr alloys at 1300°C in oxygen at pressures from 100 to 760 Torr. The various vacuum exposure periods are given by each line.

Oxidation at low partial pressures.—The abrupt decrease in the rate of oxidation in going from the high- to low-pressure regions is due to a transition to selective oxidation of chromium to Cr_2O_3 at low pressures. When neglecting the edge effects, the difference in oxidation rates reflects the improved oxidation resistance of Cr_2O_3 scales compared with the duplex scales.

An accurate analysis of the kinetic data is made difficult by the fact that part of the total weight gain is due to the edge oxidation. Furthermore, some evaporation of chromium oxide takes place, although this may be relatively small at the reduced pressures.

The oxidation at low pressures is, as a first approximation, independent of oxygen pressure. This is consistent with the fact that the main part (the flat surfaces) of the surfaces is covered with Cr_2O_3 and that oxidation of unalloyed chromium to Cr_2O_3 is also independent of oxygen pressure. A slight tendency toward increased net weight gain with decreasing oxygen pressure may possibly reflect an effect of decreased oxide (CrO_3) evaporation with decreased oxygen pressure. However, this must be confirmed by additional measurements.

The approximate parabolic rate constant at 10 Torr O_2 yields an activation energy of about 50 kcal/mole. This may be compared with the value of 59 kcal/mole for high-purity chromium (5). It has been concluded that growth of Cr_2O_3 is governed by chromium diffusion through the scale (5).

The reason for the edge effects is not clear. It may be speculated that they are due to the large surface-to-bulk ratio at the edges. This will result in a fast depletion of chromium in the alloy phase at the edges

and correspondingly make conditions favorable for CoO and subsequent spinel formation.

Acknowledgment

The authors wish to thank Mr. R. O. Dodds, whose assistance in the various experimental phases of this work made this publication possible. This work was supported by NASA under Research Grant NGR-36-002-070.

Manuscript submitted April 9, 1969; revised manuscript received *ca.* May 30, 1969.

Any discussion of this paper will appear in a Discussion Section to be published in the June 1970 JOURNAL.

REFERENCES

1. P. Kofstad and A. Z. Hed, *This Journal*, **116**, 225 (1969).
2. P. Kofstad and A. Z. Hed, *ibid.*, **116**, 229 (1969).
3. A. Morkel and H. Schmalzried, *Z. Phys. Chem. Neue Folge*, **32**, 76 (1962).
4. P. Kofstad and A. Z. Hed, To be published.
5. W. C. Hagel, *Trans. ASM*, **56**, 583 (1963).

Magnetochemistry of Manganese in Fluorapatite and Chlorapatite

J. A. Parodi

General Electric Company, Lighting Research Laboratory, Nela Park, Cleveland, Ohio

ABSTRACT

Magnetic susceptibility determinations were made on apatites of the composition, $Ca_{10-\alpha}Mn_\alpha X_2(PO_4)_6$, where α varies from 0.1 to 5.0 and X is Cl or F. Values of the effective magnetic moment close to 5.92 are evidence for all of the manganese being divalent, and linear change of lattice parameters and refractive indices with manganese concentration indicate complete solid solution of manganese. For both chlorapatite and fluorapatite the Weiss constant varies linearly with manganese concentration, with the magnetic interaction being somewhat larger for the former. The linear variation of the Weiss constant is interpreted as indicating a constant distribution ratio of manganese between the two cation sites in the apatite structure.

Knowledge of the environment of manganese in halophosphate phosphors is important to an understanding of its function as an activator. While it is true that this problem has been the object of a moderate amount of research, the question of the crystalline environment of manganese and its interaction with its surroundings is still not settled. It is clear from electronic paramagnetic resonance (EPR) studies (1-3) that manganese preferentially occupies cation sites of trigonal symmetry in fluorapatite, the Ca(I) sites, when its concentration is roughly two orders of magnitude less than amounts used in lamp phosphors. EPR studies by Piper and Prener on single crystals of chlorapatite (4) show that manganese is distributed among the four Ca(I) and six Ca(II) sites. Ohkubo and Mizuno (5) interpret EPR spectra of synthetic polycrystalline "$3[Ca_3(PO_4)_2]$ · $Ca(F_{1-x}, Cl_x)$: Mn (ratio of Mn- to Ca-ion is 1:200)" as indicating that Mn^{++} gradually shifts from the Ca(I) site to the Ca(II) site as x increases from 0 to 0.18. Johnson (6) has interpreted polarized luminescence experiments, as well as EPR measurements, as indicating that luminescent Mn^{++} is at Ca(I) positions in fluorapatite and at Ca(II) positions in chlorapatite. Johnson's crystals contained two or four orders of magnitude less manganese than commercial halophosphate phosphors.

Unfortunately all of the above researchers investigated materials with very low manganese content, so that one cannot with confidence extrapolate their conclusions to halophosphates containing much higher concentrations of manganese. The distribution of manganese between the two cation sites may be a function of manganese concentration. For a given paramagnetic ion the value of the Weiss constant, Δ, determined by magnetic susceptibility measurements, is dependent on the crystalline environment of the ion (7). Thus, a determination of Δ for Mn^{++} would be expected to yield information not only on the distribution of manganese between the Ca(I) and Ca(II) positions, but, hopefully, also on the manner in which manganese interacts with its surroundings. The following work is concerned with the magnetic susceptibility of $Ca_{10-\alpha}Mn_\alpha X_2(PO_4)_6$, where X is F or Cl and α varies from 0.1 to 5.0.

Experimental

Preparation of materials.—Calcium, manganese chlorapatites were produced from appropriate mixtures of manganous orthophosphate, calcium orthophosphate, calcium carbonate, and ammonium chloride in 50% excess. The mixtures were fired for 1 hr in telescoping fused silica crucibles in a stream of nitrogen passed over NH_4Cl at 300°. Firing temperature ranged from 1000° for low manganese content to 850° for high manganese concentration.

Fluorapatites were prepared from similar mixtures except that stoichiometric proportions of calcium fluoride were used in place of ammonium chloride. They were fired two times for 1 hr in a purging atmosphere of CO/CO_2 = 1/10 at temperatures ranging from 950° to 1100°.

The resulting apatites were pure white to cream colored depending on manganese concentration. They sintered, but the chlorapatites were easily converted to free flowing powders by heating in water. Presumably a little calcium chloride cement was produced during firing. The fluorapatites were ground by mortar and pestle and passed through a 100 mesh silk screen.

$Mn_3(PO_4)_2$ was prepared by firing a mixture of $MnNH_4PO_4 \cdot H_2O$ and $MnCO_3$ two times at 850° in a nitrogen atmosphere. $Ca_3(PO_4)_2$ was prepared by firing a mixture of phosphor grade $CaHPO_4$ and $CaCO_3$ in nitrogen at 1000°.

Magnetic susceptibility.—The Faraday method (8), with a Mettler microbalance and pole caps after the design of Heyding, Taylor, and Hair (9), was used

for the magnetic susceptibility determinations. Mercury tetrathiocyanatocobaltate, $HgCo(CNS)_4$, and trisethylenediamine nickel thiosulfate, $Nien_3S_2O_8$, were used as calibration standards (10, 11). The sample container, which was made of fused silica, was a cylindrical bucket (7 mm ID x 8 mm) attached to a rod (20 cm x 2 mm diameter) by means of a stirrup. During measurement the sample container was surrounded by an atmosphere of nitrogen. As no trace of ferromagnetism was evident in any of the samples measured, the susceptibilities reported here are averages of determinations at several different values, usually ten, of the magnetic field. Susceptibility determinations were made at four different temperatures: room temperature and the boiling points of nitrogen, ethane, and dichlorodifluoromethane. The boiling points at 1 atm pressure are 77.3°, 184.6°, and 243.4°K, respectively.

Analytical.—Unit cell dimensions were determined by a standard x-ray diffraction technique.

Refractive indices were determined with the aid of a microscope by immersion in standard refractive index oils.

Manganese was determined either volumetrically by the bismuthate method (12), or spectrophotometrically after oxidation to permanganate by potassium periodate (13).

For the few chlorapatites subjected to complete compositional analysis, calcium was determined gravimetrically as the oxide after a double precipitation as the oxalate (14), phosphate was determined gravimetrically as magnesium pyrophosphate after a molybdate separation and a double precipitation as magnesium ammonium phosphate (14, 15), and chloride was determined by the Volhard method (16).

Results and Discussion

Refractive index as a function of manganese concentration is given in Fig. 1. It is seen that the refractive index increases linearly with manganese content. Figure 2 shows that the unit cell volume for the chlorapatites decreases regularly with increasing manganese concentration. In Fig. 3 it is seen that the spacing of the (211) plane of fluorapatite decreases progressively with increasing manganese concentration. Chemical analyses of the calcium manganese chlorapatites (Table I) show only small deviations from stoichiometry, indicating the presence of only minor proportions of impurity phases. It is, thus, reasonable to conclude that, for the purpose of magnetic susceptibility determinations, all of the manganese is in solid solution in a single apatite phase.

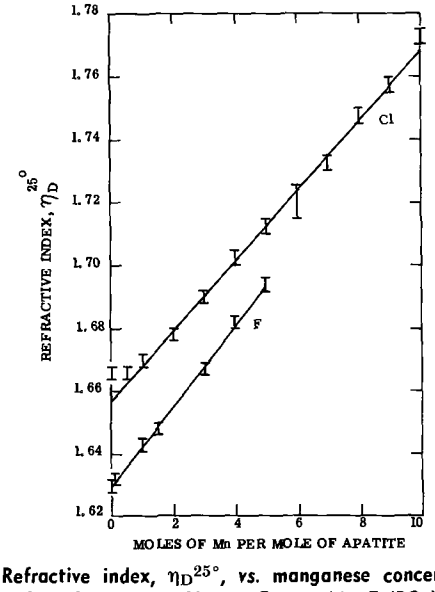

Fig. 1. Refractive index, $\eta_D^{25°}$, *vs.* manganese concentration in $Ca_{10-\alpha}Mn_\alpha Cl_2(PO_4)_6$, curve Cl, and $Ca_{10-\alpha}Mn_\alpha F_2(PO_4)_6$, curve F.

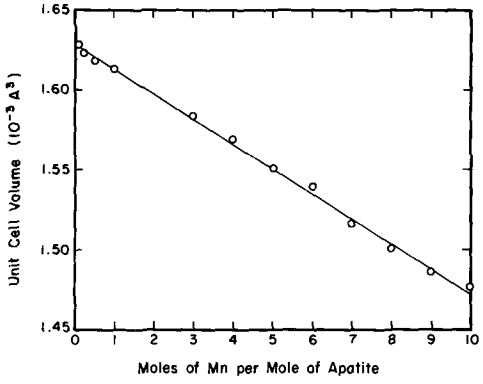

Fig. 2. Unit cell volume of $Ca_{10-\alpha}Mn_\alpha Cl_2(PO_4)_6$ *vs.* concentration of manganese.

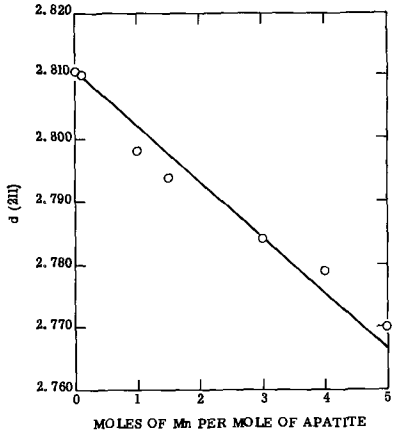

Fig. 3. Distance between (211) planes of $Ca_{10-\alpha}F_2(PO_4)_6$ *vs.* concentration of manganese.

Magnetic susceptibilities are listed in Tables II and III. The average standard deviation of a single measurement is 0.2%.

The temperature dependence of the magnetic susceptibility for these apatites follows the Curie-Weiss law, which has the form

$$\chi = \frac{C}{T+\Delta} + A \qquad [1]$$

Here C is the Curie constant, Δ is the Weiss constant which is expressed as an additive correction to the temperature, and A is the experimentally determined diamagnetic susceptibility of the apatite: —0.3604 x 10^{-6} cgs units for chlorapatite and —0.3406 x 10^{-6} for fluorapatite. A rearrangement of the above equation gives

$$T = -\Delta + \frac{C}{\chi + A} \qquad [2]$$

so that Δ is determined experimentally by plotting the absolute temperature against the reciprocal of the paramagnetic susceptibility. A best fit of the data to a straight line is easily and most accurately done by a least squares calculation on a computer. This was done

Table I. Chemical analysis of $Ca_{10-\alpha}Mn_\alpha Cl_2(PO_4)_6$

Manganese concentration	Weight per cent				
α	Ca	PO_4	Cl	Mn	Total
1	34.7	54.5	5.8	4.8	99.8
5	18.1	51.8	5.8	23.8	99.5
7	10.8	50.6	5.8	31.7	98.9
10	0.0	48.9	6.8	43.9	99.6

Table II. Magnetic susceptibility of $Ca_{10-\alpha}Mn_\alpha Cl_2(PO_4)_6$

α	Run No.	T_0, °K	$10^6\chi_0$	T_1, °K	$10^6\chi_1$	T_2, °K	$10^6\chi_2$	$10^6\chi_3$*
0	1	R. T.	−0.3598					
	2	R. T.	−0.3608					
	3	R. T.	−0.3619					
	4	R. T.	−0.3591					
0.1	1	298.8	0.8598	243.1	1.134	184.8	1.610	4.241
	2	297.7	0.8620	241.5	1.144	183.3	1.605	4.228
	3	297.3	0.8706	241.5	1.143	182.5	1.612	4.272
	4	296.1	0.8696	241.8	1.145	182.2	1.619	4.240
0.2	1	295.3	2.097	242.2	2.623	183.2	3.575	8.812
	2	295.6	2.090	242.1	2.618	182.8	3.559	8.800
	3	295.8	2.091	243.4	2.610	183.0	3.554	8.819
0.5	1	296.1	5.822	242.7	7.144	183.4	9.472	22.27
	2	295.1	5.845	242.5	7.149	183.3	9.455	22.34
	3	294.6	5.862	242.7	7.140	182.8	9.443	22.27
1.0	1	294.0	12.38	244.0	14.84	183.8	19.49	44.44
	2	294.7	12.34	243.7	14.83	183.2	19.55	44.40
	3	295.9	12.29	248.9	14.67	182.9	19.60	44.48
2.0	1	294.6	24.24	243.4	29.10	183.7	37.91	81.58
	2	295.2	24.16	242.8	28.96	183.3	37.68	81.73
	3	297.2	23.98	242.9	28.93	183.6	37.58	81.98
3.0	1	296.1	35.89	241.5	43.13	182.8	55.26	114.1
	2	296.1	35.93	242.4	43.08	182.8	55.42	114.2
	3	296.0	35.87	242.2	43.00	183.3	55.22	114.1
4.0	1	295.8	46.47	242.7	54.81	181.6	70.18	138.5
	2	293.7	46.52	242.1	55.06	182.2	70.04	138.9
	3	295.1	46.28	243.1	54.64	181.5	69.85	138.5
5.0	1	294.9	55.95	241.9	66.01	183.5	83.42	159.7
	2	293.1	56.05	242.0	65.93	183.4	83.34	159.1
	3	294.1	56.04	243.9	65.84	182.9	83.32	159.3

* Temperature = 77.3°K.

Table III. Magnetic susceptibility of $Ca_{10-\alpha}Mn_\alpha F_2(PO_4)_6$

α	Run No.	T_0, °K	$10^6\chi_0$	T_1, °K	$10^6\chi_1$	T_2, °K	$10^6\chi_2$	$10^6\chi_3$*
0	1	R. T.	−0.3406					
	2	R. T.	−0.3394					
	3	R. T.	−0.3397					
	4	R. T.	−0.3434					
	5	R. T.	−0.3399					
0.1	1	299.2	1.058	242.0	1.380	183.2	1.931	5.005
	2	300.2	1.071	244.0	1.378	184.6	1.920	4.983
	3	299.2	1.065	243.4	1.376	184.0	1.925	4.961
1.0	1	297.2	13.65	242.9	16.61	183.5	21.88	50.86
	2	296.4	13.61	243.2	16.57	183.6	21.84	50.62
1.5	1	298.2	20.84	242.7	25.41	183.4	33.09	75.37
	2	297.0	20.96	243.4	25.36	183.6	33.15	75.48
3.0	1	295.8	40.16	243.3	48.54	184.6	63.08	138.6
	2	296.9	40.15	242.8	48.58	183.3	63.14	138.5
	3	295.6	40.21	243.1	48.55	183.8	63.09	138.3
4.0	1	297.5	51.43	243.2	61.96	183.9	79.86	170.4
	2	298.4	51.33	243.3	62.01	183.7	79.96	171.2
	3	298.3	51.40	243.5	61.98	183.8	79.93	170.4
5.0	1	298.8	61.83	242.9	74.83	183.3	96.23	200.3
	2	298.1	61.84	243.3	74.48	183.8	95.97	200.6
	3	297.9	61.85	243.5	74.54	183.5	95.94	200.2

* Temperature = 77.3°K.

Table IV. Weiss constant for $Ca_{10-\alpha}Mn_\alpha Cl_2(PO_4)_6$ and $Ca_{10-\alpha}Mn_\alpha F_2(PO_4)_6$

α	Chlorapatite* Δ, °K	σ	Fluorapatite† Δ, °K	σ
0.1	2.9	0.4	1.9	0.6
0.2	2.9	0.4		
0.5	5.5	0.4		
1.0	9.3	0.0	5.4	0.3
1.5			7.7	0.0
2.0	15.8	0.3		
3.0	24.5	0.2	13.3	0.2
4.0	34.0	0.7	19.0	0.4
5.0	41.3	0.5	22.1	0.3

* For chlorapatite, $\chi = \dfrac{C}{T + \Delta} - 0.3604 \times 10^{-6}$.

† For fluorapatite, $\chi = \dfrac{C}{T + \Delta} - 0.3406 \times 10^{-6}$.

for the data in Tables II and III, and the results are given in Table IV and Fig. 4.

Before discussing the significance of the Weiss constant determination, it is necessary to ascertain the oxidation state of the manganese. From the method of preparation and the color of the samples, as well as the fact that manganese substitutes for divalent calcium in apatite, one might assume with reasonable certainty that all of the manganese is divalent. However, the value of the effective magnetic moment is the best indication of the oxidation state of manganese. We have seen that the experimental susceptibilities obey a Curie-Weiss law, which, substituting fundamental constants for the Curie constant, C, can be written

$$\chi_M = \frac{N\beta^2\mu_{eff}^2}{3k(T + \Delta)} = \frac{4N\beta^2 S(S + 1)}{3k(T + \Delta)} \qquad [3]$$

where χ_M is the temperature dependent molar paramagnetism. Rearranging and putting in numerical values for the constants, the effective magnetic moment is expressed in terms of experimentally determined parameters

$$\mu_{eff}^2 = 8.060\ (T + \Delta)\ \chi_M \qquad [4]$$

Results of this calculation appear in Tables V and VI. From equation [3], $\mu_{eff}(Mn^{+2}) = 5.92$ and $\mu_{eff}(Mn^{+3}) = 4.90$, so that, therefore, the experimental magnetic moments of Tables V and VI establish the fact that all of the manganese is divalent. Further, we see that,

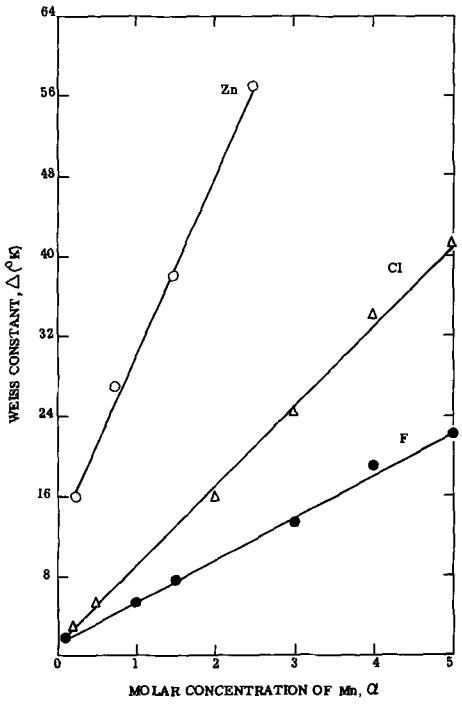

Fig. 4. Weiss constant of manganese in fluorapatite and chlorapatite, $Ca_{10-\alpha}Mn_\alpha X_2(PO_4)_6$, curves F and Cl, and in zinc silicate, $Zn_{12-\alpha}Mn_\alpha(SiO_4)_6$, curve Zn, vs. molar manganese concentration α.

Table V. Effective magnetic moment of manganese in $Ca_{10-\alpha}Mn_\alpha Cl(PO_4)_6$

α	Wt. % Mn	μ_{eff}	$100\dfrac{5.92 - \mu_{eff}}{5.92}$
0.1	0.48	5.83	1.5
0.2	0.92	5.94	0.3
0.5	2.48	5.77	2.5
1.0	4.8	5.97	0.8
2.0	9.68	5.91	0.2
3.0	14.66	5.93	0.2
4.0	19.39	5.93	0.2
5.0	23.8	5.93	0.2

$\mu_{eff}^2 = \dfrac{3k}{N\beta^2}(T + \Delta)\ \chi_M = 8.060\ (T + \Delta)\ \chi_M$.

$\chi_M = \dfrac{54.94}{N_1}(\chi + 0.3604 \times 10^{-6})$ where N_1 is the weight fraction of Mn in the apatite.

Table VI. Effective magnetic moment of manganese in $Ca_{10-\alpha}Mn_\alpha F_2(PO_4)_6$

α	Wt. % Mn	μ_{eff}	$100\frac{5.92-\mu_{eff}}{5.92}$
0.1	0.56	5.78	2.4
1.0	5.32	5.92	0.0
1.5	8.15	5.92	0.0
3.0	15.81	5.93	0.2
4.0	20.63	5.93	0.2
5.0	25.50	5.87	0.8

$\mu_{eff}^2 = \frac{3k}{N\beta^2}(T + \Delta)\chi_M = 8.060\ (T + \Delta)\chi_M$.

$\chi_M = \frac{54.94}{N_1}(\chi + 0.3406 \times 10^{-6})$ where N_1 is the weight fraction of Mn in the apatite.

as is to be expected for an S state transition metal ion, the "spin-only" formula [3] is obeyed very closely.

Van Vleck (7) interprets the Weiss constant as primarily a manifestation of distortions by interatomic forces. It is not an atomic property as is clear from the fact that it varies markedly from one compound to another of a given paramagnetic ion, whereas μ_{eff} is relatively constant. Its origin can be twofold: Δ can arise from (*i*) Heisenberg exchange interaction (direct or super-) between magnetic dipoles and/or (*ii*) interaction of the orbital angular momentum with asymmetric crystalline electric fields. In the case of S state ions such as Mn^{++} and Fe^{+++}, which have no orbital angular momentum, Δ is due only to exchange interaction and should approach zero at infinite magnetic dilution. It is clear that spin-spin interaction will be a function of the kinds and arrangements of intervening diamagnetic ions. To be specific, differences in the crystalline environment of Mn^{++} between fluorapatite and chlorapatite should appear as different values of the Weiss constant.

Inspection of Fig. 3, which is a plot of Δ against manganese concentration, reveals that there is indeed a difference in the exchange interaction between the two structures. The interaction of Mn^{++} in chlorapatite is substantially greater than in fluorapatite. In both cases, Δ is a linear function of manganese concentration and its sign is positive.

In the apatite structure there are four calcium ions of one kind, Ca(I), and six of another, Ca(II), per unit cell (17-19). The first of these, which is the same in both fluor- and chlorapatite, is a site of trigonal symmetry in which Ca^{++} is in the center of a skewed triangular prism of oxygen ions. In the second site each calcium ion is in a reflection plane perpendicular to the trigonal axis and is surrounded by an irregular polyhedron of one halide and five oxygen ions. In fluorapatite the fluoride ion is at the center of a regular triangle of calcium ions of the second kind, whereas in chlorapatite the chloride ion is shifted along the C_0 axis to a position somewhat less than half the distance from one mirror plane of calcium ions to the next.

From the crystal structure it is clear that differences in Δ can only be caused by interactions of Mn^{++} in locations near the halide ions. The larger values of the Weiss constant in chlorapatite are, therefore, caused by the presence of manganous ions at Ca(II) positions. From geometrical considerations one would expect Mn^{++} ions at the Ca(II) sites to be less well shielded from one another by intervening anions in chlorapatite and, therefore, to interact more strongly. Although there are six Ca(II) locations available in both apatites for occupation by Mn^{++}, it is extremely unlikely that, at the higher concentrations especially, all of the manganese would preferentially seek out these positions. On the other hand it is not possible at the highest concentration for all of the manganous ions to be in Ca(I) sites. It is, therefore, more reasonable to assume a distribution between the two sites in both chlorapatite and fluorapatite. From the observation that Δ is a linear function of manganese concentration from $\alpha = 0.1$ to 5.0, it is concluded that the distribution ratio of Mn^{++} between Ca(I) and Ca(II) sites is constant with change in manganese content. It is not possible to determine, from the data presented here, the numerical value of the distribution ratio, nor whether it differs from fluorapatite to chlorapatite.

The conclusion that manganese substitutes for both types of calcium ions is in agreement with the EPR results of Piper and Prener for much lower manganese concentration in chlorapatite (4), but it does not agree with the EPR studies on fluorapatite (1-3) which place Mn^{++} at Ca(I) positions. It would appear that manganese shifts from Ca(I) positions to a distribution between Ca(I) and Ca(II) as its concentration in fluorapatite increases from about Mn/Ca = 10^{-3} to 10^{-1}.

The positive sign of Δ indicates that the exchange interaction is antiferromagnetic. Griffith (20) considers the case of direct exchange between ions of a pair, the interaction given by $-J\bar{S}_1\cdot\bar{S}_2$. J is a constant commonly called the "exchange integral" and $\bar{S}_1$ and $\bar{S}_2$ are the spin vectors for the two ions. He obtains a spin Hamiltonian for the pair

$$H = -\tfrac{1}{2}JS(S+1) + 2\beta\bar{H}\cdot\bar{S} + \tfrac{3}{4}J$$

which shows that in zero magnetic field there are a singlet and a triplet state with energy separation, J. For positive J the triply degenerate state lies lower and the interaction is ferromagnetic, whereas for negative J the spin multiplet is inverted and the exchange interaction is antiferromagnetic. Griffith derives an expression for the magnetic susceptibility

$$\chi = \frac{N\beta^2}{k\,[T - (J/4k)]}$$

which is equivalent to the Curie-Weiss law

$$\chi = \frac{N\beta^2\mu^2}{3k(T+\Delta)}$$

so that $\Delta = -J/4k$. Thus, Δ is positive for antiferromagnetic and negative for ferromagnetic direct exchange.

Interaction via an intervening anion between two cations with half filled d-orbitals, *i.e.*, superexchange, is always antiferromagnetic (21, 22). This is readily understood if we consider the linear combination, $Mn^{++}-O^{=}-Mn^{++}$. There is an overlap of a $p\sigma$ orbital of $O^{=}$ with the d-orbitals of the Mn^{++} ions. The transfer of a p-electron to one Mn^{++} ion must be into an empty half of a d-orbital, so that by the Pauli exclusion principle, the p-electron left behind must have a spin parallel to those of the Mn^{++} d-electrons. In order for the remaining p-electron to transfer to the Mn^{++} ion on the opposite side, therefore, the spins of the latter must be opposed to the spins of the first Mn^{++} and the exchange is antiferromagnetic. When the angle made by Mn-O-Mn is 90° rather than 180° as in the above example, it should be clear from geometrical considerations that direct cation-cation exchange is more significant and cation-anion-cation exchange is less significant. The over-all effect is still antiferromagnetic and is greater for oxides than chlorides because of the shorter cation-cation distance in the former (23).

It is clear that the greater the overlap of the ligand wave function with the paramagnetic cation wave function, *i.e.*, the more covalent the bond, the greater is the superexchange. On this basis one would expect superexchange between Mn^{++} ions to be greater through chloride ions than through fluoride ions. In the two apatites, however, by virtue of the fact that the fluoride and chloride ions occupy different posi-

tions relative to Ca(II), the cation-anion overlap is probably greater for the former. This might be sufficient to create at the halide site more superexchange in fluorapatite, and the geometrical factors will almost certainly cause greater direct exchange in chlorapatite. The net effect, as we have seen, is a substantially larger antiferromagnetic exchange interaction for Mn^{++} in chlorapatite.

It is of interest to compare the magnetic interaction of manganese in the apatites with that of manganese in zinc silicate. For this purpose the results of Larach and Turkevich (24) are plotted, together with the present data on apatites, in Fig. 3. It is seen that Δ for Mn^{++} is much larger in zinc silicate than in the apatites. The stronger interaction can be explained on the basis of a difference in bonding.

The bonding between Ca^{++} ions and coordinating anions in apatite has more ionic character than Zn-O bonds in zinc silicate. Cation to anion distances in the apatites are very close to the sums of the corresponding ionic radii of Goldschmidt (25) and Pauling (26). Further, the value of the hyperfine splitting constant for Mn^{++} in the Ca(I) position, about 93 oersteds for an X-band EPR spectrometer, indicates relatively strong ionic bonding (1-3). Van Wieringen (27) has shown that the hyperfine splitting of Mn^{++} is large in ionic compounds, 99 and 91 oersteds in CaF_2 and CaO, and relatively small in covalent compounds, 65 and 59 oersteds in ZnSe and CdTe. In zinc silicate a hyperfine splitting of 84 oersteds (28) indicates that the bonding is intermediate between that of compounds that are usually considered strongly ionic and strongly covalent. Also the Zn-O distance of 1.92Å (29) corresponds more closely to the sum of the covalent radii (30) than to the sum of the ionic radii. The result of this difference in character of bonding is a larger Weiss constant for Mn^{++} in zinc silicate: greater superexchange because of greater overlap of the wave functions and greater direct exchange because of smaller intervening anions.[1]

It would be of interest to determine Δ for Mn^{++} in apatites containing both F^- and Cl^-. In halophosphate phosphors a relatively low concentration of Cl^- has a profound effect on the wavelength of Mn^{++} emission. For example Apple and Ishler (31) report a Mn^{++} emission peaking at 5720Å in calcium fluorophosphate phosphor, 5860Å in calcium chlorophosphate, and 5830-5850Å[2] in calcium chlorofluorophosphate in which about 10% of the fluoride has been replaced by chloride. One wonders whether a similar disproportionate effect on the exchange interaction of manganese would occur. Apple and Ishler (31) have interpreted changes in the luminescence emission of Mn^{++} in chlorophosphates and chlorofluorophosphates quenched from 1150° as due to possible redistribution of Mn^{++} between the Ca(I) and Ca(II) sites. In view of the above discussion one might expect to see a change in Δ for quenched samples. Also it is not inconceivable that the presence of antimony would cause a change in Δ, either by creating a difference in manganese distribution between the two cation sites and/or causing an environmental change which would disturb the exchange interaction.

Acknowledgments

The author is indebted to Paul A. Hurst and David W. Allen for invaluable assistance in the preparation of materials and carrying out the susceptibility determinations, to Miss Jeanette R. Cooper for determinations of the unit cell volume, and to Mrs. Mary Bradford and G. Dragt for wet chemical analyses.

Manuscript received June 18, 1969.

Any discussion of this paper will appear in a Discussion Section to be published in the June 1970 JOURNAL.

[1] Tetrahedral covalent radii of O, F, and Cl are 0.66, 0.64, and 0.99Å, respectively (30), whereas the corresponding ionic radii are 1.40, 1.36, and 1.81Å (26).

[2] Estimated from Fig. III of ref. (31).

REFERENCES

1. P. H. Kasai, *J. Phys. Chem.*, **66**, 674 (1962).
2. Y. Ohkubo, *J. Phys. Soc. Japan*, **18**, 916 (1963).
3. V. M. Vinokurov, M. M. Zaripov, and V. G. Stepanov, *Soviet Phys.*-Solid State (*Engl. Transl.*), **6**, 866 (1964).
4. W. W. Piper and J. S. Prener, To be published.
5. Y. Ohkubo and H. Mizuno, Abstract, International Conference on Luminescence, Budapest, 1966, "Electron Paramagnetic Resonance of Mn^{2+} Ions in Calcium Halophosphates."
6. P. D. Johnson, "Luminescence of Organic and Inorganic Materials," p. 563, H. P. Kallmann and G. M. Spruch, Editors, John Wiley & Sons, New York (1962).
7. J. H. Van Vleck, "The Theory of Electric and Magnetic Susceptibilities," p. 304, Oxford Univ. Press (1932).
8. P. W. Selwood, "Magnetochemistry," 2nd ed., p. 11, Interscience Publishers Inc., New York (1956).
9. R. D. Heyding, J. D. Taylor, and M. L. Hair, *Rev. Sci. Instr.*, **32**, 161 (1961).
10. B. N. Figgis and R. S. Nyholm, *J. Chem. Soc.*, **1958**, 4190.
11. N. F. Curtis, *ibid.*, **1961**, 3147.
12. I. M. Kolthoff and E. B. Sandell, "Textbook of Quantitative Inorganic Analysis," 3rd ed., p. 677, Macmillan Co., New York (1952).
13. E. B. Sandell, "Colorimetric Determination of Traces of Metals," 2nd. ed., p. 430, Interscience Publishers Inc., New York (1950).
14. J. I. Hoffman and G. E. F. Lundell, Bur. Standards *J. Res., Nat. Bur. Std.*, **20**, 608 (1938).
15. J. I. Hoffman and G. E. F. Lundell, *J. Assoc. Offic. Agr. Chemists*, **8**, 184 (1924).
16. I. M. Kolthoff and E. B. Sandell, *op. cit.*, p. 546; J. R. Caldwell and H. V. Moyer, *Ind. Eng. Chem., Anal. Ed.*, **7**, 38 (1935).
17. St. Náray-Szabó, *Z. Krist.*, **75**, 387 (1930).
18. M. Mehmel, *ibid.*, **75**, 323 (1930); *Z. Phys. Chem.*, **15A**, 223 (1931).
19. C. A. Beevers and D. B. McIntyre, *Mineral Mag.*, **27**, 254 (1956).
20. J. S. Griffith, "The Theory of Transition-Metal Ions," p. 276, Cambridge Univ. Press (1961).
21. P. W. Anderson, "Magnetism," Vol. I, Chap. 2, p. 48, G. T. Rado and H. Suhl, Editors, Academic Press, New York (1963).
22. J. B. Goodenough, "Magnetism and the Chemical Bond," p. 168, Interscience Publishers Inc., New York (1963).
23. *Op. cit.*, p. 182.
24. S. Larach and J. Turkevich, *Phys. Rev.*, **89**, 1060 (1953).
25. V. M. Goldschmidt, "Geochemische Verteilungsgesetze der Elemente," Skrifter det Norski Videnskaps-Akad. Oslo I. Matem.-Naturvid Klasse (1926).
26. L. Pauling, "The Nature of the Chemical Bond," 3rd ed., p. 514, Cornell University Press, Ithaca, New York (1960).
27. J. S. van Wieringen, *Discussions Faraday Soc.*, No. 19, 118 (1955).
28. Nancy H. K. Perkins, "Electron Paramagnetic Resonance of Mn^{+2} in Single Crystals of Zn_2SiO_4," Ph D. Thesis, Cornell University, 1965.
29. R. W. G. Wyckoff, "Crystal Structures," Vol. II, Tables VIII B, 9 and VIII B, 10, Interscience Publishers Inc., New York.
30. M. L. Huggins, *Phys. Rev.*, **28**, 1086 (1926); L. Pauling and M. L. Huggins, *Z. Krist.*, **87**, 205 (1934).
31. E. F. Apple and W. E. Ishler, "Luminescence of Organic and Inorganic Materials," p. 576, H. P. Kallman and G. M. Spruch, Editors, John Wiley & Sons, New York (1962).

Crystal Growth and Ferroelectric Properties of Single Crystals from the Ternary Systems of $KNbO_3$-$NaNbO_3$-$BaNb_2O_6$ and $RbNbO_3$-$NaNbO_3$-$BaNb_2O_6$

D. F. O'Kane,* G. Burns, E. A. Giess, B. A. Scott, A. W. Smith, and B. Olson

IBM Research Division, Yorktown Heights, New York

ABSTRACT

Good optical quality single crystals with a tungsten bronze crystal structure were grown by the Czochralski method from melts in the ternary systems of $(KNbO_3)_x$ $(NaNbO_3)_y$ $(BaNb_2O_6)_z$ and $(RbNbO_3)_x$ $(NaNbO_3)_y$ $(BaNb_2O_6)_z$, where $x < 0.34$, $y < 0.34$, and $z > 0.66$. X-ray, chemical, and differential thermal analyses were performed on the pulled crystals. The dielectric properties and twin structure of the crystals have been examined. Some compositions contain no microtwins while retaining the favorable electrooptic properties associated with $NaBa_2Nb_5O_{15}$.

A number of new electrooptic materials, such as $KSr_2Nb_5O_{15}$ (1) and $NaBa_2Nb_5O_{15}$ (2, 3), with a tungsten bronze structure have been reported to have improved linear electrooptic coefficients and are capable of efficient second harmonic generation. These materials do not suffer laser damage as has been the case with $LiNbO_3$, and some compositions can be grown as large optically homogeneous single crystals. In particular, $NaBa_2Nb_5O_{15}$ shows a great deal of promise, but a severe problem results from the presence of microtwins (4) which are difficult to remove and tend to degrade the optical quality.

The ferroelectric and electrooptic properties of tungsten bronze-type ferroelectric crystals pulled from melts of $K_xNa_{1-x}Ba_2Nb_5O_{15}$ have been reported (5). These compositions have many of the favorable properties of $NaBa_2Nb_5O_{15}$, including relative ease of growth. When $x \geq 0.7$ the difficulties of microtwinning are eliminated, resulting in better optical quality crystals. At $x = 0.8$, the ferroelectric transition temperature is 420°C, the room temperature dielectric constant is 55, and the electrooptic coefficient is 4.0×10^{-11} m/V. The latter value is 10% higher than $NaBa_2Nb_5O_{15}$. Laser induced optical inhomogeneities cannot be observed after extended exposure.

The present study is an extension of the work on $K_xNa_{1-x}Ba_2Nb_5O_{15}$ to include other compositions in the ternary system of $KNbO_3$-$NaNbO_3$-$BaNb_2O_6$ and to examine the effect of substituting $RbNbO_3$ for $KNbO_3$. We have studied single crystals pulled from melts of $(KNbO_3)_x$ $(NaNbO_3)_y$ $(BaNb_2O_6)_z$ and $(RbNbO_3)_x$ $(NaNbO_3)_y$ $(BaNb_2O_6)_z$ where $x < 34$, $y < 34$, and $z > 66$. These limits represent the approximate location of the ferroelectric tungsten bronze structures in the ternary systems. The two ternary systems are shown in Fig. 1 and 2. The compositions of interest melt in the range of 1390°-1460°C.

A knowledge of the ternary phase diagrams is necessary to understand what compositions can be expected by pulling crystals from a melt. There are three binary systems which are important to the behavior of the two ternary systems. These are the $NaNbO_3$-$BaNb_2O_6$, $KNbO_3$-$BaNb_2O_6$, and $RbNbO_3$-$BaNb_2O_6$ systems. Scott *et al.* (6) have examined the $NaNbO_3$-$BaNb_2O_6$ phase diagram and found an orthorhombic tungsten bronze structure which extends from 62 to 83 m/o (mole per cent) $BaNb_2O_6$ and eutectics at 23 and 85 m/o $BaNb_2O_6$. The maximum melting (1438°C) bronze composition was near 66.7 m/o $BaNb_2O_6$($NaBa_2Nb_5O_{15}$). Giess *et al.* (5) reported tetragonal tungsten bronze structures at 66.7 m/o $BaNb_2O_6$ in the $KNbO_3$-$BaNb_2O_6$ and $RbNbO_3$-$BaNb_2O_6$ systems. The compounds, $KBa_2Nb_5O_{15}$ and $RbBa_2Nb_5O_{15}$, decompose peritectically at 1391° and 1395°C, respectively.

Experimental Procedures

The starting materials were K_2CO_3, Na_2CO_3, $BaCO_3$, and Nb_2O_5 from the Johnson-Matthey Company, Grade

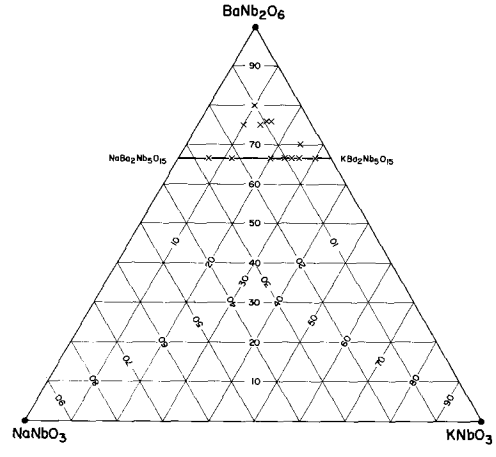

Fig. 1. Ternary system composed of $KNbO_3$, $NaNbO_3$, and $BaNb_2O_6$. The numbers indicate the mole per cent of each component. The points (x) show the melt compositions used for crystal growth.

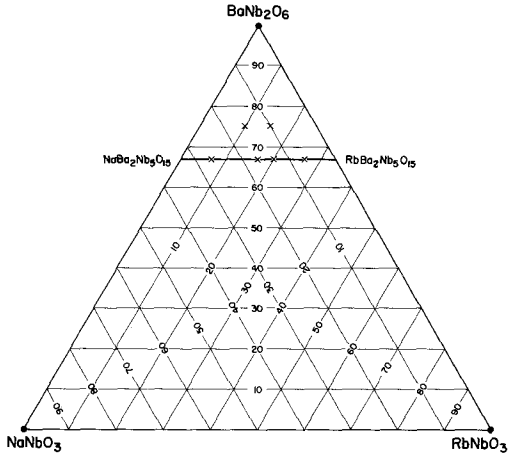

Fig. 2. Ternary system composed of $RbNbO_3$, $NaNbO_3$, and $BaNb_2O_6$. The numbers indicate the mole per cent of each component. The points (x) show the melt compositions used for crystal growth.

* Electrochemical Society Active Member.

I, with less than 10 ppm impurities, except for Nb_2O_5 which contained less than 0.03 w/o (weight per cent) Ta. The Rb_2CO_3 (99%) from Alfa Inorganics was found to contain Na, Al, Mg, Si, and Ca in quantities of less than 100 ppm. In some cases the Rb_2CO_3 was dried in CO_2 before using. Differential thermal analysis (DTA) was used to establish the freezing points of various compositions and to examine the melting and freezing behavior of pulled single crystals. Two gram powder samples of the pulled crystals or annealed powder samples were loaded in platinum capsules containing a thermocouple well in the bottom. The sample and alumina reference material were heated and cooled at 5°C/min.

Each composition was prepared by heating stoichiometric quantities of the starting materials to 1400°-1500°C in a 100 ml platinum crucible. A Czochralski type crystal pulling system (8) was used to obtain single crystals. A 23 kw r.f. generator supplied power to melt the charge in the platinum crucible, which was insulated by alumina pellets. Oxygen was passed into the system at 0.3 liters/min to avoid reduction of the crystals, which would result in a blue discoloration. Crystal growth was started with a seed crystal mounted on the pulling shaft. In many cases the seed was a single crystal of $NaBa_2Nb_5O_{15}$ with the c-axis oriented along the direction of crystal growth. Pull rates were about 2-6 mm/hr with a rotation rate of 40-60 rpm. The temperature gradient above the melt surface was about 18°C/mm for the first 5 mm and 1°C/mm for the next 50 mm. The system was usually cooled at 5°C/hr for the first 300°C and then at 15°C/hr to room temperature. Thus, the crystals were well annealed after growth, and cracking was not a serious problem. Rapid cooling did cause cracking normal to the c-axis.

Crystal growth of single phase ternary compositions was no more difficult than the growth of $NaBa_2Nb_5O_{15}$. The growth rates that were used appeared to be adequate to establish equilibrium conditions between the melt and freezing crystal, although none of the ternary compositions studied was found to be congruently melting; the crystal compositions always differed from the starting melt compositions. Some estimate of the change in composition can be seen in Fig. 3 and 4 which show the melt and pulled crystal compositions. The pulled crystal composition is the analyses obtained on the first 30g or less of crystal pulled from a 400g melt. These data are also listed in Tables I and II. The melt compositions with 66.7 m/o $BaNb_2O_6$ are part of the $K_xNa_{1-x}Ba_2Nb_5O_{15}$ or $Rb_xNa_{1-x}Ba_2Nb_5O_{15}$ pseudo-joins in the ternary systems. The evaporation of K_2O and Na_2O from melts of $K_xNa_{1-x}Ba_2Nb_5O_{15}$, where x = 0.7, 0.8, was not found to be significant. Pulled crystals from compositions held above the melting point for 20 to 430 hr showed no significant difference in chemical composition or Curie temperature. Also, the same shift in composition as shown in Fig. 3 was found

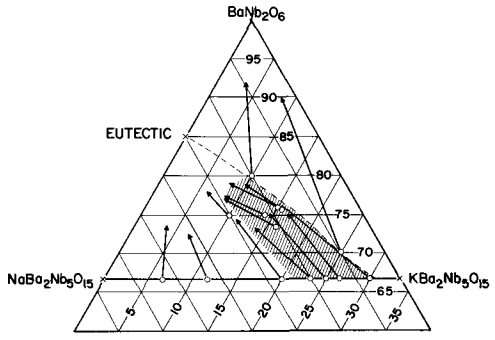

Fig. 3. Section of the ternary system of $KNbO_3$-$NaNbO_3$-$BaNb_2O_6$ showing the melt compositions (⊙) and the composition of pulled crystals (←) from each melt. The dashed line indicates the approximate location of the phase boundary between the $BaNb_2O_6$ and bronze phases. The shaded area is the region with a tetragonal bronze structure.

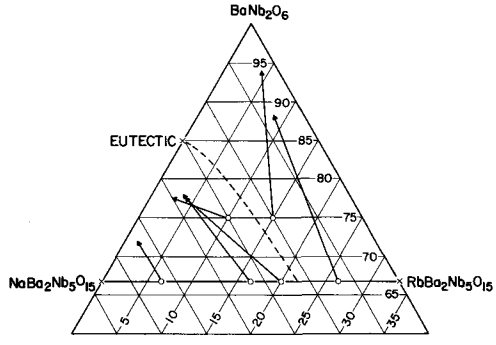

Fig. 4. Section of the ternary system of $RbNbO_3$-$NaNbO_3$-$BaNb_2O_6$ showing the melt compositions (⊙) and the compositions of pulled crystals (←) from each melt. The dashed line indicates the approximate location of the phase boundary between the $BaNb_2O_6$ and bronze phases.

for crystals grown by slowly cooling melts in sealed crucibles where no evaporation could take place.

Three Bridgman crystal growth runs were made to determine the phases present in particular compositions, the order in which the phases freeze out, and the lattice parameters and chemical composition of the first to freeze material. Two 300g samples of $(KNbO_3)_{16}$ $(NaNbO_3)_{11}$ $(BaNb_2O_6)_{73}$ and $Rb_{0.7}Na_{0.3}Ba_2Nb_5O_{15}$ and one 36g sample of $K_{0.85}Na_{0.15}Ba_2Nb_5O_{15}$ were loaded in platinum tubes which were lowered at 3 mm/hr through a platinum resistance heated furnace from a uniform zone at 1480°C into a colder zone with a gradient of 1.2°C/mm. Below 1200°C, the tubes were cooled at 50°C/hr. This method did not produce single crystals greater than 1 mm (3).

Table I. Composition and properties of crystals pulled from melts of $(KNbO_3)_x$ $(NaNbO_3)_y$ $(BaNb_2O_6)_z$

Melt composition, m/o			Crystal composition from chemical analyses, m/o			Crystal properties		Lattice parameters	
$KNbO_3$	$NaNbO_3$	$BaNb_2O_6$	$KNbO_3$	$NaNbO_3$	$BaNb_2O_6$	T_w, °C	T_c, °C	a_o, Å	c_o, Å
15	9	76	7.9	13.0	79.1	247	548	12.469*	4.001
6.7	22.6	66.7	3.5	22.6	73.9	217	538	12.471*	4.001
11.7	21.6	66.7	6.6	20.9	72.5	175	519	12.473*	4.003
10	15	75	5.6	16.1	78.3	148	492	12.492*	4.006
20	13.3	66.7	11.1	14.3	74.6	70	469	12.499*	4.011
16	11	73	8.4	14.5	77.1	‡	457	12.502	4.011
23.3	10.0	66.7	13.6	13.1	73.3	‡	453	12.508	4.012
15.5	8.7	75.7	9.9	11.2	78.9	‡	447	12.502	4.011
14	11	75	8.1	14.4	77.5	‡	441	12.499	4.008
25	8.3	66.7	14.2	10.6	75.2	‡	432	12.514	4.015
26.7	6.6	66.7	16.3	8.3	75.4	‡	420	12.514	4.017
30	3.3	66.7	14.8	9.1	76.2	‡	—	12.532	4.021
10	10	80	3.3	4.8	91.2	—	—	$BaNb_2O_6$ structure	
25	5	70	8.3	1.6	90.1	—	—	$BaNb_3O_8$ structure	

* Pseudo-tetragonal parameter, optical interference patterns indicate biaxial symmetry.
‡ No twins at 20°C.

Table II. Composition and properties of crystals pulled from melts of $(RbNbO_3)_x$ $(NaNbO_3)_y$ $(BaNb_2O_6)_z$

Melt composition, m/o			Crystal composition from chemical analyses, m/o			Crystal properties				
								Lattice parameters		
$RbNbO_3$	$NaNbO_3$	$BaNb_2O_6$	$RbNbO_3$	$NaNbO_3$	$BaNb_2O_6$	T_W, °C	T_c, °C	a_o, A	b_o, A	c_o, A
6.7	26.6	66.7	1.5	26.5	72.0	240	558	17.609	17.633	3.998
16.7	16.6	66.7	3.8	18.4	77.8	140	505	17.662	—	4.007
16.7	16.6	66.7	5.1*	19.1*	75.8*	—	—	17.662	—	4.007
10	15	75	2.4	20.0	77.6	158	496	17.647	17.660	4.005
20.0	13.3	66.7	4.0	18.6	77.4	85	460	17.665	—	4.006
26.7	6.6	66.7	8.3	3.2	88.5	—	—	‡	—	‡
15	10	75	4.2	1.8	94.0	—	—	‡	—	‡

* Crystal from the frozen melt.
‡ Major phase was $BaNb_2O_6$.

Lattice constants were determined by the powder method with a silicon internal standard on a Guinier x-ray focusing camera with copper K_α radiation. The standard deviation of sine squared theta values was about 0.1%. Thus, the 3σ limits are 0.02 and 0.006Å for a_o and c_o, respectively. A Buerger precision camera with filtered molybdenum radiation was used in single crystal studies.

The pulled crystals were oriented by x-ray methods to within a ½ degree of the c-axis and cut on a diamond saw. The polished c-plane surface was examined for strain and microtwins on a Leitz polarizing microscope. The temperature (T_W) at which the microtwins disappear was measured on a microscope hot stage. For the orthorhombic crystals, microtwins were removed by cooling 5 x 5 x 5 mm^3 or smaller crystals through the tetragonal to orthorhombic phase transition with pressure applied along the [100] axis of the orthorhombic cell. The pressure was applied by a stainless steel vise which was mounted on a Leitz heating stage. The crystal surface was observed under the microscope during cooling.

The symmetry of the crystals was examined optically at 20°C on a microscope with convergent plane-polarized light and a Bertrand lens. The interference patterns established the uniaxial (tetragonal) or biaxial (orthorhombic) symmetry of the crystals.

The pulled crystals were analyzed for Rb or K, Na, Ba, and Nb using the methods shown in Table III. The weight per cent of each element was converted to the mole per cent of the niobates. The analysis for Nb served as a check on the assumption that the elements were in the niobate form.

The crystals pulled from melts of $K_{0.8}Na_{0.2}Ba_2Nb_5O_{15}$ were poled by applying an electric field of 3000 V/cm along the c-axis of the tetragonal structure at 100°C.

The small signal dielectric constants were measured on poled, oriented, single crystals at 10^4 Hz. The temperature was measured continuously from room temperature to a point above the Curie temperature. Figure 5 shows a circuit diagram of the system used. It has proved to be reliable, simple, and convenient. The voltage across R is proportional to C if $R << 1/\omega C$, which is easy to arrange. A Princeton Applied Research JB6 is used as a narrow band amplifier-oscillator and the y-scale of the x-y recorder is calibrated with known capacitors. The arrangement is similar to that described by Triebwasser (9).

Temperatures of −113° and −80°C were needed for 90° phase matched second harmonic generation with a 1.06μ Nd YAG laser for crystals from melts of $K_xNa_{1-x}Ba_2Nb_5O_{15}$ where $x = 0.8$ and 0.7. Crystals from melts of $K_{0.2}Na_{0.8}Ba_2Nb_5O_{15}$ and $Rb_{0.2}Na_{0.8}Ba_2Nb_5O_{15}$ phase matched near 80°C.

Table III. Chemical analyses

Element	Dissolution	Method	Accuracy
Na	$HF-HNO_3$	Flame photometry	±5%
Rb	$HF-HNO_3$	Atomic absorption	±3%
K	$HF-HNO_3$	Atomic absorption	±3%
Ba	$Li_2B_4O_7$ fusion	Precipitated as $BaSO_4$	±1%
Nb	KOH fusion	Polarographic reduction of Nb^{+5} to Nb^{+4}	±2%

Results and Discussion

$KNbO_3$-$NaNbO_3$-$BaNb_2O_6$ *system.*—Czochralski pulled tungsten bronze crystals were obtained from 12 different compositions in the $KNbO_3$-$NaNbO_3$-$BaNb_2O_6$ system. The maximum crystal diameter was 20 mm while the average crystal diameter and length were 8 and 30 mm, respectively. A single crystal pulled from a melt of $K_{0.2}Na_{0.8}Ba_2Nb_5O_{15}$ is shown in Fig. 6. The pulled crystals appeared to be chemically homogeneous based on Curie temperature measurements along the crystal length and the use of the crystals for electro-optic measurements. The small size of the crystals (30g or less) in relation to the melt (400g) minimized compositional changes in the crystal.

The section of the ternary system of $(KNbO_3)_x$ $(NaNbO_3)_y$ $(BaNb_2O_6)_z$ where $x < 34$, $y < 34$, and $z > 66$ is shown in Fig. 3. This shows the composition of the starting melts and the pulled crystals obtained from these melts. After the crystals were pulled, three phases were usually found in the frozen melts; these were the tungsten bronze, $BaNb_2O_6$, and the perovskite $KNbO_3$. Freezing points determined from DTA cooling curves on seeded samples along the pseudo-join between $NaBa_2Nb_5O_{15}$ and $KBa_2Nb_5O_{15}$ are shown in Fig. 7. These show a discontinuity at $K_{0.65}Na_{0.35}Ba_2Nb_5O_{15}$ and a minimum at $K_{0.825}Na_{0.175}Ba_2Nb_5O_{15}$. Above $x = 0.825$

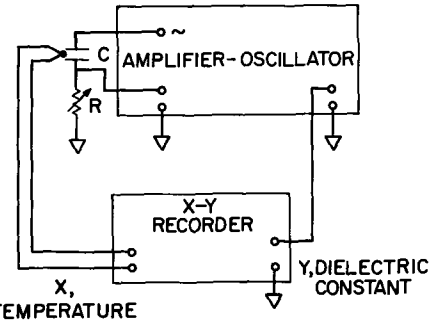

Fig. 5. Circuit diagram for the continuous measurement of dielectric constant vs. temperature. A Princeton Applied Research JB6 is used as a narrow band amplifier-oscillator. The voltage across R is proportional to C if $R << 1/\omega C$.

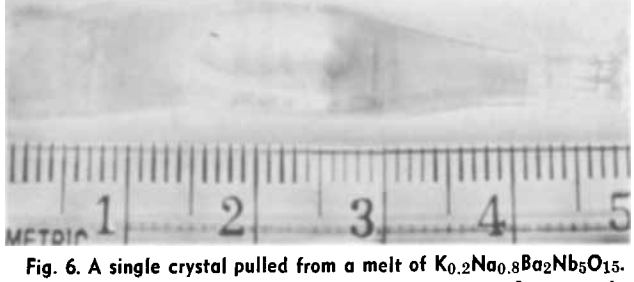

Fig. 6. A single crystal pulled from a melt of $K_{0.2}Na_{0.8}Ba_2Nb_5O_{15}$. Growth was along the c-axis. The small divisions are 1 mm each.

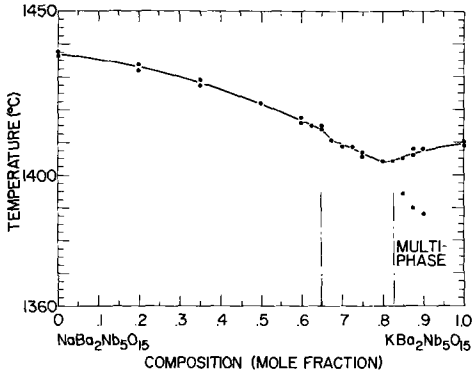

Fig. 7. Liquidus temperature vs. composition for DTA samples on the pseudo-join of $K_xNa_{1-x}Ba_2Nb_5O_{15}$. Two samples were run for most compositions. In the multiphase region a transition occurred below the liquidus temperature.

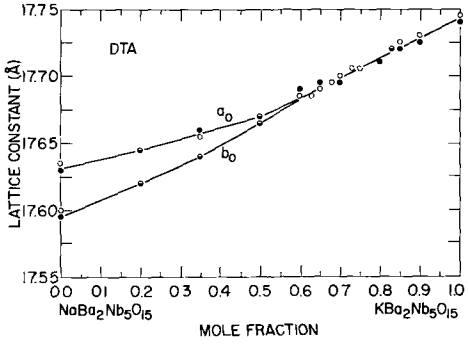

Fig. 8. Lattice constants for frozen melts of DTA samples on the pseudo-join of $K_xNa_{1-x}Ba_2Nb_5O_{15}$. Measurements were made on material from the top (●) and bottom (○) of the DTA tube.

in $K_xNa_{1-x}Ba_2Nb_5O_{15}$ the frozen DTA samples were multiphase. However, it was still possible to pull single phase bronze crystals from melts with $x \leq 0.9$. At room temperature, the pulled bronze crystals were tetragonal when the melt had $0.6 < x \leq 0.9$ and orthorhombic for $x \leq 0.6$. The chemical analysis data on the pulled crystals show that the melts become richer in $KNbO_3$ during crystal growth. Crystal growth from a 400g melt of $(KNbO_3)_{15.5}$ $(NaNbO_3)_{8.7}$ $(BaNb_2O_6)_{75.7}$ produced a tetragonal tungsten bronze phase in the initial 30g and then a $BaNb_2O_6$ rich phase. This indicated that the melt was very close to the phase boundary between the bronze and $BaNb_2O_6$ phases. A $BaNb_2O_6$ rich phase was found in crystals pulled from melts of $x = 10$, $y = 10$, $z = 80$ and $x = 25$, $y = 5$, $z = 70$.

Figure 3 shows that the pulled crystals from the tungsten bronze region were higher in $BaNb_2O_6$ and lower in $KNbO_3$ than the melt, while the $NaNbO_3$ content changed only slightly. We attempted to locate a maximum melting composition in the ternary system in order to obtain more homogeneous crystals and to operate under more favorable growth conditions. However, only small differences are believed to exist between the melting points of all compositions containing more than 66 m/o $BaNb_2O_6$. The melting behavior of some pulled crystals is described in Table IV. The melting points of pulled crystals exceed the peritectic decomposition temperature of $KBa_2Nb_5O_{15}$ (1391°C) and are less than the melting point of $BaNb_2O_6$ (1459°C). None of the crystals melted as sharply as the $NaBa_2Nb_5O_{15}$, indicating some difference between the liquidus and solidus temperatures.

Lattice parameter data for the tungsten bronze crystals are shown in Table I. Pseudo-tetragonal parameters are tabulated for crystals with slight orthorhombic splittings. Figure 8 shows the lattice constants (a_o and b_o) for frozen melts of DTA samples on the pseudo-join of $K_xNa_{1-x}Ba_2Nb_5O_{15}$. Only small differences are observed between material from the top and bottom of the DTA tube. Above $x = 0.6$ the room temperature structure is tetragonal. In this region, the lattice constant (a_o) is based on the orthorhombic cell which is $\sqrt{2}$ times larger than the tetragonal a_o. These results along with the chemical analyses on the tetragonal crystals pulled from melts with $x > 0.6$ define the approximate region of the tetragonal bronze structure in the ternary system (Fig. 3).

Table IV. Melting ranges for K-Na-Ba and Rb-Na-Ba niobate crystals

Crystal composition, m/o				Melting range, °C
$KNbO_3$	$RbNbO_3$	$NaNbO_3$	$BaNb_2O_6$	
6.6	—	20.9	72.5	1399-1434
11.1	—	14.3	74.6	1407-1422
3.3	—	4.8	91.9	1412-1447
—	1.5	26.5	72.0	1428-1441
—	4.0	18.6	77.4	1421-1443
—	2.4	20.0	77.6	1425-1436
$NaBa_2Nb_5O_{15}$				1438

Additional data on the ternary phase diagrams were obtained from x-ray and chemical analysis data on the Bridgman ingots. The Bridgman cooling of $(KNbO_3)_{16}$ $(NaNbO_3)_{11}$ $(BaNb_2O_6)_{73}$ resulted in a bronze and a $KNbO_3$ rich phase in the frozen ingot. The first to freeze material (orthorhombic bronze structure) had the same composition and lattice parameters (Table V) as a Czochralski pulled crystal from a melt of the same composition (Table I). The last to freeze section in the Bridgman tube had about 95% of a $KNbO_3$ rich phase with a blue color. The Bridgman growth from the $K_{0.85}Na_{0.15}Ba_2Nb_5O_{15}$ melt resulted in the initial freezing of a tetragonal bronze crystal which had a composition lower in $NaNbO_3$ content than that predicted from the location of the phase boundary between the bronze and $BaNb_2O_6$ phases. The last to freeze section had approximately equal quantities of the bronze and $KNbO_3$ rich phases. These results and the data on pulled crystals indicate that the phase boundary between the $BaNb_2O_6$ and tungsten bronze regions extends from the eutectic at $(NaNbO_3)_{15}$ $(BaNb_2O_6)_{85}$ in that binary over to $x > 0.90$ on the $K_xNa_{1-x}Ba_2Nb_5O_{15}$ pseudo-join.

$RbNbO_3$-$NaNbO_3$-$BaNb_2O_6$ *system.*—Six compositions from the $(RbNbO_3)_x$ $(NaNbO_3)_y$ $(BaNb_2O_6)_z$ ternary system were examined in the region of $x < 34$, $y < 34$, and $z > 66$. The melt compositions and pulled crystals are shown in Fig. 4. The results of chemical analyses on each pulled crystal are summarized in Table II.

The solubility of $RbNbO_3$ in the tungsten bronze structure is considerably less than that of $KNbO_3$. The highest concentration of $RbNbO_3$ was found in a crystal of $(RbNbO_3)_{5.1}$ $(NaNbO_3)_{19.1}$ $(BaNb_2O_6)_{75.8}$ which was taken from a frozen melt of $Rb_{0.5}Na_{0.5}Ba_2Nb_5O_{15}$. Pulled material from a melt of $Rb_{0.8}Na_{0.2}Ba_2Nb_5O_{15}$ contained primarily $BaNb_2O_6$. The first to freeze section from the $Rb_{0.7}Na_{0.3}Ba_2Nb_5O_{15}$ ($x = 23.3$, $y = 10.0$, $z = 66.7$) Bridgman sample had a $BaNb_2O_6$ structure with the composition shown in Table V. The phase boundary between the bronze and $BaNb_2O_6$ phases probably extends from the 85 m/o $BaNb_2O_6$-15 m/o $NaNbO_3$ eutectic to about $Rb_{0.65}Na_{0.35}Ba_2Nb_5O_{15}$. All the tungsten bronze pulled crystals containing Rb were orthorhombic at room temperature. Their lattice parameters are listed in Table II. If the tetragonal structure exists at room temperature, it is in a much smaller region of the ternary system than the corresponding $KNbO_3$ system.

Microstructure.—Optical examination at 20°C showed interference figures characteristic of uniaxial symmetry for all crystals grown from melts of $K_xNa_{1-x}Ba_2Nb_5O_{15}$ where $0.6 < x \leq 0.9$ and from melts near $(KNbO_3)_{16}$ $(NaNbO_3)_{11}$ $(BaNb_2O_6)_{73}$. Other bronze crystals from

Table V. Chemical analyses and lattice parameters of Bridgman crystals

Melt composition, m/o				First material to freeze: Composition from chemical analyses, m/o				First material to freeze: Tungsten bronze lattice parameters		Last material to freeze	
$KNbO_3$	$RbNbO_3$	$NaNbO_3$	$BaNb_2O_6$	$KNbO_3$	$RbNbO_3$	$NaNbO_3$	$BaNb_2O_6$	a_o, Å	c_o, Å	Major phase	Minor phase
16	—	11	73	8.8	—	12.3	78.9	12.499*	4.010	$KNbO_3$	Bronze
28.3	—	5.0	66.7	20.8	—	4.3	74.9	12.534	4.021	$KNbO_3$	Bronze
—	23.3	10.0	66.7	—	7.7	4.3	88.0	$BaNb_2O_6$ structure		Bronze	$RbNbO_3$

* Pseudo-tetragonal parameter, optical interference pattern indicates biaxial symmetry.

the $KNbO_3$-$NaNbO_3$-$BaNb_2O_6$ and $RbNbO_3$-$NaNbO_3$-$BaNb_2O_6$ systems were biaxial.

The typical appearance of the microtwins in pulled crystals is shown in Fig. 9. The lines are parallel to the [110] and [110] directions of the orthorhombic cell. Microtwinning results from the tetragonal to orthorhombic phase transformation and has been described for $NaBa_2Nb_5O_{15}$ (4). Table I shows that higher $KNbO_3$ concentrations in the bronze structured crystals from the $KNbO_3$-$NaNbO_3$-$BaNb_2O_6$ system cause a shift in the orthorhombic transformation (T_W) below 77°K and the resulting absence of microtwins. Although microtwins in $NaBa_2Nb_5O_{15}$ can be removed by applying pressure along the [100] axis of the orthorhombic cell while cooling below 300°C, it is not easily accomplished and can produce strain and cracking of the crystal. For example, Byer (10) describes the improvement in optical quality of detwinned $NaBa_2Nb_5O_{15}$ above 300°C. In the case of the $RbNbO_3$-$NaNbO_3$-$BaNb_2O_6$ system, the transformation (T_W) was lowered to 85°C in a crystal from a melt of $Rb_{0.6}Na_{0.4}Ba_2Nb_5O_{15}$. Results on other compositions are shown in Table II. The microtwins in the crystal from the melt of $Rb_{0.2}Na_{0.8}Ba_2Nb_5O_{15}$ are shown in Fig. 9. The microtwins were removed from this crystal by heating to 300°C and then cooling under pressure. The orthorhombic tungsten bronze crystals containing K or Rb appear to be easier to detwin that $NaBa_2Nb_5O_{15}$. Fewer crystals cracked, possibly because less pressure was required to detwin the K and Rb crystals. Also, the difference between the lattice parameters, a_o and b_o, decreases as the K and Rb concentrations increase.

Sensitivity to laser damage.—There are 10 possible cation (A^+, A^{+2}) sites available in the tungsten bronze type structure (11). These are: two α sites which have 12 oxygen ions coordinating the site; four β sites with 15 oxygen ions; and four γ sites with 9 oxygen ions. In the case of $NaBa_2Nb_5O_{15}$ (4), the β sites are believed to be filled by Ba, the smaller α sites are occupied by Na, and the smallest sites (γ) are unoccupied. Concentrations of more than 66.7 m/o $BaNb_2O_6$ in all the pulled crystals means there are more than 4 Ba ions per unit cell in the tungsten bronze structure. The extra Ba ions, which number as high as 0.41/cell for the $(KNbO_3)_{9.9}$ $(NaNbO_3)_{11.2}$ $(BaNb_2O_6)_{78.9}$ crystal, are believed to occupy the α sites along with the A^+ cations (Na, K, or Rb). For each Ba ion on an α site, there is a corresponding vacant α site. On this basis the crystals cannot be considered filled since there are some vacant α sites and completely vacant γ sites. The maximum number of Ba ions per unit cell in the tungsten bronze Rb crystals was 4.38 for the crystal of $(RbNbO_3)_{3.8}$ $(NaNbO_3)_{18.4}$ $(BaNb_2O_6)_{77.8}$.

A crystal of $(KNbO_3)_{16.3}$ $(NaNbO_3)_{8.3}$ $(BaNb_2O_6)_{75.4}$ grown from a melt of $K_{0.8}Na_{0.2}BaNb_5O_{15}$ was examined for laser damage (5) with a one-half watt argon laser (4880Å) focused with a 30 mm lens. When the electric field of the laser beam was directed along the c- and a-axes in separate runs, no optically induced inhomogeneities were observed after 15 min of exposure. Under the same conditions, $LiNbO_3$ damaged within seconds.

Dielectric properties.—The dielectric constant, ϵ, *vs.* temperature, T, and $10^4/\epsilon$ *vs.* T data for the crystals of $(KNbO_3)_{5.6}$ $(NaNbO_3)_{16.1}$ $(BaNb_2O_6)_{78.3}$ and $(RbNbO_3)_{3.8}$ $(NaNbO_3)_{18.4}$ $(BaNb_2O_6)_{77.8}$ are shown in Fig. 10 and 11. The data above the transition temperature, T_c, can be fitted to the Curie-Weiss expression, $\epsilon = (2\pi/A)(T - T_o)^{-1}$ where $2\pi/A$ is the Curie constant, c, and T_o is the paraelectric Curie temperature. The slopes, c, obtained from plots of T *vs.* $1/\epsilon$ above T_c are shown in Table VI for the two crystals. The T *vs.* $1/\epsilon$ data below T_c also give an intercept, T_o, which is approximately equal to the intercept obtained from the data above T_c. This suggests that the transition is second order. Also, thermal hysteresis which is characteristic of first order transitions was not observed in the ϵ *vs.* T curves for any of the crystals listed in Tables I and II. In the perovskite ferroelectrics, $BaTiO_3$ and $KNbO_3$, which undergo a first order transition, T_o is below T_c and thermal hysteresis in T_c is observed on heating and cooling. The A values for the two bronze crystals in Table IV are 2.2 x 10^{-5}/°C and 0.8 x

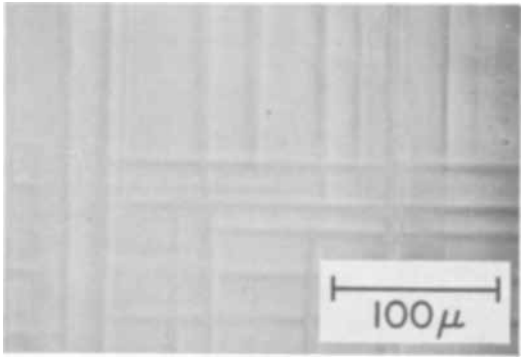

Fig. 9. Twin structure in crystals pulled from melts of $K_xNa_{1-x}Ba_2Nb_5O_{15}$ ($x \leq 0.6$) and $Rb_xNa_{1-x}Ba_2Nb_5O_{15}$ ($x \leq 0.6$) viewed along the c-axis. Lines are parallel to the [110] directions of the orthorhombic cell.

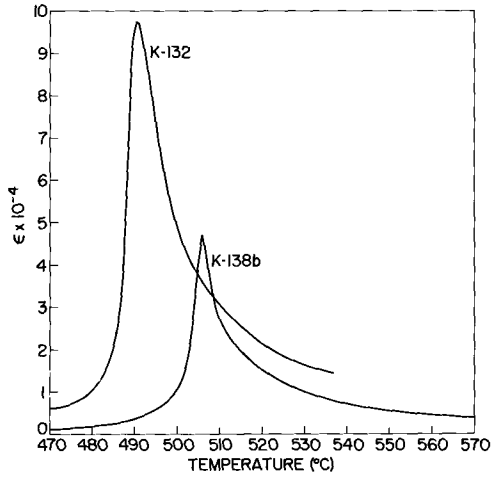

Fig. 10. Dielectric constant along the c-axis *vs.* temperature for crystals K-132 $(KNbO_3)_{5.6}$ $(NaNbO_3)_{16.1}$ $(BaNb_2O_6)_{78.3}$ and K-138b $(RbNbO_3)_{3.8}$ $(NaNbO_3)_{18.4}$ $(BaNb_2O_6)_{77.8}$.

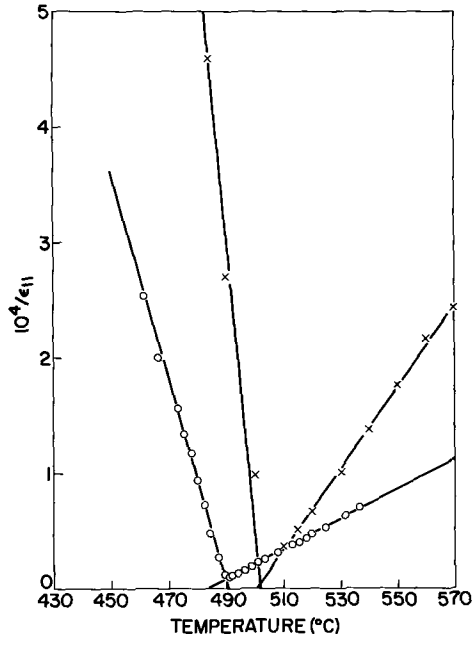

Fig. 11. $10^4/\epsilon_{11}$ *vs.* temperature for crystals K-132 $(KNbO_3)_{5.6}$ $(NaNbO_3)_{16.1}$ $(BaNb_2O_6)_{78.3}$ and K-138b $(RbNbO_3)_{3.8}$ $(NaNbO_3)_{18.4}$ $(BaNb_2O_6)_{77.8}$.

10^{-5}/°C, which are approximately the same as for the perovskites and other tungsten bronze compositions (12). Increasing the concentrations of K or Rb in the bronze crystals caused a lowering of the ferroelectric transition temperature (Tables I and II).

Burns (13) has described the effects on T_c of the quenching of $NaBa_2Nb_5O_{15}$ and also of crystals pulled from melts of $K_xNa_{1-x}Ba_2Nb_5O_{15}$. Smaller changes in T_c were observed for compositions containing more K. An ordering effect dependent on the ionic size was suggested as a possible explanation. The ionic sizes of the cations are: Ba^{++} = 1.35Å, Na^+ = 0.95Å, K^+ = 1.33Å, and Rb^+ = 1.48Å. The substitution of K^+ for Na^+ could be expected to produce less ordering.

Summary

Single crystals with an orthorhombic tungsten bronze structure were grown from a range of solutions in the ternary systems of $(KNbO_3)_x$ $(NaNbO_3)_y$ $(BaNb_2O_6)_z$ and $(RbNbO_3)_x$ $(NaNbO_3)_y$ $(BaNb_2O_6)_z$. A small solid solution region with a tetragonal bronze structure at room temperature was found in the former system. Chemical analyses of the pulled crystals indicated the approximate location of the phase boundary between the bronze and $BaNb_2O_6$ structures in each system.

Microtwins were absent at 20°C in the tetragonal bronze crystals near $(KNbO_3)_{14}$ $(NaNbO_3)_{12}$ $(BaNb_2O_6)_{74}$. These crystals also had the best optical quality. Other bronze compositions in the two ternary systems had lower tetragonal to orthorhombic transformation temperatures than $NaBa_2Nb_5O_{15}$. The microtwins in the K and Rb orthorhombic bronze crystals were less difficult to remove than those present in $NaBa_2Nb_5O_{15}$.

For the systems studied in this paper efficient phase matched second harmonic generation for 1.06-0.53μ above room temperature was obtained only in crystals with an orthorhombic bronze structure, such as those from melts of $Rb_{0.2}Na_{0.8}Ba_2Nb_5O_{15}$ and $K_{0.2}Na_{0.8}Ba_2Nb_5O_{15}$. The tetragonal bronze phase matched below room temperature.

Substitution of K or Rb for Na resulted in a lowering of the Curie temperature and a retention of the sharp transition at the Curie temperature. Analysis of the ϵ *vs.* T data for two representative crystals indicated second order transitions at the ferroelectric to paraelectric transition.

Table VI. Curie temperatures and ferroelectric constants for K-Na-Ba and Rb-Na-Ba niobate crystals

Crystal composition	T_c, °C	Above T_c $c \times 10^{-5}$, °C	Above T_c $A \times 10^5$, °C
$(KNbO_3)_{5.6}$ $(NaNbO_3)_{10.1}$ $(BaNb_2O_6)_{78.3}$	492	7.7	0.8
$(RbNbO_3)_{3.8}$ $(NaNbO_3)_{18.4}$ $(BaNb_2O_6)_{77.8}$	506	2.8	2.2

Acknowledgment

The authors would like to thank K. H. Nichols, B. A. Jenkins, C. F. Guerci, and R. M. Potemski for their technical assistance. This work was partially supported by the Army Research Office, Durham, North Carolina, under Contract DA-31-124-ARO-D-205.

Manuscript submitted May 22, 1969; revised manuscript received July 18, 1969. This was Paper 54 presented at the New York Meeting, May 4-9, 1969.

Any discussion of this paper will appear in a Discussion Section to be published in the June 1970 JOURNAL.

REFERENCES

1. E. A. Giess, G. Burns, D. F. O'Kane, and A. W. Smith, *Appl. Phys. Letters*, **11**, 233 (1967).
2. J. E. Geusic, H. J. Levinstein, J. J. Rubin, S. Singh, and L. G. Van Uitert, *ibid.*, **11**, 269 (1967).
3. D. F. O'Kane, E. A. Giess, G. Burns, and B. A. Scott, *Bull. Am. Phys. Soc.*, **12**, 1079 (1967).
4. L. G. Van Uitert, H. J. Levinstein, J. J. Rubin, C. D. Capio, E. F. Dearborn, and W. A. Bonner, *Mater. Res. Bull.* **3**, 47 (1968).
5. G. Burns, E. A. Giess, D. F. O'Kane, B. A. Scott, and A. W. Smith, *J. Appl. Phys.*, **40**, 901 (1969).
6. B. A. Scott, E. A. Giess, and D. F. O'Kane, *Mater. Res. Bull.*, **4**, 107 (1969).
7. E. A. Giess, B. A. Scott, G. Burns, D. F. O'Kane, and A. Segmuller, *J. Am. Ceram. Soc.*, To be published.
8. D. F. O'Kane, G. Burns, B. A. Scott, and E. A. Giess, *This Journal*, **115**, 1081 (1968).
9. S. Triebwasser, *Phys. Rev.*, **101**, 993 (1956).
10. R. L. Byer, S. E. Harris, D. J. Kuizenga, J. F. Young, and R. S. Feigelson, *J. Appl. Phys.*, **40**, 444 (1969).
11. A. Magneli, *Arkiv Kemi*, **1**, 213 (1949).
12. G. Burns, D. F. O'Kane, E. A. Giess, and B. A. Scott, *Solid State Commun.*, **6**, 223 (1968).
13. G. Burns and D. F. O'Kane, *Phys. Letters*, **28A**, 776 (1969).

Silicon Epitaxial Layers with Abrupt Interface Impurity Profiles

Dinesh C. Gupta* and Roy Yee

General Telephone and Electronics Laboratories, Inc., Woburn, Massachusetts

ABSTRACT

Silicon epitaxial layers of good quality have been deposited on silicon substrates by the pyrolysis of silane at low temperatures. Studies to minimize the degradation of the impurity profile of an epitaxial silicon layer caused by various sources or processes are reported. Auto doping and system doping during deposition have been minimized by using techniques such as sealing the backsides of the substrates, sealing the susceptor, and using two-temperature cycle depositions. Impurity profiles of the layers deposited by the above methods are compared with the profiles of the layers obtained from more conventional deposition conditions.

The use of hyperabrupt junctions is becoming increasingly important for the fabrication of fast variable capacitive diodes and integrated circuits. This requires obtaining and controlling sharp impurity gradients at the substrate-epitaxial layer interface. The doping sources that tend to degrade the interface impurity gradient can be categorized as follows (1):

1. Impurities originating from the reaction chamber, *i.e.*, its walls, fixtures, gas lines, etc.
2. Impurities present in the silicon epitaxial growth source, *e.g.*, $SiCl_4$, $SiHCl_3$, or SiH_4.
3. Impurities originating from autodoping, *i.e.*, the inclusion of impurities within the epitaxial layer that are obtained from the substrate etching.
4. Impurities originating from the hot susceptor, if r.f. heating is used.
5. Impurities due to out-diffusion from the substrate, or the buried layers, during high temperature epitaxial growth.

The investigation reported here seeks to minimize each impurity source by using special techniques or procedures.

Apparatus and Techniques

Apparatus.—The furnace arrangement used to achieve the epitaxial deposition of silicon from the pyrolysis of silane is depicted in Fig. 1. The system uses only gaseous sources for the dopants as well as the silicon source, excluding, of course, the comparison source, silicon tetrachloride. The gases are spectroscopically analyzed for impurity content and concentrations. The dopant gases are controlled by a pneumatically pulsed gas chromatography sampling valve, however, in the results presented here, no intentional doping from dopant sources was used. The reaction chamber is a multiple slice, cold wall, vertical gas flow system capable of handling six 1-in. diameter slices (2). In the investigations reported here, however, only three slices plus a control slice were used for each run. All runs, whether using SiH_4 or $SiCl_4$, were made in the same reaction chamber to maintain identical geometric conditions. The susceptor on which the slices were placed, was fabricated from n-type, arsenic-doped, 0.5 ohm-cm silicon, and was heated by a 4 MHz r.f. coil located externally to the reaction chamber. As a precautionary measure the system was kept moisture-tight using stainless steel gas lines, fittings, etc., since traces of water vapor can cause etching of silicon at epitaxial growth temperatures (3) which may produce autodoping effects.

Silicon epitaxy source.—A widely used process to deposit epitaxial silicon layers is the hydrogen reduction of silicon tetrachloride (4). The hydrogen reduction of trichlorosilane has also been investigated (5). In both cases, however, the deposition temperatures are quite high, and achieving abrupt impurity gradients becomes difficult. Efforts have been made therefore to deposit layers at reduced temperatures using the pyrolysis of SiH_4 (6-8) and improved impurity gradients have been achieved using substrate resistivities as low as 0.007 ohm-cm (7).

The use of SiH_4 as the silicon source is well suited for minimizing autodoping and out-diffusion, for the following well-known reasons. First, silane has no HCl as a decomposition product, and consequently the amount of autodoping should be considerably reduced as compared to the hydrogen reduction of the silicon halides. Second, it is possible to reduce out-diffusion effects by lowering the epitaxial growth temperature to more than compensate in the diffusion length for the increase in diffusion time required to deposit a given layer thickness at the reduced temperature. To take advantage of this fact, the silicon source must be capable of being efficiently decomposed at the lower growth temperature. The decomposition of silane is indeed more favorable thermodynamically than silicon tetrachloride in the temperature range used here, namely, 900°-1000°C. The heat of formation for silane at these temperatures is about one order of magnitude lower than that for silicon tetrachloride (8, 9).

Control of autodoping.—We propose here that the autodoping can be controlled by back-sealing the substrates prior to deposition by using an insulating, etch-resistant film, *e.g.*, silicon oxide, silicon nitride, etc., on the back side of the silicon slices. In these studies, a 15,000Å thick layer of thermally grown silicon dioxide was used for back-sealing.

Control of susceptor doping.—The susceptor is heated and etched by HCl prior to the deposition cycle and during conventional H_2-$SiCl_4$ deposition.

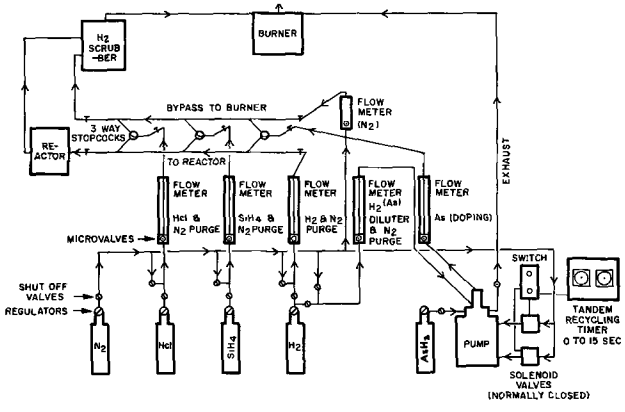

Fig. 1. Schematic of silane system

* Electrochemical Society Active Member.

Therefore, it becomes a source for impurities, especially since its resistivity is usually relatively low for efficient r.f. coupling. By sealing its surface with an epitaxially deposited layer of high purity silicon, or with an insulating etch-resistant film, a reduction of impurities from this source can be achieved.

Out-diffusion.—The resistivity of the substrate, or of buried layers, is controlled by the device design so that out-diffusion from these sources during epitaxial deposition can be controlled effectively only by maintaining the deposition temperature as low as possible to achieve good quality epitaxial layers.

The choice of SiH_4 as the silicon epitaxy source permits lower deposition temperatures, and consequently a reduction in the amount of out-diffusion from the substrates. In fact, depositing at about 1000°C compared to 1175°C will decrease the diffusion constant of the substrate dopant (in this case, arsenic) by about an order and a half in magnitude (10).

High-Low Temperature Cycle Depositions

A completely different approach for achieving good quality epitaxial layers with reduced redistribution of doping impurities is to carry out the initial nucleation growth at high temperatures and complete the deposition at a reduced temperature. This method is called the coating technique (11), or the high-low temperature cycle technique.

By this technique, a reduction in growth temperature to 850°C for silane depositions is possible, while still maintaining good quality layers with abrupt doping profiles at the interface.

Analysis and Discussion of Results

Using the special techniques described above to enhance the abruptness of impurity gradients, silicon n/n^+ epitaxial layers were deposited at temperatures of 900°-1000°C using silane as the silicon source. The impurity distributions are compared with those obtained in layers deposited using more conventional deposition conditions, namely, silicon tetrachloride as the silicon source, and the deposition temperatures in the range of 1175°-1250°C.

The quoted temperatures are optical pyrometer temperatures, emissivity uncorrected; however, the pyrometer was calibrated against a Pt + 10% Rh thermocouple, as described in the Appendix.

The substrates used for these studies were (111) oriented, mechanically and chemically polished, and had dislocation counts of less than 100 dislocations/cm^2. The arsenic concentration in the substrates was approximately 3.5×10^{19} atoms/cc.

To achieve good quality epitaxial layers, it was necessary to *in-situ* HCl etch the slices prior to deposition. After etching, the system was purged with hydrogen for a time sufficiently long to adequately remove any HCl vapors remaining in the system.

Impurity profiles were determined by diode voltage-capacitance measurements (12) on diffused or Schottky barrier diode structures. The values of the impurity concentrations reported for the surface of the layers were obtained by the spreading resistance probe measurements (13).

Deposition rate.—The dependence of the deposition rate on the growth temperature for various volume percentages of SiH_4 in H_2 is shown in Fig. 2. As the temperature is lowered, the percentage of SiH_4 should be lowered to achieve good quality epitaxial layers. The activation energy of the system is found to be 30 kcal/mole from 850° to 1100°C. Joyce and Bradley (3) have reported a value of 37 ± 1 kcal/mole as the activation energy from 950° to 1100°C. At temperatures higher than 1100°C, the reaction is found to be independent of the SiH_4 concentration, indicating that the pyrolysis of SiH_4 is complete, and a constant growth rate results. Figure 3 gives the dependence of the deposition rate at 1000°C on the volume per cent of SiH_4 in H_2.

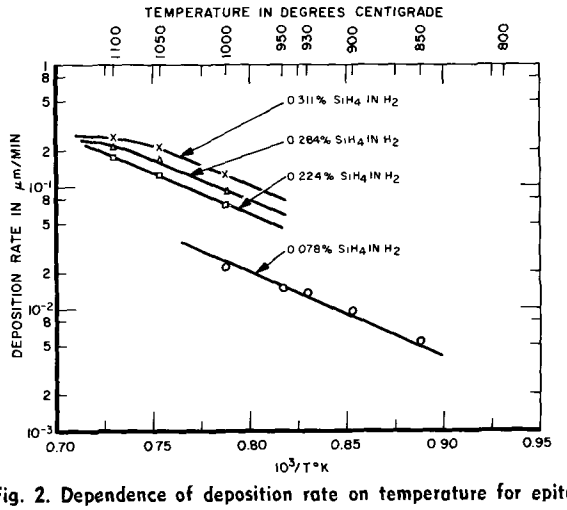

Fig. 2. Dependence of deposition rate on temperature for epitaxial layers using silane.

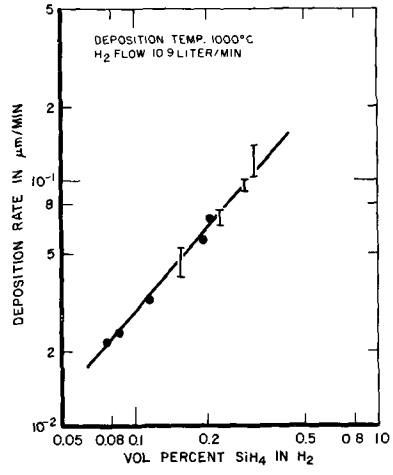

Fig. 3. Effect of SiH_4-H_2 ratio on deposition rate

Impurity profiles resulting from use of special techniques.—The effect of the back side sealing of the substrates on the impurity profiles of the layers is shown in Fig. 4 through 6. Figure 4 gives the impurity profiles of two epitaxial layers obtained by the de-

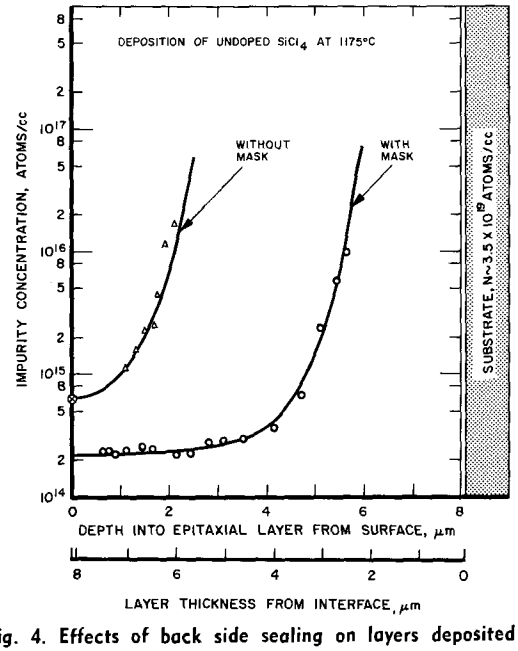

Fig. 4. Effects of back side sealing on layers deposited by the decomposition of silicon tetrachloride.

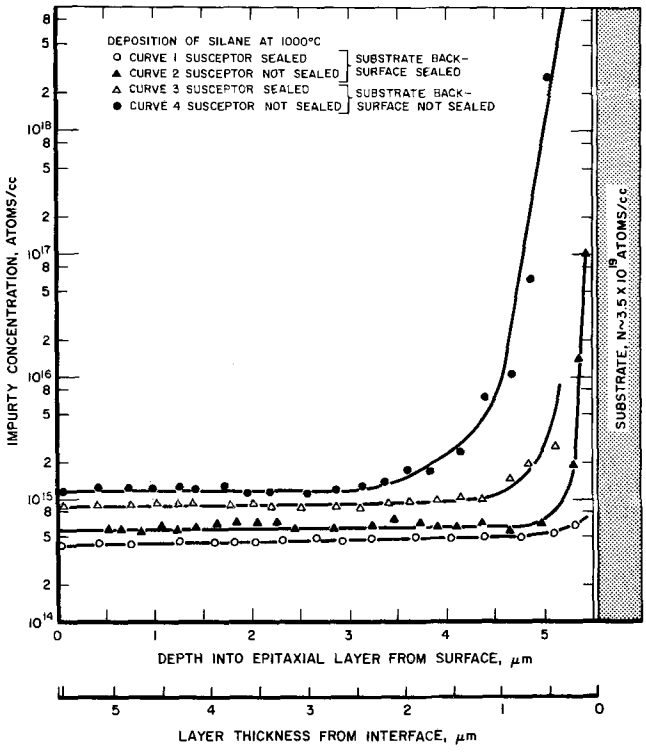

Fig. 5. Effects of substrate back-surface and susceptor sealing on layers deposited by the pyrolysis of silane.

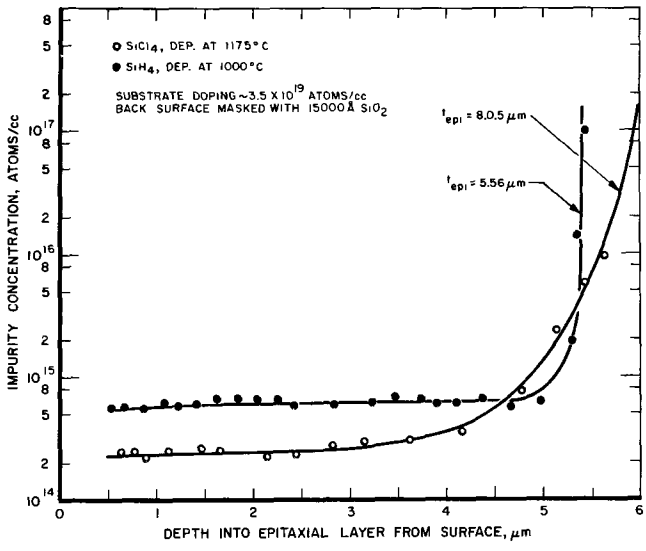

Fig. 6. Comparison of $SiCl_4$ and SiH_4 deposition with the substrate back-surface sealed.

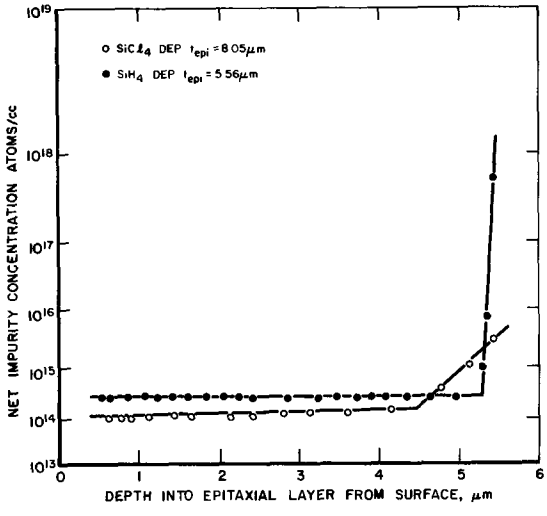

Fig. 7. Arithmetic probability plot of the impurity profiles shown in Fig. 6.

composition of $SiCl_4$. Curve 1 had the back side of the substrate sealed while in curve 2 the back side was not sealed.

In Fig. 5, the impurity profiles of the two epitaxial layers deposited with the silane process are depicted. Curve 2 had the back side of the substrate sealed, while in curve 4 the back side was not sealed.

It is clear from these results that back-sealing the slices reduces the amount of impurity doping at the interface significantly. These impurity profiles, improved as they are, still reflect the two remaining impurity sources, namely, autodoping from the susceptor and out-diffusion from the substrates. The effect of autodoping from the susceptor has been determined from two runs deposited under the condition of having the susceptor sealed as well as having the slices back-sealed in one run, and not back-sealed in the other. These two profiles are shown in Fig. 5, denoted by curves 1 and 3, respectively. Some improvement in the impurity profiles are noted over runs made without susceptor sealing, but this improvement is not as significant as that due to back-sealing. The extra doping near the interface can be accounted for by out-diffusion from the substrate. The diffusion length for the silane layers is about 0.3 μm as discussed below.

The effect of out-diffusion is also shown in Fig. 6, where comparison is made of the impurity profiles of the layers deposited by $SiCl_4$ process at 1175°C and SiH_4 process at 1000°C with the substrate back-surface sealed. The increase in the abruptness of the impurity gradient is attributed to not only the reduction of autodoping from the front side due to the nonexistence of HCl vapors in the silane system, but also to the decrease in the arsenic diffusion constant by about one and a half orders of magnitude that results from the reduction in growth temperature from 1175° to 1000°C. The layer deposited from silane also has a higher impurity concentration near the layer's surface, which shows that even though less impurity doping occurs near the interface using the silane process, the silane source used here is less pure than the silicon tetrachloride source.

Figure 7 shows an arithmetic probability plot of the impurity profiles of the layers shown in Fig. 6. Complementary error function diffusion processes, *e.g.*, out-diffusion, are readily identifiable from this type of plot since they appear as straight lines on the graph (14). One obtains a diffusion length of 1.8 μm for the deposition at 1175°C with $SiCl_4$ while for the deposition from SiH_4 at 1000°C, a diffusion length of only 0.3 μm is obtained. These results reflect the decrease in the diffusion constant of arsenic as mentioned previously. The change in the slope in the lines can be explained in terms of the model suggested by Kahng *et al.* (15) in which the impurity doping from the back side, in their case, and from the front side, in our case, is redeposited from the gas phase to give an exponential distribution. A net profile similar to the plots of Fig. 7 can be obtained by the addition of the exponential distribution for autodoping, represented by

$$N = N_o^* \exp(-x/L_2)$$

and the error function distribution for the out-diffusion during the deposition, represented by

$$N = (N_s/2)\ \mathrm{erfc}\ (x/L_1)$$

These distributions are shown in Fig. 8.

High-low cycle epitaxy.—Using a high-low temperature cycle as discussed earlier, the deposition temperature can be reduced further, *e.g.*, it was possible to deposit good quality epitaxial silicon at temperatures as low as 1000°C using the decomposition

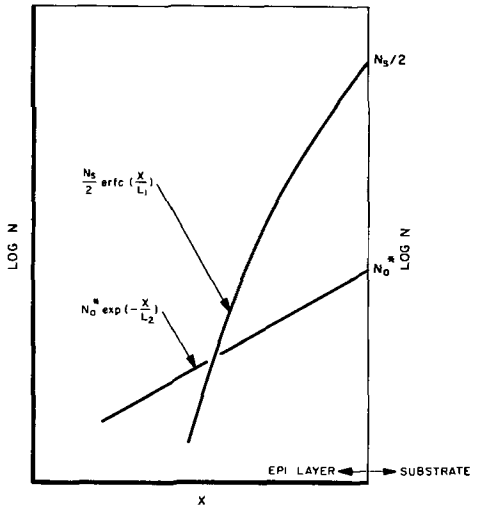

Fig. 8. Theoretical net impurity distribution of layers with autodoping and out-diffusion.

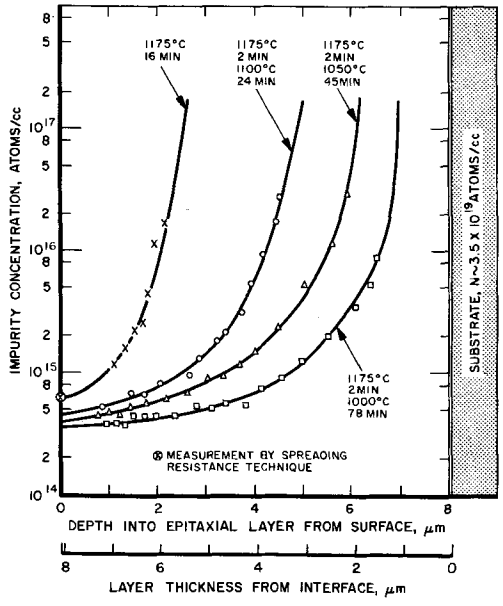

Fig. 9. Impurity profiles of the layers deposited in $SiCl_4$ system using high-low temperature cycle.

of silicon tetrachloride and this technique. The impurity profiles on the layers are shown in Fig. 9. The coating was performed at 1175°C for 2 min in each case. Note the improvement in the impurity gradient of the layers with the reduction in temperature of the low cycle. The back sides of the substrates in these cases were not sealed. Using the same technique, it was possible to deposit good quality layers at a temperature as low as 850°C with the pyrolysis of silane. Coating in the latter case was performed at 1000°C. Figure 10 shows the results. The back sides of the substrates were not sealed. It is interesting to note that the abruptness of the gradient is very nearly the same for depositions carried out at 1000°C with substrate back-surface sealed as it is for depositions at 850°C with an initial coating for 2 min at 1000°C but without the back side sealed.

Surface quality.—The surface quality of silicon deposited by the pyrolysis of silane has been found to be quite good for deposition temperatures as low as 950°C and it is possible to obtain mobilities in the layers approaching that of bulk silicon (16). Below 950°C the surfaces contain nuclei of different orientations. At temperatures below 850°C, nucleation was found to be incomplete and polycrystalline growths were obtained as shown in Fig. 11. The density of nuclei on the surface of the layer was about thirty

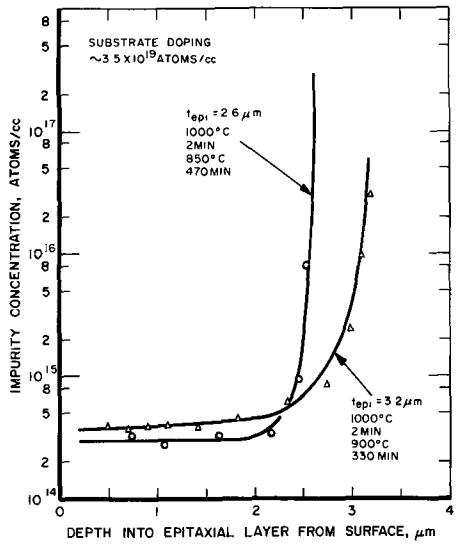

Fig. 10. Impurity profiles of the layers deposited in SiH_4 system using high-low temperature cycles.

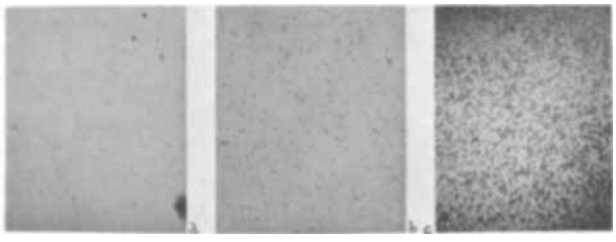

Fig. 11. Photomicrographs showing surfaces of layers deposited by silane at temperatures: (a) 900°C, (b) 850°C, (c) 800°C. Magnification 500X.

times less for layers deposited at 900°C than that deposited at 850°C.

Conclusions

In conclusion, a sharp transition between the doping levels of the substrate and the epitaxial layer can be achieved by low temperature epitaxial depositions using the pyrolysis of silane. Most suitable temperatures for this type of deposition are found to be in the range of 950°-1000°C where the film quality is good and the times of deposition are reasonable. Using the coating technique the deposition temperature can be lowered to 850°C without deteriorating the film quality. An even sharper transition between the doping concentration of the substrate and the layer can be obtained regardless of silicon source, *i.e.*, $SiCl_4$ or SiH_4, if autodoping from the substrate is controlled by sealing its back surface. Additional abruptness is possible if the surface of the susceptor is sealed using a film of high purity silicon or some etch-resistant dielectric material, *e.g.*, silicon oxide, silicon nitride, etc.

Acknowledgments

The authors wish to acknowledge the helpful discussions with Dr. P. Wang. Thanks are due to L. Ramos and P. Keating for conducting the experimental work, to R. Vagnini and G. Voyk for fabrication of diodes, and to J. Chan for measurements.

Manuscript submitted Oct. 3, 1968; revised manuscript received May 20, 1969. This, in part, was Paper 75 presented at the Boston Meeting, May 5-9, 1968.

Any discussion of this paper will appear in a Discussion Section to be published in the June 1970 JOURNAL.

REFERENCES

1. T. Basseches, S. K. Tung, R. C. Manz, and C. O. Thomas, *Metallurgy of Semiconductor Materials*, **15**, 69 (1962).

2. J. Porter, V. Sils, P. Wang, and N. Cerniglia, Presented at the Detroit Meeting, Oct. 1961.
3. T. L. Chu and R. L. Tallman, *This Journal*, **111**, 1306 (1964).
4. H. C. Theuerer, *ibid.*, **108**, 649 (1961).
5. J. M. Charig and B. A. Joyce, *ibid.*, **109**, 957 (1962).
6. B. A. Joyce and R. R. Bradley, *ibid.*, **110**, 1235 (1963).
7. S. R. Bhola and A. Meyer, *RCA Rev.*, **24**, 511 (1963).
8. S. E. Meyer and D. E. Shea, *This Journal*, **111**, 550 (1964).
9. K. J. Miller, R. C. Manz, and M. J. Grieco, *ibid.*, **109**, 643 (1962).
10. C. S. Fuller and J. A. Ditzenberger, *J. Appl. Phys.*, **27**, 544 (1956).
11. S. Nakanuma, *IEEE Trans. on Electron Devices*, **ED-13**, 578 (1966).
12. Dinesh C. Gupta, *Solid State Technol.*, **11**, 31 (Feb. 1968).
13. R. G. Mazur and D. H. Dickey, *This Journal*, **113**, 255 (1966).
14. V. Sils, R. W. Berkstresser, P. Wang, and T. A. Longo, *Electrochem. Technol.*, **2**, 138 (1964).
15. D. Kahng, C. O. Thomas, and R. C. Manz, *This Journal*, **110**, 394 (1963).
16. Dinesh C. Gupta, *ibid.*, **116**, 670 (1969).

APPENDIX

The deposition temperature in the above studies was measured by an optical pyrometer (emissivity uncorrected), however, the optical pyrometer was calibrated by obtaining, at the pyrometer, the radiation which was dependent on the silicon ingot's surface emissivity with a platinum, platinum +10% rhodium thermocouple as follows:

A 5 ft long muffle furnace was used as a heat source to heat an ingot of silicon placed at one end of the furnace tube. Contacting the face of this silicon ingot was the thermocouple, while at the other end of the furnace tube the optical pyrometer was placed and focused onto the same silicon face to which the thermocouple was attached. An inverted cone was used as a lens shade to minimize stray radiation entering the optical pyrometer.

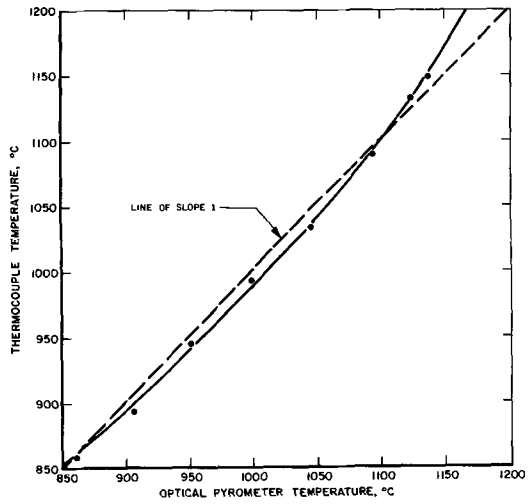

Fig. 12. Calibration of optical pyrometer with platinum, platinum +10% rhodium thermocouple.

The furnace temperature was allowed to stabilize at various temperature values, as measured on the thermocouple, within the range of 800°-1150°C, and the corresponding measurements were taken by the optical pyrometer. The results are plotted in Fig. 12. It can be seen that the optical pyrometer temperatures quoted are probably correct to within ±15°C, and for the range of temperatures most pertinent to this work tend to be actually lower than the quoted temperatures. This result is not necessarily in conflict with the results normally reported, viz., that the optical pyrometer temperature is usually lower than the actual temperature, since as can be seen in Fig. 12, deviations at the higher temperatures do indicate this condition. In most cases reported with regard to epitaxial growth, the temperatures are in this higher temperature range.

Studies in the Adamantine Family of Semiconductors

IV. The $Zn_xCd_{1-x}SnAs_2$ Semiconducting Alloy System: Phase Diagram and Preparation

B. R. Pamplin and J. S. Shah[1]

School of Physics, Bath University of Technology, Claverton Down, Bath, England

ABSTRACT

The results of a DTA study of the alloy system $Zn_xCd_{1-x}SnAs_2$ are presented and a pseudobinary phase diagram is deduced showing the liquidus, solidus, and order-disorder transition lines as a function of Cd content. The use of zone refining techniques to prepare single phase samples for further study is also described.

The II IV V_2 compounds are closely related structurally and electronically to the well known tetrahedrally bonded, diamond and sphalerite structure group IV and III V semiconducting compounds. They have been the subject of several reviews (1-3). $CdSnAs_2$ is isoelectronic and isomorphous with InAs from which it may be derived by cross-substitution (4) and to which it has similar electronic properties [*i.e.*, a room temperature electron mobility of 22,000 $cm^2/V.s$ at $n = 10^{17}$ per cc (5)]. It has a markedly lower lattice thermal conductivity [70 mw/cm°C (6)], and thus it and its solid solutions are of technological interest as thermoelectric materials.

Most pairs of isostructural II IV V_2 compounds are expected to be isomorphous in the solid state provided the electronegativities and atomic sides of corresponding atoms differ by not more than 10-15%, especially if one or two of the atomic species are the same. Previous papers in this series (7, 8) reported the x-ray evidence for complete solid solution between $ZnSnAs_2$ and $CdSnAs_2$ and also for the pseudoternary system $InAs-ZnSnAs_2-CdSnAs_2$.

This paper reports our study of the phase diagram $Zn_xCd_{(1-x)}SnAs_2$ and techniques evolved for the preparation of single phase samples at different compositions in this alloy system with a brief mention of the ternary alloys.

Properties of the End-Component Compounds

Several papers have reported relevant work on the components of the pseudobinary phase diagram $ZnSnAs_2$ (1-4, 9-14) and $CdSnAs_2$ (4, 5, 9, 10, 15, 16).

[1] Present address: H. H. Wills Physics Laboratory, The University, Bristol, England.

Early work on $ZnSnAs_2$ by Pfister and Folberth (11, 14) established that it may exist at room temperature in two forms. The stable form has the chalcopyrite structure EI_1 (space group $D_{2d}^{12} - I\bar{4}2d$) in which the diamond structure pattern of atomic sites is readily recognized, subject to a slight tetragonal distortion. The other, metastable, form has the sphalerite structure B3 (space group $T_d^2 - F\bar{4}3m$). This is derived from the first by disordering or randomizing the Zn and Sn atomic sublattices and thus restoring cubic symmetry. The fcc As atomic sublattice is substantially unaffected by the order-disorder transition occurring between these two structures. Most reported values for the temperature of the order-disorder transition lie in the range 532°-650°C (12-15). Russian work (1) indicates that it may be as high as 700°C; there may be a certain degree of hysteresis resulting in a slightly lower disorder-order transition temperature. At 778°± 3°C the compound melts incongruently, probably through a peritectic transition (13). Thus, this end of the phase diagram cannot properly be represented as a single component of exact composition $ZnSnAs_2$. But we feel that the difficulty is really a small perturbation and that to a first approximation it may be overlooked.

$CdSnAs_2$ is usually assumed to be a straightforwardly chalcopyrite structure compound which melts and freezes congruently at 595°±2°C. However some recent Russian work is mentioned (1) in which a disorder temperature 10°-20°C below the melting point is suggested because quenched $CdSnAs_2$ was observed to have a sphalerite structure.

Differential Thermal Analysis Techniques

In the DTA technique a differential temperature measurement compares the specimen with a standard substance whose properties are well behaved in the temperature range studied. Because our compounds are decomposed by heating in air, we kept our powdered sample in a vacuum-sealed quartz ampoule. Our standard, silver, was similarly encapsulated. Both ampoules were mounted close together in a cylindrical pyreofilite holder and the required signals derived from a chromel-alumel differential thermocouple and a sample thermocouple. The differential signal was recorded using a solid state chopper preamplifier. The sample temperature was recorded to an absolute accuracy of better than ±3°C.

The specially constructed tube furnace in which the holder fitted snugly had a 5 in. zone of temperature uniform to ±2°C. It was controlled by a saturable reactor with a programmed proportional temperature controller. Heating rates from 1°C/min to 10°C/min were used and 4°C/min was found to be the best compromise. The accuracy of the arrangement was tested by finding the melting points of Ag, Sb, InSb, $ZnSnAs_2$, and $CdSnAs_2$. Our measurements gave 965°, 630°, 528°, 778°, and 595°C, respectively. The value for Ag is about 4°C higher than the accepted value but the other results are in good agreement with the accepted values so no correction has been applied to our subsequent observations.

The samples used were for the most part the same annealed powders used in the x-ray lattice parameter work (7). These were chosen to lie at compositions $x = n/8$ ($n = 0, 1, 2, \ldots 8$) through the system because these are the compositions expected to show further ordering of the disordered chalcopyrite phase (17).

Results and Discussions

Typical heating and cooling curves are presented in Fig. 1 and the arrest temperatures recorded in Table I. The differential thermocouple line on the chart shows a clear but wide peak, arrest C on heating and F on cooling, coresponding to the solidus and liquidus, respectively, and one or two small peaks. Reading the arrest temperatures from the chart is necessarily rather subjective. Where possible we have followed the recommendation of Partridge *et al.* (18) and taken the temperature corresponding to the maximum rate of deflection on the rising side of the peak. Where this does not give a clear value we have erred toward lower temperatures for the heating curves and higher temperatures for cooling curves.

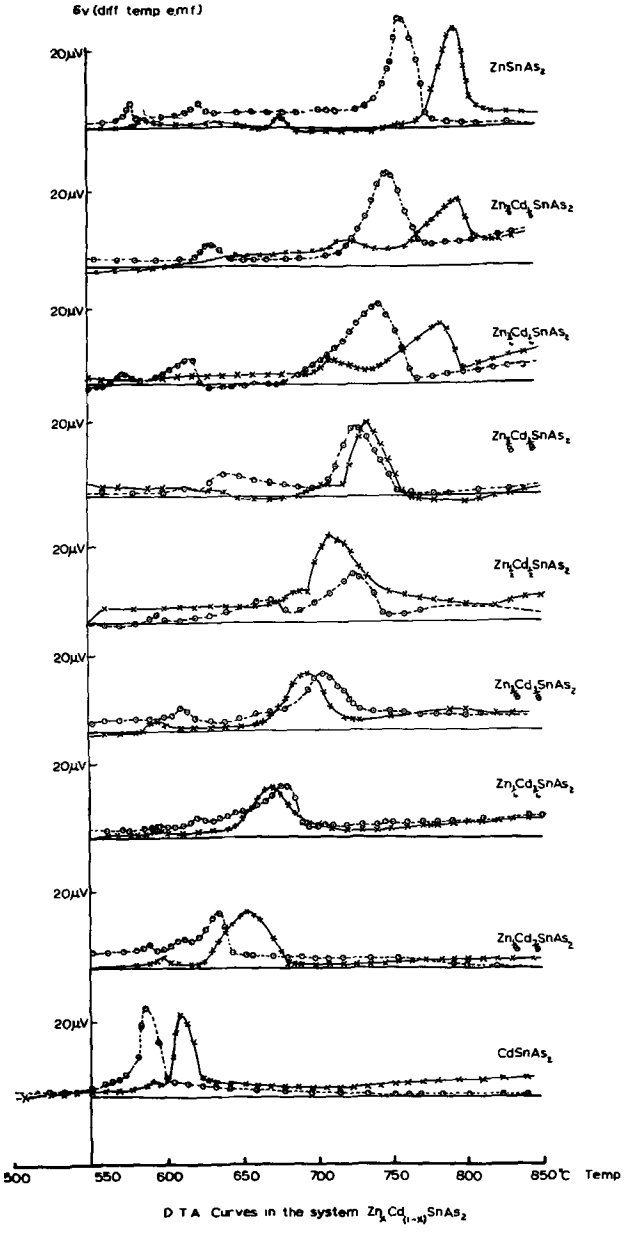

Fig. 1. Differential thermal analysis heating and cooling curves in the system $Zn_xCd_{1-x}SnAs_2$. —x—, Points while heating at 4°C/min; - - ○ - -, points while cooling at 7°C/min.

Arrest B is taken to be due to the order-disorder transition. Arrests A and D, which are often larger in area than B, are supposed, following the suggestion of Gasson *et al.* (12), to be due to SnAs and SnAs + As

Table I. Arrest temperatures

		Arrest temperatures, °C						
		Heating				Cooling		
	Compositions	A	B	C	End of melting	D	E	F
1	$ZnSnAs_2$	584	670	778	820	560	628	778
2	$Zn_{7/8}Cd_{1/8}SnAs_2$	—	707	765	810	—	638	772
3	$Zn_{3/4}Cd_{1/4}SnAs_2$	—	700	735	800	—	640	765
4	$Zn_{5/8}Cd_{3/8}SnAs_2$	—	690	720	765	623	690	752
5	$Zn_{1/2}Cd_{1/2}SnAs_2$	—	675	695	770	600	680	745
6	$Zn_{3/8}Cd_{5/8}SnAs_2$	595	—	665	725	—	620	730
7	$Zn_{1/4}Cd_{3/4}SnAs_2$	595	—	645	720	595	620	690
8	$Zn_{1/8}Cd_{7/8}SnAs_2$	580	—	625	680	580	610	690
9	$CdSnAs_2$	565	—	595	620	—	—	595

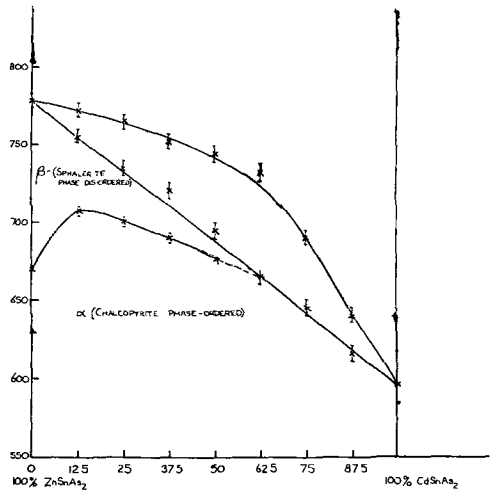

Fig. 2. Proposed equilibrium phase diagram for the $Zn_xCd_{1-x}SnAs_2$ alloy system. △, disorder-order transition temperatures; ▼ order-disorder transitions, liquidus and solidus temperatures.

phases. Electron probe microanalysis of directionally frozen and zone refined ingots confirmed the presence of these phases.

In Fig. 2 we show a proposed equilibrium diagram for $Zn_xCd_{1-x}SnAs_2$ alloys. Its general character is the same as for mixed III V alloys (such as InAs-GaAs). The two phase region between the solidus and liquidus is 50°C deep and 20 a/o (atomic per cent) wide in the middle of the system. The liquidus is taken from arrest F on cooling and the solidus from arrest C on heating. The extra line, from arrest B, divides the chalcopyrite phase region from the sphalerite structural region. This phase supposes the alloys are pseudobinary, which, since $ZnSnAs_2$ does not melt congruently, cannot be exactly true. However, we feel that the analysis of these results in terms of a two component system is basically sound and is supported by the growth studies reported in the next section.

Arrest B for $ZnSnAs_2$ itself may be attributed to the disorder-order transition but the same conclusion cannot fairly be made for the alloys which by virtue of the phase diagram we propose must freeze at best to give a graded composition ingot and at worst a non-equilibrium mixture of phases. Thus no disorder-order line is drawn in Fig. 2.

It is noted that arrests and transition temperatures observed by other workers (12, 13, 15, 16) on $ZnSnAs_2$ and $CdSnAs_2$ are generally in good agreement with our results and consistent with this phase diagram.

Preparation of Single Phase Specimens

The proposed phase diagram indicates that complete solid solution exists between the two chalcopyrite structure components below the order-disorder temperature and solid solution with the sphalerite structure between this line and the solidus for zinc rich alloys. The diagram also implies that the tie lines in the two phase region between the solidus and liquidus lie in the plane of the diagram. This would mean that an alloy of composition x frozen directionally (or zone refined) under equilibrium growth conditions would be graded from a first to freeze zinc rich composition to a last to freeze cadmium rich tail.

It is well known that alloy material with a phase diagram like that proposed must be frozen very slowly indeed if inhomogeneity due to constitutional supercooling is to be avoided. Dismukes and Ekstrom (19) have extended the conventional analysis of constitutional supercooling to the Ge-Si alloy system. They find the maximum permissible growth rate v cm/sec for a temperature gradient G °C/cm is given by

$$v = \frac{G \cdot D}{m(c_l - c_s)}$$

where m = the slope of the liquidus, c_l = solute concentration (*i.e.*, concentration of one of the components of the solid solution) in liquid, c_s = solute concentration in solid, and D = diffusion coefficient for solute in solution.

We have applied this formula to our system; taking m, c and c_s from our phase diagram, G = 20°C/cm (measured value) and assuming $D = 10^{-4}$ cm²/sec (as a typical figure in the absence of data) we find v must not exceed $5 \cdot 10^{-5}$ cm/sec or 1 mm/hr for alloys near the middle of the alloy system.

During the course of this work we made fifty ingots of these alloys. Some were quenched, some directionally frozen (DF), and some zone refined (ZR), but all on x-raying contained an adamantine phase which, judging by the relative intensities of the x-ray powder photograph lines, accounted for the majority of the material. This adamantine phase always had a variable composition, the powder photograph lines were blurred in quenched specimens and showed a graded ingot in DF and ZR ingots. These facts strongly support the main features of the proposed phase diagram. However, all ingots contained at least a trace of impurity phase. Arsenic condensed in the colder portions of the sealed tube. SnAs and SnAs + As phases were found on electron probe microanalysis of the latter portions of DF and ZR ingots. Surprisingly neither Zn_3As_2 or Cd_3As_2 (or their alloys) were ever found.

In the early stages of the work it was felt that a slight excess of As should be added to provide a gaseous atmosphere over the hot solid and liquid. However the best results were obtained when about 2% excess zinc was added to react with the SnAs phase. ZR and DF ingots containing excess zinc had a higher percentage of single phase graded composition chalcopyrite structure material. But unfortunately none of these ingots was near being a single crystal.

Several other growth techniques were tried in an attempt to produce single crystals. All, including halogen assisted vapor transport, failed. Liquid encapsulated zone refining using KI + 2LiI produced material similar to the ZR material described above.

The best material obtained, which was used in the electrical measurements (20) was produced by ZR in a vitreous carbon boat in a sealed tube kept at an ambient temperature of 570°C to inhibit sublimation of arsenic. The zone speed was 0.1 mm/hr. Figure 3 shows a photomicrograph confirming the disappearance of SnAs rich second phase material when the zone speed was reduced from 10 to 0.1 mm/hr. The boundary is quite sharp indicating that constitutional undercooling due to poling up of impurity rejected by the growing crystal is severe enough to cause the growth interface to reach a eutectic in the four components (Zn, Cd, Sn, As) phase field at just about the growth rate predicted above.

In view of the ease with which the alloys in the $InAs\text{-}ZnSnAs_2\text{-}CdSnAs_2$ system anneal from as quenched powdered alloys to a single sphalerite phase condition (7), hot and cold pressing was also used to prepare specimens for electrical measurements. The most successful technique involved the addition of 0.1% by weight of camphor to the compact before pressing under 5000 psi at 250°C for 10 min pumping at the same time to drive out the camphor binder. These pressed disks were 16 mm diameter and 3 mm thick and after sintering at 550°C for a few hours were suitable for cutting into 10 x 3 x 2 mm specimens. The electrical properties of the compressed powders compared consistently with the ingot material.

Conclusion

We are confident that the proposed phase diagram, Fig. 2, represents correctly the gross features of the $Zn_xCd_{1-x}SnAs_2$ system. The existence plane of this adamantine phase in the proper four component phase field is thought to be quite narrow and to deviate from the line given by the formula by about 2% toward the

Fig. 3. Photomicrograph of the surface of a zone refined ingot of nominal composition $ZnCdSn_2As_4$ showing that the second phase present when the zone speed was 10 mm/hr and disappeared when the speed was reduced to 0.1 mm/hr. Magnification approx. 150X.

zinc rich side for the maximum melting point composition near the zinc end of the line.

Acknowledgments

We wish to thank the Central Electricity Generating Board for supporting this work.

Manuscript received Feb. 23, 1968; revised manuscript received July 3, 1969.

Any discussion of this paper will appear in a Discussion Section to be published in the June 1970 JOURNAL.

REFERENCES

1. A. S. Borschevskii, N. A. Goryunova, F. F. Kesamently, and D. N. Nasledov, *Phys. Status Solidi*, **7**, 9 (1967).
2. B. Ray, *R. A. E. Tech. Memos.* 773 and 777 (1966).
3. B. R. Pamplin, Special report SAMSS 66/8, Scientific Advisers (1966).
4. C. H. L. Goodman, *J. Phys. Chem. Solids*, **6**, 305 (1958).
5. N. A. Goryunova, S. Mamsev, and V. D. Prochukhan, *Dokl. Acad. Nauk (USSR)*, **142**, 623 (1961).
6. P. Leroux-Hugon, *Compt. Rend.*, **256**, 118 (1963).
7. B. R. Pamplin and J. S. Shah, Part II, *Nature*, **207**, 180 (1965).
8. B. R. Pamplin. J. S. Shah, and R. A. L. Sullivan, Part III, *This Journal*, **112**, 1249 (1965).
9. C. H. L. Goodman, *Nature*, **179**, 828 (1957).
10. N. A. Goryunova and V. D. Prochukhan, *Soviet Phys.-Solid State (Engl. Transl.)*, **2**, 161 (1960).
11. O. G. Folberth and H. Pfister, *Acta. Cryst.*, **13**, 199 (1960).
12. D. B. Gasson, F. J. Holmes, I. C. Jennings, B. R. Marathe, and J. E. Parrott, *J. Phys. Chem. Solids*, **23**, 1291 (1962).
13. H. Borchers and R. G. Maier, *Z. Metall.*, **17**, 775 and 1006 (1963).
14. H. Pfister, *Acta. Cryst.*, **16**, 153 (1963).
15. K. Masumoto and S. Isomura, *J. Phys. Chem. Solids*, **26**, 163 (1965).
16. A. J. Strauss and A. J. Rosenberg, *J. Phys. Chem. Solids*, **17**, 278 (1961).
17. B. R. Pamplin, Part I, *J. Phys. Chem. Solids*, **25**, 675 (1964).
18. E. P. Partridge, V. Hicks, and G. W. Smith, *J. Am. Chem. Soc.*, **63**, 454 (1941).
19. J. P. Dismukes and L. Ekstrom, *Trans. Met. Soc. A.I.M.E.*, **233**, 672 (1965).
20. J. S. Shah, Ph.D. Thesis, Bath University of Technology (1967).

Marker Techniques for Studying the Mechanism of Scaling of Metals Based on the Use of the $O^{18}(p,n)F^{18}$ Nuclear Reaction[1]

J. B. Holt and L. Himmel

Lawrence Radiation Laboratory, University of California, Livermore, California

ABSTRACT

A general mechanistic approach to the study of scaling reactions is proposed which dispenses with the conventional inert marker. Instead, radioisotopes of the reacting components are used to establish the nature of the diffusing species in the solid reaction products formed on metal surfaces at high temperatures. For investigating the mechanism of oxidation of metals, O^{18} is employed as a tracer and the stable isotope is subsequently activated by proton bombardment *via* the nuclear reaction $O^{18}(p,n)F^{18}$. The basis for the technique is outlined and its application to the scaling of iron and of zirconium is described. The experiments with iron establish conclusively that, at temperatures up to 1050°C, iron is the only diffusing component in the dense, adherent wüstite layer which forms adjacent to the metal. Direct evidence is also presented for the vapor phase transport of oxygen by a dissociative mechanism during the growth of porous, non-adherent wüstite scales on iron in H_2/H_2O atmospheres. It is shown that oxygen is mobile in thick ZrO_2 scales formed on Zr in a water vapor atmosphere at 1200°C; however, the unusual form of the O^{18} distribution in the scale indicates that open channels must have existed in the outer portion of the scale during oxidation which allowed direct penetration of oxygen to levels deep within the ZrO_2 layer. The advantages and limitations of the present technique are discussed with particular reference to conventional marker methods. Major sources of difficulty in the interpretation of inert marker experiments are identified and a set of experimental requirements is given which, if satisfied, should permit reliable transport information to be obtained using conventional marker techniques.

The mechanism of a heterogeneous chemical reaction, such as the oxidation of a metal, can be considered established, at least in principle, if the rate-determining step in the reaction is known and if the manner in which the reactants are transported to and from the various phase boundaries in the system can be specified. Information of this kind cannot generally be obtained from kinetic studies alone. In fact, even under conditions where diffusion-controlled kinetics are observed, it is often not possible to decide, unambiguously, whether the reaction is sustained by the outward migration of metal ions through the scale, or by the inward diffusion of the nonmetallic component. The dominant or faster diffusing species can, of course, be predicted if self-diffusion or ionic conductivity data are available for both components over the entire stability range of the product phase. Unfortunately, reliable data of this type currently exist for only a few oxide and sulfide systems (1-3).

When the necessary transport data are not available, inert marker techniques are customarily employed to determine the nature of the mobile component in the growing scale. Marker methods were first introduced by Pfeil (4) in 1929 in his classic work on the scaling of iron, and they have been applied subsequently to a great many gas-solid (1) and solid-solid reactions (5-7) but often, as experience has demonstrated, with puzzling or conflicting results. Although several sources of difficulty in the conduct and interpretation of inert marker experiments have now been recognized (8-13), the feeling persists that the results of marker studies may not be trustworthy and should not be accepted without caution. The present work was undertaken in an attempt to develop a generalized marker technique that circumvents some of the problems encountered with conventional marker methods. The results have also permitted us to define in detail the experimental conditions that must be met in order to obtain reliable transport information from inert marker studies.

Instead of employing inert markers which, ideally, do not take part in the reaction, the technique described below utilizes radioactive isotopes that are themselves components of the product scale layer. For oxygen, which does not have a suitably long-lived radioisotope, the stable isotope O^{18} is used and this is subsequently activated by proton bombardment *via* the nuclear reaction $O^{18}(p, n)F^{18}$. The approach is, in essence, equivalent to carrying out a simultaneous transport experiment for both the metallic and nonmetallic component under the actual conditions encountered during the growth of the scale layer. It differs from the conventional marker technique in that the relative mobilities of the two components are determined not simply from the position or location of the marker, but from the distribution of the radioactive species in the product phase. Additional information concerning the mode of transport of the reactants may also be obtained from an analysis of these distributions. Specifically, it now becomes possible to determine whether the transport of oxygen (or other components) takes place by normal lattice diffusion, by migration along grain boundaries or other structural discontinuities in the scale, or as a result of transport through the vapor phase. Such information is not directly obtainable from conventional marker experiments but is frequently of vital importance in the interpretation of marker studies, as we shall demonstrate.

First, we briefly discuss conventional or inert marker techniques, following which the basis for the present method is outlined. Application of the technique is illustrated with reference to two scaling reactions, the oxidation of iron to wüstite, in which the cation is the mobile component, and the oxidation of zirconium, in which the growth of the ZrO_2 layer is generally considered to proceed by the inward transport of oxygen ions.

[1] Work performed under the auspices of the U.S. Atomic Energy Commission.

Inert Marker Techniques

The basic principle involved in a conventional marker experiment is quite straightforward (1, 8). It is assumed that the original gas/solid interface between two reacting materials can be marked in such a manner that it remains distinguishable after reaction has occurred. The position of the original marked interface is then located with respect to the final boundaries of the product phase. This establishes directly the fraction of the total amount of reaction product formed at the respective phase boundaries. Two limiting situations may immediately be recognized: (*a*) the metallic component is the faster diffusing species, in which case the reaction occurs exclusively at the scale/gas interface, and as a consequence the inert marker is located at the metal/scale boundary; (*b*) the nonmetallic component is much more mobile, reaction takes place entirely at the metal/scale phase boundary, and the marker is therefore found at the scale/gas interface. In both instances, the final position of the marker coincides with the original marked interface between the solid and the gas.

It might be thought that the intermediate situation in which both components have roughly comparable mobilities would be even more general. If such were the case, the marker would be found imbedded in the scale part way between the scale/gas and metal/scale boundaries. In nonstoichiometric oxides (sulfides, nitrides, *etc.*), however, the defect concentrations in the metal ion sublattice generally far exceed those in the anion sublattice or *vice versa*, and hence the rates of mass transport of the two components frequently differ by orders of magnitude. The likelihood that this intermediate situation would often be encountered in practice must therefore be considered quite remote.

Nevertheless, the literature abounds with apparent examples of this type. Even in such a well-documented system as the oxidation of iron to wüstite, for which evidence from many different sources overwhelmingly favors the cation as being the faster diffusing species (2, 14-16), markers have been found within the wüstite layer, often at a considerable distance from the iron/wüstite boundary (11, 17-20). Markers have also been observed within the NiO scale formed on nickel (21, 22), the FeS layer on iron (10), and the Ag_2S scale grown on silver (9, 23, 24). In each of these systems, it is definitely known from self-diffusion or other transport measurements that the mobility of the cation in the bulk oxide or sulfide is much greater than that of the corresponding anion (1, 2, 25, 26). These few examples illustrate the need for considerable care, not only in the planning and execution but especially in the interpretation of inert marker experiments.

It now seems clear, in fact, that the location of the marker may not be determined solely by the relative mobilities of the two constituents in the scale, but that the marker position is often strongly influenced by other conditions which arise during the growth of the scale (1, 8-12). Whenever inert markers have been observed within the reaction product formed on a metal substrate, the scale, almost without exception, has been found to consist of two physically distinct but crystallographically identical layers, an inner porous region adjacent to the metal and an outer layer, in contact with the gas phase, which is dense and compact. In duplex scales of this type, the inert marker is always found at or near the boundary between the porous and compact regions of the scale. The conclusion that has frequently but erroneously been drawn in such instances is that the dense outer portion of the scale is formed by the outward migration of metal ions and that the inner porous layer grows as a result of the inward diffusion of the nonmetallic component through the scale. In other words, comparable mobilities are assigned to both constituents in the scale lattice.

As noted previously, simple interpretations such as this are often found to be in direct conflict with theoretical predictions or with the results of self-diffusion measurements. While there can be little doubt that transport of the nonmetallic constituent has indeed taken place during the growth of the inner porous layer in duplex scales, no justification exists for assuming that this transport has occurred by normal lattice diffusion. A far more satisfactory interpretation may be given which not only explains the origin of the duplex scale but is also consistent with evidence obtained from other sources. This alternate interpretation, due to Meussner and Birchenall (10), Mrowec and Rickert (27), and others (9, 28-30), is briefly as follows.

It is assumed that the dense outer portion of the scale is formed by the outward migration of metal ions while the scale is still relatively thin and in intimate contact with the metal. As the scale continues to thicken, however, it becomes increasingly difficult for adherence between the scale and the metal to be maintained, and at some critical stage the scale may become partially detached from its substrate. The actual stage at which this happens depends on many factors, including the nature and magnitude of the stresses that originate in the scale during growth, the plasticity of the scale, and the purity of the metal. Nevertheless, should the compact scale become physically separated from the metal, the inert marker, which is surrounded by the scale, may be carried off along with it. Dissociation of the detached scale will then take place until the equilibrium partial pressure of the reacting gas is established within the void created at the interface. As a consequence, the nonmetallic component will be transported from the separated portion of the scale to the underlying metal through the vapor phase, and a new scale layer may then form beneath the marker. Certain details of this process remain to be clarified, but it is not difficult to visualize how repeated detachment of the scale, along with dissociative vapor transport, could lead eventually to the formation of an inner porous scale layer, thereby offering an explanation for why the marker is found near the junction between the porous and compact segments of the scale. According to this latter interpretation, the cation is the diffusing species in the scale lattice; transport of the nonmetal, which is indicated by the position of the marker, is thought to occur not by normal lattice diffusion but, rather, through the vapor phase.

Evidence will be presented which lends further support to this interpretation. It thus appears that, whenever porous or nonadherent scales are formed, the possibility that a dissociative mode of transport may be operative should not be overlooked in interpreting the results of marker studies. As long as the scale remains dense and adherent, however, the position of the marker will generally give a true reflection of the relative mobilities of the two reacting species in the scale layer (1, 8, 10). To avoid complications introduced by the formation of porous, nonadherent scales it is always advisable, in carrying out marker experiments, to adjust the experimental conditions so that compact, adherent scales are obtained. A full discussion of the various experimental factors involved will be postponed until the results of the present work have been described.

Techniques Utilizing Radioactive Components of the System as Markers

The inert marker can be eliminated entirely from the experimental procedure if use is made of radioactive isotopes of the two chemical constituents involved in the reaction. The theoretical and experimental basis for this approach was first outlined by Bardeen *et al.* (31) in their study of the oxidation of copper using radioactive Cu^{64}. Bardeen *et al.* plated a thin film of Cu^{64} on a copper disk, partially oxidized it to Cu_2O, and then removed successive layers of the oxide by etching, measuring the activity of Cu^{64} in each layer. They showed that the concentration of Cu^{64}

was highest at the Cu_2O/gas interface and decreased progressively toward the Cu/Cu_2O boundary. They also demonstrated, using the Wagner theory of oxidation (2, 32), that this was the distribution to be expected if the growth of the oxide were sustained by the diffusion of vacant Cu^+ ion sites from the outer surface of the oxide toward the Cu_2O/Cu interface, or, equivalently, by the outward migration of Cu^+ ions. On the other hand, had oxygen been the mobile constituent, the distribution of Cu^{64} would have remained sharp, being confined to a narrow zone at the metal/scale interface.

Although the primary purpose of their work was to provide experimental confirmation for the Wagner theory, it is clear that the method employed by Bardeen *et al.* also serves as a valuable marker technique. This has been recognized by several investigators. Using basically the same experimental approach, for example, Schnizlein and co-workers (33) have established that oxygen is the mobile component in the oxide layer formed on uranium metal at 200°C. Similarly, Jarry *et al.* (34) have shown that Ni is the faster diffusing species in the NiO scale grown on Ni at 1000°C, but that, in the reaction between fluorine and Ni at 600°-700°C, F appears to be the migrating species.

In most experiments of this kind thus far reported which involve the growth of thick scales on metals, only the distribution of the radioactive cation has been investigated (31, 33-38). In a few cases, however, the radioactive isotope S^{35} has been utilized in studying the mechanism of sulfidization (39-41) of metals and alloys. There are, as we shall see, a number of advantages in using both components of the system as tracers, particularly since this should provide a rigid cross-check on the consistency of the results. In Fig. 1, the distributions of the radioactive components which would be expected in the scale layer are illustrated schematically for the two limiting situations mentioned above, namely: (*a*) the cation is the mobile species (Fig. 1a and 1b); and (*b*) the anion is mobile (Fig. 1c and 1d). The expected positions of inert markers are indicated in both cases.

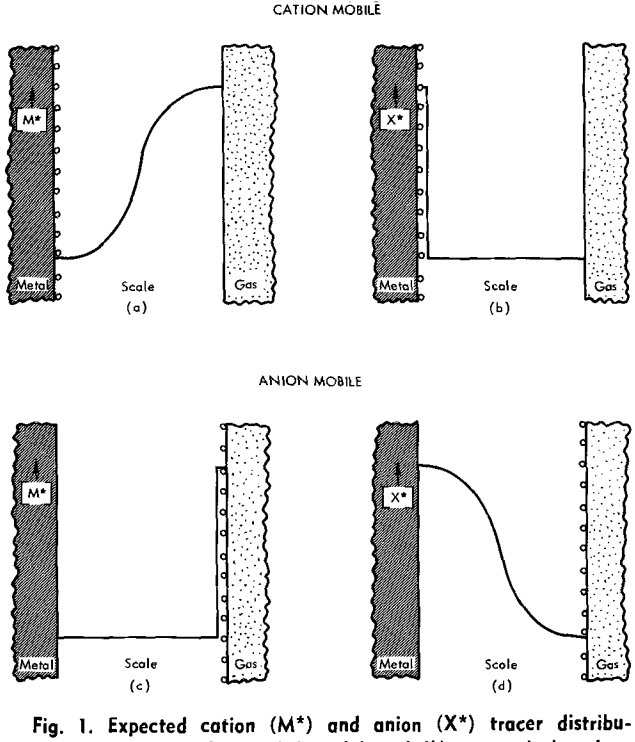

Fig. 1. Expected cation (M*) and anion (X*) tracer distributions in the scale under conditions (*a*) and (*b*), respectively, where the cation is the diffusing component. The corresponding distributions in situations where the anion is the mobile species are indicated by (*c*) and (*d*), respectively. The open circles represent the expected positions of inert markers in each case. Schematic.

Consider first the commonly encountered situation in which the mobility of the cation in the scale far exceeds that of the nonmetallic constituent. If a thin deposit of the radioactive metal is applied to the surface of the sample before oxidation, it will subsequently be found distributed throughout the scale in essentially the manner shown by Bardeen *et al.* (Fig. 1a). On the other hand, if a thin reaction layer containing a radioisotope of the nonmetal is first formed on the surface to mark the original interface and the reaction is then allowed to continue in a normal or inactive environment, the final distribution of the radioactive anion will be that shown in Fig. 1b. In this case the radioactive nonmetal functions as a truly inert marker; its distribution therefore remains sharp and its location, at the metal/scale interface, coincides with that of a more conventional Pt wire marker.

The corresponding tracer distributions in circumstances where the anion is the mobile component are given in Fig. 1c and 1d. Here, the radioactive cation behaves as a inert marker and remains at the scale/gas interface, while the anionic component is distributed continuously throughout the scale, its activity being greatest at the metal/scale phase boundary and lowest at the external surface. The point which bears emphasis is that the diffusing species in any given system is readily and unambiguously identified by the fact that it is distributed in a predictable manner over a major portion of the thickness of the scale. It should be noted, however, that when only one radioactive marker is employed, say the nonmetallic component, its distribution must be determined fairly accurately since the concentration of the radioactive anion in the scale will always be greatest at the metal/scale interface, regardless of which component is the mobile species (*see* Fig. 1b and 1d). Thus, it would not be sufficient merely to detach the scale mechanically from the metal substrate and count the activity on both its surfaces, as has been the practice in previous work in which the radioisotope S^{35} was used as a marker in sulfidization studies (39-41).

Because a suitable radioisotope of oxygen is lacking, some modification in technique is required in order to determine the anion tracer distribution in oxide scales. The method proposed here is based on the use of the nuclear reaction $O^{18}(p, n)F^{18}$ and represents an extension of the charged-particle activation technique previously developed by Condit and Holt (42-44). In effect, the stable isotope O^{18} is used as a marker in precisely the same manner as would a radioactive component, except that the tracer is activated after reaction with the metal has been completed. This is accomplished by proton bombardment of the O^{18} which yields the radioactive isotope F^{18}. The latter has a half life of 110 min and decays with the emission of a 0.67-MeV positron. These characteristics permit the O^{18} distribution in the scale to be determined by simple autoradiographic procedures.

Other charged-particle activation techniques have been employed for this same purpose. Amsel and Samuel (45), for example, have utilized the nuclear reaction $O^{18}(p, \alpha)N^{15}$ to study the mechanism of anodic oxidation of aluminum, while Cox and Roy (46) and their colleagues (47) have used the $O^{17}(He^3, \alpha)O^{16}$ reaction in similar fashion to explore the transport of oxygen in thin ZrO_2 films formed on Zr. Application of these reactions involves measurement of the energy spectrum of the α-particles produced during the nuclear reaction when the oxide, which contains O^{18} or O^{17}, is bombarded with monoenergetic protons or He^3-particles, respectively. Since the depth below the surface down to which activation occurs is limited, these reactions cannot be used to determine the stable tracer distribution in thick oxide scales unless a multiple sectioning technique is employed (48-50). However, great sensitivity can be achieved and hence these activation reactions are ideally suited to the study of the mechanism of growth of thin oxide films on metals. Using

the $O^{18}(p, \alpha)N^{15}$ reaction, Amsel and Samuel have been able to determine the concentration of O^{18} as a function of depth with a spatial resolution of 60Å in anodic oxide films on Al. The resolution claimed by Cox and Roy is about 300Å.

The two scaling reactions which we have chosen to illustrate the application of the present technique were selected because the relative mobilities of metal and oxygen ions in the respective oxides, wüstite (Fe_xO) and ZrO_2, were believed to be sufficiently well established that little doubt should have arisen concerning the interpretation. Actually, the system we chose initially as being representative of a scaling reaction in which oxygen diffusion predominates was the conversion of magnetite (Fe_3O_4) to hematite (Fe_2O_3) (14, 15). It soon became apparent, however, that the migrating species in the Fe_2O_3 layer formed on magnetite is iron and not oxygen. A detailed report of this investigation will be published elsewhere (51).

Experimental Procedure

Iron samples were machined from an ingot of zone-refined iron obtained from Battelle Memorial Institute through the courtesy of the American Iron and Steel Institute. These specimens had the form of a rectangular parallepiped approximately 2 cm × 1 cm × 2 mm thick. All surfaces of each specimen were metallographically polished, cleaned and degreased ultrasonically, and then "marked" with O^{18}. This was done by oxidizing in an atmosphere ($P_{O_2} \cong 130$ Torr) enriched to 30% in O^{18} for roughly 1 min at about 1050°C. The thin ($\sim 20\mu$) oxide layer formed during this period constituted the O^{18} marker. The O^{18} was then pumped out of the system and replaced by normal O^{16}; oxidation was then allowed to continue at the same temperature and pressure as before.

One of the O^{18} marked iron specimens was oxidized for roughly 45 min; this produced a compact, adherent scale about 300μ thick. After slowly cooling to room temperature, one of the surfaces of this specimen was beveled at a shallow angle by shimming up one edge and grinding on 600-grit Carborundum paper. The entire cross section of the scale was thus exposed on the beveled surface, giving an effective magnification of about 30. Similarly marked specimens were oxidized under the same conditions for considerably longer periods in an attempt to produce porous scales. Instead of beveling, cross sections of these samples were prepared by slicing with a string saw and polishing on a vibratory diamond-impregnated lap.

Zirconium specimens about 1.5 cm × 1.0 cm × 2 mm thick were cut from a piece of high-purity crystal-bar Zr sheet supplied by the Wah Chang Corporation. These specimens were marked by exposing them to an atmosphere enriched to 30% O^{18} for roughly 20 min at 750°C ($P_{O_2} \cong 120$ Torr). Subsequent oxidation in a normal environment was carried out at about 1200°C in a flowing water vapor atmosphere using argon as a carrier gas. Under these conditions, in 1 hr a dense, black, adherent layer of ZrO_2 about 180μ thick was produced. The scale was beveled prior to irradiation in the same manner as described above.

The 90-in. cyclotron at the Lawrence Radiation Laboratory was used to irradiate the samples with 2.7-MeV protons at a beam current of about 5 μA for times of the order of 30-45 min. At this beam energy, which is only slightly above the threshold energy (2.59 MeV) for the $O^{18}(p, n)F^{18}$ reaction, the O^{18} is preferentially activated to F^{18} and there are no interfering or competing reactions. This was confirmed by monitoring the decay of the radiation emitted by the samples, which showed that: (*a*) only a single radioactive species was present, and (*b*) the half life (110 min) corresponded to that of F^{18}. During irradiation the samples were mounted in a water-cooled target holder which was oscillated back and forth across the stationary proton beam in order to ensure that all portions of the specimen received the same total integrated exposure. Other details of the irradiation procedure have been described previously (42-44). Within about 30 min to an hour after irradiation, contact autoradiographs were prepared using Kodak Type A autoradiographic plates or, when greater resolution was desired, Type AR-10 stripping emulsion.

A number of other experiments have been carried out in order to obtain direct evidence for possible vapor phase transport of oxygen during the growth of wüstite scales on iron. For this purpose, high-purity iron specimens of both rectangular and cylindrical geometry have been employed, as well as an iron alloy containing 1 a/o (atomic per cent) Pt. These specimens were polished, degreased, and then marked with O^{18} by heating them for about 2 min at 800°C in a 30% enriched O^{18} atmosphere ($P_{O_2} \cong 120$ Torr). Preoxidation in O^{18} was deliberately carried out at a temperature below the α-γ transformation in iron in order to reduce the possibility of spalling of the oxide film during subsequent cooling; in addition, the samples were cooled relatively slowly by gradually reducing the furnace power. The marked specimens were then transferred to another system where they were oxidized either partially or completely to wüstite in a flowing H_2O/H_2 atmosphere which contained only the natural abundance of O^{18} (0.23%). The pertinent oxidizing conditions were: temp = 1015°C, $P_{H_2O}/P_{H_2} = 3.2$. In all cases the samples were slowly heated to furnace temperature in high-purity argon before the H_2O-H_2 gas mixture was admitted, and, at the conclusion of each run, the specimens were furnace cooled in argon. Cross sections of the samples were prepared by cutting them with a string saw, after which the specimens were given a standard metallographic polish.

Results and Their Interpretation

Cation migration in adherent oxide scales formed on iron.—The compact adherent scale produced on rectangularly shaped, zone-refined iron specimens in an oxygen atmosphere at 1050°C was found to consist almost entirely of wüstite; the thin surface layers of Fe_3O_4 and Fe_2O_3 which were also present represented only about 5% of the total thickness of the scale. The wüstite layer in contact with the metal was also free of porosity except near the extreme edges and corners of the specimen. A low-power photograph of the beveled surface of this specimen is shown in Fig. 2, together with the corresponding autoradiograph obtained after proton activation. It is immediately apparent that the O^{18} originally incorporated at the surface of the metal has remained fixed in this position during the subsequent thickening of the scale in a normal O^{16} environment.

This offers convincing proof that the growth of the wüstite layer is occasioned by the outward transport of Fe ions, or, in this case, by the migration of vacant Fe^{++} ion sites from the Fe_3O_4/Fe_xO phase boundary toward the Fe/Fe_xO interface. The O^{18}, being immobile, behaves precisely like an inert marker and is therefore concentrated in a sharply defined band at the Fe/wüstite interface (*see* Fig. 1b). Further verification of the sharpness of the O^{18} distribution is provided by the microdensitometer profile, also reproduced in Fig. 2, which was obtained by scanning the original autoradiographic plate in a direction normal to the metal/scale boundary on an Ansco recording densitometer. The abrupt cutoff in activity at both boundaries of the O^{18}-marked zone allows us to conclude with confidence that the mobility of oxygen ions in the rocksalt-type wüstite lattice must be at least two orders of magnitude smaller than that of iron at 1050°C. It follows that, in previous investigations in which Pt wires or other types of inert markers have been found imbedded within the wüstite layer (11, 17-20), the transport of oxygen past the marker must have occurred by some mechanism other than lattice diffusion. Additional

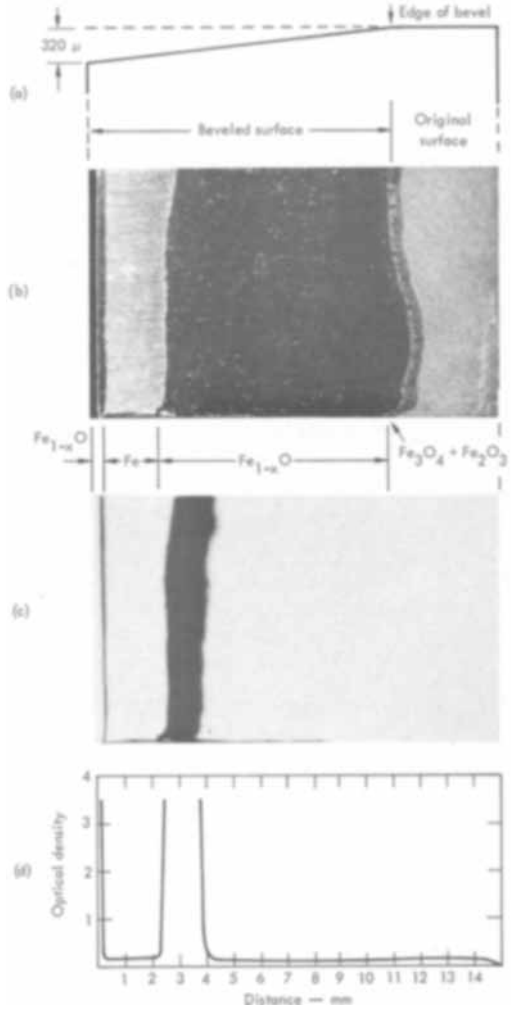

Fig. 2. O^{18} distribution in marked zone-refined iron specimen oxidized for 45 min at 1050°C in 1 atm O_2. (*a*) Plan view of beveled specimen; (*b*) low-power photograph of beveled surface; (*c*) corresponding autoradiograph after proton activation; (*d*) microdensitometer scan of autoradiograph.

experiments are described below which indicate that a vapor transport mechanism was operative.

Oxygen transport in ZrO_2 scales formed on Zr.—The 180μ-thick scale formed on high-purity Zr in a water vapor atmosphere at 1200°C had the characteristic black color usually associated with reduced or oxygen-deficient ZrO_2. Traces of the white stoichiometric oxide could be seen only at the extreme corners and edges of the specimen. The structure of the scale and the underlying metal is shown in cross section in Fig. 3a. Three distinct layers may be noted. The outermost (dark gray) layer is ZrO_2, the intermediate layer is the oxygen-stabilized α-Zr(O) solid solution (h.c.p.) and the innermost zone corresponds to the β-Zr(O) solid solution (b.c.c.) which has undergone transformation to α-Zr on cooling. Although no cracks or fissures were observed on examining the external surface of the scale under a low-power microscope, many elongated voids appear on a polished cross section (Fig. 3a), particularly in the outer portion of the scale. However, careful examination has revealed that a true diffusion barrier does exist at the metal/scale boundary. This is evident from Fig. 3b which shows that the oxide in contact with the oxygen-stabilized α-Zr(O) layer is perfectly adherent and free from any porosity.

Despite great care taken during metallographic preparation, many of the voids which are seen in Fig. 3a are believed to be artifacts. They represent areas within which small crystallites have mechanically broken out of the scale during polishing, thus giving an exaggerated appearance to the size and shape of the voids. Nonetheless, it must be presumed that the outer portion of the scale is not completely dense, and that relatively open channels which would have permitted direct access of oxygen probably existed in the outer part of the scale while oxidation was proceeding.

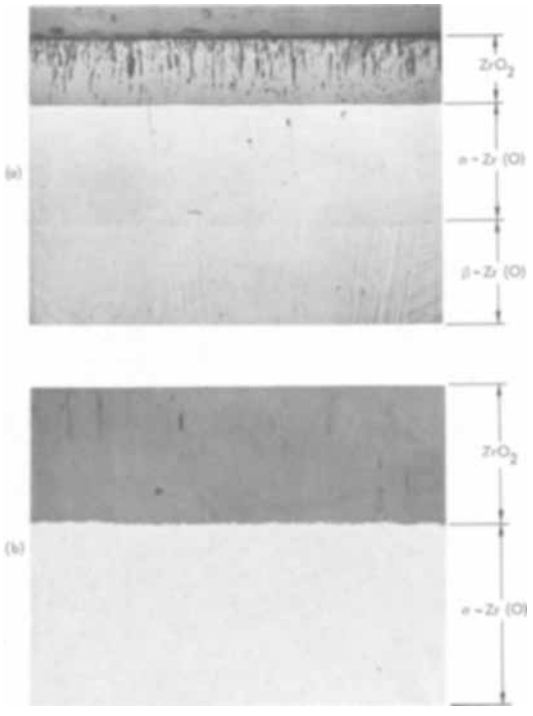

Fig. 3. Cross section of scale formed on crystal-bar Zr sheet at about 1200°C in a water vapor atmosphere. (*a*) Over-all structure showing the separate layers of ZrO_2, α-Zr(O), and β-Zr(O), 50×; (*b*) appearance of ZrO_2/α-Zr(O) interface, 250×. Unetched. Polarized light.

The autoradiograph obtained from an O^{18}-marked specimen after beveling and irradiation is presented in Fig. 4b. Included in this figure is a matching photograph of the beveled surface (Fig. 4a) and a microdensitometer profile (Fig. 4c) showing the optical density of the autoradiographic plate as a function of distance measured along the beveled surface. This particular specimen has been beveled in such a manner that only a portion of the intermediate oxygen-stabilized α-Zr(O) layer has been exposed on the beveled surface near the extreme left-hand edge of the sample.

The features of major interest here are the following: (*a*) the O^{18} tracer, initially confined to a thin ($\sim 2\mu$) layer on the metal surface, is now spread out along the bevel over a distance of about 3.5 mm from the α-Zr/ZrO_2 interface, corresponding to a distance of about 100μ in the direction normal to the interface, which is slightly over one half the total thickness of the scale; (*b*) down to a depth of about 80μ below the external surface of the scale, the O^{18} concentration is constant at a level corresponding to the natural abundance (0.23%) of O^{18}. The O^{18} distribution in the apparently dense portion of the scale near the metal interface is thus seen to be qualitatively similar to the distribution shown in Fig. 1d. This clearly establishes that the growth of the oxide layer involves the inward migration of oxygen through the ZrO_2 lattice. The actual form of the O^{18} profile in the ZrO_2 layer is unusual, however, in that, on proceeding toward the external surface, the O^{18} concentration falls off much more rapidly with distance than would be expected if oxygen were the only mobile constituent, or if oxygen transport through the scale took place only by normal solid-state diffusion processes.

The defect structure and extent of the departure from stoichiometry in ZrO_2 are still not well estab-

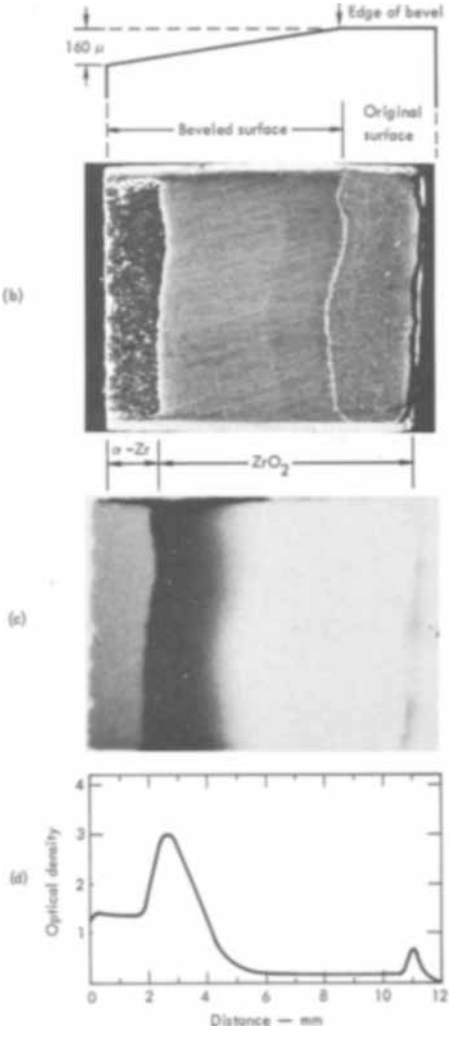

Fig. 4. O^{18} distribution in marked crystal-bar Zr specimen oxidized for 1 hr at about 1200°C in water vapor. (*a*) Plan view of beveled specimen; (*b*) low-power photograph of beveled surface; (*c*) matching autoradiograph after irradiation; (*d*) microdensitometer trace of autoradiograph.

lished (2, 52-55) either for the monoclinic form, which is stable below about 1200°C, or the tetragonal and cubic modifications, which are stable at higher temperatures. Although Madeyski and Smeltzer (56) have recently measured the self-diffusion coefficient of oxygen in pure monoclinic ZrO_2 between 800° and 1000°C using the gaseous exchange technique, comparable tracer self-diffusion data for Zr are not available, nor have the partial ionic conductivities for both components been determined. The possibility that the transport of Zr ions may make some contribution to the growth of the scale at high temperatures therefore cannot be dismissed *a priori* (2, 53, 57). It can easily be demonstrated, however, that, in order to account for the anomalous O^{18} distribution shown in Fig. 4 on a model involving counter-current diffusion of both ion species, the mobility of Zr ions in ZrO_2 must be even greater than that for oxygen. The available evidence (1) argues against such an interpretation. The inert marker experiments of Chirigos and Thomas (58) and Mallett and Albrecht (59) imply, for example, that, in oxygen at temperatures up to 950°C, the growth of ZrO_2 scales on Zr proceeds by the inward migration of oxygen without any noticeable participation on the part of cations. Had we carried out marker experiments using radioactive Zr as well as O^{18}, it could have been established whether or not the same holds true for the growth of the scale in a water vapor atmosphere, as appears probable.

The structural characteristics of the scale provide another and perhaps more reasonable explanation for the unusual form of the O^{18} distribution. When examined in polarized light, the ZrO_2 layer is found to consist of tiny lath-shaped crystallites, each oriented with their long axes parallel to the growth direction. The ease with which many of these crystallites seem to be dislodged during metallographic preparation suggests that they may not be firmly joined to one another; in fact, judging from the voids seen in cross section (Fig. 3a), it appears that more or less continuous channels exist along crystallite boundaries, especially in the outer portion of the scale. If so, normal O^{16} in the gas phase may penetrate deeply into the interior of the scale along these channels and exchange with the O^{18} which is present in the dense scale layer near the α-Zr/ZrO_2 interface. This, in turn, could lead to a rapid depletion of the O^{18} content in the outer scale layer and give rise to a tracer profile of the general form shown in Fig. 4. Comparison of Fig. 3a and Fig. 4 indicates that the region below the external surface within which voids are most apparent does indeed correspond, at least roughly, to the zone of constant background activity on the autoradiograph.

It is worth mentioning at this point that a simple and direct test of this proposed scaling mechanism could be obtained experimentally by reversing the order of oxidation, *i.e.* by oxidizing first in H_2O^{16} to produce a thick scale and then admitting H_2O^{18} shortly before cooling the sample. If channels or fissures which allow direct access of oxygen are present in the scale during growth, radioactivity produced by the $O^{18}(p, n)F^{18}$ reaction will be observed to a considerable depth below the surface; on the other hand, if the scale is truly dense and compact, the O^{18} will be confined to the extreme surface of the scale layer. By systematically varying the thickness of the scale layer formed in normal oxygen, the exact stage in the oxidation process at which mechanical breakdown on the scale occurs could also be determined. Such experiments might prove highly instructive, particularly if correlated with the results of weight gain measurements.

The mechanism by which oxygen is transported through the supposedly dense portion of the scale adjacent to the metal remains open to speculation. It has frequently been suggested in the past (46, 57, 59-64) that grain or crystallite boundaries may provide preferred paths for oxygen diffusion even in completely compact ZrO_2 scales grown on Zr. We had hoped that the autoradiographs themselves might furnish some basis for distinguishing between a grain boundary and a volume diffusion mechanism; however, the maximum resolution obtainable was not nearly sufficient to discern individual crystallite boundaries. In principle, the dominant transport mode could also be deduced from the shape of the O^{18} concentration *vs.* distance profile. The O^{18} concentration in the scale, c, relative to that at the metal/scale boundary, c_0, can easily be determined from the microdensitometer trace (Fig. 3c) by calibrating the original autoradiographic film. The resulting c-x curve is presented in Fig. 5.

It may be observed from Fig. 5a that, within a distance of about 25μ from the metal/scale boundary, the data can be fitted reasonably well by a straight line on a plot of $\ln c/c_0$ *vs.* x, which is suggestive of a line or short-circuiting diffusion process. A clear-cut distinction between a grain boundary and a bulk transport mechanism cannot be made, however, inasmuch as a rather good straight line is also obtained on a probability plot (Fig. 5b). This ambiguity may have arisen because: (*a*) the O^{18}-marked layer originally applied to the metal surface was not sufficiently thick to maintain a constant O^{18} concentration at the metal/scale interface throughout the experiment so that the appropriate boundary conditions were not satisfied; (*b*) no account has been taken of the fact that the diffusion

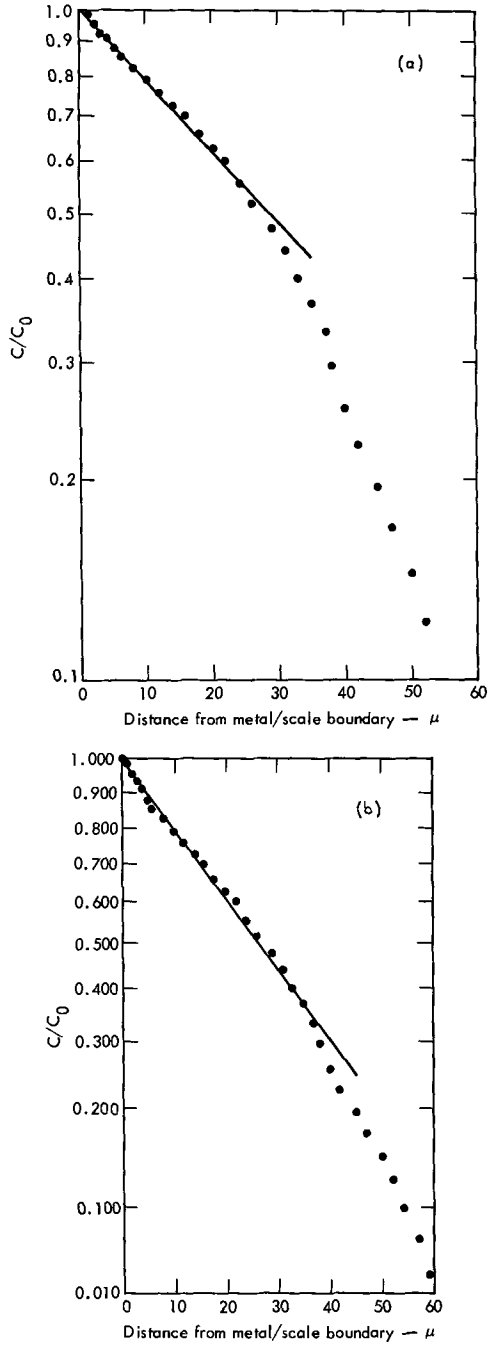

Fig. 5. The O^{18} concentration in the ZrO_2 layer as a function of the distance from the ZrO_2/α-Zr(O) interface: (*a*) ln c/c_0 *vs.* x; (*b*) probability plot of the data shown in (*a*).

of the O^{18} tracer into the growing scale layer is occurring at a moving rather than a stationary boundary; (*c*) the diffusion coefficient may be a sensitive function of the composition or stoichiometry; and (*d*) the O^{18} distribution was perturbed by exchange with gaseous O^{16} in deep-lying channels or fissures. It is evident that a more thorough study will be required in order to identify the operative transport mode decisively.

Although definite proof is lacking, the available evidence seems to suggest that most of the oxygen which eventually reaches the metal is transported through the dense part of the scale along short-circuiting paths of high diffusivity rather than by a volume diffusion process. The oxide scale formed at 1200°C in a water vapor atmosphere exhibits an average grain or crystallite size of the order of 1μ. If the structure of the scale is idealized by assuming it to consist of a columnar array of uniformly sized crystallites each 1μ × 1μ on a side, nearly one oxygen ion in every 10^3 would be located at a crystallite boundary. This means that virtually all of the mass transport needed to account for the observed rate of growth of the scale could be supplied by diffusion along crystallite boundaries if the grain boundary diffusion coefficient were as small as 10^4 times the volume diffusion coefficient of oxygen ions in ZrO_2. Considering that 1200°C is still a relatively low temperature compared to the melting point of ZrO_2 ($T_M \approx 3000$°C; $T/T_M \approx 0.49$), a ratio of the grain boundary to the lattice diffusivity of 10^4 is not at all unreasonable.

The conditions favoring grain boundary transport are greatly improved at lower temperatures, particularly in view of the marked reduction in the average crystallite size which is noted below about 1000°C. According to Lightstone and Pemsler (64), for example, the average grain diameter in ZrO_2 scales produced by oxidizing Zr in pure O_2 at 800°C is only about 300Å. These same authors investigated the transport of O^{18} in ZrO_2 scales formed on Zr at temperatures between 600° and 900°C using an argon ion beam to sputter oxygen atoms from the scale into a mass spectrometer where they could be analyzed directly. Their results were shown to be consistent with a short-circuit diffusion mechanism for oxygen transport. By making use of the $O^{17}(He^3, \alpha)O^{16}$ nuclear reaction, Cox and Roy (46) determined the distribution of O^{17} in relatively thin (<4μ) ZrO_2 scales formed by oxidizing first in O^{16} and then in O^{17} at 400° and 500°C. They, too, concluded that oxygen transport through the scale could not have been controlled by a simple volume diffusion process, and that grain or crystallite boundaries may provide the most likely paths for oxygen diffusion.

This raises some question regarding the interpretation to be placed on the values for the diffusion coefficient of oxygen which have been derived from an analysis of the diffusion-controlled oxidation kinetics of Zr at temperatures between 400° and 1050°C (65-67). Along with Cox and Roy (46), we believe that these derived or calculated values do not represent bulk diffusion coefficients; instead, they probably correspond to the product of the grain boundary diffusion coefficient and the effective cross-sectional area of high-diffusivity paths in the scale. Significantly, the calculated coefficients yield an activation energy for oxygen diffusion of only 28-31 kcal/mole, whereas the activation energy reported by Maydeski and Smeltzer (56) for relatively large-grained ZrO_2 is 56 kcal/mole. Furthermore, in the temperature range between 800° and 1000°C, the derived oxygen diffusion coefficients are between 3 and 4 orders of magnitude larger than the self-diffusion coefficients measured directly by Maydeski and Smeltzer. Cox and Roy have pointed out still another discrepancy, *viz.* that the calculated diffusion coefficients are in fortuitously good agreement with oxygen self-diffusion data for calcia-stabilized zirconia; since the latter contains nearly 15% oxygen ion vacancies and since the maximum departure from stoichiometry in pure ZrO_2 appears to be of the order of 0.1% or less (1, 55), no such agreement would be expected if oxygen diffuses by the same mechanism in both materials.

Evidence for Vapor Phase Transport of Oxygen during Growth of Wüstite on Iron in H_2-H_2O Atmospheres

Oxidation of high-purity iron samples with rectangular geometry.—Iron samples having rectangular or platelike geometry may be completely converted to wüstite without developing extensive internal porosity except near corners and edges; generally, a thin porous zone is also observed in the exact midplane of the specimen, as indicated in Fig. 6a. The O^{18} distribution in a wüstite sample which had been marked in the usual fashion prior to oxidation is shown in Fig. 6b. In regions well removed from the corners and edges, the O^{18} distribution is sharp and is confined to the midplane of the specimen, thus again confirming that iron is the diffusing species. Close inspection of the auto-

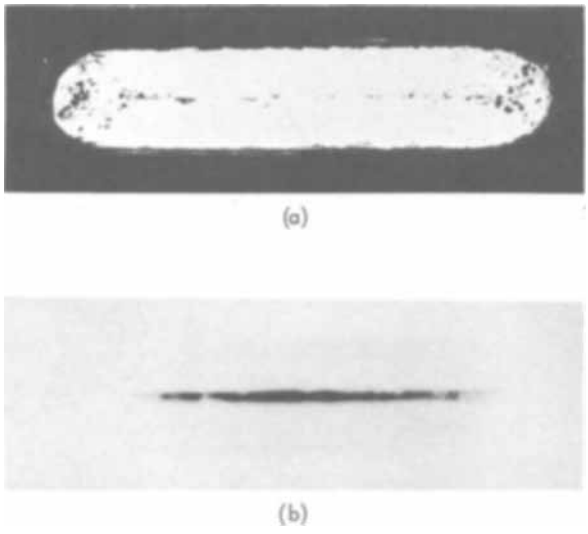

Fig. 6. O^{18} marker experiment on a rectangularly shaped zone-refined Fe specimen completely converted to wüstite by oxidizing at 1015°C in an H_2/H_2O atmosphere. (*a*) Cross section of oxidized specimen; (*b*) matching autoradiograph after proton activation of O^{18}.

radiograph (Fig. 6b) reveals that there are, in fact, two separate but parallel zones on either side of the midrib in which the O^{18} is concentrated. Apparently, the O^{18}-marked layers initially present on the two large flat faces of the iron sample did not quite meet in the center when the metal was entirely consumed.

The O^{18} distribution in the porous regions of the scale near the specimen edges is significantly different. This is evident from the autoradiograph in Fig. 7, which shows that the O^{18} tracer is spread out over a considerably greater area near the outside (right-hand) edge of the sample than it is in the denser central portion of the scale. Enhanced transport of oxygen must, therefore, have occurred at the corners and edges. This could not have been produced by the migration of some type of oxygen defect—either oxygen vacancies or interstitials—in the wüstite lattice since the relative mobilities of iron and oxygen ions in wüstite cannot be appreciably different near the corners and edges than in other regions of the scale. Furthermore, the average wüstite grain diameter is about 2-3 mm so that, if enhanced penetration of oxygen took place along grain boundaries, this would undoubtedly have been detected on the autoradiograph. No evidence for preferential grain boundary migration was found, however. We are thus led to the conclusion that the most likely mode of transport of oxygen in the porous regions of the scale is through the vapor phase *via* a dissociative mechanism (29, 30, 68).

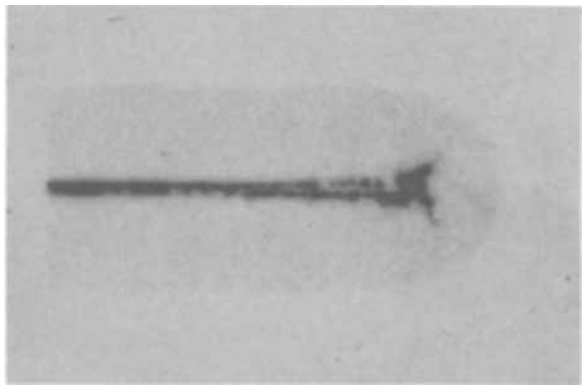

Fig. 7. Same as Fig. 6 except that the autoradiograph now shows the O^{18} distribution near the extreme (right-hand) edge of the sample.

Oxidation of high-purity iron samples having cylindrical geometry.—The local loss of adherence that occurs at the corners and edges of platelike specimens results in partial relief of stresses which are set up in the scale during growth. This, combined with the inherent plasticity of wüstite, allows the oxide formed on the large flat faces of the specimen to remain in good contact with the receding metal surfaces. Thick, compact, adherent wüstite layers, may, therefore, be produced on rectangularly shaped specimens. In samples having cylindrical form, the scale is under greater lateral constraint, but, more importantly, stresses cannot be relieved by edge cracking. As a consequence, rupture and partial separation of the scale from the metal are observed at isolated points around the circumference of the specimen at a much earlier stage in oxidation process. This sequence of affairs is illustrated in Fig. 8, which shows cross sections of the scale formed on O^{18}-marked, 7-mm-diam × 2.5-cm-long iron specimens at several intermediate stages during com-

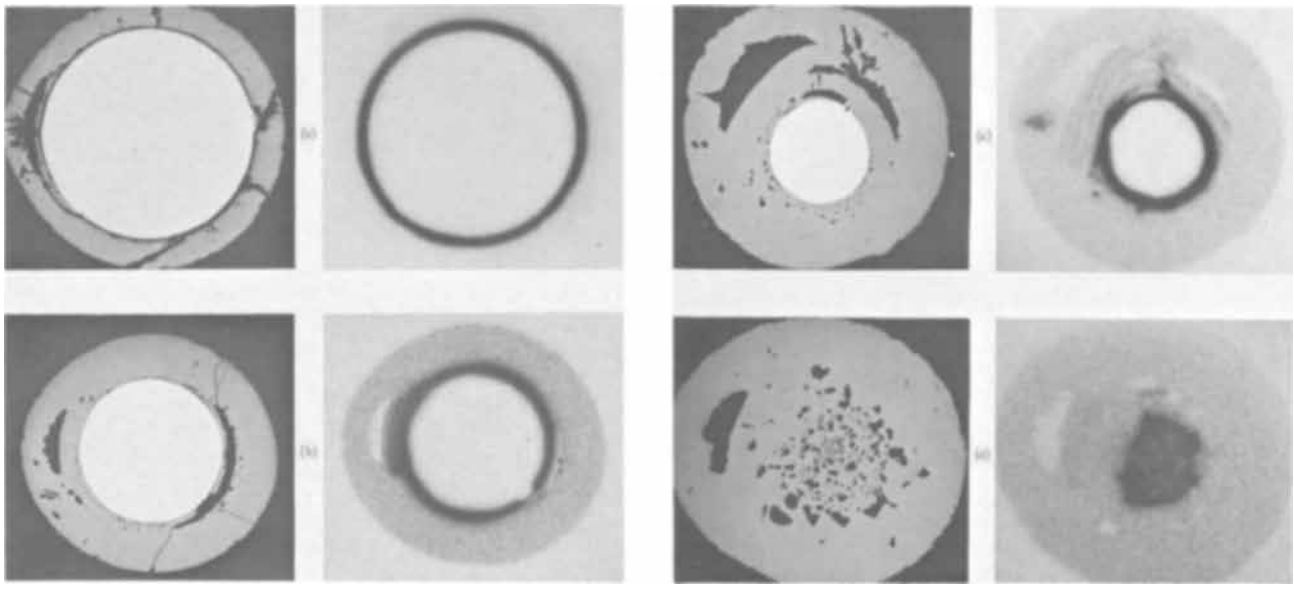

Fig. 8. Oxidation of O^{18}-marked 7-mm-diam, zone-refined iron cylinders at 1015°C in H_2/H_2O. Cross sections of the specimens and the corresponding autoradiographs are shown at various stages of oxidation to wüstite. (*a*) Oxidation time 4½ hr; (*b*) 17 hr; (*c*) 44 hr; (*d*) 90 hr.

plete reaction to wüstite at about 1000°C; the corresponding autoradiographs obtained after proton activation are also presented for comparison.

In general, the internal porosity developed in cylindrical specimens is far more extensive than that found in rectangularly shaped samples (compare, for example, Fig. 6b and 8d). The appearance of porosity in the scale is often accompanied by a smearing out of the O^{18} distribution near the metal/scale interface, and a rough correlation seems to exist between the amount of internal porosity and the extent of broadening of the O^{18} distribution. In completely oxidized cylindrical specimens, the central region over which the O^{18} tracer is distributed may occupy as much as 30% of the total volume of the oxide. The relative size of this centrally activated region increases with increasing specimen diameter and is greater near the ends of the cylinder than near the center, depending, no doubt, on the exact stage at which loss of adherence occurs between the scale and the metal. Similarly, the shape of this activated region also varies since separation of the scale from the metal does not take place simultaneously at all points around the circumference. These observations can be explained satisfactorily only by assuming that oxygen is transported through the vapor phase from detached portions of the scale to the underlying metal.

It should be pointed out that no O^{18} is observed in the vicinity of many of the large internal voids seen near the external surfaces of the scale (Fig. 8). This is somewhat puzzling. In order to be able to detect the vapor phase transport of O^{18}, however, the marked oxide must be detached cleanly from the surface of the metal along with the contiguous portion of the scale. This may not happen if the bond between the metal and the oxide is sufficiently strong. Instead, cracks may propagate through the oxide rather than along the metal/scale interface and the O^{18} may then remain bound to the metal. Indications that the detachment of the scale may actually occur in this manner can be found in Fig. 8. Juenker *et al.* (11) have proposed a similar method of scale detachment based on their metallographic observations.

Oxidation of an Fe-1 *a/o* Pt *alloy.*—Highly porous wüstites are obtained when dilute Fe-Pt alloys are oxidized to completion under the same conditions as those employed for zone-refined iron. The appearance of a completely oxidized Fe-1 a/o Pt specimen of rectangular shape is shown in cross section in Fig. 9a. (compare with Fig. 6a). In addition to the voluminous porosity, the interior portion of scale contains a fairly uniform dispersion of elemental Pt particles about 10μ in diameter. Proton activation of this sample yielded the autoradiograph shown in Fig. 9b, which reveals that the O^{18} distribution is spread out to a much greater extent on both sides of the midplane than it is in the dense, pure wüstite specimen illustrated in Fig. 6b. It is also evident that the interior portion of the scale over which the O^{18} is distributed coincides roughly with the zone of fine porosity shown in the accompanying photograph.

Solid-state diffusion of oxygen in the Pt-containing wüstite may be ruled out as a possible means of oxygen transport on the basis of the following argument. Platinum is believed to be virtually insoluble in wüstite and hence it should have little or no influence on the defect structure of the oxide. If dissolved, however, the substitution of Pt ions for iron in the wüstite lattice would either increase the concentration of iron ion vacancies or leave this concentration unchanged since the normal valence states of Pt are +2 or +4. The failure to detect even the slightest evidence for the preferential transport of oxygen along grain boundaries in high-purity, coarse-grained wüstite makes it reasonable to dismiss such a mechanism in this case as well, despite the fact that the average size of the wüstite grains in the highly porous region of the Pt-bearing

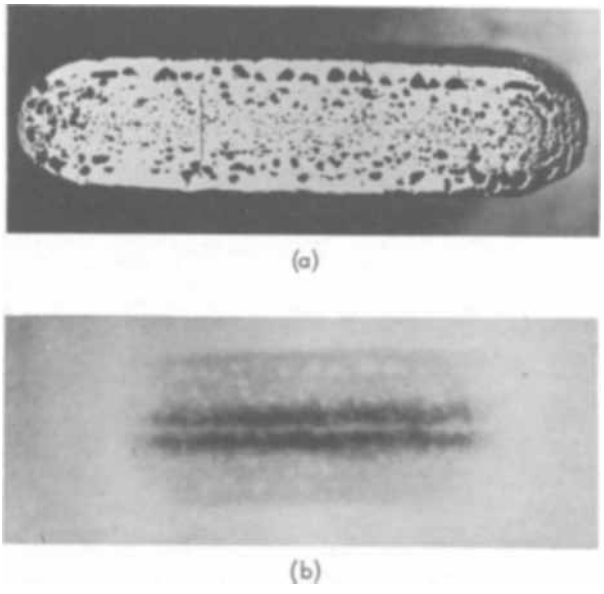

Fig. 9. O^{18} marker experiment on a rectangularly shaped Fe-1 a/o Pt alloy completely converted to wüstite in a H_2/H_2O atmosphere at 1015°C. *(a)* Cross section of oxidized specimen; *(b)* matching autoradiograph after irradiation.

scale is perhaps an order of magnitude smaller than that in the pure wüstite. Hence, by analogy with preceding examples, we again conclude that the major transport of oxygen took place through the vapor phase. Dissociative transport mechanisms thus appear to play an even more significant role in the oxidation of alloys than with pure metals, partly because impurities in the metal exert a strong influence on the degree of adherence of the scale.

Thick, non-adherent scales formed on iron in air.—The morphology of the scale produced by oxidizing a rectangularly shaped iron specimen for a relatively long time in air at about 1000°C after marking with O^{18} is shown in cross section in Fig. 10a. Complete separation of the scale from the metal has occurred along one of the large faces of the sample, thus allowing the scale on the opposite surface to grow without constraint and maintain contact with the metal. Detach-

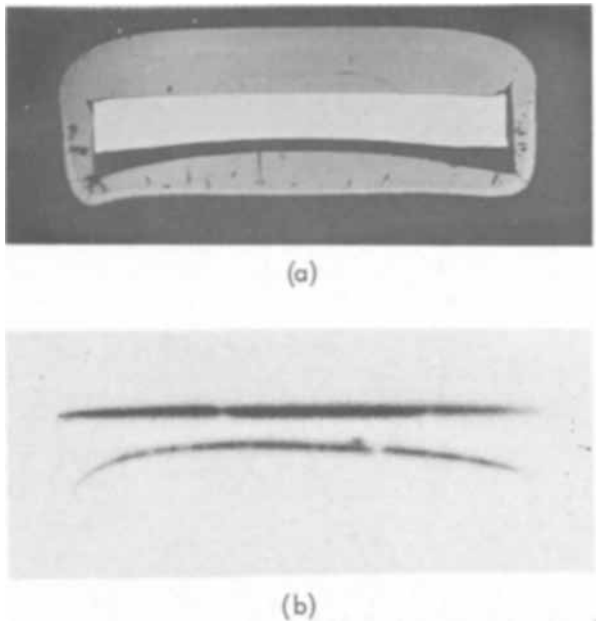

Fig. 10. O^{18} marker experiment on a rectangularly shaped zone-refined iron specimen partially oxidized in air at about 1000°C. (a) Cross section; (b) corresponding autoradiograph.

ment of the scale along this (bottom) surface apparently took place in step-wise fashion during growth as a result of the inward propagation of cracks originating at corners and edges (10, 11). It is significant, however, that, although the scale formed on the bottom surface is completely nonadherent, no internal porosity is seen except near the very edges. The nonadherent portion of the scale consists mostly of Fe_3O_4 and Fe_2O_3, which establishes that detachment of the scale occurred at temperature and not during subsequent cooling (15, 17).

The autoradiograph obtained when this specimen was activated is presented in Fig. 10b. Somewhat surprisingly, the O^{18} distribution is sharp even on the nonadherent side, where the tracer is concentrated at the surface of the oxide adjacent to the metal; faint vestiges of activity can also be found on the metal itself. It is clear that extensive transport of oxygen through the vapor phase did not occur in this experiment. Detachment of the scale from the metal is therefore not the only condition that must be met in order for a dissociative transport mechanism to operate. A suitable vapor species must also be present. Since vapor phase transport is observed when iron is oxidized to wüstite in H_2/H_2O atmospheres but not in dry air, it appears that some vapor species involving both oxygen and hydrogen, *e.g.* H_2O, is responsible. Fujii and Meussner (70) had earlier reached this same conclusion based on a detailed study of the mechanism of oxidation of Fe-Cr alloys in water vapor.

Discussion

The general approach outlined in earlier sections of this report involves study of the radioisotopic distributions of both chemical components in the growing scale layer. This approach has been illustrated here only by employing one of the two constituents, *viz.* oxygen, as a tracer. Wherever possible, however, it is suggested that both chemical species be utilized in order to provide a check on the internal consistency of the results. Establishing the distribution of the metallic as well as the nonmetallic component becomes particularly important when working with reaction products whose defect structures are unknown and for which little or no ionic transport data are available. In studying the oxidation of Zr at high temperatures, for example, the possibility that the diffusion of Zr ions may make some contribution to the growth of the scale could not be ruled out with certainty based only on consideration of the O^{18} distribution in the ZrO_2 layer.

Suitable radioisotopes exist for nearly all metals, the most notable exceptions being Ti and Al. Conveniently long-lived radioisotopes are also available for most nonmetallic elements of interest such as sulfur, carbon, phosphorus, boron, silicon, the halogens, *etc.* The only important exception, aside from oxygen, is nitrogen. Condit *et al.* (69) have recently shown, however, that the $N^{15}(\alpha,n)F^{18}$ nuclear reaction can be employed to study the distribution of nitrogen in solids in exactly the same way as the $O^{18}(p,n)F^{18}$ reaction has been utilized here. It is evident, therefore, that the use of the components of the system itself as markers constitutes a perfectly general technique which can be applied to virtually every class of scaling reactions on metals. With little modification, the same approach can also be used to study the mechanism of solid-liquid and solid-solid reactions (70), as well as such processes as the conversion of a lower to a higher oxide, sulfide, *etc.* (51). Application of the technique of the scaling of alloys may prove to be somewhat more difficult, however, because of the complex morphology of the oxide scales formed in alloy systems.

Judging from the examples presented above, the use of the $O^{18}(p,n)F^{18}$ nuclear reaction to study the mechanism of oxidation of metals offers a number of advantages over conventional marker techniques. In dense, adherent scales, for example, not only can the diffusing species be identified unambiguously but, in systems in which oxygen is the mobile component, valuable information concerning the mode of transport may also be deduced from the shape of the O^{18} concentration profile. This is illustrated by the work on the oxidation of Zr which, although not conclusive, indicates that oxygen may be transported through the compact portion of the scale along grain or crystallite boundaries. The unusual form of the O^{18} distribution in thick ($\sim 200\mu$) scales produced on Zr in a water vapor atmosphere has also furnished evidence that cracks or fissures which allow oxygen to penetrate deeply into the scale must have been present in the outer portion of the ZrO_2 layer. So detailed a picture of the transport processes that occur during the oxidation of Zr under the particular conditions employed in these experiments could hardly have been derived simply by observing the location of an inert marker.

The utilization of O^{18} as a tracer which can be detected by autoradiographic methods through subsequent proton activation thus provides the unique capability of determining whether the transport of oxygen takes place by diffusion through the solid reaction product or by some other means. In this respect, the $O^{18}(p,n)F^{18}$ nuclear reaction is definitely to be preferred over other charged-particle activation techniques such as those developed by Amsel and coworkers at the Ecole Normale in Paris (45, 48-50, 71) or by Cox and his collaborators at Chalk River, Ontario (46, 47). The experiments dealing with the growth of wüstite on iron in H_2/H_2O atmospheres dramatically illustrate this point. We have shown, for example, that oxygen is practically immobile in the wüstite lattice itself but that it is transported to the underlying metal at a rapid rate through the vapor phase under conditions which lead to the formation of porous scales. It is precisely because information of this type cannot be obtained from inert marker studies that the interpretation of conventional marker experiments must be carried out with great care. In fact, the failure to give due recognition to vapor phase transport processes is no doubt responsible for many of the incorrect conclusions which have been drawn from the results of inert marker experiments.

Certain limitations of the proton activation technique should also be noted (42, 50). Since autoradiographic procedures are employed, the accuracy with which the O^{18} distribution in the scale can be measured is partly determined by the resolution obtained on the film. This, in turn, is dependent on the thickness of the radioactive source, *i.e.* the depth of activation at the surface of the sample, the intimacy of contact between the emulsion and the sample, the characteristics of the film itself, and various other factors (72, 73). By controlling the energy of the proton beam just above the threshold energy for the $O^{18}(p,n)F^{18}$ reaction and irradiating with the beam at a grazing angle to the surface of the specimen, the depth of activation can be held to within 1μ; using the best stripping emulsions, it is possible, under these conditions, to obtain a resolution of the order of 5μ. This means that such features as the preferential transport of oxygen along grain boundaries would not be distinguishable unless the average grain diameter in the scale were greater than about 10μ.

The half life of F^{18} (110 min) is sufficiently long to make sectioning procedures practicable. However, the cross section for the $O^{18}(p,n)F^{18}$ reaction does not vary smoothly with energy but instead exhibits a number of sharp resonances (74). As a result, the activity measured at different depths below the surface cannot be related in a simple manner to the concentration of O^{18} at each level. Since sectioning methods are less satisfactory than might be supposed, the use of autoradiographic procedures becomes almost mandatory. A lower limit is thus imposed on the thickness of the oxide scale which can be employed in marker studies of this kind. Even if 100% enriched O^{18} were used, enough activity for proper autoradiographic detection

would probably not be obtained if the thickness of the O^{18}-marked layer initially formed on the metal surface were much less than 1μ. To establish the distribution of O^{18} in the scale with sufficient reliability, the final or over-all thickness of the oxide layer would have to be about an order of magnitude greater, *i.e.* roughly 10μ. The technique is therefore not nearly as well suited for investigating the early stages of oxidation of metals, as are the activation methods developed by Amsel *et al.* or Cox and co-workers.

By employing a radioisotope of the metallic component as a marker, it should not only be possible to check the interpretation of the O^{18} marker experiments but, in systems in which the cation is the faster diffusing component, supplementary information concerning the transport mechanism may also be obtained. The wüstite scales formed on iron at high temperatures are sufficiently coarse grained, for example, that preferential migration of iron along grain boundaries should be discernible on an autoradiograph if it contributes significantly to the growth of the scale. The scale may also be sectioned to determine the tracer distribution, analysis of which should reveal whether a bulk or a short-circuiting diffusion mechanism is operative. If normal lattice transport is indicated and there are no other complications, the cation diffusion coefficient calculated from the slope of the ln c *vs.* x^2 plot should agree reasonably well with the self-diffusion coefficient measured by more conventional techniques (35, 36, 38). This would provide still another check on the assumed transport mechanism. Complications may arise, however, as was shown by Carter and Richardson (37), who studied the oxidation of Co using Co^{60} as a tracer. They observed an anomalous distribution of Co^{60} near the metal/scale interface; Birchenall (75) later suggested that this may be associated with the development of porosity in the scale. It may be interesting, therefore, to compare the Fe^{55} or Fe^{59} distribution in an apparently dense pure wüstite scale with the distribution seen in the porous wüstite scales obtained by oxidizing dilute Fe-Pt alloys under the same conditions.

Based on our observations and those of others, it would seem that the proper approach to the conduct of inert marker studies is to choose the experimental conditions in such a way that complications introduced by the formation of porous scales are avoided or at least minimized. Although the factors which govern the loss of adherence between the scale and the metal, as well as the development of porosity in the scale, are still not fully understood, enough experience has been gained to permit several working rules to be set down. These are as follows:

1. Metal specimens with rectangular or platelike geometry should be employed and their lateral dimensions should preferably be of the order of ten times the thickness or greater.

2. The highest purity metals available should be selected since even trace amounts of impurities may have a deleterious effect on the adherence between the scale and the metal.

3. The surfaces of the specimens should be polished and scrupulously cleaned before the inert marker is applied.

4. High-melting noble metals such as Pt or Ir, vapor deposited on the surface of the sample in the form of thin discontinuous films, appear to provide the most satisfactory markers (8, 76). Radioisotopes of these metals (*i.e.*, Pt^{197} or Ir^{192}) are also suitable (37). If Pt wires are used, these should be lightly sintered or spot-welded to the metal so that they are in intimate contact with the surface. The wires should also be of sufficiently small diameter ($<25\mu$) that they do not interfere with normal diffusional flow during the growth of the scale (10).

5. Preliminary experiments should be carried out on unmarked specimens of identically the same size, shape, and purity in order to establish the range of conditions, *i.e.* time, temperature, oxygen pressure, *etc.*, under which compact, adherent scales are produced. The actual marker studies should be performed under these same conditions and the expectation that the scale grown on the marked samples is, in fact, free from internal porosity should be verified by metallographic examination.

6. In working with metals which undergo phase transformations at temperatures below those employed in the actual marker experiments, it is advisable to bring the metal specimen to the desired temperature in an inert (or reducing) atmosphere before admitting oxygen into the system. This will avoid any possibility that the scale formed during warmup, and the marker along with it, becomes detached from the metal surface due to volume changes accompanying the phase transformation in the metal. The same applies to systems whose oxides exhibit crystallographic transformations.

7. Temperature fluctuations in the oxidation furnace should be kept to a minimum to avoid introducing thermal stresses which could lead to premature rupture or loss of adherence of the scale. Whenever possible, the specimens should also be cooled in such a way as to prevent excessive spalling of the scale.

8. Since the presence of water vapor may accelerate vapor transport, steps should be taken to ensure that the reacting gases are dry.

By taking these simple precautions it should be possible, in most instances, to obtain a reliable measure of the relative mobilities of the metallic and nonmetallic components in the scale from inert marker experiments. These same precautions should also be observed when using O^{18} as a marker, if the objective is simply to establish the nature of the mobile constituent in the pure, dense product phase. On the other hand, if it is desired to investigate the details of the scaling mechanism over as wide a range of conditions as possible, including those which lead to the formation of porous or nonadherent scales, a somewhat different approach is called for. The physical characteristics of the scale now assume overriding significance; in this connection, the importance of good metallography as an essential aid in the interpretation of marker experiments can hardly be overestimated. It will also be appreciated that, by making proper use of O^{18} as a tracer, much may be learned concerning the physical nature of the scale as it exists at the oxidizing temperature. For example, to determine whether or not rupture of the scale has occurred in a manner which allows direct access of oxygen to the underlying metal, O^{18} may be admitted to the system shortly before the specimen is cooled to room temperature. Any cracks into which O^{18} had penetrated will then be revealed on the resulting autoradiograph by the presence of activity along their borders; these cracks should therefore be distinguishable from those which might have originated on cooling.

In conclusion, it should be mentioned that in addition to its usefulness in studying the mechanism of oxidation processes, the $O^{18}(p, n)F^{18}$ nuclear reaction may also be employed to advantage in many other types of investigations, *e.g.* in the determination of metal-oxygen phase diagrams, studies of the solubility and diffusivity of oxygen in metals, measurement of oxygen self-diffusion coefficients in bulk oxides (44, 77), and in studying the preferential segregation and mobility of oxygen along grain boundaries or other structural discontinuities (43).

Acknowledgments

The authors wish to thank the entire staff of the 90-in. cyclotron at the Lawrence Radiation Laboratory for their help in carrying out these experiments. In all phases of this work, we have profited greatly from discussions and useful comments offered by R. H. Condit. The assistance of F. Vanderhoofen and M. Y. Almassy in the preparation of specimens is also gratefully acknowledged.

Manuscript submitted March 17, 1969; revised manuscript received *ca.* July 23, 1969.

Any discussion of this paper will appear in a Discussion Section to be published in the June 1970 JOURNAL.

REFERENCES

1. P. Kofstad, "High-Temperature Oxidation of Metals," John Wiley & Sons, Inc., New York (1966).
2. K. Hauffe, "Oxidation of Metals," Plenum Press, New York (1965).
3. F. A. Kröger, "The Chemistry of Imperfect Crystals," North-Holland Publishing Co., Amsterdam (1964).
4. L. B. Pfeil, *J. Iron Steel Inst.*, **119**, 501 (1929); *ibid.*, **123**, 251 (1931).
5. H. Schmalzried, *Z. Physik, Chem., N. F.*, **33**, 111 (1962).
6. R. E. Carter, *J. Am. Ceram. Soc.*, **44**, 116 (1961).
7. C. Kooy, *Pure Appl. Chem.*, **9**, 441 (1964).
8. S. Mrowec, *Z. Physik. Chem., N. F.*, **29**, 47 (1961).
9. S. Mrowec and T. Werber, *Acta Met.*, **8**, 819 (1960).
10. R. A. Meussner and C. E. Birchenall, *Corrosion*, **13**, 677t (1957).
11. D. W. Juenker, R. A. Meussner, and C. E. Birchenall, *Corrosion*, **14**, 39t (1958).
12. M. Cagnet and J. Moreau, *Acta Met.*, **7**, 427 (1959).
13. J. Moreau and M. Cagnet, *Rev. Met.*, **55**, 1091 (1958).
14. L. Himmel, R. F. Mehl, and C. E. Birchenall, *Trans. AIME*, **197**, 827 (1953).
15. M. H. Davies, M. T. Simnad, and C. E. Birchenall, *ibid.*, **191**, 889 (1951).
16. C. E. Birchenall, *Metallurgical Reviews*, **3**, 235 (1958).
17. B. W. Dunnington, F. H. Beck, and M. G. Fontana, *Corrosion*, **8**, 2 (1952).
18. I. Pfeiffer, *Z. Metallk.*, **49**, 267 (1958).
19. H. Engell and F. Wever, *Acta Met.*, **5**, 695 (1957).
20. K. Sachs, *Metallurgia*, **54**, 11 (1956).
21. B. Ilschner and H. Pfeiffer, *Naturwiss.*, **40**, 603 (1953).
22. J. A. Sartell and C. H. Li, *J. Inst. Metals*, **90**, 92 (1961/1962).
23. L. Czerski and S. Patzau, *Arch. Hutnictwa*, **1**, 353 (1954).
24. H. Rickert, *Z. Physik. Chem., H. F.*, **23**, 355 (1960).
25. K. Hauffe, "Reaktionen in und an Festen Stoffen," Springer-Verlag, Berlin (1955).
26. R. H. Condit, Ph.D. Thesis, Princeton University, University Microfilms #60-4974 (1960).
27. S. Mrowec and H. Rickert, *Z. Physik. Chem., N. F.*, **28**, 422 (1961).
28. A. Dravnicks and H. McDonald, *J. (and Trans.) Electrochem. Soc.*, **94**, 139 (1948).
29. S. Mrowec and T. Werber, *Acta Met.*, **7**, 696 (1959).
30. F. Maak and C. Wagner, *Werkstoffe Korrosion*, **12**, 273 (1961).
31. J. Bardeen, W. H. Brattain, and W. Shockley, *J. Chem. Phys.*, **14**, 714 (1946).
32. C. Wagner, in "Atom Movements," pp. 153ff, American Society for Metals, Cleveland (1951).
33. J. G. Schnizlein, J. D. Woods, J. D. Bingle, and R. C. Vogel, *This Journal*, **107**, 783 (1960).
34. R. L. Jarry, J. Fisher, and W. H. Gunther, *ibid.*, **110**, 346 (1963).
35. G. W. Castellan and J. W. Moore, *J. Chem. Phys.*, **17**, 41 (1949).
36. W. J. Moore and B. Selikson, *ibid.*, **19**, 1539 (1951).
37. R. E. Carter and F. D. Richardson, *Trans. AIME*, **203**, 336 (1955).
38. S. M. Klotsman, A. N. Timofeev, and I. Sh. Trakhtenberg, in "Surface Interactions Between Metals and Gases," V. I. Arkharov and K. M. Gorbunova, Editors, pp. 84ff, Consultants Bureau, New York (1966).
39. H. Pfeiffer and B. Ilschner, *Z. Elektrochem.*, **60**, 424 (1956).
40. J. Mikulski, S. Mrowec, and T. Werber, *Bull. Acad. Polon. Sci.*, **7**, 737 (1959); *ibid.*, **7**, 547 (1959); *ibid.*, **8**, 179 (1960).
41. J. Milulski, S. Mrowec, I. Stronski, and T. Werber, *Z. Physik. Chem., N. F.*, **22**, 20 (1959).
42. R. H. Condit and J. B. Holt, *This Journal*, **111**, 1192 (1964).
43. J. B. Holt and R. H. Condit, "Materials Science Research," Vol. 3., pp. 13ff, Plenum Press, New York (1966).
44. J. B. Holt, *Proc. Brit. Ceram. Soc.*, No. 9, p. 157 (July 1967).
45. G. Amsel and D. Samuel, *J. Phys. Chem. Solids*, **23**, 1707 (1962).
46. B. Cox and C. Roy, *Electrochem. Technol.*, **4**, 121 (1966).
47. R. W. Ollerhead, E. Almqvist, and J. A. Kuehner, *J. Appl. Phys.*, **37**, 2440 (1966).
48. A. Choudhury, D. W. Palmer, G. Amsel, H. Curien, and P. Baruch, *Solid State Commun.*, **3**, 119 (1965).
49. D. W. Palmer, *Nucl. Inst. Methods*, **38**, 187 (1965).
50. G. Amsel and D. Samuel, *Anal. Chem.*, **39**, 1689 (1967).
51. L. Himmel and J. B. Holt, *Acta Met.*, To be published.
52. D. L. Douglass and C. Wagner, *This Journal*, **113**, 671 (1966).
53. R. W. Vest, N. M. Tallan, and W. C. Tripp, *J. Am. Ceram. Soc.*, **47**, 635 (1964).
54. R. W. Vest and N. M. Tallan, *J. Am. Ceram. Soc.*, **48**, 472 (1965).
55. P. Kofstad and D. J. Ruzicka, *This Journal*, **110**, 181 (1963).
56. A. Madeyski and W. W. Smeltzer, *Mater. Res. Bull.*, **3**, 369 (1968).
57. J. N. Wanklyn, *Electrochem. Technol.*, **4**, 81 (1966).
58. J. Chirigos and D. E. Thomas, WAPD-53, Westinghouse Electric Corp., Pittsburgh, Pa. (1952).
59. M. W. Mallet and W. M. Albrecht, *This Journal*, **102**, 407 (1955).
60. E. A. Gulbransen and K. F. Andrew, *Trans. AIME.*, **209**, 394 (1957).
61. S. Aronson, *This Journal*, **108**, 312 (1961).
62. W. W. Smeltzer, R. R. Haering, and J. S. Kikaldy, *Acta Met.* **9**, 880 (1961).
63. R. J. Hussey and W. W. Smeltzer, *This Journal*, **111**, 564 (1964).
64. J. B. Lightstone and J. P. Pemsler, *Proc. 6th Intern. Symp. Reactivity Solids, Schenectady, N. Y., 1968*, To be published.
65. J. Debuigne and P. Lehr, *Mem. Sci. Rev. Met.*, **60**, 911 (1963).
66. C. J. Rosa and W. C. Hagel, *J. Nucl. Mater.*, **27**, 12 (1968).
67. C. J. Rosa and W. C. Hagel, *Trans. Met. Soc. AIME*, **242**, 1293 (1968).
68. C. T. Fujii and R. A. Meussner, *This Journal*, **110**, 1195 (1963).
69. R. H. Condit, J. B. Holt, and L. Himmel, *ibid.*, **114**, 1100 (1967).
70. J. B. Holt, in "Sintering and Related Phenomena," G. C. Kuczynski, N. A. Hooton, and C. F. Gibbon, Editors, pp. 169-188, Gordon and Breach (1967).
71. G. Amsel, G. Beranger, B. de Gelas, and P. Lacombe, *J. Appl. Phys.*, **39**, 2246 (1968).
72. R. H. Condit, in "Techniques of Metals Research," Vol. 2, Pt. 2, R. F. Bunshah, Editor, John Wiley & Sons, New York, In press.
73. D. F. Stein, *Trans. Met. AIME*, **239**, 1721 (1967).
74. H. Mark and C. Goodman, *Phys. Rev.*, **101**, 768 (1956).
75. C. E. Birchenall, *This Journal*, **103**, 620 (1956).
76. L. Czerski, S. Mrowec, and T. Werber, *Arch. Hutnictwa*, **3**, 37 (1958).
77. J. S. Sheasby and B. Cox, *J. Less-Common Metals*, **15**, 129 (1968).

Technical Notes

Reaction Kinetics of Partially Decomposed Barium Titanyl Oxalate

Thomas S. Montgomery

Robert McCullough Research Center, Ling-Temco-Vought, Inc., Dallas, Texas

The intermediates formed from partially decomposed barium titanyl oxalate tetrahydrate, $BaTiO(C_2O_4)_2 \cdot 4H_2O$ have been studied. Several thermal decomposition mechanisms have been previously proposed by several investigators (1-5). Gallagher and Thomson (4) proposed that an anhydrous compound decomposes between 300° and 400°C producing barium carbonate and titanium(IV) oxide which, in turn, reacts at 600°-700°C to form barium titanate. Infrared analyses of compositions similar to these proposed intermediates and reaction products have been obtained previously (6-11).

In this investigation the solid state reaction kinetics between the intermediates, $BaCO_3 + TiO_2$ was examined in the 400°-700°C range. The reaction rate data was analyzed using equations corresponding to reaction mechanisms of several types. The equations representing differing models have been reviewed (12).

Experimental Procedure

Barium titanyl oxalate tetrahydrate was prepared by the method of Clabaugh *et al.* (13, 5), and heated to selected temperatures. The partially decomposed phases were analyzed by infrared spectrophotometry using the double beam mode over the range 400-4000 cm^{-1}. Isothermogravimetric analyses (TGA) were obtained at selected temperatures over the 400°-700°C range.

Isothermal analyses of weight loss *vs.* time were obtained from material calcined to 400°C, pressed at 10,000 psi and the pellets stabilized at 400°C. The pellets were elevated to the desired isothermal temperature within 10 min and the extent of the solid state reaction was monitored by per cent weight loss. The complete reaction of $BaCO_3 + TiO_2 \rightarrow BaTiO_3 + CO_2\uparrow$ requires 15.9% weight loss. The pellets were weighed immediately after being thermal stabilized at 400°C and immediately after the run. Close correlation between calculated and observed weight loss was noted for the higher temperature evaluations where the material obviously was completely reacted.

Results and Discussion

Infrared analysis.—The infrared spectra was evaluated for the barium titanyl oxalate which had been calcined at several temperatures in the 400°-700°C range. The spectra in the 200°-400°C range was considered only qualitatively so as to observe the change in spectra up to the 400°C region. It was observed that the major change in absorption peak positions occurs at 400°C, and that above this temperature the peak positions are established and only the intensity changes (Fig. 1).

The absorption peaks observed in the 400°-700°C region near 1430, 1020, 860, and 695 cm^{-1} are associated with the V_3, V_1, V_2, and V_4 vibrations, respectively, which have been previously assigned to $BaCO_3$ (6, 7). An absorption peak near 540-560 cm^{-1} may be compared both to the V_1 (or Ti-O stretch frequency) of $BaTiO_3$ (10) or the unassigned frequency of TiO_2 (11). For cubic and tetragonal $BaTiO_3$ the asymmetric absorption band V_1 extends from about 800 to 475 cm^{-1}, with a center of 540 cm^{-1}, and a half width of 165 cm^{-1} (10).

The area under the V_3 (1430 cm^{-1}) $BaCO_3$ peak decreases as the calcining temperature is increased. This correlates with the thermogravimetric data (4) showing the reaction is proceeding and the amount of the carbonate present is decreasing. The amount of TiO_2 decrease or $BaTiO_3$ increase could not be related as the only vibration mode observed for both phases

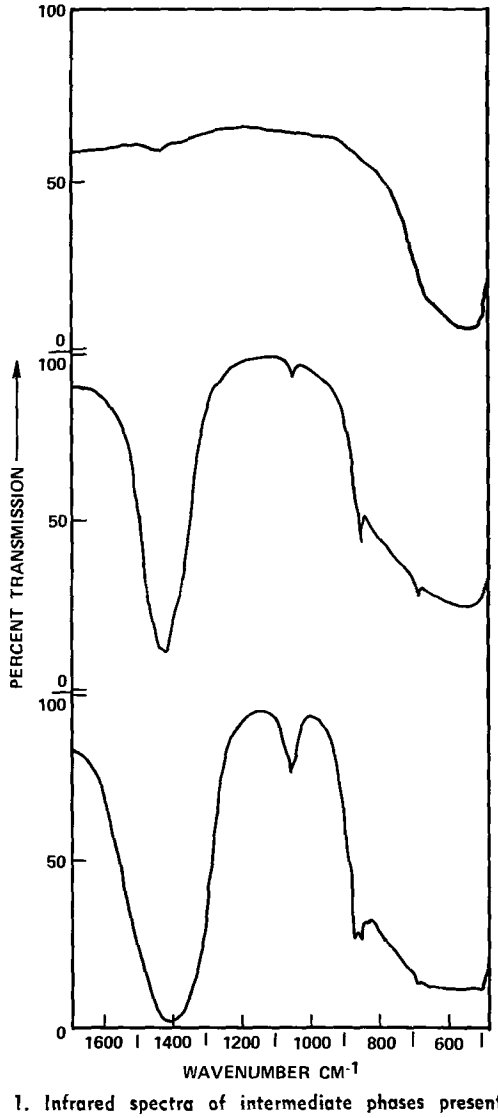

Fig. 1. Infrared spectra of intermediate phases present. Note the decrease in relative intensity of the $BaCO_3$ peaks (in text) with increasing temperature. Upper-700°C, middle-550°C, lower-450°C.

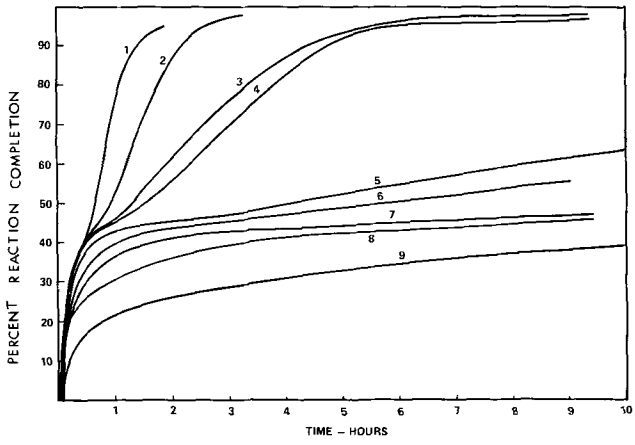

Fig. 2. Decomposition curves of $BaCO_3$ and TiO_2 phases reacting to form $BaTiO_3$. 1, 680°C air; 2, 680°C vacuum; 3, 650°C air; 4, 650°C vacuum; 5, 600°C air; 6, 600°C vacuum; 7, 550°C air; 8, 550°C vacuum; 9, 500°C air.

is near 500 cm^{-1}. The broad absorption peak in the 500-700 cm^{-1} region is retained as the temperature is increased toward 700°C. [Remaining fundamental modes for TiO_2 occur at 388 and 183 cm^{-1} and for $BaTiO_3$ at 400, 183, 12 cm^{-1} (6, 7, 10).] X-ray diffraction analysis of the phases present for heating at 550°C for 20 hr to 50% reaction completion showed only a major $BaTiO_3$ peak and four lines to match $BaCO_3$.

Reaction kinetics.—The relation between per cent reaction completion, temperature, environment, and duration of run until no further weight loss was observed is shown in Fig. 2. The 100% reaction completion represents the 15.9% weight loss for the reaction $BaCO_3 + TiO_2 \rightarrow BaTiO_3 + CO_2\uparrow$. The isothermal decomposition or reaction completion data were subjected to diffusion controlled equations. Rate constants calculated from the equations showed a drift with time (14).

The reactants, viz., $BaCO_3$, TiO_2 (anatase), and/or TiO_2 (rutile), have densities which are 4.31, 3.9, and 4.18-4.25, respectively. The presence of either anatase or rutile and $BaCO_3$ reacting to form a final phase, $BaTiO_3$ ($\rho = 6.02$), having lower molar volume may undergo contraction; and the formation of a discontinuous product layer. Laidler (15) proposes that reaction at a phase boundary may be the rate-determining step when a discontinuous product phase occurs. The relation between the fraction reaction completed and time for a phase boundary controlled reaction is

$$k_{PB}t = 1 - (1 - X)^n$$

where $n = 1/3$ for spherical shaped grains, and X is the amount of reaction completion. The rate constant data obtained for the phase boundary equation represented by the contracting sphere model ($n = 1/3$) is plotted in Fig. 3 and shows constancy of the rate constant after 40 and 55% reaction completion of the 680° and 650°C air runs, respectively.

The kinetics of the anatase-rutile transformation have been extensively studied (16, 17). In a 2-hr period, conversion of anatase to rutile is 60% completed at 680°C, whereas it is only 15% completed at 650°C (16). This may then be related to the reaction between $BaCO_3$ and TiO_2 to form $BaTiO_3$. The initial 2-hr period shows that the reaction is nearly (95%) completed at 680°C, whereas only 60% of the reaction is completed at 650°C in air. The per cent rutile formed at 600°C is negligible and the per cent $BaTiO_3$ formed

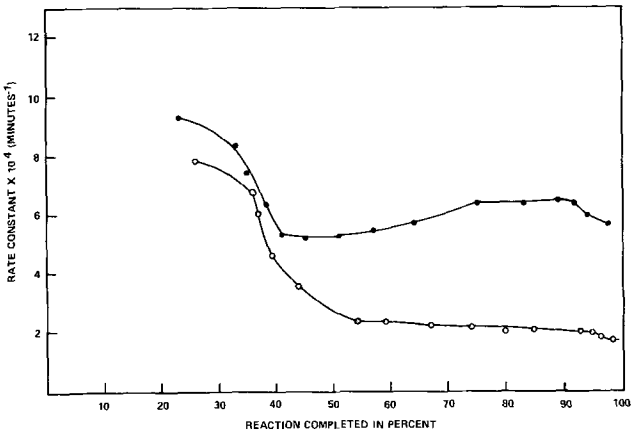

Fig. 3. Analysis of the rate constants using the phase boundary model, $[1 - (1 - \alpha)^{1/3}] = kt$, for the reaction of $BaCO_3$ and TiO_2 to form $BaTiO_3$ in air, ●, 680°C; ○, 650°C.

in the solid state reaction at 600°C is considerably less (<50%) than at the higher temperatures. This suggests that the reaction shows the Hedvall effect (18) and is controlled in part by the kinetics of the anatase-rutile conversion.

Manuscript submitted May 27, 1969; revised manuscript received July 17, 1969.

Any discussion of this paper will appear in a Discussion Section to be published in the June 1970 JOURNAL.

REFERENCES

1. B. V. Strizhov *et al.*, *Zh. Prikla. Khim.*, **33**, 2009 (1960).
2. O. Saburi, Report, Murata Manufacturing Co., Ltd., Nagaoka-Cha, Kyoto, Japan, June 27, 1961 (in Japanese).
3. P. K. Gallagher and F. Shrey, *J. Am. Ceram. Soc.*, **48**, 567 (1963).
4. P. K. Gallagher and J. Thomson, Jr., *ibid.*, **48**, 644 (1965).
5. F. W. Wlassich, LTV Research Center, Report No. 0-71000/7R-17, Nov. 1967.
6. B. M. Gatehouse, S. E. Livingstone, and R. S. Nyholm, *J. Chem. Soc.*, **1958**, 3137.
7. H. H. Adler and P. F. Kerr, *Am. Mineralogist*, **48**, 839 (1963).
8. J. D. C. Yates, *J. Phys. Chem.*, **65**, 746 (1961).
9. K. E. Lewis and G. D. Parfitt, *Trans. Faraday Soc.*, **62**, 204 (1966).
10. J. T. Last, *Phys. Rev.*, **105**, 1740 (1957).
11. W. G. Spitzer, R. C. Miller, D. A. Kleinman, and L. E. Howard, *ibid.*, **126**, 1710 (1962).
12. (a) D. L. Branson, *J. Am. Ceram. Soc.*, **48**, 591 (1965).
    (b) S. F. Hulbert and M. J. Popowich, "Kinetics and Mechanism of the Reaction Between TiO_2 and $SrCO_3$," Paper presented at International Symposium on Ceramics, Alfred, N.Y., June 1967.
13. W. S. Claubaugh, E. M. Swiggard, and R. Gilchrist, *J. Res. Nat. Bur. Stds.*, Research Paper 2677, **56**, (May 1956).
14. T. S. Montgomery, LTV Research Center, Report No. 0-71000/9R-3, March 1969.
15. K. J. Laidler, "Chemical Kinetics," 2nd ed., pp. 316-381, McGraw-Hill Book Co., New York (1965).
16. A. W. Czanderna, C. N. Ramachandra Rao, and J. M. Hoeing, *Trans. Faraday Soc.*, **54**, 1069 (1958).
17. (a) R. D. Shannon and J. Pask, *Am. Mineralogist*, **49**, 1707 (1964).
    (b) A. Navrotsky and O. J. Kleppa, *J. Am. Ceram. Soc.*, **50**, 626 (1967).
18. J. A. Hedvall, *Chem. Rev.*, **15**, 139 (1934).

Stability of Aluminum Oxide Films on Germanium Devices

S. Krongelb

IBM Watson Research Center, Yorktown Heights, New York

Recent work has indicated that Al_2O_3 films can be deposited and used as insulating layers on semiconductor surfaces (1-3). This material can meet the need for an insulator deposited at relatively low temperatures, for, as Aboaf (2) has shown, Al_2O_3 can be formed at 420°C by the pyrolysis of aluminum isopropoxide. The present work will demonstrate that Al_2O_3 deposited by pyrolysis or by sputtering is superior to SiO_2 made at a comparable temperature by the reaction of tetraethyl orthosilicate (TEOS) and oxygen (4) in that the Al_2O_3 is far less susceptible to water pickup and much more stable under bias-temperature stressing than the SiO_2. The combination of Al_2O_3 deposited over SiO_2 will be shown to have particularly desirable characteristics for germanium device technology.

Sample Preparation

The SiO_2 films were made at 450°C by the reaction of TEOS and oxygen (4). Al_2O_3 was formed either pyrolytically from $Al(OC_3H_7)_3$ at 420°C in a nitrogen ambient as described by Aboaf (2), or by r.f. sputtering from a 99.9% pure Al_2O_3 cathode in an argon atmosphere. The substrate temperature in the latter process was estimated to be about 400°C.

Fixed-charge and surface-state densities were determined from C-V measurements made and interpreted as described by Sedgwick (5). These properties on single-layer insulators were evaluated on a structure consisting of a 2-5 ohm-cm n- or p-type (110) Ge substrate on which about 2200Å of the desired oxide had been deposited. A 30-mil diameter evaporated Al dot completed the device. The insulating film for the double-layer measurements consisted of about 1000Å of SiO_2 deposited directly on the germanium and covered with about 1500Å of the appropriate Al_2O_3. Electrical stability was evaluated on the basis of the change in fixed-charge density after a 1 hr bias-temperature stress at 150°C with fields up to 10^6 V/cm under both positive and negative bias. Charge transport during stress was measured as described by Kerr (6).

Moisture resistance was appraised by comparing the water content of the films before and after temperature-humidity (T & H) stressing at 85°C and 85% relative humidity. The amount of water in the films was determined from the infrared absorption in the 3μ region by the methods of Pliskin and Lehman (7), using films deposited on infrared transparent (high resistivity) silicon substrates. The single-oxide films were about 5000Å thick while the double-layer samples consisted of about 4000Å of SiO_2 covered by 1500Å of the appropriate Al_2O_3. The latter structure was designed primarily to determine the effectiveness of Al_2O_3 in preventing water absorption by the highly susceptible SiO_2. All spectra were obtained on a Beckman IR-10 spectrometer operated in the double-beam mode. With the above samples, an absorption corresponding to an optical density of 0.004 or greater per micron of oxide could readily be measured.

Results and Discussion

Electrical properties.—Sedgwick (5) has shown that the Ge-insulator interface is characterized by the presence of both fixed charges and fast acceptor states. These parameters are given in Table I for the various insulating films under consideration. It is noted that, except for pyrolytic Al_2O_3 directly on Ge, all the films give rise to a positive fixed charge and moderate surface-state densities. (Sputtered Al_2O_3 directly on Ge is not included because the sputtering process introduces excessive surface state densities which leads to an uninterpretable MOS characteristic.) The presence of negative fixed charge in Al_2O_3 on Ge and the reduction in fixed charge when Al_2O_3 is deposited over SiO_2 have been previously reported (2, 8). It should be noted that the fixed charges cited in Table I are effective values calculated from C-V data on the assumption that all the charge lies at the Ge-insulator interface. This effective charge describes the effect of the real charges in the insulating film on the semiconductor surface, but the actual charges, especially for the two-layer structures, are very likely not all located at the semiconductor interface.

Changes in the electrical surface properties as a result of bias-temperature stressing are given in the last column of Table I. The shifts for most samples fall within a factor of two of the values cited, and for the SiO_2 films are in a direction indicating ion motion. The magnitude of the shift for the +10V stress on SiO_2 may be greater than for −10V, but the difference is generally within the factor-of-two spread of the data. More significantly we have found that the observed C-V shift on a given SiO_2 device represents only a half to a quarter of the charge transport which was actually measured on that device during stressing. Our hypothesis, based on work currently in progress, is that the C-V shift represents the net effect of the transported charge combined with partial neutralization and trapping at the SiO_2-Ge interface. In fact, a smaller stress field can actually cause larger apparent C-V shifts. This behavior is attributed to the fact that while essentially complete ion transport still takes place at lower fields, the trapping effect is reduced. The C-V data cited here probably understate the instability inherent in this SiO_2 film deposited on germanium.

With Al_2O_3, either directly on the semiconductor or applied over SiO_2, the C-V shift is significantly reduced. These small shifts can occur is either direction for either polarity of applied stress so that the C-V data still represent a combination of effects, probably ion motion, trapping, and annealing (small shifts of comparable magnitude have been noted on heating without bias). However, ion motion in the presence of Al_2O_3 is markedly reduced as has been verified by direct measurement of charge transport during the stressing of Al_2O_3 and Al_2O_3-SiO_2 structures. The observed transport is small and comparable to or less than the C-V shifts. The C-V data thus do provide a valid evalua-

Table I. Typical electrical interface properties of various oxide films

Oxide	Fixed charge per cm²	Surface states per cm²	Change under stress in fixed charge per cm²
SiO_2 by TEOS and oxygen at 450°C	3×10^{12} pos	1.5×10^{12}	2×10^{12}
Al_2O_3 by pyrolysis in N_2 at 420°C	2×10^{12} neg (variable)	Up to 12×10^{12}	0.4×10^{12}
Pyrolytic Al_2O_3 over 450°C SiO_2	0.7×10^{12} pos	1.0×10^{12}	0.3×10^{12}
Sputtered Al_2O_3 over 450°C SiO_2	1.2×10^{12} pos	1.4×10^{12}	0.3×10^{12}

Table II. Water content of various films before and after temperature and humidity exposure

Material	Initial O.D./μ* SiOH	Initial O.D./μ H_2O	After T & H O.D./μ SiOH	After T & H O.D./μ H_2O	Days in T & H environment
SiO_2 (by TEOS process at 450°C)	0.04	0.013	0.076	0.095	5
Al_2O_3 (pyrolytic)	0.008**		0.013**		59
Al_2O_3 (sputtered)	<0.004**		<0.004**		29
SiO_2 protected by pyrolytic Al_2O_3	0.03	0.007	0.029	0.010	26
SiO_2 protected by sputtered Al_2O_3	0.02	<0.004	0.014	<0.004	33

* Optical density per micron of film.

tion of the stability of these films, and the magnitude of the shift is at a level which is acceptable for bipolar devices. While the single layer of Al_2O_3 does have good electrical stability, the two-layer structures are more attractive for device applications because of the lower surface-state densities associated with them.

Water pickup.—The water content of the various films before and after T & H exposure is summarized in Table II. Water content is expressed in terms of infrared optical density per micron of film; where SiOH and H_2O absorption can be resolved, both optical densities are given. [A convenient rule of thumb is that the weight fraction of water in SiO_2 is approximately equal to the optical density of the SiOH absorption per micron of oxide (9).]

The results show that SiO_2 deposited by the reaction of oxygen and TEOS has a high water content initially and readily picks up additional water during the T & H stressing. These findings are consistent with previously reported adverse effects resulting from room-temperature exposure to high humidity (4). The pyrolytic Al_2O_3 films, on the other hand, contain relatively little water initially and are only slightly affected by T & H exposure. The water content of the sputtered films is below the detectability limit of the Beckman IR-10 spectrometer even after stressing. In comparing the effects of T & H exposure on SiO_2 and Al_2O_3, it should further be noted that the SiO_2 films become saturated with water after only a few days of stressing, whereas the data for the Al_2O_3 films represent the effects of a month or more of T & H exposure.

Low water content in a film after T & H stressing has generally been taken as an indication that the film will protect the underlying materials from the effects of ambient moisture. This passivating property of the Al_2O_3 films can be seen directly from the last two entries in Table II. These samples consist of 4000Å of SiO_2 which is covered over by 1500Å of the indicated Al_2O_3. The dominant contribution to the I-R absorption in these structures comes from water in the SiO_2, and the data accordingly are expressed as the optical density per micron of SiO_2. The fact that there is no increase in water content after T & H stressing is attributed to the passivating qualities of the Al_2O_3. A slight decrease in water content is in fact noted, but the difference is close to the reproducibility limit of our measurements and further work is required to establish whether the change is really significant. The data in Table II also show that SiO_2 which is covered by Al_2O_3 has a lower initial water content than does unprotected SiO_2. This difference is probably real and may be explained by noting that some water is driven off under the conditions of the Al_2O_3 deposition. Subsequent exposure to the atmosphere does not result in reabsorption of moisture because the SiO_2 is now protected.

Conclusion

The two-layer structure of Al_2O_3 over SiO_2 deposited on germanium has been shown to have a relatively stable semiconductor interface under bias-temperature stressing. Superior moisture resistance, when compared to a single SiO_2 layer deposited at comparable temperatures, has also been demonstrated for the two-layer structure. While Al_2O_3 alone also exhibits good electrical stability and moisture resistance, it has drawbacks in that (*i*) Al_2O_3 cannot be sputtered directly onto the semiconductor surface without excessive surface damage, and (*ii*) pyrolytic deposition of Al_2O_3 on Ge results in a high and variable density of surface states. The two-layer structure overcomes these problems and appears promising for device work.

Acknowledgments

This work was performed with the assistance of B. J. Agule and B. J. Stoeber. The cooperation of J. A. Aboaf, E. F. Baran, C. W. Casey, and J. P. Hoekstra, who prepared the various Al_2O_3 films, and of V. Maniscalco, who performed the aluminum evaporation, is also gratefully acknowledged.

Manuscript received March 7, 1969; revised manuscript received *ca.* July 7, 1969. This was Paper 311 presented at the Boston Meeting, May 5-9, 1968.

Any discussion of this paper will appear in a Discussion Section to be published in the June 1970 JOURNAL.

REFERENCES

1. S. K. Tung and R. E. Caffrey, *This Journal*, **114**, 275C (1967).
2. J. A. Aboaf, *ibid.*, **114**, 948 (1967).
3. A. Waxman and K. H. Zaininger, *Appl. Phys. Letters*, **12**, 109 (1968).
4. S. Krongelb, *Electrochem. Technol.*, **6**, 251 (1968).
5. T. O. Sedgwick, *J. Appl. Phys.*, **39**, 5066 (1968).
6. D. R. Kerr, Paper No. 14 presented at the Cleveland Meeting, May 1966.
7. W. A. Pliskin and H. S. Lehman, *This Journal*, **112**, 1013 (1965).
8. T. O. Sedgwick, and J. A. Aboaf, *IEEE Trans. Electron Devices*, **15**, 1015 (1968).
9. W. A. Pliskin, Private communication.

Brief Communication

Making Formed Contacts to Semiconductors Using a Programmable Power Supply

T. M. Baleshta*[1]

Surface Science Group, Mineral Sciences Division, Mines Branch, Department of Energy, Mines and Resources, Ottawa, Ontario, Canada

An effective way of obtaining good ohmic contacts is by the formed (welded)-contact method. A formed contact can be made either by discharging a capacitor, with a series resistance to provide constant current characteristics through a point contact (1), or by applying a succession of current pulses through a point contact from a high-impedance power source (2). For those workers who do not have access to commercial bonding equipment, the following contact forming technique may be useful.

A programmable d-c power supply, having both constant voltage and constant current regulation, with automatic crossover from constant voltage to constant current, is an ideal high-impedance current source that can be used to make formed contacts. A power supply with these characteristics is, for example, the Lambda Electronics Corporation Model No. LH125. This power supply is capable of supplying a voltage from 0 to 40V and a current from 0 to 3A, and has a voltage-to-current crossover delay of 1 msec. The contact-forming procedure is to use the power supply in place of the capacitor in the capacitor-discharge technique, but without the series resistance since the constant-current mode of the power supply provides this feature. The output voltage of the power supply is set to a value which will give an initial current pulse (thermal transient) that starts the contact-forming process, and the output current of the power supply (current limiting) is set to provide post heating of the contact. Postheating allows the contact area to remain molten for a short time (a few seconds) resulting in a stable and reproducible contact. When the lead wire touches the semiconductor, the power supply will hold its programmed voltage for 1 msec before automatically crossing over to the current-limiting mode.

A number of formed contacts were successfully made to low-resistance (1-ohm) samples of FeS_2 and PbS. The voltage of the power supply was set so that an initial current pulse of approximately 10A started the forming of the contacts; then a postcurrent of 1A was maintained through the contact for a few seconds to complete the forming. The lead wires used were gold and copper, both having diameters of 0.005 in. The resulting contacts were mechanically strong and voltage-current characteristics showed them to be ohmic.

Manuscript received June 24, 1969.

Any discussion of this paper will appear in a Discussion Section to be published in the June 1970 JOURNAL.

REFERENCES

1. R. Bray and A. Many, Chap. 7.4 in "Solid State Physics," Vol. 6, K. Lark-Horovitz and V. A. Johnson, Editors, Academic Press, New York (1959).
2. A. C. Sims, *J. Electron. Control*, **3**, 139 (1957).

* Electrochemical Society Active Member.
[1] Present address: Electronics Dept., Algonquin College of Technology, Ottawa, Ont., Canada.

Anodes for Refuelable Magnesium-Air Batteries

R. P. Hamlen,* E. C. Jerabek, J. C. Ruzzo, and E. G. Siwek

Physical Chemistry Laboratory, General Electric Company, Research & Development Center, Schenectady, New York

ABSTRACT

The aim of this work was to select a suitable anode and electrolyte combination for the operation of a replaceable anode magnesium-air battery. Various combinations were considered from the standpoint of cell voltage, parasitic consumption of metal, and the volume of reaction product sludge formed. Packaging materials were also tested to prevent the sludge from falling to the bottom of the cells and to minimize magnesium hydroxide formation on the cathodes. The anode package selected consisted of AZ61 magnesium alloy covered on each surface with Vexar expanded polyethylene and glycerinated cellulose. Sodium chloride solutions, between 7 and 18%, were satisfactory electrolytes, the latter being superior as a result of a lower resistive drop in the electrolyte and a shorter voltage transient on changing current densities.

The purpose of this work was to select an anode alloy and an electrolyte-separator system for use with magnesium-air cells. The cells are to be employed in a battery with replaceable anodes and electrolyte (1, 2). This system differs from the silver chloride-magnesium sea water cell in that the product is primarily a hydroxide rather than a chloride, and all of the magnesium hydroxide (or hydroxychloride) product must be contained within the cell rather than being flushed out. The over-all pH in the cell is higher, although at the magnesium electrode it may be lower as a result of the poorer circulation in the cells.

Since the product sludge must remain within the cell, the total ampere-hour discharge between refuelings is determined by the volume of sludge per ampere-hour and by the total cell volume available for containment of the sludge. The arrangement of the cell must be such that the bottom portion of the magnesium is not completely masked by fallen reaction product. In addition, the cell must be such that the depleted anode and the reaction products can be conveniently removed from the cell without damaging the cathodes. The voltage should be as high as possible, consistent with a reasonable coulombic efficiency, and the voltage transient on increasing from a low to a high current density should be minimized and the time interval over which it occurs should be as short as possible. The experiments described below were aimed at selecting an appropriate anode, electrolyte, and separator combination.

Experimental

Voltage and gassing behavior.—Several different magnesium alloys were selected for testing, based on previous air cell work and on the recommendations of the Dow Chemical Company. In addition to these, two samples of aluminum were obtained from the Metals Research Laboratories of the Olin Mathieson Chemical Company. These had been formerly recommended for use as a substitute for magnesium in silver chloride-magnesium torpedo batteries, and had been found to operate with slightly lower voltages, but with higher efficiencies. The various metals were compared using a small cell of 10 cm^2 active area arranged as shown in Fig. 1. A platinum-Teflon Niedrach-Alford [Ref. (3)] cathode was used, the gap between the magnesium and the cathode was ¼ in., and a flow meter was arranged so that the gas flow out of the cell could be measured. A calomel reference electrode was connected to the cell through a side arm halfway between the electrodes. A mercury-wetted 60 Hz on-off switch was placed in series with the load as a means of measuring the resistance of the whole cell and of the magnesium half cell. This resistance was measured by measuring the initial voltage recovery using an oscilloscope when the load was removed. The oscilloscope was also used for evaluation of the transient behavior of the magnesium when switching current levels. Otherwise the cell was operated at constant current. For these tests, the electrolyte was 7% sodium chloride solution. Electrolyte pumped through the cell due to gas evaluation was returned to the cell *via* the electrolyte recirculation arm shown in Fig. 1.

Figure 2 gives the polarization curves for the various alloys. The aluminum was Type A-6 alloy from the Olin Metals Laboratory. The voltage for the Gemag alloy (Magnesium Elektron, Limited) was the highest over the whole range. However, the gassing results, shown in Fig. 3, show that at relatively low current densities the gassing rate is higher than that for any of the other alloys. This means that at low current drains of a few milliamperes per square centimeter large fraction of the magnesium would be consumed in self-discharge. The dashed line in Fig. 3 represents the

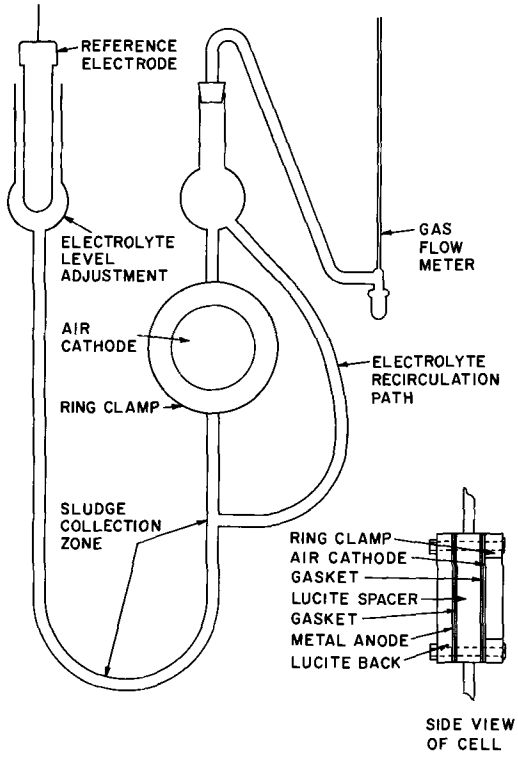

Fig. 1. Metal-air cell of 10-cm^2 area with circulating electrolyte

Key words: batteries, magnesium, air cathodes, anodes.
* Electrochemical Society Active Member.

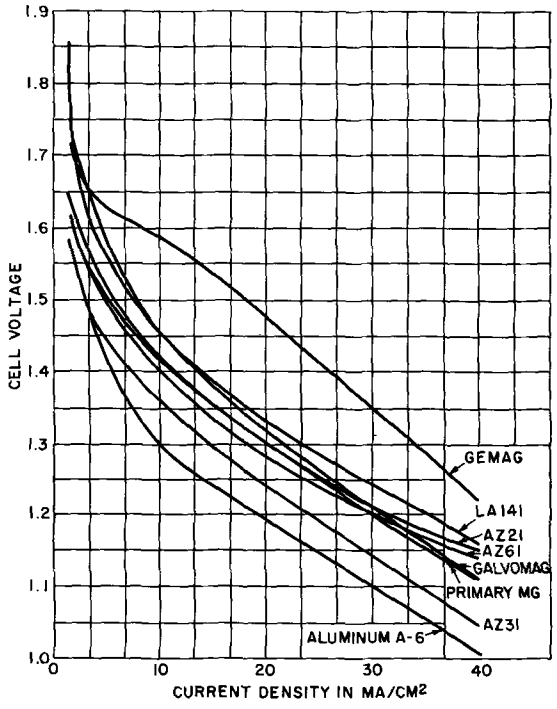

Fig. 2. Voltage vs. current density for various alloys

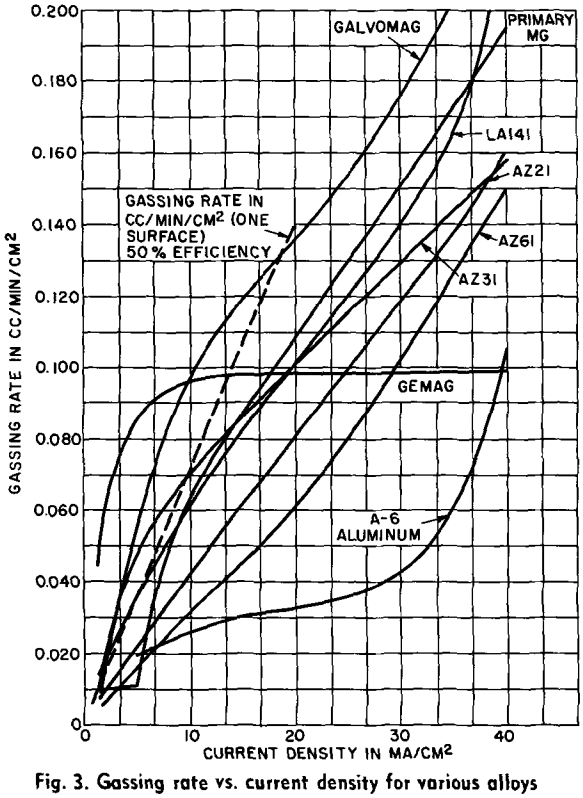

Fig. 3. Gassing rate vs. current density for various alloys

gassing rate at which 50% of the metal would be consumed in the self-discharge reaction. The farther below this line the curve for a sample is, the higher its efficiency should be. The aluminum sample should be better than the others on the basis of efficiency in the intermediate current density range, although its voltage is lower than the others. During these experiments, it was observed that the gassing rate at a given current density was somewhat dependent on the prior operation of the cell, possibly as a result of changes in surface area or electrolyte concentration. This may account for some of the irregularities of the curves in Fig. 3.

Of the magnesium samples, AZ61 represents a good compromise between voltage and gassing behavior, and is one of the readily available alloys. This is the alloy which is used in water-activated magnesium-silver chloride torpedo batteries.

Sludge volume measurements.—The volume of sludge produced for a given alloy and electrolyte system was determined as follows. A sample of alloy was operated in a small cell between air electrodes 5.7 cm high and 7.6 cm wide (43 cm^2). The thicknesses of the alloy samples ranged from 10 to 80 mils, and the gap between the electrodes was about ¼ in. The volume of liquid contained was about 14 cc. The cell was operated at constant current at ambient temperature for a specified time, and then the residual matter was washed out of the cell and off the anode into graduated centrifuge tubes. The volume of sludge was measured after centrifugation. This sludge was frequently observed to be nonhomogeneous, consisting of layers of light-colored hydroxide or hydroxychloride, and dark-colored matter containing fine particles of unreacted metal. In addition to measuring the sludge volume, observations were also made on the nature of the reaction product (tightly or loosely packed within the cell) and on the ease of removal of the magnesium anode.

Results and Discussion

Table I summarizes the results of some of the tests, which were conducted primarily with AZ31 and AZ61 magnesium alloys. The table gives the sludge volumes in cubic centimeters per ampere-hour. It was desired to find the combination giving the minimum sludge volume, since this would yield the maximum number of ampere-hours for a given cell size. The results for AZ31 in 7% sodium chloride show that there is considerable variation in results obtained from tests conducted under similar conditions. There does not appear to be any large change in sludge volume with increased sodium chloride concentration. However, the average for AZ61 in 7% sodium chloride, 3.8 cc/A-hr, is lower than that for AZ31, 4.7 cc/A-hr.

Various electrolytes and additives were employed during these tests. Some of the observations follow.

Magnesium ion in solution.—When a solution of a salt containing magnesium ion, such as magnesium chloride or bromide, was used as the electrolyte, magnesium hydroxide precipitated in and on the cathode. This caused a rapid decrease in cell output.

Calcium chloride.—With a solution of calcium chloride, the magnesium rapidly passivated. This probably resulted from the deposition of a layer of calcium hydroxide on its surface.

Thickeners.—Two per cent Jaguar gum (Stein, Hall and Company, Incorporated) was added to 7% sodium chloride solution to observe the effect of drastically in-

Table I. Sludge volume measurements

Test No.	Alloy	Electrolyte	Current, amperes	Current density, mA/cm^3	Ampere-hours	Sludge volume, cc/A-hr
12	AZ31	7% NaCl	1.00	23	5.5	5.5
23	AZ31	7% NaCl	1.00	23	3.5	5.0
37	AZ31	7% NaCl	1.20	28	6.0	3.6
27	AZ31	14% NaCl	1.00	23	3.9	4.4
33	AZ31	21% NaCl	1.20	28	6.0	4.0
11	AZ31	Sat'd NaCl	0.42	10	7.1	4.9
13	AZ31	Sat'd NaCl	1.00	23	5.5	5.8
20	AZ61	7% NaCl	1.00	23	3.5	4.6
41	AZ61	7% NaCl	1.20	28	6.0	3.7
49	AZ61	7% NaCl	0.40	9	6.0	3.0
35	AZ61	21% NaCl	1.20	28	6.0	3.5
15	GEMAG*	7% NaCl	1.00	23	3.7	6.8
22	Galvomag**	7% NaCl	1.00	23	3.5	4.9
26	LA141 Mg***	7% NaCl	1.00	23	1.9	6.4
21	OML A6 Al****	7% NaCl	1.00	23	3.5	~9

* A proprietary GE alloy produced by Magnesium Elektron, Ltd.
** A Dow Chemical Company cathodic protection alloy.
*** A lithium-magnesium alloy from Brooks and Perkins.
**** Olin Metals Laboratory aluminum.

creasing the electrolyte viscosity. When the cell was operated, the hydrogen evolved from the magnesium carried most of the viscous electrolyte out of the top of the cell.

Precipitation aids.—Separan NP10 (Dow Chemical Company) and polyacrylic acid added to 7% sodium chloride each caused the formation of tightly packed sludge. This is a disadvantage form the standpoint of the removal of spent anodes.

Chelating agents.—Versene (the sodium salt of ethylenediamine tetraacetic acid) and Versene Fe-3 [the sodium salt of N-N-di (2-hydroxy-ethyl) glycine—both from Dow Chemical Company], potential chelating agents for magnesium ion, were considered because of the possible effect on sludge volume. There does appear to be a slight advantage using Versene Fe-3 (2%, plus 7% NaCl), the sludge volume being 3.3 cc/A-hr on AZ61 (average of 6 tests) compared to 3.8 cc/A-hr in 7% sodium chloride alone. However, the presence of Versene Fe-3 caused increased corrosion of copper and nickel cell components.

During these experiments, it was observed that magnesium hydroxide was precipitated in and on the cathode after a few hours of operation. This caused the performance to deteriorate with time. The precipitation results from the fact the hydroxyl ion is formed at the cathode, and therefore the solubility for magnesium ion is lowest at this point. In order to reduce the problem, samples of microporous filters and cellophane were placed between the anode and the cathode during cell operation. The original intent was to place a single permanent layer over the face of the cathode in contact with the solution. However, it was found that the magnesium hydroxide layer precipitated on the electrolyte side of this filter caused an increase in the internal resistance of the cell. Because of this, it was decided that each anode should be bagged in the appropriate separator material.

The bagging materials considered were: Acropor AN-200 microporous filter (Gelman Company), glycerinated and unglycerinated cellulose, and glycerinated and unglycerinated fibrous casing (all from Union Carbide Corporation). Cellulose and fibrous casing were both superior to the microporous filter medium from the standpoint of keeping magnesium hydroxide precipitate off of the cathode. Glycerinated cellophane was the least expensive of the separator materials considered and is recommended for this system.

An additional problem pertaining to the sludge was the manner in which it distributed itself vertically in the cell. If nothing was introduced to keep the sludge from dropping to the bottom of the cell, the bottom of the cell would not discharge due to increased electrolytic resistance where the sludge would fill the electrolyte gap. To compensate for this situation, various large-pore materials were introduced between the cellophane and the magnesium anode. The materials employed were cellulose felt (Kendall Company, Grade EU 101), open-cell polyurethane foam (Scott Paper Company), and various grades of Vexar expanded polyethylene (Du Pont). The material finally selected was a grade of Vexar, 30ADS49, having a thickness of 0.1 cm and diamond-shaped openings about 0.8 cm across. It was found that with felt the escape of the hydrogen gas generated was somewhat cut off, so that the internal resistance of the cell was increased by the resulting gas pockets. One of the grades of Scott foam performed as satisfactorily as the Vexar, but it was less convenient to handle and to assemble into anode packages.

Electrical contact.—Electrical contact between cells was achieved by means of a clip attached to the top of each magnesium anode. This clip had two U-shaped ears which fitted into mating contacts attached to the adjacent cathode. Clips of tin-plated nickel were found to be satisfactory. The clip was riveted to the top of each anode using brass rivets. A coating of neoprene paint (Adhesive Products Corporation) was applied over the whole clip, except for the U-shaped part, and over an adjacent ¼-in. strip of magnesium. A completed anode package is shown in Fig. 4.

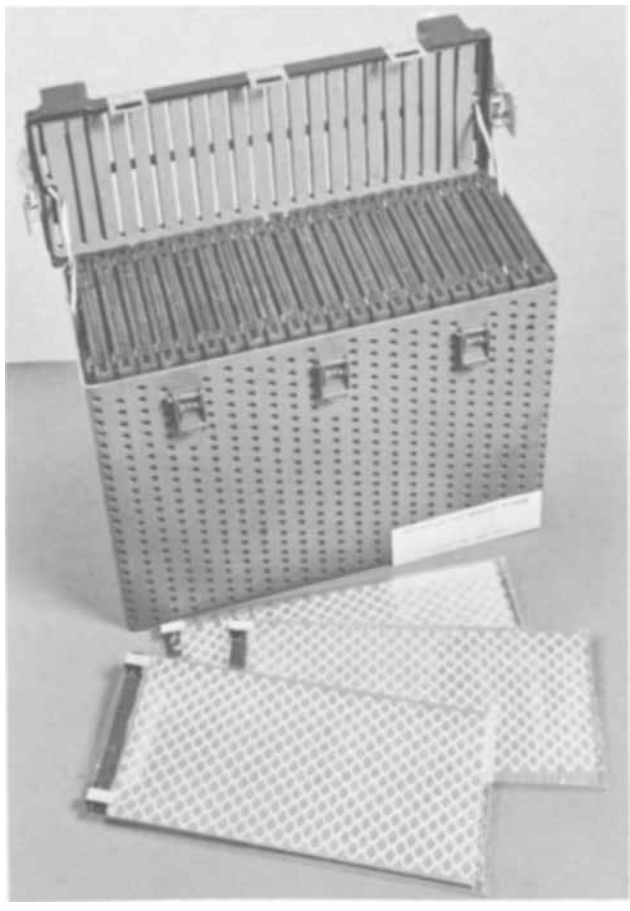

Fig. 4. Complete anodes and battery

Transients.—One of the problems usually encountered with cells having magnesium anodes is the temporary drop in voltage observed when the current is increased. This has been studied by Robinson and King [Ref. (4)] and results from the nature of the film formed on magnesium in basic solutions.

AZ61 alloy had a shorter transient time than AZ31 alloy, and each of these was considerably shorter than that for the A6 aluminum alloy. The alloy with the shortest transient time of any was the GEMAG alloy, which also showed the highest voltage. This high voltage and short transient time result from a very high rate of self-discharge, which keeps the surface relatively free of magnesium hydroxide. Because of this, the coulombic efficiency was found to be very low at the relatively low average drain rates under consideration, so that this alloy could not be used in the present application. Similar behavior was observed for the LA141 alloy. The load was resistive, so that the current reached the new value gradually. The duration of the voltage transient can be anywhere from a fraction of a second to a minute or more, depending on the relative currents before and after switching, the *p*H, the temperature, electrolyte concentration, and the extent of discharge of the anode. The *p*H at the anode can be lowered drastically when the magnesium hydroxide builds up in the cell. With *p*H paper, it has been found immediately after discharge to be as low as 8.0. Figures 5 and 6 show the transient behavior of anodes at various states of discharge using 7% sodium chloride when an initially low level was switched first to an intermediate current level, and second to a high current level. The figures show that when switching

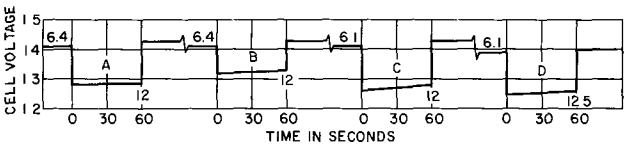

Fig. 5. Transient behavior in 7% NaCl solution—low to intermediate current—2.3A (6.4 mA/cm²) to 4.3A (12.0 mA/cm²)—after: A, 6 A-hr; B, 12 A-hr; C, 18 A-hr; D, 24 A-hr. The numbers indicate current densities in mA/cm².

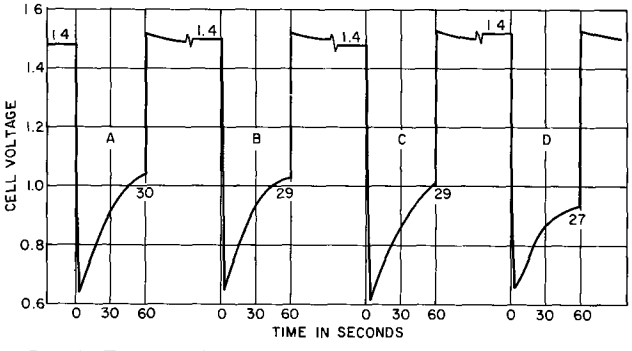

Fig. 6. Transient behavior in 7% NaCl solution—low to high current—0.5A (1.4 mA/cm²) to 10.9A (30 mA/cm²)—after: A, 6 A-hr; B, 12 A-hr; C, 18 A-hr; D, 24 A-hr. The numbers indicate current densities in mA/cm².

between intermediate current levels there is relatively little effect, but that when switching to a high load near the end of discharge there can be a major effect.

Anode thickness and life.—In these cells, it was desired to employ an anode 9.2 cm wide and 21.3 cm high, which would fit into a 0.5-cm gap between two air electrodes. It was necessary to select the thickness of the anode such that it would deliver the proper life but not allow the formation of so much product sludge that the anode could not be removed from the cell at the end of discharge. On the basis of the sludge volume measurements and life tests on thinner electrodes, a thickness of 35 mils was selected. Figures 7 and 8 give polarization curves for these large AZ61 electrodes, spaced ⅛ in. from a cathode, in various sodium and lithium chloride solutions. These data show that the voltage is highest in 18% lithium chloride, primarily as a result of the lower resistance of the electrolyte. In 7% lithium chloride the voltage at higher current densities is higher than for 7% sodium chloride, while in 18% lithium chloride the voltage drops appreciably. This probably results from the relatively low solubility

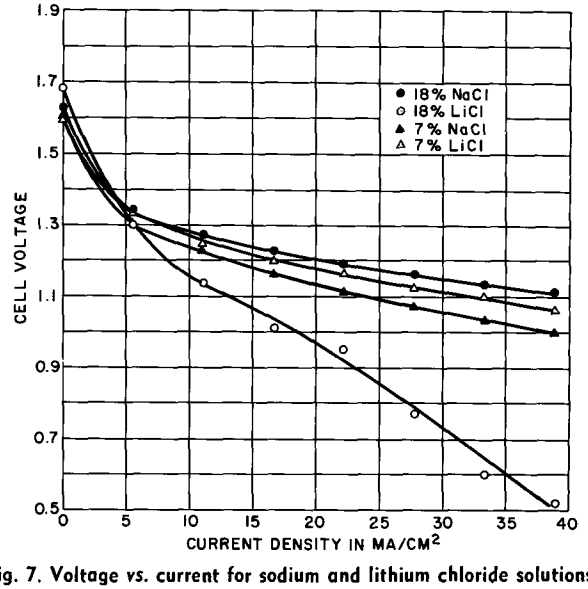

Fig. 7. Voltage vs. current for sodium and lithium chloride solutions

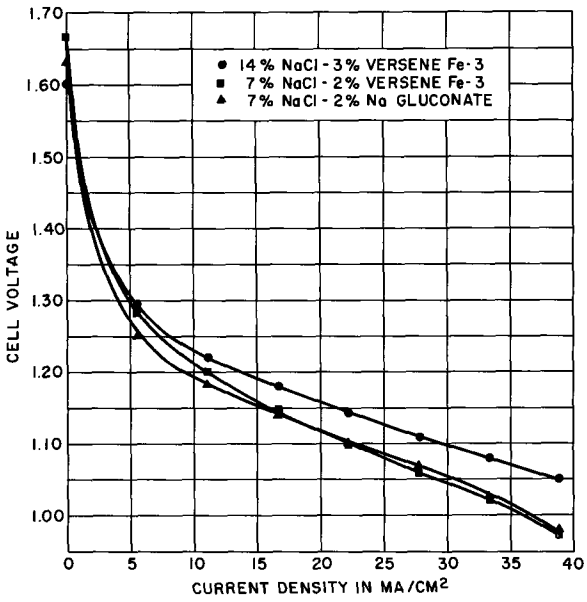

Fig. 8. Voltage vs. current using additives

of lithium hydroxide, which may precipitate on the air electrode. Figure 8 gives the results in solutions of sodium chloride containing Versene Fe-3 and sodium gluconate, each of which might be expected to chelate the magnesium to some extent. Each of these resulted in a slight decrease in voltage. In these tests the data for each of the curves were obtained from the averages of five different tests.

A series of 35-mil thick AZ61 anodes were packaged with Vexar and glycerinated cellulose and were operated in double-faced cathode compartments at a current of 2A (5.6 mA/cm²). The maximum number of ampere-hours obtained was slightly over 30, at which point the magnesium was completely consumed and the cell was solidly packed with sludge. In order to allow for removal of the depleted anode package, it was necessary to stop at about 24 A-hr of operation. At this point the anode package could be removed with less difficulty. During operation it was necessary to add about 45 cc of electrolyte over the 12-hr period to keep the voltage above 1V. When water, rather than a sodium chloride solution, was added to the cell during operation, the output voltage (on a resistive load) was decreased rather than increased. The same effect was observed when drying. There appears to be an osmotic effect relating to the fact that hydroxyl ion is produced inside the cathode during operation and, when the cell is rinsed with water rather than electrolyte, some of this water is imbibed by the electrode and causes it to be partially flooded. If the electrode is dried after rinsing, the performance on a second charge is restored to near the initial level.

Battery operation.—Figure 4 is a photograph of a 23-cell magnesium-air battery employing these anodes. It was designed for a ½A, 28V load for 9 min, and a 12A, 22V load for the following 1 min. This cycle would repeat itself continuously for 12 hr, at which time the anode would be replaced. After the initial electrolyte charge, the voltage on the first few cycles is usually low during the high current drain period until the electrolyte temperature increases. After the temperature reaches 120°F, the voltage during the high current period reaches 22V in about 3 sec using 18% sodium chloride. It was found that the duration of this transient was shorter with 18% rather than 7% sodium chloride. In the latter, the duration of this transient could be as long as 1 min near the end of discharge.

During operation a portion of the water evaporates and is carried out of the cell by the air circulating through it. As was mentioned above, this necessitates the addition of a total of about 45 cc of electrolyte to

each cell during the 12-hr operating period. The amount of water necessary varies with the operating temperature, since at higher ambient temperature more water will be lost by evaporation. If water is not added, the magnesium is not consumed uniformly and the cell voltage falls because of the greater demand on the bottom portion of the magnesium. Starting at an ambient temperature of about 80°F, it was sufficient to add about 15 cc of water to each cell at 3-hr intervals.

Acknowledgments

The authors thank C. E. Kent and J. L. Manganaro of this laboratory for helpful discussions, as well as J. L. Robinson of the Dow Chemical Company. This work was supported in part by the United States Marine Corps.

Manuscript submitted March 5, 1969; revised manuscript received July 17, 1969.

Any discussion of this paper will appear in a Discussion Section to be published in the June 1970 JOURNAL.

REFERENCES

1. C. E. Kent and W. N. Carson, Jr., *Proc. Ann. Power Sources Conf.*, **20**, (1966).
2. C. E. Kent, *ibid.*, **21**, (1967).
3. L. W. Niedrach and H. R. Alford, Jr., *This Journal*, **112**, 117 (1965).
4. J. L. Robinson and P. F. King, *ibid.*, **108**, 36 (1961).

Determination of the Water Vapor Permeability and Continuity of Ultrathin Parylene Membranes

M. A. Spivack and G. Ferrante

Union Carbide Corporation, Bound Brook, New Jersey

ABSTRACT

A method has been developed to determine the water vapor permeability of very thin dielectric films over a large range of thicknesses. It is shown that the permeability of poly(chloro-*p*-xylylene) unsupported thin films is the same throughout the range of thicknesses tested: 292-73,388Å. The results agree with values reported on 2 x 10^{-3} cm thick samples under similar test conditions and with 8 x 10^{-3} cm thick samples obtained by standard flow methods. The results also compare favorably with the water vapor permeability of other polymeric materials. Since the permeability obtained [2.0 x 10^{-9} cm^3 (STP)-cm/sec-cm^2-cm Hg] indicates that thick (8 x 10^{-3} cm) films are structurally continuous, then ultrathin (<300Å) films of poly(chloro-*p*-xylylene) must also be free of voids. In addition, the method is sensitive enough to detect discontinuities as small as 1μ in diameter.

An important function of an encapsulating coating in electronic assemblies is to provide a moisture and gas barrier which prevents corrosion of construction materials or alteration of device parameters. At the same time it also should afford electrical insulation. All materials absorb and are permeable to moisture and gases to some extent and cannot be considered truly hermetic; however, the rates at which these processes occur may be low enough so that ideality can be approached. It is generally agreed that the major volatile contaminant is water vapor (1, 2).

This paper describes a method of determining the permeability of a dielectric film, poly(chloro-*p*-xylylene) (parylene C), to water vapor over a wide range of film thicknesses. The method involves producing free-standing membranes of the material and determining the water vapor transmission (WVT) rate at the particular film thickness. Since parylene C is nonwetting, the permeability should be the product of the WVT rate and the membrane thickness (3). Previous work with hydrophobic polymer films as thick as 70 x 10^{-3} cm (4) and as thin as 4 x 10^{-3} cm (5) has validated this assumption. No reference was found where films of less than 4 x 10^{-3} cm in thickness were used.

Deviations from this predicted behavior indicate discontinuities in the film's structure (6); therefore, by comparing the calculated permeability over a range of film thicknesses, this technique can also be used to determine whether the film contains pinholes at any particular thickness level.

Experimental

Permeability cell.—The method for determining the WVT rate had to be sensitive enough to allow accurate measurements and yet had to be nondestructive to the sensitive membranes. The simplest, most reliable, and most reproducible method was thought to be a weighed cell technique (7) with water contained inside the membrane sealed cell.

This reversed Payne Cup (water inside, desiccant outside) was modified by attaching a manometric sidearm to the cell which was completely sealed with mercury, except for a capillary bleed tube threaded through the mercury seal. The purpose of the sidearm was to provide a means of equalizing the *total* pressure across the membrane without appreciably affecting the WVT rate. (If a few millimeters of pressure differential is allowed to exist, the thinner membranes buckle to an appreciable extent.)

One can then determine permeability (P) from

$$P = \frac{q\tau}{At\,(VP_1 - VP_2)} = Q_f\tau \qquad [1]$$

where q is the quantity of gas diffusing through a film of surface area A and thickness τ, in time t with a difference $(VP_1 - VP_2)$ between the partial pressures of the diffusing gas on the two sides of the membranes (8). The usual units associated with this type of measurement are cm^3 (STP)-cm/sec-cm^2-cm Hg.

The procedure used to prepare the cell is as follows. The membrane is prepared and attached to the cell with a silicone adhesive *after* water has been inserted but *before* the sidearm is sealed with mercury. The ensemble is then allowed to come to thermal equilibrium (usually overnight, which also allows the adhesive to set). The bleed tube is inserted into the sidearm and the cell is then completely sealed (except for the bleed) with mercury. The sealed cell is placed into a desiccator which in turn is in a temperature-controlled room (23.0° ± 0.5°C). At periodic intervals

Key words: encapsulation, membrane, parylene, passivation, permeability, pinholes, polymers, thin films, water vapor.

(from 1 to 10 days), the entire cell is weighed on a balance (accurate to 0.1 mg) to measure the loss of water.

To determine the total driving force across the cell, two relative humidity monitors were used. The first was inserted into the desiccator with the various permeation cells. The second, an electrohydrometer, was used to check the relative humidity *inside* the permeation cell by sealing the hygrometer probe within the cell. The relative humidity was always found to be 100% inside and 0% outside the cell. Therefore, the pressure difference of Eq. [1] was always ~21 mm Hg.

From 6 to 12 individual cells were checked for WVT rate per membrane thickness. Usually, five weighings were taken per population sample, ranging from 1- to 10-day intervals after the start of testing to insure that a steady state has been achieved.

Membrane preparation.—The dielectric film used in these studies was poly(chloro-*para*-xylylene) or parylene C. The unsupported membranes were prepared by a vacuum process as described by Gorham (9). By this method films were deposited onto glass substrates which had been previously treated with a parting agent, such as a vacuum-evaporated alkali halide. (The results obtained were found to be independent of the parting agent used.) Following deposition of the polymer, the parting agent was activated by dissolving in water and the membrane was lifted from the substrate *via* an annular mount.

Membrane thickness.—The methods used to measure the membrane thickness were interferometry and optical absorbance. Interference fringes were used in the bulk of this work (10, 11); however, below about 800Å thickness, no fringes are discernible and, therefore, optical absorbance methods were used.

Discussion and Results

True film permeability.—The value of interest is the WVT through the film only, independent of other parallel and series diffusion pathways. In the permeability cell previously described, the escape of vapor from the cell is controlled not only by the resistance of the membrane but also by the air spaces within the cell and the surrounding desiccator. In addition, there are parallel escape routes such as through the capillary bleed tube and possible leakage through the seal used to attach the membrane to the cell.

To determine the WVT due solely to the thin membrane (Q_f, see Eq. 1), an equivalent electrical conductance analog may be made which yields

$$Q_f = \frac{Q_o\,(Q_{obs} - Q_x)}{Q_o + Q_x - Q_{obs}} \qquad [2]$$

Q_f is the conductance through the film and is the quantity of interest. Q_o is the series conductances controlled by the geometry of the system and can be measured by observing the WVT rate using a "zero" thickness film (open cell). Q_x is the conductance through all parallel diffusion routes, measurable by using a film of infinite thickness (10-mil aluminum foil). With a membrane on the cell, the quantity actually measured is Q_{obs} (observed).

Thickness variation effects.—WVT rates were measured on sample populations ranging from 292 to 78,388Å in thickness. In all cases it was observed that steady state was reached in less than a day (the shortest measuring time used) and that the rate of loss of water vapor remained constant throughout the length of the test (up to 3 weeks).

Table I shows the results obtained for each membrane thickness, including the open (zero thickness) and closed cell (infinite thickness) "end points." Also shown in Table I is the true WVT rate through the films (Q_f) as calculated from Eq. [2] and the permeability (P) as determined from Eq. [1]. The errors indicated on both Q_f and P are standard deviations.

Table I. Permeability constant for various thicknesses of parylene C films

Film thickness (Angstroms)	Observed flux, Q_{obs} (grams/day)	Film flux, Q_f (grams/day	Permeability constant, $P \times 10^9$ [cm³ (STP)-cm/sec-cm²-cm Hg]
0 (Q_o)	0.3873 ± 0.040	—	—
292 ± 75	0.2207 ± 0.0228	0.5077 ± 0.1910	2.38 ± 1.48
836 ± 13	0.1091 ± 0.0064	0.1500 ± 0.0185	1.97 ± 0.27
1946 ± 18	0.0529 ± 0.0016	0.0599 ± 0.0032	1.83 ± 0.11
3701 ± 55	0.0308 ± 0.0016	0.0323 ± 0.0023	1.87 ± 0.16
6080 ± 10	0.0207 ± 0.0011	0.0208 ± 0.0014	1.98 ± 0.14
7470 ± 100	0.0179 ± 0.0013	0.0177 ± 0.0015	2.08 ± 0.16
11,069 ± 920	0.0136 ± 0.0007	0.0130 ± 0.0009	2.27 ± 0.34
23,100 ± 293	0.0064 ± 0.0006	0.0055 ± 0.0007	1.98 ± 0.28
78,388 ± 1400	0.0027 ± 0.0006	0.0017 ± 0.0007	2.06 ± 0.86
(Q_x)	0.0010 ± 0.0001	—	—

Table II. Water vapor permeability constants of various polymers

Polymer	Permeability constant, P* cc(STP)-cm / sec-cm²-cm Hg	Reference
Cellulose acetate	1.2-3.1 × 10^{-6}	(8, 14)
Polystyrene	1.2 × 10^{-7}	(8)
Silicones	2.4-4.3 × 10^{-8}	(1)
Polyurethanes	1.3-4.7 × 10^{-8}	(1)
Polyethylene (low density)	1.1-1.8 × 10^{-8}	(8, 14, 16)
Epoxies	1.0-1.3 × 10^{-8}	(1)
Poly(ethylene terephthalate)-(Mylar)	1.0 × 10^{-5}	(1)
Polypropylene	3.8-4.0 × 10^{-9}	(1, 8)
Poly(tetrafluoroethylene)-(Teflon)	3.5 × 10^{-9}	(16)
Poly(vinylidene chloride)-(Saran)	3.1 × 10^{-9}	(17)
Poly(chloro-*p*-xylylene)-(parylene C)	2.0 × 10^{-9}	This work
Polyethylene (high density)	1.6-1.8 × 10^{-9}	(8, 16)

* At 23°C on 3-8 × 10^{-3} cm thick films.

It is seen (Table I) that the permeability, within error limits, is the same for the 292Å film as it is for the 78,388Å film. The average value from all the thicknesses is 2.03 ± 0.17 x 10^{-9} cm³ (STP)-cm/sec-cm²-cm Hg. This value agrees exactly with the results obtained by Lee (12) on 2 x 10^{-3} cm thick samples in similar ambients. This value also agrees with results obtained from 5-8 x 10^{-3} cm thick samples measured by a flow technique (ASTM-E96-63T) at a temperature of 38°C if an activation energy of 17 kcal/mole is assumed for the diffusion process.[1]

The greatest error in permeability (P) is seen to occur at the extremities of thickness. For the very thin films, the thickness uncertainty and Q_o values contribute to the large error; the end point substantially contributes in the case of the thicker films. Even with the larger uncertainties at the two thickness extremes, the permeability at each thickness deviates from the over-all average by only ± 8.5%.

Comparison with other polymers.—The water vapor permeabilities of various polymers are shown in Table II. All the values indicated were either measured at, or corrected to, 23°C and were measured on films 5-8 x 10^{-3} cm thick. Cellulose acetate is given as an example of a water-permeable polymer having a permeability constant of about 10^{-6} (units as previously defined). Polystyrene, which is a good insulator, is shown to be a poor water barrier. The common encapsulating material (silicones, urethanes, epoxies) have permeabilities in the low 10^{-8} range while poly(vinylidene chloride) exhibits a constant of about 3.1 x 10^{-9}. The water vapor permeability of parylene C is shown to be low and about the same as for very high density polyethylene.

Induced faults.—To test the sensitivity of these measurements in detecting film discontinuities, a hole of a particular size was mechanically induced into a given thickness population sample. Different sizes were in-

[1] A value of 19.2 kcal/mole is reported for poly(ethylene), 16.4 kcal/mole for poly(propylene), and 15 kcal/mole for poly(vinyl acetate) (13).

duced into different populations. The smallest hole was about 33μ in diameter (8.8 x 10^{-4} mm^2); the actual areas were measured by a planimeter on photomicrographs.

In all cases, the films with holes showed a marked increase in permeability over structurally continuous control samples.

The rate of water vapor loss through a unit area of induced hole was then compared to the size of the hole. Extrapolation of this data has shown that a discontinuity of about 1μ in diameter should be detectable within the error limits of the method.

Summary and Conclusions

A modified Payne Cup has been used to measure the water vapor permeability and continuity of thin parylene C films over relatively large surface areas. Free-standing films less than 300Å in thickness and more than 10 cm^2 in area can be tested by this method.

It was found that the permeability of parylene C unsupported thin films is the same throughout the range of thicknesses tested, 0.03-7.34 μm. The value of permeability obtained by this static method, 2.0 x 10^{-9} cm^3 (STP)-cm/sec-cm^2-cm Hg, agrees with other investigations using 2 x 10^{-3} cm thick films and with the value measured by standard flow methods on 8 x 10^{-3} cm thick films if an activation energy of 17 kcal/mole is assumed for the diffusion process.

In comparison to other polymeric materials, thick films of poly(chloro-*p*-xylylene) are shown to have a water vapor transmission rate about equivalent to very high density polyethylene and are somewhat superior to commonly accepted good water barrier films such as poly(vinylidene chloride), poly(ethylene terephthalate), and poly(tetrafluoroethylene).

Based on the hypothesis that these thick films (2-8 x 10^{-3} cm) are structurally continuous, then ultrathin ($<$ 300Å) films of parylene C must also be free of voids. Furthermore, extrapolation of data obtained from mechanically induced holes shows that voids of about 1μ in diameter should be detectable by this technique.

The combination of low water vapor permeability, structural continuity, and the vapor deposition nature of its application indicates that poly(chloro-*p*-xylylene) should be suitable for the protective dielectric in semiconductor devices or as an encapsulant for larger circuit board modules.

Manuscript submitted July 19, 1968; revised manuscript received July 24, 1969. This was Paper 473 presented at the Montreal Meeting, Oct. 6-11, 1968.

Any discussion of this paper will appear in a Discussion Section to be published in the June 1970 JOURNAL.

REFERENCES

1. J. J. Lucari and E. R. Brands, *Machine Design*, **39** (12), 192 (1967).
2. E. B. Hakim and R. Canepa, "Preliminary Investigation of Plastic Encapsulated Transistors" (U.S. Army Electronics Command, Ft. Monmouth, N.J., AD660349, Sept. 1967).
3. R. M. Barrer, "Diffusion In And Through Solids," p. 432, Cambridge University Press, London (1952).
4. K. D. Londenslagel and S. F. Roe, *Modern Packaging*, **139** (Feb. 1967).
5. G. S. Banker, A. Y. Gore, and J. Swarbrick, *J. Pharm. Pharmac. 18 Suppl.*, 205S-211S (1966).
6. S. Sacharow, *Plastics in Australia*, **11** (Jan. 1968).
7. A. C. Nevins, *J. Textile & Inst.*, T269 (Aug. 1950).
8. S. Sacharow, *Plastics Design & Processing*, **20** (Sept. 1965).
9. W. F. Gorham, *J. Polymer Sci.*, **4**, 3027 (1966).
10. O. S. Heavens, "Optical Properties of Thin Solid Films," p. 96 Dover Publications, Inc., New York (1965).
11. W. Niegisch and W. Beach, Private communication.
12. S. M. Lee, "Polymeric Films for Semiconductor Passivation" (NASA Contract #NAS 12-2011), March 1969, p. 51.
13. H. G. Spencer, *Proc. Paint Research Institute*, **37**, 757 (1965).
14. P. M. Hauser, A. D. McLaren, *Ind. Eng. Chem.*, **40**, 112 (1948).
15. A. W. Meyers, V. Tammela, V. Stannett, and M. Szwarc, *Modern Plastics*, **37** (10), 139 (1960).
16. P. W. Morgan, *Ind. Eng. Chem.*, **45**, 2296 (1953).
17. M. C. Slone and F. W. Reinhart, *Modern Plastics*, **31** (10), 203 (1954).

Development of an Electrochemical Acid Generator

Lloyd H. Shaffer[*,1] **and R. A. Knight**[*]

American Machine & Foundry Company, Stamford, Connecticut

ABSTRACT

Acidification of the feed streams to desalination plants is often desirable. To provide for this, an electrochemical system has been developed, combining both fuel cell and electrodialysis technology. The heart of the system is a cell which produces dilute streams of acid and base, and the whole apparatus is referred to as an "acid generator." The acid generator is a self-contained system, and requires only electricity and the desalination plant feed stream as inputs. As developed, it produces an acidified sea water stream (product), a partly desalted stream, and an alkaline stream. The anode hydrogen supply for the catalytic membrane electrode is evolved at the cathode. The acid produced is used in the prevention of scale in water processing equipment such as evaporators. Acidification of the saline feed stream releases carbon dioxide. The carbon dioxide released is used along with the alkaline cathode effluent to prepare a softened sea water for an intermediate or "buffer" stream. A small amount of product water (1%) from the evaporator is used to maintain the cathode NaOH concentration at approximately 0.1-0.3*N*. The power requirements for the cell are quite modest, about 0.5 kwhr/1000 gal for the acidification of sea water to a level of 100 ppm, and the device is readily adapted to automatic operation.

Acidification of the feed streams to desalination plants is often desirable. The reasons for this in the case of a plant designed to distill sea water are illustrated by the equations below.

$$Ca^{++} + 2HCO_3^- = CaCO_3\downarrow + CO_2\uparrow + H_2O \quad [1]$$

$$HCO_3^- = CO_2\uparrow + OH^- \quad [2]$$

$$Mg^{++} + 2OH^- = Mg(OH)_2\downarrow \quad [3]$$

Normal sea water (19 parts per thousand Cl^-) contains small but significant quantities of calcium, magnesium, and carbonate (Table I). When sea water is heated, CO_2 is driven off, and as a result the water becomes more alkaline. As bicarbonate ion decreases the carbonate ion concentration increases, and $CaCO_3$ and $Mg(OH)_2$ coprecipitate on the intake or first-stage heat transfer surfaces. The problem can be avoided through a replacement of HCO_3^- by mineral acid. The quantity of mineral acid needed is small, 0.0835 parts per thousand as HCl or 0.1112 parts per thousand as H_2SO_4. However, either because of a remote location or the particular size of a given operation, mineral acid may not always be conveniently or economically available. For example, a 1.25 million gal/day (GPD) plant, built in the early 1960's, required roughly a tank car of sulfuric acid per month for scale control. Delivery of this quantity of acid to a test site near San Diego was easily arranged but, when the plant was reassembled on an island in the Caribbean, acid pretreatment was abandoned. This necessitated a lower operating temperature and, as a result, the capacity of the plant was downgraded to 750,000 GPD (1). To provide for the replacement of HCO_3^- by mineral acid, an "acid generator" has been developed (2, 3).

The acid generator (Fig. 1) requires as inputs: electricity, about 0.5 kwhr/1000 gal, and the desalination plant feed stream. The device combines both fuel cell technology and electrodialysis techniques. The various interior compartments in the acid generator are separated by ion exchange membranes, and the cathode hydrogen is consumed on a catalytically active anode. This union of the two technologies is responsible for the rather modest amount of electrical energy, 0.05 kwhr, needed to produce an equivalent of acid and base. A summary of estimated power requirements and operating costs based on present technology is given in Table II.

Table I. Scale-forming constituents in sea water

Sea water: Cl^- = 19 g/kg, ρ_{20} = 1.0243	
Ca^{++}	0.4001 g/kg = 0.0100 m/liter
Mg^{++}	1.2720 g/kg = 0.0523 m/liter
HCO_3^-	0.1397 g/kg = 0.00229 m/liter (100.7 ppm as CO_2)
$SO_4^=$	2.649 g/kg = 0.02755 m/liter

NOTE: Oceanographer's Normal S.W., Cl^- = 19.381 g/kg (Sverdrup, Johnson & Fleming); Millstone Pt. S.W., Cl^- ~ 16.5-17.0 g/kg, CO_2 ~ 80 ppm.

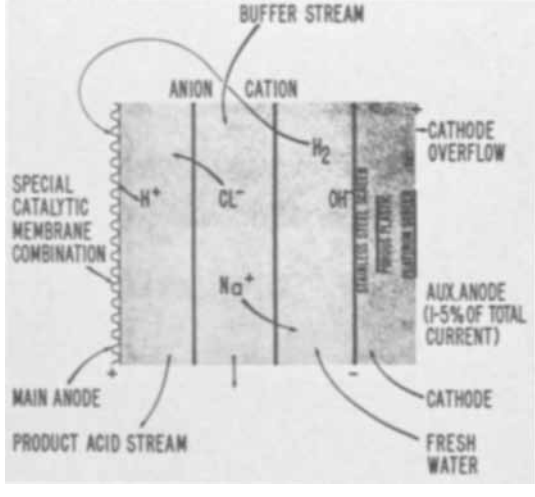

Fig. 1. Catalytic acid generator

* Electrochemical Society Active Member.
[1] Present address: Clairol, Incorporated, 90 Commerce Road, Stamford, Connecticut.

Table II. Power requirements and costs

Acid
85 ppm (as HCl)
1000 gal = 1.0243 × 8.345 × 10^3 = 8550 lb
85 × 10^{-6} × 8550 = 0.726 lb HCl
= 9.03 g-equiv./1000 gal

Current
9.03 equiv./1000 gal = 10.08 A-day/1000 gal

Power
volt/cell @ 20 asf ≃ 3.0
10.08 A-day × 3.0V × 24 hr/day = 0.725 kwhr/1000 gal
Requirement, allowing for losses and auxiliaries:
0.5-1.0 kwhr/1000 gal

Estimated cost
0.5 ¢/1000 gal

During operation of the acid generator, hydrogen is oxidized on the catalytic anode and hydrogen ions are introduced into the anode stream through the ion exchange membrane portion of the catalytic membrane electrode (Fig. 2). The anode compartment is separated from the buffer (saline) stream by an anion permeable membrane. Negative ions migrate through it to maintain electrical neutrality in the anode compartment. The buffer compartment serves two purposes: it helps isolate the anode and cathode systems; it acts as the source for the ions that must be supplied to the electrode compartments to make up for the charge introduced by the electrode reactions. When the acid generator is used in conjunction with sea water processing plants, a saline stream suitable for use in the buffer compartment is obtained by treating a portion of the main feed with alkali from the cathode compartment. The cathode compartment is separated from the buffer stream by a cation exchange membrane. The cathode alkalinity is controlled by feeding a small amount, about 1%, of the product fresh water to the cathode stream. The cathode hydrogen is circulated to the anode. To make up for the inevitable small losses, an auxiliary anode was added so that excess hydrogen could be generated at the cathode. Provisions were made for operating the auxiliary anode in two modes: low, 1% of main anode current, for normal operation; and high, 10-20 times normal, for start-up.

A variety of systems were tried during the development of a functional automatic acid generator. The problems encountered have been: electrode design and materials of construction, separation of hydrogen from the cathode stream, method of circulating hydrogen through a series of cells, and methods to soften sea water for use in the buffer stream. After investigating these problems on a small scale in 450-6000 GPD units, a 30,000 GPD unit was designed and constructed to be compatible with a Maxim[2] high-pressure tube bundle evaporator. The 450 GPD unit was rectangular in design, with a 3- x 14-in. working area. The 6000 and the 30,000 GPD units were constructed from rings of PVC 9.5 in. and 11.4 in. ID, respectively.

[2] AMF-Cuno/Maxim Millstone Point Sea Water Test Station, Waterford, Conn.

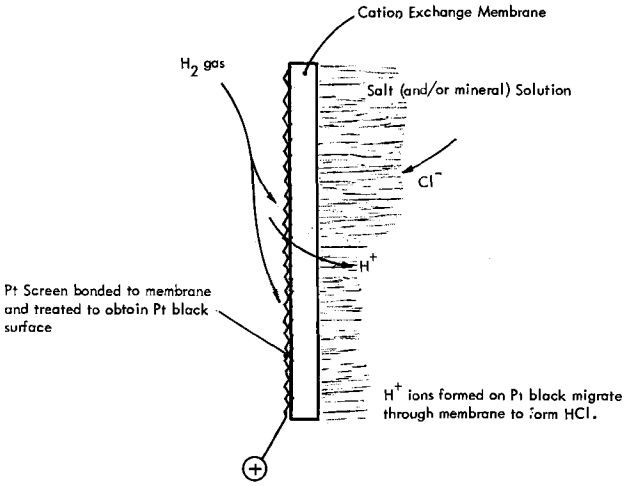

Fig. 2. Catalytic membrane electrode

Experimental

Catalytic membrane electrode.—The catalytic membrane electrode (CME) illustrated in Fig. 2 was prepared by bonding a platinized platinum/10% rhodium, 80 x 80 mesh screen to a cation permeable membrane which had been precoated with a slurry of platinum black powder (1.4 mg/cm²). The cation permeable membrane used here was a thermoplastic material prepared by first grafting styrene to a polyethylene base and then sulfonating the styrene. The chemical principles involved have been given by Chen and Mesrobian (4). A review of the principal electrochemical characteristics of leading commercial membranes is found in "Principles of Desalination" (5). The electrode was activated by cathodic reduction in 10% H_2SO_4, replatinization in 3% chloroplatinic acid, and a final cathodic reduction in 10% H_2SO_4. Electrodes prepared in this manner are capable of operating at 25-30 mA/cm² (3 x 10^{-7} equiv./sec/cm²) without excessive overvoltage or oxidation of chloride. Typical polarization curves are given in Fig. 3. In the short term, the curves are linear and reversible up to 40 mA/cm². However, at any current above ~25 mA/cm², a gradual and irreversible increase in voltage is noticeable after a few hours. The somewhat poorer polarization obtained on the large electrodes is thought to be due to the difficulties in obtaining a uniform platinum black deposit. Higher current densities are possible at higher platinum loadings. CME's were also constructed using as the current collector platinized titanium in the form of woven screen and expanded mesh. Tantalum in both forms was also used. A titanium electrode proved to be satisfactory, and was successfully tested in excess of 500 hr without degradation of performance. The tantalum was easier to handle and to bond than the titanium and, further, it appeared to give slightly better electrode performance. These electrodes were used only in the 450 GPD unit. The reason for this was that at the time of construction the only suitable electrode material available in large sizes was the platinum/10% rhodium mesh.

The elements of the catalytic membrane electrodes: the cation permeable membrane, the platinum black, and the platinized screen current collector, were bonded with a laboratory press. The conditions for bonding were 350°F at 800 psi. Electrodes for the three units mentioned above were prepared using these conditions. After the original construction was completed, it was found that lower temperatures could be used if the membrane was first equilibrated in formamide instead of distilled water. It is obvious that at the high-temperature condition the membrane loses its gel water, causing shrinkage and possible separation of the bond between current collector and membrane. The formamide has about the same dielectric constant as water and has a boiling point compatible to the bonding temperature. The net result of equilibrating the membrane in formamide is that the membrane is dimensionally stable during the heating cycle. Best re-

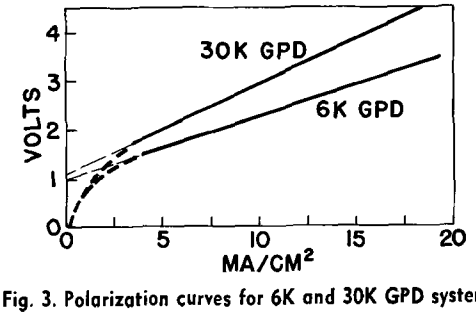

Fig. 3. Polarization curves for 6K and 30K GPD systems

sults were obtained when the bonding was done by placing the membrane electrode assembly between Pyrex plate glass platens.

Auxiliary hydrogen circuit.—To operate the acid generator, it is necessary to supply hydrogen in excess of the anode demands. This replaces hydrogen lost because of the solubility of the gas in the cathode effluent and also compensates for losses due to leakage. Provision was made for the hydrogen evolution at the cathode to exceed the rate of consumption in the main cell by adding an auxiliary anode to the system. The auxiliary anode was separated from the main cathode by a porous polyethylene plastic battery separator material. This is necessary to prevent the oxygen generated at the anode from mixing with the hydrogen generated in the adjacent cathode. The oxygen generated at the auxiliary anode was discarded. The excess hydrogen was controlled by adjustment of the current circulating in the auxiliary circuit. Hydrogen was recovered from the cathode effluent by passing the foaming liquor into a closed stilling chamber. The excess hydrogen generated was controlled so that a minimum amount of power was used to make up losses due to leakage and the solubility of hydrogen in the cathode effluent. Solubility losses depend on catholyte compartment normality (reciprocal of liters of cathode fresh water per Faraday) and they can in principle be quite small. The solubility of hydrogen in water is 1.54 ppm at 25°C and 760 mm; and, if the catholyte were maintained at 0.1*N*, the loss due to solubility would be 0.77%.

Buffer stream system.—In order for the acid generator to function, the anode must be separated from the cathode. This was accomplished by placing a cation permeable membrane in front of the cathode and an anion permeable membrane in front of the anode (CME)—*see* Fig. 1. The central compartment or "buffer" is required only to conduct electricity and to supply appropriate ions to the anode and cathode compartments. To avoid the complications that might have arisen due to the use of sea water, for example the precipitation of magnesium and calcium compounds, much of the early testing of the 450 GPD generator was performed using 0.5-1.0*N* NaCl. However as soon as the original system had been debugged, a precipitation system to soften the sea water was designed. This system used the sodium hydroxide produced at the cathode as follows: sea water and the sodium hydroxide were mixed in a heated precipitation tank at about 115°F and, simultaneously, the solution was saturated with carbon dioxide (available from the acidified sea water stream). This treatment resulted in the rapid and near total precipitation of both magnesium and calcium as magnesium hydroxide and calcium carbonate, respectively. The resulting solution (including precipitate) was allowed to overflow into a holding tank where it was permitted to cool to 90°F before passing through the buffer compartment. The system is shown schematically in Fig. 4. It was found after a short time that hydroxyl ion in the buffer stream (conc. $\sim 10^{-3}$ m/liter) was migrating into and through the anion membrane and causing the precipitation of alkaline earth metals carried by the untreated anode stream. This difficulty was circumvented by raising the product hydrochloric acid concentration from 0.003*N* (100 ppm) to 0.1-0.15*N*. This was accomplished by recirculating a part of the product stream in a feed and bleed arrangement. The high acidity introduces a current efficiency loss which depends on the selectivity of the anion membrane. The matter is discussed more fully in the Results and Discussion section. The complete system, shown in Fig. 4, was tested for 460 hr on sea water without signs of membrane fouling.

450 GPD cell.—Much of the initial testing of the acid generator was done on a unit sized for 450 GPD. The cells in this unit had tapered ends to facilitate fluid distribution and the working portions were 3- x 14-in. rectangles. The individual compartments had a thickness of ½ in. Figure 5 is a perspective view of the 450 GPD unit; it shows both the electrochemical cell and its relationship to the auxiliary liquid/gas system. Operating data, obtained both in preliminary tests on the cell and during extended tests on the entire system, are given in Table III.

6000 GPD cell.—In addition to the 450 GPD cell, two very much larger units were built and tested. Rectangular cells would also have been preferred for these; but, due to limitations of materials available for construction, sections of plastic pipe were selected for the larger unit. The first multiple unit consisted of six cells, featuring common hydrogen and cathode compartments as shown in Fig. 6. The initial compartment components were thick rings of polyethylene pipe. This was not satisfactory: the pipe sections had a tendency to cut the membranes and catalytic membrane electrodes at the inner circumference of the sealing edge, and the forces necessary to hold the unit together caused distortion of the cross sections of the polyethylene rings. It seemed desirable to avoid having the CME flex over a sharp edge and further to make sure that sealing would take place at a low total applied force. A gasket having the following features (Fig. 7) was evolved: (*a*) a filled (hard) PVC spacer ring, (*b*) beveled inner edges, (*c*) O-ring sealing surfaces.

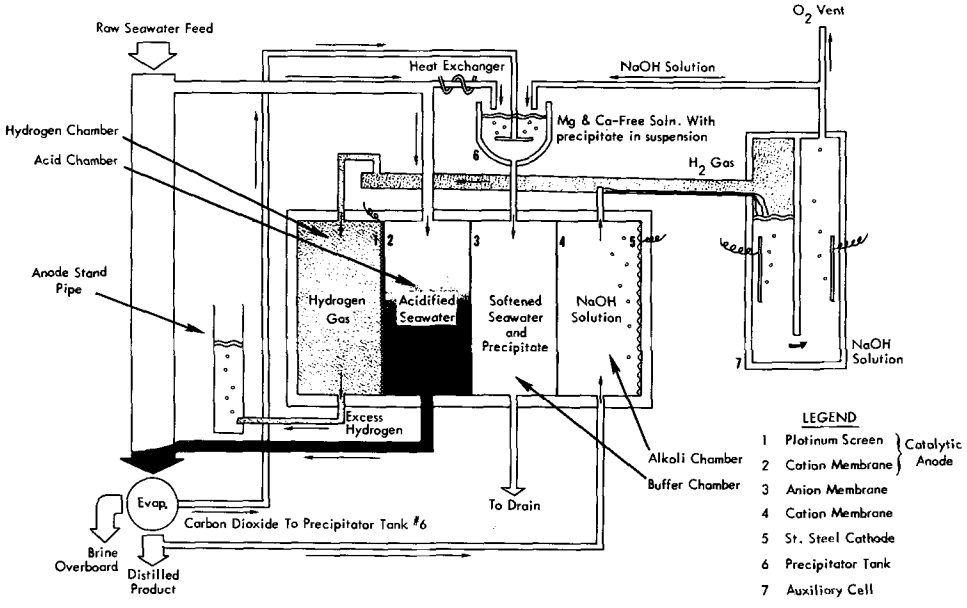

Fig. 4. Acid generator flow scheme.

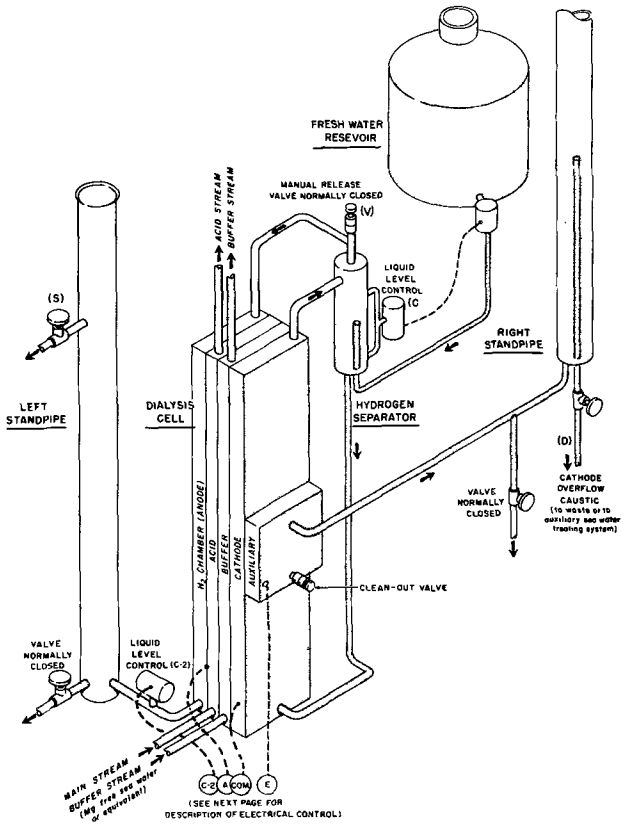

Fig. 5. Single-cell acid generator hydraulic system (450 GPD)

Experimentation with the new ring design showed that a pressure of 100-150 psi was sufficient to seal the electrodes and membranes. A six-cell multiple unit (Fig. 6) was constructed using these PVC-O-ring spacers. Calibrated deflection load springs were used to seal the cell to the desired pressure. No electrical, hydraulic, or mechanical difficulties were experienced during a total of 530 hr of testing. Relevant electrochemical data are summarized in Table III.

30,000 GPD cell.—A still larger unit, 30,000 GPD capacity, was built using the principles developed in the construction of the two small acid generators. The larger unit used ½-in. PVC spacers rather than ¾ in. as in the 6000 GPD device and it was a larger diameter, 11.4 in. instead of 9.5 in. The large unit contained 22 cells arranged as 11 pairs in series. The complete unit was tested over an extended period of time during a Navy-sponsored test of an acid-fed system. There were some minor electrical and mechanical difficulties which appeared to be due to the large round cell section; however, these did not cause any system shutdowns during the 2200-hr test period. Typical electrochemical operating data are also given in Table III.

Results and Discussion

Typical operating data for the cells described above are given in Table III. To facilitate comparison between the various units, all data have been reduced to terms based on one cell and/or the operating unit area as appropriate. The minimum power, tabulated in column 6, represents the main cell kwhr required to treat 1000 gal of feed water (9.03 equiv. of HCl at current and voltage conditions stated). The estimated total power includes an allowance for the pumps and auxiliaries actually used.

Preliminary tests on the 450 GPD acid generator cell were made with all compartments filled with 1.0*N* NaCl (Table III—line 1). Later, to simulate operation on sea water, the anode and buffer compartments were filled with 0.5*N* NaCl (Table III—line 2), and a more dilute saline fluid, 0.171*N*, was used in the cathode compartment to simulate 0.1*N* NaOH. After the com-

Table III. Summary of operating data

Cell	Product rate, ml/sec	Product composition	Current, amp	Cell voltage	Current efficiency, %	Min. power per 1000 gal feed, kwhr	Est. tot. power per 1000 gal, kwhr	Current density, mA/cm²	Linear velocity across CME, cm/sec	Buffer composition	Catholyte composition
450 GPD (1) Three-compartment cell, 42-in.² working area, ½-in. thick compartments.	19	1.0*N* NaCl	5.4	2.1	100	0.50	—	19.9	1.97	1.0*N* NaCl	1.0*N* NaCl
	24	0.003*N* HCl 0.5*N* NaCl	4.9	3.1	100	0.72	—	18.1	2.5	0.5*N* NaCl	0.171*N* NaCl
	~21	0.0022*N* HCl Sea water 2-3 × 10⁻³*N* HCl	5	3	—	—	—	~18	~2	0.47*N* NaCl	0.1*N* NaOH
6000 GPD (6) Three-compartment cells, 70.8-in.² working area, ¾-in. thick compartments.	0.56	Sea water 0.155*N* HCl	9.95	3.4	87	0.98	2.6	21.7	~0.8	Softened sea water 32% strength	0.244*N* NaOH
30,000 GPD (22) Three-compartment cells, 104-in.² working area, ½-in. thick compartments.	0.59	Sea water 0.143*N* HCl	10.0	4.17	82 (86)*	1.24 (1.00)*	2.3	14.9	~1	Softened sea water 32% strength	0.269*N* NaOH

* Avg. during 2000 hr run.

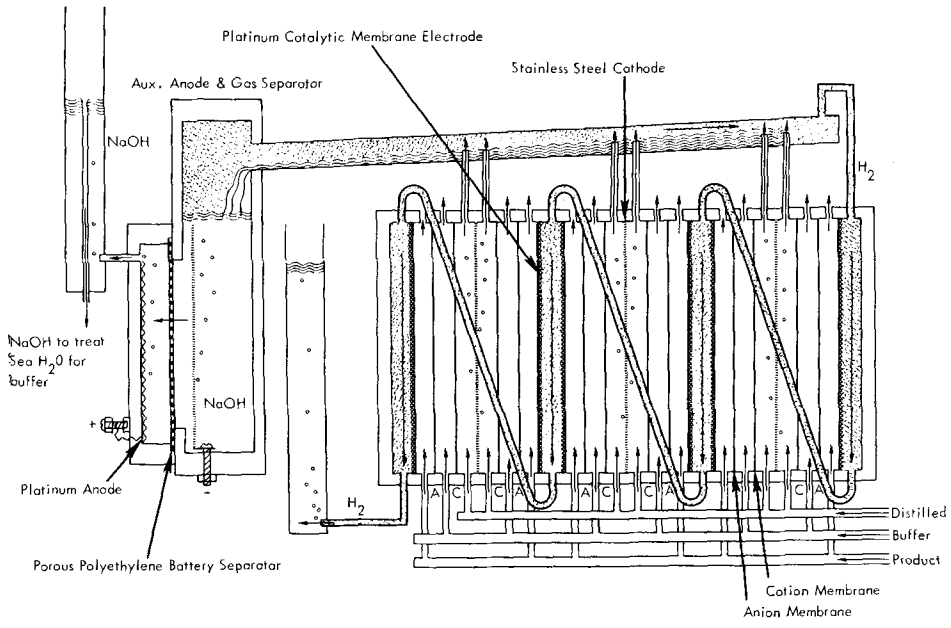

Fig. 6. Multicell acid generator hydraulic system (6000 GPD).

pletion of these tests of cell performance, a semi-automated system such as is shown in Fig. 5 was set up and operated at AMF's Millstone Point Test Station, using sea water feed to the anode compartment.

The early sea water tests were designed to be essentially equivalent to the saline water test, line 2, Table III, and an indication of the approximate operating conditions has been entered for comparison (line 3). The data available on these tests do not permit a meaningful calculation of current efficiency; however, given the physical and chemical conditions prevailing in the test cell, it is certain that it was near 100%. The somewhat lower efficiency figures recorded for the larger-scale runs are related to the high product acidity and to the fact that the anion membrane is less than 100% selective. During the first 750 hr of actual sea water operation, the buffer stream circulated from a reservoir whose salinity was maintained at 0.47*N* by daily additions of 0.6 lb of NaCl. However, during a subsequent 1000 hr, a variety of cycles for using the cathode alkali to prepare a softened sea water for buffer feed were investigated. The net result has already been described (Fig. 4). It was impossible to achieve steady long-term operation unless the buffer Ca and Mg were held to extremely low levels, 1 and 4 ppm, respectively. And at the high *p*H, ~11.5, necessary to maintain these low concentrations, ~2% of the negative ion current between buffer and product will be carried by OH^- rather than Cl^-. Hydroxyl ion migration must be prevented. In exploratory tests, long before these was any indication of electrical difficulties, visual observations showed precipitate formation in and on the anion exchange membrane. This is due primarily to the reaction between OH^- transported and Mg^{++} in the unsoftened anode stream. A 50-100 fold increase in the product acidity avoids the problem but introduces a modest electrical inefficiency. Based on published data (6), it was calculated that, in the highly acid saline product (approx. the equivalent of 0.15*N* HCl and 0.47*N* NaCl), up to 2/3 of the positive ion current will be carried by H^+; and, if the anion membrane selectivity is 82%, the apparent current efficiency of the acid generating cell will be, at best, 88%. Efficiency results for the tests conducted on the two larger devices are in agreement with this expectation.

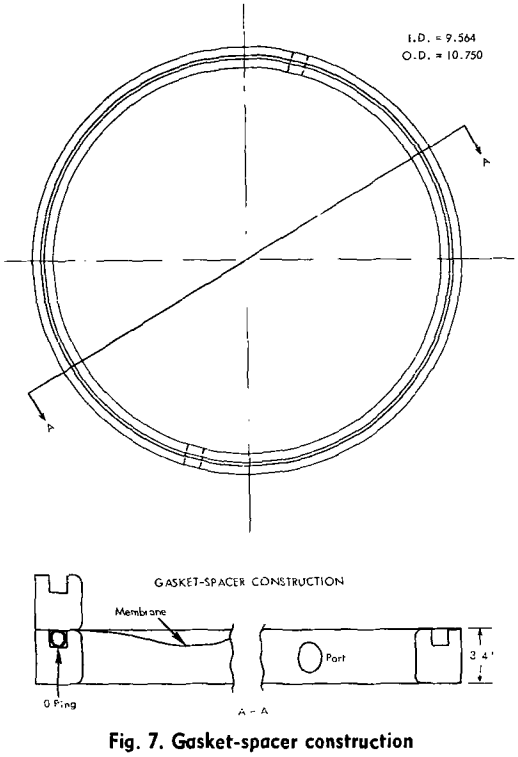

Fig. 7. Gasket-spacer construction

The almost total removal of Mg and Ca that is required introduces, in addition, another kind of electrical penalty. Mg and Ca between them account for 21% of the positive charge in sea water. Whenever current sufficient to generate the equivalent amount of alkali is passed through the cell, 21% of the original positive and negative ions will be removed from the circulating buffer stream because the buffer is set up as a desalting compartment. It had been expected that the feed and bleed buffer loop, if carefully adjusted, could be made to deliver to the cell a softened stream that was about 80% of sea water strength. In practice, there was a 70% loss in buffer salinity and a corresponding increase in power consumption. The buffer compartment ordinarily accounted for about 1/3 the total cell resistance and the large reduction in salinity therefore was equivalent to an increase of 67% in power consumption. This fact, perhaps more than any other, was responsible for the increase in minimum required power in going from the smaller to the two larger systems tested. Clearly, the buffer stream system or an alternative to it should receive a great deal of attention in any future acid generator designs.

The operating data reported for the 6000 GPD unit were derived from a set of current efficiency measurements that were made near the beginning of a 500-hr run. The high estimated total power is the result of the use of oversize pumps in assembling the 6000 GPD

configuration. When the same pumps were used in an even larger unit, a slightly lower total power figure was obtained. The data recorded for the 30,000 GPD unit are representative of conditions at the end of over 2000 operating hours. The data fairly represent the running record with two exceptions. First, during 90% of the operating time the apparent stack resistance was 15% lower than at the end and, second, the current efficiency average over 2000 hr was 85.6 ± 2%. Allowing for these two factors brings the estimated minimum power to 1.00 kwhr/1000 gal in good agreement with the figure found in operations with the 6000 GPD unit.

Conclusions and Recommendations

A self-contained device for the acidification of desalination plant feed streams has been developed. The acid generator requires as inputs electricity and the desalination plant feed stream. Substantial units of 6000 and 30,000 GPD have operated at a total power level of 2.5 kwhr/1000 gal. There are indications that this could be cut in half. The large systems tested suffer from two correctable defects. First, the cells in future units should be long thin rectangles or lozenges to get better flow distribution and to avoid problems associated with buffer precipitate settling in the quiescent portions of the round cell sections used here. And, second, further work on the catholyte/buffer system is required. Flow rates, stream ratios, and the like must be readjusted to produce a high salinity buffer stream before any significant cell power reduction is possible. Further, if the pH of the buffer can be lowered by only 1 unit, additional improvements in power requirements can be realized.

Manuscript submitted Nov. 22, 1968; revised manuscript received Aug. 11, 1969. This was Paper 223 presented at the Boston Meeting, May 5-9, 1968.

Any discussion of this paper will appear in a Discussion Section to be published in the June 1970 JOURNAL.

REFERENCES

1. S. F. Mulford, "Scale Control in Sea Water Evaporators," Saline Water Conversion Progress Report No. 133, U.S. Govt. Printing Office (1964).
2. L. H. Shaffer and R. A. Knight, Can. Pat. 756,595, "Water Treatment Systems" (1967).
3. L. H. Shaffer, Paper 223 presented at Electrochem. Soc. Meeting, Boston, May 5-9, 1968.
4. W. K. W. Chen and R. B. Mesrobian, *J. Polymer Sci.*, **23**, 903 (1957).
5. L. H. Shaffer in "Principles of Desalination," Edited by K. S. Spiegler, pp. 207-213, Academic Press, New York (1966).
6. H. S. Harned and B. Owen, "The Physical Chemistry of Electrolyte Solutions," 3rd Ed., pp. 697, 699, ACS Monograph Series, Reinhold Publishing Corp., New York (1958).
7. H. U. Sverdrup, M. W. Johnson, and R. H. Fleming, "The Oceans," Prentiss Hall Inc., Englewood Cliffs, N.J. (1942).

A Preliminary Investigation of Fluidized Bed Electrodes

J. R. Backhurst, J. M. Coulson, F. Goodridge, and R. E. Plimley

Department of Chemical Engineering, University of Newcastle upon Tyne, Newcastle upon Tyne, England

and M. Fleischmann

Department of Chemistry, Southampton University, Southampton, England

ABSTRACT

The paper describes results of preliminary experimental observations on a fluidized bed electrode. This consists of a bed of electrically conducting spherical particles fluidized by electrolyte flow. The present results are confined to the cathodic reduction of m-nitro benzene sulfonic acid to metanilic acid in aqueous sulfuric acid. The investigations have demonstrated that charge is dispersed throughout the bed such that an electrochemical reaction takes place at the particulate surface. Results show that the fluidized electrode is capable of scaling up electrode processes having low exchange currents to give high over-all currents in relatively small cell volumes.

The electrochemical industry, in terms of output, is a large and expanding one, due more to an increasing demand for its conventional products, however, rather than to their diversification. The field of organic chemicals manufacture for instance still lies almost wholly outside the industry and, to a large extent, this is due not so much to the unwillingness of manufacturers to break new ground as to the lack of commercial cells of sufficiently high capacity to make the majority of interesting organic reactions economically attractive.

The range of specific surface area of working electrode offered by industrial electrochemical cell design at the present time is between 1 and 30 ft^2/ft^3 of cell volume, and this has proved quite adequate for those reactions, such as chloride ion discharge, which take place at current densities of between 100-1000 A ft^{-2}. On this basis, the cells operate at 1000-3000 A ft^{-3}. Many organic electrode reactions of industrial significance, however, take place at current densities of only 1-10 A ft^{-2} and at this level the present generation of cells would operate with an intensity of only 3-10% of current practice. The higher investment necessary to offset the reduced performance of each cell is usually unrealistic. One solution of this difficulty lies in new cell designs of higher specific area.

Such problems are not confined to electrochemical engineering; they are met, and in many cases have been overcome, in every branch of chemical engineering. Many of the solutions which have been found have now become well-established techniques and their translation to the electrochemical case could well prove fruitful. In this context, the fluidized bed concept is particularly attractive in that it has been immensely successful in the closely analogous field of heterogeneous catalysis. The analogy, however, is only partial and is unable to anticipate the ability of a fluidized bed system to perform the function of an elec-

trode. The necessary experimental evidence for this was the first objective of the work described in the present paper and, once demonstrated, a series of experiments of a somewhat probing nature was carried out on a sufficiently broad basis to enable a tentative evaluation of the possibilities of fluidized bed electrodes to be made.

Observations have been made on the reduction of m-nitrobenzene-sulfonic acid to metanilic acid in a fluidized cathode of copper and copper-coated glass particles. Several parameters have been probed, including particle size, bed expansion, location of the current feeder, and bed geometry. The beds used were capable of supporting currents of up to about 5000 A ft^{-3} at an electrode potential corresponding to a current density of 5 A ft^{-2} at a plane electrode. This represents a reaction intensity equal to current industrial practice despite the much lower current density value.

Experimental

A series of experiments was designed to discern the broad pattern of behavior of the fluidized bed electrode with variation in the many physical and geometrical factors which might influence it. Of these, the following were thought to have priority of investigation: (i) bed dimension both parallel and perpendicular to the direction of current flow, (ii) particle size, (iii) bed voidage, (iv) electrode potential.

Although it is accepted that the nature of the electrode reaction and electrode surface will also determine the behavior of the bed, it was decided to limit the investigation initially to one system and extend the work to others in the light of the results obtained.

Choice and investigation of test reaction.—The cathodic reduction of m-nitrobenzene sulfonic acid was used throughout the experimental investigation because:

(a) it does not suffer markedly from side reactions;
(b) it has been extensively investigated and documented (1-5);
(c) it is associated with current densities (1-50 A ft^{-2}) appropriate to the context of the investigation;
(d) it occurs in aqueous solution and, with proper choice of electrode potentials, in the absence of gas evolution;
(e) it takes place on a variety of metal surfaces (4), and in particular in the case of copper is unaffected by the metal grade (1).

The reaction can be represented by

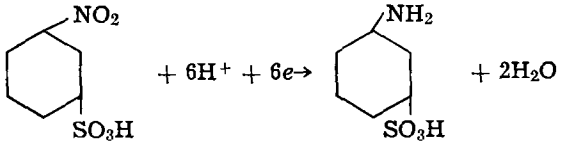

In order to compare the gain in performance of the fluidized bed electrode over conventional planar systems, an initial examination of the reaction was made to provide data on current density and current efficiency.

Polarization curves for the reaction were obtained with a spherical solid copper cathode, 1.2 in. diameter, arranged centrally in a vertically cylindrical Vyon diaphragm, of internal diameter 2.0 in., which was concentric with a cylindrical lead anode. Both catholyte and anolyte were of composition 0.125M m-nitrobenzene sulfonic acid and 1M sulfuric acid. Observations were made using a potentiostat, which, by adjusting the cell terminal voltage, maintained the copper sphere at any selected electrode potential. The value of the potential was measured with respect to a saturated calomel reference electrode connected to a Luggin capillary probe, the tip of which was located at the equator of the copper sphere. An examination of the contours of electrode potential over the rest of the sphere using a second Luggin probe and saturated calomel reference electrode revealed that deviations from the equatorial value were negligible. Results for both static and flowing electrolytes are shown in Fig. 1 which represent the average values obtained from a large number of experiments including some carried out subsequently on sheet copper electrodes. The polarization curves presented are of the same form as those reported by other workers (1).

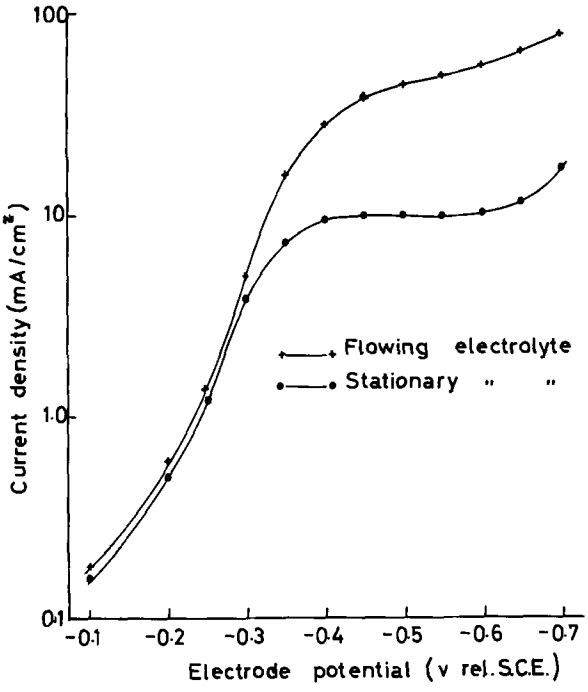

Fig. 1. Polarization data for the reduction of m-nitrobenzene sulfonic acid at a copper electrode.

The limiting current density in Fig. 1 may be identified with a region controlled by the rate of diffusion of m-nitrobenzene sulfonic acid to the electrode surface, since approximate calculation based on a diffusion layer thickness of 5 x 10^{-3} cm and a diffusivity of 0.7 x 10^{-5} cm^2 sec^{-1} gives a limiting current density of the same order of magnitude as that observed. Values presented by the Russian workers, however, are low by a factor of ten on this basis. In the present study, no explanation is offered for this discrepancy; in relation to later discussion, it is important only to remark that in this region currents are enhanced by efficient mass transfer.

The current efficiency of the reaction was also examined, the metanilic acid being determined by potentiometric titration with sodium nitrite in the presence of potassium bromide as an accelerator. The titrations were carried out directly on samples of catholyte at ambient temperature. Details of the procedure have been described by Khomutov and Filippova (2). The results are given in Table II and are in general agreement with Russian work.

At negative potentials exceeding 0.70V (SCE) the current efficiency falls off rapidly since the predominating reaction at higher potentials is increasingly that of hydrogen production. It should be pointed out that, although it is appreciated that higher current efficiencies are attainable at elevated temperatures, since the emphasis of the study was on the physical form of the electrode rather than on the chemistry of the reaction, it was felt more convenient to conduct the work at ambient temperatures.

Electrode materials.—A particulate copper cathode comprising either solid copper, copper-coated glass, or copper-coated polystyrene spheres was used throughout the investigation. Details of the particles are given in Table I.

The plated particles served two purposes. First, they allowed the particle size range to be extended beyond

Table I. Specifications of spherical particles used in the fluidized bed cathodes

Material	Size range, microns	Mean particle size, microns	Density, g cm^{-3}	Geometric surface area of material
Solid copper	75-90	82.5	8.9	81.2 cm^2 g^{-1}
	90-105	97.5	8.9	68.7 cm^2 g^{-1}
	125-150	137.5	8.9	48.6 cm^2 g^{-1}
Copper-coated glass	176-249	212	3.0	94.1 cm^2 g^{-1}
	452-520	486	3.0	41.0 cm^2 g^{-1}
Copper-coated polystyrene	355-420	387	1.2	76 cm^2 cm^{-3}
	850-1000	925	1.2	32 cm^2 cm^{-3}

150μ, the limit of availability of solid copper particles of acceptable sphericity, and, second, and more important, they provided experimental data on the performance of a supported form of electrode material which would show obvious, and in some cases essential, economies if the fluidized bed electrode were to be exploited commercially.

The plating of the glass and polystyrene beads was carried out by a method due to Shorokhova (6).

When not in use, the batches of particles were kept under water to prevent their oxidation.

In all cases, the anodes were made from lead sheet.

Fluidized bed cells.—Experimental observations were made on two forms of cell, one in which the electrical connection to the bed, henceforth called the current feeder, and the counterelectrode were concentric, and one in which they could be considered plane-parallel. They were both in essence research tools and were not considered to be prototypes of an industrial design. The details of construction of the cells are as follows:

(*i*) *Concentric configuration.*—The cell, henceforth referred to as cell I, is shown in Fig. 2. It was constructed from a flanged glass tube, 12 in. in length and 2 in. OD, the ends of which were closed by two circular perspex plates, thickness 3/8 in. The space was divided into anode and cathode compartments by a cylindrical diaphragm made from the flanged Vyon tubes, wall thickness 0.08 in. and outside diameter 1 in., bolted together at the flange with a flow distributor, also of Vyon, thickness 1/16 in., clamped between them. The fluidized bed, which was contained by the diaphragm and supported by the distributor, was introduced into the cell by removing the upper perspex plate.

The current feeder, which consisted of an 1/8-in. diameter copper rod mounted axially in the diaphragm, was supported by the lower perspex plate, into which it was cemented, and further located by the distributor through which it passed as a tight fit.

The electrode potential of the fluidized bed, which in terms of individual particles could well be extremely complex in nature, is given a characteristic value which was chosen to be that of the feeder with reference to electrolyte below the distributor. For this purpose a Luggin capillary was located as shown in Fig. 2, and readings were taken against a saturated calomel electrode. All potentials in this paper are expressed relative to a saturated calomel electrode.

A second cell of this type (cell II) was made in which the diaphragm, and hence the bed, diameter was increased to 3 in. These cells were particularly useful for calculating bed performance outside the entrance region, and, by maintaining separation of the anolyte and catholyte, for investigating current efficiency in terms of $-NO_2$ reduction. Another modification was introduced into a third cell, of diaphragm diameter 1 in., by fitting two distributors, one above the other, so that two beds, arranged in series with respect to catholyte flow, and parallel with current flow, could be examined. The reason for such a system will be made clear later.

(*ii*) *Plane parallel configuration.* The cell (cell III) is shown in Fig. 3. The internal diameter of the cell was 3 cm, and the length of tube available to the fluidized beds was approximately 12 cm. The flow distributor, which also supported the bed, was a sintered disk of porosity 3. The upper portion of the cell was constructed from a standard Quickfit B55 cone and socket joint. Two of the three nozzles it carried allowed insertion of the electrical leads to the current feeder and counterelectrode, and the third provided a gas

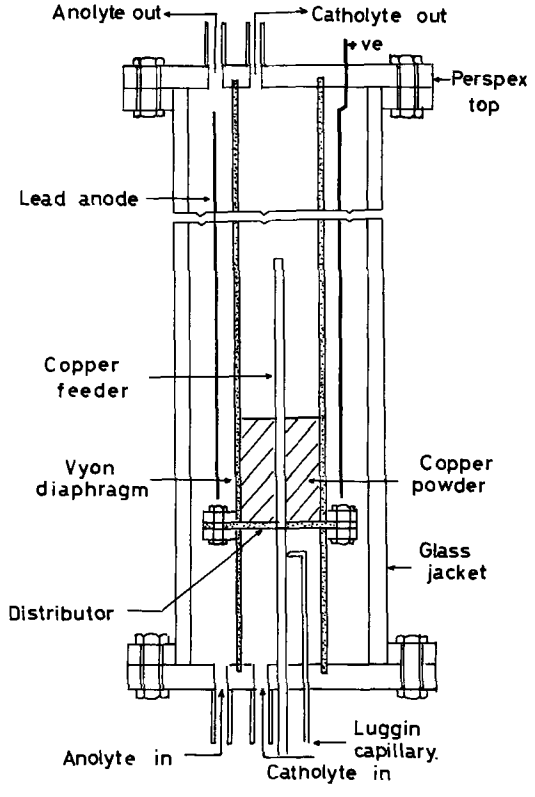

Fig. 2. Diagrammatic section of the cylindrical fluidized bed cell. Cell I.

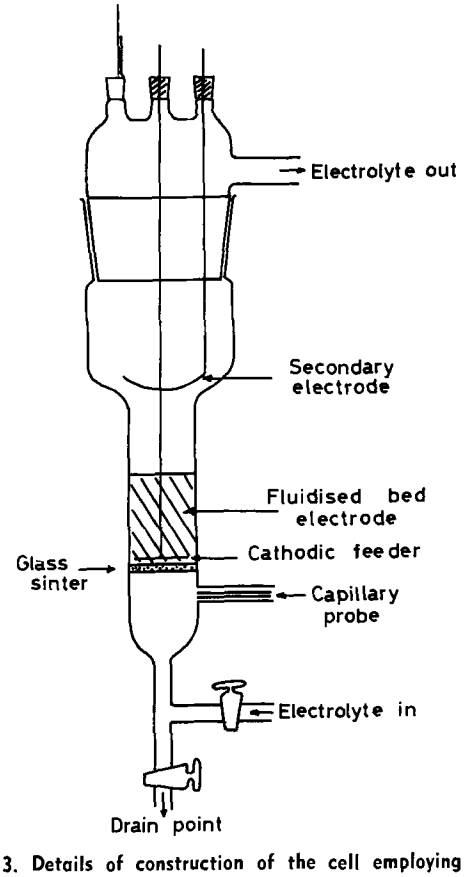

Fig. 3. Details of construction of the cell employing a plane-parallel electrode configuration. Cell III.

vent. In addition, the gas vent was used for the insertion of a Luggin capillary probe connected externally to a SCE by means of which the potential profile in the electrolyte could be observed relative to the potential of the current feeder. For this purpose the probe was supported such that its position in a vertical sense could be adjusted at will. The feeder was a flat spiral of 16 s.w.g. copper wire to which electrical connection was made by an insulated length of copper wire passing into the cell as shown in Fig. 3. When in position the plane of the feeder was perpendicular to the axis of the cell, but its axial location could be varied continuously. The counterelectrode consisted of lead sheet, shaped into a hemispherical shell, and was located above the free surface of the fluidized electrode.

The electrode potential of the bed was again characterized by the electrode potential of the feeder measured against that of the electrolyte below the distributor using a saturated calomel reference electrode.

In this form of cell the anolyte and catholyte compartments were not separated, the therefore current efficiencies could not be assessed owing to degradation of the cathodic product at the anode. Its main function was to provide information on the effect of current feeder location on electrode performance, and to enable an examination of the potential profile in the electrolyte to be made, for which purpose the visual observation afforded by the design, but not possible in the concentric configuration, simplified experimentation considerably.

(iii) The double concenrtic fluidized bed cell. The cell, cell IV, is shown in Fig. 4. It was constructed from a perspex tube of internal diameter 1.25 in. A sintered glass disk acted as a combined flow distributor and bed support. A Vyon tube of outside diameter 0.75 in. was sealed down onto the sinter such that a cathodic bed was supported in the annulus and an anodic bed of platinum coated glass particles was located inside the Vyon tube, the same electrolyte stream fluidizing both compartments.

The current feeders were coarse mesh cylindrical gauzes of copper and platinum wire for the cathodic and anodic beds, respectively. They were located adjacent to the Vyon diaphragm in a position corresponding to the top surface of the bed in the plane-parallel configuration.

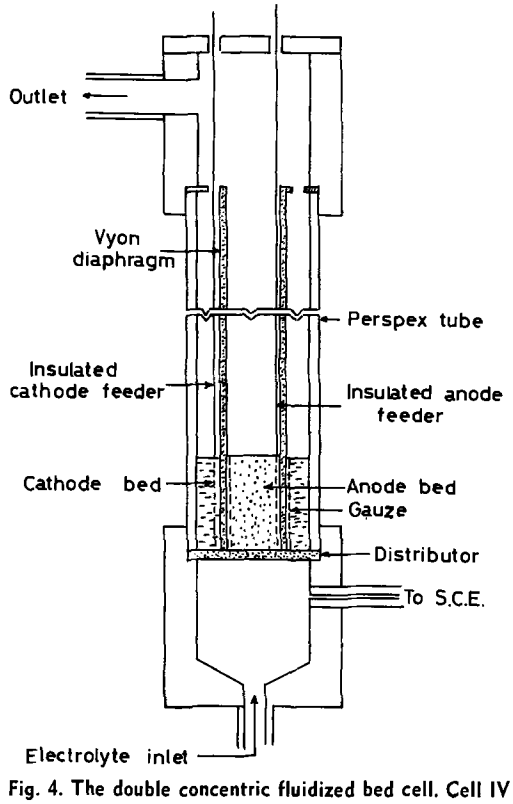

Fig. 4. The double concentric fluidized bed cell. Cell IV

The same method of electrode potential measurement was employed as in cell III, *i.e. via* a capillary located underneath the distributor. The cell was used to investigate the effect of bed expansion on electrode performance using copper-coated glass particles in the size range 450-520μ

Electrolyte circulation system.—The flow circuit was designed so that cells of either form could be inserted without modification. A diagram of the circuit is shown in Fig. 5.

The electrolyte was contained in the reservoir, capacity 5 liters, from which it was circulated through the cell by a peristaltic pump. Flow pulsations were reduced by an air vessel sealed by a mercury leg. The flow to the cell was indicated by a rotameter with a titanium float, and flow control was exercised manually by adjusting the supply and bypass valves 1 and 2. Effluent from the cell passed back to the reservoir along the return line. During extended runs with the concentric fluidized bed cell for the purpose of establishing current efficiencies, product oxidation was eliminated by running the system with a stagnant anolyte. Used electrolyte was discarded and replaced by fresh material sufficiently frequently to avoid significant depletion of the concentration of m-nitrobenzene sulfonic acid by reduction. The temperature of the electrolyte was maintained at 25°C, within acceptable limits, by means of a "Variac" transformer supplying an electric heating tape wrapped around the lower part of the reservoir.

Electrical supply.—The electrical power supply was taken directly from a rectifier. Two types were used according to the magnitude of the current load required. These were a "D-C Mobile" with maximum output 10A at 100V, and a Westinghouse silicon rectifier rated at 150A and 12V. Both were capable of continuous manual control within their ranges of current and potential.

Results and Discussion

Bed voidage.—A detailed investigation of the effect of bed voidage on the behavior of a fluidized bed electrode was carried out in cell IV, with the feeder located adjacent to the Vyon diaphragm. Observations for copper-coated glass particles in the size range 450-520μ are exemplified in Fig. 6 taken from a 40-g bed over a range of feeder potentials. The general shape of these curves has been confirmed subsequently by other workers (7). The form of the curves is not yet explained but an intensive examination of a proposed mechanism for current distribution in the bed now in progress shows early promise of doing so.

In drawing conclusions from these results, it should be borne in mind that the total current supported by the electrode reflects only the rate of reaction and not the type. The key factor in determining the latter is

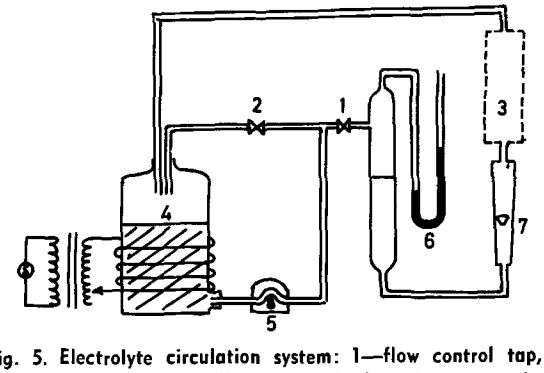

Fig. 5. Electrolyte circulation system: 1—flow control tap, 2—by-pass control tap, 3—cell, 4—heated electrolyte reservoir, 5—peristaltic pump, 6—"smoothing" vessel for electrolyte flow and manometer, 7—flowmeter.

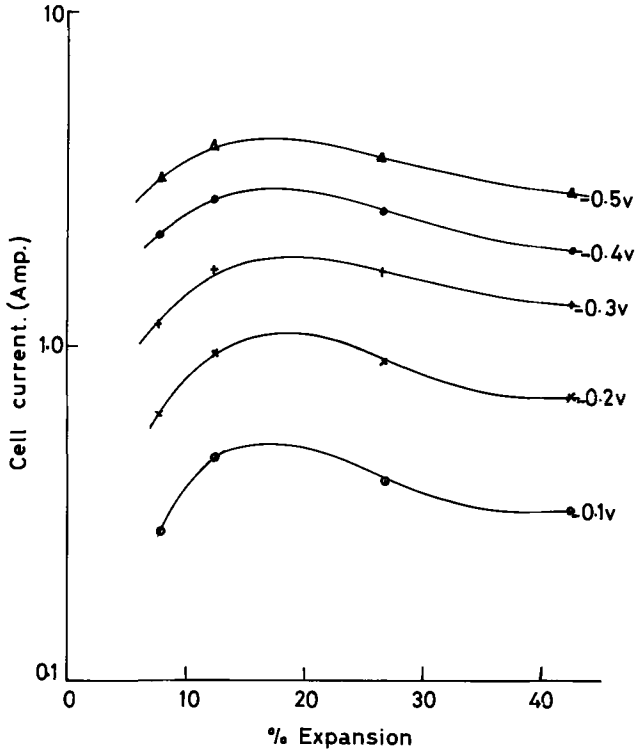

Fig. 6. Variation of cell current with expansion in the double concentric fluidized bed cell.

the potential distribution in the system and it does not therefore follow that the maximum current condition necessarily offers the best electrode performance in terms of desired reaction, although measurement of current efficiency has shown that in this particular case they do occur identically. In this connection it is also important to note that the potential distribution in the bed will show a strong dependence on the method adopted to characterize it. In the present work, it will be remembered, this was chosen to be the difference in potential between the feeder and the electrolyte prior to entry to the bed. If another method were adopted, by making reference, for example, to the electrolyte at some point within the bed, the variation of current or current efficiency with bed voidage could assume an entirely different form. Similar arguments may account for the fact that semiqualitative observations made with the concentric configurations displayed more pronounced maxima than those of the curves in Fig. 6.

From a practical point of view, however, the experimental results serve to draw attention to the importance of bed voidage in establishing the maximum operating performance of a fluidized bed electrode, and investigations so far indicate that this would be achieved with a voidage in the vicinity of 0.50-0.58 (5-25% expansion).

Scale-up.—From an electrical point of view the dimensions of the bed can be scaled up in two ways, either parallel to the direction of current flow in the cell or at right angles to it. Both cases have been investigated using cells of concentric configuration.

The effect of increasing the bed dimension at right angles to current flow was investigated in cell I and the results are presented in Fig. 7(a), (b), and (c) in terms of the variation of total cell current with static height of bed over a range of particle size and electrode potential. In general, the curves show that the total current supported by the bed scales up linearly with height except over an initial region, corresponding to low bed height, where the relationship takes on a nonlinear form. This initial region may well reflect a hydrodynamic entrance effect, since this would explain not only why the region is not typical of the

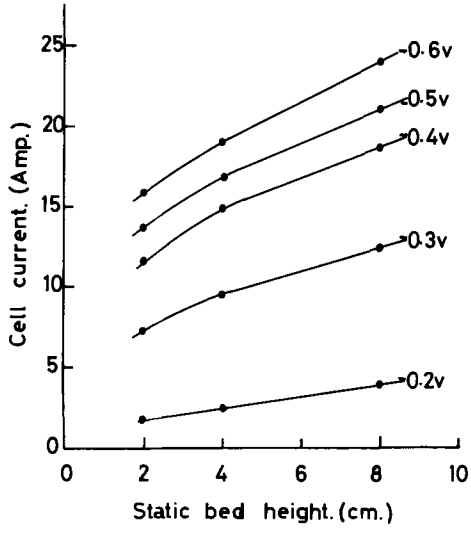

Fig. 7(a). The effect of static bed height on the total current supported by a fluidized cathode composed of copper-coated glass particles, 452-520μ diam.

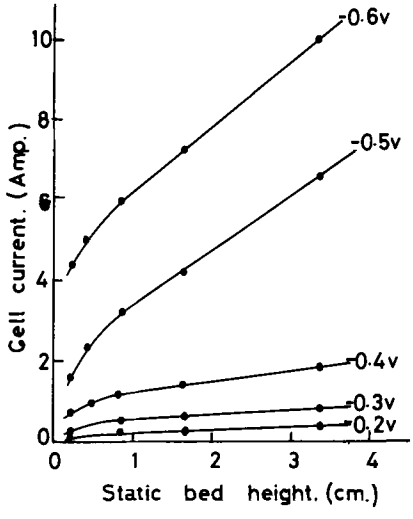

Fig. 7(b). The effect of static bed height on the total current supported by a fluidized cathode composed of solid copper particles, 125-150μ.

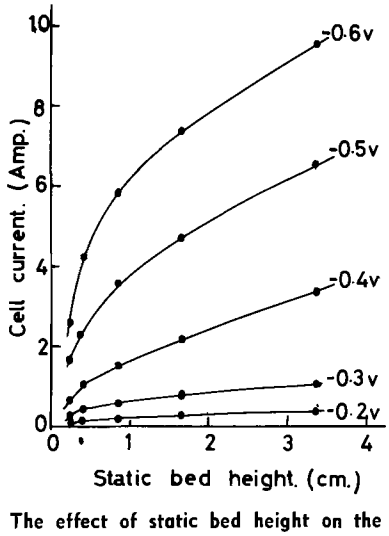

Fig. 7(c). The effect of static bed height on the total current supported by a fluidized cathode composed of solid copper particles, 75-90μ diam.

bulk of the bed but also the fact that its extent is independent of the electrode potential of the feeder and apparently only determined by physical characteristics of the particles.

The data of Fig. 7(a), (b), and (c) have also been used to determine the performance of the fluidized bed electrode in terms of specific current. Specific current, i_s, is defined as the current supported by the fluidized electrode per unit of volume it would occupy if it were in the static state, and it is therefore related to point values of the slope, dI/dh, of the curves in Fig. 7(a), (b), and (c) by

$$i_s A = dI/dh$$

where A is the cross-sectional area of the bed in a plane at right angles to its axis. By inserting values of dI/dh appropriate to the linear portion of the curves only, values of i_s were obtained from which entrance effects were eliminated.

The data obtained in this way have been divided by the specific area of the particles to produce a "pseudo current density" and are presented in Fig. 8, where they are plotted against the equivalent plane electrode current density. This latter term is defined here as the current density which is observed at a plane electrode operating at a potential equal to that chosen to characterize the fluid bed potential. This presentation of results takes account of the variation of the superficial area of the particulate electrodes and therefore makes comparison between different particle sizes and electrode dimensions more meaningful. It should be emphasized again, however, that strictly there can be no direct comparison made between a continuous electrode surface and a particulate form on the basis of a single value of potential since in general the latter will exhibit a potential distribution of varying complexity. A detailed investigation of the potential distribution is at present in progress, but at this stage the simple comparison made in Fig. 8, bearing in mind its somewhat qualitative nature, serves to give a feeling of the intensity of the performance of the fluidized bed electrode.

As a general comment, the specific current of the fluidized bed is seen to increase nonlinearly with the plane electrode current density, and is an indication that the bed is not uniformly active. The nature of the nonuniformity, however, cannot be deduced at this stage owing to the somewhat complex form of the polarization curves of the test reaction.

Considering the copper-coated glass spheres, it is seen from Fig. 8 that in the low current density region, roughly corresponding to the Tafel region, a performance significantly superior to the solid copper spheres is attained.

The effect of scaling up in a direction parallel to the current flow was determined by comparing the performance of cell I, of electrode diameter 1 in., with that of cell II, electrode diameter 3 in., for solid copper particles of size 125-150μ.

The relevant results again appear in Fig. 8, where it appears that the performance of cell II is better than cell I. However, similar weight beds were used in each cell so that comparable bed heights in cell II are approximately 1/9 of those in cell I. The effect of this is that the values of dI/dh have not reached a steady value as all the bed heights considered have been in the entrance region. For this reason, no definite conclusions may be drawn about the performance of cell II.

The data obtained from copper-coated glass particles in cells I and IV and those from solid copper powder on cells I and II have been interpreted in terms of the activity of the fluidized bed electrode by plotting the effective specific area against the plane electrode current density and in this form are shown in Fig. 9. On this basis, Fig. 9 shows that the performance of the copper-coated glass particles is superior to the solid copper powder within the range of parameters investigated.

Emphasis must again be made regarding the effect on the plotted results of the measured value of electrode potential. While in cells I and II the measured potential may be expected to approximate the true value of electrode potential, this is certainly not the case in cells III and IV. With special regard to the latter cells, the reading taken as electrode potential, and used subsequently to determine the plane electrode current density, will incorporate an IR drop through the bed which may become significant at higher potential values. For example, an IR drop of 0.025V incorporated at an observed reading of 0.35V effectively reduces the equivalent plane electrode current density from 16.5 to 9.3 A/ft^2. The effect at higher observed readings, corresponding to higher currents, would have a similar effect since, although the variation of current density with electrode potential is not so great at higher potentials, the IR drop will be greater in this case. The net effect of these considerations is to raise the effective specific areas for all points greater than an approximate plane electrode current density of 10 A/ft^2.

Potential distribution.—Potential distribution in the electrolyte in the fluid bed cathode was examined using cell III by means of a movable Luggin capillary probe connected to a SCE. Potentials were measured

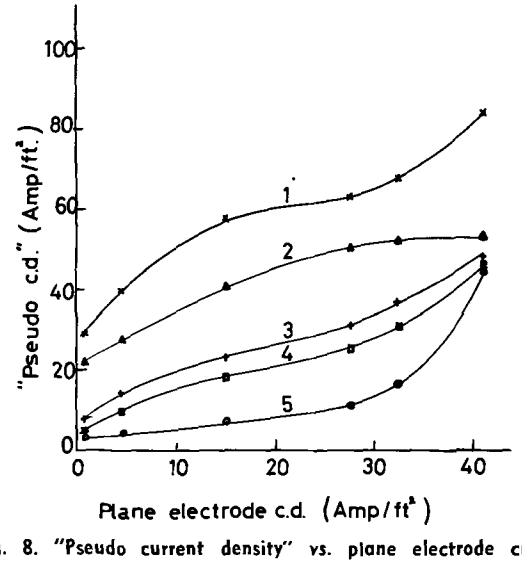

Fig. 8. "Pseudo current density" vs. plane electrode current density for various electrode materials: 1. 450-520μ copper-coated glass in Cell IV; 2. 450-520μ copper-coated glass in Cell I; 3. 125-150μ solid copper powder in Cell II; 4. 75-90μ solid copper powder in Cell I; 5. 125-150μ solid copper powder in Cell I.

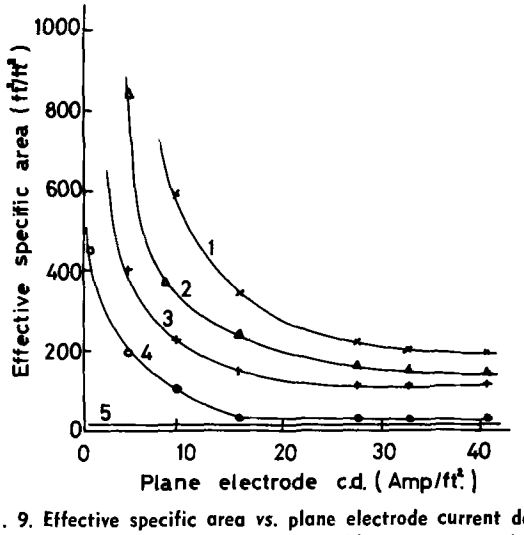

Fig. 9. Effective specific area vs. plane electrode current density for various electrode materials: 1. 450-520μ copper-coated glass in Cell IV; 2. 450-520μ copper-coated glass in Cell I; 3. 125-150μ solid copper powder in Cell II; 4. 125-150μ solid copper powder in Cell I; 5. typical industrial cell.

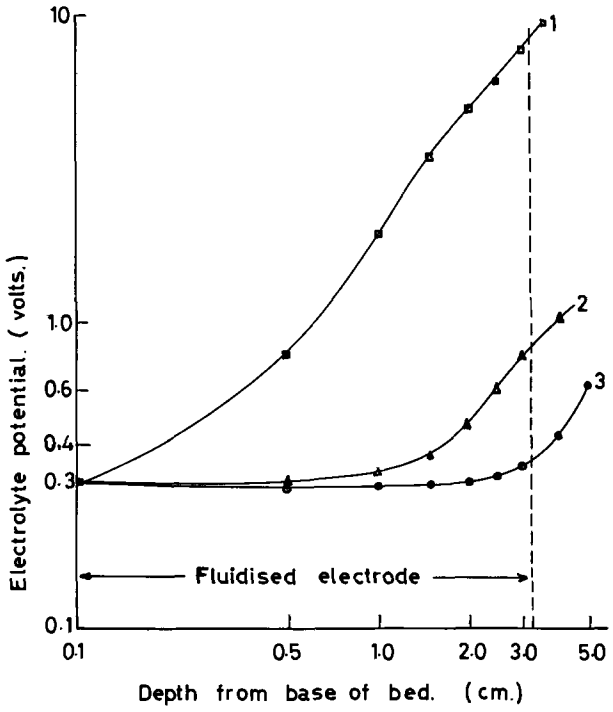

Fig. 10. Variation of potential in the electrolyte in a fluidized bed with reference to the electrode potential of the feeder. Observations were made with a Luggin probe connection to a SCE in Cell III. The feeder potential was —0.3V.

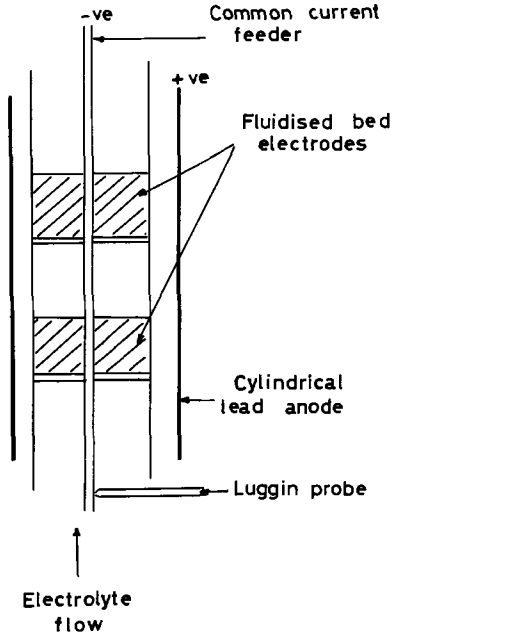

Fig. 11. Diagrammatic representation of a two-tier fluidized bed electrode. Bed diameter = 1 in.

with respect to the feeder. The results plotted in Fig. 10 correspond to three different feeder locations. As would be expected, an increase in potential in all three cases were observed in passing upward through the bed toward the anode. The rate of increase, however, is markedly different in the three cases, and in particular the total potential drop across the bed with the current feeder located in the center is greater than that with the feeder at the surface of the bed by an order of magnitude although the total cell current, 0.7A, was the same in both cases. This observation indicates that the bed is much more active in the proximity of the feeder than at points removed from it under the particular electrochemical and physical conditions obtaining. It may well imply after further investigation that, in good fluid bed electrode design, power consumption may be reduced, without in general impairing cell performance, by locating the feeder on that side of the bed nearer the counterelectrode.

The curve describing potential distribution with the feeder located near the distributor, although corresponding to the same feeder potential (0.3V) as the other two, is not strictly comparable to these since the total cell current in this case was 8.0A, some ten times greater than that observed in the other two. Although the difference in feeder location would be predicted to cause an increase in current with the feeder in this position, as well as a larger drop in potential, this change in location of the feeder cannot by itself explain the whole effect, as otherwise one would expect some significant difference between the performance with the feeder in the other two locations. It is felt, and there is more evidence to support this point of view, that the behavior of the bed in this region is of a localized nature due to an entrance effect. This has not been fully explored as yet, but its investigation is of some importance because of the obvious implications in improved electrode design. Supporting evidence was obtained from a two tier cell design shown diagrammatically in Fig. 11. The total cell current observed at all potentials examined was higher when a given weight of bed was distributed between the tiers than when it comprised a single bed. In addition, and already given mention, Fig. 7(a), (b), and (c) show typical entrance region behavior in that the performance of the bed, in terms of total cell current, increases uniformly with bed height except for a small region near the distributor which is characterized by abnormally high performance.

Current efficiency.—A series of current efficiency tests were carried out in cell I over a range of current feeder potentials using solid copper spheres, of size range 125-150μ in a bed of static height 4.9 cm (80g of bed material). The results are given in Table II, together with those for a single sphere electrode in flowing electrolyte for ease of comparison.

It is to be expected that the bed in all probability displays a complex spatial distribution of electrode potential, or, in other words, that every particle will not be operating on the same part of the plane electrode polarization curve no matter how well one attempts to control the potential of the current feeder. This is a natural consequence of the requisite potential gradients necessary to drive current through the dispersed and continuous phases. It could well be expected, however, that under the conditions of shallow potential gradients expected at relatively low total cell currents a better approach to a uniform working potential would exist than at high total currents. The data of Table II bear this out in a qualitative way in that they show, within experimental error, that at low current feeder potentials, approximating to the Tafel region, the current efficiency obtained in the bed is identical to that on the plane electrode. At higher negative potentials, within the limiting current region and where there is an onset of hydrogen evolution,

Table II. Variation of current efficiency with potential in the reduction of 0.125M m-nitrobenzene sulfonic acid in 1M H_2SO_4 at a fluidized bed cathode of solid copper particles and at a solid copper, single sphere electrode

Cathodic potential, volts	Current efficiency, % Fluidized electrode	Single sphere electrode
−0.20	78	77
−0.25	74	75
−0.30	70	70
−0.40	67	68
−0.50	62	65
−0.60	57	61
−0.70	50	57

the bed shows a significant drop in efficiency compared to the plane electrode. Assuming that hydrogen is the only other product, this suggests that parts of the bed are operating further into the hydrogen evolution region than the control potential indicates. This is not unreasonable at high currents since, in the electrode configuration under consideration, the potential profiles in the dispersed and continuous phases could diverge somewhat in regions removed from the feeder, depending on their relative conductivities. Investigations in progress tend to support this explanation. The current efficiency values quoted in the present paper have also been confirmed by other workers (7).

Electrode materials.—In the previous sections it has been noted that results are not quoted for copper-coated polystyrene beads. In general it was found that the behavior of a fluidized bed constituted of such particles had poor hydrodynamic qualities, the reason for which could be traced to their low over-all density. The movement of these particles within the bed had a "lethargic" quality which could have serious disadvantages in the application of the fluidized bed electrode in the broadest sense. One means of imparting a high density to the particles would be to give them a heavier coating of electrode material or base metal, but this to some extent would lose the advantage of using cheap nonconducting spheres as electrode carriers.

On the other hand, the solid metal spheres and coated glass beads were both satisfactory, and indications are that a minimum over-all density of 2.8 g/cm^3 is desirable.

Conclusions

The investigations have demonstrated the ability of a fluidized bed of conducting particles in contact with a current feeder to disperse charge throughout the bed such that an electrochemical reaction takes place at the particulate surface. In this way, the fluidized bed electrode is capable of scaling up electrode processes having low exchange currents so as to give high over-all currents in commercially reasonable cell volumes. As would be expected, the performance of such an electrode depends on the degree of fluidization and shows a maximum in the vicinity of 5-25% expansion (0.50-0.58 voidage). Within this region a bed of copper-coated glass beads, particle size 452-520μ, supported a specific current some 20 and more times greater than that expected of a typical commercial cell when operating at a current density of the order of 7 A ft^{-2}.

Of the materials used in the bed, coated glass beads appear to be superior in performance to solid metal particles, although the reason for this is not clear. This observation has important implications when considering the use of expensive electrode materials and in selecting over-all particle densities suitable for optimum process flow conditions.

Scale up of the bed in a direction perpendicular to current flow in the cell gives a linear increase in cell capacity, but in a direction parallel to the current flow falls short of a linear relationship, and hence size in this direction appears to be limited to about 1 in. for the types of cell considered. It is questionable, however, whether there is any need to scale up beyond this value in a parallel direction; otherwise the problem of ohmic losses in the electrolyte and diaphragm may become crucial. For instance, a bed of cross section 1 ft^2 and depth 1 in. constituted of copper-coated particles already supports a current in excess of 300A under conditions where a plane electrode would support less than 10 A/ft^2. It would probably be better therefore to think in terms of multiple cells or their equivalent rather than the scaling up of a single electrode.

It is realized that the conclusions drawn apply strictly only to the particular reaction investigated, namely the reduction of an aromatic nitro group at room temperature at a copper cathode. Other forms of cathodic and anodic reactions are under investigation, however, and observations made so far are in accord with the present conclusions.

Acknowledgments

One of the authors (J. R. B.) wishes to express his thanks to the Science Research Council for the award of an Advanced Course Studentship under which this work was carried out. The authors also wish to thank Dr. D. B. Chambers for some confirmatory experimental work carried out prior to the submission of this paper, and to all their colleagues for invaluable discussion on the subject matter of this paper.

NOMENCLATURE

A	Area of cross section of a cylindrical fluidized bed electrode in a plane perpendicular to its axis, ft^2.
h	Height of a fluidized bed electrode measured in the static condition, ft.
I	Total cell current, amperes.
i_s	Specific current, amperes ft^{-3}.

Manuscript submitted Dec. 26, 1968; revised manuscript received June 26, 1969.

Any discussion of this paper will appear in a Discussion Section to be published in the June 1970 JOURNAL.

REFERENCES

1. N. E. Khomutov and I. V. Kasatonova, *Zhur. Prikl. Khim.*, **34**, 840 (1961).
2. N. E. Khomutov and Filippova, *Td. M.Kh.T.I.*, **32**, 45 (1961).
3. N. E. Khomutov and T. N. Shornyakova, *Zhur. Prikl. Khim.*, **36**, 1521 (1963).
4. N. E. Khomutov and T. N. Shornyakova, *ibid.*, **39**, 195 (1965).
5. N. E. Khomutov and T. N. Shornyakova, *ibid.*, **36**, 1772 (1963).
6. V. I. Shorokhova and L. L. Kuz'min, *Int. Chem. Eng.*, **4**, 451 (1964).
7. C. J. B. (Projects) Ltd., Leatherhead, Surrey, Private communication (1968).

The Oxidation of Water-Soluble Organic Fuels Using Platinum-Tin Catalysts

K. J. Cathro

Division of Mineral Chemistry, C.S.I.R.O., Port Melbourne, Victoria, Australia

ABSTRACT

Electrodeposited platinum-tin mixtures show enhanced activity toward the oxidation of methanol, formaldehyde, and formic acid when compared with platinum black. This increased activity is particularly noticeable with formaldehyde, the anode polarization being decreased by 0.4V at a current density of 100 mA/cm^2.

The use of platinum-rhenium electrodeposits as an anode catalyst for the oxidation of methanol has been described (1-3). It was suggested (2, 3) that the improvement in performance over a platinum black catalyst was due to the direct reaction of an oxide of rhenium with chemisorbed fuel residues, followed by electrolytic reoxidation of the reduced rhenium oxide. After reviewing the standard oxidation potentials of several metal-metal oxide systems, it seemed likely that other platinum-metal oxide combinations would give enhanced activity toward methanol oxidation. Several elements were codeposited electrolytically with platinum, and the mixed deposits tested, in the first instance, for catalytic activity toward the oxidation of methanol and formaldehyde in 0.5M sulfuric acid. The more active catalysts were examined also for their ability to oxidize formic acid, for, although this is not an economical fuel, it can occur in actual battery systems as a partial oxidation product of formaldehyde (4). Of the combinations tested, platinum-tin was the most promising catalyst.

The addition of tin to platinum to improve its performance as an oxidation catalyst has been patented (5, 6), but little detailed information is given as to the characteristics of these catalysts. The present study gives results for the oxidation of methanol, formaldehyde, and formic acid over a range of temperature and fuel concentration.

Experimental

The cells used were those described previously (3), but in this series of tests polarization curves were obtained galvanostatically, using a stabilized power supply and suitable ballast resistors. Cyclic voltammetry was employed on a few occasions, using a potentiostat and waveform generator made in these laboratories, the curves being recorded on an X-Y plotter. Electrode potential was measured by means of a voltage follower/precision voltmeter combination, while current was measured on a suitable multirange ammeter. A mercury-mercurous sulfate reference electrode was used throughout: its potential was checked frequently against a calomel reference. The magnitude of the *IR* correction was estimated by noting the initial change in potential when a current pulse was applied to the system.

The methanol, formic acid, and sulfuric acid used were of analytical reagent grade. Reagent-grade formaldehyde is stabilized with methanol, so a methanol-free formaldehyde solution was prepared by refluxing paraformaldehyde with water. The fuel concentration was held at 1M and the temperature at 60°C unless stated otherwise: the sulfuric acid concentration was 0.5M in all cases. Electrode performance was sufficiently stable for all tests at a given tin composition to be run on the one electrode. Oxygen-free nitrogen was bubbled through all test solutions (except for the 1000-hr endurance test) before and during polarization runs.

Electrode preparation.—Catalysts were prepared by electrodeposition at controlled potential from mixed solutions of chloroplatinic acid and stannic chloride, the deposition potential being, in most cases, +0.05V to the standard hydrogen electrode (NHE). The initial platinum concentration in the plating solution was 10 g/liter; this would have decreased by less than 5% during a platinum run. The deposit composition was controlled by varying the tin concentration between zero and 12.8 g/liter and the deposits were gray to black in color. Iridium and rhodium substrates of 1 cm^2 foil were used; these metals were chosen to permit the stripping of the deposit in *aqua regia* without dissolution of the substrate. With platinum foil there is danger of attack on the substrate, especially as platinum-tin deposits dissolve more slowly than the platinum-rhenium catalysts described previously.

Platinum analyses were made using the stannous chloride method (7), while tin determinations were made polarographically after hydrolytic separation of tin using an aluminum hydroxide carrier.

Results

The polarization observed when methanol, formaldehyde, and formic acid are oxidized on a platinum deposit is reduced by the inclusion of tin in the deposit, as shown in Fig. 1(a), 1(b), and 1(c), together with the data for platinum-rhenium (3). The improvement in catalytic activity of the deposits over that of platinum black is quite clear, as is the superiority of platinum-tin codeposits (over platinum-rhenium) for the oxidation of formaldehyde and formic acid.

Some of the factors affecting catalyst activity were studied in more detail, with the results set out below.

Catalyst loading.—The loading was varied from 0.09 to 6.2 mg/cm^2 by variation of the plating time between 1 and 30 min. It is possible to get heavier deposits by plating for a longer time, but the adhesion of such deposits is poor, and they tend to crack and fall off the substrate. The thinner deposits show good adhesion.

The effect of catalyst loading on activity is shown in Fig. 2, the current density at fixed potential (0.3V *vs.* NHE for methanol, 0.15V for formaldehyde, 0.2V for formic acid) being plotted against loading. For methanol and formaldehyde the current density is proportional to $L^{0.85}$, where L is the catalyst loading in mg/cm^2. The results for formic acid scatter more, but show a similar trend. The near proportionality of activity to catalyst loading indicates that the deposits are porous and only a small decrease in available area results from increasing the thickness of the deposit.

Catalyst composition.—The composition of the deposit was varied by changing the tin concentration as described above. The fraction of tin in the deposit was proportional to the tin in solution up to approximately 3 g/liter, but thereafter became independent of the tin concentration—*see* Fig. 3.

The effect of catalyst composition on activity is shown in Fig. 4. There is an optimum composition at approximately 5% tin by weight [8 a/o (atom per cent)] for the catalyst loading of 5 mg/cm^2 used. This

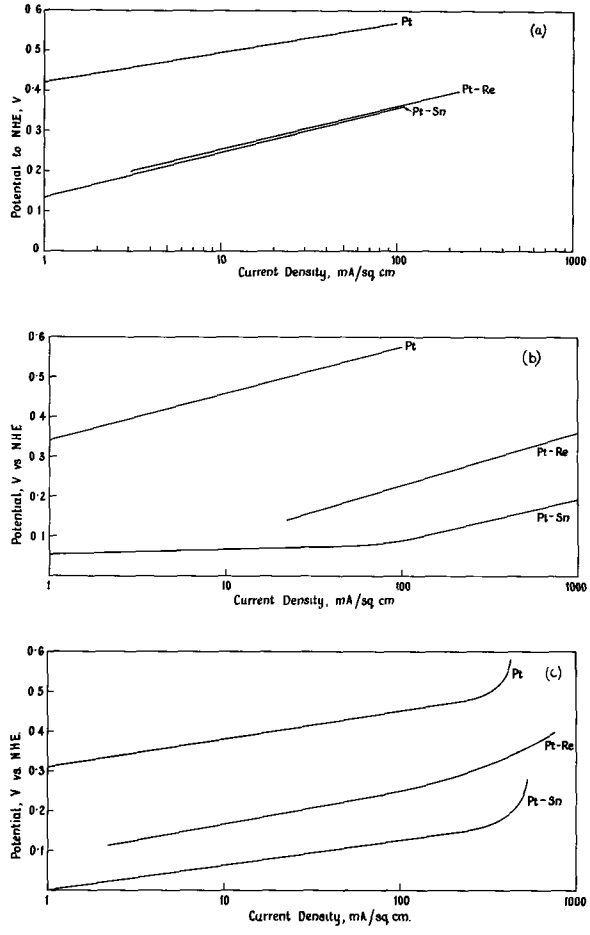

Fig. 1. Polarization curves for a platinum-tin catalyst. At 60°C, catalyst loading 7±1 mg/cm^2; platinum-tin catalyst: 6.2% Sn. (a) For 1M methanol, (b) for 1M formaldehyde, (c) for 1M formic acid.

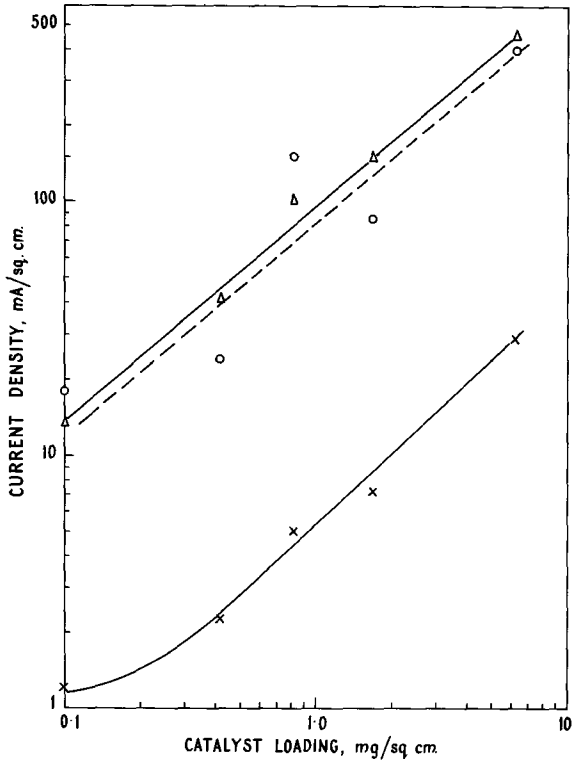

Fig. 2. Effect of catalyst loading on electrode performance. At 60°C, 1M fuel, catalyst 6.2% Sn. ×, Methanol at +0.3V to NHE. △, Formaldehyde at +0.15V to NHE. ○, Formic acid at +0.02V to NHE.

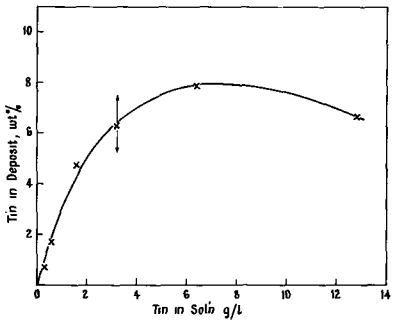

Fig. 3. Effect of plating solution composition on tin in deposit. Electrodes plated at +0.05V to NHE. Platinum = 10 g/liter initially in all cases.

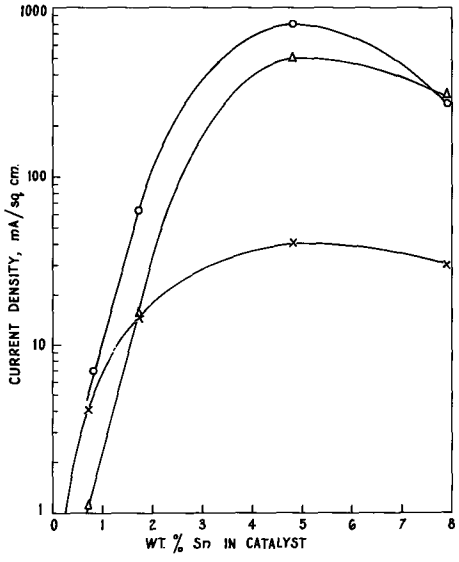

Fig. 4. Effect of catalyst composition of electrode performance. At 60°C, 1M fuel, catalyst 4.7 mg/cm^2. ×, Methanol at +0.3V to NHE. △, Formaldehyde at +0.15V to NHE. □, Formic acid at +0.2V to NHE.

is similar to the optimum of 11% by weight (11.4 a/o) observed for the platinum-rhenium system (3).

A further effect of an increasing fraction of tin is shown in Fig. 5. It can be seen that the electrode tends to become passive at a potential of approximately 0.3V to NHE if it contains an appreciable percentage of tin. Generally similar results are observed with formaldehyde and formic acid, except that the passivation potential is approximately 0.25V.

Deposition potential.—Catalyst deposits were made at potentials of +0.25, +0.05, zero, and −0.1V to NHE, the plating solution *p*H being 0.7, and tin concentration of 3.2 g/liter. Hydrogen was evolved freely at −0.1V. The effect of deposition potential on activity is shown in Table I.

The primary effect of a decrease in potential, all other factors being held constant, is to increase the

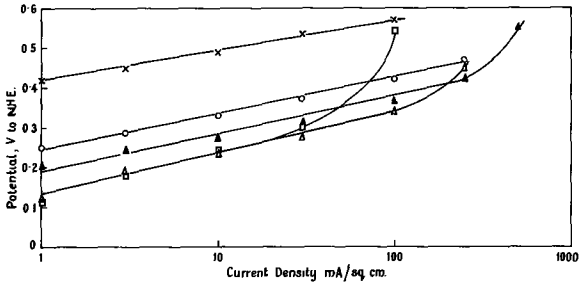

Fig. 5. Effect of catalyst composition on passivity. For 1M methanol, 60°C, 4.7 mg/cm^2. ×, No tin. ○, 0.7% Sn. ▲, 1.7% Sn. △, 4.8% Sn. □, 7.9% Sn.

Table I. Effect of deposition potential on catalyst activity

Plating potential volts to NHE	Catalyst		Current density, mA/cm², at stated potential		
	Loading, mg/cm²	Tin, %	Methanol at 0.3V	Formaldehyde at 0.15V	Formic acid at 0.20V
+0.25	2.5	6.8	13	650	78
+0.05	6.2	6.2	38	500	440
zero	11.2	2.7	38	200	300
−0.1	18.3	2.1	38	450	340

catalyst loading, but decrease the fraction of tin in the deposit. These variations of loading and composition make interpretation of the results more difficult, but if activity is assumed to be proportional to $L^{0.85}$ over the whole range of loadings, and if the effect of tin composition on activity is taken as that shown in Fig. 4, an approximate correction for these variations can be made. If this is done it is clear that there are not any large (order of magnitude) changes in specific activity with change in plating potential.

Electrolyte temperature and fuel concentration.—At fixed potential, current density increases with increase of both temperature and fuel concentration, as shown in Fig. 6 and 7.

Operating time.—One long-term run of 1000 hr duration has been made using methanol as fuel, the electrode potential at a current density of 20 mA/cm² being shown as a function of time in Fig. 8. There is a fairly rapid decay over the first hundred hours, followed by a period of nearly steady performance, with only a slight further loss in activity.

Platinum-tin deposits can be polarized to high potentials—of the order of 1.5V to NHE—at least for short periods, without significant loss in activity when returned to the normal working potential of 0.2-0.3V. This is in contrast to the platinum-rhenium system, where operation at potentials more positive than 0.5V leads to a rapid and irreversible loss in activity, probably due to loss of rhenium from the catalyst (3).

Discussion

It has been suggested that the mixed catalysts which show increased activity toward the oxidation of methanol gain their activity from the direct reaction of metal oxide with chemisorbed fuel residues, the reduced oxide then being electrolytically reoxidized (2, 3, 8, 9). The $Sn(OH)_2/Sn(OH)_4$ couple has a standard potential of + 0.075V to NHE at 25°C in acid solution (10) so it could act in this way.

It could be objected that the improvement in activity is due to the tin modifying the platinum black

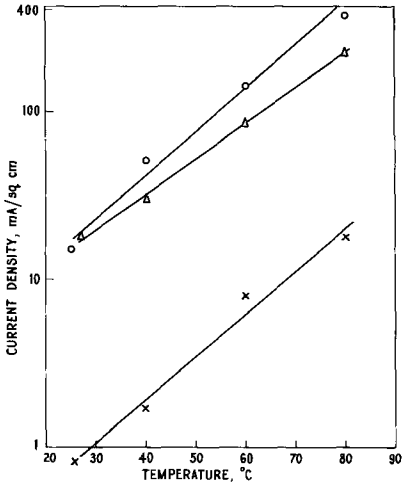

Fig. 6. Effect of electrolyte temperature on performance. At 1.7 mg/cm² catalyst, 5.3% Sn, 1M fuel. ×, Methanol at +0.3V to NHE. △, Formaldehyde at +0.15V to NHE. ○, Formic acid at +0.2V to NHE.

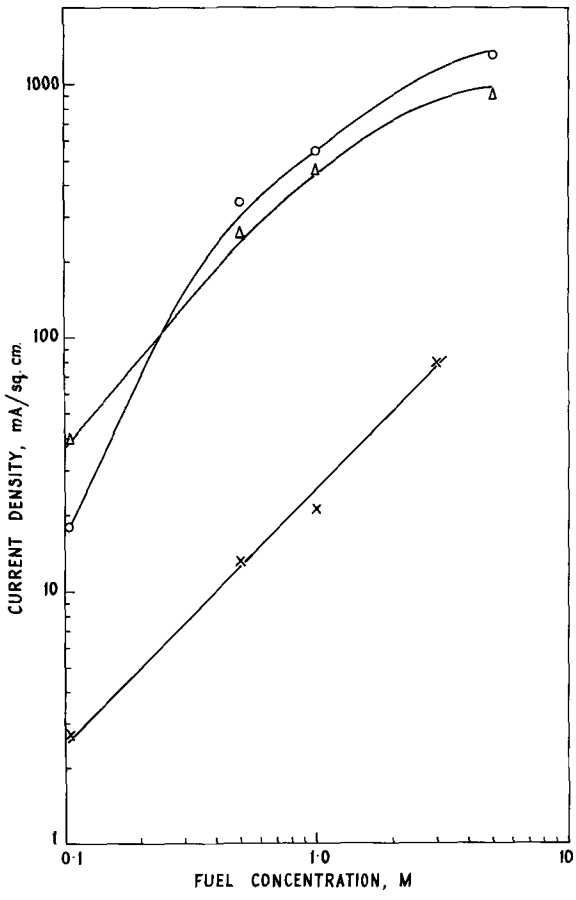

Fig. 7. Effect of fuel concentration on performance. At 60°C, 6.5 mg/cm² catalyst, 5% Sn. ×, Methanol at +0.3V to NHE. △, Formaldehyde at + 0.2V to NHE. ○, Formic acid at +0.2V to NHE.

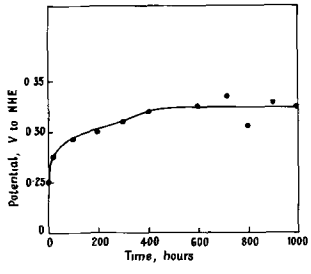

Fig. 8. Effect of operating time on electrode performance. At 60°C, 13 mg/cm² catalyst, 5.3% Sn, using 2M methanol.

so as to produce an increase in surface area. The maximum possible surface area for platinum black would be for the case where every atom was a surface atom. This area can be calculated from the relation $1/A = S/N \cdot n$ where A is the specific surface in m²/g, S is the site density in atoms/m², N is Avogadro's number, and n is the atomic weight of platinum. If a value of 1.1 x 10^{19} atoms/m² is assigned to S (11), A is 270 m²/g. The surface area of a typical electrodeposited platinum black can be estimated from the charge necessary to oxidize adsorbed hydrogen, and is 18 m²/g. Now the increase in catalytic activity may be seen (from Fig. 1) to be approximately three orders of magnitude, whereas the maximum possible increase in specific surface is a factor of 15. It is unlikely, then, that the improved activity of these catalysts is due to an increase in the specific surface area of the platinum black.

Some further evidence in favor of the redox mechanism was obtained from potential-time curves made at a constant current for platinum-tin electrodes in 0.5M sulfuric acid. Two of these are shown in Fig. 9. The curve for the platinum-tin deposit shows a large

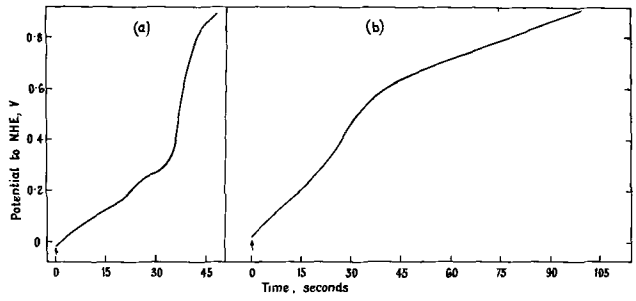

Fig. 9. Chronopotentiometry on platinum and platinum-tin: (a) 8.3 mg/cm² Pt black, (b) 9.6 mg/cm² Pt-Sn (3.3% Sn). Both in 0.5M sulfuric acid at 60°C. Current density = 10 mA/cm².

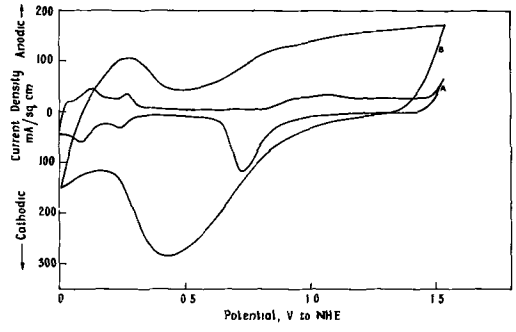

Fig. 10. Cyclic voltammetry on platinum and platinum-tin. In 0.5M sulfuric acid at 60°C, sweep rate 0.2V/sec. Curve A: 3.1 mg/cm² Pt. Curve B: 3.6 mg/cm² Pt-Sn (4.5% Sn).

increase in the charge necessary to oxidize the electrode, especially at potentials below 0.6V, while that used to oxidize the adsorbed hydrogen has decreased. The differences between platinum black and platinum-tin are even more clearly visible in the cyclic current-voltage curves of Fig. 10. These curves, representing the current flowing to a 1 cm² electrode cycled between zero and +1.6V to NHE show that oxide formation and reduction appears to extend to lower potentials on the platinum-tin electrode. These results give some support to the postulate that a redox oxide system is the cause of improved catalyst activity.

It is clear from Fig. 1 that the platinum-tin deposit is able to catalyze the oxidation of formaldehyde and formic acid more effectively than does a platinum-rhenium deposit. This could be related to the more favorable redox potential of the tin oxide system, as compared to the rhenium oxides. However, it is clear also that the rate of oxidation of methanol is very similar on both catalysts. To account for this it may be suggested that the rate of oxidation of methanol is limited by the rate of chemisorption rather than the rate of oxidation of the chemisorbed residues. Alternatively, the different compounds may give rise to different chemisorbed species, that for methanol being more difficult to oxidize.

Biegler and Koch (12) measured the adsorption rates of methanol on smooth platinum, and calculations based on the initial value of the rate show that it should be possible to chemisorb methanol sufficiently rapidly to achieve a current density of about 100 mA/cm², using 0.2M methanol at 25°C, with a catalyst loading of 1.7 mg/cm². The measured current density is 3 mA/cm² under these conditions, which makes it unlikely that chemisorption is the rate-limiting step. Breiter (13) has shown that the adsorbed intermediate has the same oxidation state in each case, but this does not prove that the species are identical. It is suggested that the chemisorbed methanol is less easily oxidized than the intermediates from formaldehyde and formic acid.

In terms of stability and activity, platinum-tin electrodeposits are effective catalysts for the oxidation of methanol, formaldehyde, and formic acid. The only property that might cause difficulty is the tendency to become passive at potentials of 0.2-0.3V. This can be overcome by the use of a ternary platinum-rhenium-tin deposit, and catalysts of this type have been used with some success in fuel cell systems operated on methanol or formaldehyde.

Acknowledgment

Helpful discussion with Dr. R. Woods in regard to the maximum possible surface area of platinum black is acknowledged.

Manuscript submitted Feb. 3, 1969; revised manuscript received July 1, 1969.

Any discussion of this paper will appear in a Discussion Section to be published in the June 1970 JOURNAL.

REFERENCES

1. O. J. Adlhart and K. O. Hever, U.S. Army Electronics Res. & Dev. Lab., Contract DA36-039 SC-90691. Report No. 4, 1/10/63-31/3/64.
2. B. L. Tarmy and associates, U.S. Army Electronics Res. & Dev. Lab., Contract DA36-039 AMC-00134(E). Report No. 3, 1/1/63-30/6/63.
3. K. J. Cathro, *This Journal*, **5**, 441 (1967).
4. K. J. Cathro, D. F. A. Koch, and H. R. Skewes, *Mechanical & Chemical Engineering Trans. Inst. Engineers, Australia*, p. 17 (May 1967).
5. U.S. Pat. 3,340,097.
6. Brit. Pat. 1,106,708.
7. G. H. Ayres and A. S. Meyer, *Anal. Chem.*, **23**, 299 (1951).
8. C. E. Heath, *Proc. Journées Internationales D'Etude Des Piles à Combustible, Brussels*, 1965, p. 99.
9. J. A. Shropshire, *This Journal*, **112**, 465 (1965).
10. M. Pourbaix, "Atlas D'Équilibres Electrochimiques à 25°C," p. 476, Gauthier-Villars & Cie, Paris.
11. L. Spenadel and M. Boudart, *J. Phys. Chem.*, **64**, 204 (1960).
12. T. Biegler and D. F. A. Koch, *This Journal*, **114**, 904 (1967).
13. M. W. Breiter, *J. Electroanal. Chem.*, **15**, 221 (1967).

Technical Notes

Phase Equilibrium Studies of Lithium Halide-Containing Electrolytes

Carl E. Johnson and Melvin S. Foster

Chemical Engineering Division, Argonne National Laboratory, Argonne, Illinois

The application of fused-salt mixtures as electrolytes in electrochemical cells has resulted in increased interest in their physical and chemical properties. A knowledge of these properties is important in selecting appropriate electrolytes since the choice depends on a variety of factors. For example, cells having low-melting cathode materials require low-melting electrolytes. Also, electrolytes with high electrical conductivities are needed to reduce ohmic losses within the cell. Fused alkali halides generally meet these requirements. Because thermodynamic stability with respect to the anode material is also an important consideration, electrolytes generally have been sought from among low-melting halide salts of the anode metal.

The electrochemical data of Hamer *et al.* (1) indicate, however, that under certain circumstances a mixed-cation electrolyte could be used in a galvanic cell. These data show that if the operating temperature of the cell or battery is restricted to temperatures below 500°C, it should be possible to use mixtures of alkali halides (lithium, potassium, rubidium, or cesium, but not sodium) as electrolytes for cells having lithium as the anode metal. Galvanic cells with lithium anodes are of particular interest because of their advantages of higher cell voltages and lower metal solubility in fused salts.

For a specific salt system, it would be highly advantageous to have a method of locating the minimum temperature, its corresponding chemical composition, and the general topological characteristics of the system with a minimum of effort. Such knowledge would greatly facilitate the choice of appropriate electrolytes for the electrochemical cells of interest. Although a more detailed investigation of the electrolyte composition in the region immediately surrounding the minimum-temperature composition would also be needed to ascertain the effects of slight compositional changes on the solidus temperature, such an investigation would be expedited by having a general knowledge of the characteristics of the system.

Accordingly, a study was undertaken to evaluate the usefulness of a perturbation theory, the conformal ionic solution theory (2), in calculating the complete liquidus surface of reciprocal salt systems, *i.e.* systems having two anions and two cations. This theory requires only limited information: the melting point, the heat of fusion, and the standard Gibbs free energy of formation of each component, and the eutectic temperature of each of the four nonreciprocal pairs in the system. The theory of conformal ionic solutions as applied to this problem has been outlined by Blander and Topol (3); a brief summary is given here.

For a reciprocal system

$$AC + BD \rightleftarrows AD + BC \qquad [1]$$

the excess free energy of mixing, $\Delta G_M{}^E$, for the three salts AC, BC, and BD necessary to define the system is given by

$$\Delta G_M{}^E = X_A X_D \Delta G^\circ + X_D \Delta G_{12}{}^E + X_C \Delta G_{34}{}^E + X_A \Delta G_{13}{}^E + X_B \Delta G_{24}{}^E + X_A X_B X_C X_D \Lambda \qquad [2]$$

where the X's are ion fractions and ΔG° is the standard Gibbs free energy change for Reaction [1]. The cation fraction of B is $X_B = n_B/(n_A + n_B)$ and the anion fraction of D is $X_D = n_D/(n_C + n_D)$ where n_A, n_B, n_C, n_D are the numbers of moles of the ions indicated. The expression for the excess free energy of mixing of the binary mixture of the salts i and j ($\Delta G_{ij}{}^E$), where AD is salt 1, BD is 2, AC is 3, and BC is 4, has been truncated to include only second-order terms, so that

$$\Delta G_{12}{}^E = X_A X_B \lambda_{12} \qquad [3]$$

and

$$\Delta G_{34}{}^E = X_A X_B \lambda_{34} \qquad [4]$$

The mixing parameters, λ_{ij}, depend only on the properties of the binary systems. The term Λ is approximated from quasi-lattice theory by

$$\Lambda = -(\Delta G^\circ)^2/2 \; ZRT \qquad [5]$$

where Z is a coordination number between 4 and 6. With the relation

$$RT \ln \gamma_i = \frac{\partial(n_k + n_e)}{\partial n_i} \Delta G_M{}^E = \frac{\partial(n_k + n_e)}{\partial n_k} \Delta G_M{}^E + \frac{\partial(n_k + n_e)}{\partial n_e} \Delta G_M{}^E \qquad [6]$$

where k and e are the constituent ions of component salt i, the activity coefficients, γ_i, of any component may be calculated from Eq. [2].

The liquidus temperature, T, is the temperature at which a solid component such as AD is in equilibrium with a solution in which the component has an activity, a. If we assume that the heat of fusion, L_i, for any component, i, is independent of temperature, then

$$R \ln a_i = -L_i (1/T - 1/T_{oi}) = R \ln X_k X_e \gamma_i \qquad [7]$$

where T_{oi} is the melting point of the pure salt.

Values of λ_{ij} are calculated from the known phase diagrams of the four nonreciprocal binary systems. For a given binary system, ij, the simplified assumption was made that

$$RT \ln \gamma_i = \lambda_{ij} N_j{}^2 \qquad [8]$$

and

$$RT \ln \gamma_j = \lambda_{ij} N_i{}^2 \qquad [9]$$

where N_i, N_j are mole fractions. Equations [8] and [9] were used with Eq. [7] to yield the following:

T (eutectic)

$$= [\lambda_{ij}(1 - N_i)^2 + L_i]/[(L_i/T_{oi}) - R \ln N_i] \qquad [10]$$

$$= (\lambda_{ij} N_i{}^2 + L_j)/[(L_j/T_{oi}) - R \ln (1 - N_i)] \qquad [11]$$

Using the measured eutectic temperature and the heats of fusion and melting points of the pure components as fixed points, Eq. [10] and [11] were solved simultaneously for λ_{ij} and the eutectic composition.

To derive the liquidus temperatures, Eq. [5], [6], and [7] were solved for the precipitation tempera-

Table I. Crystallization temperatures for the LiCl-LiI-KI system

Series I mole ratio LiCl:LiI 1:1		Series II mole ratio LiCl:LiI 3:7		Series III mole ratio LiI:KI 6:4	
m/o KI	Temp (°C)	m/o KI	Temp (°C)	m/o LiCl	Temp (°C
30.0	399.5	20.0	341.3	20.0	330.0
35.0	392.1	25.0	338.0		
47.3	436.8	31.5	330.0		
		38.3	346.1		

tures, T_i, of solid AD (component 1) to yield:

$$T_1[(L_1/T_{oi}) - R \ln X_A X_D] = L_1 + (1 - X_B X_C)\Delta G^\circ = X_B(X_B X_D + X_A X_C)\lambda_{12} + X_B X_C(X_B - X_A)\lambda_{34} + X_C(X_B X_D + X_A X_C)\lambda_{13} + X_B X_C(X_C - X_D)\lambda_{24} + X_B X_C(X_B X_D + X_A X_C - X_A X_D)\ [-(\Delta G^\circ)^2/2ZRT_1] \quad [12]$$

The liquid-solid equilibrium temperature for each of the components can be similarly calculated. For a given composition, that component with the highest liquidus temperature was selected as the component precipitating at the calculated liquid-solid equilibrium temperature. If this precipitation temperature is higher than the normal melting point for that specific component, the presence of a liquid-liquid miscibility gap is indicated. Equation [12] was solved with the aid of a CDC-3600 computer (program available on request), and the output data were fed to a Calcomp-580 incremental plotter for display.

One of the salt systems being considered for use as an electrolyte in lithium-anode galvanic cells is LiCl-LiI-KI. This system was chosen for investigation after a preliminary examination had indicated that it had a minimum melting point of 264°C, one of the lowest observed for ternary alkali halide mixtures. This ternary system, which consists of the binary eutectic systems LiCl-LiI, LiCl-KI, and LiI-KI, forms one half of the reciprocal LiCl-KI system. Therefore, it afforded an opportunity to test the usefulness of the conformal ionic solution theory for obtaining the required information with a minimum of experimental effort.

The theoretical calculations for the LiCl-LiI-KI system indicated a minimum temperature of 276°C at a composition of 6 m/o (mole per cent) LiCl, 62 m/o LiI, 32 m/o KI. This information was used to design eight thermal analysis experiments. These experiments, which were performed using apparatus and techniques that have been described elsewhere (4), provided solid-liquid equilibrium data for three pseudo-binary mixtures (Table I) which traversed the predicted minimum temperature-compositional regime.

A contour diagram of the liquidus isotherms for the LiCl-LiI-KI system, given in Fig. 1, was constructed

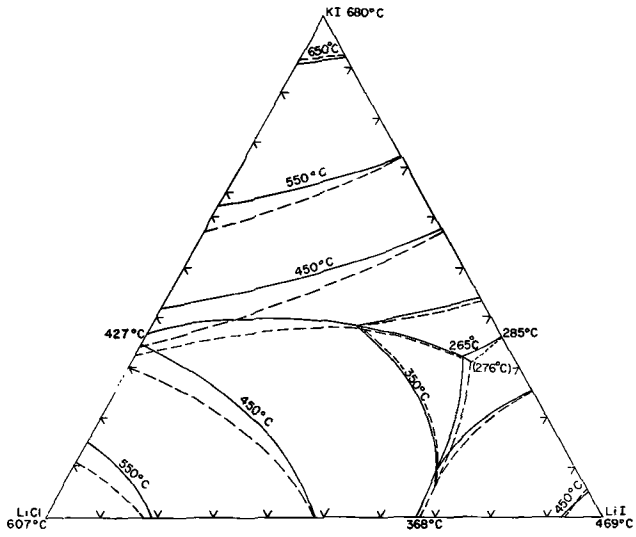

Fig. 1. LiCl-LiI-KI ternary system

from the pseudo-binary data of Table I and data for the three binary component systems. Superimposed on the figure, as dashed lines, are the isotherms predicted by the conformal ionic solution theory. It should be pointed out that the lack of agreement between calculation and experiment for the LiCl-KI binary is principally the result of the very limited experimental data available for this system. The experimental data indicated a eutectic composition of 8.5 m/o LiCl, 59 m/o LiI, 32.5 m/o KI; subsequent chemical analysis confirmed this composition. A single thermal analysis experiment at this composition showed no breaks other than a minimum at 265°C.

The good agreement between the calculated and experimental values and the few experiments required to obtain the necessary data make it clear that the conformal ionic solution theory offers significant saving of experimental effort in the selection of low-melting electrolyte mixtures.

Manuscript received June 30, 1969.

Any discussion of this paper will appear in a Discussion Section to be published in the June 1970 JOURNAL.

REFERENCES

1. W. J. Hamer, M. S. Malmberg, and B. Rubin, *This Journal*, **103**, 8 (1956).
2. M. Blander and S. J. Yosim, *J. Chem. Phys.*, **39**, 2610 (1963).
3. M. Blander and L. Topol, *Inorg. Chem.*, **5**, 1641 (1966).
4. C. E. Johnson, C. E. Crouthamel, and S. E. Wood, *ibid.*, **3**, 1487 (1964).

Heat Balances in Mercury-Cathode Chlorine Cells

Scott Lynn*

Department of Chemical Engineering, University of California, Berkeley, California

Substantial quantities of heat are released in both the electrolyzer and the decomposer of a mercury-cathode chlorine cell. Because the mercury stream leaving the one usually enters the other with little change in temperature, the two are not thermally independent. Nevertheless, it is generally convenient to treat the heat balances in the two pieces of equipment separately, with the matching of the mercury temperatures being the final constraint on the problem.

Many papers have appeared in recent years in which various commercially available mercury cells are described in detail. Sommers (8, 9) has described many cells for the purpose of comparison and Gardiner (2) has discussed at length the application of design principles to the development of a specific cell in re-

* Electrochemical Society Active Member.

cent years. The reader is referred to their work for a description of specific design features or operating conditions which may be imperfectly approximated by the generalized treatment of heat balances which follows.

Electrolyzer

In the electrolyzer, part of the sodium chloride in the brine stream is being continuously converted by electrolysis into chlorine and sodium amalgam.

$$NaCl(aq) + Hg \rightarrow Na(Hg) + \frac{1}{2}Cl_2(g) \qquad [1]$$

The enthalpy change of this endothermic reaction, ΔH_E, is +327.0 kj/mole Na. In typical commercial practice, the brine enters the cell nearly saturated (~0.26 w.f. NaCl) and at a temperature of 50°-70°C. It leaves the cell depleted by 10-20% and heated to 70°-90°C. The mercury enters the cell containing virtually no sodium, at 100°-125°C. It leaves the cell at the same temperature as the exiting brine with a sodium content of 0.15-0.45 w/o (weight per cent).

The heat balance for the electrolyzer may be written

$$E\bar{I}A_c = \frac{\bar{\epsilon I}A_c}{nF}\left[\Delta H_E + Cp_B M_{NaCl}\left(\frac{1-x_2}{x_1-x_2}\right)(t_2-t_1) + Cp_{Hg}M_{Na}\left(\frac{t_2'-t_1'}{x_2'-x_1'}\right) + \frac{\Delta H_v}{2}\left(\frac{p_{H_2O}}{\pi-p_{H_2O}}\right)\right] + A_o U_{av}(t_{av}-t_s) \qquad [2]$$

The symbols are listed in the Nomenclature and the value of the various physical properties and other quantities are given in Table I.

It is convenient to divide Eq. [2] by $\epsilon\bar{I}A_c/n\mathbf{F}$ and to evaluate the resulting terms individually:

$$\frac{n\mathbf{F}}{\epsilon}E = \Delta H_E + F_1(x, \Delta t) + F_2(x', \Delta t') + F_3(t_2) + F_4(t, t_s) \qquad [3]$$

where

$$F_1 = Cp_B M_{NaCl}\left(\frac{1-x_2}{x_1-x_2}\right)(t_2-t_1)$$

$$F_2 = Cp_{Hg}M_{Na}\left(\frac{t_2'-t_1'}{x_2'-x_1'}\right)$$

$$F_3 = \frac{\Delta H_v}{2}\left(\frac{p_{H_2O}}{\pi-p_{H_2O}}\right)$$

and

$$F_4 = \frac{n\mathbf{F}}{\epsilon\bar{I}A_c}A_o U_{av}(t_{av}-t_s)$$

The term F_1 corresponds to the increase in sensible heat of the brine. This quantity is a function of the temperature rise and the flow rate. The latter varies inversely with the change of sodium chloride content from cell inlet to outlet. F_2 corresponds to the change in sensible heat of the mercury stream and is directly analogous to F_1. F_3 is the heat required to saturate the chlorine leaving the cell with water vapor. F_4 is the rate of heat loss to the surroundings by natural convection and radiation.

In evaluating these terms, assumptions about the magnitudes of the quantities used must be made. Many of these are arbitrary and may be at variance with known data for a given cell. They are discussed in detail in the Appendix.

The functions F_1-F_4 are plotted in Fig. 1A-D for various values of the temperature and composition parameters. To determine the outlet temperature for operation of a cell, one must know the cell voltage, current efficiency, current density, the inlet temperatures of brine and mercury, and the change in com-

Table I. Physical properties and thermal quantities for heat-balance calculations on mercury-cathode cells

Quantity	Conditions	Value	Source
Cp_{H_2O}	70°C	4.186 j/g °C	(4)
Cp_B	0.26 w.f. NaCl @ 70°C	3.280 j/g °C	(3)
Cp_{Hg}	100°C	0.1375 j/g °C	(3)
D	Decomposer diameter	0.8m	Assumed
ΔH_D	25°C	−122.6 kj/mole Na	(7)
ΔH_E	25°C	+327.0 kj/mole Na	(7)
ΔH_v	0.24 w.f. NaCl @ 75°C	42.03 kj/mole H_2O	(4)
$\Delta H_v'$	0.5 w.f. NaOH @ 120°C	40.37 kj/mole H_2O	(4)
K	Decomposer volume/cell current	0.0075 m³/kA	Assumed
p_{H_2O}	0.24 w.f. NaCl @ 75°C	0.80 $p°_{H_2O}$	(5)
p'_{H_2O}	0.5 w.f. NaOH @ 120°C	0.172 $p°_{H_2O}$	(5)
U_{av}	Average for electrolyzer	14.0 w/m² °C	(6)
U'_{av}	Average for decomposer	23.4 w/m² °C	(6)

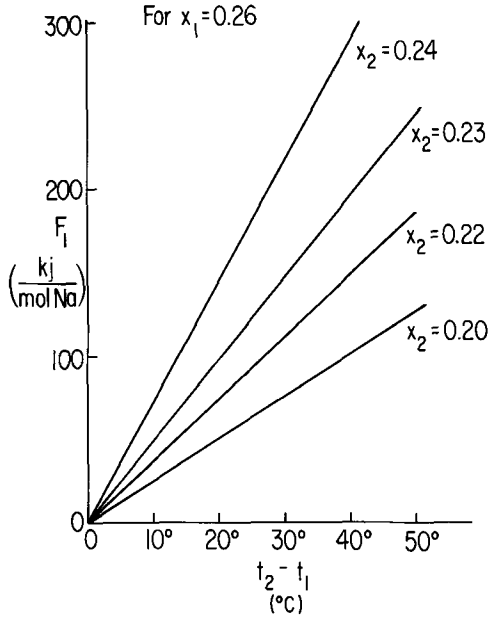

Fig. 1A. Heat effects in electrolyzer: heat content of brine

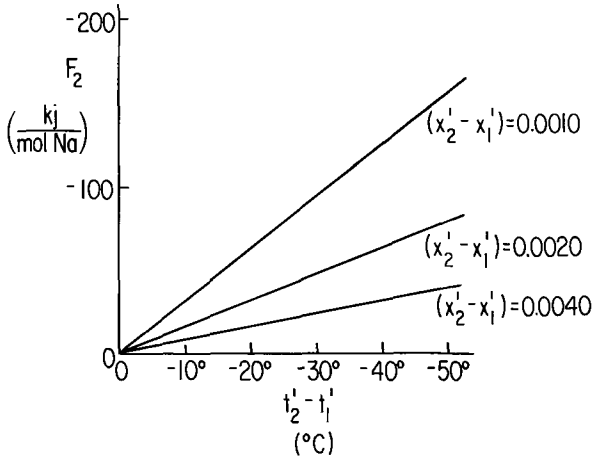

Fig. 1B. Heat effects in electrolyzer: heat content of mercury

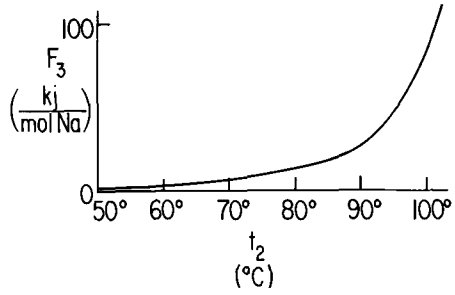

Fig. 1C. Heat effects in electrolyzer: heat to vaporize water

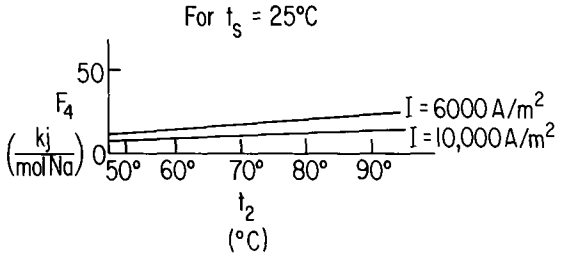

Fig. 1D. Heat effects in electrolyzer: heat loss to surroundings

position which will occur in both streams. By trial and error, one then finds the outlet temperature which satisfies Eq. [3].

Decomposer

In the decomposer, sodium amalgam reacts with water to form sodium hydroxide and hydrogen:

$$Na(Hg) + H_2O \rightarrow NaOH + \frac{1}{2}H_2 + Hg \qquad [4]$$

When enough additional water is supplied to make 50% caustic, the enthalpy change, ΔH_D, of this exothermic reaction is —122.6 kj/mole Na. In most modern cells, the decomposer is a packed bed of graphite chunks having dimensions in the range of 5-15 mm. The volume of the packing varies from 0.005 to 0.010 m³/kA of cell current.

The heat balance in the decomposer may be written

$$-\Delta H_D = F_5(\Delta x', \Delta t') + F_6(x_{NaOH}, t_o') + F_7(x_{NaOH}, t_o') + F_8(t_o', t_s') \qquad [5]$$

where

$$F_5 = Cp_{Hg}M_{Na}\left(\frac{t_o' - t_2'}{x_2' - x_1'}\right)$$

$$F_6 = Cp_{H_2O}M_{NaOH}\left(\frac{1 - x_{NaOH}}{x_{NaOH}}\right)(t_o' - t_s)$$

$$F_7 = \frac{\Delta H_v'}{2}\left(\frac{p'_{H_2O}}{\pi - p'_{H_2O}}\right)$$

$$F_8 = \frac{n\mathbf{F}}{\epsilon \bar{I} A_c}A_o'U_o'(t_o' - t_s) = \frac{n\mathbf{F}}{\epsilon}\left(\frac{4K}{D}\right)U_o'(t_o' - t_s)$$

Equation [5] equates the heat of reaction to the sum of F_5, the increase in sensible heat of the mercury; F_6, the increase in sensible heat of the water; F_7, the heat required to saturate the hydrogen with water vapor; and F_8, the heat lost to the surroundings by convection and radiation.

Because of the stirring effect of the hydrogen and the very long residence time of the caustic solution, there is very little variation in either temperature or caustic concentration in a decomposer. For purposes of calculation both may be assumed constant at the values at the outlet. The assumptions made in making the calculations are given in the Appendix. The functions F_5-F_8 are plotted in Fig. 2A and B as functions of the concentration and temperature parameters. Knowing the temperature of the entering amalgam and its change in sodium content, one finds by trial and error a value of t_2' which satisfies Eq. [5].

Example

Danna (1) cites the data in Table II as being typical of the Olin E-11 mercury cell.

From the data in Table II, one may find the values of F_5-F_8 listed in Table III by trial and error from Fig. 2A and B.

Danna (1) reports the temperature of the mercury leaving the decomposer to be 125°C. Lowering the value of t_1' would increase the difference between the

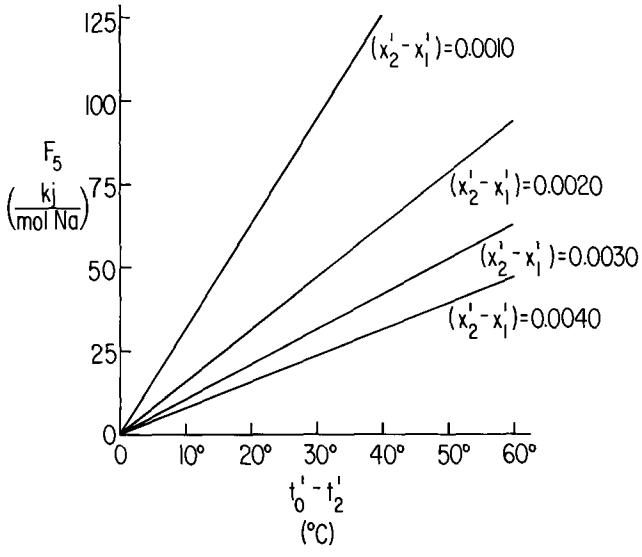

Fig. 2A. Heat effects in decomposer: heat content of mercury

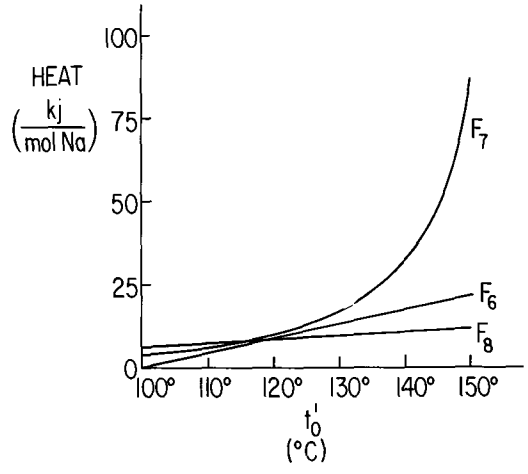

Fig. 2B. Heat effects in decomposer: F_6—heat content of caustic, F_7—heat to vaporize water, F_8—heat loss to surroundings.

heat leaving the cell $\left(\Delta H_E + \sum_{i=1}^{4} F_i\right)$ and the power input $(n\mathbf{F}E/\epsilon)$. The discrepancy may be due to a loss of heat by the amalgam stream between the cell outlet and the decomposer inlet or to the manner in which the data were averaged.

Conclusions

The calculations tabulated in Table III show that in the decomposer of this mercury-cathode chlorine

Table II. Typical operating data for the Olin E-11 mercury cell (1)

E = 4.26V	t_1 = 47°C	x_1 = 0.260	x_1' = 0.0003
$\bar{I}$ = 10.0 kA/m²	t_2 = 88°C	x_2 = 0.220	x_2' = 0.0021

Table III. Example of heat balance calculations using data from Table II

Let t_o' = 132°C	Let t_1' = 132°C
F_5 = 77 kj/mole Na	F_1 = 153 kj/mole Na
F_6 = 18	F_2 = −77
F_7 = 18	F_3 = 24
F_8 = 10	F_4 = 14
123 kj/mole Na	ΔH_E = 327
	441 kj/mole Na

$\frac{n\mathbf{F}E}{\epsilon}$ = 434 kj/mole Na for E = 4.26V and ϵ = 95%.

cell about 63% of the heat of reaction is carried out by the mercury stream. The mercury will in general be well above 100°C, a fact which must be taken into account in the design of the mercury pump and piping system. The sensible heat of the mercury stream (F_2) entering the electrolyzer adds significantly (about 72%) to the heat ($n\mathbf{F}E/\epsilon - \Delta H_E$) which is dissipated there. Heat losses to the surroundings play a small role in either balance, being less than 10% of the energy released in the decomposer and also less than 10% of the sensible heat of the brine (F_1) in the electrolyzer.

APPENDIX

In deriving Eq. [3] and [5], a number of simplifying assumptions were made, some arbitrarily and some to facilitate the calculations. In calculations for a specific cell, the reader may wish to change them to fit his own case.

The heats of reaction and all physical properties were assumed constant over the range of temperatures considered. The heats of vaporization were calculated for 75°C for brine and 120°C for caustic using the enthalpy data of Keenan and Keyes (4) and the vapor pressure data of MacMullin (5). In writing the expression for F_3, it is assumed that the water vapor leaving the cell is in equilibrium with the exit brine with respect to temperature. The variation of vapor pressure with brine composition is not large in the range of interest, so a constant ratio of $p_{H_2O}/p^o_{H_2O}$ was taken. The vapor pressure of 50% caustic was calculated in a similar manner.

The external area, A_o, of the electrolyzer was arbitrarily assumed to be 2.2 times the area of the cathode, A_c. Half of this area was assumed to be covered with rubber 8 mm thick and to have the heat-transfer characteristics of a horizontal plate facing up (6). The other half was assumed to be a horizontal plate facing down (6). The heat-transfer coefficients due to convection and radiation, and the thermal resistance of the rubber covering were the only factors considered to be of importance in estimating the heat loss from the cell. The surroundings were assumed to be at 25°C. A more extensive treatment was not considered justified in view of the small fraction of the total heat balance which is represented by F_4.

The decomposer was assumed arbitrarily to be a vertical cylinder with a diameter of 0.8m. Only the sides were considered in the heat-transfer area, but transfer by both radiation and convection was assumed to occur (6). K, the ratio of the volume of the decomposer to the cell current, was taken arbitrarily to be 0.0075 m^3/kA.

NOMENCLATURE

A_c	Area of cathode
A_o	Area of electrolyzer (assumed to be 2.2 A_c)
A_o'	Area of decomposer
Cp	Heat capacity
D	Diameter of decomposer (assumed to be 0.8m)
E	Cell voltage, anode stem to cathode plate
F	Function from Eq. [3] or [5]
$\mathbf{F}$	Faraday, 96,500 A-sec
ΔH	Enthalpy change of Eq. [1] or [4]
ΔH_v	Heat of vaporization of water
$\bar{I}$	Cathodic current density
K	Ratio of decomposer volume to cell current
M	Molecular weight
n	Electrons exchanged in reaction [1] or [4]
p_{H_2O}	Vapor pressure of water over brine
$p^o_{H_2O}$	Vapor pressure of pure water
p'_{H_2O}	Vapor pressure of water over caustic
t_1, t_2	Brine temperature at inlet and outlet of electrolyzer
t_1', t_2'	Mercury temperature at inlet and outlet of electrolyzer
t_{av}	$(t_1 + t_2)/2$
t_o'	Temperature decomposer
t_s	Temperature of surroundings
U	Over-all heat transfer coefficient
x_1, x_2	Weight fraction NaCl at inlet and outlet of electrolyzer
x_1', x_2'	Weight fraction Na in mercury at inlet and outlet of electrolyzer
ϵ	Current efficiency
π	Atmospheric pressure

Manuscript submitted April 1, 1969; revised manuscript received Aug. 8, 1969. This was Paper 173 presented at the New York Meeting, May 4-9, 1969.

Any discussion of this paper will appear in a Discussion Section to be published in the June 1970 JOURNAL.

REFERENCES

1. P. A. Danna, Olin Mathieson Chemical Co., Personal communication, July 1969
2. W. C. Gardiner, *Electrochem. Technol.*, **1**, 71 (1963).
3. International Critical Tables, McGraw-Hill, New York (1928).
4. J. H. Keenan and F. G. Keyes, "Thermodynamic Properties of Steam," John Wiley & Sons, Inc., New York (1948).
5. R. B. MacMullin, *This Journal*, **116**, 416 (1969).
6. W. H. McAdams, "Heat Transmission," 2nd Ed., McGraw-Hill Book Co., Inc., New York (1952).
7. "Selected Values of Chemical Thermodynamic Properties," Circular 500, National Bureau of Standards (1952).
8. H. A. Sommers, *Electrochem. Technol.*, **5**, 108 (1967).
9. H. A. Sommers, *ibid.*, **6**, 124 (1968).

Erratum

In the paper "β-Silicon Carbide Films" by P. Rai-Choudhury and N. P. Formigoni which was published on pp. 1440-1443 of the October 1969 issue of the JOURNAL, Vol. 116, No. 10, the caption for Fig. 2, p. 1441, should read as follows: "Electron diffraction pattern of a β-SiC film grown on (100) Si substrate; the film is discontinuous showing a strong (100) orientation."

Electrochemical Dissociation of Water Vapor in Solid Oxide Electrolyte Cells

I. Thermodynamics and Cell Characteristics

H. S. Spacil* and C. S. Tedmon, Jr.*

General Electric Research and Development Center, Schenectady, New York

ABSTRACT

This paper describes the dissociation of water vapor in high-temperature, solid oxide electrolyte cells. The characteristics of these cells are related to a composition-dependent open-circuit voltage, which can be obtained from thermodynamic considerations, to ohmic resistance, and to mass transport overvoltages. The problem of maintaining a heat balance in a system consisting of such cells is considered in terms of the heat loss through the leads connecting the cells with the surroundings. A conclusion is that the electrical energy requirement for dissociation can be reduced substantially by series connection of individual cells within the high-temperature region of the system, but that ohmic resistance limits the optimized current density through the electrolyte to values well below the maximum values that are feasible.

A recent development in the science and technology of solid oxide electrolyte cells is the application of such cells for the electrochemical dissociation of water vapor (1-3). The practical motivation for this application is the generation of inexpensive and pure hydrogen (3-4). It is the purpose of this paper to provide a definitive quantitative description of the thermodynamic and electrochemical characteristics of these cells for the various possible modes of operation. In a subsequent paper (5), the authors discuss materials, design, and fabrication problems of such cells, in the contexts of both single cells, and also multicell batteries, or "stacks."

In the first section of this paper, a generalized thermodynamic treatment of a high-temperature electrochemical cell system is presented. The analysis, subject only to the restrictions that it applies to electrochemical cells with invariant electrolytes and gaseous reactants and products, yields relationships between cell parameters in a form that is especially useful for consideration of steady-state systems which show large composition changes in going from reactants to products. In addition, this approach, in its general form, is independent of the nature of the electrode reactions. This feature is useful in dealing with water vapor dissociation cells, since these can be operated in various modes, each having different restrictions on the electrode reactions. It should be noted that this treatment would also be applicable to high-temperature fuel cell systems, but, due to the specialized nature of these, a different and more detailed analysis has been shown to be useful (6).

In succeeding sections, appropriate parameters for characterization of gas compositions at the cathode and anode are presented. Then these are used to apply the thermodynamic analysis specifically to water vapor dissociation cells employing oxygen ion electrolytes; two possible anode reactions are treated separately. Predictions of cell characteristics are compared with experimental results.

The final section of this paper presents a quantitative analysis of system heat balance. The general problem here is closely related to that of any high-temperature electrochemical, thermoelectric, or thermionic system, namely, the transmission of electric power between the high-temperature portion of the system and the ambient temperature surroundings while minimizing heat losses through the transmission leads. Results are presented for a representative system and used to demonstrate the necessity for achieving intercell connections in the high-temperature region, as well as for optimizing lead geometry.

* Electrochemical Society Active Member.
Key words: dissociation, water vapor, oxide electrolyte.

General Thermodynamics

A generalized high-temperature electrochemical cell system is shown schematically in Fig. 1. A single cell will be considered initially. Gaseous reactants, with molar flow rates $\dot{m}_{in}$ and temperatures T_{in} react electrochemically in an isothermal zone at temperature T to form gaseous products with molar flow rates $\dot{m}_{out}$ and temperatures T_{out} and to generate heat at a net rate $\dot{Q}$. A current I is supplied to the cell at a voltage E; with this convention, positive values of I and E represent a consumption of energy at a rate $\dot{W} = EI$, in watts, by the cell. The electrolyte composition is assumed to be invariant, as will be the case with solid oxides, and the gases are assumed to be thermally perfect so that their enthalpy contents are independent of pressure.

The net flow rate of some substance, or combination of substances, into or out of the system will be of interest. For the specific case of water vapor dissociation, this will be the net flow rate of water vapor which is dissociated at the cathode. In the general case, this substance can be termed the critical component, and its molar flow rate denoted by $\dot{m}^*$. This flow rate then provides a base to which other mass and energy flow rates can be referred. This steady-state approach is useful when considering the effects of irreversible phenomena, such as heat loss, as is shown subsequently.

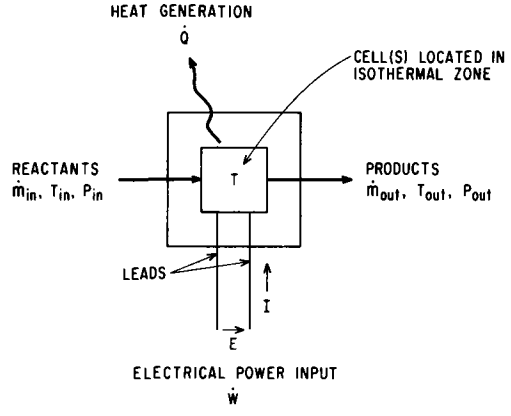

Fig. 1. Generalized high-temperature electrochemical system

Gibbs free energy change.—For the electrochemical reaction at temperature T, the rate of Gibbs free energy change for the system is $\dot{G}_T$. The partial molar Gibbs free energies of the species present can be summed to give this quantity relative to $\dot{m}^*$ as

$$\dot{G}_T/\dot{m}^* = \Delta G^{o*}{}_T + \sum_{out} [RT \sum_{s} x_s \ln (x_s P_{out})] \dot{m}_{out}/\dot{m}^* - \sum_{in} [RT \sum_{s} x_s \ln (x_s P_{in})] \dot{m}_{in}/\dot{m}^* \quad [1]$$

where $\Delta G^{o*}{}_T$ is the difference between the standard Gibbs free energies of formation of the products and reactants at temperature T, per mole of the critical component entering or leaving the cell. The summation over the index s is a summation of the product of the mole fraction x_s of each molecular species present in the product and reactant streams, and the logarithm of the same mole fraction multiplied by the total pressure, P_{out} or P_{in}, of each stream. The factor R is the gas constant per mole. The two summations are obviously entropy terms and, for equal total pressures on both sides of the electrolyte, will represent the entropy of mixing each reactant and product stream.

By neglecting frictional energy losses in the gas streams, an extension of the usual expression for the reversible electrical work obtainable in an isothermal process (7) allows an average open-circuit voltage for the cell to be obtained as

$$\overline{E}_o = (\dot{G}_T/\dot{m}^*)/z^*\mathbf{F} \quad [2]$$

where z^* is the equivalents per mole (in terms of electrons transferred through the external circuit) of the critical component, and $\mathbf{F}$ is the Faraday constant in coulombs per equivalent; $\dot{G}_T/\dot{m}^*$ must be expressed in consistent units of joules/mole. This voltage is a purely thermodynamic quantity since cell geometry and flow directions do not enter into its definition. We have termed it an average voltage since it applies to a cell in which finite changes occur in the composition of the gases passing through the cell. This composition change results from a finite cell current so that $\overline{E}_o$ varies with cell current for given reactant flow rates. Thus only the static value of $\overline{E}_o$ at zero current will be equal to the open-circuit voltage due to unchanged reactants as introduced into the cell. Appendix I shows that the value of $\overline{E}_o$ given by [2] is that of a cell with uniform current density, and which is so large that end effects can be neglected. The first of these conditions applies approximately to real single cells in which electrolyte resistivity causes the major voltage drop across the cell, and to "stacks" of series-connected cells of equal area with the same current flowing through each cell. The second condition applies to cells whose linear dimension perpendicular to the electrolyte surface is small compared to the linear dimension parallel to the direction of gas flows; this criterion is generally satisfied by the geometry of real cells. To the extent that $\overline{E}_o$ represents the average open-circuit voltage of a real cell, it could be measured experimentally in the absence of mass transport or adsorption effects by a current interruption technique. Also, with the polarity conventions used, $\overline{E}_o$ is a minimum voltage that must be overcome in order to drive current through the cell; a negative value for $\overline{E}_o$ thus indicates a cell that will operate spontaneously.

Enthalpy change.—The rate of enthalpy change for the system is $\dot{H}$, which can be expressed relative to $\dot{m}^*$ as

$$\dot{H}/\dot{m}^* = \Delta H^{o*}{}_T + \sum_{out} [x_s (H^o{}_{T_{out}} - H_T{}^o)_s] \dot{m}_{out}/m^* - \sum_{in} [x_s (H^o{}_{T_{in}} - H_T{}^o)_s] \dot{m}_{in}/\dot{m}^* \quad [3]$$

where $\Delta H^{o*}{}_T$ is the difference between the standard enthalpies of formation of the products and reactants at temperature T, per mole of the critical component entering or leaving the cell. The summation over the index s is a summation of the product of the mole fraction x_s of each molecular species present in the product and reactant streams, and the difference in standard molar enthalpy content for that species. The latter is the difference between the enthalpy content at the stream temperature, $H^o{}_{T_{out}}$ or $H^o{}_{T_{in}}$, and the enthalpy content at the cell temperature, $H^o{}_T$.

By analogy with $\overline{E}_o$, the rate of enthalpy change can be related to a voltage, for convenience in formulation of the expression for the net heat generation rate, by

$$\overline{E}_H = (\dot{H}/\dot{m}^*)/z^*\mathbf{F} \quad [4]$$

where $\dot{H}/\dot{m}^*$, like $\dot{G}_T/\dot{m}^*$, must be expressed in consistent units of joules/mole. Reactant and product stream temperatures must be specified to evaluate $\overline{E}_H$. If these temperatures were the same as the cell temperature, then the last two terms on the right-hand side of Eq. [3] vanish, and the resultant value of $\dot{H}/\dot{m}^*$ applies to the electrochemical reaction at temperature T. Under these conditions, the value of $\overline{E}_H$ from Eq. [4] can be denoted by $\overline{E}_H(T)$; a positive value of $\overline{E}_H(T)$ indicates an endothermic cell reaction, while a negative value indicates an exothermic cell reaction. While the value of $\overline{E}_H(T)$ does not apply to the complete cell system with reactants and products at temperatures which differ from the cell temperature, this value does provide a guide to heat effects in the cell itself.

Electrical and thermal characteristics.—The total current I through the cell is the product $z^*\dot{m}^*\mathbf{F}$. Denoting the total active electrolyte area by A, the average current density $\bar{j}$ is I/A. Neglecting lead resistances for the moment, and with the sign convention of Fig. 1, the total cell voltage can be written in terms of $\bar{j}$ as

$$E = \overline{E}_o + r\bar{j} \quad [5]$$

where r is the apparent specific resistance of the cell. This quantity is the resistance of a hypothetical cell of unit area which has the same electrical characteristics as the actual cell. It will, in general, include contributions from electrode resistance and nonohmic overvoltages, but in many high-temperature cells the latter are often small or negligible (6). The energy input to the cell, per mole of the critical component, is $\dot{W}/\dot{m}^*$, which can be rewritten as $z^*\mathbf{F}E$. Thus the energy input is directly proportional to E, and will be influenced by both $\overline{E}_o$ and r. Finally, neglecting energy losses due to friction in gas flow, the net heat generation rate, $\dot{Q}$, will be the sum of $-\dot{H}$ and $\dot{W}$. This rate can be then expressed per unit of cell area in terms of $\bar{j}$ as

$$\dot{Q}/A = (-\overline{E}_H + \overline{E}_o + r\bar{j})\bar{j} \quad [6]$$

Equations [2], [4], [5], and [6] have been presented for a single cell. If the system of Fig. 1 were extended to include several cells in parallel, these same equations would apply to each cell. If several cells in series are considered, the equations still apply on the average to each cell, even though no one particular cell would necessarily have the voltage and heat generation rates given by these equations which are based on over-all compositional changes. The energy input per mole of the critical component will likewise be given by $z^*\mathbf{F}E$ regardless of the actual cell arrangement.

Water Vapor Dissociation in Oxide Electrolyte Cells

Taking the amount of water vapor dissociated at the cathode as the critical component, z^* is 2 for an electrolyte conducting by O^{--} ions, so that the electri-

cal energy requirement per mole of water vapor dissociated is then 2 $\mathbf{F}E$. This will be true regardless of the nature of the anode reaction.

Solid oxide electrolytes based on stabilized zirconia having a cubic fluorite structure typically exhibit resistivities (due to O^{--} conduction) of the order of 10 ohm-cm at temperatures of 1000°C; the energy of activation for the conduction process is about 20 kcal/mole (8). These electrolytes can readily be fabricated in thicknesses down to about 0.5 mm; the electrolyte contribution to the specific resistance is the product of resistivity and thickness, and thus should be of the order of 0.5 ohm-cm^2 for the conditions quoted. Current densities in the range of 1-2 A/cm^2 should then cause the $r\bar{j}$ term in Eq. [5] to contribute about 1V to the value of E. The exact value of $\bar{E}_0$ can therefore be expected to have a significant influence on the total cell voltage. Theoretical and experimental values for $\bar{E}_0$ are presented in the following sections. Heat balance considerations, however, can strongly affect system performance; a detailed discussion is presented in a subsequent section, and continued in Part II (5).

Characterization of cathode gas.—Since water vapor and hydrogen are the only species present at the cathode, the mole fraction of water vapor at the cathode, y_C, can be used to describe the composition of the gas mixture at this electrode. Superscripts i and f are used to denote the initial (entering) and final (exiting) compositions, respectively. The flow rate of reactants to the cathode can conveniently be described in terms of the average current density that would be required to dissociate all of the water vapor entering the cell, plus the amount of water vapor that would be present if the hydrogen entering the cathode side of the cell (to prevent cathode oxidation) were in the form of water vapor. Denoting this current density by J_C, the value of $\bar{j}$ can be expressed as

$$\bar{j} = J_C(y_C{}^i - y_C{}^f) = J_C y_C{}^i x_C \qquad [7]$$

where x_C is the fraction of entering water vapor dissociated in the cell. Since x_C cannot exceed unity, the maximum value of $\bar{j}$ is thus $J_C y_C{}^i$.

Since $y_C{}^i$ and x_C characterize the initial composition and the composition change taking place in the cathode gas, the value of $\bar{E}_0$ for an oxygen anode cell will depend on these two quantities. The factor J_C cancels from Eq. [1], as it should if $\bar{E}_0$ is a purely thermodynamic quantity, when molar flow rates are expressed in [1] in terms of J_C, $y_C{}^i$, and either x_C or $y_C{}^f$. Appendix II indicates the nature of this substitution.

Oxygen Anode Dissociation Cell

The most straightforward type of dissociation cell is one in which the anode reaction involves the formation of O_2, and is

$$O^{--}\ (\text{electrolyte}) \rightarrow \frac{1}{2}O_2(\text{gas}) + 2e^-\ (\text{electrode})$$

Calculated voltages.—The value of $\bar{E}_0$ for an oxygen anode cell at a given temperature will depend on the initial composition of the cathode gas. Figures 2 and 3 show the variation of $\bar{E}_0$ as a function of x_C for this type of cell, calculated using Eq. [1] and [2] for three different initial compositions of the cathode gas at a single temperature, and for four different temperatures at the same initial composition, and a total anode pressure of 1 atm. The values at the left side of each plot, where x_C is zero, are the static open-circuit voltages that would be observed with no current flow. Figure 3 clearly shows the advantages of dissociation at higher temperatures as regards decreasing the open-circuit voltage. The value of $E_H(T)$ is about 1.29V for operating temperatures around 1000°C. This is of course due to the endothermic nature of the dissociation of water vapor to its elements, which is the overall cell reaction in this case. Since $\bar{E}_H(T)$ is greater in magnitude than $\bar{E}_0$, reference to Eq. [6] shows that at low current densities the cell itself is endothermic.

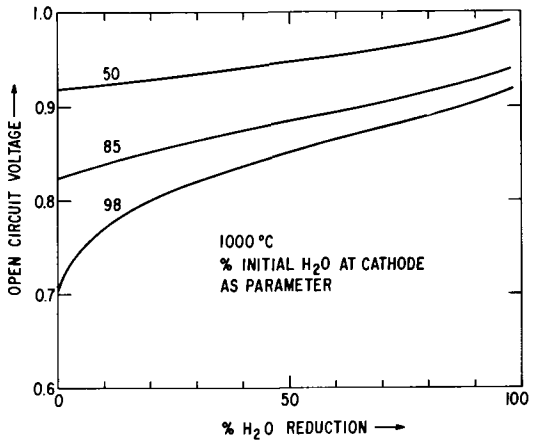

Fig. 2. Computed average open-circuit voltages for water vapor dissociation in an oxygen anode cell at various initial H_2O concentrations.

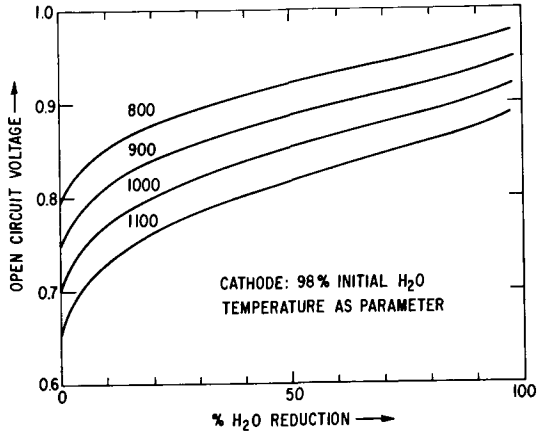

Fig. 3. Computed average open-circuit voltages for water vapor dissociation in an oxygen anode cell at various cell temperatures.

Depolarized Anode Dissociation Cell

The open-circuit voltage of a dissociation cell can be reduced by introducing a reducing fuel gas to the anode so that the anode reaction becomes

$$O^{--}\ (\text{electrode}) + \text{fuel (gas)} \rightarrow \text{oxidized fuel (gas)} + 2e^-\ (\text{electrode})$$

The low oxygen potential of the fuel in this type of cell will obviously reduce $\bar{E}_0$, as compared to an oxygen anode cell, and can thus reduce the energy required for dissociation.

Characterization of anode gas.—Fuels derived from hydrocarbons are of the most interest. Two parameters useful to describe such fuels in high-temperature cells are the normalized hydrogen-to-carbon ratio, and the relative oxidation. These quantities, denoted by h and y_A, respectively, can be most simply expressed in terms of the atom fractions of total carbon, hydrogen, and oxygen content in the fuel gas. Representing the latter by f_C, f_H, and f_O, the values of h and y_A as fractions are given by

$$h = f_H/(f_C + f_H) \qquad [8]$$

$$y_A = 2(f_O - f_C)/(2f_C + f_H) \qquad [9]$$

The relative oxidation can thus be considered as a normalized quantity that is proportional to the extent that CO and H_2 in a fuel gas have been converted to

CO_2 and H_2O. Neither of these parameters, nor the resulting open-circuit voltage, is sensitive to the presence of an inert diluent in the fuel gas. Any diluent present, however, may affect mass transport in the gas phase. The flow rate of reactants to the anode, exclusive of diluent, can then be conveniently described in terms of the current density that would be required to oxidize all of the carbon plus hydrogen entering the anode side of the cell if this carbon and hydrogen were in the form of CO and H_2. Denoting this current density by J_A, the value of $\bar{j}$ can be expressed as

$$\bar{j} = J_A(y_A{}^f - y_A{}^i) = J_A(1 - y_A{}^i)x_A \qquad [10]$$

where superscripts i and f indicate initial (entering) and final (exiting) compositions, respectively, and x_A is the fraction of the entering fuel oxidized in the cell. Diluent flow rates can be expressed relative to J_A in any desired fashion, such as a ratio of diluent to entering fuel. Since x_A cannot exceed unity, an additional constraint on the cell in this case is that the value of $\bar{j}$ cannot exceed $J_A(1 - y_A{}^i)$. The value of $\bar{E}_0$ will now depend on $y_A{}^i$ and x_A as well as on $y_C{}^i$ and x_C.

Calculated voltages.—The value of $\bar{E}_0$ at a given temperature will now depend on the initial compositions of both the cathode and anode gases, including the value of h for the fuel. Figure 4 shows the *loci* of values of constant $\bar{E}_0$ values, obtained using Eq. [1] and [2], in the x_C-x_A plane for specific initial gas compositions at 1000°C employing a substitution similar to that outlined in Appendix II. The value of −0.365V at the origin, where x_C and x_A are both zero, is the static open circuit that would be observed with no current flow.

The value of $\bar{E}_H(T)$ for a depolarized anode cell will be much smaller in magnitude than for an oxygen anode cell; the over-all cell reaction involves simultaneous fuel oxidation as well as water vapor dissociation, and the enthalpy changes at cathode and anode nearly cancel. There is a slight dependence of the enthalpy change on x_C; typical values of $\bar{E}_H(T)$ for the same conditions as given in Fig. 4 are from −0.05 to −0.06V. Thus the over-all cell reaction is slightly exothermic, but the effect is generally overshadowed by the enthalpy content changes of reactants and products if these enter and leave the cell system at different temperatures.

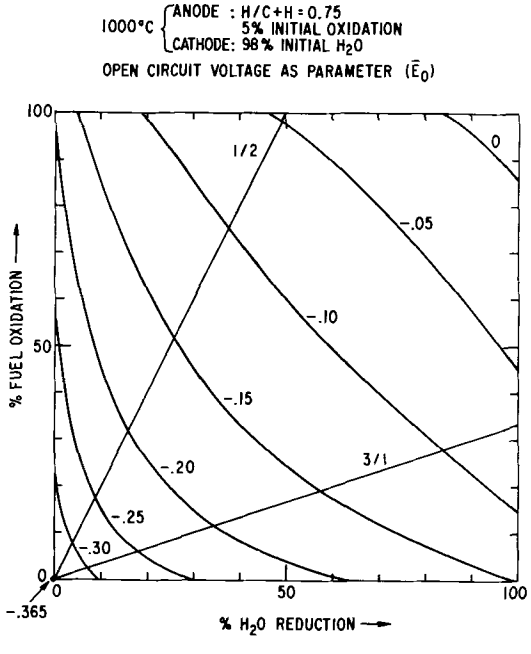

Fig. 4. Computed average open-circuit voltages for water vapor dissociation in a depolarized anode cell. Operating lines at fuel/water vapor flow rate ratios of 1/2 and 3/1 are superimposed.

Operating lines.—Equations [7] and [10] must describe the same current density. They can thus be combined to give the relation

$$J_C y_C{}^i x_C = J_A(1 - y_A{}^i)x_A \qquad [11]$$

This is a straight line in the x_C-x_A plane, and can be superimposed on a plot of $\bar{E}_0$ values as shown in Fig. 4 to give an operating line that will be followed by the cell with a constant ratio of fuel to water vapor flow rates. For a slope of unity, the operating line will describe cell operation which can simultaneously dissociate all the water vapor and oxidize all the fuel; generally either water vapor or fuel will be a limiting reactant. Figure 4 illustrates operating lines for fuel/water vapor flow rate ratios of 1/2 (fuel oxidation limiting at 50% water vapor reduction) and 3/1 (water vapor reduction limiting at 33% fuel oxidation).

Self-driven dissociation cells.—The cell voltage E of a short-circuited depolarized anode cell will obviously be zero. Applying this conditon to Eq. [5] and combining [5] and [7] yields the condition for x_C in this mode of operation as

$$-\bar{E}_0/x_C = rJ_C y_C{}^i \qquad [12]$$

Since $\bar{E}_0$ can be negative for a depolarized anode cell, the left-hand side of [12] can be positive. This self-driven mode of operation has been observed experimentally; the cell becomes, in effect, a fuel cell with water vapor as the oxidant. The operating line specified by Eq. [11] can be used to solve [12] graphically. But, even without following such an approach in detail, it is apparent that the low open-circuit voltages limit this type of operation to small current densities with the electrolytes generally available. Hence these cells are not discussed further here.

Experimental Results

Figure 5 is a schematic cross section through the active portion of a dissociation cell. Details of the construction and fabrication of such cells are presented in Part II (5). Yttria-stabilized zirconia 0.5-0.6 mm thick was normally used as the electrolyte. Cathodes were made from porous nickel, while anodes consisted either of various porous electronically conducting oxides for oxygen anode cells, or porous nickel for depolarized anode cells. Cells were operated in electrically heated furnaces, with control thermocouples attached to the outer electrode.

Cell measurements.—The cell voltage was measured by potential probes attached to the electrodes, eliminating voltage drops in the current leads. Although Fig. 5 shows current leads attached only to one end of the electrodes, most experimental cells had current leads at both ends of the electrodes. Materials for current leads, and contact resistances between these and electrodes, are discussed elsewhere by the authors (9). The auxiliary electrodes allow measurements of open-circuit voltages $E_0{}^i$ and $E_0{}^f$ that are related to the cathode and anode gas compositions at the entrance

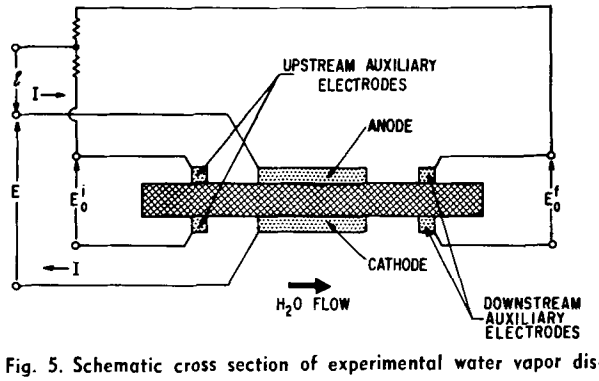

Fig. 5. Schematic cross section of experimental water vapor dissociation cell.

and exit ends of the cell. A simple resistance network, as shown, provided a linear average of these two voltages; this average is very nearly $\bar{E}_0$. Thus the difference between this experimentally measured value of $\bar{E}_0$ and E is the total overvoltage $\mathcal{E}$. In the absence of nonohmic overvoltages, the value of $\mathcal{E}$ will be equal to $r\bar{j}$, so that the slope of a plot of $\mathcal{E}$ against $\bar{j}$ should yield r.

Typically, E, ϵ, and either E_0^f or the average value of E_0^i and E_0^f were measured while the current was automatically swept from zero to a preset maximum (limiting ϵ to a maximum of 1.5-2V to prevent electrolysis of the zirconia), and back to zero over a time of about 25 min. Negligible hysteresis to the voltages was observed, and cell temperature remained constant to better than 5°C.

The value of $\mathcal{E}$ was, in general, not a linear function of current density, as it should be if it represented only a resistive voltage drop. In these cells, this can be ascribed primarily to mass transport overvoltages in the gas phase, within the pores of the electrodes. These effects, which are also encountered in measurements of high-temperature fuel cells, are detailed elsewhere in this context, as well as a discussion of the effects of electrode resistances (6). A conclusion of the cited study is that a value of r can be derived by suitably processing data on the variation of $\mathcal{E}$ with current density. The resultant value of specific resistance will contain an averaged contribution from mass transport effects. This is typically of the order of 0.05 ohm-cm² for the 0.15-mm thick electrodes generally employed, and is not a strong function of temperature since gaseous diffusion is not a thermally activated process.

Additional measurements were made on selected cells. These included leakage rate at operating temperatures, and electrode specific resistivity, as discussed in connection with high-temperature fuel cells (6). Leakage rates were of the order of 25 mA/cm² when expressed as an equivalent current density and can be neglected in comparison to the imposed current density. These leakage tests could also be used to show that electronic conductivity in the electrolyte was less than 1% of the total conductivity. Nickel electrodes showed specific resistivities of about 0.05 ohm/sq, and various oxide anodes exhibited specific resistivities of about 0.15 ohm/sq for 0.15-mm thicknesses. The contributions due to mass transport and electrode specific resistivity (which depend on cell geometry) were taken into account when calculating the cell specific resistances employed in subsequent sections.

Oxygen anode cells.—Figure 6 shows typical voltage/current density characteristics for an oxygen anode cell operated with an excess water vapor flow. The value of $J_C y_C{}^i$ was about 3 A/cm², so that at most only about 35% of the entering water vapor was dissociated at maximum current. The entering cathode gas nominally contained 50% water vapor so that the cell could be operated in a reverse direction (negative current density, with the sign convention used) while oxygen was supplied to the anode side; under these conditions, the cell becomes a hydrogen/oxygen fuel cell. The sign of the total overvoltage must then be reversed, but its significance remains the same.

The value of E at zero current is about 0.88V; this is close to the static value of $\bar{E}_0$ that would be expected from Fig. 2. The discrepancy is most probably due to deviations of the cathode feed from the nominal composition. Figure 2 also indicates that for the operating conditions of this cell, $\bar{E}_0$ should increase by only about 0.03V at most from the static value. Thus the shape of E with current density should closely parallel that of $\mathcal{E}$ for operation in the forward direction, with a constant separation for the two curves not varying by more than 0.03V. This can be verified by direct measurement in Fig. 6.

Although E is not symmetric with current density about the zero current point, $\mathcal{E}$ is symmetric about this point to within about 0.02V at 1 A/cm². The causes of the nonlinearity of $\mathcal{E}$ have already been mentioned. The symmetry of this voltage about the zero current point demonstrates that activation-type overvoltages are small, compared to resistive voltages, since these would not be symmetric with respect to direction of current flow if large. On the other hand, mass transport overvoltages at the cathode would arise primarily from water vapor/hydrogen interdiffusion, and would be expected to be symmetric. There should, of course, be no such overvoltage at the oxygen anode in the absence of a diluent, and comparison of the properties of the O_2 anode with those computed for a porous Cl_2 electrode shows that the anode pore sizes are sufficiently large to rule out any mass transport overvoltage due to viscous drag forces (10).

The asymmetry of E in Fig. 6 can then be ascribed chiefly to the fact the $\bar{E}_0$ is not symmetric with respect to the direction of current flow. This is most likely due in this case to deviations of the initial cathode gas composition from its nominal value.

Depolarized anode cells.—Figure 7 presents typical voltage/current density characteristics for a depolarized anode cell operated with limited water vapor and fuel flows. The value of $y_C{}^i$ was 0.85, and hydrogen was used as the fuel with a value for $y_A{}^i$ of 0.03. Flow rates were adjusted so that both $J_C y_C{}^i$ and $J_A(1 - y_A{}^i)$ were

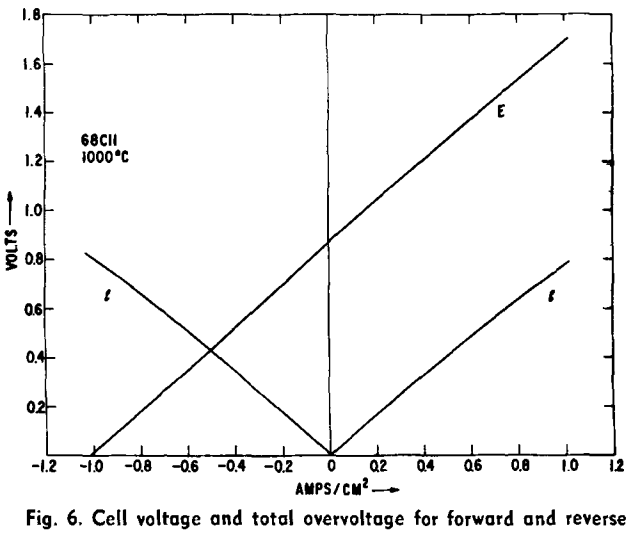

Fig. 6. Cell voltage and total overvoltage for forward and reverse operation of an oxygen anode cell with excess water vapor.

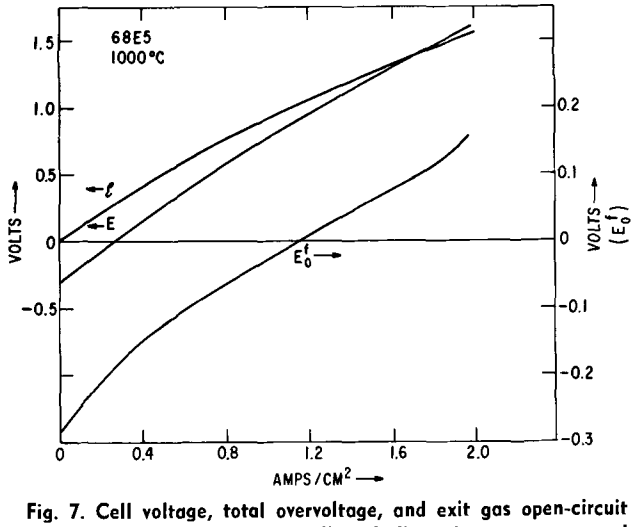

Fig. 7. Cell voltage, total overvoltage, and exit gas open-circuit voltage for depolarized anode cell with limited water vapor and fuel.

about 2.6 A/cm². Thus, at maximum current, about 75% of the entering water was dissociated and a similar amount of the entering fuel oxidized. Water vapor and fuel flows were in the same direction along the length of the tubular cell. Thus E_o^f could be measured to provide an indication of the change in water vapor dissociation, relative to fuel oxidation, at the exit end of the cell where both cathode and anode gases had their final composition. The value of E_o^i will be constant and equal to the static value of E_o^f, about —0.28V (this can be verified by direct measurement). Thus the value of $\overline{E}_o$ can be obtained by averaging the value of E_o^f with this static value.

The static value of E is negative at about —0.3V, which is generally consistent with Fig. 4 even though initial gas compositions are not identical. The static value of E in this cell is about 1.2V below that of the oxygen anode cell just described; this is a specific demonstration of the generalization that the low oxygen potential of the fuel in a depolarized anode cell reduces the amount of electrical energy (other factors being equal) required to dissociate a mole of water vapor.

Also, in contrast to the oxygen anode cell, Fig. 4 indicates that, for the depolarized anode cell being considered here, $\overline{E}_o$ should increase at maximum current by about 0.25V. Thus E should increase more rapidly with current density than $\mathcal{E}$. This is clearly shown in Fig. 7, which also shows that $\overline{E}_o$ (as measured by the average value of E_o^f) increases from —0.28 to —0.06V at 2 A/cm². Further, the change in sign of E_o^f at current densities above 1.2 A/cm² is direct evidence of the fact that the water vapor/hydrogen ratio in the exiting cathode gas is lower than the same ratio in the exiting hydrogen-base fuel gas at the anode side of the cell as a result of O^{--} transfer through the electrolyte.

It is apparent from Fig. 7 that $\mathcal{E}$ is more nonlinear for the present cell than for the oxygen anode cell with the characteristics of Fig. 6, even taking into account the different voltage scales of these two figures. The depolarized anode cell, however, has two electrodes at which mass transport overvoltages can occur, while the oxygen anode has only one. A greater degree of nonlinearity would therefore be expected for the former type of cell. It should be noted that the magnitude of mass transport overvoltages is fairly sensitive to electrode structure since these have connected porosities of only 15-30%.

System Heat Balance

It has been demonstrated that the characteristics of dissociation cells can be accounted for in terms of their average open-circuit voltage, specific resistance (ohmic), and mass transport overvoltage. Although the last is nonlinear in current density, its effect can be approximated by adding a constant to the specific resistance, provided this constant is small compared to the ohmic portion of r.

The determination of the actual system performance, *i.e.* the value of $\dot{W}/\dot{m}^*$, cannot be carried out unless the system satisfies some heat balance criterion. Consider again the system of Fig. 1. In this system, the reactant and product flows are depicted as completely separate from the leads. A real system may not have this separation, since gas and current flows may follow the same path to the cells, but the separation is useful to allow a first approximation to a heat balance which is informative as to effect of cell characteristics and lead materials on system performance. This approximation consists of the assuming that (*a*) the net heat generation rate is given by Eq. [6], which from Eq. [3] and [4] contains the effects of reactant and product temperatures as well as the enthalpy change at the cell temperature, and (*b*) the only heat loss from the cells is through the leads themselves, since in principle the thermal insulation and radiation shielding around the cells can be made sufficiently good to reduce all other heat losses to an arbitrarily low value. The latter assumption will be increasingly valid as system size increases, but the leads will always remain as a relatively high thermal conductivity path to the surroundings since they must in general be fabricated from metals or alloys exhibiting high electrical conductivity at all temperatures between that of the cells and the surroundings.

The question of multicell systems also arises. Without losing generality, any such system can be considered to consist of a set of "stacks," each containing N cells connected in series both electrically and chemically; the set of stacks are in parallel chemically and either in series or parallel electrically. The total area of all cells is still represented by A, and all intercell electrical connections must be made entirely within the hot zone at the cell temperature.

Thermal effects in leads.—Figure 8a represents a single lead of length L_l and cross section A_l extending through the thermal insulation around the cells. The thermal conductivity K of the lead material will be much higher than that of the thermal insulation, so that heat flow through the latter can be neglected, resulting in a one-dimensional problem. The lead carries the total current I which causes Joulean heating of the lead itself. The temperature T_l of the lead must be evaluated as a function of position x along the lead from a value of T at the inner (hot) end to a value of T_o at the outer (ambient) end. Then the heat loss from the cells into each lead will be proportional to A_l and to the product of K and the temperature gradient dT_l/dx in the lead at the inner end, denoted by a subscript (0). As indicated in Fig. 8a, K is a function of temperature, and thus of position along the lead.

Figure 8b shows the heat flows into and out of a thin slice of the lead, and the heat generation rate in the slice due to Joulean heating. The latter will be proportional to the square of the current and the lead resistivity ρ, which like K is a function of temperature. In the steady state, the net heat flow out of the slice must be equal to the heat generation rate in the slice, allowing a differential equation for T_l to be obtained as

$$A_l \frac{d}{dx}\left(K\frac{dT_l}{dx}\right) + \frac{I^2\rho}{A_l} = 0 \qquad [13]$$

Electrical and thermal conductivities in metals.—At ambient temperatures and higher, free electrons are responsible for both electrical and thermal conductivity in metals; in contrast to nonmetals, very little contri-

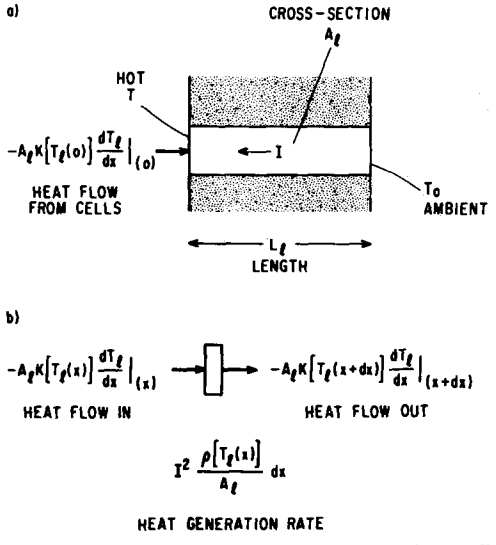

Fig. 8. (a): Schematic representation of lead, and heat flow from cells into inner end of lead. (b): Differential heat flows within lead.

bution is made to thermal conductivity by the metal atoms. As a result, a simple treatment (11) based on free electron mean path lengths in a metal predicts that electrical and thermal conductivity should be related by

$$K = \lambda\sigma T \qquad [14]$$

where λ is the Lorenz Number, with a value of 2.45 x 10^{-8} (V/°K) (2). In this treatment, the electrical conductivity itself is inversely proportional to $T + \theta$, where θ is a temperature characteristic of the metal. Two limiting cases are then possible, and are described briefly.

Pure metals.—For pure metals, θ/T is generally much less than unity as a consequence of free electron mean path length being determined primarily by thermal vibrations of the metal atoms. Then it can be shown that, for these materials, the product of the thermal coefficient of resistivity α and the resistivity ρ should be constant, independent of temperature. Available data show that this product has an average value of from about 6 x 10^{-9} ohm-cm/°K for silver to 6 x 10^{-8} ohm-cm/°K for nickel.

Alloys.—In alloys, free electron mean path length is influenced mainly by the spacing between solvent and solute atoms, causing θ/T to be much greater than unity. Then for, such materials, the resistivity ρ should be constant and independent of temperature. Many alloys based on ferrous metals or copper which contain substantial amounts of alloying additions (20% or more) have resistivities of the order of 1 x 10^{-4} ohm-cm over a fairly wide temperature range.

These electrical characteristics of pure metals and alloys as just described are approximations but are not grossly in error. For example, the resistivity of an alloy may vary by a factor of 1.5 from room temperature to 1000°C. In contrast, the resistivity of a pure metal can change by a factor of 5 or 6 over the same temperature range while its temperature coefficient-resistivity product remains constant to within 25%. The value of these approximations is that they allow relatively simple solutions of Eq. [13] in closed form, simplifying the problem of examining the effects of these two classes of lead materials on the operating point of a cell system as determined by heat balance criteria.

Heat loss and power loss in leads.—The pure metal and alloy approximations can each be introduced in turn into Eq. [13], along with the relationship of Eq. [14]. Solutions to [13] are then possible which allow evaluation of the rate of heat loss through each lead. For simplicity, two identical leads can be considered; the total heat loss from the cells through both leads will be denoted by $\dot{Q}_l$. The heat balance criterion is then

$$\dot{Q}/A = \dot{Q}_l/A \qquad [15]$$

where $\dot{Q}/A$ is given by Eq. [6].

Solutions for T_l as a function of x also allow the lead resistance R_l to be evaluated by integration of ρ over the length of the lead. The total power dissipation in each lead is then I^2R_l, and the power dissipation in two identical leads, denoted by P_l, is twice this value. The energy input to the system per mole of water vapor dissociated is now no longer given by $2\mathbf{F}E$, but must include this power dissipation. Then $\dot{W}/\dot{m}^*$ is

$$\dot{W}/\dot{m}^* = 2\mathbf{F}E + P_l/\dot{m}^* \qquad [16]$$

where E is given by Eq. [5].

The results of the solution of Eq. [13], transformed into a form appropriate for use in [15] and [16], contain a single geometrical parameter which involves total cell area, lead length, and lead cross section. This parameter, s, is given by

$$s = A/(A_l/L_l) \qquad [17]$$

In terms of s, expressions for $\dot{Q}_l/A$ and $P_l/\dot{m}^*$ can then be obtained as

$$\dot{Q}_l/A = 2\lambda^{1/2}TJ_C y_C{}^i x_C \frac{\cos\left(\frac{1}{\lambda^{1/2}}\alpha\rho\frac{s}{N}J_C y_C{}^i x_C\right) - T_o/T}{\sin\left(\frac{1}{\lambda^{1/2}}\alpha\rho\frac{s}{N}J_C y_C{}^i x_C\right)} \qquad [18]$$

$$= \lambda\frac{1}{\rho}s(T^2 - T_o{}^2) - \rho\frac{s}{N^2}(J_C y_C{}^i x_C)^2 \qquad [18b]$$

and

$$P_l/\dot{m}^* = 4\mathbf{F}\lambda^{1/2}(T + T_o)\frac{1}{N}\frac{1 - \cos\left(\frac{1}{\lambda^{1/2}}\alpha\rho\frac{s}{N}J_C y_C{}^i x_C\right)}{\sin\left(\frac{1}{\lambda^{1/2}}\alpha\rho\frac{s}{N}J_C y_C{}^i x_C\right)} \qquad [19a]$$

$$= 4\mathbf{F}\lambda\frac{s}{N^2}J_C y_C{}^i x_C \qquad [19b]$$

where [18a] and [19a] apply to the case of pure metals, and [18b] and [19b] to alloys.

Determination of system performance.—Equations [6], [7], and [18a] or [18b] can most readily be used to find the value of J_C, *i.e.* the water vapor flow rate, that satisfies [15] for any set of operating conditions. This is a nonlinear problem that can be solved by any convenient numerical method. The resultant value of J_C can then be used in Eq. [16] with [19a] or [19b] to determine $\dot{W}/\dot{m}^*$. This process can be repeated for a number of different values of the parameter s to yield the variation of $\dot{W}/\dot{m}^*$ with s. A minimum value of $\dot{W}/\dot{m}^*$ would be expected for some value of s, representing the minimum possible energy input to the system per mole of water vapor dissociated, for the assumed conditions.

System performance at heat balance.—Heat balance calculations were made on a depolarized anode cell system with water vapor and fuel inputs similar to those noted in Fig. 4, except that the fuel was assumed to contain 46% nitrogen (from air), resulting from partial combustion of a hydrocarbon to generate the fuel. Some preheating of the input streams was assumed, as well as a small amount of heat exchange to lower the temperature of the output streams. The assumed operating conditions were 95% water vapor dissociation, with a 10% excess of fuel input relative to water vapor input. In line with experimental results, the specific resistance of the cells was taken as 0.67 ohm-cm^2 at 1000°C and as 0.44 ohm-cm^2 at 1100°C.

The quantity $(\dot{W}/\dot{m}^*)/2\mathbf{F}$ having the dimensions of volts, and denoted by $\bar{E}$, was used rather than $\dot{W}/\dot{m}^*$ to describe the energy input to the system. This is the average voltage of a single cell having the properties of a cell in the system, including the effects of power dissipation in the leads; it can also be compared directly with the cell voltage for electrolysis of liquid water. Figure 9 shows the variation of performance with s at 1100°C for three different conditions: (*a*) single cells with alloy leads ($\rho = 10^{-4}$), (*b*) 10 cell stacks with alloy leads ($\rho = 10^{-4}$), and (c) 10 cell stacks with pure metal leads ($\alpha\rho = 10^{-8}$). As expected, there is an optimum lead geometry giving rise to the lowest dissociation energy, at the bottom of a rather shallow minimum. The virtues of the multicell stack in reducing the minimum dissociation energy by about a factor of two are apparent. Also, the minimum dissociation energy for 10 cell stacks does not depend on the nature of the lead material. Although this result certainly is not apparent in view of the widely different expres-

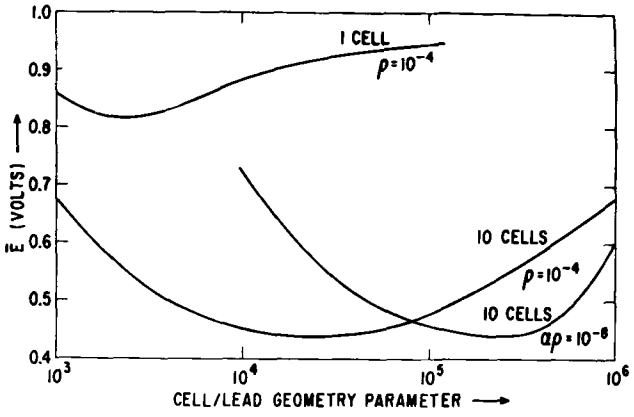

Fig. 9. Variation of average system cell voltage with cell/lead geometry parameter.

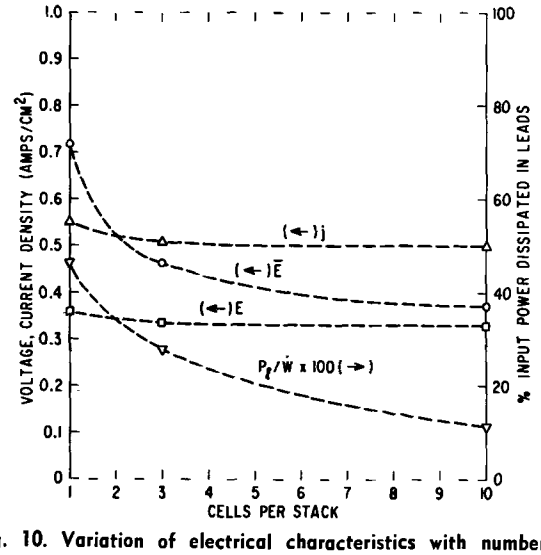

Fig. 10. Variation of electrical characteristics with number of cells per stack in a system optimized for minimum energy requirement.

sions for heat loss and power dissipation in the leads for the two cases considered, it is not unreasonable in view of the coupling between thermal and electrical conductivities. Thus there is no advantage, from an energy requirement standpoint, of preferring either type of material.

Figure 10 shows the best possible system performance, *i.e.* at the minima of curves similar to those of Fig. 9, for operation at 1000°C as a function of the number of cells per stack. Values of current density, cell voltage, and the percentage of total input power dissipated in the leads at these minima are also included. Calculation of best performance at other temperatures leads to similar results, differing primarily in the magnitude of the current density. The value of $\bar{E}_o$ is close to zero, while $\bar{E}_H$, representing mainly reactant preheating, is about 0.35V for the assumed conditions.

If minimization of energy cost is the chief criterion in dissociation, Fig. 10 illustrates the incentive for developing techniques of fabricating multicell stacks. Part II describes some of the materials problems inherent in this task. The cost of cells themselves will enter into the over-all cost of dissociation, however, and in this connection cells should be operated at as high a current density as possible to minimize the total cell area for a given system capacity. Figure 10 shows that current densities for best performance do not approach those that can safely be passed through the electrolyte as demonstrated by single-cell operation. However, the current density for best performance decreases by only 10% in going from 1 to 10 cells per stack while the energy requirement for dissociation decreases by almost 50%.

A system need not be operated at its best performance, in terms of energy requirement, if higher current densities are desirable to decrease cell area. The leads can be made larger in cross section, increasing the heat loss, effectively operating to the left of the minima shown in Fig. 9. The possible advantages of this procedure will depend on the economics of the particular system involved. Alternatively, since the value of the current density is dependent on the specific resistance of the electrolyte/electrode combinations, this parameter can be reduced to increase the current density at best performance. To some extent, increasing the cell temperature—probably with about 1150°C as an upper limit—is one way of accomplishing this reduction. Other possible approaches, and some of their limitations, are presented in Part II (5).

Manuscript submitted April 21, 1969; revised manuscript received July 17, 1969. This was Paper 356 presented at the Montreal Meeting, Oct. 6-11, 1968.

Any discussion of this paper will appear in a Discussion Section to be published in the June 1970 JOURNAL.

REFERENCES

1. H. S. Spacil and C. S. Tedmon, Jr., Paper 356 presented at Fuel Cell Symposium, Electrochem. Soc. Meeting, Montreal, Oct. 6-11, 1968.
2. H. S. Spacil and C. S. Tedmon, Jr., Paper 357 presented at Fuel Cell Symposium, Electrochem. Soc. Meeting, Montreal, Oct. 6-11, 1968.
3. *Chem. Eng. News*, **46**, 48 (1968).
4. D. W. White and H. S. Spacil, Paper 358 presented at Fuel Cell Symposium, Electrochem. Soc. Meeting, Montreal, Oct. 6-11, 1968.
5. H. S. Spacil and C. S. Tedmon, Jr., *This Journal*, **116**, 1627 (1969).
6. H. S. Spacil and C. S. Tedmon, Jr., "The Relationship of Performance and Materials Properties in High Temperature Zirconia Electrolyte Fuel Cells," presented at Meeting of Comite International de Thermodynamique and Cinetique Electrochimies, Detroit, Sept., 1968.
7. *See*, for example, "Thermodynamics for Chemists," Glasstone, 202 ff., D. van Nostrand (1947).
8. B. C. H. Steele, B. E. Powell, and P. K. R. Moody, *Proc. Brit. Ceram. Soc.*, No. 10.
9. C. S. Tedmon, Jr., H. S. Spacil, and S. P. Mitoff, *This Journal*, **116**, 1170 (1969).
10. D. A. J. Swinkels and R. N. Seefurth, *This Journal*, **115**, 994 (1968).
11. *See*, for example, "Quantum Theory of Matter," Slater, 41 ff., McGraw-Hill (1951).

APPENDIX I

The active area of an electrolyte can be described in terms of a normalized parameter ζ. This can be defined in terms of y_C, the fractional amount of water vapor in the gas at the cathode; the value of ζ is set at zero where $y_C = y_C{}^i$ and unity where $y_C = y_C{}^f$. Consider the area δA to be the area of electrolyte between y_C and $y_C + \delta y_C$, which in turn are associated with ζ and $\zeta + \delta\zeta$. A function a_ζ can be defined as

$$a_\zeta = \lim_{\delta\zeta \to 0} \frac{\delta A}{\delta\zeta} \qquad [I\text{-}1]$$

and the infinitesimal area dA becomes

$$dA = a_\zeta d\zeta \qquad [I\text{-}2]$$

The average current density between 0 and ζ is

$$\bar{j}(\zeta) = \frac{1}{A}\int_0^\zeta j a_\zeta d\zeta \qquad [I\text{-}3]$$

where j is the local value of current density at any point on the electrolyte. But from the definition of y_C, this same average current density is

$$\bar{j}(\zeta) = J_C(y_C{}^i - y_C) \qquad [I\text{-}4]$$

Equating these two expressions, differentiating, and re-

arranging gives

$$a_\zeta d\zeta = -AJ_C \frac{1}{j}\, dy_C \qquad [I\text{-}5]$$

Any quantity U having a local value which is a function of y_C will then have an average value $\overline{U}$ that can be expressed as

$$\overline{U} = \frac{1}{A}\int_0^A U dA = \frac{1}{A}\int_0^1 U a_\zeta d\zeta$$

$$= -J_C \int_{y_C{}^i}^{y_C{}^f} \frac{U}{j}\, dy_C \qquad [I\text{-}6]$$

This immediately gives $\overline{j}$ as

$$\overline{j} = -J_C\,(y_C{}^f - y_C{}^i) \qquad [I\text{-}7]$$

which is in agreement with Eq. [7]. Further, using [I-7] the average $\overline{U}$ can be expressed as

$$\overline{U} = \frac{1}{y_C{}^f - y_C{}^i}\int_{y_C{}^i}^{y_C{}^f} \frac{U}{(j/\overline{j})}\, dy_C \qquad [I\text{-}8]$$

Clearly, if $j/\overline{j}$ is approximately unity, the average value U is given by

$$\overline{U} \approx \frac{1}{y_C{}^f - y_C{}^i}\int_{y_C{}^i}^{y_C{}^f} U dy_C \qquad [I\text{-}9]$$

which is simply the average of U over y_C

From the Nernst equation, the local value of the open-circuit voltage, E_o, for an oxygen anode cell will be proportional to the natural logarithm of the water vapor/hydrogen ratio plus a constant, or

$$E_o \sim \ln\left(\frac{y_C}{1-y_C}\right) + k_1 \qquad [I\text{-}10]$$

Integrating [I-10] as indicated in [I-9] gives

$$\overline{E}_o \sim [y_C{}^f \ln (y_C{}^f) - y_C{}^i \ln (y_C{}^i) + (1-y_C{}^f)\ln(1-y_C{}^f)$$

$$- (1-y_C{}^i)\ln(1-y_C{}^i)]/(y_C{}^f - y_C{}^i) + k_1 \qquad [I\text{-}11]$$

But, as shown in Appendix II, substitution into Eq. [1] and [2] yields the result that $\overline{E}_o$ as defined by Eq. [2] involves terms containing $y_C{}^i$ and $y_C{}^f$ exactly the same as those of [I-11].

It can also be shown (6) that for fuel gases based on hydrocarbons, the local open-circuit voltage for a depolarized anode cell will be described approximately by

$$E_o \sim \ln\left(\frac{y_C}{1-y_C}\right) - \ln\left(\frac{y_A}{1-y_A}\right) + k_2 \qquad [I\text{-}13]$$

But y_A will be coupled to y_C by the O^{--} flow through the electrolyte in this case, so that E_o is still a function of y_C only. Thus the integration of [I-9] still applies. The mole fractions of the various species in the fuel gas can likewise be described in terms of y_A, with the result that Eq. [2] again yields a value of $\overline{E}_o$ consistent with that of the constant current density case.

APPENDIX II

The oxygen anode cell can be considered specifically to illustrate the form of the expression resulting from substituting appropriate flow rates and compositions into Eq. [1]. Using the nomenclature of the text, the molar flow rates of gases entering the cathode are

$$\dot{m}_{H_2O,\,in} = \frac{J_C A y_C{}^i}{2F} \qquad [II\text{-}1]$$

and

$$\dot{m}_{H_2,\,in} = \frac{J_C A (1-y_C{}^i)}{2F} \qquad [II\text{-}2]$$

Likewise, the molar flow rates of gases leaving the cathode are

$$\dot{m}_{H_2O,\,out} = \frac{J_C A y_C{}^f}{2F} \qquad [II\text{-}3]$$

$$\dot{m}_{H_2,\,out} = \frac{J_C A (1-y_C{}^f)}{2F} \qquad [II\text{-}4]$$

There is no reactant entering the anode, while the molar flow rate of gas leaving the anode is

$$\dot{m}_{O_2,\,out} = \frac{J_C A (y_C{}^i - y_C{}^f)}{4F} \qquad [II\text{-}5]$$

The total pressures at the cathode and anode are P_C and P_A, respectively, although P_C will cancel from the final expression. Taking the water vapor dissociated at the cathode as the critical component, the flow rate m^* is, by difference,

$$\dot{m}^* = \frac{J_C A (y_C{}^i - y_C{}^f)}{2F} \qquad [II\text{-}6]$$

With this choice for the critical component, it is apparent that ΔG^{o*}_T is the negative of the standard free energy of formation of one mole of water vapor at temperature T, or

$$\Delta G^{o*}_T = -\Delta G^o_{H_2O,\,T} \qquad [II\text{-}7]$$

The result of substituting the expressions of [II-1] through [II-7] into Eq. [1], and noting that y_C and $1 - y_C$ are the mole fractions of H_2 and H_2O, respectively, is then

$$\dot{G}_T/\dot{m}^* = -\Delta G^o_{H_2O,\,T} + RT \ln (P_A)/2$$

$$+ RT\,[y_C{}^f \ln (y_C{}^f)$$

$$+ (1-y_C{}^f)\ln(1-y_C{}^f) - y_C{}^i \ln (y_C{}^i)$$

$$- (1-y_C{}^i)\ln(1-y_C{}^i)]/(y_C{}^i - y_C{}^f) \qquad [II\text{-}8]$$

This expression can be evaluated with only a knowledge of $\Delta G^o_{H_2O,\,T}$ which can be obtained from a source of tabulated values.†

The treatment of a depolarized anode cell is similar to the preceding, but the mole fractions of the species present must be calculated taking the water gas shift reaction into account. The parameters h and y_A as defined in the text are convenient to use since the mole fractions of CO, CO_2, H_2, and H_2O in the anode gas can readily be expressed in terms of these parameters. In this case, P_A will also cancel from the final expression.

With expressions of the mole fractions of the various species present in the gas streams entering and leaving the cathode and anode, Eq. [3] can be evaluated with a knowledge of the various enthalpy content difference terms $H^o_{T_{out}}$-H^o_T and $H^o_{T_{in}}$-H^o_T. Since only differences in molar enthalpy content are involved, tabulated values with respect to any convenient reference temperature, such as 298°K, may be used.‡

In the preceding, the difference $y_C{}^i - y_C{}^f$ has been used to characterize the composition change in the cathode gas; this of course can be replaced by the product $y_C{}^i x_C$ (with an analogous treatment for the anode gas) to obtain expression relating $\overline{E}_o$ to x_C or x_C and x_A.

† Standard Gibbs free energy values used were from "Thermochemistry for Steelmaking," Vol. I, Elliott and Gleiser, Addison-Wesley (1960).

‡ Enthalpy content values used were obtained from the preceding source.

Electrochemical Dissociation of Water Vapor in Solid Oxide Electrolyte Cells

II. Materials, Fabrication, and Properties

H. S. Spacil* and C. S. Tedmon, Jr.*

General Electric Research and Development Center, Schenectady, New York

ABSTRACT

Following the thermodynamic and electrochemical description of high-temperature electrolytic dissociation of water vapor discussed in Part I, this paper is concerned with materials problems, design, and fabrication of both single-cell and multicell devices. Oxygen anodes and depolarized anodes are both considered, and it is concluded that the most feasible system is that employing discontinuous electrolyte segments and depolarized anodes.

The thermodynamic and electrochemical basis for the high-temperature electrolytic dissociation of water vapor was presented in Part I of this paper (1). This part of the paper is concerned with materials problems, fabrication, and performance of both single-cell devices and multicell stacks, or batteries. Two general systems were discussed in Part I, *viz.* operation with oxygen anodes and operation with depolarized anodes. With respect to materials, each system has certain features in common and some features that are much different. Both systems have the same cathode reaction and consequently the cathode and also the electrolyte may be made from the same materials. Factors influencing the choice of cathode and electrolyte materials are discussed in the following sections. The principal differences between the two systems lie in the anode reaction and anode material. Figure 1 shows schematically the operation of a zirconia electrolyte water vapor dissociation cell operating with an oxygen anode. The dominant characteristic of this mode of operation, from a materials viewpoint, is that the anode and anode leads must be chemically and physically stable in an oxidizing environment at elevated temperatures. In many respects, the materials requirements for the oxygen anode are similar to those for zirconia fuel cell cathodes (2). This is discussed in more detail in subsequent sections of this paper. Operation of zirconia electrolyte water vapor dissociation cells with depolarized anodes is shown schematically in Fig. 2. In this mode of operation, an excess of fuel over the stoichiometric requirement is employed to maintain a reducing atmosphere over the anode. Carbon monoxide is indicated as the fuel; other fuels are also feasible. Consequently, a different set of materials requirements is involved. The effect of these parameters on the fabrication and performance of both single- and multicell devices is discussed later.

It was shown in Part I that, in order to achieve an optimal thermal balance and to minimize the energy requirements for the system, it would be necessary to utilize multicell stacks in a practical system rather than single-cell devices. The latter, however, are much easier to fabricate and test. Furthermore, the investigation and interpretation of cell reactions is more straightforward with single-cell devices. Consequently, both single-cell devices and multicell stacks have been built and tested.

Electrolytes and Cathodes

The choice of materials for the cathodes and electrolyte of the cells is largely independent of the mode of operation and the number of cells in the device. With some designs of multiple-cell stacks, it is conceivable that the choice of the cathode material could be influenced by the necessity of having to make the series connections between anode and cathode. However, this will not usually be a problem.

Electrolyte.—In cells having either oxygen anodes or depolarized anodes, the electrolyte performs the dual function of providing both oxide ion conductivity and structural strength to the device.

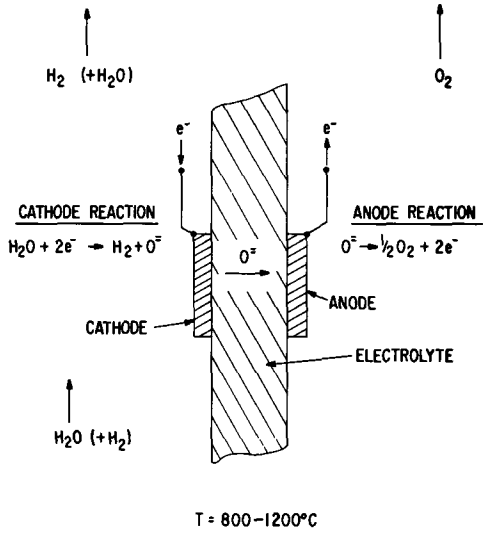

Fig. 1. Schematic illustration of solid oxide electrolyte water vapor dissociation cell with oxygen anode.

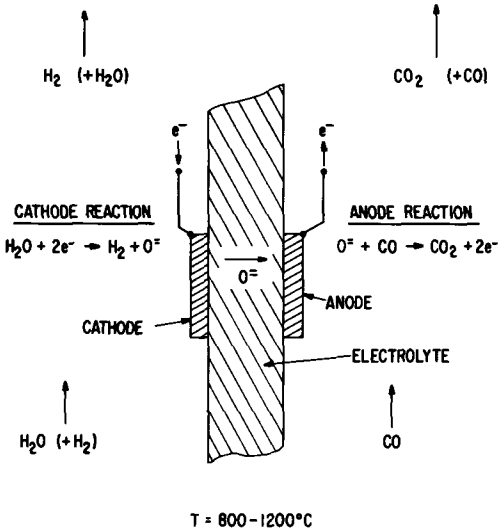

Fig. 2. Schematic illustration of solid oxide electrolyte water vapor dissociation cell with depolarized anode.

* Electrochemical Society Active Member.

Key words: dissociation, water vapor, oxide electrolyte.

The electrolyte material must satisfy several criteria. It must be fabricable into a gas-impermeable structure and possess high oxide ion conductivity and low electronic conductivity. Also, the fabrication methods used for these cells require sintering of the electrolyte to at least 95% of theoretical density at temperatures below the melting point of the electrodes (*ca.* 1450°C). Finally, the isothermal ionic conductivity should be independent of oxygen partial pressure over the wide range encountered, which may be as much as 20 orders of magnitude.

The cells which are discussed are based on a stabilized zirconia electrolyte. Other oxide ion conductors are known, such as yttria-doped thoria, or ceria-doped lanthana. The properties of zirconia are much better characterized and understood, however, and consequently it has been used. Zirconium dioxide can be stabilized into the cubic fluorite structure by the addition of various oxides such as CaO, MgO, Y_2O_3, and other rare earth oxides. In the cubic phase, the cations from the stabilizing oxide occupy sites in the zirconium cation sublattice. Since the stabilizing cation has a lower valence than the host Zr^{+4} ions, anion vacancies are created to preserve charge neutrality. As a first approximation, the oxide ion conductivity depends on the concentration of anion vacancies (3-5), and hence on the concentration and valance of the stabilizing cation. Since the concentration of vacancies is fixed by composition, it follows that at a given temperature the oxide ion conductivity is fixed by composition and therefore is substantially independent of oxygen partial pressure, at least over the range of oxygen pressures of interest here (4, 5). Figure 3 is a plot of ionic conductivity *vs.* reciprocal absolute temperature for various stabilized zirconias. Except for the case of yttria-stabilized zirconia, for which data for two compositions are presented, the curves shown for each material are for the optimal concentration of the stabilizing oxide. In each such material, lesser or greater amounts of the stabilizing oxide will result in a material with lower ionic conductivity. Thus, for the case of yttria-stabilized zirconia, 10 m/o (mole per cent) Y_2O_3 has been found to maximize ionic conductivity, while the addition of

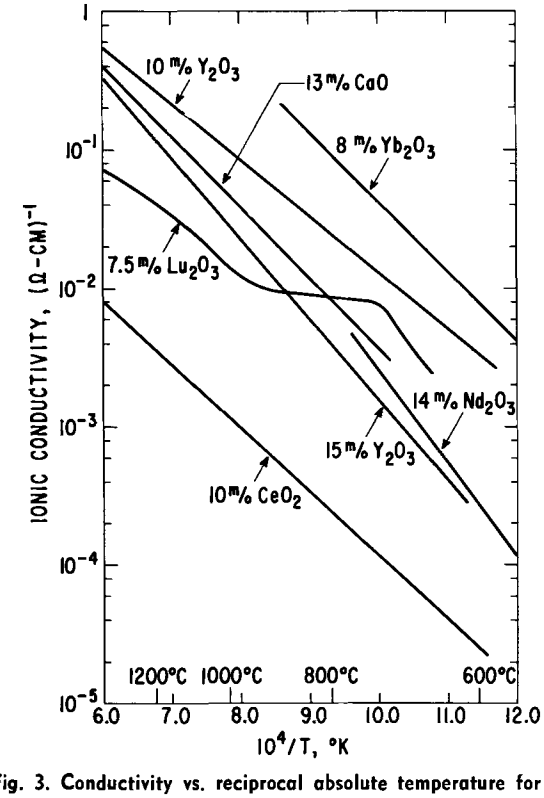

Fig. 3. Conductivity vs. reciprocal absolute temperature for various stabilized zirconias. References: ZrO_2-CeO_2 (6); ZrO_2-Y_2O_3 (7); ZrO_2-Nd_2O_3, ZrO_2-Yb_2O_3 (8); ZrO_2-Lu_2O_3 (9).

15 m/o Y_2O_3 results in decreased conductivity. The curvature in the plot for the Lu_2O_3-stabilized zirconia suggests that its conductivity may not be entirely anionic. The electronic conductivity of these stabilized zirconias is of the order of 0.1% of the ionic conductivity for oxygen partial pressures of interest.

In these experiments, zirconia stabilized with 10 m/o Y_2O_3 (termed "YSZ") was used as the electrolyte material. It is apparent from the data shown in Fig. 3 that the ytterbia-stabilized material has a higher conductivity, but cost and availability render the YSZ more practical. About 1 m/o Fe_3O_4 is added to the electrolyte to increase sinterability. This addition enables the zirconia to be sintered to about 95% theoretical density at temperatures as low as 1225°C. The addition of the iron does not measurably contribute to the electronic conductivity of the electrolyte down to oxygen partial pressures as low as 10^{-20} atm.

Details on the processing of the electrolyte material and the fabrication of cells are described subsequently; it is prepared in tubular form, about 1 cm in diameter, with a 0.5-mm wall thickness. It would be desirable, of course, to have the electrolyte as thin as possible in order to minimize total cell resistance. Leaktight tubes of YSZ with walls as thin as 0.125 mm have been prepared, but the thicker-wall tubes are a more optimal compromise between conductivity and strength.

The addition of the iron oxide as a sintering agent to the YSZ is satisfactory when the cells are operating with noncarbonaceous fuel gases. In practical application, it is likely that carbonaceous fuel gases would be used. For this purpose, the iron oxide addition is unsatisfactory; cells with Fe_3O_4-doped electrolyte show a gradual decline in performance with time, due to increased electrolyte resistance. This is apparently due to an interaction between carbon atoms from the gas and iron in the electrolyte. Cobalt oxide has been found to be an alternate sintering aid which does not interact with carbon. It can be added in about the same amounts as the iron oxide and provides sinterability in the same temperature range. Its contribution to the electronic conductivity of the electrolyte is negligible.

Cathode.—It was pointed out above that the half reaction occurring at the cathode was independent of the mode of operation, *i.e.* independent of whether depolarized anodes or oxygen anodes were used. Consequently, the choice of cathode materials is not generally going to be influenced by the mode of operation.

In both types of systems, cathodes have been made from a porous Ni-YSZ cermet, containing about 20 w/o (weight per cent) YSZ. The purpose of the latter in the electrode is to prevent sintering and growth of the Ni particles. Similar electrodes consisting of Co-20 w/o YSZ have been employed. Cell performance was found to be independent of the antisintering material in the cathode.

Both Ni and Co have the advantage of being chemically stable in H_2O/H_2 mixtures containing large amounts of H_2O. Figure 4 is a plot of the maximum H_2O content for stability of the metal indicated in an H_2O/H_2 gas mixture, as a function of temperature (10). Both Ni and Co are stable in atmospheres containing more than 90% H_2O. In contrast, for example, Fe would be severely limited as an electrode for this application. Manganese has a similar limitation, and Cu, though stable in H_2O-rich atmospheres, is limited by melting point. Consequently, Ni and Co are the only practical choices.

Details on the fabrication of the cathode on single-cell and multicell devices are discussed in a subsequent section on fabrication.

Single-Cell Devices

Single cells with oxygen anodes.—Cells operating with oxygen anodes resemble fuel cells in many respects. The electrochemical reactions occurring at the anode are effectively reversed, but the operating en-

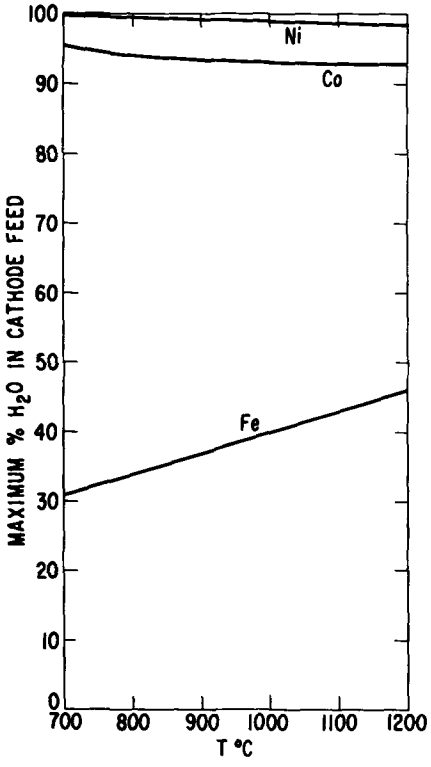

Fig. 4. Temperature dependence of the maximum water vapor content in H_2O/H_2 mixtures for stability of the metals shown.

vironment is similar, as are the criteria for chemical and mechanical stability of the anode, which would function as a cathode in a fuel cell. Basically, the anode must be made from a material which is chemically stable in air or in contact with zirconia to temperatures at least as high as 1000°C. In a previous paper (2), operational criteria were identified for fuel cell cathode materials, and quantitative relationships between cathode materials and cell operating characteristics were discussed. Many of the conclusions arrived at in that study are applicable to the problem of selection of oxygen anode materials for the zirconia electrolyte water vapor cells. It was concluded that the only practical class of materials to consider for fuel cell cathodes were the electronically conducting oxides. The same conclusion is valid for the selection of materials for anodes for these cells. Figure 5 presents conductivity data as a function of temperature for various electronically conducting oxides. The perovskite oxides—$LaCoO_3$, Sr-doped $LaCoO_3$, and $PrCoO_3$—are of particular interest because of their high values of conductivity. Unfortunately, the first two react with zirconia to form reaction products which are deleterious to cell operation; $PrCoO_3$ anodes, however, can function efficiently for long periods of operation at temperatures as high as 1000°C (2). Zirconia electrolyte water vapor dissociation cells with porous $PrCoO_3$ oxygen anodes have been built and tested. The $PrCoO_3$ is applied from an aqueous slurry to a thickness of about 0.2-0.3 mm, dried, and sintered *in situ* as the cell is heated up, resulting in a porous electrode. As was the case with fuel cells, such an electrode cannot be thermally cycled because of the large difference in thermal expansion between the $PrCoO_3$ and the zirconia.

For water vapor dissociation cells which are electrolyte limited, that is, cells in which the electrolyte resistance dominates the total resistance of the cell, the specific resistance of the cell as viewed from the terminals is given approximately by the relation

$$r = r_e + f(r_a + r_c) \qquad [1]$$

where r_e, r_a, and r_c are the specific resistances of the electrolyte, anode, and cathode, respectively, and f is a constant which takes into account the fact that the

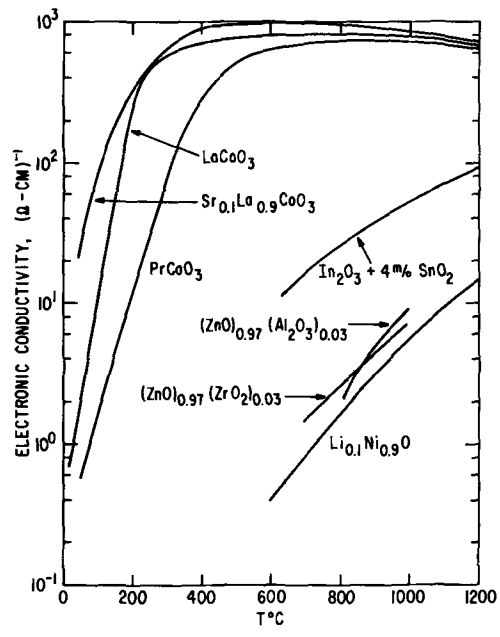

Fig. 5. Electrical conductivity vs. temperature for various electronically conducting oxides.

current distribution varies along the length of the electrodes (f = 0.08-0.3). This specific resistance, r, with units of ohm-cm^2, is the resistance of a hypothetical cell 1 cm^2 in area which has the electrical properties of the actual cell under consideration. Equation [1] can be derived by a straightforward, although tedious, analysis of a one-dimensional distributed current network (11). From a knowledge of the resistivities of the cell components and the geometry of the system, values of r can be calculated. Measurements of these resistivities have been reported elsewhere (12).

Water vapor dissociation cells with oxygen anodes have been built and tested. Satisfactory performance was obtained; up to about 95% of the incoming water vapor could be coulometrically reduced. Specific resistance of a cell can be computed from Eq. [1] and compared with experimentally determined values. The results are presented in Fig. 6, as a function of reciprocal absolute temperature. This figure presents the apparent specific resistance, which includes any contributions that may be present as a result of mass transport or activation overvoltages. Part I of this paper

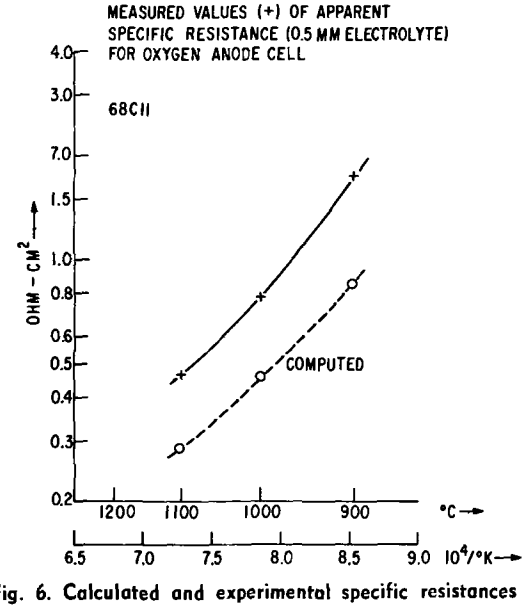

Fig. 6. Calculated and experimental specific resistances of oxygen anode cell as a function of reciprocal absolute temperature.

discussed the reasons for expecting both of these to be small compared to resistive voltage drops, at least under the usual testing conditions. This expectation is confirmed by Fig. 6 which shows that the measured value of the apparent specific resistance is approximately proportional to calculated values. The reason for the discrepancy is discussed in the following section, but, since neither mass transport nor activation overvoltages will have the same activation energy as the electrolyte resistivity, Fig. 6 shows that these effects are not significant.

Single cells with depolarized anodes.—A schematic illustration of a cell operation with a depolarized anode was presented in Fig. 2. The material requirements for cells of this type are more readily met, since the anode, as well as the cathode, is exposed to an atmosphere which is reducing to several metals, particularly Ni and Co. The anode reaction for this mode of operation is the oxidation of the fuel, such as CO. Porous Ni or porous Co electrodes, containing about 20 w/o zirconia, are acceptable anodes.

Depolarized anode cells have also been built and tested, using various fuel gases at the anode. These cells function satisfactorily, giving coulometric dissociation of the input water. Equation [1] can also be evaluated for cells of this type. Figure 7 is a plot of computed specific resistance and measured specific resistance, as a function of reciprocal absolute temperature for a typical depolarized anode cell operating on a hydrogen fuel. This figure, like Fig. 6, presents the apparent specific resistance which will include any contributions from mass transport and activation polarization effects. As with oxygen anode cells, these should be small under testing conditions. Figure 7 shows that the measured value of the apparent specific resistance is approximately proportional to the calculated value, except for a deviation at the lower temperatures (about 800°C) where activation polarizations might be expected to become significant.

The origin of the increase in measured values of specific resistance over calculated values, for both oxygen anode and depolarized anode cells, is not entirely understood, but probably lies at least in part in a form of constriction resistance at the electrode/electrolyte interfaces. Both electrodes consist of fine particles, and current flow through the electrolyte in the vicinity of the interfaces will be constricted to some region near the three-phase gas/electrode/electrolyte boundary.

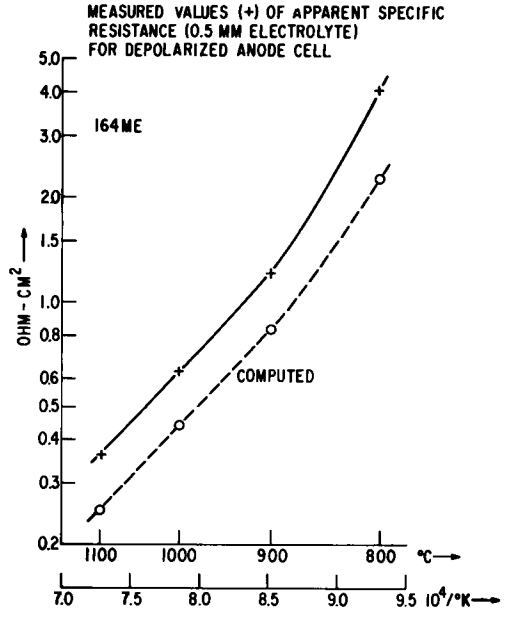

Fig. 7. Calculated and experimental specific resistances of a depolarized anode cell as a function of reciprocal absolute temperature.

This problem has been considered for solid electrolyte cells (13), and the result is that an effective thickness of the electrolyte, which will be larger than the geometrical thickness, must be used to calculate the specific resistance of the electrolyte. This in turn will result in the observed proportionality of Fig. 6 and 7.

Multicell Stacks

General design considerations.—There are two general designs for multiple-cell stacks, whether for use as fuel cells or as water vapor dissociation cells. In the first case, the electrolyte is continuous. This design is attractive because the electrolyte thus provides a convenient structural element. A schematic illustration of this type of device is shown in Fig. 8. The series connection between anodes and cathodes must be made by a lead, such as a wire, passing through the electrolyte. This connection must be made, of course, without introducing a leak.

The second general design that has been proposed for multiple-cell stacks is the case in which the electrolyte is not a continuous member. Figure 9 presents schematically several possible configurations for stacks of this type. The anode-cathode series connection may be made directly, as indicated in Fig. 9(a), and 9(c), or by means of an intermediate metal ring, or collar, as shown in Fig. 9(b).

Multicell stacks with oxygen anodes.—The continuous electrolyte design will be considered first; as was mentioned above, this design has the advantage that the electrolyte can provide structural strength. Further-

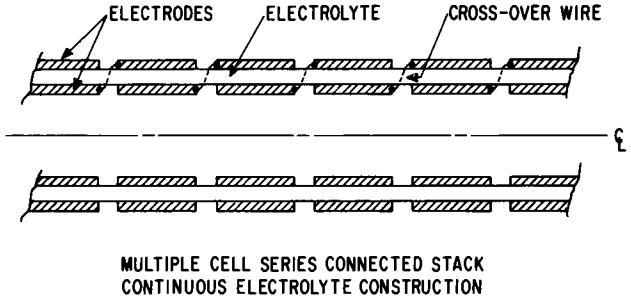

Fig. 8. Schematic illustration of a water vapor dissociation "stack" built upon a continuous electrolyte.

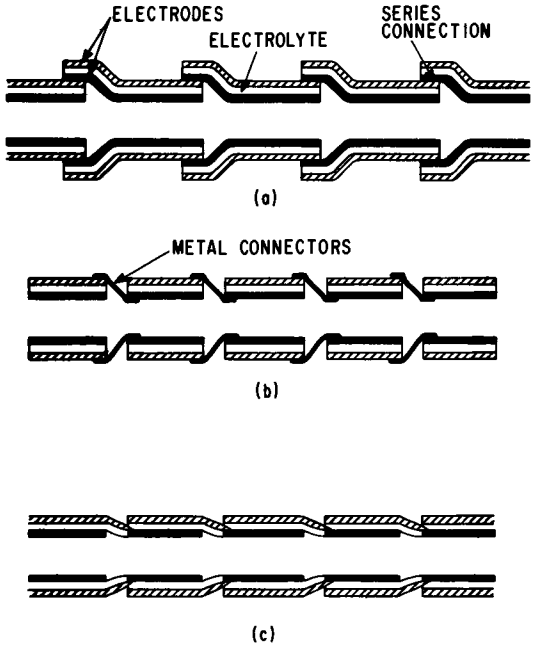

Fig. 9. Schematic illustration of various methods of construction of water vapor dissociation "stacks" built with discontinuous electrolyte.

more, the cathodes and anodes are completely separated, which allows flexibility in the choice of electrode materials. The material used for the series connection between adjacent cells, however, is exposed to an oxidizing environment on the anode side of the cell and a reducing environment on the cathode side. This condition, at temperatures of the order of 1000°C, requires the use of a noble metal such as Pt or Pd. These metals can be used as wires for the series connections. The principal problem is to bring the wire through the electrolyte without introducing leaks. Fortunately, both Pt and Pd have coefficients of thermal expansion comparable to that of stabilized zirconia. Although Pd is less costly than Pt, its use in this application imposes a substantial economic penalty, which is essentially prohibitive.

Several multicell stacks of this type have been built and tested. It was necessary to have the electrolyte be at least 0.75 mm thick in order to have no leaks at the juncture of the crossover wire. The increased electrolyte thickness increases its resistance to an unacceptable level. Consequently it is concluded that this is not a feasible approach.

Multicell stacks with oxygen anodes using a discontinuous electrolyte design, as in Fig. 9(a), are impractical because of the problem of establishing the direct series connection between anode and cathode. The oxygen partial pressure variation across the connecting section will typically be 15 orders of magnitude; the cathode must be protected against oxidation by the product oxygen, and the anode must be protected against reduction by the product hydrogen. Thus, an electronically conducting barrier would have to be interposed between the anode and the cathode of adjacent cells where these overlap. Since this barrier itself would now have to be resistant to both oxidizing and reducing conditions, again only Pt or Pd could be used. If a design like that in Fig. 9(b) is used, the collar, or ring, must be made from either Pt or Pd, which is economically unsatisfactory.

Multicell stacks with depolarized anodes.—The problems associated with multicell stacks fabricated with a continuous electrolyte are essentially the same as described above, with the exception that metals such as Ni or Co can be considered for the series connection since the anode environment will not be oxidizing to these. This alleviates the economic restriction. Both Ni and Co, however, have thermal expansion coefficients about 50% larger than that of stabilized zirconia, thus making the problem of establishing a leaktight connection more difficult.

Operation with depolarized anodes significantly relaxes conditions on materials for multicell stacks with discontinuous electrolyte segment. Either Co or Ni may be used in the anode and cathode, and a direct connection between electrodes may be established. The type of stack which has proven most satisfactory is presented schematically in Fig. 10. It is recognized that this design is a variation of that shown in Fig. 9(b). The solid Ni connections provide a leaktight series connection. The device is an integral unit. Three-cell and ten-cell stacks have been built and tested. Figure 11(a) is a photograph of a three-cell stack; a ten-cell stack is shown in Fig. 11(b). These devices

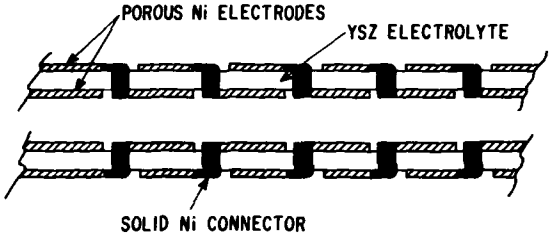

Fig. 10. Schematic illustration of water vapor dissociation "stacks" built and tested in these experiments.

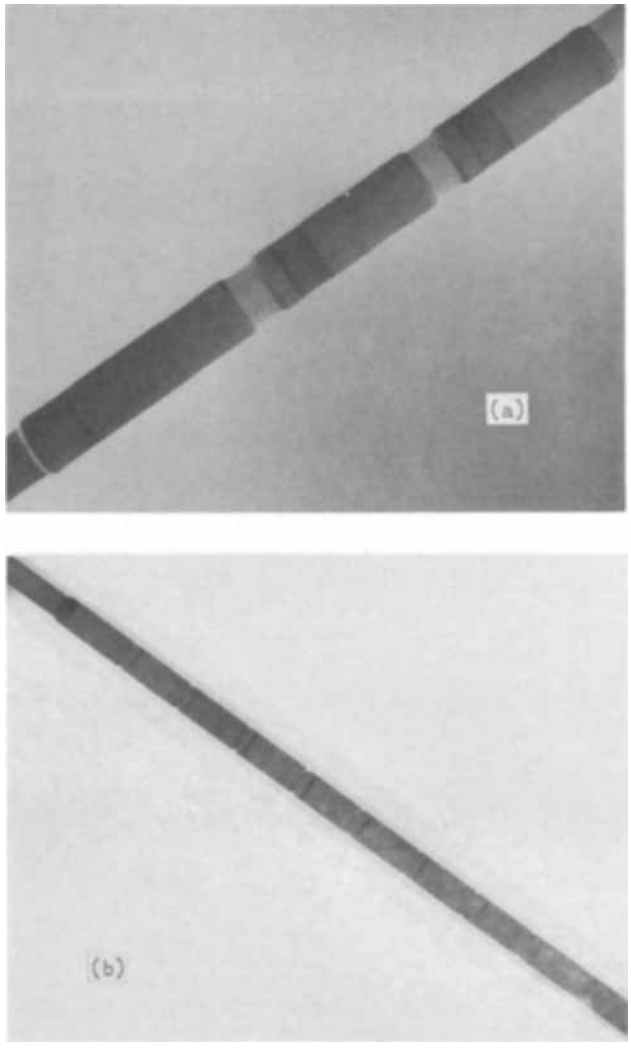

Fig. 11. (a) Photograph of typical three-cell water vapor dissociation "stack." 2/3X. (b) Photograph of typical ten-cell water vapor dissociation "stack." 3/16X.

have acceptable mechanical strength and are leaktight under pressure at room temperature.

The individual cells in multicell stacks cannot be instrumented as fully as single cells; it is not feasible to employ more than one pair of auxiliary electrodes for the entire stack, or to establish potential connections to each cell. Electrical testing is thus limited to determination of the total stack voltage, E, and, with the auxiliary electrodes, the open-circuit potential, E_o^f, at the exit end of the cell for parallel water vapor and fuel flows. The latter quantity is a single-cell measurement, as discussed in Part I.

Figure 12 is typical of the results obtained for a three-cell stack operated with H_2 fuel. Water vapor and fuel flow rates are normally expressed in terms of the current that would be required for complete dissociation of the water vapor and complete oxidation of the fuel in an equivalent single cell. The static (zero current) value of E_o^f is —0.22V, in good agreement with calculated values. The static voltage of E of —0.65V is three times the single-cell value, indicating no significant leakage at temperature under these conditions. Application of current to the stack causes E_o^f to increase and become positive at about 6.5A. At this point, the H_2O/H_2 ratios at the exit ends of the cathode and anode should be equal. Since the equivalent single-cell current is the stack current multiplied by the number of cells per stack, the observed value agrees reasonably well with the extent of water vapor dissociation and fuel oxidation that would occur at 6.5A for the given flow rates. Direct measurement of H_2 flow rates from

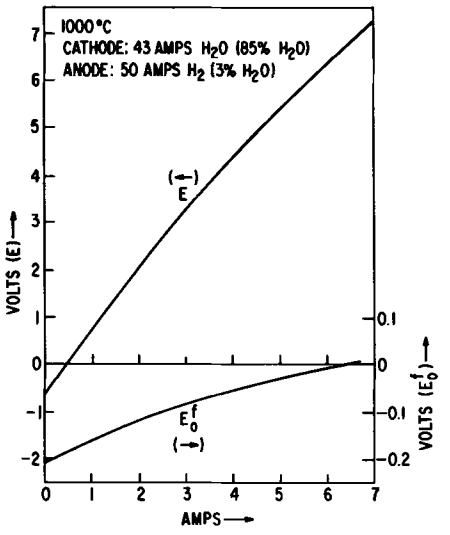

Fig. 12. Total and auxiliary electrode voltages for three-cell "stack." The active cell area is about 4 cm^2.

the cathode confirm coulometric water vapor dissociation.

Part of the nonlinearity of the stack voltage is due to the variation in average open-circuit voltage of the cells with current. The remainder is probably due to mass transport effects at the electrodes, of the type discussed elsewhere by the authors (12). An average slope, however, gives a stack resistance of about 1.0 ohms. Since the nominal cell area is 4 cm^2, the specific resistance for the device is about 1.3 ohm-cm^2, about twice that for single cells. A portion of this discrepancy can be ascribed to the different cell geometry, as well as to the interconnections and lead resistance, but the major portion cannot be accounted for at this time.

Another test of interest to stack performance is measurement of the resistance across anode-anode or cathode-cathode insulating gaps. This has been carried out, in appropriate atmospheres, on segments removed from complete stacks. The gap resistances have the proper magnitude, and show a temperature dependence paralleling that of the electrolyte. Thus any short-circuiting of adjacent cells across the gaps is due only to the electrolyte resistivity, and can be controlled by maintaining a sufficiently high value of the gap width/electrolyte thickness ratio.

The use of Ni series connections between cells allows the possibility of H_2 permeation through this material. Calculated permeation rates based on data for Ni sheet (14) are typically a few STP cc/min for current stack designs, but experimental results based on direct H_2 flow measurements indicate permeation rates an order of magnitude higher. The actual rates are undoubtedly sensitive to the structure of the Ni, and would be expected to depend on such factors as porosity and extent of grain boundaries. Although a quantitative evaluation of this effect is not possible, it must be considered in the design, fabrication, and testing of multiple cell stacks.

Fabrication Technology

For all the cells that have been described, there are two basic fabrication operations. The first is preparation of powders, and essentially involves those steps required to take the raw materials and process them into a form suitable for plasma-spraying.

The crossover leads for depolarized anode stacks were made from 99.6% purity Ni powder obtained from the Sherritt-Gordon Company. This powder, which has a particle size between 20 and 40μ, can be plasma-sprayed directly without any further preparation.

The Ni-YSZ cermet electrodes are prepared by mixing reagent-grade NiO with YSZ in the desired ratio, followed by spray-drying the powder. Spray-drying is a standard ceramic processing method which involves spraying through a nozzle a liquid-based suspension of the powder. The suspension is prepared by mixing the powders together in a water-alcohol solution to which a commercial suspending agent is added. This mixture is then fed through the nozzle on the spray-dryer into a large tank through which hot air is circulating, typically at a temperature of *ca.* 500°F. Droplets of the suspension are thus dried as they enter the tank and are subsequently size-classified. The result of this operation is agglomerated drops of very fine NiO and YSZ particles. The mix is screened to produce agglomerate particles of about 50μ size; the screened material is then calcined in air at 1325°C to impart additional strength. Following calcining, the material is ready for plasma-spraying.

Plasma-spraying is also a standard ceramic processing operation and is essentially a melting and casting operation. The prepared powders are fed into a plasma torch, in which they are rapidly melted and deposited onto a cool substrate. In these experiments, the substrate was a rotating air-cooled hollow aluminum mandrel. A Metco plasma gun was used, and a He/H_2 gas mixture was used to produce the plasma.

After plasma-spraying, the NiO in the electrode will be reduced in H_2 at about 400°C to produce a Ni-YSZ electrode. This general powder preparation procedure accomplishes several purposes. First, the use of very fine particulate NiO, rather than Ni powder, results in a fine Ni grain size in the reduced electrode. The YSZ addition prior to spray-drying affords the maximum degree of particle mixing. However, the blended mix has a particle size before spray-drying that is too small to permit satisfactory flow and melting in the plasma-spray operation. Thus the spray-drying step results in intimately mixed, very fine particles of the constituent powders bound together as a relatively coarse agglomerate suitable for plasma-spraying.

Essentially the same procedure is used for Co-YSZ electrodes.

Electrolyte powders are also prepared by spray-drying (15). Starting materials consist of unstabilized zirconia (Zircoa "A"), 99% purity Y_2O_3, and reagent-grade Fe_3O_4 powders. These powders, in the as-received condition, are all too fine for plasma-spraying, and therefore are initially spray-dried. As with the electrode powders, this operation produces an intimately mixed powder agglomerate which is then screened to a 50μ particle size. The material is calcined in air in the range of 1350°-1500°C, depending on the exact composition being prepared. It is then ready for plasma-spraying. The stabilization of the zirconia occurs during the melting and freezing of the powder in the plasma-spray operation.

For cells with oxygen anode, the $PrCoO_3$ powder is prepared by reacting Pr_6O_{11} with CoO at 1400°C in air. X-ray diffraction analysis of the products indicated essentially complete reaction. The oxide was then ground to a particle size on the order of 25μ. Oxygen anodes were applied to the cells from an aqueous slurry of the perovskite powder. $PrCoO_3$ electrodes can also be fabricated by plasma-spraying, but this procedure tends to yield an electrode that is insufficiently porous.

An important design parameter in the fabrication of water vapor dissociation cells is the electrode/electrolyte thickness ratio. The Ni-YSZ (or Co-YSZ) electrodes have thermal expansion coefficients which are characteristic of the metal; *i.e.*, $\alpha_{1000°C}$ (Ni) $\approx 15 \times 10^{-6}$ $°C^{-1}$, compared to a value of $\alpha_{1000°C}$ (YSZ) $\approx 10 \times 10^{-6}$ $°C^{-1}$ for the electrolyte. In addition, the cermet is much stronger than the pure metal (Ni or Co) at temperatures of cell operation. The electrolyte, being entirely ceramic, is also strong at elevated temperatures. Because of the differential thermal expansion, stresses arise at the electrode/electrolyte interface which can lead to mechanical failure of the cell. The

interfacial stresses can be relieved by incremental plastic flow of the electrode, if it is thin enough relative to the electrolyte. It has been empirically determined that an electrode/electrolyte thickness ratio of 1/4 is satisfactory. On cells with oxygen anodes, the $PrCoO_3$ electrode is only partially sintered and therefore quite porous. Consequently, in spite of its large coefficient of thermal expansion—$\alpha_{1000°C}$ ($PrCoO_3$) $\approx$ 28 x 10^{-6} $°C^{-1}$—interfacial stresses which arise are relieved by mechanical failure of the electrode, rather than in the electrolyte. Such failure does not occur on heating, fortunately, but cracking and spalling of the oxygen anode during cooling is a serious problem and generally these cells can be tested only once without applying a new $PrCoO_3$ anode.

A typical processing schedule for water vapor dissociation cells would then be as follows. First the metal leads (Ni) are plasma-sprayed onto a rotating aluminum mandrel. Masking is provided as required. Then the inner electrode (usually the cathode) is applied by plasma-spraying. It is reduced to a cermet in H_2. Plasma-spraying of the electrolyte then takes place; as plasma-sprayed, the YSZ is about 90% theoretical density, which is not sufficient to make it leaktight. The aluminum mandrel is removed by leaching in a KOH solution, and the cell is fired at 1225°C, which results in the YSZ sintering to about 95% theoretical density, rendering it leaktight.

The outer electrode (usually the anode) on depolarized cells or self-driven cells is applied by plasma-spraying; on cells with oxygen anodes, the $PrCoO_3$ is hand-applied.

Summary

The design, fabrication, and performance of zirconia electrolyte water vapor dissociation cells has been considered. Although not of practical value, single-cell devices are important because they provide a convenient means of evaluating cell performance and electrode reactions. Single-cell devices with both oxygen and depolarized anodes were tested.

An analysis of design and materials factors for multicell stacks led to the conclusion that the most feasible system was that employing discontinuous electrolyte segments and depolarized anodes.

Acknowledgment

The authors gratefully acknowledge the assistance of the various members associated with the Fuel Cells Program.

Manuscript submitted April 21, 1969; revised manuscript received July 17, 1969.

Any discussion of this paper will appear in a Discussion Section to be published in the June 1970 JOURNAL.

REFERENCES

1. H. S. Spacil and C. S. Tedmon, Jr., *This Journal*, **116**, 1618 (1969).
2. C. S. Tedmon, Jr., H. S. Spacil, and S. P. Mitoff, *This Journal*, **116**, 1170 (1969).
3. K. Kiukkola and C. Wagner, *This Journal*, **104**, 379 (1957).
4. W. D. Kingery, J. Pappis, M. E. Doty, and D. C. Hill, *J. Am. Ceram. Soc.*, **42**, 393 (1959).
5. H. Schmalzried, *Z. Electrochem.*, **66**, 572 (1962).
6. J. Millet and M. Guillon, *Bull. de la Direction des Etudes et Recherches, Ser. B, Reseaux Electriques No. 2*, p. 117 (1967).
7. D. W. Strickler and W. G. Carlson, *J. Am. Ceram. Soc.*, **47**, 122 (1964).
8. H. Tannenberger, H. Schachner, and P. Korges, *Intern. Meeting on the Study of Fuel Cells, Part III, Brussels, 1965*, p. 19.
9. F. Petri, *Z. Chem.*, **5**, 437 (1965).
10. Data taken from C. E. Wicks and F. E. Block, Bull. 605, U. S. Bureau of Mines.
11. *See*, for example, "Electronic Circuits and Tubes," Cruft Lab. Harvard Univ., McGraw-Hill, New York (1947) or "Electronics for Scientists," Malmstedt *et al.*, Benjamin, New York (1962).
12. H. S. Spacil and C. S. Tedmon, Jr., "The Relationship of Performance and Materials Properties in High Temperature Zirconia Electrolyte Fuel Cells," Presented at Meeting of Comité International de Thermodynamique et de Cinetique Electrochimies, Detroit, Sept. 1968.
13. H. Tannenberger and H. Siegert, Paper presented at ACS Fuel Cell Symposium, Chicago, 1967.
14. W. Fischer, *Z. Natur.*, **22A**, 1581 (1967).
15. C. W. Krystiniak, U.S. Pat. 3,429,962 (Feb. 1965) and 3,373,719 (Nov. 1968).

The Microstructure of Sintered Silver Electrodes

II. At the End of 1-Hour Rate Discharges

Charles P. Wales*

Electrochemistry Branch, Naval Research Laboratory, Washington, D. C.

ABSTRACT

A single discharge of a Ag electrode at the relatively fast 1-hr rate resulted in Ag particles smaller than those present in the unused sintered electrode. As an electrode was cycled in 35% KOH at 25°C, the active material tended to clump together while void spaces became larger. At the same time the average size of Ag particles gradually increased, although particle size remained small at the surface of a discharged electrode. These changes were accompanied by a gradual decrease in discharge capacity. The small Ag particles that formed during fast (1-hr) discharges could be oxidized more readily and more completely during a charge than the large Ag particles that formed during slow (20-hr) discharges. Therefore the capacity decreased more slowly when an electrode was cycled using fast discharges.

The present investigation concerns changes in the structure of silver electrodes when the electrodes were given a series of complete discharges at the 1-hr rate. The silver electrode is the positive electrode of silver-zinc and silver-cadmium storage batteries. These batteries are important as high capacity power sources and for their ability to be discharged at high current densities.

When a silver electrode is discharged at a high current density, such as the 1-hr discharge rate, electrode

* Electrochemical Society Active Member.

Key words: silver electrode; microstructure; storage batteries.

capacity is generally maintained at a higher value over a series of cycles than when a low discharge c.d. is used. The present paper shows that this difference in capacity results from changes in the microstructure of the electrodes, and that discharge c.d. has an important effect on structure. The structural changes that occurred as charged Ag electrodes were being reduced during discharge at the 1-hr rate have been described in the previous paper in this series (1). An earlier paper was concerned with the structures obtained when electrodes of the same original construction were discharged at the relatively low c.d. required for the 20-hr discharge rate (2).

Experimental Procedure

Since the experimental procedure has already been described (1), only a brief account is given here. Sintered Ag electrodes were charged individually at the 20-hr rate of constant current until oxygen began to evolve. Then an electrode was discharged at the 1-hr rate to a final potential of −500 mV *vs.* the Ag/Ag_2O reference electrode. This potential was equivalent to approximately 1.0V for a typical Ag-Zn cell. The cycling was done at 25°C in an excess of 35% KOH solution.

Samples for microscopic examination were cut from discharged electrodes that had been cycled from 1 to 30 times. After a sample had been washed and dried, it was impregnated with an epoxy resin while under a vacuum. Then a cross section of the sample was prepared by grinding and polishing. Finally a sample was examined by optical microscopy and the appearance of significant areas recorded by photography.

Results of Microscopic Examinations

Structure of unused sintered Ag electrodes.—Figure 1 shows an unused sintered Ag electrode, in order to have a base for illustrating the early changes that occur with use. All photographs in this paper are of cross sections through an electrode. The photographs, therefore, also show cross sections through the individual particles or crystals in the electrode. Since the structure of an unused electrode has already been described (2), only a brief account is given here. Ag was present in a wide range of sizes from approximately 0.5 to 100μ. Most Ag particles were small and had their smallest dimension in the range 1.5 to 2μ. It was estimated that only 5% of the active material consisted of particles that were over 15μ. The general appearance of the electrode structure was fairly uniform, although the large particles were not evenly distributed throughout the electrode. Many of the small particles were grouped together in clusters. Some clusters of small particles are shown in Fig. 1. Voids were small and well distributed in the unused electrode.

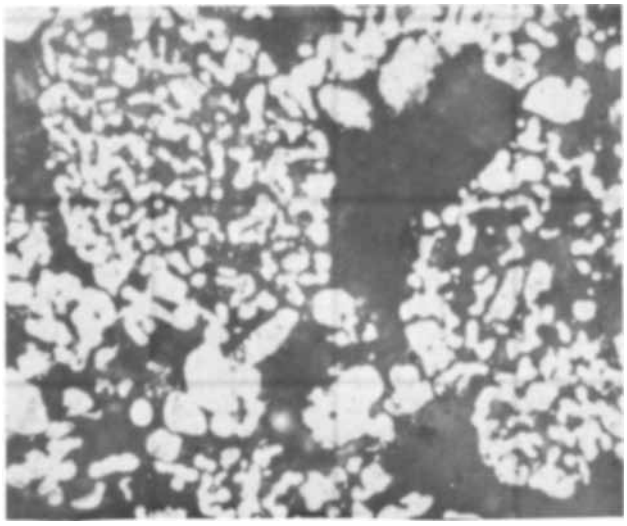

Fig. 1. Particles of Ag active material (white) in an unused sintered Ag electrode. The dark background is the impregnation plastic that has filled void areas in the electrode. Lines forming the squares are 30μ apart.

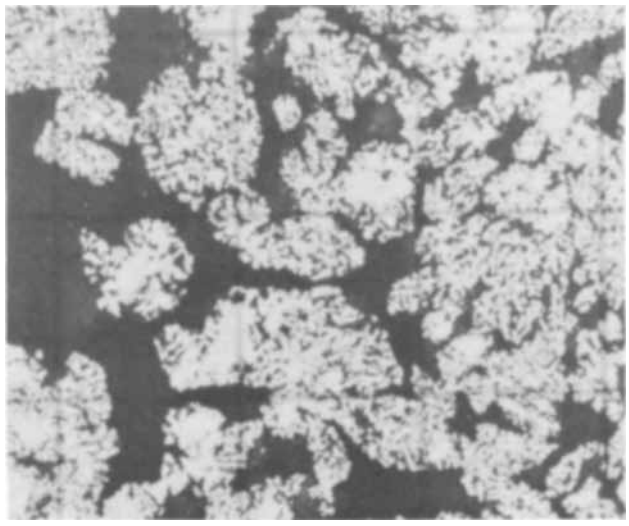

Fig. 2. Typical Ag particles present at the end of the first discharge at the 1-hr rate in 35% KOH solution. Compare with Fig. 1 at the same magnification.

Structure of discharged electrode after 1 cycle.—The average size of the Ag particles had become much smaller, and the individual particles were closer together, after charging an unused sintered electrode at the 20-hr rate to oxygen evolution and giving it a single discharge at the 1-hr rate. Figure 2 illustrates the sponge-like structure produced by the discharge at cycle 1. The changes in particle size can be seen by comparing the discharged electrode shown in Fig. 2 with the unused electrode shown in Fig. 1. Groups of particles were in larger clumps after the first discharge. (The increased size of the clumps was more apparent when the electrodes illustrated in Fig. 1 and 2 were compared at a lower magnification.) The majority of the Ag particles produced during the first discharge were quite small and had irregular, elongated shapes.

Some larger Ag particles had also formed during the first discharge, but were less common than the small particles. The area shown in Fig. 2 does not include any of these large particles that had formed during the first discharge, but it does include some even larger particles that were residual from the original electrode. These large Ag particles had failed to oxidize completely during the previous charge and were often found in the center of groups of the small particles. It is likely that some of the small Ag particles had nucleated from these large Ag particles during the discharge.

The metallic Ag grid of an unused electrode had a smooth surface, but changes occurred during the first cycle. Part of a grid member is included in Fig. 3. Small Ag particles had deposited on the surface of the grid during the discharge. Another change during the first cycle was that some penetrating attack had occurred on the grid surface. This attack probably took place during the charge, while an oxide layer was forming on the grid surface.

Deposit of small particles on surface of large particles.—Changes that took place at the grid surface resembled the changes taking place at the surface of the largest Ag particles. Figure 4 gives a full cross section through an electrode in an area that did not contain a grid member. This shows the appearance of an electrode at the end of the second consecutive discharge at the 1-hr rate, following slow charges at the 20-hr rate. The small Ag particles that formed during a fast discharge were not large enough to be seen individually at the low magnification used for Fig. 4. The bright, featureless areas included in Fig. 4 are some of the largest particles residual from the particles originally present in the unused

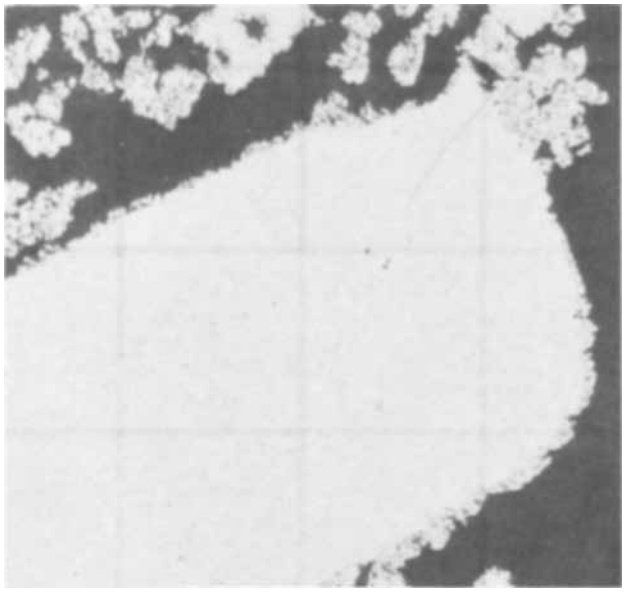

Fig. 3. Another area of the electrode shown in Fig. 2 at the end of cycle 1 discharge. Large white object is a cross section of a grid member. One electrode surface is at the right side of the photograph. Lines forming the squares are 60μ apart.

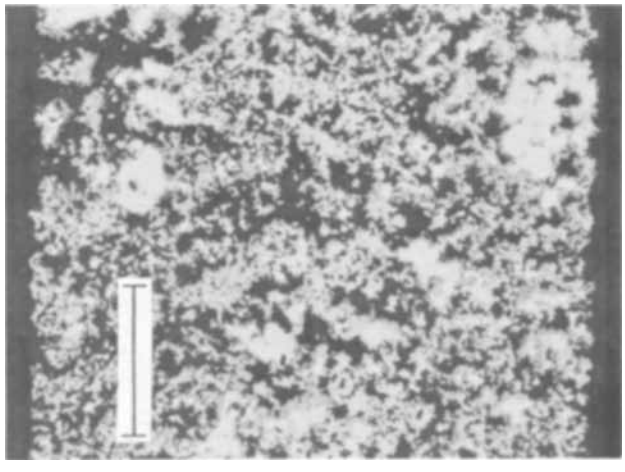

Fig. 4. Cross section of an electrode at the end of cycle 2 discharge. Electrode surfaces are at the sides of photograph. Largest Ag particles shown here had not oxidized completely during the previous two charges. Marker indicates 250μ.

electrode. As mentioned above, these very large particles were incompletely oxidized during charges. Only the surface of the largest particles was oxidized during the first charge. This surface oxide layer was reduced during the next discharge, and a layer of small Ag particles formed from the oxide layer.

The deposit of small particles gradually became thicker on the surface of large particles as an electrode was cycled. Comparison of discharged electrodes at cycles 2 and 1 showed that the number of small Ag particles present on the grid and on the large particles had increased noticeably during cycle 2. This deposit of small particles continued to grow as an electrode was cycled. Comparison of Fig. 5 with Fig. 4 shows that the deposit had become much thicker by cycle 30.

Growth of voids and clumps of particles.—The Ag particles in an electrode gradually clumped together as the electrode was cycled, and the formation of large clumps was accompanied by the development of large voids between the clumps. These changes are illustrated in Fig. 4 and 5. A comparison was made of particle distribution in discharged electrodes at cycles 1, 2, 5, 15, 27, and 30. This comparison indicated that the greatest increase in void size and in clumping of Ag particles took

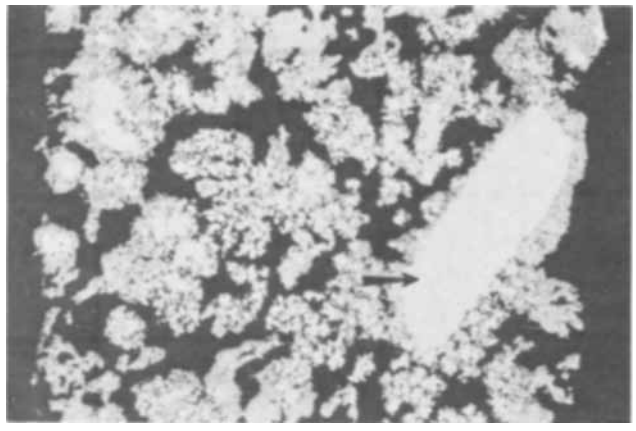

Fig. 5. Cross section of an electrode including a grid member (arrow) at the end of cycle 30 discharge at the 1-hr rate. Electrode surfaces are at the sides of photograph. Comparison with Fig. 4 at the same magnification shows changes in thickness of deposit on the grid and on the largest Ag particles. Note also the changes in voids and in Ag particle distribution.

place during the first 15 cycles. The increases were particularly evident between cycle 5 and 15. The size of voids and clumps increased more slowly from cycle 15 to 30 than from cycle 1 to 15.

Note that the discharge capacity gradually decreased when Ag electrodes were cycled using the 1-hr discharge rate (Fig. 6). This slow capacity decrease took place simultaneously with the gradual change in electrode structure. The capacity of electrodes that were discharged at the 20-hr rate has been included in Fig. 6 for comparison.

Structure of discharged electrode after 15 cycles.—The greatest change in electrode structure took place during the first cycle, with small Ag particles forming throughout the electrode during the rapid discharge. The small Ag particles were gradually replaced by larger particles when an electrode continued to be cycled, and clumps of particles gradually increased in size. The change in average particle size with cycling was less noticeable in some areas of a discharged electrode than in other areas. Figure 7 illustrates some of the Ag particles present in a discharged electrode at cycle 15. Comparison with Fig. 2 shows that the porous, sponge-like structure within the clumps of small particles was much the same in discharged electrodes at cycles 1 and 15, and that there was little change in the size of the small pores in these clumps.

A few of the larger particles that formed during discharge, gradually becoming more numerous as the number of cycles increased, are included in Fig. 7. The replacement of the small particles which formed dur-

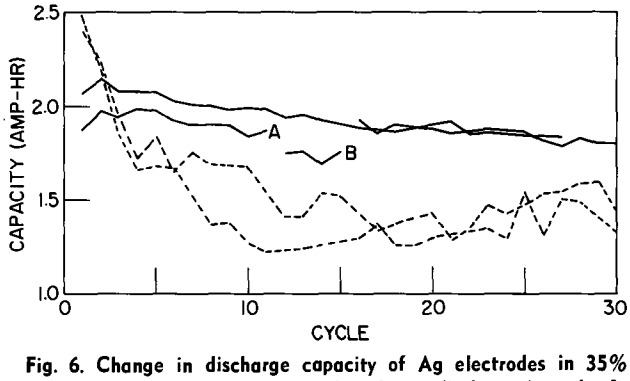

Fig. 6. Change in discharge capacity of Ag electrodes in 35% KOH at 25°C, showing two electrodes always discharged at the 1-hr rate (solid lines) and two electrodes of the same construction always discharged at the 20-hr rate (dashed lines). All charges were done at the 20-hr rate. At point A one cell stood discharged 74 days and at point B the electrolyte in this cell was replaced.

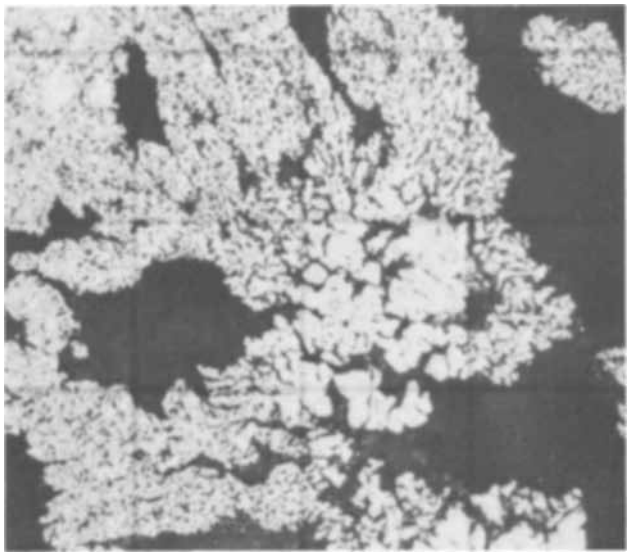

Fig. 7. Area of an electrode at the end of cycle number 15 discharge showing several sizes of Ag particles that have formed. Comparison with Fig. 2 indicates that voids have become larger as groups of Ag particles have clumped together. Lines forming squares are 30μ apart.

ing the first discharge was a slow process. The larger Ag particles were comparatively rare in the early cycles, but by cycle 15 approximately 10-15% of the active material in a discharged electrode consisted of such particles.

The large Ag particles which gradually replaced the small particles were distributed unevenly in the electrode. As much as 40-50% of some areas consisted of large particles at cycle 15, although the average for the whole electrode was only 10-15%. These larger particles were most often found in the interior of the discharged electrode and near the grid, but almost never at or near an electrode surface. These large Ag particles which formed during discharge could usually be distinguished readily from the even larger Ag particles that remained residual from the unused electrode, since there were easily recognizable differences in the structure and size of the two types.

Structure of discharged electrode after 30 cycles.—The large Ag particles occupied 30-40% of the volume of an electrode at the end of cycle 27 or 30 discharge. A typical view is shown in Fig. 8. Comparison with Fig. 7 shows that the finely divided, sponge-like structure had become less common as the number of cycles had increased. The proportion of a discharged electrode that consisted of large particles had increased by a factor of 2 or 3 in the period between cycle 15 and 30. Some of the larger Ag particles are shown at higher magnification in Fig. 9. Void space was less than usual in regions where many of these particles had clumped together. Distribution of the large particles had become very uneven. As much as 85% of some areas consisted of the large particles at the end of cycle 30, while only 10% of the other areas contained large particles.

Although many large particles had formed by the end of cycle 30 discharge, the areas near the surface of an electrode still consisted almost entirely of small Ag particles. An example of the small particles at the surface is given in Fig. 10. Small particles of this size had been found at the end of every discharge, beginning with the first discharge. As an electrode was given additional cycles, the smallest Ag particles were gradually replaced by larger particles except in areas near the electrode surface. Another change was that groups of needle-like dendrites were less common in the later cycles than they were in the early cycles. The needle-like dendrites had cross sections which were the same size as the particles shown in Fig. 10.

The average size of Ag particles increased as distance of the particles from the surface increased in electrodes that had been cycled repeatedly. The small Ag particles which were present at the surface of a discharged electrode have already been illustrated by Fig. 10. The particles which were found in regions close to the surface were larger, and some of these particles are shown in Fig. 11. The shapes of Ag particles shown in Fig. 10 and 11 were similar despite the differences in size. Although the particles shown in Fig. 11 were not of an uncommon size, it was more usual for the Ag in a discharged electrode to be present as the larger particles which were illustrated in Fig. 9.

Electrode of unusually low porosity.—There was one exception to the earlier statement that large Ag particles were almost never found at or near the electrode surface. Samples were taken from one electrode which only gave three-fourths the capacity of the other electrodes. It was found that the Ag particles were packed more closely in this electrode than was usual. The structure after five charge-discharge cycles was dif-

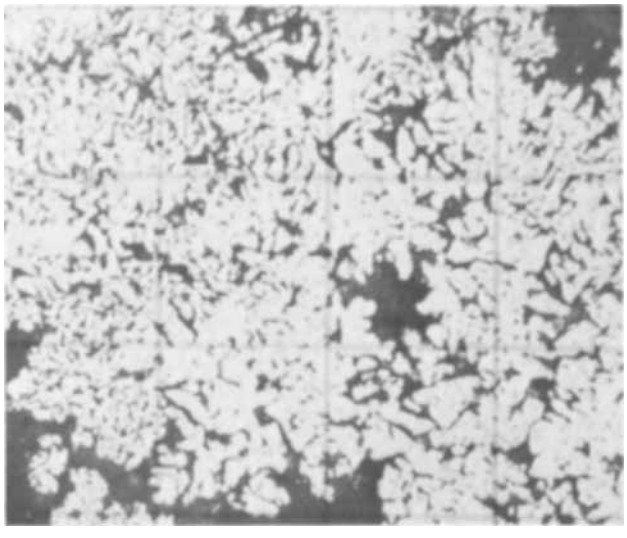

Fig. 8. Area of an electrode at the end of cycle 27 discharge including large and small Ag particles. Compare with Fig. 1, 2, and 7, all at the same magnification. Average size of Ag particles present at the end of a discharge has gradually increased with cycling.

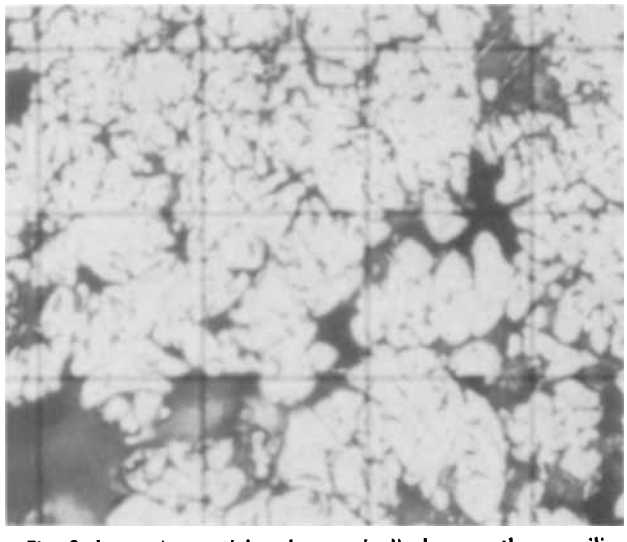

Fig. 9. Large Ag particles that gradually became the prevailing form in the interior of a discharged electrode as the number of cycles increased. A different area of the sample shown in Fig. 8 and at higher magnification. Lines forming squares are 15μ apart.

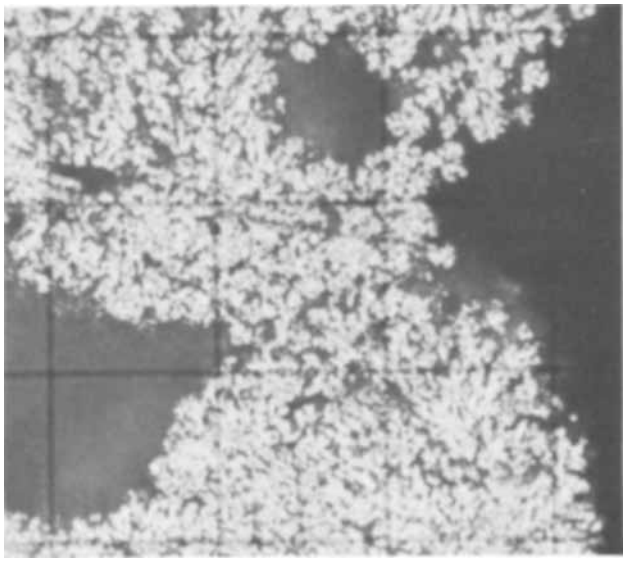

Fig. 10. Small Ag particles present at the end of cycle 30 discharge at the 1-hr rate. Right side of photograph is a surface of the electrode. Small Ag particles were always found in electrodes discharged at the 1-hr rate, but gradually became less common with cycling. Same magnification as Fig. 9.

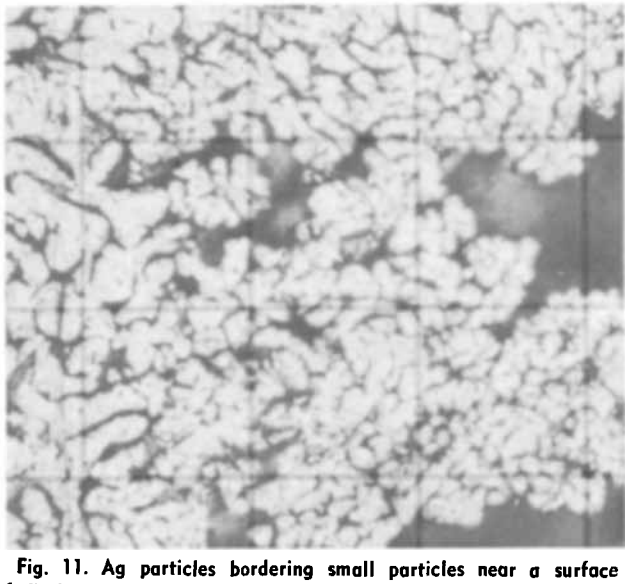

Fig. 11. Ag particles bordering small particles near a surface of discharged electrode. The surface is out of view to the right of the photograph. Same sample and magnification as Fig. 10.

ferent from the structure found in all other electrodes that were examined. The range of particle sizes was similar to the range found in other electrodes at cycle 5, but larger Ag particles were more numerous than smaller particles. Many of the large particles were present near the electrode surface, in contrast to the usual absence of large particles near a surface. The reason for the abnormal structure was not determined, but it is believed that the close packing of Ag particles contributed to the low capacity obtained from this electrode.

Discussion

Dependence of particle size on discharge c.d.—The present investigation of the microstructure of Ag electrodes has demonstrated that two identical electrodes can be converted by a single discharge into electrodes having structures and charge acceptance quite different from each other. These changes result from simply using different rates of discharge current. When the first discharge of a sintered Ag electrode was done at the relatively high c. d. required for the 1-hr discharge rate, the Ag particles that were produced during reduction of the oxides were smaller than the particles present in the unused electrode (Fig. 1 and 2). On the other hand, over half of the Ag that was produced during a slow discharge formed as large granular particles when the first discharge was done at the 20-hr rate (2). These large granular particles were approximately 10 times as large as the particles in the unused electrode. The results of x-ray diffraction have also indicated that Ag particle size varied inversely with the c. d. (3).

Table I summarizes the structural changes that took place during discharges. Table I is based on both the present and earlier work (1, 2).

It was concluded from the shapes of the Ag particles that a dendritic type of growth occurred during a fast discharge. Dendritic growth would be expected to occur when appreciable concentration gradients were set up in the electrolyte and when concentration of soluble Ag species was low near the surface where metallic Ag was forming. There would be more time for diffusion to take place through the electrolyte during a slow discharge. This would promote the growth of large Ag particles which lack obvious dendritic shapes when c. d. was low. Work on electrodeposition of Ag from various media, such as aqueous solutions of several different Ag salts (4, 5), or a LiCl-KCl eutectic (6), has shown that the mechanism of Ag deposition changes at high current densities. The same should be true when Ag forms in a KOH solution, as in the present work.

Dependence of capacity on particle size.—The size of the particles which were present in these electrodes was very important, since small Ag particles can be oxidized more readily and more extensively than large particles. This means that an electrode consisting of small Ag particles can be charged more rapidly and to a greater capacity than an electrode consisting of large particles. After large Ag particles had formed during a slow discharge, the original capacity of an electrode was not regained readily by using fast discharges. The central portions of large particles remained as metallic Ag at the end of a charge, instead of being oxidized. Discharge c. d. is an important factor to consider, therefore, when it is necessary to obtain a large capacity from Ag-Zn and Ag-Cd storage batteries over a period of several cycles.

The slow decrease in capacity that occurred when the Ag electrodes were discharged at the relatively fast 1-hr rate (Fig. 6) resulted mainly from the average size of Ag particles gradually growing larger as an electrode was cycled. The clumping of Ag particles into groups of increased size may also have been a factor in the slow capacity decrease, as well as loss of

Table I. Major effects of c.d. on the structures produced in Ag electrodes during discharge. Electrodes were cycled in 35% KOH at 25°C, with all charges done at the 20-hr rate

Always discharged at 1-hr rate	Always discharged at 20-hr rate
Ag_2O formed first on surface of AgO clumps during a discharge, then within clumps. Only one-fourth of the AgO was reduced to Ag_2O before Ag began to form.	Ag_2O formed on surface of AgO clumps and within AgO clumps simultaneously during a discharge. Over half of the AgO was reduced to Ag_2O before Ag began to form.
Ag formed throughout electrode at cycle 1 discharge, but in later discharges Ag formed first at electrode surface with formation gradually moving inward. Ag formed into particles smaller than those in unused electrode. Average size of Ag particles gradually increased with cycling.	Ag formed throughout electrode at scattered sites during a discharge, with a slight preference for formation at or near electrode surface. Ag formed into particles considerably larger than those in unused electrode. Size of Ag particles did not increase greatly after first discharge.
When electrode was 65% discharged more AgO was present than Ag_2O. At end of discharge some AgO and Ag_2O remained.	When electrode was 65% discharged only small amount of AgO was still present. At end of discharge no oxides were found.
There was little attack on grid during cycling.	Grid cross section decreased in size because of gradual attack during cycling.

active material through shedding or through oxides dissolving in the electrolyte and not reprecipitating back on the electrode. As the number of cycles increased, many of the larger Ag particles attained sufficient size that they did not oxidize completely during a charge. The increased size of these Ag particles may have resulted from particles growing together during a fast discharge. The first formation of metallic Ag occurred at the surfaces of an electrode during a fast discharge (1) and only small Ag particles were found in these areas.

Another indication of the relationship between capacity and particle size was that a greater capacity loss occurred during the first few cycles when the slow 20-hr discharge rate was used than when a rapid discharge rate was used (Fig. 6). Most of the Ag particles that formed during the slow discharges were at least an order of magnitude larger than the particles that formed during 1-hr rate discharges (2). The greatest change in particle size occurred during the first discharge regardless of which discharge rate was used.

Influence of discharge c. d. on grid corrosion.—The grid corrosion rate was decreased by using fast discharges instead of slow discharges. When the slow, 20-hr discharge rate was used, the grid gradually decreased in size as a result of penetrating attack at the grid surface (2). On the other hand, attack on the surface of the grid was noticeably less after using the higher c. d. of the 1-hr discharge rate for 5 cycles than it was after 5 cycles at the 20-hr rate. The average thickness of a grid member, after 30 cycles using the 1-hr discharge rate, was still approximately the same as the original thickness. Some penetrating attack had occurred, however, and the grid surface was no longer smooth.

The deposit of small Ag particles which formed on the grid surface during a discharge at the 1-hr rate gradually increased in thickness when discharges were repeated (Fig. 3 and 5). During a charge the small Ag particles in this deposit tended to be oxidized before the grid surface was oxidized. Oxidation of the deposit formed a protective oxide coating on the grid surface, so that less oxidation and, therefore, less attack of the grid occurred during a charge that followed a fast discharge.

Importance of particle size when manufacturing Ag electrodes.—Unfortunately, the mechanism which resulted in forming a protective oxide coating on the grid also formed protective coatings on the surface of the largest Ag particles present in the original sintered electrode. These oxide coatings prevented complete oxidation of large Ag particles in a charge and, therefore, prevented full utilization of the Ag active material in an electrode. The increasing thickness of the deposit of small particles that formed on the large Ag particles residual from the unused electrode was illustrated in Fig. 4 and 5.

Nothing that has been observed thus far has indicated that any advantage is obtained by including large Ag particles in the electrodes. Although the maximum thickness of the oxide layer on Ag particles was often greater than 5μ at the end of a charge, a minimum thickness of only 1-2μ was common. Therefore Ag particles having a diameter as large as 2-4μ can be expected to oxidize completely during a charge, if the particles have access to the electrolyte, and slightly larger particles should oxidize almost completely. It should be advantageous to grade particle size carefully when manufacturing sintered Ag electrodes and have a maximum particle size no larger than 3-4μ. Small changes in the size of particles present in an unused electrode will only affect the first few cycles, because the particle size of the Ag produced during a discharge is strongly dependent on discharge conditions and the particles tend to reach a limited size range when electrodes are cycled repeatedly.

Gradual clumping of particles.—Cycling was always accompanied by the slow formation of large voids as the particles clumped together into larger groups (Fig. 5, 7). The discharge rate had no apparent effect on the formation of voids and the clumping of particles. The voids and clumps seemed to grow at the same rate and to be approximately the same size, whether the 1-hr or 20-hr discharge rate was used for the same number of cycles.

Charge-discharge efficiency.—The electrodes which were discharged at the 1-hr rate gave only about 90% of charge capacity on the first discharge (not including the part of charge capacity used in evolving oxygen), since the silver oxides were not completely reduced during the fast discharge. Beginning with cycle 2, however, all discharges at the 1-hr rate gave nearly 100% of the capacity of the preceding charge. Approximately the same amount of oxide remained at the end of each discharge at the 1-hr rate. On the other hand, the electrodes which were discharged at the 20-hr rate always gave close to 100% of the capacity accepted during the previous charge.

The difference in the charge-discharge efficiency accounted for the electrodes which were discharged at the 1-hr rate giving less capacity at cycle 1 than the electrodes discharged at the 20-hr rate (Fig. 6). The electrodes which were discharged at the 1-hr rate were giving more capacity by cycle 3 than those discharged at the 20-hr rate, since capacity had decreased rapidly during the first few cycles using slow discharges. Based on a theoretical capacity of approximately 2.9 A-hr for the electrodes used in this work, it can be seen from Fig. 6 that in the first few cycles the electrodes discharged at the 1-hr rate gave 65-75% of the capacity theoretically possible, and these electrodes were giving 60-65% of theoretical capacity at cycle 30. Although the electrodes discharged at the 20-hr rate had given approximately 85% of theoretical capacity at cycle 1, they were only giving 45-55% of theoretical capacity at cycle 10.

Low capacity in impure electrolyte.—The capacity loss shown at point A of Fig. 6 was assumed to be due to carbonate content of the electrolyte becoming high during the 74 days of inactivity. Although the cell containing this electrode was closed, holes for the wire leads were not sealed tightly and CO_2 from the atmosphere could enter the cell. Carbonate could also result from the cellulosic separators reacting with the KOH solution. The electrode capacity improved markedly when the old KOH solution was replaced with fresh solution. The first discharge after replacing the electrolyte gave 113% of the capacity of the previous charge (measuring charge capacity to the beginning of oxygen evolution). An unusually large quantity of silver oxides must have remained in this electrode at the end of the preceding discharge. The concentration gradients in the electrolyte probably had become unusually high during discharges at the 1-hr rate after carbonate had increased and KOH concentration had decreased. The electrolyte has a strong influence on crystallization and should be studied in detail.

Conclusions

When sintered Ag electrodes were charged at the 20-hr rate and discharged at the 1-hr rate in 35% KOH solution at 25°C, the following changes took place:

1. As the oxides were reduced during the first discharge, the Ag particles which formed had a much smaller average size than the Ag present in the unused electrode. These small particles which formed during a fast discharge contrasted with the large granular particles of Ag, approximately 10 times as large as those in the unused electrode, which formed during a slow discharge at the 20-hr rate.

2. The capacity of an electrode decreased more slowly when electrodes were cycled using the 1-hr discharge rate than when using the 20-hr rate, because the small Ag particles which formed during a

fast discharge could be oxidized more readily and more completely during a charge.

3. Small particles of Ag formed on the surfaces of a grid during discharges at the 1-hr rate, and tended to protect a grid from serious attack. When the 20-hr discharge rate was used, however, a grid gradually decreased in size as a result of the grid surface being attacked repeatedly.

4. During the first discharge, the Ag formed into clumps of particles that were larger than the clumps originally present. As an electrode was cycled, the clumps of Ag particles gradually increased in size while large void spaces developed and small voids became less common.

5. The proportion of a discharged electrode that consisted of small Ag particles slowly decreased as larger Ag particles gradually developed in the interior of the electrode with cycling. Although the larger particles were comparatively rare in the first few cycles, approximately 30-40% of a discharged electrode consisted of the larger Ag particles at cycle 30.

Acknowledgment

The author wishes to thank Mr. A. C. Simon for the help and advice he has given during this work.

Manuscript submitted May 16, 1969; revised manuscript received Aug. 1, 1969. This was Paper 27 presented at the Detroit Meeting Oct. 5-10, 1969.

Any discussion of this paper will appear in a Discussion Section to be published in the June 1970 JOURNAL.

REFERENCES

1. C. P. Wales, *This Journal*, **116**, 729 (1969).
2. C. P. Wales and A. C. Simon, *ibid.*, **115**, 1228 (1968).
3. C. P. Wales and J. Burbank, *ibid.*, **112**, 13 (1965).
4. G. Wranglen, *Electrochim. Acta*, **2**, 130 (1960).
5. W. Mehl and J. O'M. Bockris, *J. Chem. Phys.*, **27**, 818 (1957).
6. J. W. Faust and H. F. John, *This Journal*, **108** 109 (1961).

Differential Capacitance and Cyclic Voltametric Studies on Smooth Lead in H_2SO_4 Solutions

Thomas F. Sharpe*

Electrochemistry Department, Research Laboratories, General Motors Corporation, Warren, Michigan

ABSTRACT

Differential capacitance and cyclic voltametric curves for smooth lead electrodes, in the presence of organic additives, are given and discussed. The results of these experiments are compared with respect to the effectiveness of the additives as expanders in the lead-acid system.

The use of lignin and other naturally occurring organic materials as expanders for the negative plate in the lead-acid system is well known (1), and several studies have been made to correlate expander activity with organic structure. Ritchie (2) reported that the effectiveness of pure organic compounds as expanders appears to be directly related to the ease with which they can be degraded to "humic substances." The best results were obtained with carbohydrates and some homologous phenolic compounds. Other studies (3) suggested that catechol residues in the lignin molecule provide expander action. Recently the Physics Department of the Research Laboratories of General Motors Corporation tested homologs of the phthalein series and found them (4) to possess various degrees of expander activity.

Most expander studies have been based on determining their effect on the charge and discharge efficiency of experimental cells or full-size batteries (2, 3). Although such tests give little insight regarding the exact mechanism by which the expander functions, it has been suggested (5) that the expander operates by an adsorption process.

One method for studying adsorption at an electrode surface is to obtain curves showing the relationship between differential capacitance and electrode potential. The purpose of this work was to determine the extent to which organic additives, having known degrees of expander activity, alter the shape of such curves obtained with smooth lead electrodes in H_2SO_4 solutions. Also included in this study were cyclic voltametric experiments to measure the electrical current that flowed throughout the potential range at which the differential capacitance measurements were made.

Experimental

The spherical test electrodes for this study were of high-purity (99.999+%) lead and were prepared in the manner described elsewhere (6). The Pyrex measuring cell contained a glass frit to separate the counterelectrode (a portion of a lead-acid-battery positive plate) from the test electrode. The test electrode compartment of the cell was provided with ground glass openings to accommodate the test electrode assembly, pre-electrolysis electrodes, and Hg/Hg_2SO_4 reference capillary. Solutions were prepared from reagent-grade H_2SO_4 and deionized, doubly distilled water, and were pre-electrolyzed for 16 hr using platinum gauze electrodes.

The a-c impedance bridge used for the capacitance measurements is similar to that reported in the literature (7). A battery-operated potentiostat (8) was used to control the potential of the test electrode against the reference electrode, and the a-c signal was eliminated from the potentiostat circuit by means of a filter choke. Data were obtained by balancing the a-c signal (10 mV peak to peak) shown on the screen of a Tektronix Oscilloscope, Type 502-A, with the direct-reading resistance and capacitance components of the bridge.

For the cyclic voltametric experiments, the test electrodes were subjected to a voltage-time sweep by feeding a signal from a sweep generator (8) into a Wenking 63TR potentiostat. The current trace during the sweep was displayed on the screen of the oscilloscope and was recorded with a Tektronix Oscilloscope Camera.

* Electrochemical Society Active Member.

The organic materials used in this study were ammonium lignosulfonate and pure compounds of the phthalein series, and were found (4) to possess expander activity in the following order. Rhodamine B < pyrogallolsulfonephthalein < gallein < ammonium lignosulfonate < coerulein. All materials were tested at a concentration of 10 ppm and at room temperature.

Results and Discussion

Differential capacitance measurements.—Differential capacitance curves for spherical lead electrodes, obtained at a-c frequencies of 500 and 5000 Hz in 1.25 sp gr H_2SO_4, are given in Fig. 1. The capacitance measurements were started at —600 mV (*vs.* NHE), in the region of hydrogen evolution, and were made at 25-mV intervals up to about 150 mV beyond the $Pb/PbSO_4$ reversible potential (—345 mV *vs.* NHE). Steady values of the capacitance were found within a few minutes after changing the potential of the test electrode.

As evident from Fig. 1, all the organic materials lowered the capacitance values to some extent. The lowering of the capacitance can be attributed to adsorption of the organic molecules at the electrode surface. Over the potential region in which they are adsorbed, the molecules can alter the thickness of the double layer and/or the dielectric constant of the medium within it, thereby changing the values for the differential capacitance. Coerulein, the best expander of the compounds tested, appreciably lowered the capacitance throughout the entire potential region cathodic to the $Pb/PbSO_4$ reversible potential. Furthermore, the pseudocapacitance associated with the formation of $PbSO_4$ at the electrode surface was markedly suppressed and shifted to more anodic potentials. At the other extreme, rhodamine B, the poorest expander, moderately lowered the capacitance only at high cathodic potentials, thereby indicating that it is adsorbed only in this potential region.

From a practical standpoint, therefore, the results indicate that the measurement of the differential capacitance of smooth lead electrodes in the presence of organic materials can be used to select those substances that will be most effective as organic expanders for the negative plate in the lead-acid system. As expander activity increases, the differential capacitance decreases throughout the entire cathodic potential region. From a theoretical interest, however, further experiments are required to determine such factors as coverage, heats of adsorption, and orientation of the organic molecules at the electrode surface.

Cyclic voltametric experiments.—Typical oscilloscopic traces of cyclic voltametric curves for spherical lead electrodes in pure, 1.25 sp gr H_2SO_4 are given in Fig. 2. The sweeps were started at —600 mV (*vs.* NHE) after the electrodes were allowed to stand at this potential for 5 min. A new electrode was used for each sweep, and the arrows in Fig. 2-a indicate the direction of the sweep. Because of the low magnitude of the cathodic current relative to the anodic current, it was often necessary to set the oscilloscope at a higher sensitivity (Fig. 2-b) to obtain an accurate measurement of the cathodic current. Current densities at various potentials could be calculated from the areas of the lead electrodes (ranging from 0.02 to 0.05 cm^2) and the current values displayed on the traces.

In cyclic voltammetry, the question arises as to how much of the measured current is used for charging and discharging the double layer. The double-layer current (i_{dl}, in $\mu A/cm^2$) is calculated by the expression

$$i_{dl} = C\frac{dv}{dt}$$

where C is the double-layer capacitance ($\mu f/cm^2$) and dv/dt is the sweep rate (V/sec). Assuming that for a smooth Pb electrode C is close to 20 $\mu f/cm^2$, the double-

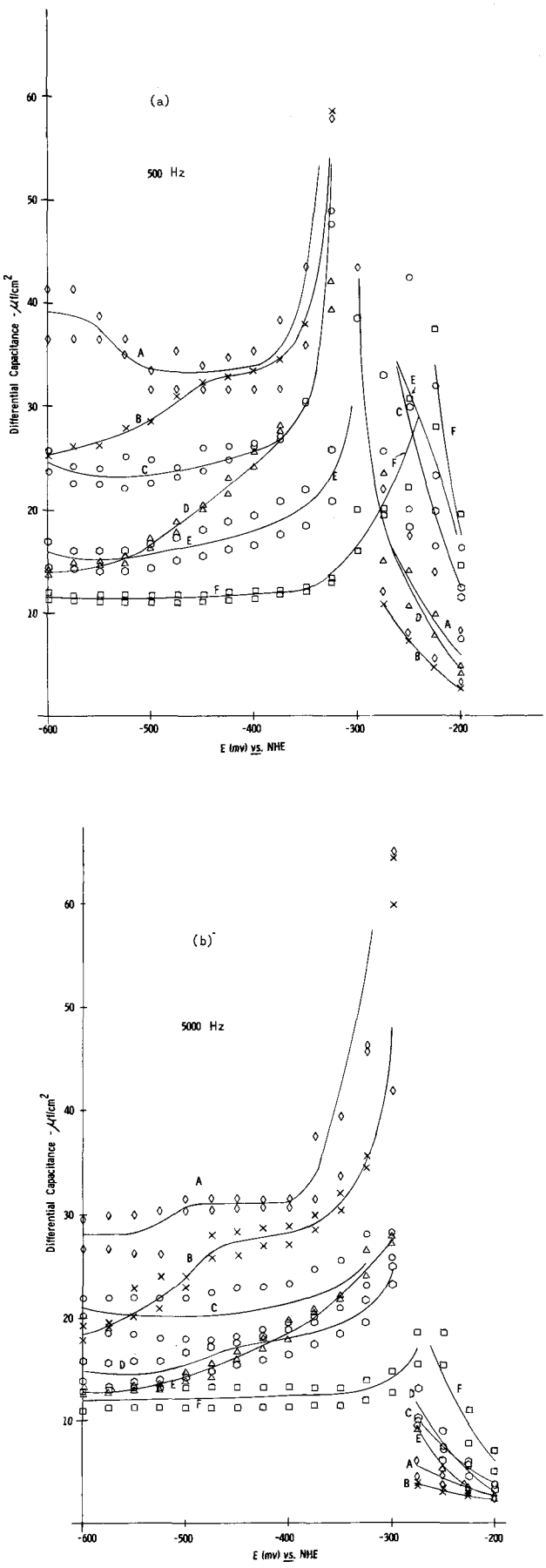

Fig. 1. Differential capacitance curves obtained at a-c frequencies of *(a)* 500 and *(b)* 5000 Hz for the lead electrode in 1.25 sp gr H_2SO_4. ◇ = no additive (curve A); X = rhodamine B (curve B); ○ = pyrogallolsulfonephthalein (curve C); △ = gallein (curve D); ⬡ = ammonium lignosulfonate (curve E); □ = coerulein (curve F). All additives were tested at 10 ppm.

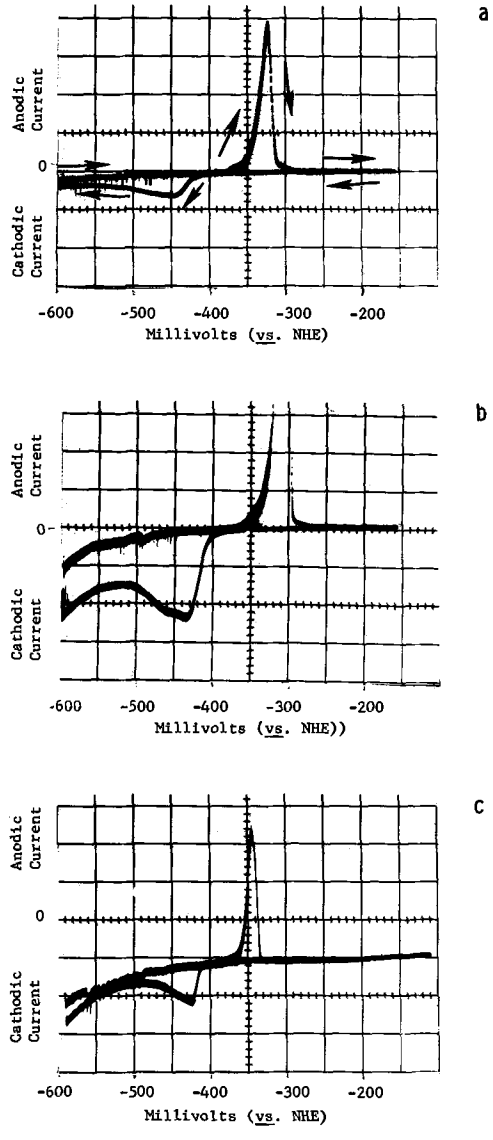

Fig. 2. Oscilloscope traces of cyclic voltametric curves for the lead electrode in pure 1.25 sp gr H_2SO_4. Sweep rate = 62.5 mV/sec for a and b; 3.5 mV/sec for c. Oscilloscope sensitivity = 0.2 mA/cm for a; 0.05 mA/cm for b and c.

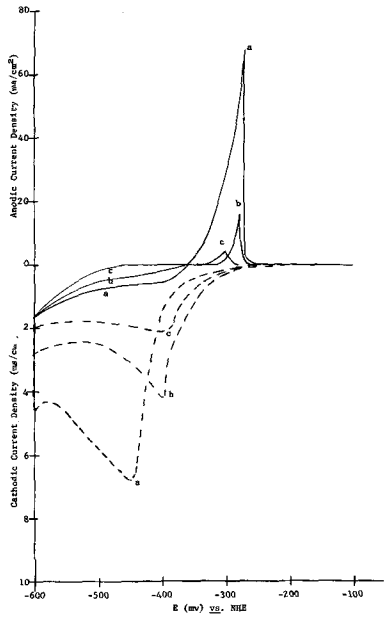

Fig. 3. Current density vs. electrode potential at various sweep rates for the lead electrode in pure 1.25 sp gr H_2SO_4: a = 62.5 mV/sec, b = 13.5 mV/sec, and c = 3.5 mV/sec.

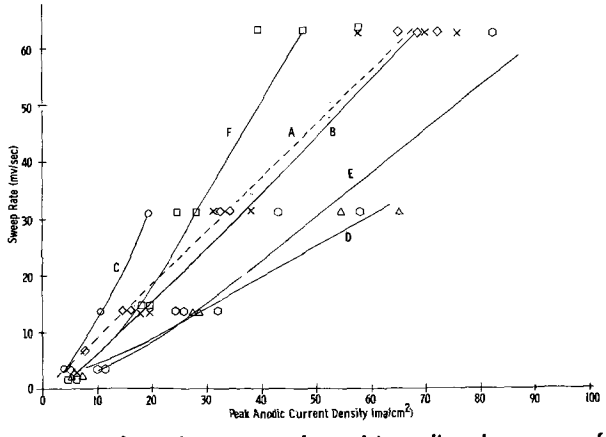

Fig. 4. Peak anodic currents observed in cyclic voltamograms for the lead electrode in 1.25 sp gr H_2SO_4. ◇ = No additive (curve A); X = rhodamine B (curve B); ○ = pyrogallolsulfonephthalein (curve C); △ = gallein (curve D); ○ = ammonium lignosulfonate (curve E); □ = coerulein (curve F). All additives were tested at 10 ppm.

layer current, even at the highest sweep rate (62.5 x 10^{-3} V/sec) used in these studies, is only about 1 μA/cm^2. This was a negligible portion of the total current and could therefore be disregarded.

The effect of sweep rate on the shape of the cyclic voltametric curve for lead in pure H_2SO_4 is given in Fig. 3. The anodic sweep is represented by a solid line, and the cathodic sweep is given by a broken line. The peak in the anodic current corresponds to the formation of $PbSO_4$. The peak height varies linearly with sweep rate (broken line, Fig. 4), which is in agreement with theory since the $PbSO_4$ behaves as an adsorbed intermediate (9) at the electrode surface.

During the cathodic sweep, the $PbSO_4$ produced in the anodic sweep is reduced to lead, and hydrogen is evolved at the electrode surface. The current for the reduction of $PbSO_4$ appears to merge with the current for hydrogen reduction.

In the presence of the additives, the anodic current peak height, measured at a given sweep rate, varied over a wide range of experimental values (Fig. 4), and no correlation could be made between expander activity and peak height. Since the peak height is proportional to the pseudocapacitance associated with the formation of $PbSO_4$, it would be expected, from the results given in Fig. 1, that as expander activity increased, the peak height would decrease. The absence of such a trend is disconcerting, and no explanation is currently available.

There was, however, a correlation between expander activity of the organic additives and the current measured during the cathodic sweep. As expander activity increased, the current for the reduction of $PbSO_4$ and hydrogen decreased. The trend was consistent over a range of sweep rates, and typical results are shown in Fig. 5. The decrease in the cathodic current, like the lowering of the differential capacitance, is attributed to adsorption of the additives at the electrode surface.

The adsorption of an organic expander at a smooth lead electrode is undoubtedly distributed differently than that at a lead-acid battery negative plate. Because of its porous nature, the negative plate possesses reaction sites having a wide range of activity. Unlike the smooth lead electrode where the adsorption may be distributed over most of the electrode surface, adsorption at the negative plate may occur only at the most active reaction sites. The reduction of $PbSO_4$ and hydrogen would be inhibited at these sites, thereby forcing the electrochemical reaction to occur over the rest of the electrode surface. Such a mechanism would also tend to retard crystal growth which could account for

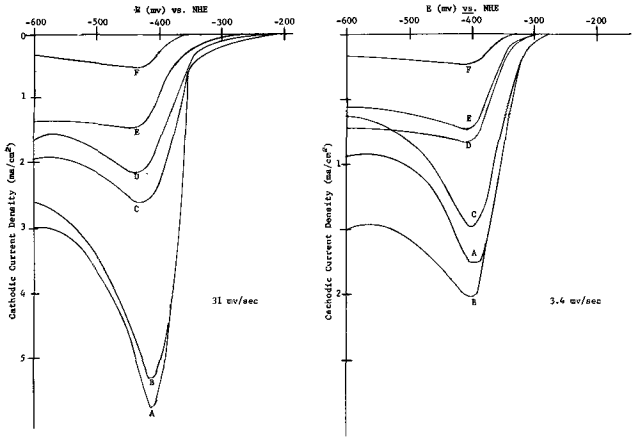

Fig. 5. Currents observed during cathodic sweep of lead electrodes in 1.25 sp gr H_2SO_4. A = no additive, B = rhodamine B, C = pyrogallolsulfonephthalein, D = gallein, E = ammonium lignosulfonate, F = coerulein. All additives were tested at 10 ppm.

the fine structure that is observed (10) when the expander is added to the negative plate.

Acknowledgments

The author wishes to thank Messrs. D. P. Krause, R. L. Williams, and R. F. Hill, and Dr. W. J. Mayer, all of the Physics Department of the Research Laboratories, General Motors Corporation, for supplying the organic compounds used in this study and for helpful discussions pertaining to their expander activity. He is also grateful to Dr. J. L. Griffin of the Electrochemistry Department of the Research Laboratories, General Motors Corporation, who designed and constructed much of the electronic instrumentation used in this study.

Manuscript received July 23, 1969. This was Paper 41 presented at the Detroit Meeting, Oct. 5-10, 1969.

Any discussion of this paper will appear in a Discussion Section to be published in the June 1970 JOURNAL.

REFERENCES

1. E. J. Ritchie, *Trans. Electrochem. Soc.*, **92**, 229 (1947).
2. E. J. Ritchie, *This Journal*, **100**, 53 (1953).
3. A. Hayashi and Y. Namura, *Kami-pa Gikyoshi*, **21**, 393 (1967).
4. D. P. Krause, W. J. Mayer, and R. L. Williams, Unpublished data.
5. E. Willihnganz, *Trans. Electrochem. Soc.*, **92**, 281 (1947).
6. T. F. Sharpe and S. G. Meibuhr, *J. Chem. Ed.*, **46**, 103 (1969).
7. R. S. Hansen, R. E. Minturn, and D. A. Hickson, *J. Phys. Chem.*, **60**, 1185 (1956).
8. Designed and constructed by J. L. Griffin, Electrochemistry Dept., Research Labs., General Motors Corp., Warren, Mich.
9. B. E. Conway, "Theory and Principles of Electrode Processes," p. 138, The Ronald Press Co., New York (1965).
10. A. C. Zacklin, *This Journal*, **98**, 325 (1951).

A Reversible Solid-State Battery with $RbAg_4I_5$ as Electrolyte[1]

Mario De Rossi, Gianfranco Pistoia, and Bruno Scrosati*

Istituto Elettrotecnico, Università di Roma, Rome, Italy

ABSTRACT

A solid-state reversible cell of the type $Ag(Hg)/RbAg_4I_5/I_2$, TBAI, C, has been developed. The anodic and cathodic contact polarizations have been minimized by amalgamation of the silver electrode and the use of a suitable mixture made of tetrabutylammonium iodide (TBAI), iodine, and graphite, respectively. The cell has an open-circuit voltage of 0.56V at 25°C, a total volume of 5 cm^3, an internal resistance of 30 ohms, short-circuit current of 1.5 A/dm^2, and is rechargeable with high coulombic efficiency.

Solid-state batteries have been widely studied in recent years because they possess some remarkable advantages with respect to conventional systems such as potentiality for extreme miniaturization, large temperature ranges of operation, and long shelf life. Because of these characteristics, solid electrolyte batteries could be very profitably used in transistorized circuits, space applications, and so on.

The most serious shortcoming of this type of cell, however, has been, until very recently, the high value of the internal resistance which has limited its practical utilization to microwatt power applications (1, 2).

Silver halides, which have been considered until a short time ago to be among the best ionic conductors, have a specific conductivity which is 6-8 orders of magnitude less than that of conventional battery electrolytes (*see* Table I).

The operative possibilities of a solid-state cell were first shown by Lehovec and Broder (3) who described a cell made of a silver anode, an AgI solid electrolyte, and a cathodic mixture of iodine and graphite. This cell has an open-circuit voltage (OCV) of about 0.7V at room temperature and yields short-circuit current densities in the range of $\mu A/cm^2$. Also described is the behavior of a high-temperature cell of the type:

$$Ag/AgI/Ag_2S,C \qquad [1]$$

to take advantage of the fact that AgI is highly conductive in its high-temperature α form (4) as shown in Table II.

Cell [1] has an OCV of 0.2V at 200°C, current densities up to 0.18 A/cm^2, but very short shelf life.

In 1958 Weininger (5) described a "bead" cell made of a small bead of AgI and two electrodes, silver and tantalum wires, inserted into the electrolyte. The mini-

Table I. Specific conductivity of silver halide solid electrolytes and of a conventional battery aqueous electrolyte at 25°C

Electrolyte	χ ohm^{-1} cm^{-1}	Reference
AgI	2×10^{-6}	(16)
AgCl	1×10^{-7}	(17)
AgBr	3×10^{-7}	(18)
Aqueous solution of H_2SO_4 30%	0.8	(19)

* Electrochemical Society Active Member.

[1] This work was sponsored by the Consiglio Nazionale delle Ricerche under contract C.N.R. No. 115/0860/1894.

Table II. Specific conductivity of AgI at various temperatures (16, 20)

Temp, °C	χ ohm^{-1} cm^{-1}
20	1.66×10^{-6}
60	4.98×10^{-6}
120	7.10×10^{-5}
144	3.40×10^{-4}
144.6*	1.31
200	1.57
500	2.52

* $\beta \rightarrow \alpha$ transition point.

aturized cell yields an OCV of 0.68V and current densities of about 14 μA/cm^2. The high-temperature behavior of the cell and its recharge possibilities are also discussed.

Subsequently, Weininger (6) built the cell

$$Ag/AgI/Ta, I_2 \qquad [2]$$

working in the temperature range 150°-550°C and having as cathodic material either iodine or a chemical compound able to furnish free iodine at high temperature, such as cesium polyiodides. Cell [2] has an OCV of 0.67V, capacity of 10 mA-hr, and short-circuit currents up to 18 mA.

In 1959 Smyth (7) described a solid electrolyte cell consisting of a silver anode, an AgCl electrolyte film a few microns thick, and a cathode composed of $KICl_4$, carbon black, and grease binder. The use of $KICl_4$ as a low-pressure source of chlorine makes the cell very stable with a shelf life of ten years.

The Smyth cell has an OCV of 1.04V at 25°C and an internal resistance of about 10^5 ohms, a capacity of 2 coulombs, and short-circuit current densities of the order of 15 ÷ 30 μA/cm^2.

Recently, Foley has made a very comprehensive review of solid electrolyte galvanic cells (8).

In the cells so far described, the high internal resistance remains the most serious problem, which has been partially overcome by high-temperature and thin electrolyte film techniques.

In very recent years, several attempts have been made to improve the conductivity of silver halides and to synthesize highly conductive solid electrolytes (8).

In 1964 Takahashi and Yamamoto (9) described the cell

$$Ag/Ag_3SI/I_2, C \qquad [3]$$

The specific conductivity of Ag_3SI at 25°C is 10^{-2} ohm^{-1} cm^{-1} (10), much higher than that of the silver halides (*see* Table I). Cell [3], in fact, can yield short-circuit current densities as high as 10 mA/cm^2 at room temperature. Unfortunately, the electrolyte cannot be used for battery purposes since it has high electronic conductivity (8). In 1967 Bradley and Greene (11) and, subsequently, Owens and Argue (12), described a new group of solid electrolytes of the type MAg_4I_5, where

Table III. Specific conductivity of $RbAg_4I_5$ at 25°C

χ ohm^{-1} cm^{-1}	Reference
0.124	Bradley and Greene (11)
0.210	Owens and Argue (12)
0.250	This work

M is K, NH_4, Rb, and possibly Cs, having a specific conductivity, due only to silver ions, as high as 0.2 ohm^{-1} cm^{-1} at 25°C (*see* Table III).

The advantage of these electrolytes for an improved solid-state battery is obvious and in 1968 Scrosati, Boddy, and De Rossi (13) described a cell of the type

$$Ag(Hg)/RbAg_4I_5/I_2, C \qquad [4]$$

having an amalgamated silver anode, $RbAg_4I_5$ solid electrolyte, and a cathodic iodine-graphite mixture.

Cell [4] has at 25°C an OCV of 0.58V, a total volume of ~2 cm^3, short-circuit currents up to 4 mA, and a total available charge of 130 coulombs (*see* Table IV). The internal resistance of the cell is about 300 ohms. This value, even if much lower than that of the operative solid electrolyte batteries previously described, is still higher than that one would have expected on the basis of the conductivity value of the electrolyte. The relatively high value of the internal resistance in cell [4] is probably due to interfacial effects between the iodine-graphite mixture and the electrolyte.

In 1968 Argue, Groce, and Owens (14) described a solid-electrolyte battery of the type:

$$Ag/RbAg_4I_5/RbI_3, C \qquad [5]$$

formed by a mixture of silver, carbon, and $RbAg_4I_5$ as anode, $RbAg_4I_5$ as electrolyte, and a mixture of RbI_3, carbon, and $RbAg_4I_5$ as cathode.

The use in cell [5] of a polyiodide in the place of iodine seems to have overcome the contact cathodic polarization observed in cell [4], thus allowing the former to yield higher current densities (*see* Table IV).

Nevertheless, some of the performances of the cell [5] described in the paper by Argue, Groce, and Owens are rather surprising. For instance the internal resistance of a low current drain cell is reported to be (2 ± 1) ohm, while in the discharge of a battery of 5 cells in series, having an OCV of 3.30V, on 100 kohm load, load voltages ranging from 3.29 to 3.26V are reported at 25°C. From these experimental data, realistic cell resistance appears to range from 60 to 250 ohms.

In this work, a solid state reversible cell with $RbAg_4I_5$ as electrolyte and in which the cathodic polarization is minimized by the use of suitable cathodic mixture is described. Furthermore, a method to obtain an improved electrolyte and some of the electrical properties of the electrolyte are also reported.

Experimental

Materials.—All the chemicals used were reagent grade. The electrolyte, $RbAg_4I_5$, was prepared by slow

Table IV. $RbAg_4I_5$ solid electrolyte cells

Reference	Scrosati, Boddy, De Rossi (13)	Argue, Groce, Owens (14)			This work		
Type of cell	Ag(Hg)/$RbAg_4I_5$/I_2, C	Ag/$RbAg_4I_5$/RbI_3, C			Ag(Hg)/$RbAg_4I_5$/I_2, TBAI, C		
Drain		Low current	Medium current	High current	Low current	Medium current	Short-circuit current
OCV (volts)	0.58	0.66	—	—	0.56	—	
Operating temperature (°C)	25	25	25	25	25	25	
Electrolyte thickness (mm)	2	0.51	0.48	0.43	1.5	1.5	
Cell diameter (cm)	2.5	1.16	1.22	2.44	2	2	
Cell volume (cm^3)	2	0.23	0.14	0.77	5	5	
Capacity (mA-hr)	~0.5	0.8	—	—	7	—	
Cell resistance (ohms)	300	60-250[a]	60[a]	0.20[a]	30	30	
Operating time		144 hr[b]	20 sec	8 msec	85 hr[b]	30 min[b]	
Load resistance		100 kohm	600 ohms	2.43 ohms	6 kohm	600 ohms	
Cell weight (grams)	5	0.7	0.5	3.2	10	10	
Short-circuit current	3 mA						~50 mA

[a] Operative cell resistance.
[b] Operating time to 70% of OCV.

heating of a stoichiometric mixture of AgI and RbI to melting and then quenching. All these operations were performed under vacuum. Subsequently the solid product was ground and left at 165°C for about 20 hr. The powder was then compressed into pellets for the experiments. The procedure is similar to that described by Argue and Owens (12) with the difference that in the present case the melting and the quenching were done under vacuum to eliminate all the possible volatile impurities. The vacuum procedure does not change the composition of the final product, as has been proved by x-ray powder patterns, and seems to improve the $RbAg_4I_5$ conductivity (*see* Table III).

Cell structure.—The cell in its essential structure may be represented as

$$Ag/RbAg_4I_5/I_2 \qquad [6]$$

The main problems in cell [6] are the contact polarizations (13) which have been minimized in the present case by the use of an amalgamated silver disk as anode (13) and of a cathodic mixture made of powdered graphite, iodine, and tetrabutylammonium iodide (TBAI). It is known that alkylammonium salts are able to retain molecular iodine (15). The function of TBAI in the cathodic mixture is therefore to prevent tarnishing reactions by free iodine on the electrolyte when the cell is not operative. Iodine is released by TBAI during discharge and retained during charge.

In order to reduce contact resistance further, the cathodic mixture is melted, uniformly spread on the electrolyte, and allowed to solidify.

The actual cell structure is therefore

$$Ag\ (Hg)/RbAg_4I_5/I_2, TBAI, C \qquad [7]$$

Measurements.—Voltage and current determinations have been performed by a Keithley Model 610C electrometer. Conductivity measurements have been performed by the use of a cell made of two amalgamated silver disks of 1 cm diameter in contact with the electrolyte pellet. A-C conductivity was determined by a Tinsley bridge, Type 4896. Polarization studies were made by an AMEL potentiostat, Model 551.

Results

Electrolyte characteristics.—The a-c specific conductivity has been found to be 0.250 $ohm^{-1}\ cm^{-1}$ at 25°C, a value about 20% higher than that reported by Argue and Owens (12). This is probably due to the vacuum technique used in the present research in the preparation of the electrolyte.

In Fig. 1 is shown a current-voltage curve of the electrolyte obtained with two amalgamated silver electrodes at 25°C. The a-c resistance of the electrolyte sample, previously measured, was 2.9 ohms. From the data of Fig. 1, the d-c resistance appears instead to be about ten times higher, *i.e.* 27 ohms. At high current drains the polarization is much higher, thus suggesting that cells having $RbAg_4I_5$ as electrolyte should be used preferably in the low and medium current drain ranges (from μA to mA).

Figure 2 shows the typical current-voltage curve of the electrolyte obtained at 25°C with two platinum electrodes. The decomposition potential of $RbAg_4I_5$ is 0.67 ± 0.01V at 25°C.

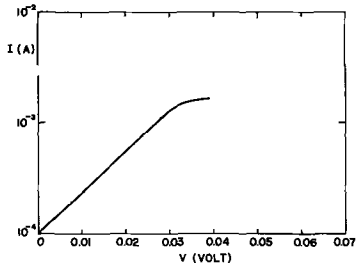

Fig. 1. Current-voltage curve for $RbAg_4I_5$ at 25°C (silver electrodes).

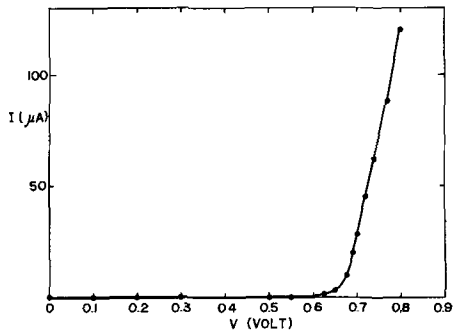

Fig. 2. Current-voltage curve for $RbAg_4I_5$ at 25°C (platinum electrodes).

Cell characteristics.—The OCV of the cell

$$Ag/RbAg_4I_5/I_2, C \qquad [8]$$

at 25°C has been found to be 0.683V (13) in good agreement with the theoretical value of 0.688V derived from the thermodynamic free energy of formation of silver iodide.

To minimize contact polarization effects, cell [7], the over-all reaction of which should be

$$Ag\ (Hg) + \tfrac{1}{2}\ I_2 \rightleftharpoons AgI \qquad [9]$$

has been taken into consideration.

The OCV of cell [7] is 0.56V at 25°C and its variation with temperature is shown in Fig. 3. The temperature dependence is 0.0006 V/°C. The cell structure is shown in Fig. 4. The cell consists of an amalgamated silver disk in contact with a pellet of $RbAg_4I_5$, ~ 2.0 cm diameter and ~ 0.15 cm thickness. The cathodic mixture is spread on the electrolyte surface. The total volume of the operative cell is ~ 5 cm^3 and the total weight ~ 10g.

From current-voltage plots at room temperature, the internal resistance was determined to be about 30 ohms (*see* Fig. 5 which applies to the initial behavior

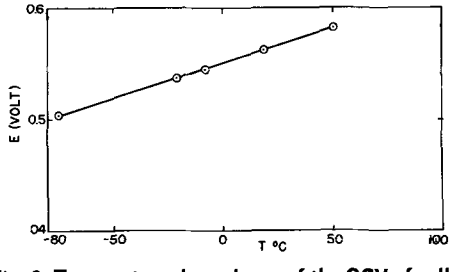

Fig. 3. Temperature dependence of the OCV of cell [7].

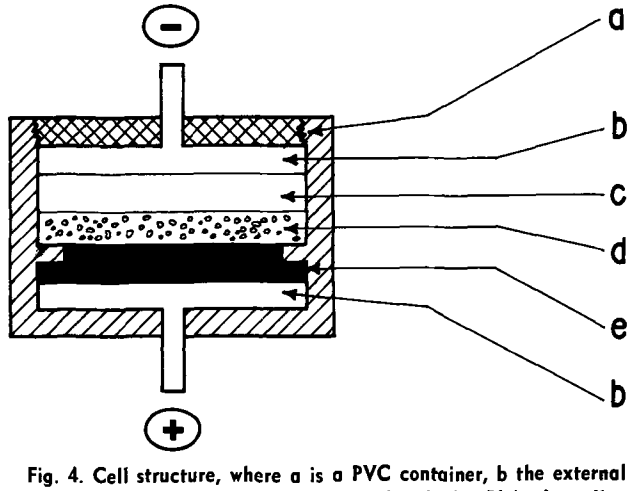

Fig. 4. Cell structure, where a is a PVC container, b the external contact, c the amalgamated silver anode, d the $RbAg_4I_5$ pellet, and e the cathodic mixture.

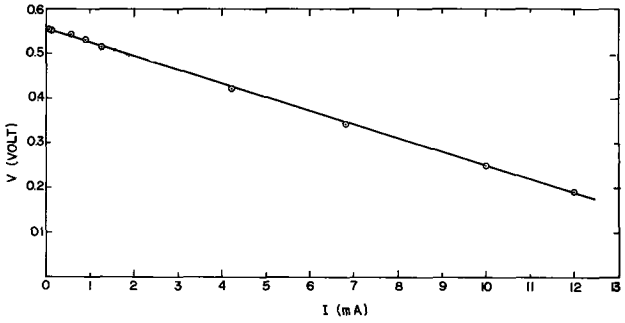

Fig. 5. Current-voltage curve for cell [7] at room temperature

of the cell). According to the a-c conductivity of $RbAg_4I_5$, the cell resistance, due to the electrolyte only, should be of the order of 0.2 ohm. The total resistance of the cell in its operative assembly is about 3 ohms, as measured by the a-c bridge. The higher value found experimentally could be explained on the basis of the data reported in Fig. 1 and of a certain residual contact resistance.

For long-time discharges, the internal resistance of the cell increases mainly because during discharge AgI, whose conductivity is very low, is formed (13).

In Fig. 6 and 7 are shown typical discharge curves at various loads and various temperatures.

Cell [7] is capable of delivering short-circuit current of ~ 50 mA (~ 1.5 A/dm²). The cell characteristics and performances at 25°C are summarized in Table IV which also gives reported data on other $RbAg_4I_5$ solid electrolyte cells.

Attempts at recharging the cell have been successful as shown in Fig. 8. The cell was discharged at 50°C through 150 ohms to 0.2V (curve a). Following this initial discharge the cell was charged at an applied voltage of 0.6V and then discharged through 1000 ohms to 0.35V (curve b). This was followed by a second charge and so on as shown in curves c and d.

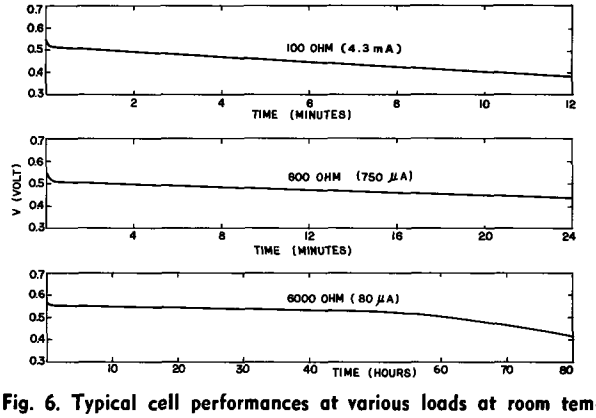

Fig. 6. Typical cell performances at various loads at room temperature.

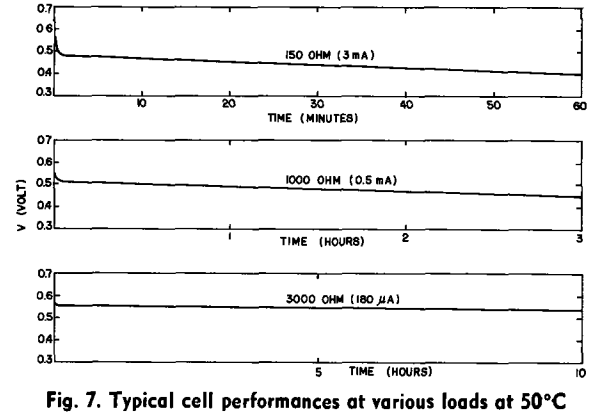

Fig. 7. Typical cell performances at various loads at 50°C

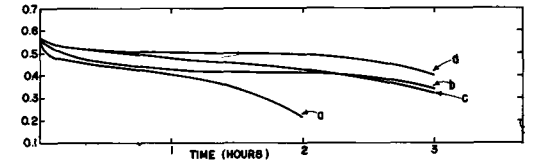

Fig. 8. Discharge curve of cell [7] charged and discharged at 50°C, where a is the first discharge at 150 ohms load and b, c, and d are the second, third, and fourth discharge curves, respectively, at 1000 ohms load.

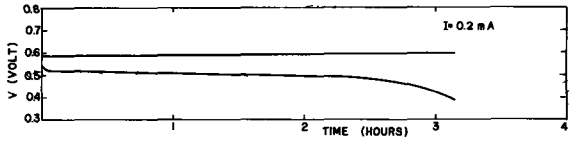

Fig. 9. Charge-discharge first cycle of cell [7] at 0.2 mA constant current and at 25°C.

The fourth charge was carried on at an applied voltage of 0.65V and the following discharge was unsatisfactory. The cell was disconnected and the negative electrode region showed a dendritic deposit of silver. This circumstance, and perhaps also the fact that the applied voltage in the fourth charge was close to the decomposition potential of the electrolyte, may explain the failure of the fifth discharge process.

This evidence indicates that the charge process preferably should be carried out at low current densities to obtain the best efficiency.

In Fig. 9 is reported a charge-discharge cycle at 25°C and at a constant current of 0.2 mA, showing a very high coulombic efficiency.

Conclusions

From the above reported data it is inferred that the cell described in this work shows clear improvements with respect to the system previously developed in our laboratory (13). Among them, the most significant is the minimization of the contact cathodic polarization.

Cell [7] also has some advantages over the battery studied by Argue, Groce, and Owens (14) at least in the low and medium current drain ranges (*see* Table IV).

Furthermore, the system described in this work shows possibilities of being recharged with high current efficiencies and, because of this and the use of iodine instead of RbI_3 in the cathodic mixture, its cost should be lower than other $RbAg_4I_5$ solid electrolyte cells.

Furthermore, cell [7] may be printed since all its components may be deposited either by evaporation (silver) or by solidification (electrolyte and cathodic mixture).

On the other hand, the cell of Argue and co-workers has a higher OCV and seems to be capable of surprisingly high current pulses, *i.e.* 90 A/dm².

Acknowledgment

The authors wish to thank Dr. P. J. Boddy of the Bell Telephone Laboratories for his helpful suggestions.

Manuscript submitted June 9, 1969; revised manuscript received July 21, 1969.

Any discussion of this paper will appear in a Discussion Section to be published in the June 1970 JOURNAL.

REFERENCES

1. J. N. Mrgudich, Solid electrolyte batteries, "The Encyclopedia of Electrochemistry," Edited by C. A. Hampel, pp. 185-197, Reinhold Publishing Corp., New York (1957).
2. M. De Rossi and B. Scrosati, *L'Elettrotecnica*, **54**, 779 (1967).
3. K. Lehovec and J. Broder, *This Journal*, **101**, 208 (1954).
4. C. Tubandt, *Z. Anorg. Allgem. Chem.*, **115**, 105 (1921).

5. J. L. Weininger, *This Journal*, **105**, 439 (1958).
6. J. L. Weininger, *ibid.*, **106**, 475 (1959).
7. D. M. Smyth, *ibid.*, **106**, 635 (1959).
8. R. T. Foley, *ibid.*, **116**, 13C (1969).
9. T. Takahashi and O. Yamamoto, *Denki Kagaku*, **32**, 610 (1964).
10. T. Takahashi and O. Yamamoto, *Electrochim. Acta*, **11**, 779 (1966).
11. J. N. Bradley and P. D. Greene, *Trans. Faraday Soc.*, **63**, 424 (1967).
12. B. B. Owens and G. R. Argue, *Science*, **157**, 308 (1967).
13. B. Scrosati, P. J. Boddy, and M. De Rossi, *Ric. Sci.*, **38**, 1366 (1968).
14. G. R. Argue, I. J. Grove, and B. B. Owens, Uncorrected preprint, 6th International Power Sources Symposium, Brighton, Sept. 1968.
15. R. Jasinski, "High Energy Batteries," Plenum Press, New York (1967).
16. K. H. Lieser, *Z. Physik. Chem., N.F.*, **B-9**, 302 (1956).
17. D. J. G. Ives and G. J. Janz, "Reference Electrodes," p. 185, Academic Press, New York (1961).
18. A. S. Miller and R. J. Maurer, *J. Phys. Chem. Solids*, **1**, 191 (1956).
19. G. W. Vinal and D. N. Craig, *J. Res. Nat. Bur. Stds.*, **13**, 689 (1934).
20. C. Tubandt and F. Lorenz, *Z. Physik. Chem.*, **B-7**, 513 (1914).

On the Passivity of Iron-Chromium Alloys

III. Effect of Potential

Robert P. Frankenthal*

Edgar C. Bain Laboratory for Fundamental Research, United States Steel Corporation, Research Center, Monroeville, Pennsylvania

ABSTRACT

The kinetics of growth of the primary and of the secondary passivating films have been examined for an Fe-24% Cr alloy in 2*N* H_2SO_4 over a potential range of several hundred millivolts above the activation potential. From these data it has been possible to evaluate the effectiveness of an adsorbed film and of an oxide film in causing passivity. It is concluded that the type of film that gives rise to passivity, as well as the mechanism of anodic dissolution during the passivation process, is potential dependent: At the activation potential an adsorbed film is responsible for passivity by inhibiting the direct, activated transfer of ions from the metal surface into solution; at high potentials an oxide film acts as the passivating agent with the current limited by the rate of diffusion of ions through the film; in a 200 mV intermediate region the adsorbed film is responsible for initiating passivity, but the steady-state film is an oxide. In addition the data indicate that the rate of growth of both the primary and the secondary films is potential dependent; at sufficiently low potentials the rate constant for primary film formation is greater than that for secondary film formation, while at higher potentials the rate constant for secondary film formation becomes greater.

In the first of this series of papers (1), we showed that on an Fe-24% Cr alloy in H_2SO_4 at least two distinct, potential-dependent films are formed during the passivation process: the primary passivating film is formed reversibly at the primary activation potential, while the secondary film forms at more positive potentials, and is very stable and resistant to reduction. In subsequent work (2), we studied the kinetics of primary film growth at the primary activation potential, showed that at this potential a small fraction of a monolayer gives rise to a high degree of passivity, and presented a preferential-dissolution/adsorption mechanism for the passivation process that agreed quantitatively with the observed experimental behavior.

In this paper we extend the experimental work over a potential range of several hundred millivolts above the activation potential. Specifically we investigate the decay of the anodic current and the growth of the primary and secondary films with time at different potentials. From these data it has been possible to determine the effectiveness of a given quantity of film as a passivating agent at each potential. It is shown that none of the prevalent theories of passivity, the adsorption theory (3), the bulk oxide theory (4), or the sequential adsorption, bulk oxide theories (5, 6), is applicable over the entire potential range of passivity. Instead evidence is presented to show that at the activation potential passivity can be attributed to a film formed by an adsorption process; at high potentials an oxide is responsible; in between there exists a 200 mV region in which an initial, adsorbed film causes a large decrease in the anodic current, but is not the steady-state film which is an oxide. It is also shown that a change in the mechanism of anodic dissolution during the passivation process occurs at the same potential at which the change from passivation by an adsorbed film to passivation by an oxide film takes place. The variation of anodic current and of film growth with time and with potential is shown to be in agreement with the above conclusions.

* Electrochemical Society Active Member.

Experimental

The alloy, electrolyte solution, electrochemical cell, electrical circuitry, specimen preparation, general procedure, and justification therefore have been described in detail previously (2). Therefore, only some essential facts and procedures are summarized here.

The alloy investigated was a high-purity, vacuum-melted Fe-24% Cr ferritic alloy. The electrolyte solution was 2*N* H_2SO_4 (pH 0.02) made from reagent-grade sulfuric acid and doubly distilled water. Further purification by passing the solution over activated charcoal did not affect the results and was generally omitted.

The basic experiment consisted of the following steps: The specimen surface was cleaned by a combination of cathodic reduction and anodic dissolution, following which the specimen was put on open circuit until the steady-state corrosion potential (± 0.5 mV) was achieved; the potential was then switched to that under study and the current-time (i-t) transient was recorded; after any given time the film that had been formed could be cathodically reduced at constant

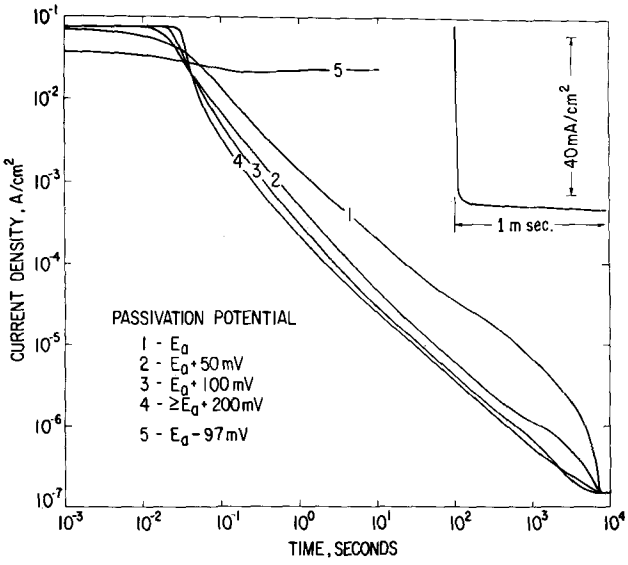

Fig. 1. Anodic current-time transients at different passivation potentials, illustrating variation with potential up to E_a + 200 mV and independence of potential at higher values. Curve 5 is the transient at the potential corresponding to the maximum current in the anodic loop; the insert is a linear plot of the first millisecond of this transient.

current (chronopotentiometry); the resulting potential-time (E-t) curve was recorded and the coulombic film thickness calculated.

All potentials are reported relative to the standard hydrogen electrode (SHE).

Results

The potentiostatically determined steady-state polarization (E-i) curve for this system has been given previously (2); the primary activation potential, E_a, was defined (1) as the potential at which the first increase in the anodic current is observed on going from the passive region to the anodic loop under conditions of reversibility. This corresponds to the minimum in the cathodic loop and lies between −0.108 and −0.109V (2).

Some typical anodic current-time transients are shown in Fig. 1. To obtain the transients at those potentials at which hydrogen evolution occurs simultaneously with the anodic reaction, it was assumed that the steady-state anodic current is the same as at potentials at which no hydrogen evolution occurs;[1] the hydrogen-evolution current, which then is equal to the difference between the measured steady-state current and the anodic steady-state current, was subtracted from the measured current at any given time to obtain the anodic current at that time. At potentials greater than E_a the initial current exceeds the capacity of the potentiostat and thus up to about 0.05 sec the transients are influenced by the characteristics of the circuit. At current densities greater than 4 mA/cm² the iR-drop correction exceeds 2 mV. At potentials more positive than E_a + 200 mV, the transients are independent of potential after about 0.05 sec. Similar observations have also been made by Nagayama and Cohen (7) for iron in borate buffer and by Rahmel and Schwenk (8) for an 18-8 austenitic stainless steel in 1N H_2SO_4 and in 0.5M Na_2SO_4. In neither case, however, did the authors report the results of any experiments within 200 mV of E_a.

A set of potential-time (E-t) curves measured during cathodic reduction after passivation at E_a has been shown previously (2). Similar curves are observed at higher potentials; for sufficiently short times

[1] This assumption is based on the observation that no discernable dissolution took place on a specimen potentiostated at E_a + 2 mV for 24 hr.

[2] Reference (2) erroneously gives the current density as 1 μA/cm²; it should be 10 μA/cm².

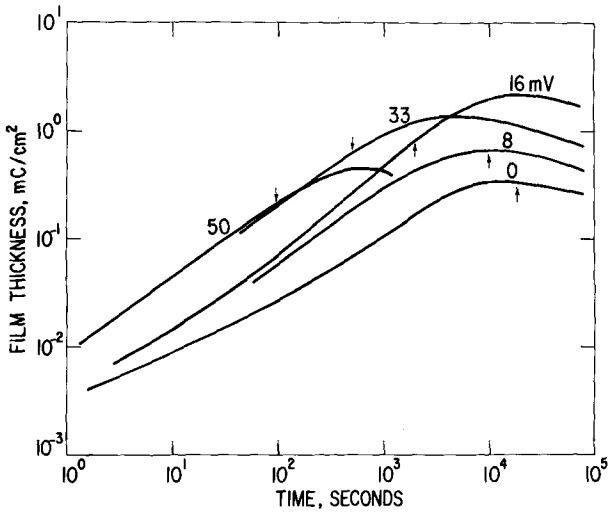

Fig. 2. Film thickness-time transients at different potentials. Passivation potential relative to E_a is given next to each curve. Time at which secondary film was first detected by an increase in the reduction potential is indicated by the arrow on each curve; at longer times true film thicknesses are greater than measured ones (see text).

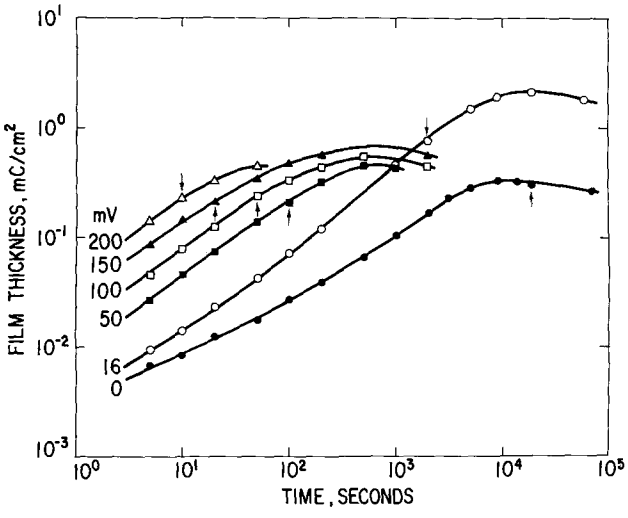

Fig. 3. Film thickness-time transients at different potentials. Passivation potential relative to E_a is given next to each curve. Time at which secondary film was first detected by an increase in the reduction potential is indicated by the arrow on each curve; at longer times true film thicknesses are greater than measured ones (see text).

the reduction potential is the same as for the primary film at E_a; the first increase in the reduction potential appears at shorter times as the passivation potential is increased (Fig. 2 and 3) and the magnitude of the change in the reduction potential increases with increasing passivation potential (Table I).

The coulombic thickness of the film is equal to the product of the time to reach the inflection point in the E-t curve and the current density for film reduction, which was 10 μA/cm².[2] To correct for hydrogen

Table. I. Effect of the passivation potential on the reduction potential. Time of passivation was 100 sec

Passivation potential, mV	Reduction potential, V
E_a	−0.123
E_a + 50	−0.124
E_a + 100	−0.128
E_a + 150	−0.131

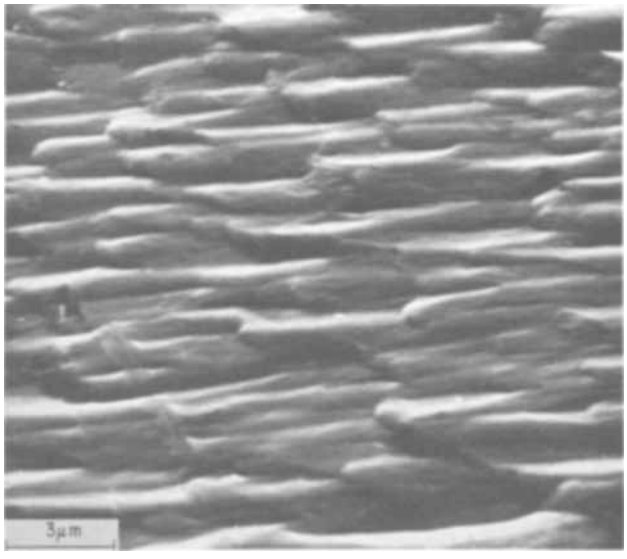

Fig. 4. Scanning electron micrograph of a surface after cleaning by anodic dissolution. Orientation-dependent etch is indicative of a film-free surface.

reduction that occurs concurrently with film reduction, 2.3 $\mu A/cm^2$, corresponding to the rate of hydrogen reduction at E_a, was added to the 10 $\mu A/cm^2$ for film reduction. Thus a current density of 12.3 $\mu A/cm^2$ was actually used. Plots of film thickness *vs.* time (Q-t curves) are shown in Fig. 2 and 3 for various potentials up to E_a + 200 mV. At more positive potentials secondary film was present before the initial point could be established.

The increase in the reduction potential is accompanied by a change in the Q-t plot for any given passivation potential (Fig. 2 and 3). At the activation potential the increase in the reduction potential does not occur until after the steady-state thickness[3] has been achieved and then this increase is accompanied by a decrease in the apparent film thickness. At higher potentials the increase in the reduction potential is detected at shorter times, before the maximum in the Q-t curve has been reached, and occurs roughly at the time at which the log Q-log t plots cease to be linear.

To determine whether the increase in the reduction potential is associated with increased difficulty of film reduction, *i.e.*, secondary film formation (1, 2), the following experiment was performed: After the film was reduced chronopotentiometrically the potential was switched to −0.205V, the potential of maximum anodic current, and the time for the current to reach its steady-state, *i.e.*, its maximum, value was monitored. This time is shortest when the reduction potential is that normally associated with the primary film; this time increases with increasing reduction potential, which in turn increases with increasing potential and time of passivation. An additional observation is that the maximum measured film thickness at E_a + 16 mV is considerably greater than that at higher potentials.

Scanning electron microscope examinations were made of many surfaces of different orientations after the specimens were anodically etched at −0.205V, the potential of maximum anodic current. A typical example of the orientation-dependent etch that is normally observed is shown in Fig. 4. This surface has been heavily etched; similar effects are also observed after lesser amounts of anodic attack.

Validity and accuracy of film thickness measurements.—Additional evidence has been obtained that strengthens the conclusions in the previous paper (2) and permits clarification of some ambiguities: (*i*) It was not possible to prove that a film formed at potentials negative of the corrosion potential was not present at all times over at least part of the surface. The orientation-dependent etch that is observed (Fig. 4) after anodic dissolution is characteristic of a film-free surface (9). Therefore, it is highly unlikely that any film initially present is not removed during the etch that is always used to clean the surface prior to each experiment. (*ii*) Cohen (10) has kindly pointed out that we had not considered the possibility of film formation at the corrosion potential after the anodic etching treatment. If after the etch the potential is switched to the corrosion potential and then back again to the etching potential, the anodic current-time transient (No. 5) shown in Fig. 1 is observed; the insert in this figure shows the first millisecond of the transient. After an initial current jump in less than 10 μsec due to charging of the double layer, the current rapidly decays to the steady-state value. If any film is formed at the corrosion potential, an increase in the current with time, rather than a decrease, would be expected as the film is removed by the etch and as is observed for an initially passivated specimen. From this it is concluded that no film is formed during the time the specimen is held at the corrosion potential. These results, as well as those presented previously (2), establish that the cathodic reduction procedure measures all the film on the surface.

The accuracy of the film-thickness measurement depends on the accuracy of the hydrogen-reduction correction. While the latter cannot be assessed quantitatively, the possible errors can be examined. Since the correction used is the experimentally determined cathodic current density, it must be the minimum correction, *i.e.*, the true cathodic current density cannot be less than the measured value. The correction perhaps should be greater for the following reasons: (*i*) If the anodic current density at E_a is greater than that assumed, the cathodic current density must also be greater in order to get the net measured current density. This error cannot be great for reasons given in the first footnote in the "Results." (*ii*) The reduction potential is about 15 mV negative of E_a; consequently the cathodic current density at this potential should be somewhat greater than at E_a. A correction for these possible errors would make the true film thickness less than that measured. Assuming that the steady-state film thickness at the activation potential cannot be appreciably less than a monolayer, the error of neglecting these additional corrections has no effect on the basic interpretation of the data. Another correction may arise from a change in hydrogen reduction kinetics in going from a filmed to a bare metal surface as the reduction proceeds. Since there is little change in the reduction potential until close to the end point, it appears that the fraction of the total current applied to hydrogen reduction remains relatively constant until close to the end point and that a significant error will occur only for very thin films.

Discussion

The purpose of this paper is to determine how the effectiveness of a given type and quantity of film as a passivating agent changes with increasing potential and the mechanism by which this film hinders anodic dissolution. In addition, it must be shown that the variations of i and Q with E and t are consistent with these findings and the resulting conclusions; the effect of potential on the i-t transients is treated in a section of this Discussion while a rate equation that accounts for the observed Q-t-E relationships is presented in an Appendix.

Effectiveness of adsorbed and of oxide films as passivators.—The primary film is the same at all passivation potentials because it exhibits the same reduction potential at each passivation potential. The data (Fig.

[3] While not easily discerned in Fig. 2 and 3, a steady state does exist over the time range from 8 to 15 ks.

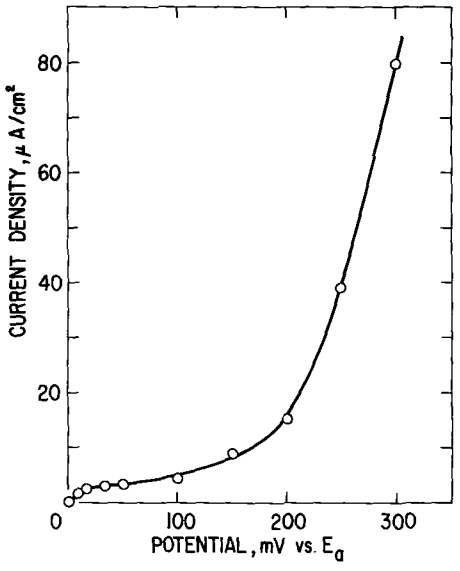

Fig. 5. Effect of a 0.36 mC/cm² film on the anodic current density at different potentials, showing the change from passivation by an adsorbed film to passivation by an oxide film at a potential of approximately E_a + 200 mV (see text).

2 and 3) show that for any given time the thickness of this film increases with potential. At the activation potential the steady-state film is 0.36 mC/cm² thick corresponding to one to three monolayers (2); we have shown (2) that the mechanism by which this film is formed and by which the decay of the anodic current can be described involves an adsorption process. At higher potentials, *e.g.*, at E_a + 16 mV, the steady-state film is many monolayers thick and it must be an oxide, because it is difficult to envision stable, separate layers of anions and cations each with a charge density of several millicoulombs/cm²; the interdiffusion of the ions to form an oxide is almost a certainty.

Although the steady-state film at potentials above the activation potential appears to be an oxide, the passivation mechanism need not necessarily involve the formation of an oxide, but may be an adsorption process such as occurs at the activation potential. To determine whether an adsorption process or the formation of an oxide film is responsible for passivity at potentials above E_a, we analyze the data in Fig. 1-3 in the following manner: At E_a the steady-state thickness of 0.36 mC/cm², corresponding to an adsorbed film, is also the minimum thickness that affords complete passivity, the anodic current density reaches its minimum value at the same time as the film thickness reaches this value; hence we arbitrarily choose this thickness as our reference. We determine the time required to reach this thickness at each potential (Fig. 2 and 3); from Fig. 1 we determine the residual anodic current density flowing at this time. This current density is plotted as a function of the potential, relative to E_a (Fig. 5) with the current normalized to zero at E_a.[4] As might be expected, the ability of this quantity of film (0.36 mC/cm²) to afford protection against anodic dissolution decreases with increasing potential. Nevertheless, over the first 200 mV this film does afford excellent protection by reducing the current density to less than 0.01% of its initial value (the value at 10^{-3} sec in Fig. 1). Above E_a + 200 mV the effectiveness of this quantity of film rapidly decreases, with the residual current at E_a + 500 mV being approximately 1 mA/cm²; thus at the higher potentials a thicker film, *i.e.*, an oxide film, is required to cause a reasonable degree of passivity.

The potential region in the neighborhood of E_a + 200 mV is most important one for this system, inasmuch as a radical change is observed in three distinct phenomena: (*i*) The film formed by the adsorption process becomes ineffective as a passivating agent above this potential; (*ii*) The preferential-dissolution/adsorption theory is not valid above this potential (2); (*iii*) The *i-t* plots become independent of potential above this potential (Fig. 1). These phenomena are consistent not only with a change in the type of film that gives rise to passivity, but also with a change in the mechanism of anodic dissolution during the passivation process. At lower potentials the preferential-dissolution/adsorption theory considers the direct, activated transfer of the ion from the metal into solution; the theory predicts a potential-dependent current-time transient (see next section) as is observed (Fig. 1). At higher potentials, at which an oxide film is required to give rise to passivity, the current-time transients are independent of potential. The latter may be explained by a mechanism involving ionic transport through a thin oxide film, the rate of which should depend only on the field across the film and not on the potential (9, 11).

We conclude that at the activation potential a film formed by an adsorption process is the primary source of passivity and that this film functions by inhibiting the direct, activated transfer of ions from the metal surface into solution. At sufficiently high potentials ($> E_a$ + 200 mV) a much thicker film, an oxide, is required; this film functions as a passivating agent by limiting the rate of anodic dissolution to the rate of diffusion of ions through the film under the influence of the field across the film. In the intermediate range ($E_a < E < E_a$ + 200 mV) the film formed by the adsorption process is responsible for lowering the current to a very small fraction of its initial value, that is it initiates passivity, while the steady-state film is an oxide and is responsible for the final decrease in the current.

Effect of potential on current-time transients.—It was stated above that the preferential-dissolution/adsorption theory predicts the effect of potential on the current-time transients for $E \leq E_a$ + 200 mV (Fig. 1); this is shown in this section.

From Eq. [3A] in the Appendix it can be seen that, if the rate of the backward reaction is sufficiently small

$$Q_j = Q_{s,j}(E)\,[1 - \exp(-k_j t^m)] \qquad [1]$$

where Q_j is the quantity of film associated with the j'th type of site[5] at any time t and potential E, $Q_{s,j}$ is the maximum or steady-state film thickness at the j'th type of site at that potential, k_j is the time-independent proportionality constants associated with film growth at that type of site and potential, and m is a constant; it is also shown in the Appendix that $k_j \sim \exp(\mathcal{K}E)$, where $\mathcal{K}$ is a constant, and that $Q_{s,j}$ is an unknown function of E.

The preferential-dissolution/adsorption theory [2] states that the anodic current density

$$i = A \exp(bE) \sum_j n_j \exp\left(-\frac{\Delta G_j^{\ddagger}}{RT}\right) \qquad [2]$$

where n_j is the number of unpassivated sites of type j per unit area, $\Delta G_j^{\ddagger}$ is the activation energy for anodic dissolution from that type of site, and A and b are constants. Since n_j is a function of both potential and time, the current density becomes a complicated function of both these variables. For less than monolayer coverage

$$n_j = n_j^{\circ}\left(1 - \frac{Q_j}{Q_j^{\circ}}\right) \qquad [3]$$

[4] Since at the higher potentials some secondary film is present at the time that 0.36 mC/cm² is measured, the true thickness is greater and the time to reach the desired thickness is actually shorter; thus the current density plotted in Fig. 5 should be greater. At E_a + 200 mV the error in the current density has been estimated to be 4 μA/cm² by extrapolating the straight line segment of the log Q – log t plot to 0.36 mC/cm².

[5] The preferential-dissolution/adsorption theory (2) considers kink, ledge, and terrace sites.

where n_j^o is the initial number of sites of type j and Q_j^o is the coulombic thickness corresponding to complete coverage of the n_j^o sites. Substituting for Q_j from Eq. [1], and rearranging

$$\frac{n_j^o - n_j}{n_j^o} = \frac{Q_{s,j}(E)}{Q_j^o}\{1 - \exp[-k_j^o t^m \exp(\mathcal{K}E)]\} \quad [4]$$

where k_j^o is the standard proportionality constant. Because of the interference of the secondary film, the function $Q_{s,j}(E)$ cannot be determined; thus the variation of n_j with E and the variation i with E cannot be calculated. It may be observed, however, that the term $\exp(bE)$ increases less rapidly with E than n_j decreases due to the term $\exp[-k_j^o t^m \exp(\mathcal{K}E)]$ in Eq. [4]. Thus for any given time, i must decrease as E increases, as is observed in this potential range, $E_a \leqq E < \sim E_a + 200$ mV. As discussed above, at higher potentials a different mechanism must apply.

Secondary film formation.—The difference between the primary and the secondary passivating films is characterized by the fact that the former is produced reversibly, while the latter is formed irreversibly and is exceedingly difficult to reduce. The existence of any secondary film can be determined sensitively by measuring the reduction potential of the film, an increase of as little as 1-2 mV being easily reproducible and indicative of irreversibility and of the presence of the secondary film. The conclusion that these changes in the reduction potential are real and due to the formation of the secondary film is in agreement with the results of the experiment in which we monitored the time for the current to reach its steady-state value at −0.205V after cathodic reduction. The slower approach to the steady state for films having higher reduction potentials is most easily explained by assuming that the reduction process did not reduce all the surface film, *i.e.*, the secondary film, and that the remainder is removed during the anodic dissolution process. Evidence for incomplete reduction is clear at the higher potentials ($E \geqq E_a + 50$ mV) at which it appears that the maximum film thickness is less than at $E_a + 16$ mV (Fig. 3); this is not only unlikely, but it clearly is not so since these maxima occur at times of less than 1000 sec while the current does not reach its steady-state value until approximately 8000 sec (Fig. 1). Since at the higher potentials secondary film formation begins before film growth has stopped, it is not possible to determine chronopotentiometrically the total film thickness at steady state. These have, however, been determined ellipsometrically at various potentials (12).

In Fig. 2 we see that the quantity of primary film present at the time that secondary film growth begins increases with potential, at least up to $E_a + 16$ mV. It is reasonable to assume that at higher potentials the total quantity of primary film formed is at least as great. Since the maximum reducible film thickness is less at higher potentials, some of the primary film must either be converted to secondary film or dissolve in the electrolyte solution. Since there is no evidence for the latter and since primary film growth always precedes secondary film formation, we conclude that the primary film undergoes a reaction to form the secondary film and that the latter is not produced directly from the metal.

The kinetic data of Fig. 2 and 3 can best be interpreted if we assume that the rate of formation of the secondary film, as well as that of the primary film, is potential dependent, and that at potentials close to the activation potential the rate constant for primary film formation is greater than the rate constant for secondary film formation, while at higher potentials ($E > E_a + 20$ mV) the rate constant for secondary film formation becomes greater. It follows that at those potentials at which the rate of growth of the primary film is greater than that of the secondary film, the apparent or measured thickness should increase until primary film growth ceases. This does happen at potentials $E_a + 8$ and $E_a + 16$ mV (Fig. 2). However, at the higher potentials at which the rate of secondary film growth is greater, the apparent thickness reaches a maximum soon after secondary film growth commences.

Because of the irreversibility of secondary film formation, the techniques employed in this study do not permit a quantitative study of the kinetics of the growth of this film. Therefore, we cannot make extensive comments on its composition and structure or suggest a mechanism for its growth.

Of interest, however, is the work of Caplan, Harvey and Cohen (13) who found for an Fe-26%Cr alloy that the film reduction potential increased sharply when the surface was subjected to highly oxidizing conditions; they attributed this to the formation of a nonstoichiometric oxide containing high valency chromium. The present work and previous work (1) are consistent with this interpretation. However, secondary film formation is detected at potentials as low as −0.108V; whether tetravalent or hexavalent chromium exist at this potential cannot be calculated since the reversible potential for the oxidation of $Cr^{III}(s)$ to Cr^{IV} or to Cr^{VI} in a $Cr^{III}(s)$ matrix, as well as the activity of the higher valent chromium species in the film, is not known.

The presence, and possibly the effect, of H and of H_2O in the passive films must also be considered (14-17). Essentially the same phenomena as those reported here have also been observed during the anodic oxidation of the noble metals (18). While variations in interpretation of the data exist, most basically involve the chemisorption of OH^- or $O^=$ followed by compound formation and oxidation to a higher valence state.

Conclusions

The kinetics of growth of the primary passivating film and of the secondary film on an Fe-24% Cr alloy in H_2SO_4 have been studied over a potential range of several hundred millivolts above the activation potential. The data have permitted a direct evaluation of the effectiveness of an adsorbed film and of an oxide film in giving rise to passivity. It is concluded that an adsorbed film is responsible for passivity at the activation potential; in the potential region $E_a < E < E_a + 200$ mV this same film is responsible for initiating passivity; however, the steady-state film is an oxide. Above $E_a + 200$ mV the adsorbed film is not an effective passivator and an oxide film is required to initiate and maintain the passive state. In the low-potential region ($E < E_a + 200$ mV) anodic dissolution during the passivation process occurs by the direct, activated transfer of the ions from the metal into solution. At higher potentials dissolution most likely occurs by the field-assisted diffusion of ions through the oxide film.

As a result of the change in the mechanism of passivity with potential, it is insufficient to state the type of film or process associated with passivity. It is necessary to define the relevant potential or potential range and the variation of film thickness, composition, structure, and mechanism of formation with potential.

The data also indicate that the rate of growth of both the primary and the secondary films is potential dependent; at potentials close to the activation potential the rate constant for primary film growth is greater than that for secondary film formation, while at higher potentials the rate constant for secondary film growth becomes greater and as a result a limiting apparent film thickness is observed before the steady state is achieved.

APPENDIX

Rate equation for primary film growth.—Previously (2) we proposed a mechanism for the passivation process at potentials below $E_a + 200$ mV in which it is assumed that dissolution occurs at different rates from different types of surface sites and that the most active

sites are passivated preferentially. Therefore, the kinetics of film growth are treated by considering each type of site and the total film as the sum of its parts, *i.e.*

$$Q = \sum_j Q_j \qquad [1A]$$

In the previous paper we restricted ourselves to three types of sites, kinks, ledges and terraces; in this paper this restriction will not be necessary. However, we restrict ourselves to the growth of no more than a monolayer of film and to the region in which no secondary film is present

We propose the following rate law for film growth at the j'th type of site at constant potential E as being consistent with the observed kinetics and with the reversibility of the film formation process

$$\left(\frac{\partial Q_j}{\partial t}\right)_E = (Q_{s,j} - Q_j)\, k_j m t^{m-1} - Q_j k_j' p t^{p-1} \qquad [2A]$$

where t is the time, $Q_{s,j}$ is the maximum or steady-state film thickness at the j'th type of site at a given potential, k_j and k_j' are time-independent proportionality constants[6] associated with film growth and film reduction, respectively, at that type of site, and m and p are constants; $Q_{s,j}$, k_j, and k_j' are potential dependent with k_j increasing and k_j' decreasing as the potential is increased. This rate equation is strictly valid only for film growth on each set of contiguous sites of the j'th type. Kinks are not likely to be contiguous; however, they occupy only 0.01% of the total sites, while terraces occupy 90% and ledges 10% of the total surface (2). This equation predicts a decreasing rate of film growth with increasing film thickness, as is observed. At sufficiently high potentials the second term on the right side of Eq. [2A] becomes negligible. Equation [2A] can be integrated analytically only when $m = p$. In that case, remembering that when $t = 0$, $Q_j = 0$, and summing over all types of sites

$$Q = \sum_j \frac{k_j Q_{s,j}}{k_j + k_j'} - \sum_j \frac{k_j Q_{s,j}}{k_j + k_j'} \exp\left[-(k_j + k_j')t^m\right] \qquad [3A]$$

For small values of the argument the exponential in Eq. [3A], may be expanded and all terms after the first in k_j, k_j' and t neglected so that Eq. [3A] reduces to

$$Q = \{\sum_j k_j Q_{s,j}\}\, t^m \qquad [4A]$$

Taking the logarithms of both sides of Eq. [4A]

$$\log Q = \log \{\sum_j k_j Q_{s,j}\} + m \log t \qquad [5A]$$

This equation predicts a linear relationship between log Q and log t as is observed for the growth of the primary passivating film (Fig. 2 and 3) with $m = 0.70 \pm 0.05$. At potentials close to E_a the linear log Q — log t relationship does not hold as well as at higher potentials. This may be either (*i*) because the constants m and p are not equal and hence Eq. [2A] cannot be integrated analytically, or (*ii*) because k_j' increases more rapidly than k_j decreases with decreasing potential. In the latter case the expansion of the exponential to obtain Eq. [4A] may not be valid for a sufficient time to observe the linear behavior predicted by Eq. [5A].

From Eq. [5A] we see that the film thickness at time 1 sec gives the time-independent apparent proportionality constant

$$k = \sum_j k_j Q_{s,j} \qquad [6A]$$

which is plotted in Fig. 6 as a function of potential. To understand completely the variation of k with E, it is necessary to know independently the variation of each $Q_{s,j}$- and each k_j-term with E. These are not known. However, it appears that at potentials well above the activation potential Q_s increases only slowly with potential (12) and hence the semilogarithmic variation of k with E is due to the variation of the k_j-terms with E. From Fig. 2 it is evident that as the potential approaches E_a, Q_s rapidly decreases, which may be the cause for the negative deviation from semilogarithmic behavior at the low potentials; the reasons given for the deviation from the linearity predicted by Eq. [5A] may also be involved.

[6] It can be shown that k_j is related to the conventional rate constant k_c by the relationship $k_c = k_j t^m$.

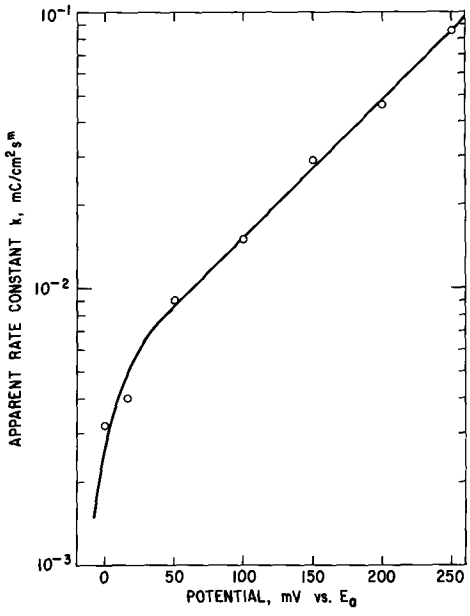

Fig. 6. Variation of the apparent rate constant k for primary film growth with potential, illustrating semilogarithmic behavior and negative deviations therefrom as the potential approaches E_a.

Acknowledgments

The author wishes to thank Mrs. A. C. Broz for skillfully performing the experimental work, C. Brickner for taking the scanning electron micrographs, and Drs. S. Barnartt, C. A. Johnson, and R. A. Oriani, all of this Laboratory, for helpful discussions.

Manuscript submitted May 16, 1969; revised manuscript received *ca.* Aug. 25, 1969. This was Paper 66 presented at the Detroit Meeting, Oct. 5-9, 1969.

Any discussion of this paper will appear in a Discussion Section to be published in the June 1970 JOURNAL.

REFERENCES

1. R. P. Frankenthal, *This Journal*, **114**, 542 (1967).
2. R. P. Frankenthal, *ibid.*, **116**, 580 (1969).
3. H. H. Uhlig, *Z. Elektrochem.*, **62**, 626 (1958); *Protection of Metals*, **2**, 431 (1966).
4. K. J. Vetter, "Electrochemical Kinetics," English translation, pp. 748-789, Academic Press, New York (1967).
5. N. Hackerman, *Z. Elektrochem.*, **62**, 632 (1958).
6. T. P. Hoar, *Corrosion Sci.*, **7**, 341 (1967).
7. M. Nagayama and M. Cohen, *This Journal*, **109**, 781 (1962).
8. A. Rahmel and W. Schwenk, *Arch. Eisenhuettenw.*, **31**, 189 (1960).
9. D. A. Vermilyea, "Advances in Electrochemistry and Electrochemical Engineering," Vol. 3, p. 211, P. Delahay, Editor, Interscience Publishers, New York (1963).
10. M. Cohen, Private communication.
11. K. Hauffe, "Oxidation of Metals," English Edition, pp. 125-137, Plenum Press, New York (1965).
12. J. R. Ambrose and J. Kruger, Private communication.
13. D. Caplan, A. Harvey, and M. Cohen, *This Journal*, **108**, 134 (1961).
14. G. Okamoto, M. Nagayama, T. Ishikawa, and T. Shibata, "Second International Congress on Metallic Corrosion," New York 1963, N.A.C.E., p. 558 (1966).
15. G. Okamoto and T. Shibata, *Nature*, **206**, 1350 (1965).
16. H. T. Yolken, J. Kruger, and J. P. Calvert, *Corrosion Sci.*, **8**, 103 (1968).
17. M. C. Bloom and L. Goldenberg, *Corrosion Sci.*, **5**, 623 (1965).
18. J. P. Hoare, "The Electrochemistry of Oxygen," Chap. II, Interscience Publishers (J. Wiley), New York (1968).

Anodic Films on Zinc and the Formation of Cobwebs

R. W. Powers*

General Electric Research and Development Center, Schenectady, New York

ABSTRACT

When a zinc anode in a strongly alkaline electrolyte is observed under a microscope, two different films can be noted under appropriate conditions. Although both have been identified as zinc oxide, type I is white and forms by precipitation from a supersaturated layer of electrolyte covering the electrode. Type II, on the other hand, seems to form directly on the electrode surface. Its color can range from light gray to black. During dissolution of the type II film, entities appear which resemble spiderwebs under the microscope. These so-called cobwebs seem to form by the gathering together of the darkening agent in this film. They are mainly zinc, are electronically conducting, and can be oxidized. Cobwebs appear to have a relationship to the hydrogen evolution that occurs at potentials anodic to the zinc rest potential. They are important, in addition, because during subsequent electrodeposition they accelerate the formation of spongy zinc at low cathodic potentials and of dendritic zinc at higher ones.

When zinc is anodized under certain conditions in a strongly alkaline solution such as 7.0 Molar (M) aqueous potassium hydroxide, entities form which resemble spiderwebs under the microscope. Such structures as shown in Fig. 1 have been called zinc cobwebs. In this paper, a discussion of the relationship between the different anodic films that form on zinc and the current-potential curve is used as a basis for considering the mechanism of the formation of these cobwebs. In addition, this paper is concerned with their composition and properties as well as their effects on other phenomena that occur with the alkaline zinc electrode.

Experimental Procedure

Most of the experimental work in this study was carried out potentiostatically in a cell in which a test electrode can be observed under a microscope during the passage of an electric current. This technique is described in detail elsewhere (1). The test electrode is arranged horizontally facing upward and is viewed through a very thin glass window in the cell with a bench microscope equipped with dark field objectives. The zinc electrode potential was controlled with a Jaissle potentiostat. Ramp and triangular waveforms used in scanning the electrode potential were taken from a multiturn potentiometer driven by a clock motor. When required, a gas lift pump operated by ultrapure hydrogen circulated the electrolyte. All measurements were made at room temperature, 23° ± 1°C.

Two kinds of zinc electrodes were used. Polycrystalline ones were punched from rolled zinc sheet designated as Mix 60 by the supplier, the New Jersey Zinc Company. It is about 99.99% pure. Such specimens were electropolished in a 20% sulfuric acid bath in order to render them structureless at the beginning of an experiment. However, most test electrodes were prepared by cleavage from a single-crystal zinc rod in liquid nitrogen. This procedure produces a mirror-like surface which lies in the basal plane. Even after some etching, the single-crystal surface presents a rather uniform background against which cobwebs can be viewed in contrast to the more variegated background of polycrystalline specimens. Single crystals from two sources were used. Some were grown by the Bridgman method in graphite molds from zinc initially 99.9995% pure. Others were grown by Research Crystals, Incorporated, of Richmond, Virginia, from zinc 99.9999% pure. The latter crystals were pulled from the melt by the Czochralski technique.

The electrolyte used throughout this work was an aqueous 7.0M potassium hydroxide solution. For most experiments, 0.25 mole of zinc oxide was dissolved per liter of solution to produce a definite zinc equilib-

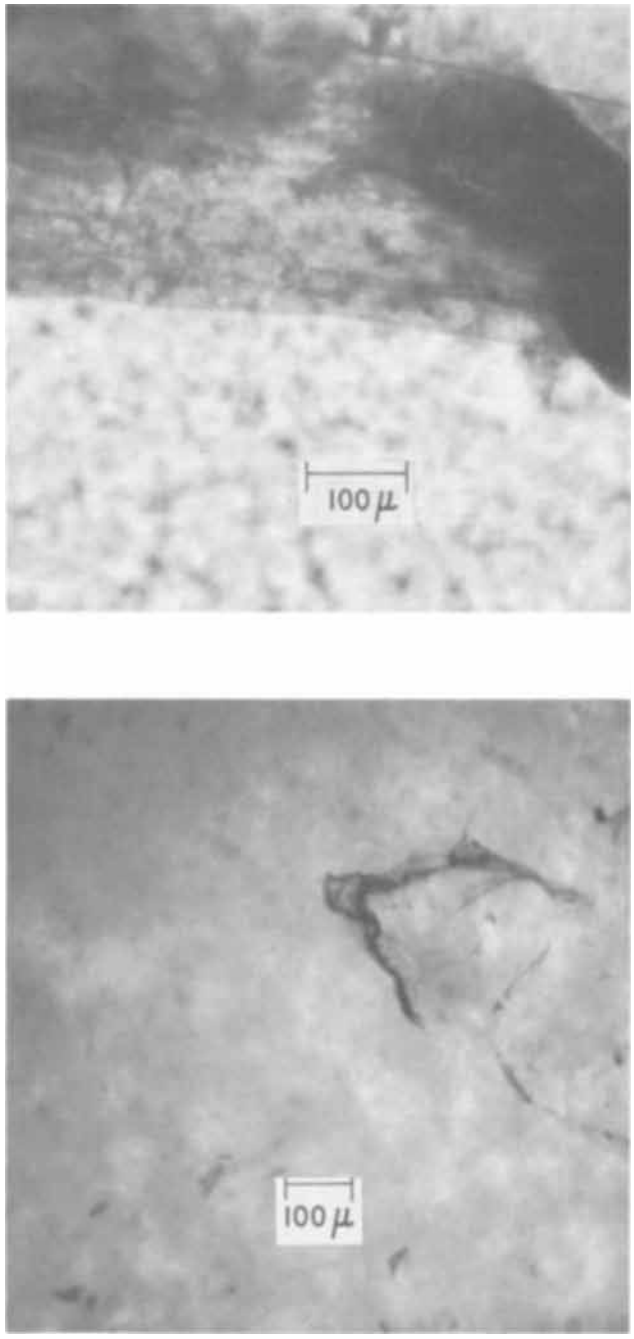

Fig. 1. Zinc cobwebs. Dark field. *Top*—100X, *bottom*—60X.

* Electrochemical Society Active Member.

rium potential and to reduce pitting of the zinc electrode surface when first exposed to electrolyte under open-circuit conditions. The occurrence of such pitting makes the interpretation of microscopic observations much more difficult. Solutions were prepared either from distilled water or from special conductivity water (2). These alkaline solutions were filtered through Gelman No. AN-200 Acropor membranes with 0.2μ pores in order to remove the larger particles of iron compounds present in reagent-grade KOH. Although atomic absorption analysis of these solutions before and after filtration indicates that only about 10% of the iron is thus removed, this treatment reduces the hydrogen evolution rate and thus makes microscopic observation easier. The filtration was carried out in a closed system in order to prevent the absorption of carbon dioxide and of oxygen. Solutions were deaerated by bubbling with purified argon.

The zinc electrode potential was measured against a mercury-mercuric oxide electrode in pure KOH of the same concentration as that used in the test cell. The electrode potentials cited in this paper are with reference to this electrode unless stated otherwise.

Experimental Results and Their Interpretation

i-U curves and the nature of the anodic films.—The conditions for the formation of zinc cobwebs are probably best understood after considering the relationship between the current-potential (*i-U*) curve and the nature of the anodic films formed under different circumstances. Some aspects of these relationships were discussed in a previous paper (3). The results to be presented confirm and extend the interpretations given there.

In Fig. 2, there is shown an *i-U* curve taken on a single-crystal specimen at the very slow potential scan rate of 0.05 mV/sec with convection nearly absent. The scan was started at the rest potential and was terminated at — 0.97V. Photomicrographs of the electrode surface were taken at the potentials indicated with capital letters beside the *i-U* curve. These are presented in Fig. 3. All were taken of the same specimen field with the same incident light intensity and exposure time. The pits produced during the dissolution of zinc at low anodic potentials (Fig. 3A-D) were usually shaped in the form of nearly regular hexagons. With increasing potential, hexagonal pits within hexagonal pits can be seen. The formation of these rather large, regularly shaped pits as shown in this series of photomicrographs constitutes an almost ideal background for viewing the initial stages of the formation of a precipitated film. The pattern of dissolution pits

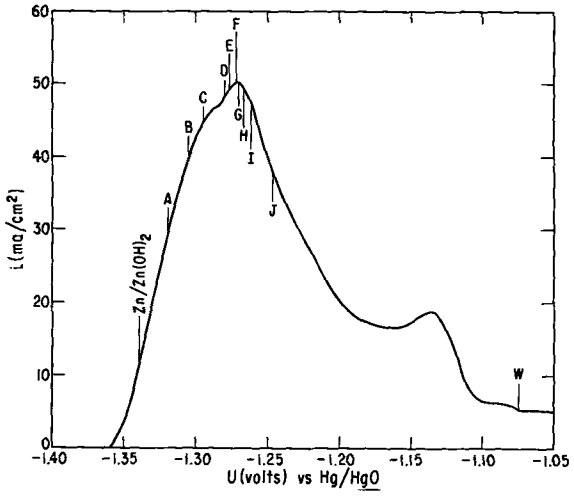

Fig. 2. Current-potential curve for cleaved zinc single crystal in 7M KOH + 0.25M ZnO taken during anodic sweep at 0.05 mV/sec under nearly convectionless conditions.

did vary somewhat from specimen to specimen. With some, highly irregular hexagonal troughs were formed over much of the electrode surface. In such instances, light scattered from the precipitated particles is difficult to distinguish from the background of light scattered off the specimen surface. As shown in a previous paper, the dissolution facets observed on specimens from still another crystal at a ten times faster potential scan rate were more uniformly developed over the entire surface (3). Here also the onset of precipitation was harder to observe than in the photographs presented in Fig. 3.

Various stages in the formation of a film by precipitation from a layer of electrolyte supersaturated with zincate are shown in Fig. 3D-G. Small white precipitate particles were noticed at potentials slightly below that at which the first maximum in the *i-U* curve occurs. They first appeared on areas of the surface where it was highly stepped or pitted. Here the local current density as well as the supersaturation are expected to be the greatest. The peak current occurred at a slightly lower potential than that previously reported where the sweep rate was ten times higher (3). This precipitated film has been called type I to distinguish it from another anodic film with very different properties (3).

The latter, called type II, appears to form directly on the electrode surface. It is more or less transparent and ranges in color from light gray to black (3). The darkening of the specimen surface, noted at potentials only slightly greater than that corresponding to the first current maximum (Fig. 3H *et seq.*), is attributed to the formation of type II beneath the type I. Corresponding to the growth of type II, the darkening increases with increasing potential or anodizing time.

That the anodic film, formed as described above, is really duplex is shown by observation of the specimen with an intense light source. On increasing the light intensity sevenfold over that used to obtain the photographs shown in Fig. 3, to the maximum obtainable with a metal halide arc light, the outer precipitated film can readily be seen as shown on Fig. 4. This photomicrograph was obtained at the potential corresponding to W on Fig. 2. The film is somewhat porous. Holes and crevices can be seen in it. The particles are coarser and more translucent than those noted near the potential of the first current peak. The thickness of this type I film is not uniform over the surface. Consequently only a portion of the field appears in focus. Some out-of-focus areas are indicated by arrows on Fig. 4.

After placing the specimen on open circuit following the experiment described above, the electrolyte was circulated and the disintegration of the outer film was followed particle by particle. After most of it was so removed, the underlying film, where buckled and torn, was evident as shown on Fig. 5. Patches of torn film as large as those shown on this figure are not commonplace when anodizing is *followed* by stirring. As shown previously though, large areas of such film are readily noted if the electrolyte is stirred *during* the anodizing to suppress the formation of type I film (3).

In experiments similar to that described above, some dark blue pieces of film have been observed beneath the very porous outer portion during disintegration of type I. These blue particles appear to be precipitate that has been consolidated into a nearly nonporous mass and are often surrounded completely by very porous precipitate. They likely give rise to the frequently noted over-all bluish appearance of anodic films on zinc.

Type I film was identified as zinc oxide by x-ray diffraction. Concordant results were obtained on three specimens prepared under different conditions. For the preparation of one specimen, the potential applied to a single crystal was scanned from the rest value to −1.24V, slightly beyond that corresponding to the first current peak. The electrolyte was not stirred. The precipitate particles on the electrode were small and

the layer of film was very thin. An example of aged precipitate was prepared by scanning to −1.08V at 0.05 mV/sec from the rest value. The film appeared similar to that shown in Fig. 4. For the third specimen, the potential was scanned to −1.11V. Although the electrolyte was circulated in this latter case, a precipitate appeared on a small portion of the electrode surface where the stirring was not vigorous. After anodizing, electrodes were removed from the cell as rapidly as possible, immersed in 30% KOH solution to remove soluble zincate, rinsed with distilled water, and dried in a stream of nitrogen. Although the intensities of the diffraction lines were less for the first specimen, the pattern for all three corresponded to the same compound, zinc oxide. It is not likely that the diffraction patterns observed resulted from the transformation of a film of zinc hydroxide after removal of the electrode from the electrolyte. According to Dietrich and Johnston, ϵ-zinc hydroxide, the most stable modification, is kinetically stable almost indefinitely at room temperature against transformation to zinc oxide and water (4). Moreover, even though the films on these specimens were duplex, the diffraction patterns must be attributed to the outer layer as x-ray diffraction patterns were not obtained from the type II film formed under the conditions described above. The results reported here are in accord with those of Nikitina, who found that at 20°C the precipitate from a 7M KOH solution supersaturated with zincate was zinc oxide. She did report in addition that zinc hydroxide can precipitate from solutions of lower KOH concentration or even from 7M KOH at lower temperatures (5).

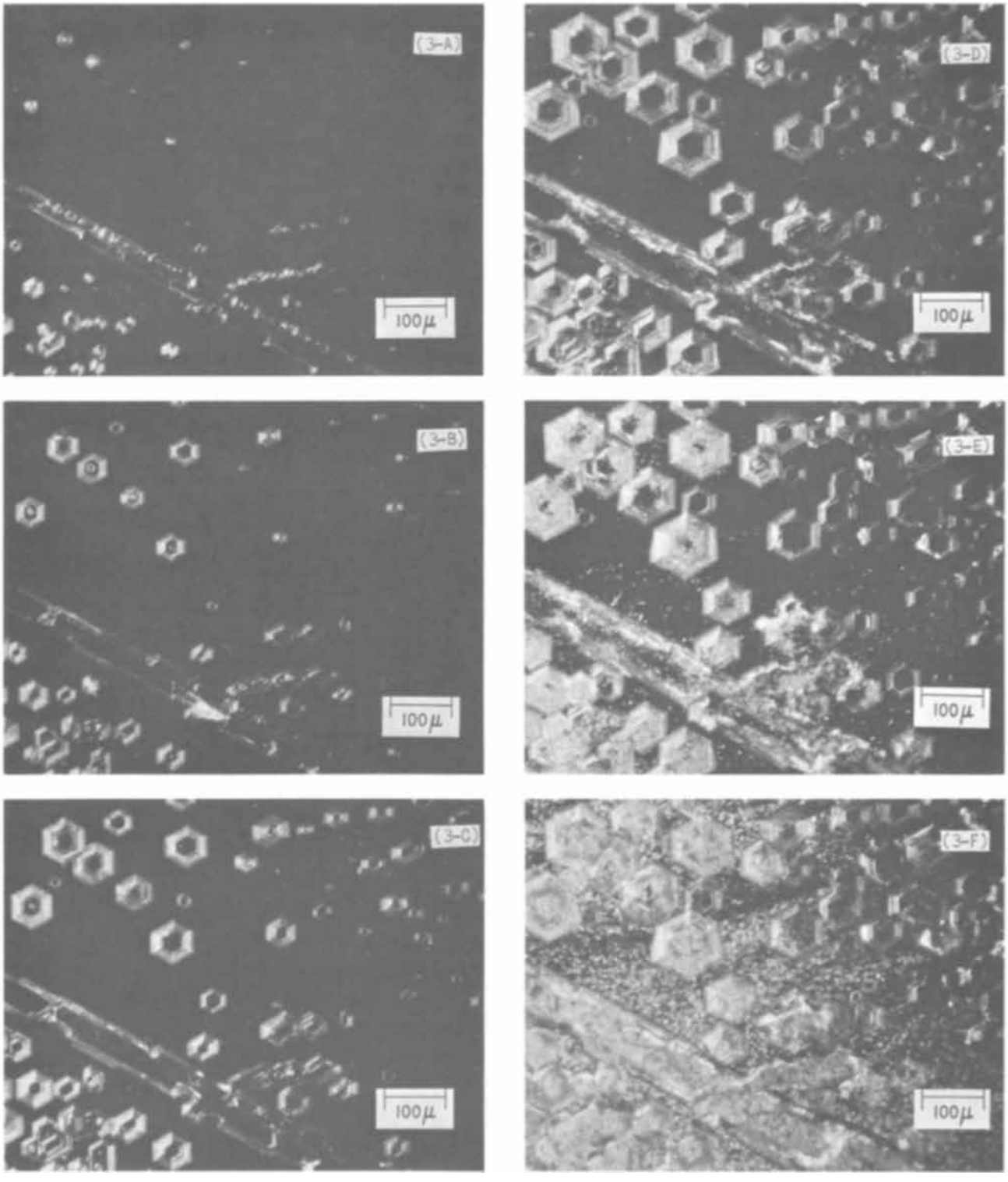

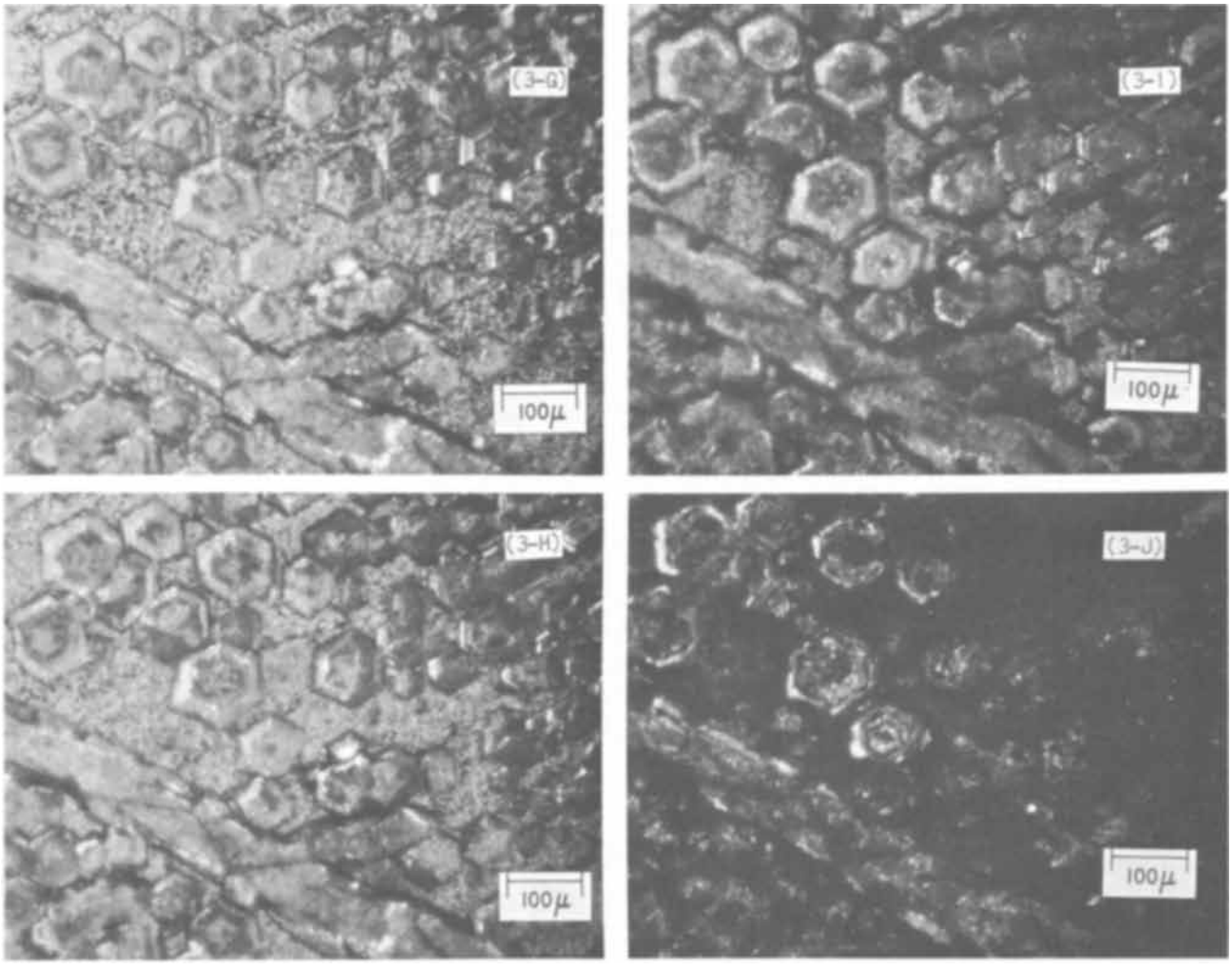

Fig. 3. Morphological changes in a zinc electrode during an anodic sweep. Dark field. 100X. Letters correspond to potentials indicated on Fig. 2 (A-J).

Type II film was also found to be zinc oxide. A single-crystal electrode, after subjection to a potential of −0.37V for 25 min, was coated with a gray film, the structure of which was established by electron diffraction. As noted previously, this procedure for preparing type II film minimizes the formation of the precipitated type (3). A reflection pattern of zinc and zinc oxide was obtained showing the presence of both epitaxial and polycrystalline zinc oxide. It was not possible to get an identifiable pattern from a rumpled type II film produced by scanning the potential of a single-crystal electrode up to −1.21V while stirring the electrolyte. This thin film may have been partially destroyed during the washing and drying operations following removal from the viewing cell.

As discussed in a previous paper, dark anodic films on zinc have been studied by a number of authors, all of whom identified them as zinc oxide (3). They were the subject of very intensive investigation by Huber who showed that the darkening was associated with the presence of excess zinc (6-9). He observed bleach-

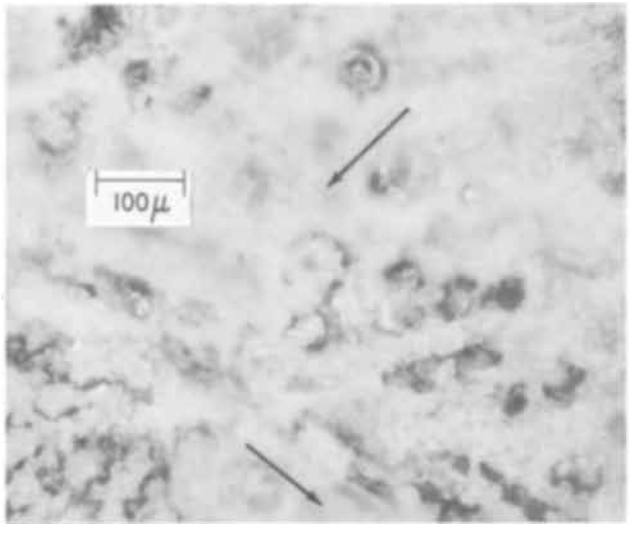

Fig. 4. Type I film. Dark field. 112X.

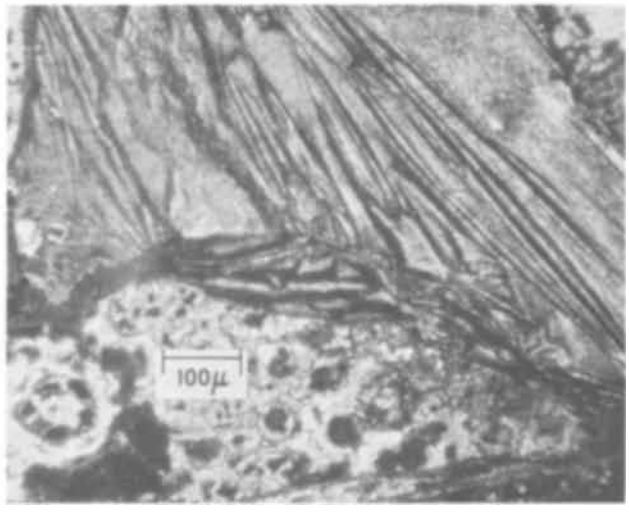

Fig. 5. Buckled type II film. Dark field. 100X.

ing on heating such films in air above 200°C and darkening again after heating in the presence of zinc vapor (8). Huber, and later Fry and Whitaker, also found the electrical conductivity of such dark zinc oxide films to be much greater than bleached ones (9, 10). The important finding of the present work is evidence for their formation at potentials close to the equilibrium value, −1.34V. The presence of a very thin layer of type II film on the zinc electrode at potentials as low as −1.30V was noted several times. During anodic potential scans with forced circulation of the electrolyte, small pieces of type II film were observed as they were partially lifted above the electrode surface and waved about by the moving electrolyte. As most previous work on dark anodic films was done at constant current, their formation was usually noticed at the oxygen evolution potential after passivation. Kaesche, however, working in dilute solutions, 1M Na_2CO_3 and 0.1M $NaHCO_3$, found evidence from constant current charging and reduction curves for the formation of an electroreducible film, presumably zinc oxide, close to the equilibrium potential (11).

The height of the second peak shown on Fig. 2, the one near −1.14V, is but 60% of that reported previously (3). The anodizing conditions were similar except that the specimens were cleaved from different single crystals. With some polycrystalline electrodes, the height was found to be nearly as great as for the first peak. Thus there is considerable variation depending on the specimen source. As this second peak occurs both in the presence as well as the absence of type I film, it likely arises from some limitation imposed by the conductivity of type II. Since zinc oxide is a semiconductor, one can speculate that small variations in the impurity content of the zinc from which the anodic film is formed may affect the degree of doping and consequently the conductivity.

Cobweb formation.—The entities called cobwebs were first observed following partial dissolution of anodic films formed during a potential scan carried to passivation. They appear to be a relatively insoluble portion of type II film and seem to form by the gathering together of the dark material in this film. Cobwebs behave as if under tension and, as the lighter-colored material is dissolved, they coalesce first into a string and then into a wad. The effect of stirring the electrolyte above them is similar to the action of a broom on spiderwebs. Some of these points can be seen from the dark field photomicrographs shown in Fig. 1. These photographs of cobwebs are unusual only as to the extent of the field lying within the same focal plane.

Probably the observation of cobwebs has been aided by the electrolyte flow pattern during stirring in the cell used for microscopic viewing (1). In this cell, the specimen caps the bottom of a hollow Teflon cylinder filled with electrolyte. A gas lift pump induces flow of electrolyte in a rectangular channel above this cylinder and parallel to the specimen surface. The flow immediately above the specimen is counter to that in the channel. This causes the dissolution of the film to be first evident on what normally would be considered the downstream side. The important point is that this circulation pattern tends to concentrate insoluble material instead of dispersing it as with most other methods of stirring.

The formation of cobwebs has been observed under a wide variety of experimental conditions. Formation occurred after anodizing at potentials ranging from −1.23 to 0.5V. However, the delicate webbing shown in Fig. 1 has been observed only on those specimens anodized at lower potentials. Cobweb formation took place on single crystals of 99.9995 and 99.9999% purity as well as on polycrystalline specimens of 99.99% purity. Formation did not appear affected by the use of lots of KOH of different purity levels or whether use was made of unfiltered KOH solutions in comparison with those filtered to remove iron compounds. Solvent purity did not appear important as both ordinary laboratory distilled water and conductivity water have been used for solution preparation without affecting cobweb formation (2). Special cleaning of the test cell in boiling concentrated nitric acid did not affect their formation. Further, it was not changed by the use of argon in place of hydrogen to operate the gas lift pump. The only positive correlation noted was with the color of the anodic film. Few cobwebs were observed if the anodizing was stopped when the film was white, *i.e.* when the electrode was covered with type I film only. However they were always seen when the film appeared dark, *i.e.* after sufficient quantity of type II film formed beneath the type I to cause the duplex film to darken. A potential scan is not required in order to form cobwebs. In fact, the most efficient procedure found for producing delicately webbed cobwebs in relatively high yield consists in stepping the potential from the rest value to −1.16V for 5-7 min, followed by circulation of the electrolyte under open-circuit conditions.

The composition and properties of cobwebs.—These facts—that a dark type II film is required for cobweb formation; that their formation is apparently not affected by changes either in the specimen purity or in the electrolyte purity; and that cobwebs can be prepared again and again on the same specimen, apparently without exhaustion, by anodizing followed by dissolution of the anodic film—suggest they are zinc and not an impurity.

Many of the experiments described above were carried out after various attempts to identify cobwebs directly by x-ray diffraction and by conventional chemical analysis failed. However, subsequent attempts using a microprobe x-ray analyzer and atomic absorption analysis were largely successful.

The specimen for microprobe analysis was prepared by anodizing at −1.16V for 5-7 min, followed by stirring the electrolyte for a couple of minutes. These steps were repeated four times so that many cobweb fragments were present on the surface of the single-crystal electrode. The microprobe gave a qualitative indication of the presence of zinc and iron only, although an effort was made to detect the presence of many other elements including copper, nickel, lead, cadmium, tin, gold, aluminum, and silicon.

Atomic absorption spectroscopy was used to get a more quantitative analysis. Specimens were anodized as described above. However, the electrolyte was stirred for a longer time in order to dislodge most of the cobwebs from the specimen surface. After 5-20 anodizing steps, the electrolyte was filtered through a Gelman Acropor membrane to collect the cobweb fragments. The membrane was washed with a 7.0M KOH solution to remove soluble zincate and then thoroughly rinsed with distilled water. One half of the filter membrane, containing no cobweb fragments, served as a control. Both this control and the other half of the membrane containing the cobwebs were placed in 5-7 ml quantities of 0.3M HCl for analysis.

The results of four different analyses for zinc and iron by atomic absorption spectroscopy are indicated in Table I. There was a considerable variation in the quantity of cobwebs available for analysis from one experiment to another—undoubtedly due in part to

Table I. Cobweb analysis by atomic absorption spectroscopy

Experiment		Quantities in μg Zn	Fe
1	Cobwebs	6.3	2.7
	Control	1.5	1.5
2	Cobwebs	16.8	1.6
	Control	10.5	0.8
3	Cobwebs	130	2.2
	Control	4.5	0.8
4	Cobwebs	41	2.1
	Control	5.3	2.1

their relatively rapid dissolution in the alkaline electrolyte. Since in all but one experiment the amount of iron in the specimen was greater than in the control, it must be inferred that cobwebs do contain some iron in agreement with the microprobe results. However in experiments 3 and 4 where the quantities analyzed were relatively large and in which therefore the accuracy should be greater, the amount of iron was but a few per cent of that for zinc. It does not seem unreasonable to assume that zinc in the cobwebs might function as a scavenger for iron compounds in the electrolyte. This would account for the presence of a small amount of iron as detected by both analytical techniques.

Cobwebs are good electronic conductors. This was documented by an adaptation of an old experiment. If a piece of pure zinc is placed in a solution of concentrated alkali, its reaction with the electrolyte to produce hydrogen will usually be slow. If, however, the zinc is touched with a platinum wire, the evolution of hydrogen from the platinum wire with simultaneous dissolution of the zinc occurs rapidly. The platinum wire need not touch the zinc directly. Another electronic conductor may be interposed between the two to yield the same result. To demonstrate the good electronic conductivity of cobwebs, a large one, formed on a cleaved single-crystal electrode, was interposed between the zinc specimen and a platinum wire. The tip of a 0.003-in. wire, the motion of which was controlled by a micromanipulator, was brought near the cobweb as shown in Fig. 6A. No hydrogen was evolved near the tip of this wire when out of contact with the cobweb. When contact was established by moving the wire in a horizontal direction, fine hydrogen bubbles were evolved from the wire in great quantity as shown in Fig. 6B. Great care was taken to avoid direct contact between the zinc specimen and the platinum wire. In these photomicrographs, only the tip of the platinum and the top of the cobweb are in focus. These results demonstrate conclusively that cobwebs are good electronic conductors.

Similar experiments may demonstrate yet another point. In Fig. 7, the photomicrograph shows that a portion of a cobweb, indicated by the arrow, disappeared after contact with a platinum wire. One interpretation of this observation is that oxidation of the cobweb has occurred. Although a cobweb mass in contact with the specimen base has considerable mechanical strength, as evidenced by difficulties in removing it with jeweler's tweezers, nonetheless there is a possibility that the disappearance was caused by mechanical dispersion associated with the evolution of hydrogen bubbles. Not all contacts with a platinum wire led to the disappearance of a cobweb at the point of contact. However, the fact that cobwebs can be oxidized was shown numerous times by another experiment. When the electrode potential of a specimen covered with cobweb fragments was stepped from the rest value to an anodic potential between −1.0 and 0V, fragments were greatly reduced in size within a few minutes. This disappearance of cobweb fragments by electrochemical oxidation is shown in Fig. 8. This experiment does not prove conclusively that cobwebs are metallic zinc as oxidation from an intermediate valence state is conceivable. However, the former interpretation seems the simpler one of this and the preceding experiment.

Some effects of cobwebs.—An important source of interest in cobwebs stems from their effects on the morphology of zinc electrodeposits. From the information presented above—that cobwebs are small pieces of electronic conductor which can protrude beyond

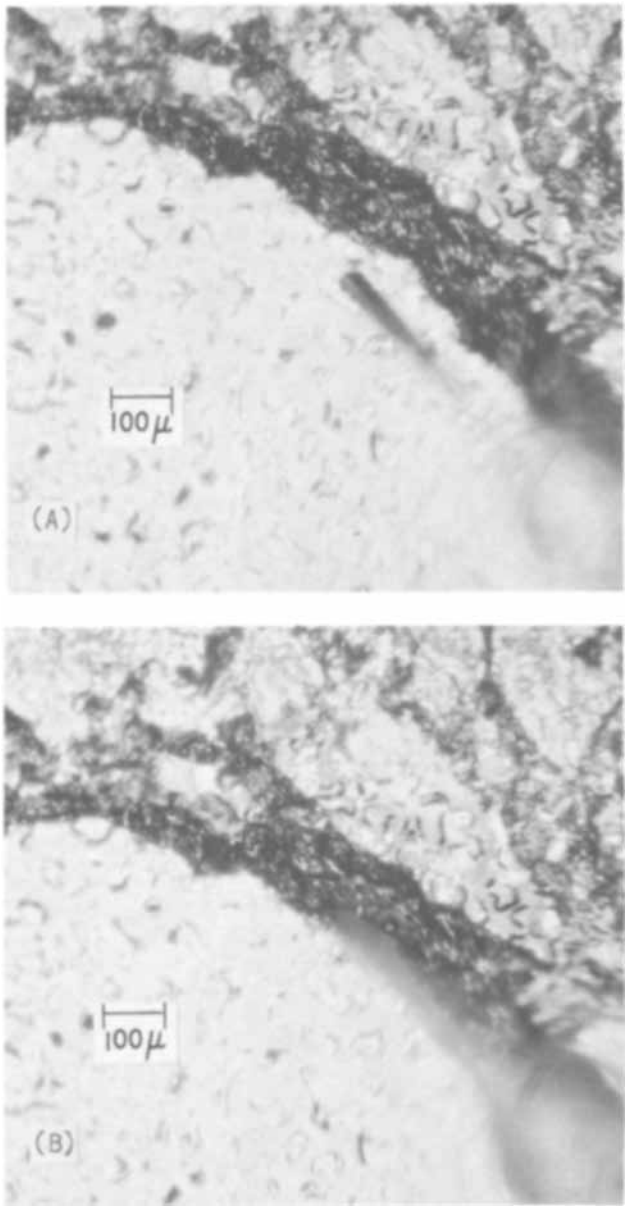

Fig. 6. Hydrogen evolution from a platinum wire touching a cobweb. Dark field. 78X. A—No contact, B—contact.

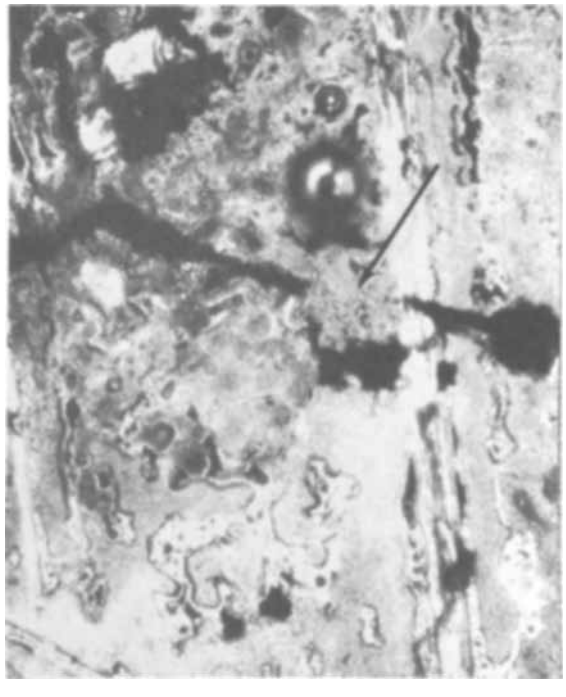

Fig. 7. Disappearance of a cobweb after contact with a platinum wire. Dark field. 90X.

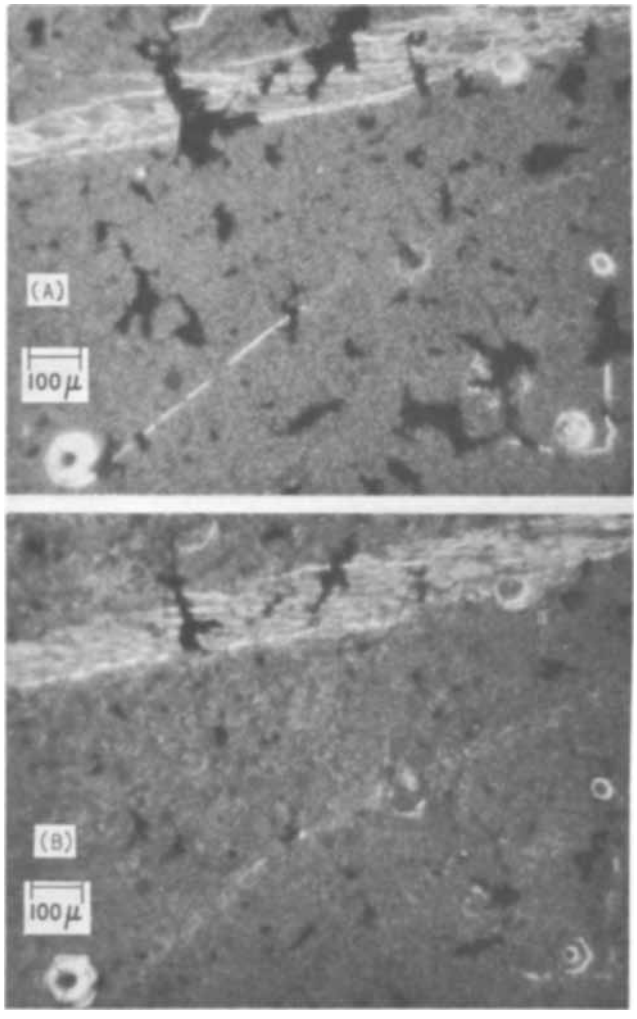

Fig. 8. Disappearance of cobwebs on application of a high anodic potential. Dark field. 62X. A—At rest potential, B—after 70 sec at 0 volt.

the bulk of the zinc electrode into the electrolyte—it is perhaps not surprising that they should affect the early stages of the formation of both spongy and dendritic zinc during subsequent electrodeposition. However, since a satisfactory discussion of this topic would unduly lengthen this paper, information about these effects will be published elsewhere.

Nonetheless, one other phenomenon related to dark anodic layers and to cobwebs is discussed—namely, that hydrogen evolution which occurs at potentials anodic to the zinc rest potential. Several years ago, Sanghi and Fleischmann documented the strange polarization behavior of zinc in dilute KOH solutions (12). Their data for 0.1M KOH saturated with zincate showed the unusual feature of a cathodic current in the region of potential between —1.07 and —0.83V *vs.* a normal mercury-mercuric oxide electrode. They attributed this current to hydrogen discharge. Thus, in the potential range between —1.3 and 0.3V, the current is cathodic below —1.28V due to zinc deposition and hydrogen discharge. It is anodic between —1.28 and —1.07V owing to zinc dissolution and film formation. It is cathodic again in the range —1.07 and —0.83V as noted above. Finally, it is anodic again above —0.83V. Sanghi and Fleischmann speculated about the role of anodic films in catalyzing hydrogen evolution. Further, they pointed out that this hydrogen evolution should also occur in more concentrated solutions but under these conditions the cathodic reaction rate would probably be less than that for anodic dissolution. In this event, the current meter, which indicates a net current only, would register an anodic one. Similar findings were made by Kaesche, using 0.01M $NaHCO_3$ and 0.01M NaOH solutions (11).

Often during anodic scans, a large quantity of bubbles, assumed to be hydrogen, were observed to issue from the electrode at potentials around —1.0V, *i.e.* just cathodic to the equilibrium potential for hydrogen. In some cases, the rate of gas evolution appeared larger than that noted during electrodeposition at potentials 200 mV cathodic to the zinc rest potential. The rate did vary greatly from specimen to specimen though. In a number of instances, this hydrogen seemed to issue from cobweb fragments produced during a previous anodizing experiment. The evolution of hydrogen from dark anodic layers has also been noted by Oxley (13). On standing at open-circuit potential, hydrogen evolution occurs preferentially on cobweb fragments as shown in Fig. 9.

Concluding Remarks

The experiments previously cited—that cobwebs are derived from type II film, that film associated with the active to passive transition; that hydrogen is evolved from them; and that cobwebs accelerate the formation of both spongy and dendritic zinc during electrodeposition—certainly show that these entities have relationships with many of the important phenomena connected with the alkaline zinc electrode.

The observations of cobwebs and associated phenomena described in this paper have been greatly facilitated by a number of favorable circumstances. The recent availability of potentiostats of relatively high current capability permit anodic film formation under more closely controlled conditions. The use of a high-intensity light source is a great help in viewing strongly light-absorbing anodic films. A kind of stirring pattern in the test cell that tends to concentrate, rather than disperse, insoluble material is an advantage. Stirring also causes motion of small cobweb fragments that directs attention to their presence. The use of single-crystal surfaces to produce a more uniform background makes cobweb observation easier. Absence of these special conditions and techniques would have made this study much more difficult.

Acknowledgments

The author is grateful to the International Lead Zinc Research Organization, Incorporated, New York, N. Y., for partial financial support of this work. He wishes to thank V. J. DeCarlo for growing zinc single crystals used in this study. Tracy Lamanec provided a qualitative analysis of cobwebs using a

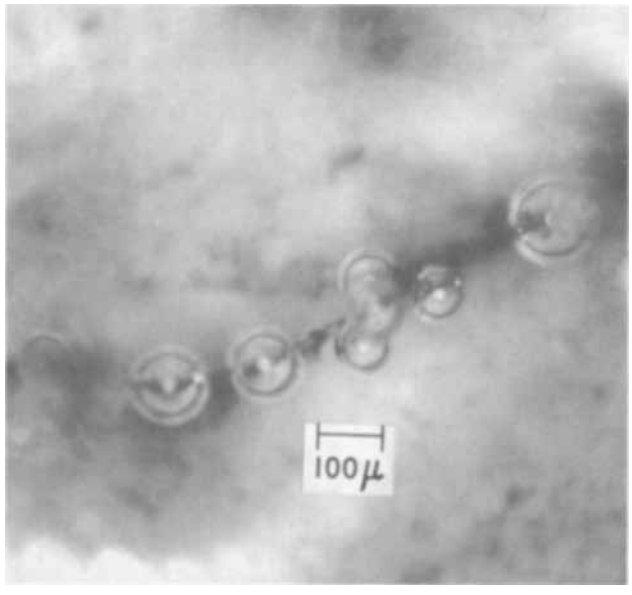

Fig. 9. Hydrogen bubbles on a cobweb. Dark field. 80X

microprobe x-ray analyzer, while David Fisher and John Bartlett did the atomic absorption analysis. The identification of the anodic films by x-ray and electron diffraction was the work of William Dorfeld and Louis Osika.

Manuscript submitted April 24, 1969; revised manuscript received Aug. 8, 1969. This was Paper 369 presented at the Montreal Meeting, Oct. 6-11, 1968.

Any discussion of this paper will appear in a Discussion Section to be published in the June 1970 JOURNAL.

REFERENCES

1. R. W. Powers, *Electrochem. Technol.*, 5, 429 (1967).
2. R. W. Powers, *ibid.*, 2, 163 (1964).
3. R. W. Powers and M. W. Breiter, *This Journal*, **116**, 719 (1969).
4. H. G. Dietrich and J. Johnston, *J. Am. Chem. Soc.*, **49**, 1419 (1927).
5. Z. Ia. Nikitina, *J. Appl. Chem. USSR*, **31**, 209 (1958).
6. K. Huber, *Helv. Chim. Acta*, **26**, 1037 (1943).
7. K. Huber, *ibid.*, **26**, 1253 (1943).
8. K. Huber, *ibid.*, **27**, 1443 (1944).
9. K. Huber, *This Journal*, **100**, 376 (1953).
10. H. Fry and M. Whitaker, *ibid.*, **106**, 606 (1959).
11. H. Kaesche, *Electrochim. Acta*, **9**, 383 (1964).
12. I. Sanghi and M. Fleischmann, *ibid.*, **1**, 161 (1959).
13. J. Oxley, Leesona Moos Lab. First Quarterly Rpt. to NASA, June-Sept. 1964, Contract No. NAS 5-3908.

The Kinetics of Dissolution of II-VI Semiconductor Compounds in Nonoxidizing Acids

L. D. Locker*,[1] and P. L. deBruyn

Department of Metallurgy and Materials Science, Massachusetts Institute of Technology, Cambridge, Massachusetts

ABSTRACT

The dissolution of ZnS, CdS, ZnSe, and $Zn_{0.85}Cd_{0.15}S$ in acid solutions has been studied under conditions where the group VI anions yield only H_2S or H_2Se. The activation energies depend on the particular compound, the acid, and the solvent. However, for ZnS the activation energy is independent of purity and crystal structure. For dissolution of high-purity compounds in aqueous H_2SO_4, the activation energies (kcal/mole) are: ZnS(9.5), CdS(14.2), ZnSe(11.7). The factors that determine nonoxidative dissolution kinetics are analyzed, and a model is presented. This case is compared to the mechanism of elemental and compound semiconductor dissolution where electron transfer occurs, and there is a relatively large change in the oxidation states between reactants and products.

The atomic processes that occur on the surface of a solid during dissolution depend on the type of bonding in the solid and on the particular species in solution (1-5). For the electrochemical dissolution of semiconductors, these processes have been studied extensively. However, little attention has been given to the mechanism of dissolution of semiconductors in nonoxidizing solutions.

The relationship of structure and bonding to the dissolution mechanism can be illustrated by several cases. For example, the dissolution of alkali halide crystals, such as LiF, is analogous to evaporation in that atoms are removed by dissociation from kink sites on the surface (1, 2). If the initial rate of dissolution in pure solvents is expressed by the equation

$$R_o = \nu \exp(-E/RT) \quad [1]$$

then for the alkali halides ν is a frequency factor that depends on the surface area and the distribution of active sites, and the activation energy E is the energy for dissociation of surface atoms. In the anodic dissolution of semiconductors, the rate is often controlled by the transport of holes from the bulk of the semiconductor to the surface. The pre-exponential term in Eq. [1] will then be a function of the bulk charge carrier concentration, the charge of the carriers, the diffusion coefficient, and the characteristic diffusion length in the solid. The activation energy will be influenced by space charge effects in the solid as well as by the bonding and structure of the particular semiconductor. All factors that have an influence on the charge carrier concentration will affect the rate of dissolution (*e.g.*, illumination, n- or p-type impurities, temperature, injection by a p-n junction, and reduction of oxidants such as ferricyanide ions on the surface).

For heavily doped n-type germanium, Gereth and Cowher (3) have reported that the rate of anodic dissolution is controlled by the supply of hydroxyl ions from the electrolyte, rather than by charge carriers in the solid. Therefore, the activation energy may depend on space charge layers in the solution rather than in the semiconductor. The pre-exponential in Eq. [1] will then be proportional to the hydroxyl ion concentration. In addition, for the spontaneous dissolution of germanium in oxygen-saturated media, Harvey and Gatos (4) found that the rate is independent of carrier concentration or illumination. In oxidative dissolution such as this, when diffusion is not rate limiting, it is bond breaking in an oxide surface complex that determines the activation energy. ν is then related to the frequency of thermal vibrations in the solid.

To distinguish between oxidative and nonoxidative dissolution, Simkovich and Wagner (5) showed for PbS and ZnO that doping of the solid and deviations from stoichiometry do not have a significant effect on the rate of dissolution in nonoxidizing acids, such as aqueous HCl. However, Ag_2S as an acceptor and Bi_2S_3 as a donor in PbS, or Li_2O as an acceptor and Al_2O_3 as a donor in ZnO do significantly affect the rate of dissolution in concentrated nitric acid. The oxidative dissolution can be characterized by the formation of elemental sulfur as a reaction product in the case of PbS.

Based on the above results, it can be concluded that in nonoxidative dissolution the rate constant and the activation energy in Eq. [1] are related to processes that occur at the solid-liquid interface. To investigate

* Electrochemical Society Active Member.
[1] Present address: Bell Telephone Laboratories, Murray Hill, New Jersey.

these processes in acid solutions, the dissolution of the II-VI compounds ZnS, ZnSe, CdS, and solid solution $Zn_xCd_{1-x}S$ has been studied as a function of both the structure and composition of the solids, and the properties of the solution. The over-all chemical reaction describing the dissolution process is

$$A_{II}B_{VI}(s) + 2H^+ = A_{II}^{++} + H_2B_{VI}(g) \quad [2]$$

with A_{II} representing the group IIB cation and B_{VI} the group VI anion. The II-VI compounds are particularly suitable for studying nonoxidative dissolution kinetics for several reasons:

1. It has already been shown that in well-agitated systems the rate is controlled by a heterogeneous surface reaction rather than by transport in the solution (6).
2. The reaction products do not form passive films that could inhibit the dissolution process.
3. The compounds can be prepared in allotropic crystalline modifications, and have a complete range of solid solubility.

Experimental

Materials.—All of the polycrystalline II-VI compounds were prepared by precipitation from a soluble salt of the group IIB cation. To produce a crystalline solid, the precipitate was dried, and annealed in H_2B gas or in an inert atmosphere. The method of preparation, impurity content, B.E.T. surface area, and crystal structure of each material are summarized in Table I. The composition of the crystallized solid solution was determined by comparing the measured lattice parameters to those reported by Ballentyne (7). In addition, chemical analyses for both zinc and cadmium were done after completely dissolving the solid in cold concentrated hydrochloric acid or in nitric acid. These two analytical methods gave results that were within 4%. The composition determined by x-ray analysis is reported in Table I. Reagent-grade chemicals and high-conductivity water (6.0×10^{-7} ohm^{-1} cm^{-1}) were used to prepare the acid solutions.

Apparatus and procedure.—Except for dissolution of ZnSe, rate measurements were made at constant pressure by continuously increasing the volume of the system as vapor was evolved. The pressure regulating system was similar to the one described by Cremer (8), although modifications were needed to keep the pressure constant to within 0.1 mm Hg while automatically recording the volume (9). The evolution of as little as 3×10^{-7} moles of vapor could be detected. This sensitivity is required in order to study the dissolution of the sparingly soluble II-VI compounds.

A 200-ml baffled Pyrex reactor flask, shown in Fig. 1, was immersed in a constant-temperature bath controlled to within 0.1°C. All experiments were carried out at a stirring speed of 1200 rpm. A 3g solid sample (± 0.1 mg) was held in a thin-walled Pyrex crucible before the start of each reaction so that it did not contact the acid in the flask. Fifty milliliters of acid

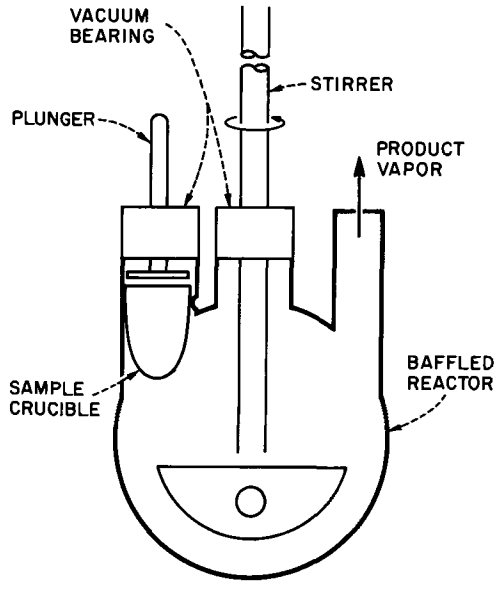

Fig. 1. Stirred reactor and sample crucible

solution were degassed by lowering the pressure until the solution boiled. The solution was then saturated by flushing the system with H_2S vapor. With the stirrer on, the reaction started instantaneously when the plunger pushed the sample crucible into the acid solution.

Dissolution experiments performed at constant pressure and temperature have definite advantages compared to experiments at constant volume. All of the vapor produced in the reaction goes into the gas phase since the solution is already saturated at a fixed constant pressure. Also, the evaluation of the constants in an empirical rate equation is easier when both temperature and pressure are constant during an experiment. In principle, the constant-pressure apparatus could have been used for the ZnSe experiments, but the large quantities of H_2Se needed to flush the system made this impractical. Although the ZnSe experiments were done at constant volume, the same reactor was used for all experiments and the sample was introduced in the same way as described above.

The concentration of acid, zinc ions, and cadmium ions was determined after equilibrium was reached in each experiment. For both zinc and cadmium, volumetric analysis was used, with ethylenediaminetetracetic acid as a complexing agent. In addition, when the cadmium ion concentration was too small to be determined by volumetric methods, analyses were done with a Jarrel-Ash flame photometer.

Results

Typical examples of the kinetic data collected in this investigation are displayed in Fig. 2 and 3. The dependence of the dissolution rate of high-purity ZnS

Table I. Preparation and properties of materials

Material	Method of preparation	Impurity content (spectroscopic analysis)	Crystal structure (observed values)	Surface area (m^2/g)
ZnS	$Zn(NO_3)_2 + H_2S$	10 ppm: Pb 3 ppm, Cu 0.2 ppm, Ni 0.3 ppm, Fe 1 ppm	Cubic $a_o = 5.38$Å	28.8
ZnS	$ZnSO_4 + H_2S$	2%: Cd 1%, Fe 0.1%	75% cubic-25% hex. (approximate)	5.5
CdS	$Cd(NO_3)_2 + H_2S$	10 ppm	Hexagonal $a_o = 4.12$Å $c_o = 6.94$Å	0.94
ZnSe	$Zn(Cl)_2 + (NH_4)_2Se$	10 ppm	Cubic $a_o = 5.60$Å	0.63
$Zn_xCd_{1-x}S$ $X = 0.85$	$Zn(C_2H_3O_2)_2 + Cd(C_2H_3O_2)_2 + H_2S$	No analysis	Hexagonal $a_o = 3.86$Å $c_o = 6.30$Å	1.2

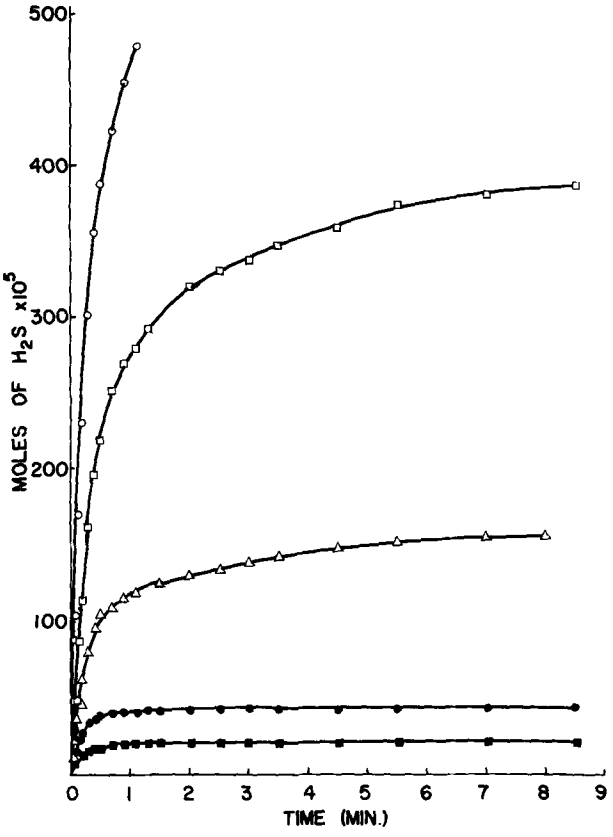

Fig. 2. Effect of sulfuric acid concentration on the dissolution of high-purity ZnS: ■ 0.5M; ● 1.0M; △ 2.0M; □ 3.0M; ○ 4.0M; T = 25°C; p_{H_2S} = 0.88 atm.

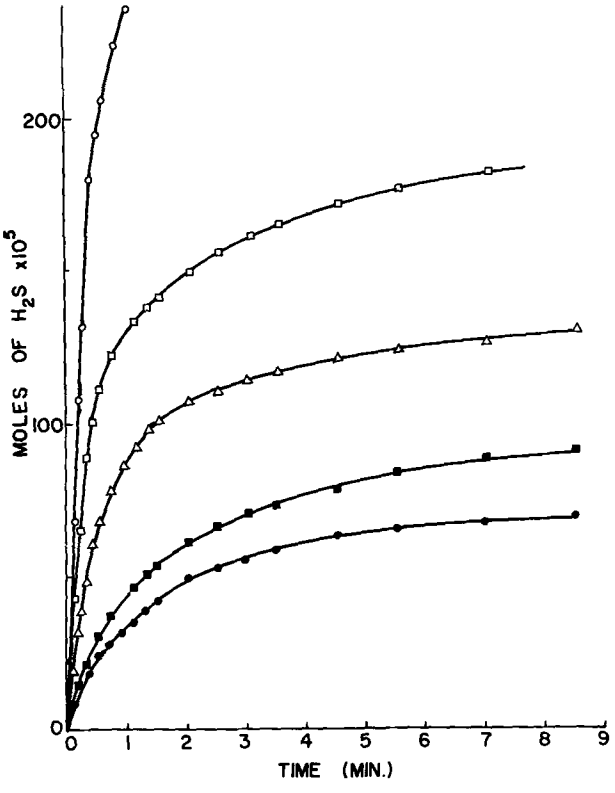

Fig. 3. Effect of temperature on the dissolution of high-purity ZnS in aqueous H_2SO_4: ● T = 0.2°C p_{H_2S} = 0.26 atm; ■ T = 10.0°C p_{H_2S} = 0.15 atm; △ T = 25.0°C p_{H_2S} = 0.27 atm; □ T = 40.0°C p_{H_2S} = 0.25 atm; ○ T = 59.0°C p_{H_2S} = 0.40 atm; [H_2SO_4] = 1.0M.

on sulfuric acid concentration at fixed temperature and hydrogen sulfide pressure is illustrated in Fig. 2. Figure 3 shows the variation of the dissolution rate with temperature at constant sulfuric acid concentration (1M). In all the investigations, the dissolution was allowed to proceed to conclusion so that information on the equilibrium state may also be obtained. This information is needed in order to determine the kinetic parameters of the reverse (precipitation) reaction. Although the general shape of the dissolution curves does not change with the composition of the leaching solution (aqueous sulfuric acid, alcoholic sulfuric acid, or aqueous hydrochloric acid), the dissolution rate in aqueous sulfuric acid is found to depend more strongly on temperature than in the other two solutions.

Our experiments confirmed the finding of Romankiw and deBruyn (6) that the dissolution process is independent of the rate of agitation of the reacting mixture beyond a critical stirring speed of 750 rpm. This experimental observation suggests that the net dissolution rate is not diffusion controlled. If we now assume that the dissolution process is controlled by a chemical reaction at the solid-liquid interface, then the rate of dissolution R (moles/m^2 sec) may be expressed as follows:

$$R = \frac{1}{A}(dn_{H_2B}dt) = k_1[H_2SO_4]^{\alpha} - k_{-1}[A_{II}SO_4]^{\beta}p^{\gamma}{}_{H_2B} \quad [3]$$

In writing Eq. [3], we assume the leaching agent to be sulfuric acid. The various symbols introduced in this expression are identified in the Nomenclature at the end of this paper. It is important to note that the formal rate constants k_1 and k_{-1} for the forward and reverse reactions, respectively, include the activity coefficients of the reacting species. The symbol A without subscript refers to the surface area (m^2) of the solid/liquid interface. The square brackets, [], imply molar concentrations of the reactants; the quantity [H_2SO_4] refers to the stoichiometric sulfuric acid concentration and not to the molar concentration of the undissociated species.

Spectrophotometric studies (10) of the composition of aqueous sulfuric acid solutions show that, except in extremely dilute solutions, the $SO_4^{=}$ ion is not a major constituent and that the concentration of undissociated H_2SO_4 is negligibly small in solutions of molarity less than 14M. At moderate concentrations, it is the HSO_4^- ion which predominates and the properties of such solutions are essentially that of a 1:1 electrolyte consisting of H^+ and HSO_4^- ions. An analysis of all pertinent thermodynamic data on this system in the temperature range 0°-50°C (11) shows that the H^+ ion concentration is proportional to the stoichiometric acid concentration in the concentration range 0.1-6M which includes the experimental concentrations (0.5-5M) used in this investigation. The sulfuric acid concentration term in Eq. [3] may therefore be replaced by the actual concentration of H^+, the proportionality constant relating [H^+] to [H_2SO_4] being approximately 0.8.

To determine the order of the forward reaction, that is, the magnitude of the constant α, we focus attention on the initial stage of the dissolution reaction. Equation [3] may now be transformed to read

$$R_o = k_f A_o[H_2SO_4]_o^{\alpha} \exp(-E_f/RT) \quad [4]$$

where R_o is the initial dissolution rate in moles/sec and is given by the initial slope of the experimental curves in Fig. 2. A check on the measured value of R_o was obtained by a numerical curve fitting technique (9). By plotting values of R_o against initial acid concentration ([H_2SO_4]$_o$), it was clearly established that α equals unity regardless of the composition of the solid phase and of the liquid phase. This first-order dependence of the dissolution rate on acid concentration was previously observed by Romankiw and deBruyn (6) for ZnS in aqueous sulfuric acid solutions. These

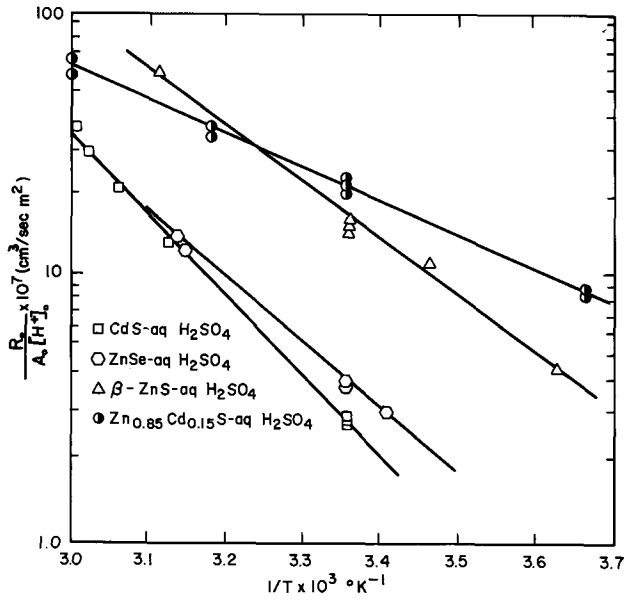

Fig. 4. Arrhenius plot for calculation of the activation energies for dissolution of II-VI compounds in aqueous H_2SO_4.

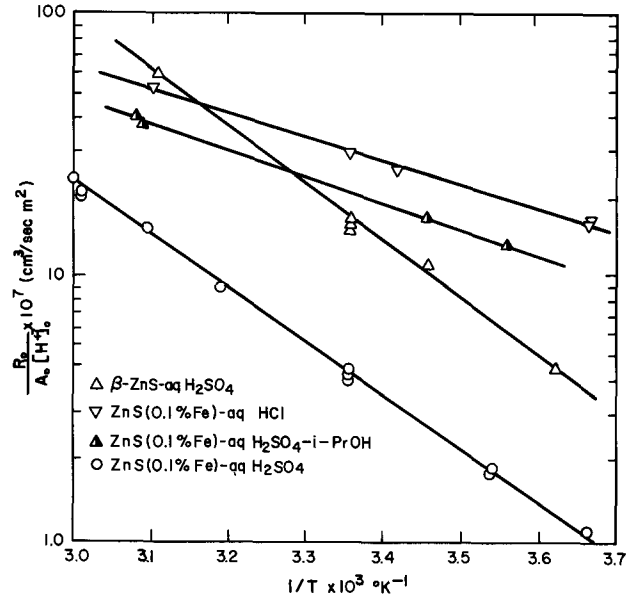

Fig. 5. Arrhenius plot for calculation of the activation energy for dissolution of ZnS in different solutions.

authors used an identical analytical procedure for evaluating α.

The activation energy E_f for the forward (dissolution) reaction was then determined by preparing plots of log $(R_o/A_o[H_2SO_4]_o)$ = log k_1 against $1/T$ as shown in Fig. 4 and 5. The magnitude of k_f, a reaction

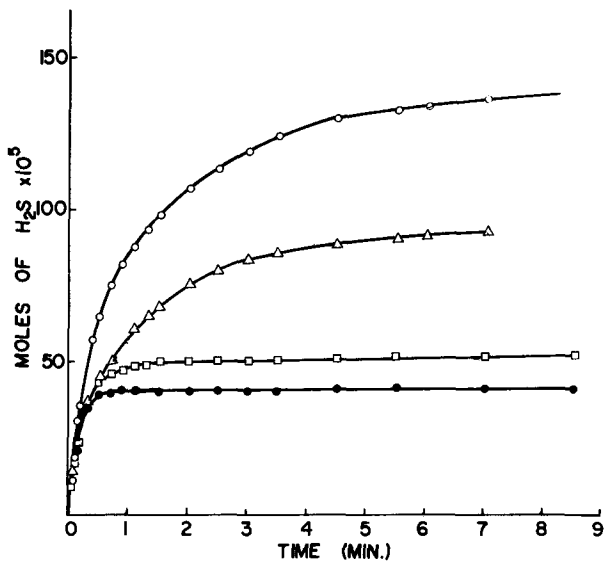

Fig. 6. Effect of H_2S pressure on the dissolution of high-purity ZnS in aqueous H_2SO_4: ● p_{H_2S} = 0.27 atm; △ p_{H_2S} = 0.32 atm; □ p_{H_2S} = 0.82 atm; ○ p_{H_2S} = 1.01 atm; T = 25°C; $[H_2SO_4]$ = 1.0M.

rate constant which is independent of temperature, may then be calculated.

At constant pressure of H_2B, it follows directly from Eq. [3] that for equilibrium conditions

$$d \log [A_{II}^{++}]_e / d \log [H^+]_e = \beta \qquad [5]$$

where the subscript e denotes that the equilibrium concentrations of the reacting species are to be used. Equation [5] shows how the constant β for the reverse (precipitation) reaction may be evaluated from experimental data such as found in Fig. 2. It also follows from Eq. [4] that, if the initial concentration of the acid is fixed in a series of experiments in which the pressure of the H_2B gas is allowed to vary, then at equilibrium, for $\alpha = 1$,

$$\log \left\{ \frac{[H_2SO_4]_o - [A_{II}SO_4]_e}{[A_{II}SO_4]_e{}^{\beta}} \right\} = \gamma \log p_{H_2B} + \log \frac{k_{-1}}{k_1} \qquad [6]$$

and therefore

$$\frac{d \log \{([H_2SO_4]_o - [A_{II}SO_4]_e)/[A_{II}SO_4]_e{}^{\beta}\}}{d \log p_{H_2B}} = \gamma \qquad [7]$$

Once β is known, the constant γ may be evaluated from the information contained in experimental rate curves such as those plotted in Fig. 6. From the appropriate plots suggested by Eq. [5] and [7], it has been established that the rate of the reverse reaction varies with the *square root* of both the concentration of the A_{II}^{++} ion in solution and the H_2B pressure. The activation

Table II. Activation energies and rate constants

Material	Solution composition	E_f (kcal/mole)	k_f (liters/sec m²)	E_r (kcal/mole)	k_r (moles liters/atm)$^{1/2}$ / sec m²
ZnS (0.1% Fe)	aq. H_2SO_4	9.9 ± 1.0*	2.7 ± 0.4 × 10^1	6.7 ± 1.0	1.9 ± 0.5 × 10^0
	aq. 20%-i-PrOH≠ 80% H_2SO_4	5.0	8.9 × 10^{-3}	1.6	5.3 × 10^{-4}
	aq. HCl	4.5	5.4 × 10^{-3}	—	—
β-ZnS	aq. H_2SO_4	9.5	3.8 × 10^0	5.8	7.5 × 10^{-2}
CdS	aq. H_2SO_4	14.2	6.8 × 10^3	6.7	1.7 × 10^1
ZnSe	aq. H_2SO_4	11.7	1.0 × 10^2	6.8	4.8 × 10^1
$Zn_{0.85}Cd_{0.15}S$	aq. H_2SO_4	5.7	2.9 × 10^{-2}	5.3	3.4 × 10^1

* Precision noted for the first value applies to others in same column.
≠ i-PrOH represents isopropanol.

energy (E_r) of the reverse (precipitation) reaction was then determined by solving Eq. [6] for k_{-1} at different temperatures and then plotting log k_{-1} against $1/T$.

All the pertinent kinetic parameters obtained by the above analysis of the experimental data are collected in Table II. It should be mentioned that in performing this analysis no correction has been made for the dependence of the activity coefficient of the reacting species on temperature. However, the stoichiometric activity coefficients for sulfuric acid and also hydrochloric acid in the concentration range 0.5*M* (Molal) to 5*M* are relatively insensitive to changes in temperature (12). The magnitudes of the activation energies E_f and E_r will therefore not be altered significantly if such corrections are made.

It is interesting to note for Table II that the values of E_r for ZnS, ZnSe, and CdS agree to within ±1 kcal/mole. During the asymptotic approach to equilibrium shown in Fig. 2, 3, and 6, the solid must form simultaneously with the dissolution. The reverse reaction involves either precipitation of new particles or growth on the already existing solid. In either case, the data suggest that the process of solid formation is not simply the reverse of the dissolution process. No attempt has been made to study the reverse reaction in detail, since the initial rate data used to calculate k_f and E_f are not affected by these complexities.

In Table II it can be seen that the activation energy E_f for dissolution in aqueous H_2SO_4 is different for each of the high-purity II-VI compounds. However, for the high-purity β-ZnS, the activation energy is almost the same as for the material containing 0.1% Fe. The latter solid also showed some wurtzite lines in its x-ray diffraction pattern which did not appear in the high-purity β-ZnS. These results indicate that the activation energy is not sensitive to impurity content or crystal structure, but the over-all rate of dissolution does depend on these factors due to changes in the number of reactive surface sites.

The dependence of the dissolution rate on the properties of the solution are also shown in Table II. For the same solid ZnS(0.1% Fe) in different solutions, there is a large change in the activation energy. Therefore, changing the solution, and with it the properties of the solid-liquid interface, influences the activation energy for the rate-controlling step.

The relatively low activation energy for dissolution of the solid solution $Zn_{0.85}Cd_{0.15}S$ may be related to other observations made on this material. For example, even after heat treatment, the x-ray diffraction peaks of the crystallized solid were not nearly as sharp as for the pure ZnS or CdS. It was found that the Zn/Cd ratio in the solution was several times higher than the ratio in the starting material. Therefore it is possible that the method of preparation sufficiently influences the surface properties of the solid to affect the activation energy for dissolution.

The results show that the rate of nonoxidative dissolution depends on both the properties of the solid and the solution. These data bear out the introductory remarks that any proposed mechanism of nonoxidative dissolution of semiconductors must account for the influence of processes at the solid-liquid interface.

Discussion

Figure 7 shows the steps that occur during dissolution of the II-VI compounds in nonoxidizing acids. Since agitation has no influence on the rate of dissolution of the II-VI compounds in aqueous H_2SO_4, and the activation energies are higher than the 3-6 kcal/mole expected for transport processes, it is unlikely that diffusion is the rate-controlling step. Furthermore, a quantitative estimate of the rate of diffusion of H^+ can be made using the equation

$$\frac{1}{A}(dn_{H_2B}/dt) = -D([H^+]_o - [H^+]_i)/d \qquad [8]$$

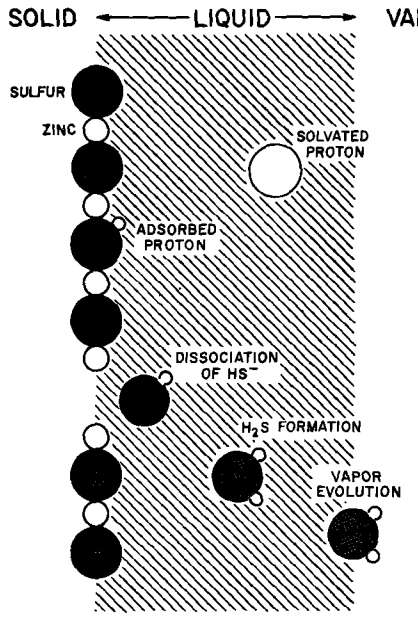

Fig. 7. The mechanism of dissolution of II-IV compounds in nonoxidizing acids.

where $[H^+]_i$ is the concentration of hydrogen ions near the solid surface. Values of $[H^+]_i = 0$, $[H^+]_o = 2$ moles/liter, $d = 10^{-3}$ cm, and $D = 10^{-5}$ cm²/sec, give a rate of 10^{-5} moles/(sec cm²). The chosen values of the effective boundary layer thickness, d, and the diffusivity, D, are likely to be within an order of magnitude for this system. Experimentally, for the II-VI compounds in aqueous H_2SO_4, the initial rates were no larger than 10^{-9} moles/(sec cm²). For the dissolution of ZnS in hydrochloric acid or in alcoholic H_2SO_4, the initial rates were approximately 10^{-5} moles/(sec cm²), so that the exclusion of diffusion control here is not as certain. However, it is the fact that the surface reaction is much slower for dissolution of ZnS in aqueous H_2SO_4 than in the other solutions, rather than the magnitude of the activation energy in the latter case, that is important. This fact is used below as evidence that a slow adsorption step is a plausible mechanism for the dissolution of the II-VI compounds in nonoxidizing aqueous H_2SO_4.

If the over-all rate of the dissolution reaction is controlled by the adsorption of hydrogen ions, or the protonated solvent, onto the surface then

$$R_o = k_f A_o [H^+]_i \exp(-E_A/RT) \qquad [9]$$

E_A is the activation energy for adsorption of the hydrogen ions at the interface. The concentration $[H^+]_i$ is related to the concentration in the bulk solution by the equation

$$[H^+]_i = [H^+]_o \exp(-\psi_\delta/RT) \qquad [10]$$

where ψ_δ is the potential of the ion at the distance of closest approach, before adsorption onto the surface. As hydrogen ions adsorb there is a change in potential equal to $(\psi_o - \psi_\delta)$, where ψ_o is the potential of the solid surface relative to the bulk solution. Also there is an energy change, Φ, when a proton interacts with the surface atoms to form some compound. This free energy change will depend on the activity of the solid surface, but it is independent of the surface charge. As shown in Fig. 7, it is assumed that the hydrogen ions adsorb preferentially on the sulfur sites, and that the surface reaction product dissociates as HS^-. This ion then reacts with a hydrogen ion to form H_2S which is transported away from the solid, and is finally evolved at the liquid-vapor interface. The observation that the H_2S/Zn^{++} mole ratio is greater than 1 is reasonable if adsorption occurs preferentially at the sulfur sites.

In terms of the adsorption theory of dissolution, where no electron transfer is involved in the rate-controlling step, the rate equation becomes

$$R_o = k_f A_o [H^+]_o \exp\left\{-\frac{\mathbf{F}}{RT}[\Phi + (\psi_o - \psi_\delta) + \psi_\delta]\right\} \quad [11]$$

The activation energy for dissolution, with the adsorption step controlling is

$$E_A = \mathbf{F}(\Phi + \psi_o) \quad [12]$$

E_A is made up of a chemical and an electrostatic contribution. The former can be related to the bonding, surface energy, and other solid properties that may effect Φ. The latter term depends on the interaction between the charged solid surface and the ions in solution. Changes in the activity of the surface due to the structure or the composition of the solid will generally be small, and Φ will not be appreciably changed. This is the reason for the small difference between the activation energies for pure β-ZnS and ZnS(0.1% Fe). The model also explains the results of Simkovich and Wagner (5), that impurities in the solid have little effect on the rate of nonoxidative dissolution. The low activation energy for $Zn_{0.85}Cd_{0.15}S$ is probably due to a state of disorder of the surface that is sufficient to affect the chemical potential for proton adsorption.

The maximum difference of about 5 kcal in the activation energies for dissolution of ZnS, ZnSe, and CdS is due primarily to the electrostatic interaction at the solid-liquid interface. This also must account for the changes in the activation energy when the same solid ZnS is dissolved in different solutions. For hydrochloric acid as the solvent, there is also the possibility that specific interactions of chloride ions occur on the surface, and alter both the surface charge and the distribution of active sites. This would lead to changes in both the rate constant and the activation energy. Although the concept of a dielectric constant for the solution near the solid surface has little meaning, the polarizability of the solvent and the potential drop across the Helmholtz layer are essential factors in the mechanism of nonoxidative semiconductor dissolution.

Conclusion

The experimental results, analyzed in terms of an activated adsorption model for the dissolution of II-VI compounds, explain why the rate of dissolution in nonoxidizing solutions is not affected by the electrical properties of the solid. It is the space charge in the solution rather than in the solid that is important.

Even in the case of oxidative semiconductor dissolution, it is known that adsorption affects the kinetics by increasing or decreasing the rate of the controlling step. For example, in the oxidative dissolution of InSb, which exhibits crystallographic polarity in the <111> direction, aliphatic amines preferentially adsorb on the Sb(111) surface and inhibit the rate by interfering with dissociation of the surface complex that controls the rate of dissolution (13). Richards and Crocker (14) found that Ag^+ reveals etch pits on the As(111) surface of GaAs for the same reason. In these two cases, it is the rate constant k_1 in Eq. [1] that is lowered. According to Harvey and Gatos (4), adsorbed halide ions catalyze the reduction of oxygen on the surface of Ge by supplying one electron. Based on the mechanism of dissolution proposed by Harvey and Gatos, this adsorption effects E as well as k_1 in Eq. [1]. Adsorbed ions can also change the rate of anodic dissolution of semiconductors when charge transfer in the solid is the rate-controlling step. The reduction of ferricyanide ($Fe(Cn_6^{-3})$ to ferrocyanide ($Fe(CN_6^{-4})$ on the germanium surface leads to an increase in the anodic dissolution rate. This is explained by Efimov (15) by the supposition that the electron required for the reduction comes from the valence band, creating an additional hole near the germanium surface. The process is analogous to the effect of illumination on the charge transfer controlled anodic dissolution.

In nonoxidative dissolution of the II-VI compounds, it is the adsorption that is the rate-controlling step. The adsorption model may be useful in explaining the results of etching studies in nonoxidizing solutions. According to this model, preferential adsorption occurs on the anion sites so that this face would be expected to dissolve faster than the corresponding cation face when the II-VI compounds are etched in the (111) orientation. Therefore, etch pits should appear on the cation faces. Studies of the adsorption kinetics of ions at the semiconductor-electrolyte interface and a more complete understanding of the changes in solvation that occur in the layer of solution near the solid surface would permit this adsorption theory of semiconductor dissolution to be developed further. These same effects are important in a broader scope of electrochemistry, such as with anodic oxide films and battery electrode behavior, so that the adsorption mechanism of nonoxidative semiconductor dissolution may be of more general importance.

Manuscript submitted March 7, 1969; revised manuscript received Aug. 8, 1969.

Any discussion of this paper will appear in a Discussion Section to be published in the June 1970 JOURNAL.

REFERENCES

1. I. Gallily and S. K. Friedlander, *J. Chem. Phys.*, **42**, 1503 (1965).
2. M. B. Ives, *J. Phys. Chem. Solids*, **24**, 275 (1963).
3. R. Gereth and M. E. Cowher, *This Journal*, **114**, 147C (1967).
4. W. W. Harvey and H. C. Gatos, *ibid.*, **105**, 654 (1958).
5. G. Simkovich and B. Wagner, *ibid.*, **110**, 513 (1963).
6. L. T. Romankiw and P. L. deBruyn, "Unit Operations in Hydrometallurgy," M. Wadsworth, Editor, p. 45, Gordon and Breach (1965).
7. D. W. G. Ballentyne and B. Ray, *Physica*, **27**, 337 (1961).
8. E. Cremer *et al.*, *Radex-Rundschau*, **1953**, 495.
9. L. D. Locker, Ph.D. Thesis, M.I.T. (1965).
10. T. F. Young, *Record Chem. Progr.*, **12**, 81 (1951).
11. L. T. Romankiw, S. M. Thesis, M.I.T. (1962).
12. H. S. Harned and B. B. Owen, "The Physical Chemistry of Electrolytic Solutions," Third Ed., Reinhold Publishing Corp., New York (1958).
13. H. C. Gatos and M. C. Lavine, *J. Phys. Chem. Solids*, **14**, 169 (1960).
14. J. L. Richards and A. J. Crocker, *J. Appl. Phys.*, **31**, 600 (1960).
15. E. A. Efimov, "Electrochemistry of Germanium and Silicon," Sigma Press (1963).

NOMENCLATURE

A	Surface area of solid (m^2)
A_o	Surface area of solid at start of reaction (m^2)
A_{II}	Atom of group IIB (Zn, Cd)
A^{++}, A_{II}^{++}	Ion of A_{II} in solution
$[A^{++}]_e$	Ion concentration at equilibrium (moles/liter
B, B_{VI}	Atom of group VIB (S, Se)
d	Diffusion path length (cm)
D	Diffusivity (cm^2/sec)
E	Activation energy (kcal/mole)
E_A	Activation energy for proton adsorption (kcal/mole)
E_f	Activation energy for dissolution reaction (kcal/mole)
E_r	Activation energy for precipitation reaction (kcal/mole)
$\mathbf{F}$	Faraday constant
$[H_2SO_4]_o$	Acid concentration at start of reaction (moles/liter)
$[H_2SO_4]_e$	Acid concentration at equilibrium (moles/liter)
$[H^+]_i$	Hydrogen ion concentration at solid-liquid interface (moles/liter)
k_1	Formal forward rate constant $\left(\frac{\text{liters}}{m^2\ \text{sec}}\right)$

k_{-1} Formal reverse rate constant $\left[\frac{\text{moles}}{\text{m}^2\,\text{sec}} \cdot \left(\frac{\text{liters}}{\text{moles}}\right)^{1/2} \cdot \left(\frac{1}{\text{atm}}\right)^{1/2}\right]$

k_f Rate constant for dissolution (liters/sec m^2)

k_r Rate constant for precipitation (moles liter/atm)$^{1/2}$/sec m^2

n_{H_2B} Moles of vapor evolved in reaction

p_{H_2B} Pressure of H_2B vapor (atm)

R_0 Initial rate of dissolution (moles/sec)

R Over-all reaction rate (moles/m^2 sec)

T Temperature (°K)

ν Frequency factor

ψ_δ Electrostatic potential of proton at solid-liquid interface relative to bulk solution

α, β, γ Constants

ψ_0 Electrostatic potential of proton on solid surface relative to bulk solution

Φ Change in chemical potential during proton adsorption

Interpretation and Significance of Heats of Activation for Electrochemical Reactions Exhibiting Anomalous Tafel Slopes

B. E. Conway and D. J. MacKinnon

Department of Chemistry, University of Ottawa, Ottawa, Ontario, Canada

ABSTRACT

Heats of activation for electrochemical reactions studied over a wide range of temperatures are considered in relation to the temperature dependence of the Tafel slope factor b. Experimentally, b is found to have anomalous temperature dependence, *i.e.*, other than the classical form $RT/\alpha\mathbf{F}$, for hydrogen evolution at Hg, Cd, Pb, Ni, and Pt and the consequences of this behavior in calculation of heats of activation are evaluated. Curvature of the electrochemical Arrhenius plots is shown to arise for certain of the cases treated and is discussed in relation to the problem of detection of proton tunneling at low temperatures. Other difficulties associated with temperature dependence of coverage by atomic H and temperature-dependent structure changes in the solvent are considered.

Heats of activation in electrode processes, unlike those for gas phase and in certain cases solution reactions, cannot be easily related to the mechanism of the reaction. This arises because only an apparent energy of activation (1) is measured by such experimental derivatives as $d \ln i_0/d(1/T)$ (involving the exchange current density i_0), $(d\eta/dT)_i$, $(d\eta/d\ 1/T)_i$ or $(d\eta/d \ln T)_i$, where η is the overpotential at a current density i related to i_0 by the familiar equation $i = i_0 \exp \eta/b$, where b is the Tafel slope. However, in a number of situations, variations of heats of activation for a given reaction, *e.g.*, over a series of metals, or on account of isotopic substitution, or with temperature, can be useful as a basis for evaluation of such factors as chemisorption in relation to the electronic character of the metal (2) or the role of quantum-mechanical tunnel effects in proton transfer (3) through the estimation of frequency factor ratios.

Normally the apparent heat of activation $\Delta H^{o\neq}_R$ at the reversible potential differs from the "true," kinetically significant quantity $\Delta W^{o\neq}$ (for zero metal-solution p.d.) according to the relation (1)

$$\Delta H^{o\neq}_R = \Delta W^{o\neq} - \beta \Delta H^o \qquad [1]$$

where ΔH^o is the enthalpy change in the single (half-cell) reaction

$$H^+_{aq} + e_M \rightleftharpoons \tfrac{1}{2} H_2 \qquad [2]$$

and β is a symmetry factor. It is well known that ΔH^o, for obvious reasons, is not a thermodynamically measurable quantity, although it may be estimated with varying degrees of uncertainty depending on the value assigned to the surface potential and the basis for assignment of individual ionic free energies of hydration (4).

Usually the apparent heat of activation is evaluated at zero overpotential from the derivative $(\partial \ln i_0/\partial\ 1/T)_{\eta=0}$ or from the temperature coefficient of overpotential at a given current density (5). At finite overpotential η, the derivative $(\partial \ln i/\partial\ 1/T)_\eta$ also gives the effective heat of activation at potential η which differs from that deduced for the reversible potential by the energy $\beta\eta\mathbf{F}$. These relations which give $\Delta H^{o\neq}_R$ in terms of $\Delta W^{o\neq}$ and ΔH^o apply when the Tafel slope b of the process is given by $b = RT/\beta\mathbf{F}$ and $\beta \neq f(T)$.

In the present and other (6) recent work, we have investigated the temperature dependence of the Tafel slopes of the hydrogen (h.e.r.) and bromine evolution reactions over a wide range of temperatures (including low temperatures down to −125°C) in order to establish the correct form of the temperature dependence of b. It has been found (6) that b is rarely given by the "defining" relation quoted above and usually b is less temperature dependent than is implied by $b = RT/\beta\mathbf{F}$ with β a constant equal to approximately 0.5. Under some conditions b can be almost independent of temperature (6-9), while for other conditions b may even increase with decreasing temperature. Inspection of early papers in the literature reveals qualitatively similar observations, but the results were usually poorly reproducible and were obtained in insufficiently purified solutions. Also, the variation of b or β with T was not systematically examined.

Generally (6), when $b \neq RT/\beta\mathbf{F}$, the Tafel slope can be represented empirically by

$$b = \frac{RT}{\beta\mathbf{F}} + c \qquad [3]$$

where c is a temperature independent constant and β can be > 0.5. It appears coincidental that $b = 0.116$ at room temperature, *e.g.*, for the h.e.r. at Hg, so that b is apparently $RT/\beta\mathbf{F}$ with $\beta = 0.5$. Over a wider range of temperature, including low temperatures down to −100°C in methanol and ethanol (3, 6), and higher temperatures up to 65°C at Hg in methanol, b is not represented by the usual simple relation $b = RT/\beta\mathbf{F}$ but by Eq. [3].

The consequences of this situation with regard to the evaluation and significance of $\Delta H^{o\neq}_R$ are investi-

gated in the present paper in relation to experimental results on the kinetics of cathodic hydrogen and anodic bromine evolution measured over a wide range of temperatures. The interpretation of temperature variations of $\Delta H^{o\neq}_R$ are of interest in regard to (*a*) the role of proton tunneling (10, 11), in the h.e.r.; (*b*) the effects of solvent structure changes on $\Delta H^{o\neq}_R$ in hydrogen-bonded media as the temperature changes; and (c) the role of temperature-dependent solvent orientation (12, 13) at the electrode interface in the kinetics of the h.e.r. Hence, it is important to establish first the effect of anomalous temperature variations of *b* in relation to their effects, if any (see below), in determining the form of the temperature dependence of $\Delta H^{o\neq}_R$. Heats of activation were therefore determined for a number of metals at which the Tafel constant *b* shows (3, 6) unusual variations with temperature.

Experimental

General.—Since heats of activation were required together with Tafel slopes, steady-state, point-by-point kinetic measurements were made galvanostatically by the "rapid" procedure (14). This method has been shown to be preferable to the "slow" procedure where variations of potential over long times (up to 2 hr) are followed at each current density. The essential experimental procedure and apparatus have been adequately described elsewhere (2). The electrolysis cell for Hg was provided with glass coils in the working and reference electrode compartments, through which thermostated water could be circulated at various temperatures. Methanolic solutions of HCl were used in most of the work in order to be able to reach low temperatures. Most kinetic measurements were carried out at a series of descending temperatures but some runs were conducted at successively ascending as well as descending temperatures.

Preparation and purification of solutions.—In order to attain low temperatures, it is necessary to use either nonaqueous (3) or concentrated acid solutions (15). Tafel lines obtained in the latter media exhibit kinks associated with specific adsorption (16) but at higher concentrations (*ca.* 7.0*N* in HCl for example) linear behavior is exhibited over several decades of current density but the *b* values are higher than $2RT/F$ presumably on account of anion adsorption. In order to avoid the high concentrations of acid that are required in water to reach low temperatures, nonaqueous solutions were employed.

The solutions chosen for the present work were the following: (*i*) 0.5*N* HCl-methanol-h; 0.5*N* HCl-ethanol-h; (*ii*) 0.5*N* DCl-methanol-d for isotope effect studies; and (*iii*) 0.4M $(C_3H_7)_4NBr$ in acetonitrile for Br^- discharge. The choice of HCl and DCl was an obvious one since both could be easily prepared in the dry, gaseous state. The choice of the system 0.4M $(C_3H_7)_4NBr$-acetonitrile was governed by the desire to study a one-electron discharge process (other than that involving protons) in a nonhydrogen-bonded solvent in order to avoid anomalous changes of activation energy which can arise in H-bonded solvents due to changes of association with temperature.

Methanol-h solutions (CH_3OH) containing HCl were prepared by the procedure previously described (3). Ethanol-h (C_2H_5OH) was prepared from the undenatured material by refluxing over, and then distilling from, dried calcium oxide. The material thus obtained was then subjected to the purification treatment previously described (3) for methanol. Methanol-d (CH_3OD) was prepared from magnesium methoxide and 99.8% D_2O as described previously (3).

Gaseous DCl was prepared by the action of D_2O on redistilled benzoyl chloride, b.p. 197°C (17). Any traces of benzoyl chloride entrained in the evolution of DCl gas were removed by two traps.

For the anodic reaction of Br^- ion at graphite, spectroscopic grade acetonitrile was used as the solvent. Recrystallized and dried (18) $(C_3H_7)_4$ NBr was dissolved in the acetonitrile until a maximum concentration of 0.4M was reached.

Purification of gases.—Hydrogen gas for the reference electrode and for bubbling in the cathode compartment during the h.e.r. runs was rigorously purified before use according to previously described procedures (2, 3). N_2 used in the anode compartment was also purified (19).

Preparation of the electrodes under study.—Platinum and nickel.—These electrodes were prepared from spectroscopically pure wires of platinum and nickel by a standardized method in order to ensure the best reproducibility of the measurements. The wires were cleaned first by washing for 24 hr in thiophene-free benzene under reflux, and then sealed, after drying, in glass bulbs in a stream of the purified hydrogen gas (2, 3). The bulbs were broken just prior to the experiment in the usual way (2, 3).

Lead and cadmium.—These electrodes were prepared by melting rods of the spectroscopically pure metals in a crucible under a hydrogen flame. The molten metals, which retained brilliant oxide-free surfaces, were then drawn into 2 mm capillaries and allowed to solidify. The tubes were then cut to expose the desired metal surface.

Mercury.—Specially distilled mercury (A.C.S. grade from Johnson-Matthey and Mallory Ltd.) was used directly without further purification.

Graphite.—Pyrolytic (nonporous) ultra-pure graphite rod obtained from the General Electric Company was used for the studies on bromide discharge, and was mounted in a specially fabricated Teflon holder connected to a Tru-bore sliding glass tube which could be fitted in the head of the working electrode compartment of the cell.

Counter and reference electrodes.—Special consideration had to be given to the counterelectrode since the electrolyte used was methanolic or ethanolic HCl (or DCl); thus, in the presence of Cl^- ion, oxidation of the alcohol by Cl_2 could arise especially during the pre-electrolysis purification which was carried out for a period of at least 10 hr at a current density of 2 mA-cm^{-2}. Although a closed stopcock between the anode and cathode compartments decreased the possibility of migration of oxidation products, etc. from the anode to the cathode, it was felt that such oxidation should be eliminated.

It was found that a large silver gauze anode met this requirement satisfactorily by reacting with Cl^- ion from the solution, forming an insoluble film of silver chloride as the anode reaction. A fresh silver electrode was prepared before each run and a standardized cleaning procedure using aq. NH_3 was followed. Platinized platinum gauze over which hydrogen gas was bubbled was also tried but did not lead to satisfactory results.

The reference electrodes were a pair of platinized platinum hydrogen electrodes which operated satisfactorily in alcoholic solutions (20) and were repeatedly checked against one another. The reversibility of the hydrogen reference electrode at low temperatures (down to −90°C) was checked in a series of special experiments as follows: (*a*) Qualitatively, by bubbling nitrogen rather than hydrogen gas at one of a pair of electrodes. The electrodes recovered their initial zero potential difference within a minute or two if the nitrogen was replaced by hydrogen gas. (*b*) Quantitatively, by variation of the partial pressure of hydrogen by dilution with nitrogen at one of the electrodes.

For the anodic reaction of Br^- at graphite, the silver-silver bromide reference half-element was used. Electrodes were prepared in pairs according to the procedure given by Ives and Janz (21).

Temperature control.—For the low temperature experiments the cell was cooled by immersion in a large

Dewar flask containing a "low-boiling" (30°-60°C) petroleum ether/liquid nitrogen mixture [cf. ref. (3)]. The temperature of the cooling bath was measured by means of a pentane thermometer at the beginning and end of each run and was found to vary by no more than 1°C. As the experiments were carried out over a total temperature range of up to 160°C, this means of temperature control was considered adequate.

The shorter temperature range (24°-65°C) involved in the experiments at mercury necessitated more accurate control of the temperature [cf. ref (3)]. For these runs, thermostated water was circulated through the cell at a pre-set constant temperature in the usual way.

Potentiodynamic measurements.—These were carried out using conventional circuitry (22) at Ni and Pt at low temperatures in methanolic solutions in order to examine if quantitative H-coverage measurements could be made, as they can in aqueous solutions at noble metals. Well resolved H peaks could not be detected presumably owing to the competitive adsorption of CH_3OH (23).

Results

Exchange current densities as a function of temperature.—Linear logarithmic behavior was observed in the over-potential (η)-current density (i) relation for the h.e.r. at Ni, Pt, Cd, and Pb. Good linear Tafel relations were also observed for the Br_2 evolution reaction at graphite. At Ni, however, in the h.e.r., two linear regions were observed in the η-log i plots (Fig. 1). At the lower current densities, the slope for this part of the η-log i relation increased with increasing temperature while for the section at high i, b decreased with increasing temperature. At approximately −40°C both regions have the same slope and a single Tafel line over some 4 decades of i is observed. In CH_3OD/DCl, the isoinclinal temperature for the log i-η relation is nearer to room temperature. The activation energy behavior was evaluated by plotting the logarithm of the exchange current i_o (see below) as a function of $1/T$.

The log i_o, pertaining to the experimental region[1] of current-potential behavior actually observed, was obtained for each temperature by calculation rather than graphical extrapolation using the experimental Tafel parameters a and b which give, when $\eta = 0$, log $i_o = -a/b$.

Nickel.—In this case, two lines for log i_o *vs.* $1/T$ were obtained (Fig. 2) corresponding to the two Tafel regions of Fig. 1. The plot for the high c.d. region shows a departure from linearity at approximately −40°C and gives a mean apparent value of $\Delta H^{o\neq}_R$ of 10.4 kcal-mole^{-1} as shown in Fig. 2. The plot for the low c.d. region exhibits curvature at the high temperature end and gives limiting values of $\Delta H^{o\neq}_R$ of 7.1 in the upper region and 3.9 kcal-mole^{-1} for the lower section.

Platinum.—As in the case of the low c.d. region at nickel, the electrochemical Arrhenius plots for platinum exhibit marked curvature especially at higher over-potentials; $\Delta H^{o\neq}_R$ varies from *ca.* 8 kcal-mole^{-1} (+25° to −46°C) to *ca.* 3.5 kcal-mole^{-1} (−46° to −125°C) (Fig. 3a). The corresponding plot for the experiment conducted over a range of ascending temperatures is shown in Fig. 3b and exhibits surprisingly an apparent negative activation energy at the high temperature end.

Lead.—The kinetic results obtained at this metal give an apparent negative energy of activation at values of $1/T > 3.9 \times 10^{-3}$ °K^{-1} but normal behavior at the higher temperatures. Thus $\Delta H^{o\neq}_R$ for $1/T < 3.9 \times 10^{-3}$ °K^{-1} is + 6.3 kcal-mole^{-1}.

[1] The value of log i_o so calculated may not be identical with that actually obtaining at $\eta = 0$ in an experimentally inaccessible range (e.g., at Pb or Hg) of current densities near the reversible potential. It refers, however, correctly to the process actually occurring at higher potentials.

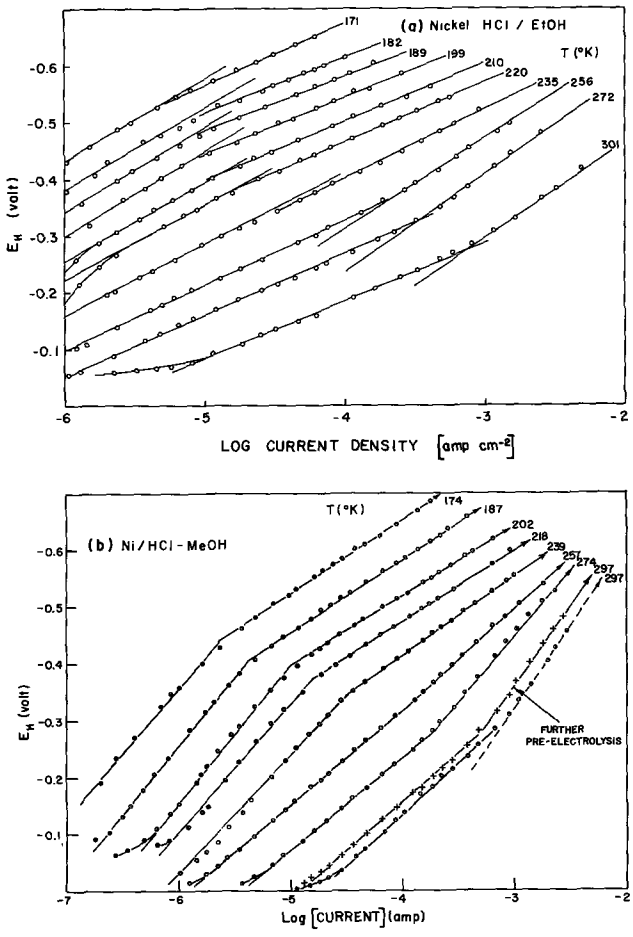

Fig. 1. Current-potential relations for the h.e.r. at Ni in alcoholic HCl solutions down to low temperatures. (a) 0.5*N* ethanolic HCl. (b) 0.5*N* methanolic HCl.

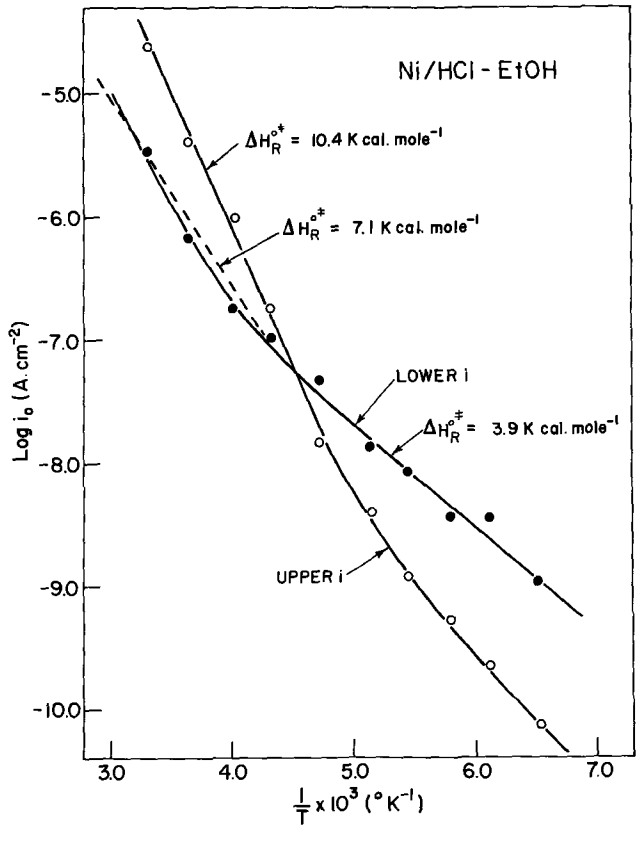

Fig. 2. Electrochemical Arrhenius plots for the two regions of Fig. 1 (h.e.r. at Ni in alcoholic HCl solutions).

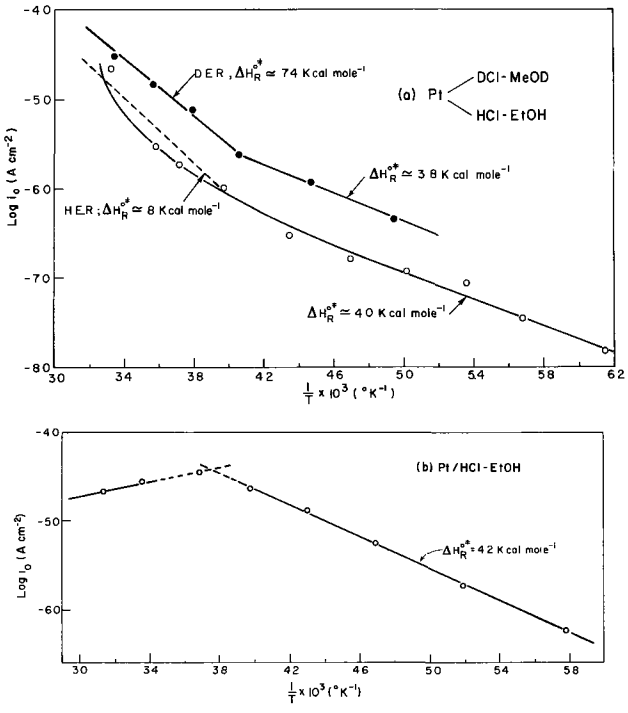

Fig. 3. (a) Electrochemical Arrhenius plots for the h.e.r. at Pt in alcoholic HCl and DCl solutions. (b) As in (a) but for a series of ascending temperatures.

Cadmium.—The log i_o *vs.* (1/*T*) plots for methanol-h and d exhibit a break at approximately 4.0 x 10^{-3} °K^{-1}, where log i_o becomes practically independent of temperature particularly in the H-solvent. The values of $\Delta H^{o\neq}_R$ calculated from the data for the h.e.r. at the high temperature end (*i.e.*, $1/T < 4.0 \times 10^{-3}$ °K^{-1}) is 7.1 kcal-mole^{-1} while that for the d.e.r. is 11.5 kcal-mole^{-1}.

Apparent activation energies as a function of η.—Values of $(\log i)_\eta$ were plotted as a function of (1/*T*) for each of the metals under consideration for various values of η. From these plots, values for $\Delta H^{o\neq}_\eta$ are obtained (5) for each η value and can then be plotted as a function of η; such relations can ideally be represented by the equation

$$\Delta H^{o\neq}_\eta = \Delta H^{o\neq}_R - \beta\eta\mathbf{F} \qquad [4]$$

where $\Delta H^{o\neq}_R$ is the value of the activation energy at zero over-potential.

Nickel; high c.d. region.—Figure 4a shows a plot of (log *i*) *vs.* (1/*T*) for η values ranging from 0 to −0.6V. $\Delta H^{o\neq}_\eta$ decreases as η increases as required by Eq. [4] and the nonlinearity of the $(\log i)_\eta$ *vs.* (1/*T*) plot gradually disappears as η increases, becoming more or less linear over the entire temperature range at the higher η values. A plot of the derived $\Delta H^{o\neq}_\eta$ *vs.* η is shown in Fig. 4b.

Nickel; low c.d. region.—The results are shown in Fig. 5, but, contrary to the above equation, $\Delta H^{o\neq}_\eta$ now increases as η increases and there is curvature in the plot which becomes more pronounced as η becomes more negative.

Platinum.—The plot of $(\log i)_\eta$ *vs.* (1/*T*) is shown in Fig. 6a; it is evident that there is some resemblance to the results for the low c.d. region at nickel shown in Fig. 5. Figure 6b shows a plot of $\Delta H^{o\neq}_\eta$ *vs.* η and indicates again an apparent negative value of β, the symmetry factor, in Eq. [4].

Lead.—Plots of $(\log i)_\eta$ *vs.* (1/*T*) were constructed as in Fig. 4, 5, and 6 and as η increases the apparent negative activation energy at the lower temperatures disappears and the relations become linear and normal at approximately −0.7V.

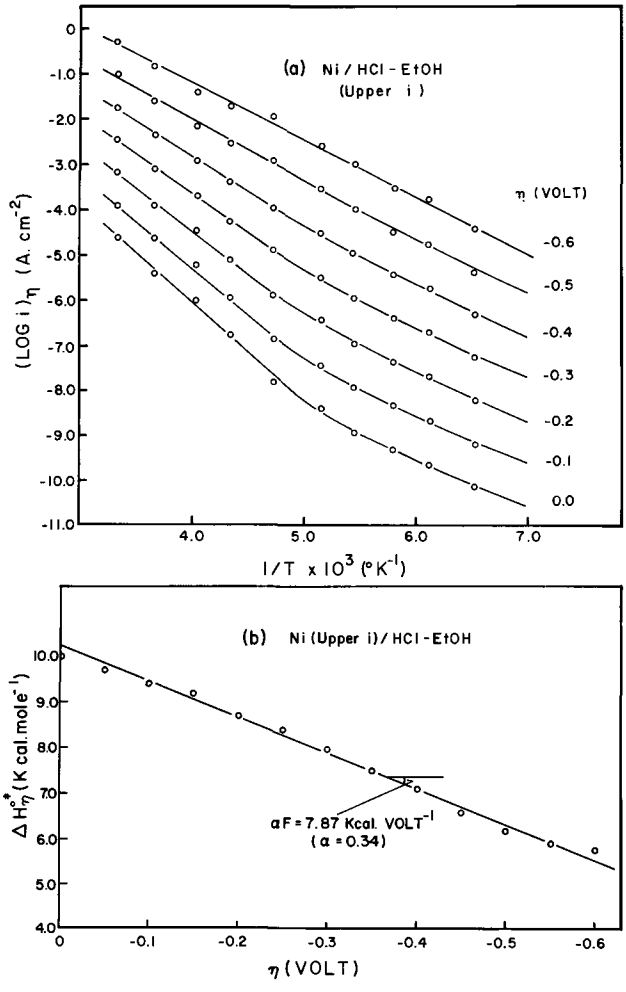

Fig. 4. (a) Plots of $(\log i)_\eta$ *vs.* 1/*T* for the upper Tafel regions in Fig. 1a. (b) Dependence of $\Delta H^{o\neq}_\eta$ (from Fig. 4a) on η (Eq. [4]).

Cadmium.—The results for this case are similar to those for lead, except that the slopes of the Arrhenius plots have, under all conditions, a normal sign.

Mercury.—The behavior of Hg was in close agreement with that evaluated previously (3) in this laboratory.

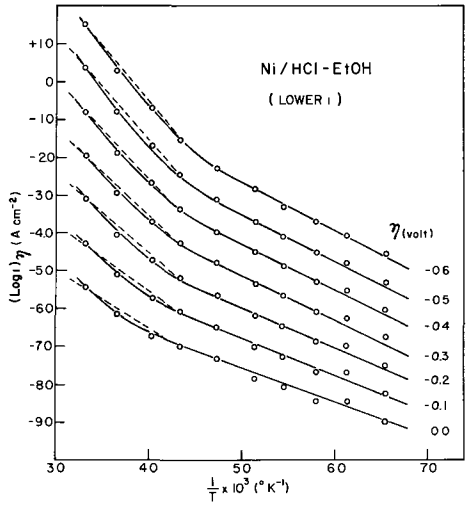

Fig. 5. Plots of $(\log i)_\eta$ *vs.* 1/*T* for the lower Tafel regions of Fig. 1a.

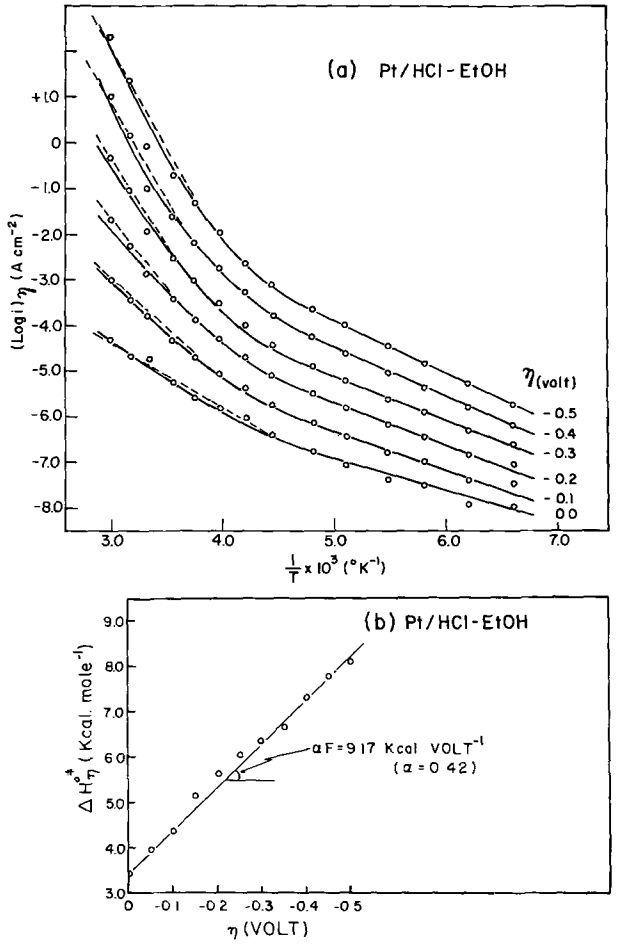

Fig. 6. (a) Plots of $(\log i)_\eta$ *vs.* $1/T$ for the h.e.r. at Pt in ethanolic HCl. (b) Dependence of $\Delta H^{o\ddagger}_\eta$ (from Fig. 7a) on η.

Corresponding data for deuterium evolution.—The polarization curves were similar to those for the h.e.r. at the above metals but b values were usually somewhat greater than the corresponding values for the h.e.r. Comparative electrochemical Arrhenius plots for the d.e.r. are shown in Fig. 7 and 3a for some of the metals referred to above.

Anodic reaction of Br^- at graphite.—The purpose of this part of the work was to provide, for comparative purposes, some results over a range of low and intermediate temperatures for a "one-electron" charge transfer process not involving reaction of H or D. After various exploratory studies, the most suitable system for this experiment was found to be 0.4M $(n\text{-}C_3H_7)_4$ NBr in spectroscopically pure acetonitrile. The Tafel slopes are found to be almost independent of T and the log i *vs.* $1/T$ plots exhibit normal behavior, giving excellent linear relations over a range of some 75°K for various η values.

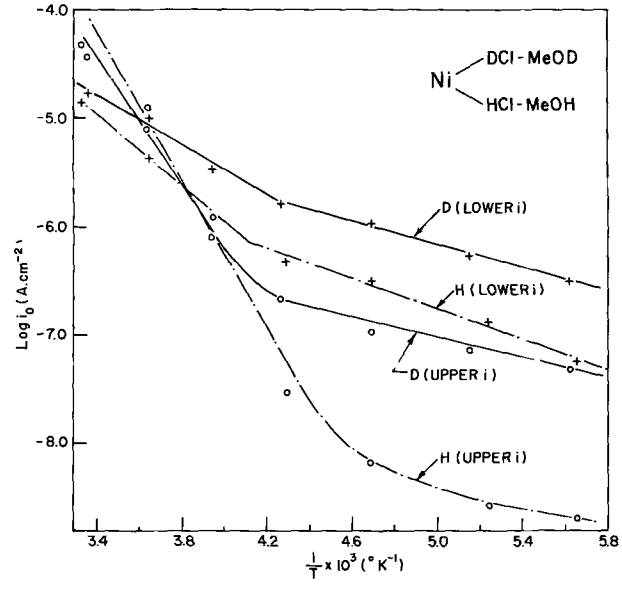

Fig. 7. Comparative electrochemical Arrhenius plots for h.e.r. and d.e.r. at Ni in methanolic solutions (*cf.* Fig. 3a).

Discussion

Illustrative numerical calculations of $\Delta H^{o\ddagger}_R$.—It was thought desirable to make illustrative evaluations of $\Delta H^{o\ddagger}_R$ for various situations in which complications may arise, *e.g.*, if β is $f(T)$ or if b is not simply equal to $RT/\beta\mathbf{F}$. Results are therefore presented here of numerical calculations of activation energies in which various means of expressing $\Delta H^{o\ddagger}_R$ have been used, corresponding to cases encountered experimentally. The following approach was employed: the usual relation

$$i_o = k \exp[-\Delta H^{o\ddagger}_R/RT] \qquad [5]$$

assuming a constant reactant ion concentration, was used and a value of 10.0 kcal-mole^{-1} was arbitrarily chosen for $\Delta H^{o\ddagger}_R$ and i_o values were calculated for a series of T values. These values were then put into the equation

$$\log i = \log i_o + \eta/2.3\, b \qquad [6]$$

where b was assumed to take one of the four possible forms listed below:

$b = RT/\beta\mathbf{F}$; where $\beta = 0.5 =$ const.; this is the simple form usually assumed for b, so that $\Delta H^{o\ddagger}_R$ should be recovered without complications; this is simply a "reference" case.

$b = (RT/\beta\mathbf{F}) + c$, where c was taken as a constant equal to 0.04V and $\beta = 0.71$ (to give $b = 0.116$ at $T = 298$°K; *cf.* the actual results obtained at Hg in methanol).

$b = (RT/\beta\mathbf{F}) + c$, where c was taken as a constant (*cf.* the observed experimental behavior described above for certain metals), that is, β is linear in T.

$b = c' - 2.3\ RT/\beta\mathbf{F}$; *i.e.*, b increases as T decreases, as found for example for Pt and in the low c.d. region at Ni when anion adsorption is significant.

For each of the cases listed above, $\Delta H^{o\ddagger}_R$ and $\Delta H^{o\ddagger}_\eta$ were recovered by the following methods and the calculated results were compared (Fig. 8):

(a) $d \log i_o/d(1/T) = -\Delta H^{o\ddagger}_R/2.3R$; this is the kinetically most convenient way of obtaining the heat of activation.

(b) $d(\log i)/d(1/T) = -(\Delta H^{o\ddagger}_R - \beta\eta\mathbf{F})/2.3R$ for various η values.

(c) $(d\eta/dT)_i = -\Delta H^{o\ddagger}_\eta/\beta\mathbf{F}T$.

(d) $(d\eta/d \log T)_i = -2.3\ \Delta H^{o\ddagger}_\eta/\beta\mathbf{F}$.

Case 1: $b = RT/\beta\mathbf{F}$; $\beta = 0.5$ and constant (Fig. 8 and 9). This case is trivial in that a value of $\Delta H^{o\ddagger}_R = 10.0$ kcal-mole^{-1} was chosen to calculate the i_o values from which $\Delta H^{o\ddagger}_R$ will obviously be recovered with the required starting value. However, this provides a basis for comparisons among the remaining three cases. For this case, the values of $\Delta H^{o\ddagger}_\eta$ calculated by method b are in agreement (as they must be) with values of $\Delta H^{o\ddagger}_\eta$ calculated from methods c and d.

Case 2: $b = (RT/\beta\mathbf{F}) + c$ which is the form of the b *vs.* T plot experimentally observed at Hg where $\beta = 0.71$ and $c = 0.04$V. A plot of $(\log i)_\eta$ *vs.* $(1/T)$ is shown in Fig. 8. Unlike their counterparts in case 1, the plots exhibit curvature which is more pronounced at the higher η values. Thus $\Delta H^{o\ddagger}_\eta$ must be determined for particular values of $(1/T)$ and the derived values are hence temperature-dependent. The plots of η *vs.* log T for this case 2 are shown in Fig. 10 and values of $\Delta H^{o\ddagger}_\eta$ calculated by method b are found not to be in agreement with values of $\Delta H^{o\ddagger}_\eta$ computed by methods c and d; however, the results of c and d are

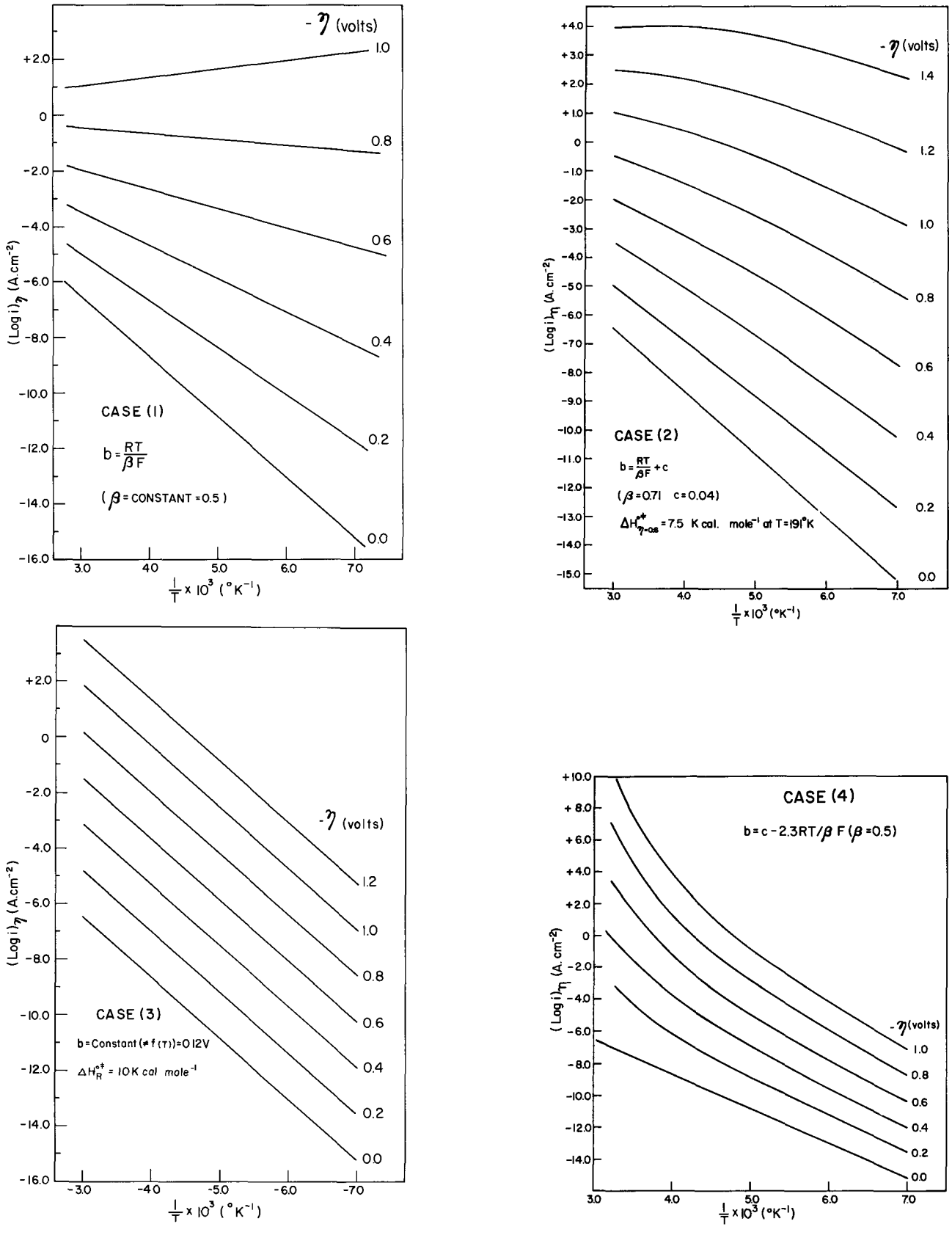

Fig. 8. Plots of (log i)$_\eta$ *vs.* $1/T$ for the four test cases examined by numerical computation

in agreement with each other.

The results derived from plots of log i_o *vs.* $1/T$ agree of course for all cases since here $\eta = 0$ (log i = log i_o at $\eta = 0$) and thus the form of b does not enter into the calculation (see lowest lines for $\eta = 0$ in Fig. 8).

Case 3: b = const. = 0.120V. Here β is changing with temperature so that $b \neq f(T)$. Thus $b = RT/\beta\mathbf{F}$ with $\beta = kT$, say.

The (log i)$_\eta$ *vs.* $1/T$ plot shown in Fig. 8 will obviously give the assumed reference value of 10.0 kcal-mole^{-1} at all η values and hence $\Delta H^{o\neq}{}_\eta$ is independent of η. When values of $\Delta H^{o\neq}{}_\eta$ are however, evaluated from the plots of $(\eta)_i$ *vs.* log T (Fig. 11), they are found to be a function of temperature (or c.d.) as follows by taking tangents to the curves in Fig. 11. Values of $\Delta H^{o\neq}{}_{\eta=0.8}$, calculated for various c.d. values, are

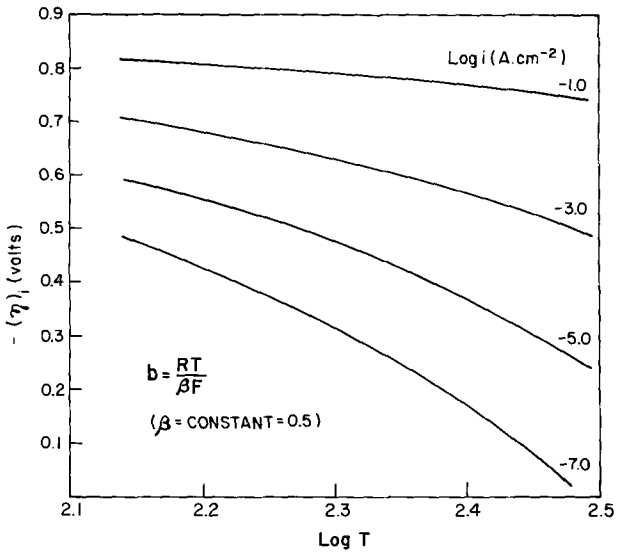

Fig. 9. Plots of $(\eta)_i$ vs. log T for case 1

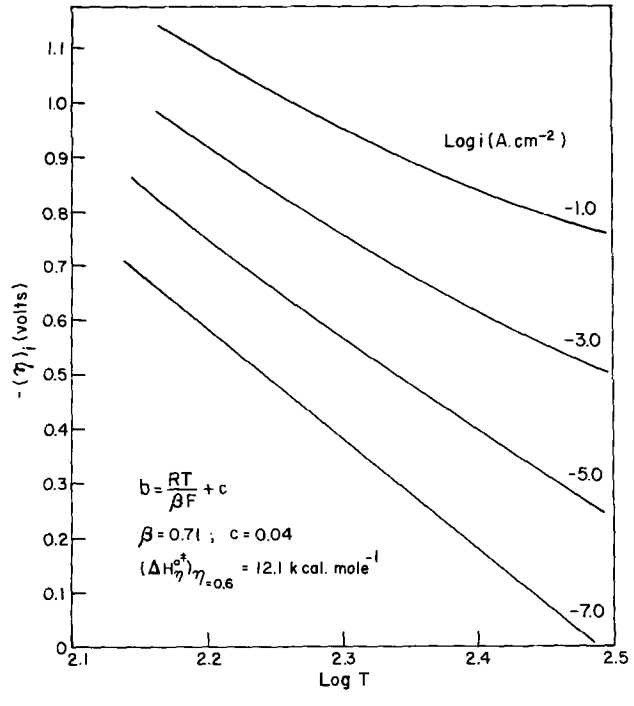

Fig. 10. Plots of $(\eta)_i$ vs. log T for case 2

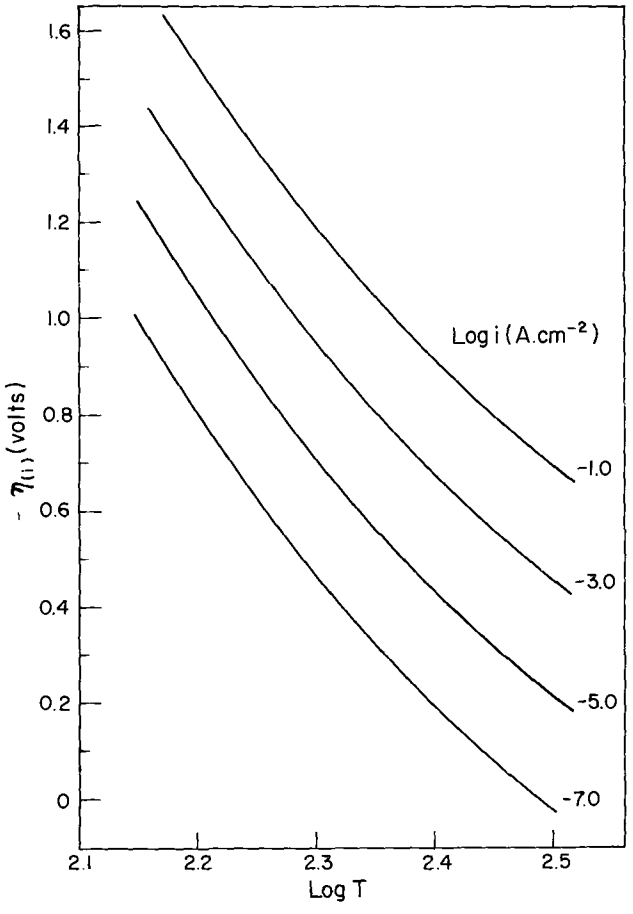

Fig. 11. Plots of $(\eta)_i$ vs. log T for case 3

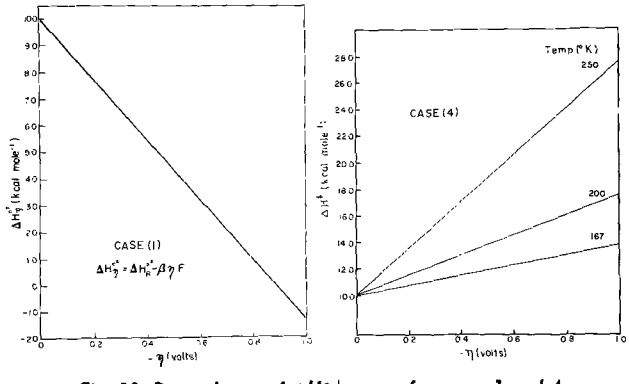

Fig. 12. Dependence of $\Delta H^{o\ddagger}_{\eta}$ on η for cases 1 and 4

found to vary by about 1 kcal-mole^{-1} when derived by methods *c* and *d*. Thus, from Fig. 11 $\Delta H^{o\ddagger}_{\eta=0.8}$ = 9.6-10.6 kcal-mole^{-1} over 7 decades of *i*.

Case 4: *b* increases with decreasing T according to a relation of the form $b = c' - 2.3\ RT/\beta\mathbf{F}$ where $\beta = 0.5$ and constant. It is shown in the present work that this case is encountered experimentally. The plots of $(\log i)_\eta$ *vs.* $1/T$ for case 4 are shown in Fig. 8 and, except for $\eta = 0$, the Arrhenius plots are curved in a manner not unlike that observed experimentally at Pt and for the low c.d. region at Ni. The curvature increases with increasing η. From Fig. 12, it can be shown that $\Delta H^{o\ddagger}_{\eta}$ increases linearly with η for a given value of T, the rate of increase becoming greater at higher temperatures. This is to be contrasted with the results for the conventional case 1, also shown in Fig. 12.

In Fig. 13, *b* is shown comparatively as a function of T for cases 1 to 4, reflecting the various cases encountered experimentally (6) for the variation of *b* with T.

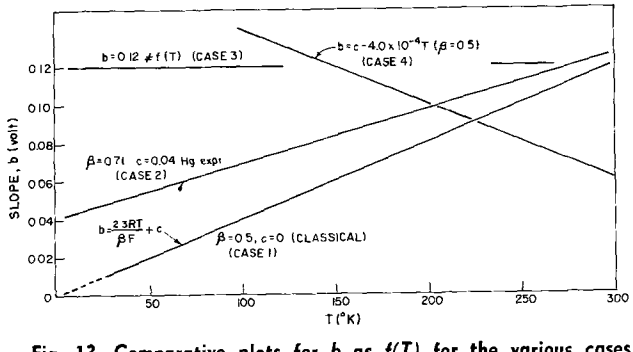

Fig. 13. Comparative plots for *b* as *f(T)* for the various cases considered and encountered experimentally [*cf.* ref. (6)].

Analytical treatment.—The above treatment based on numerical calculation has led to a number of interesting conclusions regarding the variation of $\Delta H^{o\ddagger}_{R}$ with T, so that further analytical exploration of this matter seems justified in order to examine the exact

relations between the true and apparent heats of activation for cases where $b \neq RT/\beta\mathbf{F}$.

We assume the general relation

$$\ln i = \ln i_o + \eta/b \qquad [7]$$

The conventional case, previously assumed generally applicable, is when $b = RT/\beta\mathbf{F}$ and $\beta \neq f(T)$. This gives the well known results (1, 5)

$$\frac{d \ln i_o}{d\ 1/T} = -\frac{1}{R}(\Delta W^{o\ddagger} - \beta\Delta H^o) = -\Delta H^{o\ddagger}_R/R \qquad [8]$$

where ΔH^o is the enthalpy in change reaction [2] and $\Delta W^{o\ddagger}$ is the true (but experimentally inaccessible) heat of activation when the metal-solution potential difference $\phi = 0$.

$$(\partial\eta/\partial T)_i = -\frac{1}{\beta\mathbf{F}T}[\Delta H^{o\ddagger}_\eta] = -\frac{1}{\beta\mathbf{F}T}[\Delta H^{o\ddagger}_R - \beta\eta\mathbf{F}] \qquad [9]$$

and

$$-\Delta H^{o\ddagger}_R = \beta\mathbf{F}\left(\frac{\partial\eta}{\partial \ln T}\right)_i - \beta\eta\mathbf{F} \qquad [10]$$

For a number of the experimentally investigated cases, $b = RT/\beta\mathbf{F} + c$, so that

$$\ln i = \ln i_o + \eta \Big/ \left(\frac{RT}{\beta\mathbf{F}} + c\right) \qquad [11]$$

which gives, upon differentiation

$$\left(\frac{\partial\eta}{\partial T}\right)_i = \frac{R}{\beta\mathbf{F}} \ln\frac{i}{i_o} - \left(\frac{RT}{\beta\mathbf{F}} + c\right)\frac{d \ln i_o}{dT} \qquad [12]$$

so that substituting for $\ln (i/i_o)$

$$(\partial\eta/\partial T)_i = \left(\frac{R}{RT + \beta c\mathbf{F}}\right)\cdot\eta - \left(\frac{RT}{\beta\mathbf{F}} + c\right)\left(\frac{d \ln i_o}{dT}\right) \qquad [13]$$

Expressing $\ln i_o$ in terms of a combined constant k, the true heat of activation $\Delta W^{o\ddagger}$ at $\phi = 0$ and the metal-solution p.d. ϕ_r at the reversible potential, we write

$$\ln i_o = \ln k - \frac{\Delta W^{o\ddagger}}{RT} + \phi_r \Big/ \left(\frac{RT}{\beta\mathbf{F}} + c\right) \qquad [14]$$

Then differentiating w.r.t. T and noting $\phi_r\mathbf{F} = -\Delta G^o$ and $\frac{\mathbf{F}\, d\phi_r}{dT} = \Delta S^o$ for the hydrogen half-cell reaction [2]

$$\frac{d \ln i_o}{dT} = \frac{\Delta W^{o\ddagger}}{RT^2} + \frac{\beta R}{(RT + \beta c\mathbf{F})^2}[\Delta G^o] + \frac{\beta}{(RT + \beta c\mathbf{F})}[\Delta S^o] \qquad [15]$$

which on rearrangement gives

$$\frac{d \ln i_o}{dT} = \frac{\Delta W^{o\ddagger}}{RT^2} + \frac{1}{(RT + \beta c\mathbf{F})^2}[\beta R\Delta H^o + \beta^2 c\mathbf{F}\,\Delta S^o] \qquad [16]$$

or

$$\frac{d \ln i_o}{d\ 1/T} = \frac{-\Delta W^{o\ddagger}}{R} - \frac{\beta T^2}{(RT + \beta c\mathbf{F})}\left[\frac{R\Delta G^o}{RT + \beta c\mathbf{F}} + \Delta S^o\right] \qquad [17]$$

which enables Eq. [8] to be recovered in the conventional case where $\beta c\mathbf{F} = 0$.

Returning to the evaluation of $(\partial\eta/\partial T)_i$, $d \ln i_o/dT$ can now be substituted in Eq. [13] giving, after elementary algebra

$$\left(\frac{\partial\eta}{\partial T}\right)_i = \left(\frac{R}{RT + \beta c\mathbf{F}}\right) - \left(\frac{RT + \beta c\mathbf{F}}{\beta\mathbf{F}}\right)\frac{\Delta W^{o\ddagger}}{RT^2} - \frac{1}{\beta\mathbf{F}(RT + \beta c\mathbf{F})}[\beta R\Delta H^o + \beta^2 c\mathbf{F}\Delta S^o] \qquad [18]$$

It is clear that of the two derivatives $d \ln i_o/dT$ or $d \ln i_o/d\ 1/T$ neither can give directly an apparent heat of activation which is a simple sum of $\Delta W^{o\ddagger}$ and $\beta\Delta H^o$ as is the case (Eq. [1]) when b is simply $RT/\beta\mathbf{F}$ with β constant. Similarly, $(\partial\eta/\partial T)_i$ is a complex quantity not simply related to $\Delta H^{o\ddagger}$ by Eq. [9] through $\beta\eta\mathbf{F}$, nor does it involve a sum of ΔG^o and $T\Delta S^o$ terms that can be expressed in terms of ΔH^o with $\Delta W^{o\ddagger}$. Thus when b is not simply given by the quantity $RT/\beta\mathbf{F}$, as now must be recognized to be the case experimentally under most conditions [ref. (6-9) and the present work], it cannot be expected that $\Delta H^{o\ddagger}_R$ from Eq. [8] based on $d \ln i_o/d\ 1/T$ will be identical with the quantity evaluated from $-\beta\mathbf{F}T\left(\frac{\partial\eta}{\partial T}\right)_i$ by adding $\beta\eta\mathbf{F}$ (Eq. [9]).

Bockris and Matthews (24) have again [cf. ref. (25)] referred to the question of incompatibility of activation energies of *ca.* 11 kcal · mole^{-1}, observed at mercury in alcoholic solutions, with values of $\eta > 1$V (since $\beta\eta\mathbf{F}$ is then already *ca.* 11.5 kcal · mole^{-1}). However, this value of $\Delta H^{o\ddagger}_R$ seems well authenticated (25, 27) and is also found from the results of Bockris and Parsons (26). This difficulty is only an apparent one, and is connected as we have pointed out elsewhere in discussion (25) with the question of temperature dependence of α or β, or the form of b as $f(T)$ discussed above; a general explanation was given previously (25). From the above calculations which are applicable to the case of Hg since b is experimentally (6) of the form $(RT/\beta\mathbf{F}) + c$ (with $c = 0.04$), it becomes clear how conclusions about barrier height cannot usually be made simply on the basis of the experimental derivatives $(\partial\eta/\partial T)_i$ or $d \ln i_o/d\ 1/T$, both of which evidently give complex quantities not simply related to either the apparent activation energy $\Delta H^{o\ddagger}_R$ at $\eta = 0$ or the true activation energy $\Delta W^{o\ddagger}$ at zero metal-solution p.d.

While some of the experimental results quoted (6) here involve a Tafel slope of the form $b = (RT/\beta\mathbf{F}) + c$, the possibility that $b = RT/\beta\mathbf{F}$ but with β varying with T must also be recognized (6). In such a case, the apparent activation energy is

$$\Delta H^{o\ddagger}_R + \beta\mathbf{F}\, d\phi_r/d\ 1/T + \frac{\mathbf{F}\phi_r}{T}(d\beta/d\ 1/T) \qquad [19]$$

which differs from the barrier height at $\eta = 0$ by

$$\frac{\beta\mathbf{F}}{T}(d\phi_r/d\ 1/T) + \frac{\mathbf{F}\phi_r}{T}(d\beta/d\ 1/T) \qquad [20]$$

Coverage effects in $\Delta H^{o\ddagger}_R$.—In addition to the fact that the measured value of $\Delta H^{o\ddagger}_R$ is an apparent value on account of the variation of the reference electrode potential and of b with temperature, a further complication arises with processes involving an adsorbed intermediate. In such cases, the coverage θ, *e.g.*, by H atoms, can vary with temperature and give an important contribution to the apparent heat of activation. The significance of θ in the kinetic expression for the exchange current was discussed by Devanathan and Selvaratnam (28).

For the kinetics of the h.e.r. at the reversible potential

$$i_o = k_1 C_{H^+}(1 - \theta_H)\exp[-\Delta G^{o\ddagger}_1/RT]\exp[-\phi_r/b] \qquad [21]$$

when the reaction is proceeding by a rate-determining discharge step; $\Delta G^{o\ddagger}_1$ and ϕ_r are the true free energy

of activation (corresponding to $\Delta W^{o\ddagger}$) and the metal-solution p.d. at the reversible potential. Alternatively, for an electrochemical H atom desorption step

$$i_o = k_2\,\theta_H C_{H^+} \exp\,[-\Delta G^{o\ddagger}_2/RT] \exp\,[-\phi_r/b] \quad [22]$$

or for an atom recombination step

$$i_o = k_3\,\theta_H{}^2 \exp\,[-\Delta G^{o\ddagger}_3/RT] \quad [23]$$

where k terms are combinations of constants but do not include the free energies of activation. In any of these cases, it is clear that $d \ln i_o/d\ 1/T$ will involve not only the $\Delta W^{o\ddagger}$ terms in $\Delta G^{o\ddagger}$ and $d\phi_r/d\ 1/T$ but also, depending on the type of mechanism involved, $d \ln (1-\theta_H)d\ 1/T$ or $d \ln \theta_H/d\ 1/T$. For a discharge process occurring at low coverage by H, (*i.e.*, $1-\theta_H \to 1$) no significant additional effect will arise. For the electrochemical desorption or recombination steps, however, (except at $\theta_H \to 1$) θ_H can obviously vary with temperature and in general θ_H has the form

$$\frac{K_1 C_{H^+} + \exp\,[-\phi_r \mathbf{F}/RT]}{1 + K_1 C_{H^+} \exp\,[-\phi_r \mathbf{F}/RT]} \quad [24]$$

for quasi-equilibrium in the discharge step at a "Langmuir" surface; here K_1 is the "chemical part" of the electrochemical equilibrium constant for the step $H^+_{aq} + e + M \leftrightharpoons M\,H_{ads}$ at the reversible potential ϕ_r and is related to the standard free energy of adsorption of H, ΔG^o_H in the usual way. The apparent activation energy will now be a function of the variation of θ_H with T and of ϕ_r with T, both in the kinetic term exp $-\phi_r/b$ and in the quasi-equilibrium expression for θ_H. The "chemical part" of the variation of θ_H with T obviously arises from the variation of K_1 with T, *i.e.*, from the heat of adsorption of H. Limitingly, for low θ_H at the reversible potential ϕ_r

$$\theta_H = K_1 C_{H^+} \exp\,[-\phi_r \mathbf{F}/RT]$$
$$= C_{H^+} \exp\,[-\Delta G^o_H/RT].\exp\,[-\phi_r \mathbf{F}/RT] \quad [25]$$

or

$$\ln \theta_H = \ln C_{H^+} - \Delta H^o_H/RT + \Delta S^o_H/R - \phi_r \mathbf{F}/RT \quad [26]$$

Then

$$d \ln \theta_H/d\ 1/T = -\Delta H^o_H/R - \frac{\mathbf{F}}{RT}(d\phi_r/d\ 1/T) - \frac{\mathbf{F}\phi_r}{R} \quad [27]$$

The latter two terms are the ones that also arise in the evaluation of the true activation energy of any electrode process and, as in the conventional case considered above, are together equal to $1/R$ times ΔH^o, the heat change in the half-cell process corresponding to the over-all reaction $H_3O^+ + e \to H_2O + \frac{1}{2} H_2$; the latter heat differs from ΔH^o_H since that term refers to the electrochemical discharge and adsorption partial process $H_3O^+ + M + e \to H_2O + M\,H_{ads}$. Hence

$$d \ln \theta_H/d\ 1/T = -\Delta H^o_H/R + \Delta H^o/R \quad [28]$$

Now, in the absence of any variation of coverage terms with temperature,

$$d \ln i_o/d\ 1/T = -(\Delta W^{o\ddagger}/R - \beta \Delta H^o/R) = -\Delta H^{o\ddagger}_R/R$$

so that when the variation of θ_H with temperature is allowed for in Eq. [21] for example

$$\frac{d \ln i_o}{d\ 1/T} = 1/R\,[-\Delta W^{o\ddagger} + \beta \Delta H^o - \Delta H^o_H + \Delta H^o] \quad [29]$$

$$= -1/R\,[\Delta W^{o\ddagger} + \Delta H^o_H - (1+\beta)\,\Delta H^o] \quad [30]$$

It is evident that $\Delta H^o_H - \Delta H^o$ is simply the energy of adsorption ΔH^o_{ads} of H from half a mole of H_2 so that

$$d \ln i_o/d\ 1/T = -1/R\,[\Delta W^{o\ddagger} + \Delta H^o_{ads} - \beta \Delta H^o]$$
$$= -1/R\,[\Delta H^{o\ddagger}_R + \Delta H^o_{ads}] \quad [31]$$

Since ΔH^o_{ads} is usually a negative quantity, the over-all apparent heat of activation could be negative when $\Delta H^{o\ddagger}_R + \Delta H^o_{ads} < 0$. Such a case has been observed in the present work.

Forms of electrochemical Arrhenius plots for the H.E.R.—Plots of log k *vs.* $1/T$ for the rate constant of a reaction, particularly one involving proton transfer, can deviate from linearity on account of (*a*) changes of solvent structure and hydrogen bonding with temperature; (*b*) proton tunneling; and (*c*) changes of mechanism (Fig. 14). The first two factors generally tend to produce opposite directions of deviation from linearity in the Arrhenius plots. Here we discuss qualitatively the form of the observed plots for Ni, Pt, Pb, and Cd.

The η-log i behavior at Ni shows two Tafel regions (Fig. 1); the upper one gives a Tafel slope b which initially decreases with T, while the lower region gives b values which continuously increase with decreasing T and which have high values $> 2.3 \times 2\ RT/\mathbf{F}$. This suggests that the lower region is affected by specific adsorption of anions but there is a relatively sudden desorption as η is increased. This view is supported by the fact that experiments in methanolic $HClO_4$ showed (6) only one Tafel region with b values almost equal to those for the upper region of the η-log i plots in methanolic HCl.

For the high c.d. region at Ni (Fig. 2), d log $i_o/d\ 1/T$ is progressively smaller at low temperatures than at high, *i.e.*, the relation shows "concave" curvature at the low temperature end. Also the b values for this region after falling initially with decreasing T, begin to increase again at the lowest temperatures ($<-75°C$). Both these aspects of the low temperature behavior are characteristic of participation of proton tunneling in parallel with the classical transfer process. However, the present work also shows that similar effects arise in the deuterium reaction at Ni (Fig. 7) and furthermore the Tafel slopes for the d.e.r. are higher, rather than lower, [cf. ref. (29)] than those of the h.e.r. Hence, the low temperature behavior in the log i_o *vs.* $1/T$ plots cannot be satisfactorily explained in terms of proton tunneling. We must therefore suppose that the effect arises for reasons such as preferred orientation of solvent at the lower temperatures; solvent structure change would, however, it might be supposed, lead to enthalpy effects opposite to those observed here at low temperatures, *i.e.*, $\Delta H^{o\ddagger}_R$ would tend to be larger rather than smaller.

The effects of anion adsorption are obviously of importance here, as they are in determining the Tafel slopes. Generally, at low temperatures, anion adsorption is found to be greater. For the upper lines at Ni, however, the role of anion adsorption effects must be

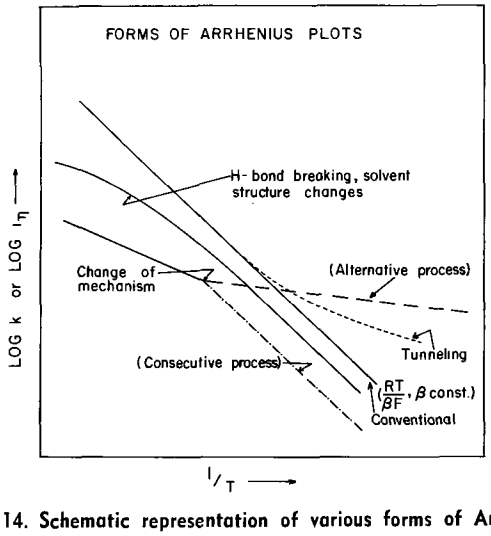

Fig. 14. Schematic representation of various forms of Arrhenius plots.

presumed absent if the change of Tafel slope is attributed to desorption of anions at high η values (*cf.* the results for the $HClO_4$ solutions; it is to be noted also that as the temperature is lowered, the potential corresponding to the change of slope is increased; this is as expected if anion desorption is involved). Under these circumstances, since tunneling has been discounted by the earlier argument, it may be suggested that the anomalous Arrhenius plots of Fig. 4 arise because of a temperature-dependent activation entropy $\Delta S^{o\neq}$ or frequency factor term of the type discussed by Caldin and Harbron (30). For the discharge step, $\Delta S^{o\neq}$ will be expected to be positive for charge neutralization and release of solvent electrostriction [*cf.* the positive (corrected) volume of activation (31)], so that with increasing solvent-structure as temperature is lowered, $\Delta S^{o\neq}$ may be expected to become relatively more positive and the rate relatively less decreased as the temperature is lowered. This would give the correct form of the curvature for the plots of Fig. 4.

A similar effect could also arise if, at lower temperatures, the methanol solvent becomes more strongly adsorbed resulting in weakening of H adsorption. In the step $H_3O^+ + MH_{ads} + e \rightarrow H_2$ this should lead to decreasing $\Delta H^{o\neq}_R$.

It may be anticipated that the behavior at Pt and Ni will be complicated by the temperature dependence of H coverage θ_H discussed above since it is well-known that the energy of adsorption of H (in Eq. [31]) can vary with θ_H and also be dependent on anion adsorption; the combination of these effects could be complex and lead to the observed temperature dependence of $d \log i_o/d\ 1/T$ for Pt and the lower Tafel regions at Ni where Cl^- adsorption effects are apparently important.

The $\log i_o$ *vs.* $1/T$ plots for Pt and for the low c.d. region of Ni (Fig. 3a and 2) exhibit curvature at the high temperature end, an effect which becomes more pronounced at high values of η. This appears to be due to the progressive desorption (15, 16) of Cl^- ions which occurs at the higher temperatures and larger η values. Such an effect is consistent with the high values of Tafel slope b and the anomalous temperature dependence of the b values (b increases with decreasing T, Fig. 1). At Pt, for increasing temperatures in the cycle of measurements, irreversible adsorption of Cl^- ion seems to be indicated (compare the two diagrams of Fig. 3).

The Arrhenius plots for Pb and Cd may also be interpreted in terms of specific adsorption of Cl^- and the apparent negative activation energy observed for Pb could receive an explanation in terms of temperature dependent H coverage in the presence of adsorbed anions. Although the activation energy for the h.e.r. at Cd falls appreciably at the lower temperatures, again similar effects set in with the d.e.r. at only slightly lower temperatures so that proton tunneling is not clearly indicated at this metal.

Acknowledgments

Grateful acknowledgment is made to the National Research Council for support of this work and for the award to one of us (D.M.) of a Graduate Research Scholarship.

Manuscript received May 20, 1969. This was Paper 233 presented in part at the New York Meeting, May 4-9, 1969.

Any discussion of this paper will appear in a Discussion Section to be published in the June 1970 JOURNAL.

REFERENCES

1. M. I. Temkin, *Zh. Fiz. Khim.*, **22**, 1081 (1948).
2. B. E. Conway, E. M. Beatty, and P. A. D. de Maine, *Electrochim. Acta.*, **1**, 39 (1962).
3. B. E. Conway and M. Salomon, *Discussions Faraday Soc.*, **39**, 223 (1965); *J. Chem. Phys.*, **41**, 3169 (1964).
4. H. F. Halliwell and S. C. Nyburg, *Trans. Faraday Soc.*, **59**, 1126 (1963).
5. J. N. Agar, *Discussions Faraday Soc.*, **1**, 81 (1947); F. P. Bowden and J. N. Agar, *Ann. Rept. Chem. Soc. Lonaon*, **35**, 90 (1938).
6. B. E. Conway and D. J. MacKinnon, *Trans. Faraday Soc.*, In press.
7. H. P. Stout, *Trans. Faraday Soc.*, **41**, 64 (1945).
8. J. N. Butler, *This Journal*, **112**, 226 (1965).
9. J. O'M. Bockris and E. C. Potter, *J. Chem. Phys.*, **20**, 614 (1952).
10. B. E. Conway and M. Salomon, *Ber. Bunsenges.*, **68**, 331 (1964).
11. R. P. Bell, *Proc. Roy. Soc. London*, **A139**, 466 (1933); R. P. Bell, J. A. Fendley, and J. R. Hulett, *ibid.*, **A235**, 453 (1956); E. F. Caldin and E. Harbron, *J. Chem. Soc.*, 3454 (1962).
12. J. O'M. Bockris, M. A. V. Devanathan, and K. Müller, *Proc. Roy. Soc. London*, **A274**, 55 (1963).
13. B. E. Conway and L. G. M. Gordon, *J. Phys. Chem.*, In press (Nov. 1969).
14. A. M. Azzam, J. O'M. Bockris, B. E. Conway, and H. Rosenberg, *Trans. Faraday Soc.*, **46**, 918 (1950).
15. J. O'M. Bockris and D. B. Matthews, *Electrochim. Acta.*, **11**, 143 (1966).
16. Z. A. Jofa and V. Stepanova, *Zh. Fiz. Khim.*, **19**, 125 (1945).
17. "Handbook of Prep. Inorg. Chem.," Vol. I, p. 129, 2nd edition; G. Brauer, Editor, Academic Press, New York (1963).
18. B. E. Conway, R. E. Verrall, and J. E. Desnoyers, *Trans. Faraday Soc.*, **62**, 2738 (1966).
19. J. J. MacDonald and B. E. Conway, *Proc. Roy. Soc. London*, **A269**, 419 (1962).
20. *E.g.* see J. O'M. Bockris, *Discussions Faraday Soc.*, **1**, 229 (1947).
21. D. J. G. Ives and G. J. Janz, "Reference Electrodes: Theory and Practice," Academic Press, New York (1961).
22. F. Will and C. A. Knorr, *Z. Elektrochem.*, **64**, 258, 270 (1960).
23. S. S. Beskozovainaya, Y. B. Vasilev, and V. S. Bagotskii, *Electrochim. Acta.*, **12**, 1323 (1967); V. S. Bagotskii and Y. B. Vasilev, *ibid.*, **11**, 1439 (1966).
24. J. O'M. Bockris and D. B. Matthews, *J. Chem. Phys.*, **44**, 298 (1966).
25. B. E. Conway and M. Salomon, *Discussions Faraday Soc.*, **39**, 270 (1965).
26. J. O'M. Bockris and R. Parsons, *Trans. Faraday Soc.*, **47**, 914 (1951).
27. S. Minc and J. Sobkowski, *Bull. Acad. Polon. Sci.*, **8**, 29 (1959).
28. M. A. V. Devanathan and M. Selvaratnam, *Trans. Faraday Soc.*, **56**, 1820 (1960).
29. B. E. Conway, *Can. J. Chem.*, **37**, 178 (1959); St. G. Christov, *Electrochim. Acta*, **4**, 194; 306 (1961); **9**, 575 (1964).
30. E. F. Caldin and E. Harbron, *J. Chem. Soc.*, **1962**, 3454.
31. G. J. Hills and D. R. Kinnibrugh, *This Journal*, **113**, 1111 (1966); see also L. I. Kristalik, *ibid.*, **113**, 1117 (1966) and B. E. Conway, *ibid.*, **113**, 1118 (1966).

Split-Ring Disk Study of the Anodic Processes at a Copper Electrode in Alkaline Solution

B. Miller*

Bell Telephone Laboratories, Incorporated, Murray Hill, New Jersey

ABSTRACT

The anodic oxidation of copper in hydroxide solutions has been reexamined with the rotating ring and split-ring disk techniques. A soluble Cu(III) species has been identified in the anodic region at the onset of oxygen evolution. This species has also been generated at gold rings from disk-produced Cu(II). Passivation processes in the copper(I) and (II) oxidation regions have been analyzed by means of the corresponding ring currents.

The anodic corrosion of copper electrodes in hydroxide solutions has been variously investigated (1-12), particularly by means of galvanostatic charging curves, following Hickling and Taylor (3). Generally, two clear steps were found in the traces before oxygen was evolved, and, from the results of subsequent examinations and/or by reasonable correspondence of the measured potentials to calculated thermodynamic values, these were assigned to the electrode reactions Cu/Cu_2O and $Cu/Cu(OH)_2$ (and/or Cu/CuO). In an early work, Müller (1) concluded that a further oxidation step of copper occurred in strong base (around 0.7V *vs.* NHE in 5*N* NaOH at 12°C) to produce a higher oxide, Cu_2O_3, whose qualitative chemistry he examined.

The potential of the CuO/Cu_2O_3 couple was further measured at a platinum electrode in various hydroxide normalities by Delhez (13) at 0°C, yielding a value of 0.81V *vs.* NHE at *p*H 14. The low temperature chosen for this study is indicative of the aqueous instability of the higher oxidation state; using a solubility product prediction (14), Delhez calculated a potential for Cu^{+3}/Cu^{+2} of about 2.3V. In highly concentrated base, 13-16.8*N* NaOH, solutions of Cu(II) have yielded at Pt anodes deposits of the sodium salt of the Cu(III) anion at moderate current efficiencies (15, 16). A chemistry of Cu(III) complexes from oxidations in basic solution has been known for some time (17).

Citations of the involvement of higher oxidation states in the direct electrochemical studies (1-12) have, however, been few. For example, Ohse (7) suggested the formation of higher oxides on the basis of the potential transients he observed in cathodically current-pulsing previously anodized copper. Shams El Din and Abd El Wahab (8) found that a new step appeared on cycling copper electrodes galvanostatically (alternate full anodic and cathodic charging) and attributed this to a soluble Cu(II) product. They concluded that this material was oxidized to a film, suggested as Cu_2O_3, on which oxygen evolution then proceeded. A potential step in the subsequent cathodic current stage and the slow open-circuit decay of the copper potential from oxygen evolution levels provided the evidence for the higher oxide actually being formed since it does not appear separately from oxygen evolution in the anodic half cycle. The latter fact is apparent from the charging current studies of most workers in the 0.1-1.0M OH^- range; the anodization of a clean copper surface does not lead to a readily distinguishable step between the Cu(II) and O_2 evolution processes. On a sintered powder electrode a further step was cited (11), but attributed to "peroxide" processes. The chemical and magnetic behavior of the compounds produced by oxidation (17) is, however, in keeping with a Cu(III) formulation.

Direct observation by electrochemical current-potential measurements has not clearly settled the issue of whether the Cu(III) species is formed before or along with oxygen evolution in the more dilute alkali solutions. Both chemical and anodic oxidation of Cu(II) in concentrated base suggest that it is produced, but the detection of such processes by purely electrochemical techniques at copper anodes has been inferential because of the oxygen interference. A different approach, as exemplified by the rotating ring-disk and split-ring disk methodology applied to anodic corrosion processes at a disk (18, 19) appeared desirable. The disk, taken alone, yields results comparable to those referred to above on single electrodes. However, the use of the annular ring, detecting products transported from the disk (20-22), offers the possibility of simultaneously characterizing solubilized species, even those of relatively short lifetime ($\sim 10^{-2}$ sec). Ring currents or split-ring current ratios may be used to determine electrons transferred (18, 19).

In the present work, the transitions of a copper surface on anodization in alkali have been reexamined for the purpose of identifying the oxidation states produced and characterizing the passivation processes in each stage. Even where the transitions involve the formation of films, the ring amperometric sensitivity is sufficient to detect the soluble portion and to characterize its oxidation state by a proper combination of split-ring reactions. For example, in the case of a supposed Cu(III) species, the observation of two different reduction steps to known lower states, taking care to avoid or compensate for the ring reduction of concurrently generated oxygen, confirms the oxidation state. The oxidation behavior of anodically generated Cu(II) at noble metal rings, compared to the behavior of saturated solutions of Cu(II), supplements results from Cu(III) generation at the disk. Ring-disk conclusions on oxidation states are based on amperometric results on the electrode and the contacting solution and do not require comparison to thermodynamically calculated potentials or subsequent examination of the passive films by chemical or physical methods. In addition, the well-understood collection efficiency properties of the system (23) make feasible the quantitative determination of the electrode-solution mass distribution.

Experimental

The electrode employed was a copper disk-gold split-ring design fabricated with 99.99% copper according to procedures described elsewhere (18, 19, 24). A similar electrode with a gold disk was used to examine possible solution impurity reactions and the interference due to oxygen at ring or disk. The electrodes were polished, using 0.3μ Linde A as the final stage. Both electrodes had nominally the same dimensions, with disk, internal ring, and external ring diameters of 0.476, 0.524, and 0.642 cm, respectively. For such geometry with a conventional continuous ring, the theoretical collection efficiency, N, is 0.34 (23). The individual half-rings therefore have values (N_1 and N_2) of about 0.165, taking into account an approximate 1-2% loss

* Electrochemical Society Active Member.

of active area in the insulating ring divisions. The mechanical drive assembly (24), operating circuitry (18), and cell configuration (19) are described elsewhere. Solutions were prepared from reagent grade sodium hydroxide and showed a satisfactory absence of impurity reactions over the potential range and current sensitivities employed.

Results

The behavior of a stationary copper electrode in a controlled-potential sweep at 20 mV/sec in 1*N* NaOH is shown in Fig. 1. The first anodic peak is very much smaller than the second (by a factor of about 25). Depending on the sweep rate and cycling history, a third inflection is observed on the rise into oxygen evolution at about +0.5V *vs.* SCE and, on reversal of the sweep, a small net cathodic peak can be observed at the high potential end. The inflection, but not the net cathodic peak, is normally detectable when the electrode is rotated at speeds typical of the measurements to be cited later (600-3000 rpm).

At the current density necessary to polarize the electrode beyond 0V *vs.* SCE in a galvanostatic experiment, any process occurring in the region of oxygen evolution to the extent shown by the inflection in Fig. 1 would be obscured. On the other hand, low current reduction or open-circuit decay experiments, such as those cited earlier, would more readily detect a transition corresponding to the high potential cathodic process shown in Fig. 1.

With the copper disk rotated at 1000 rpm, the addition of potentiostated gold half-rings to the experiment produces the results shown in Fig. 2 for three ring potentials. The typical rotating disk current-potential trace corresponding to Fig. 1 is shown at the top with the three transitions of interest labeled I, II, and III. The lower traces represent a collection of half-ring currents *vs.* disk potential for runs in which a pair of such traces with different half-ring potentials was obtained in each experiment. For a half-ring held just positive of the first two disk transitions (0.00V), anodic ring current (a) is seen for I and only residual current for II. At the point of oxygen evolution, labeled III, a cathodic peak (b) is seen which is absent in blank experiments with an all-gold system and which is therefore not due to oxygen reduction. This peak is still observed at positive ring potentials of several tenths of a volt. When the half-ring is held at a high positive potential (0.55V) corresponding to the beginning of oxygen evolution, anodic ring currents (c) and (d) are seen for both disk peaks. At the other extreme, when the half-ring is held sufficiently negative (−0.90V) to reduce all copper species back to metal and oxygen to hydroxyl ions, cathodic ring currents (e) and (f) are seen for the two disk peaks. The first, (e), is not apparent at the reduced gain necessary to have (f) on scale in Fig. 2 since it is of the same magnitude as (a) which is shown on a 100× more sensitive axis. The reduction of oxygen at the −0.90V half-ring obscures any other concurrent process at the right end of the trace.

The qualitative conclusions about the ring processes consistent with the above experiments are:

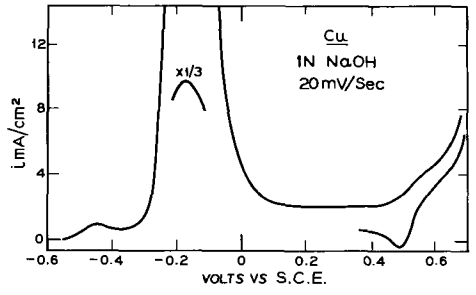

Fig. 1. Potentiodynamic sweep of a stationary copper electrode from −0.55V to oxygen evolution, then reversal to +0.35V.

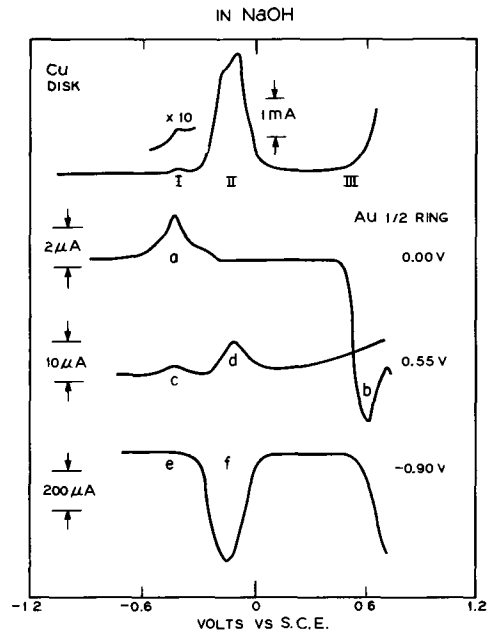

Fig. 2. Traces from top: 1, potentiodynamic sweep of copper disk in 1N NaOH, disk potential axis common to all traces; gold half-rings held at indicated potentials during disk sweeps; 2, 0.00V; 3, +0.55V; 4, −0.90V.

a,	Cu(I)	→ Cu(II)
b,	Cu(III)	→ Cu(II)
c,	Cu(I)	→ Cu(III)
d,	Cu(II)	→ Cu(III)
e,	Cu(I)	→ Cu(O)
f,	Cu(II)	→ Cu(O)

The remainder of the results to be presented is divided into two parts. The first deals with the confirmation of the above identification of species and with the measurement of the electrode-solution mass distribution in disk transitions I and II by means of the ring processes (a, e, and f). The second summarizes further evidence for the presence of a Cu(III) species and treats the current-potential characteristics of the Cu(II)-Cu(III) couple in 1*N* NaOH.

Anodic transitions I and II.—Experimentally, in a disk-ring amperometric study of a film-controlled electrode-solution mass distribution, the passive-active transitions are more readily analyzed if a constant disk anodization current is used to control the coulombs passed than if the potential is swept. This corresponds here to passivating transition I and returning to active dissolution in the rising portion of transition II where a much larger charge is required to polarize the electrode beyond the 0.0V *vs.* SCE region. Such an experiment, starting with a disk cathodically stripped immediately before anodization, is shown in Fig. 3 in which the bottom trace is the disk potential, E_d, *vs.* time at 280 μA/cm^2 (i_d = 50 μA) and the two potential plateaus (−0.49 and −0.35V) correspond to transitions I and II, respectively. The upper trace is the current, i_{r-}, through shorted half-rings operated at −0.8V, where all soluble copper species are reduced to metal, corresponding to reactions e and f. The calculated collection efficiency for the shorted half-rings is 0.33. Thus, for 50 μA i_d, the calculated current for a ring reaction which is the reverse of that at the disk is 16.5 μA, and this is the value obtained at the −0.35V plateau of II. Beyond the time scale of the trace, both i_{r-} and E_d are unchanging; currents approaching 2000 μA are required to initiate filming (see disk current peak height in Fig. 2).

If the experiment is run with shorted half-rings set at +0.3V (equivalent to *a*), the traces of Fig. 4 are obtained. Ring current is obtained only for I and is of less than 5 μA peak, the same order of magnitude as

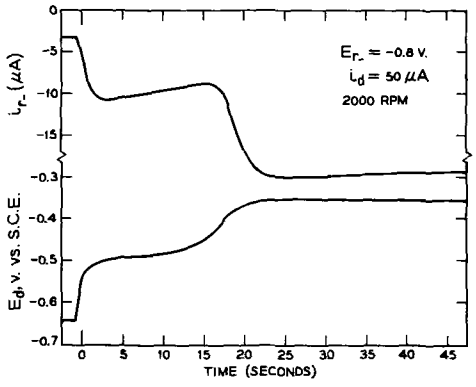

Fig. 3. Constant current anodization of Cu disk in 1N NaOH with shorted half-rings held at —0.8V. Lower trace, disk potential; upper trace, cathodic ring current.

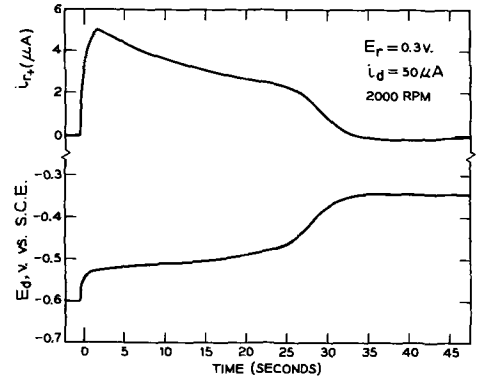

Fig. 4. As in Fig. 3, with shorted half-rings held at +0.3V. Lower trace, disk potential; upper trace, anodic ring current.

the cathodic ring maximum on the initial anodization in Fig. 3. The disk transition times for repeated constant currents are variable and depend on cycling history and initial polishing. However, the measurements which yield collection efficiencies by reflecting geometric areas, such as the cathodic ring current for II in Fig. 3, are constant and independent of the variations in the coulombs necessary to passivate I. The anodic and cathodic ring currents corresponding to I are also slightly variable, introducing some uncertainty in determining the anodic to cathodic ring current ratios so as to identify the species in the product flux. To avoid this difficulty, the split-ring experiment was run as shown in Fig. 5. The major feature is that the half-ring traces are mirror images of each other until the disk reaction II begins to contribute, at which point the cathodic half-ring current rises to that calculated from collection efficiency while the anodic half-ring current drops to the residual level. The product of I must be Cu(I) which is one-electron oxidizable and

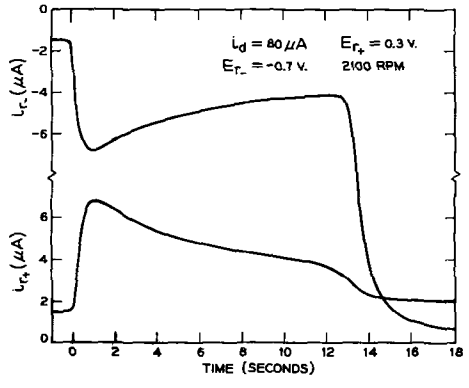

Fig. 5. Split ring anodic (i_{r+}) and cathodic (i_{r-}) limiting currents for 448 μA/cm² copper anodization in 1N NaOH.

reducible to Cu(II) and Cu(O), respectively. The Cu(I) flux never reaches the theoretical value predicted by the collection efficiency, indicating film formation, presumably Cu_2O. As soon as the double layer charging portion of the i-t plot is complete and copper current flows, the current declines from the peak, which is offset from zero time mainly by the cumulative effects of double layer capacity and the transit time from disk to ring.

Using only the data of any of the split-ring experiments as in Fig. 5, it is possible to compute additional features of the anodization process I. The product oxidation state identity has already been established above by the mirror symmetry. The cathodic ring current for II gives the electrode (geometric) collection efficiency. The time for the transition I, t_I, is given by the inflections of both traces at the 13 second region. The total coulombs at the disk for I is $i_d t_I$. For complete solubility and ring reaction involving the same number of electrons as the disk reaction producing the ring reactant, the theoretical current-time integrals at the half-rings would be $n_- i_d t_I$ and $n_+ i_d t_I$, where n_- and n_+ are the geometric collection efficiencies of the half-rings being used as cathode and anode. Thus, the fractions of disk coulombs resulting in dissolved Cu(I) and Cu_2O film are, respectively

$$\frac{\int i_{r+}\,dt}{n_+ i_d t_I} \quad \text{and} \quad 1 - \frac{\int i_{rt}\,dt}{n_+ i_d t_I}$$

all the quantities involved being controlled or measured in the single disk anodization as followed in Fig. 5. For this experiment, n_- and n_+ are 0.165, and the soluble fraction was 0.21 and the film 0.79. Conversion into a film thickness of Cu_2O using a bulk density of 6.0 g/cm³ and an electrode area of 0.178 cm² yields 57Å at the point of the disk potential polarization to reaction II.

Figures 3-5 indicate that, during constant current anodizations which would, according to the Levich equation, give Cu(I) surface concentrations of approximately 2.4-3.7 x 10^{-4}M, the measured ring peaks are actually equivalent to values of ~ 1 x 10^{-4}M. To examine whether lower disk current densities would produce Cu(I) species detectable at ring currents corresponding to the collection efficiency, *i.e.*, with no precipitation at the disk, linear anodic current scans were run as shown in the i_{r_-} and i_{r_+} *vs.* i_d traces of Fig. 6. The initial parts of the i_{r_+} and i_{r_-} traces deviate from linearity at the lowest measurable $\Delta i_r/\Delta i_d$, and no free dissolution is detectable. The region of Cu_2O formation ends at about 80 μA i_d. Free dissolution is readily seen, for example, in Ag_2O formation (25) in the same hydroxide concentration, but the solubility level of that oxide is considerably higher. The peak heights for the ring currents of Fig. 3-4 do indicate considerable supersaturations, reflecting the step current nature of the oxide formation; the maximum i_{r_+} reached in

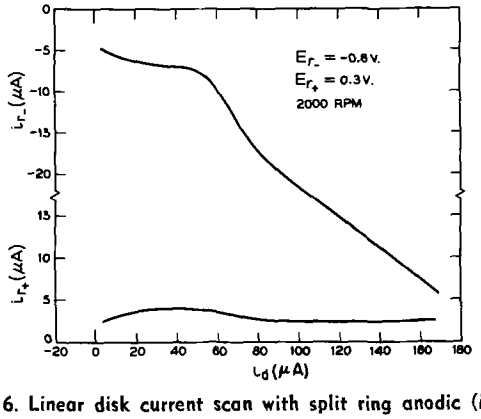

Fig. 6. Linear disk current scan with split ring anodic (i_{r+}) and cathodic (i_{r-}) limiting currents for Cu(I) → Cu(II) and Cu(I) → Cu(O) in 1N NaOH.

scans carried out as in Fig. 6 is only a fraction of the peak from the step experiment.

The transition in E_d (not shown in Fig. 6) to reaction II in the linear current scan occurs in the 70 μA i_d region. It is to be noted that when the free dissolution of the electrode occurs after this shift in reaction, the cathodic ring current *vs.* disk current trace becomes linear with a slope given by the geometric collection efficiency and with an extrapolation back to zero disk current which passes through the residual current origin of the ring trace. The oxidation state of reaction II cannot be identified by the cathodic ring behavior alone, since this reaction is always the reverse of the disk reaction and the numbers of electrons transferred cancel in the relation $i_r = \frac{n_r}{n_d} \mathrm{N} i_d$, where n_r and n_d are the numbers of electrons involved at ring and disk, respectively. Since the one electron oxidation of Cu(I) occurs in the same potential region as process II, Cu(II) can be considered to be confirmed within these experiments. Ratio experiments involving 1 and 2 electron reductions and possibly a 1 electron oxidation were not carried out for II since they were obtained for I and III, the regions of experimentally interesting uncertainty. Although structure is seen for transition II in both the ring and disk traces during disk potential scans, the possible involvement of both $Cu(OH)_2$ and CuO cannot be determined from the solution (ring) side.

Anodic transition III.—The third transition is most easily distinguished from the oxygen evolution reaction by monitoring its product at the ring, since the effect it has on the disk current during potential scan is limited to an inflection, as in Fig. 1. Moreover, the flux seen in ring reduction back to Cu(II) decays rapidly at either constant disk potential or constant disk current and thus it is not possible to obtain a ring current-potential curve of the product by sweeping ring potential for a steady state disk condition. The process appears experimentally similar to the Cu_2O step I, where film formation and passivation at the lowest accessible currents prevent the attainment of any steady-state condition except a filmed surface from which Cu(I) solubility is practically undetectable. Accordingly, the identification of the disk-produced species in III was approached by examining the peak ring or split-ring currents at various fixed ring potentials during successive disk polarizations.

After cycling the disk electrode several times, the peak ring currents at a given ring potential were found to be reproducible. The half-ring currents at different half-ring potentials during a typical charging of the disk into oxygen evolution are shown in the left oscilloscope picture of Fig. 7. The disk electrode was initially carried into oxygen evolution at a constant current ($> \sim 2$ mA) sufficient to passivate transition II. It was then allowed to decay on open circuit to a potential just above that at which it would depassivate and then charged back into oxygen evolution (E_d axis of Fig. 7) at a very much smaller current (100 μA). For E_r + 0.2V the half-ring current trace shows a cathodic peak, whereas the −0.6V cathodic half-ring current is still rising at that point. At the more positive potential oxygen reduction does not interfere, but at −0.6V it certainly does, as noted in blank studies with the all gold electrode and confirmed by the fact that the −0.6V half-ring current continues to increase while the +0.2V half-ring current drops as the copper species is passivated. Thus, at the E_d corresponding to the peak of the +0.2V trace, the ratio $i_{r-0.6}/i_{r+0.2}$ is 3.3, and for the same kind of experiment, $i_{r-0.8}/i_{r+0.2}$ is 3.8. For the traces shown, the quantity $\Delta i_{r-0.6}/\Delta i_{r+0.2}$ is 2.8 for the straight lines found between E_d of 0.56-0.58V. As will be shown, +0.2V is just negative enough to give a limiting current for product reduction to Cu(II). Therefore, at potentials of −0.6 to −0.8V where reduction to Cu(O) should be at a limiting current, the

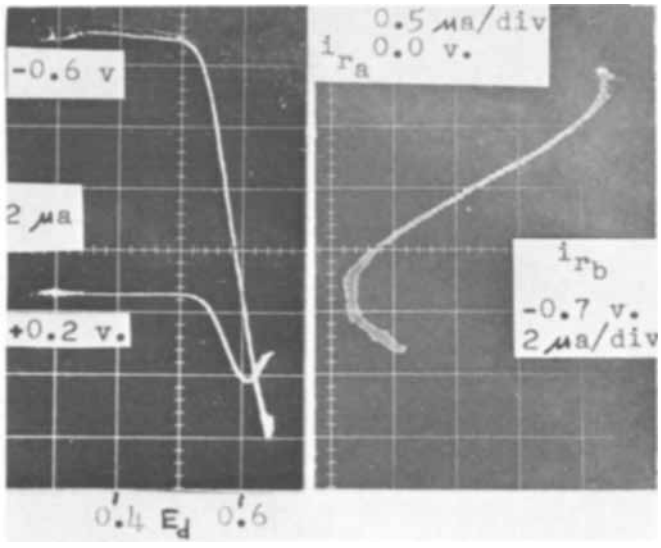

Fig. 7. Left side, split ring currents at −0.6 and +0.2V for 100 μA polarization of the disk to the positive potentials indicated; 1000 rpm in 1*N* NaOH; right side, same conditions as left side except split ring currents at 0.0 and −0.7V are plotted against each other.

contribution from oxygen makes the nominal three electron (Cu(III) → Cu(O)) to one electron (Cu(III) → Cu(II)) ratio greater than 3, especially for measurements made at the more positive disk potentials.

The same type of experiment is conducted in the right-hand portion of Fig. 7, with one half-ring current plotted *vs.* the other to improve the readability of data requiring simultaneous measure of the currents. For repeated experiments with one ring at 0.0-0.2V and the more cathodic ring at −0.7V, the slope of the linear region is 3.0 ± 0.5, the reproducibility being limited by the variable oxygen interference during the reduction of Cu(III) and the transient nature of the process. The same considerations also hold for experiments carried out by sweeping the disk potential and measuring ring current peak heights as at b, Fig. 2, for various ring potentials, where the ring currents can be made larger than in the above galvanostatic modes.

These factors make the assignment of the oxidation state as Cu(III) less certain than that for Cu(I), because in the latter case the ring reactions are free from competitive processes. A current-potential curve for the III → II reaction, if the III → II assignment is accepted, is, however, more readily derived from the galvanostatic or potentiodynamic sweep experiments described than the qualitative identification, since the relevant ring potentials are all positive of oxygen reduction.

Peak d in the survey of Fig. 2 is attributed to the oxidation reaction Cu(II) → Cu(III). Accordingly, ring current-potential curves were also obtained in the anodic direction, taking into account the oxygen evolution at the ring. The individual experimental results yielding the points used to extract the current-potential curves are next summarized and the derived behavior for the Cu(II) ⇆ Cu(III) couple then presented.

Ring oxidations.—In a saturated solution of $Cu(OH)_2$ or CuO in 1*N* NaOH, it is difficult to distinguish the oxidation wave before oxygen evolution from a blank experiment. However, the i_d peak in transition II represents a high level of supersaturation, and current levels near this value and comparably high surface concentrations of Cu(II) can be maintained at a steady state at a rotating disk. Thus, with a galvanostated disk, controlled potential sweeps of the ring may be made on concentrations of Cu(II) which are higher than those of a saturated solution by the ratio of the steady-state anodic disk current obtainable at a given rotation speed to that of a disk with a Cu(II) film (0.1

$< E_d <$ 0.4). Controlled potential ring scans from +0.4 to 0.7V, first with an open-circuited disk and then with a constant disk current about 75% of the peak transition II, are given in Fig. 8. The current-potential curve for Cu(II) → Cu(III) may be obtained by subtraction. Such a subtraction technique using a bulk saturated solution would involve differences near the experimental reproducibility, considering also that the "blank" (equivalent to i_d = 0, Fig. 8) would have to be obtained on a different solution, copper-free.

Oxidation data may be obtained, as mentioned above, by experiments yielding peak d, Fig. 2. For a 2.5M NaOH solution, in which the peak currents for transition II are approximately three times those in 1M hydroxide, some of the actual experimental traces and the point-by-point derived i-E curve are shown in Fig. 9. Two pairs of oscilloscope traces are shown, the lower of each being the disk current, whose broad peak's reproducibility is indicated by comparison of the two runs on the cycled disk. The lower ring trace gives a 0.50V E_r point on the plot; the upper ring trace, for which the residual level of oxygen evolution begins to become substantial, is at 0.70V, close to or at the limiting current region. The current-scale sensitivity ratios are 30:1 for the shorted half-rings and disk in the oscilloscope traces of Fig. 9, and it is obvious from both Fig. 8 and Fig. 9 that the collection efficiency, even accounting for a one-electron ring reaction and a two-electron disk reaction, is well below the geometric value. For example, the limiting i_r in Fig. 9 is about 0.50 mA and the disk current 9 mA, giving a collection efficiency of 2(0.5/9) = 0.11 *vs.* the 0.33 known for the electrode. The origin of the loss cannot be specified precisely. There are many possible sources of complication: for example, surface instability of Cu(III) and alteration of the anodic properties of the ring. The latter can also be affected by the possible deposition of oxide on the ring surface from the supersaturated flux of Cu(II) from the disk. There appears to be no simple relation of the ring-disk process to rotation speed, and this indicates multiple complications. However, the potential dependence of the ring current is reproducible, and, as will be seen, the independently determined oxidation and reduction currents at the ring have a sensible relation.

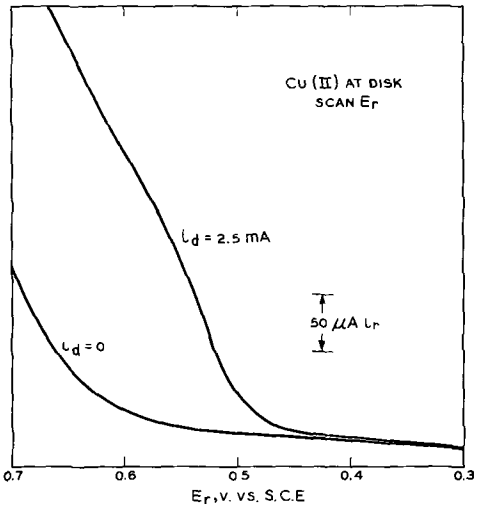

Fig. 8. Ring current-potential curves obtained by 20 mV/sec ring scan at constant disk currents in transition II region. Blank (zero disk current) scans for the 1N NaOH 1500 rpm conditions also shown.

Ring reductions.—The reduction curves were obtained by sweeping the disk potential at a fixed ring potential and by anodizing the disk at constant current with fixed ring potential as already described, the ring potentials being systematically changed for each scan. The family of curves derived from the latter approach (see also the left-hand traces of Fig. 7) is shown in Fig. 10. The ring potential was changed by 50 mV in successive runs at constant disk currents of 50 μA. The 50 μA current was chosen to give a disk-potential rate of change not appreciably greater in the region of interest than the scan rates suitable for disk potentiodynamic experiments. The passivation of Cu(III) generation at high disk potentials is clearly shown. The height of the reduction peak above the residual level was used to construct the current-potential curve.

Current-potential curves for Cu(III)-Cu(II) *in 1N* NaOH.—Figure 11 gives the curves derived from the disk potentiodynamic scans with fixed ring potentials in 1N NaOH solution. The upper curve is the collection of ring current reduction peaks as in b, Fig. 2, and the lower curve, the ring current oxidation peaks, as in d, Fig. 2. Treating the Fig. 11 curves as ring polarograms for the reduction and oxidation of constant fluxes of Cu(III) and Cu(II), respectively, $E_{1/2}$ values of +0.45 and +0.54V *vs.* SCE at 24°C are obtained.

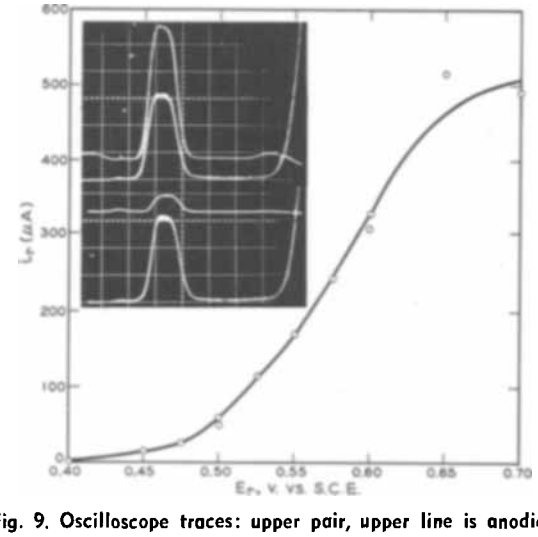

Fig. 9. Oscilloscope traces: upper pair, upper line is anodic ring current at +0.70V vs. disk potential during sweep through transition II to oxygen evolution, as shown in lower disk current line, rotation speed 1000 rpm; lower pair, identical experiment, upper line ring current at +0.50V. Plot, ring current peaks from oscilloscope traces as shown in insert plotted vs. ring potential.

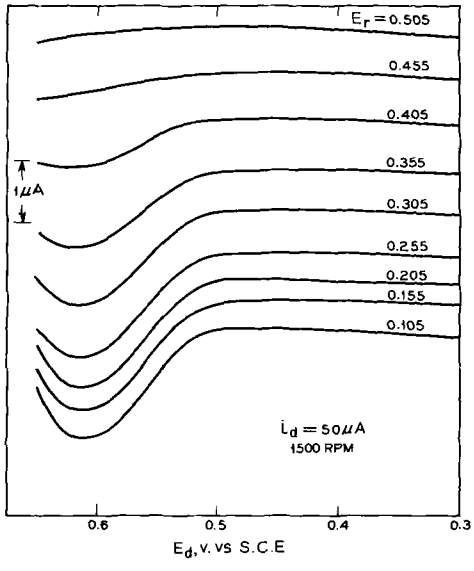

Fig. 10. Series of 280 μA/cm² constant current anodizations of the disk after zero current decays from oxygen evolution; ring currents plotted vs. disk potential for 9 constant ring potentials in 1N NaOH.

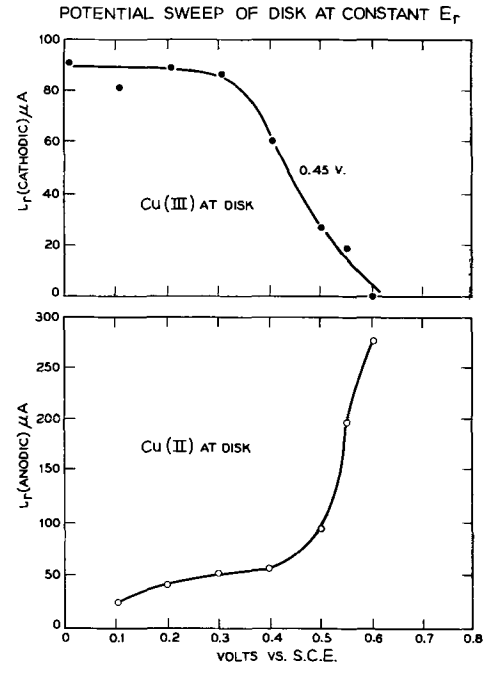

Fig. 11. Upper plot, peak cathodic currents at ring during transition III of disk potential sweep plotted against fixed ring potentials; 20 mV/sec sweep at disk, 600 rpm in 1*N* NaOH; lower plot, peak anodic currents at ring during transition II.

For the galvanostatically controlled disk, Fig. 8 and 10, the curves derived are shown in Fig. 12. $E_{1/2}$ values for reduction and oxidation are +0.40 and +0.56V *vs.* SCE, respectively. These and the values from Fig. 11 are in reasonable congruence with the value obtained potentiometrically by Delhez (13), approximately 0.48V on the present SCE scale at the lower temperature (0°C) required for stability of the Cu(III) oxide phase. In the best-defined current-potential curves, the value of $E_{3/4}$-$E_{1/4}$ is about 70-85 mV compared to the reversible 56 mV. Further speculation about kinetic parameters is not warranted by the nature of the data, accessible, as they are, only by transient or difference techniques.

Summary and Discussion

The oxidation states and corresponding electrode/solution mass distributions have been measured for the anodization of copper in 1*N* NaOH utilizing the split-ring disk technique. By means of the split-ring limiting current ratio approach, it has been possible to identify species in nonsteady reactions at the disk, a passivating surface. Successive one-electron stages have been identified, with the first and third involving film formation from their onset, while the second, or Cu(II) stage, is a solution precipitation process with a considerable range of active dissolution.

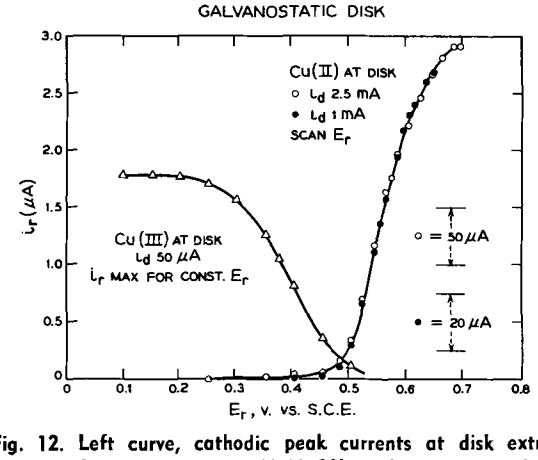

Fig. 12. Left curve, cathodic peak currents at disk extracted from Fig. 10 experiments in 1*N* NaOH; right curve; anodic ring currents from Fig. 8-type experiments representing ring current-potential curve for stated disk current corrected for blank (i_d=0) curve.

The data from a single split ring-disk anodization involving initial disk Cu_2O formation and subsequent reactivation of the electrode on polarization to Cu^{+2}-OH^- complex generation yield a variety of information. The oxidation states are identified, the passivating film thickness and the material solubilized are determined, and the time-dependence of this mass distribution between electrode and solution is measured. Cu_2O films form to a thickness of about 60Å under the anodization conditions studied, with no prefilm free dissolution detectable at the sensitivities accessible.

The high levels of supersaturation found for Cu(II) in the second stage of anodization make it possible to examine, at the ring, steady-state concentrations that could only be reached at much higher hydroxide levels under normal equilibrium conditions. This makes it possible to see the oxidation of Cu(II) distinguished from the residual level of oxygen evolution at a gold ring. Four combinations of current or potential-sweep control at the disk with static or swept potentials at the ring have yielded representative anodic and cathodic current-potential curves for the Cu(II)-Cu(III) couple. These ring-disk techniques for the identification of species and the quantitative measure of interfacial material balance appear widely applicable in the study of corrosion processes where generated species may have relatively short lifetimes in the bulk solution or passivation processes are concurrent.

Manuscript submitted May 12, 1969; revised manuscript received *ca.* July 31, 1969. This was Paper 57 presented at the Chicago Meeting, Oct. 15-19, 1967.

Any discussion of this paper will appear in a Discussion Section to be published in the June 1970 JOURNAL.

REFERENCES

1. E. Müller, *Z. Elektrochem.*, **13,** 133 (1907).
2. W. Feitknecht and H. V. Lenel, *Helv. Chim. Acta,* **27,** 775 (1944).
3. A. Hickling and D. Taylor, *Trans. Faraday Soc.,* **44,** 262 (1948).
4. S. E. S. El Wakkad and S. H. Emara, *J. Chem. Soc.,* **1953,** 3508.
5. J. S. Halliday, *Trans. Faraday Soc.,* **50,** 171 (1954).
6. F. Bouillon, J. Piron, and J. Stevens, *Bull. Soc. Chim. Belg.,* **67,** 643 (1958).
7. R. W. Ohse, *Z. Phys. Chem. N.F.,* **21,** 406 (1959).
8. A. M. Shams El Din and F. M. Abd El Wahab, *Electrochim. Acta* **9,** 113 (1964).
9. V. N. Flerov, *Zhur. Fiz. Khim.,* **37,** 1733 (1963).
10. A. M. Borshchevski, V. V. Skorcheletti, and T. I. Mikhaleva, *Zhur. Priklad. Khim.,* **39,** 1427 (1966).
11. V. A. Plokhov and V. N. Flerov, *ibid.,* **40,** 325 (1967).
12. M. N. Ronzhin and A. L. Golubev, *Korriziya Metal. i. Splavov,* Sb. 166 (1965); *C.A. 64,* 18954 g.
13. R. Delhez, *Bull. Soc. Roy. Sci. Liege,* **30,** 446 (1961).
14. A. F. Clifford, *J. Am. Chem. Soc.,* **79,** 5404 (1957).
15. G. Rozovskis, *Lietuvos TSR Mokslu Akad. Darbai Ser. B,* 19 (1963); C.A. **61,** 2709 f.
16. G. Rozovskis and A. Misevicius, *Lietuvos TSR Mokslu Akad. Darbai Ser. B,* 73 (1965); *C.A. 64,* 1636.
17. L. Malatesta, *Gazz Chim. Ital.,* **71,** 467, 580 (1941).
18. B. Miller, *This Journal,* **116,** 1117 (1969).
19. B. Miller and R. E. Visco, *ibid.,* **115,** 251 (1968).
20. A. N. Frumkin and L. N. Nekrasov, *Doklady Akad. Nauk. SSSR,* **126,** 115 (1959).
21. A. N. Frumkin, L. N. Nekrasov, V. Levich, and Ju. Ivanov, *J. Electroanal. Chem.,* **1,** 84 (1959).
22. L. N. Nekrasov and N. P. Berezina, *Doklady Akad. Nauk. SSSR,* **142,** 855 (1962).
23. W. J. Albery and S. Bruckenstein, *Trans. Faraday Soc.,* **62,** 1920 (1966).
24. R. H. Sonner, B. Miller, and R. E. Visco, *Anal. Chem.,* **41,** 1498 (1969).
25. B. Miller, Paper 291 presented at the Montreal Meeting of the Society, Oct. 6-11, 1968.

Multilayer Oxide Films on Anodized Platinum

S. D. James*

Electrochemistry Division, Chemistry Research Department,
U. S. Naval Ordnance Laboratory, White Oak, Maryland

ABSTRACT

A voltammetric study is described of conditions governing the production and stability of anodically formed bulk oxide on Pt in dilute H_2SO_4. The range of anodizing conditions covered in 1 or 2*N* H_2SO_4 was: current-density, up to 10 A/cm^2; temperature, 11°-93°C; duration, up to 18 hr. The oxidizability of the Pt anode (with respect to formation of bulk oxide) was subject to considerable hysteresis. Provided a potential of about 2.15V, RHE was exceeded, electrode oxidizability seemed to be controlled largely by the amount of strain energy present in the Pt surface. The electrolytic formation and reduction of thick bulk oxide layers effected large increases in electrode roughness factor (up to 100X or more).

Superficial, monolayer-type oxide films on platinum electrodes which have been anodized in aqueous solution are very well known although far from completely characterized. The literature on this type of film which is rapidly reduced at about 0.7V, RHE has recently received thorough reviews (1).

In addition, a number of facts indicate that, as the potential or current-density of the anodization is raised, qualitative changes occur in the nature of this film. For instance several workers (2-5) have found sharp changes of slope at about 1.8V, NHE in H_2SO_4 or $HClO_4$ for plots of Q (mC/cm^2) *vs.* E (Q is the charge required for cathodic reduction of a surface oxide formed at potential E). Schuldiner and Warner (6) have also argued for the penetration of oxygen atoms at room temperature into several monolayers of a Pt anode. By examining the chemical reducibility of platinum oxides by propane, Mayell (7) obtained evidence for a potential-dependence in the nature of the oxide. Tafel plots at a Pt anode in H_2SO_4, $HClO_4$ (8-11), and NaCl (12) show two linear portions separated by a transition region where potential increases anomalously rapidly with current. This transition is associated with the incipient participation of anions in the electrode reaction (in H_2SO_4 and $HClO_4$) caused perhaps by a qualitative change in the nature of the superficial oxide film (13). The work of Kasatkin and Rakov (11) at a Pt anode in 10*N* H_2SO_4 at −60°C is particularly interesting. At this low temperature they were able to examine the polarization curve over the large range of 2-12V, NHE (10^{-6} — 1 A/cm^2). In this voltage range they found five points in the Tafel plot where radical changes in slope occurred reflecting intense passivations. To explain these results they assume the electrode substrate to be essentially unchanged as Pt/PtO while, with increasing potential, this surface is supposed to become invaded by a phantasmagoria of no fewer than eight, progressively more oxygenated, adsorbed radicals. Many studies have shown the important influence of the state of surface oxidation on the electrode kinetics of inorganic (14) and organic (15) reactants at Pt.

Somewhat more graphic evidence for the macroscopic oxidation of Pt anodes has been accumulated in various corrosion investigations (16-28).

The purpose of the present investigation was to inquire more closely, by the voltammetric technique, into the conditions influencing the production and stability of anodically formed phase oxides.

Experimental

The platinum microelectrode under study was a 0.4 mm diameter thermocouple wire of extreme purity sealed through the side of a lead-free soda lime glass tube. Internal contact was made by a spot-welded Ni wire. The electrode was ground such that Pt and glass were flush and then polished with Fisher Polishing Alumina (40μ) to a bright finish. A photomicrograph of the electrode surface at a magnification of X340 revealed it as a planar, quite well-shaped ellipse having semi-axes of 0.0220 and 0.0178 cm (±2%) *i.e.*, an apparent area of 1.23 x 10^{-3} cm^2 (±4%). This electrode was used throughout all the work reported in this paper. For the sake of simplicity, current densities are quoted as though the area were exactly 10^{-3} cm^2, *i.e.*, true current densities are 0.81 of those reported. On the other hand, surface charge densities (mC/cm^2) reported need no such correction.

Anodizations (confined to d.c.) were done in air-saturated 1 or 2*N* H_2SO_4, at constant current in a 3-electrode system. The range of anodizing conditions covered was: current density, up to 10 A/cm^2; duration, up to 18 hr; temperature, 11°-93°C. The counter-electrode was a Pt wire, and the reference electrode was a reversible hydrogen electrode in the same solution (RHE). After anodizing, the microelectrode was rinsed with water and placed in a separate cell for voltammetric study in N_2-saturated 2*N* H_2SO_4 at 25°C. The voltammograms were obtained with a Sargent XXI polarograph employing scans from 1.00 to 0.05V, RHE, at 3 mV/sec in a 2-electrode system. The counter (and reference) electrode was again the RHE which, at the currents obtaining during the cathodic scans, was completely unpolarized. All potentials are quoted *vs.* RHE on the Stockholm convention.

The use of so tiny a working electrode (10^{-3} cm^2) was very advantageous, not merely in reducing to manageable proportions the current corresponding to such high current densities but also in minimizing the associated iR drop concentrated in the solution close to the microelectrode.[1] Even so, at *e.g.*, 10 A/cm^2 in 1*N* H_2SO_4 at 25°C, $iR_c \approx 0.6$V and thus, to get a reasonably accurate idea of the working electrode's potential under these extreme conditions, the value of R_c was required with some precision. Using a General Radio impedance bridge Type 1608-A, determinations were made of the resistive component of the working electrode's impedance in roughly 2*N* H_2SO_4 ($\rho = 2.58$ ohm-cm at 25°C). This resistance, extrapolated to infinite frequency, was 30 ohms (±2). This value was then compared with that calculated from the solution resistance and the electrode dimensions, using the established formula for a constriction resistance (29). The latter quantity was 32 ohms (±1). The correct R_c in this solution was taken as 32 ohms and in other solutions it was calculated as $R_c = 12.4\rho$ (±5%). This use of a small working electrode plus the careful sub-

* Electrochemical Society Active Member.

[1] The constriction resistance R_c near a microelectrode of area A is proportional to $A^{-1/2}$ (29) while the current i corresponding to a given current-density varies directly with A. Hence the ohmic potential drop, iR_c, corresponding to a given current density, is proportional to $A^{1/2}$ and is thus ten times smaller at a 10^{-3} cm^2 than at a 10^{-1} cm^2 electrode.

Table I. Chronological series of oxide film formations on the platinum electrode

Conditions of anodic formation of oxide film								Cathodic dissolution of oxide film*					
								First oxide		Second oxide			
Time at which anodizing begun			H_2SO_4				Anodizing Potential	Peak	Redn	Peak	V	Redn	Charge
Run	Day	Hour	N	°C	A/cm²	Duration	V, RHE	V	charge	1st	2nd	Q_{2A}	Q_{2B}
Ia. Contrasting oxidizability before and after first formation of second oxide (k_9)													
k_7	June 14	1415	1	25	10	15 min	2.59 to 2.86	0.65	1.3				
k_8	June 14	1612	2	25	10	73 min	3.16 to 3.35	0.63	1.9				
k_9	June 14	1745	1	25	1	16.7 hrs	to 2.29	0.60	5.5		0.16		16
o_3	June 20	1130	1	25	10	5 min	2.20 to 2.15	0.58	5.0		0.22		2.4
Ib. Decay in oxidizability after u_5 (curve A of Fig. 1)													
u_4	June 26	1249	2	25	10	5 min	2.68 to 2.91	0.65	2.0				
u_5	June 26	1319	2	93	10	63 min		0.57	2.3	0.32	0.19	2.4	11.2
u_6	June 26	1444	2	25	10	1 min		0.63	5.6	0.34	0.24	2.0	3.5
u_7	June 26	1459	2	25	10	1 min		0.66	5.6		0.23		1.5
u_8	June 26	1513	2	25	10	1 min		0.62	4.5		0.22		0.4
u_9	June 26	1552	2	25	10	1 min		0.62	4.5		0.23		0.2
Ic. Decay in oxidizability after u_{10} (curve B of Fig. 1)													
u_{10}	June 26	1740	2	93	1	17.9 hrs		0.52	9.9	0.33	0.18	11	29
v_1	June 27	1224	2	27	10	1 min	2.36 to 2.33	0.59	15.5	0.27		3.6	
v_2	June 27	1341	2	27	10	1 min	2.36 to 2.40	0.60	11.6	0.23		1.3	
v_3	June 27	1358	2	27	10	5 min		0.60	9.4	0.32		6.3	
v_4	June 27	1411	2	27	10	5 min		0.61	8.1	0.40		1.9	
v_5	June 27	1430	2	27	10	5 min		0.61	6.4	0.40		0.8	

* Voltammograms at 3 mV/sec in 2N H_2SO_4 at 25°C. Redn charges are mC per cm² of apparent area.

traction of ohmic potential drops made it possible to exceed the current densities of Shibata (31) and Kozawa (35) by nearly 100 fold (*vide infra*) and still know the electrode potential with fair accuracy. Neither of these authors quoted his anodization potentials.

The charge, Q, corresponding to reduction of an anodically formed film was gotten from the area under the appropriate peak in the cathodic voltammogram using that at the prereduced electrode as a base-line. The area was derived from weighing tracing paper scissored to duplicate the peak. Charges are quoted as mC/cm² of apparent area unless otherwise stated.

Results and Discussion

The voltammetric identification of phase oxides on anodically pretreated Pt appears to have begun with some experiments of Obrucheva and Nesterova mentioned by Ershler (30). They found two clear-cut arrests, at 0.7 and 0.4V, RHE, in cathodic chronopotentiograms on smooth Pt in N H_2SO_4 after preanodization at 0.1 A/cm², but only the usual 0.7V arrest after anodizing at 0.001 A/cm². They described the second, 0.4V arrest as displaying all the characteristic properties of a phase transition and attributed it to the reduction of a phase oxide. This type of study was continued by Shibata (31) who, after constant current (0.1 A/cm²) anodization in N H_2SO_4 at 25°C, inspected his oxidized electrodes chronopotentiometrically in N_2-saturated H_2SO_4. His cathodic curves displayed two well-defined arrests. The first, at about 0.6V, NHE, corresponded to a surface charge of about 4 mC/cm² and was certainly due to the reduction of the monolayer-type oxide film. Similarly, high charges have been observed previously at this potential (2, 32). The second arrest at 0.3V, NHE, lengthened with duration of the preanodization (after an induction period of about 30 min) and was 36 mC/cm² for an electrode which had been preanodized at 0.1 A/cm² for 28 hr. The only arrest previously described in the literature at this potential is that caused by monolayer hydrogen adsorption, accounting on smooth Pt for 0.5 mC/cm² at the most (33). The charge $i\tau$, for the second arrest was independent of cathodic i over at least 10 to 600 μA/cm² (34), and this arrest thus arises in a surface film of some kind. Even allowing a roughness factor of 2.5 (33) a film equivalent to 36 mC/cm² corresponds to associating at least 30 oxygen atoms with each surface Pt (2). By no possible stretching of the Pt atom oxidation number can a film of this kind be visualized as a superficial monolayer. In fact Shibata (34) later studied these films by an electron diffraction technique and concluded they were a PtO_2 phase oxide. Shibata's study of this low-potential arrest during the reduction of Pt electrodes subjected to excessive prior anodization was extended by Kozawa. After constant current anodization in 1N H_2SO_4, Kozawa recorded voltammograms in N_2-saturated 1N H_2SO_4 from 0.9 to 0.0V, NHE (35). As well as the normal cathodic peak at 0.6V, he got a second peak at 0.2V the height of which increased with the duration, current density, and temperature of the anodic pretreatment. As in Shibata's experiments, the charge corresponding to this low-potential peak, under extreme conditions, greatly exceeded that of the first peak. In Kozawa's anodizations, the upper extremities of his parametric variations were: current-density, 0.3 A/cm²; duration, 30 min; temperature, 50°C. No second cathodic peak was obtained after anodizing under similar conditions in N NaOH. Films corresponding to about 10 mC/cm² have been reported on Pt anodized in M KOH, in a somewhat obscurely presented Russian paper (36). Other voltammetric studies where phase oxides were certainly involved include those of Fleischmann *et al.* (5) and Nagel and Dietz (22).

In the present work, symbols Q_1 and Q_2 correspond to the charges involved in the voltammetric reduction of the two main films formed by the preanodization. Q_1, associated with the 0.6V peak, is due to the film formed in brief, relatively mild anodizations. This film, which will be termed the first or monolayer oxide, has been the object of most previous experimentation.

Q_2, derived from the peak at about 0.2V, is due to a film that appears only after more vigorous anodization. This film is referred to as the second or phase oxide. Under certain conditions, especially after prolonged and intense preanodization, the Q_2 peak splits and a peak at about 0.3V begins to appear. The corresponding Q's of the forked second peak are designated as Q_{2A} (0.3V) and Q_{2B} (0.2V).[2]

Hysteresis in Oxidizability (Second Oxide)

At the outset of the present work, an attempt was made to duplicate in outline the results of Kozawa (35) and Shibata (31) in dilute H_2SO_4 (1 or 2N) at 25°C. This initial attempt was strikingly unsuccessful. In spite of anodizing for much longer periods and at much higher current-densities than these workers used, the subsequent voltammograms exhibited only the usual 0.6V, first oxide peak. The most intense anodizations employed in this initial effort were those described in Table Ia as runs k_7 and k_8 at 10 A/cm²

[2] In considering the magnitude of these Q's it may be helpful to note that, if the film is a monolayer of platinum oxide, the electrode roughness factor must be $R \approx Q/0.2n$ where Q = surface charge in mC/apparent cm² and n = number of electrons withdrawn from each surface Pt during oxidation. This equation derives from an average value of 1.2×10^{15} Pt at./cm² for the three major planes of the face-centered cubic Pt lattice (2). Thus Q = 1.6 mC/cm² corresponds to R = 2 or 4 for monolayers of PtO_2 (n = 4) or PtO (n = 2) respectively.

in 1 and 2*N* H_2SO_4, respectively. In these runs, current densities greater by nearly two orders of magnitude than those successfully used by Shibata and Kozawa were fruitless, *i.e.*, $Q_2 = 0$. At this relatively early stage of the electrode's history, Q_1 was about 1.6 mC/cm^2, corresponding to a roughness factor of 2 to 4.[2] Finally, second oxide formation was obtained in run k_9 after an extremely prolonged (17 hr) anodization at 25°C in 1*N* H_2SO_4 at a potential of 2.29V, RHE. After this treatment the cathodic scan showed a sharp second peak at 0.16V with $Q_2 = 16$ mC/cm^2. In general it was found that Q_2 increased with the duration, current density, and temperature of the anodic pretreatment in agreement with Kozawa's data (35).

After the second oxide had once been formed on the electrode, it became relatively much easier to make it again. This sharply contrasting oxidizability before and after the successful run k_9 is shown in Table Ia. Before k_9, the extremely intense anodization of k_8, where the anode potential was maintained for 73 min between 3.16 and 3.35V, RHE, was fruitless. After k_9, the much milder treatment of o_2, where the potential was between 2.20 and 2.15V for only 5 min, gave a sharp second peak in the cathodic voltammogram with $Q_2 = 2.4$ mC/cm^2. Apart from the great hysteresis in oxidizability evident in Table Ia, it is obvious that the magnitude of the anode potential, provided it exceeds a certain minimum value of about 2.15V, RHE, has a relatively minor influence on second oxide formation. A hysteresis in the anodic oxidizability of Pt was briefly alluded to by Nagel and Dietz (22). They noted that during a sequence of electrolytic oxidations and reductions the anodizing time required to form a brown layer of phase oxide fell from 15 hr to 1 hr and ascribed this behavior to a gradual loosening ("Auflockerung") of the metal surface.

A pronounced hysteresis or effect of recent past history on electrode oxidizability was evident throughout the present work and introduced a strong element of irreproducibility into the data. In general, the easy formation of second oxide at the Pt electrode was favored if a thick layer of second oxide had recently been reduced to metal at this electrode. This activating effect for the anodic growth of the phase oxide was unstable and decayed at rates which varied widely according to experimental conditions. Two examples of this decay are shown in Fig. 1. The conditions applicable to these experiments are detailed in Table Ib (refers to curve A of Fig. 1) and Ic (curve B of Fig. 1). Electrode oxidizability was measured as the amount, Q_2, of second oxide formed during brief (1 or 5 min) test-anodizations in 2*N* H_2SO_4 at 25°C and 10 A/cm^2. Both the test-anodizations and the intervening periods of open-circuit storage were conducted in the same N_2-saturated 2*N* H_2SO_4 at 25°C. The time-zero of curves A and B coincides with the cathodic reduction of phase oxides equivalent to 14 mC/cm^2 (run u_5) and 40 mC/cm^2 (run u_{10}) for A and B, respectively. Halfway through curve B the test-anodization was lengthened from 1 to 5 min. In both curves, electrode oxidizability fell to zero inside 3 hr, the thicker, prior oxide of curve B being associated with an appreciably more lasting oxidizability. The procedure of characterizing electrode behavior with test-anodizations (and their associated cathodic voltammograms between 1.00 and 0.05V, RHE) seemed itself to hasten the decline in oxidizability. In one case, oxidizability survived for 48 hr in N_2-saturated 2*N* H_2SO_4 at 25°C and about 0.9V, RHE open-circuit potential, only to fall almost to zero in an hour under the influence of two test-anodizations. In another case, 67 hr of quiescence under similar open-circuit conditions sufficed to render the electrode quite inert even to the first test-anodization. Thus it would seem that after the reduction of a thick second oxide ($Q_2 >$ about 20 mC/cm^2) the Pt electrode, if undisturbed, remains oxidizable for two to three days. If, however, the electrode is subjected to the oxidation-reduction cycling involved in the procedure used to obtain Fig. 1, the oxidizability decays to zero in a matter of only several hours.

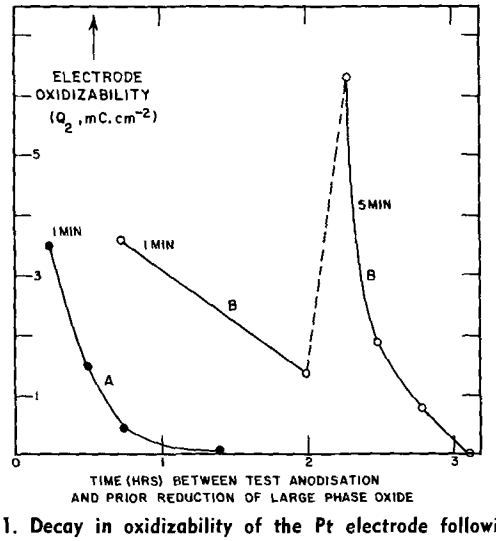

Fig. 1. Decay in oxidizability of the Pt electrode following reduction of a thick second oxide at this electrode. Q_2 is the amount of second oxide formed during brief test-anodizations at 10 A/cm^2 in 2*N* H_2SO_4 at 25°C for the labeled duration. Time zero of curves A and B was cathodic reduction of second oxides equivalent to 14 and 40 mC/cm^2, respectively.

The hysteresis in electrode oxidizability noticed in the present work was not reported in the voltammetric studies of previous workers (31, 35). An explanation of this fact and of the hysteresis itself in terms of electrode surfaces possessing varying degrees of mechanical strain can be supported by considerable evidence. Before each anodization, Kozawa (35) polished his Pt electrode with fine emery paper and rinsed it with water. This mechanical abrasion may well have introduced sufficient strain into the metal surface to act as active centers for the incipient formation of phase oxide. Shibata's pretreatments (31a) included no abrasion but just prior to anodizing, his electrodes were aged in an atmosphere of H_2 gas at 20°C for two weeks. Since Pt is subject to hydrogen embrittlement (37) Shibata's electrode surfaces also may have been significantly strained. Hence, if mechanical strain does in fact activate the Pt surface for the growth of phase oxide, it is not surprising that the oxidations of Shibata and Kozawa were both easier and more reproducible than those of the present work. This work employed no strain-producing pretreatments, and this could explain the initial failure to evoke second oxide. The first successful anodization of the present work was very prolonged (17 hr at 1 A/cm^2 in 1*N* H_2SO_4 at 25°C), and it was suggested by Schuldiner (38) that this extended period of O_2 liberation permitted considerable penetration of the Pt surface by oxygen atoms. The fact that oxygen atoms can readily reach positions below a Pt surface has been demonstrated by low-energy electron diffraction (39). Schuldiner and Warner (6, 40) have shown that such dermasorbed oxygen can strongly affect the catalytic behavior of a Pt electrode. Furthermore Hoare (41) got evidence from x-ray diffraction work, for a perceptible expansion of the lattice parameters at a Pt surface after forming a dermasorbed oxygen layer. Thus it is reasonable to suppose that the production of such a layer during extended anodization might render the electrode strained and oxidizable. It is not clear why, *e.g.*, run k_8, at 10 A/cm^2 (3.2V, RHE) for 73 min failed to activate the Pt surface since, according to Schuldiner (6) significant quantities of dermasorbed oxygen enter a Pt surface even in short anodic pulses ($\approx 10^{-3}$ sec) at potentials above 1.5V, RHE. Apparently the amount of penetration into the Pt by dermasorbed oxygen necessary to activate the surface with respect to second oxide formation is orders of magnitude greater than that acquired in short pulse

polarizations. Thus even a 73-min treatment may fail while a 17-hr treatment succeeds. From the very limited data available on the stability of dermasorbed oxygen layers on Pt electrodes (42) one would expect an oxidizability, dependent on the presence of such a layer, to persist for about two days rather than the hours illustrated in Fig. 1. However, as already stated, the imposition of test-anodizations seemed to accelerate the decline in electrode oxidizability and that of an undisturbed electrode did in fact survive for two to three days. For the persistence of oxidizability after reduction of a thick phase oxide to be due to the retention of dermasorbed oxygen for some time in surface layers, the freshly reduced Pt coating deposited during this reduction must be porous. Thus the active (containing dermasorbed oxygen) layer underneath has access to solution and is able to display its oxidizability.

There is an alternative explanation of the decay curves of Fig. 1. This again assumes the oxidizability to be caused by mechanical strain in the electrode surface but supposes this strain to arise during the reduction of the phase oxide rather than during its formation. The electrodeposition of metals is known to give catalytically active layers rich in both dislocations and point defects (43). Moreover, Piercy (44) has demonstrated that Pt can be loaded with a type of defect which anneals out at room temperature at rates not incompatible with the data of Fig. 1. Whether Pt layers electrodeposited from phase oxides under the conditions of this work could contain such defects is a moot point. That such layers are certainly different in structure from Pt black deposits obtained conventionally was shown by Shibata (34) using the electron diffraction technique. Also, for the anodic oxidation of propane, it was found that reduced PtO_2 was much more active than platinum blacks prepared by reduction from aqueous solution (49).

Structure and Stability of Anodic Films

Figure 2 shows cathodically scanned voltammograms in N_2-saturated, 2N H_2SO_4 at 25°C after the following chronological pretreatments of the Pt electrode: curve 1, prereduction in the same solution at 0.05V, RHE, *i.e.*, curve 1 shows the residual or background current; curves 2 to 6, preanodization at 93°C in 2N H_2SO_4 at 10 A/cm^2 (2.36V, RHE) for: curve 2, 5 min; 3, 30 min; 4, 1.75 hr; 5, 3.3 hr; 6, 17 hr. The splitting of the second peak, beginning in curve 4 (1.75 hr) was not observed by previous workers (31, 35) whose anodizations did not approach in severity those of the present work. Figure 3, depicting the growth of the three main films, was derived from Fig. 2 by measuring the areas under the three main peaks of this linearly scanned voltammogram to get the charges involved in forming the corresponding films. Figure 3 gives an over-all picture of film growth in a log-log plot. However, due to the successive formation and reduction of the phase oxide layers, Q_{2B}, there was a stepwise increase in electrode roughness factor, from run to run, during the experiments from which this figure is derived. In Fig. 4 an attempt was made to correct for

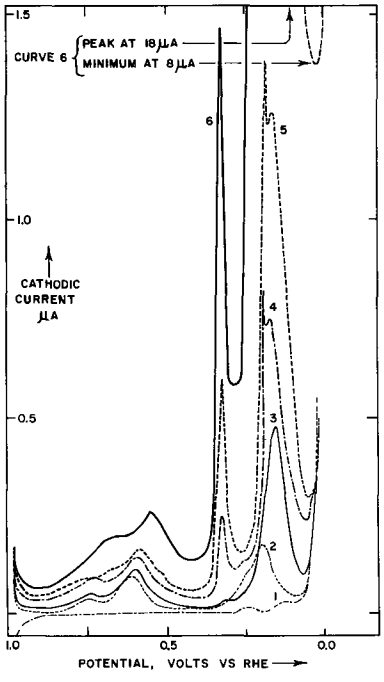

Fig. 2. Voltammetric stripping curves for the Pt electrode in N_2-saturated 2N H_2SO_4 (25°C, 3 mV/sec) after the following chronologically listed pretreatments. Curve 1, prereduction in this solution at 0.05V, RHE; curves 2 to 6, preanodization at 93°C in 2N H_2SO_4 at 10 A/cm^2 (2.36V, RHE) for: 2, 5 min; 3, 30 min; 4, 1.75 hr; 5, 3.3 hr; 6, 17 hr.

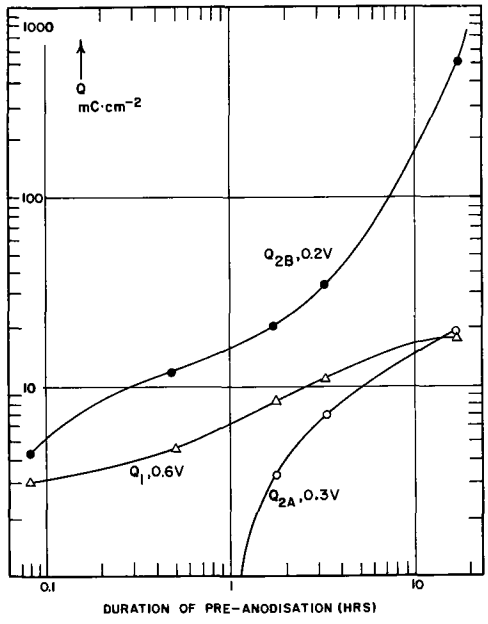

Fig. 3. Growth of anodic films on the Pt electrode vs. anodizing time. Growth curves derived from Fig. 2 are drawn for the three main peaks and labeled according to peak potential. Reduction charges Q refer to 1 cm^2 of apparent area.

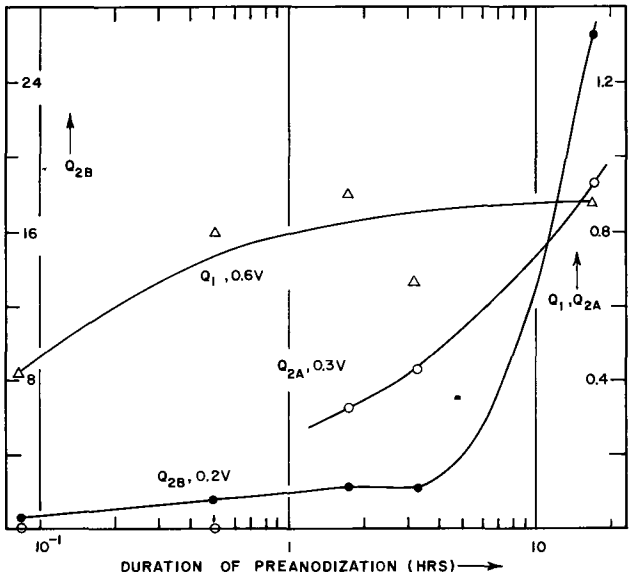

Fig. 4. Growth of anodic films on the Pt electrode vs. anodizing time. Data are those of Fig. 3 corrected for varying roughness factors, *i.e.*, reduction charges, Q, on the ordinate refer to mC/cm^2 of true area.

this varying surface area and report the Q's of Fig. 3 in terms of mC/real cm². This was done as follows. For any particular run, i, the approximate formula previously quoted,[2] *i.e.*, $R \approx Q/2n$ was applied, putting Q equal to the value of Q_1 obtained in the previous run. This gives the roughness factor appropriate to the anodization of run i. The value of R used was the average between those corresponding to monolayers of $PtO(n = 2)$ and $PtO_2(n = 4)$. Dividing the mC/apparent cm² values for run i by this value of R gives the mC/real cm² values plotted semilogarithmically in Fig. 4. The calculated values of R varied from 7.4 just before the first anodization (5 min) to 20 just before the last anodization (17 hr) of Fig. 4. Since all anodizing was done at constant current, the current density was a factor of three smaller in the last run. In spite of this variation in A/cm², the electrode potential was constant throughout this whole series of experiments (Fig. 4) at 2.36V, RHE (±0.01V).

It is evident from Fig. 3 and 4 that, after a few hours at constant potential, the rate of formation of phase oxide, Q_{2B}, increases greatly and, if continued, would have totally converted the anode to platinum oxide. In contrast Ramaley (50) in preliminary work in 1M $HClO_4$ at 25°C found that between 1.8 and 2.2V, NHE the amount of second oxide formed was determined by and varied almost linearly with the potential. This behavior seems appropriate to the formation of interfacial rather than 3-dimensional oxide.

The largest Q of Fig. 4, *viz.*, 25 mC/real cm² for Q_{2B} after 17 hr of anodizing would, if it arose from a monolayer oxide, necessitate associating about 70 oxide ions with each surface Pt. Thus Q_{2B} patently originates in a multilayer or phase oxide. While no chemical or spectral analysis of this oxide was attempted, the similarity of its appearance and mode of preparation to oxide analyzed by previous workers (25, 26) makes it highly probable that it was hydrated PtO_2. The 25 mC/real cm² oxide layer of Fig. 4 was orange-colored, amorphous looking, and very tightly adherent. After cathodic reduction of this thick film, the whole surface of the electrode was dull and pockmarked with innumerable tiny craters. An electrochemical determination of surface area at this stage gave $Q_1 = 68$ mC/apparent cm² (after a 1 min preoxidation at 2.00V, RHE in 2*N* H_2SO_4 at 27°C) corresponding to a roughness factor of 85 to 170.[2]

The Q_1 values of Fig. 3 and 4 derive from the first or monolayer oxide, the object of most previous study. Q_{2A} corresponding to the peak at about 0.3V (in Fig. 2) first observed in the present work is of comparable size to Q_1 so perhaps Q_{2A} similarly derives from a monolayer type oxide, formed at a species of external site on the Pt comparable in abundance to that responsible for Q_1 but much less easily oxidizable.

The detailed mechanism of reduction of these composite oxide films is of interest. The first reduction peak at about 0.6-0.7V in Fig. 2 is attributed to monolayer oxide. This film returns to the metallic state at the interface between bulk Pt and bulk Pt oxide. Then nothing happens until about 0.5V lower when the phase oxide starts to reduce. As pointed out by one of the referees, if this reduction begins at the oxide-acid interface it might sandwich most of the phase oxide between layers of impervious Pt metal. If this happened it is hard to see how the rest of the oxide could ever get reduced (which it does). So presumably either phase oxide reduction occurs wholly at the Pt-Pt oxide interface or reduction at the oxide-acid side deposits a highly porous metal. This latter is quite possible in view of the great roughening found in this work after such reductions.

Stability of Anodic Films

To potentiostatting at 0.5V, RHE.—The stability of the second oxide layer was examined at a controlled electrode potential of 0.5V, RHE in N_2-saturated 2*N* H_2SO_4 at 27°C. It was first established that anodizing at 10 A/cm² for 5 min in 2*N* H_2SO_4 at 93°C resulted in reproducible subsequent cathodic voltammograms such as curve 2 of Fig. 5, where $Q_2 = 7.0$ mC/cm². Curve 1, at a prereduced electrode acts as a base line for calculating the peak areas. Curve 2 was obtained in a separate cell 2-3 min after the anodization. Then curves 3 and 4 were recorded after the same anodic pretreatment. However, in recording these curves, voltage-scanning was arrested at 0.5V, RHE in order to potentiostat the electrode at this voltage. After pausing at this voltage for 104 min (curve 3) and 16.5 hr (curve 4) voltage-scanning was resumed to record the second oxide peaks. Q_2 for curves 3 and 4 was 3.8 and 1.9 mC/cm², respectively, compared with 7.0 for the normally treated electrode of curve 2. These results show that the second oxide is certainly unstable at 0.5V, RHE although its removal is still far from complete, even after 16 hr. It is apparent from Fig. 4 that the second oxide reduction regions of curves 3 and 4 were quite ill-defined[3] in comparison with those usually obtained (*c.f. e.g.* Fig. 2).

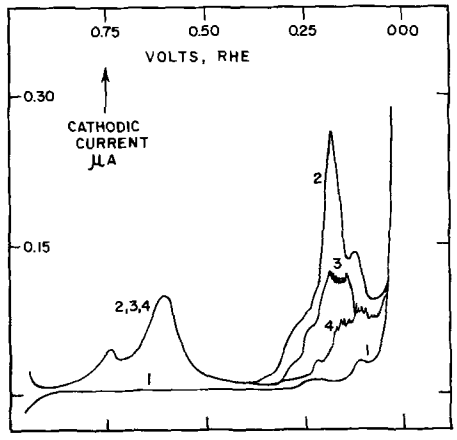

Fig. 5. Stability of second oxide layer at 0.5V, RHE exhibited by voltammetric stripping curves in N_2-saturated 2*N* H_2SO_4 (25°C, 3 mV/sec) after the following pretreatments: curve 1, prereduction in the solution at 0.05V, RHE; curve 2, anodization for 5 min at 10 A/cm² at 93°C in a separate portion of 2*N* H_2SO_4; curves 3 and 4, same as curve 2 except cathodic scanning was arrested at 0.5V, RHE to potentiostat at this value for 104 min and 16.5 hr in curves 3 and 4, respectively.

To soaking in 2N H_2SO_4 at 93°C.—It was first established that anodizing for 30 min at 10 A/cm² in 2*N* H_2SO_4 at 93°C resulted in reproducible subsequent voltammograms with $Q_1 = 5$ and $Q_2 = 17$ mC/cm². This procedure was then repeated, interposing a soaking period of 18 hr at 93°C in fresh, unelectrolyzed 2*N* H_2SO_4 between anodization and cathodic examination of the electrode. In this latter case, Q_1 had fallen to 1.7 and Q_2 to 10 mC/cm². Thus the first oxide was removed somewhat faster than the second.

Temperature Dependence of Cathodic Peak Potentials

Figure 6 shows a series of voltammograms in N_2-saturated 2*N* H_2SO_4 at 25°, 57°, and 93°C obtained in

[3] In these regions, the Sargent XXI recorder pen became subject to a "chatter" which occurred neither in curves 1 and 2 nor in those parts of curves 3 and 4 anodic to 0.25V, RHE. The origin of this effect is obscure to this author. From the experimental procedure described above, it would appear that there is a distinct difference between curve 2 on the one hand and 3, 4 on the other in that second oxide reduction in curve 2 occurred at an "anodically cleaned" electrode, i.e., one on which a monolayer oxide had been freshly reduced (45). In curves 3 and 4, 105 min and 16.5 hr, respectively of potentiostatting at 0.5V, RHE had intervened between this anodic cleaning and the resumption of voltage scanning. This is plenty of time for the electrode to have become grossly recontaminated by adsorbable solution impurities (45). To obviate this difference the electrode was given an anodic cleaning for 0.5 min at 1.7V, RHE just before continuing curves 3 and 4. However this had no effect on the pen-chatter.

that order. Each of these curves was preceded by an identical 5-min anodization in 1*N* H_2SO_4 at 10 A/cm² and 25°C. So the oxide film was similarly formed in each case but the temperature of its cathodic stripping was varied. The relative areas of the second oxide peaks in Fig. 5 are of no account. Q_2 actually fell continually in this chronological series of runs from 5.7 mC/cm² in curve 1 to 1.0 in curve 6 due presumably to the declining oxidizability discussed above. The main interest of Fig. 6 attaches to the temperature coefficient of the peak potentials. In going from 25° to 93°C, the potentials of the first and second oxide peaks became 100 and 120 mv, respectively, more positive. Both these values of peak-potential shift, of course, are relative to the unknown change of the reference electrode potential between 25° and 93°C (reference electrode was RHE, *i.e.*, reversible hydrogen electrode in the same solution). Thus the absolute magnitudes of the shifts are of little significance. It is surprising, however, that the difference between the two shifts is only 20 mv. Judging irreversibility by the potential span between onset of oxidation of the reduced electrode and incipient reduction of the oxidized electrode, one arrives at 1.0 − 0.7 = 0.3V for the first oxide and 2.1 − 0.3 = 1.8V for the second oxide. Thus it would be expected that the energy of activation and hence temperature coefficient of overvoltage should be much higher for the second than for the first oxide, giving rise to a much more substantial change in the separation of the first and second oxide peak potentials than the 20 mv actually observed in the 68°C interval.

In connection with the above discussion of the temperature dependence of oxide reduction potentials, a recent article by Marvin and Petrii (51) is of relevance. In this work galvanostatic (potential-time) curves were obtained for the cathodic reduction of PtO_2 prepared chemically by $NaNO_3$ oxidation of H_2PtCl_6 at 550°C. Chronopotentiograms were secured at different current densities (in terms of A/g of PtO_2) in 1*N* solutions of H_2SO_4 and NaOH at 20° and 95°C. Tafel plots derived from the plateau potentials of the charging curves invariably sloped by about 120 mV per decade of A/g. The only data really comparable with that of the present work were the temperature dependence of the plateau potentials. In 1*N* H_2SO_4 the plateau potential, *vs.* the respective RHE in each case, was about 330 mV higher at 95° than at 20°C. In the present work the second oxide peak potential, in 2*N* H_2SO_4 *vs.* RHE, was about 120 mV higher at 92.5° than at 25°C. Thus the data of the present work (Fig. 6) exhibits a significantly smaller temperature dependence for the second oxide reduction potential. Perhaps this reflects a significant difference in structure between chemically and anodically prepared PtO_2.

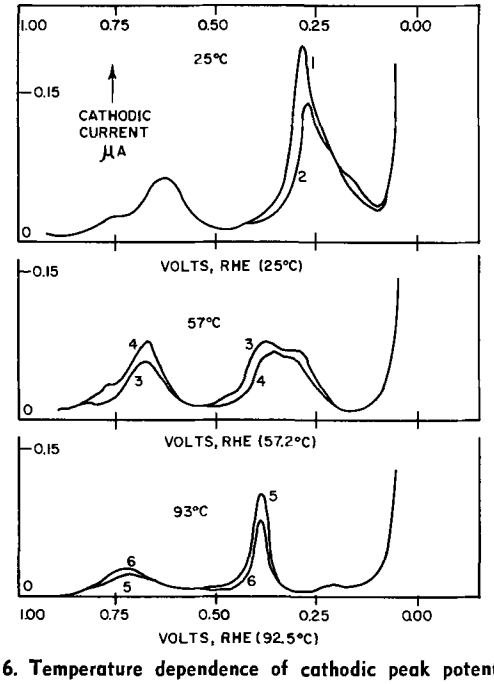

Fig. 6. Temperature dependence of cathodic peak potentials in voltammetric stripping of oxide films. Curves 1 to 6 (obtained chronologically) in N_2-saturated 2*N* H_2SO_4 (25°C, 3 mV/sec) were each preceded by an identical 5-min anodization in 1*N* H_2SO_4 at 25°C and 10 A/cm².

Low-Temperature Production of Second Oxide

Shibata's most intense anodizations (0.6 A/cm² for 60 min) failed to evoke the second oxide unless the temperature were higher than 21°C (31). He concluded that the monolayer oxide, when formed below 21°C, has a tight structure which prevents oxide growth into the interior of the metal. With the much higher anodic current densities used in the present work, it was shown that second oxide could result from anodizations as cool as 11°C, the lowest temperature at which oxidizability was studied. In one run, at 11°C in 2*N* H_2SO_4, anodizing at 10 A/cm² for 5 min (at a potential of 2.58-2.72V, RHE) yielded a sharp second oxide peak with Q_2 = 3.8 mC/cm². It was found in general that with declining anodizing temperature both the ease and reproducibility of second oxide formation was greatly diminished.

Behavior of First Oxide (0.6V Film)

The variation, in Table I of Q_1, the first oxide value, from run to run, is also of interest. This oxide is generally accepted as a monolayer-type film, and the magnitude of Q_1 is proportional to the true area of the electrode.[2] Just before run u_{10}, anodizing for 1 min at 10 A/cm² gave Q_1 = 4.5 mC/cm² (runs u_8, u_9) compared with Q_1 = 15.5 for an identical anodization immediately following u_{10}. Then, while standing in 2*N* H_2SO_4 at 25°C, Q_1 declined from this high value, falling to 3.3 mC/cm² after only 5 hr (only the early stage of this fall in Q_1 appears in Table I). The large (X3.5) increase in Q_1 caused by the reduction of the 40 mC/cm² second oxide of u_{10} is a strong indication of the phase nature of this film since the formation and dissolution of a monolayer type oxide are unlikely to effect so thoroughgoing a disruption of the surface. Thus high area Pt black catalysts for both organic hydrogenations (46) and anodic hydrocarbon oxidation (49) result from reducing PtO_2 to Pt. The fall of Q_1 from 15.5 to 3.3 mC/cm² in the 5 hr subsequent to u_{10} reflects a quite drastic reconsolidation of the disrupted Pt surface. This rate of area change seems very high by comparison with the limited data available on Pt black recrystallization in aqueous solutions (47) where, typically, 60 hr at 150°C in 90% H_3PO_4 was needed to effect 80% reduction in the electrochemically determined surface area. A major difference between the present work and the cited recrystallization study (47) lies in the storage conditions. In the latter, storage was at open-circuit while in the present work, storage was regularly punctuated by the brief anodization-cathodization treatments required to monitor the electrochemical area. It was already shown above that electrode behavior can be drastically modified by these test anodizations which greatly accelerated the decline of electrode oxidizability. Perhaps these test redox cycles have a significant effect also on the rate of consolidation of the Pt surface. Possibly Shibata's observation cited above (34), *viz.*, that a Pt surface electrodeposited from a second oxide film is more intensely strained and smaller in grain size than one prepared conventionally by deposition from chloroplatinic acid, has relevance to this point. Thus a highly strained finely divided surface should have a high recrystallization rate.

In recent work (45) it was shown that the activating effect on platinum electrodes of brief (≈1 min) anodic-cathodic cycles was due almost entirely to the impurity desorption effected by this treatment. However this was

apparently not true for the longer preanodizations of Shibata (31a). He anodized three 1 cm^2 Pt electrodes in 1*N* H_2SO_4 (25°C) at 0.1 A/cm^2 for 0.25, 1 and 28 hr, respectively, and then measured their activity by the magnitude of the hydrogen-evolution-reaction current at them for a definite small overpotential in 1*N* HCl. In each case the electrode activity fell off with time from roughly the same initial high value, but the rate of this decay was profoundly different for the three electrodes. After 30 hr in the 1*N* HCl, activity had fallen to 0.80, 0.028, and 0.018 of the initial high value for the electrodes preanodized for 28, 1, and 0.25 hr, respectively. This behavior led Shibata to discard the impurity desorption theory of electrode activation and postulate that the Pt surface had undergone a superficial structural change whose lifetime increased with the severity of the preoxidation.

The present work suggests another explanation of Shibata's data. Chronopotentiometric reduction of his electrodes showed that the preoxidations had yielded second oxide layers on them to the extent of about 0.4, 4, and 36 mC/cm^2 after the 0.25, 1, and 28-hr preanodizations, respectively. Since the present work has shown that the reduction of second oxide layers of this order of thickness can cause large increases in electrode roughness factor, it is virtually certain that the three electrodes encompassed a large spread of roughness factor (probably up to 10X). Thus the varying rates of decay in electrode activity are explained as follows. If, as is usually the case (1a, 48) contamination by adsorbing impurities from the solution was diffusion controlled, then the rate of uptake of contaminant by the electrodes was proportional to their geometrical areas which were identical. Hence percentage contamination of true area was slower for the rougher electrodes. All of Shibata's decay curves were characterized by an initial steady value of activity (the same for all three electrodes), then a more or less sudden fall, and a final slow leveling out. These curves closely resemble others obtained for the hydrogen evolution reaction at Pt under very similar conditions in 2*N* H_2SO_4 (45). In this latter work, the decay in activity was proven to arise from the adsorption of solution contaminants. It would seem that Shibata's currents started out with a measure of diffusion control, but as time (contamination) proceeded the true area diminished to the point where kinetic control predominated. With complete kinetic control the current should fall in direct proportion to the true area. This decay in current should naturally be slowest for the electrode with the highest roughness factor. Thus it would seem that Shibata's electrochemical activations comprised merely "anodic cleaning" and were not basically different from more conventional brief anodizations.

Note added in proof: Both Professor Conway himself and one of the referees of this paper considered that similarities between this work and a recent paper [Conway and Gilroy, *Can. J. Chem.*, **46**, 875 (1968)] merit further discussion. In my opinion the area of contact between the two studies is quite small. The main thrust of the present work is directed at the phase or second platinum oxide, an orange-brown layer which in extreme cases can be scraped off the metal in palpable lumps. The reduction charge (Q_{2B}) of this oxide can reach 25 mC/real cm^2 (Fig. 4). Its reduction peak potential is 0.4 to 0.5V below that of the first or monolayer oxide (Fig. 2) at a voltage scanning rate of 0.2 V/min.

Conway's Fig. 2 shows differentiated galvanostatic reduction curves for a Pt electrode in M H_2SO_4. If the prior potential exceeded 1.6V, RHE his oxide reduction curves at high current densities split into two clear peaks (OX.1 and OX.2). His total oxide reduction charge never exceeded 1.0 mC/real cm^2, *i.e.*, there is room for both OX.1 and OX.2 to coexist on the purely external surface of Pt. The scanning rate of Conway's Fig. 2 was ≈400 V/sec and OX.1/OX.2 peaks are separated by 0.1V. At lower scanning rates the peaks merged into one. This contrasts strongly with my Fig. 2 where the 1st and 2nd oxide reduction peaks differ by 0.5V at a scanning rate of 0.2 V/min, *i.e.*, X10^5 slower than Conway's.

To sum up, the following data of the present work show that a much clearer distinction exists between my 1st and 2nd oxides than between Conway's OX.1 and OX.2: (*a*) the very large mC/real cm^2 for Q_{2B} compared with Q_1; (*b*) the large voltage separation of reduction peaks for Q_1 and Q_{2B}; (c) the independent behavior of Q_1 and Q_{2B} *vs.* anodization time in my Fig. 3 and 4. I think there is little doubt that the 1st and 2nd peaks in my Fig. 2 refer to monolayer and phase oxide, respectively. On the other hand, OX.1 and OX.2 probably refer to two different energy sites on the external surface of Pt, *i.e.*, to a fine structure in the monolayer oxide. Possibly the fine structure apparent in my Fig. 2 in the 1st oxide reduction peak (*i.e.*, a small prewave at 0.7V before the main one at 0.6V) may relate to Conway's OX.1 and OX.2.

Manuscript submitted Feb. 13, 1969; revised manuscript received July 3, 1969. This paper was presented at the 19th Meeting of CITCE, Detroit, Sept. 22-27, 1968. This work was based on data obtained at Brookhaven National Laboratory, Upton, New York, in work done under the Auspices of the United States Atomic Energy Commission.

Any discussion of this paper will appear in a Discussion Section to be published in the June 1970 JOURNAL.

REFERENCES

1. (a) S. Gilman, in "Electroanalytical Chemistry," p. 111, A. J. Bard, Editor, Marcel Dekker, New York, (1967); (b) J. P. Hoare in "Advances in Electrochemistry and Electrochemical Engineering," p. 201, P. Delahay, Editor, Interscience Publishers, New York (1967).
2. J. S. Mayell and S. H. Langer, *This Journal*, **111**, 438 (1964).
3. S. Gilman, *Electrochim. Acta.*, **9**, 1025 (1964).
4. M. Becker and M. W. Breiter, *Z. Elektrochem.*, **60**, 1080 (1956).
5. M. Fleischmann, J. R. Mansfield, and Lord Wynne-Jones, *J. Electroanal. Chem.*, **10**, 511 (1965).
6. S. Schuldiner and T. B. Warner, *This Journal*, **112**, 212 (1965).
7. J. Mayell, *ibid.*, **113**, 385 (1966).
8. T. R. Beck and R. W. Moulton, *ibid.*, **103**, 247 (1956).
9. M. A. Gerovich, R. I. Kaganovich, V. M. Vergelesov, and L. N. Gorokhov, *Doklady Akad. Nauk. SSSR*, **114**, 1049 (1957).
10. E. A. Efimov and N. A. Izgaryshev, *Zhur. Fiz. Khim.*, **30**, 1807 (1956); **31**, 1141 (1957).
11. E. V, Kasatkin and A. A. Rakov, *Electrochim. Acta.*, **10**, 131 (1965).
12. C. Suzuki, M. Yoshida, H. Onoue, and T. Matsuno, *J. Electrochem. Soc. (Japan)*, **34**, 376 (1966).
13. M. W. Breiter, *Chem. Ing. Tech.*, **35**, 376 (1963).
14. For example, S. D. James, *Electrochim. Acta.*, **12**, 939 (1967).
15. Yu. B. Vasil'ev and V. S. Bagotskii, "Fuel Cells, Their Electrochemical Kinetics," p. 77, Consultants Bureau, New York, 1966 (Russian edition, Nauka Press, Moscow, 1964).
16. A. De La Rive, *Pogg. Ann.*, **41**, 157 (1837); **45**, 417 (1838).
17. J. P. Hoare, *Electrochim. Acta.*, **9**, 599 (1964).
18. R. Ruer, *Z. Physik. Chem.*, **44**, 81 (1903).
19. P. Brouillet and I. Epelboin, *Rev. met.*, **51**, 693 (1954).
20. A. N. Frumkin, *Trans. Faraday Soc.*, **55**, 156 (1959).
21. C. Marie, *J. Chim. phys.*, **6**, 475 (1908).
22. K. Nagel and H. Dietz, *Electrochim. Acta.*, **4**, 1 (1961).
23. L. Stuchlik, *Ber.*, **37**, 2913 (1904)
24. E. Briner and A. Yalta, *Helv. Chim. Acta.*, **26**, 1829 (1943).
25. S. Altmann and R. H. Busch, *Trans. Faraday Soc.*, **45**, 720 (1949).
26. E. Galloni and R. H. Busch, *J. Chem. Phys.*, **20**, 198 (1952).
27. T. Inoue. *Denki Kagaku*, **25**, 381, 418, 576 (1957); *C. A.*, **52**, 1808f, 13466i, 13478g (1958); Transl. of third article available from: Info. Div., B.N.L., Upton, N. Y., 11973 (BNL-Tr-168).

28. C. L. Mantell, "Electrochemical Engineering," p. 333, 349, McGraw Hill Book Co., New York (1960).
29. R. Holm, "Electric Contacts Handbook," 3rd ed., p. 13, Springer-Verlag, Berlin (1958).
30. B. Ershler, *Discussions Faraday Soc.*, **1**, 269 (1947).
31. S. Shibata, *Bull. Chem. Soc. Japan*, (*a*), **36**, 525 (1963); (*b*), **40**, 696 (1967).
32. W. Visscher and M. A. V. Devanathan, *J. Electroanal. Chem.*, **8**, 127 (1964).
33. For example, F. Will, *This Journal*, **112**, 451 (1965).
34. S. Shibata, Private communication.
35. A. Kozawa, *J. Electroanal. Chem.*, **8**, 20 (1964).
36. Yu. S. Gorodetskii, *Zhur. Fiz. Khim.*, **38**, 2717 (1964).
37. E. Gileadi, M. A. Fullenwider, and J. O'M. Bockris, *This Journal*, **113**, 926 (1966).
38. S. Schuldiner, Private communication.
39. C. W. Tucker, *J. Appl. Phys.*, **35**, 1897 (1964).
40. S. Schuldiner and T. B. Warner, *This Journal*, **112**, 853 (1965).
41. J. P. Hoare, S. G. Meibuhr, and R. Thacker, *ibid.*, **113**, 1078 (1966).
42. S. Schuldiner, T. B. Warner, and B. J. Piersma, *ibid.*, **114**, 343 (1967).
43. I. Uhara *et al.*, *J. Phys. Chem.*, **67**, 996 (1963).
44. G. R Piercy, *Phil. Mag.*, **5**, 201 (1960).
45. S. D. James, *This Journal*, **114**, 1113 (1967).
46. V. Voorhees and R. J. Adams, *J. Am. Chem. Soc.*, **44**, 1397 (1922).
47. J. F. Connolly, R. J. Flannery, and B. L. Meyers, *This Journal*, **114**, 241 (1968).
48. P. Delahay, "Double Layer and Electrode Kinetics," p. 118, Interscience (Wiley), New York (1965).
49. E. J. Cairns and E. J. McInerney, *This Journal*, **114**, 980 (1967).
50. L. Ramaley, Private communication.
51. R. V. Marvet and O. A. Petrii, *Elektrokhimi.*, **3**, 518 (1967).

Concentration Polarization and Mass Transfer Influence on the Kinetics of Two Stepwise-Proceeding Electrode Reactions under Galvanostatic Conditions

I. H. Plonski
Institute for Atomic Physics, Bucharest, Romania

ABSTRACT

The previous system of equations derived for the kinetics of two stepwise-proceeding electrode reactions under galvanostatic conditions is extended for the case when both concentration polarization and mass transfer of the intermediate and final ion are taken into account.

In a previous paper (1) the two stepwise-proceeding electrode reactions

$$M \rightleftarrows M^{z_1+} + z_1 e \qquad \text{(I)}$$

$$M^{z_1+} \rightleftarrows M^{(z_1+z_2)+} + z_2 e \qquad \text{(II)}$$

were considered under galvanostatic conditions. Neither concentration polarization nor mass transfer were taken into account. In the reactions concerned, M is the metal, M^{z_1+} is the intermediate ion, $M^{(z_1+z_2)+}$ the final ion, and z_1 and z_2 are the number of electrons involved in the first and second step, respectively. The kinetic equations for this system are

$$\frac{d\eta}{dt} = \frac{1}{C}\left[i + i_{o2}\, e^{-\alpha_{c2}\eta} - i_{o1}\, e^{\alpha_{a1}\eta} - \frac{[M^{z_1+}]}{[M^{z_1+}]_o}\left(i_{o2}\, e^{\alpha_{a2}\eta} - i_{o1}\, e^{-\alpha_{c1}\eta}\right)\right] \qquad [1]$$

and

$$\frac{d[M^{z_1+}]}{dt} = \frac{i_{o1}}{z_1\mathbf{F}} e^{\alpha_{a1}\eta} + \frac{i_{o2}}{z_2\mathbf{F}} e^{-\alpha_{c2}\eta} - \frac{[M^{z_1+}]}{[M^{z_1+}]_o}\left(\frac{i_{o1}}{z_1\mathbf{F}} e^{-\alpha_{c1}\eta} + \frac{i_{o2}}{z_2\mathbf{F}} e^{\alpha_{a2}\eta}\right) \qquad [2]$$

Here η is the overvoltage, t the time, C the double layer capacity, i the current density, i_{o1} and i_{o2} the exchange current densities for the first and second step, respectively, $\mathbf{F}$ the Faraday number, $[M^{z_1+}]$ and $[M^{z_1+}]_o$ the intermediate ion concentration at the electrode surface during the electrolysis and at equilibrium, respectively, and $\alpha_{a1} = \frac{\beta_1 z_1 \mathbf{F}}{RT}$, $\alpha_{c1} = \frac{(1-\beta_1) z_1 \mathbf{F}}{RT}$, $\alpha_{a2} = \frac{\beta_2 z_2 \mathbf{F}}{RT}$, and $\alpha_{c2} = \frac{(1-\beta_2) z_2 \mathbf{F}}{RT}$, R the gas constant, T the absolute temperature, and β_1 and β_2 the symmetry factors for the first and second step, respectively.

The above system of equations is approximately valid under the following specific assumptions:

1. The final ion concentration is practically constant at the electrode surface; this holds for processes occurring with current densities far below the limiting diffusion current density, or for processes when the overvoltage reaches its steady state long before the end of the transition time. When the time of electrolysis is prolonged, the increase of the final ion concentration at the electrode surface will generate a concentration polarization attended by the mass transfer of the final ion into the bulk of the solution.

2. If the intermediate ion does not leave the electrode surface, because it exists only as a result of the reversible process between the surface metal and the final ion, $M \rightleftarrows M^{z_1+} \rightleftarrows M^{(z_1+z_2)+}$; in other words, there will be no intermediate ion in the bulk of the solution, and therefore no mass transfer. In this case all conclusions regarding the intermediate ion concentration refer only to the surface concentration.

3. If the diffusion current for the intermediate ion is great enough to assure a constant concentration of the intermediate ion in the whole solution. In this case the same conclusions apply to the bulk concentration, too.

4. When the intermediate ion concentration is very low and one can neglect its diffusion flux into the bulk of the solution in comparison to the rate of its further electrochemical oxidation.

With the exception of these particular cases the concentration polarization due to the change of the final ion concentration at the electrode surface and mass transport processes of both the final ion and intermediate ion must be taken into account.

The complete system of equations for this case is

$$\frac{d\eta}{dt} = \frac{1}{C}\left[i + i_{o2}\frac{[M^{(z_1+z_2)+}]}{[M^{(z_1+z_2)+}]_o} e^{-\alpha_{c2}\eta} - i_{o1}\, e^{\alpha_{a1}\eta} - \frac{[M^{z_1+}]}{[M^{z_1+}]_o}\left(i_{o2}\, e^{\alpha_{a2}\eta} - i_{o1}\, e^{-\alpha_{c1}\eta}\right)\right] \qquad [3]$$

$$\frac{d[M^{z_1+}]}{dt} = \frac{i_{o1}}{z_1\mathbf{F}}\, e^{\alpha_{a1}\eta} + \frac{i_{o2}}{z_2\mathbf{F}}\,\frac{[M^{(z_1+z_2)+}]}{[M^{(z_1+z_2)+}]_o}\, e^{-\alpha_{c2}\eta} - \frac{[M^{z_1+}]}{[M^{z_1+}]_o}\left(\frac{i_{o1}}{z_1\mathbf{F}}\, e^{-\alpha_{c1}\eta} + \frac{i_{o2}}{z_2\mathbf{F}}\, e^{\alpha_{a2}\eta}\right) + D_1\left(\frac{\partial M_1}{\partial x}\right)_{x=0} \quad [4]$$

and

$$\frac{d[M^{(z_1+z_2)+}]}{dt} = \frac{i_{o2}}{z_2\mathbf{F}}\left(\frac{[M^{z_1+}]}{[M^{z_1+}]_o}\, e^{\alpha_{a2}\eta} - \frac{[M^{(z_1+z_2)+}]}{[M^{(z_1+z_2)+}]_o}\, e^{-\alpha_{c2}\eta}\right) + D_2\left(\frac{\partial M_2}{\partial x}\right)_{x=0} \quad [5]$$

Here $[M^{(z_1+z_2)+}]$ and $[M^{(z_1+z_2)+}]_o$ are the concentrations of the final ion at the electrode surface during electrolysis and at equilibrium, respectively, D_1 is the diffusion coefficient for the intermediate ion, D_2 is the diffusion coefficient for the final ion, M_1 and M_2 are the concentrations of the intermediate and final ion, respectively, being functions of both time t and the distance from the electrode surface, x. Obviously, $M_1(0, t) = [M^{z_1+}]$ and $M_2(0, t) = [M^{(z_1+z_2)+}]$. The terms $D_1\left(\frac{\partial M_1}{\partial x}\right)_{x=0}$ in Eq. [4] and $D_2\left(\frac{\partial M_2}{\partial x}\right)_{x=0}$ in Eq. [5] represent the rate of the appearance (or disappearance) of the respective ion at the electrode surface due to mass transfer or, in other words, the diffusion currents at the electrode surface, divided by $z_1\mathbf{F}$ and $z_2\mathbf{F}$, respectively.

The mathematical problem consists in solving Fick's equation

$$\frac{\partial M_1}{\partial t} = D_1\,\frac{\partial^2 M_1}{\partial x_2} \quad [6]$$

for the initial and boundary conditions

$$M_1(x, 0) = [M^{z_1+}]_o$$

$$M_1(t, \infty) = [M^{z_1+}]_o$$

$$\left(\frac{\partial M_1}{\partial x}\right)_{x=0} \quad \text{given by Eq. [4]}$$

and also

$$\frac{\partial M_2}{\partial t} = D_2\,\frac{\partial^2 M_2}{\partial x_2} \quad [7]$$

for the initial and boundary conditions

$$M_2(x, 0) = [M^{(z_1+z_2)+}]_o$$

$$M_2(t, \infty) = [M^{(z_1+z_2)+}]_o$$

$$\left(\frac{\partial M_2}{\partial x}\right)_{x=0} \quad \text{given by Eq. [5]}$$

Equations [3]-[7] form a mixed system of equations with ordinary and partial derivatives which has only approximate numerical solution.

The solution of the first boundary problem of Fick's equation for the initial and boundary conditions

$$M_1(x, 0) = [M^{z_1+}]_o = \text{constant}$$

$$M_1(0, t) = [M^{z_1+}] = \text{function of } t$$

is

$$M_1(x, t) = \frac{1}{2\pi}\int_0^\infty \frac{1}{\sqrt{D_1 t}}\left\{e^{-\frac{(x-\xi)^2}{4D_1 t}} - e^{-\frac{(x+\xi)^2}{4D_1 t}}\right\}[M^{z_1+}]_o\, d\xi + \frac{D_1}{2\sqrt{\pi}}\int_{t_o}^{t} \frac{x}{[D_1(t-\zeta)]^{3/2}}\, e^{-\frac{x^2}{4D_1(t-\zeta)}}\, M_1(\zeta)\, d\zeta \quad [8]$$

where ξ and ζ are integral variables. Solution [8] is valid for $x \geq 0$ and $t \geq t_o$, with $-\infty < t_o < +\infty$; $M_1(x, t)$, given by Eq. [8], is differentiable once with respect to t, and twice with respect to x, and satisfies the initial and boundary conditions for $t = 0$ and $x = 0$.

Assuming a solution, $M_1(x, t)$, differentiable also at the boundary, its differential will be calculated as a limiting process. By introducing $y = (x - \xi)/2\sqrt{D_1 t}$ and $-2\sqrt{D_1 t}\, dy = d\xi$ in the first integral of Eq. [8], and $y = x/2\sqrt{D_1(t-\zeta)}$ and $(4\sqrt{D_1}(t-\zeta)^{3/2}\, dy)/x = d\zeta$ in the second integral of Eq. [8], one can obtain for $x > 0$ and $t > 0$ the differential

$$\frac{\partial M_1}{\partial x} = \frac{[M^{z_1+}]_o\, e^{-\frac{x^2}{4D_1 t}}}{\sqrt{\pi D_1 t}} + \frac{2}{x\sqrt{\pi}}\int_{\frac{x}{2\sqrt{D_1 t}}}^{+\infty} (1 - 2y^2)\, e^{-y^2}\left[M_1\left(t - \frac{x^2}{4D_1 y^2}\right)\right] dy \quad [9]$$

We define for $t > 0$ and $x = 0$

$$\left(\frac{\partial M_1}{\partial x}\right)_{x=0} = \frac{[M^{z_1+}]_o}{\sqrt{\pi D_1 t}} + \lim_{x\to 0}\left\{\frac{2}{x\sqrt{\pi}}\int_{\frac{x}{2\sqrt{D_1 t}}}^{+\infty} (1 - 2y^2)\, e^{-y^2}\left[M_1\left(t - \frac{x^2}{4D_1 y^2}\right)\right] dy\right\} \quad [10]$$

The second term of the right-hand side of Eq. [10] may be obtained numerically by computing a great enough number of integrals for decreasing values of x until its value remains constant within the desired approximation. The same route may be taken to compute $\left(\frac{\partial M_2}{\partial x}\right)_{x=0}$. Unfortunately, the computation is long and intricate.

As a good first approximation, Fick's Eq. [6] and [7] are solved by assuming $M_1(0, t)$ and $M_2(0, t)$ to be constant within a very short interval of time. In this case the solutions are

$$\left(\frac{\partial M_1}{\partial x}\right)_{x=0} = \frac{[M^{z_1+}]_o - [M^{z_1+}]}{\sqrt{\pi D_1 t}}, \quad \text{for } t > 0 \quad [11]$$

and

$$\left(\frac{\partial M_2}{\partial x}\right)_{x=0} = \frac{[M^{(z_1+z_2)+}]_o - [M^{(z_1+z_2)+}]}{\sqrt{\pi D_2 t}}, \quad \text{for } t > 0 \quad [12]$$

The same expressions [11] and [12] are then assumed to be valid also when $[M^{z_1+}]$ and $[M^{(z_1+z_2)+}]$ are time dependent. Using such an approximation, the mass transfer effect is overestimated: the real values of $[M^{z_1+}]$ and $[M^{(z_1+z_2)+}]$ which would be obtained by the correct solving of Eq. [9] and [10], respectively, will be between the values obtained by using Eq. [11] and [12] in conjunction with Eq. [3]-[5] and those obtained by assuming $\left(\frac{\partial M_1}{\partial x}\right)_{x=0} = 0$ and $\left(\frac{\partial M_2}{\partial x}\right)_{x=0} = 0$. Consequently, the following results are valid in a qualitative sense.

Equations [3] to [5] in conjunction with Eq. [11] and [12] are solved numerically for different values of the parameters concerned, given on Fig. 1 and 2.[1]

[1] Some unusual values are taken for concentrations and diffusion coefficients in order to obtain visible effects of concentration polarization and mass transfer processes in a rather convenient period of time.

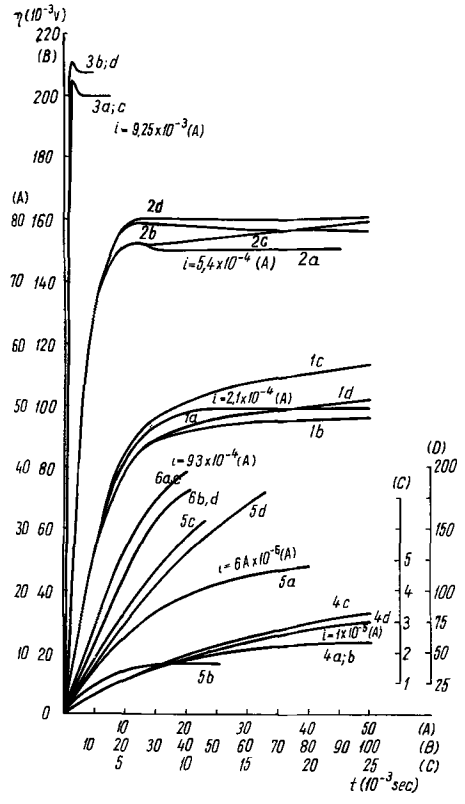

Fig. 1. Overvoltage, η, *vs.* time, *t*, for $z_1 = z_2 = 1$, $\beta_1 = \beta_2 = 0.5$, and different values of *i* pointed on the curves. Curves 1-3: $i_{o1} = 1x10^{-4}$(A), $i_{o2} = 1x10^{-5}$(A); 1-2(O_A—A_A); 3(O_C—A_C). O = ordinate, A = abscissa. Index "a": $D_1 = 0$, $\frac{d[M^{z+}]}{dt} = 0$; b: $D_1 = 1x10^4 cm^2/sec$, $\frac{d[M^{z+}]}{dt} = 0$; c: $D_1 = D_2 = 0$, $\frac{d[M^{z+}]}{dt}$ given by Eq. [5]; d: $D_1 = 1x10^4$ cm²/sec, $D_2 = 1x10^2$ cm²/sec.

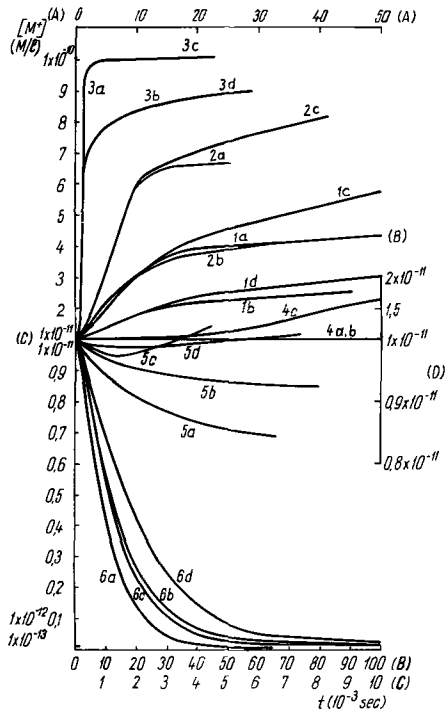

Fig. 2. Intermediate ion concentration, $[M^+]$, *vs.* time, *t*, for the same parameters as in Fig. 1. Curves: 1-3 (O_A—A_A); curve 4 (O_B—A_B); curve 5 (O_D—A_B); curve 6 (O_C—A_C).

In order to point out the effect of both the concentration polarization and the mass transfer processes, the following cases are treated first separately and then together.

(*A*). Neither concentration polarization nor mass transfer are taken into account (curves a, Fig. 1 and 2). The cases are discussed in the previous paper (1) and are given here only for comparison.

(*B*). The influence of intermediate ion mass transfer when the final ion concentration is assumed to be constant (curves b, Fig. 1 and 2).

For $i_{o1} > i_{o2}$, the mass transfer occurs from the electrode surface into the bulk of the solution. At $i < i_{cr}$, [*i* critical denoted by i_{cr} represents the value of *i* from which the $\eta - t$ curve becomes peak shaped in the absence of mass transfer influence (1)], the $\eta - t$ curve is located below the curve when no mass transfer is assumed (Fig. 1, curve 1b), and above it at $i > i_{cr}$ (Fig. 1, curves 2b and 3b). The $[M^{z_1+}] - t$ curves are located below curves a at all current density values (Fig. 2, curves b).

For $i_{o1} < i_{o2}$, the mass transfer takes place from the bulk of the solution to the electrode surface. At all current density values, both $\eta - t$ curves (Fig. 1, curves 5b and 6b) and $[M^{z_1+}] - t$ curves (Fig. 2, curves 5b and 6b) are located above curves a.

The case of $i_{o1} = i_{o2}$ is out of question because $[M^{z_1+}] = [M^{z_1+}]_o$ = constant (1).

As one can see from the represented curves, at all current density values, the mass transfer of the intermediate ion manifests its influence as a delay in the approach to the steady state. Also, as was expected, the mass transfer effect appears sooner with an increase of *i*.

It can be seen from Eq. [4] in conjunction with Eq. [11] that the corrective term for the intermediate ion mass transfer vanishes with increasing time, because after some time the gradient between the concentration at the electrode surface and in the bulk of the solution remains practically constant, but the time increases; consequently η and $[M^{z_1+}]$ will tend to their steady-state values. The physical meaning that the diffusion current at the electrode surface becomes very small is that the concentration gradient at the electrode surface and its neighborhood decreases in time, the front of diffusion being shifted toward the bulk of the solution.

(*C*). The effect of the change of final ion concentration, when no mass transfer is taken into account.

As one can see from Eq. [3] to [5], the terms containing the change of final ion concentration contain the negative exponential of the overvoltage. Hence, these terms are under two opposite influences when both $[M^{(z_1+z_2)+}]$ and η increases. Consequently, due to this fact and to the complexity of the system, it is difficult to forsee the effect of the change of final ion concentration on the behavior of η and $[M^{z_1+}]$ when *t* or *i* increase.

From the computed curves it may be noticed that for all cases $i_{o1} > i_{o2}$ (curves 1c, 2c, and 3c), $i_{o1} = i_{o2}$ (curve 4c) and $i_{o1} < i_{o2}$ (curves 5c and 6c), η surpasses its value when $[M^{(z_1+z_2)+}]$ is assumed constant, increases continuously and, as far as the computation was made, no steady state is attained. Also, it can be seen that at high current densities, that is at high values of the overvoltage (curve 3c and 6c, Fig. 1) the effect of concentration polarization on the overvoltage is not noticeable within the computed time used; this is probably due to the fact that, since the mentioned exponential term is very small, the computation (the electrolysis) must be extended to longer times in order that the final ion concentration be high enough to balance the η effect.

From Fig. 2 it can be noticed that for $i_{o1} > i_{o2}$ (curves 1c, 2c, and 3c), $i_{o1} = i_{o2}$ (curve 4c), and $i_{o1} < i_{o2}$ (curves 5c and 6c), the intermediate ion concentration is at all times greater than its value corresponding to case "a." Also, for $i_{o1} > i_{o2}$ and $i_{o1} = i_{o2}$, the $[M^{z_1+}]$ is

continuously increasing; for $i_{o1} < i_{o2}$, the $[M^{z_1+}]$ decreases at the beginning, then increases over its equilibrium value. At high current densities the same discussion is valid as for the η behavior.

The different features of $[M^{z_1+}] - t$ curves is due to the fact that for $i_{o1} > i_{o2}$ and $i_{o1} = i_{o2}$, both the increase of η and the increase of $[M^{(z_1+z_2)+}]$ lead to the increase of $[M^{z_1+}]$, so that at all times $[M^{z_1+}]$ is greater than its value corresponding to case *a*. Contrarily, for $i_{o1} < i_{o2}$, the increase of η leads to the decrease of $[M^{z_1+}]$, but the increase of $[M^{(z_1+z_2)+}]$ leads to the increase of $[M^{z_1+}]$. As a result all the curves representing the decrease of $[M^{z_1+}]$ in time are attenuated in comparison with curves a, and after some time the influence of the final ion concentration manages to balance the influence of the overvoltage, and the intermediate ion concentration begins to increase.

(*D*). The real system of equations is solved when concentration polarization and both mass transfer processes are taken into account.

As one can see from the curves d, Fig. 1 and 2, the effect of the final ion mass transfer, represented by the corrective term

$$\sqrt{\frac{D_2}{\pi t}}\,([M^{(z_1+z_2)+}] - [M^{(z_1+z_2)+}]_o) = D_2\left(\frac{\partial M_2}{\partial x}\right)_{x=0}$$

in Eq. [5], consists in attenuating the effect of concentration polarization mentioned in case c.

It can also be noticed that when the time increases, the difference between curves d and a or b becomes greater.

The fact that a steady state is not attained is valid for the times for which the computation was done. In order to see the correct behavior of $\eta - t$ and $[M^{z_1+}] - t$ curves at large values of time the computation should be extended. Anyhow, it may be proved mathematically that a steady-state will not be attained for $[M^{z_1+}]$ and $[M^{(z_1+z_2)+}]$ because the cases of $\frac{d[M^{z_1+}]}{dt} = 0$, $\frac{d[M^{(z_1+z_2)+}]}{dt} = 0$ and $\frac{d\eta}{dt} \neq 0$ and also $\frac{d[M^{z_1+}]}{dt} = 0$, $\frac{d[M^{(z_1+z_2)+}]}{dt} = 0$, and $\frac{d\eta}{dt} = 0$ lead to absurd relations. The case of $\frac{d\eta}{dt} = 0$, $\frac{d[M^{z_1+}]}{dt} \neq 0$, and $\frac{d[M^{(z_1+z_2)+}]}{dt} \neq 0$ is possible, but in order to see which of the cases, this one or the case of $\frac{d\eta}{dt} \neq 0$, $\frac{d[M^{z_1+}]}{dt} \neq 0$, and $\frac{d[M^{(z_1+z_2)+}]}{dt} \neq 0$ is true, the computation must be extended to longer times. Moreover, it is preferable to use the numerical approximate solution of Eq. [10], which is more exact (see the Appendix).

Conclusions

The main effect of intermediate ion mass transfer is to delay the reaching of the steady state, without a qualitative alteration of the shape of $\eta - t$ or $[M^{z_1+}] - t$ curves.

The influence of the concentration polarization due to the change of the final ion concentration attended by the mass transfer of the final ion consists of the fact that both the overvoltage and the intermediate ion concentration exceed their values, valid when the final ion concentration is assumed to be constant, the latter at last increasing continuously.

Acknowledgments

The author is indebted to Dr. N. Moldovan and E. Ciupitu, of the Institute of Atomic Physics, Bucharest, Romania, for mathematical assistance and programming the computer.

Manuscript submitted Feb. 28, 1969; revised manuscript received July 1, 1969.

Any discussion of this paper will appear in a Discussion Section to be published in the June 1970 JOURNAL.

APPENDIX

1. Let us assume that after some time $\frac{d[M^{z_1+}]}{dt} = 0$ and $\frac{d[M^{(z_1+z_2)+}]}{dt} = 0$, *e.g.*, the rates of disappearance of the intermediate and final ion from the electrode surface by electrochemical reactions are equal to the rates of their supply at the electrode surface. Then, $[M^{(z_1+z_2)+}] \to [M^{(z_1+z_2)+}]_x$ and $[M^{z_1+}] \to [M^{z_1+}]_x$; with increasing time,

$$\frac{[M^{z_1+}]_o - [M^{z_1+}]_\infty}{\sqrt{\pi D_1 t}} \to 0;$$

$$\frac{[M^{(z_1+z_2)+}]_o - [M^{(z_1+z_2)+}]_\infty}{\sqrt{\pi D_2 t}} \to 0$$

and Eq. [4] and [5] become

$$\frac{i_{o1}}{z_1\mathbf{F}}\,e^{\alpha_{a1}\eta} + \frac{i_{o2}}{z_2\mathbf{F}}\,\frac{[M^{(z_1+z_2)+}]_\infty}{[M^{(z_1+z_2)+}]_o}\,e^{-\alpha_{c2}\eta} - \frac{i_{o2}}{z_2\mathbf{F}}\,\frac{[M^{z_1+}]_\infty}{[M^{z_1+}]_o}\,e^{\alpha_{a2}\eta} = 0 \quad [4']$$

and

$$\frac{[M^{z_1+}]_\infty}{[M^{z_1+}]_o} = \frac{[M^{(z_1+z_2)+}]_\infty}{[M^{(z_1+z_2)+}]_o}\,e^{-(\alpha_{a2}+\alpha_{c2})\eta} = \frac{[M^{(z_1+z_2)+}]_\infty}{[M^{(z_1+z_2)+}]_o}\,e^{-2\alpha\eta} \quad [5']$$

(for $\alpha_{a1} = \alpha_{a2} = \alpha_{c1} = \alpha_{c2} = \alpha$)

By introducing [5'] in [4'] we obtain $\frac{i_{o1}}{z_1\mathbf{F}}\,e^{\alpha\eta} = 0$ which is absurd for both $\frac{d\eta}{dt} = 0$ and $\frac{d\eta}{dt} \neq 0$.

2. For the case of $\frac{d\eta}{dt} = 0$; $\frac{d[M^{z_1+}]}{dt} \neq 0$; $\frac{d[M^{(z_1+z_2)+}]}{dt} \neq 0$, we have

$$\frac{[M^{z_1+}]}{[M^{z_1+}]_o} = \frac{i + i_{o2}\,\frac{[M^{(z_1+z_2)+}]}{[M^{(z_1+z_2)+}]_o}\,e^{-\alpha_{c2}\eta_\infty} - i_{o1}\,e^{\alpha_{a1}\eta_\infty}}{i_{o2}\,e^{\alpha_{a2}\eta_\infty}} \quad [3'']$$

By introducing [3''] into [4] and [5] we obtain a possible system of two equations, which may represent the increase of the intermediate ion concentration on account of the increase of the final ion concentration, for very high values of time.

$$\frac{d[M^{z_1+}]}{dt} = \frac{i_{o1}}{z_1\mathbf{F}}\,e^{\alpha_{a1}\eta_\infty} + \frac{i_{o2}}{z_2\mathbf{F}}\,\frac{[M^{(z_1+z_2)+}]}{[M^{(z_1+z_2)+}]_o}\,e^{-\alpha_{c2}\eta_\infty} - \frac{i + i_{o2}\,\frac{[M^{(z_1+z_2)+}]}{[M^{(z_1+z_2)+}]_o}\,e^{-\alpha_{c2}\eta_\infty} - i_{o1}\,e^{\alpha_{a1}\eta_\infty}}{i_{o2}\,e^{\alpha_{a2}\eta_\infty}} \left(\frac{i_{o1}}{z_1\mathbf{F}}\,e^{-\alpha_{c1}\eta_\infty} - \frac{i_{o2}}{z_2\mathbf{F}}\,e^{\alpha_{a2}\eta_\infty}\right) - \frac{[M^{z_1+}]_o}{\sqrt{\pi D_1 t}} \left[\frac{i + i_{o2}\,\frac{[M^{(z_1+z_2)+}]}{[M^{(z_1+z_2)+}]_o}\,e^{-\alpha_{c2}\eta_\infty} - i_{o1}\,e^{\alpha_{a1}\eta_\infty}}{i_{o2}\,e^{\alpha_{a2}\eta_\infty}} - 1\right] \quad [4'']$$

$$\frac{d[M^{(z_1+z_2)+}]}{dt} = \frac{i_{o2}}{z_2\mathbf{F}}\left(\frac{i_{o1}}{i_{o2}}\,e^{\alpha_{a2}\eta_\infty} - \frac{[M^{(z_1+z_2)+}]}{[M^{(z_1+z_2)+}]_o}\,e^{-\alpha_{c2}\eta_\infty}\right) - \frac{1}{\sqrt{\pi D_2 t}}\,([M^{(z_1+z_2)+}] - [M^{(z_1+z_2)+}]_o) \quad [5'']$$

REFERENCE

1. I. H. Plonski, *This Journal*, **116**, 944 (1969).

Methods for Characterizing the Structure and Electrochemical Behavior of Teflon-Bonded Pt Electrodes

J. Giner,* J. M. Parry,* S. Smith, and M. Turchan

Tyco Laboratories, Incorporated, Waltham, Massachusetts

ABSTRACT

Experimental measurements designed to test a specific model of the Pt-Teflon bonded electrode are described. The model assumes that the catalyst agglomerates are filled with electrolyte and that the Teflon binder creates hydrophobic channels, providing effective gas penetration. The electrochemical measurements of surface area and distribution of adsorbed charge formed by reduction of CO_2 or oxidation of C_3H_8 were carried out for a series of electrodes of different structure. Comparisons are made with BET surface area and pore volume distribution. The results presented are consistent with the proposed model.

The Teflon-bonded electrode (1, 2) represents a very efficient structure which allows extensive utilization of the catalyst and therefore very high current densities at relatively low polarization. Although this electrode has been extensively used in fully engineered fuel cells and in many catalyst screening programs, relatively little is known about its working mechanism. In particular, the degree of utilization of the catalyst under various working conditions is an unknown factor.

Based on our experience with this type of electrode, we have developed a qualitative description of the mechanism based on a double-porosity model (3, 4). We assume that the catalyst particles form porous, electronically conductive agglomerates which under working conditions are completely flooded with electrolyte. These catalyst agglomerates are held together by the Teflon binder which also creates hydrophobic gas channels. When current is drawn from the electrode, reactant gas diffuses through the hydrophobic channels, dissolves in the electrolyte contained in the agglomerates, and reacts on available sites of the catalyst particles. The number of sites available depends on the rate of diffusion and the rate of reaction on those sites near the surface of the agglomerate. The model, of course, assumes that all the catalyst particles are in good electronic contact with the external circuit and good ionic contact with the electrolyte. Efficient utilization of the catalyst surface then is defined by mass transport rates in the agglomerate.

We can further separate (5) the utilization of the catalyst surface into a "transversal utilization" of the electrode, which depends on the internal *IR* drop, and a "radial utilization" of the flooded agglomerates, which depends on the slow diffusion of the reactant gas in electrolyte flooding the agglomerate.

In the present paper, we present details of experimental tests to assess the validity of this model and describe the development of methods to determine some of the characteristic parameters of the electrode. A mathematical treatment of the model is given elsewhere (5). We have measured (*a*) that fraction of the catalyst surface which maintains the necessary electronic and ionic contacts for normal operation; (*b*) the effect of Teflon content on the electrode structure and electrode performance; (*c*) the values of microporosity of the flooded agglomerate and macroporosity of the electrode; and (*d*) the effective size of the agglomerate (*i.e.*, the length that the reactant gas diffuses into the flooded agglomerate under the effect of a concentration gradient). We have also examined the effect of the resistance of the electrolyte from the front to the back face of the electrode.

* Electrochemical Society Active Member.

The work discussed here was carried out in the course of a program to determine the intrinsic catalytic activity of different Pt blacks for the anodic oxidation of propane. The working conditions were those under which the propane oxidation is most efficient (85% H_3PO_4 and 150°C). Although some of the results obtained are specific to these conditions, most of the conclusions should be valid in understanding those mechanisms that enable the Teflon-bonded structure to operate efficiently as a gas diffusion electrode in a fuel cell under more general conditions.

Experimental

The Teflon-bonded electrodes were prepared by sieving the commercial Pt black (Englehard Industries) through a 325-mesh screen, and mixing the desired proportions with Teflon 30 dispersion and water. The resulting paste was rolled out to a thin sheet, and pressed into gold-plated tantalum screen (50-mesh, 3-mil wire). Electrodes with 20 ± 1 mg Pt, and varying Teflon ratios (15-50% by weight PTFE), were cut out in disks of 1.13 cm^2 geometric surface area, dried for several hours under vacuum at 100°C, and finally sintered at 250°C for 5 min under N_2.

The electrochemical measurements were carried out in 85% H_3PO_4 at 150°C using the "floating electrode" technique (6) with prepurified N_2 and C_3H_8 (99.99%).

The "floating electrode" cell, as modified for this work, is shown in Fig. 1. The body of the cell consisted of a Pyrex U-tube fitted with a working electrode compartment and a counterelectrode compartment. The working electrode was supported in an electrode holder on a ring of Pt wire and kept in position by a slight downward pressure of a spring of Pt wire, which was also the electronic contact to the electrode. A Teflon collar sliding on the main support compressed the spring, keeping the electrode in position. The reference electrode was a "dynamic hydrogen electrode" (7) situated inside the main support tube. The difference between this reference and the reversible hydrogen electrode was found by calibration against a hydrogen "floating electrode" at open circuit in each experiment. It was found to be constant within a millivolt each day, with a value between 35 and 50 mV. The distance between the Luggin capillary tip and the floating electrode is fixed by the electrode holder configuration and was, therefore, identical for each test. This distance was approximately 2 mm—about twice the external diameter of the capillary.

A liquid seal filled with H_3PO_4 provided a gastight working electrode compartment.

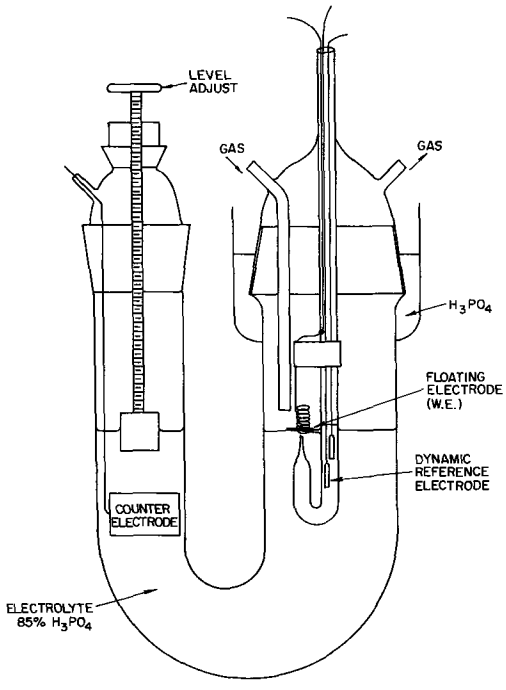

Fig. 1. Floating electrode cell

The level of the electrolyte was raised to "float" the electrode on the surface by lowering a Teflon plunger in the counterelectrode compartment.

The "floating electrode cell" was placed in an oven and maintained at 150°C. The gases (N_2, C_3H_8) were humidified over water at 93.50° ± 0.05°C (corresponding to 600 mm Hg) to keep the electrolyte concentration at its optimum value (8) of 85%.

Electrochemical measurements (described in detail below) were made using a Wenking fast rise potentiostat and a laboratory-built galvanostat. The switching from potentiostatic to galvanostatic mode was achieved with High Speed Mercury Relays. While in the galvanostatic mode, the *IR* drop between floating electrode and the tip of the Luggin capillary was determined using an interrupter technique. The voltage-time curves during galvanostatic studies were recorded on a X-Y recorder.

All quoted potential values are referred *vs.* the reversible hydrogen electrode and are corrected for *IR* drop (resistance between working electrode and Luggin capillary tip was usually about 0.6-0.9 ohm).

Effect of Teflon content on electrode performance.—Before proceeding to more detailed experiments, it was necessary to show that the Teflon content of the electrodes was at a level where the major assumptions of the model were realized in practice. Accordingly, polarization curves for the anodic oxidation of propane were measured for a series of electrodes prepared from the same batch of a commercial platinum black (using the same catalyst load of 20 mg/cm^2) but with Teflon contents varying from 15 to 50% by weight.

The measurements were carried out potentiostatically starting from 200 mV, at 50-mV increments, after waiting 5 min at each potential.

It can be seen from Fig. 2 that, in the range of 20-40% Teflon, the electrochemical activity using the current/geometric cm^2 at 400 mV *vs.* RHE as an indicator is practically identical. At both 15 and 50% Teflon, the activity has dropped off. At 15%, the electrode is "too hydrophilic" so that there are long gas diffusion paths. At 50% Teflon, the electrode is "too hydrophobic" so that there is poor electrolyte contact. The value of the peak current/geometric cm^2 increases with Teflon content in the range of 20-40% Teflon. This would indicate that the peak current is a function of electrode structure, while the current at 400 mV is more indicative of the intrinsic activity of the black. The remainder of the tests described here were carried out with 30% Teflon electrodes unless otherwise noted.

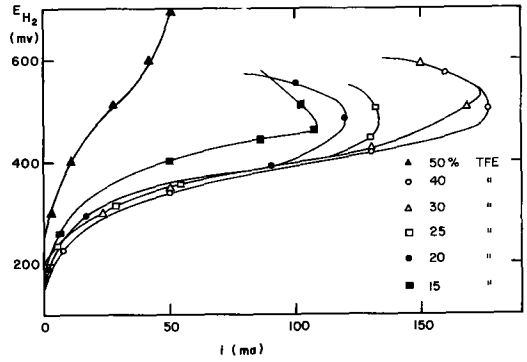

Fig. 2. Effect of Teflon content on performance of Teflon-bonded platinum electrode.

Determination of the surface area.—One of the most important factors that needs to be determined is the real surface area of the electrode that is in contact with the electrolyte and has a conductive path to the current-collecting screen under normal fuel cell operating conditions (in this case a floating electrode). For these and all the following experiments, nitrogen was used as the inert gas.

The conventional method of determining the electrochemical surface area of a Pt electrode is the determination of the extent of hydrogen adsorption (Q_H). Unfortunately, with electrodes of this type, this method gives ambiguous results due to the hydrogen evolution. As is shown in Fig. 3, hydrogen evolution can occur at potentials well above the reversible hydrogen potential. This occurs because the electrode structure permits very rapid diffusion of H_2 away from the surface so that the equilibrium H_2 partial pressure corresponding to the electrode potential is never attained. The extent of hydrogen evolution varies with the rate of nitrogen flow and the electrode structure so that the reliability of the data is affected. For this reason, we have determined the surface area by the reduction of potentiostatically chemisorbed oxygen. For these measurements, it is necessary to select a potential and adsorption time at which sizeable and reproducible chemisorption occurs, but at which no oxide formation or oxygen dissolution into the Pt lattice occurs. An adsorption potential of 1050 mV and adsorption time of 3 min were found most convenient for these measurements. The amount of charge (Q_{PtO}) determined by galvanostatic stripping at 10 mA/cm^2 was found to be very reproducible if the potential and time are well controlled, as shown in Fig. 4. The errors associated with random variation in the adsorption potential and adsorption time were carefully examined. Figure 5 shows the effect on the charge of changing the adsorption potential by a series of 20-mV increments. For convenience, the change is

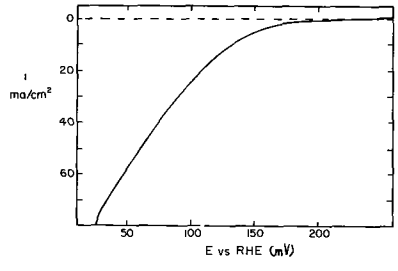

Fig. 3. H_2 evolution from PTFE-bonded Pt electrode under fuel cell conditions with N_2 flow; 85% H_3PO_4, 150°C; potential sweep: 10 mV/min.

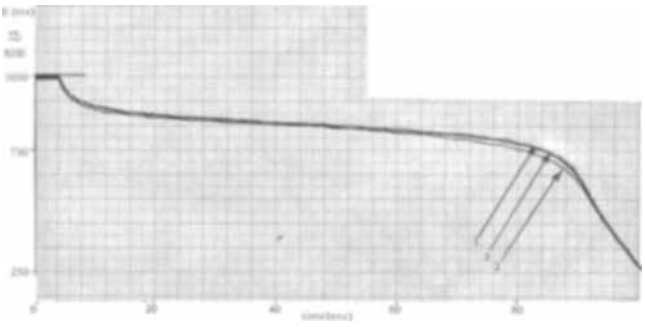

Fig. 4. Reproducibility of "electrochemical surface" determination by cathodic reduction of Pt-O. Pt-Teflon (20% TFE), 85% H_3PO_4, 150°C.

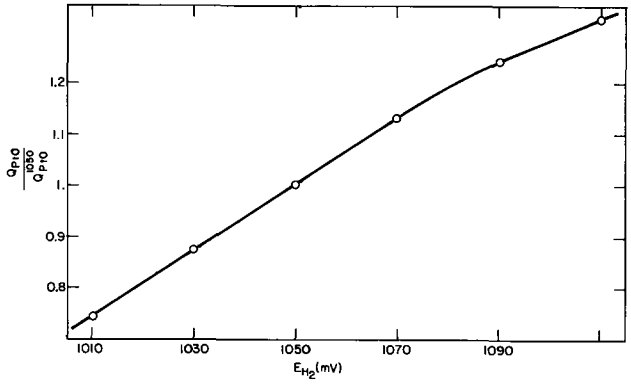

Fig. 5. Effect of potential on charge of chemisorbed oxygen

referred relative to the charge at 1050 mV. It can be seen that for a change of 10 mV (which is well above the maximum random variation to be encountered) the difference is about 7%. Figure 6 shows the effect on charge of varying the waiting time at 1050 mV. About 96% of the "steady-state" coverage is reached in 5 min, while in 3 min the coverage is 92%. In order to avoid the strongly bound oxygen which is formed after long waiting times, it was decided to measure all the charges after 3 min. Since this does not correspond to a steady-state coverage, it was necessary to control the adsorption time to better than 5 sec in order to obtain reproducible results.

A correlation between Q_{PtO} and Q_H was obtained by making measurements on the Teflon-bonded electrodes in a submerged rather than a floating position. Under these conditions, no hydrogen evolution is observed since only small quantities of dissolved H_2 are needed to satisfy the thermodynamic requirement at potentials above the reversible electrode. Table I shows that an average value for the Q_H/Q_{PtO} ratio is 0.58. Based on a saturation coverage of hydrogen on Pt of 0.21 mcoulomb/cm² of real surface, it can be concluded that 1 mcoulomb of adsorbed charge under the specified conditions of potential and time corresponds to 2.8 cm² of surface.

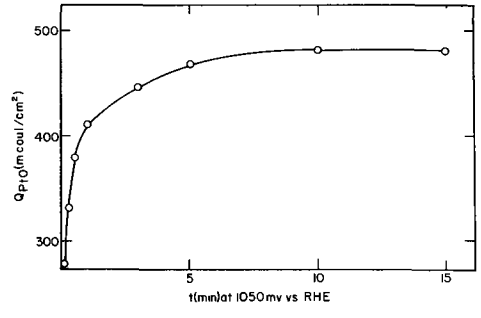

Fig. 6. Effect of waiting time at E = 1050 mV on galvanostatically determined Q_{PtO}.

Table I. Comparison of oxygen coverage formed at 1050 mV with hydrogen coverage (submerged electrode)

Electrode	% Teflon	Oxygen charge, mcoulombs/cm²	Hydrogen charge, mcoulombs/cm²	Q_H/Q_{PtO}
95C	20	484	291	0.61
94F	25	510	306	0.60
72A	30	540	297	0.55
98E	40	512	287	0.56
106D	14	532	307	0.58

Table II. Comparison of "electrochemical surface area" and BET surface area of Pt-Teflon electrodes (40% PTFE)

Electrode	Time in use (hours)	Measured Q_{PtO} (mcoulombs/cm²)	Calculated electrochemical surface (cm²/cm²)	Measured BET surface (cm²/cm²)
98B	0.5	825	2.3×10^3	2.6×10^3
98B	48	470	1.3×10^3	1.4×10^3
108E	0.5	650	1.8×10^3	3.3×10^3
108E	24	420	1.2×10^3	1.2×10^3

Long-term surface decrease.—When working at 150° in phosphoric acid, one of the problems encountered is the decay of surface area which is greatest in the first few hours, and then continues for days at a slower rate, as shown in Fig. 7. This surface decrease is due to sintering rather than loss of platinum as was shown by weighing the electrode after use. As is discussed later, this behavior was confirmed by BET measurements. X-ray diffraction measurements also showed an increase in crystallite size. All the surface measurements discussed here were carried out in a short enough period of time to be able to disregard change in area, due to sintering.

Comparison of electrochemical surface area and BET area.—By comparing the BET value of the surface with the electrochemical surface, calculated using the relationship between Q_{PtO} and real surface area of 2.8 cm²/mcoulomb, it is possible to determine the fraction of available Pt (*i.e.*, fraction of Pt which is both wet with electrolyte and in good electronic contact with the current collector). Table II shows a comparison of the electrochemical surface area and BET surface area for two 40% Teflon-bonded electrodes measured shortly after immersion and at various times up to 2 days in the electrolyte. In the case of electrode 98B, the initial and final values of the BET area and that determined electrochemically are surprisingly close. In the case of electrode 108E, the electrochemical surface area is 55% smaller than the ini-

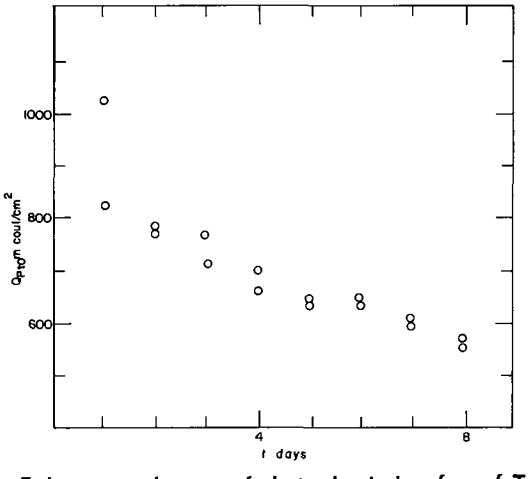

Fig. 7. Long-term decrease of electrochemical surface of Teflon-bonded electrode in 85% H_3PO_4 at 150°C.

tial BET value, but after use both surfaces are equal. This can be interpreted by saying that in good performing electrodes all the Pt surface is electrochemically available, at least at the current density of 10 mA/cm², used for the cathodic reduction of the PtO. The difference between the initial values with electrode 108E can be due to excessive wetproofing, which is highly probable since 40% Teflon content is about critical for this catalyst. For the comparisons of Table II, the surface area of the Teflon particles can be neglected since it is much smaller than that of Pt.

Comparison of electrochemical surface of completely immersed electrode under fuel cell conditions.—We have shown that the same value for the electrochemical surface area is obtained for the electrode in both the floating and fully submerged conditions. Table III shows the Q_{PtO} values for a number of electrodes with Teflon content varying from 14 to 40% under both circumstances. Complete wetting of the submerged electrode was ensured by evolving H_2 at the electrode for 2 min to remove any inert gases by a purging action; residual H_2 was readily oxidized before the surface area measurement. It can be seen that in this range of Teflon content both values are practically equal, indicating that all the Pt surface is electrochemically available in the floating electrode. This comment is strictly true only at the measuring current density of 10 mA/cm² but probably holds at significantly higher current densities, as is discussed below.

Effect of current density on cathodic stripping of chemisorbed oxygen under fuel cell conditions.—In order to study the Pt utilization at different current densities and to obtain an indication of the value of the *IR* drop in the electrolyte within the electrode structure, experiments were made in which the oxygen film formed potentiostatically at 1050 mV was reduced at a series of current densities. It can be seen from Table IV that the effect of current density on Q_{PtO} from 10-100 mA/cm² is only 3.7%. Analysis of the galvanostatic stripping curves shows no significant differences between the 10 and 100 mA/cm² curves. All these data indicate that up to 100 mA/cm² no measurable *IR* losses exist.

[1]According to our model, and using a specific conductivity of 0.55 ohm^{-1} cm^{-1} for 85% H_3PO_4 at 150°C (9), the ionic resistance between the electrolyte side and the gas side of an electrode with 50% macroporosity and 80% microporosity (as defined below) and 0.2 mm thick should be between 0.1 and 0.2 ohm-cm² depending on the tortuosity factor.

These results and calculations show again that practically 100% of the catalyst is wetted by the electrolyte. The much lower fraction of 2-5% of wetted catalyst reported by Austin and Almaula (10) can be due to the use of inefficient electrodes, in spite of the high currents obtained when used as H_2-anodes. Hydrogen oxidation can be misleading because of the very large exchange currents of this reaction on Pt, especially in acid solutions, so large that even electrodes with a very poor Pt utilization can deliver several A/cm². From this point of view, the oxidation of propane (Fig. 2) is a reaction more suited to test the utilization of a catalyst in a porous electrode structure because of its low exchange current.

The determination of microporosity and macroporosity.—For the mathematical treatment of Teflon-bonded electrodes, microporosity and macroporosity are extremely important. As microporosity we define the fraction of the flooded agglomerate, which is occupied by the electrolyte, while macroporosity can be defined as the fraction of the electrode which is not filled by the flooded agglomerate. According to the latter definition, the volumes occupied by Teflon, wire, and gas are added together, which is convenient for the mathematical treatment of Teflon-bonded electrodes when the gas transport along the unflooded pores is fast.

These definitions of macro- and microporosity are operational definitions different in general from the more frequently used concepts.

Both so defined "microporosity" and "macroporosity" can be determined by a careful gravimetric procedure involving the accurate determination of the weight of all the components of the dry electrode and of the amount of electrolyte which can be adsorbed in the electrode.

Table V shows these values for a large series of electrodes obtained with the same amount of Teflon but with different kinds of platinum black. It can be seen that microporosity changes from 80-90%, while macroporosity changes between 50 and 72%. A value of 80% for microporosity has also been reported by Horowitz (11) who also assumes the same qualitative model.

The accuracy of the gravimetric measurements on the electrode is poor due to the possible formation of droplets on the electrode surface. In order to improve the accuracy of these determinations, spheres of 0.9-cm diameter were prepared using mixtures of 30% Teflon by weight and commercial Pt black. In this way, the external surface of the mass is minimized and the error due to droplets is reduced. After sintering, the density of these spheres is the same as the calculated density of the Pt-Teflon mixture on the electrodes. Table VI shows the results obtained with two of

Table III. Comparison of "electrochemical surface area" of floating electrode and submerged electrode

Electrode	% TFE	Q_{PtO} floating, mcoulombs/cm²	Q_{PtO} submerged, mcoulombs/cm²
106D	14	520	530
95C	20	525	500
94F	25	496	510
72A	30	530	540
114A	30	650	665
140D	30	575	575
98E	40	518	512
98A	40	480	480
109A	40	585	580
108E	40	440	435

Table IV. Variation of Q_{PtO} with cathodic stripping current

Current density, mA/cm²	Q_{PtO} (mcoulombs/cm²)
10	757
30	756
50	753
70	724
100	730

Table V. Macroporosity and microporosity of Pt-Teflon electrodes (30% Teflon)

Electrode	Electrode thickness, (10^{-3} cm)	Macroporosity, β (%)	Microporosity, θ (%)
138B	16.0	65	82
141B	15.0	64	85
141D	15.0	71	80
144C	19.0	62	87
144D	17.0	55	90
144E	18.0	49	91
144F	17.0	63	89
145A	16.0	72	81
145C	16.0	58	87

Table VI. Macroporosity and microporosity of Pt-Teflon spheres (30% PTFE)

Sphere	Pt content (mg)	Teflon content (mg)	H_2O content (mg)	Macroporosity, β (%)	Microporosity, θ (%)
#1	438.8	207.3	193.3	46	89
#2	504.6	216.2	213.1	40	90

these spheres. It can be seen that the values of microporosity and macroporosity measured on the spheres are in good agreement with the values obtained with the electrode.

Agglomerate size.—During the present work, no attempts were made to determine the agglomerate size which is an important characteristic of the Teflon-bonded electrode since it determines in part (5) the radial utilization of the catalyst in the agglomerate. However, methods have been devised to do these determinations in the immediate future. A first, direct method of determining the diameter of the agglomerate is the use of a scanning electron microscope. A second method is an indirect method based on the reduction of CO_2 which, under the conditions of the present work (85% H_3PO_4 and 150°C) can be made to occur under exclusive diffusion control. This work will be the subject of another publication.

Conclusions

From this work, the following conclusions can be reached:

1. The conventional method of determining the surface area of Pt electrodes using anodic charging curves is not appropriate to determine the area of Teflon-bonded Pt electrodes under normal fuel cell conditions, due to excessive H_2 evolution
2. A method based on galvanostatic reduction of potentiostatically chemisorbed oxygen can be developed to great precision.
3. Under normal fuel cell conditions, all the Pt surface of Teflon-bonded electrodes in good electronic contact with the current collection grid is found to be in good ionic contact with the bulk of the electrolyte, indicating that the model of the flooded agglomerate is correct.
4. The *IR* drop between the front and back of the electrode, even at 100 mA/cm^2, is negligible for an electrode with 30% Teflon.
5. The microporosity of Teflon-bonded electrodes is about 80-90%, while the macroporosity varies from 50 to 72%.
6. Under the conditions used in this work, the performance (current density at a practical potential of 400 mV *vs.* RHE) of a Pt-Teflon electrode as a propane anode in 85% H_3PO_4 and at 150°C is almost independent of Teflon content in the range 20-40%, although the peak current increases with increasing Teflon content. The performance decreases sharply for Teflon contents of 15 and 50%.
7. In 85% H_3PO_4 and at 150°C, a decrease of the Pt surface is observed which can be completely attributed to sintering. This surface decrease is accompanied by growth of crystallite size which occurs even at potentials much below those at which PtO can be formed.

Acknowledgments

We are pleased to acknowledge support of this work by the U.S. Army Mobility Equipment Research and Development Center, Fort Belvoir, Virginia, under Contract DAAE-15-67-c-0048.

Manuscript submitted May 15, 1969; revised manuscript received Aug. 14, 1969. This was Paper 328 presented at the Montreal Meeting, Oct. 6-11, 1968.

Any discussion of this paper will appear in a Discussion Section to be published in the June 1970 JOURNAL.

REFERENCES

1. L. W. Niedrach and H. R. Alford, *This Journal,* **112,** 117 (1965).
2. R. G. Haldeman, W. P. Coman, S. H. Langer, and W. A. Barber, "Fuel Cell Systems," Advances in Chemistry Series No. 47, p. 106, American Chemical Society (1965).
3. J. Giner, Report to U.S. Army Engineer Research and Development Labs., Fort Belvoir, Va., Contract No. DA 44-009-AMC-410(T) (Oct. 31, 1965).
4. J. Giner, *Proc. Ann. Power Sources Conf.,* **21,** 10 (1967).
5. J. Giner and C. Hunter, *This Journal,* **116,** 1124 (1969).
6. J. Giner and S. Smith, *Electrochem. Technol.,* **5,** 61 (1967).
7. J. Giner, *This Journal,* **111,** 376 (1964).
8. W. T. Grubb and L. W. Niedrach, *Proc. Ann. Power Sources Conf.,* **17,** 69 (1963).
9. Monsanto Chemical Co., Tech. Bull. I-239.
10. L. G. Austin and S. Almaula, *This Journal,* **114,** 927 (1967).
11. H. H. Horowitz, *ibid.,* **114,** 650 (1967).

Samarium, Europium, and Ytterbium Electrode Potentials in LiCl-KCl Eutectic Melt

K. E. Johnson[1] and J. R. Mackenzie[2]

Department of Chemistry, Sir John Cass College, London, England

ABSTRACT

Samarium, europium, and ytterbium displace the alkali metals from their molten chlorides, forming the divalent species Sm(II), Eu(II), and Yb(II) in solution. Progressive coulometric reduction of solutions of $SmCl_3$, $EuCl_3$, and $YbCl_3$ in LiCl-KCl at 450°C enabled the redox potentials to be measured *vs.* 1m Pt(II)-Pt(0): Sm(III)-Sm(II) −1.729 ± 0.006V; Eu(III)-Eu(II) −0.554 ± 0.007V; Yb(III)-Yb(II) −1.375 ± 0.003V. Potentials of ytterbium systems starting from both $YbCl_3$ and $YbCl_2$ were followed over a ~200°C interval and from $\partial E^{\circ\prime}/\partial T(\mathrm{Yb}) - \partial E^{\circ\prime}/\partial T(\mathrm{Ag}) = 0.66 \times 10^{-3}$V deg^{-1}, ΔS° and ΔH° for the reaction $YbCl_3 \rightarrow YbCl_2 + \frac{1}{2}Cl_2$ in LiCl-KCl at 450°C were found to be 22 cal/deg^{-1} mole^{-1} and 54.5 kcal/mole^{-1}, respectively, close to the values for pure $YbCl_3$ decomposition. No evidence of disproportionation of Sm(II), Eu(II), and Yb(II) was found but scrupulous precautions were needed to keep the solvent free from impurities which readily react with the highly reducing ions, especially Sm(II). Considerable experimental details are included.

The existence of the divalent state for some rare earth elements is evident by the formation of well-defined crystalline halides, LnX_2. The stability of LnX_2 with respect to disproportionation is given by the free energy

$\Delta G^\circ_{\mathrm{disp.}} = 2\Delta G^\circ_{f(LnX_3)} - 3\Delta G^\circ_{f(LnX_2)}$ and, using a value of $\Delta S^\circ_{\mathrm{disp.}}$ for $NdCl_2$ of −15 eu, Polyachenok and Novikov (1) estimated $\Delta G^\circ_{\mathrm{disp.}}$ for all the solid rare earth dichlorides. Their calculations suggest that $PmCl_2$, $SmCl_2$, $EuCl_2$, $TmCl_2$, and $YbCl_2$ should be stable, and $NdCl_2$ and $ErCl_2$ might also exist. It is known that all the divalent rare earth ions may be incorporated into alkaline earth fluoride crystals (2).

Instability of the species Sm(II), Eu(II), and Yb(II) in the liquid state has been postulated to account for incomplete reduction of trihalides by hydrogen (3-5), but it has been pointed out (6) that the disproportionation reaction may be augmented by reaction of the rare earth metal with the material of the reaction vessel. Recent tensimetric studies (7-9) of $SmCl_3$, $EuCl_3$, and $YbCl_3$ showed that $LnCl_3$ was unstable with respect to dissociation into $LnCl_2$ and chlorine rather than $LnCl_2$ being unstable with respect to disproportionation.

From boiling points and other thermal data Polyachenok and Novikov (10) found $\Delta G^\circ_{1400^\circ}$ for the disproportionation of $SmCl_2$ (gas) to be +30 kcal/mol $SmCl_2$. Large positive values of $\Delta G^\circ_{\mathrm{disp.}}$ were also indicated for $EuCl_2$ and $YbCl_2$ but ΔG°_{1330} for $NdCl_2$ was −14 kcal/mol in agreement with the observation that $NdCl_2$ yielded only $NdCl_3$ and Nd on sublimation.

The rare earth dichlorides are soluble in water, but all except $EuCl_2$ rapidly reduce the solvent with evolution of hydrogen. In molten chloride solvents stable solutions might be expected in the light of the thermodynamic data reviewed above. Thermographic studies (11) of the systems KCl-$SmCl_3$-$SmCl_2$ and KCl-$YbCl_3$-$YbCl_2$ indicated the formation of compounds $LnCl_2 \cdot 2KCl$ and $LnCl_3 \cdot 3KCl$ and complex ions $LnCl_4^{-2}$ and $LnCl_6^{-3}$ were postulated to exist in the melts. There was no mention of instability of $SmCl_2$ and $YbCl_2$. Contrary to this, Campbell (12) postulated disproportionation of Sm(II), Eu(II), and Yb(II) in molten LiCl-KCl eutectic. He first estimated the standard redox potentials from chronopotentiometric data. Then, after exhaustive cathodic reduction of the Ln(III) species at controlled potential, the rate of change in concentration of Ln(III) and Ln(II) was obtained by monitoring the change in redox potential with time. Chronopotentiograms for the reduction of Ln(III) were recorded after successive exhaustive reductions and reoxidations at controlled potential. The quantity $i\,\tau_{1/2}$ (i = cathode current density, τ = transition time) decreased at each cycle, and this was said to rule out an oxidation process as responsible for the slow drift of redox potential. Dark deposits, formed in the vicinity of the electrode, were tentatively identified as the rare earth metal and taken as confirmation of a disproportionation process.

Theoretical calculations of emf's of formation cells in pure chlorides (13) do not support a disproportionation of solid or liquid $SmCl_2$. The Sm(III) − Sm(II) and Sm(II) − Sm(O) potentials calculated were −1.443 and −3.891V at 450°C and −1.171 and −3.559V at 1000°C. The present study was aimed at measuring the electrode potentials of Sm, Eu, and Yb in molten LiCl-KCl eutectic. Although only the redox potentials were obtained, the stability of the divalent halides in solution in LiCl-KCl has been established. The need to maintain solvent and solute of high purity became apparent in the investigation, and it seems pertinent to include in considerable detail the means of accomplishing this and to derive the possible magnitude of errors in the formal potentials.

Basic Equipment

Vacuum manifold.—The system employed a single-stage rotary pump in conjunction with a 1½ in. mercury diffusion pump. The rotary pump was of the air ballast type, and the system was capable of maintaining pressure lower than 5 x 10^{-5} Torr. In view of the corrosive nature of the gases pumped through the system, however, particular attention was paid to trapping, and adequate protection of the pumps was only assured by the use of three liquid nitrogen traps each with a cold region some 20 cm in length. These were interposed between the manifold and pump in a "back to back" arrangement.

Measurement of pressure down to 10^{-3} Torr was made with Pirani gauges placed in the high vacuum manifolds and in the backing systems. Lower pressures entailed the use of a Penning gauge. The gauge heads

[1] Present address: Department of Chemistry, University of Saskatchewan, Regina, Saskatchewan, Canada.
[2] Present address: Department of Chemistry, The University, Southampton, England.
Key words: samarium, europium, ytterbium, redox, melt, disproportionation.

were protected from chlorine and hydrogen chloride by further trapping. In consequence all pressures quoted later in this text refer to the partial pressure of "permanent" gases in the vacuum system.

Argon purification.—The purification reagents were contained in four stainless steel tubes (¾ in. OD and 32 in. in length) assembled in pairs. One pair was charged with copper made by hydrogen reduction of cupric oxide "wire," the other with tightly packed turnings of titanium-zirconium alloy. Each tube was closed by silver-soldering stainless steel plates across the ends and was connected into the system by side arms of copper. Either 3/16 in. OD copper tube or glass was used throughout with connections made by Simplifix couplings wherever possible. Silicone rubber pressure tubing was used for connections between copper tube and glass apparatus. Pressures lower than 5×10^{-3} Torr were readily attained in the system even with the reagent tubes at 700°C.

Hydrogen chloride.—This was generated from Analar hydrochloric and sulfuric acids. The concentrated acids were allowed to drip from dropping funnels down the two arms of a Y-shaped column packed with porcelain helices. Hydrogen chloride, generated as they mixed in the vertical section, was partially dried by counter current contact with sulfuric acid, and by bubbling through the concentrated acid in a wash bottle. The latter also constituted a rough indication of the rate of flow. Final drying was effected by passage through molecular sieve cooled in a slush bath of dry ice and acetone.

Chlorine.—Tank chlorine was scrubbed with H_2SO_4, dried by passage over freshly fused $CaCl_2$, and then over anhydrous $MgClO_4$. Although $FeCl_3$ was condensed with HCl in the final drying of that gas, it possibly remained as a contaminant of Cl_2.

Furnaces.—Generally, Nichrome V in either strip or wire was wound on mullite formers, using a lathe to obtain uniform tension and spacing of turns. On smaller furnaces, where finer wire was used, turns per inch were increased near the end of each tube for a distance equal to about 1½-2 times the diameter of each tube. This helped to offset the greater loss of heat at the ends of the tube and to ensure a more uniform hot zone.

For the argon purification furnace, some 25 ft of stainless steel sheathed Pyrotenax cable, taking a total load of 2 kw at 230V, was run backwards and forwards down a 2 ft length of 2 in. diameter mullite tube and held in position by Nichrome straps.

The two vertical tube furnaces employed for melt purification and electrochemical measurement were each suspended by a pulley and counterweight system in vertical Dexion guides to enable them to be raised or lowered as required.

Temperature measurement and control.—Temperatures were measured with calibrated T1/T2 alloy thermocouples and a Cropico potentiometer, also used for electrochemical measurements.

Temperature control of the argon purification furnace was maintained by a Fielden controller of the on/off type.

A more elaborate proportional control system was used for melt purification and electrochemical measurement to attain a temperature stability within the melt better than ±0.2°C. A T1/T2 alloy thermocouple with a cold junction cooled in ice was used as sensing element and was placed close to the furnace windings. The signal actuated an A.E.I. T.C.3. Proportional Controller the output from which, after amplification by a magnetic pre-amplifier operated a 2 kw saturable core reactor (Savage Transformers). This system (Fig. 1) had the advantage of high stability over long periods and was little affected by fluctuations in supply voltage. Operating temperatures could be easily altered, and,since the slave unit was a current control device,

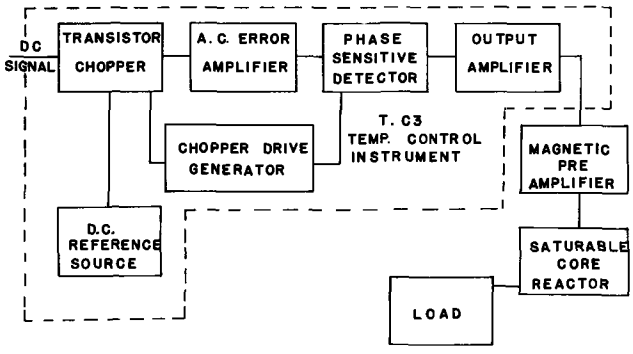

Fig. 1. Proportional temperature control system

there was little need for careful matching of load resistance to supply voltage. Heavy gauge windings could consequently be used on the furnaces without employing an intermediate matching transformer.

Coulometers.—Either a Metrohm coulometer or one of the following systems was used for the coulometric generation of solute species.

In the first system a Wadsworth Potentiostat (Southern Instruments Ltd.) was used to deliver constant current to the electrolytic cell during measured periods of time by maintaining a constant potential across a 2000 ohm potentiometer placed in the anode circuit of the cell. The current was monitored by measuring the iR drop across a 10 ohm standard resistor.

In the second system current of approximately the desired value was supplied from an H.T. battery to the cell via a resistance net-work and iR drop across a suitable resistor in series with the cell integrated over the time of generation by a mechanical integrator (Electro Methods). Calibration of this instrument was achieved by substituting a 10 ohm standard resistor for the cell and monitoring the current at short intervals over a period of an hour or more. Over narrow ranges of current a substantially linear response was observed and a precision of better than 0.2% was obtainable in the measurement of charge (14).

Preparation of Solvent

Reagents

Preliminary investigation showed that Analar KCl as supplied could contain 2-5 %ww of water removable by oven drying at 140°C, but no significant weight loss was observed on subjecting dried LiCl from freshly opened bottles to the same treatment. The entire contents of new 250g bottles of LiCl were weighed into a 5 kg jar and the calculated amount of finely powdered, oven dried, KCl added. The jar was then sealed and the contents well mixed by tumbling.

Apparatus

A filter tube containing the eutectic powder was supported inside a glass envelope by a flanged glass adaptor and provision made to collect melt either in the round bottom of the envelope for immediate electrochemical study, or in narrow, vertical, extension tubes fused to the bottom. Constrictions in the walls of these tubes enabled portions of melt each 50-70 ml in volume to be sealed off out of contact with the atmosphere. Vacuum or argon could be applied independently above or below the column and hydrogen chloride or chlorine could also be passed up the column and out to waste via a sulfuric acid guard trap.

The whole of the above assembly was supported at the flanges by a water-cooled brass annulus placed above a vertical tube furnace.

Procedure.—Hydrogen chloride treatment.—During early experiments the procedures adopted for melt purification closely followed those of Laitinen *et al.* (15). It was found, however, that extended periods of vacuum drying at room temperature did little to re-

duce the water content of the mixture. Therefore the temperature was raised slowly under vacuum immediately subsequent to charging the apparatus, while a manifold pressure of less than 10^{-3} Torr was maintained above and below the column of powder. With the onset of rapid evolution of water vapor the temperature was held steady until fluidization ceased and the pressure had returned to the above figure, when heating was resumed. At 300°C, after leaving overnight under vacuum, hydrogen chloride was admitted to the system and passed up through the powder at a pressure slightly in excess of atmospheric and the temperature again raised until sintering and finally melting took place. Under these conditions further copious evolution of water was apparent from the appearance of condensation in the upper portions of the filter tube, and the pressure above the filter was reduced to *ca.* 5×10^{-2} Torr for intervals of a few minutes to remove it.

After the greater part of the hydrogen chloride had been pumped off at pressures of the order of 10^{-3} Torr, vacuum was applied below the sinter and the melt slowly allowed to filter into the receiver. Careful admission of argon above the melt allowed the rate of filtration to be controlled.

Chlorine treatment.—The procedure adopted in the use of chlorine for melt pretreatment largely followed that already described for hydrogen chloride. Removal of dissolved chlorine prior to filtration was accomplished by evacuation above the sinter, 2-3 hr at a pressure of 5×10^{-4} Torr sufficing to remove all traces of the yellow coloration attributable to the gas in solution. Some HCl remained in Cl_2-treated melts, however.

With chlorine treatment no carbonaceous material was formed as melting occurred and it may be concluded that the heavy metal impurities, filtered off in this residue after hydrogen chloride treatment (16), were retained in solution.

Magnesium treatment.—Magnesium turnings were introduced prior to filtration while a stream of argon was bubbled through the melt in the filter. The best scavenging of the melt took place if Mg was left in contact overnight under vacuum.

Electrolysis.—Electrolysis was used as an alternative to Mg treatment.

The electrode assembly comprised a cylindrical tungsten cathode mounted in a tubular glass skirt coaxial with a graphite anode. The latter was a sliding fit in the short extension inside the skirt of the Pyrex tube supporting the assembly from a long tip cone joint (B34). This was sealed off to form a stopper to fit the top of the normal filter tube assembly used in gas pretreatment and was provided with two tungsten-to-glass seals. Molybdenum wires, one passing down the inside of the support tube, the other down the outside, welded to the tungsten lead-ins, enabled vacuum-tight electrical connection to be made with the two electrodes. Holes provided in the top of the skirt and of the support tube served the dual purpose of providing passage for these wires and of equalizing pressures throughout the assembly when in use. When in position in the filter tube the bottom of both electrodes finished about 1 cm above the sintered disk.

The glass skirt was cleaned in hot 40% perchloric acid and then well washed with distilled water before drying. The tungsten cathode was electropolished by anodization at 20V in 5*N* aqueous sodium hydroxide containing *ca.* 2 %wv of sodium nitrite. It was then well washed in distilled water and vacuum dried. New spectroscopic quality graphite rods were used as anodes, but it was necessary first to out-gas these by heating under high vacuum (10^{-5} Torr) to 500°C and then allowing them to cool in an atmosphere of chlorine.

Electrolysis of Cl_2-treated melt under a pressure of $<5 \times 10^{-3}$ Torr was carried out at 2.5V. Currents of the order of 40-60 mA were observed initially, but these decayed over periods of 6-12 hr by a factor of ten to values corresponding to cathode current densities less than 1.0 $\mu A/mm^2$.

Precautions.—All glassware was washed with hot detergent (R.B.S. 25 or Quadrilene) followed by boiling with either 30% perchloric acid or 1:1 hydrochloric acid and water, several rinses with hot distilled water and oven drying at 140°C. Water was removed from tubes by heating them with electrothermal heating tape throughout the melt pretreatment.

Preparation of Rare Earth Halides

The preparation of the trichlorides and dichlorides of Sm, Eu, and Yb has been mentioned briefly in connection with spectroscopic studies (17, 18). Details are discussed elsewhere (19).

Electrochemical Procedure

Metal ion-metal potentials.—Each electrode compartment was prepared by fusing a filter tube to the lower end of a "long tip" B19 cone, the upper end of which was joined to a B19 socket. A small hole in the wall of the compartment some 5 cm above the frit provided ingress for the argon atmosphere in the flask.

Platinum electrodes were made from 1 cm^2 foil attached to Pt wire sealed in 2 mm bore Pyrex tubing. The Pyrex sheath passed through a silicone rubber bung which served to support the electrode inside the compartment.

A samarium electrode was prepared by welding Pt to Sm with a strip of gold foil between the two metals.

A 250 ml multinecked, Quickfit flask received the HCl-treated and filtered melt which was then maintained at a temperature of 450° ± 2°C by a heating mantle controlled by an energy regulator of the Simmerstat type. Three electrode compartments were introduced, two bearing Pt and one Sm. A current of 5 mA was passed between the Pt electrodes to generate a Pt(II)-Pt(0) reference electrode.

In later experiments the third compartment was made from boron nitride[3] in the form of a blind tube which was a push fit in a short length of Pyrex tube fused to the lower end of a B19 cone assembly and was prevented from dropping through the former by a slight rim left at the open end. To permit ingress of the melt through the impermeable boron nitride a number of fine holes (0.1 mm diameter) were drilled through the blind end. The compartment, previously vacuum dried overnight at 450°-500°C, was filled by applying vacuum directly to its top.

Ytterbium electrodes consisted of pieces of ingot suspended from tungsten wire; 1 mm diameter dysprosium wire was polished with fine carborundum paper prior to use as an electrode.

Redox potentials.—The cell is depicted in Fig. 2 and the closure detailed in Fig. 3. It comprised a stainless steel center disk surrounded by a water-cooled aluminum alloy annulus and clamped to the flange of the glass envelope with an "O" ring seal forming a vacuum-tight joint. A Pyrex glass adaptor, fitted to a central tapered hole through a vacuum tight silicone rubber sleeve, enabled the apparatus to be connected to the argon and vacuum system by ball and socket joints, and a B10 cone joint at the top of the adaptor provided for the insertion of a thermocouple pocket. Additional holes accommodated Viton A "O" rings forming the seals for glass tubes passing through the disk. These tubes constituted the electrode compartments and terminated in glass frits at their lower ends, the upper ends being provided with B10 sockets. Each tube was sealed and locked into position by compression of the "O" rings by a duralumin annulus held in position by a clamping bar and set screws.

To adjust electrode height within the melt Pyrex hypodermic syringes of 2 ml capacity were used; a

[3] Kindly supplied by Dr. R. Biddolph of Messrs. Borax Consolidated Ltd.

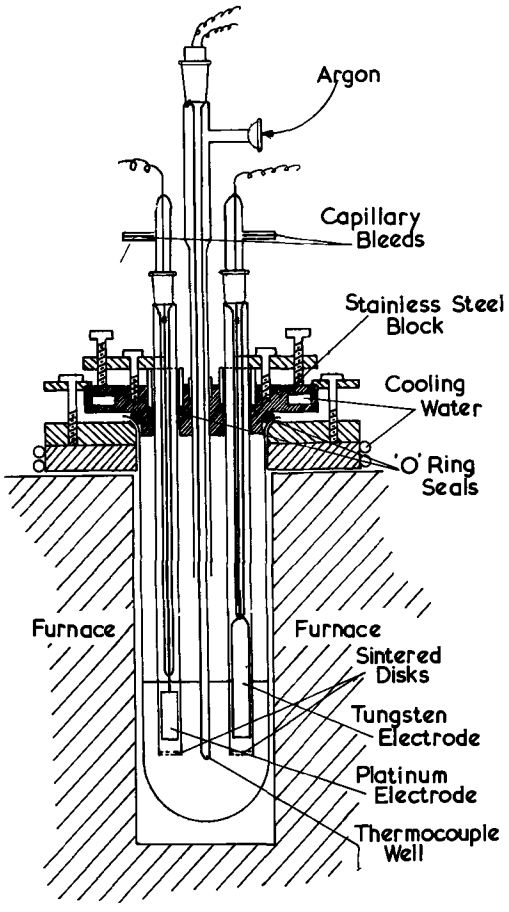

Fig. 2. Components of cell used in electrochemical measurements

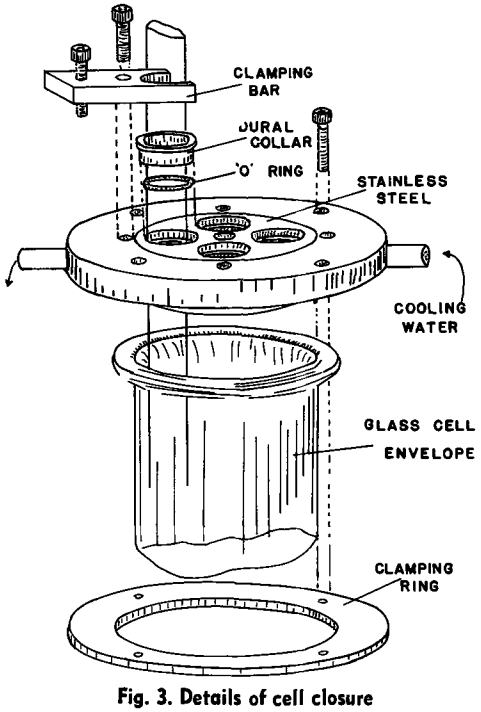

Fig. 3. Details of cell closure

B10 cone was fused to the outlet of each syringe barrel together with a short capillary side arm, while the plunger was joined to the upper end of the electrode stem.

Tungsten electrodes, made from 006-in. foil, were electropolished by anodization at 20V in 5*N* NaOH containing 1 %wv $NaNO_2$, and were vacuum dried and stored under dry argon.

Table I. Sm electrode potential vs. 1m Pt(II)-Pt(0) reference

Time, min	No. of coulombs	Potential, v
0	0.135	−3.370
10	0.135	−3.371
20	0.135	−3.364
25	0.135	−3.363
30	0.135	−3.366
30	0.336	−3.369
34	0.336	−3.366
45	0.336	−3.363
45	3.325	−3.366

Solvent was filtered into the cell envelope after the greater part of the dissolved gas had been pumped off. Argon was admitted and the filter tube assembly replaced by the electrolytic cell head with stoppered compartments above the melt level. The apparatus was then evacuated and left overnight in the furnace while the remaining hydrogen chloride was pumped off at pressure $\sim 1 \times 10^{-3}$ Torr. Argon was admitted at just above atmospheric pressure and the compartments immersed to 2-3 cm. A platinum electrode was inserted into one compartment, a tungsten one into another and solute (50-150 mg) weighed into the third before insertion of an indicator electrode (Pt or W). Throughout these operations a steady stream of argon was passed through the apparatus to prevent ingress of atmospheric oxygen and moisture.

When each compartment had filled to a depth of *ca.* 2 cm, its depth of immersion was adjusted until the level of its contents coincided with that of the bulk of the melt. Electrodes were then lowered into position and a thermocouple pocket introduced. While the temperature stabilized at 450°C, the Pt foil of the reference electrode was anodized (600 sec at 10 mA).

At the conclusion of each experiment electrodes were withdrawn from the melt and the stoppered compartments, complete with contents, were removed and allowed to cool in a dessicator. In the case of reference electrodes, solvent adhering to the outside was scraped away and the lower portion of each compartment was cut off and weighed. The contents were removed by boiling with water, dried glass reweighed, and the weight of solution obtained. Where it was more important to retain the compartment contents in an anhydrous state, cooling was carried out in a nitrogen filled drybox and the glass of the compartment carefully broken away from the solidified melt.

Results

Metal ion-metal potentials.—After anodizing for 1 min at 5 mA, a samarium electrode in a glass compartment had a potential of −2.9V[4] *vs.* a Pt(II)-Pt(0) reference electrode which decayed to −2.5V after 5 min, but could not be read again. On dismantling the apparatus, it was found that the immersed Sm was corroded, the Sm compartment had disintegrated into yellowish-green and black fragments; the flask bore heavy etches and dark brown stains; the orange color of Pt(II) in the reference compartment was lost, but the frit was covered by a gray residue; the bulk of the electrolyte was dark red and, on cooling *in vacuo*, formed a jade green solid which evolved hydrogen and left a turbid colorless solution when added to water.

Using a boron nitride compartment, a samarium electrode was inserted and anodized at 1.5 mA for various times. The consequent potentials appear in Table I.

The samarium electrode was corroded, and the melt in the compartment embrittled a piece of platinum immersed in it and, according to its persistent flame reaction, the platinum was impregnated with lithium. A silver spiral electrode, substituted for the corroded Sm electrode, assumed a stable potential which became more positive on successive anodizations. The time for stabilization after anodization decreased

[4] The IUPAC convention is used for electrode potentials.

from 50 min for the first to 15 for the fourth. Additional experimental evidence for the extreme reactivity of metallic samarium with molten alkali chlorides was provided in the following manner. Small portions of both caesium and potassium chorides (approximately 2g) were oven dried and then sintered first in a stream of dry hydrogen chloride, then under high vacuum, the temperature being finally raised until melting took place. The pellet of solidified material was transferred to a clean molybdenum boat and a bright chip of samarium ingot (*ca.* 20 mg) was placed on top. Boats were heated under a stream of pure dry argon in a clear silica combustion tube. As melting of the alkali halide occurred, the samarium metal was observed to dissolve with some violence with the formation of a very dark red to black solution. On cooling the solid product assumed a violet coloration.

Europium corroded very rapidly in the LiCl-KCl melt and a tungsten electrode inserted in the Eu compartment registered a potential of ~ -3V. Ytterbium corroded to an apple green solution and registered a potential of -3.0 to -3.5V. Dysprosium immediately blackened on immersion, then slowly corroded to give a pale violet solution containing Dy in some form and a dark solid. The Dy electrode had a potential of -2.809 ± 0.002V *vs.* 1M Pt(II)-Pt(0), and this potential was only transiently changed by anodization.

Redox potentials.—Samarium.—The potential of a tungsten indicator electrode in a solution initially containing $SmCl_3$ (at 450°C) was monitored as the Sm(III) was progressively reduced coulometrically. In two experiments out of some 30, stable potentials were measured and Nernst plots for one of these is shown in Fig. 4. Although the dark red color characteristic of Sm(II) persisted for some hours in other experiments no other reliable potential data were obtained.

Europium.—The details of four experiments in which platinum was employed as the cathode in progressive coulometric reduction of $EuCl_3$ in solution are presented in Table II.

The average of the first two experiments is an intercept of -0.554 ± 0.007V. One plot is shown in Fig. 5.

Ytterbium.—Nernst plots for four experiments at 450°C are combined in Fig. 6. Again, the concentrations were varied by progressive coulometric reduction at tungsten of vacuum sublimed $YbCl_3$ in solution. Details of these experiments appear in Table III together with two results obtained using less pure $YbCl_3$. The average of the points in Fig. 6 is a slope of 0.148V and an intercept of -1.375 ± 0.003V.

Table II. Europium redox potentials at 450°C

	Eu concentration, *M*	Cl in $EuCl_3$, %	Intercept, V
1.	0.22	40.2	−0.547
2.	0.26	40.9	−0.559
3.	0.092	38.8	−0.573
4.	0.14	38.4	−0.547

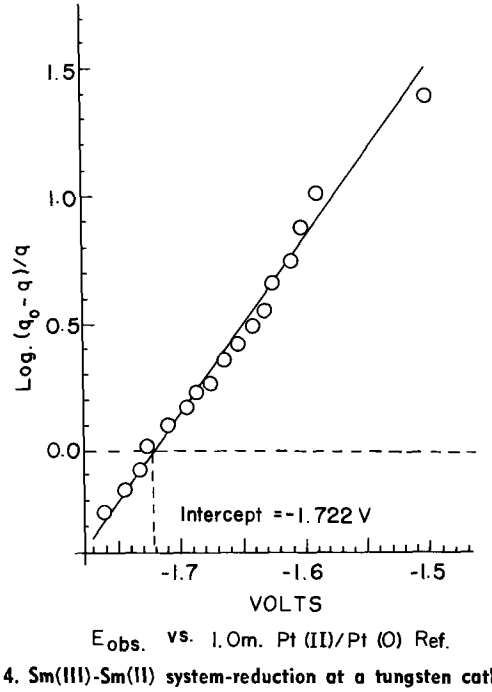

Fig. 4. Sm(III)-Sm(II) system-reduction at a tungsten cathode at 450°C.

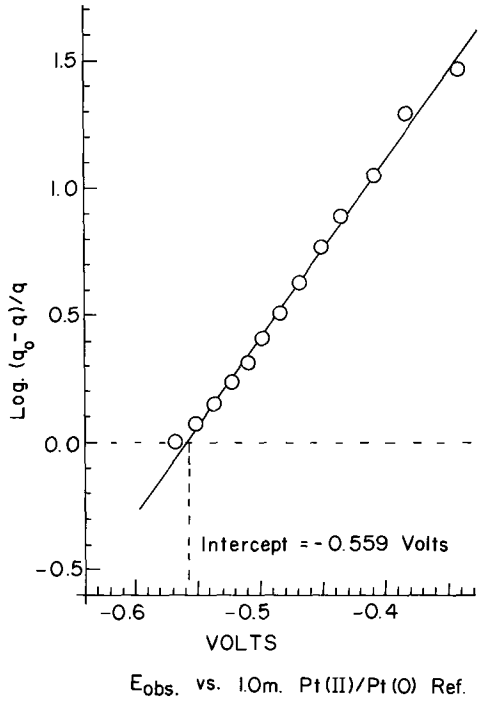

Fig. 5. Eu(III)-Eu(II) system-reduction at a platinum cathode at 450°C.

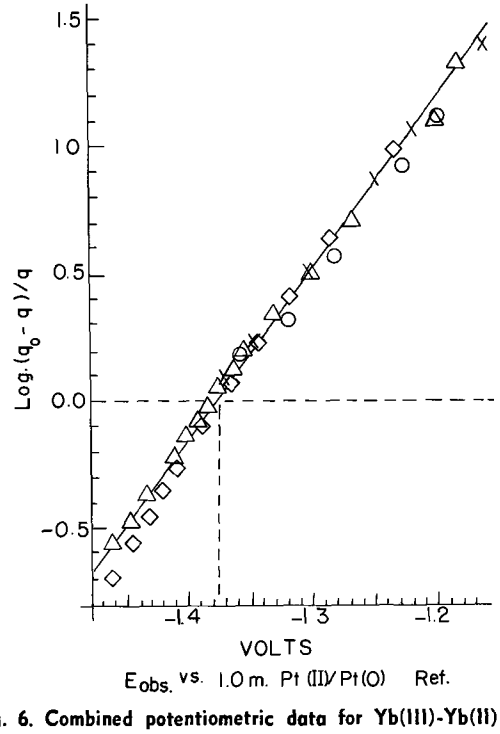

Fig. 6. Combined potentiometric data for Yb(III)-Yb(II) system. Nernst plots of four experiments at 450°C.

Table III. Ytterbium redox potentials at 450°C

	Yb concentration, m	Cl in $YbCl_3$, %	Slope of regression line, V	Intercept.* V
1.	0.18	37.94	0.130	−1.376
2.	0.052	37.94	0.154	−1.364
3.	0.04	37.26	0.136	−1.380
4.	0.12	37.92	0.137	−1.374
5.	0.054	35.25	0.169	
6.	0.07	29.2	0.124	

* The intercept is that of the least squares line of theoretical slope.

Table IV. Temperature dependence of Yb(III)-Yb(II) potential

	log Yb(III)/ Yb(II)	Potential at 458°C *vs.* 0.05m Ag(I)-Ag(0) Observed V	Calculated V	Isothermal coefficients $\left(\frac{\partial E}{\partial T}\right)_P$ mv deg^{-1}	$\left(\frac{\partial E^{o'}_{Yb}}{\partial T}\right)_P - \left(\frac{\partial E^{o'}_{Ag}}{\partial T}\right)_P$ mv deg^{-1}
1.	0.267	−0.432	−0.427	1.02	0.75
2.	0.002	−0.460	−0.465	0.92	0.70
3.	−0.105	−0.480	−0.480	0.89	0.69
4.	−0.378	−0.518	−0.519	0.87	0.71

Since Ag(I) solutions are more stable at the higher temperatures than Pt(II) solutions, a Ag(I)-Ag(0) reference electrode was employed in studies of the temperature dependence of the potential. In one experiment a solution of $YbCl_3$ was partially reduced and potentials measured over a cycle from 360° to 600°C at 10° temperature intervals. Then the $YbCl_3$ was further reduced and the cycling repeated. In a second experiment a solution of $YbCl_2$ was partially oxidized, cycled, further oxidized and recycled. No hysteresis was observed in the emf *vs.* temperature relations, and the potential values observed at 450°C agreed well with those calculated from the standard potential of −1.375V as obtained above. Figure 7 and Table IV summarize the data.

Discussion

Metal ion-metal potentials.—It is clear that samarium displaces the alkali metals from their fused chlorides. The potential of the samarium electrode in the boron nitride compartment is close to the lithium potential measured by Liu (20) with a tungsten indicator electrode (−3.320V). The red solution contained Sm(II) which could be oxidized to Sm(III) at a silver anode. The lithium formed would alloy with platinum, but not silver, and be capable of vicious attack on Pyrex glass.

Europium and, less violently, ytterbium also displaced Li from LiCl-KCl to form solutions of the divalent ions. The (II)-(0) potentials of these three metals in LiCl-KCl must therefore be more negative than the lithium potential, as are the predicted reduction potentials of the pure dichlorides (6, 13). The measurements with dysprosium were inconclusive: the calculated Dy(III)-Dy(0) potential of −2.901V (13) suggests that Dy(III) may be involved but then corrosion by Li^+ oxidation becomes ruled out.

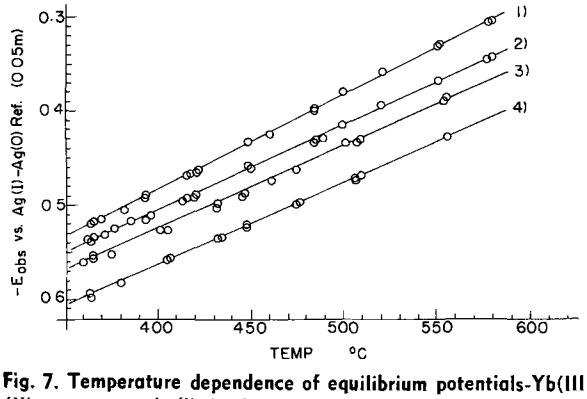

Fig. 7. Temperature dependence of equilibrium potentials-Yb(III)-Yb(II) system *vs.* Ag(I)-Ag(0) reference at the same temperature.

Redox potentials.—Stable equilibrium potentials for the three systems were linearly dependent on $\log_{10}$ Ln(III)/Ln(II) calculated on the basis of 100% current efficiency (see Appendix) for the reduction processes. Nernst slopes were close to 0.143V = 2.303 RT/F at 450°C, indicating a one electron process. Confirmation of the identity of the reduced species was provided by spectroscopic studies which showed that solutions obtained by electrolytic or magnesium reduction of the trichlorides or directly from the dichlorides had identical broad band uv-visible spectra (17) now accepted as Laporte-allowed $4f^n \rightarrow 4f^{n-1}5d$ transitions of divalent lanthanide ions.

The large number of unsuccessful experiments with samarium emphasizes that this study was at the limit of the materials and techniques adopted, primarily because one species is a highly mobile ion with the reducing power of aluminum metal. Only traces of oxidizing impurities such as hydrogen, heavy metal, or silicate ions in solution or adsorbed on the glass would upset the system, and any deterioration of the glass, once begun, appeared to proceed relentlessly.

The least difficulty was experienced with the ytterbium system but the less pure $YbCl_3$ samples (5 and 6) gave rise to curved Nernst plots and turbid green solutions. It is likely that Yb_2O_3 and YbOCl were present in such impure samples.

High-purity $EuCl_3$ was not easy to prepare and initial experiments with nominally pure material gave curved Nernst plots. All samples had mild reducing properties suggesting the presence of $EuCl_2$ as well as the expected oxide and oxychloride. One odd observation was the slight turbidity of solutions of the $EuCl_3$ in LiCl-KCl but the clarity of its aqueous solutions.

The formal potentials (on a molal scale) at 450°C are summarized in Table V together with those for some other related systems.

Thermodynamic calculations.—From the redox potentials one can calculate the free energy change for the reaction

$$LnCl_3(soln.) \rightleftharpoons LnCl_2(soln.) + \tfrac{1}{2}Cl_2(g)$$

In Table VI the results are compared with calorimetric and tensimetric data for the reaction

$$LnCl_3 \rightleftharpoons LnCl_2 + \tfrac{1}{2}Cl_2$$

The calculated differences in free energies of solution of trivalent and divalent chlorides are small and reasonable using Polyachenok's data (Line 1-Line 2) but large (Line 1-Line 3) if the calorimetric data, obtained with less pure materials and with greater errors, are employed.

Differentiation of the Nernst equation and substitution of the working concentrations of ions leads to a mean value of (0.71 ± 0.02) × 10^{-3} volt/deg^{-1} for

Table V. Standard potentials in LiCl-KCl at 450°C

System	Potential $E^{o'}_m$, V	Error	Reference
Li(I)-Li(0)	−3.320	0.002	(20)
	−3.364		This work
Mg(II)-Mg(0)	−2.580	0.002	(20)
Al(III)-Al(0)	−1.767	0.009	(20)
Sm(III)-Sm(II)	−1.729	0.006	This work
Yb(III)-Yb(II)	−1.375	0.003	This work
Ag(I)-Ag(0)	−0.727	0.002	(20)
HCl-$\frac{1}{2}H_2$	−0.710	0.005	(22)
W(II)-W(0)	−0.585		(23)
Eu(III)-Eu(II)	−0.554	0.007	This work
Pt(II)-Pt(0)	0		(20)
$\frac{1}{2}Cl_2$-Cl$^-$	+0.306	0.002	(21)

Table VI. Thermodynamic aspects of $LnCl_3 \rightleftharpoons LnCl_2 + \frac{1}{2}Cl_2$
ΔG° in kcal · mol^{-1} at 450°C

	$SmCl_3$	$LnCl_3$ $EuCl_3$	$YbCl_3$	Method	Reference
1.	46.9	19.6	38.8	Potentiometric	This work
2.	42.6	18.4	37.5	Tensimetric	(8)
3.	31.0	11.6	20.5	Calorimetric	(6)
1-2.	4.3	1.2	1.3		
1-3.	15.9	8.0	18.3		

$\left(\frac{\partial E^{o'}_{Yb}}{\partial T}\right)_P - \left(\frac{\partial E^{o'}_{Ag}}{\partial T}\right)_P$. This becomes 0.66×10^{-3} volt/deg^{-1} on the mole fraction concentration scale (24) and taking $\left(\frac{\partial E^{o'}_{Ag}}{\partial T}\right)_P = 0.292 \times 10^{-3}$ volt/deg^{-1} (25) we obtain $\Delta S^\circ = \mathbf{F}T\left(\frac{\partial E^{o'}_{Yb}}{\partial T}\right)_P =$ 22 cal/deg^{-1}·mol^{-1} and $\Delta H^\circ = -\mathbf{F}E + \mathbf{F}T\left(\frac{\partial E^{o'}_{Yb}}{\partial T}\right)_P$ = 54.5 kcal/mol^{-1} for the redox reaction in solution in satisfactory agreement with values extrapolated from Polyachenok's work of 18 cal·deg^{-1}/mol^{-1} for ΔS° and 51.5 kcal/mol^{-1} for ΔH° for the dissociation of pure $YbCl_3$ (8).

Acknowledgment

This work was supported by the Ministry of Technology, London.

APPENDIX

Errors in Redox Potential Measurements

(*a*) *Restricted solubility and current efficiency.*—Where solubility of the reduced species is limited, passage of charge q_s may saturate the solvent with Ln(II) and for $q > q_s$

$$E = E^{o'} + \frac{RT}{\mathbf{F}} \ln (q_o - q) + \text{const.}$$

which means a sharp increase in Nernst slope. If Ln(III) is sparingly soluble, a similar departure from the ideal equation applies at $q < q_o - q_s$.

Where the added solute contains Δq_o of insoluble material the deviation, ΔE, of the observed potential from the expected linear relation may be written as a series

$$E = -RT\left(\frac{\Delta q_o}{q_o - q} - \frac{\Delta q_o^2}{2(q_o - q)^2} + \ldots\right)$$

Provided $q < \frac{1}{2}q_o$, linearity and slope of the E *vs.* $\ln(q_o - q)/q$ plot are little affected even at 20% contamination. The error in $E^{o'}$ can be shown to be ~ -0.6 mV per 1%.

Loss of current efficiency obeys a similar equation and introduces an error in $E^{o'}$ of +1 mV per 1% loss provided $q < \frac{1}{2}q_o$.

(*b*) *Solute impurities.*—If the solute initially contains reduced species equivalent to the passage of a charge Δq_o then

$$E = E^{o'} + \frac{RT}{\mathbf{F}} \ln \frac{q_o - (q + \Delta q_o)}{q + \Delta q_o}$$

The deviation is negative and gives rise to pronounced curvature of the E *vs.* $\ln(q_o - q)/q$ plot and the magnitude of $\Delta E^{o'}$ is much larger in this case. However, the systematic errors in $E^{o'}$ taken from linear plots appear to be less than the random errors.

Manuscript submitted Feb. 11, 1969; revised manuscript received July 30, 1969. This was Paper 190 presented at the New York Meeting, May 4-9, 1969.

Any discussion of this paper will appear in a Discussion Section to be published in the June 1970 JOURNAL.

NOMENCLATURE

ΔG° disp., ΔG°_f,	Gibbs free energy of disproportionation, formation, etc. kcal/mol^{-1}.
i,	current density, A/cm^{-2}.
τ,	transition time, sec.
E,	electrode potential according to IUPAC convention, V.
$\left(\frac{\partial E}{\partial T}\right)_P$, $\left(\frac{\partial E^{o'}}{\partial T}\right)$	isothermal coefficients of measured and formal potentials, mV/deg^{-1}.
$E^{o}_{m'}$,	formal potential on molal concentration scale, V.
ΔS°, ΔH°,	standard entropy and enthalpy, cal deg^{-1} mole^{-1} and kcal/mole^{-1}, respectively.
q, q_o,	charge, coulombs.
ΔE,	deviation of electrode potential, V.

REFERENCES

1. O. G. Polyachenok and G. I. Novikov, *Zhur. neorg. Khim.*, **8,** 1567 (1963).
2. D. McClure and Z. J. Kiss, *J. Chem. Phys.*, **39,** 3251 (1963).
3. G. Jantsch and N. Skalla, *Z. anorg. Chem.*, **193,** 391 (1930).
4. G. Jantsch, N. Skalla, and H. Jawarek, *Z. anorg. Chem.*, **201,** 207 (1931).
5. G. Jantsch, N. Skalla, and H. Grubitsch, *ibid.*, **212,** 65 (1933).
6. L. Brewer, L. A. Bromley, P. W. Gilles, and N. Lofgren, "The Chemistry and Metallurgy of Miscellaneous Materials," L. L. Quill, Editor, McGraw Hill Book Co., New York (1950).
7. G. I. Novikov and A. K. Baev, *Zhur. neorg. Khim.*, **7,** 1349 (1962).
8. O. G. Polyachenok and G. I. Novikov, *ibid.*, **9,** 773 (1964).
9. O. G. Polyachenok and G. I. Novikov, *ibid.*, **8,** 1526 (1963).
10. O. G. Polyachenok and G. I. Novikov, *ibid.*, **8,** 2631 (1963).
11. G. I. Novikov, O. G. Polyachenok, and S. A. Frid, *ibid.*, **9,** xx (1964).
12. G. M. Campbell, Ph.D. Thesis 1963, Vanderbilt University, Univ. Microfilms Inc. No. 64, 4739.
13. W. J. Hamer, M. S. Malmberg, and B. Rubin, *This Journal*, **112,** 750 (1965).
14. J. J. Lingane, "Electroanalytical Chemistry," p. 347, Interscience Publishers, Inc., New York (1958).
15. H. A. Laitinen, W. S. Ferguson, and R. A. Osteryoung, *This Journal*, **104,** 516 (1957).
16. D. K. Roe, Ph.D. Thesis University of Illinois, 1959.
17. K. E. Johnson, J. R. Mackenzie, and J. N. Sandoe, *J. Chem. Soc.*, **1968,** A2644.
18. K. E. Johnson and J. N. Sandoe, *Can. J. Chem.*, **46,** 3457 (1968).
19. K. E. Johnson and J. R. Mackenzie, *J. Inorg. Nucl. Chem.*, In press.
20. H. A. Laitinen and C. H. Liu, *J. Am. Chem. Soc.*, **80,** 1015 (1958).
21. H. A. Laitinen and J. E. Pankey, *ibid.*, **81,** 1053 (1959).
22. H. A. Laitinen and J. A. Plambeck, *ibid.*, **87,** 1202 (1965).
23. K. E. Johnson and J. R. Mackenzie, *Anal. Chem.*, **41,** 1483 (1969).
24. H. A. Laitinen, R. P. Tischer, and D. K. Roe, *This Journal*, **107,** 546 (1960).
25. E. J. Salstrom, *J. Am. Chem. Soc.*, **56,** 1272 (1934).

Current Distribution on a Rotating Disk Electrode

Vinay Marathe and John Newman

Inorganic Materials Research Division, Lawrence Radiation Laboratory, and Department of Chemical Engineering, University of California, Berkeley, California

ABSTRACT

The radial variation of deposit thickness on a rotating disk electrode was measured for deposition of copper from a solution 0.1*M* in $CuSO_4$ and 0.1*M* in H_2SO_4. The results confirm the theory of nonuniform current distribution on such electrodes below the limiting current.

The basic theory of the rotating disk electrode was developed by Levich in 1942. Since then, considerable work has been done to refine the theory of this electrode system. It has been widely used for the study of electrode processes and mass transfer in electrochemical systems. Measurement of diffusion coefficients and bulk concentrations and the study of moderately fast electrode reactions are some of the common applications. Theoretically predictable velocity and concentration profiles and elimination of natural convection effects due to strong forced convection make it suitable for the above-mentioned and other applications. Furthermore, the current density is uniform at the limiting current.

Recently, Newman (6) has shown that below the limiting current the current density is nonuniform and can be obtained by solving for the concentration and potential distribution simultaneously (subject to electrode kinetic boundary conditions). The convective diffusion equation for the diffusion layer can be replaced by an integral equation (7, 8, 13) relating the reactant concentration and the normal derivative of the reactant concentration at the electrode surface

$$i = \frac{n\mathbf{F}D}{1-t_+}\frac{\partial c}{\partial y}\Big|_{y=0} = \frac{n\mathbf{F}D}{1-t_+}\left(\frac{a\nu}{3D}\right)^{1/3}\sqrt{\frac{\Omega}{\nu}} \left\{ \frac{c_\infty - c_0(0)}{\Gamma(4/3)} - \frac{r}{\Gamma(4/3)}\int_0^r \frac{dc_0}{dr}\Big|_{r=x}\frac{dx}{(r^3-x^3)^{1/3}} \right\} \quad [1]$$

where i is the current density on the disk and c_0 and c_∞ are the surface and bulk concentrations of the reactant.

The potential distribution outside the diffusion layer satisfies Laplace's equation and can be expressed as a series solution, from which one obtains

$$\Phi_0 = \frac{RT}{Z\mathbf{F}}\sum_{n=0}^{\infty} B_n P_{2n}(\eta) \quad [2]$$

and

$$i = -\kappa_\infty \frac{\partial \Phi}{\partial y}\Big|_{y=0} = -\frac{\kappa_\infty}{r_0\eta}\frac{RT}{Z\mathbf{F}}\sum_{n=0}^{\infty} B_n P_{2n}(\eta) M_{2n}'(0) \quad [3]$$

Here η and ξ are rotational elliptic coordinates defined by

$$y = r_0\xi\eta \text{ and } r = r_0\sqrt{(1+\xi^2)(1-\eta^2)}$$

and Φ_0 is the ohmic drop extrapolated to the disk surface, $P_{2n}(\eta)$ is the Legendre polynomial of order $2n$, and $M_{2n}(\xi)$ is a Legendre function satisfying

$$\frac{d}{d\xi}\left[(1+\xi^2)\frac{dM_{2n}}{d\xi}\right] = 2n(2n+1)M_{2n}$$

with boundary conditions

$$M_{2n} = 1 \text{ at } \xi = 0 \text{ and } M_{2n} = 0 \text{ at } \xi = \infty$$

The disk, being metallic, should be at a uniform potential V (applied voltage), and therefore

$$V = \Phi_0 + \eta_s + \eta_c \quad [4]$$

where η_s and η_c are the surface and concentration overpotentials; these are computed from

$$\eta_c = \frac{RT}{Z\mathbf{F}}\left[\ln\left(\frac{c_0}{c_\infty}\right) + t_+\left(1-\frac{c_0}{c_\infty}\right)\right] \quad [5]$$

$$i = i_0\left(\frac{c_0}{c_\infty}\right)^\gamma\left[\exp\left\{\frac{\alpha Z\mathbf{F}}{RT}\eta_s\right\} - \exp\left\{-\frac{\beta Z\mathbf{F}}{RT}\eta_s\right\}\right] \quad [6]$$

where i_0 is the exchange current density, γ is the slope of a logarithmic plot of exchange current density *vs.* concentration, and α, β are electrode kinetic parameters.

Simultaneous solution of Eq. [1] through [6] yields the current distribution. Results obtained by iterative calculation have been described in the literature (6, 8). The current distribution depends on the parameters

$$N = -\frac{nZ\mathbf{F}^2Dc_\infty}{RT(1-t_+)\kappa_\infty}r_0\sqrt{\frac{\Omega}{\nu}}\left(\frac{a\nu}{3D}\right)^{1/3} = \Gamma(4/3)\,i_{\lim}\frac{Z\mathbf{F}}{RT}\frac{r_0}{\kappa_\infty}$$

$$\delta = i_{avg}\frac{Z\mathbf{F}}{RT}\frac{r_0}{\kappa_\infty}$$

$$J = i_0\frac{Z\mathbf{F}}{RT}\frac{r_0}{\kappa_\infty}$$

and α, β, γ, and t_+. N, δ, and J can be considered as the dimensionless limiting, average, and exchange current densities, respectively.

The aim of this work was to study the current distribution experimentally for comparison with theoretical results. Newman's theory is valid for metal deposition from a single salt and for the reaction of a minor component with excess supporting electrolyte. The metal deposition reaction from copper sulfate-sulfuric acid at copper electrodes was chosen for experimental work.

Experimental Technique

The metal deposition reaction will result in a copper deposit on the electrode surface, and this will be proportional to the current distribution if the density (g/cm^3) of the deposit is uniform. Experimental measurements of the deposit thickness would thus yield the current density distribution.

To maintain the theoretically predicted velocity profiles, the deposit thickness should be very small compared to the momentum boundary layer ($\approx 5 \times 10^{-2}$ cm). The active surface of the disk should be considerably smaller than the total surface and the cell size for approximating the assumptions of the hydrodynamic and potential distribution models. These restrictions limit the application of several thin film

measurement techniques like radiographic methods, ultrasonic testing methods, and eddy-current testing. Tolansky (12) has reported the measurement of electrodeposited films by employing interferometry. In our experiments, the deposits were found to be fairly bright but not smooth enough to give an interference pattern. Additives for obtaining bright and smooth deposits could not be employed in the present work since they could alter the transport properties and the electrode kinetic parameters of the system.

In this work, the deposit distribution was measured with a precision optical instrument by sectioning the electrode at a plane passing through its axis. The electrode was embedded in a hard epoxy resin to prevent burring of the deposit during machining.

Design of the Rotating Disk Electrode System

Disk electrodes of various shapes and designs have been used in the past. In a review on the rotating disk system, Riddiford (10) has summarized the various designs and recommended several design criteria based on theoretical and experimental considerations. These criteria attempt to attain the theoretical hydrodynamic model and concentration profile by minimizing the edge effects and ensuring laminar flow. The potential distribution is valid for a finite disk embedded in an infinite insulating plane with walls and counterelectrode at infinity. This can be achieved for a disk electrode if it satisfies the above-mentioned criteria and if the polarization is confined to the disk electrode. Angell, Dickinson, and Greef (2) have measured the potential distribution for disk electrodes satisfying Riddiford's criteria and found the results to be in qualitative agreement with Newman's theory (5, 6). The disk electrode was carefully designed (3) to meet the criteria set up by Riddiford and others. Only the central portion of the lower surface of the disk is active. A rotating disk electrode is shown in Fig. 1. The disk electrode specifications are:

Outside diameter, cm	4
Active surface diameter, cm	0.5
Disk thickness, cm	0.1
Shaft diameter, cm	0.8

The Lucite cell is 14 cm in diameter and 10 cm high. It has a circular inset in the bottom for the anode. The copper anode is 7.5 cm in diameter, *i.e.* more than 200 times larger than the cathode (this confines the polarization effects to the cathode). The electrical connection to the anode is through a screw at the bottom of the cell, and the opening is made liquid tight with a rubber ring in a groove.

The central copper portion of the rotating disk electrode is machined to dimensions and cast in epoxy resin. The epoxy, on curing, is machined to the dimensions (specified earlier) and shape shown in Fig. 1.

Experimental Set-Up and Procedure

A Lambda Model 2B regulated power supply was used as a constant current source. The current was measured with a Keithley Model 610R electrometer to an accuracy of ±2%. Electrical connection to the rotating disk electrode was achieved by means of a mercury well. The disk was mounted on a spindle with ⅜-in. 24 TPI left-handed threads. The spindle was tightly fitted in two ⅞-in. OD New Departure RC bearings. To minimize eccentricity, the bearings were mounted inside a heavy brass bearing case. The spindle was coupled to the shaft of a variable speed motor (Bodine Electric Company, Type NSE 11R, with a gear ratio of 10-1) controlled by a precision d-c voltage power supply. The speed of rotation was determined by a General Radio Type 631-BL strobotac with an accuracy of ±1%. The temperature was maintained at 25.0° ± 0.1°C by immersing the cell in a water bath.

Since the rugosity of the disk surface should be considerably less than the momentum boundary layer thickness, the disk surface was subjected to the following treatment before deposition:

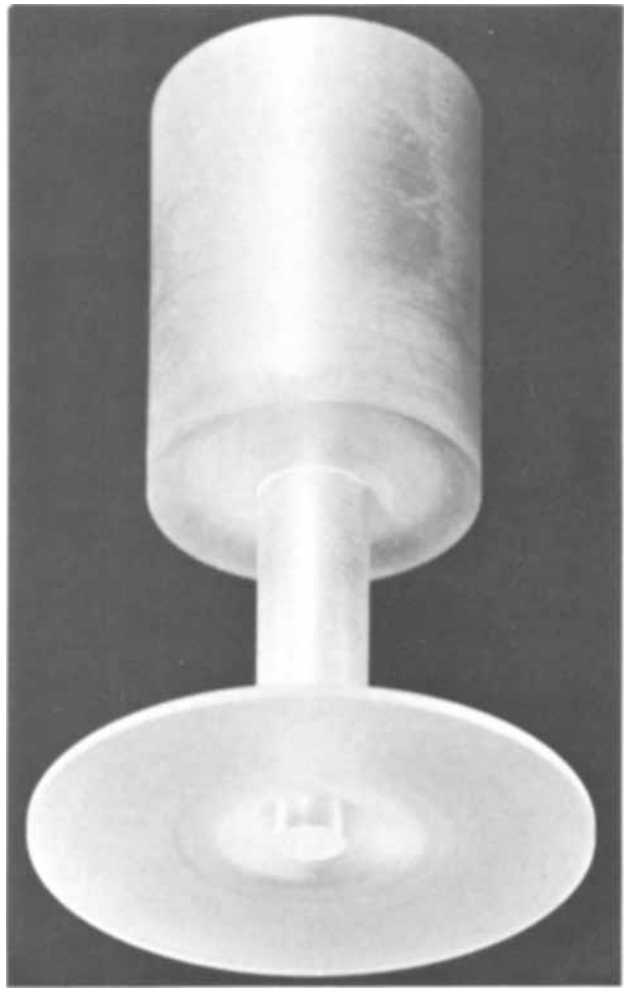

Fig. 1. The rotating disk electrode

1. The disk surface was polished successively on No. 0, 00, 000, and 0000 emery papers using kerosene as a lubricant. The last paper has a grain size of 15-20μ.
2. The electrode surface was polished on a wheel mounted with canvas cloth (Diamond Abrasive 1μ) at moderate speeds with kerosene as lubricant.
3. The surface was next polished on a wheel mounted with Microcloth using γ-alumina (0.05μ) as the grinding compound.
4. The electrode surface was cleaned with isopropyl alcohol or carbon tetrachloride.
5. The electrode was rinsed with distilled water followed by the electrolyte.

For ease and accuracy of measurement, a fairly nonuniform and smooth deposit is desirable. With copper sulfate only, the deposit was very rough and, with considerable excess of sulfuric acid, the deposit was not sufficiently nonuniform to measure the variation in deposit thickness accurately. Consequently, the electrolyte concentration chosen was 0.1*M* copper sulfate and 0.1*M* sulfuric acid. As mentioned earlier, the deposit thickness should be considerably less than the momentum boundary layer thickness ($\approx 5 \times 10^{-2}$ cm). Consequently, the time of deposition was chosen such that the maximum deposit thickness was less than 2×10^{-3} cm. Deposition times were 15-30 min.

After deposition, the disk electrode was washed with water followed by isopropyl alcohol. It was then embedded in an epoxy resin made up of:

100 parts by weight of Resin 826 (Shell Chemical Company)
10 parts by weight of LP3 (accelerator, Thiokol Chemical Company)

15 parts by weight of D40 (catalyst, Furane Plastics Company)

The embedding was done by pumping the resin down into a vacuum to eliminate bubbles and gaps at boundaries and curing at 65°C for 16 hr. One half, toward the axis, was machined off on a milling machine, leaving about 5/1000 in. for polishing and etching.

The sectioned electrode was polished as described earlier for surface treatment. It was then etched (etchant: 50 parts distilled water, 50 parts ammonium hydroxide, and 20 parts of 30% hydrogen peroxide) so that the deposit could be distinguished from the electrode due to differences in grain structure. The deposit was then observed with a metallographic microscope and microphotographs (X 1000) of the deposit layer obtained at various points by a Polaroid camera attached to the metallograph.

Results

The theoretical current distribution depends on the parameters N, J, δ, α, β, γ, and t_+ defined earlier. For computing N and J, data on ν, D, κ_x, and i_0 are needed. Kinematic viscosities (ν) and diffusion coefficients (D) were obtained from a correlation of physical properties for the copper sulfate-sulfuric acid system by Selman, Hsueh, and Newman (11). Conductivities were obtained from data reported by Richardson and Taylor (9). Data on transference numbers t_+ for the copper sulfate-sulfuric acid system were not available, so these were back-calculated from limiting current density measurements by Selman (unpublished). The exchange current density was extrapolated from the data of Mattsson and Bockris (4). The kinetic parameters α, β, and γ were also obtained from the work of Mattsson and Bockris (4) and the values used are

$$\gamma = 0.42$$
$$\alpha Z = \alpha_a = 1.5$$
$$\beta Z = \alpha_c = 0.5$$

From the microphotographs of the deposit along a disk diameter, the variation in thickness was measured. Table I gives the results of such measurements at three values of δ. These results are plotted along with the theoretical current distribution from Newman's theory (6) in Fig. 2, 3, and 4. Measurements closer to the limiting current density were rendered difficult due to powdery deposits.

Discussion and Conclusions

The experimental results are in good agreement with Newman's numerical results.

Recently, Albery and Ulstrup (1) have reported their experimental work with ring-disk electrodes in $NaBr-HClO_4$ solutions. Bromine is produced on the disk electrode, and the ring electrode is supposed to be maintained at such a potential that all the bromine reaching it is destroyed. They have developed a theoretical expression for the ring current in terms of the electrode geometry and the concentration profile at the outer edge of the disk. For some values of the concentrations and currents, the observed collection efficiencies are lower than the theoretical value for a uniform current density on the disk electrode, while a higher value would be expected if the current density were higher near the edge of the disk. Albery and Ulstrup postulate that the discrepancy may be due to the omission of the migration term in the convective diffusion equation by Newman.

Table I. Experimental values of the deposit thickness

Electrolyte: 0.1M copper sulfate – 0.1M sulfuric acid
T = 25°C, Ω = 300 rpm, r_0 = 0.25 cm
κ_x = 0.051 ohm^{-1} cm^{-1}, ν = 0.9439 × 10^{-2} cm^2/sec
Z = 2, α = 0.75, β = 0.25, γ = 0.42
N = 22.2, J = 0.382, i_0 = 1 mA/cm^2, i_{lim} = 65 mA/cm^2

r/r_0	Experimental t/t_{avg} δ = 4.82	δ = 12.3	δ = 17.12
0	0.8367	0.7417	0.7655
0.2	0.8571	0.7748	0.8078
0.4	0.8816	0.8165	0.8481
0.6	0.945	0.8912	0.9079
0.8	1.016	1.0022	1.006
1.0	1.323	1.7024	1.465

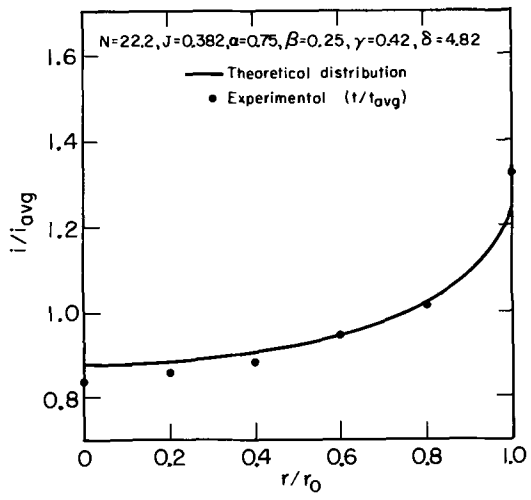

Fig. 2. Current distribution at 19.4% of the limiting current density.

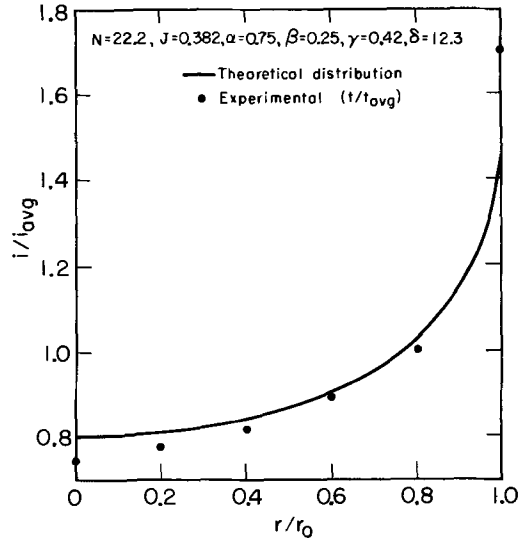

Fig. 3. Current distribution at 49.5% of the limiting current density.

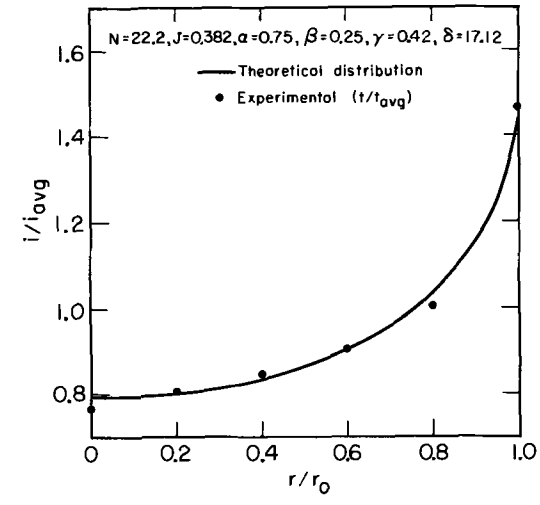

Fig. 4. Current distribution at 69% of the limiting current density.

It should be noted, however, that their system does not satisfy one of the basic requirements of Newman's theory—that the disk be embedded in an infinite, insulating plane. A straightforward way to use a ring-disk electrode for quantitative study of nonuniformities of current distribution would be to keep the two electrodes at the same potential and operate them as a sectioned electrode. The different current densities are then a measure of a nonuniform current distribution. Operation of the ring electrode as a collector for the species produced at the disk electrode would be expected to accentuate the nonuniform current distribution on the disk electrode. Further discussion of the results of Albery and Ulstrup will be submitted shortly.

The experimental method in the present work is a direct approach to testing Newman's theory, and the results seem to confirm it within the limits of experimental accuracy.

Although the theory is strictly applicable only to solutions of a single salt or solutions with an excess of supporting electrolyte, the present system is halfway between, having equal concentrations of sulfuric acid and copper sulfate. Nevertheless, the general conclusion must still apply that, below the limiting current, the current density is higher near the edge of the disk, although the appropriate values of the parameters of the theory are rendered uncertain. In this case, it appears to the authors that the parameter N is best evaluated from the experimental limiting current density.

The nonuniform current distribution arises from the nonuniform ohmic potential drop in the solution outside the diffusion layer; no approximations have been introduced in this regard. For a rotating disk electrode this tendency toward nonuniformity of the current distribution is countered, to a greater or lesser extent, by the limitations of electrode kinetics and mass transfer in the diffusion layer. In the diffusion layer, approximations were introduced appropriate to single-salt solutions or supporting-electrolyte solutions; the more general problem is formulated in Ref. (14). These approximations cannot have a drastic effect on the predicted behavior of the system; the one which first comes to mind would be that on limiting currents (15).

The observation, noted in the experimental section, that an excess of sulfuric acid led to a fairly uniform deposit is, of course, in harmony with theoretical predictions. We could still have used an excess of supporting electrolyte if we had increased the electrode radius in proportion to the increase in conductivity. This would have required redesign of the cell (there being some concern about the resulting swirling produced by the larger disk) and was decided against. For small disks used in kinetic studies with an excess of supporting electrolyte, a uniform current distribution would be expected unless the exchange current density is large. For engineering systems, nonuniformity of current distribution should not be ignored.

Acknowledgment

This work was supported by the United States Atomic Energy Commission, AEC Contract W-7405-eng-48.

NOMENCLATURE

a	0.51023
B_n	Coefficients in series for potential distribution
c	Concentration of reactant, mole/cm^3
c_o	Concentration at the disk surface, mole/cm^3
c_x	Bulk concentration, mole/cm^3
D	Diffusion coefficient, cm^2/sec
$\mathbf{F}$	Faraday's constant, coulomb/equiv.
i	Normal current density at electrode surface, A/cm^2
i_o	Exchange current density, A/cm^2
i_{avg}	Average current density, A/cm^2
i_{lim}	Limiting current density, A/cm^2
J	Dimensionless exchange current density
n	Number of electrons produced when one reactant ion or molecular reacts
N	Dimensionless limiting current density
r	Radial coordinate
r_o	Radius of the active surface of the disk, cm
R	Universal gas constant, j/mole-deg
t	Thickness of deposit
t_+	Transference number of the reactant
t_{avg}	Average deposit thickness over the disk electrode
T	Absolute temperature, °K
V	Potential of the disk electrode, volts
y	Coordinate normal to the disk, cm
z_i	Charge number of species i
Z	$-z_+z_-/(z_+-z_-)$ for single salt $-n$ with excess supporting electrolyte
α, β, γ	Kinetic parameters
δ	Dimensionless average current density
η_c	Concentration overpotential, volts
η_s	Surface overpotential, volts
κ_x	Bulk conductivity, ohm^{-1}cm^{-1}
ν	Kinematic viscosity, cm^2/sec
Φ	Electrostatic potential, volts
Φ_o	Ohmic drop extrapolated to the disk surface, volts
Ω	Angular velocity, radians/sec

Manuscript submitted Feb. 28, 1969; revised manuscript received *ca.* July 18, 1969.

Any discussion of this paper will appear in a Discussion Section to be published in the June 1970 JOURNAL.

REFERENCES

1. W. J. Albery and J. Ulstrup, *Electrochim. Acta,* **13,** 281 (1968).
2. D. H. Angell, T. Dickinson, and R. Greef, *ibid.,* **13,** 120 (1968).
3. Vinay Marathe, "Current Distribution on a Rotating Disk Electrode," M.S. Thesis, Univ. of California, Berkeley, June 1968 (UCRL-18264).
4. E. Mattsson and J. O'M. Bockris, *Trans. Faraday Soc.,* **55,** 1586 (1959).
5. John Newman, *This Journal,* **113,** 501 (1966).
6. John Newman, *ibid.,* **113,** 1235 (1966).
7. John Newman, *ibid.,* **114,** 239 (1967).
8. W. R. Parrish and John Newman, *ibid.,* **116,** 169 (1969).
9. H. K. Richardson and F. D. Taylor, *Trans. Electrochem. Soc.,* **20,** 179 (1911).
10. A. C. Riddiford, *Advances in Electrochemistry and Electrochem. Eng.,* **4,** 47 (1966).
11. J. R. Selman, Limin Hsueh, and John Newman, "Physical Properties of $CuSO_4$-H_2SO_4 Solutions," *Inorganic Materials Research Division Annual Report 1966,* p. 49 (UCRL-17330, March 1967).
12. S. Tolansky, *J. Electrodepositors' Tech. Soc.,* **27,** 171 (1951).
13. Daniel E. Rosner, *This Journal,* **113,** 624 (1966).
14. John Newman, *Intern. J. Heat Mass Transfer,* **10,** 983 (1967).
15. John Newman, *Ind. Eng. Chem. Fundamentals,* **5,** 525 (1966).

The Transport Entropy of Hydrogen Ion in the Water-Ethanol System

II. The Heats of Transport of HCl and the Transported Entropy of H^+

J. Lin

Department of Chemistry, Boston College, Chestnut Hill, Massachusetts

ABSTRACT

The entropy of transport of 0.01 molal HCl, S^*_{HCl}, was measured in the H_2O-C_2H_5OH system from the initial and final thermoelectric power of the quinhydrone-hydrogen ion thermocell at a mean temperature of 25°C. The variation of S^*_{HCl} with the composition of the solvent system was studied and its implication on the solvent structure and on the mechanism of H^+ ion transport across a temperature gradient is discussed. The transported entropy of H^+ ion, $\bar{\bar{S}}_{H+}$, at 25°C was also calculated from the S^*_{HCl} obtained and from the initial thermoelectric power of the hydrogen-hydrogen ion thermocell in water-ethanol mixtures given by Lin and DeHaven in Part I.

In the first paper of this work, Lin and DeHaven (1) (hereafter referred to as Part I) have suggested that studies of the solvent effect on the thermoelectric properties of thermocells may reveal interesting information concerning the structure of the solvent system and the mechanism of hydrogen ion transfer across a temperature gradient. In this connection the initial thermoelectric power of the hydrogen-hydrogen ion thermocell and the cation transport number of HCl were measured in the water-ethanol system. In the present paper we calculate the molar heat of transport of HCl and the transported entropy of hydrogen ion from the measurement of the initial thermoelectric power ϵ_0 and the final thermoelectric power ϵ_∞ of the quinhydrone (QH)-hydrogen ion thermocell at a mean temperature of 25°C, as a function of X, the weight per cent of ethanol in the H_2O-C_2H_5OH solvent mixture.

Application of the potentiometric method to study the thermal diffusion process taking place within an electrochemical cell from its initial (homogeneous) state to the final (Soret) steady state was first demonstrated successfully by Agar and Breck (2) in 1955. However, since the effect under consideration (change of thermoelectric power from the initial homogeneous state to the final steady state) is small, the electrode used must be extremely reproducible and stable and so far the electrode systems which have been studied are only a few, namely; $Tl(Hg)/Tl^+$ (3), $Cd(Hg)/Cd^{++}$ (3), $Ag/AgCl/Cl^-$ (4), $Fe(CN)_6^{-3}/Fe(CN)_6^{-4}$ (5), and QH/H^+ (6) systems. All these studies were conducted in the aqueous solvent and have given a remarkably consistent result which compared well with other independent measurements such as the conductometric method (7). In the present study, we have used the quinhydrone electrode to measure the heat of transport of 0.01 molal HCl in the water-ethanol system from 0 to 100 w/o (weight per cent) ethanol at an average temperature of 25°C.

The electrode reaction of the thermocell, $(T)\,Pt/Q, H_2Q, HCl(0.01M), H_2O(100\text{-}X), C_2H_5OH(X)/Pt(T+\Delta T)$, where Q is quinone, H_2Q hydroquinone, X ethanol weight per cent, $T = 20°C$ and $\Delta T = 10°$, is given by

$$\frac{1}{2}Q - \frac{1}{2}H_2Q + H^+ + e^- = 0 \qquad [1]$$

and following the notation of Part I, $\epsilon_0(X)$ and $\epsilon_\infty(X)$, may be written as

$$\mathbf{F}\,\epsilon_0 = \frac{1}{2}(S_{H_2Q} - S_Q) - \bar{\bar{S}}_e - S_{H+} - t_{H+}S^*_{H+} + t_{Cl-}S^*_{Cl-} \qquad [2]$$

$$\mathbf{F}\,\epsilon_\infty = -\bar{\bar{S}}_{H+} - \bar{\bar{S}}_e + \frac{1}{2}(\bar{\bar{S}}_{H_2Q} - \bar{\bar{S}}_Q) \qquad [3]$$

and

$$\mathbf{F}\,(\epsilon_\infty - \epsilon_0) = -t_{Cl-}S^*_{HCl} - \frac{1}{2}(S^*_Q - S^*_{H_2Q}) \qquad [4]$$

where the transported entropy $\bar{\bar{S}}$ is defined as $\bar{\bar{S}} = S^* + S$.

For the sake of simplicity in Eq. [2], [3], and [4] the explicit dependence of thermoelectricities, entropies, and transport numbers on X have not been shown. It is noticed in Eq. [4] that the entropy of transport of HCl may be computed from the difference of ϵ_∞ and ϵ_0 provided that the term $\frac{1}{2}(S^*_Q - S^*_{H_2Q})$ is known. Although data on the values of S^*_Q and $S^*_{H_2Q}$ are not available, since Q and H_2Q are much alike, S^*_Q and $S^*_{H_2Q}$ are expected to be not much different. Indeed, the term $\frac{1}{2}(S^*_Q - S^*_{H_2Q})$ is small and is shown to be 0.05 e.u. in aqueous solvent by Breck, Cadenhead, and Hammerli (6) (by the substitution of the molar entropy of transport of acids obtained from the Soret measurement (7) into Eq. [4]). For the case where $X \neq 0$, addition of alcohol will give rise to a different solvent structure, and both S^*_Q and $S^*_{H_2Q}$ are expected to be dependent on X. However, again due to similarity between Q and H_2Q, it is likely that both S^*_Q and $S^*_{H_2Q}$ may depend on X to much the same extent at all X. Therefore, in this study, we have also assumed that $\frac{1}{2}(S^*_Q - S^*_{H_2Q})$ is small at all X and that for all practical purposes we may rewrite Eq. [4] as

$$\mathbf{F}\,(\epsilon_\infty - \epsilon_0) = -t_{Cl-}S^*_{HCl} \qquad [5]$$

Since the left-hand side of Eq. [5] is experimentally measurable, S^*_{HCl} may be calculated by using the values of t_{Cl-} reported in Part I.

In aqueous solvents, since the isothermal temperature coefficient of the electrode system used is in most cases known, the transported entropy of the ion reversible to the electrode system may be derived by the measurement of ϵ_∞ (*e.g.*, Eq. [3]). For the present study, this is hardly the case, and it is not possible to derive $\bar{\bar{S}}_{H+}(X)$ from the present measurements alone. However, $\bar{\bar{S}}_{H+}(X)$ may still be computed by using the initial thermoelectric powers, $\epsilon_H(X)$, of the hydrogen-hydrogen ion thermocell reported in Part I. The equation which governs $\epsilon_H(X)$ may be written as

(Eq. [5] in Part I).

$$\mathbf{F}\,\epsilon_H = \frac{1}{2}S_{H_2} - \bar{\bar{S}}_e - \bar{\bar{S}}_{H^+} + t_{Cl^-}S^*_{HCl} \qquad [6]$$

Since S_{H_2} (1 atm) and $\bar{\bar{S}}_e$ are available, S^*_{HCl} and $\bar{\bar{S}}_{H^+}$ may be readily obtained. The corresponding molar heats of transfer, Q^*_{HCl} may then be calculated by the formula $Q^*_{HCl} = TS^*_{HCl}$.

Experimental

Procedures on the preparation of solutions other than $X = 100\%$ have been described in Part I. For $X = 100\%$, the solution was prepared by mixing the commercial absolute alcohol (d^{25}_4 measured = 0.7850) with an appropriate amount of 12N HCl. The exact composition was calculated to be $X = 99.9\%$ and the concentration of the solution, 0.01000M.

The initial thermoelectric powers, $\epsilon_0(X)$, were measured by the "static method" using the N-shaped cell (8) with platinum electrodes. Cell solutions were prepared by the method described by previous authors (6, 8). The quinhydrone (Fisher reagent grade) was washed several times with the acid solution prior to its addition into the cell solution. The isothermal residual emf of the cell was usually of the order of ± 50 μV and was corrected from the thermal emf readings. Results of the measurements are shown in Table I.

Measurements of final thermoelectric powers, $\epsilon_\infty(X)$, are somewhat more difficult. Mainly due to the necessity of avoiding the occurrence of convection and also to keep the measurement within reasonable bounds of time, it was always found convenient to employ a sandwich type cell with a thickness of approximately 1 cm. In the present study, the cell used is also a sandwich type cell. However, the present cell is assembled mechanically rather than like the conventional redox cell which is usually sealed together chemically using an adhesive. As shown in Fig. 1, the cell consisted of two gold disks (as electrodes) and a Plexiglass ring. In between the gold disks and the Plexiglass ring, Teflon gaskets were used to prevent leakage. The whole cell was then assembled with 4 nylon screws together with the copper jackets. There are several advantages of such a cell design. First of all, since Teflon gaskets were used to prevent leakage, the present design enables one to avoid the difficulty of finding an inert glue to seal the cell. The problem associated with this difficulty is important for the present solvent study. Not only because ethanol itself is a good solvent, but also because of the fact that quinhydrone is a strong redox agent, we have found that the cell solution interacts (especially for $X > 35\%$) with practically all the adhesives or cements that may be used to seal the cell properly. This interaction is troublesome as indicated by the fact that the thermal emf observed becomes increasingly erratic with increasing alcoholic concentration when the cell is sealed chemically (for example by the use of epoxi cement or

Table I. Thermoelectric powers and molar entropies of transport of 0.01M HCl

ϵ_0 and ϵ_∞ for (T) Pt/Q, H_2Q, HCl(0.01M), H_2O(100-X), C_2H_5OH(X)/Pt(T + ΔT) thermocell

Wt %	t_{Cl^-}[a]	ϵ_H (mV/deg)[a]	$-\epsilon_0$ (mV/deg)	$-\epsilon_\infty$ (mV/deg)	S^*_{HCl} (e.u.)
0	0.174	0.150	0.630	0.708	10.3
4.9	0.176	0.156	0.644	0.678	4.5
17.9	0.146	0.140	0.746	0.731	−2.4
34.2	0.177	0.163	0.878	0.841	−4.8
48.7	0.205	0.202	0.853	0.839	−1.6
63.4	0.244	0.248	0.818	0.808	−0.9
77.8	0.300	0.348	0.716	0.702	−1.1
92.0	0.424	0.551	0.495	0.464	−1.7
99.9	0.239[b]	—	0.615	0.703	8.5

[a] Taken from Part I.
[b] Calculated from Eq. [4] in Part I.

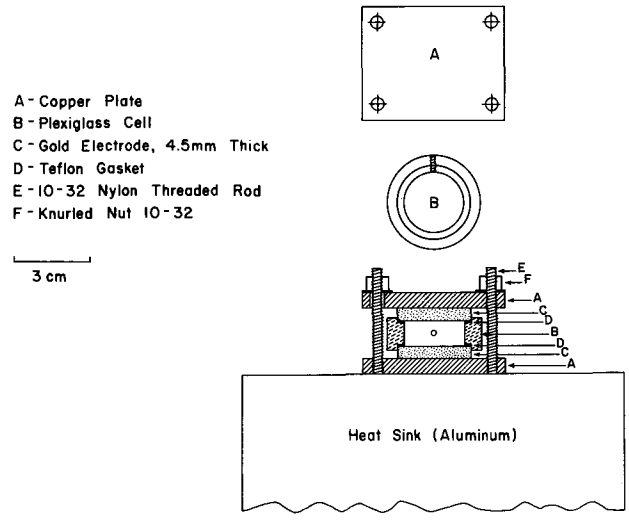

Fig. 1. Thermocell

pliobond adhesive). Second, the copper jackets used in assembling the cell serve also as a useful "thermal blanket" for the electrodes and thus provide a more stable temperature for the electrode. Using the "temperature tower" (5, 6) along with YSI Model 71 temperature controller and Type 423 thermistors, we were able to keep the temperature of the electrode constant within 0.01° ~ 0.02° and the temperature difference to within 0.02°.

The quinhydrone electrode has been applied to many alcoholic media (9), including methanol by Ebert (10), ethanol by Larsson (11), and n-butanol by Seltz and Silverman (12). Unfortunately Larsson's reference concerning the application in ethanol media is not readily available and we were not able to consult this reference. It has been reported (10) that hydrochloric acid (especially for concentrations higher than 0.1N) has a tendency to chlorinate quinone and give rise to difficulties in emf measurements. In nonaqueous solvent systems, this chlorination reaction is perhaps even more prominent and as reported by Ebert (10), it was necessary to extrapolate his readings to "zero time." In the present study, however, we have found that electrode systems are quite stable and even for the ethanol concentration as high as 99.9% by weight, the ϵ_0 value may be reproduced within $\pm$ 7 μV/deg and the ϵ_∞ value to within $\pm$ 5 μV/deg. It is also interesting to note that no such difficulty was observed by Breck, Cadenhead, and Hammerli (6), where they have carried their thermocell measurements in aqueous solvent up to as high as 1.0N in HCl. The results of ϵ_∞ measurements are shown in Table I.

Results and Discussion

Although the initial thermoelectric powers were measured by the static method, just to see how thermocells approach their steady states, we have undertaken a few experiments to investigate the kinetic behavior of the thermocell. Figure 2 represents a result of such a study on the 34.2% alcohol solvent system. The technique used here was the same as that used in the conductance study of Sagert and Breck (13), that is first a "dummy cell" is placed in the temperature tower for thermal equilibrium (usually requiring about 2 hr) and then is quickly replaced by the working cell. The time $t = 0$ in Fig. 2 is the "hypothetical" instant (the instant when the replacement was completed) at which a temperature gradient is applied to the cell. As expected, due to the complexity of the system, the kinetic curve is not as simple as that observed in an aqueous solvent (6). Although no theory is as yet available for the description of such a kinetic curve, some qualitative explanations of Fig. 2 may be provided. It may be reasonable to assume that thermal diffusion of the acid should be more rapid and

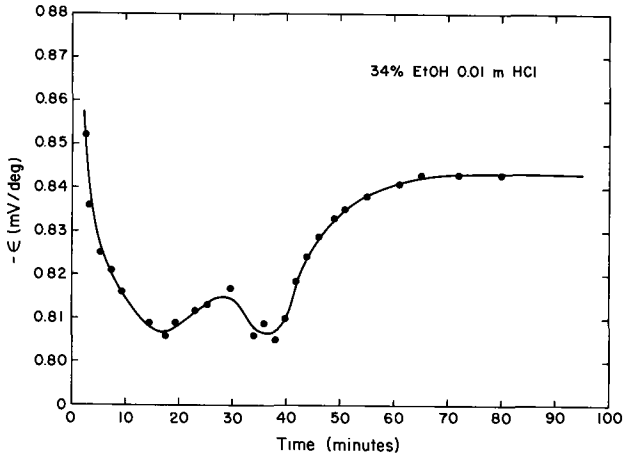

Fig. 2. Plot of the thermoelectric powers against time

thus predominate in the early stages giving rise to a smooth curve for a short time. When t is large, all the diffusion currents (over-all) approach zero and eventually the system reaches a steady state characterized by the flat portion of the curve. In between the short time and long time periods there might be a "competing" diffusion among all the species, hence a rather unusual behavior. In view of the shape of the curve, no attempt has been made to compute the effective diffusion coefficient for HCl and the over-all characteristic time of the thermocell. Also, no attempt has been made to obtain the ϵ_0 value by extrapolating the curve.

Using Eq. [5] and the $t_{Cl^-}(X)$ obtained in Part I, $S^*_{HCl}(X)$ values were computed and entered in Table I. Substituting $S^*_{HCl}(X)$ into Eq. [6], $\bar{\bar{S}}_{H^+}(X)$ may be obtained and the results are shown in Table II. Assuming that entropies of transport are additive, and also using a convention that $S^*_{Cl^-}(X) = 0$ at 0.01M, we note that $S^*_{HCl}(X)$ is just the conventional $S^*_{H^+}(X)$.

It is worth noting that the present value of $\bar{\bar{S}}_{H^+}$ at $X = 0$, which is calculated by the use of ϵ_H value from Part I agrees well with the result of Breck, Cadenhead, and Hammerli (6) who obtained $\bar{\bar{S}}_{H^+}$ at 0.01M HCl from their ϵ_∞ in water by using the isothermal temperature coefficient of the emf of the cell H_2/HCl/QH given by Harned and Wright (14). Agreement of this sort indeed is useful in cross checking the nonisothermal and the isothermal measurements.

Although studies on the solvent effect on the thermal diffusion of electrolytes, at present, are still minimal, it is nevertheless desirable to attach more importance than hitherto to the role of the solvent. The study of Becsey and Bierlein (15) should serve as an interesting example. Using the method of wave-front-shearing interferometry, Becsey and Bierlein have measured heats of transport of $CdSO_4$, $AgNO_3$, $BaCl_2$, and KI in both H_2O and D_2O and found that heats of transport observed in H_2O are substantially higher than that observed in D_2O. Their findings are indeed significant, for according to Eastman (16), heats of transport might be related to the reversible thermal effects which must occur in the vicinity of an ion as it moves through the solvent. Since a more randomly constituted solvent system will experience a greater fall in entropy while in the electrostatic field of the moving ion, the fact that entropies (or heats) of transport in H_2O are higher than D_2O is indeed consistent with the accepted concept that D_2O has more structure than H_2O (17). For the H_2O-C_2H_5OH system, although ethanol and water resemble each other fairly closely in hydrogen bonding facility (18), the structures to which these bonds can give rise are very dissimilar in the two cases and appear to be mutually exclusive. Thus, as reflected in the study of ionic Walden products (19), it is generally believed that addition of ethanol to water initially will enhance the structure of the solvent system. This structure enhancement reaches a maximum near $X = 20 \sim 30\%$ and then at a higher concentration, the structure of the solvent system is gradually reduced.

Table II. Transported entropy of 0.01M hydrogen ion and the relative ionic sizes

Wt % Ethanol	$\bar{\bar{S}}_{H^+}$	$-\Delta\bar{\bar{S}}_h$	D^a	$-\frac{\partial \ln D^b}{\partial \ln T}$	$\frac{r(X)}{r(X=0)}$
0	14.0	12	78.5	1.37	1.000
4.9	12.7	13.2	75.5	1.44	0.994
17.9	12.1	13.9	68.0	1.58	1.149
34.2	11.0	14.9	58.5	1.66	1.309
48.7	10.7	15.3	49.5	1.69	1.534
63.4	9.7	16.3	41.5	1.71	1.738
77.8	7.3	18.7	34.0	1.77	1.914
92.0	2.2	23.8	27.5	1.85	1.944

[a] Interpolated from the data given in ref. (19).
[b] Taken from Part I.

In the present study, to show how S^*_{HCl} varies with X and for the convenience of comparisons, S^*_{HCl} is plotted *vs.* X in Fig. 3 along with the limiting ionic Walden product of H^+ taken from Spivey and Shedlovsky (19). The correlation is indeed striking in spite of the fact that S^*_{HCl} takes an abrupt jump at $X = 100\%$, a phenomenon which will be discussed later. In terms of Becsey and Bierlein's findings, the decrease in S^*_{HCl} for small X value is consistent with the expectation that the addition of a small amount of ethanol would promote the structure of the solvent system. After an initial decrease, S^*_{HCl} goes to a minimum at around $X = 30\%$ and then increases to stay at a fairly small magnitude up to X is almost 100% ethanol. The exact position of the minimum of S^*_{HCl} is, however, at a higher $X(\sim 30\%)$ than that predicted by the ionic Walden product ($\sim 20\%$). According to Eastman's picture, as the ion passes by a given solvent molecule, the molecule is first oriented by the ionic field and then takes up a random orientation when the ion recedes, and so it follows that heat is liberated ahead of an ion and absorbed behind it, or as concluded by Eastman, all ionic heats (or entropies) of transport should be positive.

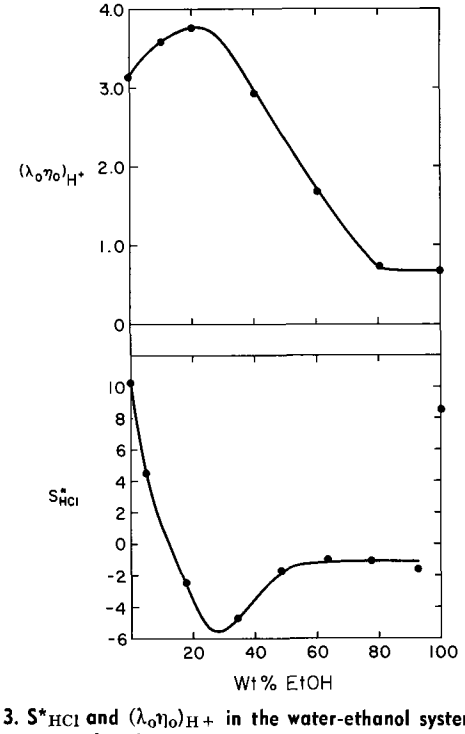

Fig. 3. S^*_{HCl} and $(\lambda_0\eta_0)_{H^+}$ in the water-ethanol system. Data on $(\lambda_0\eta_0)_{H^+}$ are taken from ref. (19).

However, negative ionic heats of transport have been observed (20) and it is now understood that for a more satisfactory interpretation of the entropy of transport, the structure-making and structure-breaking effects of the ion must be included in the consideration. For a structure-maker, there is a further reduction of the entropy of solvent molecules ahead of the ion and therefore an additional evolution of heat. But for a structure-breaker, the entropy of solvent molecules increase and may actually give rise to a negative heat of transport. The structure-breaking effect of an ion may arise if the dipole orientation by the ionic field is not compatible with the normal hydrogen-bonded structure of the solvent system and as a result some hydrogen bonds are therefore broken. Under such a circumstance the increase in the entropy of the solvent molecules due to other modes of motion may be more significant than the reduction of entropy due to dipole orientation. Chloride ions are notorious for such a structure-breaking effect in water (21) and judging from the present result it is likely that this may very well be the case in the ethanol-water system also. The S^*_{HCl}'s observed are negative for X greater than approximately 15% up to more than 90%. The large negative value for S^*_{HCl} at $X \sim 30\%$ is perhaps not unexpected since at this solvent composition the solvent system is believed to have a maximum structure (compared to the other compositions) and it is likely that the restriction imposed on the compatibility of dipole orientation may be most stringent.

As mentioned in Part I, we have anticipated that solvent study on the heat of transport may reveal interesting information concerning the mechanism of ionic transport across a temperature gradient. The fact that S^*_{HCl} increases abruptly at $X = 99.9\%$ is thus interesting and may be explained in terms of the mechanism of H^+ transport suggested by Breck and Lin (1, 20). Transport of H^+ occurs not only by a simple migration mechanism but more significantly by a chain mechanism where H^+ may be transferred from a hydronium ion to an adjacent solvent molecule which is favorably oriented, *i.e.*, by the reaction $H_3O^+ + H_2O \rightarrow H_2O + H_3O^+$ in water or its equivalent $ROH_2^+ + ROH \rightarrow ROH + ROH_2^+$ in pure alcohol. Thus, a transport of entropy may arise not only from the alternate ordering and disordering effects of the ionic field on the solvent structure, but more significantly from transport of entropies of reaction as hydrogen bonds are alternately made and broken. In an aqueous solvent, where the "absolute" ionic entropies of transport have been convincingly determined (20) this additional entropy of transport is indicated by the fact that entropy of transport of H^+ is abnormally high compared with other univalent ions.

For the present solvent system, although the convention that $S^*_{Cl^-}(X) = 0$ for 0.01*M* HCl will by no means serve the purpose of a standard state, it is nevertheless useful in judging the relative magnitude of the ionic entropy of transport at each solvent composition. Thus, the very fact that the conventional $S^*_{H^+}$'s at higher alcoholic concentrations (50-90%) are much smaller than those measured in the aqueous solvent and also in pure alcohol has indeed indicated that the suggestion by Breck and Lin may be fairly accurate, namely, that the high values of $S^*_{H^+}$ are due primarily to a proton transfer mechanism. It is true that for a large X, H^+ may be transported by the reaction, $H_3O^+ + EtOH \rightarrow H_2O + EtOH_2^+$; but it is known (18) from the equilibrium data that the rate of the reverse reaction in this case greatly exceeds that of the forward reaction. Under such circumstances only a simple migration mechanism should be operative and according to the suggested mechanism, the observed entropy of transport of H^+ would be small. In pure alcohol, H^+ may be effectively transported by the reaction $EtOH_2^+ + EtOH \rightarrow EtOH + EtOH_2^+$ and therefore a much larger ionic entropy of transport for H^+ is obtained as compared with the previous case.

Finally we discuss the transported entropy of H^+ computed in Table II. The transported entropy of an ion is the entropy carried by the moving ion under a limiting case of an isothermal condition. Following Khoroshin and Temkin (22), one may write

$$\bar{\bar{S}} = S_g + \Delta S_h + S^* = S_g + \Delta\bar{\bar{S}}_h \qquad [7]$$

where; S_g, entropy of the gaseous ion; ΔS_h, entropy of hydration of the gaseous ion; and $\Delta\bar{\bar{S}}_h$, transported entropy of hydration.

The transported entropy of hydration, $\Delta\bar{\bar{S}}_h$, which includes the contribution of the entropy of transport, was found to be better approximated by Born's model of hydration than the entropy of hydration ΔS_h in the aqueous solvent; that is, denoting Z as the ionic valence and r as the ionic radius, it was found by Breck and Lin (20) that $\Delta\bar{\bar{S}}_h$ correlates better with Z^2/r than ΔS_h. This is interesting and may be interpreted as follows. In Born's theory, apart from other approximate features, the solvent is treated as a dielectric continuum. However, in reality since a strong ionic field acts over a fairly short distance in the vicinity of the ion, the continuum model could best serve as a crude approximation. Therefore, correlations between ΔS_h and Z^2/r are in general less than satisfactory. For the case of $\Delta\bar{\bar{S}}_h$, it is slightly different since here we are considering a moving ion. A moving ion sees only an "average" dielectric medium and consequently, the continuum assumption is less critical. Thus, it is not surprising that a better correlation exits between $\Delta\bar{\bar{S}}_h$ and Z^2/r.

In the present study, S_g at 25°C may be computed from the Sackur-Tetrode equation to be 26.00 e.u. for H^+. If indeed, $\Delta\bar{\bar{S}}_h$ of H^+ may be approximated by the Born theory, it is then expected that $\Delta\bar{\bar{S}}_h$ should be proportional to $(\partial \ln D/\partial \ln T) \cdot (1/Dr)$. Thus taking $(\partial \ln D/\partial \ln T)$ and D from Part I, it is possible, within the frame of the Born theory, to estimate the relative size of H^+ as a function of the composition of the solvent system. Results of such a calculation are presented in Table II along with the pertinent parameters. It is seen that the present results predict a progressive increase (except at $X = 4.9\%$) of the ionic size when the concentration of ethanol increases. In view of the fact that ethanol molecules are larger compared with water molecules, this seems likely if r is interpreted as the "effective" radius. For it may be reasonable to expect that water molecules in the primary hydration layer will be gradually replaced by ethanol as the concentration of ethanol increases. An experimental check on this result should be interesting.

Comments

By the very nature of entropy as an "indicator" of order-disorder phenomena, it is felt that thermoelectric studies on the electrolytes in the mixed solvent system should be useful in elucidating such phenomena as ion-ion, ion-solvent, and solvent-solvent interaction. The present article does not pretend to be exhaustive, rather we hope it would be a useful example. There is a lot more remaining to be done in the immediate area; for example, to study the concentration dependence of $S^*_{HCl}(X)$ and to carry on a similar study with ions of quite different natures such as the tetraalkyl ammonium ions. Also in the present study, although the assumption that $\frac{1}{2}(S^*_Q - S^*_{H_2Q})$ is small, is hopefully a reasonable one, it is nevertheless desirable to have an experimental check on such an assumption. Work along this line is in progress in our laboratory.

To be more conclusive on the problem of the mechanism of H^+ transport across a temperature gradient, more studies on other acids will be needed. It is worth

mentioning that the mechanism suggested by Breck and Lin is sufficiently similar to the mechanism of H^+ transport under an electric field, *i.e.*, considering the transport of H^+ as a sort of "structural diffusion." In view of the fact that in these two cases the driving forces involved are quite different, this is an interesting thing to know. An electric field (for example a d-c field) will tend to align the solvent dipole and thus create more order, whereas a temperature gradient would tend to create more disorder by way of setting up a thermal energy gradient among the solvent molecules.

To evaluate the ionic entropy of transport on an "absolute" basis, a study of the problem of standard state is necessary. We plan to discuss this subject in a forthcoming article.

Acknowledgment

The author wishes to thank Professor Andre J. de Bethune for his reading of the manuscript. This work was supported by the Office of Saline Water, U. S. Department of the Interior, under Grant No. 14-01-0001-1466.

Manuscript submitted May 29, 1969; revised manuscript received *ca.* Aug. 15, 1969.

Any discussion of this paper will appear in a Discussion Section to be published in the June 1970 JOURNAL.

REFERENCES

1. J. Lin and J. J. DeHaven, *This Journal*, **116**, 805 (1969).
2. J. N. Agar and W. G. Breck, *Nature*, **175**, 298 (1955).
3. J. N. Agar and W. G. Breck, *Trans. Faraday Soc.*, **53**, 167, 179 (1957).
4. J. Chanu, "Transport Processes in Statistical Mechanics," I. Prigogine, Editor, Interscience Publishers, New York, London (1958).
5. W. G. Breck and J. Lin, *Trans. Faraday Soc.*, **61**, 1511 (1965).
6. W. G. Breck, G. Cadenhead, and M. Hammerli, *Trans. Faraday Soc.*, **61**, 505 (1965).
7. See for example; J. N. Agar, "Thermogalvanic Cells," in *Adv. Electrochem. Electrochem. Eng.*, **3**, 31 (1963).
8. W. G. Breck, *Trans. Faraday Soc.*, **59**, 729 (1963).
9. G. J. Janz and D. J. G. Ives, in "Reference Electrodes," p. 270, D. J. G. Ives and G. J. Janz, Editors, Academic Press, New York (1961).
10. L. Ebert, *Ber. Deut. Chem. Ges.*, **58**, 175 (1925).
11. E. Larsson, Dissertation, Lund, 1924.
12. H. Seltz and L. Silverman, *Ind. Eng. Chem. Anal. Ed.*, **2**, 1 (1930).
13. N. H. Sagert and W. G. Breck, *Trans. Faraday Soc.*, **57**, 436 (1961).
14. H. S. Harned and D. D. Wright, *J. Am. Chem. Soc.*, **55**, 4849 (1933).
15. J. G. Becsey and J. A. Bierlein, *J. Chem. Phys.*, **46**, 391 (1967).
16. E. D. Eastman, *J. Am. Chem. Soc.*, **50**, 283 (1928).
17. See for example; R. W. Stoughton, *Ann. Rev. Phys. Chem.*, **16**, 297 (1965).
18. F. Franks and D. J. G. Ives, *Quart. Rev.*, **20**, 1 (1966).
19. H. O. Spivey and T. Shedlovsky, *J. Phys. Chem.*, **71**, 2165 (1967).
20. W. G. Breck and J. Lin, *Trans. Faraday Soc.*, **61**, 2223 (1965).
21. H. S. Frank in "Chemical Physics of Ionic Solutions," p. 53, B. E. Conway and R. G. Barradas, Editors, John Wiley & Sons, Inc., New York (1966).
22. A. V. Khoroshin and M. I. Temkin, *Zhur. Fiz. Khim.*, **26**, 773 (1952).

Technical Note

EMF and Voltammetric Measurements on the U(IV)/U(III) Couple in Molten LiF-BeF_2-ZrF_4

H. W. Jenkins,[1] G. Mamantov,* D. L. Manning, and J. P. Young

Department of Chemistry, University of Tennessee, Knoxville, Tennessee, and Analytical Chemistry Division, Oak Ridge National Laboratory, Oak Ridge, Tennessee

Knowledge of the U(IV)/U(III) ratio in molten LiF-BeF_2-ZrF_4 [65.6-29.4-5.0 m/o (mole per cent)] is of considerable importance to the Molten Salt Reactor program of the Oak Ridge National Laboratory. This ratio reflects the presence of (or lack of) reducing conditions, desirable in order to minimize corrosion in the reactor. We have shown previously (1) that the reduction of uranium (IV) in molten LiF-BeF_2-ZrF_4 at 500°C is a reversible one-electron process occurring at approximately −1.5V (*vs.* Ni/NiF_2,$X_{Ni(II)}$ = 1). Other aspects of the electrochemistry of uranium in the same melt have been discussed elsewhere (2, 3). A review of electrode reactions in molten fluorides is available (4). Determination of small concentrations of U(III) in the presence of large amounts of U(IV) by direct voltammetry or chronopotentiometry (forward or current-reversal) was found to be not feasible. Spectrophotometric studies on U(IV) and U(III) in this melt (5, 6), have shown that U(IV) has analytically useful absorption bands at 640 and 1090 nm, and that U(III) absorbs strongly at 360 nm and exhibits a weaker band at 890 nm.

The emf studies on the U(IV)/U(III) couple described below were conducted as part of developing an emf series of measured potentials in molten fluorides (7). Simultaneously with the emf measurements, a simple voltammetric method was developed for the determination of the U(IV)/U(III) ratio when U(IV) >> U(III). The U(IV)/U(III) ratio in the same samples was also measured by spectrophotometry.

Experimental

The electrochemical measurements were conducted in a drybox-furnace combination that was described previously (8). The instrumentation employed and the Ni/Ni(II) reference electrode in boron nitride

* Electrochemical Society Active Member.
[1] Oak Ridge Associated Universities Fellow, University of Tennessee, Knoxville, Tennessee.

have also been described (1, 8). The melt in the reference electrode compartment consisted of anhydrous nickel fluoride (mole fraction 10^{-4}-10^{-3}) dissolved in LiF-BeF_2-ZrF_4 of the same composition as the bulk melt. It was necessary to relate the potential of each reference electrode to a common reference point since previous work (8) has shown that a junction potential exists across the boron nitride sheath. It should be emphasized that this junction potential is constant to within a few mV for periods of 1-2 weeks or longer, provided the temperature is kept constant. The common reference used in this work is the standard electrode potential of the nickel(II)/nickel couple where the standard state of nickel(II) is taken to be the hypothetical unit mole fraction solution (9). The potential of each reference electrode was determined with respect to a nickel(II)/nickel electrode in the bulk of the melt prior to the addition of solute species. A sample of the melt was taken to determine the nickel(II) concentration in the bulk of the melt. The nickel (II) in the bulk of the melt was removed by reduction with zirconium metal. The potential of the reference electrode was related to the standard electrode potential of the nickel(II)/nickel couple by means of the Nernst equation.

The potential of the U(IV)/U(III) couple was measured at a platinum wire indicator electrode. The U(IV) was added to the melt as LiF-UF_4 (73-27 m/o). The U(III) concentration was varied by the controlled reduction of U(IV) with a zirconium rod that could be immersed in the melt. It was established from stability of emf measurements and from variations in the voltammetric peak current that homogeneity of solutions was attained by waiting about 1 hr between additions and measurements; the melt was stirred periodically (either manually or mechanically) during that time. The emf measurements were recorded over a 15-30 min period to insure the stability of the values. All measurements were made at 500°C. At the time of each emf measurement, a sample of the melt was taken in a graphite windowless cell (6), allowed to solidify, and transferred to a heated spectrophotometric facility. The complete operation was performed without exposing the sample to the atmosphere; such exposure would probably alter the oxidation state of the solute. On remelting the sample in a helium atmosphere, its spectrum was obtained. The absorbance of U(IV) was determined at 640 nm and that of U(III) at 360 or 890 nm depending on its concentration level. The U(IV)/U(III) ratios determined by spectrophotometry were used in the Nernst equation to determine the standard potential of this redox couple and also for comparison with the U(IV)/U(III) ratios determined voltammetrically.

Results and Discussion

A summary of emf measurements on the U(IV)/U(III) couple *vs.* a Ni(II)/Ni reference electrode is shown in Table I, column 2. All potentials are in accordance with the Stockholm sign convention. Also given in Table I are the emf values corrected *vs.* a unit mole fraction Ni(II)/Ni electrode (column 3). A plot of the corrected emf values *vs.* the log of the U(IV)/U(III) ratio (from spectrophotometry) resulted in a straight line which exhibited the theoretical Nernstian slope of 0.153V (at 500°C). The standard electrode potential determined by extrapolation to a U(IV)/U(III) ratio of unity is -1.480 ± 0.01V. This value is in reasonably good agreement with the value of -1.517V calculated by Baes (9) from thermodynamic data obtained in a somewhat different melt, namely LiF-BeF_2 (66-34 m/o).

Values for the U(IV)/U(III) ratios determined by the new voltammetric method are shown in the last column of Table I. In the voltammetric measurements, current-voltage curves for the U(IV) → U(III) reduction are recorded *vs.* a platinum electrode which is poised at the equilibrium potential (E_{eq}) of the melt. The equilibrium potential, in turn, depends on the U(IV)/U(III) ratio. The fixed reference potential is generated internally; it is the voltammetric equivalent of the standard electrode potential (E_o), *i.e.*, the potential at which the U(IV)/U(III) ratio is unity at the electrode surface. The potential E_o is the potential corresponding to the current value that is 85% of the peak current. This holds true for a reversible couple in which the oxidized and reduced forms are soluble and the concentration of the reduced form is much smaller than that of the oxidized form (10). This is the case for the U(IV)-U(III) system in this melt (1). It follows from the Nernst equation

$$E_{eq} - E_o = \Delta E = \frac{RT}{n\mathbf{F}} \ln \frac{\text{U(IV)}}{\text{U(III)}}$$

that the difference between E_{eq} and E_o is a measure of the U(IV)/U(III) ratio. It is seen that both oxidation states may be determined from the voltammetric peak current and the position of the voltammogram on the potential scale (it is assumed that iR drop as well as polarization of the reference electrode are eliminated through the use of an auxiliary electrode).

The agreement with spectrophotometric results is quite good, considering the instability of U(III) in both experimental systems. U(III) could not be maintained for more than 24 hr. This is believed to be due in part to the diffusion of oxygen through the dry box gloves which oxidizes U(III) to U(IV).

The voltammetric method is particularly useful in nonaqueous solvents where reference electrodes are frequently not readily available, or the standard potentials may not be known. This method is being employed in highly radioactive molten salt solutions; the use of a Ni(II)/Ni reference electrode contained in boron nitride for this purpose may not be feasible.

Acknowledgments

This work was supported by the U.S. Atomic Energy Commission under contract with the Union Carbide Corporation and Contract AT-(40-1)-3518.

Manuscript submitted March 14, 1969; revised manuscript received *ca.* Sept. 5, 1969.

Any discussion of this paper will appear in a Discussion Section to be published in the June 1970 JOURNAL.

REFERENCES

1. G. Mamantov and D. L. Manning, *Anal. Chem.*, **38**, 1494 (1966).

Table I. Determination of the uranium(IV)/uranium(III) ratios*

$\frac{U(IV)}{U(III)}$ ratio**	$E_{ref} - E_{U(IV)/U(III)}$, V	$E°_{Ni(II)/Ni} - E_{U(IV)/U(III)}$, V	$\frac{U(IV)}{U(III)}$ ratio†
138.0	0.882	1.152	180
29.4	0.987	1.257	29.6
11.8	1.075	1.345	10.0
6.7	1.078	1.348	7.1

* Mole fraction of total uranium 2.9×10^{-3}.
** Determined by spectrophotometry.
† Determined by voltammetry.

2. G. Mamantov and D. L. Manning, *J. Electroanal. Chem. and Interf. Electrochem.*, **18**, 309 (1968).
3. D. L. Manning and G. Mamantov, *ibid.*, **17**, 137 (1968).
4. G. Mamantov, "Electrode Reactions in Molten Fluorides," in "Molten Salts: Characterization and Analysis," G. Mamantov, Editor, M. Dekker (1969).
5. J. P. Young, G. Mamantov, and F. L. Whiting, *J. Phys. Chem.*, **71**, 782 (1967).
6. J. P. Young, *Inorg. Chem.*, **6**, 1486 (1967).
7. H. W. Jenkins, Ph.D. Dissertation, University of Tennessee, 1969.
8. H. W. Jenkins, G. Mamantov, and D. L. Manning, *J. Electroanal. Chem. and Interf. Electrochem.*, **19**, 385 (1968).
9. C. F. Baes, Jr., in SM-66/60, "Thermodynamics," Vol I, IAEA, Vienna (1966).
10. R. S. Nicholson and I. Shain, *Anal. Chem.*, **36**, 706 (1964).

DISCUSSION SECTION

This Discussion Section includes discussion of papers appearing in the *Journal of The Electrochemical Society*, Vol. 116, No. 1, 2, and 6, January, February, and June, 1969.

pH Changes at Anion Selective Membranes under Realistic Flow Conditions

T. R. E. Kressman and F. L. Tye
(pp. 25-31, Vol. 116, No. 1)

Allyn H. Heit[1] and **Richard Prober**[2]: Kressman and Tye's painstaking experiments provide additional insight into the mechanism for fouling of anion selective membranes in electrodialysis. Their data leave little doubt that, at conditions of high current density, organic species accelerate the functional failure of the membranes, as evidenced in practice by depressed selectivity and increased ohmic resistance. Indeed, in view of that it is surprising that OH^- transport through anion selective membranes eventually becomes stabilized (as indicated in Kressman and Tye's paper, Fig. 6 and 8).

However, in our opinion, the data do not warrant the conclusion that "the main limitation on electrodialysis is not polarization per se but poisoning of the anion-selective membranes." Even with especially purified feed solutions, high current densities could not be sustained longer than a few hours (see their Fig. 8). Thus, feed pretreatment to remove organic matter and thereby prevent membrane poisoning cannot be justified. In desalination by electrodialysis, the membranes must serve for several years; hence unpoisoned membranes are an idealization not attainable in practice over a useful fraction of the membrane lifetime.

The pH changes observed by Kressman and Tye are bulk-phase effects, and the pH at the membrane-solution interfaces may be significantly greater than in the bulk solution. For example, Kressman and Tye's data (Fig. 6) that, in NaCl solutions significant OH^- transfer began at current densities of 10 mA/cm^2, imply an average mass transfer coefficient (D/δ) of 15 cm/hr through the hydrodynamic boundary layer on the donating solution side of the anion exchange membranes (Eq. [2]). Then, assuming that the coefficient for OH^- transfer through the diffusion boundary layer on the receiving solution side of the membrane is of the same order of magnitude, we calculate that the alkalinity at the receiving solution-membrane solution interface must (on the average) have been about 0.0042*N* (pH 11.6) in order to maintain a bulk-stream alkalinity of 0.0027*N* (pH 11.4) at the stated feed-and-bleed rates.

The transport of OH^- ions through anion selective membranes at high current density brings about an undesirable side effect in electrodialysis of naturally occurring brackish waters. Sparingly soluble calcium and magnesium compounds precipitate where the OH^- concentration is greatest, that is, on the receiving stream face of the anion exchange membranes, unless the receiving stream (concentrate) feed is acidulated. We have observed such precipitation particularly with feed water of pH 7.4-7.7 and marked by 100-150 ppm of HCO_3^- ion. We have also observed that type of precipitation on the donating stream (diluate) side of the anion selective membranes with a feed stream containing 800-900 ppm (as $CaCO_3$) of hardness, despite the donating stream feed and effluent both having bulk pH values less than 7.0.

It must be remembered that pH changes occur as the result of depletion of electrolyte content in the diffusional boundary layers adjacent to the membrane surfaces. The effect is not confined to anion exchange membranes. We have observed pH changes even when the anion membrane is replaced by a nearly neutral (in fact, slightly cation selective) cellulosic membrane, as in the transport depletion process. Indeed, pH changes in electrodialysis were noted at an early period when the only material available to serve the membrane requirements of electrodialysis cells were nitrocellulose or regenerated cellulose or possibly animal tissue. Bethe and Toropoff[3] reported a passage of current through a multichambered electrodialysis stack, wherein the chambers are defined by nonselective membranes, resulted in effluents emerging from the stack at acidic or alkaline pH, depending on whether the individual stream issued, in effect, from a dilution or concentration chamber.

T. R. E. Kressman and **F. L. Tye**: Heit and Prober are not correct in inferring from our data that organic poisoning occurs only at high current densities. We believe that it happens at all current densities including zero. The effects shown in Fig. 9 resulted from poisoning runs at 5 mA/cm^2 which we would regard as a very moderate current density. The related phenomena of organic poisoning of strongly basic anion-exchange resins takes place in the absence of current and in further work[4] we have established that anion-selective membranes are also poisoned in the absence of current.

Heit and Prober should not presume that hydroxyl ion transport through the anion-selective membrane was stabilized. We state that "the apparently steady, reproducible and reversible conditions obtaining for the data on Permaplex A-20 in Fig. 6 must have occurred because the amount of organic matter accumulated by the membrane during the runs was small relative to the amount already on the membrane at the start of this series." This surely indicates that we do not regard the situation as genuinely stabilized. We have little doubt that had the experiments represented in Fig. 8 been continued for longer times that the current density necessary to maintain a receiving

[1] Ionac Chemical Company, Division of Sybron Corporation, Birmingham, N. J.
[2] The Permutit Company, Division of Sybron Corporation, Princeton, N. J.
[3] Bethe and Toropoff, *Z. Phys. Chem.*, 88, 686 (1914).
[4] T. R. E. Kressman and F. L. Tye, *Electrochim. Acta*, In press.

stream alkalinity of 0.0027*N* would have had to be reduced. In other work[4] where operation was continued for several hundred hours conditions did not stabilize.

We have not commented on the justifiability of feedwater pretreatment as a practical procedure as inferred by Heit and Prober's second paragraph. In fact, as they admit, we have shown that organic poisoning occurs even with purified solutions.

We believe that our work shows that the attainment of higher current densities which are economically desirable in electrodialytic water treatment is not restricted by inherent hydrodynamic, mass transport, and electrical migration factors, but by the effect on them of membrane poisoning. We are at variance with nothing else that Heit and Prober write nor do we think that their remarks in any way detract from this conclusion.

An Investigation of the Difference Between NaCl and $NaClO_3$ as Electrolytes in Electrochemical Machining

James P. Hoare, Mitchell A. LaBoda, Michael L. McMillan, and Augustine J. Wallace, Jr.

(pp. 199-203, Vol. 116, No. 2)

P. J. Boden[5] and **J. M. Evans**[6]: The intensive study carried out by the authors into the behavior of electrolytes for electrochemical machining is very welcome since it is a serious attempt to solve the problems of the process via a fundamental electrochemical investigation. We have found great experimental difficulties in measuring anode potential under high flow rate conditions and were, therefore, impressed by the rotating disk technique which they employed. Our own conclusions conflict with those of the authors somewhat, and we would like to advance some of our own results.

As we have already stated,[6] we believe that the sole criterion for determining the ability of an electrolyte to produce good machining tolerances is the aggressiveness of its anion toward any passive film formed in the stray current region. Chlorate anions impose only mild attack on passive films formed in their presence, whereas the chloride anions break down the film more severely. In their paper the authors mentioned the absence of the protective γ-Fe_2O_3 in sodium chloride electrolyte. Work at Nottingham[7] seems to indicate that this film exists in chloride solutions but is almost totally pitted in the higher strength solutions (15-20% w/w).

We were surprised to read that the flow of solution has little effect on the machining rate. Turner and Cuthbertson[8] showed that the machining current varied with flow and our calculations indicate that the flow required to give polished surfaces of iron in NaCl solution varies according to the well-known empirical relationship

$$I = K(V)^n$$

where V is the velocity of the electrolyte, $n = 0.5$, and I = current density at which polishing occurs.

Since chlorates and nitrates are potential fire hazards, work has been concentrated on attempting to simulate the desirable cutting properties of these electrolytes through modification of a sodium chloride base solution. Our research has led to the conclusion that wild cutting is merely a function of heavy pitting of a passive film and, if these pits can be blocked then an improvement in machining properties may be achieved. In the case of nickel and nickel-based alloys, this has been achieved by making small additions of anions to the chloride solution so that insoluble salts can be produced in the stray current region. Additions such as carbonate, phosphate, and ferricyanide have been made to chloride solutions and the reduction in stray current attack (SCA) has been superior to that produced in chlorate electrolyte. This work is being reported in greater detail elsewhere, but it is apparent that the effectiveness of the addition is directly related to the solubility of the nickel salt it produces. Indeed, oxygen-containing anion additions, bicarbonate, sulfate, and nitrate produced a relatively small change in SCA due to the formation of soluble nickel salts. The mechanism by which these salts produce the improvement thus appears to be one of pit blocking. Also, provided that small additions are made, *i.e.*, the weight of salt added does not exceed a critical quantity, the surface finish ahead of the tool is unaffected and bright surface finishes can still be achieved at high efficiencies.

A second point which should be noted is that these additions generally increase the alkalinity of the chloride solution and should reduce corrosion of exposed parts of the E.C.M. machines.

J. P. Hoare, M. A. LaBoda, and A. J. Wallace, Jr.: We wish to thank Boden and Evans for their interest in our work, but we would like to take advantage of this opportunity to point out a number of areas in which these authors may have misinterpreted the results of our work.

In NaCl solutions, we maintain that a protective film is not present on iron specimens, although from cathodic stripping studies,[9] we also detect the presence of a nonprotective film. The important word here is "protective."

In the present paper being discussed,[10] we did not say that the metal removal rate was independent of the electrolyte flow rate. It is the steady-state polarization curve that is independent of the speed of rotation of the disk electrode. Actually, in a previous report,[11] it was pointed out that above a given flow rate, where good machining takes place, the increase in metal removal rate varies so slowly with increasing flow rates it is not economical to operate at higher rates. In this range, the metal removal rate may be considered to be approximately independent of flow rate. At the low flow rate and where the ECM properties are more strongly dependent on flow rate, interest is lacking because such experimental conditions do not give efficient ECM operation.

We would like to point out that polishing is not obtained in Cl^- ion electrolytes on most common structural metals except the 300 series stainless steels. Any polishing obtained with Cl^- ion solutions was obtained[6] in the poor ECM range of current densities (50 A/in.^{2}). Economically interesting metal-removal rates take place in the current range between 300 and 1200 A/in.^{2} (3).

Our experience has been that when the electrolyte contains high concentrations of Cl^- ion, nothing can modify the aggressive nature of such an electrolyte to the point where one obtains machining rates and excellent surface finishes on steel and nickel alloys equivalent to the results achieved with chlorate electrolytes. It may be possible to obtain bright surfaces of varying quality under certain conditions with many electrolytes, but only with the chlorate does one find the mirror-bright finish over such a large range of materials and experimental conditions.

In the absence of any detailed report of the experimental conditions, structures of cells, and experimental results, it is impossible to comment further on the work of Boden and Evans with respect to their additions of $CO_3^=$, $PO_4^=$, CrO_4^-, etc., to Cl^- ion-based electrolytes.

[5] Department of Metallurgy, The University of Nottingham, University Park, Nottingham, England.
[6] P. J. Boden and J. M. Evans, *Nature*, 222, 337 (1969).
[7] V. Ashworth, Private communication, Nottingham University (1969).
[8] T. S. Turner and J. W. Cuthbertson, *Production Engineer*, 45, 270 (1966).
[9] J. P. Hoare, *This Journal*, Submitted for publication.
[10] J. P. Hoare, M. A. LaBoda, M. L. McMillan, and A. J. Wallace, Jr., *This Journal*, 116, 199 (1969).
[11] M. A. LaBoda and M. L. McMillan, *Electrochem. Technol.*, 5, 340 (1967).

Effects of Oxidizable Anion Adsorption on the Anodic Behavior of Platinum

Sigmund Schuldiner
(pp. 767-771, Vol. 116, No. 6)

Sigmund Schuldiner replying to the discussion of his paper by K. J. Vetter and J. W. Schultze which appeared on page 824 of the June 1969 Discussion Section v: Vetter and Schultze[12] in a discussion of my paper on the effects of oxidizable anion adsorption on the anodic behavior of platinum have unfortunately based their analysis on a series of erroneous interpretations of data published in several papers from this Laboratory.[13-16] Their incorrect use of our data has led them to a mechanistic interpretation of the reaction of Pt-O_{ad} with dissolved H_2 which can easily be shown to be false.

In their discussion, Vetter and Schultze claim that we state [14, 16] that the mean value of the reaction rate of Pt-O_{ad} + H_2 is 1.2 mA/cm^2. In fact, we make no such statement, and the Vetter and Schultze claim that we did is not correct. In my paper[14] it was pointed out that the rate of the Pt-O_{ad} + H_2 reaction was measured on three separate Pt bead electrodes of different catalytic activity for this reaction. The actual rates for the Pt-O_{ad} + H_2 reaction for each of these electrodes was 0.4, 1.2, and 8 mA/cm^2, respectively. Warner and Schuldiner[16, 17] clearly showed that the rate of the Pt-O_{ad} + H_2 reaction is strongly dependent on the electrode thermal treatment and/or chemical etching. Platinum is a "demanding" catalyst for the reaction. However, my work[15] showed also that the steady-state hydrogen oxidation reaction is independent of the electrode history of Pt. Hence, each electrode gave the same limiting (0.04-0.7V *vs.* NHE) rate of oxidation of H_2 of 2 mA/cm^2.

If the Vetter and Schultze electrochemical mechanism for the reaction of Pt-O_{ad} + H_2 were correct, then the electrode which had a reaction rate of 0.4 mA/cm^2 for this reaction would have a limiting current density for the H_2 oxidation reaction of 0.4 mA/cm^2. Similarly, the electrode with a reaction rate of 1.2 mA/cm^2 would have an H_2 limiting oxidation current density of 1.2 mA/cm^2, and the electrode with a reaction rate of 8 mA/cm^2 would have an H_2 limiting oxidation current density of 2 mA/cm^2. The precision (within 10%) of determining both the reaction rate of the Pt-O_{ad} + H_2 reaction and the limiting H_2 oxidation rate are high enough so that the differences indicated for each electrode would be easily distinguishable in my experimental results. Since all three electrodes gave 2 mA/cm^2 limiting H_2 oxidation current density, the conclusion is that the electrochemical Pt-O_{ad} + H_2 mechanism proposed by Vetter and Schultze is incorrect.

Vetter and Schultze further err in using our data in Fig. 4,[16] by applying an incorrect relation between their supposed Pt-O_{ad} coverage (θ) and potential (E). The data in our Fig. 4[16] shows the transient relation between θ and E, whereas our potentiostatic data in footnotes 14 and 15 concerns the steady state. A steady-state relation between potential and fraction of surface covered with adsorbate can be obtained from our Fig. 2.[15] If one assumes, as does Vetter and Schultze, that this adsorbate is oxygen (or oxide) then one can obtain a relation between θ and E. Using the equation for the rate of reduction of Pt-O_{ad} proposed by Vetter and Schultze[12]:

$$i_- = k_- c_{H+} \exp(a_- \theta - 2.3\, E/b_-)$$

and using their values of $a_- = 13.8$, $b_- = 60$ mV, k_- = constant, c_{H+} = concentration of hydrogen ions, and applying this to the steady-state relation between θ and E[15] one obtains the results shown in Table I. The data for 1M H_2SO_4 shown in the last column show that i_- (k_- and c_{H+} are constants) is not constant from 0.51 to 0.87V. In fact these data show a very rapid decrease in current density from 0.51 to 0.87V. This decrease is contradictory to the data found in footnotes 14 and 15 that showed a steady-state limiting current density from 0.04 to 0.7V. The actual experimental current density decrease at 0.87V[14, 15] was one third of the 0.7V value. The calculated data shown in Table I give a decrease in current density from 0.7 to 0.87V of almost two orders of magnitude. Thus, again it is shown that the analysis used by Vetter and Schultze and their conclusion that the reaction of Pt-O_{ad} + H_2 is electrochemical is incorrect.

Table I. Steady-state relations

θ	E, V	$i_-/k_-c_{H^+}$
0.23	0.51	-7.8×10^{-8}
0.38	0.61	-1.3×10^{-8}
0.40	0.70	-5.7×10^{-10}
0.46	0.79	-4.0×10^{-11}
0.57	0.87	-8.9×10^{-12}

In their analysis of the formic acid reaction, their data (Fig. 2, footnote 12) shows that at a θ of 0.16 and E of 1V, $i \approx 10^{-4}$ A/cm^2. Not enough detail is given to indicate if these are transient or steady-state measurements. My steady-state potentiostatic measurements (Fig. 2, footnote 15) showed that at 1V the steady-state value of what Vetter and Schultze would call θ is 0.71, and i for the formation of oxygen is 5×10^{-7} A/cm^2 (Fig. 1, footnote 15). Here again, it appears that Vetter and Schultze and I are referring to two different experimental conditions. Under steady-state conditions, the rate of oxidation of water to oxygen is orders of magnitude slower than under the conditions used by Vetter and Schultze.

Vetter and Schultze have assumed that steady-state and transient θ and E relations are identical and have based their analysis on an indiscriminate use of both experimental cases. The fact is, however, that transient and steady-state values of these parameters have been shown experimentally to be quite different.

In point of fact, the Vetter and Schultze analysis demonstrates that the Pt-O_{ad} + H_2 reaction is not an electrochemical reaction. This further supports our conclusion[16] that this is a direct chemical reaction between adsorbed oxygen atoms and dissolved molecular hydrogen. This reaction is experimentally[16] independent of potential up to 0.9V, and since the reaction is chemical and independent of potential, one can reasonably predict that the reaction rate is essentially independent of potential up to at least 1.2V positive to NHE.[14, 15] In any case, at potentials below 0.9V where no extrapolation of the rate of the Pt-O_{ad} + H_2 reaction is required, I feel that Vetter and Schultze have offered strong support to my major conclusion[13-15] that the initiation of passivation of the hydrogen oxidation reaction at 0.7V *vs.* NHE is caused by anion adsorption rather than adsorbed oxygen atoms, an oxide, or another oxidation product of water.

[12] K. J. Vetter and J. W. Schultze, *This Journal*, 116, 824 (1969).
[13] S. Schuldiner, *This Journal*, 116, 767 (1969).
[14] S. Schuldiner, *This Journal*, 115, 362 (1968).
[15] S. Schuldiner, *This Journal*, 115, 897 (1968).
[16] T. B. Warner and S. Schuldiner, *This Journal*, 115, 28 (1968).
[17] T. B. Warner and S. Schuldiner, *This Journal*, 114, 1120 (1967).

Highly Refractive Glasses to Improve Electroluminescent Diode Efficiencies

A. G. Fischer* and C. J. Nuese

RCA Laboratories, Princeton, New Jersey

ABSTRACT

A series of low-melting arsenic-chalcogen-halogen glasses were developed, with refractive indexes between 2.4 and 2.9. Despite severe thermal expansion mismatch, it was possible to form stable glass domes on planar electroluminescent diodes by using glass compositions which permit strain relief by thermoplastic flow. By reducing internal reflection losses, external efficiencies were routinely increased by factors from 4-6 for GaAs, $GaAs_{1-x}P_x$, and $Al_xGa_{1-x}As$ diodes, resulting in external efficiencies as high as 7.2% for a solution-grown $Al_xGa_{1-x}As$ diode.

In planar-shaped electroluminescent diodes which emit near-bandgap radiation, large absorption losses and a small critical angle usually limit the external emission to a few per cent of the junction emission. In such diodes, most of the radiation is internally reflected at the crystal surface and strongly absorbed. This loss mechanism can be significantly reduced by shaping the diode to eliminate total internal reflection (*e.g.*, in the form of a hemisphere or Weierstrass sphere), or by capping the diode with a properly shaped transparent material with a refractive index as close as possible to that of the semiconductor (~3.5). An improvement in the external efficiency by a factor of up to 26 is theoretically possible (1) by either of these techniques.

In practice, a factor of 10 improvement has been attained for GaAs diodes shaped as hemispheres (1) (but not free of absorption). However this technique requires excessively thick semiconductor wafers as well as rather tedious shaping procedures, and hence is not particularly well suited for large-scale production. Furthermore, for $GaAs_{1-x}P_x$ or $Al_xGa_{1-x}As$ diodes, which are usually prepared as thin layers on thick GaAs substrates, the epitaxial layer is too thin for shaping, and the GaAs substrate strongly absorbs emission from the higher-energy-gap epitaxial layer. For these reasons, the use of a properly shaped transparent encapsulant for planar electroluminescent diodes is particularly attractive.

Transparent resin domes have been used routinely on diode light sources; however their low refractive index ($\leq$1.8) limits efficiency improvements to less than a factor of three (2). A transparent optical As-S-Br glass of high refractive index ($n = 2.4$) was used earlier by Fischer (3) as an imbedding medium for studies on ZnS electroluminescent particles. However, apart from the primary requirements for a high refractive index and low absorption, such a glass must fulfill two more conditions in order to be practical for dome fabrication on electroluminescent diodes:

(*a*) The viscosity *vs.* temperature behavior of the glass must permit it to be moldable at temperatures low enough to prevent chemical reactions between the glass and the diode, or melting of the solder contacts.

(*b*) The viscosity of the glass must be low enough at room temperature to permit thermoplastic flow. This flow can then relieve the strain caused by the large difference in the thermal expansion coefficients of the glass and the semiconductor, thereby preventing the glass dome from cracking off the crystal.

In this paper we describe a series of optical glasses consisting of various combinations of arsenic, sulfur, selenium, tellurium, bromine, and iodine, which meet the conditions discussed above. Such glasses, when used as spherical domes on planar diodes which emit near-bandgap light, have been found to increase external efficiencies by as much as a factor of 6. Through the use of these glasses, room-temperature external efficiencies were increased from 0.03 to 0.16% for vapor-grown $GaAs_{1-x}P_x$ diodes, from 0.4 to 2.1% for Zn-diffused GaAs diodes, and from 1.7 to 7.2% for a solution-grown $Al_xGa_{1-x}As$ diode. The preparation and properties of these glasses, their fabrication as domes on planar electroluminescent diodes, and the optical and electrical properties of the glass-encapsulated diodes are discussed below.

Preparation and Properties of Arsenic-Chalcogen-Halogen Glasses

Composition.—A yellow glass consisting of arsenic ($n \approx 4$), sulfur ($n \approx 1.95$), and bromine ($n \approx 1.66$) in approximately equal parts (weight per cent) has been used previously to match the refractive index of ZnS (3). However, our present studies have found that this glass is not suited for electroluminescent diode encapsulation because of a large thermal expansion mismatch between the glass and the diode, and because of the brittleness of the glass at room temperature. The purpose of our present study of arsenic-chalcogen-halogen glasses has been to overcome the thermal mismatch problem of the previous glass, and to increase the refractive index to more closely match that of $GaAs_{1-x}P_x$ ($n \approx 3.5$).

To increase the refractive index, sulfur can be replaced partly or totally by selenium ($n \approx 3$) and/or tellurium ($n \approx 4$), and bromine can be replaced by iodine ($n \approx 3.3$). But with such substitution, the absorption edge shifts to longer wave lengths, toward the red and infrared (Fig. 1), and the glasses finally become black in color. All observed properties of these glasses appear to change smoothly with changes in

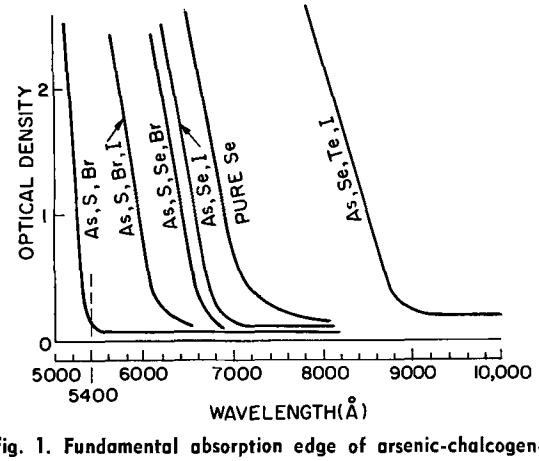

Fig. 1. Fundamental absorption edge of arsenic-chalcogen-halogen glasses.

* Electrochemical Society Active Member.

composition. However, for the glasses to be practical for electroluminescent diode encapsulation, many ranges of composition must be avoided, as described below:

(i) Arsenic-rich compositions provide glasses with undesirably high softening temperatures (>200°C). High-temperature fabrication steps can melt ordinary solder contacts. Such glasses are also too brittle at room temperature to prevent cracking.

(ii) Halogen-rich compositions (especially those with iodine) yield glasses which are moldable at a suitably low temperature, but which solidify very rapidly upon cooling, so that they are also too brittle at room temperature. (These are labeled "short" glasses since they have a short temperature range of usable viscosity, in contrast to "long" glasses which have a long temperature range of useful viscosity). At higher halogen concentrations, these glasses are no longer brittle at room temperature, but soften at relatively low temperatures (about 50°C) which may be attained by the diodes during high-level operation. Still higher bromine content leads to glasses which are liquid at room temperature.

(iii) Compositions rich in sulfur provide desirable "long" glasses. However, too much sulfur lowers the refractive index, and also leads to devitrification upon long standing.

Because of such limitations, many different glass compositions were prepared and evaluated in order to select those best suited for electroluminescent diode encapsulation. A representative series of compositions examined for this purpose during the course of our studies is presented in Table I. Obviously, a more extensive materials-oriented study of the arsenic-chalcogen-halogen glasses would be interesting; however, the complexity of the As-S-Te-Se-Br-I glass system over wide compositional ranges precludes such a detailed investigation. Furthermore, the properties listed above were found to provide adequate guidance for the preparation of several glass compositions which were successfully used to improve electroluminescent diode efficiencies.

Two glasses in particular were found useful for diode encapsulation. A yellow glass consisting of As (10g), S (13.5g), and Br (≈2 cc) has a refractive index of 2.4 and is transparent to light with wave length greater than about 5400Å (*see* Fig. 1). A red glass consisting of As (10g), S (8g), Se (15g), and Br (≈1.8 cc), has a higher refractive index of 2.5-2.7, but transmits light only in the red and infrared spectral range. The infrared glasses which are rich in Se have a very high refractive index ($n \approx 2.9$). However they have not been successful to date because of large absorption losses due to the formation of a second phase, as observed by scanning electron microscopy.

Table I. Representative glass composition series

Type	Arsenic	Chalcogen		Halogen		Comments
	g	S		Br		$n \sim 2.4$
		g				
	10	10		1.8-2 cc		Small uncontrolled amounts of Br are lost during preparation
	10	11				
	10	12				
Yellow glass	10	13				
	10	13.5				← This glass gave best results
	10	14				
	10	15				
		S	Se	I	Br	$n \sim 2.5$-2.7
		g	g			
	10	10	10	Same as above		
Red glass	10	8	15	Up to 15		← Best results
	10	6	20	mole % Br can be replaced by I		Residual absorption increases with Se and I (second phase?)
	10	4	25			
	10	0	35			
		Se	Te	I	Br	$n \sim 2.9$
		g	g	g		
IR glass	10	35		3	*ca.* 0.3 cc	High absorption (second phase?)
	10	32	5	3		

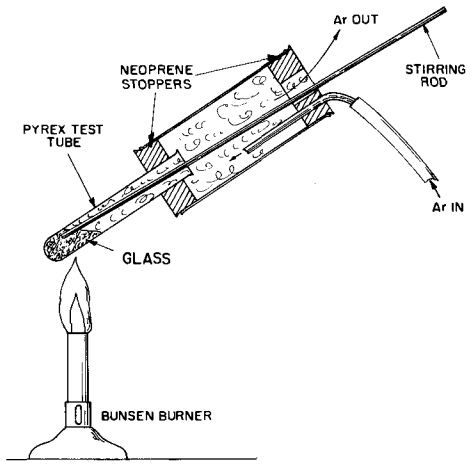

Fig. 2. Set-up for preparation of glasses.

Preparation.—The general preparation of all arsenic-chalcogen-halogen glasses proceeds basically as follows. High-purity elements[1] (99.999%) are used, and surface oxides are removed by heating in hydrogen (for Se or Te), or by heating in vacuum (for S). Bromine is dried with $CaCl_2$ or "molecular sieve," and iodine is dried by storing it in a closed vessel with P_2O_5.

Using the simple apparatus shown in Fig. 2, the arsenic is reacted with the chalcogens and iodine (when used) under argon with intense stirring. This may require heating to 600°C. The mixture is then allowed to cool to about 50°C, and bromine is added with a pipette.[2] The mixture is reheated and stirred vigorously as soon as the viscosity is low enough. At a temperature where the glass is sufficiently liquid (~200°C), one homogenizes (restirs) the composition, and lets it settle to allow bubbles to escape. Since the glass must be of high optical quality, great care is needed in this homogenization to prevent bubbles and schlieren. This preparation method is simple and inexpensive; however a small amount of bromine is always lost, the exact quantity of which depends primarily on the specific techniques of the preparer. One batch of a particular glass is sufficient to encapsulate about 100 diodes.

The reproducibility of the glasses described here could almost certainly be improved by preparation in evacuated quartz ampoules; however the danger of explosion with sealed ampoules would require careful attention.

Evaluation.—Refractive indexes were determined by the Chaulnes method (4), where the displacement of a visual image is measured with and without a plane-parallel glass plate between the sample and the observer. They ranged from 2.4 for the yellow arsenic-sulfur-bromine glasses to 2.9 for the *IR*-translucent black glasses containing Se, Te, and I.

The very important residual absorption at energies less than that of the fundamental absorption edge was monitored for each glass by measuring two large planar wafers, one 1 mm thick, the other 2 mm thick, to separate reflection from absorption losses. The absorption of a 1-mm thick wafer should not exceed 2% for useful glasses. High absorption coefficients were

[1] Suppliers: As, Se, Te: American Smelting and Refining Co., South Plainfield, N. J. S: United Mineral & Chemical Corp., 129 Hudson St., New York, N. Y. Br: Matheson, Coleman & Bell, East Rutherford, N. J.

[2] The amount of bromine required to provide adequate room-temperature thermoplasticity for any of the glass compositions is empirically determined by adding bromine in 0.2-cc increments to the molten mixture until the glass no longer cracks off the Pyrex tube upon cooling to room temperature. The final test for thermoplasticity is strong adhesion of a glass dome to a Kovar header.

found to correlate with the occurrence of small precipitated rods as seen under the scanning electron microscope, and are still excessive at present (>3%) in Se-, Te- and I-rich glasses. Suppression of this second phase by ultrasonic stirring during preparation appears to be promising.

To measure the thermal expansion curves, a very simple and inexpensive dilatometer was constructed (Fig. 3). The average expansion coefficient for the glasses was found to be 230 x 10^{-7}/°C, as compared to 48 x 10^{-7}/°C for GaAs (Fig. 4). This large mismatch in thermal expansion coefficients clearly illustrates the need for thermoplasticity of the glass at room temperature to prevent cracking.

Fabrication of Glass Domes on Diodes

To produce small manageable pieces from the large glass ingots, the test tube containing the glass is submerged in liquid nitrogen and then placed into hot water. The glass cracks into fragments several millimeters in diameter. A selection of equally sized pieces is then heated on a microscope slide until they melt into slightly flattened droplets. After cooling, the beads are carefully examined to eliminate those with flaws.

The electroluminescent diode to be dome-encapsulated is then heated in air to about 170°C under a microscope. A glass bead is lifted with vacuum tweezers and, by means of micromanipulators, placed onto the heated diode, where it rapidly melts. If it is not accurately centered on the diode, it can be gently pushed sideways to improve its positioning. If the glass is not transparent to visible light, such as the ones used on infrared-emitting diodes, an infrared image converter can be mounted on the microscope, and the infrared emission of the forward-biased diode can be used to aid in the centering procedure. After the dome is correctly placed, the diode is inverted during cooling to round the slightly flattened dome (Fig. 5).

These free-flowing glass droplets attain their shape under the influence of surface tension, gravity, viscosity, and wetting adhesion forces. The surface of the resulting dome is perfectly smooth. Domes which are formed using molds (silicone rubber molds were found best) have slightly rough surfaces and have not yielded efficiencies as high as the freely formed spheres.

Properties of Dome-Encapsulated Diodes

To evaluate the effectiveness of the glass domes for increasing the efficiency of electroluminescent diodes, numerous Zn-doped GaAs and $GaAs_{1-x}P_x$ diodes were encapsulated for each of the glass mixtures, and their external quantum efficiency was measured before and after glassing. Room-temperature external efficiencies were routinely measured with a large-area (1-in. diameter) calibrated silicon solar cell (Hoffman 2A) placed immediately adjacent to the diode. Efficiencies were also checked in an integrating sphere for several of the more successful glasses.

The room-temperature external emission *vs.* current characteristics for a representative GaAs and a $GaAs_{0.6}P_{0.4}$ electroluminescent diode, before and after encapsulation, is presented in Fig. 6 and Fig. 7. The yellow As-S-Br domes for these diodes were formed naturally, without mold, as described previously and as illustrated in Fig. 5. The hemispheres were about 0.10 in. in diameter, whereas the diodes were 0.020-0.025 in.

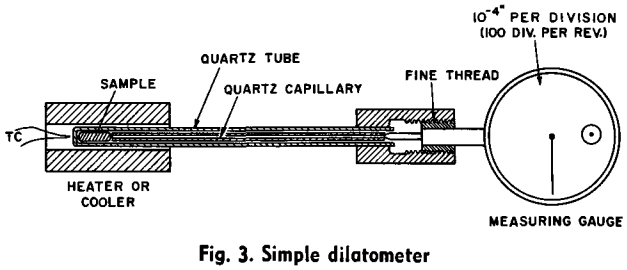

Fig. 3. Simple dilatometer

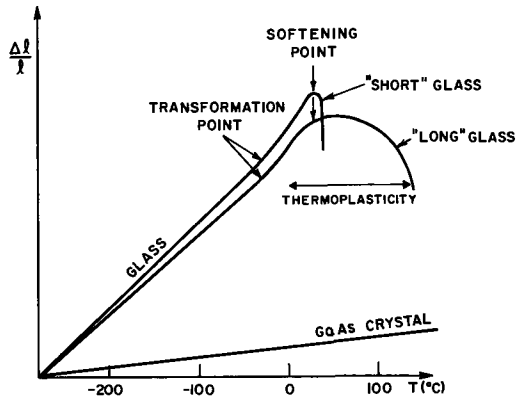

Fig. 4. Thermal expansion curves of glasses. (Probe force: 20g)

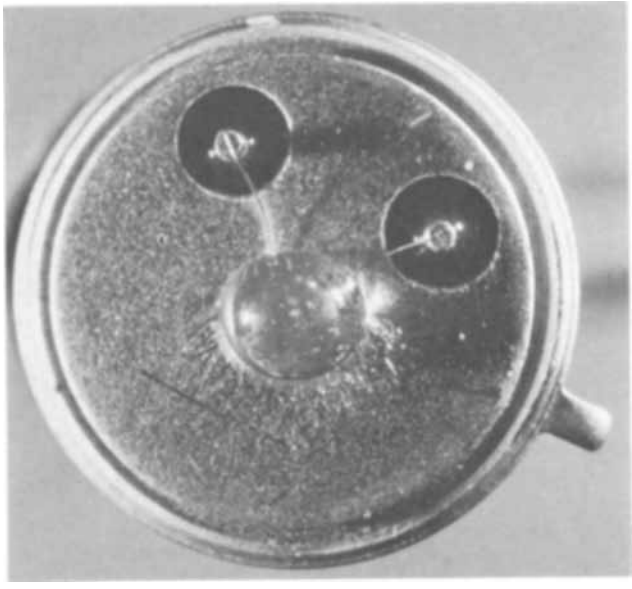

Fig. 5. Photograph of encapsulated diode on TO-5 header

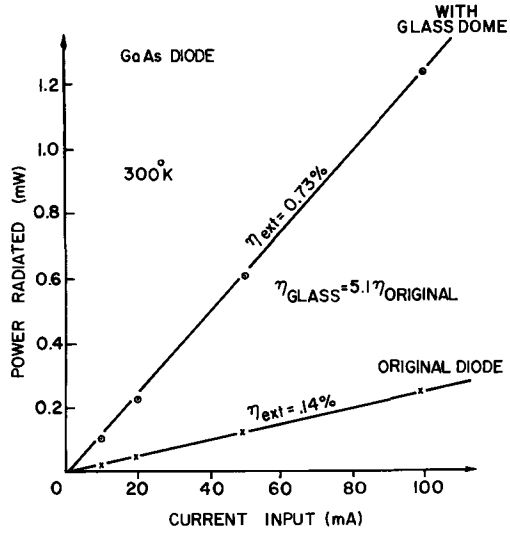

Fig. 6. Power radiated *vs.* input current for encapsulated GaAs diode. $T = 300°K$.

square. For both the GaAs and $GaAs_{0.6}P_{0.4}$ diodes of Fig. 6 and 7, external efficiencies are shown to increase by a factor of 5.1-5.3 after glassing. Removal of the glass encapsulant with methylene iodide was found to restore the efficiency to its former value, suggesting that a chemical interaction between the diode and the glass is not the cause of the efficiency increase. In general, improvements of room-temperature efficiencies varied between 4 and 6 for such diodes, which

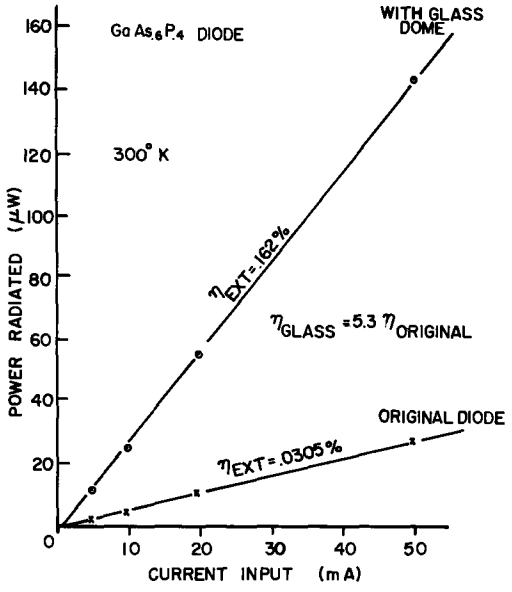

Fig. 7. Power radiated vs. input current for $GaAs_{0.6}P_{0.4}$ diode. $T = 300°K$.

are somewhat less than a value of 7 calculated for a perfectly shaped, nonabsorbing glass with a refractive index of 2.4 (2), but which are nevertheless about twice as high as values for organic resin domes. The external emission of the encapsulated diodes depends strongly on the precise shape of the dome, its centering over the diode, and the optical clarity of the glass itself.

In general, the relative efficiency improvement for encapsulated diodes depends also on the sample geometry and the optical quality of the diode prior to glassing. If a diode contains optical scattering centers, or deviations from surface planarity (*e.g.*, pits, hillocks, cleavage ridges, *etc.*), trapped light may escape *via* reflection or refraction from these inhomogeneities. However, this additional component of external emission is significant only for semiconductors with very little absorption, where the light can bounce around, such as for red-light-emitting GaP diodes. For such GaP diodes, which presently yield highest visible-light efficiencies, our glasses provide an efficiency improvement of only about a factor of 2, since the initial emission is *not* significantly limited by light trapped *via* total internal reflections. The same holds true for SiC light diodes,[3] where the index matching ($n_{SiC} \sim 2.6$) is almost perfect, but where the improvement factor (2-3) is nevertheless disappointing.

However, for the zinc-doped GaAs and $GaAs_{0.6}P_{0.4}$ diodes studied here (including those in Fig. 6 and 7), beneficial effects from optical inhomogeneities are very unlikely, since the near-bandgap radiation is readily absorbed. In particular, the GaAs substrate adjacent to the $GaAs_{1-x}P_x$ epitaxial layer would immediately absorb any of the high-energy light attempting to bounce around within the semiconductor. This is also the case for Si-compensated $Al_xGa_{1-x}As$ diodes grown from solution on GaAs substrates. The $Al_xGa_{1-x}As$ layer itself absorbs little of the light (5); however absorption in the GaAs substrate is large. Glassing of such a diode therefore resulted in an external efficiency improvement by a factor of 4.2, from 1.7 to 7.2% at room temperature (5). Our results with GaAs, $GaAs_{1-x}P_x$, and $Al_xGa_{1-x}As$ diodes suggest that large improvements will be obtained for all diodes which are initially limited by large absorption losses and a small critical angle. It should be noted that the glass domes do not provide similarly large improvements in the brightness (luminosity/area) of visible-light emitting diodes, because of magnification of the diode area by the spherical glass dome.

Besides improving diode efficiencies, an additional advantage of the glass domes is the ease with which their shape can be varied to provide different far-field emission patterns (2). For example, the small spheres which are formed naturally during cooling provide a rather broad spatial pattern not significantly unlike that of the original diode, but occasionally as broad as that shown in Fig. 8a (78° half-width). On the other hand, a large hemisphere (molded in silicone rubber) provides a somewhat more beam-like pattern due to the focussing action of the "lens" formed by the spherical glass surface (Fig. 8b). The unusual bulges in the patterns of Fig. 8 arise from irregular curvatures in the experimental glass domes examined here. Prior to glassing, the spatial emission pattern for all diodes was approximately that of a $(1\text{-}\cos^3\theta)$ distribution, with a half-width of 65°.

The current-voltage characteristics of several GaAs and $GaAs_{1-x}P_x$ electroluminescent diodes were evaluated, before and after encapsulation, in order to determine the existence of any leakage current caused by the glass or by any possible reaction of the glass with the diode surface. As shown for the representative $GaAs_{0.6}P_{0.4}$ diode in Fig. 9, there was no measurable leakage current caused by the glassing process for currents in the investigated range between 10^{-6} and 10^{-1}A. Similar results were obtained on a series of 10 different GaAs and $GaAs_{1-x}P_x$ encapsulated diodes.

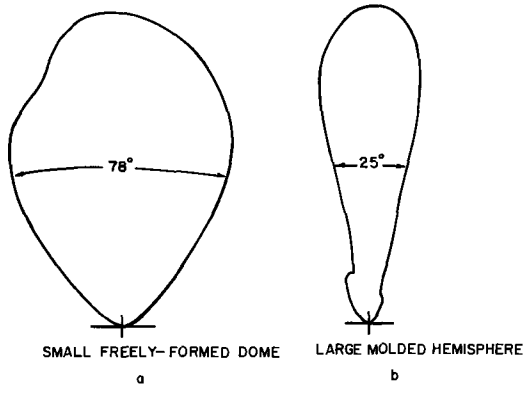

Fig. 8. a—Far-field pattern of diode with small, naturally formed dome; b—far-field pattern of large, molded hemispherical dome.

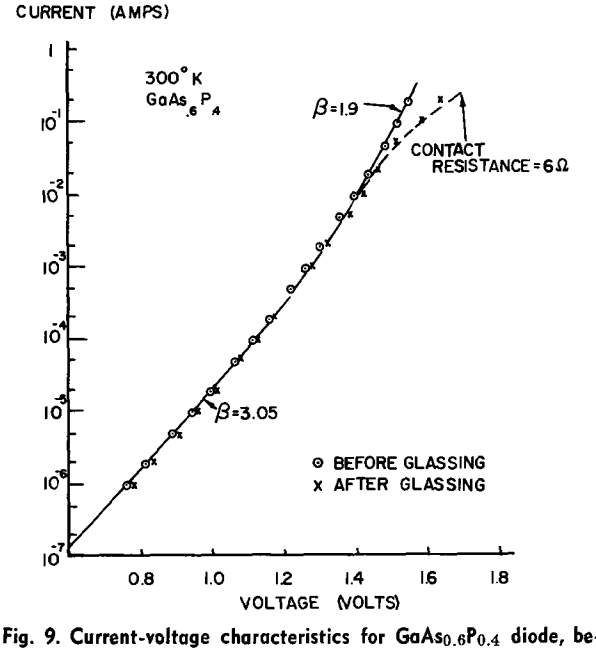

Fig. 9. Current-voltage characteristics for $GaAs_{0.6}P_{0.4}$ diode, before and after encapsulation.

[3] Supplied by General Electronic Co., Miniature Lamp Division, Cleveland, Ohio.

Note however, in Fig. 9, the deviation of the two curves at high currents. The shift to larger voltages after glassing represents an ohmic series resistance of about 6 ohms, which is almost certainly due to loosening of the current leads during the mounting of the glass dome, or by relative thermal motion during cooling. The increased contact resistance is not inherent to the glassing process itself, since diode geometries can be readily employed with current leads connected to the bottom of the diode, where they would not be weakened by the glassing process.

Conclusions

A series of arsenic-chalcogen-halogen glasses were developed with low melting temperatures and with refractive indexes between 2.4 and 2.9. The glasses are chemically stable and have absorption edges between 5400 and 9000Å. Despite the severe expansion mismatch, it was possible to form stable glass domes on planar electroluminescent diodes by employing glass compositions which permit strain relief by thermoplastic flow. Room-temperature external efficiencies were routinely increased by factors from 4 to 6 by dome-encapsulating electroluminescent diodes of GaAs, $GaAs_{1-x}P_x$, and $Al_xGa_{1-x}As$. With these glass domes, room-temperature external quantum efficiencies were increased from 0.03 to 0.16% for vapor-grown $GaAs_{1-x}P_x$ diodes, from 0.4 to 2.1% for Zn-diffused GaAs diodes, and from 1.7 to 7.2% for a solution-grown $Al_xGa_{1-x}As$ diode, close to earlier predictions (6).

Acknowledgments

The authors wish to thank H. Kressel and I. Ladany for the use of their integrating spheres and for supplying solution-grown *e-l* diodes for encapsulation. We also wish to acknowledge the capable assistance of J. J. Gannon for numerous measurements.

Manuscript submitted April 23, 1969; revised manuscript received *ca.* Aug. 11, 1969. This paper was presented at the Device Research Conference, Rochester, N. Y., June 23, 1969.

Any discussion of this paper will appear in a Discussion Section to be published in the June 1970 JOURNAL.

REFERENCES

1. W. N. Carr and G. E. Pittman, *Appl. Phys. Letters*, **3**, 173 (1963); W. N. Carr, *Infrared Physics*, **6**, 1 (1966).
2. C. J. Nuese, J. J. Tietjen, J. J. Gannon, and H. F. Gossenberger, *This Journal*, **116**, 248 (1969).
3. A. G. Fischer, *ibid.*, **109**, 1043 (1962).
4. *See, e.g.*, A. Miller, *J. Opt. Soc. Amer.*, **58**, 428 (1968).
5. H. Kressel, F. Z. Hawrylo, and N. Almeleh, *J. Appl. Physics*, **40**, (1969).
6. A. G. Fischer, *Solid State Electron.*, **2**, 245 (1961).

The Synthesis of Bulk GaP from Ga Solutions

T. S. Plaskett

IBM Research Division, Yorktown Heights, New York

ABSTRACT

The synthesis of solid ingots of high-purity GaP by reacting PH_3 with molten Ga at 1000°-1200°C is described. Actual growth parameters were measured during synthesis and compared with the values predicted from solution growth theory. Growth rates of about 1.7×10^{-5} cm/sec were possible with this system for a solution saturated with P at 1200°C. Some properties of the synthesized material are presented.

Many GaP single crystal growth techniques (1, 2) for preparing material for electronic applications require large solid starting ingots of high-purity GaP. However, most high-purity GaP is only available in granular or platelet form or as a spongy mass with considerable entrapped Ga. Solid ingots have been synthesized from the elements under high temperatures and pressures (3-5) where the melt approaches the stoichiometric composition,[1] but under these conditions there is the problem of contamination from the container material. Solid ingots of high purity have also been produced by reacting P_2 or some gaseous phosphorus compound with Ga at lower temperatures, but over an extended period of time.

In this paper a method to synthesize high-purity solid ingots of GaP at a low temperature and in a reasonable but short time is described. The growth parameters under these conditions were measured and are compared with the theoretical values predicted from constitutional supercooling considerations. Some properties of the synthesized ingot are also given.

Growth Considerations

The reaction of molten Ga with PH_3 can be described as

$$Ga + PH_3 \rightleftarrows GaP + 3/2\ H_2 \qquad [1]$$

The usual procedure is to let the GaP that is formed by the reaction dissolve into the Ga at a hot region and then precipitate at the coldest region. Essentially, the growth or precipitation is from dilute solution (at 1200°C, for example, Ga dissolves about 12% by weight of GaP). The growth of solid material without any entrapment of Ga is therefore limited by the onset of constitutional supercooling (hereafter abbreviated to cs), which is encountered at high growth rates. The conditions that are required to prevent cs during growth from dilute solutions are quite severe.

Both Hurle, *et al.* (6), and Tiller (7) have analyzed growth from solution from the standpoint of cs. Hurle *et al.* in their analysis included the effect of stirring and showed that for the growth of III-V compounds the condition for no cs can be expressed, in a slightly rearranged form, as

$$\frac{G_L}{f} \geqq -\frac{mC_L}{D} \exp \Delta \qquad [2]$$

where G_L is the temperature gradient in the liquid ahead of the solid-liquid interface

f is the growth rate

m is the slope of the liquidus curve

D is the liquid diffusion coefficient

C_L is the excess concentration of the III (or V) component in the melt and is defined as $C_L = C_{III} - 0.5$, and

[1] GaP melts at 1467°C and has a dissociation pressure at the melting point of about 35 atm.

Table I. Growth parameters

Temp, °C	Slope of liquidus m, °C/mole fraction	Excess Ga conc.* C_L, mole fraction	Theoretical G_L/f values for the onset of cs °C-sec/cm²	Measured G_L/f values at various synthesis temperatures, °C-sec/cm²
800	2.6×10^4	0.498	2.6×10^8	
900	1.2×10^4	0.493	1.2×10^8	
1000	4.5×10^3	0.480	4.3×10^7	1.4×10^7
1100	2.6×10^3	0.446	2.3×10^7	2.0×10^7
1200	1.9×10^3	0.395	1.5×10^7	2.3×10^7
1300	8.7×10^2	0.325	5.7×10^6	
1400	7.4×10^2	0.220	3.3×10^6	

* $C_L = (C_{III} - 0.5)$ where C_{III} is the concentration of the Ga in the compound and C_L is excess concentration of Ga in the Ga-P solution.

Δ is defined by the relationship, $\Delta = f\delta/D$ where δ is the thickness of the boundary layer of excess solvent at the solid-liquid interface.

If we now consider only a system where there is good stirring in the solution, then δ approaches zero and Eq. [2] reduces simply to

$$\frac{G_L}{f} \geq \frac{mC_L}{D} \qquad [3]$$

Some typical values for G_L/f for the system Ga-P are shown in Table I. The values are similar to those obtained from the analysis of Tiller (7). In both cases, the solubility data of Hall (8) and Rubenstein (9) were used to determine m and C_L. A value of 5×10^{-5} cm²/sec was used for D similar to that used by Tiller (7). From this analysis it is apparent that extremely high-temperature gradients are required if solid ingots are to be synthesized at a reasonable rate. As the concentration of the solution increases, the severity of the growth condition G_L/f decreases. At the stoichiometric composition, *i.e.*, no excess Ga, the ratio is zero since no Ga build-up would exist ahead of the interface and therefore no cs. If only partial stirring exists, the G_L/f values shown in Table I are increased by the factor exp Δ.

Experimental

The reactor used in this investigation is shown in Fig. 1. A 30g charge of Ga is placed in a pyrolytic BN crucible (1.5 cm diameter and 6 cm deep) which in turn fits into a quartz tube. The bottom of the quartz tube is cooled by a blast of air to provide the steep temperature gradient. A 10% PH_3 in Ar mixture is injected through the top of the quartz tube down to a few millimeters inside the crucible at a rate between 50-100 ml/min. A small diameter inlet tube is used to maintain a high velocity of the gas in order to prevent decomposition of the PH_3 prior to entering the hot reactor.

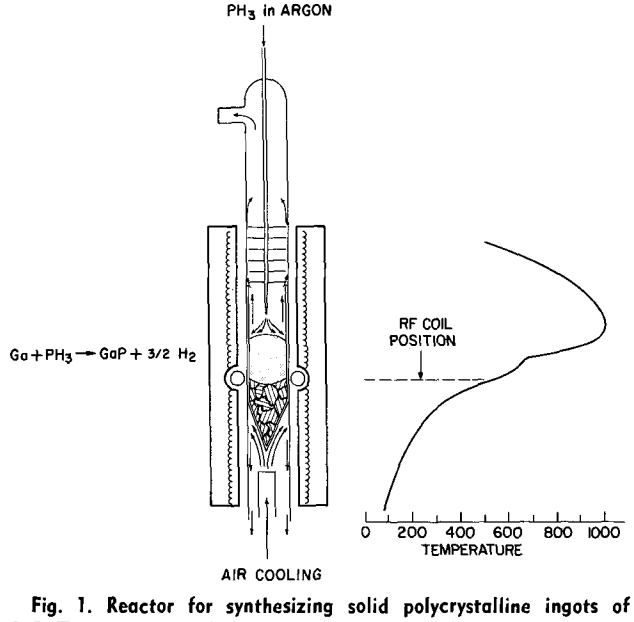

Fig. 1. Reactor for synthesizing solid polycrystalline ingots of GaP. Temperature profile in furnace shown at right.

The reactor is heated by a single turn rf coil and resistance heated furnaces are placed above and below the coil. The coil is initially positioned near the bottom of the crucible. This produces intense concentrated heat below the surface of the solution thus generating strong convective currents to provide the necessary mixing. The mixing also ensures that the GaP that is formed at the surface is dissolved throughout the solution instead of crusting over the surface and preventing further reaction. The strong blast of air at the bottom of the crucible provides the steep temperature gradient and also maintains the growing interface at a position slightly below the coil. The actual temperature profile in the furnace is shown in Fig. 1. Once a steady-state condition is reached, which takes about 6 hr, the reactor is moved through the furnace at a rate of about 1.7×10^{-5} cm/sec. The time for synthesis for the 30g charge of Ga is about 3 days.

A 10% PH_3 in Ar gas mixture was used. At concentrations lower than this, it was not possible to saturate the solution at 1200°C. An estimate of the composition required is that the partial pressure of P_2 in the gas stream must exceed the vapor pressure of P_2 over the saturated solution. For Ga-P solution at 1200°C the vapor pressure (10) is about 1×10^{-2} atm. The partial pressure of P_2 in the 10% gas mixture is 5×10^{-2} atm.

With this system, doped ingots can be synthesized either by adding the dopant to the gas stream or to the Ga prior to synthesis. GaP ingots doped with C were synthesized by adding CH_4 to the gas stream. Si, Te, Zn, Sn, and Bi doped ingots were synthesized by adding the dopant to the Ga.

A temperature exploration during synthesis was made by a thermal probe. A thin-walled quartz tube, closed at one end, was inserted down the center of the crucible. During synthesis, a thermocouple was moved through the tube. The GaP actually synthesized around the tube, and therefore the temperature profile in the solid as well as the solution was measured.

Results and Discussion

Ingot morphology.—A typical GaP ingot synthesized in this system over a period of about 3 days is shown in Fig. 2. The ingot weighs about 40g. Typical sections cut from near the top and from just above the cone of the ingot are shown. No entrapped Ga is visible. If the reactor is run at a lower temperature, some entrapped Ga is detected in the lower portion of the ingot. A typical crystalline structure of an ingot taken from the center portion is shown in Fig. 3. Occasionally near the top of the ingot a section consisted of a few large grains, but this was not reproducible. Single crystal growth would not be expected in this system because of the lack of growth stability. With the presence of convective stirring, violent growth fluctuations would be expected at the solid-liquid interface. Single crystal growth from solution requires extremely good stability, which is obtainable only at much slower growth rates. Some of the factors that determine growth stability have been discussed quantitatively by Tiller (7).

Chemical purity.—Except for Si, the impurity content was below the level of detection by emission spectrographic analysis. The impurities were best detected by photoluminescence studies. A detailed paper on the photoluminescence properties of this material is presented elsewhere (11). Briefly, the major impurities determined by photoluminescence were N, S, C, and Si. The S and C levels, as determined by electrical measurements, were below 3×10^{16} at./cc. The Si con-

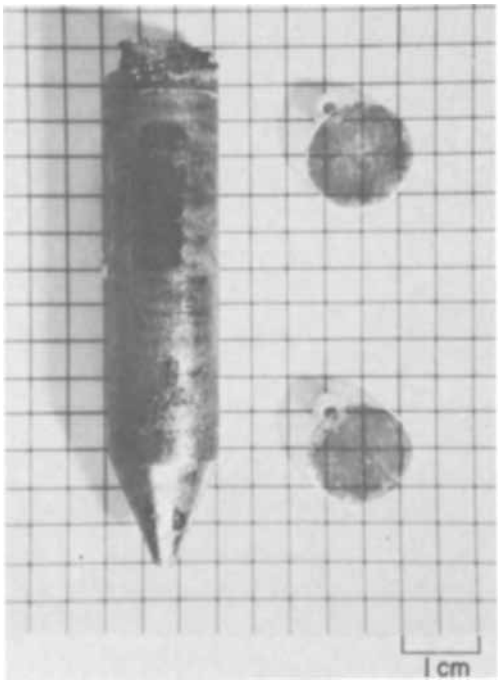

Fig. 2. Typical synthesized ingot. Polished sections shown are taken from top and bottom of another ingot.

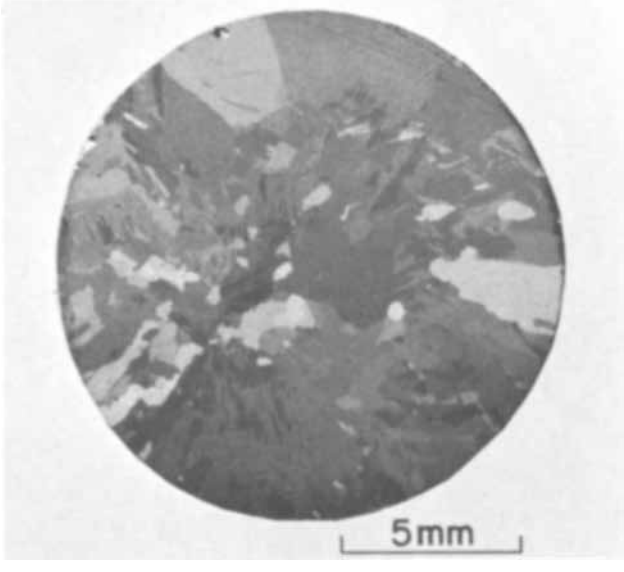

Fig. 3. Typical grain structure of an ingot. Cross section shown taken from the center portion of an ingot.

tamination is from the quartz. It was found that by operating the reactor at a lower temperature the Si could not be seen in photoluminescence. The S and C contaminations are from the PH_3-Ar gas mixture. It was possible, however, to obtain gas mixtures in which the only contaminant observed in the synthesized GaP was N (by photoluminescence) and this was probably introduced from the BN crucible. Some of the C may also be attributed to contamination from the BN crucible.

Growth conditions.—The growth conditions during synthesis were determined from the thermal probe measurements made during one run. The temperature profiles at various times after the start of synthesis, both in the ingot and solution, are shown in Fig. 4. After the start of synthesis each curve has two distinct inflection points. The lower inflection point designates the position of the solid-liquid interface while the top inflection point designates the position of the surface of the Ga solution. Some of the growth parameters

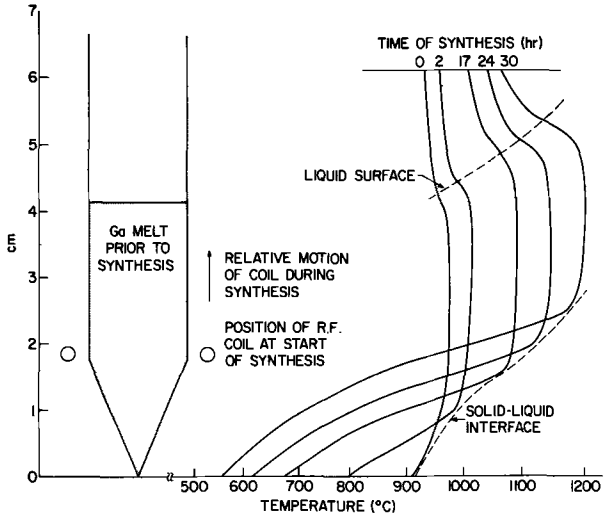

Fig. 4. Temperature profile in the solution and the ingot during synthesis.

determined from the thermal probe data are shown in Table II. The temperature of the solution increased as synthesis progressed since the rf power was not decreased proportionately to the amount of solution that was left. After the initial synthesis in the cone was complete, the growth rate and temperature gradient became essentially constant at about 1.7×10^{-5} cm/sec and about 320°-380°C/cm, respectively. If we assume that G_s, the temperature gradient obtained from the curves, is equal to G_L, the temperature gradient in the liquid at the solid-liquid interface,[2] then the G_L/f values can be calculated. Values calculated from the experimental data are shown in Table I for the temperature range used during synthesis. At the lower temperature, *i.e.*, the first quarter of the ingot to synthesize, the G_L/f values are below the predicted values for cs. This agrees quite well with the experimental evidence since entrapped Ga was occasionally observed in this region of the ingot. At the higher temperatures, *i.e.*, the remainder of the ingot, the G_L/f values are greater than the predicted value for cs and in this portion no entrapped Ga was observed.

Conclusion

A method of synthesizing high-purity GaP at reasonable rates of growth from dilute Ga solutions is described. It was demonstrated that it is possible to maintain sufficiently steep temperature gradients in a growth system to prevent cs. With the present system, the maximum temperature gradient possible was about 380°C/cm. It was found experimentally that with this gradient growth rates of about 1.7×10^{-5} cm/sec were possible for a Ga solution saturated with P at about 1200°C, without entrapping Ga. The G_L/f ratio necessary to prevent cs agrees fairly well with the theoretical value.

[2] This assumption is good for metallic crystal growth where heat transfer is only by conduction. However, for transparent materials such as GaP, heat is also transferred by radiation. O'Hara *et al.* (12) have shown that this can cause the gradient in the liquid to exceed that in the solid.

Table II. Measured growth parameters

Time after start of synthesis, hr	Interface position from cone, cm	Temperature of solid-liquid interface, °C	Temperature of reaction surface, °C	G_s °C/cm	f cm/sec
0	0	—	—	—	—
2	0.98	988	1016	210	1.7×10^{-5}
17	1.55	1080	1092	320	1.7×10^{-5}
23.5	2.01	1137	1145	380	1.7×10^{-5}
29.5	2.47	1188	1200	380	1.7×10^{-5}

The ingots were polycrystalline because of the severe growth conditions during synthesis. Considerably more growth stability would be required for single crystal growth.

Acknowledgment

The author is grateful to Messr. A. H. Parsons for technical assistance and to W. A. Kahn and J. J. Dempsey for the construction of the reactor.

Manuscript received July 11, 1969. This was Recent News Paper 608 presented at the Montreal Meeting, Oct. 6-11, 1969.

Any discussion of this paper will appear in a Discussion Section to be published in the June 1970 JOURNAL.

REFERENCES

1. T. S. Plaskett, S. E. Blum, and L. M. Foster, *This Journal*, **114**, 1303 (1967).
2. S. E. Blum and R. J. Chicotka, *ibid.*, **115**, 298 (1968).
3. S. E. Blum, R. J. Chicotka, and B. K. Bischoff, *ibid.*, **115**, 324 (1968).
4. J. P. Besselere and J. M. Le Duc, *Mat. Res. Bull.*, **3**, 797 (1968).
5. S. J. Bass and P. E. Oliver, *J. Crystal Growth*, **3**, 286 (1968).
6. D. T. J. Hurle, O. Jones, and J. B. Mullin, *Solid-State Elec.*, **3**, 318 (1961).
7. W. A. Tiller, *J. Crystal Growth*, **2**, 69 (1968).
8. R. N. Hall, *This Journal*, **110**, 385 (1963).
9. M. Rubenstein, Paper 65 presented at the Los Angeles Meeting of the Society, **109**, 69C (1962).
10. D. Richman, *J. Phys. Chem. Solids*, **24**, 1131 (1963).
11. T. N. Morgan, T. S. Plaskett, and G. D. Pettit, *Phys. Rev.*, **180**, 845 (1969).
12. S. O'Hara, L. A. Tarshis, and R. Viskanta, *J. Crystal Growth*, **3**, 583 (1968).

The Use of Metal-Organics in the Preparation of Semiconductor Materials

I. Epitaxial Gallium-V Compounds

H. M. Manasevit and W. I. Simpson

Autonetics Division of North American Rockwell Corporation, Anaheim, California

ABSTRACT

Single-crystal GaAs, GaP, $GaAs_{1-x}P_x$ and $GaAs_{1-x}Sb_x$ films have been grown on GaAs and a number of insulating substrates by the decomposition of alkyl-gallium compounds in the presence of arsine, phosphine, arsine-phosphine, and arsine-stibine mixtures. Both triethylgallium and trimethylgallium have been used successfully in the preparation of GaAs. This process makes compound semiconductor film growth compatible with methods used for the growth of elemental semiconductors and eliminates many of the difficulties inherent in multitemperature-zone processes.

A key factor in the fabrication of many semiconductor devices is the production of single-crystal material of high purity and quality. Films of Ga-V compounds are normally harder to produce than films of elemental semiconductors. Most of the CVD methods for epitaxy already reported (1, 2) involve at least a two-temperature process: (*a*) at T_1, the formation of volatile Ga compounds by the reaction in hydrogen of metallic Ga or the Ga-V compound itself with a halide or water vapor (3) as a transporting agent; and (*b*) at $T_2 < T_1$, the deposition of the compound on a substrate in an atmosphere containing the Group V constituent. When transporting agents are used to produce high-purity epitaxial films of gallium arsenide (GaAs) on GaAs and a number of other semiconductor substrates, etching may also occur; and the early stages of epitaxial growth probably involve some doping of the growing film with impurities in the substrate or, in heteroepitaxial semiconductor systems, with the major elemental constituents of the substrate. This may result in the production of an interfacial alloyed layer in a system such as GaAs on Ge, for example.

Although the transport technique is amenable to closed-tube methods, many advantages to open-tube processes can be cited; and the latter approach is most often used. However, the nature of the reactions involved in the production of the III-V compounds necessitates that the two temperature zones be carefully controlled for reproducible growth to occur. In addition, depending on the growth technique used, it can be important to keep some of the reactants separate (1) until they reach the deposition zone, so that source materials are not affected.

This paper describes a process which requires only one hot temperature zone for the *in situ* formation and growth of the semiconductor compound directly on the heated substrate. This occurs in an atmosphere essentially free of an etching specie and is sufficient not only for growth on some semiconductors but also for growth on insulating substrates.

In this process, compound semiconductor films are produced by reacting organo-Ga compounds and Group V hydrides. Because of the use of the more volatile organo-Ga compounds, *i.e.* triethylgallium (TEG) and trimethylgallium (TMG), it has been possible to meter appreciable quantities of these room-temperature liquids into the reactor by bubbling a carrier gas through them. They can then be mixed in the reactor with different arsine (AsH_3), phosphine (PH_3), arsine-phosphine (AsH_3-PH_3), or arsine-stibine (AsH_3-SbH_3) concentrations controlled independently by simple flowmeter adjustments. Selenium or sulfur may be added as n-type dopants from tanks containing hydrogen selenide (H_2Se) or hydrogen sulfide (H_2S), respectively, diluted with a carrier gas; and p-type doping is obtained by passing the carrier gas over diethylzinc (DEZ) (4) equilibrated at 0°C in a stainless-steel container.

Experimental

Apparatus.—The apparatus consists principally of a single vertical 60-mm OD quartz tube 38 cm long containing a silicon-carbide-covered carbon pedestal which can be inductively heated; stainless-steel bubblers containing the liquid metal-organic compounds and SbH_3; appropriate flowmeters for monitoring the carrier gas,

group V hydride(s), and dopant flows; burn-off area for hydrogen; and a manifold made from ¼-in. stainless steel tubing. Provisions are made for bypassing the quartz reactor and keeping the reactants separate until the gases are equilibrated and ready to be mixed for film formation. A schematic of the apparatus is shown in Fig. 1.

Temperatures, observed on the SiC-coated pedestal, were estimated by comparing the readings of an infrared thermometer with those of an optical pyrometer at pedestal temperatures greater than 750°C, establishing an average emissivity value for the system (0.75), and then extrapolating infrared thermometer signal readings to still lower temperatures. Film thickness was determined either from measurement of an infrared reflectance interference pattern or from angle-lapping and staining multilayer structures.

Materials.—Triethylgallium (TEG) and trimethylgallium (TMG), both air- and water-sensitive liquids, were obtained commercially. The TMG was additionally purified by vacuum-trap distillation until tensiometrically homogeneous fractions were obtained [vapor pressure of TMG at 0°C = 64.5 mm, literature value = 64.5 mm (5)]. The AsH_3 concentrations were nominally 5 or 10% in H_2 and the PH_3, 10% in H_2. SbH_3 was stored under H_2 and equilibrated at −78°C. H_2Se was diluted to 500 ppm in H_2. Diethylzinc (DEZ) was purged with H_2 at −23°C for about 30 min and then stored at 0°C under H_2 until used for doping studies. During doping, the bubbling tube was kept above the liquid.

Ge (111) and GaAs semi-insulating substrates of several orientations were mechanically polished and then chemically polished just before use. Natural faces of flux-grown BeO and ThO_2 were used without polishing after being cleaned with trichloroethylene, water, and methanol rinses. Solvent-cleaned, mechanically polished, essentially scratch-free, basal-plane (0001) Verneuil sapphire (Al_2O_3) and (111), (110), and (100) slices of spinel ($MgAl_2O_4$) cut from Czochralski boules were used as substrates without further treatment.

Procedure.—In the early stages of the investigation, only TEG was commercially available, and it was used in a preliminary study to determine the feasibility of preparing GaAs films by the use of organo-Ga compounds. Thin single-crystal films of GaAs were formed on freshly etched Ge wafers by bubbling H_2 at about 1 liter/min through TEG at about 60°C for 1 hr and decomposing the gases at 700°C on the Ge wafers in an atmosphere containing AsH_3. The crystal character of the overgrowth of GaAs/Ge is shown in Fig. 2, and single crystallinity was confirmed by reflection electron diffraction.

When TMG (bp = 55.6°C at 760 mm) became available, the deposition procedure became more controllable because of its greater volatility as compared with TEG (bp = 143°C at 760 mm). Conditions now considered sufficient for growing good-quality (111) GaAs on appropriately oriented substrates of Ge, GaAs,

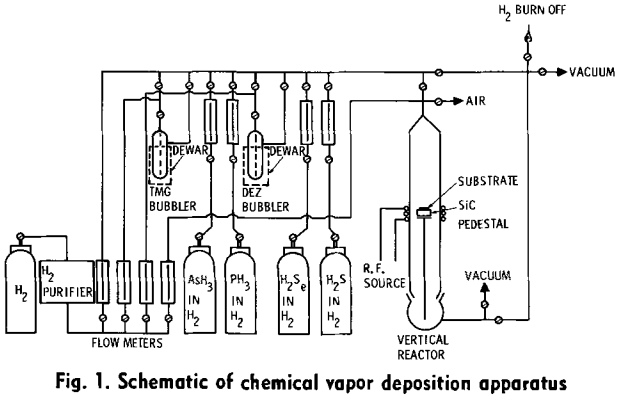

Fig. 1. Schematic of chemical vapor deposition apparatus

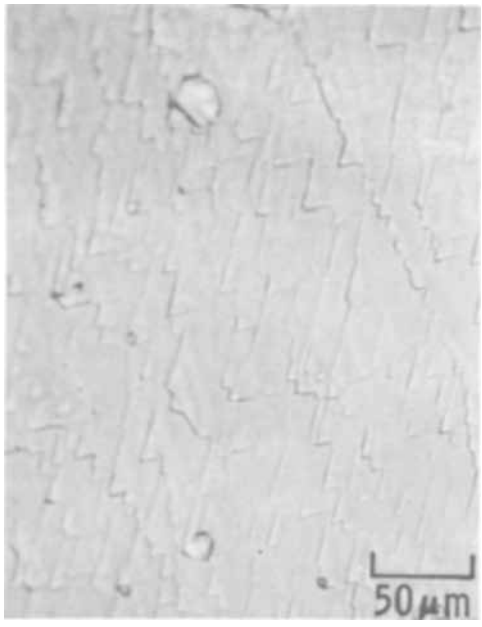

Fig. 2. Surface structure of (111) GaAs growth on (111) Ge (the film was produced from TEG and AsH_3).

and single-crystal insulators incorporate the following typical ranges of concentrations and parameters: TMG 0.2-0.8%; arsine (10%) flow rate about 100-400 ml/min; total H_2 flow rate about 1.5 liters/min; and pedestal temperature 650°-750°C. When the substrate is GaAs, the AsH_3 flow is started independently of the TMG with the pedestal at about 600°C to establish an arsenic atmosphere and help prevent decomposition of the substrate; at the desired deposition temperature, the TMG is introduced to form the GaAs deposit. It was determined for the apparatus in use that better films are produced if the group V hydrides are introduced into the reactor prior to the addition of the TMG for growth on insulating substrates also. Hydride flow is also continued when the deposition is completed and until the temperature has dropped to about 600°C.

The structural nature of the deposit, indicated by the general appearance as viewed in the optical microscope, was determined by x-ray diffraction and/or electron diffraction analysis. The presence and relative compositions of As, P, and Sb in the films were determined with the electron microprobe.

The electrical properties of the films were evaluated from measurements made on Hall samples etched in the GaAs films by standard photolithographic techniques. The carrier concentrations were deduced from the Hall coefficient R_H according to $n = 1/eR_H$, and the Hall mobility was determined from the product $\mu_H = \sigma R_H$, where σ is the electrical conductivity.

Results and Discussion

Using the aforementioned procedures, single-crystal films of GaAs, GaP, and solid solutions of gallium arsenide-phosphide ($GaAs_{1-x}P_x$) and gallium arsenide-antimonide ($GaAs_{1-x}Sb_x$) can be produced on Ge, GaAs, and/or a number of single-crystal insulating substrates.

GaAs *epitaxy.—Film orientation and crystal quality.* As described in a previous publication (6), epitaxial growth of GaAs has been achieved on a number of insulating substrates. The results from that paper are summarized in Table I. Figure 3 shows the surface of a 30-μm film on (0001) Al_2O_3 and the triangular pattern characteristic of (111) growth. The GaAs surface appears rough at thicknesses greater than about 6 μm and displays a rosette pattern, somewhat noticeable in Fig. 3 but more apparent at slightly lower magnifications. Similar growth occurs on (111) $MgAl_2O_4$ and a

Table I. Orientation relationships between GaAs and single-crystal oxides

Substrate plane	Parallel relationships
(0001) Al_2O_3	(111) GaAs || (0001) Al_2O_3
(100) $MgAl_2O_4$	(100) GaAs || (100) $MgAl_2O_4$
(111) $MgAl_2O_4$	(111) GaAs || (111) $MgAl_2O_4$
(10$\bar{1}$0) BeO	(100) GaAs || (10$\bar{1}$0) BeO
(10$\bar{1}$1) BeO	(111) GaAs || (10$\bar{1}$1) BeO
(0001) BeO	(111) GaAs || (0001) BeO
(100) ThO_2	(100) GaAs || (100) ThO_2

natural (10$\bar{1}$1) BeO face (Fig. 4). A typical reflection electron diffraction pattern and x-ray Laue pattern for (111) GaAs growth on (0001) Al_2O_3 are shown in Fig. 5. In (a), strong Kikuchi lines are evident and support the single-crystal nature of the overgrowth; in (b), extra spots not due to the substrate can be identified and correlated with the (111) GaAs overgrowth (6).

Simultaneous growth on (0001) Al_2O_3 and on the (111)"A" and (111)"B" faces of GaAs demonstrated that the surface of the film grown on Al_2O_3 resembled the growth on the GaAs "A" face. This suggests that bonding at the Al_2O_3-GaAs interface involves an As bridge, perhaps between metal ions at the substrate surface and the succeeding Ga layer in the film. If so, one might expect different epitaxial relationships to exist between GaAs and Al_2O_3 and between Si and Al_2O_3 (7), in which bonding seemed to be related to a filling-in of metal-ion sites with bonding to the oxygen ions. Preliminary experiments involving GaAs growth on a few other sapphire orientations support the contention that different epitaxial relationships do exist in the different systems, despite the similar cubic-type structure and lattice parameters for Si (5.43A) and GaAs (5.65A).

This contention was further supported in recent studies by the observed growth of (100) GaAs on Czochralski (110) $MgAl_2O_4$,[1] a rather surprising result when compared with the GaAs-spinel relationships reported in Table I. It was also found that the epitaxy is sensitive to the quality of the spinel; for when some Verneuil spinel ($MgO \cdot 3.3Al_2O_3$) was used as a substrate, the intersection of grain boundaries with the crystal surface was readily revealed by the GaAs overgrowth (Fig. 6).

[1] This observation was made during studies being supported in part by the NASA contract No. NAS12-2010.

Fig. 3. The surface structure of a 30-μm GaAs film growth on (0001) Al_2O_3.

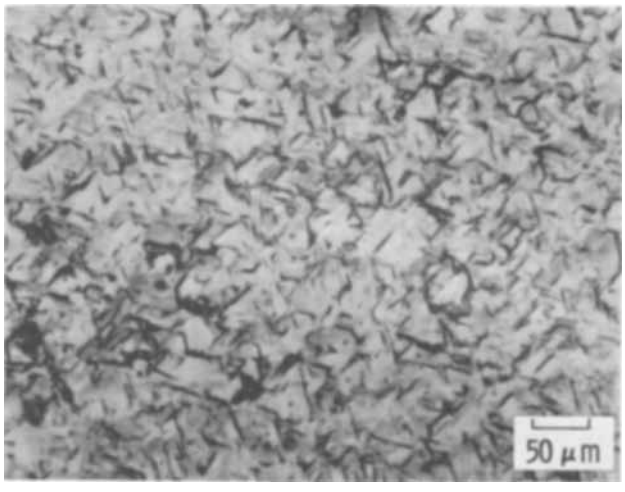

Fig. 4. Surface structure of (111) GaAs deposit on natural (1011) face of BeO.

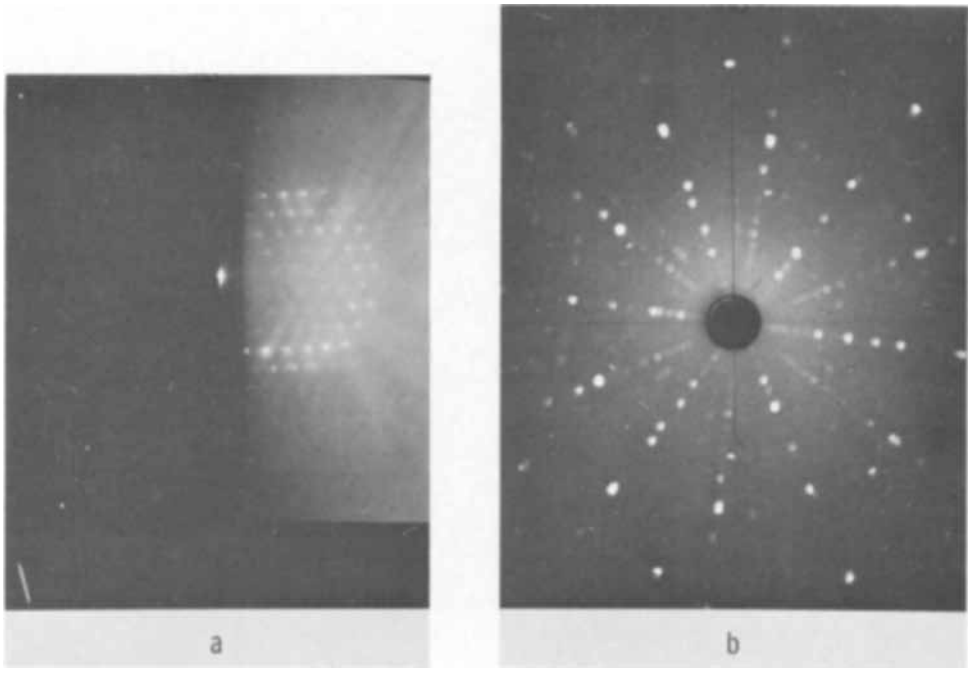

Fig. 5. a—Reflection electron diffraction pattern, and b—x-ray Laue pattern for (111) GaAs growth on (0001) Al_2O_3.

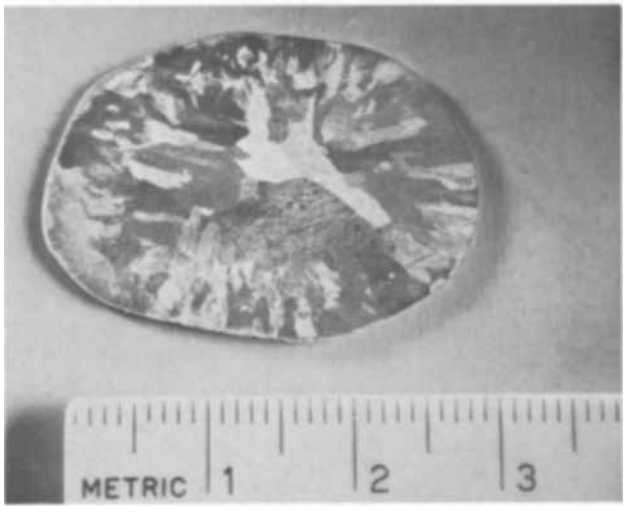

Fig. 6. The effect of grain boundaries in the Verneuil $MgO \cdot 3.3Al_2O_3$ on the growth of GaAs.

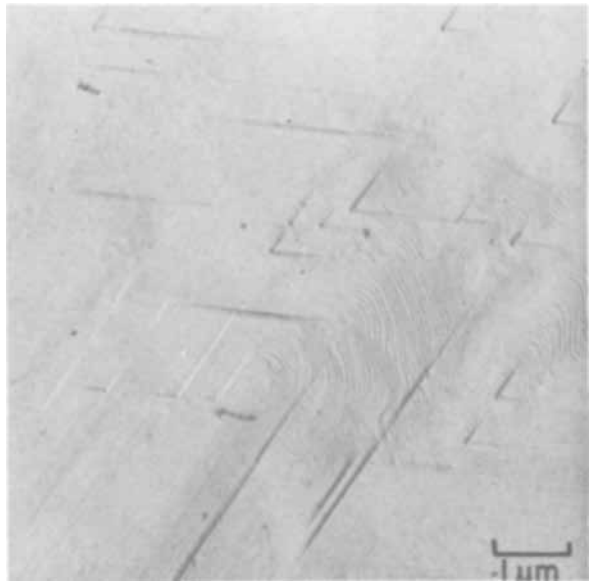

Fig. 7. Replica electron micrograph of (111) GaAs film growth on (0001) Al_2O_3.

As was observed for the silicon growth on (0001) Al_2O_3 (8), a high degree of twinning may exist in (111) GaAs films grown on (0001) Al_2O_3 if the deposition conditions are not optimized. One sample was measured as having a twin density of 7.8%. The technique for twin density measurement has been previously described (8). A replica electron micrograph for a 10-μm film is shown in Fig. 7. An indication of some twinning in the film can be seen. Growth steps in the epitaxial film are also evident. However, the reflection electron diffraction pattern for the film (similar to Fig. 5a) does not support the high twin density value. This correlates with the observation (based on measured charge carrier mobility values) that film quality can improve with film thickness. X-ray techniques provide an average value of twin density for the complete film thickness (8), while reflection electron diffraction basically reveals surface quality. With proper deposition conditions, mirror-smooth GaAs films with no detectable twins (as determined by x-ray evaluation) are being grown on (0001) Al_2O_3 and (111) $MgAl_2O_4$.

Some of the defect structure in films with microtwinning grown on insulators can be revealed by a light polishing-etch such as 1:1:4 hydrogen peroxide-water-sulfuric acid. The triangular pattern shown in Fig. 8a was produced by dipping a mechanically polished 14-μm (111) GaAs film grown on (111) $MgAl_2O_4$ for 10 sec into a freshly prepared 1:1:4 solution. Two minutes of etching (Fig. 8b) (about 2.5 μm removed) revealed a relatively uniform continuation of the defect structure. However, after 5 min of etching, only very small pyramids were evident (Fig. 8c) at the surface of the remaining 7-μm thick film. This also suggests an improvement in film quality with thickness for GaAs grown on $MgAl_2O_4$.

Studies of GaAs grown on BeO have been limited to the natural faces of flux-grown crystals. Attempts to reuse the bare natural faces of the BeO substrates without repolishing have been only partially successful. When GaAs films are etched off with HNO_3-HF mixtures, the substrates seem less amenable to (100) GaAs regrowth but slightly better for (111) GaAs growth on the $(10\bar{1}1)$ face. The $(10\bar{1}0)$ surface is apparently changed significantly by the sequence involving film growth and subsequent removal by the acid mixture.

Effects of deposition parameters on GaAs *film growth.* —At any one temperature, the growth rate of (111) GaAs on Al_2O_3 has been found to be essentially linear with TMG concentration when it is decomposed in an atmosphere containing As and at least a 10-fold excess of AsH_3 over TMG in the gas stream entering the

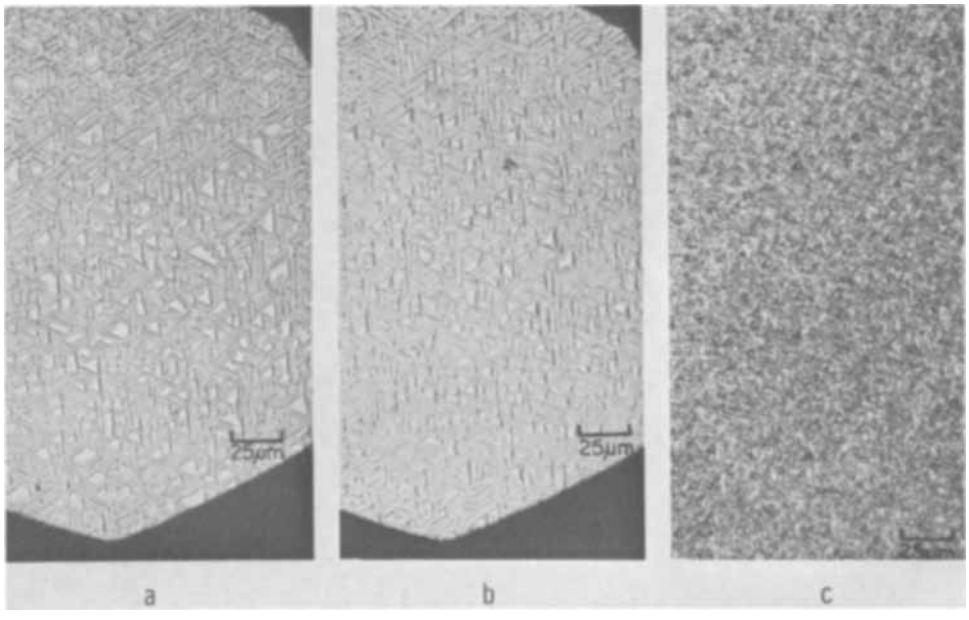

Fig. 8. Structure revealed in a 14-μm (111) GaAs growth on (111) $MgAl_2O_4$ by etching with 1:1:4 hydrogen peroxide-water-sulfuric acid mixture for a total of: a—10 sec, b—2 min, c—5 min (7 μm removed).

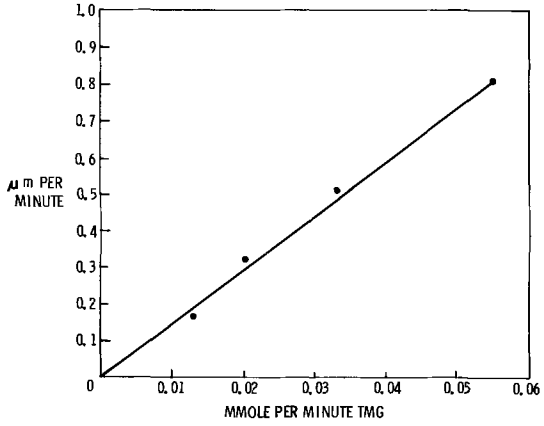

Fig. 9. Growth rate at 725°C of (111) GaAs on (0001) Al_2O_3 as a function of TMG concentration.

reactor. Typical growth rates at 725°C are depicted in Fig. 9 for different concentrations of TMG carried into the reactor per minute. With higher concentrations and temperatures, considerable turbulence is evidenced near the vicinity of the heated pedestal.

In the temperature range 600° to about 800°C, the growth rate was found to be essentially constant for TMG additions of 0.02 and 0.03 mmole/min but dropped off somewhat at about 825°C (Fig. 10). Films grown on Al_2O_3 at 800° and 825°C were less perfect than those grown at 675°C, as determined by reflection electron diffraction (Fig. 11).

Electrical properties of GaAs *films.*[2]—Hall coefficient measurements were used to examine the electrical properties of the GaAs films. Undoped specimens up to ~5 μm thick produced from one combination of TMG and AsH_3 exhibited high resistivity, about 10^3-10^5 ohm-cm. The addition of H_2Se to the gas stream containing the TMG and AsH_3 produced on pyrolysis n-type films with net carrier concentrations as high as 6.2×10^{18} electrons/cm³, obtained when the H_2Se flow rate was about 100 ml/min. The addition of "excess" H_2Se caused the electron mobility to decrease slightly and changed the appearance of the GaAs deposit. These surface changes are shown in Fig. 12(a-f). The change in crystal character may be due to the formation of another compound such as Ga_2Se_3, As_2Se_3, or an alloy, as the solubility limit of Se in GaAs is exceeded.

The addition of DEZ to the gas stream provided p-type GaAs growths with net carrier concentrations up to 2.8×10^{19} holes/cm³, resistivities of 0.003 ohm-cm,

[2] An up-to-date and more complete description of the electrical properties of GaAs films grown by the TMG-AsH_3 process will appear in a subsequent paper by A. C. Thorsen.

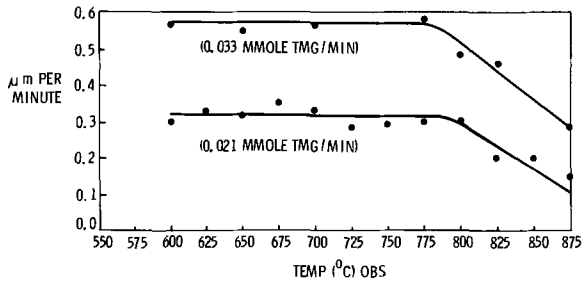

Fig. 10. Effect of substrate temperature on rate of growth of (111) GaAs on (0001) Al_2O_3.

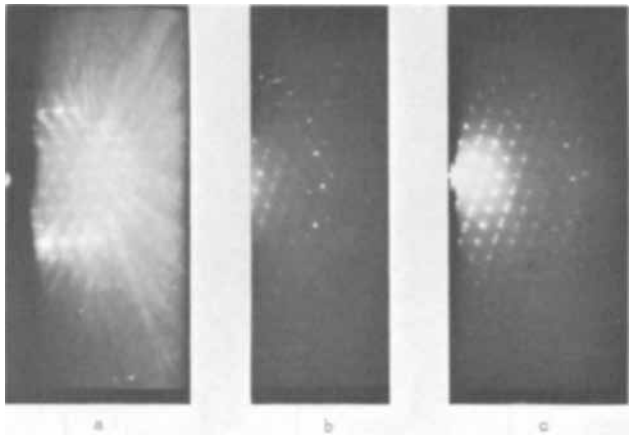

Fig. 11. Reflection electron diffraction photographs of (111) GaAs/(0001) Al_2O_3 films grown at: a—675°C, b—800°C, c—825°C.

and room temperature mobilities of about 75 cm²/V-sec. The highest doping level was reached when the H_2 flow over the DEZ was about 35 ml/min. Further additions of zinc as DEZ also caused a change in the surface character, as noted in Fig. 13(a-d).

Mobilities of Se-doped GaAs films grown on (0001) Al_2O_3 early in our studies were found to be dependent on film thickness. Films less than about 8 μm thick exhibited average mobilities usually less than 2000 cm²/V-sec, while films about 8-25 μm thick had average mobility values of about 4000 cm²/V-sec for carrier concentrations of about 4×10^{16} cm^{-3}.

Mobilities of about 5000 cm²/V-sec at $n = 1 \times 10^{16}$ cm^{-3} have recently been measured for GaAs films not intentionally doped. Experiments are also in progress to compare the properties of the growth of GaAs on GaAs with the films grown on the insulators. The effect

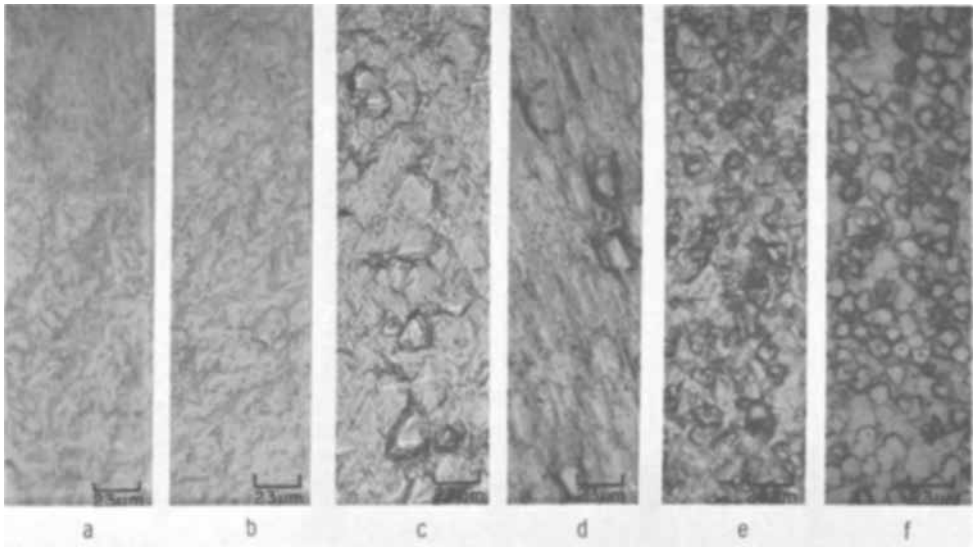

Fig. 12. Effect on appearance of GaAs growth at 725°C on (0001) Al_2O_3 of increases in H_2Se concentration. The doped H_2 flow rates were: a—10 ml/min, b—50 ml/min, c—100 ml/min, d—150 ml/min, e—200 ml/min, f—325 ml/min.

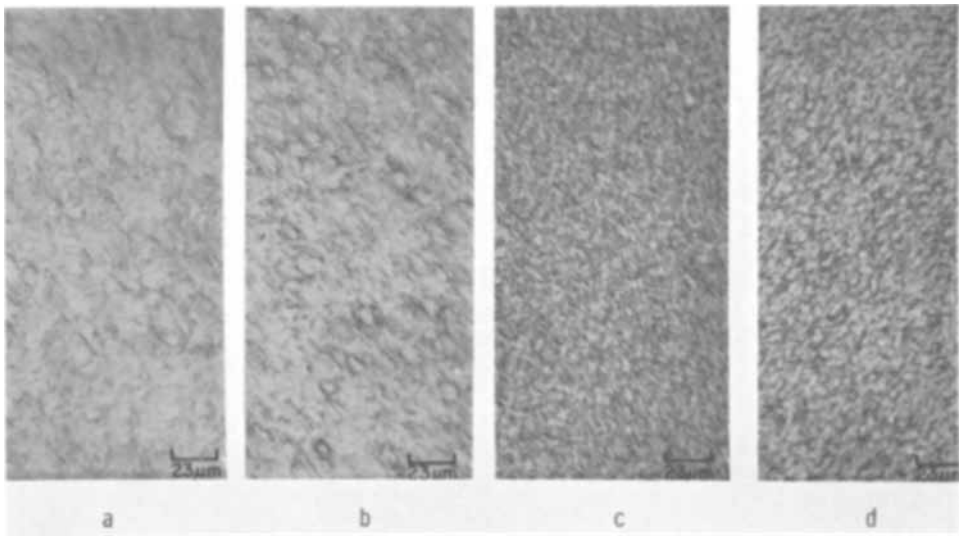

Fig. 13. Effect on appearance of GaAs growth at 725°C on (0001) Al_2O_3 of increases in DEZ concentrations. The H_2 flow rates over DEZ were: a—5 ml/min, b—25 ml/min, c—35 ml/min, d—75 ml/min.

of the purity of the starting materials on film properties is also being studied.

Films of GaAs grown on insulating substrates have been found to possess a much lower degree of residual stress than that found for Si on Al_2O_3 (9, 10) and $MgAl_2O_4$ (11). This is not unexpected, since the mean linear thermal expansion coefficients for GaAs (6.4 x 10^{-6}/°C) (12) and sapphire ($\perp$ to c-axis, 7.7 x 10^{-6}/°C, between 20°-500°C) (13) are not too far apart at room temperature. Essentially, no bowing could be observed for a 35-μm GaAs film grown on a 10-mil Al_2O_3 substrate. However, a 1-μm film did curl a 5-μm Al_2O_3 platelet concave downward, indicating that the residual stress in the GaAs is compressive. Further studies of the stresses in the films and their effect on electrical properties are in progress.

By varying the amounts and types of dopants introduced into the gas stream during crystal growth, multilayer epitaxial structures have been fabricated on Al_2O_3. A four-layer (p^+, p, n, n^+) 48-μm thick structure was grown on (0001) Al_2O_3, photolithographically processed, and etched into mesas with relatively large p-n junction areas of about 6 x 10^{-4} cm^2. An I-V characteristic of one of these "grown" diodes is shown in Fig. 14. Capacitance-voltage measurements indicated that the junctions were transitionary between graded and abrupt.

GaP *and* $GaAs_{1-x}P_x$ *epitaxy*.—Although the emphasis to date has been on the preparation of films of GaAs on insulating substrates, some experiments have been carried out with the TMG-AsH_3 and/or PH_3 reaction to prepare films of GaP and $GaAs_{1-x}P_x$ mixed compounds on GaAs and on insulating substrates.

However, it is apparent that controlling the growth of single-crystal films of GaP on insulators is more difficult than the control of GaAs film growth. Whereas GaAs films only 1 μm thick are single crystal on Al_2O_3, GaP films of the same thickness have to date exhibited only highly preferred orientation on (0001) Al_2O_3 while exhibiting single crystallinity on GaAs. However, the films on Al_2O_3 have improved in quality with additional thickness growth, producing surfaces that were identified as single-crystal (111) orientation by reflection electron diffraction. The electron diffraction pattern for the surface of such a film (7.5 μm thick) grown on (0001) sapphire is shown in Fig. 15. The pattern is sharp, and good structure is indicated.

GaP growth on a thin sapphire platelet caused curling of the platelet in a concave downward direction, which indicated the residual stress in the GaP film to be compressive.

Additions of PH_3 to the AsH_3-TMG mixtures normally used for growing GaAs films will produce thin single-crystal $GaAs_{1-x}P_x$ films on (0001) Al_2O_3. In these preliminary studies, single-crystal films with the compositions $GaAs_{0.9}P_{0.1}$ and $GaAs_{0.4}P_{0.6}$ have been grown on (0001) Al_2O_3 and (111) $MgAl_2O_4$. Additional studies are in progress.

Multilayers of single crystals of GaAs and GaP have also been fabricated on Al_2O_3. Figure 16a shows the multilayer structure revealed by a bevel section through a GaAs/GaP/GaAs/Al_2O_3 film. The order of the surface structure in Fig. 16b indicated a single-crystal com-

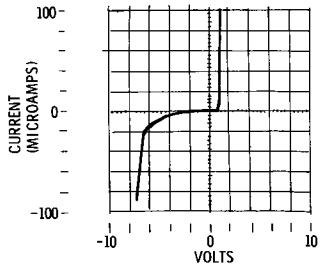

Fig. 14. I-V curve of GaAs/Al_2O_3 (p^+pnn^+) diode

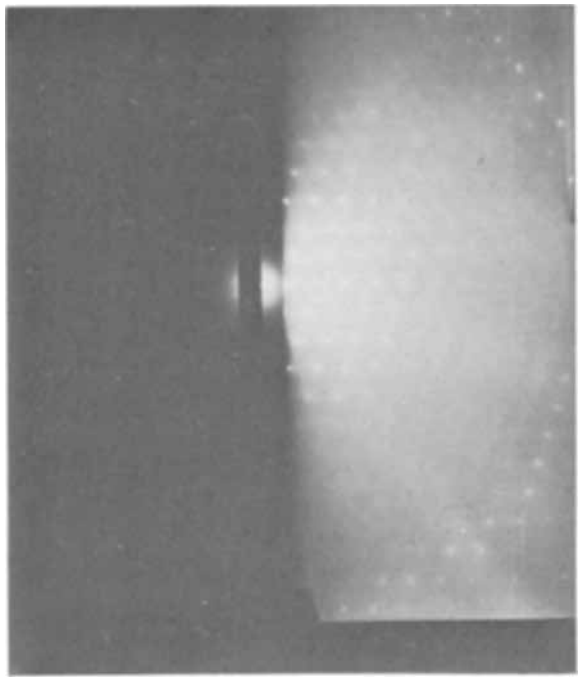

Fig. 15. Reflection electron diffraction evidence for (111) growth of GaP on (0001) Al_2O_3 at 700°C.

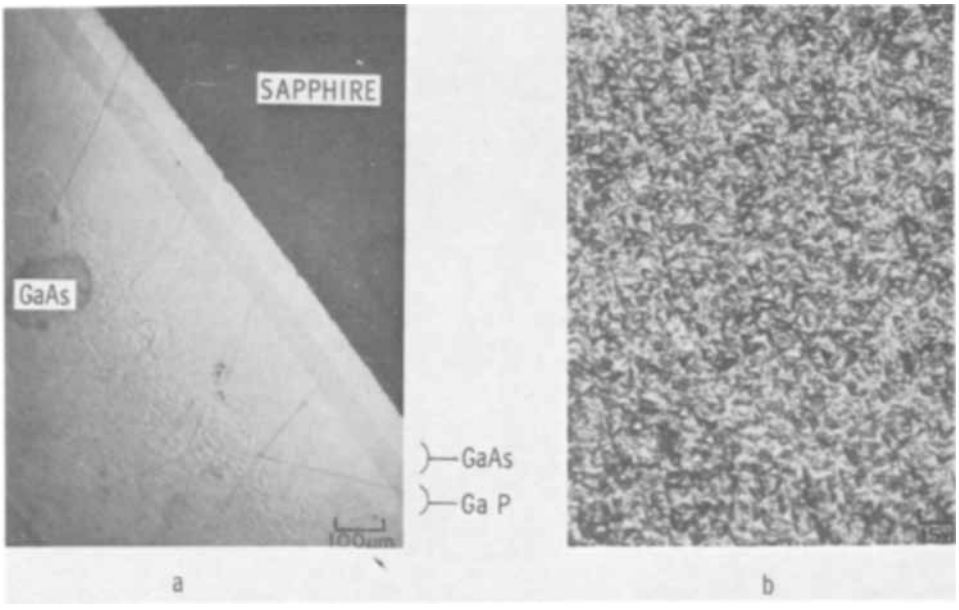

Fig. 16. a—A multilayer GaAs/GaP/GaAs/Al_2O_3 composite as revealed by angle-lapping, b—surface of the composite.

posite. This was confirmed by x-ray diffraction procedures.

$GaAs_{1-x}Sb_x$ *epitaxy*.—A few experiments relating to $GaAs_{1-x}Sb_x$ epitaxy were performed at 725°C on (100) GaAs and (0001) Al_2O_3. Single-crystal films with approximate compositions in the range $GaAs_{0.9}Sb_{0.1}$ to $GaAs_{0.7}Sb_{0.3}$ were obtained when the TMG-AsH_3-SbH_3 ratios were arbitrarily changed by either reducing the arsenic flow or increasing the flow rate of hydrogen bubbling through the liquid SbH_3. Better growth, as determined by reflection electron diffraction, was obtained on (100) GaAs than on (0001) Al_2O_3 at the higher concentrations of Sb. Epitaxial films of $GaAs_{1-x}Sb_x$ can also be achieved by using trimethylantimony in place of SbH_3 (14).

Reaction mechanisms.—The use of the metal-organic for semiconductor film formation was not without concern for the possibility of major carbon contamination. Graham (15) reported that the pyrolysis of TMG at 520°C in an argon carrier gas produced a metallic-looking film containing 8.0% carbon. Plust (16) described the production of Ga of semiconductor purity by photolysis of TEG, but Graham obtained gray-black solids containing metallic Ga using Plust's process. In order to prevent the formation of nonvolatile carbonaceous side-products, two steps were initially taken: (*a*) the use of H_2 as the carrier gas as a means for tying up free radicals that may be assumed to be involved in the mechanism for the pyrolysis of TMG; and (*b*) the use of the Group-V hydride(s) in excess over the stoichiometric amount required to react with a given amount of TMG, as represented, for example, by reaction [1] for the formation of GaAs:

$$(CH_3)_3Ga + AsH_3 \rightarrow GaAs + 3CH_4 \qquad [1]$$

The AsH_3 in excess (or other group V hydride) probably reacts with the TMG before it has a chance to pyrolyze, thus avoiding the formation of undesirable products. It also provides an As atmosphere to help prevent the dissociation at elevated temperatures. The relatively low temperatures used for GaAs formation also apparently prevent C from being a major contaminant in the GaAs films. If C were there as a minor contaminant, it would most probably be due to impure starting materials or caused by improper handling in the deposition apparatus.

Harrison *et al.* (18) performed an experiment in which TMG and AsH_3 were mixed at room temperature in 1:1 molecular proportions in the vapor state for 18 hr and then heated to about 200°C. This produced a red film which was postulated to be stoichiometric GaAs. Unfortunately, the experiment was not evaluated sufficiently. If the rate of formation and quantity of methane had been measured, then one would have more confidence in the study of the stoichiometry of reaction [1]. There may have also been a reaction between AsH_3 and a gray film which Harrison reported had formed on the walls of the tube at room temperature. This film may have been a reaction product between TMG and Pyrex, which has been previously observed (19). It was in the belief that reaction [1] was the predominant reaction that studies of reactions between the metal-organics and the hydrides were begun. Knowledge of Harrison's prior investigation at low pressures came to light afterwards.

A few experiments in our laboratories were also performed using $AsCl_3$ and TMG as the reacting materials. Epitaxy was not achieved on the insulators, and this approach was soon discarded. It may be that the reaction is complicated by the formation of HCl, produced by the reduction of $AsCl_3$ by H_2

$$2AsCl_3 + 3H_2 = 1/2As_4 + 6HCl \qquad [2]$$

Further reaction by TMG with HCl could produce in the first stage of the reaction the compound methyl gallium dichloride

$$2(CH_3)_3Ga + 4HCl \rightarrow (CH_3GaCl_2)_2 + 4CH_4 \text{ (20)} \qquad [3]$$

followed by complete dealkylation

$$(MeGaCl_2)_2 + 2HCl \rightarrow 2CH_4 + 2GaCl_3 \qquad [4]$$

HCl could also obstruct epitaxy if the growth rate of the depositing film is less than its etching rate by the HCl.

Summary

The decomposition of alkylgallium compounds (R_3Ga), *e.g.* trimethylgallium or triethylgallium, in the presence of arsine, phosphine, arsine-phosphine, or arsine-stibine has produced single-crystal growth of the corresponding Ga-V compounds on single-crystal insulating substrates as well as on GaAs, GaP, and/or Ge. A reasonable explanation for the formation of the Ga-V compound is expressed by the reaction, *e.g.* for the production of GaAs

$$(CH_3)_3Ga + AsH_3 \xrightarrow[650°\text{-}750°C]{} GaAs + 3CH_4$$

This technique obviates the use of multiple temperature zones for the CVD process, simplifies the procedure considerably, and makes compound semiconductor film growth compatible with the growth of elemental semi-

conductors, such as Si and Ge. This compatibility has made it possible to fabricate and study, *via*, CVD and appropriate masking techniques, various combinations of single-crystal compound and elemental semiconductor layers on the same insulating substrate. New degrees of freedom and new concepts in device design are now apparent which may make optimum use of the differences in the physical, electrical, and optical properties of different semiconductors.

Acknowledgments

The authors wish to thank F. M. Erdmann for assisting in the growth of the layers; Dr. R. L. Nolder, L. A. Moudy, and E. R. Goldman for electron and x-ray diffraction analyses; Dr. A. C. Thorsen for the electrical measurements; G. W. Johnson, J. L. Healy, and D. Medellin for the angle lapping and some of the photomicrographs; R. W. Stewart for electron microprobe analyses; J. P. Wendt and Dr. B. T. French for the device processing and evaluation of the 4-layer GaAs diode; S. B. Austerman for the BeO crystals; and Dr. R. P. Ruth for his most helpful discussions, encouragement, and direction in the described program.

Manuscript submitted April 14, 1969; revised manuscript received *ca.* Aug. 15, 1969. This was Paper 63 presented at the Boston Meeting, May 5-9, 1968.

Any discussion of this paper will appear in a Discussion Section to be published in the June 1970 JOURNAL.

REFERENCES

1. J. J. Tietjen and J. A. Amick, *This Journal*, **113**, 724 (1966).
2. J. R. Knight, D. Effer, and P. R. Evans, *Solid-State Electron.*, **8**, 178 (1965).
3. M. Michelitsch, W. Kappallo, and G. Hellbardt, *This Journal*, **111**, 1248 (1964).
4. R. W. Conrad and R. W. Haisty, *ibid.*, **113**, 199 (1966).
5. E. Wiberg, T. Johannsen, and O. Stecker, *Z. Anorg. Allgem. Chem.*, **251**, 114 (1943).
6. H. M. Manasevit, *Appl. Phys. Letters*, **12**, 156 (1968).
7. H. M. Manasevit, R. L. Nolder, and L. A. Moudy, *Trans. TMS-AIME*, **242**, 465 (1968).
8. R. L. Nolder, D. J. Klein, and D. H. Forbes, *J. Appl. Phys.*, **36**, 3444 (1965).
9. C. Y. Ang and H. M. Manasevit, *Solid-State Electron.*, **8**, 994 (1965).
10. D. J. Dumin, *J. Appl. Phys.*, **36**, 2700 (1965).
11. P. H. Robinson and D. J. Dumin, *This Journal*, **115**, 75 (1968).
12. M. E. Straumanis, J. P. Krumme, and M. Rubenstein, *ibid.*, **114**, 640 (1967).
13. J. B. Austin, *J. Am. Ceram. Soc.*, **14**, 795 (1931).
14. H. M. Manasevit, Unpublished data.
15. W. A. Graham and A. R. Gatti, A. D. Little, Inc., Cambridge, Mass., Final Report, Contract AF19(604)-4975, Dec. 31, 1960.
16. H. G. Plust, U.S. Pat. 2,898,278, Aug. 4, 1959.
17. N. N. Greenwood and M. Wallbridge, *J. Chem. Soc.*, **1963**, 3912.
18. B. Harrison and E. H. Tompkins, *Inorg. Chem.*, **1**, 951 (1962).
19. H. M. Manasevit, Ph.D. Thesis, "Study of Reactions of Silyl Bases with Selected Lewis Acids," p. 44, Illinois Institute of Technology, Chicago, Ill., June 1959.
20. G. E. Coates, "Organo-Metallic Compounds," 2nd Ed., p. 151, John Wiley & Sons, Inc., New York (1960).

Stresses in SiO_2 Films Obtained from the Thermal Decomposition of Tetraethylorthosilicate—Effect of Heat-Treatment and Humidity

J. A. Aboaf*

IBM Watson Research Center, Yorktown Heights, New York

ABSTRACT

The interference fringe method was used for measurement of stresses in SiO_2 films deposited on Si and Ge substrates. An attempt has been made to deduce both the amount of stress resulting from intrinsic stress and the stress arising from mismatch of temperature coefficient of expansion. From measurement at room temperature of stress in SiO_2 films deposited by thermal decomposition of tetraethylorthosilicate at 725°C in forming gas (less than 0.2 x 10^9 dynes/cm^2), or at 450°C in oxygen ($+1.5 \times 10^9$ dynes/cm^2), it is concluded that the intrinsic stress is tensile. The mechanical properties of the SiO_2 films prepared by these two methods were assumed to be similar to those of bulk vitreous silica. An explanation is offered for the observed increase in the room temperature tensile stress of the 450°C-SiO_2 film on heat-treatment to 700°C, and to the following decrease in tensile stress on heat-treatment to 800°C. A decrease in the room temperature stress in the 450°C-SiO_2 film occurs on exposure of the film to a humid ambient.

It is well known that dielectric and metal films deposited on substrates by a variety of methods are in a state of stress. Hoffman (1) in a recent review on stresses in films has dealt extensively with the measurement and origin of the stress.

The control of both the magnitude and sign (tensile or compressive) of stresses in thin film insulators deposited on semiconductors is of primary importance in the fabrication of semiconductor devices and circuits. Excessive stress in films can cause (*i*) bowing of the semiconductor substrates, with subsequent difficulty in photolithographic processes, (*ii*) the appearance of slip lines (due to plastic flow of the semiconductor) with deleterious effects in the subsequent processing of the devices, and (*iii*) cracking and peeling of the insulating films.

Stresses in thin films result from the difference in thermal coefficient between the film and substrate, from structural modifications resulting from heat treatment, and from the built-in intrinsic stress. Little is known about the intrinsic stress of films except that

* Electrochemical Society Active Member.

it is dependent on the deposition parameters and appears to be intimately related to the nucleation and growth of the film. In this study, the intrinsic stress of films has been deduced by subtracting from the experimentally measured stress, the calculated contribution resulting from the difference in thermal expansion between the film and substrate, assuming for the coefficient of expansion of the film the value of the bulk material when available.

The present investigation was undertaken to measure the room temperature stress in pyrolytic SiO_2 thin films, the changes in stress on densification of these films when heat-treated at high temperatures, and the effects on stress resulting from exposure to a humid ambient.

Experimental

Substrates.—Glang *et al.* (2) have shown that silicon wafers could be used for the measurement of stress in thin films. In the present study, <111> silicon (Monsanto Corporation) and <111> germanium (IBM Corporation) substrates were used. Wafer thicknesses were approximately 8 mils, and wafer diameters were approximately 1 in. The germanium wafers were p-type, either 0.1 ohm cm or 3-8 ohm cm and were polished on both sides; the silicon wafers 0.1 ohm cm were polished on one side. Only wafers exhibiting uniform curvatures were used. They were cleaned in 1:1 HF:H_2O prior to oxide deposition. Oxides were deposited on the concave face of the wafers (for Si, the polished face).

Film deposition.—The films were deposited by the pyrolytic decomposition of tetraethylorthosilicate in a forming gas atmosphere (10% H_2-90% N_2) at 730°C (3) (H. T. SiO_2), and in oxygen at 450°C (4) (L. T. SiO_2). Thickness uniformity was better than ± 5%.

Three deposition rates 50, 100, and 200 Å/min were used for the L. T. SiO_2. The H. T. SiO_2 was deposited at 200 Å/min. The thickness of the films used for stress measurement was approximately 4000Å.

Measurement of stress.—The method used for measurement of stresses in films and the mathematical details of the stress analysis have been described by Finegan and Hoffman (5), and consists of measuring the shape of the substrate and of the substrate film by the interference fringe technique. The change in the shape of the substrate indicates strain in the wafer, which in turn is a measure of the stress in the film.

In order to measure the stress in the films it is assumed that the substrate wafer is elastic, uniformly thick, thin compared to its radius, and that its deflection is small as compared to its thickness. This was the case in the experiments described below. However, in some cases when the thickness of the film was high and the stress at the temperature of deposition was higher than the yield stress of the substrate, the substrate deformed irreversibly (6); consequently the condition of elasticity is not met, and the theory of bending plates could not be applied.

We have used an experimental apparatus quite similar to that of Finegan and Hoffman (5). The shape of the wafers at room temperature, as determined by the Newton's ring technique, is to be parabolic. The substrate rests film side down on an optical flat and is illuminated by sodium light. The interference fringe pattern produced is photographed with a Polaroid camera (Fig. 1), and subsequently another interference fringe pattern is obtained after stripping the film from its substrate. This is the reference pattern. The relative position of the fringes on both fringe patterns (corresponding to a distance of 1.2 cm on the wafer) is measured in two perpendicular directions, making sure that the substrate film and the substrate reference data are taken in the same relative position. For each set of data, a computer program is used to fit a parabola by the method of least squares and to calculate the force per unit width in the two directions. The average of these two values, divided by the thickness of the film, is the stress in the film at room temperature.

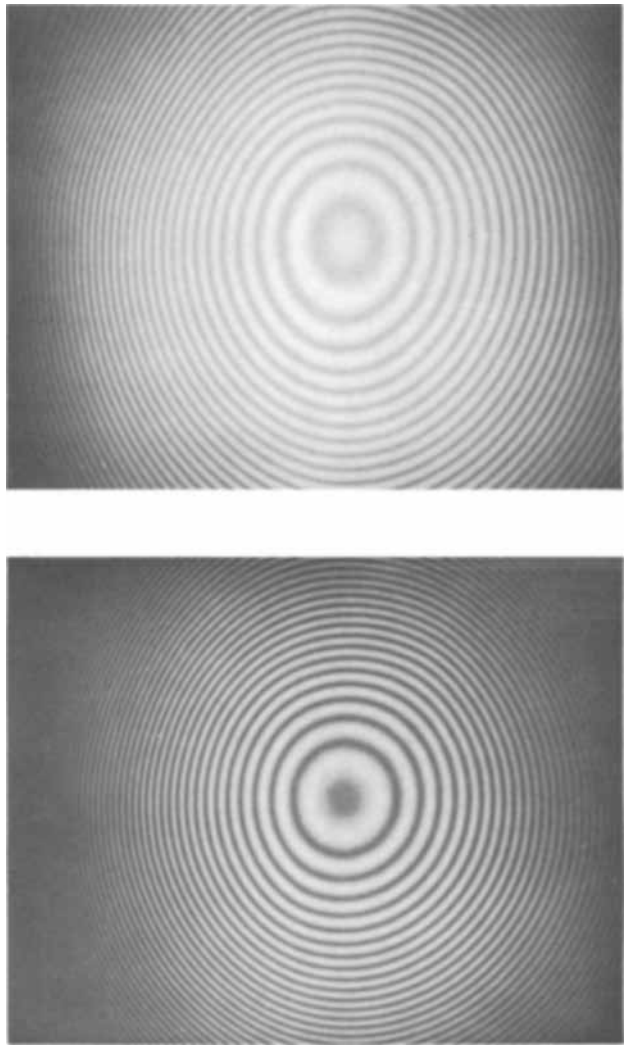

Fig. 1. Interference fringe pattern of uniformly curved silicon wafer: Top, without SiO_2 film; bottom, with 450°C SiO_2 film.

The sensitivity of the measurement is such that it is possible to detect for the wafer and film thicknesses used a minimum stress of 2.5×10^8 dynes/cm^2. The error involved in the stress measurement is dependent on the error of three independent variables: film thickness, substrate thickness, and the difference in the number of fringes. The error was calculated to be less than 15%.

The thickness of the films is measured independently either by Vamfo (7) or by double beam interferometry. Young's modulus data for the silicon and germanium substrates (necessary to calculate the room temperature stress in the films) were taken from Glang (2) and Fine (8).

Results

Wafer curvature without films.—At an early stage during this study it was found that not all wafers could be used. The interference fringe pattern of the wafers varied from well-defined (Fig. 1) to hopelessly distorted (Fig. 2) concentric rings. The yield of wafers showing a uniform circular or elliptical pattern varied from batch to batch; yields as low as zero and as high as 80% were encountered. This effect is probably due to the stresses induced during polishing. Annealing at temperatures of up to 800°C reduced yield still further.

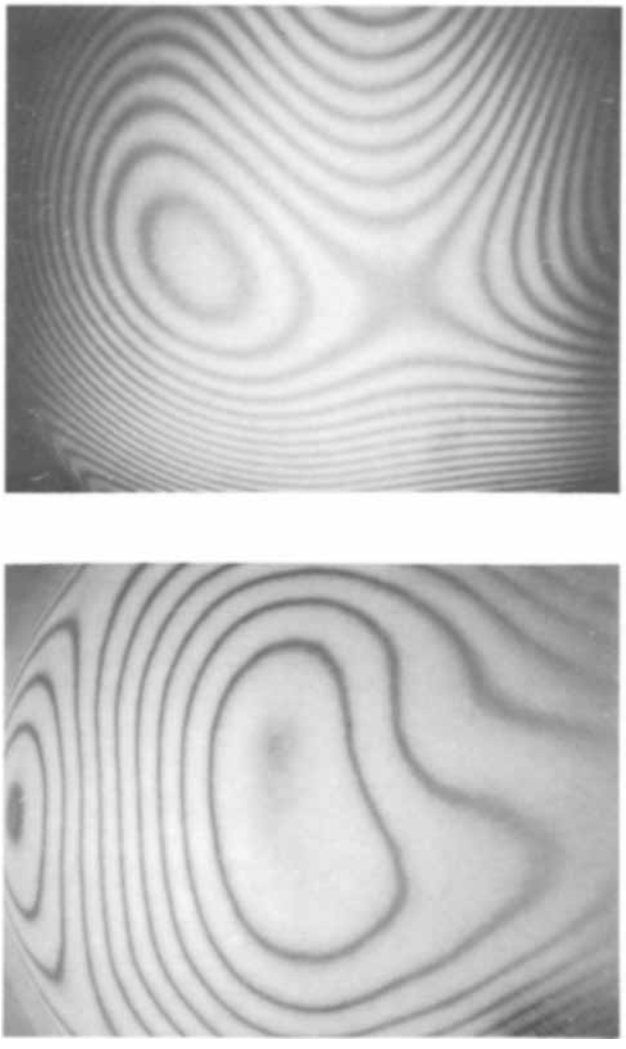

Fig. 2. Interference fringe pattern of distorted wafers

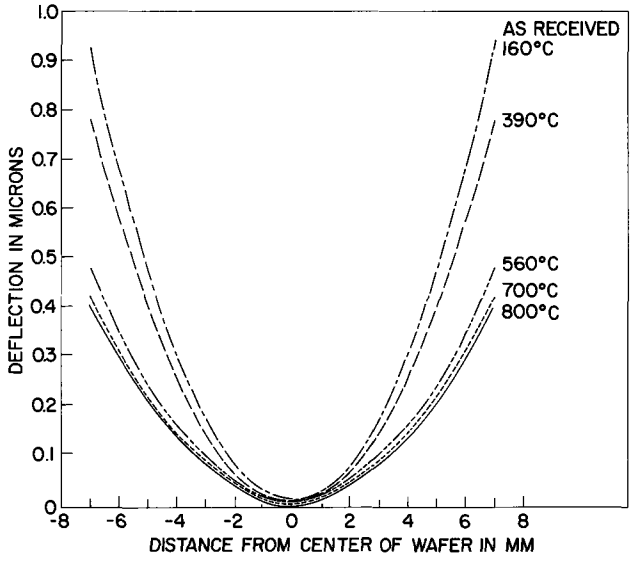

Fig. 3. Room temperature curvature of silicon wafer (Monsanto 5 ohm-cm) after heat-treatment in forming gas for ½ hr at various temperatures.

All results given in this study were obtained with wafers showing a well-defined fringe pattern of concentric rings with and without the dielectric film (Fig. 1).

The curvature of a silicon wafer is shown in Fig. 3 after several annealing treatments at different temperatures. It is seen that the wafer flattens with increasing temperature. For the measurement of stress it was not necessary to anneal every substrate. In fact, the curvature of the wafer after annealing at a certain temperature is identical to that obtained after deposition of the oxide at this temperature and successive stripping of the film. However, when heat-treatment of oxides at different temperatures were made, the wafers were annealed at 800°C for 4 hr prior to deposition of the oxide film. The change in the stress at room temperature of the oxide was then measured on basis of the same reference wafer.

Stress at room temperature of SiO_2 *films.*—A film deposited on the inner surface of a curved substrate is in tension if the film causes a decrease in the radius of curvature of the substrate, and in compression in the reverse case. In the first case, the sign of the stress is taken to be positive, and in the second case negative.

The stress at room temperature in SiO_2 films deposited on silicon and germanium is shown in Table I.

The reproducibility in the stress at room temperature is much better for the H. T. SiO_2 than for the L. T. SiO_2. It has not been possible to differentiate the stress at room temperature for L. T. SiO_2 deposited at 50, 100, 200 Å/min. The stress at room temperature for SiO_2 films deposited at 380° and 520°C fell within the range given for the 450°C-SiO_2.

Room temperature stress of SiO_2 *as a function of high-temperature annealing.*—L. T. SiO_2 films on silicon were heat-treated at 700° and 800°C in a forming gas atmosphere. The change in the room temperature stress for a typical specimen is shown in Table II.

The room temperature stress in the film increases after the 700°C heat-treatment and decreases after the 800°C treatment. Compared to the room temperature curvature at 450°C, the room temperature curvature at 700°C has increased, while that after the 800°C has decreased.

The stress at room temperature in the film reaches a plateau value rapidly after a few minutes at 700°C; at 800°C, the plateau value is reached more slowly. The thickness of the SiO_2 film after the 700°C treatment is reduced by 8%, and after the 800°C treatment by 11%, compared to that of the as-deposited sample.

L.T. SiO_2 films, 4000Å thick, on germanium crack on heat-treatment at 700°C. Films deposited on silicon do not crack after heat-treatment at 800°C.

Effect of a humid ambient on the room temperature stress of L.T. SiO_2.—L.T. SiO_2 films on silicon were treated in a humidifier at 85°C and 85% relative hu-

Table I. Stress at room temperature in SiO_2 films

	L.T. SiO_2	H.T. SiO_2
On silicon wafers	Tension $+0.9$ to $+2 \times 10^9$ dynes/cm²	Less than 0.2×10^9 dynes/cm²
On germanium wafers	Compression -0.2 to -1×10^9 dynes/cm²	Compression -1.7 to -2×10^9 dynes/cm²

Table II. Change in room temperature stress

Film treatment	Min	Room temperature stress, dynes/cm²
450°C-SiO_2 on silicon		$+1.5 \times 10^9$
Heat-treated at 700°C	5	$+2.3 \times 10^9$
Heat-treated at 700°C	15	$+2.2 \times 10^9$
Heat-treated at 700°C	30	$+2.5 \times 10^9$
Heat-treated at 800°C	5	$+1.1 \times 10^9$
Heat-treated at 800°C	15	$+0.7 \times 10^9$
Heat-treated at 800°C	30	$+0.3 \times 10^9$
Heat-treated at 800°C	60	$<0.2 \times 10^9$
Heat-treated at 800°C	90	$<0.2 \times 10^9$

midity. The change in the room temperature stress for a typical specimen is as follows:

SiO_2 as deposited	$+1.2 \times 10^9$
after 5 hr in 85°C, 85% RH	$+0.4 \times 10^9$
after 21 hr in 85°C, 85% RH	$+0.5 \times 10^9$

The decrease in room temperature stress occurs with no change in thickness of the film.

Discussion

Intrinsic stress in SiO_2 *films.*—Schwuttke and Howard (9), Blech *et al.* (10), Drum and Rand (11), and more recently Lathlaen and Diehl (12) have interpreted their stress measurements in SiO_2 films as function of various parameters (temperature, rate of deposition, etc.) as being due to various values of coefficient of expansion for SiO_2 films. A different interpretation is given below based on our experimental results.

The measurement of stress in the film at room temperature does not differentiate between stresses generated by the difference in thermal expansion between the film and substrate, and intrinsic stress. The total stress, S, as measured at room temperature is

$$S = (\alpha_{\text{film}} - \alpha_{\text{sub}}) \frac{E_f}{1 - \gamma_f} (T_2 - T_1) + \sigma_i$$

α thermal coefficient of expansion of the film or substrate
E modulus of elasticity of the film
γ_f Poisson's ratio for the film
$T_2 - T_1$ temperature of deposition of film -- room temperature
σ_i intrinsic stress.

Let us assume that the mechanical properties of the high-temperature SiO_2 films are similar to those of bulk vitreous silica. α, E, and γ for SiO_2 are taken respectively equal to 0.55×10^{-6}, 7.2×10^{11} dynes/cm^2, and 0.17 (13). The average coefficient of expansion of silicon between any two temperatures is taken from Maissel (14). Using these values, it is possible to calculate the intrinsic stress, taking for the room temperature stress in H.T.-SiO_2 films on silicon substrates, the experimental value. The intrinsic stress is tensile and its value is $\sim + 2.1 \times 10^9$ dynes/cm^2.

One can also make the assumption that the intrinsic stress in SiO_2 films is the same whether deposition occurs on silicon or on germanium wafers. Under this assumption, using the above equation and using the coefficient of expansion for germanium (15), the stress expected in SiO_2 on germanium substrates can be estimated. This stress is compressive, equal to -1.8×10^9 dynes/cm^2 and is in excellent agreement with the experimental value (Table I). The qualitative results obtained for films on germanium are in agreement with those made by x-ray diffraction by Segmuller (16).

If the above assumptions are used to estimate the room temperature stress of L.T. SiO_2 on germanium, the agreement between the calculated value and the experimental value is not as good; this is not unexpected considering the porous properties of the low-temperature oxide (4).

Annealing effects.—The room temperature stress in L.T. SiO_2 films when these are heat-treated successively to 700° and 800°C suggest that two effects occur: the first one in conjunction with the increase in tensile stress and the second one with the decrease in tensile stress to an essentially stress free film at room temperature.

The increase in tensile stress is attributed to the densification of the film because of loss of moisture contained in the film and to the closing of pores during heat-treatment to 700°C. In fact, the infrared spectra of low-temperature SiO_2 shows a water content as measured at the 3650 cm^{-1} band of 6% (0.060 optical density/micron). After the heat-treatment, the water content is 1% (0.010 optical density/micron) and the oxide is 8% thinner. It is interesting to note that this effect occurs without the shifting of the Si-O stretching band (1065 cm^{-1}) to higher frequencies.

The subsequent decrease in tensile stress as measured at room temperature after heat-treatment at 800°C may be attributed to a structural densification which results in the shifting of the 1065 cm^{-1} Si-O band to a value of 1075 cm^{-1}. The water content in the film after the 800°C treatment remains at the level reached after the 700°C treatment: the oxide thickness decreases by another 3%. Pliskin and Lehman (17) noted Si-O frequency shifts after densification of films by heat-treatment. Mackenzie (18) has interpreted volume shrinkage in bulk vitreous silica primarily to variation in the mutual orientation of SiO_4 tetrahedra.

The stress at room temperature and the intrinsic stress (stress at temperature) for low temperature SiO_2 films deposited at 450°C and annealed at 700° and 800°C are given in Table III. It is interesting to note that the intrinsic stress in the low temperature oxide is practically equal to that of the oxide which has been heat-treated at 800°C: *i.e.*, on heat-treatment at 800°C, it appears that the stress built into the films during deposition has not been released; this result cannot be explained. The intrinsic stress in the films at 450°, 700°, and 800°C was calculated as shown above on basis of the experimental values of stress at room temperature and of the mechanical properties of bulk SiO_2.

The cracking on heat-treatment of a 4000Å thick SiO_2 film deposited on germanium (this does not occur for films deposited on silicon) might be due to the large stress resulting from the larger thermal coefficient of expansion of germanium as compared to that of silicon. However, the estimated stress at temperature is almost the same for the SiO_2 film on germanium heat-treated at 700°C and for the SiO_2 film on silicon heat-treated at 800°C; only in the first case does the film crack. It does not appear thus that the high stress is the cause of cracking. It is possible, as suggested by Krongelb (4), that on heat-treating at high temperature, the moisture contained in the film tends to react as the interface between the germanium and SiO_2, forming gaseous GeO, which upon escaping would rupture the film.

Humidity effects on stress in SiO_2 *films.*—Drift of stress due to weathering for SiO_2 films deposited by the silane-NO process was reported by Drum and Rand (11). For our films, a large decrease in the room temperature stress occurs on exposure to a humid ambient. Densification (*i.e.*, decrease in the volume of the film) does not, however, occur. The Si-O absorption band shifts from 1065 to 1075 cm^{-1}. Pliskin (17) observed that increase in water content in electron gun evaporated SiO_2 film results in a shifting of the Si-O stretching band toward higher frequencies, and interpreted the phenomenon as being due to strain, varia-

Table III. Stress at room temperature and intrinsic stress for SiO_2 films

	Stress at room temperature (experimental) dynes/cm^2	Stress at* temperature (intrinsic stress) dynes/cm^2
L.T. SiO_2	$+1.5 \times 10^9$	$+2.5 \times 10^9$
L.T. SiO_2 heat-treated at 700°C for 30 min in forming gas	$+2.2 \times 10^9$	$+4.3^{**} \times 10^9$
L.T. SiO_2 heat-treated at 800°C for 1 hr in forming gas	$+0.2 \times 10^9$	$+2.5^{\dagger} \times 10^9$

* Calculated on basis of the experimental results and the assumptions made in text.
** If no densification would occur, the stress at temperature should have been $+3.4 \times 10^9$ dynes/cm^2 (experimental stress at room temperature + stress induced in heating the sample from 25° to 700°C).
† If no densification would occur, the stress at temperature should have been $+3.8 \times 10^9$ dynes/cm^2.

tion in band energy, and purity. It is suggested that the decrease in stress is related to the breakdown of the film structure as SiO_2 tetrahedra reacts with H_2O to form silanol groups (4) and a more open structure.

The presence of an intrinsic stress in vapor deposited SiO_2 films has been shown but not explained. Klokholm (19) has interpreted the intrinsic stress in metal systems as being due to the annealing and shrinkage of disordered material underneath the surface of the growing film. Unfortunately, we do not know the structure of SiO_2 films and how their structure differs according to the method of preparation. Recent experimental and theoretical advances in x-ray diffraction (20) have yielded new information on the structure of bulk SiO_2. The use of these techniques might be useful for SiO_2 films.

Conclusion

On the basis of room temperature stress measurements in SiO_2 films deposited on silicon and germanium, it has been possible to estimate the intrinsic stress in vapor deposited SiO_2 films by assuming for the values of the mechanical properties of the films deposited at high temperature those of the bulk properties of vitreous silica; the intrinsic stress derived is the same for both substrates.

The heat-treatment effects of low-temperature films occur in two stages: first, an increase in tensile stress occurring with loss of moisture contained in the film, densification, and no variation in the Si-O stretching band; second, a decrease in tensile stress occurring gradually and resulting in a shift toward higher frequencies of the Si-O band.

The room temperature stress in low-temperature films decreases sensibly on exposure to a humid ambient with no densification of the film. The intrinsic stress in these films is not explained.

Acknowledgment

The author wishes to thank Dr. R. A. Laff for reading and discussing the manuscript. Also, Drs. E. Klokholm, F. H. Dill, T. O. Sedgwick, and S. Krongelb for many discussions during the course of this study. E. Bassous and S. Krongelb provided the SiO_2 films. B. J. Agule ran the infrared spectra. The technical assistance of E. F. Baran is greatly appreciated. The author wishes to thank also L. Berenbaum for his initial collaboration during this work.

Manuscript submitted April 21, 1969; revised manuscript received Aug. 13, 1969. This was Recent News Paper 603 presented at the Montreal Meeting, Oct. 6-11, 1968.

Any discussion of this paper will appear in a Discussion Section to be published in the June 1970 JOURNAL.

REFERENCES

1. R. W. Hoffman, "Physics of Thin Films," Vol. 3, pp. 211-273, Academic Press, New York (1966).
2. R. Glang, R. A. Holmwood, and R. L. Rosenfeld, *Rev. Sci. Instr.*, **36**, 7 (1965).
3. E. L. Jordan, *This Journal*, **108**, 478 (1961).
4. S. Krongelb, *Electrochem. Technol.*, **6**, 251 (1968).
5. J. D. Finegan and R. W. Hoffman, "8th National Symposium on Vacuum Technology Transactions," p. 935, Pergamon Press, New York (1961).
6. J. A. Aboaf, *This Journal*, **116**, 1736 (1969).
7. W. A. Pliskin and E. E. Conrad, IBM *J. Res. & Dev.*, **8**, 43 (1964).
8. M. E. Fine, *J. Appl. Phys.*, **24**, 338 (1953).
9. G. H. Schwuttke and J. K. Howard, *ibid.*, **39**, 1581 (1968).
10. I. A. Blech, J. Guyaux, and G. Cooper, *Rev. Sci. Instr.*, **38**, 638 (1967).
11. C. M. Drum and M. J. Rand, *J. Appl. Phys.*, **39**, 4458 (1968).
12. R. Lathlaen and D. A. Diehl, *This Journal*, **116**, 620 (1969).
13. Corning Glass Works, Engineering with Glass, General Properties Chart, 1962, p 26.
14. L. Maissel, *J. Appl. Phys.*, **32**, 211 (1960).
15. R. K. Kirby, National Bureau of Standards, personal communication, February, 1967.
16. A. Segmuller, *IBM J. Res. & Dev.*, **12**, 421 (1968).
17. W. A. Pliskin and H. S. Lehman, *This Journal*, **112**, 1013 (1965).
18. J. D. Mackenzie, *J. Am. Ceram. Soc.*, **46**, 10 (1963).
19. E. Klokholm, *This Journal*, **115**, 823 (1968).
20. R. L. Mozzi, MIT Thesis, October, 1967.

Some Properties of Vapor Deposited Silicon Nitride Films Obtained by the Reaction of $SiBr_4$ and NH_3

J. A. Aboaf*

IBM Watson Research Center, Yorktown Heights, New York

ABSTRACT

Silicon nitride films, easily etchable in buffered HF (75 Å/min) and usable as gallium diffusion masks, are deposited at 800°C by the $SiBr_4$ and NH_3 reaction (ratio $SiBr_4$ to NH_3 of 1:13) in a forming gas atmosphere. The chemical composition of the films, deposited between 500° and 800°C, as measured by chemical and electron microprobe analysis, is nearer to $Si(NH)_2$ than to Si_3N_4. The 800°C films are impervious to moisture. The room temperature stress in the films deposited on silicon is very high ($+1.2 \times 10^{10}$ dynes/cm^2) and cannot be lowered by decreasing the temperature of deposition or the $SiBr_4$ to NH_3 ratio. The intrinsic stress of the films is highly tensile and is much higher than that in vapor deposited SiO_2 films: germanium wafers tend to warp with formation of slip lines. Films of Si_3N_4 composition containing —NH groups are obtained at 800°C when the ratio of $SiBr_4$ to NH_3 is 1:4.

The purpose of this study is to evaluate the reaction of $SiBr_4$ vapor and NH_3 at different temperatures in a forming gas atmosphere in view of obtaining silicon nitride films of the following characteristics: (*a*) films useful as diffusion masks against gallium at 800°C for 16 hr; (*b*) films easily etchable in buffered HF; and (*c*) films of low tensile stress or possibly compressive stress.

Silicon nitride films are prepared by various methods: reaction between silane and ammonia at temperatures above 750°C (1-3), and at low temperature

* Electrochemical Society Active Member.

by a radio frequency glow discharge reaction (4), or sputtering (5). These methods lead to silicon nitride films of Si_3N_4 composition; they are resistant to moisture and are good masks against shallow diffusion of B, P, As, and Ga (6); they are essentially insoluble in buffered HF and only slightly soluble in concentrated HF.

Mixed nitride-oxide films (7) are prepared by adding a few per cent in volume of oxygen to silane and ammonia gases. These films etch faster in HF, but this method of deposition cannot be used when the substrate is germanium because of the oxidizing atmosphere.

Silicon nitride films obtained from the reaction between $SiCl_4$ and NH_3 can be deposited on silicon at temperatures ranging between 550° and 1250°C (8, 9). A similar reaction is studied here.

Experimental

Deposition conditions.—The deposition of nitride films is carried out in a horizontal resistance furnace, 15 in. long. The furnace tube is made of quartz with an outside diameter of 59 mm; a quartz liner of 55 mm inside diameter is used and is changed every few runs. The hollow substrate holder, also of quartz, has a flat top and curved bottom and rests on the bottom of the furnace tube liner. The temperature on the top surface of the substrate (the deposition temperature) is calibrated against the temperature registered by a thermocouple placed inside. During an experimental run only the inside temperature is recorded.

A schematic of the apparatus is shown in Fig. 1. High-purity ammonia (Precision Gas Products Company) flows into the quartz tube through a nozzle situated at a distance of about 2 in. from the uniform hot zone. This geometry is necessary in order to minimize the reaction of $SiBr_4$ and NH_3 prior to reaching the hot zone. Silicon bromide, semiconductor grade (Alfa Organics Company) is kept at room temperature in a bubbler. Forming gas is used to transport the silicon bromide into the furnace and as the diluting gas. "High purity" forming gas is not satisfactory: a germanium wafer, when heated in this atmosphere at 800°C, shows a "hazy" surface resulting from an attack of the germanium. This reaction is probably due to residual H_2O in the gas. Accordingly, prior to entering into the furnace tube, the forming gas is purified by flowing it first through a platinum bed heated at approximately 400°C and then a liquid nitrogen trap (for condensation of H_2O). No etching of germanium surfaces is observed under these conditions.

Germanium nitride is found to form by the reaction of ammonia and a germanium halide between 400°-600°C (10). Electron microscopy of the surface of a <110> germanium wafer after exposure to an ammonia atmosphere for 30 min at 800°C reveals well-defined 6-facets pits. No attack of the germanium surface due to NH_3 is noticeable using the procedure described below.

The substrate wafers, silicon or germanium, are placed on the holder and the quartz tube evacuated to 20μ pressure. Purified forming gas is then introduced in the tube and the substrate holder pushed into the hot zone. When the desired temperature is reached, the ammonia is introduced in the tube and within one minute the bromide follows. As soon as the deposition is completed, the bromide and ammonia valve are closed and the substrate pulled out to the cooler zone of the furnace; subsequently, the tube is opened.

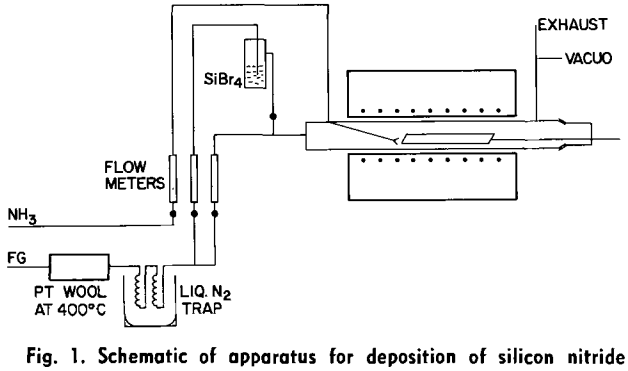

Fig. 1. Schematic of apparatus for deposition of silicon nitride ($SiBr_4$ + NH_3).

Chemical analysis.—Films, 6000-10,000Å thick deposited on germanium or platinum plates, are used for the determination of nitrogen and silicon. The nitrogen in the films is analyzed by the well-known Kjeldahl method. The silicon is determined by absorption spectrophotometry after reaction of the specimen with ammonium molybdate and subsequent reduction of the silicomolybdate.

Stress measurement.—Details of the experimental set-up of the problems regarding the choice of substrates are described elsewhere (11). Silicon wafers are used as substrate on the basis of the data reported by Glang *et al.* (12). The films are deposited on (111), n-type, 0.1 ohm cm silicon wafers, 8 mils thick. Measurements are made at room temperature using the interference technique described by Hoffman (13).

Gallium diffusion.—Lines, 2 mils wide, are made in silicon nitride films deposited at 800°C on germanium by photolithography and etching in buffered HF. A 500Å thick film of SiO_2 (deposited by the pyrolysis of tetraethylorthosilicate at 450°C in oxygen) is then deposited on the wafer. SiO_2 is not a mask against gallium diffusion, but serves to prevent the gallium from attacking the germanium surface.

The diffusion is conducted for 16 hr in a two-zone evacuated furnace with the gallium source at 750° and the specimen at 800°C; the vacuum is held at approximately 1 x 10^{-5} mm. The resulting surface concentration of gallium is 4 x 10^{18} atoms/cc.

Results

The silicon nitride films deposited on silicon or germanium are clear, transparent, and hard. Thickness variation (2000Å thick film) from one edge of a wafer to the other, and from wafer to wafer (2 wafer system) is less than 5%. The films are amorphous; electron diffraction shows only a pattern of diffuse rings. The surface of the films, as seen in electron microscopy, is particularly smooth. The refractive index of the film deposited at 800°C is 2.0.

In Fig. 2, an Arrhenius plot shows the rate of deposition of silicon nitride films for the following conditions: $SiBr_4$ 0.1 x 10^{-3} mole, NH_3 1.3 x 10^{-3} mole, forming gas as carrier gas, 5 l/min. Between 550° and 800°C there is a linear dependence of log rate *vs.* $1/T$. The slope indicates an activation energy of 19 kcal/

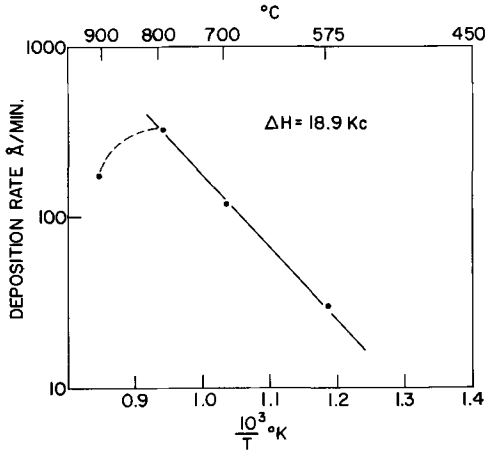

Fig. 2. Deposition rate of silicon nitride as a function of temperature. $SiBr_4$ 0.1 x 10^{-3} mole, NH_3 1.3 x 10^{-3} mole, carrier gas forming gas 5 l/min.

Table I. Etch rate of silicon nitride films

Temperature of deposition of silicon nitride films. NH_3 to $SiBr_4$ Ratio of 13:1	Etch rate in buff HF—25° Å/min	Etch rate in conc. HF—25°C Å/min
800	75	1350
700	150	—
575	1100	—

mole. The rate at 900°C decreases probably because of a depletion of the $SiBr_4$ at an upstream point, prior to reaching the deposition zone of interest.

The etch rate of the silicon nitride films ($NH_3/SiBr_4$ ratio of 13:1) is shown in Table I. It is worth noticing that in concentrated HF the etch rate is 1 order of magnitude higher than that for the nitride deposited by the silane process (1).

An MIS capacitance voltage measurement at 150 kHz made on a Ge-800°C nitride-Al sandwich results in a large density of negative fixed charge and/or surface states. The hydrogen used during deposition appears to induce surface states at the interface as was shown by Sedgwick (14). The same measurement made on a Si-800°C nitride-Al sandwich results in surface charge values of + 4 x 10^{12} charges/cm^2. The value of the dielectric constant is about 8 as computed from the maximum capacitance value of the MIS capacitance and the thickness of the oxide.

Stress measurements.—Stress measurements are made, at room temperature, on silicon wafers on which approximately 2000Å thick films are deposited. The stress at room temperature in films deposited at a $NH_3/SiBr_4$ ratio of 13:1 and at 800°C is tensile and equal to 1.3 x 10^{10} dynes/cm^2.

The stress in films deposited at different ammonia to bromide ratios is shown in Fig. 3. Films deposited at a ratio below 10:1 seem to contain an excess silicon; their etch rate is quite low, and the film cannot be totally removed with HF; consequently, they are not considered.

The room temperature stress of silicon nitride films deposited on silicon in the same apparatus by the reaction between SiH_4 and NH_3 in forming gas at 800°C, at a deposition rate of 125 Å/min, and a ratio of NH_3/SiH_4 of 20 results comparable to that of films obtained by the bromide process.

The room temperature stress in silicon nitride films on silicon deposited between 500° and 800°C at a $NH_3/SiBr_4$ ratio of 13:1 is given in Fig. 4. The stress is tensile and appears to be independent of the temperature of deposition.

The room temperature stress in silicon nitride films is one order of magnitude higher than that for SiO_2 films obtained by the pyrolytic decomposition of tetra-

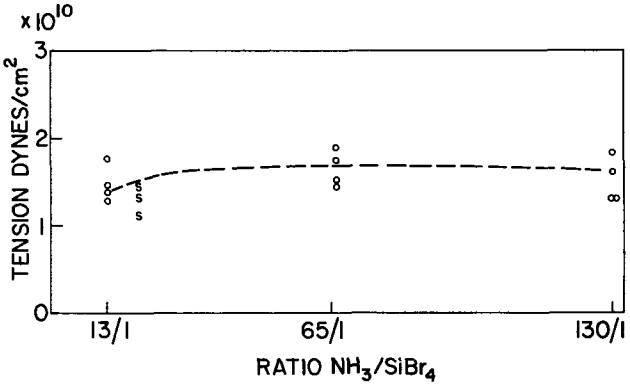

Fig. 3. Room temperature stress in silicon nitride films deposited on silicon wafers as a function of $NH_3/SiBr_4$ ratio. Films deposited at 800°C, approx. 2000Å thick. o, Bromide process; s, silane process.

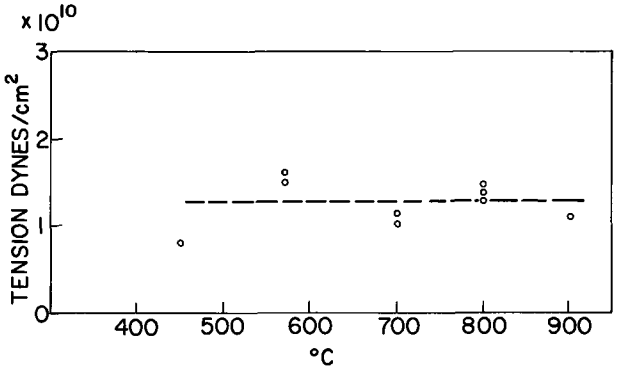

Fig. 4. Room temperature stress in silicon nitride films deposited on silicon wafers as a function of temperature of deposition. Films approx. 2000Å thick. $SiBr_4/NH_3$ = 1:13.

ethylorthosilicate (11). While some data on the mechanical properties of single crystal silicon nitride (5) and polycrystalline silicon nitride of various porosities are available (15, 16), no data on amorphous silicon nitride can be found in the literature. Consequently, it is not possible to separate the stresses generated by the difference in thermal expansion between the film and substrate and that due to the intrinsic stress as it was done for SiO_2 films (11).

It would be interesting, however, to know at least qualitatively the sign of the intrinsic stress, or stress at temperature in the silicon nitride films. A nitride film is deposited at 800°C on a 2-mil thick, flat germanium wafer and its curvature observed *in situ* through a window situated at the end of the deposition tube. The wafer bows upward (with the nitride in the concave side). Thus, at the temperature of deposition, the intrinsic stress in the film is tensile.

Figure 5 shows the curvature (at room temperature) of a 2-mil thick (110) germanium which is coated with a 2200Å thick silicon nitride film at 800°C; for comparison that of a 2-mil thick germanium wafer on which is deposited a 7200Å thick SiO_2 film at 800°C by the thermal decomposition of tetraethylorthosilicate in forming gas is also shown. These wafers curve during deposition at 800°C and are found to be warped after being brought down to room temperature. From the large deflection brought about by the silicon nitride film, it can be concluded that the intrinsic stress in the nitride film is much higher than that estimated for SiO_2 (2.1 x 10^9 dynes/cm^2) (11). A visual inspection of the germanium wafers show that the germanium is plastically deformed; slip lines can be seen on the wafers. It is thus possible to conclude also that the intrinsic stress in both films is higher than the yield stress of germanium at 800°C. For a (110) germanium wafer, slip lines occur in the (111) plane in the <110>

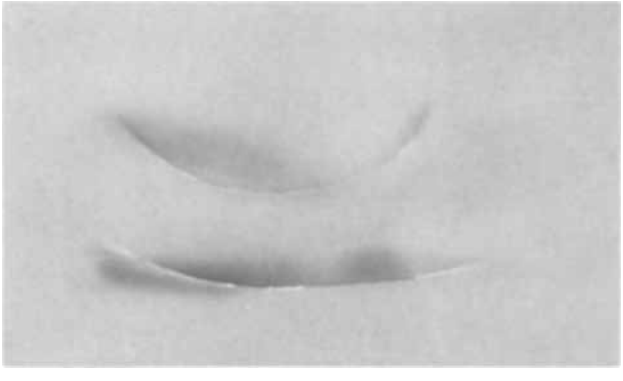

Fig. 5. Top, 2000Å thick silicon nitride film on 2-mils thick <110> germanium wafer; bottom, 7200Å thick SiO_2 film on 2-mils thick <110> germanium wafer (tetraethylorthosilicate process, 800°C).

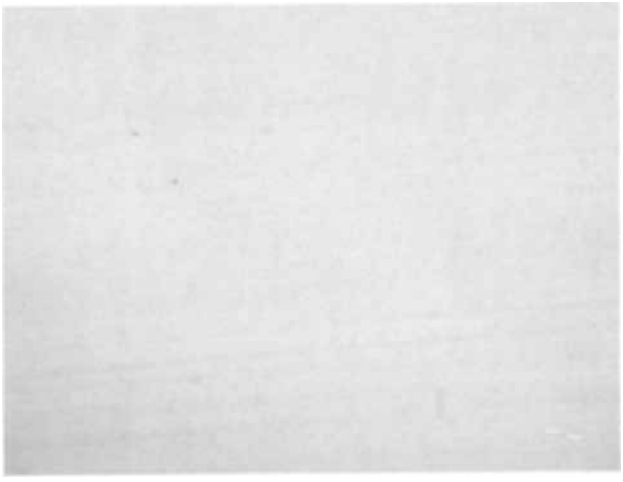

Fig. 6. Slip lines in germanium wafer <110>, direction <110> as seen at the interference microscope. Magnification 150X.

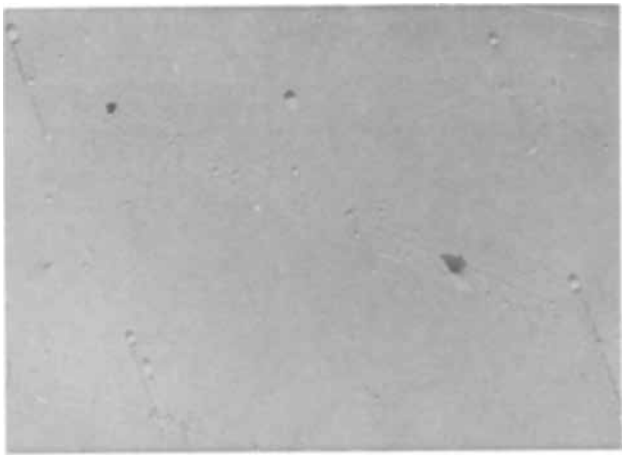

Fig. 7. Slip lines in germanium wafer <110>, direction <$1\bar{1}0$> as seen at the electron microscope. Magnification 9750X.

direction (Fig. 6). In Fig. 7, an electron microscope replica of the surface shows slip lines and a large number of pits (probably random dislocations along the length of the slip lines).

Diffusion masking.—Silicon nitride films on germanium deposited at 800°C ($SiBr_4/NH_3$ = 1/13) act as masks against gallium at 800°C for 16 hr. However, the germanium wafers covered with 1100Å thick silicon nitride + 500Å thick SiO_2 curve during the 16-hr diffusion with evidence of warping as explained in the preceding paragraph. It appears that the intrinsic stress in the silicon nitride, coupled with that of the SiO_2 film (10), are higher than the yield stress of germanium. The deformation of the wafers makes them unsuitable for device preparation.

Depositing the nitride at substrate temperatures of 700°C or less does not reduce the stress. Also, the stress is not reduced by increasing the ammonia to bromide ratio. However, a 300Å thick nitride film is a mask against gallium diffusion. This film is satisfactory; the silicon nitride + 500Å SiO_2 films do not warp the wafer during a 16-hr diffusion, and no slip lines could be found under examination with an interference microscope.

Chemical analysis.—A summary of the chemical analysis of silicon nitride films (about 8000Å thick) deposited on platinum or germanium is given in Table II. The chemical analysis is accurate to about 5% relative to the amount determined, the electron microprobe analysis to 2%.

The chemical analysis of the silicon nitride films deposited by the reaction of silane and ammonia at

Table II. Chemical analysis of silicon nitride films
All figures in weight per cent

Films deposited at 800°C : $SiBr_4$ + NH_3 reaction**

Run	1	2	3	4	5	6	7	8A	8B*	9A	9B*	10*
Si	48	—	47.6	56.4	53.2	47.3	54.7	44.7	48	47.8	48	42
N	—	50	—	44.8	50.1	51.8	45.5	56	—	51.2	—	—
Br									1			

Films deposited at 575°C : $SiBr_4$ + NH_3 reaction**

Run	1	2	3
Si	50.6	48.9	—
N	56	—	60

Films deposited at 800°C : SiH_4 + NH_3 reaction***

Run	1	2
Si	61.3	58.3
N	41.8	45.5

Bulk Si_3N_4 Si 59.3 N 38.8

* Analysis made by electron probe.
** $SiBr_4/NH_3$ ratio = 1/13.
*** SiH_4/NH_3 ratio = 1/20.

800°C ($NH_3/SiBr_4$ ratio of 20:1) shows that the atomic ratio of silicon to nitrogen is equal to 3/4 and agrees with that of Doo (17). For the nitride deposited by the silicon bromide and ammonia reaction at 800°C ($SiBr_4/NH_3$ = 1:13), this ratio appears to be 1/2. The only compound close to this atomic ratio described in the literature is the silicidiimide $Si(NH)_2$. It is formed in the liquid phase from $SiBr_4$ and NH_3 and is reported to be amorphous (19). Some properties of the silicidiimide and the nitride films deposited here are compared below. The infrared absorption spectra of the films (Fig. 8) shows not only the Si-N stretching vibration at 860 cm^{-1}, but also two other bands at 3350 and 1200 cm^{-1} which can be ascribed to the stretching and bending vibration of the NH group (18).

There is disagreement as to the mode of decomposition of the silicidiimide. According to Billy (19), the amorphous silicidiimide starts losing NH_3 at 80°C in a nitrogen atmosphere and is transformed into Si_3N_4 at 540°C; on the other hand, Glemser and Naumann (20), on basis of their thermogravimetric data, find the existence of two intermediate species before reaching Si_3N_4 at 1250°C, *i.e.*,

$$Si(NH)_2 \xrightarrow{300°C} Si_3N_5H_3 \xrightarrow{650°C} Si_2N_3H \xrightarrow{1250°C} Si_3N_4$$

(In these compounds, the percentage in weight in Si

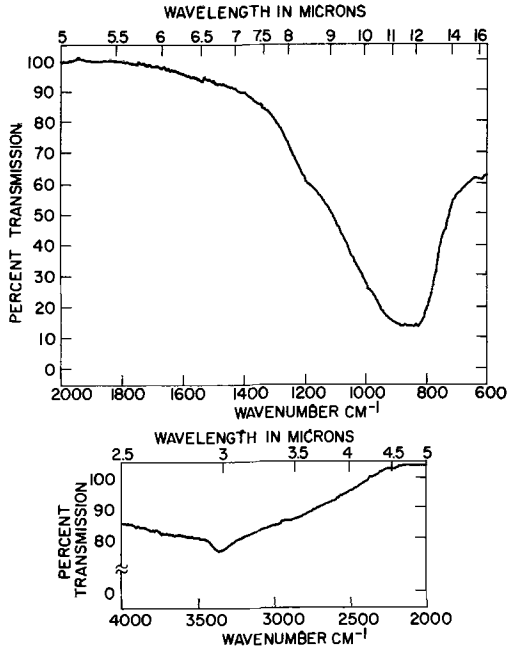

Fig. 8. Infrared absorption spectra of silicon nitride film deposited at 800°C ($SiBr_4/NH_3$ = 1:13).

is respectively 48.3, 53.4, 56.6 and 60; in N, respectively 48.3, 44.5, 42.4 and 40.)

Silicon nitride films, deposited on silicon by the bromide process at 800°C ($SiBr_4/NH_3$ = 1/13), were heat-treated in a forming gas atmosphere for 3 hr at 1300°C. The silicon composition in the films, as measured by the electron microprobe, do not change; however, the 3350 and 1200 cm^{-1} infrared absorption bands cannot be detected; accordingly, -NH groups are lost during heat-treatment. An electron diffraction study of the heat-treated films shows these films to be still amorphous.

The silicidiimide, formed in the liquid phase by the reaction of $SiBr_4$ and NH_3, absorbs water vapor readily (20). However, an infrared test of a film subjected to an 85°C and 85% relative humidity ambient, for 24 hr, shows no moisture pick up (minimum detectable 0.004 optical density per micron at 3650 cm^{-1}).

While composition and infrared properties suggest the film to be $Si(NH)_2$, other properties such as decomposition and water absorption do not confirm it. Also, it was possible to deposit at 800°C silicon nitride films of Si_3N_4 composition using a $SiBr_4$ to NH_3 ratio of 1:4. These films do not show any free silicon (electron microprobe analysis), but their infrared spectra shows -NH bands.

In conclusion, it appears that the reaction of $SiBr_4$ and NH_3 gives rise to amorphous films of various silicon, nitrogen content according to the temperature of deposition and to the ratio of $SiBr_4$ and NH_3; also, that the reaction in the vapor phase is different from that occurring in the liquid phase.

Conclusion

Silicon nitride films, readily etchable in buffered HF and usable as diffusion masks at 800°C for gallium were deposited by the $SiBr_4$ and NH_3 reaction at 800°C. The chemical composition of the films ($SiBr_4/NH_3$ = 1/13) is nearer to $Si(NH)_2$ than to Si_3N_4. It has not been possible to decrease the very high stress in the films (1.3 x 10^{10} dynes/cm^2) either by decreasing the temperature or by changing the $SiBr_4$ to NH_3 ratio.

Acknowledgment

The author wishes to thank Drs. R. A. Laff and T. O. Sedgwick for discussions and for reviewing the manuscript. The author is indebted to B. L. Olson for the chemical analysis, J. D. Kuptsis for the electron microprobe analysis, B. J. Agule for the MOS curves and infrared absorption spectra, and H. N. Yu for the diffusion experiments. The technical assistance of E. F. Baran is very much appreciated.

Manuscript submitted April 30, 1969; revised manuscript received Aug. 13, 1969.

Any discussion of this paper will appear in a Discussion Section to be published in the June 1970 JOURNAL.

REFERENCES

1. V. Y. Doo, D. R. Nichols, and G. A. Silvey, *This Journal*, **113**, 1279 (1966).
2. T. L. Chu, C. H. Lee, and G. A. Gruber, *ibid.*, **114**, 717 (1967).
3. K. E. Bean, P. S. Gleim, and R. L. Yeakley, *ibid.*, **114**, 733 (1967).
4. R. C. G. Swann, R. R. Mehta, and T. P. Cauge, *ibid.*, **114**, 713 (1967).
5. S. M. Hu and L. V. Gregor, *ibid.*, **114**, 826 (1967).
6. V. Y. Doo, IEEE Transactions on Electron Devices, July 1966.
7. T. L. Chu, J. R. Szedon, and C. H. Lee, *This Journal*, **115**, 318 (1968).
8. M. J. Grieco, F. L. Worthing, and B. Schwartz, *ibid.*, **115**, 525 (1968).
9. B. E. Deal, P. J. Fleming, and P. L. Castro, *ibid.*, **115**, 300 (1968).
10. H. Nagai and T. Niimi, *ibid.*, **115**, 6 (1968).
11. J. A. Aboaf, *ibid.*, **116**, 1732 (1969).
12. R. Glang, R. A. Holmwood, and R. L. Rosenfeld, *Rev. Sci. Instr.*, **36**, 7 (1965).
13. J. D. Finegan and R. W. Hoffman, 8th National Symposium on Vacuum Technology Transactions, 935, Pergamon Press, New York (1961).
14. T. O. Sedgwick, *J. Appl. Phys.*, **39**, 5066 (1968).
15. G. G. Deeley, J. M. Herbert, and N. C. Moore, *Powder Met.*, **8**, 145 (1961).
16. N. L. Parr and E. R. W. May, Special Ceramics, Heywood Co., Ltd., London.
17. V. Y. Doo and D. R. Kerr, NASA, CR 995, 1967.
18. C. N. Rao, "Chemical Applications of Infrared Spectroscopy," chap. 5, Academic Press, New York.
19. M. Billy, *Ann. Chim.*, **4**, 795 (1959).
20. O. Glemser and P. Naumann, *Z. Anorg. Chem.*, **298**, 134 (1959).

Technical Notes

Structure of Silicon Monoxide

S. C. H. Lin and M. Joshi

IBM Burlington, Components Division, Essex Junction, Vermont

The electrical properties of silicon oxide films depend on the method of preparation, which determines the composition and the structure of the films. The structure of thin films of silicon monoxide obtained by the method of evaporation has been studied by researchers using electron diffraction (1), infrared spectroscopy (2, 3), and the electron microprobe (4). The electron diffraction and the electron microprobe studies indicate that the films consist of mixtures of Si and SiO_2. On the other hand, the infrared absorption spectroscopy results show that the films are predominantly mixtures of SiO, SiO_2, and a little Si_2O_3. All these studies are quite recent in comparison with the x-ray study (5) of bulk amorphous SiO, which is used as a source for evaporation. Brady (5) proposed, in 1958, that the bulk amorphous SiO is a material of stoichiometric mixture of SiO_2 + Si. Because of the controversy, we found it necessary to re-examine the atomic structure of SiO by x-ray diffraction.

Even after we made considerable improvement in the accuracy of the x-ray data, Brady's conclusion retains its essential validity. (Our SiO samples and Brady's samples were obtained from the same company.)

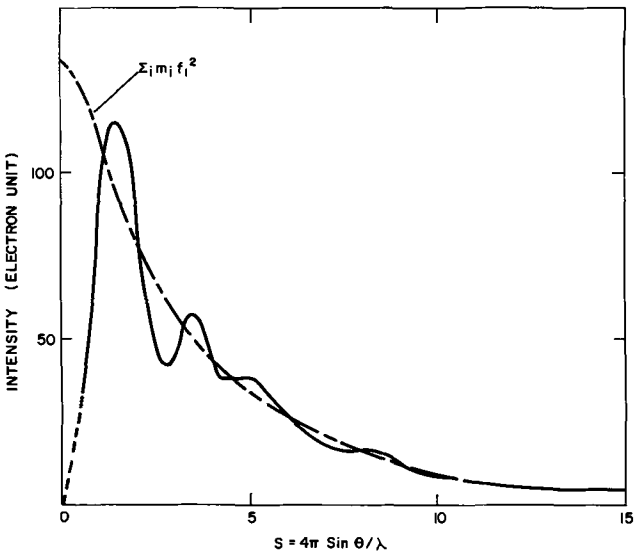

Fig. 1. X-ray intensity spectrum of silicon monoxide after correction and scaling.

Experimental

The first few peaks in the electron radial distribution function (RDF) are sensitively determined by the high angle data in the x-ray intensity curve. We took the following steps to minimize the errors in the RDF.

1. The intensity data were recorded over a considerably wider range of $S = 4\pi \sin \theta/\lambda$. $S_{max} = 15$ in our data; $S_{max} = 12$ in Brady's data.

2. Long-time step counting, 20 min/0.25° step, was performed to minimize the high angle range ($S > 5$) errors.

3. Intensity patterns were corrected only for polarization. Incoherent scattering correction was not felt necessary as the scattered x-ray entered the monochromotor before entering the counter. In our case, we have obtained in the electron unit a satisfactory normalization of the relative intensity curve throughout the total angular range. Information could not be obtained regarding this point from Brady's paper. Effective numbers of electrons $K_{Si} = 15$ and $K_O = 7$ and a sample density of 2.16 g/cm^3 were used in our radial distribution calculation.

4. The diffraction patterns were recorded with MoKα radiation. We used a scintillation counter, a monochromotor, and a pulse height analyzer for measuring scattered intensity.

Results and Discussion

The x-ray intensity curve we obtained is illustrated in Fig. 1. Curve a in Fig. 2 represents the following electron radial distribution:

$$R(r) = \sum_i \sum_j 0.5\, K_i K_j [4\pi r^2 n_{ij}(r)] = K_{Si}K_O[4\pi r^2 n_{Si-O}(r)] + 0.5\, K_{Si}K_{Si}[4\pi r^2 n_{Si-Si}(r)] + 0.5\, K_O K_O [4\pi r^2 n_{O-O}(r)]$$

Here the symbols are according to the usual notation (6). Our $R(r)$ curve is somewhat different from Brady's curve, as can be seen in Fig. 2. Peaks I and IV have almost identical positions in both curves. Peaks

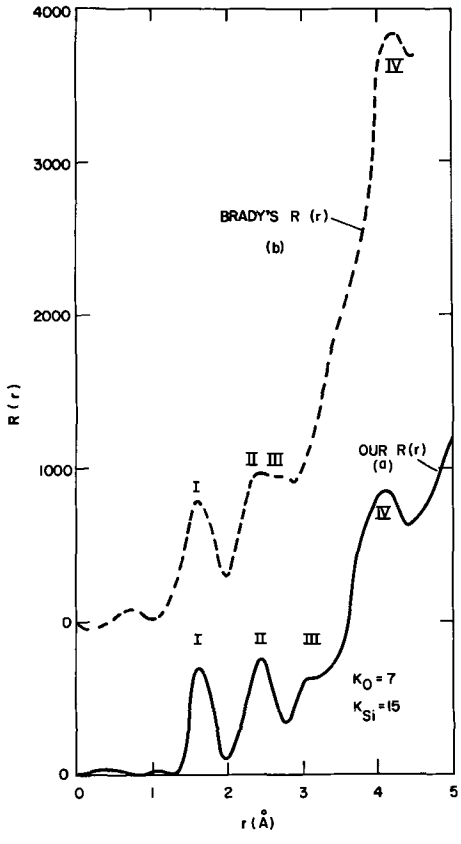

Fig. 2. Electron radial distribution curve of silicon monoxide compared with Brady's curve.

II and III are clearly separated, and are identifiable in our $R(r)$ curve. This separation gives considerable credence to Brady's model for SiO structure; namely, SiO is a mixture of amorphous Si and SiO_2.

Following Brady's line of argument, Peak I, at 1.63Å, is attributable to Si-O pairs from silica alone. The peak area is 210 e^2, which corresponds to 4 oxygen atoms around a silicon atom. Peak II has an area of 300 e^2 at 2.45Å. If this peak is due to the Si-Si pair from amorphous silicon alone, the silicon neighbor number becomes 5.3, which is large for an amorphous silicon. Since the O-O peak in vitreous silica locates at approximately 2.6Å, we would assume that this small O-O peak is hidden within the large Si-Si peak, since silicon atoms scatter twice as strongly as oxygen atoms. If half of the O-O peak area ½(0.5 x 7 x 7 x 6) = 74 is subtracted from the peak area, the rest of the area, 226 e^2 gives the correct value of 4 for the number of silicon-silicon neighbors. Peak III, at 3.05Å, is attributed to Si-Si pairs in SiO_2 and has an area approximately 240 e^2 which corresponds to 4.3 Si-Si pairs (7). Peak IV, at 3.94Å, in the radial distribution curve corresponds to the second Si-Si peak in amorphous silicon (1). The peak area calculations are summarized and compared with that of amorphous silicon and vitreous silica in Table I.

We find that the composition of the bulk SiO is a mixture of amorphous silicon and vitreous silica, as

Table I. Comparison of peak positions and areas of radial distribution function of SiO with amorphous silicon and vitreous silica

Peak	Pair distance r_{ij} (Å)	Pair I-J	Peak area A_{ij} (e^2)	No. of neighbors $n = \frac{A_{ij}}{m_i K_i K_j}$	Corresponding values in amorphous silicon		Corresponding values in vitreous silica	
					r	n	r	n
I	1.63	Si-O	210	4			1.63	4
II	2.40	O-O	(74)	(6)			2.6	6
		300 = Si-Si	(226)	(4)	2.35	4		
III	3.05	Si-Si	240	4.3			3.1	4
IV	3.95				3.85	12	4.0	

proposed by Brady. This chemical composition is not much different from the thin films of silicon monoxide as determined through electron diffraction (1) and electron microprobe (4).

Manuscript received July 16, 1969.

Any discussion of this paper will appear in a Discussion Section to be published in the June 1970 JOURNAL.

REFERENCES

1. M. V. Coleman and D. J. D. Thomas, *Physica Status Solidi*, **22**, 593 (1967).
2. I. R. Rawlings, *Brit. J. Appl. Phys.* (*J. Phys. D.*) *Ser. 2*, **1**, 733 (1968).
3. W. A. Pliskin and H. S. Lehman, *This Journal*, **112**, 1013 (1965).
4. E. W. White and R. Roy, *Solid State Commun.*, **2**, 151 (1964).
5. G. W. Brady, *J. Phys. Chem.*, **63**, 1119 (1959).
6. S. C. H. Lin, *Physica Status Solidi*, **34**, No. 2 (1969).
7. E. H. Henninger, R. C. Buschert, and L. Heaton, *J. Phys. Chem. Solids*, **28**, 423 (1967).

Electrical Resistivity of Tungsten Films Prepared by WF_6 Reduction

A. F. Mayadas, J. J. Cuomo,* and R. Rosenberg

International Business Machines Corporation, Thomas J. Watson Research Center, Yorktown Heights, New York

This note is concerned with a study of tungsten films prepared by hydrogen reduction of tungsten hexafluoride. The observations reported here of large-area epitaxy of tungsten on sapphire are in esssential agreement with earlier structure work of the Autonetics group (1); however, we find that the very low deposition rates and high temperatures specified in the earlier work are not essential to achieving epitaxial single-crystal films. Resistivity studies for this class of films have not been previously reported; some of the present results are of particular interest in that they indicate a high degree of perfection in the single-crystal deposits.

Details of the film deposition apparatus are shown in Fig. 1. With the exception of the quartz mixing chamber and the quartz reaction tube, the system is constructed wholly of stainless steel and is completely helium leaktight, since preliminary observations had indicated that the presence of gaseous impurities is detrimental to film/substrate adhesion. Provisions were available for purging of the system with purified hydrogen, and, in order to eliminate contaminants, a hydrogen flow was maintained during periods when the system was idle. The hydrogen and WF_6 flow were controlled by a leak valve. For any one deposition, the film thickness was estimated from the WF_6 valve setting which was calibrated to W deposition rate. After each run, film thickness was measured to an estimated accuracy of $\pm 7\%$ by Tolansky interferometry.

The WF_6, obtained from the General Chemical Division of Allied Chemical Corporation, was of high-purity grade. The graphite susceptor was of spectroscopically pure graphite and prior to use it was completely coated at high temperature with tungsten to prevent outgassing during film deposition.

Oxidized silicon, sputtered Al_2O_3 on oxidized Si, and single-crystal α-Al_2O_3 (sapphire) wafers were used as substrates. These were cleaned in a hot concentrated solution of $H_2SO_4 + K_2Cr_3O_7$.

Typically, three substrates were placed in the system which was then purged for about 1 hr with hydrogen. The substrates were then preheated to 1000°C for 2 min, allowed to cool to the operating temperature, and held there for 10 min. WF_6 was controllably introduced through the leak valve. Deposition times ranged from 1 to 20 sec.

Structural determination was made by x-ray diffraction (Laue) and low angle electron diffraction techniques. Single crystal films were epitaxially grown on sapphire[1] at temperatures of 500°C or higher and rates as high as 6000 Å/sec. Most of the sapphire substrates were cut perpendicular to the normal growth direction which is approximately 70° off c-axis. A few substrates characterized by a c-axis normal were also used. The orientation relationships were similar to those reported earlier (1); that is, {111} W || {0001} Al_2O_3, and [110] W || [$2\bar{1}\bar{1}0$] Al_2O_3. A sample pattern is shown in Fig. 2A. As the deposition temperature was decreased below 450°C, the tungsten deposit became polycrystalline with a preferred {111} orientation (*see* Fig. 2B). On sputtered Al_2O_3 or oxidized silicon substrates, the tungsten deposit was polycrystalline with grain sizes of the order of 300-500Å. Above 500°C, a {111} texture was prevalent (Fig. 2C) with an increased tendency toward a random structure as the temperature was lowered (Fig. 2D).

Deposition parameters and structural observations for several films are summarized in Table I, while surface structure of some etched single-crystal films is shown in Fig. 3.

Electrical Resistivity

The electrical resistivity of several films was measured both at room temperature (296°K) and at 4.2°K, and resistivity ratios (RR $\equiv \rho_{296°K}/\rho_{4.2°K}$) computed. Measurements were of the standard 4-point in-line type.

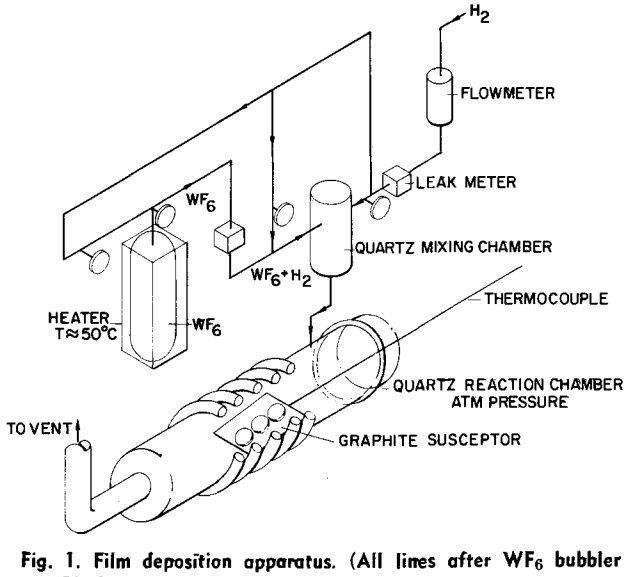

Fig. 1. Film deposition apparatus. (All lines after WF_6 bubbler are at 50°C.)

[1] A few films were also deposited on freshly cleaved MgO substrates. The cleavage planes are {100} and structure studies showed that {100} W || {100} MgO and [110] W || [100] MgO, at a substrate temperature of 500°C.

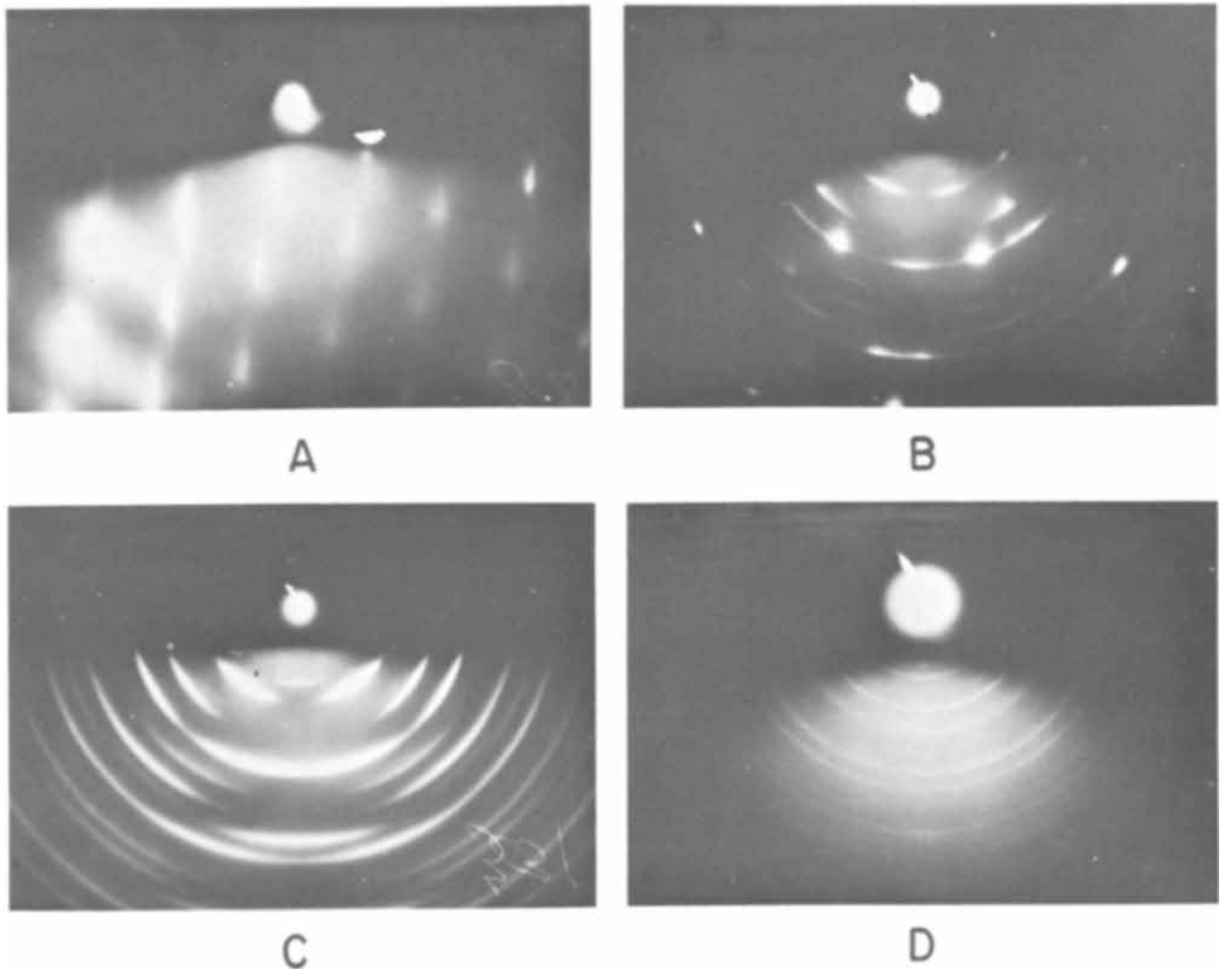

Fig. 2. A—Electron diffraction pattern from single-crystal W film (film M) on sapphire substrate (~ 70° off c-axis). Substrate temperature T_s = 510°C. B—Electron diffraction pattern from polycrystalline W film (film F) on sapphire substrate; T_s = 460°C. C—Electron diffraction pattern from polycrystalline W film (film C) on SiO_2; T_s = 520°C. D—Electron diffraction pattern from polycrystalline W film (film A) on SiO_2; T_s = 460°C.

Polycrystalline films.—Polycrystalline films, *i.e.* those deposited on thermally grown SiO_2 and sputtered Al_2O_3, exhibited room temperature resistivities, $\rho_{296°K}$, about 30-100% higher than the published bulk value of 5.3 μohm · cm (2), and low resistivity ratios: about 2-4. Substrate temperature (in the range 450°-650°C did not appear to affect these electrical characteristics. Some representative measurements are shown in Table I. In view of the fact that even the thicker polycrystalline films are characterized by such low resistivity ratios, it is safe to conclude that the (Fuchs) thickness size-effect (3) plays only a negligible role in determining the RR and virtually none in determining $\rho_{296°K}$; the poor electrical characteristics must therefore be discussed in terms of structural disorder in these films.

That the low RR's for polycrystalline films are due to grain-size effects is strikingly illustrated by the observation that samples B (polycrystalline) and J (single crystal) were deposited simultaneously with the two substrates placed side by side in the three-position susceptor (Fig 1), so that chemical impurities

Table I. Summary of Data

Film	Substrate	Substrate temp, °C	Thickness, A	ρ 296°K μohm · cm	ρ 4.2°K μohm · cm	ρ 296°K/ρ 4.2°K	Structure
A	Ox · Si*	460	2300	15.85	7.38	2.14	Random fine-grained
B	Ox · Si	520	3500	12.36	5.75	2.15	Random fine-grained
C	Ox · Si	520	6380	9.57	3.91	2.45	Preferred (111), fine-grained
D	Sputt. Al_2O_3**	460	2450	14.11	7.15	1.98	Random fine-grained
E	Sputt. Al_2O_3	520	4060	13.50	6.03	2.24	Random fine-grained
F	S.C. Al_2O_3***	460	2420	8.26	2.12	3.90	Preferred (111)
G	S.C. Al_2O_3	520	1500	6.90	1.72	4.00	Single-crystal
H	S.C. Al_2O_3	510	2300	6.76	0.539	12.53	Single-crystal
I	S.C. Al_2O_3	520	3500	5.40	0.261	20.69	Single-crystal
J	S.C. Al_2O_3	520	3810	5.78	0.329	17.53	Single-crystal
K	S.C. Al_2O_3	520	4100	5.51	0.194	28.39	Single-crystal
L	S.C. Al_2O_3	510	4210	5.53	0.277	19.92	Single-crystal
M	S.C. Al_2O_3	510	6600	5.60	0.131	42.86	Single-crystal

* Oxidized silicon.
** Al_2O_3 sputtered onto oxidized Si.
*** Sapphire.

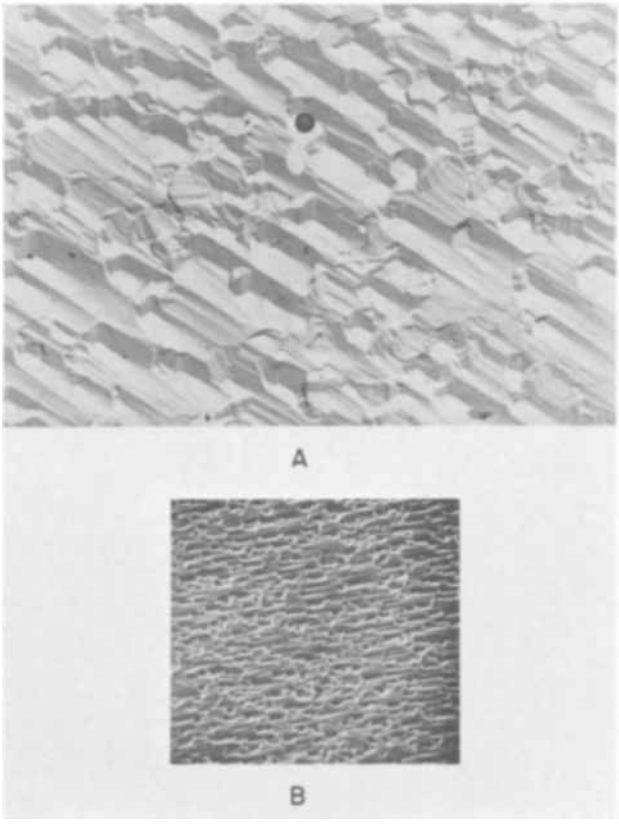

Fig. 3. A—Surface replication electron micrograph of a single-crystal W film after mild etch in potassium ferricyanide/potassium hydroxide solution. (Diameter of black sphere is 5000Å). B—Scanning electron micrograph, same film as in A. (Magnification X970).

should be present in about the same concentration in both films. Yet the RR for the polycrystalline sample is markedly lower than that for the single crystal. This difference between single-crystal and polycrystalline films deposited simultaneously was reproduced many times and was found not to depend on substrate position in the susceptor.

Epitaxial single-crystal films.—As noted in the section on film structure, a substrate temperature of about 500°C is required to obtain epitaxy. Early observations by us also indicated that the resistivities of the 500°C films were almost identical to the 600°C films, so the succeeding discussion is limited to only the 500°C films on sapphire.

Measurements of $\rho_{296°K}$ on these single-crystal films were generally within a few per cent of the bulk resistivity and were essentially independent of thickness in the range 1500-10,000Å. Measured values of $\rho_{4.2°K}$ (and hence RR), however, were strongly dependent on thickness. The RR's were generally quite high (*see* Table I, sample G through M) so that for these films the magnitude of the thickness size-effect resistivity must be estimated in order to assign a number to the intrinsic film resistivity at 4.2°K, ρ_i (*i.e.*, the resistivity the film would possess if it were infinitely thick), and intrinsic electron mean free path at 4.2°K, l_i. To extract this information by use of the Fuchs size-effect theory, the surface scattering parameter p which is the fraction of specularly reflected electrons must be known. Although available evidence indicates $p \approx 0$ is generally a good approximation, no specific data on surface scattering in tungsten are available. Furthermore, it is unlikely that the simple Fuchs theory (which postulates the existence of an isotropic scalar electron relaxation time) can quantitatively predict the thickness dependence in a complex material such as tungsten whose Fermi surface is known to consist of both a highly anisotropic electron "jack" and a hole octahedron (5). For these reasons, only qualitative estimates of ρ_i and l_i can be expected for these films.

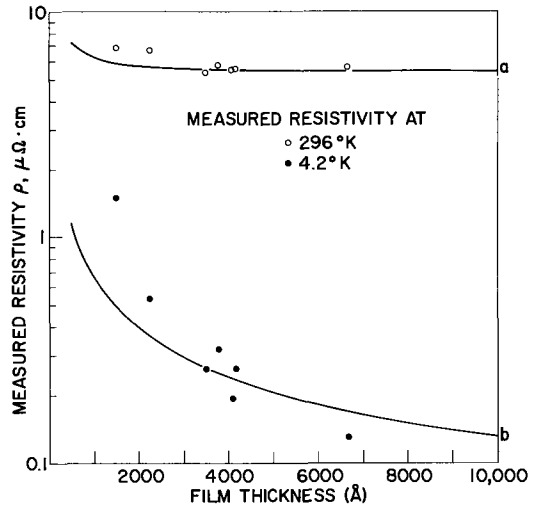

Fig. 4. Thickness dependence of measured resistivity for single-crystal films at 296° and 4.2°K. Solid lines are calculated Fuchs size-effect curves; Curve a: $p = 0$, $\rho_i = 5.3$ μohm · cm, $l_i = 413$Å; Curve b: $p = 0$, $\rho_i = 0.0437$ μohm · cm, $l_i = 50{,}000$Å.

In Fig. 4, the measured resistivities for the single-crystal films of Table I are plotted against thickness. Also shown are resistivity *vs.* thickness curves calculated[2] from the Fuchs theory for $p = 0$, with ρ_i and l_i selected to fit the data. It can be seen that, as expected, only a small size-effect is observed at room temperature and a reasonable fit can be made to the solid curve (curve a) drawn for the values $\rho_i = 5.3$ μohm · cm and $l_i = 413$Å which has previously been reported for bulk tungsten (7). At 4.2°K, a much stronger thickness dependence is found which has been fitted to the solid curve for $\rho_i = 0.0437$ μohm · cm, $l_i = 50{,}000$Å (curve b).

There seems to be a tendency for the data points corresponding to thinner films to fall above the solid curve, while those for the thicker films fall below. This may be due to the fact that thinner films getter more chemical impurities from the system and therefore have smaller l_i's; however, substantially more data points are required to study the details of the thickness dependence. It should be mentioned that x-ray topographic examination (8), sensitive to dislocations and local strain, has revealed no essential difference between our thick and thin films on sapphire (regardless of orientation): both appear to be high-quality single crystals.

A significant conclusion of the present work is that the high resistivity in the polycrystalline tungsten films is not due to impurities but to grain boundary scattering of electrons, since polycrystalline and single-crystal films deposited simultaneously have quite different resistive characteristics.

Acknowledgments

The authors are grateful to J. B. Bartivic for aid with sample preparation, J. C. DeLuca for aid with resistivity measurements, C. Aliotta for electron microscopy, J. Angilello for x-ray diffraction, and E. I. Alessandrini for electron diffraction.

Manuscript submitted April 2, 1969; revised manuscript received Aug. 20, 1969.

Any discussion of this paper will appear in a Discussion Section to be published in the June 1970 JOURNAL.

[2] The calculation scheme, which has been published earlier (6), assumes the general validity of Matthiessen's Rule at room temperature and makes use of the fact that the product $\rho_i l_i$ is a constant for any (reasonably) pure metal. The value $\rho_i l_i = 2.185 \times 10^{-11}$ ohm-cm², obtained by Fawcett and Griffiths (7) from anomalous skin-effect measurements on tungsten, was used in the calculation.

REFERENCES
1. Arnold Miller, G. D. Barnett, G. R. Pulliam, and R. G. Warren, Conference on Advanced Electronic Materials, August 1962, Philadelphia, Pa.; "Metallurgy of Advanced Electronic Materials," Vol. 19, p. 263, Interscience Publishers, Inc., New York (1963).
2. G. K. White and S. B. Woods, *Phil. Trans.*, **215A**, 35 (1959).
3. K. Fuchs, *Proc. Cambridge Phil. Soc.*, **34**, 100 (1938).
4. *See, e.g.*, D. S. Campbell in "The Use of Thin Films in Physical Investigations," p. 315, Academic Press Inc., New York (1966).
5. *See, e.g.*, T. L. Loucks, *Phys. Rev.*, **139**, A1181 (1965).
6. A. F. Mayadas, *J. Appl. Phys.*, **39**, 4241 (1968).
7. E. Fawcett and D. Griffiths, *J. Phys. Chem. Solids*, **23**, 1631 (1962).
8. J. K. Howard, IBM Components Div., East Fishkill, N. Y., Private communication.

Epitaxial Gallium Arsenide from Trimethyl Gallium and Arsine

P. Rai-Choudhury*

Westinghouse Electric Corporation, Research and Development Center, Pittsburgh, Pennsylvania

Gallium arsenide is used in devices such as Gunn oscillators, high-voltage varactors, lasers, tunnel diodes, *etc.* Epitaxial techniques are being developed in which gallium arsenide with controlled doping is deposited from the vapor or liquid phase on gallium arsenide as well as sapphire substrates. Most deposition techniques reported to date use some form of transport mechanism *via* a halide (1). Relatively high volatility and the absence of any transport agents (such as HCl) make trimethyl gallium an attractive source of gallium for the vapor growth of GaAs. For instance, trimethyl gallium has a vapor pressure of 0.25 atm at room temperature, compared to 3.4×10^{-36} atm for gallium and 0.49 atm for $GaCl_3$ (2). Manasevit and Simpson (3) have reported on the use of organometallics in the preparation of III-V compounds. Manasevit has also reported on some structural aspects of the single-crystal growth of GaAs on a number of single-crystal, insulating, oxide susbtrates (4). In this communication, use of trimethyl gallium for the growth of epitaxial GaAs on gallium arsenide and sapphire substrates is reported.

A conventional horizontal rf heated reactor having a graphite susceptor was used. The substrates used were semi-insulating GaAs of (100) orientation and sapphire of (0001) orientation. The sawed GaAs substrates were lapped with 5μ alumina powder and chemically polished to remove 75μ from the depositing surface. The chemical etchants used were conc H_2SO_4: 30% H_2O_2 : H_2O :: 5:1:1. X-ray topography of the polished wafer indicated that the polished surface is damage free. Sapphire substrates were mechanically polished and annealed in H_2 for 2 hr at 1400°C prior to film growth. The trimethyl gallium [$(CH_3)_3Ga$] sources were used as received from the supplier (typical purity in ppm: Si 50 to 100; Cu, Ag, Ca, Pb, and Na < 1; Mg 1). Palladium-purified hydrogen was bubbled through the trimethyl gallium and was reacted with arsine (AsH_3) to form the epitaxial GaAs layer. The resistivity, the net carrier concentration, and the mobility of these films were measured by van der Pauw technique (5). Examination by reflection and transmission electron diffraction and microscopy was used to assess film perfection. The layers and substrates were also analyzed by a spark source mass spectrometer.

Figure 1 shows a diffraction pattern of a GaAs film grown on GaAs substrates having an (100) orientation. The film was grown at about 700°C using $(CH_3)_3Ga$ and AsH_3 with partial pressures of 7.5×10^{-4} atm and 1.0×10^{-2} atm, respectively. Depending on gas velocity, the growth rate of the films was varied from 0.69 to 0.11 μ/min. The film from which Fig. 1 was obtained was grown at 0.11 μ/min and the resulting surface of the epitaxial layer was extremely smooth and free of any visible defects. Transmission electron microscopy examinations of the films were compared to those obtained from layers grown by a conventional $AsCl_3$-Ga-H_2 system; the appearance of the deposits from the two systems is comparable. Films produced by both processes were found to contain isolated amorphous precipitates. The study of these defects is in progress and the results will be reported subsequently. Figure 2 show an electron diffraction pattern of a GaAs film grown under conditions identical to that of Fig. 1 but on a sapphire substrate. The films were epitaxial, the orientation relationship between film and substrate being

$$(111)_{GaAs} \| (0001)_{Al_2O_3} \text{ and } [1\bar{1}0]_{GaAs} \| [11\bar{2}0]_{Al_2O_3}$$

All the films grown on GaAs substrates were n-type with a net carrier concentration of 2.6×10^{17} to 9.0×10^{17} atoms/cm^3 and a mobility of 1740 to 2550 cm^2/V sec. Most of the films grown on sapphire were found to be n-type (however, hot-probe analysis was not always definitive), with one of the best films having a net carrier concentration of 6.5×10^{17} atoms/cm^3 and a mobility of 2480 cm^2/V sec. The layers were analyzed by a spark source mass spectrometer and the results are compared in Table I with those from a semi-insulating GaAs substrate as well as with epitaxial GaAs from a $AsCl_3$-Ga-H_2 system.

It should be emphasized that the impurity concentrations listed here are essentially surface concentra-

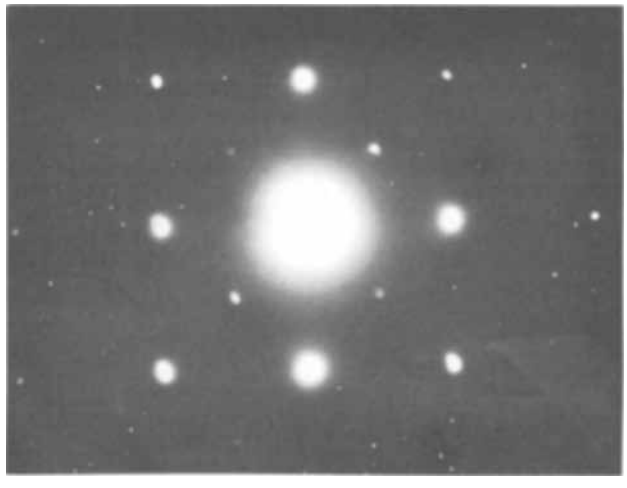

Fig. 1. Transmission electron diffraction pattern of GaAs films grown on semi-insulating GaAs substrate of (100) orientation.

* Electrochemical Society Active Member.

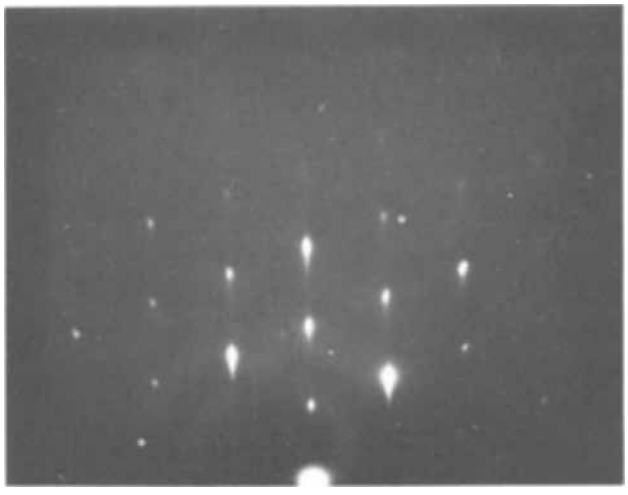

Fig. 2. Reflection electron diffraction pattern of GaAs films grown on sapphire substrate of (0001) orientation; (111)GaAs || (0001) Al_2O_3, [1$\bar{1}$0] GaAs || [11$\bar{2}$0] Al_2O_3.

tion in the case of epitaxial layers and might therefore contain some adsorbed impurities difficult to clean. The impurity concentrations in the substrate material, however, are more reliable since the entire epitaxial layer was sparked off before analysis. Since the carbon contamination level in the present system is comparable with the $AsCl_3$-Ga-H_2 system, it appears that the carbon contamination from the trimethyl gallium is probably insignificant. Metallographic examination of the surface of the epitaxial layers also supports this view. Carbon contamination from TMG is also unlikely from thermodynamic considerations. The over-all reaction may be written as

$$(CH_3)_3Ga(g) + \frac{1}{4}As_4(g) + \frac{3}{2}H_2(g) = GaAs(s) + 3\,CH_4(g)$$

The CH_4 formed may decompose to give graphite and hydrogen. At 1000°K, for example, the equilibrium partial pressure of CH_4 for the reaction

$$CH_4(g) = C(s) + 2\,H_2(g)$$

Table I. Impurity concentrations in GaAs in ppm

Element	Layers from $(CH_3)_3Ga$-AsH_3-H_2 system	Layers from $AsCl_3$-Ga-H_2 system*	Semi-insulating GaAs substrate
C	238.4	100-569	8.79
N	1.78	Not detectable	0.07
O	220.4	307-1042	0.52
Si	4.46	—	0.19
S	1.47	Not detectable	0.27
Fe	1.60	Not detectable	Not detectable
Cu	2.24	Not detectable	Not detectable
Zn	0.89	Not detectable	Not detectable

* The GaAs layer grown in the $AsCl_3$-Ga-H_2 system had a net carrier concentration of 1.1 × 10^{16} atoms/cm³ and a mobility of 3400 cm²/V sec.

is 9.7 x 10^{-2} atm which is considerably above the $(CH_3)_3Ga$ partial pressures used for growth of GaAs. Therefore, CH_4 will not decompose to graphite.

In summary, the epitaxial GaAs produced from trimethyl gallium and arsine is of good quality metallographically, but requires some improvement in purity. The electrical parameters such as mobility and net carrier concentrations of GaAs on sapphire are comparable with those of GaAs grown on semi-insulating GaAs substrates.

Acknowledgments

The author wishes to thank W. Cifone, J. H. Rieger, D. L. Barrett, and Dr. R. W. Ure for assistance with the experimental work.

Manuscript received Aug. 29, 1969.

Any discussion of this paper will appear in a Discussion Section to be published in the June 1970 JOURNAL.

REFERENCES

1. "Proceedings of the International Symposium on Gallium Arsenide," Institute of Physics and Physical Society Conference Series No. 3, Sept. 1966.
2. O. Kubaschewski and E. Evans, "Metallurgical Thermochemistry," Pergamon Press (1958).
3. H. M. Manasevit and W. I. Simpson, Paper 63 presented at Electrochem. Soc. Meeting, Boston, May 5-9, 1968; Extended Abstract, Vol. 5, p. 154.
4. H. M. Manasevit, *Appl. Phys. Letters*, **12**, 156 (1968).
5. L. J. van der Pauw, *Philips Res. Repts.*, **13**, 1 (1958).

The Electrochemical Behavior of Titanium

Effect of pH and Chloride Ions

N. T. Thomas* and Ken Nobe*

School of Engineering and Applied Science, University of California, Los Angeles, California

ABSTRACT

The anodic and cathodic behavior of titanium in sulfuric acid in the absence and presence of chloride ions have been investigated. Two stable corrosion potentials were observed. One was in the active region, the other in the passive region. Neither corrosion potential was appreciably affected by chloride ions or pH changes between pH 0.25-2.00. The corrosion current of active titanium was not affected significantly by chloride ions up to 3.5% NaCl but decreased with increase in pH. Passivation parameters decreased with increase in pH but either remained unchanged or decreased only slightly with addition of chloride ions. The rate of the h.e.r. in the Tafel region was not appreciably affected by chloride ions. The differential capacitance of titanium in solutions of pH 0.25-2.00 ranged from 150 to 200 $\mu f/cm^2$ at the active corrosion potential and was a reasonably constant value, 25 $\mu f/cm^2$, at the passive corrosion potential. For the negative potential range a maximum capacitance, 222 $\mu f/cm^2$ at $-0.490 \pm 0.010V$ *vs.* SCE which was approximately the primary passivation potential, and a minimum capacitance, 73 $\mu f/cm^2$ at $-0.985 \pm 0.012V$, were observed. At potentials more positive than the primary passivation potential, the capacitance decreased monotonically with increase in potential and reached a value of 7 $\mu f/cm^2$ at 3.2V.

Titaninum and titanium alloys are promising new lightweight structural materials with good corrosion resistance in a number of different environments. As a result, there has been a growing literature on the corrosion and passivation behavior of titanium (1-10). This is a study of the anodic behavior of titanium in sulfuric acid solutions of pH from 0.25 to 2.00 in the absence and presence of chloride. In addition, the effect of chloride ions on the hydrogen evolution reaction has been examined.

Experimental

Electrodes made from Ti 65A (TMCA) were used for the experiments. The analysis of the impurities was given by TMCA as 0.023%C, 0.25%Fe, 0.01% N_2, 0.005% H_2, and 0.2% O_2. Cylindrical electrodes of about 1.4 cm in length were cut from 1.25-cm diameter rod. The surface area of each electrode was about 5.5 cm^2. A smooth electrode surface was obtained by slicing the surface on a lathe with a carbide cutting tool. The electrodes were degreased with hot benzene in a soxhlet column for at least 4 hr, then annealed under vacuum at 700°C for 1 hr and furnace cooled. After this, the electrodes were stored in a desiccator until use.

A description of the instrumentation, the electrochemical cell, and the electrode assembly have been given previously (11). Anodic polarization was performed potentiostatically with an Anotrol Controller (Model 4100). Galvanostatic polarization was used for the study of the h.e.r. Electrode potentials were measured with Keithley Electrometers (Model 602 and 610B). Differential capacitances were determined with the d-c pulse method.

Solutions of 1*N* H_2SO_4 were prepared by diluting reagent-grade concentrated sulfuric acid with double-distilled water. Solutions of different pH values were then obtained by adding appropriate quantities of 20*N* NaOH to the 1*N* H_2SO_4 solutions. The chloride solutions were prepared by adding appropriate amounts of sodium chloride to solutions of 1*N* H_2SO_4.

The solutions were deaerated with prepurified nitrogen for at least 12 hr before an experimental run. The electrodes were activated in 1*N* HF for 1 min, generously washed with double-distilled water, and then introduced into the deaerated solution. The electrode was rotated continuously with a tangential velocity of 6.6 cm/sec. The corrosion potential was monitored until steady state was achieved for at least 2 hr. Then, polarization of the electrode was begun. The temperature of the cell was maintained at 24° ± 1°C. Saturated calomel electrodes were used as reference electrodes.

Results and Discussion

Steady state was achieved within 2 min for anodic polarization between the corrosion potential and the primary passivation potential. Between the latter and the Flade potential, 10-20 min were required to reach steady-state conditions. In the passive region, ½-1 hr were required. For each experimental point, polarization was observed for at least an additional 5 min after steady state was observed and occasionally, as a check, polarization was maintained an additional 3 hr. For cathodic polarization, the hydrogen evolution reaction in the Tafel region reached steady state within 5 min at each polarization point.

Open-circuit behavior.—The corrosion potentials for nonactivated electrodes in 1*N* H_2SO_4 ranged between 400-700 mV *vs.* SCE indicating self-passivation when titanium was immersed in the electrolyte. A few electrodes were observed to self-activate, and a typical case is shown in Fig. 1. A similar potential-time behavior was observed by Tsvetnova *et al.* (6) for high-

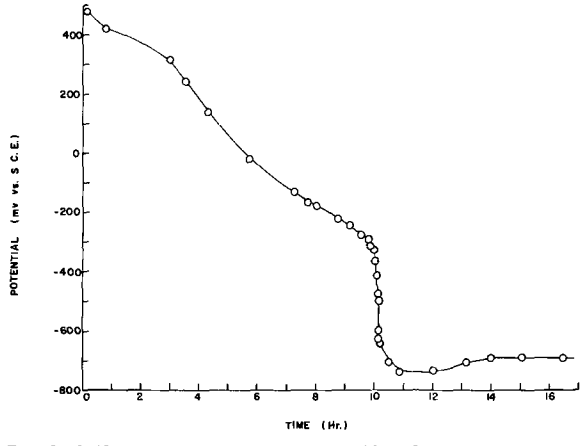

Fig. 1. Self-activation of titanium in 1*N* H_2SO_4 from the passive corrosion potential.

* Electrochemical Society Active Member.

Table I. Effect of pH on the electrochemical behavior of titanium

pH	Active corrosion potential	Corrosion current	Passive corrosion potential	Primary passivation potential	Critical current	Passive current at 800 mV	Capacitance at active corrosion potential	Capacitance at passive corrosion potential
	mV *vs.* SCE	μA/cm^2	mV *vs.* SCE		μA/cm^2		μf/cm^2	
0.25	−680 ± 10	9.0 ± 0.7	650 ± 20	−520	22.6 ± 1.5	0.50 ± 0.02	150 ± 10	23 ± 1
0.50	−675	6.0	670	−540	12.7	0.40	195	25
1.00	−665	2.9	680	−560	3.5	0.33	202	28
1.50	−675	2.0	680	−600	2.5	0.27	205	20
2.00	−700	1.1	685	−630	0.8	0.22	198	25

purity titanium in 5*N* H_2SO_4. However, they observed an activation time which was much shorter than the ones in this investigation, indicating that the activation time increases with increase in pH.

The corrosion potentials of electrodes activated in 1*N* HF were considerably more negative than the corrosion potentials of electrodes which self-passivated. Table I gives both the active and passive corrosion potentials of titanium in solutions ranging from pH 0.25 to 2.00 and shows that there was no significant dependence of the corrosion potentials of titanium with pH. These are in accord with those of other investigators (2, 12). Peters and Myers (2), who activated their electrodes by cathodic polarization, observed a small pH dependence of the active corrosion potential.

After anodic polarization of titanium in the pH range studied, the electrode remained passive. An active corrosion potential could be obtained again by cathodic polarization. These results along with those of Schlain *et al.* (12), who obtained active corrosion potentials by conducting experiments on titanium in deaerated solutions lasting 15 days, indicate that in sufficiently acidic solutions passive titanium will eventually become active at open circuit. The activation process is accelerated by cathodic polarization, and almost instantaneous activation is achieved by a brief immersion of titanium in HF.

For pH solutions of 2.00 and above, active corrosion potentials could not be achieved within a reasonable time duration by either cathodic polarization or activation in HF. The corrosion potential of titanium (activated in HF) in pH solutions of 2.00 was approximately 50 mV above the primary passivation potential immediately after immersion. Thereafter, the corrosion potential increased slowly with time until the stable steady-state passive corrosion potential was achieved. However, active corrosion potentials for this pH could be achieved by first activating titanium in HF, immersing in 1*N* H_2SO_4, and then adjusting the pH by the addition of a concentrated solution of NaOH.

The corrosion currents of active titanium were determined by extrapolation of the Tafel line for the h.e.r. to the corrosion potential. As shown in Table I, the corrosion current decreased with increase in pH.

Anodic and cathodic behavior of titanium in the absence of chloride ions.—The anodic behavior of titanium in sulfuric acid at various pH values is shown in Fig. 2. The critical current densities, I_{cc}, the primary passivation potentials, ψ_{pp}, are shown in Fig. 3 and 4, and the passive current densities are presented in Table I. It is shown that these parameters decrease with increase in pH in accord with the results obtained by others (1-5). As shown in Fig. 3 and 4, the values of $\partial\psi_{pp}/\partial pH = -0.06V$ with $\partial \log I_{cc}/\partial pH = -0.84$, where I_{cc} is in μA/cm^2, were obtained in this investigation for the pH range between 0.25-2.00. These results were in good agreement with those of Peters and Myers (2) who obtained $\partial\psi_{pp}/\partial pH = -0.06V$ and $\partial \log I_{cc}/\partial pH = -0.77$ for titanium in sulfuric acid solutions of higher concentrations than those used in this investigation.

The primary passivation potential of titanium in 1*N* H_2SO_4 was in agreement with Tsvetnova and Krasil'shchikov (8) but their critical current was greater than that observed in this investigation. Passive currents were in agreement with the latter investigators but were lower than the values of Peters and Myers (2) since their results were not obtained at steady-state.

The cathodic polarization of titanium in 1*N* H_2SO_4 is shown in Fig. 5. The Tafel slope and exchange current density for the hydrogen evolution reaction were 150 mV and 1.7 x 10^{-8} A/cm^2, respectively. It is seen that at about −1.0V, the experimental polarization points begin to deviate from the linear Tafel curve of the h.e.r. suggesting the inception of another electrode reaction. Steady state for each experimental point at current densities exceeding the linear Tafel region was achieved in 10-15 min compared to the 5 min required within the Tafel region. The complete set of results and the analysis of the kinetics of the h.e.r. on titanium will be given elsewhere (13).

Effect of chloride ions.—Figure 5 shows the effect of chloride ions on the cathodic polarization of titanium

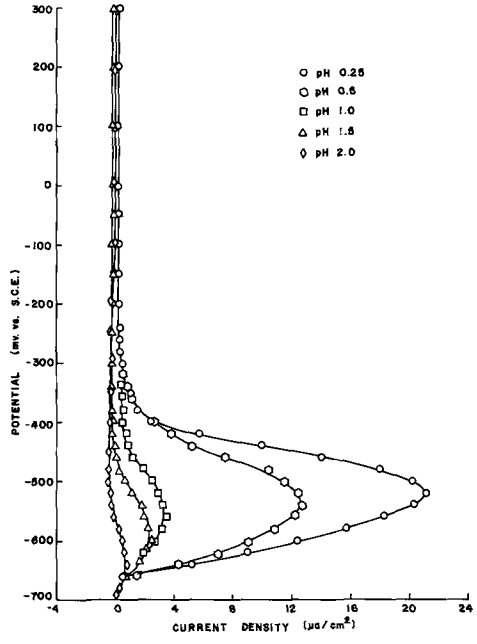

Fig. 2. Effect of pH on anodic behavior

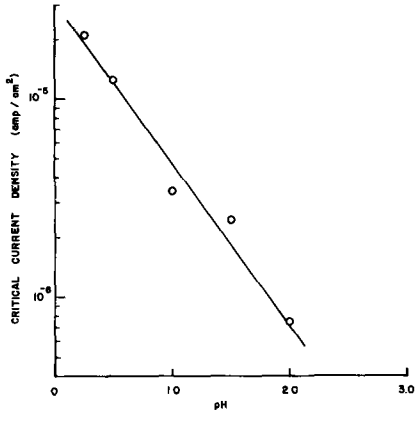

Fig. 3. Effect of pH on the critical current density

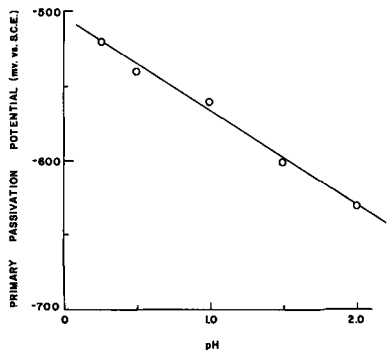

Fig. 4. Effect of pH on the primary passivation potential

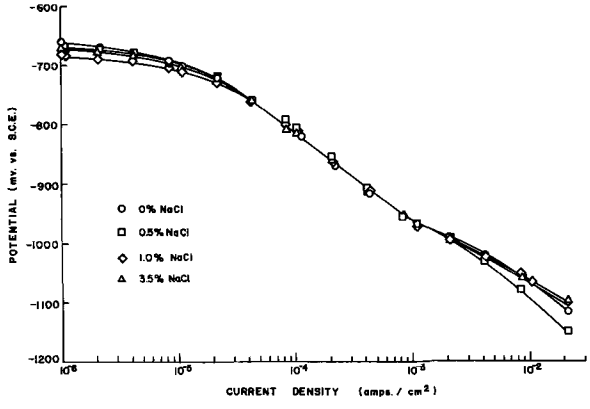

Fig. 5. The effect of chloride ions on cathodic polarization of titanium in 1*N* H_2SO_4.

in 1*N* H_2SO_4. As shown, chloride ions have no appreciable effect on the electrochemical behavior of titanium in the Tafel region of the h.e.r. However, in the low and high current density range, chloride ions have a small effect. Table II shows that the corrosion current was not affected significantly with addition of chloride ions.

The effect of chloride ions on the anodic behavior of titanium in 1*N* H_2SO_4 is shown in Fig. 6. The passivation parameters at each chloride ion concentration are presented in Table II. The active and passive corrosion potentials and the primary passivation potentials of titanium were not appreciably affected by chloride ions even for 5.8% NaCl. There was a slight decrease in the critical current density of titanium in the presence of chloride ions which was also observed by Levy (1). At the potential of 800 mV, which was well within the passive region, there was a small decrease in the passive current density with increase in chloride ions. That is, chloride ions facilitated the anodic passivity of titanium.

The above result was further substantiated by the following experiment. First, titanium in 1*N* H_2SO_4, initially at the active corrosion potential, was passivated by potentiostatically changing the potential of the electrode to 800 mV *vs.* SCE. After the steady-state passive current was attained, a small known amount of a concentrated sodium chloride solution (1*N* H_2SO_4)

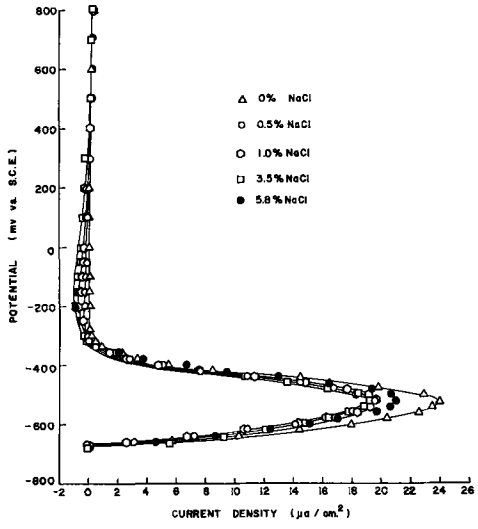

Fig. 6. Effect of chloride ions on the anodic behavior of titanium in 1*N* H_2SO_4.

was added to the electrolyte. Then, the new steady-state passive current was measured. The same procedure was followed after each incremental addition of concentrated sodium chloride solution. The result of this experiment also showed that the passive current density decreased with increase in the concentration of chloride ions.

In general, the passivation characteristics of titanium were more greatly affected by pH changes than changes in the concentration of chloride ions in accord with the results of Griess (4).

In the lower potential range of the passive region, a small cathodic current, which increased with increase in chloride ions, was observed, indicating a net reduction reaction in this potential range.

Subsequent to anodic polarization of titanium in the presence of chloride ions, the passive corrosion potential was assumed. Extensive cathodic polarization could not reactivate titanium to the active corrosion potential in contrast to the results of titanium in the absence of chloride ions.

Differential capacitance.—The capacitances of titanium at the active and passive corrosion potentials in the absence and presence of chloride ions are presented in Tables I and II. Table I shows that the capacitance of titanium in a solution of pH 0.25 was 150 ± 10 $\mu f/cm^2$ which is unusually large for the double-layer capacitance. In the pH range of 0.50-2.00, the capacitance remained essentially constant at 200 $\mu f/cm^2$. This large capacitance at the active corrosion potential may be a pseudocapacitance due to an adsorbed electroactive intermediate (*e.g.*, hydrogen atoms) (14, 15). On the other hand, the capacitance at the passive corrosion potential was approximately 25 $\mu f/cm^2$ throughout the pH range investigated.

In the presence of chloride ions up to 1% NaCl, the capacitance of titanium at the active corrosion potential, as shown in Table II, was the same as in the absence of chloride ions. However, for 3.5 and 5.8% NaCl solutions,

Table II. Effect of chloride ions on the electrochemical behavior of titanium (pH = 0.25)

% NaCl	Active corrosion potential	Corrosion current	Passive corrosion potential	Primary passivation potential	Critical current	Passive current at 800 mV	Capacitance at active corrosion potential	Capacitance at passive corrosion potential
	mV *vs.* SCE	$\mu A/cm^2$	mV *vs.* SCE		$\mu A/cm^2$		$\mu f/cm^2$	
0	−680 ± 10	9.0 ± 0.7	650 ± 20	−520	22.6 ± 1.5	0.50 ± 0.02	150 ± 10	23 ± 1
0.5	−670	10.0	650	−520	19.6	0.45	147	22
1.0	−675	11.0	640	−520	19.7	0.45	150	23
3.5	−675	11.0	665	−520	19.2	0.44	138	22
5.8	−680	—	680	−520	21.0	0.33	132	21

the capacitance of titanium decreased slightly. Table II shows that, at the passive corrosion potential, the capacitance of titanium remained essentially the same in the absence and presence of chloride ions.

The capacitance *vs.* potential behavior in the potential range from −1.15 to 3.2V *vs.* SCE is shown in Fig. 7. A capacitance maximum and minimum were observed in the negative potential range. The maximum capacitance, observed at −0.490 ± 0.010V which was approximately the primary passivation potential, was 222 μf/cm^2. The minimum capacitance, observed at −0.985 ± 0.012V, was 73 ± 2 μf/cm^2. As shown in Fig. 5, the deviation from the Tafel line for the h.e.r. commenced at approximately the potential of the capacitance minimum. It is interesting to note that this potential corresponds closely to the potential of zero charge for titanium, −0.945V *vs.* SCE, calculated by Antropov (16). However, at present, no significance is attached to the agreement between this p z c value and the potential at the capacitance minimum. Further investigation of this point is in progress.

The capacitance behavior between 0-3.2V (C = 7 μf/cm^2 at 3.2V) was in good agreement with the results of Kuznetsova *et al.* (17). As do the latter workers, it seems reasonable to attribute this decrease in capacitance in the above potential range to the increase in thickness of the oxide film. Thomashov *et al.*'s analysis of the passive film on titanium indicated that, for the passive potential range of this investigation, the surface was covered with a mixed oxide of Ti_2O_3 and TiO_2 (18).

The capacitance behavior in the neighborhood of the primary passivation potential was similar in magnitude and shape to the faradaic capacitance of titanium in 5*N* H_2SO_4 determined by Brynza *et al.* (19) with a-c impedance measurements. These investigators utilized an equivalent circuit model of the double-layer capacitance in parallel with the faradaic impedance which consisted of the faradaic capacitance and faradaic resistance in series. For the potential range in the neighborhood of the active-passive transition, Vorob'ev and Ershler (7) observed that the double-layer capacitance of titanium in sulfuric acid was reasonably constant at approximately 25 μf/cm^2. In view of this result, it seems reasonable to assume that the large capacitances observed in the active-passive transition potential range and obtained by the d-c pulse method correspond to a faradaic capacitance or, more specifically, an adsorption pseudocapacitance.

Two linear regions in the potential-time curve would be observed when a d-c current pulse is passed through a circuit equivalent to that described above for a-c impedance measurements. Since the d-c current pulse was developed by a mechanical pulser (11) with a rise time slower than 10 μsec, the initial part of the potential transient, which was the charging curve for the double-layer capacitor, could not be obtained. The second linear region, which occurs at a later time than the first, corresponds to the faradaic capacitance (pseudocapacitance, in this case). This pseudocapacitance has been surmised to result from adsorption of an electroactive species which initiates the passivation of titanium (19).

Conclusion

1. Titanium in deaerated H_2SO_4 exhibited a stable passive corrosion potential and a stable active corrosion potential.

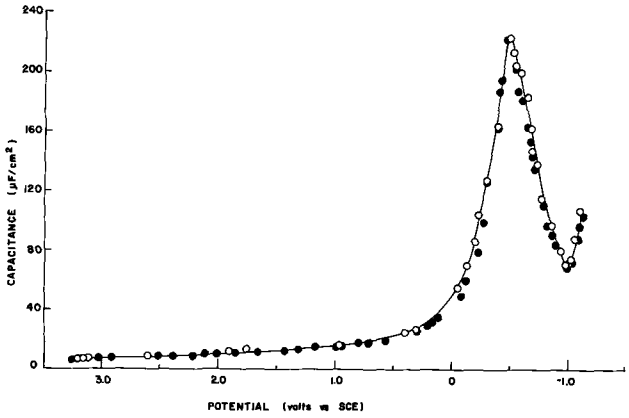

Fig. 7. Differential capacitance vs. potential for titanium in 1*N* H_2SO_4.

2. The passivation characteristics of titanium in H_2SO_4 were dependent on the pH, but did not vary appreciably with the concentration of chloride ions.

3. The capacitance-potential behavior of titanium in 1*N* H_2SO_4 showed a maximum at −0.490 ± 0.010V and a minimum at −0.985 ± 0.012V.

Acknowledgment

This work is part of the continuing University of California research program in sea water desalination.

Manuscript submitted May 19, 1969; revised manuscript received *ca.* Aug. 10, 1969. This was Paper 406 presented at the Montreal Meeting, Oct. 6-11, 1968.

Any discussion of this paper will appear in a Discussion Section to be published in the June 1970 JOURNAL.

REFERENCES

1. M. Levy, *Corrosion*, **23**, 236 (1967).
2. J. M. Peters and J. R. Myers, *ibid.*, **23**, 326 (1967).
3. M. Stern and H. Wissenberg, *This Journal*, **106**, 755 (1959).
4. J. C. Griess, *Corrosion*, **24**, 96 (1968).
5. N. D. Tomashov, G. P. Chernova, and R. M. Al'tovskii, *Russ. J. Phys. Chem.*, **35**, 523 (1961).
6. R. V. Tsvetnova, S. L. Dyatkina, S. N. Sheremet'eva, A. R. Kel'n, and A. I. Krasil'shchikov, *ibid.*, **37**, 544 (1963).
7. V. N. Vorob'ev and B. V. Ershler, *ibid.*, **38**, 1072 (1964).
8. R. V. Tsvetnova and A. I. Krasil'shchikov, *ibid.*, **39**, 109 (1965).
9. A. P. Brynza and V. P. Fedash, *Protection of Metals*, **4**, 228 (1968).
10. M. Levy and G. N. Sklover, *This Journal*, **116**, 323 (1969).
11. R. R. Sayano and Ken Nobe, *Corrosion*, **22**, 81 (1966).
12. D. Schlain, C. B. Kenahan, and D. V. Steele, *This Journal*, **102**, 102 (1955).
13. N. T. Thomas and Ken Nobe, *ibid.*, To be submitted.
14. J. O'M. Bockris and H. Kita, *ibid.*, **108**, 676 (1961).
15. B. E. Conway and E. Gileadi, *Trans. Faraday Soc.*, **58**, 2493 (1962).
16. A. T. Petrenko, *Russ. J. Phys. Chem.*, **36**, 815 (1962).
17. E. G. Kuznetsova, T. I. Borisova, and V. I. Veselovskii, *Soviet Electrochemistry*, **4**, 142 (1968).
18. N. D. Tomashov, R. M. Al'tovskii, and M. Ya. Kushnerev *Dokl. Akad. Nauk. SSSR, Phys. Chem. Section*, **141**, 927 (1961) (Transl.).
19. A. P. Brynza, V. P. Fedash, and V. N. Kovtun, *Protection of Metals*, **2**, 31 (1966).

Orientation Dependence of the Aluminum Oxide Dielectric in Film Capacitors

Ferenc E. Rosztoczy*,[1] and Mildred H. Read

Bell Telephone Laboratories, Incorporated, Murray Hill, New Jersey

ABSTRACT

An investigation of the anodization of evaporated aluminum films and the reliability of aluminum oxide film capacitors made with and without a manganese oxide layer between the dielectric and the metal top electrode has been made. A correlation appears to exist between the degree of orientation of the polycrystalline aluminum film and the anodization characteristics or performance of the capacitors. The dielectrics with the highest anodization voltages or those which resulted in the highest performance capacitors were formed on the most randomly oriented aluminum films.

It has been demonstrated that the addition of a semiconducting layer of manganese oxide between the dielectric and the metal top electrode improves those properties of film capacitors which are dependent on the dielectric strength (1, 2). As a result, tantalum film capacitors with manganese oxide (TMM capacitors: Substrate—Ta-Ta_2O_5-MnO_x-Metal) show lower leakage currents and excellent performance during accelerated life testing at 50% of the formation voltage and 85°C (3). The self-healing property of the TMM capacitor structure also permits the use of larger areas and lower formation voltages, either of which results in larger capacitance values (1). It also allows the fabrication of tantalum oxide film capacitors on substrates with rough surfaces. Preliminary results indicated similar improvements in yield and life test performance when a manganese oxide layer is added to thin-film capacitor structures based on evaporated SiO or anodic Al_2O_3 dielectric (2). Aluminum oxide capacitors did occasionally exhibit low yields and poor performance (4, 5), and sometimes aluminum films could not be anodized to voltages over 100V (6). It is the purpose of this paper to describe the properties of aluminum oxide film capacitors formed on smooth glass as well as on unglazed ceramic substrates, and to show that the quality of the finished aluminum oxide film capacitors with and without the addition of manganese oxide layer between the anodic film and the counter-electrode depends to a large extent on the degree of orientation of the aluminum film.

The advantage of using aluminum instead of tantalum for thin-film capacitors would be its higher conductivity, which makes it more desirable for high-frequency applications. Its shortcoming is the significantly smaller dielectric constant [21-28 for the tantalum oxide (7, 8) *vs.* 8-11 for aluminum oxide (5, 8)].

Experimental

Figure 1 shows the 15 spot test pattern and the cross section of an AMM capacitor structure. One- by three-inch glass (Corning #7059) or unglazed high alumina ceramic slides (American Lava #614) were used as substrates. The aluminum pattern was usually generated with photoetching techniques using KMER with J100 stripper to remove the KMER without scratching the aluminum. In some cases, the aluminum pattern was evaporated through a mask. To obtain adherent aluminum films, it was important to use freshly cleaned slides and to degas them prior to the deposition of the aluminum film. The cleaning of the slides included an ultrasonic wash in a cold and then in a 75°C Igepal 710 solution (Antara Chemical Company), a boil in 10% hydrogen peroxide, and finally a rinse in overflowing, boiling, deionized water.

The aluminum films were anodized in 30% ammonium pentaborate ethylene glycol solution at room temperature. The anodization voltage was gradually increased during a 10-15 min period to the desired value which was maintained for 30 min. During anodization on certain aluminum films, slow oxygen gas formation started around 100V, which increased if the voltage was raised further. The capacitors on these slides had low breakdown voltages. Within each aluminum evaporation group, the slides tended to behave similarly during anodization.

Study of the x-ray wide-film Debye-Sherrer diffraction photographs of aluminum slides having different anodization characteristics showed that, while the aluminum oxide was amorphous in all cases, there was significant difference in the degree of (111) crystal orientation of the aluminum films. That is the degree to which the (111) plane is parallel to the substrate surface, or, alternatively, the degree to which the [111] fiber axis is normal to the substrate surface. Three typical x-ray diffraction pictures for aluminum films evaporated on glass substrates are presented in Fig. 2. Picture a represents slides where the aluminum exhibits the least orientation. Most of the lines are uniform in intensity, although the (111) line shows an arc. Picture c shows only arcs indicating a high degree of orientation, while picture b is typical for the "in between" slides. The lines are continuous but strongly arced.

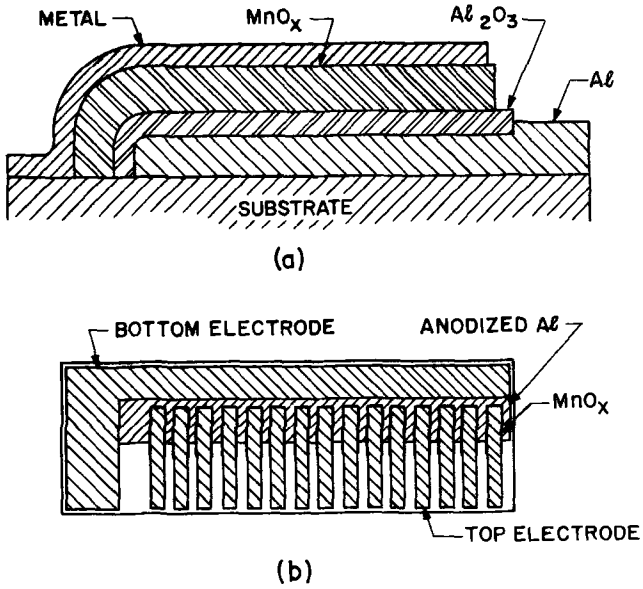

Fig. 1. (a) Cross section of AMM capacitor, (b) 15 spot capacitor pattern.

* Electrochemical Society Active Member.
[1] Present address: Varian Associates, Palo Alto, California.

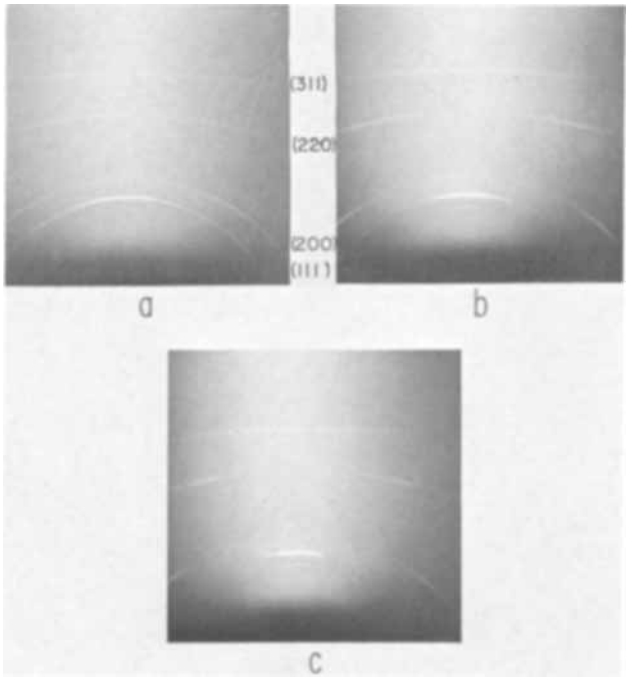

Fig. 2. X-ray photographs showing the different degree of (111) orientation in aluminum film: (a) least oriented—continuous lines with gentle arcing, (b) medium oriented—continuous lines with strong arcing, (c) most oriented—no continuous lines, only arcs.

The sharp lines would indicate a crystallite size of about 1000Å with some larger crystals giving rise to spots. In all the samples, the (111) line is stronger than expected for randomly oriented material and a certain degree of orientation appears to be present in all samples as shown by the tendency of the (111) line to appear as an arc.

Electron micrographs of platinum-carbon replicas of the aluminum film surface indicate that the crystallites are generally around 2000Å, but in each sample there are crystals about 3000-5000Å in diameter and these are much thicker than the bulk of the film (Fig. 3). The area of these larger crystals is about 1-5% of the total area. The crystallite faces tend to be parallel to the surface of the substrates. The planes on the less oriented films make larger angles to the substrate than on the more oriented films. In the case of the oriented samples, with the flattest planes, the crystallites seem to merge together in some instances (Fig. 3b).

The oxygen formation around 100V occurred on the aluminum films with the highest degree of (111) orientation, while aluminum films having a low degree of preferred orientation could be anodized to over 300V without oxygen evolution.

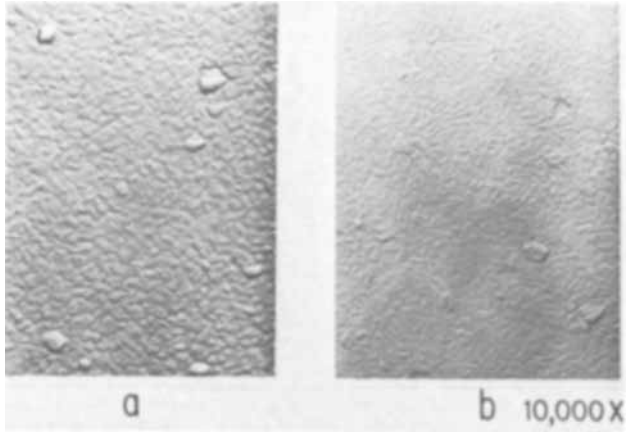

Fig. 3. Electron microscope photographs showing the effect of different degree of (111) orientation in aluminum film: (a) least oriented—planes make larger angles to substrate, (b) most oriented—planes more nearly parallel to substrate. 5500X.

A preliminary study of the evaporation conditions for aluminum films indicated that those films showing the least orientation (consequently, the most suitable ones for capacitor fabrication) were deposited in the following manner:

(a) The slides were heated to 250°C under vacuum.

(b) At a pressure in the 10^{-6} Torr range, a few hundred Angstroms of aluminum were evaporated on the hot substrate.

(c) The slides were cooled to room temperature in an argon atmosphere of about 0.2 Torr.

(d) The system was evacuated again to less than 10^{-5} Torr, and aluminum, sufficient to form 5000Å film, was evaporated on the unheated aluminum coated substrates.

A Ta_2O_5 or Ti layer on the glass substrate did not seem to affect the degree of orientation of the aluminum films.

The manganese oxide was deposited pyrolytically, by spraying an aqueous solution of 2% Mn $(NO_3)_2$ with 5% Superoxol (H_2O_2) onto the anodized aluminum-coated substrates whose temperature was maintained at about 200°C. The thickness of the resulting manganese oxide was varied between 2000 and 8000Å. The pattern of the manganese oxide was etched in HNO_3-H_2O_2 solution after the top electrodes, aluminum, gold, or nichrome-gold, had been evaporated through a mechanical mask.

Results

Yield of 15 spot AMM capacitors (AMM: Substrate—Al-Al_2O_3 MnO_x-Metal electrode).—During the preparation of the capacitors, it was found that a high degree of (111) orientation of the aluminum films seemed to limit the formation voltage. The aluminum films were, therefore, split into three groups according to the degree of orientation (*see* Fig. 2). Table I summarizes the initial yields which were obtained for 5000-pf capacitors formed at 130V on the three different types of aluminum films using the 15 spot test pattern shown in Fig. 1(b). The yield is based on the percentage of capacitors with a leakage current of less than 1 A/f at 75V. The table also lists the percentage of shorted capacitors and the average leakage current of the capacitors.

The results indicate that the degree of orientation of the aluminum films has a significant influence on the yield and the number of shorts of the aluminum oxide film capacitors. When the MnO_x was deposited at 170°C, the yield dropped from 100% found for films with a low degree of orientation to less than 50% for films with the highest degree of orientation. Raising the spraying temperature to 245°C also results in lower yields and in 4-10 times higher leakage currents, with this effect being more pronounced for capacitors formed on films showing a high degree of orientation.

Yield of 15 spot AM capacitors (AM: Substrate—Al-Al_2O_3-Metal electrode).—The observation that the

Table I. Effect of crystal orientation and spraying temperature on the properties of AMM capacitors (130V anodization, gold top electrode)

No. of capacitors	Degree of orientation	Spraying temp, °C	Shorts at 75V, %	Yield at† 75V, %	I_{75}* NAmp
30	Least	170	0	100	0.05
30	oriented	245	0	97	0.18
45	Medium	170	0	100	0.76
30	oriented	245	3.3	93.5	7.80
15	Most	170	6.7	47	36
15	oriented	245	76.7	0	—

† Percentage of capacities with leakage currents at 75V less than 1 A/f.

* I_{75}: Average leakage current at 75V in amperes/farad.

crystal orientation in the metal film has an important effect on the anodization properties of the aluminum suggested that it might be possible to use the less oriented aluminum films as determined by anodization characteristics for the development of aluminum oxide film capacitors without a layer of manganese oxide. Table II presents data for AM capacitors on glass, and on glass with either a layer of 500Å of titanium or Ta_2O_5. Both layers had initially been introduced to improve the adherence of the aluminum film to the glass substrate. The yield for the AM capacitors on glass substrates was 97% at 75V and the average leakage was about 0.7×10^{-9}A. (The slides were anodized to 130V.) Even at 100V, 90% of these capacitors had leakage currents in the 10^{-9}A range. The results were similar for AM capacitors on glass with a Ta_2O_5 layer. However, a titanium layer between the glass and the aluminum resulted in a lower yield (55% at 75V) and leakage currents which were about 10-15 times higher. This was attributed to the fact that the ammonium pentaborate-ethylene glycol used to anodize the Al is not a suitable anodizing solution for titanium at higher voltages, and the metallic titanium which was unprotected by Al_2O_3 (because of pinholes on the aluminum film) was responsible for the high leakages.

Life test performance of 15 spot AMM and AM capacitors.—AMM capacitors using the less oriented aluminum films formed at 130V with gold top electrodes were life tested at 85° and 110°C for 16 weeks. Testing voltages of 50, 65, and 70V and −20V were applied between the aluminum and the top electrode. The results of the life tests are presented in Table III. No failures occurred in 16 weeks at 50V, 85°C, or −20V, 85°C; 97% of the capacitors survived the test period at 65V, 85°C. About 7% failure occurred at 50V, 110°C, and 65V, 110°C; 90% of the capacitors survived 70V, 85°C for 16 weeks. These results are very similar to those reported for TMM capacitors formed at the same anodization voltage (9). But it should be mentioned that AMM capacitors have only about half the capacitance density (0.044 μf/cm²) as TMM capacitors (0.1 μf/cm²) if the same formation voltage is used. In the case of the reverse voltage where the aluminum was negative, the AMM capacitors survived 20V for 16 weeks at 85°C, indicating that these capacitors are less unsymmetrical than the tantalum film capacitors.

Table IV presents accelerated life test results for AM capacitors anodized at 130V. No failures were observed for 4 weeks at 50V, R.T., or at 50V and 85°C, or at 30V, 110°C for the capacitors that had no underlay. For the AM capacitors with Ta_2O_5 underlay, no failures were observed at 30V, 110°C, or at 40V, 85°C. One out of 13 capacitors failed in 4 weeks at 60V and 85°C. One out of 13 capacitors failed in 4 weeks at 50V and 85°C. The AM capacitors with titanium underlay showed similar results. No failures were observed at 30V and 85°C, or at 30V and 110°C; one out of 13 failed at 50V and 85°C.

Table II. Properties of AM capacitors. Effect of Ta_2O_5 or Ti underlay (130V anodization, 5000 pf, gold top electrode, 0.007 DF)

Underlay	75 Volts Shorts, %	75 Volts Yield, %	75 Volts Leakage current*	100 Volts Shorts, %	100 Volts Yield, %	100 Volts Leakage current*	No. tested
None	0.8	97	0.14	1.7	90	0.4	120
Ta_2O_5	1.0	97	0.1	1.0	91	0.4	105
Ti	1.3	55	1.8	1.3	25	4.4	75

* The leakage current is in amperes/farad.

Table III. 16 Weeks accelerated life test results of AMM capacitors (130V anodization, gold top electrode)

Voltage, d.c.	Temp, °C	Survivors, %	No. of capacitors tested
50	85	100	30
50	110	93	30
65	85	97	60
65	110	93	45
70	85	90	30
−20*	85	100	15

* Aluminum negative.

Table IV. 4 Weeks accelerated life test results of AM capacitors (130V anodization, gold top electrode)

Voltage, d.c.	Temp, °C	Failures	No. of capacitors tested	Underlay
30	85	0	14	None
30	110	0	15	None
40	85	0	14	None
50	25	0	15	None
50	85	0	11	None
30	110	0	15	Ta_2O_5
40	85	0	15	Ta_2O_5
50	85	1	13	Ta_2O_5
30	85	0	14	Ti
30	110	0	15	Ti
50	85	1	13	Ti

Large AMM capacitors.—The excellent results found for the 5000-pf capacitors with an area of 0.1 cm² indicated that aluminum films showing a low degree of orientation might be suitable for the preparation of much larger capacitors by using larger areas and lower anodization voltages as for the TMM type (1, 3).

Two small groups of AMM capacitors on glass substrates and anodized to 130V, between 0.07 and 0.32 μf in size, were put on life test at 50V and room temperature for 1 week. The voltage was then raised weekly by 10V. The results presented in Fig. 4 indicate that no failures occurred below 110V. In the first group of four with an average size of 1.6 cm², 0.07 μf, corresponding to a capacitance density of about 0.044 μf/cm², the first failure occurred at 110V and two capacitors survived 140V for 3 days. In the second group of six capacitors, with an average size of 7.2 cm², 0.32 μf, no failures occurred within 8 weeks, by which time the test voltage had been increased to 120V. Four capacitors on unglazed alumina substrate which showed a 25% higher capacitance density were life tested at 50V and room temperature. All survived 16 weeks.

The possibility of using lower anodization voltages for obtaining high capacitance density AMM capacitors has also been investigated. Four AMM capacitors, between 1 and 1.5 μf in size (5-7 cm²) were prepared on glass substrates using 25V anodization. The finished capacitors were put on life test for 4 weeks at 10V and room temperature, and at 20V for an additional 4 weeks. All capacitors survived the 8 weeks of testing (*see* Fig. 5).

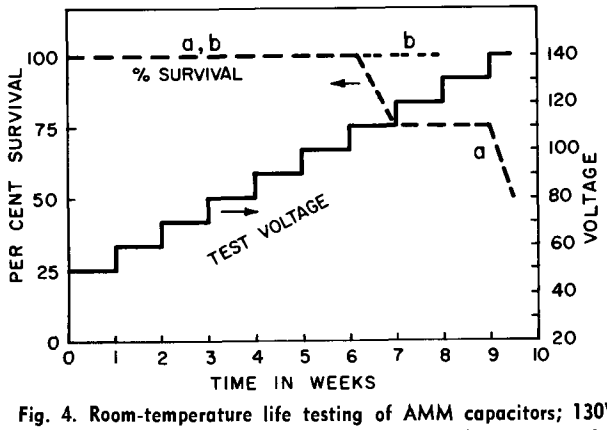

Fig. 4. Room-temperature life testing of AMM capacitors; 130V anodization, aluminum top electrodes: (a) 4 samples, average size 0.7 μf; (b) 6 samples, average size 0.32 μf.

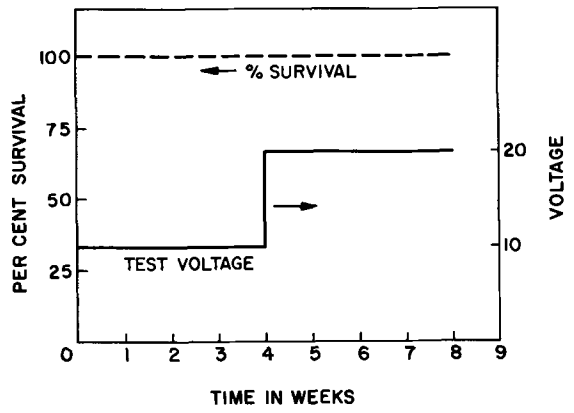

Fig. 5. Room-temperature life testing of AMM capacitors; 25V anodization, aluminum top electrodes, size 1-1.5 μf, 4 samples.

Effect of Anodization Voltage on the Properties of Aluminum Oxide Film Capacitors

In order to gain more information about the anodization behavior of evaporated aluminum films, a number of samples on glass substrates were anodized to 25, 130, 200, and 300V using the usual 30% ammonium pentaborate-ethylene glycol solution. In Fig. 6 the reciprocal capacitance density for the different anodization voltages has been plotted *vs.* the formation voltage. As in the case of tantalum oxide film capacitors, the reciprocal capacitance shows a linear dependence on the formation voltage.

As contrasted with the tantalum oxide film capacitors (10), the performance of the aluminum oxide film capacitors improves with increasing anodization voltage, at least up to 300V.

The results listed in Tables V and VI show how the anodization voltage affects the leakage current, the yield, and the number of shorts of AM and AMM capacitors. Analysis of the results for the AM capacitors shows that the leakage current remains below 1 A/f for all three formation voltages when the capacitors are measured at 75% of the formation voltages. For the AMM capacitors, the voltage where the current exceeds 1 A/f is lower than the AM type and it appears to be closely related to the reforming voltage which is about 70% of the formation voltage. The correlation is especially noticeable in the case of the 300V capacitors where the AMM capacitors were reformed at 210V. Below 210V the AMM type shows lower leakage currents than the AM capacitors and better yield, but at 225V the average leakage current is 200 $\times$ 10^{-9}A for the AMM *vs.* 3 $\times$ 10^{-9}A for the AM capacitors.

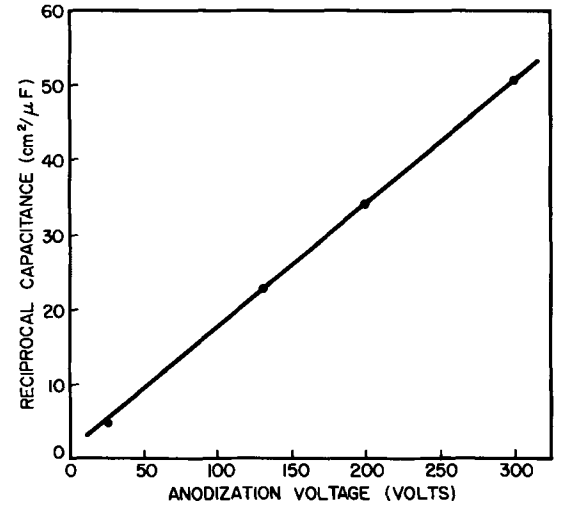

Fig. 6. Change of reciprocal capacitance as a funtion of anodization voltage for aluminum thin film capacitors.

Table V. Leakage current (amperes/farad) of AM and AMM capacitors, anodized to different voltages

Anod. volt.	Cap. type	50V	75V	100V	125V	150V	175V	200V	225V
130	AM	0.036	0.08	0.36	—	—	—	—	—
200	AM	0.024	0.04	0.12	0.18	1.0	—	—	—
300	AM	—	0.04	0.06	0.10	0.11	0.17	0.37	1.0
130	AMM	0.018	0.03	0.12	5[1]	—	—	—	—
200	AMM	0.012	0.03	0.10	1.2	32[2]	—	—	—
300	AMM	0.01	0.017	0.02	0.02	0.05	0.09	0.12	67[3]

[1] Reformed only to 110V.
[2] Reformed only to 130V.
[3] Reformed only to 210V.

Table VI. Initial yield of AM and AMM capacitors anodized to different voltages

Anod. volt.	Cap. type	75V S*	75V Y†	100V S	100V Y	125V S	125V Y	150V S	150V Y	175V S	175V Y	200V S	200V Y	225V S	225V Y
130	AM	0	14	1	13	—		—		—		—		—	
200	AM	0	15	0	15	0	13	0	10	—		—		—	
300	AM	0	15	0	15	0	15	0	14	0	13	1	13	1	12
130	AMM	0	15	0	14	0	7[1]	—		—		—		—	
200	AMM	0	15	0	14	0	11	0	1[2]	—		—		—	
300	AMM	0	15	0	15	0	15	0	15	0	15	0	14	0	0[3]

* Short: No. of shorts out of 15 capacitors tested.
† Yield: No. of capacitors with leakage current less than 1 A/f out of a total of 15.
[1] Reformed only to 110V.
[2] Reformed only to 130V.
[3] Reformed only to 210V.

Frequency Dependence of Dissipation Factor and Humidity Effect

The capacitance and the dissipation factor of a number of capacitors have been measured at frequencies between 0.1 and 50 kHz. Typical results for AM and AMM capacitors are plotted in Fig. 7 and 8. The upper curve, for a 7600-pf AMM capacitor, reveals a shallow minimum of 0.022 at about 2 kHz for the dissipation factor and, above 50 kHz, the curve shows a 45° slope due to the series resistance of the manganese oxide. The dissipation factor for the AM capacitor is much lower, about 0.007 at 1 kHz, and it remains virtually unchanged because of the low series resistance of the electrodes. [When anodized to 150V, the dissipation factor of TM capacitors increased from less than 0.01 to 0.26 in the same frequency range (10), due to the series re-

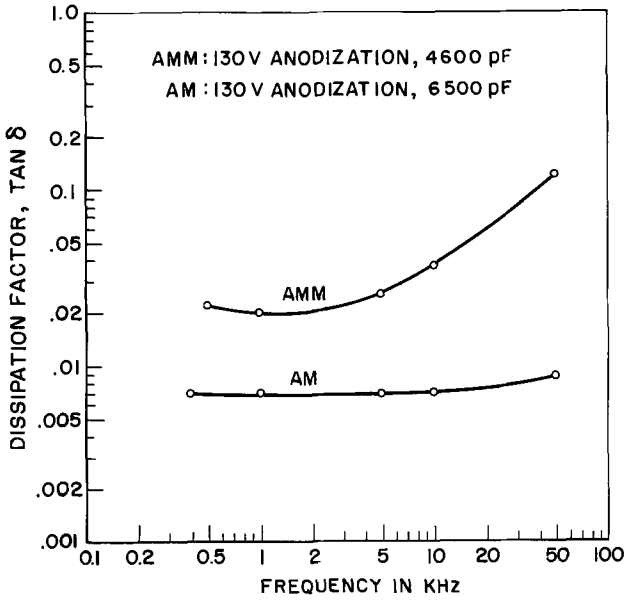

Fig. 7. Frequency dependence of tan δ for AM and AMM capacitors.

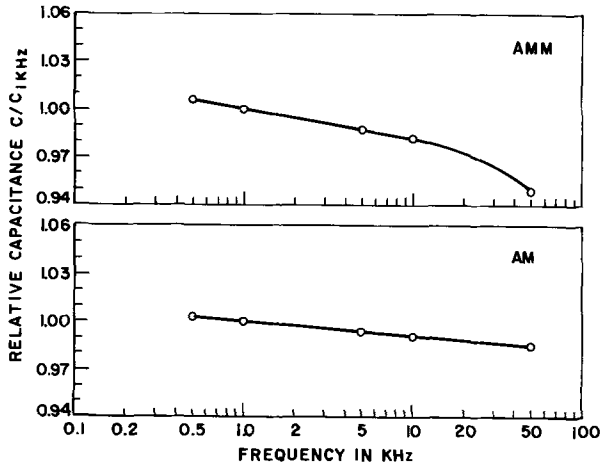

Fig. 8. Frequency dependence of capacitance for AM and AMM capacitors.

sistance of the tantalum film anode.] The capacitance of the AM capacitors decreases by about 2% between 500 Hz and 50 kHz while the AMM capacitors show a somewhat larger drop in this frequency range. [TM capacitors showed 5% decrease in the same range according to Vromen and Klerer (10).]

When measured at zero and 87% relative humidity (*see* Table VII), the AM capacitors with gold counterelectrode showed a change in capacitance of approximately 1%. For AMM capacitors it varied from 0.08 to 4%, which wide spread seems to be related to the manganese oxide. This is very similar to observations made on TMM capacitors. [With gold counterelectrode and 130V anodization, TM capacitors showed 0.79-2.46% change in capacitance by humidity according to Klerer, Orr, and Farrell (11).]

Conclusions

It was found that the quality of aluminum oxide film capacitors made either with or without a semiconducting manganese oxide layer between the dielectric and the counterelectrode depends to a large extent on the degree of the (111) orientation in the aluminum anode. The yield of AMM capacitors anodized to 130V was 100% using aluminum films with a low degree of orientation, compared to 47% for films showing a high degree of orientation.

Capacitors formed on aluminum with a low degree of orientation showed no failure during an accelerated life test period of 16 weeks at 50V, 85°C, and 97% of these capacitors survived life testing at 65V, 85°C. Aluminum oxide film capacitors prepared without a manganese oxide layer showed 97% yield, and no failure was observed during 4 weeks of life testing at 50V and 85°C. The results suggest that aluminum oxide film capacitors can be prepared which are equal in quality to tantalum oxide film capacitors; but, due to the lower dielectric constant of aluminum oxide, their capacitance density is only half that of tantalum oxide film capacitors anodized to an equivalent voltage. Aluminum oxide film capacitors offer an advantage over tantalum oxide film capacitors (12) in cases where low resistivity capacitor anodes are needed. AM capacitors have a very flat dissipation factor *vs.* frequency curve; at 50 kHz, the dissipation factor is still only 0.0085. They should be suitable for high-frequency application.

In aluminum oxide film capacitors up to 300V the breakdown voltage appears to be proportional to the anodization voltage.

The moisture effect is about 1% in AM capacitors, and it is somewhat variable in AMM capacitors. Some AMM capacitors were prepared with a moisture response of less than 0.1%.

Table VII. Moisture response of aluminum oxide film capacitors when cycled between zero and 87% relative humidity (130V anodization, gold top electrode, 5000 pf)

Type	Underlay	DF	ΔC,* %	Spray No.	Evap. No.
AMM	—	0.018	0.10	1	1
AMM	—	0.017	0.10	1	2
AMM	Ta_2O_5	0.017	0.08	1	5
AMM	—	0.022	0.37	2	5
AMM	Ta_2O_5	0.021	0.30	2	6
AMM	—	0.018	1.4	3	3
AMM	Ta_2O_5	0.020	1.4	4	7
AMM	Ta_2O_5	0.021	3.2	4	7
AMM	—	0.020	4.0	5	2
AMM	—	0.014	0.12	6	3
AM	Ti	0.006	0.94	—	8
AM	Ti	0.007	0.85	—	8
AM	Ta_2O_5	0.006	1.0	—	9
AM	—	0.006	1.2	—	10
AM	Ta_2O_5	0.006	1.0	—	11

* ΔC: Capacitance change; average values for the 15 capacitors on one slide.

Acknowledgment

The authors wish to acknowledge the assistance of A. J. Masessa in some of these experiments.

Manuscript submitted Dec. 9, 1968; revised manuscript received Aug. 8, 1969.

Any discussion of this paper will appear in a Discussion Section to be published in the June 1970 JOURNAL.

REFERENCES

1. D. A. McLean and F. E. Rosztoczy, *Electrochem. Technol.*, **4**, 523 (1966).
2. F. E. Rosztoczy and D. A. McLean, *This Journal*, **113**, 16C, (1966); Recent News Paper presented at Electrochem. Soc. Meeting, Buffalo, Oct. 10-14, 1965.
3. B. H. Vromen and F. E. Rosztoczy, IEEE Microelectronics Symposium, St. Louis, July 1966, Proc. pp. 3C 1-10.
4. M. S. Hunter, *Electrochem. Technol.* **1**, 151 (1963).
5. D. A. McLean, N. Schwartz, J. K. Werner, and M. Gresh, "Improved Electrolytic Capacitors," Contract Da-36-039 sc-74996, Final Report, Jan. 15, 1960.
6. W. McMahon and G. I. Parisi, Private communication.
7. J. Klerer, *This Journal*, **112**, 896 (1965).
8. L. Young, "Anodic Oxide Films," pp. 186 and 213, Academic Press, New York (1961).
9. F. E. Rosztoczy and A. J. Masessa, Unpublished results.
10. B. H. Vromen and J. Klerer, *IEEE Trans.*, **PMP-1**, #1 (1965).
11. J. Klerer, W. H. Orr, and D. Farrell, *Proc. Electron. Components Conf.*, **1966**, 348.
12. D. A. McLean and F. E. Rosztoczy, *This Journal*, **112**, 58C, (1965); Paper 10A presented at Electrochem. Soc. Meeting, San Francisco, May 9-13, 1965, Extended Abstracts, **2**, pp. 29-31.

The Effect of CO_2 on the Viscosity of Alkaline Electrolytes

T. I. Overthrow, J. N. Miller, and N. A. Hampson

Chemistry Department, Loughborough University of Technology, Leicestershire, England

Alkaline electrolytes are of general interest in many battery applications including zinc cells, fuel cells, and others. Electrolytes are frequently based on KOH (4-10M) in which the OH^- concentration may fall to about 3M at the end of discharge. CO_2 pickup is a problem in all cases. This note records a preliminary investigation of this effect.

Experimental

Measurements were made using an Ubbelohde viscometer (BS/IP/SL No. 1) in a thermostat at 59.90° ± 0.05°C. The characteristic constants of the viscometer were determined by measuring the flow times of toluene and water (1). Solutions were made up in distilled water using AnalaR grade reagents, and filtered through sintered glass disks. The flow time of each solution was measured at least three times: each mean relative viscosity value was subject to a standard error of *ca.* 2%.

Results

The relationships between the relative kinematic viscosities (ν/ν_0) of the solutions and their compositions are summarized in the figure. The three solutions represented by "0% conversion" were:

(i) NaOH (8g — 2.5M) — Na_2CO_3 (15.2g — 1.8M) — H_2O (76.8g — 53.2M)

(ii) NaOH (11.6g — 3.6M) — NaCl (16.3g — 3.5M) — H_2O (72.1g — 49.7M)

(iii) KOH (11.2g — 2.5M) — K_2CO_3 (21.3g — 1.9M) — H_2O (67.5g — 47.1M)

In each system, measurements were also made on solutions whose compositions corresponded to the progressive conversion of NaOH (KOH) to Na_2CO_3 (K_2CO_3), due allowance being made for the water which would be produced if the conversion was effected using CO_2.

Discussion

The curves in Fig. 1 indicate that the effect of CO_2 in alkaline battery electrolytes is to increase the electrolyte viscosity. It can be seen that the complete carbonation of the available OH^- in a spent electrolyte containing *ca.* 3M OH^- would be to increase the viscosity with respect to the hydroxide component by up to *ca.* 40%. The presence of an inert electrolyte (NaCl) does not eliminate the viscosity increase.

The result of this increase in viscosity would be to increase the diffusion layer thickness which in turn would decrease the limiting current density and accelerate the onset of passivation (anodic or cathodic).

The magnitude of such a reduction in the limiting current would be difficult to predict theoretically for a particular system, especially for a flowing system (2). Whatever the magnitude, however, the effect of the increase in viscosity would be undesirable.

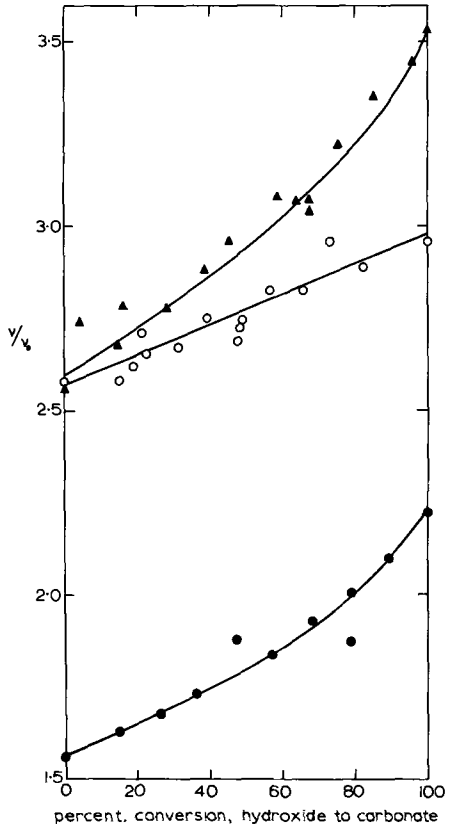

Fig. 1. Variations in the relative kinematic viscosities of aqueous solutions accompanying the conversion of NaOH (KOH) to Na_2CO_3 (K_2CO_3): ▲, system (i); ○, system (ii); ●, system (iii).

Acknowledgment

The authors are indebted to Dr. E. Blumenthal of I.C.I. Mond Division, Northwich, Cheshire, England, for his advice.

Manuscript submitted June 23, 1969; revised manuscript received Sept. 7, 1969.

Any discussion of this paper will appear in a Discussion Section to be published in the June 1970 JOURNAL.

REFERENCES

1. British Standard 188 (1957).
2. V. Levich, *Acta Phisicochem. URSS*, **17**, 257 (1942) (CA37,6561); **19**, 117 (1944) (CA39,2257).

A Laboratory Cell for the Continuous Generation of Sodium Amalgam

Scott Lynn*

Department of Chemical Engineering, University of California, Berkeley, California

and H. Hunter Paalman

Research Laboratories, The Dow Chemical Company, Walnut Creek, California

The sodium amalgam produced in commercial chlorine cells is a chemically interesting commodity whose potential as a reducing agent is largely wasted when it is used to make sodium hydroxide and hydrogen. MacMullin (1) described a number of alternative uses, none of which has become widespread in the 18 years since his article appeared. However, because of the growing imbalance between caustic production and need, research in this area continues.

Sodium amalgam may be made from sodium and mercury for small-scale laboratory use, but this method becomes tedious if large quantities are required. Electrolytic generation is then preferable. However, operation of a small chlorine cell is fraught with annoyance. The chlorine must be disposed of; the anodes wear and must be frequently adjusted; chlorinated brine is corrosive, *etc.* These problems prevent a chlorine cell from being a reliable piece of laboratory equipment.

Sodium amalgam may also be generated by the electrolysis of sodium hydroxide in a cell with a flowing mercury cathode and a nickel anode. The anodic product is oxygen; the nickel electrode does not corrode and never needs adjustment. The electrolyte is relatively noncorrosive and is easily pumped. Minimal corrosion occurs when the cell is not in use.

The equipment sketched in Fig. 1 has been found by the authors to be useful for generating sodium amalgam at the rate of 3.7-5.6 g moles Na/hr (100-150A). The cell was made from two ¼- x 5- x 17-in. plates of nickel and mild steel, respectively. The active electrode area was 45 sq. in. Two 1½- x 5- x 17-in. Lucite blocks, milled out as shown in Fig. 2, formed the inlet and outlet headers. Neoprene gaskets used in assembly of the cell also served to set the spacing between the electrodes. The cell was sloped at an angle of about 10° to allow the mercury to flow by gravity; the caustic electrolyte flowed through the cell countercurrent to the mercury. The slope and caustic flow rate were sufficient to minimize blanketing of the anode by the evolving oxygen.

The caustic was pumped with an Eastern Model D-11 centrifugal pump equipped with a packing gland. A side stream was pumped through a filter to pick up scale dislodged by chemical action of the amalgam. A heat exchanger kept the operation in the temperature range of 50°-60°C. This limitation was imposed by the use of Lucite as a material of construction.

The current was supplied by a General Electric Model 6RS-945-P1 single-phase, full-wave rectifier and was unfiltered. Two rectifiers were used in parallel when higher amalgam production was required. Current was measured by using a 200A precision shunt and a null-balance potentiometer. The cell voltage was typically in the range of 3.5-4.8V.

The mercury pump was an Ingersoll-Rand ¾ KRV-B centrifugal sump pump having a capacity of 1 gpm at a head of 12 ft. To provide a constant head for the required mercury flow of 50-250 ml/min, the flow from the mercury pump was throttled with four 1/16-in. orifice plates in series (*see* Fig. 3). The larger stream of mercury flowed up through a vented, adjustable, constant-overflow standpipe and was returned to the pump. The standpipe vent line dipped into the pool

* Electrochemical Society Active Member.

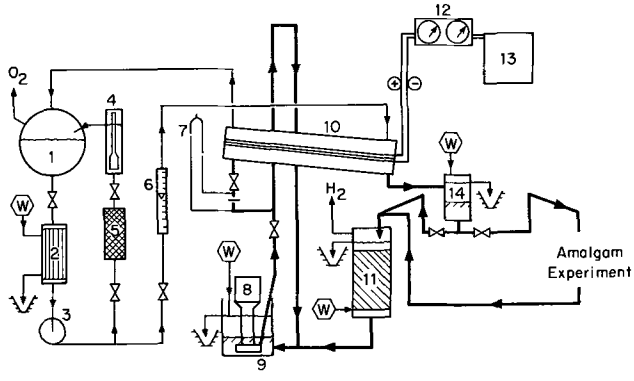

Fig. 1. Equipment for the continuous generation of sodium amalgam: ____ caustic circuit, ▬▬ mercury circuit, ⟨W⟩ water, ⫶⫶ sewer; 1—caustic tank, 2—caustic cooler, 3—caustic pump, 4—caustic hydrometer, 5—caustic filter, 6—caustic meter, 7—mercury flow meter, 8—mercury pump, 9—mercury sump, 10—amalgam cell, 11—decomposer, 12—current-voltage meters, 13—rectifier, 14—amalgam wash pot.

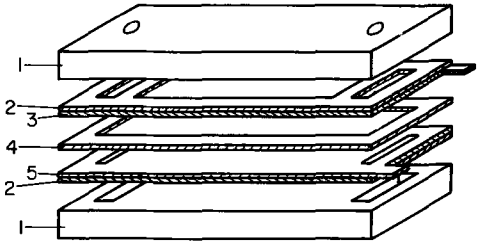

Fig. 2. Detail of cell: 1—Lucite blocks, milled and tapped; 2—neoprene gaskets; 3—nickel anode; 4—neoprene electrode spacer-gasket; 5—steel cathode. (Note: Assembly bolts around periphery of cell not shown.)

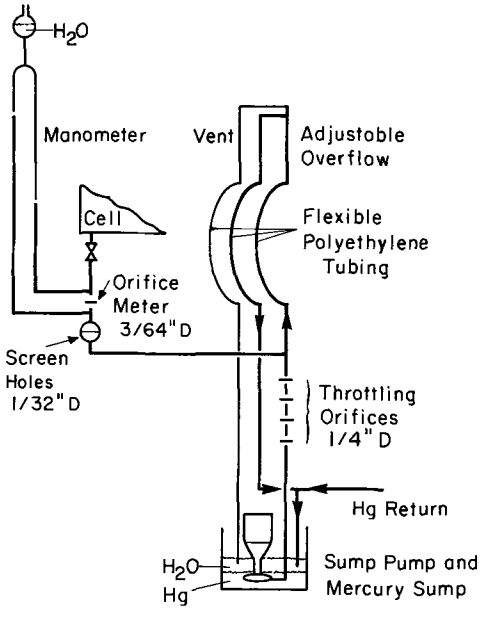

Fig. 3. Detail of mercury flow-control system.

of water covering the mercury in the sump. The downflow of mercury in the return line thereby pulled water with it, preventing the build-up of solid caustic and the discharge of mercury vapor into the room which would have resulted from venting with air. The smaller flow of mercury went to the cell through a metering orifice. The quantity of mercury flowing to the cell was varied by adjusting the height of the standpipe. This method of regulating the flow was adopted to replace a needle valve which was found to be a very unstable control device for this service.

The sodium amalgam produced could be used as desired in experimentation or could be returned to the pump through a decomposer made of a 1-ft section of 3-in. industrial glass pipe packed with granular graphite and heated with an internal steam coil to about 100°C.

The hydrogen evolved from the decomposer was measured with a soap-bubble flow meter. At steady state, this flow was a convenient method of monitoring the sodium content of the mercury stream returning to the pump. When no experimentation was in progress, the hydrogen flow could be used to determine the cell efficiency. When a reaction was being studied, the hydrogen flow was used to determine the extent of depletion of the amalgam. Oxygen containing a small amount of hydrogen was produced in the cell and was also measured with a soap-bubble flow meter. Hydrogen evolution at the cathode is the only possible side reaction in this system. The flow of oxygen could thus be used to determine the cell efficiency independently; the two methods of measurements generally agreed within 1%.

The primary variable affecting current efficiency was found to be the caustic concentration. When this was kept above 30 w/o (weight per cent) NaOH, the efficiency was consistently 97-99%. At lower electrolyte concentrations, cell performance became progressively worse. Another factor of importance in maintaining a high current efficiency was providing enough mercury to cover the cathode plate completely. This requirement set an upper limit on the amalgam concentration which could be produced at a given current and cell slope. Typical of the present system was 0.2% Na maximum at 100A. Modification of the cell design at the expense of simplicity would allow operation with a nearly level cathode and eliminate this restriction.

When the cell was first constructed, it operated at a very low current efficiency. Replacement of 316 stainless steel with mild steel in the mercury piping led to the satisfactory behavior reported above. Although the matter was not pursued, it is possible that some chromium was picked up by the mercury and caused the difficulty. Thereafter, the use of stainless steel was avoided throughout the system where possible. However, it was used in the caustic pump and other portions of the caustic piping system without trouble.

Manuscript received Jan. 9, 1969.

Any discussion of this paper will appear in a Discussion Section to be published in the June 1970 JOURNAL.

REFERENCE

1. R. B. MacMullin, *Chem. Eng. Progr.*, **46**, 440 (1950).

DISCUSSION SECTION

This Discussion Section contains discussion of a paper appearing in the *Journal of The Electrochemical Society*, Vol. 116, No. 3, (March 1969).

Plating Stresses from Electroless Nickel Deposition on Beryllium

R. M. Shemenski, J. G. Beach, and R. E. Maringer
(pp. 402-409, Vol. 116, No. 3)

Konrad Parker[1]: The paper presents numerous data and calculations, indicating that the internal stresses in electroless nickel deposits on beryllium can vary according to the plating conditions used by different platers. Each group of three beryllium strips plated by one of the four platers developed stress values in the nickel beryllium composite varying less than ± 10%. Nevertheless, the authors conclude that "since the resulting microstructures were similar, any effect of plating conditions should be minimal."

Recently, Baldwin and Such[2] stated: "The internal stress of the electroless deposits can be controlled by adjustment of the bath composition, particularly pH, so that it can be of any desired value between 16,000 psi (tensile) and 8000 psi (compressive). Wherever deposits having zero or compressive stress are considered beneficial, they can be produced but at a concomitantly lower plating rate."

We have started an investigation to determine the effect of the plating variables on stress in a closely controlled Kanigen® laboratory system. We have found that the masking of thin metal strips on one side can induce tensile bending prior to plating and during removal after plating. For more accurate bow-out measurements we are, therefore, plating both sides of the strips, then masking one side and stripping the deposit from the other.

Our results to date, which will be presented in detail later, show that the stress in electroless nickel deposits on beryllium and other substrates can be controlled by the plating conditions to be either tensile or compressive. Factors affecting the phosphorus content of the deposit such as pH are of primary influence in regard to the magnitude and direction of the internal stress produced. The stress in the as-plated condition is, therefore, not primarily due to differences in thermal expansion coefficients as the authors assume, but is induced to an appreciable degree during plating. It is also likely that the thermal expansion coefficient of the plate is not constant, but varies with the composition of the nickel alloy.

We confirm the authors' statement that electroless nickel deposits contract when annealed to 190°C; thus, by imparting a compressive stress in the deposit during plating, a practically stress-free state can be achieved after annealing. It would be most interesting if the authors could provide the phosphorus content of the nickel alloy coatings used in their investigation. The reason for the random variation of their stress data might then become apparent.

R. M. Shemenski, J. G. Beach, and R. E. Maringer: The authors wish to thank Mr. Parker for his remarks concerning our study on electroless nickel deposition on beryllium. It was unfortunately not within the

[1] Kanigen® & Coating Research, General American Research Division, General American Transportation Corp., 7448 North Natchez Ave., Niles, Ill. 60648.

[2] *Trans. Inst. Metal Finishing*, **46**, 73-80 (1968).

scope of this investigation to study the plating process itself. Rather, the study was designed to evaluate the product that would result in actual mirror production, not under idealized laboratory conditions. The authors are aware that plating conditions have a significant effect on the properties of an electroless nickel deposit, and in fact this is discussed in the paper. We are pleased to hear that research on the residual stresses in Kanigen® is continuing in GATX.

Each participating commercial plater was informed of the purpose of this study and was urged to use his best technology and his greatest care in plating the test specimens. The authors had no control over this phase of the study and so had to assume that these precautions were observed, just as one would expect these platers to handle an actual mirror. The reasons for feeling that this assumption was satisfactory and that gross effects due to handling or masking were minimal were also discussed in the paper.

The interpretation made by Mr. Parker of the results reported in the paper, that the residual stresses in the as-plated condition were primarily due to differences in the coefficients of thermal expansion, is not correct. It was explicitly stated that the authors recognized that: (*a*) the plating process itself, (*b*) metallurgical instability, and (c) differences in the coefficients of thermal expansion between plate and substrate, all contributed to the residual stress level attained in an electroless-nickel/beryllium substrate system. Therefore, this study acknowledged the importance of the plating process in developing residual stresses, but was limited to calculating the stress levels to be expected from present commercial practice.

The authors agree that more research on the deposition of electroless nickel is needed and that better control of the important parameters in the plating process should improve the dimensional stability of the coating. The role of phosphorus content, as discussed by Mr. Parker, is surely an important area.

Erratum

Drs. H.-E. Gumlich and U. Scherz want to point out that the review paper on "Optical Transitions in II-VI Compounds Containing Transition Elements," Paper 9 given at the Spring Meeting of The Electrochemical Society in Boston, May 5-9, 1968, by H.-E. Gumlich was based on a cooperation of H.-E. Gumlich and U. Scherz, which might not clearly enough be stated by citing U. Scherz (5). Essential parts of this paper are also contained in a review paper given by U. Scherz at the meeting of the Deutsche Physikalische Gesellschaft in Berlin, 1967. Only an abstract of this review has been printed as cited by (5) in the Boston paper by H.-E. Gumlich.

---

can be created, erased, and moved anywhere in thin sheets of magnetic material without interconnection. They may interact with one another in a controlled fashion and their presence or absence can be detected. Therefore, devices employing the new technology could be made to perform a variety of functions—logic, memory, switching, counting—all within one solid magnetic material.

The energy needed to manipulate the bubbles can be applied either by current-carrying conductors or picked up from a surrounding magnetic field by microscopic "ferromagnetic antennae" in printed patterns distributed over the surface of the material.

Physical Organic Chemist—Ph.D. 1952—Extensive industrial and contract experience in polymers, dielectrics and electrochemical technology. Highly creative and diligent. Strong interest in materials evaluation and applications. Reply Box C-22.

Physical Chemist, Ph.D. 1958—Research experience in electrodeposition, instrumentation, corrosion, metallurgy, batteries, fuel cells, organic and inorganic processes. Research or Teaching Position. Reply Box C-23.

Positions Wanted

Society members of any class may, at no cost and for the purposes of professional employment, place not more than three identical insertions per calendar year, not to exceed 8 lines each. Count 43 characters per line, including box number, which the Society will assign.

Certificates, Pins, and Keys Now Available

The Society announces the availability of the following items:

Membership Certificates	$ 3.00
Gold Membership Pin	$ 7.50
Gold Membership Key	$15.00

Those interested should send their order accompanied by check to The Electrochemical Society, Inc., 30 East 42 St., New York, N. Y. 10017.

POSITIONS WANTED

Please address replies to the box number shown, c/o The Electrochemical Society, Inc., 30 East 42 St., New York, N.Y. 10017.

Electrochemist—M.S. (1957)—seeks position in R & D. 12 years of varied battery R & D experience including alkaline secondaries, fuel cells, molten salt and metal air batteries. Patents and Publications. Reply Box C-7.

Inorganic-Physical Chemist—M.S. 1958 seeks leadership position. Experience in hydrometallurgy of Cb and Cu, electroless deposition, preparation of metal powders. Project leader in testing of electrodeposits, alumina reduction. Publications, computer programming, supervisory experience. Reply Box C-18.

Electrochemist—seeks administrative opportunity—18 years' manufacturing and R & D experience, including photochemistry, computer technology, energy conversion devices, adhesives, plastics, analysis, and technical supervision. Law training, industrial teaching, and product display experience. Reply Box C-19.

Electrochemist—Ph.D. 1962—8 years' experience in electrochemistry, electrolytic coating of polymeric materials, electrochemical processes, homogenous and heterogenous catalysis, electrokinetics, fuel cells, and batteries. Reply Box C-20.

Electrochemist—B.A. 1959—graduate studies—desires challenging position in small- to medium-size company. Ten years' basic and applied research in batteries, corrosion, electrodeposition. Reply Box C-21.